Structures Congress 2011



Edited by
Dana Ames, P.E.
Theodore L. Droessler, P.E.
Marc Hoit, Ph.D.

ASCE

SEI
ASCE
STRUCTURAL ENGINEERING INSTITUTE

Structures Congress 2011

PROCEEDINGS OF THE 2011 STRUCTURES CONGRESS

April 14–16, 2011
Las Vegas, Nevada

SPONSORED BY
The Structural Engineering Institute (SEI)
of the American Society of Civil Engineers

EDITED BY
Dana Ames, P.E.
Theodore L. Droessler, P.E.
Marc Hoit, Ph.D.

Published by the American Society of Civil Engineers

Copyright and Disclaimer

ISBN: 978-0-7844-1171-1

Any statements expressed in these materials are those of the individual authors and do not necessarily represent the views of ASCE, which takes no responsibility for any statement made herein. No reference made in this publication to any specific method, product, process or service constitutes or implies an endorsement, recommendation, or warranty thereof by ASCE. The materials are for general information only and do not represent a standard of ASCE, nor are they intended as a reference in purchase specifications, contracts, regulations, statutes, or any other legal document.

ASCE makes no representation or warranty of any kind, whether express or implied, concerning the accuracy, completeness, suitability, or utility of any information, apparatus, product, or process discussed in this publication, and assumes no liability therefore. This information should not be used without first securing competent advice with respect to its suitability for any general or specific application. Anyone utilizing this information assumes all liability arising from such use, including but not limited to infringement of any patent or patents.

Copyright © 2011 by the American Society of Civil Engineers.
All Rights Reserved.

ASCE and American Society of Civil Engineers—Registered in U.S. Patent and Trademark Office.

American Society of Civil Engineers
ASCE International Headquarters
1801 Alexander Bell Drive
Reston, VA 20191-4400 USA

Call Toll-Free in the U.S.: 1-800-548-2723 (ASCE)
Call from anywhere in the world: 1-703-295-6300
Internet: http://www.pubs.asce.org

Preface

Preparation for the 2011 Structures Congress required significant time and effort from the members of the Local Planning Committee, the National Technical Program Committee, and the staff at SEI. Therefore, much of the success of the conference is a reflection of the level of effort by this group of volunteers.

The committee would like to acknowledge the critical support of the sponsors, exhibitors, presenters, and participants who contributed to the success of the conference through their participation.

The Structures Congress technical program consists of over 100 concurrent technical sessions on topics that are redefining structural engineering in the areas of bridge and transportation structures, buildings, strategies for today's global economy and advances in research. The CASE Spring Risk Management Convocation and the Forensic Specialty Track supplement the Congress. All of these help enforce networking, interacting and forming partnerships with our structural peers.

Sharing in the success of the 2011 Structures Congress are our cooperating organizations, CASE, SEAOC, SEASoN, ACI, Las Vegas Chapter, ACEC Nevada, Southern Nevada Post Society of American Military Engineers, ASCE San Francisco Section, ASCE Los Angeles Section, ATC and ASCE Southern Nevada Branch.

On behalf of our dedicated volunteers and SEI staff, we would like to thank you for spending your valuable time attending the 2011 Structures Congress. It is our hope that you and your colleagues will benefit greatly from the information provided and make professional connections that lasts for years. By increasing communication skills, helping the practicing engineer expand his or her knowledge, leadership, and influence, we believe that delegates will learn how to excel in this new and exciting environment.

Dana Ames and Theodore L. Droessler
Co-Chairman, Local Planning Committee

Acknowledgments

Local Planning Committee

Dana Ames, P.E., S.E.
Co-Chairman
R2H Engineering, Inc

Theodore L. Droessler, P.E.
Co-Chairman
Clark County Department of
Development Services, Building Division

Curt Haldeman, P.E.
Granite Construction Company

Arvid Handegard, P.E.
Jacobs Engineering

Chuck Joseph, P.E.
Jacobs Engineering

Ron Lynn, C.B.O.
Clark County Department of
Development Services, Building Division

Daniel Paulis, P.E.
CH2M HILL

Aly Said, Ph.D.
University of Nevada, Las Vegas

Kaushal Shah, P.E., S.E.
BergerABAM

Craig Smart, P.E.
HDR

Ying Tian, Ph.D.
University of Nevada, Las Vegas
(UNLV)

Table of Contents

Bridges

Seismic Reliability and Performance Assessment of Bridges

System-Level Calibration of Bridge Component Damage States 1
K. R. Mackie

Seismic Fragility Estimates and Optimization of Retrofitting Strategies for Reinforced Concrete Bridges: Case Study of the Fabela Bridge in Toluca, Mexico 13
V. Bisadi, M. Head, and P. Gardoni

Effect of Ground Motion Suite Size on Uncertainty Estimation in Seismic Bridge Fragility Modeling 23
B. G. Nielson and W. C. Pang

Reliability and Redundancy of Bridge Systems under Lateral Loads 35
G. Anitori, J. R. Casas, and M. Ghosn

Long Term Structural Health Monitoring of Bridges

Anomaly Detection without Structural Behavior Models 47
I. F. C. Smith

Damage Detection and Localization in Structures: A Statistics Based Algorithm Using a Densely Clustered Sensor Network 53
Elizabeth L. Labuz, Shamim N. Pakzad, and Liang Cheng

Bridge Structural Health Monitoring Specification: 2020

Monitoring of Long Term Bridge Performance (LTBP) Program Bridges 65
Steven M. Petroff, Marvin W. Halling, and Paul J. Barr

Data-Driven Methods for Threshold Determination in Time-Series Based Damage Detection 77
Ruigen Yao and Shamim N. Pakzad

A Characterization of Traffic and Temperature Induced Strains Acquired Using a Bridge Monitoring System 89
Mustafa Gul, H. Burak Gokce, and F. Necati Catbas

Proposed Data Specifications for Bridge Structural Health Monitoring Sensor Data 101
Stephen Prusaczyk, Richard Christenson, John Dewolf, Alireza Jamilapour, and John Bartoletti

Cable Supported Bridges

Wind Engineering Studies for a Cable-Stayed Bridge in Talavera de la Reina, Spain 113
F. Nieto, S. Hernández, J. Á. Jurado, F. Pereira, and A. Díaz

Assessing and Retrofitting Steel Bridges for Fatigue

Detection of Critical Fatigue Cracks in Steel Bridge Materials with Remote Acoustic Emission Monitoring **123**
Jianguo Yu and Paul Ziehl

Improved Method for Bonding CFRP Overlays to Steel for Fatigue Repair **133**
Fatih Alemdar, Adolfo B. Matamoros, Caroline R. Bennett, Ron Barrett-Gonzalez, and Stanley T. Rolfe

Fatigue Repair of the Arkansas River Bridge **145**
Y. Zhao, K. W. M. Roddis, G. Ramirez, and J. P. Jones

Experimental Investigation of Bridge Response

Experimental Study of Shear Capacity of Reinforced Concrete Slabs **152**
Eva Lantsoght, Cor van der Veen, and Joost Walraven

Seismic Response of Bearings for Quasi-Isolated Bridges—Testing and Component Modeling **164**
J. S. Steelman, L. A. Fahnestock, J. M. LaFave, J. F. Hajjar, E. T. Filipov, and D. A. Foutch

Measurements of a Steel Orthotropic Deck under Crawl Loading **179**
S. Roy, R. S. D. Alapati, N. K. Manandhar, and J. W. Fisher

Innovative Bridge Design and Construction Approaches

Simplified Erection Guidelines for Double I-Girder Systems during Bridge Construction **190**
Quihong Zhao, Baolin Yu, and Edwin G. Burdette

Feasibility Analysis of Using UHPC in Prestressed Bridge Girders **203**
Christopher W. Taylor, Kristin F. Montoya, David W. Jáuregui, Craig M. Newtson, and Brad D. Weldon

Innovative Bridge Analysis Approaches

Effect of Secondary Elements on Load Distribution in Prestressed Bridge Girders **215**
M. R. Roddenberry, J. Chipperfield, and K. S. Tawfiq

Bridges Subjected to Impact Loads of Moving Vehicles Obtained from Vehicle Dynamics **227**
S. Jerath and S. B. Gurav

Elastic Nonlinear Analysis of Plane Truss Bridges **239**
Morteza A. M. Torkamani and Jyh-Hung Shieh

Innovative Seismic Analysis of Bridges

Seismic Analysis of Bridge Columns under Axial, Flexure, Shear, and Torsional Loadings **252**
T. Ravi S. Mullapudi and Ashraf Ayoub

Effect of Abutment Shear Keys on the Seismic Response of Bridges 265
M. W. Salveson and B. V. Fell

Computational Analyses of Quasi-Isolated Bridges with Fusing Bearing Components 276
E. T. Filipov, J. F. Hajjar, J. S. Steelman, L. A. Fahnestock, J. M. LaFave, and D. A. Foutch

Seismic Analysis of Integral Abutment Bridges Including Soil-Structure Interaction 289
Qiuhong Zhao, Reza Vasheghani-Farahani, and Edwin G. Burdette

Buildings

Long Span Stadium Roofs

Erection of the Cable Net Roof for the London 2012 Olympic Stadium 304
N. Cole and P. Hulme

Challenges of Retrofitting an Existing Domed Stadium with a New Retractable Roof—BC Place Stadium, Vancouver, BC 314
David M. Campbell and Karen A. Lynch

Design of the Retractable Roof for the Florida Marlins' New Ballpark 324
Stephen E. Blumenbaum and Aaron C. White

Wind Induced Torsional Loads on Buildings

Evaluation of Wind-Induced Torsional Loads on Buildings by North American and European Codes and Standards 337
M. Elsharawy, T. Stathopoulos, and K. Galal

Wind-Induced Torsional Loads on Low-Rise Buildings 349
M. Elsharawy, K. Galal, and T. Stathopoulos

Floor Vibration Serviceability

Floor Vibration Characteristics of Long Span Composite Slab Systems 360
T. Andres Sanchez, Brad Davis, and Thomas M. Murray

Impedance Modeling for Prediction of Train Induced Floor Vibrations 371
M. Sanayei, N. Zhao, P. Maurya, J. A. Moore, J. A. Zapfe, and E. M. Hines

Simplified Methods for Estimating the Response of Floors to a Footfall 383
C. J. Middleton and J. M. W. Brownjohn

Efficient Design of Floor Structures Using Active Vibration Control 404
M. J. Hudson, P. Reynolds, and D. Nyawako

Structural Performance in Fire

A Comparison between the Single Plate and Angle Shear Connection Performance under Fire 416
Serdar Selamet and Maria E. Garlock

Effects of Thermal Expansion and Support Restraints on Performance of Composite Floors in Fire 427
H. Mostafaei and F. Alfawakhiri

RC Bearing Walls Subjected to Elevated Temperatures 439
M. J. McGinnis, K. A. Mueller, Y. C. Kurama, and K. P. Graham

Experimental Evaluation of Composite Floor Assemblies under Fire Loading 451
Purushotham Pakala, Rustin Fike, Emily Wellman, Venkatesh Kodur, and Amit Varma

Behavior of Steel Columns under Fire Loading 463
Lisa Choe, Amit H. Varma, and Andrea Surovek

Integrating Life Cycle and Carbon Assessments

Carbon Emissions and Building Structure: What the Structural Engineer Needs to Know about Carbon in the 21st Century 472
Mark D. Webster, Helena Meryman, and Dirk M. Kestner

Life Cycle Assessment Using ATHENA Impact Estimator for Buildings: A Case Study 483
Elizabeth Stek, Dave DeLong, Terry McDonnell, and Jose Rodriguez

Integrating Life Cycle and Carbon Assessments: What Life Cycle Assessment Can Teach Structural Engineers about Design and Specification 495
Frances Yang

Infrastructure Sustainability: Streamlining Life Cycle Assessment for Practicing Bridge Engineers 507
Jeralee L. Anderson

Tall Building Design in Seismic Regions: Design Philosophies and Global Perspectives

Deflection Limits in Tall Buildings—Are They Useful? 515
Rob Smith

Structural Analysis and Design Challenges of the Ping An Tower under Consideration of the Upcoming China Code 528
Dennis C. K. Poon, Ling-en Hsiao, Yi Zhu, Steven Pacitto, Steve Zuo, Torsten Gottlebe, and Shenming Wang

Non-Linear Time History Analysis for the Performance Based Design of Shanghai Tower 541
Dennis C. K. Poon, Ling-En Hsiao, Yi Zhu, Leonard Joseph, Steve Zuo, Guoyong Fu, and Onur Ihtiyar

Reinforcing Topics for Concrete Structures

Effect of Stirrups on the Contribution of Concrete Compressive Strength and Tensile Steel to the Shear Strength of RC Beams Using Artificial Neural Networks 552
Hassan El-Chabib

Cyclic Response of Concrete Frame Members Reinforced with Ultrahigh Strength Steel 560
H. Tavallali, A. Lepage, J. Rautenberg, and S. Pujol

Nominal Shear Strength Limits for Short Diagonally-Reinforced Concrete Coupling Beams 571
Steven Barbachyn, Yahya C. Kurama, and Lawrence C. Novak

Existing Masonry Buildings Evaluation and Retrofit

A Simple Method in the Preliminary Assessment of Historic Masonry Buildings 583
James S. Cohen

Problems in the Repair of Historic Brick Masonry Buildings 594
James S. Cohen

Reliability Analysis of Masonry Members under Compression 605
S. Kazemi, M. Mahoutian, H. Moosavi, and Y. Korany

Wood Light Frame Design

Is Roof Eave Blocking Required to Transmit Wind/Seismic Forces? 616
Felix Martin

Truss Plates for Use As Wood-Concrete Composite Shear Connectors 626
Peggi L. Clouston and Alexander C. Schreyer

Effect of Support Restraint on Wood-to-Wood Joist Hanger Connection 636
William T. Bolduc and Samaan Ladkany

Contextualizing the Load Duration-Dependent Strength of Wood Members 650
G. R. Searer, T. F. Paret, and R. J. Kristie

The 14th Edition AISC Steel Construction Manual

The AISC 2010 *Specification* and the 14th Edition *Steel Construction Manual* 661
Larry Muir and Cynthia J. Duncan

Seismic Design of Cold Formed Steel and Metal Building Systems

Development of Seismic Design Provisions for Steel Sheet Sheathed Shear Walls 676
C. A. Rogers, N. Balh, C. Ong-Tone, I. Shamim, and J. DaBreo

Seismic Design of Diagonal Strap Bracing Using AISI S213 688
Greg Greenlee

Earthquake Simulator Testing of Metal Building Systems 693
C. M. Uang, M. D. Smith, and W. L. Shoemaker

Seismic Force Distribution for Metal Building Systems with Mezzanines 705
M. D. Smith and C. M. Uang

Innovations in Steel Plate Shear Walls

Behavior of Steel Plate Shear Walls with In-Span Plastic Hinges **716**
Ronny Purba and Michel Bruneau

Recent Experimental Research on Steel Plate Shear Walls in NCREE **724**
Chao-Hsien Li, Jing-Tang Chang, Keh-Chyuan Tsai, and Chih-Han Lin

Design and Testing of Coupled Steel Plate Shear Walls **736**
D. J. Borello and L. A. Fahnestock

Seismic Design and Analysis of Self-Centering Steel Plate Shear Walls **748**
Patricia M. Clayton, Daniel M. Dowden, Ronny Purba, Jeffrey W. Berman, Laura N. Lowes, and Michel Bruneau

Modular Construction of Steel Plate Shear Walls for Low and Moderate Seismic Regions **758**
Robert G. Driver and Hassan Moghimi

Nonlinear Seismic Analysis for Everyday Application

Nonlinear Dynamic Analysis of Structures Using Modal Superposition **770**
K. K. F. Wong

Use of Nonlinear Analysis in the Context of the ASCE 7 Seismic Load Provisions **782**
Finley A. Charney

Seismic Retrofit of Pre-Northridge Steel Moment Frame Building Using Nonlinear Static Analysis per ASCE 41-06 **791**
Methee Chiewanichakorn, Luis Toranzo, and Aaron Reynolds

Seismic Vulnerability Assessments of Marine Structures Using Non-Linear Static Analysis Procedures **803**
Edward H. Stehmeyer III

Use of Protective Systems to Achieve High Seismic Performance Goals

Seismic Design of a 15 Story Hospital Using Viscous Wall Dampers **815**
James Newell, Jay Love, Mark Sinclair, Yu-Ning Chen, and Amarnath Kasalanati

Seismic Analysis and Rehabilitation of a 15 Story Pre-Northridge Steel Moment Resisting Frame Building **827**
Timothy Graf, James O. Malley, Mark Sinclair, James Newell, Colin Blaney, Moisey Fraynt, Chia-Ming Uang, and Tamer Ahmed

"The Bowls Project"—A Prototype for Full Scale Testing As an Alternate Approval Process for Small Scale Base-Isolated Structures **839**
Gordon Wray, Mark Sinclair, and Michael H. Ramage

Seismic Isolation: Applications of WorkSafe Technologies Ball-N-Cone Isolator **852**
A. M. Nacamuli and K. M. Sinclair

Soil Structure Interaction and Seismic Isolation at Nuclear Facilities

Probabilistic and Deterministic Seismic Soil Structure Interaction Analyses for the Lotung Quarter-Scale Containment Model 864
D. W. Eggers, S. Bolourchi, and F. Ostadan

Seismic Isolation of Safety-Related Nuclear Structures 876
A. S. Wittaker, Y.-N. Huang, R. L. Mayes, and R. P. Kennedy

Site Response Analyses 886
C. J. Constantino, T. W. Houston, and M. C. Constantino

Detailing Issues for Steel Structures

Simple Shear Connections—Not So Simple 898
Erik Anders Nelson

Designing and Detailing Welded Skewed T-Joints 909
T. Green and T. Schlafly

Finite Element Analyses of Super Composite Column and Its Connections for Ping An International Financial Center Tower 918
Dennis C. K. Poon, Ling-en Hsiao, Zhu Yi, Steve Zuo, Steve Pacitto, Torsten Gottlebe, and Jianhai Liang

Steel Detailing Practices: Using Global Variation to Envision Innovation 929
K. Simonen

Lateral Force Systems

Out-of-Plane Stability of Buckling-Restrained Braces 938
Tsuyoshi Hikino, Taichiro Okazaki, Kouichi Kajiwara, and Masayoshi Nakashima

Dynamic Response of a Steel Concentrically Braced Frame 950
Taichiro Okazaki, Dimitrios G. Lignos, Tsuyoshi Hikino, and Kouichi Kajiwara

Self-Centering Buckling-Restrained Braces for Advanced Seismic Performance 960
David J. Miller, Larry A. Fahnestock, and Matthew R. Eatherton

Building Specific Seismic Strengthening and Design

A Celebration of Structure As Architecture—The Cathedral of Christ the Light 971
Mark Sarkisian, Peter Lee, and Eric Long

Performance-Based Seismic Evaluation of Ping An International Finance Center 983
Dennis C. K. Poon, Ling-en Hsiao, Yi Zhu, Steven Pacitto, Steve Zuo, Torsten Gottlebe, and Rohit Srikonda

Enhanced Seismic Design of the New San Bernardino Court 994
M. Sarkisian, P. Lee, L. Hu, and C. Doo

Seismic Retrofit of a Higher-Education Building Using Advanced Analysis to Optimize Use of Existing Building Components 1007
Devon Lumbard, James Newell, Qi-Song "Kent" Yu, and James O. Malley

Business and Professional Practice

Effect of I-35 Minnesota Bridge Failure on Bridge Inspection and Evaluation Program

Impact of I-35W Bridge Failure on State Transportation Agency Bridge Inspection and Evaluation Programs 1019
S. Alampalli and K. C. Rehm

Simple Check for Yielding in Truss Bridge Gusset Plate Connections 1027
J. W. Berman, B. S. Wang, A. Olson, C. W. Roeder, and D. E. Lehman

SE Licensure

Lessons Learned from the Utah Experience: Suggestions for Implementing a Structural License and Practice Act in Your State 1036
Barry Kay Arnold

The New 16-Hour NCEES Structural Exam—How We Got Here 1049
E. T. Huston and T. L. Miller

Thinking about Engineering

The Intentionality of Design 1059
Jon A. Schmidt

Philosophy of Structural Building Codes 1067
William M. Bulleit and Dave K. Adams

What Does It Mean to Be Sustainable? 1074
Tonatiuh Rodriguez-Nikl

Connection Details Engineering

Connection Details—Practicing Engineers and the Code 1086
C. Wilcox, B. Nuttall, and T. Barnett

Education

Failure Case Studies and Forensics in Engineering Education: Best Practices

Using Failure Case Studies to Teach Reinforced Concrete Design 1098
Norbert Delatte

Lessons Learned through the Development of an Undergraduate Course on Civil Engineering Failures 1108
K. A. Salyards

Using the Hyatt Regency Skywalk Collapse Case Study in Engineering 1118

Education
John W. Lawson and Pamalee A. Brady

Use of Failure Case Studies in a Construction Planning and Estimating Course **1130**
P. A. Bosela and N. J. Delatte

Advances in Structural Engineering

Engineered Biobased Composites for Construction: Material Development, Multiscale Modeling, and Long-Term Durability **1147**
W. V. Srubar III and S. L. Billington

An Evaluation of Anchorage Systems for Fiber-Reinforced Polymer (FRP) Laminates Bonded to Reinforced Concrete Elements **1157**
S. V. Grelle and L. H. Sneed

Analysis of RC Structures with Carbon-Nanofiber Concrete **1169**
T. Ravi S. Mullapudi and Ashraf Ayoub

Energy Structures and Non Structural Components

Seismic Response of Ceiling Piping Partition Non Structural Systems

Experimental and Analytical Studies of Hospital Piping Assemblies Subjected to Seismic Loading **1179**
Arash E. Zaghi, E. “Manos” Maragakis, Ahmad Itani, and Elliott Goodwin

Design of a Test-Bed Structure for Shake Table Simulation of the Seismic Performance of Nonstructural Systems **1191**
Siavash Soroushian, Manos Maragakis, Ahmad Itani, Gokhan Pekcan, and Arash E. Zaghi

Seismic Performance Evaluation of Highway N High-Voltage Substation **1203**
Dongming Yan, Genda Chen, and Dennis Bouse

Structural Performance Criteria for Alternative Energy Production Systems

Performance Indicators for Structures and Infrastructure **1215**
Dan M. Frangopol and Duygu Saydam

Performance Indicators for Offshore Wind Farms **1227**
A. Longabard, G. Tsiatas, and L. Manuel

Marine Hydrokinetic Energy Generation Systems and Their Performance Indicators **1236**
H. S. Tang and S. Skraatz

Design and Reliability of Transmission Tower and Wind Turbine Structures

Design Loads for Transmission Towers under Skewed Wind Loading **1246**
T. G. Mara and T. C. E. Ho

Design and Evaluation of Non Structural Components and Non Buildings

New Approaches in Fixing Technology: Approvals Follow Design Guides, Shown by Example of Anchor Channels 1258
Matthias Roik

Design of Sports Lighting Support Structures—Will Your Structures Perform to Expectation? 1269
Brian R. Reese

Parametric Investigation of Seismic Interaction between Precast Concrete Cladding Systems and Moment Resisting Frames 1286
Andrew Baird, Riccardo Diaferia, Alessandro Palermo, and Stefano Pampanin

Evaluation of Fatigue Resistance of Multi-Sided Sign and Traffic Signal Structures 1298
Y. C. Park, S. Roy, R. Sause, and J. W. Fisher

Extreme Loads

Advances in Concrete for Blast Resistant Structures

Use of Empirical Constitutive Properties to Develop a Resistance Function for Reinforced Masonry 1310
R. S. Browning and J. S. Davidson

Material Characterization of Fiber Reinforced Concrete for Improved Blast Performance 1320
W. F. Heard, P. K. Basu, N. Nordendale, and J. Hoemann

The Evaluation of Pre-Stressed Pre-Cast Panels Subjected to Blast 1337
A. Billek and S. Marjanishvili

Innovative Methods to Defeat Blast Loads: Windows and Doors

Development of Design Recommendations for Edge-Bolted Laminated Glass 1347
D. Duke, B. T. Bewick, T. Casey, and S. R. Misko

Design and Testing of Cable Catchment Systems for Historic Window Blast Protection 1359
Seda Dogruel and Caroline Field

Testing and Analytical Evaluation of Doors 1375
Michael J. Lowak, Jay S. Idriss, and James W. Wesevich

ASCE 7-10 Snow, Rain, and Flood Loads

ASCE 7-10 Changes to Flood Load Provisions 1411
William L. Coulbourne

General Provisions, Load Combinations, and Dead Live and Atmospheric Ice Loads

ASCE Standard 7-10 Dead and Live Loads 1418
Harry B Thomas

Load Combination Requirements in ASCE Standard 7-10: New Developments 1425
Therese P. McAllister and Bruce R. Ellingwood

Introduction of Performance Criteria into Chapter 1 of ASCE 7-10 1432
Ronald O. Hamburger

ASCE 7-10 Wind Loads

ASCE 7-10 Wind Loads 1440
Ronald Cook, Larry Griffis, Peter Vickery, and Eric Stafford

State of the Practice for Blast Resistant Design of Structures

Overview of UFC 3-340-02 *Structures to Resist the Effects of Accidental Explosions* 1454
Patrick F. Acosta

Design of Windows for Blast Loading—Moving Forward 1470
D. Duke, J. S. Shull, and R. S. Browning

Design Guidelines for Post-Installed Mechanical Anchors in Concrete Subjected to Impact Loads 1484
Daniel Gavahi and Sharon Gallant

Current State of Practice of Bridge and Tunnel Vulnerability Assessments/Evaluations

Analysis Techniques for Terrorist Risk Assessment and Mitigation of Bridges 1496
A. M. Coughlin

Case Study of Bridge and Tunnel TVAs: Since the Blue Ribbon Panel Recommendations for Bridge and Tunnel Security Were Issued 1506
Joseph M. Englot

Blast Design

Blast Amelioration Systems: Effect of Topological Parameters on Performance of Layered Metallic-Lattice Sandwich Panels 1518
John Przywara and Kapil Khandelwal

Blast Analysis and Testing

Damage Size Prediction of Reinforced Concrete Slabs under Blast Loads Using Artificial Neural Networks 1530
Ahmed Ibrahim, Hani Salim, and Ian Flood

Blast Test of Full-Size Wall Barriers Reinforced with Enamel-Coated Steel Rebar 1538
Dongming Yan, Genda Chen, Jason Baird, Huawei Yin, and Mike Koenigstein

Modeling and Testing of Laminated Window Systems under Blast Loading 1552
B. Lusk, H. Salim, K. Perry, M. Nawar, W. C. Wedding, S. Kiger, and A. Ibrahim

Forensics

Forensic Investigation of Crane Failures: Case Studies and Lessons Learned

Attaching Tower Cranes to Buildings in New York City **1561**
Dan Eschenasy

Collapse of the I-280 Maumee River Bridge Launching Gantry in Toledo, Ohio **1570**
Paul E. Kassabian, Michael McCall, Donald O. Dusenberry, and William P. Konicki

Wind Vulnerability for Critical Facilities

Vulnerability Assessments of Structural Frames for Critical Facilities **1583**
William L. Coulbourne

Wind Vulnerability Assessment of Roof Systems and Rooftop Equipment for Critical Facilities: A Preliminary Protocol for Design Professionals **1594**
Thomas L. Smith

Wind Risk Assessments for Cladding and Glazing in Critical Facilities **1606**
Paul E. Beers

A Preliminary Proposal for a Probabilistic Performance-Based Hurricane Engineering Framework **1618**
Michele Barbato, Francesco Petrini, and Marcello Ciampoli

ASCE 7-10 Changes to Wind Provisions and Our Approach to Forensics **1630**
Wiliam L. Coulbourne and Philip Line

Performance of Structures under Extreme Loads through Field Observations and Analytical Investigations

Assessment of Seismic Performance of Structures in 2010 Chile Earthquake through Field Investigation and Case Studies **1637**
O. Kwon, A. S. Elnashai, B. Gencturk, S. Kim, S. Jeong, and J. Dukes

Bridge Performance during the 2010 M8.8 Chile Earthquake **1649**
P. W. Yen, G. D. Chen, I. Buckle, T. Allen, D. Alzamora, J. Ger, and J. G. Arias

Performance of Structures in the January 2010 M_w7.0 Haiti Earthquake **1660**
Steven M. Baldridge and Justin D. Marshall

February 27, 2010 Chile Earthquake: Preliminary Observations on Structural Performance and Implications for U.S. Building Codes and Standards **1672**
John W. Wallace

Structural Repair and Strengthening of Foundations and Slabs-on-Grade

Engineering Aspects in Evaluation of Pile Capacity by Dynamic Testing **1686**
Mark R. Svinkin

High School Slab on Grade Settlement Evaluation and Permanent Structural Slab Repairs **1698**

Aaron R. Lewis, Sean M. Homem, Michael F. Hughes, and Giuliana Zelada-Tumialan

Performance Issues in Buildings and Structures

Loose Mortar-Set Roof Tile Falsehood **1710**
Mel Underwood

Non-Destructive Examination Techniques of Tubular Steel Pole Sports Lighting Structures **1722**
Brian R. Reese

Old Masonry under Seismic Loads: Stiffness Identification and Degradation **1736**
T. Zimmermann, A. Strauss, and R. Wendner

Commonality Test Methodology for Residential Structures in Katrina Canal Breaches Class Action **1748**
Erik L. Nelson, Marco A. DeLeon, and Gregory G. Schober

Forensic Remediation Measures

Tendon Failure Investigation and Drying in a Two-Way Unbonded Post-Tensioned Roof Slab **1759**
Andrea E. Shear, James P. Donnelly, and Matthew E. Lewis

Saving the Bodie Island Lighthouse: Preservation and Rehabilitation Challenges in a 140-Year Old Coastal Structure **1771**
Robert A. Bass and Jacqueline R. Bass

Snow Removal Strategies of Lightweight, Flat Roof Structures **1782**
Anthony M. Dolhon and Rahul Ratakonda

Las Vegas Structures

Nevada Geology and Assessment of Seismic Hazards

Earthquake Hazard Class Mapping by Parcel in Las Vegas Valley **1794**
J. N. Louie, S. K. Pullammanappallil, A. Pancha, T. West, and W. K. Hellmer

Hoover Dam Bypass Project

Design of the New Mike O'Callaghan Pat Tillman Memorial Bridge at Hoover Dam **1806**
David Goodyear

Research in Nevada Universities

Evaluation of Concrete Shear Strength for FRP Reinforced Beams **1816**
M. Zeidan, M. A. Barakat, Z. Mahmoud, and A. Khalifa

When the Roof Collapses **1827**
William T. Bolduc

Characterization of High Strength Steel Fiber Reinforced Concrete and Self **1839**

Consolidating Concrete Mixtures with Various Steel Volume Fractions for Infrastructure

A. T. Berhe and S. G. Ladkany

Effect of Different Parameters on the Tensile Strength of Adhesive Anchors **1850**

S. E. Robinson and A. M. Said

Viva Las Vegas: Structural Challenges

CityCenter Aria Tower—Engineering the Iconic Casino in Las Vegas **1862**

Dennis Poon, Kim Lin, Leonard Joseph, Guoyong Fu, and Allen LaSala

New Research and Novel Applications

Dynamic Monitoring of Civil Structures Using Advanced Sensing Systems and Techniques

Implementation of a Multiagent-Based Paradigm for Decentralized Real-Time Structural Health Monitoring **1875**

K. Smarsly, K. H. Law, and D. Hartmann

Electrical Resistance and Seismic Behavior of Carbon Nanofiber RC Bridge Columns **1886**

R. N. Howser, H. B. Dhonde, and Y. L. Mo

Polystyrene-MWCNT Based Nanocomposite Multifunctional Strain Sensor: Dynamic Monitoring of Civil Engineering Structures **1900**

V. S. M. Vemuru, R. K. Srivastava, A. Srivastava, S. Nagarajaiah, and P. M. Ajayan

Life Cycle Performance under Multiple Hazards

Long-Term Seismic Performance of RC Bridge Piers in an Aggressive Marine Environment **1907**

M. Akiyama and Dan M. Frangopol

Probabilistic Optimization of the Management of Corroding RC Structures **1915**

E. Bastidas-Arteaga, F. Schoefs, and M. Sánchez-Silva

Structural Risk Evaluation for Offshore Platforms under Major Accidental Events **1925**

Liangsheng Wang, Ali Sari, and Fraser Munro

Life Cycle Performance Metrics for Aging and Seismically Vulnerable Bridges **1937**

Citlali Tapia, Jayadipta Ghosh, and Jamie E. Padgett

A Probabilistic Framework for Performance-Based Durability Engineering: Application to Corrosion in Reinforced Concrete **1949**

M. M. Flint and S. L. Billington

Multi Hazard Modeling and Response of Structures

A Framework for Performance-Based Engineering in Multi-Hazard Coastal Environments **1961**

M. C. McCullough and A. Kareem

Lifetime Seismic Performance of Aging Structural Systems **1973**

Fabio Biondini, Elena Camnasio, and Alessandro Palermo

Resilience of Structures, Infrastructure, and Communities under Seismic Hazard

The Role of Critical Infrastructure in Community Resilience to Disasters **1985**

Scott B. Miles

Resilience Modeling and Simulation of Smart Grids **1996**

Min Ouyang and Leonardo Dueñas-Osorio

Conceptual and Analytical Differences between Resiliency and Reliability for Seismic Hazards **2010**

Ross B. Corotis

The State of Art of Community Resilience of Physical Infrastructure **2021**

G. P. Cimellaro, Chris S. Renschler, Amy Frazier, Lucy A. Arendt, A. M. Reinhorn, and Michel Bruneau

Measuring, Monitoring, and Evaluating Post-Disaster Recovery: A Key Element in Understanding Community Resilience **2033**

J. S. Bevington, A. A. Hill, R. A. Davidson, S. E. Chang, A. Vicini, B. J. Adams, and R. T. Eguchi

Resilience As Optimization Criterion for the Rehabilitation of Bridges Belonging to a Transportation Network Subject to Earthquake **2044**

Dan M. Frangopol and Paolo Bocchini

Advances in Shape Memory Materials Bridge Applications

Seismic Repair of RC Bridge Piers Using Shape Memory Alloys **2056**

Moochul Shin and Bassem Andrawes

Seismic Protection of Bridge Structures Using Shape Memory Alloy-Based Isolation Devices **2066**

O. E. Ozbulut and S. Hurlebaus

A Shape Memory Polymer Based Self-Healing Syntactic Foam Sealant for Expansion Joint **2078**

Guoqiang Li and Tao Xu

Progress of the SEI Disproportionate Collapse Standards and Guidance Committee

Report of the Terminology and Procedures Sub-Committee (SC1): Recommendations for Design against Disproportionate Collapse of Structures **2090**

U. Starossek, R. Smilowitz, M. Waggoner, K. J. Rubenacker, and Marco Haberland

Advances in Structural Analysis: Multiscale Mechanics and Advanced Simulation Methods in Structural Engineering

A Framework for Optimizing Civil Infrastructure Resiliency **2104**

D. A. Reed, Z. B. Zabinsky, and L. N. Boyle

A Special Solution for Lateral-Resisting Systems Capable of Multiple Seismic Performances 2113
Tomaso Trombetti, Stefano Silvestri, Giada Gasparini, and Ilaria Ricci

Blast Vulnerability Evaluation of Concrete Masonry Unit Infill Walls Retrofitted with Nano Particle Reinforced Polyurea: Modelling and Parametric Evaluation 2126
M. Irshidat, A. Al-Ostaz, A. H.-D. Cheng, and C. Mullen

Seismic Analysis of Nuclear Facilities

Overview of ASCE 4 Revision 2 2142
O. Gurbuz, S. A. Short, and M. W. Salmon

Benchmark Analysis of Seismically Induced Fluid-Structure Interaction in Liquid-Containing Tanks with Insufficient Freeboard 2153
F. G. Abatt

Modeling and Analysis for Seismic Evaluation of Nuclear Structures 2166
S. A. Short, O. Gurbuz, A. S. Whittaker, and M. Shams

Sliding and Rocking of Unanchored Components and Structures: Chapter 7.6 ASCE 4 Revision 2 2178
S. R. Jensen and O. Gurbuz

Recent Developments in Simplified Nonlinear Static Procedures for Seismic Evaluation and Design of Structural Systems

Applicability of Nonlinear MDOF Modeling for Design 2190
Michael Valley

Seismic Evaluation of Steel Moment Frames and Shear Walls Using Nonlinear Static Analysis Procedures 2204
D. G. Lignos, C. Putman, F. Zareian, and H. Krawinkler

Applicability of Nonlinear Static Procedures to RC Moment-Resisting Frames 2216
Michalis Fragiadakis, Dimitrios Vamvatsikos, and Mark Aschheim

Prediction of Nonlinear Response—Pushover Analysis versus Simplified Nonlinear Response History Analysis 2228
Helmut Krawinkler, Dimitrios G. Lignos, and Chris Putman

Bridge Reliability and Fragility Issues

Kalman Filter-Based Identification of Bridge Fragility Parameters 2240
Swagata Banerjee, Chao Chi, and Masanobu Shinozuka

Sensitivity of Reliability Index of Bridge Girders to Random Variables and Average Daily Truck Traffic 2251
O. Kwon, E. Kim, and S. Orton

Coastal Bridge Reliability during Hurricane Events: Comparison of Fragility Curves by Static and Dynamic Simulation 2263
Navid Ataei and Jamie E Padgett

RAPID Assessment of Effect of Haitian Earthquake

Effects of the January 2010 Haitian Earthquake on Selected Equipment and the Implications for the Seismic Design of Critical Non-Structural Components Required for Post-Earthquake Recovery Operations in Developing Countries **2275**
Nathan C. Gould, Barry J. Goodno, Phillip L. Gould, and Philip Caldwell

Structural Analyses to Replicate the Observed Damage to Engineered Buildings from the January 2010 Haiti Earthquake **2285**
D. Zhang, G. Federico, K. Telleen, A. Schellenberg, R. Fleischman, and J. Maffei

What Can We Learn from the Great Structural Designers?

Conceptual Transparency: Examples from the Work of Robert Maillart and Jörg Schlaich **2297**
E. M. Hines

Félix Candela and the Origins of Inspiration **2309**
Maria E. Moreyra Garlock and David P. Billington

The Influence of Engineering Organization on Design and Construction Processes at Tennessee Valley Authority Dams of the 1930s **2320**
A. B. Liel

Remote Sensing of Structural Damage

A Comprehensive Assessment of Building Damage after the January 12, 2010 Haiti Earthquake **2332**
Ronald T. Eguchi, Stuart Gill, Shubharoop Ghosh, Walter Svekla, Galen Evans, and Joaquin Toro

Advanced Computation Techniques in Structural Engineering

Procedures for Fatigue Crack Growth Monitoring and Fatigue Life Prediction Using Acoustic Emission Data and Neural Networks **2341**
F. F. Barsoum, E. v. K. Hill, Y. Zhang, A. Korcak, and J. Suleman

Experimental Validation of Design Concepts and Analytical Methods for Collapse-Resistance of Structures Subjected to Explosive and Abnormal Loading

Large-Scale Experimental Evaluation of Building System Response to Sudden Column Removal **2353**
Wei-Jian Yi, Sashi K. Kunnath, Fan-Zhen Zhang, and Yan Xiao

New Methods for Progressive Collapse Testing and Simulation **2358**
David Vaughan, David Milner, and James Gran

Recent Advances in Structural Engineering

Visualisation—A Conceptual Design Aid **2370**
Yaqub Rafiq

Open Sourcing the Design of Civil Infrastructure (OSD-CI): A Paradigm Shift 2382
T. Kijewski-Correa

Assessment and Reduction of Transportation Structure Vulnerability: Past, Present, and Future 2394
Sena Kumarasena and Raymond Daddazio

Non Building Structures

Wind Effects of Non Building and Special Structures

Unresolved US Code Compliance Issues for Wind Energy Structures: The Need for Research 2406
Nestor A. Agbayani, Rolando E. Vega, and James Newell

Seismic Blast Vibration and Modular Weight Management Aspects of Petrochemical Structure Designs

Analysis of Nonbuilding Structures Connected by Large Diameter Pipe while Subjected to Seismic Loads 2417
Eric Wey, Dawar Naqvi, David Glasscock, and Ankur Sepaha

Blast Resistant Design: Engineering Level Frame Analysis 2432
W. L. Bounds, Amol Ganpatye, and George Miller

Designing Foundations for Vibrating Machinery: Dealing with Soil and Software Issues 2443
Amy Petrash, William Bounds, and Silky Wong

Weight Management Considerations for Onshore Modularized Petrochemcial Facilities 2458
Silky S. K. Wong, Alan Shive, and Harry Warren

Design, Investigation, and Repair of Large Non Building Structures

Repair and Retrofit of a Failed Deep Underground Sewage Pump Station 2473
Prasad Samarajiva and Narendra Gosain

SCR Pile Cap Foundation Design Using STAAD v8i and Excel 2485
Jonathan Meyer

Concrete Shear Strength of Elevated Water Storage Tank Pedestals 2496
Atis A. Liepins and Gunjeet Juneja

Metal Liquid Storage Tanks on Sloped Foundations: What Could Possibly Go Wrong? 2509
Richard A. Dethlefs, Zeno Martin, and Aaron J. Sterns

Seismic Retrofit of Non Building Structures

Considerations for Retrofitting Existing Pipe Bridges 2520
Xiapin Hua

Structural Strengthening of Aloha Stadium 2532
C. M. Moe, C. Paulson, G. R. Searer, A. A. Erickson, and B. Wonneberger

Seismic Design Retrofit and Detailing for Special Structures 2545
Crystal Roe Starr

Special Structures

Engineering of Monumental and Unusual Stairs

Floating Stair Using High Performance Structural Materials 2555
Mark C. Waggoner

Staircase Vibrations Due to Human Activity 2562
Rami Eid, Michael Seica, David Stevenson, and Brian Howe

How to Keep Monumental Stairs from Vibrating 2572
Daniel J. Huntington and Jon W. Mooney

The Feature Stair at Louis Vuitton in Crystals at CityCenter 2585
Crispin Howes, Michal Krynski, and Stephan Kordt

The Spiral Stairs at the Art Gallery of Ontario 2594
Crispin Howes and Eric Gordon

Engineering Live Entertainment

Large Temporary Structure for Special Event 2605
M. G. Paschetto, T. D. Heidersdorf, and D. M. Campbell

Assessing Existing Theater Structures and Rigging Infrastructure for Large Production Demands 2613
T. D. Mills, M. G. Paschetto, and D. M. Campbell

Touring Stages for Outdoor Concert Productions 2624
Karen A. Lynch and Paul A. Gossen

Posters

Understanding Wall/Slab Bending Moment and Shear Transfer in Liquid Containing Structures 2632
Leonel I. Almanzar-Micheli and Jordan Morris

On the Application of the Meck Plot in Elastic Buckling 2640
Tadeh Zirakian

A New Approach to Office Construction: Deacero Headquarters, Monterrey, Mexico 2647
Anton Nelson, Brendan McPhail, Elliot Weinstock, and Juan Porral

CityCenter's Long Span Porte Cochères 2659
Dennis Poon, I. Paul Lew, and John Barry

Accuracy of Applying "Stiff-Girder" Approach in Reinforced Concrete Bridges **2671**
M. AbdelLatef

Influence of the Guide Specifications for LRFD Seismic Bridge Design in Alabama **2683**
Paul J. Coulston and Justin D. Marshall

High Quality, Two-Nodes Component-Based Modeling of Semi-Rigid Beam-to-Column Connections for Computer-Oriented Analysis **2695**
T. W. Aure and S. Taye

Evaluation of the ASCE 7-05 Standard for Dual Systems: Response History Analysis of a Tall Buckling-Restrained Braced Frame Dual System **2707**
L. J. Aukeman and P. Laursen

Florida Tampa International Airport Interchange Steel Bridges Design **2718**
Arun P. Khatri, Allan Berry, and Dongzhou Huang

Experiment of Slender Confined Masonry Panels under Monotonic and Cyclic Loading **2730**
Y. H. Tu, T. H. Chuang, P. C. Lin, P. W. Weng, and Y. T. Weng

ASCE 31 and 41: Apocalypse Now **2741**
T. F. Paret, G. R. Searer, and S. A. Freeman

Seismic Evaluation of an Existing Low Ductility Braced Frame Building in California **2756**
Jeremy T. Callister and Robert G. Pekelnicky

Seismic Damage Analysis Model for RC Structures Based on Concrete Plastic Damage Model **2768**
Z. H. Li, J. Teng, and X. F. He

Performance Evaluation of Shear Walls in Existing Wall-Type Precast Reinforced Concrete Residential Buildings with New Openings **2780**
J. Takagi, S. Minami, and K. Kitayama

Structure Failure Mechanism Study Based on Vulnerability Theory **2792**
Zhiqiang Zhang, Guanxing Su, Jihong Ye, and Xiaofeng "Bill" Zhang

Vibration Reduction of a Stadium Corridor Using Tuned Mass Dampers **2807**
Zhiqiang Zhang, Guowei Zhou, Aiqun Li, and Xiaofeng "Bill" Zhang

The Road Less Traveled—Middlebury, Vermont's Design-Build Cross Street Bridge Project **2818**
Gregory S. Goodrich

Three-Dimensional Effects in Progressive Collapse Modeling **2829**
Honghao Li and Sherif El-Tawil

Alternate Path Progressive Collapse Analysis of Steel Stud Bearing Wall Structures **2840**

Nabil A. Rahman, Ayman Elfouly, and Michael Booth

Seismic Behavior of Steel Reinforced Concrete Beam-Columns and Frames **2852**

Mark D. Denavit, Jerome F. Hajjar, and Roberto T. Leon

Effect of Structure, Soil, and Ground Motion Parameters on Structure-Soil-Structure Interaction of Large Scale Nuclear Structures **2862**

L. M. Anderson, S. Carey, and J. Amin

Performance Test of Secondary Mass Dampers for Vibration Control of Tall Buildings **2874**

H. Kim, J.-W. Park, D.-K. Kim, and S. Hwang

A New Structural Modification Approach for Seismic Protection Based on Adaptive Negative Stiffness Device: Conceptual Analysis **2892**

D. T. R. Pasala, A. A. S. Sarlis, Satish Nagarajaiah, A. M. Reinhorn, M. C. Constantinou, and D. Taylor

Behavior of Shear Tab Connections under Column Removal Scenario **2905**

H. Daneshvar and R. G. Driver

Effect of Regular Perforation Patterns on Steel Plate Shear Wall Column Demands **2917**

Hassan Moghimi and Robert G. Driver

Analysis of Creep Buckling of Steel Columns Subjected to Fire **2929**

M. A. Morovat, J. Lee, M. D. Engelhardt, T. A. Helwig, and E. M. Taleff

Punching Shear Failure in Progressive Collapse Analysis **2941**

Y. Mirzaei and M. Sasani

Experimental Evaluation of an Innovative Isolation System for a Lightweight Steel Moment Frame Building at E-Defense **2951**

Nhan D. Dao, Keri L. Ryan, Eiji Sato, Taichiro Okazaki, Stephen A. Mahin, Arash E. Zahgi, Kouichi Kajiwara, and Taizo Matsumori

UPV Method for Detecting Properties of Carbon-Nanofiber Concrete **2963**

T. Ravi S. Mullapudi and Ashraf Ayoub

Award Winning Bridges in California Owned and Designed by Caltrans **2971**

Carl Huang, Craig Copelan, Ric Maggenti, and Alfred R. Mangus

Documentaries As a Tool to Inform the Public about Major Infrastructure Projects in California **2983**

Craig Copelan, Alfred R. Mangus, and Ric Maggenti

The Effects of Deteriorating Bridges on Bridges on the Bridge Network Connectivity **2993**

Keivan Rokneddin, Jayadipta Ghosh, Jamie E. Padgett, Leonardo Duenas Osorio

A Study on the Minimum Column-to-Beam Moment Ratio of Steel Moment Resisting Frame with Various Connection Models **3008**

Se Woon Choi and Hyo Seon Park

Steel Plate Shear Walls with Controlled Infill Tension Fields **3018**
J. Neal and B. Qu

The Renovation of Franklin Field/The Creation of the George A. Weiss Pavilion **3029**
Paul A. Gossen and Steven P. Emery

Comparison of Hybrid and Emulative Precast Concrete Shear Walls for Seismic Regions **3033**
B. J. Smith, Y. C. Kurama, and M. J. McGinnis

Evaluation of Ground Motion Scaling Methods for Analysis of Structural Systems **3045**
A. P. O'Donnell, O. A. Beltsar, Y. C. Kurama, E. Kalkan, and A. A. Taflanidis

Three-Dimensional Tests of Two-Story, One-Bay by One-Bay, Steel Concentric Braced Frames **3057**
Keith Palmer, Charles Roeder, Taichiro Okazaki, Carol Shield, and Dawn Lehman

Design of Normal Strength Concrete Mixtures with Recycled Concrete Aggregates **3068**
A. M. Knaack and Y. C. Kurama

Buckling Behavior of Shell Elements Subjected to Inelastic Reversed Cyclic Loading **3080**
Max Stephens, Peter Dusicka, and Gregory Lewis

Seismic Evaluation of Bridge G-947 in Clark County, Nevada Using Nonlinear Static Procedures **3092**
Ahmad Saad, Aly Said, and Barbara Luke

Development of Concrete/Cold Formed Steel Composite Flexural Members **3099**
N. Wehbe, A. Wehbe, L. Dayton, and A. Sigl

An Experimental Study on the Mechanical Properties of Pultruded CFRP Plates at Elevated Temperatures **3110**
Ke Wang, Ben Young, and Scott T. Smith

Inverse Identification of Micromechanics and Fracture Mechanics-Based Damage Evolution Law of Brittle Composites **3120**
Shen Shang and Gun Jin Yun

Progressive Collapse Analysis of RC Structures Including Beam Axial Deformation **3132**
Ali Kazemi and Mehrdad Sasani

Effects of Troweling on Shrinkage of Concrete Treated with an Evaporation Reducer **3141**
Vikram C. S. Majeti, Christian Dominguez, and Craig M. Newtson

I35W Bridge Collapse: Lessons Learned and Challenges Revealed **3153**
S. Hao

Characterization of Mortar Using Calcified Cell-$CaCO_3$by Microbial Biomineralization **3171**

Wha-Jung Kim, Woo-Young Chun, Jun-Seok Park, and Chang-Joon Lee

This page intentionally left blank

System-level calibration of bridge component damage states

K. R. Mackie[1]

[1]Assistant Professor, Department of Civil, Environmental, and Construction Engineering, University of Central Florida, Orlando, FL 32816-2450; PH (407) 823-2857; email kmackie@mail.ucf.edu

ABSTRACT

Post-earthquake repair costs and repair times are important for evaluating the performance of bridges in a fundamentally different way than the traditional component-level metrics such as bearing displacements and column ductility demands. Repair costs and times are metrics that address the system-level response of bridges to a suite of seismic events, especially when cast probabilistically in the form of fragility curves. Traditionally, bridges are assessed and fragilities are generated according to enumerated component damage states (e.g., DS1 is minor damage). However, the level of system functionality that corresponds to each component damage state and whether individual components have risk or performance consistent with the system are of considerable interest in seismic assessment. In this paper, repair costs and times are calculated for a typical multi-span reinforced concrete highway overpass bridge in California. This system-level information is then used to back calculate consistent component damage states. The initial damage states are compared to the back-calculated states for forward prediction on different bridge configurations, and it is shown that it is difficult to achieve consistent performance using constant component damage states.

INTRODUCTION

For the highway overpass bridges that comprise most regional transportation systems, there are two principal concerns that contribute to economic-based decision making. The total expected loss after an earthquake includes not only the cost associated with damage to the structure itself, but also the cost associated with the loss of function. Functional loss is particularly relevant in the case of a highway network system because the indirect losses to an urban area might greatly exceed the direct losses. Estimated costs due to repair and the loss of function are the subjects of large-scale simulations on urban regions and transportation networks. The goal of such simulations is to provide an economic impact analysis of damage to a transportation system in an extreme event, such as an earthquake, on an urban area. The economic impact can be defined in terms of damaged and failed links in the transportation network and link costs associated with traffic flow. Direct losses to the region include damage to components (bridges) as well as time delays in the damaged network. Indirect losses are due to the interruption of goods and services to those businesses affected by the earthquake. (Mackie 2010)

While downtimes may contribute more directly to the accumulation of indirect losses in the network after an event, they are also the most difficult to quantify because they are largely based on emergency response, resource management, and the decisions of reconnaissance, engineering, and management personnel. Therefore, the focus of the study presented in this paper is primarily on the direct costs associated with repair of the bridge to functionality. This task is achieved by performing a performance-based earthquake engineering (PBEE) analysis on individual bridge configurations. PBEE assessment is performed for both direct repair costs as well as repair efforts. The PBEE assessment procedure is briefly described in this paper; however, the emphasis is on quantifying the relationship between system and component limit states; therefore, references are provided for more detailed reading on the details of the procedure itself.

HAZUS (FEMA 1999) contains five damage limit states (DS1 to DS5) that are defined in terms of observable damage and response of different bridge components, such as piers, abutments, shear keys, and foundations. The five states are intended to correspond to the bridge states of none, minor, moderate, excessive, and complete, respectively. The performance that defines the boundaries of each particular state are subjective in nature and not necessarily easy to quantify based on either observed states of damage, nor based on quantitative results obtained from, for example, nonlinear finite element analysis. In addition, it may be desirable to be able to consistently group or identify different bridge components into the same damage states as the entire system. This would require a consistent risk or performance definition for both the component and system damage states. In general, while components are commonly described using component damage states (Padgett 2007, Nielson 2005, Mackie et al. 2008), there is no clear map between these and the corresponding performance of the system or vice versa.

In this paper, an implementation of the Pacific Earthquake Engineering Research (PEER) Center performance-based earthquake engineering framework (Cornell and Krawinkler 2000) is used to generate probabilistic estimates of repair cost and repair time. The complete analysis is accomplished using the local linearization repair cost and time methodology (LLRCAT), described by Mackie et al. (2009) and depicted conceptually in Figure 1. In the LLCAT methodology, each bridge system is disaggregated into independent structural or non-structural components or subassemblies defined as PGs that are damaged, assessed, and repaired together using a specific combination of different repair methods. Demands on the bridge system (and components) are determined using 3D nonlinear time history analysis under multiple-component earthquake excitation. The descriptor of earthquake intensity is designated an intensity measure (IM) and the measure of response is designated an engineering demand parameter (EDP). The damage in each of the PGs is characterized according to several discrete damage states (DSs) that are defined by distributions of critical EDPs. Different repair methods are employed for the various damage states of each PG or bridge component. The repair methods for each PG require a combination of several repair quantities (Qs). Repair quantities for all PGs are then combined with due consideration of the correlation between components. Repair costs (RC) are obtained through a unit cost (UC). Repair times (RT) are obtained through a production rate (PR). The PRs are in terms of crew

working days (CWD), representing one working day for a normal sized crew and can be combined later by construction management experts to obtain total site construction times.

$$\text{RC: } \lambda(RC > rc) = \int_{im}\int_{dm}\int_{edp} G(uc \cdot q|dm)dG(dm|edp)dG(edp|im)|d\lambda(im)|$$

$$\text{RT: } \lambda(RT > rt) = \int_{im}\int_{dm}\int_{edp} G(lpr|dm)dG(dm|edp)dG(edp|im)|d\lambda(im)|$$

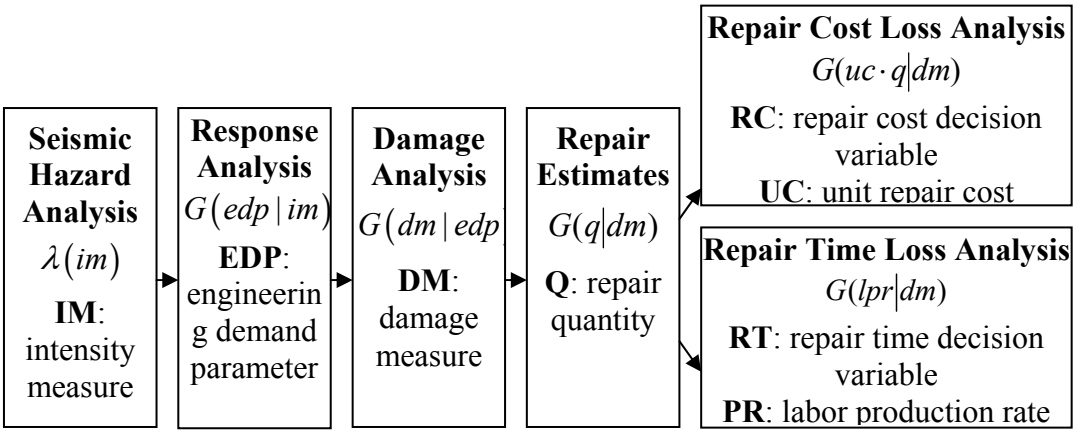


Figure 1. Schematic representation of the LLRCAT methodology.

BRIDGE CONFIGURATIONS

The two bridges considered in this study are from a series of bridge types presented by Ketchum et al. (2004) that were intended to be typical of post-tensioned concrete box girder construction in California. Specifically, the two configurations with common deck sections and single column bents were selected for this study. The two configurations are designated as Type 1A and Type 11B. The bridges have 3 internal spans of 150' and 2 external spans of 120' with a total length of 690'. The bridges are cast-in-place, pre-stressed (CIP/PS) 2-cell box girder bridges with the superstructure supported on neoprene bearing pads under each of the three box webs. The only difference is the clear column heights and column diameters; the Type 1A has 22' column heights and 4' column diameters, and the Type 11 has 50' column heights and 6' column diameters.

The testbed bridge is broken down into performance groups (PGs) for each major bridge superstructure, substructure, and foundation component. Each performance group represents a collection of structural components that act as a global-level indicator of structural performance and that contribute significantly to repair-level decisions. Performance groups are not necessarily the same as load-resisting structural components. For example, non-structural components may also form a performance group, since they also suffer damage and contribute to repair costs. The notion of a performance group also allows grouping several components together for related repair work. The correlation between repair items from the PGs is

handled at the demand model level in the methodology. A total of 27 PGs are considered for the testbed bridge: columns based on maximum displacement (1 PG per column), columns based on residual displacement (1 PG per column), deck/superstructure (1 PG per bridge span), abutment (1 PG per abutment), bearings (1 PG per abutment including all bearings), shear keys (1 PG per abutment including both external shear keys), approach (1 PG per approach), abutment piles (1 PG per abutment), and pile groups (1 PG per column). Further details regarding the testbed bridge and the analytical model that was developed for simulation are contained in Mackie et al. (2008).

REPAIR COSTS AND TIMES

Normalized costs of repair are obtained by using the repair cost ratio (RCR) between the cost of repair and the cost of original new construction. This ratio is useful for comparing the performance of different bridge design options for new construction. For the evaluation of existing structures, the RCR including demolition costs might be more useful. Constructing a new bridge on the same site after an earthquake would require both demolition of the damaged bridge and construction of its replacement. The cost of new construction can be obtained using different methods. Ketchum et al. (2004) computed construction costs based on quantity estimates for each of the testbed bridge models. Also, Caltrans bridge cost estimates for planning purposes are based on the deck and type of construction and provide a range of cost/SF of deck area. The cost of new construction was adjusted by the price index to make comparisons between current 2007 cost data and the new construction costs reported in Ketchum et al. (2004) that were based on 2003 cost estimates.

The unit costs (UC) for the individual repair items used in this paper study are given in Mackie et al. (2008). It is assumed that unit costs are constant regardless of the quantity. A simple lump sum contingency estimate can be used to display the magnitude of total repair cost uncertainty due to possible fluctuations in unit cost in this case. Repair times are also computed on the basis of each repair quantity Q. For any repair item, a probability of 50% that $Q > 0$ indicates that the associated repair time should be added to the total repair time for the project. Repair tasks that use the same repair items are assumed to occur simultaneously. So, when the repair times are added up, this estimate more closely approximates repair duration instead of repair effort. The repair task durations are based on estimated schedules from damage scenarios (Mackie et al., 2008). The repair durations were related to the individual repair quantities by summing the different tasks associated with each repair quantity. The mobilization required for several of the items dominated the repair time. For example, preparing the material and safety plan for methacrylate deck overlay takes 20 working days, while the actual cleaning and treating of the bridge deck takes only 2 working days.

Due to the methodology, the outputs from the methodology are the intensity-dependent first and second moments of the repair times and costs. In addition, final repair costs can be disaggregated into contributions from each repair quantity or performance group (for the expected costs as well as the cost variance). Retaining an intensity-dependent format, the total repair cost ratio for both bridge types is shown in

Figure 2. The ordinate is plotted in units of the percent of the replacement cost. The plot shows that both the first and second moments vary with intensity and that the RCR of the two bridge configurations is not necessarily equal, even when the structure-independent site intensity (measured in terms of the peak ground velocity) is the same. There is a range of intensities (80 < PGV < 180 cm/s) for which both bridges exhibit approximately constant RCRs. This is due to the fact that most of the superficial concrete repairs have been made (epoxy inject cracks, repair spalls, etc.) and do not continue to accumulate with increasing intensity until more serious damage occurs. For the range of intensities considered during the analysis, only Type 1A experiences a jump in RCR due to excessive deformation and damage to the columns.

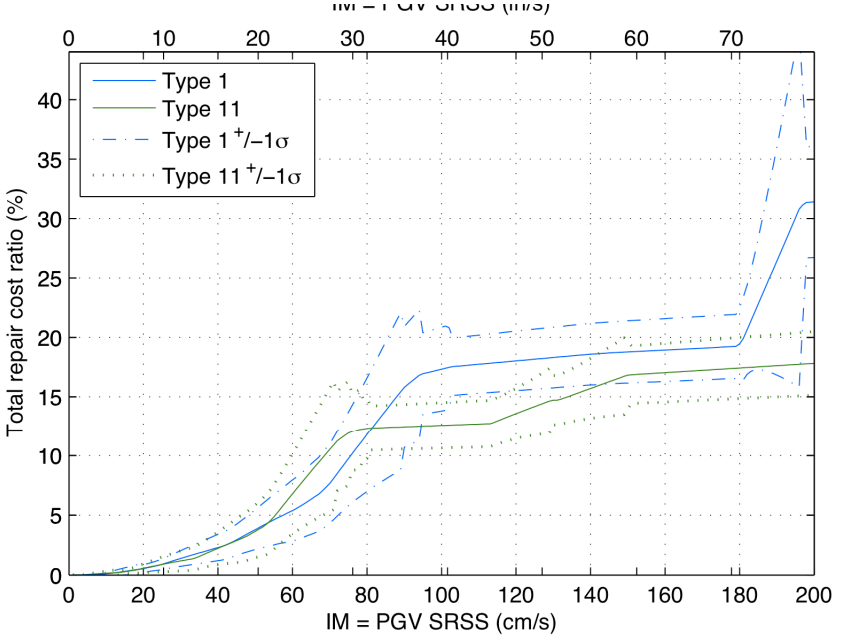


Figure 2. Intensity-dependent repair cost ratio for two bridge configurations.

COMPONENT DAMAGE STATE STUDIES

From data compiled for the Northridge earthquake, the HAZUS (Basöz and Mander 1999) document reports a modified repair cost ratio (RCR) as a function of damage for typical bridges. The HAZUS damage states of slight, moderate, extensive, and complete have mean RCRs of 12%, 19%, 48%, and 100%, respectively. As these were observations made on the inventory and damage cases observed in the region, they range all the way from 0 to 100%. However, the two bridge configurations in this study are intended to be of newer design and construction, and therefore considerably more ductile and less prone to shear and other brittle failures. Therefore, the target RCR levels were modified slightly for this study and are 2%, 5%, 15%, 30%, and 50% for DS1-DS5, respectively.

It is ostensible from Figure 2 that each repair quantity (and therefore each PG) contributes differently to the expected system-level metric of repair cost (or repair time). Not only this, but the relative contribution from each Q differs as the intensity

of the earthquake event changes. To better understand the discrepancy between the component damage states (presented in subsequent sections), the relative contributions of each PG for both bridge types are presented first. Figure 3 shows the disaggregation of the cumulative expected cost at each intensity for Type 1A. Because the repair cost is cumulative and normalized at each intensity, the range is always between 0 and 1 with the distance between lines indicating the contribution of each PG. For example, at and intensity of 120 cm/s, PGs 5 and 6 are the largest contributors (left and right abutment deck end displacement). However, at small intensities such as PGV < 25 cm/s, before gap closure occurs at the abutments, there is zero contribution from these PGs. The data at extremely small intensities (PGV < 10 cm/s) should not be considered as accurate, because the quantities are all being normalized by approximately zero.

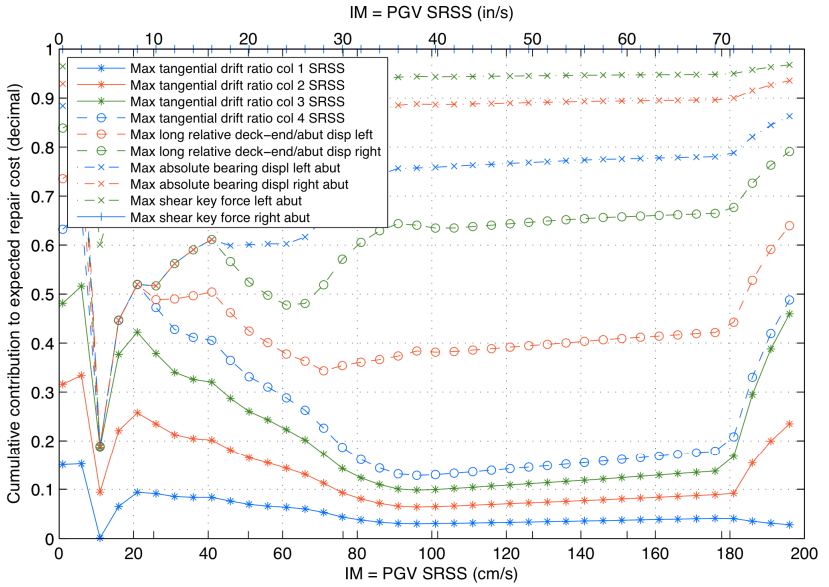


Figure 3. Disaggregation of expected repair cost by performance group (cumulative) for Type 1A.

Figure 4 shows similar information for Type 11B. It is immediately apparent from comparing the two figures that the range of intensities at which the relative importance of the columns and abutments is significantly different. In Type 11B, the columns have a minimal relative contribution to the total cost until a PGV of approximately 110 cm/s (does not imply small repairs and patching are not being performed earlier, only that the relative cost is small compared to the total). The majority of intensities considered in the study have repair costs governed by the abutments for Type 11B.

For each target system RCR, the corresponding distribution of intensity was calculated for each (distribution was assumed to be defined by the first two moments). Using this intensity distribution and the original probabilistic seismic demand models, the distribution of EDPs was obtained for each state and PG. The cumulative distribution function of this EDP was plotted for each PG to illustrate the component-level states that are consistent with the system-level states. It should be

noted that the variance is not strictly correct because it contains a contribution from the uncertainty obtained from the RCR-IM relationship, but only a forward estimate obtained from the demand model.

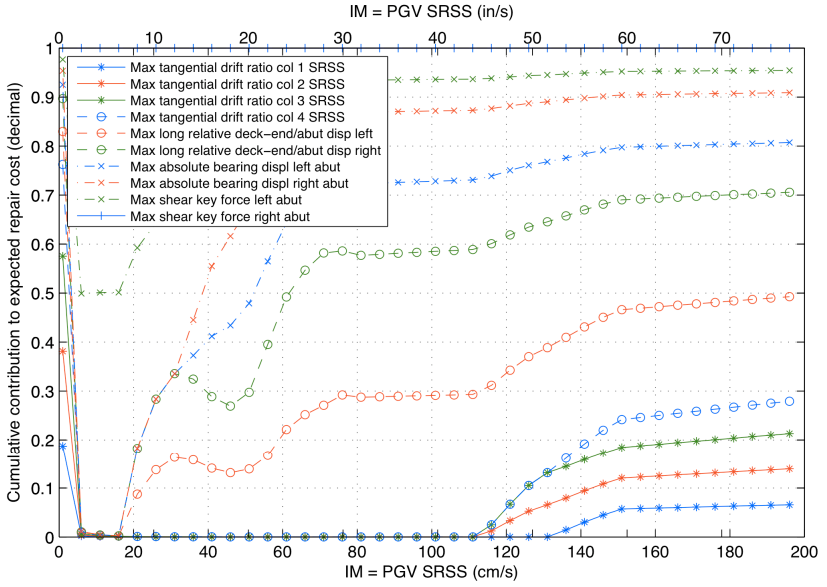


Figure 4. Disaggregation of expected repair cost by performance group (cumulative) for Type 11B.

Because the damage state median values are most often parameterized in terms of the geometric and material properties of the bridge (there is not a single EDP value that describes the onset of damage in columns for example), it is more logical to compare normalized damage fragility curves. The medians were normalized by the largest damage state median of the original damage states for each given PG. Note, in the original formulation, each PG may have a different number of damage states; however, in the proposed (new) comparison, there are a fixed number of damage states. Only the new damage states that fall within the range of system values for a given bridge are shown. For example, for Type 1A, there are only 4 states in the range of intensities considered, whereas for Type 11B, there are only 3 states.

The normalized median values are shown for Type 1A for the first 21 PGs in Figure 5. The remainder of the performance groups are not shown as the particular bridge model was run with elastic springs at the base of the bents; therefore, there are no residual pile deformations to trigger the foundation PGs. For the column PGs (1-4 for maximum, 5-8 for residual), the damage state medians consistent with the system RCR values selected are generally lower than the original damage state medians. This is because the original column damage states have only a lower level state followed by the more extreme cases immediately preceding collapse.

However, for the abutment damage states, the damage state medians consistent with the system are considerably higher, indicative of the fact that they trigger at lower intensities. The larger values (some on the order of two times the original) indicate that the consistent damage states should trigger at higher deformations level to limit the contribution of the abutment to the system RCR. These

relative contributions can be seen in the original disaggregation by PG in Figure 3 and Figure 4. The normalized median values for Type 11B are shown in Figure 6. Similar trends to Type 1 can be observed, although it is also immediately apparent that by normalizing the medians alone, there is no agreement between the consistent component damage state medians between the two bridges.

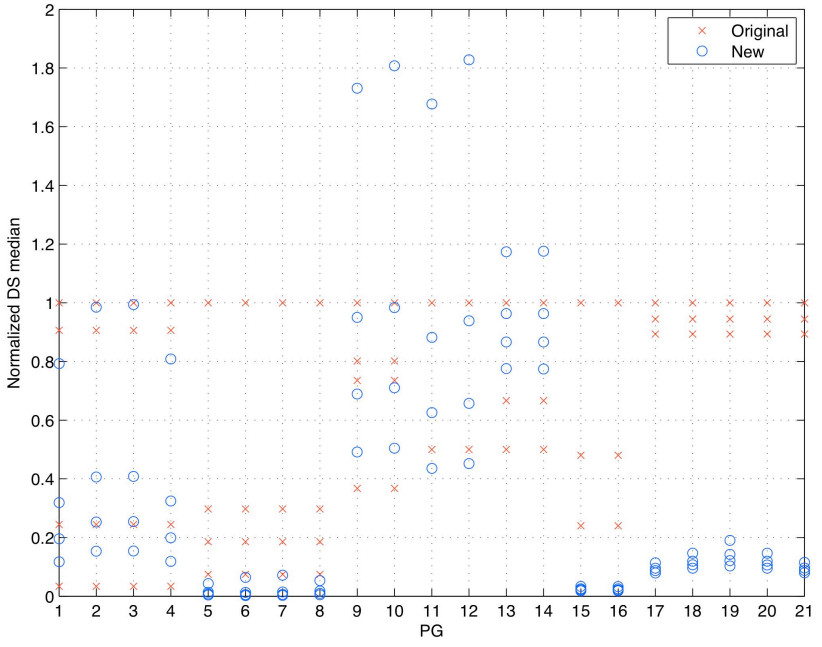


Figure 5. Normalized damage state medians for all performance groups of Type 1A (original and proposed).

The normalized damage state fragilities are shown for PG 2 (second column considering maximum drift ratio) in Figure 7 for both bridge configurations. The median values in the plot correspond directly to Figure 5 and Figure 6. As mentioned previously, there are four damage states that occur within the range of intensities considered for Type 1 and three damage states for Type 11. The only agreement between damage states DS3 and one could argue that DS1 of Type 1 matches DS2 of Type 11. Normalizing the damage states accounts for the differences in the performance of the columns between the two bridge configurations (i.e., in a similar manner as the original damage state medians were parameterized in terms of the bridge properties). However, as the consistent damage states are based on the system RCR, the normalization has no effect on the relative contributions of the columns to the system RCR. This is analogous to saying that the component to system map is different between the two bridges and should not be assumed constant, i.e., the columns do not always contribute a fixed percent to the system RCR, nor will the columns necessarily have the same state of damage or functionality as the rest of the bridge, as has been assumed in the past (Mackie and Stojadinovic 2004).

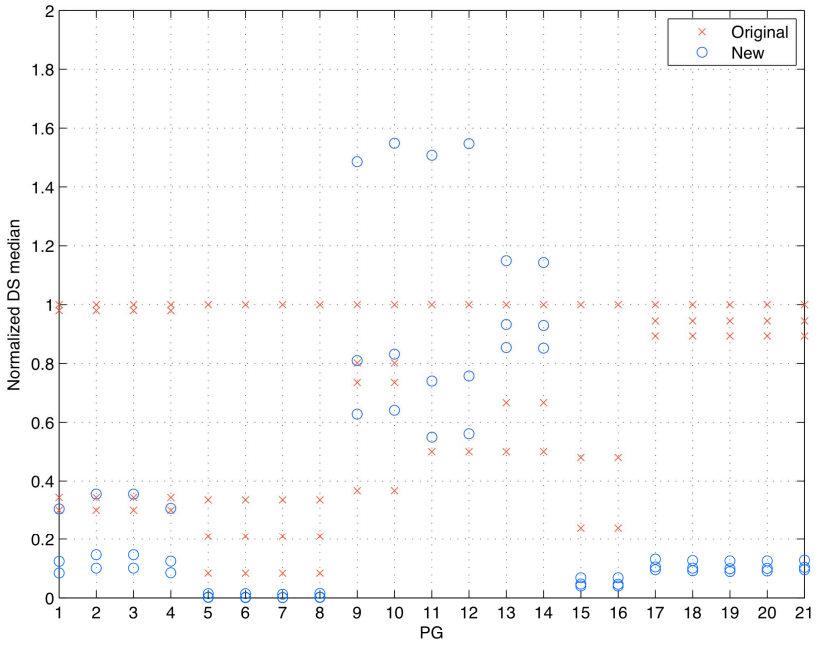


Figure 6. Normalized damage state medians for all performance groups of Type 11B (original and proposed).

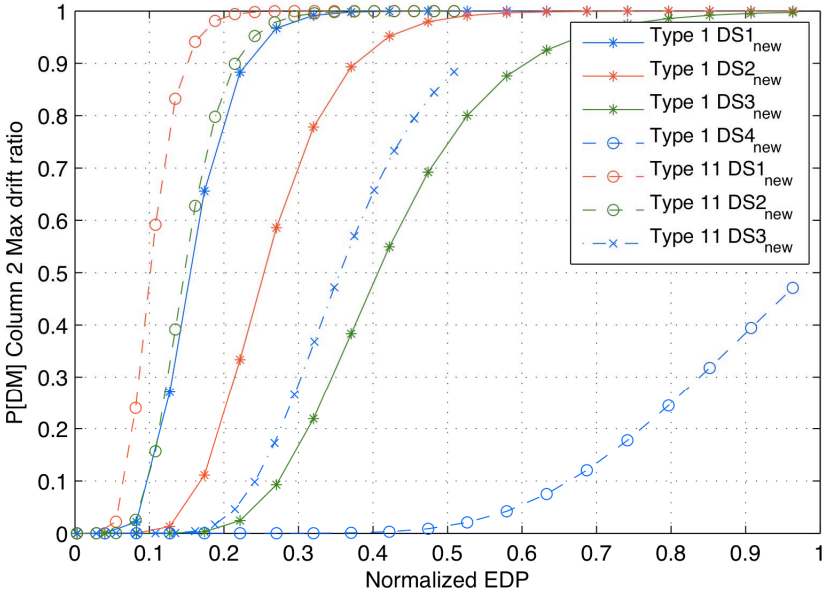


Figure 7. Comparison of normalized damage state fragilities at constant RCRs for performance group 2 (Column 2 maximum drift ratio).

The normalized damage state fragilities are shown for PG 9 (left abutment relative longitudinal displacement) in Figure 8 for both bridge configurations. As with

the column comparison, there is limited agreement between consistent damage states for each of the two bridge types. DS2 for Type 1 and DS1 for Type 11 are among those with approximate correspondence. For Type 1, DS2 corresponds to an intensity of 57 cm/s and DS1 for Type 11 is 38 cm/s. As an index into the disaggregation figures, the intensities correspond to decreases in the importance of the abutment PGs and a region where they are not the dominant contributor to the RCR. However, DS3 has an intensity of 88 cm/s and 134 cm/s for Type 1 and Type 11, respectively. In this region of intensities, the column contributions are approximately constant and the dominant RCR driver is the abutment PGs.

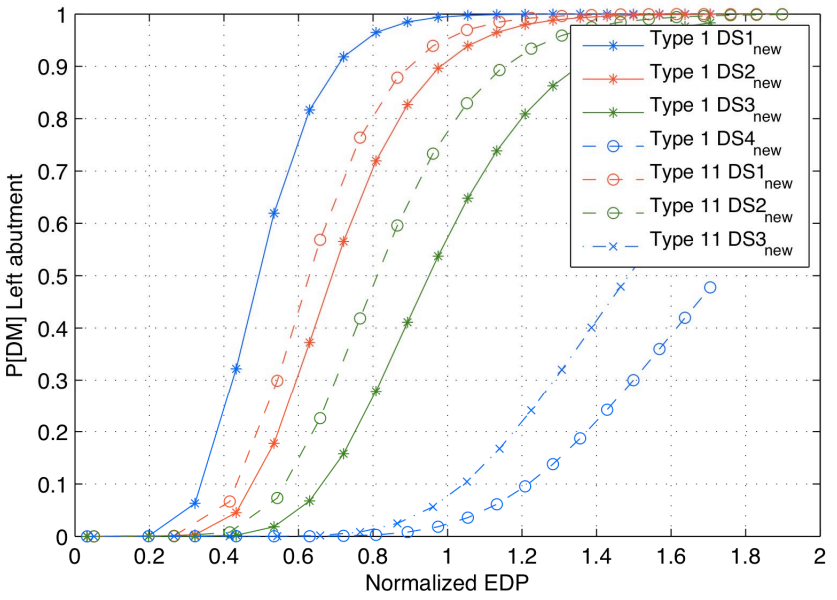


Figure 8. Comparison of normalized damage state fragilities at constant RCRs for performance group 9 (Left abutment relative longitudinal displacement).

A similar exercise could be performed for selected repair time performance levels. However, the repair times tend to be piecewise constant with finite ramps (in CWD-IM space). Therefore, and more intuitively, the system time and cost states were correlated to one another. The solid lines in Figure 9 show this correlation. In addition, approximate plus/minus one standard deviation lines are have been computed. The radial lines emanating from the original show constant intensities (only for the first three states). The Type 11 curve exhibits smaller RCR values throughout (radial lines to the left of Type 1). The two bridge types have a radial line that coincides for the third state, as consistent with the previous discussion.

A critical consideration not mentioned thus far is that a complete comparison between the original and consistent component damage states can only be performed by recomputing the system RCR-IM curve for each bridge. Using the current methodology; however, the exact same result would be obtained because of the local linearization that takes place between the median of the damage state and the repair quantities. This is akin to interpolation; however, the assumption is that the turning points in the locally linear relationship are defined by the original damage states; a

key assumption. Truly, one would need to return to basic damage scenarios based on the new consistent damage states and perform repair design, quantity take off, and cost estimation. This is prohibitive at this time, even for a single selection of component states, particularly because the state of damage defined by these consistent states may not have distinct meaning (onset of certain types of damage) at the damage scenario and repair design phases.

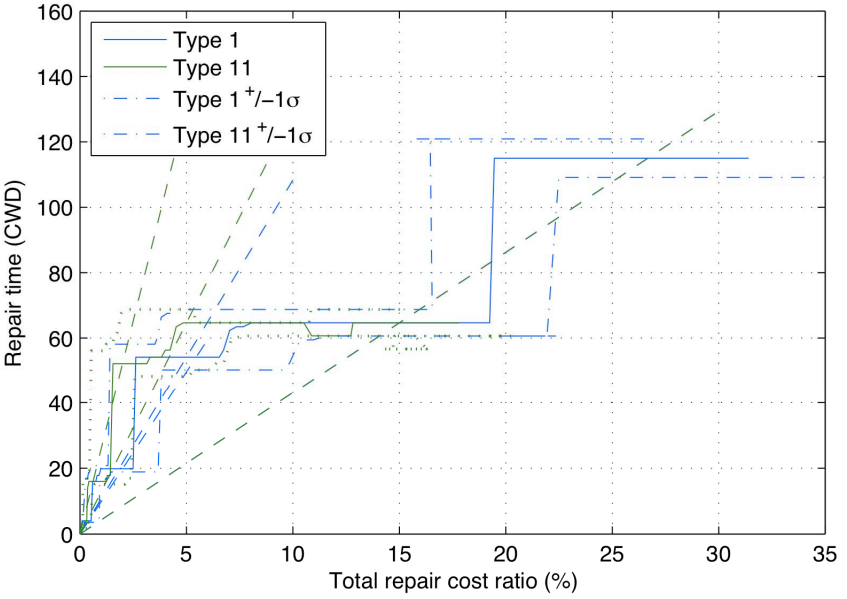


Figure 9. Consistency between RCR and RT estimates with radial lines of constant intensity.

Another important consideration is that the second moment of the consistent component damage states computed here is only approximate and that there is only a single permutation of component damage states that would allow one to arrive at the specified system RCR or RT level. This of course is not true and a more complete parameter estimation analysis would be required to investigate the best fit or most likely value of the median for each PG and damage state that would lead to the RCR distribution (in a probabilistic sense). However, in the absence of a mathematical expression for the DM-Q relationship, this becomes tedious for all but simulation approaches. This topic will be further explored in future work.

CONCLUSIONS

Post-earthquake repair costs and repair times are important system-level metrics for evaluating the performance of bridges. They are the result of the aggregation of costs and repair actions to individual performance groups (PGs) within the structure. In this framework, it is desirable to have a consistent definition of performance between PGs, as well as between the PGs and the system. The results in this paper represent a first step toward quantifying such a consistent relationship between component and system limit states. Here the consistency metric is selected

as different levels of repair cost that are then correlated to repair times. While it is straightforward to ascertain the PG damage state medians that are consistent with different levels of system performance using the LLRCAT methodology, the results indicate that significant challenges remain. Specifically, due to the linearization of the damage to repair model, the proposed damage state medians are merely linear interpolations between the existing median values. Therefore, when performing a separate analysis using the new damage states (in lieu of more scenarios and cost estimation), the same results will be generated. The second major shortcoming is that the component states (while consistent) are not constant between different bridge configurations. This leads to results of questionable usefulness when performing network vulnerability studies. The results demonstrate that the differences in the PG medians is largely due to the relative contributions of the performance groups to the repair cost ratio. However, the relative contributions change with intensity as well as bridge type. Therefore, at this time, more work is necessary to better understand the driving mechanisms behind the component to system level mapping.

REFERENCES

Basöz N, and Mander J. (1999). "Enhancement of the highway transportation lifeline module in HAZUS." National Institute of Building Sciences.

Cornell, C.A., and Krawinkler, H. (2000). "Progress and Challenges in Seismic Performance Assessment." *PEER Center News*, 3(2).

HAZUS, (1999), Earthquake Loss Estimation Methodology, SR2 edition. Washington, DC: National Institute of Building Sciences for Federal Emergency Management Agency.

Ketchum, M., Chang, V. and Shantz T. (2004). "Influence of Design Ground Motion Level on Highway Bridge Cost." *PEER Lifelines 6D01 Report*, Pacific Earthquake Engineering Research Center, University of California, Berkeley.

Mackie, K.R., Wong, J-M., and Stojadinovic, B. (2009). "Post-earthquake Bridge Repair Cost and Repair Time Estimation Methodology." *Earthquake Engineering and Structural Dynamics*, 39(3): 281-301.

Mackie, K.R. (2010). "Sensitivities in repair cost and repair time metrics for seismic bridge response." In Proceedings of ASCE Structures Congress (19th A&C Specialty Conference), May 12-15, 2010. Orlando, FL.

Mackie, K., Wong, J-M., and Stojadinovic, B. (2008). "Integrated Probabilistic Performance-based Evaluation of Benchmark Reinforced Concrete Bridges." *Report No. 2007/09*, Pacific Earthquake Engineering Research Center, University of California, Berkeley.

Mackie, K., and Stojadinovic, B. (2004). "Fragility curves for reinforced concrete highway overpass bridges." In Proceedings of the 13th World Conference on Earthquake Engineering, August 1-6, 2004. Vancouver, Canada.

Nielson, B.G. (2005). "Analytical fragility curves for highway bridges in moderate seismic zones." Ph.D. thesis, Georgia Institute of Technology, Atlanta GA.

Padgett, J. (2007). "Seismic vulnerability assessment of retrofitted bridges using probabilistic methods." Ph.D. thesis, Georgia Institute of Technology, Atlanta, GA.

Seismic fragility estimates and optimization of retrofitting strategies for reinforced concrete bridges: Case study of the Fabela Bridge in Toluca, Mexico

V. Bisadi[1], M. Head[2] and P. Gardoni[3]

[1] PhD Student, Zachry Department of Civil Engineering, Texas A&M University, College Station, TX 77843-3136; PH (979) 204-5028; email: vahid_bisadi@tamu.edu
[2] Assistant Professor, Zachry Department of Civil Engineering, Texas A&M University, College Station, TX 77843-3136; PH (979) 862-5687; FAX (979) 845-6554; email: mhead@civil.tamu.edu
[3] Associate Professor, Zachry Department of Civil Engineering, Texas A&M University, College Station, TX 77843-3136; PH (979) 845-4330; email: pgardoni@civil.tamu.edu

ABSTRACT

Seismic fragility estimates are computed for the Fabela Bridge, a five-span single-column bent reinforced concrete bridge, located in Toluca, Mexico based on previously developed probabilistic models for the capacity and demand of typical reinforced concrete bridges. The seismic fragility estimates are computed considering deformation failures in the columns. The approach used in this study properly accounts for epistemic and aleatory uncertainties of the problem. The properties of the bridge used to develop the fragility curves are estimated by matching the frequencies of a 3D finite element model to field data. For this purpose, a 3D finite element model of the studied bridge is created based on the available information of the bridge including drawings and field observations. Then the model is updated based on the modal frequencies obtained from measured accelerations in a series of forced vibration tests on the bridge. Fragility curves are generated to assess the seismic vulnerabilities of the current bridge. Different retrofit strategies are also applied to the bridge model to generate new fragility curves for a retrofitted bridge. The optimal retrofit strategies are determined based on the developed fragilities.

INTRODUCTION

Several cases of bridge failures with single column piers during past earthquakes demonstrate that this type of bridges is vulnerable to ground motions. One of the most important failure cases is the failure of Hanshin Expressway viaducts during the 1995 Kobe earthquake (Hashimoto et al. 2005). Fragility estimates are helpful to quantify

the vulnerability of bridges subjected to seismic loads. This paper estimates seismic fragility of the Fabela Bridge, a five-span bridge with single column concrete piers, located in Toluca, Mexico. Considering the high volume of daily traffic that pass over the Fabela Bridge, its survival after earthquakes is very important. The fragility estimates for the Fabela Bridge are developed based on the current condition of the bridge, which is evaluated based on the results of vibration data resulting from forced vibration tests on the bridge.

This study estimates the fragilities of the bridge in different performance levels. Column drift is used as a measure to define performance levels. Seismic demands on the bridge are estimated using the probabilistic demand model proposed by Gardoni et al. (2003). The seismic demands on the bridge are related to the structural properties of the bridge. Therefore, accurate estimation of the structural properties plays an important role in developing reliable fragility curves. In this study, preliminary values are considered for structural properties based on the available information in construction drawings. Then, the considered values are updated by matching the vibration frequencies of a finite element model of the bridge to those obtained from field data.

An appropriate way to investigate the effectives of retrofit strategies is to evaluate their effect on the reduction of failure probability. Comparison of fragility curves before and after retrofitting the structure reveals the effectiveness of the retrofit strategy. In this study, four retrofit strategies are considered for the studied bridge: steel jacketing and concrete jacketing over the plastic hinge region at the bottom of the columns and also steel and concrete jacketing on all the heights of the columns. The effect of each of these strategies is studied on the fragility curves and based on the results a retrofit strategy is recommended to reduce the vulnerability of the Fabela Bridge to earthquake loads.

This paper has seven sections. First, the preliminary properties of the Fabela Bridge that are obtained from the design drawings are presented. The second section presents the results of the conducted vibration tests on the bridge. Then the updating process of structural properties using vibration data is discussed. Next, the details of each retrofit strategy are presented. Then we present the fragility estimates of the Fabela Bridge and investigate the effect of each retrofit strategy on the fragility curves. Finally, the last section presents the conclusions of this study.

PROPERTIES OF THE STUDIED BRIDGE

The Fabela Bridge is a five-span single-column concrete bridge that is located in Toluca, Mexico. Figure 1 shows the elevation of the Fabela Bridge and its geometrical properties. Three lanes of traffic pass over the bridge. The width of superstructure is 10.95m and it is composed of cellular prestressed concrete girders and a concrete slab. The Fabela Bridge has four single column circular piers with different heights. The diameter of columns are 2m and the height of columns A,B, C and D in Figure 1 are 5.90m, 6.87m, 7.55m and 7.28m, respectively. Columns are continuous to the deck. Joints 1, 3 and 5 in Figure 1 are specified as fixed joints in design drawings and joints 2, 4 and 6 are specified as moveable joints. Elastomeric bearings are used at all joints. Shallow foundations support the piers.

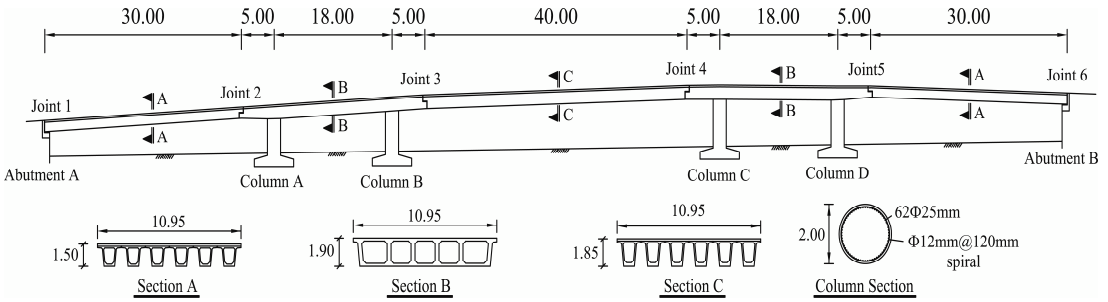


Figure 1. Elevation of the Fabela Bridge (dimensions are in meters unless otherwise mentioned).

VIBRATION TESTS

Vibration test data by Bisadi et al. (2011) has been used in this study. Two accelerometers on the bridge deck have been used to record the transverse accelerations during vibration tests with sampling time of 0.005 second. One of them was installed on the deck at the top of Column B and the other one was installed 20m away from the first one near the center of the bridge. Vibration tests were conducted using a two-axle truck with the weight of 164kN. The truck moved on the bridge with various speeds varying from 10km/h to 40km/h.

After recording accelerations, baseline correction and an eighth order bandpass filter are applied on them. The highpass and lowpass frequencies in the bandpass filter are considered equal to 0.3 and 20 Hz, respectively. Also, Hanning window (Oppenheim and Schafer 1989) is applied on the recorded accelerations to make the start and end points of the records match. Then, Fourier spectra of accelerations are computed and vibration frequencies are determined.

Four transverse vibration frequencies are obtained from recorded accelerations and are equal to 1.190Hz, 2.127Hz, 2.872Hz and 3.473Hz. It should be noted that these frequencies are limited to those transverse mode shapes of the bridge that produce vibrations at the location of accelerometers and are not necessarily the first four transverse vibration frequencies of the bridge. For example, the installed accelerometers do not capture vibration modes in which only the end parts of the deck (between joints) vibrate.

UPDATING STRUCTURAL PROPERTIES

Deterioration of bridge components during time makes changes in structural properties such as the stiffnesses of components that in turn change the vibration characteristics of the bridge. This is one of the reasons that the vibration frequencies of a model created based on the construction drawings does not match those obtained from measured data in field. Also, there are always some errors in the modeling assumptions that cause approximations in the results of analytical models. In this study, an analytical model is created first based on construction drawings and then structural properties in the model are updated to match the model vibration frequencies to those obtained from field data. The first part of this section describes the details of the finite element model of the Fabela Bridge and the second part explains the method used for updating structural properties of the created model.

Analytical modeling

Pushover analyses on the finite element model of the bridge are required in this study to compute the deterministic part of the demand model. Therefore, an appropriate finite element model of the bridge is needed. A 3D nonlinear finite element model of the Fabela Bridge is created in finite element package OpenSees (McKenna & Fenves 2009). Elastic frame elements are used to model bridge deck. The mass of the deck is considered as concentrated masses at the deck element nodes. Following Naeim & Kelly (1999) a bilinear force-displacement relationship is used for modeling the elastomeric bearings. Bridge foundations are modeled using translational and rotational linear springs based on the relations recommended in FEMA 356 (2000). For modeling of bridge abutments, Caltrans (2006) recommendation are used for the calculation of abutment stiffness in both longitudinal and transverse directions.
Columns of the bridge are modeled by assigning fiber sections to displacement beam-column elements in OpenSees. Confined concrete material properties are assigned to the core concrete of the columns and unconfined concrete material properties are assigned to the cover concrete. Confinement effectiveness coefficients are calculated based on the relations developed by Mander et al. (1988). Five percent damping are considered for the structure in the analytical model.

Updating method

The goal of updating structural properties is to match the model vibration frequencies to those obtained from field data. To achieve this goal the following error function has to be minimized:

$$e = \sum_{i=1}^{n} \frac{\hat{f}_i^2 - f_i^2}{f_i^2} \tag{1}$$

where e = the error term; $\hat{f}_i$ = vibration frequency of mode i from finite element model; f_i = target vibration frequency of mode i from field data; and n is the number of considered modes. Since four transverse vibration frequencies obtained from field data in this study, $n=4$ in the above equation. It should be mentioned that the vibration frequencies of the first four modes in the finite element model that cause displacements at the location of installed accelerometers are considered to compute error function.

The value of the $\hat{f}_i$ in Equation 1 depends on a vector of structural properties, **x**, that is used in the finite element model. Therefore, the value of **x** that minimizes the error term in Equation 1 has to be found. To effectively update the value of **x**, sampling based techniques such as Markov Chain Monte Carlo (MCMC) simulation technique (Gilks et al. 1996) can be used. In this study, we use MCMC simulation technique with the Geweke method (Geweke 1991) for convergence criteria.

Table 1 shows the initial, updated and target vibration frequencies. Table 2 shows the structural properties that are considered in updating process and their initial and updated values. Updated structural properties are used to estimate probabilistic capacity and demand models and fragility of the Fabela Bridge.

Table 1: Initial, updated and target frequencies.

	Vibration Frequency (Hz)			
	Mode 1	Mode 2	Mode 3	Mode 4
Initial	1.283	1.721	1.888	2.113
Updated	1.147	2.174	2.484	3.507
Target	1.190	2.127	2.874	3.473

Table 2: Initial and updated structural properties.

		Value	
Parameter	Unit	Initial	Updated
Foundation-transverse stiffness	kN/m	9.20×10^{5}	1.74×10^{6}
Foundation-rotational stiffness	kNm/rad	1.05×10^{7}	1.14×10^{7}
Abutment transverse stiffness	kN/m	9.15×10^{4}	7.37×10^{4}
Bearing stiffness at Joints 1,3 & 5	kN/m	8.41×10^{3}	8.88×10^{3}
Bearing stiffness at Joints 2,4 & 6	kN/m	6.05×10^{3}	2.73×10^{3}
EI of Columns	kNm^2	1.96×10^{7}	2.49×10^{7}
EI of Deck	kNm^2	1.26×10^{9}	1.00×10^{9}

RETROFIT STRATEGIES

Four retrofit strategies are considered in this study and the effects on them on the fragility curves of the bridge are investigated. The first retrofit strategy is using steel jackets over the plastic hinge length at the bottom of bridge columns. Steel jacketing is the most common retrofit technique for concrete columns in bridges (Priestley et al. 1996; Tamai et al. 2000). Using steel jacketing increases the confinement stress that helps increase the ultimate strain and compressive stress of concrete. It is especially helpful for the unconfined concrete at the cover where there is no confinement stress. In this study, steel jacketing with 10mm thickness is considered for the first retrofit strategy. The second studied retrofit strategy in this paper is concrete jacketing at plastic hinge length at the bottom of the columns. Similar to steel jacketing, this retrofit strategy provides additional confinement at the location of the plastic hinge region at the bottom of the columns. For this retrofit strategy, using 12mm transverse reinforcement at center to center distance of 80mm is considered for the jacket. The third and fourth retrofit strategies are using steel and concrete jacketing over all the height of the columns, respectively, where all of the retrofit strategies are listed and described in Table 3. Figure 2 shows the cross section of the considered jackets in different strategies.

Table 3: Retrofit strategies considered in this study.

Retrofit Strategy	Description
Strategy 1	Steel jacketing on plastic hinge
Strategy 2	Concrete jacketing on plastic hinge
Strategy 3	Steel jacketing on whole column length
Strategy 4	Concrete jacketing on whole column length

FRAGILITY ESTIMATION

This study employs probabilistic demand models to estimate the fragility of the Fabela Bridge in three performance levels. Commonly accepted values of 1, 2 and 4% are used for the mean of column drifts at insignificant damage, moderate damage and severe damage performance levels, respectively. The failure of the bridge at each

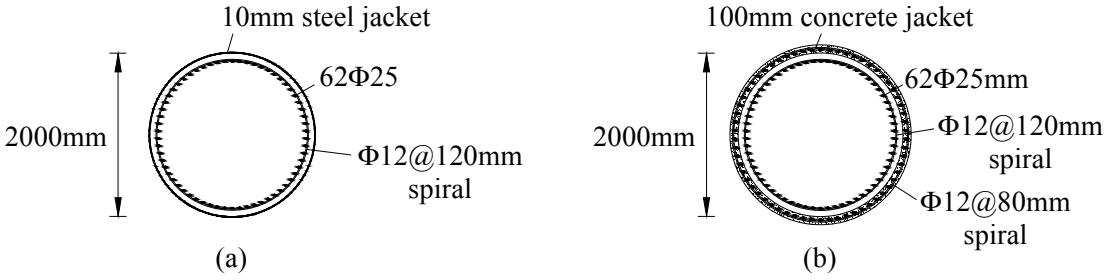


Figure 2. Properties of the considered jackets: (a) steel jacket (b) concrete jacket

performance level is defined as the failure of at least one column of the bridge. The limit state function for each column of the bridge in each performance level is defined as follows:

$$g_{i,j}(\mathbf{x},\boldsymbol{\Theta}) = C_j - D_{i,j}(\mathbf{x},\boldsymbol{\Theta}),\ i = A,B,C,D \tag{2}$$

where C_j= corresponding drift to performance level j; $\boldsymbol{\Theta}$=set of model parameters; and $D_{i,j}(\mathbf{x},\boldsymbol{\Theta})$= probabilistic demand model for column i at performance level j.

Multivariate probabilistic demand models proposed by Gardoni et al. (2003) are used in this study. The demand models are composed of the following three terms:

$$D_i(\mathbf{x},\boldsymbol{\Theta}_i,\boldsymbol{\Sigma}) = \hat{d}_i(\mathbf{x}) + \gamma_i(\mathbf{x},\boldsymbol{\theta}_i) + \sigma_i\varepsilon_i \quad i = A,B,C,D \tag{3}$$

where $\boldsymbol{\Sigma}$ =covariate matrix of the demand model and $\hat{d}_i(\mathbf{x})$= deterministic demand model for column i. $\gamma_i(\mathbf{x},\boldsymbol{\theta}_i)$=correction terms to consider bias inherent in the deterministic capacity model; σ_i= standard deviation of the model error; and ε_i = a random variable with normal distribution, zero mean and unit standard deviation. The deterministic demand part of the above models is computed based on a modification proposed by Gardoni et al. (2003) of the capacity-demand-diagram methods based on the inelastic design spectrum method originally developed by Chopra and Goel (1999). The correction terms for the demand models consist of explanatory functions and have the following form:

$$\gamma(\mathbf{x},\boldsymbol{\theta}) = \sum_{j=1}^{p_k} \theta_j h_j(\mathbf{x}) \tag{4}$$

where $h_j(\mathbf{x})$ are explanatory functions for demand models and have been defined in Gardoni et al. (2003).

Figure 3 shows the fragility curves of the Fabela bridge in different performance levels. Figure 3 reveals that the effect of the studied retrofit strategies on the fragility curves of the Fabela Bridge is not considerable. It is due to the good condition of the unretrofitted structure, which has enough capacity subject to the applied seismic loads and retrofit plans do not help it very much. The other reason is that the drift corresponding to each performance level is considered the same for original and retrofitted structure in this study. Further research is needed for defining the drifts corresponding to performance levels more accurately. However, Figure 3 reveals that the effect of the studied steel jacketing on the reduction of probability of failure of the Fabela Bridge is more than the studied concrete jacketing. It is also found that using the jackets along the entire height of the columns do not have any effect on the fragility curves rather than using the jackets on the plastic hinge length of the columns. It is illustrated in Figure 3 because the fragility curves of the retrofit strategies 3 and 4 match on the fragility curves of the retrofit strategies 1 and 2, respectively. Figure 4 shows the variation of the probability of failure of the structure with the drift capacity of the columns. Although there is not a considerable difference between the probability of failure of the original structure and retrofitted structure with different strategies in Figure 4, but that difference increases while pseudo acceleration increases.

SUMMARY AND CONCLUSIONS

This paper estimated the fragility curves for a five-span single-column concrete bridge in Toluca, Mexico. The results of experimental vibration tests were used to update the structural properties of studied bridge to obtain the current condition of the Fabela Bridge. Four retrofit strategies were proposed to decrease the failure probability of the studied bridge. The first two retrofit strategies were using steel and concrete jacketing over the plastic hinge area of the columns, respectively. The third and forth studied retrofit strategies were similar to the first two strategies but the steel and concrete jackets were considered along the entire height of the column. Fragility of the original structure and retrofitted structure with different retrofit strategies were estimated using Monte Carlo simulation. Three different performance levels of insignificant damage, moderate damage and severe damage with corresponding drift values of 1%, 2% and 4% were considered in this study. The results showed that the studied strategies did not help reduce the probability of failure considerably because of the existing good condition of the studied bridge. The existing good condition of the studied bridge was obvious based on the results from the vibration data, where the updated properties are for the most part better than what was specified in design drawings. The updated stiffness of the columns, which has an important role in affecting the probability of failure, was concluded to be more than its value based on design drawings. However, despite the small effect of the retrofit strategies on the probability of failure of the bridge, using steel jacketing over the plastic hinge length of the columns was found to be the most effective retrofit strategy among the studied strategies. The results showed that using jacketing on the entire column height does

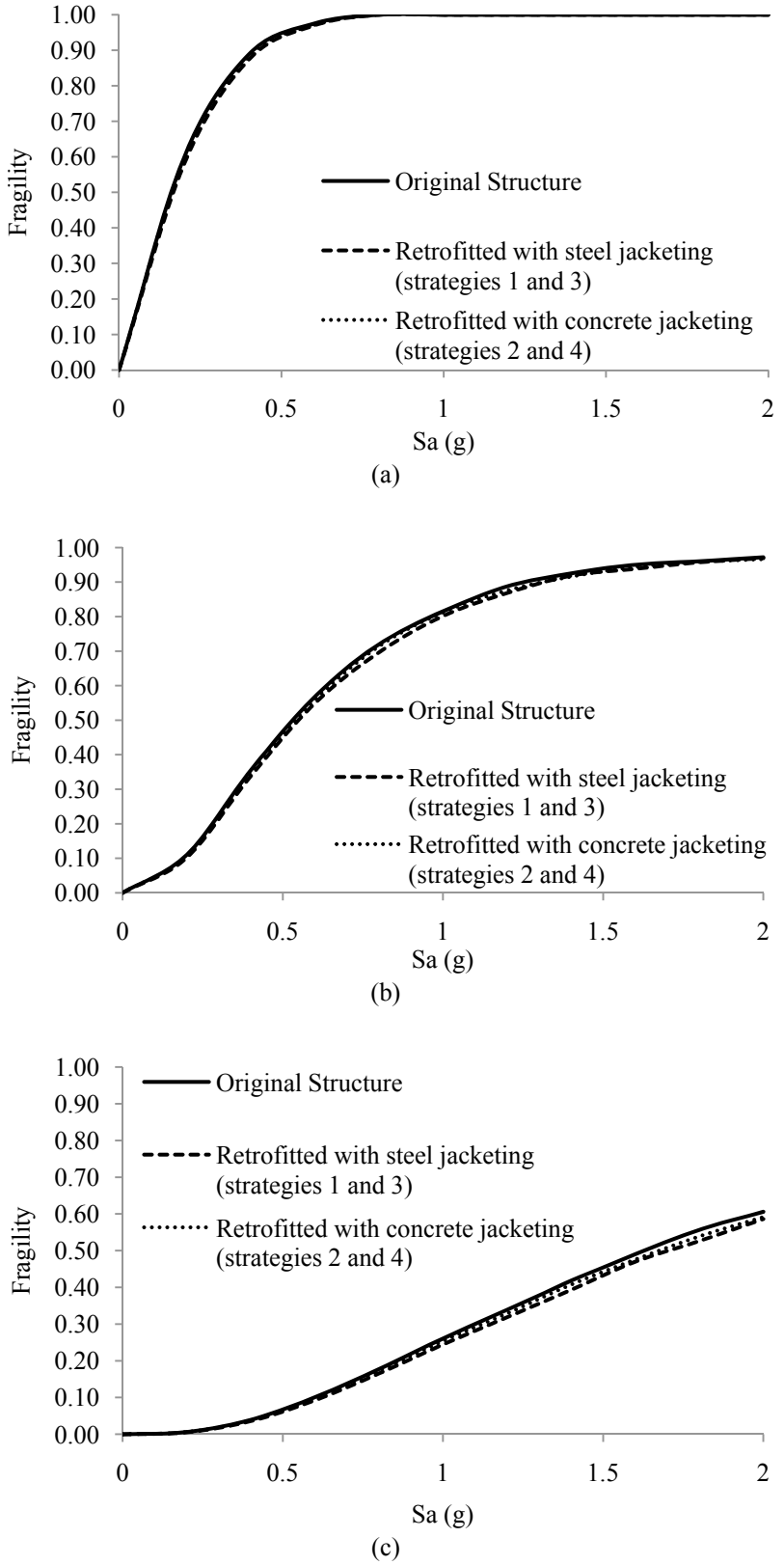
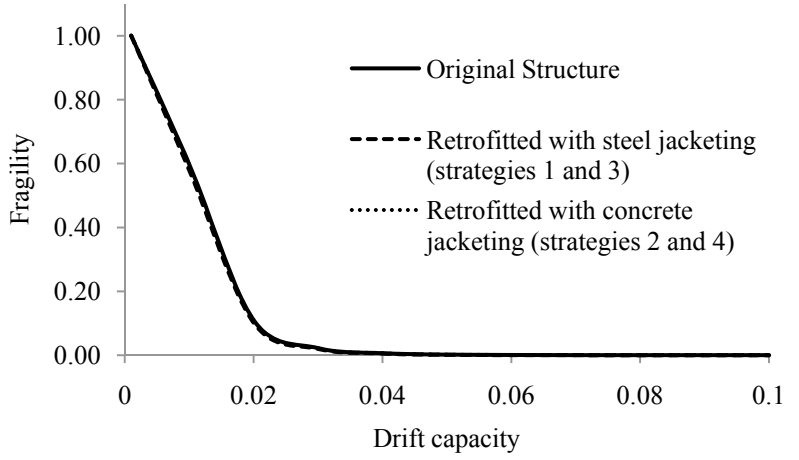
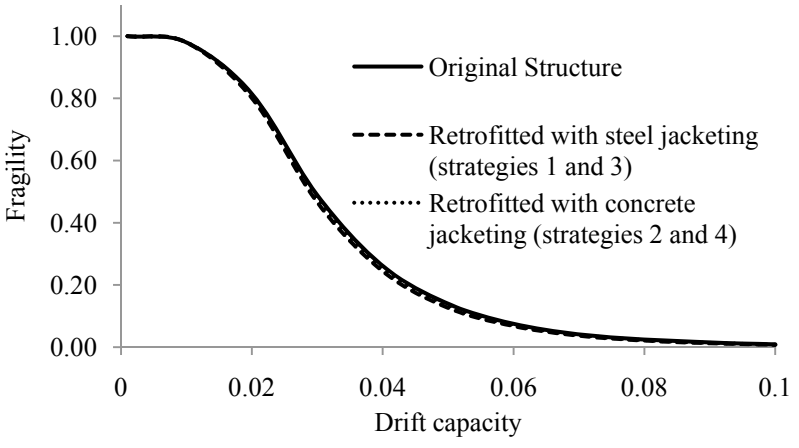


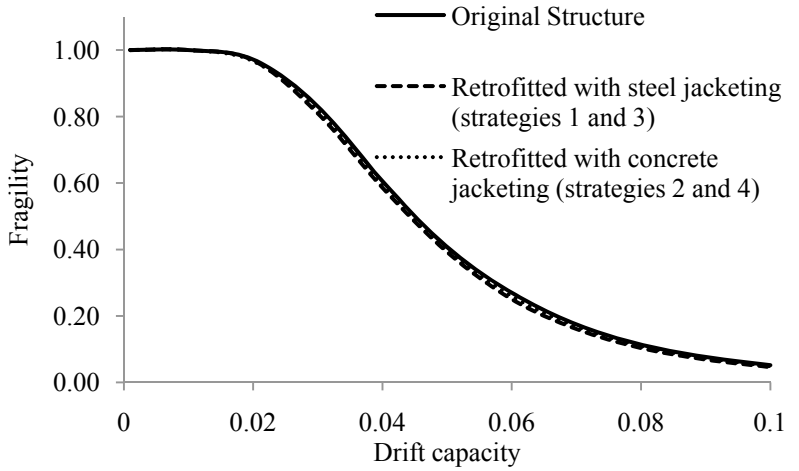
Figure 3. Fragility curves of the Fabela Bridge: (a) insignificant damage (b) moderate damage (c) severe damage



(a)



(b)



(c)

Figure 4. Variation of the failure probability with drift capacity of columns: (a) Sa=0.2g (b) Sa=1.0g (c) Sa=2.0g

not cause any additional reduction in the probability of failure than using jacketing over the plastic hinge length. Future work will include investigating the effect of the retrofit strategies on the corresponding drifts to performance levels, which are important parameters in the determination of the failure probability.

REFERENCES

Bisadi, V., Head, M., Gardoni, P., Hurlebaus, S., De Leon, D. (2011). "Fragility estimates for the Fabela Bridge in Mexico incorporating vibration field data." Accepted for publication in: *Proceeding of ICASP 11*, Applications of Statistics and Probability in Civil Engineering. Zurich, Switzerland.

Chopra, A.K., Goel R.K. (1999). Capacity-Demand diagram methods for estimating seismic deformation of inelastic structures: SDF systems, Report Number PEER-1999/02, Pacific Earthquake Engineering Research Center, University of California, Berkeley, California.

FEMA. (2000). Prestandard and commentary for the seismic rehabilitation of buildings. FEMA 356, Federal Emergency Management Agency, Washington, D.C.

Gardoni, P., Mosalam, K. M., Der Kiureghian A. (2003). "Probabilistic seismic demand models and fragility estimates for RC bridges." *J. Earthquake Eng.*, 7(Sp. Issue 1), 79 - 106.

Geweke, J. (1991). Evaluating the accuracy of sampling-based approaches to the calculation of posterior moments. *Bayesian statistics*, J. M. Bernardo, J. O. Berger, A. P. Dawid, and A. F. M. Smith, eds., Oxford University Press, Oxford, 169-193.

Gilks, W. R., S. Richardson, & D. J. Spiegelhalter (1996). *Markov Chain Monte Carlo in Practice: Interdisciplinary Statistics*, Chapman & Hall/CRC.

Hashimoto, S., Fujino Y., Abe, M. (2005). "Damage analysis of Hanshin Expressway viaducts during 1995 Kobe Earthquake. II: Damage mode of single reinforced concrete piers." *J. of Bridge Eng.*, 10(1), 54-60.

Mander, J. B., Priestley M. J. N., Park R. (1988). "Theoretical stress-strain model for confined concrete." *J. of Struct. Eng.*, 114(8), 1804-1826.

McKenna, F., Feneves, G. L. (2010). "Open system for earthquake engineering simulation." Pacific earthquake engineering research center, version 2.2.2.

Naeim, F., Kelly J. M. (1999). *Design of seismic isolated structures: from theory to practice*, John Wiley & Sons, New York.

Oppenheim, A.V., Schafer R.W. (1989). *Discrete-Time Signal Processing*, Prentice-Hall, 447-448.

Priestley, M. J. N., Seible, F., and Calvi, G. M. (1996). Seismic design and retrofit of bridges, Wiley, New York.

Tamai, S., Sato., T., Okamoto, M. (2000). "Hysteresis model of steel jacketed RC columns for railway viaducts." *Proc. 16th Congress of IABSE*, Lucerne, Switzerland, Sep. 18-21.

Effect of Ground Motion Suite Size on Uncertainty Estimation in Seismic Bridge Fragility Modeling

B.G. Nielson[1] and W.C. Pang[2]

[1]Lowry Hall, Clemson University, Clemson, SC USA 29634-0911; PH +1(864) 656-3312; E-mail: bryant.nielson@ces.clemson.edu,
[2]Lowry Hall, Clemson University, Clemson, SC USA 29634-0911; PH +1(864) 656-0014; E-mail: wpang@clemson.edu

ABSTRACT

Seismic fragility modeling of highway bridges is becoming a well developed and accepted field among engineers. Within any fragility estimate exists many sources of uncertainty. One source of uncertainty which is key to robust fragility modeling is the aleatory uncertainty which exists within the ground motion suite itself. One obvious question an analyst must ask pertains to the appropriate number of ground motions which must be used to appropriately capture this aleatory uncertainty. This study looks to add to the existing knowledge base, established by previous research, by explicitly looking at the resulting uncertainty estimates as the size and make-up of the ground motion suite is altered.

To explore this issue of ground motion suite size four bridge models which are representative of bridges in the Central and Southeastern United States (CSUS) are developed. Median value estimates for all bridge modeling parameters are utilized and held constant and no uncertainty in component capacities is used in an effort to decouple the aleatory uncertainty in the ground motions from the epistemic uncertainty present in typical modeling parameters. Utilizing a suite of 160 recorded ground motions as a pool, numerous subsets of this suite are created and used to generate fragility curves. To keep variation in median and dispersion estimates reasonable this preliminary study recommends that a suite of 80 or more ground motions be used. Such information is essential as fragility modeling gets closer to being an everyday reality for the practicing engineer.

INTRODUCTION

As time passes more and more researchers and engineers across the country are becoming involved in the seismic fragility assessment of highway bridges. Of the three general approaches to fragility curve development (i.e. expert (ATC 1985; ATC 1991), empirical (Basoz and Kiremidjian 1999; Shinozuka et al. 2000b), analytical (Jernigan and Hwang 2002; Mackie and Stojadinovic 2006; Nielson and DesRoches 2007b; Shinozuka et al. 2000a)), the analytical procedure using full nonlinear time history analysis has become quite popular (Aygun et al. 2011; Oh-Sung and Elnashai 2010; Pan et al. 2010; Simon et al. 2010). One specific requirement of this approach is the assembly of a suite of ground motions which is of sufficient size so as to

adequately capture the underlying seismic demand on the bridge structure and to also be representative of the underlying stochastic process of the seismic hazard (Mackie et al. In Press). Thus, a fragility analyst is charged with assembling the correct type and number of ground motions to ensure that the epistemic uncertainty captured in the analysis is not too large.

For design purposes, the suite size for buildings can be taken as either three or seven depending on the specific application (ASCE 2010). However, ground motion suite sizes for fragility analysis must also be able to quantify and minimize the uncertainty in the estimates as well. To this end, the correct number of ground motions to be used is not something which is well understood or agreed upon by those working in the field. Some have used as few as 20 ground motions if the ground motions are selected to meet certain criteria (Wen and Wu 2001). However, many of the recent studies have used between 80 and 100 ground motions to meet the needs of the analysis (Mackie and Stojadinovic 2004; Nielson and DesRoches 2007a; Pan et al. 2010; Simon et al. 2010).

The current study takes a closer look at the impact ground motion suite size has on both fragility median and dispersion estimates. This is done by using an assembled suite of 160 recorded ground motions which are then repeatedly sampled to generate subsets of ground motions of different sizes. These subsets are then used to generate system level fragility curves for four different bridge models which identify some clear consequences of suite size.

GROUND MOTION SUITE

The base ground motion suite used for this study consists of 160 recorded ground motions which are taken from the PEER Next Generation Attenuation strong ground motion database (PEER 2010). This is the same suite which has been used in a previous bridge fragility based study (Mackie et al. In Press). The suite was assemble using a binning approach wherein the bins were divided into large (L) and small (S) earthquake magnitudes (M) and also long (L) and short (S) site-to-source distances (R). Furthermore, an equal representation of time histories from NEHRP soil types C and D was also sought (ASCE 2010). Figure 1 gives a visual understanding of the make-up of each bin. As seen in this figure, a magnitude of 6.5 is taken as the cut-off between large and small earthquakes while 30 km is taken as the cut-off between long and short distances. Thus, 20 ground motions for each soil type are given for each bin.

To provide a more complete picture of the suite make-up, the response spectra for pseudo-acceleration (S_a) and pseudo-velocity (S_v) are given for each ground motion in Figure 2. The 10^{th}, 50^{th}, and 90^{th} percentile spectra are also provided to illustrate the variability which is inherent in the compiled suite. The main energy content seen in the pseudo acceleration spectra is seen in the range of periods from 0.2 to 0.5 seconds. The spectral velocity is more dominated by the range of periods from 0.5 to 1.0 seconds. The rationale for creation of the ground motion subsets is provided later in the manuscript.

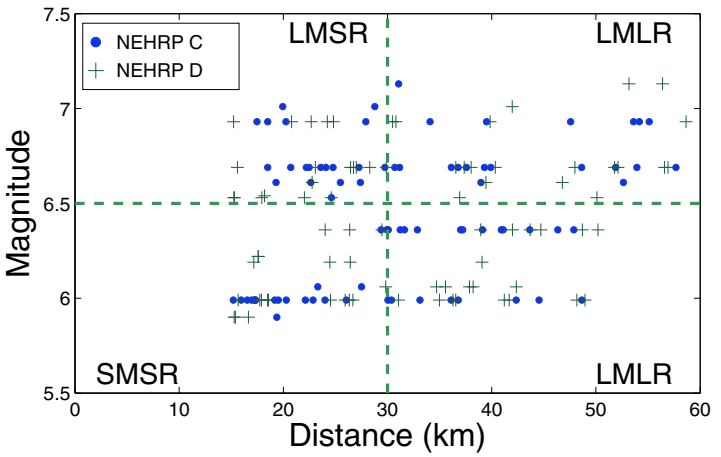
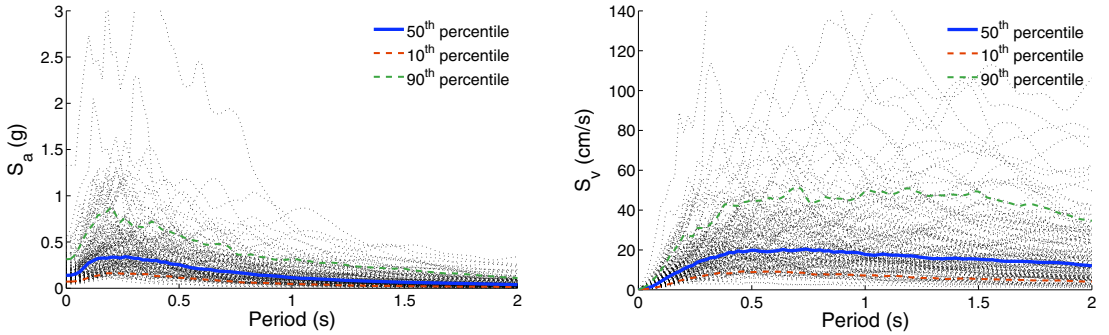


Figure 1. Suite of 160 ground motions with equal sized magnitude (M)-distance (R) bins.



(a) (b)

Figure 2. Response spectra for ground motion suite (a) spectral acceleration (b) spectral velocity

CASE STUDY BRIDGES

Two bridge classes common to the Central and Southeastern United States (CSUS) were selected for evaluation – namely the multi-span simply supported (MSSS) steel girder bridge and also the multi-span continuous (MSC) concrete girder bridge. Thorough descriptions of each bridge class and appropriate modeling parameters can be found in Nielson (2005). However, a basic description including typical details of these bridge classes is given in Figure 3. Each bridge is three spans with equal length approach spans (12.2 m) which are supported on three-column bents. The columns are circular reinforced concrete columns which are poorly detailed for resisting seismic forces. The steel girder bridge uses high-type steel bearings while the concrete girder bridge uses elastomeric bearings and pre-cast AASHTO I-girders. The girders are made continuous with a cast-in-place continuity diaphragm. Most of the bridge components are modeled to capture nonlinear behavior (bents, abutments, bearings and impact) while the superstructure uses linear models.

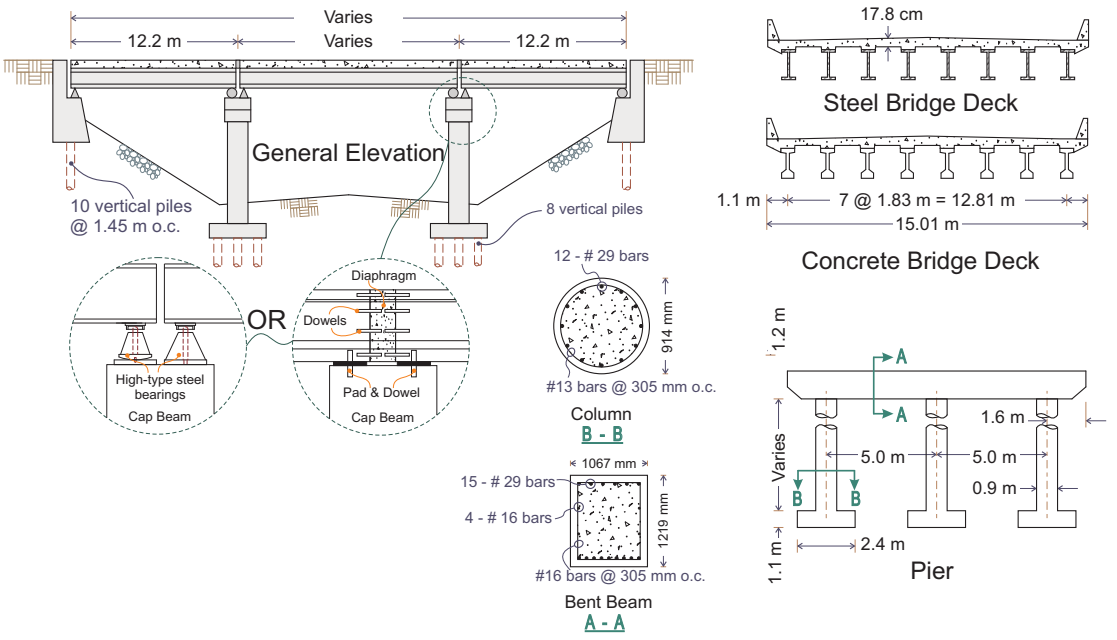


Figure 3. Typical details for MSSS steel girder and MSC concrete girder bridges

Two bridge models from each of the two bridge classes were generated to cover a wider range of structural periods to see if it had any impact on the findings. The center span lengths and columns heights were varied to ensure that different periods were realized. Table 1 provides a brief summary of the characteristics of each of the bridge models used in this study. One may note that the columns have either a 5.0 m or 7.0 m height which are the two most commonly occurring heights for bridges in the CSUS (Nielson 2005). The span lengths are either 16.25 m or 32.5 m. For the MSSS Steel bridge models the first longitudinal modal period is either 0.371 s or 0.252 s and are denoted as long period and short period respectively. The concrete girder bridges have fundamental periods of 0.719 s for the long period and 0.489 s for the short period bridge.

The ground motion intensity measure (IM) used for the computed fragility curves for the bridges labeled as long is peak ground velocity (PGV) and the IM for the bridges labeled as short is peak ground acceleration (PGA). In all cases these IMs were selected because they were deemed to be the most efficient (i.e. the smallest dispersion estimates).

Table 1. Basic properties of the four evaluated bridges

Bridge No.	Bridge Description	Center Span Length (m)	Column Height (m)	Long* Period (s)	Trans** Period (s)
1	MSSS Steel – Long	32.5	7.0	0.371	0.358
2	MSSS Steel – Short	16.25	5.0	0.252	0.224
3	MSC Concrete – Long	32.5	7.0	0.719	0.553
4	MSC Concrete Short	16.25	5.0	0.489	0.374

* Long ➔ longitudinal ** Trans ➔ transverse

RESULTS

The probability that a bridge structure exceeds a prescribed damage state or fails to meet a performance expectation, conditioned on a seismic intensity measure (i.e. PGA, PGV, S_a and etc.), can be expressed using a fragility curve. A common way of determining the non-performance (fragility) of a bridge is to express the damage state in terms of demand (D) exceeding capacity (C) or $C < D$. If both the capacity and demand are lognormally distributed, the fragility (F_R) or conditional probability of failure for a given damage state can be computed using the following equation:

$$F_R(C < D \mid IM) = 1 - \Phi\left(\frac{\ln(m_C) - \ln(m_D)}{\sqrt{\beta_C{}^2 + \beta_D{}^2}}\right) \tag{1}$$

where m and β are the median and logarithmic standard deviation (i.e. the uncertainty), and subscripts C and D denote the capacity and demand, respectively. IM is the intensity measure, i.e. PGA or PGV.

Four damage states are defined in this study: slight, moderate, extensive and complete damage. The details of the damage state definition and description can be found elsewhere (Nielson 2005).

The median of the demand parameters (curvature ductility of columns and deformation of bearings) is estimated using a power equation (Cornell et al. 2002):

$$\begin{aligned} D &= b_o \left(IM\right)^b \varepsilon = m_D \varepsilon \\ \ln(D) &= \ln(b_o) + b\ln(IM) + \ln(\varepsilon) = \ln(m_D) + \ln(\varepsilon) \end{aligned} \tag{2}$$

where b_o and b are the regression constants. ε is a normally distributed error term with a zero mean. The demand uncertainty arises from the inherent randomness in the ground motions which is quantified by the logarithmic variance of ε (or variance of $\ln(\varepsilon)$).

In order to investigate the influence of the ground motion suite size on the estimation of the demand uncertainty (β_D), the bridge fragility curves were generated using eight different ground motion suite subset sizes (16, 24, 32, 48, 64, 80, 96, and 120 ground motions). Figure 4 shows four examples of ground motion subsets. For each ground motion subset, 20 ground motion suites (realizations) were randomly assembled by selecting an equal number of ground motions from each bin, grouped by moment magnitude and site-to-source distance. Thus if an analyst were to use only 16 ground motions using the binning approach, then each ground motion in a given bin would have equal probability of being selected for the suite. The demand parameters estimated using these ground motion suites were then used to generate component and system level fragility curves. It should be noted that the fragility curves presented in this paper do not include the capacity uncertainty (β_C). This allows one to quantify the effect of demand uncertainty on the fragility estimation without the influence of the capacity uncertainty.

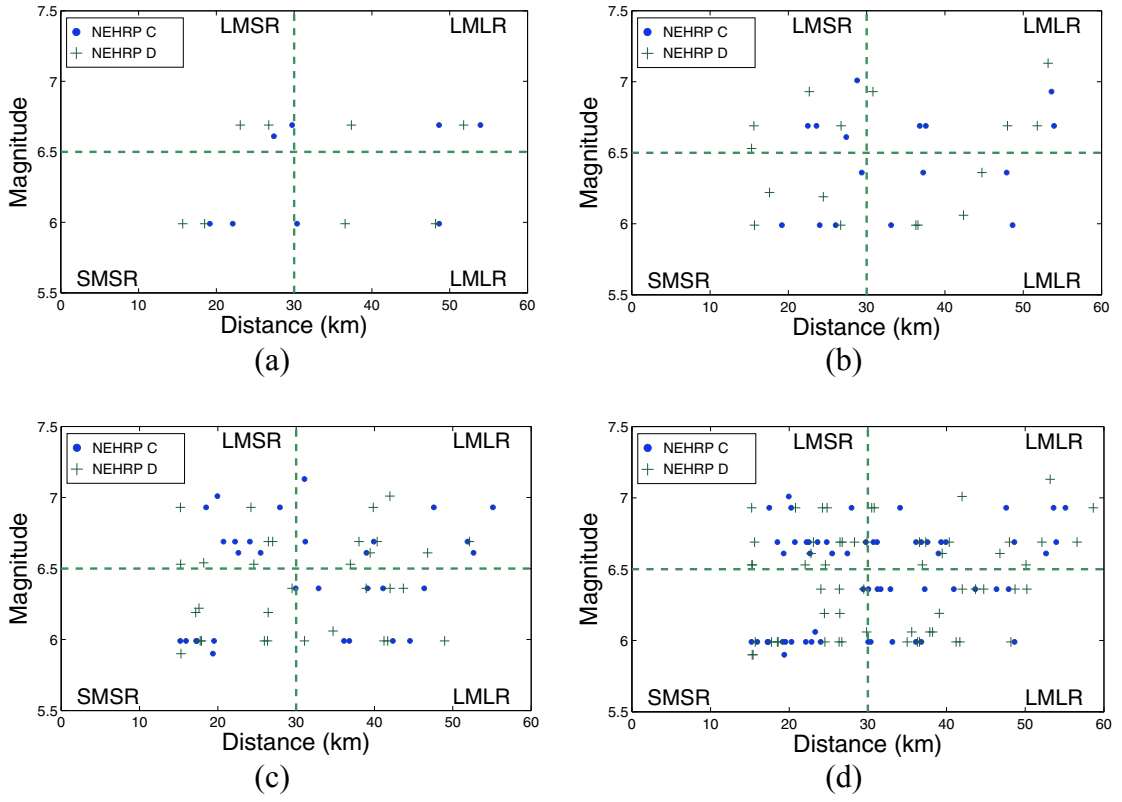


Figure 4. Examples of ground motion subsets (a) 16, (b) 48, (c) 80 and (d) 120

Figure 5 shows four representative sets of moderate damage state system fragility curves for bridge type 2 (MSSS Steel – Short) estimated using 16, 48, 80 and 120 ground motions. For all ground motion subsets, twenty fragility curves are determined and plotted in Figure 5 along with the 10^{th} and 90^{th} percentiles. These percentiles are bounds which represent the error band in the estimation of the fragility curve. It is clear to see that as the number of ground motions increases, the error band of the fragility curve reduces. Significant error may exist if one uses only 16 ground motions to generate the fragility curve for bridge type 2. Also shown in the figure is the fragility curve determined using all 160 ground motions. The fragility curve produced using all 160 ground motions is assumed to be the "true" or benchmark fragility curve. For example, if only 16 ground motions were used to estimate the fragility of a type 2 bridge located at a site with PGA equal to 0.5g (see Figure 5a), the probability of exceeding the moderate damage state may range from 0.44 to 0.96 while the "true" exceedance probability is approximately equal to 0.62.

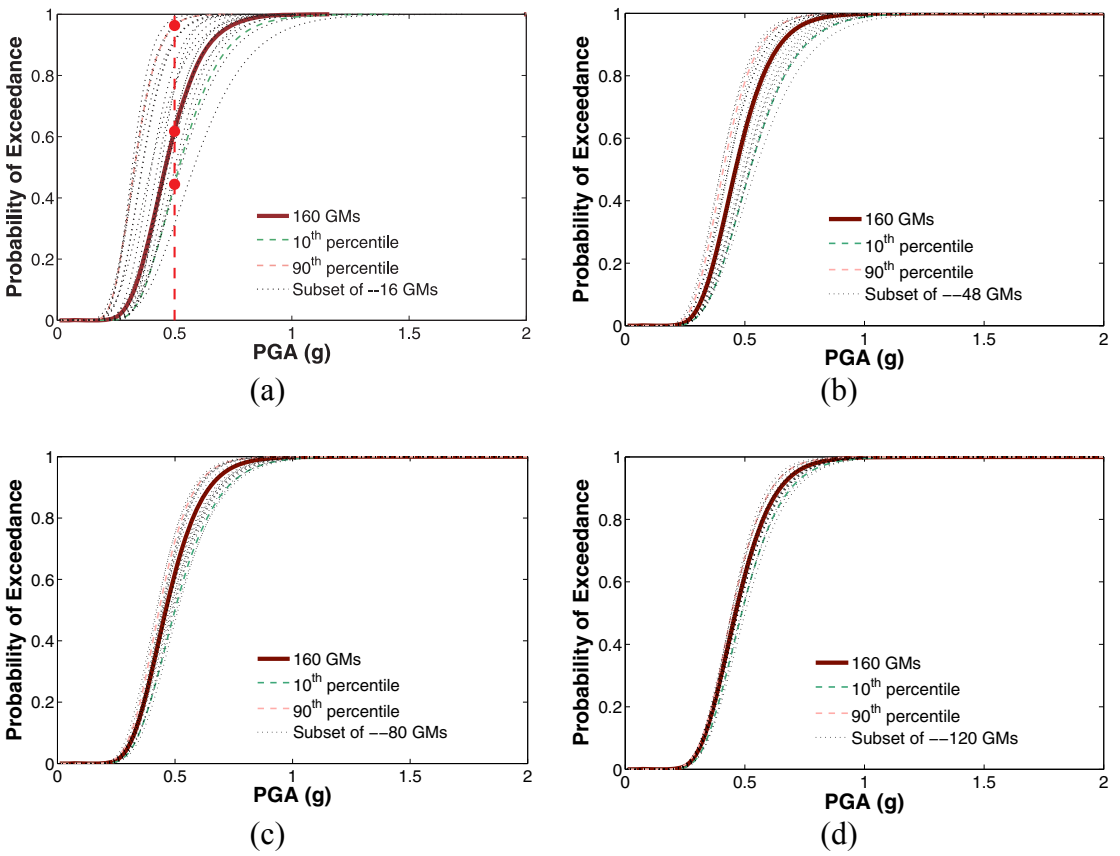


Figure 5. Bridge type 2 – Moderate damage state using the following number of ground motions (a) 16 , (b) 48, (c) 80 and (d) 120

Figure 6 gives the fragility curves for bridge type 2 at a complete damage state for the same four representative suite sizes (i.e. 16, 48, 80, 120). A comparison between the moderate damage state and complete damage state reveals that the error bands for the complete damage state is larger than that of the moderate damage state. This same trend exists for the other damage states and the other bridge types as well. This increase in the error band width with higher damage states is to be expected since the seismic demands generally stay close to the linear elastic range for the lower damage states. However, the demands of the higher damage states are usually associated with the highly nonlinear region of the structure response. The more nonlinear the structure becomes the more sensitive it will be to specific ground motion characteristics such as duration and intensity. Thus a larger variation in the demand and the subsequent fragility curves is expected.

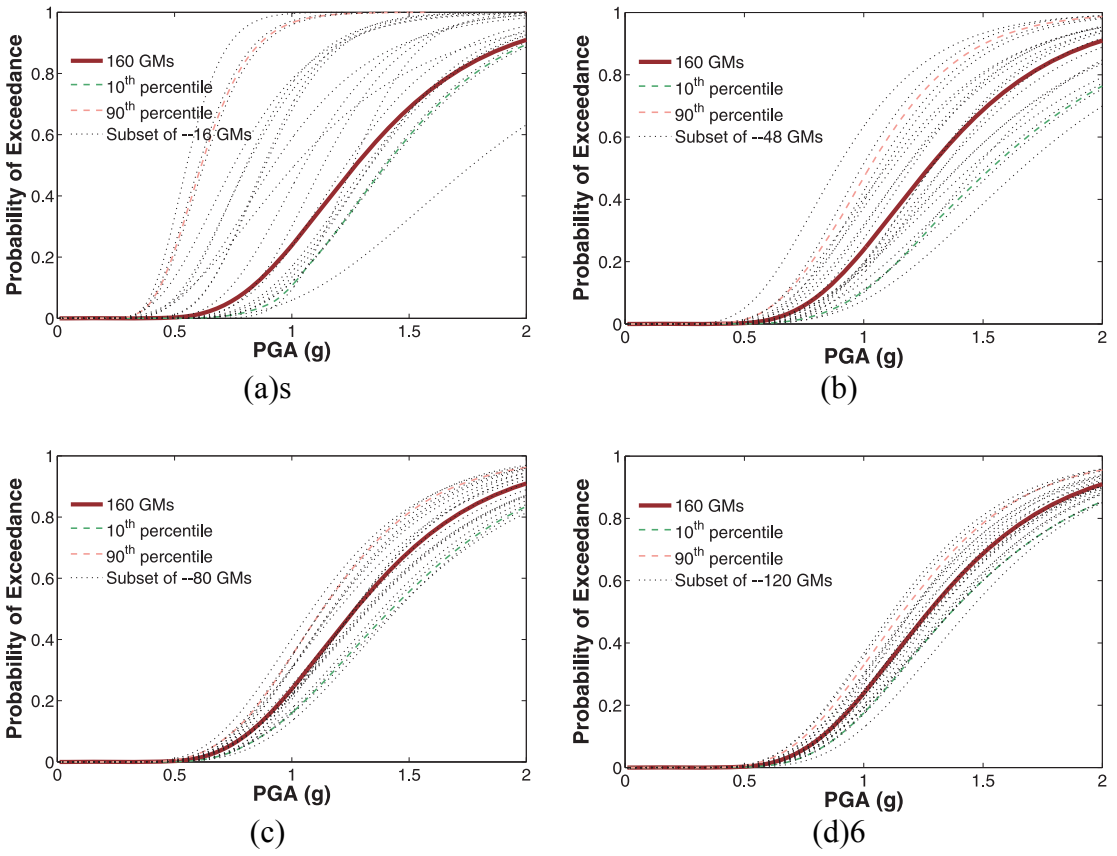


Figure 6. Bridge type 2 – Complete damage state using the following number of ground motions (a) 16 , (b) 48, (c) 80 and (d) 120

For illustration purposes Figure 7 is provided for the moderate damage state for bridge type 3 (MSC concrete – long). The combined effect of bridge construction type and ground motion suite size can be seen by comparing the fragility curves shown in this figure with those found in Figures 5 and 6 (MSSS steel - short). At a given damage state and for the same number of ground motions, the variation in the fragility estimation is larger in the type 3 concrete bridge than that of the type 2 steel bridge. This larger variation in one type over the other type can be attributed to the levels of contribution one gets from each of the bridge components. For example, the steel bearings and the concrete columns in the MSSS steel bridge both make significant contributions to the overall computed system fragility. The resulting dispersion values (for the 160 ground motions) are 0.31 for slight damage to 0.34 for complete damage. By comparison, computed dispersions for the MSC concrete bridge range from 0.56 for slight damage to 0.54 for complete damage where the columns play a much more significant role on the overall system fragility estimates. This inherent increase (approx 50%) in the dispersion estimates, which was also seen in a previous study (Nielson 2005), appears to map over to a larger variation in the fragility estimates for the type 3 bridge for a given ground motion suite size.

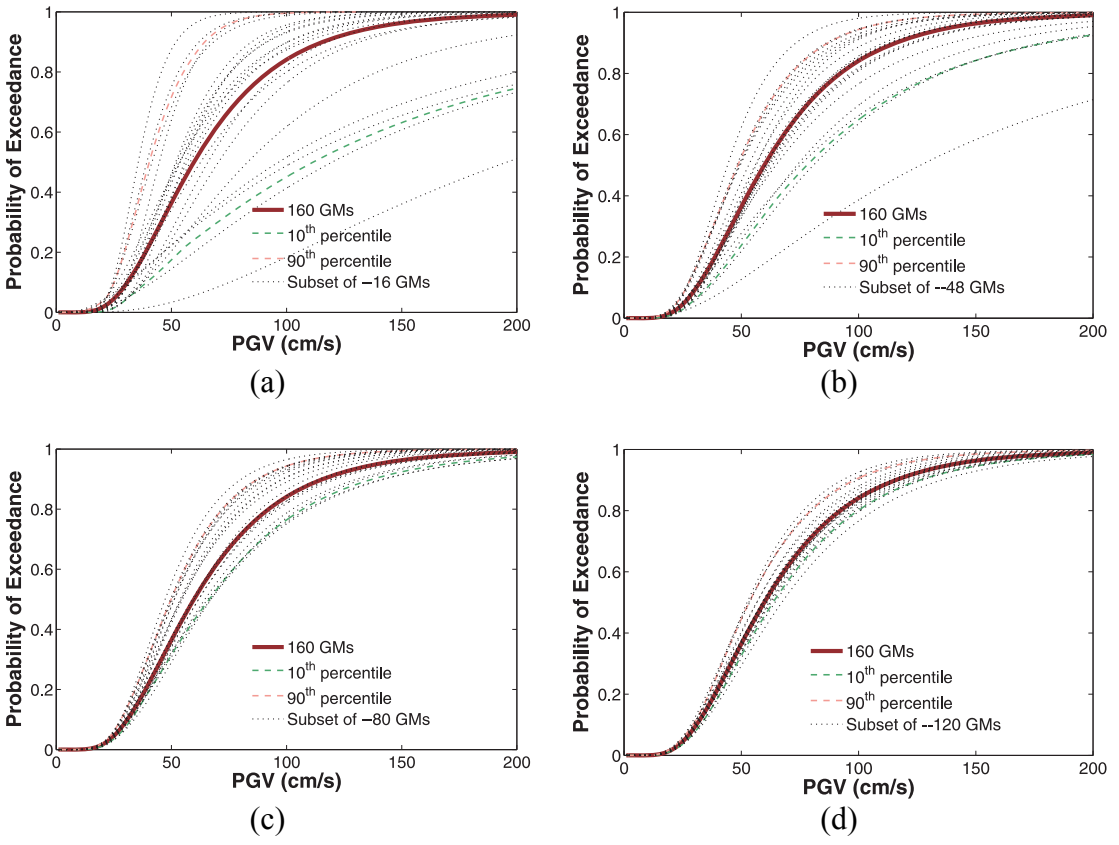


Figure 7. Bridge type 3 – Moderate damage state using the following number of ground motions (a) 16 , (b) 48, (c) 80 and (d) 120

Figure 8 illustrates the influence on the number of ground motions on the dispersion of the median estimates of the fragility curves for the four bridge types considered in this study. As expected, the dispersion of the median estimates of the fragility curves reduces as the number of ground motions increases. A similar trend is observed for the dispersion estimates of the fragility curves (Figure 9). The dispersion in the median estimates explains the horizontal spread of the fragility curves seen in figures 5 to 7 whereas the dispersion of the dispersion estimates of the fragility curves describes the variation of the slope of the fragility curves observed in the same figures. Since the calculated dispersions in Figure 9 are direct estimates designed to capture the aleatory uncertainty in the ground motion suite, then the scatter seen in these estimates represents the epistemic uncertainty associated with suite size and selection. The results of this preliminary study seem to suggest that, in order to obtain reliable estimates of both the median and dispersion of a fragility curve, a large number of ground motions (80 or more) should be used to perform the dynamic time history analysis. Using this number of ground motions, the bands on the dispersion estimates are no more than ±20% of the "true" dispersion. However, if only 16 or 24 ground motions are used then the error can be as large as 60-70% (See Figure 9).

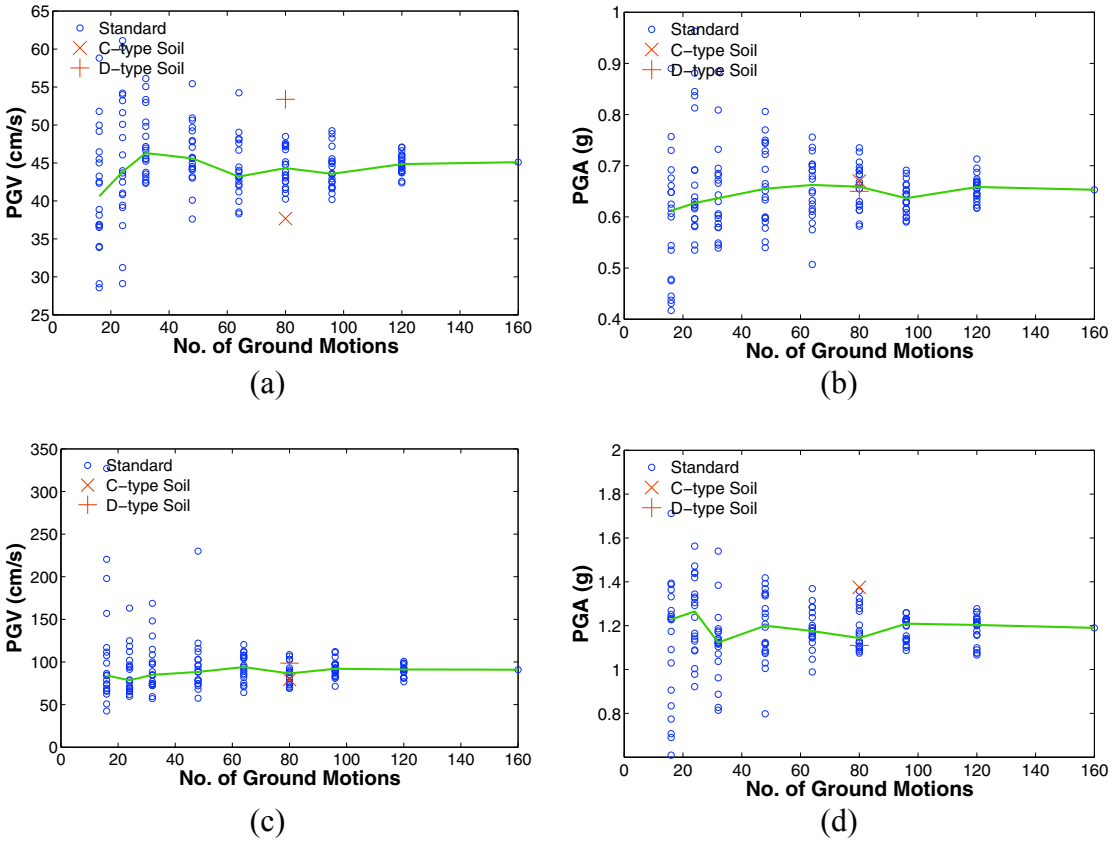


Figure 8. Fragility median estimates for extensive damage state for bridge types (a) 1 , (b) 2, (c) 3 and (d) 4

CONCLUSIONS

This paper presents the results of a study to examine the effects of ground motion suite size on the aleatory uncertainty estimates of bridge fragility curves. Four bridge types were considered in this study, namely MSSS steel and MSC concrete bridges each with a long and a short fundamental period. The variation of the median and dispersion of the bridge fragility curves for four damage states were estimated using eight different ground motion suite subsets, ranged from 16 to 120 ground motions. The results show that using ground motion suites with 24 or less ground motions can result in erroneous bridge fragility estimation. In order to obtain reliable estimates of both the median and dispersion of a fragility curve, a relatively large number of ground motions, in the order of 80 or more, are needed.

The number of ground motions suggested for use may possibly be reduced if a more selective process is used to assemble the ground motion suite. When one uses a simple four-bin approach (M-R), three of the bins lend themselves to providing low intensity ground motions. As such, a subset of 16 ground motions may produce a suite of ground motions which are all low intensity but it can also produce a subset which has a higher percentage (up to 25%) of high intensity ground motions. This results in the high variability in the median and dispersion estimates seen in this

study. Placing specific intensity requirements on the M-R bins may result in less variability in the responses and if this happens the size of the ground motion suite may be eligible for reduction. This will be investigated in future studies.

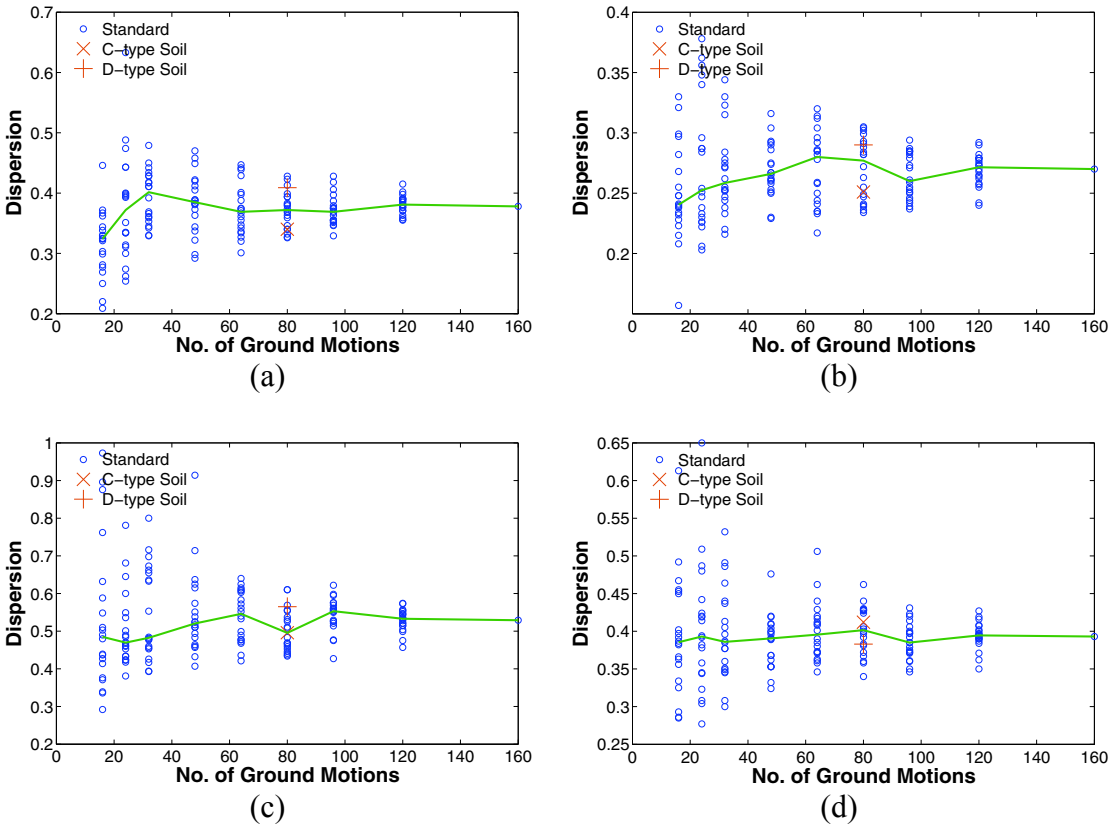


Figure 9. Fragility dispersion estimates for extensive damage state for bridge types (a) 1 , (b) 2, (c) 3 and (d) 4

REFERENCES

ASCE. (2010). *Minimum Design Loads for Buildings and Other Structures, ASCE 7-10*, ASCE, Reston, VA.

ATC. (1985). "Earthquake Damage Evaluation Data for California." *ATC-13*, Applied Technology Council, Redwood City, CA.

ATC. (1991). "Seismic Vulnerability and Impact of Disruption of Lifelines in the Conterminous United States." *ATC-25*, Applied Technology Council, Redwood City, CA.

Aygun, B., Dueas-Osorio, L., Padgett, J. E., and Desroches, R. (2011). "Efficient longitudinal seismic fragility assessment of a multispan continuous steel bridge on liquefiable soils." *Journal of Bridge Engineering*, 16(1), 93-107.

Basoz, N., and Kiremidjian, A. S. "Development of Empirical Fragility Curves for Bridges." *5th US Conference on Lifeline Earthquake Engineering*, Seattle, WA, USA.

Cornell, A. C., Jalayer, F., Hamburger, R. O., and Foutch, D. A. (2002). "Probabilistic Basis for 2000 SAC Federal Emergency Management Agency Steel Moment Frame Guidelines." *Journal of Structural Engineering*, 128(4), 526-532.

Jernigan, J. B., and Hwang, H. "Development of Bridge Fragility Curves." *7th US National Conference on Earthquake Engineering*, Boston, Mass.

Mackie, K., and Stojadinovic, B. "Fragility Curves for Reinforced Concrete Highway Overpass Bridges." *13th World Conference on Eartquake Engineering*, Vancouver, B.C. Canada.

Mackie, K. R., Cronin, K. J., and Nielson, B. G. (In Press). "Response Sensitivity of Highway Bridges to Randomly Oriented Multi-Component Earthquake Excitation." *Journal of Earthquake Engineering*.

Mackie, K. R., and Stojadinovic, B. (2006). "Post-earthquake functionality of highway overpass bridges." *Earthquake Engineering and Structural Dynamics*, 35(1), 77-93.

Nielson, B. G. (2005). "Analytical Fragility Curves for Highway Bridges in Moderate Seismic Zones," PhD, Georgia Institute of Technology, Atlanta.

Nielson, B. G., and DesRoches, R. (2007a). "Analytical seismic fragility curves for typical bridges in the central and southeastern United States." *Earthquake Spectra*, 23(3), 615-633.

Nielson, B. G., and DesRoches, R. (2007b). "Seismic Fragility Methodology for Highway Bridges Using a Component Level Approach." *Earthquake Engineering & Structural Dynamics*, 36(6), 823-839.

Oh-Sung, K., and Elnashai, A. S. (2010). "Fragility analysis of a highway over-crossing bridge with consideration of soil-structure interactions." *Structure and Infrastructure Engineering*, 6(1-2), 159-78.

Pan, Y., Agrawal, A. K., Ghosn, M., and Alampalli, S. (2010). "Seismic fragility of multispan simply supported steel highway bridges in New York State. II: Fragility analysis, fragility curves, and fragility surfaces." *Journal of Bridge Engineering*, 15(5), 462-472.

PEER. (2010). "NGA Strong Motion Database." Pacific Earthquake Engineering Research Center.

Shinozuka, M., Feng, M., Q., Kim, H.-K., and Kim, S.-H. (2000a). "Nonlinear Static Procedure for Fragility Curve Development." *Journal of Engineering Mechanics*, 126(12), 1287-1296.

Shinozuka, M., Feng, M., Q., Lee, J., and Naganuma, T. (2000b). "Statistical Analysis of Fragility Curves." *Journal of Engineering Mechanics*, 126(12), 1224-1231.

Simon, J., Bracci, J. M., and Gardoni, P. (2010). "Seismic response and fragility of deteriorated reinforced concrete bridges." *Journal of Structural Engineering*, 136(10), 1273-1281.

Wen, Y. K., and Wu, C. L. (2001). "Uniform Hazard Ground Motions for Mid-America Cities." *Earthquake Spectra*, 17(2), 359-384.

Reliability and redundancy of bridge systems under lateral loads

Anitori G.[1], Casas J.R.[1] and Ghosn M.[2]

[1]School of Civil engineering, Technical University of Catalonia, Barcelona, Spain; email: giorgio.anitori@gmail.com, joan.ramon.casas@upc.edu
[2]The City College of New York/CUNY, New York, USA;
email: mghosn@ccny.cuny.edu

ABSTRACT

A methodology is proposed to analyze the structural redundancy of bridge systems under lateral loads. The paper compares the results obtained from a probabilistic approach to those of a simplified deterministic analysis. A non-linear finite element analysis based on a 3-D frame model is performed for an example bridge considered to be representative of the behavior of structures with integral column-superstructure connections. The analysis accounts for material non-linearity using realistic models for the stress-strain relationships of the different constituents. The quantification of the available redundancy levels is evaluated using reliability as well as deterministic criteria previously proposed in NCHRP 458.

INTRODUCTION

The design of bridges has traditionally been performed on a member by member basis and little consideration is usually provided to the remaining capacity of the system after the failure of one structural element. As a consequence of several tragic collapses that followed the failure of single elements, the evaluation of the structural redundancy and robustness of bridges has become of primary importance.
The evaluation of the safety of structural members and systems and the calibration of bridge design and evaluation specifications are based on meeting target reliability levels (ISO 2394; 1998 and AASHTO LRFD; 2008). The target reliabilities are usually specified to match the performance of previous successful designs and are related to the expected social and economic consequences of failures as well as society's risk tolerance.
Target reliability indices are the bases for calibrating load and resistance factors and partial coefficients used in limit state design. Alternatively, the reliability index, β, can be calculated for each structure individually by evaluating the probability of limit state exceedance, P_f. The relationship between the two parameters may be represented by $P_f = \Phi^{-1}(-\beta)$ where Φ is the Normal cumulative distribution function (see figure 1). The reliability index can be used as a measure of the reliability of structural members as well as structural systems and accounts for both

the margin of safety implied by the design procedure and the uncertainties in estimating member strengths and applied loads.

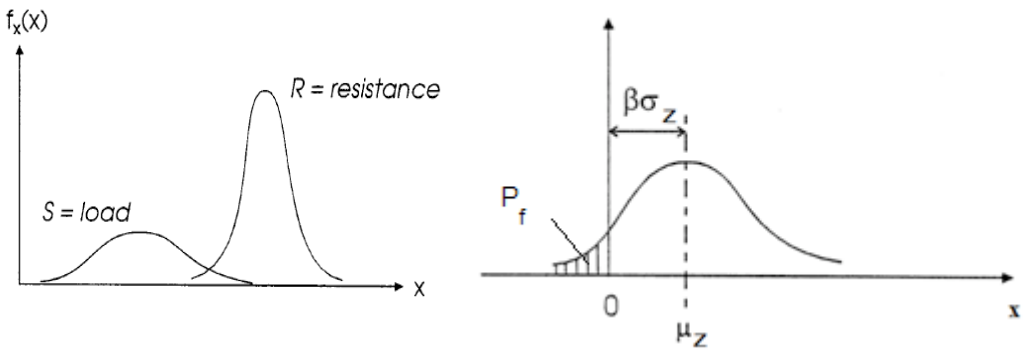


Figure 1. Representation of probability based evaluation of structural safety a) Probability distribution of load and resistance and b) probability distribution of limit state function.

Measures of Redundancy. Ghosn (1998) and Liu et al. (2000) defined redundancy as the capability of the system to continue to carry loads after the failure of one main member. Accordingly, Ghosn (1998) defined three measures of redundancy. Two measures compare the performance of an initially intact bridge system to the capacity of the first member to resist failure. The third measure compares the performance of a damaged system where a main load carrying member has been removed from the system. These measures are given in eq. (1) as:

$$\begin{aligned} R_u &= LF_u / LF_1 \\ R_f &= LF_f / LF_1 \\ R_d &= LF_d / LF_1 \end{aligned}, \qquad (1)$$

where:

LF_1 is the load that causes the failure of the first member;

LF_u is the load that causes collapse of the system;

LF_f is the load that causes the functionality limit state of the initially intact structure to be exceeded;

LF_d is the load factor that causes the collapse of a damaged structure which has lost a main load carrying member.

Ghosn (1998) also proposed three reliability measures of redundancy which are defined in terms of reliability indices as given in eq. 2:

$$\begin{aligned}\Delta\beta_u &= \beta_{ult.} - \beta_{member} \\ \Delta\beta_f &= \beta_{funct.} - \beta_{member} \\ \Delta\beta_d &= \beta_{damaged} - \beta_{member}\end{aligned} \quad (2)$$

Where β_{member} represents the reliability index related to the failure of one member $\beta_{ult.}$ the reliability index related to the collapse of the structure, $\beta_{funct.}$ the reliability index related to the loss of functionality of the structure, $\beta_{damaged}$ the reliability index related to the collapse of the damaged structure.
These relative reliability indices give measures of the additional safety provided by the system compared to the safety against first member failure.
The evaluation of the redundancy of typical bridge systems is illustrated in this paper using the example bridge described below.

EXAMPLE BRIDGE

An efficient approach for designing bridges against lateral loads consists of using integral connections between the columns and superstructures to form a monolithic structure with a higher resistance to lateral loads compared to bridges with typical bearing connections. The example bridge considered in this study is a four-span bridge where the longer span is 48m (see figure 2). The superstructure is a post-tensioned multibox girder with diaphragms above the piers and is rigidly connected to the columns (see figure 2).

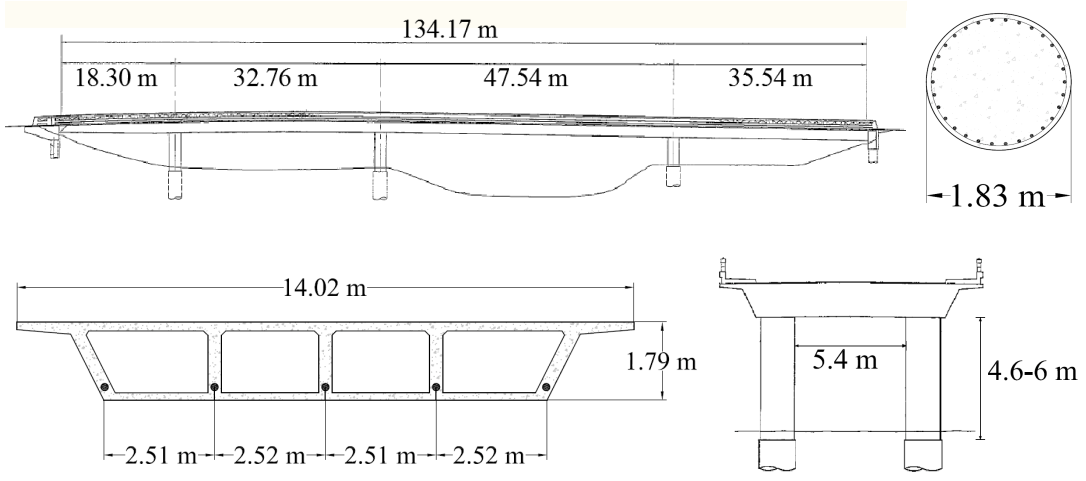


Figure 2. Example Bridge Configuration
a) Bridge profile, b) column cross section,
c) Cross section of bridge superstructure and d) pier profile.

Structural model. A FEM model based on one-dimensional beam elements has been developed to perform the nonlinear analysis of the bridge system. The mesh follows the 3-D space frame model proposed by Hambly (1991) and McLean et al. (1998), in which each element is provided with the proper stiffness characteristic (for longitudinal bending, torsion, distortion, and local transversal bending) as well as nonlinear strength properties in bending. Figure 3 shows the mesh for the 3-D space frame model.

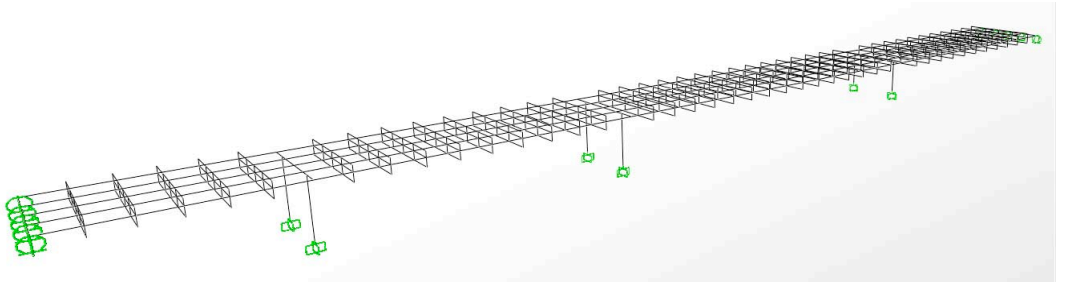


Figure 3. 3-D space frame model.

Material Nonlinearitity. Realistic stress-strain relationships are considered to simulate material non linearity. In particular Mander's (1984) model was adopted for confined and unconfined concrete, and Simple's (SAP2000 manual 2008) model for reinforcing and prestressing steel (see figure 4).

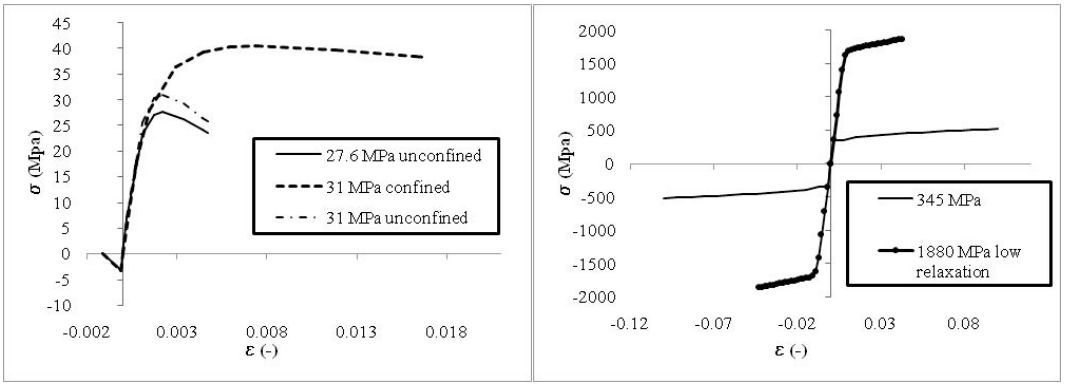


Figure 4. Stress-strain curves
a)concrete (Mander's model) and b) steel (Simple's models).

These realistic models are used to generate moment-curvature relationships for each bridge member. The generated relationships are subsequently simplified and modeled as tri-linear curves for implementation into the lumped plasticity model. As shown in figure 5, the model accounts for the effect of the axial load on the moment-curvature curves of the columns.

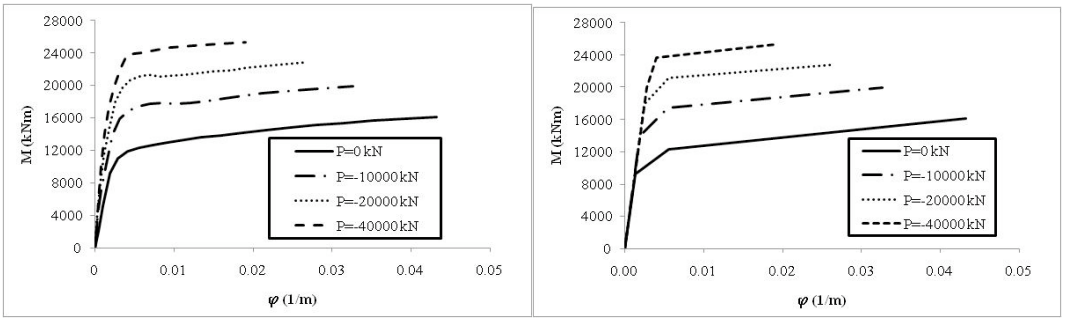


Figure 5. Moment curvature curves for different axial loads a) Original curves and b) simplified tri-linear curves.

Pushover Analysis. In order to represent the capacity of the structure a displacement-controlled nonlinear static analysis is performed. As shown in figure 6, a set of lateral forces is applied over each bent and the lateral displacement of a control point situated over the central pier is measured.

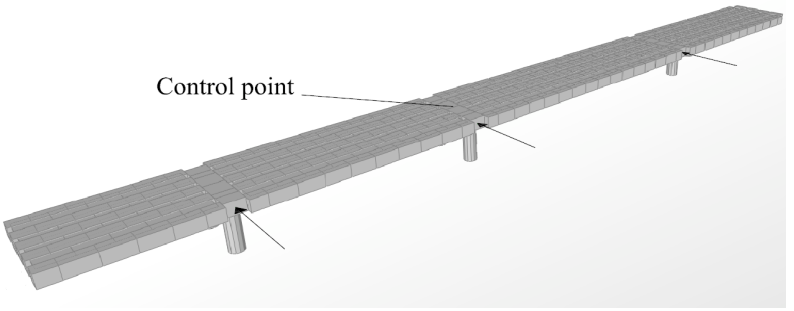


Figure 6. Lateral load distribution and control point.

The lateral distribution of forces is found by $f_{\mathrm{mod},i} = P_i \, \phi_i \Big/ \sum P_j \, \phi_j$,which accounts for the modal displacement of the more significant mode of vibration, more detail can be found in Anitori, (2009).

The P-delta effects are considered in the analysis to account for the geometric nonlinearity. This feature accounts for the second order moments due to the lateral displacement of members under axial load.

Damage scenarios. The analysis of the bridge is performed for the originally intact structure as well as for different damage scenarios. The damage scenarios represent the condition of the structure following an extreme event such as the collision of a truck in a column causing its brittle failure, the effects of a severe earthquake which may produce hinging in the column connections, or foundation settlement. The damages considered in this paper are represented by the failure of one column, which can be partial (loss of bending capacity at the connection but axial capacity remains) or total (the contribution of the element to the load carrying capacity of the bridge is totally removed). In this paper only the results related to the most critical damage scenario are presented which is the total failure of the column in the end bent (figure 7).

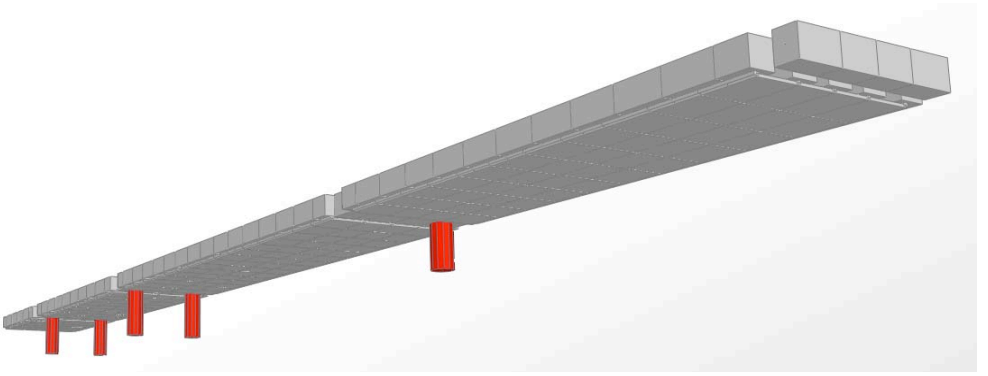


Figure 7. Most critical damage scenario (column in pier 3 totally damaged).

DETERMINISTIC ANALYSIS OF REDUNDANCY

A deterministic approach is necessary to permit the evaluation of structural redundancy using simple yet accurate methods. This is an important requirement if redundancy is meant to be used by practicing engineers as part of the bridge design and evaluation process.

Deterministic Redundancy criteria. The proposed deterministic criteria are based on the research conducted under the auspices of the U.S. National Cooperative Highway Research Program (NCHRP) in Report NCHRP 458 which developed approaches for the redundancy and reliability analysis of bridge superstructures and substructures. Liu et al., (2000) performed simplified reliability analyses of a large set of typical bridge bents and used those results to propose the following deterministic criteria which have been calibrated to meet a minimum level of system safety based on the performance of designs that have historically shown good system performance. The criteria are presented in terms of the redundancy measures previously defined in Eq. (1) and consist of the following:

$$\begin{aligned} R_u &= LF_u / LF_l \geq 1.20 \\ R_f &= LF_f / LF_l \geq 1.20 \\ R_d &= LF_d / LF_l \geq 0.50 \end{aligned} \tag{3}$$

The load factors LF_1, LF_f, LF_u and LF_d are respectively the expected value of the lateral load at which the first member fails, the system exhibits a maximum lateral displacement greater than column height/50, the originally intact system reaches collapse, and system that has exhibited major damage collapses. If the deterministic criteria provided in eq. (3) are met, the system may be defined as redundant.

Analysis of results. To deterministically evaluate redundancy following the procedure just presented only two analyses are needed (one for the intact and one for the damaged system). The analyses are performed at the nominal values for all the variables.

Figure 8 shows the results for the intact and for the damaged case, and table 1 summarizes the redundancy ratios found.

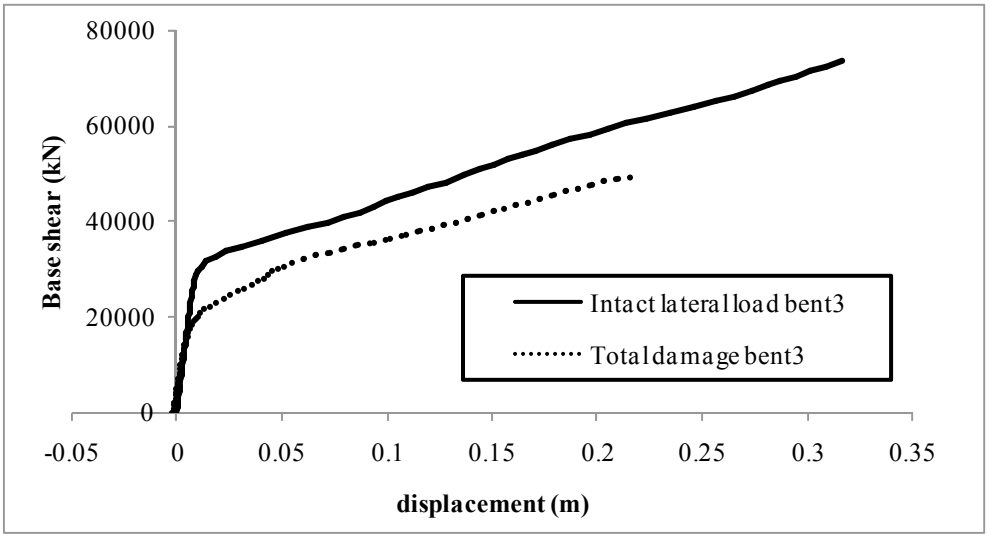


Figure 8. Load vs. displacement curves for intact and damaged system.

Table 1. Summary of redundancy analysis.

Event	Displacement	Force	Ratio	Ratio limit
First component failure	0.59 cm	20899.59 kN		
System collapse	26.54 cm	66217.67 kN	Ru=3.17	1.20
Excessive displacements (H/50)	12.00 cm	47064.74 kN	Rf=2.25	1.20
Collapse of damaged system (after removal of column in bent 3)	21.81 cm	49368.58 kN	Rd=2.38	0.50

As seen in Table 1, for this bridge the deterministic criteria set in Eq. (3) are fully satisfied for all three limit states. Thus, the structure can be defined as being redundant.

PROBABILISTIC APPROACH

The probabilistic approach for evaluating bridge redundancy consists of performing simulations that account for the uncertainties associated with estimating the most important parameters that control the evaluation of the structure's capacity to resist lateral load. The parameters considered in this study are the ones that define the material properties. These are considered to control the variability of the

response of the structure. These parameters are treated as random variables having the statistical properties listed in table 2.

Table 2. Random variables properties.

Variable	Description	Bias	COV	Distribution
f'c	Concrete compressive strength	1.15	0.15	lognormal
fcu	Concrete stress at crushing	1.00	0.10	normal
fy	Reinforcing steel yielding stress	1.10	0.11	lognormal
ε_u	Reinforcing steel ultimate strain	1.33	0.15	lognormal
fu	Reinforcing steel ultimate stress	1.10	0.11	normal

Generation of samples. The Latin Hypercube Sampling (LHS) method has been selected to generate a representative number of samples for the parameters considered as random variables Florian A. (1992). This LHS procedure is a modification of the Monte Carlo Sampling (MCS) method but overcomes the problem of performing a large number of analyses by selecting the samples from a partitioned domain divided into segments of equal probabilities as compared to MCS that selects samples randomly in the domain of probabilities of each variable (see figure 9).

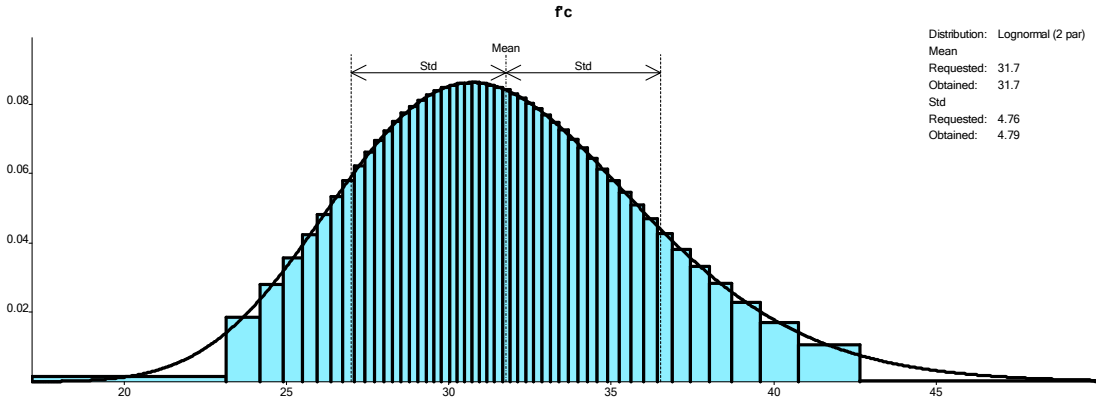


Figure 9. Partitioning of a variable domain into segments of equal probability.

Although, LHS can give accurate values for the mean and standard deviation of the limit state function, it cannot give accurate estimates of the probability of failure, because the number of unsafe runs is not sufficient to represent low probable events such as those associated with estimating the probability of failure of structural systems. Thus, the probability of failure is evaluated by fitting the response into a probability distribution function and then evaluating the probability that this response is lower than an established safety limit.

In the present study following a sensitivity analysis performed on simple models, the probability domains of the random variables are divided into 50 equi-probable segments.

In order to find the reliability indexes for first member failure, ultimate capacity of the intact system, the functionality limit state and the capacity of the damaged system respectively denoted as β_{member}, $\beta_{ult.}$, $\beta_{funct.}$ and $\beta_{damaged}$, the probability distributions of the capacity of the system to resist lateral loads for each limit state respectively represented by LF_1, LF_f, LF_u, and LF_d are obtained from the implementation of the LHS scheme.

Analysis of results. Figure 10 shows the capacity curves for the 50 runs performed for the intact structure and for the damaged structure.

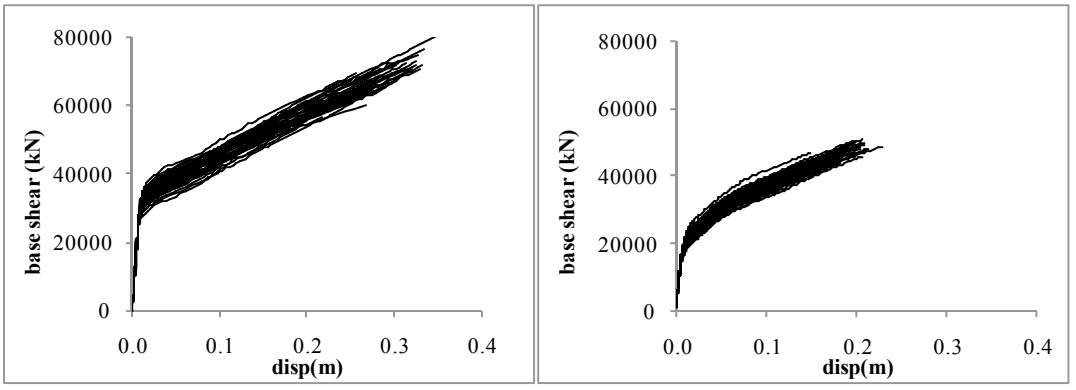


Figure 10. Probabilistic results for a)intact system and b)damaged system.

The capacities to resist lateral loads for the four limit states previously defined are fitted into appropriate probability distributions. The most adequate distribution is obtained using statistical tests on the goodness-of-fit. Table 3 summarizes the results which are also illustrated in figure 11.

Table 3. Response results.

Variable	Mean	COV	Probability distribution
LF1	20217.63	0.07	Log-normal
LFf	45259.32	0.18	Min.Extreme
LFu	65802.53	0.11	Weibull
LFd	44986.32	0.11	Min. Extreme

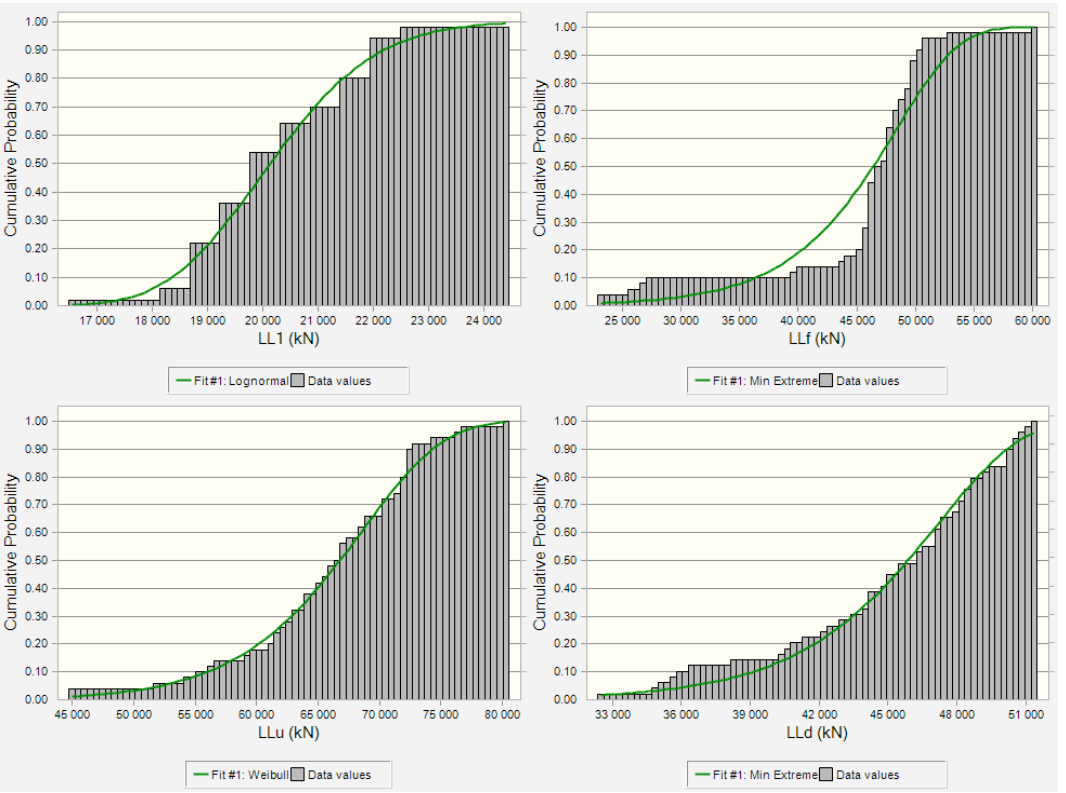


Figure 11. Fitting of response data by probability functions for a)LF1, b) LFf, a)LFu and b) LFd.

The expected applied lateral load is assumed to be equal to the seismic design load and is calculated by the following expression:

$$LL = \frac{m\, a(T_i)}{q} \tag{4}$$

where:

- m is the total mass of the structure;
- $a(T_i)$ is the acceleration related to the fundamental period of the most significant mode of vibration of the structure. In this paper, this acceleration is found from the CALTRANS 2006 design spectra for a type C soil;
- q is the ductility factor accounting for the dissipating behavior of the structure and is equal to 3.5.

A reduced expected lateral force is considered for the damaged state according to Liu et al.(2000) which suggests that a lateral load expected in a 2-year return period. The following formula is used to relate the 2-year load to the design-life load be used for that limit state:

$$LL_2 = 0.38\, LL\,. \tag{5}$$

In the analysis, the applied lateral forces are considered as deterministic. The resulting relative reliability indices are shown in table 4.

Table 4. Relative reliability index for the three limit states.

Event	RRI	RRI Limit
System collapse	$\Delta\beta_u$=2.61	0.50
Excessive displacements (H/50)	$\Delta\beta_f$ =1.02	0.50
Total damage of bent 3 column	$\Delta\beta_d$ =1.23	-2.00

The results confirm the high redundancy level of the structure especially for the damaged system. In fact, the loss of one member in the case of integral design can lead to a significant number of alternative load paths leading for high level of redundancy for the damage limit state

COMPARISON BETWEEN PROBABILISTIC AND DETERMINISTIC APPROACHES

The results of the two methods proposed to evaluate bridge redundancy are compared to verify that the two approaches are consistent. In that aim, the redundancy ratios are calculated for each run of the probabilistic simulation, then the average and the coefficients of variation are calculated for each LF_u/LF_1, LF_f/LF_1 and LF_d/LF_1 ratio. Table 5 shows the results and and demonstrates that they are very similar to the ones obtained by the deterministic approach.

Table 5. Comparison of redundancy ratios.

	Deterministic	Probabilistic	
		mean	COV
Ru	3.17	3.28	0.15
Rf	2.25	2.25	0.17
Rd	2.38	2.19	0.19

CONCLUSION

This paper uses non-subjective and quantifiable measures to evaluate the redundancy of bridge systems subjected to lateral loads. A deterministic and a probabilistic approach for the analysis of bridge redundancy are used. Integral bridge designs which have been recently used in seismic zones to achieve high lateral load capacity and high ductility levels have been demonstrated to produce highly redundant structures so that the system would not be likely to collapse following the failure of one column.

The deterministic approach has been demonstrated to provide good accuracy in estimating the level of redundancy as compared to the more rigorous probabilistic approach. The accuracy and ease of implementation of the deterministic approach in routine design would facilitate the consideration of redundancy during the design of new bridges and the load capacity evaluation of existing bridges.

ACKNOWLEDGEMENTS

The authors acknowledge the financial support provided by the Spanish Ministry of Research and Innovation through projects BIA2010-16332 and IPT-370000-2010-029. Thanks are also due to Professor Franco Bontempi and Dr. Stefania Arangio for supporting the work which was presented as part of the diploma thesis of the first author. The third author acknowledges the financial support provided by the Spanish Ministry of Education during his sabbatical leave at the Technical University of Catalonia (UPC) under the scholarship SAB2009-0164.

REFERENCES

AASHTO, (2008). AASHTO LRFD *Bridge Design Specifications*, Washington, DC.

Anitori, G. (2009). *Redundancy of bridge systems under lateral loads,* Diploma thesis, UPC, Barcelona.

CALTRANS, (2006). *Seismic Design Criteria* ver.1.4, Sacramento CA.

CSI, (2008). SAP2000 manual *Material stress-strain curves.* Berkeley CA.

Ghosn, M., Moses, F. (1998). *Redundancy in highway bridge superstructures NCHRP report 406*, Transportation research board, Washington DC.

Hambly, E.C. (1991). *Bridge deck behavior*, Taylor & Francis, New York.

ISO 2394 (1998). *General principles on reliability for structure*, Geneve.

Florian, A. (1992). "An efficient sampling scheme: Updated Latin Hypercube Sampling." *Probabilistic Engineering Mechanics* 7, 123-129.

Liu, W. D., Ghosn, M., Moses, F., Neuenhoffer A. (2000). *Redundancy in highway bridge substructures*, NCHRP Report 458, Transportation Research Board, Washington DC.

Mander, J. B., Park, R., Prisley, M. J. N. (1984). "Theoretical stress-strain model for confined concrete." *Journal of structural engineering*, ASCE. 114(3), p. 1804-1826.

McLean, D., Kuebler, S. E., Mealy, T. E. (1998). *Seismic performance and retrofit of multicolumn bridge bents*, Washington state department of transportation.

Anomaly Detection without Structural Behavior Models

I.F.C. Smith, F.ASCE

Applied Computing and Mechanics Laboratory, Swiss Federal Institute of Technology (EPFL), IMAC-IIC-ENAC, Station 18, CH-1015 Lausanne, Switzerland; Ian.Smith@epfl.ch

ABSTRACT

Measurement-data interpretation is especially costly when structural modeling is required. This paper summarizes results of three studies of anomaly detection without structural behavior models. In the first study, five signal-analysis methods were compared using an eight-year temperature/traffic loading vs. time history on a simulation of a two-span beam with four cases of damage scenarios occurring after four years and nine months. Moving principal-component analysis was identified to be able to detect damage most reliably. In the second study, ten signal analysis methods were compared using the same loading vs. time history as the first study. Fifteen cases of variations in daily temperature, traffic loading and sensor noise were used in this comparison. Results showed that moving principal-component analysis and robust regression detect damage more effectively than the other methods, especially in the presence of outliers and missing data. The third study involved the application of temperature cleansing methods to increase damage detectability and decrease detection time when using moving principal components analysis. The advantages of this method were compared with those of the robust regression method. Both methods are complementary. Complex relationships between frequency filtering, sensor/damage locations, traffic loading and noise were found to determine detectability and detection time. This has lead to several avenues for further study.

INTRODUCTION

It is difficult to convince practicing engineers to commit money to long-term structural health monitoring. Often the most important issue is neither the cost of purchasing and placing sensors nor the cost of data storage. Engineers are hesitant because of difficulties associated with data interpretation. Data interpretation is particularly arduous when detailed structural models are necessary for structural identification, especially when complete information is not readily available from design and construction phases.

Less cumbersome approaches to structural health monitoring involve the application of signal-analysis methodologies to monitoring data. Such methodologies do not require structural behavior models. Over the years, tens of research papers

have proposed strategies such as auto-regressive methods (Omenzetter and Brownjohn 2006), (Lu and Gao 2005), (Nair et al. 2006), Fourier analyses (Balan et al. 2000), wavelet methods (Moyo and Brownjohn 2002), (Sun and Chang 2002), robust regression (Jajo 2005), principal component analysis (Posenato et al. 2008), correlation analysis (Ide et al. 2007), instance-based methods (Berry and Linoff 2000) and Box-Jenkins analysis (Moyo and Brownjohn 2002) for anomaly detection. An ASCE state-of-the-art report that provides further detail of such methods is in preparation (ASCE 2010).

Few research projects involved a systematic comparison of several methodologies. Furthermore, comparison of results between projects was hindered by differences in sensitivity to damage (and other anomalies), sensor locations and signal noise level. Also, practical structural-engineering contexts are much different than other measurement contexts due to the presence of yearly and daily temperature cycles, large numbers of outliers (up to 20%) and common situations where data are missing. Finally, some methods indicate the presence of an anomaly only after several days, sometimes weeks, following its occurrence.

This paper provides a summary of three comparative studies of signal analysis methods that have been applied to two structural cases. Each study is described below. For further details, the reader is referred to the original papers.

STUDY ONE

This study (Posenato et al. 2008) examined results from five data analysis techniques in terms of their ability to detect four damage scenarios. Due to difficulties in retrieving databases from real structures with a range of damage severities, a finite-element model of a beam was used to evaluate the efficiency of algorithms to detect damage. The behavior of a bridge (a continuous beam over two 5m spans) was simulated in healthy and various damaged states. A thermal load simulated structural behavior under varying environmental conditions. In the FE model, it was possible to simulate both thermal and applied moving loads as well as damaged elements in one or more sections of the beam with stiffness reductions. The response was measured by means of a ‘virtual’ monitoring system installed in the structure. The monitoring system was composed of six pairs of elongation sensors; six sensors were located at the lower surface and six at the upper surface. Cracks were simulated in order to model local degradation in material properties. Structural behavior was studied in both healthy and damaged states to test the ability of five statistical algorithms to detect when and where damage occurs. Four damage severities were simulated.

Each simulated time series was representative of a structural response measured at predefined sensor locations over eight years, assuming four measurements per day (11000 measurements). Damage occurred after 1750 days. The time series showed harmonic variations due to seasonal variations of temperature in both healthy and damaged states. However, no obvious correlation to

damage formation was directly observed from the elongation-sensor time histories. Only in cases of severe damage was a small shift of periodicity observed. As a consequence, signal-analysis methods are required to interpret data in order to detect damage.

The example deformation history in this study had harmonic variability due to the seasons and therefore, the training period was taken to be two years and the size of the moving window was one year. Once a sequence of values exceeded a threshold defined statistically from observed variations during the undamaged state, damage was assumed to be detected.

Results have shown that two signal-analysis methods, moving principal component analysis and the moving correlation method work more effectively than other methods for long-term structural health-monitoring tasks such as the example in this study. These approaches can be applied over long periods to a range of structural systems in order to discover anomalous states even when there are large quantities of data. For quasi-static monitoring of civil structures, these new methodologies perform better than wavelet methods, short term Fourier transform and the instance-based method. Another important characteristic is adaptability. Once new behavior is identified, adaptation allows detection of further anomalies.

STUDY TWO

In this research (Posenato et al. 2010) compared ten methods in terms of their ability to detect damage in the presence of noise, outliers and missing data. Also, clustering methods are evaluated for their ability to reduce difficulties associated with computational complexity. The loading history was the same as for Study One. Fifteen cases of variations in daily temperature, traffic loading and sensor noise were used in this comparison.

The following algorithms were compared:

- Auto Regressive with Moving Average (ARMA)
- Box-Jenkins (BJ)
- Seasonal ARIMA
- Discrete Wavelet Transform (DWT)
- Wavelet Packet Transform (WPT)
- Robust Regression Analysis (RRA)
- Instance Based Method (IBM)
- Short-term Fourier Transform (SFT)
- Correlation Anomaly Scores Analysis
- Moving Principal Components Analysis (MPCA)

While all ten methods are able to detect damage when there are no noise sources, outliers and missing data, few remain able in their presence, especially at levels that are typically expected in civil-engineering situations. Full-scale bridge

examples were also used to illustrate the most promising methods. For details of this study the reader is referred to the original paper.

This study has resulted in the following conclusions:

- Moving Principal Component Analysis and Robust Regression Analysis are useful for identifying and localizing anomalous behavior in civil engineering structures. These approaches discover anomalous states over long periods of time even when there are large quantities of data.
- For quasi-static monitoring of civil structures with noise in measurements, MPCA and wavelet packet transform perform better than other wavelet methods, auto regressive analysis, instance-based methods and correlation anomaly scores. MPCA out-performs WPT since it can distinguish between permanent and temporary anomalies.
- Robust regression has shown lower performance than MPCA and wavelet analysis but has the advantage of being insensitive to outliers and missing data.
- MPCA combined with Interquartile Range Analysis accommodates outliers in the measurements.
- MPCA can also be adapted to situations when measurements are missing completely and when a single measurement is missing.
- A clustering algorithm extends the use of MPCA to those applications where a significant number of sensors are present in the structure, thus allowing the MPCA to remain tractable for full scale applications.

STUDY THREE

The third study (Laory et al. 2011) compared damage detectability and time to detection for moving principle component analysis with the robust regression method. Comparisons were carried out when removing seasonal variations, for various damage locations with respect to sensors and for various levels of noise and traffic loading. A case study of a 80m-span steel-truss railway bridge was used to illustrate results.

This study resulted in the following observations:

- The time to detection of RRA was shorter than that of MPCA.
- MPCA provided greater damage detectability than RRA.
- Removing seasonal variations decreased the damage detectability of MPCA.
- Removing seasonal variations had a small influence on damage detectability of RRA.
- Decreases in traffic loading increased damage detectability of both MPCA and RRA.
- When damage detectability was high (in case of high damage levels and low traffic loading), Removing seasonal variations may shorten the time to damage detection of MPCA.

- The negative effect of traffic loading and damage level on time to detection using RRA was less than that using MPCA.

From these observations the following conclusions have been drawn:

- Moving principal component analysis (MPCA) is generally better than robust regression analysis (RRA) in terms of damage detectability. On the other hand, RRA is better than MPCA in terms of time to damage detection.
- RRA is not sensitive to seasonal variations.
- For MPCA, there is a trade-off between damage detectability and time to damage detection when removing seasonal variations.

From evaluating the performance of MPCA and RRA, it is recommended that these two methods should be considered complementary since they are most appropriate in different contexts.

CONCLUSIONS

Choice of the right behavior-model-free analysis method for measurement-data interpretation depends on factors such as the presence of outliers, missing data, noise, the extent of damage that needs to be detected and the maximum allowable time to detection. In many cases, there will be several complementary methods that can be used in parallel. These studies have revealed that MPCA and RRA are useful and complementary methods and therefore, they deserve a place in the computational toolboxes of engineers who interpret continuous-monitoring data taken from measurements of civil-engineering structures.

More work is required in the areas of definition of the training period, window sizes, damage detection thresholds and matching the best measurement system configuration to the data-interpretation methods that are employed. These topics are the subjects of current research.

ACKNOWLEDGEMENTS

This research was funded by the Swiss Commission for Technology and Innovation and the National Science Foundation. PhD students Dr. Daniele Posenato and Irwanda Laory are thanked for their contributions. Dr Thahn Trinh helped in the third study. The University of Genoa (Prof. A. Del Grosso and Dr. F. Lanata) contributed to definition of the load/temperature history for the first two studies. Our industrial partner is Smartec SA, Lugano and we are grateful to Dr Daniele Inaudi for his support.

REFERENCES

ASCE (2010). Structural Identification of Constructed Systems, Structural Identification Comittee, American Society of Civil Engineers. In Press.

Balan, R., I. Daubechies and V. Vaishampayan (2000). "The analysis and design of windowed Fourier frame based multiple description source coding schemes." *Ieee Transactions on Information Theory* **46**(7): 2491-2536.

Berry, M. J. A. and G. Linoff (2000). *Mastering data mining : the art and science of customer relationship management*. New York, Wiley Computer Pub.

Ide, T., S. Papadimitriou and M. Vlachos (2007). Computing correlation anomaly scores using stochastic nearest neighbors. *The 2007 Seventh IEEE International Conference on Data Mining*. Omaha NE, USA, IEEE**:** 523-528.

Jajo, N. (2005). "A Review of Robust Regression and Diagnostic Procedures in Linear Regression." *Acta Mathematicae Applicatae Sinica (English Series)* **21**(2): 209-224.

Laory, I., Trinh, T.N. and Smith, I.F.C. (2011) "Evaluating two model-free data interpretation methods for measurements that are influenced by temperature, *Advanced Engineering Informatics*, in press.

Lu, Y. and F. Gao (2005). "A novel time-domain auto-regressive model for structural damage diagnosis." *Journal of Sound and Vibration* **283**(3-5): 1031-1049.

Moyo, P. and J. M. W. Brownjohn (2002). "Detection of anomalous structural behaviour using wavelet analysis." *Mechanical Systems and Signal Processing* **16**(2-3): 429-445.

Nair, K. K., A. S. Kiremidjian and K. H. Law (2006). "Time series-based damage detection and localization algorithm with application to the ASCE benchmark structure." *Journal of Sound and Vibration* **291**(1-2): 349-368.

Omenzetter, P. and J. M. W. Brownjohn (2006). "Application of time series analysis for bridge monitoring." *Smart Materials and Structures* **15**(1): 129-138.

Posenato, D., P. Kripakaran, D. Inaudi and I. F. C. Smith (2010). "Methodologies for model-free data interpretation of civil engineering structures." *Computers & Structures* **88**(7-8): 467-482.

Posenato, D., F. Lanata, D. Inaudi and I. F. C. Smith (2008). "Model-free data interpretation for continuous monitoring of complex structures." *Advanced Engineering Informatics* **22**(1): 135-144.

Sun, Z. and C. C. Chang (2002). "Structural Damage Assessment Based on Wavelet Packet Transform." *Journal of Structural Engineering* **128**(10): 1354-1361.

Damage Detection and Localization in Structures: A Statistics Based Algorithm Using a Densely Clustered Sensor Network

Elizabeth L. Labuz[1], Shamim N. Pakzad[2], and Liang Cheng[3]

[1]Graduate Student, Department of Civil and Environmental Engineering, Lehigh University, 117 ATLSS Drive, Bethlehem, PA 18015; PH (610) 758-4543; FAX (610) 758-5553; email: elabuz@lehigh.edu
[2]P.C. Rossin Assistant Professor, Department of Civil and Environmental Engineering, Lehigh University, 117 ATLSS Drive, Bethlehem, PA 18015; PH (610) 758-6978; FAX (610) 758-5553; email: pakzad@lehigh.edu
[3]Associate Professor, Department of Computer Science and Engineering, Lehigh University, 326 Packard Lab, Bethlehem, PA 18015; PH (610) 758-5941; email: cheng@cse.lehigh.edu

ABSTRACT

Damage prognosis for structural health monitoring is a challenging and complex research topic in civil engineering. Early and accurate damage detection is essential to maximizing the useful life of structures. The use of densely clustered sensor networks provides promising applications in the analysis of structural components and identification of local damage. The proposed localized damage detection method utilizes a linear regression analysis to monitor changes in the linear behavior of a structure with the onset of damage. The structural responses at various sensor locations along a structure are compared to those of other locations and pair-wise influence coefficients are estimated. These coefficients serve as damage indicators when damaged values are compared to healthy-state values. By statistically comparing the change in influence coefficients, structural damage can be accurately and effectively identified. The method is verified using simulations and an experimental prototype of a local beam-column connection, as well as a simulated model of a two-span bridge girder.

INTRODUCTION

Structural health monitoring (SHM) plays an integral role in maintaining the integrity of important civil, mechanical, and aerospace engineering systems. Structures experience a number of dynamic influences on a daily basis ranging from typical ambient vibrations to more extreme wind and earthquake loadings. Whether the damaging effects of these load cases are visible immediately or appear more gradually in time, it is important to be able to detect the damage before it becomes detrimental to the entire structure and its surroundings. Not only will money be saved by being able to repair more manageable damages at earlier detection, but also fatal catastrophes can be prevented. As an increasing number of structures are beginning to reach the limit of their service lives, the need for effective, efficient, and affordable damage detection methods is becoming more apparent.

Traditional non-destructive evaluation (NDE) techniques include but are not limited to visual inspection, liquid penetrant, magnetic particle, radiography, eddy

currents, ultrasonic waves, acoustic emission, and infrared thermography (Trimm 2007). While these methods are useful in certain circumstances, they require *a priori* knowledge of the location of damage and are subject to the trained eye of the inspector. Also, in order to implement these techniques one must have direct access to the location of damage, which may be difficult to reach. Furthermore, NDE techniques are costly, difficult to use with complex equipment, and provide only a temporary means of SHM.

Both advancements in sensor technologies as well as improved understanding of the modal properties of structures have given rise to vibration-based damage identification methods. These methods find a basis in the vibration behavior of a structure, namely the connection between the modal parameters of a structural system—natural frequencies, mode shapes, and modal damping—and its physical properties—mass, stiffness, and damping (Doebling *et al* 1998; Alvandi and Cremona 2006). Parametric changes signify changes in the physical properties, i.e. structural damage in the form of mass or stiffness loss. Also, the advancements of wireless networks make it possible to implement these vibration-based methods on a semi-permanent basis for continuous monitoring of structures.

However, current SHM practices involving global-based damage detection require knowledge of specific structural properties, including mass, stiffness, or damping ratio, for which it is often difficult to determine correct values (Koh *et al* 1995; Morassi and Rovere 1997; Sohn and Law 1997; and Ratcliffe 1997). Additionally, global detection techniques, which are based on global properties, are not sensitive to local damage and, therefore, cannot determine damage locations. Other proposed local damage detection methods, for example the damage locating vector (DLV) method (Bernal 2002), also require the knowledge of structural properties or require homogeneity of the structural properties as in the two-dimensional gapped smoothing method (Yoon *et al* 2005).

An effective damage detection method has been proposed that is sensitive to local damage (Labuz *et al* 2010). The method uses vibration responses collected via densely clustered sensors to achieve localized damage detection without the need for exact knowledge of structural properties. Influence coefficients, obtained from linear regression between pairs of node responses, are used as the index for determining the existence of damage. This study presents both simulated and experimental results to demonstrate the effectiveness of the proposed local damage detection method.

DAMAGE DETECTION ALGORITHM

The algorithm implemented is based on the assumption that a structure exhibits linear behavior, and is thus applicable for identifying damage in structures that fall within this category. In order to capture this behavior, linear regression analysis is used to find pair-wise influence coefficients, α_{ij}, between two nodes i and j, based on the structural response data u_i and u_j at time instance t_k with ε_{ij} and β_{ij} being time-variant and invariant linear regression parameters along with α_{ij} to be estimated as follows:

$$u_j(t_k) = \beta_{ij} + \alpha_{ij} \cdot u_i(t_k) + \varepsilon_{ij}(t_k).$$

The structural response will change as damage occurs, which is then reflected in the influence coefficients. Therefore, the comparison of the resulting influence coefficients from the initial undamaged state with those of the damaged state of the structure serves as a *damage indicator* when it yields a significant change in the value of the coefficients from state to state. This characteristic allows for the identification of the damage location by observing the pattern of influence coefficients exhibiting significant changes. Because this method only involves processing of the structural response, this is an output-only method and, thus, can be easily applied regardless of loading conditions. Figure 1 outlines the procedure for the damage detection algorithm.

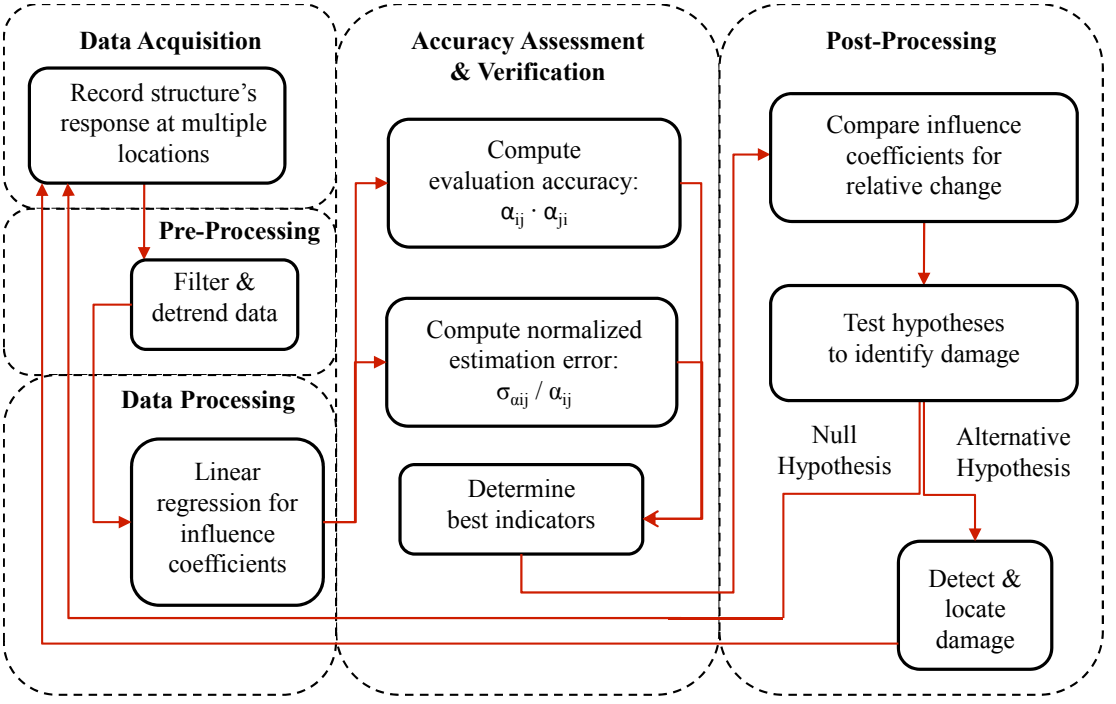


Figure 1. Damage detection algorithm procedure.

INFLUENCE COEFFICIENTS AND NORMALIZED ESTIMATION ERROR

Once the coefficients have been calculated, the accuracy of the data must be assessed and verified before damage detection can be performed. By minimizing the error in the parameters, the occurrence of false alarms will also be minimized. Two parameters are considered for this purpose: the evaluation accuracy and the normalized estimation error associated with each pair-wise coefficient. The product of influence coefficients α_{ij} and α_{ji}, yields the evaluation accuracy, EA_{ij}, of these coefficients, indicating which node responses are linearly related to one another with the least amount of regression error, ε_{ij}, and thus are more accurate predictors. An evaluation accuracy of 1.0 signifies a strong accuracy of estimation, while a product of less than 1.0 corresponds to progressively higher values of noise and nonlinear behavior of the physical structure.

The second parameter that is used for data verification is normalized estimation error, which is calculated by

$$\gamma_{ij} = \frac{\sigma_{\alpha_{ij}}}{\alpha_{ij}}.$$

Normalized estimation error allows for a direct comparison of the amount of error exhibited within the measured data. A low estimation error will correspond to a more accurate predictor. Based on these two parameters the strongest damage indicating influence coefficients are identified for use in damage detection. These coefficients are post-processed and monitored for significant changes to localize the damage.

SIMULATED BEAM-COLUMN CONNECTION

A simulated model is used to demonstrate the application of this method. Consider a simple beam-column connection, representing a local joint, with nine node locations, as shown in Figure 2. The column portion of the joint is fixed at both ends while the beam cantilevers out from the centerline of the column. Two simulation conditions were performed which include (1) an undamaged baseline condition and (2) a damaged condition, characterized by a 40% reduction in the beam stiffness. For each of these models, displacement data was simulated for a white noise excitation applied at the free end of the beam in the y-direction. Measurement noise was accounted for by adding additional noise to the response.

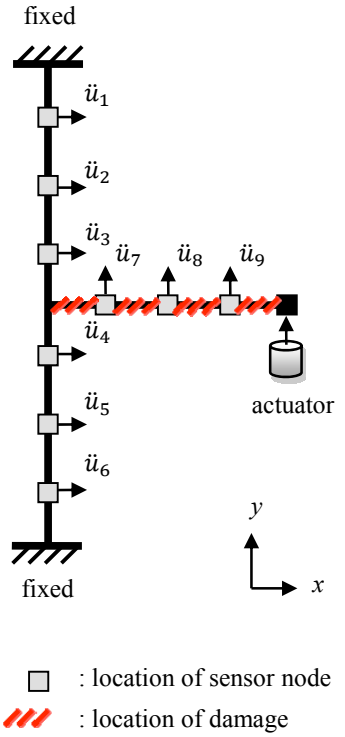


Figure 2. Local beam-column joint with nine node locations used for simulated beam-column model.

SIMULATION RESULTS

The algorithm was then applied to the simulated displacement data and the parameters were extracted. A selection of the influence coefficient changes are shown in Figure 3. The influence coefficients $\alpha_{ij},\ 1 \leq i,j \leq 6$ all experience very small (less than 1%) changes between the undamaged and damaged states. This implies that the physical relationship between these nodes has not changed. However, the coefficients of nodes 1 through 6 paired with nodes 7, 8, and 9 show relative changes between 30-40%. When nodes are on opposite sides of the damage, i.e. nodes 1 through 6 are on the undamaged column, while nodes 7, 8 and 9 are on the damaged beam, the physical relationship between the paired nodes change. The beam experiences more flexibility in the form of higher displacements, whereas the column nodes see small displacements similar to the undamaged state. This physical change is reflected in a more significant relative change in the value of influence coefficients. Furthermore, the influence coefficients $\alpha_{ij}, 7 \leq i,j \leq 9$ also experience changes in coefficients between 3-10%. This signifies that the physical properties of the structure between α_{78}, α_{79}, and α_{89} have changed. Therefore, damage must exist between these nodes. This is consistent with the known damage condition. Thus, the application of influence coefficients and local damage indicators is demonstrated.

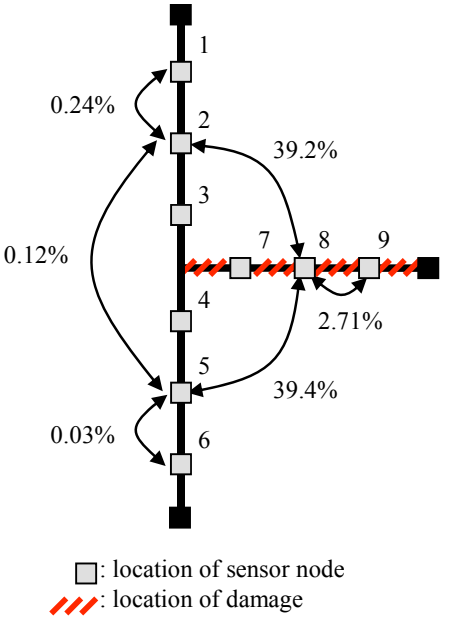


Figure 3. Relative change in pair-wise influence coefficients for the simulated beam-column structure.

EXPERIMENTAL BEAM-COLUMN CONNECTION

A small-scale steel beam-column connection, based on the simulated model, was constructed in the ATLSS Center at Lehigh University and was used for experimental verification of the algorithm. As is shown in Figure 4, the two ends of the column have fixed supports and the beam cantilevers from the centerline of the column. The intention was to model the beam-column connection area in which this prototype

represents only a portion of these members. The free end of the cantilever was attached to an actuator and excited by harmonic force at a 15 Hz forcing frequency, and the acceleration responses were collected at each of the nine sensor nodes. Furthermore, to avoid nonlinear behavior of the elements, an amplifier controlled the amplitude of the excitations. This portion of the experiment served to establish a baseline response for the undamaged structure.

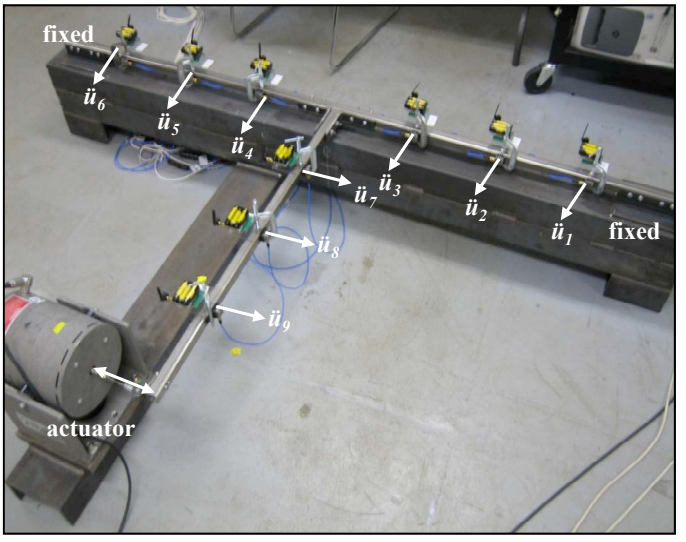


Figure 4. Experimental beam-column instrumented with nine tethered accelerometers.

For the second portion of the experiment, the beam member was replaced by a member of 40% reduced wall thickness in order to simulate damage to the structure. The excitations were repeated similarly to the undamaged case.

Acceleration data at each sensor location was collected at a 200 Hz sampling rate and 0.005 sec time step, with each test lasting 10 seconds total. Both the undamaged and damaged structures were tested 50 times, for a total of 100 tests, each containing 2000 samples per sensor location. All data was pre-processed and influence coefficients were computed to locate the damage.

EXPERIMENTAL BEAM-COLUMN RESULTS

Once the 72 influence coefficients were calculated from the acceleration data, they were assessed to identify the most significant indicators to be used for damage detection. This involves two parameters: evaluation accuracy, *EA*, and normalized estimation error, γ. By inspection of these parameters, eight different trends can be identified in the undamaged and damaged parameters, with lower estimation errors coinciding with greater evaluation accuracies and vice versa. These trends have been designated as eight different regions, whose mean values are presented in Table 1. Region 1 in the table corresponds to the least estimation error and highest accuracy, and region 8 corresponds to the greatest estimation error and lowest accuracy. Parameters in region 1, consisting of $\alpha_{ij},\ 7 \leq i,j \leq 9$, are the most accurate and have the least error. This is a reasonable outcome as nodes 7, 8, and 9 are all located in a

row along the same structural element (the beam). Therefore, the accelerations at node 7, for example, will be more highly correlated to those at node 8 or 9.

Table 1. Average Estimation Error (γ) and Evaluation Accuracy (*EA*).

Region	Influence Coefficients	γ_{ii} Average	EA_{ij} Average
1	α_{78}, α_{79}, and α_{89}	0.0002	0.9999
2	α_{23} and α_{45}	0.0015	0.9947
3	α_{27}, α_{28}, α_{29}, α_{37}, α_{38}, α_{39}, α_{47}, α_{48}, α_{49}, α_{57}, α_{58}, and α_{59}	0.0044	0.9554
4	α_{12}, α_{13}, α_{46}, and α_{56}	0.0057	0.9377
5	α_{17}, α_{18}, α_{19}, α_{67}, α_{68}, and α_{69}	0.0074	0.8997
6	α_{24}, α_{25}, α_{34}, and α_{35}	0.0093	0.8379
7	α_{14}, α_{15}, α_{26}, and α_{36}	0.0114	0.7903
8	α_{16}	0.0161	0.6626

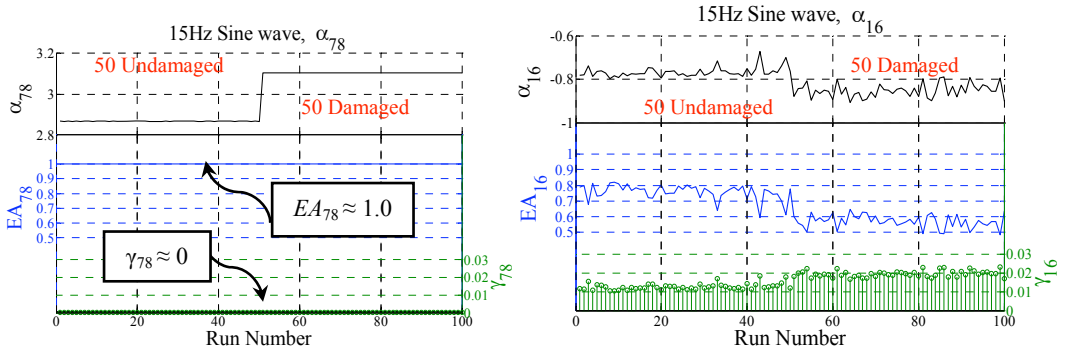
On the contrary, region 8, which consists of parameter α_{16}, exhibits the poorest accuracy and the greatest estimation error. This can be accounted for by the fact that each of these nodes is located at either end of the column near the fixed connections. These boundary conditions create large additional noise, which contributes to the fact that α_{12} or α_{56} exhibit lower accuracy than α_{78} or α_{89} despite the similar configuration of the nodes with respect to one another. Figures 5(i) and (ii) show examples of α, *EA*, and γ results from regions 1 and 8, respectively. Figure 5(i) shows that the *EA* is almost equal to unity and the γ is almost equal to 0 for region 1, while Figure 5(ii) shows a much lower *EA* and a noticeably higher γ for region 8. Moreover, Figure 5(i) shows a more decisive change in the influence coefficient value than Figure 5(ii). Based on similar data for all 8 regions, it can be concluded that regions 1 through 4 contain useful damage indicators. On average, these influence coefficients exhibit accuracy greater than 93% and estimation error less than 0.006.

The experimental results of the relative changes in the influence coefficients, α_{ij}, between the undamaged and damaged tests are shown briefly in Figure 6. Observing these coefficient changes is the first step in post-processing the data. The changes associated with α_{78}, α_{79}, and α_{89}, which are 8%, 12%, and 4% respectively, are potential indicators of a property change between nodes 7 and 9. This is consistent with the damage, or stiffness reduction, that was created along the full length of the beam portion of the test structure.

The coefficients of region 2, α_{23} and α_{45}, experienced 3% and 8% changes. This is less consistent with what would be expected in comparison to the very low (less than 1%) changes that were seen in the simulated results. One major cause of this is ambient noise, which is difficult to control in an experimental setting, but even more so in a real structure.

Influence coefficients from region 3 were more in line with the prediction of the simulated results, with the exception of α_{49} (2%) and α_{57} (3%), which were low compared to the 5-40% range of the others. Again, these two discrepancies are likely accountable to noise. However, the majority of the coefficients in this region showed noticeable fluctuations from the undamaged state to the damaged state. These changes, along with the model results, show that nodes on opposite sides of the damage location experience the largest changes, which is consistent with the simulated results. Again,

the changes in coefficients point to the location of damage in the structure (i.e. damage between nodes 2 and 7, 3 and 8, and so forth).



(i) **(ii)**

Figure 5. Comparison of *α*, *EA*, and *γ* results: (i) Region 1 and (ii) Region 8.

While the results for the first three trend regions were mostly consistent with the simulated results, the remaining regions were not as consistent. A prime example is region 6, consisting of parameters α_{24}, α_{25}, α_{34}, and α_{35}. According to the model, these coefficients, whose nodes are all located on the same side of the damage, should experience very little fluctuation from the undamaged to damaged states. However, their experimental changes range from 12-20%. Recall that in the previous verification stage region 6 showed the third lowest accuracy and the third highest error; therefore, these coefficients are not considered to be significant damage indicators and can be neglected.

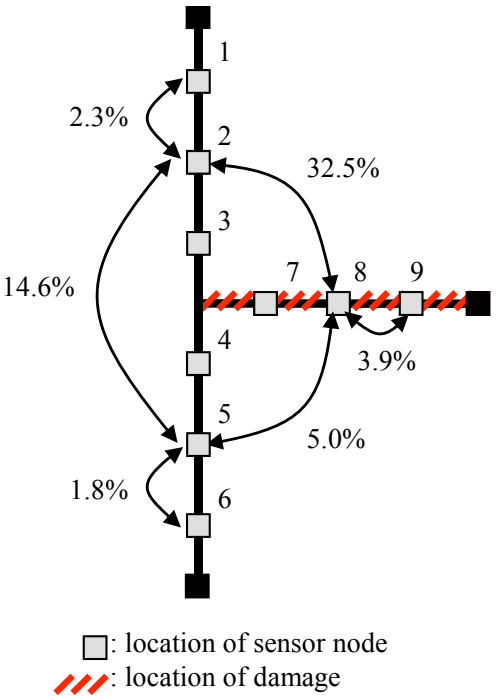


Figure 6. Relative change in pair-wise influence coefficients for the experimental structure.

SIMULATED TWO-SPAN GIRDER

In order for the proposed damage detection method to be adequately verified for practical application, it must be applied to more complex structures. Therefore, a small-scale two-span steel bridge girder has been simulated. The girder was modeled as a two-dimensional frame with short columns with fixed supports and uneven spans as shown in Figure 7. This configuration was chosen as it can model the behavior of a bridge girder, as well as that of a building frame. Furthermore, the uneven spans allow for more variety in the results and damage scenarios. The model has 21 total nodes, which coincide with the sensor locations, with six at each corner joint and nine at the center joint. A white noise excitation was applied in the x-direction to produce displacement responses at each node. Measurement noise was accounted for by adding random noise to the response. Two simulation conditions were considered which include (1) an undamaged baseline condition and (2) a damaged condition, characterized by a 50% reduction in the stiffness of an 8-inch portion of the center column between node C7 and the beam as noted in Figure 7. It is important to note that this corresponds to only a 0.7% decrease in stiffness of the column as a whole. The rest of the structure maintains the same stiffness properties as the undamaged structure.

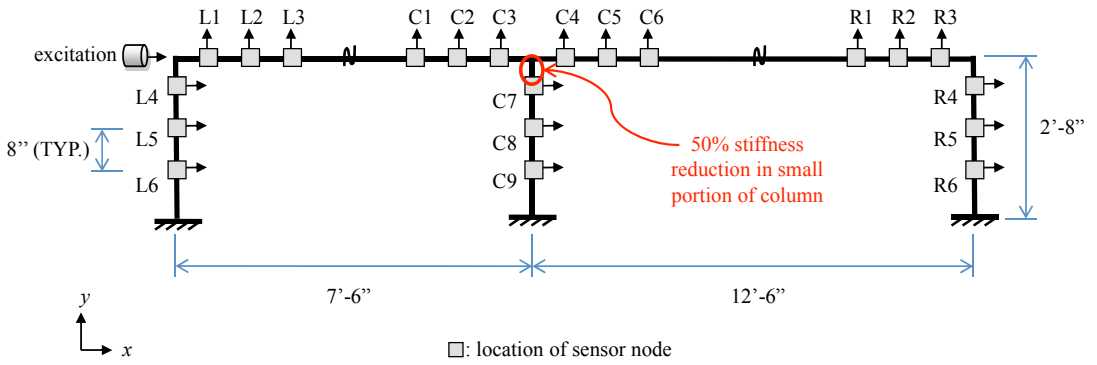


Figure 7. Simulated two-span bridge girder with 21 sensor node locations.

SIMULATION RESULTS

Results were generated considering 100 (50 undamaged, 50 damaged) separate sets of 2000 simulated samples per node. The damage detection algorithm was then applied to the simulated displacement data and the influence coefficients were determined. The plots in Figure 8 demonstrate pair-wise relationships that show (i) the significant change in coefficients on opposite sides of the damage (C2 to C8) versus (ii) the negligible change in coefficients on the same side of the damage (L5 to L6). Even with added noise, both examples show high accuracies and low errors. Thus, both coefficients are considered as significant damage indicators. These change patterns are consistent with those found in the beam-column simulations and experiments.

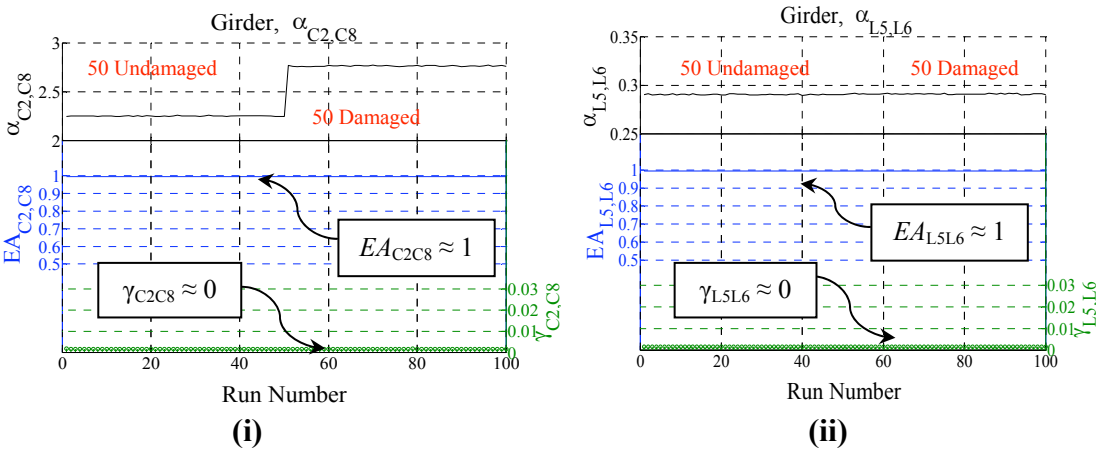


Figure 8. Comparison of α, EA, and γ for (i) nodes surrounding damage and (ii) nodes remote from damage.

Figure 9 shows the average change in influence coefficients throughout the structure resulting from the damage. As can be seen, the center beam nodes (C1 through C6) change more than two or three times that of the other nodes. This is consistent with the known 50% localized stiffness reduction at the central connection. Therefore, the algorithm is sufficient in identifying the general location of damage within the structure as a whole, even though the overall stiffness reduction of the structure was negligible.

Furthermore, the modal properties of the structure change insignificantly with the occurrence of damage at the central joint. This can be seen in Table 2, which shows the modal frequencies of the first three modes for the undamaged and damaged conditions. The percent changes range from approximately 0.5% to 1.5%. These minor changes would be undetectable in any modal-based global detection method with consideration of reasonable errors. However, the proposed localized method detects the damage effectively regardless of minimal changes in global properties.

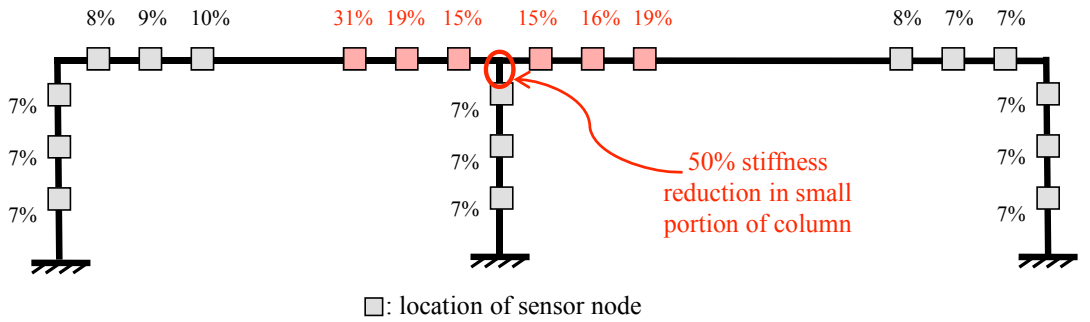


Figure 9. Average relative change in pair-wise influence coefficients for the simulated beam-column structure.

Table 2. Modal frequencies in Hz for the undamaged and damaged models.

	Undamaged	Damaged	% Change
Mode 1	2.67 Hz	2.64 Hz	1.16%
Mode 2	4.45 Hz	4.42 Hz	0.59%
Mode 3	6.81 Hz	6.70 Hz	1.53%

CONCLUSION

A densely clustered sensor network was successfully implemented for local damage detection of both a simulated model and experimental prototype of a steel beam-column connection. The proposed output-only method effectively used linear regression to estimate influence coefficients from vibration-induced acceleration responses of the structure. Changes in the influence coefficients correctly reflected changes in the vibration properties of the structure, thus, revealing the existence and location of damage. Although the experimental structure exhibited more noise error than the simulated results, both the simulation and the experiments identified the location of damage.

Additionally, results showed a significant difference in performance between coefficients with high EA and low error and those with low EA and high error. Therefore, coefficients must be evaluated for strong damage indicating characteristics as this noticeably contributes to the effectiveness of damage detection. In real-world applications earlier damage detection will allow for more manageable repairs and reduce the risk of structural failures.

Finally, a structure in the form of a bridge girder with two unequal spans was simulated. This model was used to investigate the application of the algorithm for more complex structures with more realistic damage scenarios. Using simulated displacement data and applying the algorithm, the resulting influence coefficients correctly identified the central local joint as the location of damage. This is especially significant because both global stiffness and modal frequencies of the structure remained nearly unaffected by the occurrence of damage. This suggests that other detection methods that are based on global properties would fail to detect this damage, whereas the proposed method identified not only the existence but also the location of the damage.

ONGOING AND FUTURE WORK

While the localized damage detection method has been shown to be effective for the scenarios presented, it is important to continue to verify this method for increasingly complex and realistic structures. Although only one damage scenario is presented for the two-span girder simulation, ongoing research involves the investigation of a variety of damage combinations and loading cases. Also, an experimental prototype similar to the simulated girder will be constructed and tested at Lehigh University using three types of sensors: tethered piezoelectric accelerometers, wireless piezoelectric accelerometers, and strain gauges. Moreover, it is important to determine the smallest amount of damage to which this algorithm is sensitive.

ACKNOWLEDGMENTS

The research described in this paper is partially supported by the National Science Foundation through Grant No. CMMI-0926898 by Sensors and Sensing Systems program, and by a grant from the Commonwealth of Pennsylvania, Department of Community and Economic Development, through the Pennsylvania Infrastructure Technology Alliance (PITA).

REFERENCES

Alvandi, A., and Cremona, C. "Assessment of vibration-based damage." *Journal of Sound and Vibration* 292 (2006) 179–202.

Bernal, D., M.ASCE. "Load Vectors for Damage Localization." *Journal of Engineering Mechanics* (Jan 2002): 7-14.

Chen, J., and Gupta, A.K. (2000). *Parametric change point analysis*. Birkhäuser, Boston.

Doebling, Scott W., Farrar, Charles R., and Prime, Michael B. "A Summary Review of Vibration-Based Damage Identification Methods." *The Shock and Vibration Digest* 30 (Mar 1998): 91-105.

Koh, C.G., See, L.M., and Balendra, T. "Damage Detection of Buildings: Numerical and Experimental Studies." *J. Struct. Engrg.* 121(8), (Aug 1995): 1155-1160.

Labuz, E. L., Chang, M., Pakzad, S. "Local Damage Detection in Beam-Column Connections Using a Dense Sensor Network," *Proc. of 19th Annual Structures Congress*, Orlando, FL (May 2010).

Morassi, A., and Rovere, N. "Localizing a Notch in a Steel Frame from Frequency Measurements." *J. Engrg. Mech.* 123(5) (May 1997): 422-432.

Ratcliffe, C.P. "Damage Detection Using a Modified Laplacian Operator on Mode Shape Data." *Journal of Sound and Vibration* 204(3) (1997): 505-517.

Sohn, H., and Law, K.H. "A Bayesian Probabilistic Approach for Structure Damage Detection." *Earthquake Engineering and Structural Dynamics* 26 (1997): 1259-1281.

Trimm, Marvin. "An overview of nondestructive evaluation methods." *Journal of Failure Analysis and Prevention* 3(3) (2003): 17-31.

Yoon, M.K., Heider, D., Gillespie Jr., J.W., *et al.* "Local damage detection using the two-dimensional gapped smoothing method." *Journal of Sound and Vibration* 279 (2005): 119-139.

Monitoring of Long Term Bridge Performance (LTBP) Program Bridges

Steven M. Petroff[1] Marvin W. Halling[2] , Ph.D, P.E., F.ASCE;
Paul J. Barr[3], Ph.D., M. ASCE;

ABSTRACT

The Long Term Bridge Performance (LTBP) Program, sponsored by the Federal Highway Administration, is currently in the pilot phase. During this phase, seven bridges distributed throughout the United States have been subjected to an initial round of of bridge performance testing. This preliminary testing was conducted to establish a baseline for comparison with future bridge testing, monitoring, and evaluation. Long term instrumentation systems have been designed and installed at these sites. This paper will focus on three of the pilot bridges. For each bridge, the preliminary testing conducted and long-term instrumentation layout will be provided.

INTRODUCTION

Utah State University (USU) was contracted with Rutgers University and the Federal Highway Administration (FHWA) under the Long-Term Bridge Performance (LTBP) Program to conduct preliminary testing and carryout long-term monitoring on bridges selected for the pilot study west of the Mississippi River. Researchers at Virginia Tech are supervising the testing of the bridges east of the Mississippi River. Through these tests, the program will collect, store, and analyze data to be used for improved maintenance and bridge owner decisions.

Following a rigorous selection process, each bridge underwent extensive preliminary testing including dynamic, live load, NDE/NDT, material testing, in addition a detailed visual inspection. This initial data, along with years of maintenance records, were analyzed to determine an appropriate long-term instrumentation. Preliminary testing for six of the pilot bridges is currently complete. Current scheduling plans are to conduct the preliminary testing on the final pilot bridge in February 2011. Long-term monitoring systems have been installed on four of the seven bridges with systems planned for the remaining three. The focus of this paper will be on the pilot bridges located in Utah, California, and Minnesota. These three bridges are located west of the Mississippi river and therefore fall under the responsibility of Utah State University to conduct preliminary testing and long-term monitoring.

[1] Research Engineer, Department of Civil and Environmental Engineering, Utah State University, 4110 Old Main Hill, Logan Utah 84322; PH (435) 797-3827; email: steven.petroff@usu.edu
[2] Associate Professor, Department of Civil and Environmental Engineering, Utah State University, 4110 Old Main Hill, Logan Utah 84322; PH (435) 797-3179; email: marv.halling@usu.edu
[3] Associate Professor, Department of Civil and Environmental Engineering, Utah State University, 4110 Old Main Hill, Logan Utah 84322; PH (435) 797-8249; email: paul.barr@usu.edu

UTAH PILOT BRIDGE

Bridge Description

The Utah Pilot Bridge is a single span, pre-cast, pre-tensioned, bulb-tee concrete girder bridge. The bridge carries two lanes of northbound I-15 traffic over Cannery Street in Perry, Utah. The bridge is located approximately 97 km (60 miles) north of Salt Lake City, Utah. It was built in 1976. The deck is made of 203 mm (8 in.) thick reinforced concrete with a varying asphalt overlay ranging from 152 mm (6 in.) to 203 mm (8 in.). The total clear span length of the bridge is 24.38 m (80 ft) with actual girder lengths of 25.15 m (82.5 ft). The bridge has a total width of 13.56 m (44.5 ft) and a roadway width of 12.8 m (42.0 ft) comprised of two 3.66 m (12 ft) wide travel lanes, in addition to 1.83 m (6 ft) and 3.66 m (12 ft) wide shoulders. Figure 1 shows an elevation view of the Utah Pilot Bridge



Figure 1: Elevation view of the Utah Pilot Bridge.

Preliminary Testing

Dynamic Testing

Dynamic testing allowed for the determination of the first four modal frequencies and corresponding damping ratios. For the Utah Pilot Bridge, an electromagnetic harmonic shaker was used to provide forced vibrations. This method of excitation was chosen because of its ability to provide highly accurate and known excitations, which improves analysis and determination of modes and frequencies.

A 4-channel data acquisition demonstration version module was used to record sensor response. One of the four channels was used to record the forced vibration input into the bridge. The remaining three channels were connected to 1Hz velocity transducers and used to record the bridge response. The real time FFT, windowing, anti-aliasing, and other controls of the data acquisition module allowed for easy viewing of the bridge response. Multiple testing scenarios were run in order to provide specific information of the bridge and to study the capabilities of the data acquisition module. Analysis of the recorded data yielded information on the first four modes, and their associated frequencies and damping ratios, see Table 1.

Table 1: Dynamic response summary

Mode	Frequency	Damping
1	6.78	4.16%
2	7.86	3.89%
3	9.55	3.49%
4	14.36	2.99%

Live Load Testing

In addition to dynamic testing, a quasi-static live load test was also conducted on the Utah Pilot Bridge. Two heavily loaded, three axle dump trucks were used to provide the load for the test. Due to the high average daily traffic, around 22,000 vehicles per day, a complete closure of the bridge was not possible. UDOT required that the test be conducted on a Sunday morning, when traffic volume was at a minimum. In order to have the testing system ready for the load test, installation of sensors occurred prior to the day of testing. Before testing began, all sensors were checked to verify they were reading properly.

A Bridge Diagnostics Inc. (BDI) wireless structural monitoring system was used to record the bridge response. The system was composed of a base station CPU that communicated with six wireless nodes. Each node was capable of monitoring four sensors. In all, seven deflection sensors and twenty surface mounted strain sensors were monitored throughout the test. At each strain gauge location, two gauges were installed vertically over the height of the girder. One strain gauge was installed on the bottom flange of the girder and one was installed at the top of the web, as shown in Figure 2. Figure 3 shows a plan view of the bridge with the locations of installed sensors.

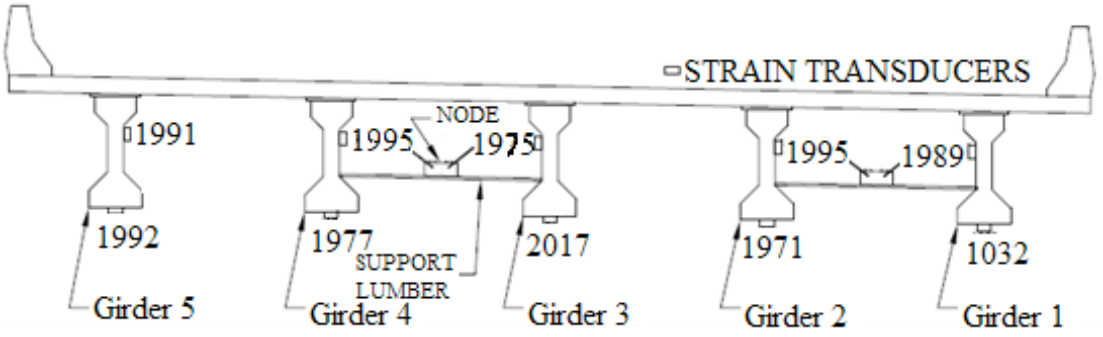


Figure 2. Cross-sectional view of Section A-A with gauge identification numbers.

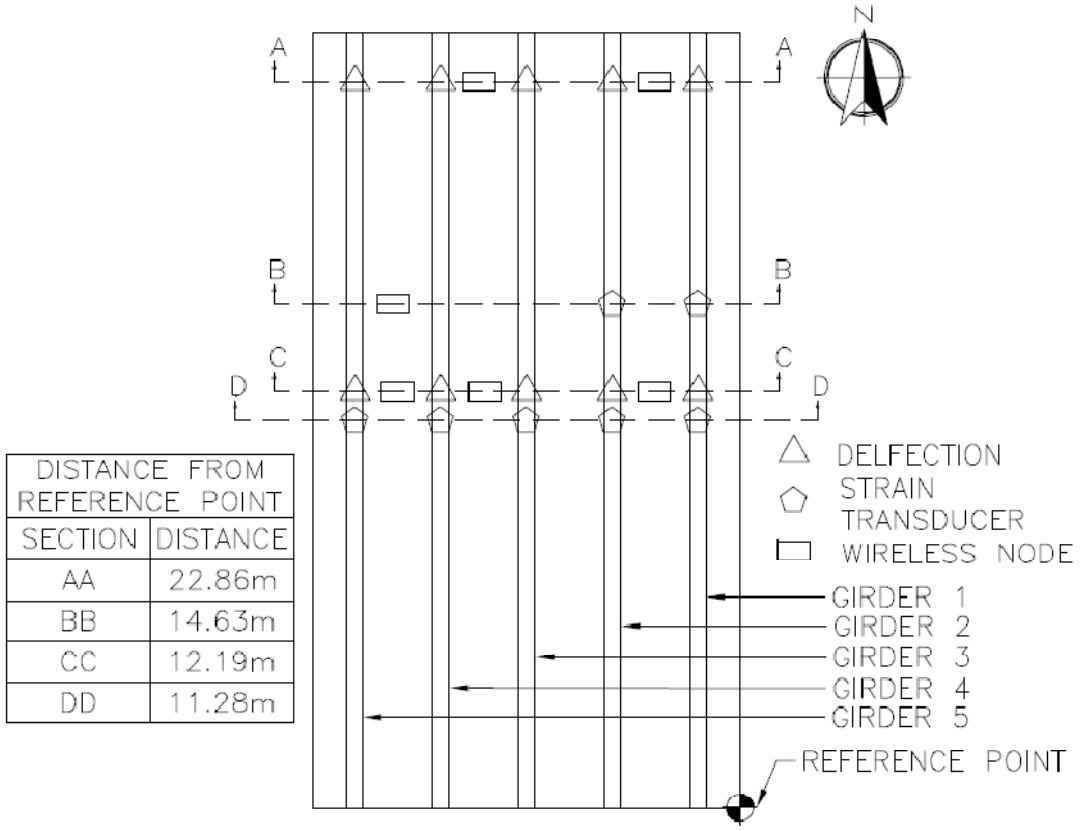


Figure 3: Plan View of instumenation with sectional divisions.

Additional Preliminary Tests

Other tests conducted on the Utah Pilot Bridge included NDE/NDT, material testing, and a detailed visual inspection. The NDE/NDT and material testing focused their scope to deck evaluation. Due to the thick asphalt overlay, the NDE/NDT tests did not produce useable results. Material testing required the removal of the asphalt overlay to access the concrete deck. Individual tests on the deck through the material testing included: chloride ion penetration, half-cell potential, corrosion resistance, and Schmidt Hammer testing.

Long-Term Monitoring Plan

Following the preliminary testing and evaluation, an instrumentation plan was developed to monitor long-term bridge response. Preliminary testing provided essential information for determining the sensor type, quantity and location. The final decision of make and model of instrument to use was based on the type of information desired for a particular response category. Sensors chosen included velocity transducers, foil strain gauges, vibrating wire strain gauges, tilt meters, thermocouples, weather station, and a traffic camera. The weather station includes an ambient air temperature probe, relative humidly probe, solar radiation pyranometer, a wind speed/direction anemometer, and a precipitation gauge that records if a precipitation event is occurring and the duration of the event. The traffic camera is capable of high quality streaming data, recording video footage and still shots based on a triggered event. All data is remotely accessible via an internet connection. Power

for the system is provided via solar panels and a battery backup array. The data acquisition system is a Campbell Scientific CR5000 with an AM16/32B multiplexer, an AVW200 Vibrating Wire Spectral Analyzer, and a wireless CalAmp 882 CDMA Cellular modem. The weather station, traffic camera, and solar panels are installed on an instrumentation tower. The tower is secured to a solid foundation and is adjacent to the instrumentation cabinet, as shown in Figure 4.



Figure 4: Left: Instrumentation tower, box, and fence. Right: Data Acquisition box.

CALIFORNIA PILOT BRIDGE

Bridge Description

Constructed in 1975, the California Pilot Bridge carries two lanes of southbound I-5 traffic over Lambert Road. Lambert Road is located in Sacramento County, approximately 50 km (30 miles) south of the city of Sacramento. This portion of I-5 is located on an important connecting route between Sacramento and San Francisco. For that reason, the average daily traffic on the structure is 25,000 vehicles per day with approximately 21% of that being attributed to truck traffic.

The bridge superstructure is a two span, cast-in-place, post-tensioned, box-girder structure. Span length is 39.62 m (130 ft) long for a total of 79.25 m (260 ft). The bridge has a skew of 8°. A single pier at midspan supports the bridge. The deck is 203 mm (8 in.) thick and made of reinforced, cast-in-place concrete with a clear polymer overlay. The roadway width is 12.8 m (42 ft) with two 3.66 m (12 ft) wide travel lanes, and 1.83 m (6 ft) and a 3.66 m (12 ft) wide shoulders. Figure 5 shows an elevation view of the bridge looking from the west to the east.



Figure 5: Elevation view of California Pilot Bridge.

Preliminary Testing

Dynamic Testing

Following the success of the Data Physics demonstration module used for the dynamic test of the Utah Pilot Bridge, an 8 channel data acquisition system was used for the dynamic test on the California Pilot Bridge. This increase in sensor capacity allowed for more simultaneously monitored channels during each test setup. No lane closures were needed to conduct the dynamic test on the California Pilot Bridge. In contrast to the Utah Pilot Bridge, all the instruments were placed inside of the box girder cells, as seen in Figure 6, thus providing safe access for the researchers at all times, regardless of the traffic on the bridge deck. The electromagnetic harmonic force shaker, used to provide the necessary excitation, was also located inside one of the box girder cells.

One challenge that was prevalent during the dynamic test was the difficulty in filtering out the heavy impact of truck traffic on the bridge. Since there were no lane closures, on the bridge during the dynamic test, traffic flowed at the posted freeway speed limit. This created a considerable amount of noise that required rigorous filtering and windowing in the data analysis software. Test settings were selected that used tight filtering around specific frequencies, multiple averages, and a very small frequency step for the shaker excitation. These settings reduced the magnitude of noise after the test.



Figure 6: View of shaker and instruments inside box girder cell.

Live Load Testing

For the California Pilot Bridge a combination of quasi-static and dynamic live load tests were performed. Two different types of heavily loaded trucks were used to provide the load for the test. A three-axel super dump truck was used in combination with an 18-wheel side dump. Both were loaded to the legal limit for their axle configurations. Due to the high average daily traffic a complete closure of the bridge was not possible. However, Caltrans and the California Highway Patrol allowed for a controlled slow down that provided windows of eight to ten minutes of no traffic on the bridge. During each testing window, trucks were positioned on the bridge according to predetermined load paths and slowly driven across the structure.

A Bridge Diagnostics Inc. (BDI) wireless structural monitoring system was used to record the bridge response. The system was composed of a base station CPU that communicated with fourteen wireless nodes. Each node was capable of supporting four sensors. On this bridge, a total of eight deflection sensors, forty-two surface mounted strain sensors, two string-pot displacement sensors, and one uniaxial rotation sensor was used. Figure 7 shows the bridge instrumentation plan.

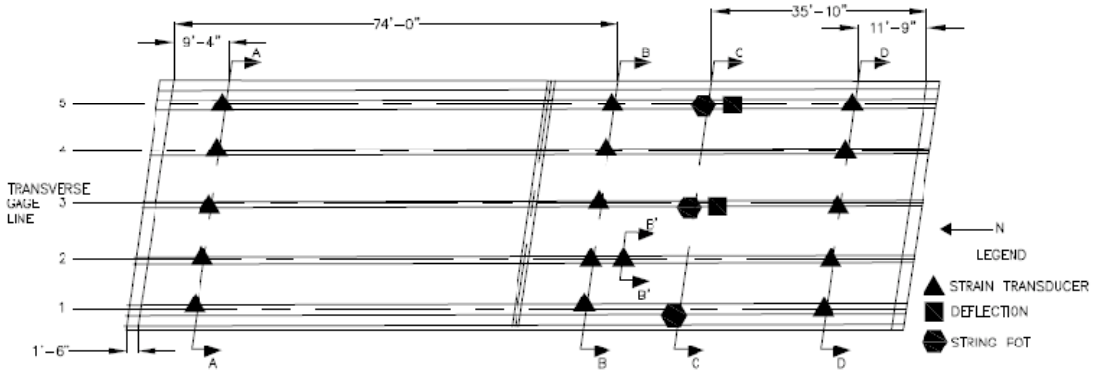


Figure 7: Instrumentation plan for California Live load Testing. Top figure is North Span, bottom figure is South span.

Additional Preliminary Tests

Other preliminary tests and evaluations conducted on the California Pilot Bridge include NDE/NDT, material testing, and a detailed visual inspection. The NDE/NDT and material testing focused their scope to deck evaluation. The thin polymer over lay initially applied on the bridge deck was essentially worn off over most of the bridge, especially in the travel lanes. This allowed for all testing to be conducted directly on the exposed, bare concrete deck. Additional nondestructive testing was conducted to determine voids in the post-tensioned ducts.

Long-Term Monitoring Plan

The California Pilot Bridge long-term monitoring plan was developed after the initial testing was performed. Preliminary testing provided valuable information for determining the sensor type, quantity and location. Sensors chosen were similar to those of the Utah Pilot Bridge and include velocity transducers, foil strain gauges, vibrating wire strain gauges, tilt meters, thermocouples, and a traffic camera. The traffic camera is capable of high quality streaming data, recording video footage and

still shots off a trigger, and remotely accessible via an internet connection. Power for the data acquisition system is provided via an AC connection.

The data acquisition system is a Campbell Scientific CR5000 with three AM16/32B multiplexers, an AVW200 Vibrating Wire Spectral Analyzer. The CR5000 was chosen because of its high frequency sampling rate and capability to run multiple sensors with varying types of measurement protocols. The multiplexers were used to expand the channel capabilities of the CR5000 for thermocouple, tilt meter, and vibrating wire strain gauge sensors. A single program controls the sampling rate, type, and analysis processing for each of the sensors.

Overall, the California Pilot Bridge was instrumented with sixteen foil strain gauges, four vibrating wire strain gauges, four velocity transducers, three tilt meters, fourteen thermocouples placed adjacent to fourteen foil strain gauges, and a total of twenty thermocouples installed over the depth of the deck at two locations. Sensor locations are distributed across the length of the bridge as well as along the exterior and the interior of two of the cells. Locations were chosen based on the analysis of the preliminary test data. Figure 8 shows a typical sensor location for an interior and exterior installation. The traffic camera is installed on an instrumentation tower located approximately 15.24 m (50 ft.) south of the south bridge abutment.



Figure 8: Typical monitoring sensor location at California Pilot Bridge.

MINNESOTA

Bridge Description

The Minnesota Pilot Bridge is located approximately 145 km (90 mi.) north of Minneapolis, Minnesota. The bridge carries State Road 123 over the Kettle River.

State Road 123 runs through the town of Sandstone, Minnesota. The bridge is listed on the Minnesota Historical Bridge inventory and much of the land under the bridge is part of a state park. These two factors stress the importance that this bridge and location have on the people of Minnesota.

The structure is 122 m (400 ft) long and 12.2 m (40 ft) wide. The original deck was 146 mm (5.75 in.) thick with a 76 mm (3 in.) bituminous overlay. In 1984, the deck was replaced with a 178 mm (7 in.) thick reinforced concrete deck with a thin polymer overlay. The south side has a large parapet section for a sidewalk and higher railing. The original design had a 102 mm (4 in.) diameter gas line passing through the sidewalk. In the 1984 reconstruction, the gas line was moved to a location under the first interior girder from. The sidewalk is 1.27 m (5 ft) wide. The deck carries two 3.66 m (12 ft.) wide travel lanes and two 1.22 m (4 ft) wide shoulders. Figure 9 shows a cross-sectional view of the deck and parapets and Figure 10 shows an elevation view of the bridge.

As seen in Figure 10, the bridge superstructure is pinned at two intermediate supports, each 30.5 m (100 ft) from either end of the bridge. The main span has a total length of 61 m (200 ft). There are piers on either side of the river. The east most pier is supported on an elastomeric bearing whereas the west support is pinned. Expansion joints are located at both ends of the bridge, as seen in Figure 10. Figure 11 is a photograph of the Minnesota Pilot Bridge.

Constructed in 1948, the Minnesota Pilot Bridge was designed as a truss arch bridge. Maintenance records document a complete remodeling and overhaul of the entire structure in 1984. Since that time, typical maintenance has been performed on the bridge.

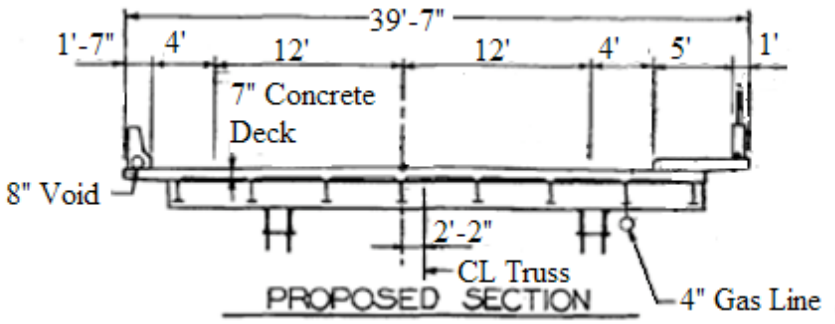


Figure 9: Scross-sectional view of the Minnesota Pilot Bridge

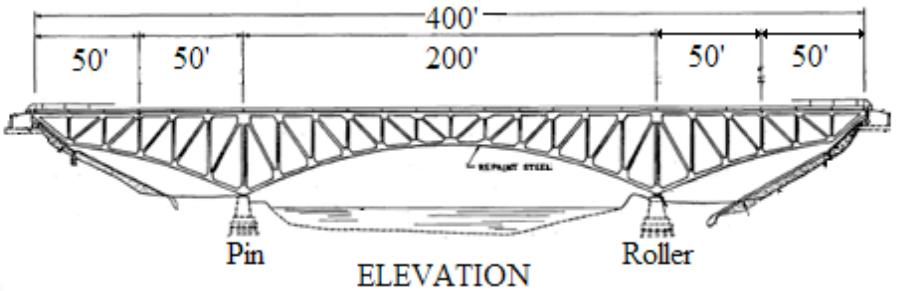


Figure 10: Elevation view of the Minnesota Pilot Bridge



Figure 11: Photograph of the Minnesota Pilot Bridge.

Preliminary Testing

Dynamic Testing

In order to accurately monitor the dynamic response of this relatively large structure, a data acquisition system capable of recording 24 channels was used. The system provided the necessary input variables for controlling the type of test and an easy to read real-time output for system verification. The average daily vehicle traffic on this bridge is relatively low, approximately 2,000 which allowed for fairly easy filtering, windowing and anti-aliasing of data. The greatest disturbance to dynamic measurements during the day was the presence of two large under bridge inspection trucks. The engines from these trucks created a large harmonic vibration that required very tight filtering to eliminate the influence of the trucks on the data. For this reason, testing through the night proved to yield the highest quality data. Researchers were able to conduct multi-hour tests with essentially no traffic on the bridge. During those tests, coherence between the electromagnetic shakers and sensors was consistently above 0.95.

Three shaker orientations were used to determine the maximum number of modes. The shakers were first oriented to vertically excite the bridge. Following that, two variations of horizontal shaking were applied. The first was a purely transverse loading. The second had the shakers oriented at 45°, to excite transverse and longitudinal modes. Interestingly, the orientation of 45° produced the greatest information for transverse modes. In total, nine distinct modes were identified. Table 2 contains a summary of this modal information.

Table 2: Summary of Minnesota Dynamic Test Results

Mode #	Frequency	Run Used	Prominent Direction	Damping Ratio
1	1.71	44	Transverse	1.46
2	2.44	20	Vertical/ Longitudinal	2.43
3	3.76	11	Vertical	0.96
4	4.37	47	Transverse	2.46

5	5.04	12	Vertical	0.71
6	5.53	22	Vertical	1.64
7	6.46	6	Vertical	2.63
8	7.67	13	Vertical	0.90
9	9.76	14	Vertical	0.57
10	10.16	14	Vertical	0.81

Live Load Testing

A joint effort between USU and Bridge Diagnostics Inc. (BDI) was employed to conduct the live-load test on the Minnesota Pilot Bridge. The reason for a joint effort was due to the large size of the structure and the need for a large amount of instrumentation on the structure. Researchers at USU worked jointly with BDI to assist in developing an installation plan for the bridge and in carrying out the test. BDI supplied a testing system that included 128 total sensors distributed across the North Truss, South Truss, and Floor System of the bridge. USU supplied another system with an additional 32 sensors, distributed in an area that covered the western third of the bridge structure. In all, the data acquisition system consisted of 160 strain sensors and ten displacement transducers.

Loading for the test was provided by two large under bridge inspection units (UBU's). These units were already on site to provide access for the visual inspection and instrument installation where a ground based boom lift was not adequate. During the test, these trucks were driven into position and slowly driven across the bridge. Uninterrupted access of the bridge deck was allowed due to controlled closures of the bridge travel lanes for periods of ten to fifteen minute intervals. Traffic control was set up at both ends of the bridge and coordinated closure of the traveling lanes with researchers conducting the live load test. Figure 12 shows the two trucks used for loading during the live load test.



Figure 12: Trucks driving across the Minnesota Pilot Bride during the Live-Load test.

Additional Preliminary Tests

Other preliminary tests conducted on the Minnesota Pilot Bridge include NDE/NDT, material testing, and a detailed visual inspection. The NDE/NDT and

material testing focused their scope to deck evaluation whereas the visual inspection was performed for the entire structure.

Long-Term Monitoring Plan

Though still in its preliminary approval stage, a plan for the long-term instrumentation of the Minnesota Pilot Bridge has been designed. An overview document has been sent to the MnDOT for approval and comments. Initial reviews of the plan have been very positive. The plan proposed by the LTBP team will include a combination of foil strain gauges, tiltmeters, vibrating wire strain gauges, velocity transducers, thermocouples, deck thermal gradient devices, linear displacement sensors (joint, bearing, and structure expansion), and a traffic camera.

Similar to the Utah and California Pilot Bridges, a data acquisition system capable of both dynamic and static measurements will be used. It is anticipated that multiple multiplexers and vibrating wire interfaces will be used to efficiently record the sensor readings from the many instruments planned for installation. An instrumentation tower is expected to be installed west of the bridge to house the traffic camera.

CONCLUSION

As part of the Federal Highway Administration's (FHWA) Long Term Bridge Performance Program (LTBP), Utah State University was contracted to perform initial testing on three bridges located in Utah, California and Minnesota. The responsibility of USU was to conduct a Live Load test, a Dynamic test, prepare a Long-Term Monitoring plan, and carry out the long-term monitoring.

Results from the initial testing provided a current estimation the current bridge structural health. Long-term monitoring is currently underway. Early monitoring results show excellent comparison with preliminary testing results. Changes in future bridge behavior will be used to determine long-term trends for bridge performance.

ACKNOWLEDGEMENTS

This publication was supported by a subcontract from Rutgers University, Center for Advanced Infrastructure & Transportation (CAIT), under DTFH61-08-C-00005 from the U.S. Department of Transportation – Federal Highway Administration (USDOT-FHWA). Any opinions, findings, and conclusions or recommendations expressed in this publication are those of the author(s) and do not necessarily reflect the views of Rutgers University or those of the U.S. Department of Transportation – Federal Highway Administration.

The authors would also like to acknowledge the cooperation and assistance of personnel from the Transportation departments of Utah, California, and Minnesota.

Data-driven methods for threshold determination in time-series based damage detection

Ruigen Yao, Graduate Student, Department of Civil and Environmental Engineering, Lehigh University, Bethlehem, PA 18015. ruy209@Lehigh.edu
Shamim N. Pakzad, Assistant Professor, Department of Civil and Environmental Engineering, Lehigh University, Bethlehem, PA 18015. pakzad@Lehigh.edu

ABSTRACT

Structural vibration monitoring has received a lot of attention from the research community in the past few years. The objective is to create automatic structural assessment techniques that can be realized through programmed vibration analysis. Till now many vibration-based damage features have been proposed, yet to truly automate the damage identification process, reliable damage threshold construction techniques are also need. In this paper, two data-driven methods based on resampling and nearest neighbor rule are applied for threshold construction for damage features from autoregression (AR) analysis of vibration signals. Both threshold calculation techniques are rooted in empirical feature probability estimation. The proposed thresholds are then tested on features extracted acceleration measurements collected from a 5 DOF test specimen. The resampling method is applied to Mahalanobis distance of AR model coefficients, while the nearest neighbor rule is used on a combination of coefficient distance feature and the residual autocorrelation feature. Both methods perform well in this case study.

KEYWORDS: Structural health monitoring; damage detection; time series analysis; autoregressive modeling; statistical pattern recognition; Mont Carlo method.

INTRODUCTION

For years researchers have been working on automatic damage detection in the hope of reducing a structure's maintenance cost by minimizing human involvement in the process. The rapid development in vibration data acquisition systems for the infrastructure has stimulated a vast interest in vibration-based damage detection and structural assessment, and accordingly a lot of literature are produced [Doebling et al. 1998]. Modal properties are among the earliest damage indicators adapted to this end [Alvin et al. 2003; Doebling 1998], but were found to be insensitive to local damage

and computationally expensive. Recently, time series analysis for vibration signals is being investigated in hope of establishing a more sensitive vibration-based damage detection approach [Farrar et al. 1999].

Time series analysis techniques have long been applied to fault detection in mechanical systems [Fassois and Sakellariou, 2007] before they were introduced into the field of civil engineering. This is essentially a data-driven approach that will 'let the data speak for itself'. The general strategy of time- series based damage detection includes five steps: 1) obtain data from baseline/healthy state structure; 2) extract a statistical quantity/damage feature Q from the data via time series analysis; 3) obtain data from current/unknown state structure; 4) extract the Q quantity from the data using the same method; 5) compare Q from the unknown state with that from baseline state using hypothesis testing. If the difference is statistically significant, the system is deemed damaged. The critical quantity Q can be a function of estimated time series model properties or signal spectrum.

Several time-series analysis methods have already been employed to identify damage in civil structures [Sohn and Farrar, 2001; Worden and Manson, 2007; Gul and Catbas, 2009]. The results reported in these papers are encouraging, since structural damage does result in a substantial change in the Q quantity in all cases. The main problem is that the extracted Q quantity can be affected by many other non-relevant factors such as environmental noise and excitation levels, and will suffer some oscillation even when the structural conditions remain the same. Therefore, it is important to set the damage threshold properly such that the number of false alarms and missed cases is minimized.

Statistical hypothesis testing [Koch 1999] is the recognized standard approach for threshold determination. It assumes that the features follow a certain probability distribution, and the threshold is set at a point beyond which the chance for a feature value to occur is small. This approach is theoretically optimal as long as the assumed feature distribution is valid. Hypothesis testing may do well for fault identification in machinery, as the excitation force is well known and the damage types are well-defined. For civil engineering applications, however, there are more uncertainties. When the probability distribution of damage features are too complex to be accurately represented by analytical distribution functions available, threshold constructed using hypothesis testing will yield poor results in damage identification and an alternative approach is needed.

In this paper a data driven threshold determination scheme using cross-validation and resampling techniques [Good, 1999] will be introduced and applied to the Mahalanobis distance [Mahalanobis 1936] feature described in Section 2. This feature is shown to be unstable, and its distribution is unknown. Yet the data-driven method

still yields an effective threshold. Also the Mahalanobis distance feature is paired with the autocorrelation feature to improve the damage detection performance of time-series based methods. A nearest-neighbor approach [Duda et al. 2000] is used to set the significance threshold for the feature pair.

The paper is organized as follows: Section 2 is dedicated to a brief review of time-series analysis techniques for damage detection. The damage features can be obtained from either autoregressive (AR) model coefficients or AR model residuals, and hypothesis tests are devised according to their respective theoretical distributions.

In section 3, new data driven approaches for threshold determination are presented. Section 4 contains an application of the Mahalanobis distance feature to detect damage in a lab specimen, and the results using the new threshold construction scheme are presented. Section 5 includes a discussion of feature combination and its application to the same specimen as in section 4.

DAMAGE DETECTION METHODS USING TIME SERIES ANALYSIS

Autoregressive (AR) model is perhaps the most widely adopted time series analysis tool [Brockwell and Davis, 2002]. The definition of a univariate AR model of order p is as below:

$$x(t) = \sum_{j=1}^{p} \phi_{xj} x(t-j) + \epsilon_x(t). \quad (1)$$

In this equation, $x(t)$ is the time series to be analyzed, ϕ_{xj} are the AR model coefficients, and $\epsilon_x(t)$ is the model *residual*. This model basically attempts to express the value of signal at time t as a linear combination of its previous values up to lag p.

According to classical structural dynamics theory, the discretized structural response under random excitation can always be approximated by an AR process of large order. Damage features from AR modeling can be grossly divided into two categories; model coefficients based and model residual based. AR model coefficients can be estimated directly from the data using one of the standard algorithms, and the residual sequence can henceforth be obtained from eqn. (1). In the remainder of this section, two damage features, one from each category, will be presented.

Mahalanobis distance of AR model coefficients

It has been proved that if the signal is really an AR process, then any regular coefficients estimator$\{\phi_{xj}\}$ from the signal is asymptotically unbiased and normally distributed with covariance matrix $\sigma_e^2\Gamma_p^{-1}$[Brockwell and Davis, 2009]. Therefore, a metric that represents the deviation in the probability space of normal distribution seems a good choice of damage feature. Mahalanobis distance is such a metric defined from the definition of multivariate normal distribution. The estimator of the Mahalanobis distance between a potential outlier vector x_ξ and baseline sample set can be obtained as

$$D_\zeta = (x_\xi - \bar{x})\hat{\Sigma}^{-1}(x_\xi - \bar{x}).$$

where $\bar{x}$ is the average of the baseline sample feature vectors, and $\hat{\Sigma}$ the estimated covariance matrix. When applying this method, the baseline signals are first segmented (often with large overlap) and for each segment an AR coefficient vector are estimated. Signals from current structural state are processed likewise and for each coefficient vector obtained its Mahalanobis distance to the baseline coefficients set will be computed. These Mahalanobis distance features are then compared with the Mahalanobis distances within baseline set. When the structural system is damaged, it is expected that the Mahalanobis distance feature for AR coefficients will increase significantly (Fig 1).

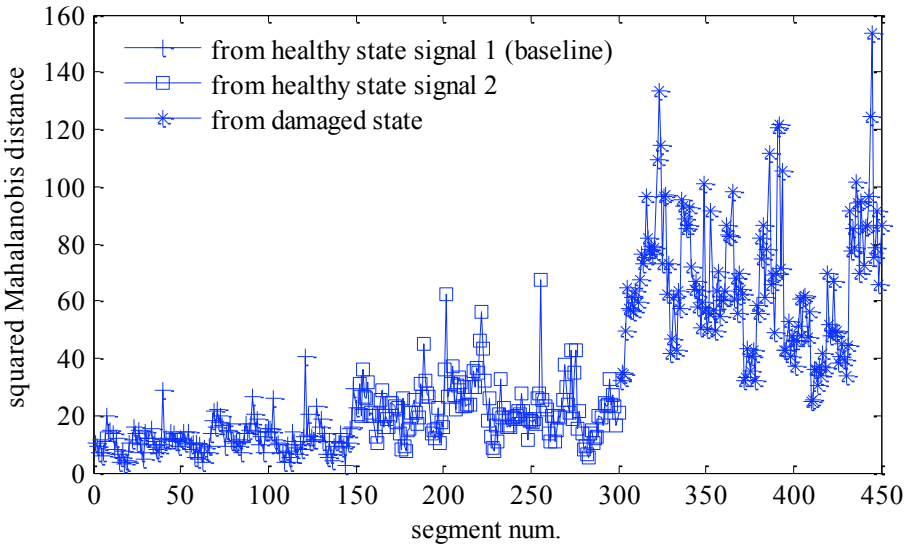


FIG. 1. MAHALANOBIS DISTANCE OF MODEL COEFFICIENTS. SEGMENT SIZE IS 350. THE OVERLAP BETWEEN CONSECUTIVE SEGMENTS IS 300.

Auto-correlation function (ACF) of AR model residuals

It is clear from (1) that if the AR model used to filter the signal is the same as the model from which the signal is generated, the residual series should be a white noise. Otherwise, the residual series will carry certain identifiable patterns that can be captured by its autocorrelation function. ACF can be estimated from residual sequence as:

$$\hat{\rho}(\tau) = \frac{\sum_{i=1}^{i=N-\tau+1}[\epsilon(i+\tau)-\bar{\epsilon}]\,[\epsilon(i)-\bar{\epsilon}]}{\sum_{i=1}^{i=N}[\epsilon(i)-\bar{\epsilon}]^2}.$$

From the baseline signal a baseline AR model can be estimated, which will then be fitted to new signals from unknown structural state. If the structural condition is unchanged, the ACF will resemble a Dirichlet delta function. It can be shown that for large N the sample autocorrelations of a white noise sequence at nonzero lags are approximately identically and independently distributed $N(0,1/n)$ [Brockwell and Davis, 2009], hence the 95% confidence bounds can be drawn at $\pm 1.96/\sqrt{n}$, as 1.96 is the .025 quantile of the standard normal distribution. Accordingly, the system can be identified as damaged when the number of ACF function value outside the bounds become statistically significant (Fig.2).

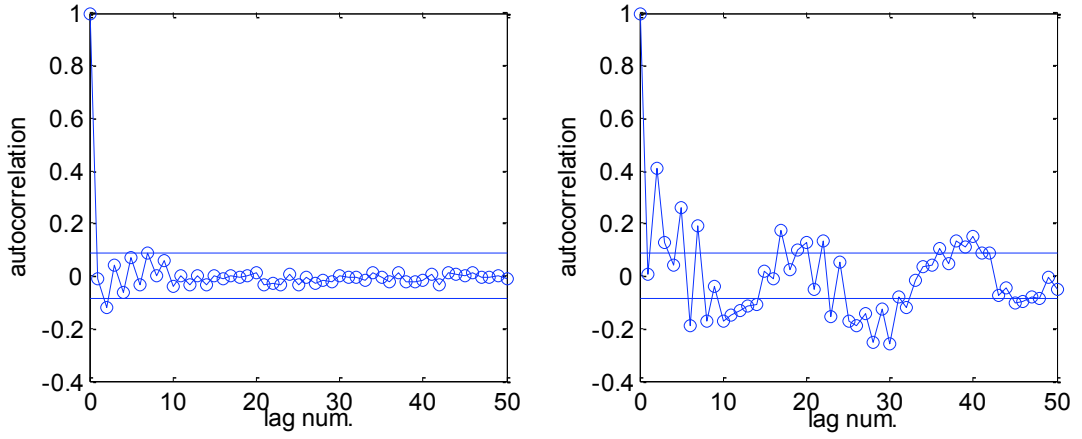


FIG. 2. RESIDUAL AUTOCORRELATION AS DAMAGE INDICATOR; LOTS OF OUTLIERS APPEAR WHEN MODEL NO LONGER FIT THE DATA WELL. THE LENGTH OF RESIDUAL SEQUENCE IS 520.

THRESHOLD CONSTRUCTION SCHEMES FOR DAMAGE FEATURES FROM TIME SERIES ANALYSIS

A desirable threshold is one that strikes up a balance between false alarms and missed cases. Now in most engineering practices this value is determined in an *ad hoc*

manner. Statistical hypothesis testing has been tried for automatic threshold construction, but its effectiveness is not guaranteed unless the actual feature distribution is the same as assumed. Here, tow data-driven methods will be introduced for threshold construction.

Threshold calculated from resampling: the 'cross-one-out' method

From Fig. 2 it is clear that the Mahalanobis distance feature suffers from large fluctuations within the baseline sample set. Also, when the baseline samples are extracted from vibration signal segments with overlap, the sample set is in fact not a very good representation of the actual feature probability space. Therefore, hypothesis testing exploiting the multivariate normal distribution will tend to yield a conservative threshold.

The first problem is perhaps resulted from environmental variations and statistical modeling and estimation deficiencies and cannot be helped; one solution to the second problem is to use vibration signals without overlap for feature extraction. However, when the data available is limited, this method is not practicable.

To address this problem here a 'cross-one-out' resampling technique is adopted. First a segment is cut from the baseline signal at a random time point and reserved for testing, and sample segments of the same size are cut with a preset overlap from the remaining signal. The Mahalanobis distance between the AR model coefficients of left-out segment and those of the sample set is then computed and stored. This process is repeated for a large number of times and the value beyond which 5% of the tests occur is used as threshold in subsequent analysis. This is essentially an estimation of the feature distribution by recomputing the statistic for many a time by leaving out a certain portion of observation, and can be viewed as a combination of jackknife and cross-validation technique [Shao and Tu, 1995].

Other methods have been proposed for threshold determination of Mahalabnobis distance feature; a Monte Carlo method has been used [Sohn, 2001] to produce the desired threshold by calculating the 5% quantile of empirical feature distribution of simulated coefficient vectors whose components are drawn independently from standard normal distribution. However, as noted in previous text, the AR coefficients are not mutually independent and may not have a unit variance. The assumption of this simulation is not well-grounded, thereby this approach is not used here though reported successful in a couple of literatures.

Empirical density estimation for multiple features; the nearest neighbor rule

Threshold determination becomes complicated when there is more than one feature in the algorithm. Fortunately, the nearest neighbor rule (Fig. 3) provides an intuitive way for empirical density estimation, from which damage threshold can be derived.

Suppose a dataset $\{x_i\}$ is generated from a certain probability distribution $p(x)$, then an empirical estimate of the probability density at x_i can be obtained exploiting the condition below

$$\hat{p}(x_i) \propto 1/\min d^n(x_i, x_j) \ (i \neq j).$$

Here n stands for the feature vector dimension, and (x_i, x_j) is the distance between point x_i and x_j. It is clear that the larger the distance from a point to its nearest neighbor, the smaller is its probability to occur.

A decision strategy for multiple features can hence be established as follows; for each feature vector from unknown state, search for its nearest neighbor in the baseline feature set and record the squared Euclidean distance. When the number of feature vectors above threshold exceeds a certain amount, the system is identified as damaged.

Therefore, the only thing remains to be determined for applying this strategy is the threshold value and its corresponding significance level. In the application presented in Section 5, a 5% significance level threshold is used. The threshold value for the test (unknown state) sets is four times the distance value D^* that has 5% of within-baseline nearest neighbor distances above it. This decision is based on following considerations; assume that both baseline and test features follows a same unimodal distribution that decays exponentially with respect to the distance to feature mean, then around 2.5% of the total features will be expected to have squared nearest neighbor distance beyond $2D^*$ given that the baseline and test set are of equal size. Since in the proposed decision strategy only baseline features are used for nearest neighbor search, this will increase the threshold to $4D^*$ because only half of the samples remain. To simply data processing, here the threshold is tested against 5% of the test features instead of 2.5% of the total features. It is but a slight relaxation

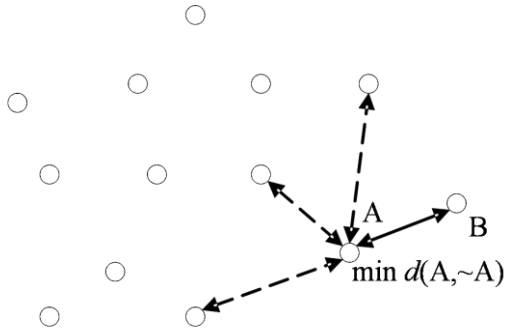


FIG. 3 ILLUSTRATION OF THE NEAREST NEIGHBOR RULE

of conditions, as few of the baseline features will go beyond this critical value.

APPLICATION OF THE RESAMPLING THRESHOLD CONSTRUCTION SCHEME

The damage detection algorithms are applied to acceleration measurements collected from a 5 degree-of-freedom structure (Fig 4) subjected to base excitation. Wired accelerometers are mounted to the shaking table and each floor. Damage is simulated by adding weight to the 4th floor. For each structural scenario, two sets of acceleration signals are recorded from two random excitation experiments. The sampling frequency is 100 Hz for all datasets.



FIG. 4 THE PLEXIGLASS 5 DOF LAB SPECIMEN

Fig 5 displays some of the results from Mahalanobis distance method. (a) is the result from 2nd floor response using threshold from proposed technique; (b) is the result from 4th floor response using threshold from proposed technique; (c) is the result from 4th floor response using threshold from hypothesis testing based on multivariate normal assumption. The significance level in all cases is 5%.

The AR model order adopted is 5, and 350-point segments are cut from acceleration signals with 300 overlap. It is obvious from Fig. 5 (a) and (b) that the change in feature value becomes more prominent at sensing locations more close to structural damage. Also, a comparison between Fig. 5 (b) and (c) shows that the threshold determination technique proposed here does yield a superior performance to that of frequentist hypothesis testing. In all the plots in Fig. 5 logarithmic scale is used for the y axis in order to decrease the oscillation of feature values.

Because in this case a controllable artificial excitation source is used in all the experiments, the overall statistical characteristic of Mahalanobis distance feature does not vary much over time. When this method is applied for damage detection from ambient vibration responses, this feature can become even more unstable. However, this resampling-based technique is still proved reliable in a couple of experiments on a space truss under ambient load, on the condition that there is enough data available.

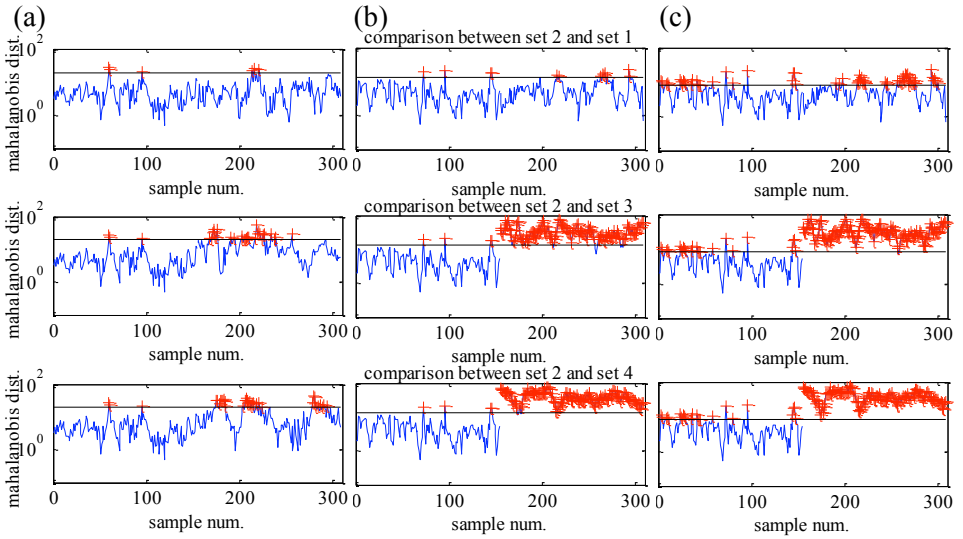


FIG. 5 DAMAGE DETECTION USING THE MAHALANOBIS DISTANCE OF AR MODEL COEFFICIENTS.

FEATURE COMBINATION

Most of the current research on damage detection by time series analysis employs only a single feature, or a set of features from either residual analysis or model parameter analysis. More damage sensitive methods can probably be established by taking features from both categories into consideration, as they in some sense reflect different aspects of the vibration signals. Thus here the two features mentioned in section 2 will be combined for damage identification.

To begin with, two feature pair sets of equal size are extracted from baseline and unknown signal, respectively. The extraction of Mahalanobis distance feature is still the same as before, i.e. for baseline signal feature values are generated using the 'cross-one-out' method introduced in Section 3, and for unknown state signal they are obtained using the routinely procedure described in Section 2. Note here that the logarithm of the distance is used to reduce the oscillation of feature values. Correspondingly, the residual sequence of each signal segment is obtained by filtering each data segment with the AR model estimated from the whole baseline signal. The autocorrelation feature value is then computed from the formula below;

$$Q_2 = \sum_{i=-10}^{10} |\rho(i)|$$

Where $\rho(i)$ is the ACF of the residual sequence. The segment size and overlap length adopted are still 350 and 300.

Fig 6 contains two scatter plots of baseline and test feature clusters extracted from acceleration responses at 4th floor of the lab specimen afore mentioned. Test features in the left plot come from healthy state, while those in the right one are from damaged state. It can be seen that when the structural condition remains same, the two clusters largely overlap each other; when damage has occurred, the test cluster will drift away from the baseline.

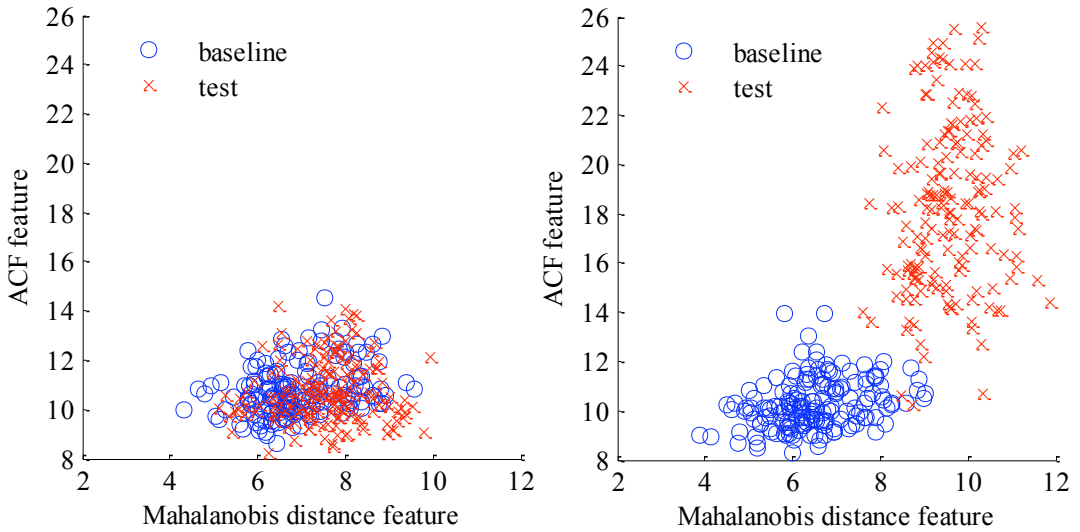


FIG.6 SCATTER PLOTS OF DAMAGE FEATURE PAIRS.

The nearest neighbor scheme is applied here to determine the damage threshold, and the results are summarized in table 1. The value before the slash is the number of outliers, and after the slash is the decision on structural state. The notation in statistical hypothesis testing is used; H_0 denotes healthy state, while H_1 denotes damaged state. Feature variables are all normalized beforehand with respect to the corresponding baseline standard deviation so that contribution of the two features to damage identification is equal. In each comparison the size of both baseline and test set is 166, and the threshold value for the number of outliers is accordingly set at 9. For each sensor location different AR model order is used to better fit the data. The performance of this algorithm is excellent in this case, with only one false alarm for the healthy state and perfect recognition for damaged case. It seems that the responses at 1st and 4th floor are most affected by the simulated damage.

TABLE 1 DAMAGE IDENTIFICATION RESULT USING NEAREST NEIGHBOR SCHEME.

Sensor location / Dataset num.	` 1st floor	2nd floor	3rd floor	4th floor	5th floor
1 (healthy state; baseline)					
2 (healthy state; validation)	$7/H_0$	$7/H_0$	$7/H_0$	$3/H_0$	$14/H_1$
3 (damaged state)	$126/H_1$	$78/H_1$	$32/H_1$	$161/H_1$	$88/H_1$
4 (damaged state)	$112/H_1$	$37/H_1$	$27/H_1$	$159/H_1$	$30/H_1$

CONCLUSION

For this case studies presented in this paper, thresholds based on data driven techniques are proved successful. They tend to generate fewer false alarms than frequentist hypothesis testing, yet still correctly report damage for most tests. All of these techniques employ some sort of empirical density estimation. Although the procedure is somewhat computationally complex, it provides a relatively reliable way to construct thresholds for features with large variation or of unknown distribution and thus automate the process of damage detection.

However, it must be stated that neither improved schemes for threshold construction, nor combination of features, can replace the quest for features that are more stable and damage-sensitive. Features are always the most important topic in damage detection. Adjusting threshold determination methods and combining features can help well-chosen features to perform better, but they cannot save a bad feature from yielding bad performance. Such features based on autoregression on single node response are innately ‘fragile’ because the information is limited and can be affected by other factors. When the loading condition or operation environment of the structure monitored is subjected to change, features based on longer data or data from several sensing locations will probably be more reliable. This will be a good subject for future research.

ACKNOWLEDGMENTS

The research described in this paper is partially supported by the National Science Foundation through Grant No. CMMI-0926898 by Sensors and Sensing Systems program, and by a grant from the Commonwealth of Pennsylvania, Department of Community and Economic Development, through the Pennsylvania Infrastructure Technology Alliance (PITA).

REFERENCES:

[1] Alvin, K. F., Robertson, A. N., Reich, G. W., and Park, K. C., (2003). "Structural system identification: from reality to models." *Computers & Structures.* Volume 81, Issue 12, pp. 1149-1176.

[2] Brockwell, P. J., Davis, R.A. (2002). *Introduction to Time Series and Forcasting*, 2nd ed. Springer, NY

[3] Brockwell, P. J., Davis, R.A. (2009). *Time Series: Theory and Methods*, 2nd Edition, Springer, NY.

[4] Doebling, S. W., Farrar, C.R., and Prime, M. (1998). "A Summary Review of Vibration-Based Damage Identification Methods." *The Shock and Vibration Digest*, Vol. 30, No. 2, pp.91-105.

[5] Duda, R. O., Hart, P. E., and Stork, D. G. (2000). *Pattern recognition*, Wiley-Interscience, 2nd Edition.

[6] Farrar, C. R., Duffey, T. A., Doebling, S. W., Nix, D. A. (1999). A Statistical Pattern Recognition Paradigm for Vibration-based Structural Health Monitoring, 2nd International Workshop on Structural Health Monitoring ,Standford , CA.

[7] Fassois, S. D. and Sakellariou, (2007). J. S, "Time-series methods for fault detection and identification in vibrating structures." *Phil. Trans. R. Soc. A*, Vol. 365, pp. 411-448.

[8] Good, P. I. (1999). *Resampling Methods: A Practical Guide to Data Analysis*, Birkhauser.

[9] Gul, M. and Catbas, F.N. (2009). "Statistical Pattern Recognition for Structural Health Monitoring Using Time Series Modeling: Theory and Experimental Verifications." *Mechanical Systems and Signal Processing*, Vol. 23, Issue 7, pp. 2192-2204.

[10] Koch, K., (1999). Parameter Estimation and Hypothesis Testing in Linear Models, Springer; 2nd Edition.

[11] Mahalanobis, P.C. (1936). "On The Generalized Distance in Statistics." *Proceedings National Institute of Science*, India, Vol. 2, No. 1., pp. 49-55.

[12] Shao, J. and Tu, D. (1995). *The Jackknife and Bootstrap*, New York: Springer-Verlag.

[13] Sohn, H., Farrar, C. R. (2001). "Damage Diagnosis Using Time Series Analysis of Vibration Signals." *Smart Materials and Structures*, Vol.10, No 3, pp. 446–452.

[14] Sohn, H., Farrar, C. R., Hunter, N.F. and Worden, K. (2001). "Structural Health Monitoring Using Statistical Pattern Recognition Techniques." *Journal of Dynamic Systems, Measurement and Control* ,Vol. 123, Issue 4, 706-711.

[15] Worden, K. and Manson, G., (2007). "the Application of Machine Learning to Structural Health Monitoring." *Phil. Trans. R. Soc*, A 365, pp. 515–537.

A CHARACTERIZATION OF TRAFFIC AND TEMPERATURE INDUCED STRAINS ACQUIRED USING A BRIDGE MONITORING SYSTEM

Mustafa Gul[1], H. Burak Gokce[2], and F. Necati Catbas[3]

[1] Post-doctoral Researcher, Department of Civil, Environmental and Construction Engineering, University of Central Florida, Orlando, Florida, 32816; Ph: 407-823-4122, Email: mgul@mail.ucf.edu

[2] PhD Candidate, Department of Civil, Environmental and Construction Engineering, University of Central Florida, Orlando, Florida, 32816; Ph: 407-823-4122, Email: hgokce@mail.ucf.edu

[3] Associate Professor, Department of Civil, Environmental and Construction Engineering, University of Central Florida, Orlando, Florida, 32816; Ph: 407-823-3743; Email: catbas@mail.ucf.edu

ABSTRACT

This study reviews different data analysis approaches to demonstrate possible means for getting information at different levels from the most commonly used strain sensors in an SHM system for short term and long term applications. The different methods are discussed from a real life monitoring study. First, the test bridge is presented with a brief introduction of the monitoring system and the sensor locations. Then, pre-processing and evaluation of raw strain data is discussed to identify the functionality of the installed sensors. Afterwards, strain data characterization by means of traffic and temperature induced strains is shown for more in-depth data analysis techniques. Finally, a new damage identification methodology based on strain correlation is discussed briefly. It is shown that there should be a suite of techniques and features to be available for implementation in SHM systems since one particular technique/feature may not be very reliable or sufficient for a particular case and/or structure.

INTRODUCTION

Structural Health Monitoring (SHM) is the research area focusing on condition assessment of different types of structures. One of the objectives of SHM systems is to provide an automated tool for tracking the health of a structure by combining different sensing technologies and data analysis techniques. As the SHM technology becomes more available and affordable with the recent developments in sensing and computing technologies, the challenges regarding analysis and management of the acquired data also increase.

In the last decades, the aging transportation network has directed the interest of civil engineering community to bridge health monitoring due to the critic nature of these structures. Different studies for bridge health monitoring can be found in literature from different perspectives such as damage detection, reliability, maintenance-cost, structural identification (Brownjohn et al. 1995; Aktan et al. 1996; Enright and Frangopol 1999; Fujino 2002; Catbas et al. 2007).

The implementation of the sensors and data acquisition systems can be considered as the first step for developing an SHM system. The next step is establishing the data collection and data analysis methodologies to assess the condition of the structure. The data analysis methodologies can be utilized for different objectives such as visual checks, statistical analysis, traffic characterization, environmental effect characterization and damage identification. After the data collection and analysis step, the last step for the SHM system is the decision making for repair and maintenance operations. These steps can help the infrastructure owners by indicating the worsening conditions such as graduate deterioration or instantaneous damage. This information which is generated with the help of SHM system can also be used by the owners in scheduling repairs or preventive maintenance to maximize the service life of the structure. Moreover, the root causes of the problems can be identified and future designs can be improved using the information generated using the monitoring system.

Objective and Scope

The objective of this study is reviewing different data analysis approaches to demonstrate possible means for getting information at different levels from the most commonly used strain sensors in an SHM system for short term and long term applications. First, the real life structure is discussed with the monitoring system and the sensor locations. Then, pre-processing and evaluation of raw strain data is discussed to identify the functionality of the installed sensors. Afterwards, strain data characterization by means of traffic and temperature induced strains is shown as fundamental applications for comprehensive data analysis techniques. Finally, a new damage identification methodology based on strain correlation is discussed briefly.

EXPERIMENTAL SETUP AND DATA COLLECTION FROM SUNRISE BOULEVARD BRIDGE (SBB)

The west bound of the Sunrise Boulevard Bridge (SBB) in Ft. Lauderdale, Florida (Figure 1) is selected to implement a comprehensive SHM system. Monitored span of this bascule type movable bridge, which was constructed in 1989, has a total span length of 35.7 m, a width of 16.3 m and carries three traffic lanes. The bridge opens every 30 minutes when requested and usually less than 10-15 times a day.

The instrumentation plan is designed to monitor the most critical electrical, mechanical, and structural components of the bridge. The current installation consists of strain gages, accelerometers, tiltmeters, strain rosettes, pressure gages, etc. with a total number of 162 sensors. In this paper, data from 36 Hitec-weldable-dynamic strain gages (at a data collection rate of 250 Hz) and 36 Geokon low speed vibrating wire strain gages (collecting data every 15 minutes) is used. These strain gages are located on top and bottom flanges of the main girders (48), floor beams (16) and stringers (8). More details about full instrumentation plan can be found in Catbas et al. (2010). The locations for the strain gages and corresponding nomenclatures are given in an inset in Figure 2. For example, WN refers to West North and ES refers to East South. Three pre-scheduled 5 minute-long time slots (morning, early and late afternoons), corresponding to peak hours of operation, are selected for daily high speed data collection. Low speed strain data is collected once in every 15 minutes. In

the following sections different data analysis methodologies will be discussed to extract useful information from high and low speed strain data.



Figure 1: Sunrise Boulevard Bridge (SBB)

PRE-PROCESSING AND EVALUTION OF RAW STRAIN DATA

Visual check of the raw strain data can be considered as the first step to detect non-working and malfunctioning strain gages. This process consists of viewing a graphical representation of real-time or archived data from a sensor channel and inferring from the predicted behavior of that sensor, whether or not that sensor channel is working properly. A common issue with the strain gage is the sensor drift, which can be defined as general trend of the data to shift to higher or lower readings during the collection. It is important to note that the condition of a sensor is not a constant. For example, a once working sensor may become a non-working sensor if it encounters some sort of trauma. For this reason, visual checking of the raw strain data is a continuous process for data quality control. In Figure 2, a video time frame and corresponding strain data coming from EN3 top and bottom flanges are shown. In these plots, it is seen that the strain level is coming back to its original level after the bus crosses the bridge. It should be noted here that visual check of the data may not be feasible in case of an automated SHM system and the above mentioned procedures for checking the data should be automated for such applications.

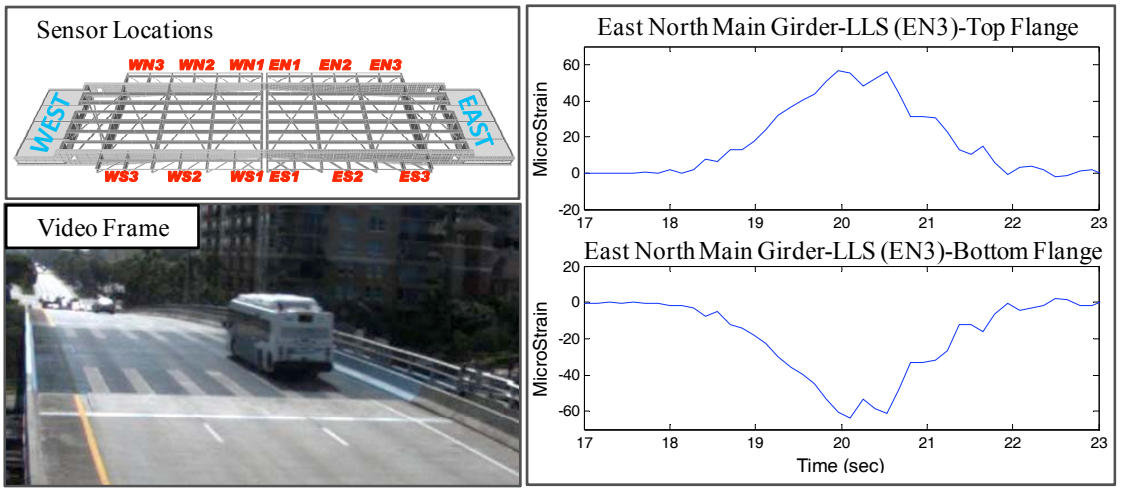


Figure 2: SBB sensor location nomenclature, video frame and corresponding strain data from EN-3

CHARACTERIZING TRAFFIC INDUCED STRAINS

Extracting statistical information, such as maximum, minimum, mean, standard deviation, correlation and root mean square can be considered as another type of data analysis approach, which helps the engineer, not only to understand the data behavior, but also to interpret the data. In addition to these advantages, statistics also help for identification of traffic behavior by identifying the truck induced stress levels, ADTT numbers etc. Figure 3 shows the daily maximum and minimum strains coming from the bottom flange of the East South stringer from the period of October 15 to January 15. Since the stringers are the starting point of the load distribution and have smaller cross-sections, higher strain values at stringers are observed compared to some of the other components such as floor beams and main girders. Higher strain values were observed mainly during the rush hour times of each day. Extreme value distribution can also be obtained using the statistical information about the strain. A three months strain data histogram coming from East South stringer is shown in Figure 4 that can be utilized for system reliability estimation and fatigue analysis.

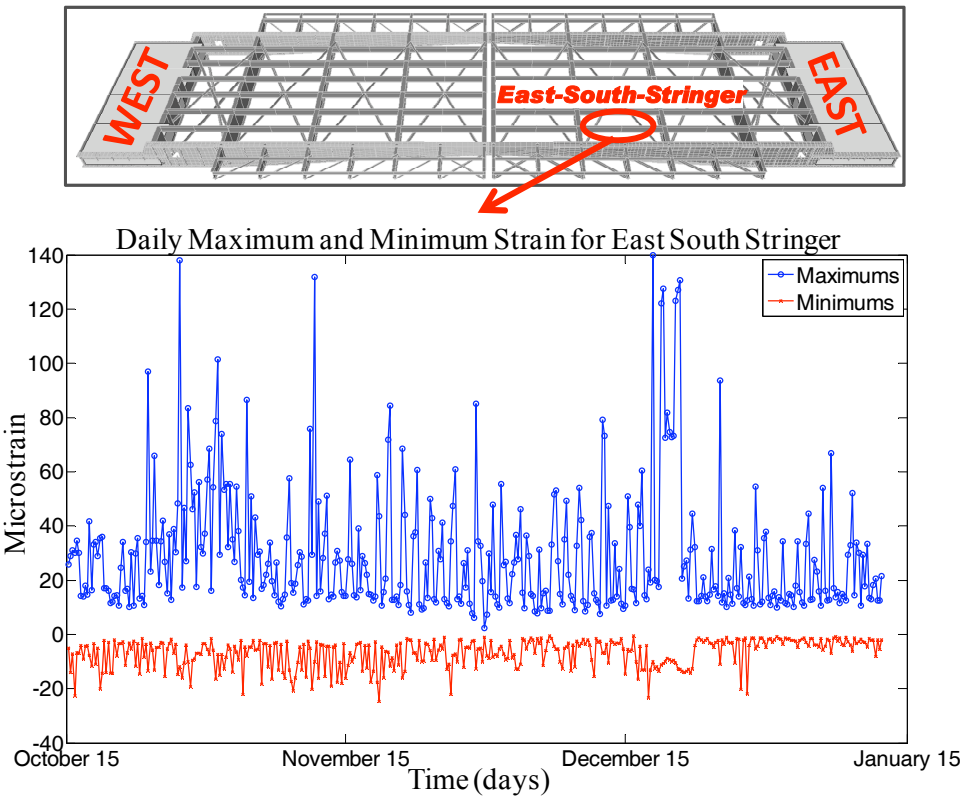


Figure 3: Daily maxima and minima strain for each day from East South stringer

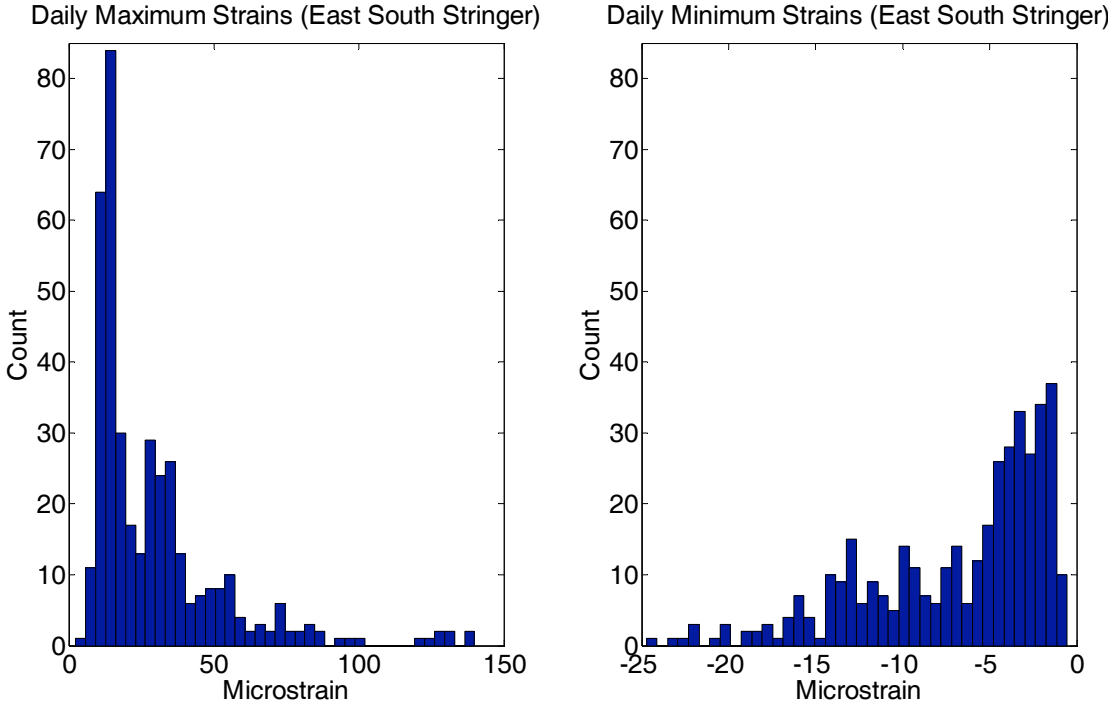


Figure 4:Three months strain data histogram from East South stringer

CHARACTERIZING TEMPERATURE INDUCED STRAINS

Slow speed strain gages were employed to measure stress-induced strain and temperature data simultaneously. Some previous studies showed that the daily or seasonal temperature effects may create critical stress levels, even higher than traffic induced stresses. Therefore, the strain temperature relationship is extremely important for long term monitoring. With a long term strain-temperature data, it is possible to obtain daily and seasonal cycles over the time. Fitting some models to this data may offer an effective tool for prediction of the stress cycles on the structure as well.

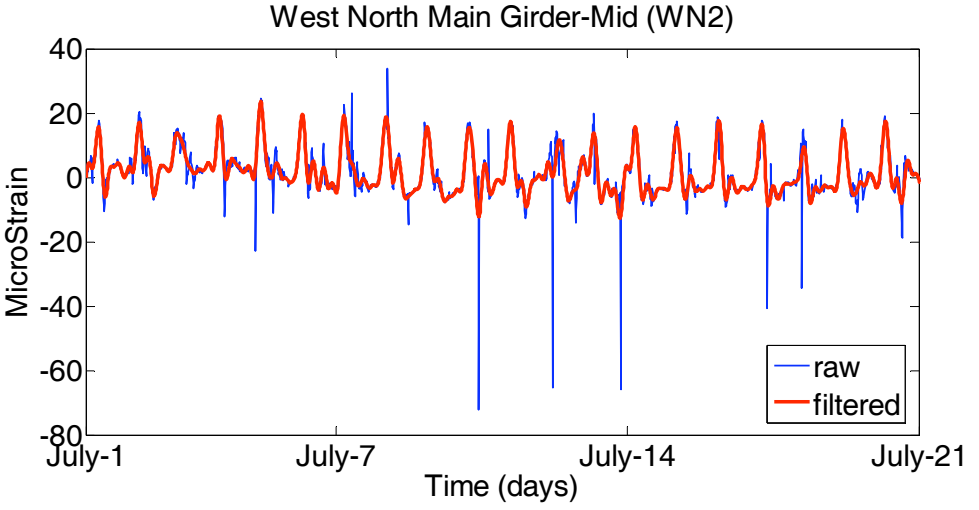


Figure 5:WN2 vibrating wire strain gage raw and filtered data (July 1–July 21)

When the three-week data set, shown in Figure 5, from vibrating wire strain gages was inspected, it was seen that there were some spikes in the data. In a fixed bridge, these can be attributed to vehicular traffic; however, in this case, opening and closing of the bridge was the main reason for these high strain values in addition to possible truck induced effects. These strain values were not created due environmental effects; therefore, filtering these spikes out of the data enabled a better correlation of the temperature and structural response (Figure 6). A low pass filter was designed to eliminate the effects of traffic and opening-closings. These outliers were eliminated to see only the effects due to environment inputs to the bridge. From Figure 6, a 30% strain temperature correlation is seen before filtering the strain data. After filtering the data, the correlation between the strain and temperature is increased to 60% which can be more clearly observed.

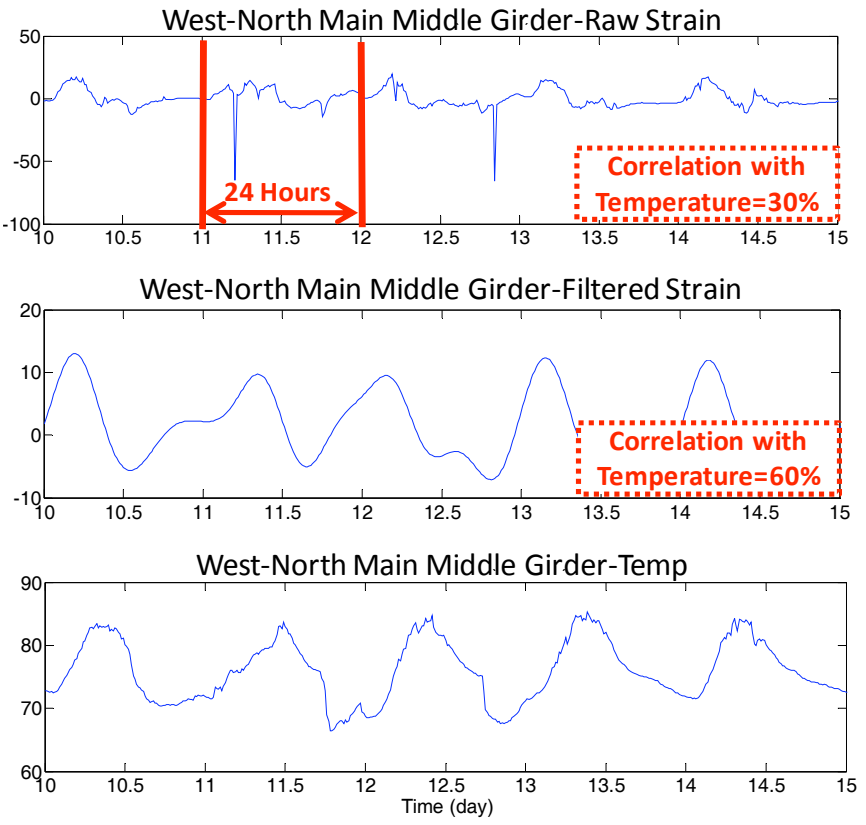


Figure 6:WN2 strain and temperature raw and filtered data (July 8–July 13)

Because of the cyclic nature of the temperature and its correlation with strain, it would be appropriate to investigate the temperature and strain responses by means of Fourier Series with the expansion form as given below.

$$f = a_0 + \sum_{n=1}^{N} a_n \sin(n\omega t) + b_n \cos(n\omega t)$$

The main idea here is to characterize the temperature induced strains and be able to make predictions for the future stress levels of the structure with expected temperatures with this characterization. For this reason, strain and temperature models using Fourier Series with eight terms (*N=8)* can capture the observed daily cycles efficiently as shown in Figure 7. Furthermore, it is seen that the correlation is raised to a level of 80% when the Fourier models of temperature and strain are considered. This increase promises for better characterization of temperature induced strains thereby an accurate strain temperature model can be created with long term monitoring data.

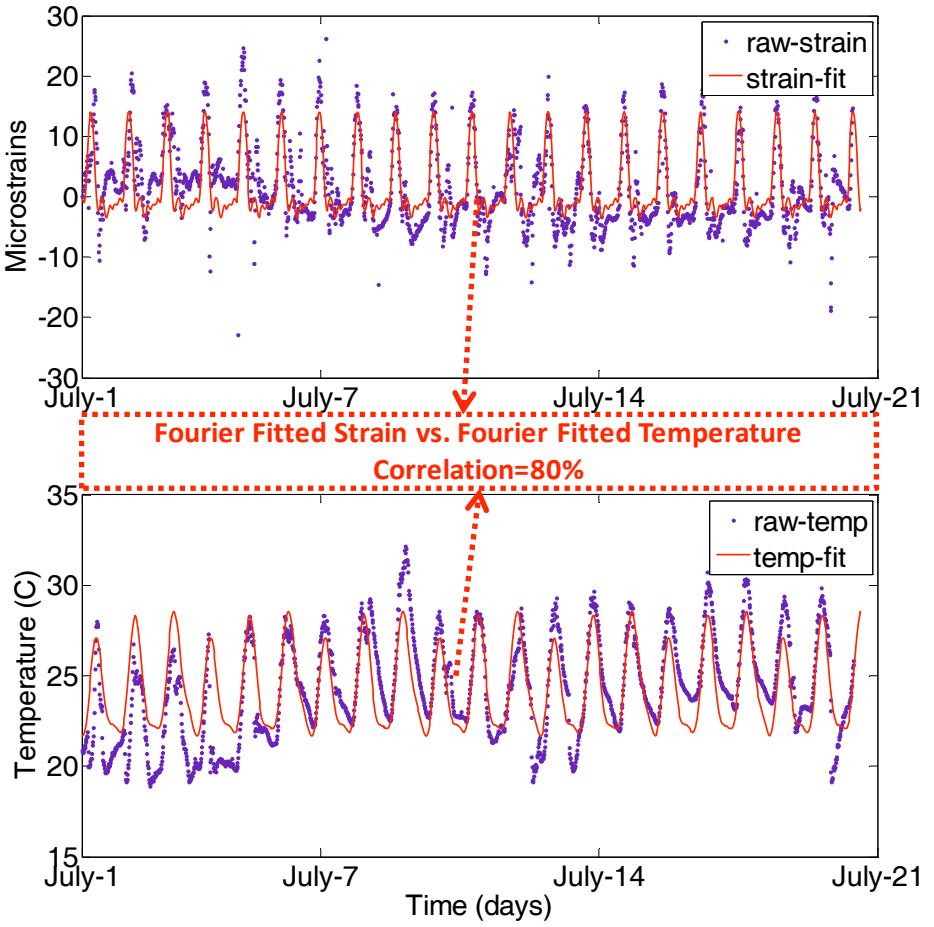


Figure 7:WN2 vibrating wire strain gage raw and Fourier fitted strain and temperature data

ANALYSIS OF STRAIN DATA FOR DAMAGE IDENTIFICATION

After collecting the basic statistical information from each sensor channel for each data set, some data analysis methods can be used for structural damage identification. In this part of the study, strain correlation based damage identification is presented. Cross correlation which is a measure of similarity of two data sets in vector form giving a value between +1 and -1. Having similar behavior in data sets gives higher correlation while low correlation indicates either low or no correlated response. General cross correlation coefficient formula is as follows:

$$\rho_{X,Y}=\frac{\sum_{i=1}^{n}(x_i-\bar{X})\times(y_i-\bar{Y})}{(n-1)\times S_X\times S_Y}$$

where $\bar{X}$ and $\bar{Y}$ are means and S_X and S_Y are the standard deviations of each vector. Ideally, the strain channels should have a correlation with the neighbor, or symmetric locations, and the outcome of this correlation will show consistency in the strain levels. In the light of this information, the authors decided to investigate the possible change in the correlation coefficients due to structural changes on the movable bridge.

Structural Alterations on SBB

The Live Load Shoes (LLS) are the support locations of the main girders when the bridge is in closed position (Figure 8). If misaligned or improperly balanced, the bridge may not fully sit on the LLS. In that case, the dead load and traffic load are transferred to the gears and shafts, which cause damage to mechanical assemblies. Small gaps also lead the girders to pound on the live load shoes, which results in further misalignment, additional stresses, fatigue damage, and excessive wear. For this study, LLS shim removal (Figure 8) is chosen as a damage scenario based on the inspection reports of bascule type of movable bridges in Florida. The West South LLS (WS3) shims which are removed to see the effect of a gap around 3.2 mm up to 4.8 mm.

Results

Correlation coefficients of the strain channels are tracked for a 25 different data sets before, during and after damage from a three weeks period. First, 10 data sets are collected in 10 days to illustrate the before damage correlation coefficients. Then, five data sets are collected for LLS shims removal case on same day due to time consideration to illustrate the during damage correlation coefficient. Finally, 10 more data sets were collected in a 10 day period to see if the correlation coefficients are becoming their original level.

The correlation coefficient change between the ES3 and WS3 strain gages during the three weeks period are shown in Figure 8. It can be easily seen that the correlation coefficients before damage case are around -0.8, during LLS damage are around -0.3and after damage these coefficients came back to the -0.8 level again but

this time with a smaller standard deviation. The reason behind this is the significant effect of the maintenance. The trends of the correlation coefficients are also tracked for different strain gages but they are not presented here for the sake of brevity. More data and results will be reported in another publication which is dedicated to this approach and results.

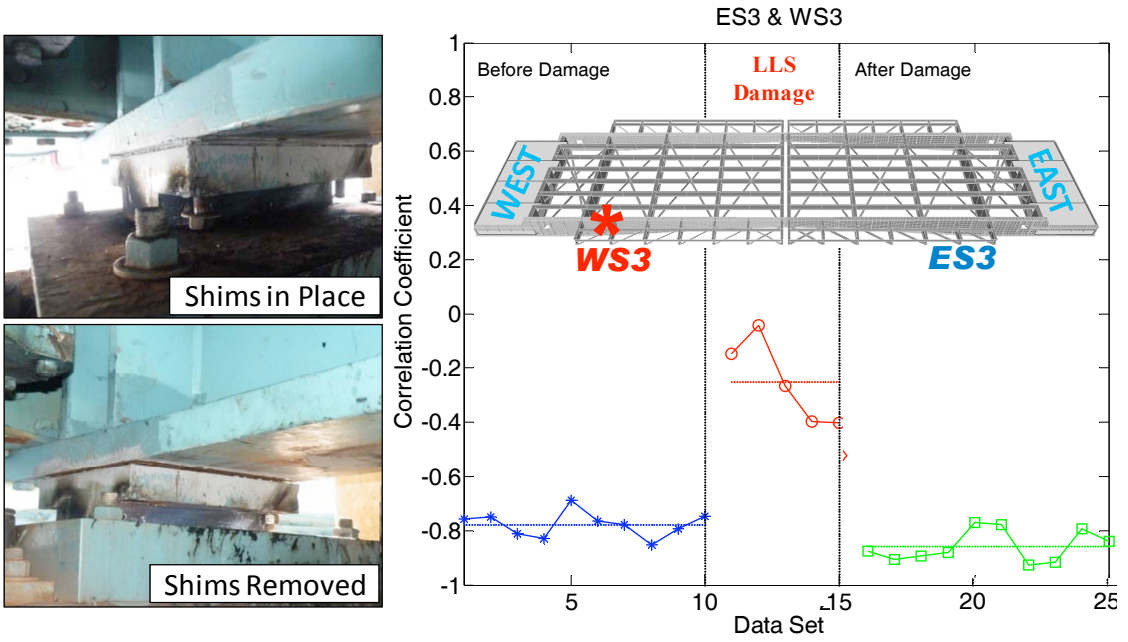


Figure 8:LLS shims and correlation coefficient change before, during, after damage

SUMMARY AND CONCLUSIONS

In this paper, different data analysis approaches are presented to extract meaningful information from high and slow speed strain data. It is observed that raw data analysis is necessary to identify functionality of the sensors and to evaluate data quality whereas statistical analysis is a fundamental step for advanced analysis methodologies. Moreover, traffic induced strain analysis is important to identify traffic characteristics that can be used for identifying fatigue cycles, ADTT numbers and extreme value distributions for structural reliability estimation. In addition, strain and temperature are crucial to continuously monitor and fit different models to make predictions because structural components subjected to high stresses or stress reversals due to temperature cycles. Finally, an effective way of handling strain data by means of correlation based damage identification methodology is presented. Based on the results, it is seen that this new methodology can help to track and detect any

permanent change by means of strain measurements under any traffic loading. It is shown that there should be a suite of techniques and features to be available for implementation in SHM systems since one particular technique/feature may not be very reliable or sufficient for a particular case and/or structure.

ACKNOWLEDGMENTS

The research project described in this paper is supported by the Florida Department of Transportation (FDOT) and Federal Highway Administration (FHWA). The writers would like to thank and cordially remember Mr. Marcus Ansley, P.E. for his support and guidance throughout the project. The writers would like to express their profound gratitude to Dr. Hamid Ghasemi of FHWA for his support of this research. The support of both agencies and their engineers is greatly recognized and appreciated. The opinions, findings, and conclusions expressed in this publication are those of the authors and do not necessarily reflect the views of the sponsoring organizations. Several graduate students and research collaborators are also to be acknowledged for their contributions at different levels for this study.

REFERENCES

Aktan, A. E., D. N. Farhey, D. L. Brown, V. Dalal, A. J. Helmicki, V. J. Hunt and S. J. Shelley (1996). "Condition Assessment for Bridge Management." Journal of Infrastructure Systems, ASCE **2**(3): 108-117.

Brownjohn, J. M., A. Zasso, G. A. Stephen and R. T. Severn (1995). "Analysis of Experimental Data from Wind-Induced Response of a Long Span Bridge." Journal of Wind Engineering and Industrial Aerodynamics **54/55**: pp. 13-24.

Catbas, F. N., S. K. Ciloglu, O. Hasancebi, K. A. Grimmelsman and A. E. Aktan (2007). "Limitations in Structural Identification of Large Constructed Structures." Journal of Structural Engineering **133**(8): pp. 1051-1066.

Catbas, F. N., M. Gul, R. Zaurin, H. B. Gokce, T. Terrell, T. Dumlupinar and D. Maier (2010). "Long Term Bridge Maintenance Monitoring Demonstration on a Movable Bridge. A Framework for Structural Health Monitoring of Movable Bridges," Final Project Report to Florida Department of Transportation (FDOT).

Enright, M. P. and D. M. Frangopol (1999). "Condition Prediction of Deteriorating Concrete Bridges Using Bayesian Updating." Journal of Structural Engineering, ASCE **125**(10): 1118-1125.

Fujino, Y. (2002). "Vibration, Control and Monitoring of Long-Span Bridges – Recent Developments and Practice in Japan." Journal of Construction Steel Research **58**: 71-97.

Proposed Data Specifications for Bridge Structural Health Monitoring Sensor Data

Stephen Prusaczyk[1], Richard Christenson[2], John Dewolf[3], Alireza Jamilapour[4], and John Bartoletti[5]

[1] Department of Civil and Environmental Engineering, University of Connecticut, 261 Glenbrook Road Unit 2037, Storrs, Connecticut 06269-2037; PH (860) 486-2992; FAX: (860) 486-2298; email: stephen.prusaczyk@engr.uconn.edu
[2] Department of Civil and Environmental Engineering, University of Connecticut, 261 Glenbrook Road Unit 2037, Storrs, Connecticut 06269-2037; PH (860) 486-2270; FAX: (860) 486-2298; email: rchriste@engr.uconn.edu
[3] Department of Civil and Environmental Engineering, University of Connecticut, 261 Glenbrook Road Unit 2037, Storrs, Connecticut 06269-2037; PH (860) 486-2270; FAX: (860) 486-2298; email: dewolf@engr.uconn.edu
[4] Division of Research, Connecticut Department of Transportation, 280 West Street, Rocky Hill, CT 06067; PH (860) 258-0392; email: alireza.jamalipour@ct.gov
[5] Parsons Brinkerhoff, 148 Eastern Boulevard, Suite 200, Glastonbury, CT 06033; PH (860) 659-0444; email: bartoletti@pbworld.com

ABSTRACT

Bridge structural health monitoring involves the collection and analysis of systematic measurements obtained from installed sensors on the bridge. While there are many quality certification systems available for civil engineering systems, e.g. American Society for Testing and Materials (ASTM), typical bridge monitoring specifications do not explicitly address performance requirements. As the applications of bridge structural health monitoring becomes more varied and advanced it will become necessary to ascertain the quality of measured data in order to check its suitability for new and varied applications.

The quality of measured data has a direct impact on the results obtained from data analysis in structural health monitoring. The quality of measured data for a bridge monitoring system should meet three basic criteria: First, measured data should be devoid of anomalies such as signal clipping, intermittent noise spikes, temporary signal dropouts, and spurious trends. Second, the errors, including aliasing and quantization, and system noise should be within an acceptable range. Lastly, the measured data should satisfy required assumptions, such as stationarity and normality.

Data qualification is defined as validating the quality of measured data and quantifying errors and noise to ensure the measured data sufficiently satisfies the above mentioned criteria. Despite the tremendous impact the quality of measured data has on bridge structural health monitoring, data qualification has not been formalized for bridge monitoring to provide a basis for bridge monitoring data specifications. This paper proposes measures of data qualification that can be used as a foundation for data specifications in bridge structural health monitoring. This paper will use data collected from monitored bridges in the Connecticut Long Term Bridge Monitoring program as examples of issues faced when using long term bridge monitoring data acquisition systems.

INTRODUCTION

Structural health monitoring of highway bridges has proven to be extremely beneficial for engineers, state agencies, and researchers. These systems allow for determination of structural integrity to supplement physical inspections. Physical inspections can be limited by lack of physical access to areas on the structure, availability of manpower, or economic reasons. Also, the frequency of physical inspections may not observe the onset of damage and be able to prevent catastrophic structural failure (DeWolf et al. 1995a, DeWolf et al. 1995b). Structural health monitoring, as a supplement to bridge inspections, can be used to determine the condition of the entire structure on a continuous and long term basis. Also, unlike physical inspections, structural health monitoring can provide inspectors with actual values for stress, accelerations, or any other parameter being measured (DeWolf et al. 2002). With a combination of structural health monitoring and physical inspections, the health of a bridge structure can accurately be tracked over time.

Bridge health monitoring systems allow the collection and analysis of data which can describe the behavior of bridges over long periods of time. This analysis can help bridge owners such as state agencies determine optimal bridge maintenance and replacement strategies (DeWolf et al. 1995a). Vibration based monitoring is of particular use for damage detection and monitoring deterioration of structures (DeWolf et al. 1991a, DeWolf et al. 1998, DeWolf et al. 2002). Vibration monitoring has been shown to effectively assess the global condition of highway bridges (DeWolf et al. 1991b, DeWolf et al. 1992, DeWolf et al. 1995a, DeWolf et al. 1995b). Strain monitoring has also been effectively implemented to determine the levels of stress and structural performance of particular structural members and connections (DeWolf et al. 1995b, DeWolf et al. 1998, DeWolf et al. 2002). This type of analysis had been used to determine whether or not a bridge structure is behaving as designed (DeWolf et al. 1998). The analysis of bridge data can provide additional information on the structural health of the bridge and supplement bridge inspections (DeWolf et al. 2002). The benefits of bridge monitoring are generally recognized by the bridge engineering community with an increasing number of applications throughout the country (DeWolf et al. 1995a, DeWolf et al. 1995b).

A number of different types of structural health monitoring systems have been installed and used on highway bridges (DeWolf et al. 1995, DeWolf et al. 1995 Application). As observed, the applications of bridge structural health monitoring are becoming more and more varied and advanced. Bridge monitoring systems are applied to different types of bridges, employ a variety of sensor types, and acquire the data in a variety of manners.

There are numerous quality certification systems available for civil engineering systems, e.g. American Society for Testing and Materials (ASTM), American Society of Civil Engineers (ASCE), and American Association of State Highway and Transportation Officials (AASHTO). In particular, AASHTO presents the code for the structural performance of bridges. AASHTO presents engineers with the loads to be applied to bridge structures along with design considerations to be taken (AASHTO 2009). In 2008, the Federal Highway Administration (FHWA) also has implemented a Long Term Bridge Performance (LTBP) program to better understand long term performance of highway bridges and the associated issues (FHWA 2011).

The design and implementation of a structural health monitoring or the long term performance of bridge structures is not included in these specifications. Furthermore, typical bridge monitoring specifications do not explicitly address performance requirements for the sensor data.

This paper presents proposed specifications for highway bridge structural health monitoring sensor data. The proposed specifications are based on experiences with bridge monitoring systems installed on a variety of bridges in Connecticut over the past decade as part of a joint research program between the Connecticut Department of Transportation and the University of Connecticut. The proposed set of specifications are intended to serve as a starting point from which further discussions can be based to ensure future bridge structural health monitoring systems can achieve their maximum potential.

PROPOSED SPECIFICATIONS

The basis for the proposed bridge structural health monitoring specifications for sensor data has been provided by the experiences of the Long Term Bridge Monitoring Program in Connecticut. Long Term Bridge monitoring in Connecticut is a joint research effort of the Connecticut Department of Transportation and the University of Connecticut. Since 1994, six bridges in Connecticut have been installed with bridge monitoring systems (DeWolf et al. 2006, Olund et al. 2009, DeWolf et al. 2009). Recently, some of the data acquisition equipment on the bridges has been updated. There are a variety of bridges being monitored, using a number of different types of sensors, and, over the course of the research, a range of data acquisition systems. Both concrete and steel bridges are being monitored, with superstructure types varying from box girders, traditional slab-on-girder, to truss. The sensors installed on these bridges include: foil, vibrating wire and piezoelectric strain gages; piezoelectric and capacitive accelerometers; RTD temperature sensors; tilt meters; and linear variable differential transformer (LVDT) displacement transducers and string potentiometers. Both wired and wireless sensors are used in the research. The diversity of this monitoring program is drawn upon in the proposed specifications.

Critical to any bridge monitoring efforts is the data analysis used to identify the structural health of the bridge. The quality of measured data has a direct impact on the results obtained from data analysis in structural health monitoring. Structural health monitoring techniques such as peak picking (DeWolf et al. 1991a, DeWolf et al. 1998,) require data undistorted in the frequency domain. Strain monitoring of structures requires data in the time domain that is void of excessive noise and data anomalies (DeWolf et al. 1998, DeWolf et al. 2002). As structural health monitoring analyses continue to improve and advance, the reliance on high quality data becomes more critical.

The quality of measured data for a bridge monitoring system should meet three basic criteria: First, measured data should be devoid of anomalies such as signal clipping, intermittent noise spikes, temporary signal dropouts, and spurious trends. Second, the errors, including aliasing and quantization, and system noise should be within an acceptable range. Third, the measured data should satisfy required assumptions, such as stationarity and normality. Verifying assumptions such as stationarity and normality are necessary prior to data analysis, however, this

particular criteria is inherent to the bridge's loading and subsequent response and is not part of the proposed bridge structural health monitoring specifications. The proposed specifications, as discussed in this paper, will address: data anomalies, including signal clipping, intermittent noise spikes, temporary signal dropouts, spurious trends, and periodicies; errors, associated with aliasing and quantization; and measurement noise associated with the sensor, cabling or data acquisition hardware.

Data Anomalies. The presence of data anomalies in a bridge health monitoring system should be checked and documented once the system is installed, and at regular intervals during the life of the system. The bridge monitoring system should be devoid of any data anomalies. Data anomalies may include signal clipping, intermittent noise spikes, temporary signal dropouts, spurious trends, and periodicity. While it is difficult to anticipate these anomalies, their presence can be eliminated through changes of the system or appropriate post processing of the data. These aforementioned data anomalies are indentified through the inspection of collected data in both the time and frequency domains.

One anomaly is signal clipping, which occurs when the maximum value of the sensor or data acquisition system is exceeded. This anomaly can be seen as a flat top when the signal is viewed in the time domain. Signal clipping can be avoided by properly selecting sensors and data acquisition systems that can handle the expected measurements from the bridge. If signal clipping is not prevented in the original installation of the structural health monitoring system, the sensors and data acquisition system should be replaced with a system that can handle the measurements.

Another anomaly that can occur during the collection of data from a highway bridge is intermittent noise spikes. This likely occurs when the cables connecting the components of the structural health monitoring system incur relative motion. As with signal clipping, intermittent noise spikes are noticed in the time domain of the measured data. Intermittent noise spikes are characterized by random large spikes in the time history. To avoid the presence of intermittent noise spikes, all cables in the system should be securely fixed/tied down. The connections of all cables should also be inspected to ensure a snug fit.

An example of intermittent noise spikes was observed on the Sikorsky Bridge monitoring system. The Sikorsky Bridge, National Bridge Index (NBI) #761, pictured in Figure 1, is a five span steel plate girder bridge spanning a distance of approximately 1800 feet over the Housatonic River in Stratford/Milford Connecticut. This bridge carries the limited access traffic of The Merritt Parkway (Route 15) north and southbound. The sensors installed on this bridge include piezoelectric accelerometers, foil strain gages, LVDTs, and tilt meters. A 16-bit data acquisition unit is used to collect data from the 48 sensors installed on the bridge. Figure 1 shows the time history for an accelerometer (Accelerometer 1) located on the southernmost span (Span 1) of the Sikorsky Bridge. While the normal response of the bridge is less than 0.1g, three intermittent spikes are observed in the 10 second interval with amplitudes around 1g. This suggests that there may be an issue with the cables connecting the sensors to the data acquisition unit for the Sikorsky Bridge system.

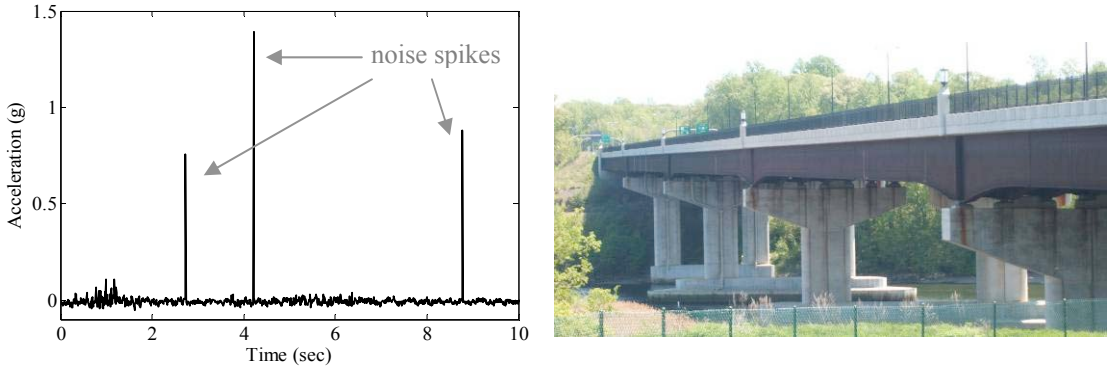


Figure 1. Intermittent Noise Spikes from Sikorsky Bridge System – Accelerometer 1, Span 1, 10 second Time History and Picture of Southbound Bridge.

A third anomaly, temporary signal dropouts, can occur when the measured signal suddenly vanishes into the noise floor of the data for a period of time. This data anomaly can be attributed to a number of different components in a structural health monitoring system. It can be a problem with the wiring or connections of the system, or a problem with the sensors themselves. If temporary signal dropouts occur the system should be carefully inspected for issues.

A spurious trend is a time varying change in the mean value of a set of data. When strain gages are not compensated for changes in temperature a spurious trend can occur. These temperature trends can be resolved by using full bridge strain sensors, or by removing any bias in the post processing of the data. Spurious trends are of significance when they do not occur because of a change in temperature. In this case, the sensor should be carefully inspected.

The final data anomaly addressed here that can be experienced in a bridge health monitoring system is a periodicy. A periodicy is a signal added to the actual signal that repeats at a regular interval. In bridge health monitoring this is likely due an improperly grounded system. This ground loop results in a 60 Hz periodic signal. The existence of a periodic signal can be most easily observed as a large spike in the frequency domain of the data set. If a periodic signal is encountered in a bridge monitoring system the grounding of all AC electrical components should be checked.

An example of periodicies was observed during the recent installation of a bridge health monitoring system installed on an I-91N overpass in Meriden CT. The Meriden Bridge, NBI #03051, shown in Figure 2, is a single span slab-on-girder bridge with a total span of 85 feet. The sensors installed on this bridge include 18 foil strain gages, 4 piezoelectric strain sensors, 8 piezoelectric accelerometers, 4 capacitance accelerometers, and 4 resistance temperature detectors. Data is collected using a 24-bit data acquisition unit. A 60 Hz periodicy was initially observed in the measured strain gage data. An auto-power spectral density function of the foil strain gage located at the top midspan of the center girder (M1) is shown in Figure 2. The auto-power spectral density function transforms the time domain strain measurement into the frequency domain. The auto-power spectral density function is a measure of the energy content of the signal as a function of frequency. From the plot in Figure 2, it is obvious that there is significant energy localized at 60 Hz.

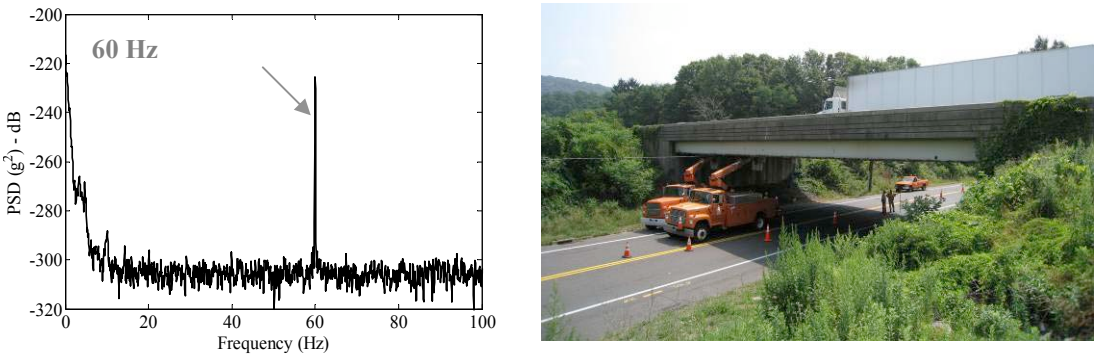


Figure 2. Periodicy Observed on Meriden Bridge System –
Auto-Power Spectral Density Function of Strain Measurement and Picture of Bridge.

Five data anomalies have been identified for the proposed specifications that may be encountered when working with a bridge structural health monitoring system. The existence of all or any of these anomalies should be checked initially for the system as well at regular time intervals and the appropriate action should be taken to eliminate any anomalies when identified.

Aliasing and Filtering. The potential for aliasing exists when digitally measuring analog signals. Aliasing occurs when a high frequency signal appears as a lower frequency signal. Once measured data is aliased, it is impossible to reconstruct the original signal or even tell that the sample has been aliased. It is therefore imperative to be proactive and prevent aliasing from occurring in the first place. This can be done by either carefully selecting the sampling rate or installing anti-aliasing filters.

In order to eliminate aliasing using the sampling rate, a rule of thumb is that data should be sampled at a rate ten times higher than the resonant frequency of the sensor. This is not an issue with certain sensors that have low resonant frequencies. For example, a tilt meter with a resonant frequency of 2 Hz should be sampled at 20 Hz. Piezoelectric accelerometers, however, can have resonant frequencies of 3500 Hz. This would require sampling the data at a rate of 35 kHz. Due to system capabilities and data storage this may not be feasible. In such cases anti-aliasing filters can be employed. Appropriate anti-aliasing filters the measured data prior to the analog to digital conversion such that the frequency content of the measured signal larger than the Nyquist frequency (one half of the sampling rate) is effectively removed. It is recommended that all dynamic measurements be passed through anti-aliasing filters to prevent aliasing. Current technology allows standard implementation of 8-pole filters which can effectively prevent aliasing.

The bandwidth of the filter used in an anti-aliasing filter must be carefully selected. Of first concern, as identified above, is that the bandwidth of the filter be less than the Nyquist frequency, or one half of the sampling rate. Depending on the natural distortion of the specific filter used, the usable bandwidth will be some frequency less than the Nyquist frequency.

An example of an anti-aliasing filter that leads to a restricted bandwidth was experienced on the Flyover Bridge monitoring system. The Flyover Bridge, NBI #05868, located in Hartford, Connecticut, is shown in Figure 3. This bridge is a multi-span, continuous, double steel box girder bridge with a composite concrete deck. The

original data acquisition system had a two-pole low-pass filter with a cutoff frequency of 2 Hz used for anti-aliasing. With a sampling rate of 100 Hz, this filter provided sufficient anti-aliasing protection. However, the 2 Hz cutoff frequency of this filter resulted in measured data with distorted frequency content above this 2 Hz. A new data acquisition system on the bridge provides a bandwidth of 500 Hz. Figure 3 shows a plot of the auto-power spectral densities of an accelerometer (A4) located on the fourth span (Span 4) of the bridge from both the original and the current system. It is observed in the auto-power spectral density functions that the original signal was attenuated above 2 Hz. While this was not a problem for the original structural health monitoring analysis that considered only the fundamental frequency of the bridge, at 1.5 Hz, current approaches (Scianna, et al., 2011) are using multiple lower frequency modes.

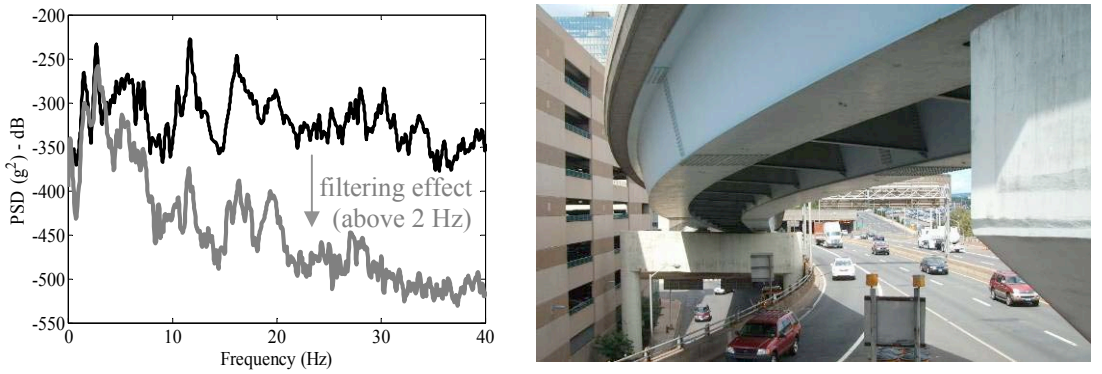


Figure 3. Filtering Issues – Accelerometer 4 on Flyover Bridge Auto-Power Spectral Density Function and Picture of Bridge.
(Original Data Acquisistion (DAQ) – gray; Current DAQ – black)

Quantization. Quantization error is inherent to analog sensors and digital processing. When a continuous analog signal is saved as a digital signal, the amplitude of each sample is expressed using a finite number of bits in binary terms by the analog to digital (A/D) converter. A round-off error is created due to this conversion, which is called quantization error. The quantization error can be reduced by using an analog to digital converter with a high total number of bits. Common A/D converters available today are 24-bit. These seem to minimize quantization error sufficiently, providing accurate data results.

An example of quantization is observed between the original and current monitoring systems on the Cromwell Bridge. The Cromwell Bridge, NBI #03078, shown in Figure 4, is located in Cromwell, Connecticut. The bridge carries I-91S traffic over the Mattabessett River. The bridge is a three-span, simply supported, slab-on-girder bridge. In November of 2004, the original structural health monitoring system was installed on the Cromwell Bridge. The original system consisted of 20 strain gages and a 16-bit data acquisition system. In July 2010, a new 24-bit data acquisition system replaced the original system. This improved the resolution of the sensor measurements from 1 με (microstrain) to 0.06 με. Figure 4 shows comparative time histories for strain gage 8. The original data was recorded at 10 Hz, while the new data is recorded at 1600 Hz and passed through an 8-pole Butterworth filter with a cutoff frequency of 100 Hz. Figure 4 above shows the time history response of a

vehicle crossing over the bridge for the original system with 1 με resolution and a vehicle crossing over the bridge with the finer 0.06 με resolution of the current system. The finer resolution can provide more accuracy of the dynamic response of the structure for both health monitoring and weigh-in-motion calculations.

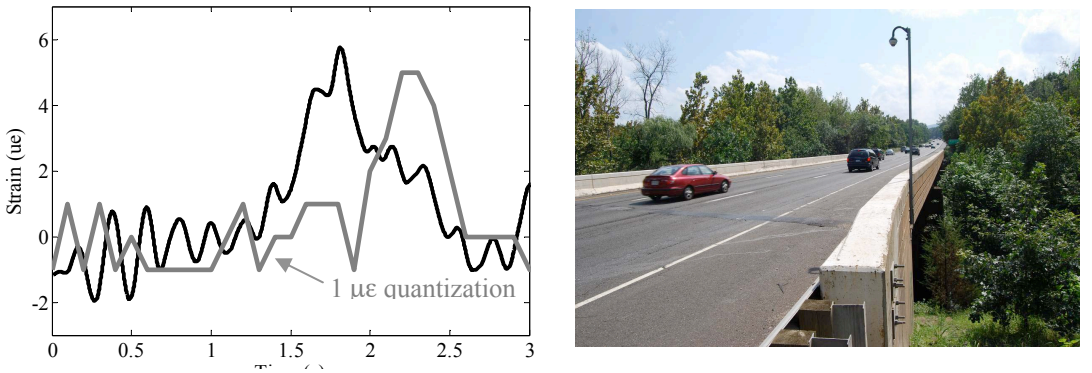


Figure 4. Quantization of Cromwell Bridge System and Picture of Bridge (Original Data Acquisistion (DAQ) – gray; Current DAQ – black)

Measurement Noise. It is important to reduce the amount of noise in a structural health monitoring system. Noise measured in a signal may be due to the sensors, data acquisition system, means of data transmission such as cables, or any other intermediary in the system between the system and data acquisition unit.

Large levels of noise in a system can hide the actual response of the bridge being measured. This reduces the usefulness of the measurement. The amount of noise in a signal is quantified by the signal-to-noise ratio (SNR). A signal-to-noise ratio is defined as the ratio of signal power to the noise power corrupting the signal, and can be presented as the ratio of the variance of these two signals.

There are a number of ways to effectively reduce the amount of noise in a bridge health monitoring. First, sensors with a measurement range only slightly larger than the peak values to be measured should be used. Also, cable lengths should be kept as short as physically possible. Lastly, the signal being sent to the data acquisition unit should be amplified to a similar magnitude as the analog voltage input.

Another issue for bridge monitoring applications is the definition of what exactly constitutes noise in the measurement. For applications in Connecticut when the excitation is considered the vehicles passing over the bridge, noise might be considered to include additional sources of ambient vibration including wind excitation, vehicles on adjacent bridges or roadways, fluids in any piping attached to the bridge, etc. As such, to identify SNR in the field measurements are taken from the bridge during high or peak travel times and in the late night/early morning when, using traffic cameras and remote data capture, it can be confirmed there is low or no traffic on the bridge, which is meant to closely represent the noise floor.

What has been observed from field measurements on a number of the bridges in Connecticut is that a range of higher frequency signal content is present in both the high and low traffic periods. The SNR determined using the signals with this higher

frequency energy content is correspondingly low. This higher frequency energy in the low traffic signal may likely be due to high frequency vibrations due to the other ambient vibration sources cited above. The higher frequency energy content should, in such a case, not be considered when determining the SNR. It is proposed that the SNR be calculated for measured signals filtered at a cutoff frequency where a distinction between the high and low traffic periods can be distinguished in the frequency domain.

The previously mentioned Sikorsky Bridge system is considered again for this example. The plots in Figure 5 show the acceleration recorded by Accelerometer 1 of Span 1 at periods of both high and low traffic excitation. The plot on the left shows the acceleration measurements including the high frequency content. The corresponding SNR is calculated to be 1.6. The high and low traffic periods are both observed to contain similar levels of energy above 30 Hz for this particular bridge span. The plot on the right is for the time histories filtered in post processing to remove energy content above 30 Hz. The SNR is calculated from this signal to be 36.3. This example illustrates the importance of understanding the frequency content of the measured signals when quantifying noise and in subsequent structural health monitoring calculations.

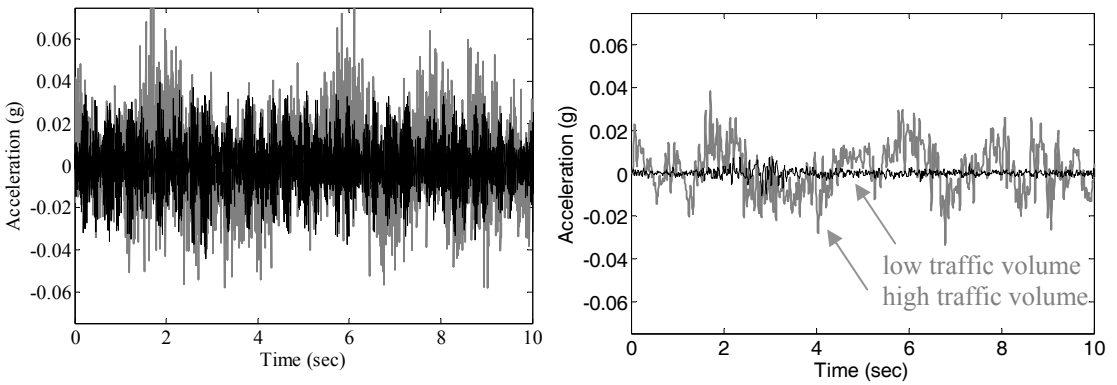


Figure 5. Inherent Noise Levels in Sikorsky Bridge System Accelerometer 1 Span 1 – Left with high frequency content; Right with high frequency content removed (High Traffic Volume – gray; Low Traffic Volume – black)

CONCLUSION

The previously described data anomalies along with considerations for aliasing, quantization and noise should be considered to derive a set of specifications for the installation and implementation of structural health monitoring on bridge structures and in particular specifications for the measured data from these systems.

Specification 1 – Data Anomalies. In dealing with data anomalies, the presence of any and all data anomalies experienced with the system should be checked periodically and documented accordingly. If a data anomaly is experienced, the proper action should be taken to fix the problem. To avoid signal clipping, expected measurements for strain, acceleration and any other parameter should be

approximated before the installation of a permanent system. This can be done through thorough structural analysis or the installation of temporary sensors once the bridge is constructed. Once the maximum expected values are determined, sensors should be carefully selected that are able to capture the dynamic behavior of the structure. If a temporary signal dropout occurs the most likely issue is a poor cable connection. The connections between all elements in the structural health monitoring system should be carefully inspected periodically and particularly if a signal dropout is experienced. To avoid intermittent noise spikes all cables in the system should be adequately fixed/tied down to avoid relative motion. If intermittent noise spikes are experienced, the cables should be checked to insure adequate support. Spurious trends in strain gages can be eliminated by specifying temperature compensating strain gages. Spurious trends due to temperature variations in other types of sensors can be effectively managed in the post processing of the data. When a large spike is encountered in the frequency domain for a sensor at 60 Hz, there may be an issue with the grounding of the system. All wiring during the installation of the health monitoring system should be performed carefully and grounded properly. The structural monitoring system design documents should be reviewed, signed, and sealed by a professional Electrical Engineer to avoid electrical issues with the system.

Specification 2 – Aliasing and Filtering. As previously mentioned, aliasing of data can deem a set of random measurements useless. It is therefore essential that anti-aliasing filters be implemented on all dynamic sensors. These filters should be carefully selected so that the data collected is not distorted in regions of research interest.

Specification 3 – Quantization. Quantization error in a health monitoring system can be eliminated through the use of an analog to digital converter with a high total number of bits. Current technology allows the use of analog to digital converters with 24 bits.

Specification 4 – Noise. By minimizing the volume of noise in a structural health monitoring system, the best quality data can be obtained and analyzed. A number of different approaches should be taken to minimize the noise in an installed bridge health monitoring system. First, the expected peak measurement values should be determined as previously mentioned for eliminating signal clipping. Sensors should then be selected that have a measurement range only slightly larger than these peak values. Also, cable lengths should be kept to a minimum to minimize the chances of external noise getting into the system. Noise can also be minimized by ensuring that the signal sent to the data acquisition unit is amplified to a similar magnitude as the analog voltage input. Many new data acquisition units are able to consider a small voltage range, minimizing noise from the data acquisition system. The frequency content of the measured signal should be used to identify and help classify what constitutes noise and the signal in the measured signals.

These specifications are intended to provide a guide to the design of structural health monitoring systems for the use on highways bridges. The specifications should be updated and adapted to take advantage of advancements in technology and current practices.

ACKNOWLEDGEMENT

The authors gratefully acknowledge the Federal Highway Administration and the Connecticut Department of Transportation for funding of this project through the State Planning and Research (SPR) program, project SPR-2256.

REFERENCES

AASHTO LRFD Bridge Design Specifications. Washington, D.C.: American Association of State Highway and Transportation Officials, 2009.

Federal Highway Administration. "About-LTBP: Long-Term Bridge Performance Program."Web.07Jan.2011.http://www.fhwa.dot.gov/research/tfhrc/programs/infrastructure/structures/ltbp/about.cfm

DeWolf, J.T., M. Accorsi and P.N. O'Leary. 1991a. Bridge Performance from Vibrational Monitoring. Proceedings of the International Conference on New Dimensions in Bridges and Flyovers, Singapore, 93-99.

DeWolf, J.T., P.N. O'Leary, D.A. Bagdasarian. 1991b. Bridge Vibration Monitoring and Analysis. Annual Meeting of the South Carolina Section of the American Society of Civil Engineers, Greenville, SC, 12 pages.

DeWolf, J.T., P.N. O'Leary, and D.A. Bagdasarian. 1992. Failure Prevention in Bridges through Continuous Vibrational Monitoring. Fourth International Conference on Structural Failure, Product Liability and Technical Insurance, Technical University of Vienna, Vienna, Austria. Published by Elsevier, 1993, pp. 357-364

DeWolf, J.T., P.E. Conn and P.N. O'Leary. 1995a. Continuous Monitoring of Bridge Structures. International Association for Bridge and Structural Engineering Symposium: Extending the Lifespan of Structures, San Francisco, CA, pp. 935-940.

DeWolf, J.T., and R.G. Lauzon. 1995b. Application of Monitoring Technology to Bridge Assessment. Fifth International Conference on Structural Failure, Product Liability and Technical Insurance, Technical University of Vienna, Vienna, AUSTRIA, pp. 413-423.

DeWolf, John T., Michael P. Culmo, and Robert G. Lauzon. "Connecticut's Bridge Infrastructure Monitoring Program for Assessment." Journal of Infrastructure Systems 4.2 (1998): 86-90. Print.

DeWolf, J. T., R. G. Lauzon, and M. P. Culmo. "Monitoring Bridge Performance." Structural Health Monitoring 1.2 (2002): 129-38.

DeWolf, J.T., J.K. Olund, C. Liu and A.J. Cardini. 2006. The Long Term Structural Health Monitoring of Bridges in the State of Connecticut. Third European Workshop on Structural Health Monitoring, Granada, Spain, pp. 372-378.

DeWolf, J.T., Cardini, A.J., Olund, J.K. and D'Attilio, P.F. (2009). "Structural Health Monitoring of Three Bridges in Connecticut," Transportation Research Board 88th Annual Meeting, Washington DC, January 11-15, 2009.

Olund, J.K., Cardini, A.J., D'Attilio, P., Feldblum, E. and DeWolf, J.T. (2006). "Connecticut's Bridge Monitoring Systems," NDE Conference on Civil Engineering, St. Louis, MO, 173-179.

Scianna, A.M., Jang, S., and Christenson, R.E. (2011). "Model-free modal flexibility-based damage detection strategy for in-service highway bridges", SPIE Smart Structures/NDE, San Diego, CA (accepted).

Wind Engineering Studies for a Cable-Stayed Bridge in Talavera de la Reina, Spain

F. Nieto[1] (M.ASCE), S. Hernández[2] (F.ASCE), J.Á. Jurado[3], F. Pereira[4] and A. Díaz[5]

[1]University of La Coruna, School of Civil Engineering, Campus de Elviña, 15071, La Coruna, Spain; PH: +34 981167000; FAX: +34 981167170; email: fnieto@udc.es
[2]University of La Coruna, School of Civil Engineering, Campus de Elviña, 15071, La Coruna, Spain; PH: +34 981167000; FAX: +34 981167170; email: hernandez@udc.es
[3]University of La Coruna, School of Civil Engineering, Campus de Elviña, 15071, La Coruna, Spain; PH: +34 981167000; FAX: +34 981167170; email: jjurado@udc.es
[4]University of La Coruna, School of Civil Engineering, Campus de Elviña, 15071, La Coruna, Spain; PH: +34 981167000; FAX: +34 981167170; email: fpereira@udc.es
[5]Former member University of La Coruna, School of Civil Engineering, Campus de Elviña, 15071, La Coruna, Spain; PH: +34 981167000; FAX: +34 981167170; email: adiaz@udc.es

ABSTRACT

The recently designed highway for by-passing the city of Talavera de la Reina in Spain is currently under construction. The main structural element in the project is a cable-stayed bridge which for sure will become a landmark in the region. The bridge has a main span of 318 m, comprising a concrete box deck 36 m width and a single inclined pylon 164 m high.
The singularity of the bridge has recommended a comprehensive analysis regarding wind effects on the structure. The aerodynamic coefficients of the deck have been obtained from wind tunnel tests and they have also been computed using CFD software considering two different turbulence models. Also the flutter functions have been evaluated by means of sectional model tests and the flutter velocity has been obtained. It has been found that the bridge enjoys a safe design for wind actions.

INTRODUCTION

Long span bridges are wind prone structures which can suffer from a number of different phenomena such as: flutter, vortex-shedding, buffeting and so on. In cable-stayed bridges wind effects must be considered along the design process as they can suffer adverse effects. Some examples of cable-supported bridges which have suffered adverse wind effects are the Kessock Bridge in the United Kingdom which showed important deck oscillations due to vortex-shedding (Owen et al., 1996) or the Vasco de Gama Bridge in Portugal (Mendes and Branco; 1998) whose design had to be carefully checked as at the early design stage. Also the Great Belt Bridge showed

vortex-shedding excitation which entailed the application of mitigation measures before its inauguration.
Engineers have nowadays a set of tools to tackle with wind effects in bridges: code stipulations, sectional model wind tunnel test, boundary layer wind tunnel tests of complete bridge aeroelastic models and numerical simulations using CFD software. These approaches do not exclude each other, nevertheless they are complementary and the combined application of all of them allows a better comprehension of the bridge performance. In this work, the application of some of the mentioned tools in the design of a cable-stayed bridge in Spain is commented and the main results are presented.

BRIDGE DESCRIPTION

Talavera de la Reina is a middle size city located in central Spain in the route connecting Madrid (Spain) and Lisbon (Portugal). Actually a new highway for by-passing the city at its Southern limit is being constructed and its main structural element is cable-stayed bridge. In figure 1 two images of the bridge location are provided.



Figure 1. Bridge location

In the figure 2 several images of the structure are showed. The bridge has only one span of 318 m. At one side there is a pylon which has 164 m of height and a studied geometry from the aesthetics point of view. From the pylon two planes of cables connect both sides of the deck and at its back zone there are another two planes of cables which balance the pylon by transmitting the forces to the foundation. The ruled surfaces shape of these set of cable results very attractive. As it is shown at figure 2, the deck is a multi-cell box girder of concrete with two lateral cantilevers. Its width is 36 m and its depth is 2.77 m. The upper slab of the deck resists the traffic of vehicles and the lateral cantilevers are for the pedestrians. The bridge enjoys a formal design that can be appreciated in several images of a virtual model that are presented in figure 3.

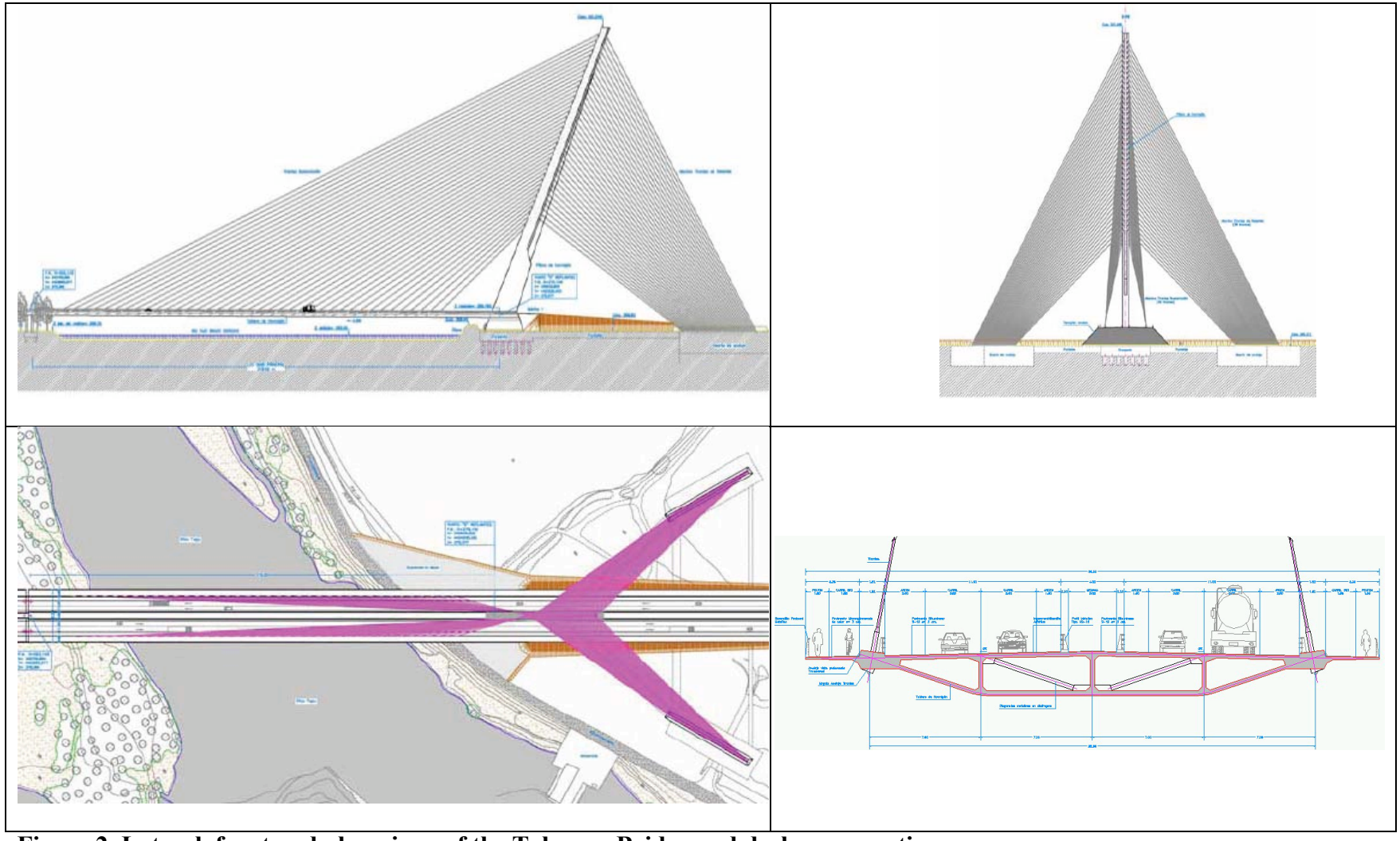


Figure 2. Lateral, front and plan views of the Talavera Bridge and deck cross-section.

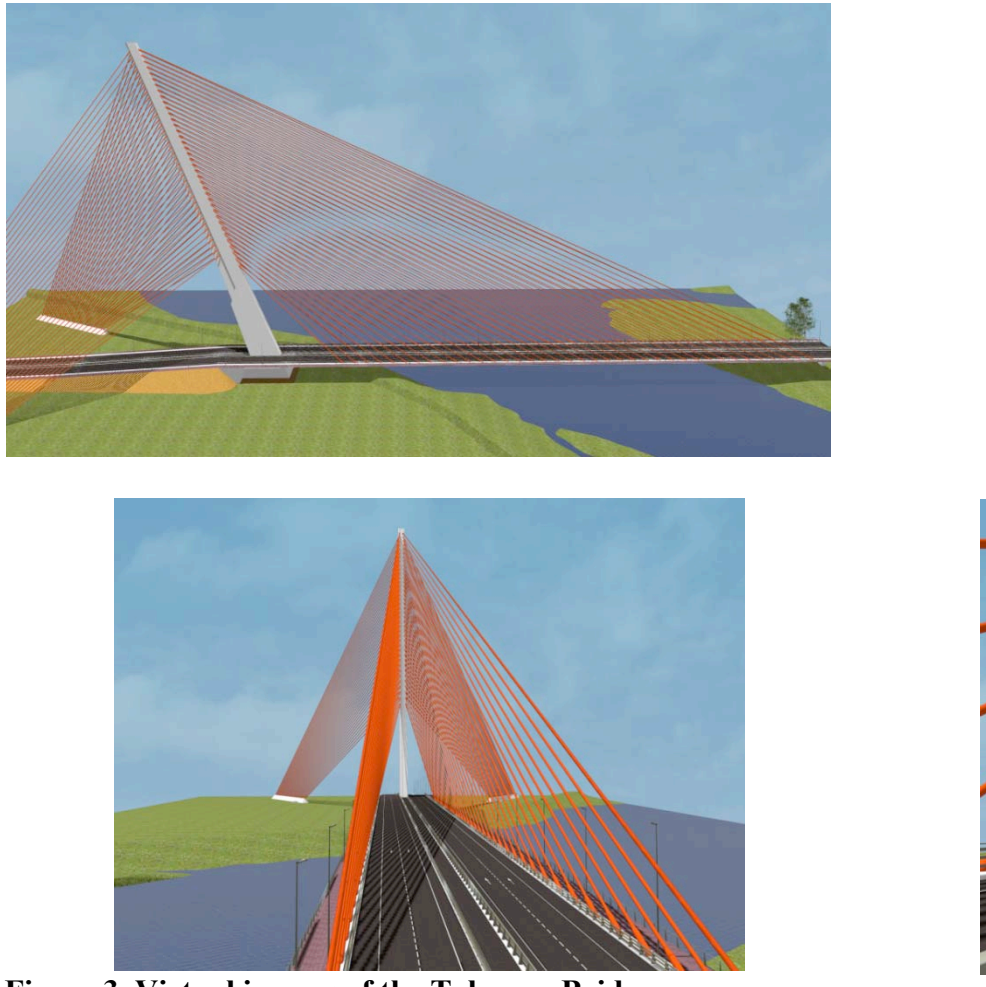


Figure 3. Virtual images of the Talavera Bridge

AERODYNAMIC COEFFICIENTS

Aerodynamic coefficients are important information required to carry out aeroelastic analysis aimed to identify the safety level of cable supported bridges against wind induced phenomena. They allow the calculation of the static action caused by the wind. They are also present in the expression of buffeting forces, therefore studies of bridge behaviour under turbulent flow need to obtain previously that set of coefficients. And they also give qualitative information about the expected flutter performance of a deck cross-section as to avoid one degree of freedom instability the first derivative of lift and moment coefficients must be positive according to the criteria of figure 6; additionally, the greater the value of those derivatives is the lower the flutter critical wind speed of the structure is (Larose and Livesey, 1997; Diana et al., 2007). The aerodynamic coefficients are obtained by carrying out a test of a fixed deck sectional model measuring in the wind tunnel the drag force D, the lift L and the moment M (see figure 6 for positive sign convention) that exerts air flow over the model. The dimensionless values of these actions use the dynamic pressure of wind and the deck width B to determine the following coefficients:

$$C_D = D/(\tfrac{1}{2}\rho U^2 B)$$
$$C_L = L/(\tfrac{1}{2}\rho U^2 B)$$
$$C_M = M/(\tfrac{1}{2}\rho U^2 B^2)$$

Experimental evaluation. The wind tunnel of the School of Civil Engineering of the University of La Coruña used for the experiments appears on figure 5 The test section of the tunnel has one square meter, which is enough for testing the sectional model of the Talavera Bridge at a geometric scale 1/100. A picture of the model is shown also in figure 5 and it has the same geometry as the real prototype considering barriers and any element which can affect to the aerodynamic responses.

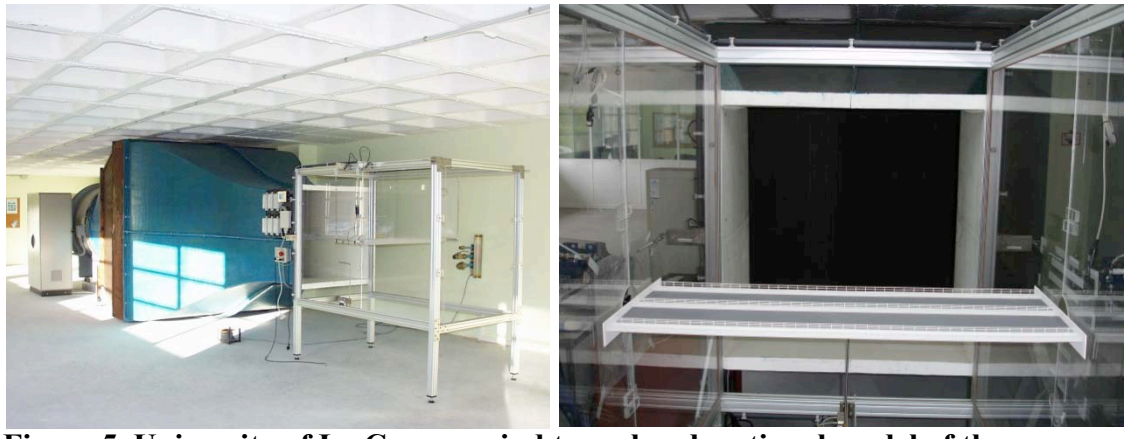


Figure 5. University of La Coruna wind tunnel and sectional model of the Talavera Bridge.

In figure 6 the aerodynamic coefficients obtained experimentally for the Talavera Bridge cross-section are presented along with the sing convention employed in this work. It can be seen that both lift and moment coefficients present low positive slopes in the range of analyzed angles of attack (-8º, +8º), which is an indication of a good flutter performance.

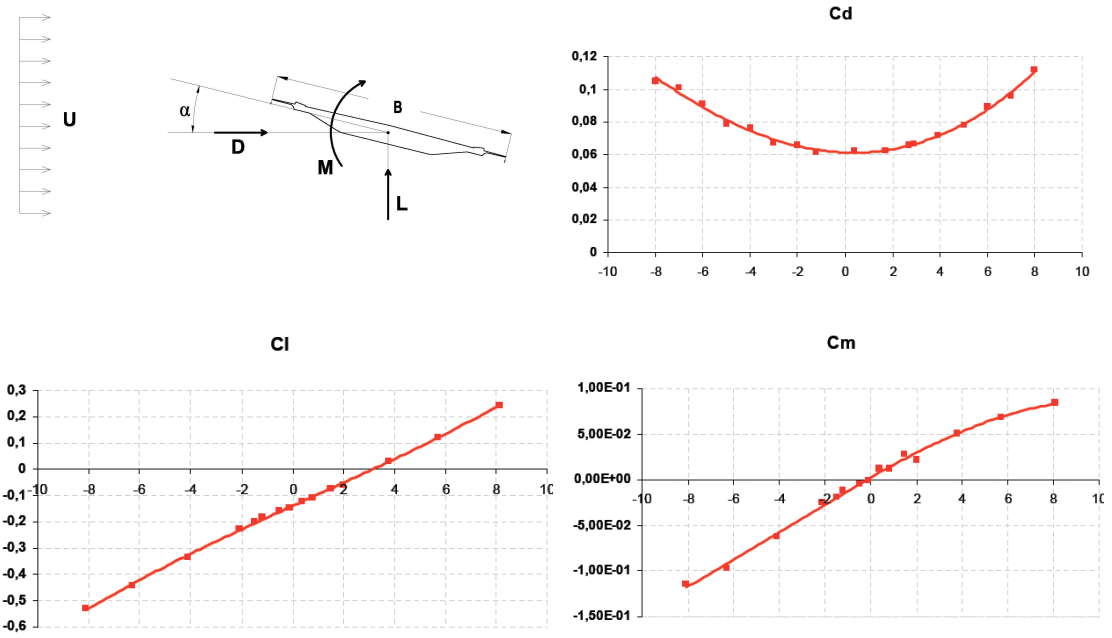


Figure 6. Sign criteria and experimental aerodynamic coefficients.

Numerical evaluation. In recent years the number of applications of CFD (Computational Fluid Dynamics) in bridge engineering has grown as numerical methods are capable of providing time-effective information in the preliminary aerodynamic design of bridge decks (Cochran and Derickson, 2010; Nieto et al., 2010). Two CFD simulations have been carried out by the authors with the aim of evaluating the general performance of numerical methods in the evaluation of aerodynamic coefficients in bridge decks. In first place, the aerodynamic coefficients were computed for a 2D model of the geometry of the cross section without barriers (bare deck section) considering steady state and k-ε turbulence model with enhanced wall treatment. A second CFD model was considered, including the barriers in the 2D model and adopting k-ω SST turbulence model. Some authors have suggested that amongst the RANS (Reynolds Averaged Navier-Stokes) turbulence models k-ω offers more accurate results in bridges than k-ε as the later over-produces the turbulence kinetic energy near the walls and it may change the flow patterns (Sun et al, 2005). In figure 7 the results computed for both models are presented along with the experimental results for validation. It can be seen that both turbulence models offer a good approximation to the experimental values from a qualitative point of view. More in detail, k-ω provides a more accurate simulation especially for the moment coefficient. On the other hand, the drag coefficient evaluated considering the k-ε model is very close to the wind tunnel result.

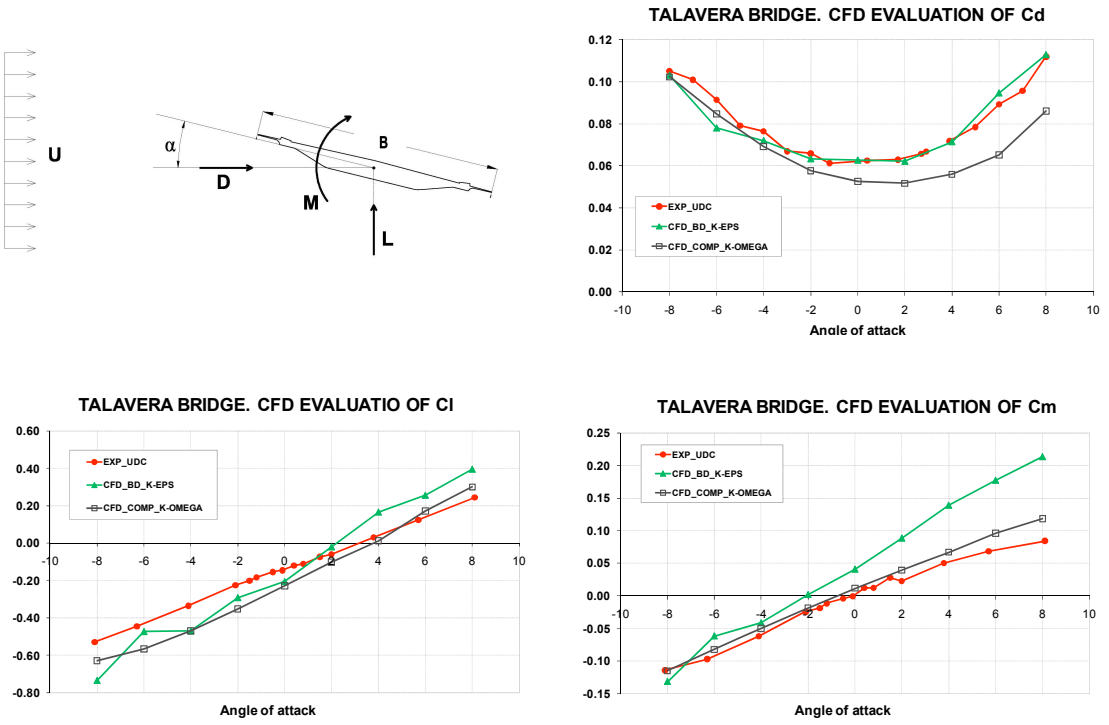


Figure 7. Comparison between experimental and CFD aerodynamic coefficients.

FLUTTER RESPONSE

The set of eighteen flutter derivatives is important information required to carry out aeroelastic analysis of bridges aimed to identify the safety level against wind induced instability. Flutter derivatives are the components of the aeroelastic damping and stiffness matrices that relate the lift, drag and moment forces to the vector of displacements and velocities of bridge deck, as it can be seen in the next equation. The standard way to evaluate flutter derivatives is using wind tunnel tests, although currently CFD evaluation of flutter derivatives is a field of research (Ge and Xiang, 2008).

$$\mathbf{f}_a = \begin{Bmatrix} D_a \\ L_a \\ M_a \end{Bmatrix} = \frac{1}{2}\rho U^2 KB \cdot \begin{pmatrix} P_1^* & -P_5^* & -BP_2^* \\ -H_5^* & H_1^* & BH_2^* \\ -BA_5^* & BA_1^* & B^2A_2^* \end{pmatrix} \begin{Bmatrix} \dot{v} \\ \dot{w} \\ \dot{\varphi}_x \end{Bmatrix} + \frac{1}{2}\rho U^2 K^2 \cdot \begin{pmatrix} P_4^* & -P_6^* & -BP_3^* \\ -H_6^* & H_4^* & BH_3^* \\ -BA_6^* & BA_4^* & B^2A_3^* \end{pmatrix} \begin{Bmatrix} v \\ w \\ \varphi_x \end{Bmatrix}$$

$$\mathbf{f}_a = \mathbf{C}_a \dot{\mathbf{u}} + \mathbf{K}_a \mathbf{u}$$

where B is the deck width, ρ is the air density, U is the mean wind speed, $K = B\omega/U$ is the reduced frequency with ω the frequency of the response, and $P^*_i(K)$, $H^*_i(K)$, $A^*_i(K)$ $i = 1...6$ are the flutter derivatives which are functions of K. $\mathbf{K}_a$ and $\mathbf{C}_a$ are aeroelastic stiffness and damping matrices.

In this work the free vibration approach with the sectional model of the deck supported by eight vertical and four horizontal springs was used. The complete set of eighteen coefficients A^*_i, P^*_i, H^*_i (i = 1,…6) was identified. The stiffness of the springs determines the vibration frequencies of the system that together with the wind velocity in the tunnel, U and the model width, B, determines the range of reduced velocities, U^*, in order to be able to obtain flutter functions. Two spring sets were used in order to vary the natural frequencies of the model and include a wider range of reduced velocities. In tables 1 and 2 the main data of the sectional model and the range of reduced velocities considered in this work are summarized. Also figure 8 shows the obtained flutter functions for Talavera de la Reina Bridge.

Table 1: Properties and natural frequencies of the sectional model of Talavera Bridge.

	SECTIONAL MODEL MASS			3.2 kg		
	SECTIONAL MODEL INERTIA			5.1 kgm^2		
	MODEL WIDTH			0.36 m		
	DISTANCE d			0.47 m		
	VERTICAL SPRINGS		HORIZONTAL	MODEL FREQUENCIES (rad/s)		
	TOP	BOTTOM	SPRING	LATERAL	VERTICAL	TORSIONAL
TEST 1	130 N/m	96 N/m	102 N/m	13.6	16.6	35.7
TEST 2	600 N/m		300 N/m	21.1	26.1	67.9

Table 2: Range of reduce velocity for flutter derivatives.

	RANGE OF REDUCED VELOCITY		
	A5,A6,H5,H6,P1,P4	A1,A4,H1,H4,P5,P6	A2,A3,H2,H3,P2,P3
TEST 1	8<U*<26	6<U*<21	3<U*<7
TEST 2	5<U*<16	4<U*<10	1<U*<4

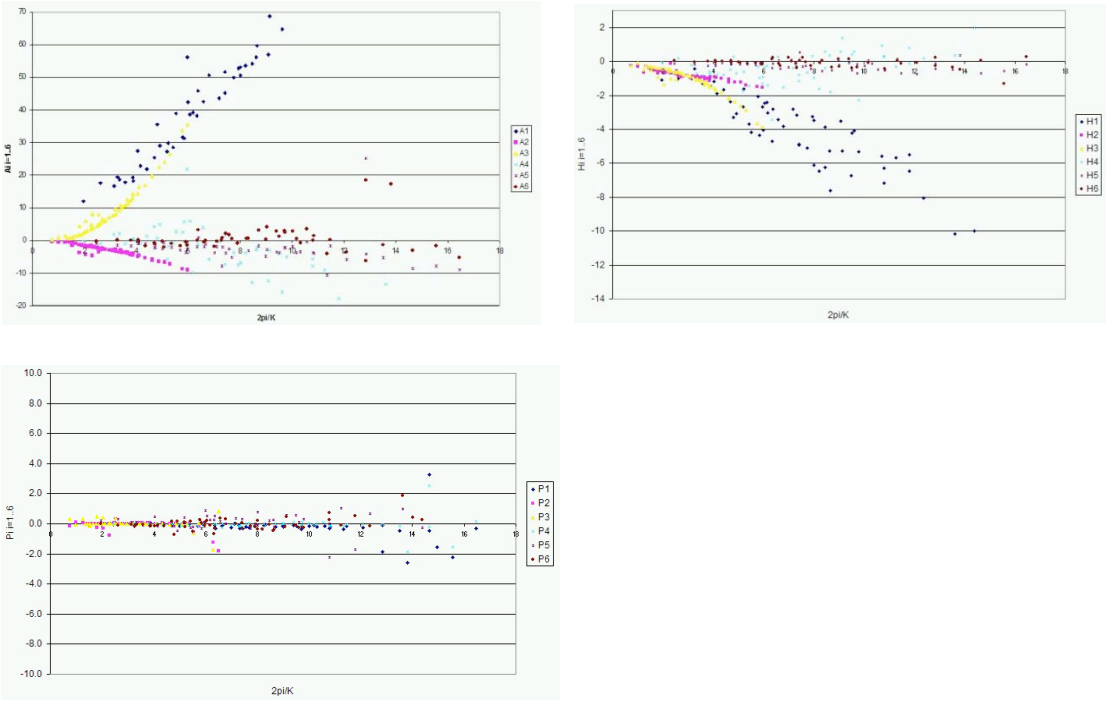


Figure 8. Flutter derivatives of the Talavera de la Reina Bridge.

Once flutter derivatives are obtained, flutter speed of the complete bridge can be calculated by solving of a non linear eigen-problem which comes from the dynamic equilibrium equation for the deck.

The imaginary part β of the eigenvalues μ counts on the frequency ω, while the real part α of the eigenvalues is associated with the damping ratio ζ. The condition of flutter corresponds to the lowest wind speed U_f which gives one eigenvalue with vanished real part. Figure 9 shows graphs with the evolution of the eigenvalues of the problem for increasing wind velocities. It is observed that the critical flutter velocity for the Talavera Bridge is 77 m/s.

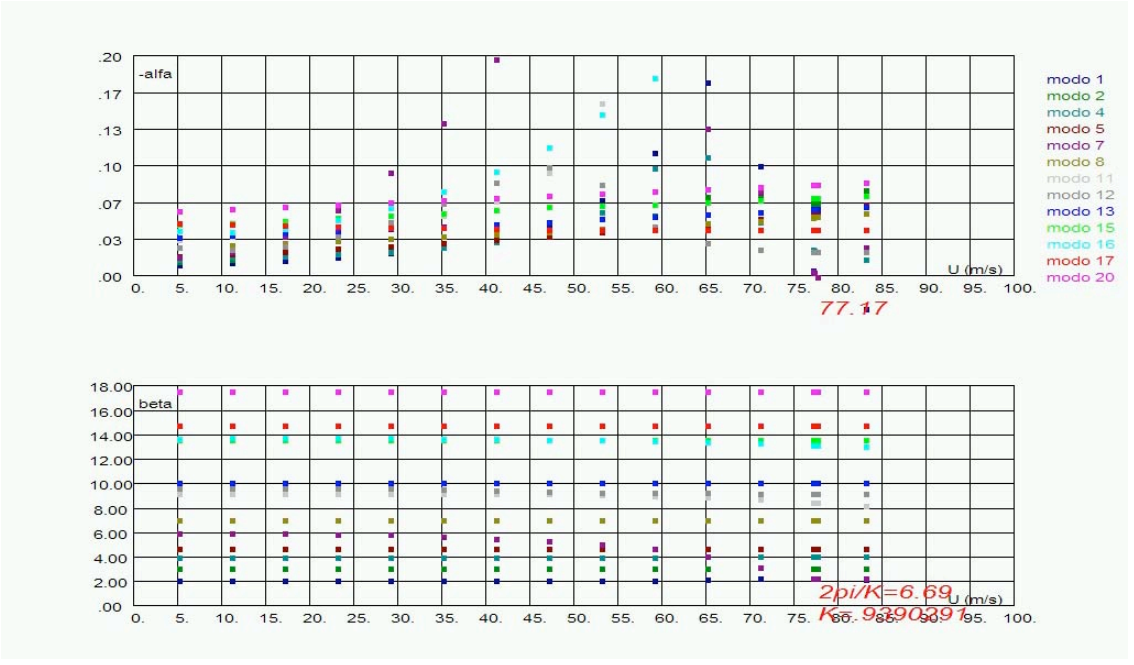


Figure 9. Evolution of eigenvalues with respect to wind velocity *U* until flutter condition with a null damping.

CONCLUSIONS

The main characteristics of the Talavera de la Reina cable-stayed Bridge have been described and virtual images of the bridge have been presented.

The aerodynamic coefficients of the deck have been obtained by means of sectional model wind tunnel tests in the range of angles of attack (-8º, +8º). CFD has been also employed to compute the aerodynamic coefficients considering a 2D model, steady state and two different RANS turbulence models. In both cases the numerical results are close to the experimental ones.

The flutter derivatives have been obtained using the free vibration approach. The flutter velocity obtained has been 77 m/s (277 km/h) which is well above 500 years return period wind speed at the deck level (41.5 m/s or 149 km/h).

In general, the Talavera de la Reina Bridge enjoys a safe design for wind actions.

REFERENCES

Cochran L. and Derickson R. (2010) "A physical modeler's view of Computational Wind Engineering". The Fifth International Symposium on Computational Wind Engineering. North Carolina: Chapel Hill.

Diana G., Belloli M., Rocchi D., Resta F. and Zasso A. (2007) "Sensitivity analysis on the effects of different aerodynamic devices on the behaviour of a bridge deck". 12th International Conference on Wind Engineering, Cairns, Australia.

Ge Y.J. and Xiang H.F. (2008) "Computational models and methods for aerodynamic flutter of long-span bridges". *Journal of Wind Engineering and Industrial Aerodynamics*; 96: 1912-1924.

Larose G.L. and Livesey F.M. (1997) "Performance of streamlined bridge decks in relation to the aerodynamics of a flat plate". *Journal of Wind Engineering and Industrial Aerodynamics*; 69-71: 851-860.

Mendes P.M. and Branco F.A. (1998) "Numerical wind studies for the Vasco da Gama Bridge, Portugal". *Structural Engineering International;* 8(2): 124-128.

Nieto F., Hernández S., Jurado J.Á. and Baldomir A. (2010) "CFD practical application in conceptual design of a 425 m cable-stayed bridge". *Wind and Structures, An International Journal*; 13(4): 309-326.

Owen J.S., Vann A.M., Davies J.P. and Blakeborough (1996) "The prototype testing of Kessock Bridge: response to vortex shedding". *Journal of Wind Engineering and Industrial Aerodynamics*; 60: 91-108.

Sun D., Wright N.G., Owen J.S. and Liaw K. (2005). "identification of 18 flutter derivatives using CFD turbulence modelling". The Fourth European & African Conference on Wind Engineering, Prague, Czech Republic.

Detection of Critical Fatigue Cracks in Steel Bridge Materials with Remote Acoustic Emission Monitoring

Jianguo Yu [1], Paul Ziehl [2]

[1] Department of Civil and Environmental Engineering, University of South Carolina, 300 Main Street, Columbia, SC 29208; PH (803) 777 8368; Fax (803) 777 0671; email: yu22@cec.sc.edu
[2] Department of Civil and Environmental Engineering, University of South Carolina, 300 Main Street, Columbia, SC 29208; PH (803) 777 8018; Fax (803) 777 0671; email: ziehl@cec.sc.edu

Abstract

Catastrophic failure of steel bridge components can occur if the fatigue cracks reach critical levels. The purpose of the study described is to characterize the acoustic emission (AE) corresponding to crack extension from the stable to the unstable stage in steel bridge material. AE monitored fatigue tests were conducted using specialized compact tension (CT) specimens made of ASTM A572G50. A combined approach involving Swansong II filters and investigation of waveforms is employed in the discrimination of AE signals caused by cracks or noise. This approach is appropriate for data filtering and interpretation of sparse data as may be expected from field tests where wireless monitoring is essential. The results indicate that AE parameters from reduced datasets can provide warning for critical fatigue cracks under different test conditions. The transition of fracture mechanisms is reflected in the reduced AE dataset.

Keywords: Acoustic emission (AE); fatigue cracks; stress intensity; bridge health monitoring

1. Introduction

As described in the ASCE 2009 Report Card (ASCE, 2009), a large number of bridges are structurally deficient and functionally obsolete. Traffic flow and environmental factors induce cyclic loads and may initiate fatigue cracks in steel components, as shown in Figure 1. In the case of fracture critical regions, the cracks may result in the failure of the entire bridge if they come into the stage of unstable propagation. AE techniques have shown promise for nondestructive evaluation of fatigue damage in steel materials (Sinclair and Connors 1977, Ohira et al. 1980, Gong et al. 1992, Bassim et al. 1994, Chen and Choi 2004, Oh et al. 2004) and civil infrastructure in general (Ziehl 2008, Yu et al. 2010).

Crack growth behavior is determined by the type of material and the set of loading conditions. Stephens (2000) demonstrated that for positive load ratios increasing of the mean load level can accelerate crack growth. Vasudevan and Sadananda (2001) presented that the crack growth curves have a tendency to merge at the upper end of load ratios where the stress intensity range approaches the threshold. Based on these two former studies, crack growth behavior under different load ratios are

demonstrated in Figure 2. For a given material the set of loading conditions decides the crack growth behavior. Substantial differences in crack growth behavior occur for different load ratios. With a specific load ration, R, the crack growth rate curve (crack growth rate versus stress intensity range) is unique. Each crack growth rate curve has three stages: threshold region, stable propagation and unstable propagation. Stage III may result in catastrophic failure. The critical crack is the transition point between stage II and stage III. The transition points on the crack growth rate curves are shifted to lower stress intensity range as the load ratio increases. The correlation between AE characteristics and critical fatigue cracks should be obtained for steel bridge material prior to the widespread application of AE for structural health monitoring and prognosis.

Previous efforts have focused on the prediction of fatigue life through the AE characteristics corresponding to the crack propagation behavior within the stable stage (Hamel et al. 1981, Daniel et al. 1997, Roberts and Talebzadeh 2003). It would be difficult and time consuming to test under every loading condition to determine specific relationship between AE and crack growth behavior. Additionally, the AE signals corresponding to the transition of crack propagation stages may not be collected if the study focuses only on the stable stage. Lindley et al. (1978) presented an improved correlation model that covers both stage II and stage III. This model involved fracture toughness, K_c, which depends on the thickness of the material subjected to cyclic loads (Dowling 2007). For the actual bridge components with different dimensions, and subject to variable-amplitude loads, the models presented in former studies require substantial tests for data correlation.

The possibility exists that AE may characterize critical crack growth because a common nature exists in each transition of crack propagation from stage II to stage III. For each crack growth rate curve as shown in Figure 2, two driving forces, stress intensity range and maximum stress intensity, govern the crack growth behavior (Vasudevan and Sadananda 2001, Yu and Kujawski 2010). The cyclic driving force, stress intensity range, dominates stages I and II under plane strain conditions. The stress intensity and size of the plastic zone ahead of the crack tip increase as the crack advances. After the fracture toughness has been reached, the static driving force (maximum stress intensity) controls stage III under plane stress conditions. It has been reported that AE parameters have demonstrated major jumps when the stress intensity reached a certain value (Chen and Choi 2004).

Emission identification is a necessary step to obtain accurate AE evaluation of fatigue damage. In addition to active crack growth, AE sensors are also sensitive to the noises from grating between fracture surfaces, friction between target structure and fixtures, and the environment. The grating emission can be minimized by collecting and analyzing signals in the vicinity of the peak load (Sinclair and Connors 1977, Lindley et al. 1978). The spatial filtering techniques based on source location, guard sensors and time of arrival (Berkovits and Fang 1995, Daniel et al. 1997, Lopez Pumarega et al. 2003) can be employed to separate extraneous noise from crack bursts in laboratory testing, based on the prediction that the crack initiates ahead of the notch tip and grows along the notch plane. Waveform-based techniques also have been proposed to distinguish the AE signals (Martin 1995, Hamstad and McColskey

1997, Choi et al. 2000, Pullin et al. 2005). Because typical parameters such as rise time, duration, amplitude, and counts in a burst-type waveform are employed to identify the signals, the waveform-based techniques are suitable for both laboratory studies and field tests where sparse data sets are required.

In this paper, the AE characteristics associated with the crack growth behavior of the material used for in-service bridges were collected through conventional fatigue crack testing. AE parameters that fit for indicating crack extension from stage II to stage III were determined based on test results and association of AE signal characteristics with crack growth behavior. The critical damage level of fatigue cracks and corresponding critical level of AE signals were characterized for the successful application of structural damage evaluation. The application of passive piezoelectric based sensing is described for cyclically loaded compact tension (CT) specimens. The specimens are representative of steel bridge construction and were specially designed and fabricated for this purpose. The plan dimensions of the CT specimens were considerably increased from those traditionally used. This was done to minimize reflections that could lead to difficulties with interpretation of the AE signals. Tests for collecting AE from grating and extraneous noise were also performed. Signals were filtered through a combined approach involving Swansong II Filters and visual investigation of waveforms. The cleaned dataset was interpreted using linear elastic fracture mechanics (LEFM).

2. Experimental procedures

CT specimens, made of structural steel ASTM A572 Grade 50, were used in AE-monitored conventional fatigue tests. The geometry of the specimens is displayed in Figure 3. The thickness of the specimens was selected to be representative of bridge construction. Custom fixtures were designed and fabricated to mount the CT specimens. The cyclic tension loads were applied to the specimen using a servo-hydraulic mechanical testing machine and the surface cracks were monitored optically with a high resolution recording microscope. A clip gage was employed to measure the crack mouth opening displacement (CMOD) to clarify crack opening and closure and to determine the crack length. The measurement locations of the clip gage are at the edge of the specimen as shown in Figure 3.

Instruments manufactured by Mistras Group were employed to detect, collect and process AE signals. Standard resonant sensors of type R15I-AST with integral 40 dB preamplification were utilized to detect and collect the signals associated with crack growth behavior. The layout of the five sensors is shown in Figure 3. Sensors were attached to the specimen with vacuum grease and held in place with plastic clamps. AE data was processed and displayed through a 16-channel Sensor Highway II-Remote Asset Integrity Monitor system. The axial displacement, axial loads and CMOD were introduced into the signal processor along with AE signals.

Pencil lead break (PLB) tests were performed before each fatigue test to check the status of each sensor and the location capability of the sensor arrangement. In addition, waveforms and their characteristics obtained in the PLB tests were used as a frame of reference from genuine hits for data filtering.

3. Data filtering procedures

In the application of passive piezoelectric sensing techniques, genuine hits from cracking and "false" hits from noise can both be recorded. One type of "false" hit is induced by the grating between fracture surfaces, another is from extraneous noise. The extraneous noise mainly comes from the hydraulics, machine start and stop, slippage and abrasion of the load train according to the test setup. To minimize grating emission signals the data collected below 80% of the peak load was removed from the dataset. This approach to filtering the grating emission is of interest to the field evaluation of bridges where it is important that sparse data be used for interpretation. To reduce the "false" hits induced by the test setup in loading and unloading procedures, pins in the specimen fixtures were wrapped with cloth and gaps between the specimen and fixture were filled with plastic shims. While this greatly reduced the extraneous noise, the noise could not be completely eliminated through these simple methods.

Verification tests were performed to determine the intensities of the friction emission using a specimen with crack length of 40 mm. In these tests the maximum load in the cycles was decreased to a lower level. The lower peak load was selected to be insufficient to produce crack growth. All of the AE events at this lower peak load were therefore assumed to be due to friction emission. Emission having the characteristics of friction emission was then filtered from the dataset used for later evaluation. To obtain a high threshold of friction emission and a conservative evaluation of the crack growth detection, the maximum emission in each signal bin was scanned. This amplitude threshold (60 dB) was determined to minimize friction emission from the dataset.

The waveforms and their characteristics obtained from friction emission tests and PLB tests were employed as a reference to identify the "false hits" for data filtering.. The technique of the Swansong II filter was employed to further filter the friction signals based on the relationship between amplitude and duration of AE events. For the specific Swansong II filter in this study, "false" hits are defined by their peak amplitude and duration. Typical parameters in AE waveforms include peak amplitude, rise time, duration, and emission counts. The waveforms from fatigue cracks, friction emission and PLB tests are also demonstrated in Figure 4. The waveforms caused by friction generally have long duration and poorly defined peak amplitudes. In fatigue cracks and PLB tests, the shorter duration and higher peak amplitude are indicative of genuine AE, as is the clean front-end of the waveform.

4. Results and discussion

The characteristics of the AE associated with the parameters of fracture mechanics are useful for damage evaluation of in-service structures. The collection and interpretation of signal characteristics are essential to achieve a successful application of the AE technique to the structure of interest. Based on the filtered datasets, AE parameters were associated with corresponding parameters in crack growth behavior to obtain their critical values which indicate crack development from the stage of stable propagation to the stage of unstable propagation.

The maximum stress intensity and cumulative hits versus load cycles in the test for CT1 are displayed in Figure 5. It can be observed that the cumulative hits increased dramatically after the maximum stress intensity, K_{max}, passes through the value of 81.4 MPa$\sqrt{\text{m}}$. As load ratio, R, is 0.02, the stress intensity range, $\Delta K = (1 - R)K_{max}$, is equal to 79.8 MPa$\sqrt{\text{m}}$.

The rapid increases ('jumps') as shown in Figure 5, which also exist in the CT2 test results, are not attributable to friction signals but mainly from the transition of fracture mechanisms (Daniel et al. 1997). As shown in the photo embedded in Figure 5, the smooth fracture surface indicates that plane strain dominates the crack growth, while the rough surface indicates that plane stress dominates crack growth. This phenomenon exists in many steels. In this transition zone the variation of the cyclic plastic zone and strain intensification were reflected in the AE dataset.

The crack length and cumulative counts versus load cycles from the CT2 test results are shown in Figure 6. The cumulative counts increased exponentially similar to that of the crack length as the number of load cycles increased. The increment of cumulative counts became visibly larger after the crack length was beyond 20.8 mm.

It has been shown in this study that for typical steel bridge materials AE characteristics corresponding to crack growth behavior were caused by different cyclic loading conditions. In addition, AE cumulative hits and cumulative counts work well for the determination of critical fatigue crack growth. Additional parameters such as signal strength and hit rate will also be investigated to increase the robustness of the correlations.

5. Conclusions

Passive piezoelectric sensing techniques were utilized to monitor fatigue crack growth in CT specimens that were specially designed and fabricated to be representative of steel bridge construction. Reference tests such as friction emission and pencil lead breakage were performed to obtain reference waveforms from friction and simulated cracks. A Swansong II filter combined with a waveform-based approach was used to minimize "false" signals in the AE dataset. The correlation between AE characteristics and crack growth behavior was built through the association of AE parameters with corresponding parameters in fracture mechanics. Based on this study, the following conclusions can be drawn:

1. AE characteristics associated with crack growth behavior can effectively determine the critical level of fatigue crack growth under different cyclic loading conditions. AE cumulative hits and cumulative counts can provide warning signs at the critical point where fatigue cracks come into the stage of unstable propagation. The critical values of the AE parameters depend on the loading conditions.

2. AE can characterize and reflect crack growth behavior such as the transition between fracture mechanisms in steels that are representative of bridge construction.

3. Friction emission testing can provide reference waveforms to aid in the differentiation of noise from cracking, but did not provide all-inclusive reference

parameters for data filtering. This is because the loads are decreased to keep the crack length constant during the friction emission testing.

4. The combination of a Swansong II filter with a waveform-based approach was found to be appropriate for data processing and interpretation. This combined method holds promise not only in the laboratory studies but also in field testing. It is important to define the waveforms associated with background noise and crack growth if this method is to be used.

6. Acknowledgements

This work is performed under the support of the U.S. Department of Commerce, National Institute of Standards and Technology, Technology Innovation Program, Cooperative Agreement Number 70NANB9H9007. The authors wish to acknowledge those involved at Mistras Group, especially Valery Godinez; and joint venture partners University of Miami (Antonio Nanni) and Virginia Tech (Dan Inman).

We also thank DRPA, Virginia DOT, South Carolina DOT and Florida DOT for providing access to bridges and related information for this project.

7. References

ASCE (2009). *2009 Report card for America's infrastructure*.

Bassim, M. N., Lawrence, S.S., and Liu, C.D. (1994). "Detection of the onset of fatigue crack growth in rail steels using acoustic emission." *Engineering Fracture Mechanics*, 47(2), 207-214.

Berkovits, A., and Fang, D. (1995). "Study of fatigue crack characteristics by acoustic emission." *Engineering Fracture Mechanics*, 51(3), 401-416.

Chen, H. L., and Choi, J. H. (2004). "Acoustic emission study of fatigue cracks in materials used for AVLB." *Journal of Nondestructive Evaluation*, 23(4), 133-151.

Choi, J., Luo, J. J., and Daniel, I. M. (2000). "Analysis of acoustic emission waveforms from propagating fatigue crack." *Review of Progress in Quantitative Nondestructive Evaluation*, 19, 351-358.

Daniel, I. M., Luo, J. J., Sifniotopoulos, C. G., and Chun, H. J. (1997). "Acoustic emission monitoring of fatigue damage in metals." *Symposium on Quantitative Nondestructive*, 16, 451-458.

Dowling, N. E. (2007) *Mechanical behavior of materials: engineering methods for deformation, fracture, and fatigue*, 3rd ed., Pearson Education, NJ.

Gong, Z., Nyborg, E. O., and Oommen, G. (1992). "Acoustic emission monitoring of steel railroad bridges." *Materials Evaluation*, 50(7), 883-887.

Hamel, F., Bailon, J. P., and Bassim, M. N. (1981) "Acoustic emission mechanisms during high-cycle fatigue." *Engineering Fracture Mechanics*, 14(4), 853-860.

Hamstad, M. A., and McColskey, J. D. (1997). "Wideband and narrowband acoustic emission waveforms from extraneous sources during fatigue of steel." *Journal of Acoustic Emission*, 15(1-4), 1-18.

Lindley, T.C., Palmer, I.G., Richards, C.E. (1978). "Acoustic Emission Monitoring of Fatigue Crack Growth." *Materials Science and Engineering* , 32, 1-15.

Lopez Pumarega, M. I., Armeita, M. A., Ruzzante, J. E., and Piotrkowski, R. (2003). "Relation between amplitude and duration of acoustic emission signals." *Review of Quantitative Nondestructive Evaluation*, 22, 1431-1438.

Martin, C. A., Van Way, C. B., Lockyer, A. J., and Kudva, J. N. (1995). "Acoustic emission testing on an F/A-18 E/F titanium bulkhead." *Proc. SPIE*, 2444, 204-211.

Oh, K. H., Jung, C. K., Yang, Y. C., and Han, K. S. (2004). "Acoustic emission behavior during fatigue crack propagation in 304 stainless steel." *Key Engineering Materials*, 261-263, 1325-1330.

Ohira, T., Kishi, T., and Horiuchi, R. (1980). "Acoustic emission during fatigue crack propagation in structural materials." *International Acoustic Emission Symposium*, 5, 137-145.

Pullin, R., Holford, K. M., and Baxter, M. G. (2005). "Modal analysis of acoustic emission signals from artificial and fatigue crack sources in aerospace grade steel." *Key Engineering Materials*, 293-294, 217-224.

Robert, T.M., and Talebzadeh, M. (2003). "Fatigue life prediction based on crack propagation and acoustic emission count rates." *Journal of Constructional Steel Research*, 59, 679-694.

Sinclair, A. C. E., and Connors, D. C. C. (1977). "Acoustic emission analysis during fatigue crack growth in steel." *Materials Science and Engineering*, 28, 263-273.

Stephens, R. I., Fatemi, A., Stephens, R. R., and Fuchs, H. O. (2000) *Metal Fatigue in Engineering*, 2nd ed., John Wiley & Sons, NY.

Vasudevan, A.K., and Sadananda, K. (2001). "Analysis of fatigue crack growth under compression-compression loading." *Int. J. Fat.*, 23, s365-s374.

Yu, J., and Kujawski, D.(2010). "Analysis of stress distribution in compression precracking." *International Journal of Structural Integrity*, 1(2), 140-152.

Yu, J., Ziehl, P., Zarate, B., Caicedo, J., et al. (2010). "Quantification of fatigue cracking in CT specimens with passive and active piezoelectric sensing." *Proc. SPIE*, 7649, 76490R1-12.

Ziehl, P. H. (2008). "Applications of acoustic emission evaluation for civil infrastructure." *Proc. SPIE*, 6934, 1-8.



Fig. 1 Illustrations of fatigue cracks in steel bridges

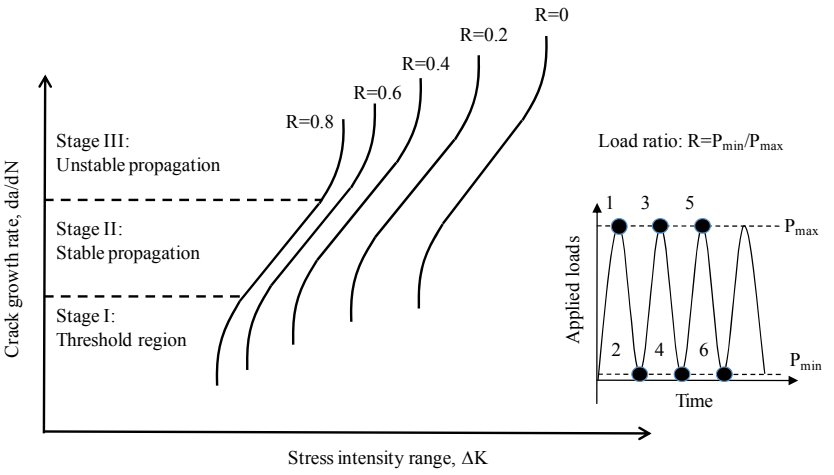


Fig. 2 Schematic illustrations of crack growth behavior with different load ratios

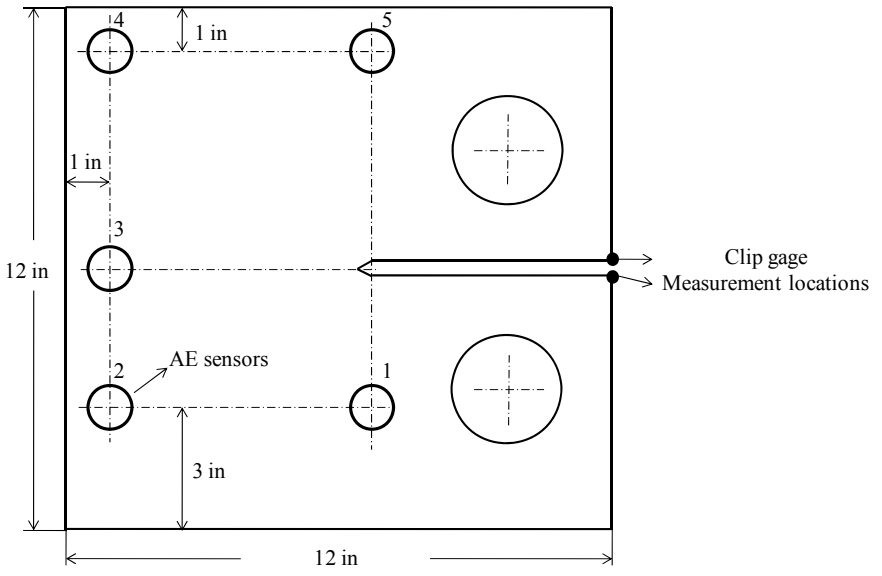


Fig. 3 Geometry of CT specimen and arrangement of sensors

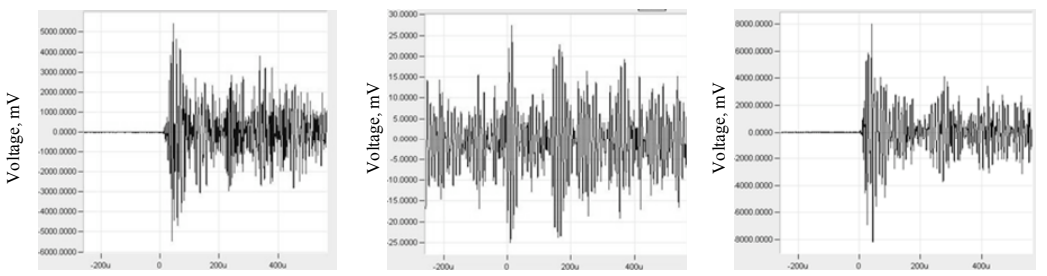


Fig.4 Waveforms from fatigue cracks, friction, and PLB tests.

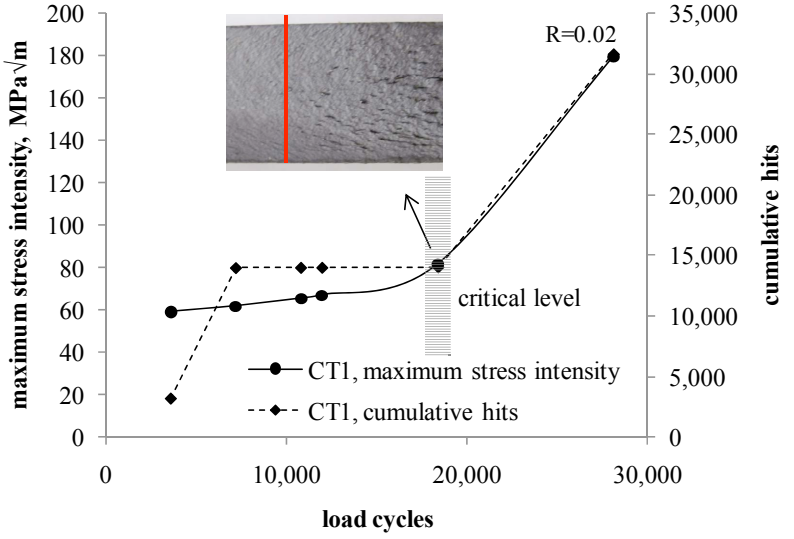


Fig.5 CT1 maximum stress intensity and cumulative hits vs. load cycles

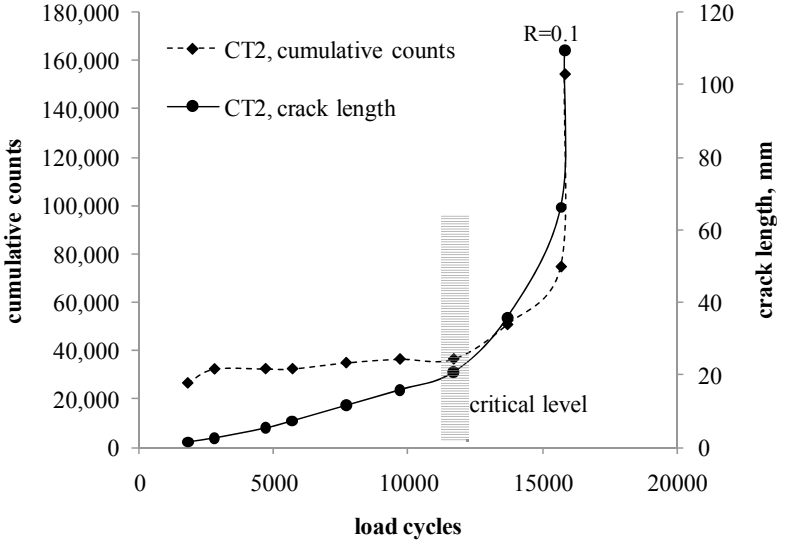


Fig. 6 CT2 crack length and cumulative counts versus load cycles

Improved Method for Bonding CFRP Overlays to Steel for Fatigue Repair

Fatih Alemdar[1], Adolfo B. Matamoros[2], Caroline R. Bennett[3], Ron Barrett-Gonzalez[4], and Stanley T. Rolfe[5]

[1] Department of Civil, Environmental, and Architectural Engineering, University of Kansas, 1530 W. 15th St., 2150 Learned Hall, Lawrence, KS 66045, Tel. 785-864-3268, Fax. 785-864-5631, alemdar@ku.edu
[2] Department of Civil, Environmental, and Architectural Engineering, University of Kansas, 1530 W. 15th St., 2150 Learned Hall, Lawrence, KS 66045, Tel. 785-864-3761, Fax. 785-864-5631, abm@ku.edu
[3] Department of Civil, Environmental, and Architectural Engineering, University of Kansas, 1530 W. 15th St., 2155 Learned Hall, Lawrence, KS 66045, Tel. 785-864-3235, Fax. 785-864-5631, crb@ku.edu
[4] Department of Aerospace Engineering, University of Kansas, 1530 W. 15th St., 2120 Learned Hall, Lawrence, KS 66045, Tel. 785-864-4267, Fax. 785-864-3597, barrettr@ku.edu
[5] Department of Civil, Environmental, and Architectural Engineering, University of Kansas, 1530 W. 15th St., 2150 Learned Hall, Lawrence, KS 66045, Tel. 785-864-3767, Fax. 785-864-5631, srolfe@ku.edu

ABSTRACT

Experiments and computer simulations were carried out at the University of Kansas to investigate the use of composite materials for strengthening and repair of fatigue-vulnerable steel bridges. Prefabricated CFRP overlays were attached to welded coverplate specimens using a layer of epoxy resin. The specimens were then subjected to three-point bending under cyclic loading at a constant stress range. Early tests showed that bonding CFRP overlays to steel was an effective method to reduce the stress demand in areas susceptible to fatigue damage, and that this strengthening method could lead to substantial increases in crack initiation life. Fatigue tests also showed that maintaining the bond between the CFRP overlays and the steel was the most critical factor in the effectiveness of this strengthening technique. It was observed that the presence of a layer of breather fabric embedded within the layer of epoxy resin was the most important parameter affecting bond behavior under fatigue loading.

This paper describes monotonic and fatigue tests carried out to evaluate the effect of the presence of breather fabric and thickness of the resin layer on bond strength and on the performance of the resin layer under fatigue loading. It was found that the mode of failure of the resin under monotonic and fatigue loading changed significantly due to the presence of the breather cloth. Although the presence of breather cloth had a negligible effect on the bond strength of thin resin layers, its effect on strength increased with the thickness of the resin layer. It was also found that the presence of the breather fabric had a very significant effect on the post-peak behavior of monotonic tests, which partially explains its beneficial effect on behavior under fatigue loading.

BACKGROUND

Techniques to repair connections vulnerable to fatigue damage in steel bridges must be developed considering the specific geometry and other relevant characteristics of the particular connection detail. This is particularly the case for fatigue repairs using composite material overlays, in which the geometry and location of the overlays should be optimized for the shape of the connection detail. Nonetheless, several studies have found that regardless of geometry a critical factor in the implementation of this repair technique is maintaining the bond between the composite material and the steel for the intended fatigue life of the repair. There is a wealth of studies investigating bond between resins and metal.

Two studies closely related to the type of repair discussed in this paper were carried out by Nozaka et al. (2005; 2005a), who investigated the effectiveness of carbon-fiber-reinforced polymer (CFRP) strips for increasing fatigue life of steel girders. Testing described in Nozaka et al. (2005) was

designed to compare how several types of adhesives and laminates would perform in different configurations. Two different CFRP types and a total of five adhesives were evaluated. A testing rig was used which consisted of a W14x68 girder 14.1-ft long with a large hole and a wide slit machined at mid-span to represent a crack in the tension flange and to focus the tensile force in that area. CFRP strips were bonded onto individual steel plates which were then bolted to the tension flange of the girder. Specimens were then loaded monotonically in four-point bending under displacement control. Nozaka et al. found that the specimens did not fail due to tensile failure of the CFRP, but rather due to a mixture of tensile failure and debonding.

In a continuation study, Nozaka et al. (2005 a) evaluated several options to properly test the bond strength of CFRP strips. Two commonly used tests use single-lap and double-lap specimens. These have been extensively used to test the shear strengths of adhesives to metals. One of the concerns expressed by Nozaka et al. was that a single-lap test would cause the joint to rotate. This is due to the misalignment of neutral axis between the separate parts, and it results in a peeling stress along with a shear stress acting on the interface between the resin and the steel girder. Therefore a single-lap specimen would not result in a failure due to solely shear stress, but rather a combination of shear and peeling stress. To evaluate the various bond tests Nozaka et al. (2005) started by investigating the stresses on a fatigue-damaged girder repaired with composite materials. The model consisted of two CFRP strips bonded to the inner surface of the tension flange of the girder. One CFRP strip was located on each side of the web.

The specimen was modeled using ABAQUS (2007) with the CFRP modeled as an elastic material, and the steel and adhesive modeled as elastic-perfectly-plastic materials. By modeling the specimen in this fashion it was possible to calculate the shear, peeling, and normal stresses. By comparing the shear stresses near the CFRP, with and without the CFRP strip, it was possible to determine that the stress was reduced when the CFRP strip was applied. These effects contributed to the transfer of forces from the girder flange to the CFRP. It was also shown that shear and peeling stresses increased on both edges of the strip due to an edge effect, which can cause debonding.

Nozaka et al. explored alternate specimen types to properly test the bond of the CFRP. In an attempt to minimize peeling stress during testing, three separate test specimens were considered. The chosen specimen consisted of a 0.5 in. thick plate of 12 in. length. The thickness of the end of the plate was increased in an attempt to align the neutral axis of each section. Restraints were then applied to the end of the specimen to limit rotation.

The first step of testing was to examine the effect of varying steel thickness. Three different thicknesses were tested including 0.5, 0.7 and 1.0 in. By examining the results it was found that changing the steel thickness had no major effect on the shear stress. With further investigation it was found that the tensile stress in the steel adherent was beyond the yield strength of the steel (Nozaka et al., 2005 a). This occurred before the CFRP strip failed; therefore this type of specimen could not be used for testing. For this reason it was concluded that single-lap specimens were inadequate to measure the true bond strength of CFRP strips bonded to steel (Nozaka et al. 2005 a).

Nozaka et al. (2005) concluded that the test specimen had to be attached to the girder by bonding the CFRP strips to steel plates which were then bolted to the tension flange of the girder. This test arrangement was also used for the testing in their previous study. A large hole and slit was machined at the mid span of the girder to represent a fatigue crack in the tension flange. By doing this the applied compression force would be isolated through the crack, optimizing the effect on the crack. The specimen was then tested under four-point loading with supports 5.0 in. from the edges of the girder.

The studies by Nozaka et al. (2005; 2005 a) highlight the fact that when composite overlays are utilized, depending on the geometry of the overlay, there can be a combination of tensile (peel) and shear stresses transferred along the interface between the steel and the composite overlay, and that the relative magnitude of the two actions is dependent on the geometric configuration of the overlay and the connection being repaired. This aspect is of particular significance when using composite overlays to repair welded connections.

Several studies conducted at the University of Kansas have investigated the concept of using composite materials to strengthen fatigue-vulnerable connections in steel bridge structures. An example

of the type of specimen used at Kansas to evaluate this strengthening technique is shown in Fig. 1. The specimen consists of two plates welded together and subjected to three point bending under fatigue loading. This specimen was chosen because a severe discontinuity exists at the point where the two plates are welded, and the stress concentrations in the discontinuity lead to fatigue failure under cyclic loading.

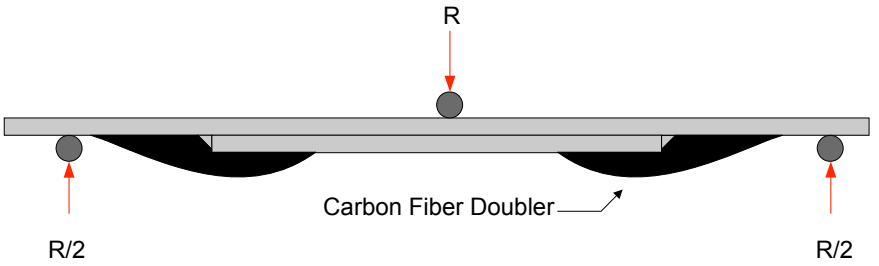


FIGURE 1 Three-Point Bending Fatigue Specimen Strengthened with Composite Overlays

Computer simulations of the specimen shown in Fig. 1 performed for this study using the finite element analysis software ABAQUS showed that attaching overlays made with composite materials to areas of the specimen affected by stress concentrations (areas adjacent to the welds) led to significant reductions in the localized stress demand. This effect is shown in Fig. 2, which shows the maximum stress demand at the weld region of the specimen for configurations with and without a composite overlay. The finite element results indicated that the composite overlays were effective in providing an alternate load path to the force transmitted between the two steel plates, spreading the stress demands over a larger area and consequently reducing the stress gradient.

One of the most significant challenges associated with the implementation of this retrofit technique is developing a fabrication process that results in stiff overlays that are properly bonded to steel elements. Although composite plies can be applied directly in the field, better results are obtained by prefabricating the overlays in shop and subsequently attaching them to a bridge. However, this fabrication sequence brings about challenges, for example, because the composite overlay may not align perfectly with the steel, and because a method of properly bonding the overlay to the steel must be developed. In this study, composite overlays were prefabricated following the procedure described by Kaan (2008) and attached to three-point bending specimens shown in Fig. 1 by means of a layer of epoxy resin between the composite overlay and the steel. Finite element models were developed to investigate the effect of varying the thickness of the layer of epoxy resin on the stress demand at the toe of the weld, and on the shear and tensile stresses at the interface between the resin layer and the steel (Petri 2008).

Stress demands calculated using the finite element model are shown in Fig. 3. In the case of the three-point bending specimen, the thickness of the resin layer had a significant effect on the peel stress between the epoxy resin and the steel. A similar effect was observed for the peel stress between the epoxy resin and the composite overlay. The magnitude of the maximum peel stress was significantly different on each side of the epoxy resin layer and it was found to increase with decreasing thickness of the epoxy resin layer.

Kaan (2008) and Alemdar performed tests to experimentally evaluate the results from the finite element study. Results are illustrated in Fig. 4. The diamond shapes in Fig. 4 represent the initiation life of four control specimens tested at nominal stress ranges of 20 and 28 ksi at the weld toe (Kaan, 2008). Average initiation life of the control specimens tested at a nominal stress range of 20 ksi was 425,000 cycles. The horizontal line with points labeled TRI 06 corresponds to a fatigue test performed by Kaan (2008) and later by Alemdar (round marker) as part of this study. Kaan and Alemdar used a single three-point bending specimen strengthened with composite overlays, cycled at a nominal stress range of 20 ksi. Kaan (2008) performed his test with a layer of epoxy resin 1/16 in. thick. The X-shaped markers correspond to points at which Kaan (2008) observed debonding of the composite overlay. Each time after debonding was observed, the specimen was inspected and the overlay re-attached. Kaan (2008) loaded

the specimen for a total of 2.1 million cycles without any observable fatigue crack. There were a total of 5 debonding events, with an average of 431,500 cycles between debonding events. Loading of the specimen was later continued by Alemdar (shown by the round markers in Fig. 4). He used a ¼ in. thick epoxy resin layer with embedded breather cloth. Alemdar was able to load the specimen for an additional 1.5 million cycles without any debonding events. After loading for 1.5 million additional cycles (for a total of 3.7 million cycles) the overlay was removed and an inspection showed that there were no observable fatigue cracks.

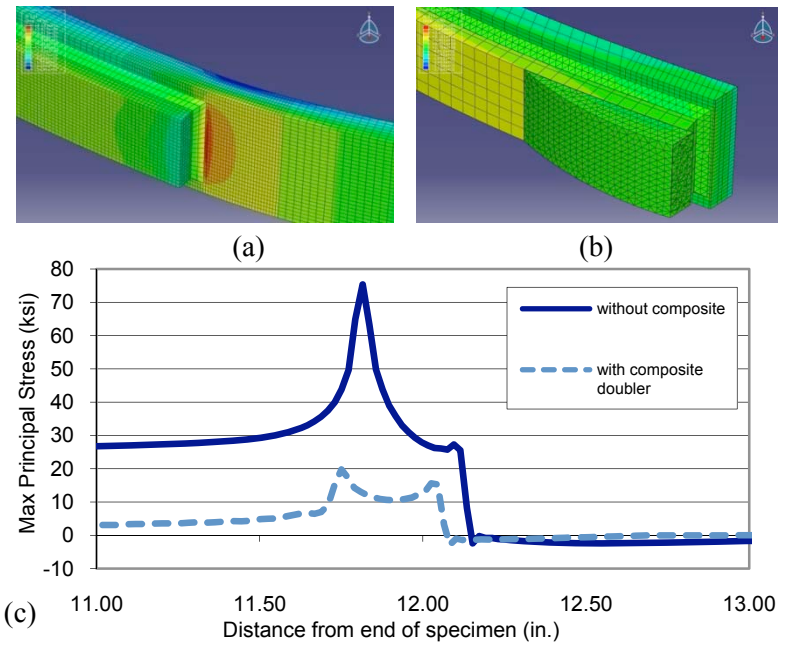


FIGURE 2 Calculated Maximum Principal Tensile Stress for Specimens With and Without Composite Overlays.

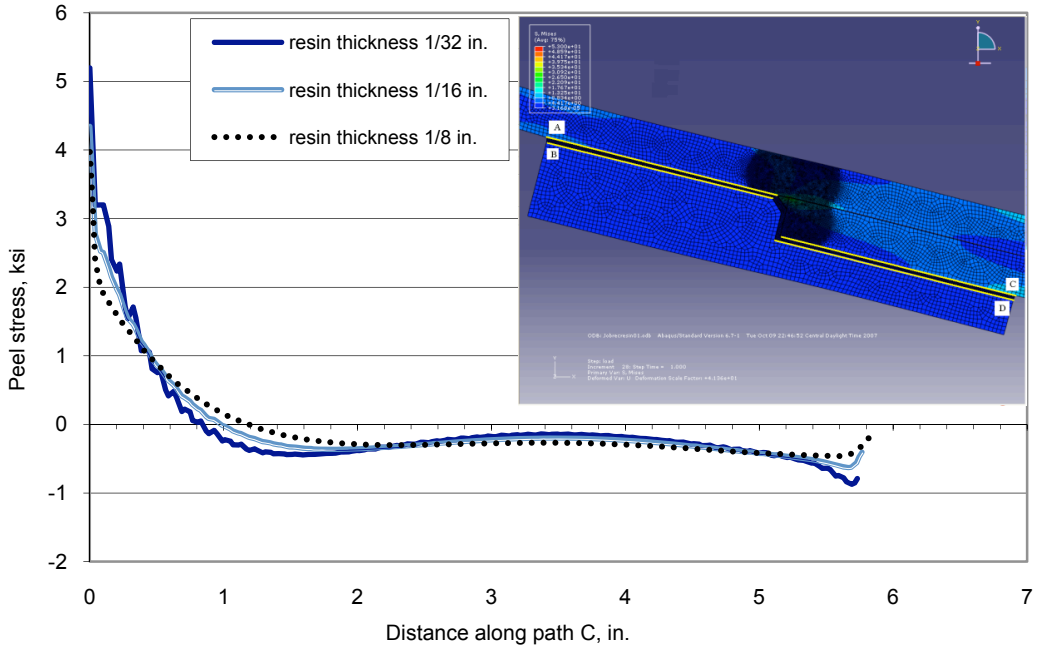


FIGURE 3 Peel stress demand along path C for various thicknesses of epoxy resin layer.

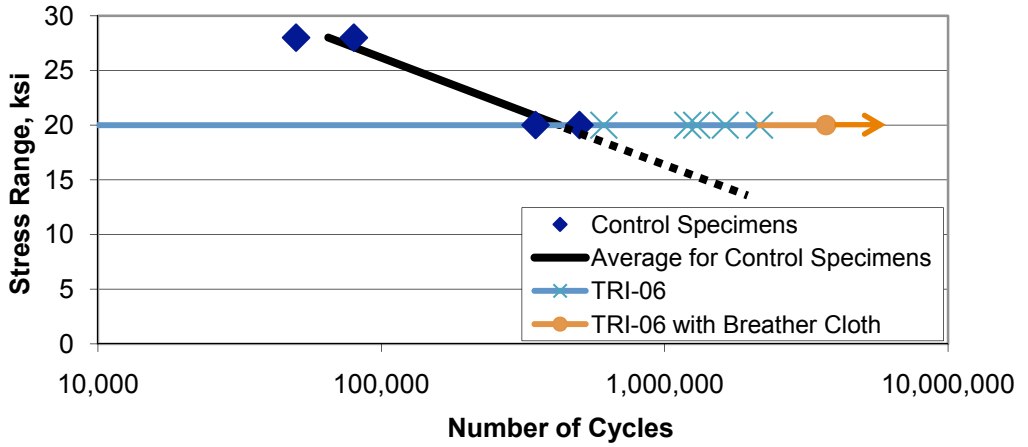


FIGURE 4 Crack Initiation Life for Three-point Bending Specimens Tested by Kaan and Alemdar.

The tests performed by Alemdar and Kaan (2008) showed that the use of composite overlays increased the initiation life of the specimen from 425,000 cycles to infinite fatigue life, confirming the observations from the finite element analyses. The aforementioned tests also showed that the presence of breather cloth increased the fatigue life of the epoxy resin layer from an average of 431,000 cycles to infinite fatigue life. Proper bond is critical to the performance of this strengthening method because if an overlay debonds, the specimen continues to cycle in the unreinforced configuration until a repair is implemented. For this reason, and because the observed fatigue life of specimens with breather cloth was significantly higher than those without breather cloth, a series of experiments was undertaken to study the effects of embedding breather cloth on the bond strength and fatigue life of the epoxy resin layer.

EXPERIMENTAL STUDY

The effects of embedding breather cloth on the strength and fatigue life of the epoxy resin layer were further studied by performing two series of monotonic tests. The monotonic tests were designed to simulate the state of stress in the epoxy resin layer of three-point bending specimens. For the first series of tests a composite overlay similar to those used to strengthen the plate-coverplate specimen was attached through a steel plate using a layer of epoxy. The test apparatus and its dimensions are shown in Fig. 5.

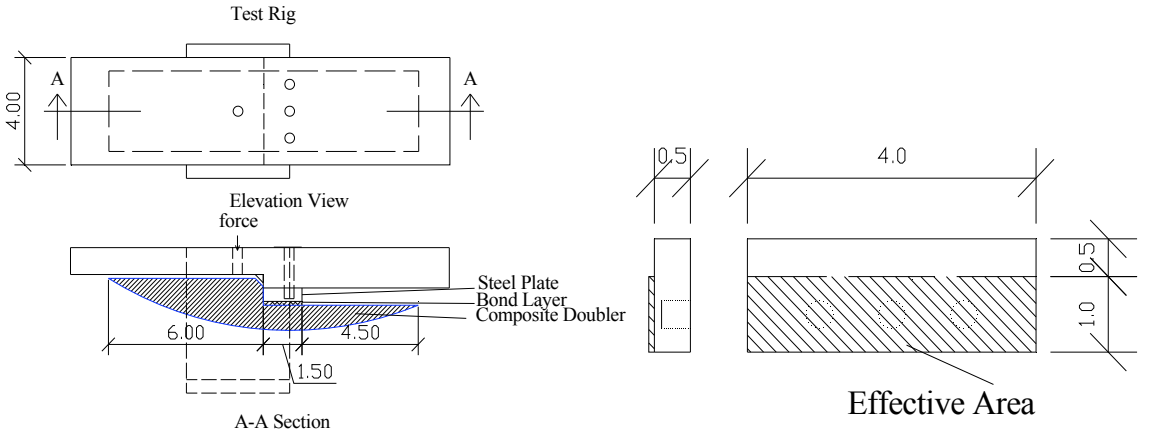


FIGURE 5: Test Apparatus for Peel Tests (all dimensions shown in inches.)

Properties of the materials used in the experiments are presented in Table 1. Monotonic tests were performed according to the following protocol. The composite overlay was bonded to the steel plate with a layer of epoxy of a pre-determined thickness. The steel plate was subsequently bolted to the reaction apparatus, which was attached to the testing machine. The specimen was loaded using a pin that was pushed through a hole in the plate (Fig. 6), inducing a state of stress in the resin layer that combined the effects of direct tension and bending (Fig 7). The part of the plate opposite the loading pin was machined to avoid direct contact between the composite and the reaction plate (Fig. 6).

Finite element analyses were performed to compare the state of stress in the resin layer of the monotonic tests and the resin layer of the three-point bending specimen. Results from the finite element analysis are shown in Fig. 7. Although the stresses shown in Fig. 7 do not constitute a perfect match of those in Fig. 3, important features are repeated. In both cases, the normal stresses vary following a gradient from tension to compression, indicative of combined tension and bending, with peak values at the edge of the resin layer.

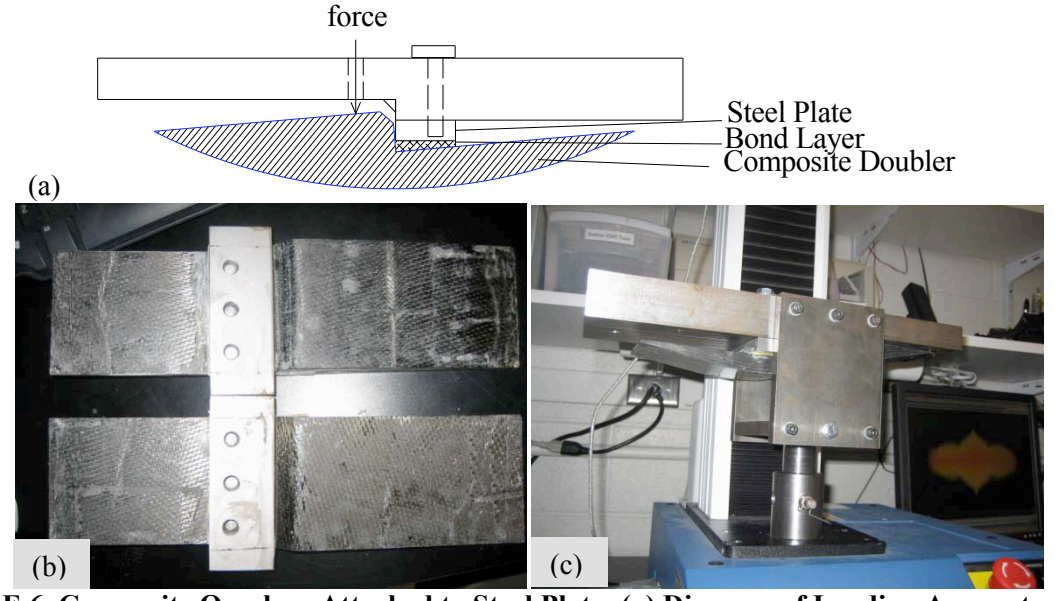


FIGURE 6. Composite Overlays Attached to Steel Plate: (a) Diagram of Loading Apparatus, (b) Steel Plates Bonded to Composite Overlays, (c) Reaction Apparatus Installed in Testing Machine.

RESULTS

For the first series of monotonic tests, in which the resin layer was used to bond a steel plate to the composite overlay, most failures were due to delamination within the composite overlay instead of loss of bond between the resin layer and the steel (Fig. 8). This was likely due to the fact that the resin used to bond the composite to the steel (Hysol ®) was stronger than the resin used to fabricate the composite overlay. Measured load-deflection relationships for the specimens tested are shown in Fig. 8. The dashed lines in Fig. 8 correspond to resin layers with embedded breather cloth, while the solid lines correspond to specimens without breather cloth. As shown in Fig. 8, the average peel stress ranged between 100 and 300 psi.

The failure of one of the specimens without breather cloth illustrates one of the most important effects of embedding breather cloth within the resin layer. Due to the low viscosity of the resin, large voids formed in the resin layer during fabrication, resulting in much weaker bond between the resin layer

and the steel. This was the only instance in which failure occurred due to loss of bond between the resin layer and the steel instead of debonding of the composite.

Table 1 : Material Properties

CFRP			
Number of Layers in Coupon	Number of Coupons	Avg. Modulus of Elasticity GPa (ksi)	Standard Deviation GPa (ksi)
1	3	85.8 (12,438)	10.0 (1,445)
3	4	75.3 (10,926)	10.9 (1,581)
5	3	61.7 (8,944)	0.3 (42)
9412 Hysol® Resin			
Coupon Thickness mm (in.)			
6.4 (0.25)	6	2.1 (303)	0.2 (25)

The main objective of the study was to evaluate the bond between the resin layer and the steel, therefore, the test was modified to avoid premature failure due to delamination of the composite. In a second series of tests, the composite overlay was replaced by a steel plate, guaranteeing that failure would be caused by loss of bond between the epoxy and the steel.

The steel plate used to replace the composite overlay had dimensions of 1-½ in. wide, 4 in. long, and ½-in. thick. Only a 1-in. wide strip of the steel plate was bonded to the resin. The remaining ½ in. was covered with Teflon tape to prevent bond with the steel (Fig. 5). In the same manner as the first group of tests, there were specimens with and without breather cloth embedded in the epoxy resin layer.

The specimens were prepared according to the following procedure. The surface of the two plates was roughened with a grinder and subsequently cleaned with acetone and methanol. The edge of the area to be bonded was covered with adhesive tape in order to build a dam for the resin. In specimens with embedded breather cloth, the cloth was cut leaving a hole to allow placing of a spacer to maintain consistent thickness of the resin. At this point the resin was mixed and poured in the bond area. When cloth was used, it was verified that the cloth absorbed the resin evenly, and that sufficient resin was absorbed by the cloth. The second steel plate was then placed on top of the resin pool making sure that the plate was in contact with the spacer. Pressure was maintained with a clamp throughout the curing process.

A total of 14 peel tests were performed to evaluate the effect of resin layer thickness and presence of breather cloth on the average tensile stress at failure. Resin layers tested had thicknesses of 1/16 in., 1/8 in., and 1/4 in. Specimen characteristics and the average peel stress at failure are summarized in Table 1. The average peel stress was calculated as the maximum measured force divided by the effective bond area. This simple quantity was considered adequate to establish a basis of comparison between the different configurations.

Load-displacement curves for the peel tests are shown in Fig. 9. Curves with dashed lines correspond to specimens with cloth, while solid lines correspond to load-deformation curves for specimens without cloth. In general, specimens with breather cloth achieved significantly higher deformations at failure. Another observed trend was that specimens without breather cloth exhibited sudden failure leading to a total loss in bond between the two plates. Specimens with breather cloth retained a residual capacity of approximately 30% of the maximum stress.

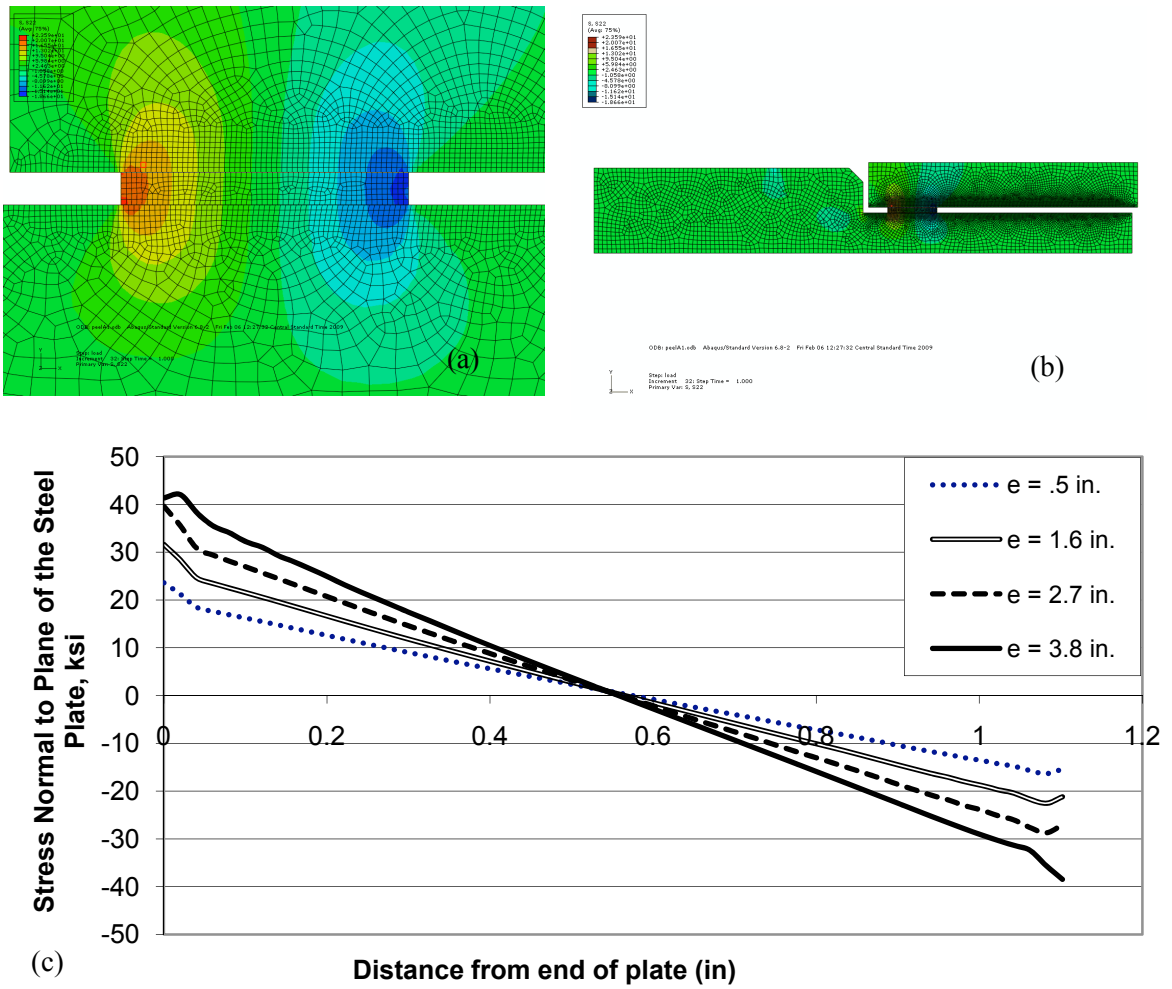


FIGURE 7. Stress Demand on the Resin Layer (a) Finite Element Fringe Showing Stresses Normal to the Plane of the Plate, (b) Finite Element Mesh, (c) Calculated Tensile (Peel) Stress at the Steel-Resin Interface for Various Pin Eccentricities (in units of in.).

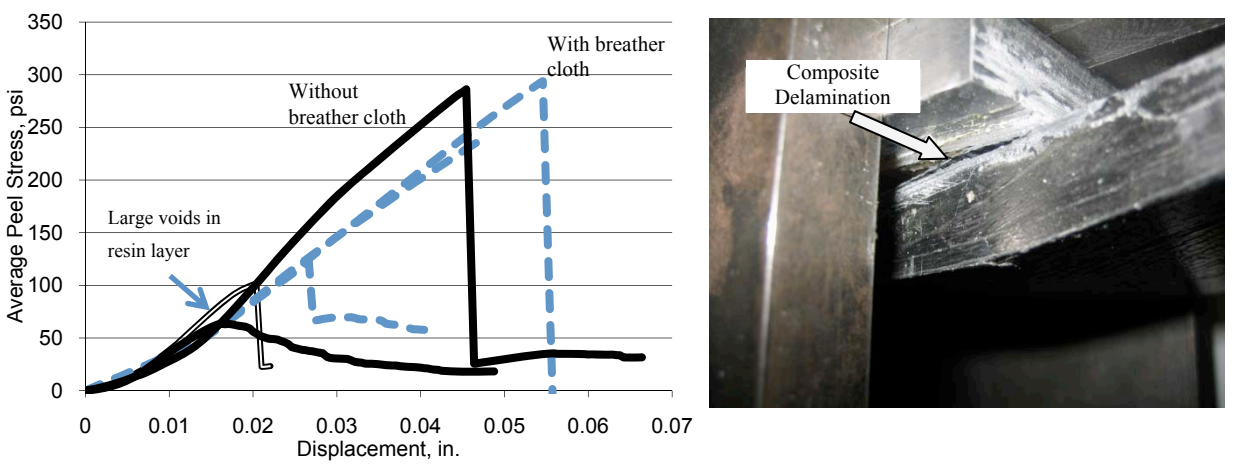


FIGURE 8. Monotonic Peel Tests of Epoxy Resin Layer with Composite Overlays.

TABLE 1 Results from Peel Tests of Steel Plates

Specimen Designation	Thickness (in.)	Cloth (y/n)	Average Peel Stress (psi)
1	0.0625	n	737.4
2	0.0625	n	601.4
3	0.0625	y	644.9
4	0.0625	y	677.4
5	0.1250	n	501.1
6	0.1250	n	360.6
7	0.1250	n	512.9
8	0.1250	y	488.3
9	0.1250	y	584.6
10	0.1250	y	535.4
11	0.2500	n	274.6
12	0.2500	n	371.1
13	0.2500	y	381.7
14	0.2500	y	434.3

Figure 10 shows the resin layer of specimens with and without breather cloth after failure. It is apparent that while the resin layer without cloth developed voids (Fig. 10a), the resin layer with breather cloth did not. Furthermore, it was observed that failure occurred through the middle of the resin layer in the resin layer with breather cloth, with residues remaining attached to both steel plates. This is an indication that the tensile strength of the resin was the limiting factor, and not the bond strength between the steel and the resin.

Figure 11 shows the appearance of the steel plates after failure for specimens with a resin layer thickness of 1/8 in. and 1/4 in. Another feature observed was that in specimens with thinner resin layers, failure tended to occur through the middle of the resin layer, while in specimens with thicker resin layers the tendency was for a greater amount of resin to remain attached to one of the two plates.

Figure 11 shows the relationship between the tensile (peel) strength of the resin layer and the thickness of the resin layer for specimens with and without breather cloth. Figure 11 shows that the strength of the resin layer decreased with increasing thickness, and that the reduction in strength with thickness was less pronounced for specimens with breather cloth. Also, it was observed that for specimens with very thin resin layers the presence of breather cloth had a negligible effect on strength, while for layers 1/4 in. thick, the difference in strength was on the order of 25%. These results suggest that using a resin layer with a thickness of at least 1/8 in. with embedded breather cloth will provide the best results. The observed benefits of breather cloth were: a lower propensity to develop voids in the resin layer; higher strength (for layers with a thickness of at least 1/8 in.); and a significant residual strength after cracking, which is likely to slow crack growth under fatigue loading.

CONCLUSIONS

Results of a study on improved methods for bonding CFRP overlays to steel specimens showed that excellent performance for this type of fatigue repair could be achieved by prefabricating composite overlays and attaching them to the steel structures using a layer of epoxy resin with embedded breather cloth. Monotonic tests were performed to develop a better understanding of the effects of the thickness of the resin layer and the presence of breather cloth on the fatigue life of the epoxy resin layer. It was found that use of breather cloth eliminated the presence of large voids in the resin layer, which can act as a trigger for fatigue cracks and significantly reduce the fatigue life of the bond layer. Although thicker

epoxy resin layers resulted in lower peel strength, thicker layers were less susceptible to problems due to large voids. Another benefit associated with the use of breather cloth was in terms of ductility. The monotonic tests showed that after failure of the resin took place, the breather cloth was capable of tying together the two sides of the failure surface, resulting in a residual capacity of approximately 30% of the strength of the resin. In terms of fatigue behavior, this type of post-peak behavior indicates that breather cloth likely has the effect of retarding the growth of fatigue cracks that form within the bond layer. Both of these effects result in a significant improvement in the bond strength under fatigue loading between composite overlays and steel elements, which are consistent with the improvements in fatigue life observed in fatigue tests of three-point bending specimens.

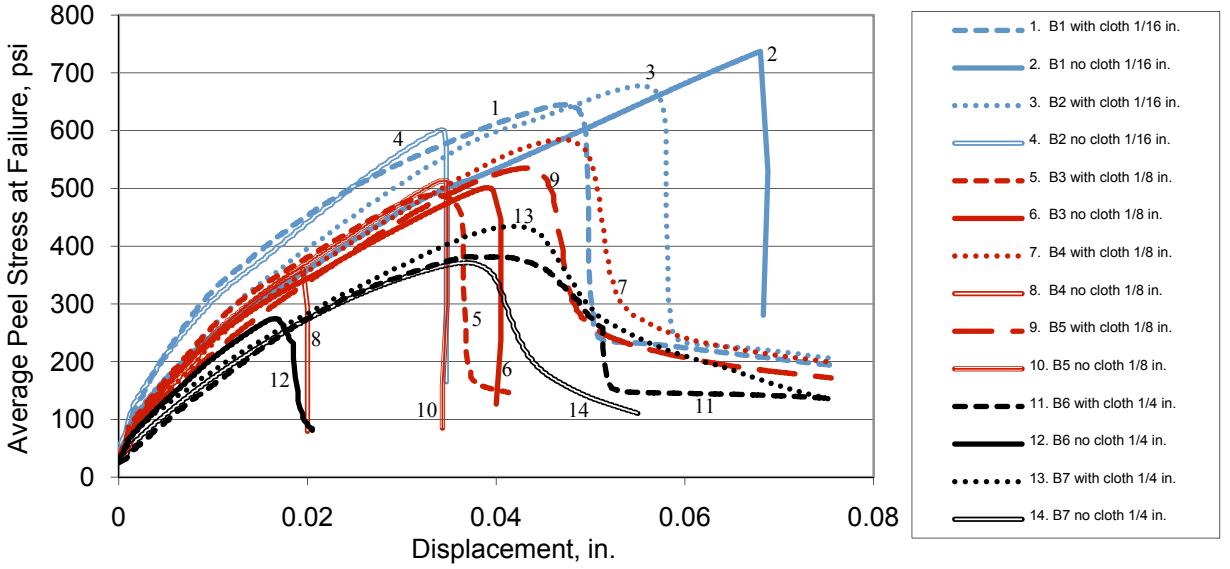


FIGURE 9. Monotonic Peel Tests of Epoxy Resin Layer with Steel Plates.

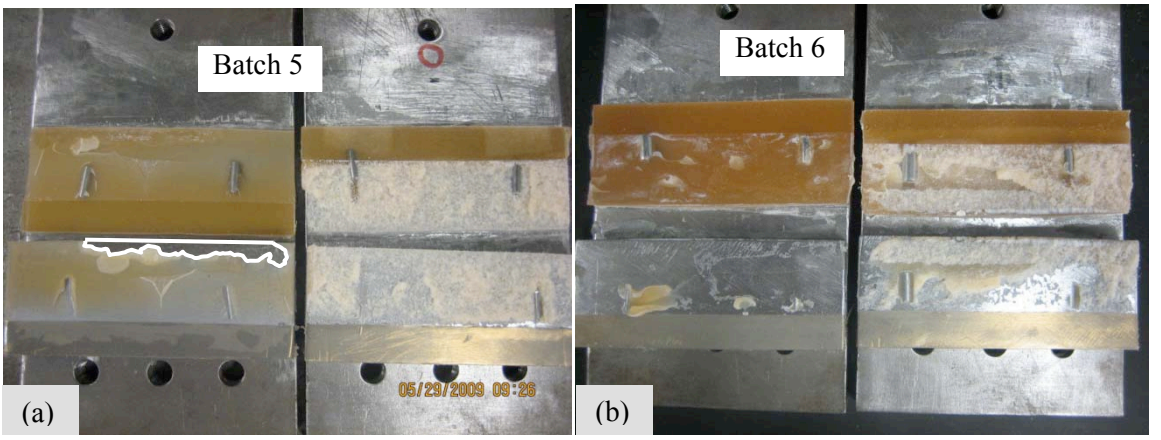


FIGURE 10 Appearance of Resin Layer after Failure for Specimens from (a) Batch 5 (1/8-in. thick) and (b) Batch 6 (1/4-in. thick).

In summary, computer simulations and fatigue tests performed in this study showed that composite overlays were capable of significantly extending the fatigue life of steel structures as long as

adequate bond was maintained between the overlays and the steel. Excellent bond performance under fatigue loading was achieved by attaching prefabricated composite overlays to the steel using a layer of epoxy resin with embedded breather cloth with a thickness of at least 1/8 in.

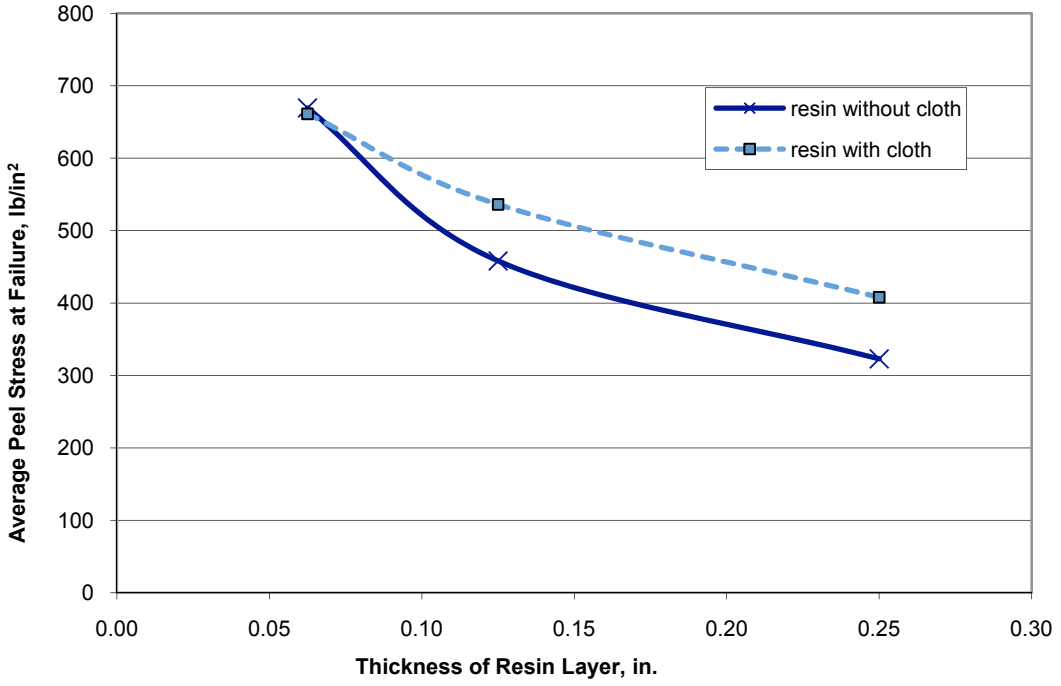


FIGURE 11 Effect of Resin Layer Thickness on Peel Strength of Epoxy Resin Layer.

REFERENCES

ABAQUS/*Standard manual*, version 6.7. (2007). Hibbitt, Karlsson, and Sorensen, Inc., Pawtucket, R.I.

Kaan, B. (2008). "Fatigue Enhancement of Category E' Details in Steel Bridge Girders using CFRP Materials," MS Thesis, University of Kansas at Lawrence.

Nozaka, K., Shield, C., Hajjar, J. (2005). "Effective bond length of carbon-fiber-reinforced polymer strips bonded to fatigued steel bridge I-girders." *Journal of Bridge Engineering*, 10(2), 195-205.

Nozaka, K., Shield, C., Hajjar, J. (2005 a). "Design of a test specimen to assess the effective bond length of carbon fiber-reinforced polymer strips bonded to fatigued steel bridge girders." *Journal of Composites for Construction*, 9(4), 304-312.

Petri, B. (2008). "Finite Element Analysis of Steel Welded Coverplate Including Composite Doublers," MS Thesis, University of Kansas, Lawrence.

ACKNOWLEDGMENT

The authors are grateful for support from the Kansas Department of Transportation (KDOT) and the University of Kansas Transportation Research Institute (KU TRI). The authors would also like to appreciatively acknowledge support provided through Pooled Fund Study TPF-5(189), which includes the

following participating State DOTs: Kansas, California, Iowa, Illinois, New Jersey, New York, Oregon, Pennsylvania, Tennessee Wisconsin, and Wyoming, as well as the Federal Highway Administration.

Fatigue Repair of the Arkansas River Bridge

Y. Zhao[1], K. W. M. Roddis[2], G. Ramirez[3], J. P. Jones[4]

[1] Yuan Zhao, Ph.D., P.E., Bridge Design Engineer, Texas Department of Transportation, Bridge Division, (512) 416-2632, yuan.zhao@txdot.gov. Formerly, Doctoral Candidate, University of Kansas.
[2] W. M. Kim Roddis, Ph.D., P.E., Professor and Chair, Department of Civil and Environmental Engineering, The George Washington University, (202) 994-4901, roddis@gwu.edu. Formerly, Professor, University of Kansas.
[3] Guillermo Ramirez, Ph.D., P.E., Assistant Professor, Department of Civil Engineering, The University of Texas at Arlington, (817) 272-2683, willy@uta.edu. Formerly, Assistant Professor, University of Kansas.
[4] John Patrick Jones, P.E., Manuals, Modeling and Policy Engineer, Kansas Department of Transportation, Bureau of Design, State Bridge Office, (785) 368-7175, jjones@ksdot.org.

BACKGROUND

Since the Kansas Department of Transportation (KDOT) started its fracture critical bridge inspection program around the mid-1980s, many welded steel bridge details at the diaphragm (or floorbeam) to girder connections were found to have developed fatigue cracks, often due to the cause of out-of-plane distortion. While proper fatigue design philosophy has been developed and incorporated into the current AASHTO bridge design specifications, repair of existing bridges with fatigue cracking remains a challenge to the bridge engineering community, especially when the repair details happen to reside in locations with geometrical complexity, or when cracking is compounded by corrosion or impact damage.

Beginning 1996, a series of research studies were performed through the collaborative effort between the KDOT State Bridge Office and the University of Kansas (KU). Five candidate structures were selected to examine the overall fatigue problem experienced by the KDOT steel bridges, using state-of-art finite element (FE) modeling technique. Two of these five bridges were then strain gauged, both before and after the repair, to ensure that the fatigue details were eliminated and the chosen repair method was effective.

This paper discusses the research and repair findings of the first case study sponsored by KDOT, the Arkansas River Bridge.

FATIGUE CRACK DEVELOPMENT

The Arkansas River Bridge was constructed in 1955 on highway K-96 over the Arkansas River in Hutchinson, Kansas. It is a 1020-ft long noncomposite steel bridge with three continuous units and 17 equal spans (Figure 1). The superstructure consists of a typical girder-floorbeam-stringer system and has an 8 ¼ in. concrete deck (Figure 2). The total bridge cross section width is 60.42 ft, including four 12 ft driving lanes, two 2 ft shoulder lanes, and two 4.21 ft side walks. All main structural members are rolled steel sections.

During the 1995 and 1996 bridge inspections, the KDOT Special Inspection Team noticed fatigue crack development at about 110 welded connections in the bridge.

Based on the location of occurrence, cracks were categorized into three major types: Type 1 broken welds at the stringer bottom flange to floorbeam top flange attachment (Figure 3), Type 2 vertical cracks at either the stringer-to-floorbeam or floorbeam-to-girder connections next to the expansion joints (Figure 4), and Type 3 horizontal cracks at the floorbeam to exterior girder connections due to out-of-plane distortion (Figure 5).



Figure 1 The Arkansas River Bridge

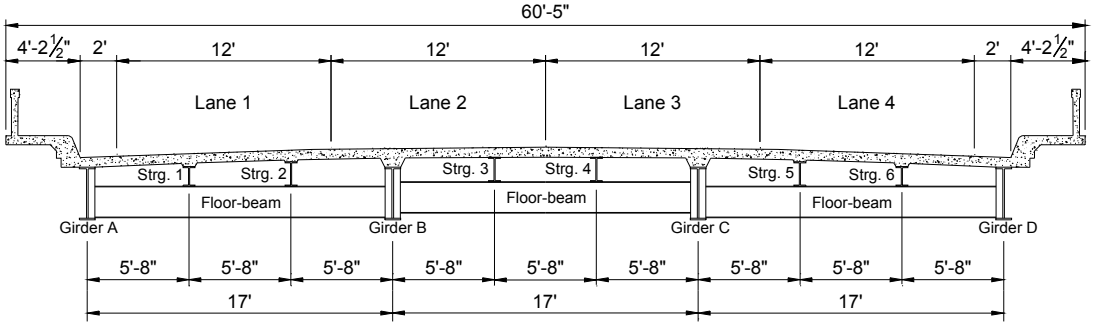


Figure 2 Bridge Cross Section

For Type 1 cracks, since the load path from stringer to floorbeam would not be interrupted even if the welds were completely detached, no major repair was deemed necessary at this crack location. Type 2 cracks could affect the bridge load-carry capacity to some extent, but no collapse mechanism should form due to the structural redundancy at the bridge piers. As a result, instead of applying local repair at each individual crack locations, a simple strengthening solution was proposed by adding new floorbeams next to the existing floorbeams at the expansion joints. Type 3 cracks were found only at the intermediate floorbeam to exterior girder connections. The

floorbeams of the Arkansas River Bridge were attached to the girder connection stiffeners by a 4 in. horizontal weld at the coped top flange, two 4 in. vertical welds at the top and bottom of the web, and five 2 in. slot welds along the web depth. This detail subjected the top horizontal welds to high cyclic stresses when the supporting girders deflected differently on the opposite ends of the floorbeam. Cracks were all found to have started from the outside edge of the connection stiffener, and then propagated following the weld path along the width of the stiffener plate. There are 68 floorbeam to exterior girder connections in this bridge, 39 of them had developed Type 3 cracks by 1996. Since this type of cracking could grow directly into the girder web and cause section loss of the main load-carrying members, it was considered the primary focus of the research and repair investigation, during both the FE modeling and field instrumentation.

It is interesting to point out that Type 3 cracks were not found at the two interior girders, apparently due to the lower fatigue stresses developed at the floorbeam to interior girder connections. Type 3 cracks were not found at the end of the units or negative moment regions either, as no differential girder deflection should develop at the support locations.

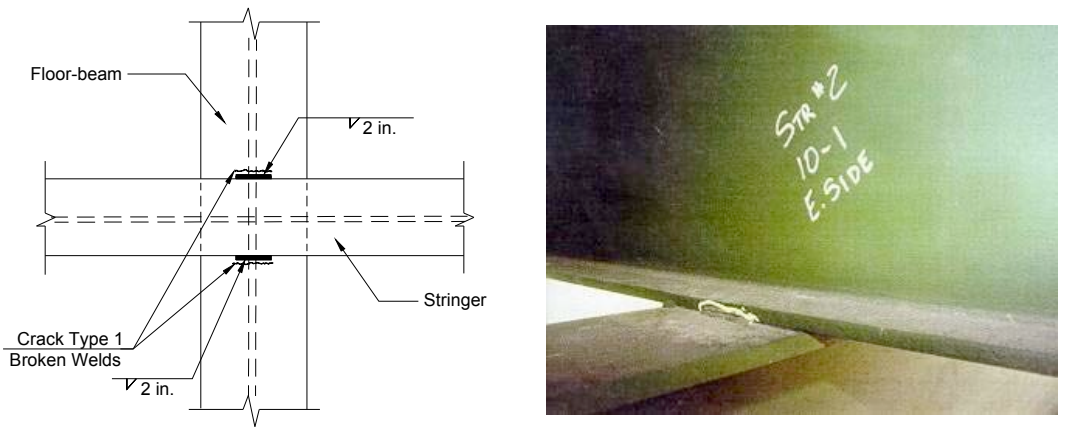


Figure 3 Crack Type 1

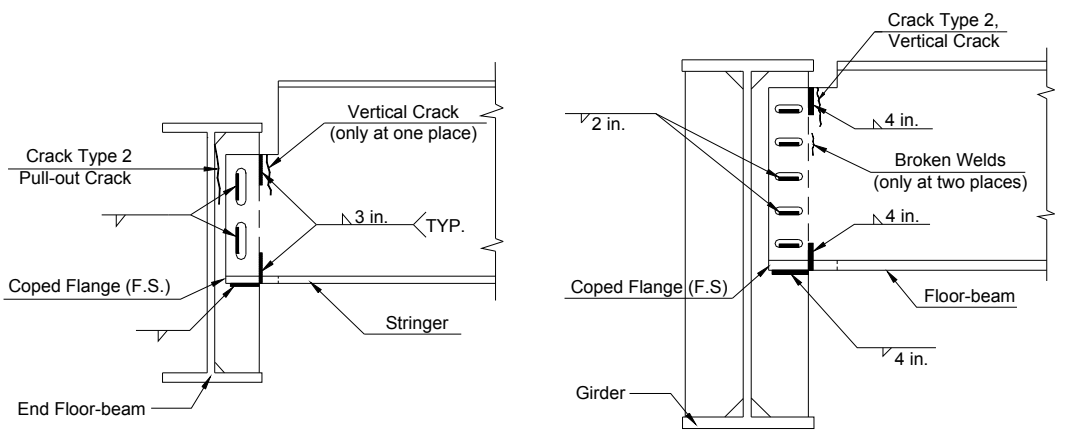


Figure 4 Crack Type 2

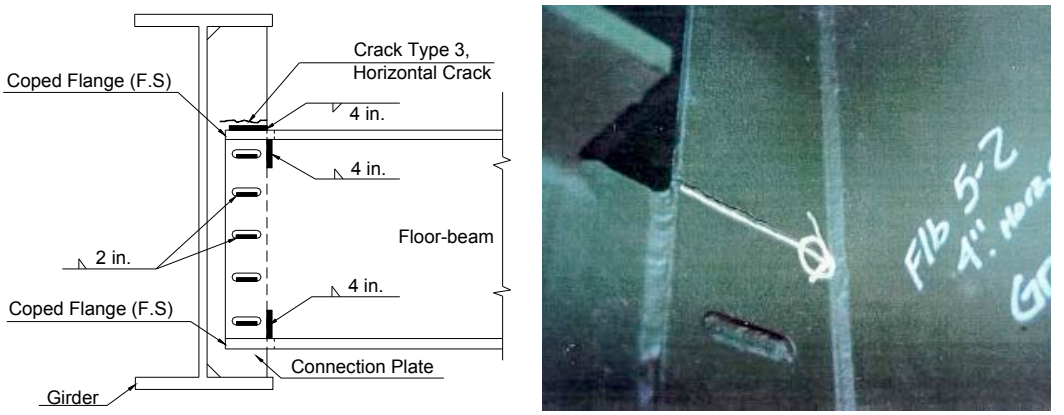


Figure 5 Crack Type 3

FINITE ELEMENT MODELING

Two consecutive spans of the 2nd unit from Pier No. 10 to Pier No. 12 were chosen for the FE study, due to the fact that they were found with the most cracks in the bridge. Computer program ANSYS was used for the FE modeling and analysis. All bridge superstructure components were first built into a large coarse model, and the mostly stressed floorbeam to girder connection was then "cut out" and analyzed further at the submodel level with refined element mesh. An AASHTO HS15 fatigue truck plus 10% impact was used for load application. Wheel loads were placed along the center of driving lane close to Girder D, and moved in 5 ft increments from Pier No. 12 to Pier No. 10 for a total of twenty load cases.

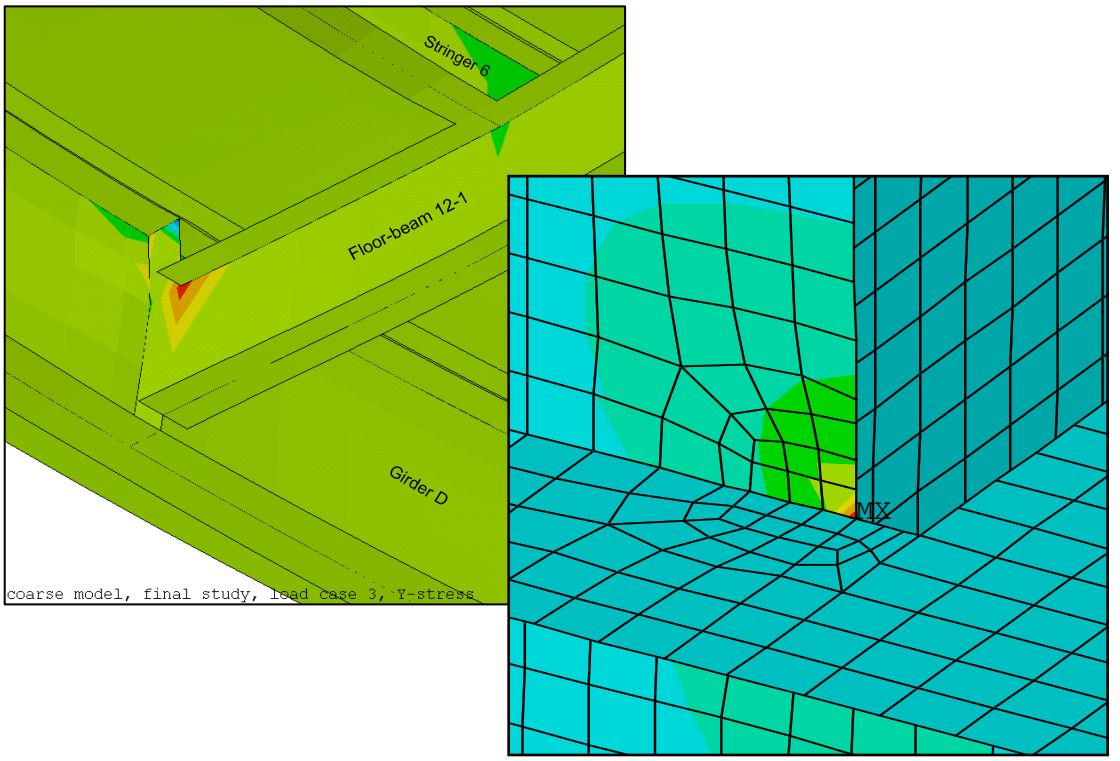


Figure 6 FE Models (Left: Coarse Model, Right: Submodel)

From the coarse-to-sub model analysis, the largest stress variation was found at Floorbeam 12-1 to Girder D connection, right at the edge of the connection stiffener where it was welded to the floorbeam top flange (Figure 6). The maximum stress occurred at Load Case 3, 34.2 ksi; and the minimum stress occurred at Load Case 15, -1.3 ksi. This resulted in a total stress range of 35.5 ksi. There is no specific fatigue detail category that matches the case of the Type 3 crack detail in the Arkansas River Bridge, but it is reasonable to conclude based on the available codes and specifications that the detail resistance would not be any better than Category C. The constant amplitude fatigue threshold (CAFT) of Category C is 10 ksi. Taking into account the occasional heavy truck loading, the current AASHTO LRFD specifications require the detail stress ranges to be designed below ½ CAFT if an infinite life is required. As a result, the stress range that occurred at the Type 3 crack locations in the Arkansas River Bridge was much higher than the detail capacity, even for a finite fatigue life design. The hot-spot revealed by FE modeling matched what had occurred in the actual bridge, and the stress results explained why more than 50% of the floorbeam to exterior girder connections had already developed Type 3 cracks.

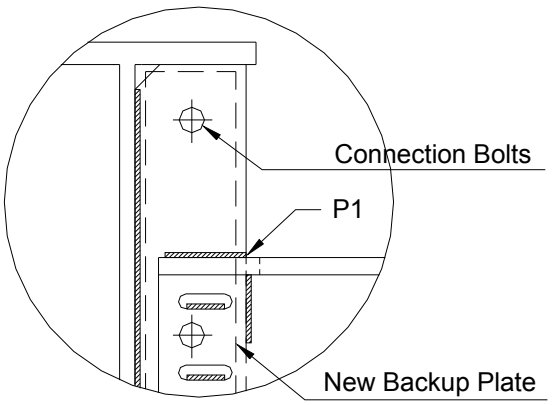


Figure 7 Repair Plan 1

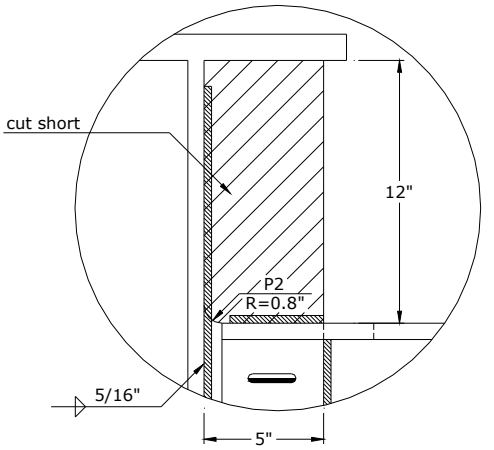


Figure 8 Repair Plan 2

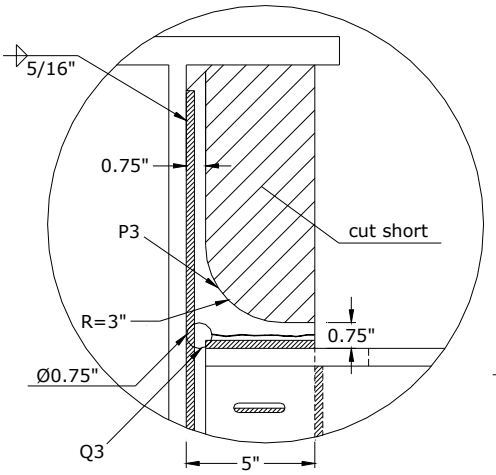


Figure 9 Repair Plan 3

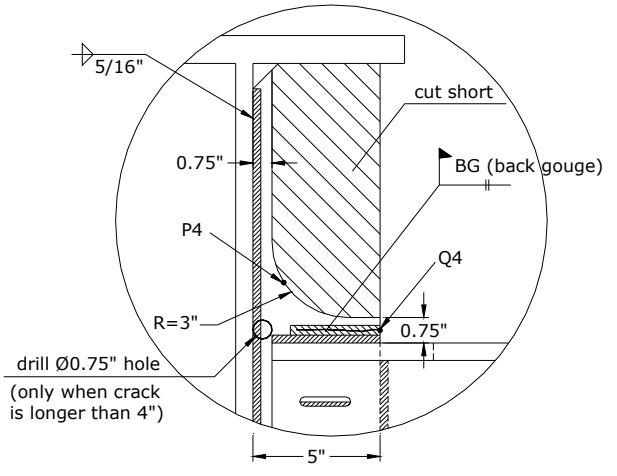


Figure 10 Repair Plan 4

Once the FE model was validated, repair analyses were followed, again using the coarse-to-submodel approach. Four different repair plans were investigated. Repair plan 1 was to bolt a backup plate to the existing stiffener to splice the cracked surfaces (Figure 7). Interestingly, the FE analysis results showed that for the uncracked locations, the maximum stress range was reduced by 40%, but still at a high magnitude of 20.7 ksi and located at the same concentration point on the outside edge of the existing stiffener. For the cracked locations, an increasing horizontal stress was observed at the bottom circumference of the repair hole drilled at the crack tip. This may allow cracks to develop at the stiffener to girder web welds. Repair plan 2 was to cut short the stiffener completely from above the floorbeam top flange, including all the cracks and weld attachments (Figure 8). The maximum stress range was found to be 33.0 ksi at the curved transition between the horizontal and vertical cut surfaces. Although this is a Category A detail, the predicted stress range was higher than CAFT. Surface finish of the repair was also a concern, as there had been cases where rough surfaces were left in place and caused new crack development at the repaired details. Repair plan 3 was to cut short the stiffener partially and drill a hole at the inside stiffener edge in order to capture the crack when it proceeded to that point (Figure 9). Although this repair was much simpler compared to Repair plan 2 from the construction perspective, the FE analysis indicated that high fatigue stress could develop at either the crack tip or the repair hole, and thus lead to further crack growth along the welds. The fourth repair plan was to partially cut short the stiffener and reweld the crack (Figure 10). The stress variation at the outside stiffener edge was found significantly reduced, from 35.5 ksi to 2.2 ksi, due to the fact that a large portion of the stiffener plate above it was removed so the geometry constraints were relieved. The maximum stress range now shifted to the mild curved edge with a magnitude of 23.7 ksi. If the cut edge was properly finished, a fatigue resistance consistent with Category A detail could be obtained. However, infinite fatigue life might not be reached because the maximum stress range was only slightly lower than CAFT and higher than ½ CAFT.

The fatigue lives allowed by the four different repair methods were then calculated, based on the stress range results obtained from the FE models. Since a new Hutchinson Bypass would be constructed soon to serve the main artery of the city, traffic volume of the Arkansas River Bridge was expected to decrease in the future. Repair plan 4 was found to yield a longer life than the other three repairs. The estimated fatigue live was 15 yr, 30 yr, or 60yr, respectively, if the future truck traffic was assumed 100%, 50%, or 25% of the 1996's.

Based on the analytical study, Repair plan 4 was chosen eventually during the final repair design of the bridge, due to its advantages over the other three repairs in terms of overall stress reduction and fatigue life extension. Although the softening mechanism has been previously used in the crack repair of other bridges, its application in this particular crack configuration is probably the first of its kind.

FIELD INSTRUMENTATION

To verify the computational results and the effectiveness of the repair, field tests were performed at selected connections, both before and after the repair of the Type 3 cracks. Two sand trucks, each has an equivalent weight of an HS15 truck, were supplied by KDOT. Traffic was closed and construction work was also temporarily suspended during the tests. A total of 21 loading conditions were tested prior to the retrofit, and a total of 15 loading conditions were tested after the retrofit. Each loading condition was executed twice.

Figures 11 and 12 show the strain gauges installed prior to and after the retrofit, respectively. The measured stress range data from the pre-retrofit test turned out to match very well with the FE results. The direct stress measurements from the post-retrofit test turned out to be higher than the FE results. This was probably due to the difference between the dimensions assumed in the analytical models and the actual resulting geometries at the repair details. A two-step scaling procedure was then used in order to realistically bracket the stress ranges for future fatigue life estimate. At the time the field tests were conducted, construction of the Hutchinson Bypass had been finished, so an updated traffic forecast indicated only 5% truck traffic for the Arkansas River Bridge for the next 20 years. An estimated fatigue life of 25-65 years was then obtained for the repaired details, based on the scaled stress measurement and the updated traffic count. This was also very close to what was predicted by the FE repair analysis, and the result was considered acceptable by the KDOT engineers.

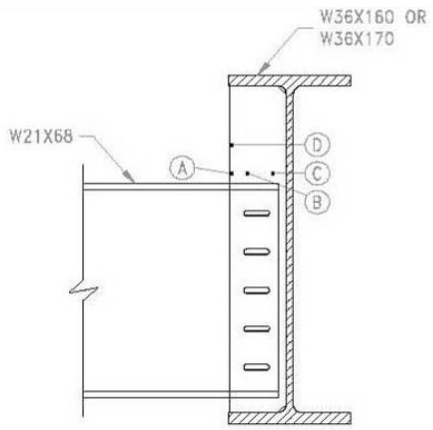


Figure 11 Strain Gauges Installed before the Retrofit

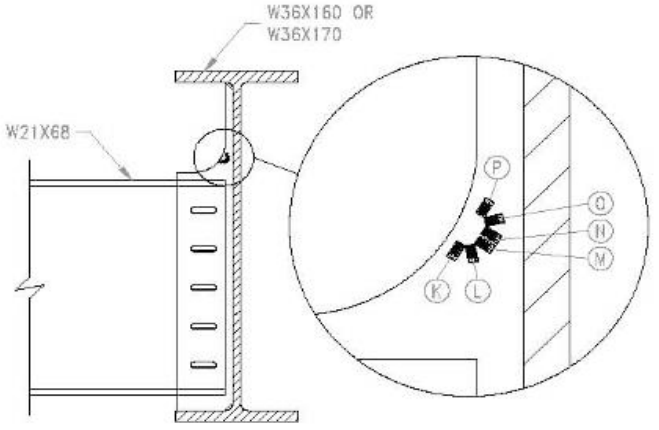


Figure 12 Strain Gauges Installed after the Retrofit

SUMMARY

The bridge was repaired in 2003 and no crack development or reinitiation has been reported to this date. The research effort not only helped put the bridge back to normal service, but resulted in a significant saving to KDOT and the taxpayers. The total structural repair cost is $500,000, in contrast to the estimated $5 million for bridge replacement. The research approach and the repair method also provided useful guidance to the repair of other KDOT bridges, as well as bridges of other state DOTs that developed similar crack scenario.

Experimental Study of Shear Capacity of Reinforced Concrete Slabs

Eva Lantsoght[1], Cor van der Veen[1] and Joost Walraven[1]

[1]Concrete Structures, Delft University of Technology, Stevin II-North 2.06, Stevinweg 1, 2628 CN Delft, The Netherlands; PH 0031(0)152787449; FAX 0031(0)152787438; email: E.O.L.Lantsoght@tudelft.nl

ABSTRACT

When assessing the capacity of existing reinforced concrete slab bridges under the increased traffic loads prescribed in the current codes, shear may become the critical failure mode. To better evaluate the shear capacity of reinforced concrete slab bridges, a series of experiments is carried out on continuous one-way slabs loaded close to the support. Eight continuous slabs of 5m x 2,5m x 0,3m are tested. The loading position is taken at different *a/d* ratios. Six slabs with a standard concrete mixture and two slabs with a higher strength concrete are tested. The influence of the loading history, the shear span to depth ratio and the concrete compressive strength is discussed. Conclusions on the influence of these parameters on the one-way shear capacity of reinforced concrete slabs are drawn.

INTRODUCTION

Over the past decades traffic loads have increased significantly. Therefore, the capacity of existing reinforced concrete bridges, designed for lower traffic loads, is currently under discussion. In particular the shear capacity of existing slab bridges is sometimes found to be insufficient, if checked with the current codes.

The governing design methods present a lower bound solution and usually are a conservative prediction of the shear capacity. Generally structural members are designed in such a way that flexural failure will occur before shear failure. Regarding existing structures, residual bearing capacity is expected from factors such as the increase of the concrete strength due to decades of further hydration of the cement and possibly a higher concrete strength under long-term loading. The shear capacity of deck slabs loaded close to the supports might also be higher than expected. Most publications about shear in reinforced concrete concentrate either on one-way shear in beams or on punching shear (two-way shear) in slabs. One-way slabs typically are designed using beam shear formulas. For loads close to the supports and very wide slabs a certain effective width b_{eff} is assumed. This effective width represents the width of the support which carries the load. The shear stress v is taken as uniformly distributed over the effective width. In practice this load spreading for wheel loads is assumed to occur under 45° from the load towards the support, Figure 1. A minimum value of $2d$ for loads in the middle of the width and of d at the edge and corner of the slab is used in practice. Even though the design values of the shear capacity are

found to be very low and sometimes insufficient, previous small-scale testing (Regan, 1982) has shown a considerable additional shear capacity for slabs under concentrated loads close to the supports.

To investigate this phenomenon an extensive experimental program is conducted at Delft University of Technology, The Netherlands. The variables in this test program are:

- the shear span to depth ratio (*a/d*),
- the reinforcement layout,
- the concrete compressive strength,
- the width of the slab,
- the position of the load along the width,
- the size of the loading plate,
- the type of support (simple or continuous),
- the type of reinforcement (deformed bars versus plain bars),
- the support layout (line support or bearing) and
- the loading history.

More background to the test program can be found in (Lantsoght et al., 2010b). The influence of the size of the wheel load, the amount of transverse flexural reinforcement, the type of the support (simple or continuous) and a comparison with code provisions and with Regan's method (Regan, 1982) for the first four tested slabs is given in (Lantsoght et al., 2010a).

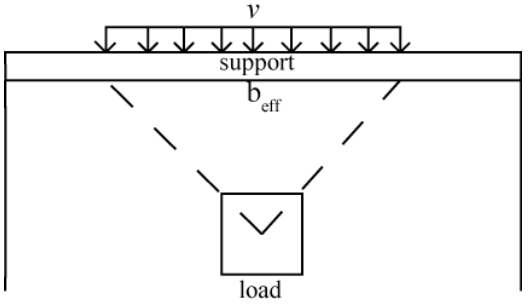


Figure 1: Effective width assuming 45° load spreading, top view showing concentrated load and line support.

EXPERIMENTS

Test setup. Slabs of 5m x 2,5m x 0,3m representing bridge decks on scale 1:2 are tested. A sketch of the top view and side view of the test setup is presented in Figure 2. The load can be moved along the width and span of the slab and can be placed both close to support 1 (sup 1 in Figure 2) and support 2 (sup 2 in Figure 2). Loading plates of 200mm x 200mm and 300mm x 300mm are used to simulate a wheel load. The supports are line supports and consist of a steel beam of 300mm wide, a layer of plywood eccentric from the center line of the steel, away from the span, and a layer of felt of 100mm wide. Support 1 represents a simple support. Prestressing bars are used to restrain the rotation at support 2, simulating a continuous support. The prestressing force is applied before the start of every test. When the load increases during testing (ΔP), the rotation over support 2 increases ($\Delta\theta$). The prestressing bars

counteract the increase in rotation, which leads to an increase in the force in the prestressing bars (ΔF_{ps}). The mechanics of the increasing force in the prestressing bar during testing is shown in Figure 3. In reality, the settlement of the support (felt and plywood) and the elongation of the prestressing bars result in $\Delta\theta \neq 0^{o}$.

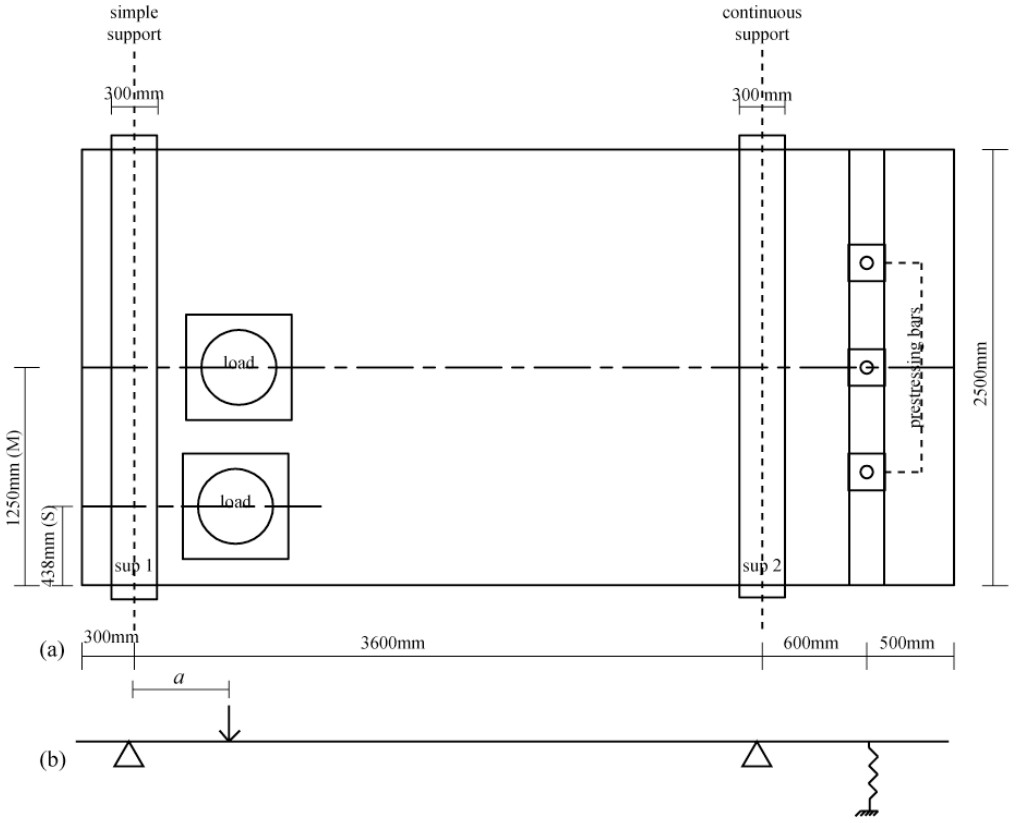


Figure 2. Sketch of test setup, (a) top view, (b) side view, dimensions in mm.

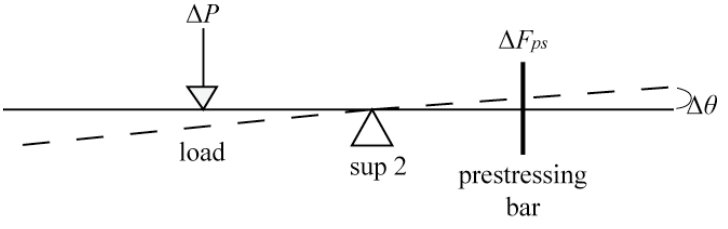


Figure 3. Increase in force in prestressing bar during testing.

Specimens. An overview of the properties of the eight tested slabs can be found in Table 1, in which:

f_c' the cube compressive strength of the concrete at the age of testing the slab,
f_{ct} the splitting tensile strength of the concrete at the age of testing the slab,
ρ_l the amount of flexural reinforcement in the span direction,
ρ_t the amount of flexural reinforcement in the transverse direction,
a/d the shear span to depth ratio,

a the distance between the center of the load and the center of the support,
d the effective depth,
M/S the position of the load along the width; middle (M) or side (S),
A_{load} the size of the square loading plate.

Table 1. Properties of slabs S1 to S8.

Slab	f_c' (MPa)	f_{ct} (MPa)	ρ_l (%)	ρ_t (%)	a/d	M/S	A_{load} (mm x mm)
S1	35,8	3,1	0,996	0,132	2,26	M	200 x 200
S2	34,5	2,9	0,996	0,132	2,26	M	300 x 300
S3	51,6	4,1	0,996	0,258	2,26	M	300 x 300
S4	51,7	4,2	0,996	0,182	2,26	S	300 x 300
S5	48,2	3,8	0,996	0,258	1,51	M	300 x 300
S6	50,6	3,9	0,996	0,258	1,51	S	300 x 300
S7	82,1	6,2	0,996	0,258	2,26	S	300 x 300
S8	77,0	6,0	0,996	0,258	2,26	M	300 x 300

On every slab six tests were carried out, except for S3 (five tests), S5 (five tests) and S8 (three tests). M denotes initial loading at the middle of the slab width. S denotes initial loading at the side at 438mm from the free edge, Figure 2. In case of M-loading, subsequent S-loading is carried out on a fully cracked and locally failed slab which indicates the residual capacity for S-loading. In case of S-loading, subsequent M-loading is carried out on a fully cracked and locally failed slab which indicates the residual capacity for M-loading.

The maximum aggregate size was 16mm. Slabs S1 to S6 contained blast furnace cement and S7 and S8 contained Portland cement, blast furnace cement and fly ash. During casting, two slabs were cast simultaneously. As a result, there are always two slabs (for example S1 and S2) which were made out of the same concrete mixture and thus have the same concrete properties. Two types of concrete were used: normal strength concrete with a target value for f_c' of 43MPa (C28/35) for slabs S1 – S6 and high strength concrete with a target value for f_c' of 73MPa (C53/65) for slabs S7 and S8.

The layout of the reinforcement of S1 and S2 is shown in Figure 4(a) and Figure 4(b). The layout of S3 and S5 – S8 is shown in Figure 4(c) and the layout of S4 is shown in Figure 4(d). Reinforcement S500 with an average yield stress of 580MPa and ultimate stress of 710MPa is used. The amount of flexural reinforcement ρ_l was determined as necessary to resist a bending moment created by a load of 2MN (maximum capacity of the jack) at position M along the width and 600mm along the span (a/d = 2,26). The amount of transverse flexural reinforcement ρ_t is traditionally taken as 20% of ρ_l. In this series of tests 13,3% of ρ_l is used in S1 and S2 and 25,9% of ρ_l is used in S3, S5, S6, S7 and S8. In S4 the amount of transverse flexural reinforcement is only doubled in the vicinity of the supports, Figure 4(d).

The influence of the support is important for a/d-values of 2,5 and less (Kani, 1964). Slabs S1 – S4, S7 and S8 were loaded at 600mm from the center of the

support, resulting in an *a/d*-ratio of 2,26. Slabs S5 and S6 were loaded at 400mm from the center of the support, resulting in an *a/d*-ratio of 1,51.

The different sizes of the loading plate were chosen to simulate different sizes of tires. The 200mm x 200mm load is a 1:2 scale representation of the 400mm x 400mm axle load used in load model 2 of EN1991-2:2002.

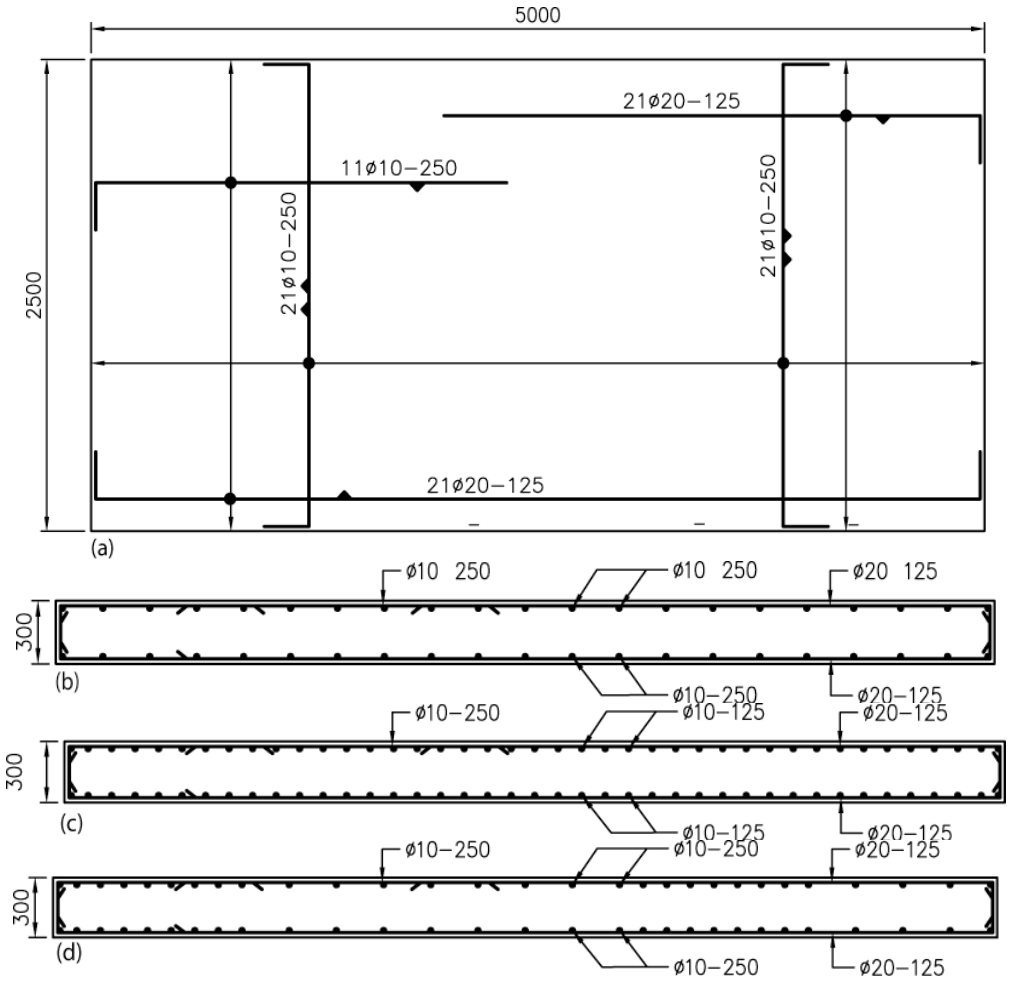


Figure 4. Reinforcement layout: (a) plan view of slabs S1 and S2, (b) cross-section of slabs S1 and S2, (c) cross-section of slabs S3, S5-S8, (d) cross-section of slab S4.

Test results. The values of the peak loads obtained for S5 to S8 are summarized in Table 2, in which the following abbreviations are used:

b_r	the distance between the load and the free edge taken along the width,
SS	the load is placed close to the simple support,
CS	the load is placed close to the continuous support,
P_u	the peak load,
s	the test gives a shear capacity, obtained on a virgin specimen,
r	the test gives a residual shear capacity, obtained on a predamaged specimen.

The results of slabs S1 up to S4 can be found in Lantsoght et al. (2010a).

Table 2. Results of tests of S5 to S8.

Name	*a/d*	b_r (mm)	SS/CS	P_u (kN)	s/r
S5T1	1,51	1250	CS	1804	s
S5T2	1,51	438	CS	1395	r
S5T4	1,51	1250	SS	1755	s
S5T5	1,51	438	SS	1295	r
S5T6	1,51	438	SS	1286	r
S6T1	1,51	438	CS	1446	s
S6T2	1,51	438	CS	1423	s
S6T3	1,51	1250	CS	1897	r
S6T4	1,51	438	SS	1366	s
S6T5	1,51	438	SS	1347	s
S6T6	1,51	1250	SS	1384	r
S7T1	2,26	438	SS	1121	s
S7T2	2,26	438	CS	1172	s
S7T3	2,26	438	CS	1136	s
S7T4	2,26	1250	CS	1128	r
S7T5	2,26	438	SS	1063	s
S7T6	2,26	1250	SS	1011	r
S8T1	2,26	1250	SS	1481	s
S8T2	2,26	1250	CS	1356	s
S8T5	2,26	438	SS	868	r

Figure 5 shows how the peak load is determined from the measured load-deflection diagram during testing. Typical brittle shear failures (Figure 5(a)) are observed as well as shear failures with a limited amount of post-peak ductile behavior (Figure 5(b)).

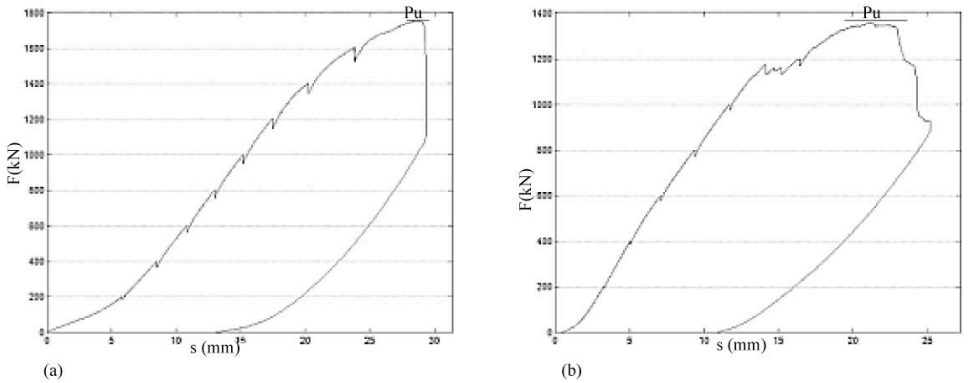


Figure 5: Determination of the peak load (P_u) for (a) S5T4, brittle failure and (b) S8T2, with post-peak ductility.

Figure 6 shows the loading sequence and the meaning of s and r. First, test S5T1 is carried out with the load close to the continuous support and results in a virgin shear capacity denoted by "s". This test causes local failure and heavy damage to the slab at the side of the continuous support. An example of damage caused by testing the shear capacity is shown in Figure 7. Next, S5T2 is carried out on the damaged slab. The result of this experiment is influenced by the cracking and failure caused by S5T1 and therefore gives a residual shear capacity, denoted r. Bridges which might have been in service for several decades, do not have locally failed areas like the specimens tested for residual capacity. As a result, the measured residual shear capacity is a conservative lower bound of the capacity of existing bridges that are fully cracked in bending and might have been overloaded in the past.

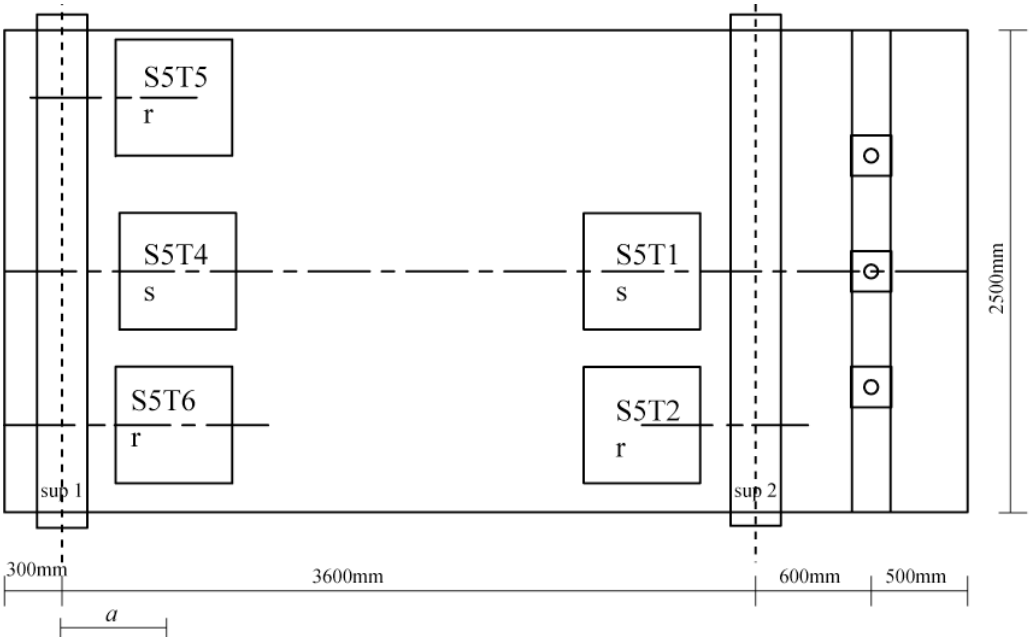


Figure 6: Explanation of s and r.



Figure 7. Cracking caused by S2T1, bottom face.

RESULTS AND DISCUSSION

Loading history. The residual shear capacity gives a lower bound estimate of the shear capacity of bridge slabs which are fully cracked in bending and have been in service for several decades. Therefore experiments were carried out slabs locally

failed due to previous testing, with results denoted by "r" in Table 2, loading sequence shown in Figure 6. To study the influence of predamaging, the results of tests on S3 and S4, on S5 and S6 and on S7 and S8 are compared. For these pairs of slabs, all parameters were held constant, only the load history was altered. It was observed that the width of cracks due to previous testing increased during testing for residual capacity. In only one case the test gave a 5% higher residual capacity, as shown in Table 2 for S5T1 and S6T3 (tests in the middle of the width at the continuous support). All other comparisons gave lower residual capacities, as expected. The results per pair of slabs are given in Table 3, in which:

P_r the capacity obtained in an experiment for residual shear capacity, denoted r in Table 2,

P_s the capacity obtained in a shear capacity experiment on an undamaged slab, denoted s in Table 2.

The overall average is a residual capacity of 84% of the undamaged shear strength. This result is surprisingly high, as it was not expected that slabs which had been tested up to their ultimate capacity and showed cracks of sometimes a few centimeters wide (Figure 7) would be able to resist again considerable levels of loading.

Table 3. Residual capacity.

Slabs	P_r/P_s
S3 – S4	0,80
S5 – S6	0,95
S7 – S8	0,78

Shear span to depth ratio. The shear span to depth ratio is known as an important parameter influencing the shear capacity of reinforced concrete beams. This influence is traditionally shown in Kani's valley (Kani, 1964). The influence of the shear span to depth ratio on reinforced concrete slabs subjected to point loads is less clear. A 45º load spreading as shown in Figure 1 leads to a decreasing effective width for a decreasing distance to the support. The theoretical ultimate shear stress v_u remains the same, but the smaller effective width would lead to a smaller maximum shear load $V_u = v_u b_{eff} d$. Therefore, the shear span to depth ratio (a/d) was studied in this series of experiments.

The slabs S3 and S5 are similar with regard to their properties. They are both loaded at the middle (M), but for different values of a/d (2,26 and 1,51 respectively). Also, the slabs S4 and S6 are similar. They are both loaded at the side (S) but for different values of a/d (2,26 and 1,51 respectively). Only test results obtained on virgin specimens, denoted by s in Table 2, are considered. Figure 8 shows the results as a function of a/d. It is clear that in all cases the shear capacity increases with decreasing value of a/d.

In EN1992-1-1:2005 the shear span to depth ratio is incorporated for small shear spans. §6.2.2 (6) prescribes: "For members with loads applied on the upper side within a distance $0{,}5d \le a_v \le 2d$ from the edge of a support (or center of bearing where flexible bearings are used), the contribution of this load to the shear force V_{Ed} may be multiplied by $\beta = a_v/2d$. … This is only valid provided that the longitudinal reinforcement is fully anchored at the support. For $a_v \le 0{,}5d$ the value $a_v = 0{,}5d$

should be used." For slabs S3 and S4 β = 1 is obtained and for S5 and S6 β = 0,66. A 51% increase in shear capacity is expected using this procedure. Comparing the test results shows an average increase in capacity of 26% with a coefficient of variation of 6%. The observed increase in shear capacity for slabs is thus less than expected on the basis of the factor β from the EN 1992-1-1:2005. This factor was derived based on results from shear tests on beams.

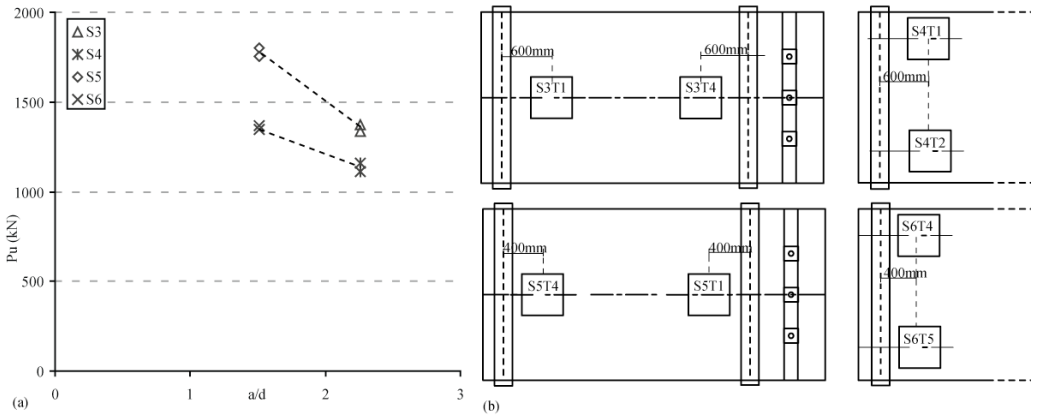


Figure 8. Influence of distance of load to support on shear capacity for normal strength concrete.

A possible reason for the influence of the shear span to depth ratio is related to the formation of a direct compression strut between the load and the support. When the load is applied close to the support, an internal compression strut can develop between the load and the support. Hence, another mechanism of shear transfer is activated: the strut-and-tie action, in which the beam transfers the force between the load and the support through a direct compression strut.

When applying this concept to the shear capacity of slabs under concentrated loads, a lower increase in capacity for decreasing *a/d* could be explained. The width of the element influences the possibility of developing a direct compression strut between the load and the support. A three-dimensional strut-and-tie model can now develop. In beams, the only possible load path is directly from the load to the support at small *a/d* ratios. In slabs, different load paths can develop. As a result of these different load paths, the average value of *a/d* will be larger, Figure 9.

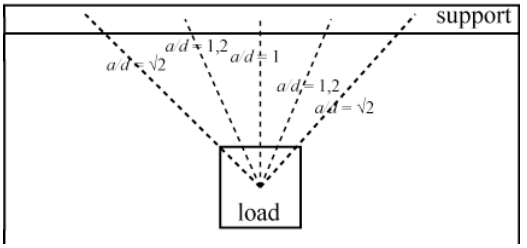


Figure 9: Larger average *a/d* ratio for slabs as compared to beams.

Concrete compressive strength. Traditionally, the concrete tensile strength is seen as the most important factor influencing the shear strength of beams. For design purposes, the tensile strength is calculated based on the concrete compressive strength with a square root (for example, ACI 318-08) or cube root (for example EN 1992-1-1:2005) relationship. Design methods for the punching shear resistance of concrete slabs also involve the concrete compressive strength.

To experimentally study the influence of the concrete compressive strength on the one-way shear capacity of slabs, the results of S2, S3, S4, S7 and S8 are compared. S2, S3 and S4 are produced with normal strength concrete, while S7 and S8 are produced with high strength concrete. The results are shown in Figure 10. All tests were carried out at a/d = 2,26. S2 contained less transverse flexural reinforcement (ρ_t in Table 1), but it has been previously shown that the influence of ρ_t on the ultimate load is small (Lantsoght et al., 2010a). Only the results of the undamaged slabs (denoted s in Table 2) are used. No increase in capacity with increasing compressive strength is observed. An increase in scatter is observed for the test results with high strength concrete. The measured average increase in shear capacity for S3 and S4 versus S7 and S8 is 0,46% for an increase in concrete compressive strength of 54%. The expected increase in capacity is 24% for a square root relationship between the concrete compressive strength and the tensile strength and 15% for a cube root relationship. The experimental data do not reflect this observation. The splitting tensile strength increased even with 47%, as shown in Table 1. Comparing S2, S3/S4 and S7/S8 leads to the similar conclusions.

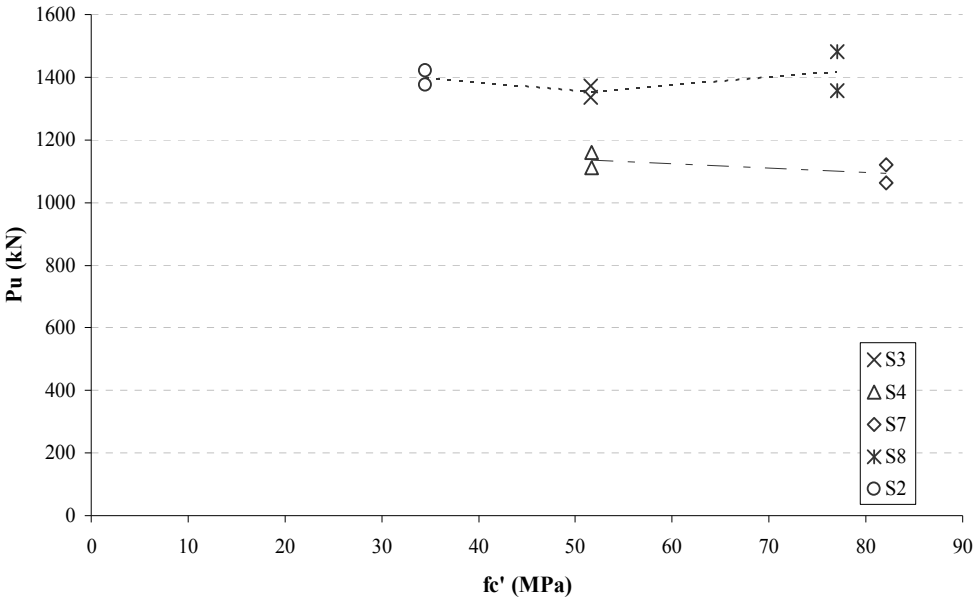


Figure 10. Influence of the concrete compressive strength (cube strength), for *a/d* = 2,26, for loading at the middle (upper series) and loading at the side (lower series).

The concrete compressive strength influences the shear capacity of beams because it directly influences the concrete tensile strength, the dowel capacity limited to the tensile strength of the concrete cover supporting the dowel, the aggregate interlock capacity and the strength of the compression zone. However, for high strength concrete the aggregate interlock capacity is reduced. The aggregate itself is then the weakest element through which the shear crack passes. The result is a very smooth crack surface. It was observed in S7 and S8 that the shear crack indeed cut through the aggregates. (Sherwood et al., 2007) suggest that 70% of the shear capacity is carried by aggregate interlock. The reduced aggregate interlock capacity of the high strength concrete might explain why no increase in shear capacity is observed for an increasing concrete strength. However, the relation between high strength concrete and their aggregate interlock capacity is still a point of discussion. The same observation has been made by (Angelakos et al., 2001). They reported: "high cylinder strengths do not necessarily result in high values of failure shear stress".

Another possible explanation is that the mechanism of shear transfer works in a different way for slabs under point loads than for beams in shear. Due to the width of the element, redistribution of forces can occur. Therefore, a three-dimensional strut-and-tie model should be developed in order to explain the observations.

CONCLUSIONS

To evaluate the capacity of existing reinforced concrete slab bridges a series of large-scale experiments on reinforced concrete slabs have been carried out. Test results concerning the loading history, the shear span to depth ratio and the concrete compressive strength are discussed. The results and conclusions are summarized in the following:

1. Heavily cracked and locally failed slabs still have about 84% of the shear capacity of an undamaged slab when loaded again in the vicinity of an already failed region.
2. The shear capacity clearly increases for a decrease in distance to the support, but the increase is smaller than expected based on the Eurocode formula for beam shear.
3. No increase in capacity with increasing concrete compressive strength was observed. The smaller aggregate interlock capacity in high strength concrete might explain this.

The experimental results show that the mechanism of shear transfer in slabs under wheel loads is different from the mechanism in beams. Redistribution of forces along the width might result in a three-dimensional system of forces which needs to be evaluated through a three-dimensional strut-and-tie model.

Future work includes:

- experiments on slabs with a different width,
- experiments on slabs reinforced with plain bars, and
- experiments on slabs supported by elastomeric bearings.

ACKNOWLEDGEMENTS

The funding for this research provided by the Dutch Ministry of Transport, Public Works and Water Management (Rijkswaterstaat) is gratefully acknowledged.

REFERENCES

ACI Committee 318, (2008). *Building Code Requirements for Structural Concrete (ACI 318-08) and Commentary*, American Concrete Institute, Farmington Hills, MI, USA.

Angelakos, D., Bentz, E. C., and Collins, M. P. (2001). "Effect of concrete strength and minimum stirrups on shear strength of large members." *ACI Structural Journal*, 98(3), 290-300.

CEN, (2002). *Eurocode 1 – Actions on Structures - Part 2: Traffic loads on bridges, EN 1991-2,* Comité Européen de Normalisation, Brussels, Belgium.

CEN, (2005). *Eurocode 2 – Design of Concrete Structures: Part 1-1 General Rules and Rules for Buildings*, *EN 1992-1-1*, Comité Européen de Normalisation, Brussels, Belgium.

Kani, G. N. J. (1964). "The Riddle of Shear Failure and Its Solution." *ACI Journal Proceedings*, 61(4), 441-467.

Lantsoght, E. O. L., van der Veen, C., and Walraven, J. (2010a). "Experimental study of reinforced concrete bridge decks under concentrated loads near to supports." *Proceedings of the 13th International Conference and Exhibition on Structural Faults and Repair*, Edinburgh, UK.

Lantsoght, E. O. L., van der Veen, C., and Walraven, J. (2010b). "Shear tests of reinforced concrete slabs with concentrated loads near to supports." *Proceedings of the 8th fib international PhD Symposium in Civil Engineering*, Technical University of Denmark, Kgs. Lyngby, Denmark, 81-86.

Regan, P. E. (1982). *Shear Resistance of Concrete Slabs at Concentrated Loads close to Supports*. Polytechnic of Central London.

Sherwood, E. G., Bentz, E. C., Collins, M. P., (2007). "Effect of aggregate size on beam-shear strength of thick slabs." *ACI Structural Journal*, 104(2), 180-190.

Seismic Response of Bearings for Quasi-Isolated Bridges – Testing and Component Modeling

J. S. Steelman[1], L. A. Fahnestock[2], J. M. LaFave[3], J. F. Hajjar[4], E. T. Filipov[1], and D.A. Foutch[5]

[1]Graduate Research Assistant, Dept. of Civil and Environmental Engr., University of Illinois at Urbana-Champaign, 205 N. Mathews Ave. Urbana, IL61801; email: jsteelm2@illinois.edu, filipov1@illinois.edu
[2]Assistant Professor, Dept. of Civil and Environmental Engr., University of Illinois at Urbana-Champaign, 205 N. Mathews Ave. Urbana, IL 61801; PH (217) 265-0211; email: fhnstck@illinois.edu
[3]Associate Professor, Dept. of Civil and Environmental Engr., University of Illinois at Urbana-Champaign, 205 N. Mathews Ave. Urbana, IL 61801; PH (217) 333-8064; email: jlafave@illinois.edu
[4]Professor and Chair, Dept. of Civil and Environmental Engr., Northeastern University, 360 Huntington Avenue, Boston, MA 02115; PH (617) 373-3242; email: jf.hajjar@neu.edu
[5]Professor Emeritus, Dept. of Civil and Environmental Engr., University of Illinois at Urbana-Champaign, 205 N. Mathews Ave. Urbana, IL 61801; PH (217) 333-6359; email: dfoutch@illinois.edu

ABSTRACT

In areas of moderate seismicity, such as Mid-America, there is interest in developing alternate bridge design and construction methodologies to the typical approaches that are employed in high-seismic regions. One such method is to design so that various bearing components will exceed their ultimate capacities during a major seismic event in a specific sequence, leading to a global bridge structure response similar to a seismically-isolated system. Because the bridge would typically exhibit a stiff response, only developing an isolated response during major earthquakes, the bridge superstructure response may be described as quasi-isolated. This paper presents results for elastomeric bearing components obtained for an experimental program performed to investigate and characterize various bearing types that are being used for quasi-isolated designs. The elastomeric bearings investigated displayed approximately linear elastic response before sliding with a friction coefficient in the range of 0.3 – 0.45, at a shear strain in the range of 150 – 250%. The experiments also investigated the response of anchored retainer brackets used to prevent transverse motion for service loads and small earthquakes to characterize the combined effects of shear and overturning up to and including rupture of the concrete anchor. The test data indicate that the required horizontal force delivered by a bearing to a retainer to cause a failure of the anchor is slightly higher than the ultimate pure tensile strength of the anchor.

INTRODUCTION

Seismic isolation has been implemented as an effective means of earthquake damage mitigation in structural engineering, with some of the earliest patents dating back to the turn of the 20th century, and increasing frequency from the 1970s onward (Buckle and Mayes, 1990). Isolation systems have typically been used in high-seismic areas, such as the west coast of the United States, Japan, and New Zealand, where additional design and construction costs are justifiable in light of the seismic hazard. For bridges outside of high-seismic areas, however, commonly employed components to permit thermal displacements of superstructures inherently possess properties suitable for isolation systems. Consequently, a quasi-isolated design that relies on thermal expansion devices to also provide seismic energy dissipation can be an appealing alternative within the suite of earthquake protection design options, providing the benefits of reduced force demands, as long as the structural system is designed to account for the associated increased displacements of an isolated response.

The Illinois Center for Transportation (ICT), working in conjunction with the Illinois Department of Transportation (IDOT), is currently investigating the behavior of bridge systems to calibrate and refine IDOT's Earthquake Resisting System (ERS) methodology. The IDOT ERS philosophy relies on prescribed sequential "fusing" (i.e., exceeding ultimate capacity) of specific components, arranged by levels ranging from 1 to 3 (Tobias et al., 2008). The dual use of thermal expansion components for seismic energy dissipation is a key feature of the IDOT ERS. Level 1 requirements are intended to provide a force capacity threshold to ensure elastic response to service loads and small to moderate earthquakes, and Level 2 requirements address displacement demands following Level 1 fusing.

IDOT bridges commonly employ elastomeric bearings to permit thermal deformations of the superstructure. The experimental program includes tests of two types of elastomeric bearings: steel-reinforced elastomer only (IDOT Type I), and steel-reinforced elastomer combined with a flat Teflon sliding surface (IDOT Type II). Both types of elastomer bearings include stiffened L-shaped retainer brackets to restrain transverse motion of the superstructure. The first tests of the experimental program focused on the response of the components of Type I bearings and individual retainer response.

EXPERIMENTAL TESTING SETUP

The experimental tests were performed at the Newmark Structural Engineering Laboratory at the University of Illinois, using a testing apparatus shown in Figure 1, designed to realistically reflect field conditions for the typical, full-scale bridge bearing specimens.

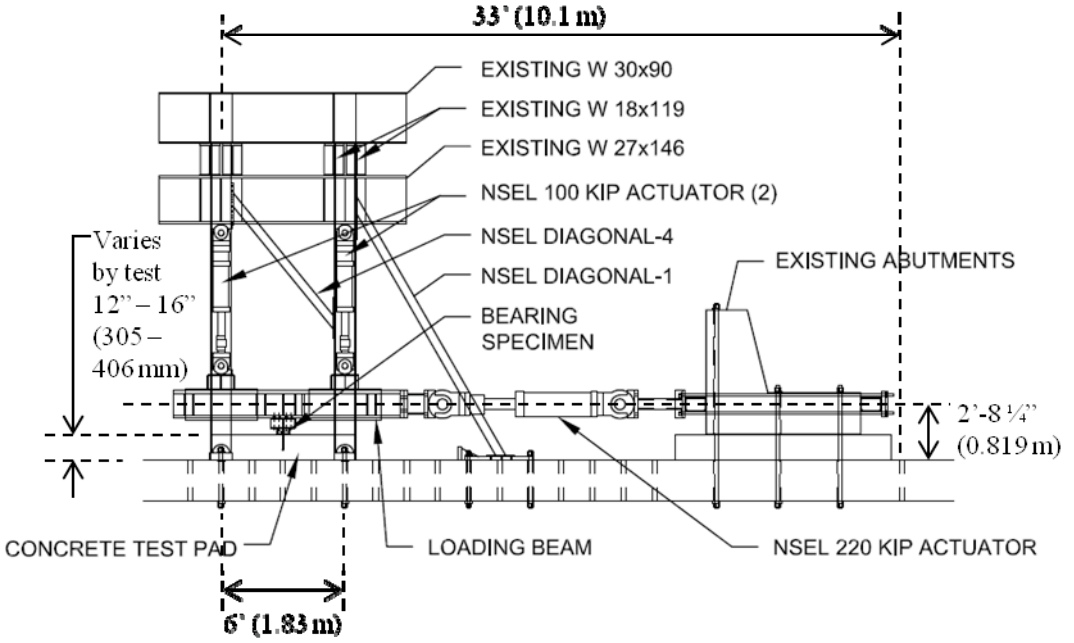


Figure 1. Testing Setup Elevation

The primary objective of the testing program was to simulate large lateral deformations of elastomeric bearings that may occur due to seismic excitation. Based on preliminary analyses of full bridges in conjunction with a review of literature documenting previous tests of elastomeric bearings (Stanton and Roeder, 1982; Roeder et al., 1987; Kulak and Hughes, 1992; Mori et al., 1999), a target of 400% shear strain was selected for the testing program. The largest bearings included in the testing program were comprised of 5 layers of 5/8" (15.9 mm) elastomer layers, for an equivalent rubber thickness of 3.125" (79.4 mm), and an associated 400% shear strain of 12.5" (317.5 mm). A 30" (762 mm)-stroke, 220 kip (980 kN) capacity actuator was employed to provide the required 25" (635 mm) horizontal displacement capacity for fully reversed cyclic tests.

The vertical loading and support was designed to capture the lateral response realistically. Vertical loading was imposed on the bearings using a pair of 100 kip (445 kN) capacity actuators reacting against a steel frame secured to the laboratory strong floor with pretensioned anchors. The use of a pair of actuators allowed the vertical load to be maintained at a specified target of simulated gravity load, regardless of the lateral displacement of the bearing. Concrete pads were cast to simulate typical bridge substructures, including a brushed finish as specified by IDOT (IDOT, 2007), to ensure that the frictional response of elastomers bearing on concrete was captured realistically. A concrete pad is secured to the strong floor during a test by using pretensioned anchors around the perimeter of the pad.

The experimental results presented in this paper are for specimens and parameters listed in Table 1. Dimensions of test specimens conformed to standards used by IDOT, and full details for the test specimens may be found in the IDOT Bridge Manual (IDOT, 2009). The specimens in Table 1 represent only a portion of the

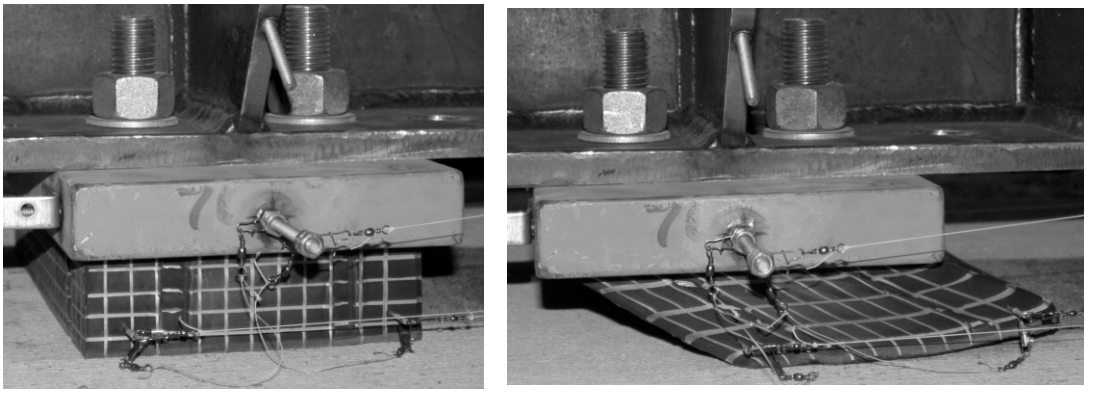
complete testing program. The complete program also includes tests of 13c bearings, Type II 7c bearings, and fixed bearings, with tests performed on bearings oriented to simulate both longitudinal and transverse loading for all types of bearings.

Table 1. Partial Test Matrix

Test	Specimen	Protocol	Vertical Load (MPa)
1	Type I 7c #1	Monotonic	3.45
2	Type I 7c #1	Monotonic	3.45
3	Type I 7c #1	Monotonic	3.45
4	Type I 7c #1	Monotonic	3.45
5	Type I 7c #1	Monotonic	2.59
6	Type I 7c #1	Monotonic	1.38
7	Type I 7c #1	Monotonic	3.45
8	Type I 7c #2	Cyclic	1.38
9	Type I 7c #3	Cyclic	3.45
10	Type I 7c #2	Cyclic	5.52
11	Retainer	Monotonic	N/A

ELASTOMERIC BEARING EXPERIMENTS

Displacements of Type I and Type II bearings include both shear deformations in the elastomers, and frictional sliding, so deformations are referred to using "equivalent shear strain" for convenience. For the Type I bearings, sliding occurs at the elastomer-concrete interface. The first experiments imposed horizontal displacements simulating deformations parallel to a bridge span. Images captured at the initiation of lateral displacement and incipient sliding are shown in Figure 2.



(a) Initiation of Lateral Displacement **(b) Incipient Sliding**

Figure 2. Still Captures of Test Specimen #1 during Test #1

The bearing shown in Figure 2 is a typical Type I 7c bearing, composed of a steel top plate bonded to a block of steel-reinforced elastomer during vulcanization. The top steel plate measures 8" x 14" in plan, and 1-1/2" thick (203 x 356 x 38.1 mm), and the reinforced elastomer is composed of 5 layers of elastomer, each measuring 7" x

12” x 3/8” (178 x 305 x 9.53 mm), with each layer separated by a 3/32” (2.38 mm) thick steel shim. With 5 layers of 3/8” elastomer, the equivalent rubber thickness of the bearing is 1.875” (47.6 mm), corresponding to a maximum displacement during tests of 7.5” (190.5 mm). The steel top plate is tapped with four holes so that the plate can be bolted to the bottom flange of a steel girder in the field, which was simulated with a built-up steel plate fixture for the experiments. Lines were drawn on the sides of the elastomer so that deformations could be more easily seen. Horizontal lines correspond to locations of internal steel shims, and vertical lines were added to construct a grid of approximately square spaces. Steel studs were welded to the top plate, and needles were inserted into the elastomer so that string potentiometer lines could be attached and used to record displacements of the specimen.

Elastomeric bearings used by IDOT are designed based on vertical load limitations of 1.38 to 5.52 MPa (200 to 800 psi). Based on discussions with an internal technical review panel assembled within IDOT, a typical simulated gravity load was set at 3.45 MPa (500 psi). Initial tests to identify fundamental constitutive response were performed by imposing monotonic horizontal shear deformations from rest up to 400% equivalent shear strain. Data from the initial tests is shown in Figure 3 through Figure 5.

All tests in Figure 3 were performed with a common simulated gravity load of 3.45 MPa (500 psi). All loading was removed from test specimens for approximately 1 day between tests so that the elastomer could recover from any scragging that may have developed in a previous test. In the case of these tests, however, deterioration of the bearing elastomer was not limited to hyperelastic material response. When the elastomer is ground against the surface of the concrete, portions of the elastomer are permanently removed by abrasion, in particular at the leading edge of the elastomer base in the direction of motion. The bearing edge appeared chamfered at a roughly 45º angle after the first test. The mechanism appeared to stabilize in the succeeding tests however, based on the difference in lateral force versus displacement evident between Test 1 and Tests 2 and 3.

Large deformations of elastomers reported in the literature typically consider bearings with different construction details (e.g., use of both top and bottom plates to secure bearing to super- and substructures) and material properties (high damping versus low damping elastomers). Consequently, one of the primary points of interest for these bearing experiments was to establish the response of bearings that have not been specifically designed for seismic effects when subjected to deformations larger than typical non-seismic limitations of 50 – 70% shear strain. In general, elastomers are expected to stiffen significantly when subjected to large deformations, regardless of whether the elastomeric material would be classified as high-damping or low-damping. For the tests represented in Figure 3 through Figure 5, a material softening branch was not observed, and a stiffening branch appeared to be precluded by the initiation of sliding.

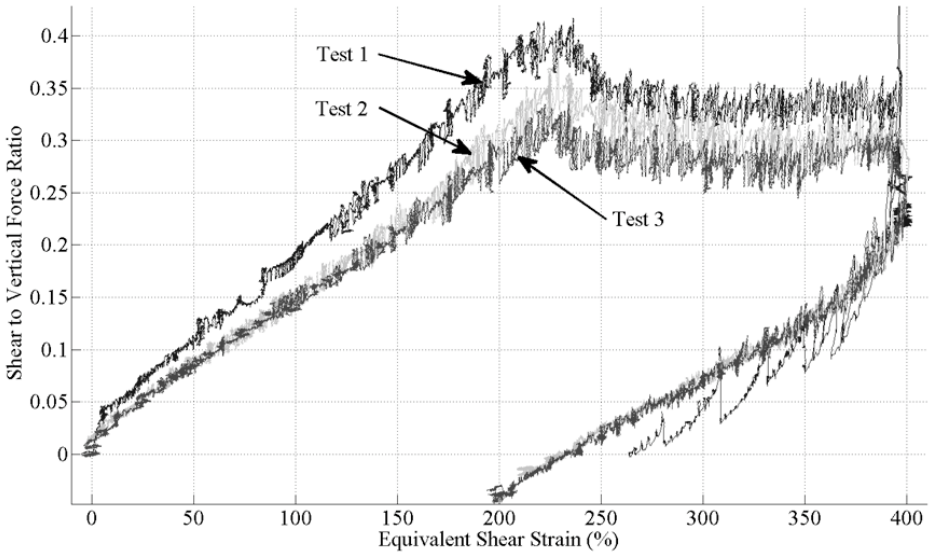


Figure 3. Successive Monotonic Tests of Type I bearing, all tests with 3.45 MPa (500 psi) simulated gravity load

To investigate the response of the bearing when subjected to varying gravity load cases, a series of monotonic tests were performed in the opposite direction from the first three tests. Tests were performed successively, with the typical delay between tests to allow for scragging recovery, in a sequence of 3.45, 2.59, 1.38, and 3.45 MPa (500, 375, 200, and 500 psi). As would be expected, the slip load of the bearings decreases as the applied vertical load decreases, and so the lower vertical load also results in less shear deformation, and a larger proportion of sliding for the imposed monotonic displacement, as seen in Figure 4. The variation in slip load is not, however, linearly scaled with imposed vertical load. Whether due to a reduced curling of the elastomer base with the lower gravity load, or differences at a microscopic level of interaction at the interface of the elastomer and roughened concrete, the data shown in Figure 5 indicate that the coefficient of friction is correlated inversely with the applied vertical load. At a load of 3.45 MPa, based on Figure 3 and Figure 5, the coefficient of friction for sliding is approximately 0.3 – 0.35, and slightly higher at 2.59 MPa, tending to fall at or slightly above 0.35. When the vertical load is decreased further, to 1.38 MPa, the coefficient of friction increases to approximately 0.45.

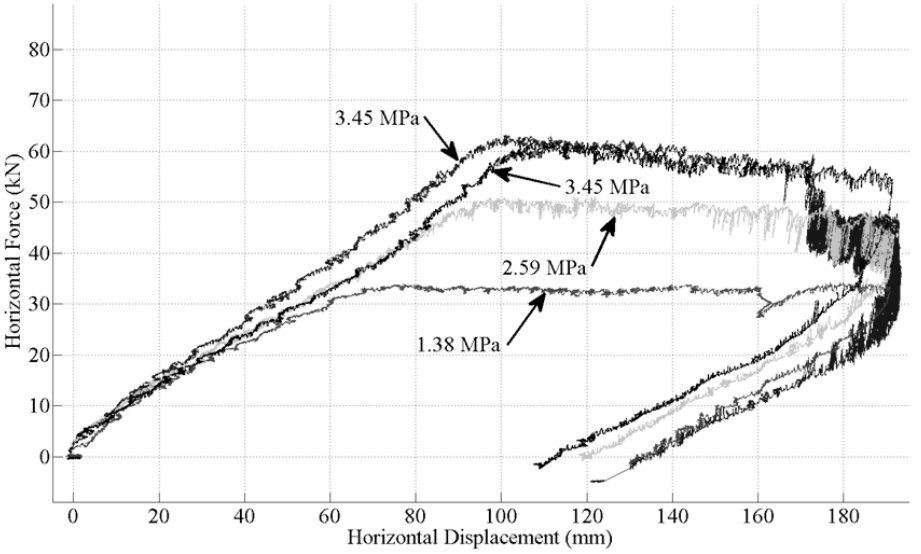


Figure 4. Successive Monotonic Tests of Type I bearing, varying simulated gravity load, load versus displacement

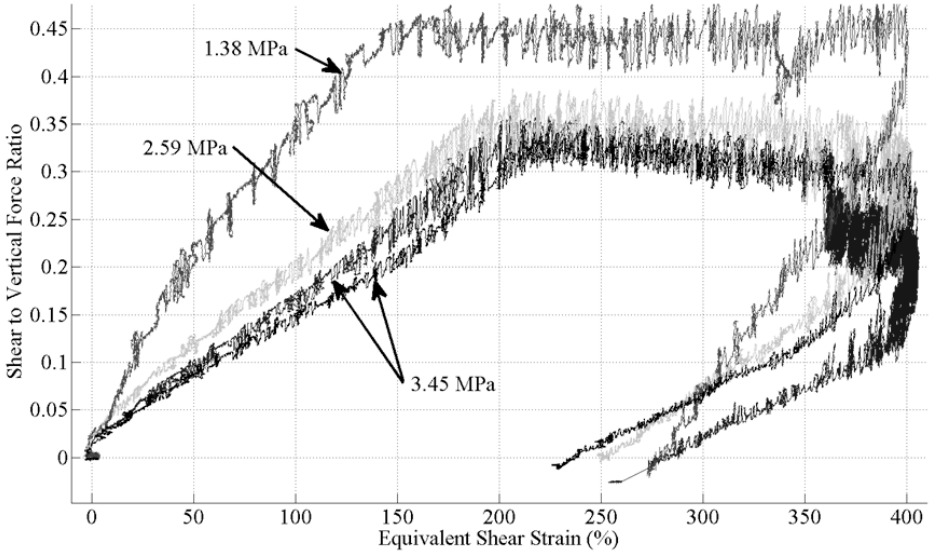


Figure 5. Successive Monotonic Tests of Type I bearing, varying simulated gravity load, horizontal to vertical load ratio versus shear strain

To investigate the cyclic response of Type I bearings, tests were also performed with cyclic loading protocols as follows: seven fully reversed cycles @ 25% and 50% equivalent shear strain, three fully reversed cycles @ 100%, 200%, 300%, and 400% equivalent shear strain. Tests were also performed for several levels of simulated gravity load. The first test, using a new bearing, was conducted with a simulated gravity load of 1.38 MPa (200 psi), and provided the data shown in Figure 6. The next test, also using a new bearing, was conducted with a simulated load of 3.45 MPa (500 psi), and generated the data shown in Figure 7. Finally, the bearing that had

been tested with a 1.38 MPa simulated gravity load was retested with the maximum permissible simulated gravity load of 5.52 MPa, shown in Figure 8.

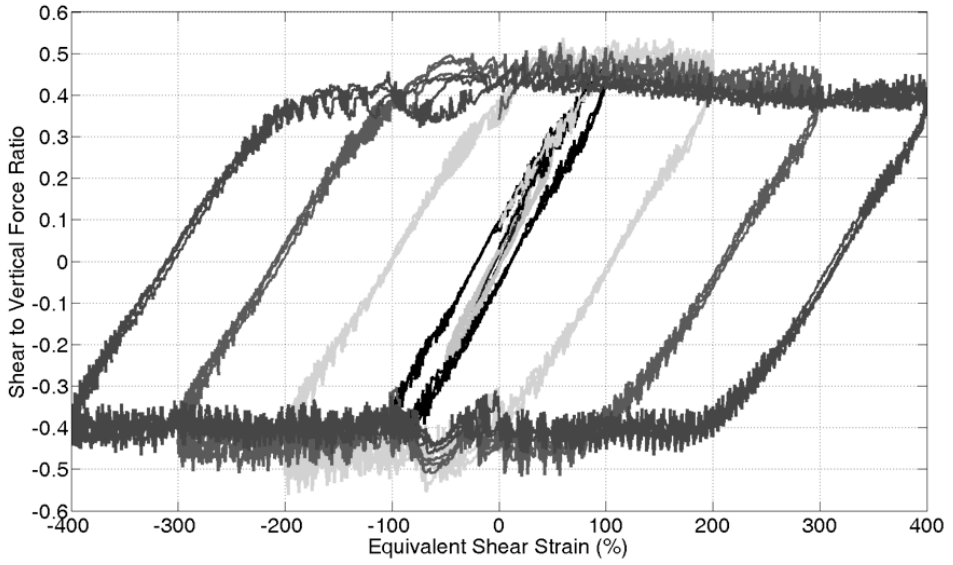


Figure 6. Cyclic Tests of Type I bearing, 1.38 MPa simulated gravity load

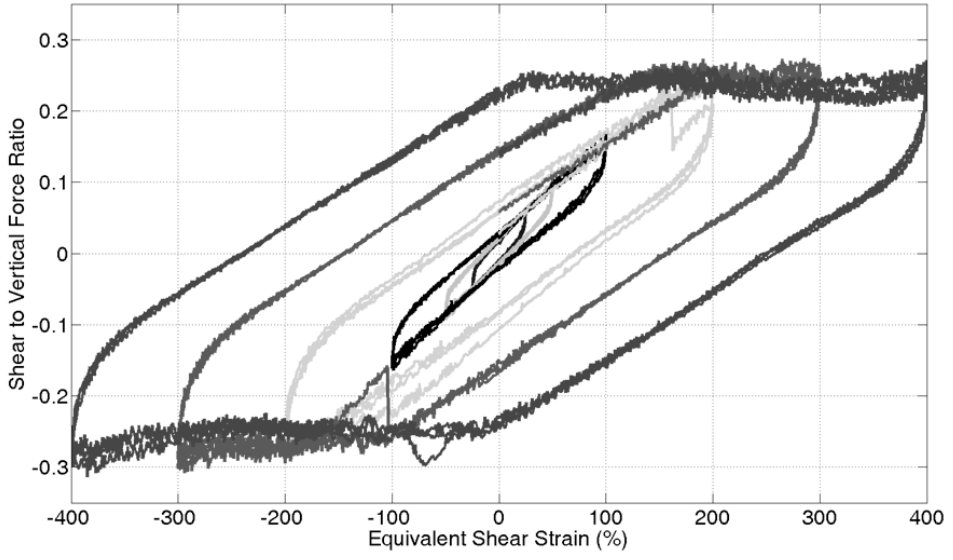


Figure 7. Cyclic Tests of Type I bearing, 3.45 MPa simulated gravity load

The three sets of test data reflect results similar to the monotonic tests for similar testing parameters. For example, the slip coefficient for the bearing subjected to the lightest simulated gravity load was significantly higher than for the tests at higher gravity loads, similar to Figure 5. The values ranged from approximately 0.4 – 0.5 at 1.38 MPa, to approximately 0.2 – 0.25 at 5.52 MPa. Other aspects of the response can only be observed in the cyclic tests, rather than the monotonic, such as the apparent degradation of bearings with successive cycles. Rather than being

consistent across all results, however, the influence of the cyclic degradation appears to be correlated to the testing parameters.

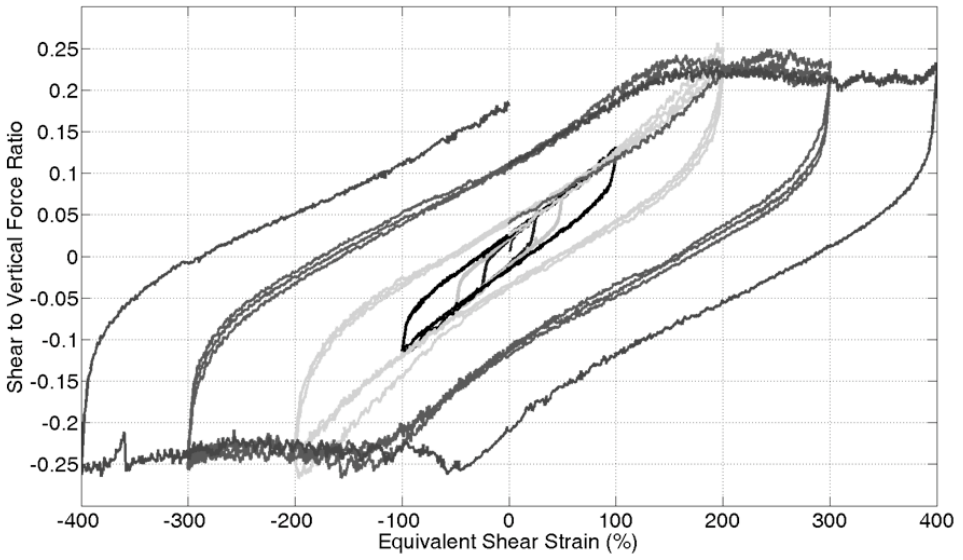


Figure 8. Cyclic Tests of Type I bearing, 5.52 MPa simulated gravity load

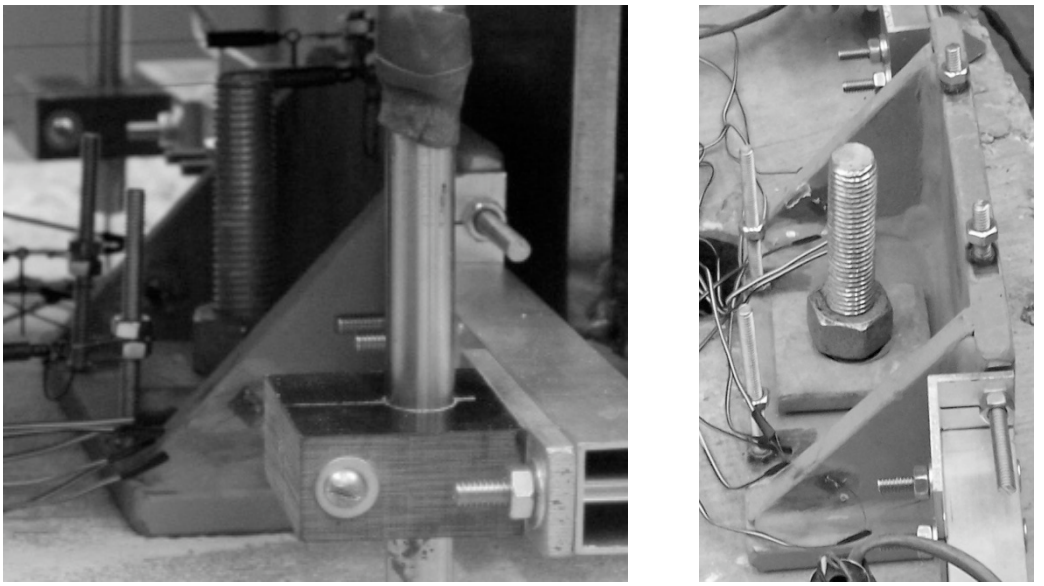
The data in Figure 6 show a continuous degradation in slip force with increasing cycles, suggesting that the degradation is tied to the bearing's travel on an abrasive surface. For the other two cases, however, in Figure 7 and Figure 8, degradation does occur on successive cycles, so long as the maximum displacement does not increase. When the maximum displacement increases for a new stage of the loading protocol, however, the frictional resistance increases at the maximum and minimum limits of displacement. This suggests that the degradation is partially influenced by abrasion of the elastomer base, but also by the condition of the concrete surface, so that "clean" surfaces which the bearing is traveling over for the first time possess greater frictional resistance than locations where the bearing has already deposited portions of elastomer by previous abrasions.

Regardless of the source of these variations, the effect appears to be minor overall. For large deformations, there is a stable response of linear elastic loading followed by frictional slip, with no visible damage other than minor abrasion of the elastomer base for gravity load up to 3.45 MPa. The test with 5.52 MPa was terminated prematurely for reasons other than the condition of the testing specimen. However, upon inspection following the test, the bearing had been deformed and ground against the concrete so severely that the edge of the lowest internal shim was visible.

RETAINER BRACKET EXPERIMENTS

To resist lateral translations of the bridge superstructure under service conditions and small seismic events, IDOT uses a standard detail for a stiffened L bracket, with a single holddown anchor installed into the concrete substructure. Figure 9 shows the

first tested retainer bracket mounted in the testing setup, prior to the test, and dismounted after the test is performed. Displacements were measured during the test with a combination of four string potentiometers and two LVDTs mounted with brackets to the sides of the retainer. Visible damage was limited to the threaded anchor and the concrete near the embedded anchor.



(a) Installed and Instrumented Prior to Test **(b) Dismounted After Test**

Figure 9. Still Captures of Retainer #1

A schematic view of the test setup prior to the start of the test is shown in Figure 10. The anchor is installed to an embedment of 9 inches (230 mm). The top plate of a Type I bearing was simulated by using the steel fixture of the testing frame to push against the face of the retainer.

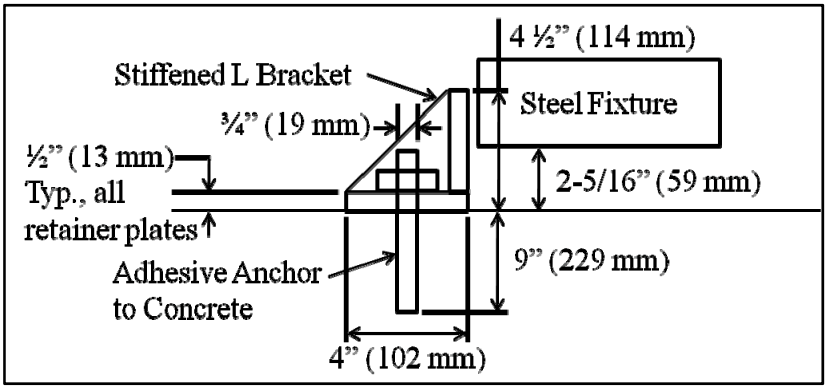


Figure 10. Schematic of Retainer Test Setup, Prior to Test

The contact height of the steel fixture caused the retainer to rotate as well as slide, as shown in Figure 11, and inducing the loading shown on the free-body diagram in Figure 12.

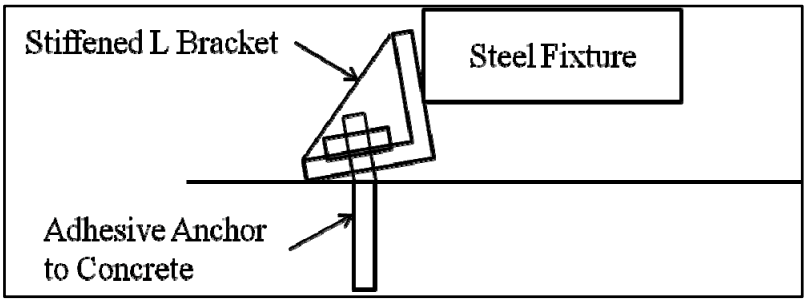


Figure 11. Schematic of Retainer Test at Incipient Failure of Anchor

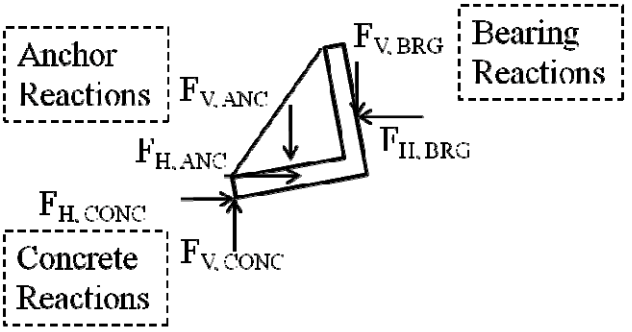
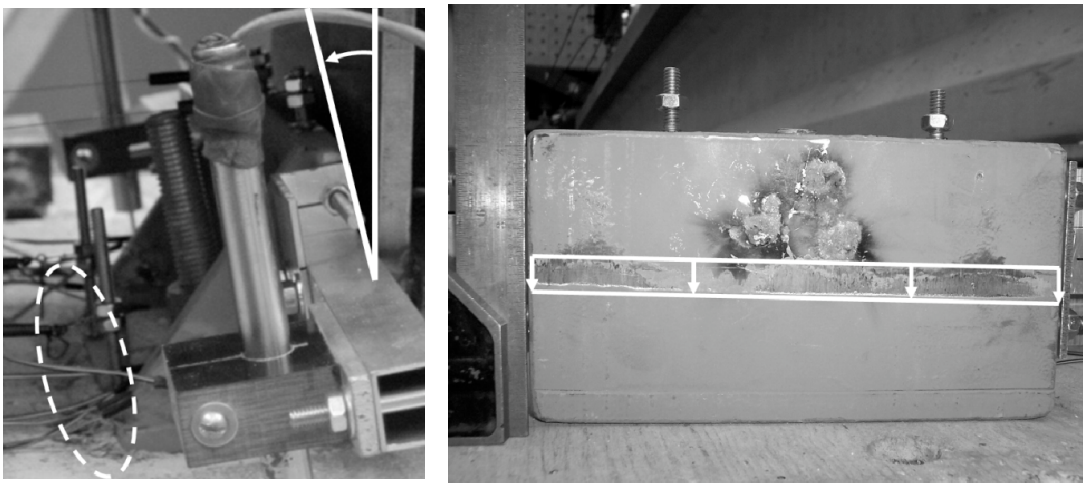


Figure 12. Free-Body Diagram of Reactions on Retainer at Incipient Anchor Failure



(a) Mounted, at Incipient Failure **(b) Face of Retainer After Test**

Figure 13. Still Captures of Retainer #1 Overturning Effects

As the retainer began to rotate, the toe of the retainer was driven into the concrete, as seen in Figure 13(a). An oval in the lower left of the image has been drawn to highlight the concrete being crushed at the toe of the retainer. The gap opening at the top of the retainer due to rotation is also indicated on the right-hand side of the image. Simultaneously, the retainer was developing a vertical load, at the contact location of the steel fixture, also contributing to the prevention of retainer rotation, and relieved by intermittent slips of the steel fixture along the vertical face of the retainer. This effect was evidenced by jumps in the vertical load recorded during the experiment,

combined with the scraping of paint where the steel fixture slipped against the retainer, shown in Figure 13(b).

The maximum horizontal force recorded during the retainer test was 29.6 kips (132 kN), using a 3/4" (19 mm) threaded anchor to the concrete test pad. Anchor material was specified as ASTM F1554, Grade 36, however, random selection of three anchor samples for tension tests indicated that the material was likely rejected Grade 55 material. Ultimate strengths obtained from the three tension test specimens were 84.7, 73.9, and 73.5 ksi (584, 510, and 507 MPa). Dividing the maximum horizontal force by the effective area of the threaded anchor (per ASTM F1554), the resulting stress is 88.5 ksi (610 MPa), slightly higher than the average ultimate strength of the tension test specimens.

The typical IDOT design procedure for the retainer used in this test would have estimated the "fuse" capacity to be 9.5 kips (42.3 kN) for Grade 36 material, or 11.9 kips (52.9 kN), even if Grade 55 had been assumed. These values are determined by accounting for tension demands on the concrete anchor with a reduced resistance factor. The current design approach neglects shear resistance at the toe and induced vertical load on the bearing plate on the retainer face. With respect to the overarching design strategy, this test indicated that the force required to transition to a quasi-isolated response would be approximately 3 times greater than expected, regardless of material strength assumed, indicating that the calculation methodology to estimate fuse strength of retainers should be calibrated for future versions of the IDOT ERS to prevent the development of unexpectedly high lateral forces in the structural system.

COMPUTATIONAL MODELING

Computational modeling is in development using Abaqus (2010), which will use the experimental data for calibration. The computational models will then be used to consider variations in parameters beyond those tested, such as material strength of various components, to investigate the associated effects on the bearing response. Preliminary models of elastomeric bearings are 2D plain strain models, with quad elements used for elastomeric material and the steel top plate, and beam elements used to model the thin internal steel shims. The Yeoh (1993) model was selected to capture the hyperelastic response of the elastomer. The top steel plate and internal shims are tied rigidly to the surrounding elastomer elements, and both the base and sides of the elastomer are modeled with hard contact and friction slip interactions relative to the rigid part representing the concrete test pad. Images showing the bearing with 3.45 MPa gravity load applied at the start and at the end of a monotonic displacement are shown in Figure 14 and Figure 15.

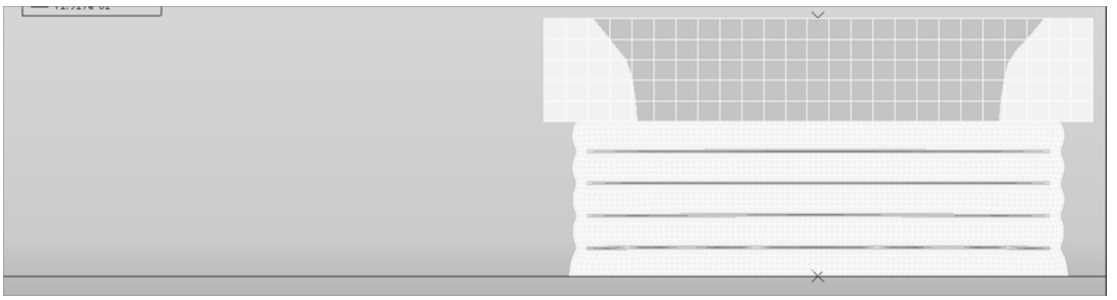


Figure 14. Type I 7c Bearing Model, Gravity Load Only

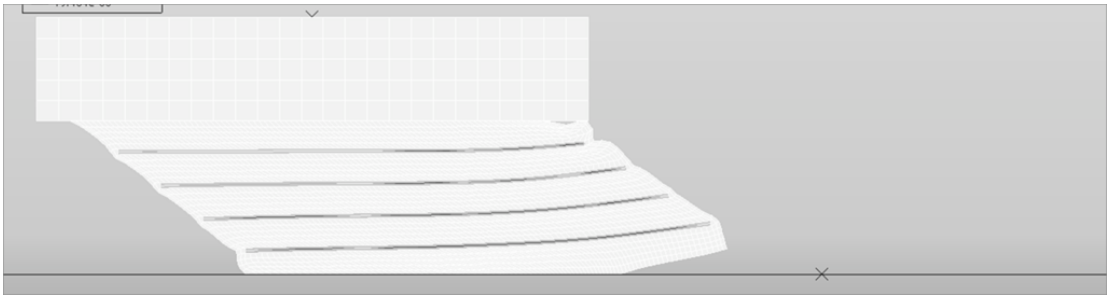
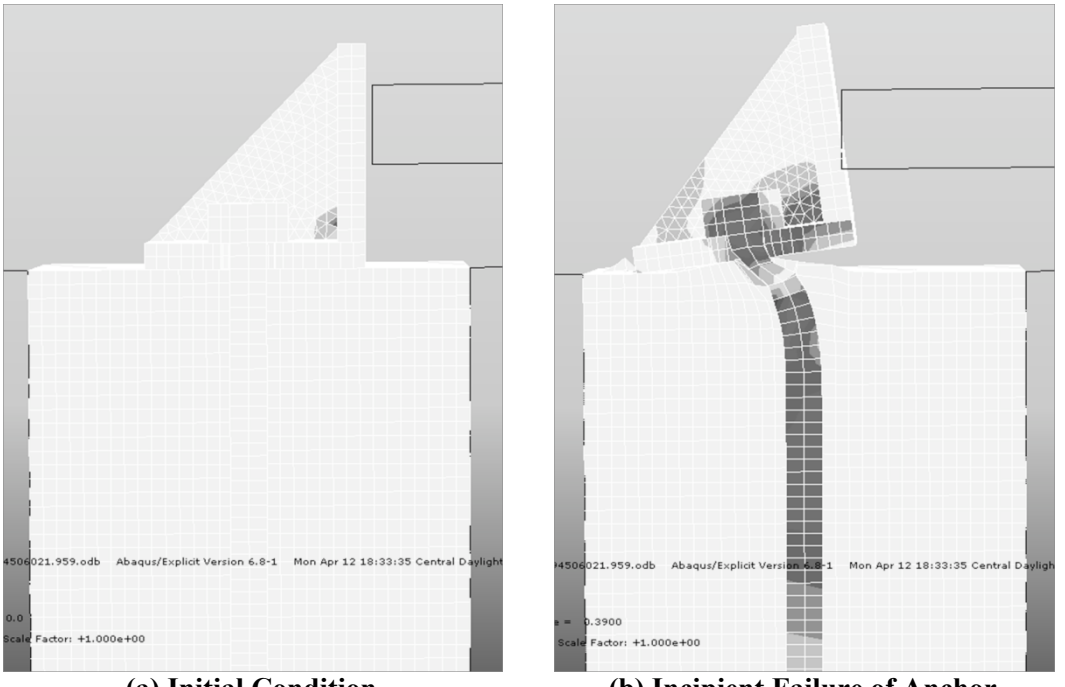


Figure 15. Type I 7c Bearing Model, Displaced to 400% Equivalent Shear Strain



(a) Initial Condition **(b) Incipient Failure of Anchor**

Figure 16. Computational Retainer Model

The preliminary retainer model includes a damage evolution model with element removal for the steel, to capture the degradation and rupture of the concrete anchor. The bottom and side of the retainer are modeled with contact interactions to permit contact and separation of the bearing top steel plate on the side, and the concrete surface on the bottom, using both hard contact for normal interactions and friction sliding for tangential interactions. Screen captures of the initial condition and

incipient failure of the anchor from the retainer model in Abaqus are shown in Figure 16, above.

CONCLUSIONS

The experimental testing program has generated data indicating that typical Type I bearings used by IDOT, incorporating low damping elastomers, can generally be characterized with linear elastic response for light to moderate loads, even at large displacement demands on the order of 250% shear strain, because the elastomer is permitted to slide on the concrete substructure, thereby precluding a stiffening branch. A stiffening branch may, however, begin to appear in the constitutive response for very large gravity loads.

Furthermore, repeated monotonic tests on a single bearing, along with cyclic tests incorporating multiple reversed cycles up to 400% equivalent shear strain, indicate that the bearings are remarkably resilient. Scragging and deterioration effects appear minor in most cases. The bottom surface of the elastomer is visibly worn and roughened by being dragged across concrete through multiple cycles of large displacements, but the visible abrasions appear to have only a minor influence on force-displacement response. Furthermore, delamination was not observed externally, and the only visible damage extending to the internal shims was for the case of the highest tested vertical load.

Characterization of retainer response can be relatively complex. The retainer is subject to overturning resistance at the toe, as well as an induced vertical load at the bearing plate. The orientations and magnitudes of the loads are therefore somewhat difficult to predict, and the fuse capacity of the sacrificial retainer during a major seismic event may be significantly underestimated by current design techniques in use by IDOT. The data indicate that for the retainer tested, the shear resistance is equivalent to slightly more than the full ultimate capacity of the concrete anchor.

The data presented in this paper are representative of only an initial set of experiments. The completed experimental program will also include experiments of larger, 13c Type I bearings, Type II 7c bearings, and fixed bearings. All bearing types and sizes are tested for loading in both longitudinal and transverse orientations. The complete set of experiments will be used to calibrate a suite of computational models, and the parametric variations of the computational models will be used to formulate appropriate models to capture the response characteristics of quasi-isolated full bridge structures in global bridge models.

ACKNOWLEDGMENTS

This article is based on the results of ICT R27-70, *Calibration and Refinement of Illinois' Earthquake Resisting System Bridge Design Methodology.* ICT R27-70 was conducted in cooperation with the Illinois Center for Transportation (ICT); IDOT; Division of Highways; and the U.S. Department of Transportation, Federal Highway

Administration (FHWA). The contents of this article reflect the view of the authors, who are responsible for the facts and the accuracy of the data presented herein. The contents do not necessarily reflect the official views or policies of the ICT, IDOT, or FHWA. The authors would like to thank the members of the project Technical Review Panel, chaired by D. H. Tobias, for their valuable assistance with this research.

REFERENCES

Abaqus FEA (2010). SIMULIA website, Dassault Systèmes, Vélizy-Villacoublay, France. http://www.simulia.com/products/abaqus_fea.html

Buckle, I. G., and Mayes, R. L. (1990). "Seismic Isolation: History, Application, and Performance---A World View." *Earthquake Spectra*, EERI, 6(2), 161-201.

Illinois Department of Transportation (IDOT). (2009). *Bridge Manual*, Springfield, Illinois.

Illinois Department of Transportation (IDOT). (2007). *Standard Specification for Road and Bridge Construction*, Springfield, Illinois.

Kulak, R. F, and Hughes, T. H. (1992). "Mechanical Tests for Validation of Seismic Isolation Elastomer Constitutive Models," *DOE Facilities Programs, Systems Interaction, and Active/Inactive Damping, Eds. C.-W. Lin et al.*, ASME Publication PVP Vol. 229, 41-46.

Mori, A., Moss, P. J., Cooke, N., and Carr, A. J. (1999). "The Behavior of Bearings Used for Seismic Isolation under Shear and Axial Load," *Earthquake Spectra,* EERI, 15(2), 199-224.

Roeder, C. W., Stanton, J. F., and Taylor, A. W. (1987). *Performance of Elastomeric Bearings*. National Cooperative Highway Research Program 298. Washington, D.C: Transportation Research Board.

Stanton, J. F., and Roeder, C. W. (1982). *Elastomeric Bearings Design, Construction, and Materials*. National Cooperative Highway Research Program 248. Washington, D.C: Transportation Research Board, National Research Council.

Tobias, D. H., Anderson, R. E., Hodel, C. E., Kramer, W. M., Wahab, R. M., and Chaput , R. J. (2008). "Overview of Earthquake Resisting System Design and Retrofit Strategy for Bridges in Illinois." Practice Periodical on Structural Design and Construction, ASCE, 13(3), 147-158.

Yeoh, O. H. (1993). "Some Forms of the Strain Energy Function for Rubber." *Rubber Chemistry and Technology*, American Chemical Society, Vol. 66, 754-771.

Measurements of a Steel Orthotropic Deck under Crawl Loading

S. Roy[1], R.S. D. Alapati[2], N.K. Manandhar[3] and J.W. Fisher[4]

[1]ATLSS Center, Lehigh University, 117 ATLSS Drive, Bethlehem, PA 18015-4729; PH (610) 758-5822; FAX (610) 758-5553; email: sor3@lehigh.edu
[2]ATLSS Center, Lehigh University, 117 ATLSS Drive, Bethlehem, PA 18015-4729; PH (610) 758-6273; FAX (610) 758-5553; email: rsa307@lehigh.edu
[3]ATLSS Center, Lehigh University, 117 ATLSS Drive, Bethlehem, PA 18015-4729; PH (610) 758-6255; FAX (610) 758-5553; email: nkm209@lehigh.edu
[4]ATLSS Center, Lehigh University, 117 ATLSS Drive, Bethlehem, PA 18015-4729; PH (610) 758-5537; FAX (610) 758-5553; email: jwf2@lehigh.edu

ABSTRACT

Recently a full scale prototype of a steel orthotropic deck was evaluated for a signature bridge in the ATLSS Engineering Research Center, Lehigh University. The deck was innovatively designed to be integral with the existing deck framing system. Since fatigue critical live load stresses at welded connections in an orthotropic deck can be produced by different loading dispositions, the response of the prototype deck was determined under a rolling tandem axle bogie in eight transverse positions. Global displacements at the specimen boundary were simulated by three under deck hydraulic actuators. The deck was instrumented using more than 300 sensors at critical locations. A 3D finite element model of the prototype deck was analyzed corresponding to the discrete axle positions and compared with experimental results. The prototype testing and the analytical studies provided critical understanding of the complex behavior of the deck and the influence surface/response envelopes under local wheel loads.

INTRODUCTION

Background. Steel orthotropic deck form is a natural choice for long span bridges, both for new design and rehabilitation. This light weight redundant deck form helps in reducing dead load stresses on the supporting cables, thereby increasing the life cycle of the main supporting elements and the bridge. In addition, a thin wearing surface on the orthotropic deck provides sufficient overlay for durability, improved riding quality and low maintenance. Despite these advantages and successful implementation of this deck system around the world, the use of orthotropic deck form in the United States has been limited, primarily because of increased efforts required for advanced analysis and design, relatively high initial cost owing to intensive fabrication, and higher possibility of in-service fatigue cracking from a large number of welded connections. Particularly several of the welded details are the bulkhead/sub-floor beam to rib connections and the rib to deck welds that are subjected to complex in-plane and out-of-plane deformations under localized wheel

loads (Gajer et al. 1996). Response of orthotropic decks are mostly manifested locally under wheel loads. Depending on the longitudinal and transverse disposition of loads, the deck elements can be subjected to a complex combination of in-plane and out-of-plane stresses that are significantly larger compared to the global nominal stresses. The critical live load stresses at a connection can be produced by different loading dispositions, and accordingly designing orthotropic deck requires a knowledge of the influence surface under wheel loads.

Recently the fatigue performance of a full scale prototype of an orthotropic deck was evaluated at the ATLSS Engineering Research Center, Lehigh University. The deck was proposed to replace the upper level deck of a signature double-decker bridge and was innovatively designed to be integral with the floor system and the stiffening truss. The test specimen comprised a quarter of the deck between the panel points of the stiffening truss, and included part of one floor beam and two stringers. To determine the critical live load disposition for the fatigue test, the deck response was determined under a rolling tandem axle bogie that was moved across the deck at about 5 mph. The tandem configuration was as per the AASHTO specification and the bogie was rolled in eight transverse positions. Global displacements at the boundary of the prototype deck were simulated by three actuators located under the floor beam and the two stringers. The deck was instrumented using more than 300 sensors at critical locations. A 3D finite element model of the prototype deck was analyzed corresponding to the discrete tandem axle positions and compared with experimental results to understand the complex behavior of the deck and to develop influence surface/response envelopes under local wheel loads. The prototype testing and the analytical studies provided critical understanding of the behavior of an orthotropic deck that was integral with the deck framing system, and provided valuable information for design improvement and optimization in achieving more than 100 years service life.

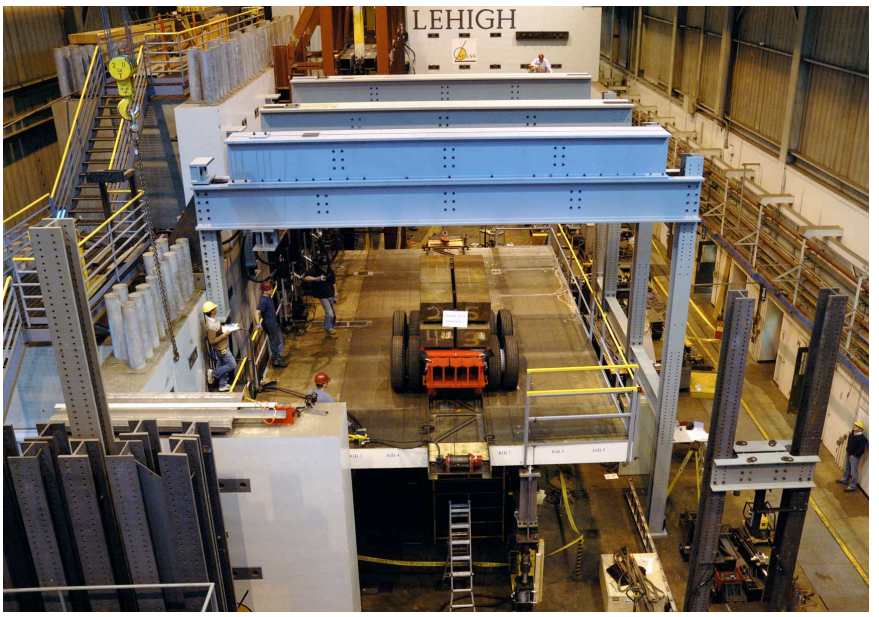


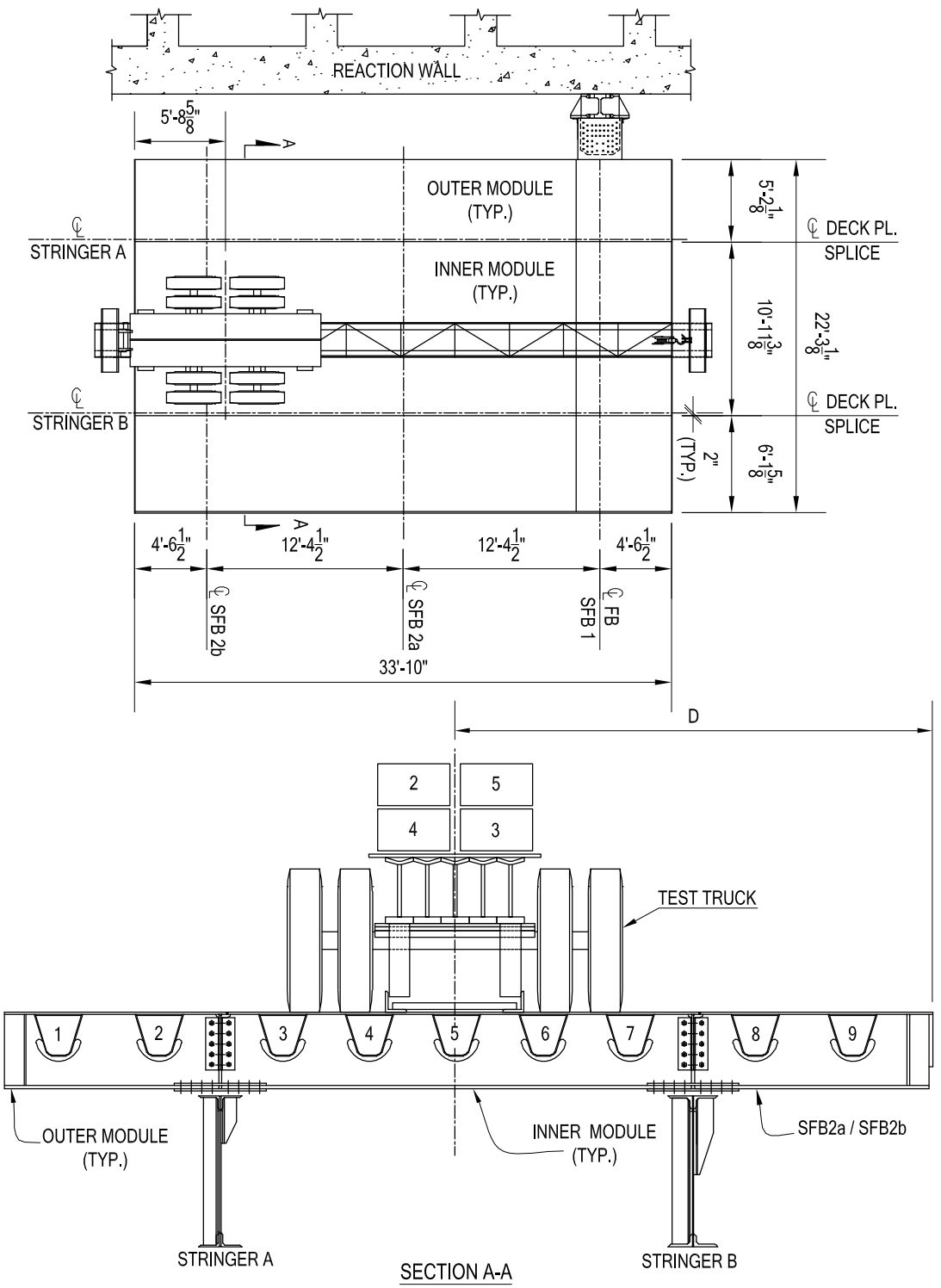
Figure 1. Test setup in the ATLSS Center, Lehigh University.

Test setup. The test setup at the multi-directional testing facility in the ATLSS Engineering Research Center, Lehigh University is shown in Figure 1. To reproduce realistic conditions, the test setup comprised part of the upper level floor framing of the bridge including full size stringers and floor beams. The horizontal members of the transverse box at each node of the stiffening truss constituted the floor beams to the upper and lower decks. These members consisted of built-up box sections that were evidently quite stiff and were expected to form fixed end connections with the vertical members. Accordingly, the west end of the floor beam in the prototype deck was rigidly connected to the strong wall to simulate fixed end support. The stringers, framing into the floor beam in the bridge, were cantilevered off the floor beam in the setup. The east end of the floor beam and the south ends of the stringers were supported by actuators reacting vertically against the strong floor to impose continuity boundary condition only in the vertical direction. The top and bottom clevises of the actuators were arranged such as to allow axial displacement of the stringers and the floor beam. The play in the clevises allowed sufficient movements in the other four degrees of freedom. Another 4 ft 6½ in of the stringers were cantilevered to the north of the floor beam to support a part of the deck that was included to simulate the transverse field splices.

Description of prototype deck. The prototype deck was 6.8 m (22 ft 3 in) wide and 10.3 m (33 ft 10 in) long, and included a standard inner module, and two outer modules, and typical longitudinal and transverse field welds between the deck panels. No wearing surface was provided on the 16 mm (5/8 in) thick deck plate. The typical inner module consisted of five trapezoidal ribs at 635 mm (2 ft 1 in) spacing. The outer module had two ribs at 2 ft 5 in spacing. The ribs were 305 mm (1 ft) deep and 8 mm (5/16 in) thick.

The deck was made integral with the supporting stringers and floor beams using stringer extensions and sub floor beams. The prototype deck contained three transverse sub-floor beams at 3.8 m (12 ft 4½ in) centers. One sub-floor beam was fastened to the main floor beam and identified as SFB1. The other intermediate sub-floor beams, identified as SFB2a and SFB2b, were 560 mm (22 in) deep and had 16 mm (5/8 in) thick web. The sub-floor beams were provided with cutouts for pass-through ribs. At the sub-floor beam connections, the ribs were provided with full depth internal bulkheads (diaphragms). The bulk-head plates were 8 mm (5/16 in) thick. The edges of the orthotropic deck were maintained free.

The prototype deck was fabricated with ASTM A709 Grade 50 steel.



Position		1	2	3	4	5	6	7	8
D	(ft)	8.8	9.8	10.3	10.9	11.3	11.9	12.9	14.1
	(m)	2.7	3.0	3.1	3.3	3.4	3.6	3.9	4.3

Figure 2. Crawl test plan.

CRAWL TESTS

Crawl truck. The response of the prototype deck was determined under a bogie with tandem axles that was rolled along the deck at a slow rate of about 0.038 mph. The bogie represented the tandem axles of a tractor-trailer with tandem configuration in accordance to HL-93 loading of the AASHTO LRFD Bridge Design Specifications. The axles were spaced 1.2 m (4 ft) apart. A pair of wheels were attached to each axle. The center-to-center distance between the wheel pairs in the transverse direction was 1.8m (6 ft). Retreaded truck tires, pressurized to 0.6 MPa (90 psi), were used on the wheels. To compare with the recommendations of the AASHTO Specifications, the tire contact for each wheel was measured on the laboratory floor. The average measurement of tire contact area was approximately 0.276 m × 0.532 m (10.88 in × 20.97 in).

The self-weight of the crawl truck was 7 tons (14.1 kip). The crawl truck was loaded with four steel billets identified in Figure 2 that weighed 9.1 kip, 10.6 kip, 10.5 kip and 9.4 kip respectively. The combined weight of truck and four billets was 24.5 tons (53.7 kip), which was about 2.2 times the trailer axle load of the AASHTO notional fatigue truck. The loads at each wheel pair of the loaded truck, measured using a portable scale (provided by PennDOT), were respectively 13.0 kip, 13.5 kip, 13.2 kip and 14.1 kip in clock wise rotation from front-left to rear-left wheel pairs.

Test procedure. To determine the load positions that produced the most critical live load stresses in the deck elements, the crawl truck was rolled along the deck in eight transverse positions. The centerline of the truck was positioned between ribs 3 and 7, which resulted in the outer wheel pairs being located between ribs 2 and 8. In the first position, the left wheels were located symmetrically above stringer extension B. In subsequent positions, the truck was positioned such that either one wheel or a wheel pair was located symmetrically on the deck plate in between the stiffening ribs, or over a rib. A typical position (position 5) is shown in Figure 2, where the right wheel pairs are located symmetrically on the deck plate between ribs 6 and 7. A truss along the length of the deck was used underneath the test truck to guide the truck in a straight line (Figure 2). The truck was pulled by a hydraulic winch attached to one end of the guide truss with the rope hooked underneath the test truck. For each position the truck was pulled forward and backward at an average speed of about 0.065 km/h (0.038 mph).

Instrumentation and data acquisition: The deck was extensively instrumented using about 400 data channels to determine the global response of the test deck and to monitor the local stresses at the fatigue sensitive rib-to-sub floor beam and rib-to-deck connections. About 250 bondable or weldable encapsulated metallic resistance strain gages of 6 mm (¼ in) gage length in uniaxial, biaxial and rosette configurations were installed.

Most of the strain gauges were installed on SFB1 and SFB2a at junctions with ribs 2, 3, 7 and 8, to capture the variation of stresses around the cutout and in the bulkhead plate. A typical arrangement of strain gauges at SFB2a and Rib 7 intersection is shown in Figure 3 All gages at the sub floor beam were placed back to back on the north and south faces of the web, to measure out-of-plane bending

stresses, except for the two rosettes at the cutouts in SFB2a below the ribs that were provided only on the south face. Rosettes were installed adjacent to cutouts abutting the sub-floor beam-to-rib weld, to measure the principal stresses at the cutout stress concentration, that could lead to fatigue cracking.

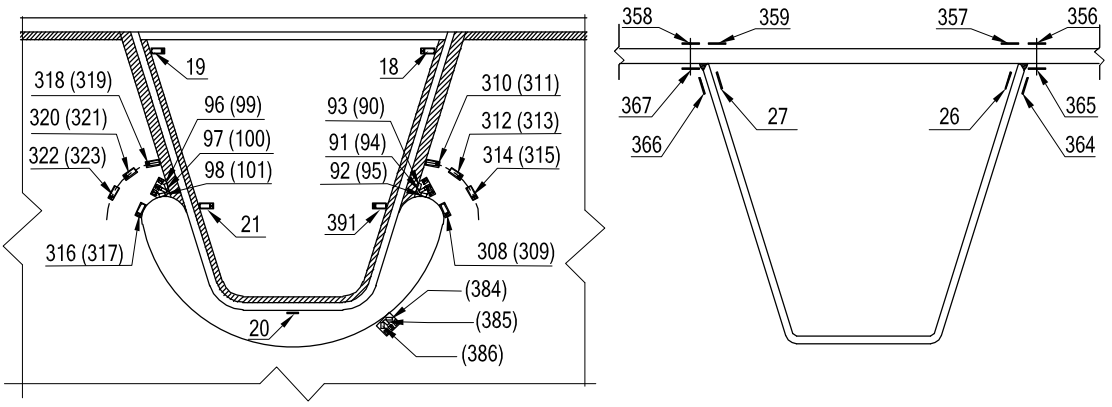


Figure 3. Typical gauge arrangement: (a) SFB2a; (b) Rib 7.

On the internal bulkhead plates in ribs 3 and 7, four strain gages were installed abutting the bulkhead-to-rib weld as shown in Figure 3. High temperature resistant weldable strain gages of 6 mm (1/4 in) length were used at the bulkhead plates so that they could survive the heat generated during the welding of subfloor beams to the ribs and the ribs to the deck plate. Two strain gauges of same type were installed on the internal face of rib wall in Rib 7 near the rib-to-deck weld at two sections 49.5 in and 99.0 in north of SFB2a. Conventional strain gauges were placed on the outer face of the rib wall, matching these internal gauges, to measure out-of-plane bending of rib wall. Similar back-to-back strain gauges were provided on the deck plate to the west of rib-to-deck welds at the same section (channel numbers 364 and 366), also to capture the bending stresses in the deck plate under wheel loads. The gauge arrangement at the section 49.5 in north of SFB2a is shown in Figure 3

Additional strain gauges were installed on: the deck plate at center line of sub floor beams; at deck splices; at soffit of ribs 3 to 7; at copes and seat angles of stringer extension; and at floor beam to wall connection plates. In addition, displacement of the deck was measured by Linear Variable Displacement Transducers (LVDT) at 10 locations. One LVDT was installed under SFB2a at the mid span between Stringer Extensions A and B, while the remaining nine LVDTs were installed underside the deck at the mid span section between SFB1 and SFB2a.

Data collection was performed by Campbell Scientific CR9000 digital data loggers.

FINITE ELEMENT ANALYSES

Modeling. FEA of the prototype deck including the floor beams and stringers was conducted using a commercially available package ABAQUS (Dassault Systèmes. 2010) to better understand the response characteristics of the deck. The model included all features of each component. The welded and bolted connections were not

modeled; instead all welded and bolted connections in a component were considered as integral and all bolted connections between components were displacement constrained. The boundary conditions were defined consistent with the test setup. Solid 20 node second order isoparametric reduced integration serendipity elements were used for modeling the components. The model consisted of 691,000 elements, 4,400,00 nodes and 13,200,000 degrees of freedom.

Analyses. The model was analyzed for the for eight discrete load dispositions in the longitudinal direction simulating the crawl tests. All eight transverse positions were analyzed. The loads were applied as pressure on 10 in × 20 in tire footprints according to the AASHTO LRFD Bridge Design Specifications.

All analyses were conducted on a distributed memory parallel execution computer cluster of 16 machines, each having eight central processing units (cpu). The analyses were linear elastic and used direct solver.

A deformed configuration of the model is shown in Figure 4

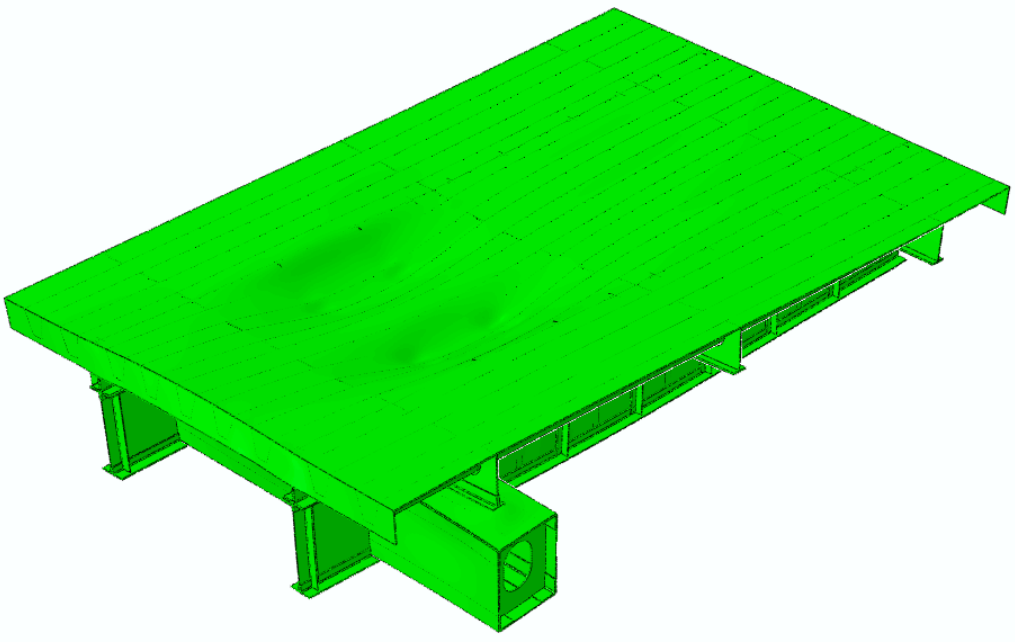


Figure 4. Deformed configuration of deck.

DISCUSSION OF RESULTS

Rib-to-deck connection. Response of the rib-to-deck plate connection under longitudinally and transversely varying wheel positions are shown in Figure 5 and Figure 6 with respect to Rib 7 at the instrumented section 49.5 in and 99.0 in north of SFB2a. These figures show the variation of stress measured at a gauge as the crawl truck traversed along the deck in transverse position 5 from south to north. The horizontal axis of the plots show the position of the crawl truck centerline (center of the wheels) with respect to SFB2a, which is taken as origin. Also shown on the plots

are the results obtained from FEA and the truck positions corresponding to the peak stresses.

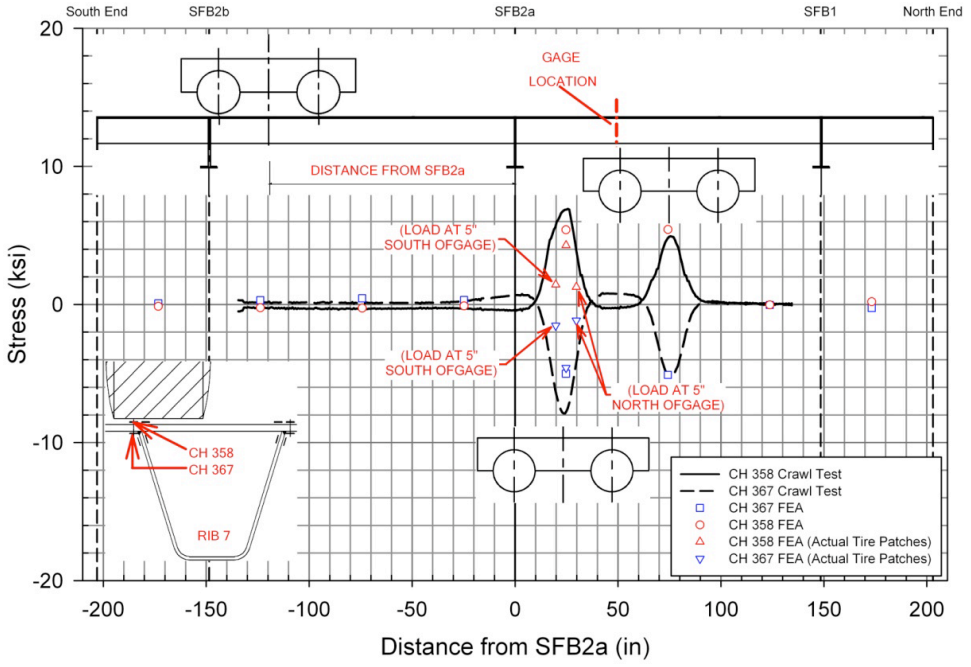


Figure 5. Crawl test result in deck plate at rib-to-deck connection: Position 5

Typically the response of the rib-to-deck connection at a section was manifested by the presence of wheel load in the vicinity of the section. As the truck rolled across the deck, peak stresses were observed at the wheel locations. Figure 5 shows the normal stresses in the transverse direction measured at the back-to-back uniaxial gauges on the deck plate that were located ahead of the rib-to-deck plate weld toe. As is evident, peak stresses occurred at these gauges when the wheels of the crawl truck were at the section. In this particular position one of the tires in both wheels was directly over the gauges. The stresses were negligible when the wheels were away from the section, and changed rapidly as the wheel was in the vicinity. This observation was also verified by FE simulations, where wheel loads were positioned at 5 in on either side of the section, and rapid change in stresses were noted. Tensile and compressive stresses of almost equal magnitude developed at the top and bottom gauges respectively, indicating almost pure bending of the deck plate under wheel loads. Two peaks occurred due to the passage of the crawl truck — one due to the front wheel and the other due to the rear wheel — indicating that the deck plate experiences two stress cycles due to the passage of one tandem axle.

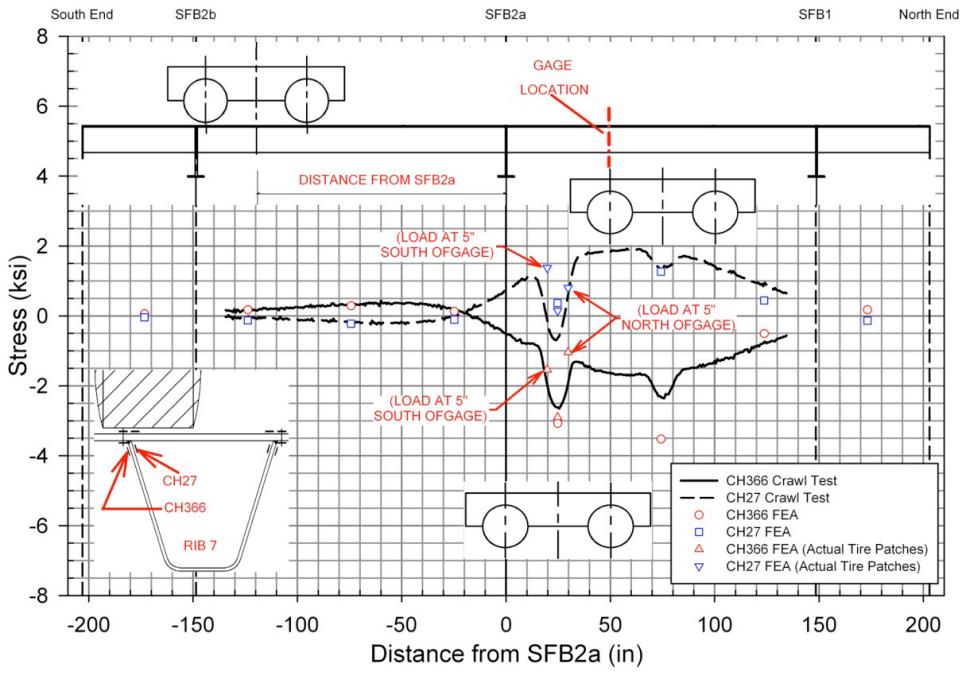


Figure 6. Crawl test result in rib wall at rib-to-deck connection: Position 5

Figure 6 shows the normal stresses at the faces of the rib wall measured in the back-to-back uniaxial gauges located near the rib-to-deck connection. Stresses in the gauges were negligible when the truck was on the span between SFB2a and SFB2b. However, tensile and compressive stresses of almost equal magnitude developed in the internal and external gauges respectively, as the truck approached SFB2a and was on the span between SFB2a and SFB1, except as follows. When one of the wheels was in the vicinity of the section of interest, the stresses changed rapidly. With the wheel at the section, the tensile stress in the inner gauge became compressive and the compressive stress in the outer gauge increased. This change was more noticeable when only one wheel was on the span and the other wheel was on SFB2a. It is evident that the rib wall was predominantly subjected to bending due to wheel loads, except at a section under the wheel, where significant axial compressive stresses developed in the rib wall. The FEA simulations generally agreed well with the measurements, except when the rear wheel was on the section.

Sub-floor beam-to-rib connection. Figure 7 shows the stresses measured in the (near) horizontal legs of the back-to-back rosettes at the rib-cutout in SFB2a for position 5. These gauges were identified as CH98 on the north face and CH101 on the south face. The stresses were predominantly in plane as the crawl truck rolled across the span between SFB2a and SFB2b from the south. As the truck approached the sub-floor beam, the stresses in the north gauge reduced compared to the south gage, indicating bending of the sub-floor beam along with Rib 7. The bending stresses existed while the truck was on the span between SFB1 and SFB2a. The maximum bending stresses occurred when the truck was on the span SFB1-SFB2a, with one wheel on the subfloor beam. The figure also indicates that for a single passage of test

truck, the rib-cutout in SFB2a experienced only one stress cycle, and the sub-floor beam does not experience the effects of individual axles.

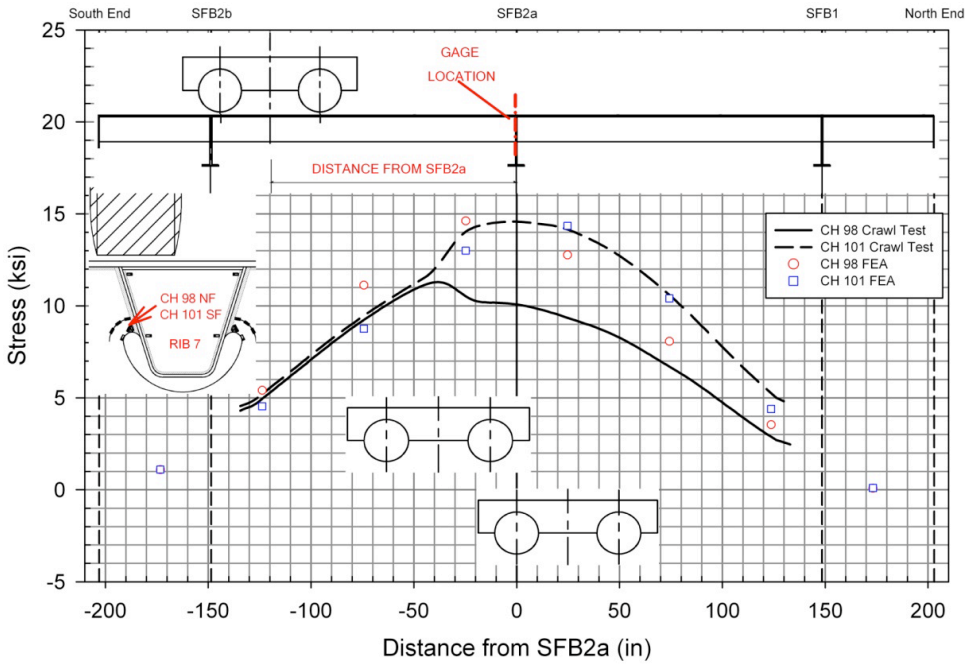


Figure 7. Crawl test result in deck plate at rib-to-deck connection: Position 5

Effect of transverse disposition of load. To demonstrate the effects of transverse and longitudinal disposition of the crawl truck, the stresses measured in the back-to-back uniaxial gauges (CH27 and CH366) on Rib 7 wall are tabulated in Table 1, for positions 3, 4, 5 and 6 under both truck axles. The gauge CH27 was on the inner face and gauge CH366 was on the outer face of the west wall. In position 3 both walls of Rib 7 were under the wheels. In position 4, one wheel was on the deck plate in the middle of Rib 7 and the other wheel was in between ribs 6 and 7. In position 5, one wheel was on the west wall of Rib 7 and the other wheel was on the east wall of Rib 6. In position 6, one wheel was on deck plate in between ribs 6 and 7, and the other wheel was on deck plate in Rib 6.

As is evident from Table 1, the stresses obtained in the rib under the front and the rear axles were not same, although loads on both axles were similar. In particular, the results in position 4 appears interesting. In this position the wheels were located symmetrically about the west rib wall, which resulted in only in-plane stresses in the rib wall, when the front axle was on the section. When the rear axle was on the section, the magnitude of in-plane stress remained the same, whereas a significant bending stress (causing tension on the inside face) developed in the rib wall. Existence of this bending stress can be explained from Figure 6, which shows that the wheel loads generated bending stresses at sections away from the loaded section. This suggests that the front axle contributed to the stresses at the section loaded by the rear axle, and resulted in the difference in observed stresses.

The table also shows that as the transverse position of the axles changed, the stresses changed in the rib, sometimes causing reversal in bending stresses. For

example, the position 5 generated bending stress in the rib wall that is compressive on the inside face, where as the positions 4 and 6 generated bending stresses that are tensile on the inside face. Due to the presence of high tensile welding residual stresses at the weld toe, the entire reversal can be effective in causing fatigue damage.

The maximum bending stress occurred in the rib wall in position 6, where the rib was eccentrically loaded.

Table 1.

	Stresses due to front axle (MPa)				Stresses due to rear axle (MPa)			
Crawl Test Positions	Gage #27	Gage #366	Bending	In-plane	Gage #27	Gage #366	Bending	In-plane
3	-1.38	-11.03	+/-4.83	-6.20	-11.03	-5.52	-/+2.76	-8.27
4	-5.52	-5.52	+/-0.00	-5.52	13.79	-24.82	+/-19.30	-5.52
5	-19.30	-5.52	-/+6.89	-12.41	-15.17	9.65	-/+12.41	-2.76
6	19.30	-26.89	+/-23.09	-3.79	13.79	-15.86	+/-14.82	-1.03

CONCLUSIONS

The measurements indicated that the response of the rib-to-deck connection at a section was manifested by the presence of wheel load in the vicinity of the section. The measurements also showed that the critical live load stresses varied with different loading dispositions in the transverse direction, as well as with the longitudinal position of the axle loads. Accordingly, designing orthotropic deck requires a knowledge of the influence surface under wheel loads. The deck connections experience one stress cycle due to the passage of each axle. The stresses were predominantly in sub-floor beams. A single passage of tandem axle produced only one stress cycle at the rib-cutout. The 3D finite element analyses provided good correlation with the measurements and provided valuable insight into the complex behavior of the deck and helped in developing the influence surface. The positions of hydraulic actuators for fatigue testing of the deck were determined based on these crawl test results.

ACKNOWLEDGEMENTS

The authors gratefully acknowledge the sponsors and the engineers of this project, and the support staff of the ATLSS Engineering Research Center at Lehigh University for their respective contributions.

REFERENCES

Gajer, R.B., Patel, J., and Khazem, D., (1996). “Orthotropic steel deck for the Williamsburg Bridge reconstruction.” *Proceedings of the 14th structures congress*, Vol. 1, 14-18.

Dassault Systèmes. (2010). Abaqus 6.10: Analysis User's Manual. Providence, RI: Dassault Systèmes Simulia Corp.

Simplified Erection Guidelines for Double I-Girder Systems during Bridge Construction

Qiuhong Zhao[1], Baolin Yu[2] and Edwin G. Burdette[3]

[1] Steel Research Laboratory, Department of Civil and Environmental Engineering, the University of Tennessee, Knoxville, TN 37996-2010; PH (865) 974-7711; e-mail: qzhao@utk.edu

[2] Steel Research Laboratory, Department of Civil and Environmental Engineering, the University of Tennessee, Knoxville, TN 37996-2010; PH (865) 974-7724; e-mail: byu5@utk.edu

[3] Department of Civil and Environmental Engineering, the University of Tennessee, Knoxville, TN 37996-2010; PH (865)974-7704; e-mail: eburdett@utk.edu

Abstract

In the current design specifications, only the individual girder inside the double girder system is checked for lateral torsional buckling between the intermediate cross-frames. However, the overall lateral torsional buckling of double girder systems may be critical under bridge erection, due to the limited lateral bracing present at this stage. Therefore, close attention should be paid to the overall stability of double I-girders during construction, and research has been conducted for the simply supported case and the cantilever case under self-weight only. The results are presented in this paper.

Through extensive finite element analyses, established formulas on the overall lateral torsional buckling capacity of simply-supported double girder systems were verified and then modified for the cantilever case. A stability index L/S was developed for estimating the stability of double girder systems under erection, which equals to the ratio between the girder span L and the girder spacing S. Formulae were then derived for the maximum span L_{max} and the maximum stability index $(L/S)_{max}$, beyond which the double girder system would lose stability under its self-weight. Parametric studies were conducted to determine the dominant parameters for L_{max} and $(L/S)_{max}$ for various girder sections with different spacing. A quick and reliable method was also established to check the stability of double girder systems under erection using the L/S ratio.

Introduction

Double I-girder systems are widely used in highway and railroad multi-girder bridges, which consist of two I-girders connected by intermediate cross-frames as well as top and bottom diagonal braces. During the construction stage, the double

girder system is erected before the concrete deck is added, and it is subjected only to the self-weight of the girder and weight of construction equipment and workers, which are much smaller than the service loads. However, since the lateral supports provided by the concrete deck at the top flange are generally weak until concrete hardens, the system is particularly vulnerable at this stage, due to its slenderness and relatively low lateral and torsional stiffness (Kozy and Tunstall, 2007; Hastings, 2010). Therefore, close attention should be paid to the stability of the double girder system during the erection stage.

Traditionally, the stability check of a double girder system has focused on evaluating the stability of each single girder within the unbraced length between the cross-frames (Yura et al, 2008). However, in terms of overall integrity, there is the possibility of overall lateral torsional buckling of the entire girder system, especially when the two girders are closely spaced. An example was shown as the recent Marcy Bridge collapse in New York with overall lateral torsional buckling failure of a tub girder system (Yura and Widianto, 2005), as shown in Figure 1 below, which could be considered similar to a closed-spaced double girder system. On the other hand, the stability of steel girders under erection is usually considered a construction issue to be addressed by contractors and/or the subcontractors, who may not have either the time or expertise to conduct a thorough stability analysis during construction. Therefore, it is important to develop simplified erection guidelines to assist the erectors in conducting a quick and reliable check on the stability of double girder systems under erection.



FIGURE 1 The collapse of the Marcy Bridge in New York (Exponent, 2009)

There had not been much research conducted on the overall buckling of double girder systems until the occurrence of the Marcy Bridge collapse. Kozy (Kozy and Tunstall, 2007) noticed the danger of overall lateral torsional buckling of the tub girder under construction, and a case study on a three-span continuous composite steel plate girder bridge was conducted using finite element buckling analysis and non-linear incremental collapse analysis. It was concluded that overall lateral torsional buckling could control the strength of a double girder system and should be considered in the design. Yura also did considerable research on the overall lateral torsional buckling of double girder systems (Yura et al, 2008; Yura and Widianto, 2005), where a thorough analysis was conducted to determine the lateral and torsional stiffness of double girder system, and a formula

was derived for the lateral torsional buckling capacity of a simply-supported double girder system:

$$M_g = C_b \frac{\pi}{L}\sqrt{EI_y GJ + \frac{\pi^2 E^2 I_y C_w}{L^2}} \quad (1)$$

Eq. 1 was simplified by Yura into Eq. 2 by combining the dominant parameters

$$M_{gs} = C_b \frac{\pi^2 SE}{L^2}\sqrt{I_y I_x} \quad (2)$$

where M_g = global lateral torsional buckling capacity of double girder system; M_{gs} = simplified global buckling capacity; C_b = moment diagram modification factor; L = span length; E = modulus of elasticity; G = shear modulus of elasticity; I_x, I_y = moment of inertia about horizontal and vertical centroidal axes, respectively; S = girder spacing; C_w = warping constant. It was also concluded that for a simply supported double girder system, the C_b factors under a uniform distributed load (C_b = 1.12) and under a concentrated load at midspan (C_b =1.35) for single girders were applicable based on finite element analyses (Yura et al, 2008).

Derivation of Simplified Erection Guidelines for Double Girder System

Eq. 2 provided the theoretical basis to check the lateral torsional buckling of double girder systems under erection. For any double girder system under the girder self-weight, the maximum external bending moment (M_u) increases with the girder span L, while the global lateral torsional buckling capacity (M_{gs}) decreases with the girder span L. Therefore, a certain span limit L_{max} exists, beyond which $M_u \geq \phi M_{gs}$ and global lateral torsional buckling of the double girder system will occur, as shown in Figure 2.

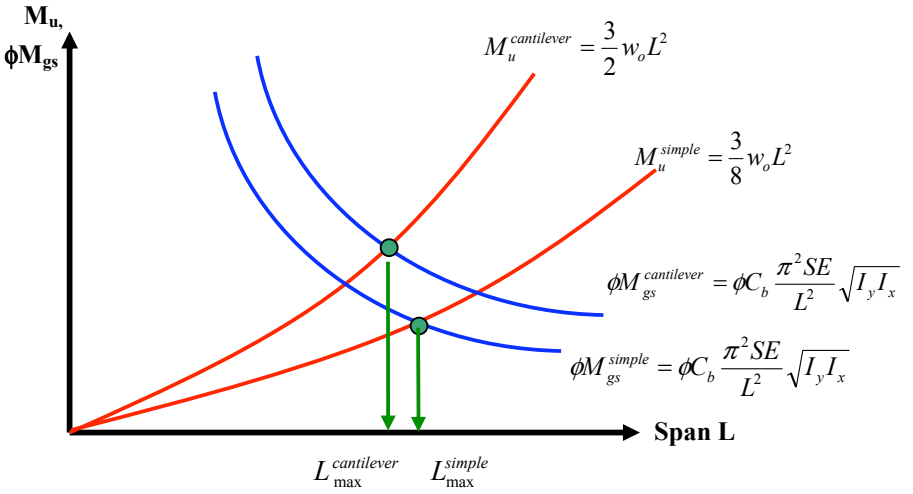


FIGURE 2 Span limit L_{max} for double girder systems under erection

Considering Load Combination IV in the AASHTO LRFD code, which equals to 1.5 times the girder self-weight, the maximum external bending moment (M_u^{simple}) for the simply supported case during the erection stage would be

$$M_u^{simple} = \frac{1}{8} \times (2 \times 1.5 w_o) L^2 = \frac{3}{8} w_o L^2 \quad (3)$$

where, w_o= uniform load on one girder due to self-weight, $w_o = A \cdot D_{steel}$; A = area of single girder section; D_{steel} = steel density. From Eq. 2, the design lateral torsional buckling capacity for simply supported double girder systems would be

$$\phi M_{gs}^{simple} = \phi C_b \frac{\pi^2 SE}{L^2} \sqrt{I_y I_x} \quad (4)$$

where ϕ = 1.0 resistance factor, C_b = 1.12 for simply supported girder under uniform load. Solving $M_u^{simple} = \phi M_{gs}^{simple}$, L_{max} for a simply supported double girder system is given below

$$L_{\max}^{simple} = 1.32 \cdot \sqrt[4]{\frac{\pi^2 SE}{w_o} \sqrt{I_x I_y}} \quad (5)$$

Similarly, considering Load Combination IV in the AASHTO LRFD code, the maximum external bending moment for the cantilever case during the erection stage would be

$$M_u^{cantilever} = \frac{1}{2} \times (2 \times 1.5 w_o) L^2 = \frac{3}{2} w_o L^2 \quad (6)$$

By extending Eq. 2 to the cantilever case, the design lateral torsional buckling capacity for cantilever double girder systems would be

$$\phi M_{gs}^{cantilever} = \phi C_b \frac{\pi^2 SE}{L^2} \sqrt{I_y I_x} \quad (7)$$

where ϕ = 1.0 resistance factor, C_b = 2.04, which according to Timoshenko's *Theory of Elastic Stability* (Timoshenko and Gere, 1961), is the lower bound of C_b for a cantilever single girder under uniformly distributed load. Solving $M_u^{cantilever} = \phi M_{gs}^{cantilever}$, L_{max} for a cantilever double girder system is

$$L_{\max}^{cantilever} = 1.08 \cdot \sqrt[4]{\frac{\pi^2 SE}{w_o} \sqrt{I_x I_y}} \quad (8)$$

Eq. 5 and Eq. 8 could be used to check the double girder free span under erection with the maximum allowable span L_{max}, and prevent the overall lateral torsional buckling of double girder system under erection. However, in Yura's studies, Eq. 1 and Eq. 2 were only verified by finite element analysis on a few simply-supported cases, and no analyses were conducted on the cantilever cases to verify the applicability of Eq. 2 as well as the C_b factor. Therefore, it was unclear if these formulae were applicable for a wide range of double girder systems under both simply-supported and cantilever situations, which are the two most common cases during erection. Finite element analyses were then conducted on a wide range of double girder systems in order to 1) check the accuracy of the formulae for the simply supported case; 2) extend the formulae to the cantilever case, which are described in the following section.

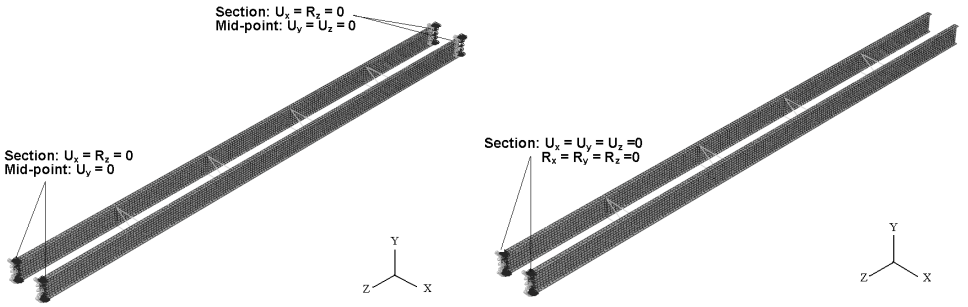
Verification of Capacity Formulae for Double Girder Systems through FEA

A group of double girder systems with various section properties were investigated in order to cover the typical range in actual bridge projects. The flange varied from 305mm x 25mm to 914mm x 38mm, and the web varied from 1245mm x 13mm to 2400mm x 17mm, which was similar to the previous research conducted by the authors on single girders (Hastings, 2010). The girder spacing varied from 1.83m to 4.27m, based on the large database obtained from literature survey (Brockenbrough and Merritt, 2006; Mabsout et al, 1997; Mabsout et al, 2002). The girder span was chosen such that the girder is still in the elastic stage under its self-weight. According to a parallel study (Zhao et al, 2010), the section area and spacing of cross-frames were chosen such that the stiffness and strength requirements for bracing were satisfied (Yura, 2001), which would barely affect the stability of double girder system.

Finite element analysis program ABAQUS was used to model the double girder system and conduct the static and buckling analysis (ABAQUS, 2008). The girders were modeled with four-node shell elements S4R, and the intermediate cross-frames were modeled with two-node truss elements T3D2 with a pin connection at both ends (Kozy and Tunstall, 2007; Yura et al, 2008). The mesh size of each model was proportional to the span. The steel material was M 270, Gr. 50W, modeled as a elastic material with a modulus of elasticity of 2.01GPa and a Poisson's ratio of 0.30.

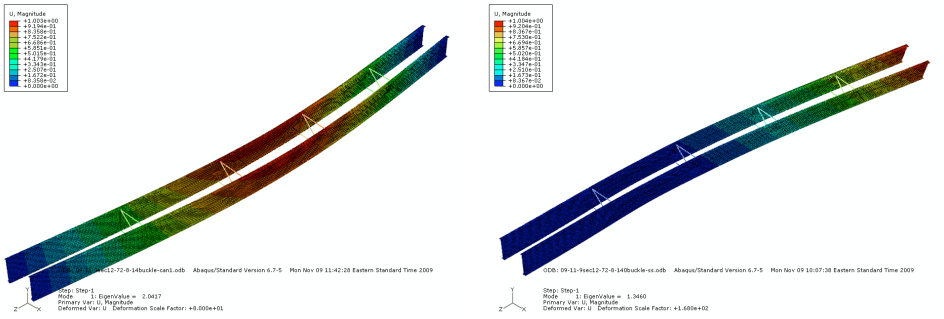
Load Combination IV of the current AASHTO LRFD specifications (1.5D) was used. In order to avoid the effects of loading location, the external load was applied as a uniform body force (force per volume) to the girder model with a value of $1.5W_{steel} = 115{,}454\ N/m^3$, where W_{steel} is the weight density of steel. For the simply supported model, the torsional rotations and lateral displacements normal to the web were restrained with free warping for all the nodes at both end sections. The vertical displacements of the midpoints at both end sections were restrained, while the longitudinal displacement was restrained at one end section and free at the other. For the cantilever model, one end was fixed by constraining all 6 degrees of freedom for each node, and the other end was free with no constraints (White and Jung, 2007). A view of the finite element model is shown in Figure 3.

Elastic static analyses under 1.5D were firstly conducted to calibrate and verify the finite element model. Eigenvalue buckling analyses were then conducted to obtain the overall lateral torsional buckling capacity of each double girder system, as well as indentify major buckling modes. The Eigen values (λ) and mode shapes of the double girder system are shown in Figure 4 for the simply supported case and the cantilever case respectively. It is obvious that, for both cases, the primary buckling mode (mode 1) is lateral torsional buckling of the double girder system as a whole, instead of buckling of individual girders between the cross frame (Mode 2 and 4 for the simply supported case, Mode 3 and 11 for the cantilever case). Therefore, the Eigen values (λ) corresponding to the global buckling mode was used to calculate the critical buckling moments in later study.

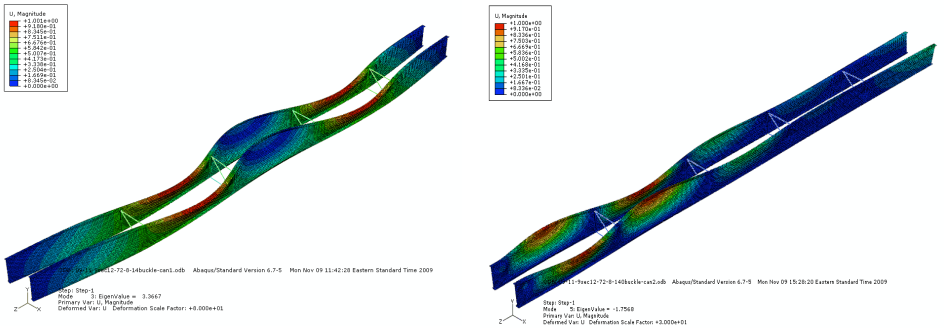


a. Simply supported Case b. Cantilever Case

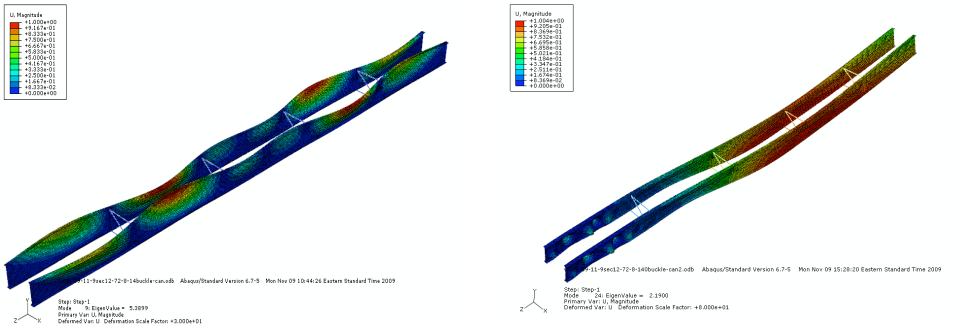
FIGURE 3 Finite element model of double girder systems



Mode 1 ($\lambda = 2.04$) Mode 1 ($\lambda = 1.35$)



Mode 2 ($\lambda = 3.37$) Mode 3 ($\lambda = 1.76$)



Mode 4 ($\lambda = 3.56$) Mode 11($\lambda = 2.19$)

a. Simply supported case b. Cantilever case

FIGURE 4 Eigen values and mode shapes of double girder system

The critical elastic lateral torsional buckling moment (M_{cr}) of each double girder system was calculated by multiplying the Eigen values (λ) with the maximum external bending moment along the girder span, and then compared with Yura's formula in Eq. 2 (M_{gs}) for both the simply supported and the cantilever case, as shown in Table 1 below. It is obvious that for the simply supported case with a uniform load (C_b = 1.12), the discrepancies between the FEA results and Yura's formula for most models are below 5%, and Yura's formula turned out to be quite accurate for simply supported double girders. On the other hand, there were considerable differences (30-40%) between the finite element results and Yura's formula for the cantilever case with C_b = 2.04. A modification factor C_d was then introduced to account for the differences, which might be due to factors such as the rigidity of the cross-frame connection or the difference in the moment distribution between a cantilever double girder system with lateral movement and a single cantilever. The C_d values for each model are listed in Table 1, with an average of 1.37 and a standard deviation of 0.04.

TABLE 1 Lateral torsional buckling capacity of double girder system

Model #	Lateral Torsional Buckling Capacity (kN-m)					
	Simply Supported Case			Cantilever Case		
	FEA M_{cr}	Yura M_{gs} (C_b=1.12)	Diff (%)	FEA M_{cr}	Yura M_{gs} (C_b=2.04)	$C_d = M_{cr}/M_{gs}$
1	2870	3014	4.7	7789	5489	1.42
2	3192	3424	6.8	8534	6236	1.37
3	4120	4491	8.3	10864	8179	1.33
4	4778	5233	8.7	12481	9531	1.31
5	4013	4213	4.8	10885	7674	1.42
6	4535	4844	6.4	12178	8823	1.38
7	5167	5562	7.1	13818	10131	1.36
8	5912	6497	9.0	15298	11833	1.29
9	3936	4067	3.2	10654	7407	1.44
10	5128	5422	5.4	13843	9876	1.40
11	7588	8157	7.0	20325	14857	1.37
12	9494	10196	6.9	24657	18572	1.33
13	7808	8305	6.0	21020	15127	1.39
14	8463	9124	7.2	22670	16619	1.36
15	10263	11125	7.7	27367	20263	1.35
16	9638	10548	8.6	25347	19212	1.32
17	8588	8901	3.5	23185	16212	1.43
18	9233	9856	6.3	24791	17951	1.38
19	11150	11974	6.9	29876	21809	1.37
20	11795	12816	8.0	31363	23344	1.34
21	9174	9442	2.8	24827	17198	1.44
22	9944	10528	5.5	26780	19176	1.40

23	11982	12751	6.0	32221	23225	1.39
24	12619	13733	8.1	33773	25014	1.35
25	14398	15003	4.0	38750	27326	1.42
26	15382	16158	4.8	40442	29431	1.37
27	15224	15887	4.2	40965	28938	1.42
28	16042	17206	6.8	42959	31340	1.37
29	18469	19135	3.5	49863	34854	1.43
30	21491	22962	6.4	57726	41825	1.38
31	21511	22411	4.0	56861	40821	1.39
32	23122	24272	4.7	60883	44209	1.38
33	19290	19886	3.0	51190	36220	1.41
34	22886	23863	4.1	60415	43465	1.39
35	22439	23254	3.5	59414	42356	1.40
36	26624	27905	4.6	69855	50827	1.37
37	22027	22685	2.9	58447	41319	1.41
38	26138	27222	4.0	69003	49583	1.39
39	25582	26491	3.4	67726	48251	1.40
40	27654	28833	4.1	72975	52518	1.39
41	35089	36535	4.0	92709	66546	1.39
42	33743	35226	4.2	89056	64162	1.39
43	32384	33547	3.5	85752	61103	1.40
44	37383	39138	4.5	98507	71287	1.38
45	39465	41070	3.9	104308	74807	1.39
46	37969	39600	4.1	100192	72128	1.39
47	36396	37674	3.4	96367	68621	1.40
48	42022	43953	4.4	110726	80057	1.38
49	36767	37909	3.0	97471	69049	1.41
50	42435	44228	4.1	111930	80558	1.39
51	38965	40232	3.1	103217	73279	1.41
52	41478	43107	3.8	110618	78516	1.41

Therefore, Yura's formula could be extended into the following form for cantilever double girders under a uniformly distributed load:

$$M_{gs}^{cantilever} = C_d C_b \frac{\pi^2 SE}{L^2} \sqrt{I_y I_x} \tag{9}$$

where $C_d = 1.37$ the modification factor; $C_b = 2.04$. Accordingly, the L_{max} formula for cantilever double girder system would be modified into the following form:

$$L_{\max}^{cantilever} = 1.17 \cdot \sqrt[4]{\frac{\pi^2 SE}{w_o} \sqrt{I_x I_y}} \tag{10}$$

Verification of Simplified Erection Guidelines for Double Girder System

Based on Eq. (10), a parametric study was conducted to investigate the effects of girder geometric properties on the span limit L_{max} for the cantilever case, with parameters shown in Table 2. The same tendency will be observed for the simply-supported case since the L_{max} values are proportional.

TABLE 2 Parametric studies on L_{max} of double girders under erection

Case #	Flange Width b_f (mm)	Flange Thickness t_f (mm)	Web Depth D_w (mm)	Web Thickness t_w (mm)	Girder Spacing S (m)
1	305 - 914	25 - 38	1245	13	1.83 – 4.27
2	305	25	1245- 2400	13 - 17	1.83 – 4.27
3	305	25 - 51	1245	13	1.83 – 4.27
4	305	25	1245	10- 25	1.83 – 4.27

In Case 1 analyses, the web depth and thickness were held constant, while the flange width, the flange thickness and the girder spacing varied in order to investigate the effects of flange width and girder spacing on the span limit L_{max}, and the results are shown in Figure 5. In Case 2-4 analyses, the investigation was mainly on the effects of web depth, flange thickness and web thickness on the span limit L_{max}. From the parametric studies, it is clear that the span limit L_{max} increases with the flange width, the flange thickness, the girder spacing, and the web depth, while L_{max} decreases with the web thickness, probably because increasing web thickness would lead to a much faster increase of girder self-weight and external bending moment than the increase of girder lateral bucking capacity, therefore the net result is a decrease in the span limit L_{max}.

From the analyses, the flange width and girder spacing were found to be the two most important parameters for L_{max}, where L_{max} increased 45-54% when the flange width increased from 305mm to 914mm, and L_{max} increased 23% when the girder spacing increased from 1.83m to 4.27m. In comparison, the web depth, flange thickness and web thickness only had limited influence on L_{max}, since the maximum differences in L_{max} are 5.9%, 5.9% and 8.9% respectively.

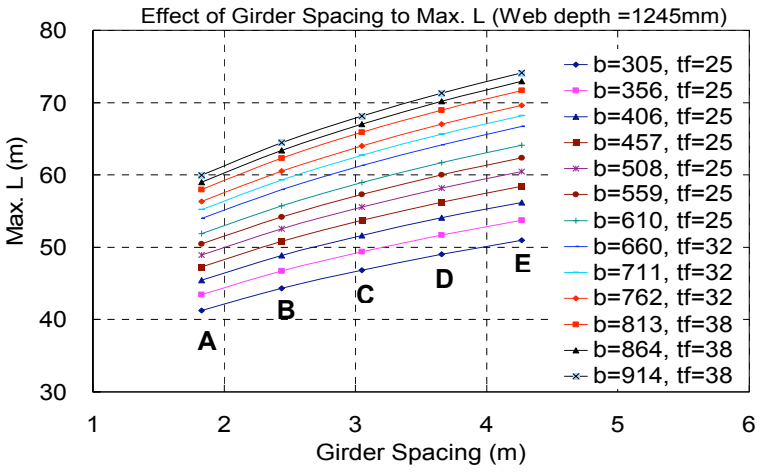


FIGURE 5 Effect of girder spacing and flange width on max. span (Case 1)

Since simplified erection guidelines have been developed for single steel I-girder under erection using the L/b ratio, where L is the unbraced length and b is the compression flange width (Hastings et al, 2010), similar erection guidelines could also be established for double girder system by introducing a stability index. From the previous parametric studies, the girder spacing S, which is the distance between the centers of two I-girders, has great influence on the lateral torsional stiffness of the double girder systems and could be taken as the "flange width" of the whole system. A stability index was then introduced as L/S, which is the ratio between the girder span L and the girder spacing S. For each double girder system, a unique $(L/S)_{max}$ ratio exists, beyond which the system would have global lateral torsional buckling under its self-weight. For any given double girder geometry, the $(L/S)_{max}$ ratio for the simply supported system as well as the cantilever system would be shown in Eq. 11 and 12 below, which are proportional to each other, as shown in Eq. 13.

$$(L/S)_{\max}^{simple} = 1.32 \cdot \sqrt[4]{\frac{\pi^2 E}{w_o S^3}\sqrt{I_x I_y}} \tag{11}$$

$$(L/S)_{\max}^{cantilever} = 1.17 \cdot \sqrt[4]{\frac{\pi^2 E}{w_o S^3}\sqrt{I_x I_y}} \tag{12}$$

$$(L/S)_{\max}^{simple} = 1.125(L/S)_{\max}^{cantilever} \tag{13}$$

Due to the complicated formula, checking the possibility of lateral torsional buckling of the whole double girder system directly with $(L/S)_{max}$ ratio might not be easy. Data from the previous parametric study were then re-processed in order to investigate the effect of each parameter on the $(L/S)_{max}$ ratio, and more importantly, identify the upper and lower limits of $(L/S)_{max}$ for a quick stability check. Results are shown in Figure 6 and 7, where it is clear that the $(L/S)_{max}$ increases with the flange width, the flange thickness, and the web depth, while decreases with the girder spacing and the web thickness. The flange width and girder spacing would affect the $(L/S)_{max}$ ratio much more than the web depth, flange thickness and web thickness.

If the geometry of a cantilevered double girder system falls into the parametric study, the $(L/S)_{max}$ ratio could be directly read or interpolated from the curves in Figure 6, in order to conduct a preliminary check on double girder system stability. Moreover, for cantilever double girder systems, the absolute lower bound of the $(L/S)_{max}$ ratio, below which lateral torsional buckling of the whole system would not occur under erection, could be conservatively taken as 10. The absolute upper bound of the $(L/S)_{max}$ ratio, beyond which lateral torsional buckling of the whole system would occur under erection, unless temporary supports are provided, could be conservatively taken as 35. According to Eq. 13, the absolute lower and upper bound of the $(L/S)_{max}$ ratio for simply supported double girder system could be conservatively taken as 11 and 40.

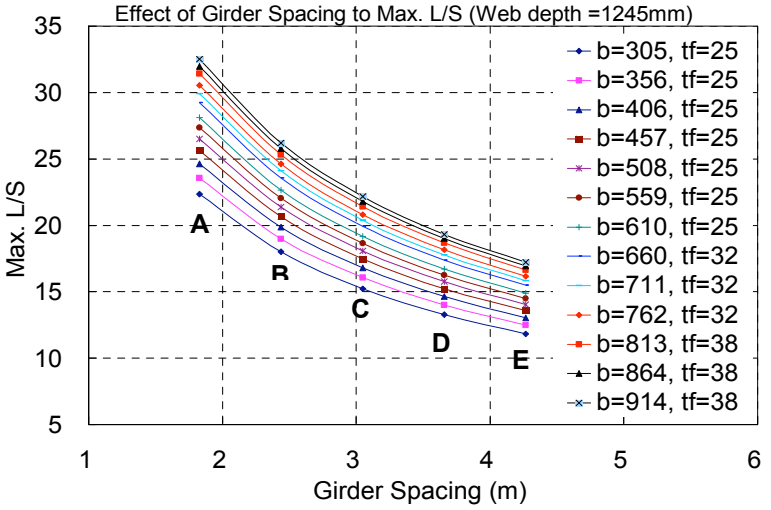
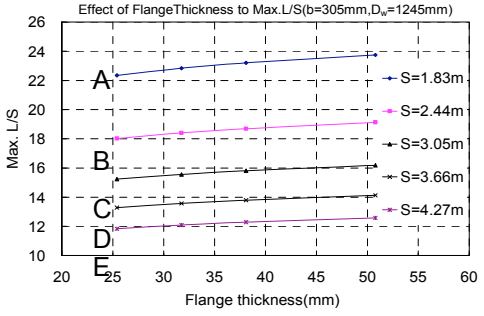
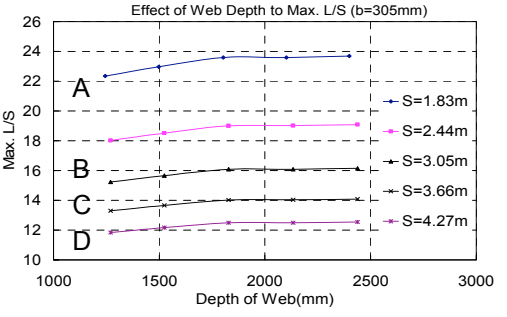


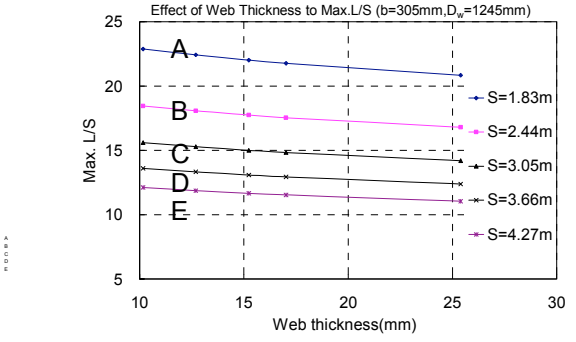
FIGURE 6 Effects of girder spacing and flange width on max. L/S (Case 1)



(a) Effect of flange thickness (Case 2)



(b) Effect of web depth (Case 3)



(c) Effect of web thickness (Case 4)

FIGURE 7 Effects of web depth, flange thickness and web thickness on max. L/S

Conclusion

The work presented here supports the following conclusions:

1. Based on buckling analyses of double girder systems with a wide range of section properties, Yura's formula (Eq. 2) for the overall lateral torsional buckling capacity of double girder systems turned out to be quite accurate for the simply supported case under uniformly distributed load ($C_b = 1.12$);
2. Based on buckling analyses, Yura's formula was modified for cantilever

double girders under uniformly distributed load (C_b = 2.04), by introducing a modification factor C_d =1.37;

3. For double girder systems under erection, formulae for span limit L_{max} were derived for both the simply supported and the cantilever cases, beyond which lateral torsional buckling of the whole system would occur under girder self-weight;
4. A stability index L/S, which is the ratio between the girder span to the girder spacing, was introduced for the convenience of checking the possibility of lateral torsional buckling of double girders under erection. Formulae for the $(L/S)_{max}$ ratio were also derived;
5. Parametric studies were conducted to investigate the effects of various geometric parameters on the L_{max} and $(L/S)_{max}$ ratio. The flange width and girder spacing were found to have the most influence, while the web depth and thickness, and the flange thickness, only had minimal effects;
6. For the shapes investigated, double girders with an L/S ratio less than 10 for the cantilever case, and 11 for the simply supported case, should not require a stability check. Double girder systems with an L/S ratio larger than 35 for the cantilever case, and 40 for the simply supported case, would probably need temporary support during erection;
7. If a double girder system falls into the range in Figure 7, then $(L/S)_{max}$ could be directly read or interpolated from Figure 7, in order to conduct a preliminary check on system stability. For the simply supported case, the values should be increased by 12.5%.

REFERENCES

1) ABAQUS. *ABAQUS/standard user's manuals.* Hibbitt, Karlsson, and Sorenson, Inc., Pawtucket, R.I., 2008
2) Exponent Engineering and Scientific Consulting. Pedestrian Bridge Collapse. http://www.exponent.com/pedestrian_bridge_collapse/. Accessed June 10, 2009.
3) Brockenbrough, R. L. and F. S. Merritt. *Structural Steel Designer's Handbook.* McGraw – Hill, New York, 2006.
4) Hastings, J. S., Zhao Q.*, and E. G. Burdette. "Girder Stability during Steel Bridge Erection". *J. of Bridge Engineering*, November, Volume 15, Issue 6, 2010, pp. 759-762.
5) Kozy, Brian and S. Tunstall. "Stability analysis and bracing for system buckling in twin I-girder bridges." *Bridge Structures,* 3(3), 2007, pp. 149-163.
6) Mabsout, M. E., K. M. Tarhini and G. R. Frederick. "Finite element analysis of steel girder highway bridges." *Journal of Bridge Engineering*, 2(3), 1997, pp. 83-87.
7) Mabsout, M. E., I. Y. Naddaf and K. M. Tarhini. "Load Reduction in Steel Girder Bridges." *Practice Periodical of Structural Design and Construction,*

7(1), 2002, pp. 37-43.

8) Timoshenko, S., and J. Gere. *Theory of elastic stability,* McGraw-Hill, New York, 1961.
9) Yura, Joseph, T. Helwig, R. Herman and C. Zhou. "Global lateral buckling of I-shaped girder systems." *Journal of Structural Engineering.* 134(9), 2008, pp. 1487-1494.
10) Yura, J. A., and J. A. Widianto. "Lateral buckling and bracing of beams – A re-evaluation after the Marcy bridge collapse." *Proc. Structural Stability Research Council, Montreal,* 2005, pp. 277-294.
11) Yura, J. A. "Fundamentals of Beam Bracing". *Engineering Journal*, First Quarter, 2001, pp. 11-26.
12) White, D. W., and S. Jung. "Effect of web distortion on the buckling strength of non-composite discretely-braced steel I-section members." *Engineering Structures,* 29(8), 2007, pp. 872–1888.
13) Zhao Q., Yu B., Burdette E. G., and Hastings J. S. "Monitoring Steel Girder Stability for a Safer Bridge Erection", *J. of Performance of Constructed Facilities*, ASCE, December, Volume 23, Issue 6, 2009, pp. 391-398.

FEASIBILITY ANALYSIS OF USING UHPC IN PRESTRESSED BRIDGE GIRDERS

Christopher W. Taylor[1], Kristin F. Montoya[1], David V. Jáuregui[2], Craig M. Newtson[2], and Brad D. Weldon[3]

[1]Graduate Research Assistant, Department of Civil Engineering, PO Box 30001 MSC-3CE, New Mexico State University, Las Cruces, NM 88003, Ph. 575-646-3801, e-mail: cwtaylor@nmsu.edu, kfajardo@nmsu.edu
[2]Associate Professor, Department of Civil Engineering, PO Box 30001 MSC-3CE, New Mexico State University, Las Cruces, NM 88003, Ph. 575-646-3801; e-mail: jauregui@nmsu.edu, newtson@nmsu.edu
[3]Assistant Professor, Department of Civil Engineering, PO Box 30001 MSC-3CE, New Mexico State University, Las Cruces, NM 88003, Ph. 575-646-3801; e-mail: bweldon@nmsu.edu

ABSTRACT

Ultra high performance concrete (UHPC) is an emerging material which develops very high compressive strengths and exhibits improved tensile strength and durability properties. Recent construction of three UHPC bridges in the United States has sparked interest in the use of UHPC for prestressed bridge girders in several states. UHPC offers many advantages including longer spans, improved durability, and smaller structural members, making it an appealing material to use in prestressed bridge construction. This paper presents a case study conducted to investigate the feasibility of implementing UHPC in bridge design in New Mexico. Using a modified LFD procedure, bridge designs were developed considering the compressive strength, modulus of rupture, and modulus of elasticity of UHPC as well as design requirements for flexure and shear, girder cross-section geometry, and prestressing strand area. Comparisons with as-built bridge configurations show that using UHPC with compressive strengths between 100 MPa and 150 MPa may potentially lead to a reduction in required girder lines and reduce or eliminate mild steel shear reinforcement. Compared to regular concrete, a cubic yard of commercially available UHPC can cost as much as 10 times more, making designers and precasters hesitant to adopt this material. An economic analysis, assuming that local materials can be used to produce UHPC, indicates that the initial high cost can be offset by careful selection of materials, reduced construction time and maintenance, and the increased service life of the structure. Costs were evaluated based on local material prices, design parameters of the bridge, modified production practices, and a projected maintenance schedule. This study aids in the development of design procedures and recommendations for implementing UHPC as a prestressed concrete girder material.

INTRODUCTION

Ultra High Performance Concrete (UHPC) is an emerging material which develops very high compressive strengths (up to 200 MPa) and also exhibits improved tensile strength (up to 50 MPa) and durability properties (Graybeal 2006). Several characteristics of UHPC offer advantages for structural applications, specifically prestressed concrete bridges, including:

- Increased strength and ductile behavior allowing the concrete to deform and support flexural and tensile forces, even after initial cracking.

- Durability characteristics similar to those of an impermeable material reducing the effects of corrosion and concrete contamination.
- A higher resistance to abrasion than that of normal strength concrete (NSC).
- Reduced creep and shrinkage, making the material very suitable for applications in prestressed concrete.
- The ability to replicate both the macro- and micro-texture of the formwork, resulting in high-quality textured or smooth surfaces.

Historically, conventional structural design has used concrete to support large compressive loads with steel reinforcement to resist tensile forces. Using UHPC, steel reinforcement may be reduced or eliminated. Additional advantages for using UHPC include: reduced material quantities; smaller geometry and weight of members; simpler detailing and construction; reduced maintenance; and longer lifespan. Recent events have shown the importance of durable long-lasting infrastructure. The use of UHPC helps to achieve goals of higher standards for U.S. infrastructure and meeting the increasing demands for reduced labor, materials, construction time, and environmental impact, while increasing safety, security, durability, and service life.

This paper describes an investigation regarding the feasibility of UHPC for prestressed concrete bridges in New Mexico using typical New Mexico Department of Transportation (NMDOT) bulb-tee girders. A parametric design study was conducted for a simple span bridge using both high performance concrete (HPC) and UHPC. Based on the actual bridge drawings and specifications, girder designs were developed with the aid of CONSPAN®, a commercially available, comprehensive design program for prestressed concrete bridges. Due to the unique characteristics of UHPC, both 15 mm and 18 mm strands were considered in the re-design. HPC versus UHPC bridge designs were compared based on the required number of girders (i.e., concrete volume), number of prestressing strands, deck thickness, and shear detailing. Due to the high cost of UHPC (up to 10 times the cost of NSC), the design goal was to optimize the usage of UHPC in the bridge girders. Additionally, using the design results, an economic analysis was conducted that considered the life-cycle costs of UHPC and the use of local New Mexico materials.

BRIDGE CASE STUDY

The simple span bridge investigated in this paper was the I-25/Doña Ana Interchange located near Las Cruces, New Mexico (Figure 1). This bridge was designed using HPC. The parametric flexure and shear study compared the as-designed/as-built bridge with HPC and a modified bridge that is re-designed using UHPC. Several UHPC material characteristics identified from literature influence prestressed concrete girder design. These characteristics include: modulus of elasticity, modulus of rupture (i.e., allowable tensile stress), creep, and shrinkage. Both the modulus of elasticity and modulus of rupture were considered based on literature findings related to UHPC properties. Creep and shrinkage were calculated by the current AASHTO specifications because without specific material testing, modified design values cannot be accurately determined (AASHTO 2007).

UHPC PARAMETRIC STUDY: FLEXURE

The I-25/Doña Ana Interchange Bridge (Figure 1) is a simple span structure with a length of 34.29 m and no skew. The cross-section has six typical NMDOT BT-63 girders, spaced at 2.21 m (Figure 2), and a 191 mm cast-in-place deck of conventional concrete with a compressive strength of 27.6 MPa. The deck is 13.11 m wide with travel way dimension of 12.19 m, allowing for two traffic lanes, and an overhang of 1.03 m. The beams are braced by intermediate 9.53 mm steel bent plate diaphragms at the third points along the span. The traffic barrier is a 1.07 m concrete guard rail.



Figure 1: Photograph of I-25/Doña Ana Interchange (North Bound).

For ease of comparison, several parameters were kept constant including: deck width; ratio of deck overhang to girder-to-girder spacing (46.6%); deck compressive strength; harped strand pattern; and girder length. Parameters that were varied included: number of girder lines; deck thickness; release and final girder compressive strengths; modulus of elasticity; modulus of rupture (i.e., allowable tensile stress); and diameter of prestressing strands. The BT-63 in the design plans has modified dimensions; however, the other girder sizes (e.g., BT-54) considered in this study were based on NMDOT standard dimensions. The bridge was designed based on the Load Factor Design (LFD) method of the AASHTO Standard Specifications (17th edition) and the 2002 interims. Thus, comparisons made with UHPC are made using the LFD method.

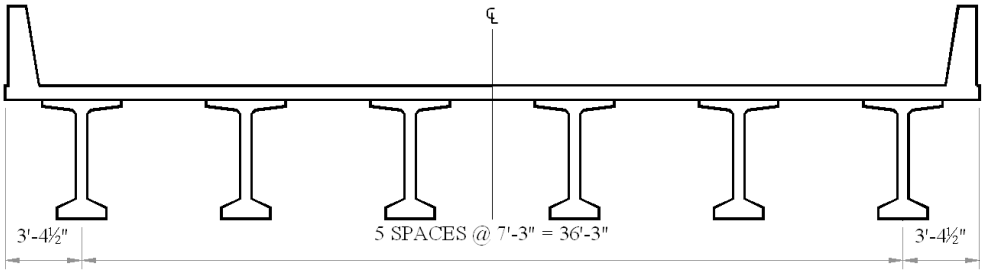


Figure 2: Cross-Section of I-25/Doña Ana Interchange.

For each cross-sectional configuration, final compressive strengths of 65.5, 103.4, 120.7, 137.9 and 155.1 MPa were used; however, only the results for 155.1 MPa are presented in this paper. For each compressive strength, the required number of 15 mm and 18 mm strands was determined based on the modulus of elasticity estimated from equations found in literature. In addition, the modulus of rupture was calculated by the AASHTO code and then prestressing strands are manually removed so that tensile stress limits from the literature control the number of strands for the serviceability limit state.

Effects of Modulus of Elasticity

Two design equations from the literature were used to estimate the modulus of elasticity for UHPC. The first is from the Association Française de Génie Civil (AFGC) French specification (2002) and is:

$$E_c = 262{,}000\sqrt[3]{f'_{ATT}} \text{ (psi)} \quad (1)$$

where, f'_{ATT} is the compressive stress of UHPC after thermal treatment. The second equation is given in Graybeal (2005) as:

$$E_c = 46{,}000\sqrt{f'_c} \text{ (psi)} \quad (2)$$

These equations were considered to evaluate the influence of the modulus of elasticity on UHPC girder design. Equation 1 assumes that the specimen undergoes thermal treatment. Equation 2 can be used to predict the modulus of elasticity regardless of the curing method (Graybeal 2005).

Using Equations 1 and 2 for the modulus of elasticity, the required number of strands is similar, with Equation 2 occasionally resulting in fewer strands. Equation 1 gives larger values for the modulus of elasticity than Equation 2; therefore, the fewer strands required using Equation 2 can be attributed to the smaller modular ratio between the NSC deck and the UHPC girders.

Calculating the modulus of elasticity using Equation 2 results in larger live load deflections than Equation 1. However, it was found that live load deflections are not a controlling limit state for any of the viable bridge designs in this study. Thus, Equation 2 was adopted to compute the final design values for the UHPC modulus of elasticity in this study. This equation results in the fewest strands and adequate stiffness to control live load deflections. Additionally, Equation 2 is applicable over a large range of compressive strengths, 27.6 to 193.1 MPa.

Effects of Modulus of Rupture

Equations presented in the literature for the modulus of rupture are based on those developed for the commercially available UHPC material Ductal®. These equations are sensitive to the curing method used. In this study, it was assumed local materials would be used for the UHPC mixture proportions. Thus, to analyze the effects of the UHPC's increased strength in tension, limiting values for tension reported in the literature were used. For the range of compressive strengths considered herein, Gowripalan and Gilbert (2000) suggest the lower bound value for tensile strength of 8.0 MPa. Graybeal (2008) uses 9.0 MPa as a limiting value for tensile strength. It is important to note that in much of the literature, UHPC is considered to have a range of compressive strengths from 150.0 to 220.0 MPa (Ahlborn *et al.* 2008, Graybeal 2008, Gowripalan and Gilbert 2000), which is higher than the range of compressive strengths considered in this study (ranging from 103.4 to 137.9 MPa). Therefore, the tension stress limit was assumed to be 8.0 MPa as recommended by Gowripalan and Gilbert (2000) when no specific data is available.

It should be noted that the limiting value of 8.0 MPa is a characteristic value for flexural tensile strength that has a safety factor of four compared to measured values from direct and flexural tension tests (Gowripalan and Gilbert 2000). Due to the conservative nature of this value, it is reasonable to assume that this limiting value is applicable to all the final compressive strengths used in this study.

Prestressing Strand Dimensions

Two sizes of prestressing strands were used in this study, 15 mm diameter and 18 mm diameter. The primary difference is the cross-sectional area. The 18 mm strands provide 35% more cross-sectional area than the 15 mm strands, with only a 17% increase

in diameter. The advantage of the larger prestressing strands is the labor savings and the increased prestressing force available using fewer strands (Schuler 2009).

UHPC PARAMETRIC STUDY: SHEAR

The shear design of UHPC girders differs significantly from the design of HPC girders. The steel fibers contained in a typical UHPC mixture contribute to the shear capacity of the section at the ultimate limit state (i.e., after the girder section cracks). The combined contribution of the concrete and steel fibers to shear capacity can be sufficient to carry factored shear forces without the need for traditional, transverse mild steel stirrups. Thus, the mild steel reinforcement may be reduced or eliminated according to AFGC Section 7.3.2 (2002).

Desgin Shear Strength Procedure for Steel Fiber Reinforced UHPC

The shear strength procedure described in this section is based on the "Recommendations for the Design of UHPC" by MIT. This procedure uses the French based AFGC recommendations and the research conducted at MIT on Ductal®. The formalized procedure can be found in the white paper produced by Dr. Franz-Josef Ulm of MIT for the Mars Hill Bridge built in Wapello County, Iowa (Ulm 2004).

For the shear portion of this study, shear loads and forces were calculated using the AASHTO LRFD specifications. Justification for using LRFD methods is twofold. First, LRFD uses state of the art methods for determining the anticipated shear failure angle, θ, based on the Modified Compression Field Theory. Secondly, the procedures developed by Ulm (2004) use the LRFD load factors to determine the factored shear force on the UHPC girder.

The ultimate limit state (ULS) for shear is based on the premise that crack-bridging steel fibers carry a part of the shear load, very similar to shear reinforcement. The design strength of the section is expressed as:

$$\varphi_V V_R^{ULS} = \varphi_c V_c + V_p + \varphi_f V_f + \varphi_s V_s$$

where, $\varphi_v V_R^{ULS}$ is the design shear; φ_c is a strength reduction factor, taken as 0.66 to account for material variability; V_c is the contribution of the concrete; V_p is the contribution of the harped prestressing strands; φ_f is a strength reduction factor, taken as 0.66 to account for non-ideal randomization of the fibers; V_f is the contribution of the steel fibers; $\varphi_s$is the LRFD strength reduction factor for shear, taken as 0.9; and V_s is contribution of the mild steel stirrup. For prestressed concrete applications, the concrete contribution to shear strength is expressed as:

$$V_c = 0.09\sqrt{f_c'}\, b_w\, z$$

where, f'$_c$ is the 28 day design compressive strength of the concrete; b_w is the web width; and z is the lever arm at the ultimate moment equal to the distance between the centroid of the compression block and the centroid of the prestressing strands (Graybeal 2006). The term V_p represents the vertical force component of the harped prestressing strands after losses and the steel fiber contribution to shear strength is given as:

$$V_f = \frac{A\,\sigma_p}{\tan(\theta)}$$

where, A is the area of the shear plane (i.e., effective fiber area), and is computed as 90% of the web width multiplied by the lever arm at ultimate moment (i.e., $A = 0.9 b_w z$). The term σ_p is the residual tensile strength carried across the shear crack from the time of

cracking until a limiting strain is achieved. According to Graybeal (2006), the value for residual tensile stress is determined experimentally from tension tests. In the absence of experimental data for the UHPC and the girders of this parametric study, typical values from literature were examined and a conservative value of 6.9 MPa. This is a reasonable value to assume without experimental testing because it is below the expected tensile cracking limit of the UHPC. The final term is tan(θ), which is the tangent of the compression strut angle in the shear area measured from the horizontal (θ has a lower bound of 30°). Under the LRFD code option in CONSPAN®, θ is calculated directly and is output. The method used by CONSPAN® to calculate θ is specified in LRFD Art. 5.8.3.4.2.

Finally, if mild steel stirrups are required then V_s is computed according to LRFD Equation 5.8.3.3-4:

$$V_s = \frac{A_v f_y (\cot\theta + \cot\alpha)\sin\alpha}{s}$$

where, A_v is the area of the transverse reinforcement (i.e., stirrups); f_y is the yield strength of the mild steel (equal to 414 MPa); θ is as described above; α is the angle of the transverse reinforcement (taken as 90°); and s is the spacing of the stirrups.

Results using 15 mm Diameter Strands

The as-designed bridge has 36 - 15 mm strands; 24 straight, 6 harped, and 6 debonded-partial length strands (in the top flange) to control stresses and provide the required flexural moment capacity. For the parametric study, only harped strands were used to obtain consistent comparisons. Harped strand patterns were developed in a two step process. First, CONSPAN® was used to determine an initial strand pattern. This initial pattern was then modified manually by adding and removing strands and adjusting the harped strand pattern to ensure that the final strand pattern was a sound design. In this manner a straight/harped strand pattern was generated for the as-designed bridge. The resulting pattern required a total of 28 - 15 mm strands (26 straight, 2 harped) as shown in Figure 3. The difference in strands between the as-designed and baseline bridge occurs at two locations. There are two less straight strands in the bottom bulb for the baseline bridge girder. Also the as-designed bridge girder plans call out 6 debonded-partial length strands in the top flange. For the purpose of the parametric study six BT-63 girders with 28 (26 straight, 2 harped) - 15 mm diameter strands was considered to be the baseline design of the I-25/Doña Ana Interchange Bridge.

Using LFD, Equation 2 to estimate the modulus of elasticity, and limiting the modulus of rupture to AASHTO provisions (i.e., the higher tensile strength of UHPC is not considered), the number of girder lines and the girder size decrease from six BT-63 girders to five BT-54 girders, for a total savings of 23% in girder concrete volume. This concrete volume reduction results in a 71% increase in the required number of 15 mm strands for UHPC compressive strengths 155.1 MPa. The deck thickness was increased by 13.3%.

Increasing the limit of the modulus of rupture to 8.0 MPa, decreases the number of girder lines from six BT-63 girders to four BT-63 girders, for a total savings of 33% in girder concrete volume with a 50% increase in the required number of 15 mm strands and a 26.7% increase in the deck thickness. This configuration saves an additional concrete volume of 11% compared to five BT-54 girders that are viable under the LFD code.

These comparisons show that with the increase in compressive strength and the improved tensile strength of UHPC, greater concrete savings are possible in the girders that are not possible with HPC. Allowable live load deflections were checked and satisfy serviceability requirements.

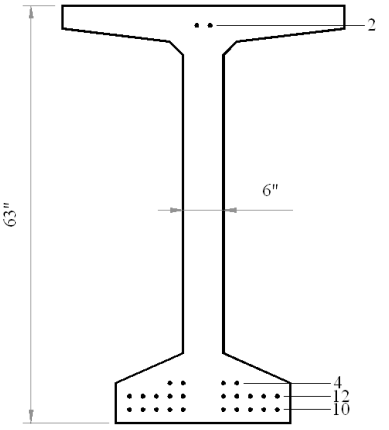


Figure 3: End Cross-Section of Baseline Design (BT-63) with 28 - 15 mm Strands Using HPC.

Shear Design

Using the final bridge configuration using four UHPC typical BT-63 girders, the shear capacity of the section can be determine following the procedure described above.

The computed shear failure angle at the critical section was below the limiting value of 30°; thus, the angle used to determine the steel fiber contribution to the strength of the section was taken as 30°. Recall that the fiber contribution is not related to the compressive or tensile strength of the concrete, but is a function of the shear failure plane and residual tensile stress in the fibers after the concrete cracks. It should further be noted that the fiber contribution to the shear capacity is much larger compared to the concrete and the harped strand contribution. The fiber contribution represents approximately 77.2% of the design shear strength of the girder section.

The girder section has sufficient capacity to carry the ultimate shear forces with no change to the cross-sectional geometry.

Results using 18 mm Diameter Strands

For the purpose of the parametric study six BT-63 girders with 22 (20 straight, 2 harped) 18 mm diameter strands is considered to be the baseline design of the I-25/Doña Ana Interchange.

Using LFD, Equation 2 to estimate the modulus of elasticity, and limiting the modulus of rupture to AASHTO provisions (i.e., the higher tensile strength of UHPC is not considered), the number of girder lines decreases from six BT-63 girders to four BT-63 girders using UHPC, for a total savings of 33% in girder concrete volume. This concrete volume reduction results in a 55% increase in the required number of 18 mm strands and 26.7% increase in the deck thickness.

Increasing the limit of the modulus of rupture to 8.0 MPa decreases the number of girder lines and the girder size from six BT-63 girders to four BT-54 girders, for a total savings of 38% in girder concrete volume. This concrete volume reduction results in a 109% increase in the required number of 18 mm strands and 26.7% increase in the deck thickness. This configuration saves an additional concrete volume of 5% compared to four BT-63 girders that are viable under the LFD code.

These comparisons show that the improved compressive and tensile strength of UHPC in combination with 18 mm strands, will yield greater concrete savings that are not possible with HPC and 15 mm strands. Allowable live load deflections were checked and satisfy serviceability requirements.

Shear Analysis

Using the final bridge configuration with four UHPC typical BT-54 girders, the shear capacity of the section was determined following the procedure described above.

The typical BT-54 girders have a 150 mm web thickness and have insufficient capacity at the critical section. Two options are possible to meet the required shear strength capacity:

1. Increase the web width 25 mm. If this option is selected, girder concrete reduced by 33%. The increase of width did not change the amount of prestressing strands required for flexure.
2. Use No. M16 mild steel stirrups at 610 mm on center, shown in Figure 4. If this option is selected there will be a 38% reduction in required amount of girder concrete.

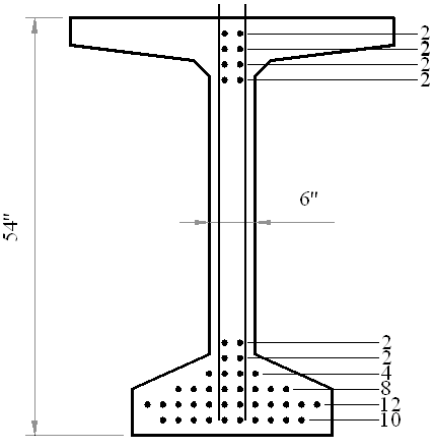


Figure 4: End Cross-Section of Four BT-54 Girders with 48 - 18 mm Strands Using UHPC.

Confinement Steel

The bursting force effect is addressed in LFD Art. 9.22. According to this article, stirrups and nominal reinforcement should be placed over a distance at least equal to the depth from the end of the beam. If 18 mm strands are used, the final bridge configurations required stirrups in this region of the beam. Thus the inclusion of confinement steel would be a simple task and would not significantly add to the total overall cost of a UHPC girder. However, if 15 mm strands are used, the final bridge configurations do not require stirrups to provide adequate shear strength in the bursting region.

ECONOMIC ANALYSIS

For the economic analysis, the as-designed bridge is compared to the re-design of the bridge using UHPC girders.

Cost Comparison of UHPC Girders

The cost of one BT-63 girder with HPC is approximately $2,602, based on a cost of $\$163/m^3$. For one BT-63 girder with UHPC the cost is approximately $14,260, estimating the cost of UHPC using local materials at $\$896/m^3$. The cost of one BT-54 girder with UHPC is $13,180.

The smallest number of girders possible was found to be four BT-54 girders. This design was only possible with the use of 18 mm strands. If it is not possible to use 18 mm strands, five BT-54 girders is the best choice.

When 18 mm strands are used, the design shear capacity was insufficient with a 150 mm web. To have adequate shear capacity either the web thickness of the BT-54 girder would have to be increased in width by 25 mm or mild steel stirrups would be required. Based on the cost of concrete, if the web thickness is increased, the cost of the girder concrete increases by approximately $1,080.

Prestressing Strand Comparison

Strand size greatly affects the overall design which in turn affects the cost. In this case, using 18 mm strands is almost twice as expensive as using the 15 mm strands. This

cost was developed based on a strand unit cost of $1.18/m for 15 mm stands and $2.13/m for 18 mm stands.

The cost of the 15 mm strands in the baseline bridge is $6,860. The total cost of 15 mm strands in a bridge configuration with four BT-63 girders is $6,680, which is a 0% increase compared to the baseline design. The total cost of 18 mm strands in a bridge configuration with four BT-54 girders is $13,570, which is a 49.4% increase over the baseline design.

Steel Fibers Constituent Costs

The steel fibers are the most expensive constituent in UHPC. In this study, a cost analysis was performed for a beam that has steel fibers at 2% by volume with minimal mild reinforcement that is used for composite action with the deck. The total material cost for a single BT-63 girder is $14,680 with 2% fiber content. To reduce this cost, the possibility of reducing the steel fibers content from 2% to 1% by volume could be explored. However, additional testing would be required for this option.

Mild Steel Costs

When developing the costs for UHPC girder designs, some assumptions had to be made. It was assumed that all mild reinforcement could be removed for the UHPC girders except for deck composite action mild steel. Another assumption was that the amount of reinforcing needed for the BT-54 girders was the same as the amount needed for the BT-63 girders. This is justified because the difference in the amount of mild steel is small, approximately 0.7 kg. The cost of the mild reinforcement was determined based on a unit cost of $0.88 per kg.

The amount of mild reinforcement needed was obtained from the plans of the I-25/Doña Ana Bridge. The total cost of mild steel for the baseline design is $1,475. The only cost of steel for the four BT-63 girders is $45, this is the mild steel to provide composite action with the NSC deck. The total cost of mild steel for the four BT-54 girders is $75, this is for the composite action with the deck and bulb confinement. Recall, the cost of UHPC required to provide sufficient shear capacity by increasing the web thickness was $1,170. It is clear that using mild steel stirrups is more cost effective.

Normal Strength Concrete Deck Cost

The NMDOT has standard concrete deck details specified in section 4.3.1 of the NMDOT Bridge Procedures and Design Guide (2005). The thickness of the NSC deck varies with the effective span beam girders, while the spacing and amount of mild steel deck reinforcement remains constant, as the spacing increases between girders, the thickness of the deck increases, thus increasing in volume. The cost of NSC was estimated to be $\$131/m^3$.

The deck of the as-designed bridge has a thickness of 190 mm, width of 13.11 m and a length of 34.60 m. The cost of the as-designed deck is $11,447. The increase in cost for a four BT-54 or four BT-63 girders is 13.3%.

Total Cost for I-25/Doña Ana Interchange

An overall cost comparison table was developed and shown in Table 1. It is evident that the four BT-63 girders design is the least expensive design that uses UHPC with a total cost of $120,014. The total cost for four BT-54 girders is $124,030, this is 3.3%

higher than the four BT-63 girder design. The best design based on initial cost is six HPC BT-63 girders.

Table 1: I-25/Doña Ana Interchange Comparison Final Costs.

	6 HPC BT-63 Girders (15 mm strands)	4 UHPC BT-63 Girders (15 mm strands)	4 BT-54 Girders (18 mm strands)	4 Modified BT-54 Girders (18 mm strands)
Girder Conc.	$15,610	$57,040	$52,720	$57,030
Strands	$6,860	$6,860	$13,570	$13,570
Mild Reinf.	$8,850	$180	$300	$300
Labor Cost	$38,817	$43,130	$43,130	$43,130
Deck Conc.	$11,297	$12,804	$14,310	$14,310
Total Cost	$81,434	$120,014	$124,030	$128,340

Future Worth

The typical life span of bridge girders is designed for 75 years. Based on Ahlborn *et al.* (2008), it was assumed that the life span of the UHPC girders would be twice as long as that of the HPC girders. Based on the life spans stated above, the current bridges will need girder replacements in 75 years. Consideration of the life-cycle cost is important in this study. If the only financial parameter considered is initial cost it is clear that HPC is the least expensive. However life-cycle costs of HPC and UHPC should also be considered.

The future worth of these bridges is determined by:

$$F = P(1+i)^n \tag{3}$$

where, F is the future worth after n years; P is the present worth; i is the inflation rate taken as 3.85% (based on 2009 inflation rate); and n is the life span of the bridge, taken as 75 years for the HPC girders and 150 years for the UHPC girders.

The future worth is then adjusted to a net present value (NPV) and is determined by:

$$NPV = F(1+r)^{-n}$$

where, F is the future worth calculated by Equation 3; r is the discount rate, taken as 3.85% and n and described previously.

Table 2 provides a summary of the future worth analysis. The value $162,868 is twice the present value of the bridge. The reasoning behind this is that if the HPC were to be built today the initial cost would be $81,434 to construct the bridge and $81,434 would have to be set aside in savings. This money, set aside at an interest rate of 3.85% will generate the future cost of the HPC bridge in 75 years. Within a 75 year life span there will be no cost to rebuild the UHPC bridges. Therefore, there is a life-cycle cost benefit to using UHPC for the I-25/Doña Ana Interchange. The least expensive option is four UHPC BT-63 girders with 15 mm strands.

The last column of Table 2 shows the cost of four modified (i.e., increased web width) UHPC BT-54 girder. This cross-section is required to provide adequate shear strength if mild steel stirrups are excluded. Compared to the cost of four typical BT-54 girders it is 3.5% more expensive to increase the web width than to use mild steel stirrups.

Table 2: I-25/Doña Ana Interchange Future Worth.

	6 HPC BT-63 Girders (15 mm strands)	4 UHPC BT-63 Girders (15 mm strands)	4 UHPC BT-54 Girders (18 mm strands)	4 Modified UHPC BT-54 Girders (18 mm strands)
Present Value	$81,434	$120,014	$124,030	$128,340
Future Worth	$1,384,509	$34,690,156	$35,851,130	$37,096,892
Net Present Value	$81,434	$120,014	$124,030	$128,340

There are many variables that influence the cost of UHPC. Mixture proportions, the curing regimen, the percent volume are all factors that can be optimized to lower the cost of UHPC. However, further research is needed to investigate these different parameters. In addition, design standards and specifications are not readily available for using UHPC. Thus, many of the properties of UHPC are not fully utilized. Once additional research and more design applications using UHPC have been conducted, a better understanding of this material will exist, in which we can fully optimize the manner in which we use this material. This will once again lower the cost.

From the bridge analyzed in this economic analysis, it can be seen that the initial cost of implementing UHPC is high. However, if the lifecycle costs are included UHPC has the potential to save money.

CONCLUSIONS AND RECOMMENDATIONS

Based on the results of this study, the following conclusions were drawn:

- UHPC girders with traditional 15 mm diameter strands require fewer girder lines and less concrete material as compared to high strength concrete.
- Larger diameter prestressing strands (i.e., 18 mm) strands can further reduce the member sizes and thus, the required concrete material.
- Incorporating the tensile strength of UHPC into the design can significantly impact the number of required prestressing strands.
- The required shear capacity can be achieved by considering the shear capacity of the crack-bridging fibers. In cases when the required tensile strength cannot be met by the UHPC contribution alone, traditional transverse mild steel reinforcement can be included in critical regions, or the size of the structural member can be modified (i.e., increasing the girder web width). Note that the amount of required traditional transverse mild steel reinforcement is significantly reduced compared to a high strength concrete girder.
- UHPC has the potential to reduce the life-cycle costs of bridge girders. UHPC is expected to provide at least twice the service life expected from HPC. Savings are made at 75 years when the HPC girder bridge has to be replaced and the UHPC girder bridge does not.

UHPC has the potential to offer many advantages for structural design applications. These properties enable the design and construction of bridges with longer spans, improved durability, and smaller structural members. The improved durability properties also improve the longevity of bridges, potentially doubling the service life of the structure.

As more research is conducted on this new material, design procedures and equations to model the behavior of UHPC will become available which could potentially further impact the efficiency of UHPC.

ACKNOWLEDGEMENTS

The authors would like to thank Bryce Simons, Ray Trujillo, Ted Barber, Ben Najera, Jim Camp, Keli Daniell, and Virgil Valdez (Research Bureau, NMDOT) for their guidance and support throughout the project. The authors also acknowledge the assistance of several individuals: Dr. Benjamin Graybeal, FHWA Turner-Fairbank Research Center; Dr. Franz Josef Ulm, Massachusetts Institute of Technology; Dean Bierwagen, Iowa Department of Transportation; Brian Moore, Wapello County Engineer; Brain Keierleber, Buchannan County Engineer and Ned Johnson, Buchannan County; Dr. Sri Sritharan, Iowa State University, and Brian Silvis, Virginia Department of Transportation for their assistance gathering information and answering questions. Shannon Applegate and Steven Ruiz of Coreslab, Albuquerque, NM; Steve Darrah, BASF The Chemical Company; and Megan May, Fibercon International assisted in determining cost of materials used in this study. The findings and conclusions in the paper are those of the authors and do not necessarily reflect the views of the organizations or the individuals acknowledged above.

REFERENCES

American Association of State Highway Transportation Officials, *AASHTO LRFD Bridge Design Specification,* Customary U.S. Units 4th Edition, Washington D.C., 2007.

Ahlborn, T.M., Peuse, E.J., Misson, D.L. Ultra-High-Performance-Concrete for Michigan Bridges Material Performance-Phase I. Research Report RC-1525. Michigan Department of Transportation, 2008.

Gowripalan, N. and Gilbert, R.I., Design Guidelines for UHPC Prestressed Concrete Beam. The University of New South Wales, January 2000.

Graybeal, B., *Flexural Behavior of an Ultrahigh-Performance Concrete I-Girder*. ASCE Journal of Bridge Engineering,Vol.13, No. 6, pp. 602-610. November-December 2008.

Graybeal, B. *Material Property Characterization of Ultra High Performance Concrete*. FHWA-HRT-06-103, McLean, VA, 2006.

Graybeal, B.A "*Characterization of the Behavior of Ultra-High Performance Concrete*." PhD Dissertation, University of Maryland, College Park, 2005.

New Mexico Department of Transportation, *Bridge Procedures and Design Guide.* September 2005.

Service d`études techniques des routes et autoroutes of the Association Française de Génie Civil (AFGC/SETRA), *Interim Recommendations,* January 2002.

Schuler, G. *Producer's Experience with 10,000 psi Concrete and 0.7-in. Diameter Strands* March/April 2009. http://www.hpcbridgeviews.com/i54/Article4.asp. Accessed Nov. 20, 2009.

Ulm, F.-J. Bending & Shear Design of Iowa DOT Sample Bridge – Update. Design Review of Mars Hill Bridge, Massachusetts Institute of Technology for the Iowa Department of Transportation. May 24, 2004.

Effect of Secondary Elements on Load Distribution in Prestressed Bridge Girders

M.R. Roddenberry[1], J. Chipperfield[2], and K.S. Tawfiq[3]

[1]Department of Civil and Environmental Engineering, FAMU-FSU College of Engineering, 2525 Pottsdamer St., Rm A128, Tallahassee, FL 32310-6046; PH (850) 410-6125; FAX (850) 410-6142; email: mroddenberry@eng.fsu.edu
[2]Department of Civil and Environmental Engineering, FAMU-FSU College of Engineering, 2525 Pottsdamer St., Tallahassee, FL 32310-6046, email: chippjo@eng.fsu.edu
[3]Department of Civil and Environmental Engineering, FAMU-FSU College of Engineering, 2525 Pottsdamer St., Rm A129, Tallahassee, FL 32310-6046; PH (850) 410-6143; FAX (850) 410-6142; email: tawfiq@eng.fsu.edu

ABSTRACT

Secondary bridge elements, such as barriers, curbs, or diaphragms, are not accounted for when calculating the distribution of load effects to interior and exterior girders, using the American Association of State Highway and Transportation Officials (AASHTO) Load and Resistance Factor Design (LRFD) Bridge Design Specifications (AASHTO 2007). This paper shows that including the effect of barriers changes the distribution of loads and, therefore, bending moments in girders. The Florida Department of Transportation (FDOT) Structures Research Lab made field strain measurements on two bridges: a Florida Bulb-T girder bridge and an AASHTO Type IV girder bridge. The Florida Bulb-T bridge strain measurements were taken before and after barriers were placed, and the AASHTO girder bridge was tested only with the barriers. The bridge test results were used to calibrate finite element models, which showed that the barrier, the barrier joint, and the diaphragms affect both interior and exterior girder strains.

INTRODUCTION

Since the 1930s, bridge engineers have used the concept of distribution factors to evaluate the distribution of live loads to, in the case of a girder bridge, the interior and exterior girders. The live load Distribution Factors (DF) are specified in AASHTO LRFD Bridge Design Specifications, and they do not account for secondary stiffening elements, e.g., barriers, diaphragms, and sidewalks.

It is possible that, by considering the effect of secondary stiffening elements, the distribution factors could be decreased, giving the bridge a higher load rating with the ability to theoretically carry larger loads (heavier trucks). Although it may not be desirable to count on secondary elements for design, because the elements may become damaged, it may be beneficial for the purpose of permitting to allow heavy trucks to cross on a temporary basis.

Higher levels of accuracy can be obtained from modifications to the original DF equations, which consider different variables not taken into account in the AASHTO LRFD equations (Eamon and Nowak 2005). Some researchers found that

the secondary stiffening elements such as barriers and diaphragms were able to reduce live load distribution factors significantly. This is dependent on the geometry of the bridge. A lot of bridges today, in essence, could carry increased loads due to the stiffening elements (Akinci et al. 2008).

Abendroth et al. (1995) discusses the effectiveness of diaphragms in prestressed concrete bridges. One of the reasons for having intermediate diaphragms in bridges is to reduce the risk of overturning of the girders during construction. Green et al. (2004) explained that the addition of intermediate diaphragms reduced deflections by about 19% in straight bridges. This shows a positive correlation with the addition of intermediate diaphragms the stiffer the girders become.

Mabsout et al. (1997) observed a 5% to 30% increase in the capacity of an interior girder due to sidewalks and railings. Cai and Shahawy (2004) studied the effects of diaphragms, bearing stiffness, and skew angles on load distribution and strains. An increase in diaphragm stiffness reduced the maximum strain up to 30%.

Akinci et al. (2008) knew the barrier effect caused a decrease of about 30% in the DF and wanted to see if the joints in the barriers change the distribution. When discontinuous barriers were present, there was an increase in stresses at the bottom of the girder. "Discontinuous parapets have full depth joints or gaps that may be introduced at locations other than the deck joints to reduce transverse parapet cracking" (Akinci et al. 2008).

Much research has been done on the effects of the barriers and diaphragms on a bridge, but with very little focus on the barrier joints. This research examines what effects the barrier joint has on the bridge both locally and globally. Field tests on two bridges in service and finite element modeling were performed to make comparisons and draw conclusions. Field test data is not reported herein; the data was used to calibrate the finite element models for the before-barrier and after-barrier conditions.

STRUCTURES CONSIDERED

Two bridges were examined in this study: a Florida Bulb-T girder bridge (Bridge 1) and an AASHTO Type IV girder bridge (Bridge 2). Erected in 2003, Bridge 1 is a prestressed concrete girder bridge with a cast-in-place, reinforced concrete slab. It has an overall width of 58'- 2.875". The bridge consists of six FBT78 (Florida Bulb-T 78 inch) girders, spaced at 9'-11.25", and an 8.25" thick slab (see Figure 1). The bridge accommodates two 11'-9.75" lanes, two 9'-10.125" shoulders, and two F-shaped traffic barriers. A typical unit contains three spans between expansion joints, with the slab being continuous over the two interior piers. The center span is where the test data was collected and, therefore, was the focus for this research. The span length is 152', with a center-to-center spacing between bearing pads of 149'-6". The prestressed girder concrete had a specified 28-day strength, f'_c, of 8,500 psi and a theoretical modulus of elasticity, MOE, of 5,306 ksi; the deck had a specified strength of 4,500 psi with MOE of 3,863 ksi; and the barriers had a specified strength of 3,336 psi with MOE of 3,292 ksi. The bridge's barriers have 0.788" wide joints at the midspan and at each pier, and diaphragms at the piers provide horizontal bracing for the girders.

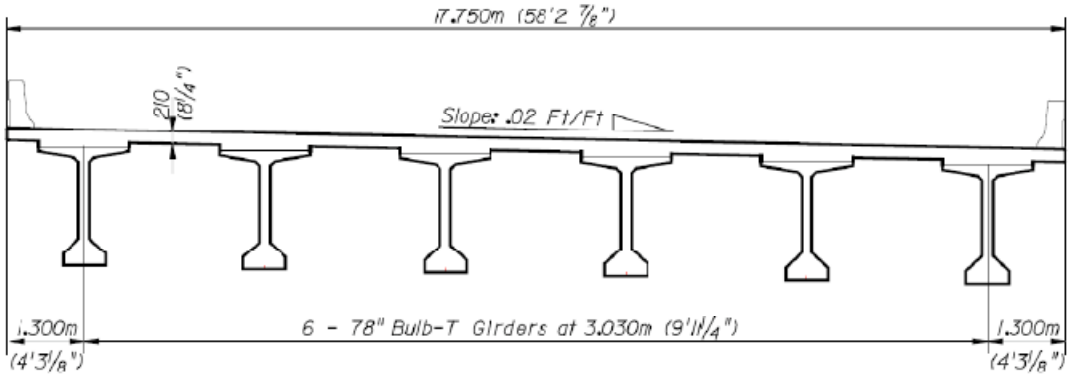


Figure 1. Cross section of Bridge 1.

Bridge 2, constructed in 1981, is a simply supported 118'-8" span which consists of a reinforced concrete slab and thirteen AASHTO Type IV girders equally spaced at 4'-5" (see Figure 2). The 59'-1" width includes three 12' lanes of traffic, two 10' shoulders, and two F-shaped barriers. The girder concrete had a specified strength of 5,000 psi, and the deck and barriers had a specified strength of 5,500 psi. The barriers have a joint at midspan, and diaphragms are located at 39'-4" from each approach slab (approximately third-points on the span). The modulus of elasticity of the concrete is stated in the plans: 3,860 ksi for the barriers and deck, and 3,627 ksi for the girders. The girders contain 49-0.5" diameter pretensioned 270 ksi low-relaxation strands.

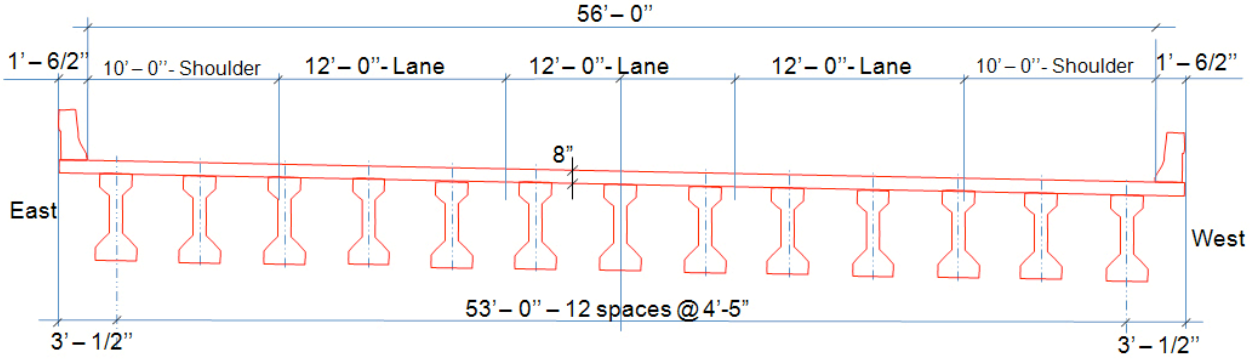


Figure 2. Cross section of Bridge 2.

OBJECTIVE OF STUDY

The Florida Department of Transportation (FDOT) Structures Research Lab made field measurements on both bridges. On Bridge 1, measurements were taken both before and after the barriers were placed, whereas on Bridge 2, measurements were taken only for the post-barrier condition. The bridges were incrementally loaded with the FDOT test vehicle and varying amounts of 2-ton blocks. The trucks were placed in order to create large bending moments in the exterior and first interior girders at midspan. Strain gages were used to measure longitudinal strains on the bottom of the

girders at midspan. These strains were used to validate and calibrate the finite element models.

Finite element modeling (FEM) of the bridges was conducted to determine how much effect the secondary elements have on live load distribution. Specifically reported herein are the results concerning the effect of the barriers, barrier joints, and diaphragms. FEMs were made for the case of no barriers, barriers without a midspan joint, barriers with a midspan joint, and barriers with third-point joints; models were also made with and without diaphragms. The objective was to determine how the diaphragms and different barriers affect the live load distribution and if the effects are local or global.

FINITE ELEMENT MODELING AND ANALYSIS

The FEMs of the bridges included the structural components that add to the stiffness of the bridge, namely the deck, barriers, diaphragms, and girders. The two bridges were modeled using the same techniques and element types; Solid 65 elements were used for 3-D modeling of reinforced concrete. This element is defined by eight nodes, each having three degrees of freedom with translations in the nodal x, y, and z directions. These elements allowed for the modeling of reinforcement as a smear, using a "real constant", by adding the total amount of reinforcement by a percentage of the volume it takes up in each element. The real constants were applied in each element in up to three directions. Because solid elements were used instead of shell or beam elements, the models were very large. FEM strains were compared to the load tests and were then used to make conclusions about the barrier, barrier joint, and diaphragm effects. Figure 3 shows a typical model.

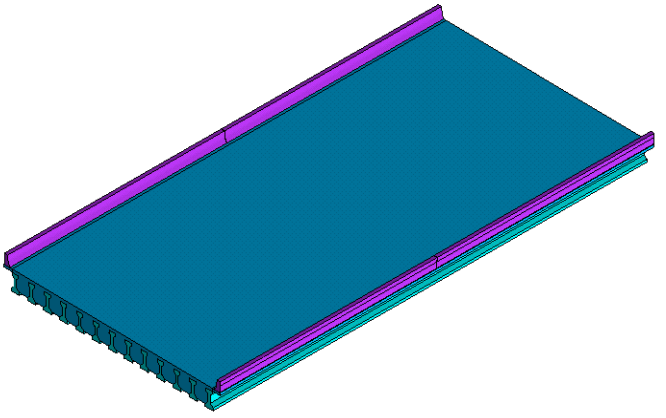


Figure 3. Typical Finite Element Model.

The theoretical material properties from the bridge plans were adjusted slightly to calibrate the models. For Bridge 1 FEM, the girder's MOE was taken as 5,306 ksi. For the deck and diaphragms, it was taken as 3,863 ksi; and for the barrier, 3,292 ksi. For Bridge 2, the MOE for the girders was 3,000 ksi and for the deck, diaphragms, and barriers was 3,200 ksi. Poisson's ratio of 0.2 was used for all concrete. The reinforcing steel MOE was 29,000 ksi with a Poisson's ratio of 0.35 for both bridges.

This study focused on live load distribution and, therefore, dead load effects were not modeled.

RESULTS

Barrier Effects. For Bridges 1 and 2, three FEMs were analyzed for each: no barriers, barriers without joints, and barriers with joints. For Bridge 1, FEMs simulate the FDOT load test truck loaded with 30 2-ton blocks. This load case was used to calibrate the FEM to the load test results. From Figure 4, compared to 90.4 με for the bridge with no barrier, the continuous barrier caused 87.5 με -- about a 3.2% decrease -- in the first interior girder (Girder 4-5) strains. When a joint in the barrier was added, the strain was 87.1 με, which is almost no change in strain.

Figure 5 shows the effects of the barrier and joint on the exterior girder (Girder 4-6). Compared to no barrier, the addition of the barrier causes an overall reduction in strain along the length of the girder. For the maximum strain, no barrier causes 101.9 με, whereas a continuous barrier causes 92.7 με. With a joint in the barrier, localized strain increases occur in the vicinity, longitudinally, of the joint – the maximum strain of 103.6 με is about the same strain when there is no barrier.

For Bridge 2, FEMs simulate the FDOT load test truck loaded with 36 2-ton blocks; this load case was used to calibrate the FEM to the load test results. Although Bridge 2 has diaphragms, in order to isolate the effect of the barriers, the diaphragms were not modeled in the first FEMs. Figure 6 shows that the continuous barrier decreases the maximum strain in the first interior girder (Girder 12) by 15.8%, from 125.3 με to 105.5 με, when compared to the no barrier case. The strain decreased, longitudinally along the entire span length when barriers were added. Also, the barrier without a joint causes a 7.5% lower maximum strain (105.5 με) than the barrier with a joint, and it affected the strains over about 40% of the span length.

From Figure 7, for the exterior girder (Girder 13), the addition of the barrier decreases the maximum strain by 20.2%, from 149.8 με to 119.6 με, compared to no barriers. The strain decreased longitudinally along the entire span length when barriers were added. With a joint in the barrier, the maximum strain of 170.7 με is 42.7% higher than without a joint in the barrier. The importance of these results is that the jointed barrier causes a girder strain that is 14% higher than without the barrier.

Diaphragm Effects. Figures 8 and 9 show the effects of diaphragms on Bridge 2 girder strains. The maximum strains with diaphragms (located at third-points) and barriers (with a joint at midspan) present decreased from 114.0 με to 106.0 με (7.0%) and from 170.7 με to 142.4 με (16.6%) in interior and exterior girders 12 and 13, respectively, compared to having barriers but no diaphragms.

Abendroth et al. (1995) mentioned that the vertical load distribution is independent of the type and location of the intermediate diaphragms. Cai and Shahawy (2004) reported that increasing the stiffness of diaphragms reduces maximum strain. The strain decrease effects from the diaphragms act globally along the length of the girder, reducing the strains along the span.

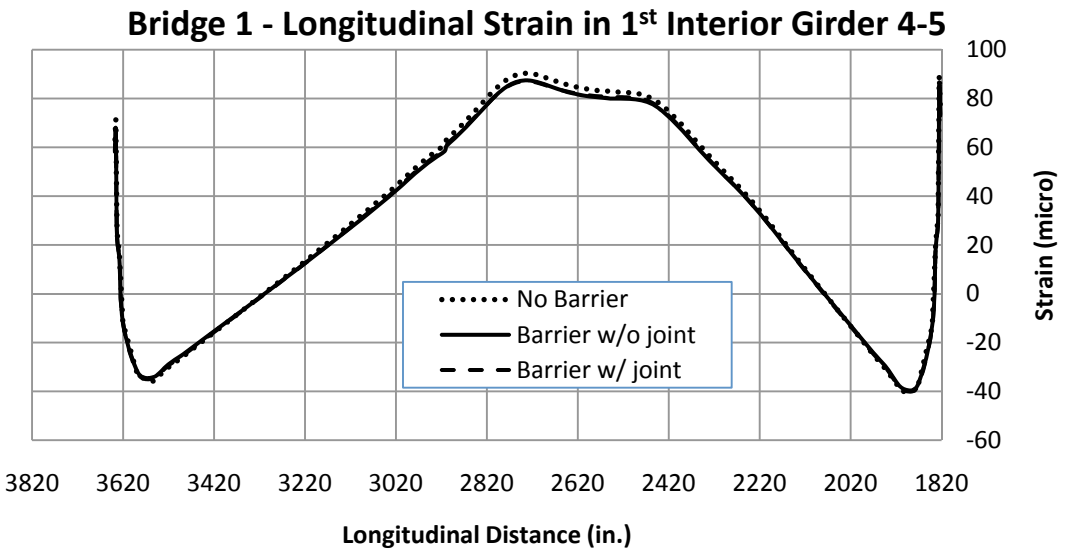


Figure 4. Bridge 1, strains in first interior girder 4-5 due to barrier and barrier joint at midspan.

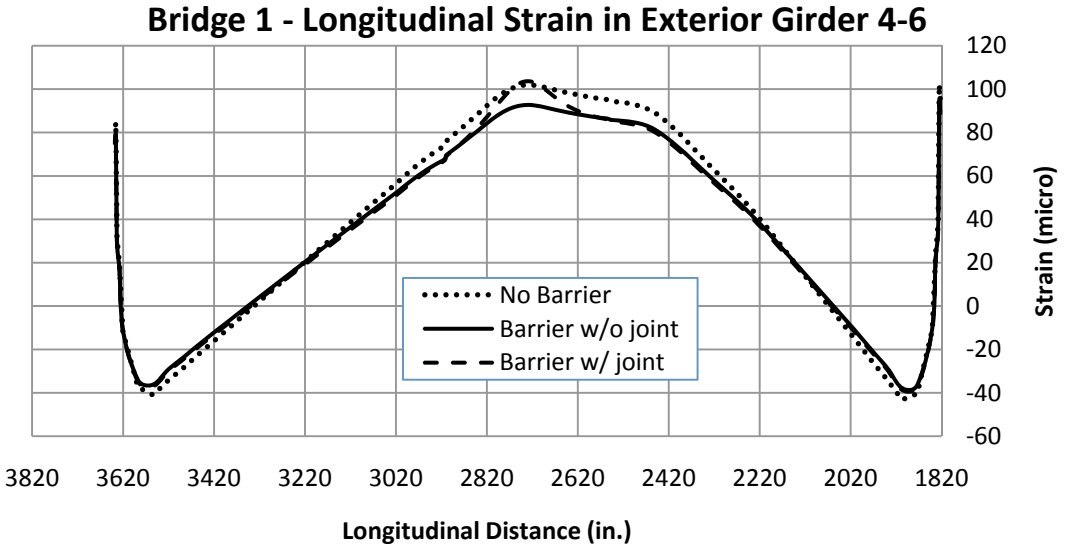


Figure 5. Bridge 1, strains in exterior girder 4-6 due to barrier and barrier joint at midspan.

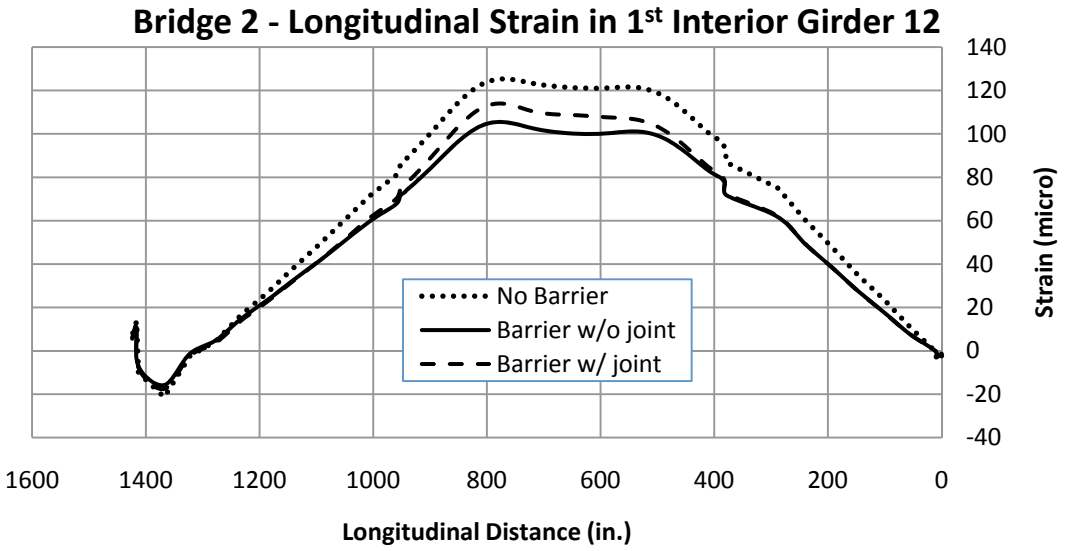


Figure 6. Bridge 2, strains in first interior girder 12 due to barrier and barrier joint at midspan.

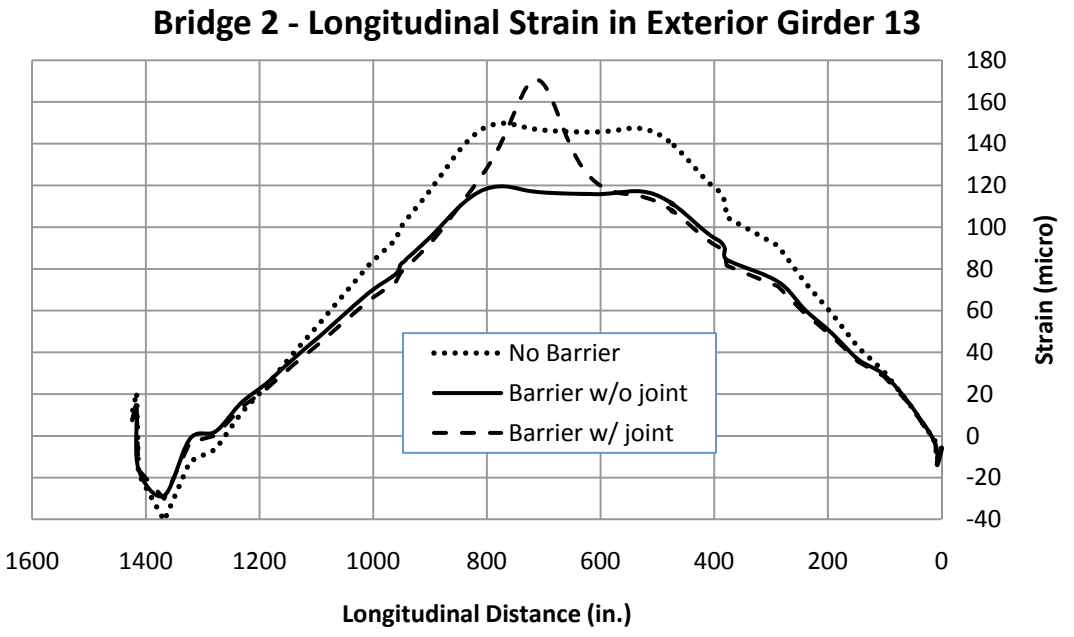


Figure 7. Bridge 2, strains in exterior girder 13 due to barrier and barrier joint at midspan.

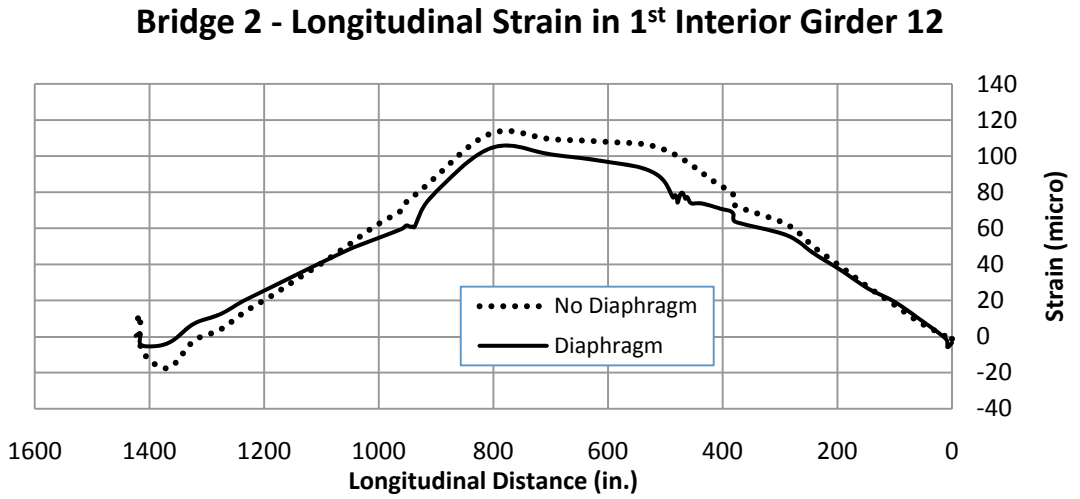


Figure 8. Bridge 2, strains in first interior girder 12 due to diaphragms, with barrier and joint.

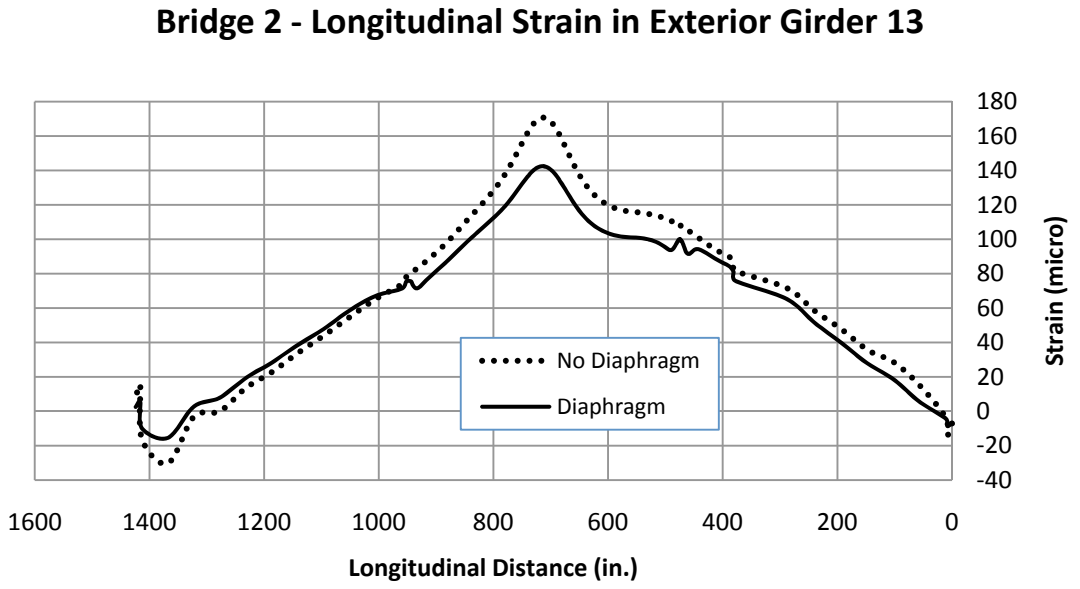


Figure 9. Bridge 2, strains in exterior girder 13 due to diaphragms, with barrier and joint.

Figures 10 and 11 show the longitudinal strains with no barriers, both with and without diaphragms. The strain decreases 16.38% and 22.53% in interior and exterior girders 12 and 13, respectively, when diaphragms are added. The increase in strain when the diaphragm is removed is much larger than when the diaphragm was removed with the barriers present, for both the first interior and exterior girders.

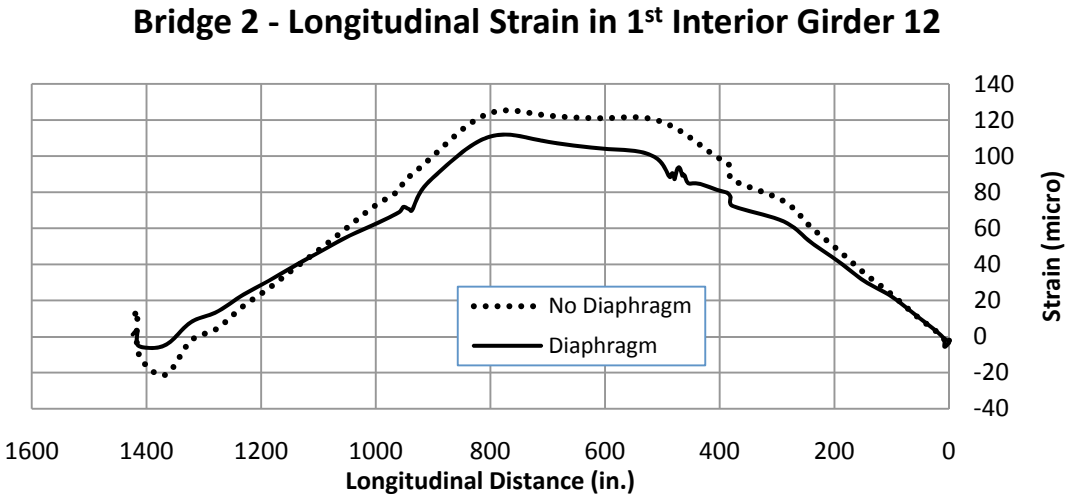


Figure 10. Bridge 2, strains in first interior girder 12 due to diaphragms, without barriers.

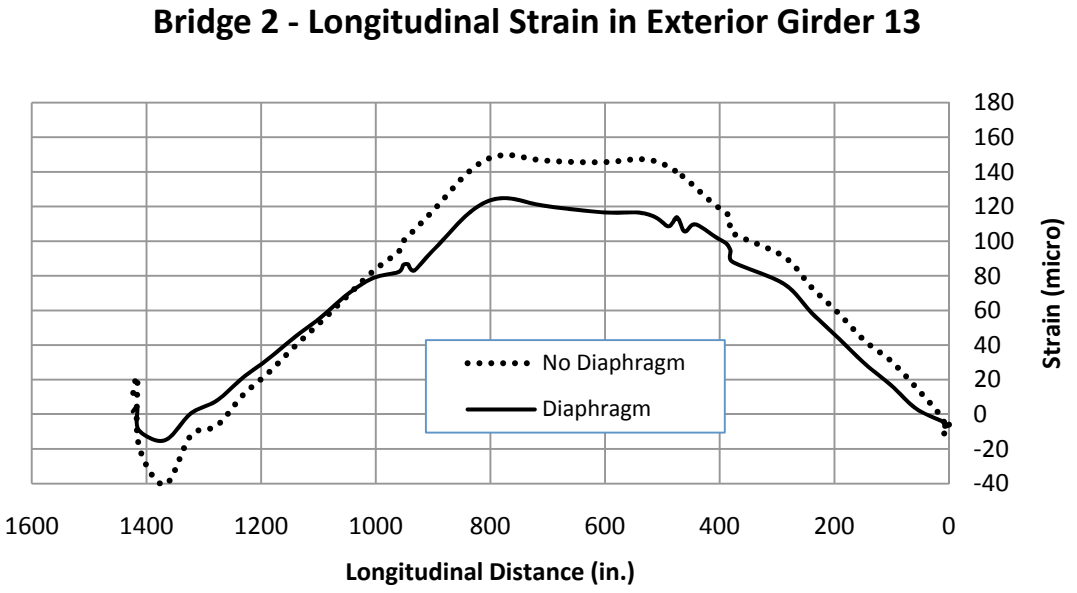


Figure 11. Bridge 2, strains in exterior girder 13 due to diaphragms, without barriers.

RECOMMENDATIONS

Figures 12 and 13 show, for Bridge 1, the effect on girder strains of barrier joints placed at third-points, compared to no joints and a joint at midspan. Placing the joints at third-points would move the localized strain increase away from the midspan (place of maximum moment). For this scenario, the maximum strain is still located at midspan. The third-point barrier joints have a localized effect only and contribute

only to the area around the joint location. The localized strain increase over the joint located around 2420 in. is larger because that is the side that the load is on.

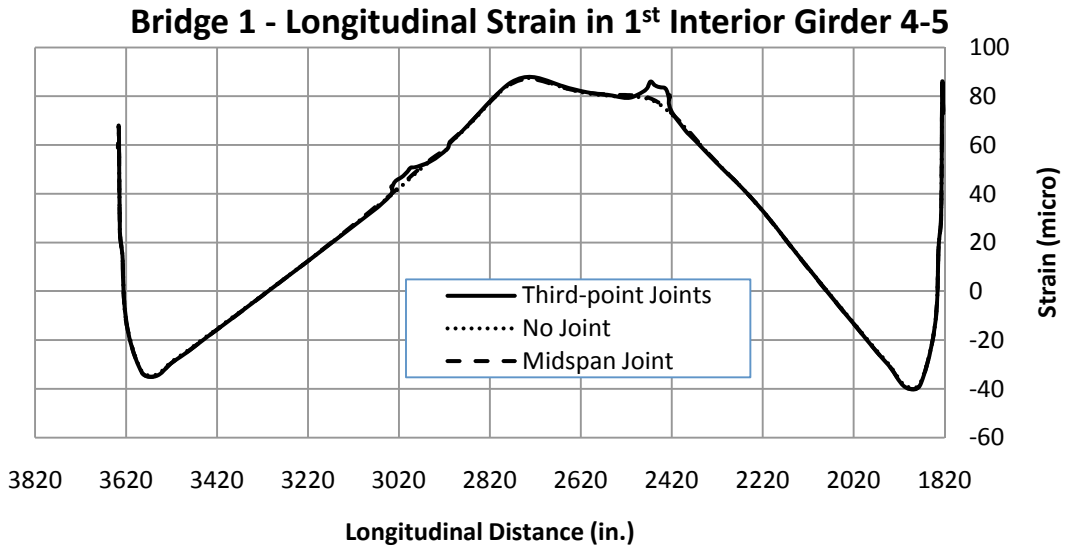


Figure 12. Bridge 1, strains in first interior girder 12 due to third-point barrier joints.

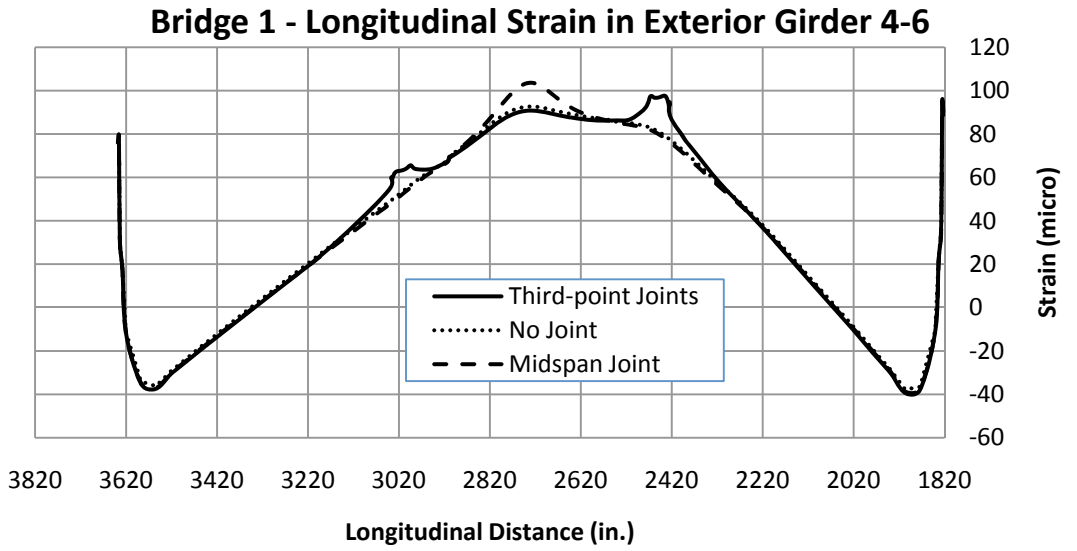


Figure 13. Bridge 1, strains in exterior girder 13 due to third-point barrier joints.

For existing bridges, if the joint is not necessary, it would be possible to retroactively fill in the joint with concrete or grout to create a continuous barrier condition. This would eliminate the strain concentration on the exterior girder of

bridges. For the joint fill to be effective, the concrete would need to have an adequate bond with the already existing barrier concrete.

CONCLUSIONS

The following conclusions may be made based upon the finite element models of the two bridges:

1. The addition of barriers reduces the strains in the exterior girder.
2. Intermediate diaphragms cause a decrease in the longitudinal girder strains globally, along the span of the bridge.
3. A joint in the barrier causes a localized strain increase in the exterior girder, in the longitudinal vicinity of the joint.
4. If barrier joints are deemed necessary, placing them at third-points along the span may be better than at midspan.
5. The effects of the barriers being added to the bridge are global, changing the strains along the span of the bridge.
6. A joint in the barrier has a small effect on the interior girder strain, and the effect spreads over one-third of the span length. The joint greatly affects the exterior girder strain, and the effect is local near the joint.
7. For load testing, using strain gages for measurement, special attention should be paid to the location of barrier joints that are present, so that their effects can be properly assessed, i.e., by the addition of extra strain gages or by extra monitoring around the longitudinal vicinity of the joints.

REFERENCES

Abendroth, R. E., Klaiber, F. W., and Shafer, M. W. (1995). "Diaphragm Effectiveness in Prestressed - Concrete Girder Bridges." *Journal of Structural Engineering,* ASCE, 121(9), 1362-369.

Akinci, N. O., Liu, J., and Bowman, M. D. (2008). "Parapet Strength and Contribution to Live Load Response for Superload Passages." *Journal of Bridge Engineering*, ASCE, 13(1), 55-63.

AASHTO LRFD Bridge Design Specifications, 3rd Edition, Washington, D.C. (2007).

Cai, C. S., Shahawy, M. (2004). "Predicted and Measured Performance of Prestressed Concrete Bridges." *Journal of Bridge Engineering,* ASCE, 9(1), 4-13.

Eamon, C. D., and Nowak, A. S. (2005). "Effects of Edge-Stiffening and Diaphragms on Reliability of Bridge Girders." *Journal of Bridge Engineering*, 10(2), 206-214.

Green, T., Yazdani, Y., and Spainhour, L., (2004). "Contribution of Intermediate Diaphragms in Enhancing Precast Bridge Girder Performance." *Journal of Performance of Constructed Facilities*, 18(3), 142-46.

Mabsout, M. E., Tarhini, K. M., Frederick, G. R., and Tayar, C. (1997). "Finite – Element Analysis of Steel Girder Highway Bridges." *Journal of Bridge Engineerin*g, 2(3), 83-87.

Mabsout, M. E., Tarhini, K. M., Frederick, G. R., and Kobrosly, M. (1997). "Influence of Sidewalks and Railings on Wheel Load Distribution in Steel Girder Bridges." *Journal of Bridge Engineering*, 2(3), 88-96.

Bridges Subjected to Impact Loads of Moving Vehicles Obtained from Vehicle Dynamics

S. Jerath[1], Ph.D., P.E., F.ASCE and S. B. Gurav[2], Ph.D.

[1]Professor of Civil Engineering, University of North Dakota, 243 Centennial Drive, Stop 8115, Grand Forks, ND 58202-8115; PH (701) 777-3564; FAX (701) 777-3782; email: sukhvarshjerath@mail.und.edu

[2]Sargent & Lundy LLC, 55 East Monroe Street, Chicago, IL 60603; PH (312) 269-6304; FAX (312) 269-6539; email: sanjay.b.gurav@sargentlundy.com

ABSTRACT

In this paper the cumulative effect of road surface roughness, vehicle dynamics, vehicle weight and speed is considered to find the impact factor for highway bridges. AASHTO HS20-44 vehicle is considered running on a very good road. The roughness of the road surface profile is found by using the power spectral density function. The AASHTO truck is modeled as a 12 degree of freedom system to consider the vehicle dynamics. First the forces coming on the bridge deck are calculated taking into account the road surface roughness, then the forces are input to find the vertical deflection by orthotropic plate theory. The deflection obtained is compared with the static deflection to find the impact factor. The impact factor thus obtained is compared with the impact factor calculated from the AASHTO formula. This study shows that the AASHTO formula underestimates the impact factor.

INTRODUCTION

Moving loads cause vibrations in the bridges, the resulting deformations and stresses are much higher than the static deformations and stresses. Peculiar feature of the moving loads on the highway bridges is that they are variable both in space and time. An impact factor, I, given by AASHTO is: $I = \frac{50}{L+125}$, where I is the impact factor with a maximum value of 30%. L is the length in feet of the portion of the span that is loaded to produce maximum stress in the member. Impact factor given by AASHTO depends only on the span length of the bridge, whereas, road surface profile, weight, speed, dynamics of a vehicle, and bridge geometry all affect the impact factor when moving loads are traveling on a bridge. The objective of this paper is to calculate the increased forces that act on a bridge deck by considering the road surface roughness, and the vehicle dynamics for an AASHTO HS20-44 truck at various speeds. The increased forces are applied on a bridge deck considered as an orthotropic plate to calculate the deflections. Bridges decks act differently in longitudinal and transverse directions because of their structural configuration and hence can be modeled as orthotropic plates. The increased forces and deflections are compared with the static forces and deflections to calculate the impact factor.

ROAD SURFACE ROUGHNESS

Road surface roughness is one of the factors that affect the impact factor for a bridge design. Dodds and Robson (1973) developed the Power Spectral Density (PSD) function to describe the road surface roughness as follows:

$$S(\phi) = A\left(\frac{\phi}{\phi_0}\right)^{-w} \quad (1)$$

Where, $S(\square)$ = PSD (m^2/cycle/m), $\square$ = wave number (cycle/m), A = roughness coefficient (m^3/cycle), $\square_0$ = discontinuity frequency = $\left(\frac{1}{2\pi}\right)$(cycles/m), and w = roughness exponent. The roads are classified as motorways, principal roads, and minor roads. Each of these classifications is further divided into very good, good, average, poor, and poor categories. In this paper the roughness exponent, w, has been taken as 2 for simplifying the road surface roughness. Jerath and Gurav (2008) used the PSD procedure to develop the road surface profile that is used here to find the roughness profile of a very good road for a T-beam bridge deck shown in Figure 1.

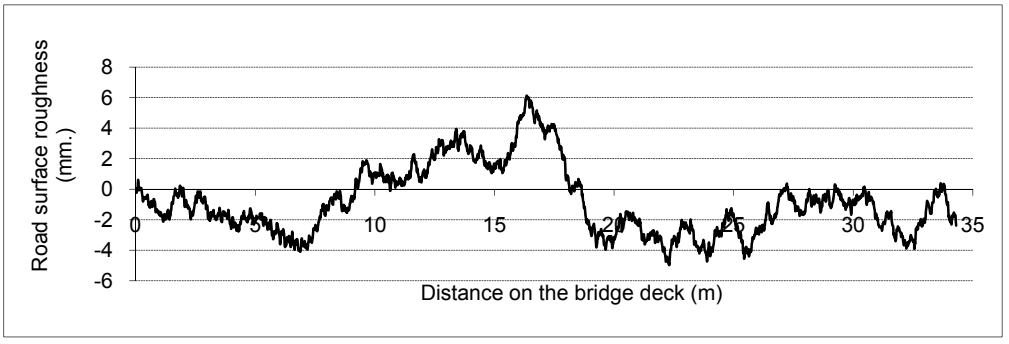


Figure1. Road surface roughness of a very good road for a T-Beam bridge

The data points are shown on the horizontal axis along the length of the bridge deck. Span length of the bridge in consideration is 112.5 ft (34.29 m) and it is divided into 2048 (2^{11}) sample points in Figure 1. The vertical axis shows the vertical distance between the tip of the road surface at a point from an imagined zero surface level in meters. The variation of the road surface is +6 to -5 mm (0.24 to -0.20 in.) for a very good road along the length of the bridge deck. The road surface roughness is used as input to the AASHTO HS20-44 vehicle model to calculate the forces that will act on a bridge deck.

VEHICLE DYNAMICS

The AASHTO HS20-44 truck is modeled as consisting of five rigid masses: tractor, semi-trailer, steer wheel/axle set, tractor wheel/axle set, and trailer wheel/axle set shown in Figures 2 and 3. Tractor and semi-trailer are assigned three degrees of freedom (y, θ, $\square$) individually. Two degrees of freedom (y and $\square$) are assigned to each wheel axle set. Thus there are 12 degrees of freedom (DOF) in the vehicle.

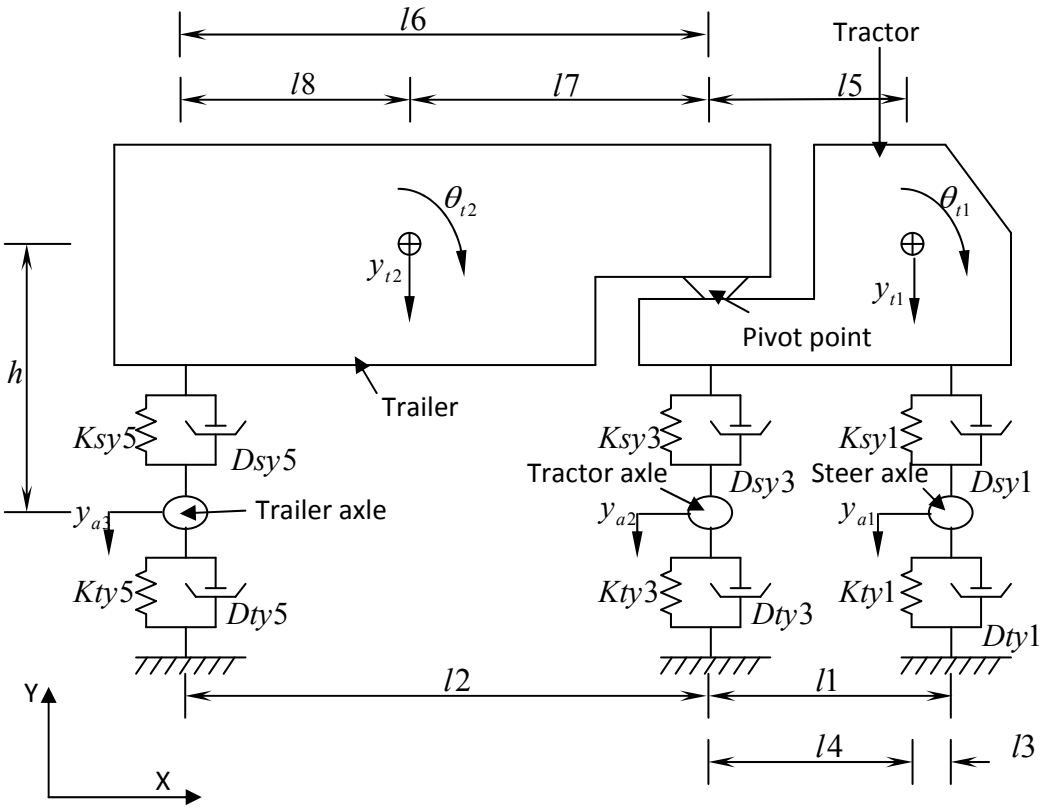


Figure2. Side elevation of AASHTO HS20-44 vehicle model

The equations of motion for the system are derived using Lagrange's formulation:

$$\frac{d}{dt}\left(\frac{\partial T}{\partial \dot{q}_i}\right)+\frac{\partial D}{\partial \dot{q}_i}-\frac{\partial T}{\partial q_i}+\frac{\partial V}{\partial q_i}=Qnc_i \qquad (2)$$

Where T, D, and V are total kinetic energy, dissipation energy, and potential energy of the vehicle consisting of springs, dampers, and masses shown in Figures 3 and 4. q_i and $\dot{q}_\iota$ are the generalized displacements and velocities, and Q_{nci} is a generalized force, I = 1,2,------, 11,12. The masses and the degrees of freedom of each rigid body are as follows:

y_{t1}, m_{t1}= Tractor vertical displacement and mass; ϕ_{t1}, I_{xt1}= Tractor roll displacement and mass moment of inertia about X axis; θ_{t1}, I_{zt1}= Tractor pitch displacement and mass moment of inertia about Z axis; y_{t2}, m_{t2}= Trailer vertical displacement and mass; ϕ_{t2}, I_{xt2}= Trailer roll displacement and mass moment of inertia about X axis; θ_{t2}, I_{zt2}= Trailer pitch displacement and mass moment of inertia about Z axis;

y_{a1}, m_{a1}= Steer axle vertical displacement and mass; and ϕ_{a1}, I_{xa1}= Steer axle roll displacement and mass moment of inertia about X axis; y_{a2}, m_{a2}= Tractor axle vertical displacement and mass; ϕ_{a2}, I_{xa2}= Tractor axle roll displacement and mass moment of inertia about X axis; y_{a3}, m_{a3}= Trailer axle vertical displacement and mass; and ϕ_{a3}, I_{xa3}= Trailer axle roll displacement and mass moment of inertia about X axis.

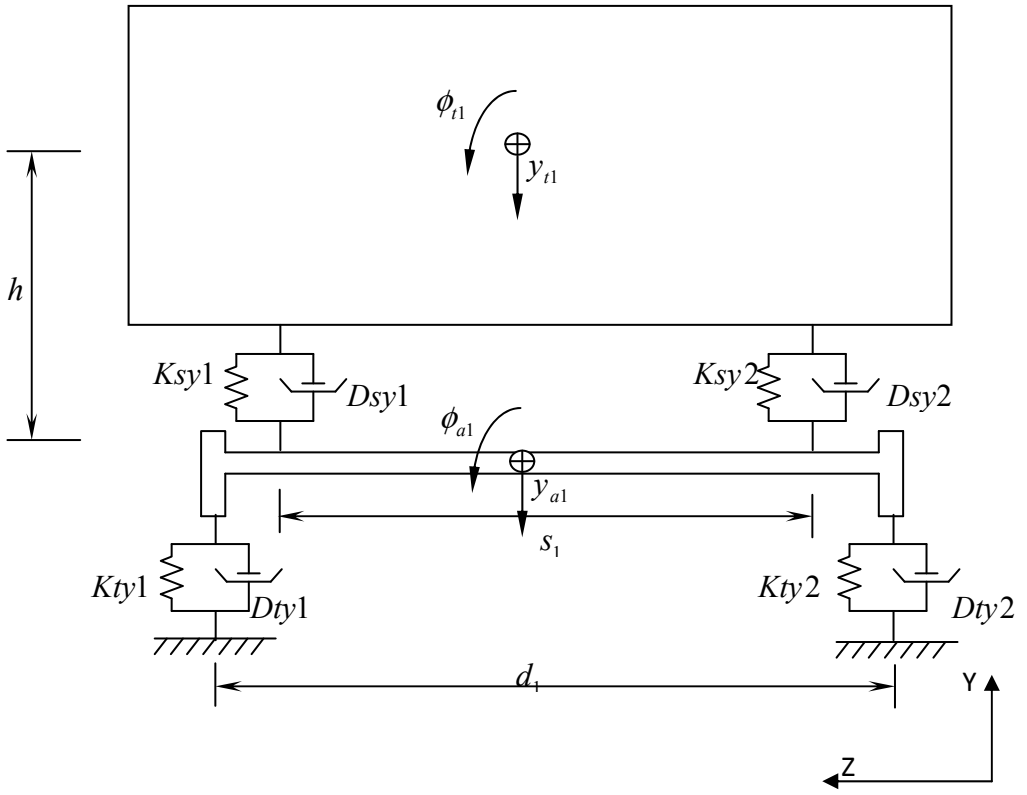


Figure3. Front elevation of AASHTO HS20-44 vehicle model

The relative displacements at the spring locations are given by

Suspension springs:

$$U_{sy1} = \left(y_{t1} - y_{a1} - \frac{l_3}{l_5} y_{t2} \right) + \left(s_1 / 2 \right)\left(\phi_{t1} - \phi_{a1} \right) + l_3 \theta_{t1} - l_7 \frac{l_3}{l_5} \theta_{t2}$$

$$U_{sy2} = \left(y_{t1} - y_{a1} - \frac{l_3}{l_5} y_{t2} \right) - \left(s_1 / 2 \right)\left(\phi_{t1} - \phi_{a1} \right) + l_3 \theta_{t1} - l_7 \frac{l_3}{l_5} \theta_{t2}$$

$$U_{sy3} = \left(y_{t1} - y_{a2} + \frac{l_4}{l_5} y_{t2} \right) + \left(s_2 / 2 \right)\left(\phi_{t1} - \phi_{a2} \right) - l_4 \theta_{t1} + l_7 \frac{l_4}{l_5} \theta_{t2} \qquad (3)$$

$$U_{sy4} = \left(y_{t1} - y_{a2} + \frac{l_4}{l_5} y_{t2} \right) - (s_2 / 2)(\phi_{t1} - \phi_{a2}) - l_4 \theta_{t1} + l_7 \frac{l_4}{l_5} \theta_{t2}$$

$$U_{sy5} = \left(y_{t2} - y_{a3} - \frac{l_8}{l_7} y_{t1} \right) + \left(s_3 \big/ 2 \right)(\phi_{t2} - \phi_{a3}) - l_8 \theta_{t2} - l_5 \frac{l_8}{l_7} \theta_{t1}$$

$$U_{sy6} = \left(y_{t2} - y_{a3} - \frac{l_8}{l_7} y_{t1} \right) - \left(s_3 \big/ 2 \right)(\phi_{t2} - \phi_{a3}) - l_8 \theta_{t2} - l_5 \frac{l_8}{l_7} \theta_{t1}$$

Tire springs:

$$U_{ty1} = y_{a1} + \left(d_1 \big/ 2 \right) \phi_{a1} + (u_{sr1})$$

$$U_{ty2} = y_{a1} - \left(d_1 \big/ 2 \right) \phi_{a1} + (u_{sr2})$$

$$U_{ty3} = y_{a2} + \left(d_2 \big/ 2 \right) \phi_{a2} + (u_{sr3}) \qquad (4)$$

$$U_{ty4} = y_{a2} - \left(d_2 \big/ 2 \right) \phi_{a2} + (u_{sr4})$$

$$U_{ty5} = y_{a3} + \left(d_3 \big/ 2 \right) \phi_{a3} + (u_{sr5})$$

$U_{sr1\text{----}6}$ = Vertical displacement of road surface, it is considered positive if upwards.

The total kinetic energy, $T = \sum T_i$ of the system is

$$T = \frac{1}{2} m_{t1} \dot{y}_{t1}^2 + \frac{1}{2} Ix_{t1} \dot{\phi}_{t1}^2 + \frac{1}{2} Iz_{t1} \dot{\theta}_{t1}^2 + \frac{1}{2} m_{t2} \dot{y}_{t2}^2 + \frac{1}{2} Ix_{t2} \dot{\phi}_{t2}^2 + \frac{1}{2} Iz_{t2} \dot{\theta}_{t2}^2 + \frac{1}{2} m_{a1} \dot{y}_{a1}^2 + \frac{1}{2} Ix_{a1} \dot{\phi}_{a1}^2$$

$$+ \frac{1}{2} m_{a2} \dot{y}_{a2}^2 + \frac{1}{2} Ix_{a2} \dot{\phi}_{a2}^2 + \frac{1}{2} m_{a3} \dot{y}_{a3}^2 + \frac{1}{2} Ix_{a3} \dot{\phi}_{a3}^2 \qquad (5)$$

The total potential energy, $V = \sum V_i$ of the system is

$$V = \frac{1}{2} K_{sy1} U_{sy1}^2 + \frac{1}{2} K_{sy2} U_{sy2}^2 + \frac{1}{2} K_{sy3} U_{sy3}^2 + \frac{1}{2} K_{sy4} U_{sy4}^2 + \frac{1}{2} K_{sy5} U_{sy5}^2 + \frac{1}{2} K_{sy6} U_{sy6}^2$$

$$+ \frac{1}{2} K_{ty1} U_{ty1}^2 + \frac{1}{2} K_{ty2} U_{ty2}^2 + \frac{1}{2} K_{ty3} U_{ty3}^2 + \frac{1}{2} K_{ty4} U_{ty4}^2 + \frac{1}{2} K_{ty5} U_{ty5}^2 + \frac{1}{2} K_{ty6} U_{ty6}^2 \qquad (6)$$

The dissipation energy, $D = \sum D_i$ of the system is

$$D = \frac{1}{2}D_{sy1}\dot{U}_{sy1}^2 + \frac{1}{2}D_{sy2}\dot{U}_{sy2}^2 + \frac{1}{2}D_{sy3}\dot{U}_{sy3}^2 + \frac{1}{2}D_{sy4}\dot{U}_{sy4}^2 + \frac{1}{2}D_{sy5}\dot{U}_{sy5}^2 + \frac{1}{2}D_{sy6}\dot{U}_{sy6}^2$$

$$+\frac{1}{2}D_{ty1}\dot{U}_{ty1}^2 + \frac{1}{2}D_{ty2}\dot{U}_{ty2}^2 + \frac{1}{2}D_{ty3}\dot{U}_{ty3}^2 + \frac{1}{2}D_{ty4}\dot{U}_{ty4}^2 + \frac{1}{2}D_{ty5}\dot{U}_{ty5}^2 + \frac{1}{2}D_{ty6}\dot{U}_{ty6}^2 \qquad (7)$$

Substituting the relative displacements in terms of 12 DOF from Equations (3) and (4),and using Equations (2), (5), (6), and (7), we get twelve equations of motion given by Gurav (2006). These equations of motion can be written in matrix form as

$$[M]\{\ddot{q}\} + [C]\{\dot{q}\} + [K]\{q\} = \{F\} \qquad (8)$$

Where, $[M]$ = global mass matrix; $[C]$ = global damping matrix; $[K]$ = global stiffness matrix; and $\{F\}$ = global force matrix. The generalized displacements and their derivatives are given by

$$\lfloor q \rfloor = \lfloor y_{t1}\ \theta_{t1}\ \phi_{t1}\ y_{t2}\ \theta_{t2}\ \phi_{t2}\ y_{a1}\ \phi_{a1}\ y_{a2}\ \phi_{a2}\ y_{a3}\ \phi_{a3} \rfloor$$

$$\left\lfloor \dot{q} \right\rfloor = \left\lfloor \dot{y}_{t1}\ \dot{\theta}_{t1}\ \dot{\phi}_{t1}\ \dot{y}_{t2}\ \dot{\theta}_{t2}\ \dot{\phi}_{t2}\ \dot{y}_{a1}\ \dot{\phi}_{a1}\ \dot{y}_{a2}\ \dot{\phi}_{a2}\ \dot{y}_{a3}\ \dot{\phi}_{a3} \right\rfloor \qquad (9)$$

and $$\left\lfloor \ddot{q} \right\rfloor = \left\lfloor \ddot{y}_{t1}\ \ddot{\theta}_{t1}\ \ddot{\phi}_{t1}\ \ddot{y}_{t2}\ \ddot{\theta}_{t2}\ \ddot{\phi}_{t2}\ \ddot{y}_{a1}\ \ddot{\phi}_{a1}\ \ddot{y}_{a2}\ \ddot{\phi}_{a2}\ \ddot{y}_{a3}\ \ddot{\phi}_{a3} \right\rfloor$$

The MATLAB was used to get the solutions of $\{q\}$ and its derivatives. From these displacements the suspension forces in the springs and tire forces are calculated. The spring suspension and tire forces are given by

$F_{syi} = K_{syi}U_{syi} \pm F_{yi}$ - Suspension spring force.

$F_{dsyi} = D_{syi}\dot{U}_{syi}$ - Damping force in the suspension.

$F_{tyi} = K_{tyi}U_{tyi}$ - Tire spring force.

$F_{dtyi} = D_{tyi}U_{tyi}$ - Damping force in the tire.

i = 1 to 6, and F_{yi} = Friction force at the ith suspension.

The data regarding distances, stiffness of the springs and tires, damping coefficients, and friction forces required to solve Equation (8) are given by Gurav (2006).The calculated tire forces are shown in Table 1. The ratio of the tire forces and the static forces give the impact factors for various speeds of the vehicle. The impact tire force varied from 24.72% for the trailer axle tires to 51.74% for the tractor axle tires when the speed of the vehicle was increased from 40 to 90 mph (64 to 144 km/hr). The increased forces are considered for the analysis to find the deflection of the deck of a simply supported T-Beam concrete bridge of span 112.50 ft (34.29 m)

and width of 42.66 ft (13.00 m). The analysis of the bridge is performed by using the orthotropic plate theory.

Table 1. Comparison of tire forces at different speeds for HS20-44 truck on a T-beam bridge deck.

Speed (mph)	Static (Kips)	Fty1 (Kips)	%Impact	Static (Kips)	Fty3 (Kips)	%Impact	Static (Kips)	Fty5 (Kips)	%Impact
40	3.99	4.67	17.16	15.97	21.53	34.80	15.99	19.94	24.72
45	3.99	4.71	17.98	15.97	24.23	51.74	15.99	19.82	23.92
50	3.99	4.74	18.79	15.97	22.29	39.54	15.99	19.20	20.09
55	3.99	4.58	14.76	15.97	21.73	36.08	15.99	18.86	17.96
60	3.99	4.82	20.73	15.97	22.28	39.51	15.99	19.23	20.27
65	3.99	4.72	18.19	15.97	22.64	41.75	15.99	19.64	22.83
70	3.99	4.79	19.95	15.97	22.82	42.88	15.99	19.81	23.87
75	3.99	4.86	21.90	15.97	23.94	49.91	15.99	19.34	20.93
80	3.99	4.87	22.06	15.97	23.10	44.63	15.99	19.51	22.00
85	3.99	5.08	27.27	15.97	23.30	45.92	15.99	19.89	24.36
90	3.99	5.17	29.57	15.97	23.84	49.28	15.99	19.44	21.59

Note: Fty2, Fty4, and Fty6 are same as Fty1, Fty3, and Fty5 respectively. 1 Kip = 1000 lbs =4.5 kN, 1 mph = 1.6 km/hr.

ORTHOTROPIC PLATE THEORY UNDER MOVING LOADS

In this the bridge deck is modeled as an orthotropic rectangular plate with two edges simply supported and the other two edges as free shown in Figure 4. The strain energy of an orthotropic plate is given by Timoshenko (1959) as

$$U = \frac{1}{2}\int_0^a\int_0^b \left[D_x\left(\frac{\partial^2 w}{\partial x^2}\right)^2 + \left(D_x v_{yx} + D_y v_{xy}\right)\frac{\partial^2 w}{\partial x^2}\frac{\partial^2 w}{\partial y^2} + D_y\left(\frac{\partial^2 w}{\partial y^2}\right)^2 + 4D_{xy}\left(\frac{\partial^2 w}{\partial x \partial y}\right)^2 \right] dxdy \qquad (10)$$

Where, $D_x = \frac{E_x h^3}{12(1 - v_{xy}v_{yx})}$, $D_y = \frac{E_y h^3}{12(1 - v_{xy}v_{yx})}$ and $D_{xy} = \frac{G_{xy} h^3}{12}$

E_x = Modulus of elasticity in X direction, E_y = Modulus of elasticity in Y direction,

v_{xy} = Poisson's ratio associated with a strain in the Y direction for a load in the X

direction, v_{yx} = Poisson's ratio associated with a strain in the X direction for a load in the Y direction, G_{xy} = Shear modulus of the plate.

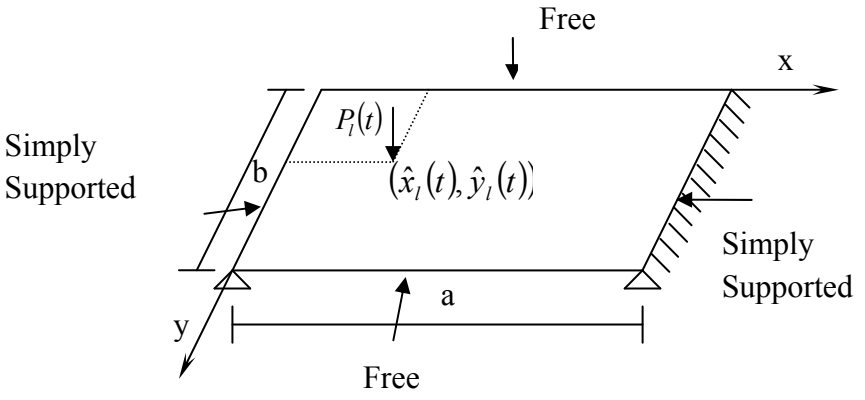


Figure4. Orthotropic plate with moving load

The kinetic energy of the plate is given by

$$T = \frac{1}{2}\int_0^a \int_0^b \dot{w}(x,y,t)^2 \rho h dx dy \tag{11}$$

Where, ρ = Mass density of material of the plate, h = Thickness of the plate.

The work done due to damping in the plate is given as

$$W_c = -\int_0^a \int_0^b w(x,y,t) c_b \dot{w}(x,y,t) dx dy \tag{12}$$

Where, c_b = Damping coefficient of the plate.

The external work done by the force $P_l(t)$ can be written as

$$W = \int_0^a \int_0^b \sum_{l=1}^{N_p} P_l(t)\delta(x-\hat{x}_l(t))\delta(y-\hat{y}_l(t))w(x,y,t) dx dy \tag{13}$$

Where, $P_l(t)$, $(l = 1,2,...,N_p)$ = Moving loads, $\hat{x}_l(t), \hat{y}_l(t)$ = Coordinates of the position of moving load $P_l(t)$, $\delta(x-\hat{x}_l(t))$, $\delta(y-\hat{y}_l(t))$ = Dirac Delta function.

The displacement function of the plate can be written as a summation of the normal mode function in the X and Y coordinates as,

$$w(x,y,t) = \sum_{m,n} w_{mn}(x,y) q_{mn}(t) \tag{14}$$

Where, $w_{mn}(x,y) = Y_{mn}(y)\sin\left(\frac{m\pi x}{a}\right)$ = Normal modes of the plate, $q_{mn}(t)$ = The corresponding generalized coordinates.

By using the Lagrange's equation,

$$\frac{d}{dt}\left(\frac{\partial T}{\partial \dot{q}}\right) - \frac{\partial T}{\partial q} + \frac{\partial U}{\partial q} - \frac{\partial W_c}{\partial q} = \frac{\partial W}{\partial q} \tag{15}$$

Equation of motion is given by

$$\{M\}\{\ddot{q}\} + \{C\}\{\dot{q}\} + \{K\}\{q\} = \{P\} \tag{16}$$

Where,

$$M = \int_0^a \int_0^b w^2{}_{mn}(x,y)\rho h dx dy \tag{17}$$

$$C = \int_0^a \int_0^b w^2{}_{mn}(x,y) c_b dx dy \tag{18}$$

$$K = \int_0^a \int_0^b \left[\begin{array}{l} D_x\left(\frac{\partial^2 w_{mn}}{\partial x^2}\right)^2 + \left(D_x v_{yx} + D_y v_{xy}\right)\frac{\partial^2 w_{mn}}{\partial x^2}\frac{\partial^2 w_{mn}}{\partial y^2} \\ + D_y\left(\frac{\partial^2 w_{mn}}{\partial y^2}\right)^2 + 4D_{xy}\left(\frac{\partial^2 w_{mn}}{\partial x \partial y}\right)^2 \end{array} \right] dx dy \tag{19}$$

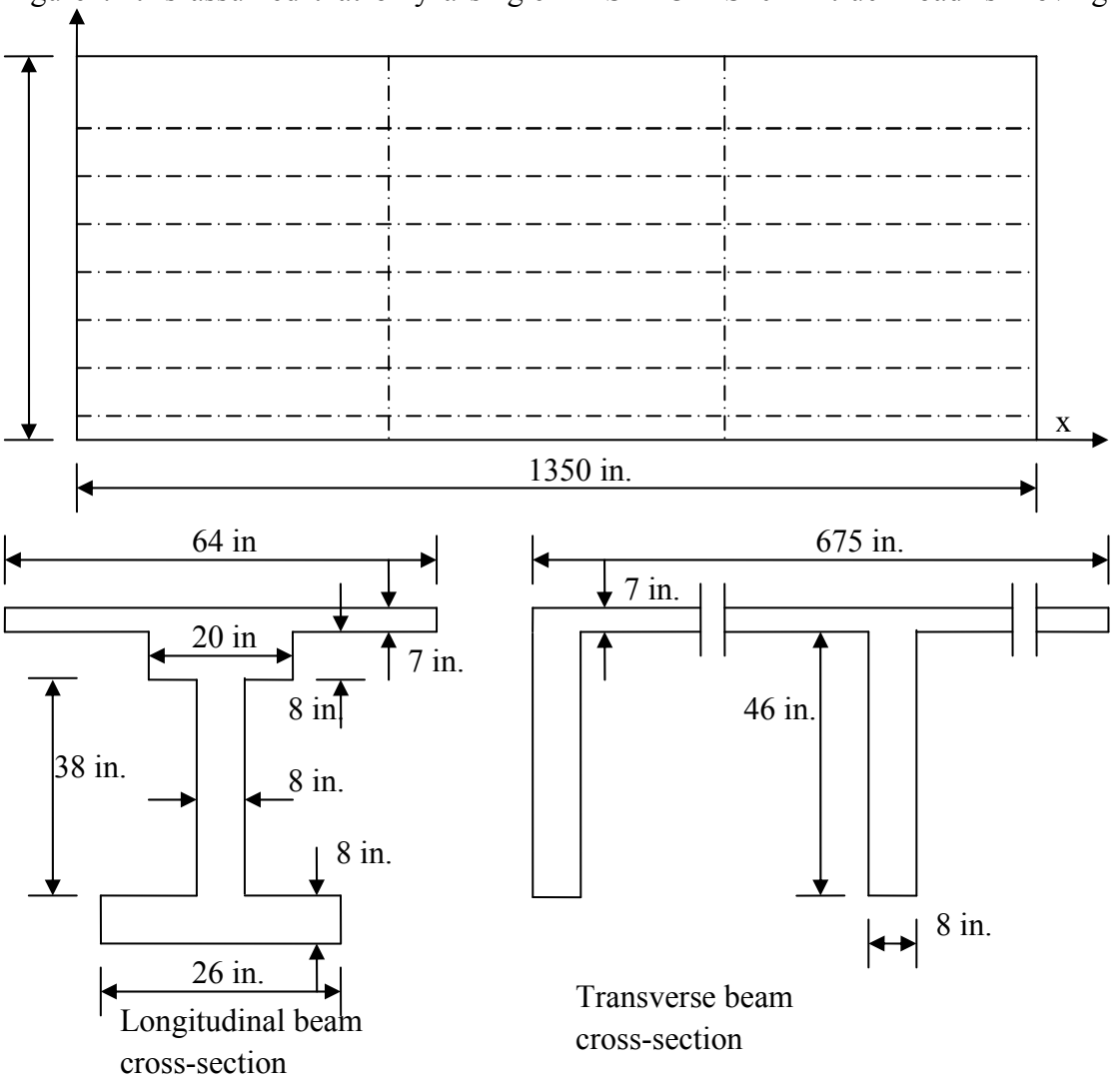
$$P = \int_0^a \int_0^b \sum_{l=1}^{N_p} P_l(t)\delta(x - \hat{x}_l(t))\delta(y - \hat{y}_l(t)) w_{mn}(x,y) dx dy \tag{20}$$

The equation of motion (16) is solved for the generalized coordinate q_{mn} by MATLAB. The normal modes of the plate $w_{mn} = Y_{mn}(y) sin\left(\frac{m\pi x}{a}\right)$ required in the Equation (16) are obtained from the eigenvalue analysis of the orthotropic plate given by Gurav and Jerath (2006).

ANALYSIS OF T-BEAM BRIDGE BY ORTHOTROPIC PLATE THEORY

A simply supported T-Beam bridge of span 112.5 ft = 1350 in. (34.29 m) and width of 42.66 ft = 512 in. (13.00 m) is considered as shown in Figure 5. The bridge is built on a very good road whose road surface roughness profile is shown in

Figure1. It is assumed that only a single AASHTO HS20-44 truck load is moving



1 in. = 25.4 mm

Figure5. Simply supported T-Beam bridge

along the center line of the bridge deck at different speeds. The tire forces that have a cumulative effect of road surface roughness and vehicle dynamics from Table 1 are multiplied by 2 to get the total axle force for the steer, trailer, and tractor axles. The axle forces are shown in Table 2 at different speeds.

The physical properties of the bridge deck in Figure 5 are:

a = 112.5 ft (34.29 m), b = 42.66 ft (13.00 m), h = 0.58 ft (176.78 mm), mass density ρ = 4.658 slugs/ft^3 (2400 kg/m^3), υ_{xy} = 0.2, D_x = 2.3285x10^9 lb.ft (3.1574x10^9 N. m), D_y = 0.2575x10^9 lb.ft (0.3492x10^9 N.m), $2H$ = 0.0342x10^9 lb.ft (0.0464x10^9 N.m).

Table 2. Axle load of AASHTO HS20-44 truck on the T-beam bridge deck.

Speed mph (km/hr)	Total axle load					
	Steer axle		Tractor axle		Trailer axle	
	lbs	kN	lbs	kN	lbs	kN
40 (64)	9340	42.03	43060	193.77	39880	179.46
45 (72)	9420	42.39	48460	218.07	39640	178.38
50 (80)	9480	42.66	44580	200.61	38400	172.80
55 (88)	9160	41.22	43460	195.57	37720	169.74
60 (96)	9640	43.38	44560	200.52	38460	173.88
65 (104)	9440	42.48	45280	203.76	39280	176.76
70 (112)	9580	43.11	45640	205.38	39620	178.29
75 (120)	9720	43.74	47880	215.46	38680	174.06
80 (128)	9740	43.83	46200	207.90	39020	175.59
85 (136)	10160	45.72	46600	209.70	39780	179.01
90 (144)	10340	46.53	47680	214.56	38880	174.96

The maximum vertical displacements at the center of th T-Beam bridge deck under AASHTO HS20-44 moving with different speeds are calculated by the orthotropic plate theory and are shown in Table 3. The static displacement in the Table 3 is obtained by assuming the vehicle is moving at 5 mph (8 km/hr). The impact factor for the vertical deflection is in the range of 36.81% to 43.96% in the Table 3, whereas the impact factor given by the AASHTO formula for the bridge is $\frac{50}{112.5+125} = 21.05\%$. Thus the AASHTO formula underestimates the impact factor.

Table 3. Maximum vertical displacements at the center of the bridge deck

Speed mph (km/hr)	Vertical displacement in. (mm)	Static vertical displacement in. (mm)	Impact %
40 (64)	0.299 (7.595)	0.218 (5.537)	36.81
45 (72)	0.314 (7.976)	0.218 (5.537)	43.96
50 (80)	0.305 (7.747)	0.218 (5.537)	39.56
55 (88)	0.301 (7.645)	0.218 (5.537)	37.91
60 (96)	0.306 (7.772)	0.218 (5.537)	40.11
65 (104)	0.304 (7.722)	0.218 (5.537)	39.01
70 (112)	0.299 (7.595)	0.218 (5.537)	36.81
75 (120)	0.302 (7.671)	0.218 (5.537)	38.46
80 (128)	0.301 (7.645)	0.218 (5.537)	37.91
85 (136)	0.308 (7.823)	0.218 (5.537)	41.21
90 (144)	0.312 (7.925)	0.218 (5.537)	42.86

CONCLUSIONS

- The road surface roughness of various types of highways ranging from very good roads on motorways to poor category on minor roads can be generated by using the power spectral density function.
- An AASHTO HS20-40 vehicle is modeled successfully as a 12 degree of freedom system to account for the effect of vehicle dynamics for calculating the dynamic force coming from the tires on the road surface.
- The solution of the equation of motion gives the vehicle spring suspension forces and the tire forces acting on the road. The impact of the tire forces varied from 24.72% for the trailer axle tires to 51.7% for the tractor axle tires when the speed of the vehicle is increased from 40 to 90 mph (64 to 144 km/hr).
- The cumulative effect of the road surface roughness, vehicle dynamics, weight and speed of the vehicle is found in the vertical deflection at the center of a simply supported T-Beam bridge deck by orthotropic plate theory. The impact factor varied from 38.81% to 43.96%, whereas the impact factor from ASSHTO formula is 21.05% for this bridge, which is an underestimation.
- It is recommended to further study the effect of number of vehicles traveling in different lanes and various speeds. In this study only one vehicle is traveling along the center line of the bridge deck.

REFERENCES

American Association of State Highway and Transportation Officials (AASHTO). (1989). *AASHTO standard specifications for highway bridges*, Washington, D.C.

Dodds, C.J., and Robson, J.D. (1973). "The description of road surface roughness." *Journal of Sound and Vibration*, 31(2), 175-183.

Gurav, S.B. (2006). *Design analysis of bridges under moving loads*, Ph.D. dissertation submitted to the University of North Dakota, Grand Forks, ND.

Gurav, S.B., and Jerath, S. (2006). "Dynamic analysis of bridges under moving loads." *Proceedings of the 7th International Conference on Short and Medium Span Bridges*, Montreal, QC, Canada.

Jerath, S., and Gurav, S.B. (2008). "Road surface roughness generation by power spectral density in bridge design." *Proceeding of the ASCE 2008 Structures Congress*, Vancouver, BC, Canada.

Timoshenko, S., and Woinowsky-Krieger, S. (1959). *Theory of plates and shells*, 2 ed., McGraw-Hill, New York.

ELASTIC NONLINEAR ANALYSIS OF PLANE TRUSS BRIDGES

Morteza A.M. Torkamani[1], and Jyh-Hung Shieh[2]

[1] Department of Civil and Environmental Engineering, University of Pittsburgh, 932 Benedum Hall, 3700 O'Hara Street, Pittsburgh, PA 15261-2294; PH (412) 624-9881; FAX (412) 624-0135; email: torkmani@pitt.edu

[2] Deptartment of Civil and Environmental Engineering, University of Pittsburgh, 949 Benedum Hall, 3700 O'Hara Street, Pittsburgh, PA 15261-2294; PH (412) 624-9870; FAX (412) 624-0135; email: jsst63@pitt.edu

ABSTRACT

There are, enormous number of, steel truss bridges in the U.S. and around the world. Elementary theory of structural analysis or linear elastic small displacement finite element method is typically used for analysis and design of these bridges. However, steel bridges may face large deflections and inelastic displacements due to unexpected live loads and/or unfavorable environmental conditions. Therefore, there is a need for the second- or higher-order elastic and/or inelastic analysis of these bridges. This article presents a methodology for the elastic large displacement analysis of plane trusses that are novel in bridge engineering practice.

Higher-order stiffness matrices and finite element procedure is used for the elastic nonlinear analysis of plane truss structures. The higher-order stiffness matrices are derived and formatted by using the updated Lagrangian description and the finite element concept. Then a numerical method, a modified Riks-Wempner approach, is used for the solution of geometric nonlinear plane truss problems. First, background on nonlinear truss analysis, the scope of this work, and the assumptions pertinent to this research are given. Second, the stiffness matrices, for nonlinear elastic plane truss analysis, are presented by using the incremental equation of equilibrium that is derived from first variation of increment of total potential energy. Third, a modified Riks-Wempner method is used for programming and software development. Numerical examples and results are presented next. The accuracy of the software developed is checked by comparing the results of numerical examples with theoretical results and examples published by other authors. In this research, the concept of Object-Oriented technology and C++ programming language are used for coding and software developed.

INTRODUCTION

To reflect the real behavior of structures under ultimate or abnormal loading conditions, nonlinear analysis should be adopted instead of linear analysis, since most structures exhibit some nonlinear behavior before reaching their limits of resistance. In the analysis of structural systems, two different types of structural nonlinearities have been identified. They are material nonlinearity and geometric nonlinearity. In this work, geometric nonlinearity for plane trusses is considered and the load-deflection paths of several trusses are traced and compared to existing literature and benchmark problems.

Nonlinear analysis of truss structures has been widely investigated by many researchers during the last four decades. However, because of the space limitation a literature review is not provided in this article.

SCOPE AND OBJECTIVES

The purposes of this research are: (1) to present the finite element formulation and derivation of higher-order nonlinear stiffness matrices that may be used for the analysis of plane truss systems under large strain conditions, (2) to apply a numerical procedure that is a variation of the modified Riks-Wempner method with higher-order nonlinear stiffness matrices for solving geometric nonlinear plane truss problems, (3) to develop a software package using C++ language capable of providing geometric nonlinear analysis for plane trusses, and

(4) to check the accuracy and reliability of the theoretical developments and software developed in this study by comparison of the results from two examples presented in this work with published literature.

ASSUMPTIONS

The following assumptions are made in order to solve the problems more effectively: (1) The members of the structures are straight, free of residual stress and imperfections. The longitudinal axis of each member is collinear with the centroidal axis of the cross-sections, (2) The nodes of each truss element are assumed to be hinged. The truss elements can resist axial force, but not bending moment or shear force, (3) Only deformations occurring in the plane of the truss structure are considered; local buckling is not taken into account, (4) The cross sections of members are symmetric about the plane of the truss (x-y plane), and are always normal to the x-axis of the members during deformation of the members, and (5) The cross-sections of members always stay in the plane of the truss, and large strains are allowed.

COORDINATE SYSTEMS

Lagrangian formulation is recommended in the analysis of solids and structures since it may represent a more natural and effective analytical approach than an Eulerian formulation. An Eulerian formulation is generally adopted in the analysis of fluid mechanics problems focused on the motion of the material through a stationary control volume. However, if problems arise with the use of a free surface analysis, an arbitrary Lagrangian-Eulerian formulation provides an effective solution because it allows the modeling of general free surfaces and interactions between fluid flows and structures (Bathe 1996).

There are two primary types of Lagrangian descriptions in geometric nonlinear analysis. They are *total* and *updated* Lagrangian descriptions. In the *total* Lagrangian description, all quantities are referred to the initial configuration of the element, *i.e.,* the initial configuration is selected as the reference configuration. Fig. 1 shows this initial configuration, which is called C_0. Although this type of description is easy to apply, a major disadvantage is that it leads to incorrect description of the equilibrium path when large deflections exist.

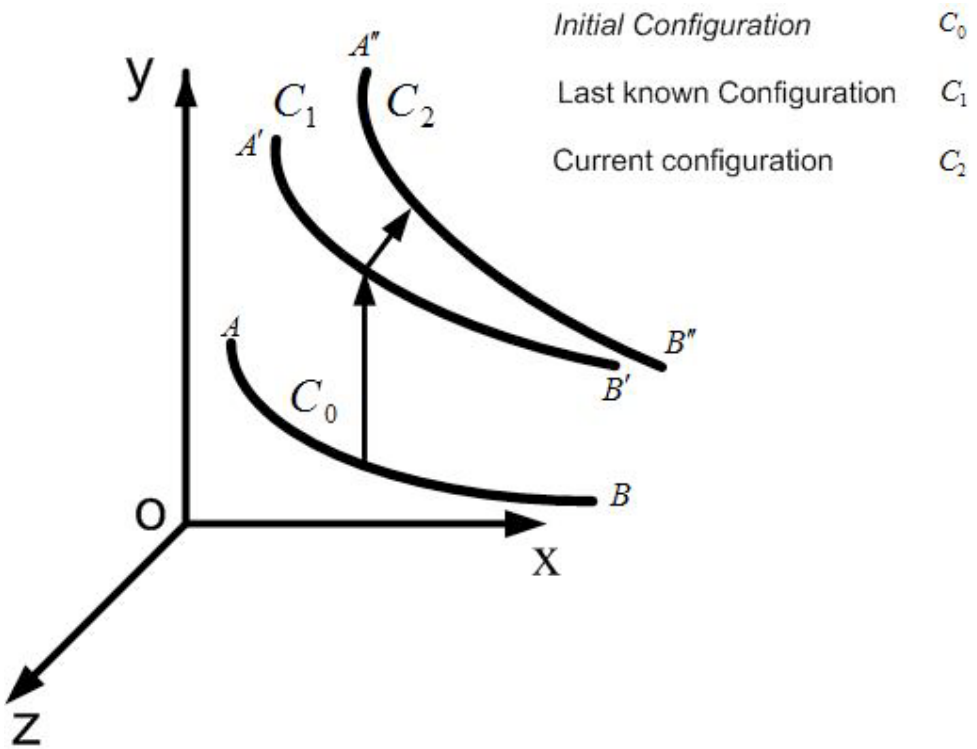


Fig. 1: Displacement of a Continuous Media from C_0 to C_2

In the *updated* Lagrangian description, all quantities are referred to the last configuration of the element, *i.e.,* the last configuration is chosen as the reference configuration (called C_1, see Fig. 1). This method generates a more accurate result than the first one. In the present study, this method is adopted, since its efficiency in dealing with the numerical computation is proven as compared to the total Lagrangian description (Torkamani and Sonmez 2001, Yang *et al*. 2007).

GENERAL FORMULATION

The elementary theory of structural analysis has been widely used for the calculation of internal forces, displacements, stresses, and strains of structures in order to select the proper member sizes for such systems. The shortcoming of elementary theory is its inability to represent the real behavior of the structures. For instance, the elastic behavior of cable nets, the calculation of the buckling load of a steel structure, and the nonlinear material behavior of a concrete building all fall in this category. In addition, it should be noted that the results obtained on the basis of elementary theory are questioned for many cases because the elementary theory of structures uses the most simple way to describe the behavior of structures. Moreover, in the elementary theory, the effects of the large deformations are ignored when considering the equations of equilibrium or motion.

Updated Lagrangian Formulation

In the updated Lagrangian formulation, the description of the continuous media up to the C_1 configuration is calculated (see Fig. 1). Furthermore, the media is in equilibrium at C_1 configuration. The deformation from the C_0 to C_1 is large. By increasing the external load, the continuous media deforms from the C_1 to C_2 configuration.

The incremental equilibrium equation is derived by applying the principle of minimum of increment of total potential energy. The increment of total potential energy from C_1 to C_2 configuration, considering C_1 configuration as the reference point, is given by

$$ {}^{2}_{1}\Delta\pi = \int_{{}_1V} ({}^{1}_{1}\tau_{ij} + \frac{1}{2}\,{}_1\tau_{ij})\,{}_1\varepsilon_{ij}\,{}^{1}dV - \int_{{}_1V} ({}^{1}_{1}f_i + \frac{1}{2}\,{}_1f_i)\,{}_1u_i\,{}^{1}dV - \int_{{}_1S} ({}^{1}_{1}t_i + \frac{1}{2}\,{}_1t_i)\,{}_1u_i\,{}^{1}dS \tag{1} $$

The stress, body force, surface traction, finite strain and displacement increments of a point P from C_1 to C_2 are written as:

$$ {}^{2}_{1}\tau_{ij} = {}^{1}_{1}\tau_{ij} + {}_1\tau_{ij} \tag{2} $$

$$ {}^{2}_{1}f_{ij} = {}^{1}_{1}f_{ij} + {}_1f_{ij} \tag{3} $$

$$ {}^{2}_{1}t_i = {}^{1}_{1}t_i + {}_1t_i \tag{4} $$

$$ {}^{2}_{1}\varepsilon_{ij} = {}^{1}_{1}\varepsilon_{ij} + {}_1\varepsilon_{ij} \tag{5} $$

and

$$ {}^{2}_{1}u_i = {}^{1}_{1}u_i + {}_1u_i \tag{6} $$

where ${}^{2}_{1}\tau_{ij}$ denotes the stresses, ${}^{2}_{1}f_{ij}$ the body forces, ${}^{2}_{1}t_i$ the surface tractions, ${}^{2}_{1}\varepsilon_{ij}$ the finite strains, and ${}^{2}_{1}u_i$ the displacements. All of these terms are at the C_2 configuration with respect to the C_1 reference configuration. In this study, a left superscript denotes the configuration of occurrence, and a left subscript the configuration of reference. The strain increments ${}_1\varepsilon_{ij}$ may be decomposed into linear and nonlinear parts:

$$ {}_1\varepsilon_{ij} = {}_1e_{ij} + {}_1\mu_{ij} \tag{7} $$

where ${}_1\varepsilon_{ij}$ denotes the increment of finite strain from configuration C_1 to C_2 with respect to the C_1 reference configuration and the linear part of strain increment ${}_1e_{ij}$ is defined as

$${}_1e_{ij} = \frac{1}{2}\left(\frac{\partial\ {}_1u_i}{\partial\ {}^1x_j} + \frac{\partial\ {}_1u_j}{\partial\ {}^1x_i} \right) \tag{8}$$

The nonlinear part ${}_1\mu_{ij}$ is expressed as

$${}_1\mu_{ij} = \frac{1}{2}\left(\frac{\partial\ {}_1u_k}{\partial\ {}^1x_i}\ \frac{\partial\ {}_1u_k}{\partial\ {}^1x_j} \right) \tag{9}$$

If one expands Eq. (1), takes the first variation of the expended equation, and sets the first variation of the increment of the total potential energy equal to zero, one would have $\delta\ {}^2_1\Delta\ \pi = 0$. On the other hand, the first variation of Eq. (7) may be written as:

$$\delta\ {}_1\varepsilon_{ij} = \delta\ {}_1e_{ij} + \delta\ {}_1\mu_{ij} \tag{10}$$

Substituting Eq. (10) in $\delta\ {}^2_1\Delta\ \pi = 0$ and taking advantage of virtual work equalities, one has the following incremental equilibrium equation

$$\int_{{}_1V} C_{ijkl}\ {}_1e_{kl}\ \delta\ {}_1e_{ij}\ {}^1dV + \int_{{}_1V} C_{ijkl}\ {}_1\mu_{kl}\ \delta\ {}_1e_{ij}\ {}^1dV + \int_{{}_1V} C_{ijkl}\ {}_1e_{kl}\ \delta\ {}_1\mu_{ij}\ {}^1dV$$

$$+ \int_{{}_1V} C_{ijkl}\ {}_1\mu_{kl}\ \delta\ {}_1\mu_{ij}\ {}^1dV + \int_{{}_1V} {}^1_1\tau_{ij}\ \delta\ {}_1\mu_{ij}\ {}^1dV + {}^1_1R = {}^2_1R \tag{11}$$

where ${}^2_1R$ and ${}^1_1R$ denote the virtual works done by the external loads acting on the continuous media at the C_2 and C_1 configuration, respectively.

Since all of the terms in Eq. (11) refer to the last calculated configuration, C_1, the left subscript 1 for e_{ij} , μ_{ij}, C_{ijkl}, ${}^1R$, ${}^2R$, and the left superscript 1 for V are dropped to simplify the equation as presented in the following forms

$$\int_V C_{ijkl}\, e_{kl}\, \delta e_{ij}\, dV + \int_V C_{ijkl}\, \mu_{kl}\, \delta e_{ij}\, dV + \int_V C_{ijkl}\, e_{kl}\, \delta \mu_{ij}\, dV$$

$$+ \int_V C_{ijkl}\, \mu_{kl}\, \delta \mu_{ij}\, dV + \int_V {}^1\tau_{ij}\, \delta \mu_{ij}\, dV + {}^1R = {}^2R \tag{12}$$

Finite Element Model

First, the stiffness matrices for a geometrically nonlinear elastic plane truss element suitable for updated-Lagrangian analysis using the incremental equations of equilibrium given by Eq. (12) is derived.

Considering the nodal displacements defined in Fig. 2, the displacements *u(x)* and *v(x)* may be written as the following forms

$$u(x) = [N_u]\{d\} \tag{13}$$

$$v(x) = [N_v]\{d\} \tag{14}$$

where

$$[N_u] = \left[1 - \frac{x}{L},\ 0,\ \frac{x}{L},\ 0 \right] \tag{15}$$

$$[N_u] = \left[\ 0,\ 1-\frac{x}{L},\ 0,\ \frac{x}{L}\ \right] \tag{16}$$

$$\{d\}^T = \{u_1, v_1, u_2, v_2\} \tag{17}$$

In Eqs. (15) and (16), $[N_u]$ and $[N_v]$ are vectors of shape functions for axial and lateral displacement of a truss element with length L. Note that the element force vector corresponding to the element nodal displacement vector, Eq. (17), is written as

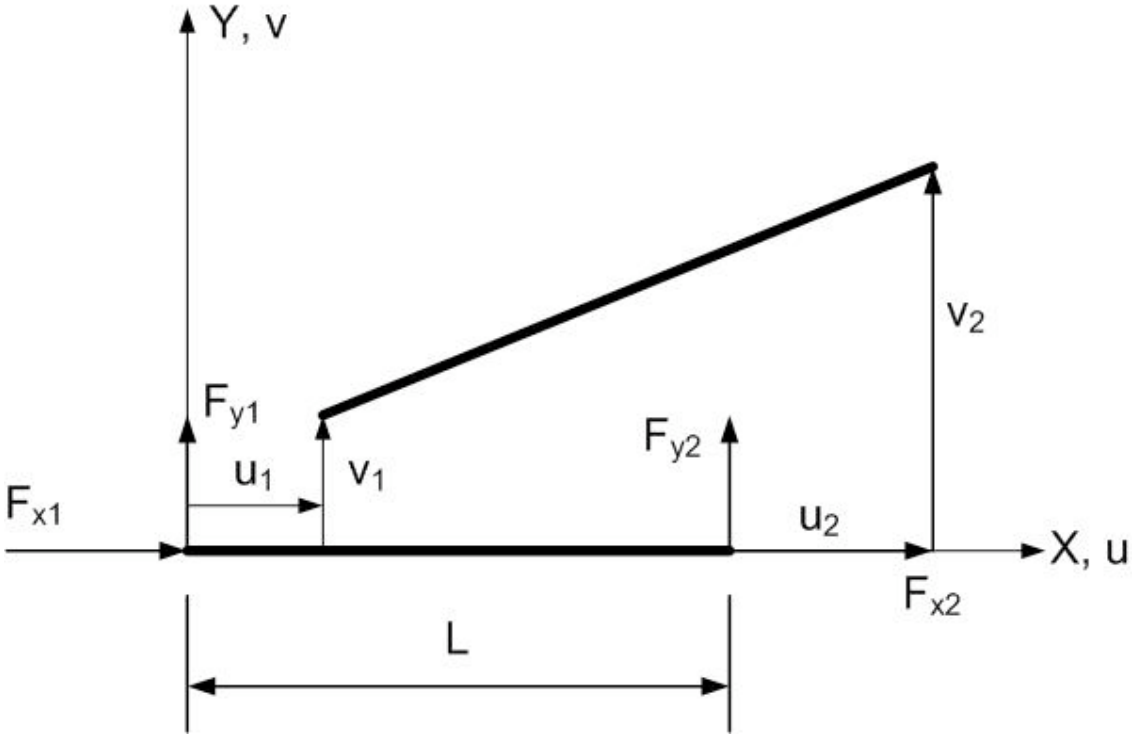


Fig. 2: Coordinate Systems of a Plane Truss Element

$$\{f\}^T = \{F_{x1}, F_{y1}, F_{x2}, F_{y2}\} \tag{18}$$

See Fig. 2 for notations used in this article.

Equilibrium Equations for Truss Element

The incremental equation of equilibrium, Eq. (12), is now applied to a truss element. A truss element is a special case of a continuous media, therefore; C_{ijkl} becomes E and ε_{ij}, e_{ij}, μ_{ij} and ${}^1\tau_{xx}$ are given by Eqs. (19) to (22):

$$\varepsilon_{ij} = \varepsilon_{xx} \tag{19}$$

$$e_{ij} = e_{xx} \tag{20}$$

$$\mu_{ij} = \mu_{xx} \tag{21}$$

$${}^1\tau_{xx} = \sigma_0 \tag{22}$$

where E is the modulus of elasticity of the material. According to Eqs. (19) to (22), Eq. (12) is then given by

$$\begin{aligned}&\int_V E e_{xx}\delta e_{xx}\,dV+\int_V E\mu_{xx}\delta e_{xx}\,dV+\int_V E e_{xx}\delta\mu_{xx}\,dV\\&\int_V E\mu_{xx}\delta\mu_{xx}\,dV+\int_V {}^1\tau_{xx}\delta\mu_{xx}\,dV+{}^1R={}^2R\end{aligned}\tag{23}$$

Furthermore, based on Eqs. (13) and (14), Eqs. (7) to (9) may be written as

$$e_{xx}=\frac{\partial u}{\partial x}=[N_u']\{d\}\tag{24}$$

$$\mu_{xx}=\frac{1}{2}\left[\left(\frac{\partial u}{\partial x}\right)^2+\left(\frac{\partial v}{\partial x}\right)^2\right]=\frac{1}{2}\left(\{d\}^T[N_u']^T[N_u']\{d\}+\{d\}^T[N_v']^T[N_v']\{d\}\right)\tag{25}$$

$$\varepsilon_{xx}=e_{xx}+\mu_{xx}=\frac{\partial u}{\partial x}+\frac{1}{2}\left[\left(\frac{\partial u}{\partial x}\right)^2+\left(\frac{\partial v}{\partial x}\right)^2\right]\tag{26}$$

$$\varepsilon_{xx}=[N_u']\{d\}+\frac{1}{2}\left(\{d\}^T[N_u']^T[N_u']\{d\}+\{d\}^T[N_v']^T[N_v']\{d\}\right)\tag{27}$$

The first variation of Eq. (24) and Eq. (25) is expressed, respectively, as

$$\delta e_{xx}=\{\delta d\}^T[N_u']^T\tag{28}$$

and

$$\delta\mu_{xx}=\{\delta d\}^T[N_u']^T[N_u']\{d\}+\{\delta d\}^T[N_v']^T[N_v']\{d\}\tag{29}$$

where $[N']=\frac{dN}{dx}$.

Substituting Eqs. (24) to (29) into Eq. (23) and, rearranging the results, yields

$$\begin{aligned}&\{\delta d\}^T\int_V E[N_u']^T[N_u']\{d\}\,dV\\&+\{\delta d\}^T\int_V\frac{E}{2}[N_u']^T\left(\{d\}^T[N_u']^T[N_u']+\{d\}^T[N_v']^T[N_v']\right)\{d\}\,dV\\&+\{\delta d\}^T\int_V E\left([N_u']^T[N_u']+[N_v']^T[N_v']\right)\{d\}[N_u']\{d\}\,dV\\&+\{\delta d\}^T\int_V\frac{E}{2}\left([N_u']^T[N_u']+[N_v']^T[N_v']\right)\{d\}\{d\}^T\left([N_u']^T[N_u']+[N_v']^T[N_v']\right)\{d\}\,dV\\&+\{\delta d\}^T\int_V\sigma_0\left([N_u']^T[N_u']+[N_v']^T[N_v']\right)\{d\}\,dV\\&+\{\delta d\}^T\{{}^1f\}=\{\delta d\}^T\{{}^2f\}\end{aligned}\tag{30}$$

Nonlinear Incremental Stiffness Matrices

Canceling out the term $\{\delta d\}^T$, and extracting the term $\{d\}$ from the integrals of the first variation of the increment of total potential energy, Eq. (30), and integrating yields

$$\left([k_0]+[k_p]+[k_1]+[k_2]+[k_3]\right)\{d\}=\{{}^2f\}-\{{}^1f\}\tag{31}$$

where

$$[k_0] = \int_L E\,A\,[N_u']^T\,[N_u']\,dx \tag{32}$$

$$[k_p] = P\int_L \left([N_u']^T\,[N_u'] + [N_v']^T\,[N_v']\right)dx \tag{33}$$

$$[k_1] = \int_L \frac{E\,A}{2}\,[N_u']^T\left(\{d\}^T[N_u']^T\,[N_u'] + \{d\}^T[N_v']^T\,[N_v']\right)dx \tag{34}$$

$$[k_2] = \int_L E\,A\left([N_u']^T\,[N_u'] + [N_v']^T\,[N_v']\right)\{d\}[N_u']\;dx \tag{35}$$

$$[k_3] = \int_V \frac{E\,A}{2}\left([N_u']^T\,[N_u'] + [N_v']^T\,[N_v']\right)\{d\}\{d\}^T\left([N_u']^T\,[N_u'] + [N_v']^T\,[N_v']\right)dx \tag{36}$$

Rewriting Eq. (31) leads to the following desired incremental force-displacement relationship:

$$[k_I]\{d\} = \{f\} \tag{37}$$

where

$$[k_I] = [k_0] + [k_p] + [k_1] + [k_2] + [k_3] \tag{38}$$

and

$$\{f\} = \{^2f\} - \{^1f\} \tag{39}$$

The incremental-stiffness matrix $[k_I]$ consists of five matrices that connect the incremental-element displacement $\{d\}$ to the corresponding incremental element force $\{f\}$.

Each term of the incremental stiffness matrix $[k_I]$, as given in Eq. (38), is presented in matrix form in Appendix A.

The first matrix $[k_0]$ is the conventional linear stiffness matrix for uncoupled axial behavior and is constant. The second matrix $[k_p]$ is the initial stiffness matrix which depends on the axial force *P* presented at the beginning of each incremental load step.

Considering the other three terms of Eq. (38), it is noted that the elements of the matrices $[k_1]$ and $[k_2]$ are the linear function of the incremental element displacements. The last matrix $[k_3]$ is a quadratic function of the incremental element displacements. This matrix is symmetric.

SOLUTION OF NONLINEAR EQUILIBRIUM EQUATIONS

In order to obtain the non-linear incremental equilibrium equations, the global stiffness matrix must be assembled from the incremental element stiffness matrices after they are transformed to the global coordinate system by using the transformation matrix. The non-linear incremental equilibrium equation may then be written as

$$\{F\} = [K]\{D\} \tag{40}$$

where $[K]$ denotes the global nonlinear stiffness matrix, $\{D\}$ represents the vectors of the incremental nodal displacements, and $\{F\}$ represents the vectors of the incremental nodal forces. In general there are three primary procedures for the solution of nonlinear structural analysis. They are the pure (linear) incremental method, the nonlinear incremental method (incremental-iterative procedure), and the direct method. Among these, the linear incremental method is the easiest procedure to implement, but its results are not accurate for problems involving large displacements and rotations, because of the large errors which accumulate in each incremental step. Therefore, this method is not popular and will not be discussed further.

The most effective methods for the solution of the Eq. (40) are the incremental-iterative methods, since iterations are performed at each incremental step during the solution procedure, thus; the accumulation of errors is small. Depending on the efficiency and accuracy of the solution desired, there are five various types of nonlinear solution approaches. They are the Newton-Raphson method, displacement control method, generalized displacement control method, work control method, and arc-length method. Each of these methods has its own advantages or disadvantages and also distinctive variations. More extensive information on evaluating these methods can be found in Wong and Tin-Loi (1990), Yang and Kuo (1994), and Torkamani and Sonmez (2008).

In the direct method, the deformation corresponding to any load along the load deformation curve can be obtained by applying the total load in one step and iterating to convergence. The secant stiffness matrix is used in this method.

Since the incremental-iterative methods can solve the nonlinear problem in a step-by-step fashion, equilibrium of the nodal points is achieved at each increment or step through an iterative process. For most problems, the incremental-iterative methods would be preferred. In this work, one is interested in not only load-deflection curves of geometrically nonlinear problems, but also the buckling load and post-buckling behavior of a structural system. Therefore, the arc-length method, an incremental-iterative method, is recommended and used to solve the post-buckling problems and is adopted in this research. To calculate the variation of the nonlinearity of the structure, the arc-length method adds an extra constraint equation to control the step size for each incremental load. One version of the arc-length method, called the modified Riks approach, was proposed by Tsai and Palazotto (1990) to analyze the shell structures. Later, Xu and Mirmiran (1997) combined a co-rotational finite element and a modified version of the Riks-Wempner method to analyze prestressed arches. This study uses the modified Riks-Wempner method with variable stiffness matrix to solve nonlinear plane truss problems.

NUMERICAL EXAMPLES AND RESULTS

To test the efficiency, accuracy and validity of the theory and the software package that are developed in this study, 2 plane truss problems are examined and presented in this article. The results of these examples are compared to the theoretical solutions, if available, or the results of the other theories that are published in the literature. Problems that are presented in this section are considered to have large deflections and to behave elastically and be geometrically-nonlinear.

Example No. 1 - Shallow Truss

This example is a two member truss that was previously analyzed by Papadrakakis (1983). Because of its low aspect ratio, this is considered a shallow truss. The theoretical solution of this benchmark problem is derived and presented in Eq. (41).

$$P = \frac{2EA}{L}(h-u)\left[\left(1+\left(\frac{u}{L}\right)^2-\frac{2uh}{L^2}\right)^{-\frac{1}{2}}-1\right] \tag{41}$$

In Eq. (41), u is the vertical displacement of node B and h is the total height of the truss before application of any load. Fig. 3 shows the undeformed configuration of the truss with solid lines with the applied load P acting at node B.

The following data are used in this example: the modulus of elasticity E = 2.06 × 10^8 kN/m^2 (29,870 ksi), the length of each member L = 11 m (36 ft 1.08 in), members have a circular cross-section with an area A = 0.00169 m^2 (26.2 in^2), and the rise angle $\alpha = 3.326^\circ$. Member and local buckling effects are disregarded in this example.

The results of Example No.1 that are obtained in this study using modified Riks-Wempner method are compared to the theoretical solution given by Eq. (41). Fig. 3 shows the relations between the applied load P and the displacement of node B; the theoretical solution and numerical results have very good agreement. This

example demonstrates a typical snap-through phenomenon. The load-deflection curves (Fig. 3) indicate that at 338.04 kN (75,991.4 lb) applied load, a limit-point load is reached. This limit-point load is referred to as the system buckling load. When the applied load is zero and the vertical displacement of point *B* is 0.695 m (2 ft 3.36 in), the structure becomes flat. In an experimental case, the structure snaps through such a deflection and reaches the point of zero applied load and the vertical displacement of 1.4 m (4 ft 7.12 in). At this point the structure hangs down below the horizontal level without any applied load.

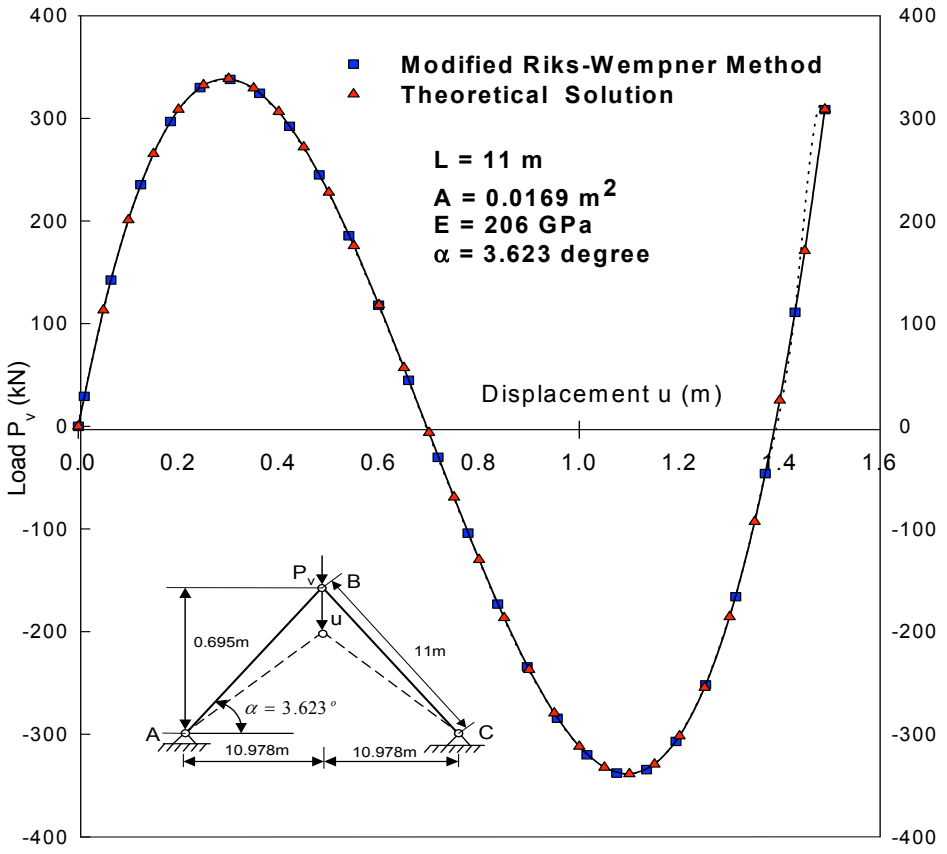


Fig. 3: Load-Displacement Relation for Shallow Truss

Example No. 2 - Strut Structure

Thompson and Hunt (1973) analyzed this structure for imperfection-sensitivity in the buckling of a reticulated or triangulated column. Later, Rosen and Schmit (1979) investigated the influence of local imperfections on the behavior of the global structure, and Kondoh and Atluri (1985) studied the relation between local buckling and global instability.

The configuration of this structure is shown in Figs. 4 and 5. This structure is composed of 35 members, all of which have a circular cross-section, and an identical modulus of elasticity of $E = 68.964 \times 10^6$ kN/m^2 (10,000.72 ksi). The influence of member and local buckling are not considered in the nonlinear analysis of this example. Table 1 lists the cross-sectional areas for all of the members. It is noted that this strut structure is not strictly symmetric with respect to the X axis (see Fig. 4), therefore, the effective neutral axis of the strut is slightly above the horizontal axis passing through nodes 1 and 19 (Kondoh and Atluri 1985).

Table 1: Cross-section of area for each member of Thompson's strut structure from Kondoh and Atluri (1985).

Member's Number	Cross-sectional area for each member cm^2
1-13, 17-21	54.84
14-16	54.84
22-35	51.61

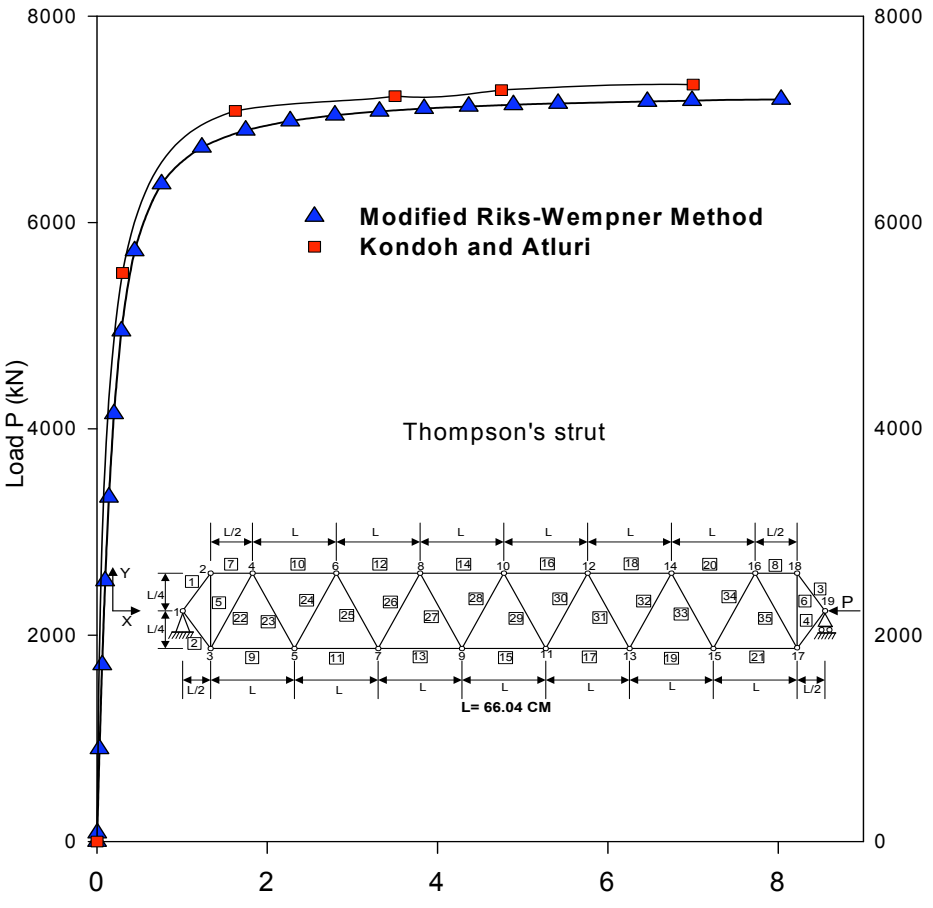


Fig. 4: Load-Displacement Relation for Thompson's Strut Truss, Node 10

The purpose of this example is to track the load-deflection curves for the displacement of node 10 in the vertical direction, and node 19 in the horizontal direction corresponding to the compressive load *P* applied at node 19. Figs. 4 and 5 show the load-deflection curves for node 10 and 19, respectively. It is observed that the structure exhibits global buckling behavior at a load of about 6,915.88 kN (1,556,143.46 lb). After this point, the stiffness of the structure is approaching zero, and the equilibrium path remains stable. The solutions obtained in the present work appear to be close in agreement compared to those of Kondoh and Atluri (1985).

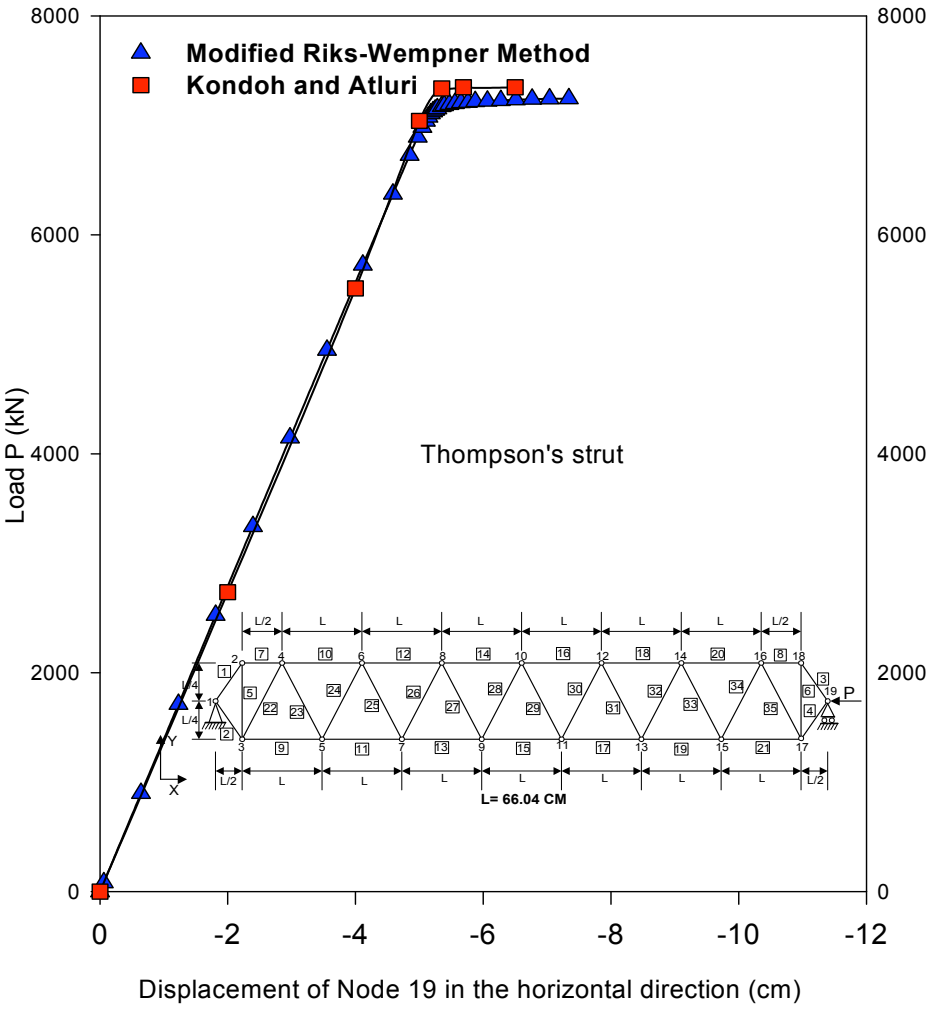


Fig. 5: Load-Displacement Relation for Thompson's Strut Truss, Node 19

SUMMARY AND CONCLUSIONS

The strain-displacement relation with the consideration of large or finite strain for plane trusses is considered in this work. Based on this relation, the incremental stiffness matrices for the higher-order analysis of elastic plane trusses were derived using the minimization of incremental total potential energy and variational principle. In addition, a nonlinear analysis procedure for predicting the load-displacement of plane truss structures subjected to geometric nonlinearity and elastic behavior has been developed and implemented in a computer package.

An algorithm for the modified Riks-Wempner method with variable stiffness matrix has been applied to finite element analysis to trace the full load-deflection path of two examples. Some modification was added in the modified Riks-Wempner method in order to let the load-deflection curve pass the limit points.

The presented numerical examples confirm that the results obtained by developed software are in agreement with the theoretical solution and examples published by other authors.

The first example is shallow two member truss subjected to a vertical concentrated load *P*. This problem is used as benchmark to examine the accuracy of the software. The results of the first example are identical to those given by the theoretical solution. The second example is the strut structure previously analyzed by Kondoh and Atluri (1985). As presented here, the result of this example also demonstrate a reasonable agreement compared to Kondoh and Atluri's work.

In conclusion, the reliability of the model and the software package that are developed during the course of this research are examined through two numerical examples showing reasonable accuracy. The methodology developed in this work provide the bases for further research and development; further research is focused on the problems of inelastic post-buckling analysis. In addition, more rigorous investigations on the stress-strain, force-deflection relationship for the truss systems must be done.

APPENDIX A - INCREMENTAL STIFFNESS MATRICES

The elastic stiffness matrix [k_0], the geometric stiffness matrix [k_p], and the stiffness matrices [k_1], [k_2], and [k_3] are given as:

Matrix: [k_0]

$$[k_0] = \frac{EA}{L}\begin{bmatrix} 1 & 0 & -1 & 0 \\ 0 & 0 & 0 & 0 \\ -1 & 0 & 1 & 0 \\ 0 & 0 & 0 & 0 \end{bmatrix} \tag{42}$$

Matrix: [k_p]

$$[k_p] = \frac{P}{L}\begin{bmatrix} 1 & 0 & -1 & 0 \\ 0 & 1 & 0 & -1 \\ -1 & 0 & 1 & 0 \\ 0 & -1 & 0 & 1 \end{bmatrix} \tag{43}$$

Matrix: [k_1]

$$[k_1] = \frac{EA}{2L^2}\begin{bmatrix} \Delta u & \Delta v & -\Delta u & -\Delta v \\ 0 & 0 & 0 & 0 \\ -\Delta u & -\Delta v & \Delta u & \Delta v \\ 0 & 0 & 0 & 0 \end{bmatrix} \tag{44}$$

where, $\Delta u = u_2 - u_1$ and $\Delta v = v_2 - v_1$.

Matrix: [k_2]

$$[k_2] = \frac{EA}{2L^2}\begin{bmatrix} 2\,\Delta u & 0 & -2\Delta u & 0 \\ 2\,\Delta v & 0 & -2\Delta v & 0 \\ -2\,\Delta u & 0 & 2\Delta u & 0 \\ -2\,\Delta v & 0 & 2\Delta v & 0 \end{bmatrix} \tag{45}$$

Matrix: [k_3]

$$[k_3] = \frac{EA}{2L^3}\begin{bmatrix} \Delta u^2 & \Delta u\Delta v & -\Delta u^2 & -\Delta u\,\Delta v \\ \Delta u\,\Delta v & \Delta v^2 & -\Delta u\,\Delta v & -\Delta v^2 \\ -\Delta u^2 & -\Delta u\,\Delta v & \Delta u^2 & \Delta u\Delta v \\ -\Delta u\,\Delta v & -\Delta v^2 & \Delta u\,\Delta v & \Delta v^2 \end{bmatrix} \tag{46}$$

REREERENCES

Bathe, K. J., (1996). "*Finite Element Procedure*," Prentice-Hall, New York.

Kondoh, K., and Atluri, S. N. (1985). "Influence of the Local Buckling on Global Stability: Simplified, Large Deformation, Post-Buckling Analysis of plane Trusses," *Computers and Structures*, 21(4), 613-627.

Papadrakakis, M. (1983). "Post-Buckling Analysis of Trusses," *Journal of Structural Engineering,* ASCE, 109(9), 2129-2147.

Rosen, A. and Schmit, L. A. (1979). "Design-Oriented Analysis of Imperfect Truss Structures Part 1: Accurate Analysis," *International Journal for Numerical Methods in Engineering*, 14, 1309-1321.

Thompson, J. M. T. and Hunt, G. W. (1973). "*A General Theory of Elastic Stability*," William Clowes and Sons Ltd, Great Britain, 277-283.

Torkamani, M. A. M., and Sonmez, M. (2001). "Inelastic Large Deflection Modeling of Beam-Columns," *Journal of Structural Engineering, ASCE*, 127(8), 876-887.

Torkamani, M. A. M., and Sonmez, M. (2008). "Solution Techniques for Nonlinear Equilibrium Equations," *18th Analysis and Computation Specialty Conference, Structures Congress, ASCE*, Vancouver, BC, Canada, April 24-26, CD-ROM.

Tsai, C. T., and Palazotto, A. N. (1990). "A Modified Riks Approach to Composite Shell Snapping Using a Higher-Order Shear Deformation Theory," *Computers and Structures*, 35(3), 221-226.

Wong, M. B. and Tin-Loi, F., (1990). "Geommetrically Nonlinear Analysis of Elastic Framed Structures", *Computers and Structures*, 34(4), 633-640.

Xu, Z., and Mirmiran, A. (1997). "Looping Behavior of Arches Using Co-rotational Finite Element," *Computers and Structures*, 62(6), 1059-1071.

Yang, Y. –B., and Kuo, S. –R. (1994). "*Theory and Analysis of Nonlinear Framed Structures*," Prentice Hall, Singapore.

Yang, Y. –B., Lin, S. P., and Wang, C. M. (2007). "Rigid Element Approach for Deriving the Geometric Stiffness of Curved Beams for Use in Buckling Analysis," *Journal of Structural Engineering, ASCE*, 133(12), 1762-1771.

Seismic Analysis of Bridge Columns under Axial, Flexure, Shear and Torsional Loadings

T Ravi S Mullapudi[1] and Ashraf Ayoub[2]

[1]PhD Candidate, Department of Civil and Environmental Engineering, N 107, Engineering Building 1, University of Houston, Houston, Texas, 77204; PH (713) 743 4250; FAX (713) 743 4260; email: tsmullapudi@uh.edu
[2]Associate Professor, Department of Civil and Environmental Engineering, N 107, Engineering Building 1, University of Houston, Houston, Texas, 77204; PH (713) 743 4285; FAX (713) 743 4260; email: asayoub@uh.edu

ABSTRACT

This study presents an inelastic non-linear three dimensional (3-D) beam element with axial, bending, shear force and torsion interaction for seismic analysis of Reinforced Concrete (RC) bridge columns. As a result of these load combinations the structural performances of RC bridge columns defer in strength, deformation capacity and failure modes. The shear mechanism along the beam is modeled by using Timoshenko beam approach with curved 3-D frame elements. The values of the concrete strength in principal directions 1, 2 and 3 are affected by the strain state in the other directions. The problem consists in solving a system of equations by combining the equilibrium conditions, compatibility conditions and constitutive laws of materials at section and structural level. The model is validated with the experimental tests subjected to real time earthquake motions.

INTRODUCTION

The behavior of the earthquake on the reinforced concrete (RC) structures is dependant on time, frequency of occurrence, and intensity. It is well known that RC structures are subjected to multi-directional loadings under earthquake ground motion. The multi-directional loading conditions are caused by multi-dimensional earthquake motions and structural configurations like spandrel beams, skewed bridges, curved bridges and bridges with outrigger beams (Figure 1). The analytical modeling of the behavior of structures under bending, shear and axial force interaction has received considerable attention in recent years because the shear failure in bridges is sudden and brittle and can potentially fail at lower ductility under the gravity loads. The establishment of nonlinear constitutive models for RC elements under combined loadings and the development of corresponding nonlinear finite element models are essential to predict the correct behavior of RC structures. The past three decades saw new constitutive models in an effort to improve the general performance of the structures and elements. In these models, the equilibrium equations assume the stresses in the concrete struts and steel bars to be smeared. Similarly, the strains of steel and concrete are also smeared, and are obtained by

averaging the strains along a steel bar that crosses several cracks. The constitutive laws of concrete and steel bars were developed through large-scale panel testing, and relate the smeared stresses to the smeared strains of the element (Hsu and Zhu 2002). In this current research Softened Membrane Model (SMM) was implemented (Mullapudi, 2010). In this model, the tension stiffening effect of concrete was taken into account with a shear stress contribution along the crack direction. This model was further extended by developing the Hsu/Zhu ratios (Poisson effect) (Zhu and Hsu 2002), which can help to predict accurately the entire response of the specimen, including both the pre and post-peak responses.

An RC element with combined loading including torsion is a more sensitive problem than shear because it is a three dimensional (3-D) problem, which is the combination of the two dimensional shear problem and an additional shear caused by torsion (Figure 2). The equilibrium and compatibility of the 3-D element with the warping of the tube wall causes additional bending in the concrete struts. Vecchio and Selby (1991) have developed a finite element program for 3-D analysis with an eight node regular hexahedral element. In their constitutive material model they have used the Modified Compression Field Theory. In this research a generalized 3-D frame element with the Softened Membrane Model is implemented. Every section of the frame element is subdivided into different regions to account for 1-D, 2-D and 3-D material responses.

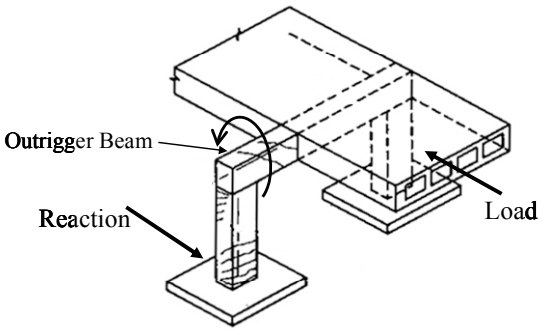


Figure 1. Torsion in outrigger beam

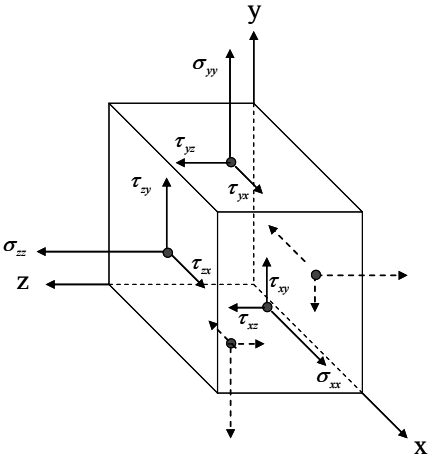


Figure 2. 3-D Stress distribution

FINITE ELEMENT FORMULATION

The finite element model is based on the recently developed force method of analysis (Spacone et al. 1996). The force-based formulation proved to overcome most of the difficulties associated with the standard displacement approach and generally has superior robustness and requires lower number of model degrees of freedom for comparable accuracy when dealing with RC members. This model was developed based on the Timoshenko type force formulation with the assumption that plane sections remain plane. The element comprises two node frame element which follows a directrix line between nodes 1 and 2 (Figure 3). Each element is divided into several

sections along the length of the element and also into several fibers across the cross section of the member. The response at each fiber is calculated from the response at the directrix with the help of plane sections which remain plane.

The general 3-D beam element with rigid body modes is shown in (Figure 4) and; without rigid body modes in shown in (Figure 5).

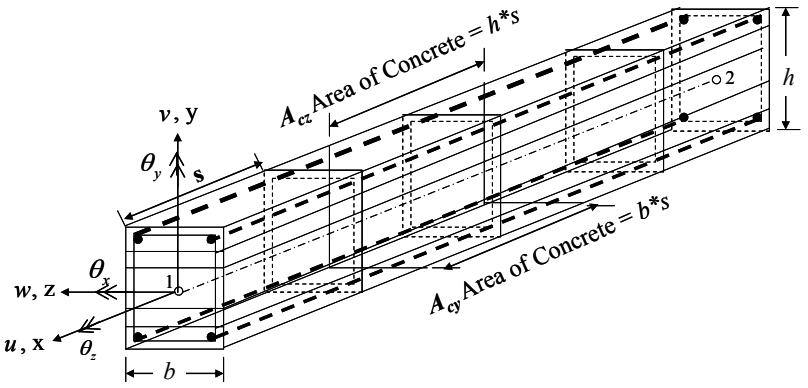


Figure 3. 3-D Fiber element formulation

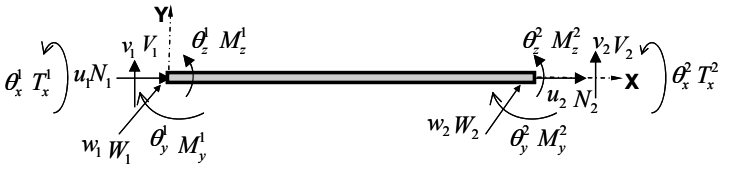


Figure 4. Displacements and forces with rigid body modes

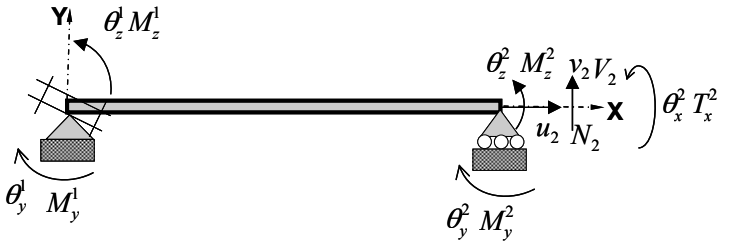


Figure 5. Displacements and forces without rigid body modes

The section behavior is evaluated through fiber discretization with appropriate material constitutive models. The constitutive behavior of the concrete fibers is described in subsequent sections. To account for dynamic effects, the Newmark method is adopted and is briefly described in the next section. The model was developed using the finite element program FEAPpv (Taylor 2005).

DYNAMIC BEHAVIOR FORMULATION

The nonlinear dynamic behavior is analyzed following the well known Newmark method (Newmark 1959). Accordingly, the following equilibrium equation

is solved for:

$$\hat{k}_j \Delta d_j = \Delta \hat{F}_j \tag{1}$$

where Δd_j is the displacement increment at time step j, and the dynamic stiffness $\hat{k}_j$ is evaluated as

$$\hat{k}_j = k_j + \frac{\gamma}{\beta \Delta t} c + \frac{1}{\beta (\Delta t)^2} m \tag{2}$$

whereas the k_j is the static stiffness, m is the mass matrix, c is the Rayleigh damping matrix, and Δt represents the time increment from steps j to $j+1$. In the current model the coefficients $\gamma = 0.5$ and $\beta = 0.25$ were selected for considering the average acceleration method, which is unconditionally stable.

The dynamic residual load increment $\Delta \hat{F}_j$ is evaluated as

$$\Delta \hat{F}_j = \Delta F_j + \left(\frac{1}{\beta \Delta t} m + \frac{\gamma}{\beta} c \right) \dot{d}_j + \left[\frac{1}{2\beta} m + \Delta t \left(\frac{\gamma}{2\beta} - 1 \right) c \right] \ddot{d}_j \tag{3}$$

where $\dot{d}_j$ and $\ddot{d}_j$ are the velocity and acceleration respectively at time step j.

The damping matrix is determined based on the Rayleigh-type formulation expressed as a linear combination of the mass matrix m and the stiffness matrix k as

$$c = \alpha_m m + \beta_k k \tag{4}$$

whereas the parameters α_m and β_k are calculated based on the natural frequencies of the first modes and their damping ratios. For a nonlinear system, the incremental procedure described in Equation. 1 needs to be accomplished using an iterative procedure.

Reyleigh damping with first five modes were considered in the analysis. Three damping ratios were used in the analysis based on the condition of the member. A damping ratio of 2% was used when the structure was in the elastic stage and only slight cracking was observed. A damping ratio of 4% was used when the considerable cracking was observed. A damping ratio of 8% was used when the reinforcement of the member yielded until the failure. A time step of 0.01 sec has been used in the earthquake analysis.

CONCRETE CONSTITUTIVE MODEL

Constitutive laws depend upon the type of region of the cross section in which the material model is used. A smeared stress-strain curve with smearing behavior is used for the response of the reinforcing bar. The cross section is divided into a number of sub divisions based on the appealing three stress state. They are 1-D, 2-D and 3-D regions (Figure 6). 1-D regions are subjected only to normal stresses, 2-D regions are subjected to normal and transverse stress in one direction, and 3-D regions are subjected to normal stress and transverse stress in two directions.

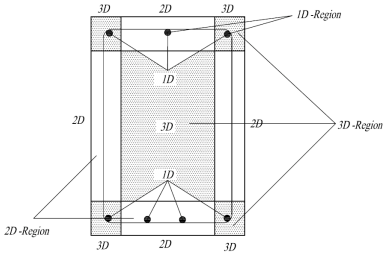


Figure 6. Sectional regions definition

3-D regions have six stresses $\{\sigma_{3D}\}$ and corresponding strains $\{\varepsilon_{3D}\}$; however the current beam formulation only considers three stress $\{\sigma\}$ and strain $\{\varepsilon\}$ components while the other three stress and strain components are derived by solving the equilibrium conditions.

$$\{\sigma_{3D}\}=\begin{bmatrix}\sigma_x & \sigma_y & \sigma_z & \tau_{xy} & \tau_{yz} & \tau_{xz}\end{bmatrix}^T \quad \{\varepsilon_{3D}\}=\begin{bmatrix}\varepsilon_x & \varepsilon_y & \varepsilon_z & \gamma_{xy} & \gamma_{yz} & \gamma_{xz}\end{bmatrix}^T \quad (5)$$

$$\{\sigma_{UN}\}=\begin{bmatrix}\sigma_y & \sigma_z & \tau_{yz}\end{bmatrix}^T \qquad \{\varepsilon_{UN}\}=\begin{bmatrix}\varepsilon_y & \varepsilon_z & \gamma_{yz}\end{bmatrix}^T \quad (6)$$

The unknown stress components σ_{UN} should be zero to satisfy the internal equilibrium between the reinforcing steel and concrete, which will result in the corresponding three unknown strain values ε_{UN}. Since the constraint condition is nonlinear, the determination of the corresponding strains requires an iterative solution procedure.

Concrete strains ε_{3D} were used to calculate the principal strains, or Eigen values, and principal strain directions, or Eigen vectors, with the Jacobi method.

To rotate the stress and strain vectors from global x-y-z co-ordinate system to 1-2-3 co-ordinate system with an angle of $[\alpha_1]$:

$$[R(\alpha_1)]=\begin{bmatrix} l_1^2 & m_1^2 & \mathrm{n}_1^2 & l_1m_1 & m_1n_1 & n_1l_1 \\ l_2^2 & m_2^2 & \mathrm{n}_2^2 & l_2m_2 & m_2n_2 & n_2l_2 \\ l_3^2 & m_3^2 & \mathrm{n}_3^2 & l_3m_3 & m_3n_3 & n_3l_3 \\ 2l_1l_2 & 2m_1m_2 & 2n_1n_2 & l_1m_2+l_2m_1 & m_1n_2+m_2n_1 & n_1l_2+n_2l_1 \\ 2l_2l_3 & 2m_2m_3 & 2n_2n_3 & l_2m_3+l_3m_2 & m_2n_3+m_3n_2 & n_2l_3+n_3l_2 \\ 2l_3l_1 & 2m_3m_1 & 2n_3n_1 & l_3m_1+l_1m_3 & m_3n_1+m_1n_3 & n_3l_1+n_1l_3 \end{bmatrix} \quad (7)$$

In a fiber-based element formulation, the process of the state determination at the fiber level requires the calculation of the fiber stresses $\begin{bmatrix}\sigma_x & \sigma_y & \sigma_z & \tau_{xy} & \tau_{yz} & \tau_{xz}\end{bmatrix}^T$ from the strain state $\begin{bmatrix}\varepsilon_x & \varepsilon_y & \varepsilon_z & \gamma_{xy} & \gamma_{yz} & \gamma_{xz}\end{bmatrix}^T$. Because the SMM has been implemented in a Timoshenko-type beam element, the values of ε_x, γ_{xy}, γ_{xz} are typically known, while the lateral strain ε_y, ε_z values must be evaluated from the equilibrium. Due to the nonlinear behavior of the concrete and

steel, an iterative procedure is needed to determine the lateral strain ε_y and ε_z.

STRESS STATE DETERMINATION

The constitutive equations depend on the strain state and the region of the cross section. The principal strains ε_1, ε_2 and ε_3 are found from the global strains using the Jacobi method and the equivalent uniaxial strains $\bar{\varepsilon}_1, \bar{\varepsilon}_2$ and $\bar{\varepsilon}_3$ are derived based on Hsu/Zhu ratios (Jeng and Hsu, 2009). Local concrete material stiffness is derived based on the material Young's Modulus and the Hsu/Zhu ratio. The global stiffness in Cartesian direction is calculated by transforming the local stiffness to global direction. The global stiffness in *y*, *z* and *yz* direction are condensed in the element formulation and, during this process the stresses in axial, flexure and shear direction are coupled together.

The values of the concrete uniaxial strains in principal directions 1, 2 and 3 have eight cases, namely 1-Tension, 3-Compression; 1-Tension, 3-Tension; 1-Compression, 3- Compression; 1- Compression, 3-Tension; 1-Tension, 2-Compression; 1-Tension, 2-Tension; 1-Compression, 2- Compression and 1-Compression, 2-Tension. The strength in one direction is affected by the strain state in the other direction. Because of the lateral tensile strain, principal compressive strength of the concrete reduces or softens.

For the first case, the equivalent uniaxial strain of concrete $\bar{\varepsilon}_1$ in principal direction 1 is in tension, and the equivalent uniaxial strain $\bar{\varepsilon}_3$ in principal direction 3 is in compression. The equation for compressive strength and strain reduction factor ζ is given by (Hsu and Zhu 2002):

$$\zeta = \left(\frac{5.8}{\sqrt{f_c^{'}(MPa)}} \le 0.9 \right) \left(\frac{1}{\sqrt{1+400\bar{\varepsilon}_1}} \right) \left(1 - \frac{|\beta|}{24^{\circ}} \right) \tag{8}$$

$$\beta = 0.5 \tan^{-1} \left(\frac{\gamma_{13}}{\varepsilon_1 - \varepsilon_3} \right) \tag{9}$$

The ultimate stress in the orthogonal directions is therefore $\zeta f_c^{'}$ at a softened strain $\zeta\varepsilon_0$, where ζ is the softening coefficient, β is the deviation angle in degrees which is the difference between the applied stress angle α_1 and the rotating angle α_r, $\bar{\varepsilon}_1$ is the lateral tensile strain and γ_{13} is the shear strain in 1-3 direction. Similar relations were applied in remaining seven cases.

NUMERICAL CORRELATIONS WITH EXPERIMENTAL RESULTS

SIMULATION OF PRAKASH et al. (2010) COLUMN H/D(6)-T/M(0.2)

The 3-D model was used to simulate the behavior of a reinforced concrete bridge column (Column H/D(6)-T/M(0.2)) tested by Prakash et al. (2010) at the

Missouri S&T. Column was analyzed with an applied torsion to moment (T/M) ratio of 0.2. The aspect ratio height to diameter (H/D) of the column is 6 and the spiral reinforcement ratio of 0.73% and longitudinal reinforcement ratio of 2.1% with a concrete compressive strength of 41.2 MPa (6.0 ksi) was used in the analysis. Yield strength of longitudinal steel of value 490 MPa (71.0 ksi) and yield strength of transverse reinforcement of value 525 MPa (76.1 ksi) were used.

Flexural cracks first appeared near the bottom of the column and their angle became more inclined at increasing heights above the top of the footing. The appearance of the cracks increased with an increase in applied loading. The longitudinal bars yielded at about 38 inches from the base of the column. The model failed by yielding of the longitudinal and transverse reinforcement followed by core degradation. The load-displacement curve matched well with the experiment (Figure 7).

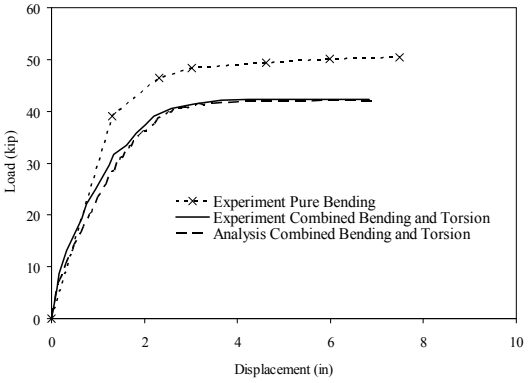


Figure 7. Monotonic load-displacement curve

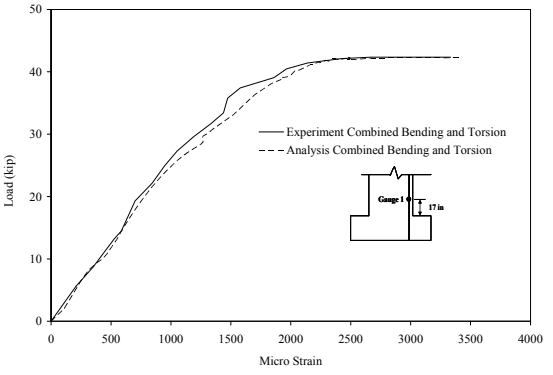


Figure 8. Longitudinal steel strain distribution

Figure 7 shows the comparison of the column performance with pure bending ((T/M =0) and combined loading (T/M =0.2). Because of the induced torsion the bending strength and stiffness have been reduced considerably.

Figure 8 shows the longitudinal steel strain distribution at 17 inches above the foundation. The longitudinal strain increased with the increase of the lateral load on the column. The experimental strain gauge readings matched well with the analytical results and the current model captured the yielding rather well.

SIMULATION OF LAPLACE et al. (2001) COLUMN 9F1 UNDER SHAKE TABLE TESTING

The model was used to simulate the behavior of the circular RC bridge column 9F1 subjected to the real time 1940 Imperial Valley (El Centro) earthquake excitation tested by Laplace et al. (2001) at the University of Nevada, Reno. An axial load of 356 kN (80 kip) was applied constantly to the column. The column is loaded in single curvature. The actual test specimen has a 406.44 mm (16 in) diameter and is 1.83 m (72 in) long from the top of the footing to the centerline of the applied load. The reinforcement consisted of twenty No. 4 longitudinal bars, and 6.5 mm (0.25 in) spiral transverse reinforcement spaced at 38.1 mm (1.5 in). A concrete compressive strength of $f_c^{'}$=37.4 MPa (5.4 ksi) and tensile strength of f_t=2.0 MPa (0.3ksi) are used to analyze the reinforced concrete column. A yield stress of longitudinal and transverse reinforcement of f_y=458.2 MPa (65.0 ksi) and f_y=397.4 MPa (57.6 ksi) respectively are used in the analysis. The Young's modulus of concrete and steel are E_c = 37500 MPa (5440 ksi) and E_s = 200,000 MPa (29000 ksi) respectively.

9F1 Column was analyzed with the 2.5xEl Centro earthquake motions and the comparisons of the experimental results with the flexural element and the currently developed shear element are presented in Figure 9 - Figure 14. At 2.5xEl Centro earthquake motion the flexural element is unable to predict accurately the displacement amplitude and the resisting load capacity (Figure 9 and Figure 11) but the shear element is able to predict well (Figure 10 and Figure 12). At this El Centro motion longitudinal bar has yielded more than 2 times the 1.0xEl Centro earthquake motion at gauge 1 location and is fairly accurate compared to experimental values (Figure 13). Transverse steel bar at gauge 2 location as shown in Figure 14 is not yielded and agreed well with the experimental results.

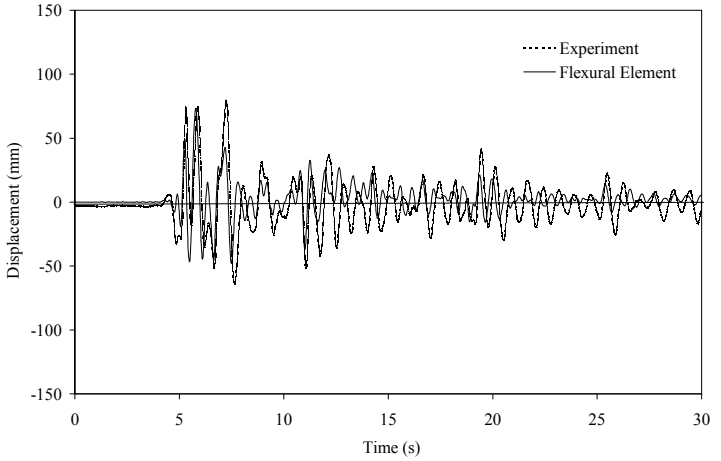


Figure 9. Time history with the flexural model

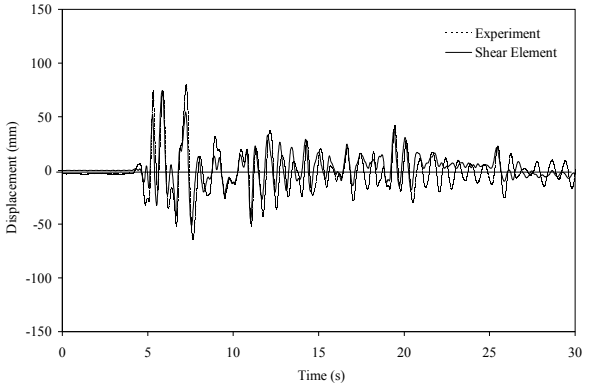


Figure 10. Time history with the shear model

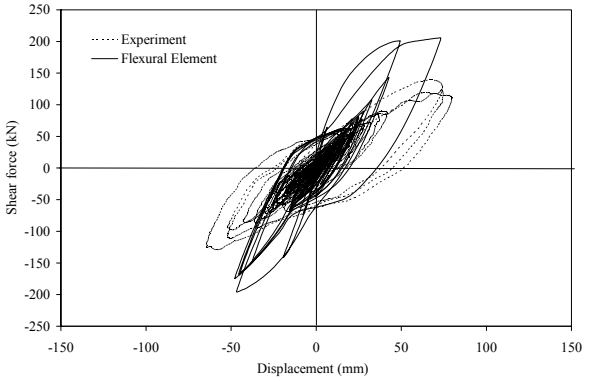


Figure 11. Shear force versus tip displacement with the flexural model

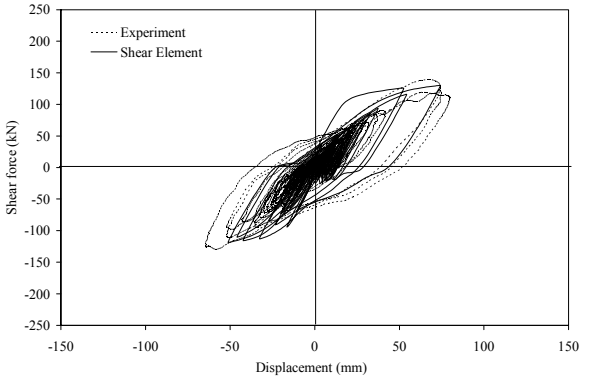


Figure 12. Shear force versus tip displacement with the shear model

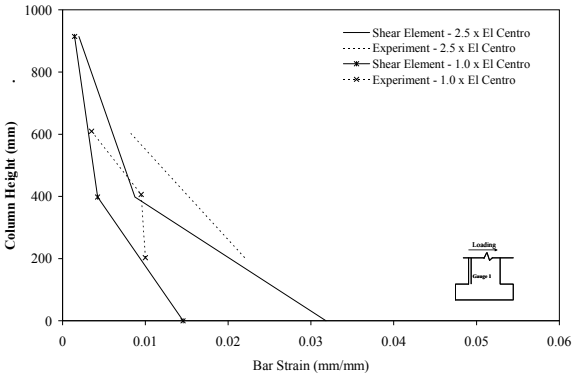


Figure 13. Longitudinal steel bar strain profile at gauge 1 location

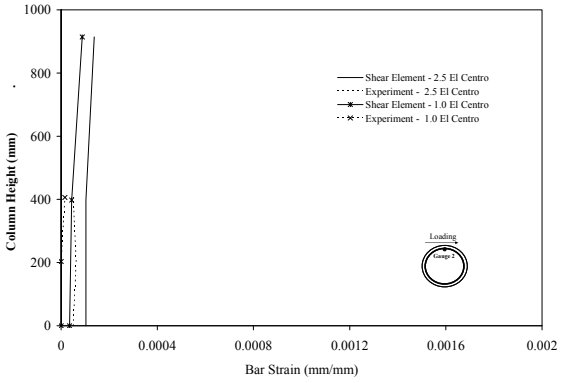


Figure 14. transverse steel bar strain profile at gauge 2 location

SIMULATION OF ARIAS-ACOSTA AND SANDERS (2010) COLUMN C1 UNDER SHAKE TABLE TESTING

Arias-Acosta and Sanders (2010) have conducted bidirectional shake table testing's of bridge columns under combined effect of axial, shear, bending and torsion at University of Nevada, Reno (UNR). The 3-D model was used to simulate the behavior of the circular RC bridge columns C1 subjected to the real time bidirectional 1992 Petrolia at Mendocino earthquake excitations.

The column is tested under cantilever type loading. The actual test specimen has a 406.44 mm (16 in) diameter and is 1.83 m (72 in) long from the top of the footing to the centerline of the applied load. The reinforcement consisted of twenty No. 4 deformed longitudinal bars, and 6.5 mm (0.25 in) spiral transverse reinforcement spaced at 38.1 mm (1.5 in). A concrete compressive strength of $f_c^{'}$=30.0 MPa (4.5 ksi) and tensile strength of f_t=1.7 MPa (0.2ksi) are used to analyze the reinforced concrete column. A Yield stress of longitudinal and transverse reinforcement of f_y=447.0 MPa (64.0 ksi) and f_y=420.0 MPa (60.0 ksi) respectively

are used in the analysis. The Young's modulus of concrete and steel are E_c = 30000 MPa (4350 ksi) and E_s = 200,000 MPa (29000 ksi) respectively.

A unique inertial loading system named Bidirectional Mass Rig (BMR) was developed for shake table testing of single column under biaxial motions (Figure 15). The purpose of this setup is to distribute the mass on BMR (Figure 16) such that the mass center and stiffness center of the loading frame differs from each other and induces torsion on column under bidirectional earthquake excitation.

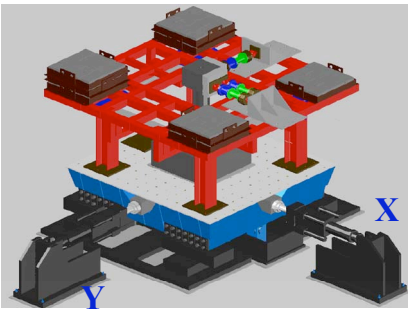


Figure 15. Bidirectional Mass Rig (BMR)

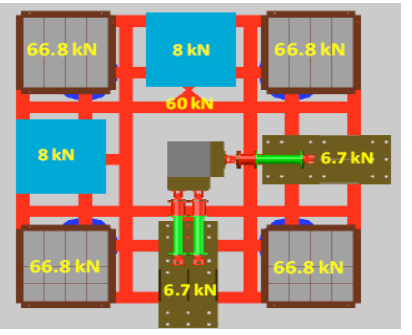


Figure 16. Mass distribution on BMR

The C1 Column was analyzed with the 0.6 x Petrolia earthquake motions in X and Y directions (Figure 15). The ground motion is considered as near fault ground record with asymmetric peak velocity pulses along X and Y directions. The comparison of the experimental results with the currently developed shear element is presented in Figure 17 and Figure 18. At 0.6 x Petrolia motion, shear element is fairly accurate to predict the load - displacement behavior in X –direction (Figure 17) and in Y – Direction (Figure 18). The behavior of the specimen was controlled by biaxial effect of bending including the induced torsion. The longitudinal bar yielding was observer after 0.6 x Petrolia motion and agreed well with the experimental results.

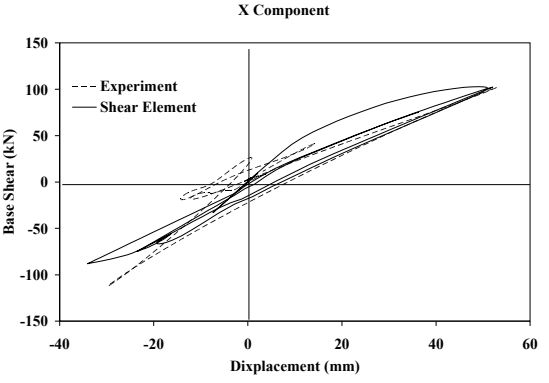


Figure 17. Force-disp. in X – Direction

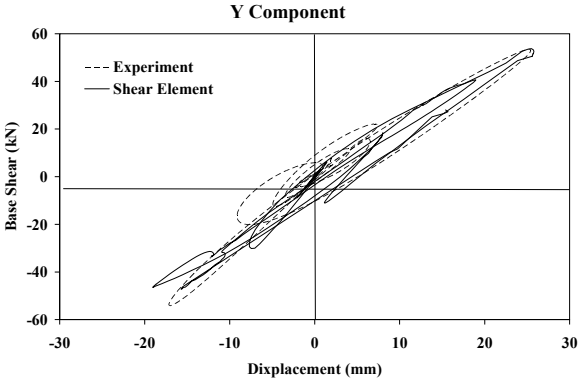


Figure 18. Force-disp. in Y – Direction

CONCLUSIONS

This work represents a new approach for the dynamic analysis of structures made up of non-linear materials under combined loadings including torsion. A Fiber based 3-D beam element was developed to analyze reinforced concrete structures with the incorporation of mechanisms of shear deformation and strength. The section deformations are determined from the strain state using the classical plane section hypothesis. The proposed model is able to capture the interaction between axial, flexural, shear and torsional responses. The results of a numerical correlation with the experimental data of bridge piers show that the model is able to capture the failure mechanism and provides accurate results.

ACKNOWLEDGEMENTS

This study was supported by grant number 0530737 from the Network for Earthquake Engineering Simulation (NEES), which support is gratefully acknowledged.

REFERENCES

Arias-Acosta, J., Sanders, D.H., 2010, "Shake Table Testing of Bridge Columns Under Combined Actions*",* ASCE & AISC Analysis and Computation Conference / Structures Congress/North American Steel Construction Conference (NASCC), Orlando, FL, May 12- 14.

Hsu, T.T.C., and Zhu, R. H., 2002, "Softened Membrane Model for Reinforced Concrete Elements in Shear" Structural Journal, American Concrete Institute, Vol 99, No 4, pp.460-469.

Jeng, C.H and Hsu, T.T.C., 2009, "A softened membrane model for torsion in reinforced concrete members", Engineering Structures, Vol. 31, No. 9, pp. 1944-54

Laplace, P., Sanders, D., and Saiidi, M.S., 2001, "Experimental Study and Analysis of Retrofitted Flexure and Shear Dominated Circular Reinforced Concrete

Bridge Columns Subjected to Shake Table Excitation" Report No. CCEER 01-6, Department of Civil Engineering, University of Nevada, Reno, Nevada.

Mullapudi, T.R.S., 2010, "Seismic Analysis Of Reinforced Concrete Structures Subjected To Combined Axial, Flexure, Shear And Torsional Loads", PhD. thesis, Department of Civil and Environmental Engineering, University of Houston, Houston, 328 pp.

Newmark, N. M., 1959, "A Method of Computation for Structural Dynamics," Journal of the Engineering Mechanics Division, ASCE, pp. 676-94.

Prakash, S., Belarbi, A., and You, Y., 2010 "Seismic performance of circular RC columns subjected to axial force, bending, and torsion with low and moderate shear", Engineering Structures, Vol. 32, pp. 46-59.

Spacone, E.; Filippou, F. C.; and Taucer, F. F., 1996, "Fiber Beam-Column Model for Nonlinear Analysis of R/C Frames, Part I: Formulation," Earthquake Engineering and Structural Dynamics, V. 25, pp. 711-725.

Taylor, R. L., 2005, "FEAP User Manual v2.0." Department of Civil and Environmental Engineering, University of California, Berkeley, 2005, http://www.ce.berkeley.edu/~rlt/feap/.

Vecchio, F.J.; Selby, R. G., 1991, "Toward Compression-Field Analysis of Reinforced Concrete Solids," Journal of the Structural Engineering, ASCE, V. 117, No. 6, June. , pp. 1740-1758.

Zhu, R. H., and Hsu, T.T.C., 2002,"Poisson Effect of Reinforced Concrete Membrane Elements" Structural Journal, American Concrete Institute, Vol 99, No 5, pp.631-640.

Effect of Abutment Shear Keys on the Seismic Response of Bridges

M.W. Salveson[1] and B.V. Fell[2]

[1]Department of Civil Engineering, California State University, Sacramento, 6000 J Street, Sacramento, CA 95819-6029, USA; PH (916) 278-6812; FAX (916) 278-7957; email: salveson@ecs.csus.edu
[2]Department of Civil Engineering, California State University, Sacramento, 6000 J Street, Sacramento, CA 95819-6029, USA; PH (916) 278-8139; FAX (916) 278-7957; email: fellb@ecs.csus.edu

Abstract

Seismic analysis results of typical post-tensioned concrete bridges are presented considering the nonlinear behavior of transverse abutment shear. Current Caltrans and AASHTO bridge design criteria present overly general assumptions for the boundary conditions provided by abutment shear keys. This work uses a suite of ground acceleration time histories to compare the code specified assumptions to a more rigorous abutment shear key model that includes the lateral gap between the superstructure and the keys as well as the non-linear material response of the key itself. With the exception of the abutment shear key elements, the bridges are modeled using linear-elastic frame elements, as is typical in practice. Results of a sensitivity analysis are presented for typical parameters, including: record variability, bridge skew, bridge length, and bent heights. The analysis results precede a discussion which demonstrates the necessity for experimental work on this topic to verify the adequacy of the existing design code.

Introduction

Bridges are critical structures in the network of highways and roadways connecting cities, towns, businesses and communities. Extensive earthquake damage to bridges creates a lasting effect on local and state economies as well as public confidence in the general infrastructure of the transportation system. The resulting economic losses and disruption of earthquakes are neither acceptable to the public nor cost-effective from a repair perspective. Understanding the effects of earthquakes on bridges has been a focus of the research and design communities, resulting in novel analysis techniques and improved design provisions. A somewhat recent thrust has been to accurately model bridge end conditions, including the effects of the abutment and soil behavior (Romstad et al, 1995, Goel and Chopra, 1997, Shamsabadi et al, 2005, Huang et al, 2008) on the longitudinal stiffness and strength of the structure.

Conversely, modern Californian seismic design codes include the lateral stiffness, strength and damping effects of bridge end abutments in the analysis of the overall structure, albeit in a more simplified manner by assigning a stiffness to the abutment shear keys in proportion to the lateral stiffness of the bridge bents. While the current design methodology may be appropriate for ordinary configurations, little research has verified these lateral stiffness values. Moreover, the shear keys are viewed more as a brittle fuse during the seismic response of the structure, rather than a ductile, energy dissipating element. Thus, not only is there a need to investigate the lateral elastic stiffness of shear keys, which will influence the distribution of seismic forces, but there is also an opportunity to develop an energy dissipating element from the shear key response. The latter requires examining the nonlinear response of these elements designed with modern practices while also developing innovative reinforcement details to improve the ductility of the shear keys.

The paper begins by introducing the motivation for the current study, including common geometries and loading on bridge abutment components. Next, it presents the analytical modeling approach and associated ground motions along with results from a parametric study of several bridge geometries. Finally, the results are discussed in the context of current code-based modeling assumptions and the need for future experimental and analytical work.

Background and Motivation

Abutment shear keys, shown schematically in Figure 1, are typically designed as brittle elements if the abutment is supported on piles, with the assumption that they will lose strength capacity during a large seismic event. In the case of spread footing conditions, the keys are still considered brittle elements, albeit with a larger strength capacity so as to ensure they remain intact. Current editions of the Caltrans Seismic Design Criteria (SDC) provide a complete set of seismic design guidelines for post-tensioned reinforced concrete bridges.

Regardless of foundation type, however, the lateral stiffness of the component is taken as 50% of the total stiffness of the adjacent bent or pier group. Thus, the transverse abutment stiffness is currently modeled in an ad-hoc manner by using the stiffness of adjacent bents rather than the physical size, reinforcing details and other parameters associated with the abutment keys. Considering this, there is a need to investigate the appropriateness of using pier and bent stiffnesses to inform geometrically-unlike abutment key rigidities. Furthermore, regardless of the accuracy of current Caltrans Criteria, within a performance based engineering perspective, it would be valuable to develop a rational procedure for the design and analysis of the transverse behavior of the superstructure at the abutment.

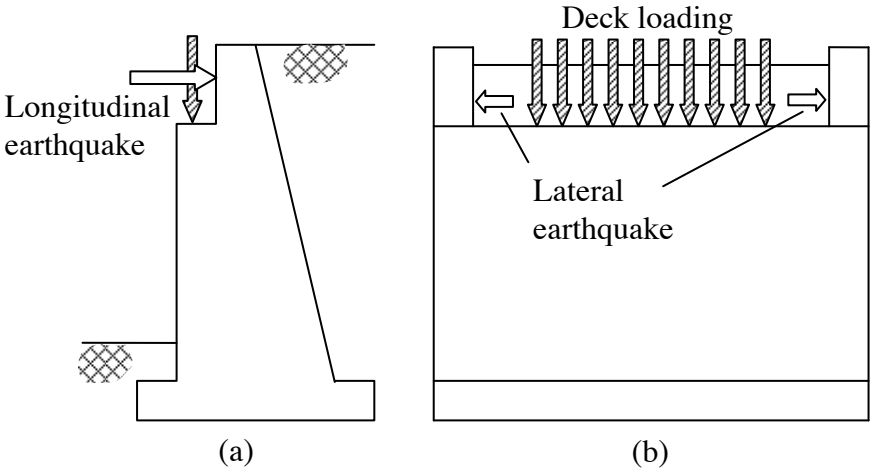


Figure 1: Typical (a) Longitudinal and (b) Lateral abutment and shear key details and loading

The current procedure to calculate lateral earthquake design loads for California bridges is dependent on a site-specific, elastic spectral acceleration demand (i.e., site-specific hazard curves found in Appendix B of the SDC). In considering the elastic stiffness of a typical bridge system, a large degree of uncertainty is associated with the abutment shear keys in the case of moderate to severe earthquake events. While the stiffness of the bridge bent and abutment stiffness in the longitudinal (or normal) direction are considered less variable due to a large amount of research conducted on each respective subassembly, the lateral behavior of abutments have not been rigorously investigated. Thus, the current seismic design criterion assumes that the lateral abutment stiffness is 50% as stiff as the nearest bents (section 7.8.2 in the SDC). This assumption is driven by the fact that end conditions (typically a shear key) will soften considerably at the Maximum Credible Earthquake (MCE) level, while, on the other hand, provide significant elastic rigidity during low and moderate level seismic events. In this light, an advancement of bridge design methodologies would be to incorporate a lateral stiffness model into the seismic design criterion for abutments, similar in form to the longitudinal model proposed by Romstad et al, (1995).

Archetype Bridge Geometry

Post-tensioned box girder concrete bridge geometry can be adapted to meet a wide variety of physical constraints. Thus, it is difficult to capture the behavior of all concrete bridges with the parametric study presented in this paper. Rather, the current investigation is meant to query key geometrical features that, when coupled with the boundary conditions at the abutments, may influence the overall response of the structure. This may inform future analytical studies with a wider range of geometric, material and loading scenarios.

An archetype bridge geometry (Geometry A) was designed for a high seismic risk site in Riverside, CA. For simplicity, the structure is considered to be on a tangent in both the horizontal and vertical directions. It is a relatively short, three span structure, such that modifications to the abutment boundary conditions will have a noticeable effect on the overall structure response. Key properties of the archetype structure are listed in Table 1. An elevation view of the bridge is shown in Figure 2, while the cross-sections of the columns and bridge superstructure are shown in Figure 3.

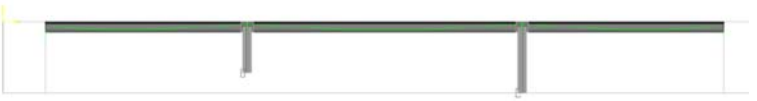
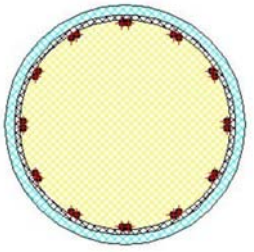
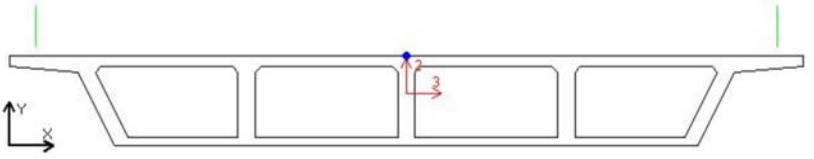


Figure 2 – Elevation View of Bridge Geometry "A"

Three dissimilar bridge configurations were analyzed, each representing a change to a key geometric feature likely to influence the structural response. Geometry B modifies Geometry A with a large (45 degree) skew at the bents and abutments. Geometry C modifies Geometry A by substantially decreasing the length of the end spans of the bridge. Geometry D modifies Geometry A by doubling the length of the bridge columns.



(a)



(b)

Figure 3 – Column (a) and Superstructure (b) Cross Sections

Table 1 – Baseline Bridge Properties

SUPERSTRUCTURE	
Bridge Length:	320 feet
Number of Spans:	3
Span 1 Length:	95 feet
Span 2 Length:	130 feet
Span 3 Length:	95 feet
Concrete Strength:	$f_c' = 4000$ psi
Superstructure Depth:	5.245 feet
SUBSTRUCTURE	
Columns per Bent:	2
Column Diameter:	4 feet
Bent 2 Height:	20 feet
Bent 3 Height:	30 feet
Concrete Strength:	$f_c' = 5000$ psi

Modeling Approach and Development

Dynamic Model

The bridge was modeled using a refined mesh of one dimensional elements, including linear elastic frame elements (for the bridge superstructure and columns), linear elastic truss elements (for the abutment springs), and special non-linear shear key elements (discussed later in this section). See Figure 4. The model was constructed in compliance with all applicable SDC recommendations and requirements.

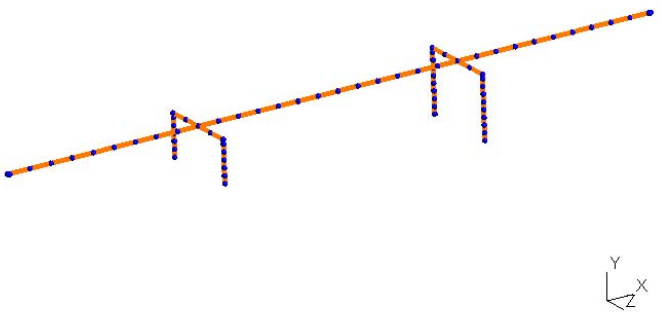


Figure 4 – Bridge Mesh

The equation of motion for a linear elastic system subjected to a ground acceleration is described by the differential equation $\mathbf{ma} + \mathbf{cv} + \mathbf{ku} = -\mathbf{ma}_g$, where $\mathbf{m}$ is the mass matrix (lumped, for this work), $\mathbf{c}$ is the viscous damping matrix, $\mathbf{k}$ is the stiffness matrix, $\mathbf{a}$ is the vector of nodal accelerations, $\mathbf{v}$ is the vector of relative nodal

velocities, $\mathbf{u}$ is the vector of relative nodal displacements, and $\mathbf{a}_g$ is a vector associated with the ground accelerations. In design practice, the analysis is commonly performed with modal design response spectrum, as opposed to a suite of ground acceleration time histories.

To utilize a non-linear shear key, the differential equation must first be recast in the more general form: $\mathbf{ma} + \mathbf{cv} + \mathbf{f}_s(\mathbf{u}) = -\mathbf{ma}_g$. Here, the stiffness term $\mathbf{ku}$ has been replaced with the nonlinear displacement response $\mathbf{f}_s(\mathbf{u})$. It is also necessary to abandon the direct use of a response spectrum, as the use of a response spectrum explicitly assumes a linear elastic system. Instead, a suite of ground acceleration time histories such that the non-linear differential equation is solved at each time step. For this work, the unconditionally stable constant average acceleration time integration technique was used.

Finally, it should be noted that developing the viscous damping matrix $\mathbf{c}$ is somewhat challenging. For a linear modal analysis, an appropriate damping ratio can be specified for each mode (typically 5% of critical damping). For the non-linear time history used here, the damping matrix must be constructed directly. For simplicity, a mass-proportional matrix was used that corresponds to a 5% damping ratio for the first mode of vibration.

Time History

The time histories used for the analyses have been selected from a suite of ground motions produced for the PEER Transportation Research Program (TRP) for broad-band ground motions. For the TRP study, the broad-band ground motions were selected for relatively generic structures, and sites with M = 7, R = 10 km, and a soil site (Jayaram, N. and Baker J.W., 2010). Considering that this is a preliminary study, 7 pairs of ground motions were selected from the 40 pairs created for the larger TRP program. It is expected, however, that future analyses will use the entire package of ground motions. The ground motions were scaled to an appropriate Caltrans Acceleration Response Spectrum at the first mode period of 1.3 seconds. See Figure 5.

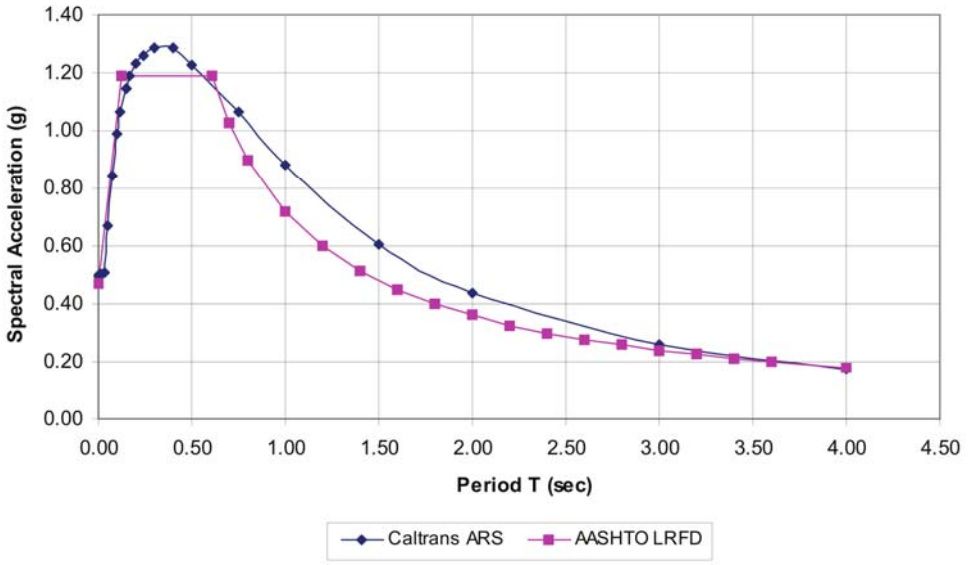


Figure 5 – Caltrans Acceleration Response Spectrum

Constitutive Model

Standard constitutive models, consistent with the latest version of the Caltrans SDC, were used for most of the bridge model. Gross section properties were used to represent the post-tensioned superstructure and cracked section properties were used to model the substructure. Moduli of elasticity for members were calculated using the concrete compressive strength according to the relation $E_c = 57{,}000\sqrt{f_c'}$.

Longitudinal springs were placed at the abutments, consistent with the requirements of the SDC, Section 7.8.1, "Longitudinal Abutment Response." For the linear elastic model, transverse springs were placed at the abutments, consistent with the requirement of SDC, Section 7.8.2, "Transverse Abutment Response." The effects of compliant soils at foundations were not considered for this analysis. Therefore, foundation supports were assumed to be rigid.

For the non-linear model, a rate-independent force-deformation model is assumed for each of the two shear keys at each abutment. The model includes a gap between the bridge superstructure and the shear keys, a short, stiff, linear portion as the key itself deforms elastically, and a perfectly plastic portion to represent the post failure behavior of the key. See Figure 6.

The model requires three parameters: an initial gap size (typically one inch), an ultimate shear key force, and the stiffness of the shear key. The shear key force and shear key stiffness remain unchanged throughout the analysis. The gap size is allowed to increase, however, as the shear key fuses and deforms plastically. A portion of a single load cycle resulting in an increased gap is shown in Figure 6.

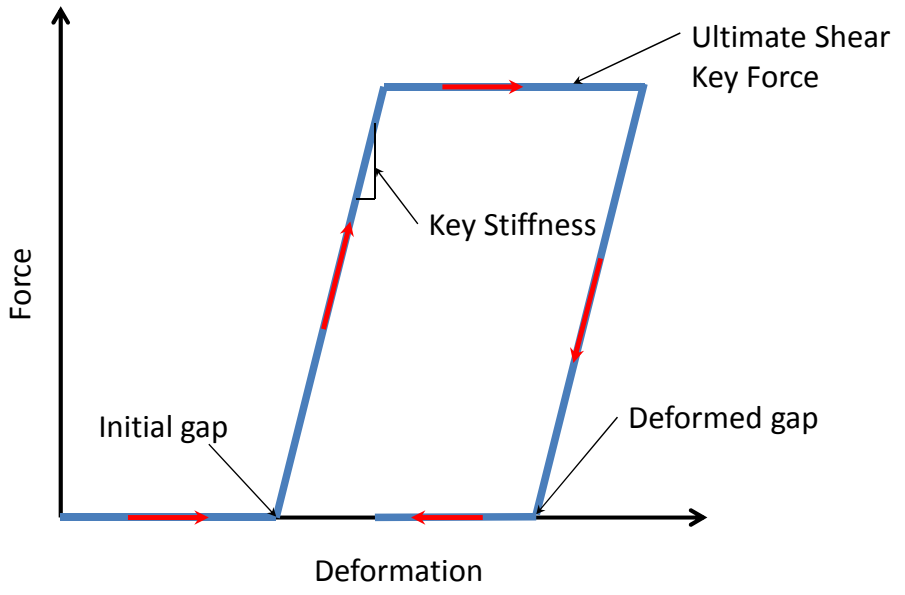


Figure 6 – Nonlinear Shear Key Constitutive Model

The ultimate shear key force is determined from the theoretical capacity of the key itself, typically using the shear friction method ($F_{key} = \mu A_s f_y$), where A_s is the cross sectional area of the reinforcing steel crossing the shear key failure plane and $f_y$is the yield strength of that steel (typically 60 ksi). The value of μ depends on the construction details (e.g. monolithic construction versus the use of construction joints). For the bridge analyzed in this study, it is assumed that $\mu = 1.0$ and $F_{key} = 237$ kips.

The key stiffness will be quite high relative to the rest of the model. For this analysis, a plane stress finite element model was used, resulting in a key stiffness of approximately 108,000 kips per inch. See Figure 7.

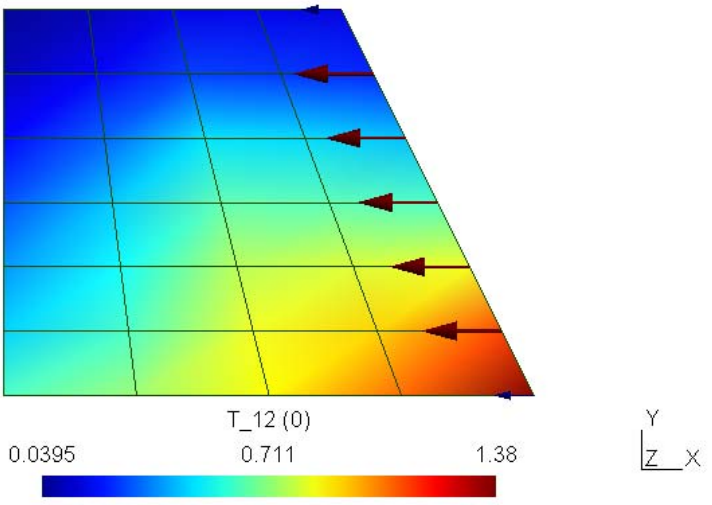


Figure 7 – Shear Key Finite Element Element Model

Analytical Results

For each of the four bridge configuration, two cases were considered for the time history analyses: 1) a standard linear elastic representation of the transverse shear keys, and 2) the nonlinear shear key model discussed in the previous section. For each time history analysis, the maximum lateral displacement of the columns was recorded. Results for each time history are shown in Table 2. A summary of all results are shown in Table 3

	Geometry A		Geometry B		Geometry C		Geometry D	
Time History	*Linear*	*Nonlinear*	*Linear*	*Nonlinear*	*Linear*	*Nonlinear*	*Linear*	*Nonlinear*
FN1	4.634	5.687	4.475	5.144	5.539	6.197	3.296	4.277
FN13	7.069	4.171	8.253	6.466	6.055	4.373	8.807	5.030
FN34	7.142	6.243	7.912	6.678	7.576	5.757	9.719	7.399
FP1	4.753	4.504	4.477	4.610	4.513	5.237	3.516	4.610
FP13	6.494	3.928	6.702	4.455	4.327	2.902	10.842	4.166
FP28	5.604	5.554	5.385	5.339	5.559	5.416	4.341	7.406
FP34	5.194	5.222	4.873	4.929	5.205	5.345	4.159	6.212

Table 2 – Max Column Displacements (inches)

The results associated with the linear analyses are surprisingly similar to the results associated with the nonlinear analyses. In fact, the linear analyses yield results that are more conservative than their nonlinear counterparts (as explicitly assumed in the SDC) and produce a wider range of displacements across the suite of ground motions.

This by no means implies that the standard linear elastic methodology accurately represents the nonlinear abutment response. Rather, it suggests that the existing methodology may not spoil the overall structural response for normal ordinary bridges. The large observed displacement standard deviation associated with the linear model for a bridge with unusually long columns suggests the need for additional investigations into bridges with highly flexible substructures.

	Geometry A		Geometry B		Geometry C		Geometry D	
	Mean	*Std Dev*	*Mean*	*Std Dev*	*Mean*	*Std Dev*	*Mean*	*Std Dev*
Linear	5.842	0.981	6.011	1.489	5.539	1.004	6.383	3.018
Nonlinear	5.044	0.797	5.374	0.808	5.032	1.010	5.586	1.308
Ratio	1.2	1.2	1.1	1.8	1.1	1.0	1.1	2.3

Table 3 – Summary of Results (inches)

Summary and Future Work

While several investigations have examined the longitudinal stiffness of bridge abutments (Romstad et al, 1995, Goel and Chopra, 1997, Shamsabadi et al, 2005, Huang et al, 2008) there has not been a rigorous experimental study on the lateral abutment stiffness. Goel and Chopra (1997) reported field data from the instrumented US 101/Painter Street Overpass and partly investigated this stiffness; however, only two ground motions are discussed while only one produced significant inelastic response.

Therefore, combined with the results from this study, a more rigorous and complete analytical and experimental study may be warranted. The fundamental objective will be to develop and validate new seismic design procedures for bridge structures including accurate models of bridge abutment keys. As the earthquake engineering community moves more towards performance based design criteria, sophisticated models will become a valuable tool in accurately assessing the behavior of bridges under extreme loading events. Medium and large-scale experimental investigations should be included, supported by several analytical research thrusts including non-linear dynamic analyses using a larger set of ground motions than presented here and elastic modeling approaches to inform modifications to design procedures.

Acknowledgements

The authors would like to thank Mr. Steven Johnson, P.E. for his assistance with the development of appropriate properties for the bridge model. Mr. Johnson is an accomplished bridge engineer with Dokken Engineering in Folsom, California.

References

Goel, R.K. and Chopra, A.K. (1997). "Evaluation of bridge abutment capacity and stiffness during earthquakes." Earthquake Spectra, 13(1), 1-23.

Huang, J., Shield, C.K. and French, C.E. (2008). "Parametric study of concrete integral abutment bridges." Journal of Bridge Engineering, 13(5), 511-526.

Jayaram, N., and Baker, J. W. (2010). "Ground-Motion Selection for PEER Transportation Research Program." Proceedings, 7th International Conference on Urban Earthquake Engineering (7CUEE) & 5th International Conference on Earthquake Engineering (5ICEE), Tokyo, Japan, 9p.

Romstad, K., Kutter, B., Maroney, B., Vanderbilt, E., Griggs, M. and Chai, Y. H. (1995). "Experimental measurements of bridge abutment behavior." Report No. UCD-STR-95-1, Department of Civil and Environmental Engineering, University of California, Davis.

Shamsabadi, A., Ashour, M. and Norris, G. (2005). "Bridge abutment nonlinear force-displacement-capacity prediction for seismic design." Journal of Geotechnical and Geoenvironmental Engineering, ASCE, 131(2), 151-161.

Caltrans Seismic Design Criteria (SDC) Version 1.6, Caltrans. (2010).

Computational Analyses of Quasi-Isolated Bridges with Fusing Bearing Components

E. T. Filipov[1], J. F. Hajjar[2], J. S. Steelman[1], L. A. Fahnestock[3], J. M. LaFave[4], and D.A. Foutch[5]

[1]Graduate Research Assistant, Dept. of Civil and Environmental Engr., University of Illinois at Urbana-Champaign, 205 N. Mathews Ave., Urbana, IL 61801; PH (217) 333-5230; email: filipov1@illinois.edu, jsteelm2@illinois.edu
[2]Professor and Chair, Dept. of Civil and Environmental Engr., Northeastern University, 360 Huntington Avenue, Boston, MA 02115; PH(617) 373-3242; email: jf.hajjar@neu.edu
[3]Assistant Professor, Dept. of Civil and Environmental Engr., University of Illinois at Urbana-Champaign, 205 N. Mathews Ave., Urbana, IL 61801; PH (217) 265-0211; email: fhnstck@illinois.edu
[4]Associate Professor, Dept. of Civil and Environmental Engr., University of Illinois at Urbana-Champaign, 205 N. Mathews Ave., Urbana, IL 61801; PH (217) 333-8064; email: jlafave@illinois.edu
[5]Professor Emeritus, Dept. of Civil and Environmental Engr., University of Illinois at Urbana-Champaign, 205 N. Mathews Ave., Urbana, IL 61801; PH (217) 333-6359; email: dfoutch@illinois.edu

ABSTRACT

Computational systems analyses are described for bridge systems that employ quasi-isolation by using a set of fixed bearings in addition to isolation bearings such as elastomeric bearings with an elastomer-concrete sliding interface or elastomeric bearings with a PTFE (Teflon) to stainless steel sliding interface. The system uses stiffened L-shaped retainer brackets that limit transverse displacement of elastomeric bearings and the bridge is intended to respond predictably, reliably, and elastically under service loading (including small seismic events), but for larger seismic events, certain bridge bearing components are intended to "fuse" and experience nonlinear behaviors that can allow for passive quasi-isolation of the bridge superstructure. To facilitate the computational modeling, experimental findings from ongoing research are being used to formulate phenomenological element models that simulate nonlinear fusing behaviors in the bridge bearings and auxiliary components. Furthermore the substructure pier elements, the bridge foundations and the abutment backwalls were modeled as they can exhibit nonlinear behaviors under large loadings. A parametric study is being carried out to investigate the effectiveness of the isolation system for various bridge structures and bearing combinations, and the findings will provide guidance for confirmation and further development of quasi-isolation design strategies.

INTRODUCTION

The concept of a quasi-isolation system for bridges has come from ongoing research to calibrate and refine the Earthquake Resisting System (ERS) methodology currently in use by the Illinois Department of Transportation (IDOT). The project

which is a joint effort of the Illinois Center for Transportation (ICT) and IDOT, is investigating a system of prescribed sequential "fusing" (i.e., exceeding ultimate capacity) of specific components such that more critical components remain in service after an earthquake, and structural collapse is prevented (Tobias et al., 2008). The core of this proposed ERS is an extension of a common bridge design methodology employed in high seismic regions of the United States, where the substructure and superstructure should remain elastic while a fusing mechanism is implemented at the interface between the two (AASHTO 2000, AASHTO 2009). The central objective of the IDOT study, is to observe the progression of damage in common bridge configurations when subjected to large seismic motions and the concomitant quasi-isolated response of the global bridge system as various components transition from elastic behavior to alternate forms of response.

The ongoing experimental work at the University of Illinois (Filipov et al. 2010), is aimed at investigating the nonlinear behavior of: (1) IDOT Type I bearings fabricated using an elastomer reinforced with steel shims placed directly on a concrete substructure, allowing for the possibility of sliding during an earthquake; (2) IDOT Type II bearings that consist of a bottom steel plate connected to the substructure and vulcanized to an elastomer, a steel reinforced elastomeric bearing, a top plate vulcanized to the elastomer and coated on the top side with PTFE, and a stainless steel plate carrying the girded load directly on to the PTFE surface; (3) low-profile fixed bearings with anchor bolts and pintles that prevent movement during ordinary service operations, but are designed to fail at higher earthquake loads; and finally (4) L shaped retainers that are designed as fuse components to fracture the attached anchor bolt during a seismic event. Preliminary experimental results documented in (Steelman et al. 2011) are being followed by a comprehensive component analysis using Abaqus (Abaqus FEA 2010), and the findings will be used to finalize the models for simulating the bearings and ancillary components.

The base global bridge system described herein, incorporates nonlinearities in the bearing components, substructures, foundations and abutment backwalls, and is being be used to study the effectiveness of quasi-quasi isolated systems. A study by (Bignell and LaFave 2009) has shown the seismic fragility of bridges in Southern Illinois and it is believed that isolation would be a cost effective solution to provide safer infrastructure. Dynamic nonlinear analyses with different ground motions will be completed for various IDOT bridges that differ in superstructure girder type and length, intermediate sub-structure type and height, and the type of isolation bearings installed.

MODELING OF A BASIC BRIDGE PROTOTYPE

The global system models are being analyzed using the open source, nonlinear seismic analysis program Open System for Earthquake Engineering Simulation (OpenSees 2006). The system models incorporate linear elastic behavior for all elements in the bridge superstructure, such as the beams, cross-bracing, deck, and parapets. The girders are modeled as linear beam-column elements based on the specified section properties, and the deck is modeled using four-node shell elements with linear elastic behavior. Low-profile fixed bearings are implemented at one of

the intermediate piers, while Type I or Type II elastomeric expansion bearings are used at the other pier and the abutments. Figure 1 shows the finite element mesh for the basic prototype bridge which has three 15.2m (50') spans bridge with 4.6m (15') tall multi-column piers. The rendering shows the scaled deflection of the bridge when the superstructure is loaded in the longitudinal direction. The right pier experiences a larger deflection than the left, since it is equipped with fixed bearings. The prototype bridge deck is 12.8m (42') wide, which allows for two lanes of traffic, it has six W27x84 Gr. 50 composite girders and a 20.3cm (8") concrete deck.

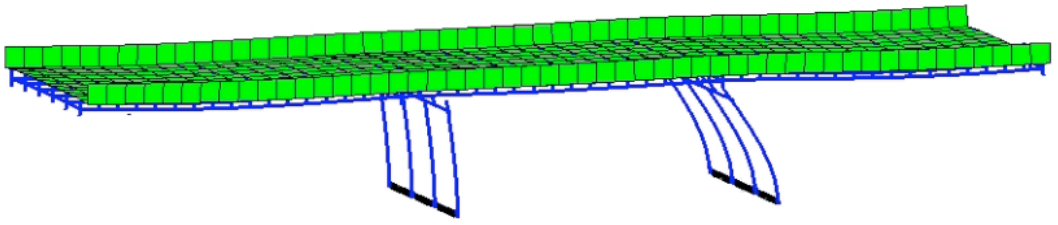


Figure 1. Basic bridge prototype model created using OpenSees

To formulate the parametric study, the basic bridge will be modified as shown in Table 1. Variations will include using a different type and length of superstructure and also different substructure types and heights; further modeling the bridge with Type I or Type II bearings will result in a total of 24 distinct bridge model configurations. Each model variation will be subjected to several suites and intensities of ground motions, and the behavior will be investigated in both the longitudinal and transverse directions.

Table 1. System analysis matrix

		Bridge Type 1 Steel - Short				Bridge Type 2 Steel - Long				Bridge Type 3 Concrete - Short				Variations
Parameter	**Alternatives**	1	2	3	4	5	6	7	8	9	10	11	12	
Span Length & Bridge Type (ft)	50' - 50' - 50'	*	*	*	*									3
	60' - 60' - 60'									*	*	*	*	
	80' - 120' - 80'					*	*	*	*					
Intermediate Sub-Structure	Continuous Wall	*	*			*	*			*	*			2
	Multi Column Pier			*	*			*	*			*	*	
Intermediate Sub-Structure Height	Short - 15'	*		*		*		*		*		*		2
	Tall - 40'		*		*		*		*		*		*	
Movement Bearings	Type I Elastomeric	All (12) of the above bridges will be modeled with												2
	Type II Elastomeric	Elastomeric Type I & Type II Bearings												

Bearings and ancillary components

The OpenSees program allows for the implementation of user defined materials and elements that can be modified to exhibit specific behaviors. C++ programming was used to create models that augment the capabilities of OpenSees, and thus allow for modeling of complex nonlinear behaviors such as the sliding of elastomeric bearings and PTFE bearings, and the plastic deformation and failure of the retainers and fixed bearings. The bearing models are still in a preliminary

development phase, but have been formulated based on similar studies in literature and the ongoing experimental testing by (Steelman et al. 2011). The bearing and component behaviors will be updated and refined as the experimental test are completed in the near future.

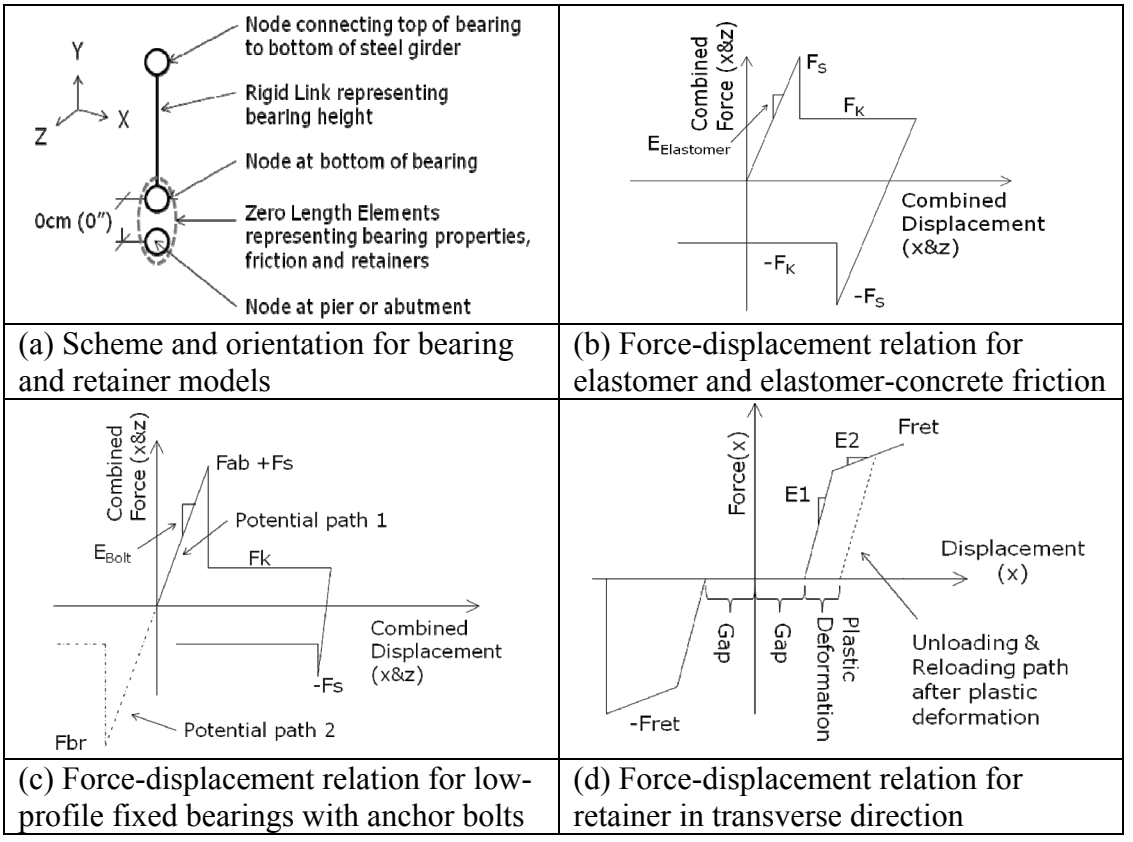
A zero-length bi-directional element was created to combine the force-displacement definitions for the *x* and *z* translation DOFs, so that the force in these directions is governed by their combined displacement. This allows a user to capture phenomenon such as friction break off, as it occurs simultaneously in both the x and z directions. Figure 2 (a) shows the general orientation under which the zero length bi-directional element is to be used. Four uniaxial materials (preferably linear elastic) can be used to define the element's translation in the y direction, as well as rotations about the *x*, *y* and *z* axes. In contrast to the bearings, the retainer models are created to act only in the transverse direction of the bridge.

Elastomer and Elastomer-Concrete/PTFE-Stainless Steel Friction: This element combines the effects of the elastomer along with the stick-slip friction behavior experienced either at an elastomer-concrete interface (for Type I bearings), or a PTFE-stainless steel interface (for Type II bearings). Initially the nonlinear friction response at a bearing is modeled through a "static configuration" with an elastic response, which is effective until the static friction break-off force (*Fs*) is reached at the elastomer-concrete interface. At this point slip occurs and the model enters a "kinetic configuration" where the force at the elastomer-concrete interface is reduced to the kinetic friction force (*Fk*) as shown in the force-displacement relation in Figure 2 (b). This kinetic configuration is maintained until the elastomer force falls below the kinetic friction force, in which case the bottom of the bearing comes to a stop relative to the concrete below and the model returns to the "static configuration". The static and kinetic forces (*Fs* and *Fk)* are governed by the applied axial force on the bearing(N), multiplied by the coefficients of friction at the interface surface (μ_S and μ_K respectively). Therefore, different static and kinetic forces may be expected at each substructure depending on the carried axial load and bearing type. At this time coefficients of static and kinetic friction (μ_S and μ_K) have been set constant at 0.35 and 0.15, however recently completed experiments shown that these coefficients could be dependent on the applied axial load, and could have a broad range of values.

Low-Profile Fixed Bearings with Anchor Bolts: As shown in Figure 2 (c) these bearings are initially modeled as elastic until the horizontal force exceeds the combined anchor bolt shear failure force (*Fab*) plus the static friction break-off force at the steel plate-concrete (*Fs*) interaction surface. This would cause anchor bolt failure and sliding, and the fixed bearing model will thereafter be governed only by a friction behavior similar to that described in the text above. At this time coefficients of static and kinetic friction (μ_S and μ_K) for the steel bearing plate to concrete substructure interface, have been set constant at 0.62 and 0.40 based on previous literature.

Retainers: The phenomenological retainer component has an initial gap that must be closed by the bearing's top plate before the retainer is engaged and force is observed.

Once this initial gap is closed, the force-displacement behavior of the retainer is modeled as elastic, up until plastic deformation begins, as shown by the backbone force-deformation relationship in Figure 2 (d). At this stage the component model experiences linear strain hardening until it reaches a peak breaking force (*Fret*). As plastic deformation is accumulated by the retainer assembly model, the retainer contact point is moved away from its initial configuration, and the gap between the initial position of the bearing top plate and the retainer increases. Furthermore, it is important to note that the positive and negative force-displacement curves are used to separately model the two retainers, therefore the incremental plastic deformations are specific to each retainer and once the breaking force is reached in a retainer, its effects are entirely removed from the model. This initial retainer model is based on the assumption of tension-shear failure in the anchorbolt that holds the retainer to the concrete substructure. Recent experimental testing has shown that although this model seems to provide a reasonable approximation of the force-displacement behavior, the actual capacity of the retainer assembly may be significantly higher than was initially calculated.



(a) Scheme and orientation for bearing and retainer models

(b) Force-displacement relation for elastomer and elastomer-concrete friction

(c) Force-displacement relation for low-profile fixed bearings with anchor bolts

(d) Force-displacement relation for retainer in transverse direction

Figure 2. Bearing element scheme and force-displacement relations

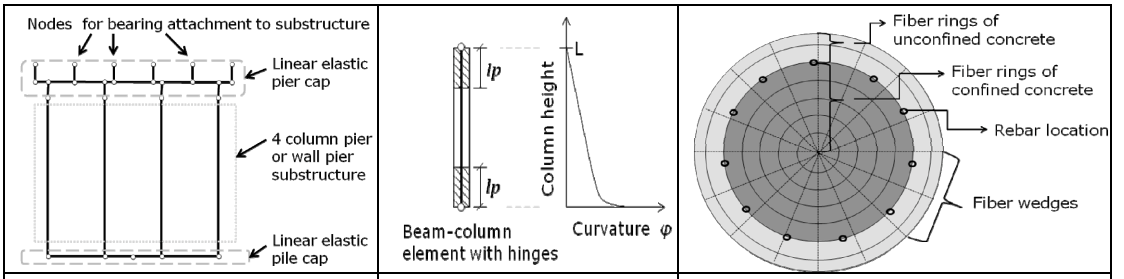
Substructures

The substructure layout is shown in Figure 3 (a) the pier and pile caps are relatively stiff compared to the columns or wall, and are thus modeled as linear elastic elements. The column and wall piers can however experience nonlinear phenomena

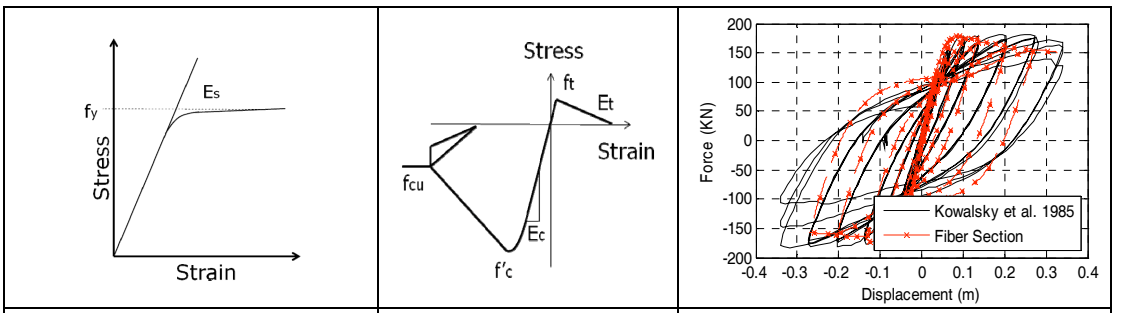
such as cracking and flexural yielding when subjected to high lateral loads. Different elements, element discretizations and fiber sections were investigated to find an appropriate method for modeling a single cantilever, and dual curvature columns. The lumped plasticity model proposed by (Scott and Fenves 2006) was used, as it presents a higher curvature at the plastic hinge regions as shown in Figure 3 (b), which well matches concrete column behavior. The plastic hinge length is defined per (Berry et al. 2008), as $l_p = 0.05L + 0.1 f_y d_b / \sqrt{f_c'}$ in MPa ($l_p = 0.05L + 0.008 f_y d_b / \sqrt{f_c'}$ in psi) is used, where L is distance from the critical section to the point of contraflexure, *fy* is the longitudinal rebar yield strength, *db* is the longitudinal rebar diameter, and *fc'* is the concrete strength.

A fiber section, Figure 3 (c), was used to model the nonlinear material behavior in the plastic hinge regions of the column. To provide consistently reliable results the section was discretized to have 15 fiber wedges, 15 fiber rings of confined concrete, 5 fiber rings of un-confined concrete and the necessary number of fibers to simulate each rebar individually. The reinforcement was modeled by using the OpenSees Steel 02 - material (Figure 3 (d)), while the un-confined and confined concrete were modeled using the OpenSees Concrete 02 material (Figure 3 (e)). Some constants used in the column analysis include using 1.25 for the confined to un-confined concrete ratio, $ft = -0.12 f_c'$ for the concrete tensile capacity and $E_C = 4730\sqrt{f_c'}$ in MPa ($E_C = 57,000\sqrt{f_c'}$ in psi) for the concrete modulus of elasticity.

Modifying the material properties, as well as column and section geometries, it was possible to validate the lumped plasticity model against experimental findings from (Ang et al. 1989), (Chai et al. 1991), and (Kowalsky et al. 1999). A sample cyclic force-displacement validation of the (Kowalsky et al. 1999) test FL 3 is shown in Figure 3 (f) with the analytical results based on the described fiber model. The wall substructures are modeled in the same fashion for out-of-plane loading, where a rectangular fiber section is used in a beam-column element with hinges. For in-plane behavior of the wall a spring is used to model shear deformations and a linear elastic member is used to model flexural deformation of a cracked section of the wall. The wall capacity and stiffness are significantly less in the out-of-plane direction, thus this direction is also more important, and the model is validated against experiments from (Haroun et al. 1993) and (Abo-Shadi et al. 1999) for the out-of-plane loading. Both the column piers and wall piers have significantly higher shear capacities than the bearings' fuse capacities so shear failure is not expected to occur.



(a) Substructure Scheme	(b) Element and curvature distribution	(c) Fiber sections used at hinge locations



(d) Steel 02 model	(e) Concrete 02 model	(f) Sample validation

Figure 3. Definitions and validation for pier column substructure

For the parametric study it was important to define the limit states of concrete piers, so cracking, and steel yielding effects are carefully monitored. Figure 4 shows a force-displacement hysteresis for a typical IDOT cantilever column that would be used for a short bridge structure. The analyzed column is 4.6m (15') tall from base to point of load application, it has a 0.91m (3') diameter, 24.12MPa (3500psi) normal weight concrete, and eleven #9 longitudinal bars with 3.81cm (1.5") clear cover.

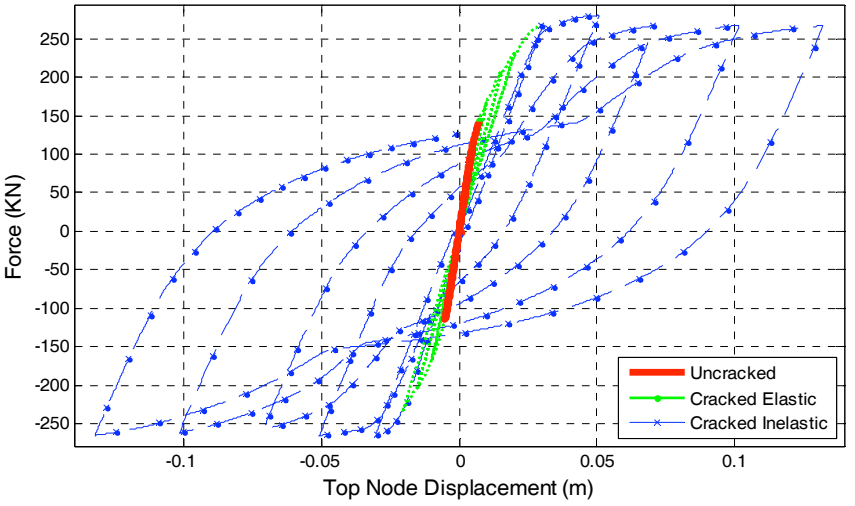


Figure 4. Limit states for typical IDOT column in force-displacement

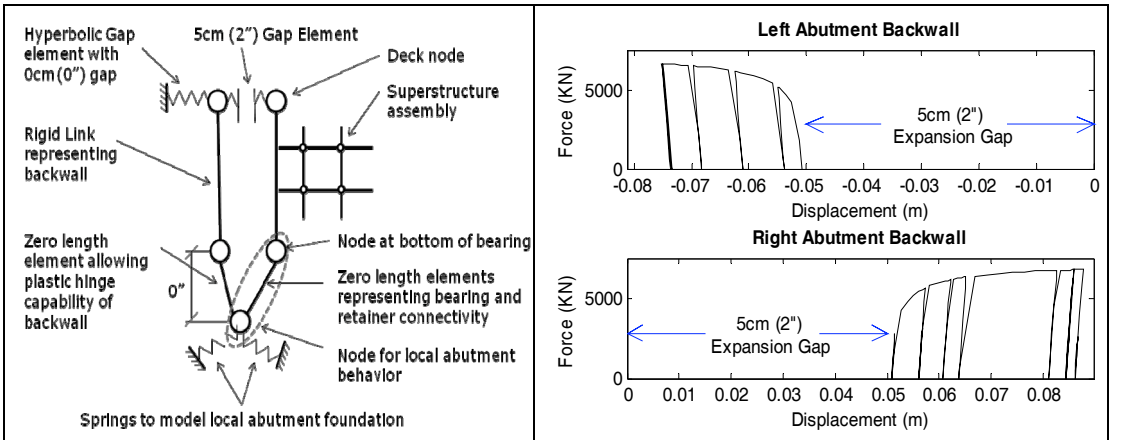
Foundations

Intermediate substructure and abutment foundation response is included in the system models based on a separate study of the bridge foundations and soils that was carried out with a geotechnical pile group analysis program. The typical abutment foundation for bridges in Illinois is defined as (11) HP12x63 piles at a 13.7m (45') depth, with a 1.2m x 1.8m x 12.8m (4'x6'x42') concrete pile cap. A row of four piles is battered towards the superstructure at a 1 to 3 slope, a row of five piles is placed straight and two piles are placed in the wing walls. The typical foundation for the intermediate substructure has three rows of four HP12x63 piles at a 13.7m (45')

depth, with a 0.76m x 3.7m x 10.7m (2.5'x12'x35') pile cap, and all piles being straight. Soil types were modeled as (i) a stiff rocky soil modeled as a fixed base, (ii) stiff clay or medium stiff sand, modeled with 0.072–0.096MPa (1500–2000psf) shear strength, and (iii) a soft clay or loamy soil, modeled with a 0.014-0.024MPa (300–500psf) shear strength. The soil-foundation interaction behavior was calculated for the foundations and different soil types as curvilinear force-displacement relations. The foundation is then simulated in OpenSees as a zero-length element that restrains the bottom node of each substructure using springs for lateral and rotational stiffness as per (Finn 2005).

Abutment backwalls

Abutment backwalls are placed at a distance from the bridge deck, allowing for an expansion gap, and are a very important component of the bridge seismic behavior. When subject to longitudinal movement, the bridge is reasonably flexible and as soon as the 5cm (2") gap is closed the superstructure contacts the backwall and experiences nonlinear behaviors both from the structural concrete backwall as well as the soil backfill behind the abutment elements. As shown in Figure 5 (a), the backwall structural element is modeled using a rigid link connected to a bilinear zero length element that simulates the flexural stiffness and capacity of a 0.61m (2') concrete wall with a reinforcement ration of 0.11%. The nonlinear soil behavior is defined as per (Shamsabadi et al. 2007), and is modeled using the OpenSees hyperbolic gap material assuming the backfill is a compacted, dense sand with an ultimate passive resistance of 262.7KN per meter (18 kips per foot) of backwall, similar to what can be expected for typical Illinois bridges. The backwall and backfill system produces the force-displacement behavior as shown in Figure 5 (b), when the prototype bridge is subjected to a 975 year return period longitudinal earthquake ground motion. The backwall can have a substantial effect on the bridge response as described in the design recommendations from (AASHTO 2009), both for longitudinal and transverse bridge loading, since twisting about the vertical axis of the superstructure could lead to substantial deck to backwall interactions.



(a) Scheme and orientation of backwall and abutment elements

(b) Force displacement behavior of the two abutments for a dynamic analysis

Figure 5. Backwall scheme and sample force displacement behavior

PRELIMINARY BRIDGE ANALYSES

Transient nonlinear dynamic modeling is carried out using the OpenSees program. Due to the high degree of nonlinearity an adaptive algorithm was created, such that when non-convergence was encountered the time-stepping solution algorithm, and the integrator were altered in an attempt come to an acceptable solution for the system displacement. The base bridge model (bridge #1 with bearings Type I per Table 1) was simulated using a synthetic earthquake record with a 975 year return period, generated for Paducah, KY (Fernandez and Rix 2006), where the seismic hazard is dominated by large magnitude, but infrequent, seismic events in the New Madrid seismic zone. Figure 6 shows the bearing forces and residual displacement (distance from initial bearing seat location to the new location where the bearing is seated) vs. time plots for an intermediate bearing (bearing carrying girder #3), at each of the four substructures.

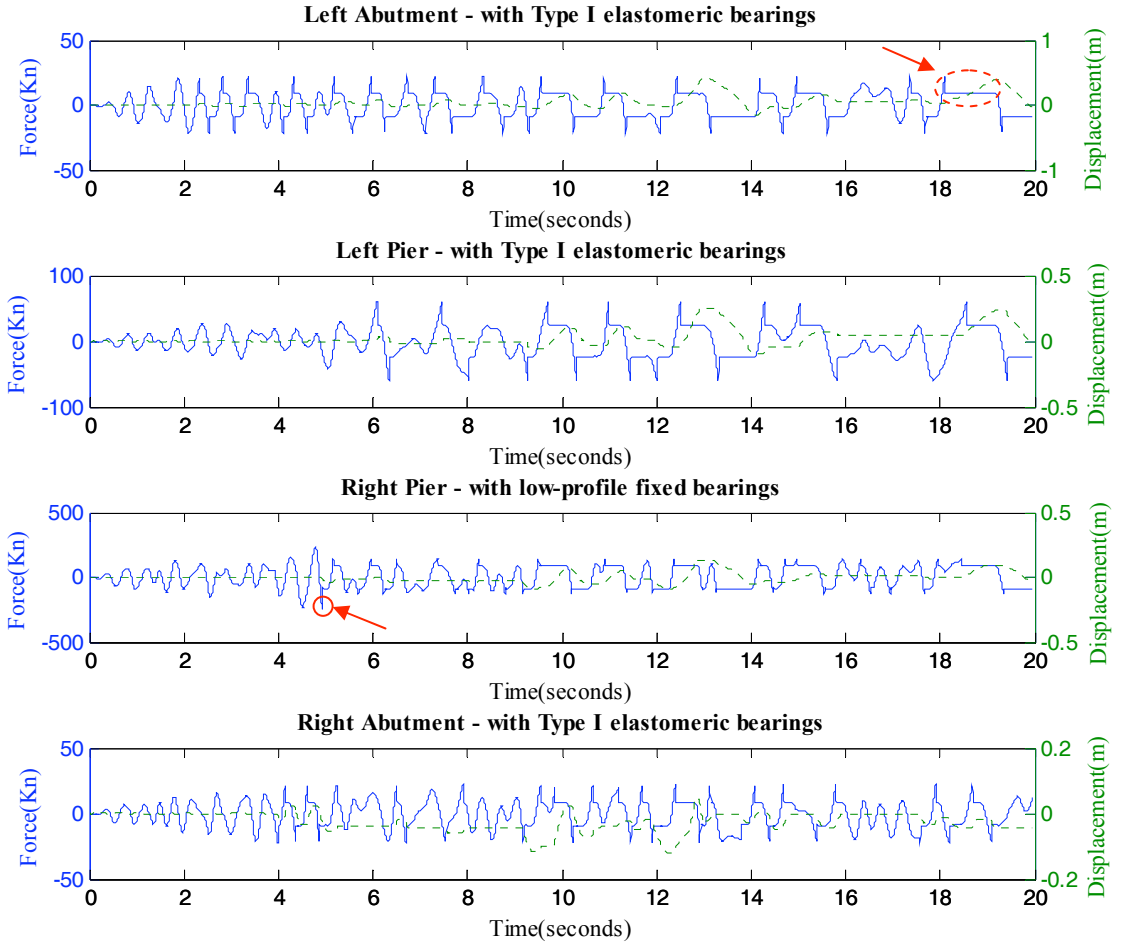


Figure 6. Force (solid) and relative displacement (dashed) at bearing locations vs. time step

Since the intermediate pier bearings have a larger tributary area and carry a larger load, the break-off friction forces for the intermediate piers are significantly higher than those for the abutments. Furthermore it is also interesting to see that since

the right pier has the fixed bearing, it also experiences an interesting response that incorporates a pintle failure at about the 4.8 seconds in the dynamic analysis. At that time the bearing experiences a maximum force of 251KN (56.4kips), and thereafter the forces in the bearing are significantly smaller since the anchorbolt is no longer in place. The sliding behavior of the bearings can easily be observed as pointed out in the left abutment plot between 18 and 19.4 seconds. When the static friction force is reached in the bearing, the force drops down to the kinetic friction force and the bearing slides from a 0.04m to a 0.39m residual displacement. Notice that since the fixed bearings have a higher initial break-off force as well as higher coefficients of friction, they tend to experience less sliding and residual displacement than the rest of the bearings. This leads the superstructure to twist about the vertical axis located at the right pier as it is sliding in the transverse direction. Testing in the longitudinal direction exhibits similar sliding behavior as in Figure 6, however since the bridge is symmetric, there is no twisting behavior, and the bearing displacements are greatly limited by the backwall.

To carry out the parametric study, the different bridge models will be analyzed for varying earthquake hazards. A number of factors affect the response of a bridge including the magnitude of the earthquake, the source mechanism, the distance from the epicenter to the bridge site, the attenuation of the seismic motions with distance, the soil type at the bridge site, and the bridge configuration. For the bulk system analysis it was decided to use suites of (10) 975 year return period synthetic ground motions for each Cape Girardeau, MO, and Paducah, KY provided by (Fernandez and Rix 2006). These ground motions are then scaled to match different degrees of earthquake intensity by using the procedure from the (Sommerville et al. 1997) SAC report where the weighted sum of the squared error between the average spectrum and the target design spectrum is minimized.

To study the three dimensional behavior of the bearings and the full bridge system, the models will all be analyzed for longitudinal, transverse and bi-directional loading application. This will permit for the investigation of the bearing assemblies to different loading directions and will also employ the use of the retainers and backwall as necessary. Bi-directional loading and twisting due to the bridges' asymmetries will also give valuable information about torsional loading of the substructures and the global three dimensional behavior. Although vertical ground motions will not be used for preliminary analysis, since the bearing behaviors are greatly governed by axial load it would be useful to perform research for near-field loadings where vertical accelerations could be significant (Elgamal and He 2004).

A baseline set of analyses has been completed using strong ground motions in the transverse direction to show that the computational approach is effective. Figure 7 shows the same bridge as defined before, subjected to a suite of truncated ground motions that have been scaled to different intensities. The graphs show that with higher intensity shaking there would be higher displacement as expected, and there would also be a larger standard deviation of the data for stronger ground motions. The graphs in Figure 7 also show that the displacements at the right pier are smaller than those at the abutments or left pier. This is to be expected, since the preliminary values for coefficients of friction for the fixed bearings at the right pier are high and there is also the initial capacity of the anchorbolt.

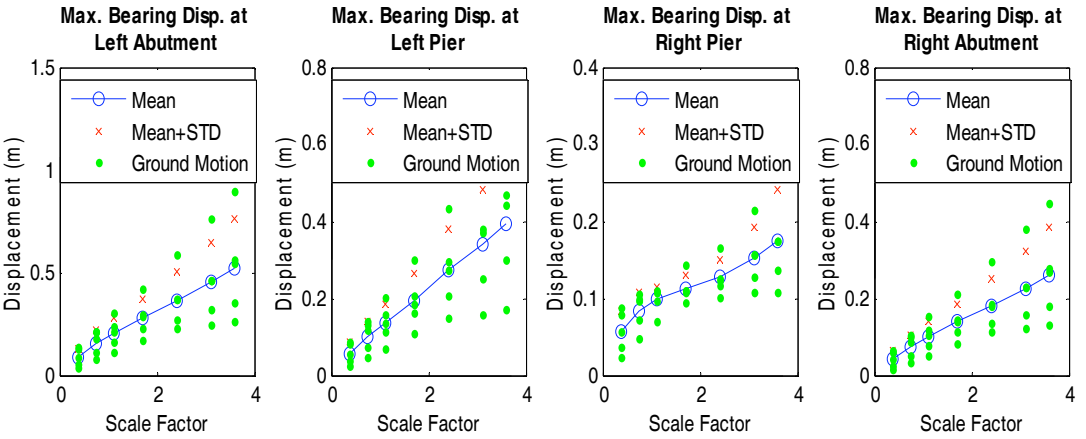


Figure 7. Maximum displacement for a middle bearing at each substructure, when bridge is subject to transverse ground motion loading

SUMMARY AND CONCLUSIONS

The computational models are currently based on preliminary assumptions about the bearing and fuse behaviors. Information in the literature, computational component analysis data, and future experimental results are all expected to provide valuable additional input on how to appropriately model the bearing and ancillary component fusing behaviors. Using well calibrated and validated bearing models, the computational analysis will provide valuable insight about the performance of different bride elements in the global structural response. Typical bridge substructures, foundations and abutment backwalls have been studied, and the bridge model has been built to account for a variety of nonlinear behaviors that can occur as a result of strong ground motions. Initial results have shown that the bearing friction force has a large influence of the superstructure displacement in the transverse direction, and the abutment backwall tends to limit longitudinal displacements. A baseline set of analyses incorporating a suite of ground motions have been completed and current research is aimed at performing parametric studies to investigate the performance of quasi-isolation systems for different bridge structures.

ACKNOWLEDGMENTS

This article is based on the results of ICT R27-70, *Calibration and Refinement of Illinois' Earthquake Resisting System Bridge Design Methodology.* ICT R27-70 was conducted in cooperation with the Illinois Center for Transportation (ICT); IDOT; Division of Highways; and the U.S. Department of Transportation, Federal Highway Administration (FHWA). The contents of this article reflect the view of the authors, who are responsible for the facts and the accuracy of the data presented herein. The contents do not necessarily reflect the official views or policies of the ICT, IDOT, or FHWA. The authors would like to thank the members of the project Technical Review Panel, chaired by D. H. Tobias, for their valuable assistance with this research.

REFERENCES

Abaqus FEA (2010). SIMULIA website, Dassault Systèmes, Vélizy-Villacoublay, France. http://www.simulia.com/products/abaqus_fea.html

Abo-Shadi, N.A., Saiidi, M., and Sanders, D.H. (1999). "Seismic Response of Bridge Pier Walls in the Weak Direction." Report to the Multidisciplinary Center for Earthquake Engineering Research (MCEER), Report No. CCEER-99-3, Center for Civil Engineering Earthquake Research, University of Nevada, Reno.

American Association of State Highway and Transportation Officials (AASHTO). (2000). *Guide specifications for seismic isolation design with interims*, Washington, D.C.

AASHTO. (2009). *Guide specifications for LRFD seismic bridge design*, Washington, D.C

Ang B.G., Priestley, M.J.N., and Paulay, T. (1989). "Seismic Shear Strength of Circular Reinforced Concrete Columns." *ACI Structural J.*, 86(1), 45-59.

Berry, M.P., Dawn, E.L. and Lowes, L.N. (2008). "Lumped-Plasticity Models for Performance Simulation of Bridge Columns." *ACI Structural J.*, 105(3), 270-279.

Bignell, J., and LaFave, J. (2009). "Analytical fragility analysis of southern Illinois pier supported highway bridges." Earthquake Engineering & Structural Dynamics, 39(7), 709-729.

Chai, Y., Priestley, M.J.N., and Seible, F. (1991). "Seismic Retrofit of Circular Bridge Columns for Enhanced Flexural Performance," *ACI Structural J.*, 88(5), 572-584.

Elgamal, A. and He, L. (2004). "Vertical Earthquake Ground Motion Records: An Overview", *J. of Earthquake Engineering*, 8(5), 663-697.

Fernandez, J. A. and Rix, G. J. (2006). "Probabilistic Ground Motions for Selected Cities in the Upper Mississippi Embayment." School of Civil and Environmental Engr., Georgia Inst. of Technology, Atlanta, GA. http://geosystems.ce.gatech.edu/soil_dynamics/research/groundmotionsembay/

Filipov, E. T., Steelman J. S., Hajjar, J. F., LaFave J. M., and Fahnestock L. A. (2010). "Bridge Bearing Fuse Systems for Regions with High-Magnitude Earthquakes at Long Recurrence Intervals." Paper No. 1834, *Proceedings of the 9th US and 10th Canadian Conference on Earthquake Engr.*, Toronto, Canada, EERI, Oakland, CA

Finn, W.D.L. (2005). "A study of piles during earthquakes: Issues of design and analysis." *Bulletin of Earthquake Engineering*, 3(2), 141–234.

Haroun, M. A., Pardoen, G.C., Shepard, R., Haggag, H.A., and Kazanjy, R.P. (1993). "Cyclic Behavior of Bridge Pier Walls for Retrofit." Final Report to the California Department of Transportation, University of California at Irvine, RTA No.59N974, Irvine, CA,

Kowalsky, M.J.; Priestley, M.J.N.; and Seible, F. (1999). "Shear and Flexural Behavior of Lightweight Concrete Bridge Columns in Seismic Regions." *ACI Structural J.*, 96(1), 136-148.

OpenSees (2006). OpenSees website, Pacific Earthquake Engineering Research Center, University of California, Berkeley, CA. http://opensees.berkeley.edu/OpenSees/home/about.php

Scott, M.H., and Fenves G.L. (2006), "Plastic Hinge Integration Methods for Force-Based Beam–Column Elements." *J. of Structural Engineering* 132(2), 244–252.

Shamsabadi, A., Rollins, K. M., and Kapuskar, M. (2007). "Nonlinear soil-abutment-bridge structure interaction for seismic performance-based design." *J. of Geotechnical and Geoenvironmental Engineering*, 133(6), 707-720.

Sommerville, P., Smith, N., Punyamurthula, S., Sun, J., Woodward-Clyde Federal Services (1997). "Development of Ground Motion Time Histories for Phase 2 of the FEMA/SAC Steel Project" Report No. SAC/BD-97/04, SAC Joint Venture, Sacramento, California

Steelman J. S., Fahnestock L. A., LaFave J. M., Hajjar, J. F., Filipov, E. T., and Foutch D. A. (2011), "Seismic Response of Bearings for Quasi-Isolated Bridges – Testing and Component Modeling" Paper No. 855, 2011 Structures Congress, Las Vegas, NV, April 14 - 16, SEI

Tobias, D. H., R. E. Anderson, C. E. Hodel, W. M. Kramer, R. M. Wahab, R.J. Chaput (2008). "Overview of Earthquake Resisting System Design and Retrofit Strategy for Bridges in Illinois." *Practice Periodical on Structural Design and Construction 13, (3), 147-158*

SEISMIC ANALYSIS OF INTEGRAL ABUTMENT BRIDGES INCLUDING SOIL-STRUCTURE INTERACTION

Qiuhong Zhao[1], Reza Vasheghani-Farahani[2] and Edwin G. Burdette[3]

[1] Steel Research Laboratory, Department of Civil and Environmental Engineering, the University of Tennessee, Knoxville, TN 37996-2010; PH (865) 974-7711; e-mail: qzhao@utk.edu

[2] Department of Civil and Environmental Engineering, the University of Tennessee, Knoxville, TN 37996-2010; PH (865)974-4384; e-mail: rvashegh@utk.edu

[3] Department of Civil and Environmental Engineering, the University of Tennessee, Knoxville, TN 37996-2010; PH (865)974-7704; e-mail: eburdett@utk.edu

ABSTRACT

Integral abutment bridges are jointless bridges in which the deck is continuous and connected monolithically with the abutment walls supported typically by a single row of piles. Part of the research results from an ongoing project is presented in this paper, which focuses on the effects of two major parameters on the seismic behavior of an integral abutment bridge in Tennessee by considering soil-structure interaction around the piles and in back of the abutments: (1) clay stiffness (medium vs. hard) around the piles, and (2) level of compaction (loose vs. dense) of the abutment wall backfilling. Modal and nonlinear time history analyses were performed on a three dimensional detailed bridge model using the commercial software SAP2000, which clearly showed that (1) compacting the backfilling of the abutment wall will increase the bridge dominant longitudinal natural frequency considerably more than increasing the clay stiffness around the piles; (2) the maximum deflection and bending moment in the piles under seismic loading will happen at the pile-abutment interface; (3) under seismic loading, densely-compacted backfilling of the abutment wall is generally recommended since it will reduce the pile deflection, the abutment displacement, the moments in the steel girder, and particularly the pile moments; (4) under seismic loading, when the piles are located in firmer clay, although the pile deflection, the abutment displacement, and the maximum girder moment at the pier and the mid-span will decrease, the maximum pile moment and the maximum girder moment at the abutment will increase.

INTRODUCTION

Integral abutment bridges are jointless bridges in which the deck is continuous and connected monolithically with the abutment walls supported typically by a single row of piles. A typical integral abutment bridge is illustrated in Figure 1.

The advantages of these bridges include reduced maintenance costs compared to jointed bridges with expansion joints and abutment bearings, reduced corrosion and material degradation at the joints (FHWA, 1986), increased structural capacity during seismic events (Hassiotis et al, 2006), the elimination of uplift due to dead loads (Wasserman and Walker, 1996), the provision of reserve live load capacity by distributing the loads along the continuous and full depth diaphragm at bridge ends,

as well as faster and simpler construction. (Wasserman and Walker, 1996; Hopper and Gomes , 1996)

During the analysis and design of integral abutment bridges, the biggest uncertainties generally lie in the nonlinear soil-abutment and soil-pile interactions, since the magnitude and nature of the soil and structural deformations and stresses are interdependent (Faraji *et al, 2001).* Therefore, it is meaningful to investigate the nonlinear soil-abutment and soil-pile interactions during seismic events, and identify the main factors affecting bridge behavior.

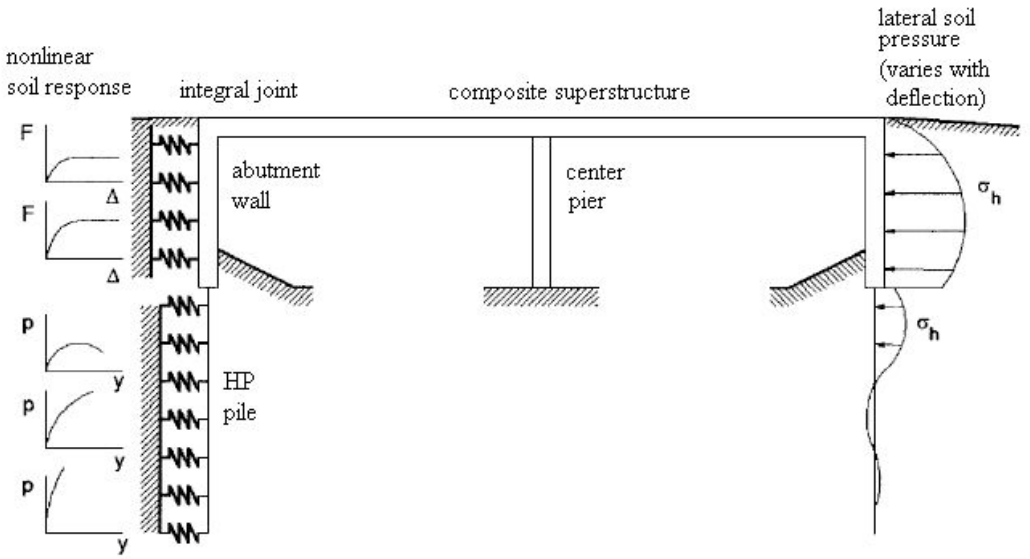


Figure 1 Typical integral abutment bridge

BACKGROUND

Behavior of integral abutment piles under realistic soil constraints

Burdette et al. investigated experimentally the response of integral abutments supported by steel H-piles and prestressed concrete piles, respectively. It was found that a pile embedment length of 305 mm into the abutment was sufficient to assure pile-abutment integrity, when the pile deflection did not exceed the design limit of 25.4 mm specified by the Tennessee Department of Transportation (TDOT). Beyond this limit, some cracking of the pile-abutment interface was observed, which was more extensive in stiffer soils but still did not cause the loss of integrity at significantly larger displacements, even in extremely stiff soils (Burdette et al, 2000). It was also found that the prestressed concrete pile cracked just below the pile-abutment interface when the deflection at the ground surface approached 25.4 mm, which significantly reduced the section stiffness but did not greatly affect the overall behavior. It was then concluded that the current deflection limit was conservative and a value of 38 mm would appear to be reasonable (Burdette et al, 2007)

Soil-structure interaction of integral abutment bridges under thermal loading

Many researchers have studied the soil-pile and soil-abutment interaction in integral abutment bridges, the first dealing with thermal analysis. Faraji et al. presented a

thermal analysis of an integral abutment bridge which explicitly incorporated nonlinear springs for cohesionless soil behind the abutment walls and adjacent to the supporting piles. A parametric study was conducted on the compaction effects, where it turned out that soil compaction behind the abutment wall would double the peak axial forces and moments in the deck, while reducing the peak pile moments by half. Also, soil compaction adjacent to the piles affected the moments in the HP piles, without any significant influence on the abutment wall or bridge deck. (Faraji et al, 2001).

Khodair and Hassiotis studied soil-pile interaction in integral abutments under thermal loading experimentally and numerically, and found that the influence of lateral loads imposed by the superstructure on the piles was confined within a small volume of soil around the piles. (Khodair and Hassiotis, 2005)

Civjan et al. studied effects of backfill properties and soil restraints on integral abutment piles with regard to bridge distortions, and maximum moments developed in the piles caused by thermal loading. It was found that the bridge expansion was predominantly affected by the backfill conditions, whereas the bridge contraction was influenced by the pile restraint conditions. It was also shown that the pile moments were minimized when denser backfill and smaller pile restraint were provided (Civjan et al , 2007)

Seismic response of integral abutment bridges

Several researchers have also investigated seismic response of integral abutment bridges (e.g. (Goel, 1997), (Dehne and Hassiotis, 2003) and (Spyrakos and Loannidis, 2003). Goel studied earthquake characteristics of integral abutment bridges, in which he measured the dynamic properties of a two-span concrete bridge from motions recorded during an actual earthquake, and indicated that the vibration period elongated and the damping ratio increased by a factor of more than two as the intensity of the ground motion increased. (Goel, 1997)

Dehne and Hassiotis conducted seismic analysis on an integral abutment bridge, through which it turned out that accurate modeling of the soil-structure interaction was required to evaluate the effects of longitudinal and transverse earthquake excitation on the response of integral abutment bridges. It was concluded that an integral abutment bridge system with the dense compacted soil behind the abutment wall and loose sand around the piles would have the best performance characteristics. (Dehne and Hassiotis, 2003)

Spyrakos and Loannidis studied seismic behavior of a single-span post-tensioned integral abutment bridge including soil-structure interaction, in which they assessed the significance of soil-structure interaction on the mode shapes and seismic response of the bridge. Sensitivity studies were conducted to investigate the effect of foundation stiffness on the overall dynamic and seismic response of the bridge system. It turned out that the vibration frequencies changed about 20 percent in extreme cases, and the foundation stiffness did not affect significantly the seismic response of the bridge. They also found that the existence of backfill had a significant effect on the dynamic characteristics and seismic response of the bridge. (Spyrakos and Loannidis, 2003)

ANALYSIS OF AN INTEGRAL ABUTMENT BRIDGE IN TENNESSEE

This paper focuses on the seismic behavior of a two-span integral abutment steel bridge in the State of Tennessee, with an emphasis and sensitivity study on the effects of the levels of sand compaction in back of the abutments and clay stiffness around the piles. Clay is the common type of soil in most locations in Tennessee, which has not been studied enough on seismic response of integral abutment bridges yet. A 3-D model of an integral abutment bridge was constructed with seismic soil springs around the piles and behind the abutments. The commercial design/analysis software SAP2000 is used for convenience of application of research results for the design engineers.

1) BRIDGE MODEL

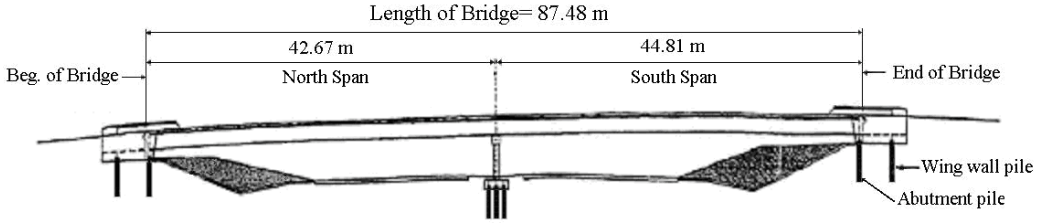
The bridge is located on Massman Drive across I-40 in Nashville, Tennessee, with a north span of 42.67 m and a south span of 44.81 m. The bridge superstructure consists of five steel plate girders with a height of 1.63 m and center to center spacing of 2.97 m, supporting a 0.21 m thick concrete deck above. The bridge substructure consists of two 2.87 m height and 0.91 m thick integral abutments supported each by ten HP10×42 steel piles oriented in the strong axis bending. Views of the bridge and also its abutment details are shown in Figure 2.

2) FINITE ELEMENT MODEL

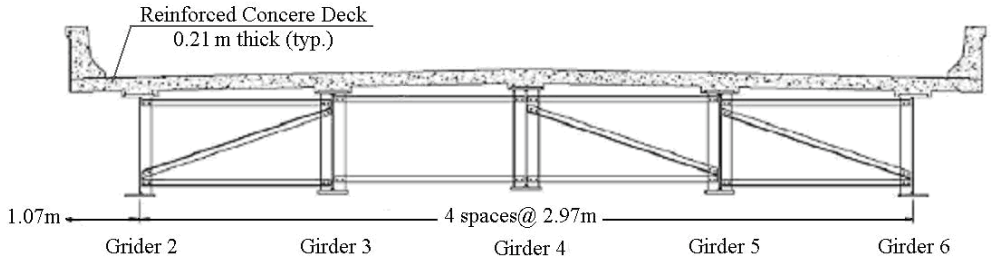
A 3-D finite element model (FEM) of the bridge was constructed using SAP2000 software. The deck, abutments and pile caps are modeled as shell elements while the steel plate girders, piers, bent cap and piles are modeled as beam elements. To account for the composite action of the superstructure, rigid link elements are inserted between the deck nodes and the girder nodes. A rigid connection is assumed at the conjunction of the steel girders and the abutments, as well as between the piles and the abutments, reflecting the fact that the steel girders and piles were cast rigidly in the concrete there. Nonlinear link elements are used to model the nonlinear soil reactions around the piles and in back of the abutments. For the analyses, a damping coefficient of 0.05 is considered in the bridge model. The 3-D finite element model of the bridge is shown in Figure 3.

3) NONLINEAR SOIL SPRINGS

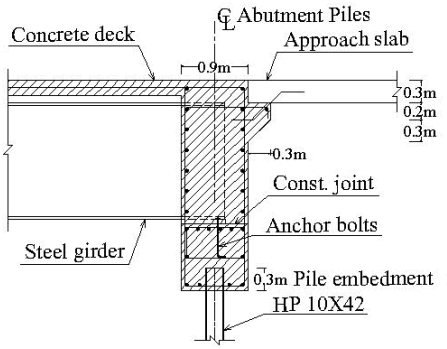
The soil around the piles is considered clay, which is common in most locations in Tennessee. Properties of medium clay and hard clay are selected from the geotechnical reference (Coduto, 1999) in order to represent soil characteristics in Tennessee. The abutment wall backfilling is cohesionless clean sand with properties based on experimental test data obtained at Brigham Young University (Cummins, 2009) for both the loosely and densely-compacted cases. Therefore, four different soil cases are defined for the sensitivity study, as shown in Table 1.



(a) Longitudinal Profile



(b) Deck cross section



(c) Abutment details

Figure 2 Massman Drive Bridge in Nashville, TN

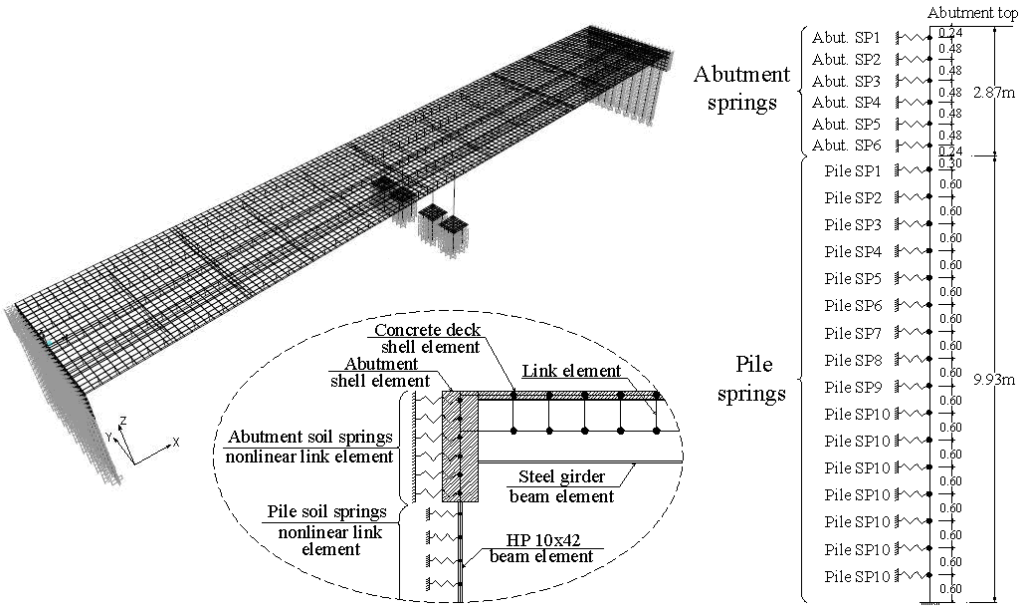


Figure 3 Massman Drive Bridge modeled in SAP2000

Table 1 Soil properties for the sensitivity study

Case	Soil around piles	Abutment backfill
1	Medium Clay ($c_u = 37.5\,kPa, \gamma = 14.61\,kN/m^3$)	Loosely-compacted clean Sand ($\phi = 37^o, c = 0, \gamma = 16.50\,kN/m^3$)
2	Medium Clay ($c_u = 37.5\,kPa, \gamma = 14.61\,kN/m^3$)	Densely-compacted clean Sand ($\phi = 40.5^o, c = 0, \gamma = 18.30\,kN/m^3$)
3	Hard Clay ($c_u = 200\,kPa, \gamma = 18.14\,kN/m^3$)	Loosely-compacted clean Sand ($\phi = 37^o, c = 0, \gamma = 16.50\,kN/m^3$)
4	Hard Clay ($c_u = 200\,kPa, \gamma = 18.14 kN/m^3$)	Densely-compacted clean Sand ($\phi = 40.5^o, c = 0, \gamma = 18.30\,kN/m^3$)

c_u = undrained shear strength of undisturbed clay; γ = effective soil density

Nonlinear soil springs around the piles

The procedures given in the American Petroleum Institute (API) are followed to define the p-y curves for clay material and model the nonlinear soil springs around the piles (American Petroleum Institute, 1993). The ultimate unit lateral bearing capacity of clay p_u is shown by EQ (1):

$$p_u = \begin{cases} 3c_u + \gamma X + J\dfrac{c_u X}{D} & for\ X < X_R \\ 9c_u & for\ X \geq X_R \end{cases} \quad (1)$$

Where p_u= ultimate resistance, *kPa* (psi), c_u = undrained shear strength, *kPa* (psi), D= pile diameter, *mm* (in.), γ = effective soil density, MN/m^3 (lb/in^3), *J*= dimensionless empirical constant, X = depth below soil surface, *mm* (in.), X_R = depth below soil surface to bottom of reduced resistance zone, *mm* (in.) and determined by EQ (2):

$$X_R = \frac{6D}{\dfrac{\gamma D}{c_u} + J} \quad (2)$$

After determining p_u, the *p-y* (load vs. deflection) curves for soil springs along the pile length are generated from Table 2. Note that $y_c = 2.5\varepsilon_c D$, where ε_c is the strain at 50% of soil ultimate resistance from undrained compression tests of undisturbed soil samples. For $c_u = 37.5$ and 200 kPa used in the analyses, corresponding ε_c values of 0.01 and 0.005 are selected. 0) For the different soil springs along the pile length shown in Figure 3 as Pile SP1, Pile SP2… the *p-y* curves are determined as shown in Figure 4 for the hard clay, in which *y* is the lateral displacement of the pile.

Table 2 Load-deflection curves for clay soil under cyclic loading (API, 1993)

$X > X_R$		$X < X_R$	
p / p_u	y / y_c	p / p_u	y / y_c
0	0	0	0
0.5	1.0	0.5	1.0
0.72	3.0	0.72	3.0
0.72	∞	$0.72\,X / X_R$	15.0
------	------	$0.72\,X / X_R$	∞

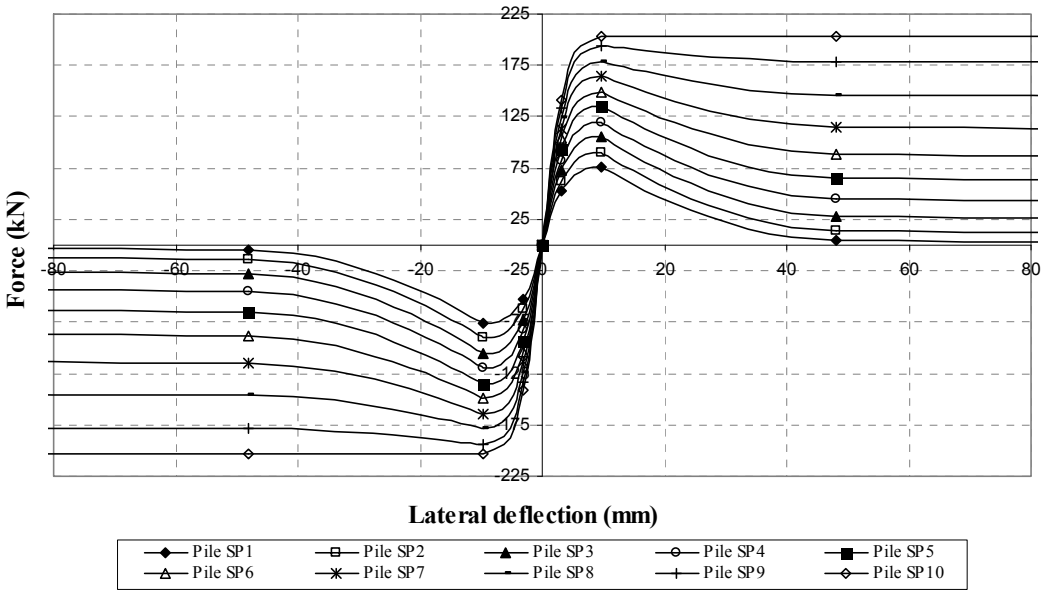


Figure 4 Force-deflection curves of pile springs under cyclic loading for hard clay

Nonlinear soil springs in back of the abutments

Based on a comprehensive study on nonlinear soil-abutment interaction for seismic design of bridges by Shamsabadi et al. (2007), a simplified hyperbolic force-displacement relation was proposed by EQ (3) and shown in Figure 5.

$$F(y_i) = \frac{F_{ult}(2Ky_{\max} - F_{ult})y_i}{F_{ult}y_{\max} + 2(Ky_{\max} - F_{ult})y_i} \tag{3}$$

where y = lateral displacement of the abutment, K= average soil stiffness as shown in Figure 5, F_{ult} = maximum abutment force (per unit length of the wall) developed at a maximum displacement of $y_{\max}$. For cohesionless soil backfilling F_{ult} can be determined by

$$F_{ult} = 0.5K_{pe}\gamma h^2 \tag{4}$$

where K_{pe}= seismic passive earth pressure coefficient, γ = soil density and h = height of the wall.

To determine the seismic passive earth pressure coefficient, a log spiral procedure is used following Shamsabadi et al. (2007) or NCHRP 12-70 (2008). Based on the location of the bridge, peak ground acceleration (PGA) and horizontal seismic coefficient (K_h) are determined. Then, a log spiral procedure using the NCHRP Figures is used to obtain K_{pe} for different abutment backfilling soils.

Based on the experimental test results obtained at Brigham Young University (Cummins, 2009), $y_{\max} = 0.024H$ for loosely-compacted clean sand backfilling and $y_{\max} = 0.03H$ for densely-compacted clean sand backfilling where H was the height of the pile cap. Moreover, considering the test results two values of K = 120 kN/cm/m and K = 180 kN/cm/m have been selected for loosely-compacted clean sand backfilling and densely-compacted clean sand backfilling, respectively. These K values are then adjusted for the 2.87 m wall height according to the Caltrans specifications (Caltrans, 2006) and K = 120(2.87m)/1.68m = 205 kN/cm/m and K = 180(2.87m)/(1.68m) = 307.5 kN/cm/m were assigned for loosely-compacted backfilling and densely-compacted backfilling, respectively.

Following the approach above, as shown in Figure 6, force displacement relations for unit length of the wall for two different cases of loosely-compacted and densely-compacted sand backfilling are determined and modeled by nonlinear link elements in the bridge model.

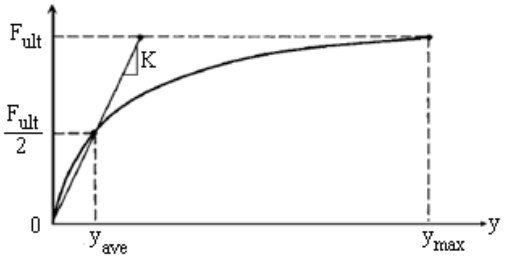


Figure 5 Hyperbolic force-displacement formulation

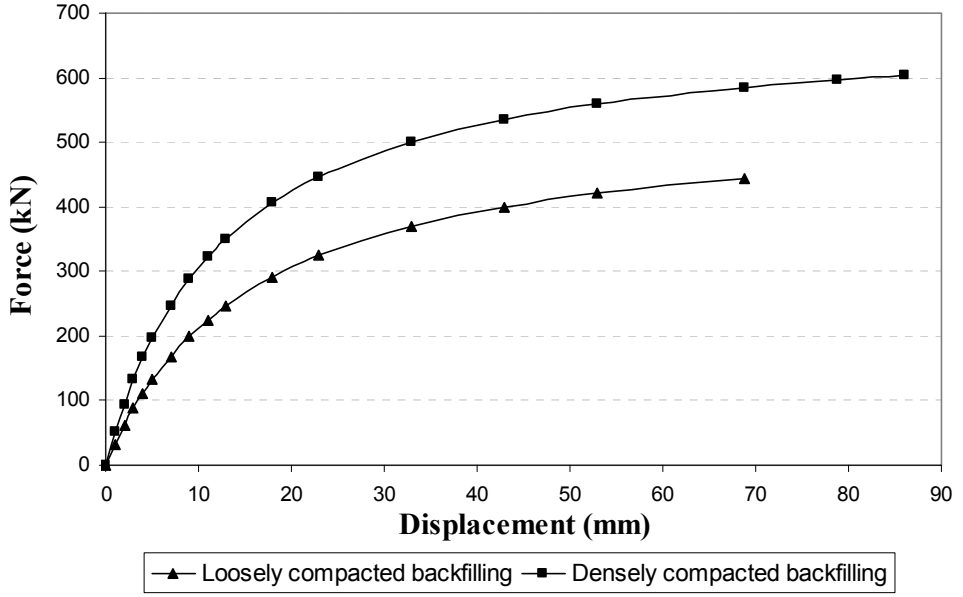


Figure 6 Force displacement relations for abutment backfilling

4) MODAL ANALYSIS AND SENSITIVITY STUDIES

In order to evaluate the effect of different clay materials around the piles and different levels of soil compaction in back of the abutments on dynamic properties of the integral abutment bridge, modal analysis is performed using the three dimensional finite element model of the bridge for the 4 cases defined in Table 1. The results of the modal analyses include different mode shapes in all three directions, but in this paper, since the focus was to investigate the effect of soil material around the piles and the levels of soil compaction in back of the abutments, only the longitudinal mode shapes are presented and discussed, which are numbered only considering the longitudinal direction modes instead of all the modes. These longitudinal mode shapes, for two different cases of piles in medium clay and hard clay, are shown in Figures 7 and 8, respectively, and the corresponding natural frequencies are shown in Table 3.

Table 3 Natural frequencies of Massman Drive Bridge for longitudinal modes (Hz)

Longitudinal Mode #	Case 1	Case 2	Case 3	Case 4	Case 1&2	Case 3&4	Case 1&3	Case 2&4
	Medium clay Loose backfill	Medium clay Dense backfill	Hard clay Loose backfill	Hard clay Dense backfill	Diff %	Diff %	Diff %	Diff %
1	2.07	2.09	2.10	2.14	1	2	2	2
2	4.67	5.54	5.17	5.83	19	13	11	5
3	7.61	7.70	7.83	7.94	1	1	3	3
4	9.24	9.24	19.66	19.66	0	0	113	113

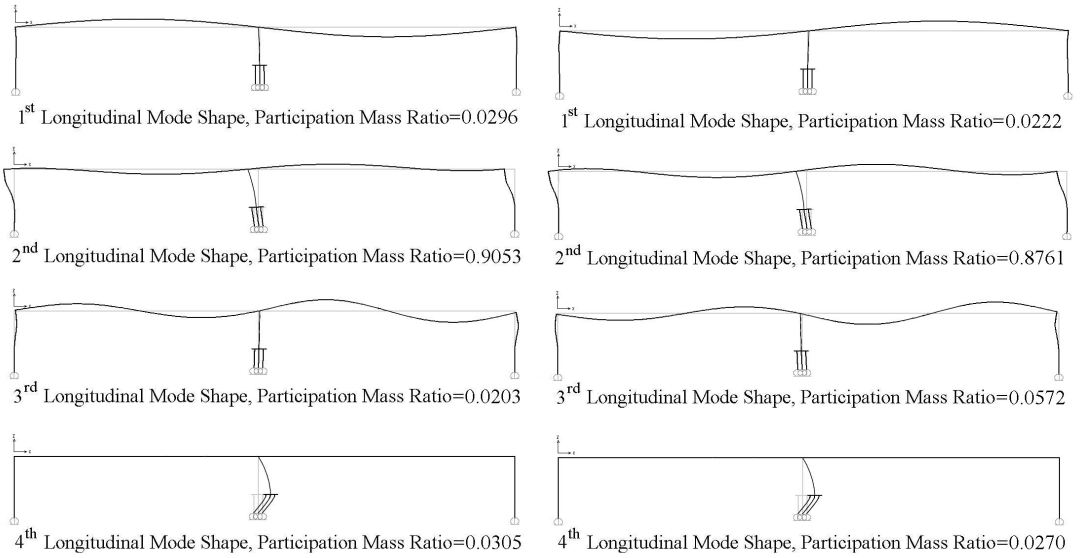
**Positive means increasing*

As shown in Figures 7 and 8, the longitudinal mode which contributes the most to the seismic analysis is primarily the second mode with frequency shown in Table 3. From Table 3, it is clear that the dominant frequency increases by about 19% and 13% for the piles in medium clay and hard clay respectively, when the sand backfilling varies from loosely to densely compacted. The dominant frequency increases by about 11% and 5% for loosely-compacted sand backfilling and densely-compacted sand backfilling respectively, when the clay around the piles varies from medium to hard. Therefore, the bridge dominant longitudinal natural frequency will increase considerably by compacting the sand backfilling of the abutment wall.

5) SEISMIC ANALYSIS AND SENSITIVITY STUDIES

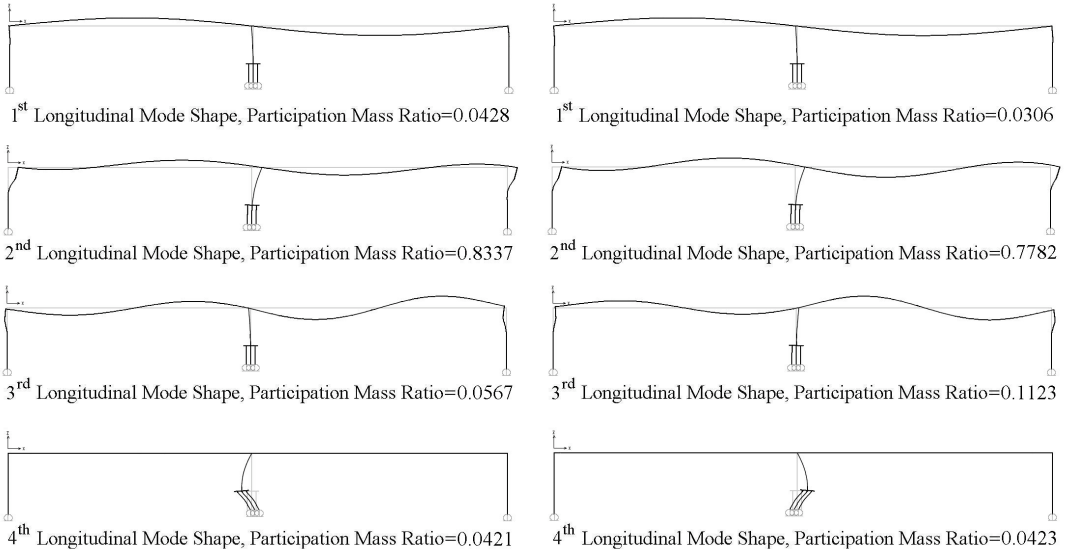
The Massman Drive Bridge is located in Nashville, Tennessee, which is in a low seismic region with peak ground acceleration (PGA) equal to 0.086g. In order to obtain a better understanding of the seismic response of integral abutment bridges in Tennessee, the Memphis region is considered instead with peak ground acceleration equal to 0.39g. The bridge is studied using the IMPVALL/I-ELC180 component of El Centro earthquake (Imperial Valley, 1940) scaled to the PGA of 0.39g. Nonlinear time history analyses are performed using the scaled component of El Centro earthquake applied in the longitudinal direction of the bridge. The same four cases defined in Table 1 are considered here, similar to the modal analyses, to investigate

the effect of clay stiffness around the piles and the levels of sand compaction in back of the abutments on seismic behavior of the bridge. The results of the nonlinear time history analyses are presented in Figures 9 and 10 for maximum pile deflections and maximum pile moments, and in Tables 4 and 5 for maximum abutment displacement and maximum girder moments.



(a)Loosely-compacted backfilling (b) Densely-compacted backfilling

Figure 7 Longitudinal mode shapes of bridge model for piles in medium clay



(a) Loosely-compacted backfilling (b) Densely-compacted backfilling

Figure 8 Longitudinal mode shapes of bridge model for piles in hard clay

Maximum pile deflection and abutment displacement

The maximum lateral deflections of the piles during the time-history analysis were compared, and the most critical pile was identified. The maximum deflection along the height of this pile is plotted in Figure 9 for all four cases, where it is obvious that the maximum lateral deflection of the pile along the length is always located at the pile-abutment interface. The maximum value of this deflection from all cases is 19.7 mm for **case 1**, with medium clay around the piles and loosely-compacted sand backfilling behind the abutments, a value less than the limiting value of 25.4 mm proposed by the Tennessee Department of Transportation (TDOT). The minimum value from all cases was 8.6 mm for **case 4**, with hard clay around the piles and densely-compacted sand backfilling behind the abutments. Therefore, it is clear that the pile deflection is affected by the soil stiffness both behind the abutment and around the piles, and the pile deflection will decrease when the soil stiffness increases, in other words, when the abutment backfilling is compacted or the piles are located in firmer clay, or both.

The maximum lateral displacements at the top and the bottom of the abutment walls during the time-history analysis are shown in Table 4 for all four cases. The maximum wall lateral displacements are generally larger at the bottom and match well with the pile deflection.

Maximum moments along abutment piles

The maximum moments along the piles during the time-history analysis were compared and the most critical pile was also identified. The maximum moment along the height of this pile during the time-history analysis is plotted in Figure 10 for all four cases, where it is obvious that the maximum moment is always located at the pile-abutment interface. The maximum value of this maximum moment from all cases is 240.99 kN.m for **case 3**, with hard clay around the piles and loosely-compacted sand backfilling behind the abutments. The minimum value from all cases is 129.40 kN.m for **case 2**, with medium clay around the piles and densely-compacted sand backfilling behind the abutments.

Therefore, it is clear that the pile moment is affected by the stiffness of the soil behind the abutment and around the piles in a different way from pile deflection. It is clear that the maximum pile moment will decrease when the abutment backfilling is compacted and increase when the piles are located in firmer clay. The maximum pile moment will be reduced about 25% and 18% by densely compacting the abutment backfilling, when the piles are in medium and hard clay, respectively.

Maximum moments in steel girders

The maximum positive and negative moments in steel girders during the time-history analysis are shown in Table 5 for all the cases. The maximum positive girder moment is generally located at the middle of the longer south span (44.81 m), and the maximum negative girder moments are generally located at the pier and the abutments.

For the steel girder moments at the middle of south span and at the pier, the maximum values happen in **case 1**, with medium clay around the piles and loosely-compacted sand backfilling behind the abutments, while the minimum values happen

in **case 4**, with hard clay around the piles and densely-compacted sand backfilling behind the abutments. For the steel girder moments at the abutments, the maximum value happens in **case 3**, with hard clay around the piles and loosely-compacted sand backfilling behind the abutments, while the minimum value happens in **case 2**, with medium clay around the piles and densely-compacted sand backfilling behind the abutments.

Therefore, it seems that the steel girder moments along the bridge, i.e., inside the span and at the pier will generally decrease with the soil stiffness both behind the abutment and around the piles, similar to the pile deflection and abutment displacement. On the other hand, the maximum steel girder moments at the abutment will decrease when the abutment backfilling is compacted and increase when the piles are located in firmer clay, similar to the pile moment, since these two moments are closely related.

Based on the analyses results, it is recommended to compact the backfilling behind the abutments densely for the integral abutment bridges in clay soil, in order to control the pile deflection, the abutment displacements, the maximum bending moments in the pile as well as the maximum bending moments in the steel girders.

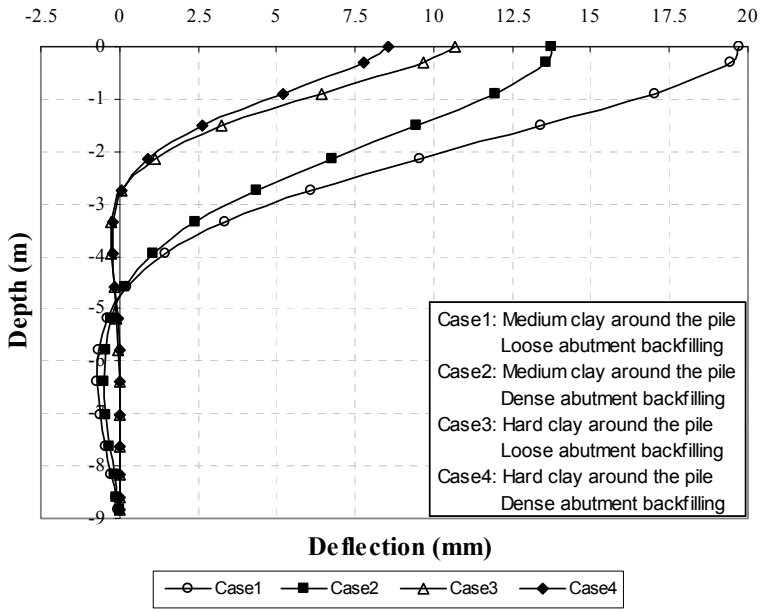


Figure 9 Maximum lateral deflections of abutment steel HP piles

Table 4 Maximum abutment displacement

Case	Description	North abutment (mm)		South abutment (mm)	
		Top of wall	Bottom of wall	Top of wall	Bottom of wall
Case 1	Medium clay Loose backfill	-17.6*	-19.4	17.6	-19.7
Case 2	Medium clay Dense backfill	-11.4	-13.4	11.4	-13.7
Case 3	Hard clay Loose backfill	-10.2	-10.8	10.2	-10.7
Case 4	Hard clay Dense backfill	-8.0	-8.5	8.0	-8.6

** Negative means toward the soil, positive means away from the soil*

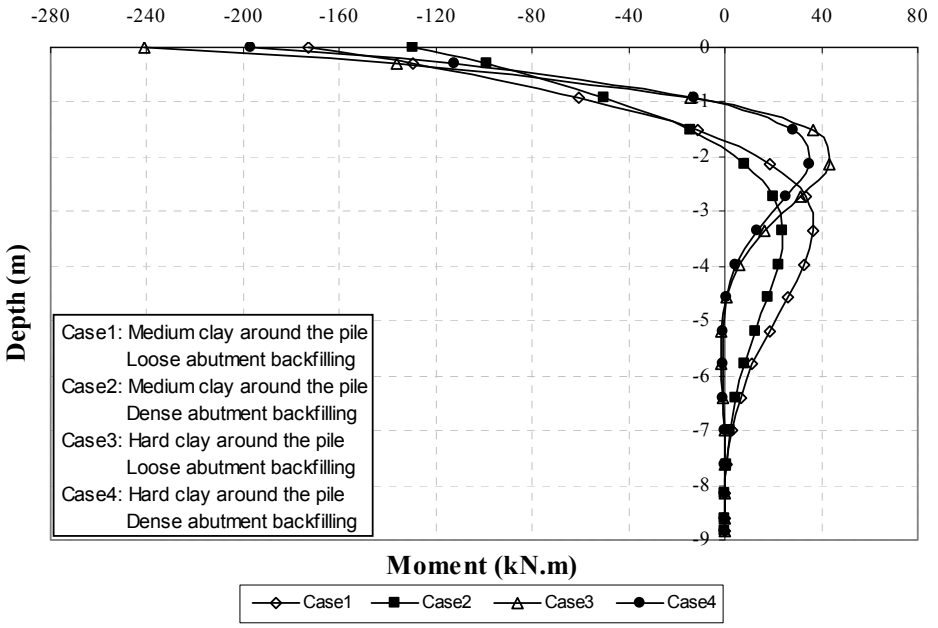


Figure 10 Maximum moment distribution in abutment steel HP piles

Table 5 Maximum moments in steel girders

Moment M_u (kN.m)	Case 1	Case 2	Case 3	Case 4	Case 1&2	Case 3&4	Case 1&3	Case 2&4
	Med. clay Loose backfill	Med. clay Dense backfill	Hard clay Loose backfill	Hard clay Dense backfill	Diff %	Diff %	Diff %	Diff %
M_u^- @Pier	2239.84	2193.99	2059.25	2027.54	-2	-2	-8	-8
M_u^+	1656.05	1498.06	1545.41	1446.94	-10	-6	-7	-3
M_u^-@ Abutment	1465.38	1391.57	1563.15	1509.39	-5	-3	7	8

**Positive means increasing; Negative means decreasing*

CONCLUSION

For the bridge discussed in this paper located in the State of Tennessee, the following conclusions can be drawn from the dynamic and seismic analyses:

(1) Compacting the sand backfilling behind the abutment wall will increase the dominant longitudinal frequency of the bridge considerably more than increasing the clay stiffness around the piles.

(2) Under seismic loading, the maximum pile deflection and the maximum abutment wall displacement are both at the pile-abutment interface. This deflection is affected by the soil stiffness both behind the abutment and around the piles, and will decrease when the abutment backfilling is compacted or the piles are located in firmer clay, or both.

(3) Under seismic loading, the maximum moment in the pile is at the pile-abutment interface. The pile moment will decrease when the abutment backfilling is compacted and increase when the piles are located in firmer clay. Therefore, this

moment is maximum for the case with piles in hard clay and loosely-compacted backfilling, and minimum for the case with piles in medium clay and densely-compacted backfilling.

(4) The maximum steel girder moments at the pier and the mid-span will generally will decrease when the abutment backfilling is compacted or the piles are located in firmer clay, similar to the pile deflection and abutment displacement. However, the maximum steel girder moments at the abutments will decrease when the abutment backfilling is compacted and increase when the piles are located in firmer clay, similar to the pile moment.

(5) When the piles are located in firmer clay, although the pile deflection, the abutment displacement, and the maximum girder moment at the pier and the mid-span will decrease, the maximum pile moment and the maximum girder moment at the abutment will increase.

(6) Densely-compacted backfilling behind the abutments is generally recommended, since it will reduce the pile deflection, the abutment wall displacement, the steel girder moments, and particularly the pile moment.

ACKNOWLEDGEMENT

The research presented in this paper is funded by the Tennessee Department of Transportation (TDOT) and the Federal Highway Administration. Their financial support is gratefully acknowledged. The authors would also like to thank Mr. Ed Wassermann and Mr. Tim Huff for providing resources and technical help during the research activities. Any opinions, findings or conclusions expressed in this paper are those of authors and do not necessarily reflect the view of the sponsoring agencies.

REFERENCES

American Petroleum Institute (API). (1993). *"Recommended Practice for Planning, Designing, and Constructing Fixed Offshore Platforms—Working Stress Design.*" 20th Ed., API RP2A-WSD, Washington, D.C.

Burdette, E.G., Deatherage, J.H. and Goodpasture, D.W. (2000). "*Behavior of Laterally Loaded Piles Supporting Bridge Abutments-Phase I*." Center for Transportation Research, University of Tennessee, Knoxville.

Burdette, E.G., Deatherage, J.H. and Goodpasture, D.W. (2007). "*Behavior of Laterally Loaded Piles Supporting Bridge Abutments-Phase II*." Center for Transportation Research, University of Tennessee, Knoxville.

Caltrans (2006). *"Seismic Design Criteria*." California Department of Transportation.

Civjan, S.A., Bonczar, C., Brena, S.F., Dejong, J. and Crovo, D. (2007). "Integral Abutment Bridge Behavior: Parametric Analysis of Massachusetts Bridge." *Journal of Bridge Engineering*, ASCE, Vol. 12, No. 1, January/February, pp. 64-71.

Coduto, D.P. (1999) *Geotechnical Engineering Principles and Practice*. Prentice-Hall, Saddle River, New Jersey.

Cummins, C.R. (2009) *"Behavior of a Full-Scale Pile Cap with Loosely and*

Densely-Compacted Clean Sand Backfill under Cyclic and Dynamic Loadings." Master Thesis, Brigham Young University, April.

Dehne, Y. and Hassiotis, S. (2003). "Seismic Analysis of Integral Abutment Bridge-Scotch Road I-95 Project." *16th ASCE Engineering Mechanics Conference*, University of Washington, Seattle, July.

Faraji, S., Ting, J.M., Crovo, D.S. and Ernst, H. (2001). "Nonlinear Analysis of Integral Bridges: Finite Element Model." *Journal of Geotechnical and Geoenvironmental Engineering,* ASCE, Vol. 127, No. 5, May, pp. 454-461.

FHWA/RD-86/102 *(1986). Seismic Design of Highway Bridge Foundations*., Federal Highway Administration.

Goel, R.K. (1997). "Earthquake Characteristics of Bridges with Integral Abutments." *Journal of Structural Engineering*, ASCE, Vol. 123, No. 11, November, pp. 1435-1443.

Hassiotis, S., Khodair, Y., Roman, E., and Dehne, Y. (2006). *"Evaluation of Integral Abutments*." FHWA-NJ-2005-025.

Hopper, E.J. and Gomes, J.P. (1996). "*Field Study of an Integral Backwall Bridge*." Virginia Transportation Research Council, VTRC 97-T7, October.

Khodair, Y.A. and Hassiotis. S. (2005). "Analysis of Soil-Pile Interaction in Integral Abutment." *Journal of Computers and Geotechnics*, Elsevier, Vol. 32, pp. 201-209.

NCHRP 12-70 (2008). "*Seismic Analysis and Design of Retaining Walls, Buried Structures, Slopes and Embankment*." National Cooperative Highway Research Program, Transportation Research Board, Washington.

Reese L.C., Wang, S.T., Isenhower, W.M. and Arrellaga, J.A. (2004). "*Computer Program LPILE Plus Version 5.0 Technical Manual*, A Program for the Analysis of Piles and Drilled Shafts under Lateral Loads." Austin, Ensoft, Inc., July.

Shamsabadi, A., Rollins, K.M. and Kapuskar, M. (2007). "Nonlinear Soil-Abutment-Bridge Structure Interaction for Seismic Performance-Based" Design. *Journal of Geotechnical and Geoenvironmental Engineering*, ASCE, Vol. 133, No.6, June, pp. 707-720.

Spyrakos, C. and Loannidis, G. (2003). "Seismic Behavior of a Post-Tensioned Integral Bridge Including Soil–Structure Interaction." *Journal of Soil Dynamics and Earthquake Engineering*, Elsevier, Vol.23, pp. 53-63.

Wasserman, E.P., and Walker, J.H. (1996). "Integral Abutments for Steel Bridges." *Highway Structures Design Handbook*, Vol. 2, American Iron and Steel Institute, Chicago, IL.

Erection of the cable net roof for the London 2012 Olympic Stadium

N. Cole (CEng, MICE)[1] and P. Hulme (BEng)[2]

[1] Design Engineer; On Behalf of Watson Steel Structures Ltd. Ramboll, 60 Newman St, London, W1T 3DA; Tel: +44 (0)20 7631 5291; Fax +44 (0)20 7323 4645
email: nicholas.cole@ramboll.co.uk
[2] Contracts Manager; Watson Steel Structures Ltd, Lostock Lane, Lostock, Bolton, Lancashire, BL6 4BL; Tel: +44 (0)1204 699 999; Fax +44 (0)1204 694 543
email: paul.hulme@watsonsteel.co.uk

ABSTRACT

Designed by Populous (architects) and Buro Happold (structural engineers) and fabricated and erected by Watson Steel Structures Ltd, the roof over the London 2012 Olympic Stadium covers an area of more than 24,500m^2. The construction of the cable net roof posed many complex engineering problems, culminating in the erection of the 14 lighting towers, perched on the leading edge of the roof and supported by a secondary cable net. The entire main cable net, including access gantries, was lifted in one operation involving the simultaneous operation of 28 pairs of strand jacks to lift and pre-stress the cable net roof structure. The design of the staged lifting procedure meant that no additional strand jacks were required for the connection of other cables. An innovative method of lifting the lighting towers into position, using a single crane, was developed to save time and avoid the use of a second crane in a tight location.

This paper covers the fabrication of the roof elements, the staged erection and pre-stressing of the main cable net and also the erection of the stadium's signature lighting towers.

INTRODUCTION

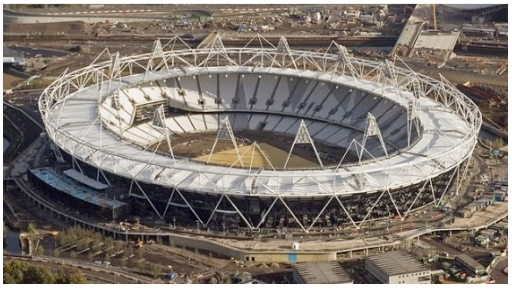
a)  b) 

Figure 1 – London Olympic Stadium ((a) Photographer: Phil Wright)

The roof over the 80,000 capacity London 2012 Olympic Stadium (Figure 1) forms the crown over a highly efficient stadium design, incorporating only 10,000t of steelwork for the entire stadium structure. The form of the roof is commonly known as a 'Bicycle wheel' cable net roof, as shown in Figure 2, and was first used for stadium roof designs in the early 1980's. As with a bicycle wheel, the radial cables are pre-stressed between the compression ring (rim) and tension ring (hub) to avoid any slack cables under extreme load cases and provide the strength and stiffness required to span over the seats below. The pre-stress also serves to provide geometric stiffness to the compression truss and resists global buckling of the truss.

Stadium roof statistics:

- The roof covers an area of approximately 20,000m^2.
- There are over 14,000m of spiral strand cables ranging from 80mm diameter to 25mm diameter.
- The compression truss weighs approximately 2500t.
- Each of the 14 lighting towers contains up to 45 lights that were installed and operational prior to erection of the towers.
- Lifting equipment with a total capacity of 6800t was required to pre-stress the 600t primary roof cable net.
- The largest crane used on site was a 1350t capacity, Liebherr LR11350 crawler crane, the largest in the UK at the time.

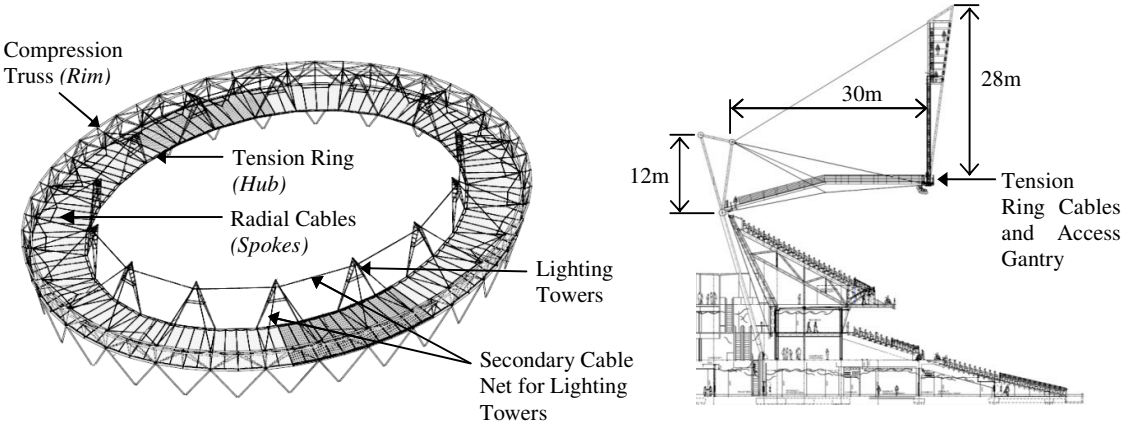


Figure 2 – Roof structure definitions **(Images: Buro Happold, Populous)**

The cable net roof consists of 28 'major' radial gridlines forming the main roof support, with an additional 84 'minor' gridlines for the support of the PVC coated polyester fabric covering. This divides the roof into 112 gridlines at approximately 6m spacing at the leading edge of the roof. The tension ring consists of ten 60mm diameter cables that are connected to steel 'nodes' (Figure 4) that also support the access gantry and the lighting tower bases.

Throughout the design and construction of the 2012 Olympic Stadium roof 'demountability' was a key consideration. It is intended that the stadium will be converted for use on a smaller scale following the 2012 Olympics, which will most likely involve the removal of the current roof for replacement with a smaller permanent roof.

FABRICATION

Compression Truss

The final forces developed in the cable net are a direct result of the accuracy that the compression truss has been fabricated and built to and, as a result, tight tolerance requirements were specified for the length of individual members and the angle of the end plates. The chord members were fabricated in a continuous run in the workshop (Figure 3a), with each segment being fabricated slightly oversize and the 'pipe flange' bearing connections machined to fit with the previous segment, following a survey of the previous end plate. The first fabricated segment was kept in the factory and used for the fabrication of the last segment to ensure correct fit up of all pieces. This method ensured that the final piece could be installed with minimal adjustments to the adjacent temporary truss supports and to a high degree of accuracy.



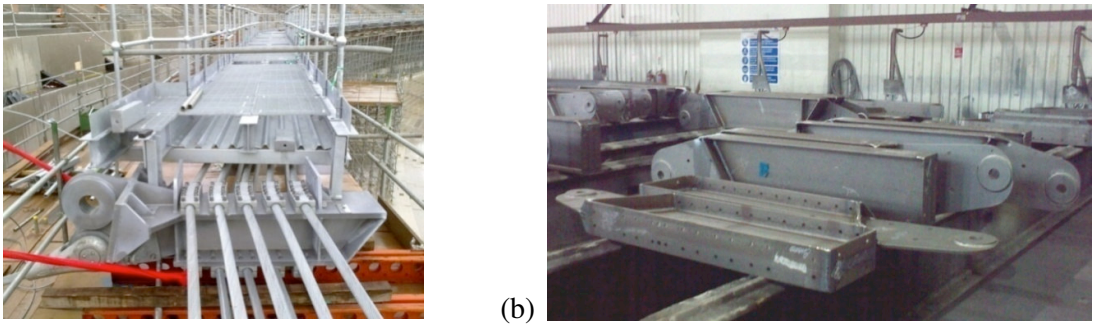
(a) (b) (c)

Figure 3 – Compression truss (a) Chords fabricated in factory to provide exact fit up; (b) Site assembled 'bay' (36m) being lifted out of site erection jig; (c) Final piece of compression truss being installed

Surveys of the compression truss were continuously taken during construction to check the tolerances. However, with over 40mm radial expansion of the truss due to the winter-summer temperature variation and a 6 month construction program, the steelwork temperature had to be measured at the time of each survey and used to alter the theoretical model for comparison with the survey.

Nodes

Typically, the tension ring/ radial cables for roofs of this form are connected by cast steel nodes, incorporating all cable connections and clamping details. For the 2012 Olympic Stadium, it was found that significant material and cost savings could be made by fabricating the nodes from a combination of plate material for the major nodes and standard beam sections for the minor nodes (Figure 4). Cable clamps were manufactured separately as cast items and bolted to the nodes on site. An additional feature of the design of the nodes was the incorporation of permanent fabricated plates for the connection of the temporary strand jack cables during erection. These can be seen at the rear of the top flanges of the nodes and are mostly concealed by the gantries and fabric roof covering when complete (Figure 4a and Figure 11). These permanent connection points simplified the erection and will also aid the deconstruction in several years time.



(a) (b)

Figure 4 – (a) Major node showing cables connected with clamps and gantry installed (b) Minor nodes during fabrication

Cable Clamps

The design of the cast cable clamps was rationalised to allow a single clamp mould to be used for all major nodes and a second mould for the minor nodes. These moulds had tapered cable grooves to accommodate the full range of cable kink angles around the oval roof shape. The clamps were installed with aluminium sleeves wrapped around the cables to reduce localised bearing stresses on the surface of the cable strands.

Following the requirements of EC3 1-11, a test rig, mimicking the final condition of the clamps was built in the steel fabricators workshop and a piece of test cable and two cable clamps were tested (Figure 5). The tests were carried out at varying axial loads in the cable to measure any effect of the reduction in cable diameter, due to Poisson's ratio, that may reduce the clamping force. The ultimate clamp slip resistance was measured for each load condition and it was found that the variation in load had negligible effect on the overall slip resistance.

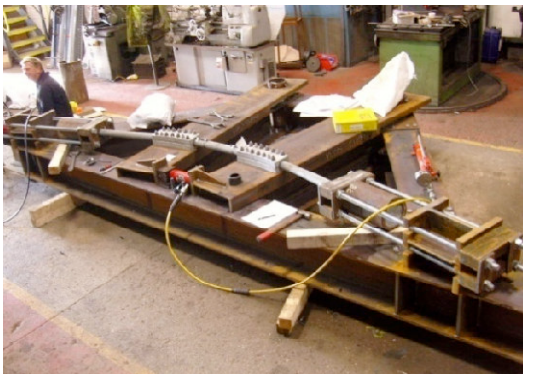


Figure 5 – Cable clamp test rig in steel fabricators workshop

PREPARING FOR THE BIG LIFT

Following completion of the precast terracing and compression truss, a scaffold was erected on the terrace, directly below the final position of the tension ring. The tension ring cables and nodes were laid out onto the temporary scaffold and connected, followed by the access gantry which is connected to the top of the nodes. The gantry, running the entire length of the tension ring, was lifted with the cable net to avoid the 112 additional lifts that would have been required for its installation in the air. An added advantage of lifting the gantries with the cable net was that it provided instant access to the roof and strand jacks as soon as the roof was lifted. Each gantry segment was, therefore, designed to allow a large range of movement in all axes to avoid any damage to the units during the lift operation.

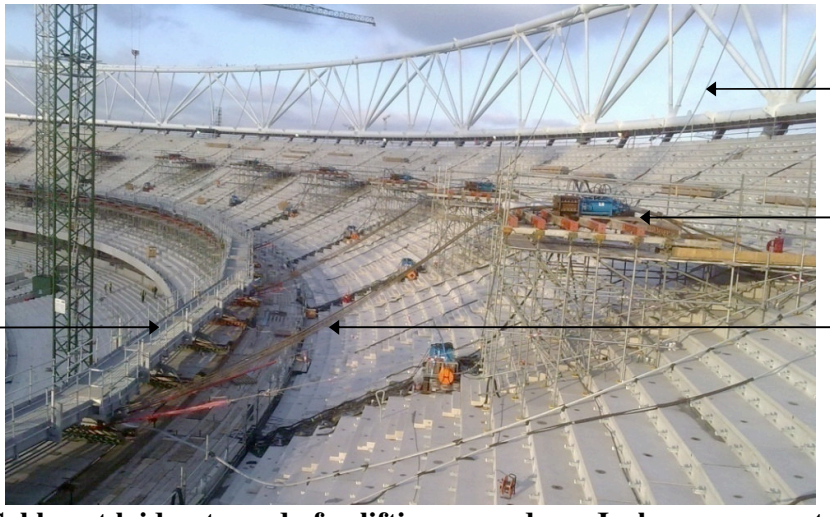


Figure 6 – Cable net laid out, ready for lifting procedure. Jacks are connected to the 28 main suspension cables.

The 112 lower radial cables were connected directly to the tension ring nodes and laid across the terrace, whilst the 28 main suspension cables were hung from the top chord of the compression truss and connected to pairs of strand jacks midway up the terrace. The jacks were connected to each other, and to the suspension cables, via bespoke jacking beams (Figure 7) and the temporary steel strands linked the jacks to the strand termination plates on the major nodes. The strand jacks, supplied by Fagioli Ltd, varied in capacity between 100t and 180t and were required to pre-stress the most highly loaded cables up to 2600kN, giving a total lifting capacity in excess of 6800t.



Figure 7 - Strand jack arrangement

LIFTING OPERATION

Due to the hierarchy of major and minor cables, it was only necessary to pull from the 28 major gridlines using pairs of linked strand jacks. Each strand jack is an electronically operated hydraulic ram that uses a system of mechanical grips to climb along the temporary jacking strands. The jacking operation used 'flying jacks' (Figure 7 and Figure 8) to pull the free ends of suspension cables towards the tension ring until the final connection could be made. The use of flying jacks simplified the temporary works that would have been required for the more standard system of jacks mounted on the compression truss as they used the permanent load paths without imposing any additional temporary loads on the structure.

The jacking process involved the simultaneous operation of all 56 jacks, controlled from the main control cabin on the ground. The operation of the jacks was carried out to a tightly prescribed routine that had been developed from the simulation in the analysis model. The position of each of the 28 major nodes was monitored at regular intervals using pre-programmed survey instruments and compared with the theoretical positions from the analysis model. In addition, each jack gave a continuous load readout which was also recorded and compared to the model results throughout the operation. This combined force/ geometric surveying allowed any small deviations from the intended lifting procedure to be corrected quickly.

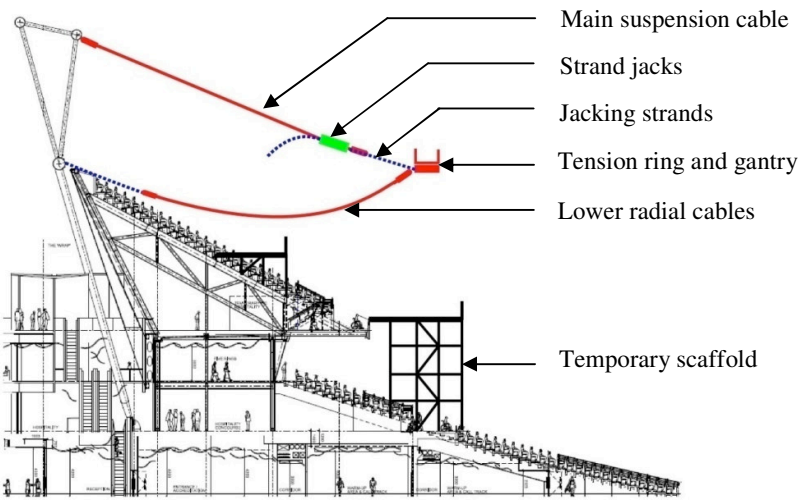


Figure 8 - Diagram showing intermediate jacking stage

The lift operation was conducted in several stages that had been analysed in detail previously:

1. Lift jacks from platforms individually and operate until they are suspended
2. Operate jacks until full tension ring lifts off
3. Operate jacks until tension ring reaches intermediate height (Figure 8).
4. Connect lower cables to compression truss
5. Complete jacking to full height, pre-stress cable net and insert pins in upper cables



Figure 9 - Initial lift off of tension ring

It was critical that the tension ring lifted off vertically from the scaffold platform as there was only a small allowance for horizontal movement on the surface of the scaffold (Figure 9). This was further complicated by the fact that, due to the oval shape of the stadium, the natural shape of the tension ring is in the form of a saddle under its self weight and the forces in the suspension cables vary around the stadium. This resulted in the North and South ends of the tension ring raising 7.5m clear of the scaffold before the East and West sides lifted off (Figure 10).



Figure 10 – Saddle shape of tension ring at the point of lift off

It took one day to lift the entire tension ring clear of the scaffold platform with a further day to raise the cable net 10m to the level of the bottom chord of the compression truss. This position was selected as the shortest distance between the tension ring and the bottom chord of the compression truss to reduce the lower cable connection loads. In this position, all the lower cables could be connected using either manually operated tirfors (pulling wires) or small manually operated hydraulic jacks. Once all the cables had been connected, the final lift and pre-stressing operations took a further day. The whole operation from the start of the lift to insertion of the last pin (Figure 11) was completed in less than 4 weeks and met both the positional and force tolerances that had been set on the cable net structure.

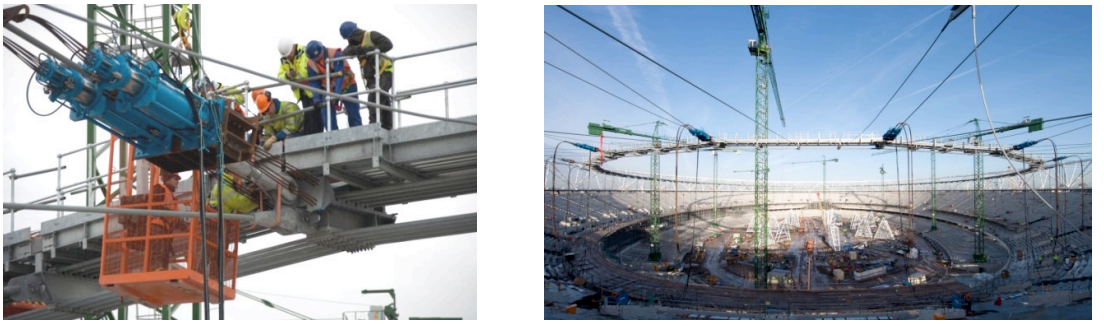
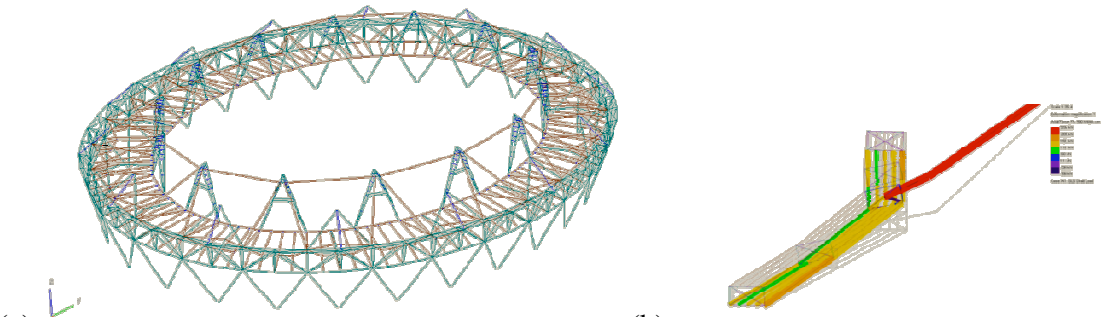


Figure 11 - Insertion of pins following final pre-stressing (Photographer: Adam Wilson)

ERECTION ANALYSIS

The roof erection analysis was carried out by the steelwork fabricator and was independently checked by the consultant engineers. The roof erection process involves a vertical range of movement in excess of 20m, during which time the cable net is highly flexible. For this reason, GSA, dynamic relaxation, analysis software was used for the analysis due to its ability to solve highly non linear problems.

Some additional software was written to solve the particular geometric requirements at each of the jacking stages. This calculated the distribution of cable forces to allow a perfectly vertical lift off of each tension ring node without affecting the plan position of the remaining nodes. It also minimised the forces required to connect the lower radial cables allowing connections to be made using hand operated equipment rather than high capacity jacks. These results were then inputted back into the main analysis model for confirmation.



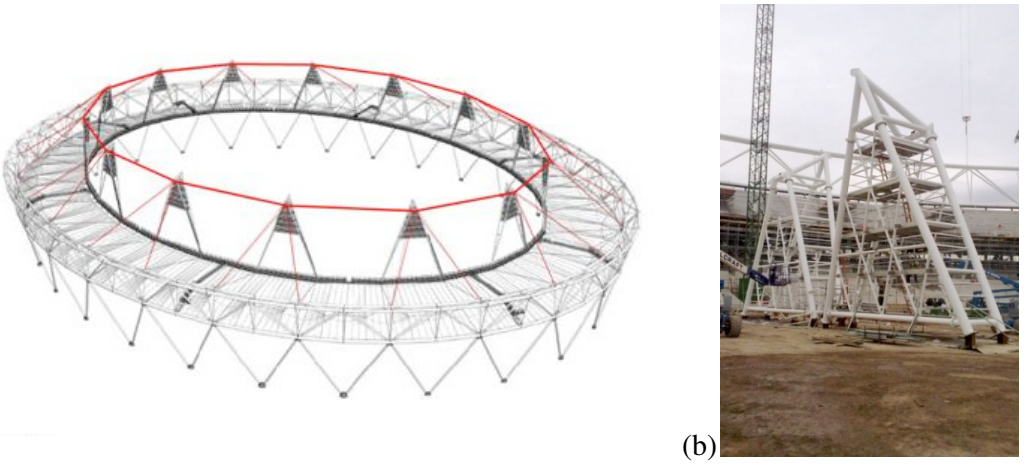
(a) (b)

Figure 12 – (a) Full roof analysis model (b) Localised twist on tension ring cables at lift off

Localised effects on the gantries and cables, as the tension ring lifted off, were analysed (Figure 12) and the results used to detail the connections to allow for adequate movement in all directions.

LIGHTING TOWERS

The 14 lighting towers sit on the tension ring major nodes and are supported by a secondary cable net. The secondary cable net functions in a similar manner to the primary net, with an upper tension ring, made up of 2 cables, spanning between the tops of the towers pulling the towers towards the centre of the field of play and radial backstay cables that are pre-stressed back to the compression truss (Figure 13).



(a) (b)

Figure 13 – (a) Lighting tower cable net (b) Construction of lighting towers at ground level

The stability system of this form of cable net is such that none of the 14 towers are stable until the final cable has been connected and pre-stressed. Several options were explored for the temporary stability of the towers and the final scheme saw them erected with a 40m long temporary strut connecting each tower back to the compression truss (Figure 14).

The tops of the lighting towers were constructed at ground level (Figure 13) and were fully fitted out with lights and electrical connections prior to lifting up onto the roof.

Each lighting tower weighed less than 35t but, due to the length of the reach over the tension ring, the main lift was completed using a 600t crawler crane fitted with a 30m luffing jib and 90t of superlift ballast (Figure 14). An innovative solution was developed to lift in the 6t temporary strut, to avoid the use of a second crane in a congested work area. This involved using two independent hooks from the same crane, an operation rarely done on this scale. The main hook supported the lighting tower itself, whilst a second hook, from the luffing jib, carried the temporary strut and could be operated, independently, to lower the strut into position.



Figure 14 - Lighting tower supported from main hook with temporary strut hung from luffing jib

For the erection of the lighting towers a staged analysis was performed for the addition of each tower. In each analysis stage the towers were checked for the 1 in 5 year wind load to ensure that the permanent design loads would not be exceeded in the temporary condition. This analysis included each stage of the lift on the crawler crane under an operational wind speed of 20m/s.

As for the main cable net lift, the erection of the lighting towers had been extensively analysed and was conducted with positional monitors on the tension ring and all lighting towers and force monitoring equipment on several members relaying data to be compared with the analysis results.



Figure 15 – Lighting towers supported on temporary struts prior to installation of lighting tower support cables

Following installation of all 14 towers on their temporary supports, the secondary cables were lifted into position and pre-stressed using small hollow ram hydraulic jacks. Before the temporary struts could be removed, it had to be verified that the cables had been pre-stressed to the required load and that the stability of the lighting towers had been transferred to the cable net system. A survey of the cable forces showed that in some locations the forces deviated significantly from the required values.

The analysis model was updated to reflect the surveyed geometry of the compression truss and lighting towers and it became apparent that small out of tolerances of the top chord of the compression truss resulted in large out of tolerances in the lighting tower cable forces due to the geometry of the backstay cables. To rectify the problem, the original cable net form finding process was repeated with the new model to provide new lighting tower cable lengths. These lengths were then used to provide adjustments for the adjustable turnbuckles, located on every backstay cable. Following the adjustments, the cable forces were re-surveyed and, to the relief of the engineers, had been corrected to the theoretical values.
The final erected geometry of the roof and lighting towers was verified by the main contractor using a full 3D laser scan of the entire stadium structure. The cable net pre-stress forces were also independently checked by a team from Porto University in Portugal using cable vibration measurements to calculate the natural frequencies and forces in the cables.

CONCLUSION

The detailed analysis results that had been prepared prior to the lift operations ensured quick checking of how the structure was behaving and gave the design and construction team added confidence in what was a technically challenging procedure. The lighting towers, perched on the roof edge in an apparent permanent state of instability, are testament to the challenges tackled by the construction team in realising a cutting edge design.

The successful completion of this complex engineering structure relied on the close coordination between consultants and contractors for every stage of the works to ensure that the project would be constructed safely as it was well outside the envelope of standard construction works.

ACKNOWLEDGEMENTS

Client: The Olympic Delivery Authority (ODA)
Architect: Populous (UK)
Structural Engineer: Buro Happold (UK)
Main Contractor: Sir Robert McAlpine (UK)
Steelwork Contractor: Watson Steel Structures Ltd (UK)
Strand Jacking Contractor: Fagioli Ltd (UK)
Cable Supplier: Bridon Cables (UK)
Steel Casting Foundry: William Cook Cast Products (UK)
Software: Analysis: GSA, Steelwork detailing: X-Steel

REFERENCES

Goppert, K (2007). "A Spoked Wheel Structure for the World's Largest Convertible Roof – The New Commerzbank Arena in Frankfurt, Germany." *Structural Engineering International 4/2007, Structures Worldwide*. IABSE.

Goppert, K (2007). "Structures for Stadium Projects." IABSE E-Learning Project *http://www.elearning-iabse.org/l22/index.html*

Holgate, A (1996). "The Art of Structural Engineering: The Work of Jorg Schlaich and his Team." Edition Axel Menges.

Lewis, W. J (2003). "Tension Structures: Form and Behaviour." Thomas Telford Ltd.

Challenges of Retrofitting an Existing Domed Stadium with a New Retractable Roof – BC Place Stadium, Vancouver, BC

David M. Campbell P.E., M.ASCE[1], and Karen A. Lynch P.E., M.ASCE[2]

[1] Principal and President of Geiger Gossen Hamilton Campbell Engineers P.C.
2 Executive Blvd Suite 410, Suffern, NY 10901 (845)368-3330 Fax(845)368-3366;
e-mail: dmc@geigerengineers.com
[2] Associate of Geiger Gossen Hamilton Campbell Engineers P.C.
2 Executive Blvd Suite 410, Suffern, NY 10901 (845)368-3330 Fax(845)368-3366;
e-mail: kal@geigerengineers.com

ABSTRACT-

BC Place Stadium in Vancouver, BC opened in 1983 as the first domed stadium in Canada covered by the largest air-supported roof in the world. As part of a major revitalization project the stadium dome is being replaced with a new retractable roof structure. The new roof, designed and engineered by an international team, is under construction with completion scheduled in late 2011. The new roof, designed for the 1 in 100 year snow and wind loads and current seismic requirements, is supported by the original stadium superstructure. The new roof structure is a post-tensioned radial cable truss, clad with tensile membrane with a center retracting pneumatic membrane.

The paper presents features of the new roof and addresses some of the unique challenges encountered in this unprecedented project. While the challenges overcome in the roof construction, now nearing completion, are worthy and manifold, this paper is limited to roof design due to required brevity. The roof construction will hopefully merit future publication.

INTRODUCTION-

BC Place Stadium is located in downtown Vancouver along the North Shore of False Creek. The original construction was undertaken on a relatively open site in what was then an industrial enclave at the fringe of the Vancouver urban center. The stadium development was a catalyst in the transformation of the False Creek eastern basin to a vibrant mixed use urban area. Indeed this success provided the first of many significant challenges to the revitalization of the stadium as construction access to the site had become highly constrained. What had been a relatively open site in the early 1980's is now a high trafficked urban site. Moreover, the greatest asset of the facility is its location and the surrounding land. These conditions were key in the decision to revitalize the existing stadium rather than to pursue a new build to respond to the increased demands and expectations for multi-purpose stadium facilities. Not coincidently, with consideration of a general refurbishment of the facility was consideration of the future of the stadium's air-supported roof; which had reached the end of its originally anticipated service life. Moreover in replacing the

roof the Owner hoped to transform the image of the venue. Consequently, the roof replacement became a major driver of the facility revitalization.

An initial feasibility study of roof replacement identified the key challenges. Site constraints and the facility's configuration all but necessitated supporting a new roof on the existing stadium superstructure. Evolution of the Building Code of British Columbia, based upon the National Building Code of Canada, was such that any new passive roof structure is subject to much greater snow loads and seismic demands. Moreover, the primary virtue of the active air-supported roof structure is its extremely minimal mass and its nearly 'invisible' dynamic demand on the supporting structure, it was likely that any passive structure with the capacity to carry the very significant design roof snow load of 2.2 kPa would create undue demands on the existing stadium superstructure. Site constraints also limited access for construction and erection. The primary objectives in design were to meet the Owner's desire to create a dramatic change in the building architecture and to minimize lost use of the venue.

The roof structure developed by the roof design team, Geiger Engineers with Schlaich Bergermann and Partner, Tensys and RWDI, responded to these and other significant challenges.

BC PLACE NEW ROOF STRUCTURE-

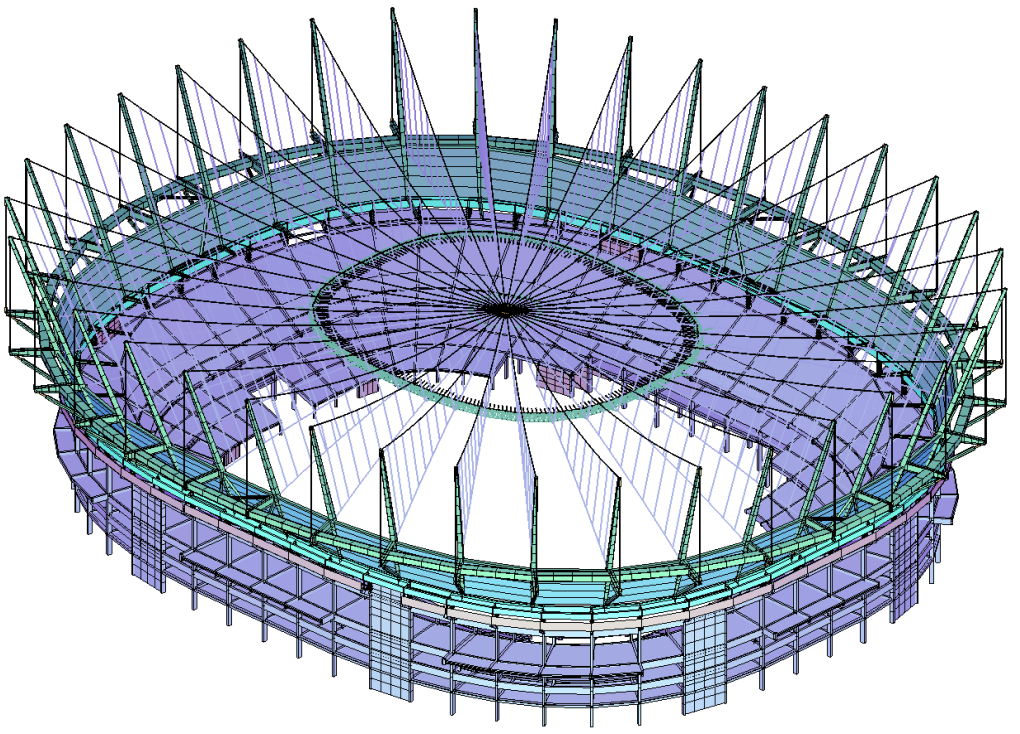


Figure 1. Stadium Superstructure with Primary Roof Structure, Membrane and All Cladding Removed

The new roof, developed to meet these criteria, is a tensioned membrane clad radial cable truss structure with a retractable center. The roof membrane is supported at the bottom radial cable chords.

The primary structural system is comprised of 36 structural steel masts supporting the radial cable truss, post-tensioned within a steel compression ring. The system is illustrated in Figures 1 & 2. The primary structure is exposed and featured architecturally realizing the desire of the Owner to transform the image of the stadium in its revitalization.

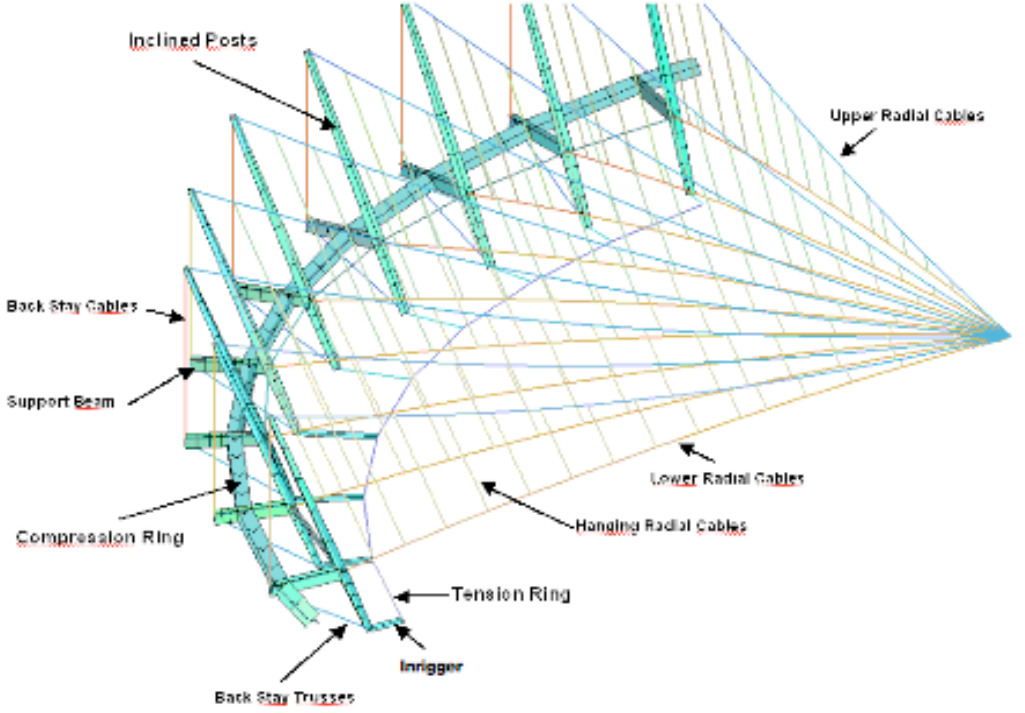


Figure 2. One Quarter of Primary Roof Structure, All Cladding Removed

To minimize the demand on the supporting structure the new roof structure is a 'closed system' (as was the original air-supported roof), equilibrating horizontal forces of the cable truss internally and only relying on the existing stadium superstructure for vertical support and to resist applied lateral loads. The tangential horizontal moment on a mast assembly resulting from the upper radial cables is resisted by the vertical separation of the tension and compression rings. The former is at the base of the roof and the latter nominally 12.5 m above this elevation. As the stadium plan and the original ring geometry was developed as a super-ellipse to equilibrate the air-supported roof's skew-symmetric cable layout the 36 sided polygons of the new rings would not follow this form, but rather were form-found with the cable truss prestress to provide a funicular equilibration of the cable forces. This resulted in the distinct architecture of the system with the exterior compression ring and interior tension ring nested in plan. The configuration concentrates structural material at the perimeter where it is easiest to erect and allowing the roof span to be solely cables. See Figure 3.

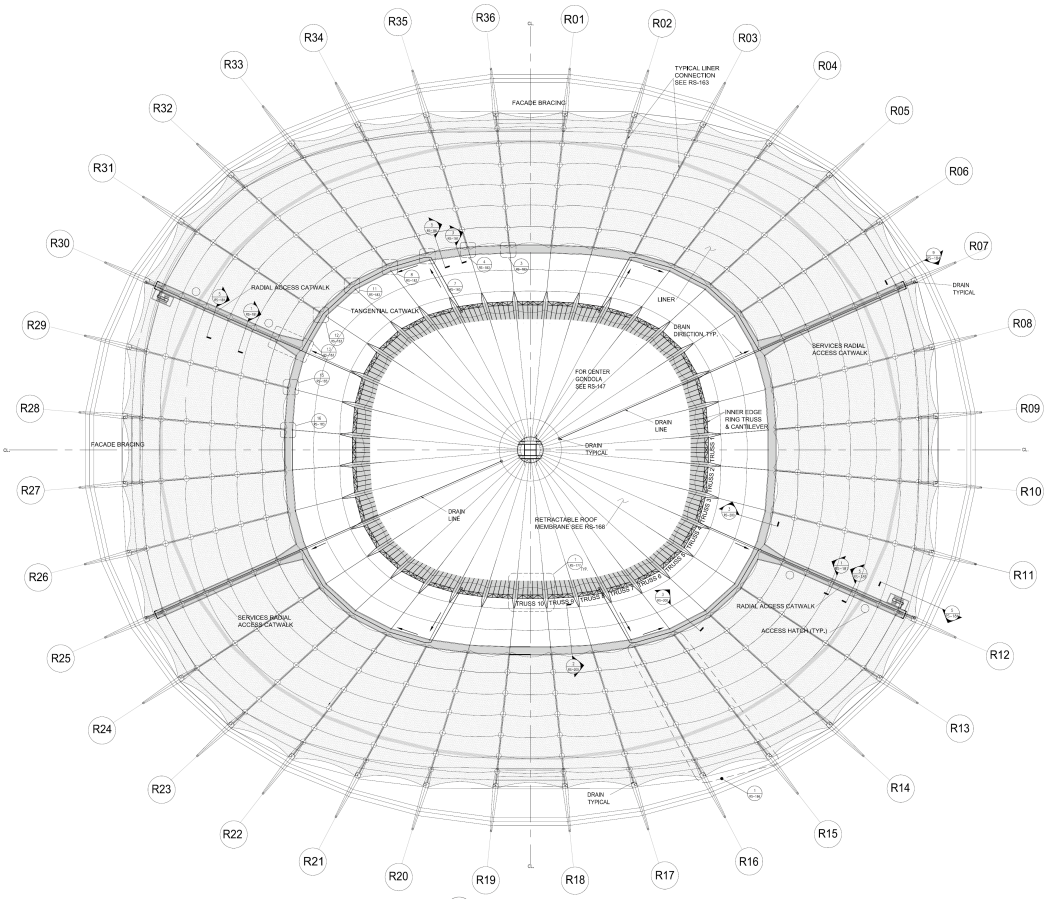


Figure 3. Stadium Reflected Ceiling Plan

The roof cladding consists of three systems, chosen for their low mass, functionality, serviceability, and suitability: 1) A retractable membrane roof over the field comprised of fluorocarbon composite fabric. 2) The fixed roof canopy, covering the balance of the roof, comprised of ptfe coated fiberglass roof membrane supported by steel arched ribs that span between radial bottom chord cables and 3) The clerestory façade comprised of ETFE film membrane panels and louvers.

RETRACTABLE ROOF-

The retractable roof, covering nominally 7,500 m^2, is comprised of pneumatically inflated cushions, which span between radial bottom chord cables. The interior space between the top and bottom membranes of the cushions is pressurized by compressors in the roof's center house. Internal operating pressure of the cushions is 500 Pa and is increased to a maximum of 2,000 Pa when the design snow load is present. (For reference, the operating pressure of the original air-supported roof was 270 Pa with a maximum of 700Pa.)

The retractable roof is a prefabricated membrane assembly supported by trolleys that ride on the radial bottom chord cables. When retracted, the membrane cushions are deflated and collected to the center node where they are stowed in a 20 m diameter receptacle for protection from weather. The roof is intended to be closed (fabric deployed) through the winter season and retracted during appropriate weather in the summer season. The deployed roof laps over a 'shelf' at the perimeter of the fixed canopy roof and seals to it by means of a pneumatic cushion.

FIXED ROOF CANOPY-

The fixed roof canopy is a ptfe-coated fiberglass fabric membrane supported on tied steel arch ribs. The ribs span between the radial bottom cable chords of the primary roof structure. The roof membrane is the same generic material as the existing air-roof. An acoustic liner is provided covering nominally 50% of the roof area.

At the inside edge of the fixed roof canopy is a glazed ring, cantilevered from the inner ring girder truss providing a "shelf" for retractable roof overlap. The glazed shelf is pitched to drain to a continuous gutter around the edge girder truss, which is drained via radial pipes to the roof perimeter. A personnel access walkway is provided on top of the ring to service retractable roof winches, seals, gutters and drains.

The outer roof perimeter is supported by built-up steel hollow members with trapezoidal cross-section spanning between masts. The top of the edge beams is a perimeter walkway. A continuous steel perimeter gutter is attached to the inside of edge beam below the fabric panel clamp-line.

ROOF SUPPORT AND MAST BEARING SYSTEM-

The primary structure is supported upon a new cast-in-place concrete transfer girder built within the original air-supported roof's precast compression ring. Additional steel columns were added parallel to the upper deck's outer column line to support the transfer structure and the new roof loads. See Figure 4. This work was completed in the Phase 1 of the project in 2009, while the facility remained in use. As the existing ringbeam was used as the air-supported roof's snow melt air distribution plenum, alternative snow melt air ducting was required for the winter of 2009-2010 during which time the facility was the host venue for the 2010 Olympic Winter Games Opening and Closing Ceremonies.

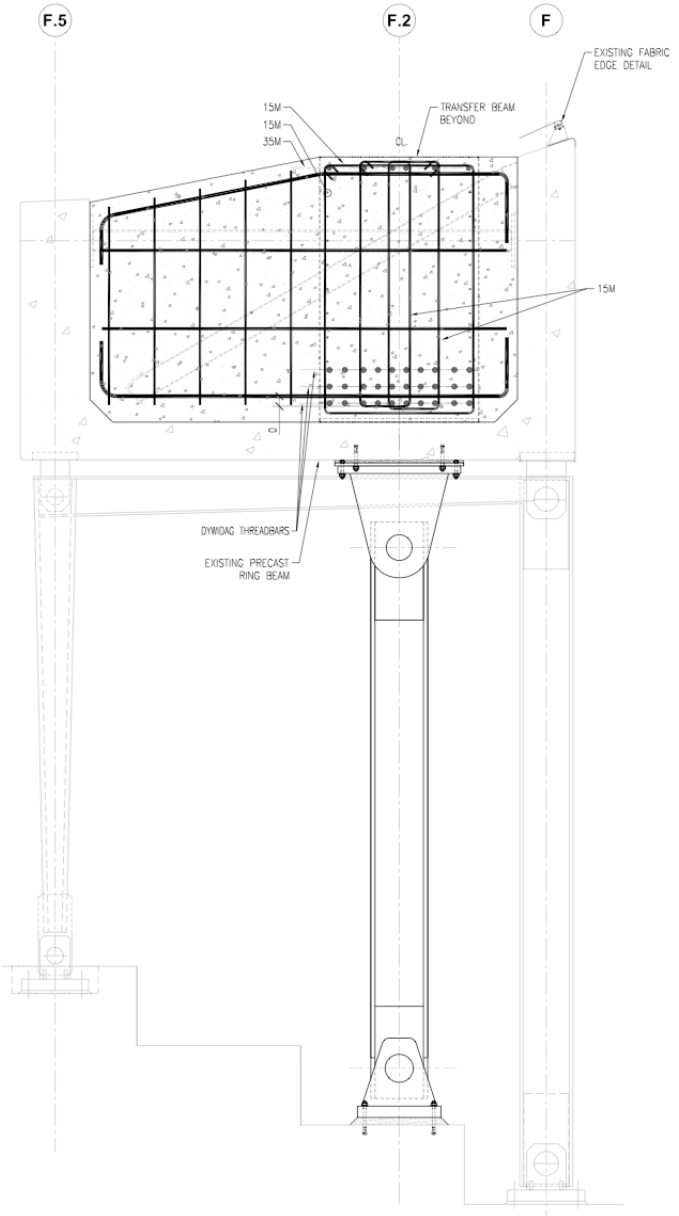


Figure 4. Section thru Existing Ring Beam and Transfer @ Support, Phase 1

The roof system is supported on 36 radially-guided slide & rotation bearings and laterally supported in the tangent direction at four braced bays at the cardinal points in plan. This uncoupling of the roof from the supporting structure allows for the relatively large deformations of the rings necessary to resist various load conditions without transfer of lateral loads to the existing supporting superstructure. However these large deformations, as much as 450mm, created challenges in supporting the mast bearings throughout their range of motion and in detailing the secondary façade clerestory structure. See Figure 5.

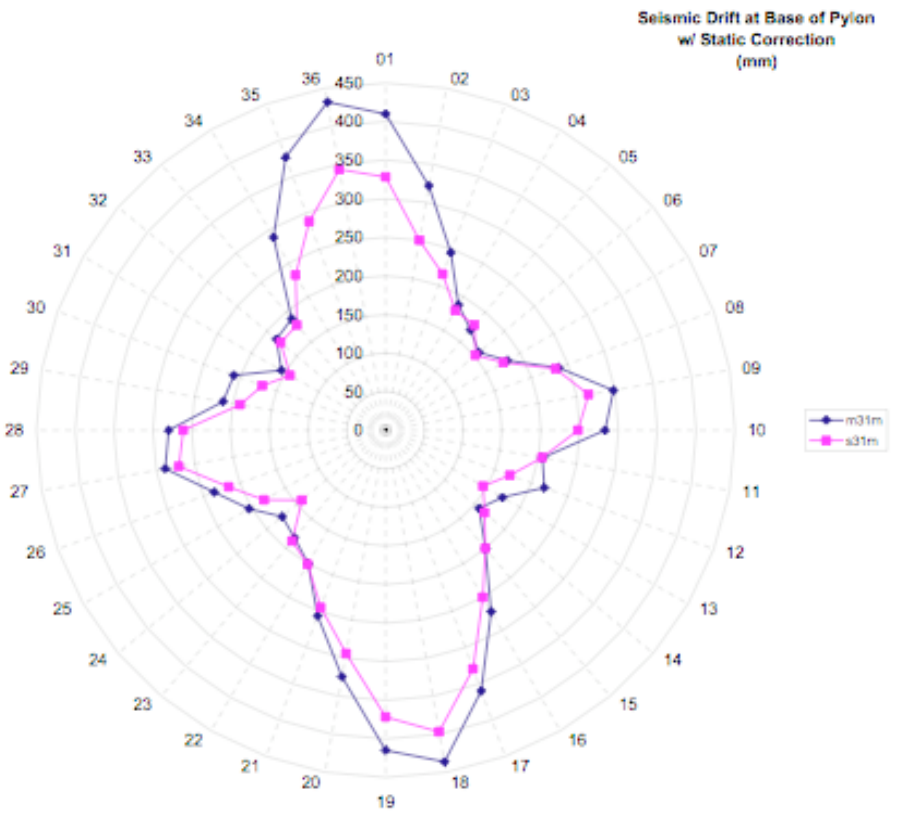


Figure 5. Radar Chart Unsigned Maxima of Seismic Drift at Mast Base Supports.

FAÇADE CLERESTORY-

The façade clerestory is composed of five horizontal panels; the panel immediately above the original precast ringbeam is a series of operable louvers for ventilation. See Figure 6. The primary elements of the façade are structural steel HSS girts spanning nominally 20 m between masts and panelized single skin ETFE foil membrane with vertical aluminum ribs. The connection of the girts to the masts must accommodate tangential expansion/contraction from zero at head to the maximum at foot of the façade. This was achieved by pinning one end of each girt and allowing a cuff at the other to slide on a horizontal 80 or 120mm spigot. This allows the foot of the façade to "float" with the masts.

Additionally, the geometry of the roof system is such that the masts are not oriented radially. Therefore the behavior of the girts is not symmetric about the mast and is unique in each location. The drainage system from the main roof, which is mounted on the masts, must also accommodate this same range of movement. A flexible membrane connects the vertical edge members of the façade to the masts thereby sealing the entire system.

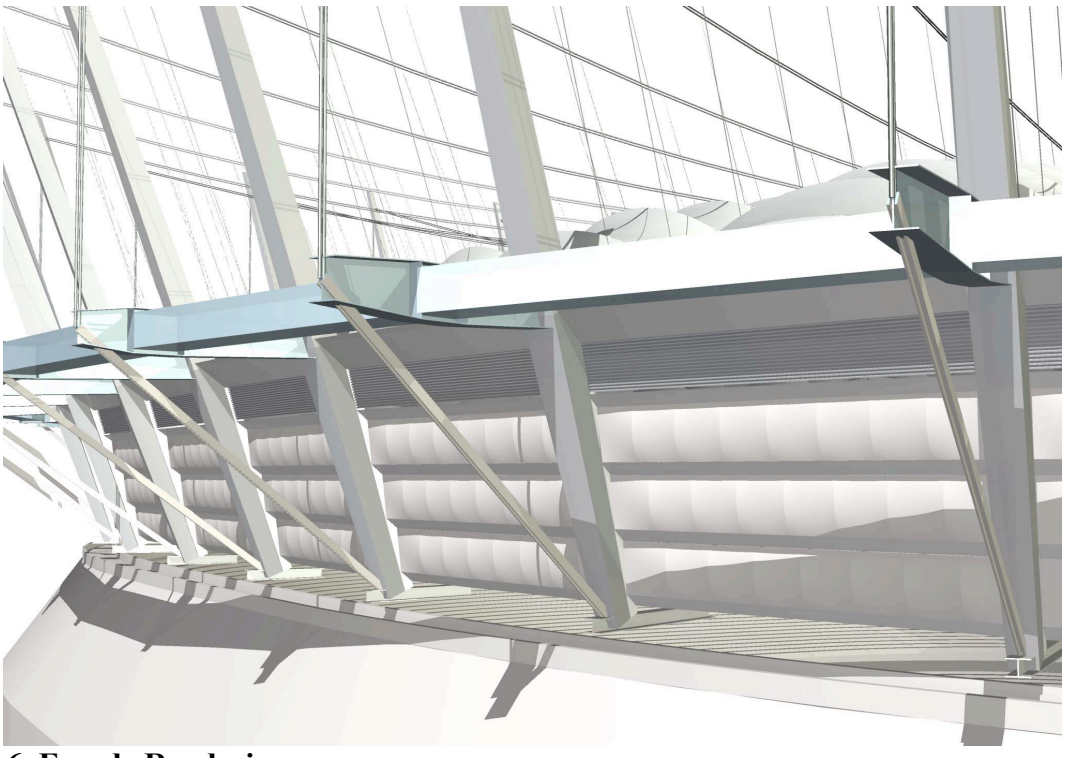


Figure 6. Façade Rendering.

LATERAL FORCE RESISTING SYSTEM-

The existing stadium superstructure is comprised of eight nominally independent reinforced concrete structures with lateral force resisting systems comprised of shear walls in the circumferential direction and moment fames in the radial direction. The new roof, as well as the original roof, is a single integrated structure supported on these eight structures. The dynamic characteristics of the roof system are intentionally quite different from that of the supporting stadium superstructure. A response spectrum analysis was performed modeling the existing stadium superstructure with the new roof. In final design, seismic demand governed some of the roof members, the roof's eccentrically braced frames, the travel of the mast bearings, and necessitated stiffening of the storey between the top of the reinforced concrete structure and the transfer girder at the original ring beam level.

The original roof's ring was supported on intentionally flexible moment frames therefore radial lateral stiffening frames were added to control drift (Hamilton, 1987). See Figure 7. The RSA indicated that the new roof and transfer structure contributed to approximately 10% of the overall base shear of the stadium. Evaluation of the existing stadium by Genivar, the structural engineer for the base structure, indicated the necessity of reinforcing the upper stadium columns supporting the roof as well as a general upgrade to the stadium's seismic force resisting systems, mostly as a consequence of the changes in code from the time of original construction. These innovative structural upgrades were designed by Genivar and, while of interest, are beyond the purview of the limited scope of this paper.

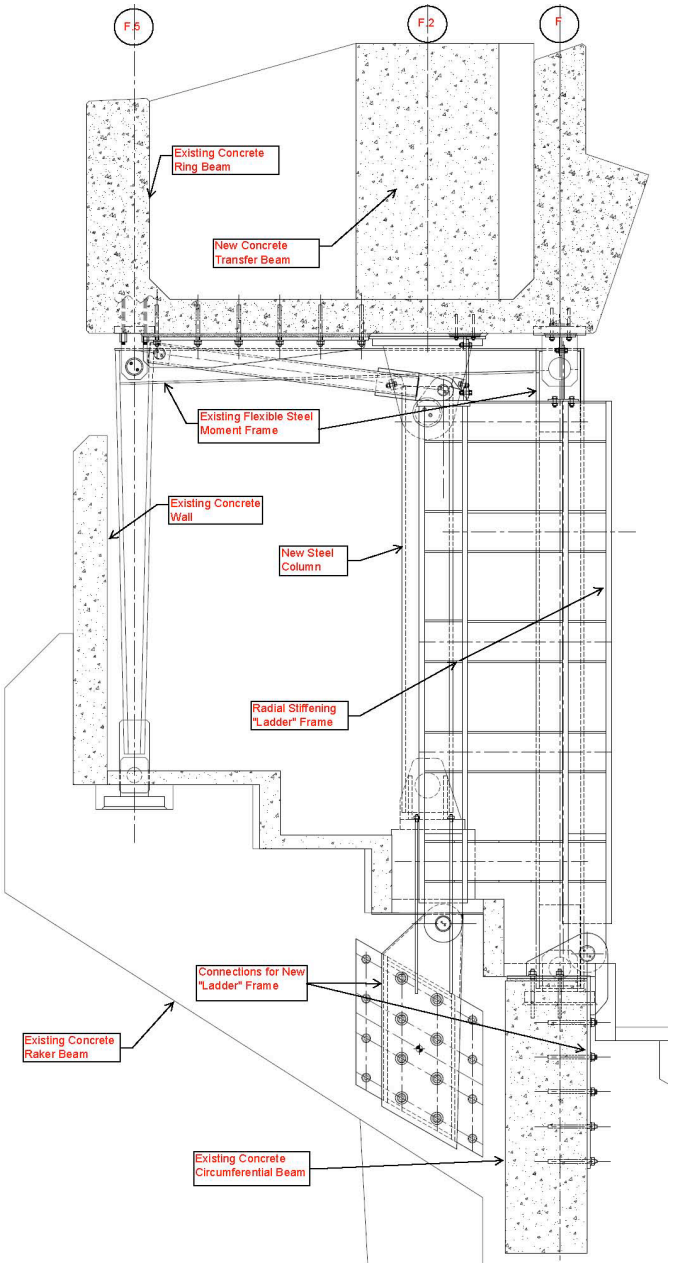


Figure 7. Section thru Existing Ring Beam and Transfer @ Support with Ladder Frames

The transfer of lateral load from the four braced bays to the existing shear walls presented some challenges as the roof's braced bays do not coincide with the shear wall locations. In plan, the two systems are more than two bays (28.6m) apart and the vertical distance from the new bearings, on top of the ringbeam, to the shear wall is 3.5m. During Phase 1, a built-up steel section was cast into the new concrete transfer beam and rigidly connected at the existing column lines. In order to allow movement of the mast and simultaneously transfer lateral load, a pivot strut was connected from the base of the mast at the braced bay to the Phase 1 embed. Below

the ringbeam, another beam was welded to the underside of the embed and bolted to the shear wall system. This series of beams, which in addition to the elevation change has two changes in plan orientation, resists the lateral load from half of the roof.

CONCLUSION-

The renovated BC Place Stadium is nearing completion. Roof construction, more challenging than it's design, is scheduled for completion in the Fall of 2011. The revitalized stadium presents a new image inside and out for sports and for exhibitions with its new retractable roof. The facility was closed for renovations for nominally 16 months.

REFERENCES-

Hamilton, K., et.al. (1987). "Comparison of Air-Supported Roofs on the Vancouver, B.C. and Indianapolis Stadium**."** *Proceedings, IASS Conference, Beijing*.

Design of the Retractable Roof for the Florida Marlins New Ballpark

Stephen E. Blumenbaum, P.E. and Aaron C. White, P.E.

Walter P Moore, 201 East Kennedy Boulevard, Suite 300, Tampa, Florida 33602; PH (813) 838-2424; FAX (813) 838-2289; email: sblumenbaum@walterpmoore.com, awhite@walterpmoore.com

ABSTRACT

When the Florida Marlins began planning for a new baseball-only facility, the presence of a retractable roof was essential. The team owner had a vision for a modern structure different than many of the recently-constructed retro-ballparks. That vision included a retractable roof that was foreseen as more than an umbrella for field and fans. Armed with this direction, the design team embarked on devising a roof structure that could survive major hurricanes economically, while still satisfying the architectural and operational demands of the ballpark.

The new ballpark, currently under construction and moving towards an opening day in April 2012, is situated near downtown Miami, Florida. On the one hand, the design team was challenged to support an architecture that did not overwhelm the surrounding residential neighborhood. On the other hand, traditional approaches to resisting hurricane-force winds forecast the need for either a potentially obtrusive or more costly structure.

To resolve this dilemma, the roof team implemented an innovative storm preparation strategy to survive major tropical events. Leveraging the experience gained from previous collaboration on several retractable roofs, the team approached their design holistically, with each consultant balancing the efficiency and cost associated with their scope against the roof as a whole. The engineers also collaborated heavily with the project wind consultant to determine cost-effective operating parameters. Because of its unconventional functionality, the resulting three-panel roof, with spans up to 560 feet, exemplifies a new generation of retractable roof design. This session will present the challenges encountered, and solutions provided, by the structural team in charge of designing this new type of roof.

OWNER REQUIREMENTS

Early in the project the design team was made aware of certain key parameters that ultimately would influence the roof design significantly. First, the look of the ballpark ought to be a notable departure from the focus on nostalgic features of other recently-completed ballparks. This directive harmonized with the owner's interest in work from 20th artisans specializing in surrealism and abstract art, as well as Miami's own vibrant art deco culture. In response to this interest, the design team expressed the entire stadium with bold, sculpted shapes.

Second, there was a strong interest in having a roof with increased functionality versus other baseball venues. Many Major League Baseball stadiums are designed to function only in two positions: open and closed. As such, their only purpose is that of shelter from precipitation.

However for the Marlins Ballpark, the team added a new function: variable shade positioning. This new capability would place the new stadium squarely in a new generation of sport venue – one that could adjust fan and player comfort in real-time. This implied more frequent use than roofs on other baseball stadiums.

Finally, in response to the design team's recommendation, ownership explicitly included in the project the provision that the stadium would not be used as a hurricane shelter. Unlike most design parameters that typically constrain a design team, this allowed the team to incorporate an innovative feature, discussed later in this paper, into the stadium's function that saved roof steel tonnage and construction cost.

SITE CONSTRAINTS

External Site Constraints

The Marlins Ballpark is located in the Little Havana district of Miami, on a site that was home to the now-demolished Orange Bowl. The urban setting, coupled with the requirement for a retractable roof, required a relatively compact stadium. Seating will be limited to approximately 37,000 patrons – one of the smallest venues in Major League Baseball. Parking garages flank the stadium on the north and south sides, leaving the west side of the site available for storing the roof. Furthermore, the plan area facilitated a tri-panel, telescoping retractable roof, which is a design used successfully at other baseball stadiums. Fewer panels would have required more real estate or perhaps dictated less roof movement, both of which were undesirable options.

Additionally, the surrounding buildings in Little Havana are mostly one or two-story residential and commercial structures. Throughout the design process, the team remained sensitive to the possibility that the ballpark could "overpower" its surroundings. To guard against this possibility, the roof's profile needed to be kept to a feasible minimum.

Finally, the design team selected an orientation for the track supporting the retractable roof based on the fact that downtown Miami is located east of the stadium and the moveable glass wall in the outfield would expose a view of downtown. To provide unobstructed views of Miami through the outfield wall, the track is oriented in the East-West direction, which requires the roof to span in the North-South direction.

Internal Operations

The usage of the ballpark within the stadium influenced the design of the retractable roof as well. The primary need is the ability to span across the playing field. Typical baseball fields inscribe a square area roughly 350 feet on a side. Add to this dimension the necessary plan distance for seating and concourses, and the minimum span for a roof usually will surpass 500 feet.

Another parameter establishing the geometry of the roof is the height required to clear batted balls. There seem to be few, if any, objective criteria for establishing the minimum

volume required to play baseball without obstructions from above. Major League Baseball publishes detailed ground rules for how to call certain plays when the ball strikes an overhead structure, but does not publish criteria on how to build the structure to avoid batted balls in the first place. Nevertheless, the design team was conscious of the nuisance of obstructed flight paths for both players and fans alike, and worked to minimize the probability that this could occur.

There has been some research in determining optimum parameters for baseball flight. (Sawicki, et al, 2003). Using parameters from this research, typical ambient conditions in Miami during baseball season, and the general flight equations including drag effects, a volume was constructed representing the maximum reasonable boundary of expected baseball flight at Marlins Ballpark. The resulting volume could be used to evaluate the impact of various panel shapes and elevations on a comparative basis, and help the designers understand specifically where trouble spots might occur.

ENVIRONMENTAL CONDITIONS

The stadium happens to be situated where one environmental condition, wind, dominates the structural design over many others. South Florida is subject to some of the highest design wind speeds in the United States, while other environmental conditions such as seismic or snow load are inconsequential. Interestingly, this afforded the design team the chance to focus on minimizing the effect of wind load, without being constrained significantly by other environmental conditions that might otherwise blunt the effectiveness of wind mitigation solutions.

As prescribed by the Florida Building Code, the design wind speed (3-second gust) for Miami - Dade County is 146 mph. Of the five other Major League Baseball stadiums that have retractable roofs, Minute Maid Park (Houston, TX) is subjected to the next-highest design wind speed of 110 mph. Since wind pressure is related to the square of velocity, a comparable roof in Miami would have experienced wind pressures 76% higher than Houston.

MECHANIZATION INTEGRATION

A variety of mechanization systems have been employed, with varying amounts of success, for North American sports venues with retractable roofs. The ability of the roof to function as specified depends in large part on the integration of the roof mechanization system with the roof structure, and the ability of the entire design team to understand how the roof behaves as a whole.

For this project, the mechanization consultant selected a traction drive system, due to considerations of cost, loading, operating frequency, and other variables. The system consists of a series of independently-driven transporters, utilizing steel wheels riding on a heavy-duty steel rail. The roof structure bears on the transporters, which in turn provide a load path for all roof reactions down to the concrete track beam.

Although cost-effective, the mechanization imposed certain demands on the roof structure above. First, quite unlike a typical building structure, where the foundation simply can be sized for whatever loads the superstructure imposes on it, here the "foundation" system worked only for a certain range of roof loads. In fact, three different configurations are evaluated: Operating (associated with a maximum wind speed of 40 mph), Parked (maximum wind speed of 95 mph), and Secured (50-year wind speed of 146 mph). Any significant deviation from preliminary estimates of wheel reactions would require a change to an entirely different, much more costly, mechanization system. The cost of the foundation for the roof structure can be represented by a step-function: an incremental increase in roof loading is accompanied potentially by a dramatic increase in mechanization cost.

Secondly, the relative stiffness in the vertical direction of the roof, mechanization, and supporting concrete track structure all contribute to the reactions on the wheels as the panels move along the track. Unlike certain systems used in the design of other ballparks, the mechanization system for the Marlins Ballpark would not have any kind of spring system. Thus, it would not be able to accommodate either appreciable deflections of the track structure (even deflections meeting code requirements) or excessive vertical stiffness of the roof.

Finally, due to its nature as a moveable structure, the retractable roof is subject to certain dynamic loads. For the rare case of a panel that may have lost the ability to brake using the transporters, bumpers are installed at the end of each rail. Therefore, each panel needs to be able to withstand the loading associated with a rapid deceleration parallel to the rail. This deceleration typically is a small fraction of the acceleration of gravity.

Another unusual load case occurs if a panel hits an obstruction on one of its rails, but the transporters on the other rail continue traveling. The time required to notify the transporters on the still-moving end of the panel is such that one end of the panel could move beyond the other end. In essence, this arrangement "racks" the panel beyond its design geometry.

STRUCTURAL SOLUTIONS

Roof Basics

The roof is comprised of three structurally independent roof panels: two "low" panels that can nest beneath an "upper" panel when the roof is in the open position. The panels travel in an east-west direction, supported by post-tensioned concrete track beams on concrete supercolumns. In the closed position, the roof is sealed between panels and also at the interface of the panels and the fixed roof. Each panel consists of planar trusses spanning over 500 feet from south track to north track, with three trusses per lower panel, and six trusses in the upper panel. Trusses are linked together, perpendicular to their span, with sway bracing in the vertical plane. In the bottom plane of the panels, bracing links the trusses together to resist horizontal loads. Each panel behaves essentially as a large beam, with a pin support at one end, and a roller support at the opposite end. The trusses are parallel to the first base line, resulting in a 6 3/7 degree plan skew relative to a line perpendicular to the concrete track beams.

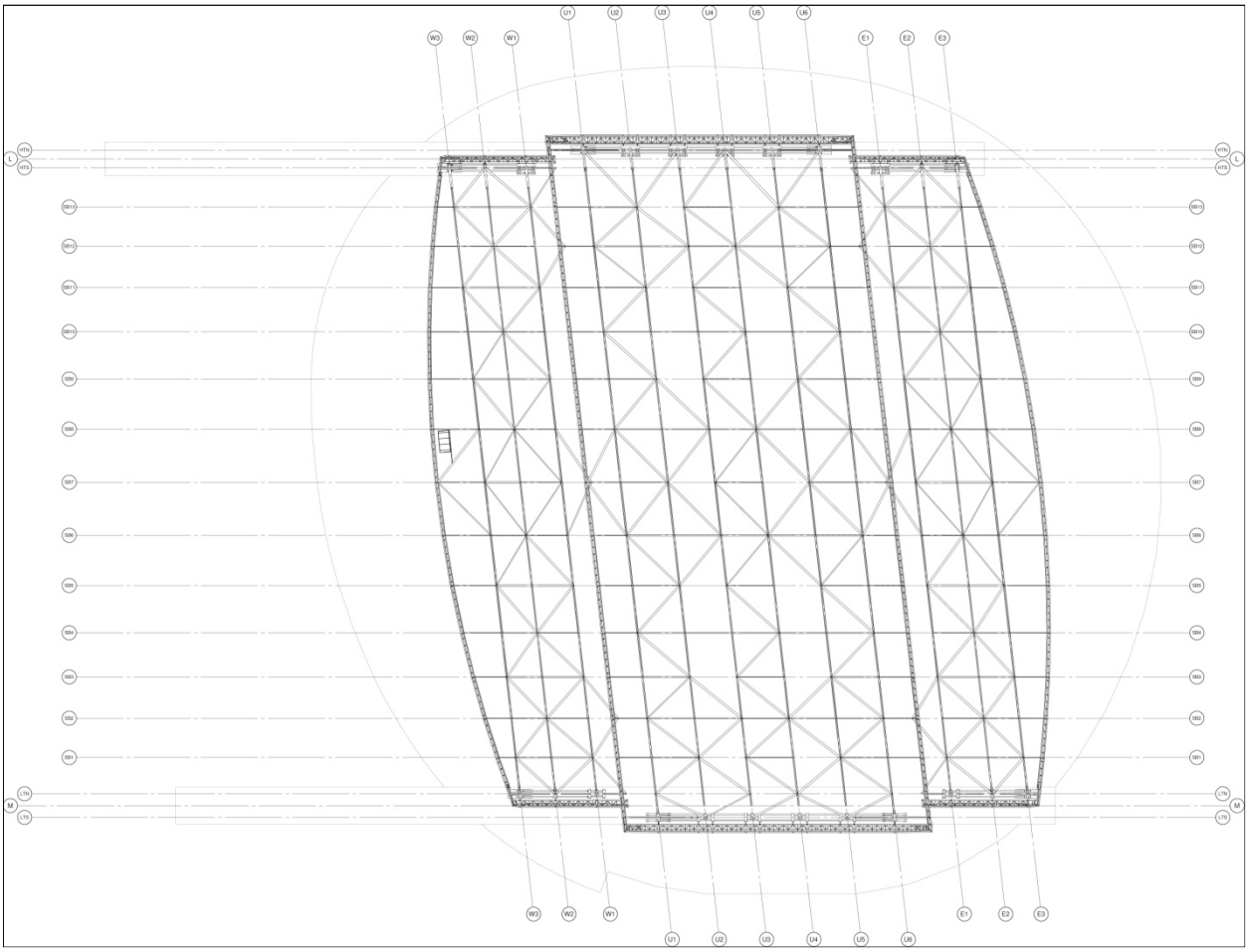


Figure 1. Plan view at bottom plane of roof panels

Walter P Moore collaborated with Populous to establish the overall shape of the roof, aiming for a sculpted, sleek look. The structure was set as high as possible to miss batted balls, but low enough on the outside to not overpower little Havana. Further, the structure had to be deep enough to span effectively and stay within preliminary tonnage estimates: the low panels are 42.5 feet deep at midspan, and the upper panel is 45 feet deep at midspan.

Once the bottom of the structure was set, and the truss height determined at midspan, there were a few options available to the design team to control the look of the roof. First, the panels were tapered towards their ends to minimize height. Second, sloping cantilevers were provided on the east and west sides of the panels beyond the last trusses to prevent the look of a boxed shape. Finally, the roller support was placed at the lower, south track, again to minimize height.

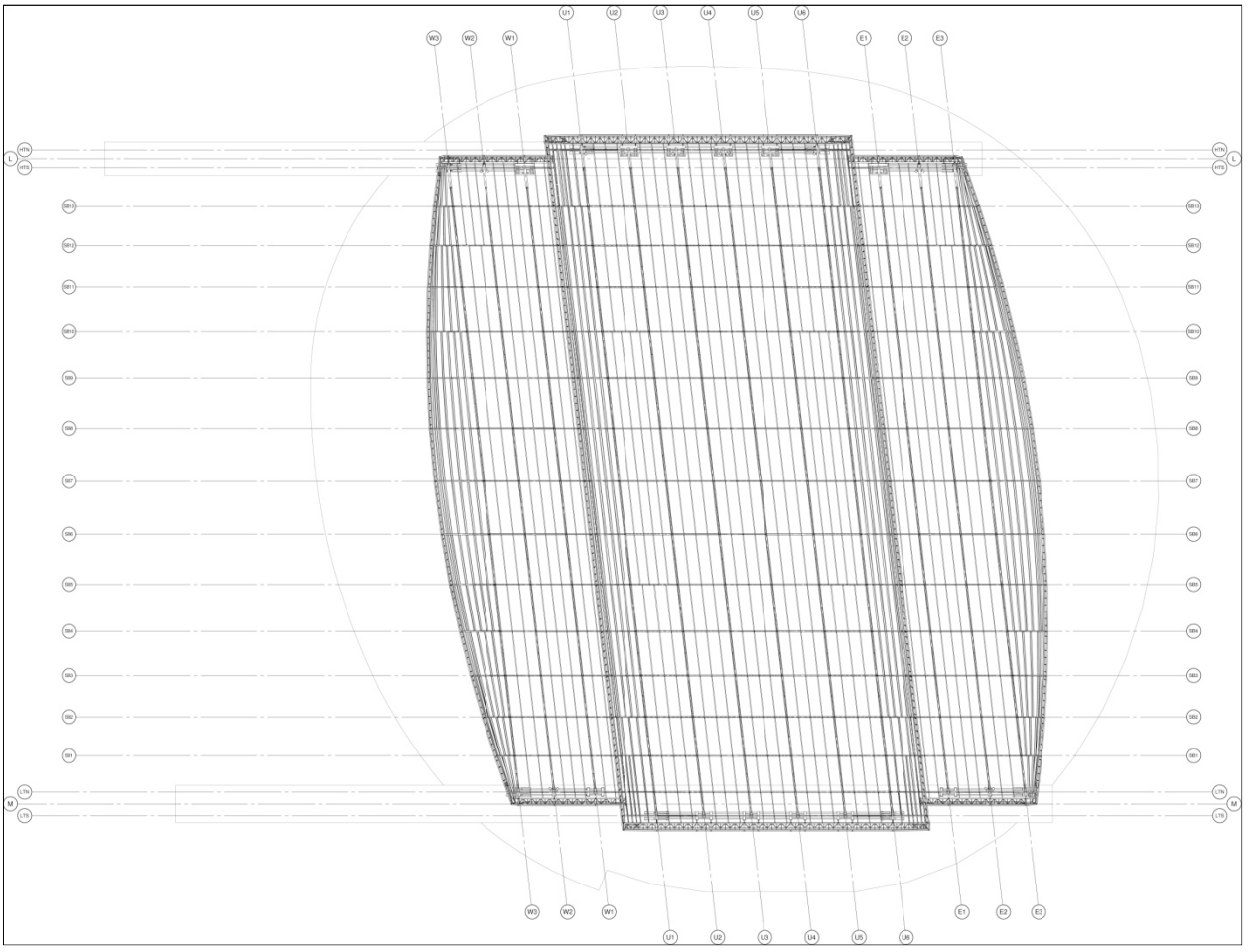


Figure 2. Plan view at top plane of roof panels

What does what

The planar trusses are a modified Pratt type, comprised of W14 web horizontal sections (ASTM A913, Grade 65) for the chords, and W12 (ASTM A992 or ASTM A572, Grade 50) web horizontal web members. The top chords are braced out of plane at panel points by W30 (ASTM A992 or ASTM A572, Grade 50) members that support purlins. The bottom chords are braced out of plane at panel points by square HSS (ASTM A500, Grade B, Fy = 46ksi) and pipe (API 5L X52, Fy = 52ksi) members. The chords are braced in-plane at panel points by the W12 web members. Within certain panels, the chords also are braced at panel half-points by sub-vertical and sub-diagonal W12 members (ASTM A992 or ASTM A572, Grade 50). The trusses are the primary load path for all vertical loads and lateral loads in the north-south direction.

To resist lateral loads in the east-west direction, a horizontal truss is formed in the bottom plane of each roof panel. Square HSS and pipe members constitute the tension and compression diagonals of the horizontal truss, and the aforementioned W14 members comprise the tension and compression chords. This arrangement is efficient from a tonnage standpoint because any compression created in the chords of the horizontal truss due to lateral loads is counteracted by

the tension in these same members resulting from resisting vertical loads. For downforce load combinations, there is compounding tension within certain members (tension due to vertical loads and lateral loads), but there is no compounding compression, as there would be if the lateral system was in the top plane of the roof panel. There is also a benefit of simplifying fabrication and erection by placing the horizontal braces in the bottom plane of the roof panel. Were these placed in the top plane of the roof panel, they would subdivide the purlins, necessitating many more purlin pieces, associated connections, and crane time.

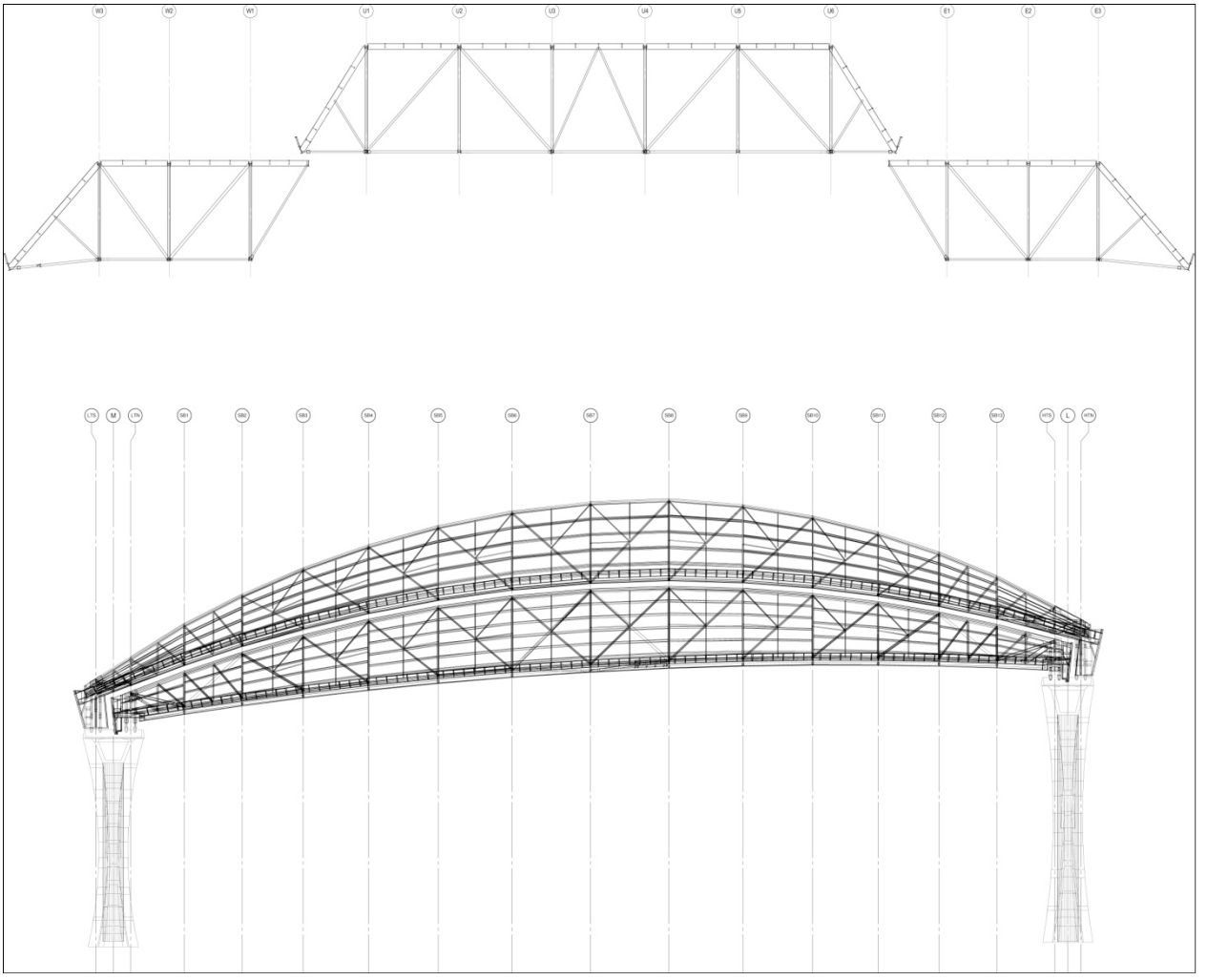


Figure 3. Section perpendicular and section parallel to roof span

Maximum cladding uplift pressures of approximately 150 psf (for 10 square feet of tributary area) are resisted by 3" steel deck (18 or 20 gage, depending on location) supported by steel beam purlins (ASTM A992 or ASTM A572, Grade 50). Purlins span to, and brace, the aforementioned W30 members. End support and sidelap fastening, although necessary only to resist uplift pressures, resulted in a certain diaphragm capacity as well. The diaphragm contributed to the resistance of lateral loads such as wind and deceleration forces. Consequently, each panel behaves like a tube for lateral loads and torque parallel to the main span. It was not prudent to ignore the deck's diaphragm stiffness, as the design team could not assume sufficient

ductility existed at the deck to steel connection to instantiate the desired behavior of uplift resistance only. Therefore, deck support and sidelap fastening has been designed not only for uplift pressures, but also for diaphragm shear.

Getting Load Down to the Track

Although the panels are shaped like arches, they cannot be allowed to act as such. From a mechanization standpoint, arch behavior is deeply undesirable, because the associated thrust loads require a more complex, more costly support system. To resist the lateral component of thrust, it is almost certain that another rail and set of wheels would be required. This in turn would necessitate a wider, probably more heavily reinforced, track structure. Also, the track structure, which is supported by concrete columns cantilevering over 100 feet above the ground, would have to resist a much larger lateral load. This would require larger, more heavily reinforced columns, and larger foundations.

Furthermore, from the perspective of the retractable roof, an arch is an indeterminate system. As such, it provides a load path that is more sensitive to relative stiffnesses of the roof structure, mechanization, and track structure. It is critical to the reliable function of the roof that the loads on the transporters are known with a reasonably high degree of confidence, and an indeterminate roof structure adds undesirable uncertainty to this estimate.

For these reasons, arching action would not be used. But how does one create a roller, and make each roof panel act as a beam? One solution to this problem is a four-bar linkage (refer to Figure 4). Imagine a rectangle (the four sides representing the four "bars") located in a vertical plane that is perpendicular to the direction of the rail. The rectangle has two long vertical sides, and two short horizontal sides. The vertical sides are structural steel W14 columns, the bottom horizontal side is represented by the transporter, and the top horizontal side is represented by the connection collecting the top and bottom truss chords at a single work point. The connections at each of the four corners are released for moment, which is accomplished by using spherical hinges.

Placed beneath one end of a roof truss, such an arrangement permits the truss end to move perpendicular to the rail, thus relieving any arch action. This release comes at the cost of horizontal reactions developing in the four-bar linkage as the linkage becomes a parallelogram to accommodate lateral movements. To minimize these horizontal thrust reactions (i.e., prevent the acute angle of the parallelogram from becoming too small), the mechanization requires 10 units of height to the rectangle for every unit of lateral displacement. Therefore, the lateral movements must be known to a high degree of accuracy before setting the final roof geometry. The resulting height required for the four-bar linkage was approximately 16 feet for the low panels, and 20 feet for the upper panel.

The layout of the bowl permitted the elevation of the south track (near right field, where there could be relatively fewer seats than near the bases) to be 30 feet lower than the north track (which is parallel to the third base line). The design team elected to place four-bar linkages at the south end of the roof, at the low track. This way, even though extra height was required at

the south end, the roof profile at the low track need not be any higher than the profile at the high track (i.e., the north end of the panel).



Figure 4. Four-bar linkage during low panel construction

As a standalone structure, the linkage is not stable. Therefore, the top horizontal bar of the linkage is attached rigidly to the truss support above the south track, and serves two purposes. First, because the connection of the panel to the north track still retains stiffness in the north-south direction, the truss becomes a tension tie for the transmission of the stabilizing shear reaction from the south track to the north track. Second, because the bar is attached rigidly to the truss, a stabilizing moment can develop to keep the transporters vertical. Thus the stability of the panel as a whole is assured, even while providing a release of the arching tendency of the panel.

Letting in the Wind

Preliminary studies performed by the wind tunnel consultant on an enclosed structure indicated maximum uplift pressures of approximately 90 psf, and maximum downforce pressures of approximately 60 psf, including the effects of internal pressure. But the design team had to consider the effects of a seal breaking between panels, and the structure undergoing an enclosure classification change from “Enclosed” to “Partially Enclosed”. In effect, the result of a seal breaking would be to change the GC_{pi} value in ASCE 7 from +/-0.18 to +/-0.55. Given that the q_z was approximately 82 psf, this meant that were the seal to break, internal pressures could

increase from about +/-15 psf to +/-45 psf. The design team had to account for this contingency in the design if the roof was to remain in a closed position during the maximum wind event, but this came with an associated cost premium to the project.

However, because the stadium would not be used as a hurricane shelter, there was no need to keep the stadium weatherproof during this extreme wind event. Therefore, the team studied the effect of maintaining a gap between panels and between panels and the fixed roof – the wind tunnel consultant explicitly incorporated the gapped position into its testing regime. The results of the wind tunnel study were encouraging: in some locations on the roof, wind pressures were reduced by as much as 70% simply by providing this gap. Regardless of wind direction, internal pressures stayed very low when the roof was configured in the gapped position. Net wind pressures typically were less than initial estimates. Use of the gapped position reduced the total roof weight by approximately 5%-10%. Also, mechanization costs were saved by reducing the need for as many transporter tiedowns to resist uplift and lateral loads.

The gapped position also acted as an insurance policy against the unexpected, but still possible, occurrence of a breach in the east wall. Were this wall to break, and were the roof in a conventional closed position, significant internal pressures (estimated to be at least 45psf, but potentially as high as 80psf) would develop, causing major uplift on the roof. Rather than face the decision of designing for this possibility (and incurring cost premiums as a result), the team could rely on the fact that even if the east wall is breached, the internal pressures change very little on account of the gapped roof.

Maintaining Stability

The roof panels were designed using the Direct Analysis Method described in AISC Specification Appendix 7. The fundamental requirements for this method are:

1. A second-order analysis that accounts for P-δ and P-Δ effects
2. Notional loads to account for geometric imperfections, or the inclusion of the geometric imperfections directly
3. Reduced stiffness of all members contributing to the stability of the structure

All three requirements were met in the design of the roof panels. In summary, the process for implementing this method was to determine notional loads that could be applied to a model with the completed, theoretical geometry and unreduced stiffness such that the resulting forces within the members closely matched the forces resulting from an analysis of a structure with initial deformations and reduced stiffness.

Appendix 7 of AISC 360-05 does not prescribe specifically how to account for the effects of geometric imperfections and inelasticity on the lateral framing system for a long-span roof structure. Building and maintaining many analysis models would be required to directly incorporate these geometric imperfections into the design. Given the infeasibility of this approach, an externally-applied set of notional loads that indirectly imposes these effects on the lateral framing system was derived and applied to a single analysis model. The notional loads

were combined appropriately with gravity and lateral loads for the design of the system. Notional loads were applied on the flat portions of the Upper and East roof panels in the North, South, East, and West directions. The effect of the notional loads on the member forces was compared to the effect of the deformed starting geometry and reduced stiffness, and then adjusted appropriately.

Several types of starting geometries were considered to represent imperfections in the roof structure: buckled shapes in the North, South, East, and West directions; purely translational parabolic shapes in the East and West directions; and purely translational shapes in the North and South directions. The imperfect starting geometries were determined from an eigenvalue buckling analysis, and then scaled to 2" of initial imperfection in the North and South directions, and 4" in the East and West directions. The purely translational parabolic shapes were determined from a parabola equation at coordinates that fall on truss panel points, and linearly interpolated for coordinates between these points. For the purely translational North and South shapes, the entire roof structure supported by the four-bar moment frames was simply shifted to the North or South by 2", and the coordinates on the four-bar linkage members were interpolated linearly down to a shift of zero at the wheels.

A reduced flexural stiffness of 0.8*EI and a reduced axial stiffness of 0.8*EA were applied to all members that contributed to the lateral stability of the panels. The magnitude of reduced stiffness was in general accordance with Appendix 7 of AISC 360-05. Conservatively, the stiffness of the deck was not considered.

The resulting notional loads generated by this study were combined as appropriate in gravity-only and gravity-plus-lateral load combinations. In general, the effect of implementing the Direct Analysis Method was to increase the demand by a few percent on members contributing to the lateral stability of the structure. The increased demand was larger for members comprising the moment frame directly above the north track. This is to be expected for at least a couple of reasons: the arch shape of each panel is asymmetric: the slope at the south track is greater than at the north. Thus, the panels naturally will tend to move in that direction under self-weight alone, even if there are no geometric imperfections. Also, these moment frames are the only restraint for any load in the north-south direction.

Achieving the Right Wheel Reactions

Sets of either two or four W14 columns, centered below each of the trusses, carry vertical loads down to the transporters. The transporters transmit compression to the wheels, which then bear directly on the rail. The transporters transmit tension to a combination of rail clamps and uplift clips, both of which hold the rail. For lateral load in the north-south direction, at the north end only, these same columns are linked together with beams to create a moment frame. Lateral loads also are carried down through the transporters, and are transmitted to the track structure through either the wheels bearing on the rails, or tie-downs connecting the transporters to the track beam.

All lateral loading is delivered at the truss work points, which are in excess of 20 feet above the wheel / rail interface. In the east-west direction, a robust load path obviously is

required to get this shear (typically several hundred kips) down to the rails. Structurally, the most efficient way to do this is to have a simple braced frame, perhaps using the aforementioned columns as boundary elements.

But a braced frame presents a problem for the retractable roof panels: it is too efficient. More specifically, a braced frame provides so much vertical stiffness relative to its strength that it severely overloads the wheels beneath its boundary elements. The result is an inefficient use of the mechanization: not enough wheels contribute to resisting lateral load. The vertical stiffness presents a second problem. As the panel moves along the rail, the individual wheels encounter "hard" and "soft" points along the track, depending on whether they are above a track column or track center span, respectively. Wheels on top of hard points tend to accumulate roof load, and wheels on top of soft points tend to shed roof load. The two main contributors to this phenomenon are the roof framing directly over the rail, and the track framing supporting the rail.

Given the size and span of the concrete track beams, it was not feasible to increase their stiffness sufficiently to use braced frames in the roof structure directly over the rail. Instead, the problem had to be solved within the roof framing. What followed was an iterative process with the following objectives: tune the stiffness to mitigate the load-sharing phenomenon and engage all the transporter wheels to resist the overturning moment, while still providing a sufficiently strong load path for the several hundred kips of shear that needed to migrate down to the rail.

The solution chosen was a set of moment frames in the east-west direction to transmit shear down to the track beam. The columns are linked together typically with heavy W18 sections. In this way, a fraction of the total shear is carried down through each subassemblage, until it is resolved as a small tension / compression couple with the two transporter wheels. At the last subassemblage, the beam to column connections are pinned, otherwise the wheels in these transporters would be overloaded.

Holistic Analysis

For the roof to function over the long term, the effects of track and roof stiffness, plus creep on the track beam, need to be understood. Creep will impact the long-term shape of the track beam, and therefore will also influence the wheel reactions. To better understand these effects, an integrated analysis model of all three roof panels plus the track and bowl structure was created.

The ratio of creep strain to initial strain was calculated, in accordance with ACI 209, to be approximately 0.93. This is the factor to apply to the sustained dead load to simulate creep-only deflections. The post-tensioning in the track structure was designed to counteract the self weight of the track. Therefore, only the dead load of the roof is effective in contributing to creep effects on the track. To simulate creep effects in the analysis model, line loads (hereinafter referred to as the "creep load") equal to the creep factor multiplied by the distributed wheel reactions due to roof weight plus superimposed dead load on the roof were applied to the rail.

Unless the dead load is constant and sustained for the same amount of time over the entire length of the rail, then the track will not experience uniform creep over its entire length.

Consequently, it would not be reasonable to apply a single case of creep load over the entire length of the rail. Moreover, it is possible that certain wheel reactions could be governed by creep occurring over only a limited length of rail. For these reasons, the following different cases of creep load were analyzed. In each case, creep load is applied on the rail only at the position specified:

- Open position
- Closed position
- Hurricane position
- 100% of creep load applied at the Open and Closed positions, and 75% percent of creep load applied along the rail between these positions
- No creep anywhere along the rail

After an initial review of the effects of creep on wheel reactions, the design team concluded that rail camber would be required to offset the adverse impact that creep would have on the wheels. The general procedure for determining the amount of camber consisted in tuning an upward-directed load that approximately balanced the deflection due to creep. The final cambered shape approximately equaled the inverse of the instantaneous deflected shape due to roof panel dead load.

Such variables result in a large number of possible results per wheel. For each roof position, the total effect is comprised of:

Total Effect = Effect of Gravity and/or Wind + Effect of Camber + Effect of Creep

For each position, and each wheel, the maximum and minimum vertical and north-south reactions were gathered from the variable combinations indicated by the above equation. This process was repeated for each wind condition. This allowed for comparison of the entire range of wheel reactions to the acceptable limits provided by the mechanization consultant.

CONCLUSION

As of January 2011, the roof of the new Florida Marlins Ballpark is under construction, with its three panels at different stages of completion, from the assembly of the Upper Panel on shoring towers, to installing steel roof deck on the lower panels. The ballpark is on track to bring a new environment for enjoying baseball to the fans of south Florida beginning in April 2012. As part of that experience, players and fans alike will be exposed to the next generation of retractable roofs for stadiums.

REFERENCES

AISC (2005). *Specification for Structural Steel Buildings*, ANSI/AISC 360-05, American Institute of Steel Construction, Chicago, IL

Sawicki, G.S., Hubbard, M., and Stronge, W.J. (2003). “How to hit home runs: Optimum baseball bat swing parameters for maximum range trajectories”, *American Journal of Physics*

Evaluation of wind-induced torsional loads on buildings by North American and European codes and standards

M. Elsharawy, T. Stathopoulos, and K. Galal

Faculty of Engineering and Computer Science, Concordia University, Montréal, Québec, Canada H3G 1M8

ABSTRACT

The common characteristics of wind-induced loads on building envelopes always vary in temporal and spatial dimensions. The variation of local wind pressures on building claddings and the total effective wind forces (base shear/overturning moment) on the main structural building systems have been investigated in the past few decades. However, very limited studies examined wind-induced torsional loads on the main resisting structural systems of buildings. This paper reviews these past studies and proceeds with a comparison of torsion provisions in three national wind loading standards, namely the American Society of Civil Engineers standard (ASCE/SEI 7-10), the National Building Code of Canada (NBCC 2010), and the European code (European 2004). Three low buildings located in an open terrain, in addition to three tall buildings located in suburban terrain were considered for this comparison. The low and tall building dimensions were selected to cover three different aspect ratios (length/width) varying from 1 to 3. The results demonstrated significant discrepancies among the provisions of these wind standards in evaluating torsional wind loads on buildings.

1. INTRODUCTION

Wind-induced torsional loads on buildings have been of concern to wind engineering researchers, structural engineers as well as code committees. An extensive literature survey demonstrates that the simplified methods introduced in the current wind load standards to evaluate wind load effects on buildings cover the effective base wind shear and overturning moment. However, more work is required to ensure that these provisions are adequate to assess wind-induced torsion, which is mainly generated as a result of non-uniform horizontal distribution of wind forces on the main wind force resisting system. Although wind-induced torsional loads on buildings may not be always the dominant load case for building design, overlooking the accurate representation of wind-induced torsional loads may lead to unrealistic spatial distribution for wind design loads. Such unrealistic loads may be conservative in certain design situations and detrimental in others. Clearly, a realistic evaluation of wind-induced design torsional loads has a significant effect on the serviceability and survivability of buildings.

This paper presents a review of the wind-induced torsional loads studies on low and tall buildings. In addition, it presents a comparison of the provisions of three well-known wind loading standards: the American Society of Civil Engineers standard (ASCE/SEI 7-10), the National Building Code of Canada (NBCC 2010), and the European code (European 2004). Three low buildings in open terrain exposure and three tall buildings in suburban terrain exposure are analyzed using the three standards. All analytical approaches provided

in these standards for the evaluation of wind loads on the buildings considered are applied and results are compared.

2. WIND-INDUCED TORSIONAL LOADS ON BUILDINGS

The majority of residential and commercial buildings worldwide are categorized as low-rise buildings. Moreover, low-rise buildings are prone to excessive damage in wind disaster events. Very limited studies examined wind-induced torsional loads on low-rise buildings as shown clearly in the comprehensive reviews by Holmes (1983), Stathopoulos (1984) and Krishna (1995). A major contribution in the development of provisions for the evaluation of wind loads on low-rise buildings was based on the research carried out at the University of Western Ontario (UWO) in the late 70's. An extensive experimental program in a boundary layer wind tunnel examined a variety of rectangular low buildings with different dimensions, roof slopes and upstream terrain exposures but wind-induced torsional loads were not examined in detail. However, wind-induced torsion has been examined in the wind tunnel for three low-rise buildings with different aspect ratios by Isyumov and Case (2000). The study recommended that applying partial wind loads similar to those implemented for the design of tall buildings will improve the design of low buildings. This study, which was the only one carried out to examine wind-induced torsional loads on low buildings, concluded that more information is essential to improve the evaluation of wind-induced torsional loads on low buildings.

Wind-induced torsional loads on tall buildings have received more attention compared to low buildings, since more complex interactions between the fluctuating wind forces and main wind force resisting systems may result in significant dynamic wind torsion for tall buildings. Moreover, any rotational motion of a building could be a reason for disturbance and for causing discomfort to building habitants. Wind tunnel studies are recognized as a reliable source of information for engineers to design such buildings. Ten multi-degree-of-freedom aeroelastic models have been tested in the wind tunnel by Greig (1980) to measure the mean and the dynamic torsional wind-induced moments. This is the first study that introduced an empirical formula for predicting the torsional wind moment on tall buildings, although this was an empirical formula based on a finite data set; indeed, to be used as a general estimator, this formula must be validated and improved through performing additional wind tunnel tests.

Isyumov and Poole (1983) tested buildings with square and rectangular cross-sections in the wind tunnel by using the weighted pneumatic averaging technique to measure the mean and dynamic torque components. This study was trying to overcome the limitation of the pressure instrumentation to measure simultaneously the wind pressure over the building surfaces. It was shown that the pressure fluctuation on the back face induced by vortex shedding has a significant contribution to the dynamic torsional moment in the studied buildings. Also, the study showed that the quasi-static assumptions can provide reasonable estimates of the dynamic torque. A comparison between measuring the base torque using a force balance method in wind tunnel and the integration of the pressures measured on the sides of the model has been published by Tallin (1985) where it was shown that although the force balance technique requires smaller computational effort, it over-estimates the torsional moment. Lythe et al. (1990) conducted a wind tunnel study, in which torsional wind loads for different building shapes (simple, complex symmetrical, and complex non-

symmetrical) were measured in detail. Instrumentation and computational limitations at the time restrained the study to only examine the mean torsional wind loads.

As a kind of simplicity and by using two dimensionless factors, the equivalent eccentricity, e, and the load reduction factor, r, the magnitudes of torsional wind loads were investigated in wind tunnel for several tall buildings with respect to horizontal loads, as reported by Xie et al. (2000). In general, it was illustrated that for most buildings the overall equivalent eccentricities are found to be more than 10% (20% for torsional sensitive buildings). Some real-life tall buildings have been tested through wind tunnel tests and results presented by Boggs et al. (2000). In general, the equivalent eccentricity for these buildings might reach up to 30% of the building width and the wind-induced torsion effects cannot be eliminated but can possibly be minimized by changing the building geometry or the structural properties of the tall buildings. The tests also showed the effects of the structural properties on the elimination the coupling between the torsional and sway vibrations.

Zhou et al. (2000) introduced a gust load factor (GLF) formulation to estimate the torsional wind response for tall buildings. This was based on data collected from High Frequency Force Balance (HFFB) wind tunnel tests. The study discussed the effect of a nonuniform mode shape on the HFFB results since the rigid model used allowed only for linear mode building shape. This GLF procedure can be used in the preliminary design stages prior to the detailed wind tunnel tests. This procedure requires also more validations, possibly through aeroelastic model testing in the wind tunnel, to become a generalized approach. More recently, the development of the solid state switching technology has allowed the use of the High Frequency Pressure Integration (HFPI) method to determine the overall wind loads on tall buildings. The effectiveness of using this method has been studied by Ho et al (1999) who compared the traditional HFFB with HFPI method. The results collected from testing two tall building models in the wind tunnel demonstrated that wind tunnel testing with HFPI method is capable of providing improved information on the overall wind-induced building forces and torsional moments.

3. WIND-INDUCED TORSION IN WIND CODES AND STANDARDS

The instantaneous variation of wind-induced forces on building envelope in both temporal and spatial dimensions may introduce significant instantaneous torsional moments about the vertical building axis. This wind-induced torsion should be accounted for during building design process. Generally, there are two main approaches in the wind loading standards for the evaluation of the actual effects of wind-induced torsional loads on buildings. The first approach is implemented by applying reduced uniform wind loads on building surfaces with additional equivalent eccentricity from the building dimensions (used in ASCE/SEI 7-10), while the other way is by applying non-uniform wind loads (used in NBCC 2010, and European 2004). The non-uniform wind loads can be simulated by either increasing the wind pressure on the building corners, by using partial wind load acting on one part of the building face, or by applying a triangular wind load on the building surfaces. Table 1 summarizes the different procedures proposed in the current issues of the wind loading codes and standards for estimating the torsional moments acting on buildings due to wind. These procedures lack the full details required for describing the torsional wind load cases. The following sections describe the different approaches used to calculate the wind-induced torsional loads in the American, the Canadian and the European wind code / standards:

Table 1: Analytical approaches provided in the current standards

ASCE/SEI 7-10	NBCC 2010	European 2004
• **Simplified(Envelope) method** (for low-rise buildings) Load cases: - Transverse direction - Longitudinal direction - Torsional case	• **Simplified (Static) method** (for low-rise buildings) Load cases: - Transverse direction - Longitudinal direction	• **Detailed method** (for all building heights) Load cases: - Transverse direction - Longitudinal direction - Torsional case (triangular load)
• **Detailed(Directional) method** (for all building heights) Four load cases using: - Reduction factor - Equivalent eccentricity	• **Detailed (Dynamic) method** (for all building heights) Four load cases using: - Partial Loads - Reduction Factors.	

3.1 American Society of Civil Engineers (ASCE/SEI 7-10)

Wind load provisions in ASCE/SEI 7-10 include two analytical methods to estimate wind forces on the main wind force resisting system (MWFRS): the simplified (envelope) method, which is applicable for low-rise (h<60 ft) buildings and the detailed (directional) method, which can be used for designing buildings of all heights. The simplified method has three main load cases, namely; transverse (perpendicular to ridge) load case, longitudinal (parallel to ridge) load case, and torsional load case. The description of the three load cases is given in ASCE/SEI 7-10 in chapter 28, Figure 28.4-1. In the third case, the torsional effects have been taken into account by applying only 25% of the full design wind pressure on half of the building faces. Exceptionally, one-storey buildings with h<30 ft and two-story buildings framed with light frame construction or designed with flexible diaphragms need not be designed for the torsional load cases. On the other hand, the detailed method has four load cases described in ASCE/SEI 7-10, chapter 27, Figure 27.4-8. In the first and third cases uniform wind loads are applied without any torsional loads. Torsional wind loads are specified in cases 2 and 4 by introducing two non-dimensional parameters, 15% equivalent eccentricity of the building dimension and 0.75 and 0.563 reduction factors respectively for the equivalent static wind pressure. Specific exemptions are provided in Appendix D of the Commentary of ASCE/SEI 7-10. Finally, it is also quoted in the Commentary that

> *"Although this is more in line with wind tunnel experience on square and rectangular buildings with aspect ratios up to about 2.5, it may not cover all cases, even for symmetric and common building shapes where larger torsions have been observed"* (C27.4.6)

3.2 National Building Code of Canada (NBCC 2010):

Among the national building codes and standards, the NBCC was the first to include in its provisions the effects of wind-induced torsional loads on buildings. In fact, there are two analytical methods stated in NBCC 2010 to predict wind-induced torsional moments on

buildings. The simplified (static) method is appropriate for low-rise buildings, while the detailed (dynamic) method is specified for all building heights. Two wind direction ranges are considered in the simplified method, i.e. the transverse (perpendicular to ridge) and the longitudinal (parallel to ridge). In this method, the external peak (gust) pressure coefficients (C_pC_g) provided for low rise buildings implicitly account for torsional loads. Based on the concept of partial loads acting on building envelope, the detailed procedure has four load cases. In Cases A and C symmetric uniform loads are considered, in order to estimate the maximum base shears and overturning moments. On the other hand, partial wind loads are recommended to create equivalent torsional building loads in Case B and Case D. Nevertheless, the choice of partial loads could be difficult for designer engineers as can be seen from the code statements quoted below:

> *"In case B, the full wind pressure should be applied only to parts of the wall faces so that the wind-induced torsion is maximized"* (note (2) to figure I-16); and
> *"… the influence of removing 50% of the case C loads from parts of the face areas that maximizes torsion, as shown in figure I-16, case D, should be investigated"* (Commentary I, 37).

3.3 European 2004: Actions on structures - General actions - Part 1-4: wind actions

The Eurocode defines one unified analytical method that can be used for predicting the wind forces on all building types regardless of height. Wind pressure and force coefficients are described in Eurocode part 4 section 7. Torsional effects are taken into account by applying non-uniform pressures and forces, as shown in European 2004, Figure 7.1. A triangular wind load is applied on the windward surface with a rectangular load on the leeward face of the building. Limited information regarding wind-induced torsional loads and only for rectangular buildings can be found in this code. In addition, European 2004 includes a rather difficult to apply statement regarding the torsional wind load case:

> *"For other cases an allowance for asymmetry of loading should be made by complete removing the design wind action from those parts of the structure where its action will produce a beneficial effect".* (Section 7.1.2 – note (b))

4. WIND-INDUCED TORSION COMPARISONS: CASE STUDIES

In this section, different building configurations were analyzed using the three codes/standards. Three low-rise buildings (gabled roof slope 4:12, width (B =16 m), and height (h = 6 m) with horizontal aspect ratios (L/B =1, 2, and 3) located in an open terrain; and three tall buildings (B = 30 m, h = 60 m) with horizontal aspect ratios (L/B =1, 2, and 3) located in suburban terrain have been analyzed for this comparison. Both simplified and detailed methods described in the ASCE/SEI 7-10 and NBCC 2010 has been applied for the three low-rise buildings, in addition to the detailed method available in European 2004. For tall buildings, the detailed method in the three codes/standards has been used to estimate wind loads. In the simplified method (ASCE/SEI 7-10), the external pressure coefficients (GC_{pf}) on building envelope are estimated for low-rise buildings using Figure 28.4-1. In the detailed method (ASCE/SEI 7-10), the roof and side wall external wind pressure (GC_{pf}) are estimated according to Figure 27.4-1. In the simplified method (NBCC 2010), external peak pressure coefficients (C_gC_p) are provided for low-rise buildings, in Figure I-7, Commentary I. The external pressure estimation by the detailed method (NBCC 2010) is taken from

Figure I-15, Commentary I. Likewise for European 2004, external pressure coefficients for vertical walls of rectangular plan buildings are calculated using Figure 7.5 and Table 7.1 available in section 7, while for the external pressure of duo pitch roofs, values are provided in the same section (Figure 7.8 and Table 7.4a). The assessment of torsional moment should be done with respect to the corresponding applied wind forces. For this reason, two load cases, maximum torsional moment with the corresponding shear force and maximum shear force with the corresponding torsional moment, were presented in this study. The wind velocity was adjusted by using Durst curve given in the ASCE/ESI 7-10 Commentary, Figure C26.5.1. This was to alleviate the effect of using the 3-sec reference wind speed in ASCE/SEI 7-10, as opposed to the mean hourly and 10-minute wind speed in NBCC 2010 and European 2004 respectively. The results are presented in terms of shear force and equivalent eccentricity. The shear coefficients and equivalent eccentricities in transverse direction were estimated as per Eq. 1 and 2 respectively.

$$C_V = \frac{\text{Base shear}}{0.5\ \rho\ V_h^2\ B\ h} \tag{1}$$

$$e\ \% = \frac{\text{Base torsional moment}}{L\ *\ \text{Base shear}} *\ 100 \tag{2}$$

It is also important to compare the magnitude of the torsional moment estimated for the three low buildings based on the application of the wind load patterns introduced (simplified and detailed methods) in the standards considered with the past wind tunnel results. The estimated torsional moment is normalized to get the torsional coefficient according to Eq. 3.

$$C_T = \frac{\text{Base torsional moment}}{0.5\ \rho\ V_h^2\ B\ L\ h} \tag{3}$$

Details of the calculation procedure are provided in Appendix I for one building configuration.

5. COMPARISON RESULTS AND DISCUSSION

Comparisons among ASCE/SEI 7-10, NBCC 2010 and European 2004 for three low-rise buildings are presented in Figure 1. The results are introduced in terms of shear coefficients and equivalent eccentricities for the load case representing the maximum torsional moment and the corresponding horizontal shear force. As clearly shown, significant differences are found among the three national codes/standards in evaluating the torsional moment, whereas smaller differences are found in evaluating shear forces. The results show that ASCE/SEI 7-10 estimates torsional loads three times higher than those of NBCC 2010 and more than twice the torsional loads calculated by the European 2004. This is attributed to the different methodologies adopted by different codes/standards in representing the actual wind distribution by an equivalent wind static load. In Figure 2, comparisons among the three codes/standards using the detailed analytical procedure for the same buildings are presented. Although significant differences of equivalent eccentricities have been found among the codes/standards, different values of shear coefficients compensate and produce more comparable torsional moments. For example, NBCC 2010 introduces the highest equivalent eccentricity value, which is equal to 25% of the building length but it also has

the smallest value for shear coefficient. Thus, it appears the detailed method fixes an appropriate equivalent eccentricity depending on the value of shear coefficient in order to produce comparable torsional moments for all cases. For instance, the detailed method (ASCE/SEI 7-10) estimated torsional coefficients for the three low buildings equal to 0.24, 0.48 and 0.73. Likewise, torsional coefficients for the same buildings evaluated by the detailed method (NBCC 2010) are 0.24, 0.45 and 0.70. Clearly, the magnitude of the torsional moments produced by the detailed method is almost the same in the two standards. However, the total wind loads required to be applied in the torsional load case by using the detailed method in the two standards and resulting from adding the shear forces and the forces resulted from the torsion are different given that ASCE/SEI 7-10 requires applying 75% of the full wind loads while NBCCE 2010 requires applying 50% of the total wind loads. This needs deeper assessment and investigation.

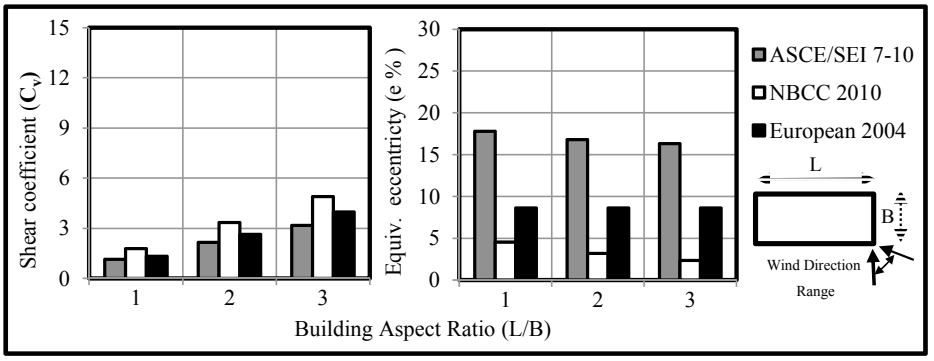


Figure 1. Simplified method - low buildings - partial wind load case (max. torsion and corresponding shear)

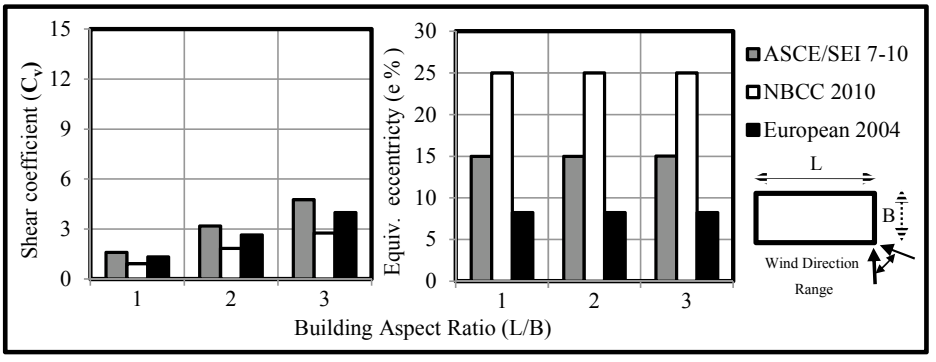


Figure 2. Detailed method - low buildings – partial wind load case (max. torsion and corresponding shear)

It is also of interest to compare the wind-induced torsion between the simplified method and the detailed method proposed in the same building code. Comparing the simplified method with the detailed method proposed by ASCE/SEI 7-10 for low-rise buildings shows a decrease of the equivalent eccentricity by about 18% and an increase of the shear coefficient by 40%. Therefore, using the simplified or detailed method of ASCE/SEI 7-10 for estimating wind design values for the main frame elements for low-rise buildings would result in similar loads. In NBCC 2010, the shear coefficient values estimated by the detailed method have smaller values compared to the simplified approach by 45%; on the other hand, the equivalent eccentricity in the detailed approach have more than four times higher

values compared to the simplified method. This is another point that requires further research to fill the gap between the detailed and the simplified method in NBCC.

As previous studies focused on estimating the effective horizontal wind loads for low rise buildings (i.e. maximum base shear) regardless of the horizontal distribution of the real wind loads (i.e. leading to maximum torsion), the current comparison shows that the three codes are successful in yielding similar values for maximum base shear loads, as can be seen in Figure 3. The values for the shear coefficients are estimated based on the full wind load cases in the simplified and the detailed method. Figure 4 presents peak torsional moment coefficients estimated by the simplified and the detailed method in the three codes/standards with the peak torsional coefficient measured in past wind tunnel tests. It can be seen that the detailed method proposed in ASCE/SEI 7-10 and NBCC 2010 succeeded to predict the wind-induced torsional moment on low buildings, particularly for small aspect ratios. However, significant difference has been found between the simplified method of ASCE/SEI 7-10 and NBCC 2010 when compared with the wind tunnel test results. The simplified method in both standards underestimates the torsional moment due to wind on low-rise buildings. However, the simplified method (ASCE/SEI 7-10) appears closer to the wind tunnel results. European 2004 underestimates the torsional moment due to wind on low-rise buildings by almost 50%.

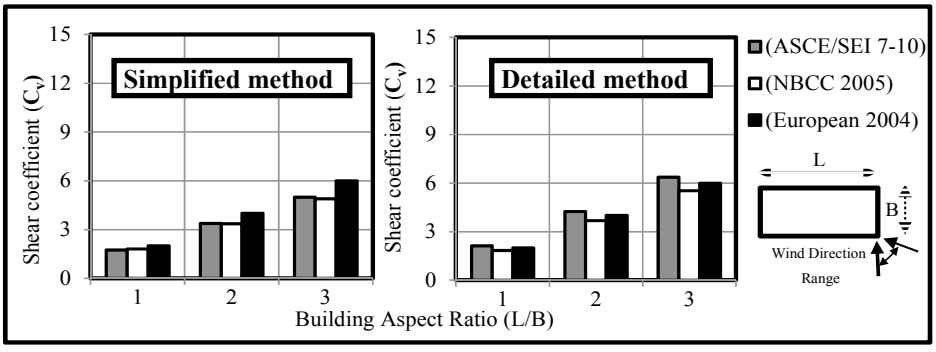


Figure 3. Simplified and detailed methods - low buildings – full wind load case (maximum shear force)

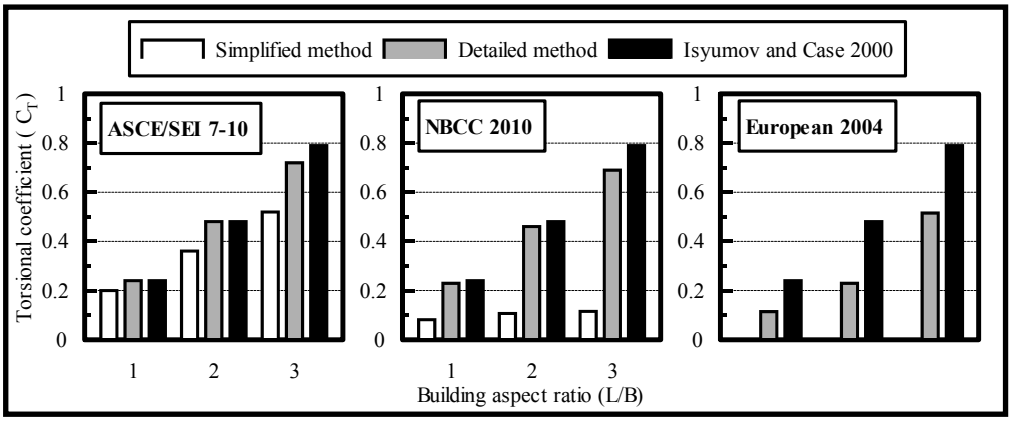


Figure 4. Peak torsional coefficients for three low buildings evaluated by the three codes/standards compared with wind tunnel results by Isyumov and Case 2000.

For tall buildings, only one analytical approach is proposed for calculating the wind loads on the main resisting frame in the three standards – see Table 1. Figure 5 presents the comparison among the provisions for the three tall buildings examined. Shear coefficients and the equivalent eccentricities are presented for the torsional load case (maximum torsion and corresponding shear force). It has been noticed that higher eccentricities are associated with lower shear coefficients. This is in line with what has been found in the low-rise building cases, (see Figure 2). For instance, the detailed method in ASCE/SEI 7-10 estimates torsional coefficients equal to 0.27, 0.54 and 0.85 for the three tall buildings considered. In a similar manner, torsional coefficients for the same buildings evaluated by the detailed method of NBCC 2010 are found equal to 0.30, 0.60 and 1.0. As previously mentioned, the magnitude of the torsional moments produced by the detailed method is almost the same in the two standards. However, the total wind loads due to shear, as well as those forces resulting from torsion, are different given that ASCE/SEI 7-10 requires applying 75% of the full wind loads while NBCC 2010 requires applying only 50% of the full wind loads. On the other hand, the European standard estimates torsional coefficients equal to 0.18, 0.39, and 0.60 for the three tall buildings. However, this is about 35% less than the other two standards; the European code requires wind loading for torsional case 40% higher than the other two codes/standards. These discrepancies need to be investigated to assess their effects on tall building design. Figure 6 illustrates the variation of the maximum base shear created by wind loads over the three tall buildings proposed by the three codes/standards, similar to Figure 3. ASCE/SEI 7-10 and NBCC 2010 show good agreement while the European 2004 provides almost 15% higher shear coefficient values.

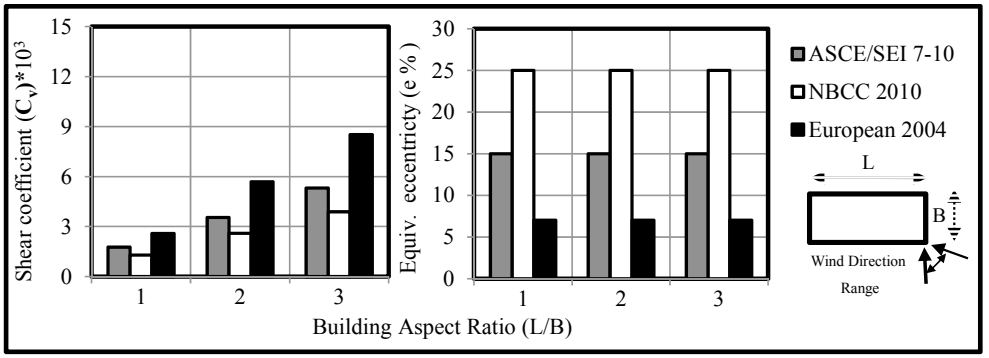


Figure 5. Detailed method – tall buildings – partial wind load case (max. torsion and corresponding shear)

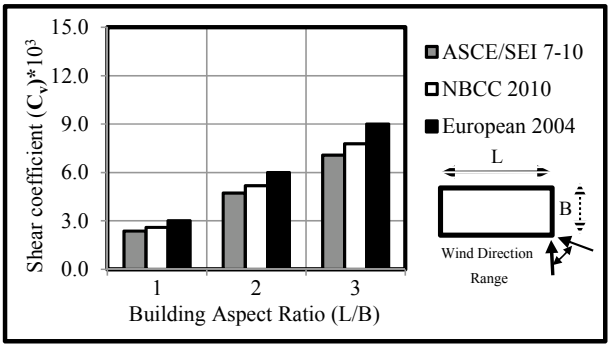


Figure 6. Detailed method – tall buildings – full wind load case (maximum shear force)

6. SUMMARY AND CONCLUSIONS

This paper reviews past studies on wind-induced torsional loads for low and tall buildings. In addition, it discusses and compares the provisions for wind-induced torsion in the Canadian, American and European wind codes/standards along with the previous wind tunnel studies. Both simplified and detailed methods provided in these codes/standards for the evaluation of wind-induced torsional loads on buildings have been used. The comparison results demonstrate the following:

a- For low buildings:
- The simplified method in ASCE/SEI 7-10 estimates torsional moments more than three times those of NBCC 2010 while twice those of the European 2004 provisions.
- Compared to the previous wind tunnel measurements, the simplified method for torsional moment in ASCE/SEI 7-10 works well for the square building; less so for buildings with higher aspect ratios. On the other hand, the simplified method in NBCC 2010 underestimates the measured torsional moment significantly.
- The detailed methods in both ASCE/SEI 7-10 and NBCC 2010 show good agreement with the torsional moment measured while the European code seems to underestimate these torsional moments for all building geometries.
- The detailed methods in both ASCE/SEI 7-10 and NBCC 2010 yield torsional moments of comparable magnitudes. However, the total wind loads due to shear forces, as well as those forces resulting from torsion are different.
- Good agreement is noticed for estimating wind-induced torsion by the simplified and the detailed method in ASCE/SEI 7-10 for low building aspect ratios; for higher aspect ratios the simplified method yields lower torsional moments.
- NBCC 2010 simplified and detailed method yields similar maximum base shear forces but very different maximum torsional loads.

b- For tall buildings:
- ASCE/SEI 7-10 estimates the maximum torsion by applying 0.75 of the maximum wind load with additional equivalent eccentricity 15% of building dimensions, while NBCC 2010 applies 0.5 of the maximum wind load with additional equivalent eccentricity of 25%. On the other hand, the European code applies 0.70 of the maximum wind load with an eccentricity of 7%. In general, these yield comparable torsional moments; however the total effective loads resulting from adding the shear force and additional force due to the torsional moment are different.
- Eurocode estimates maximum base shear somewhat higher than ASCE/SEI 7-10 and NBCC 2010.

More experimental data are required for a reliable assessment of wind-induced torsion on low-rise and tall buildings.

7. REFERENCES

ASCE/SEI 7-10. (2010). "Minimum Design Loads for Buildings and Other Structures." published by the Structural Engineering Institute of ASCE, Reston, VA

Boggs, D. W., Hosoya, N. and Cochran, L. (2000). "Sources of Torsional Wind Loading on Tall Buildings: Lessons from the Wind Tunnel." Proceedings of Structures Congress 2000, Philadelphia, Pennsylvania, USA, Sponsored by ASCE/SEI, May 8-10

Davenport, A.G., Surry, D. and Stathopoulos, T. (1977). "Wind Loading on Low-Rise Buildings: Final Report on Phases I and II." University of Western Ontario, Eng. Sci. Res. Rep., BLWT-SS8

Davenport, A.G., Surry, D. and Stathopoulos, T. (1978). "Wind Loading on Low-Rise Buildings: Final Report on Phase III." University of Western Ontario, Eng. Sci. Res. Rep., BLWT-SS8

Greig, G.L. (1980). "Towards An Estimate of Wind-Induced Dynamic Torque on Tall Buildings." Univ. of Western Ontario, M.Eng. Thesis, Sept. 1980

Ho, T.C.E., Lythe, G.R. and Isyumov, N. (1999). "Structural Loads from the Integration of Simultaneously Measured Pressures." Proc. ICWE- 10, Copenhagen, Denmark

Holmes, J. D. (1983). "Wind Loads on Low Rise Buildings – A Review." CSIRO Div. of Building Research, Highett. Victoria, Australia

Isyumov, N. and Case, P. C. (2000). "Wind-Induced Torsional Loads and Responses of Buildings." Proceedings of Structures Congress 2000, Philadelphia, Pennsylvania, USA, Sponsored by ASCE/SEI, May 8-10

Isyumov, N. and Poole, M. (1983). "Wind-induced Torque on Square and Rectangular Building Shapes" Journal of Wind Engineering and Industrial Aerodynamics, vol.13: pp.183-196

Krishna, P. (1995). "Wind Loads on Low-Rise Buildings – A Review." Journal of Wind Engineering and Industrial Aerodynamics, vol.54-55: pp.383-396

Lythe, G.R. and Surry, D. (1990). "Wind-induced Torsional Loads on Tall Buildings" Journal of Wind Engineering and Industrial Aerodynamics, vol.36: pp.225-234

NBC2010. (2010). "User's Guide – NBC 2010, Structural Commentaires (part 4)." Issued by the Canadian Commission on Buildings and Fire Codes, National Research Council of Canada

PrEN 1991-1-4. (2004). "Eurocode 1, 2004: Actions on Structures – General actions – Part 1-4: Wind actions." European Standard

Stathopoulos, T. (1984). "Wind Loads on Low-rise Buildings - A Review of the State of the Art." Engineering Structures, vol.6: pp.119-135

Tallin, A. (1985). "Analysis of Torsional Moments on Tall Buildings." Journal of Wind Engineering and Industrial Aerodynamics, vol.18: pp.191-195

Xie, J. and Irwin. (2000). "Key Factors for Torsional Wind Response of Tall Buildings." Proceedings of Structures Congress 2000, Philadelphia, Pennsylvania, USA, Sponsored by ASCE/SEI, May 8-10

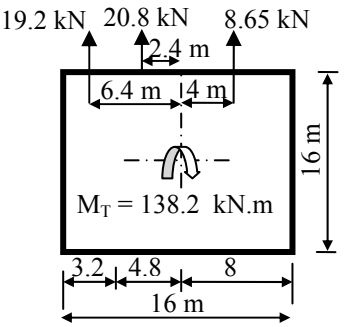
Zhou, Y. and Kareem, A. (2000). "Torsional Load Effects on Buildings under Wind." Proceedings of Structures Congress 2000, Philadelphia, Pennsylvania, USA, Sponsored by ASCE/SEI, May 8-10

APPENDIX I

Building 1: Note that the magnitude of the wind velocity does not have an effect on the results since all the values are normalized with respect to it.

A) AMERICAN SOCIETY OF CIVIL ENGINEERS (ASCE/SEI 7-10):

3-second guest wind speed = 40.2 m/s
The velocity wind pressures are computed using:
$q_z = 0.613\ k_z\ k_{zt}\ k_d\ V^2\ I = 0.613\ (0.932)(1)(0.85)(40.2)^2 =$
$= 760\ N/m^2 = 0.76\ kN/m^2$
Design pressures for the MWFRS:
$P = q_z\ [(GC_{pf}) - (GC_{pi})]$
(GC_{pf} values are taken from the table in figure (28.4-1),
Transverse direction $\theta = 18.4^o$
Width of end zone surface: a = 3.2 m.



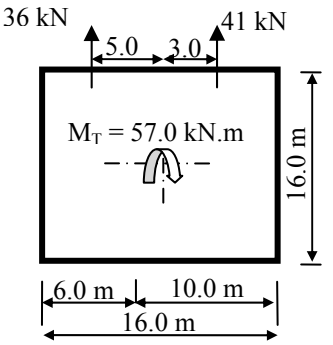
Torsional load case - transverse direction:

$$C_V = \frac{(48.65 * 10^3)}{0.5 * 1.25 * 26.645^2 * 16 * 6} = 1.14$$

$$e\% = \frac{1}{16} * \frac{138.2}{48.65} * 100 = 17.8\%$$

B) NATIONAL BUILDING CODE OF CANADA (NBCC 2010):

The equivalent hourly mean wind speed = 26.645 m/s
Calculation of wind velocity pressure q (kN/m^2):
$q = (V_{10})^2/39.2^2 = 0.462$ kN/m^2
Take the important factor =1
Calculate the exposure factor related to open terrain
$Ce = (Z/10)^{0.2} \geq 0.9$ $Ce = (7.333/10)^{0.2} = 0.94 \geq 0.9$, then Ce = 0.94
Calculation of end zones:
$y^{(6)} = 6.0$ m
Wind pressure over building surface:
$p = 1 * 0.462 * 0.94 * C_gC_p = 0.434 * C_gC_p$ (kN/m^2)
C_gC_p values obtained from figure I-7
(Commentary I, page I-13):
For $\theta = 18.4^o$



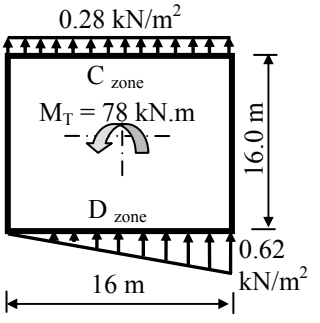
Torsional load case - transverse direction:

$$C_V = \frac{(77.0 * 10^3)}{0.5 * 1.25 * 26.645^2 * 16 * 6} = 1.8$$

$$e\% = \frac{1}{16} * \frac{57.0}{77.0} * 100 = 4.6\%$$

C) EUROPEAN 2004

The equivalent 10-minute reference wind speed = 28.2 m/s
Calculation of Wind velocity pressure:-
Fundamental basic wind speed
$V_{b,o}$= 28.20 m/s (terrain category II)
Basic wind speed $V_b = C_{dir}\, C_{season}\, V_{b,o}$ (m/s)
Mean wind $V_m(z) = 5.3542 \ln (z/0.05)$
Peak velocity pressure q (kN/m^2)
$q_b(z) = [1 + 7 * 1/\ln (z/0.05)] * 1/2 * 1.25 * V_m^2(z) = 1.0$ kN/m^2
Wind pressure on surface
$W_e = q_p(z_e) * C_p * 0.85 = 850 * C_p$ (N/m^2)
$C_{P\,(D\ zone)} = 0.72$ and $C_{P\,(C\ zone)} = 0.333$



Torsional load case- transverse direction:

$$C_V = \frac{(56.45 * 10^3)}{0.5 * 1.25 * 26.645^2 * 16 * 6} = 1.325$$

$$e\% = \frac{1}{16} * \frac{78.0}{56.45} * 100 = 8.64\%$$

Wind-induced torsional loads on low-rise buildings

M. Elsharawy, K. Galal and T. Stathopoulos

Faculty of Engineering and Computer Science, Concordia University, Montréal, Québec, Canada H3G 1M8

1. ABSTRACT

This paper presents a set of wind tunnel tests that are carried out to examine wind-induced torsional loads on low-rise buildings. Three low-rise buildings were tested in the Building Aerodynamics Laboratory located in the Engineering Complex at Concordia University, Montreal, Canada. Two low-rise buildings (scale 1:400) with a flat and 4:12 gabled roof slope (having the same dimensions) were examined in open and urban terrain exposures for a half wind direction cycle (every 15^o). In addition, a model (scale 1:200) of an actual low-rise building in Fredericton, New Brunswick, Canada and its surroundings has been tested in three wind tunnel tests. Two of latter set of tests were conducted for the building model with a complete simulation of its surroundings in open and urban terrain exposures for a complete cycle by 10^o increments. The building was also tested in an open terrain exposure without any surroundings. Peak, mean, and minimum base torsion and shear force for each azimuth were evaluated for all tests. In general, the measured results indicated that the maximum torsional moment on low-rise buildings could be simulated by applying 75% of the full wind loads (maximum shear) with additional 15% equivalent eccentricity of the facing building dimension.

2. INTRODUCTION

The majority of buildings worldwide are categorized as low-rise buildings. Low-rise buildings are prone to excessive damages in wind disastrous events. The proper design for such building depends significantly on the sufficient evaluation of the instantaneous temporal and spatial variation of wind-induced loads on building envelopes. These variations of wind-induced loads may result in significant torsion/torque about the vertical building axis. Even though for symmetric building shapes wind-induced torsional moment are found. Several studies have been carried out to evaluate the variation of local wind pressures on building claddings and the total effective wind forces (base shear/overturning moment) on the main structural building systems. However, very limited studies examined wind-induced torsional loads on low-rise buildings, as shown clearly in the comprehensive reviews by Holmes (1983), Stathopoulos (1984) and Krishna (1995). The major contribution in the development of North American provisions for the evaluation of wind loads on low-rise buildings was based on the research carried out at the University of Western Ontario (UWO) in the late 70's. An extensive experimental program in a boundary layer wind tunnel examined a variety of rectangular low buildings with different dimensions, roof slopes and upstream terrain exposures. However, wind-induced torsional loads were not examined in detail. Isyumov and Case (2000) studied wind-induced torsion

by conducting wind tunnel tests for three low-rise buildings with different aspect ratios. The study suggested (till more data are developed) that applying partial wind loads similar to those implemented for the design of tall buildings will improve the design of low buildings. This study was the only are addressing wind-induced torsional loads on low buildings. Clearly, more information is essential to improve the evaluation of wind-induced torsional loads on low buildings.

This paper presents a set of wind tunnel tests that are carried out to examine wind-induced torsional loads on low-rise buildings. One of the targets for this study is to quantify the effect of the different building geometrical parameters, as well as the effect of different terrain exposures and the surroundings on the wind-induced torsion. Thus, three low-rise buildings were tested in different terrain exposures. Two similar buildings with different roof slopes were tested in open and urban terrain exposures. In addition, a model of an actual low-rise building in Fredericton, New Brunswick, Canada and its surroundings has been tested.

3. CURRENT STATE IN BUILDING CODES

In this section, a summary of a comparison is conducted by Elsharawy et al. (2011) for peak torsional coefficient, C_T, as estimated by the application of the load patterns stated in three building standards/codes namely; the American Society of Civil Engineers standard (ASCE/SEI 7-10), National Building Code of Canada (NBCC 2010), and European code (European 2004) versus wind tunnel results reported by Isyumov and Case (2000) (see Figure 1). Three 4:12 roof-gabled low buildings with different aspect ratios, namely; L/B =1, 2, and 3 were tested by Isyumov and Case (2000) in an open terrain exposure. The simplified (envelope/static) and the detailed (directional/dynamic) methods stated in the ASCE/SEI 7-10 and NBCC 2010 as well as the detailed method available in Eurocode 2004 have been applied for their analysis. The wind velocity was adjusted by the Durst curve given in the commentary part of ASCE/ESI 7-10 in figure C26.5.1. This was to alleviate the effect of using the 3-sec reference wind speed used in ASCE/SEI 7-10 instead of the mean hourly and 10-minute wind speed used in NBCC 2010 and Eurocode 2004, respectively. The peak torsional coefficient, C_T, was calculated using the following equation:

$$C_T = \frac{\text{Peak Torsional Moment}}{0.5\ \rho\ V_h^{\,2}\ B\ H\ L} \tag{1}$$

where ρ = air density (kg/m^3), V_h = reference mean hourly wind velocity (m/s).

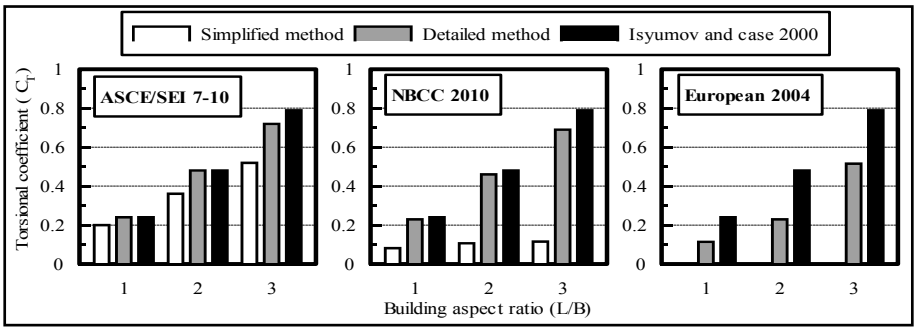


Figure 1. Comparison of torsional coefficients for three low-rise buildings with the wind tunnel tests conducted by Isyumov and case (2000), Elsharawy et al. (2011)

The comparison presented in Figure 1 demonstrates the following:

- The simplified method in ASCE/SEI 7-10 estimates torsional moments more than three times those of NBCC 2010 while twice those of the European 2004 provisions.
- Compared to the previous wind tunnel measurements, the simplified method for torsional moment in ASCE/SEI 7-10 works well for the square building; less so for buildings with higher aspect ratios. On the other hand, the simplified method in NBCC 2010 underestimates the measured torsional moment significantly.
- The detailed methods in both ASCE/SEI 7-10 and NBCC 2010 show good agreement with the torsional moment measured while the European code seems to underestimate these torsional moments for all building geometries.
- The detailed methods in both ASCE/SEI 7-10 and NBCC 2010 yield torsional moments of comparable magnitudes. However, the total wind loads due to shear forces, as well as those forces resulting from torsion are different.
- Good agreement is noticed for estimating wind-induced torsion by the simplified and the detailed method in ASCE/SEI 7-10 for low building aspect ratios; for higher aspect ratios the simplified method yields lower torsional moments.
- NBCC 2010 simplified and detailed method yields similar maximum base shear forces but very different maximum torsional loads.

The literature survey showed that the study conducted by Isyumov and Case (2000) is the only available study that addresses wind-induced torsional loads on low-rise buildings. Therefore, there is still a need to conduct more wind tunnel studies in order to enhance the understanding and modeling of wind-induced torsional loads acting on low-rise buildings. This highlights the need for the current study.

4. WIND TUNNEL TESTS

Three low-rise buildings were tested in the Building Aerodynamics Laboratory of Concordia University. Two models of low-rise buildings (scale 1:400) that have external dimensions of 152.5 mm (length) by 9.75 mm (width) and eave's height of 30 mm were constructed and tested in the wind tunnel. The first building model noted by "building I" has a flat roof while the other noted by "Building II" has a 4:12 gabled roof slope. The buildings with a flat and 4:12 roof slopes are equipped by 76 and 128 pressure taps, respectively. For "Building I" which has a flat roof, the pressure tapes are located on the side walls only since the uplift pressure on the top surface will not contribute to the base shear force and the torsional moment about the vertical building axis. "Building I" and "Building II" were tested in an open and urban terrain exposures for a half wind direction cycle (every 15^{o}). In addition, a model of a low-rise building noted by "Building III" in Fredericton, New Brunswick and its surroundings has been tested in the wind tunnel (see Figure 2). Taking into consideration the size of the full-scale building and the surrounding structures, as well as the simulation conditions of the boundary layer wind tunnel of Concordia University, a geometric scale of 1:200 was selected for the wind tunnel study. The model has external dimensions of 86.5 mm (length) by 42.5 mm (width) and a total height of 24.35 mm. The gabled roof has a slope $\theta=22.5^{o}$. The model called "Building III", is equipped with 128 pressure taps located on the wall and roof surfaces. Two tests were conducted for the building model with a complete simulation of its surroundings in open

and urban terrain exposures for a complete cycle by 10^o increments (36 wind directions). The building model was also tested in an open terrain exposure without any surroundings.

The wind velocity and turbulence intensity profile were measured using the 4-hole Cobra probe (TFI) and sampling rate of 1000 Hz. The velocity profile and the turbulence intensity simulated in the wind tunnel for open and urban terrain exposures are shown in Figure 3. The gradient wind velocities are measured as 13.2 m/s and 12.4 m/s for open and urban terrain exposures respectively. The power law exponent for the wind velocity profile simulated in these tests was 0.17 and 0.29, whereas the turbulence intensity at the mean roof height was 20.2% and 30.2% for open and urban terrain exposure, respectively. The pressure measurements on the models were conducted using a system of miniature pressure scanners from Scanivalve (ZOC33/64Px) and the digital service module DSM 3400.

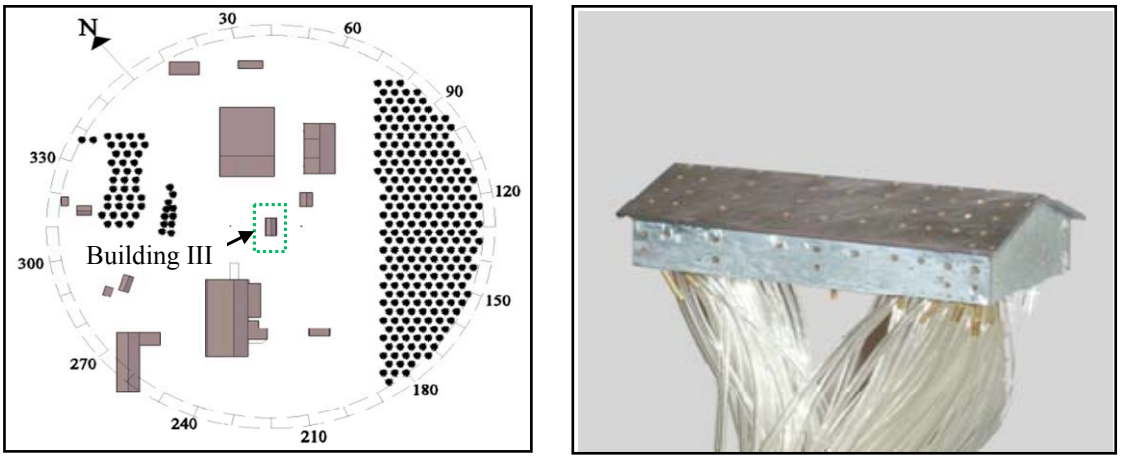


Figure 2. a) A plan of the model "Building III" with its surroundings tested in wind tunnel
b) Wind tunnel model "Building III" and location of pressure taps (Zisis and Stathopoulos (2010))

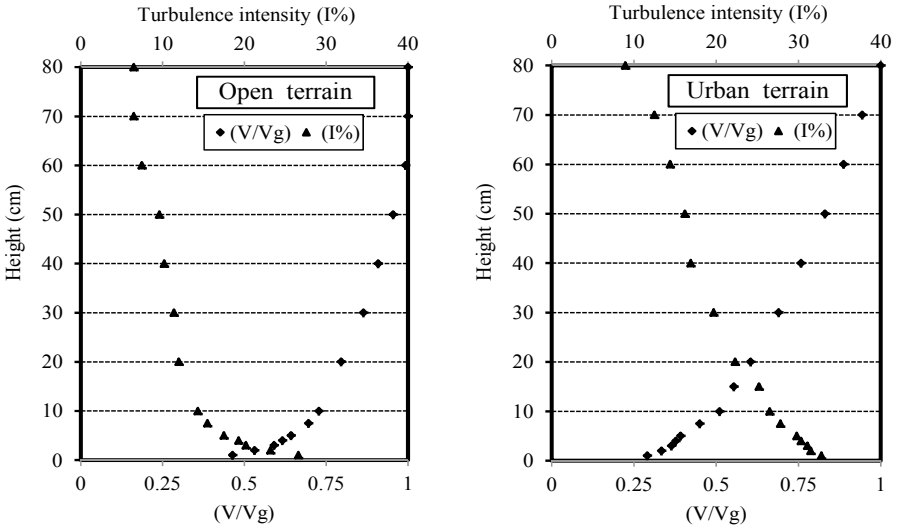


Figure 3. Wind velocity profile and the turbulence intensity simulated in wind tunnel for open and urban terrain exposure

The results of the wind tunnel tests were analysed. The measured pressures on the model surfaces are represented as differential pressure with respect to the atmospheric pressure. The wind pressure coefficient for each tap are estimated using

$$C_P = \frac{P - P_a}{0.5\ \rho\ V_h^2} \tag{2}$$

where P is wind pressure (kN/m^2), P_a is atmospheric pressure, ρ is air density (1.25 Kg/m^3) and V_h is the velocity at the mean roof building height (m/s).The instantaneous wind force corresponding to each tap is estimated by integrating the pressure coefficient over the effective area ($A_{effective}$) and multiplying it by the wind velocity pressure q_h

$$f_{tap} = C_p\ A_{effective}\ q_h \tag{3}$$

Since the vertical component (up-lift) of the force does not affect the torsional moment, the horizontal components of the wind forces acting on the inclined gable roof, in addition to the side wall forces, have been considered. The total instantaneous horizontal shear forces are calculated for each direction. The resultant shear force is estimated and normalized by using Eq. 4 below. The torsional coefficients were also estimated by normalizing the instantaneous torque according to Eq. 1. Maximum and minimum shear and torsional coefficients are estimated by applying extreme value analysis for each wind azimuth.

$$C_V = \frac{\text{Base Shear Force}}{0.5\ \rho\ V_h^2\ B\ h} \tag{4}$$

4.1 Experimental results

Three low-rise buildings are tested in the boundary layer wind tunnel. Four wind tunnel tests have been conducted for “Building I” and “Building II” with a flat and 4:12 gabled roof slopes in open and urban terrain exposures. In addition to that, three wind tunnel tests for “building III” ($\theta = 22.5^o$). The first two tests are for the building with the completed simulated surroundings in open and urban terrain exposure. To evaluate the effect of the surrounding on the wind loads, “Building III” was also tested in an open terrain exposure without any surroundings. The instantaneous base shear and torsional moment coefficients are estimated for each azimuth. Furthermore, the peaks are estimated based on extreme value analysis.

4.2 Effect of changing roof slope

Figure 4 shows the variation of peaks and means for shear and torsional coefficients with wind direction for “Building I” and “Building II” in open and urban terrain exposure. In fact, as it is well established in building codes that increasing the roof slope results in increasing the shear forces and consequently the overturning moments, similarly, the torsional moment should also be expected to increase. The test results demonstrate that increasing roof slope angle from flat to 4:12 led to an increase of the wind forces and torsional moment. The magnitude of shear and torsion for the building with 4:12 roof slope is higher by about 25% in open than urban terrain exposures.

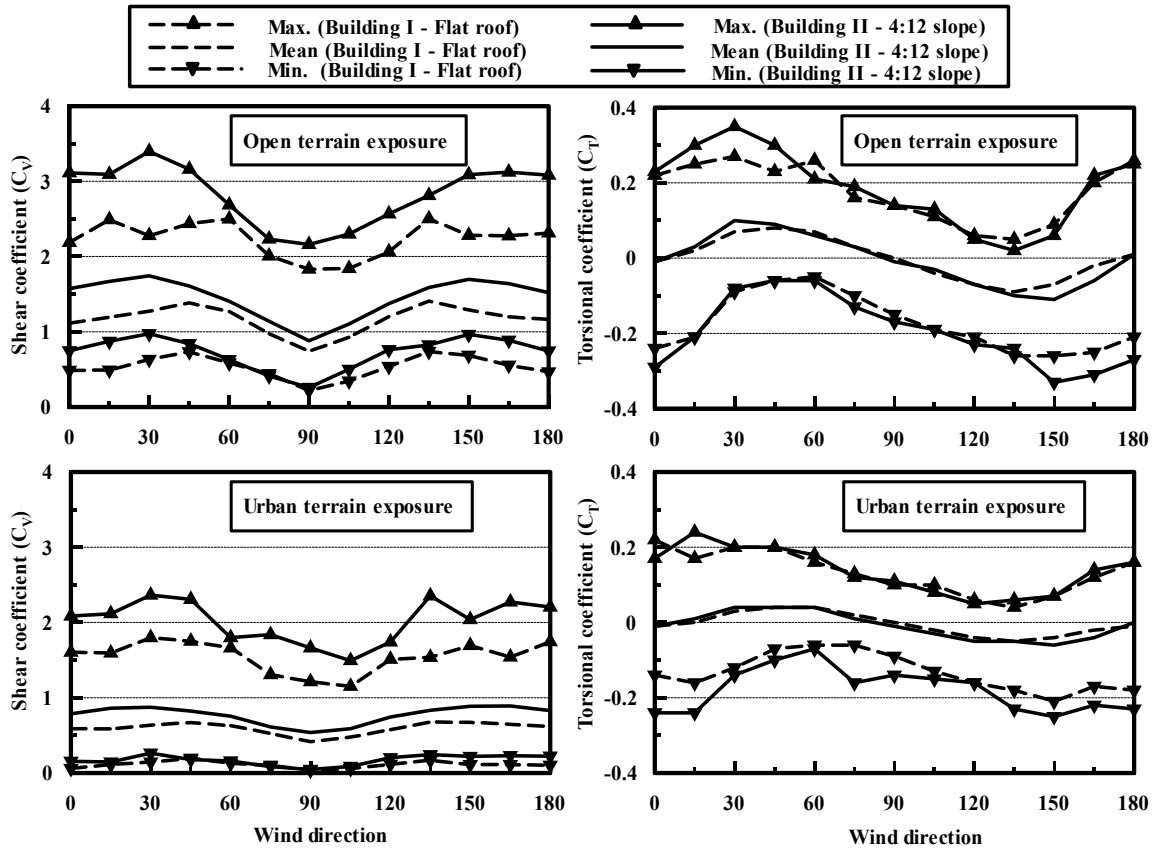


Figure 4. The variation of shear and torsional coefficients with wind direction for buildings I and II in open and urban terrain exposure

4.3 Effect of terrain exposure on base shear and torsional moment

The results for the first two buildings (flat and 4:12 roof slope) are presented in Figure 4. It can be seen that the base shear and torsional moment have been reduced in the urban terrain exposure for the same building by about 30%. Thus, the reduction in wind standards adopted for the maximum shear and overturning moment load cases should be also implemented for the torsional load case. On the other hand, the third building was tested with a complete simulation for the surroundings (local elements) in open and urban terrain exposures. The variation of peak and mean torsional coefficients for thirty six wind directions is presented in Figure 5. The results show that the effect of the terrain exposure on the torsional coefficient, C_T, is insignificant. The variation of peak base shear force with wind direction is presented in Figure 6. In general, it is expected to have a reduction in wind loads when considering the two different terrain exposures. In the current tests, the reduction of the mean wind velocity pressure in urban terrain exposure is counteracted by the effect of the high turbulence in wind flow due to the surroundings. This could be the reason of having almost the same peak torsional moment due to wind in the two terrains. This implies that there is a need to investigate the effect of the terrain exposure and the interaction with the surroundings in detail.

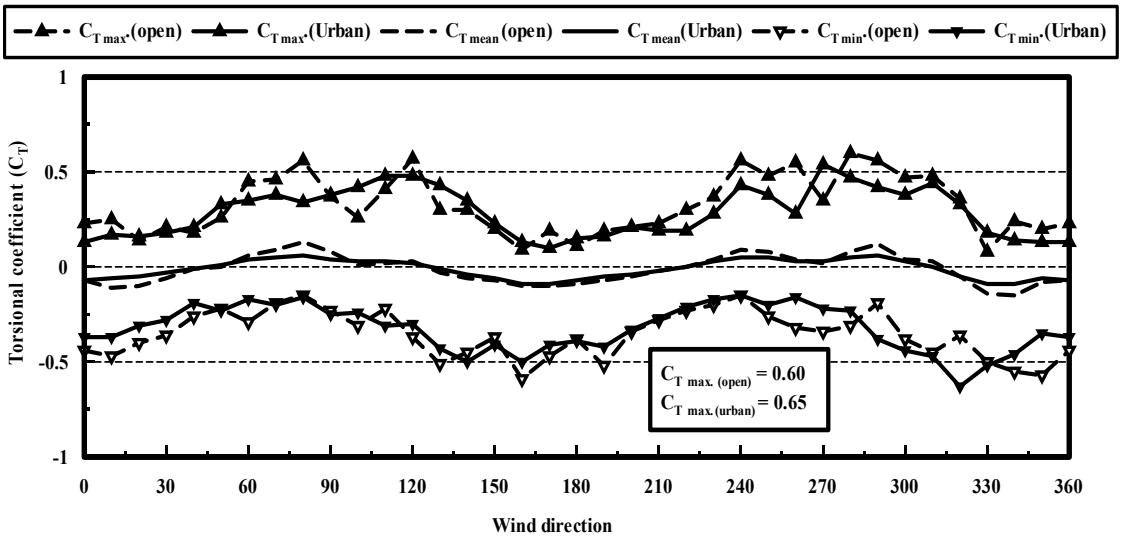


Figure 5. The variation of torsional coefficients with wind direction for building III in open and urban terrain exposures

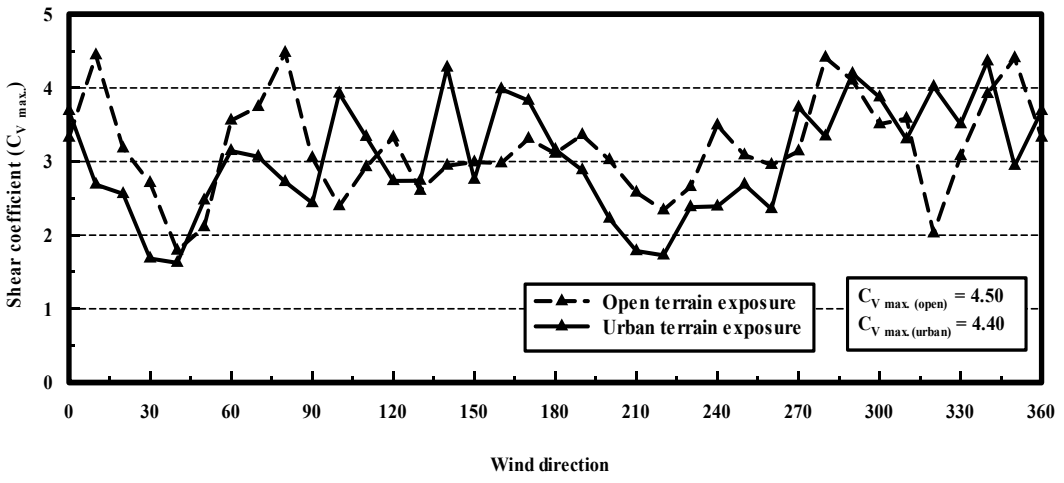


Figure 6. The variation of shear coefficient with wind direction for building III in open, and urban terrain exposure

4.4 The effect of surroundings on base shear and torsional moment

Two cases for "Building III" were investigated in the wind tunnel in open terrain exposure. The first case was the building with a complete simulation of the surroundings (scale 1:200), whereas the second case was for the building without any surroundings. In the latter case, due to the symmetry in the building's shape and the free space around the building model in wind tunnel, the data was measured only for the buildings in wind directions varying from 130^o to 220^o (every 10^o). The maximum and minimum torsional coefficients for the two cases were presented in Figure 7. It can be observed that the surroundings reduce the maximum torsional loads by about 20%.

It is also noticed that Building III in open terrain without the surroundings will gain higher base shear. The surroundings as obstacles facing the wind flow reduce the base shear by 30% for this particular building model. In general, it can be concluded that the surroundings will most likely help decrease the wind loads on buildings.

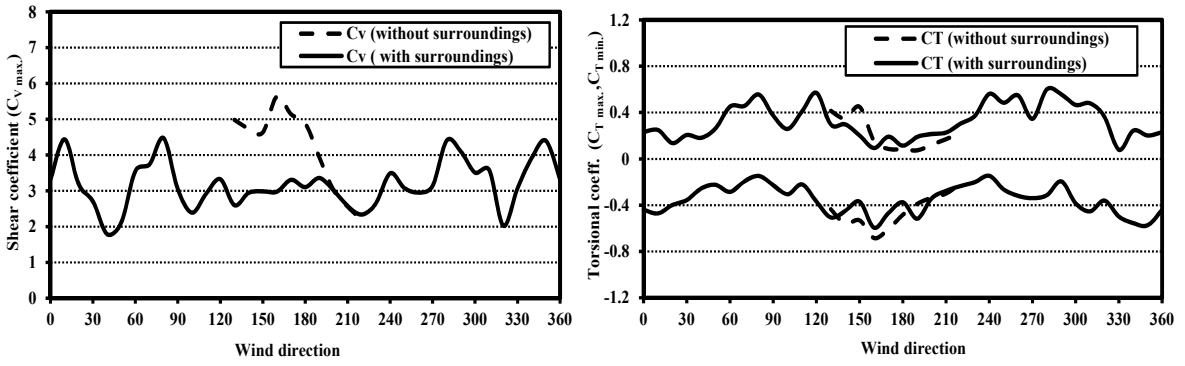


Figure 7. The effect of the surroundings on shear and torsional coefficients in an open terrain exposure

5. COMPARISON WITH STANDARDS

The wind tunnel test results for the three buildings are compared with the proposed values for base shear force and torsional moment stated by two currently updated building codes and standards, ASCE/SEI 7-10 and the NBCC 2010. The shear and torsional peaks for all tested wind directions in open terrain exposure are plotted in Figure 7 along with the result evaluated by the application of wind load patterns proposed in the codes/ standards considered. For the first two buildings (flat and 4:12 roof slope), the absolute maximum shear and torsional coefficients for thirteen wind directions are presented, whereas the peak shear and torsional coefficient are presented for thirty-six azimuths for Building III. The experimental results are compared with the provisions of the simplified (envelope/static) method and the detailed (directional/dynamic) method in the two building codes. For the simplified method calculations in ASCE/SEI 7-10, figure 28.4-1 is used to get the external pressure coefficients (GC_{pf}). The basic (transverse) and torsional load cases presented in figure 28.4-1 of ASCE/SEI 7-10 are used to estimate the maximum torsional moment and base shear for the buildings. For the detailed method calculation in ASCE/SEI 7-10, Figure 27.4-1 is used to get the external pressure coefficient, C_p, on the side walls and the roofs. The simplified method calculations in NBCC 2010 for the torsional and shear coefficients were derived based on figure I-7 where the external peak composite-gust pressures (C_pC_g) are provided for low-rise buildings. The external pressure estimation by the detailed method of NBCC 2010 follows the flowchart of figure I-15 in Commentary I. ASCE/SEI 7-10 and NBCC 2010 calculations were carried out considering the open terrain exposure C, and terrain category II, respectively.

From Figure 8, the following can be observed:

- There is a good agreement in evaluating the base shear force by the simplified and the detailed method in both standards.

- The application of the wind load patterns proposed in the detailed (directional/dynamic) method in ASCE/SEI 7-10 and NBCC 2010 is sufficient to evaluate and predict the torsional moments for all cases considered.
- The simplified (Static) method of NBCC 2010 underestimates the torsional moment in all studies cases.
- In general, the simplified method of ASCE/SEI 7-10 works well for the torsional moment, yet it becomes problematic to account for surroundings and other local elements.

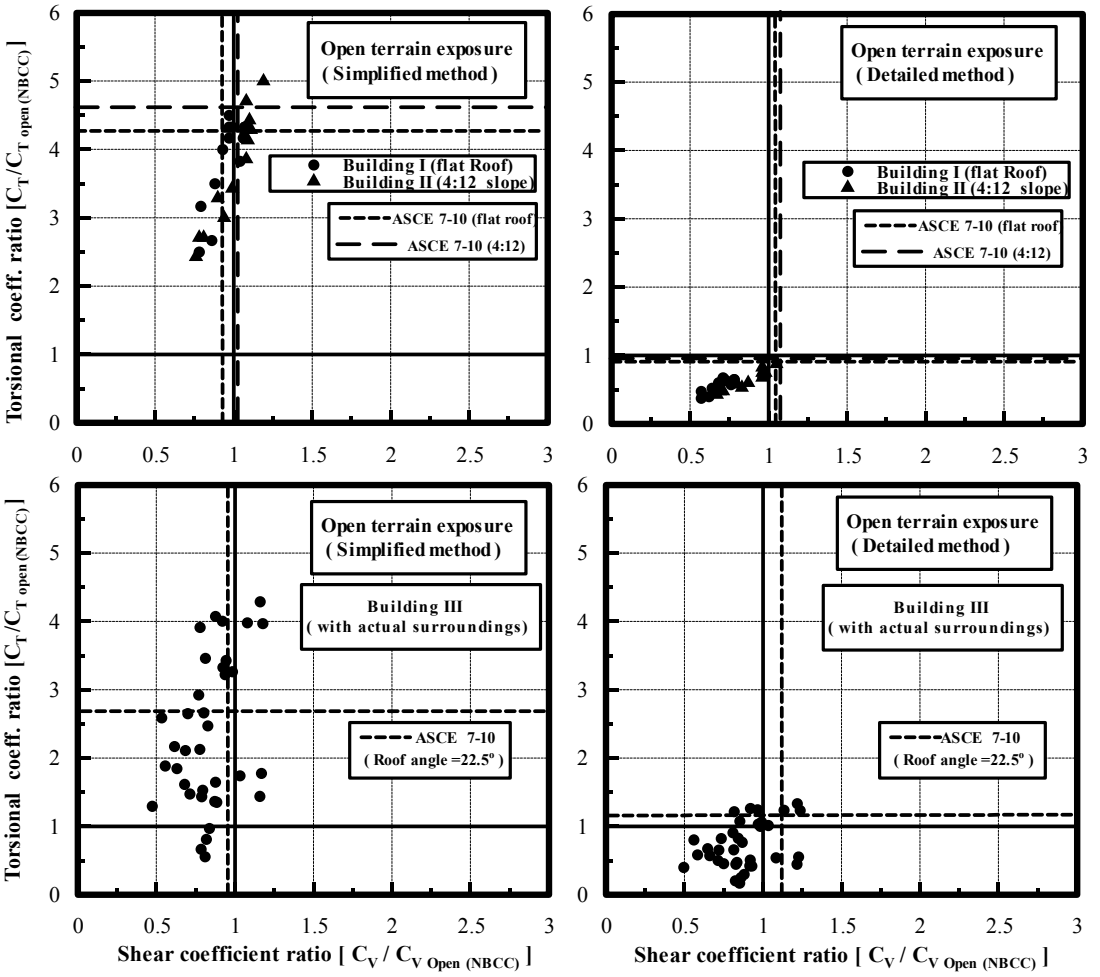


Figure 8. Comparison of wind tunnel shear (C_V) and torsional coefficients (C_T) with the values proposed in the North American codes/standards for open terrain exposure

The horizontal distribution of the instantaneous wind loads on the main wind resisting building system always causes torsional moment about the vertical building axis. The magnitude of this torsion significantly depends on the magnitude of the wind resultant and the deviation (eccentricity) ever existing between the aeroelastic wind resultant force and the building center of rigidity. The torsional load design case is generally simulated by applying reduced wind loading on parts of the building envelope generating additional equivalent eccentricity. Table 1 presents a summary for the peak shear and torsional coefficients based on the application of two North American wind standards (ASCE/SEI 7-

10 and NBCC 2010) and the results of previous and present wind tunnel tests. The shear load case is presented in a form of shear coefficient ($C_{V\ max.}$), whereas the torsional load case is described by using three parameters, namely peak torsional coefficient "C_{Tmax}", peak equivalent eccentricity "e %", and the percentage of the full wind load "Load %" required to get the maximum torsional moment. The equivalent eccentricity "e %" is calculated as

$$e\ \% = \frac{\text{Base torsional moment}}{L\ *\ \text{Base shear}} *\ 100 \qquad (5)$$

where L = building dimension facing the wind,

Table 1: Wind tunnel measurements of peak torsional moment on low buildings and comparisons with building codes and standards

Information source	Building I (flat roof) (B = 39, L = 61, H =12) m				Building II (θ = 18.4°) (B = 39, L = 61, H = 12) m				Building III (θ = 22.5°) (B = 8.5, L = 17, H =3.1) m (with surroundings)			
	Shear case	Torsional case			Shear case	Torsional case			Shear case	Torsional case		
	$C_{v\ max}$	$C_{T\ max}$	e_{max}%	Load %	$C_{v\ max}$	$C_{T\ max}$	e_{max}%	load %	$C_{v\ max}$	$C_{T\ max}$	e_{max}%	load %
Simplified ASCE/SEI 7-10	2.28	0.26	17.6	65	2.90	0.33	17.5	65	3.42	0.38	17.25	65
Detailed ASCE/SEI 7-10	3.35	0.38	15	75	3.45	0.39	15	75	4.52	0.51	15	75
Simplified NBCC 2010	2.34	0.06	2.6	100	2.86	0.07	2.5	100	3.8	0.14	3.95	100
Detailed NBCC 2010	3.22	0.4	25	50	3.22	0.4	25	50	3.62	0.45	25	50
Isyumov and Case. 2000 (B = 9.75, L=19.5, H = 4.88) m	-	-	-	-	-	0.48	-	-	-	-	-	-
Wind tunnel (open terrain)	2.5	0.27	15.20	70%	3.40	0.35	15.50	65%	4.5	0.60	15.24	87%
Wind tunnel (urban terrain)	1.8	0.20	14.82	75%	2.36	0.25	15.30	70%	4.36	0.65	14.8	84%
Reduction percent (open / urban)%	28%	26%			30%	32%			3%	10%		

The main observation from the values presented in Table 1 is that the maximum torsional loads can be produced by applying 75% from the total wind load (maximum base shear) with additional equivalent eccentricity 15% from the perpendicular building dimension to wind load.

6. SUMMARY AND CONCLUSIONS

This paper examines wind-induced torsional loads on low-rise buildings. A set of wind tunnel tests are presented. Two buildings scaled at 1:400 have the same dimensions, but "Building I" has a flat roof while "Building II" has a 4:12 gabled roof. These two buildings were tested in open and urban terrain exposure. "Building III" was scaled at 1:200 and simulates a building in Fredericton, New Brunswick with its surroundings. Three tests were conducted for the building model with a complete simulation of its surroundings in open, suburban and urban terrain exposures for a complete cycle of wind

directions by 10^o increments. This building was also tested in an open terrain exposure without any surroundings. Peak, mean, and minimum base torsion and shear force coefficients for each azimuth were evaluated. The results indicate the following:

- Changing the roof from flat to a 4:12 slope results in an increase of 30% in the total shear force and an increase of 25% in the torsional moment due to wind.
- The buildings located in urban terrain exposure are subjected to less wind loads (shear forces and torsional moments) by about 30% than those located in open terrain exposure.
- The simplified (envelope) method in ASCE/SEI 7-10 and the simplified (static) method in NBCC 2010 require more attention to account for the surrounding effects on torsional moment.
- The maximum torsional loads can be produced by applying 75% from the total wind load (maximum base shear) with additional equivalent eccentricity 15% from the perpendicular building dimension to wind load.

It should be noted that the above conclusions are drawn based on a limited number of tests with specific conditions. More data is required to develop better wind load patterns accounting for wind-induced torsional loads on low-rise buildings.

7. REFERENCES

ASCE/SEI 7-10. (2010). "Minimum Design Loads for Buildings and Other Structures." published by the Structural Engineering Institute of ASCE, Reston, VA

Davenport, A.G., Surry, D. and Stathopoulos, T. (1977). "Wind Loading on Low-Rise Buildings: Final Report on Phases I and II." University of Western Ontario, Eng. Sci. Res. Rep., BLWT-SS8

Davenport, A.G., Surry, D. and Stathopoulos, T. (1978). "Wind Loading on Low-Rise Buildings: Final Report on Phase III." University of Western Ontario, Eng. Sci. Res. Rep., BLWT-SS8

Elsharawy, M., Stathopoulos, T., and Galal, K. (2011). "Evaluation of wind-induced torsional loads on buildings by north American and European codes and standards." Proceedings of the 2011 Structures Congress, Las Vegas, Nevada, USA, Sponsored by ASCE/SEI, April 14-16

PrEN 1991-1-4. (2004). "Eurocode 1, 2004: Actions on Structures – General actions – Part 1-4: Wind actions." European Standard

Holmes, J. D. (1983). "Wind Loads on Low Rise Buildings – A Review." CSIRO Div. of Building Research, Highett. Victoria, Australia

Isyumov, N. and Case, P. C. (2000). "Wind-Induced Torsional Loads and Responses of Buildings." Proceedings of Structures Congress 2000, Philadelphia, Pennsylvania, USA, Sponsored by ASCE/SEI, May 8-10

Krishna, P. (1995). "Wind Loads on Low-Rise Buildings – A Review." Journal of Wind Engineering and Industrial Aerodynamics, vol.54-55: pp.383-396

NBC2010. (2010). "User's Guide – NBC 2010, Structural Commentaires (part 4)." Issued by the Canadian Commission on Buildings and Fire Codes, National Research Council of Canada

Stathopoulos, T. (1984). "Wind Loads on Low-rise Buildings - A Review of the State of the Art." Engineering Structures, vol.6: pp.119-135

Zisis, I., and Stathopoulos, T. (2010). "Wind-Induced Loads on the Foundation of a Low-Rise Building: Full-Scale and Wind Tunnel Experimentation." Proceedings of the 2010 Structures Congress, Orlando, Florida, USA, Sponsored by ASCE/SEI, May 12-15

FLOOR VIBRATION CHARACTERISTICS OF LONG SPAN COMPOSITE SLAB SYSTEMS

T. Andres Sanchez, M.S., E.I.T.[1] , Brad Davis, Ph.D., S.E.[2], and

Thomas M. Murray, Ph.D., P.E.[3]

[1]Ph.D. Candidate, Georgia Tech School of Civil and Environmental Engineering, 790 Atlantic Drive, Atlanta, GA 30332, USA, Phone: 540-808-7710, Fax: 404-894-2278, E-mail: telmoandres@gatech.edu

[2](Corresponding Author) Assistant Professor, University of Kentucky Civil Engineering Department, 373 Raymond Building, Lexington, KY 40506, USA, Phone: 859-257-4916, Fax: 859-257-4404, E-mail: bdavis@engr.uky.edu

[3]Emeritus Professor of Structural Steel Design, Virginia Tech Civil and Environmental Engineering, 200 Patton Hall, Blacksburg, Virginia 24061, USA, Phone: 540-731-3330, E-mail: thmurray@vt.edu

ABSTRACT

Recently developed steel-framed floor systems utilizing long-span metal deck have the potential of providing large column free areas with overall floor thicknesses approximately equal to concrete flat plates while typically imposing less dead load on the structure. The vibration serviceability of such floor systems is investigated in this paper. Two laboratory specimens, a full-scale mockup, and 13 in-situ floors were tested to measure their natural modes and responses to walking excitations. Natural modes were determined using experimental modal analysis techniques or heel-drop test results. Response to walking was determined by measuring the maximum peak acceleration due to individual walkers traversing the floor. The natural frequencies for the laboratory specimens and mockup were in the range of those measured for typical composite framing systems whereas all in-situ floors are high-frequency floors. The measured accelerations due to walking and subjective evaluations indicate that such floors will generally have adequate resistance to vibrations due to walking.

INTRODUCTION

Steel-framed floors offer several advantages compared to cast-in-place concrete floor systems, including speed of construction, economy, and flexibility for future remodeling. However, they usually require larger floor-to-floor heights than those required for concrete flat plate floors, which is the primary reason that flat plate floor systems are more commonly used in high-rise residential structures such as hotels and condominiums. Steel-framed floor systems are also perceived by the engineering community to be more vulnerable to vibration serviceability problems due to humans walking on the floor.

Very recently, new steel-framed floor systems have been developed that decrease or eliminate the floor-to-floor height disadvantage. The systems use long-span composite deck (LSCD) to span up to 9.14 m (30 ft) without interior beams, to create large column-free areas with relatively high ceilings. When used for spans approaching 9.14 m (30 ft), the composite slabs are 200 mm to 250 mm (8 in. to 10

in.) deep and use fairly deep—nominally 115 mm (4.5 in.) and deeper—composite deck that is shored during construction. The resulting UL D951 fire rated assembly achieves a two hour rating without sprayed-on fire protection while UL D501 provides a two hour rating with a gypsum board ceiling. The slabs are supported at the column lines by steel beams with the top flange either flush with the bottom of the deck or embedded in the slab to minimize the total system depth. The slab edges parallel to the deck are sometimes constructed without spandrel members to minimize the floor depth at the cladding. Other variations in the use of these floors include supporting the slab directly on CMU or steel stud walls. This construction system used in low-rise residential buildings eliminates the need of supporting beams, so the total floor depth is the slab thickness.

Intuitively, one might assume that a composite slab spanning 9.14 m (30 ft) would be subject to disturbing vibrations due to walking and, unfortunately, there is no current standard method in North America for evaluating LSCD systems for vibration serviceability. The lack of experience with such systems would undoubtedly deter some engineers from using them. Therefore, the objective of the study described herein is to investigate the floor vibration performance of LSCD systems. Experimental results and subjective evaluations from a laboratory floor specimen, a floor mock-up, a laboratory footbridge, and in-situ tests of thirteen floors of buildings currently in service are used to assess the vibration behavior of these systems.

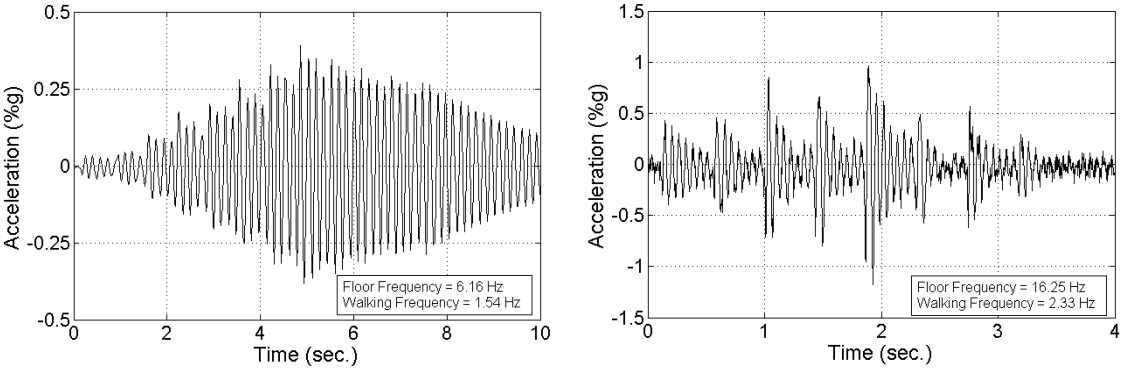
CATEGORIZATION OF FLOORS BY NATURAL FREQUENCY

Human perception of vibrations depends on the vibration frequency and therefore the natural frequency of the floor. Vibrations of floors with frequencies below about 10 Hz are much more likely to cause discomfort of the occupants than in floors with frequencies above 10 Hz (Murray et al., 1997; Smith et al., 2007). Based on this limit, floors can be classified as low-frequency or high-frequency.

The type of response to walking also depends on the natural frequency of the floor. In low-frequency floors, a walking force harmonic frequency (integer multiple of the step frequency) can match a natural frequency, resulting in a resonant response. Figure 1(a) shows an example of the typical response of these floors. The plot is the acceleration trace measured in a floor with a natural frequency of 6.16 Hz, while walking at 1.54 Hz, the fourth sub-harmonic (integer division) of the floor frequency. Therefore the fourth harmonic of the walking force matched the natural frequency. The figure shows that the response builds up with every step which causes the high acceleration response to last for several seconds.

In high-frequency floors, the acceleration response is a series of impulse responses that experience a fast decay after each step and therefore no resonant build-up. Figure 1(b) shows the trace measured in a floor with a natural frequency of 16.25 Hz, while walking at the seventh sub-harmonic of the floor frequency, 2.33 Hz. The accelerations in this floor are a sequence of short transient responses that die out before the next step. (The increased response near 2 sec. is due to the walker being nearer to midspan, not due to a resonant build-up.) An important characteristic of these systems is that generally the accelerations are not perceived by floor occupants because the vibrations decay so rapidly and because they occur at frequencies that are

outside the range in which humans are most sensitive to vertical vibrations, 4 Hz to 8 Hz (Murray et al., 1997; Smith et al., 2007). Therefore, in some cases the peak accelerations that result from each step may be larger than in low-frequency floors, however, they are not perceived by the occupants.



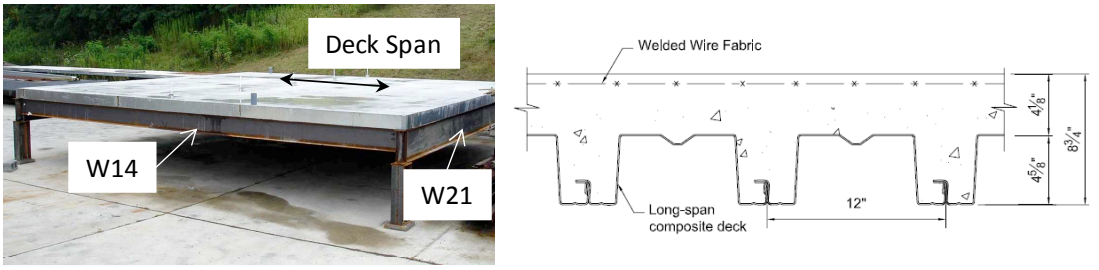
(a) Low frequency floor. **(b) High frequency floor.**

Figure 1. Sample acceleration responses.

EXPERIMENTAL PROGRAM

Floor descriptions. The program included investigations of a laboratory floor, a floor mockup, a laboratory footbridge, and thirteen floors in residential buildings.

The laboratory floor, Figure 2, was a single 9.14 m by 9.14 m (30 ft by 30 ft) bay constructed and tested at the Virginia Tech Thomas M. Murray Structural Engineering Laboratory in 2006. The 222 mm (8-3/4 in.) composite slab consisted of a 117 mm (4-5/8 in.) steel deck covered with 105 mm (4-1/8 in.) of 24 MPa (nominal 3.5 ksi) normal weight concrete. The floor was supported only at the perimeter with W530x66 (W21x44) girders and W360x32.9 (W14x22) beams which framed into W310x60 (W12x40) steel stub columns. Temporary shoring was provided at the third points of the slab to limit the dead load deflections during the concrete placement. The slab supported no nonstructural elements such as cladding or partitions.

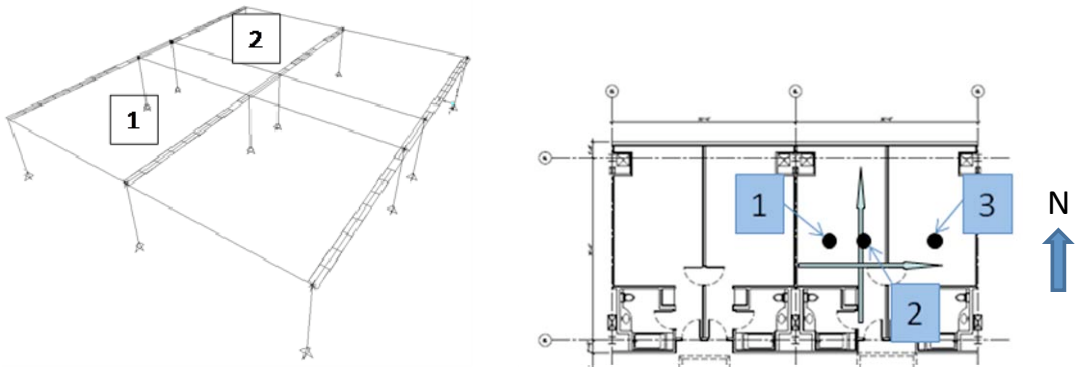


(a) Photograph. **(b) Section.**

Figure 2. Laboratory floor specimen.

The 18.5 m by 22.6 m (61 ft by 74 ft) full-scale floor mockup, located in Las Vegas, Nevada, was tested in January 2008 and again August 2008. The slab was supported by perimeter beams and interior girders to simulate a four bay (separated

by a corridor) portion of a hotel wing with 9.14 m by 9.14 m (30 ft by 30 ft) areas free of columns and beams. Figure 3(a) is an image of the mockup configuration. The mockup was constructed using a similar LSCD system described above for the four main bays and a 133 mm (5-1/4 in.) total thickness composite slab on 51 mm (2 in.) deck for the corridor. It was tested in the stages that are summarized in Table 1. During Stages 1 through 4, cladding and partitions (see Figure 3(b)) were installed below and on the slab in Bay 1 and the adjacent main bay. The partitions and cladding were constructed of light-gage steel studs with one sheet of drywall on each side. Bay 2 and its adjacent main bay were bare slabs during all stages. During Stage 4, the main north-south partitions below and above the slab in the middle of Bay 1 were removed to create a partition layout similar to that in a condominium "great room."



(a) Configuration including bay numbers.

(b) Partition locations, accelerometer locations, and walking paths.

Figure 3. Floor mockup.

Table 1. Summary of stages – floor mockup.

Stage	Partitions	Cladding	Shaker locations
0	None	None	Centers of Bay 1 and Bay 2
1	Hotel Rooms	Slip Connected to Slab	Bay 1, 7.5 ft west of center
2	Hotel Rooms	None	Bay 1, 7.5 ft west of center
3	Hotel Rooms	Supported by Slab	Bay 1, 7.5 ft west of center
4	Great Room	Supported by Slab	Center of Bay 1

The 2.13 m (7 ft) wide by 9.14 m (30 ft) long laboratory footbridge was built and tested in three stages at the Virginia Tech Thomas M. Murray Structural Engineering Laboratory during 2007 and 2008. The slab was 222 mm (8-3/4 in.) thick and consisted of a 117 mm (4-5/8 in.) deep deck and 105 mm (4-1/8 in.) of concrete topping. The slab was supported by nominally 200 mm (8 in.) CMU walls and the connections between the slab and the CMU walls were detailed to perform as moment connections. Figure 4 shows a photograph of the laboratory footbridge. Figure 5 shows the testing stages which were designed to determine the effect of different amounts of restraint being provided by the CMU walls.



Figure 4. Laboratory footbridge.

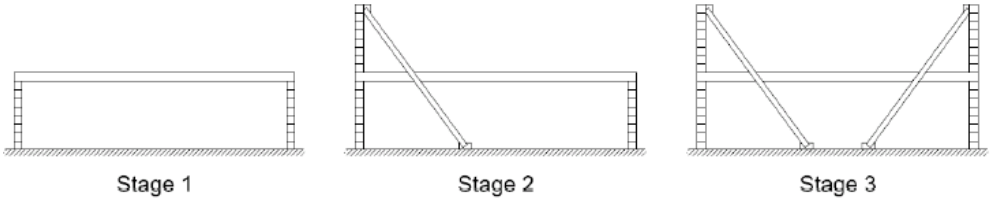


Figure 5. Laboratory footbridge stages.

In-situ tests of 13 floors in six buildings were conducted to investigate the performance of LSCD in residential structures constructed with CMU and stud walls. The buildings were under construction at the time of testing and most of the floors did not have partitions. Table 2 contains descriptions of the tested floors.

Table 2. Descriptions of in-situ floors.

Floor bay number	Bay width x span	Slab thickness mm (in.)	Concrete strength MPa (ksi)	Deck height mm (in.)	Floor support
1	6.15 m x 6.92 m (20.2 ft x 22.7 ft)	152 (6.0)	28 (4)	51 (2.0)	Stud wall - Steel beam
2					Stud wall - Stud wall
3	8.13 m x 4.48 m (26.7 ft x 14.7 ft)	152 (6.0)	28 (4)	51 (2.0)	Stud wall - Stud wall
4	4.19 m x 7.16 m (13.75 ft x 23.5 ft)	152 (6.0)	28 (4)	51 (2.0)	CMU - Concrete beam
5	9.28 m x 6.61 m (30.5 ft x 21.7 ft)	152 (6.0)	21 (3)	51 (2.0)	Stud wall - Stud wall
6	9.75 m x 7.01 m (32 ft x 23 ft)	171 (6.75)	28 (4)	51 (2.0)	CMU wall - CMU wall
7	8.96 m x 4.27 m (29.4 ft x 14 ft)	140 (5.5)	28 (4)	51 (2.0)	CMU wall - CMU wall
8	5.39 m x 6.71 m (17.7 ft x 22 ft)	152 (6.0)	28 (4)	51 (2.0)	Concrete beam – CMU
9	5.39 m x 7.52 m (17.7 ft x 24.7 ft)	152 (6.0)	28 (4)	51 (2.0)	Concrete beam – CMU
10	8.92 m x 5.11 m (29.3 ft x 16.8 ft)	152 (6.0)	28 (4)	51 (2.0)	Steel beam - Steel beam
11	6.05 m x 5.92 m (19.8 ft x19.4 ft)	152 (6.0)	21 (3)	51 (2.0)	Stud wall - Stud wall
12					
13					

Experimental methods. For other than the in-situ floors, experimental modal analyses (EMA) were performed by applying a measured dynamic force to the floors while simultaneously measuring the acceleration response at numerous locations. The measurement results were post-processed to estimate the frequency response function (FRF) which gives detailed information on the natural modes. An electrodynamic shaker was used to provide excitation because it provides higher quality FRF estimates than those obtained using other forms of excitation (Pavic and Reynolds, 1999; Reynolds and Pavic, 2000a; Reynolds and Pavic, 2000b; Hanagan et al., 2003). Dynamic forces were applied at the center of the laboratory floor and at the mockup locations indicated in Table 1. During the laboratory footbridge tests, the shaker was positioned 0.914 m (3 ft) away from one support wall. It was determined that at this location, the force drop-offs due to shaker-structure interaction were insignificant. Burst chirp (sinusoidal) force input was applied by the shaker and measured using a custom-built force transducer placed between the slab and the shaker during tests on the laboratory floor and laboratory footbridge and using an armature accelerometer during tests on the mockup. Burst chirps were used because they provide a very controlled level of force input—selected to result in accelerations approximately equal to those expected from walking, 0.5%g to 2%g—over a bandwidth including natural frequencies of interest.

Accelerations were measured at various locations on the laboratory and mockup slabs and the footbridge. The measured force and accelerometer time domain signals were converted from volts to engineering units and used to estimate the accelerance FRFs for excitation and response at various locations on the slabs. Natural frequencies were detected by visual observation of the FRF magnitude and imaginary part plots and damping ratios were determined by FRF curve fitting using ME'ScopeVES Version 3.0 (Vibrant Technology, 2001). The basic concept of FRF curve-fitting is to match a parametric mathematical model of the FRFs to the ones estimated (measured) using the FRF estimator. Natural frequencies and modal damping ratios are primary parameters of the model. If a set of natural frequencies and damping ratios is selected such that the parametric model matches the estimated FRF, then the selected natural frequencies and damping ratios are presumably good approximations of the actual values.

For the floors tested in-situ, the modal properties of the slabs were determined using unmeasured heel-drops as the input force. A single heel-drop provides a broadband force excitation with significant energy between approximately 0.5 Hz and 20 Hz. The time domain acceleration signal is transformed to the frequency domain using a fast Fourier transform (FFT) and peaks in the resulting spectrum indicate natural frequencies. However, mode shapes and damping cannot be directly inferred from unmeasured heel-drop test results.

Experiments were also performed to determine the acceleration response to walking excitation for each floor. The general approach was to first determine the natural frequencies using EMA or heeldrop tests, and where available, use the FRF magnitude to determine which mode or modes will provide the highest accelerations. A walker then attempted to walk at specific frequencies to determine the maximum acceleration response that can be reasonably expected in the bay. Walking paths were

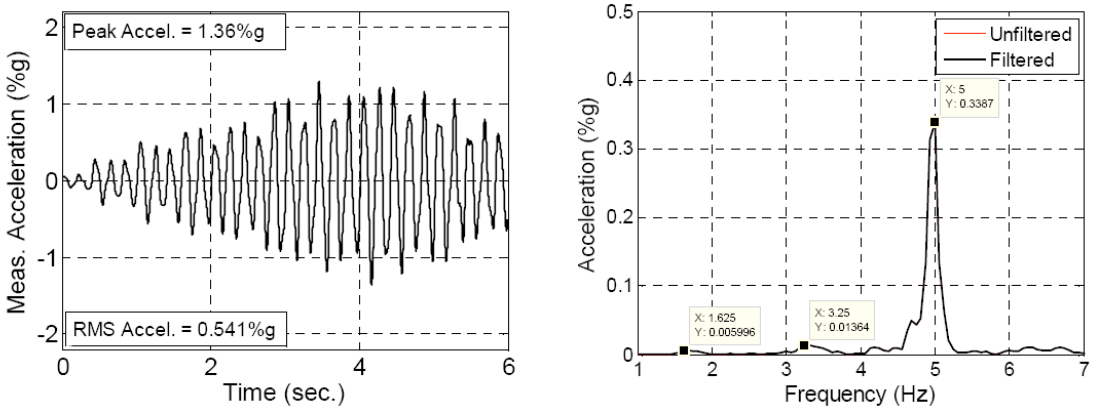
through the middle of the laboratory floor, the footbridge, the in-situ bays, and along the two paths indicated in Figure 3(b) for the mockup. Acceleration responses were measured at the middle of the laboratory floor and at eleven different locations on the laboratory footbridge, including midspan. During the mockup Stage 0 tests, the accelerations were measured at the centers of Bays 1 and 2—see Figure 3(a). During the other stages, accelerations were measured at the locations shown in Figure 3(b). Researchers also stood near mid-bay or midspan on each floor during several walking tests and offered subjective evaluations of vibration severity.

In all cases with EMA results available, one mode had a significantly larger FRF peak magnitude, indicating that it provides much higher accelerations than the other modes. Such a mode is referred to as the dominant mode. All dominant modal frequencies were far outside the range of reasonable walking frequencies (approximately 1.6 Hz to 2.2 Hz per Murray et al., 1997). However, as described previously, it is also possible to cause resonance using a harmonic of the walking force. Therefore, the walker carried a metronome and attempted to walk at a subharmonic (integer division) of the dominant frequency. Numerous walking tests were performed at the chosen subharmonic of the dominant frequency in an effort to determine the maximum acceleration due to walking that can be reasonably expected. Multiple individual walkers were used where possible. Single trips across the tested bay were performed in all cases rather than walking back and forth.

The acceleration waveforms collected from the two laboratory specimens and the mockup floor were filtered to exclude frequency content below 1 Hz to eliminate any DC offset and above 15 Hz to eliminate high frequency vibrations which are of no interest in assessing floor vibration serviceability. For the in-situ building tests, the recorded measurements where filtered to only include frequencies between 1 Hz and 35 Hz. The upper limit was increased for these floors because in many cases, the floor responses included significant contributions from modes with frequencies higher than 15 Hz.

EXPERIMENTAL RESULTS

Laboratory floor. The measured natural frequency of the laboratory floor was 4.98 Hz which is within the range of natural frequencies for low-frequency steel-framed floor systems. The measured damping ratio was 0.44% of critical damping. The measured walking acceleration waveform and spectrum for the test conducted while walking at 1.66 Hz (the third subharmonic of the natural frequency) are shown in Figure 6. The maximum peak acceleration in the time domain was 1.36%g which exceeds the 0.5%g limit for residences. However, subjective evaluators judged the floor to not have objectionable vibrations. Also note that in a real floor with the same dimensions as this laboratory specimen, the floor performance would be significantly improved with the addition of nonstructural elements, people, partition walls, and adjacent slab spans.



(a) Waveform. **(b) Spectrum.**

Figure 6. Measured acceleration response of the laboratory floor to walking.

Floor mockup. Table 3 shows the measured natural frequencies for the mockup. Interestingly, the natural frequencies only increased slightly with the addition of partitions, which indicates that the partitions added some stiffness corresponding to the added mass. However, the damping increased substantially from 0.5% of critical to 2.2% for Stages 3 and 4. As was the case for the laboratory floor, the natural frequencies are in the typical range of natural frequencies for low-frequency steel-framed floors. The table also shows the peak accelerations due to walking that were measured for all five of the mockup stages. The peak accelerations exceed the 0.5%g limit for residences, but by only a small margin in Stages 1 through 4 which most closely represent actual service conditions. Note that with additional damping from more nonstructural components, people, and connection of the partitions to the floor above, the Stage 1 through 4 responses would not exceed 0.5%g. Subjective evaluators during each stage indicated that the floor did not undergo objectionable vibrations, with most being described as "barely perceptible" or "slightly perceptible."

Table 3. Mockup measured natural frequencies, damping ratios, and accelerations due to walking.

Stage	Natural frequency (Hz)	Damping ratio (% critical)	Peak acceleration (%g)
0, Bay 1	5.55	0.5	0.768
0, Bay 2	6.00	0.5	0.966
1, Bay 1	6.35	1.3	0.626
2, Bay 1	5.93	1.3	0.559
3, Bay 1	6.03	2.2	0.527
4, Bay 1	5.72	2.2	0.599

Laboratory footbridge. Figure 7 shows the measured FRF for the three stages and Table 4 shows the natural frequencies which place each stage into the low frequency floor category. Interestingly, the natural frequencies barely changed with the addition of restraining CMU during Stages 2 and 3, probably indicating that the tops of the CMU walls moved laterally very slightly as the slab moved vertically.

The FRF peak magnitude decreased substantially, however, most likely due to the additional vibrating mass provided by the CMU walls. The peak acceleration due to walking was less than the 0.5%g limit during tests at all three Stages. Subjective evaluators indicated that the vibrations were slightly perceptible, but would not be severe enough to cause complaints. The vibration response would be further improved by the addition of nonstructural components.

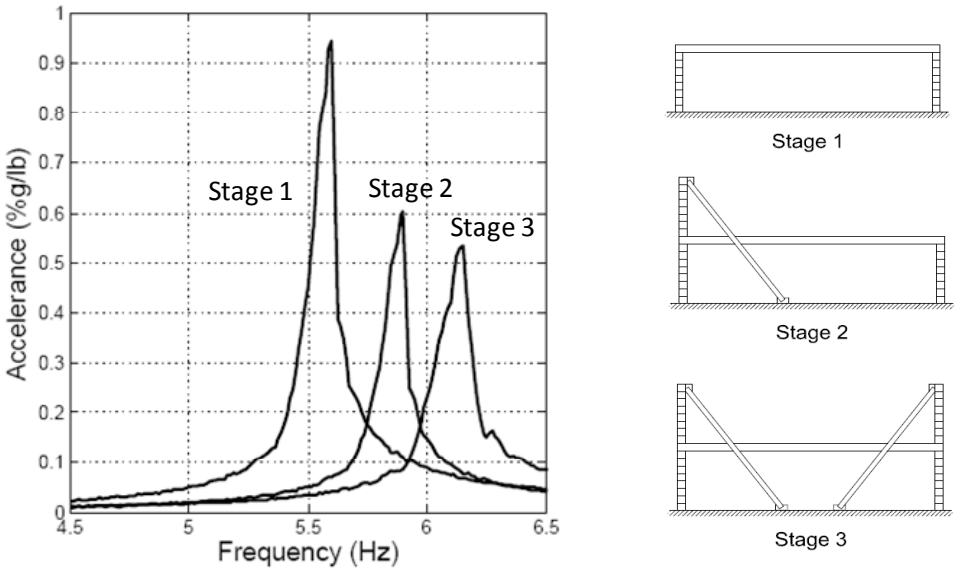


Figure 7. Measured FRFs for the laboratory footbridge (all three stages).

Table 4. Laboratory footbridge measured natural frequencies, damping ratios, and accelerations due to walking.			
Stage	**Natural frequency (Hz)**	**Damping ratio (% critical)**	**Peak acceleration (%g)**
Stage 1	5.73	1.0	0.35
Stage 2	5.89	1.3	0.39
Stage 3	6.14	1.3	0.45

In-situ tests of residential buildings. Measured natural frequencies and peak acceleration from walking tests at several subharmonics of the measured frequencies are summarized in Table 5. The accelerations shown in the table correspond to the maximum values measured in the walking tests. Except for Bays 3 and 9, partitions were not in place at the time of testing. In these two bays, the partition walls significantly increased the floor system. For these floors, the peak accelerations were less than 0.1%g during the walking tests. As shown in Table 5, all the tested floors had frequencies above the 10 Hz, meaning LSCD behave as high-frequency floors when they bear on rigid supports, as is the case of the structural walls. Because the floor frequencies are above 10 Hz, the previously mentioned 0.5%g acceleration limit for residual floors does not apply. Subjective evaluators indicated that the vibrations were imperceptible during all walking tests.

Table 5. In-situ building floors measured natural frequencies and accelerations due to walking.		
Bay number	**Natural frequency (Hz)**	**Peak acceleration (%g)**
1	13.30	1.41
2	16.80	1.32
3	26.00	< 0.1
4	11.80	1.05
5	13.50	0.60
6	14.50	0.84
7	27.80	0.94
8	11.50	1.73
9	20.50	< 0.1
10	13.50	0.38
11	13.00	2.57
12	10.50	0.78
13	10.75	0.84

The frequency results obtained from the in-situ tests are quite interesting because even though the spans are long (Table 2), the floors are very stiff. Apparently, the typical slab-to-supporting wall connection provides flexural fixity, which significantly increases the floor natural frequency. This behavior is contrary to the expected performance in steel-framed floors, where the beams and girders behave as simply supported elements with pinned connections (Murray et al., 1997; Smith et al., 2007).

DISCUSSION AND CONCLUSIONS

The laboratory floor, floor mockup, and laboratory footbridge tests indicate that LSCD have very good resistance to floor vibrations due to walking. The floors had natural frequencies that are in the range of those measured for composite slab and composite beam floor systems and far above the 3 Hz limit to avoid vandal jumping. Measured peak accelerations due to walking exceeded the 0.5%g limit for residences in most bays, but tests represent a scenario more severe than expected in service. The in-service responses should be less than 0.5%g due to the presence of nonstructural elements, people, partition walls, and partition connections to the floor above. Also, the tests were conducted with walkers traversing the least favorable path (directly through the middle of the bay) and the accelerations were measured at mid-bay, which is the location of maximum response. Subjective evaluators indicated that the responses were not severe enough to cause complaints. Therefore, it is concluded that LSCD systems have very good potential to be constructed to spans of 9.14 m (30 ft) without annoying vibrations due to human activities in residential structures. It should be emphasized, however, that LSCD designs must be evaluated during the project design phases.

The in-situ tests show that floor vibration performance is very satisfactory when the LSCD are supported by steel stud or CMU walls. For these cases, the systems

behave as high-frequency floors, with natural frequencies that in many cases well above the 10 Hz limit. Subjective evaluators indicated that the vibrations due to walking were imperceptible on these floors. Hence, it is concluded that slab and wall combinations similar to those described in this research have very good potential to be used without vibration problems. Again, it is emphasized that LSCD designs must be evaluated during the project design phases.

ACKNOWLEDGEMENTS

The writers thank Metal Dek Group® a Unit of CSi®, Columbia, South Carolina for sponsoring the research described herein. The first author acknowledges the Fulbright Commission in Ecuador for the fellowship awarded to study in the M.S. program at Virginia Tech. Finally, the second author very much appreciates the Walter P. Moore and Charles E. Via fellowships that partially funded his Ph.D. studies at Virginia Tech, which included some of the research described in this paper.

REFERENCES

Hanagan, L.M, Raebel, C.H., and Trethewey, M.W. (2003). "Dynamic Measurements of In-Place Steel Floors to Assess Vibration Performance," *Journal of Performance of Constructed Facilities*, American Society of Civil Engineers (ASCE), Vol. 17, No. 3, pp.126-135.

Murray, T.M., Allen, D.E., and Ungar, E.E. (1997). *Design Guide No. 11* "Floor Vibrations Due to Human Activity," American Institute of Steel Construction (AISC), Chicago, IL.

Pavic, A. and Reynolds, P. (1999). "Experimental Assessment of Vibration Serviceability of Existing Office Floors Under Human-Induced Excitation," *Experimental Techniques*, Vol. 3, No. 5, pp. 41-45.

Reynolds, P., and Pavic, A. (2000a). "Impulse Hammer versus Shaker Excitation for the Modal Testing of Building Floors," *Experimental Techniques*, Vol. 24, No. 3, pp. 39-44.

Reynolds, P., and Pavic, A. (2000b). "Quality Assurance Procedures for the Modal Testing of Building Floor Structures," *Experimental Techniques*, Vol. 24, No. 4, pp. 36-41.

Smith, A.L., Hicks, S.J., and Devine, P.J. (2007). *Design of Floors for Vibration: A New Approach*, The Steel Construction Institute (SCI), Ascot, Berkshire.

Vibrant Technology Inc. (2001). *ME'scopeVES Operating Manual*, Scotts Valley, CA.

IMPEDANCE MODELING FOR PREDICTION OF TRAIN INDUCED FLOOR VIBRATIONS

M. Sanayei[1], N. Zhao[2], P. Maurya[3], J.A. Moore[4], J. A. Zapfe[5], E. M. Hines[6]

[1] Professor, Dept. of Civil & Environmental Engineering, Tufts University, Medford, MA, (617) 627-4116, masoud.sanayei@tufts.edu

[2] Graduate Student, Tufts University, Medford, MA, ningyu.zhao@tufts.edu

[3] Graduate Student, Tufts University, Medford, MA, pradeep.maurya@tufts.edu

[4] Supervisory Consultant, Acentech Inc., jmoore@acentech.com

[5] Director, Noise & vibration Group, Acentech Inc., jzapfe@acentech.com

[6] Professor of the Practice, Tufts University, Dept. of Civil & Environmental Engineering; Associate, LeMessurier Consultants, ehines@lemessurier.com

ABSTRACT

Laboratory and manufacturing facilities are frequently located in areas that experience high-frequency (greater than 30 Hz) environmental vibration. Such vibrations are a concern for the proper functioning of sensitive laboratory devices, precision manufacturing equipment as well as human comfort. A simple method to accurately predict the magnitude of high-frequency floor vibrations would allow detailed vibration assessment during the conceptual design phase, and provide physical insight useful for developing vibration mitigation approaches. This paper discusses a methodology for prediction of train-induced floor vibrations in buildings using a wave propagation technique. The data obtained from an experiment carried out at Tufts University on a scale model laboratory building have been used to validate the predictions. The proposed wave propagation method successfully predicted the measured velocities and impedances of the scale model building.

INTRODUCTION

Many facilities are located in environments with substantial ambient vibration. The vibration may be from highway vehicles, trains, or other sources. Floor vibrations are of concern for precision manufacturing facilities and for laboratories where sensitive experiment is carried out. Examples of sensitive manufacturing processes include fabrication of laser devices, electronic microscopes, surgical devices, and semiconductor integrated cores. As technologies continue to evolve and become more complex, the demands on manufacturing are expected to become more rigorous. These vibrations also may be of concern for human comfort in residential settings.

This paper focuses on the experimental validation of a simple wave propagation based modeling approach for the prediction of train-induced floor vibrations. This approach can be used during the conceptual design phase of projects where owners

are concerned about environmentally induced floor vibrations—with the potential to save millions of dollars in construction costs and hundreds of thousands of dollars detailed finite element studies whose accuracy is not guaranteed in the high frequency range.

BACKGROUND

Problems associated with floor vibrations are not new. The first known study was reported almost 70 years ago (Hunaidi et al., 1997). Numerous studies have been carried out to contribute to the understanding of the problem of floor vibrations.

Bahrekazemi (2004) reported that the techniques used for vibration mitigation are location dependent. These locations are either at the vibration source, in the path, or at the structure. Ju et al. (2004), Adam et al. (2005), and Wang et al. (2003) applied these various mitigation methods for the reduction of train induced vibrations. Mitigation methods selected were based on the location including soil improvement under the embankment and construction of concrete slabs, construction of open as well as in-filled trenches and isolation of the building foundation from the ground using elastic support system. Site conditions also play a dominant role in deciding the most appropriate mitigation method.

For successful mitigation of floor vibrations, it is necessary to have accurate and efficient prediction methods. In order to predict building vibration induced by nearby trains, various approaches have been adopted. Some of these approaches include finite element modeling, numerical model based approach, utilization of transfer functions and impedance based models. Each of these methods is characterized by its own efficiency, accuracy, ease of use in application, time consumption and limitations.

Ju (2007) developed an integrated finite element model for a bridge, nearby building, soil, and train for vibration prediction. Gupta et al. (2008) developed a coupled periodic finite element and boundary element model. It was used for prediction and assessment of subway induced vibrations with respect to studying the performance of different track structures in tunnels. With et al., (2007) used transfer functions for the prediction of floor vibrations in a building. Trochides (1991) predicted excitation levels due to ground borne vibrations in buildings near subways based on the approximate impedance formulae for the tunnel and the structure and energy considerations.

In the present paper, an approach for floor vibration prediction based on impedance modeling has been used. The authors developed an analytical model based on their previous research published by Sanayei et al. (2008), Hughes et al. (2008), and Zhao et al. (2010) to predict the velocity response of the structure. Experiments using a shaker on a scale model building have been carried out to simulate train-induced vibrations. The measured floor velocities have been used to validate the wave propagation model predictions. This paper also explains the efficiency and applicability of this approach in predicting floor vibrations in buildings.

MATHEMATICAL MODEL FOR IMPEDANCE BASED APPROACH

Train-induced vibrations propagate through soil in the form of waves that are transmitted to buildings at the foundation level. The vibrations are predominantly vertical although horizontal components exist (Li et al.2009; Yanmei et al. 2010). The interaction between the ground borne vibration and the vibration induced in the building foundation is complicated. In the present paper, it is assumed that the dominant mode of transmission into the upper floors in buildings is from longitudinal waves (dilatation) in the columns, bending wave transmission is more readily blocked at the lower floors. In the mathematical model, the vibrating force is assumed to be applied only in the vertical direction at the base of the columns (Conroy, 2008). Floor plates attached to the columns radiate energy as transverse bending waves. Longitudinal waves transmitted in columns are less affected by floors of typical weights and are more importantly responsible for the transmission into the upper floors.

Modeling of Column. The partial differential equation for free vibration of a column subjected to longitudinal waves (see Figure 1) is given by (deSilva, 2000)



Figure 1. Simple bar element representing column

$$\rho A(x)\frac{\partial^2 u(x,t)}{\partial t^2}-\frac{\partial}{\partial x}[E_c A(x)\frac{\partial u(x,t)}{\partial x}]=0 \tag{1}$$

where ρ, A and E are density, cross-sectional area and modulus of elasticity, respectively. E_c is the complex modulus of elasticity representing energy dissipation as $E_c = E(1+j\eta)$ with η denotes the structural loss factor.

The steady state response is given by:

$$u(x,t)=u(x)e^{j\omega t} \tag{2}$$

By substituting (2) into (1), the spatial equation of motion thus obtained is,

$$-\rho A(x)\omega^2 u(x)-\frac{\partial}{\partial x}[E_c A(x)\frac{\partial u(x)}{\partial x}]=0 \tag{3}$$

Furthermore, for a prismatic bar element, (3) can be written as,

$$\frac{\partial^2 u(x)}{\partial x^2}+\beta^2 u(x)=0 \tag{1}$$

where

$$\beta=\omega\sqrt{\frac{\rho}{E_c}}=\frac{\omega}{c_L} \tag{5}$$

$$c_L=\sqrt{\frac{E_c}{\rho}} \tag{6}$$

β is called as wavenumber (Cremer et al., 1988), which is a measure of the phase change per unit distance of a propagating wave, and c_L is the constant axial wave velocity.

The homogeneous solution for partial differential equation is,

$$u(x) = C_1 \sin(\beta x) + C_2 \cos(\beta x) \tag{7}$$

The element stiffness matrix is computed using the stiffness method, assuming linear spring behavior $\left(\{f\} = [k_{col}]\{u\}\right)$, by first applying a unit axial displacement to the left end of the rod, and then to the right. By fixing the right end of the rod and applying a unit displacement to the left end, the coefficients C_1 and C_2 can be solved,

$$C_1 = -\frac{\cos(\beta L)}{\sin(\beta L)} \text{ and } C_2 = 1 \tag{8}$$

Therefore, the steady state displacement field for a rod fixed at one end and free at the other, similar to a founded structural column, is,

$$u(x) = -\frac{\cos(\beta L)}{\sin(\beta L)}\sin(\beta x) + \cos(\beta x) \tag{9}$$

and the corresponding force field is,

$$f(x) = -E_c A\beta\left[\frac{\cos(\beta L)}{\sin(\beta L)}\cos(\beta x) + \sin(\beta x)\right] \tag{10}$$

By fixing the left end of the rod and applying a unit displacement to the right end, the coefficients are calculated (Brett 2007),

$$C_1 = \frac{1}{\sin(\beta L)} \text{ and } C_2 = 0 \tag{2}$$

The corresponding steady state displacement field and the force field are:

$$u(x) = \frac{\sin(\beta x)}{\sin(\beta L)} \tag{3}$$

$$f(x) = E_c A\beta\frac{\cos(\beta x)}{\sin(\beta L)} \tag{4}$$

The reactions at each end, related to each displacement, are the elements of the dynamic stiffness matrix of a single column acting as a bar element, and can be written as,

$$[k_{col}] = \frac{E_c A\beta}{\sin(\beta L)}\begin{bmatrix} \cos(\beta L) & -1 \\ -1 & \cos(\beta L) \end{bmatrix} \tag{14}$$

Modeling of Floor Slab. Floors attached to the columns can be modeled as energy dissipating floors slabs. The bending theory used to describe the response of the floor is thin plate theory. Thin infinite plates are totally resistive in the sense that they carry energy away from driving point (the column). This resistance is called point force impedance and is given as:

$$Z = 8\sqrt{D}\sqrt{\rho h} \tag{15}$$

where D is the bending stiffness of a plate of thickness h

$$D = \frac{Eh^3}{12\left(1-\nu^2\right)} \tag{16}$$

In general terms, impedance is the ratio of the applied force f to the response velocity v,

$$Z = \frac{f}{v} \tag{17}$$

Thus using Newton's second law and eq. (17),

$$f = m_{eff}\ a = Z\ v \tag{18}$$

The dynamic effective mass of the plate (m_{eff}) which is dependent on the driving frequency, is given by,

$$m_{eff} = \frac{Z}{j\omega} = -\frac{j}{\omega} 8\sqrt{D}\sqrt{\rho h} \tag{19}$$

Assembly of System of Equations. The dynamic stiffness matrix of the column elements, $\left[k_{col}\right]$ and the dynamic floor participation, $\left[m_{eff}\right]$ are assembled into global system matrices $\left[K_{col}\right]$ and $\left[M_{slab}\right]$, to be used in the steady state response, $\{U\}$, of a building column subjected to a harmonic loading, $\{F\}$.

$$\left[K_{col}\right]\{U\} - \omega^2\left[M_{slab}\right]\{U\} = \{F\} \tag{20}$$

Note that the stiffness and mass matrices are both frequency dependent in that the elements change based on the driving frequency.

The frequency dependent steady state response for all the floors becomes,

$$\{U\} = \left[K_{col} - \omega^2 M_{slab}\right]^{-1}\{F\} \tag{21}$$

and the velocity is given as,

$$\{V\} = i\omega\{U\} \tag{22}$$

The vibration velocity response level at all floors is given in VdB scale as,

$$VdB = 20\log_{10}\frac{v}{v_{ref}} \tag{23}$$

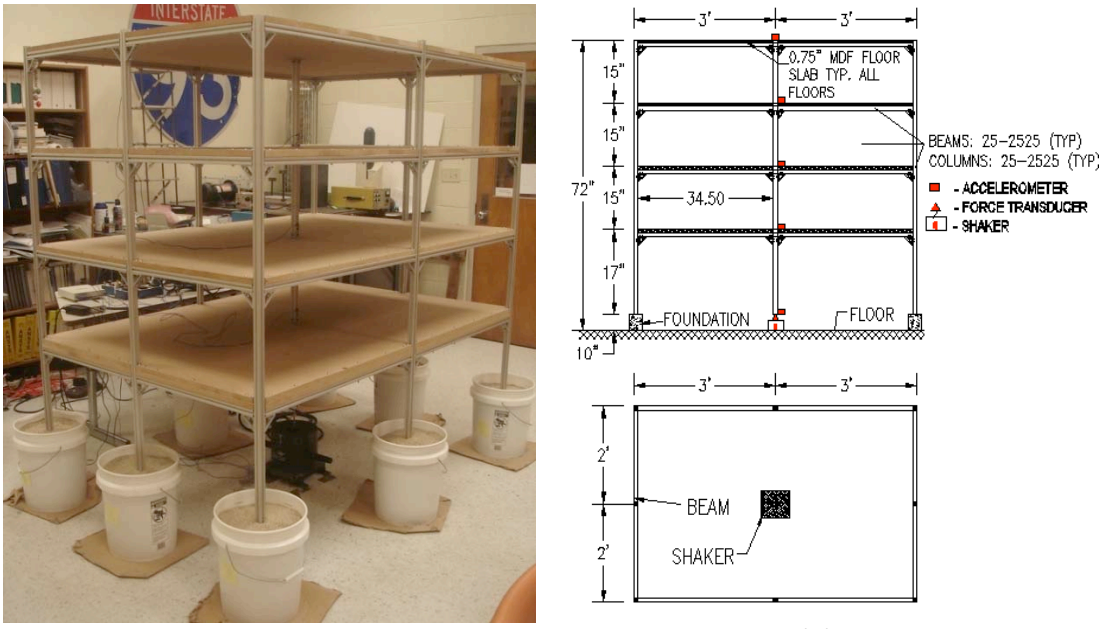
where,

$$v_{ref} = 1\times 10^{-8}\ \text{m/s} \tag{24}$$

Note that only the center column is considered in the mathematical model in (20). Therefore the sizes of the above system matrices are 5 x 5 (one for modeling of the column excitation at the base and four for the point impedances of the four floors).

EXPERIMENTATION OF SCALE MODEL BUILDING

Zhao (2009) designed and constructed a scale model building including base and 4 floors (see Figure 2). The scale model building (6' x 4' x 72") has a floor height of 17" at the base and 15" for all other floors. The model consists of 9 columns in total and 4 floor slabs. Aluminum alloy of 6105-T5 strips were used for the column while the floor slabs were constructed from medium density fiberboard (MDF).



(a) (b)

Figure 2. Scale model building with MDF floors (all dimensions in inches)

The material properties for columns and floors are summarized in Table 1.

Table 1. Materials used and its properties

Properties	Column	Floor
Material	Aluminum (6105-T5) Alloy	Medium Density Fiberboard
Young's Modulus (E)	70.3 GPa	3.15 GPa
Density (ρ)	2691 kg/m^3	700 kg/m^3
Poisson's Ratio (υ)	0.33	0.18
Loss Factor (η)	0.002	0.02

A Bruel & Kjaer Permanent Magnetic Vibration exciter type 4808 with a force rating of 112 N was used to excite the model at the base on one column. A Bruel & Kjaer force gauge type 8230 was used at the base of the column to measure the excitation force. PCB accelerometers type 352C65 were used to measure the vibrations on the floors at the center column.

The scale model building in Figure 2 consisted of base and 4 floors with accelerometers attached at each level. A Brüel & Kjær Permanent Magnetic Vibration Exciter Type 4808 was connected to the base of the center column. In order to measure the force applied to the structure, a load cell was mounted at the base of the center column. The shaker was supported by four neoprene base isolators to minimize flanking excitation to other columns. The eight (side and corner) columns that were not excited were buried in sand-filled buckets.

The scale model building in Figure 2 consisted of base and 4 floors with accelerometers attached at each level. A Brüel & Kjær Permanent Magnetic Vibration Exciter Type 4808 was connected to the base of the center column. In order to

measure the force applied to the structure, a load cell was mounted at the base of the center column. The shaker was supported by four neoprene base isolators to minimize flanking excitation to other columns. The eight (side and corner) columns that were not excited were buried in sand-filled buckets.

The scale model building was excited axially at the base of the center column for the purpose of testing and modeling the vertical propagation of structure-borne vibrations. A white noise signal was generated as the excitation source with a 50 kHz sampling rate and a sampling block of 50,000 data points. The length of each set of data was 1 second and the frequency resolution was 1 Hz. A Hanning window was applied to each set of one-second measured data in the time domain. The measured acceleration was transformed to the frequency domain using FFT function in Matlab.

Figure 3 shows the measured excitation force after taking moving average over 201points.The horizontal axis shows the range of frequency from 10 to 5000 Hz while the vertical axis shows the measured input force in N. A moving 201 point average was used to smooth the results.

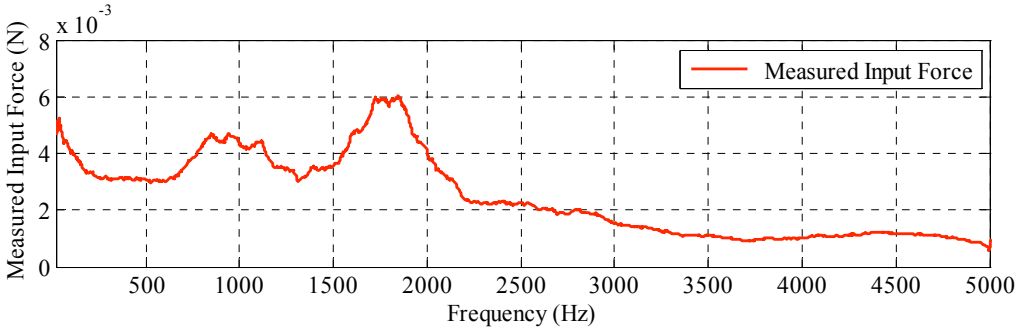


Figure 3. Force Spectrum

Acceleration measurements were made in the vertical direction on the center column at each floor, as well as at the column base. The measured data obtained from the load cell gives the measurement of the applied force at the base through shaker at the corresponding frequency. These readings were used to calculate and predict the velocity response at each level using the analytical model. The measured acceleration data were used to calculate the velocity at each floor. A moving 201 point average was used to smoothen the results. The plot comparing the predicted and measured velocity response is thus obtained. Figure 4 shows that the predicted and measured velocity response at each floor and the base of the building in the same frequency range after taking the moving average over 201 points. The vertical axis shows the velocities in VdB with a reference velocity of 10^{-8} m/s.

The ratio of measured input force to the velocity of the floor is defined as the impedance of that floor slab. If the velocity response is at the point of excitation, it is called the driving point impedance. If the response is measured at other locations within the building, it is called the transfer impedance. The data obtained through this experiment was further used to compare the predicted impedance to the impedance measured experimentally. Figure 5 shows the predicted and measured impedances at each floor and the base of the building. The vertical axis shows impedances in dB reference to 1 N-s/m.

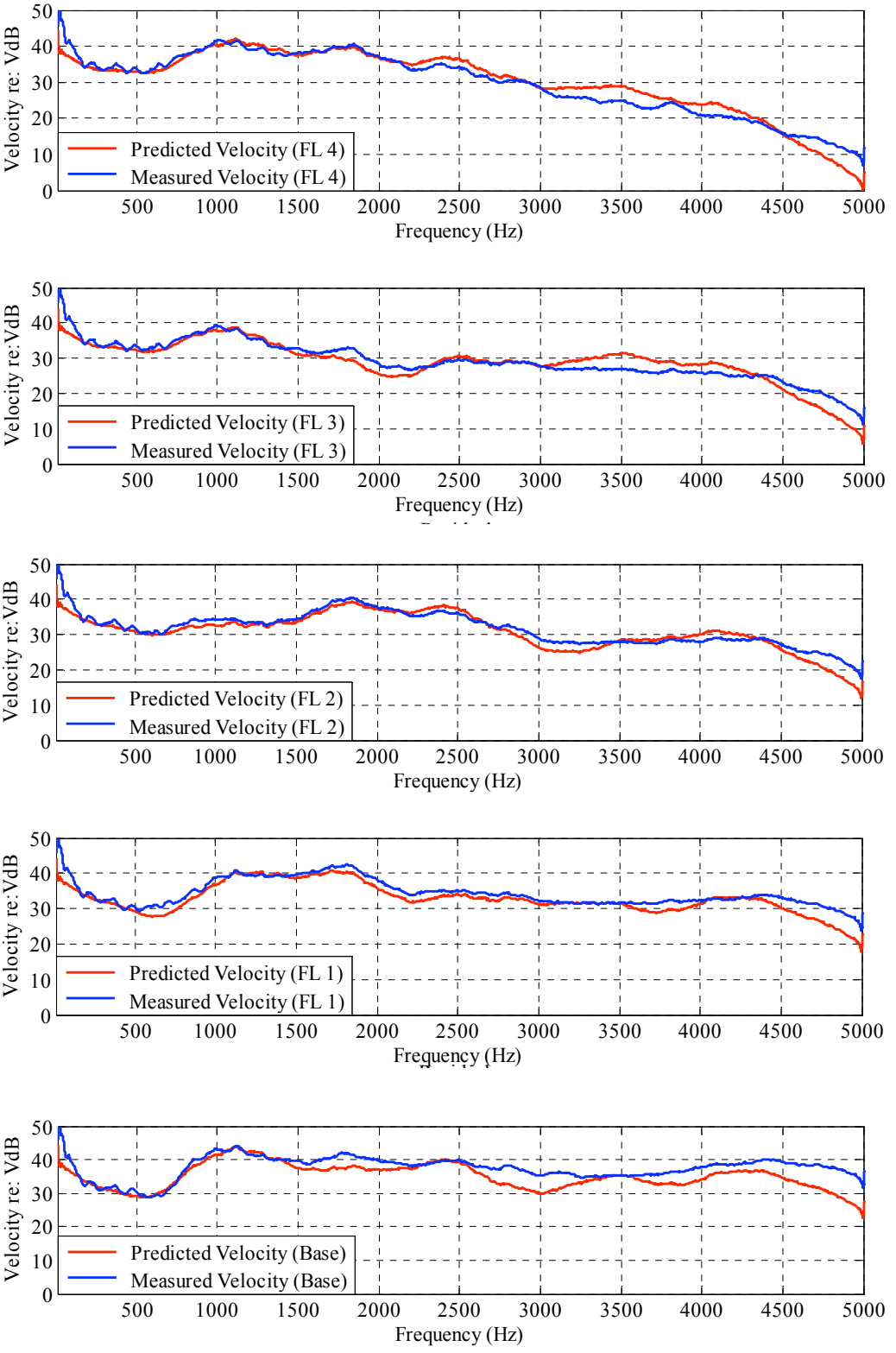


Figure 4. Predicted and Measured Velocity Response for Each Floor

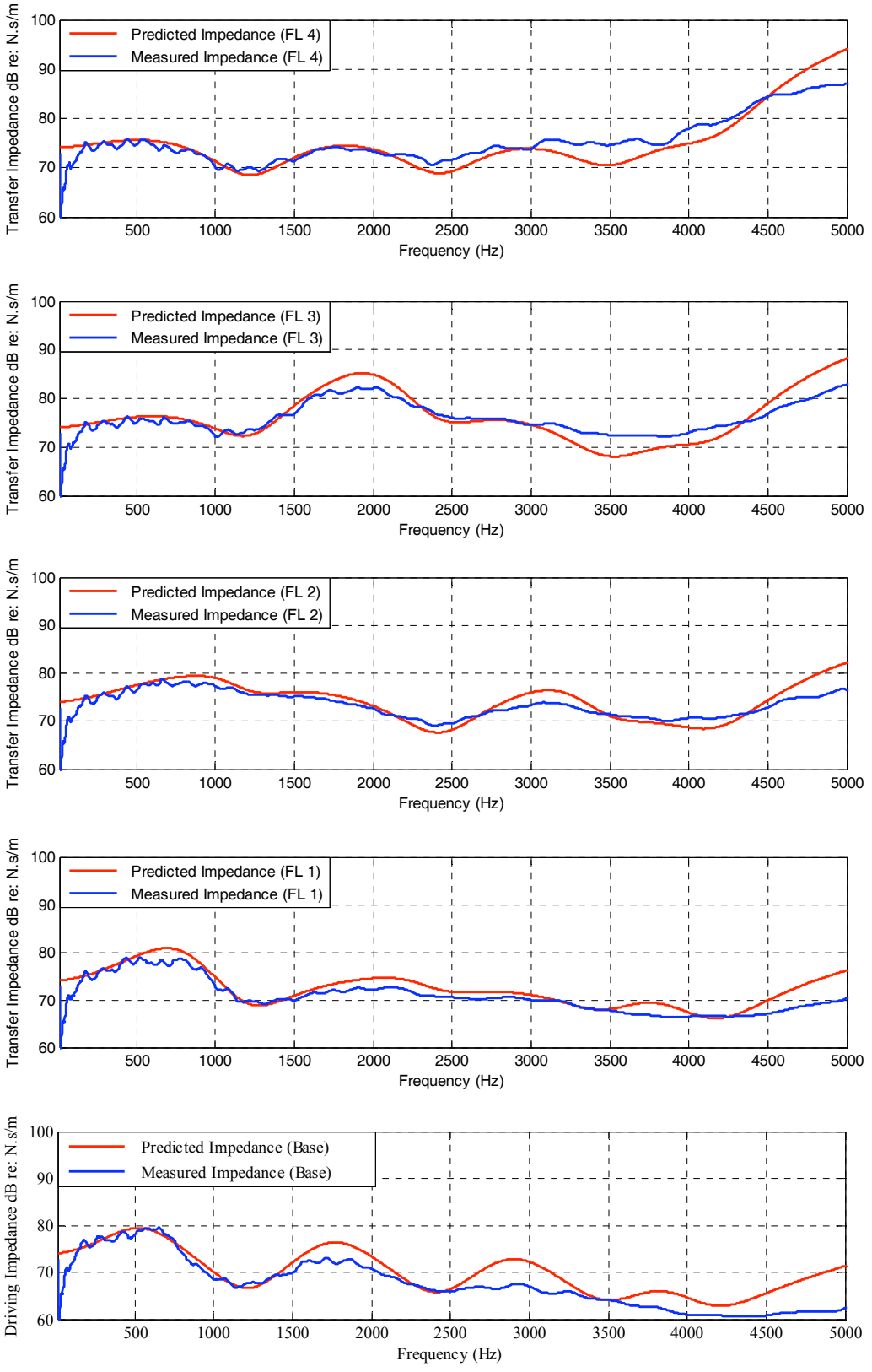


Figure 5. Predicted and Measured Impedance for Each Floor

Observations. As it can be observed from the plots (Figures 4 and 5), the predicted velocities and impedances are very good predictors of the measured values. However, there are some discrepancies found in the high frequency region. Also it can be inferred from these plots that the accuracy in the prediction of velocity and impedance is better for higher floors.

Sources of errors. The probable reason for the deviation at the higher frequency may be due shear softening of the floor slabs at higher frequencies. The predictions are expected to roll off at higher frequencies if a thick infinite plate model (Mindlin model) was used instead of a thin plate bending theory. Mindlin model accounts for shear deformation of the cross-section of the floor. Another source of error may be due to the bending phenomena that can be present in the column.

Impedance based model: advantages and limitations. The impedance based model, compared to the other approaches like finite element approach (which requires many more DOF at higher frequencies with greater cost and time to characterize an extended building structure), is simple, efficient, and provides a fast way to estimate the effects of vibrations induced by passing trains or other environmental sources.

In its present form however, the impedance based model cannot be used to predict the vibration induced in a building containing a staircase or opening in the floor slab or other kind of discontinuities and irregularities.

CONCLUSIONS AND FUTURE WORK

The impedance based model developed was verified with experimental results from a scale model building for longitudinal excitation of a building column. From the results and the observations, it can be concluded that:

1. The impedance-based model successfully predicted the velocity response of the scale model building at column locations.
2. These predictions are more accurate in the lower frequency region as compared to the high frequency region.
3. This method can be applied accurately to special cases where the train induced vibrations are mainly vertical in transmission to building columns.
4. Impedance-based modeling was used for prediction of train-induced vibrations in buildings.
5. Wave propagation models are highly efficient in terms of computation time required.

In the future, use Mindlin thick plate theory to improve modeling of the floor behavior. This model is expected to improve the accuracy of the predictions in the high frequency region. Shear deformations need to be included in the response in addition to bending deformations. Furthermore, full scale testing of a building will be performed for validations of the presented wave propagation method.

Future work also includes plans to test a full scale building during various stages of construction and fit-out. It is well known that non-structural elements can affect vibration measurements significantly. In fact, the inability to correlate basic models with real buildings at a level of acceptable accuracy, led to this study. This completed model study, will have a significant impact on future work in real buildings, helping to direct methods of measurement, and helping to discern the different effects of structural and non-structural elements.

ACKNOWLEDGEMENTS

The authors would like to thank Acentech Inc. for their volunteering time, expertise and equipment in every stage of this research. Thanks to Professor Babak Moaveni at Civil Engineering department at Tufts University for his advice and concern in this research. Also thanks to Tufts Faculty Research Awards Committee (FRAC) for their funding for this research.

REFERENCES

Adam, M., Estorff, O.V. (2005). "Reduction of train-induced building vibrations by using open and filled trenches." *Computers and structures* Jan, 83(1) pp.11-24

Bahrekazemi, M., (2004). *Train-Induced Ground Vibration and its Prediction*, PhD Thesis, Royal Institute of Technology, Stockholm, ISSN 1650-9501

Brett, C., (2007). *Predicting Train-Induced Wave Propagation in Multi-Story Buildings.* Masters Thesis- 1440206, Medford, MA: Tufts University.

Clough, R. and Penzien, J. (2003). *Dynamics of Structures* (Second (revised) ed.). Computers and Structures, Inc., Berkeley, CA.

Conroy, K.M., (2008). *Vibration transmission through Buildings with Walls using Wave Propagation Methods*, Masters Thesis No. 1450765, Medford, MA: Tufts University.

deSilva, C., (2000). *Vibration Fundamentals and Practice*. Boca Raton: CRC Press.

Xia He, Jianguo, C., Pengbo, W., Chaoyi, X., Roeck, G. D. and Degrande, G., (2009). "Experimental investigation of railway train-induced vibrations of surrounding ground and a nearby multi-story building." *Earthquake Eng & Eng Vib* Mar., 8(1), pp:137-148

Fahy, F., (1985). *Sound and Structural Vibration*, *Radiation Transmission and Response*. Academic Press, London.

Fahy, F., & Gardonio, P., (2007). *Sound and Structural Vibration, Radiation, Transmission and Response* (Second ed.). London: Academic Press.

Gupta. S., Liu, W. F., Degrande, G., Lombaert, G., Liu, W.N., (2008). "Prediction of vibrations induced by underground railway traffic in Beijing." *Journal of sound and vibration* Jul.,310 pp:608-630

Harris, M., M. & Hanson Inc. (2006). *Transit Noise and Vibration Impact Assessment,* Federal Transit Administration (FTA)

Hughes, M.F., Sanayei, M., Moore, J.A., Zapfe, J.A., and White, R.D., (2008). "Experimental Validation of Building Vibration Propagation Using a Four Story Laboratory Model," *Proceedings of the ASCE,* Structures Congress 2008, Vancouver, Canada, Apr., 24-26

Hughes, M.F., (2008). *Testing and modeling of vertical vibration propagation in a scale model building*. Masters Thesis No. 449704, Tufts University, Medford, MA.

Hunaidi O, Tremblay M., (1997). "Traffic-induced building vibrations in Montreal" *Canadian Journal of Civil Engineering*, Feb., 24(5):736-753.

Ju, S.H., Lin, H.T., (2004). "Analysis of Train Induced vibrations and vibration reduction schemes above and below the critical Rayleigh speeds by finite element method", *Soil dynamics and the Earthquake Engineering*, May, (24)993-1002

Ju, S.H., (2007). "Finite element analysis of structure-borne vibration from high-speed train." *Soil dynamics and earthquake engineering*, Oct, (27) 259-273

Li, B., Zou, T., Omenzetter, P., (2009). "Investigation of traffic-induced floor vibrations in a building." *Proc. of NZSEE conference*, Christchurch, New Zealand, Apr.

Sanayei, M., Brett, C.R., Zapfe, J.A., Ungar, E.E., and Hines, E.M., "Predicting Train-Induced Vibrations in Multi-Story Buildings," *Proceedings of the ASCE,* Structures Congress 2008, Vancouver, Canada, Apr., 24-26, 2008.

Trochides, A. (1991) "Ground-borne Vibrations in buildings near subways." *Journal of Applied Acoustics*, Jul., (32) 289-296.

Wang, J.F., Lin, C.C., Chen, B.L., (2003). "Vibration Suppression for high-speed railway bridges using tuned mass dampers", *International Journal of Solids and structures*, Oct., (40) 465-491

With, C., Bodare, A., (2007). "Prediction of train induced vibrations inside buildings using transfer functions." *Soil Dynamics and Earthquake Engineering*, Jun., 27 93-98

Xia He, Yanmei, CAO, Roeck, D. G., Degrande, G., (2007). "Environmental Problems of Vibrations induced by railway traffic" *Frontiers of Architecture and Civil Engineering in China* 1(2), pp: 142-152

Yanmei, CAO, Xia, H., (2010). "Experimental study of railway traffic induced environmental vibrations," *International Conference on Mechanic Automation and Control Engineering (MACE)*, IEEE, pp. 1850-1853,

Zhao, N., (2009). *Mitigation of Train-Induced Floor Vibrations Using a Blocking Floor in a Scale Model Building.* Masters Thesis No. 1468272, Medford, MA. Tufts University.

Zhao, N., Sanayei, M., Moore, J.A., Zapfe, J.A. and Hines, E.M., "Mitigation of Train-Induced Floor Vibrations in Multi-Story Buildings Using a Blocking Floor," *Proceedings of the ASCE,* Structures Congress 2010, Orlando, Florida, May 12-14, 2010.

Simplified Methods for Estimating the Response of Floors to a Footfall

C. J. Middleton[1] and J. M. W. Brownjohn[2]

[1]Research Associate, Vibration Engineering Section, Department of Civil and Structural Engineering, University of Sheffield.
Email: C.J.Middleton@sheffield.ac.uk

[2]Professor, Vibration Engineering Section, Department of Civil and Structural Engineering, University of Sheffield.

Abstract

Floor vibration serviceability has become an area of interest over recent years. Lightweight electronic offices, especially those with slender architectural forms, and high-technology buildings with low vibration environments can often have excessive floor vibration due to human walking. This can result in a floor which is not fit-for-purpose. There exist a number of design guides which offer simplified formulae to analyse these floors. However, the simplistic methods are often shown in be inaccurate and inappropriate. The alternative, finite element analysis (FEA), which is often considered more accurate, can be expensive to implement and time consuming. In addition, modelling techniques required for dynamic analyses are different to that required for static analysis. This is often overlooked, resulting in poor inaccurate models. An accurate, simplistic, method is required which is suitable for everyday design.

This paper examines the current simplified methods of predicting floor response to a single human walking. The inaccuracies are highlighted, as well as where the methodology is inappropriate. The paper also introduces new techniques and ideas to improve design guides in the future.

Introduction

Vibration performance of floors subject to human walking is a relatively modern concern resulting from two main factors. Firstly, throughout the last century, modern advances in construction technology have allowed for floors in new constructions to become more slender, which leads to more economical, aesthetically pleasing, designs. In offices in particular, the increased slenderness is coupled with a reduction in mass applied to the floor due to a move from a heavy traditional office to a light-weight electronic paperless office, making the floors more susceptible to excessive vibration from walking. Secondly, advances in technology have resulted in increased use of high-technology electronic devices becoming common in our

everyday lives. Components in these computers and measurement devices (e.g. in hospitals) often have sensitive vibration criteria. Thus from the standpoint of both design, vibration serviceability often governs the design of floors, influencing the member sizes and structural layout more than strength requirements.

Currently, the most accurate and efficient method for determining the response of a proposed floor design is by extracting the modal properties using finite element (FE) analysis, and calculating the response with a characteristic force model or measured walking force. However, this process is time consuming and costly. It is desirable for a cost effective method of quickly and economically assessing the floor's vibration performance to human induced walking. A number of design guides have been published which use simplified procedures to calculate the response to walking based on the response of a single vibration mode.

Unfortunately, these guides tend not to be clear in their application and are not flexible in their methods. For example, if the structure is not a simple design with a uniform structural plan, the simple rules become complex, abstract and difficult to use. Moreover, they often prove to be inaccurate, predicting responses differing widely from those obtained using finite element analysis or from direct measurement in situ.

This paper focuses on application of and problems with using the AISC design guide. It begins by briefly describing how the guide recommends calculating the modal properties. It then continues to examine the force models recommended. One of the examples within the AISC design guide is then examined by comparing it with FE analysis and with a novel method of obtaining modal mass. At each stage, any inaccuracies in the guidance are highlighted, and where possible avenues of improvement are suggested.

Current design guides

There exist a number of design guides to aid in assessing a floors performance. The most recent ones in Europe and America are:

- AISC design guide 11: Floor vibrations due to human activity (USA) (Murray, Allen, & Ungar, 1997)
- ATC design guide 1: Minimizing floor vibration (USA) (ATC, 1999)
- SCI P354: Design of floors for vibration: a new approach (UK) (Smith, Hicks, & Devine, 2009)
- CC CCIP-016: A design guide for footfall induced vibration of structures (UK) (Willford & Young, 2006)
- Hivoss: Vibration design of floors (Europe) (Hivoss, 2007)

Each guide is similar in approach: calculate modal properties, apply a force and evaluate the response; however, there are small differences in the calculation methods, which can cause large differences in the calculated responses. Due to their similarities, the areas in which errors are introduced are common across the design guides.

AISC design guide 11

The design guide is split into a number of parts. It starts by giving an overview of vibration terminology and principles and continues to discuss acceptance criteria, which are beyond the scope of this paper. The guide recommends determining the fundamental modal properties for analysis and offers methods in their calculation. For walking excitation, there are then two methods of calculation, depending on the occupancy of the floor: design for walking excitation and design for sensitive equipment. There is also a section on rhythmic excitation and the guide finishes with remedial measures for vibration problems, both of which are not within the scope of this paper.

Mode shape and modal mass

Throughout the AISC design guide, first a floor mode must be determined before any modal property is calculated. An understanding of the assumed mode shapes is essential. In addition, as modal mass is defined by:

$$M = \int_{xmin}^{xmax} \int_{ymin}^{ymax} \phi(x,y)^2 m \, dydx \qquad \textbf{Equation 1}$$

where ϕ is a mode shape function in x and y, and m is a mass distribution function, modal mass is directly linked to the mode shape, and are therefore discussed together.

In the design guide it is recommended that there is likely to be a mode governed by the floor joists (left plot of Figure 1), a mode governed by the floor girders (right plot of Figure 1) or a combination of the two.

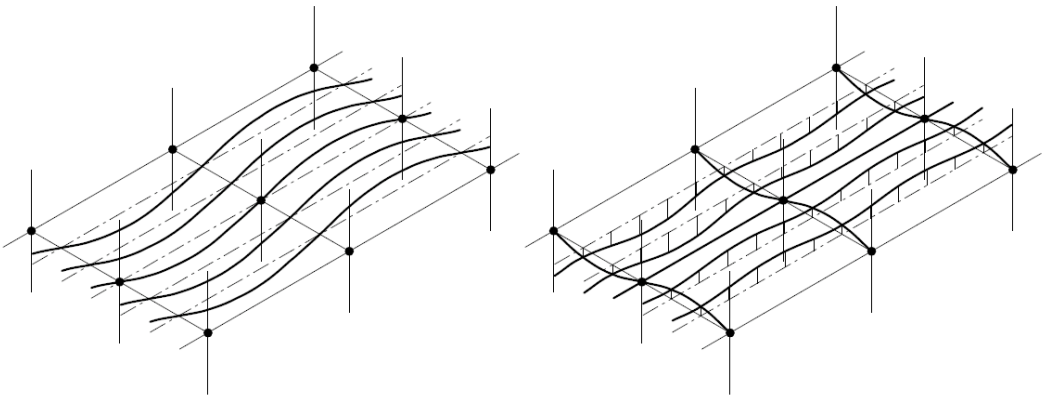


Figure 1: Joist (left) and girder (right) floor modes, illustration from SCI P354 (Smith, Hicks, & Devine, 2009).

One of the key assumptions in the AISC design guide is that partitions and non-structural elements will confine dynamic response to a localised region; i.e. only one floor bay needs to be considered and it will act as a two way slab. Finite element (FE) modal analysis of the whole empty structure, with many uniformly spaced bays, results in many closely spaced modes spanning the whole structure. The design guide recommends its simplified single panel approach over the FE analysis as it implies it is unlikely for the FE modes to exist. As this assumption would dramatically change the shape and area of a mode shape, this would also have a significant effect on the modal mass of the assumed mode. It is crucial to accurately determine the area of the floor participating in the response to calculate the modal mass.

Measured modal properties of a structure which includes partitions can be used to investigate the assumption the partitions constrain modes shapes. The left plot of Figure 2 shows the floor plan of an experimentally measured structure. The partition layout is clear, with the highlighted area showing the test area. In this case, most of the partitions are substantial heavy brick partitions. The right plot shows the first and third vibration modes, which span the whole test area and beyond. It is clear that the partitions do not break up these modes. There were also more localised modes, but a number of these also spanned partition lines. The localised modes contributed to the response more, but the global modes response was still significant enough to require consideration.

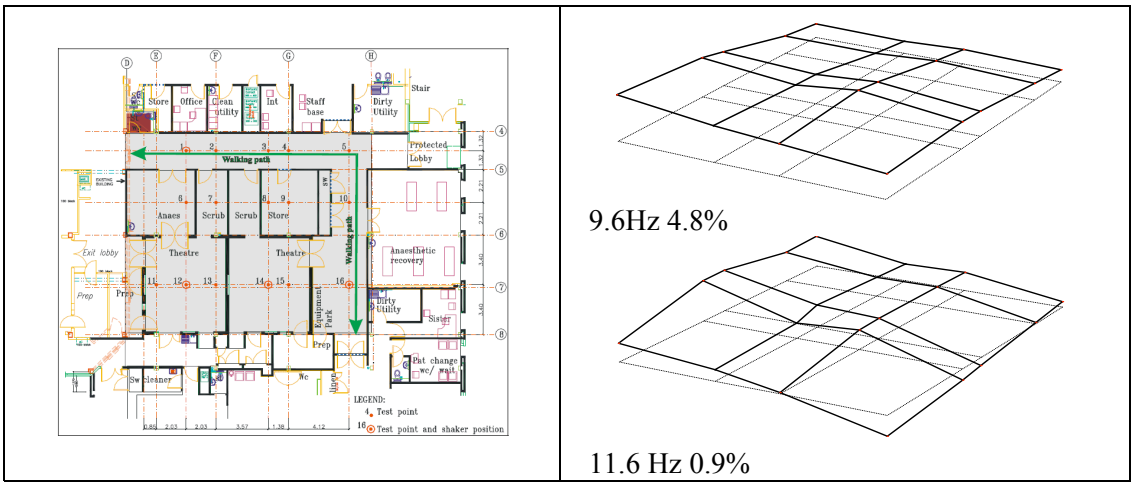


Figure 2: Partition layout (left) and the 1st and 3rd vibration modes (right) from a measured structure with brick partition walls.

The influence of partitions is not understood and is under-researched. Falati, in his PhD thesis (Falati, 1999), examined the contribution of partitions. He discovered:

- Contribution depends on if they are full height or cantilever.
- Contribution depends on their geometrical position to the mode shape.
- Full height partition acts as a flexible vertical support.

In addition to this, it would be possible to add some common sense assumptions:

- Lightweight partitions would have less influence than massive partitions
- Stiff partitions would have more influence than flexible partitions

Even trying to model partitions with finite elements is difficult due to the variability in stiffness of the connections as they are not structural. In the author's experience, partitions generally reduce the response, but to what extent is very situation-dependant. As it is difficult to predict how partitions will affect modes shapes, and in turn modal masses, it should be recommended that they are not included in the analysis, resulting in a slightly conservative response estimation.

In the AISC design guide, the modal mass is expressed as an effective panel weight:

$$W = wBL \qquad \textbf{Equation 2}$$

Where w is the distributed weight per m^2, L is the panel length and B is the effective panel width. This equation is common in all design guides, but generally it is expressed with mass, not weight. However, there are various methods of calculating B and L, but the origin of the methods is never clear or referenced. In the UK design guides it seems to be based on the beam frequency equation, empirically altered with parametric studies. In the AISC design guide it is based on a relationship between

relative stiffnesses of the structural members, but how this has been developed is not clear. It is commonly known that increasing the number of floor bays in the structure reduces the response. The AISC design guide includes this by stating: if there is an adjoining bay with a span 0.7 times this span the mass may be increased by 50%. It has been shown many times that modal mass estimations using the simplified methods are very inaccurate and are the biggest source of error in the design guides (Middleton & Brownjohn, 2007) (Middleton & Brownjohn, 2010).

Equivalent modal mass estimation

To facilitate improving the modal mass estimation methods of the design guides, a new method has been developed. This method is based on using the actual deformed shape of the vibration response to calculate a participating mass using Equation 1.

If a single bay is considered in both directions, there is generally only a single mode that needs to be considered in the analysis. As such, the shape of the response is the same as the mode shape, and this shape is very similar to the static deflection of the floor to a point load at the centre. If the static deflection is used in Equation 1, a participating mass can be found that is very similar to the modal mass.

The same idea can be applied to multiple bays. The top row of Figure 3 shows the first three modes shapes of a 3 bay structure. Each one of these modes pertains to the fundamental mode of a 1 bay structure, and as such have very closely spaced modal frequencies; in this case they are all within 0.5 Hz of each other. The bottom left plot of Figure 3 shows the initial dynamic response to an impulse applied in the centre of the middle bay. If this was animated it could be seen that this shape is preserved for a significant number of oscillations before the damping and geometrical distribution of the response effects it. It is clear that this shape is a combination of all three mode shapes, and as their frequency is closely spaced, they stay pretty much in phase for a significant number of oscillations. Due to this, it may be possible to approximate the response of the three modes using a single equivalent mode, with an equivalent modal mass. The bottom right plot of Figure 3 shows the static deflection to a point load applied to the centre of the middle bay. Again this deflected shape is very similar to the shape in the bottom left of Figure 3 and it may be used to approximate a modal mass for the equivalent mode.

For this structure the response seems to be confined to 3 bays. This is true even if the number of bays is increased and the mode shapes span the whole structure due to the way the modes sum. As such, with this structure increasing the number of bays further would not have a significant influence on the response. Interestingly, this agrees with the AISC design guides assumption that the response will be localised – but not due to non-structural elements and partitions, this is due to the support

conditions. It is likely that this is case specific and depends on the structural layout and member properties – the number of bays to consider would not always be 3.

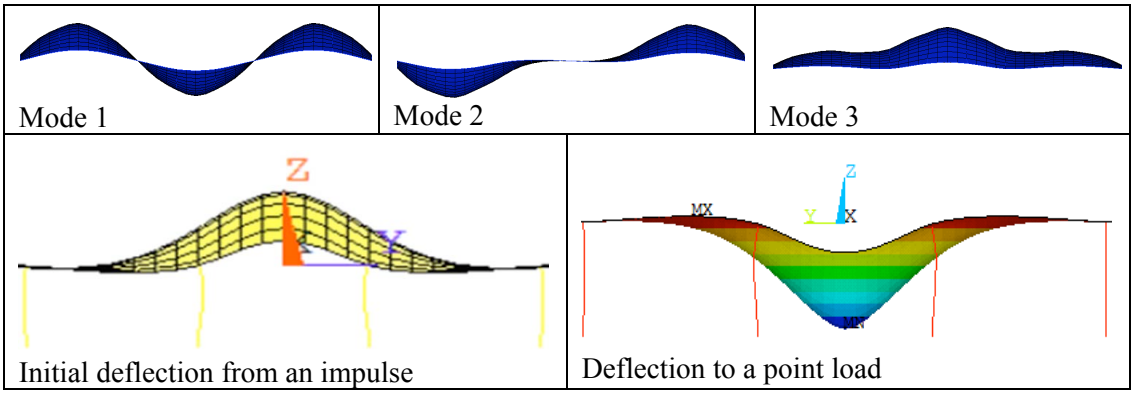


Figure 3: First 3 modes of a 3 bay floor structure (top row), the initial dynamic response to an impulse (bottom left) and the displacement to a point load at the centre of the middle bay (bottom right).

Fundamental frequency

The AISC design guide describes the fundamental natural frequency as the most important parameter in estimating the response and recommends its simplified procedure over modal analysis. The method presented is based on the two mode system shown in Figure 1; the frequency is calculated for the beam and girder mode separately, then a combined mode and the fundamental frequency is the lowest of the three.

The frequency is estimated from the static deflection due to self-weight plus any permanent live loads. In these calculations the design guide recommends increasing the static Young's modulus by a factor 1.35 due to small strains and to assume full composite action between beams and the slab. Although written in a slightly different form in the guidance, the natural frequency calculations are built up by first assuming the fundamental natural frequency of a beam as:

$$f_1 = \frac{\pi}{2}\sqrt{\frac{EI}{mL^4}} \qquad \textbf{Equation 3}$$

where is the Young's modulus, is the second moment of area, is mass per unit length . The deflection of the beam to a UDL is defined by:

$$\Delta = \frac{5}{384}\frac{mgL^4}{EI} \qquad \textbf{Equation 4}$$

where is acceleration due to gravity. Equation 4 can be substituted into Equation 3 to express the fundamental frequency in terms of deflection:

$$f_1 = \frac{17.75}{\sqrt{\Delta}}$$ **Equation 5**

which can be approximated by:

$$f_1 \approx \frac{18}{\sqrt{\Delta}}$$ **Equation 6**

where Δ is deflection in millimetres and can be defined as $\Delta = \Delta_j + \Delta_g$, where the subscripts j and g represent the joist and girder respectively. Each deflection can be considered separately to find the frequency of each mode, or both together to find the frequency of a combined mode.

The accuracy of the frequency estimate using this displacement approach depends on how well the static displacement matches the mode shape. This can be illustrated simply with a spring and mass system where the fundamental natural frequency can be defined as:

$$f_1 = \frac{1}{2\pi}\sqrt{\frac{k}{m}}$$ **Equation 7**

where k is the spring stiffness and m is its mass. The deflection of a spring to a load is defined by:

$$\Delta = \frac{mg}{k}$$ **Equation 8**

which can be substituted into Equation 8 to express the fundamental natural frequency in terms of displacement:

$$f_1 = \frac{1}{2\pi}\sqrt{\frac{g}{\Delta}}$$ **Equation 9**

Assuming a spring mass system with two masses in series, with equal masses and equal stiffnesses, the deflection can be defined as:

$$\Delta = \frac{2mg}{k} + \frac{mg}{k} = \frac{3mg}{k}$$ **Equation 10**

which, if substituted into Equation 7 to express the fundamental natural frequency in terms of displacement gives:

$$f_1 = \frac{0.5774}{2\pi}\sqrt{\frac{g}{\Delta}}$$ **Equation 11**

and the corresponding mode shape would be $x_1 = 1, x_2 = 1.5$. However, this is different from an exact analysis of a double spring mass system in series, which can be defined as:

$$f_1 = \frac{0.6180}{2\pi}\sqrt{\frac{g}{\Delta}} \qquad \textbf{Equation 12}$$

and the corresponding mode shape would be $x_1 = 1, x_2 = 1.618$. The discrepancy in result due to assuming the Equation 9 Is also suitable for a double spring mass system in series gives an error in frequency of approximately 6.5% due to the mismatch in mode shape assumption. If the spring approximation was used for a beam and plate the error would be approximately 11% and 22% respectively. The same calculation can be performed starting with the beam frequency equation and calculating the error for spring mass system and a plate, but it is not so clear to present. If the calculation is performed the error found is approximately 11% for both cases. This means that if the modal frequency is estimated using Equation 6, but the mode of vibration is predominantly a plate mode, an error of up to 11% may be introduced.

Modal damping

The AISC design guides states that until recently damping determined from filtered heel drop tests. The test were performed by performing heal drop, filtering out high frequency modes and estimating damping using logarithmic decrement. This method generally overestimated the modal damping and values ranging from 4-12% we reported. The over estimation was due to the contribution of closely spaced modes of vibration, which cause geometric dispersion of the response. When the response was filtered a number of closely spaced modes can still contribute to the response, but the separate contributions are not distinguishable in the time history response. Estimating the corresponding damping for each mode requires more sophisticated modal analysis techniques.

Damping cannot be modelled as easily as mass and stiffness; it is not related to the material properties of the structure, but derives from frictional forces in joint, connections and not structural elements (Jeary, 1985). As such, guidelines can be given for typical structures but these must be used with engineering judgement and the analyst's experience and are also amplitude-dependent. The AISC design guide recommends 2-5% for offices, 2% for shopping malls and 1% for footbridges. The large range for offices depends on its type (open plan, many partitions, traditional of electronic, etc.)

Force Modelling

For typical floors (e.g. office floors), the AISC design guide uses harmonic amplitudes from footfall forces:

$$F_i = P\alpha_i \cos(2\pi i f_p t) \qquad \textbf{Equation 13}$$

where P is the persons weight, α_i is the harmonic amplitude of the ith harmonic, f_p is the pace rathe in Hz and t is time. The values of α are given as 0.5, 0.2, 0.1 and 0.05 for the 1st, 2nd, 3rd and 4th harmonic respectively. The values of the harmonics reported in the literature vary significantly, and in any case are stochastic parameters that depending on pacing rate. A good overview is presented by Zivanovic (Zivanovic, Pavic, & Reynolds, 2005). Figure 4 shows the harmonic amplitudes for the first and second harmonic, each dot represents a different study. It is clear to see why the values have been disputed over the years. For the first harmonic, the amplitudes have a clear trend proportional with pace rate, although there is still a large degree of variation. For the second, and, although not shown, higher harmonics, the distribution is much more scattered and a line of best fit does not describe the data – it is clearly a random process. From Figure 4, one can conclude the AISC values are likely to be conservative. The problem with the harmonic method is that above the last significant harmonic (approximately the fourth harmonic) there is no force, so negligible response. As such, this method cannot be used to analyse modes above approximately 10 Hz

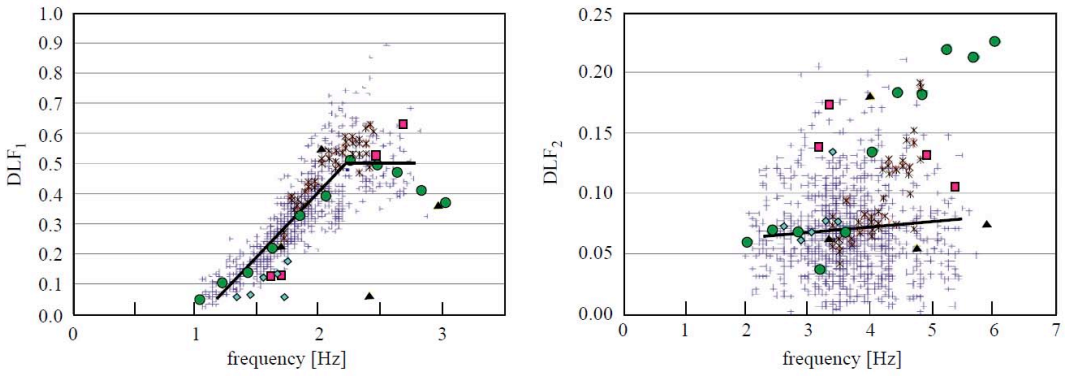


Figure 4: Harmonic amplitudes after Zivanovic (Zivanovic, Pavic, & Reynolds, 2005) for the first (left) and second (right) harmonic; each different type of dot is representing a different study. The solid line is a line of best fit.

For sensitive occupancies, the AISC design guide recommends using the kf method developed by Ungar (Ungar & White, 1979). The method is based on a pulse approximation of a footfall force, which is illustrated in Figure 5. It is assumed that disregarding the characteristic peaks and trough of a footfall force will only introduce minor errors.

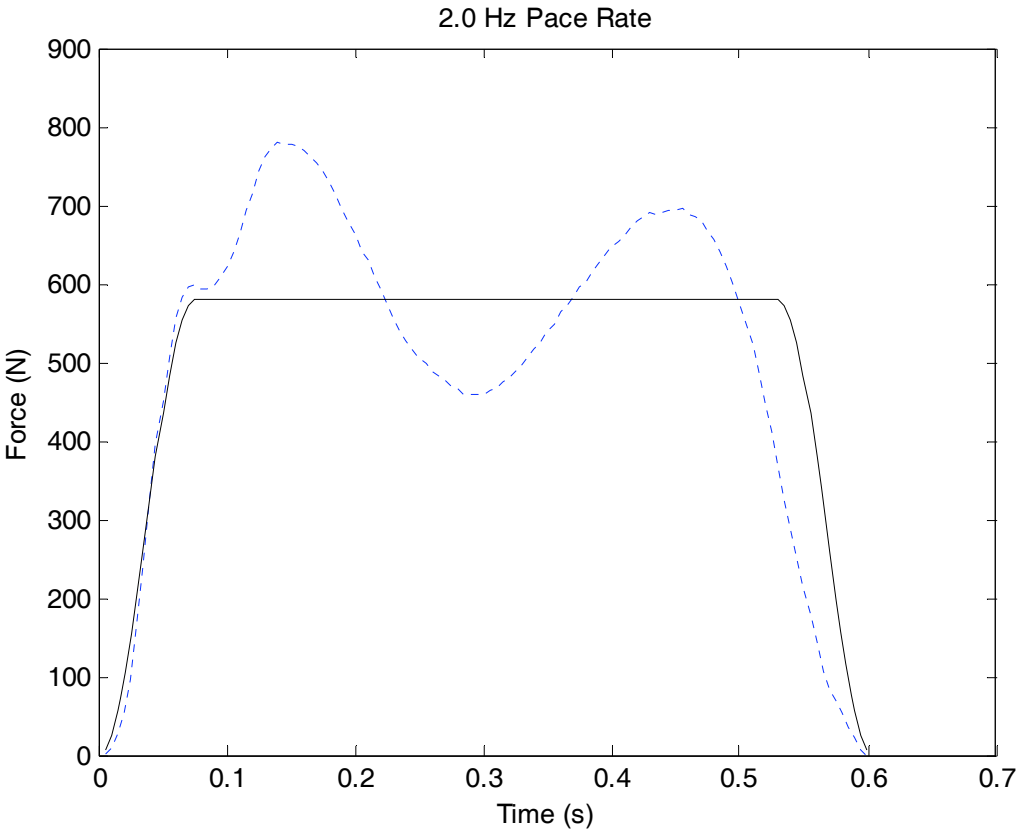


Figure 5: Measured footfall force (dotted line) with the idealised pulse over laid.

The analysis of the response is based on an amplification factor and static deflection. Although the presentation in the AISC design guide differs slightly, the velocity of the nth mode can be derived:

$$V = 2\pi f_n X_{max} \qquad \textbf{Equation 14}$$

where X_{max} is the maximum dynamic displacement and is given by:

$$X_{max} = \frac{F_m k f_0^2}{2 f_n^2} \qquad \textbf{Equation 15}$$

where F_m represents a person's dynamic force, k is the point stiffness of the floor and f_0 is related to a person's pace rate. If Equation 15 is substituted into Equation 14, the resulting velocity expression is:

$$V = \frac{\pi F_m k f_0^2}{f_n} \qquad \textbf{Equation 16}$$

which shows that an increase in the natural frequency will decrease the velocity. As frequency is related to stiffness and mass by:

$$f_n = \frac{1}{2\pi}\sqrt{\frac{k}{m}} \qquad \textbf{Equation 17}$$

reducing the mass, while the stiffness remains constant, will increase the frequency and reduce the response, which is intuitively incorrect. This method has often been shown to be inaccurate and non-representative of response to measured forces (Brownjohn & Middleton, 2008).

The reason for the inaccuracy with this method is shown in Figure 6. The kf method calculates the residual response considering no damping, i.e. the response after the duration of the pulse. The column on the left shows no damping with the top, middle and bottom row showing the force, velocity response of a 10 Hz oscillator and velocity response of a 15 Hz oscillator respectively. It can be seen that with the correct oscillator frequency, the residual response can be 0. This does not happen in the design guide as the exact amplification factor is fitted with a crude curve for the remainder of the calculation. The right column shows the response with 3% damping. It is clear that this considerably changes the response. In addition, Figure 7 shows the response of SDOF oscillators to a measured walking force. The response is clearly very different to that of the idealised pulse in Figure 6. The response of kf method does not represent the characteristic response from a walking force, and as the method disregards the response during the force (which is important in the response) it is recommended that this method is not used

The response of the 10 Hz oscillator is not intuitive and may require some further explanation. In this method the rise of the pulse is defined with a sine wave, and in this example the period of that sine wave (the rise time) matches the period of the oscillator. If displacement is considered, the oscillator would displace with exactly the same shape as the pulse force. It displacement increases with the rise and would halt at the plateau – there is no momentum and the restoring force is balanced by the static force of the pulse's plateau. The plot in Figure 6 is the velocity, which is simply the displacement response differentiated

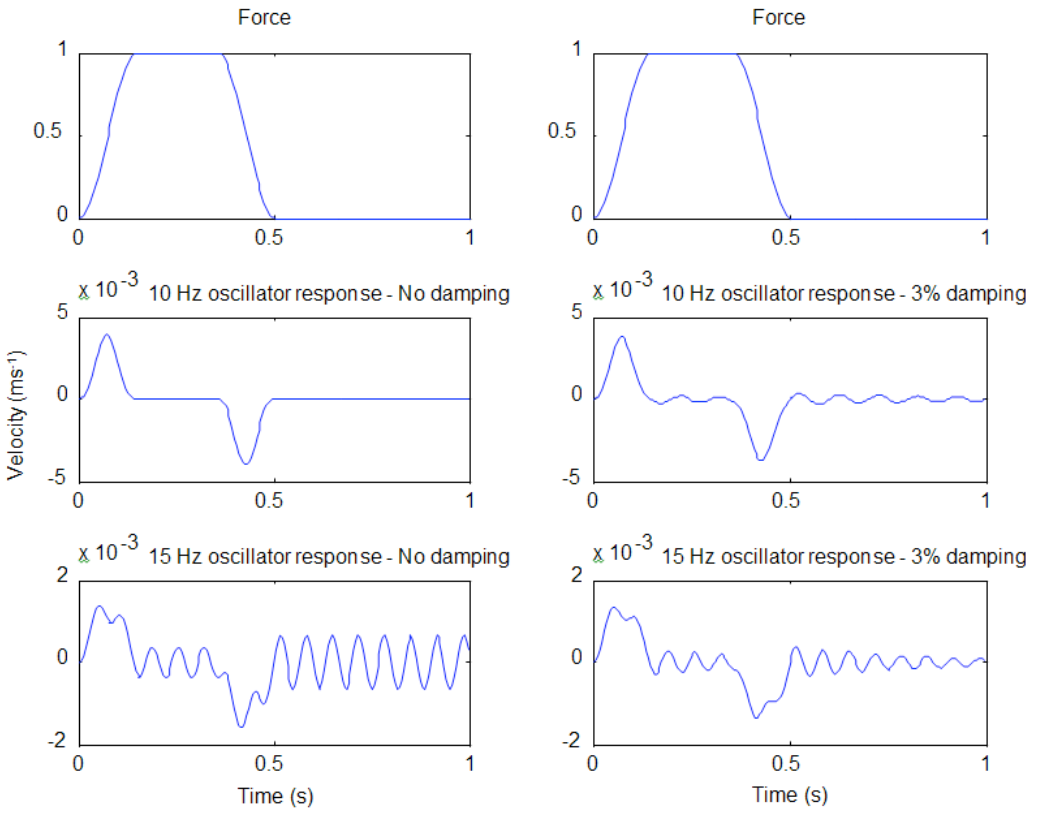


Figure 6: Velocity response of the idealised pulse. The left column is with no damping and the right column is with 3% damping. The top row is the force, the middle row is the response of a 10 Hz oscillator and the bottom row is the response to a 15 Hz oscillator.

The AISC design guide categorises floors by the occupancy. For office floors, it recommends using the harmonic method, which is only suitable for modes up to approximately 10 Hz. For sensitive floors it recommends the kf method for all frequencies. It does not make sense that there should be an overlap of frequencies, if the harmonic method is accurate below 10 Hz, then it should also be suitable for sensitive occupancies. Indeed, if a force model is accurate and characteristic of a walking force, it should be suitable for all cases.

As the response of a floor changes from a resonant response to a transient response (illustrated in Figure 7) after the fourth harmonic, a more logical step is to have a difference force model depending on floor frequency. This split is present in the UK guidance; floors are known as low frequency floors (LFFs) when the response with resonance to walking and high frequency floors (HFFs) when they response transiently. For high frequency floors, the force model used is the effective impulse developed by Arup (Willford, Field, & Young, 2006).

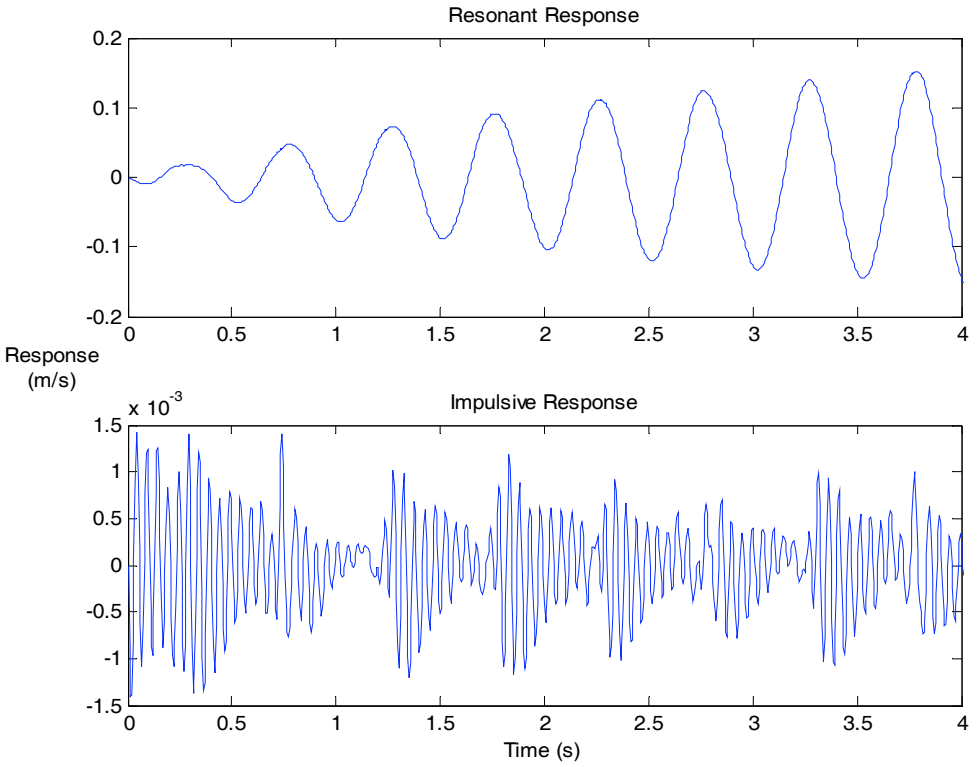


Figure 7: Low frequency (top) and high frequency (bottom) floor response to a measured force with a 2 Hz pace rate.

The effective impulse is based on the velocity response of a mass to a given impulse, which is defined as:

$$V = I/M \qquad \textbf{Equation 18}$$

where V is the velocity of a body, M is its mass and I is the impulse applied in Ns^{-1}. If the mass is set to 1, it can be seen that the resulting velocity is equal to its impulse. To obtain the effective impulse values in the design guides, measured walking forces were applied to a SDOF oscillator with a known frequency and unit mass. The resulting peak velocity is equal to an impulse that would give the same peak velocity, and is termed the effective impulse of the force. The procedure was repeated at different oscillator frequencies. As an impulse is representative of an instantaneous force, it is not suitable for resonance. Arup performed these analyses for a range of pace rates and oscillator frequencies and curve fitted the results. The empirical expression for the effective impulse with a 25% chance of exceedance is given by:

$$I_{eff} = 54 f_p^{1.43} / f_n^{1.3} \qquad \textbf{Equation 19}$$

This method has been shown to be reasonably accurate (Brownjohn & Middleton, 2008), and much more so than the kf method for HFFs. A simple test of the accuracy

can be obtained by comparing the response of an SDOF oscillator to the measured force against the response from the corresponding effective impulses.

Although Arup recommend analysing the response to just one pace, in reality there would be multiple paces. Multiple paces will be used in this example as it is more realistic. The left plot in Figure 8 shows the response of a 15 Hz SDOF oscillator to a measured walking force with a 2 Hz pace rate. This force was generated using an instrumented treadmill with metronome-prompted walking. This gives the most stable pacing rate possible, however variation does still exist. The middle plot shows the response to the corresponding curve fitted effective impulse, but with the pace rate variations kept. The characteristics of the response have been preserved, including the larger response towards the end of the signal. The plot on the right shows the response with the impulses at exactly 2 Hz, with no variation. In this case the characteristics of the response have been removed, and the peak response at the end of the signal has been eliminated. This demonstrates that not only does the force of an individual step need to be modelled appropriately, but so does the variation in timing between successive steps. This would also vary the harmonic amplitudes.

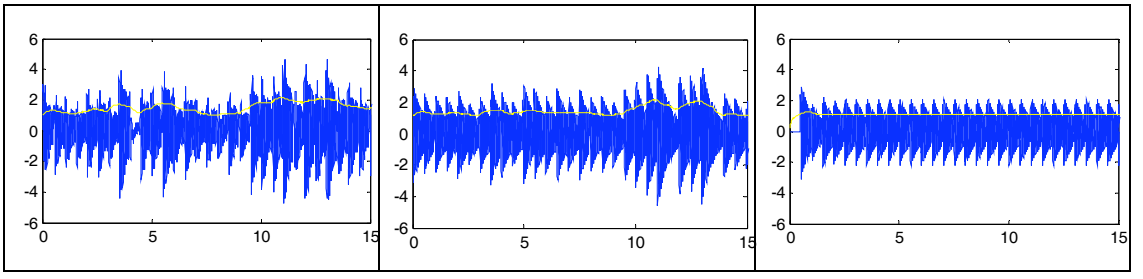


Figure 8: 15 Hz SDOF oscillator response to a measured walking force time history (left), effective impulse including pace rate variation (middle) and the effective impulse without pace rate variation (right).

With the two force models that depend on floor frequency, it is possible to calculate much more accurate responses, but as was shown, these force models are not perfect. In addition, having two models is not ideal. For lightweight floors there often exist low frequency global modes, and at high frequency, low mass local modes, with both contributing significantly to the response. Ideally, a universal force model would be appropriate, that includes variation in pace rate.

Comparison of FE analysis Vs. AISC design guide 11

To assess the accuracy of the AISC guide, example 4.3 presented in the guide will be analysed with FE analysis and with the modal mass from displacement of a point load. In the example only one bay is described, but it is implied that it is continuous over the supports. As such, the floor will be considered as 1x1 bay, 3x3 bay, 5x5 bay, 7x7 bay, 9x9 bay to see how the structural size changes response and modal

properties. Columns have not been modelled, but pinned supports have been applied, which is more in keeping with the design guides calculations, however it is commonly known that columns may have an influence on the response (Middleton & Brownjohn, Response of high frequency floors: A literature review, 2010). The 1x1, 3x3 and 5x5 bay models are shown in Figure 9.

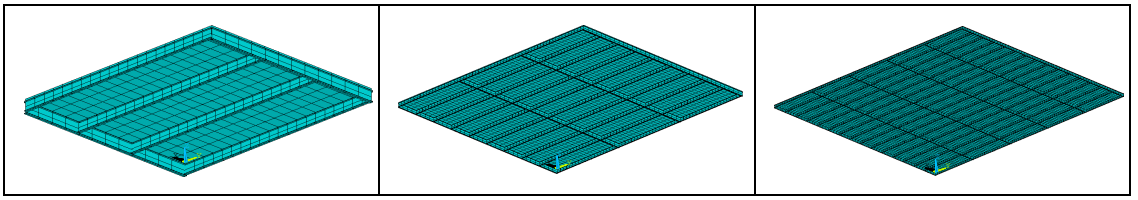


Figure 9: Underside of the FE model showing the beam locations for the 1x1 bay (left), 3x3 bays (middle) and 5x5 bays (right) models.

For each model, the FE model modal properties are extracted for the mode grouping that pertains to the first mode of a single bay. As this example is concerned with accuracy of the modal properties, not the force, the response is calculated with a unit impulse to remove any errors introduced by force assumptions in the guidance. This impulse is applied to the centre point of the middle bay and the response will be calculated assuming 3% damping.

Table 1 shows an overview of results for the 1x1 bay structure and Figure 10 shows the response time histories of the impulse excitation. It is clear that the frequencies are not too different, with a maximum of 0.75 Hz between the AISC design guide and FE analysis. However, when considering the modal mass the AISC design guide value is approximately 5 times more that from the FE analysis. This translates to the response being considerably underestimated. However, the modal mass calculated using the static deflection is very similar to value from the FEA modal analysis.

Table 1: Results comparisons for AISC design guide, FEA and modal properties from static deflection.

	AISC Example	FE with modal analysis	From static load deflection
Fundamental modal frequency (Hz)	4.15	4.9	4.6
Fundamental modal mass (kg)	46800	8500	8200
Peak velocity from 1N/s impulse (m/s)	0.23×10^{-4}	1.17×10^{-4}	1.23×10^{-4}

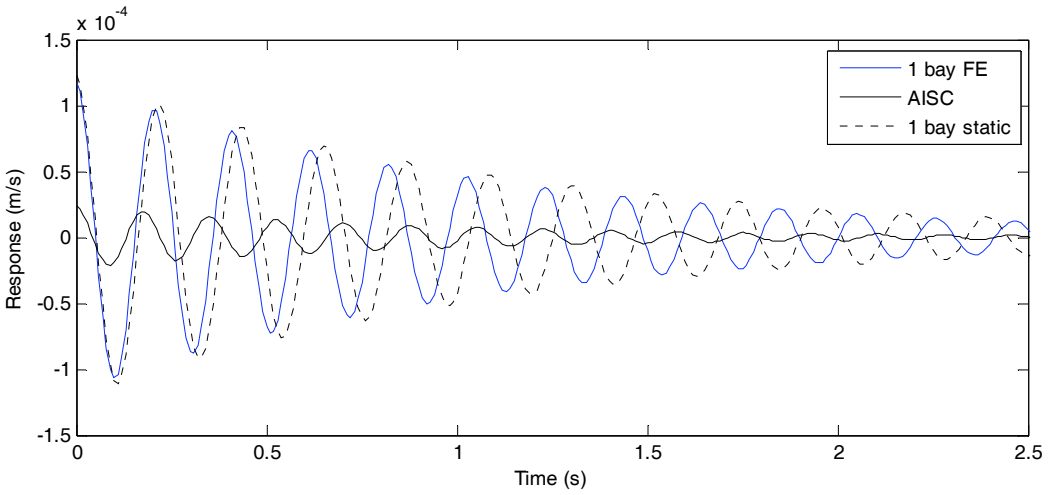


Figure 10: Time history response for the 1 bays structure for each analysis technique

The left plot in Figure 11 shows how the fundamental natural frequency changes with increasing bays using FE modal analysis and static deflection from the FE model. In both cases the frequency increases, but interestingly (although not shown here) if columns are modelled the frequency decreases. The right plot shows the % difference between the modal analysis frequency and the frequency calculated with deflection using Equation 6. Interestingly the maximum error is approximately 11 %, which is close to the maximum error when calculating natural frequency with the beam equation but using displacement from a slab. One example is not conclusive, but this indicates why there is a discrepancy in the frequency results.

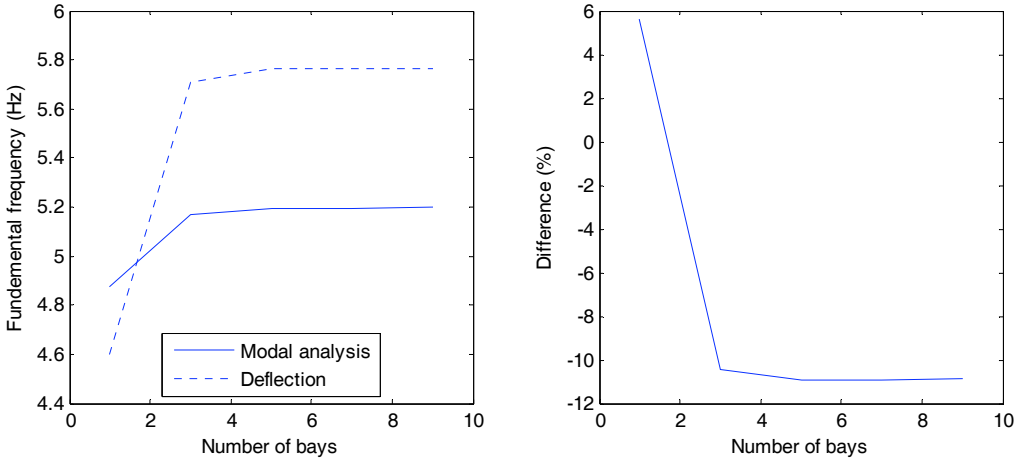


Figure 11: How fundamental natural frequency changes with increasing bays (left) and the difference in the calculation methods (right).

Figure 12 shows how the peak velocity changes due to the impulse with the number of increasing bays. In this case, the response approximately halves between 1 and 3 bays. As the response to an impulse is proportional to the mass, this means the mass participating in the response must approximately double – much more than the AISC design guide's 50% increase recommendation. In this case, after 3 bays there is no significant reduction in response with increasing the number of bays.

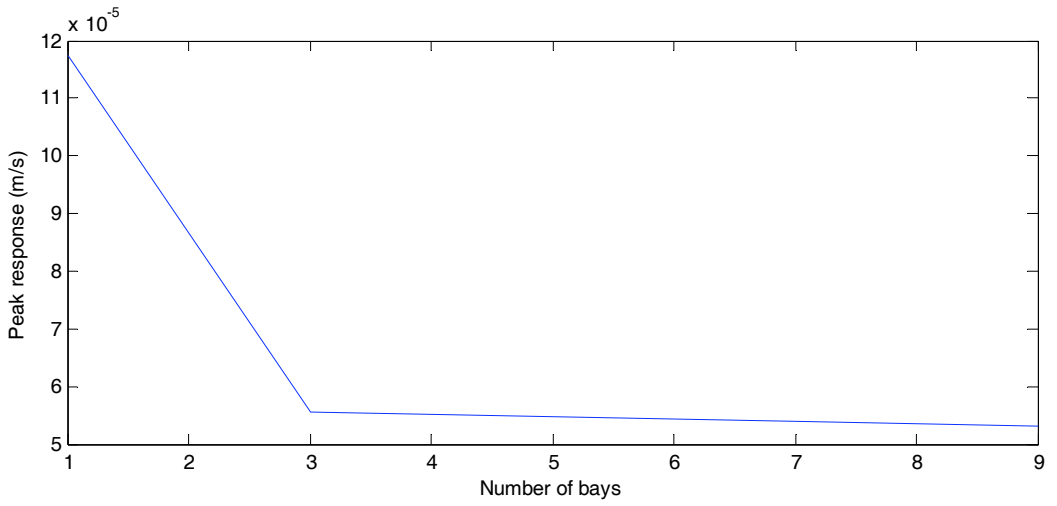


Figure 12: Peak velocity response from the unit impulse with increasing bays.

Figure 13 shows the time history response for the AISC and modal FE analysis overlaid. Due to such a large overestimation in mass, the AISC response is lower than all the FE responses, even for the largest structures. Another interesting point is that although there is a large number of closely spaced modes, the response of all the time histories appear to be dominated by one frequency. If the response of the 3x3, 7x7 and 9x9 bays are compared to the AISC design guide it is clear that they decay much quicker although they were all analysed with 3% damping. This is due to the geometrical spread of energy.

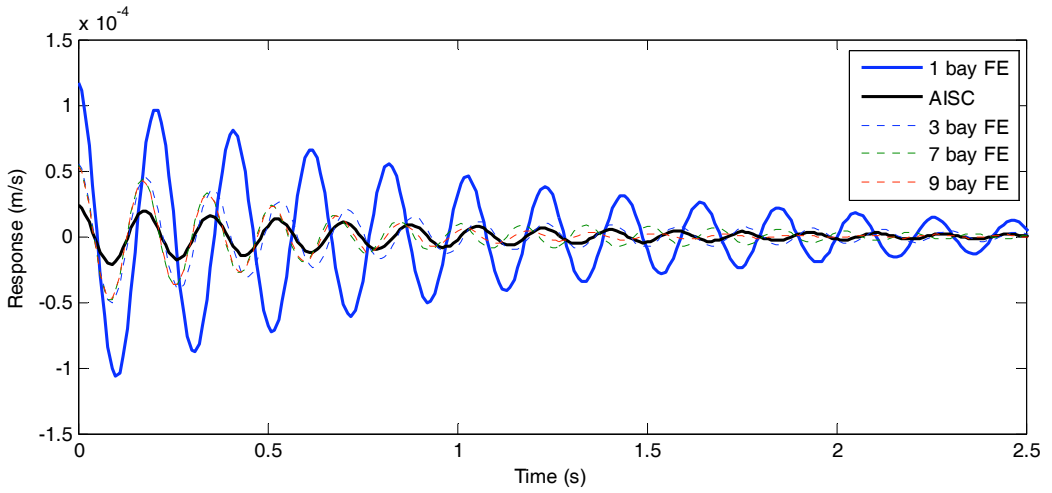


Figure 13: Time history response for the AISC and modal FE analysis overlaid. The lines for the 1 bay analyses are made thicker for clarity.

Discussion and conclusions

Although only AISC design guide was assessed in this study, all guides have similar inaccuracies in estimating modal properties, especially with modal mass. All design guides have similar procedures and calculations and it was shown that their methods are not always appropriate for assessing floor vibration response, especially for multi-bay structures.

The response of multi-bay structures is made up of many modes, but because the frequencies are closely spaced the total response appears to be dominated by one single frequency, but with a higher damping ratio due to the geometrical spread of energy. The individual closely spaced modes span the whole floor area, but the summed response results in a localised response. It appears that the combined response of all the modes is similar to a single localised mode. It seems plausible that the simplified method in the design guides based on a single mode of vibration may be able to represent accurately the response of large floors if a set of equivalent modal properties can accurately be determined. For this an equivalent mass, frequency and damping ratio is required. This paper has shown a possible method which provides a reliable equivalent mass and has shown where errors in frequency maybe introduced, although damping estimation has yet to be addressed. Past results from heel drop tests, which overestimated the damping ratios may actually be useful. Although the damping values do not match each individual mode found in a modal analysis, they may be appropriate in determining the response of an equivalent mode. Ideally, the reduction in response due to the geometric effects should be calculated and added to an appropriate damping value. Ironically, if the work within this paper is validated further, simplified floor design may do a full circle. Originally

(unintentionally) geometric damping was included in the analysis, this was then removed as it was not modal damping. One mode was always used in the response calculations, but recently the design guides have proved to be inaccurate and multi-modal analysis using FE was recommended. With the results in this paper, it may be possible to represent a number of closely spaced modes as a single mode, and if geometric dispersion is included in the damping ratio, the response is very similar to a multi-modal response. However, this time round, an appropriate equivalent modal mass is required.

Even if modal properties can be accurately determined, or if an equivalent mode can be obtained, the results are meaningless if there is not an accurate and appropriate force model. The current state-of-the-art is to have different force models for different floor frequencies. This indicates that neither model truly models the walking force. It is desirable to have a single model, which is suitable for all floors, and all structures subject to human walking.

A floor should not have a binary pass or fail, the very nature of the analysis is stochastic and should be reflected in the guidance. There is a large degree of randomness of a walking force, not only between different people, but with each step of the same person. In addition, the modal properties of the floor are not fixed. Modal analysis gives a linear fit of a non-linear structure. All structures have amplitude dependant frequency and damping. Finally, classifying a floor with a maximum response may not be characteristic of the floor. If that response is only for 5% of the floor area, it may still be acceptable.

The aim of this paper was to highlight common inaccuracies in all design guides, and to suggest possible avenues for improvements. In addition, the whole procedure of analysis and classification of the floor was discussed. Although the study presented here is large enough to be conclusive, it should serve as an indicator for future research.

References

ATC. (1999). *Minimizing floor vibration.* ATC.

Brownjohn, J. M., & Middleton, C. J. (2008). Procedures for vibration serviceability assessment of high frequency floors. *30*(6), 1548-1559.

Falati, S. (1999). *The contribution of non-structural components to the overall dynamic behaviour of concrete floor slabs.* Oxford: University of Oxford.

Hivoss. (2007). *Vibration design of floors: Guideline.* Research fund for coal and steel.

Jeary, A. P. (1985). Damping in tall buildings. *Conference on tall buildings.*

Middleton, C. J., & Brownjohn, J. M. (2007). Response of high freqeuncy floors to a footfall. *IMAC XXVI.* Orlando, Florida: SEM.

Middleton, C. J., & Brownjohn, J. M. (2010). Performance of high frequency industrial floors. *ASCE Structures Congress* (pp. 890-901). Orlando, Florida: ASCE.

Middleton, C. J., & Brownjohn, J. M. (2010). Response of high frequency floors: A literature review. *32*, 337-352.

Murray, T. M., Allen, D. E., & Ungar, E. E. (1997). *Floor vibrations due to human activity.* AISC.

Smith, A. L., Hicks, S. J., & Devine, P. J. (2009). *Design of floors for vibration: A new approach.* SCI.

Ungar, E. E., & White, R. W. (1979). Footfall-induced vibration of floors supporting sensitive equipment. *10*(3).

Willford, M. R., & Young, P. (2006). *A design guide for footfall induced vibration of structures.* The Concrete Centre.

Willford, M. R., Field, C., & Young, P. (2006). Improved methodologies for the prediction of footfall-induced vibrations.

Zivanovic, S., Pavic, A., & Reynolds, P. (2005). Vibration serviceability of footbridges under human induced excitation: a literature review. *279*, 1-74.

Efficient Design of Floor Structures Using Active Vibration Control

M. J. Hudson[1], P. Reynolds[2,3] and D. Nyawako[4]

[1] Department of Civil & Structural Engineering, University of Sheffield, UK; PH +44 114 222 5727; email: m.j.hudson@shef.ac.uk

[2] Department of Civil & Structural Engineering, University of Sheffield, UK; PH +44 114 222 5074; email: p.reynolds@shef.ac.uk

[3] Full Scale Dynamics Limited, UK; PH +44 114 222 5074; email: p.reynolds@fullscaledynamics.com

[4] Department of Civil & Structural Engineering, University of Sheffield, UK; PH +44 114 222 5727; email: d.nyawako@shef.ac.uk

ABSTRACT

Improved design methods have led to the use of more slender structural elements in the construction of many newly built structures, especially office floors. These floors satisfy ultimate limit state criteria but can attract complaints arising from excessive human-induced vibrations. Active vibration control is a technology that has been shown to significantly reduce the level of response in this situation. This paper investigates the potential increases in slenderness and associated materials savings that can be realised whilst adhering to the vibration serviceability limits through the implementation of an active vibration control system. The decentralised control setup used was found to realise significant material savings whilst still achieving desirable vibration performance.

INTRODUCTION

Floor vibrations in structures such as offices can cause disturbance and annoyance to occupants if they are sufficiently large (Hanagan, 1994; Hanagan et al., 2003; Setareh and Hanson, 1992). Advances in structural design methods have permitted more slender elements to span long distances in office structures, while meeting ultimate limit state (ULS) and deflection requirements. Furthermore, there has been a trend of employing more open-plan office layouts which have inherently less damping than traditional compartmentalised offices with full height partitions (Díaz et al., 2009; Hanagan, 1994). Consequently, these slender and open-plan structures tend to be more prone to excessive vibrations resulting from human activity. Previously, this has typically meant that floors must be designed stiffer and more

massive than ULS requirements require or that the column/beam layout must be modified to correct this problem.

Active vibration control (AVC) has been shown to have great potential for reducing the level of vibration in floor structures (Hanagan, 1994; Nyawako and Reynolds, 2009; Díaz and Reynolds, 2009, 2010). It is proposed in this paper that AVC can be incorporated at the design stage to avoid the increases in member sizes that would otherwise be required to meet vibration performance criteria.

This paper begins with an analysis of the vibration performance of a range of composite steel/concrete floor systems of differing slab thicknesses and a comparison against vibration serviceability criteria. Following on from this, the effect of utilising an AVC system on each floor system is examined. The results from this are then presented and conclusions drawn.

STRUCTURAL MODEL

A Finite Element (FE) model of a typical office floor has been developed using the commercially available software ANSYS (ANSYS, 2000). The layout of this steel-concrete composite structure has overall dimensions of 45m x 24m, based on a column grid of 15m x 6m, as shown in Figure 1. Primary beams span 6m between columns and secondary beams span 15m between columns and primary beams. A composite steel/concrete slab spans 3m between the secondary beams.

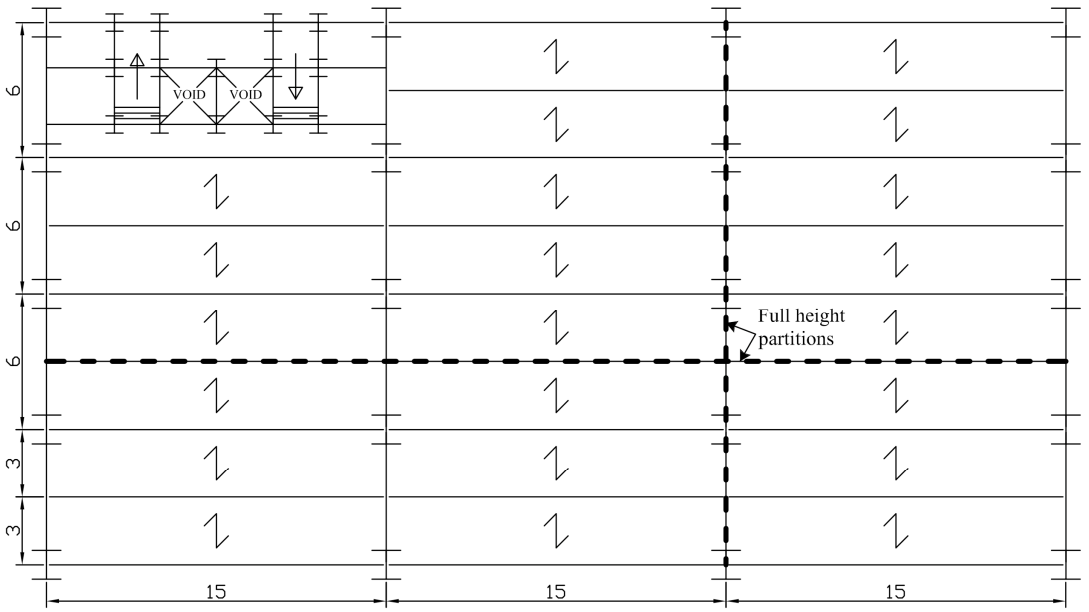


Figure 1 - Structural layout for FE model

This type of regular bay structure tends to have modes that involve movement throughout the whole floor plate. This feature yields modes with large modal mass which reduces the amplitudes of vibration. Real structures tend to have irregularities

that break up this regular grid and so have more localised modes. A lift shaft and staircase have been incorporated into the structural model to simulate this. Additionally, 2 full-height glass partitions physically connected to the floor and ceiling above have been modelled to further break up the global modes into more localised modes to make the modes more realistic for a building of this size (indicated as thick dashed line on Figure 1).

Asymmetric cellular beams were used as long-span beams because of the long distance these relatively light members can span. This is a typical feature of many modern office floors. Initial member sizes were designed through ULS and deflection requirements using a 130mm slab depth. This resulted in a secondary beams size of 748 x 152/210 x 72.2 ACB and primary beams size of 457 x 191 x 74 UB. These beam elements were modelled using BEAM44 elements so that the connection with the floor slab could be simulated through an offset (Smith et al., 2007). BEAM44 elements are uniaxial with tension, compression, bending and torsion capabilities (ANSYS, 2000). The floor slab itself was modelled using orthotropic SHELL63 elements; the change in thickness of the profiled slab was modelled by reducing the Young's modulus in the weaker direction while maintaining a constant slab thickness and (reduced) density. All connections were assumed to be fixed, an assumption that is generally valid because the vibrations caused by human excitation result in only small deflections that are not sufficient to cause significant rotation at joints (Pavić and Willford, 2005). SHELL63 elements were used to model the staircase floor and lift shaft walls, assuming concrete plates of thickness 300mm and 150mm respectively. The partitions were represented as a series of 1m long vertical BEAM4 elements with only axial stiffness of 1.0×10^8 N/m per m width (Miskovic et al., 2009). The resulting FE model is shown in Figure 2.

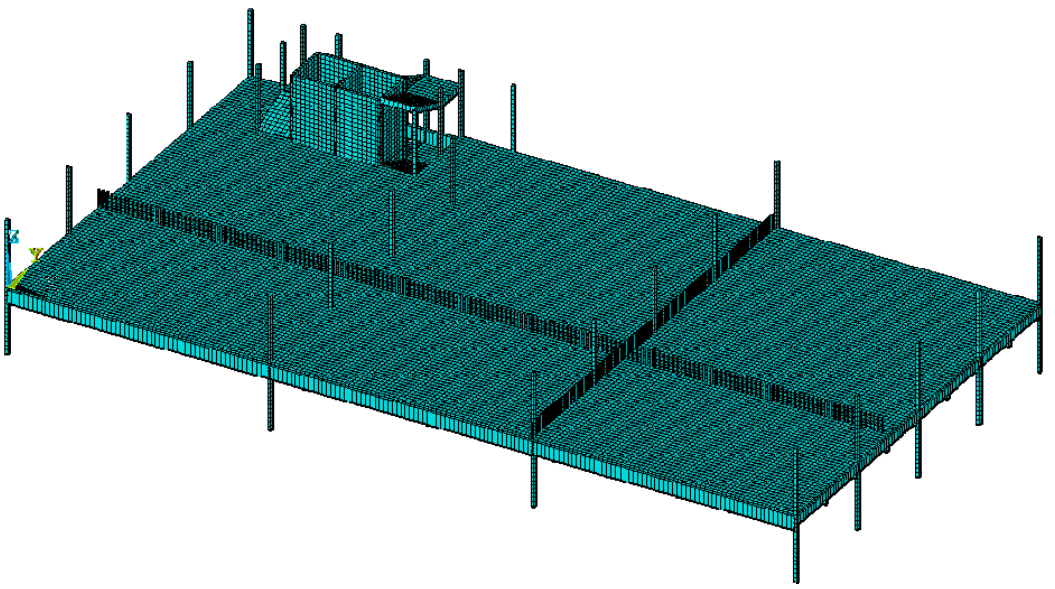


Figure 2 - FE model of structure

RESPONSE PREDICTION

The vibration performance of this structure was predicted and compared against typical vibration limits placed on office floors. Here, the Response factor, R, is used to quantify the level of vibration in the structure – this is a scalar multiple of a baseline response of 0.005m/s^2, which is close to the threshold of human perception. For quiet offices, an R factor limit of 4 is often recommended (Smith et al., 2007).

The response factor was calculated using real walking force time histories at pacing frequencies between 1.6Hz and 2.2Hz. The structural properties were modelled using the modal data extracted from the FE model with assumed modal damping of 2.5% for every mode. This damping value lies within the range recommended by the SCI P354 guidelines (Smith et al., 2007) of 1.1% for floors with only a small amount of furnishings and 3.0% for fully fitted out floors. The large areas of uninterrupted office space present here mean that the floor system is unlikely to develop modal damping as if fully fitted out, hence the slightly reduced value of 2.5% damping has been used. All modes up to 30Hz were considered even though the lowest mode had a natural frequency of 5Hz. This is a considerably higher cut-off than current guidance (Pavić and Willford, 2005; Willford and Young, 2006; Smith et al., 2007) recommends, since recent research (Živanović and Pavić, 2009; Middleton and Brownjohn, 2010) has shown that the division of floors into "low frequency" and "high frequency" can lead to a significant loss of accuracy by omitting the important contributions from some modes. The response analysis was performed using a modal superposition method to calculate the modal forces from pedestrian and the control system at different physical locations, as discussed by Hudson and Reynolds (2010).

The response factor was calculated over a 2.5m x 1m grid encompassing the whole floor structure, with the stationary pedestrian force applied and the response evaluated at each grid point. The results of this calculation for the initial floor system (with slab depth of 130mm) are shown in Figure 3a. Note that a non-linear colour mapping has been used here – the lighter areas indicate areas where $R<4$, while the darker areas indicate areas where $R\geq4$. The shading has been generated through interpolation from the response at the grid points.

It is observed that the response for this initial floor exceeds the limit of R=4 in many areas, so the floor design must be modified. A larger slab thickness was modelled because this makes the structure more massive which tends to reduce the amplitude of vibration. Furthermore, the increase in lateral stiffness acts to increase the global nature of the modes, further increasing the modal mass. The depth of the slab was therefore increased in 20mm increments in an attempt to reduce the response. The steel beam sizes were not increased, both for simplicity and because a preliminary ULS and deflection check indicated that the increase in composite action due to the increased slab depth was sufficient to cover the increased loading. The response factor results for these floor systems are indicated in Figure 3b-e and in Table 1.

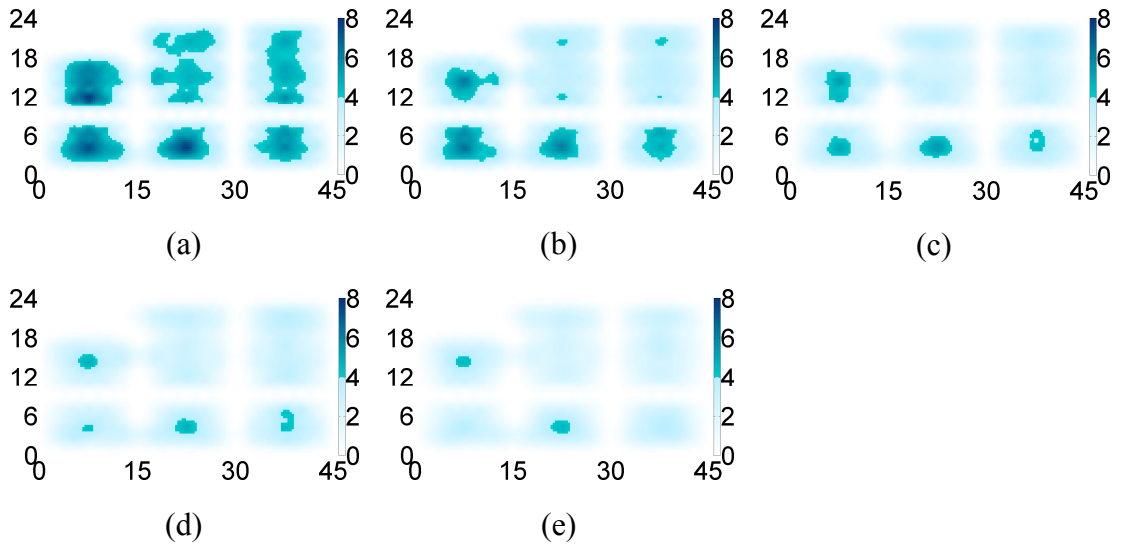


Figure 3 - Response of uncontrolled floor subject to human excitation with varying slab depth: (a) 130mm, (b) 150mm, (c) 170mm, (d) 190mm, (e) 210mm

The response of the floor only becomes acceptable in the majority of locations when the slab is increased to 210mm depth, and even at this depth there are still areas that exceed the R factor limit. However, as the R factor does not exceed 4 by a large amount or over large areas of the floor, it is considered unlikely that this would result in adverse comment.

Table 1 - Increases in R factor for various slab depths

Slab depth (mm)	Maximum R factor	Percentage of floor exceeding R=4 (%)
130	7.6	22.7
150	6.5	9.1
170	5.5	2.9
190	4.7	1.5
210	4.5	0.8

CONTROL SYSTEM

The AVC system comprises of 3 key components as shown in Figure 4: accelerometers to measure the response of the floor; actuators to apply a control force to the floor; and a controller to generate the input voltage to the actuators as a function of the response measured. The accelerometers and actuators are often collocated to avoid instability complications arising from additional phase-lags introduced in non-collocated implementations (Preumont, 2002).

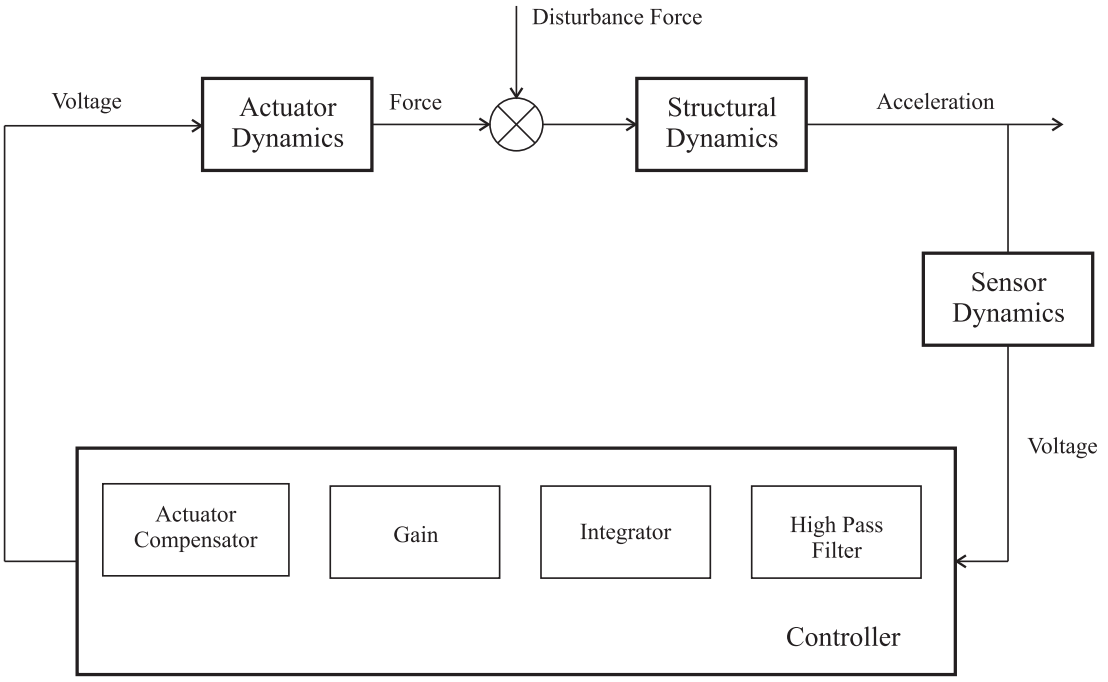


Figure 4 - Active control schematic

The actuators modelled in this study were the APS Dynamics Model 400 electrodynamic shakers that have been used in previous AVC experiments (Nyawako and Reynolds, 2009). The dynamics of the actuator have a significant effect on the performance of the AVC system; indeed, it is often one of the poles relating to the actuator dynamics that first becomes unstable as the feedback gain is increased. These dynamics were modelled by a third order transfer function – a combination of a second order spring-mass-damper model and a first order lag term that is caused by virtue of working the amplifier in 'voltage mode'. The resulting transfer function was thus approximated as (Nyawako and Reynolds, 2009):

$$\frac{F(s)}{V_{in}(s)} = \frac{-ws^2}{s^2+2\zeta_a\omega_a s+\omega_a^2 s} \cdot \frac{1}{s+\epsilon}$$

where: $F(s)$ is the force output from the actuator, $V_{in}(s)$ is the voltage input to the actuator, w is the force voltage characteristic for the actuator, s is the laplace

operator, ω_a is the natural frequency of the actuator, ζ_a is the damping ratio of the actuator and ϵ is a constant representing the lag in the voltage mode.

Direct velocity feedback with a compensator to account for the actuator dynamics was used as the control law in this study. The response of the structure was measured in terms of acceleration so the signal required integration to yield velocity. The accelerometers used in experimental work often have an offset due to the earth's gravitational field or signal conditioning electronics, hence a high pass filter is required to remove this constant before integration. This filter was modelled as a 2nd order high-pass Butterworth filter with a cut-off frequency of 1Hz. In addition, a compensator was designed to limit the detrimental dynamics introduced by the actuator.

This floor system has many modes of vibration that are locally spatially distributed. This means that there is no single point that can control and observe the vibration resulting from all the modes that are excited by human excitation. One possible solution to this problem is to use several actuators distributed across the structure, each acting independently to reduce the response at that location – a decentralised controller (Skogestad and Morari, 1989) – as shown in Figure 5. Whilst this cannot offer the capability of a 'full MIMO' (multiple input – multiple output) configuration, where the actuator voltages are computed as functions of the response at multiple locations, it does have the advantage of a simpler and more intuitive design process as well as being easier to make failure tolerant (Skogestad and Morari, 1989).

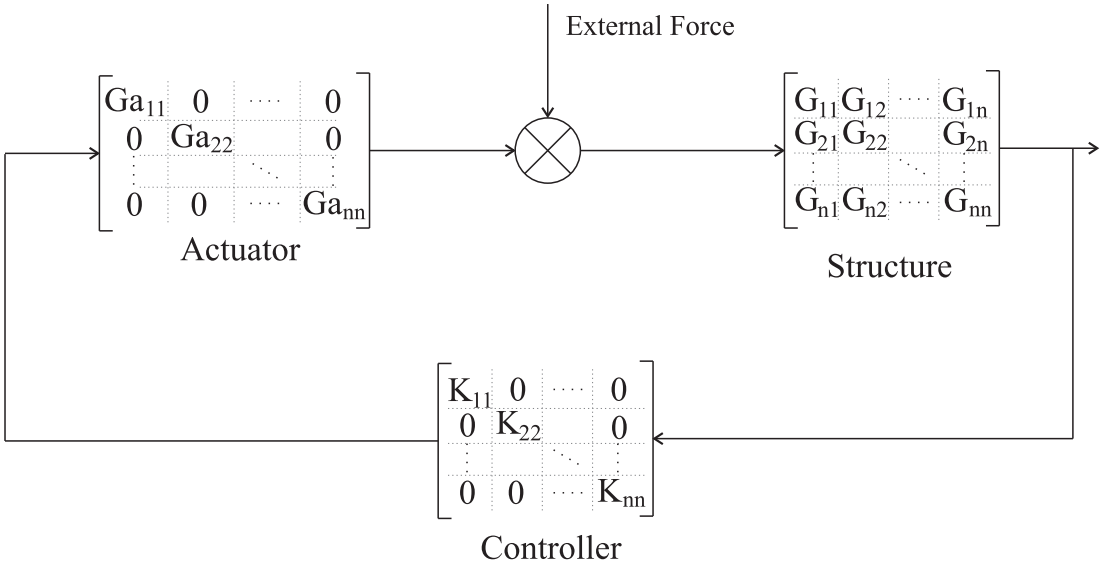


Figure 5 - Decentralised control setup

The design of a decentralised controller involves two main steps – 1) the choice of input/output pairings and 2) the design of each SISO (single input, single output) controller (Skogestad and Morari, 1989). Here, the input output pairings are intuitively chosen as the collocated actuator and sensors. With regards to the second

step – it is important to note that stability of the individual SISO loops does not guarantee stability of the overall system because of the interaction with off-diagonal terms in the structural system (Vaes et al., 2005). This means that a MIMO stability check is required; the generalised Nyquist criterion (Skogestad and Postlethwaite, 2005) was used here. Ensuring failure tolerance within the system was beyond the scope of this paper, thus the design process was simplified to one of ensuring stability while considering all control loops. Here, optimal gains for each SISO collocated actuator sensor setup were chosen to be the maximum gains that ensure at least 6dB gain margin and 30° phase margin. When combined in the MIMO setup the gains for all loops were modified by an equal percentage until the same stability margins were met in the MIMO case.

The difference in modal properties for each of the 5 floor systems means that the suitable locations of actuators and sensors differ. For this reason an actuator placement study was performed for each of the floors, the results of which are shown in Figure 6.

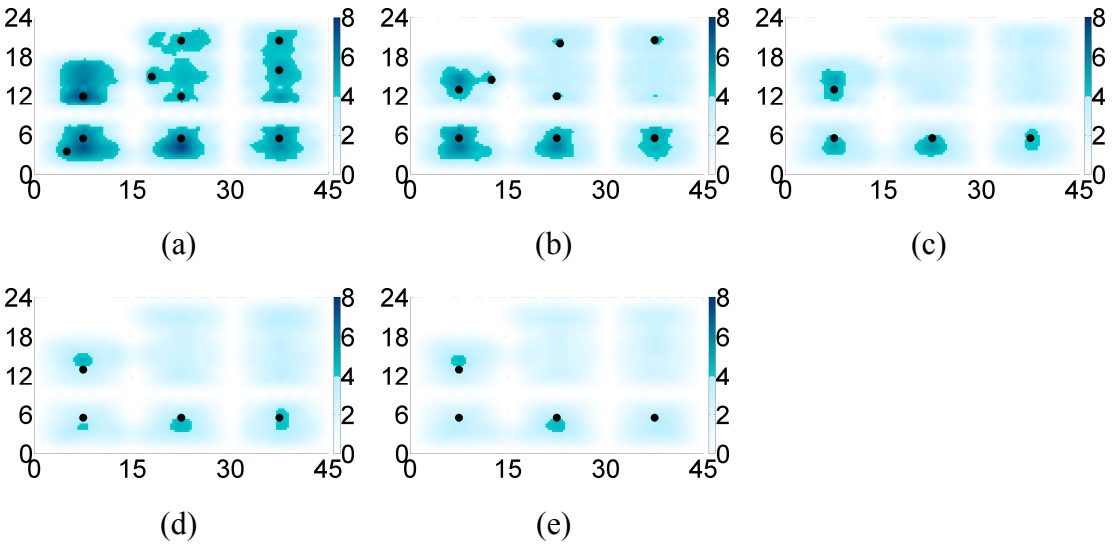


Figure 6 - Actuator locations (shown as black dots) with uncontrolled response shown as shaded

It is interesting to observe that floor system (e) required 4 actuators while the uncontrolled response was high in only 2 locations. The reason for this is that when only 2 actuators were used at the locations of large response an increase in the response at the other locations was observed. This is likely due to the off-diagonal terms in the structural system; these have an unquantified effect on the control system because they were neglected during the design of each SISO controller. Whilst the MIMO system was checked for stability, crucially, it was not checked for performance improvements. The μ-interaction measure (Grosdidier and Morari, 1986) could be used to ensure nominal performance. However, for simplicity in this paper the extra actuators were utilised as shown in Figure 6e.

RESULTS

The response factor was calculated for all 5 floor systems with AVC applied as described earlier, with the results shown in Figure 7.

The maximum response for all floors is greatly reduced. Some of the floors had small areas whose response was slightly greater than R=4. However, these small areas could be unlikely to cause adverse comment, as was also the case for the best-case uncontrolled floor. Indeed, the maximum response for the 130mm controlled structure was less than the maximum response for the 210mm uncontrolled structure at R=4.3 compared with R=4.5. The envelopes of maximum response when viewed along lines parallel to the X-axis are shown in Figure 8.

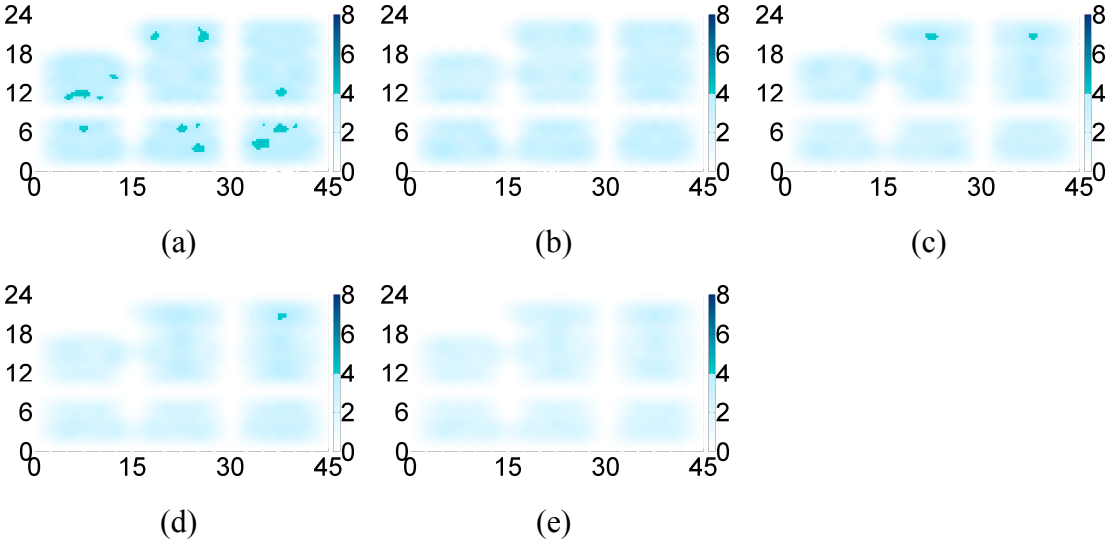


Figure 7 - Response of controlled floor subject to human excitation with varying slab depth: (a) 130mm, (b) 150mm, (c) 170mm, (d) 190mm, (e) 210mm

It is observed that for all 5 floors the response factor was reduced along the cross section by introducing AVC. While increasing the slab thicknesses tended to reduce the whole response globally, AVC targeted only the locations at which the response was greatest. In terms of dynamic performance this leads to a more efficient floor system where the response is not unnecessarily low at some locations.

It can be seen in Figure 8c that the response of the controlled floor around 18m actually exceeded that of the uncontrolled floor. This again was a consequence of using the decentralised controller without ensuring nominal performance – only nominal stability. Given that the response was predominantly reduced to below R=4 the controller can be deemed as performing suitably well.

The impact of AVC is shown even more clearly in Figure 9 which plots the maximum response factor for each floor system. Here, it is apparent that the maximum response measured for the thickest uncontrolled floor was actually greater than the maximum response for the thinnest controlled floor.

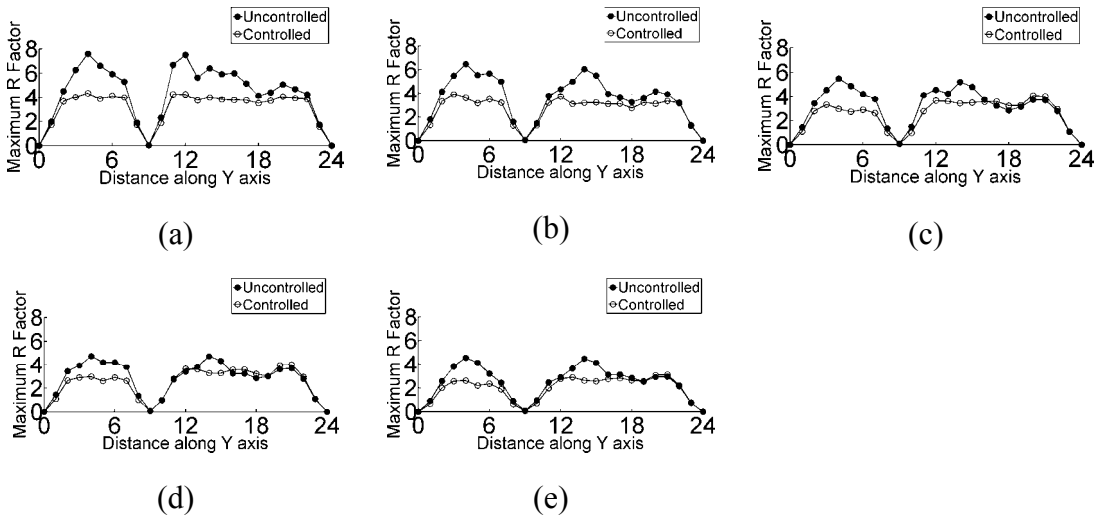


Figure 8 – Envelope of reduction in response due to AVC

This difference in slab depth for equivalently performing floors is equivalent to a 46% reduction in concrete required for the slab. The embodied energy and embodied carbon that could be saved through this reduction can be calculated by using the data provided by Hammond and Jones (2008). Here, RC40 concrete was assumed and thus it was calculated that approximately 243GJ and 35tonnes of CO_2 would be saved from the concrete not used on this floor alone.

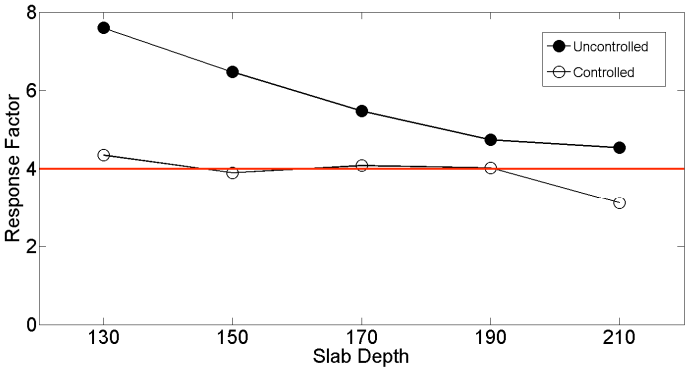


Figure 9 - Summary of response factor changes

CONCLUSIONS

This paper has demonstrated a possible application for active vibration control, utilising its ability to reduce the response of a structural floor system subject to human-induced excitation. Here, the design of a floor that performs poorly from a vibration serviceability perspective has been brought in line with recommended

limits through two distinct methods – 1) by increases to slab depth and 2) by the introduction of an AVC system. It has been shown that by using an AVC system significant material savings can be realised, amounting to 46% for the concrete in the slab.

The additional stiffness introduced through the use of partitions caused the mode shapes to become significantly localised. This actually made controlling the response a more difficult task due to controllability and observability issues. Where more global modes are involved, e.g. in smaller floor systems where it is possible that the whole floor is open-plan, it is expected that fewer actuators would be needed to achieve desirable performance improvements. On the other hand, research is currently working towards improving the performance and cost of the actuators used for AVC in floor structures. This may make it a more desirable option to use many actuators distributed across the floor system even when the modes are fairly global in nature.

This work could be extended by considering the effect of the coupling between each actuator – a result of the off-diagonal terms in the structural system. This could be achieved through the use of the μ-interaction measure or by using a full MIMO scheme with a model-based controller such as LQR, IMSC or H_∞. Also, the additional costs that the use of AVC incurs, both operational and embodied, should be quantified to permit a thorough evaluation of the benefits of including AVC in the design of new floor structures.

ACKNOWLEDGEMENTS

The authors would like to acknowledge the financial support given by the UK Engineering and Physical Sciences Research Council via Industrial CASE Award with WSP Buildings (Voucher Number 08002020), the Responsive Mode Grant (Ref. EP/H009825/1) and Platform Grant (Ref. EP/G061130/1).

REFERENCES

ANSYS, 2000. Release 11.0 Documentation for ANSYS.

Díaz, I.M., Reynolds, P., 2009. Robust saturated control of human-induced floor vibrations via a proof-mass actuator. Smart Materials and Structures 18, 125024.

Díaz, I.M., Reynolds, P., Nyawako, D., 2009. Vibration Testing and Active Control of an Office Floor, in: Proceedings of the IMAC-XXVII. Presented at the IMAC-XXVII, Society for Experimental Mechanics Inc., Orlando, Florida USA.

Díaz, I.M., Reynolds, P., 2010. Acceleration feedback control of human-induced floor vibrations. Engineering Structures 32, 163-173.

Grosdidier, P., Morari, M., 1986. Interaction measures for systems under decentralized control. Automatica 22, 309–319.

Hammond, G.P., Jones, C.I., 2008. Embodied energy and carbon in construction

materials, in: Proceedings of Institution of Civil Engineers: Energy (in press).
Hanagan, L.M., 1994. Active Control of Floor Vibrations (PhD Thesis).
Hanagan, L.M., Murray, T.M., Premaratne, K., 2003. Controlling Floor Vibration with Active and Passive Devices. The Shock and Vibration Digest 35, 347-365.
Hudson, M., Reynolds, P., 2010. Analytical and Experimental Evaluation of Active Vibration Control of an Office Floor Structure, in: Proceedings of 5WCSCM. Presented at the 5th World Conference on Structural Control and Monitoring, Tokyo, p. 10047.
Middleton, C., Brownjohn, J., 2010. Response of high frequency floors: A literature review. Engineering Structures 32, 337-352.
Miskovic, Z., Pavić, A., Reynolds, P., 2009. Effects of full-height nonstructural partitions on modal properties of two nominally identical building floors. Canadian Journal of Civil Engineering 36, 1121-1132.
Nyawako, D., Reynolds, P., 2009. Response-dependent velocity feedback control for mitigation of human-induced floor vibrations. Smart Materials and Structures 18.
Pavić, A., Willford, M., 2005. Vibration Serviceability of Post-Tensioned Concrete Floors. Appendix G in Post-Tensioned Concrete Floors Design Handbook - Technical Report 43 99-107.
Preumont, A., 2002. Vibration Control of Active Structures: An Introduction, 2nd ed, Solid Mechanics and its Applications. Kluwer Academic Publishers, The Netherlands.
Setareh, M., Hanson, R.D., 1992. Tuned Mass Dampers to Control Floor Vibration from Humans. Journal of Structural Engineering 118, 741-762.
Skogestad, S., Morari, M., 1989. Robust performance of decentralized control systems by independent designs. Automatica 25, 119–125.
Skogestad, S., Postlethwaite, I., 2005. Multivariable Feedback Control, 2nd ed. John Wiley & Sons Ltd, Sussex.
Smith, A.L., Hicks, S.J., Devine, P.J., 2007. Design of floors for vibration: A new approach (SCI P354). SCI, Ascot, Berkshire.
Vaes, D., Swevers, J., Sas, P., 2005. Experimental validation of different MIMO-feedback controller design methods. Control Engineering Practice 13, 1439–1451.
Willford, M., Young, P., 2006. A Design Guide for Footfall Induced Vibrations of Structures. The Concrete Society 016.
Živanović, S., Pavić, A., 2009. Probabilistic Modeling of Walking Excitation for Building Floors. Journal of Performance of Constructed Facilities 23, 132-143.

A Comparison between the Single Plate and Angle Shear Connection Performance under Fire

Serdar Selamet [1] and Maria E. Garlock [2]

[1] Graduate Student, Department of Civil and Environmental Engineering, Engineering Quad, Room E209A, Princeton University, Princeton, NJ 08544 U.S.A.; Phone: +1-609-258-5437, Fax: +1-609-258-1563; email:sselamet@princeton.edu
[2] Assistant Professor, Department of Civil and Environmental Engineering, Princeton University, Engineering Quad, Room E209A, Princeton University, Princeton, NJ 08544 U.S.A.; Phone: +1-609-258-2728, Fax: +1-609-258-1563; email:mgarlock@princeton.edu

ABSTRACT

The strength and stability of connections in a floor system is an integral part of a building structure. A connection is subjected to large compressive and tensile forces during heating and cooling phase of a fire, respectively. Since shear connections are only designed for gravity loads that produce shear, their behavior in a floor assembly at elevated temperatures needs to be investigated. This paper compares the behavior of three types of shear connections (single plate, single angle and double angle) under fire conditions using the finite element software ABAQUS. The single plate shear connection was validated by a full-scale building fire tested in Cardington. Adopting Eurocode and AISC provisions on the shear connection design, the Cardington connection was redesigned using the single and double angles. While the single plate connections can provide substantial rotational ductility and tensile strength, it could fail during cooling phase of a fire by bolt-hole bearing or bolt shear. The bolted double angle connections are generally more ductile in tension which is advantageous during cooling phase; however they are prone to develop prying forces which could cause the failure of the bolts. In all of the connection models, the beam near the connection experiences local buckling at elevated temperatures.

INTRODUCTION

Structural floor systems undergo significant geometric changes due to thermal expansion of steel during a fire event. Additionally, the strength and stiffness of steel reduce dramatically at elevated temperatures. Hence, connections become an integral part of building construction because they could be subjected to large axial forces, moments and strain reversal during cooling period of a fire [Ramli-Sulong et al 2007]. Current design codes [AISC 2005 and ECCS 2001] are based on isolated member tests subjected to standard fire conditions. Such tests do not reflect the behaviour of a complete building under either normal temperature or fire conditions [Wald F. et al. 2006]. The complex interaction of structural components such as

angles, plates, bolts and supporting members can be accurately captured by conducting large scale experiments or utilizing three-dimensional finite element models. The finite element modeling of the three different types of shear connections (single angle, double angle and single plate) under the same boundary conditions, loading and natural fire scenarios enables us to compare the strength, ductility and failure modes of these connections and their effect on the global behavior of the floor subassembly. This paper uses the finite element software ABAQUS [Simulia 2008]. The single plate shear connection was validated by a full-scale building fire tested in Cardington [Garlock and Selamet 2010; Wald, F. et al 2006]. Adopting AISC provisions on the shear connection design at ambient temperature, the Cardington connection was redesigned using the single and double angles.

Previously, Ramli-Sulong et al. [2007] used the component based method to estimate the axial force and moment capacity of double angle connections. However, the method was limited in capturing the ductility of the connection. Liu et al. [2002] conducted several furnace experiments with axially restrained unprotected beam with a double angle connection. He found that there were clear indications that the bolt holes in the beam web had been elongated as a result of the large bearing forces. The connections, although designed to carry only shear, developed significant moment because of the high rotations and the contact between the lower beam flange and the column. The combination of high connection moment and axial compression force causes lower flange buckling in the beam near the connection. The connection then loses its moment resistance. This paper aims to observe and compare the behavior of the three types of shear connections under a natural fire, which has not been studied previously.

SINGLE PLATE CONNECTION IN A SUBASSEMBLY

Geometry

We previously modeled a subassembly of the Cardington building test using the finite element software ABAQUS. The geometric details are given in Figure 1. The connection between the secondary beam and the girder is a single plate connection, which is designed according to Eurocode provisions [ECCS 2001] at ambient temperature. We modeled only half of the bay and used necessary boundary conditions and loading for symmetry. Further, the thermal and structural effect of the composite slab in the experiment is taken into account by applying a three-sided fire boundary on the beam and by using *Connector elements in ABAQUS, respectively. The use of *Connector elements to represent the additional flexural stiffness provided by the slab is explained thoroughly in Garlock and Selamet [2010].

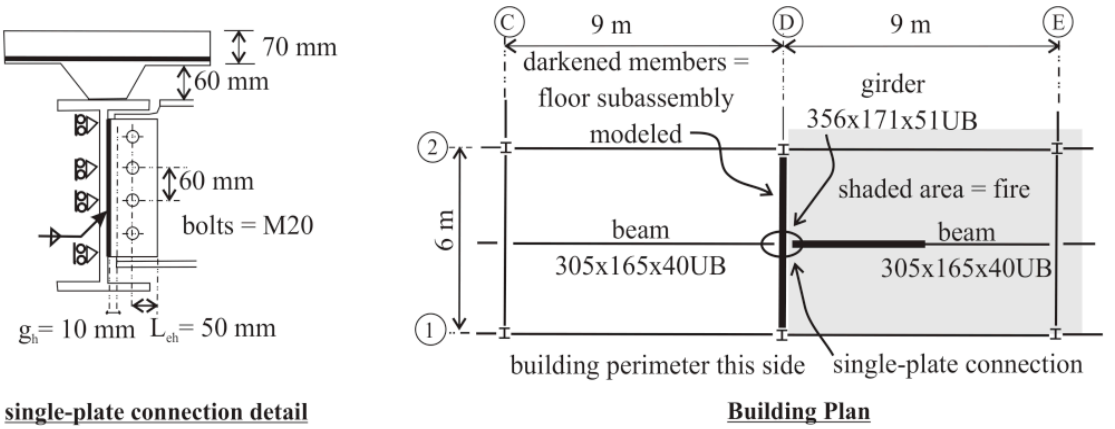


Figure 1: Details of Cardington [Wald, F. et al 2006] (a) single plate connection and (b) the building compartment and the subassembly (illustrated with thick lines).

Fire Scenario

In Cardington, a moderate fire scenario is used with the fire load of 40 kg/m^2 with wooden cribs covering the compartment floor area. In our model, the secondary beam is heated on three-sides with the average (recorded) thermocouple readings at the beam midspan taken from the Cardington test. The range of the beam midspan (structural) temperature and the gas (fire) temperature history is shown in Figure 2. The intensity of fire is slightly reduced near the connection region due to local massitivity.

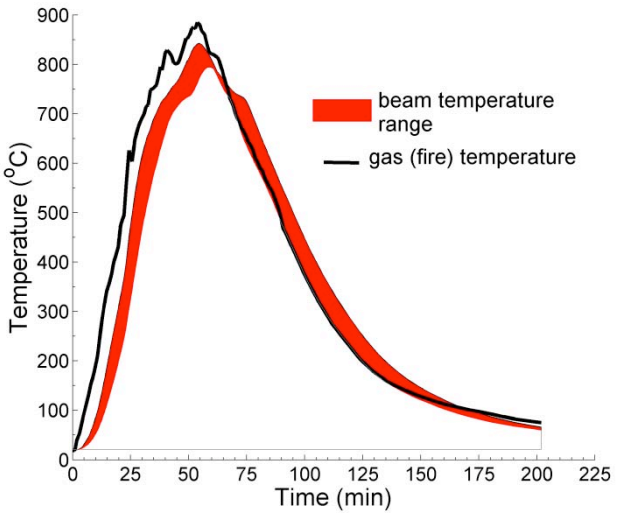


Figure 2: The temperature history of the recorded compartment fire and the range (min-max) of beam (305x165x40UB) temperature in Cardington building test.

Material Properties

In the finite element model, the steel properties of the plate, bolts, beam and girder are taken directly from the measured values at ambient temperature in the Cardington building test. Young's modulus *E* of steel is taken as 207GPa for all components. The strength and stiffness of hot-rolled steel are reduced according to Eurocode

provisions [ECCS 2001]. The elevated temperature properties of quench-tempered bolts are applied using Kirby [1995]. The steel plasticity is modeled using 'von Mises' yield criteria with isotropic strain hardening. No material softening (decreasing branch of the stress-strain curve) is included as this would greatly decrease the convergence character of the problem. Table 1 shows the ambient temperature yield and ultimate (strain hardening) strength of the subassembly components. The single plate, single angle and double angles are modeled using Grade 43 strength. Figure 3 shows the (engineering) stress-strain curve of four components at ambient temperature and 600 °C. These curves are converted to true stress and strain for the finite element analysis.

Table 1: Steel properties at ambient temperature.

Materials	**S275** (beam)	**S355** (girder)	**Grade 43** (plate/angle)	**Grade 8.8** (bolt)
yield strength (MPa)	303	396	275	695
ultimate strength (MPa)	469	544	430	869

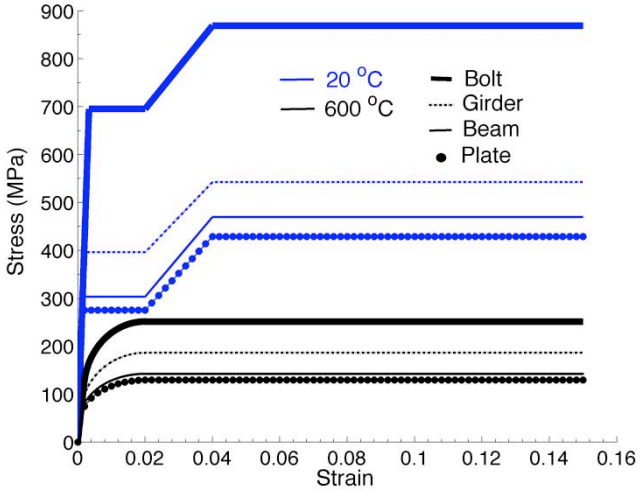


Figure 3: Eurocode steel stress-strain curves with strain hardening for plate/angle, bolts, 305x165x40UB (beam) and 356x171x51UB (girder) at 20 °C and 600 °C.

DESIGN OF SINGLE AND DOUBLE ANGLE CONNECTIONS

The single and double connections are designed for ambient temperature conditions for the Cardington building scenario using AISC provisions [AISC 2005]. The geometric details of the three connections are illustrated in Figure 4. As seen in Table 2, the connections are designed with similar shear and tensile strength according to AISC provisions. All three connections have beam web bolt-bearing as the governing limit state in shear and tension as stated in Equation J3-6a in Steel Construction Manual [AISC 2005]. The single plate and single angle connections have four bolts and are almost identical in geometry. The double angle connection has a smaller angle thickness (6 mm) and has 3 bolts centered in the beam web. Further, the bolt end distance (L_{eh}) is 50 mm in the beam web. Such geometric change is necessary to

keep the ambient temperature shear and tensile strength of the double angle connection similar to the strength of the single plate and single angle models.

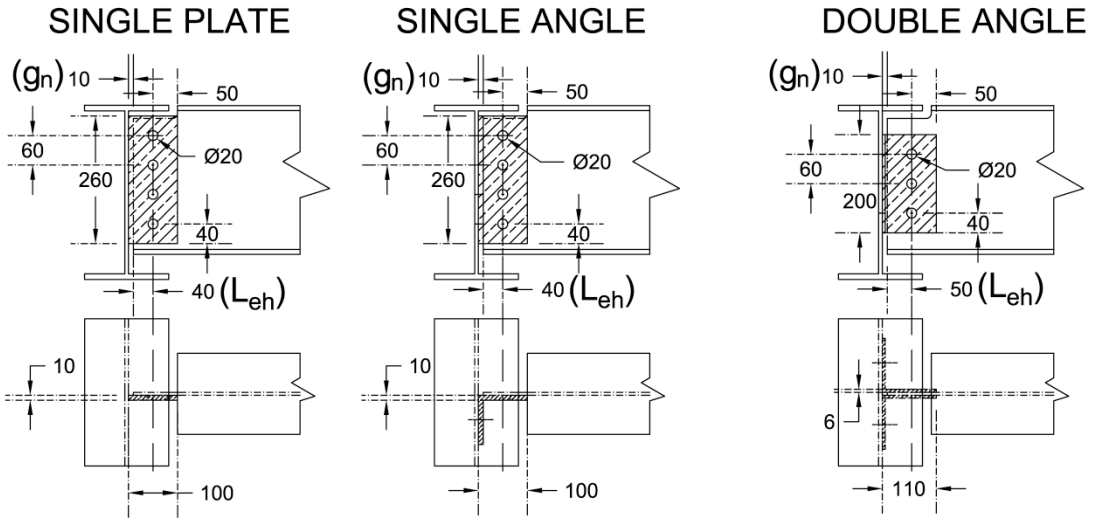


Figure 4: Geometric details of the three shear connection types (dimensions are in millimeters).

Table 2: Shear and tensile strength of single plate, single angle and double angle connections at ambient temperature.

dimensions in mm	**Shear strength (kN)**	**Tensile strength (kN)**
Single Plate (P10-260x100)	349	294
Single Angle (L10-100x100)	349	294
Double Angle (2L6-110x110)	294	296

Neither of the angle models are designed considering the prying action because the expected tensile force in the beam is not known apriori. Figure 5 shows the prying action of an angle. Here, *T* is the maximum expected tensile force in the angle (per bolt), *Q* is the prying force (per bolt) and *B* is the allowed tensile force in the bolt. The geometric parameters are *a'*, *b'* and *p* (tributary length per bolt).

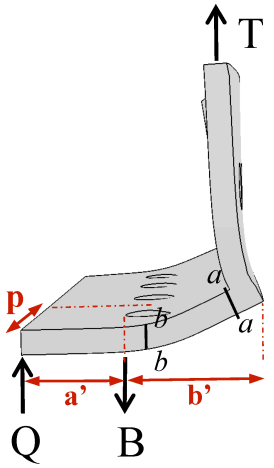


Figure 5: Prying action and illustration of forces *T*, *Q* and *B* in an angle.

The general formula for the minimum angle thickness t_{min} to avoid failure due to prying action is stated by Thornton [1985] in Equation 1.

$$t_{\min} = \sqrt{\frac{8Tb'}{pF_y(1+\delta\alpha)}} \qquad \text{Eq. 1}$$

Here, F_y is the yield strength of the angle and δ is the ratio of the net area at section *b-b* and the gross area at section *a-a* (both shown in Figure 5). The coefficient α is the ratio between the moment per unit width at section *b-b* and the moment per unit width at section *a-a*. For the single angle model; if we assume that T is equal to 400kN (:= 100kN per bolt) and B is the ultimate tensile capacity of Grade 8.8 bolts, the equation suggests that t_{min} should be about 25 mm (~1 inch) with $\alpha = 1$ and $\delta = 1$. Similarly, t_{min} = 28 mm (~1.1 inch) for the double angle model. Hence, both the single angle (t = 10 mm) and the double angle thickness (t = 6 mm) used in the model suggest that the prying action will likely occur due to large tensile forces in the beam during fire.

THE FINITE ELEMENT MODEL

Meshing

Several convergence studies for the three-dimensional finite element connection models were implemented previously by the authors [Selamet and Garlock 2010]. For the bolts and the bolt-hole regions, 20 elements are found to be sufficient to accurately represent the shear and tension capacity of the region. Further, minimum of 3 elements through the angle/plate thickness is necessary to capture the bending behavior of the angles or the plate. Generally, finer meshes are utilized around the connection region, where large concentration of forces and instabilities such as the local buckling are expected. Fully integrated (C3D8) and incompatible (C3D8I) hexagonal elements are used near connection region and at contact areas, whereas reduced integrated (C3D8R) elements are used for the rest of the subassembly.

Imperfection Study

Due to the eccentricity of single plate and single angle connections, no imperfection is introduced prior to static analysis since deformations will inherently develop as the beam starts to expand at elevated temperatures due to the unsymmetrical nature of the connection. For double angle connections, however, imperfections need to be introduced, because of the perfect symmetry at the beginning of the analysis. The imperfection geometry is found using the eigenvalue extraction method by ABAQUS. The eigenmode of the subassembly is scaled to 1% and introduced to the general static analysis.

Analysis

An uncoupled thermo-mechanical analysis is performed since the heat transfer is independent of the structural response of the subassembly. The creep property of steel is not considered; hence an uncoupled thermal and structural analysis is computationally efficient. For gravity and fire loading, a purely static analysis is

performed, where several stabilization techniques are utilized in order to establish convergence especially at the onset of the beam web and lower flange buckling at the connection.

OBSERVATIONS AND RESULTS

Out of the three subassemblies, only the single plate model failed by bolt bearing in the beam web at 123 minutes into the fire as seen in Figure 6. Both the single angle model and the double angle model (see Figure 7 and Figure 8) survived the entire fire duration without significant deformation in the beam but with excessive bending and significant plastic deformation in the angle due to the large tension in the beam. Additional details of observations are listed in Table 3.

Table 3: Response details of finite element models

PARAMETERS	SINGLE PLATE	SINGLE ANGLE	DOUBLE ANGLE
time @ analysis end (min)	123	202	202
temperature @ analysis end (°C)*	231	62	62
$P_{c,max}$ (compression-kN)**	745	750	750
$P_{t,\,max}$ (tension-kN)**	395	305	280
connection limit state	beam web bolt bearing	excessive angle bending, but no failure	excessive angle bending, but no failure
web buckling (time)	yes (@12 min)	yes (@ 11.5 min)	no
lower flange buckling (time)	yes (@ 20 min)	yes (@ 20 min)	yes but minimal (@ 20 min)
girder contact (time)	yes (@ 14 min)	yes (@ 14 min)	yes (@ 15 min)
other observations	n/a	girder top flange buckling near connection	girder top flange buckling near connection

* average beam midspan temperature
** at beam midspan

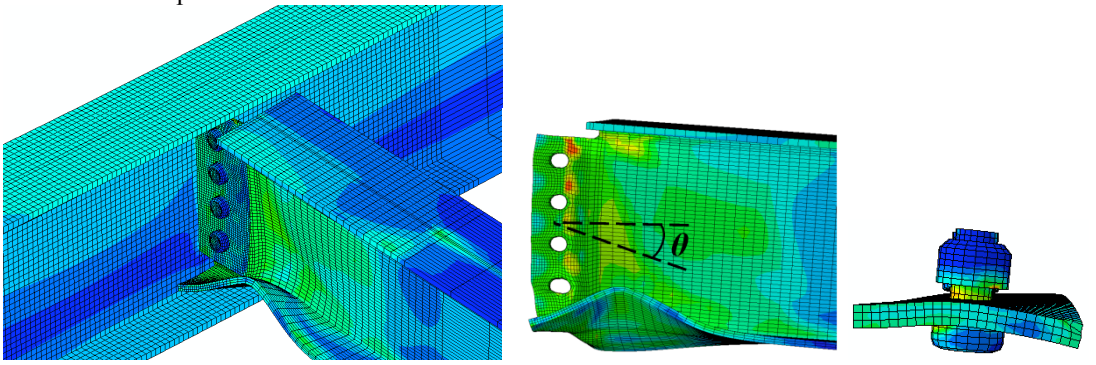


Figure 6: Mises contours and deformations of single plate connection subassembly at the end of analysis (123 minutes). θ represents the connection rotation angle.

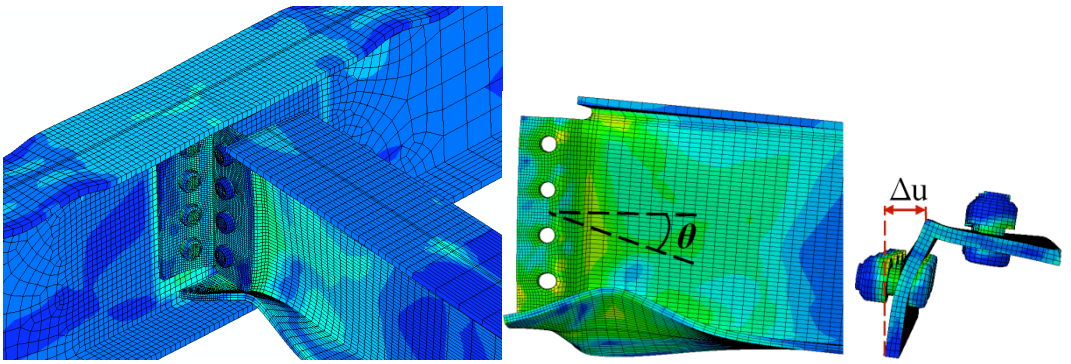


Figure 7: Mises contours and deformations of single angle connection subassembly at the end of analysis (202 minutes). Δu represents the horizontal uplift of the angle heel. θ represents the connection rotation angle.

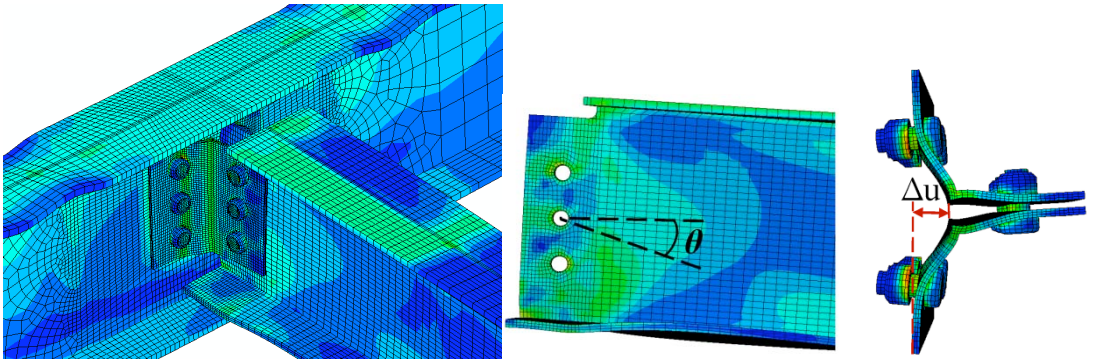
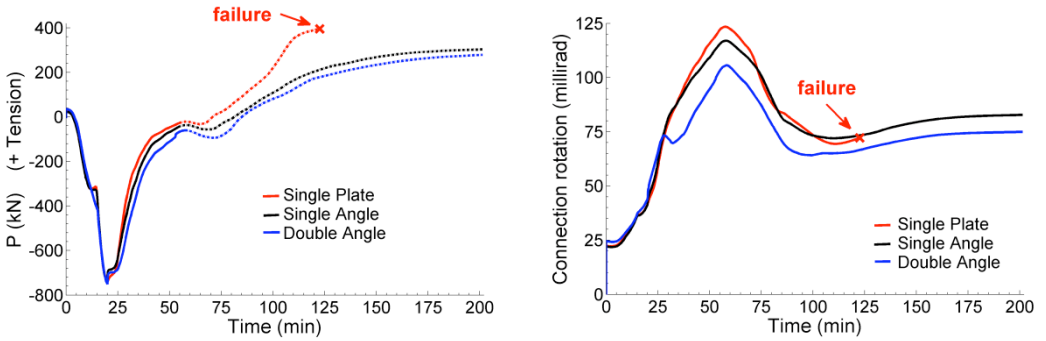


Figure 8: Mises contours and deformations of double angle connection subassembly at the end of analysis (202 minutes). Δu represents the horizontal uplift of the angle heel. θ represents the connection rotation angle.

The axial force time history in Figure 9 illustrates the differences in structural fire behavior between the angles and the plate as a shear connection. In previous papers [Selamet and Garlock 2010], we have shown that the maximum compression in the beam during heating phase of a fire was governed by the buckling capacity of the beam web and lower flange near the shear connections. The single and double angle shear connections also exhibit this behavior. All of the three subassemblies have the same axial capacity in compression which is governed by the beam lower flange buckling. The single plate and single angle connections do not provide enough lateral resistance to the beam web; hence the web buckling occurs in early stages of fire. The double angles provide significant resistance to the beam web, and we observe no web buckling in this model. The extent of lower flange buckling is similar for single plate and single angle models, but it is much less severe for the double angle because it is not preceded by the web buckling.

As seen in Figure 9, the tensile strength capacity of both the single angle and double angles is lower than that of the single plate connection. Although the maximum tensile strength of angle connections is lower, the angles exhibit ductile behavior and survive the fire. As the beam contracts during the cooling phase, the tensile resistance

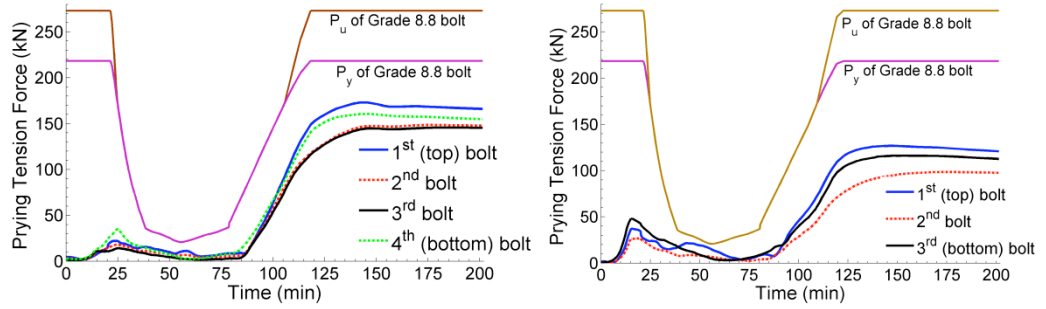
of the single plate itself (ignoring the other connection parts) is governed by the gross yielding of the plate, whereas the tensile resistance of the angles itself is governed by the bending capacity of the angle leg. The additional deformation provided by the angle leg significantly decreases the beam tensile force because it adds flexibility to the connection. Hence, the subassembly with the single angle connection survives the fire and the beam does not fail by the bolt-bearing limit state. On the other hand, the double angle connection has thinner angles (6 mm) and thus a smaller bending resistance. This model survives the fire, but experiences significant plastic deformation (see Figure 8) whereas the beam bolt region does not deform.



(a) (b)

Figure 9: (a) Axial force time history in the beam (dashed lines represent the cooling of fire) and (b) connection rotation θ (clockwise is positive, see Figures 6, 7 and 8).

All three shear connections exhibit similar moment time history (although not shown). This indicates that the moment at a shear connection is dependent mostly on the slab (composite deck) behavior and the gap distance (g_n) between the beam and girder, and it does not necessarily depend on the type of the shear connection. Since the gap distance (see Figure 5) and the *Connector resistance representing the slab structural behavior are kept the same for all models, the beam moment time history as well as the connection rotation (shown in Figure 9b) are similar for all three shear connection designs.



(a) (b)

Figure 10: Bolt tension (due to prying action) for (a) the single angle and (b) the double angle connections (due to symmetry, only 3 bolts on one angle are shown). P_u and P_y represent the ultimate and yield bolt strength, respectively.

Figure 10 plots the tension in the bolts (*B* in Figure 5), which includes the prying action for (a) the single angle and (b) double angle connections. Figure 10a shows that the bolts in the single angle exhibit significant tensile forces; however they do not reach their yield or ultimate tensile strength. The three bolts in the double angle model (Figure 10b) exhibit smaller tensile forces as expected because the tension in the beam is split evenly into two angles.

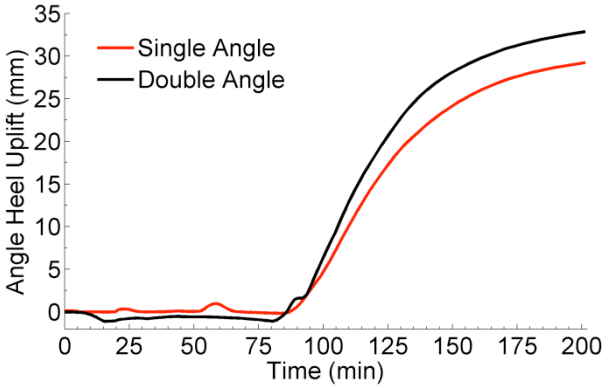


Figure 11: Angle heel uplift or relative displacement Δu (see Figure 7 and 8) for the single and double angle connections.

Figure 11 shows the uplift of the angle heel (at the top) for both models. The double angle connection experiences a larger uplift (Δu) because of its thinner angles. Since both angle models have a large Δu (~30-35 mm), we can assume that such deformation absorbs some of the beam contraction during cooling phase of the fire. Such flexibility in the connection prevents the beam web from failing by bolt-bearing limit state.

CONCLUSION

In this paper, we designed and modeled single and double angle connections using the same boundary, loading and fire scenario of the single plate connection subassembly which is adopted from the Cardington building test. The finite element models are able to capture the large deformation and the change of contact conditions accurately for the duration of fire. Our observations suggest that the angle connections have a more ductile fire response compared to the single plate although their maximum tensile strength is lower. Both the single and double angle connections survive the natural fire with significant plastic deformation in the angle legs whereas the single plate connection fails by bolt bearing in the beam web. Using different type of shear connections did not change the overall response of the subassembly during heating, but had significant influence on the overall response during cooling. We can confirm this by looking at the beam axial force diagram where the onset of the lower flange buckling and the maximum beam compression for all three connection models are almost identical. Further, the models exhibit similar connection rotation and beam midspan deflection behavior. During cooling, the shear connections have different responses in terms of failure limit state, deflection and maximum tensile strength.

During the heating phase of fire, all connections experience local buckling in the beam lower flange when the gap distance (g_n) closes and the girder-beam contact is established. The lower flange buckling also marks the maximum compression in the beam. The beam web buckling occurs in the coped beam only for connections with plates/angles on one side of the beam web (single plate and single angle).

As the beam contracts during the cooling phase of fire, the bending of the angle legs due to large tensile force in the beam creates the phenomenon called 'prying action'. The use of high strength bolts eliminates the possibility of a bolt failure in tension; however the bolt tensile forces get close to the bolt yielding capacity. The angle connections provide additional flexibility that the single plate connections do not have. The use of thin angles for the double angle connection creates significant plastic deformation in the angle, and it is recommended to use caution when selecting the angle thickness. In conclusion, we see a significant benefit using the angle connections for a more robust fire connection design.

REFERENCES

AISC (2005). *Steel Construction Manual, 13th Edition*, Chicago, IL.

European Committee for Standardization - ECCS (2001). *Eurocode 3: Design of steel structures Part 1.2: General Rules Structural fire design ENV 1993-1-2:2001,* Brussels, Belgium.

Garlock, M. and Selamet S. (2010). "Modeling and Behavior of Steel Plate Connections Subject to Various Fire Scenarios", *Journal of Structural Engineering*, 136 (7), 897-906.

Kirby, B.R. (1995). "The Behaviour of High-Strength Grade 8.8 Bolts in Fire", *Journal of Constructional Steel Research*, 33 (1-2), 3-38.

Liu, T.C.H., Fahad, M.K., Davies, J.M. (2002). "Experimental Investigation of Behaviour of Axially Restrained Steel Beams in Fire", *Journal of Constructional Steel Research*, 58 (9), 1211-1230.

Ramli-Sulong, N.H., Elghazouli, A.Y., Izzuddin, B.A. (2007). "Behaviour and Design of Beam-to-Column Connections under Fire Conditions", *Fire Safety Journal*, 42 (6-7), 437-451.

Selamet, S., and Garlock, M. (2010). "Robust Fire Design of Single Plate Shear Connections", *Engineering Structures*, 32 (8), 2367-2378.

Simulia (2008). *Abaqus Documentation version 6.8*, Providence, RI.

Thornton, William A. (1985). "Prying Action – a General Treatment", *Engineering Journal*, ASCE, Second Quarter, 67-75.

Wald, F., Simoes da Silva, L., Moore, D.B., Lennon, T., Chladna, M., Santiago, A., Benes, M., Borges, L. (2006). "Experimental Behaviour of a Steel Structure under Natural Fire", *Fire Safety Journal*, 41 (7), 506-522.

Effects of Thermal Expansion and Support Restraints on Performance of Composite Floors in Fire

H. Mostafaei[1], F. Alfawakhiri[2]

[1]Research Officer, National Research Council Canada, M-59, 1200 Montreal Rd, Ottawa, ON K1A 0R6; Hossein.Mostafaei@nrc-cnrc.gc.ca
[2]Senior Engineer, American Iron and Steel Institute, 594 Windham Lane, Naperville, IL 60563; falfawakhiri@steel.org

ABSTRACT

This paper presents results of a numerical study on the effects of thermal expansion and support restraint conditions on the performance of composite floors in fire. Previously, two full-scale composite floor specimens were tested to investigate factors, such as the supports restraint conditions, that affected the failure of the World Trade Center buildings' floors. Although higher fire resistance was expected for the restrained floors, the test results showed higher fire resistance rating for the unrestrained floor specimen. The purpose of this research was to understand the rationale behind these results numerically. The structural analysis software SAFIR was employed to evaluate the response of the composite floor specimens in fire, such as strain and stress distributions and floor deflection. The results show that the concrete spalling during the first hour of the test for the restrained specimen would have been due to concrete compression failure caused by the restraint condition and thermal expansion.

INTRODUCTION

Since the 9/11 disaster, various studies have been carried out to investigate the performance and collapse simulation of the World Trade Center (WTC) buildings subjected to the impact of the aircrafts and the following fire. Significant efforts have been extended to investigate performance of the WTC's building structures in the fire (NIST, 2005). Although damage from the impacts could have had considerable effects on the structural response of the two towers, the WTC's towers had not collapsed in fire shortly after the impacts. In fact, the WTC's north tower burned for 102 minutes, after it was hit by the aircraft, before it collapsed. As for the WTC south tower, the collapse of the structure occurred after burning for 56 minutes in fire. Therefore, fire was considered as a major factor in the collapse of the two towers.

One of the experimental studies was carried out by the National Institute of Standards and Technology (NIST) on the fire resistance and performance of the WTC's towers composite floors (Gross et al., 2005). A main objective of this experimental study was to explore "why and how WTC towers collapsed following the initial impacts of the aircraft and to determine factors that most influenced the buildings' composite floors failure". Two full-scale composite floors were tested by NIST at the Underwriters Laboratories of Canada fire testing facility in Toronto (ULC). In order to investigate the support restraining effects on fire performance of the floors, one specimen was tested with restrained supports and the other - with unrestrained supports conditions. Although higher fire resistance was expected for the restrained floors, the test results showed higher

fire resistance for the unrestrained full-scale floor specimen compared to the restrained floor. Observations during the two tests indicated more damage and spalling of concrete for the restrained floor specimen compared to the unrestrained specimen.

This paper provides results of a numerical study for the two floor test assemblies. The main objective is to investigate and understand the failure mechanism of these two full-scale specimens, which simulate the WTC's towers composite floors. The analysis was done using the SAFIR structural analysis package (Franssen, 2007). Furthermore, a post-processor was developed to generate stress and strain profiles on the cross-sections of the floors' elements.

FLOOR SYSTEM OF THE WTC TOWERS

The World Trade Center towers had a steel/concrete composite floor system. It consisted of a concrete slab and steel trusses supported at the two truss ends between the building's core columns and exterior wall columns. The steel trusses were installed in pairs with 2.0 m spacing, on center, with a nominal clear span of either 18.3m or 10.7m. Both top and bottom chords were made of double steel angles. Double round bars were used as the diagonal members of the trusses. The diagonal bars were extended beyond the top chord, in form of a "knuckle", to play the role of the shear connectors for the composite floor. In addition, bridging trusses were used, perpendicular to main trusses, in the floor system, to transfer the applied loads to the main trusses, spaced 4.0 m on center (Gross et al., 2005).

The Cafco Type D was used as the Spray-Applied Fire-Resistive Materials (SFRM) for fire protection of the WTC's floor truss steel elements. The two full-scale floors test assemblies, selected for the purpose of numerical studies in this paper, have been designed to simulate the performance of the WTC's towers composite floors in fire. Results of the numerical studies are provided in the following sections.

FLOOR TEST ASSEMBLIES

Two floor specimens were tested by the NIST at the ULC Toronto based on the ASTM E119 standard, one with restrained and one with unrestrained supports. The floor specimen configuration and dimensions are provided in Figure 1. The floor main truss, for specimen No. 1 with restrained support, the main truss for specimen No. 2 with unrestrained support and the details of the bridging truss are plotted in Figure 2.

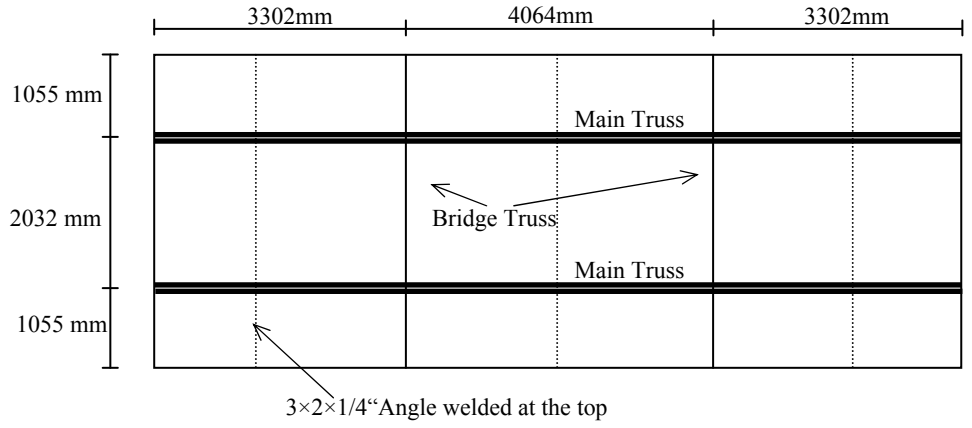
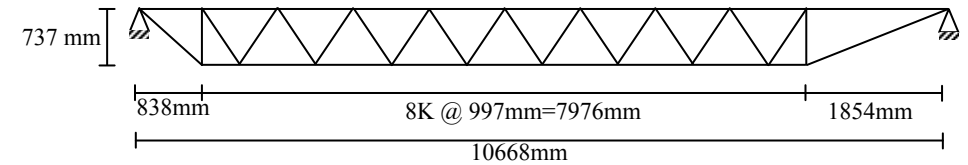
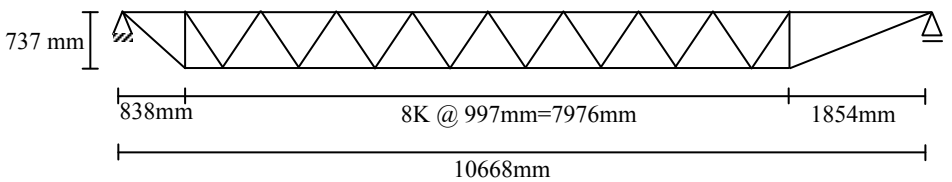


Figure 1. Configuration of the full-scale floor specimens.

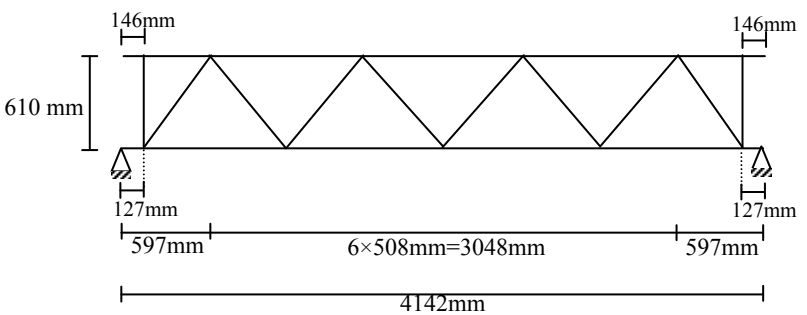
Figure 3 identifies types of the steel sections for the top and bottom chords and the diagonal members of the truss specimens. A cross-section for the truss system, including the entire steel truss section and the concrete slab, is provided in Figure 4. Top and bottom chords and diagonal elements of the main and bridging trusses were coated by 19.05 mm thickness of the available SFRM (BLAZE-SHIELD DC/F by Isolatek International). Further details of the specimens can be found in the test report by Gross et al. (2005).



a) Main truss specimen No. 1 with restrained supports.



b) Main truss specimen No. 2 with unrestrained supports.



c) Bridging truss.

Figure 2. Structural dimensions for a) main truss of specimen No. 1 and b) main truss for specimen No. 2 and c) bridging Truss.

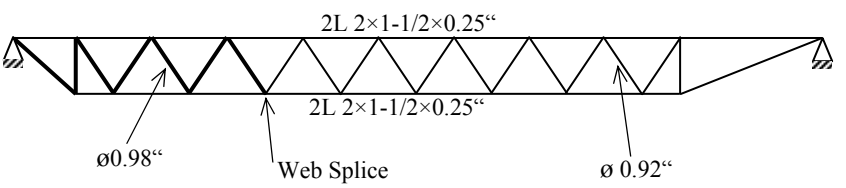


Figure 3. Sections of steel elements for the main truss.

NUMERICAL MODELING

Geometry and configuration

The floor specimens were modeled using the SAFIR software (Franssen, 2007), which is a program for analysis of structures for both structural and fire loads. Based on the support details shown in Figure 2-c, the bridging trusses have less stiffness than the main truss and would not be capable of transferring high shear force to the supports.

Therefore, it was assumed that the main structural elements transferring the applied load to the test frame would be the main trusses. The concrete slab was assumed acting as a one-way slab in the direction of the main trusses, and compositely with the main trusses. These assumptions simplified the analysis to model only the main trusses with the concrete slab, and to ignore the bridging trusses. In addition, due to the symmetrical geometry only half of the floor specimen was modeled.

Figure 5 shows the model of the main truss for specimen No. 2, with unrestrained supports and the applied load. The geometry and the element sections for restrained specimen No.1 are similar to that of specimen No. 2. Except that for specimen No. 1 the truss's right end support is restrained for horizontal displacement.

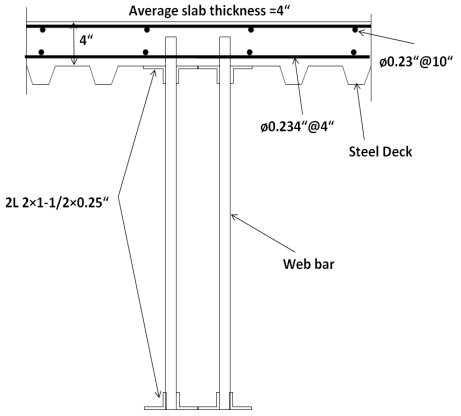


Figure 4. Cross-section of the floor system at the main truss location.

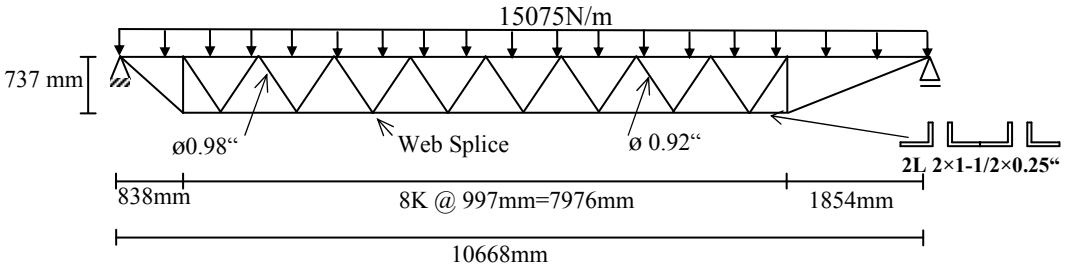


Figure 5. The main truss model for analysis of unstrained specimen No. 2.

Material mechanical properties

Bottom chord angles of the truss were made of 2 L2×1-1/2×0.25", as shown in Figure 4, with A572 steel and yield strength of f_y= 425.5 MPa. Round bars with two different diameters, 0.92" and 0.98" were used as the diagonal elements for the truss. Figure 5 shows the web splice where the diagonal round bars changed from 0.98" to 0.92" section through the truss. The yield strength for bar 0.92" is f_y= 402 MPa and for bar 0.98" is f_y= 372 MPa. The concrete slab reinforcement of the floor consists of two layers of welded wire fabric 254mm × 102mm (10 in. by 4 in.), as shown in Figure 4. W4.2 wires with a diameter of 5.8mm (0.23"), a yield strength of 492 MPa and spacing of 254mm were placed in the longitudinal direction. W4.3 wires with a diameter of 5.9mm (0.234"), a yield strength of 498 MPa and spacing of 102 mm were located in the transverse direction. For the purpose of this study only longitudinal bars were included in the analysis, based on the assumption that the floor would act as a one-way slab structure. The above steel material properties were derived from the individual material property

tests reported by Gross et al. (2005), and applied to both specimens No. 1 and No. 2. The concrete slabs of the specimens were made of lightweight concrete. Mechanical properties of the concrete are provided in Table 1 for both specimens. The concrete compression strengths were taken from the test reports and the tensile strength of concrete were estimated according to equation (1) proposed by Vecchio in Wong and Vecchio (2002).

$$f_t' = 0.33\sqrt{f_c'} \quad (1)$$

where, f_t' is the tensile strength in MPa and f_c' is the concrete compression strength at 56 days in MPa.

Table 1. Mechanical properties of the floor lightweight concrete of specimens.

Specimen	Compressive Strength at 28 Days (MPa)	Compressive Strength at 56 Days (MPa)	Tensile Strength* (MPa)
No.1	28.8	32.6	1.9
No.2	20.2	26.8	1.7

* estimated according to equation (1).

Applied loads

The total uniform load for each floor specimen consists of two load cases: the uniform self weight construction load of 2298 N/m^2 (48 psf) and an additional superimposed load of 4981 N/m^2 (104 psf). Hence, the total applied uniform load on the floor is 7279 N/m^2 (152psf). Since only one truss is modeled, due to the floors symmetrical geometry and loading, the linear uniform load on each truss is determined with multiplying the total uniform load by half of the floors' width; uniform load (per unit length) = 7279N/m^2 × 4.142 m / 2 =15075N/m, as shown in Figure 5.

Material thermal properties

In both floor specimens, the BLAZE-SHIELD DC/F was used as the SFRM in multiple coats with an average thickness of 0.75", to protect elements of the main and bridging trusses. The test report indicated that no attempt was made to control overspray of material onto the deck of the test assemblies. Thermal properties of the SFRM were obtained at different temperatures based on the test repot by Carino et al. (2005). Thermal conductivity of the SFRM changes from 0.046 W/(m.K) at 25 ^{o}C to 0.53 W/(m.K) at 1200 ^{o}C. Specific heat for the SFRM starts with 826 J/(kg.K) at 25 ^{o}C and increases up to 1392 J/(kg.K) at 1200 ^{o}C. The density of the SFRM was considered variable for the analysis from 236 (kg/m^3) at 25 ^{o}C to 432 (kg/m^3) at 1200 ^{o}C, Carino et al. (2005).

For all steel elements of the truss, STEELEC3 material model of the SAFIR was used for both thermal and material properties. As for concrete, thermal properties were derived from the study results reported by Prasad and Baum (2005). Appendix A of the report provides these properties at different temperatures for the lightweight concrete. For concrete thermal conductivity the value is varied from 1.5 W/(m.K) at 25 ^{o}C to 1.00 W/(m.K) at 1200 ^{o}C and for specific heats it is from 880 J/(kg.K) at 25 ^{o}C to 1500 J/(kg.K) at 1200 ^{o}C. The lightweight concrete of the two specimens was designed for a density of 1600 kg/m^3 (100 pcf) at ambient temperature, which is different from that of the concrete reported by Prasad and Baum (2005). Therefore, for this analysis, the

concrete density was reduced from 1600 kg/m^3 at 20 ^{o}C to 1300 kg/m^3 for 1200 ^{o}C. The reduction function was selected as those of the lightweight concrete used by Prasad and Baum (2005). Moisture content of concrete was obtained as 51 kg/m^3, based on the reported 70% relative humidity, 0.23 chemically bound water, 237 kg (522lb) cement, and concrete water mix of 127 kg (281 lb).

Heat transfer analysis

Due to the round shape cross section, finite element (FE) meshes with triangle elements were generated to model cross sections of the diagonal elements of the truss assemblies. Figure 6 shows the FE mesh for these elements. Elements with a darker color represent the steel bars and elements with a lighter color form the SFRM materials. Using SAFIR, the heat transfer analysis was carried out for the web elements while they were exposed to standard fire, ASTM E 119. The results for the temperature distributions on the cross sections at the time = 3600 seconds are plotted in Figure 7. Figure 8 shows the comparison between analysis and test results for the temperature at the surface of the web elements at different time steps.



Figure 6. FE mesh for the double bar web elements, each with diameter of 0.98".

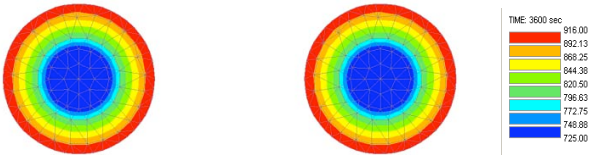


Figure 7. Temperature distribution on sections of the web elements at time = 3600 sec.

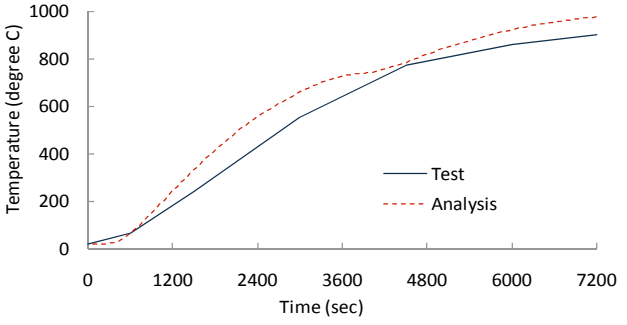


Figure 8. Temperatures on the surface of the bar, web elements, for specimen No. 1.

In this figure, although the test results show a little lower temperature profile than that of the analysis, they are in close correlation. For the structural analysis, the temperature results of the test were employed.

FE meshes with rectangular elements were assigned to both concrete and steel angles of the truss's top and bottom chords of the assemblies. Based on the total cross-section area of the longitudinal steel reinforcement wires, two fiber elements on the top and two on the bottom of the slab cross-section were assigned as the slab steel reinforcement, with each fiber away from the slab top and bottom edges in accordance with the cover concrete thicknesses. Since BEAM element, a fiber model, of the SAFIR package was used for modeling the cross sections, this lumping of reinforcement wires

into a limited number of fibers would have no effect on the results. Figure 9 shows the mesh generated for the top chord of the truss, concrete slab and steel angels. The steel deck was modeled for heat transfer analysis; however it was not included in the structural analysis as there would be no shear interaction between the deck and the concrete. The test observations for both assemblies indicated separation of the steel deck at the very early stage of the tests.

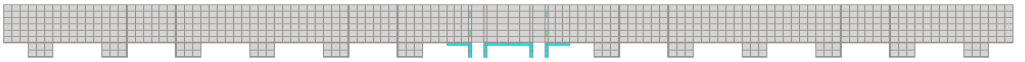


Figure 9. FE mesh for the top chord steel elements and the concrete slab.

In the initial thermal analysis, SFRM overspray was ignored, so the lower face of the floor was exposed directly to the assigned furnace temperature profile. First, the metal deck and the protected steel truss top chord angles were exposed to the furnace temperatures measured in test and the analysis was carried out. In order to impose the exact test temperatures to the angles and the metal deck, large values were assigned to the convection coefficient on hot surfaces, convection coefficient on cold surfaces and relative emissivity of the steel deck in the SAFIR input file. This would accelerate the heat transfer through the slab frontiers by convection and radiation.

In this initial analysis, the analytical results showed considerably higher temperatures, at the unexposed side of the slab, compared to that of the test data. This could be due to the separation of the metal deck from concrete, reported during the test. The gap between the concrete slab and the steel deck, which was not modeled in the initial analysis, could act as an additional insulation layer delaying the heat transfer to/through the slab. Therefore, the second analytical approach was to expose the slab directly to the measured concrete temperature profiles. However, no measurement was reported from the tests for temperatures on the bottom surface of the concrete. Therefore, an attempt was made to determine such temperatures for the bottom surface of the concrete slab. Figure 10 illustrates the developed temperature histories for both specimens. The concrete slabs were then exposed to the developed temperature histories for the heat transfer analysis.

The top chord steel angles of the specimens were subjected directly to the test temperatures, since the measurements were available. Figure 11 verifies that the temperatures on the top chord angles, measured during the test, are in exact agreement with those of the top chord mesh, determined from the analysis. The same verifications were obtained for the web elements and the bottom chords.

Figure 12 illustrates the results for temperatures at the unexposed surface of the floor assemblies. It indicates a consistent correlation between the test and the analytical results. The calculated temperature distribution in the concrete slab and top chord angles of the truss assembly No. 1 are illustrated in Figure 13.

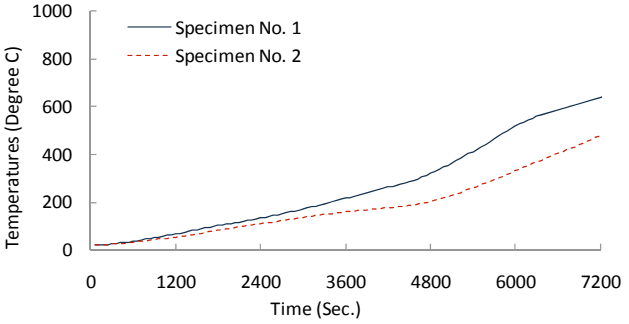
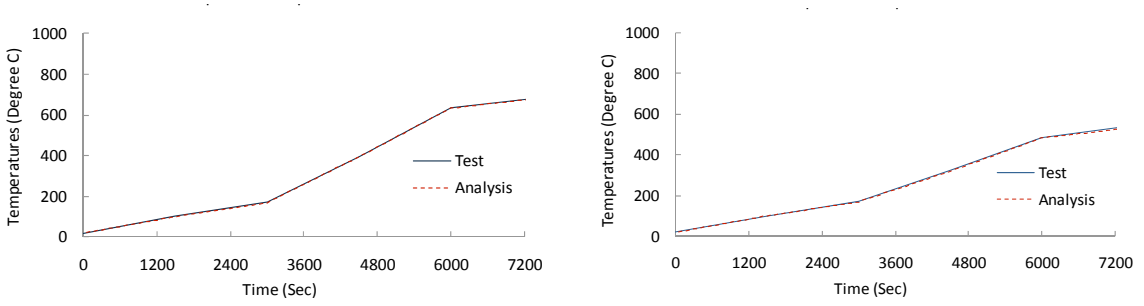
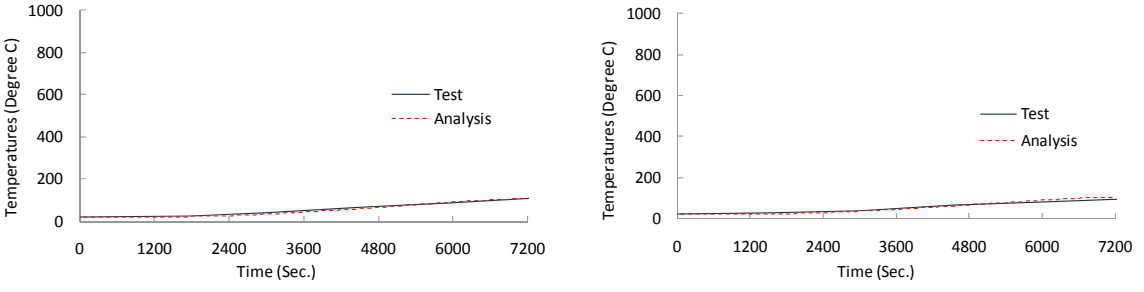


Figure 10. Developed temperature histories for bottom surface of concrete.



Specimen No. 1 Specimen No. 2

Figure 11. Temperatures on the top chord angles.



Specimen No. 1 Specimen No. 2

Figure 12. Temperature results measured and determined on the unexposed surface of concrete.

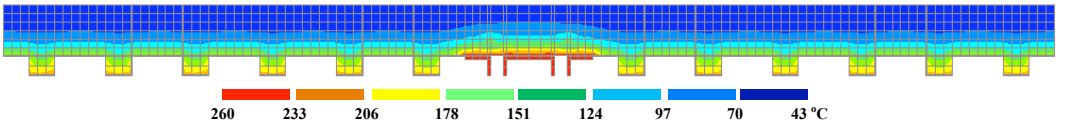


Figure 13. Temperature distribution on the top chord cross-section of the floor assembly No.1 at time = 3600 sec.

Structural analysis

Structural analysis of the two truss assemblies were carried out using the same software package, SAFIR, by employing the defined material properties for each section and the calculated temperature distributions from the heat transfer analysis. In the

structural analysis, the metal deck of the floor was not simulated since, as mentioned earlier, there was no shear interaction between the slab and the steel deck. The temperature distributions and material properties of the structural elements had minor differences in the two specimens. Hence, practically, the main difference between the two specimens was the restrained conditions of the truss end supports; that is being restrained for assembly No. 1 and unrestrained for assembly No. 2. Figure 14 shows the truss deflection, for specimen No. 1, generated by the SAFIR post-processor software, before and after fire exposure. Figures 15 and 16 compare analytical and experimental results for deflections in specimen No. 1 and No. 2, and indicate a consistent agreement between the analysis and the test results.

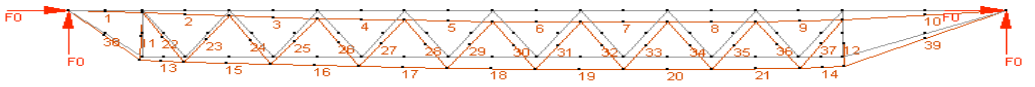


Figure 14. Truss specimen No. 1 with restrained ends before and after fire exposure.

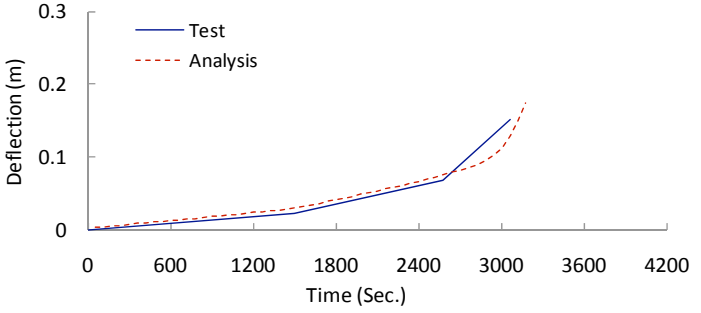


Figure 15. Deflections histories for specimen No. 1: analysis and experimental results.

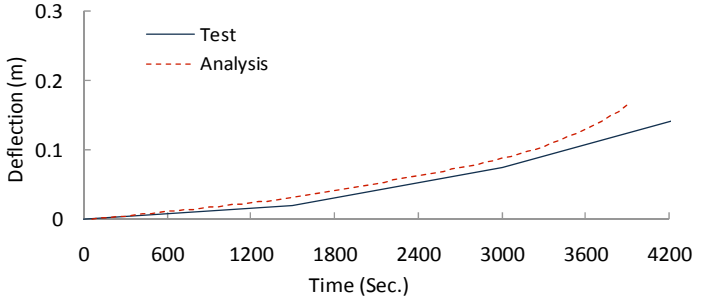


Figure 16. Deflections histories for specimen No. 2: analysis and experimental results.

The floor assemblies were able to last significantly longer in the tests, compared to the analytical results shown in Figures 15 and 16. That was because the SAFIR software would fail to converge when the structure suffered certain level of damage; which was compression failure of the top fibers/layers of the slab for this analysis. However, during the tests, the floors can sustain higher levels of damage and deformation. Observations from the test indicate significant spalling of the concrete in specimen No. 1, at both ends of the floor. This spalling occurred at about the same time as the convergence failure obtained from the analysis, preceded by sharp acceleration of deformations, as shown in Figure 15.

Figure 17 shows the total axial load in element #10 of the truss in Figure 14, for both the restrained specimen No. 1, and the unrestrained specimen No. 2. These analytical results indicate a difference of about 15 times between the restrained and unrestrained specimen axial loads, which show the considerable effects of supports restraint conditions on the structural response. The results convey the fact that the significant spalling observed during the test for specimen No. 1 would be the result of compression failure of the top fibers/layers of the concrete slab.

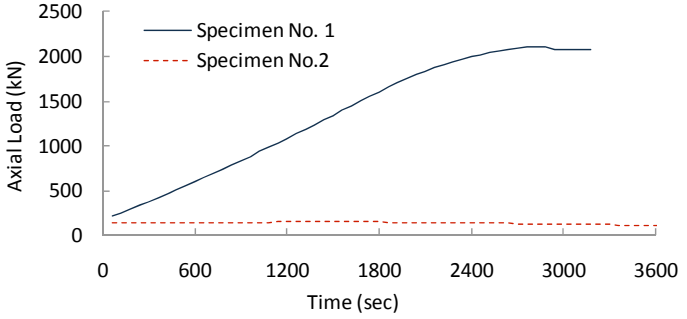


Figure 17. Axial load in element 10 of both restrained, specimen No. 1, and unrestrained specimen No. 2, assemblies (see Figure 14 for elements number).

In addition to the deformation and load response, strain and stress results for the concrete were investigated. Figure 18 and Figure 19 provide stress and strain distributions on the cross section of the concrete slab for element #10 of the restrained truss, specimen No. 1, at the time of failure. Figure 19 provides mechanical strains on the section, which is determined by SAFIR by subtraction of the thermal expansion strain from the total strain. Both results indicate that at this time step, the extreme top fibers of the concrete, cover concrete, fail in compression when concrete compression stress reaches 32 MPa or concrete compression strain achieved 0.002.

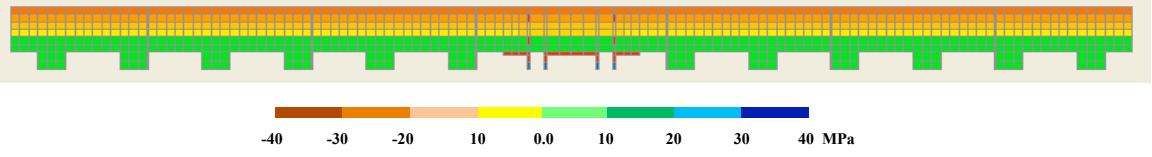


Figure 18. Stress distribution on the top chord of specimen No. 1 for element #10 of the truss at the time of concrete failure.

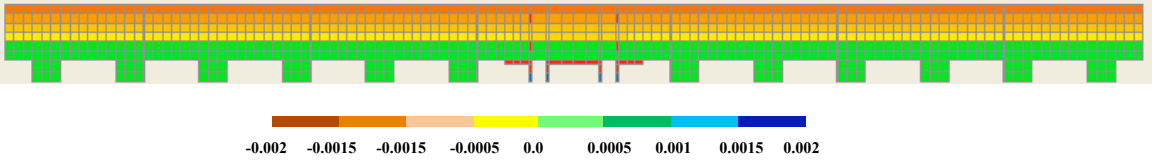


Figure 19. Mechanical strain distribution on the top chord of specimen No. 1 for element #10 of the truss at the time of concrete failure.

To study the stress and strain development, stress and strain distributions of the concrete slab were obtained for the vertical center line section of the slab at different time steps. Figures 20 through 23 illustrate the stresses and curvatures for both specimens. The analytical results clearly indicate that the stress and strain are considerably higher in the case of restrained specimen compared to that of the unrestrained assembly. It can also

be pointed out that the section experienced significantly larger curvature at the time of failure compared to that of the ambient temperature, which could be the result of large thermal expansion of the truss.

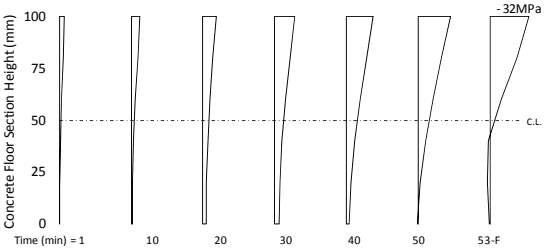


Figure 20. Stress profile at the vertical center line of the concrete slab section for specimen No. 1 at different time steps.

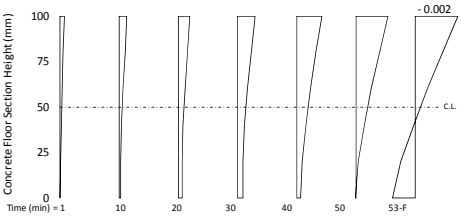


Figure 21. Mechanical Strain profile at the vertical center line of the concrete slab section for specimen No. 1 at different time steps.

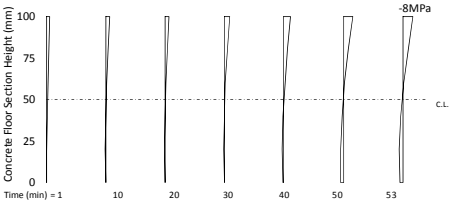


Figure 22. Stress profile at the vertical center line of the concrete slab section for specimen No. 2 at different time steps.

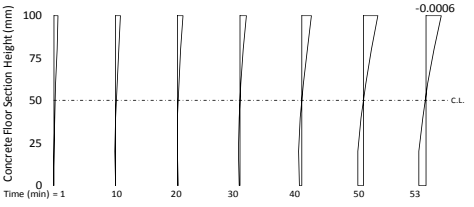


Figure 23. Mechanical Strain profile at the vertical center line of the concrete slab section for specimen No. 2 at different time steps.

Results from this numerical study and the two test assemblies indicated that overall performance of unrestrained floor specimen was better than the restrained specimen. Future comparative tests of restrained vs. unrestrained floor assemblies would be suggested to confirm if unrestrained floors perform better in other comparative tests.

In this study, no damage to the fireproofing materials of the truss, due to the initial impact and jet fuel explosion, is considered. In the 9/11 fire, the WTC towers' floors were exposed to a hydrocarbon fire load, however, in this investigation the composite floors were exposed to a standard fire, ASTM E119. In addition, the horizontal support

restraint condition for the test assembly No. 1 was only in compression. The floor specimen was free to displace in tension. However, in practice such restraint conditions would be imposed both in compression and tension.

Future studies would be recommended to investigate the above mentioned deficiencies in different scenarios.

CONCLUSIONS

A numerical study was carried out to investigate failure mechanism of the World Trade Center composite floors. The results from the analysis and the comparisons with the test results of the two full-scale floor assemblies, suggested the following conclusions:

Separation of the metal deck from the concrete slab during the fire would have decreased the heat transfer to the concrete slab.

The significant spalling of concrete and large deformation of specimen No. 1 at about 50 minutes would have been due to the thermal expansion of the truss resulting in compression failure of the top fibers of the concrete slab.

The axial load in the restrained truss assembly was significantly (about 15 times) higher than that of the unrestrained specimen.

ACKNOWLEDGMENT

Acknowledgements are extended to Mr. Joe Hum from NRC Fire Research Program for developing a post-processor software to simulate the stress and strain diagrams and his contribution in this study.

REFERENCES

Carino, N.J., Starnes, M.A., Gross, J.L., Yang, J.C., Kukuck, S.R., Prasad, K.R., Bukowski, R.W. (2005). "Passive Fire Protection", Federal Building and Fire Safety Investigation of the World Trade Center Disaster, NIST NCSTAR 1-6A, *National Institute of Standards and Technology*, 326 pp.

Franssen, J.M. (2007). User's Manual for SAFIR 2007a Computer Program For Analysis of Structures Subjected to Fire, *University of Liege*, Belgium, 79 pp.

Gross, J., Hervey, F., Izydorek, M., Mammoser, J., Treadway, J. (2005). "Fire Resistance Tests of Floor Truss Systems", Federal Building and Fire Safety Investigation of the World Trade Center Disaster, NIST NCSTAR 1-6B, *National Institute of Standards and Technology*, 202 pp.

NIST (2005). "Final Report of the National Construction Safety Team on the Collapses of the World Trade Center Tower ", Reports of the Federal Building and Fire Investigation of the World Trade Center Disaster, NIST NCSTAR 1, *, National Institute of Standards and Technology*, 298 pp.

Prasad, K., Baum H., (2005). "Fire Structure Interface and Thermal Response of the World Trade Center Towers", Federal Building and Fire Safety Investigation of the World Trade Center Disaster, NIST NCSTAR 1-5G, *National Institute of Standards and Technology*, 338 pp.

Wong, PS, Vecchio, FJ. (2002). "Vector2 & Formwork user's manual", *Department of Civil Engineering, University of Toronto*; 214 pp.

RC Bearing Walls Subjected to Elevated Temperatures

M. J. McGinnis,[1] K.A. Mueller,[2] Y. C. Kurama,[3] and K. P. Graham[4]

[1]Civil Engineering, University of Texas at Tyler, 3900 University Blvd, Tyler, TX 75799; PH: (903) 565-5870; email: mmcginnis@uttyler.edu
[2]Civil Engineering and Geological Sciences, Univ. of Notre Dame, 156 Fitzpatrick Hall, Notre Dame, IN 46556; PH: (574) 631-5380; email: kmuelle4@nd.edu
[3]Civil Engineering and Geological Sciences, Univ. of Notre Dame, 156 Fitzpatrick Hall, Notre Dame, IN 46556; PH: (574) 631-8377; email: ykurama@nd.edu
[4]Civil Engineering, University of Texas at Tyler, 3900 University Blvd, Tyler, TX 75799; email: kgraham3@patriots.uttyler.edu

ABSTRACT

RC bearing walls are one of the most common primary lateral and gravity load carrying systems in U.S. building practice. Severe exposure to fire can compromise the out-of-plane stability of these walls under service-level gravity loads, causing catastrophic overall or disproportionately large failure of the structure. Considering these issues, the authors are conducting a project with the overall objective of developing experimental and analytical evidence to demonstrate the structural design and performance of RC walls under fire. Eight full scale wall fire tests are scheduled to be completed as part of this project. This paper describes the finite element modeling of the full scale concrete wall structures, and initial pilot experiments conducted to validate the modeling approaches. The results of the finite element simulations will be paired with the experimental results of full scale walls to develop a predictive fire-resistant structural design procedure for the walls.

INTRODUCTION

The response of reinforced concrete (RC) structures to fire is a complex coupled phenomenon. Current building codes in the U.S. are based on prescriptive fire resistant design provisions for the individual components of a structure. For example, according to ACI 216.1 (ACI 2007), the fire endurance of a RC wall is governed by its ability to confine a fire over a specified period of time (rather than by its structural strength or stability) and the fire endurance for a wall can be determined similar to a RC slab. The International Building Code (ICC 2009) requires a standard "fire resistance rating" of 2 to 3 hours (depending on structure height) for exterior and interior bearing walls. While a significant amount of previous research has been conducted to establish relative fire resistance ratings for different types of structural components, the results from these efforts do not provide knowledge on the structural load bearing capacity under fire. Rational performance-based design methods and analysis tools (as an alternative to the current prescriptive methods) are needed (NIST 2005) to enable the evaluation of the structural performance of a building component under a prescribed fire loading, similar to structures under other types of loads.

This ongoing project has the following three specific objectives involving basic research on the fire resistant behavior and design of load-bearing RC wall structures: (1) to investigate the out-of-plane axial-load-moment-curvature-temperature (P-M-φ-T) behavior of RC wall cross sections under elevated temperatures; (2) to evaluate the effects of geometric, material, reinforcement, and loading parameters on the behavior of RC wall structures under fire; and (3) to develop a rational, predictive fire-resistant structural design procedure based on the research results. The current paper describes the finite element modeling of full scale concrete wall structures, and initial pilot experiments conducted to validate the modeling approaches. The results of the finite element simulations will be paired with the experimental results of full scale walls to develop a predictive fire-resistant structural design procedure for the walls.

BACKGROUND

Most of the previous experimental research on RC structures under fire is based on the ASTM E119 standard test method (ASTM 2009), which requires that the fire endurance of a building component be determined by subjecting it to increasing temperatures that vary with time as shown in Figure 1. The tests are conducted by placing the specimen inside a specially-built furnace designed to follow the ASTM E119 time-temperature (t-T) curve.

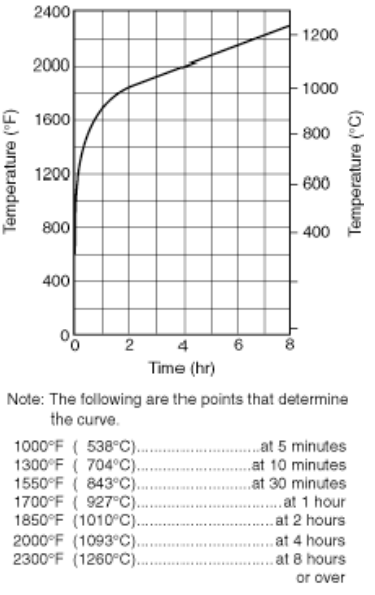


Figure 1. ASTM E119 time-temperature curve

In comparison with RC beam, column, and slab members, the previous fire engineering research on RC wall structures is limited (Lie 1972; Gustaferro and Abrams 1975; Plecnik et al. 1982; Crozier and Sanjayan 2000). The experiments conducted by Crozier and Sanjayan (2000) in Australia form the single most relevant research for the current project. A total of eighteen slender RC wall specimens were subjected to eccentric gravity loads and out-of-plane lateral loading, and then heated on one side following the ASTM E119 t-T curve using a gas-fired furnace. The wall specimens were 1.2 m (4 ft) long and 3.66 m (12 ft) high with uniform thicknesses of 75, 100 and 150 mm (3, 4, and 6 in), corresponding to wall height-to-thickness slenderness ratios of 48, 36, and 24, respectively. Concrete strengths of 48 MPa (7 ksi) and 69 MPa (10 ksi) were used with 0.25% steel reinforcement in the form of deformed wire mesh and reinforcing bars. The gravity and lateral loads were kept constant and the specimens were heated until collapse or other failure criteria (e.g., excessive deflections or deflection rates) were reached. It was found that: (1) out-of-plane thermal bowing due to one-sided fire exposure results in a significant reduction in the gravity load capacity of the walls; (2) flexural cracking allows the pore vapor pressure inside the heated concrete to be released; and thus, walls with little or no flexural cracking (i.e., with smaller M/P ratio) are more likely to experience explosive spalling than walls with significant flexural cracking; (3) higher strength concrete walls experience smaller out-of-plane thermal bowing due to higher thermal

conductivity and lower thermal expansion of higher strength concrete; and (4) the thickness of the concrete cover over the steel reinforcement has a significant effect on the load carrying capacity of the walls. These results indicate that in addition to material properties and reinforcement details (e.g., concrete cover), the dehydration of concrete and its relationships with temperature and deformation (e.g., cracking and spalling) play an important role on the behavior of RC walls under fire.

The parameters to be varied in the experimental program are: (1) wall axial load level; (2) concrete strength; (3) concrete cover to reinforcement; and (4) reinforcing details. A total of 8 specimens will be tested as shown in Table 1. Each specimen will first be subjected to a constant axial load (both low and moderate load levels will be considered as shown in Table 1), representing service gravity conditions. Then, the temperatures on the heated surface will be increased based on a pre-determined t-T curve. The application of out-of-plane bending moments will include both initial and increasing moments. Moments that subject the fire-exposed surface to flexural tension as well as flexural compression will be considered.

Table 1: Test Matrix

Specimen Number	Type of Design	Axial Load Level	Concrete Strength MPa (ksi)	Clear Cover cm (in.)	Wall Thickness cm (in.)
1	NSB	$0.10P_0$	31 (4.5)	1.9 (0.75)	38 (15)
2	NSB	$0.20P_0$	31 (4.5)	1.9 (0.75)	38 (15)
3	NSB	$0.20P_0$	31 (4.5)	3.8 (1.50)	38 (15)
4	W	$0.20P_0$	31 (4.5)	1.9 (0.75)	38 (15)
5	SB	$0.20P_0$	31 (4.5)	3.8 (1.50)	38 (15)
6	NSB	$0.20P_0$	31 (4.5)	1.9 (0.75)	38 (15)
7	NSB	$0.10P_0$	62 (9.0)	1.9 (0.75)	38 (15)
8	NSB	$0.10P_0$	62 (9.0)	3.8 (1.50)	38 (15)

NSB = Non-Seismic Boundary
W = Web
SB = Seismic Boundary
P_0=concentric axial compression strength of section at room temperature.

The test specimens represent seismic boundary regions, non-seismic boundary (i.e., end) regions, and web regions from the prototype wall designs. As described below, the web (W) region specimens have distributed reinforcement in the vertical and horizontal directions of the structure, the non-seismic boundary (NSB) region specimens have nominally spaced closed hoops, and the seismic boundary (SB) region specimens have a larger amount of hoop reinforcement in addition to the flexural steel. The finite element models described

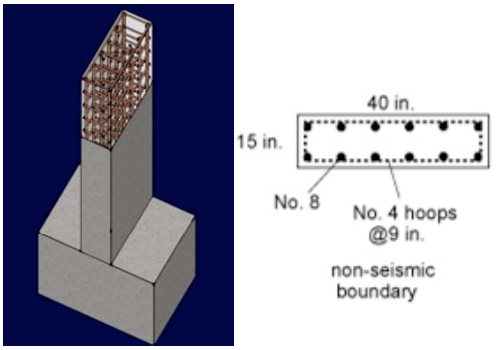


Figure 2. Full scale wall experimental details

in this paper are for the wall detailed for non-seismic applications. Since the research focuses on the out-of-plane response of RC walls under fire, the wall properties in the thickness direction are the most important. Thus, the wall thickness and reinforcement details (including concrete cover) are modeled at full scale. The test specimens model, at full-scale, a 1.0 m (40 in) long strip from the first story [3.05 m (10 ft) high] of a wall. Each specimen has a uniform thickness and uniform reinforcement details along its length and height. This will permit the tests to focus on the most important parameters (i.e., parameters in the thickness direction) affecting the wall response.

FINITE ELEMENT MODELING

Wall Model Description

A finite element model in ABAQUS (2009) was created for the pre-test analyses of the wall specimens. Prior to the laboratory experiments, these models are being used to determine the expected performance of the test specimens so that structures with the highest potential benefit to the current state of knowledge can be tested. Validation and refinement of the analytical models will be based on comparisons between the experimental data and the analytical predictions. Ultimately, the validated models will provide information beyond what could be measured in the laboratory. Furthermore, since only a limited number of structure configurations, designs, and loading histories can be tested, analytical parameter studies are conducted to extend the test data.

The current model utilizes a sequential analysis where the service level gravity load is applied to the wall first followed by a heat transfer analysis to determine the thermal effects. Other loads such as out-of-plane (i.e., in the weak direction of the wall cross-section) lateral forces and moments as well as increased axial forces can be added to the procedure.

The ABAQUS model uses standard 8-node linear brick elements for the wall concrete and 2-node truss elements for the reinforcing bars. The mechanical properties of the concrete were taken from Knaack et al. (2010a,b). This recent research at the University of Notre Dame took all of the available experimental data on North American unreinforced concrete properties under elevated temperatures and performed a statistical analysis to obtain best fit regression lines. The thermal properties of the concrete and the thermal and mechanical properties of the reinforcing steel were taken from Eurocode 2 (2005). Since the thermal conductivity and specific heat vary with temperature, multiple data points were specified in ABAQUS.

The service-level axial load was applied through a stiff steel plate rigidly connected to the top of the wall model to ensure uniform axial stresses on the concrete below. The fire load was applied through radiation and convection coefficients applied with a heat sink corresponding to the appropriate fire load over a 1.83 m (6 ft) height of the wall base. For the pre-test investigation, the thermal analysis was conducted for the full 8-hour ASTM E119 exposure so that extreme limits can be determined beforehand. To reduce the computational run time, the analyses were conducted on a 0.46 m (18 in.) wide wall model [as compared with the

1.0 m (40 in.) wide test specimens]. Similar to the full-scale walls, the base of each model was rigidly connected to a foundation block, which had fixed boundary conditions at the bottom. The temperatures were applied to one face of the wall above the foundation block at the base. Radiation and convection were considered at the back face of the wall since ambient air temperature is assumed in both the test setup and the real building scenario. The two side faces of the wall were modeled with adiabatic boundary conditions because the specimen is a "slice" from a much longer wall. This means that the temperature distribution along the length of the wall is assumed to remain relatively constant.

To validate these models for use in designing test specimens, a fire test of a simpler, smaller concrete wall panel was conducted. This validation effort is described in the next section.

Validation Experiment Description

The validation experiment consisted of testing a simple un-reinforced concrete wall panel under compression loading and simulated fire conditions similar to the fire time temperature curve specified by ASTM E119. Figure 3(a) shows a photograph of the experimental specimen that was tested. The specimen is 1.2 m (4 ft) tall, 0.91 m (3 ft) wide and 0.014 m (5.5 in) thick. The pattern of lines on the face of the specimen was used as part of the deformation measurement technique applied during the testing (digital image correlation) which is described later in this paper. The validation wall was loaded by post-tensioning (PT) bars that were placed within 65 mm diameter ducts that pass through the specimen. The load in the hydraulic jacks was held at a constant 400 kN (90 kips), simulating a service load stress in the validation wall of 6.9 MPA (1 ksi). Figure 3(b) shows a close-up of the load application region of the specimen with the 6.4 mm (0.25 in) thick steel load redistribution plates that were used to spread the load from the jacks. The validation wall was free to expand in the vertical direction.

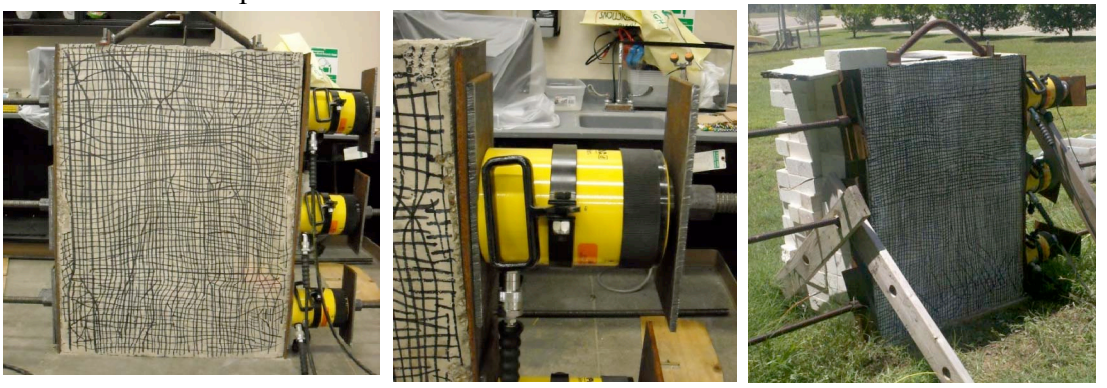


Figure 3. Validation test specimen: (a) specimen; (b) load region; (c) fire test set-up

The validation wall was comprised of concrete with f'_c equal to approximately 41 MPa (6 ksi) and was tested at an age of approximately 12 months from the casting date. The wall was stored exposed to the exterior relative humidity conditions in Tyler, TX during its aging and curing time period from July 2009 to July 2010. The curing conditions influenced the moisture movement documented during the validation test and are discussed more fully later in this paper.

Figure 3(c) shows a photograph of the test set-up for the validation wall. The fire load was applied with a venturi style burner that was outfitted with a simple baffle to spread the heated gasses across the back surface of the concrete specimen. The hot burner gasses were contained within an insulated enclosure with approximate dimensions of 1.2x0.91x0.6 m (4x3x2 ft) constructed of dry fitted refractory bricks. Figure 4 shows the time-temperature curve applied in the validation wall test. The curve plotted is the average of readings from 5 thermocouples that were distributed through the insulated enclosure behind the validation wall. Although similar to ASTM E119, the applied temperatures represent a fire with growth, free burning, and decay phases.

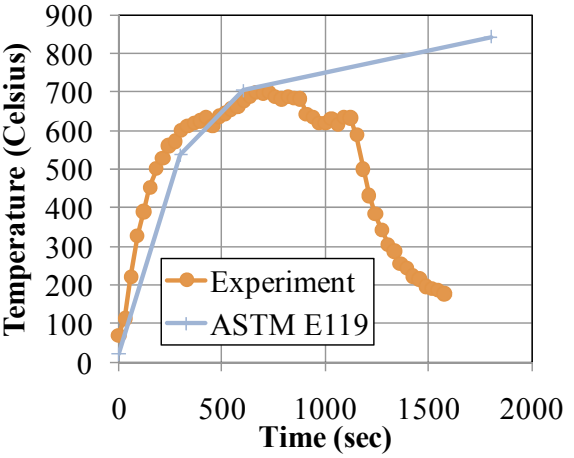


Figure 4. Validation experiment time-temperature curve

A secondary consideration in the validation experiment was to validate new approaches for data collection during fire testing. In the validation experiment, deformations (displacements and strains) were measured with 3D digital image correlation (DIC). 3D-DIC has been used to capture deformations in many civil engineering applications (e.g., Orteu 2009; McGinnis et al. 2005), including those in concrete structures (Corr et al. 2007). In this method, a stochastic pattern is applied to the surface of an object and stereo pairs of photographs of the object are captured before and after load events. The captured digital images are divided into regions that are several pixels across, called facets. Then, these facets are tracked through an image series using pattern recognition and photogrammetric triangulation principles, thus yielding essentially full-field, 3D surface displacements and strains of the view area. The accuracy of 3D-DIC scales somewhat linearly with the field of view (FOV). For the FOV used herein (approximately 1.3 m vertical by 1 m horizontal (51x40 in.), the in-plane accuracy for displacements is conservatively stated as +/-30 microns (0.0011 in). As noted, the pattern used for 3D DIC is visible in the photographs shown in Figure 3.

The full-field of temperatures on the unheated face of the specimen were measured using infrared thermography. The FLIR T400 used is capable of measuring temperatures from -20 to 1200 °C with an accuracy of ±2°C or ±2% of the reading.

Validation Model Description

Details of the validation model were selected to closely match those for the full scale walls. In particular, the material properties, heat transfer and heat input properties (radiation, convection and conduction), element type and approximate element size were similar. The geometry, boundary conditions, and loading matched the validation experiment, and the temperature loading was specified as shown in Figure 4.

Validation Results

Figure 5(a) shows the measured out-of-plane displacements of the validation wall at a time of approximately 500 seconds, and Figure 5(b) shows the output from the validation wall finite element (FE) analysis. The figures show results for approximately the upper 0.99 m (39 in) of the wall – the DIC technique did not record results for the lower 0.23 m (9 in) of the wall. It is clear that the validation wall experienced significant thermally-induced bending during the experimental test that is well captured in the FE model.

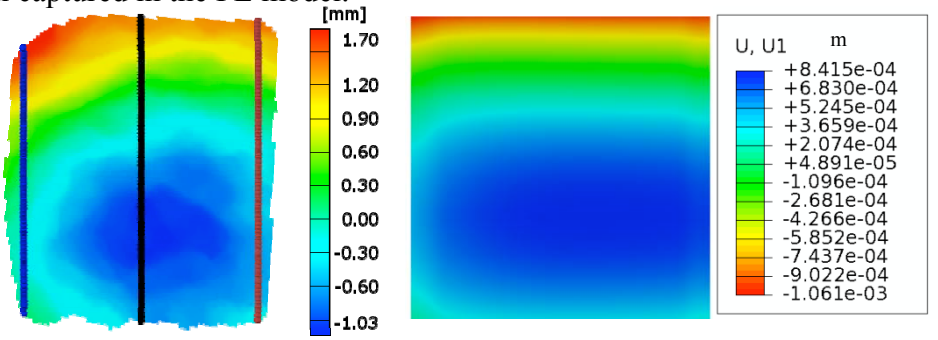


Figure 5. Out of plane displacements in validation experiment: (a) DIC; (b) ABAQUS

Figure 6 shows a comparison of the center out-of-plane displacement of the wall as measured by DIC and as calculated in the FE model. The FE model appears to be capturing the global deformation behavior well.

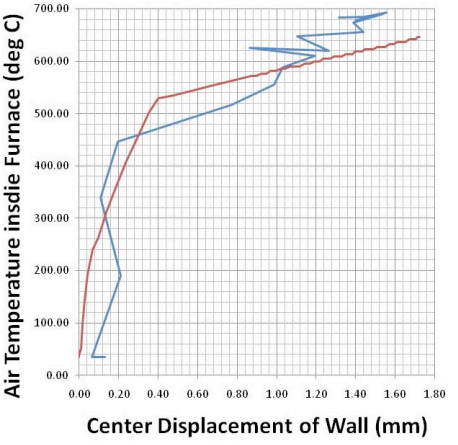


Figure 6. Comparison of center out-of-plane displacement in validation experiment

Figure 7(a) shows the vertical (i.e., y-direction) strains as measured by DIC at a fire time of 80 seconds. The figure shows that the validation wall has cracked at the location of the upper and lower PT ducts at this relatively short fire duration. The validation wall is un-reinforced and relatively thin at the duct locations, resulting in this early cracking. Figure 7(b) shows strain results from the FE model for comparison. The FE model exhibits the same cracking phenomena, albeit at a slightly later time (280 seconds). Within the first several minutes of fire loading, the model is particularly sensitive to the values used for the convection coefficient of the wall, but this dependence drops rapidly at later times when radiation dominates the heat transfer. For realistic concrete walls, the time

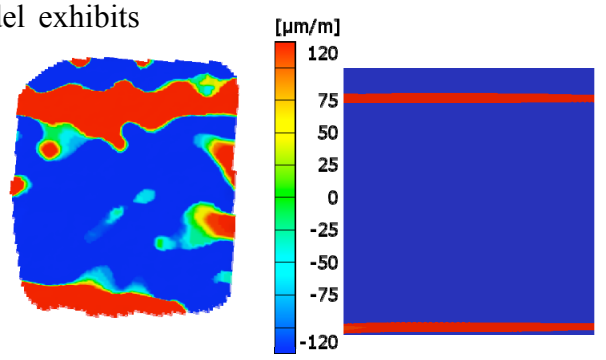


Figure 7. Y-direction strains in validation experiment: (a) DIC, (b) ABAQUS

durations will be considerably longer than in this simple validation test. Good agreement is shown between the experimentally measured values and those from the ABAQUS model.

Finally, the temperatures measured with the thermal imaging system in the validation test are compared with those computed in the FE model (Figure 8). Temperatures are shown for the unheated face at the end of the validation test. The test is for a relatively short fire duration (25 minutes, including the cool-down phase), and thus for this 14 cm (5.5 in.) thick wall, the temperatures of the unheated face do not change significantly from the ambient air temperatures (35 degrees Celsius). Good agreement is noted between measured and modeled results.

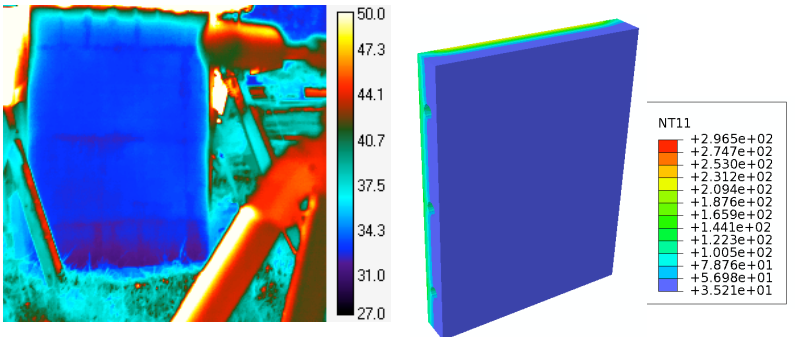


Figure 8. Cold face temperature in validation experiment: (a) measured; (b) ABAQUS

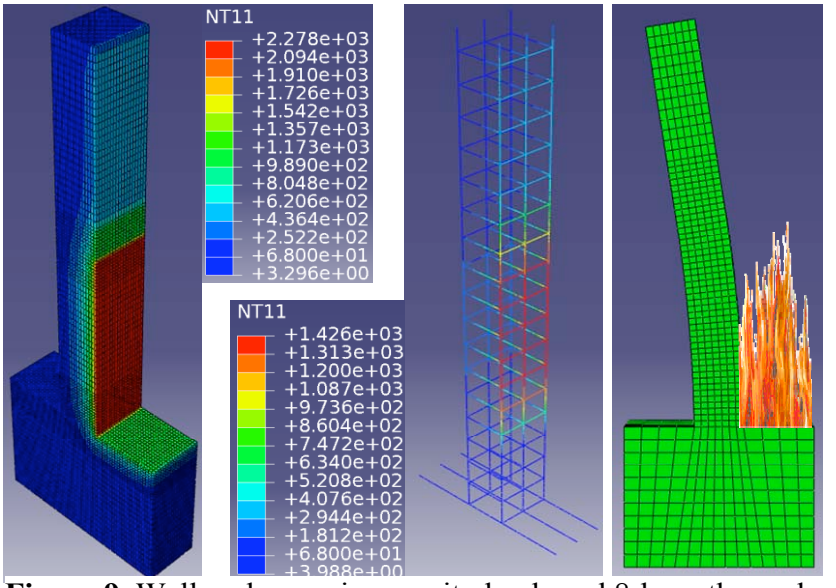


Figure 9. Wall under service gravity loads and 8-hour thermal exposure: (a) concrete temperatures; (b) steel temperatures; (c) wall deflected shape

FULL SCALE WALL MODEL RESULTS

The resulting predicted temperature distribution and deflected shape for one of the full scale wall test specimens is shown in Figure 9. In this analysis, the top of the wall was assumed free to rotate and displace laterally. Additional analyses with different boundary conditions for the wall top will be investigated in the future (e.g., fixed or partially-fixed conditions).



Figure 10. Spalling observed at the end of the validation experiment



Figure 11. Moisture leakage through wall in validation experiment

In the validation tests, spalling (see Figure 10) was observed after only a few minutes of fire exposure. This was expected, as noted, the validation specimen was stored in a high relative humidity environment and thus was at a high internal moisture state. Figure 11 shows the unheated face of the validation specimen at the completion of the test and shows significant water has migrated to the cold surface, driven by the internal temperature changes occurring in the wall. The significant role of moisture movement in spalling phenomena is well known (Consolazio 1998). It is intended that this project will include moisture movement effects in future modeling efforts. Additionally, moisture profiles through the depth of concrete walls will be captured in the experiments using a nuclear magnetic resonance imaging probe (NMR) (Beyea et al. 1997, Prado 2003, Manz et al. 2006, van der Heijden 2007).

Since the accurate modeling of this behavior is difficult in ABAQUS, two extreme models were created to investigate the possible effects of spalling. In the first model (Figure 10), it was assumed that the wall cross section remained unchanged throughout the heat transfer analysis considering no spalling. The second model assumed full spalling from the start of the analysis by removing all of the concrete cover and running the same gravity plus heat transfer analysis on a wall with reduced thickness over the complete heated region. The results from these two models bound the expected actual behavior. The maximum and minimum principal stresses of the concrete from the spalled wall model are shown in Figure 12. The pilot experiment highlighted the challenges in FE convergence after concrete cracking, and these issues as well as the others raised in this paper will receive further study as part of this ongoing project.

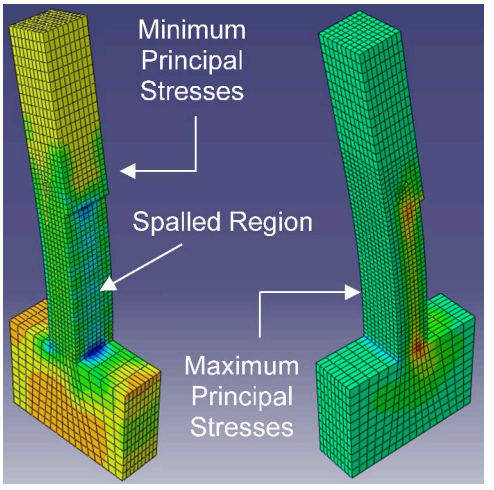


Figure 12. Maximum and minimum principle stresses of wall concrete under service gravity loads and 8-hour ASTM E119 thermal exposure (spalled model)

SUMMARY AND CONCLUSIONS

This paper presents an ongoing research effort on the behavior of reinforced concrete bearing walls under elevated temperatures from fire. General features of a series of wall test specimens are given and a preliminary finite element analysis model for the walls is described. To validate these models for use in designing the test

specimens, a fire test of a simpler, smaller concrete wall panel was conducted. A secondary consideration in the validation experiment was to explore the use of 3D digital image correlation and infrared thermography for data collection during fire testing. The measured and predicted behaviors from this pilot test are compared in the paper. Based on the results, the modeling approach appears appropriate for use in designing the experimental parameters; however, further analytical development is needed, especially on the effects of concrete spalling as well as the behavior after cracking. It is shown that the combination of full-field measurement techniques strengthens the confidence in the validity of experimental and analytical approaches.

ACKNOWLEDGEMENTS

This research is being funded by the National Science Foundation (NSF) under Grant No. CMMI 0800356. An EAGER extension to the project is also funded by the NSF under Grant No. CMMI 1049577. The support of the NSF Program Director Dr. M. P. Singh is gratefully acknowledged. In addition, the authors recognize the technical support provided by Dr. T. D. Lin, President of Lintek International, Inc. The following engineers contributed RC building design details to the project and their help is gratefully acknowledged: Thomas A. Sabol – Englekirk and Sabol; Paul J. Brienen – PCS Structural Solutions; Brian G. Morgen – Magnusson Klemencic Associates; Michael G. Allen and James O. Malley – Degenkolb Engineers; and Rashid Ahmad – Walker Parking Consultants. Strain gauges used in two of the wall specimens were donated by Hitec Products, Inc. The authors are also grateful to StresCore Incorporated, South Bend, Indiana, for allowing the casting of three of the wall specimens in their facility. The opinions, findings, and conclusions expressed in the paper are those of the authors and do not necessarily reflect the views of the NSF or the individuals/organizations acknowledged above.

REFERENCES

Abaqus/CAE. Vers. 6.9. Dassault Systèmes Simulia Corporation, 2009.

ACI 216.1, “Code Requirements for Determining Fire Resistance of Concrete and Masonry Construction Assemblies (ACI 216.1-07, TMS-216-07),” Joint ACI/TMS Committee 216, 2007.

ACI 318, “Building Code Requirements for Structural Concrete and Commentary,” ACI 318-05, ACI Committee 318, American Concrete Institute, 2008.

ASTM, “Standard Test Methods for Fire Tests of Building Construction and Materials,” ASTM E119, 2009.

Beyea, S. D., Bremner, T. W., Prado, P. J., Balcom, B. J., Gratten-Bellew, P. E., Armstrong, R. L., “Magnetic Resonance Imaging (MRI) of Moisture Distribution in Concrete,” Annual Conference of the Canadian Society for Civil Engineering, Sherbrooke, (1997).

Consolazio, G. R., McVay, J. W., Rish, J. W. III, "Measurement and Prediction of Pore Pressures in Saturated Cement Mortar Subjected to Radiant Heating," *ACI Materials Journal*, 95, (5),526-536, (1998).

Corr, D., Accardi, M., Graham-Brady, L., and Shah, S., "Digital Image Correlation Analysis of Interfacial Debonding Properties and Fracture Behavior in Concrete," *Engineering Fracture Mechanics*, V. 74, No. 1-2, 2007, pp. 109-121.

Crozier, D. and Sanjayan, J., "Tests of Load-Bearing Slender Reinforced Concrete Walls in Fire," *ACI Structural Journal*, V. 97, No. 2, 2000, pp. 243-251.

Eurocode 2: Design of Concrete Structures - Part 1-2: General Rules - Structural Fire Design. Publication no. 1992-1-2:2004. London: BSI, 2005.

Gustaferro, A. and Abrams, M., "Fire Tests of Joints between Precast Concrete Wall Panels: Effect of Various Joint Treatments," *PCI Journal*, V. 20, No. 5, September-October 1975.

ICC, International Building Code, International Code Council, Falls Church, VA, 2009.

Knaack, A., Kurama, Y., Kirkner, D., "Compressive Strength Relationships for Concrete Under Elevated Temperatures," *ACI Materials Journal*, V. 107, No. 2, March-April 2010a, pp. 164-175.

Knaack, A., Kurama, Y., Kirkner, D., "Stress-Strain Relationships for Concrete Under Elevated Temperatures," *ACI Materials Journal*, 2010b. (in print)

Lie, T., "Contribution of Insulation in Cavity Walls to Propagation of Fire," Ottawa National Research Council, 1972.

Manz, B., Coy, A., Dykstra, R., Eccles, C. D., Hunter, M. W., Parkinson, B. J., Callaghan, P. T., "A Mobile One-Sided NMR Sensor with a Homgeneous Magnetic Field: The NMR MOLE," *Journal of Magnetic Resonance*, 183, 25-31, (2006).

McGinnis, M., Pessiki, S., and Turker, H., "Application of 3D Digital Image Correlation to the Core-Drilling Method," *Experimental Mechanics*, V. 45, No. 4, 2005, pp. 359-367.

NIST, "Final Report on the Collapse of the World Trade Center Towers," National Institute of Standards and Technology," September 2005.

Orteu, J., "3-D Computer Vision in Experimental Mechanics," *Optics and Lasers in Engineering*, V. 47, No. 3-4, 2009, pp. 282-291.

Prado, P. J., "Single Sided Imaging Sensor," *Magnetic Resonance Imaging*, 21, 397-400, (2003).

Plecnik, J., Bresler, B., Chan, H., Pham, N., and Chao, J., "Epoxy-Repaired Concrete Walls Under Fire Exposure," *ASCE Journal of the Structural Division*, V. 108, No. 8, 1982, pp. 1894-1908.

van der Heijden, G. H. A., van Bijnen, R. M. W., Pel, L., Huinink, H. P., "Moisture Transport in Heated Concrete, as Studied by NMR, and its Consequences for Fire Spalling," *Cement and Concrete Research*, 37, 894-901, (2007).

Experimental Evaluation of Composite Floor Assemblies Under Fire Loading

Purushotham Pakala[1], Rustin Fike[2], Emily Wellman[3], Venkatesh Kodur[4] and Amit Varma[5]

[1]Ph.D. Candidate, Department of Civil and Environmental Engineering, Michigan State University, East Lansing, MI, pakalapu@msu.edu
[2]Ph.D. Candidate, Department of Civil and Environmental Engineering, Michigan State University, East Lansing, MI, fikerust@msu.edu
[3]M.S. Candidate, Department of Civil Engineering, Purdue University, West Lafayette, IN, eblockso@purdue.edu
[4]Professor, Department of Civil and Environmental Engineering, Michigan State University, East Lansing, MI, kodur@msu.edu
[5]Associate Professor, Department of Civil Engineering, Purdue University, West Lafayette, IN, ahvarma@purdue.edu

ABSTRACT

Composite action in floor systems plays an important role in enhancing load carrying capacity. Fire resistance of composite floors however remains an uncertain issue. As such, the fire response of composite floor assemblies during fire resistance tests is presented in this paper. Three composite floor slab assemblies were tested under different fire scenarios, connection configurations and fire protection schemes in the beam. It was observed that the concrete slab plays a major role in transferring forces from one part of the slab assembly to the other. Data from these fire resistance tests are being used to develop and validate numerical models for tracing the fire response of floor slabs.

INTRODUCTION

Composite floor assemblies are predominantly used in the construction of buildings due to the numerous advantages they offer over other floor systems. Composite floors have reduced construction costs, higher load-carrying capacity, and better fire resistance properties. The steel deck present on the top of steel framing system, acts as formwork during concrete casting, eliminating the need for external formwork and thus leads to reduced construction costs. The savings in the construction costs can be significant for multi-storey buildings. Once concrete attains its design strength, the concrete slab acts compositely with the steel beam in carrying the applied loads.

The behavior of composite floor assemblies under fire conditions is different from that at ambient temperature and extremely complex. It was observed in the Cardington test (British Steel, 1998) that the load carrying capacity of the composite floor assemblies under fire conditions was different from that obtained from the consideration of flexural theory. Hence a clear understanding of the fire behavior of the composite floor assemblies is necessary for developing rational design approaches under performance based design environment.

To develop a better understanding of the behavior of composite floor systems under fire conditions, an experimental program was undertaken at the Center for Structural Fire Engineering and Diagnostics at Michigan State University (MSU) in collaboration with Purdue University. As part of the study, fire resistance tests were conducted on three composite floor slab systems. Results of these fire tests are presented in this paper and utilized to quantify the effect of parameters such as fire scenario, fire insulation and connection type on the fire behavior of composite floor systems.

RESEARCH SIGNIFICANCE

There is lack of understanding and data on the behavior of composite floor systems, with unprotected secondary beams, under fire conditions. Previous fire resistance experiments (Bailey et.al (2000), Gillie et.al (2001), Martin Gillie et.al (2001), Gillie et.al (2002), Bailey (2004), Martin Gillie et.al (2004), Wang (2005) and Lamont et.al (2007)) have shown that real structures demonstrate higher fire resistance than predicted by element level fire resistance tests. These studies have indicated that the enhanced fire resistance can be attributed to the composite action in floor systems, and the development of tensile membrane action. During later stages of fire exposure, tensile membrane action helps in transferring forces from fire weakened steel beams to the slab and other cooler parts of the structure. Thus, overall load carrying capacity of the composite floor assembly is maintained for a longer duration. To quantify this effect there has been significant interests in recent years to develop a better understanding on the behavior of floor systems specifically with unprotected secondary beams.

There is however still a lack of understanding on the interaction between fire induced internal forces (such as tension and compression) and composite construction. To gain a better understanding into the effect of internal forces on the behavior of composite floor slab assembly, experiments were undertaken to study the fire response of composite floor systems. Results from these studies, as presented in this paper, can be used to illustrate the typical behavior of composite floor systems under fire exposure.

FIRE RESISTANCE TESTS

To overcome current knowledge gaps about understanding the enhanced fire resistance of composite floor slab assemblies, three composite floor slab assemblies were tested. The test parameters include, fire exposure, connection configuration and fire protection schemes. The experimental program and conclusions are presented in detail elsewhere (Wellman et al. 2010), and are presented briefly in the following sections.

Test specimens: The experimental program consisted of fire resistance tests on three composite floor slab assemblies designated as “Slab1”, “Slab 2” and “Slab 3”. The floor systems were 4.57m long and 3.96m wide, supported on a composite steel beam and girder framework which was 3.96m long and 2.13m wide. As shown in Fig 1 the framework was made with ASTM A992 steel and consisted of W10X15 beams and W12X16 girders. The beams were connected to the girders via shear tab connections

in Slabs 1 and 2 as shown in Fig 2, while they were connected using double angle connections for Slab 3 as shown in Fig 3. The detailing of the assembly including the design of the connections was done as per AISC specifications for structural steel buildings (AISC, 2005).

The girders in all three floor assemblies and the beam in Slab 1 were provided with 14.3 mm of Carboline Type 5GP fire protection in order to achieve a 1-hour fire resistance rating. For all insulated members fire protection thickness was measured at several locations to assure a uniform thickness. In Slabs 2 and 3, the beams were left entire unprotected.

The concrete was cast atop of Vulcraft 1.5VLR composite decking. The deck was arranged such that the ribs are oriented parallel to the girders and perpendicular to the beams. The slab had a maximum thickness of 101.6mm and a minimum thickness of 63.5mm above the ribs of the deck. The slab was provided with 6x6-W1.4xW1.4 welded wire fabric shrinkage reinforcement at a distance of 38.1mm from the top surface of the slab. The beam and girder framework was connected to the slab using 76.2mm (3 inch) long, 15.9 mm (5/8 inch) diameter shear studs with a spacing of 406.4 mm along the girder and 152.4 mm along the beam, as shown in Fig 4. The shear studs are welded to the beam and girder framework and are protruded into the slab through the steel deck by cutting holes of appropriate size in the steel deck.

The concrete on these floor assemblies was placed in two batches. Slabs 1 and 2 were cast from the same batch of concrete while Slab 3 was cast from a different batch of concrete. Light weight concrete was supplied from a local concrete batch mix plant. After placing the concrete, the test specimens were covered with a vapor proof barrier and allowed to cure at ambient conditions until achieving a constant relative humidity. The concrete was designed for a compressive strength of 28 MPa with an actual strength at testing of 42 MPa for all three Slabs.

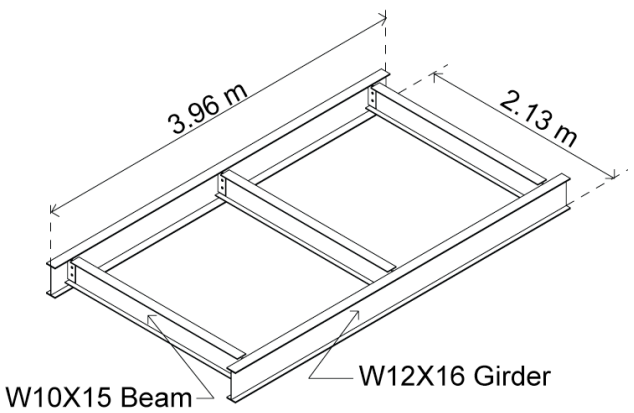


FIGURE 1 – STEEL BEAM AND GIRDER FRAMEWORK USING IN THE COMPOSITE SLAB ASSEMBLIES

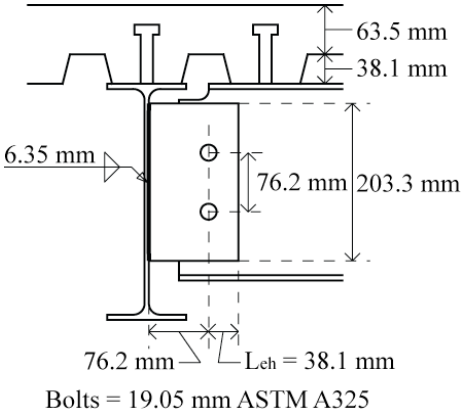


FIGURE 2 – SHEAR TAB CONNECTION USED IN FLOOR SLABS (SLAB 1 AND SLAB 2)

Test Apparatus: The fire resistance tests on the composite floor systems were carried out using the structural fire testing facility at Michigan State University. The test furnace, as shown in Fig.5, has the capacity to simultaneously apply both thermal and structural loading to the test specimen, to simulate that experienced in a real structure.

The furnace consists of a heating chamber that is 2.44 m wide, 3.05 long, and 1.78 m high. The maximum heat power the furnace can produce is 2.5 MW. Six gas burners located within the furnace provide the thermal energy, while six thermocouples, distributed throughout the test chamber, monitor the furnace temperature during a fire test. To facilitate the visual observation of the fire exposed specimen during the course of the fire test, two small view ports are provided on either side of the furnace wall.

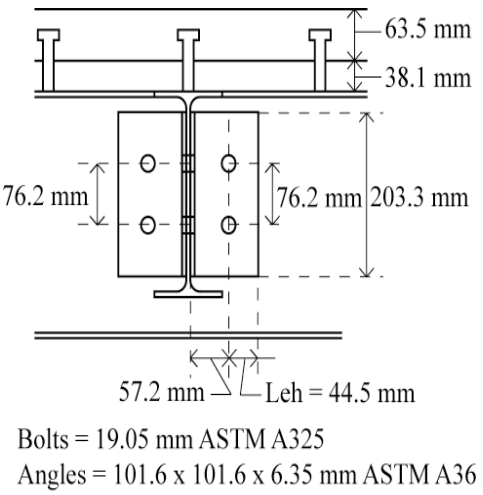


FIGURE 3 – ALL BOLTED DOUBLE ANGLE CONNECTION USED IN FLOOR SLAB 3

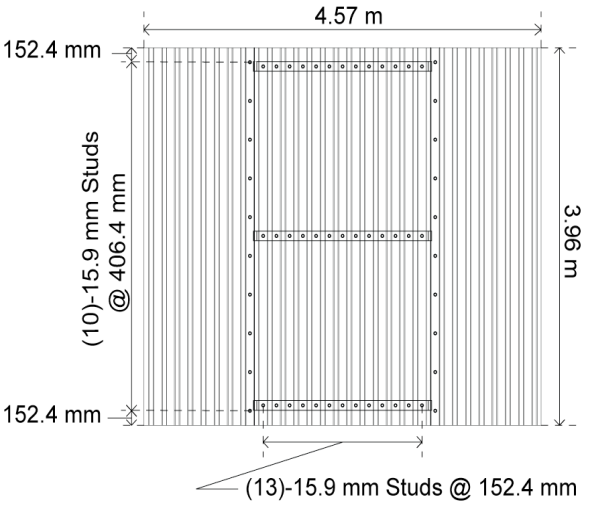


FIGURE 4 – LAYOUT OF SHEAR STUDS IN THE COMPOSITE FLOOR ASSEMBLIES



FIGURE 5 – STRUCTURAL FIRE TESTING FACILITY AT MICHIGAN STATE UNIVERSITY

Test Conditions and Procedure: The slab systems were placed on the furnace in such a way that the middle W10x15 beam was completely inside the furnace, while the ends of W12x16 girders were resting on external supports. Both the external W10x15 beams were completely outside the heating chamber of the furnace.

Loading on the slab systems was applied as five point loads, two along each external girder, and a single concentrated load at the mid-span of the interior beam. The point

loads on the girder were separated by a distance of 870 mm. Loading on the slab assemblies were computed using the ambient temperature ultimate moment capacities of the members assuming equal dead and live load then reduced for fire exposure. The calculated load value at the mid-span of beam was 133.4 kN for Slab 1 and 111.2 kN for Slab 2 and 3 while that on the girders was 22.2 kN applied at 432 mm on either side of the girder mid-span. The loading was applied 30 minutes prior to the start of the test to ensure that the deflections reached a steady state before the start of fire.

After 30 minutes of load application, Slab 1 was exposed to ASTM E119 standard fire. The load on the beam was applied and continued until the beam failed. Then the concentrated load on the beam was removed and magnitude of two point loads on each girder was increased to 44.5 kN (applied at a distance of 432 mm on either side of girder mid-span). This increased value of concentrated loads on each girder created the same moment at the girders mid-span as that experienced during the initial loading (two point loads of 22.2 kN on each girder and a load of 133.4 kN at beam mid-span). Loading was intended to continue until failure was reached in the girders; however the actuators reached their full extension and the loading value was no longer able to be maintained. At this time all loading was removed and the test ended.

Failure criteria in all the slabs was defined using the criteria recommended by BS-476 (CEN,1987), where failure is defined to be either deflection or rate of deflection. The first failure criterion corresponds to a maximum deflection greater than L/20. The second failure criterion corresponds a deflection greater than L/30 and a rate of deflection greater than $L^2/9000d$.

Slabs 2 and 3 were exposed to design fire with the initial five points loading as described above. This loading was maintained until failure was reached in the beam. Loading on the beam was removed and two point loads on each of the girders were increased to 44.5 kN. Loading was intended to continue until failure was reached in the girders, after which all loading was to be removed and the cooling curve phase initiated. However, in the case of Slab 2, the actuators reached their full extension and the loading value was no longer able to be maintained. In Slab 3, failure was reached in the girders.

The design fire used for Slab 2 and Slab 3 consisted of ASTM E119 standard fire (ASTM, 2008) for the first 110 minutes for Slab 2, and 85 minutes for Slab 3. This was followed by a decay phase with a cooling rate of 12.2 °C/minute. A summary of test parameters considered in this study are shown in Table 1.

TABLE 1: TEST PARAMETERS USED IN THE CURRENT STUDY FOR COMPOSITE SLABS

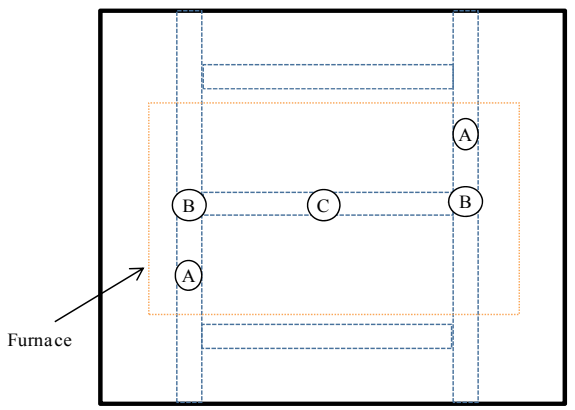
Specimen	Fire Protection (Beam, Girder)	Fire Scenario	Connection	Loading (Beam, Girders)
Slab 1	1 hour, 1 hour	ASTM E119	Shear Tab	133.4 kN, 22.2 kN
Slab 2	None, 1 hour	Design fire 1	Shear Tab	111.2 kN, 22.2 kN
Slab 3	None, 1 hour	Design fire 2	Double Angle	111.2 kN, 22.2 kN

Instrumentation: The instrumentation in the composite floor assemblies included thermocouples, strain gauges, and displacement transducers to monitor thermal and structural response of the floor assemblies. Type-K chromel-alumel thermocouples of

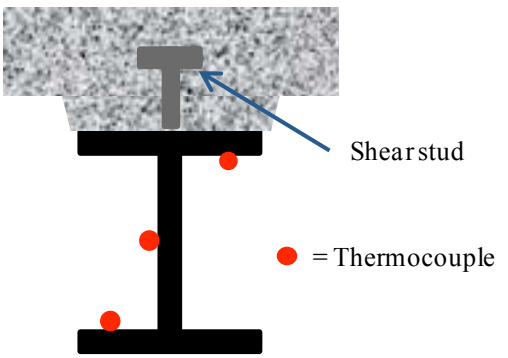
0.91 mm thick were placed on the lower and upper flanges as well as on the web of the steel beams and girders at different locations along the length. Additionally, thermocouples were placed on the ribs of the deck, shear studs and on the surface of the concrete slab. The thermocouples were placed at five different sections (labeled A,B and C) in the slab assembly. Section A is located at the quarter-span of the girder; section B is located at the intersection of beam and girder while section C is located at the mid-span of the beam. Location of thermocouples in the slab assembly along with the thermocouple layout in beam and concrete section are shown in Fig 6. Also, the furnace temperature was measured using six thermocouples distributed spatially inside the furnace in accordance with the ASTM E119 test procedures.

The vertical displacements of the slab were measured using linear varying displacement transducers (LVDT's) connected to the top surface of the slab. Also strain on the top surface of the slab was measured using strain gauges located at three locations on the slab. Location of the displacement transducers and strain gauges are shown in Fig 7.

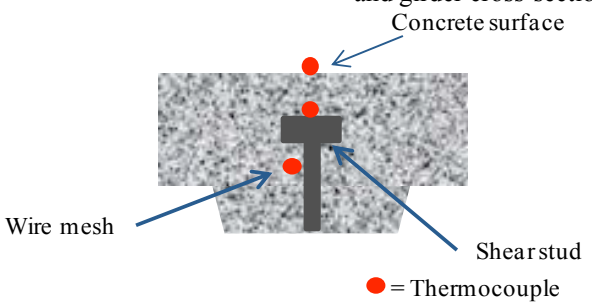
Data from the instrumentation network was recorded at five second intervals via a central data acquisition system. Also, the pressure in the vertical actuators of the furnace was also recorded as a measure of applied load. Additionally, visual observations were made to record any important events (beam buckling, insulation fall off) or at five minute intervals throughout the duration of the test.



(a) Location of thermocouple sections in the slab assembly

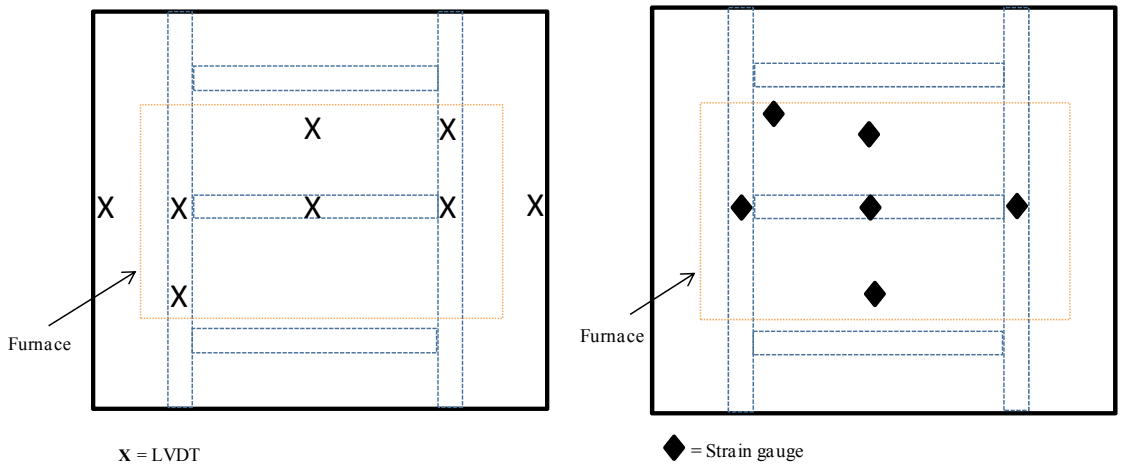


(b) Location of thermocouples along the beam and girder cross-section



(c) Location of thermocouples in the concrete slab cross-section

FIGURE 6 – LAYOUT OF THE THERMOCOUPLES IN THE FLOOR SLABS.



(a) LVDT's (b) Strain gauges

FIGURE 7. LAYOUT OF LVDT'S AND STRAIN GAUGES IN THE SLAB ASSEMBLIES

EXPERIMENTAL RESULTS

Data generated from the above fire tests can be used to study thermal and structural response of the composite slab floor assemblies under fire exposure. Thermal response, structural response, and failure patterns are presented in the following sections to illustrate the response of the assemblies to fire.

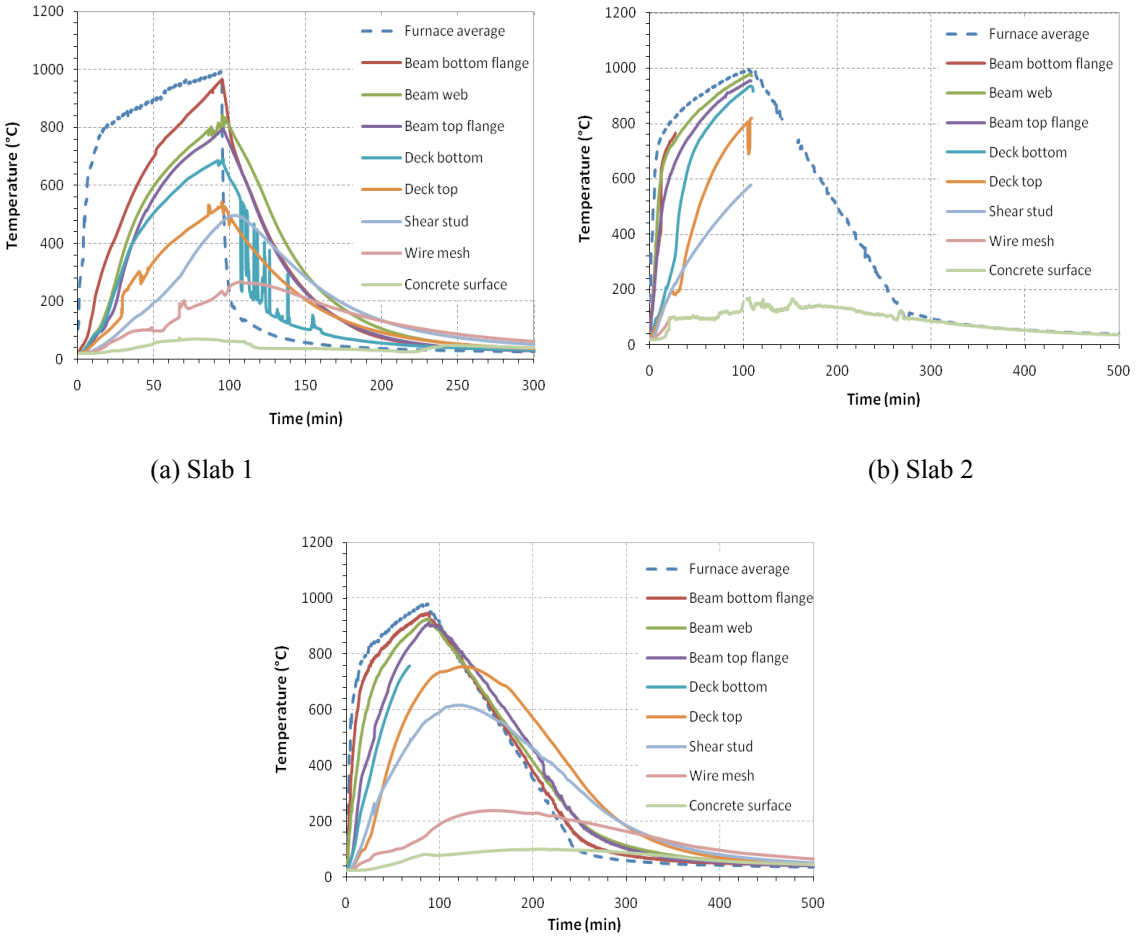
Thermal Response: Fig 8 shows the recorded temperatures at mid-span of the beam for Slabs 1, 2 and 3 during the fire test. As expected, the temperature of the unprotected beam closely followed the fire temperature, and in general, is higher than the other slab components. The maximum temperature recorded at various locations along the beam cross-section decrease from beam bottom flange to the concrete surface. This is on the expected lines because the beam is subjected to maximum fire exposure as it is closer to the fire zone and the temperatures decrease with increased distances from fire zone.

The temperatures in the deck (bottom and top) follow that of the fire, though the temperatures themselves are lower. These lower temperatures observed in the deck are due to large thermal capacity of the concrete slab, while the similarity in the temperature trends is because the bottom of the deck is directly exposed to the fire. Also the maximum temperature in the shear stud and wire mesh are lower than that of steel beam and deck because of the fact that they are located in the concrete and far from the fire zone. Also the thermal conductivity of concrete is lower as compared to steel. However the trend in the temperature variation is similar to that of the average temperature recorded in the furnace.

Structural Response: The structural response of the composite slab can be gauged through deflection time history of the slabs as seen in Fig 10. Fig 9 shows the labeling of displacement transducers used in the displacement plots. It can be seen in Fig 10 that the displacements in the beam and girders gradually increase with increasing fire

temperatures. Then the displacements start to decrease in the cooling phase of the fire (Slabs 2 and 3). The increase in deflections is caused due to the loss in stiffness of steel and thermal expansion of steel with increasing temperature. The free thermal expansion of the beam is restrained by the presence of surrounding girders. The restraint provided by the girders induces additional compressive forces in the beam. The reduced strength of the beam and restraint provided from the protected girders results in an increase in deflection.

As soon as the decay phase of the fire starts, the temperatures in the beam as well as the entire slab assembly start to decrease, allowing it to regain part of their initial strength and stiffness as well as an increase in thermal contraction. This increased strength and thermal contractions results in the decreased deflections in the entire slab assembly.



(a) Slab 1

(b) Slab 2

(c) Slab 3

FIGURE 8 – RECORDED TEMPERATURES AT MID-SPAN OF BEAM AS A FUNCTION OF FIRE EXPOSURE TIME

It can be seen from the figures that the maximum displacement occurs at the beam mid-span. Also, the deflections at the beam mid-span increase rapidly during the growth phase of the fire. This is expected because as the fire temperatures increase, the beam undergoes an increased thermal expansion as well as rapid loss in stiffness

in comparison to the protected girders. The girder mid-span deflection is slightly higher for slab with unprotected beam in comparison to the one with protected beam. This indicates that the reduction in deflection due to fire proofing the beams is not significant and leaving the beam unprotected might not significantly influence the overall behavior of slab.

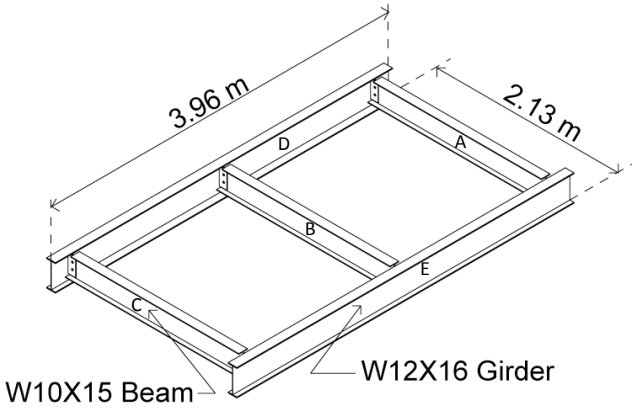
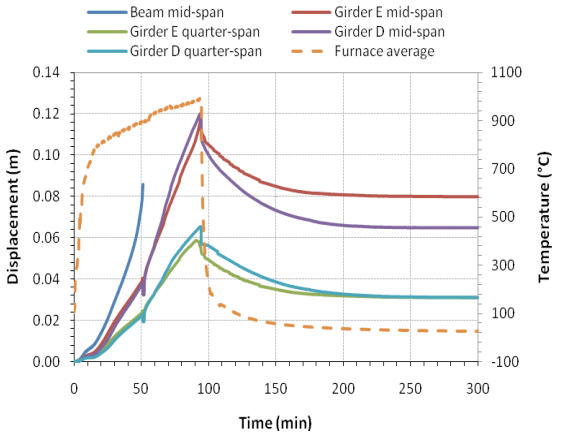
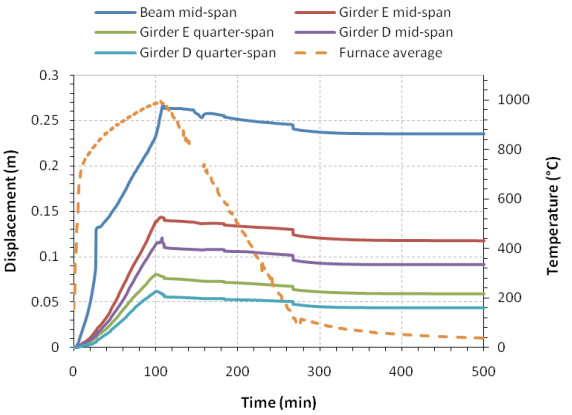


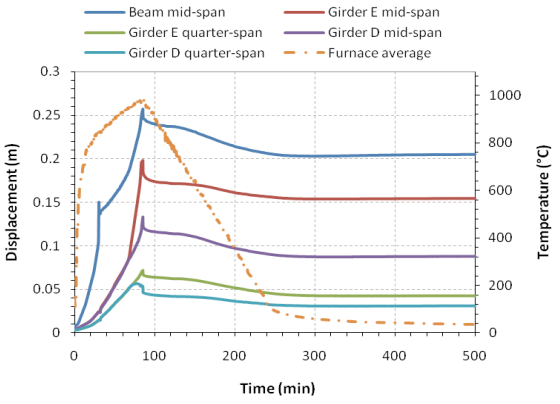
FIGURE 9 – LABELING OF BEAMS AND GIRDER IN THE SLAB ASSEMBLY USED IN DISPLACEMENT PLOTS



(a) Slab 1



(b) Slab 2



(c) Slab 3

FIGURE 10 – DEFLECTIONS RECORDED AS A FUNCTION OF FIRE EXPOSURE TIME AT DIFFERENT SECTIONS FOR THE SLAB ASSEMBLIES

A comparison of deflections of slab with shear tab connection and double angle connection shows that the deflection of girders with double angle connection is greater than that with shear tab connection. Also the rate of deflection for double angle connections is higher than that of shear tab connection. These observations indicate that the double angle connections have more flexibility in comparison to shear tab connections.

Cracking and failure patterns: In addition to the thermal and structural responses recorded through the instrumentation, visual observations were taken during the course of each fire test to note important events. For Slab 1, initial cracking was observed in the concrete slab over the beam and girders. These cracks were followed by the development of diagonal cracks from the girder and exterior beam joints with steam and boiling water emitted from the cracks. At about 51 minutes in to fire exposure, the concrete under the central load actuator failed to the concentration of forces, thus the load had to be removed. At 94 minutes in to the test, deflections in the girders accelerated and the actuators could not maintain loading, thus the test was ended at this time.

For Slab 2, cracking occurred initially in an ovular shape, in the slab, with steam and boiling water emitted from the cracks. At 27 minutes, the deflection failure criterion for the beam was reached. Beam loading was then removed and the girder loading increased. Testing then continued until 110 minutes when the actuators reached their full extension and no further loading could be applied. The cooling phase was then entered and maintained until 270 minutes when the furnace reached its ambient state. When the specimen was removed from the furnace, visible rotational deformations were present in the shear connections, along with bearing deformations of both the beam web and the plate, as well as deformations of the bolt shank.

Initial cracking of Slab 3 was over the beam, parallel to the member, as well as in ovular shape around the loading point. At 31 minutes, the maximum deflection in the beam was reached. Beam loading was then removed and girder loading increased. Testing continued until 85 minutes, when one of the girders reached its deflection failure criteria. The girder failure resulted in the development of a huge crack along the length of the girder. The cooling phase of the heating curve was entered and maintained until 265 minutes when the furnace reached its ambient temperature. When the specimen was removed from the furnace, small but visible rotational deformations were present in the shear connections.

In all three slab assemblies, cracks started forming in ovular pattern with steam emitting from the cracks. As the test progressed, cracks began to form at different locations in the slabs with initial cracks widening. At the end of the tests, all slabs had ovular cracking patterns with all the cracks present in the region between the two girders. The crack development and concentration indicates the development of tensile membrane action (tensile ring in the concrete surrounded by a compressive ring) where in the concrete slab started to carry load from the fire affected steel section and transfer it to unaffected steel sections.

CONCLUSIONS

Based on the results from the presented experimental study, the following conclusions can be drawn:

- Application of fire protection to the beams helps in reducing the heating rate of the beam as well as its deflections.
- No failure was observed in the fire exposed beam to girder connections though these connections underwent permanent deformations.
- In composite beam slab assemblies the deflection in girders are slightly higher when beams are unprotected than those with protected beams. This indicates that leaving the beams unprotected might not significantly affect the overall slab behavior.
- In composite beam slab assemblies double angle connections are more flexible than shear tab connections under fire conditions.
- Unique data generated from these floor tests can be used to validate numerical models for tracing the fire behavior of floor systems and connections under fire conditions.

ACKNOWLEDGEMENTS

This material is based upon work supported by the National Science Foundation (NSF) under grant numbers CMMI-0758409 (Michigan State University) and CMMI-0758461 (Purdue University). Any opinions, findings, and conclusions or recommendations expressed in this paper are those of the authors and do not necessarily reflect the views of the sponsors.

REFERENCES

[1] AISC, Steel Construction Manual, Thirteenth Edition. Chicago: *American Institute of Steel Construction* (AISC), 2005.

[2] ASTM. Designation: E119-08a – Standard Test methods for Fire Tests of Building Construction and Materials. West Conshohocken, PA: American Society for Testing and Materials (ASTM) International, 2008.

[3] Bailey C.G., White D.S., Moore D.B. "The tensile membrane action of unrestrained composite slabs simulated under fire conditions", *Engineering Structures*, Vol. 22, pp. 1583-1595, 2000.

[4] Bailey C.G. "Membrane action of slab/beam composite floor systems in fire*", Engineering Structures*, Vol. 26, pp. 1691-1703, 2004.

[5] British Steel "The Behaviour of a Multi-Storey Steel Framed Building Subject to Fire Attack", *British Steel plc Swinden Technology Center*, Moorgate, Rotherdam, UK 1998.

[6] CEN, BS 476-20 Fire tests on building materials and structure – Part 20: Method for determination of the fire resistance of elements of construction, *European Committee for Standardization*, Brussels, Belgium, 1987.

[7] Gillie M, Usmani A.S., Rotter J.M. "A structural analysis of the first Cardington test", *Journal of Construction Steel Research*, Vol. 57, pp.581-601, 2001.

[8] Gillie M, Usmani A.S., Rotter J.M. "A structural analysis of the Cardington British Steel Corner Test", *Journal of Construction Steel Research*, Vol. 58, pp.427-442, 2002.

[9] Lamont S, Gillie M, Usmani A.S. "Composite steel-framed structures in fire with protected and unprotected edge beams", *Journal of Construction Steel Research*, Vol. 63, pp. 1138-1150, 2007.

[10] Martin Gillie, Asif Usmani, Michael Rotter, Mark O' Connor. "Modelling of heated composite floor slabs with reference to the Cardington experiements", *Fire Safety Journal*, Vol. 36, pp. 745-767, 2001.

[11] Martin Gillie, Asif Usmani and Michael Rotter. "Bending and membrane action in concrete slabs", *Fire and materials*, Vol. 28, pp. 139-157, 2004.

[12] Wang Y.C. "Performance of steel-concrete composite structures in fire", Review Article, *Prog. Struct. Engng Mater*, Vol.7, pp. 86-102, 2005.

[13] Wellman E., Varma A.H., Fike R., Pakala P., and Kodur V., "Experimental Evaluation of Composite Floor Assemblies Under Fire Loading", *ASCE Journal of Structural Engineering*, in review.

Behavior of Steel Columns under Fire Loading

Lisa Choe[1], Amit H. Varma[1], and Andrea Surovek[2]

[1]Bowen Laboratory, School of Civil Eng., Purdue University, 1040 South River Rd, West Lafayette, IN 47907, email: lchoe@purdue.edu; ahvarma@purdue.edu.
[2]Civil and Environmental Eng., South Dakota School of Mines and Tech., 501 East St. Joseph St. Rapid City, SD 55701, email: surovek@sdsmt.edu

ABSTRACT

This paper presents the behavior of A992 wide flange steel columns under fire loading. Experimental tests were conducted to investigate the structural-thermal response of steel columns subjected to axial loads and elevated temperatures. Two identical W14X53 specimens were tested under (i) non-standard fire loading to determine the axial load capacity at elevated temperature and (ii) standard fire loading to determine the buckling temperature of the axially loaded steel column. For the non-standard fire test (Test I), the monotonically increasing axial load was imposed on the steel column under steady-state heating condition. For the standard fire test (Test II), the steel column carrying the sustained axial load was tested under transient heating condition. The structural-thermal responses of steel columns observed in Test I and Test II were compared including column end rotations, lateral and axial displacements, and steel temperatures. The measured column buckling behaviors were also compared to those obtained by 3D finite element analyses. The results indicated that the end rotations and displacements of the steel column before buckling were affected by the sequence of applied loading. Both Test I and Test II provided the similar prediction of axial load capacity and buckling temperature of the steel columns.

INTRODUCTION

In U.S., prescriptive fire ratings of building components have been obtained from ASTM E119 (2010) standard fire test or standard calculation methods based on the results of prior E119 fire tests. However, most column tests have been conducted without applying service loads. This is because the standard fire tests on the mechanically loaded steel columns are expensive and there are only a handful of column testing furnaces in the world. As a result, there is a lack of knowledge regarding fire behavior of the structural steel columns in service. This knowledge must be supported by experimental data regarding the structural-thermal responses of steel columns subjected to combined axial loads and elevated temperatures. Theses experimental test results are essential to develop structural performance-based design guidelines for steel building structures under realistic fire loading effects. The

behavior of steel building structures under fire loading depends significantly on the elevated temperature performance of the steel columns (Varma et al. 2008).

This paper presents experimental test program to investigate the inelastic behavior of A992 wide flange steel columns subjected to elevated temperatures from standard and non-standard fire loading. The 3D finite element models were also developed to predict the fire behavior of steel column prior to the tests. The experimental results can be a benchmark to validate any existing column design curves that account for the effects of surface temperatures, thermal gradients, and restraints at the columns ends.

TEST PROGRAM

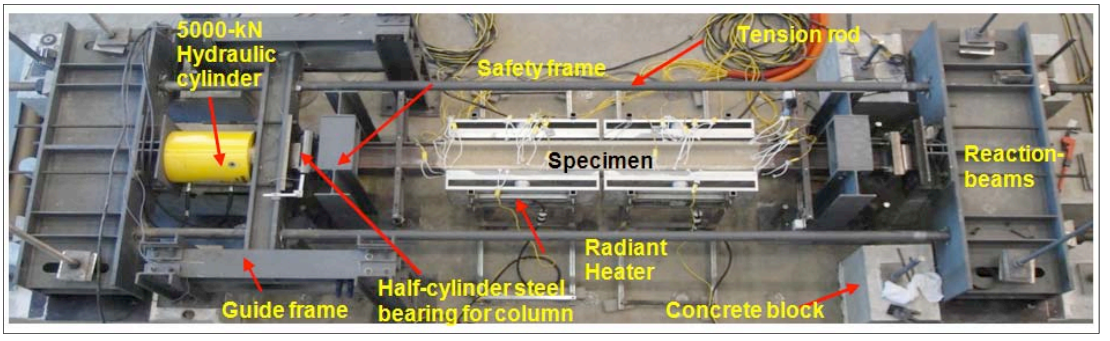
The experimental tests were conducted to determine the fundamental behavior and stability of wide flange steel columns subjected to combined axial loads and thermal loading. Test program consisted of Test I and Test II by imposing two different loading conditions including non-standard fire and standard fire, respectively. Test I was conducted such that the steel column was tested under steady-state heating condition. Note that the steel column was exposed to uniform temperature throughout the test. Test II was conducted such that the axially loaded steel column was exposed to increasing temperatures until column buckled. To do this, ASTM E119 temperature-time (T-t) relationship was used for determining the rate of heating to the specimen. Test results included: (i) axial load-displacement (P-δ), (ii) axial load-lateral displacement (P-Δ), (iii) axial load-end rotation (P-θ), (iv) temperature-axial displacement (T-δ), (v) temperature-end rotation (T-θ), and (vi) temperature-lateral displacement (T-Δ) responses. In addition, these measured responses obtained from Test I and Test II were compared.

The specimens were A992 W14X53 columns with the length of 3.45 m. They were simply supported bare steel columns with slenderness ratio (L/r_y) of 71. Mechanical properties of W14X53 columns were: yield strength of 406 MPa, ultimate tensile strength of 530 MPa, and elongation (with 8 in-gauge length) of 24.5%. Figure 1 (a) shows the self-reacting test frame that was designed for conducting the column tests, which could allow (a) easy access to install the voltage-based displacement and rotation transducers and (b) axial loads up to 4000 kN. Four concrete blocks supported the entire setup. Machine greased steel plates (A572) were placed on the blocks to minimize the friction effect on the measured axial loads. Half-cylinder steel bearings and matching saddles were used to avoid the undesired bending of tension rods.

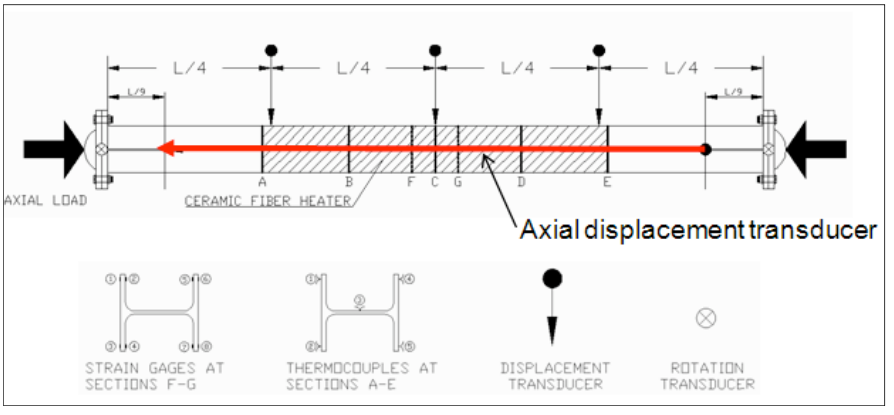
Figure 1 (a) shows the location of ceramic radiant heaters. The column was exposed to radiant heating with surface dimensions equal to 400 mm x 1000 mm. The column length subjected to high temperature during the test was 1800 mm. These heaters were placed as close as 1 cm from each side of the specimen. Namely, the flanges in the mid-portion of specimen were directly exposed to radiant heating. Figure 1 (b) shows the instrumentation layout. Three linear displacement transducers along the specimen length measured the lateral displacements. Two rotation transducers were mounted at the column ends. Two string potentiometers were

installed toward the column ends to measure the axial displacement. K-type thermocouples covered with insulation cement patch measured the steel temperatures during the test. Ceramic insulation blankets were placed on top of the steel specimen where radiant heating was not directly applied.

In Test I, the steel column was exposed to the target steel temperature of 500 ^{o}C, which maintained throughout the test. Once target temperature was achieved, axial loading was applied monotonically until the column buckling occurred. In Test II, the specimen carrying the constant axial load (60 % of ambient axial load capacity) was exposed to increasing temperatures until column buckled. The heating rate used in Test II was obtained from 2D heat transfer analysis using the standard E119 T-t relationship. For both Test I and Test II, axial load of 133 kN was applied initially to align the specimens and to ensure the concentricity of loading.



(a)



(b)

Figure 1 (a) Column test setup and (b) instrumentation layout

Steel Temperature Profile

In order to determine the heating rate used in Test II, ASTM E119 (2010) gas temperature-time (T-t) relation was considered. Using the ceramic radiant heaters, this standard gas temperature could not be directly applied to the specimen; instead,

the pre-determined steel surface temperature profile was required to operate the heaters. The applied steel temperature profile was determined before the testing, the procedure was as follows: (1) thickness of fire protection (e.g. SFRM) was assumed to be 20 mm (3/4 in.). This fire protection provided the design fire resistance rating of 1 hour for W14X53 steel column. The building code, IBC (2008) was used for the design of fire protection. (2) 2-D heat transfer analysis was conducted to obtain the steel temperatures when the specimen subjected to the standard E119 fire for 2 hours. The material properties of steel and spray fire resistant materials (SFRM) were considered as specified in Eurocode-3 (ECS 2005).

Figure 2 shows the prediction of steel temperature profile that was used for thermal loading to the W14 specimen in Test II. As shown below, when the W14X53 column with SFRM coating (with design fire rating of 1hr) is subjected to the standard E119 fire, the heated steel temperature is increased almost linearly with the rate of 6 ^{o}C/min. In Figure 2, gray and red lines represent the SFRM coating and the cross section of W14X53, respectively. Note that the flanges were exposed to the E119 fire but the web remained at ambient. Web temperature was increased by thermal conduction. The same heating condition was used in Test II.

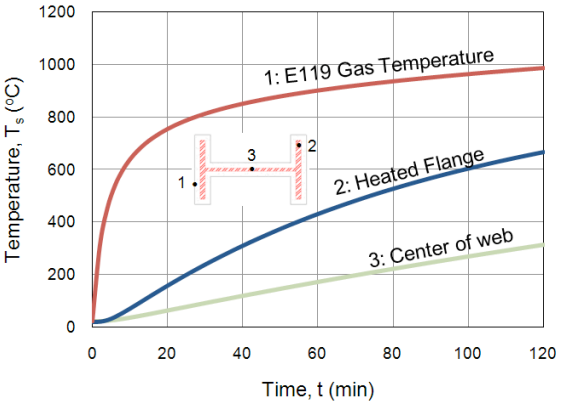


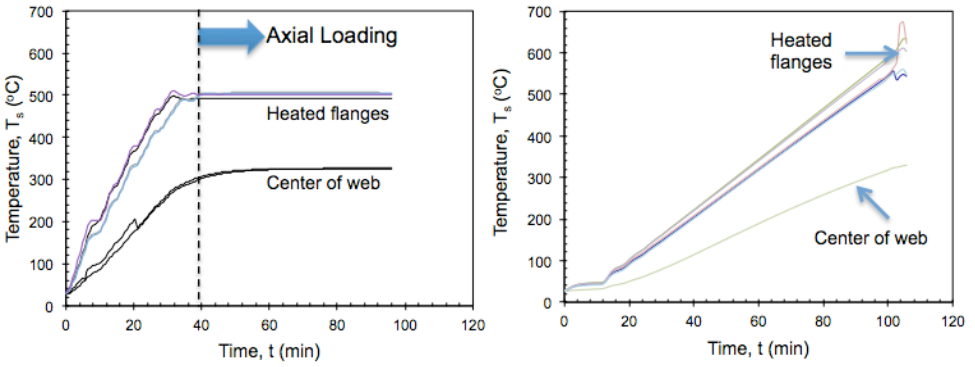
Figure 2 Temperature-time (T-t) relations obtained from 2-D heat transfer analysis

TEST RESULTS

Temperature Measurement and Loading Procedure

Figures 3 (a)-(b) show the steel temperatures of W14X53 specimens measured in Test I and Test II, respectively. In Test I, it took about 40 minutes to reach the exposed steel temperature of 500 ^{o}C followed by increasing axial loading under steady-state heating condition. In Test II, the identical W14X53 specimen was also tested under transient heating condition. As shown in Figure 3 (b), the steel

temperature was increased with the approximate rate of 6 ^{o}C/min obtained from 2-D heat transfer analysis. To compare the column behavior under two different heating conditions, the specimen used in Test II was subjected to axial load of 1450 kN, which was the maximum axial load measured in Test I.

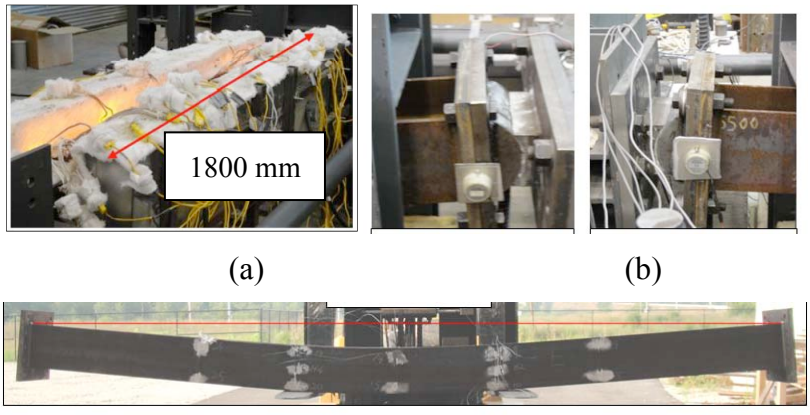


(a) (b)

Figure 3 Steel temperatures of W14X53 columns measured in (a) Test I and (b) Test II

Observation from Test I

Figures 4 (a)-(c) show photographs of W14X53 column during testing, the final end rotations, and final deflected shape, respectively. Increasing axial load slowly developed the global buckling at the steel temperature of 500 ^{o}C. When axial load reached to 1450 kN (about 60% of ambient axial load capacity), the column instability was accelerated with developing large lateral displacement. No local buckling was observed.

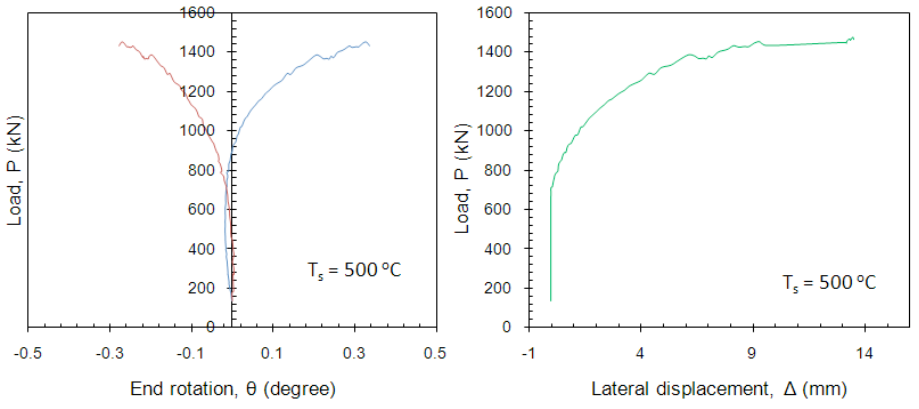


(a) (b)

(c)

Figure 4 (a) The specimen during the test, (b) final end rotations, and (c) final deflected shape obtained from Test I

Figures 5 (a)-(b) show the measured axial load-end rotation (P-θ) and the axial load-lateral displacement (P-Δ) response of W14X53 column when exposed to steel temperature of 500 °C, respectively. In Figure 5 (a), positive values indicate the rotations (θ) measured near the hydraulic cylinder; negative values indicate the far end rotation. It was observed that the magnitude of end rotation increased remarkably after the axial load was about 1450 kN. This result was also reflected in the measured lateral displacement response as shown in Figure 5 (b). Very small end rotations and lateral displacements were observed at the axial load less than 800 kN.



(a) (b)

Figure 5 (a) Axial load-end rotation (P-θ) and (b) axial load-lateral displacement (P-Δ) response obtained from Test I

Observation from Test II

Figure 6 (a)-(b) show the measured steel temperature-end rotation (T-θ) response and the measured steel temperature-lateral displacement (T-Δ) response of W14X53 column subjected to constant axial load of 1450 kN. This magnitude of axial load was the maximum axial load measured in Test I. Compared with Figures 5 (a)-(b), the specimen behavior in Test I was different from Test II. The column behavior was controlled by the sequence of loading.

As illustrated in Figures 6 (a)-(b), the W14X53 column in Test II was deflected upward at the initial stage of thermal loading (up to 250 °C), and then changed the direction. This is probably because of the temperature gradient through the cross-section that was not avoidable due to the heater layout shown in Figure 1 (a). Also, ceramic insulation blankets were placed top of the specimen only to protect the thermocouples as shown in Figure 4 (a). It was observed that the exposed temperature of top flanges were 20% higher than the bottom flanges. When the column was under transient heating condition, the temperature gradient across the cross section had a significant effect on the column behavior. Further investigation on the cause of this thermal bowing is still undergoing.

Figures 6 (a)-(b) also indicate that end rotations and lateral displacements are increased significantly in the temperature range from 500 to 550 °C. After the

exposed steel temperatures reached to 550 ^{o}C, the noticeable global buckling was observed. At that point, the hydraulic cylinder and controller could not hold the specified axial load (=1450 kN) anymore. The final deflected shape of the specimen was similar to that of the specimen observed from Test I. No local flange distortion was observed.

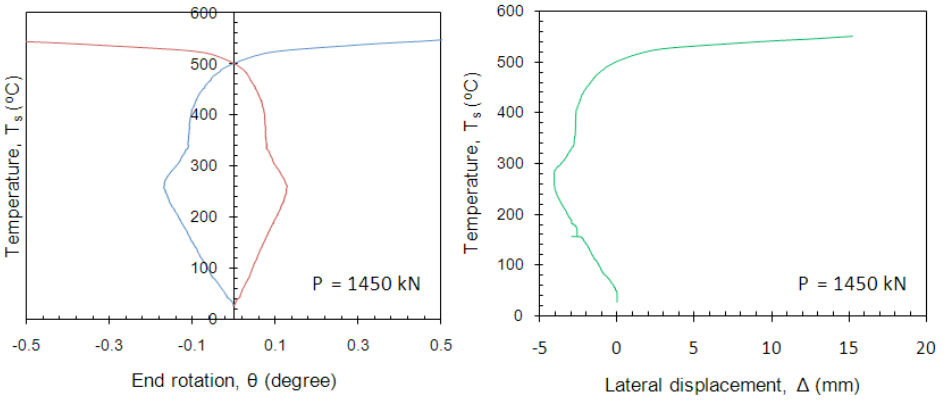


Figure 6 (a) Axial load-end rotation (P-θ) and (b) axial load-lateral displacement (P-Δ) response obtained from Test II

3D FEM PREDICTIONS AND COMPARISONS

Prior to each experimental test, three-dimensional finite element models (3D FEMs) were developed to predict the expected specimen behavior. Test I and Test II were simulated using finite element based software, ABAQUS ver. 6.10-1 (ABAQUS 2010). The modeling approaches were based on the methodology developed by Agarwal et al. (2009) and summarized in Choe et al. (2010). Eurocode-3 (ECS 2005) temperature dependent elastic, plastic, and thermal material properties of steel (i.e., σ-ε-T and α-T, where σ = stress in MPa; ε = strain; T = temperature in ^{o}C; and α =thermal expansion coefficient in $^{o}C^{-1}$) were used in the finite element models. Figure 7 (a) shows comparisons of the measured and numerically predicted axial load-displacement (P-δ) response of the W14X53 column in Test I. Similarly, Figure 7 (b) presents the exposed.

As shown in Figure 7 (a), the column specimen in Test I axially shortened with increasing axial load. The load-displacement response was similar to the column buckling at ambient temperature, but the steel stiffness and yield strength at elevated temperatures were degraded significantly. The measured axial capacity was 1450 kN (about 60% of axial capacity at ambient). In contrast, the column specimen in Test II elongated until the column was not able to maintain the sustained axial load of 1450 kN as shown in Figure 7 (b). The exposed steel temperature at column buckling was 550 ^{o}C. The specimens in Test I and Test II had a different behavior (i.e, shortening vs. elongation), but provided the similar prediction of axial capacity and buckling

temperature. Also, the comparisons in Figures 7 (a)-(b) show that the 3D finite element models reasonably predict the experimental behavior of the tested column specimens.

Figure 7 (b) shows there is slight discrepancy between the measured and calculated steel temperature-displacement (T-δ) response of the W14X53 column in Test II. This is probably due to the temperature gradient across the cross section in experiment. Temperature measured at the bottom of specimen was lower than 500 ^{o}C because of the heater layout and insulation used in Test II as described earlier. No temperature gradient was included in finite element model, and column buckling temperature was more conservative than the measured buckling temperature.

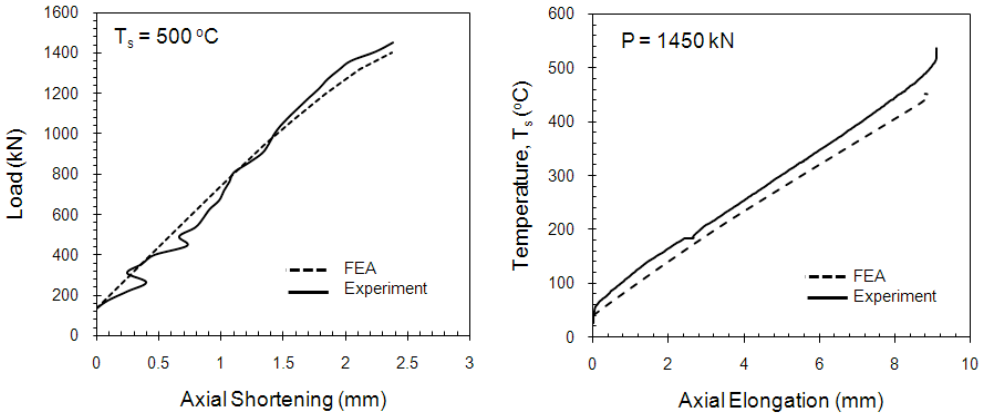


Figure 7 (a) Axial load-displacement (P-δ) in Test I and (b) Temperature-displacement (P- δ) response in Test II

SUMMARY AND CONCLUSION

This paper has presented the structural-thermal response of structural steel columns subjected to elevated temperatures. Experiments were conducted to compare the column behavior under two different heating conditions. In Test I, the W14X53 column was subjected to 500 ^{o}C and increasing axial loading until column buckling occurred. In Test II, the pre-determined steel surface temperature profile (obtained from heat transfer analysis) was used to apply thermal loading to the specimen subjected to sustained axial load (about 60% of axial load capacity). The overall behavior including end rotations, lateral displacements, and axial displacements were dissimilar between Test I and Test II. This is because the column behavior was controlled by the loading sequences. Initial thermal bowing was observed in Test II. This was because the effect of temperature gradient across the cross section in the heated region was more significant on the column behavior under transient heating condition. Test I and Test II resulted in different column axial displacements (i.e, shortening vs. elongation) before buckling, but provided the similar prediction of axial capacity and buckling temperature.

ACKNOWLEDGMENT

The research presented in this paper was funded by the National Science Foundation (Grant No. SMM-0825506 and 0825338). The project is titled " Structural Mechanics of Steel columns and Beam-Columns under Fire Loading". Experimental data, findings, and conclusions or recommendations are those of the authors only.

REFERENCE

ABAQUS (2010). *ABAQUS/Standard Version 6.10 User's Manuals: Volume I-III*, Hibbitt, Karlsson, and Sorenson Inc., Pawtucket, RI.

Agarwal, A., Varma, A.H., and Cedeno, G. (2009). "Steel columns under fire loading: stability behavior and design." *Proceedings of the Annual Stability Conference*, Structural Stability Council, Phoenix, AZ, in press, 405-429.

ASTM Standard E119 (2010). *Standard Methods of Fire Test of Building Construction and Materials*, American Society for Testing and Materials: West Conshohocken, PA, USA.

Choe, L., and Varma, A.H. (2010) "Experimental investigation of fundamental behavior of steel members under fire loading." *Proceedings of The Sixth International Conference,* Structures In Fire, East Lansing, MI.

ECS (2005). *Eurocode 3: Design of Steel Structures, Part 1.2, Structural Fire Design*, European Committee for Standardization, Brussels, Belgium.

IBC (2008). *International Building Code*. International Code Council Inc., Falls Church, VA, USA.

Varma, A. H., Hong, S., Agarwal, A., and Prasad, K., (2008). "Behavior of Steel Building Structures Under Realistic Fire Loading." *Proceedings of the 2008 Structures Congress – Vancouver, Canada*, ASCE, 12 pp.

Carbon Emissions and Building Structure: What the Structural Engineer Needs to Know about Carbon in the 21st Century

Mark D. Webster, P.E., LEED AP BD+C, M.ASCE,[1] Helena Meryman, LEED AP BD+C, M.ASCE,[2] and Dirk M. Kestner, P.E., LEED AP BD+C, M.ASCE,[3] with contributions from other members of the SEI Sustainability Committee Carbon Working Group

[1]Simpson Gumpertz & Heger, 41 Seyon St., Waltham, MA, 02453; mdwebster@sgh.com
[2] ScrapD, 169 Nevada St., San Francisco, CA 94110; helena@scrapd.com
[3] Walter P Moore, 221 West 6th St., Austin, TX 78701; dkestner@walterpmoore.com

The SEI Sustainability Committee formed a Carbon Working Group (CWG) in December 2009, chaired by this paper's lead author. The CWG is developing a white paper addressing building structure and carbon emissions which will be completed this year. The present paper is an interim report describing the CWG's findings to date.

Carbon Working Group Members:

Mark D. Webster, chair

Adam Slivers	Kathrina Simonen
Ali Mehrabian	Kenneth Bland
Dirk Kestner	Lindsey Maclise
Greg Briggs	Russ Miller-Johnson
Helena Meryman	Sandeep Mathur
Jeralee Anderson	Tona Rodriguez-Nikl

INTRODUCTION

The contribution of carbon emissions to the increase in the global average temperature is well established. It is nearly universally accepted that significant decreases in carbon dioxide and other greenhouse gas emissions must be realized in the near future, or the global community will face very troublesome and possibly even catastrophic climate-related impacts. Civil engineers have a professional duty to abide by the code of ethics adopted by ASCE. The first principle states "Engineers uphold and advance the integrity, honor and dignity of the engineering profession by: a) using their knowledge and skill for the enhancement of human welfare and the environment." The first canon instructs us that "Engineers shall hold paramount the safety, health and welfare of the public and shall strive to comply with the principles of sustainable development in the performance of their professional duties" (ASCE, 2009). To these ends, structural engineers are tasked with finding ways to reduce the climate impacts of structures. This paper provides information on the currently available data pertaining to the carbon impacts of concrete and steel. The focus is on how to use the available data to make informed choices to minimize the climate impact of the material aspects of structural design. The first step is to understand the

impacts, their relative intensities, and a little bit about climate science. The Carbon Working Group is dedicated to making this information available and usable.

BACKGROUND

The term "greenhouse effect" is used to describe how carbon and other heat-trapping gases in our atmosphere warm the Earth and its lower atmosphere. These gases allow visible light to enter, but obstruct escaping heat. Sunlight imparts energy to the Earth. When the Earth radiates this solar energy back out in the form of infrared radiation (heat), greenhouse gases (GHGs) reflect this heat in all directions, including down toward the Earth. Ice core data shows that for all of human history—roughly 200,000 years—the amount of CO_2 in the atmosphere ranged from about 190 to 290 parts per million (ppm) (Petit 1999). Most recent temperature and carbon concentration data sets show rapid increases over the past 100 years. Currently the concentration of atmospheric CO_2 is about 390 ppm and is increasing at a rate of about 2 ppm/year (ESRL 2011). Between 1910 and 2005, the global average temperature rose by 0.9 degrees Celsius, with over 60% of the rise occurring since 1970 (IPCC 2007). The scientific community is nearly unanimous that these increases are due to human activities.

While CO_2 is not the most potent GHG, it is the most abundant and therefore has the largest cumulative effect. Greenhouse gases persist in the atmosphere. Each gas has a different rate of decay. One-fifth of the CO_2 we emit today will remain in the atmosphere in the year 3011. The carbon we "spend" today will continue warming the earth for thousands of years, and so it follows that the carbon we spend tomorrow doesn't replace today's carbon, but rather is added to it, resulting in carbon build-up. The decay rate of GHGs is therefore a fundamental part of determining its global warming potential (GWP).

Many gasses contribute to the greenhouse effect, but the warming potency of the gasses varies widely. By far the most abundant greenhouse gas is carbon dioxide (CO_2), but nitrous oxide (N_2O) and methane (CH_4) are present in significant amounts and are more potent warmers. The GWP of any gas is a measure of how much it contributes to global warming compared to how much the same mass of carbon dioxide contributes. Thus, by definition, the GWP of carbon dioxide is 1. GWP depends on how well a gas absorbs infrared radiation (radiative forcing) and how quickly it decays from the atmosphere. Therefore, the GWP depends on what time-span is being considered, for example the next 10, 100 or 500 years. The 100-year time-frame is most common. At 100 years, the GWP of methane is 25 and that of nitrous oxide is 298 (IPCC4 2007).

Carbon Dioxide Equivalency (CO_2e) represents the global warming potential of a mixture of gasses in known amounts as an equivalent amount of CO_2. To convert non-CO_2 emissions into CO_2e, the mass of each gas is multiplied by its GWP and added together to find a mass of CO_2e. It is important that all the GWP values used are from the same time-scale or the result is meaningless. References to "carbon" emissions in this paper refer to CO_2e unless otherwise noted.

The relatively sudden rise in temperature caused by increasing CO_2 emissions is destabilizing the earth's weather systems, leading to more frequent and severe storms, new rainfall and drought patterns, and altered temperature patterns that will

make some areas of the planet significantly colder and some areas much warmer. The warming of the arctic regions will melt ice sheets, causing a rise in sea level, and putting low-lying coastal areas and some island nations under water.

SOURCES OF CARBON EMISSIONS

Fossil fuel use is the largest contributor to carbon emissions. The U.S. Environmental Protection Agency (EPA) reports that in 2008 the U.S. emitted about 6,960 million metric tons (Tg) of CO_2e, about 85% of which was due to fossil fuel combustion (EPA 2010). Figure 1 shows the breakdown of these fossil fuel emissions.

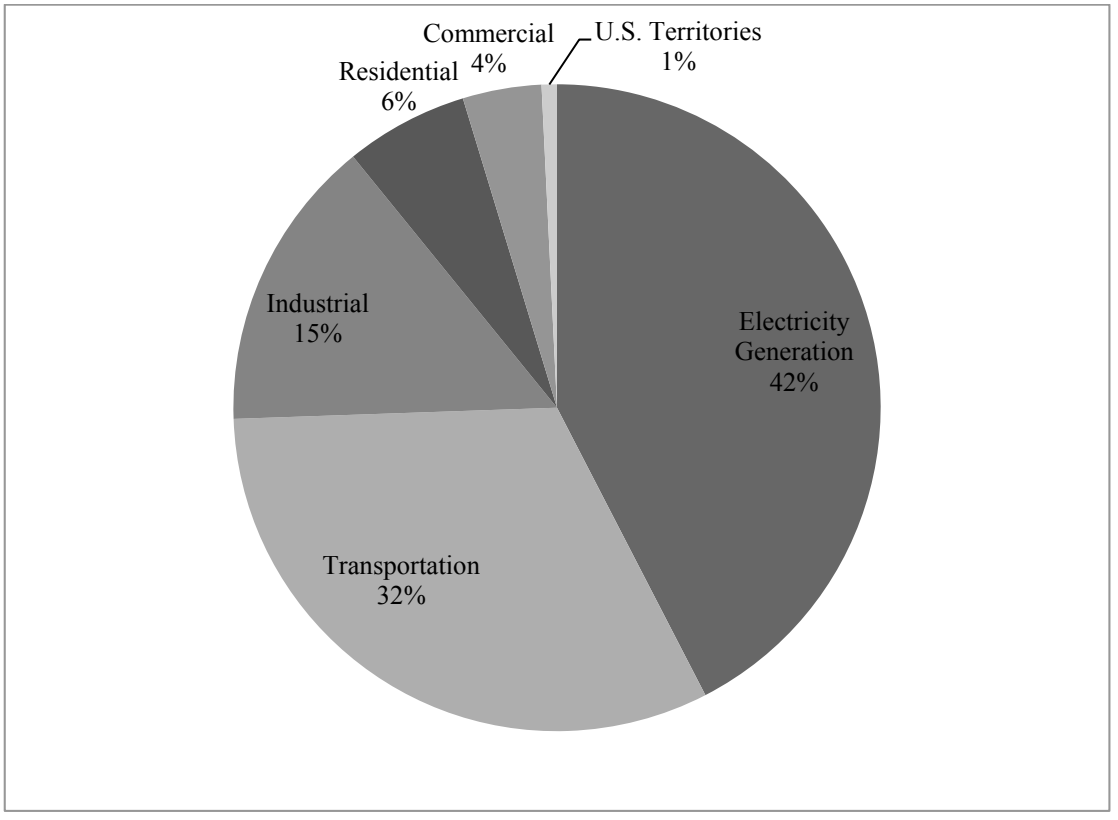


Figure 1: U.S. Carbon Emissions Due to Fossil Fuel Consumption (EPA 2010)

In addition to fossil fuel combustion, certain industrial sectors produce significant quantities of carbon emissions due to process-related chemical reactions. Iron and steel production and metallurgical coke production accounted for 69 Tg CO_2e in 2010 and cement production for 41 Tg.

RELEVANCE OF BUILDING STRUCTURE

Building structure primarily contributes to a building's carbon emissions in two ways: embodied carbon and use-phase carbon.

Embodied carbon is the sum of all carbon emissions generated during the extraction, manufacturing, fabrication, and erection of the structural system.

Sometimes end-of-life emissions are also included, such as the emissions due to building demolition and disposal of materials. Emissions due to the transport of materials from extraction to erection and also at end-of-life are typically included in the calculation for embodied carbon.

During the use-phase of a building, i.e. occupancy, carbon emissions result primarily from the consumption of on-site energy and water. The structural design of a building can impact the building's energy efficiency. For example, if strategically located, the thermal mass of concrete and masonry can help temper swings in exterior temperature, thereby reducing energy use. Another example is thermal bridging. When structural components such as steel outriggers and concrete cantilevered decks pass through the building's thermal envelope, breaking the insulation layer, significant thermal losses can occur, increasing the building's energy consumption.

Assuming a 50-year life, the global warming potential associated with the embodied impacts of a building's structural system can vary from about 1 to 16 percent of the building's total life-cycle GWP (Webster 2004). The type of construction, energy sources, and the energy efficiency of the building systems are important factors in determining the structural contribution to the impact. As buildings become more energy efficient and electricity production transitions towards renewable sources, the relative impact of building structure will increase even further.

CARBON IMPACTS OF CONCRETE AND STEEL

This interim report addresses only concrete and steel. The CWG is also studying wood, FRP, and masonry and plans to address these materials as well in its forthcoming white paper.

Concrete

Concrete's primary carbon impacts derive from cement and steel reinforcement. Reinforcement is addressed in the steel discussion below. In a typical concrete mix, the cement accounts for 12% or less of the concrete mix by weight, but represents about 95% of the carbon emissions (Kestner 2009).

Portland cement is produced in manufacturing facilities where raw materials (lime, iron, silica, and alumina, most commonly in the form of limestone and clay) are heated in a kiln to high temperatures (reaching 1450ºC) causing a chemical reaction called calcination. Calcination produces approximately 0.51 metric tons of carbon dioxide (CO_2) per metric ton of clinker produced. Ordinary portland cement is about 95% clinker and 5% gypsum. The fuel required to heat the kiln to such high temperatures contributes another 0.43 metric tons of CO_2 per metric ton of clinker produced (van Oss 2005). Using van Oss's figures, 54% of emissions are due to calcination and 46% are due to thermal or primary energy uses. It is important to note that electricity—which typically account for between 7% and 10% of total energy—is not accounted for. The carbon impact of electricity used to grind and process cement is difficult to quantify; it varies from very low for electricity from hydro power to very high for coal-based power.

The EPA reports that cement manufacturing produces roughly 1.5% of total GHGs in the United States, while the construction industry produces 6% of all U.S. GHGs (EPA 2008). These numbers are lower than the global average simply because

the U.S. is such a big consumer of energy; it is not an indication of superior performance by U.S. cement plants (Meryman, 2010). For close to a decade the cement sector has conceded to contributing around 5% of global anthropogenic CO_2 emissions. This number has been up for debate, especially considering the continued growth in cement demand. Using 2007 data from the Carbon Dioxide Information Analysis Center (CDIAC) for total fossil fuel and cement-based CO_2 emissions (30,675 million tons), cement calcination emissions (1,977 million tons), and the emissions breakdown provided above by van Oss, we can generate a more current estimate (CDIAC 2010). Globally, GHG emissions due to cement manufacturing account for over 6.4% of the major anthropogenic CO_2 emissions.

Concrete's carbon impacts can be reduced by replacing portland cement with complementary cementing materials such as fly ash and slag. As post-industrial "waste" materials, fly ash and slag have very low carbon emissions. The carbon emitted during their production does not contribute to their embodied carbon because it is attributed to the primary product, such as the electricity generated by a coal-fired power plant that produces fly ash as a waste product.

BEES 4.0, is a free life-cycle assessment program developed by the National Institute of Standards and Technologies (NIST) that can provide useful insight into the climate impact of materials. BEES includes carbon figures for a number of different concrete mixes used in a number of different types of structural elements. BEES reports figures only for assemblies of reinforced concrete elements that include assumed quantities of reinforcement and formwork. According to BEES, a reinforced concrete beam constructed with 4 ksi concrete using only portland cement as a binder has a CO_2e of 14.1 kg/ft^3. The same element using a concrete mix with 50% cement replacement with slag has a CO_2e of 10.4 kg/ft^3. Even though the reinforcement and formwork impacts are identical for both options, the carbon impact for the slag mix is 26% lower. The carbon impact of concrete alone is very much controlled by the cement content; replacing 1 ton of cement with fly ash or slag reduces the carbon impact of concrete by about 0.84 to 0.9 tons, per the following calculation:

> (0.51 tons (CO_2 from calcination) + 0.43 tons (CO_2 from thermal energy)) x 0.95 (emission factor attributed to the cement portion of concrete) x 0.95 (clinker factor)) = 0.84 tons.

Since electricity is not included in the energy emissions, this is a minimum value.

Steel

Structural steel is produced primarily in electric arc furnaces (EAFs) or basic oxygen furnaces (BOFs). According to the Steel Recycling Institute (SRI 2009), steel produced in EAFs has a total recycled content of about 90%, compared to 33% for steel produced in BOFs. In part due to its recycled content, EAFs produce fewer carbon emissions per ton of production than do BOFs.

All hot-rolled shapes produced in the United States are from EAFs (AISC 2008). HSS is currently manufactured using steel from both EAFs and BOFs. In 2008, more than half of the coil steel used to produce HSS came from BOFs (AISC 2008-1).

Most of the structural steel used for buildings in the United States is produced domestically. AISC estimates that only 9% of domestic consumption is imported (AISC 2010).

Steel deck and cold-formed framing are typically produced from the same stock material—cold-rolled sheet—and is often galvanized. Most of this steel is produced domestically in BOFs. Reinforcing steel used in masonry and concrete construction is typically produced domestically in EAFs.

The primary life-cycle stages of structural steel production are:

1. Extraction of raw materials. Raw materials include iron ore, coal, and limestone. Collection of steel scrap, another primary raw material, is included in this life-cycle stage. About 80% of post-consumer steel is recycled into new steel (World Steel 2008).
2. Steel production, including rolling and forming.
3. Shop fabrication.
4. Transportation between life-cycle stages.
5. Construction.
6. End-of-Life. Most steel removed from buildings is recycled into new steel.

Of these six life-cycle stages, the steel production stage produces the most CO_2e. EAF production produces less than half as much CO_2e as BOF production. The Steel Manufacturer's Association (SMA) estimates that EAF production emits 0.74 tons of CO_2/ton of product, while BOF production emits 1.91 tons CO_2/ton of product (SMA 2007).

AISC publishes a "carbon footprint" for domestically produced rolled shapes, all of which are produced in EAFs, of 0.73 to 0.89 tons of CO_2 per ton of steel (AISC 2010), based on the SMA study as well as a study AISC commissioned from a life-cycle assessment consulting firm. These figures assume a recycling rate of 98% and exclude fabrication. AISC's life-cycle assessment consultant recently completed a study of the fabrication of structural steel. The study found that fabrication adds about 0.19 to 0.26 tons of CO_2e per ton of steel (Weisenberger 2010). Summing the production and fabrication figures gives a range of 0.92 to 1.15 tons of CO_2e per ton of fabricated steel.

HSS sections are produced in both EAFs and BOFs, so their production emits more CO_2e than hot-rolled shapes. AISC does not publish carbon impact estimates for HSS sections. The Athena Institute, an independent life-cycle assessment consulting firm, published production and transport emissions values of CO_2 and methane for HSS sections produced in combined U.S. steel mills (Athena 2002). Unfortunately the reports do not include nitrous oxide (N_2O) emissions. Applying a GWP factor of 25 for methane, the total CO_2e for HSS amounts to 1.76 tons/ton of production.

Steel reinforcement is produced primarily in EAFs. Again using the Athena inventory data and the same approach we used for the HSS calculations, we find that the CO_2e figure for U.S. reinforcement is 0.59 tons/ton.

Athena also addressed galvanized steel deck and welded wire mesh. For these products the CO_2e figures are 1.79 and 1.35 tons/ton, respectively.

DESIGNING TO REDUCE CARBON IMPACTS

Once the structural designer understands the carbon impacts of available materials, he or she can implement carbon-reduction strategies. For most buildings, the choice of concrete or steel construction will depend upon factors other than carbon emissions. Assuming this is the case, the designer's task is to reduce the impacts of the given material.

For both concrete and steel structures, material optimization will generally reduce carbon impacts.

For steel, optimization strategies might include the following:

- Using more labor-intensive (and potentially more expensive) options such as lighter columns with continuity plates at joints rather than larger columns sized to minimize fabrication.
- Selecting braced frames for lateral-load resisting systems in place of moment-resisting frames, which use substantially greater quantities of steel. A study by Simpson Gumpertz & Heger, Inc. found that, for a representative 9-story building in Los Angeles, designing a braced-frame lateral system in place of a moment-resisting frame reduced the structural steel quantity by 37%, with a commensurate reduction in GWP.
- Designing with castellated beams rather than conventional wide flanges.
- Investigating catenary structures in place of trusses for long-span roofs.

For concrete, optimization might include:

- Strategically introducing air voids into concrete elements, such as those employed in the BubbleDeck® system.
- Investigating thin-shell arched or folded-plate structures in place of linear and planar elements.

Concrete offers additional opportunities to reduce carbon impacts by specifying material improvements, such as the replacement of cement with complementary cementing materials such as fly ash and slag. Other ways to reduce the carbon-intensive cement content include:

- Avoiding over-specifying concrete strength and designing and specifying for f'c at 56 days where feasible.
- Using larger-sized aggregates to reduce the paste volume.

Finally, steel reinforcement quantities can be reduced where it is not required. For example, reinforcement in slabs-on-grade can be eliminated by using more closely spaced control joints. Use of 75 ksi reinforcement in place of Grade 60 reinforcement can also reduce carbon impacts by reducing the reinforcement tonnage.

CARBON CALCULATION EXAMPLE

Until standardized methods of carbon impact are fully developed and implemented, we cannot be certain that carbon figures obtained from different

sources, and perhaps even from the same sources, are directly comparable. The International Standards Organization (ISO) has developed and is continuing work on standards for performing life-cycle assessments such as those used to determine carbon emissions. Carbon accounting is still in its infancy, and, although we see enough consistency in the figures developed by different organizations that we believe some convergence is underway, we realize that the figures may still vary by 50% or more depending on the assumptions and methodologies used. One problem is that the assumptions used to build the data set are usually not well explained, so it is difficult to know if it is an apples-to-apples comparison. Currently, comparisons between options using similar materials are more accurate than comparisons between different materials. For these reasons, the following exercise is intended for demonstration purposes only and is not intended to provide a definitive conclusion regarding the relative carbon impacts of the two systems.

The example shown in Tables 1 and 2 compares two alternatives for a 30-foot span in a typical office building, with loads including self weight, 10 psf for MEP and finishes, 20 psf for partitions, and 50 psf live load. The structural proportions were selected to provide a 2-hour fire rating without the need for additional fireproofing on the steel deck. Note that it is a component comparison, so does not account for possible differences in the building systems beyond the boundaries of the beams, such as girder and column differences and fireproofing materials.

Option 1: Steel Composite Beam

- W14x22 beams @ 8'-4" o.c.with 10 shear studs per beam
- 20 ga. 2-inch steel deck
- 2 inches plus 4.5 inches for a total thickness of 6.5 inches of normal-weight, 3,500 psi concrete with 25% of cement replaced by Class C fly ash
- 6x6-W2.1xW2.1 steel mesh

Table 1. Carbon account for Option 1.

Item	Unit	Quantity per Square Foot	Carbon Intensity (lb/lb or lb/cy)	Carbon (psf)	% of Total
W 14x22	22 plf	2.64 psf	1.04	2.7	22%
Deck		1.97 psf	1.79	3.5	29%
Mesh		0.29 psf	1.35	0.4	3%
Studs		0.03 psf	1.04	0	0%
Concrete	5.5 in	0.02 cy/sf	332	5.6	46%
Total				**12.3**	**100%**

Option 2: Concrete pan-formed beams

- 5-inch normal-weight 4,000 psi concrete with 25% of cement replaced by Class C fly ash

- pan-formed beams 6-inch wide by 16-inch deep (below slab) @ 72 inches o.c. (total system thickness of 21 inches)
- 1.65 psf of beam reinforcing

Table 2. Carbon account for Option 2.

Item	Unit	Quantity per Square Foot		Carbon Intensity (lb/lb or lb/cy)	Carbon (psf)	% of Total
Slab Steel		0.3	psf	0.59	0.2	2%
Beam reinf.		1.65	psf	0.59	1.0	11%
Concrete	6.64 in	0.02	cy/sf	376	7.7	87%
Total					**8.9**	**100%**

While this comparison shows that the concrete option has a lower embodied carbon impact per square foot of floor area, it addresses only an element and does not account for the full structural system. It also does not consider impacts due to the construction process or those from material transportation. However, it serves as a starting point for those who want to perform this type of calculation in their practice. A complete example would need to address the girders, vertical and lateral framing elements, as well as foundations to make an actionable assessment of the relative merits of the two systems. For even more accuracy, differences in non-structural systems, such as any additional fire-proofing required for the steel-framed option, would need to be included.

Additionally, this example is based on publicly available carbon data developed by different organizations at different times using different assumptions. Our hope is that practitioners will soon have at their disposal more reliable and comparable figures for carbon intensity that will give more credence to calculations such as these. The National Renewable Energy Laboratory is compiling a U.S. Life Cycle Inventory Database (http://www.nrel.gov/lci/) that may eventually fulfill this need. Additionally, the World Resource Institute is developing product-specific carbon footprint standards and ASTM is developing "product category rule" standards which aim to enable more accurate comparisons between products and assemblies. With supply-chain-specific product carbon footprints, designers could specify carbon as a performance metric to motivate and reward lower impact/higher efficiency manufacturing methods.

CONCLUSIONS

Structural engineers have an important role to play in reducing the carbon impact of the built environment. The structural system accounts for a significant portion of a building's life-cycle carbon impacts. Understanding the environmental impact of the structures we design is the first step in cultivating our ability to reduce and mitigate these impacts. Using currently available data is appropriate as structural engineers work to define methods to account for and report the carbon footprint of

structures. The accuracy of these analyses will improve as better LCA data becomes available. With an understanding of material carbon emissions and the limitations of current data, the structural engineer can effectively use simple calculations to make rough comparisons between options and can apply carbon-reduction strategies to reduce the structural system's carbon impacts. As the data improves and structural engineers develop their own tools to utilize it, we can look forward to having a more valued voice in the discussion of the climate impacts of materials, and improved capability to design projects to minimize those impacts.

REFERENCES

AISC 2008. American Institute of Steel Construction, "Structural Steel: An Industry Overview," December 2008.

AISC 2008-1. American Institute of Steel Construction, "Steel Quiz," *Modern Steel Construction*, June 2008.

AISC 2010. American Institute of Steel Construction, "Structural Steel: An Industry Overview," September 2010.

ASCE 2009. American Society of Civil Engineers Code of Ethics, http://www.asce.org/Content.aspx?id=7231, last accessed January 2011.

Athena 2002. The Athena Sustainable Materials Institute, *Cradle-to-Gate Life Cycle Inventory: Canadian and US Steel Production by Mill Type*, March 2002.

CDIAC 2010. Oak Ridge National Laboratory, Carbon Dioxide Information Analysis Center, "Global CO_2 Emissions from Fossil-Fuel Burning, Cement Manufacture, and Gas Flaring: 1751-2007," http://cdiac.ornl.gov/ftp/ndp030/global.1751_2007.ems, accessed January 2011.

EPA 2008. *Quantifying Greenhouse Gas Emissions from Key Industrial Sectors in the United States*. US Environmental Protection Agency, May 2008.

EPA 2010. Inventory of U.S. Greenhouse Gas Emissions and Sinks: 1990-2008 (Executive Summary). U.S. Environmental Protection Agency, April 2010 http://www.epa.gov/climatechange/emissions/downloads10/US-GHG-Inventory-2010_ExecutiveSummary.pdf.

ESRL 2011. Earth Systems Research Laboratory, Global Monitoring Division, Trends in Atmospheric Carbon Dioxide, ftp://ftp.cmdl.noaa.gov/ccg/co2/trends/co2_gr_mlo.txt, last accessed January 2011.

IPCC4 2007. Forster, P., V. Ramaswamy, P. Artaxo, T. Berntsen, R. Betts, D.W. Fahey, J. Haywood, J. Lean, D.C. Lowe, G. Myhre, J. Nganga, R. Prinn, G. Raga, M. Schulz and R. Van Dorland, 2007: Changes in Atmospheric Constituents and in Radiative Forcing. *In: Climate Change 2007: The Physical Science Basis. Contribution of Working Group I to the Fourth Assessment Report of the Intergovernmental Panel on Climate Change* [Solomon, S., D. Qin, M. Manning, Z. Chen, M. Marquis, K.B. Averyt, M.Tignor and H.L. Miller (eds.)]. Cambridge University Press, Cambridge, United Kingdom and New York, NY, USA http://www.ipcc.ch/pdf/assessment-report/ar4/wg1/ar4-wg1-chapter2.pdf.

IPCC 2007. *Climate Change 2007: The Physical Science Basis. Contribution of Working Group I to the Fourth Assessment Report of the Intergovernmental Panel on Climate Change* (Solomon, S., D. Qin, M. Manning, Z. Chen, M.

Marquis, K.B. Averyt, M.Tignor and H.L. Miller (eds.)). FAQ 3.1, Cambridge University Press, Cambridge, United Kingdom and New York, NY, USA. http://www.ipcc.unibe.ch/publications/wg1-ar4/faq/wg1_faqIndex.html.

Kestner 2009. Kestner, Dirk, *The Mysterious Role of Structure in Sustainable Design*, Greenbuild presentation, November 2009.

Meryman 2010. Meryman, Helena; Vaughan, Sarah; Kren, Alan; and Alsamsam, Iyad, "Chapter 3.2: Concrete," *Sustainability Guidelines for the Structural Engineer,* edited by Kestner, Dirk M.; Goupil, Jennifer; and Lorenz, Emily, ASCE 2010.

Petit 1999. Petit J.R., Jouzel J., Raynaud D., Barkov N.I., Barnola J.M., Basile I., Bender M., Chappellaz J., Davis J., Delaygue G., Delmotte M., Kotlyakov V.M., Legrand M., Lipenkov V., Lorius C., Pépin L., Ritz C., Saltzman E., Stievenard M. "Climate and Atmospheric History of the Past 420,000 years from the Vostok Ice Core, Antarctica," *Nature* **399**: 429-436.

SMA 2007. Steel Manufacturers Association, "Carbon 'Footprints' in U.S. Steelmaking," by John Stubbles, 2007.

SRI 2009. Steel Recycling Institute, "2008 The Inherent Recycled Content of Today's Steel," updated December 2009.

Van Oss 2005. Van Oss, Hendrik G., *Background Facts and Issues Concerning Cement and Cement Data*, United States Geological Survey, 2005.

Webster 2004. Webster, Mark, "Relevance of Structural Engineers to Sustainable Design of Buildings," *Structural Engineering International*, March 2004.

Weisenberger 2010. Weisenberger, Geoff, "The Fabrication Factor," *Modern Steel Construction*, July 2010.

World Steel 2008. World Steel Association, "Fact Sheet: Raw Materials," October 2008.

Life Cycle Assessment Using ATHENA® Impact Estimator for Buildings: A Case Study

Elizabeth Stek, LEED AP®[1], Dave DeLong, LEED AP®[2],
Terry McDonnell, PE, SE, SECB[3], Jose Rodriguez, LEED AP® BD+C[4]

[1]Halcrow Yolles, One South Dearborn, 21st Floor, Chicago, IL 60603; PH (312) 212-4209; email: elizabeth.stek@halcrowyolles.com
[2] Halcrow Yolles, One South Dearborn, 21st Floor, Chicago, IL 60603; PH (312) 212-4224; email: david.delong@halcrowyolles.com
[3]Halcrow Yolles, One South Dearborn, 21st Floor, Chicago, IL 60603; PH (312) 212-4205; email: terry.mcdonnell@halcrowyolles.com
[4]Halcrow Yolles, One South Dearborn, 21st Floor, Chicago, IL 60603; PH (312) 212-4428; email: jose.rodriguez@halcrowyolles.com

ABSTRACT

Life cycle assessment is a means of calculating the environmental impact of processes. The ATHENA® Impact Estimator for Buildings was developed by the Athena Sustainable Materials Institute and software collaborator, Morrison Hershfield as a means of applying life cycle assessment to the construction of buildings. The Impact Estimator measures the environmental impact of the new construction of a building in the areas of: Primary Energy, Global Warming Potential, Human Health Respiratory Effects, Ozone Depletion, Weighted Resource Use, Water Pollution, and Air Pollution. It is the intent of this paper to use the software to evaluate a four story office building for four proposed structural framing systems currently under construction in Chicago. The building was designed with the intent of achieving LEED® Platinum certification. The results of the four life cycle assessments will be compared. During this comparison, the authors intend to examine the software to determine its validity as a tool for making sustainable design decisions based upon structural systems.

INTRODUCTION

Sustainable development, defined in *Our Common Future* as "development that meets the needs of the present without compromising the ability of future generations to meet their own needs" (World Commission on Environment and Development, 1987), has been gaining more attention in the past few decades. In many industries, environmental consequences are now given consideration alongside economic and social consequences. One of the challenges in the sustainable development movement has been developing metrics that more effectively aid in making decisions based on how these decisions will affect the environment. One way the building industry measures sustainability is by using a technique call life cycle assessment.

Life cycle assessment (LCA) is a study of the consequences that certain products, processes, or services will have on the environment based on the byproducts, energy

and resources that they require throughout their lifespan. LCA is a relatively new tool for rating the sustainability of buildings but its use is being encouraged by the incorporation of LCA into the LEED® and Green Globes® rating systems.

It is the purpose of this paper to compare four life cycle assessments based on structural system options (S1-S4) for a four story office building constructed in Chicago using ATHENA® Impact Estimator. The results of the Impact Estimator output will be will be considered in several ways:

- Program accuracy
- Embodied vs. operating impacts
- Environmental metrics
  - Embodied Energy Consumption
  - Global Warming Potential - CO_2 equivalence
  - Smog Potential - NO_x equivalence
  - Human Respiratory Effects - PM2.5 equivalence

Program Accuracy
The Impact Estimator allows data to be inputted in two different ways: by identifying assembly type, providing geometry and live loads, which the program then uses to calculate a bill of materials ('A' models), and by input of material quantities directly ('B' models). ATHENA® Impact Estimator for Buildings V3.03 Software and Database Overview claims that these values should be within +/- 10% of a detailed manual take-down. It is the intention of the authors to investigate this claim.

Embodied vs. Operating Energy
Previous research (Hsu 2010) has shown that the embodied energy of a building is only a fraction of the operating energy. The authors intend to quantify this difference and check it against previous research.

Environmental Impacts
Through a comparison of the environmental impacts, it will be determined whether the structural system that was chosen for the office building is the most environmentally sustainable.

By comparing the above results for the four structural systems, the authors will examine the software to determine its validity as a tool for making sustainable design decisions based upon structural systems.

LIFE CYCLE ASSESSMENT FOR BUILDINGS

A building's energy use and its associated emissions have an extensive impact on the environment. In the United States, the building industry accounts for approximately 40% of the country's primary energy use (US DOE 2009). Though a majority of this is operating energy, the materials used to construct a new building have an inherent environmental cost (Johnson 2006). This cost is associated with the extraction,

manufacturing, transportation, construction and end of life disposal of the building materials and is referred to as embodied environmental impacts.

Structural elements have a greater environmental impact than many of the other building elements such as finishes, flooring, and roofing, because they are the greatest percentage of the total building material. The decision on how to structurally frame a building can therefore have a great impact in the building's environmental impact. Though this energy is only a fraction of what is used to power the building over its lifetime, as building envelope and HVAC systems become more efficient and the amount of energy required to heat, cool, and light a building decreases, the environmental impacts associated with the manufacturing and construction phases will make up an increased percentage of the total impact.

While the gathering and evaluation of the data for all of the processes involved in the extraction, manufacturing, construction and end of life disposal associated with structural components is very rigorous, new advances in LCA have made it possible for a structural engineer to compare how particular structural framing schemes will impact the environment. Programs like ATHENA® Impact Estimator for Buildings allows the design team to perform a desktop LCA of several options during the schematic design phase so that environmental impacts can be considered at the beginning of the design process when major system decisions are being made.

ATHENA® IMPACT ESTIMATOR FOR BUILDINGS

Athena Sustainable Materials Institute, a non-profit organization based in Ontario, Canada developed the ATHENA® Impact Estimator for Buildings. The Institute's mission is to promote sustainability in the built environment through the use of Life Cycle Assessment in North America. They offer two products in the United States, the Impact Estimator for Buildings and EcoCalculator for Assemblies. The EcoCalculator supplies more accessible results based on predefined calculations made with the Impact Estimator. This paper focuses on the use of the Impact Estimator to analyze a low rise office building constructed in Chicago.

The Impact Estimator was developed as a support tool to aid in the decision making process at the conceptual design stage. The software provides a cradle-to-grave (extraction through end of life disposal) life cycle assessment for a building design. It allows us to compare up to five design scenarios in terms of the following environmental impact categories set forth by the US Environmental Protection Agency for LCA in accordance with ISO 14040:

- Primary energy consumption
- Acidification (Air) Potential - moles of H^+ ions equivalent mass
- Global warming potential – $C0_2$ equivalent mass
- Human Health Respiratory Effects Potential - PM2.5 equivalent mass
- Ozone Depletion Potential – CFC 11 equivalent
- Photochemical Smog Potential - NO_x equivalent mass
- Eutrophication Potential - N equivalent mass

- Weighted Raw Resource Use

(ATHENA® Impact Estimator for Buildings, Overview)

The impact estimator takes into account any or all of the following building characteristics and life-cycle factors to measure the impact in each of the metrics listed above:

- Material manufacturing, including resource extraction and recycled content
- Related transportation
- On-site construction
- Regional variation in energy use, transportation and other factors
- Building type and lifespan
- Maintenance and replacement effects
- Demolition and disposal

(ATHENA® Impact Estimator for Buildings, Overview)

The user enters the city which best represents the location of the project (currently only seven US cities are included as options), the expected life span of the project, and the material assemblies of the project. The project location determines the electrical grid, transportation mode and travel distances for each material, as well as product manufacturing technologies. The life span of the project will affect the maintenance and replacement cost for building assemblies. For example, any assembly that has a service life, based on regional data, less than that of the whole building will have increased environmental costs associated with repair and replacement and any assembly with a service life greater than that of the structure will be credited with the environmental impact of the difference in lifespan. The material take-off can be determined in two different ways: a "deterministic" method where the model completes a quantity take-off calculation based statistical data and a "prescriptive" method where the user directly enters quantities. The bill of materials is used in conjunction with recognized material databases to determine the environmental impacts of the materials. A table of the databases and their vintage is available on the Athena Institute's website at www.athenasmi.org.

PROJECT DESCRIPTION

The building under consideration is a four story (125,000sf) owner occupied office building on the north side of Chicago, Illinois. The building has open floor plates, a semi-circular training room and an atrium acting as lobby and connector, built close to the Chicago River. To simplify the analysis, only the 79,800sf, four story, main office building will be considered and the atrium, lobby and other interstitial space will be omitted. All options share a common foundation system and are clad with a glass curtain wall which was assumed to be 80% glass and 20% spandrel with 6" of insulation. Due of the nature of the work being done in the building a live load of 80psf plus a 20psf partition load for a total of 100psf live load was used in the Athena model. At the roof level the authors also used a 100psf live load as an average of the plaza area, mechanical units and green roof. A detailed description of the foundation and structural options follow and a sketch of a typical floor layout for the office

building can be found in Appendix A. For this study, the building was assumed to have a 50yr lifespan.

Foundation System

The foundation system for this building consists of belled caissons down to stiff clay at approximately 32 feet below grade. Grade beams were installed at the perimeter of the building to accommodate frost requirements of the building location, support the first floor of the building façade, and assist with thermal insulation at the perimeter of the building. A few isolated grade beams were also installed at bays that contained steel cross-bracing. In options that have a concrete shear wall lateral system, a mat foundation was considered under the elevator cores and stairwells to support the shear walls.

Option S1: Structural Steel Framing

The framing for this scheme consists of rolled steel W shaped beams, columns and braces. The gravity floor framing system consists of 3" concrete slab on 3" steel deck supported by W18x50 floor beams (typical) acting compositely with the deck/slab. Beams are supported by W21x55 girders or frame directly into columns, depending on their location. The lateral load resisting system consists of steel cross-bracing located around the elevator shafts, stairwells and washrooms.

Option S2: Reinforced Concrete Option

The framing for this scheme consists of reinforced concrete band beams, one-way slabs, columns and shear walls. The gravity floor framing system consists of reinforced concrete band beams 8'-0" wide on 30'-0" centers (i.e. at column lines). The beams are 28" deep for the 45'-0" spans and 16" deep elsewhere. An 8" thick reinforced concrete slab (whose depth is integral with the beams) spans one-way between these beams. In the exterior bay at each end of the building, the depth of the one-way slab must be increased to 12" in order to ensure that long-term deflections in these areas fall within the limits set by the design codes. In all other locations, the 8" slab suffices. The presence of framing in adjacent bays provides additional stiffness due to the continuity of construction. Columns are typically 26" in diameter. In this scheme, the spandrel beams support only the cladding. There are no girders. The lateral load resisting system consists of 10" thick reinforced concrete shear walls around the elevator cores and stairwells.

Option S3: Post-Tensioned Option

The framing for this scheme consists of post-tensioned concrete band beams and reinforced concrete one-way slabs, columns and shear walls. The gravity floor framing consists of post-tensioned concrete band beams 8'-0" wide on 30'-0" centers (i.e. at the column lines). The floor slab is not post-tensioned. The depth of the typical floor slab is 8", and 12" at end spans, the same as for the reinforced concrete option. The beams are 24" deep for 45'-0" spans and 16" deep elsewhere. Except for the post-tensioning of the beams, this scheme is similar in arrangement and general characteristics to the reinforced concrete scheme. The use of post-tensioning allows

the depth of the beams that span 45'-0" to be reduced from 28" to 24". This depth would also be required in the middle 20'-0" span due to construction and continuity issues associated with the post-tensioning. All spandrel beams are reinforced concrete 24" deep, and mildly reinforced. The lateral load resisting system consists of 10" thick reinforced concrete shear walls around the elevator cores and stairwells, exactly as in option S2.

Option S4: Hollow Core Plank Option

The framing for this scheme consists of pre-cast hollow core concrete slabs supported on structural steel beams and columns together with steel braced frames at the building core. The gravity floor framing system consists of 14" and 10" thick hollow core slabs supported by W24 or W27 girders. The 14" thick hollow core slabs are required for the 45'-0" spans under the specified loads. The 10" thick slabs are adequate elsewhere. Columns are typically W14 sections. A 2" thick topping is required over all slabs to ensure that the floor diaphragm is capable of transferring lateral loads from wind to the braced frames. This topping must be supplemented with additional reinforcement and detailing. To increase the floor to ceiling height additional steel is added so that top of hollow core is 2" below the top of steel elevation (see Figure 1). The lateral load resisting system duplicates that of option S1.

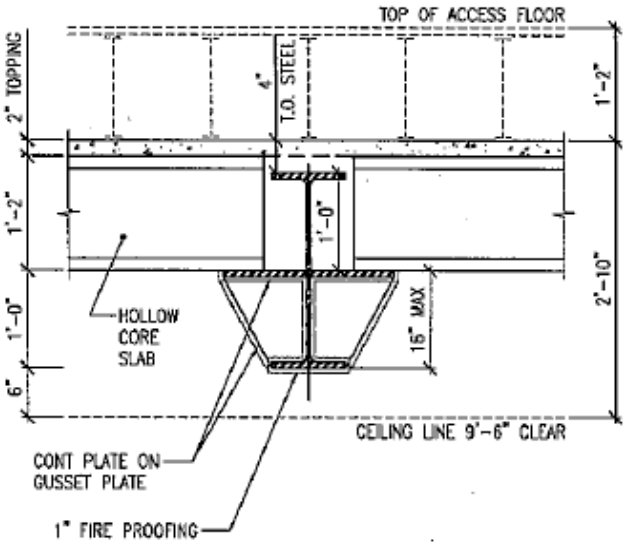


Figure 1: Option S4 connection of hollow core to floor beams (section elevation)

RESULTS

Program Accuracy

The take-off quantities resulting from Athena's assumptions ('A' models) vs. those calculated by a manual take-off ('B' models) are shown in Table 1. The Impact Estimator does not include many of the assemblies that were used in the four structural system options including: composite slab on deck, deep foundations, one-

way concrete slabs, lateral steel bracing, mat foundations, post-tensioned beams, and grade beams. Because of this it was necessary to do a manual take-off for these items, or to 'fake' them in as other assemblies which, by engineering judgment, would give approximately the same material quantities. Quantities added to the Impact Estimator because assembly options weren't available are identical in both 'A' and 'B' models. The manual take-off performed by the authors did not account for construction materials such as formwork or the curtain wall assembly, so these quantities were taken from Athena.

Table 1: Athena material quantities (A) vs. manual take-off quantities (B)

Matl	Units	S1A	S1B	A/B (%)	S2A	S2B	A/B (%)	S3A	S3B	A/B (%)	S4A	S4B	A/B (%)
Aluminum	Tons	44	44	---	44	44	---	44	44	---	44	44	---
Batt. Fiberglass	sf(1")	83009	83009	---	83009	83009	---	83009	83009	---	83009	83009	---
Concrete (total)	yd³	2410	2519	96%	7382	6295	117%	7382	6237	118%	3610	3773	96%
EPDM membrane (black, 60 mil)	lbs	4818	4818	---	4818	4818	---	4818	4818	---	4818	4818	---
Galvanized Decking	Tons	114	114	---	0	0	---	0	0	---	0	0	---
Galvanized Sheet	Tons	5	5	---	5	5	---	5	5	---	5	5	---
Galvanized Studs	Tons	4	4	---	0	0	---	0	0	---	0	0	---
Glazing Panel	Tons	248	248	---	248	248	---	248	248	---	248	248	---
Rebar, Rod, Light Sections	Tons	16	20	78%	638	295	216%	714	259	275%	77	65	119%
Screws Nuts and Bolts	Tons	25	7	373%	1	1	100%	1	1	100%	25	6	439%
Welded Wire Mesh/Ladder Wire	Tons	9	14	67%	2	6	30%	2	6	31%	16	6	261%
Wide Flange Sections	Tons	493	454	109%	0	0	---	0	0	---	491	423	116%

It can be seen in Table 1 that there are some discrepancies between the 'A' and 'B' models that are outside the +/-10% margin of error described by the Institute. In particular, the quantity of nuts and bolts that the program estimated for steel framing was an order of magnitude higher than the manual takeoff. Also the concrete volume and reinforcing quantities are significantly different for the concrete framing options from the 'A' to 'B' models. These differences affect the calculated impacts and should be kept in mind when reviewing the impact comparisons to follow.

Figure 2 shows the primary energy and global warming potential (GWP) associated with several systems. In the case of the concrete option S2, the lateral and foundation systems account for around 20% of both impacts. These systems are not inherently included in the Impact Estimator. The design team should be advised to consider the impacts that these additional structural systems can add to the gravity framing output that can be generated with ATHENA® Impact Estimator.

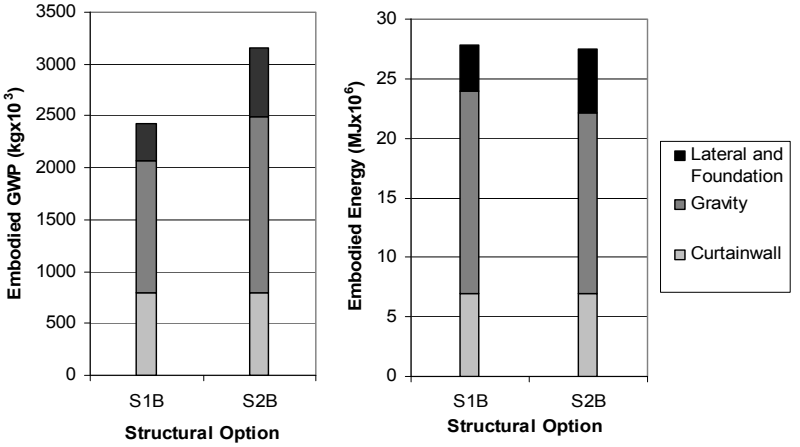


Figure 2: Primary energy and GWP impacts associated with various building systems

Embodied vs. Operating Impacts

The embodied impacts are those associated with the manufacturing of the building components, their construction on-site, and their disassembly and disposal at the end of the life of the structure. For primary energy analysis of the structural options, a majority of the embodied impact was a result of the manufacturing process (see Figure 4). Similar results were encountered for the other impacts in the study.

An energy study was performed separately with all inputs assumed equal for all options. The primary energy required to operate the building far outweighs the embodied energy of the materials used to construct the building. In all of the structural options for this office building primary energy required for operation is over ten times greater than the material embodied energy (see Figure 3), which accounted for anywhere from 6-9% of the total energy.

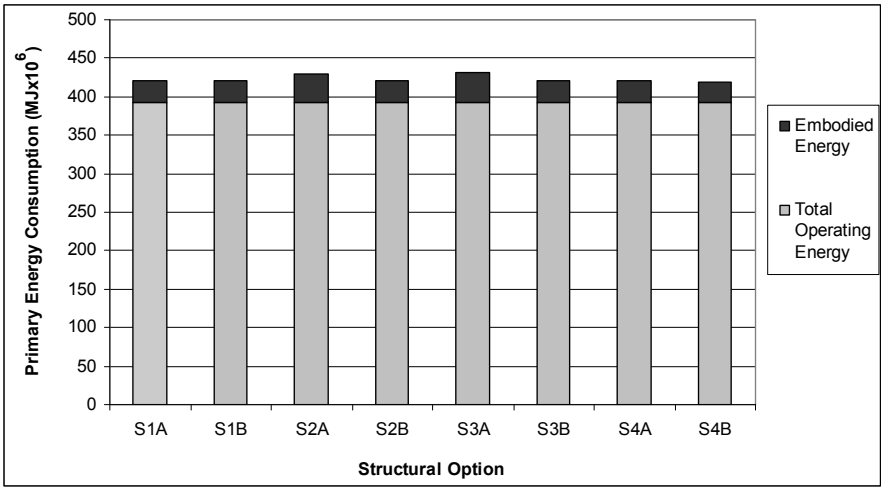


Figure 3: Embodied vs. operating primary energy consumption

When other environmental metrics are observed, the embodied impacts comprise a greater portion of the overall impact: 8-13% of the global warming potential is

associated with embodied processes as well as 19-24% of the human health respiratory effect potential (HHresp). When smog potential is considered, the embodied impacts make up a majority (60-72%) of the overall impact.

Environmental Metrics

Primary Energy Consumption

Though the energy associated with the operation of the building (roughly 90% of the total cradle-to-grave energy) is assumed equal for all of the structural options, there is variation of the embodied energy associated with each. The prescriptive or engineer determined ('B') structural options have approximately the same primary energy consumption (see Figure 4). None of them deviate more than 3% from their average. However, the embodied energy values for the 'deterministic' or program-determined ('A') concrete options, S2A and S3A, are roughly 40% higher than this average. This is consistent with the discrepancies in quantities noted earlier.

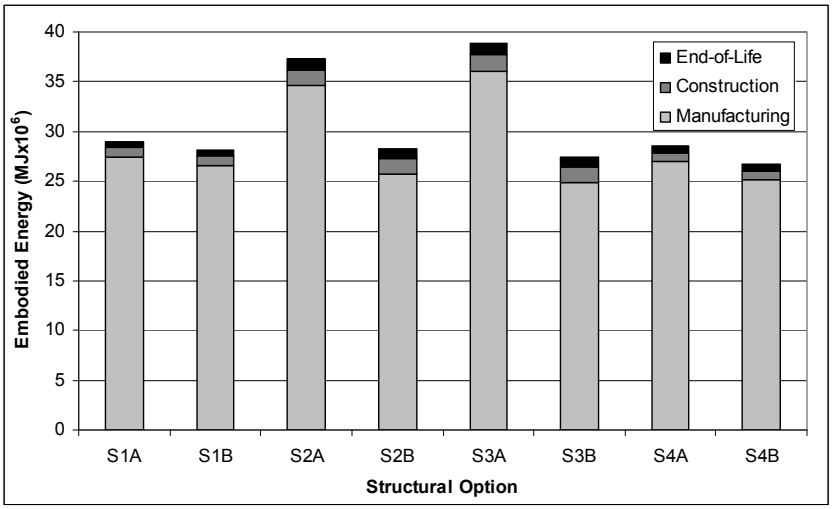


Figure 4: Embodied energy consumption

Global Warming Potential

If global warming potential is considered, the two structural steel options (S1 and S4) perform better than the concrete (S2 and S3) options (see Figure 5). This is consistent with previous LCA studies (Guggemos and Horvath 2005). Once again, the impact measurements for the deterministic concrete options are statistical outliers for reasons discussed previously.

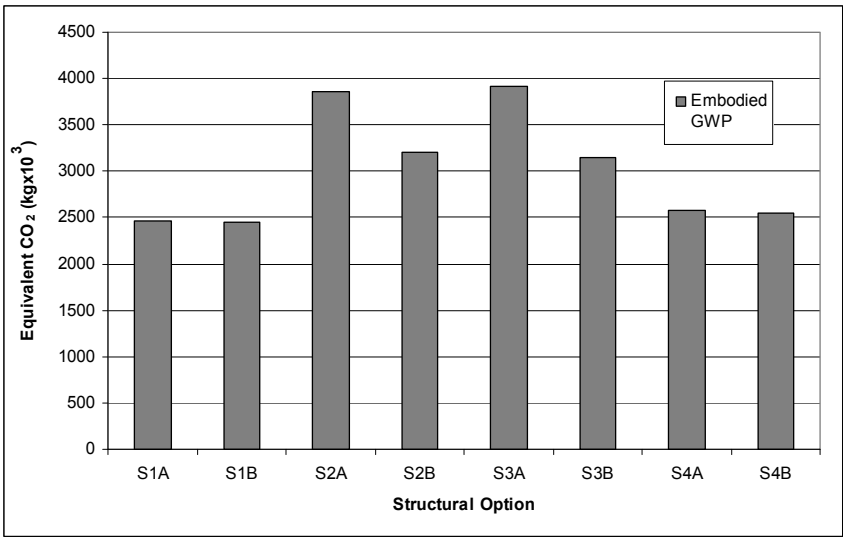


Figure 5: Comparison of global warming potential

Smog potential

Similarly to the global warming potential, the smog potential was greatest with the concrete options (S2 & S3) and least with the composite deck and steel framing option (S1) (see Figure 6).

Human health respiratory effects

Like the previous metrics, the concrete options contained the largest human health respiratory effects potential with S1 option containing the least (see Figure 6). Figure 6 also gives a comparison of embodied vs. operating impacts.

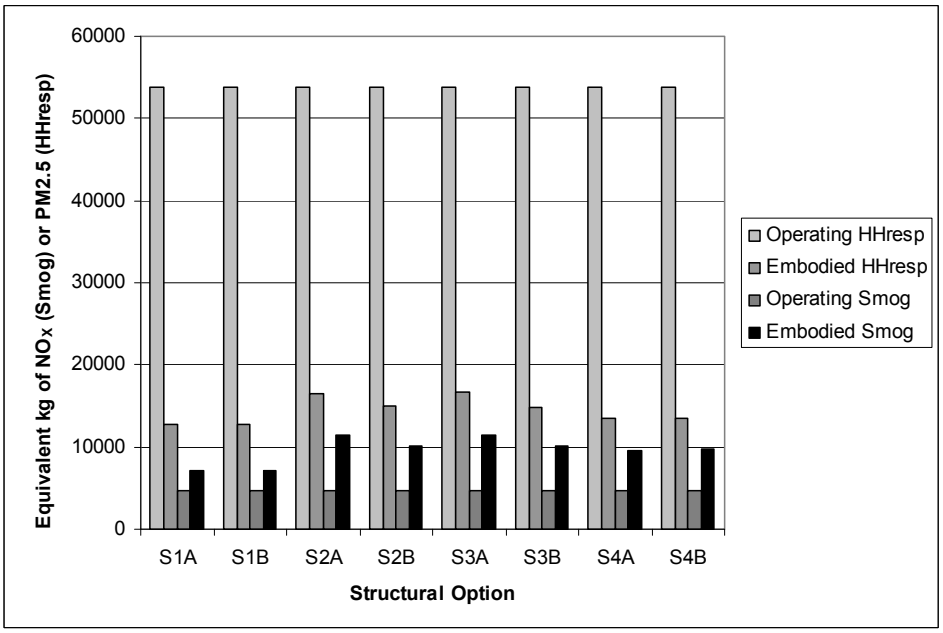


Figure 6: Comparison of human health respiratory effects potential

CONCLUSION

It is the purpose of this paper to examine the ATHENA® Impact Estimator for Buildings LCA software to determine its validity as a tool for making sustainable design decisions based upon structural systems. The intention of the authors is to view the results of the Impact Estimator output in several ways: the accuracy of the program's engineering assumptions, embodied vs. operating energy consumption, and environmental metrics. It is the conclusion of the authors that ATHENA® Impact Estimator has some inherent inaccuracies in estimating material quantities. The overestimate of the concrete volume and possibly the reinforcing quantities had the greatest influence, because it was the concrete options (S2 & S3) in the models where the quantities were determined from Athena ('A' models), that have a greater negative impact than the models where quantities were determined by the authors ('B' models). In regards to the embodied vs. operating energy, it is the conclusion that the embodied energy of the structural components comprises less than 10% of the total primary energy consumption, and in the embodied energy the extraction and manufacturing phases dominate over the construction and end of life phases. When comparing the four structural options in terms of primary energy, global warming potential, smog potential, and human respiratory effects, it is the author's conclusion that the option chosen, composite slab on deck with steel framing and cross-bracing (S1), was the best choice environmentally (see Figure 7). In conclusion, with an awareness of the limitations, ATHENA® Impact Estimator is workable tool for the comparison of structural systems at the schematic level but more work needs to be done to include a broader range of structural assemblies that are commonly used in the Chicago market.

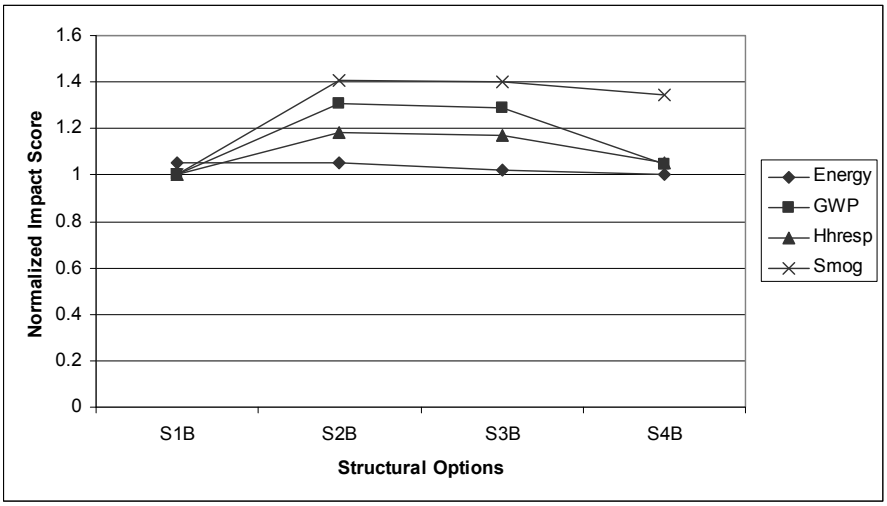


Figure 7: Summary of environmental performance of structural options.

REFERENCES

ATHENA® Impact Estimator for Buildings. Overview. <http://www.athenasmi.org/tools/impactEstimator/index.html>(Dec 2010). Athena Sustainable Materials Institute, Ontario, Canada

"ATHENA® Impact Estimator for Buildings V3.03 Software and Database Overview." (2008). Athena Sustainable Materials Institute, Ontario, Canada

Guggemos, Angela Acree and Horvath, Arpad. (2005). "Comparison of Environment Effects of Steel- and Concrete-Framed Buildings". *Journal of Infrastructure Systems*, Vol 11, No. 2, ASCE

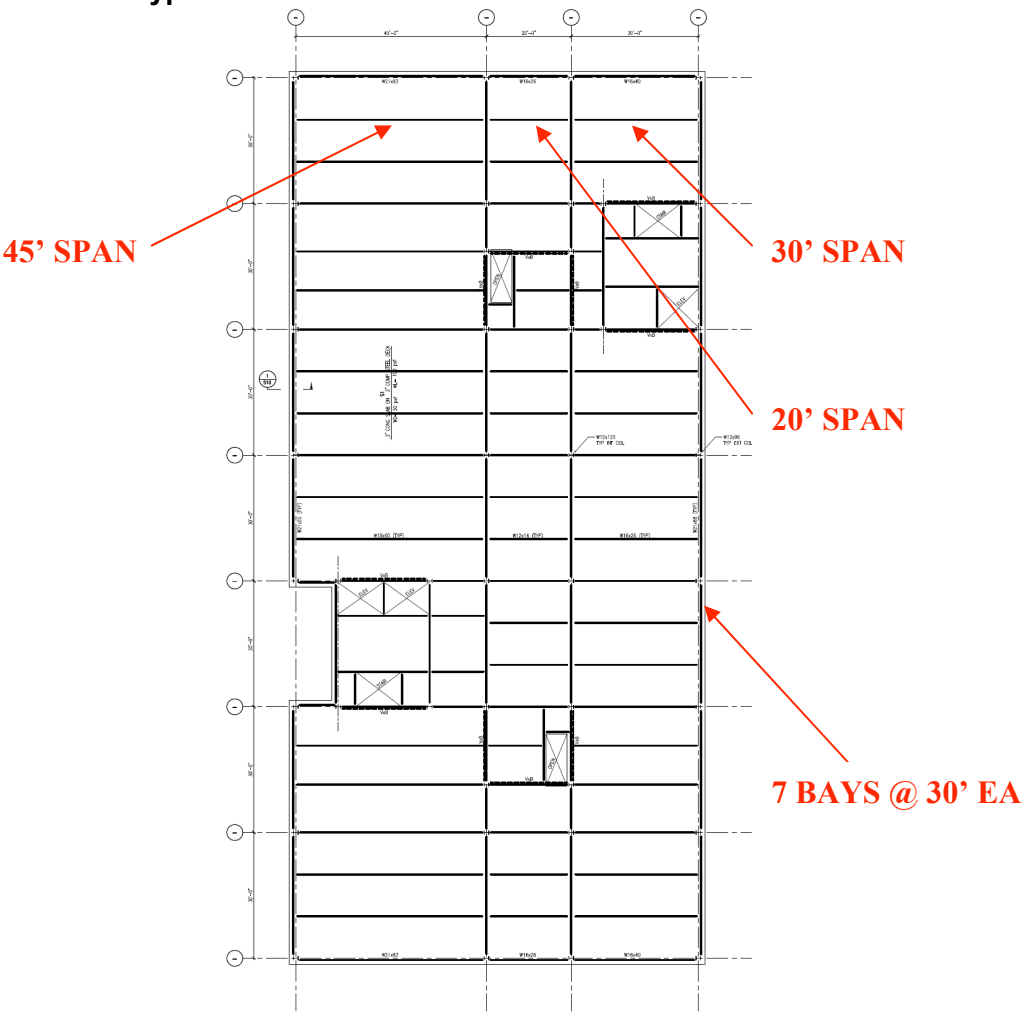
Hsu, Sophia Lisbeth. (2010). "Life Cycle Assessment of Materials and Construction in Commercial Structures: Variability and Limitations". Massachusetts Institute of Technology. Cambridge, MA

Johnson, Timothy Werner. (2006). "Comparison of Environmental Impacts of Steel and Concrete as Building Materials Using the Life Cycle Assessment Method". Massachusetts Institute of Technology. Cambridge, MA

United States. Department of Energy. U.S. Energy Information Administration. Annual Energy Review 2009, Washington, DC

World Commission on Environment and Development. (1987). "Our Common Future, Report of the World Commission on Environment and Development," *Annex to the General Assembly document A/42/427, Development and International Cooperation: Environment*

Appendix A – Typical Floor Plan



Integrating Life Cycle and Carbon Assessments: What Life Cycle Assessment Can Teach Structural Engineers about Design and Specification

Frances Yang, P.E., LEED® AP[1]

[1]Arup, 560 Mission Street, Floor 7, San Francisco, CA 94105, 415-946-0271, frances.yang@arup.com

ABSTRACT

Life-Cycle Assessment (LCA) is the method which most fully accounts for the environmental impacts of structures. The method provides feedback for our engineering design and specification choices. Three case studies will demonstrate how LCA was used in different ways to answer different questions structural engineers had in the desire to reduce the environmental impacts of their projects. One uses Athena® EcoCalculator for an existing building while the other two studies employ LCA outside of currently available software models for new structures.

INTRODUCTION

Life-Cycle Assessment (LCA) is the method which considers a range of environmental impacts of a product over a span of its life cycle stages. When used for a building, it most fully accounts for the environmental impacts of structures from the material extraction, processing and manufacture, construction, use, end of life, and transport of materials between these activities in these phases. A comprehensive set of environmental impacts includes energy use, resource depletion, toxicity to air and water, global warming potential, and ozone depletion, to name a few. Although the data needed gather such information is vast, tools in the US exist to make an LCA-based evaluation relatively simple for building designers. The way in which the structural engineer uses these tools depends on what questions they are asking.

Environmental Impacts Embodied in an Existing Building

The first study asked how much in environmental resources was already invested in the original structure and its multiple retrofits. The client sought to preserve not only the aspects of the original structure, but also the evidence that told its story as the region's first example of adaptive reuse. Reuse of existing structure is one of the most significant ways to reduce the embodied environmental impacts of construction. Structural elements of The Cannery dated back to 1967. Most structures only last 35-60 years, particularly in a region concerned with seismic safety.

Athena® EcoCalculator was chosen for this exercise because of how well the building construction materials matched the assembly choices. The simplicity of the spreadsheet-based tool also aligned with the limited time and budget, and the understanding that the client only desired a rough estimate, in only a few widely

understood metrics. Embodied energy, embodied carbon, and waste metrics were chosen to best represent the environmental concerns at hand.

Using EcoCalculator was feasible due to the availability and legibility of existing drawings documenting original construction and multiple retrofits. EcoCalculator merely required one to input total area of each assembly type. The Cannery was of typical historic brick wall and steel frame construction later retrofit with shotcrete and rigid diaphragm floors. Thus area of masonry walls, steel joist floors, steel columns, and concrete walls were the primary inputs. Sometimes the elements were found under a different assembly category than where they were found in the actual building, e.g. masonry walls were in "Interior Walls" in the EcoCalculator. The pad foundation and shotcrete were not found under the standard assemblies offered by EcoCalculator. After consulting with Athena® technical support, we felt comfortable with adding in an additional area of concrete floor equivalent to the volume of concrete foundation and using 6" cast-in-place to represent shotcrete.

Cannery_EcoCalc [Compatibility Mode]

ATHENA® EcoCalculator for assemblies

TOTAL IMPACTS BY BUILDING COMPONENT	Primary Energy (MMBtu) TOTAL	GWP (tons) TOTAL	Weighted Resource Use (tons) TOTAL	Air Pollution Index TOTAL	H2O Pollution Index TOTAL
COLUMNS & BEAMS	27073	1805	8567	253836	2008.80
INTERMEDIATE FLOORS	6540	520	2904	75608	1243.78
EXTERIOR WALLS	1242	110	605	18829	7.33
WINDOWS	1865	145	282	35385	23.33
INTERIOR WALLS	19434	1200	2065	329940	18.71
ROOF	5865	324	548	58933	647.93
WHOLE BUILDING	62019	4105	14972	772531	3949.88

C. EXTERIOR WALLS

ATHENA ASSEMBLY EVALUATION TOOL v2.2—Northern USA low-rise building

IN THE YELLOW CELLS BELOW, ENTER THE AMOUNT OF SQUARE FOOTAGE THAT EACH ASSEMBLY IS USED IN YOUR BUILDING

		Assembly R-value	Square footage	Percentage of total	Primary Energy per SF (MMBtu)	GWP per SF (lbs)	Weighted Resource Use per SF (lbs)	Air Pollution Index per SF	H2O Pollution Index per SF
Average:					0.14	22.65	71.36	2.16	0.69
6" CAST-IN-PLACE CONCRETE									
14	CIP Concrete, brick cladding rigid insulation, latex paint	21.28	0		0.20	32.74	135.13	3.32	0.0008
15	CIP Concrete, steel cladding rigid insulation, latex paint	21.09	0		0.22	49.08	118.48	3.92	4.3952
16	CIP Concrete, stucco cladding rigid insulation, latex paint	20.59	0		0.13	22.89	124.02	1.85	0.0016
17	CIP Concrete, EIFS, latex paint	15.99	0		0.10	19.22	109.74	1.61	0.0007
18	CIP Concrete, precast cladding rigid insulation, latex paint	21.00	0		0.13	25.38	146.53	1.99	0.0040
19	CIP Concrete, brick cladding, rigid insulation, vapor barrier, gypsum board, latex paint	21.84	0		0.22	33.78	138.94	3.51	0.0008
20	CIP Concrete, steel cladding, rigid insulation, vapor barrier, gypsum board, latex paint	21.65	0		0.24	50.12	122.29	4.11	4.3952
21	CIP Concrete, stucco cladding, rigid insulation, vapor barrier, gypsum board, latex paint	21.15	0		0.14	23.93	127.83	2.04	0.0016
22	CIP Concrete, EIFS, vapor barrier, gypsum board, latex paint	16.55	0		0.11	20.26	113.55	1.79	0.0007
23	CIP Concrete, precast cladding, rigid insulation, vapor barrier, gypsum board, latex paint	21.56	0		0.14	26.43	150.34	2.18	0.0040
24	CIP Concrete, rigid insulation, vapor barrier, gypsum board, latex paint	21.04	11252	100%	0.11	19.53	107.57	1.67	0.0007

Welcome and How-to | COLUMNS AND BEAMS | INTERMEDIATE FLOORS | EXTERIOR WALLS | WINDOWS | INTERIOR WALLS | ROOFS

Figure 1: Snapshot of Athena® EcoCalcutor v2.2. Input required under "Square footage" column heading. Environmental outputs in upper right hand corner.

EcoCalculator output was converted into metrics more easily understood by the client and other stakeholders. This resulted in stating that preservation of The Cannery's structure was on the scale of:

- saving enough energy to power 500 homes for one year,
- saving the amount of carbon it would take nearly 380,000 trees over 10 yrs to sequester, and
- avoiding an amount of waste that would fill 2.2 football fields

The first two conversions used the EPA Greenhouse Gas Equivalencies Calculator and the third used data from Arup's waste group regarding typical construction waste density and assumed landfilling to 3 feet high.

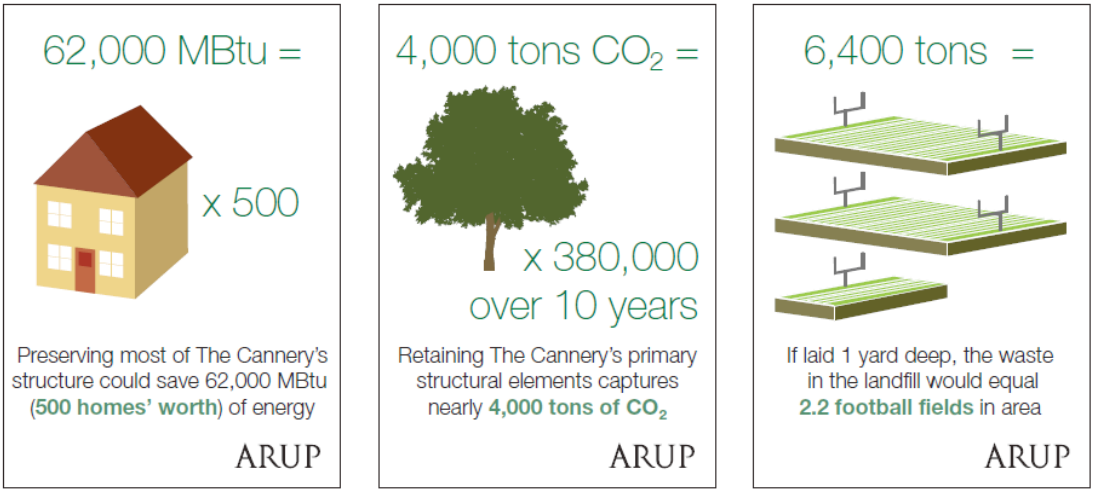


Figure 2: Representations of environmental resources invested in existing Cannery building

These results added quantitatively to the environmental piece of the preservation story the client had in mind for The Cannery building. Surveys of historic structures show the longer a building is conserved and adapted for future use, the more others will come to admire and care for it, and the more value people will find in investing future efforts to sustain its legacy (Brand 1994). The Cannery had reached its time horizon for expected replacement of the structure. However, by choosing to preserve the primary elements --masonry walls, steel framed floors with concrete slab, and foundation – it effectively reduced the embodied impacts on the environment over its lifespan. Design for enhanced seismic safety will further prolong its service life beyond the life that has repeatedly been preserved.

Embodied Carbon of Different Structural Schemes

In the second case, the study sought to answer several questions long held by structural engineers wanting to know how their role matters in sustainable design. SE's often ask themselves:

- What is the relative impact of: the choice of framing scheme, cement content in concrete mix, recycled content of steel?

- What is the relative impact of structure compared to transport, construction, and architectural components of the buildings?
- Do results change for different building types?
- With so much variation in LCA calculations, can what I do really make a difference to results?

The study chose to focus on embodied carbon from cradle to site for the sake of common language with the client and due to foreseen limitations in data for other environmental metrics. LCA then guided the quantification and comparison of three buildings that represent typical design and construction of commercial, school, and hospital structures. The bills of quantities were already available from a cost study published by The Concrete Centre in 2007.

Six different framing schemes were compared, plus two long span options for the commercial building only, for a total of 20 different structural solutions across the three building types. For each of the three building types the only variations were directly attributable to the choice of structural scheme. Thus, facade height, soffit area, and foundation differences changes were solely due to the framing option.



Figure 3: Framing options considered in study. Long span options not in hospital or school.

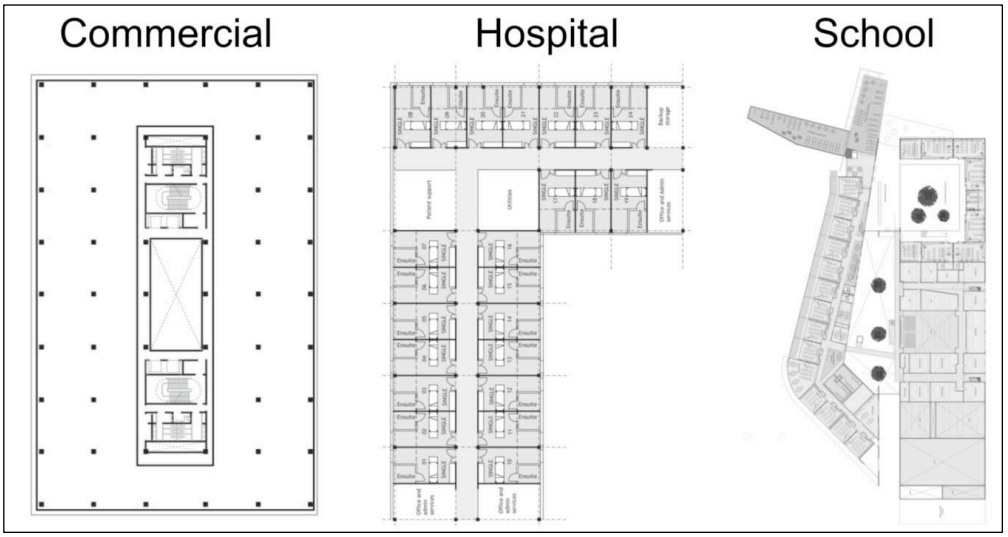


Figure 4: Plans of the three buildings studied

TABLE 1: Key characteristics of the case study buildings

	Measurement	Office	Hospital	School
Primary Parameters	Gross Floor Area (m^2)	16480	10752	13500
	Façade area / floor area	~40%	~60%	~65%
	Number of floors	6	2	2-3
	Basement?	No	No	No
	Foundations	Piles	Pads	Pads
	Number of schemes	8	6	6
	Construction impacts	12%	21%	16%
	Structure (% of total)	60%	50%	50%

Embodied CO_2 factors came from industry published figures when available (CISCF 2009). When not available, they were obtained directly from manufacturers or from life-cycle inventories (LCI) through LCA software (GaBi 2003). Development and accessibility of LCI data for construction materials has progressed much further in the UK than in the US (ICE 2008).

Results show that structure, including foundations, represented 50% or more of the whole building embodied CO_2. This was consistent across all three building types. There was no clear advantage to choosing steel over concrete or vice versa, as no structural scheme gave the lowest impact consistently. What mattered more was what was done with the scheme chosen. The amount of concrete in all buildings provided significant potential to change the embodied CO_2 of a building through specification of low cement concrete.

On the other hand, the minimum depth steel solution was consistently the highest impact solution by a large margin that was not recovered by reduction in facade area. Facade height reduction was limited by MEP needs. Thus, the least materially efficient design structurally was also the least advantageous in embodied CO_2.

Embodied CO_2 of non-structural elements was not affected significantly by changes in the structural scheme. As a general rule the embodied CO_2 of the structure can be optimised without adversely affecting the whole building impact.

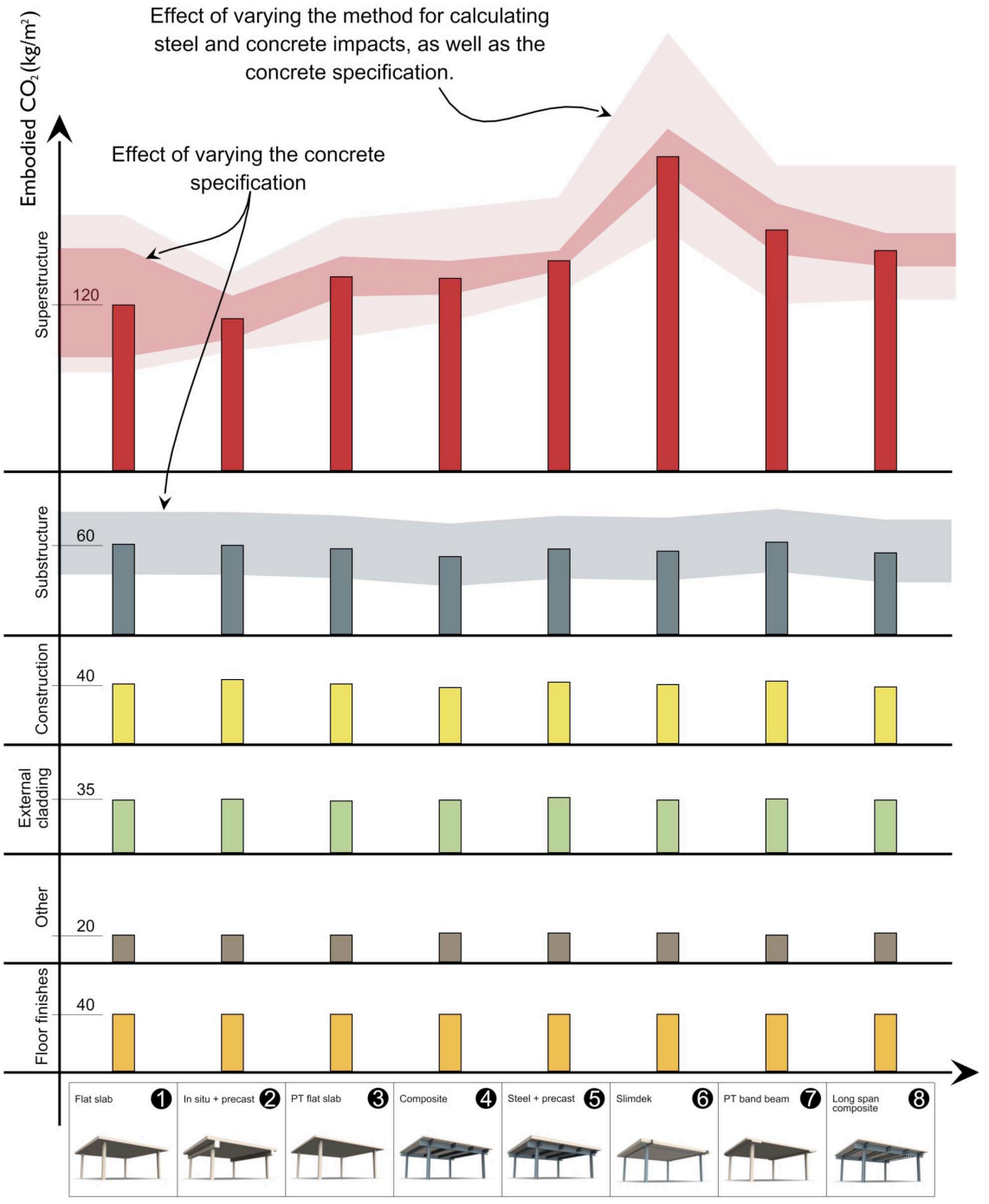


Figure 5: Breakdown of structural and non-structural elements for all framing scheme options (commercial building)

Standards such as ISO 14040 series allow broad flexibility in approach to the calculation of the materials impacts used in buildings. This has led to a range in embodied CO_2 factors that causes confusion when attempting to compare LCA results from different studies. The need for a standard methodology when evaluating buildings has been acknowledged and work has started, such as PAS 2050 in the UK

and CEN 350 in Europe. Still, the discrepancies have made some designers wonder if, until this flexibility is reigned in, attempts to quantify their efforts are futile. In this study, differences in method were separated from material specification choices to examine which design decisions, versus LCA methodology variations, will affect results.

Results showed that the real reductions to embodied carbon made through material specification and efficient design are just as great as reductions affected by changes in methodology. Thus, the role structural engineers have to play is significant to reducing climate change impacts of building construction.

Although operational and end-of-life impacts were not included in this study, the lower impact schemes would not preclude opportunities for reduction in operational impacts. Also excluded from the study are refurbishment and end of life scenarios. The potential variation introduced by these post-construction activities is very large. The design and detailing of the building can be reviewed in order to minimise operational impacts, maximise the life-span of the building elements and minimise end of life impacts.

Considering End-of-Life Options

The final study uses LCA principles to assess the effects of using framing designed for deconstruction for a parking structure. This required careful consideration of how to quantify end-of-life impacts.

The client requested an embodied carbon footprint comparison of eleven structural framing options for a parking structure in the United Arab Emirates (UAE). The comparison was based on supplied structural drawings, sample concrete mixes, and an understanding of end-of-life information and methodologies.

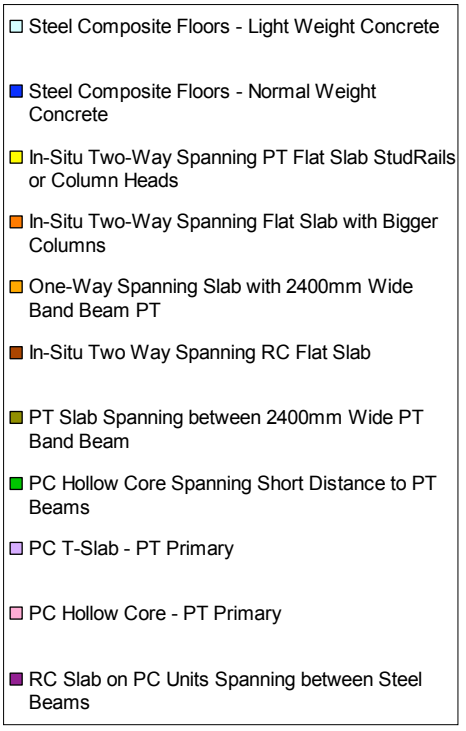


Figure 6: Eleven structural framing options under consideration

An inherent challenge for carbon footprinting projects in the Middle East region is a lack of region-specific carbon footprint data. Embodied carbon factors came from combining information for different concrete mixes and associated materials, based on UAE structural design and supply scenarios, with information provided by the Masdar project specifications manager and by regionalizing materials embodied carbon data in LCI databases.

The scope of the carbon footprint study included all material production activity including primary extraction activity, manufacture/production and transportation to site. End-of-life scenarios took into account current practice expected regionally for the different materials used in the structural design options proposed.

Recycling at end of life is based on a discounting methodology put forth by Eaton and Amato, adopted by CORUS. The formula takes into account the emissions from production of virgin steel discounted by emissions saved by future recycling. Use of this methodology reflects the likelihood of occurrence in current market conditions for rebar and structural steel sections. Other methods exist; this one seemed best suited for steel, which was the main material with an alternate end-of-life scenario in this study.

$$S_{ce} = (P_{ce} - R_{ce}) \times \frac{(1-r)}{(1-r^n)} + R_{ce}$$

Figure 7: Equation used in discounting method for taking into account materials recovery at end of life

Reuse at end of life could only realistically be applied to the precast slab on steel frame option. The other steel frame options support a composite concrete and metal deck. The metal studs that are welded onto the steel beams to achieve composite-action make reuse of the steel frame too difficult to have ever been done in practice. The most likely scenario for the steel sections in composite structures as currently constructed is demolition and recycling. The reuse of steel scenario assumed that the framing members would only be reused once, and that the concrete plank floors would be crushed and recycled as unbound aggregate, based on most likely current practice in the region.

Results from these comparisons showed that when only considering Cradle-to-Site, the deconstructable framing scheme performed the worst in carbon terms, whereas the concrete schemes performed best. All concrete on this job had aggressive cement replacement rates: 40% ground granulated blast furnace slag (GGBS) in precast, 50% GGBS in cast-in-place, and 70% GGBS in foundations. However, once the study expanded the life cycle boundary to include recycling of steel at end-of-life (and concrete crushed and used as base course), the steel schemes performed as well as the concrete schemes.

Finally, and somewhat surprisingly, when considering reuse of the steel frame, there was not enough sectional steel in the whole system to compensate for initial environmental burdens of more concrete and rebar to make it the best option in carbon terms. More concrete and rebar was needed for the less structurally efficient precast planks that do not act compositely with the steel frame.

These results points to several scenarios that would likely reap greater environmental benefit: reusing the precast planks, multiple reuse of the steel frame, using salvaged steel and using a deconstructable composite system. An example of the latter has been offered through a past Lifecycle Building Challenge (Webster, 2007). This study did not allow for investigating these scenarios, but based on current results, they emerge as logical next steps towards decreasing embodied carbon. Moreover, if an environmental impact metric besides embodied carbon was used for comparison, the ranking of schemes could have ended up quite different. For instance, steel manufacture tends to burden the environment in the category of toxicity to water much more heavily than concrete, so reuse of steel may exemplify a greater benefit if this impact were examined.

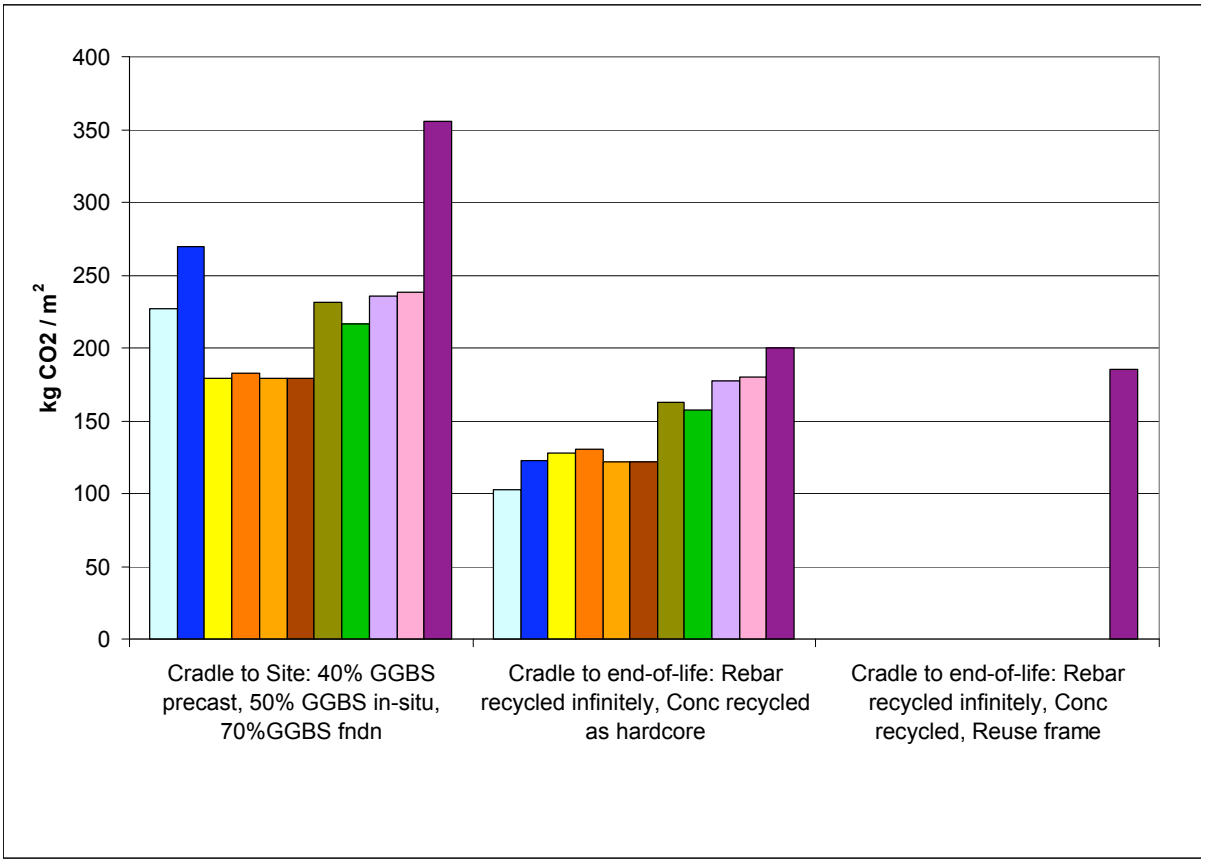


Figure 8: Comparison of framing options with and without end-of-life considerations

CONCLUSION

The first example showed that buildings embody vast repositories of energy and materials. The EcoCalculator was used to help quantify the resources tied up in a historic building. Turning these values into easily understood metrics helped the client add a layer of environmental stewardship to their value story in retrofit and preservation efforts.

In the second case, LCA principles are used to compare embodied CO_2 levels related to project choices within structural engineers' control, and bring to light the importance of their role in making more environmentally beneficial choices. Decisions in structural framing schemes, cement content in concrete mix, and recycled content were shown to have significant impact on whole building outcomes, in comparison to transport, construction, and architectural components of the buildings. Lessons learned were consistent across the three buildings that represent typical design and construction of commercial, school, and hospital structures.

The last example showed the importance of end-of-life considerations when designing for unconventional recovery of materials. The discounting methodology resulted in significant re-ranking of the environmental performance of design options. Results indicated that environmental benefits from deconstructable design has its

limits when it causes the need for more virgin material. Thus, an optimal solution would uphold both disassembly/reuse as well as optimal structural efficiency.

These varied studies show that structural engineers can use the principles and data from LCA in a variety of ways to make more informed design and specification choices. Methods should be tailored to the questions being asked. Having better understanding of LCA and using tools readily available, structural engineers have a large part to play in sustainable design.

REFERENCES

Athena® EcoCalculator v2.2 (2008), Athena Sustainable Materials Institute, Ottawa, Canada. <http://athenasmi.org/tools/ecoCalculator/index.html>

Stewart Brand (1994), *How Buildings Learn: What Happens After They're Built*, Penguin Books, New York, NY.

CISCF (2009) Concrete Industry Sustainable Construction Forum, Sustainability Performance Report The Concrete Centre, March 2009.

Cost Studies (2007-2007) Cost Model Study - Commercial Buildings. CCIP-010 The Concrete Centre, October 2007; Cost Model Study - School Buildings. CCIP-011 The Concrete Centre, December 2007; Cost Model Study - Hospital Buildings.CCIP-012. The Concrete Centre, December 2008

Eaton & Amato (1998) AMATO, A., & EATON, K. J.,:- 'A comparative Life Cycle Assessment of Modern Office Buildings.' published by the Steel Construction Institute, Ascot, Berkshire, U.K. 1998

EPA Greenhouse Gas Equivalencies Calculator <http://www.epa.gov/cleanenergy/energy-resources/calculator.html>

GaBi (2003) PE INTERNATIONAL. GaBi 4 extension database III: steel module and GaBi 4 extension database XIV: construction materials module.

ICE (v1.6a) University of Bath. Inventory of Carbon and Energy. Hammond, Geoffrey P. and Craig I. Jones, 2008. 'Embodied energy and carbon in construction materials', Proceeding of the Institution of Civil Engineers: Energy, 161 (2): 87-98

ISO 14040 (2000-2006) BS EN ISO 14040:2006 Environmental management - Life cycle assessment - Principles and framework.. [British Standard; European Standard; International Standard]; BS EN ISO 14041:1998 Environmental management. Life cycle assessment. Goal and scope definition and inventory analysis; BS EN ISO 14042:2000 Environmental management. Life cycle management. Life cycle impact assessment; BS EN ISO 14043:2000 Environmental management. Life cycle assessment. Life cycle interpretation.

PAS 2050 (2008) Specification for the assessment of the life cycle greenhouse gas emissions of goods and services, British Standards Institute October 2008

Mark D. Webster, Dirk M. Kestner, James C. Parker, Matthew H. Johnson, "Deconstructable and Reusable Composite Slab" Lifecycle Building Challenge 2007 Winner: Component, Professional - Unbuilt. <http://www.lifecyclebuilding.org/2007/winner-slab.php>

Infrastructure Sustainability: Streamlining Life Cycle Assessment for Practicing Bridge Engineers

Extended Abstract

Jeralee L. Anderson, P.E., LEED-AP, M.ASCE[1]

[1]Department of Civil and Environmental Engineering, University of Washington, Mailbox 352700, Seattle, WA 98195; PH(206) 685-7198; email: jeralee@uw.edu

ABSTRACT

Life cycle assessment (LCA) can help bridge design engineers understand, measure, and evaluate the initial and long term environmental impacts of bridge projects, such as energy use and carbon dioxide (CO_2) emissions. LCA can be a helpful tool when comparing conventional construction materials with those that claim to be more environmentally sustainable because it provides the engineer with quantified information on impacts that cannot be identified by a typical bridge life cycle cost analysis (BLCCA).

This study investigates the life cycle environmental impacts for a small single span bridge project. A life cycle inventory is completed using the PaLATE v2.1 tool as modified for use with the Greenroads™ Rating System, and reports quantities for two key indicators of environmental impact for the project: energy use and CO_2. This research demonstrates that LCA tools can provide useful environmental information quickly and easily for structural engineers, but streamlined tools also require an understanding of the inherent limitations of their data sources and analysis methods.

INTRODUCTION

Whether designing a highway bridge, a building, a retaining wall or simple pedestrian overpass, structural engineers confront many decisions for which they follow a standardized method of accounting for those decisions, or they use a set of tools to put them to practice. Simple questions like *How long will the structure last? What loads will it carry? Is it safe? How will it perform in a natural hazard?* are only a few of the technical challenges and constraints faced by practicing engineers. Every project has a unique series of these challenges. In response, countless laboratory tests, decision-making tools and quality accounting methods have been developed and refined, and have ultimately transformed the standard of practice in bridge design to what it is currently.

Now, the infusion of sustainability in all aspects of resource management, manufacturing, land use, economic development, and social culture creates a new challenge: a need for additional tools to understand and quantify the broad range of environmental impacts caused by bridge projects in their lifetimes. But while use of life cycle assessment (LCA) as a decision-making tool is on the rise in the building industry, it has yet to appear in a structural engineer's typical toolbox for infrastructure construction projects. Due to the large footprint of transportation

infrastructure, LCA tools may have substantial and positive environmental influence if systematically implemented in the transportation industry as well.

What Life Cycle Assessment Is

At its heart, LCA is simply a method of environmental accounting. When completed correctly (meaning using best available data with reasonable assumptions, good faith and a standardized method), it can provide a quantified snapshot in time of any number of selected environmental impacts based on data from almost all industries. LCA data are widely available and well established in fields like product engineering, electronics, agriculture, resource extraction, and chemical processing, all of which influence bridge building in some respect. Thus, the main strengths and potential utility of LCA lie in the breadth of its existing literature as well as its standardized methodologies, such as process-based LCA, materials flow analysis (MFA) and economic input-output (EIO) LCA.

For construction projects, industry environmental emissions data is less prevalent, less accurate, less complete and often inaccessible except by academic researchers; consequently, this is LCA's main weakness. The lack of high quality data surely invites more assumptions and thus greater uncertainties into the final step of the LCA process, interpretation of the results. This weakness, however, does not distract from the overall utility of the process of measuring and tracking environmental emissions for a project.

This paper focuses on only the first steps in the LCA process: goal and scope definition and the life cycle inventory (LCI), where data collection is the key step. The inventory results in quantified impacts, such as megajoules of total energy consumed and kilograms of carbon dioxide emitted, but does not assign any weighting to these results. Valuations are also necessarily project-specific, so this focus is intended to limit the subjectivity of the reported results.

Because LCI results are heavily dependent on input data quality and availability, it is critical that the limitations of data used on a project LCI are well understood prior to acting on or interpreting the results. Importantly, and like any tool with built-in limitations, such as pile or beam design software, the lack of data or its uncertainty should not preclude an engineer from using the method so long as its limitations are clearly understood. Even the simplest LCI provides previously unmeasured perspectives by integrating environmental issues into everyday design choices, helping to weigh alternatives, and providing new insight on tradeoffs between those alternatives.

Life Cycle Assessment Is Not Engineering Economics

An important distinction must be made between LCA and life cycle cost analysis. LCA uses a decision-making process that is similar to life cycle cost analysis (LCCA), more commonly known as engineering economics or project finance. But, while both are decision-making tools that provide quantitative results, their purposes and scope are much different. A relationship between the two methods can be drawn by their overall usefulness when used in the decision-making process, but that is where the similarities end.

Since LCCA is also not widely adopted, as shown in Ozbay (2004), it is useful to mention that the majority of the life cycle oriented literature for bridge engineering is directed at optimization models in bridge management systems at the network and project level (Morcous, 2007; Frangopol & Liu, 2007; Estes & Frangopol, 2001; Frangopol, 2004; Hegazy, Elbeltagi, & El-Behairy, 2004), for preservation and maintenance (List, 2007; Strauss et al. 2007; Naus & Johnston, 2001), and reliability analysis under environmental stressors and hazards (Lee, Cho, & Cha, 2006; Hosser et al. 2008; Padgett, Dennemann, & Ghosh, 2010). Environmental costs are typically not considered in LCCA, but Ehlen (1999) provided a model using so-called "third-party costs," defined as environmental damages, though he used values of zero in his model for these costs. A case could be made for similar applications of life cycle assessment in each of these categories, with the primary goal of measuring environmental impacts instead of simple bottom-line cost impacts. Additionally, it is likely that current applications of LCCA can be expanded to include LCA, or perhaps new applications could be developed using similar algorithms.

Mathematically, LCCA allows a designer to understand the economic impact of their design choices and construction methods at any given point in time under the concept of time value of money. The National Cooperative Highway Research Program Report 483 (Hawk, 2003) provides the most comprehensive information on life cycle thinking for bridge projects. The report gives substantial detail about the utility and application of BLCCA, including examples, a guidance manual, and software tools, and a comprehensive summary of research work done using the LCCA method on bridge projects in the United States (until date of publication). Ehlen (1997) also provides an excellent explanation of the utility of BLCCA and relevant applications for engineers. It is notable there is no such manual or tools for LCA, and due to their similar nomenclature, this is perhaps why the methods are frequently confused.

However, there is government support for life cycle thinking. In 2005, the Safe, Accountable, Flexible, Efficient Transportation Equity Act: A Legacy for Users (SAFETEA-LU) mandated that state departments of transportation (DOTs) use economic tools for decision-making in infrastructure design such as value engineering or LCCA for bridge projects valued at or above US$20 million or any federal aid project exceeding US$25 million (Federal Highway Administration, n.d). But, outside of compliance with this regulation, application of BLCCA is sparse. Thompson (2004) provides a discussion of LCCA tools for bridges and notes that it has not been applied in practice because adequate and accurate decision-support tools are still not widely available to the bridge engineering community for streamlining the process. Similar conclusions may be made about the adoption of life cycle assessment methods and tools.

According to Kendall et al (2005) and Keoleian et al. (2008), literature for bridge LCA is even less available, though some recent MFA and embodied energy work has been done in Japan (Itoh & Kitagawa, 2003), France (Le, Feraille-Fresnet, & Bouhaya, 2009) and the United Kingdom (Collings, 2006; Zhang, 2010). The most formative research projects in the United States have been process-based LCA comparisons of different concrete deck designs (Kendall et al., 2005, Keoleian et al., 2008) and the straightforward comparison of steel and concrete bridge alternatives

completed by Horvath and Hendrickson (1998) using an EIO-LCA model. Some authors have also attempted to use LCA software designed for buildings on infrastructure products (Reiner & Rens, 2006), which may not be advisable due to the different contexts of bridge and building projects. The variety of these studies makes comparing the results difficult because not only do the application regions differ, but so do the sources of data and methods or standards used. Additionally, there is currently no standardized tool that would allow results to be compared more easily.

Other groundbreaking work has been completed recently by Pacheco et. al (2010) on bridge construction processes and also for the general building construction process by Bilec, Ries and Matthews (2010). New studies on ground improvement methods are appearing from international researchers (Jefferson et al. 2010; Yee & Ooi, 2010). Possibly most relevant, Muench (2010) also provides a summary of 44 life cycle assessment models completed for roadways to date in order to determine average rules of thumb for different lifecycle stages. Unfortunately, a similar review of bridge LCAs would not be feasible considering the limited availability of results.

LCA differs substantially from LCCA in terms of its mathematical approach. For example, there is currently no consensus on the time value of environmental resources, like energy, or emissions, like CO_2, as there is a way to evaluate the time value of money: compound interest formulas. So, how inflation works, what its impacts are in the long and short term, and the economic conditions under which changes in inflation may occur, are well understood. Long range environmental consequences, on the other hand, such as the impacts of CO_2 on global warming or climate change, are not well understood and there is also great uncertainty in the availability of fossil energy reserves. These uncertainties do not reduce the importance of the LCA method, in fact, they reinforce its need. The complexity of LCA often comes from the idea that multiple criteria must be considered at the same time under the same conditions. A streamlined tool that can be applied in practical project contexts is needed.

SCOPE OF RESEARCH

This study provides preliminary results of streamlined life cycle inventory tool called PaLATE v2.1 as modified for use with the Greenroads™ Rating System. The goal of this study is to demonstrate that a tool is available that may be helpful for bridge engineers seeking to measure or include environmental criteria in their design process. The tool reports results of total energy consumed for the initial construction, materials production, future maintenance activities and transportation of materials to-and-from the site for a small single span bridge project. Results of this study will be presented at the Structural Engineers Institute Structures Congress in Las Vegas, NV, April 13-16, 2011.

Project Description

The Tonquin Avenue Bridge is located in Ocean Shores, WA and spans the 150-foot Lake Minard Canal (see Figure 1). It was built in 1970, deemed structurally deficient due to rotting of the timber superstructure and supporting piers in 2006, and was subsequently closed to traffic. This route is critical as for evacuation during a

tsunami for the community members and also provides crossing for several critical utilities such as electricity, water, and sewer.



Figure 1. Existing Tonquin Avenue timber bridge.
(Reproduced with permission courtesy of GeoEngineers, Inc.)

The new project calls for replacement of the bridge superstructure as a single span with five concrete WF58G prestressed concrete girders and cast-in-place concrete deck, abutments, piers and block retaining walls as well as new utilities (see Figure 2). The substructure is founded in beach soils and will require ground improvements, which will include dynamically placed stone columns. The bridge approaches on either side will also be removed and replaced to meet current design standards (AECOM USA, 2010).

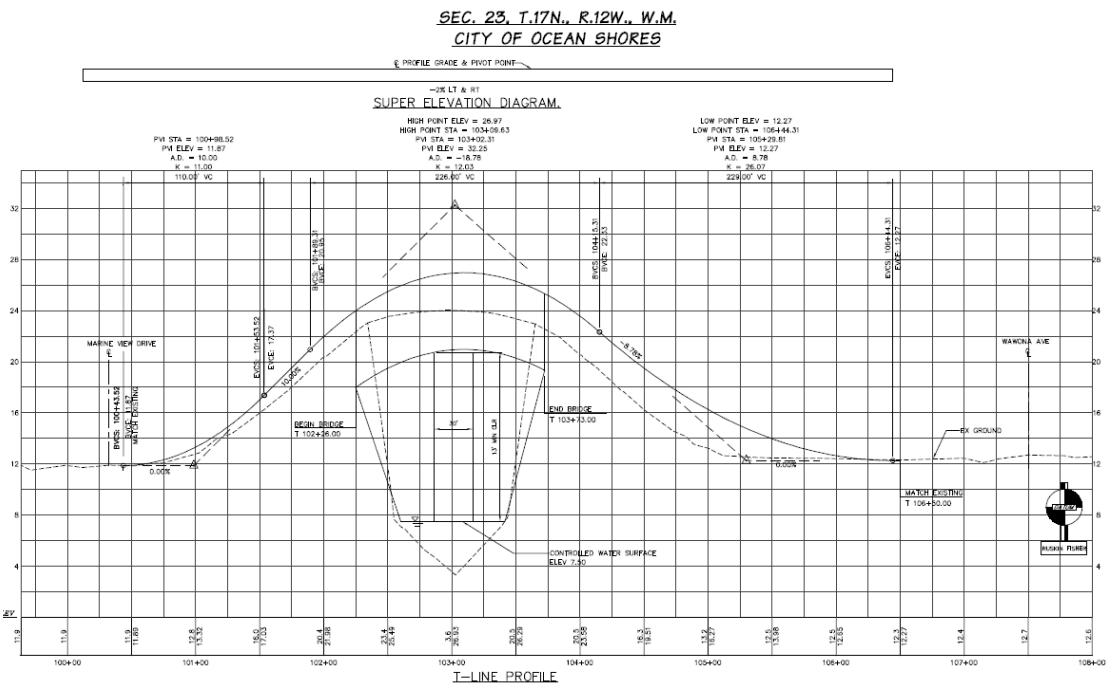


Figure 2. Proposed concrete bridge layout (in elevation).
(Reproduced with permission courtesy of AECOM USA, Inc.)

ACKNOWLEDGEMENTS

The author would like to recognize the efforts of University of Washington colleague Craig Weiland, who helped develop and revise the PaLATE v2.1 software used in this study. Also, this work would not have been possible without the helpful collaboration of Michael Hutchinson, Lyle Stone and Bruce Stirling of GeoEngineers, Inc. Finally, the author is very grateful for the contributions of Kiva Lints and Vanessa Bacurin of AECOM USA, Inc., who were instrumental in providing the project data for this study.

REFERENCES

AECOM USA, Inc. (2010). Design Report: Tonquin Avenue Bridge Replacement Project, Ocean Shores, Washington. Prepared for City of Ocean Shores, Washington. AECOM, Inc., Bellevue, WA, 57 pp.

Bilec, M. M., Ries, R. J., & Matthews, H. S. (2010). Life-cycle assessment modeling of construction processes for buildings. *Journal of Infrastructure Systems, 16,* 3, 199-205.

Collings, D. (2006). An environmental comparison of bridge forms. *Bridge Engineering,* 159, BE4, 163-168.

Ehlen, M. A. (1997). Life-Cycle Costs of New Construction Materials. *Journal of Infrastructure Systems, 3,* 4, 129-133.

Ehlen, M. A. 1999. "Life-cycle costs of fiber-reinforced-polymer bridge decks." *J. Mater. Civ. Eng.,* 113, 224–230.

Estes, A. C., and Frangopol, D. M. 2001. "Minimum expected costoriented optimal maintenance planning for deteriorating structures: Application to concrete bridge decks." Reliab. Eng. Syst. Saf., 73, 281–291.

Federal Highway Admnistration (n.d). "Fact Sheets on Highway Provisions, "SAFETEA-LU Fact Sheets – Stewardship and Oversight, <http://www.fhwa.dot.gov/safetealu/factsheets/stewardover.htm> (December 31, 2010).

Frangopol, D. M., & American Society of Civil Engineers. (2004). Life-cycle performance of deteriorating structures: Assessment, design, and management. Reston, VA: American Society of Civil Engineers.

Frangopol, D. M., & Liu, M. (January 01, 2007). Maintenance and management of civil infrastructure based on condition, safety, optimization, and life-cycle cost*. Structure & Infrastructure Engineering: Maintenance, Management, Life-Cycle Design & Performance, 3, 1, 29-41.

GeoEngineers, Inc. (2010). Final Design Report: Geotechnical Engineering Services - Tonquin Avenue Bridge Replacement Project, Ocean Shores, Washington. Report for AECOM USA, Inc., GeoEngineers, Inc., Tacoma, WA, 36pp.

Hegazy, T., Elbeltagi, E. and El-Behairy, H. (2004). Bridge Deck Management System with Integrated Life-Cycle Cost Optimization. *Transportation Research Record*, 1866, Transportation Research Board, National Research Council, 44–50.

Horvath, A. & University of California at Berkeley. (2007, 5 June) PaLATE: Pavement Life-Cycle Tool. <http://www.ce.berkeley.edu/~horvath/palate.html> (May 20, 2008)

Horvath, A. and Hendrickson, M. (1998). "Steel versus Steel-Reinforced Concrete Bridges: Environmental Assessment," *Journal of Infrastructure Systems*, ASCE, 4(3), 111-117.

Hosser, D., Klinzmann, C., & Schnetgoke, R. (2008). A framework for reliability-based system assessment based on structural health monitoring. Structure and Infrastructure Engineering, 4, 4, 271-285.

Itoh, Y., & Kitagawa, T. (2003). Using CO_2 emission quantities in bridge lifecycle analysis. *Engineering Structures, 25,* 5, 565-577.

Jefferson, I., Gaterell, M., Thomas, A.M, and Serridge, C.J. (2010). *Ground Improvement,* ICE, 163 (G11), 71-77.

Kendall, A., Dettling, J. E., Smith, V. M., Chandler, R. F., Lepech, M. D., Li, V. C., & Keoleian, G. A. (2005). Life Cycle Modeling of Concrete Bridge Design: Comparison of Engineered Cementitious Composite Link Slabs and Conventional Steel Expansion Joints. *Journal of Infrastructure Systems, 11,* 1, 51.

Keoleian, G. A., Helfand, G. E., & Kendall, A. (2008). Integrated Life-Cycle Assessment and Life-Cycle Cost Analysis Model for Concrete Bridge Deck Applications. *Journal of Infrastructure Systems, 14,* 3, 214.

Le, R. R., Feraille-Fresnet, A., & Bouhaya, L. (2009). Simplified environmental study on innovative bridge structure. *Environmental Science & Technology, 43,* 6, 2066-71.

Lee, K. M., Cho, H. N., & Cha, C. J. (July 01, 2006). Life-cycle cost-effective optimum design of steel bridges considering environmental stressors. Engineering Structures, 28, 9, 1252-1265.

List, G. (2007). A model for life cycle evaluation of highway investments. Structure & Infrastructure Engineering: Maintenance, Management, Life-Cycle Design & Performance, 3, 2, 95-101.

Morcous, G. (2007) Pareto Analysis for Multicriteria Optimization of Bridge Preservation Decisions Transportation Research Record: Journal of the Transportation Research Board, 1991, Transportation Research Board of the National Academies, Washington, D.C., 62–68

Muench, S. T. (2010). Roadway Construction Sustainability Impacts: Review of Life-Cycle Assessments. *Transportation Research Record,* 2151, 36.

Muench, S. T., Anderson, J. L., & Söderlund, M. (2010). "Greenroads: a sustainability performance metric for roadways, *Journal of Green Building, 5,* 2, 114-128.

Naus, D.J. and Johnston, M.W. (2001, October). International RILEM Workshop on Life Prediction and Aging Management of Concrete Structures. Proceedings of the International RILEM Workshop Technical Committees, Cannes, France, 16-17, October 2000. *Materials and Structures,* RILEM, 34, 458-466.

Okasha, N. M., & Frangopol, D. M. (January 01, 2009). Lifetime-oriented multi-objective optimization of structural maintenance considering system

reliability, redundancy and life-cycle cost using GA. Structural Safety, 31, 6, 460.

Ozbay, K. (2004). Life-cycle cost analysis: State of the practice versus state of the art. *Transportation Research Record,* 1864, 62-70.

Pacheco, P., Adão da Fonseca, A. P., Resende, A. and Campos, R. (2010). "Sustainability in Bridge Construction Processes" *Clean Technology and Environmental Policy,* Springer, 12, 75-82.

Padgett, J. E., Dennemann, K., & Ghosh, J. (2010). Risk-based seismic life-cycle costbenefit (LCC-B) analysis for bridge retrofit assessment. *Structural Safety, 32,* 3, 165.

Reiner, M., & Rens, K. (January 01, 2006). High-Volume Fly Ash Concrete: Analysis and Application. Practice Periodical on Structural Design and Construction, 11, 1, 58.

Strauss, A., Bergmeister, K., Hoffmann, S., Pukl, R., & Novak, D. (January 01, 2008). Adva nced Life-Cycle Analysis of Existing Concrete Bridges. Journal of Materials in Civil Engineering, 20, 1, 9.

Thompson, P.D. (2004). Bridge life cycle costing in Integrated Environment of Design, Rating and Management. *Transportation Research Record.*

Yee, K. and Ooi, T.A. (2010). "Ground Improvement – A Green Technology towards a Sustainable Housing, Infrastructure and Utilities Developments in Malaysia," *Geotechnical Engineering Journal of the SEAGS & AGSSEA*, 41 (3), 1-20.

Zhang, C. (2010). Delivering sustainable bridges to help tackle climate change. *Engineering Sustainability, ICE, 163, ES2, 89-95.*

Deflection Limits in Tall Buildings – Are they useful?

Rob Smith
Associate Principal, Arup, 12777 West Jefferson Blvd, Los Angeles, CA 90066, USA; PH +1 310 578 4598; email: rob-j.smith@arup.com

ABSTRACT

Serviceability criteria in the form of lateral deflection and acceleration limits under wind loading are often the governing structural issues for tall buildings. Whilst the basis for acceleration criteria has been the subject of research, rational refinement and consensus over recent years, deflection limits are still rather arbitrary. Current guidance on deflection limits in international design codes is very limited and is based primarily on experience with typical low and medium-rise buildings. The issues with lateral deflection in very tall buildings are different to those of low-rise buildings, and depend on structural form. Rational choice of deflection criteria for tall buildings therefore requires further consideration of the nature of the deformations and the effects they have on the functional aspects of the building.

This paper identifies the functional issues, the relevant deflection measures, and reviews current international practice. New design approaches are challenging previous design norms, and the paper describes a performance-based approach, which allows greater freedom in choosing appropriate constraints for structural and non-structural components. Whilst the subject matter is not new, the use of new design tools and processes leads us to re-examine rules of thumb previously used. The paper focuses primarily on wind events, but comparisons with seismic events are drawn.

INTRODUCTION

Lateral loading effects from wind and seismic sources usually dominates the structural design of tall buildings. As well as strength considerations, stiffness and its effect on deflection, is usually the governing criteria which determines structural element size and cost.

Structural design codes are generally written with conventional types of low-rise and medium-rise buildings in mind. High-rise buildings often have different structural forms such as outrigger systems, bundled tubes, megabracing etc. The nature of the deflection with these structural types often differs to that in low-rise buildings. At the time of writing there are a large number of buildings around the world being designed well above the height that has historically been fully considered when formulating code rules. In order to provide improved criteria for deflection performance of these buildings, it is essential to understand the nature of lateral deflections and effects on serviceability and strength.

The first part of this paper discusses the functional issues that are affected by deflections in high-rise buildings. The next part discusses factors that affect the predicted deflections. Finally, a review of recommended deflections and a design approach is given. This paper describes a performance-based approach for deflection limits, whereby the limit should be defined by consideration of the performance of all the associated non-structural and structural items.

PERFORMANCE CONSIDERATIONS RELATED TO DEFLECTION

Cladding and Facade

Cladding systems must be designed to accommodate the movements imposed upon them so as to maintain the functionality of weather-tightness, acoustic and thermal insulation and structural / mechanical integrity.

The movements of concern to cladding are local deformations, not overall deflections. The relevant local deformations are affected by the arrangement and types of fixing and the design of the joints, but may be categorised broadly as vertical compression/extension, in-plane shear, and warping.

All aspects of sources of deformation are of concern. These include

- Movements associated with continuing construction of the building after panels have been installed
- Long term (quasi-static) effects due to gravity loads, creep and shrinkage
- Medium term effects (e.g. thermal)
- Short term and dynamic effects (wind and earthquake)

Movements from all sources must be combined to determine the effect on individual panels. This is common practice amongst many specifiers of facade systems.

The movements tolerated by cladding panels are then limited by:

- Maximum movement joint size (limited by manufacturing or architectural preference)
- Size of panels
- Detailing of movement joints and connections
- Ductility of panels (which is typically low)

Interior fit-out : partition walls, architectural finishes etc

Broadly the same considerations apply to internal fit out as apply to cladding. However there may be additional racking deformations associated with:

- Relative vertical gravity and thermal shortening between internal and exterior cores, walls and columns
- Additional racking due to lateral deformation shapes of walls/cores and frames

It is common in seismic zones for partition walls to be designed for movement. For instance, soft layers can be placed at the end and head of walls, allowing in-plane movement, but restricting out-of-plane movement. Where brittle finishes are applied, and movement joints are not specified, the designer can assess shear drift for an appropriate panel size and limit drift based on guidance for low-rise buildings.

Lifts / Elevators

The considerations for lifts are different. Lifts are contained within shafts and are only sensitive to lateral movements due to wind (and earthquake). Lift cars and counterweights are laterally restrained by vertical rails within the shaft and systems can be designed to accommodate significant lateral ‘slope’. However, a major consideration is the profile of the cables and deflected lift shaft, and the need to

prevent the cables from snagging on fittings in the shaft. Cables respond dynamically to lateral vibration of the building and it is important to avoid significant resonance by ensuring the natural frequency of the cables is well separated from the natural frequencies of the building during significant building motions. This is often managed by parking the lifts during high winds so that the cable lengths are reduced to increase cable frequencies away from resonance.
The shaft size may need to be increased in order to provide adequate clearance between the cables and the shaft during strong winds, to accommodate the lateral curvature (related to deflection) of the lift shaft (and therefore building as a whole), and the sag and vibration of the cables. The geometry of the lift shaft and its deflected shape should be considered on a case by case basis and there is no single limiting value – the height is likely to be governed by the size and strength of cables. As lateral deflection limits are relaxed the sizes of lift shafts may have to increase, or other measures may be needed to reduce cable motions.

Occupant comfort

Occupant comfort is related to the perceived movement of buildings. In isolation from visual cues, humans cannot detect the quasi static lateral deflection of a tall building, sensing only the motion, normally quantified in terms of acceleration rather than displacement. Whilst there is no universally agreed limit for lateral accelerations, there are various guidelines in different design standards which are broadly similar.
Deflection checks are not adequate for assessing occupant comfort as these do not adequately cover the important dynamic factors affecting acceleration. For this reason the historic specification of a lateral 'deflection limit' (e.g. the Hong Kong concrete design code (2004) recommends a limit of H/500) as a means of guarding against excessive human perception of motion is at best indirect and empirical, and at worst could be either unsafe or uneconomic. For buildings with supplementary damping, it is possible to make a building more flexible and still achieve satisfactory accelerations.
In the case of a very tall or flexible building, the floor 'slope' might be noticed by the occupants. Perception might be might be triggered by a ball or marble starting to roll across a floor or table top, or a pendulum light fitting moving out of line with a 'vertical' feature. Criteria for such phenomena have not been developed, as traditionally it has been 'motion' (i.e. lateral accelerations) that has governed. However, this may not be the case in future for very tall buildings where human sensitivity to acceleration is lower and the floor slope becomes relatively more significant .

Acceptable damage

Normal design practice assumes that the structure will remain near-elastic for the ultimate (factored) wind load. It is also assumed that the non-structural elements will also remain largely undamaged for the unfactored wind load – typically 50 or 100 years. For seismic loading, more damage is acceptable. ASCE 41-06 (2006) provides guidance on how different shear drifts relate to different damage levels. The "immediate occupancy" damage category (typically relating to a 30-70 year seismic event) allows a small degree of damage, but the "service wind" (50 years) allows no

damage. The difference relates to the need to consider wind storms of lesser but still significant magnitude, and which remain a common occurrence.

CONSIDERATIONS IN THE PREDICTION OF DEFLECTIONS

Structural modelling of frame

Typically, structural modeling is performed with the intent of calculating force distribution within a building. A conservative approach is made which often over estimates deflections. Therefore realistic assumptions would need to made relating to items such as non-structural elements, P-delta effects, construction sequence, cracking of elements, short term elastic modulus, stiffness degradation, modelling of joints. While there are numerous text books written on this subject, there is little standardized guidance.

Loading and return period

Wind

Deflections under wind loading are normally taken at the "design wind speed". The design wind loading for tall buildings is usually taken as either 50 year (non-hurricane/cyclone/typhoon regions) or 100 year (in hurricane/cyclone/typhoon regions). Load factors used may also vary between codes and care should be taken when selecting a return period to take proper account of intended safety at the ULS limit.

For certain types of building, the peak wind loading may be associated with a lower wind speed. This occurs when the critical wind speed for vortex shedding is lower than the 50 year wind speed. In this case, the design should not only use the peak wind load for estimating deflections, but should also consider increasing this. The reason for the that the probability of the building experiencing this force is higher than for a building which does not see this vortex shedding peak.

Damping

Damping is a big factor in determining the dynamic response, which will often contribute a significant proportion of the overall deflections in wind. As discussed in Smith, Willford and Merello (2010) the values of damping conventionally recommended are typically too optimistic for very tall buildings, and appropriate values, based on improvements over the last 10 years or so in quality of understanding and measurement, should be adopted, especially where best-estimate wind speeds and responses are used for design.

Seismic

Seismic response is usually based on either the 475 or 2475 year event. The nature of seismic loading is such that a much greater shear drift is seen within the building than in wind. Interstorey drift largely matches shear drift (racking deformation) in this case. See later for definitions of drift.

DEFINITIONS OF DEFORMATION UNDER WIND OR EARTHQUAKE

The following are useful definitions to describe how a building deforms.

Total building drift ratio is defined as the peak lateral deflection at the top of a building divided by the height of the building (excluding items such as masts etc) under the design wind load. This is a crude measure of assessing the stiffness of a building and its likely performance.

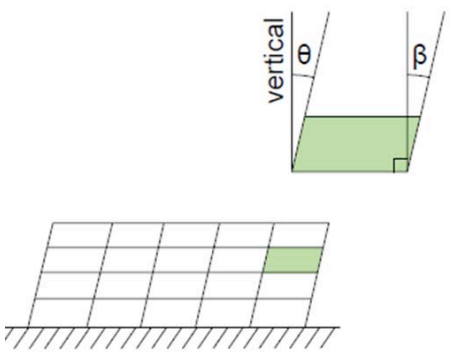
Interstorey drift is defined as the difference in horizontal displacement over one storey (floor) divided by the storey height. This is the most commonly used form of deformation criterion and many structural design standards refer to this. This can be seen as θ in Figure 1.

Floor Slope. In the context of building deflections, the slope can be defined as the average angle of the floor plate at the lower part of a panel that is considered. The slope may vary in each bay, depending on the relative vertical deflection of the columns or walls at each side of the bay. In Figure 1, this is θ – β and may vary from panel to panel.

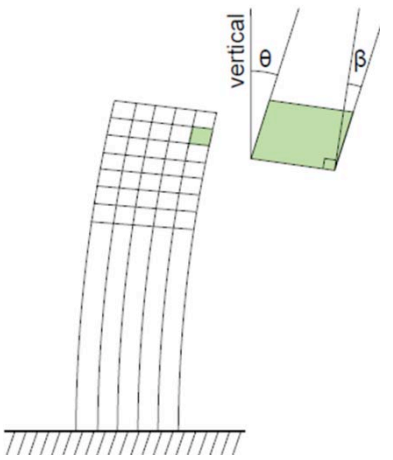
Panel deformation is a measure of the in-plane shear deformation of a wall panel. It is the difference between the interstorey drift and the local floor slope. Whilst in framed perimeter structures the floor slope will generally mean the panel deformation is less than the interstorey drift, in some cases the effect of floor slope is additive (e.g. between a core and a perimeter structure). This is a measure of the deformation that would cause damage to non-structural elements. This is β in Figure1. If one compares figures b and c, it can be seen that panel deformation may vary across a storey. A famous example of a building with a high floor slope and high interstorey drift but no panel deformation is the leaning tower of Pisa. The deformation is almost entirely in the foundation.

Racking deformation can be defined as the average panel deformation over a storey.

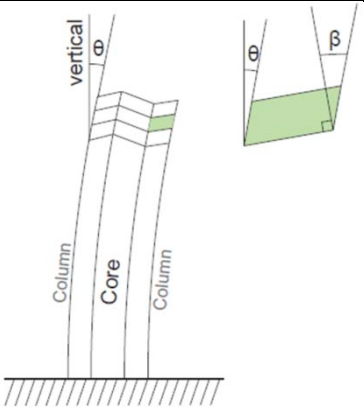
Inclination may be defined as the slope of a nominally vertical element such as a lift shaft in wind. It is the same as interstorey drift.



a/ Low rise building – interstorey drift same as panel deformation



b/ Tubular building – interstorey drift higher than panel deformation



c/ Core building – interstorey drift can be lower than panel deformation



d/ Example of building with high interstorey drift and low panel deformation

Figure 1 - Definitions of drift - based on CTBUH (2008)

EXISTING CODES AND STANDARDS

The following data has been taken from various international design and loading codes. Many modern design codes do not apply limits on lateral deflection of buildings.

Table 1 - deflection limits in international standards

Standard/ Reference	Effect	Type	Inter-storey Drift Ratio Limit	Top Deflection Limit
Chinese Standard				
JGJ3-2002 Technical specification for concrete structures of tall building	Wind (H>250m)	Concrete/ Steel/ Composite	1/500	No guidance
	Seismic (50yrs) (H>250m)	Concrete/ Steel/Composite	1/500	No guidance
JGJ 99-98 Technical specification for steel structure of tall building	Wind	Steel Structure	1/400	No guidance
	Seismic (50yrs)	Steel Structure	1/250	No guidance
DG/TJ08-015-2004 Code for design of steel – concrete hybrid structures for high – rise buildings (Shanghai)	Wind (H>250m)	Composite	1/500	No guidance
	Seismic (50yrs) (H>250m)	Composite	1/500	No guidance
Hong Kong Code				
Code of practice on Wind Effects in Hong Kong 2004	Wind	RC/Steel	No guidance	No guidance
Code of Practice for Structural use of Concrete 2004	Wind	RC	No guidance	1/500
Code of Practice for Structural Use of Steel 2005	Wind	Steel	1/400	1/500
Eurocode				
Eurocode 3 ENV 1993-1-1:2005:	Wind	Steel	No guidance	No guidance
Eurocode 8 EN 1998-1-2004	Seismic (approx 95 year)	Steel / Concrete (limits depend on finishes)	1/200 – 1/100	No guidance
British Standards				
BS 5950 – structural steel in buildings	Wind	Steel	1/300	No guidance
BS 8110 – structural use of concrete ("limit applies unless partition, claddings have been specifically detailed ..")	Wind	Concrete	1/500	No guidance
American Standards				
ASCE 7-05 – Minimum design loads for buildings and other structures	Wind		No guidance	No guidance

Standard/ Reference	Effect	Type	Inter-storey Drift Ratio Limit	Top Deflection Limit
	Seismic (2/3 of 2475 event)	Steel / Concrete	1/100 – 1/200	No guidance
Los Angeles Tall Building Structural Design Council, An alternative procedure for Seismic analysis and design of Tall buildings located in the Los Angeles region (2008)	Seismic (MCE)	All	1/33	No guidance
Japanese Code				
Building Codes of Japan and Recommendations from the Special Approval Process by a Selected Expert Review Panel (applies to any building over 60m)	Seismic	Steel	Typically: (100yr): 1/200 (500yr): 1/75 - 1/100	No guidance
		Concrete	Typically: (100yr): 1/500 (500yr): 1/200	No guidance
Guidelines for the Evaluation of Habitability to Building Vibration	Wind	Steel	Same as above	No guidance

LITERATURE REVIEW

Interstorey drift

Recommendations for criteria on drift limits have been in existence for many years. For instance "The stability of tall buildings" (Wood, 1958) gives a table of racking tests. From this, it can be seen that typically first cracks in a masonry wall would occur at around H/400, although there is considerably more movement before ultimate load is reached.

Similarly, tests by Freeman (1977) on plasterboard partitions indicated that first cracks would occur around H/300 to H/400. The paper also discusses how partitions may affect the overall damping and stiffness of the building.

One of the most comprehensive reviews of the drifts is published by the Council of Tall Buildings and Urban Habitat (1980) includes a study of the state of the art in the 1970s. Limits for interstorey drift from literature range from H/333 to H/666. Note that the latter is based upon a wind pressure of 958 Pa (20 lb/ft2) at 30m height, rather than a specific return period. Most of the drift values in this book refer to those in common usage, but little mention is made of physical testing. A later study by ASCE (Ellingwood et al 1986) shown in table 3 compiled the results of various tests to ascertain the effect of drift on damage to non-structural components. As can be seen, the critical point where damage becomes visible would appear to be H/500 to H/300.

Galambos and Ellingwood (1986) suggest that the serviceability criteria based upon 50 year winds are too onerous and it would be more suitable to use a reliability method based around the 8 year period (8 years being a typical lease period in a tall building), such that the design deflections are not exceeded more than once in that period. We do not believe that this suggestion was ever taken up in building codes.

A further study by the ASCE (1988) conducted a survey of US structural engineering practices. The study focussed on engineers treatment of drift in tall buildings of the time. Typically (41% of respondents), engineers designed to H/400 interstorey drift for the 50 year wind. A number used different numbers between H/600 and H/200.

Of course, the above has focussed on determining a deflection limit for a defined wind event, ie a deterministic approach. Generally such approaches should be calibrated against probabilistic approaches, although such procedures are not practical in normal building design.

Reid and Turkstra (1981) reviewed such a process and concluded that the most important variable apart from loading was the damage limitation threshold (ie the drift limit!) The other conclusion that can be drawn from their work is rather simple – flexible buildings are more likely to suffer damage if not detailed correctly. This is a sliding scale and not based on a single number.

Examples of buildings which have been designed outside of "normal" drift limits are given in Taranth (2009) The SRZ tower in Dubai (265m high office building, designed by Lemessuirier Consultants) did not meet a limit of H/500 in design, and this requirement was relaxed owing to the nature of the deflection (bending rather than shear). The same argument was applied to the Al Bateen Towers in Dubai (204m). See table 4.

Another building designed (but not yet built) with high drifts is the 600m Chicago Spire. While the drifts are not reported publicly (Burns et al, 2008) the first natural period is – 18 seconds. This is an indication of a very flexible building which could not meet traditional deflection limits.

Total building drift

Much of the older literature (CTBUH, 1980) focused on total building drift limits, discussing occupant comfort and dynamics. At that time, the use of damping to control building dynamics was in its infancy, as was the understanding of the sensitivity of building occupants to lateral movement. A survey of engineers in Boston, Ma indicated that total building drifts used in the 1970s was between H/1000 and H/200, with the majority using a limit of H/400. Two companies reported that buildings designed with a limit of H/200 had performed adequately in the past, although no details are given.

A key point to note that in the 1970s US design practice, there was no fixed deflection criteria. This remains true in today's practice.

Table 2 - test data from Wood (1958)

Type of frame and infill	First visible crack : deflection / height	First crack deflection (inches)	Ultimate deflection (inches)
Frame type 1 Horizontal girders 10 in x 4.5 in (I25) Vertical stanchions 10 in x 8 in (I 55) (weak direction) 6 in x 3 in x 0.5 in bolted cleat connections to top and bottom flanges of each beam			
Open bare frame	n/a	1.0	6.0
Encased frame	1/100	1.0	2.3
Encased frame with 4.5 inch brick panel	1/350	0.3	2.5
(repeat test) with 4.5 inch brick panel	1/400	0.28	2.8
Brick on edge in filling	1/400	0.27	2.0
3 in hollow clinker block	1/450	0.25	0.8
(repeat test) 3 in clinker block	1/400	0.28	0.7
3 in hollow clay block	1/275	0.4	1.5
3.5 inch brick	1/425	0.26	0.6
4.5 inch brick with door opening	1/1000	0.11	2.1
Frame type 2 (stiffer) Horizontal girders 13 in x 5 in (I35) Vertical stanchions 10 in x 8 in (I 55) (strong direction) 6 in x 4 in x 3/8 in bolted cleat connections to top and bottom flanges of each beam			
Encased frame	1/100	1.0	2.2
4.5 inch brick infilling	1/400	0.28	1.5

Table 3 - Serviceability performance levels published by ASCE (Ellingwood 1986)

Deformation as a fraction of span or height	Visibility of deformation	Typical behavior
< 1/1000	Not visible	Cracking of brickwork
1/500	Not visible	Cracking of partition walls
1/300	Visible	General architectural damage Cracking in reinforced walls Cracking in secondary members Damage to ceiling and flooring Façade damage Cladding leakage
1/200 – 1/300	Visible	Visual annoyance Improper drainage
1/100 – 1/100	Visible	Damage to lightweight partitions, windows, finishes Impaired operation of moveable components such as doors, windows, sliding partitions

SAMPLE DATA FROM BUILDINGS

The following gives examples of tall building designs.

Table 4 - Design deflections

Name of building	Lctn	Source of data	Ht (m)	Structural System	Max Lateral Deflect	Max Interstorey Drift
Central Plaza	Hong Kong	Arup	374	perimeter tube core	H/785	
West Tower	Guangzhou	Arup	432	RC Core + CFT Diagrid	H/575	h/500
Jin Mao Tower	Shanghai	Taranath	421	RC Core + SRC Column frame	H/575 (Chinese code wind)	
International Commerce Centre	Hong Kong	Arup	480	RC Core + Outrigger + SRC Column frame	H/400	h/300
2IFC	Hong Kong	Arup	420	RC Core + Outrigger + SRC Column frame	H/466	h/315
Petronas Tower	Kuala Lumpur	Taranath	452	RC Core + Outrigger + SRC Column frame	H/560 (50 year wind)	
Elysian Hotel	Chicago	Taranath	208	RC Core + outrigger + RC Mega columns	H/800	
Pinnacle	London	Arup		Braced steel perimeter with viscous dampers		h/300
St Francis Towers	Manila	Arup	210	RC core, moment frame, Damped outrigger	H/230	h/250
Al Bateen Towers	Dubai	Taranath	204	Coupled shear wall		h/300 (reported as 10 year wind)
SRZ Tower	Dubai	Taranath	265	RC Core + outrigger + frame		Approx h/350 (10 year wind)

Sources of data : Arup – internal Arup correspondence

Taranath – see Taranath (2009)

RECOMMENDATIONS

Stiffen building for the appropriate use and wind event

The degree of stiffening required for a building should consider the contents (brittle finishes, flexible panels etc) and also the nature of the climate (eg hurricane/typhoon/tropical cyclone, thunderstorm, or extra-tropical cyclone).

In a hurricane climate and with brittle finishes, it may be more appropriate to take a lower return period wind with tighter deflection criteria. This might be panel deformation of H/600 for a 10 or 20 year wind. The rationale is to concentrate on ensuring no damage in a more realistic service state. Although, in this case, the 50 or 100 year wind deflection may be high, the accumulated damage over the life of the building would be similar to that of a structure designed in a non-typhoon region.

For synoptic wind climates (non-typhoon), where detailing cannot accommodate higher deflections, panel deformations should be limited to between 1/300 and 1/500 in the 50 year wind.

Accommodate movements

In many case, non-structural items can be designed to accommodate deflections. Items which can be designed for this are cladding panels, partitions, lift cables, services etc. As has been discussed previously, overall deflection limits and interstorey drift limits can be a crude measure of the actual functional requirements, and specific 'performance based' approaches offer greater flexibility and make more sense particularly for very tall buildings. This is already common in seismic zones where construction details are modified to permit greater movement than normal with minimal damage to cladding and fit-out.

Use "panel" deformation as definition of movement

Deformations should be provided/specified for appropriate panel sizes and types to represent cladding panels or non-structural walls. Interstorey-drifts, even when considering the differing effects of shear and bending are fairly meaningless as they do not consider the internal deformation of the building.

Design for occupant comfort

Quantitative criteria for occupant comfort are expressed in terms of acceleration, not deflection, and traditional deflection limits are not a good way of attempting to satisfy comfort criteria.

REFERENCES

ASCE, "Wind Drift Design of Steel-Framed Buildings: State-of-the-Art Report" (1988) ASCE Task Committee on Drift Control of Steel Building Structures of the Committee on Design of Steel Building Structures, James M. Fisher, chmn. *Journal of Structural Engineering*, Vol. 114, No. 9, September 1988, pp. 2085-2108,

American Society of Civil Engineers. (2006) ASCE Standard 41 – 06, *Seismic Rehabilitation of Existing Buildings*.

Buildings Department, Hong Kong. (2004) *Code of practice for structural use of Concrete*

Burns J, Irwin P, Bacon D, Cicci M, Tomasetti R, Steele N. (2008) "Wind Engineering of the 600m Chicago Spire", IABSE 2008 conference Chicago. Pub International Association of Bridge and Structural Engineers, Zurich, Switzerland

Council on Tall Buildings and Urban Habitat (CTBUH) (1980) Planning and Design of Tall Buildings ,5 vols., , ASCE ,New York, N.Y ch SB-5

Council of Tall Buildings and Urban Habitat. (2008) *Recommendations for Seismic Design of High-Rise Buildings*, (available at www.ctbuh.org)

Ellingwood, B., Allen, D. E., Elnimeiri, M., Galambos, T. V., Iyengar, H., Robertson, L. E., Stockbridge, J. and Turkstra, C. J. (1986). "Structural Serviceability: A Critical Appraisal and Research Needs" (By the Ad Hoc Committee on Serviceability Research, Committee on Research of the Structural Division). *Journal of Structural Engineering*. Vol. 112, No. 12. 2646-2664.

Freeman (1977), "Racking Tests of High-Rise Building Partitions", *Journal of the Structural Division*, Vol. 103, No. 8, August 1977, pp. 1673-1685

Galambos T and Ellingwood B (1986) "Serviceability Limit States Deflections", Journal of Structural Engineering, Vol. 112, No. 1, January 1986, pp. 67-84,

Reid, S. G., and Turkstra, C. J.,(1981) "Codified Design for Serviceability,", *Structural Safety and Reliability*, Elsevier Scientific Publishing, Amsterdam, ,pp. 583-592.

Smith R, Merello R, Willford M (2010). "Intrinsic and Supplementary Damping in Tall Buildings". *Proc. Institution of Civil Engineers, Structures and Buildings April 2010 163(SB2), 111-118*

Taranath B (2009), Reinforced Concrete Design of Tall Buildings, CRC Press, Boca Raton, Fl, USA

Wood R. (1958) "The Stability Of Tall Buildings", *Proceedings of the Institution of Civil Engineers,* 1958, 11, September, 69–102

Structural Analysis and Design Challenges of the Ping An Tower under Consideration of the Upcoming China Code

Authors: Dennis C.K. Poon[1], Ling-en Hsiao[2], Yi Zhu[3], Steven Pacitto[4], Steve Zuo[5] Torsten Gottlebe[6], Shenming Wang[7]

[1]PE., Managing Principal, Thornton Tomasetti, Inc., dpoon@thorntontomasetti.com
[2]Senior Principal, Thornton Tomasetti, Inc., lhsiao@thorntontomasetti.com
[3]MSSE., Principal, Thornton Tomasetti, Inc., yzhu@thorntontomasetti.com
[4]PE., Principal, Thornton Tomasetti, Inc., spacitto@thorntontomasetti.com
[5]PE.,Vice President, Thornton Tomasetti, Inc., szuo@thorntontomasetti.com
[6]Associate, Thornton Tomasetti, Inc., tgottlebe@thorntontomasetti.com
[7]Senior Engineer Thornton Tomasetti, Inc., swang@thorntontomasetti.com

Thornton Tomasetti, Inc., 51 Madison Ave, New York NY 10010, Tel: 917-661-7800

ABSTRACT

When completed the Ping An Tower will be the second tallest building in the world and the tallest in China. Its design was being developed at the same time as the latest cycle of revisions to the China Code were being proposed and considered. Expert panel reviewers familiar with upcoming code changes considered them when commenting on the design. As a result, the analysis and design challenges experienced on the Ping An Tower provide a preview of likely effects of the forthcoming China Code. The paper will discuss and summarize extensive analyses required to satisfy the new China Code standards. The impending provisions in the China Code will establish more stringent design requirements that go beyond current international building design standards.

PROJECT DESCRIPTION

At 660m of height, the Ping An Tower will be the centerpiece of the growing Shenzhen skyline located just a few minutes north of Hong Kong. It will be the tallest tower in China upon completion in 2014. Its skyward-pointing shape is reminiscent of classic skyscraper forms like the Empire State Building and Chrysler Building in New York City while using state-of-the-art technologies for design and construction. Implementing LEED requirements for design, construction and life cycle properties will set a new standard for China building design. In 115 stories the tower will accommodate high end Class A office space, trading floors, Skylobbies and sky restaurants as well as an observation deck. An 11 story podium will house entertainment venues, high end retail stores and cultural amenities. Its 5 story deep

basement includes spaces for mechanical, electrical and plumbing services as well as extensive parking areas. *See Figure 1.*
The development will occupy an area of 12,000m^2 with a total gross floor area (GFA) of 462,000m^2 (4.95 million ft^2) with 385,000m^2 above and 77,000m^2 below grade.

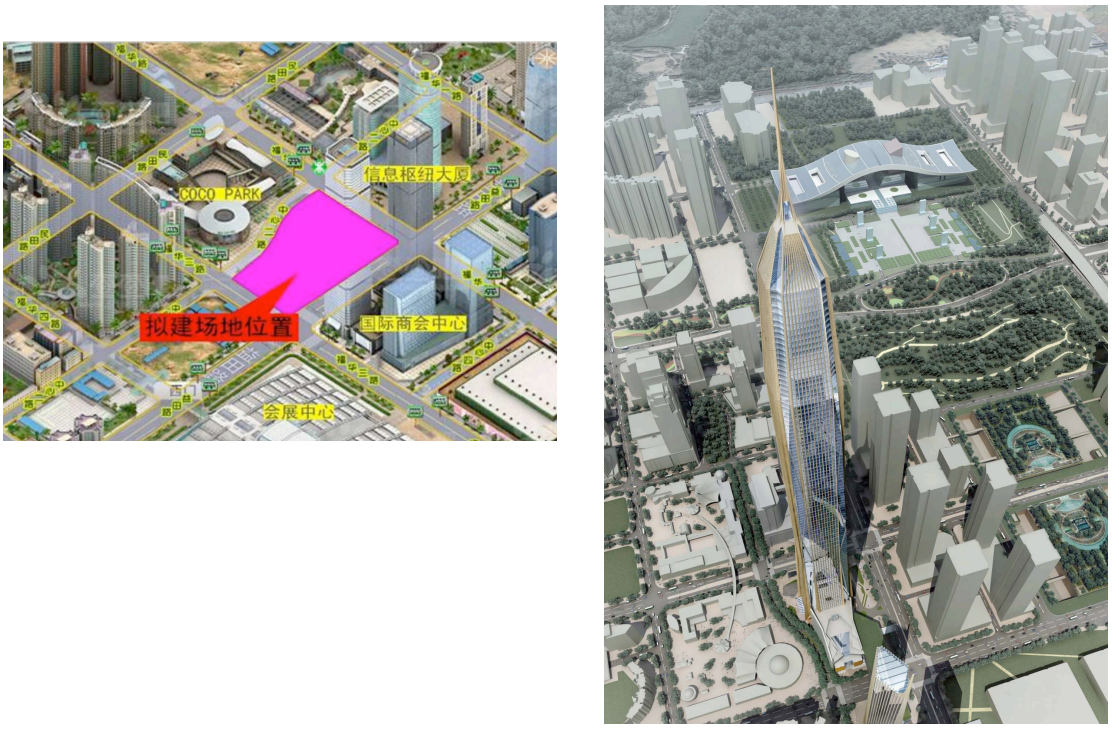
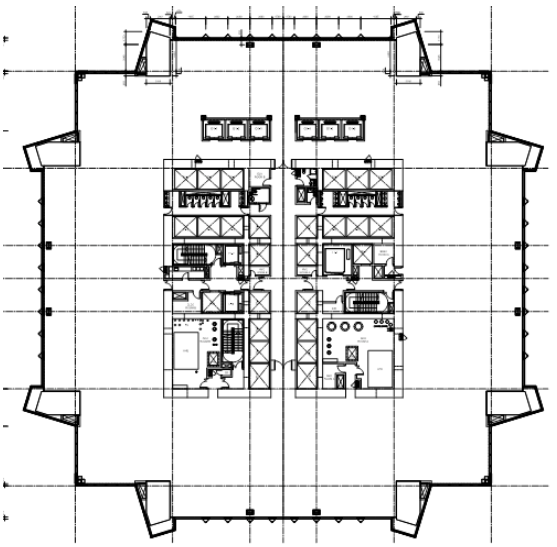


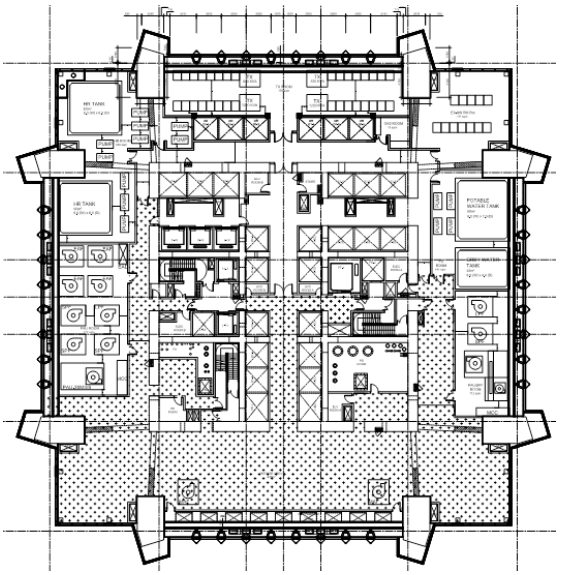
Figure 1 – Ping An Tower Site Plan and 3D Rendering
(Courtesy of KPF)

A stacked-zone approach was adopted for interior space planning. This design strategy is becoming more common for super tall structures since it provides efficiency in construction and ongoing building operation. Each zone, containing about 15 office floors, is separated from other zones by double height mechanical floors which are also designed as refuge floors in emergency events. The floor plates are square with recessed corners. Floor overall dimensions taper from the ground floor up to level 27 and then stay constant up to level 95 (while the four corners keep receding) From level 95 to 115 floor dimensions steadily reduce to produce a unique roof profile. Above the last floor a tapered structural steel frame will support a 60m tall mast (Figure 2).





Typical Office Floor Plan



Typical Mechanical Floor Plan

Figure 2 - Ping An Tower Elevation and Typical Floor Plans
(Floor Plans are Courtesy of KPF)

GEOTECHNICAL CONDITIONS AND TOWER FOUNDATION

Considering its coastal location, site subgrade conditions are fairly good: strata of clay, fine sand and coarse sand for 30m with at least 35m of decomposed rock below. The site is defined for seismic design as Type II to III. See Table *1* for typical soil strata and mechanical properties. The water table is high, just 2.2 to 4.9m below grade.

Table 1- Soil Profile

Soil Stratum Succession	Soil Stratum Name	Average Soil Stratum Thickness (m)	Average Distance to the Bottom of Stratum (m)	Saturated Undrained Internal Friction Angle (degree)	Saturated Undrained Cohesion (kPa)	Shear Wave velocity (m/s)
①	Backfill	5.45	5.45	-	-	190.3
②	Silty Clay	1.4	6.85	12.3	18.0	174.5
③-1	Clay	3	9.85	18.4	42.9	213.7
③-2	Med.Coarse Sand	2.3	12.15	-	-	245.4
③-3	Fine Sand	1.4	13.55	-	-	250.0
③-4	Silty Clay	3.15	16.7	14.8	34.9	243.4
③-5	Silty Clay	2.4	19.1	11.3	15.5	211.0
③-6	Coarse Sand	2.75	21.85			258.2
④	Grav. Clay	7.05	28.9	23.7	21.4	275.6
⑤-1	Fully Weathered Granite	5.85	34.75	26.0	16.5	336.6
⑤-2	Fully Weathered Granite	6.25	41	26.8	14.2	380.4
⑥-1	Severely Weathered Granite	14.55	55.55	-	-	458.4
⑥-2	Severely Weathered Granite	10.45	66	-	-	504.6
⑦-1	Medium Weathered Granite	6.25	72.25	-	-	663.9
⑦-2	Medium Weathered Granite	9.25	81.5	-	-	700.5
⑧-1	Slightly Weathered Granite	9.95	91.45	-	-	933.8

To support the heavy weight of the structure a bearing pile foundation was chosen. A single hand dug super caisson of approximately 9m diameter is located under each super column. It has a bearing capacity of about 543MN. Sixteen hand dug caissons of 7m diameter (bearing capacity 344MN) are located under the core. It is economical in the southern region of China to use hand dug caissons and a common practice. The caissons are about 30m long to bear on bedrock. The Ping An Tower mat is 5m thick beneath the main core and 3m thick in the surrounding area, using a concrete strength of C40 (f'c=4.9ksi). The advantage of locating large caissons under columns and core wall intersections is the direct load path from superstructure through mat to caissons and bedrock, minimizing mat thickness and excavation volume.

Figure 3a shows the pile layout and 3b the predicted mat settlement deformations.

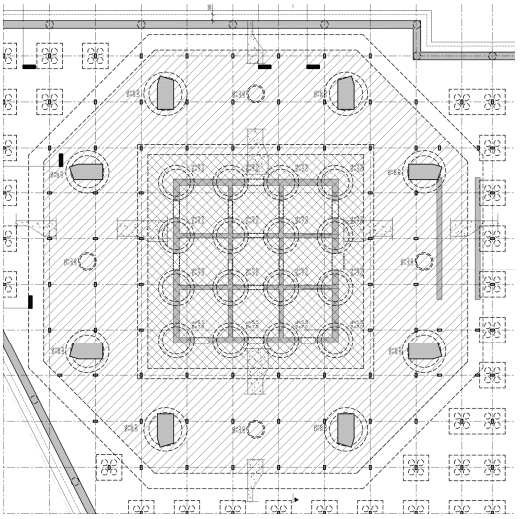


Figure 3a - Tower Mat

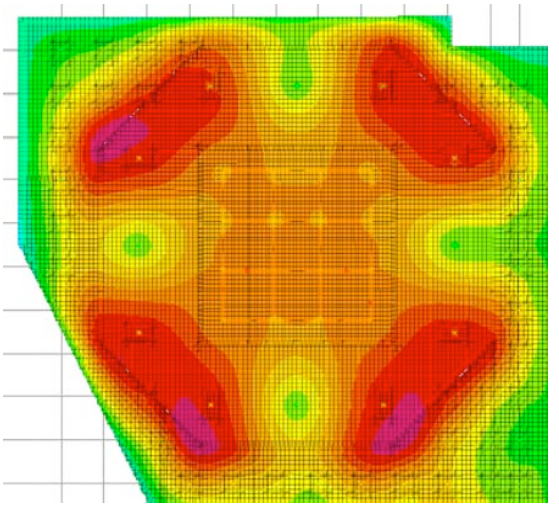


Figure 3b - Mat Settlement Contour

The anticipated settlement of the mat is greatest under super columns, at 20mm, followed by that under the core, at 14mm. To address the differential settlements between the podium and the tower mat, the design also includes delayed pour strips at basement levels, as well as recommendations for construction using specific stages and sequences.

LATERAL LOAD RESISTING SYSTEM

The eventual success of a super tall building design often hinges on selection of the most appropriate lateral load resisting system. Systems providing comparable strength and stiffness can differ by millions of dollars of construction cost, so various schemes were investigated at the beginning of the project. The goal was to find the most economical system using the least quantity of building material and weight that also provides the most efficient and flexible space layout. Among the options investigated were Tube-in-Tube, Mega Frames and various hybrid systems. The most efficient system is a "Core-Outriggers-Mega Frame" system with a reinforced concrete core, super composite columns and steel outrigger trusses. The final design uses a combination of a Core-Outriggers-Mega Frame and an Exterior Mega Frame formed by belt trusses and mega braces joining the super composite columns. The reason for that decision will be discussed later. *See Figure 4*

The two major criteria that need to be controlled for every super tall building are the limiting story drift and limiting acceleration (for comfort based on human perception). These two criteria can also be related to overturning moment and story shear.

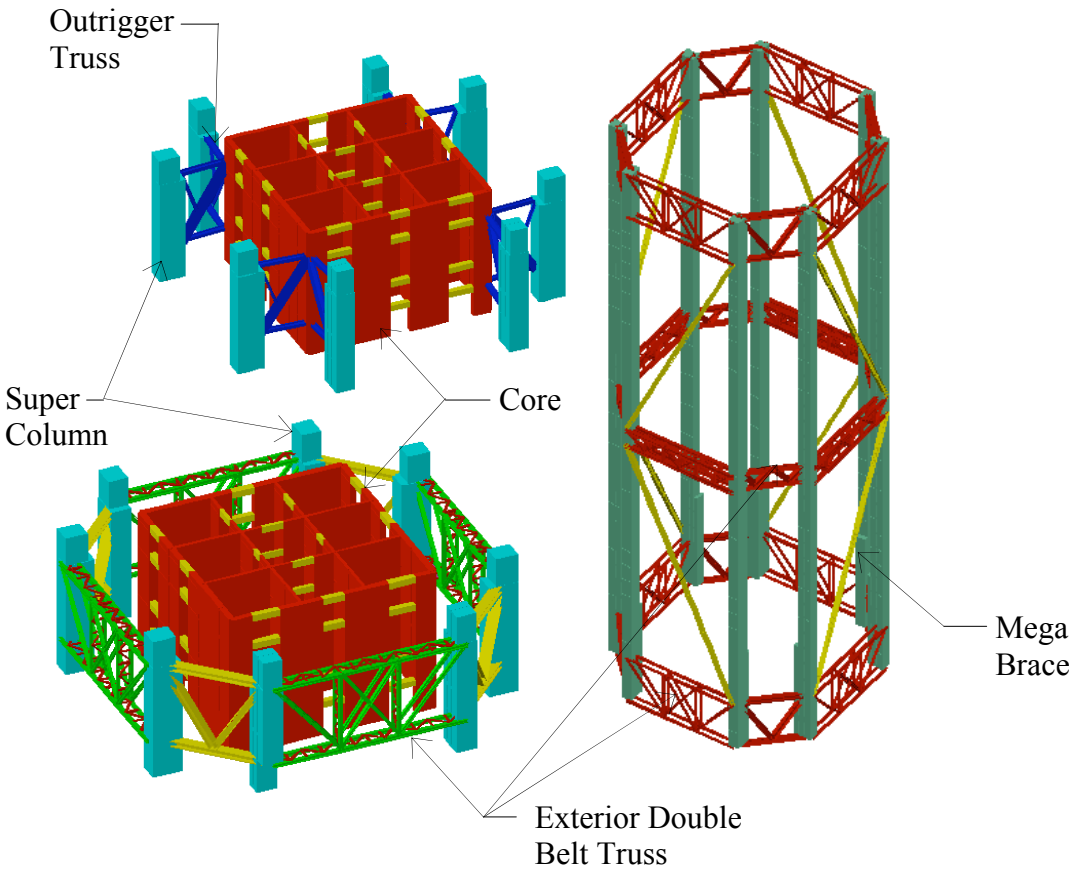


Figure 4 Lateral System Components

The concrete core is a nine-cell square in plan, 32m on each side from Zones 1 through 5. Starting with Zone 6, the four corner cells of the core are cut off to achieve an efficient office space layout. Above Level 112 parts of the south and north walls are also eliminated. See Figure 5. The flange (outermost) wall thickness varies from 1.5m at Zone 1 to 0.5m at Zone 8. Web (interior) walls vary from 0.8m to 0.4m thick. While it is unusual to change web wall thicknesses along elevator shafts, the changes address a specific seismic provision in the China code related to compression stress ratio in walls under gravity loads. Wide flange steel column shapes are embedded within boundary zones at the most highly stressed corners and ends of core walls. They serve to both strengthen the core and to provide a clear load path from outrigger forces into the core. The core walls play a critical role in resisting most of the gravity load and lateral load. To eliminate any concern about brittle shear failure when subject to a combination of high shear stress and axial stress, embedded steel plates are used to reinforce the core walls from foundation to level 12. The plates both enhance ductility and permit a reduced wall thickness.

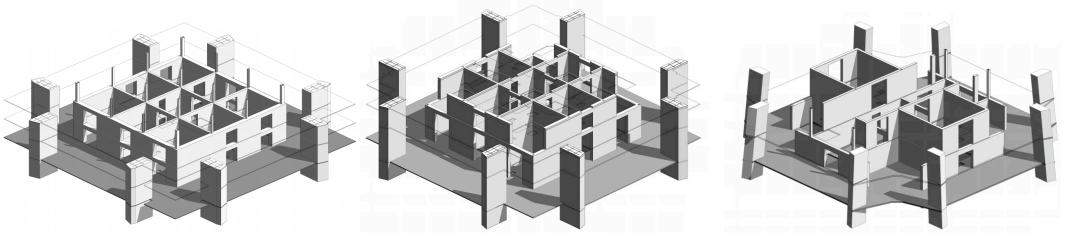


Figure 5a- zones 1~5 Figure 5b- zone 6 and above Figure 5c- above level 112

Figure 5 - Core Wall Layouts (scale varies)

It is impractical and inefficient to have a super tall tower core resist all overturning and provide all lateral stiffness by itself. The greater strength and stiffness of the whole building footprint is engaged by using outriggers at mechanical/refuge levels to tie the core to perimeter super columns. This creates a larger lever arm to resist overturning moment effects very efficiently. Their contribution to cantilever flexural stiffness can be expressed as $A*d^2$, where A is the area of the super columns and the d is the distance between them. As d gets bigger, the stiffness contributed by super columns increases dramatically. To achieve maximum outrigger effectiveness and to avoid secondary kink forces in slabs it is highly recommended to align outrigger trusses with main core wall planes. For the Ping An Tower outriggers are aligned with core flange walls. In plan, the super columns are generally rectangular, varying in size from approximately 6.0m by 3.2m at Zone 1 to 2.9m by 1.4m at Zone 8. To increase super column axial stiffness as well as axial and flexural strength, built up steel shapes are embedded within. Super columns are connected to the core through two story high steel outrigger trusses at four of the mechanical/refuge floors as shown in *Figure 6a*. Outrigger steel chords run continuously within the core walls. While this makes core wall construction more challenging, it avoids local stress concentrations from truss-to-wall transition details where outriggers and walls meet. The location and number of outrigger trusses was extensively studied and optimized. The outriggers at low zones are effective in

reducing the building fundamental period, while higher outriggers help control story drifts at upper zones.

Two-story high steel belt trusses exist at every mechanical/refuge level to connect all the super columns and form an "Exterior Mega Frame" system that provides additional lateral stiffness and strength to the overall lateral system of the tower (Figure 6a).

The current China code has a requirement similar to one in the IBC calling for a dual system approach for super tall structures. In the China code, that approach requires an exterior frame strong enough to resist 20% of the total seismic load on its own. During meetings with the China Seismic Expert Panel, this requirement was expanded based on current research and recent seismic events in China. In addition to the current strength requirement, to qualify as the second line of defense the exterior frame also must attract and resist at least 6% of the total story shear based on relative stiffness. In further meetings with the experts, the criteria became even more stringent: the secondary frame must attract and resist 6% of the total base shear (not story shear) at each level. As the comparison graphs in figure 6b show, meeting the stiffness requirement is difficult: most of the overturning moment is taken by the super columns, but most of the shear stays in the core.

A key strategy used to attract and maintain the required portion of base shear to the exterior frame was the addition of mega braces. The braces also provide additional load path redundancy and additional torsional stiffness. Another special design feature is the use of double belt trusses laced together, which were required to brace the super columns due to the eccentric alignment of the belt truss in plan with the super columns.

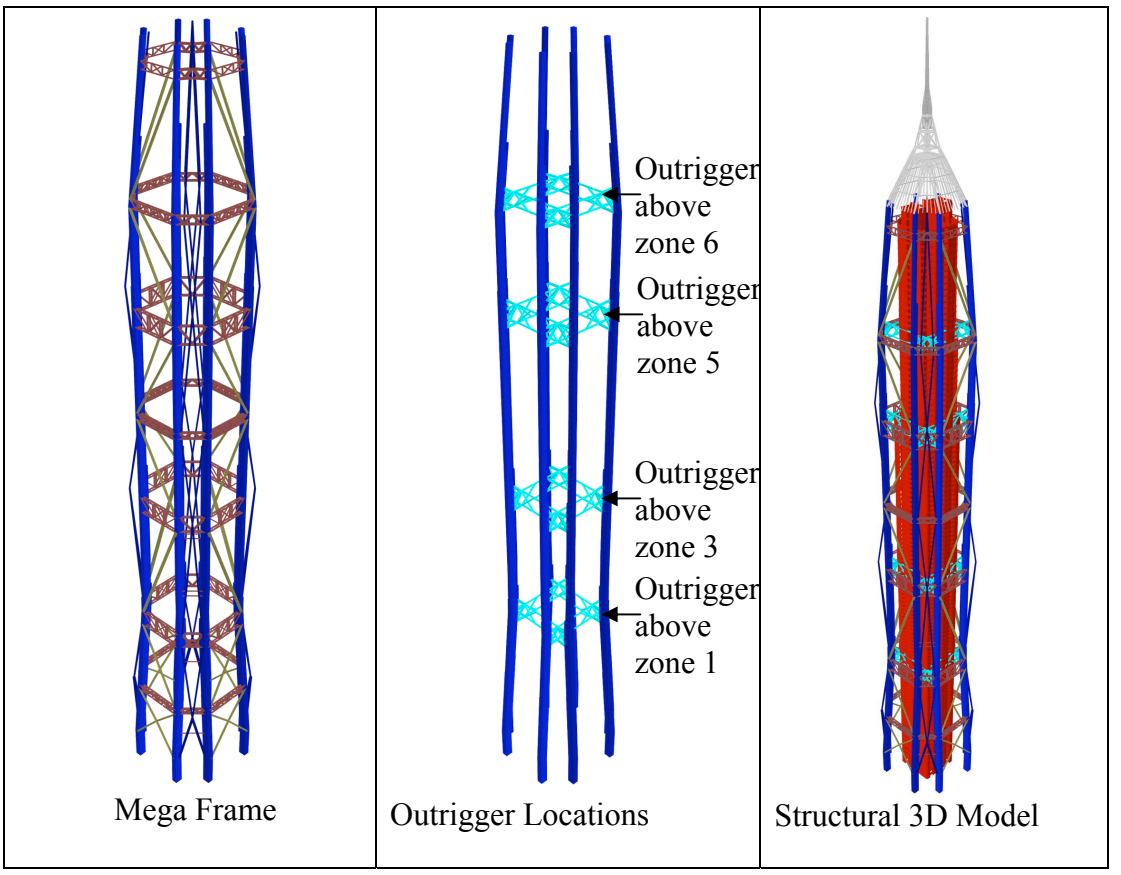


Figure 6a Exterior Mega Frame, Outriggers and Structural 3D Model

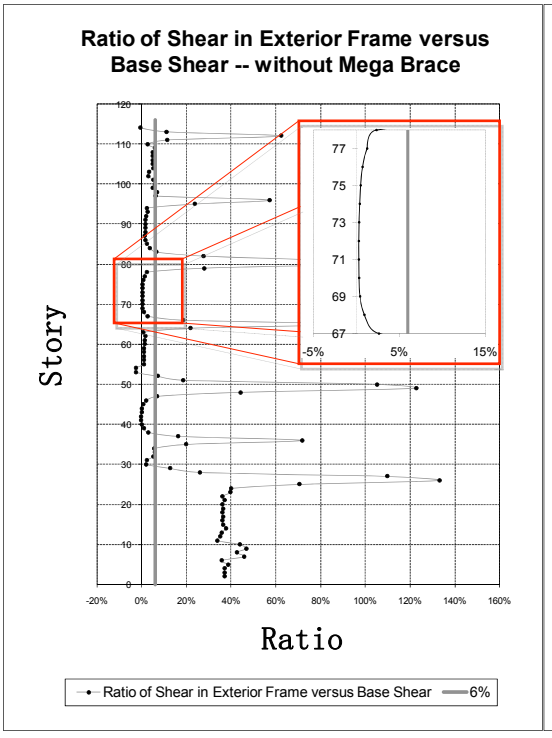


Figure 6b

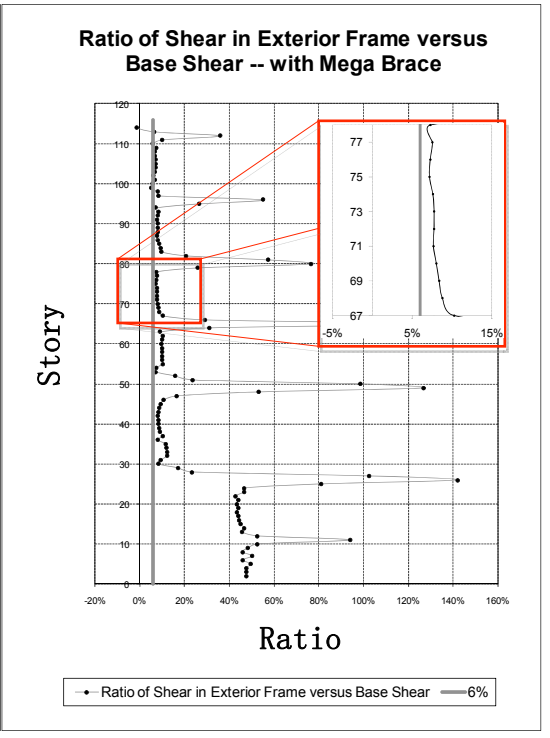


Figure 6c

Figure 6b and 6c show the ratio between the shear force in the exterior frame at every floor and the total base shear. Figure 6b corresponds to the structural system without mega braces and 6c with mega braces. As can be seen from the curves, the shear forces in Figure 6b is almost zero on typical levels, while in Figure 6c the shear forces increases to more than 6% of the base shear for most of the stories.

GRAVITY SYSTEM

The gravity supporting floor system of Ping An Tower consists of concrete filled composite metal deck slabs and steel beams composite with the slabs. Although in this region a composite slab and steel beam floor system is more expensive than a conventional reinforced concrete slab and beam system, composite framing was adopted to reduce form work, increase construction speed and reduce tower weight. Less tower weight reduces foundation costs and seismic loads. The composite slab design is controlled by gravity load bearing strength, stiffness, fire rating, diaphragm shear and acoustic requirements.

Typical office floors use a 125mm thick dovetail re-entrant composite floor deck (125mm thick concrete fill including dovetail ribs of metal deck) that provides a 2-hour fire rating according to laboratory tests. Typical mechanical/refuge levels use 180mm thick composite floor decks (180mm thick concrete fill including ribs of metal deck).

Typical office levels between mechanical levels have steel gravity perimeter columns that are continuous within one zone but stopped at mechanical levels, where the belt trusses transfer the column gravity loads into the super columns. *See Figure 7a.* This discontinuous gravity column scheme maximizes gravity loads in super columns to minimize tension forces from wind and seismic loads. It is crucial to keep the concrete super column in compression since even a small net tension force can result in a major loss of axial stiffness. By transferring column loads at every zone, perimeter steel gravity columns also have smaller column sizes that are more economical and aesthetically preferable.

The exterior mega braces large enough to attract significant shear forces also contribute to the gravity system, which poses some design challenges. First, single braces were arranged to create opposing forces upon application of gravity load (looking at any building corner elevation you see Xs or diamonds, as is shown in Figure 8a). If this had not been done, gravity would have caused the tower to twist. Second, the opposing forces required resolution for equilibrium. Kink forces in the belt truss levels (Figure 8b) must be considered in the floor system and core wall designs.

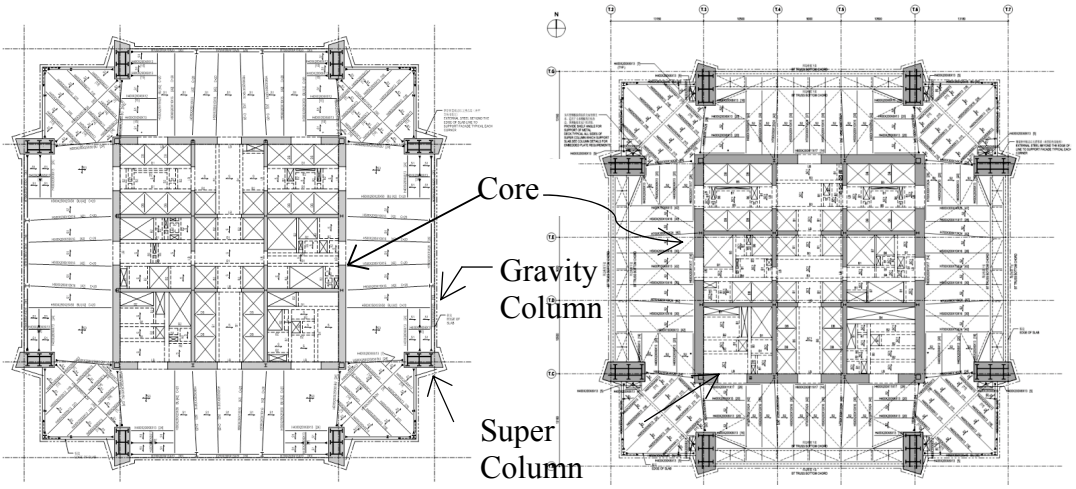


Figure 7a –Floor System at Office Level Figure 7b- Floor System at MEP Level

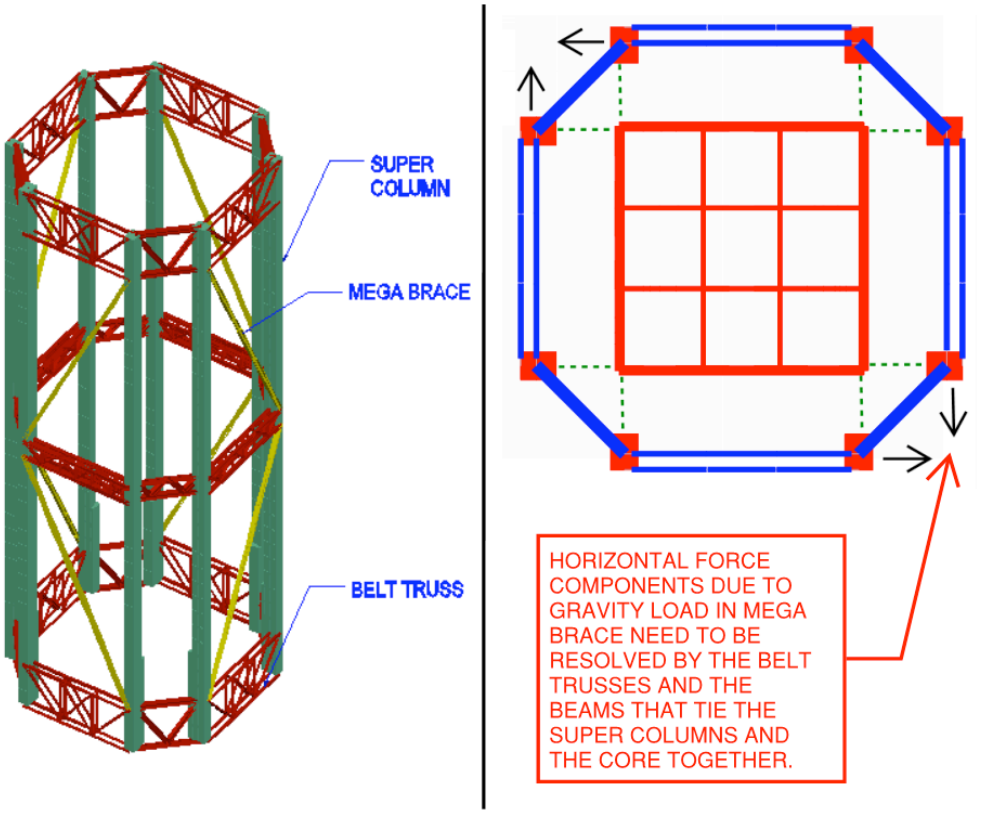


Figure 8a – Exterior Mega Brace Layout Figure 8b - Kink Force to Be Resolved

SPIRE STRUCTURE

The spire structure is located above level 115 and comprises a mast and its supporting structures, as is shown in Figure 9a.

The structural system of the spire is an industrial frame truss system, two frames in the north-south direction and two in the east-west direction, which is supported on the eight super columns (Figure 9b). Mast lateral support comes from its embedment within a steel braced socket. Overturning is resolved by a force couple through clamp mechanisms bearing against the top and bottom of the steel braced socket, which transfers the load into the steel spire support structure. The Building Maintenance Unit (window washing crane system) support structure carries the gravity load of the BMU as well as forces from the steel braced socket above.

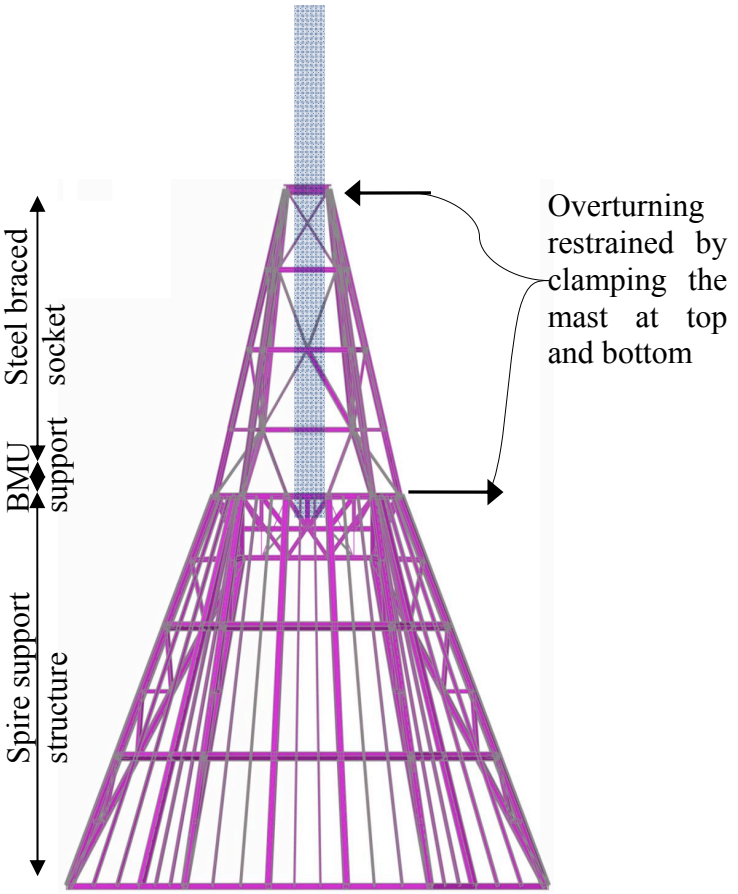


Figure 9a – Spire Structural System

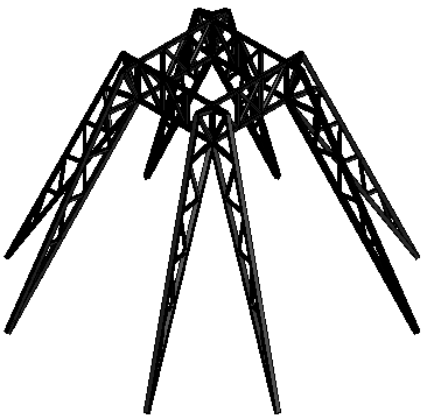


Figure 9b – Industrial frame structure to support the spire

CONCLUSION

Codes are based on research which relies on predictions, tests and experience. But these are limited to today's comprehension. Therefore engineers will constantly confront new challenges, either from unknowns or from situations and problems that are not covered by codes or other known publications. It is our responsibility to provide a product that satisfies all the requirements of public safety and that can only be achieved when research and design go hand in hand. The Ping An Tower is an example of a design that is ahead of standard conventions and meets requirements for both today and tomorrow through a unique design.

ACKNOWLEDGEMENT

We would like to thank Mr. Leonard Martin Joseph, P.E., S.E., Principal of Thornton Tomasetti, Inc, for comments and assistance during design of the structure as well as for enhancing this paper through his thoughtful suggestions.

PROJECT DESIGN TEAM CREDITS

Client: Ping An Insurance (Group) Company of China, Ltd.

Architect: Kohn Pedersen Fox Associates

Structural Engineer: Thornton Tomasetti Inc.

MEP Engineer: J. Roger Preston Group

Local Design Institute: China Construction (Shenzhen) Design International

Wind Engineering Consultant: Rowan Williams Davies and Irwin Inc. (RWDI)

Mr. I. Paul Lew, Senior Vice President, Thornton Tomasetti

REFERENCE

IBC (2006), *International building Code*, International Code Council.
ASCE-41 (2006), *Seismic Rehabilitation of Existing Buildings*, American Society of Civil Engineers, Structural Engineering Institute, Reston VA.
GB50011-2001 (2008 version), *Code For Seismic Design of Buildings,* Ministry of Housing and Urban-Rural Development of People's Republic of China.
JGJ3 (2002), *Technical Specification for Concrete Structures of Tall Buildings,* Ministry of Housing and Urban-Rural Development of People's Republic of China.

Non-Linear Time History Analysis for the Performance Based Design of Shanghai Tower

Dennis C.K. Poon[1], Ling-En Hsiao[2], Yi Zhu[3], Leonard Joseph[4], Steve Zuo[5], Guoyong Fu[6],Onur Ihtiyar[7]

[1] P.E., Managing Principal, Thornton Tomasetti Inc., DPoon@thorntontomasetti.com,
[2] Ph.D, Thornton Tomasetti Inc., LHsiao@thorntontomasetti.com,
[3] MSCE, Thornton Tomasetti Inc. 398 Han Kou Rd. Room 1402 Hang Sheng Bldg. Shanghai PRC 20001, YZhi@thorntontomasetti.com,
[4] S.E, Thornton Tomasetti Inc., 2211 Michelson Drive Suite 460 Irvine CA, 92612, LJoseph@thorntontomasetti.com,
[5] P.E., Thornton Tomasetti Inc. SZuo@thorntontomasetti.com,
[6] P.E., Thornton Tomasetti Inc. PFu@thorntontomasetti.com,
[7] MSCE, Thornton Tomasetti Inc. : Oihtiyar@thorntontomasetti.com

Thornton Tomasetti, Inc ., 51 Madison Ave, New York NY 10010, Tel: 917-661-7800

ABSTRACT:

Structural nonlinear performance of the 126-story, 632-meter tall Shanghai Tower has been studied for 2475-year return period seismic events through nonlinear time history analysis. Seven sets of ground motions were selected as representative of potential local seismic excitation and scaled to meet the provisions of China Seismic Code, GB50011-2001 (2008 version) and Shanghai Seismic Code, DGJ08-9-2003. A detailed and complex finite element model (FEM) of the structure was created within Perform 3D (2008), a widely used software program for nonlinear analysis and performance assessment of structures.

Global behavior of the structure was checked to meet serviceability requirement. For performance acceptance criteria at the individual structural element level, GB50011-2001 and ASCE 41-06 "Seismic Rehabilitation of Existing Buildings" (2006) were used as major references. The nonlinear time history analyses confirmed acceptable global and local performances of Shanghai Tower as designed.

INTRODUCTION

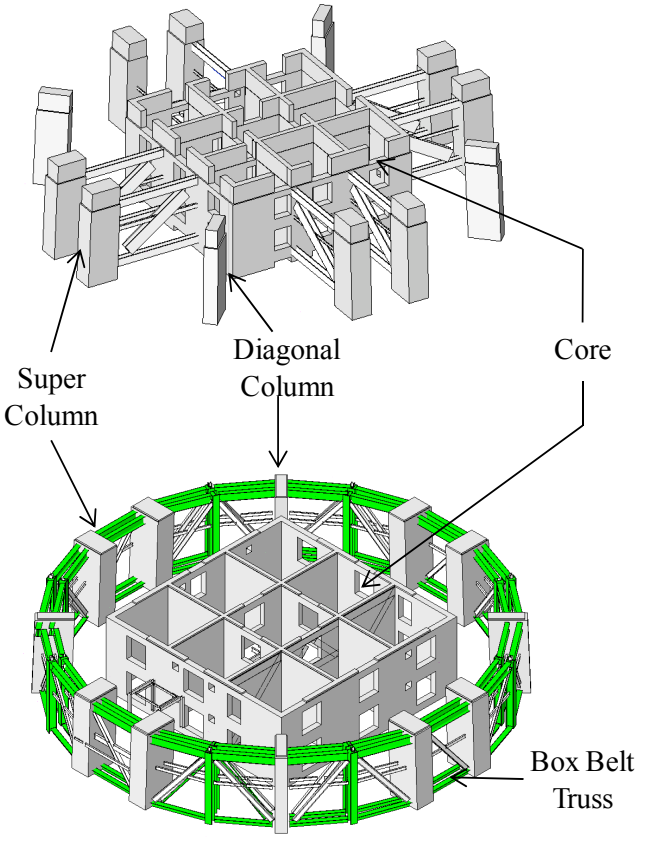
Shanghai Tower Complex, with 576,000 m^2 (6.2 million ft^2) of space and a total budget of US$2.2 billion, is a mixed-use development featuring world-class offices, luxury hotels, retail spaces, convention facilities and observation decks. Five story deep basement houses retail shops, mechanical rooms and parking spaces, as well as connections to the Shanghai Metro subway system. The 126-story, 632 meter (2,074 feet) tall tower is currently under construction and will be the world's second tallest building when completed in 2014.

The Shanghai Tower exterior facade, its most distinctive feature, is an outer skin based on a round-cornered triangle that gradually rotates in plan and reduces in size at upper levels. The tower interior spaces can be visualized as eight vertically stacked circular cylinders with gradually diminishing diameters, separated by larger two-level mechanical/refuge floors that extend to the outer skin. Figure 1 is a rendering of the Shanghai Tower Complex and surroundings.



(a)

Figure 1a - 3D Rendering of the Shanghai Tower Complex(Courtesy of Gensler)



(b)

Figure 1b - Lateral resisting System of Shanghai Tower

LATERAL SYSTEM

For supertall buildings such as Shanghai Tower, the structural lateral load resisting system must be very efficient and well integrated with the overall design. This tower uses a "Core-Outriggers-Mega Frame" system including a concrete core, outrigger trusses, super columns and an exterior mega frame using double belt trusses.

The square concrete core with 30m wide faces efficiently encloses numerous elevators and stairs needed to service tower occupants, but is not sufficient by itself to resist extreme overturning moments generated by lateral typhoon and seismic loads,

or to limit deflections to code-mandated values. The most economically feasible approach to resist overturning and improve stiffness is to engage outer columns to benefit from a bigger moment arm. So eight sets of two-story outrigger trusses aligned with inner 'web' core walls tie the core and exterior super columns together as seen in Figure 1b. In addition, the tower is wrapped by a mega frame consisting of double belt trusses at the mechanical/refuge levels linking the super columns together and transferring secondary column gravity loads to super columns. Core outer wall thickness varies from 1200mm to 600mm while inner 'web' wall thickness varies from 900mm to 500mm. Super columns slope very gradually to stay within the stacked cylinder diameters, and super column plan dimensions vary from 3.7m by 5.3m at the bottom to 1.9m by 2.4m at the roof.

PRESCRIBED CODE DESIGN

Seismic design of the Shanghai Tower followed the China Seismic Design Code , GB50011-2001 (2008 version) and Shanghai Seismic Code, DGJ08-9-2003, using a linear modal analysis procedure. Unlike some other international model code approaches, the China code defines three earthquake levels:

- Frequent Earthquake level with a return period of 50 years,
- Moderate Earthquake level with a return period of 475 years
- Severe Earthquake level with a return period of 2475 years.

The China Seismic Code only specifies simple performance goals for structures under these seismic levels as:

- " No damage" under Frequent Earthquake
- " Minor Damage, but Repairable" under Moderate Earthquake
- " No Collapse" under Severe Earthquake

Since Shanghai Tower height exceeds limits in the China code, it required a Non-Linear Time History Analysis. The structure was modeled and studied for different seismic stages by using both Abaqus and Perform 3D software. This paper presents Perform 3D results for the Severe Earthquake Level.

SELECTION OF GROUND MOTIONS

Seven sets of ground motions were selected, including two sets of synthetic seismic records. The other records were selected from earthquake events at locations that resemble the seismic characteristics of the Shanghai Tower site. All records were scaled to meet the requirements in China Seismic Code and Shanghai Seismic Code :

1. The peak ground motion in the major direction should be scaled to at least 200 gal and in the minor direction scaled to 170 gal.
2. The lowest base shear of the selected ground motion in the major direction shall be higher than 65% of the code spectrum base shear.

3. The average base shear of the selected ground motion in the major direction shall be higher than 80% of the code spectrum base shear.

Linear Time History Analysis was performed to determine the base shears of each set of ground motions and establish appropriate scale factors as shown in Table 1. Scaled ground motion records, and their response spectrum curves as generated by BiSpec (2009) are shown in Figure 2.

Table 1, Scale Factors for the Ground Motions

	Major Direction			Minor Direction	
EQ PAIRS	Scale Factor	Scaled Peak Ground Acc. (gal)	Ratio to Code Shear	Scale Factor for Minor	Scaled Peak Ground Acc. (gal)
ATS000-ATS090†	**0.94**	229	0.66	**0.94**	170
CHY004-N-CHY004-E‡	**2.04**	200	0.76	**1.75**	170
CHY016-N-CHY016-E‡	**1.94**	200	0.82	**1.81**	170
WSF-N-WSF-E‡	**2.78**	200	0.66	**2.64**	170
MEX006-007*	**1.66**	200	1.10	**1.40**	170
SHW4•	**5.71**	200	0.91	-	-
Shanghai•	**1.14**	200	1.07	-	-

† Kocaeli, Turkey, 1999/08/17
‡Chi-Chi, Taiwan, 1999/09/20, Each record is taken from different stations
* Mexico City, Mexico, 1985/09/19
• Synthesized Records from CECS 160.

Response spectra of the records show similar behavior with the China code spectrum for periods above 1 second. This range is sufficient to capture the dynamic behavior of a 600 meter tall building since the first twelve periods of the tower, with cumulative mass participation approaching 90%, lay in this range.

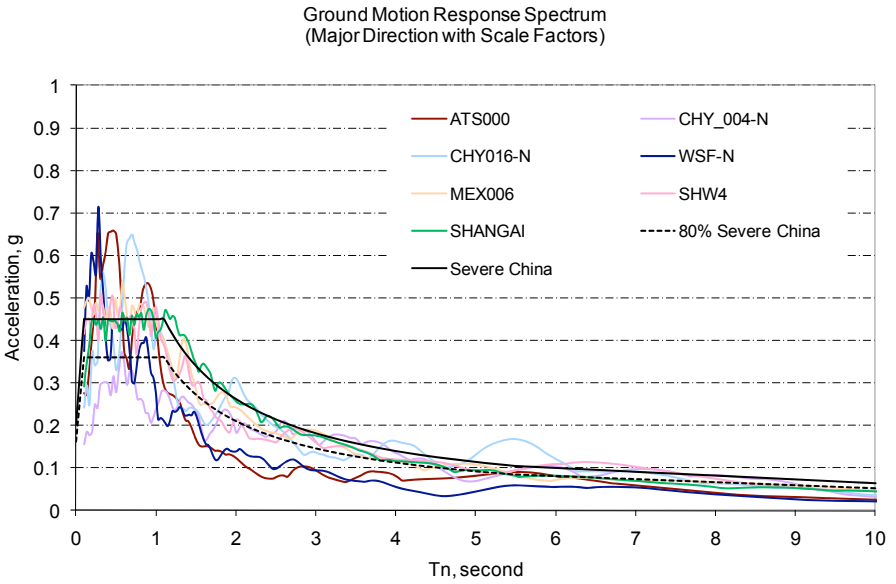


Figure 2, Ground Motion Response Spectra of the Selected Ground Motions

ANALYTICAL MODEL

General geometric and numerical modeling considerations for the nonlinear Perform 3D model were defined in the accordance with ASCE 41-06.

The components that contribute to the global lateral system were reflected in the model as shown in Figure 3. Core wall link beams, belt trusses and outrigger trusses were modeled with 2-noded frame elements that have 6 degrees of freedom at each end. Central core piers and super columns were modeled as 4-noded fiber wall elements which are analogous to shell elements in the analysis program ETABS; they have both in- and out-of-plane bending stiffness. Gravity loads were defined as line loads on core wall and super column elements. The translational and rotational mass at each level was assigned as a lumped mass at each story. All nodes at each level were connected with a rigid diaphragm. P-Δ effects were considered in the analysis. Nonlinear time history cases were run after the gravity load analysis was completed. Rayleigh damping varied between 1.5% and 2.0% for the first 10 modes of the structure. It was included to account for the energy dissipation contribution of non-structural components.

NONLINEAR BEHAVIOR

Conventional modeling techniques and assumptions vanish when the structural elements reach their nominal capacities. Engineers should strive to understand the global post-yield behavior of the structure rather than get lost in details of individual members and connections. The ASCE 41-06 document provides an important guide for challenging aspects of nonlinear modeling.

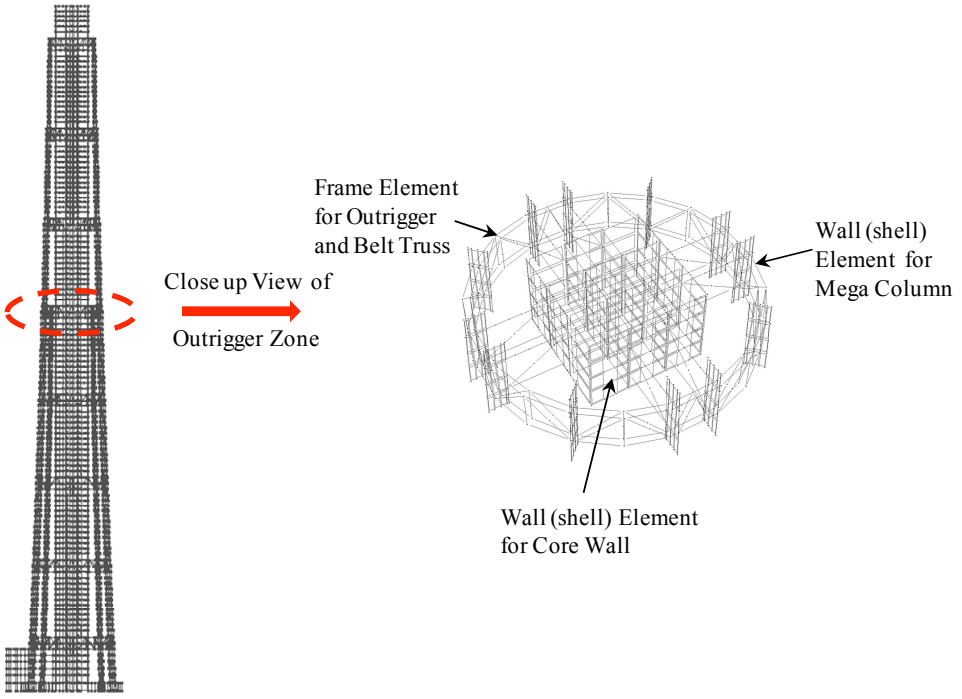


Figure 3, Shanghai Tower Analytical Model in Perform 3D

Moment-hinge methodology was used for defining nonlinearity of link beams, while fibers were used to model core walls and super (or mega) columns.

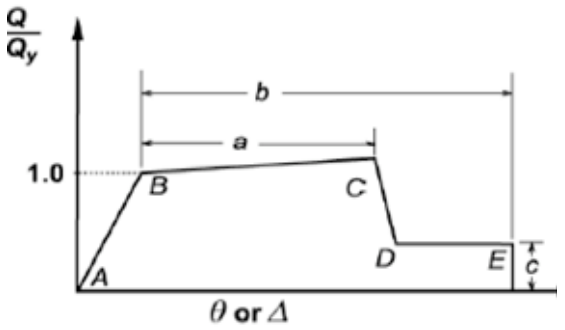
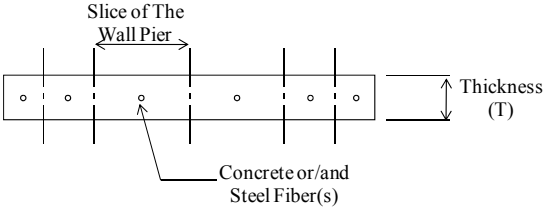


Figure 4, Generalized force-deformation curve by ASCE41-06.

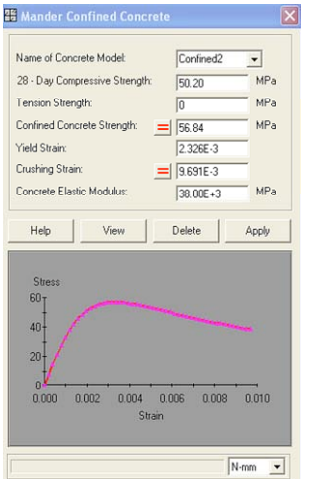
A generalized force-deformation curve proposed in ASCE 41-06 was used to model the behavior of reinforced concrete link beams. Parameters, denoted as 'a', 'b' and 'c' in Figure 4, were expressed in terms of end rotations and depended on the normalized shear stress and reinforcement type (diagonal or conventional). Following the specifications for beam members in ASCE 41-06, the designers used Perform 3D's built-in chord rotation function, which is based on moment-hinge theory, to model the nonlinearity of link beam.

For modeling the central core, we used Perform 3D fiber elements: wall slices as discrete 2D axial members with uniform nonlinearity throughout their length, as depicted in Figure 5a. These elements can be made of either steel or concrete, and their properties depend on the geometry and reinforcement ratio of the wall slice. The Mander Model (1988) was used to define the stress-strain relationship of confined and unconfined concrete. Figure 5(b) depicts the confined concrete stress-strain curve.



(a)

Figure 5a - Plane View of a Wall Pier defined with Fiber Elements



(b)

Figure 5b - Mander Model of Confined Concrete in XTRACT

Belt-truss and outrigger truss members were first defined with linear properties and were then checked to see if the demand exceeded the capacity. If so, those members were redefined with nonlinear properties.

PERFORMANCE LEVELS

Acceptance criteria specified in "Seismic Rehabilitation of Existing Buildings" (ASCE 41-06) were used. ASCE 41-06 classifies the performance of the structure into four levels. The conceptual definition for each building performance level is listed below:

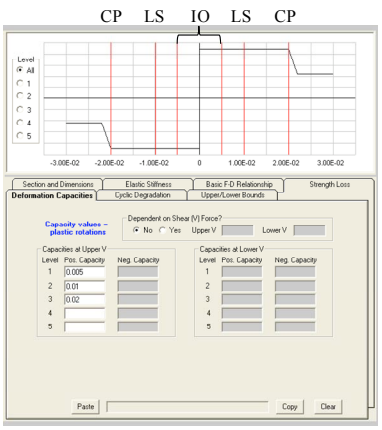


Figure 6, Definition of Performance Levels for Link Beams in Perform 3D

Operational Level (OL): Overall damage is very light and the structure almost behaves in the elastic range.

Immediate Occupancy (IO): Overall damage of the structure is light with no permanent drift. Structure retains its original strength.

Life Safety (LS): Moderate damage occurs with some permanent drift and strength loss.

Collapse Prevention (CP): Extensive damage with little residual stiffness and strength left. Structure is close to collapse.

The modeling parameters for beams, columns and coupled walls under each performance level are listed in ASCE 41-06 Tables 6-7, 6-8 and 6-18 respectively as related to plastic rotation. . These tables were used to assess the member performance of Shanghai Tower.

ANALYSIS RESULTS

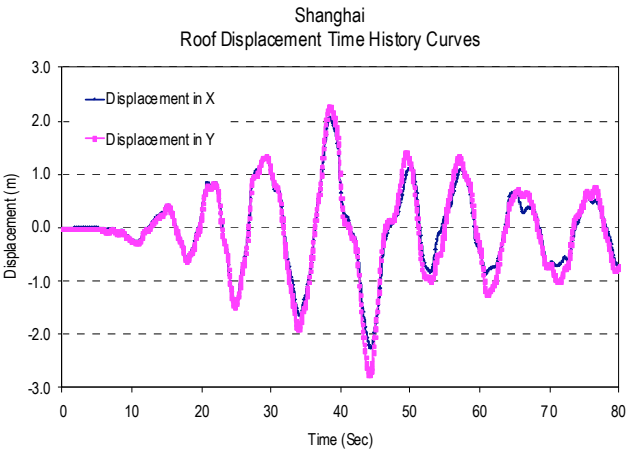
Gravity analysis was performed first, followed by time history analyses in Perform 3D. Global behavior and individual member performance was then verified.

The behaviors of the structure were fairly similar under all ground motion records. Since the fundamental building period of the tower is relatively long (about 9 seconds), it took around 20 seconds for response to build up. At the floors above the 80th floor, the wall cracking and beam yielding behaviors were much more extensive than at lower floors. At first, core wall cracking was seen locally at higher floors, followed by link beam yielding. Under continued shaking, both wall cracking and beam yielding extended through the building height before the super columns started to crack. Super column reinforcement went into tension but did not yield. Core wall reinforcement did yield locally at outrigger zones. Peak roof displacement occurred after 30 seconds. Of all seven sets of ground motions, Shanghai synthetic records generated the largest roof lateral displacement, 2.75 meters, as shown in Figure 7.

The central core system dissipated inelastic energy through link beam yielding while outrigger trusses and belt-trusses remained elastic.

Earthquae	X Dir. (m)	Y Dir. (m)
ATS000	1.24	1.21
CHY004	1.89	1.84
CHY016	2.08	2.32
WSF-E	1.46	1.60
MEX006	2.17	2.35
SHW4	2.13	2.00
Shanghai	2.26	2.75

(a)



(b)

Figure 7 (a) Maximum Roof Displacements, (b) Roof Displacement vs Time Graph to Synthesized Shanghai Record

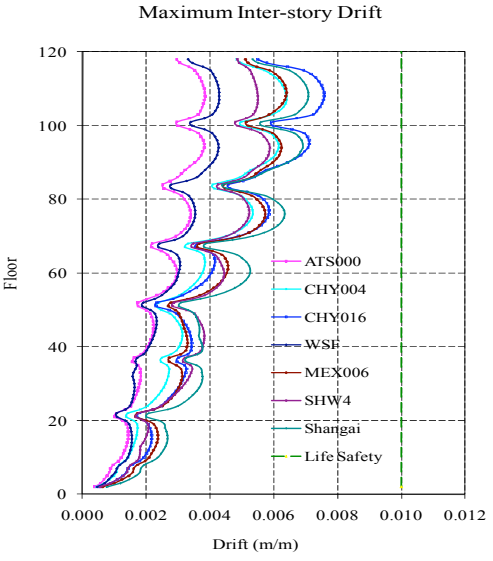


Figure 8, Story Drift Curves of Shanghai Tower

Maximum story drift curves for all ground motions are shown in Figure 8, **Story Drift Curves of Shanghai Tower**

The leftward (reduced) drift points indicate the presence of outriggers which significantly reduce story drifts. Maximum story drifts occur above 80th floor due to higher mode effects and range from approximately 0.004 to 0.008, within the acceptance limit of 0.01 set by the China Seismic Code.

A coupled wall system is composed of individual wall piers that are tied together by link beams. The link beams are the main structural elements that dissipate energy through hysteresis behavior. This is commonly seen in high rise structures, where beam deformation capability makes a significant contribution to overall ductility of the structure.

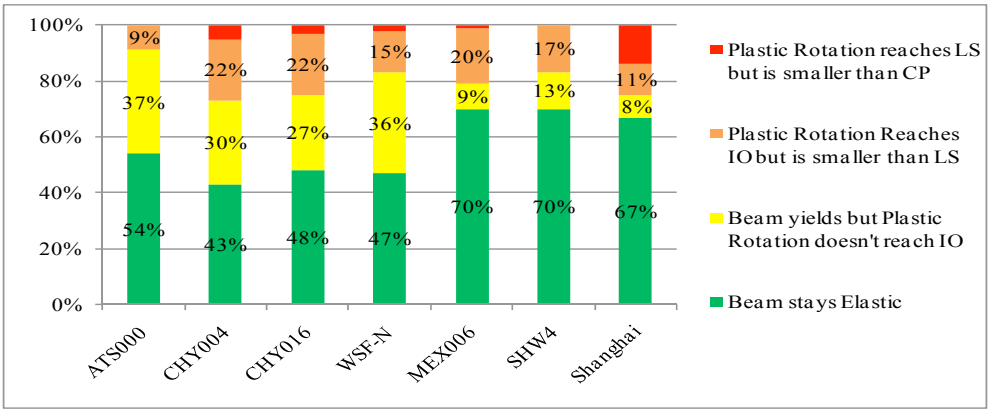


Figure 9, Performance Summary of Link Beams

Figure 9 summarizes performance of the Shanghai tower link beams. Approximately 30% to 60% of the link beams go into non-linear range, depending on the seismic event applied. Comparing maximum beam plastic rotation values to the limits given in ASCE 41-06, almost all link beams behave within LS level and none reaches the CP limit. Wall piers do crack throughout the tower but yielding of the vertical reinforcement is limited to outrigger zones only with plastic rotations being less than the IO level.

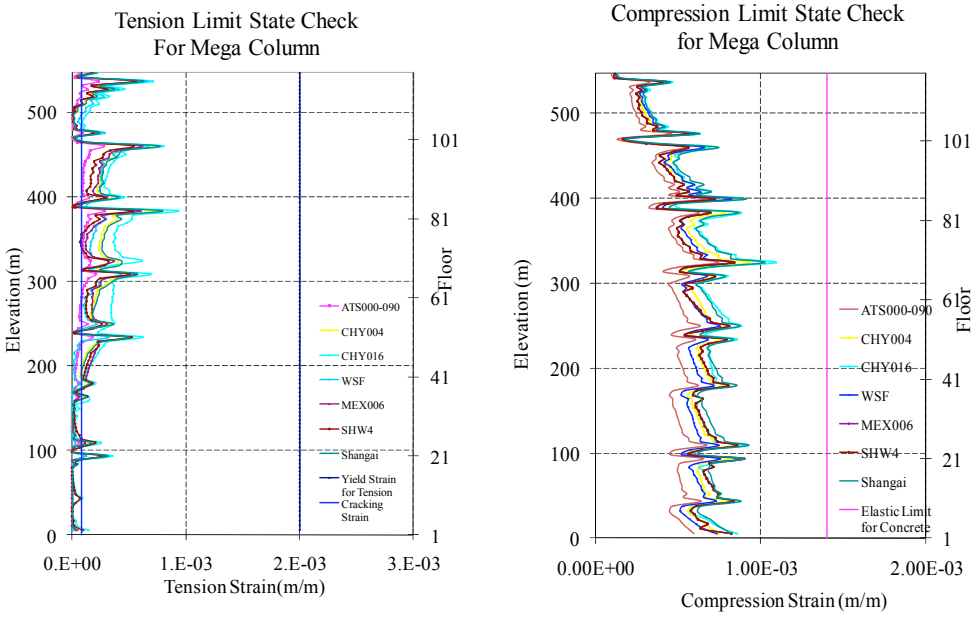


Figure 10, Maximum Tension and Compression Strains of Super Columns

Super column behavior was studied in detail as lateral stiffness of the structure heavily depends on it. These elements were mainly governed by axial forces as moments are relatively insignificant. Axial deformations were determined for each ground motion and reinforcement tension and concrete compression strains are graphed in Figure 10. Sudden changes in strain values occur at outrigger zones where forces can enter and exit the super columns via outrigger trusses. These columns

crack above the 35th floor due to relatively low gravity forces. Steel in super columns doesn't yield as maximum steel strain is determined to be around 0.001 m/m. Although axial compression forces in super column increase at lower levels, concrete compressive strains are generally 0.0005 to 0.001 because column sizes are getting larger. Overall, compression strains are not close to the crushing limit of confined concrete.

Belt trusses and outrigger trusses play important roles in terms of joining the core and super columns. These elements were assumed to stay elastic in the first run. Then maximum demands on these members were compared with their ultimate capacity. None of these members reach their buckling or yield point so inelastic behavior was not an issue.

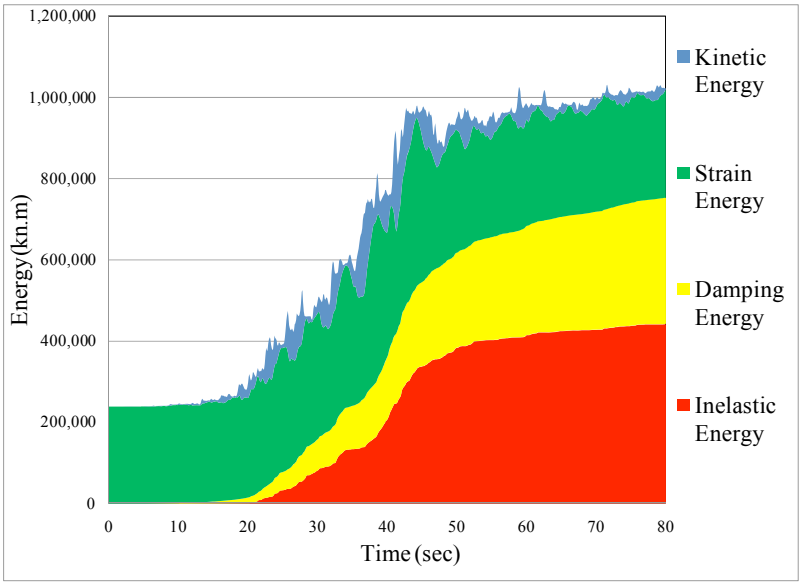


Figure 11, Energy Time Curve for Shanghai Synthesized Record

Energy generated under a seismic event is stored, absorbed, converted or dissipated by different behaviors such as kinetic, strain, damping and inelastic behavior. Energy time curves, as depicted in Figure 11 for a Shanghai synthetic record, are useful to understand its distribution. Approximately 40% to 50% of the total energy is dissipated by inelastic behavior.

CONCLUSION

Non-linear Time History Analysis of Shanghai Tower shows that this super tall structure provides an acceptable level of performance under a severe seismic event with a 2475 year return period. The maximum story drifts are within the code limit under all seven sets of ground motions. Link beams exhibit considerable yielding but plastic rotations are within the Immediate Occupancy level. Although wall piers and super columns are found to experience cracking, tension stresses in the reinforcement are below the steel yield point. Outrigger and belt-truss framing member demands are less than their ultimate capacities.

ACKNOWLEDGEMENT

We would like to acknowledge the members of the Shanghai Tower design team; Hyunjae Kwon, Zheng Gui Ma, Billy Tse and Torsten Gottlebe.

REFERENCE

ASCE-41 (2006), *Seismic Rehabilitation of Existing Buildings*, American Society of Civil Engineers, Structural Engineering Institute, Reston VA.

Bi-Spec (2009), *Program for Computing Linear and Nonlinear Spectra of Earthquake Records*, University of California, Berkeley Pacific Earthquake Engineering Research Center.

GB50011 (2008), *Code For Seismic Design of Buildings,* Ministry of Housing and Urban-Rural Development of People's Republic of China.

Mander J.B, Priestley M.J.N, Park R. (1988), *Theoretical Stress Strain Curve For Confined Concrete*, J. Structural Engineering, ASCE, 114(8), 1804-1823.

Perform 3D (2008), *Nonlinear Analysis and Performance Assessment for 3D Structures*, Computers and Structures, Inc. Berkeley California.

XTRACT (2002), *Cross Section Analysis Program for Structural Engineers v.2.6*, Imbsen Software Systems, Sacramento CA.

Effect of Stirrups on the Contribution of Concrete Compressive Strength and Tensile Steel to the Shear Strength of RC Beams Using Artificial Neural Networks

Hassan El-Chabib

Bradley University, Peoria, IL, 61625, Email: helchabib@bradley.edu

Abstract

Current shear design procedures calculate the nominal shear capacity, V_n of reinforced concrete (RC) slender beams with shear reinforcement (stirrups) by simply superimposing the shear capacity carried by concrete, V_c to that carried by stirrups, V_s. Previous studies concluded that current shear design equations do not only underestimate the resistance of concrete to shear, they also assume that the addition of stirrups does not alter the shear behaviour of RC slender beams. The addition of stirrups is known to provide confinement to concrete and therefore enhances the contribution of basic shear mechanisms to V_c. Current shear design provisions are yet to account for such enhancement and they simply calculate concrete contribution to V_n assuming that stirrups do not exist. In this paper, a previously developed artificial neural network (ANN) model trained on shear database of normal and high-strength concrete beams was used to investigate the effect of stirrups on the contribution of several basic shear design parameters to the overall shear capacity of RC beams. A sensitivity analysis was also carried out to evaluate the performance of several existing shear provisions in calculating the nominal shear capacity of reinforced concrete slender beams.

***Keywords**:* artificial intelligence, beam, slender, confinement, shear, strength.

INTRODUCTION

Most current shear design procedures and standards adopt semi-empirical and statistically derived techniques to calculate the nominal shear capacity, V_n of reinforce concrete (RC) slender beams. They simply superimpose concrete contribution, V_c (shear capacity of the beams not containing shear reinforcement) to that of stirrups, V_s. The shear capacity carried by stirrups, V_s is calculated based on the parallel truss model with 45^o diagonal shear cracks using the following equation:

$$V_s = \frac{A_v f_{yv} d}{s} = \rho_v f_{yv} b_w d \qquad (1)$$

where A_v = the cross-sectional area of stirrups, f_{yv} = yield strength of stirrups, b_w and d = the beam's effective depth and width respectively, s = spacing between stirrups, and ρ_v = ratio of shear reinforcement.

Whereas, the resistance of concrete to shear V_c, is determined based on the contribution of major shear transfer mechanisms in slender beams such as aggregate interlock, dual action, and the uncracked portion at the top of the concrete beam. It is usually calculated using semi-empirical equations, derived based on observations from experimental studies on RC beams with concrete compressive strength typically less than 40 MPa. Table 1 shows shear equations considered in this paper that are used in current shear provisions to calculate the nominal shear strength of RC slender beams.

Table 1- Shear expression of different methods

$V_n(N) = V_c + V_s = \left(0.158\sqrt{f_c'} + 17.2\rho_l\left(\frac{Vd}{M}\right)\right)b_w d + \frac{A_v f_{yv} d}{s}$ $V_c \le 0.3\sqrt{f_c'}\, b_w d \;\; ; \;\; V_s \le 0.06\sqrt{f_c'}\, b_w d \;\; and \;\; f_c' < 70 MPa$	(ACI, 11-5)*
$V_n(N) = V_c + V_s = 0.2\lambda\sqrt{f_c'}\, b_w d + \frac{A_v f_{yv} d}{s}$ $when \quad d \le 300\ mm$	(CSA, simplified method)*
$V_n(N) = V_c + V_s = \left(\frac{260}{1000+d}\right)\lambda\sqrt{f_c'}\, b_w d + \frac{A_v f_{yv} d}{s} \;\; ; \;\; V_c \le 0.1\lambda\sqrt{f_c'}\, b_w d$ $when \quad d > 300 mm$	(CSA, simplified method)*

*f_c' is the 28-day compressive strength of concrete cylinder (MPa), ρ_l is the longitudinal reinforcement ratio, V_c is the shear capacity at failure (N), and M and V are the moment and shear force, respectively at a critical section.

Such a practice assumes that the addition of stirrups does not affect the contribution of shear design parameters on V_c. Whereas, experimental studies (Mphonde, 1989 and Russo, 1997) reported that the addition of stirrups usually leads to a higher V_c than that determined for RC similar beams without shear reinforcement. Moreover, Ghana (1987) suggested that the shear failure mechanism of RC beams with shear reinforcement is fundamentally different from that of beams without shear reinforcement, and therefore V_c and V_s mutually influence each other. Furthermore, the shear fracture surface in high-strength concrete (HSC) slender members usually propagates through coarse aggregates rather than around them, and is therefore smoother than that in normal-strength concrete (NSC) members. This behavior tends to reduce shear resistance through aggregate interlock (a major shear transfer mechanism in RC beams not containing shear reinforcement), which may have serious implications in the shear design of such beams. Thus, empirical design equations, derived based on experimental data developed using NSC, needs to be cautiously evaluated for HSC.

Several studies (Mphonde, 1989, Kim, 1994, and Sarsam, 1992) also investigated the ability of various shear strength equations to predict the shear strength of reinforced concrete slender

beams with or without shear reinforcement. It was concluded that current shear design techniques are either very conservative or simply not applicable for RC beams made of HSC. This paper uses a neural network based model to investigate the performance of shear equations used by current provisions of the American Concrete Institute (ACI 318R-2008) and the simplified method of the Canadian Standards Association (CSA A23.3-05). A parametric study was also carried out to assess the ability of the above shear calculation/prediction techniques to quantitatively account for the effects of stirrups on the contribution of several basic shear resistance mechanisms to the shear strength of reinforced NSC and HSC slender beams.

ANN MODEL

Artificial neural networks (ANNs) are highly adaptive data-driven trainable systems capable of capturing hidden and complex behavior through learning from training examples. The multi-layer perceptron networks (MLP) are the most widely used ANNs in engineering applications due to their ability to implement non-linear transformations for functional approximation problems and to map given inputs into desired outputs (El-Chabib, 2006). The main objective in building an artificial neural network-based model is to train a specific network architecture using a comprehensive database to search for an optimum set of parameters for which the trained ANN can predict accurate values of outputs for a given set of inputs. Explaining the fundamental basis of ANNs is beyond the scope of this paper and details on how to build, train and simulate a neural network model can be found elsewhere [Haykin, 1994 and El-Chabib, 2005)]. A previously developed ANN model (El-Chabib, 2006) is used in this paper to investigate the effect of stirrups on the shear behavior of RC slender beams. The model was trained on shear strength results for 542 reinforced NSC and HSC slender beams with or without shear reinforcement. Results were collected from published literature and only simply supported beams with a shear span to depth ratio ($a/d \geq 2.4$) that exhibited shear failures were considered. Table 2 provides the range and average values of all parameters included in the database.

The network's architecture that was adopted consists of an input layer containing 6 variables representing the commonly known shear design parameters (d, b_w, a/d, $\rho_v f_{yv}$, ρ_l, and f'_c), an output layer with one unit representing the shear capacity (V_n), and a hidden layer of 10 processing units.

Table 2- Statistical data for shear design parameters and shear capacity of beams used in database

Parameters	Training data (542 beams)			Testing data (114 beams)		
	Minimum	Maximum	Average	Minimum	Maximum	Average
d (mm)	40.60	1097.28	332.56	95.00	930.00	366.85
b_w (mm)	38.10	457.00	196.71	38.10	457.00	215.61
a/d	2.40	6.05	3.26	2.40	5.00	3.12
ρ_l (%)	0.48	5.80	2.35	0.50	5.04	2.43
$\rho_v f_{yv}$ (MPa)	0.00	2.24	0.36	0.00	2.53	.46
f'_c (MPa)	10.50	125.30	46.26	13.70	125.00	49.05
V_n (kN)	2.69	749.30	134.34	8.38	787.55	162.32

PERFORMANCE OF SHEAR DESIGN METHODS

The performance of the ANN model as well as that of the shear equations considered in this paper was evaluated using shear results for 114 NSC and HSC slender beams. The predicted/calculated shear capacities were compared to the experimentally measured values using the average absolute error (*AAE*) and a performance factor (*PF*) calculated as follows:

$$AAE = \frac{1}{n}\sum \frac{\left|V_m - V_p\right|}{V_m} x\,100 \tag{2}$$

$$PF = \frac{V_m}{V_p} \tag{3}$$

where V_m and V_p are the measured and predicted/calculated shear capacity, respectively.

For NSC beams without shear reinforcement, the average absolute error (*AAE*) and the average of the performance factor (*PF*) for the ANN model were 11% and 1.02 compared to 25% and 1.29 for ACI (11-5) and 22% and 1.23 for the simplified method of CSA whereas those for HSC beams without shear reinforcement were, 13% and 1.02 for ANN, 33% and 1.23 for ACI (11-5), and 27% and 1.11 for the simplified method of CSA. On the other hand, the average absolute error (*AAE*) and the average of the performance factor (*PF*) for beams with shear reinforcement were as follows: 12% and 1.0 for ANN compared to 23% and 1.29 for ACI (11-5) and 19% and 1.64 for CSA-A23.3 (simplified method) in the case of NSC beams and 12% and 1.0 for ANN, 26% and 1.36 for ACI (11-5), and 22% and 1.28 for CSA-A23.3 (simplified method) in the case of HSC beams. The performance of ANN, ACI, and CSA in predicting/calculating the shear capacity of RC is shown in Figs. 1 and 2.

The figures show that the data points for the ANN model are the closest to the equity line, whereas those for ACI (11-5) and the simplified method of CSA-A23.3 are scattered over a relatively wider range, especially for beams having shear capacity values larger than 200 kN. It is also shown in the figures that ACI (11-5) and the simplified method of CSA are fairly conservative in predicting the shear capacity of RC slender beams as indicated by an *AAE* varying between 20% and 33% and an average *PF* reaching as high as 1.36 in the case of HSC beams with stirrups.

The conservative predictions provided by the CSA simplified method, and the more accurate equation of ACI-318 (11-5) for RC beams with stirrups are partially due to the fact that both methods assume that no interactions occur between stirrups and other shear transfer mechanisms, and simply calculate the shear capacity of RC beams containing stirrups by superimposing the contribution of stirrups to that of concrete. It is important to note herein that the data points located above the equity line for both ACI and CSA are for beams with either large effective depth, large amount of longitudinal and/or transverse reinforcement

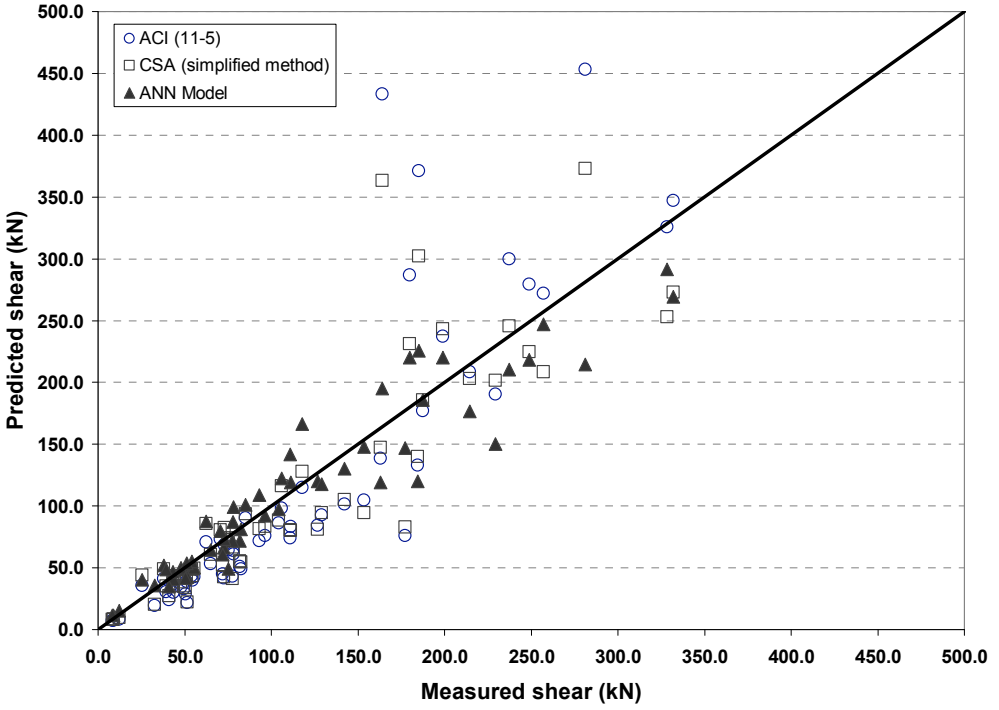


Fig. 1- Measured versus predicted shear capacity for beams without stirrups.

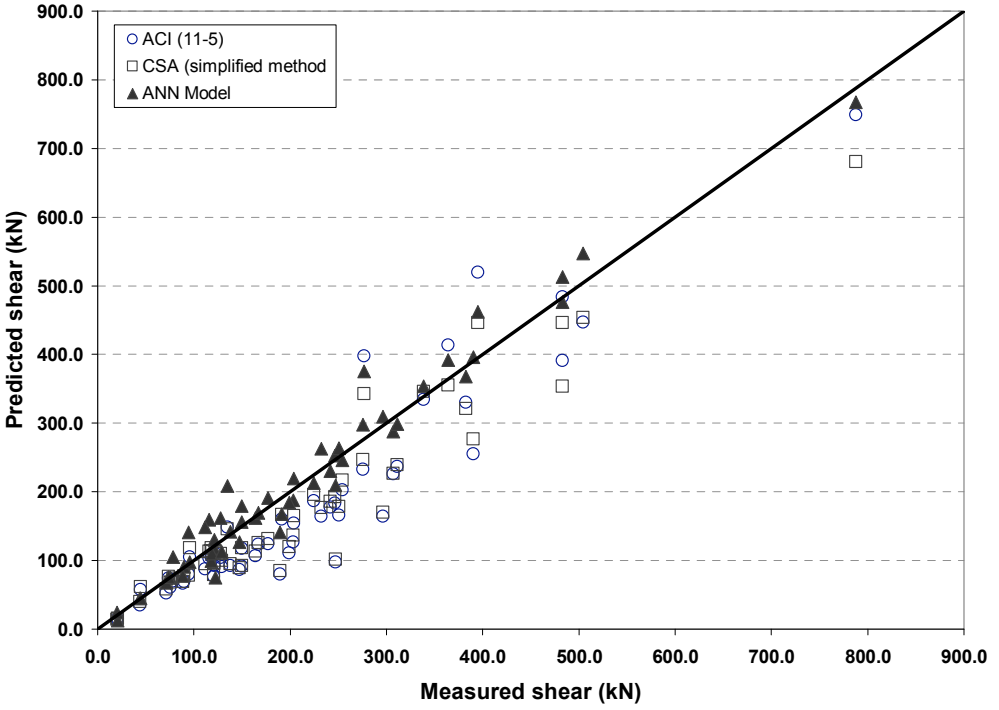


Fig.2- Measured versus predicted shear capacity for beams without stirrups.

EFFECT OF STIRRUPS ON THE CONTRIBUTION OF f'_c

The influence of stirrups on the contribution of f'_c to the shear strength of RC beams is illustrated in Fig. 3. The figure includes the shear strengths of three sets of beams as predicted by the ANN model. Beams in each set share the same properties except f'_c, and beams in different sets with similar f'_c share the same properties except for the amount of shear reinforcement, $\rho_v f_{yv}$. The first set represents the shear strength of RC beams without stirrups. The second and third sets show the shear strength of RC beams with stirrups capacity of $\rho_v f_{yv}$ = 0.344 and 1.034 respectively as predicted by ANN and as calculated by simply adding V_c and V_s. The figure clearly shows that the addition of stirrups contributes much more to the shear strength of RC beams than just the stirrups capacity of $\rho_v f_{yv}$. However, such effect decreases as the capacity of stirrups increases.

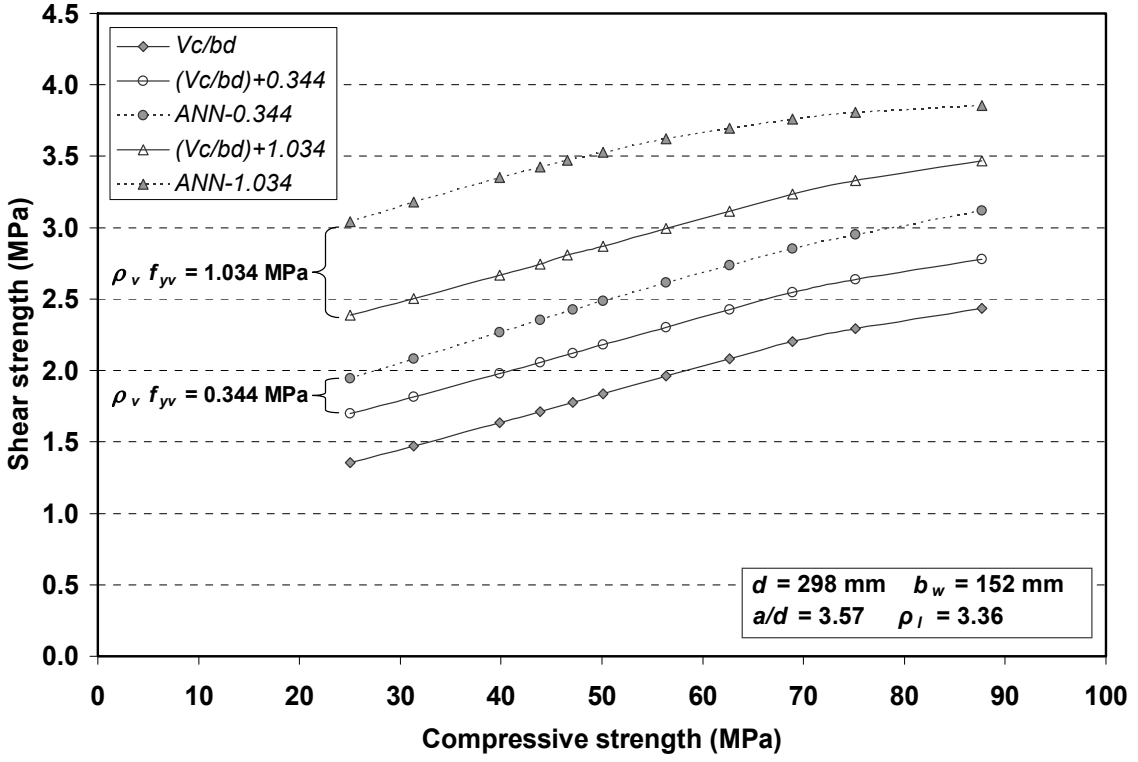


Fig. 3- Effect of stirrups on the contribution of f'_c to the shear strength of RC slender beams

EFFECT OF STIRRUPS ON THE CONTRIBUTION OF ρ_l

The influence of stirrups on the effect of longitudinal steel ratio ρ_l, is shown in Fig. 4. The figure illustrates the shear strength of three sets of beams versus ρ_l for different values of $\rho_v f_{yv}$. Beams in all three sets have similar properties except for ρ_l and $\rho_v f_{yv}$. Set # 1 contains beams without shear reinforcement ($\rho_v f_{yv}$ = 0.0), whereas sets #1 and #2 contain beams with $\rho_v f_{yv}$ = 0.754 and 1.14, respectively. The figure shows that the influence of stirrups on the contribution

of tensile steel to the shear strength of RC slender beams is independent of the stirrups capacity $\rho_v f_{yv}$. For a similar steel ratio, ρ_l and regardless of the amount of $\rho_v f_{yv}$, the addition of stirrups generates a constant increase to the shear strength of RC slender beams obtained using $V_s + V_c$. However, such increase is noticeably significant for $\rho_l > 2.5\%$. It is believed that stirrups help confining the longitudinal steel bars in place, thus preventing shear cracks from widening, and allowing an increase in dowel action.

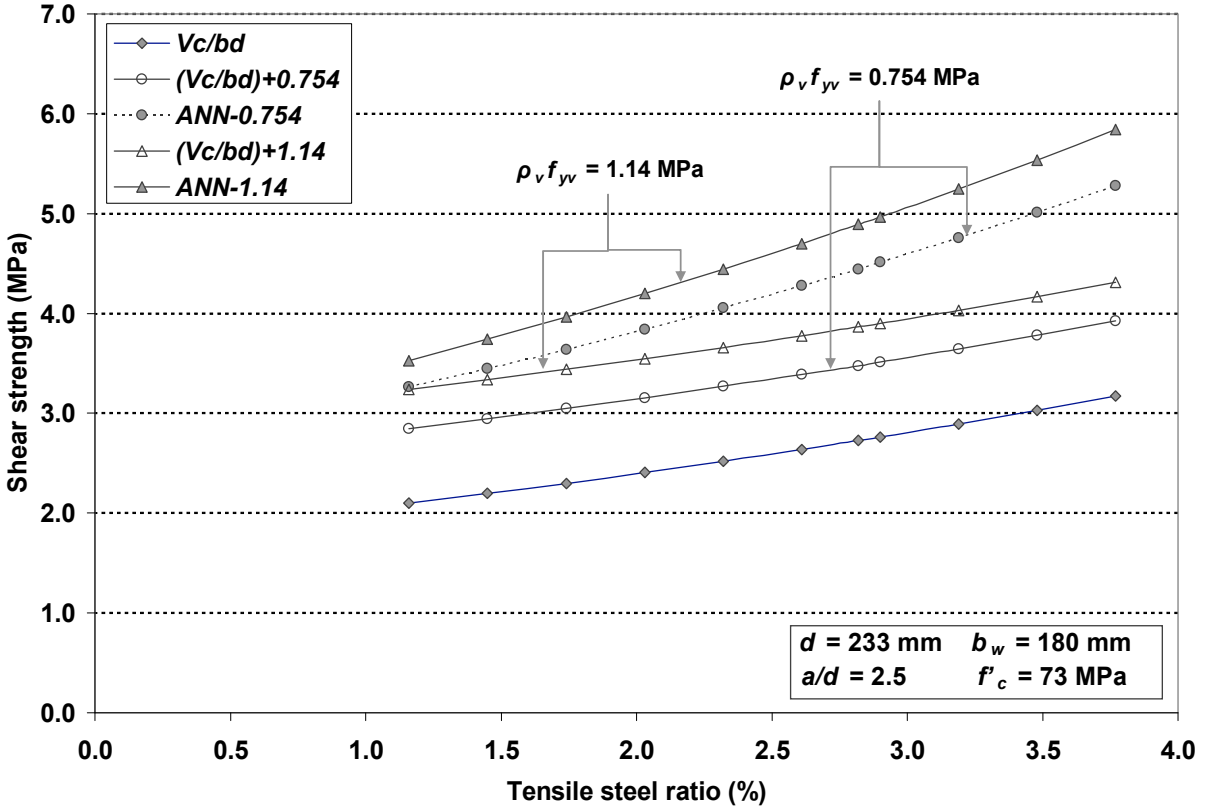


Fig. 4- Effect of stirrups on the contribution of ρ_l to the shear strength of RC slender beams

CONCLUSIONS

Results in this study obtained using the ANN model showed that the shear strength of RC slender beams with shear reinforcement depends on the amount of stirrups and it is up to 50% higher than values calculated using ACI 11-5 and the CSA simplified method. It was shown that calculating the shear strength of RC beams containing shear reinforcement by simply superimposing the capacity of stirrups to the shear capacity of a similar beam without shear reinforcement is not accurate and leads to unnecessarily conservative results.

REFERENCES

ACI Committee 318, (2008) "*Building Code Requirements for Structural Concrete*," (ACI 318-08) American Concrete Institute, Farmington Hills, Michigan, USA, 465 p.

Ghana, P.S., (1987) "*Investigating of the Mechanism of Shear Failure of Reinforced Concrete Beams,*" Magazine of Concrete Research, V. 39, No. 12, pp. 196-204.

CSA Committee A23.3, (2004) "*Design of Concrete Structures*," Canadian Standards Association, Rexdale, Ontario, Canada, 352 p.

El-Chabib, H. and Nehdi, M., (2005) "Neural Network Modeling of Properties of Cement-Based Materials Demystified," Advances in Cement Research, V. 17, No 3, pp. 91-102.

El-Chabib, H., Nehdi, M., and Said, A., (2006) "Predicting the effect of stirrups on shear strength of reinforced normal strength concrete (NSC) and high strength concrete (HSC) slender beams using artificial Intelligence," Canadian Journal of Civil Engineering, V.33, pp. 933-944.

Haykin, S., (1994) "*Neural Networks: a Comprehensive Foundation,*" Macmillan, New York, 842 p.

Kim, J.K., and Park, Y.D., (1994) "Shear Strength of Reinforced High Strength Concrete Beams without Web Reinforcement," Magazine of Concrete Research, V. 46, No. 166, pp. 7-16.

Mphonde, A.G., (1989) "*Use of Stirrups Effectiveness in Shear Design of Concrete Beams,*" ACI Structural Journal, V. 86. No. 5, pp. 541-545.

Russo, G., and Puleri, G., (1997) "*Stirrups Effectiveness in Reinforced Concrete Beams Under Flexure and Shear,*" ACI Structural Journal, V. 94, No. 3, pp. 227-238.

Sarsam, K.F., and Al-Musawi, J.M.S., (1992) "*Shear Design of High-and Normal Strength Concrete Beams with Web Reinforcement,*" ACI Structural Journal, V. 89, No. 6, pp. 658-663.

Cyclic Response of Concrete Frame Members Reinforced with Ultrahigh Strength Steel

H. Tavallali[1], A. Lepage[2], J. Rautenberg[3], and S. Pujol[4]

[1]Ph.D. Candidate, Department of Architectural Engineering, Penn State University, University Park, PA, email: hooman@psu.edu
[2]Assistant Professor, Department of Architectural Engineering, Penn State University, University Park, PA
[3]Ph.D. Candidate, School of Civil Engineering, Purdue Univ., West Lafayette, IN
[4]Assistant Professor, School of Civil Engineering, Purdue Univ., West Lafayette, IN

Abstract

For many years, the design of reinforced concrete structures in the U.S. has been dominated by the use of steel reinforcement with a specified yield strength, f_y, of 60 ksi. Using steel reinforcement with a higher yield strength would introduce several benefits to the architectural, engineering, and construction industry. Not only would it allow for members with reduced cross sectional area, saving on material, shipping, and placement costs, but it would also help to overcome steel congestion, and facilitate concrete placement. This would directly lead to a better quality of construction, improved durability, and shorter construction times. One of the primary obstacles to the use of concrete members reinforced with ultrahigh strength steel (f_y greater than 80 ksi) is the paucity of experimental data.

The applicability of using steel with f_y up to 120 ksi as primary reinforcement in concrete members is explored in this experimental study by subjecting beams and columns reinforced with ultrahigh strength steel to a cyclic loading protocol. The mechanical behavior of these members is compared to similar members reinforced with conventional steel. Test data from this study show that the use of ultrahigh strength steel is a viable option for earthquake-resistant construction.

Introduction

For many years the design of reinforced concrete structures in the U.S. has been dominated by the use of steel reinforcement with a specified yield strength, f_y, of 60 ksi. Although higher values of f_y are allowed, it has been limited to 80 ksi since 1971 (ACI 318-71). ACI 318-08 (2008) permits the use of reinforcement with f_y of 100 ksi, but only if it is used for confinement reinforcement.

Steel with yield strength in excess of 80 ksi is currently commercially available in the U.S. and is often referred to as Advanced High Strength Steel (AHSS) or Ultrahigh Strength Steel (UHSS) (ISSI, 2006; ASTM A1011, 2010). In this study, the term UHSS is used to designate steel bars having yield strength in excess of 80 ksi and a fracture elongation of 6% or more in 8 inches. Figure 1 shows representative stress-strain curves of both conventional (Grade 60) and UHSS steels. After the introduction of ASTM A1035 (2005), there has been growing interest in UHSS bars. However, there is paucity of test data describing the behavior of concrete members reinforced with UHSS bars as longitudinal reinforcement.

Research Significance

The use of UHSS as longitudinal reinforcement is explored in this study by subjecting beams and columns to cyclic load histories. Specimens reinforced with UHSS are compared to specimens reinforced with Grade 60 steel.

There is no evidence in the U.S. of structures built or rehabilitated using UHSS as primary longitudinal and transverse reinforcement and designed to take full advantage of yield strengths in excess of 80 ksi for compression and tension stresses. This under-utilization is predominantly due to the shortage of experimental data, the lack of design guides, and the lack of coverage in existing building codes. In addition, UHSS in the U.S. only recently entered mass production.

Limits on the specified yield strength of reinforcing bars in the ACI 318 Code were originated in the 1963 edition (ACI 318-63, 1963). Their introduction was primarily related to the prescribed limit on compressive strain of 0.003 for concrete and to control crack width at service load.

The ACI 318-63 Code introduced strength design provisions with restrictions on the yield strength of non-prestressing steel. In Section 1505, ACI 318-63 specified an upper limit of 75 ksi on the yield strength of reinforcement used in compression and 60 ksi for reinforcement used in tension (unless special tests satisfied crack control requirements, in which case 75 ksi was permitted).

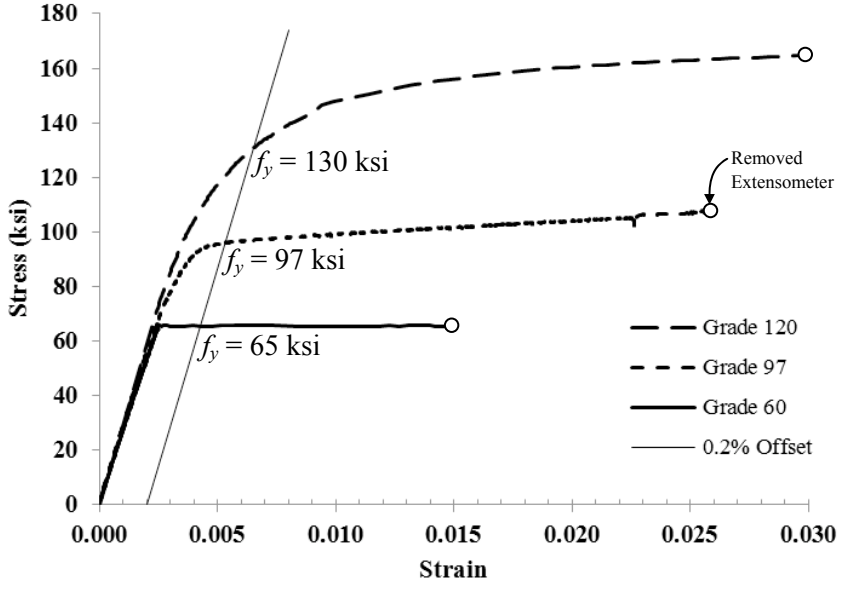


Figure 1. Measured Tensile Properties of Reinforcing Steel

In the 1971 edition of ACI 318 (1971), the limit on the specified yield strength of reinforcement (other than prestressing steel) was increased to 80 ksi for steel used in either tension or compression in order to continue accommodating the highest yield strengths covered by contemporary ASTM standards. The revised limits adopted by ACI 318-71 incorporated the findings from the extensive laboratory investigations reported in the 1960s by the eight-part report of the Portland Cement Association (Hognestad, 1961; Kaar, 1966) and by Todeschini et al. (1964). These studies were an

extension of the comprehensive column investigation initiated in 1929 by Richart and Brown (1934) under the direction of ACI Committee 105 on columns. These early efforts used longitudinal steel bars with an actual yield strength ranging from 55 ksi to 120 ksi where the fracture strain of steel typically exceeded 5%. Two conclusions about the findings of these reports are worth emphasizing: (1) in flexural members, "both maximum and average crack width are essentially proportional to reinforcing steel stress" (Kaar, 1966), and (2) "for steels with flat yield plateaus up to approximately 90,000 psi, the yield stress can be developed" in compression in tied columns (Todeschini et al., 1964).

A major effort in the 1980s and 1990s was led by Japanese researchers on the use of ductile reinforcing bars with nominal yield strengths in excess of 80 ksi for transverse and/or longitudinal reinforcement. A summary of 105 beam tests was presented by Otani, et al. (1996), who suggest that that the use of UHSS is commonplace in Japanese construction.

A design guide (ACI ITG-6R-10, 2010) recently published by the American Concrete Institute considers the use of UHSS steel conforming to ASTM A1035. However, the design stress is limited to 80 ksi for steel used in compression and to 100 ksi for steel used in tension.

Description of Experiments

To evaluate the mechanical behavior of concrete beams and columns reinforced with UHSS bars, a series of experiments was designed at Penn State University and Purdue University. The purpose of this series of tests was to evaluate the deformation capacity of such members when subjected to a cyclic loading protocol. Table 1 shows a summary of the specimens considered. The test variables include:

- Nominal yield strength of longitudinal reinforcement, (60, 97, and 120 ksi)
- Applied axial force (0 and 20% $f_c' A_g$, where f_c' is the concrete compressive strength, and A_g is the gross cross-sectional area of the specimen)

Table 1. Description of Test Specimens

Specimen		Axial Load	Longitudinal Reinforcement[a]			Transverse Reinforcement (2#3)	
		$A_g f'_c$ (%)	Top	Bottom	f_y, ksi	Spacing, in	f_y, ksi
Beams at Penn State (b=16", h=10", d=8")							
#1	CC4-X	0	4#7	4#7	60	2	60
#2	UC4-X	0	4#6	4#6	97	2	60
Columns at Purdue (b=9", h=12", d=10")							
#3	CC-3.3-20	20	3#7	3#7	60	2.5	60
#4	UC-1.6-20	20	2#6	2#6	120	2.5	60

[a] Reinforcement bars were provided by SAS Stressteel (f_y = 97 ksi) and by MMFX Technologies (f_y = 120 ksi)

The target concrete compressive strength was 6,000 psi. The geometry of typical beam and column specimens are shown in Figure 2. The specimens were loaded through the central stub so that they were in single-curvature bending. The shear span-to-effective depth ratio (a/d) for all specimens was approximately 3.

The amount of longitudinal reinforcement in each specimen was chosen so that the bending moment capacity of all specimens was approximately equal. So, for example, Specimen #3 (reinforced with 60-ksi steel) used approximately half the steel used in Specimen #4 (reinforced with 120-ksi steel). Transverse reinforcement was Grade 60 in all specimens and proportioned according to Chapter 21 of ACI 318-08.

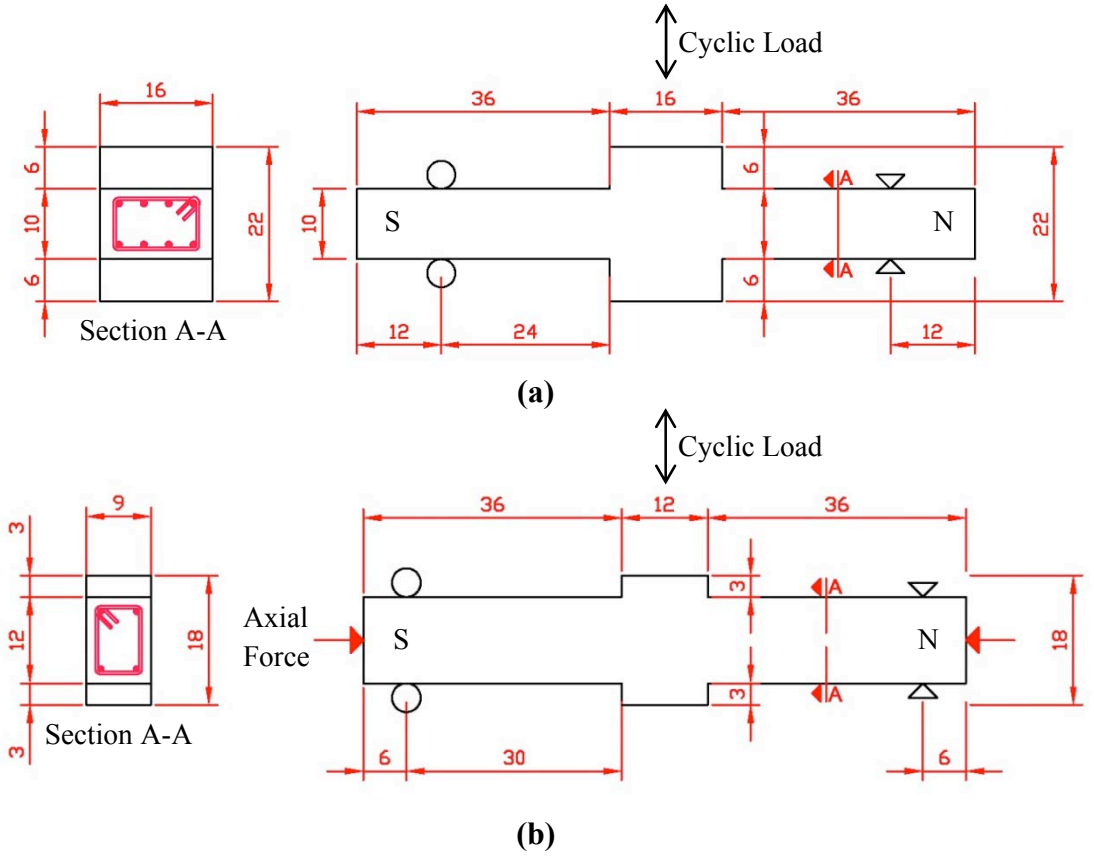


Figure 2. Geometry of Test Specimens, (a) Beams Tested at Penn State, (b) Columns Tested at Purdue (all dimensions in inches)

Loading Protocol

The drift ratio is defined here as the lateral displacement of the specimen divided by the shear span (corrected for the rotation of the central stub). The drift ratio history applied to each specimen, suggested by FEMA 461 (Applied Technology Council, 2007) is shown in Table 2 and is illustrated in Figure 3. Two cycles at each drift target are applied to the central stub at increasing amplitudes. After all cycles, the displacement is increased monotonically until failure (defined by a 20% drop in lateral-load carrying capacity from the peak value).

Table 2. Loading Protocol

Step*	Drift (%)
1	0.15
2	0.20
3	0.30
4	0.40
5	0.60
6	0.80
7	1.0
8	1.5
9	2.0
10	3.0
11	4.0
12	5.0

*Two cycles of loading in each step

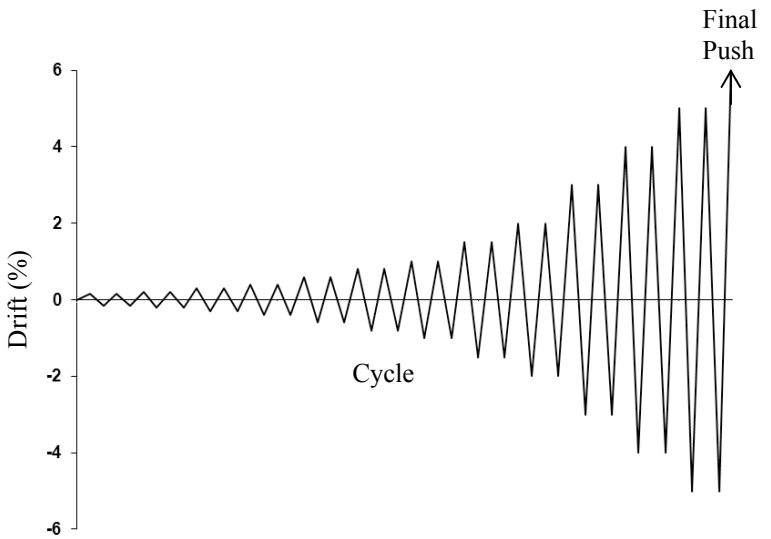


Figure 3. Loading Protocol

Experimental Results

Beams. Specimen #1, CC4-X, was designed according to ACI 318-08 requirements and built using 60-ksi steel as longitudinal reinforcement. Figure 4 shows the measured shear-drift response. The final push after all cycles from Figure 3 were completed is not shown. This specimen was capable of completing the predetermined cyclic loading protocol. At early stages of the test (up to 0.4% drift) only flexural cracks were observed. At the start of the first cycle to 0.4% drift, small inclined cracks were detected. The specimen completed cycles up to 1% without major damage. At this stage small signs of cover spalling could be observed. However the amount of spalling was small through 3% drift. In spite of wide flexural and shear cracks developing after 4% drift, the specimen completed the loading protocol without failure. In the final push, the north beam exceeded 10% drift. Figure 5 shows Specimen#1 at the end of the second cycle at 4% drift.

Specimen #2, UC4-X, had similar properties to Specimen #1 with the exception that it was reinforced longitudinally with UHSS. Figure 6 shows the measured shear-drift response without the final push. This specimen successfully completed the predetermined cyclic loading protocol. It was also capable of resisting the final push without failure up to a drift exceeding 10%. The specimen completed cycles up to 1% without major damage. The amount of spalling was small until 3% drift. In the first cycle of 3% drift, flexural cracks widened near the region of maximum bending moment. Inclined shear cracks started to grow at drifts greater than 1.5%. Large amount of concrete cover spalled off at 4% and 5% cycles. Figure 7 shows the specimen at the end of the second cycle at 4% drift.

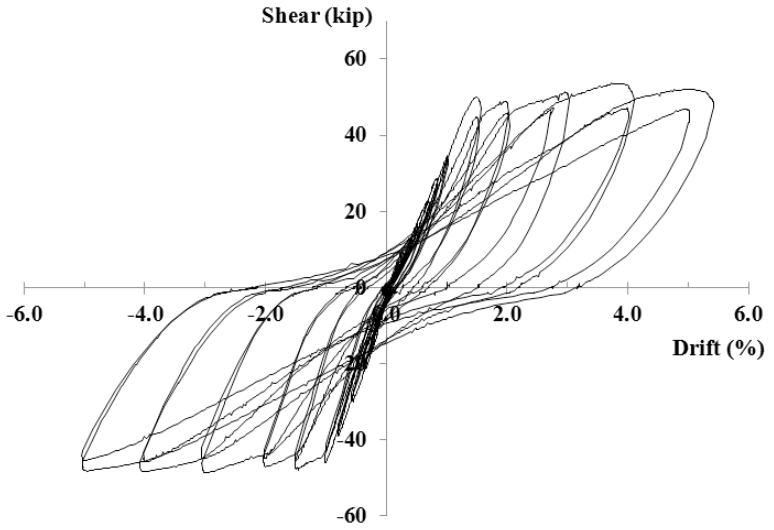


Figure 4. Shear Force vs. Drift Ratio, Specimen #1

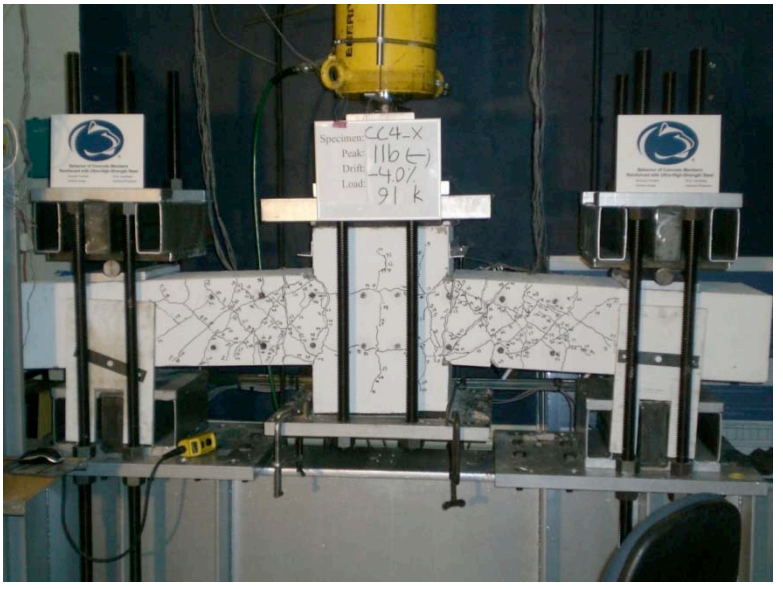


Figure 5. Specimen #1 at 4% Drift Ratio

In general both specimens had similar behavior. Specimen #1 (reinforced with Grade 60) showed a slight strength gain after yield while Specimen #2 (reinforced with UHSS Grade 97) had a nearly flat post-yield shear-drift envelope curve resembling the stress-strain curve of the steel. Both specimens completed all cycles in the loading protocol and reached drift ratios in excess of 10%. The hysteretic energy dissipated in Specimen #2 during a given post-yield hysteretic loop was smaller than the energy dissipated in the same loop for Specimen #1.

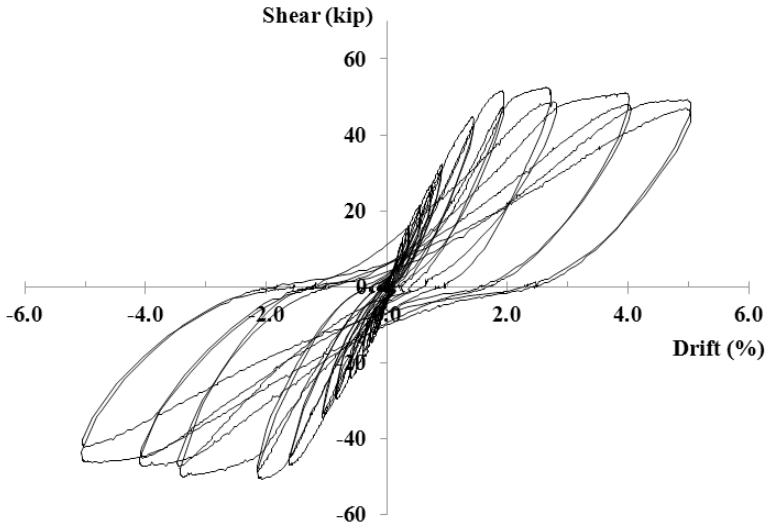


Figure 6. Shear Force vs. Drift Ratio, Specimen #2

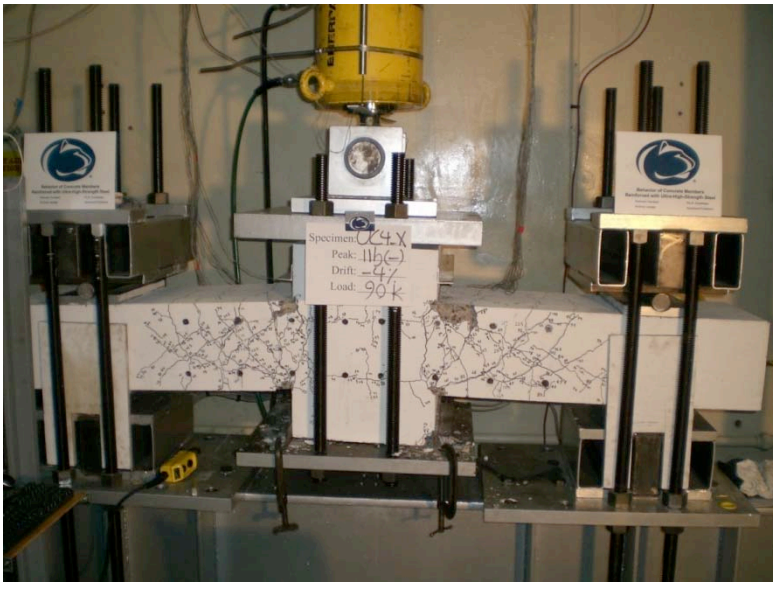


Figure 7. Specimen #2 at 4% Drift Ratio

Columns. Specimen #3, CC-3.3-20, was designed according to ACI 318 requirements. Figure 8 shows the measured shear-drift response of the specimen. It completed the first cycle at a drift ratio of 5%. At a drift ratio of approximately 1% during the second cycle to 5% drift, the longitudinal bars in compression buckled leading to a loss in lateral-load carrying capacity. A plausible explanation for the specimen failing at a drift ratio near zero is that the cracks on both sides of the specimen were open at that point. The axial load was carried predominantly by the longitudinal reinforcement, which led to buckling. Figure 9 shows the specimen at the end of the second cycle at 4% drift.

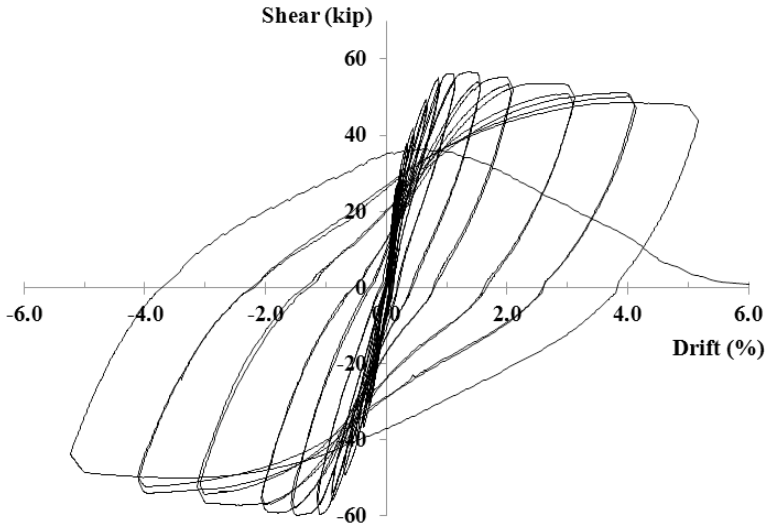


Figure 8. Shear Force vs. Drift Ratio, Specimen #3



Figure 9. Specimen #3 at 4% Drift Ratio

Specimen #4, UC-1.6-20, had properties that were similar to Specimen #3, with the exception that it was reinforced longitudinally with (approximately half as much) UHSS. Figure 10 shows the measured shear-drift response of the specimen. It completed the first half-cycle to a drift ratio of 5%, and the bars in compression buckled during the second half-cycle at that drift ratio. Testing was continued and the remaining longitudinal bars buckled at a small drift ratio (approximately 2%) during the second cycle at 5% drift ratio. Again, a plausible explanation is that the longitudinal bars need to carry a larger fraction of the axial load when the cracks in the concrete are open (typically at low drift ratios after having incurred large drift ratios). Figure 11 shows the specimen at the end of the second cycle at 4% drift.

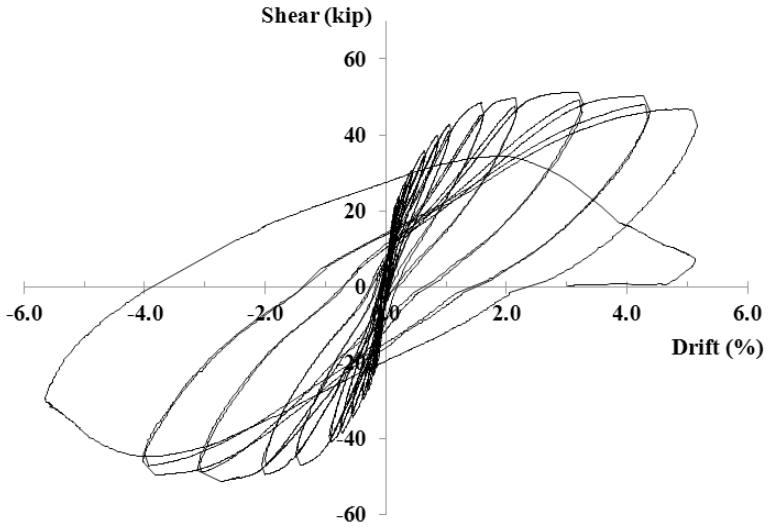


Figure 10. Shear Force vs. Drift Ratio, Specimen #4

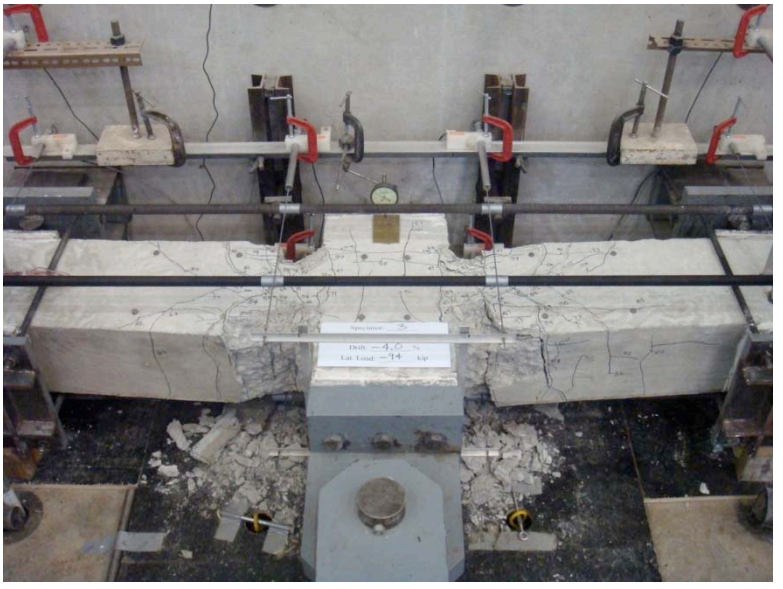


Figure 11. Specimen #4 at 4% Drift Ratio

Overall, the mechanical behavior of both columns was similar. The drift capacity of the column reinforced with Grade 60 steel and the column reinforced with UHSS Grade 120 were both 5%. However, there are at least two notable differences. The drift ratio at yield in Specimen #4 (UHSS steel) was approximately 50% higher than the drift ratio at yield in Specimen #3 (conventional steel). Also, the post-cracking stiffness of Specimen #4 is smaller than that of Specimen #3, which leads to less energy dissipation through hysteresis.

Conclusions

The test results presented here suggest that beams or columns with ultrahigh strength steel (UHSS) as longitudinal reinforcement have similar drift capacities to beams or columns reinforced with (approximately twice as much) conventional high strength steel. The tested beams tolerated drift ratios in excess of 10% without failure and the columns tested here tolerated ultimate drift ratios of 5%.

The specimens reinforced with UHSS required less steel than specimens reinforced with 60-ksi steel to reach the same moment capacity, resulting in less congestion. However, the reduction in steel caused a stiffness reduction upon unloading and reloading beyond cracking. The lower stiffness causes a reduction in energy dissipation as measured by the area of the hysteresis loops.

References

ACI 318-63. (1963). Building Code Requirements for Reinforced Concrete (ACI 318-63). ACI Standard, Reported by ACI Committee 318, American Concrete Institute, Detroit, MI, 144 p.

ACI 318-71. (1971). Building Code Requirements for Reinforced Concrete (ACI 318-71). ACI Standard, Reported by ACI Committee 318, American Concrete Institute, Farmington Hills, MI, 78 p.

ACI 318-08. (2008). Building Code Requirements for Structural Concrete and Commentary, Reported by ACI Committee 318, American Concrete Institute, Farmington Hills, MI, 465 p.

ACI ITG-6R-10. (2010). Design Guide for the Use of ASTM A1035/A1035M Grade 100 (690) Steel Bars for Structural Concrete. Reported by ACI Innovation Task Group 6, American Concrete Institute, Farmington Hills, MI, 90 p.

Applied Technology Council. (2007). FEMA 461 / Interim Testing Protocols for Determining the Seismic Performance Characteristics of Structural and Nonstructural Components. Redwood City, CA, 113 p.

ASTM A1011/A1011M-10. (2010). Standard Specification for Steel, Sheet and Strip, Hot-Rolled, Carbon, Structural, High-Strength Low-Alloy, High-Strength Low-Alloy with Improved Formability, and Ultra-High Strength. ASTM International, West Conshohocken, PA, 9 p.

ASTM A1035/A1035M-05. (2005). Standard Specification for Deformed and Plain, Low-Carbon, Chromium, Steel Bars for Concrete Reinforcement. ASTM International, West Conshohocken, PA, 5 p.

Hognestad, E. (1961). High Strength Bars as Concrete Reinforcement, Part 1 – Introduction to a Series of Experimental Reports. Journal of the PCA Research and Development Laboratories, 3:3, 23-29.

ISSI. (2006). Advanced High Strength Steel (AHSS) Application Guidelines, version 3. Prepared by the Committee on Automotive Applications, World Auto Steel, Automotive Group of International Iron and Steel Institute, Middletown, OH, 131 p.

Kaar, P. H. (1966). High Strength Bars as Concrete Reinforcement, Part 8 – Similitude in Flexural Cracking of T-Beam Flanges. Journal of the PCA Research and Development Laboratories, 8:2, 2-12.

Otani, S., Nagai, S., Aoyama, H. (1996). Load-Deformation Relationship of High-Strength Reinforced Concrete Beams. Mete A. Sozen Symposium: a Tribute from his Students, ACI SP 162, J. K. Wight and M. E. Kreger, eds., American Concrete Institute, Farmington Hills, MI, pp. 35-52.

Richart, F. E., and Brown, R. L. (1934). An Investigation of Reinforced Concrete Columns. The Engineering Experiment Station (in cooperation with the American Concrete Institute), Bulletin No. 267, University of Illinois, Urbana, IL, 91 p.

Todeschini, C. E., Bianchini, A. C., and Kesler, C. E. (1964). Behavior of Concrete Columns Reinforced with High Strength Steels. Journal of the American Concrete Institute, 61:6, 701-715.

Nominal Shear Strength Limits for Short Diagonally-Reinforced Concrete Coupling Beams

Steven Barbachyn,[1] Yahya C. Kurama,[2] Ph.D., P.E., and Lawrence C. Novak,[3] S.E.

[1]Graduate Student, Civil Engineering, University of Notre Dame, 156 Fitzpatrick Hall, Notre Dame, IN 46556; Ph: (269) 492-5426; E-mail: sbarbach@nd.edu
[2]Associate Prof., Civil Engineering, University of Notre Dame, 156 Fitzpatrick Hall, Notre Dame, IN 46556; Ph: (574) 631-8377; E-mail: ykurama@nd.edu
[3]Director of Engineered Buildings, Portland Cement Association, 5420 Old Orchard Road, Skokie, IL 60077; Ph: (847) 972-9100; E-mail: lnovak@cement.org

ABSTRACT

Sections 21.9.4.5 and 21.9.7.4 of ACI 318-08 limit the nominal shear strength, V_n of concrete coupling beams, including short beams with diagonal reinforcement, to $V_n \leq 0.83 A_{cw} \sqrt{f'_c}$ (with f'_c in MPa units, or $10 A_{cw} \sqrt{f'_c}$ with f'_c in psi units). Many experimental studies have been conducted on the design and detailing of diagonally-reinforced coupling beams for ductile behavior under seismic loading. The primary objective of the current ACI strength limit is to prevent the splitting and/or crushing of the diagonal strut in these beams. Through an analytical parametric investigation of isolated floor-level subassemblies, this paper shows that the boundary conditions utilized in the previous coupling beam experiments may not be adequate to investigate this important failure mode. The analytical model that forms the basis of the study uses a strut-and-tie representation of the forces developing inside a coupling beam under lateral loading. Multi-story coupled wall analyses are also conducted.

INTRODUCTION

Properly designed reinforced concrete (RC) coupled shear wall structures can provide large strength, stiffness, and energy dissipation under lateral loads; however, the design and construction of the coupling beams remain challenging due to the presence of large reversed-cyclic nonlinear rotation demands combined with large shear forces resulting in complex reinforcement details. For seismic conditions, Chapter 21 of ACI 318 (2008) prescribes extensive requirements for the design of coupling beams, especially for shorter beams where the nonlinear rotation and shear demands are more critical. The primary reinforcement in these beams consists of groups of diagonal bars that are confined by transverse reinforcement across the span of the beam and anchored into the walls. In addition, ACI 318 limits the nominal shear strength, V_n, of coupling beams to $V_n \leq 0.83 A_{cw} \sqrt{f'_c}$ (with f'_c in MPa units, or $10 A_{cw} \sqrt{f'_c}$ with f'_c in psi units). The commentary for this limit states: "Test results (Barney et al. 1980) demonstrate that beams reinforced as described in Section 21.9.7 have adequate ductility at shear forces exceeding $10 b_w d \sqrt{f'_c}$. Consequently, the use of a limit of $10 A_{cw} \sqrt{f'_c}$ provides an acceptable upper limit."

The main goal of the shear strength limit and transverse steel requirements in ACI 318 is to prevent the failure of the diagonal strut that develops inside a coupling

beam under lateral loading. Many experimental studies (e.g., Tassios et al. 1996; Galano and Vignoli 2000; Adebar et al. 2001; Kwan and Zhao 2002; Canbolat et al. 2005; Moretti and Tassios 2006; Wallace 2007; Fortney et al. 2008; Yun et al. 2008) have been conducted since the original study (i.e., Barney et al. 1980) that precipitated the current design and detailing requirements for diagonally-reinforced coupling beams. However, except for one beam in Adebar et al. (2001), all of the test specimens in these previous research programs were axially unrestrained. This boundary condition can provide an unconservative evaluation for the design of the beams, in particular with respect to the diagonal strut. This is because, as cracking occurs under lateral loading and the diagonal bars yield in tension, the centerline of the beam "elongates," which is resisted by the large in-plane stiffnesses of the shear walls, thus introducing compression forces into the beams. This effect is most prominent for deeper beams and especially near the base of the structure where the wall piers provide the largest restraint to the axial elongation of the beams. Furthermore, under reversed-cyclic loading into the nonlinear range, the in-plane stiffnesses of the wall piers vary by different amounts (due to differences in the wall axial forces), causing not only large compression forces, but also tension forces in the coupling beams.

Through an analytical parameter study, this paper evaluates the geometrical, reinforcement, and loading conditions that affect the behavior of diagonally-reinforced coupling beams under reversed-cyclic lateral loading. To isolate the primary load-resisting mechanisms of the structure, the analytical model uses a strut-and-tie representation based on Appendix A of ACI 318. Comparisons of the results with available test data show that, despite its simplicity, the strut-and-tie model is capable of adequately capturing the behavior of the beams. Using this model, the paper evaluates the effects of axial restraint and other parameters on the diagonal strut. Multi-story coupled wall analyses are also conducted to investigate the forces that develop in the beams.

The results from the study reveal that the reason crushing of the diagonal strut was observed in Barney et al. (1980), precipitating the current ACI 318 shear strength limit, is that these test beams had unequal areas of steel reinforcement in the two diagonals, which is not a realistic, practical detail. It is also found that the presence of a significant amount of fully-developed (i.e., achieving the yield strength of the steel) horizontal reinforcement crossing the beam-to-wall joints can induce earlier crushing of the concrete. The current ACI 318 recommendations for the horizontal reinforcement in diagonally-reinforced coupling beams are only in the ACI 318 commentary. The commentary figure (ACI 318 Fig. R21.9.7) notes partial requirements for the horizontal reinforcement as: "Horizontal beam reinforcement at wall does not develop f_y."; however, the commentary does not hold the same legal requirements as the main body of ACI 318. These recommendations could be more clearly stated to explicitly prevent the use of developed horizontal steel across the beam-to-wall joints in diagonally-reinforced coupling beams, since the tension forces in these bars could lead to increased compression stresses in the concrete.

ANALYTICAL MODELING AND VALIDATION

A nine-node two-dimensional strut-and-tie model consisting of concrete, RC, and steel members as shown in Fig. 1(a) forms the basis of the coupling beam

analyses in this paper. The steel members (solid lines) represent the primary reinforcement resisting both tension and compression forces during the cyclic loading of a beam, while the concrete members (dashed lines) are assumed to resist compression only (ignoring the tension strength of concrete). The RC members (double lines) have both steel and concrete elements. The goal is to develop a simple tool that can isolate the primary load-resisting components of a diagonally-reinforced beam; thus, allowing each component to be evaluated separately.

Nodes A, C, G, and I of the model are located where the centroids of the diagonal bar groups intersect with the top and bottom horizontal bar groups. These nodes are placed a small distance into the wall piers, providing a more realistic representation of the beam than simply placing the nodes at the beam ends. The other nodes are located equidistantly vertically and horizontally between the four corner nodes, with one node in the center so that a symmetric nine-node array is formed.

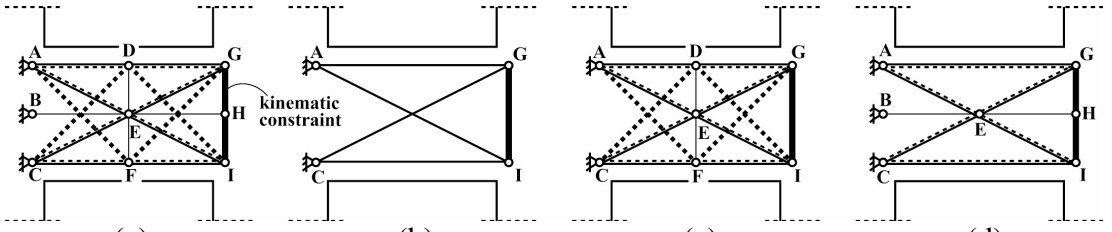


Figure 1. Strut-and-tie models: (a) nine-node model; (b) all-steel four-node model; (c) seven-node model; (d) model without concrete strut elements

RC Main Diagonal Elements. The main diagonal elements between Nodes A-E-I and C-E-G are RC elements. The steel area is equal to the total cross-sectional area, A_{sd} of the diagonal bar group. The concrete area, A_c is taken as the core area enclosed by the centerline of the ties around the diagonal reinforcement. A lower limit to A_c is set as $A_{c,min} = C_c / (0.85\beta_s f'_c)$. The calculation of $A_{c,min}$ is derived from a sectional equilibrium analysis of the beam. Assuming that all steel reinforcement is at yield and ignoring the strength of concrete in tension, the total compression stress resultant in the concrete, C_c can be found as $C_c = A_{sd} f_{yd} \cos(\alpha) + A_{sl} f_{yl} + A_{sm} f_{ym} - N_b - A_{sd}' f_{yd}' \cos(\alpha) - A_{sl}' f_{yl}'$, where, β_s=0.60 (assumed concrete strength reduction factor in accordance with Appendix A of ACI 318), A_{sd}, A_{sd}'=total areas of the tension and compression diagonal reinforcement, respectively (A_{sd}=A_{sd}' in most cases); A_{sl}, A_{sl}'=total areas of the developed tension and compression horizontal reinforcement (if present), respectively, at the top and bottom of the beam (A_{sl}=A_{sl}' in most cases); A_{sm}=total area of the developed horizontal reinforcement within the mid-depth of the beam (if present); f_{yd}, f_{yd}', f_{yl}, f_{yl}', f_{ym}=respective yield strengths for the reinforcement areas listed above; α=inclination of the diagonal bars with respect to the horizontal; and N_b=applied (external) axial force (compression negative) on the beam.

Note that C_c as described above is zero when all diagonal and horizontal reinforcement is symmetrical, no developed mid-depth horizontal bars are used (i.e., A_{sm}=0), and no external axial force is applied on the beam (i.e., N_b=0). This means that the internal resisting forces in the beam equilibrate through the reinforcing bars, with no significant compression forces in the concrete. Under this condition, a simpler "all-steel" strut-and-tie model with A_c=0 can be used, consisting of only the four corner nodes with the specified reinforcement as shown in Fig. 1(b).

RC Longitudinal Boundary Elements. The longitudinal boundary elements are RC elements between Nodes A-D-G and C-F-I. The steel area is equal to the total area of the developed horizontal bars at the top or bottom of the beam (i.e., A_{sl} or A_{sl}', which are taken as zero if the bars are not developed across the beam-to-wall joints). The concrete area is assumed to be the same as the area, A_c for the main diagonal elements (with no tension strength and an effective compression strength of $0.85\beta_s f'_c$).

Steel Longitudinal Mid-Depth Elements. The longitudinal mid-depth elements are steel elements between Nodes B-E-H with a total area of A_{sm} along the mid-depth of the beam (i.e., horizontal steel not included in A_{sl} and A_{sl}'). If the horizontal bars are not developed across the beam-to-wall joints, then, A_{sm}=0 and Nodes B and H can be removed from the model resulting in a seven-node truss as shown in Fig. 1(c).

Steel Transverse Elements. The transverse steel elements are located at the beam mid-span between Nodes D-E-F, with an assumed area equal to the total vertical leg area of the full-depth transverse reinforcement (e.g., hoops, stirrups) within one-quarter of the beam length on each side of the mid-span. This length is taken as the "tributary" length in determining the steel area lumped in the transverse elements.

Concrete Strut Elements. Four strut elements between Nodes A-F, C-D, G-F, and I-D model the concrete in compression in these regions. The concrete area in each element is taken the same as the area A_c for the main diagonals (with no tension strength and a compression strength of $0.85\beta_s f'_c$). For beams with very small length-to-depth aspect ratios, specifically $l_b/h_b<1.50$, the concrete strut elements are not used since most of the compression forces are carried through the main diagonal struts. Under this condition, the transverse elements become zero-force members, resulting in a model with just the main diagonal elements and longitudinal elements as shown in Fig. 1(d).

Assumed Loading and Boundary Conditions. The OpenSees software (Mazzoni et al. 2009) was used for the analysis of the strut-and-tie models above. The left end of the beam was fixed while the right end was free but not allowed to rotate (to result in symmetrical double curvature along the beam length). The modeling of axial restraint on the beam is described later. Gravity loads (e.g., beam self weight) were ignored and a transverse point load was applied at Node G to simulate the effects of lateral loading on the beam. The analyses were conducted in displacement control with Nodes G, H, and I (which were kinematically constrained) subjected to a prescribed reversed-cyclic transverse displacement history.

Material Idealizations. The zero-tensile-strength "Concrete01" material in OpenSees was used for all of the concrete elements. The compressive strength, set equal to $0.85\beta_s f'_c$, was assumed to be reached at a compressive strain of -0.002. Beyond this strain point, the compressive stress was assumed to remain constant to partially simulate the redistribution of the concrete stresses in an actual RC member. The "Reinforcing Steel" material, which allows for the modeling of strain hardening and Bauschinger effects, was used for the main diagonal bars. For the horizontal and transverse reinforcement, the simpler "Steel01" material was used. This material has an idealized bilinear stress-strain relationship. Two parallel Steel01 elements were

used for each longitudinal and transverse member to result in a trilinear stress-strain relationship capturing both the yield strength and the ultimate strength of the steel.

Model Validation. Comparisons between the measured and predicted lateral load versus displacement behaviors for six coupling beams tested in previous research are shown in Fig. 2. More information on the analytical model validation can be found in Barbachyn et al. (2011). In evaluating the model comparisons, it is re-emphasized that the main goal is to construct a simple tool that can isolate the most important load-resisting components of a diagonally-reinforced coupling beam, such that these components can be subsequently analyzed under different geometrical, reinforcement, and loading conditions. While it would be possible to develop more sophisticated models (e.g., using a finite element program), the strut-and-tie model remains the most effective tool for the investigation in this paper.

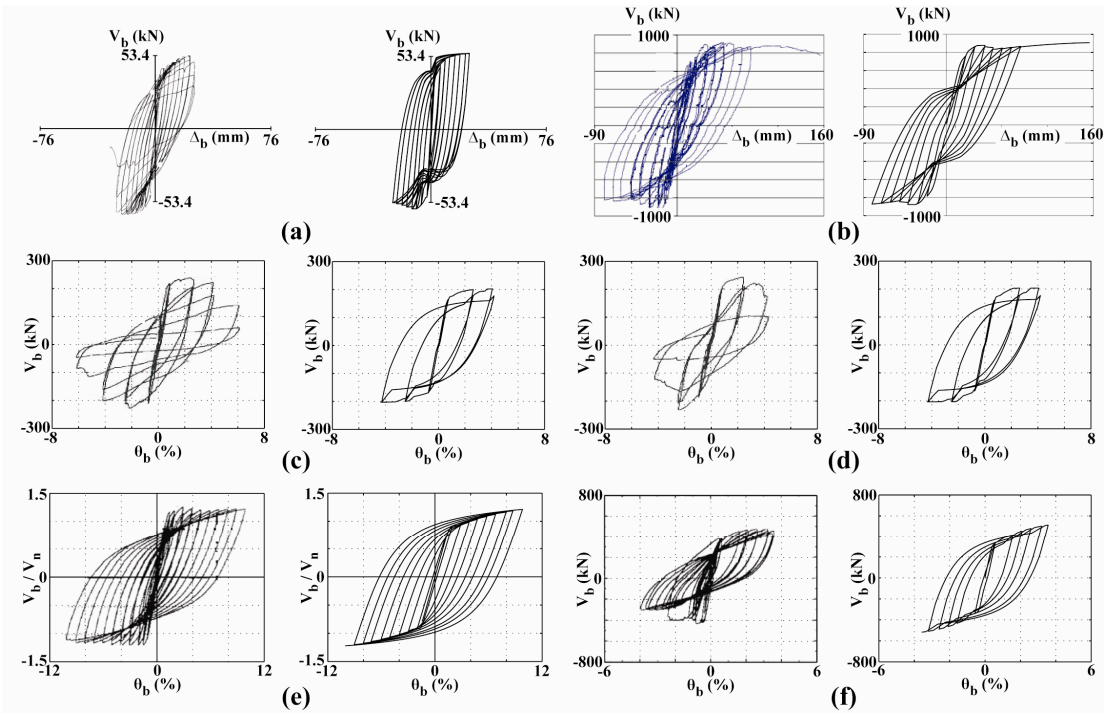


Figure 2. Measured (left) and predicted (right) coupling beam behaviors: (a) Barney et al. (1980) Specimen C6; (b) Adebar et al. (2001); (c) Galano and Vignoli (2000) Specimen P07; (d) Galano and Vignoli (2000) Specimen P12; (e) Fortney et al. (2008) Specimen DCB-2; (f) Canbolat et al. (2005) Specimen 1

PARAMETRIC INVESTIGATION

For the purposes of this investigation, a prototype 14-story building structure with plan view in Fig. 3(a) was designed for a site in Los Angeles. The wall pier details at the base are shown in Fig. 3(b) and the coupling beam elevation is shown in Fig. 3(c). Steel with yield and ultimate strengths equal to 414 and 621 MPa (60 and 90 ksi), respectively, was assumed for all of the reinforcement. The compressive strength of the concrete was assumed as f'_c=41 MPa (6 ksi).

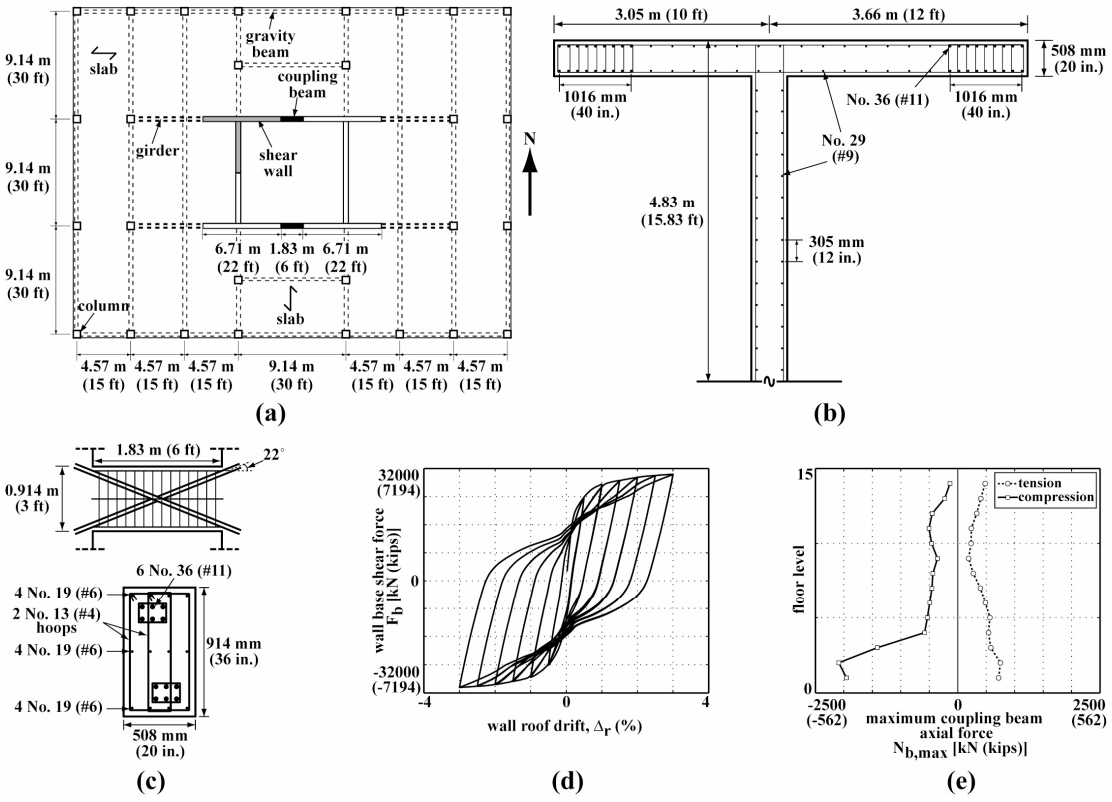


Figure 3. Prototype structure: (a) building plan; (b) wall base; (c) coupling beam (CB1); (d) base shear versus roof drift behavior; (e) maximum coupling beam axial forces

The coupling beams over the building height were assumed to be identical. This design (referred to as Beam CB1) with an aspect ratio, l_b/h_b=2.0 was used as the basis of the parametric investigation. The total area of each diagonal bar group is A_{sd}=6039 mm^2 (9.36 in^2) [6#36 (#11) bars] placed at an inclination angle of α=22°, resulting in a nominal shear strength of $V_n=2A_{sd}f_{yd}sin(\alpha)=0.62A_{cw}\sqrt{f'_c}$ (with f'_c in MPa units, or $7.5A_{cw}\sqrt{f'_c}$ with f'_c in psi units). The horizontal and transverse bars were selected according to the ACI 318 requirements. It was assumed that an adequate amount of transverse steel was placed around the diagonal bars to prevent buckling. The horizontal reinforcement [total of 12#19 (#6) bars] was not developed across the beam-to-wall joints (i.e., $A_{sm}=A_{sl}=A_{sl}'$=0 was assumed).

Two series of analyses were conducted based on Beam CB1. In the first series, the beam was assumed axially unrestrained (i.e., N_b=0) and was subjected to a series of reversed-cyclic displacements up to a maximum chord rotation of θ_b=9%. In the second series, external steel bars were modeled along the mid-depth of the beam (i.e., between Nodes B and H of the strut-and-tie model, with no connection to Node E) to simulate axial restraint conditions similar to the external bars used in the test specimen described in Adebar et al. (2001). The total area of the restraint bars was determined from a nonlinear reversed-cyclic lateral load analysis of the coupled wall structure in the E-W direction. For this multi-story wall analysis, the coupling beams were modeled using the strut-and-tie representation in Fig. 1(c) (since the horizontal bars were not developed into the walls) and the wall piers were modeled using fiber elements as described in Kurama and Shen (2008). Fig. 3(d) depicts the expected base

shear force versus roof drift angle behavior of the entire core wall structure and Fig. 3(e) shows the corresponding distribution of the maximum coupling beam axial forces over the wall height. A significant variation in the coupling beam axial forces can be seen over the height of the structure, with the largest compression forces developing near the base. Ultimately, the total area of the axial restraint bars in the coupling beam analyses was taken as A_{er}=2123 mm^2 (3.29 in^2), resulting in an axial restraint force of about -876 kN (-197 kips) at yield. This force is close to the average maximum compression force for the coupling beams over the height of the structure in Fig. 3(e). Variations in the restraint bar area were also investigated.

Note that in addition to compression, the coupling beam axial forces in Fig. 3(e) also show large tension effects. While these tension forces are not investigated further in this paper, it should be stated that they can cause more critical conditions than previously considered for the low-cycle fatigue fracture of the diagonal reinforcement.

Effect of Beam Depth. The variation of the beam depth, d_b, was simulated by changing the height of the strut-and-tie model to parametric depths equal to 0.5, 0.75, 1.25, and 1.5 times the original depth for Beam CB1, while all other properties of the beam stayed constant. The results from the investigation are shown in Figs. 4(a) through 4(f). The format of these figures is the same for all of the other parametric analysis results in this paper as follows: (a) shear force, V_b versus chord rotation, θ_b behavior for beams without axial restraint; (b) V_b versus θ_b behavior for beams with axial restraint; (c) normalized beam shear force at yield of diagonal steel, $V_{b,y}/(A_{cw}\sqrt{f'_c})$, where f'_c is in MPa units (psi units in parentheses); (d) maximum axial (i.e., horizontal) elongation of the beam, $\delta_{a,max}$ (i.e., horizontal displacement of the right end of the beam with respect to the left end); (e) maximum compression strains, $\varepsilon_{c,max}$ in the main diagonal and concrete strut elements; and (f) maximum tension strains, $\varepsilon_{t,max}$ in the main diagonal and steel transverse elements. The base case using Beam CB1 is depicted by the * markers whereas the □ markers show the parametric cases.

Looking at Fig. 4, an increase in the beam depth, d_b causes a small decrease in the normalized "yield" strength of the beam (i.e., strength at yield of diagonal reinforcement) since A_{cw} increases. As d_b is increased, the axial elongation, $\delta_{a,max}$ of the beam increases almost linearly, resulting in an increase in the tension strains, $\varepsilon_{t,max}$ of the diagonal reinforcement. The transverse steel strains remain very small throughout the parameter variation. An important observation is that for beams with axial restraint, the axial elongation and tension strains are smaller but there is a significant increase in the main diagonal and concrete strut compression strains, $\varepsilon_{c,max}$. As the depth is increased, the axially-restrained beams develop concrete strains at crushing level even though the ACI 318 nominal strength limit of $0.83A_{cw}\sqrt{f'_c}$ (with f'_c in MPa units) is not exceeded. It is concluded that the previous coupling beam experiments with no axial restraint may be unconservative for the crushing of concrete and buckling of reinforcement, especially for deeper beams.

Amount of Axial Restraint. Fig. 5 shows the analysis results where the total area, A_{er} of the axial restraint bars was varied. The variation in A_{er} was done proportionally with respect to the total area, A_{sd} of the diagonal reinforcement in the beam, ranging

from a ratio of 0 (i.e., no axial restraint) to 2.0. Note that the analysis cases presented in the other sections of the paper correspond to A_{er}/A_{sd} ratios of 0 and 0.35 (* markers in Fig. 5), and for the beam tested by Adebar et al. (2001), this ratio is equal to 1.44.

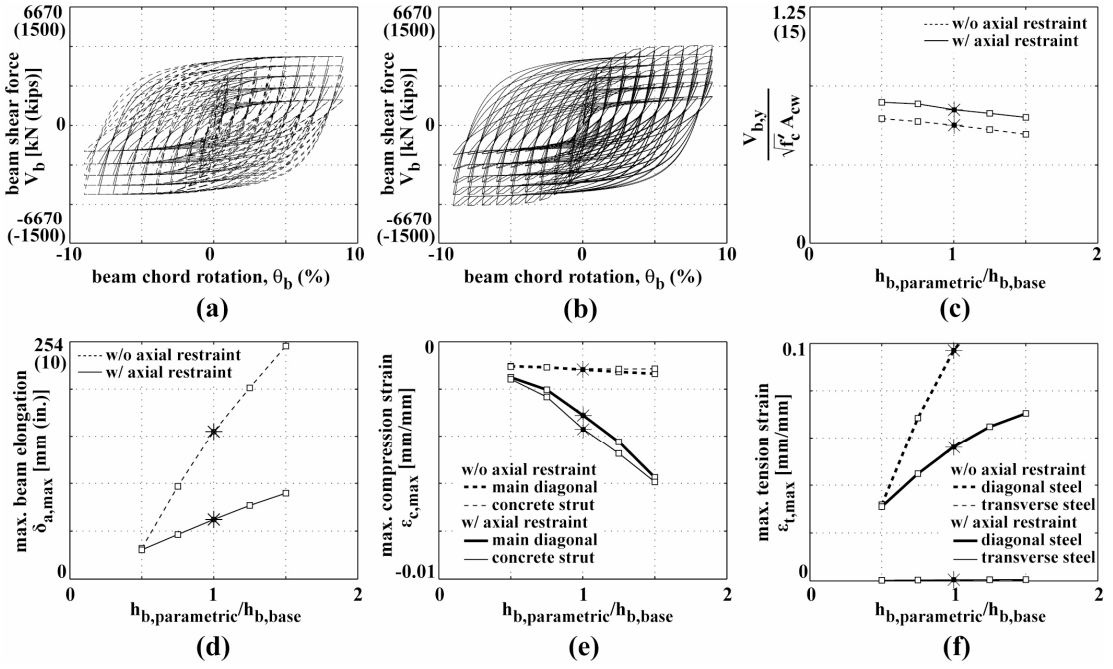


Figure 4. Beam depth, h_b: (a) without axial restraint; (b) with restraint; (c) normalized shear strength; (d) beam elongation; (e) compressive strains; (f) tensile strains

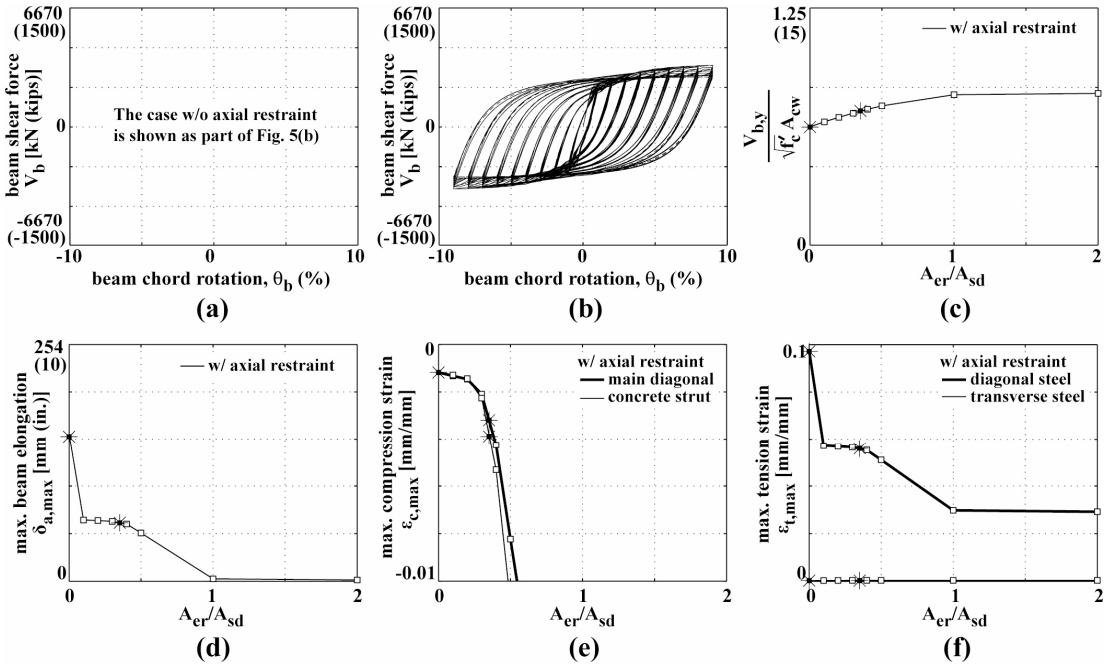


Figure 5. Amount of axial restraint: (a) no restraint; (b) with restraint; (c) normalized shear strength; (d) beam elongation; (e) compressive strains; (f) tensile strains

It can be seen from Fig. 5 that the effect of axial restraint on the lateral strength of the beam is relatively small but, as A_{er} is increased, there is a significant decrease in the axial elongations and tensile strains, and a significant increase in the compression strains. When A_{er} reaches about $1.0A_{sd}$, the axial elongation of the beam is restrained to zero and there is no additional change in the tensile or compressive strains as A_{er} is increased further. These findings confirm the need to include the restraining effect of the shear walls in the validation testing of RC coupling beams. Depending on the amount of axial restraint, beams that satisfy the ACI nominal shear strength limit can fail due to the failure of the diagonal strut.

Reinforcing Steel Areas. In this section, the reinforcing steel areas in the main diagonal and longitudinal boundary elements of Beam CB1 are varied. The concrete area A_c is kept constant in each case. As shown in Fig. 6, an increase in the main diagonal steel area, A_{sd} results in an almost proportional increase in the strength of the beam. The axial elongation of the beam is not significantly affected by this parameter; however, especially for axially-restrained beams, there is a considerable increase in the compression strains as the amount of diagonal steel is increased.

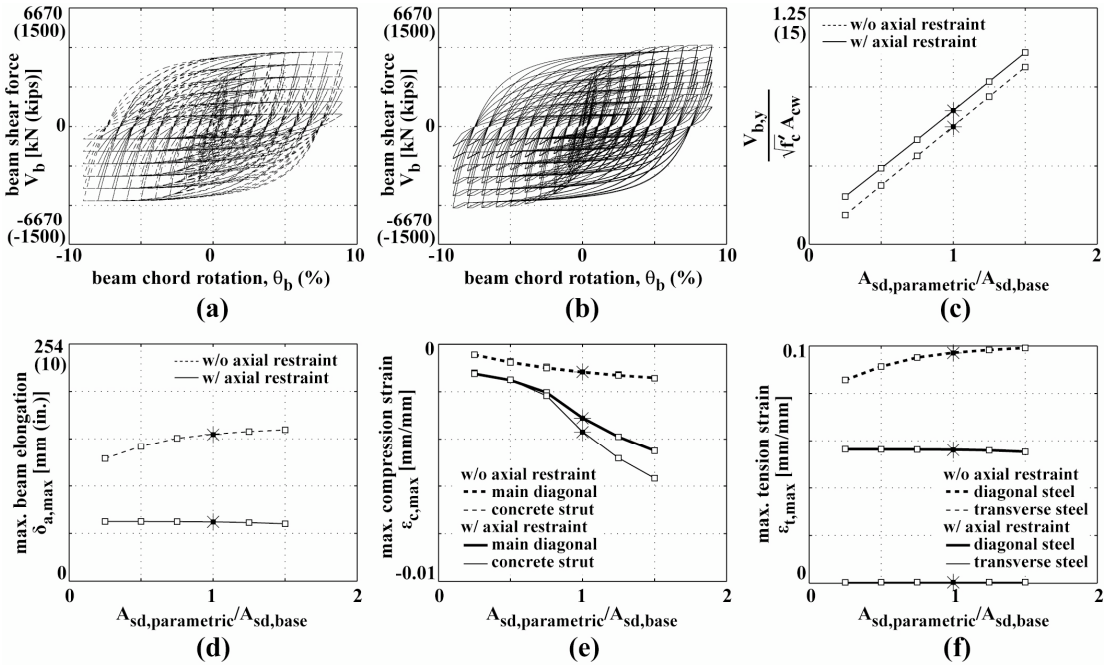


Figure 6. Main diagonal steel area, A_{sd} – symmetrical variation: (a) without axial restraint; (b) with axial restraint; (c) normalized shear strength; (d) beam elongation; (e) compressive strains; (f) tensile strains

The results in Fig. 6 correspond to cases where the reinforcement in the beam is varied symmetrically. In Fig. 7, another series of beams are analyzed where the total steel area of only one of the main diagonals is varied. While this is not a recommended design for practice, it is an important study since it shows the implications of the unsymmetrical reinforcement used in Barney et al. (1980), which had about 10% less steel in one diagonal than the other. It can be seen that as one

diagonal steel area is reduced by 10% and 20% with respect to the other diagonal, there is a significant increase in the maximum compression strains.

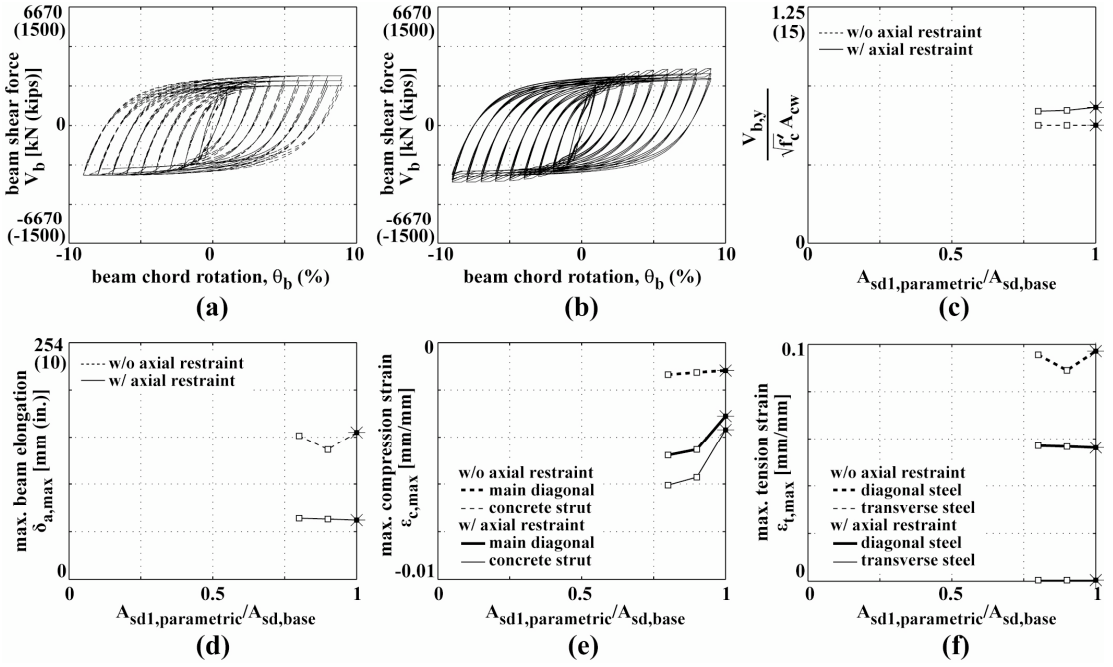


Figure 7. Main diagonal steel area, A_{sd} – unsymmetrical variation: (a) without axial restraint; (b) with axial restraint; (c) normalized shear strength; (d) beam elongation; (e) compressive strains; (f) tensile strains

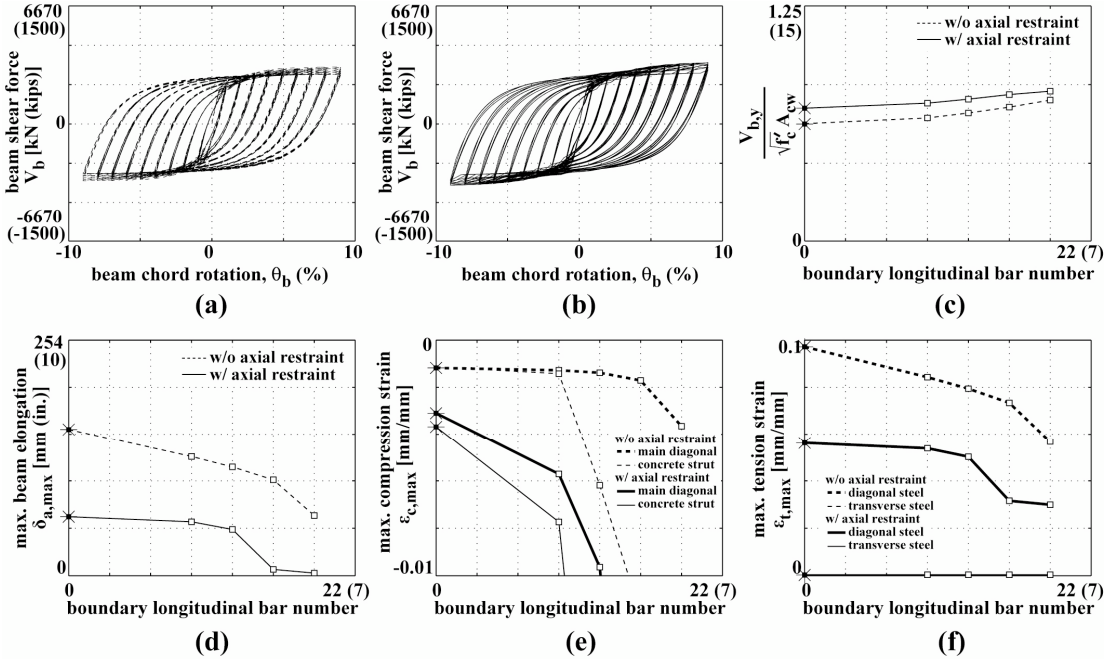


Figure 8. Boundary horizontal steel area, A_{sl}: (a) without axial restraint; (b) with axial restraint; (c) normalized shear strength; (d) beam elongation; (e) compressive strains; (f) tensile strains

Finally, the effects of the area, A_{sl} of the developed boundary horizontal reinforcement across the beam-to-wall joints are shown in Fig. 8. The analysis cases include the base case of no developed bars as well as 4 bars (top and bottom) of varying sizes [Nos. 10, 13, 16, and 19 (3, 4, 5, and 6)]. The mid-depth horizontal bar area, A_{sm} is held constant at zero. It can be seen that A_{sl} has little effect on the strength of the beam; however, as this reinforcement is increased, the compression strains in the beam also increase. If a significant amount of boundary reinforcement is developed, beams that satisfy the ACI nominal strength limit can fail due to the failure of the diagonal strut. Thus, it is not recommended to develop the horizontal bars through the beam-to-wall joints of a diagonally-reinforced coupling beam. As stated previously, this detailing requirement should be more clearly specified in ACI 318.

SUMMARY AND CONCLUSIONS

Through an analytical parameter study, this paper evaluates the geometrical, reinforcement, and loading conditions that affect the behavior of diagonally-reinforced coupling beams under reversed-cyclic lateral loading. The main findings and conclusions from the research, as limited to the variable ranges considered, are listed below.

(1) Despite its simplicity, the strut-and-tie model utilized in the paper provides a powerful tool to investigate the behavior of diagonally-reinforced coupling beams under lateral loads. For this investigation, the most significant advantage of this modeling technique is its ability to isolate the primary load-resisting components of a coupling beam.

(2) In a coupled wall structure under lateral loads, the large in-plane stiffnesses of the shear walls axially constrain the coupling beams, thus introducing significant axial forces into the beams. This effect is particularly large for the lower floor beams where compression failure of the diagonal struts can occur.

(3) Previous coupling beam experiments with no axial restraint can result in conditions that are unconservative for the crushing of the concrete and the buckling of the reinforcement. Thus, the results from these experiments cannot directly be used to validate the design and detailing of the compression diagonal.

(4) The use of unequal areas of reinforcement in the two diagonals most likely led to the failure of the compression diagonal in Barney et al. (1980), leading to the current nominal shear strength limit in ACI 318-08. Since an unsymmetrical reinforcement detail is typically unrealistic for practical applications, the ACI strength limit should be re-evaluated for coupling beams that are more representative of actual conditions.

(5) Depending on the amount of axial restraint, beams that satisfy the current nominal shear strength limit in ACI 318-08 can be unconservative due to the possibility of premature splitting and/or crushing of the diagonal strut. The axial restraint is more critical for beams with larger depth.

(6) Failure of the diagonal strut can also occur if a significant amount of horizontal steel reinforcement is developed across the beam-to-wall joints. The current ACI 318-08 commentary recommendations should be more clearly stated to

prevent the use of fully-developed horizontal steel across the beam-to-wall joints in diagonally-reinforced beams, with the possible relocation of the commentary recommendations to provisions in the main body of the ACI 318-08 document.

ACKNOWLEDGEMENTS

Funding for this research was provided by a Portland Cement Association Education Foundation Fellowship. This support is gratefully acknowledged.

REFERENCES

ACI Committee 318, "Building Code Requirements for Structural Concrete (ACI 318-08) and Commentary," American Concrete Inst., Farmington Hills, MI, 2008.

Adebar, P., Hindi, R., and Gonzalez, E., "Seismic Behavior of a Full-Scale Diagonally Reinforced Slender Coupling Beam," Technical Report, Dept. of Civil Engineering, The University of British Columbia, Vancouver, Canada, 2001.

Barbachyn, S., Kurama, Y., and Novak, L. "Design of Diagonally-Reinforced Concrete Coupling Beams," *Structural Engineering Research Report Series, NDSE-11-01*, University of Notre Dame, expected April 2011.

Barney, G., Shiu, K., Rabbat, B., Fiorato, A., Russell, H., and Corley, W., "Behavior of Coupling Beams Under Load Reversals," RD068.01B, Portland Cement Association, Skokie, IL, 1980.

Canbolat, B., Parra-Montesinos, G., and Wight, J., "Experimental Study on Seismic Behavior of High-Performance Fiber-Reinforced Cement Composite Coupling Beams," *ACI Structural J.*, 102(1), 2005, 159-166.

Fortney, P., Rassati, G., Shahrooz, B., "Investigation on Effect of Transverse Reinforcement on Performance of Diagonally Reinforced Coupling Beams," *ACI Structural J.*, 105(6), 2008, 781-788.

Galano, L. and Vignoli, A., "Seismic Behavior of Short Coupling Beams with Different Reinforcement Layouts," *ACI Structural J.*, 97(6), 2000, 876-885.

Kurama, Y. and Shen, Q., "Seismic Response Evaluation of Unbonded Post-Tensioned Hybrid Coupled Wall Structures," *Earthquake Engineering and Structural Dynamics*, 37(14), 2008, 1677-1702.

Kwan, A. and Zhao, Z., "Cyclic Behaviour of Deep Reinforced Concrete Coupling Beams," *Structures & Buildings*, 152(3), 2002, 283-293.

Mazzoni, S., McKenna, F., Fenves, G., "Open System for Earthquake Engineering Simulation (OpenSees)," Version 2.1.0 (http://opensees.berkeley.edu/index.php), Pacific Earthq. Engin. Res. Center, Univ. of California, Berkeley, CA, Jan. 2009.

Moretti, M. and Tassios, T., "Behavior and Ductility of Reinforced Concrete Short Columns Using Global Truss Model," *ACI Structural J.*, 103(3), 2006, 319-327.

Tassios, T., Moretti, M., and Bezas, A., "On the Behavior and Ductility of Reinforced Concrete Coupling Beams of Shear Walls," *ACI Struct. J.*, 93(6), 1996, 711-720.

Wallace, J., "Modelling Issues for Tall Core Wall Buildings," *The Structural Design of Tall and Special Buildings*, 16, 2007, 615-632.

Yun, H.-D., Kim, S.-W., Jeon, E., Park, W.-S., Lee, Y.-T., "Effects of Fibre-Reinforced Cement Composites' Ductility on the Seismic Performance of Short Coupling Beams," *Magazine of Concrete Research*, 60(3), 2008, 223-233.

A Simple Method in the Preliminary Assessment of Historic Masonry Buildings

James S. Cohen, MASCE, PE[1]

[1]Associate Principal, Arup, 155 Avenue of the Americas, New York, NY 10013; PH (212) 229-2669; FAX (212) 229-1056; email: james.cohen@arup.com

As part of a large infrastructure project in New York City, many load bearing brick masonry structures are located adjacent to areas undergoing excavation, tunneling and blast. Due to the numerous structures involved, simplified methods to rapidly assess stability issues of the brick masonry load bearing walls and facades have been developed. Based upon these methods, repair techniques have also been developed and successfully implemented. The methods of analysis and sample results are presented with recommended areas of improvement. The relative sensitivities of the various parameters and assumptions required are also presented.

INTRODUCTION

As part of an on-going project, it has been necessary to development a means to rapidly assess numerous historic load bearing masonry buildings, constructed during the period circa 1850 - 1910. These structures have many construction features in common despite the age range but all predating modern design code. These include: non-supporting front and rear unreinforced multi-wythe facades, unreinforced multi-wythe load bearing side walls, suspended timber frame floors, and, shallow rubble wall foundations.

Most, but not all, buildings contain commercial space at ground floor level, often framed by cast iron columns. Masonry is typically supported on the cast iron columns via masonry arches, themselves resting on cast iron plates. Public records for these buildings providing floor plans and other information are often available showing these similarities.

Other features often present in the condition of these buildings, to varying degrees, include:

- Separation of bearing walls leading to reduced bearing of the timber framing
- Deteriorated mortar in the rubble walls
- Deteriorated mortar in the brick facade
- Deteriorated mortar in the bearing walls
- Uneven settlement
- Separation of the façade to the bearing walls along vertical edges
- Cast iron tie-backs intended to tie the facades back to the interior framing and/or bearing walls, often in a corroded condition
- Lack of plumb of the overall building

Clearly, this list represents a deterioration of the building over time, detracting from the strength or stability of the building and represents a change in condition from original.

Assuming that some deterioration may be acceptable, representing a reduction in the presumed factor of safety originally incorporated into the building design, additional deterioration may be unacceptable. Such additional deterioration may be imposed by adjacent construction, including excavation, tunneling and blasting.

Constant monitoring of these older structures becomes necessary to ensure that such factors of safety are not reduced below an acceptable level; i.e., that the buildings remain stable and functional. Of particular interest is the total lean of the buildings, whether parallel to the facades or to the bearing walls.

Brick masonry is inherently difficult to analyze as a model. Typically, for new construction, brick masonry is viewed as a uniform material with fixed properties. However, the material properties of the various materials, bond of mortar, the behavior of the brick/mortar assembly, the interaction between multiple withes of the assembly and the anisoptropic behavior of the materials all create difficulties for detailed analysis.

For older buildings, these difficulties are overshadowed by the unknown condition of the various mortar joints, likely hidden deterioration, historical use of differing bricks depending upon whether they were exterior or interior, visible or hidden, and other uncertainties. In many cases, adjacent contiguous buildings, which originally formed part of a continuous structural system of row buildings have been demolished, leaving former interior bearing walls exposed. It therefore becomes necessary to simplify the assessment of the stability of the buildings where conditions may be changing daily and multiple buildings, each unique in their own way, and time is not available for refining each model for a lengthy analysis.

What follows is a simplified approach to this problem which has been used with success in determining acceptable levels of stability for these buildings.

OBJECTIVES AND BENEFITS OF SPREADSHEET APPROACH

The basic objectives are:

- Provide guidelines for allowable tilt and lean of exterior unreinforced load bearing masonry walls due to effects of adjacent construction. Outward tilt and lean only are of interest, as inward tile is resisted by the floor system, stairway core and opposing wall.
- Provide rapid feedback to changing conditions regarding building exterior wall stability
- Assess sensitivity of results to various assumptions
- Provide means for mitigating potential instability

Current methods of rapid assessment are typically based on empirical rules, such as the "middle-third" rule, whereby there is no net tension on the extreme fibers of the wall assembly. Secondary effects which may contribute to the building stability are often ignored, such as castellation of the wall, internal dead loads which may provide a counterbalancing moment and friction. Typically these methods could be time consuming as each condition would need to be separately analyzed.

The spreadsheet assessment which has been developed by its nature allows for quick reappraisal. The spreadsheet also allows for quick assessment of sensitivity of results to varying assumptions. As the analysis is rapid, it can assume short-term conditions and, finally, there is an allowance in the standardized input for altered conditions on a building-by-building basis.

BASIC ASSUMPTIONS

Basic calculation assumptions are as follows:

- Wall acts as 3-sided plate fixed along three edges.
    - With regard to vertical edges, these must be fixed as the corner masonry is typically laid in alternating fashion. To be pinned would mean failure of the corner. The base condition is assumed fixed as the full moment is assumed to be resisted through eccentric loading of the base.
- Wall material properties are constant.
- Wall thickness is constant over the height of the building (exception: bearing walls, see below).
    - Weighted averages are incorporated for the effects of window openings and varying thicknesses from pier to infill brick to allow for the averaging effect on bearing area, bending and deflection.
- Window openings are ignored.
    - For flat plate deflection (assumed, see below) the critical location for the walls will be at the base of the walls.
- Vertical deflection is not accounted for in calculations.
- Initial deflection is linearly additive to wind induced deflections.
- Initial deflection is linear; i.e., the "flat plate" remains flat.
    - Initial calculations were based upon both circular arc and parabolic shape assumptions; however, the extreme sensitivity of the results to the specific shape of the curves, which were themselves assumptions, rendered them unusable.
    - Surface profiles taken of buildings have confirmed that flat plate assumptions are reasonable.
- P-delta effect is included on initial deflection but ignored on secondary deflection.
    - The mode of failure is assumed to be either crushing or overturning, not buckling.
- Wind pressure is constant over the façade.

    - This can be adjusted but was found to not have a significant effect on results.
- There is no tensile capacity in the masonry.
    - This assumption is based upon the observed deterioration of mortar joints. Inner wythes were typically fully deteriorated, the mortar only serving to transfer compressive forces. During probes the exterior brick units of the multi-wythe walls were found to have negligible bond in most instances.
- No allowance is made for the presence of tie-rods or masonry anchors.
    - These were observed to be present; however, their effectiveness could not be determined. Prior work had indicated that these could be fully deteriorated or that their connections may be ineffective. Their presence was therefore ignored for initial assessments.
- Deflection due to wind load adds to eccentricity of dead load.
- Edge loads are resisted by shear in interlocking brick at the façade vertical corners.
- The effects of masonry cracking on the wall response are ignored.
- The stabilizing effects of any stairway are ignored.
    - Where elevators are present, these will not be part of the original structure, suggesting substantial modification has been made to the building. These calculations would therefore not be applicable.

These assumptions are used for both façades and bearing walls. Additional calculation assumptions were found to be needed for bearing walls:

- Floor and roof dead and live loads are typically supported by the bearing walls via floor joists. The joists are typically supported by pockets formed in the multi-wythe walls. These bearing loads are eccentric to the wall in a direction which is beneficial in resisting outward tilting. The center of this bearing load is assumed to be ½ bearing length; hence, for a 4-inch bearing, the dead load will be centered 2-inches from the inside face of the bearing wall. This can be adjusted.
    - This was found to be a conservative assumption. As joists deflect the center of bearing will move towards the inner face. For joists supported by ledger beams, this assumption may be overly conservative.
- Friction between the joists and masonry contributes to stability (optional).
    - It is self-evident that wood beams/joists bearing on brick will resist sliding through friction. What is unknown is the coefficient of friction to be used.
- Snow is ignored, as it is a temporary and beneficial effect.
- Live load is ignored, as it is of unknown magnitude and is beneficial.
- Bearing walls act as beams supported between floors in resisting wind load.
    - This is a necessary assumption. For a typical 5-story building, three to four wythe bearing wall is typically 60 to 75 feet deep. Only nominal wind is required to destabilize the wall if it is assumed to be supported

along the front and rear edges only. As many of these structures have been in place for over 100 years, there must be other stabilizing effects. The coefficient of friction needed to enable this behavior is found to be reasonable to minimal in value.

- The deflection from beam-action from the previous assumption is negligible.

Further calculation assumptions are made where the thickness of bearing walls reduces above the first floor:

- Wall thickness reduces from the exterior.
- Presence of piers is ignored.
- Change in mass is reflected in both dead load compressive stress and negative moment induced by the eccentricity of the missing mass.

FAILURE CRITERIA

The issue of what constitutes acceptable levels of safety needs to be addressed. The author is not aware of this issue in any current building codes due to the historical nature of the buildings.

The prime focus of the calculations is overall stability of the exterior walls. Two modes of failure were therefore considered:

1. Material failure (crushing)
2. Overall stability

With regard to material failure, choice of material properties is clearly required. Use of allowable stresses, whether from current or previous codes, was adopted.

With regard to overall stability, there is no “allowable” stability or tilt of which the author is aware.

As the wall tilts, the center of force moves from the center of the wall thickness towards the outer fibers. Assuming that no tension can exist in the brick assembly (see earlier discussion), and assuming that the stress-strain curve is linear below allowable stress levels, then the form of the stress block resulting from combined vertical and outward loading will be triangular. As the outward load increases (whether due to wind or tilt), the maximum stress in the triangular block at the outer surface will increase while the width of the stress block will decrease. It was felt that limiting the size of the stress block to cover at least one brick would therefore constitute another “failure” criteria. Therefore, as the minimum wall thickness were typically 12 inches; i.e., 3 wythe, the limiting criteria would be that the stress block would be at least 1/3 wall thickness.

It is interesting to note that, in all cases, the controlling failure criteria was this “1/3 rule”. In no instance was vertical load ever sufficient to result in allowable stresses to be reached prior to the size of the stress block reducing below acceptable levels.

Clearly, there are other limiting criteria such as joist bearing failure. Such a failure could result not by an increase in load but through a reduction in bearing length which could arise from outward movement of the wall. This and other possible failure modes, were not included in the calculations. With specific reference to joist bearing failure, this was covered through direct observation of building movement combined with internal probes to determine existing conditions prior to any potential movement.

Once the failure criteria were established, an additional factor of safety was applied. This factor of safety is applied to the results of the overall calculations; i.e., tilt, and is additional to the inherent factors of safety in allowable compressive and shear stresses.

During calculations on the specific building, basic conservative assumptions are made regarding building height, width, wall thickness, material properties and floor construction. Where measured data is known, calculations will be more precise.

Figures 1 through 5 are extracted results of sample calculations following the above assumptions. Note the available flexibility in input and results. Additionally, while fixed edges are assumed for the flat plate calculation, comparative calculations are also made for the simply supported condition.

It is found that results are very sensitive to the wind pressure loading. This is not surprising, given the height and type of construction. With regard to bearing walls, the use of friction is required to show stability. This is also not surprising, as the effects of the floors framing into the bearing walls has a stabilizing influence on the building not unlike modern floor frame to multi-story columns. What is particularly interesting is both the low value of friction needed to obtain stability and the sensitivity of the results to the value of friction coefficient chosen.

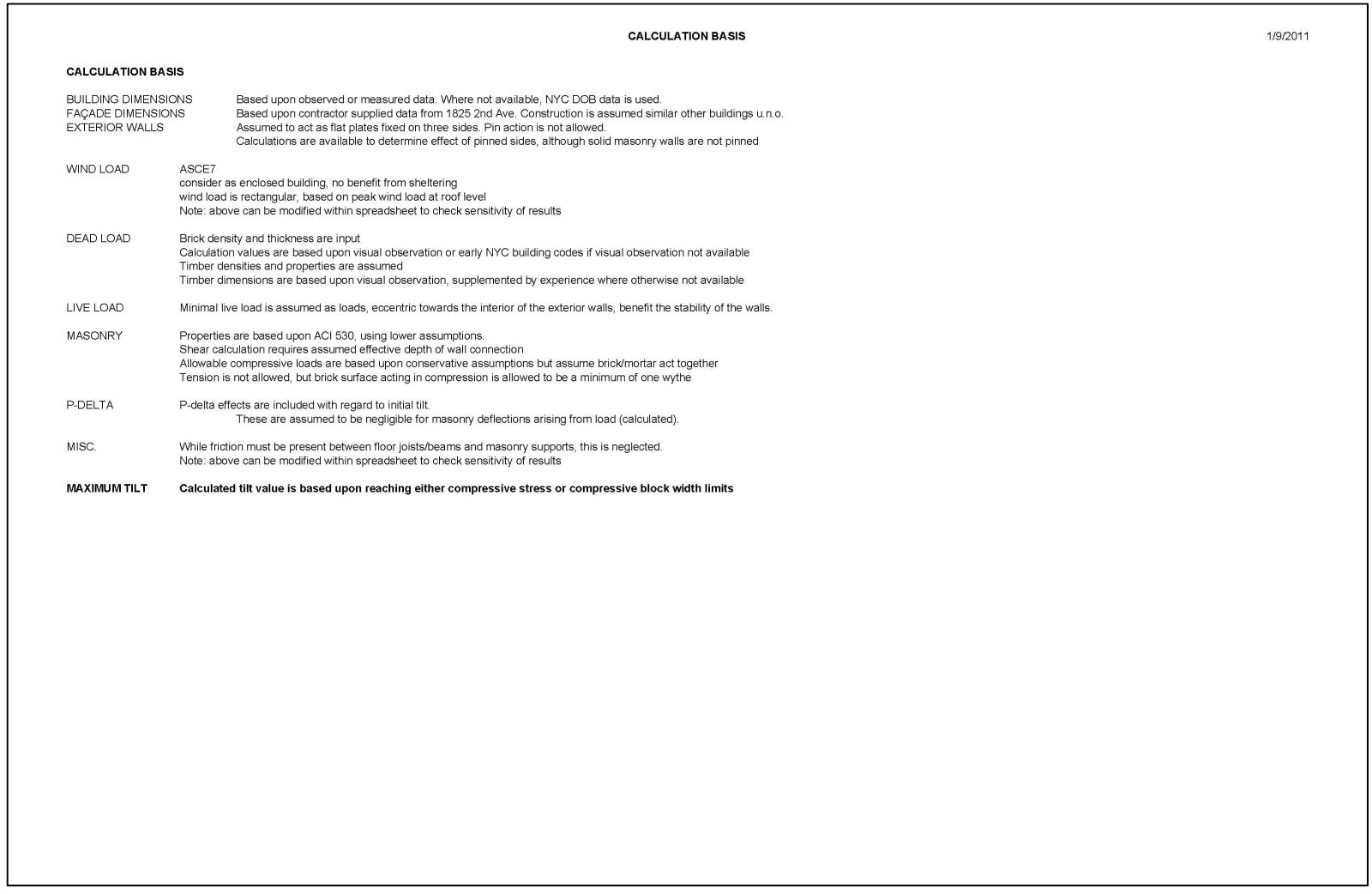
A view of the results in Figure 2 will also show that, even when only the outer wythe of the bearing wall is mobilized, in this case, less than the 1/3 of the overall thickness, the compressive stress, with all dead load included, is still below allowable values.

CONCLUSIONS

A rapid method to assess historical masonry buildings has been developed. The tool is still under development, being refined with regard to variations in building configurations, load conditions and other details. Notwithstanding, it has provided a means to quickly identify buildings requiring possible mitigation. Additional tools have been developed with regard to mitigation strategies for securing the facades against further deterioration.

ACKNOWLEDGEMENTS

The author gratefully acknowledges the support and encouragement of his colleagues during this work.

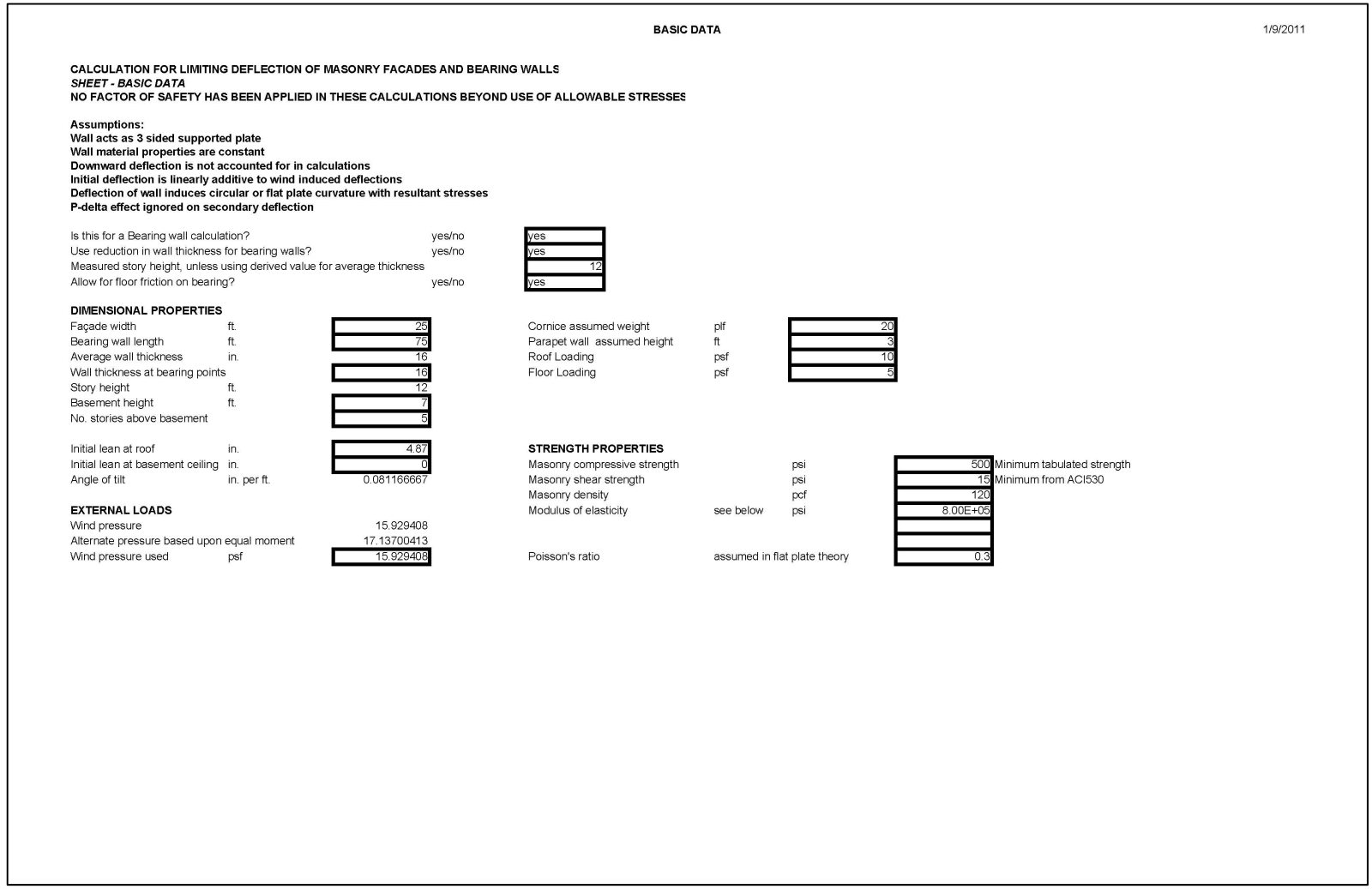


CALCULATION BASIS 1/9/2011

CALCULATION BASIS

BUILDING DIMENSIONS	Based upon observed or measured data. Where not available, NYC DOB data is used.
FAÇADE DIMENSIONS	Based upon contractor supplied data from 1825 2nd Ave. Construction is assumed similar other buildings u.n.o.
EXTERIOR WALLS	Assumed to act as flat plates fixed on three sides. Pin action is not allowed. Calculations are available to determine effect of pinned sides, although solid masonry walls are not pinned
WIND LOAD	ASCE7 consider as enclosed building, no benefit from sheltering wind load is rectangular, based on peak wind load at roof level Note: above can be modified within spreadsheet to check sensitivity of results
DEAD LOAD	Brick density and thickness are input Calculation values are based upon visual observation or early NYC building codes if visual observation not available Timber densities and properties are assumed Timber dimensions are based upon visual observation, supplemented by experience where otherwise not available
LIVE LOAD	Minimal live load is assumed as loads, eccentric towards the interior of the exterior walls, benefit the stability of the walls.
MASONRY	Properties are based upon ACI 530, using lower assumptions. Shear calculation requires assumed effective depth of wall connection Allowable compressive loads are based upon conservative assumptions but assume brick/mortar act together Tension is not allowed, but brick surface acting in compression is allowed to be a minimum of one wythe
P-DELTA	P-delta effects are included with regard to initial tilt. These are assumed to be negligible for masonry deflections arising from load (calculated).
MISC.	While friction must be present between floor joists/beams and masonry supports, this is neglected. Note: above can be modified within spreadsheet to check sensitivity of results
MAXIMUM TILT	**Calculated tilt value is based upon reaching either compressive stress or compressive block width limits**

Figure 1 - Example spreadsheet. Calculation basis.



BASIC DATA 1/9/2011

CALCULATION FOR LIMITING DEFLECTION OF MASONRY FACADES AND BEARING WALLS
SHEET - BASIC DATA
NO FACTOR OF SAFETY HAS BEEN APPLIED IN THESE CALCULATIONS BEYOND USE OF ALLOWABLE STRESSES

Assumptions:
Wall acts as 3 sided supported plate
Wall material properties are constant
Downward deflection is not accounted for in calculations
Initial deflection is linearly additive to wind induced deflections
Deflection of wall induces circular or flat plate curvature with resultant stresses
P-delta effect ignored on secondary deflection

Is this for a Bearing wall calculation?	yes/no	yes
Use reduction in wall thickness for bearing walls?	yes/no	yes
Measured story height, unless using derived value for average thickness		12
Allow for floor friction on bearing?	yes/no	yes

DIMENSIONAL PROPERTIES

Façade width	ft.	25
Bearing wall length	ft.	75
Average wall thickness	in.	16
Wall thickness at bearing points		16
Story height	ft.	12
Basement height	ft.	7
No. stories above basement		5
Initial lean at roof	in.	4.87
Initial lean at basement ceiling	in.	0
Angle of tilt	in. per ft.	0.081166667

EXTERNAL LOADS

Wind pressure		15.929408
Alternate pressure based upon equal moment		17.13700413
Wind pressure used	psf	15.929408

Cornice assumed weight	plf	20
Parapet wall assumed height	ft	3
Roof Loading	psf	10
Floor Loading	psf	5

STRENGTH PROPERTIES

Masonry compressive strength		psi	500 Minimum tabulated strength
Masonry shear strength		psi	15 Minimum from ACI530
Masonry density		pcf	120
Modulus of elasticity	see below	psi	8.00E+05
Poisson's ratio	assumed in flat plate theory		0.3

Figure 2 - Sample spreadsheet. Basic data.

BASIC DATA 1/9/2011

CALCULATION SUMMARY

STRESSES (tension [+] compression [-])

Assuming flat plate deflection		**Wall Face**	
Source		**Inside (psi)**	**Outside (psi)**
Wind	Max. stress due to uniform wind	75.55	-75.55
	Max. stress due to increasing wind	39.36	-39.36
Stretch		n/a	n/a
Lean	Max. stress due to uniform wind	50.41	-50.41
	Max. stress due to increasing wind	50.41	-50.41
Weight		-52.60	-52.60

		Wall Face	
Beam action (bearing walls only) - due to wind		**Inside (psi) (psi)**	**Outside (psi) (psi)**
Stress due to beam action between floors		6.72	-6.72
Reduction in loads if wall thickness reduces		**(psi)**	**(psi)**
Stress reduction from reduced moment arising from lean		9.13	-9.13
Stress reduction due to eccentricity of reduced mass		-22.50	22.50
Compression stress reduction due to reduced mass		10.00	10.00

Upper floor loads (bearing walls only)			
Moment	Max. stress	10.41	-10.41
Weight	Max. stress	-9.29	-9.29

Upper floor loads (facade only)			
Moment	Max. stress	0.00	0.00
Weight	Max. stress	0.00	0.00

TOTAL STRESS BEFORE REMOVING TENSILE COMPONENT
STRESSES (tension [+] compression [-])
Assuming flat plate

		Wall Face	
		Inside (psi) (psi)	**Outside (psi) (psi)**
Total	Stress (uniform wind load)	77.84	-181.61
	Stress (increasing wind load)	41.65	-145.43

TOTAL STRESSES AFTER REMOVING TENSILE COMPONENT - TENSION IS NOT ALLOWED
STRESSES (tension [+] compression [-])
Assuming flat plate

		Wall Face		**Length of Compression Block**
Source		**Inside (psi)**	**Outside (psi)**	**(in.)**
Total	uniform wind	0.00	**-415.1411468**	**3.99973778**
	increasing wind	0.00	-173.34	9.58

Note:
Length of compression block must not be negative
Length of compression block should be at least one wythe (4")
Maximum compression must not exceed maximum allowable
Factor of Safety is NOT included

Check calculation - net moment and compression from total stresses with tension must be identical to net moment and compression from total stresses with no tension

		No tension case	Tension case	
P	Total load	-830.2278646	-830.2278646	lb.
M	Total moment	-5534.924998	-5534.924998	in.-lb.

USING FACTOR OF SAFETY = 2

Initial Lean at Roof 2.435 inches
Angle of tilt 0.040583333 in. per ft.

Figure 3 - Sample spreadsheet. Results. Note the length of compression block is 1/3 the wall width.

FLAT PLATE CALCULATIONS 1/9/2011

SHEET - FLAT PLATE

Roark's Formulas for Stress and Strain
Table 26
Entry 2. Rectangular plate; three edges simply supported, one edge free

BASIC DATA

E	psi	8.00E+05	
t	in.	16	FAÇADE: ADJUSTED BASED ON AVERAGE CUBE OF t
a	ft.	60	does not include basement height
	in.	720	
b	ft.	75	
	in.	900	
a/b		0.8	

2a. Uniform over entire plate
Table of coefficients

a/b	beta	alpha	a/b			beta	alpha
0.5	0.36	0.08	0.8	FALSE	FALSE	0	0
0.667	0.45	0.106	0.8	FALSE	TRUE	0.537868	0.127636
1	0.67	0.14	0.8	FALSE	FALSE	0	0
1.5	0.77	0.16	0.8	FALSE	FALSE	0	0
2	0.79	0.165	0.8	FALSE	FALSE	0	0
4	0.8	0.167	0.8	FALSE	FALSE	0	0

Beta 0.537868
Alpha 0.127636

Maximum stress per unit applied stress 1701.848
Maximum deflection per unit applied stress 2.56E+01

2b.d. Uniformly increasing along the a side
Table of coefficients

a/b	beta	alpha	a/b			beta	alpha
0.5	0.11	0.026	0.8	FALSE	FALSE	0	0
0.667	0.16	0.033	0.8	FALSE	TRUE	0.175976	0.038333
1	0.2	0.04	0.8	FALSE	FALSE	0	0
1.5	0.28	0.05	0.8	FALSE	FALSE	0	0
2	0.32	0.058	0.8	FALSE	FALSE	0	0
2.5	0.35	0.064	0.8	FALSE	FALSE	0	0
3	0.36	0.067	0.8	FALSE	FALSE	0	0
3.5	0.37	0.069	0.8	FALSE	FALSE	0	0
4	0.37	0.07	0.8	FALSE	FALSE	0	0

Beta 0.175976
Alpha 0.038333

Maximum stress per unit applied stress 556.799 FAÇADE: AUGMENTED IF NOT FULLY EFFECTIVE
Maximum deflection per unit applied stress 7.68E+00

Roark's Formulas for Stress and Strain
Table 26
Entry 10a. Rectangular plate; three edges fixed, one edge free

BASIC DATA

E	psi	8.00E+05	
t	in.	16	FAÇADE: ADJUSTED BASED ON AVERAGE CUBE OF t
b	ft.	60	
	in.	720	
a	ft.	75	
	in.	900	
a/b		1.25	

10a. Uniform over entire plate
Table of coefficients

a/b	beta	gamma	a/b			beta	gamma
0.25	0.02	0.114	1.25	FALSE	FALSE	0	0
0.5	0.081	0.23	1.25	FALSE	FALSE	0	0
0.75	0.173	0.341	1.25	FALSE	FALSE	0	0
1	0.321	0.457	1.25	FALSE	TRUE	0.524	0.627198
1.5	0.727	0.673	1.25	FALSE	FALSE	0	0
2	1.226	0.845	1.25	FALSE	FALSE	0	0
3	2.105	1.012	1.25	FALSE	FALSE	0	0

Beta 0.524
Gamma 0.627198

Maximum stress at base per unit applied stress 1061.1
Additional deflection assumed negligible 0
Maximum shear per unit applied stress 4.52E+02

10d. Uniformly decreasing from fixed to free edge
Table of coefficients

a/b	beta	gamma	a/b			beta	gamma
0.25	0.018	0.106	1.25	FALSE	FALSE	0	0
0.5	0.064	0.195	1.25	FALSE	FALSE	0	0
0.75	0.12	0.265	1.25	FALSE	FALSE	0	0
1	0.195	0.324	1.25	FALSE	TRUE	0.273	0.390291
1.5	0.351	0.406	1.25	FALSE	FALSE	0	0
2	0.507	0.458	1.25	FALSE	FALSE	0	0
3	0.758	0.505	1.25	FALSE	FALSE	0	0

Beta 0.273
Gamma 0.390291

Maximum stress at base per unit applied stress 552.825 FAÇADE: AUGMENTED IF NOT FULLY EFFECTIVE
Additional deflection assumed negligible 0
Maximum shear per unit applied stress 2.81E+02

Figure 4 - Sample spreadsheet. Flat plate calculation.

LOADS AND DEFLECTIONS 1/9/2011

SHEET - LOAD AND DEFLECTIONS FROM WIND, WEIGHT, LEAN AND CURVATURE

COMPRESSIVE LOADS FROM DEAD WEIGHT

Cornice	assumed weight	plf	20	*From Basic Data Sheet*
Parapet wall	assumed height	ft.	3	*From Basic Data Sheet*
	weight	plf	480	assumed similar thickness and density to façade
Height		ft.	60	
Average thickness		ft.	1.33333333	
Thickness for stress calculation		ft.	1.33333333	
Density		pcf	120	
Load at base		plf	10100	
		pli	841.666667	
Average stress at base of wall		psi	52.6041667	ASSUMES UNIFORM THICKNESS ACROSS FULL WIDTH = 16 INCHES
Augmented if façade is not fully effective		psi	52.6041667	CHANGE IN STRESS ALLOWING FOR INACTIVE/ACTIVE 12 INCH SECTIONS FOR FAÇADE CALC

WIND LOAD

Net pressure	"q"	psf	10.2523247	
Load coefficient	uniform		1061.1	flat plate theory - already has reduced effectiveness of façade included
	increasing		552.825	flat plate theory - already has reduced effectiveness of façade included
Max stress	uniform	psf	10878.7417	
		psi	75.5468174	
	increasing	psf	5667.74138	
		psi	39.3593152	

MOMENT FROM LEAN

Assuming flat plate - use straight line from top of basement to roof

Deflection at roof		in.	4.87				
Deflection at basement ceiling		in.	0				
Deflection for calculation		in.	4.87				
Deflection at mid-height from top of foundation		in.	2.435				
Moment at top of foundation due to brick masonry		lb-in/ft	25811				
Additional lean from wind at mid-height CONSIDERED NEGLIGIBLE FOR FIXED EDGE CONDITION							
	uniform wind	in.	0.00E+00				
	increasing wind	in.	0.00E+00	Stress due to lean	psi	604.9453	
Total lean	uniform wind	in.	2.44E+00				
	increasing wind	in.	2.44E+00				
Moment from lean	uniform wind	lb-in/ft	2.58E+04	2.58E+04			
		lb-ft/ft	2150.9167				
	increasing wind	lb-in/ft	2.58E+04				
		lb-ft/ft	2150.9167				
Stress from lean	uniform wind	psi	50.412109				
	increasing wind	psi	50.412109				

ADDITIONAL LOAD FROM UPPER FLOOR LOADS

At ground floor	moment	lb-in/ft	-5332.1773		AVERAGE LOAD PER FOOT LENGTH
	compression	lb/ft	1782.73438		AVERAGE LOAD PER FOOT LENGTH
	stress from moment	psi	-10.414409	psi	CHANGE IN STRESS ALLOWING FOR INACTIVE/ACTIVE 12 INCH SECTIONS FOR FAÇADE CALC INCLUDED
	stress from compressi	psi	9.28507487	psi	CHANGE IN STRESS ALLOWING FOR INACTIVE/ACTIVE 12 INCH SECTIONS FOR FAÇADE CALC INCLUDED

NOTE: For façade calculations, upper floor load stresses are calculated based upon maximum thicknesses as these are beneficial to the overall stability.

Figure 5 - Sample spreadsheet. Loads and deflections.

Problems in the Repair of Historic Brick Masonry Buildings

James S. Cohen, MASCE, PE[1]

[1]Associate Principal, Arup, 155 Avenue of the Americas, New York, NY 10013; PH (212) 229-2669; FAX (212) 229-1056; email: james.cohen@arup.com

Older load bearing brick masonry structures are often in a condition of advanced deterioration and may be leaning, bowing, cracking or suffering some other form of deterioration. Problems may arise from nearby demolition, excavation or just a general lack of maintenance. Many of these may be in danger of imminent collapse. The problem of detecting problems, effecting repairs and stabilizing these buildings is presented. Case studies showing examples of these problems and possible solutions are presented.

INTRODUCTION

The aging building inventory and desire to renovate or adapt the existing building stock has led to the need to engage in the evaluation and repair of these ever-aging and deteriorating buildings. In almost all cases repairs are possible, but often the cost associated with these repairs is difficult to justify. Such difficulties may exist when repair involves partial reconstruction of the building or supporting foundations or installation of supplementary structural systems.

The following are examples of some of the issues which may be encountered during evaluation and repair.

HIDDEN DAMAGE

The original building, a masonry warehouse and manufacturing facility constructed circa 1862, consisted of four structures were at some time in their history connected and extended. At the time the author became aware of these structures a nearly total collapse of one and partial collapse of another had occurred. The collapses occurred simultaneously during an attempted renovation. A view of these buildings is given in Figure 1.

The collapse allowed a rare observation of the method of connecting the three wythes of the brick masonry wall. This can be seen in Figure 2. Although there are bonding courses, no mortar could be discerned connecting the individual wythes together.

In the rear significant vegetative growth against the buildings could easily be observed, as shown in Figure 3. Of greater significance was the growth between the wythes of the brick walls resulting in complete separation of the wythes and almost total loss of structural integrity. Figure 4 shows plant growth coming out from between the wythes at a joint in one of the walls. The growth has resulted in movement of the wall and separation of the brick.



Figure 1 - View of building frontage. Two facades are collapsed, the remaining two adjacent buildings remain intact.

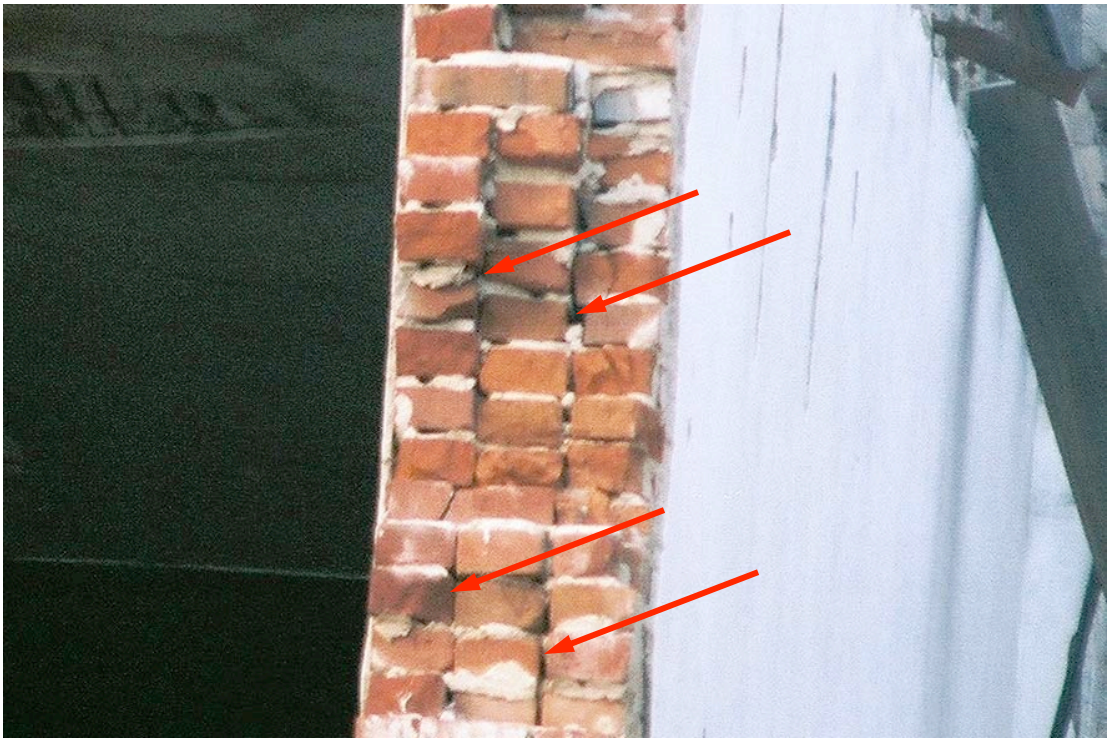


Figure 2 - Lack of mortar and separation of wythes would have been hidden.

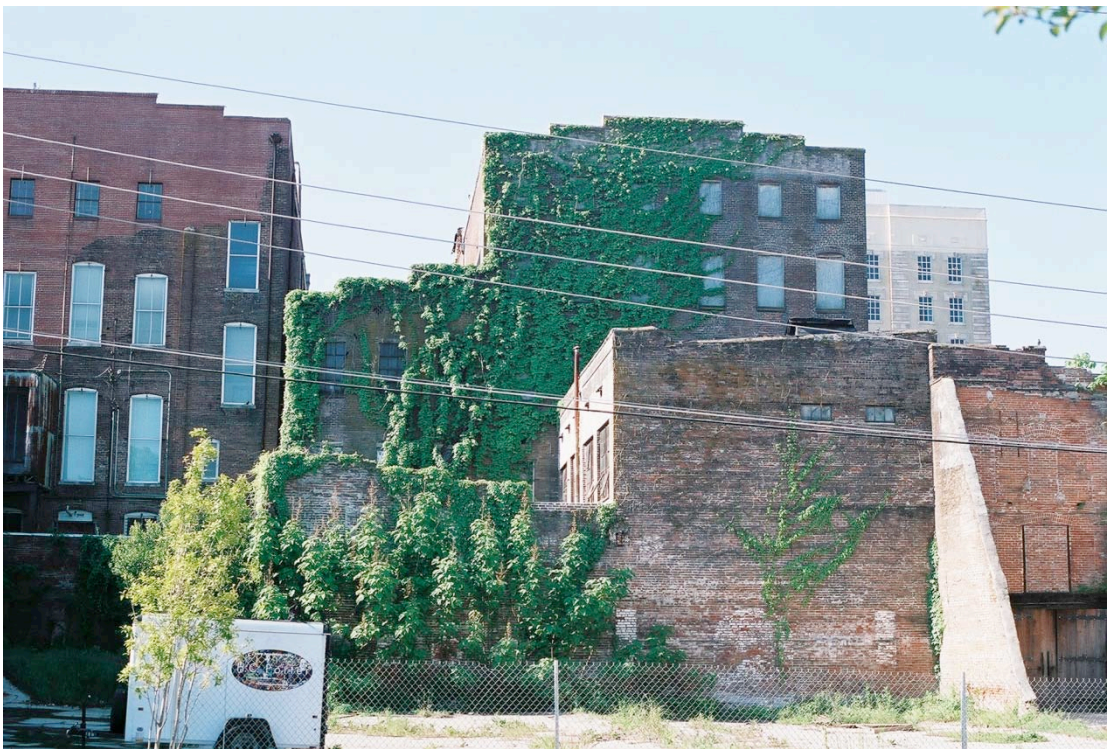


Figure 3 - Significant vegetation against the buildings. The rear of all four structures can be observed. The tree-like plant to the right has roots which commence within the brick wall and cannot be seen from the exterior.

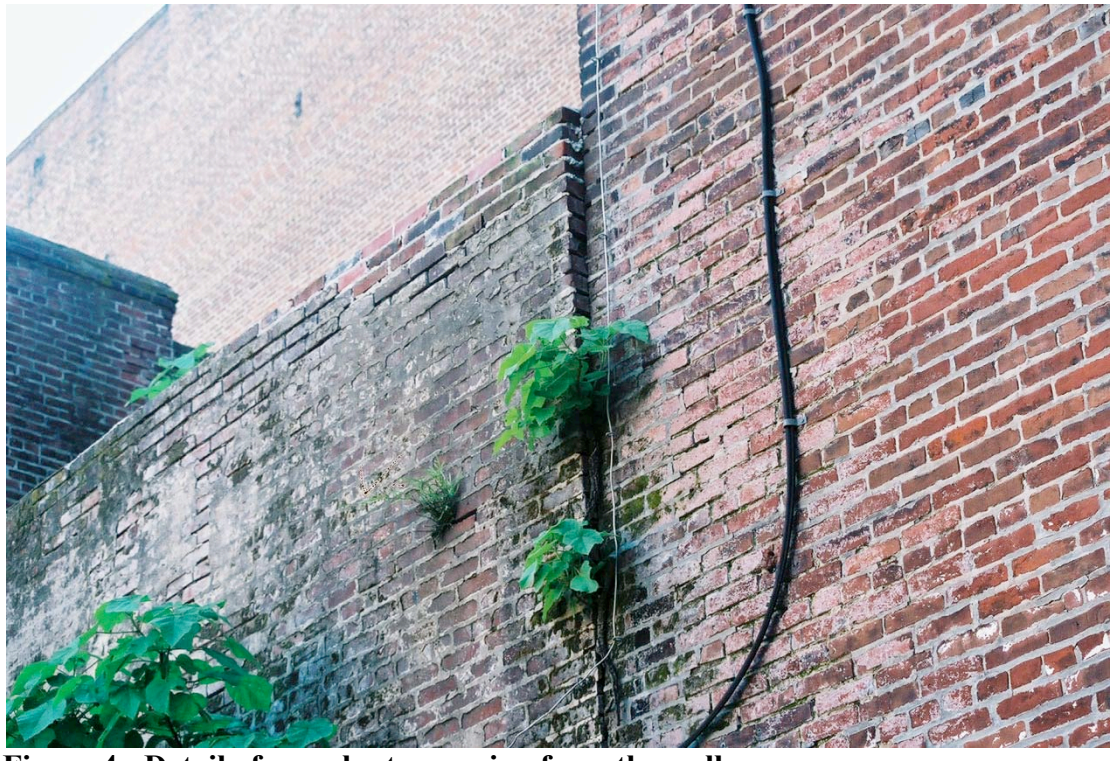


Figure 4 - Detail of one plant emerging from the wall.

In addition to these issues was significant evidence of powder post beetle attack to interior timber joists. Additionally, there was evidence of many prior collapses with missing floors and walls towards the rear of the building.

At the time of the collapse attempts were being made to repoint the masonry, but this was a surface treatment, as knowledge of the internal damage was unknown. Notwithstanding, the precipitating cause of the collapse was overloading of the roof due to ponding water, likely exacerbated by rotted joists, which were also visible at the upper levels, particularly in the vicinity of the collapse.

It is unlikely that the condition of the building at the time of collapse would have allowed for significant reclamation of the structure with the exception of the street facing Civil War era facades.

BUILDING MOVEMENT

Older buildings were generally built upon shallow foundations. Basements were generally located at foundation level. Where these are not located on firm ground, settlement over the years will occur. This is often aggravated by adjacent construction, disturbing the ground, particularly when excavation goes below the existing building's foundation line.

Buildings thus affected may lean, or tilt, typically in the direction of the adjacent construction.

Figure 5 shows underpinning which was undertaken to a building after damage had already occurred. Excavation below the level of the existing had taken place and soil had sloughed out from beneath the building. The building consequently cracked across its width and tilted towards the excavation. Underpinning was then installed to prevent further damage. In the figure the building is visible at the top, the original foundation in the center and the new underpinning beneath.

Careful observation will also show a shrinkage crack developing between the new underpinning and the original foundation wall. While drypack was applied, this was done after only a short period of time had elapsed from pouring the underpinning. Adjacent panels had already been placed and hardened. As a result, the more recent panel shrinks differentially from those adjacent. Depending upon the pattern of pours and ages of the various panels, damage to the original building will continue to occur.

Lean, or tilt, of the overall structure may occur without any evidence of adjacent excavation. Figure 7 is an illustration of extreme tilt of a building with no evident cause, other than age. The presence of the newer building provides a reference to the extent of movement experienced by the older building after completion of the new structure. This older building did, in fact, suffer a partial collapse shortly after this photograph was taken.



Figure 5 - New underpinning beneath original foundation of a building damaged by the adjacent construction. Shrinkage of the underpinning is likely to result in continued damage.

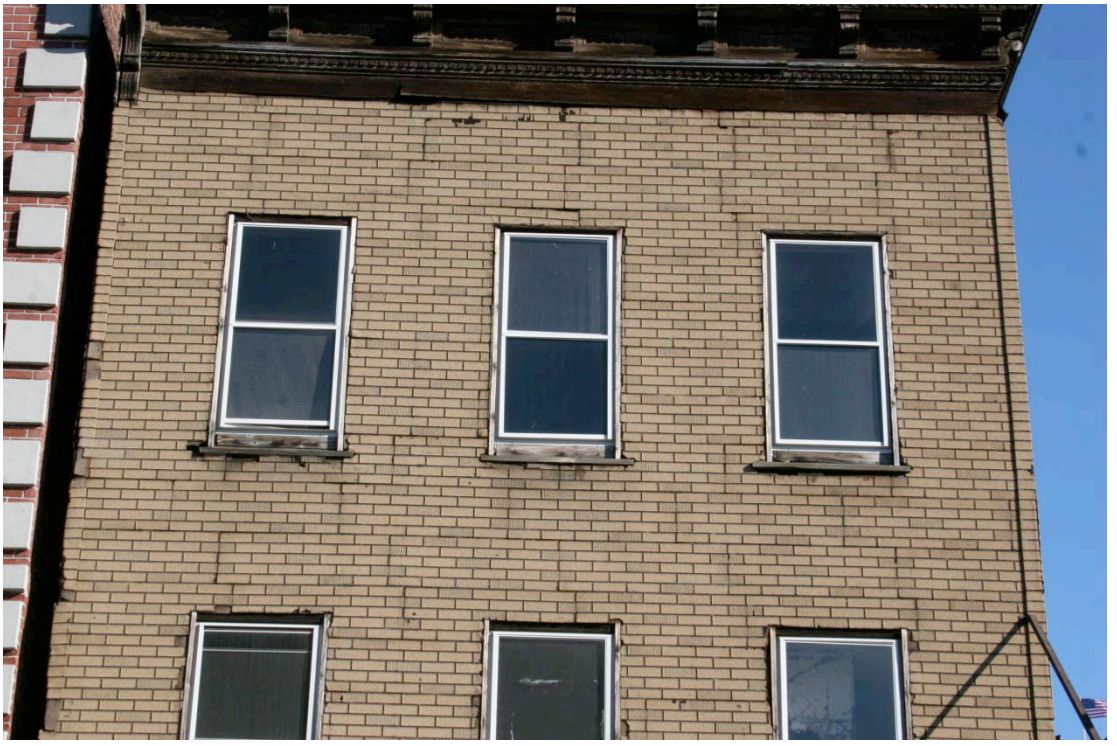


Figure 6 - Approximately 8 inches of tilt away from the newer building. The structure is also racking. A partial collapse of the side wall occurred shortly after this photograph was taken.

Frequently at issue in the repair of such structures is the desire to preserve the building for its historical value. This may hamper stabilization resulting in collapse as with the first example.

The potential for tilting is often dealt with by installing tie plates to the exterior of the building and connecting within. The intent is to tie the two outer walls together, or otherwise anchor one exterior point to an immovable point within the interior, such as a foundation or cross-wall.

Methods may involve simple plates on the exterior of a building at regular intervals, typically at floor levels. These can be unsightly and detract from the building. Sometimes decorative elements are substituted as a means to provide an aesthetically pleasing solution to the problem of attaching an external structural element to an older structure. Cast iron stars have sometimes been used for this purpose, as have other shapes.

The first problem encountered with regard to installation of tie plates is determining to what building component it is to be anchored. In addition to forces generated by any tilt, wind and other lateral loads may need to be transferred. Often this is the opposing wall, particularly for the narrower older buildings. Unfortunately, these opposing walls may not be accessible from the exterior, or the attachment may encroach on the adjacent property. Attempting to fix the tie-rod or cable to a blind side through anchors or other devices should first involve load tests to demonstrate the ability of the connection, and connecting part, to support the requisite loads.

Another issue is the pre-tension that needs to be present in the tie-rod. If cable is used, any slack present needs to be removed, as the ability of a cable to stretch may be beyond the ability of the supported wall to move without distress. This will also require regular inspection and retightening as the cable will stretch over time.

Rods need to be made snug; however, “snug” is a loose term that will require definition. The ability of the masonry to support the pretension in the rod needs to be determined. The sensitivity of the pre-tension to seemingly minor rotation of connecting threaded parts also needs determination. It is a simple matter to determine how much rotation of a nut will result in increased tension of a rod, but that is after all is first made “snug” and slack is removed.

With regard to substituting stars or other seemingly structural adornment as the anchor piece for a simple plate is also “proving” the ability of the anchor to be able to support the load. The masonry surface is unlikely to be flat and the anchor may similarly not be flat. A problem with these alternatives was recently demonstrated by a contractor’s proposal to use cast iron stars as anchors on a series of listed buildings. The loads involved were relatively low, particularly as the masonry was assumed to have only minor shear strength with which to resist the anchor load exerted by the plate on the face of the building. Notwithstanding, the decision was made to test a random sample of the stars to determine the likely breaking strength and hence factor

of safety in the completed installation. The test setup is shown in Figure 7. As the stars were uneven across their back, bearing, face, the test was arranged to see what load in bending the star arms might be able to resist.

The stars broke at widely varying loads, some as low as a few hundred pounds. Macroscopic examination of the fracture surface of these low breaks showed numerous inclusions and voids within the casting. Figure 8 shows one star following fracture. Most fractures had an evident initiation point for the failure. Maximum loads could be correlated to the size and location of these internal defects. In one instance the defect consisted of two pre-existing cracks, as was evident by the discoloration of these areas.

OCCUPANCY

It often happens that buildings may be occupied when repairs, strengthening or other mitigation strategy is being planned. This results in a desire to minimize the effects of the work and evaluation on the residents. Where the optimal solution may be to install ties across the building, the disruption to internal finishes and the need to temporarily relocate the occupants may be prohibitive.



Figure 7 - Test arrangement for cast iron star anchor

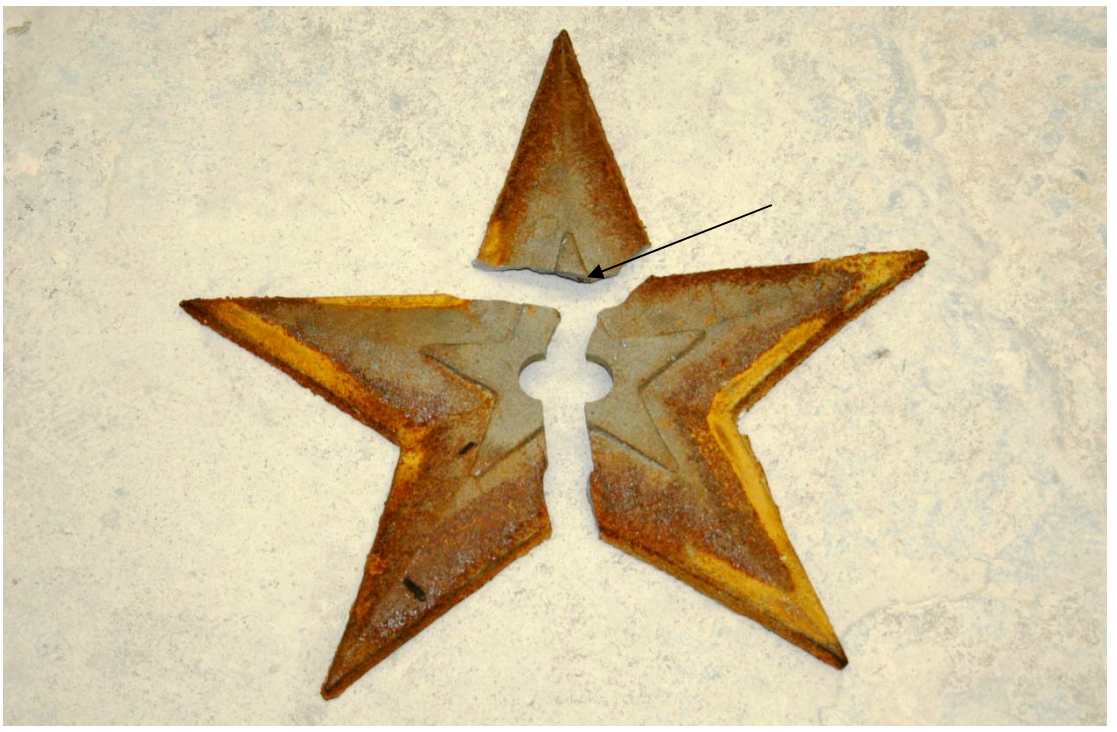


Figure 8 - Breakage of an anchor. Arrow points to defect in the casting.

While it is difficult to replace invasive inspection techniques to determine the condition of a structure, sampling methods and careful selection of probe locations may provide sufficient confidence in the results of the evaluation. Exterior observations can often lead to a more judicious selection of probe locations by identifying those areas or zones which have had seen prior repairs or alterations, or, alternatively, show the greatest tendency to water penetration or other deterioration.

Innovative solutions may be required to install the ties. As previously indicated, tie-rods or cables are often employed as a means of connecting opposing walls. These have the advantage of being located within a ceiling plenum or other hidden unused space. However, they often also typically require access to the ceiling space for installation. Alternative methods of tie the walls together may involve using the existing building elements as tie-rods. Typically floor joists are utilized for the purpose. Invasive procedures may then be limited to relatively small ceiling openings sufficient to effect a bolted connection from the externally applied tie-plate to the timber floor joist.

This latter solution can be used where the floor joist is continuous between opposing walls or are adequately tied together at interior walls to enable the forces to be transferred. Consequently, this approach is only possible for bearing walls, which also tend to have a closer spacing than the façades which run parallel to the floor joists.

Connecting to the floor joists from a façade is unlikely to have any true stabilizing effect on the façade as the bending stiffness of a floor joist in its weak is likely to be significantly lower than the stiffness of the masonry façade and the deflection available to the joist without distress will be much smaller than that available to the façade. Hence, to use the floor joists as a means of stabilizing the façade it becomes necessary to either mobilize the floor system as a diaphragm, create a strong, stiff element from the joists.

The former solution, while possible, assumes that the floor system, consisting of the sub-floor and any overlay, is sufficiently fixed to the floor joists to achieve a sufficient diaphragm for distribution of the façade tie-back loads. As the tie-rod load will necessarily be applied to the joists some vertical distance away from the sub-floor connection, it then also becomes necessary to connect the tie-rods to sufficient parallel joists in succession to avoid the possibility of rotating the joists and breaking their connection to the flooring. This may involve significant disruption to the existing ceiling finishes and, consequently, the residents.

An alternative approach is to create a truss from the parallel joists, thus converting their action from weak bending to purely tensile or compressive loads parallel to the grain of the timber. This will involve the addition of truss diagonals within the ceiling which, while disruptive, may only require removal of sufficient ceiling finishes to expose two or three joists.

An additional recent possibility for mobilizing multiple floor joists, using the floor system as a diaphragm, is the Cintec anchor. An anchor, surrounded by a fabric sock, is installed through pre-drilled oversized holes. Cementitious or other grout is injected through the middle of the anchor under low pressure. It passes through a series of grout flood holes into the fabric sock, inflating the entire assembly like a balloon. The advantage is the ability to install the anchoring system without removal of the ceiling finishes, thereby minimizing impact to the residents.

DEFINING THE STRUCTURAL SYSTEM

Older masonry buildings tended to be built to a prescriptive code, if any, such as the 1901 Building Code of the City of New York, an extract of which is presented in Figure 9.

These prescriptive codes provide a good deal of information on the potential construction of the existing building but may not be accurate on any specific structure. Alterations, repairs and strengthening strategies must be designed specific to the structure. Location of piers, details of cast iron assemblages and condition of materials can all vary.

Figure 10 below shows the results of a probe through a storefront. While it was known that there was a horizontal cast iron piece spanning between cast iron columns, it was not known that this consisted of discontinuous plates over which masonry arches were effectively spanning between columns. The system, which

appears to have been intended to use the cast iron in tension and the brick in compression, presumably also relied upon the bond between the infill masonry and the cast iron to complete the structural system.



Figure 9 - Exposed masonry arch over cast iron plate spanning between cast iron columns.

In general, sources of information contemporary to the historic building can assist in determining what structural system was envisaged by the designer or builder even if, in today's environment, such a system would not normally be implemented. These contemporaneous references can also provide information regarding construction methods, allowable loads, stresses and other physical properties of the materials in use at that time. This information is invaluable to assessing and repairing the older building.

CONCLUSIONS

Older load bearing brick masonry structures are often in a condition of advanced deterioration. Problems can arise from nearby demolition, excavation or just a general lack of maintenance. Many of these may be in danger of imminent collapse. While such structures may often be difficult to justify repairing, sufficient planning and investigation and awareness of the limitations being imposed on any investigation or repair may still lead to a successful outcome.

This paper can only present a small sample of the many issues facing repair and restoration of older buildings. It is hoped that the information and examples presented will help to inspire others.

Sec. 40.—*Walls of Unfinished Buildings.* Any building, the erection of which was commenced in accordance with specifications and plans submitted to and approved by the Department of Buildings prior to the passage of this Code, if properly constructed, and in safe condition, may be completed, or built upon in accordance with the requirements of law, as to thickness of walls, in force at the time when such specification and plans were approved.

Sec. 41.—*Walls Tied, Anchored and Braced.* In no case shall any wall or walls of any building be carried up more than two stories in advance of any other wall, except by permission of the Commissioner of Buildings having jurisdiction, but this prohibition shall not include the inclosure walls for skeleton buildings. The front, rear, side and party walls shall be properly bonded together, or anchored to each other every six feet in their height by wrought-iron tie anchors, not less than one and a half inches by three-eighths of an inch in size, and not less than twenty-four inches in length. The side anchors shall be built into the side or party walls not less than sixteen inches, and into the front and rear walls, so as to secure the front and rear walls to the side, or party walls, when not built and bonded together. All exterior piers shall be anchored to the beams or girders on the level of each tier. The walls and beams of every building, during the erection or alteration thereof, shall be strongly braced from the beams of each story, and when required, shall also be braced from the outside, until the building is inclosed. The roof tier of wood beams shall be safely anchored, with plank or joist, to the beams of the story below until the building is inclosed.

Digitized by Google

Figure 10 - Extract from the 1901 Building Code of the City of New York

Reliability Analysis of Masonry Members under Compression

S. Kazemi[1], M. Mahoutian[2], H. Moosavi[2], and Y. Korany[3]

[1] Ph.D. Student and Research Assistant, Department of Civil and Environmental Engineering, University of Alberta, Edmonton, Alberta, Canada, T6G 2W2

[2] M.Sc. Student and Research Assistant, Department of Civil and Environmental Engineering, University of Alberta, Edmonton, Alberta, Canada, T6G 2W2

[3] MCAA Chair in Masonry Systems and Associate Professor of Structural Engineering, Department of Civil and Environmental Engineering, University of Alberta, Edmonton, Alberta, Canada, T6G 2W2, email: *yasser.korany@ualberta.ca*

ABSTRACT

A structural reliability analysis was performed on concrete masonry under concentric axial compression to examine the reliability levels for masonry buildings designed to the current Canadian masonry standard CSA S304.1-04 (2004). The first order second moment method was used to carry out the analysis. Prism compressive strength for hollow and grouted concrete masonry was used as the model. Over 300 specified masonry compressive strength values were computed using test results available from North American investigations, mostly Canadian. The material and geometry statistical data needed were obtained from several Canadian concrete masonry producers. Based on the findings of this investigation, it is recommended that unreinforced masonry be assigned a material resistance factor (ϕ_m) different from reinforced masonry. For masonry members under compression, it is proposed that the current ϕ_m be increased from 0.6 to 0.65 for reinforced masonry and decreased from 0.6 to 0.5 for unreinforced masonry. The proposed factors correspond to reliability indices of 3.5 and 3.8 for reinforced and unreinforced masonry, respectively.

INTRODUCTION

The reliability of a structure is defined as the probability that it will not fail during a specified period of time under a given state of loading. The primary purpose of structural reliability is to control and manage the risk of failure to acceptable levels. In the late 1970's and early 1980's in Canada, Turkstra et al. (Turkstra and Daly 1978; Turkstra and Ojinaga 1980; and Turkstra et al. 1982) performed a series of reliability based analyses on structural masonry intended to help change the Canadian masonry design standard from the working stress method (the design approach of the time) to the limit states design approach. Test data for brick masonry walls under axial compression and out-of-plane bending were used. Turkstra proposed a value of 0.4 for the masonry material resistance factor (ϕ_m) in the early drafts of the 1994 Canadian masonry design standard (CSA S304.1-94). However, the proposed value was not adopted.

In the 1992 Drysdale's calculation published recently as an appendix to Laird et al. (2005), masonry prism strength was used as the model for a reliability analysis of masonry under compression. Compressive strength test data for two-unit high prisms were used. Recognizing that strength measured from testing two-unit high prisms is usually higher than the wall/true strength, a member variable was introduced to the reliability expression. The member variable and its coefficient of variation were judged to be 0.85 and 0.05; respectively. A masonry material resistance factor of 0.55 was proposed and adopted in the earlier edition of the Canadian masonry design standard (CSA S304.1-94). The resistance factor was later increased from 0.55 to 0.60 in the current Canadian masonry design standard (CSA S304.1-04) based on the same analysis.

The effect of workmanship on the reliability analysis of structural masonry is well recognized (Turkstra and Ojinaga, 1980; Turkstra et al., 1982; Drake et al., 2004 and Drysdale, 1992 in appendix to Laird et al., 2005). Some of the main sources of workmanship uncertainty are the thickness and filling of the mortar joints, wall plumpness, and compliance of geometry with design requirements, grouting procedures, and the level of quality control during construction. Turkstra et al. (1982) reported that the workmanship factor ranged from 1.0 for inspected masonry construction to 0.7 for uninspected masonry with coefficients of variation of 0.1 and 0.2; respectively. Turkstra and Ojinaga (1980) suggested an average workmanship factor of 0.8 with 0.15 coefficient of variation. Drysdale (1992, appendix to Laird et al., 2005) used a workmanship factor of 0.8 with a coefficient of variation of 0.2.

This paper reports on a structural reliability analysis that was performed on concrete masonry under concentric axial compression. The objective was to examine the reliability levels in the current Canadian masonry design standard (CSA S304.1-04). In this analysis, prism compressive strength for hollow and grouted concrete masonry was used as the model. Test data for the compressive strength of masonry prisms were gathered from available North American literature, mostly Canadian investigations. The material and geometrical statistical data needed for the reliability analysis were obtained from several Canadian concrete masonry producers.

TARGET RELIABILITY

The reliability of a structure is defined as the probability that it will not fail during a specified period of time for a given limit state. Structural reliability analysis is based on defining a level of safety or a reliability index β as shown in Figure 1. If the safety margin Y is the difference between the resistance R and the demand/load U, then β can be expressed in terms of the number of standard deviations, σ_Y, between $\bar{Y}$, the mean value of Y, and $Y = 0$.

$$\beta = \frac{\overline{Y}}{\sigma_Y} \qquad \text{Eq.1}$$

Structural reliability is sensitive to the value of the reliability index which is a function of a range of factors including the type of failure, estimated cost of failure

and existing levels of safety (Lawrence and Stewart, 2009). The target reliability index has to strike a balance between minimizing the probability of failure and construction cost. Higher reliability indices result in lower material resistance factors and hence higher construction cost.

A target reliability index for limit states design may be based on calibration to previous design codes, comparison to other structural materials, or acceptable risk compared to other human activities. MacGregor (1976) compared the risk of death for different activities to the risk of failure of structures. It was concluded that the probability of failure of a building should not be less than 10^{-5} per year. This corresponds to a probability of failure of 3×10^{-4} and $\beta = 3.45$ during the 30 year life of a typical building in Canada. Table A5 in the Canadian CSA S408 (1981−R2006) suggests that a value of $\beta = 4.0$ should be used for a normal importance building with a brittle type of failure. Consequently, a value of $\beta = 3.5$ is used for ductile structures with normal consequences of failure and a value of $\beta = 4.0$ is used for brittle structures with severe consequences of failure. Stewart and Lawrence (2006) proposed a reliability index value of 3.8 for structural unreinforced masonry in accordance with the Australian Standard AS 5104 (2005).

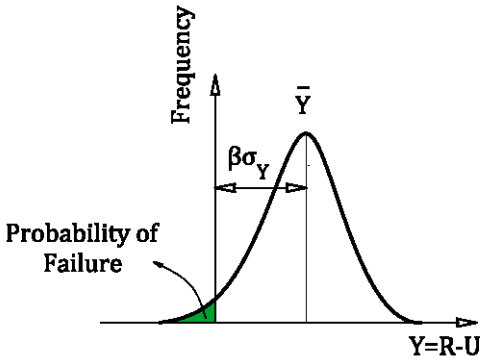


Figure. 1 Frequency distribution of the safety margin.

STRUCTURAL RELIABILITY METHODOLOGY

The first order second moment (FOSM) method has been used in structural reliability analysis since the 1970's. It is called first order in the sense that a linear function for the safety margin is used ($Y = R - U$) and second moment because it considers a special case of reliability estimation in which each variable is represented only by its mean, $\bar{Y}$, and standard deviation, σ_Y, (Melchers, 1999). Based on the FOSM method, two main approaches could be used to perform a structural reliability analysis: the separation function approach and the limit state function approach. The former was used in the current analysis.

In the separation function approach, a reasonable probability of failure is selected compared to an acceptable level of risk in other human activities. Having selected β and found the mean and coefficient of variation for resistance and load, a proper combination of the material resistance factor (ϕ) and load factor (λ) is determined.

The probability of failure, P_f, is expressed as:

$$P_f = P[\ln\left(\frac{R}{U}\right) < 0] \quad \text{Eq.2}$$

From the definition of β (Eq.1), one can write:

$$\overline{\ln(R/U)} \geq \beta\sqrt{\sigma^2_{\ln(R)} + \sigma^2_{\ln(U)}} \quad \text{Eq.3}$$

For a log-normal distribution, the coefficient of variation can be expressed as:

$$V_x^2 \cong \sigma^2_{\ln(x)} \quad \text{Eq.4}$$

Substituting in Eq.3, one can write:

$$\overline{\ln(R/U)} \geq \beta\sqrt{V_R^2 + V_U^2} \quad \text{Eq.5}$$

Where, V_R and V_U are the coefficients of variation for resistance and load, respectively.

$$\sqrt{A^2 + B^2} \cong \alpha A + \alpha B \quad \text{Eq.6}$$

Equation 6 was proposed (Lind, 1971) to linearize the right hand side of Eq.5 using a separation function α that enables treating resistance separate from load. The value of α ranges from 0.707 to 1.0 and depends mainly on the level of the reliability index and the live-to-dead load ratio. A slight change in the separation factor ($\alpha = 0.75 \pm 0.06$) was noted for a wide range of A/B ratios. A separation factor of 0.75 was used in the 1992 calculation by Drysdale (appendix to Laird et al., 2005) which is the basis for the masonry material resistance factor in both the 1994 and 2004 editions of the Canadian masonry standard (CSA S304.1-04). A value of 0.75 for the separation factor was used in the current study.

Using the separation function introduced in Eq.6, the reliability expresion (Eq.5) can be simplified as follows:

$$\bar{R}e^{-\beta\alpha V_R} \geq \bar{U}e^{\alpha\beta V_U} \quad \text{Eq.7}$$

The reliability expression in a resistance factor (ϕ) and load factor (λ) format is:

$$\phi R_n \geq \lambda U \quad \text{Eq.8}$$

Comparing Eqs. 7 and 8, ϕ can be expresed as:

$$\phi = \frac{\bar{R}}{R_n}e^{-\beta\alpha V_R} \quad \text{Eq.9}$$

Where, $\bar{R}$ and R_n are the average and nominal member strength, respectively.

Because of the interdependence of the resistance and the load factors, a correction factor less than 1.0 is applied when the target β is greater than 3.0 and greater than 1.0 when the target β is less than 3.0. Since the target β for structural masonry ranges from 3.5 to 4.0, Eq.9 is adjusted as follows:

$$\phi = C\frac{\bar{R}}{R_n}e^{-\beta\alpha V_R} \quad \text{Eq.10}$$

Where, C is a correction factor that can be derived using the procedure described by Fisher et al. (1978).

$$\mathrm{C} = \frac{1.086(1.0933 + 1.3936\ \mathrm{L/D})}{\mathrm{e}^{0.0275\,\beta}[1 + 0.03111\,\beta + (1 + 0.1313\,\beta)\mathrm{L/D}]} \quad \text{Eq.11}$$

Where, L/D is the live-to-dead load ratio.

STRUCTURAL RELIABILITY ANALYSIS

In this study, Eq.10 was used to examine the reliability levels for reinforced and unreinforced masonry designed according to the Canadian masonry standard CSA S304.1-04 under concentric axial compression. Hollow and fully grouted masonry prisms were used to represent unreinforced and reinforced masonry, respectively. Two statistical parameters need to be defined foe Eq.10, that is the mean and coefficient of variation of the resistance ratio ($\bar{R}/R_n$). These parameters were derived using a modified version of Eq.12 which was proposed by Galambos and Ravindra (1977):

$$\frac{\bar{R}}{R_n} = \frac{\bar{G}}{G_n} \times \frac{\bar{M}}{M_n} \times P \quad \text{Eq.12}$$

Where, $\bar{G}$, G_n, $\bar{M}$, M_n and P are the average geometrical property, nominal geometrical property, average material strength, nominal material strength, and professional ratio; respectively.

The compressive strength of a prism is not linearly related to the compressive strength of the unit. The British masonry code (BS 5628, 2005) and the Australian masonry standard (AS 3700, 2001) offer a relationship in which the characteristic masonry compressive strength is related to the square root of the unit strength. This implies that the square root of $\bar{M}/M_n$ should be used for computing the material statistical properties.

The effect of workmanship on the reliability of masonry structures is directly related to construction quality control. The British masonry code (BS 5628, 2005) recognizes two categories of quality control for unreinforced masonry: normal and special. Masonry partial safety factors ($\gamma_m = 1/\phi_m$) for normal inspection are higher than for special construction inspection. The effect of workmanship is more pronounced in unreinforced masonry than in reinforced masonry construction. Even with special inspection, the British code assigns lower partial safety factors for reinforced masonry

than for inspected unreinforced masonry. Based on the work by Turkstra et al. (1982), the workmanship factor *K* was taken in this analysis as 0.8 for unreinforced masonry and 0.9 for reinforced masonry with a coefficient of variation of 0.15 for both.

Considering the effect of workmanship and that prism strength is related to the square root of the unit strength, the statistical parameters for masonry resistance under compression are expressed as:

$$\frac{\bar{R}}{R_n} = \frac{\bar{G}}{G_n} \times \sqrt{\frac{\bar{M}}{M_n}} \times P \times K \qquad \text{Eq.13}$$

$$V_R = \sqrt{{V_G}^2 + \frac{1}{4}{V_M}^2 + {V_P}^2 + {V_K}^2} \qquad \text{Eq.14}$$

Where, V_G, V_M, V_P, and V_K are the coefficients of variation for geometry, material, professional, and workmanship factors; respectively. In Eq.14, the coefficient of variation of the material factor is multiplied by ¼ to account for the square root influence of the factor.

Hollow and grouted masonry prisms were used to represent masonry members under concentric axial compression. Instead of introducing a member variable based solely on judgement, prism compressive strength data were adjusted for the height-to-thickness ratio according to Table D1 of Annex D in the Canadian masonry design standard CSA S304.1-04. The adjusted values are believed to be representative of the compressive strength of masonry members.

Over 300 specified masonry compressive strength values were computed using test results for hollow and grouted concrete prisms from 31 journal articles, theses, and dissertations reporting research that has been carried out in North America, mostly in Canada. Table 4 of CSA S304.1-04 provides compressive strength values for 10-40 MPa concrete block units. A minimum grout compressive strength of 10 MPa is required for grouted masonry as per CSA A179 (2004). Experimental data points for masonry units having compressive strength lower than 10 MPa or higher than 40 MPa and for grout having compressive strength lower than 10 MPa were excluded.

The professional factor was determined by comparing the specified masonry compressive strength, computed from test data according to Annex C of CSA S304.1-04, to the nominal strength based on unit strength and mortar type as per Table 4 of CSA S304.1-04. It is well established that the professional factor computed from test results include variations of the test procedures and specimen variability in addition to the model inaccuracy (Stewart and Lawrence, 2006 and Ellingwood , 1981). Therefore, the variability in the professional factor could be expressed as:

$$V_P = \sqrt{{V_{model}}^2 - {V_{test}}^2 - {V_{spec}}^2} \qquad \text{Eq.15}$$

Where, V_P is the coefficient of variation (COV) of the professional factor, V_{model} is the COV of the model obtained from the ratio of measured to predicted strength, V_{test} represents the variation in the measured loads due to inaccuracies in the test measurements and/or the definitions of failure, and V_{spec} represents several uncertainties regarding the differences between the measured and actual parameters of the test specimens. Ellingwood (1981) suggested a value of $V_{test} = 0.02$ and $V_{spec} = 0.04$. These values are used in this study to compute the COV for the professional factor. The statistical parameters for the professional factor are summarized in Table 1.

Table 1. Statistical parameters for the professional factor.

Masonry Construction	Mean	V_{model}	V_P
Hollow	1.24	0.22	0.215
Grouted	1.34	0.22	0.215

To determine the material and geometry factors, 500 data points were collocated from five Canadian concrete block producers. The compressive strength of the blocks varied from 13 MPa to 34 MPa. The concrete block units were 390 mm in length and 190 mm in height. The block width varied from 90 mm to 240 mm in 50 mm intervals. The material ratio was obtained as the ratio of the measured compressive strength of the concrete block to its nominal compressive strength. Mortar was not considered in the analysis as part of the material ratio. To obtain the geometry ratio, the ratio between the actual and nominal cross-sectional areas was calculated. The statistical parameters for the material and geometry factors are given in Table 2.

Table 2. Statistical parameters for the material and geometry factors.

Property	Mean	Coefficient of Variation
Material (Unit Compressive Strength)	1.41	0.170
Geometry (Unit Cross-sectional Area)	1.00	0.002

Using the parameters of Tables 1 and 2, the mean and coefficient of variation for the resistance ratio ($\bar{R}/R_n$) were computed from Equations 13 and 14 for hollow and grouted masonry construction. The values are listed in Table 3.

Table 3. Statistical parameters for the resistance ratio ($\bar{R}/R_n$).

Masonry Construction	Mean	Coefficient of Variation
Hollow	1.178	0.276
Grouted	1.432	0.276

RESULTS AND DISCUSSION

Using Eq.10 and the statistical parameters in Table 3, relationships between masonry material resistance factor (ϕ_m) and the reliability index (β) were constructed and are plotted in Figure 2 for live-to-dead load ratios from 0.5 to 3.0. As can be seen from Figure 2, the relationship between ϕ_m and β is not sensitive to the live-to-dead load ratio (very close lines forming a bundle). This is consistent with the findings of other researchers (e.g. Bartlett, 2007 and Allen, 1975). The lowest values for the resistance factors occurred at a live-to-dead load ratio of three. As expected, the resistance factor decreased with increasing the reliability index. Increasing β from 3.5 to 4.0 resulted in a decrease in ϕ_m from 0.54 to 0.46 for hollow masonry and from 0.66 to 0.56 for grouted masonry. The higher ϕ_m values for grouted masonry compared to hollow masonry are attributed to the higher resistance ratio.

The target reliability index for masonry structures in the current Canadian masonry design standard CSA S304.1-04 is 3.5. While a reliability index value of 3.5 can be justified for reinforced masonry that exhibits ductile response, it is certainly not suitable for unreinforced masonry which is brittle is nature. A target reliability index of 3.8 is more appropriate for unreinforced masonry and is in conformance with the guidelines of the Canadian standard CSA S408 (1981–R2006). In Figure 2, if hollow masonry is considered representative of typical unreinforced masonry construction, the proposed reliability index of 3.8 corresponds to a resistance factor of 0.5. Considering grouted masonry to be representative of reinforced masonry construction and using a target reliability index of 3.5, the corresponding resistance factor for reinforced masonry is 0.66. Using different material resistance factors for unreinforced and reinforced masonry is not unusual and is adopted by many masonry design codes and standards (e.g. BS 5628, 2005). The Australian masonry design standard AS 3700 (2001) assigns material resistance factors of 0.45 and 0.75 for unreinforced and reinforced masonry, respectively.

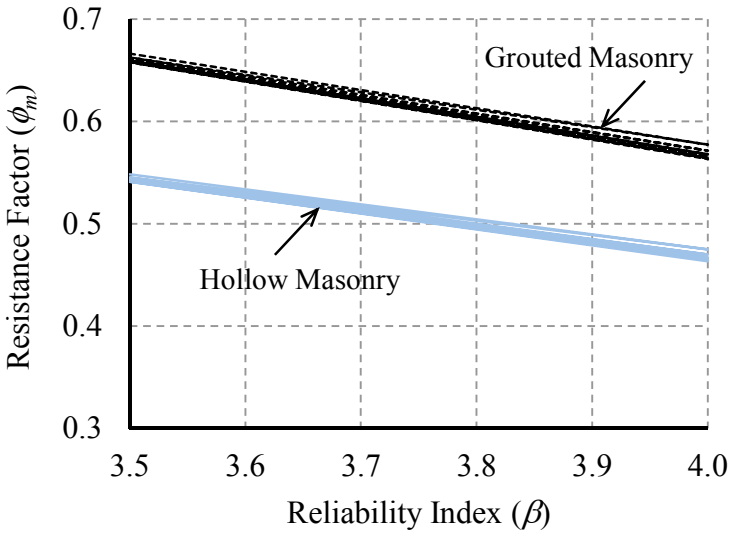


Figure 2. Relationship between the resistance factor and reliability index.

SUMMARY AND CONCLUSION

The scarcity of published research on the reliability of masonry structures in Canada suggests that the value of ϕ_m in the current and previous editions of the Canadian masonry design standard CSA S304.1 was not established on rigorous reliability analyses. It appears that calibration to the 1984 working stress design edition of the standard and engineering judgement played a greater role in selecting a value for ϕ_m.

The target reliability index of 3.5 used in the current Canadian masonry design standard is lower than the target reliability index for other comparable structural materials namely, concrete (Bartlett, 2007). While this value may be justified for reinforced masonry, it is not suitable for unreinforced masonry which lacks ductility. Following the recommendations of the Canadian standard CSA S408 (1981–R2006) and many international standards such as the Australian standard AS 5104 (2005) and considering the findings of recent research in the area of reliability of structural masonry (e.g. Lawrence and Stewart, 2009), a target reliability index of 3.8 is proposed for unreinforced masonry.

A structural reliability analysis was performed on concrete masonry under concentric axial compression to examine the reliability levels for masonry buildings designed to the current Canadian masonry standard (CSA S304.1-04). Based on the findings of this investigation, it is recommended that unreinforced masonry be assigned a material resistance factor different from reinforced masonry. For masonry members under compression, it is proposed that the current ϕ_m be increased from 0.6 to 0.65 for reinforced masonry and decreased from 0.6 to 0.5 for unreinforced masonry. This corresponds to a reliability index of 3.5 for reinforced masonry and 3.8 for unreinforced masonry. Under the current ϕ_m value of 0.6, the reliability index is 3.2 for unreinforced masonry and 3.8 for reinforced masonry.

Many researchers (e.g. Turkstra et al., 1982 and Bartlett, 2007) found that slenderness does not change the reliability index significantly. The current Canadian masonry standard addresses the slenderness effect separate from material resistance by using additional capacity reduction factors (ϕ_e and ϕ_{er}) of 0.65 and 0.75 for unreinforced and reinforced masonry construction. High eccentricity, however, is known to reduce the value of the reliability index particularly for unreinforced masonry construction (Turkstra and Ojinaga, 1980). The effect of eccentricity on the reliability level was not considered in this study and is a part of an ongoing extension to this investigation.

ACKNOWLEDGMENT

The authors wish to thank the Canadian Concrete Masonry Producers Association (CCMPA) and its member companies for providing third party test data for concrete block masonry units needed to carry out this analysis.

REFERENCES

Allen, D.E. (1975). "Limit state design - a probabilistic study." *Canadian Journal of Civil Engineering*, 2(1), 36-49.

AS 5104 (2005). *General principles on reliability for structures*. Standards Australia International, Sydney, NSW, Australia.

AS 3700 (2001). *Masonry structures*. Standards Australia International, Sydney, NSW, Australia.

Bartlett, F.M. (2007). "Canadian standards association standard A23.3-04 resistance factor for concrete in compression." *Canadian Journal of Civil Engineering*, 34, 1029-1037.

BS 5628 (2005). *Code of practice for structural use of masonry*, British Standards Institution, Bristol, UK.

CSA S304.1-04 (2004). *Design of masonry structures*. Canadian Standards Association, Ontario, Canada.

CSA S408-1981 (R2006). *Guidelines for the development of limit states design*. Canadian Standards Association, special publication, Ontario, Canada.

CSA A179 (2004). *Mortar and grout for unit masonry*. Canadian Standards Association, Ontario, Canada.

Drake, B., Stewart, M., and Lawrence, S. (2004). Variability and structural reliability of structural masonry in compression. 7th Australasian masonry conference. Newcastle, Australia, 275-284.

Ellingwood B. (1981). "Analysis of reliability for masonry structures." *Journal of the Structural Division*, 107(5), 757-773

Fisher, J. W., Galambos, T. V., Kulak, G. L., and Ravindra, M. (1978). "Load and resistance factor design criteria for connectors." *Journal of Structural Division*, ST9, 1427-1441.

Galambos, T. V. and Ravindra, M. K. (1977). "The basis for load and resistance factor design criteria of steel building structures." *Canadian Journal of Civil Engineering*, 4, 178-189.

Laird, D.A., Drysdale, R.G., Stubbs, D.W., and Sturgeon, G.R. (2005). The new CSA S304.1-04 "Design of Masonry Structures". 10th Canadian masonry symposium, Banff, Alberta, Canada.

Lawrence S. and Stewart M. (2009). Structural reliability and partial safety factors for unreinforced masonry in vertical bending. Research Report No. 274.01, Centre for infrastructure performance and reliability, The University of Newcastle, NSW, Australia.

Lind, N.C. (1971). "Consistent partial safety factors." *Journal of the Structural Division*, 97, 1651-1669.

MacGregor, J. (1976). "Safety and limit states design for reinforced concrete." *Canadian Journal of Civil Engineering*, 3, 484-513.

Melchers, R. E. (1999). *Structural reliability analysis and prediction*. John Wiley, New York.

Stewart, M.G. and Lawrence, S.J. (2006). Reliability-based code calibration of structural masonry in compression designed to Australian standards. Research Report No. 259.06, Centre for infrastructure performance and reliability, The

University of Newcastle, Australia.

Turkstra, C. and Daly, M. (1978). "Two moment structural safety analysis." *Canadian Journal of Civil Engineering*, 5, 414-426.

Turkstra, C. and Ojinaga, J. (1980). Towards a Canadian limit states masonry design code. 2nd Canadian masonry symposium, Carleton University, Ottawa, Ontario, Canada.

Turkstra, C., Ojinaga, J. and Shyu, C. (1982). Safety index analysis for a limit state Code. 2nd North American masonry conference, University of Maryland, Maryland, USA, Paper # 22.

IS ROOF EAVE BLOCKING REQUIRED TO TRANSMIT WIND/SEISMIC FORCES?

Felix Martin, S.E.

Principal Engineer, Marcon Forensics, LLC,
344 Third Street, Laguna Beach, CA 92651;
PH (949) 376-0290, FAX (949) 376-0296;
email: felix@marconforensics.com

ABSTRACT

The use of wood blocking between wood rafters or trusses has been historically accepted by engineers as necessary to act as a wood roof diaphragm boundary edge member, to transfer chord forces to the chord and to transfer wind and seismic shear forces to the shear walls.

However, the use of eave blocking has been abandoned by many design engineers who argue it is not specifically code-required and that empirical testing has shown it is not needed. They argue that chord and shear forces can be resolved through the use of other framing members and metal connectors. However, engineering mechanics and metal connector manufacturers' limits dictate that eave blocking cannot be omitted.

In low load, low heel height cases, it could be argued that eave blocking may not be needed, but where roof diaphragms transfer wind and seismic forces, design engineers omitting eave blocking do so in denial of basic engineering principles.

INTRODUCTION

Blocking between wood rafters or trusses at roof eaves (commonly known as eave blocking) has historically been standard framing practice in wood construction, particularly at open eaves. Blocking typically consists of nominal two inch wide material, normally of a depth matching the height from the bottom of the roof sheathing to the top plate of the wall.

The installation of edge blocking serves several purposes. The blocking encloses the attic space, preventing birds and vermin from entering, and it is used as a means to assure accurate dimensional spacing between the rafters or roof trusses. It also provides a load path from the roof diaphragm to the exterior walls to transfer wind or seismic forces. However, as fire requirements and aesthetic considerations have resulted in the increased use of enclosed eaves, the installation of eave blocking has been abandoned by many design engineers.

The resultant construction cost savings in both material and labor has been justified by the argument that eave blocking is not specifically required by the code (Crandell, J., Rice, R., Foley, B, and Woeste, F., 2009). This argument has been shored by results from testing sponsored by the U.S. Department of Housing and Urban Development (HUD, 2002) that appears to show edge blocking may not be "empirically" needed (as opposed to required by engineering mechanics).

Whether or not the installation of eave blocking is actually required depends on a number of factors. These may be prescriptive, required by building code statute; or, when dependent on manufactured metal connectors to transfer shear and overturning forces, by limitations placed by the connector manufacturers' specifications; or finally, as an integral part of the lateral load-resisting system, as a means to maintain a complete load path from the roof diaphragm to the shear walls.

BUILDING CODE REQUIREMENTS

Lateral Support Against Rotation

One function of eave blocking is to prevent lateral rotation of the rafters/trusses at the wall supports. The International Residential Code (IRC) did not specifically require any eave blocking to prevent rotation of rafters/trusses under the 2006 edition. Some conditions are provided in the 2009 IRC under which eave blocking is required by Section R602.10.6.2 for lateral support against rotation, but only at sections above braced wall panels. Low wind/seismic regions require partial height (to allow attic venting per R806) eave blocking, but only at rafter/truss heel heights above 9.25 inches. High wind/seismic regions required eave blocking per Figures R602.10.6.2(1), R602.10.6.2(2) or R602.10.6.2(3) for all heel heights.

That the required blocking is only partial-height for attic ventilation seems unnecessary in that the blocking is only required over braced wall panels and not elsewhere along the wall line. IRC Figures R602.10.6.2(1), R602.10.6.2(2) and R602.10.6.2(3) do not provide a load path and serve solely to prevent rotation of the rafter/truss.

Similarly, the 2009 International Building Code (IBC) under *Conventional Light-Frame Construction* Section 2308.10.6 requires the use of blocking per Section 2308.8.5, which uses heel height limits to require lateral support against rotation of the roof framing. The heel depth-to-thickness ratio for roof framing is held to a maximum unblocked ratio of 5:1. This requirement exists only to resist rotation of the roof framing and does not address the transfer of wind or seismic forces.

In conclusion, the IRC does not at present prescriptively require eave blocking to resist rotation for rafters/trusses heel heights less than 9 1/4 inches, while the IBC does not prescriptively require eave blocking for heel heights less than 6 3/8 inches.

Load Transfer

The 2006 IBC's *General Design Requirements for Lateral Force Resisting Systems* section prescribed the use of "boundary members" to transmit tension and compression forces (Section 2305.1.2). This has been historically taken by engineers to indicate a requirement for eave blocking. Since wind/seismic chord forces are typically resisted by the wall top plates, an obvious load path would be developed from the roof diaphragm to the top plates through the eave blocking to the shear wall top plate. Load eccentricities from the roof diaphragm to the top plate in this arrangement are resolved through each block's individual end nailing. Under such a configuration eave blocking meets the IBC requirement for boundary members to transmit tension and compression forces.

However, the 2009 IBC deleted Section 2305.1.2 and under newly revised Section 2306.2.1 ("Wood structural panel diaphragms") defaults the design and construction of horizontal wood diaphragms to as in accordance with the American Forest & Paper Association's *Special Design Provisions for Wind and Seismic* (2005).

AF&PA's *Special Design Provisions for Wind and Seismic* Section 4.2.6 ("Construction Requirements") requires diaphragm "boundary elements" to transmit tension, compression and shear forces but does not specifically require those to be eave blocking. In arguing for the omission of eave blocking, it has been put forth that the roof diaphragm should instead be boundary-nailed to the fascia (the new "boundary element") in order to meet the code boundary nailing requirement.

Chord forces are then assumed to transfer from the roof diaphragm to the tops of the rafter/truss (the new "boundary elements"), through the rafter/truss, and through the metal connector holding the rafter/truss to the top plate, transferring the chord forces to the shear wall top plate. The assumption is typically made without the benefit of an engineering analysis, it happens "empirically".

Because the AF&PA does not specifically require for such a transfer to take place by using eave blocking, there is no prescriptive IBC code requirement to use eave blocking to transfer tension and compression forces. While such an arrangement may not be acceptable to engineers in that it places the rafter/truss in cross-grain bending, it has been argued that it technically meets code requirements for boundary elements to transmit tension, compression and shear forces.

The resultant load path would then be from the wood diaphragm to the roof rafter/truss, through the roof rafter/truss to the metal connector, and from the connector to the wall top plates. The resultant eccentricities of this load path are generally ignored by those proposing the deletion of eave blocking, who argue the metal connector can resist the overturning by transferring the force couple through the connector flanges nailed to the sides of the roof/rater truss. This will be further discussed in the following sections.

ANALYSIS REQUIREMENTS

Diaphragm

Figure 1a below shows a standard roof framing detail for a wood framed eave, with eave blocking. Figure 1b shows the same detail, without the eave blocking but substituting standard connection hardware.

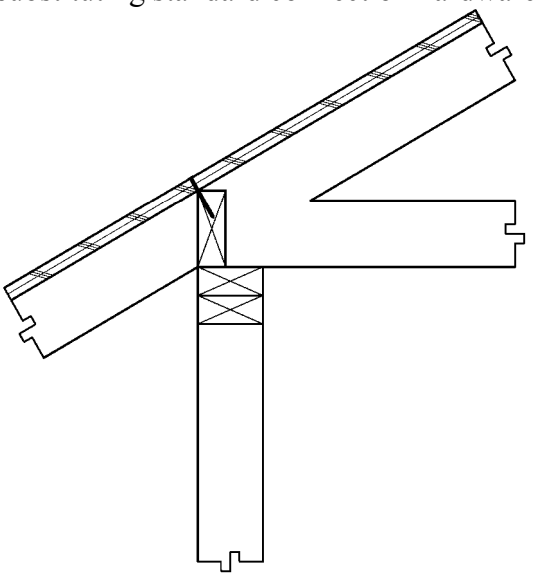


Fig. 1a – Wood Framed Eave With Eave Blocking.

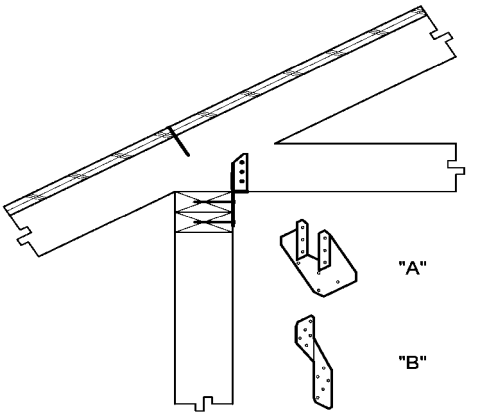


Fig 1b – Wood Framed Eave, No Eave Blocking.

Figure 1c shows again the same detail, without the eave blocking, at a masonry wall condition with standard connection hardware.

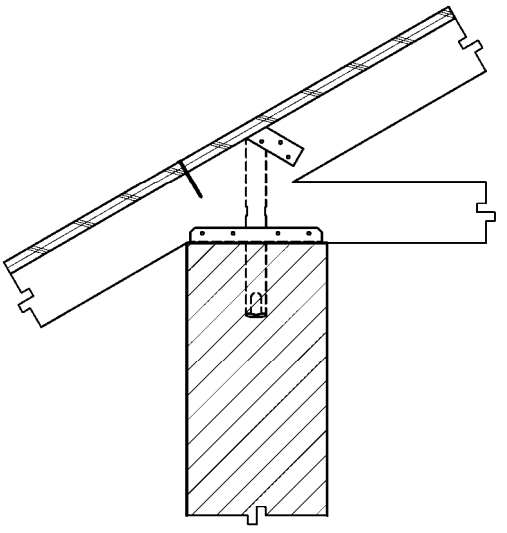


Fig. 1c – Masonry Wall Wood Framed Eave, No Eave Blocking.

In considering the need to transfer wind/seismic forces at roof eaves, two issues need to be addressed. First would be the resolution of resistant forces parallel to the direction of applied wind/seismic forces (the reaction shear forces). Second would be the resolution of resistant forces perpendicular to the direction of applied wind/seismic forces (the chord forces).

The reactive shear forces resisting wind/seismic forces for a flexible, unblocked diaphragm are typically determined from a tributary span length and a tributary wind/seismic load. Table I tabulates reactive shear values for different combinations of wind/seismic loadings (w) and different diaphragm length-to-depth ratios (L/d). Because we are only considering the analysis of eaves perpendicular to the roof framing and the roof trusses are assumed to span across the shorter dimension, the wind/seismic forces would act across the short direction of the diaphragm and we would only investigate the reactive shear forces from wind/seismic forces perpendicular to the roof framing (IBC Table 2306.3.1, Case 3 unblocked diaphragm).

Table I – Reactive Shear Forces.

Shear Flow (plf)					
L/d	0.25	0.33	0.50	0.67	1.00
w (plf)					
100	13	17	25	34	50
150	19	3	38	50	75
200	25	33	50	67	100
250	31	41	63	84	125
300	38	50	75	101	150

The results show the reactive shear forces fall within most popular sheathing thickness/nail size combinations for unblocked diaphragms. Diaphragm shear capacity would thus not seem to be a concern in eliminating eave blocking when considering reactive shear forces.

Chord forces for flexible, unblocked diaphragms are typically calculated as simple span moments between diaphragm supports, divided by the depth of the diaphragm. Table II tabulates chord forces for different combinations of wind/seismic loadings (w) and different diaphragm length-to-depth ratios (L/d), divided by the length of the diaphragm. Again considering chord forces perpendicular to framing but due this time to wind/seismic forces parallel to framing, we distributed the chord force into a "chord flow" acting along the diaphragm edge, namely, the chord force divided by the length of the diaphragm. We then compare these calculated chord flow forces along the diaphragm edge with the allowable diaphragm loading corresponding to an IBC Table 2306.3.1, Case 3 loading.

Table II – Chord Forces.

Chord Flow (plf)					
L/d	4.00	3.00	2.00	1.50	1.00
w (plf)					
100	50	38	25	19	13
150	75	56	38	28	19
200	100	75	50	38	25
250	125	94	63	47	31
300	150	113	75	56	38
350	175	131	88	66	44

The tabulated results show that the chord flow shear forces fall within most popular sheathing thickness/nailing combinations for unblocked diaphragms. In considering chord forces at diaphragms without eave blocking, diaphragm shear capacity does not appear to be a concern.

Mechanical Connectors

Typical roof wood rafter/truss to wood wall construction uses metal connectors such as those shown in Figure 1b, while typical roof wood rafter/truss to masonry wall construction uses connectors such as the one shown in Figure 1c. Available from a number of manufacturers, these connectors have load capacities (depending on the model used) of up to several hundred pounds per connector (Simpson Strong-Tie Company, 2009-2010).

The values tabulated in either Table I or Table II compare well with the allowable shear loads for these metal connectors. Provided the proper connector is selected and standard spacings are used, shear force demands from the diaphragm to the exterior walls can be met. These connectors would thus appear to meet the IBC Section 2305.1.2 requirement for the use of "boundary members" to transmit tension and compression forces.

However, where eave blocking is not used, the rafter/truss would receive the wind/seismic load from the diaphragm at the top of the rafter/truss and transfer it to the wall top plates at the base of the rafter/truss. This creates a rotational moment across the rafter/truss. Disregarding for the moment that this rotational moment induces undesirable cross-grain bending on the rafter/truss, in order for the wind/seismic load to successfully transfer into the top plates there would still need to be a free-body resolution of the rotational moment at the base of the roof rafter/truss.

The moment may be resisted by the metal connectors tying the rafter/truss to the top plates. In the case of a connector "A" as shown in Figure 1b, nailed flanges on either side of the rafter/truss could develop a resistive couple. Similarly, a connector "B" as shown in the same figure could be installed each side of the rafter/truss to resist the rotational couple. However, the rated load values for these connectors were

developed through testing that restrained the wood members from rotation. The rated load values represent capacities for straight shear transfer and do not assume a combination of shear and rotational loads. As such, the metal connectors are not approved by the manufacturer to resist rotational couples. Manufacturers specifically include catalogue warnings that the connectors are not intended to prevent cross grain bending (Simpson Strong-Tie Company, 2009-2010).

Engineers have the option to bypass the manufacturer's warnings and choose to apply engineering design concepts to analyze the connector. Such a study would have to include a complete free-body analysis and a unity equation check. Consideration would have to be given to the fact that the nails transferring the rotational couple forces would be in cross-grain shear. In addition, those intending to use "B" connectors should also consider the manufacturers' recommendation to use a minimum 2½ inch thick rafter/truss when installing the connectors opposite each other (Simpson Strong-Tie Company, 2009-2010).

Perhaps more importantly, the use of mechanical connectors such as "A" and "B" to transfer both shear and rotational forces requires a complete disregard for cross-grain bending across the rafter/truss. This condition is ignored by no-blocking proponents (Yaxley, Wilbur T., 2004) who will argue empirically for the rotational resistance provided by the fascia board, even though it is end nailed to the rafter/truss and numerically unable to provide the necessary resisting force couple. Similarly disregarded is that shear transfer may happen but only at the expense of rotational failure. A failed connection is still a failed connection.

Test results show that failure modes for anything but low-load/low-heel height conditions are generally not caused by shear failure but by some form of rotational failure (U.S. Department of Housing and Urban Development, 2004). On roof rafters this typically occurs as a cross-grain failure, an undesirable condition due to its sudden and inelastic failure mode. In roof trusses the failure is typically across the connector plates. In addition, there are no code-published allowable stress values for wood in cross-grain bending. Even if some existed, the need for an engineering analysis including a unity equation check for shear and cross-grain bending cannot be ignored.

EMPIRICAL TEST DATA

The U.S. Department of Housing and Urban Development (HUD) sponsored tests on roof truss to wall connections and reported the results in 2004. The tests involved four different attachment configurations, none using eave blocking. Two of the configurations used toe nails as the sole means of attachment. The third configuration used a combination of twenty-two toe nails and nine metal connectors. The fourth configuration used only four toe nails and nine metal connectors. The metal connectors were installed on only one side of the truss. All trusses used two-by-four inch members, so that heel heights and the resultant overturning forces were relatively small.

Test results showed a noticeable difference between toe-nail failure and metal connector failure modes. Toe-nail connection failure was defined by lower load capacities, splitting of the wood and lateral sliding of the truss along the top plate, with little out-of-plane truss rotation. Toe-nailed connections had such low capacities that out-of-plane rotations never really had the opportunity to develop to the point of failure. In essence, the toe-nailed connection failed in shear long before allowing the connection to fail in out-of-plane rotations.

Metal connector failures occurred at higher load capacities. In some cases the truss rotated out-of-plane, resulting in truss plate separations. In others, the metal connectors failed, either by failing in tension due to the overturning out-of-plane force couple, or by excessive deformation from localized buckling of the connector.

Metal connectors are load-rated by their manufacturer based on joint slip limits, rather than on failure load capacity. The HUD tests were based on failure load capacity and as such, the results report excessively high failure loads relative to manufacturer rated loads. This leads to excessively positive results that would seem to indicate the metal connectors are much more capable of resisting loads than they have been rated by their manufacturers. These findings have lead to euphoric misplaced calls for the abandonment of metal connectors allowable loads based on joint slip limits rather than by failure load analysis. In the HUD configurations tested, load failure occurred at deformations of over an inch, excessive by any measure and surely a condition that would benefit from the installation of eave blocking.

CONCLUSIONS

Roof eave blocking is not prescriptively required by either the IRC or the IBC to transfer wind/seismic forces. Eave blocking is only code-required to resist lateral rotation of the rafter/truss assemblies when prescribed height-to-width heel ratios are exceeded.

Strictly in terms of shear transfer, wood roof diaphragms in standard configurations do not appear able to develop large enough shear or chord forces to require the installation of eave blocking for additional diaphragm shear nailing. Similarly, metal truss connector shear load capacities appear sufficient to resist standard configuration shear or chord forces.

However, the use of only truss connectors in lieu of eave blocking requires a disregard of rotational bending across the rafter/truss assembly and its resultant cross-grain bending on the roof rafter/truss as well as its resultant force couple on the metal connector. A complete free-body analysis and unity equation check on both the roof rafter/truss for cross-grain bending and on the metal connector seem out of reach due to a lack of allowable wood cross-bending stress values and the fact that metal

connectors are prohibited by the manufacturer to resist cross-grain bending and that allowable shear values are based on joint slip limits.

The omission of eave blocking may be possible in some low-load, low heel-height conditions, when toe nails are used. Toe nail shear capacities are so low, cross-grain bending in low-heel conditions does not have the opportunity to develop as a concern. In other words, for low heel-height, light load cases requiring only toe-nailing at the roof rafter/truss connection to the top plate for shear transfer, cross-bending concerns could possibly be disregarded. The system would have to be designed to guarantee shear failure of the toe nailing before reaching a cross-bending failure. With some limits, low-load conditions might be possible without eave blocking.

However, once the decision to use metal connectors is made, the use of connector hardware greatly increases the shear load capacity over that of just toe-nailed assemblies. This increased shear load capacity brings about a rise in the potential for cross-grain rotational failure, either in the roof rafter or in the roof truss assembly. Any system that would use metal connectors between the roof rafter/truss and the wall top plate will require the use of eave blocking in order to avoid rotation as the failure mode.

At higher loads and particularly as the heel height increases, rotational forces and cross-grain bending cannot be ignored. In the absence of eave blocking, cross-grain rotation becomes a primary failure mechanism. Higher loads and higher heel heights also result in assembly deformations too excessive to be acceptable and well beyond the joint slip limits of the metal hardware. In designing higher-load assemblies (such as those in high wind and earthquake zones) the omission of eave blocking is not an acceptable engineering choice.

REFERENCES

American Forest & Paper Association. (2005) *Special Design Provisions for Wind and Seismic*. Section 4.2.6.

Crandell, J., Rice, R., Foley, B, and Woeste, F., (2009), "When is Roof Eave Blocking Required?", *Wood Design Focus*, Forest Products Society, Spring, Vol. 19, No. 1, pp. 10:12.

International Code Council, *International Residential Code*, (2009). Country Club Hills, IL.

International Code Council, *International Residential Code* (2006). Country Club Hills, IL.

International Code Council, *International Building Code* (2009). Country Club Hills, IL.

International Code Council, *International Building Code* (2006). Country Club Hills, IL.

Simpson Strong-Tie Company. (2009-2010). *Wood Construction Connectors.* Pleasanton, CA.

U.S. Department of Housing and Urban Development, Office of Policy Development and Research, by NAHB Research Center. (2002). *Roof Framing Connections in Residential Construction*, Washington, DC, February.

Yaxley, Wilbur T. (2004). "Forensic Engineering Analysis & Testing of Wood Truss/Wall Connections", *Journal of the National Academy of Forensic Engineers*, National Academy of Forensic Engineers, December Vol. XXI, No. 2, pp. 7:18.

Truss Plates for Use as Wood-Concrete Composite Shear Connectors

Peggi L. Clouston, Associate Member ASCE[1] and Alexander C. Schreyer[2]

[1]Associate Professor, Dept. of Environmental Conservation, University of Massachusetts, Amherst, MA 01003; PH (413)545-1884; FAX (413)545-4358; email:clouston@eco.umass.edu
[2]Lecturer, Dept. of Environmental Conservation, University of Massachusetts, Amherst, MA 01003; PH (413)545-1976; FAX (413)545-4358; email: schreyer@eco.umass.edu

ABSTRACT

Wood-concrete composite systems are well established, structurally efficient building systems for both new construction and rehabilitation of old timber structures. Composite action is achieved through a mechanical device to integrally connect in shear the two material components, wood and concrete. Depending on the device, different levels of composite action and thus efficiency are achieved.

The purpose of this study was to investigate the structural feasibility and effectiveness of using truss plates, typically used in the making of metal-plate-connected wood trusses, as shear connectors for laminated veneer lumber (LVL)-concrete composite systems. The experimental program consisted of two studies. The first study established slip-modulus and ultimate shear capacity of the truss plates when used in an LVL-concrete push out assembly. The second study evaluated overall composite bending stiffness and strength in two full size T-beams when subjected to four-point bending. One beam employed two continuous rows of truss plates and the other employed one row.

It was found that the initial stiffness of both T-beams was similar for one and two rows of truss plates but that the ultimate capacity was approximately 20% less with the use of only one row.

INTRODUCTION

The concept of connecting a wood beam to a concrete slab to achieve composite action was first implemented in the early 1930's in U.S. timber bridge construction (Doehrer and Rautenstrauch 2006). The method of interlocking the two materials was rudimentary, relying on concrete shear keys formed through slots in the wood. Although not commonly seen in the U.S. today, this construction practice is becoming popular in Europe, particularly for rehabilitation and preservation of old timber structures. A variety of connectors have been used – such as nails, screws or spikes with and without concrete shear keys – each with varying degrees of structural efficiency as well as level of ease and cost of installation (Ahmadi and Saka 1993; Ceccotti A. 1995; Blaß and Schlager 1996; Gutkowski et. al. 2008). New proprietary mechanical connectors are also being developed - such as expanded steel mesh, modified screws and sophisticated steel hardware - and are commercially sold for residential, commercial and industrial applications (Bathon and Graf 2000; Clouston et al. 2004; Clouston and Schreyer 2008).

The advantages of using Wood-concrete composites are many. Composite action between the two materials results in stronger and stiffer floors than if the two materials are unconnected, as is commonly done in light-frame construction. The use of concrete with wood also enhances sound attenuation and vibration dampening, reduces fire risks, provides a more rigid floor diaphragm, and improves floor smoothness and durability. In addition, there are benefits to the environment from encouraging the use of more timber. Wood is the only renewable building material; it requires less energy and creates less pollution in manufacturing than alternative building materials, and it stores carbon absorbed from the air. The presence of concrete in the system would add thermal mass to absorb, store, and later release heat in a building to save on operating energy.

Despite the advantages of building with this technique, little research has been directed at adapting the concept to traditional North American light-frame construction. This construction approach is typified by the prevalence of small wood framing members with a 38mm thickness (also known as 2 inch nominal lumber). The shear connectors in existence generally require thicker wood cross sections than this so as to not remove or impact too much of the wood's capacity.

To this end, the objective of this study is to investigate the structural feasibility and effectiveness of using steel truss plates - used in the making of metal-plate-connected wood trusses - as shear connectors for wood-concrete composite systems. These ready-made connectors are intended for use with 38mm framing lumber and have teeth that puncture the wood to a depth of only 9.5 mm to make the mechanical connection.

EXPERIMENTAL PROGRAM

The experimental program consists of two sequential series of tests. The first series is a standard test configuration to determine slip modulus and connector shear strength, referred to as the push-out test. The second test is a full-scale four point bending test to compare the effect on structural performance of using one row of connectors versus two rows of connectors.

Materials

The wood used for both series of tests (push-out and bending) was 44mm thick x 133mm deep 2600Fb-1.9E Eastern Species Laminated Veneer Lumber (LVL) beams manufactured by iLevel by Weyerhaeuser. The metal plate connectors were pre-manufactured, 152mm wide x 304mm long, 20 gauge, MT20 steel truss plates by MiTek. The teeth of these plates are punched in pairs and formed at right angles to the face of plate. The concrete was high strength ready-mix by Sakrete with a minimum compression capacity of 27 MPa.

The specimens were fabricated into hybrid composites as shown in Figure 1. One half of the 152mm width of the truss plates was pressed into each of the two LVL boards so that half of the connector was embedded into the lumber leaving the other half to embed into the poured concrete. Plywood was glued to the top edge of the LVL to create a 19mm space between the LVL and the concrete to mimic permanent formwork on a jobsite. Two 12mm diameter washers were placed in-between the two LVL beams which were then fastened together using 64mm decking screws. The exposed truss plates were

hand-bent to a 45 degree angle. 150mm x 150mm wire mesh was placed on top of the bent connectors to prohibit concrete shrinkage. The concrete was then cast in place and let to cure for a minimum of 28 days. Specimens were tested under ambient laboratory conditions (approximately 16°C, 40% relative humidity).

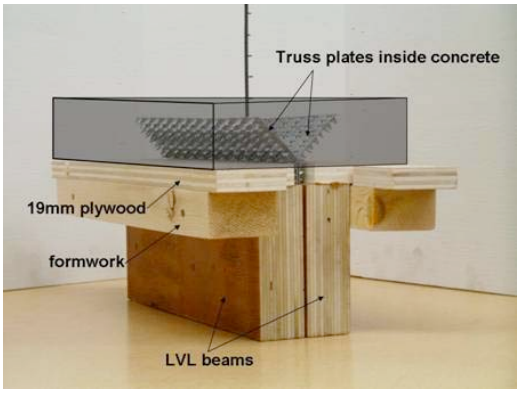


Figure 1 - LVL-concrete composite specimen

Method: Push-out tests

Five specimens were subjected to one-sided push-out tests. A schematic of the test set-up is illustrated in Figure 2. As no standard currently exists for wood-concrete composite shear tests, general guidelines of American Society for Testing and Materials standard, ASTM D 5652 were followed. The test assembly was similar to that used in previous studies (Clouston et. al. 2004 and 2005). A Linear Variable Displacement Transducer (LVDT) was placed at mid-height to measure slip displacement. Load was applied at a constant rate of 0.8 mm/min by a 133 kN capacity universal test machine under deflection control with real time data acquisition. The load was cycled first up to 20kN, then back to 8 kN and then to failure with the intent to remove slack in the specimen for accurate slip modulus measurement (similar to the ISO 6891 / DIN EN 26891 method).

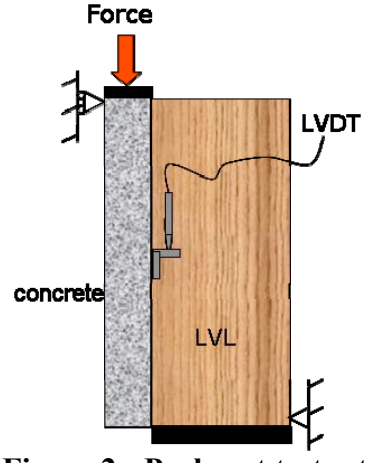


Figure 2 - Push-out test set-up

Method: Bending tests

Two T-beams were fabricated and tested in bending to investigate overall composite bending stiffness and strength. These beams used two 2743 mm long 44 mm x 133 mm LVLs as stringers. On top of these was a 19 mm plywood sheet (as permanent formwork), a 0.08 mm polyethylene (PE) sheet as moisture barrier during construction and an 89 mm thick concrete slab. Overall T-beam width was 436 mm (see Figure 3 for details).

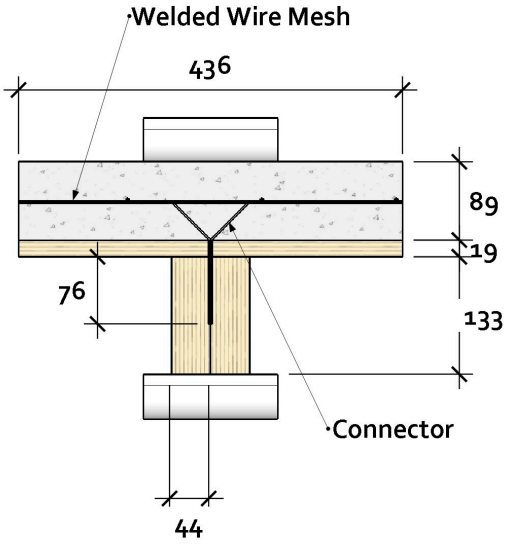


Figure 3 - Bending setup cross-section

Nailplate fasteners were pressed into the side of the LVL stringers into routed depressions, which had been recessed to a depth equal to the steel thickness. This was done so that the nailplates would sit flush with the surface of the LVL's side, therefore removing the need for spacers between both LVLs. The top portion of the nailplates that projected beyond the plywood was again bent at a 45 degree angle as illustrated in Figure 4. One of the beams featured two rows of connectors (one on each LVL) whereas the other only had one row (using staggered fasteners between the two LVLs). The top of the nailplates then served as support for a welded-wire mesh (152 mm square wire spacing), which was located approximately at ½ of the thickness of the concrete slab and tied to the nailplate fasteners. This wire mesh served solely as minimal reinforcement for crack reduction and was not intended to contribute to the composite connection.

Before adding concrete, screws were driven from below the plywood sheet to act as nonstructural connectors to hold the plywood in place. Overall, the plywood layer was not fastened to either the LVLs or the concrete in any way that would provide load transfer since it was only designed as non-structural formwork. As a final step, all seams were caulked with an elastomeric sealant so that no cement slurry could escape from the concrete mix.

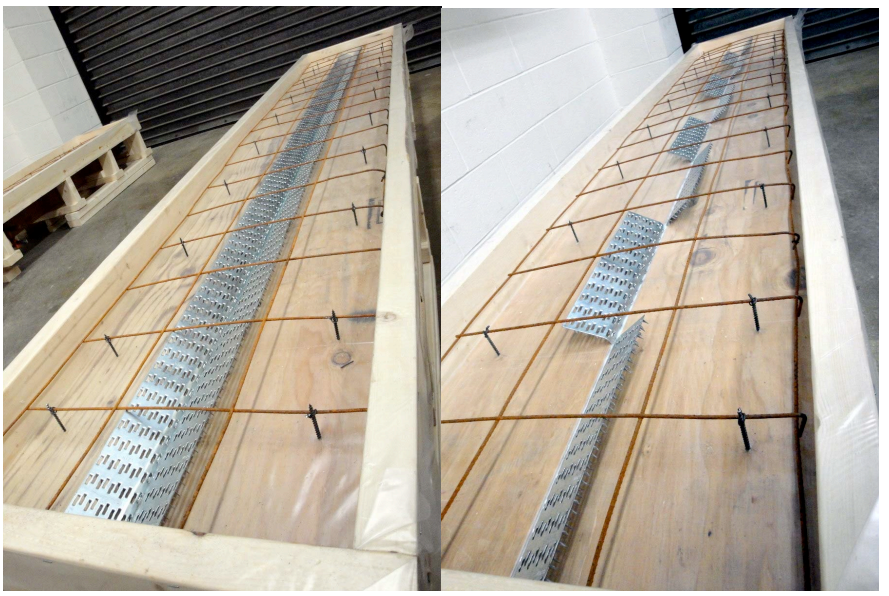


Figure 4 - Double-plated LVL beam with formwork
(left: two rows of fasteners, right: single-row with alternating fasteners)

After curing for 28 days, side formwork was removed and the beams were arranged in the 133 kN MTS testing frame using the four-point test setup illustrated in Figure 5 (see Figure 6 for a photograph). Load was applied through controlled crosshead displacement at a rate of 2.5 mm / min. Midspan displacement was recorded using an LVDT at the center of the span (on top of the concrete). All data were recorded in real-time using MTS software.

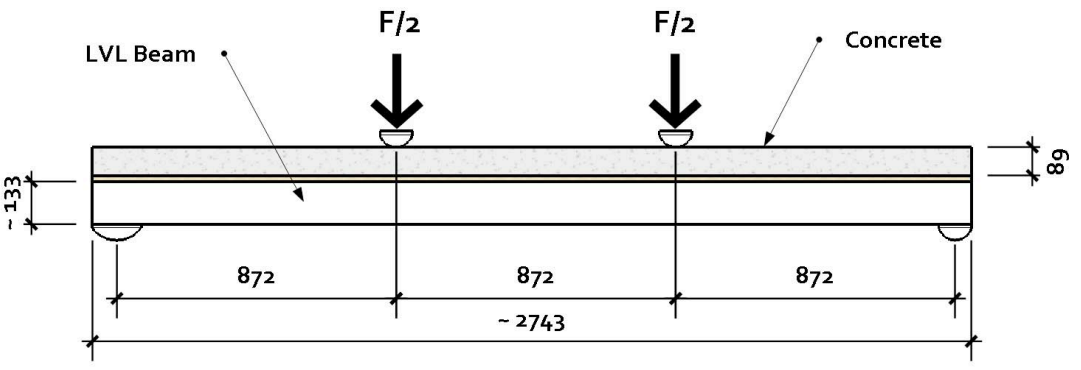


Figure 5 - T-beam bending test setup

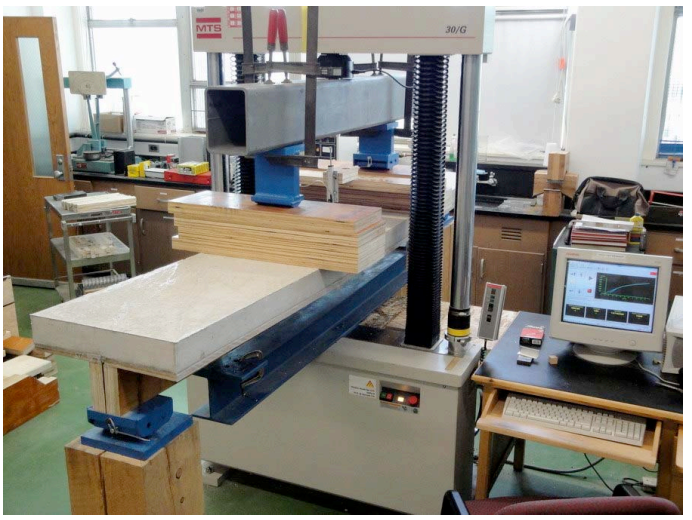


Figure 6 - T-beam in MTS test machine

RESULTS AND DISCUSSION

Push-out tests

A photograph of the failed specimen in the test fixture is provided in Figure 7. Some minor spalling of the concrete was observed but upon close inspection of the specimens (by removing the concrete and separating the LVL beams, as seen in Figure 8), it was apparent that all five specimens had failed by distortion and yielding of the truss plate at the shear interface between the plywood and the concrete. There was no obvious splitting of the wood at the location of the truss plate teeth.



Figure 7 - Shear failure of push-out specimen

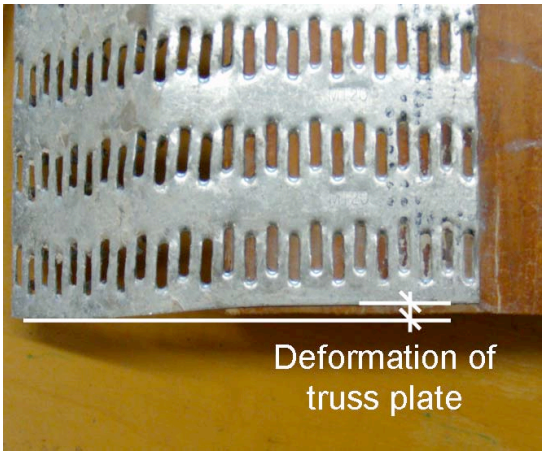


Figure 8 - Yielding of truss plate

The corresponding load / displacement curves of all five push-out specimens (reference Figure 9) indicate the ductile mechanical behavior of a steel failure mechanism (as opposed to the brittle nature of wood or concrete). Ductility was consistent for all specimens. The peak load varied moderately with a Coefficient of Variation (COV) of a 11.1%, again indicative of a reliable steel failure.

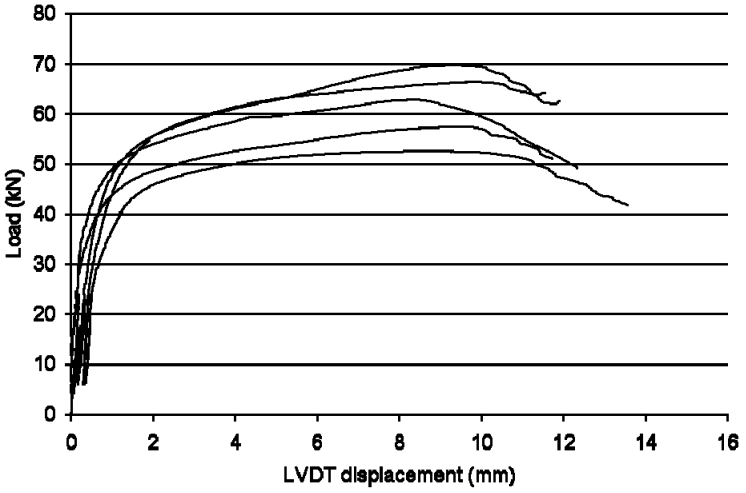


Figure 9 - Push-out tests: Load vs. LVDT displacement curves

Table 1 summarizes and quantifies the key findings of the push-out tests. The Slip Modulus, K, was determined by the slope of the linear portion of the load / displacement curve. The mean value of 128.1 kN/mm is within an expected range when compared with values previously published in the scientific literature: K=38.3 kN/mm for a notched shear key/anchor connector in 4x4 lumber (Gutkowski et. al. 2004) and K=415 kN/mm for an expanded steel mesh connector in Glulam (Clouston et. al. 2005).

Table 1 - Push-out test results

Specimen	Slip Modulus,K (kN/mm)	Peak Load (kN)
1	134.6	66.5
2	157.1	62.9
3	104.7	52.6
4	105.7	69.8
5	138.4	57.4
Mean	128.1	61.8
St. Dev.	22.6	6.9
COV	17.6%	11.1%

Bending tests

Both bending tests showed a similar failure behaviour as the push-out tests. Once all removable concrete had been broken away from the tested beams and the LVLs had been separated, it was visible (see Figure 10) that all deformation had occurred in the steel fastener in the area between the LVL beam and the concrete (i.e. the 19 mm gap created by the plywood layer). At the ends of the beam, concrete spalling and shear deformation at the LVL interface were both minimal (see Figure 11). Failure occurred mainly as shearing of the perforated steel and - at the ends of the beam - as partial tearing of the steel plate.

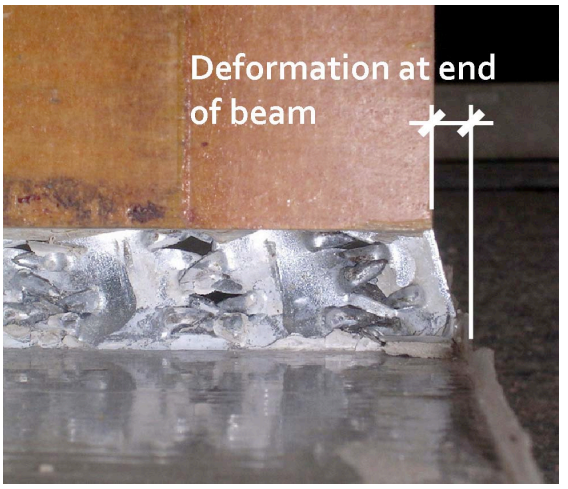


Figure 10 - Shear deformation in truss plate



Figure 11 - Tested specimens, broken apart for inspection

Load-displacement graphs for both tests (shown in Figure 12) revealed a relatively ductile failure behaviour with center-span displacements at break ranging between 40 mm and 55 mm. Ultimate failure was progressive tension failure in the LVL beam accompanied by minor crack development in the concrete. Peak load for the two specimens was 95.4 kN for the specimen with two fastener rows and 77.9 kN for the specimen with a single, alternating fastener row (i.e. 18.3 % less than the former).

It was interesting to discover that despite the drop in ultimate strength, initial beam stiffness (EI) was similar in both tests (1.88×10^9 kN·mm^2 and 1.70×10^9 kN·mm^2, respectively). This would suggest that for in-service design, the number of fasteners is not as critical as having a continuous connection. This, however, requires further tests for verification.

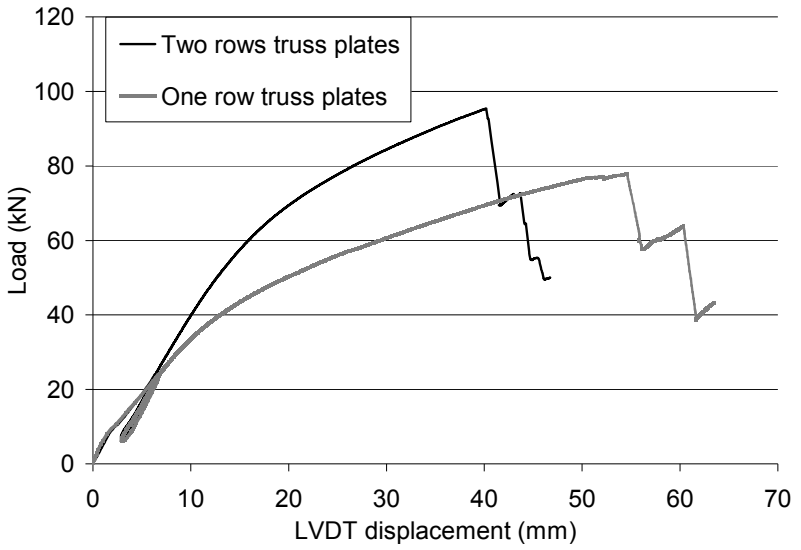


Figure 12 - Beam test graphs

CONCLUSION

An investigated was conducted into the viability of using ready-made MT20 truss plates as wood-concrete shear connectors. Two experimental test configurations were considered: push-out tests and 4-point bending tests with one row of connectors vs two rows of connectors. The push out tests indicate that the slip modulus achieved by using truss plates could be viable and within the same range of other commercially used shear connectors. It was also found that the initial beam stiffness (EI) of both T-beams with one and two rows of connectors was similar but that the ultimate capacity was approximately 20% less with the use of only one row.

REFERENCES

ASTM D5652. (2000). Standard test methods for bolted connections in wood and wood-base products. Philadelphia, Pa

Ahmadi, B.H., and Saka, M.P. (1993). "Behavior of composite timber-concrete floors." *J. Struct. Engrg.* ASCE, 119(10), 3111-3129.

Bathon, L.A., and Graf, M. (2000). "A continuous wood-concrete-composite system." *Proc., World Conference of Timber Engineering*, Whistler, B.C., 8.2.2.

Blaß, H., and Schlager, M. (1996). " Trag- und Verformungsverhalten von Holz-Beton-Verbundkonstruktionen. Teil 1" (Strength and stiffness behavior of wood concrete composite structures. Part 1). *Bauen mit Holz*, 5, 395-399 (in German)

Ceccotti, A. (1995). "Lecture E13: Timber-concrete composite structures." *STEP/Eurofortech Lecture Series*. Ed. Blass, H.J. et al. Centrum Hout, The Netherlands.

Clouston, P., Civjan, S., Bathon, L. (2004). Shear behavior of a continuous metal connector for a wood concrete composite system. Forest Products Journal 54(6) pp. 76-84

Clouston, P.; Bathon, L.; Schreyer, A. (2005). "Shear and Bending Performance of a Novel Wood-Concrete Composite System". ASCE Journal of Structural Engineering. 131(9), pp.1404-1412

DIN EN 26891, (1991). "Timber structures; joints made with mechanical fasteners; general principles for the determination of strength and deformation characteristics." (ISO 6891:1983), Deutsches Institut für Normung, e.V. Berlin, Germany

Doehrer, A. and Rautenstrauch, K. (2006). "The construction of road bridges as timber-concrete composites", Proc. WCTE 2006 - The Ninth World Congress on Timber Engineering, Portland, USA.

Gutkowski R., Brown K., Shigidi A., Natterer J. (2004). "Investigation of Notched Composite Wood-Concrete Connections," ASCE J. Struct. Engrg., 130(10), pp 1553-1561

Gutkowski R.; Brown K.; Shigidi A.; Natterer J. (2008). "Laboratory tests of composite wood–concrete beams" Construction and Building Materials (22), 1059–1066

Effect of Support Restraint on Wood-to-Wood, Joist Hanger Connection

William T. Bolduc, P.E., S.E., M. ASCE[1] and Samaan Ladkany, P.E., Ph.D.[2]

[1]Keymark Enterprises, LLC, Engineering/Software Development, 6707 Winchester Circle, Boulder, CO 80301; PH (702) 481-0742; FAX (303) 443-9054; email: bbolduc7@gmail.com
[2]Howard R. Hughes College of Engineering, Department of Civil and Environmental Engineering, University of Nevada Las Vegas, Box 454015, 4505 S. Maryland Parkway, Las Vegas, NV 89154-4015; PH (702) 301-7895; FAX (702) 895-3936; email: samaan.ladkany@unlv.edu

ABSTRACT

A common model of light gauge, metal joist hanger is tested on a wood-to-wood connection for two conditions. One condition follows the commonly used test standard for joist hangers, which allows the support beam to be restrained from horizontal and rotational movement. The second condition (unrestrained) allows the support beam to freely move horizontally and in rotation. The results show that the unrestrained case is much weaker than the standard restrained case. For the model of hanger tested, the average ultimate load for the unrestrained case was 28% of the standard restrained case. The mode of failure for the unrestrained case is different than that for the restrained case. This documents the importance of providing means of restraining the supporting beam by methods other than the connection via the joist hanger. The ASTM testing method for joist hangers may need to be adjusted to account for this possible mode of failure.

INTRODUCTION

Light gauge, metal joist hangers are widely used in wood frame construction in North America and in many areas of the world that use light wood frame construction. Most modern homes, apartments, and light commercial buildings that use light wood frame construction will also use joist hangers to connect framing members to supporting beams. A joist hanger is commonly used to connect a floor joist to a wood beam. Another common use is to connect a wood truss to a heavier “girder” truss. Although they are commonly called joist hangers, it is likely that nearly half of the usage is in roof framing, which are most commonly wood roof trusses. One of the main benefits of the joist hanger connection is that it connects to the side of the supporting beam or girder truss. This allows the supported framing member to be at the same elevation as the supporting beam or girder truss.

The use of joist hangers allows the supporting beams to be flush with the supported framing. This allows for ceilings to be free of beams placed below the ceiling level. In many cases, the architectural advantage of using joist hangers justifies the small added cost. There are also architectural trends that encourage more complex framing and more open spaces. These trends require more support beams, trusses, and engineered lumber products, all of which require greater usage of joist hangers.

The trend to more complex designs and larger open spaces increases the occurrences of joist hangers that need to carry larger loads. The manufacturers of joist hangers have developed extensive arrays of joist hanger models for various geometric conditions and load capacities. A catalog from a major hanger supplier has over 70 pages devoted to joist hangers. Some of the joist hangers can be called beam hangers or girder hangers due to the large size and load capacity.

The author has been involved in the design of wood framing for many buildings that use very complex framing to achieve the architectural requirements. The most complex cases often involve roof framing with various hips, valleys, and roof openings. These requirements often cause framing from common trusses to be supported by a girder truss. In complex cases, one end of the girder truss is then supported by another girder truss, which is then supported by a third girder truss. See Figure 1.



Figure 1. Complex (4th order) roof framing: wood trusses connected by hangers

In each case joist hangers are used to transfer the increasing loads from truss to truss. This "fourth order" framing is unusual, but becoming more common. Third order framing is not difficult to find. Second order framing occurs on most wood frame

buildings that are larger than a simple box ranch home. All of this results in increased usage of joist hangers in more heavily loaded and more critical connections.

MOVEMENT AND RESTRAINT ON SUPPORTING MEMBERS

The purpose of this research is to test the effect of support restraints on the capacity of a joist hanger connection. In actual applications the supporting member of a joist hanger is commonly a wood beam or the bottom chord of a girder truss. The supporting member is always restrained from movement to some degree. The supporting member is always restrained from moving downward by the stiffness of the beam or girder truss and the supports for the beam or girder truss. This vertical restraint is the primary restraint in the direction of load.

Secondarily, the beam or girder truss has some restraint from lateral movement (perpendicular to the beam; in the longitudinal direction of the joist). Thirdly, the beam or girder has some restrain against rotation in the plane of the joist. Movement of the supporting beam in other directions is not usually considered to be related to the downward movement from gravity loads on a joist hanger connection and is not considered in this research.

One of the primary means of providing the secondary lateral restraint and the third rotational constraint is by the connection of the supporting member to the supported joist. The supported joist or truss is usually very stiff in the longitudinal direction of the joist and quite stiff in rotation in the plane of the joist. Other building elements that are connected to the beam or girder may also provide some lateral and rotational constraints.

In actual construction, the degree of restraint provided by these other building elements has great variability. The case of a roof truss supported by a girder truss at a location away from the supports of the girder truss may have very little lateral and rotational restraint. In some cases the main restraint is provided by an attached gypsum board ceiling. In other cases the ceiling is suspended, and the truss bracing is the main constraint.

One common condition is when floor decking is directly attached to the beam or girder. The floor decking may provide substantial lateral restraint and some rotational restraint when combined with other building elements. The connections of the beam or girder at the supports in combination with the lateral stiffness and torsional stiffness of the beam or girder also provide some restraint.

This research compares two cases. In one case the supporting beam of a joist hanger connection is restrained from lateral and rotational movement by blocking and metal rods. In another case the only restraint on the supporting beam is from the joist and

the joist hanger connection. The hypothesis is that the downward load capacity of the joist hanger will be significantly less when no additional restraints are provided to the connection.

REVIEW OF TESTING STANDARDS AND CODE APPROVALS

The current standard for testing joist hangers in North America is ASTM D 7147-05. This standard also provides a method of assigning the allowable loads for joist hangers.

The standard test method loads a joist that is connected to beams (or headers) at each end. Blocking and tensile reinforcement against the blocking is used to restrain the beams from lateral and rotational movement. A 3.18 mm (1/8 inch) minimum gap is specified between the joist and the beam before loading. See Figure 2.

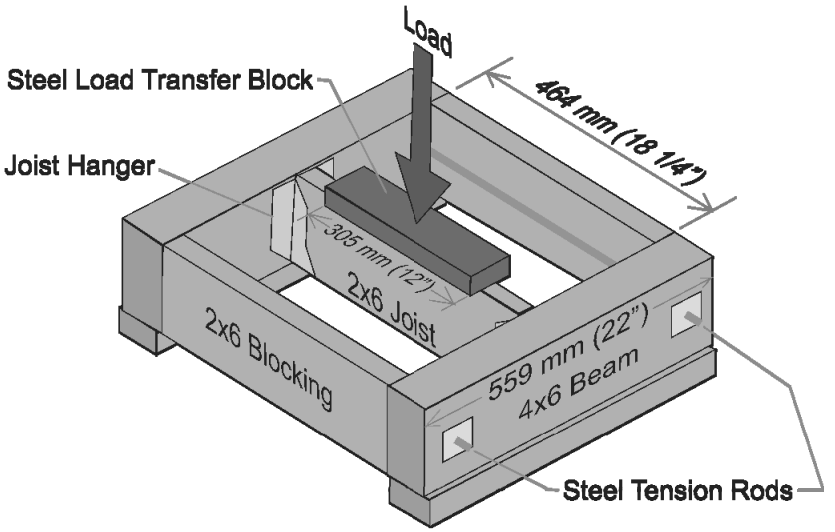


Figure 2. Standard test set-up with the actual dimensions used (restrained)

The allowable joist hanger load (for normal load duration) is specified as the lesser of the following:

The average ultimate load per joist hanger divided by 3.0, when six or more tests are performed.

The lowest ultimate load per joist hanger divided by 3.0, when less than six (but at least three) tests are performed.

The average load per joist hanger at which the measured vertical deflection is at 3.18 mm (0.125 inches).

The test method is based on a short term test. The test method specifies the rate of movement of the test machine crosshead of between 0.8 to 5.1 mm (0.03 and 0.20 in.)

per minute. The ultimate load shall not be reached in less than 5 minutes. Although the test standard uses an ultimate design value divided by 3.0, the actual safety factor is much less than 3.0, after adjusting the short term test results to a normal (ten year) duration of load.

The allowable joist hanger load is also not allowed to exceed a calculated load based on the allowable values of the steel in the joist hanger and the allowable values for the fasteners used in the connection. An addition limitation is based on the calculation of wood bearing and fasteners of the joist bearing on the seat of the hanger.

Design values for joist hangers are not listed in the *2009 International Building Code* (IBC). The use of joist hangers in the United States is usually based on the acceptance by the Building Official of an evaluation report. Evaluation reports are commonly produced by the ICC Evaluation Service, Inc. (ICC-ES) or other recognized agencies that perform technical evaluations of building products. In almost all cases, the test report for a joist hanger is produced and owned by the manufacturer of the joist hanger. The actual test reports are considered to be confidential and are not published. The test reports and other materials are submitted to the evaluation agency as justification of the design values listed in the published evaluation report. Although much testing is performed on joist hangers, very little information is published on the subject of testing joist hangers.

MATERIALS USED

The lumber, joist hangers, and nails used were purchased at retail building supply outlets. Both the lumber and the joist hangers were purchased at two different companies. The quality of both lumber and joist hangers appeared similar at both sources.

A commonly used hanger model was chosen for testing to represent the “middle of the field”. Size and load capacity was also selected to fit the available testing equipment. A “face mount” hanger was selected. A face mount hanger has no top flange, so all load must be transferred to the supporting beam by the fasteners.

The joist hanger selected was a Model HUS26 manufactured by one of the major suppliers in the United States. This hanger model is widely used and readily available in the United States. At least two manufacturers use this same model number for a joist hanger with a similar (but not identical) design and allowable capacity. The hanger model is considered to be heavier and more expensive than the lightest hangers that are commonly used. This hanger would normally be selected for a heavier required capacity, but it is not the heaviest used in this size category.

The joist hanger is made from 16 gauge galvanized steel. The measured steel thickness was 1.40mm (0.055 in.). The hanger is designed to fit a 2x6 joist but can also be used for a larger joist. This hanger is also commonly used to connect a roof truss to a girder truss. Since the bottom chord of many common trusses are 2x4 and the bottom chord of most girder trusses are 2x6 or 2x8, this size fits well with many roof trusses.

For the maximum capacity, this joist hanger model uses fourteen 89x4.12 mm (3.5x 0.162 in.) 16d common nails connecting directly from the hanger into the supporting beam. An additional six 16d common slant nails are installed into the joist at or near a 45 degree angle. These slant nails are in double shear. They penetrate the end of the joist and into the header at the slant angle.

The nails used were sold and labeled as 16d common nails and appeared to be typical of framing nails. They were measured at 89 mm (3.5 in.) long (from bottom of head to tip). The measured diameters varied from 4.01 to 4.17 mm (0.158 to 0.164 in.). The nail surface was smooth and bright. The nail shafts had eight slight, transverse indentations on each side in an area from 5 to 15 mm (0.2 to 0.6 in.) from the nail head. The head diameters were 9.1mm (0.36 in.) and the head thickness was 1.6 mm (0.062 in.).

The lumber was similar to, but somewhat more consistent than, lumber that is often used in actual construction. The lumber was purchased as #2 and better Douglas Fir. The beam (or header) members were 4x6 and the joist member were 2x6. The pieces were selected to avoid major lumber characteristics in the hanger area that may weaken the connection. Some more common characteristics such as small knots, small drying checks, and minor slope of grain were present. The lumber was graded as surface green, and all lumber was air-dried at room temperature, until the measured moisture content was between 11 and 15%. Care was taken to avoid drying below 11%.

All materials were accurately cut. All nails were driven by hand using a 0.57 kg (20 ounce) hammer. To provide consistent nailing, a pilot hole was drilled for all nails. The depth of the pilot hole was near one-third the nail length. The pilot holes were drilled with a 2.38 mm (3/32 in.) inch bit, which is 59% of the nail diameter. The *2005 National Design Specification for Wood Construction* (2005 NDS) allows pilot holes up to 75% of nail diameter without capacity reduction.

TESTING METHODS

Except as noted herein all procedures specified in ASTM D 7147-05 were followed. A 305 mm (12 in.) long steel load transfer block was used to distribute load along the top of the joist and avoid excess crushing. All assemblies were preloaded to 4.45 kN

(1000 lbf) before testing. The movement rate of the crossheads was from 3.8 to 5.1 mm (0.15 to 0.20 in.) per minute.

Six assemblies were made using the ASTM D 7147-05 arrangement (Figure 3) with blocking used to restrain the supporting 4x6 beam (or header) members from lateral or rotational movement. 9.5 mm (3/8 in.) metal rods were used as tension reinforcement just inside the blocking. This kept the 4x6 beams tight against the blocks. These assemblies are referred to as the "restrained" assemblies. The blocks were cut 6 mm (0.25 in.) longer than the 2x6 joist, so that a 3 mm (1/8 in.) gap between the joist and the beam at the joist hanger could be maintained. Polyethylene tape was applied to the each end of the joist to minimize load transfer due to friction at the end of the joist. Digital indicators were located at each joist end to measure vertical displacement of the joist with respect to the supporting beam. The measurement was taken from the mid-height of the joist to a point ¼ the beam height from the bottom of the beam.

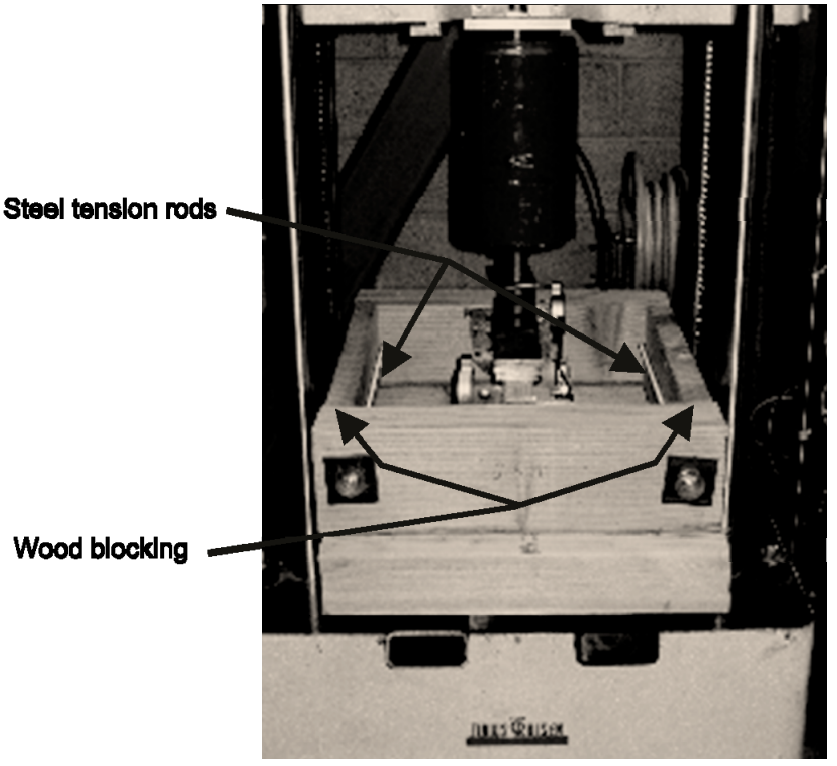


Figure 3. Restrained test configuration

Six other assemblies were made to allow unrestrained lateral movement and rotation of the supporting beam. These assemblies are referred to as "unrestrained". The only restraint against lateral movement and rotation is that provided by the joist and joist hanger connection of the joist to the beams. A heavy steel wheel was mounted to each end of the beams. The wheel is mounted to a welded steel bracket to support the 4x6 beam. The axle of each wheel is located at the centroid of the cross-section of

the 4x6 beam. This arraignment allows free rotation about the centroid and lateral movement. The steel wheel had tapered roller bearings to allow low friction and heavy loads. The steel wheels roll on smooth steel box sections that rested on the bed of the testing machine. The length of the beam was shortened to 267 mm (10.5 in.) to fit the wheels, steel brackets, and steel box sections into the testing machine. This short beam length also avoids significant bending of the beam. See Figure 4. All other aspects including the gaps and polyethylene tape are the same for both types of assemblies.

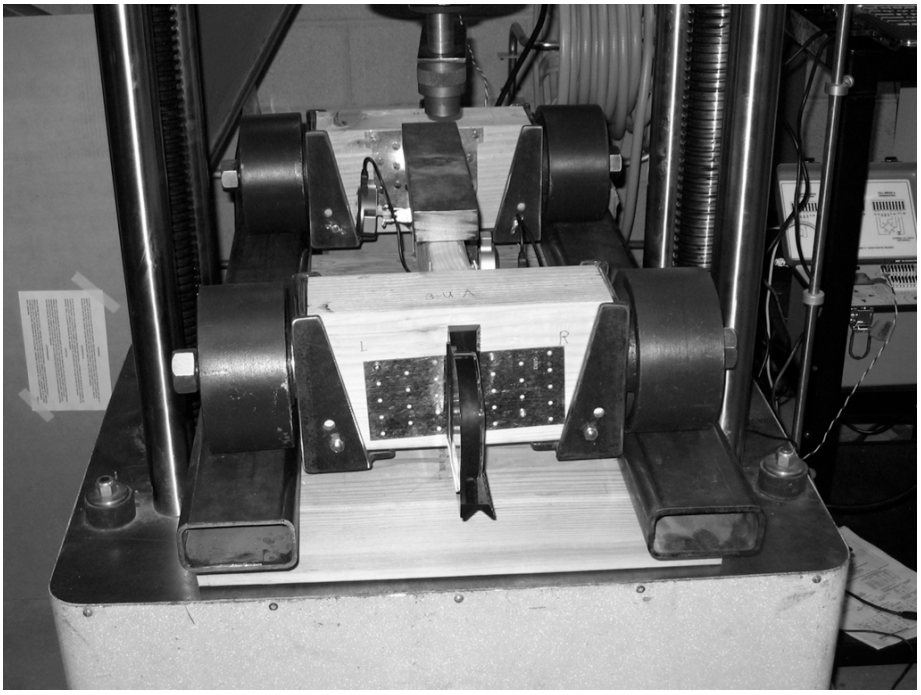


Figure 4. Unrestrained test set-up

In addition to the measurement of the vertical joist deflection, the unrestrained assemblies had digital indicators to measure the horizontal movement of the beam from the joist at each joist end. The horizontal measurement was taken against the mid height of the beams. A balance protractor was also placed on each beam to take visual measurements (within one degree) of the rotation of the beams.

RESULTS FOR RESTRAINED ASSEMBLIES

The average ultimate load per hanger was 28.7 kN (6449 lbf) for the restrained assemblies as shown in Table 1. The mode of failure for all tested restrained assemblies was wood failure (horizontal shear, splitting and bending) of the joist member that was supported by the hanger. See Figure 5. After the much shear splitting of the joist, the joist ultimately failed in tension stress due to the increase in tensile-bending stress resulting from the lack of full composite action within the joist.

Due to the wood failure (i.e. horizontal shear), the full capacity of the hanger connection was not achieved.

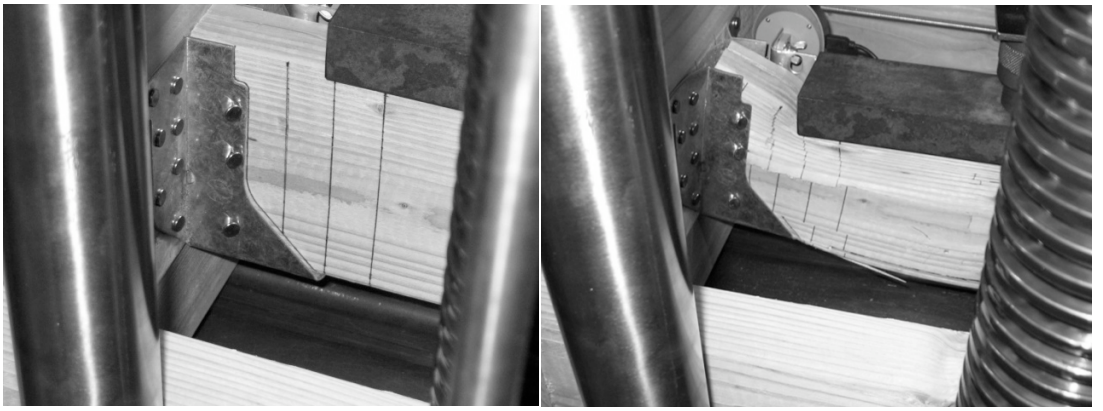


Figure 5. Before and after horizontal shear failure in joist

In test 4-R an attempt to reinforce the joist within the limits allowed by ASTM D 7147-05 was tried. It was hoped that the reinforcement might prevent the shear failure of the joist. A piece of laminated veneer lumber (LVL) was glued onto each face of the center portion of the joist. See Figure 6. The reinforcement extended to a distance up to 51mm (2 in.) from the end of each hanger, which is the maximum reinforcement allowed by ASTM D 7147-05. The result was still a shear failure in the unreinforced area without a large increase in capacity.

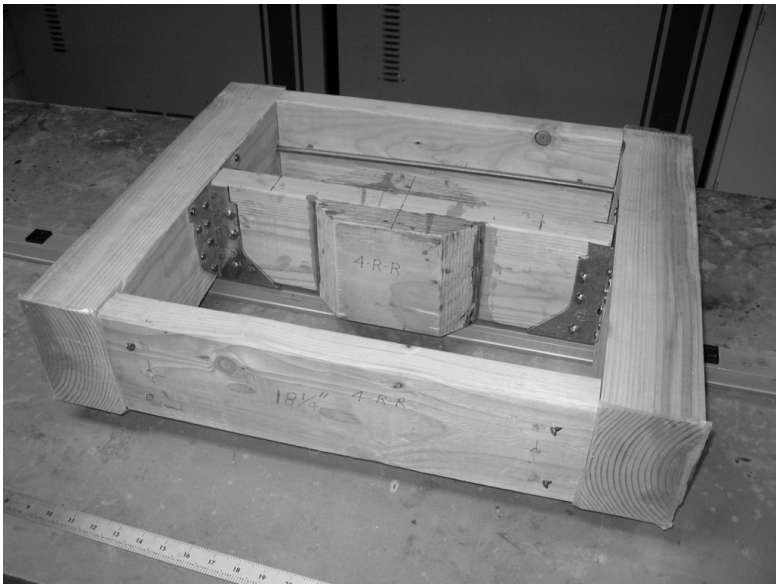


Figure 6. Assembly 4-R with reinforced joist

The average shear stress in the joist at ultimate load for the restrained assemblies can be calculated by beam theory as 8.081 MPa (1172 psi). This compares to an allowable shear stress for Douglas Fir-Larch of 1.24 MPa (180 psi), based on normal duration of load per the 2005 NDS. Based on this comparison it is not surprising that

the shear stress of the joist limited the ultimate load for the restrained assemblies. A higher ultimate load for the restrained assemblies could be expected, if a larger joist is used and/or a joist material with higher shear capacity is used, such as some engineered lumber products. This may explain why the results of these tests (average 28.7 kN or 6449 lbs) are much lower than the average ultimate value of 44.5 kN (10,000 lbs) reported in the hanger manufacturer's catalog of 2005.

RESULTS FOR UNRESTRAINED ASSEMBLIES

The average ultimate load per hanger was 8.08 kN (1817 lbf) for the un-restrained assemblies as shown in Table 1. The mode of failure for all tested un-restrained assemblies was due to movement of the hanger and the attached beam away from the end of the joist. This movement was both horizontal and rotational. This movement caused the hanger seat to rotate allowing the joist to slide down the seat and away from the beam.

Table 1. Average ultimate load for unrestrained cases is 28% of restrained cases

	Restrained Cases	
	Max. Load per Hanger	
Test	lbf	kN
1-R	6053	26.9
2-R	5658	25.2
3-R	7236	32.2
4-R	6981	31.1
5-R	6389	28.4
6-R	6377	28.8
Average	6449	28.7
COV	531	2.4

	Un-restrained Cases	
	Max. Load per Hanger	
Test	lbf	kN
1-U	1520	6.76
2-U	2274	10.12
3-U	2148	9.55
4-U	1353	6.02
5-U	2058	9.15
6-U	1548	6.89
Average	1817	8.08
COV	354	1.58

The hanger connection has some moment due to the offset of the seat of the hanger from the center of the supporting beam. When the beam is unrestrained, the only mechanism to resist this moment and prevent rotation is the connection of the beam to the hanger and to the joist. The joist cannot rotate within the plane of the joist, since it is supported at two locations. This moment is resisted by a force couple within the connection. See Figure 7.

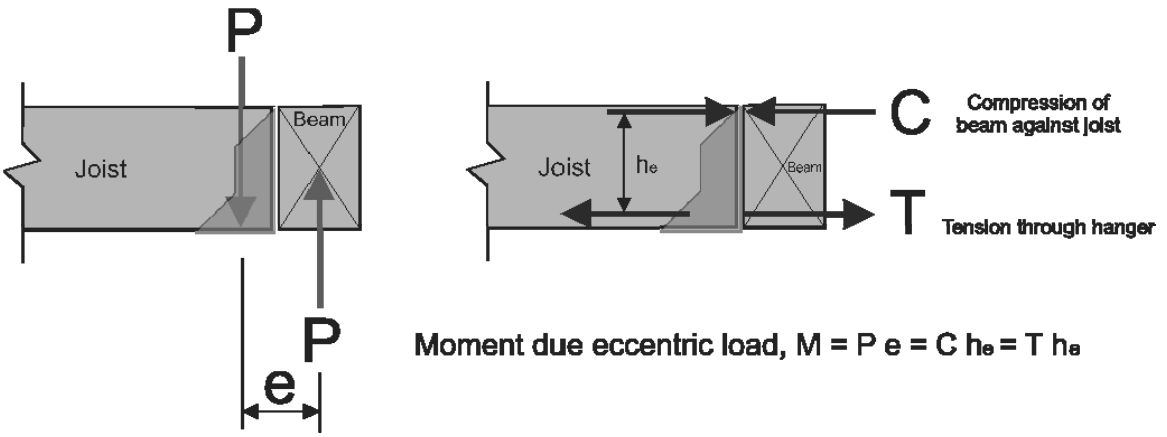


Figure 7. Forces and moment caused by the eccentric load on the hanger

During loading, the top of the beam rotates towards the joist until the small gap between by the beam and the joist closes. After the gap is closed, the upper portion of the beam bears against the joist in compression. The bottom of the beam rotates away from the bottom of the joist, but is restrained by the connection of the beam to the joist hanger and the joist hanger to the joist. This restraint results in a horizontal tension force through the joist hanger connector. See Figure 8.

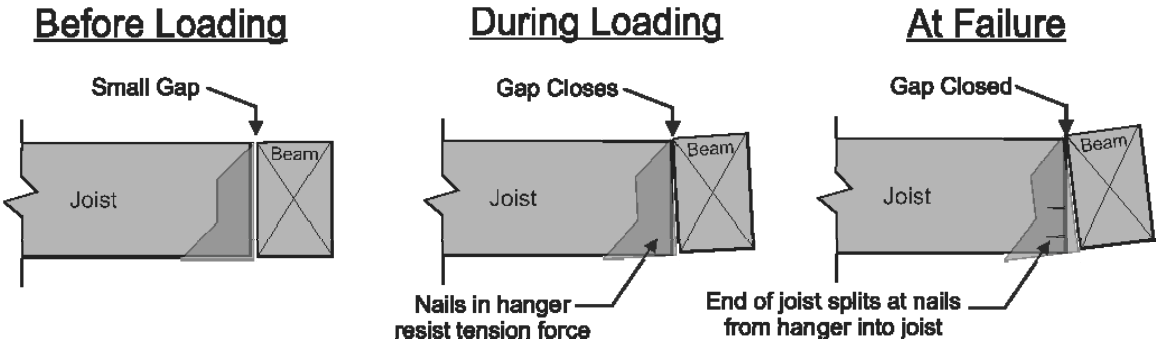


Figure 8. Mode of failure for the unrestrained case

The ultimate mode of failure is due to the nails from the joist hanger into the joist shearing through wood near the end of the joist. This shearing is parallel to the grain of the joist and very close to the joist end. See Figure 9. It is well known that nail connection into wood are weak in this mode of failure. Wood fasteners require reasonable end distances for this type of loading to achieve the design value of the fasteners.



Figure 9. Failure of unrestrained case by nails splitting out of the end of the joist

COMPARE RESULTS: RESTRAINED AND UNRESTRAINED ASSEMBLES

The average ultimate load per hanger was 28.7 kN (6449 lbf) for the restrained assemblies and 8.08 kN (1817 lbf) for the unrestrained assemblies. This difference is clearly statistically significant. This confirms the hypothesis that the downward load capacity of the joist hanger is significantly less when no additional restraints are provided to the connection. The average ultimate load for the unrestrained assemblies was 28 percent of the average ultimate load for the restrained assemblies.

The average ultimate load per hanger for the unrestrained assemblies (8.08 kN or 1817 lbf) was less than the design value for the hanger of 11.4 kN (2565 lbf), based on normal duration of load. Since the test is a short term load the difference is larger, if we compare it to a design value of 14.8 kN (3335 lbs) for a short term loading such as wind.

DISCUSSION

A scaled comparison of the testing results to the design values and the manufacturer stated average ultimate load is shown graphically in Figure 10. These results are

concerning because they shows that the ultimate strength for the unrestrained case is lower than the design values that are commonly used.

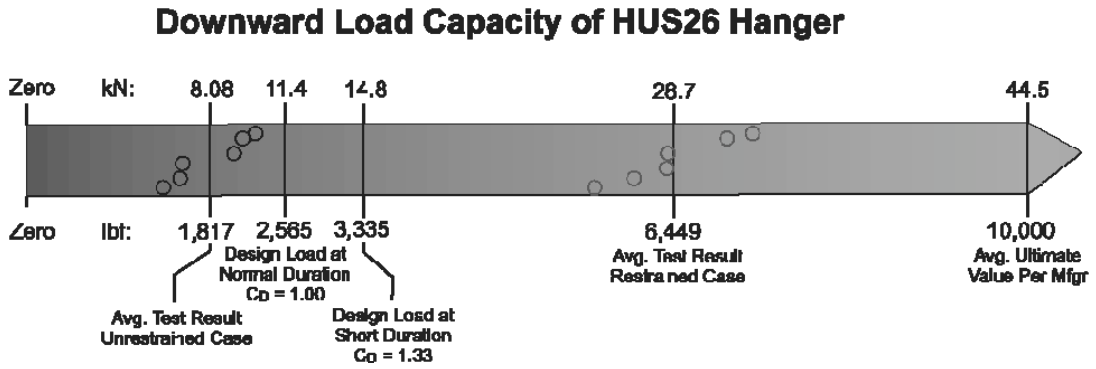


Figure 10. Scaled comparison of load values for hanger connection

It is not clear, as discussed earlier, how much lateral and rotation restraint is provided by actual construction. It is likely that the degree of constraint varies widely based on the type of connection, the related framing, and finish materials in the vicinity of the connection. Wood-to-wood connections within roof truss systems may often have less restraint than connections in floor systems.

It is likely that almost all common construction provides some level of support constraint. The unrestrained case tested is an extreme case with no support constraint. This should be considered as an extreme lower limit of what is possible.

Due to the wide variety of models of hangers it would be a mistake to assume that all hanger models will have such a large reduction in capacity without support restraints. The identified mode of failure should be very different with face-mount hangers. Hanger size may be a factor, since the length of the moment arm in the unrestrained mode of failure decreases with shorter hangers. The use of slant nailing in the connection from the hanger to the joist may weaken the connection in the unrestrained mode of failure.

The testing uncovered a mode of failure that can occur in real construction but cannot occur in the ASTM D 7147-05 testing standard. This may indicate that some changes are needed in the testing standard. Possibly an unrestrained test could be incorporated with a lower safety factor to prevent this mode of failure.

CONCLUSION

The capacity of a wood-to-wood joist hanger connection is greatly reduced if there is no lateral and rotational constraint on the supporting beam, for the model of joist hanger tested. If the supporting beam is not restrained, the mode of failure is different than what occurs by the standard testing method of ASTM D 7147-05.

The ASTM D 7147-05 testing standard allows the usage of constraints on the supporting beam. If the supporting beam is not constrained by other building elements, this may result in an over estimation of the capacity of some connections. Building designers should be aware of this so that the supporting beam is braced to provide the needed lateral and rotational resistance. Further research is needed to determine methods to provide this lateral and rotational resistance.

REFERENCES

American Forest & Paper Association, Inc., AF&PA American Wood Council. (2005). *National Design Specification (NDS) for Wood Construction 2005 Edition*. Washington, DC

ASTM International. (2005). ASTM D 7147-05 Standard Specification for Testing and Establishing Allowable Loads of Joist Hangers. West Conshohocken, PA.

ICC Evaluation Service, Inc. (2008). Acceptance Criteria for Joist Hangers and Similar Devices AC13. Whittier, CA.

ICC Evaluation Service, Inc. (2008). ESR-2549: Simpson Strong-Tie Face-Mount Hangers for Wood Framing. Whittier, CA.

ICC Evaluation Service, Inc. (2009). ESR-1881: USP Structural Connectors. Whittier, CA.

International Code Council, Inc. (2009). 2009 International Building Code. Country Club Hills, IL.

Simpson Strong-Tie Inc. (2005). Wood Construction Connectors C-2005. Pleasanton, CA.

Simpson Strong-Tie Inc. (2009). Wood Construction Connectors 2009-2010 C-2009. Pleasanton, CA.

USP Structural Connectors. (2007). Full Line Product Catalog (54th ed.). Burnsville, MN.

Contextualizing the Load Duration-dependent Strength of Wood Members

G.R. Searer[1], T.F. Paret[2], and R.J. Kristie[3]

[1] Associate Principal, Wiss, Janney, Elstner Associates, Inc., 2550 N. Hollywood Way, Suite 502, Burbank, CA 91505; Phone: (818) 303-1300; gsearer@wje.com
[2] Senior Principal, Wiss, Janney, Elstner Associates, Inc., 2000 Powell Street, Suite 1650, Emeryville, CA 94608; Phone: (510) 428-2907; tparet@wje.com
[3] Principal, Wiss, Janney, Elstner Associates, Inc., 330 Pfingsten Road, Northbrook, IL 60062; Phone: (847) 272-7400; rkristie@wje.com

ABSTRACT

Strength is defined as the capacity of a material or element to resist load and can be graphically portrayed on a load-displacement curve by the point at which the maximum load is sustained, regardless of the displacement at which it occurs. It has long been recognized that the strengths of structural materials typically exhibit some sensitivity to load duration. Most strength of materials textbooks, for example, touch on the subject of strength versus load duration and indicate that structural materials subjected to very short term loading exhibit strengths that are enhanced relative to slower loading regimens. Less well-recognized is the fact that the strengths of some structural materials under very long duration loading are substantially reduced relative to what are typically taken to be their ultimate capacities, although for years, the wood engineering community has incorporated a factor into the codes that explicitly acknowledges wood's reduced capacity under long duration loads. This paper addresses the often misunderstood phenomenon of load duration effects in wood members.

INTRODUCTION

While the building code now reflects the effects of long-duration loading for design of wood, there exists relatively little technical discussion in the literature of the general subject of the behavior of wood subjected to long-duration stresses, other than requiring that wood intended to resist long-duration stress be designed to lower stress levels than wood designed to resist only short duration loads. As a result, the engineering community-at-large does not appear to be well-versed in the actual mechanics that justify the design capacity reduction when long-term loads are to be considered. The reduction in capacity under long-term loading ought not be construed as a "loss-of-capacity", which term suggests that some increment of strength is absent when it ought to have been present, nor does it result from "decay", which suggests similarity to decay damage from biological attack. Both these terms, as well as a long list of others, wrongly suggest the existence of damage that requires repair. To the contrary, the reduced long-term capacity of wood relative to its enhanced capacity under impact and to its capacity under short duration loading is not damage, but is simply the normal and predictable effect of long-term loading.

LOAD DURATION-DEPENDENT CHARACTERISTICS OF WOOD

For more than six decades, the engineering community has incorporated a factor into building codes and standards that explicitly acknowledges wood's reduced capacity under long duration loads. While the building code provisions for design of wood reflect the effects of long duration loading -- by requiring that wood intended to resist long duration stress be designed to lower stress levels than wood designed to resist only short duration loads -- this reduction factor is one of a continuum of factors used to adjust the load-duration dependency of wood as a function of duration. As wood's capacity is deemed to be relatively lower under the influence of long duration -- essentially permanent -- loads, the load duration factors that have been established for permanent loads are less than 1.0. Similarly, in recognition of wood's enhanced capacity under short duration loads, the established load duration factors are greater than 1.0. Simply, wood (like a number of other structural materials) exhibits different strengths under different load duration regimes.

Load Duration Factors in Design

In allowable stress design, allowable stresses must be multiplied by the load duration factor (C_D) that matches the shortest duration load in each load combination. Typical load duration factors (AF&PA, 2005) are provided in Table 1 below.

Table 1. Load Duration Factors for Wood.

Load Duration	C_D	Typical Design Loads
Permanent	0.9	Dead Load
Ten years	1.0	Occupancy Live Load
Two months	1.15	Snow Load
Seven days	1.25	Construction Load
Ten minutes	1.6	Wind/Earthquake Load
Impact	2.0	Impact Load

These load duration factors are based on the *Madison Curve* (Figure 1), which was developed by the Forest Products Laboratory in Madison, Wisconsin, and have been used in design practice since the 1940s (Breyer *et al*., 2007). A similar factor, the time effect factor (λ), is used for load resistance factor design.

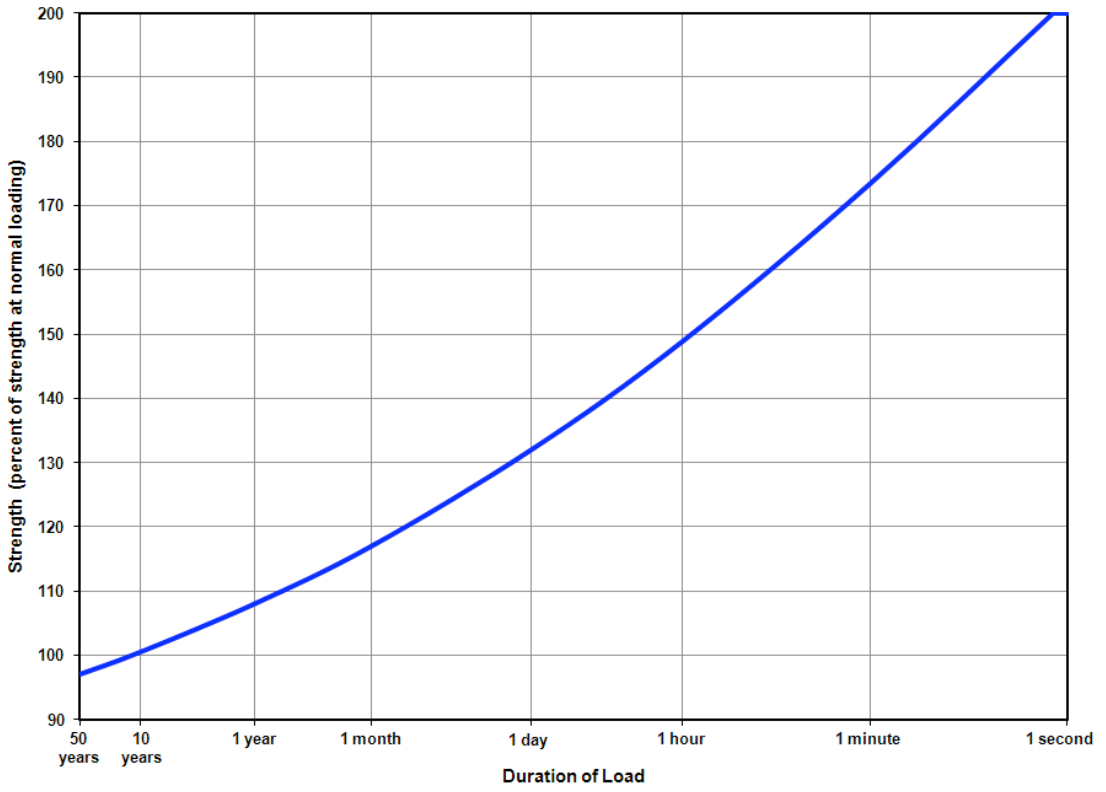


Figure 1: The *Madison Curve* -- variation of wood strength with duration of load, based on data from the Forest Products Laboratory (2010).

For most wood-framed structures, the load duration factor for permanent dead load typically does not govern the design, since design live loads in wood-supported structures tend to be as large as or larger than the design dead load. Adjustments to wood design values are linked to the cumulative time that such loads are applied; when combined with the exponential relationship between strength and load duration, AF&PA (2001) concludes, "the accumulated effects of loadings less than the maximum load the member is designed for are considered negligible and noncritical." Over the years, a number of terms have been used to describe the relationship between load duration and strength in wood, including creep rupture (Corotis and Sheehan, 1986) and damage accumulation (Murphy *et al*., 1987 and AF&PA, 2001). We note that the AF&PA no longer uses the term "damage accumulation" in their most recent commentary (2006). The discontinued use of this term appears consistent with the goal of helping to eliminate confusion regarding this phenomenon.

Failure

At the point where the demand exceeds the capacity of a wood member, regardless of whether it is long-duration demand that exceeds long-term capacity or short-duration demand that exceeds short-term capacity, the wood member will break. Figures 2 and 3 depict failures of wood members and/or structures that failed spontaneously after supporting relatively constant levels of load for many years. None of these failed structures was known to have experienced substantial changes to the loads they

supported for long periods of time prior to the occurrence of failure. Moreover, none of these members or structures exhibited decay or deterioration in the failed regions, or experienced sudden changes in moisture content, or anything else to which their spontaneous failure could be directly attributed.



Figure 2: View of a 4x16 roof purlin that failed under long-term dead load.

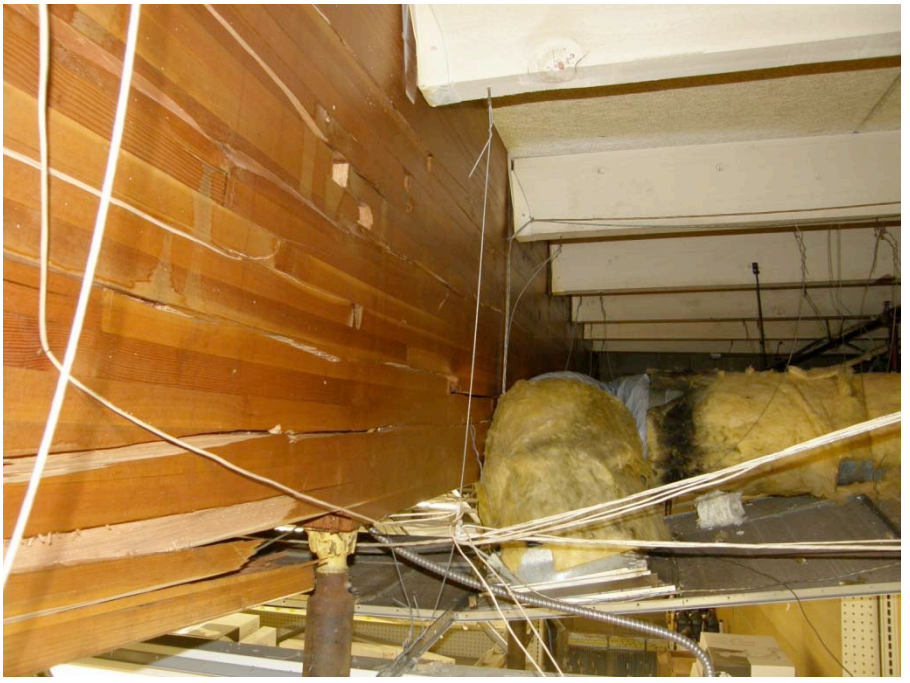


Figure 3: View of a large glu-lam beam that failed under long-term dead load.

The failure of these members is attributable to the simple fact that when load in a wood member is sustained for long periods of time, at some point the induced stresses may exceed the member's long-term capacity. Figure 4 graphically depicts an idealization of this occurrence. In the figure, the horizontal axis tracks the passage of time, the right-side vertical axis tracks the intensity of the sustained load and the left-side vertical axis tracks the member demand-to-capacity ratio (D/C). As the plot depicts, over time, the member D/C approaches and eventually reaches 1.0, even as the sustained load remains constant. At the instant of time when the member D/C rises above 1.0, the member will theoretically fail -- no decay, no sudden change in load, no external influence needed. The failure is simply a result of the time (duration) that the load has been supported by the wood member; as stated above, this time-dependent characteristic has been recognized in design practice since the 1940s. It is important to note, however, that wood itself exhibits significant variation in its mechanical properties, as discussed in greater detail in Paret *et al*. (2011), and that these variations often play a significant role in the failure of wood members.

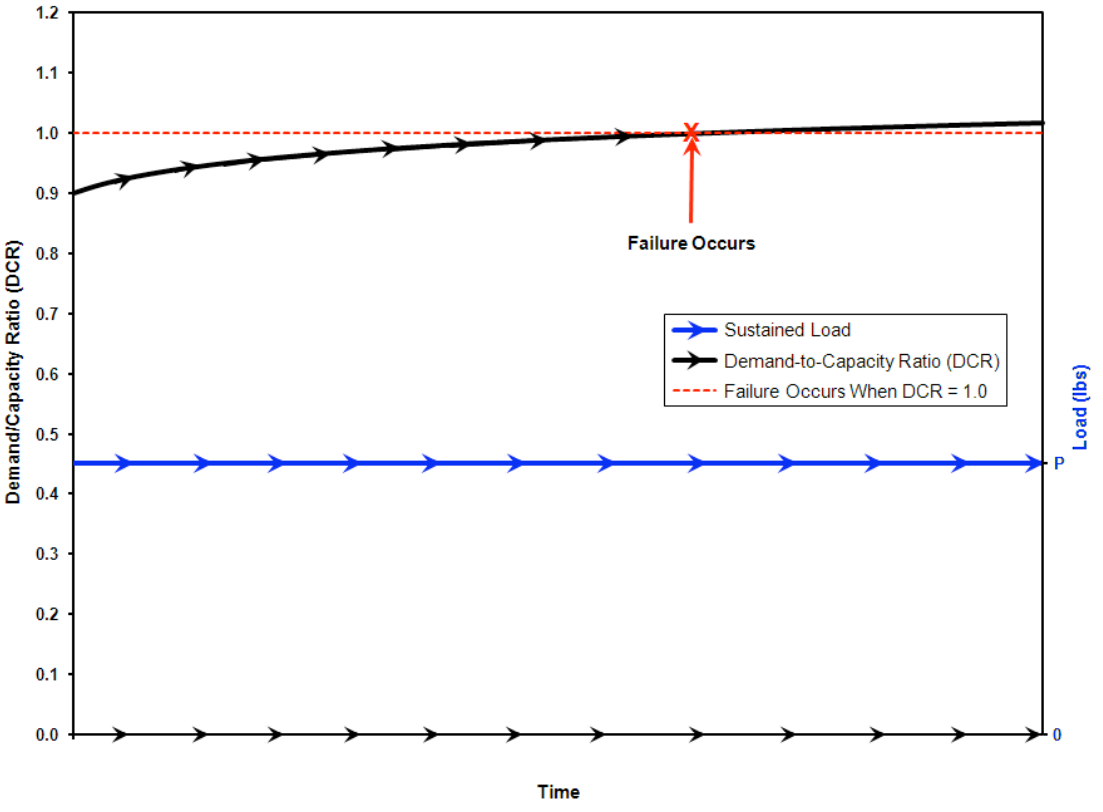


Figure 4: Although the demand remains the same, the natural time-dependent properties of wood can eventually result in failure.

OTHER STRUCTURAL MATERIALS EXHIBIT SIMILAR BEHAVIOR

A highly relevant, but similarly under-appreciated, analogy to the behavior of wood under the influence of long-duration loading can be found in concrete. Engineers almost universally understand that concrete gets stronger with time as cement hydration continues (Figure 5). Just as the 28-day compressive strength of concrete is

usually far greater than its seven-day strength, the compressive strength of concrete that is one year old is usually significantly greater than 28-day old concrete, and so on and so forth as can be seen in the figure. Regardless, a cylinder of older concrete can be made to "appear" weaker than younger concrete of the same mix design -- simply by prolonging the loading rate of the test used to determine strength of the older concrete -- because the compressive strength of concrete is sensitive to loading rate / load duration much like wood. In fact, a cylinder of concrete loaded to a fraction of its short term compressive strength will fail if the load is ramped up slowly enough or applied long enough.

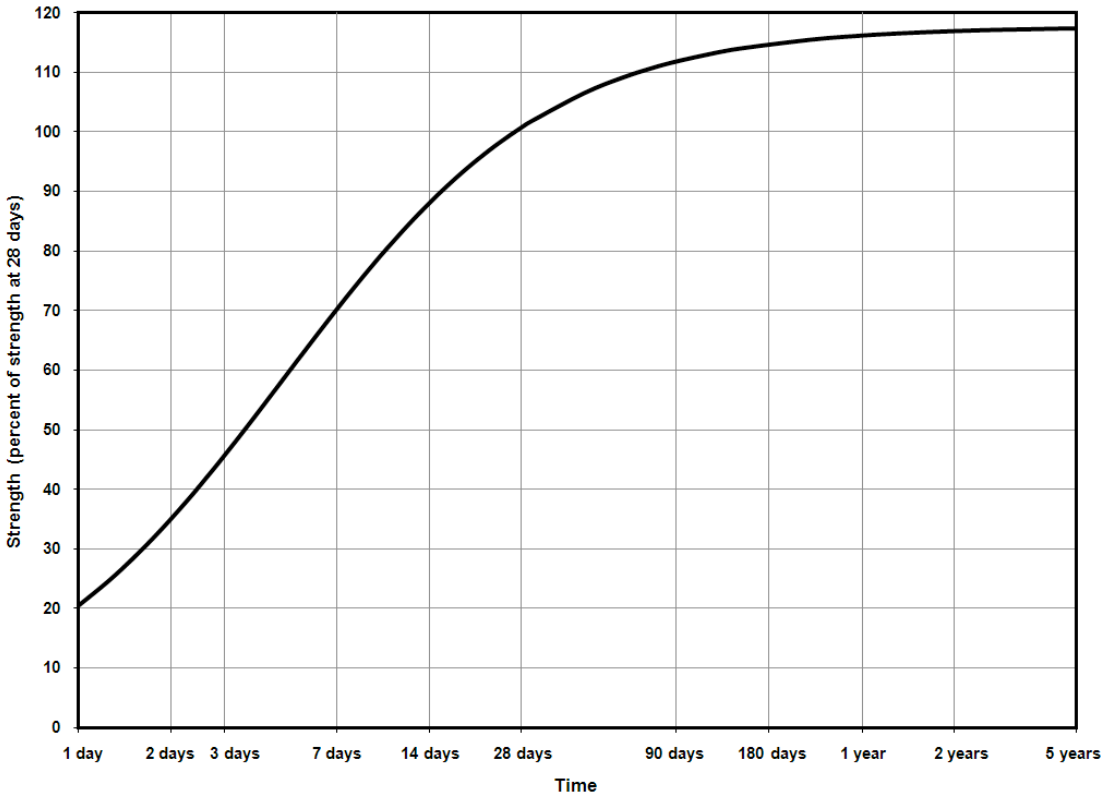


Figure 5: Increase of concrete strength with age (from Nilson, 1987).

Figure 6 shows the relationship between the compressive strength of concrete and rate of load application (from McHenry and Shideler, 1956). Like wood, concrete exhibits greater capacity under short duration loads than it does under longer duration loads, despite the acknowledged fact that the concrete exhibiting lower capacity is actually stronger (because it is older) than the concrete exhibiting greater capacity. As is the case for wood, this relationship is fundamentally a demand-side phenomenon that results from the differences in the way that the material responds to short duration and long duration loading. Concrete does get stronger over time, but it has lower strength under the influence of long duration loads than it does under short duration loads, and thus may "appear" to be weaker if the loading time is prolonged. Since concrete experiences strength gain over time, it would clearly be incorrect to characterize the lower strength that concrete exhibits under the influence of long-duration loading as a "loss-of-capacity". The same holds true for wood.

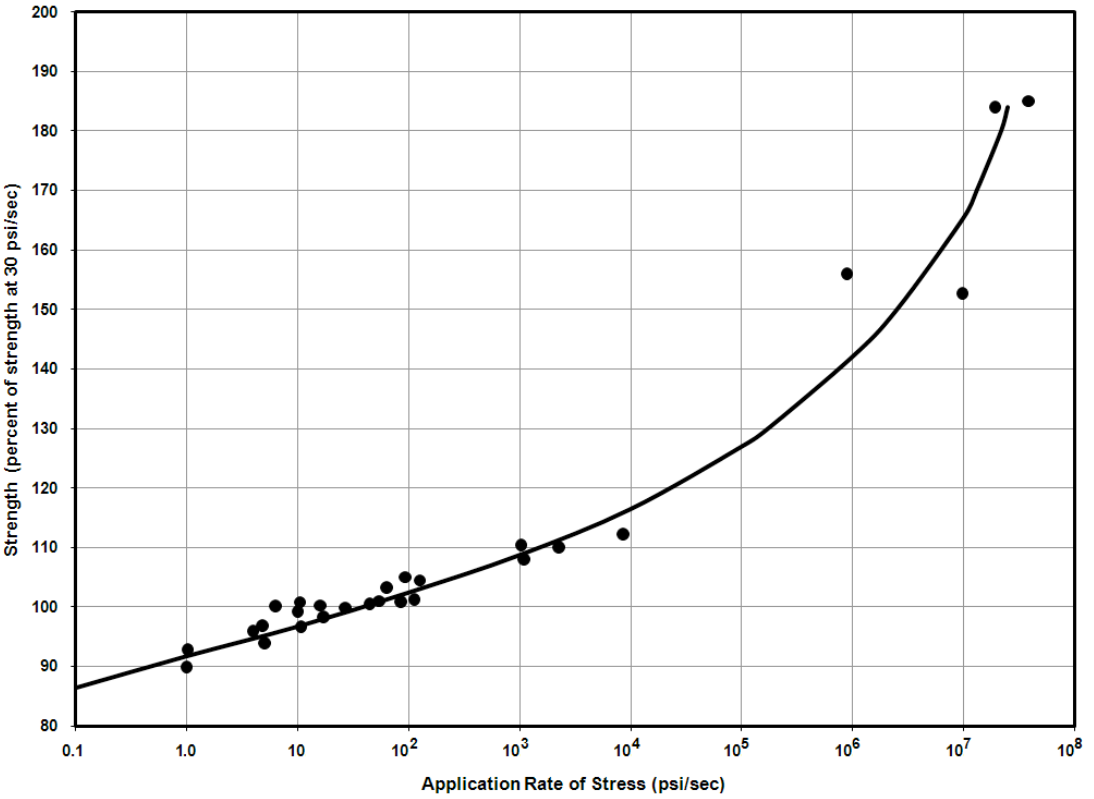


Figure 6: Variation of concrete compressive strength with application rate of load (data from McHenry and Shideler, 1956).

Steel also exhibits a similar variation of strength with loading rates, as noted in numerous studies, including Fisher and Iwankiw (2002), and as shown in Figures 7 and 8 (from Tanaka *et al*.). Like wood and like concrete, steel exhibits higher strengths under short duration loads than it does under long duration loads, but does so even more dramatically than both of the other two materials. Again, the lower strengths exhibited by steel under long duration loads are not indicative of a "loss-of-capacity", but reflect instead the sensitivity of steel to loading rate. Note that typical design procedures for routine steel structures do not consider these effects.

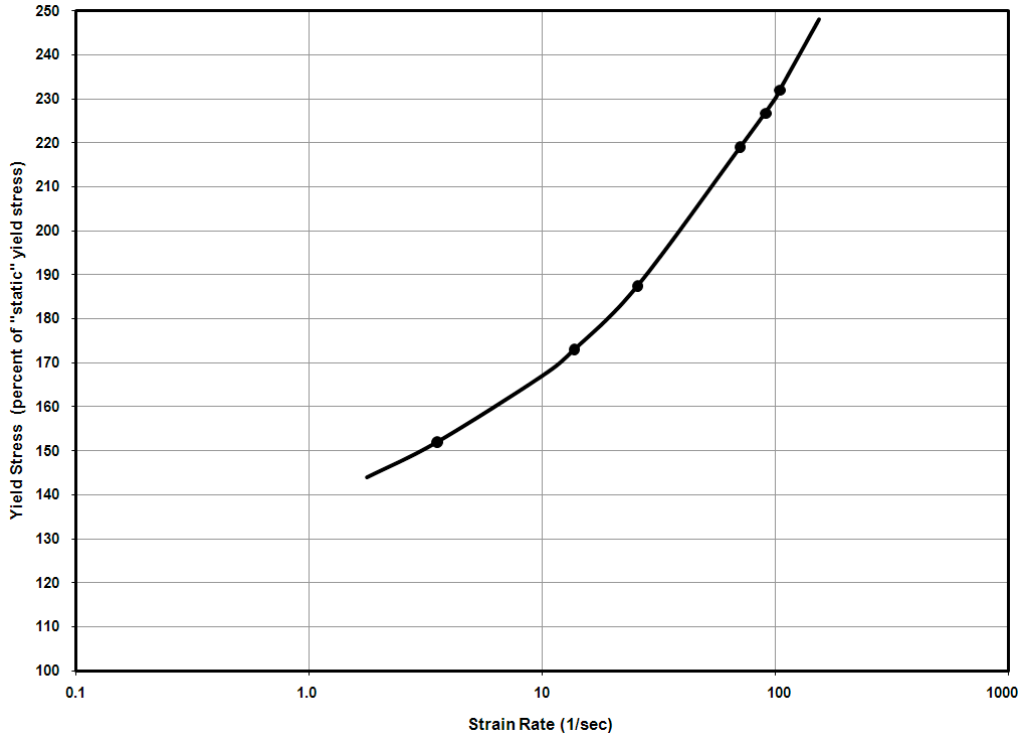


Figure 7: Variation of steel stress with strain rate: yield point data, from Tanaka *et al*., 1966.

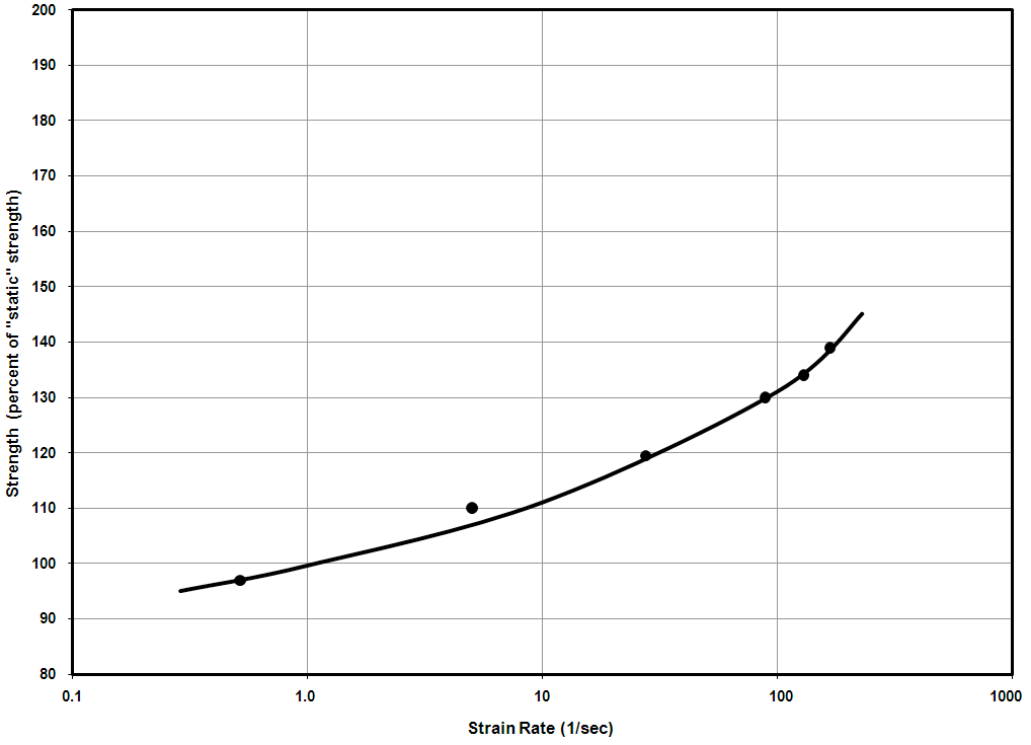


Figure 8: Variation of steel stress with strain rate: 4 percent strain data, from Tanaka *et al*., 1966.

STRUCTURAL CONTEXT IN WHICH TO VIEW THE LOAD-DURATION DEPENDENT BEHAVIOR OF STRUCTURAL MATERIALS

As presented above, commonly used structural materials exhibit similar loading rate/load-duration dependent properties despite having inherently different properties in multiple other respects. Despite these differences, however, these materials do, perhaps surprisingly, share this fundamental load duration dependency, though the different materials express this dependency somewhat differently. While a discussion of the mechanics of this dependency is beyond the scope of this paper, it remains worthwhile to contextualize the significance of this dependency to facilitate communication about what it really means when structural elements "fail" in the absence of obvious external influences. In our view, the context in which occurrences such as these should be viewed is as follows:

1. The strength of the material is a function of the length of time loads are applied.
2. Wood members (and elements of other materials with similar relationships between load-duration and strength) naturally have lower strengths for longer-term loads and higher strengths for shorter-term loads.
3. This natural response is predictable and is taken into account during design and analysis conducted in accordance with current codes. It would likely not have been appropriately considered during design prior to the 1940s.
4. Wood members (and elements of other materials with similar relationships between load-duration and strength) do not *become* stronger when they are loaded with a short-duration load; they merely *are* stronger as a result of the loading regime. Similarly, wood members (and elements of other materials with similar load-duration strength relationships) do not become weaker under long-duration loads; they merely have a lower strength associated with long-duration loads.
5. The lower strength associated with longer duration loads is neither the result of an "event" nor the consequence of "wearing out", "decay", or "deterioration", and is not something that requires repair. Note that the potential need or desire to strengthen a wood member to safely support extant sustained loads over a longer term is an issue separate and apart from "repair".

FINAL THOUGHTS

In the case of wood, the perceived lack of clarity about the net effect of long-term duration loads could potentially be eliminated simply by normalizing the load duration factors and the allowable stresses for wood so that the tabulated unmodified allowable stresses are matched with the longest duration design loads (i.e., dead load only, over the design life of the structure -- say 50 or 100 years), resulting in a 10 percent reduction in tabulated allowable stresses. For long-term loads greater than 10 years, the load duration factor would then equal 1.0, and for all loads and load combination of shorter duration, the load duration factor would be equal to the current load duration factor divided by 0.9, as shown in Table 2.

Table 2. Proposed* Load Duration Factors for Wood

Load Duration	C_D*	Typical Design Loads
Permanent	1.0	Dead Load
Ten years	1.11	Occupancy Live Load
Two months	1.28	Snow Load
Seven days	1.39	Construction Load
Ten minutes	1.78	Wind/Earthquake Load
Impact	2.22	Impact Load

* Assumes tabulated unmodified allowable stresses have been reduced by 10 percent.

As with most code provisions, providing the lowest allowable stress or lowest strength as the default would help eliminate the chance that an inexperienced engineer might forget to apply the factor, resulting in a potentially (slightly) unconservative design. Of course, given that load cases where dead loads only govern are fairly rare, and given the fairly small reduction in allowable capacity, this proposed change may not be worthwhile, but it would clarify that all wood members are not experiencing decay or deterioration simply as a result of long-term loads; merely adjusting the allowable load tables and the load duration factors by an equal but opposite factor (0.9) would eliminate any potential inference that such decay or deterioration is occurring.

CONCLUSIONS

For many structural materials, including wood, strength is dependent on the duration of loads that are applied to the material. In the case of wood, this phenomenon has been misunderstood or misrepresented on occasion as decay or deterioration, but, in reality, is not related to and should not be conflated with decay or damage from external phenomenon. Instead, the relationship between capacity and load duration is both natural and expected in wood, and the lower strength of wood under long-duration loads is not decay or deterioration any more than higher strength under shorter-duration loads is “anti-decay” or “reverse-deterioration”.

REFERENCES

American Forest & Paper Association (AF&PA), *ASD/LRFD National Design Specification for Wood Construction - ANSI/AF&PA NDS-2005*, AF&PA, Washington D.C., 2005.

American Forest & Paper Association (AF&PA), *Commentary on the National Design Specification for Wood Construction*, AF&PA, Washington D.C., 2001.

American Forest & Paper Association (AF&PA), *National Design Specification for Wood Construction with Commentary*, AF&PA, Washington D.C., 2006.

Breyer, D.E, Fridley, K.J, Cobeen, K.E., and Pollock, D.G., *Design of Wood Structures*, 6th Edition, McGraw-Hill Companies, Inc., New York, New York, 2007.

Corotis, R.B., and Sheehan, D.P., “Wood Damage Accumulation by Stochastic Load Models”, *Journal of Structural Engineering*, Vol. 112, No. 11, American Society of Civil Engineers, Reston, Virginia, 1986.

McHenry, D., and Shideler, J.J., "Review of Data on Effect of Speed in Mechanical Testing of Concrete," *ASTM Special Technical Publication No. 185*, pp. 72-82, ASTM International, West Conshohocken, Pennsylvania, 1956.

Fisher, J., and Iwankiw, N., "Appendix B - Structural Steel and Steel Connections", *World Trade Center Building Performance Study: Data Collection, Preliminary Observations, and Recommendations*, Federal Emergency Management Agency, Washington, DC, 2002.

Forest Products Laboratory (FPL), *Wood Handbook*, United States Department of Agriculture Forest Service, Madison, WI, p. 190, 2010.

Murphy, J.F., Ellingwood, B.R., and Hendrickson, E.M., "Damage Accumulation in Wood Structural Members under Stochastic Live Loads", *Wood and Fiber Science*, Vol. 19, No. 4, Society of Wood Science and Technology, Madison, WI, 1987.

Nilson, A.H., *Design of Prestressed Concrete*, John Wiley & Sons, New York, New York, p. 51, 1987.

Paret, T.F., Searer, G.R., Cobeen, K.E., and Kristie, R.J., "Strengths and Weaknesses of Wood-Framed Structures", Architectural Engineering Conference Proceedings, American Society of Civil Engineers, Reston, Virginia, 2011.

Tanaka, K., Matsuo, T., Kinoshita, M., and Maede, T., "Strength of Mild Steel at High Strain Rate", Bulletin of the Japan Society of Mechanical Engineers, Vol. 9, No. 33, 1966.

The AISC 2010 *Specification* and the 14th Edition *Steel Construction Manual*

Larry Muir[1] and Cynthia J. Duncan[2]

[1] Structural Steel Consultant, Atlanta, GA, 30340; email: larrymuir@larrymuir.com
[2]American Institute of Steel Construction, Suite 700, 1 E. Wacker Drive, Chicago, IL, 60601; PH 312-670-2400, FAX 312-896-9022; email: duncan@aisc.org

ABSTRACT

The 14th Edition of AISC's *Steel Construction Manual* will be available in the summer of 2011. The new manual includes and is based on the 2010 AISC *Specification for Structural Steel Buildings*. Because of the new specification, as well as some other modifications to the connection design procedures, the 14th Ed. Manual will include revisions to some of the existing 13th Ed. tables.

Many of the changes in the 2010 Specification are clarifications and minor adjustments, along with some important substantive changes in Chapter I, composite design, and a new Chapter N on quality control and quality assurance. Some of the other notable revisions include:

- Revised scope statement related to seismic design (Chapter A)
- Structural integrity is addressed (Chapter B)
- Stability design procedures are reorganized (Chapter C, Appendices 7 and 8)
- Revised the available shear strength values for bolts (Chapter J)
- Revised the slip-critical strength limit state for bolts (Chapter J)
- Tabulated the HSS connection design equations (Chapter K)
- New Appendix on Inelastic Analysis and Design (Appendix 1)

In addition to the changes to the Specification, several changes and improvements related to connection design were also made to the Manual. These include:

- Revised bolt value tables for both bearing and slip-critical connections (Part 7).
- Revisions and additions to the eccentrically loaded weld group tables (Part 8).
- Clarifications to the discussion of connecting elements subject to flexure (Part 9).
- Revisions to the design procedure for conventional single-plate shear connections (Part 10).
- A revised discussion on the design of flexible moment connections (Part 11).

INTRODUCTION

The AISC *Specification for Structural Steel Buildings* (AISC, 2010a) is the standard for the design, fabrication and erection of steel buildings in the U.S. and the basis of the AISC *Steel Construction Manual* (AISC, 2011). The new *Specification* is dated June 22, 2010, based on the ANSI accreditation date and the next AISC *Manual* will be the 14th

Edition of that publication and will be available in the summer of 2011. Reminiscent of the 6th Edition, the cover will be burgundy in color, and will contain some important updates. The 14th Edition continues to address both the allowable stress design (ASD) and load and resistance factor design (LRFD) methods similar to the 13th Edition. Although a concerted effort was made to minimize the number of changes in the 2010 *Specification*, ongoing research and innovation and industry practice have led to revisions and new provisions for member and connection design in the new *Specification* that are reflected in the *Manual.* The AISC *Specification* is located in Part 16 of the *Manual*, and continues to serve as the basis for the *Manual*—there would be no *Manual* without a *Specification.* New revisions to look for in the *Specification* are found in the scope statement (Chapter A), referenced material standards (Chapter A), structural integrity (Chapter B), composite design (Chapter I), quality control and quality assurance (new Chapter N), and inelastic analysis. Connection-related changes in the *Specification* occur in both weld and bolt design (Chapter J). The *Manual* covers some connection design topics not addressed specifically in the *Specification* and some of these topics have been updated, such as coped beam design, prying action, bracket plates, and single plate connections.

SCOPE

The scope statement in Chapter A of the 2010 AISC *Specification* clarifies the role of ASCE/SEI 7, *Minimum Design Loads for Buildings and Other Structures* (ASCE, 2010), by saying, "Wherever this Specification refers to the applicable building code and there is none, the loads, load combinations, system limitations, and general design requirements shall be those in ASCE/SEI 7." Further, the scope statement is now more generalized and revised to defer to the applicable building code. Previously, the scope indicated that building designs requiring an R factor of 3 or less were only required to satisfy the AISC *Specification*, and application of the AISC *Seismic Provisions for Structural Steel Buildings* (AISC, 2010b) was not required in that case. In some special cases, seismic detailing according to the AISC *Seismic Provisions* is required even when the R factor is less than 3. These cases are discussed in a new "Scope" statement appearing at the front of the 14th Edition *Steel Construction Manual*, as well as in a user note in the *Specification* Section A1.1.

NEW MATERIAL SPECIFICATIONS

Specification Section A2, Referenced Specifications, Codes and Standards, lists all of the publications and their titles that are referenced in the *Specification* or are acceptable for use with *Specification*. In addition to updating existing standards, such as AWS D1.1/D1.1M (AWS, 2008), RCSC *Specification for Structural Joints Using High Strength Bolts* (RCSC, 2009), and the AISC *Code of Standard Practice for Steel Buildings and Bridges* (AISC, 2010c), one new ASTM material standard included is ASTM A1043/A1043M (ASTM, 2005). This ASTM specification limits the yield to tensile strength (F_y/F_u) ratio to 0.8 and the Charpy V-notch toughness is 40 ft-lb @ 70 °F with CVN testing completed in accordance with ASTM A673/A673M, frequency H

(ASTM, 2004). These specifications make this an ideal material to use in seismic applications as the requirements exceed those required by the AISC *Seismic Provisions*.

Part 1 of the AISC *Manual* references this new material as well as providing dimensions and properties for new shapes that are available from suppliers. As in the past, the Dimension and Properties tables list shape designations consistent with ASTM A6 (ASTM, 2009). In the 14th Edition *Manual*, four new HP18 shapes, six new HP16 shapes, and one new MC shape (MC12×14.3) are listed.

STRUCTURAL INTEGRITY

AISC added new language to Section B3.2 of the *Specification* and in Part 2 of the *Manual* to clarify the application of the requirements given in the International Building Code. In response to the World Trade Center tragedy in 2001, the goal of the requirements is to provide some minimum robustness in the connection. The first related requirements appeared in the 2008 New York City Building Code, followed by the 2009 International Building Code. The integrity provisions given in the IBC apply to high-rise buildings assigned to Occupancy Categories III or IV. High-rise buildings are defined as those "having an occupied floor greater than 75 ft above fire department vehicle access" (AISC, 2011). The provisions also state that column splices must resist a minimum tension force and beam end connections a minimum axial tension force on the beam. Geschwindner and Gustafson (2010) examine these structural integrity requirements for single plate connections and make a comparison between the IBC and NYC methods. The AISC *Specification* states that "design for structural integrity requirements shall be based on nominal strength rather than design strength (LRFD) or allowable strength (ASD), unless specifically stated otherwise in the applicable building code." The IBC stipulates that the nominal axial tension strength of the beam end connection equal or exceed either the required vertical shear strength for ASD or 2/3 the required vertical shear strength for LRFD, but not less than 10 kips. Additionally, the *Specification* notes that limit states based on limiting deformations or yielding can be ignored when making the structural integrity check as the intent is to preclude brittle rupture failures. Bearing bolts in short slots parallel to the direction of the tension load are acceptable with the bolt assumed to be at the end of the slot.

MEMBER DESIGN

The revisions in the 2010 *Specification* are minimal related to members subject to compression, flexure, combined compression and flexure, and shear. In both Chapters E (Design of Members for Compression) and F (Design of Members for Flexure), a user note roadmap has been added at the beginning of the chapter to direct the user to the appropriate limit states for the various cross sections. For compression member design, there are two noticeable revisions. In Section E3, Flexural Members Without Slender Elements, the limit between elastic and inelastic buckling has been reformatted in terms of the elastic buckling stress, F_e, to remove a discontinuity that occurred in 2005. In Section E6, Built-Up Members, the equations to determine how many bolted or welded

connectors are required in built-up members have been revised. The formulation is based on more recent research and evaluation of all existing test data (Sato and Uang, 2007).

In Chapter F, there are slight modifications to the equations for the bending coefficient, C_b, and the limiting laterally unbraced length for inelastic buckling, L_r, as well as a new section providing an explicit local buckling check of tee stems. The equation for C_b has been modified as follows:

$$\text{2010:} \quad C_b = \frac{12.5M_{max}}{2.5M_{max} + 3M_A + 4M_B + 3M_C} \qquad \text{(F1-1)}$$

$$\text{2005:} \quad C_b = \frac{12.5M_{max}}{2.5M_{max} + 3M_A + 4M_B + 3M_C} R_m \leq 3.0 \qquad \text{(F1-1)}$$

The modifier, R_m, and the limit of 3.0 have been removed in the 2010 *Specification* equation, however, the 2005 version is still available int the commentary. The 2010 equation is only applicable to singly symmetric members in single curvature and doubly symmetric shapes. For other situations, see the 2010 *Specification* Commentary.

The equation for L_r was algebraically manipulated to remove the torsional constant, J, from the denominator of the term under the radical so there was a solution if $J = 0$. The equation for L_r has been modified as follows, with both equations giving identical results:

$$\text{2010:} \quad L_r = 1.95 r_{ts} \frac{E}{0.7F_y} \sqrt{\frac{Jc}{S_x h_o} + \sqrt{\left(\frac{Jc}{S_x h_o}\right)^2 + 6.76\left(\frac{0.7F_y}{E}\right)^2}} \qquad \text{(F2-6)}$$

$$\text{2005:} \quad L_r = 1.95 r_{ts} \frac{E}{0.7F_y} \sqrt{\frac{Jc}{S_x h_o}} \sqrt{1 + \sqrt{1 + 6.76\left(\frac{0.7F_y}{E}\frac{S_x h_o}{Jc}\right)^2}} \qquad \text{(F2-6)}$$

Section F9.4 provides a new local buckling check for tees stems in flexural compression based on the *Guide to Stability Design Criteria* (Ziemian, 2010). The 2005 *Specification* did not have provisions for the local buckling strength of stems of tee sections under a flexural compressive stress gradient. The commentary explained that the local buckling strength was accounted for in the equation for the lateral-torsional buckling limit state when the unbraced length approached zero, but this led to confusion.

The most notable revision to Chapter H (Design of Members for Combined Forces and Torsion) is a new optional solution for doubly symmetric rolled compact members subject to single axis flexure and compression. Section H1.3 provides a procedure to replace the interaction equations in Section H1.1, which can be overly conservative where the axial limit state is out-of-plane buckling and the flexural limit state is lateral-torsional buckling (Ziemian, 2010). The optional solution is permissible when the

moments are primarily about the major axis, the ratio of required flexural strength about the minor axis to the available flexural strength about the minor axis is less than 0.5, and the torsional effective length does not exceed the minor axis effective length. Using this option, the limit state of in-plane stability is checked using the usual interaction equations of Section H1.1. Additionally, the limit states of out-of-plane buckling and lateral-torsional buckling are checked using the following equation:

$$\frac{P_r}{P_{cy}}\left(1.5-0.5\frac{P_r}{P_{cy}}\right)+\left(\frac{M_{rx}}{C_b M_{cx}}\right)^2 \le 1.0 \qquad (H1-2)$$

COMPOSITE DESIGN

Chapter I, Design of Composite Members, includes some new and expanded provisions and underwent a major reorganization for the 2010 AISC *Specification*. Some of the changes include new provisions for the following topics: local buckling of filled members, compressive axial force, load transfer, diaphragms and collectors, composite beam-columns, and steel anchors. The chapter was reorganized as follows:

2005	2010
I1. General Provisions	I1. General Provisions
I2. Axial Members	I2. Axial Force
I3. Flexural Members	I3. Flexure
	I4. Shear
I4. Combined Axial Force and Flexure	I5. Combined Axial Force and Flexure
	I6. Load Transfer
	I7. Composite Diaphragms and Collector Beams
	I8. Steel Anchors
I5. Special Cases	I9. Special Cases

Section I1 includes tables providing limiting width-to-thickness ratios for compression steel elements subject to axial compression and subject to flexure in filled composite sections. These new slenderness provisions allow noncompact and slender sections in filled members, while previously they were only allowed if tested and analyzed. For axial compression, the compact/noncompact limit, λ_p, is the same as that in the 2005

AISC *Specification*. The other limits are based on an evaluation of past and more recent research (Varma and Zhang, 2009).

One important new criterion applies to both encased and filled composite columns: The available compressive strength need not be less than that specified for the bare steel member as required by Chapter E (Design of Compression Members). This revision resulted when it was discovered that occasionally the calculated available strength of a composite member could result in a lower value that the bare steel member, which is not a logical conclusion.

Section I7 provides performance language addressing the design and detailing of composite diaphragms and collector beams. Supplemental information is provided in the commentary as guidance to designers.

An additional revision that appears throughout the *Specification* is that the term steel anchor has replaced the term shear connector. Specifically, the 2010 *Specification* addresses steel headed stud anchors and channel anchors. The change in terminology in Section I8, Steel Anchors, is to be consistent with the more general provisions on anchorage in ACI 318 Appendix D. Provisions are added for edge distances of steel anchors along the axis of a composite beam for normal and lightweight concrete. New steel anchor provisions for shear, tension, and the interaction of shear and tension are also provided for other forms of composite construction, referred to as composite components.

In Section I8.2, the strength of a steel headed stud anchor is defined for a composite flexural member where steel anchors are embedded in a solid concrete slab or in a composite slab with decking. The equation is identical to the 2005 *Specification* version:

$$Q_n = 0.5 A_{sa} \sqrt{f'_c E_c} \le R_g R_p A_{sa} F_u \qquad \text{(I8-1)}$$

The revision here is in the R_p factor which has been reduced to 0.75 for the solid slab case after evaluation of existing and recent research (Pallares and Hajjar, 2010).

QUALITY CONTROL AND QUALITY ASSURANCE

The AISC *Specification* has historically addressed quality control minimally and more recent versions included provisions in Chapter M—referring to the RCSC *Specification* and AWS D1.1 for inspection guidelines. In a response to requests from the Building Seismic Safety Council, NCSEA and others, the 2010 AISC *Specification* includes a new Chapter N on Quality Control and Quality Assurance. The chapter is consistent with IBC Chapter 17, the RCSC *Specification*, and AWS D1.1, and as stated in Section N1, Chapter N "provides a plan of requirements for the minimum observation and inspection tasks deemed necessary to ensure quality in structural steel construction". The AISC *Seismic Provisions* stipulates additional quality criteria for high-seismic design. The goal of the new chapter is to provide a uniform plan with a relatively high level of assurance,

and effective consistent requirements. Chapter N also stipulates nondestructive testing requirements in Section N4, which are not available in other standards.

Quality control is implemented by the fabricator and quality assurance is provided by a third party when required by the authority having jurisdiction, applicable building code, purchaser, owner, or engineer of record. Sections N5 and N6 provide a detailed list of the tasks required to put together a quality control or quality assurance plan for structural steel buildings and composite construction, respectively. Each task is identified as a task to perform (P) or a task to observe (O). Perform means that the task must be performed for each joint or member and observe means that the task is to be observed on a random basis. Tasks assigned to be performed generally cannot be properly treated using random sampling techniques. These terms differ from common building code terminology, which assigns tasks to be observed continuously and periodically.

The chapter concludes with Section N7, Approved Fabricators and Erectors, and Section N8, Nonconforming Materials and Workmanship. Section N7 says that when a fabricator or erector participates in an approval process acceptable to the authority having jurisdiction, such as the AISC Quality Certification program, quality assurance inspections may be waived. Section N8 explains how nonconforming materials and workmanship are to be handled.

INELASTIC ANALYSIS

Appendix 1 of the 2010 AISC *Specification* is, perhaps, the first significant step towards an AISC performance based design specification. By moving some provisions to other more appropriate places in the *Specification*, Appendix 1 now addresses only inelastic analysis. In all cases, the strength limit states defined in Chapters D, E, F, G, H, I, J and K must be considered, but if they are detected by an inelastic analysis, they are not subject to the applicable provisions in the *Specification*. If a nonlinear analysis is performed, the interaction equation of Chapter N need not be checked. This chapter allows the designer to use a more sophisticated analysis.

ORGANIZATIONAL REVISIONS

Some sections of the 2010 AISC *Specification* were reorganized for ease of use and clarification with little or no modification, such as Table B4.1, Chapter C and Chapter K. Table B4.1 that provides limiting width-thickness ratios for compression elements is now split into two tables in order to clarify the different terminology that should be used for compression elements in members subject to axial compression (Table B4.1a) and in members subject to flexure (Table B4.1b). Table B4.1a refers to nonslender and slender elements while Table B4.1b refers to compact, noncompact and slender elements.

The direct analysis method that was located in Appendix 7 in the 2005 *Specification* has been moved up into Chapter C, as the method of choice for stability design. The other two methods, effective length and first-order analysis have been relegated to Appendix 7. AISC committee members suggested this reorganization because the direct analysis

method is thought to allow a more accurate determination of the load effects in the structure through the inclusion of the effects of geometric imperfections and stiffness reductions directly within the structural analysis. The method also allows use of $K = 1.0$ in calculating the in-plane column strength within the beam-column interaction equations of Chapter H. Additionally, the 2010 *Specification* includes provisions for neglecting P-δ when using the direct analysis method. It is acceptable to neglect P-δ when (1) gravity loads are supported by vertical columns, walls and frames, (2) $\delta_{max}/\Delta_{max} \leq 1.7$, and (3) one-third or less of the total gravity load on the structure is supported by columns that are part of the moment-resisting frames in the direction of translation. In no case can this apply if members are subject to compression and flexure. As in 2005, Chapter C provides a complete list of stability requirements that the stability design must account for. In 2010, one additional requirement must be considered: the uncertainty in stiffness and strength.

The provisions of Chapter K for HSS connection design have been organized into tables for plate-to-round HSS connections, plate-to-rectangular HSS connections, round HSS-to-HSS truss connections, rectangular HSS-to-HSS truss connections, round HSS-to-HSS moment connections, rectangular HSS-to-HSS moment connections, and effective weld properties for connections to rectangular HSS. Each connection type includes a figure to exemplify the variables used and the configuration. It is hoped this new arrangement will simplify HSS connection design. Section K4 includes the weld design rules for T-, Y- and cross-connections which are expanded to include moments, as well as axial loads. "Fit for purpose" design rules for overlapped connections have been incorporated where the welds may be designed to resist branch forces in HSS truss-type connections by using the effective length concept. Many HSS truss web members are subjected to low axial loads and, in such situations, this weld design philosophy works well.

CHANGES AFFECTING CONNECTION DESIGN

Though AISC strove in the cycle between 2005 and 2010 to minimize changes to the *Specification* and the *Manual*, some changes that affect connection design were made because they were felt necessary to maintain safety, improve economy, or add clarity for the user. In some instances a change in one document precipitated changes in the other.

This portion of the paper is intended to highlight some of the more significant changes that affect connection design. It is not meant to be comprehensive listing of all the changes.

CHANGES IN THE 2010 SPECIFICATION AFFECTING CONNECTION DESIGN

There are number of significant changes, which affect connections designed using the 2010 *Specification*. These changes affect the design of bolts, welds and connecting elements.

Changes to the Design of Welds

Base Metal Check for Partial-Joint-Penetration Welds

In Table J2.5, which provides the base and weld metal strengths for welded joints, the base metal strength for partial-joint-penetration welds in tension was changed to be based on the rupture strength rather than the yield strength. This change was made because the welds are sized using the rupture limit state. Limiting the base metal at the fusion line between the base metal and the weld metal to the yield strength was therefore inconsistent and unnecessarily restrictive.

Out-of-Plane Loading of Fillet Welds

The 2010 *Specification* removes the limitation that fillet welds must be loaded in-plane in order to use the directional strength increase provided by Equations J2-5 or J2-9b. Research by Gilbert Grondin of the University of Alberta and Amit Kanvinde of the University of California–Davis (Kanvinde, 2009) indicated this limitation is unnecessary. It is interesting to note that the Eccentrically Loaded Weld Group tables in Part 8 of the *Manual* have incorporated the strength increase for out-of-plane loading for quite some time.

Fillet Weld Groups of Non-Uniform Size

The design of fillet weld groups using Sections J2.4(a) and J2.4(c) has been clarified to indicate that these provisions can only be applied to uniformly sized fillet weld groups. This is important change since the load-deformation behavior is affected by variations in size as well as loading angle (Muir, 2008). Fillet weld groups composed of variously sized weld elements can be designed using Section J2.4(b), which appropriately accounts for size variations.

Changes to the Design of Bolts

Nomenclature

The most immediately obvious change to Section J3, which provides requirements for bolted connections, is one of nomenclature. To improve convenience and readability of the *Specification*, which essentially treats conventional and TC bolts as interchangeable, various bolts with common strength levels have been grouped. ASTM A325, F1852 (TC bolts), A354 Grade BC, and A449 bolts have been grouped together and referred to as Group A bolts. Similarly, ASTM A490, F2280 (TC bolts), and A354 Grade BD bolts have been grouped together and referred to as Group B bolts. These new designations should not to be confused with the existing faying surface preparation designations also referred to as Class A and Class B.

Nominal Shear Strength

A more significant change, in terms of design, is an increase in the shear strength of bolts. Historically, the shear strengths of fasteners and threaded parts provided in Table J3.2 have included a length reduction factor of 0.80. This reduction factor accounted for uneven force distributions among the bolts in end-loaded connections caused by deformation of the connection material. While this variation in load occurs only in end-loaded connections, the reduction factor is applied to all connections for simplicity. Tide (2010) reviewed available test data on which the 0.80 length reduction factor was based. Using reliability-based procedures, it was determined that if the connection length were limited to 38 in., a length reduction factor of 0.90 could accommodate the effects of differential strain. Again for simplicity the reduction is applied to both end-loaded connections up to 38 in. in length and all direct loaded connections.

Similar to provisions in previous specifications, the 2010 *Specification* includes a further reduction for longer connections. An additional length reduction factor of 0.75 is applied to connections longer than 38 in.

Since the majority of bolted connections are neither end-loaded nor greater than 38 in. long, the committee felt the economy provided by this change justified the work required to accommodate the change by the engineering profession and construction industry.

Slip Resistance

Due to new data and some uncertainty about statements made in the literature, the 2005 *Specification* contained a two tier approach to the design of slip-critical connections, which could be designed assuming slip was either a serviceability limit state or a strength limit state. This was a significant change from previous editions of the AISC *Specification* and the RCSC *Specification*, and was not viewed favorably by the committee, engineers, or the industry. Therefore, significant effort was dedicated to finding a better solution.

Several research programs were aimed at bettering the knowledge of these connections.

Gilbert Grondin of the University of Alberta conducted a survey of available data to determine appropriate resistance factors and slip coefficients. Based on this study the value of the slip coefficient, μ, for Class A faying surfaces was changed from 0.35 to 0.30 primarily to better reflect the observed behavior of connections with clean mill scale and roughened galvanized surfaces. The slip coefficient for Class B surfaces was found to be slightly conservative but the Committee decided to leave $\mu = 0.50$ for blast cleaned surfaces and blast cleaned surfaces with Class B coatings. Grondin also looks at the consequences of slip, specifically by modeling the behavior of a long-span truss utilizing oversize holes in all plies of the bolted connections. This work in conjunction with the analysis of the data, helped to lead to the resistance factors contained in the 2010 *Specification*.

Peter Dusicka of Portland State University studied the effect of multiple fills on the slip resistance. This work, which was still in process as the new specification was being

finalized, indicated the number of fillers in a joint could reduce the slip strength and lead to the inclusion of a fill factors, h_f.

Jerome Hajjar of the University of Illinois (Borello, 2009) tested a series of slip-critical bolted splice connections configured to emulate those found in long-span trusses. The nominal strength of the tested connections approached the 3-million pound capacity of the testing equipment, more accurately mirroring joints currently used in steel construction. The results confirmed that the presence of oversize holes did not cause a reduction in slip strength, a fact that was not clearly established in the literature. The tests also supported Dusicka's conclusion that multiple fillers tended to reduce the slip resistance, though with an important exception when additional bolts were added to develop the fillers.

The Hajjar tests were also configured to establish the shear strength of bolts in oversize holes with and without thick fillers, as previous tests had only included fillers up to 3/4 in. The results showed that bolts in oversize holes could develop their full design shear strength with a maximum reduction of 15% regardless of filler thickness. These tests indicated that the slip into bearing was accompanied by a significant increase in strength beyond that predicted by the slip strength, a strength beyond that extrapolated from previous tests on joints with fillers. Based on these tests, Section J5, has been modified so that the reduction factor, $[1 - 0.4(t - 0.25)]$, used to account for the presence of fills need not be less than 0.85 regardless of the thickness of the filler.

Default to Snug Tight Condition

Finally, there is an additional simple—but important—change in Section J3.1 that permits bolts to be installed to the snug tight condition when used in bearing type connections except where noted elsewhere in the *Specification*. All bolts required to be tightened to a condition other than snug-tight are required to be clearly identified on the contract documents. Note that this is not intended to preclude use of ASTM F1852 or F2280 (TC) bolts in these joints, as these are acceptable for use with the snug-tight designation, even when installed such that the spline is ruptured.

Changes Affecting Connecting Elements

The 2005 *Specification* addressed the strength of elements subjected to tension, shear, block shear and compression but did not address flexure. It was never the intention of the Committee to imply that connecting elements need not to be checked for flexure, but rather to allow these checks to be addressed when appropriate in the *Manual*, similar to other connection design limits. Though the 2010 *Specification* does explicitly address the strength of elements in flexure, the discussion is brief and merely references the *Manual* and other sources. This recognizes that flexure as we normally envision it often cannot develop in short connection elements, and consideration of flexure is a matter of engineering judgment.

CHANGES IN THE 14TH EDITION MANUAL AFFECTING CONNECTION DESIGN

There are number of significant changes, which affect connections designed using the 14th Edition of the Manual. These changes include changes due to the increased *Specification* bolt shear strengths, improvements made to the discussion on the design of coped beams, and clarifications to the prying action checks.

Specification Increase in Bolt Strengths

The increase in bolt shear strengths in the *Specification* led to widespread changes to the *Manual*. Obviously the tables providing bolt strengths in Chapter 7 had to be revised to reflect the change in the *Specification*, as did tables providing connection strengths in Chapter 10. Design Examples, available on-line, also had to be revised to remain consistent with the *Specification*. In most instances, however, the underlying design procedures used in connection design were not affected, with one notable exception— the conventional configuration of the single plate shear connection, referred to here as the conventional shear tab. While design procedures for most connections discussed in the *Manual* are based on rational models, often confirmed through testing, the design procedure for the conventional shear tab has from the start been highly empirical.

Though the effect of the increased bolt strengths was considered for a broad range of connection types, changes were only required to the procedure used for the conventional shear tab due to its inherent empiricism. The design eccentricities contained in the 13th Edition of the *Manual* were derived by dividing the observed connection strength, when governed by the bolts, by the nominal bolt strength given in by the *Specification* to determine an effective number of bolts. This effective number of bolts divided by the total number of bolts in the group is essentially the C-value provided in the Eccentrically Loaded Bolt Group tables in Part 7 of the *Manual* and can be used to determine an effective eccentricity. Since the design eccentricity was derived based on the nominal shear strength of the bolt, an increase in this value in the *Specification* reasonably precipitated an increase in the design eccentricities presented in the *Manual*. Where eccentricities were assumed to be zero in the 13th Edition, they are now assumed to be equal to half the distance separating the weld group from the bolt group, referred to as "a" in the *Manual*. In the process of reexamining the data, some changes to the prescribed ratio between the bolt diameter and the plate thickness were also made, removing the limitation altogether for shallow connections utilizing short slots and making the limit more restrictive for deeper connections utilizing standard holes.

Design of Coped Beams

The discussion in the 13th Edition of the Manual on the design of coped beams was found to be unclear and incomplete. In some instances it was not clear which limit states were likely to govern and some geometries the designer would be left without a recommendation as to the proper design procedure. The Specification Committee's Task Committee 6 worked with the Manual Committee to resolve these issues for the 14th

Edition of the Manual. The current text is more clearly written and provides a conservative catchall design procedure for conditions not meeting the geometrical constraints required of the provisions based on Yura's work. It also addresses conditions where the tension flange cope is longer than the compression flange cope.

Prying Action

Several seemingly minor, but important revisions were made to the prying action procedure in the *Manual*. The discussion of prying action in the *Manual* can be interpreted as providing essentially three different paths to determine the adequacy of a connection relative to prying action. The first assumes that the fitting geometry has not been established, the second calculates the prying force, which could then theoretically be used to check the adequacy of the connection (though this path is not fully described), and the third checks the adequacy of a connection based on a known fitting geometry. Though a thorough knowledge of the principles underlying the checks would reveal that the variable α could not exceed 1.0, this was not clearly spelled out in previous editions of the *Manual* and so was clarified in the 14th Edition. An informal survey of practicing engineers also revealed that the methods used to determine the effective connection length, p, relative to each bolt was not clearly understood nor was the upper limit that should be placed on this value. Clearer language and sketches were introduced to overcome this deficiency.

Bracket Plates

Bracket plate buckling, as described in Part 15 of the 13th Edition of the Manual, was based on a model developed by Salmon and Johnson (1996). However, the assumptions implicit in this model were not felt to accurately reflect common practice. For example the top, horizontal plate must be firmly attached to the support to satisfy the Salmon and Johnson model. However, this is not always the possible. As a result the buckling check was revised to the more general and conservative approach used in checking double copes and single plate shear connections.

CONCLUSION

As discussed here, the 2010 AISC *Specification for Structural Steel Buildings* and the 14th Edition *Steel Construction Manual* include a limited number of important updates and new topics. The AISC *Manual*, with the AISC *Specification* as its basis, continues to be the resource for steel design, fabrication and erection.

ACKNOWLEDGMENTS

Much of the information related to the changes in the *Specification* related to connection design previously appeared in the September 2010 *Modern Steel Construction* article "The 2010 AISC Specification: Changes in Design of Connections" by Larry Kloiber and Larry Muir (Kloiber and Muir, 2010).

REFERENCES

AISC (2010a), *Specification for Structural Steel Buildings*, ANSI/AISC 360-10, American Institute of Steel Construction, Chicago, IL.

AISC (2010b), *Seismic Provisions for Structural Steel Buildings*, ANSI/AISC 341-10, American Institute of Steel Construction, Chicago, IL.

AISC (2010c), *Code of Standard Practice for Steel Buildings and Bridges*, AISC 303-10, American Institute of Steel Construction, Chicago, IL.

AISC (2011), *Steel Construction Manual*, 14th Edition, American Institute of Steel Construction, Chicago, IL.

ASCE (2010), *Minimum Design Loads for Buildings and Other Structures*, ASCE/SEI 7-10, American Institute of Steel Construction, Reston, VA.

ASTM (2004), *Standard Specification for Sampling Procedure for Impact Testing of Structural Steel*, American Society for Testing and Materials, West Conshohocken, PA.

ASTM (2005), *Standard Specification for Structural Steel with Low Yield to Tensile Ratio for Use in Buildings*, American Society for Testing and Materials, West Conshohocken, PA.

ASTM (2009), *Standard Specification for General Requirements for Rolled Structural Steel Bars, Plates, Shapes, and Sheet Piling*, ASTM A6/A6M-09, American Society for Testing and Materials, West Conshohocken, PA.

AWS (2008), *Structural Welding Code—Steel*, AWS D1.1/D1.1M-2008, American Welding Society, Miami, FL.

Borello, D.J.; Denavit, M.D. and Hajjar, J.F. (2009), "Behavior of Bolted Steel Slip-critical Connections with Fillers", Newmark Structural Engineering Laboratory Report Series, Report No. NSEL-017, University of Illinois at Urbana-Champaign.

Geschwindner, L.F. and Gustafson, K.D. (2010), "Single-Plate Shear Connection Design to Meet Structural Integrity Requirements," *Engineering Journal*, AISC, Vol. 47, No. 3, 3rd Quarter.

ICC (2009), *International Building Code*, International Code Council, Country Club Hills, IL.

Kanvinde A.M., G.Y. Grondin, I.R. Gomez and Y.K. Kwan (2009), "Experimental Investigation of Fillet Welded Joints Subjected to Out-of-Plane Eccentric Loads" *Engineering Journal*, AISC

Kloiber, L.A. and Muir, L. (2010), "The 2010 AISC Specification: Changes in Design of Connections," *Modern Steel Construction*, September, Chicago.

Muir, L.S.(2008) "Deformational Compatibility in Weld Groups", Connections VI Sixth International Workshop on Connection in Steel Structures, Chicago, AISC.

NYC (2008), *New York City Building Code,* New York, NY.

Pallares, L. and Hajjar, J.F. (2010), "Headed Steel Stud Anchors in Composite Structures: Part 1. Shear," *Journal of Constructional Steel Research*, Vol. 66, No. 2, February, pp. 198–212.

Salmon, C.G. and Johnson, J.E. (1996), *Steel Structures: Design and Behavior*, 4th Edition, Harper-Collins, New York, N.Y.

Sato, A. and Uang, C.-M. (2007), "Modified Slenderness Ratio for Built-Up Members," *Engineering Journal*, AISC, Vol. 44, No. 3, 3rd Quarter.

Tide, R.H.R. (2010), "Bolt Shear Design Considerations" *Engineering Journal*, AISC

Varma, A.H. and Zhang, K. (2009), "Slenderness Limits for Noncompact/Slender Filled Members," Bowen Laboratory Report NO. 2009-01, School of Civil Engineering, Purdue University, West Lafayette, IN, August.

Ziemian, R.D. (ed.) (2010), *Guide to Stability Design Criteria for Metal Structures*, 6th Edition, John Wiley and Sons, Hoboken, NJ.

Development of Seismic Design Provisions for Steel Sheet Sheathed Shear Walls

C.A. Rogers, N. Balh, C. Ong-Tone, I. Shamim and J. DaBreo

Department of Civil Engineering and Applied Mechanics, McGill University,
817 Sherbrooke St. W., Montreal, Canada, H3A 2K6; PH (514) 398-6860;
FAX (514) 398-7361; email: colin.rogers@mcgill.ca

ABSTRACT

Seismic design provisions for use with steel sheathed cold-formed steel framed shear walls have been proposed for inclusion in the National Building Code of Canada with the associated detailing and design procedures found in the AISI S213 North American Lateral Design Standard for cold-formed steel structures. The design procedure, including recommended seismic force modification factors (R-values), was based on the results of an extensive series of monotonic, reversed cyclic and dynamic tests, as well as non-linear time history dynamic analyses of representative building structures. An approach adopted from the FEMA P695 incremental dynamic analysis procedure is being used to evaluate and improve the seismic design procedure. An overview of the process followed in the conception of the seismic design provisions is provided in this paper.

INTRODUCTION

A research project was initiated at McGill University in 2008 with the objective of developing a design method for cold-formed steel (CFS) shear walls sheathed with steel panels that could be used in conjunction with the National Building Code of Canada (NBCC) *(2005)*. The intent is for this method to be included in the Canadian section of the North American standard for cold-formed steel framing – lateral design (AISI S213) *(2007)*. An extensive program of single-storey shear wall displacement based tests was first carried out to establish a database of information. This information was then supplemented with dynamic shake table tests of single and double-storey shear wall specimens.

The equivalent energy elastic-plastic (EEEP) analysis approach was chosen to derive key design parameters for the shear walls including; nominal shear strength, resistance factor, elastic stiffness, overstrength, drift limit, ductility and test-based seismic force modification factors. This data evaluation procedure is consistent with that used to establish the Canadian wood sheathed / CFS framed shear wall design provisions in AISI S213. Single-storey shear walls of various configurations were tested under monotonic and CUREE reversed cyclic displacement based loading protocols; a selection of these walls was subjected to combined gravity and lateral loading. The walls varied in terms of framing and sheathing thickness, detailing and

aspect ratio. The shape, thickness and grade of the steel-frame members are common to the CFS industry; furthermore, these steel members are typically used for applications in which load bearing is involved. Additional test data from Serrette *et al. (1996)*, Serrette *(1997, 2002)*, Ellis *(2007)*, Yu *et al. (2007)* and Yu & Chen *(2009)* were also relied on in the development of the design method.

Using the design approach established through evaluation of the displacement based test data single and double-storey shear wall specimens were configured to be tested dynamically. These tests were the first of their kind to be carried out on steel sheathed / CFS framed shear walls. The intent was to use the results of the dynamic tests to validate and improve the accuracy of the response provided by dynamic software such as OpenSees *(McKenna et al. 2006)*, and to observe the behaviour of the double-storey specimens in order to identify whether the assumptions made in modeling, such as perimeter element design, are appropriate. The scope of the dynamic testing included five single-storey and five double-storey shear walls constructed of a typical CFS frame sheathed with 0.46 mm or 0.76 mm steel sheathing. The walls were designed as per the Canadian provisions proposed for inclusion in AISI S213. Each wall was subjected to a suite of dynamic tests ranging from impact tests to measure damping, forced vibration tests to obtain the natural period of vibration as well as ground motions representative of the seismic hazard in Canada. Dynamic models based on the results of the displacement based test walls were initially used to predict the inelastic behaviour of the walls prior to testing on the shake table such that the loading protocols could be established.

All of the test data was used in the development of non-linear time history dynamic building models that will be relied on to investigate the seismic performance of structures having a lateral system constructed with steel sheathed CFS shear walls. As a final, and still ongoing, phase to the research project non-linear time history dynamic analyses of multi-storey CFS framed structures is being carried out following an approach adopted from FEMA P695 *(2009)* on the quantification of building seismic performance factors. Input earthquake records are to be scaled to the site specific uniform hazard spectra for various cities across the county. The calculated inelastic storey drifts and the failure probabilities from the FEMA P695 incremental dynamic analysis procedure will then be utilized to evaluate and improve the seismic design procedure for steel sheathed CFS framed shear walls.

DISPLACEMENT BASED TESTING

As part of the research program 54 steel sheathed single-storey shear wall tests (18 configurations) were carried out at McGill University in 2008 *(Balh et al., 2010; Balh & Rogers 2010; Ong-Tone & Rogers 2009)*. The walls, which consisted of framing elements and a steel sheathing panel on one side measured 610 x 2440 mm, 1220 x 2440 mm, 1630 x 2440 mm and 2440 x 2440 mm in size. The frame was constructed using tracks (92.1 mm web, 38.1 mm flange) and studs (92.1 mm web, 41.3 mm flange and 12.7 mm lip) connected together with No. 8 x 12.7 mm wafer head self-drilling / self tapping screws. Simpson Strong-Tie S/HD10S hold-down devices were placed at the bottom of each chord stud to anchor the shear wall to the test frame. The shear walls varied in framing thickness (0.84 mm or 1.09 mm), sheathing thickness (0.46 mm or 0.76 mm) and detailing of the fasteners. Each panel

was attached to the frame with No. 8 x 19 mm self drilling / self tapping pan head screws spaced at 50 mm, 100 mm or 150 mm over the perimeter and at 300 mm along the field stud(s). The 1830 mm and 2440 mm long walls required the use of two sheathing panels butted together at a single internal stud. The shear walls were tested using two displacement based loading protocols; monotonic and CUREE reversed-cyclic protocol *(Krawinkler et al., 2000).* A specially constructed reaction frame, with a 250 kN capacity dynamic actuator having a displacement range of ± 125 mm, was used to test each shear wall under stroke control while measuring the resistance and relevant deformations. Detailed information on the test program can be found in the reports by Balh & Rogers *(2010)* and Ong-Tone & Rogers *(2009)*.

An additional series of 14 walls reinforced with quarter point blocking between studs and thicker chord studs was tested under a combined gravity (constant 12.5 kN / 1.22 m long wall) and lateral monotonic or reversed cyclic protocol in 2010 (Figure 1). The intent was to improve the detailing and design of the chord stud elements such that the inelastic behaviour would, for the most part, be restricted to the sheathing and its connections.



Figure 1 : Displacement based single-storey shear wall test setup

The monotonic and reversed cyclic test specimens exhibited elastic shear buckling of the sheathing panels at relatively low lateral loads followed by the development of a tension field (Figure 1). At ultimate load the failure of each test wall could often be attributed to the sheathing-to-frame connections where steel bearing, fastener pull-out, fastener pull-through and tear-out were observed (Figure 2). Unzipping of the fasteners along the perimeter of the shear wall was also common. In some cases deformations were observed in the framing elements, especially when the thicker sheathing was combined with a screw spacing of 50 mm. Twisting of the

chord studs occurred due to the horizontal component of the tension field that developed in the sheathing *(Balh & Rogers 2010; Ong-Tone & Rogers 2009)*. In addition, uplift of the track elements took place due to the vertical component of the tension field (Figure 2).



Figure 2 : Shear wall test specimens showing bearing damage at screw connections, as well as chord stud twisting and track uplift caused by tension field forces *(Balh et al. 2010)*

DYNAMIC SHAKE TABLE TESTING

To justify the proposed seismic design approach derived from these displacement based tests it was necessary to investigate the performance of representative shear walls by means of dynamic shake table tests. The scope of testing included; single-storey and double-storey walls, which were constructed of a typical screw connected CFS frame sheathed with steel sheet panels. The intent was to use the results of the dynamic tests to monitor the behaviour of the walls, to identify whether the performance is consistent with the displacement based tests, to obtain measures of damping and natural period of vibration and to validate and improve the accuracy of the force-deformation response provided by dynamic models. A 12.5 kN gravity load was first applied on the test wall once it had been constructed and assembled on the shake table. Each wall was then subjected to a suite of excitations; impact test to measure the linear-viscous damping ratio, harmonic excitation to estimate the natural period of vibration, and ground motions representative of the seismic hazard in Quebec and Vancouver Canada. Five single storey (1.22 x 2.44 m) and five double-storey (1.22 m x 5.18 m) walls were included in the scope of testing. The double-storey walls consisted of a 2.44 m high first storey wall, on top of which a 0.3 m deep CFS framed floor structure was attached followed by another 2.44 high second storey wall. The test wall was then connected to a pin supported mass structure located on the laboratory strong floor adjacent to the shake table (Figure 3). This mass structure represented the seismic mass tributary to the wall being tested. The base of the structure was also connected to the shake table such that the mass structure experienced the same dynamic excitation as the test wall.

Design of the dynamic wall specimens was initially carried out following the resistance values obtained from the displacement controlled tests with assumptions regarding the selection of the boundary elements that followed the current AISI S213

provisions for wood sheathed walls. Blocking between studs was added to the walls to limit the extent of chord stud twisting.

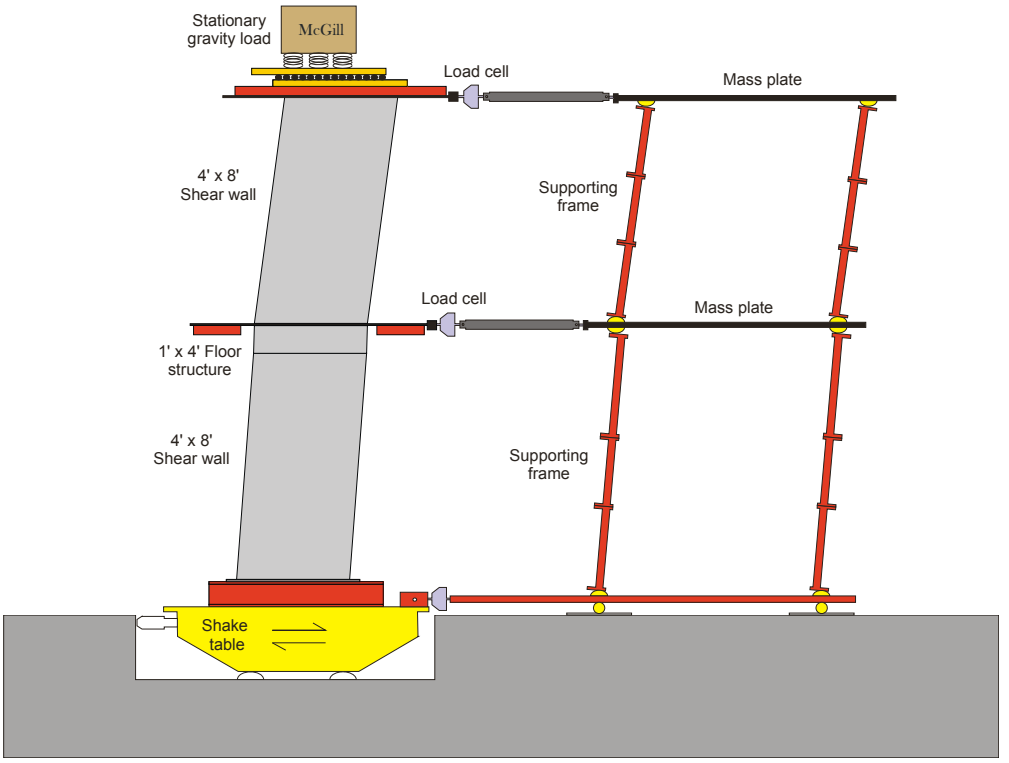


Figure 3 : Schematic of two-storey shear wall shake table dynamic test setup



Figure 4 : Dynamic double-storey shear wall test setup & failed wall specimen

The single-storey dynamic wall tests resulted in a measured performance that was similar to that obtained for the displacement based reversed cyclic tests, although the initial stiffness was somewhat smaller. However, the double-storey walls revealed a weakness in the procedure to select the chord stud members. An unexpected out-of-plane bending failure of the chord stud under compression took place due to the eccentric application of the axial force on this element. The design of subsequent double-storey walls was modified such that the axial force on the chord was considered to be applied eccentric to the centroid of the section and for the ground storey also accounted for the axial force originating in the upper storey. The eccentricity due to the location of the sheathing at the outer edge of the studs, as well as the accidental eccentricity from the gravity and seismic forces in the upper wall segment were accounted for in the design. In this fashion a beam-column design approach was taken that incorporated weak and strong axes moments as well as an axial compression force. The double-storey test wall that failed due to chord stud bending was then rebuilt and retested using the same dynamic protocol. Chord stud failure was avoided in this follow-up test; the wall exhibited the shear buckling and sheathing connection failure modes as anticipated. This shows the need for a more rigorous treatment of the chord stud design for these shear walls than what is currently found in AISI S213.

The results of the single and double-storey dynamic tests were then used to calibrate hysteretic models for use in building analyses. Some modifications were made to the initial models that were used to predict the behaviour of the dynamic shear walls prior to testing. For example, measured damping values between 5 % and 7 % of critical damping were used to aid in the selection of elastic and hysteretic damping in the model.

CURRENT DESIGN RECOMMENDATIONS

Similar to wood sheathed CFS shear walls *(Branston et al. 2006)*, the shear resistance versus deformation behaviour of steel sheathed shear walls under lateral loading is highly nonlinear. The Equivalent Energy Elastic Plastic (EEEP) method *(Park 1989; Foliente 1996)* was relied on to provide a bilinear elastic-plastic curve, which was then used to evaluate the performance of each shear wall. This approach is consistent with that used by Branston *et al. (2006)* in the development of Canadian shear wall resistance values and other related design values for the wood sheathed shear walls that are listed in the AISI S213 Standard. The EEEP method is valid for the analysis of results of both monotonic and reversed-cyclic tests. A backbone curve is constructed for the positive and negative displacement ranges of the resistance versus deflection hysteresis of each reversed cyclic test. The typical nonlinear force versus displacement response of a CFS framed shear wall is simplified for design by means of a bi-linear curve for which the plateau portion is set as the nominal shear resistance, S_y. This plateau section is established by equating the energy dissipated in testing (area under the backbone or monotonic curve) with the area under the bilinear curve, or as shown in Figure 5 by setting A1 = A2. The bilinear curve is limited by the ultimate failure displacement, assumed to occur at the 0.8 post-peak resistance, and the initial slope which is defined using the secant stiffness positioned through the

position defined by 40% of the ultimate load. El-Saloussy & Rogers *(2010)* also used the EEEP method to analyze the results from steel sheathed shear wall tests run by Yu *et al. (2007)* and Yu & Chen *(2009)*.

The EEEP analyses provided for a tabulated list of nominal shear resistance values, S_y, for CFS framed / steel sheathed shear walls. Table 1 provides these shear resistance values along with the corresponding wall configuration. Additional information on the derivation of this design information can be found in the report by Balh & Rogers *(2010)*.

Table 1. Proposed nominal shear resistance, S_y, for CFS frame / steel sheathed shear walls[1,2,8]

Assembly Description	Max. Aspect Ratio (h/w)[3]	Fastener Spacing[4] at Panel Edges (mm(in))				Designation Thickness[5,6] of Stud, Track, and Blocking (mm) (mils)	Required Sheathing Screw Size[7]
		150(6)	100(4)	75(3)	50(2)		
0.46 mm (0.018") steel sheet, one	2:1	4.13	-	-	-	0.84 (33)	8
		4.53	6.03	6.78	7.53	1.09 (43)	8
0.68 mm (0.027") steel sheet, one side	2:1	6.48	7.17	7.94	8.69	0.84 (33)	8
0.76 mm (0.030") steel sheet, one side	4:1	8.89	10.58	11.56	12.54	1.09 (43)	8
0.84 mm (0.033") steel sheet, one side	4:1	10.69	12.01	12.97	13.94	1.09 (43)	8

[1] Nominal resistance (kN/m) is to be multiplied by the resistance factor, ϕ=0.7, to obtain the factored shear resistance

[2] Sheathing is to be connected vertically to the steel frame

[3] Nominal resistances are to be multiplied by 2w/h for aspect ratios greater than 2:1 but no greater than 4:1

[4] Field screws to be spaced at 300 mm on centre

[5] Wall stud and track shall be of ASTM A653 grade 230 MPa with a minimum uncoated base thickness of 0.84 mm (0.033") for members with a designation thickness of 33 mils, and ASTM A653 grade 230 MPA with a minimum uncoated base thickness of 1.09 mm (0.043") for members with a designation thickness of 43 mils

[6] Substitution of wall stud or track is not permitted

[7] Minimum No. 8x12.7mm (1/2") self drilling / self tapping screws shall be used

[8] Tabulated nominal resistances are applicable for lateral loading only

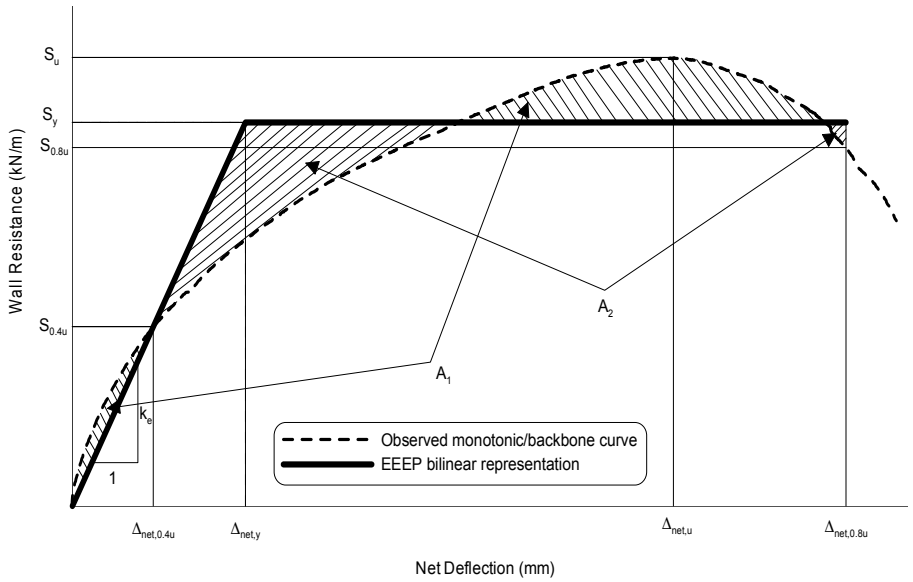


Figure 5 : Equivalent Energy Elastic-Plastic (EEEP) model *(Branston et al. 2006)*

In addition to the lateral resistance of the CFS framed shear walls two force modification factors are required for seismic design according to the NBCC. The ductility-related force modification factor, R_d, is a measure of the fuse element's ability to dissipate energy through inelastic deformation. The average value for R_d from displacement based test results was 2.87 *(Balh & Rogers 2010)*. At this time it is suggested that a value of 2.5 be considered to be consistent with the R_d value currently specified in AISI S213 for wood sheathed shear walls. A second force modification factor, R_o, represents the reserve of strength within the structure. Its calculation was based on the procedure recommended by Mitchell *et al. (2003)*. The average R_o value taken from the displacement based test results is 2.1; a value of 1.7 is suggested, again because of the R_o value for wood sheathed shear walls in AISI S213. These 'test-based' R-values require further verification by means of non-linear time history dynamic analyses of multi-storey CFS framed structures following an approach adopted from FEMA P695 *(2009)* on the quantification of building seismic performance factors.

DYNAMIC ANALYSES

The purpose of the non-linear time history dynamic analyses phase of the research is to evaluate the proposed seismic design method by predicting the performance of representative buildings during an earthquake. An approach adopted from FEMA P695 *(2009)* on the quantification of building seismic performance factors is currently being utilized to identify the probability of failure of these CFS framed structures. Input earthquake records (both synthetic and recorded) were scaled to the site specific uniform hazard spectra for various cities across the county. The OpenSees software with nonlinear dynamic analysis ability is being utilized for the purpose of modeling the tested walls and ultimately the representative building

structures. The calculated inelastic storey drifts and the failure probabilities from the FEMA P695 incremental dynamic analysis procedure will then been utilized to evaluate and improve the seismic design procedure.

Beam-column elements were used to model CFS frame components (Figure 6): elements with linear behaviour represent the chord-studs and rigid elements represent the tracks. Since tracks were attached to the relatively rigid frame during testing, and would also be attached to the foundation or floor structure in a building, using rigid elements was deemed to be realistic for their modeling. Also, track to chord stud hinge-moment connections were modeled with rotational springs. Total lateral displacement of walls was separated into two components: shear displacement representing the sheathed CFS frame displacement due to the shear force and uplift displacement representing the wall's rigid rotation because of anchor rod elongation. Zero length Springs with linear behaviour were placed at bottom of the walls to capture uplift displacement. The floor flexibility also was considered by using two linear diagonal trusses with the stiffness found from the test data.

A fictitious frame consisting of a beam-column element with "co-rotational coordinate transformation" capability and a connecting truss element was made with the gravity weight and mass load exerted at floor levels to account for the P-Δ effect of the vertical loads. The mass sourced from the mass plate and a part of the steel frame contributing to the seismic mass was lumped at top of each floor. This mass was 33.38 kN for the single-storey walls and 35.64 kN and 33.20 kN in first and second floor for double-storey walls, respectively. Rayleigh damping with 2% damping ratio was considered in the nonlinear analysis although the test-measured damping ratio in the linear domain was almost 7%.

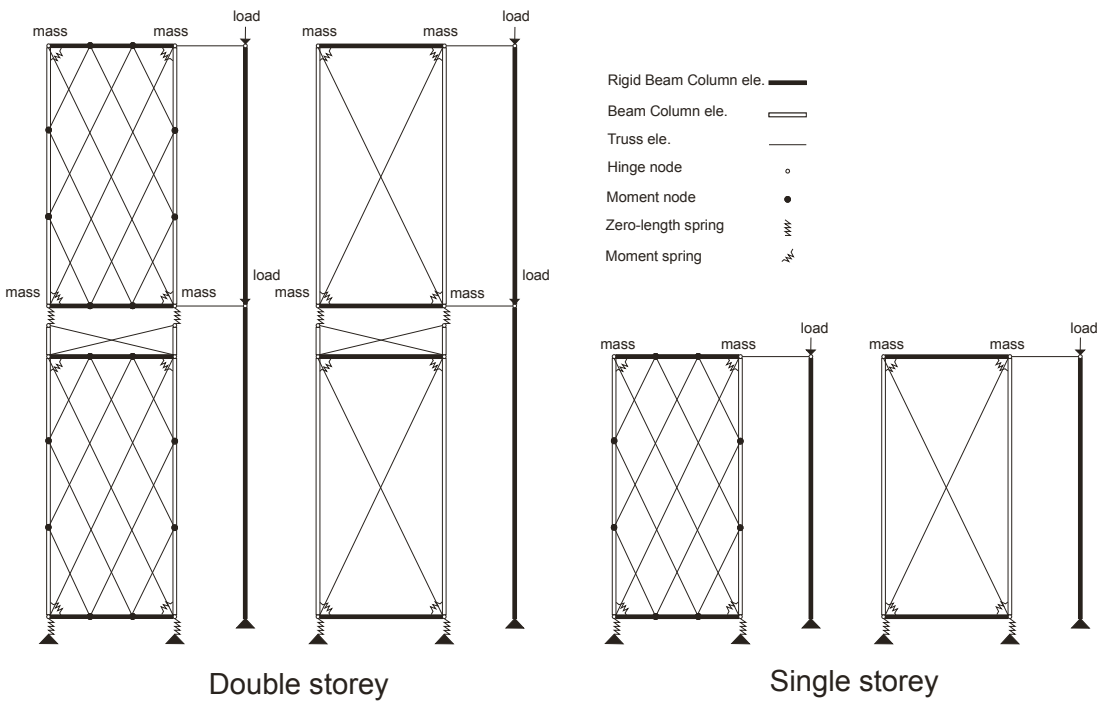


Figure 6 : Schematic of dynamic models

In order to capture the non-linear inelastic shear displacement behaviour of the walls diagonal truss elements with Pinching04 material were included in the model and calibrated to represent the characteristics of the steel sheathing and its connecting screws. Various diagonal truss element patterns are being evaluated, hence the two different schemes illustrated in Figure 6. Pinching04 material parameter values were initially extracted from the strength-displacement hystereses of the displacement based tested walls; these parameters were later modified using the dynamic test wall data such that the model and dynamic test strength and total displacement time histories matched adequately (Figure 7). Once calibration of the models with the dynamic shake table test results has been achieved models of representative building structures will be developed and used in an evaluation of the proposed design method using an approach adapted from the FEMA P695 methodology.

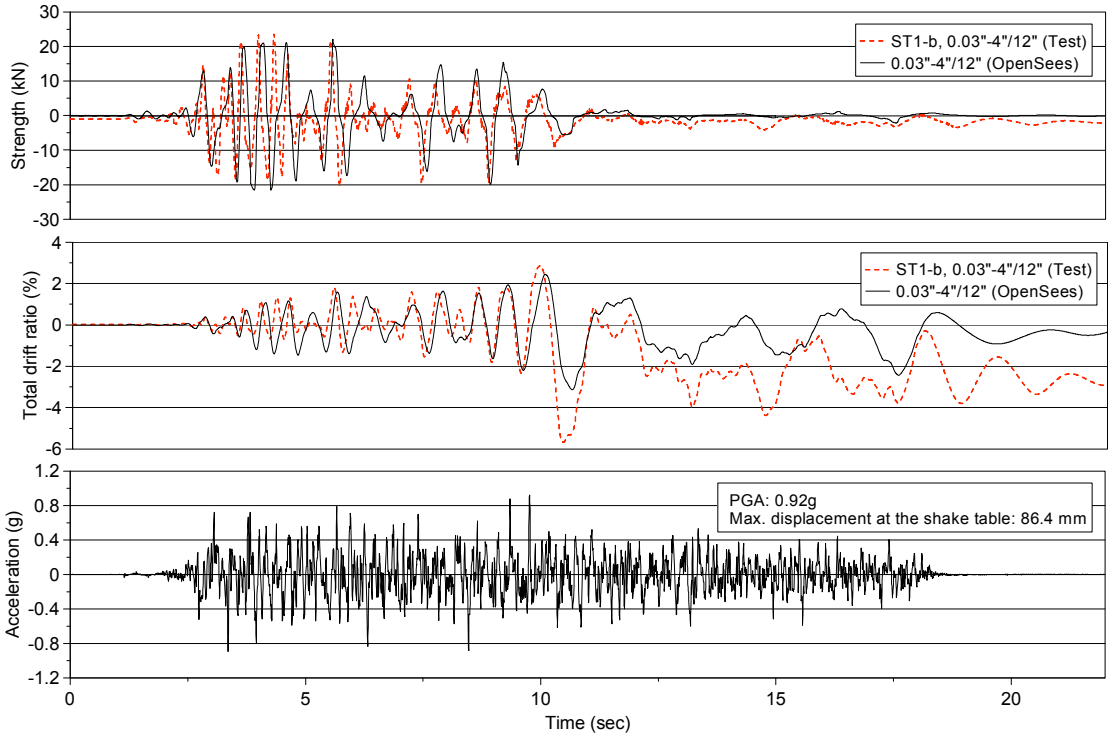


Figure 7 : Example time history of single storey dynamic shear wall test (ST1-b) and model prediction

CONCLUSIONS

To address the lack of Canadian design provisions for steel sheathed / cold-formed steel framed shear walls a test program was carried out comprising 68 single-storey steel sheathed shear walls. Two displacement based loading protocols; monotonic and CUREE reversed-cyclic were implemented for these tests. Shear wall tests completed by Yu *et al*., Yu & Chen and Ellis were incorporated with the McGill University shear wall tests to widen the database from which design values were

derived. The tests were analyzed using the EEEP method which provided a bilinear elastic-plastic curve that can be considered equivalent to the nonlinear behaviour exhibited by the shear walls. Based on the test results a resistance factor, ϕ, of 0.7 is recommended and nominal resistance values, S_y, are proposed. These nominal resistance values are only applicable for lateral loading and do not take into account the effects of gravity loads. 'Test-based' seismic force modification factors R_d and R_o of 2.5 and 1.7, respectively, are suggested for the interim design of steel sheathed shear walls. Based on the information obtained from these displacement based tests a suite of ten dynamic shake table tests was run on single and double-storey shear walls. The shake table tests have provided additional force versus deformation hysteretic data as well as time history data, damping information, and period of vibration estimates to facilitate the development of non-linear time history dynamic models that can accurately reproduce a shear wall's behaviour. These models have been calibrated with the dynamic shear wall test data and are currently being used to develop models of representative buildings that will be designed using the proposed seismic design resistances and R-values described herein. These models will be subjected to ground motion records and the results of the analyses will then be evaluated in terms of the probability of collapse as per the FEMA P695 methodology. Given the ongoing nature of this research the 'test-based' design procedure which has been proposed may be modified dependent on the findings of the final dynamic analysis phase of the study.

ACKNOWLEDGEMENTS

The authors would like to acknowledge the support provided by the Natural Sciences and Engineering Research Council of Canada (NSERC), the Canadian Sheet Steel Building Institute (CSSBI) and the American Iron and Steel Institute (AISI). Materials for construction of the test specimens were provided by Simpson Strong-Tie Co. Inc., ITW Buildex and Grabber Construction Products. Assistance with the procurement of steel framing was provided by Bailey Metal Products Limited.

REFERENCES

AISI (2007). "North American standard for cold-formed steel framing – lateral design, AISI S213", American Iron and Steel Institute, Washington, DC.

Balh. N., Rogers, C.A. (2010). "Development of seismic design provisions for steel sheathed shear walls". Research Report. Dept. of Civil Engineering & Applied Mechanics, McGill University. Montreal, QC.

Balh, N., Ong-Tone, C., Velchev, K., Yu, C., Rogers, C.A. (2010), "Development of Canadian seismic design provisions for steel sheathed CFS framed shear walls", 9th US National & 10th Canadian Conference on Earthquake Engineering. Toronto, ON, Paper No. 1016.

Branston, A.E., Boudreault, F.A., Chen, C.Y., Rogers, C.A. (2006). "Light gauge steel frame – wood structural panel shear wall design method", *Can. J. Civ. Eng.*, 33(7) 872-889.

CSA (2007). "North American specification for the design of cold-formed steel structural members, CSA S136". Mississauga, ON.

El-Saloussy, K., Rogers, C.A., (2010) "Additional cold-formed steel frame / steel sheathed shear wall design values for Canada", Research Report, Dept. of Civil Engineering & Applied Mechanics, McGill University, Montreal, Canada.

Ellis, J. (2007). "Shear resistance of cold-formed steel framed shear wall assemblies using CUREE test protocol". Simpson Strong-Tie Co. Inc, Anaheim, CA.

FEMA (2009). "Quantification of building seismic performance factors, FEMA P695", Federal Emergency Management Agency, Washington, DC.

Foliente, G.C. (1996). "Issues in seismic performance testing and evaluation of timber structural systems". Proc. International Wood Engineering Conference. New Orleans, LA, Vol. 1, 29 – 36.

Krawinkler, H., Parisi, F., Ibarra, L., Ayoub, A., Medina, R. (2000). "Development of a testing protocol for woodframe structures". Report W-02 covering Task 1.3.2, CUREE/Caltech Woodframe Project. Consortium of Universities for Research in Earthquake Engineering (CUREE). Richmond, CA.

McKenna, F., Fenves, G.L., Filippou, F.C., & Mazzoni, S. (2006). "Open system for earthquake engineering simulation (OpenSees)". Pacific Earthquake Engineering Research Center (PEER), University of California, Berkeley, CA.

Mitchell, D., Tremblay, R., Karacabeyli, E., Paultre, P., Saatcioglu, M., Anderson, D.L. (2003). "Seismic force modification factors for the proposed 2005 edition of the National Building Code of Canada". *Can. J. Civ. Eng.*, 30(2) 308 – 327.

National Research Council of Canada (2005). "National Building Code of Canada" 12th Edition. Ottawa, ON.

Ong-Tone, C., Rogers, C.A. (2009). "Tests and evaluation of cold-formed steel framing / steel sheathed shear walls". Research Report, Dept. of Civil Engineering & Applied Mechanics, McGill University. Montreal, QC.

Park, R. (1989). "Evaluation of ductility of structures and structural assemblages from laboratory testing". Bulletin of the New Zealand National Society for Earthquake Engineering, 22(3) 155 – 166.

Serrette, R.L., Nguyen, H., Hall, G. (1996). "Shear wall values for light weight steel framing." Report No. LGSRG-3-96, Santa Clara University. Santa Clara, CA.

Serrette, R.L. (1997). "Additional Shear Wall Values for Light Weight Steel Framing." Report No. LGSRG-1-97, Santa Clara University. Santa Clara, CA.

Serrette, R.L. (2002). "Performance of Cold-Formed Steel-Framed Shear Walls: Alternative Configurations," Final Report:LGSRG-06-02, Santa Clara University. Santa Clara, CA.

Yu, C., Vora, H., Dainard, T., Tucker, J., Veetvkuri, P. (2007). "Steel Sheet Sheathing Options for Cold-Formed Steel Framed Shear Wall Assemblies Providing Shear Resistance". Report No. UNT-G76234, Department of Engineering Technology, University of North Texas. Denton, TX.

Yu, C., Chen, Y. (2009). "Steel Sheet Sheathing Options for Cold-Formed Steel Framed Shear Wall Assemblies Providing Shear Resistance – Phase 2". Report No. UNT-G70752, Department of Engineering Technology, University of North Texas. Denton, TX.

Seismic Design of Diagonal Strap Bracing Using AISI S213

Greg Greenlee, P.E.[1]

[1] Engineering Partners International LLC, 9001 East Bloomington Freeway, Suite 123, Bloomington, MN; PH 952-884-0481; FAX 952-884-0491; email: ggreenlee@engineeringpartners.net

ABSTRACT

Diagonal strap bracing is a common means of providing lateral stability for a low rise commercial or residential structure in cold formed steel framing and can be used in wind and seismic design. When designing this type of force resisting system there are a number of design and serviceability considerations that should be investigated. These include loads, strap size, fastener quantity, connection detailing, and construction practices. In seismic applications it is particularly important to understand the behavior of diagonal strap bracing. Accordingly predicting the ductility of the system is critical. This presentation will discuss seismic design of diagonal strap bracing in using the provisions of AISI S213-07, the *North American Standard for Cold-Formed Steel Framing - Lateral Design*.

INTRODUCTION

Structures require a resisting system to transfer lateral loads imposed on them. Typically these loads are from wind or seismic forces. A commonly used type of lateral force resisting system in residential and low rise commercial cold-formed steel applications is diagonal flat strap bracing. When designing this type of force resisting system there are a number of design and serviceability considerations that should be investigated. These include loads, strap size, fastener quantity, connection detailing, and construction practices.

Previously the Cold-Formed Steel Engineers Institute (CFSEI) published a technical note titled *Design of Diagonal Strap Bracing Lateral Force Resisting Systems for the 2006 IBC*. The current edition of the *North American Standard for Cold-Formed Steel Framing - Lateral Design* has added guidance for the design of flat strap bracing, particularly in seismic regions. This paper re-presents some of the information from the CFSEI technical note and incorporates the new seismic provisions contained in AISI S213-07.

TYPES OF DIAGONAL STRAP BRACING

Diagonal strap bracing can be detailed in a variety of different styles. Commonly diagonal strap bracing is used on the outside flange of perimeter load bearing studs (Figure 1). Another option is to use double sided diagonal strap bracing where there

are straps on both the inside and outside flange of the studs. With either of these styles the strap may either be a wide strap connecting directly to the stud and track (Figure 2), or a narrower strap where a gusset plate is used to make the connection between the strap and the stud and track (Figure 3).

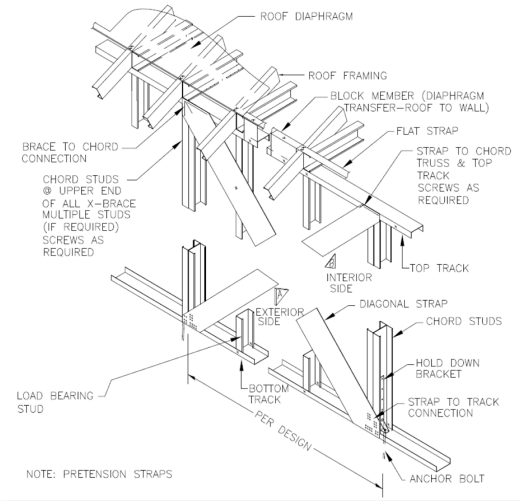


Figure used with permission of the Steel Framing Alliance

Figure 1

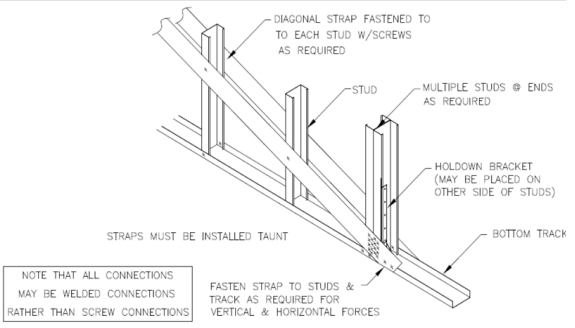


Figure used with permission of the Steel Framing Alliance

Figure 2

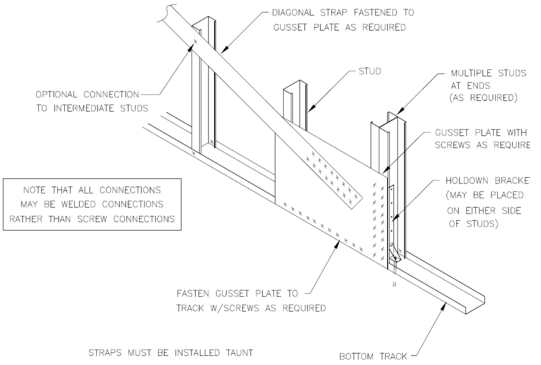


Figure used with permission of the Steel Framing Alliance

Figure 3

Wide straps that connect directly to the stud and track may be preferred over straps with gusset plates for a couple of reasons. First the gusset plates and associated fasteners add thickness to the wall which may be difficult to conceal with siding or exterior finish. Second, wider straps connecting directly to the stud and track will ultimately require fewer fasteners which will reduce installation time.

GENERAL DESIGN CONSIDERATIONS

When designing diagonal strap bracing there are a number of items to be investigated which are influenced by the type and geometry of the diagonal strap bracing. The provisions of the AISI Standard *North American Specification for the Design of Cold-Formed Steel Structural Members* (AISI S100-07) can be used to design these elements.

The width of the brace will be primarily dependent on two things. First, it must be properly sized to resist the design tensile forces in the member. Second, if it is not desirable to use a gusset plate at each end of the strap a wider strap may be required to allow the strap to connect to both the stud and track.

Connections and members must also be adequately sized to transfer loads. Where the studs are load bearing the effects of gravity loads in resisting and adding to overturning loads must be considered. Other potential design checks include induced eccentricity in the wall from a single sided strap, material over strength, and axial capacity of the chord studs. Finally, it will be necessary to properly design overturning restraints (holdowns), collectors and boundary elements.

It should be noted that because diagonal strap braces are tension only members the bottom track may be in compression between the diagonal strap and in tension outside of the brace. Often an anchor bolt is used to transfer shear loads from the bottom track to the foundation. If anchor bolts are in a compression area of the track, compressive axial capacity should be investigated. To resolve this anchor bolts may be placed in a tension area of the bottom track, or outside of the brace. Naturally this becomes an issue if the brace is located at a corner or end of a wall segment. Regardless of the anchor bolt location, bolt bearing on the web of the track and shear transfer shall be checked.

SPECIAL SEISMIC REQUIREMENTS

Special seismic requirements for diagonal strap bracing are included in Section C5.2 of AISI S213-07. These special seismic requirements are included to ensure predictability and properly controlled ductility in the system. Specifically, it gives additional requirements for material properties, connections, chord studs, anchorage and straps.

Material Properties. Industry studies have shown the yield and tensile strength of steel is generally higher than the specified minimum. This over-strength can result in performance inconsistent with the expectation of the building code. To address this

tensile and yield strength factors (R_y and R_t) have been introduced. These shall be used in the absence of verified physical properties.

Connections. As discussed above strap members are often constructed with material having a yield strength greater than specified. The design of the connections should account for this potential strap over-strength to ensure a predictable, ductile failure mode.

The available strength of connections is required to exceed the expected yield strength of the strap bracing member; but need not exceed the amplified seismic load. The expected yield strength of the strap member is equal to $A_g R_y F_y$ (applying the yield strength factor described).

Welded connections are required to be used unless:

1. An alternate connection permits gross cross section yielding of the strap member under cyclic loading per ASTM E2126
2. Calculations demonstrate gross cross section failure will occur prior to net section fracture and $R_t F_u / R_y F_y > 1.2$

These requirements apply to connections for strap members, boundary members and collectors.

Chord Studs. Similar to the requirements for connections, the available strength of the chord studs is required to exceed the expected yield strength of the strap bracing member; but need not exceed the amplified seismic load.

Anchorage. Uplift forces in the vertical boundary members shall be resisted by anchoring directly to the foundation. The track member shall not be used to resist these forces in bending.

ADDITIONAL REQUIREMENTS

The eccentricity resulting from single sided strap members shall be considered in the design. The standard defines eccentricity as half of the stud depth.

During construction it is important that the strap is installed taut. This is contained in section C5.2.4 of S213. A taut strap will ensure that the strapping immediately engages when a lateral load is applied. Pre-tensioning is a potential means to guard against loose straps. It is important, however, to ensure the strap is not overly pre-tensioned. Doing so may reduce the load carrying capacity of the strap.

RESEARCH

There have been a number of recent research programs investigating the performance of strap braced walls. The results of some of these programs have been used to develop the special seismic requirements added to AISI S213. Other programs are still ongoing, but provide important design and detailing information. The

commentary of AISI S213 provides additional insightful background information resulting from some of the more recent research programs.

REFERENCES

AISI Manual - Cold-Formed Steel Design. American Iron and Steel Institute, Washington, DC, 2008.

Comeau, G. and Rogers, C.A. (2008), *Inelastic Performance of Welded Cold-Formed Steel Strap Braced Walls*, Department of Civil Engineering and Applied Mechanics, McGill University, Montreal, Quebec, Canada

Greenlee, Greg. *Design of Diagonal Strap Bracing Lateral Force Resisting Systems for the 2006 IBC*, CFSEI Technical Note, September 2010.

International Building Code, 2006 Edition. International Code Council, Falls Church, Virginia.

Lyons, John C. *Detailing Help for Gusseted Flat Strap X-Braces*, article in the *Newsletter of the Light Gauge Steel Engineers Association (LGSEA)*. September, 2004.

North American Specification for the Design of Cold-Formed Steel Structural Members (AISI S100-07), American Iron and Steel Institute, Washington, DC, 2007.

North American Standard for Cold-Formed Steel Framing - Lateral Design (S213-07). American Iron and Steel Institute, Washington, DC, 2007.

Shear Wall Design Guide, Steel Framing Alliance, Washington, DC, 1998.

North American Standard for Cold-Formed Steel Framing - General Provisions (AISI S200-07), American Iron and Steel Institute, Washington, DC, 2007.

Velchev, K., Rogers, C. A., (2008) *Inelastic Performance of Screw Connected Cold-Formed Steel Strap Braced Walls*, Department of Civil Engineering and Applied Mechanics, McGill University, Montreal, Quebec, Canada

Wilcoski, J., 2004, *R-Factor Project Validation Test Plan.*

Earthquake Simulator Testing of Metal Building Systems

C. M. Uang, M. ASCE[1], M. D. Smith, M. ASCE[2], and W. L. Shoemaker, M. ASCE[3]

[1]Professor, Department of Structural Engineering, University of California San Diego, La Jolla, CA 92093-0085. E-mail: cmu@ucsd.edu
[2]Graduate Student Researcher, Department of Structural Engineering, University of California San Diego, La Jolla, CA 92093-0085. E-mail: mds002@ucsd.edu
[3]Director of Research & Engineering, Metal Building Manufacturers Association, 1300 Sumner Ave., Cleveland, OH 44115. E-mail: LShoemaker@thomasamc.com

ABSTRACT

Metal Building Systems (MBS) make up a substantial portion of non-residential, low-rise construction in the U.S. Given their wide spread use, it is desirable to understand their performance during a seismic event. Previous pseudo-static, cyclic testing indicates an absence of ductility in these systems. This lack of ductility arises from the inherent design concepts behind using web-tapered frames with no flange or web compactness limits, causing buckling limit states to govern the strength of the frames. In light of the lack of ductility, it is obvious that the current practice of designing MBS moment frames as Ordinary Moment Frame (OMF) systems, with R=3.5, is inappropriate. Also, simple analytical studies suggest that MBS supporting large masses, such as concrete or masonry exterior cladding or interior mezzanines, may be particularly vulnerable to the lack of ductility. For these reasons, it is desirable to develop a safe, economic, and reliable design procedure for MBS. Earthquake simulation testing of MBS has been performed to provide test data to start this development.

Three full-scale MBS specimens have been tested on the NEES/UCSD Large High Performance Outdoor Shake Table. Specimen 1 consisted of a single story MBS frame with metal side wall panels to represent the majority of MBS buildings. Specimen 2 was similar to the first, except with heavy concrete sidewall panels. Specimen 3 consisted of a MBS frame built with compact flanges, a mezzanine attached to one sidewall, and a concrete wall attached to the other. Results from each battery of tests will be presented in this paper.

INTRODUCTION

A very common form of construction in low-rise, non-residential structures is the metal building system (MBS). MBS are typically built from steel moment frames in their transverse direction and braced frames or shear walls in their longitudinal direction. The transverse frames are usually made with built-up I-sections, many times with tapered webs, which have been optimized to minimize material weight. These built-up sections are usually made without consideration of slenderness limits and frequently have slender or noncompact webs and flanges. These plates often

cause the governing limit state of the frames to be some type of buckling, a non-ductile behavior. These frames can be clad with an assortment of materials ranging from steel decking to concrete tilt-up panels.

MBS are built in a variety of locations, including high seismic zones. Currently, the building codes treat these frames as any other structural steel moment resisting system. MBS frames are usually designed as ordinary moment frames (OMF) or intermediate moment frames (IMF) as defined in ASCE/SEI 7 (ASCE, 2005) and AISC 341 (AISC, 2005b), effectively assuming an ability of the system to dissipate energy through some ductile, inelastic behavior.

While, historically, MBS perform well in large seismic events, previous pseudo-static cyclic testing at UCSD, has revealed a concerning lack of ductility in the cyclic behavior of the transverse frames used in these systems (Hong and Uang, 2006). This suggests that the assumptions made by the current building codes concerning the ductility of these systems are incorrect and the design provisions used for more traditional steel systems with rolled shapes are likely inapplicable to MBS. The research also suggested that the good past performance of these systems is due to a high level of system overstrength. Since MBS are typically very light structures, the transverse frames are usually controlled by non-seismic load combinations. This is the source of the overstrength. Thus, there is a potential lack of safety in systems with large masses, such as MBS with hard wall attachments or mezzanines, when designed according to the current code provisions (Hong and Uang, 2007). It is clear that additional seismic testing was needed to develop applicable, economic, and safe design provisions for MBS frames.

OBJECTIVE AND SCOPE

Three full-scale MBS building specimens were tested at the NEES/UCSD Large High Performance Outdoor Shake Table (LHPOST). The objective of these experiments was to test MBS frames to investigate their performance when subjected to high level seismic motions. It was desired to determine if MBS frames with heavy wall attachments or mezzanines exhibited different margins of safety against collapse than typical MBS with metal sidewalls only. Finally, the data gathered from the tests will be used to calibrate analytical models for use with a FEMA P695 (ATC, 2009) study for new design provisions.

TEST PROGRAM

NEES Shake Table

Test specimens were constructed and tested on the LHPOST. The shake table has a surface area of 7.6 m x 12.2 m and has a maximum payload of 20 MN. It is capable of motions with accelerations of up to 4 g, velocities of up to 1.8 m/s, and has a stroke of ±0.75 m.

Test Buildings

Each test specimen was to represent two interior bays of a MBS building. The specimens consisted of two 18.29 m clear span MBS frames with 6.10 m eave height and spaced at 5.49 m. Since the size of the specimens exceeded the dimensions of the table, a frame was built using W36x302 cantilevered beams and mounted to the table with adequately prestressed threaded anchoring rods. The test setup is shown in Figure 1. The frames were composed of web-tapered, built-up sections using steel plates with nominal yield stress of 379 MPa. All connections within the frames were of the bolted end-plate type. Where steel decking was used as cladding, light gauge metal girts or purlins were incorporated to mount the decking onto the frames. Each specimen had diagonal bracing in each sidewall as well as in the plane of the roof. Each frame was bolted to the testing apparatus at the column base plates. Additional mass, in the form of three 25.4 mm x 203 mm x 9.14 m steel plates, was added at the roof level to represent the remainder of the tributary mass of two full interior bays. These masses were located directly above and along each frame, above the roof decking, and were bolted to pieces connecting them to the frame rafters. The rafter flanges were laterally braced with purlins and flange braces.

Specimen 1 had only steel deck cladding at the side walls. The column flanges were laterally braced with girts and flange braces along their height. Specimen 2 had two 254 mm x 3.05 m x 6.71 m precast concrete panels at each side wall. These concrete panels represented a hard wall cladding of approximately 2.873 kN/m^2 spread over two interior bays. The walls were connected to the frame using spandrel beams bolted at the panel zones. These connections, as well as the connections of the wall base to the test apparatus, were designed to be of pin type. The column flanges were unbraced for their full height. Specimen 3 had one sidewall which resembled Specimen 2, using the same concrete panels and unbraced column flanges. The other side wall was clad with metal decking similar to Specimen 1. This sidewall also had a mezzanine attachment. The mezzanine was composed of built-up, I-beam sections with bolted connections designed as pin type. The floor mass of the mezzanine was represented with one of the 3.05 m x 6.71 m concrete

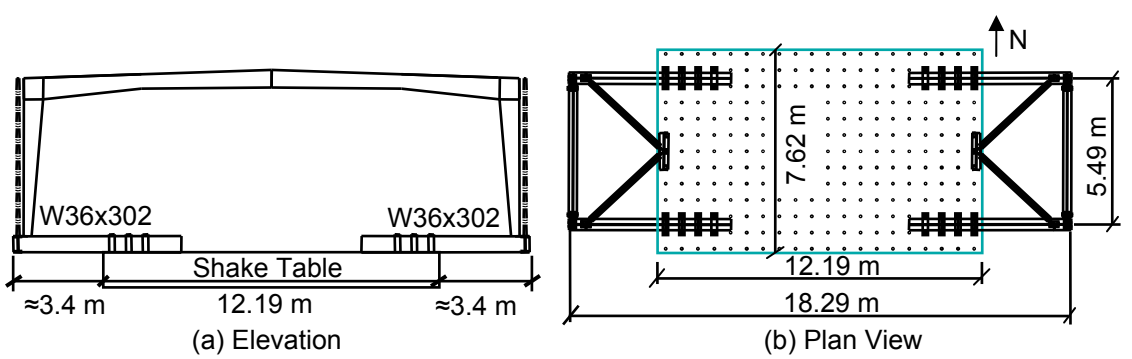


Figure 1. Test Setup

panels. Diagonal bracing was used to brace the mezzanine in the out-of-plane direction.

Each specimen was designed according to the International Building Code 2006 (ICC, 2006). Gravity loads consisted of self weight, 144 N/m^2 collateral load, 958 N/m^2 reducible roof live load, and flat roof snow load of 1,005 N/m^2. Wind loads were calculated using a wind speed of 38 m/s. The seismic load resisting system was designed and detailed as OMF with one exception. The third specimen used seismically compact flanges (AISC, 2005b) in the columns and in the rafters near the knee joint in addition to other OMF requirements. The first two specimens were designed using S_{DS} of 1.031 and S_{D1} of 0.592, while the third specimen used S_{DS} of 1.000 and S_{D1} of 0.400. Gravity load combinations controlled the rafter sizes for the first and second specimens. While wind load combinations controlled the column sizes for Specimen 1, seismic drift limitations per ASCE/SEI 7 (ASCE, 2005) controlled the column sizes for Specimen 2. Both rafters and columns for Specimen 3 were primarily sized to meet the compactness criteria set forth by the designer.

Instrumentation

Each test building was thoroughly instrumented. Strain gauges and rosettes were located at several sections along each column and rafter. Displacement transducers were used to measure slip, rotation, and uplift of the column bases and slip of the mounting frame. String potentiometers were used to measure the displacement of each frame at the roof and base as well as the mezzanine of the third specimen. Accelerometers were located at several sections along each rafter, on the mounting frame, on the roof mass plates, and in the panel zones to measure accelerations in three perpendicular directions. Over 300 separate data channels were used on each specimen.

Test Sequence

Each specimen was subjected to a variety of ground motions with the shake table. Five ground motion records were chosen from motions used in FEMA P695 (ATC, 2009). These ground motions were from 1979 Imperial Valley (H-DLT 352), 1989 Loma Prieta (CAP 000), 1992 Landers (YER 270), 1994 Northridge (LOS 000), and 1999 Chi-Chi (TCU084_001). A white noise motion and a short duration impulse type motion were used to assess the dynamic characteristics (natural periods and equivalent viscous damping) of each specimen at various times in the test sequence, intermittently between seismic record tests to detect and track accumulating damage. Prior to testing, preliminary finite element models were used to estimate the fundamental periods of each specimen. Each ground motion record was scaled such that its 5% damped pseudo-acceleration response spectrum value, at the estimated fundamental period, was some percentage of the value of the Design Basis Earthquake (DBE) response spectrum defined in ASCE/SEI 7 (ASCE, 2005), using R=1, at that same period. An example of this scaling is shown for the Imperial Valley (IV) motion in Figure 2. Tests were named using initials based on the particular ground motion record and a number representing the percentage of DBE to

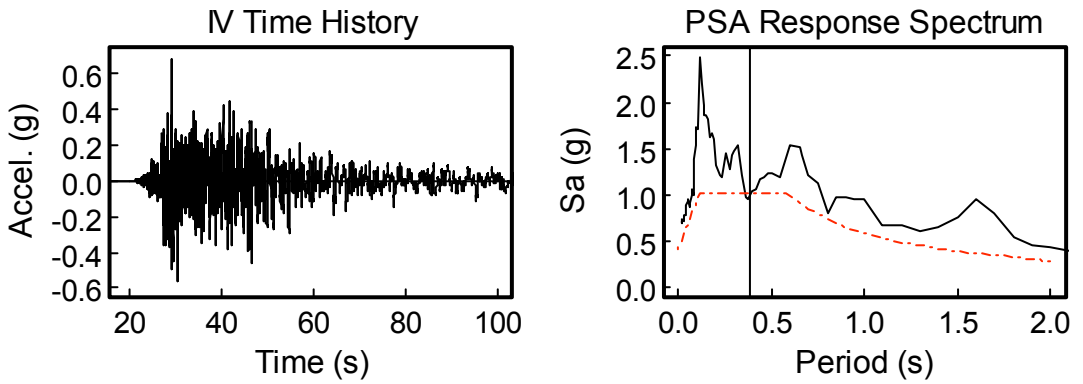


Figure 2. Imperial Valley ground motion scaled to match 100% DBE at estimated period of Specimen 1

which it was scaled, such as IV150 for the IV motion scaled to 150% DBE. Since the periods at which the records were scaled were only estimates, the actual percentage of DBE acceleration exciting the specimens varied from the number in the test name. The general test sequence for each specimen started with white noise and impulse motions, followed by each ground motion record scaled to a low percentage of DBE. For all specimens, the IV motion was used for high level tests for consistency and ease of result comparison. After the low level tests, IV tests were performed at increasing scale factors until limiting circumstances prevented further testing.

TEST RESULTS

Specimen 1

After the initial white noise and impulse tests, the fundamental period was determined to be 0.39 s. This differed from the value of 0.52 s determined from the initial analytical model. The damping ratio was determined to be about 1.5%. This measured fundamental period was used to set the scale factors for the remaining tests. After some low level ground motion records, the Imperial Valley motion was scaled up progressively to investigate the capacity of the structure. Hysteretic behavior can be seen in Figure 3 for IV100 through IV300. Testing went without problems until the IV150 test.

During the IV150 test, the anchor rods at the southeast columns sheared off. Because of this failure, the remaining three columns had to transfer the seismic loads. Despite the changed structure, no limit states were reached anywhere in the frame. After this test, a fix was made at all four column base plates using welds. These welds were placed such that minimal stiffening of the base plate connection would occur.

After the repair, testing continued with the IV200 and IV250 tests. The response of the structure until the IV250 test was essentially elastic with no limit states reached and no significant energy dissipation. During the IV250 test, the north rafter experienced a lateral-torsional buckle (LTB) at the east pinch point. This was

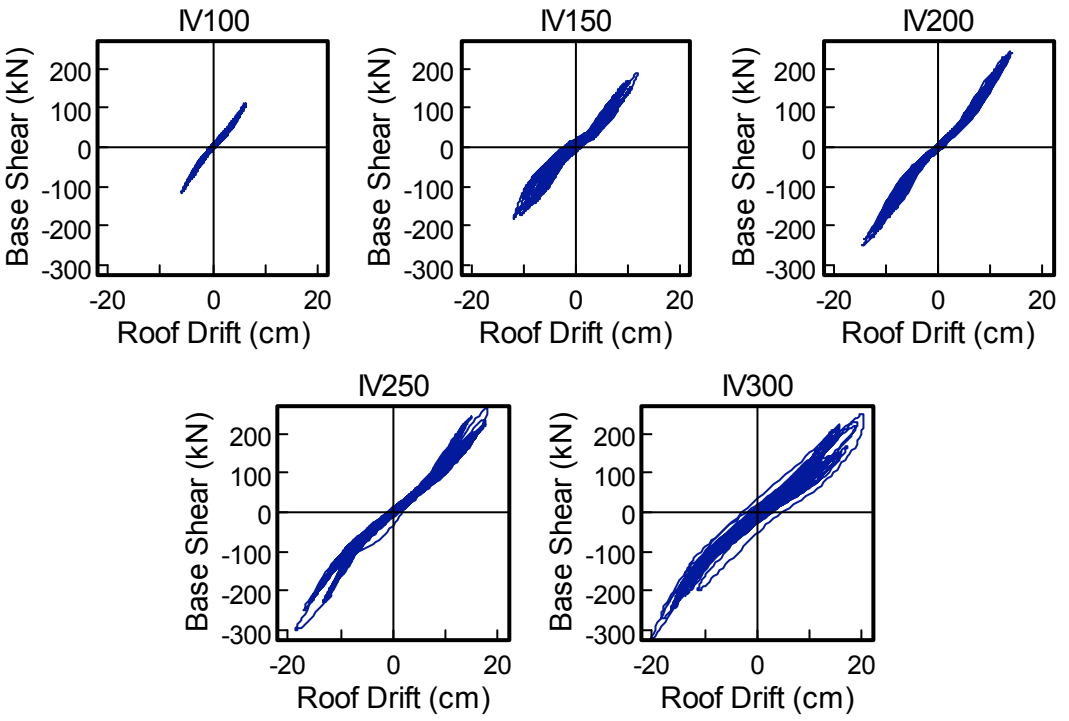


Figure 3. Specimen 1 hysteretic responses

consistent with the predicted failure mode and location. Strain gauge data from a time just prior to buckling implies a moment diagram which should cause LTB according to member strength predicted by AISC 360 (AISC, 2005a). The buckling caused large forces in the flange braces on either side of the affected unbraced length. The forces were large enough to damage the purlin at the other end of the flange brace (See Figure 4). The buckle in the rafter can be seen in Figure 4. The load-displacement curve showed a sharp drop in strength at the point of buckling, as expected. This sharp drop agrees with the nonductile behavior observed in the previous cyclic testing (Hong and Uang, 2006). After the buckle, the stiffness had degraded but the structure continued to behave elastically with a lower lateral stiffness.

Even though the structure reached a limit state, the structure was still standing and safely stable. Some weld cracking occurred at the column base fixes made previously. These welds were repaired and an additional IV300 test was performed. During this test, LTB occurred at two additional pinch point locations in the rafters. These buckles were associated with more sharp drops in strength and further degraded stiffness. In addition to the new LTBs, the initial LTB location experienced a rupture at the bottom flange (See Figure 4). This was due to low-cycle fatigue and the large lateral displacements at the LTB location. Since the structure was ruptured, it was deemed unsafe to continue testing.

During the testing this structure experienced a base shear of 224 kN when the first LTB limit state was reached. A maximum base shear of 325 kN was observed. When compared to the design base shear of 22.2 kN, a very significant amount of system overstrength is apparent. A maximum drift of 3.6% was reached during the final test.



(a) Rafter LTB



(b) Purlin Damage



(c) Flange Rupture

Figure 4. Observed damage during shake table testing of Specimen 1

Specimen 2

The fundamental period for Specimen 2 was determined to be 0.48 s. The damping ratio was determined to be between 1% and 2%. After determining the proper scaling factors for the ground motions from the fundamental period, low level testing was performed. The analytical model suggested a failure at a much lower level of base shear compared with the first specimen, so low level testing was performed at the 10% DBE level instead of 25%. Higher level testing was then performed with the Imperial Valley motion. Hysteretic behavior is shown in Figure 5. Behavior was essentially elastic until the IV100 test.

During the IV100 test, the north rafter experienced LTB at the east pinch point, the same limit state reached as the first specimen. Once again, the strength dropped sharply at the point of buckling and the structure experienced a degradation of stiffness. The LTB at the pinch point was the predicted failure mode and location.

The IV150 test caused LTB at all three remaining pinch point locations in the rafters. The LTBs all caused stiffness degradations and sharp decreases in strength. The initial LTB experienced a flange rupture in the same manor as the first specimen. Also, the large forces in the flange braces caused damage to the connections at the purlin. Photos of the flange brace damage, LTB, and flange rupture can be seen in Figure 7.

When the first limit state was reached, the base shear was 348 kN and a maximum base shear was observed at 427 kN. Compared with a design base shear of 100 kN, the system overstrength was far less in this specimen than in the first. This specimen exhibited no ductile behavior and had no significant energy dissipation. A maximum drift of 3.6% was reached during the IV150 test.

After removing the wall attachments and roof decking, this specimen was subjected to a pseudo-static pull-over test. The top of each frame was attached to a stationary point with a cable and the table was used to pull the base away from the support. This test provided a pull-over curve for the damaged structure. The measured response is shown in Figure 6, corrected for second-order effects which would have existed prior to removal of the large masses. A maximum base shear of 166 kN was observed, showing a greatly reduced strength capacity of the buckled structure. However, this post-buckling strength continued through to a very large displacement of 47 cm (7.8% drift). The extreme displacements further distorted the LTBs in the east rafter pinch points, while new top flange local buckles occurred in the western portions of the rafters. Extreme nonlinearities, eventually causing rupture, were seen in the base plates during the pull-over test. This suggests that column bases may be a source of some energy dissipation. Figure 8 - Figure 9 shows the displaced shape and various damages observed during the pull-over test.

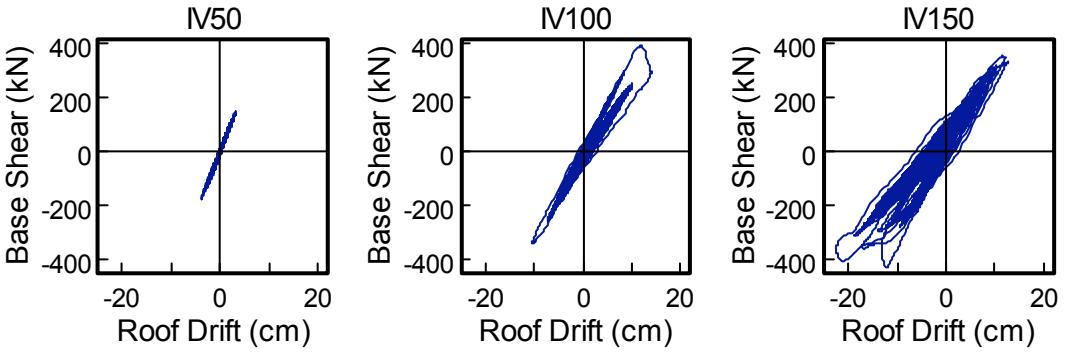


Figure 5. Specimen 2 hysteretic responses

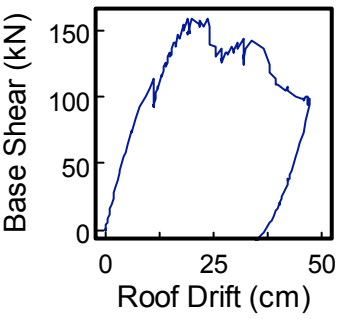


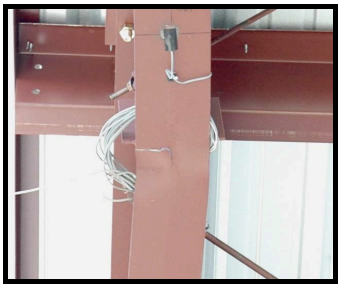
Figure 6. Specimen 2 pull-over test load-displacement response



(a) Rafter LTB



(b) Flange brace damage



(c) Flange rupture

Figure 7. Observed damage during shake table tests of Specimen 2



(a) Global deformed configuration



(b) Top flange buckle



(c) Rafter LTB

Figure 8. Observed damage during pull-over test of Specimen 2



Figure 9. Specimen 2 base plate deformation after pull-over test

Specimen 3

The third specimen had a fundamental period of approximately 0.45 s and a damping ratio of 1% - 2%. Low-level motions up to IV50 showed no inelastic behavior. Hysteretic behavior can be seen in Figure 10. During the IV100 test, elastic shear buckling occurred in the south east panel zone. Comparing moment and axial force demands calculated from the strain gauges to the panel zone strength defined by AISC equations (AISC, 2005a), this buckling was easily predicted.

After the IV100 test, additional tests were run through IV250. During these tests, all four panel zones experienced elastic shear buckling and low-cycle fatigue, eventually causing large ruptures in each web. Interestingly, during the test which caused rupture, IV200, and subsequently, the specimen exhibited significant energy dissipation as evidenced in the larger hysteretic loops seen in IV200 and IV250. Another important observation was that the structure remained elastic and undamaged outside of the panel zone areas. Panel zone damage can be seen in Figure 11.

This specimen reached its first panel zone buckling limit state at a base shear of 262 kN. Comparing this with a design base shear of 87.4 kN, it is seen that this specimen had much lower system overstrength than the first specimen. The maximum base shear reached was 405 kN and the maximum drift was 5.3%. This is the only specimen that exhibited any significant energy dissipation.

IMPLICATIONS

The results of these experiments have a few significant implications. Firstly, a low level of structural damping was observed. It would be prudent for designers of MBS to account for the structures having 1% - 2% damping, rather than the 5% assumed by the codes, when determining seismic force demands. Secondly, the differing levels of system overstrength verify that MBS with large masses have a propensity to be less reliable compared with light MBS. All three structures were designed with R=3.5. This assumes that if the structure were to remain elastic during a DBE level earthquake, the elastic demand would be about 3.5 times its design base shear. The specimens behaved primarily elastically up to this demand level. Since, for the most part, the test buildings did not exhibit ductile post-buckling behavior, it is reasonable, in design, to call the load causing the first limit state to be reached the capacity. A safety factor can be easily calculated for each specimen by dividing the

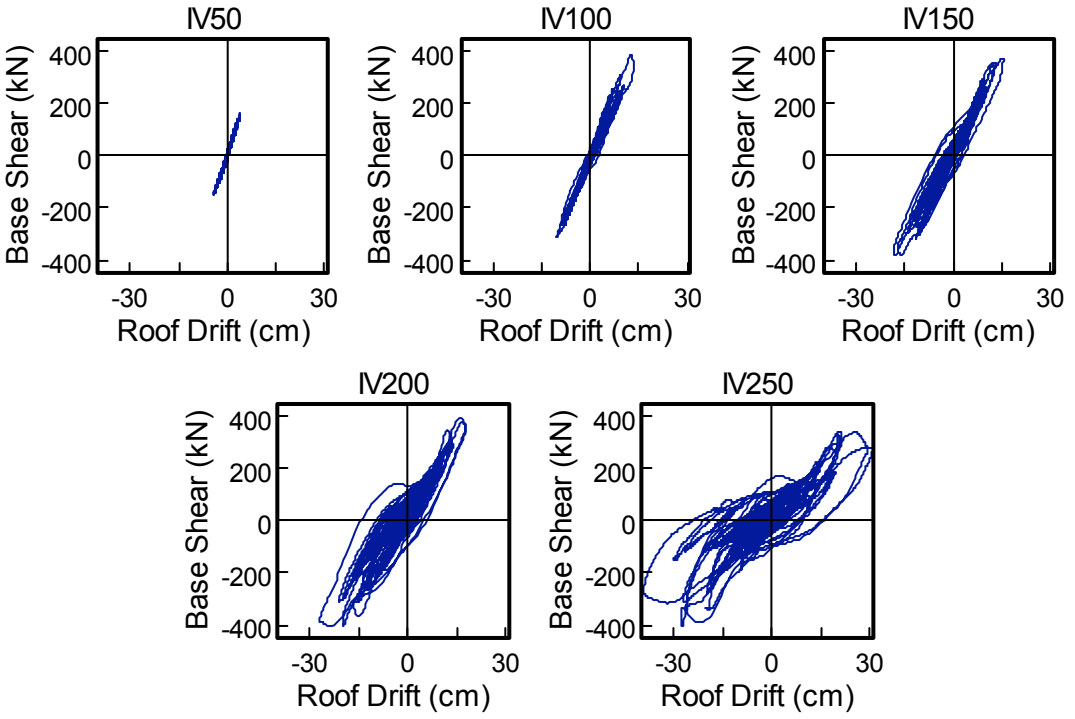


Figure 10. Specimen 3 hysteretic responses



Figure 11. Specimen 3 panel zone damage after completion of testing

observed capacity by the elastic design base shear. Safety factors for each specimen, in order, were 2.88, 0.99, and 0.86. This clearly shows that the two specimens with heavier masses were insufficient to resist DBE level earthquakes without reaching their reliable capacity. It is easily seen that the original assumption of R=3.5 is incorrect and an R=1 is likely more applicable. Use of this R value would have ensured that the structures were designed to resist the elastic DBE level forces which were demanded. However, since neither of the two specimens collapsed, perhaps a rethinking of the overall concepts of the seismic design should be considered for these elastic systems.

CONCLUSIONS

Overall, the MBS specimens were surprisingly robust. The first specimen, despite lacking ductility, showed very large system overstrength and was able to withstand a base shear approximately 290% of the DBE level without damage. Even though the second and third specimens were damaged at or below the DBE level, they remained standing and did not collapse. These results verify that the safety margin against collapse of MBS with larger masses is much lower than a typical, light MBS. They also show a significant lack of ductility in the buckling limit states. Finally, the panel zone limit states in the third specimen suggest a possible energy dissipation mechanism using shear buckling.

Currently, this research is continuing by the development of numerical models calibrated to the test data gained by these experiments. These numerical models will be used in a FEMA P695 (ATC, 2009) study. This study will test newly developed design criteria, which take into account the unique characteristics of these systems and provide an economic and safe solution for seismic design of MBS.

REFERENCES

AISC (2005a), *Specification for Structural Steel Buildings*, ANSI/AISC 360-05, American Institute of Steel Construction, Inc., Chicago, IL.

AISC (2005b), ANSI/AISC 341-05, *Seismic Provisions for Structural Steel Buildings,* American Institute of Steel Construction, Chicago, IL.

ASCE (2005), *Minimum Design Loads for Buildings and Other Structures,* American Society of Civil Engineers, New York, New York, USA, 2005;

ATC (2009), Quantification of building seismic performance factors, *Report No. FEMA-P695,* Applied Technology Council, Redwood City, CA, USA, 2009.

ICC (2006), *International Building Code 2006,* International Code Council, Country Club Hills, Illinois, USA, 2006

Hong, J.K. and Uang, C.M. (2006), *Cyclic Performance Evaluation of a Metal Building System with Web-Tapered Members, Report No. SSRP-06/23*, Department of Structural Engineering, University of California, San Diego, La Jolla, CA.

Hong, J.K. and Uang, C.M. (2007), *Development of A Seismic Design Procedure for Metal Building Systems, Report No. SSRP-07/17*, Department of Structural Engineering, University of California, San Diego, La Jolla, CA.

ACKNOWLEDGEMENT

This research was sponsored by NEES, MBMA, and AISI.

Seismic Force Distribution for Metal Building Systems with Mezzanines

M. D. Smith, M. ASCE[1] and C. M. Uang, M. ASCE[2]

[1]Graduate Student Researcher, Department of Structural Engineering, University of California San Diego, La Jolla, CA 92093-0085. E-mail: mds002@ucsd.edu
[2]Professor, Department of Structural Engineering, University of California San Diego, La Jolla, CA 92093-0085. E-mail: cmu@ucsd.edu

ABSTRACT

Metal Building Systems (MBS) are frequently constructed with mezzanines contained in their floor plans. These mezzanines can be heavy and have a significant impact on the seismic design and performance of the MBS. When a mezzanine is attached to the MBS, it is not clear to the designer whether it should be treated as a one- or two-story building. It is also not clear how the seismic forces should be distributed vertically. Validity of common assumptions about mode shapes and the first-mode dominating system response was investigated. A codified design procedure was compared with a simpler procedure commonly used by MBS designers. A parametric study suggests that the current building code procedure for vertical distribution of seismic forces may be inapplicable to the design of MBS moment frames because it does not properly address the unique dynamic characteristics of the system. The parametric study and a recommendation for a design procedure are presented in this paper.

INTRODUCTION

It is not uncommon that Metal Building Systems (MBS) are designed with partial floor mezzanines attached (See Figure 1). These mezzanines can range in size from a small fraction to almost the entire building area. In addition to a large variation in size, they can carry very light to very heavy gravity loads compared to the weight of the remainder of the structure. This variability leads to uncertainty



Figure 1. MBS with mezzanine attachment

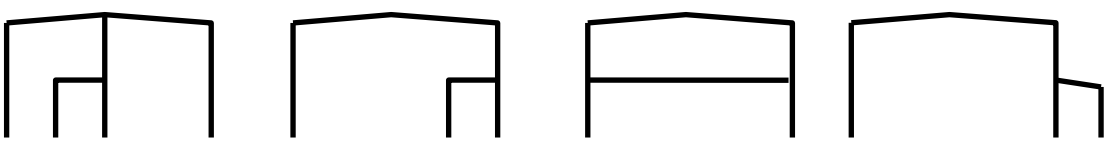
about how to treat the mezzanines when calculating seismic force demand on the MBS moment frames. The codes are not clear when to treat a mezzanine as a separate floor or as an attached mass (Bachman, et. al., 2008). If the designer treats the mezzanine as a floor, ASCE/SEI 7 (ASCE, 2005) provides a method of distributing seismic base shear to each story in the building. This method is based on some assumptions that may not apply to the whole range of mezzanine configurations found in MBS. It is desired to investigate the code method for distributing seismic loads, as well another common design method, to determine their applicability to MBS frames with mezzanines.

BACKGROUND AND THEORY

In a MBS, a partial floor mezzanine may be located in a corner, along a side or end wall, or even central to the floor area and not attached to a wall (See Figure 2). Regardless of location and orientation, one may think of a MBS with a mezzanine as a two degree-of-freedom (2-DOF) dynamic system. There are two natural modes of vibration in a 2-DOF system. The elastic response of a 2-DOF system, to a ground motion, is determined by the individual responses of each mode. Discussion will be limited to elastic response only since the current practice is to determine seismic load distribution based on elastic properties. Each mode in a classically damped building is defined by a natural period and an equivalent viscous damping ratio. These modes each vibrate the structure in a constant displaced shape with only the amplitude of the shape varying (i.e., mode shape). Each mode is treated as a single degree-of-freedom (SDOF) system subjected to the ground motion, and using superposition, the sum of their responses defines the total 2-DOF response. To perform this modal analysis, the designer must be able to determine the two periods and mode shapes.

The damping ratios, ζ_n, are usually a product of engineering judgment. ASCE/SEI 7 (ASCE, 2005) assumes 5% damping for all structures. However, recent shake table testing of three full-scale MBS, at UCSD, has revealed a damping ratio of 1% - 2% for these systems (Uang, et. al., 2011).

Determination of the natural periods and mode shapes is straightforward from dynamics. The periods and mode shapes are functions of the mass and stiffness matrices. These matrices may be derived using either flexibility or stiffness methods. The flexibility method may lend itself well to current MBS design software. Alternatively, a variation of the stiffness method, which may be appealing to MBS designers, is presented here. In developing this method, a MBS moment frame with a mezzanine attachment to one column will be used. However, this same method can be used for a frame with any mezzanine configuration or lean-to structure.



(a) Central **(b) Side** **(c) Full** **(d) Lean-to**

Figure 2. MBS mezzanine configurations

MBS designers are familiar with determining the lateral stiffness of the moment frame, k_f. Some design software automatically reports this parameter. If not readily available from design reports, it is easily obtained by applying a half-unit lateral load at each eave location, similar to the common practice used when applying seismic equivalent lateral forces. The average eave displacement corresponding to this load case is inverted to give the frame stiffness. A less available parameter is the mezzanine stiffness, k_m. This parameter can be found by restricting lateral displacement at the eaves, by placing single direction supports (rotation and vertical movement is allowed), and applying a unit lateral load at the mezzanine. The corresponding displacement of the mezzanine is inverted to give k_m. An additional parameter that will be used is α. Parameter α is the fraction of the mezzanine load that is transferred up to the remaining frame. It is obtained by the sum of reactions at the eaves, due to the mezzanine-unit load case mentioned above. It is a measurement of how much stiffer the remaining frame is compared with the column section below the mezzanine. These parameters define the 2-DOF stiffness matrix:

$$\mathbf{k} = \begin{bmatrix} k_{11} & k_{12} \\ k_{21} & k_{22} \end{bmatrix} = \begin{bmatrix} k_m & -\alpha k_m \\ -\alpha k_m & k_f - \alpha^2 k_m \end{bmatrix}$$

The 2-DOF mass matrix is much simpler to obtain:

$$\mathbf{m} = \begin{bmatrix} m_{11} & 0 \\ 0 & m_{22} \end{bmatrix} = \frac{1}{g} \begin{bmatrix} W_{mezz} & 0 \\ 0 & W_{roof} \end{bmatrix}$$

where W_{mezz} and W_{roof} are the tributary weights of the mezzanine and roof stories, respectively, and g is the acceleration of gravity.

Natural periods (T_n) and mode shapes (ϕ_n) may be determined from **k** and **m** directly through an eigenvalue analysis. Because there are only 2 modes, it is easy to obtain closed-form solutions. To aid in later investigations, two additional variables will be defined and used in the closed-form equations. The first, K_r, is the ratio of k_z to k_f. The second, M_r, is the ratio of W_{mezz} to W_{roof}. Using these parameters, the following closed-form equations for T_1, T_2, ϕ_1, ϕ_2 are provided below:

$$T_1 = 2\pi \sqrt{\frac{1}{2}\left[\frac{k_m}{m_{11}} + \frac{k_f}{m_{22}} + \frac{k_m \alpha^2}{m_{22}} - \sqrt{\frac{k_m^{\,2}}{m_{11}^2} - \frac{2k_m k_f}{m_{11} m_{22}} + \frac{2k_m^{\,2}\alpha^2}{m_{11} m_{22}} + \frac{k_f^{\,2}}{m_{22}^2} + \frac{2k_f k_m \alpha^2}{m_{22}^2} + \frac{k_m^{\,2}\alpha^4}{m_{22}^2}} \right]}$$

$$T_2 = 2\pi \sqrt{\frac{1}{2}\left[\frac{k_m}{m_{11}} + \frac{k_f}{m_{22}} + \frac{k_m \alpha^2}{m_{22}} + \sqrt{\frac{k_m^{\,2}}{m_{11}^2} - \frac{2k_m k_f}{m_{11} m_{22}} + \frac{2k_m^{\,2}\alpha^2}{m_{11} m_{22}} + \frac{k_f^{\,2}}{m_{22}^2} + \frac{2k_f k_m \alpha^2}{m_{22}^2} + \frac{k_m^{\,2}\alpha^4}{m_{22}^2}} \right]}$$

$$\phi_1 = \begin{bmatrix} 2\left(\frac{1}{\alpha} - \frac{M_r}{K_r\alpha} - M_r\alpha + \sqrt{\frac{1}{\alpha^2} - \frac{2M_r}{K_r\alpha^2} + 2M_r + \frac{M_r^2}{K_r^2\alpha^2} + \frac{2M_r^2}{K_r} + \alpha^2 M_r^2}\right)^{-1} \\ 1 \end{bmatrix}$$

$$\phi_2 = \begin{bmatrix} 2\left(\frac{1}{\alpha} - \frac{M_r}{K_r\alpha} - M_r\alpha - \sqrt{\frac{1}{\alpha^2} - \frac{2M_r}{K_r\alpha^2} + 2M_r + \frac{M_r^2}{K_r^2\alpha^2} + \frac{2M_r^2}{K_r} + \alpha^2 M_r^2}\right)^{-1} \\ 1 \end{bmatrix}$$

The Equivalent Lateral Force (ELF) method of determining seismic force demand in a structure is commonly used in MBS design. As defined in ASCE/SEI 7 (ASCE 2005), this method computes the design seismic base shear, V_b, as a function of a design response spectrum, and the fundamental natural period of the structure. The design response spectrum depends on ground motion parameters, S_{DS} and S_{D1}, which vary over the U.S. After V_b is found, a portion of this force must be distributed to each story level. The method used to distribute force relies on two assumptions. First, all of the mass is assumed to vibrate in the first mode. Second, the first mode shape is assumed. These assumptions are made because the actual force distribution depends on the stiffness of the structure, which is not known before a design is available. Both of these assumptions will be investigated to determine their validity for MBS frames with mezzanines.

Before the investigations can begin, the exact solution must be obtained. As previously mentioned, the response of an elastic structure to a ground motion is the summation of each modal response. The base shear at any time, t, for a 2-DOF system can be defined as:

$$V_b(t) = M_1^* A_1(t) + M_2^* A_2(t)$$

$$M_n^* = \frac{\left(\phi_n^T \mathbf{m}\begin{bmatrix}1 & 1\end{bmatrix}^T\right)^2}{\phi_n^T \mathbf{m} \phi_n}$$

where $A_n(t)$ is the pseudo-acceleration response of a SDOF with T_n and ζ_n (Chopra, 2007). M_n^* is the effective modal mass, or the amount of mass vibrating in the nth mode. A modal mass participation factor, M_{pn}, can be found for each mode by dividing the effective modal mass by the total mass of the system, M_{tot}. The equation for V_b may be rewritten:

$$V_b(t) = \left(M_{p1} A_1(t) + M_{p2} A_2(t)\right) M_{tot}$$

Therefore, the base shear response depends on both the modal mass participation factors and the ground motion.

The story forces **F** can also be determined from modal superposition:

$$\mathbf{F}(t) = \left(M_{p1} A_1(t) \frac{\mathbf{m}\phi_1}{\sum_{j=1}^{2} m_j \phi_{j1}} + M_{p2} A_2(t) \frac{\mathbf{m}\phi_2}{\sum_{j=1}^{2} m_j \phi_{j2}} \right) M_{tot}$$

Therefore, the story forces depend on the modal mass participations factors, the ground motion, and the mode shapes.

By assuming the first mode dominates all responses, the modal mass participation factors are set to 1 and 0 for the first and second mode, respectively. The analysis can be further simplified since the peak value of A_1, s_a, determines the demand on the structure. This peak value is found from the design response spectrum in ASCE/SEI 7 (ASCE, 2005). This simplification of **F** results in the following equation:

$$\mathbf{F}_{\max} \approx M_{tot} s_a g \frac{\mathbf{m}\phi_1}{\sum_{j=1}^{2} m_j \phi_{j1}} = V_b \frac{\mathbf{m}\phi_1}{\sum_{j=1}^{2} m_j \phi_{j1}}$$

ASCE/SEI 7 uses a method of calculating these story forces, which assumes the shape of the first mode. It is assumed to be a function of the height of each story and a parameter k, which depends on the first natural period. This assumed shape takes a linear or parabolic form depending on k, resulting in the following equation for the ELF at story i, which will be referred to as the ASCE 7 method.

$$F_i = V_b \frac{W_i h_i^k}{\sum_{i=1}^{2} W_i h_i^k}$$

where Wi is the tributary weight at story i.

Another common practice in the MBS design industry is to assume the first mode shape is equal to unity at each level, resulting in an equation for story forces that depends only on the distribution of weight, which will be referred to as the Weight method:

$$F_i = V_b \frac{W_i}{\sum_{i=1}^{2} W_i}$$

PARAMETRIC STUDY

To determine the validity of the two assumed mode shapes and the assumption that the first mode dominates response, a parametric study was performed. The parameters varied were α, K_r, and M_r. These three parameters completely determine the mode shapes and the modal mass participation factors.

Realistic bounds on these parameters were needed. When one considers a mezzanine as simply a mass attached at mid-height of a MBS frame, it is apparent that lean-to structures might also be treated this way (See Figure 1). Since lean-to structures are very light, compared to the remainder of the MBS, values of M_r approaching 0 are possible. If one considers a mezzanine which spans the full length of the frame, and attached at both end columns, values as high as 20 are reasonable. These two values set the bounds for M_r. A reasonable lower limit for K_r is likely between 1 and 2. This limit may be exceeded in some cases with centrally located mezzanines, so values approaching 0 were also considered, though most likely not common. A realistic upper bound on K_r was not able to be determined, so 50 was chosen initially. Finally, α must necessarily be bounded by 0 and 1; however some reasonable assumptions lead to tighter bounds for this study.

Firstly, this study assumes that the majority of MBS frames are designed with pinned bases. Secondly, the height of the mezzanine was assumed to be at or near 50% of the eave height. With these two assumptions, a lower bound may be set by considering a pin-pin, prismatic, column supporting the mezzanine at mid-height. This setup would result in an α of 0.5. Many times, the upper end of the column will not be pinned, and the column will be tapered, resulting in higher values of α. An actual tapered MBS frame column was modeled with a fixed upper support, resulting in an α of 0.8. Since no frame column is perfectly fixed at its upper end, this was deemed a reasonable upper bound. A value of $\alpha = 0.6$ is a good preliminary guess when calculating the above stiffness matrix. With reasonable bounds determined, both mode shapes were calculated at increments of each parameter. Modal mass participation factors were also calculated for each increment of parameter.

First-Mode-Only Assumption

It was first desired to determine if the first mode truly dominated structural response for these systems. To do so, the modal acceleration responses for each mode, as well as the modal mass participation factors were needed. The case which would have the most likely possibility of violating this assumption would be when the spectral acceleration of the first mode was as small as possible compared with that of the second mode. It was found that a reasonable upper limit on MBS frame periods is 1 s, making the scenario easy to compose. Using spectral acceleration maps from ASCE/SEI 7, a random sample of S_{DS} and S_{D1} values were computed in high seismic regions. It was found that 0.4 was a reasonable lower bound ratio of S_{D1}/ S_{DS}. Since an upper bound on the period of MBS was 1 s, S_{D1}=0.4 was taken as the spectral acceleration of the first mode and S_{DS} =1 was taken for the second mode.

Since the modal mass participation factor was calculated at each value of the three parameters, there was a very large sample of M_{p1} available to determine a reasonable value to use for investigation. The mean and standard deviation of M_{p1} were found to be 0.984, and 0.019, respectively. Since these values are based on a uniform likelihood of each parameter, these values are incorrect. However, further investigation suggests they are still reasonable values. To allow plotting, one of the three parameters needed to be removed from consideration. To do this, the mass participation factor was averaged over all α values for each value of K_r and M_r.

Figure 3 shows the range of M_{p1} values as a function of K_r. It can be seen that when $K_r > 2$, M_{p1} can vary between 95% and 100%. Therefore, it was determined that the previous values were reasonable, and a $M_{p1} = 0.984 - 0.019 = 0.965$ was assumed

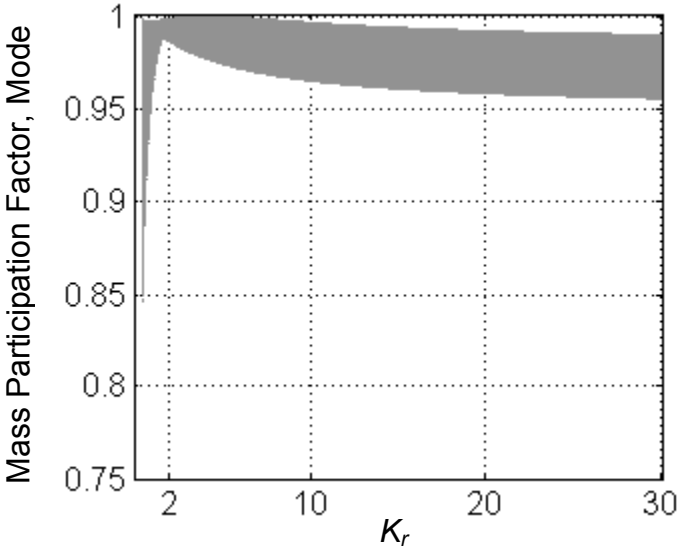


Figure 3. Range of mode 1 mass participation factor vs. K_r

with $M_{p2} = 0.035$. Using the 2-mode equation shown above for base shear, the following maximum modal base shears are found:

$$V_{b1,\max} = (0.4)(0.965)M_{tot} = 0.386M_{tot}$$
$$V_{b2,\max} = (1.0)(0.035)M_{tot} = 0.035M_{tot}$$

revealing that the second mode has a maximum contribution to total base shear of only 9.1% of the maximum contribution from the first mode. Thus, it seems reasonable to assume that the first mode dominates the response of these systems. However, the peaks of the modal responses do not always occur simultaneously so at some time, t, the response may be completely determined by the second mode. This may lead to the invalidity of this assumption when considering internal forces such as column shear or moment around the mezzanine attachment. Also, for systems with $K_r < 2$, M_{p1} becomes very small and these results are likely invalid. For the remainder of this investigation, the base shear results will be deemed sufficient to hold the first-mode-only assumption valid.

Force Distribution Methods

Next, it was desired to investigate the methods used to vertically distribute ELFs. From the parametric study and simplifying assumptions mentioned above, it was straightforward to compute the percentage of base shear assigned to each story using the exact first mode equation, the ASCE 7 method, and the Weight method. When using the ASCE 7 method, a $k = 1$ was assumed for simplification. If $k > 1$, the

error of the ASCE 7 method should be expected to increase. The error was measured by the difference between a given method and the exact equation for each parameter value. This error is the percentage of the base shear that is incorrectly assigned to a story. Again, to allow plotting, one of the three parameters needed to be removed. For each value of M_r, and K_r, the maximum error for any value of α was taken. This allowed an upper bound error envelope to be plotted for any value of M_r and K_r.

Plotting revealed that the behavior at $K_r > 30$ was approximately constant with respect to K_r. Three-dimensional plots for the error over the parameter space are shown in Figure 4 and Figure 5 for the ASCE 7 method and the Weight method, respectively. These figures show a region of high error at low values of K_r. A maximum error envelope, over all values of M_r, is shown in Figure 6. It can be seen that as K_r becomes small, the potential errors of both methods increase sharply. The change in error tapers off around $K_r = 3$. This is consistent with the region in which the first modal mass participation factor becomes significantly reduced, which may make the first mode only assumption invalid, also invalidating either method for distributing story forces. It can also be seen that when $K_r > 3$, the errors tend to depend primarily on M_r. Figure 7 shows a maximum error envelope as a function of M_r. This envelope assumes $K_r > 3$. This plot suggests that the simple Weight method for story force distribution is generally more accurate than the ASCE 7 method. As M_r approaches zero, the errors also approach zero. This is expected since $M_r = 0$ corresponds to a system with no mezzanine. Both methods exactly calculate a SDOF system. The Weight method is more accurate because its assumed mode shape more closely matches the actual mode shape.

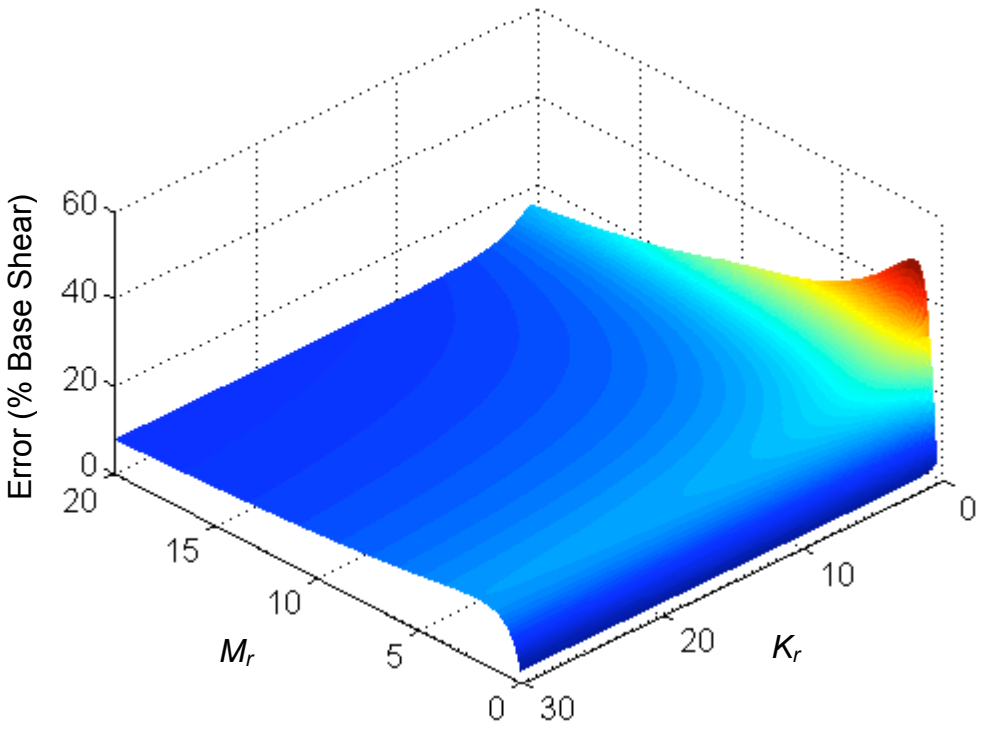


Figure 4. Error of ASCE 7 method for distribution of seismic story forces

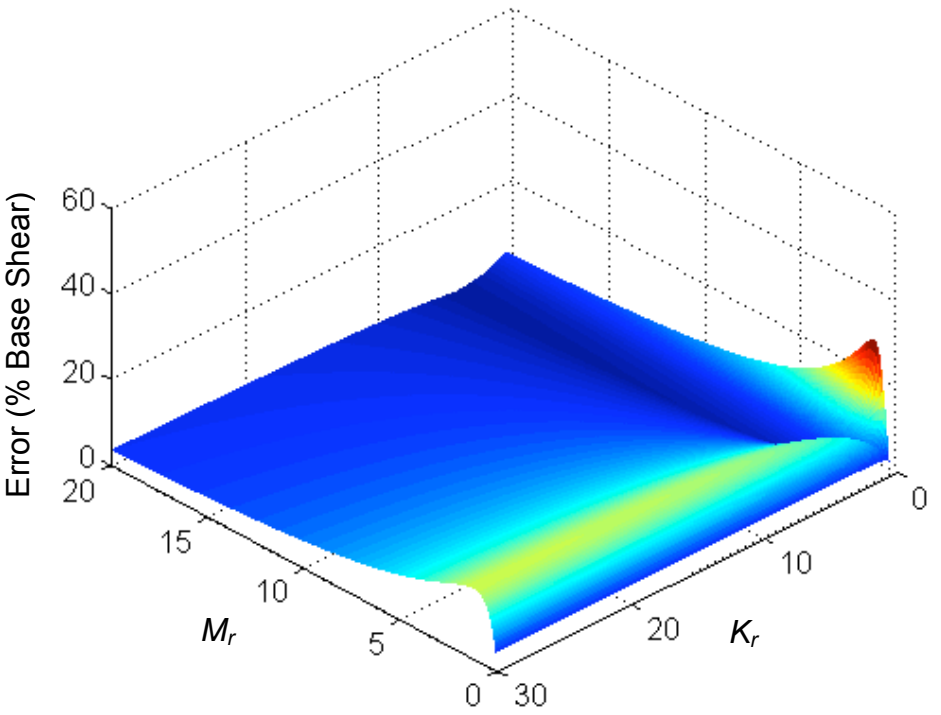


Figure 5. Error of Weight method for distribution of seismic story forces

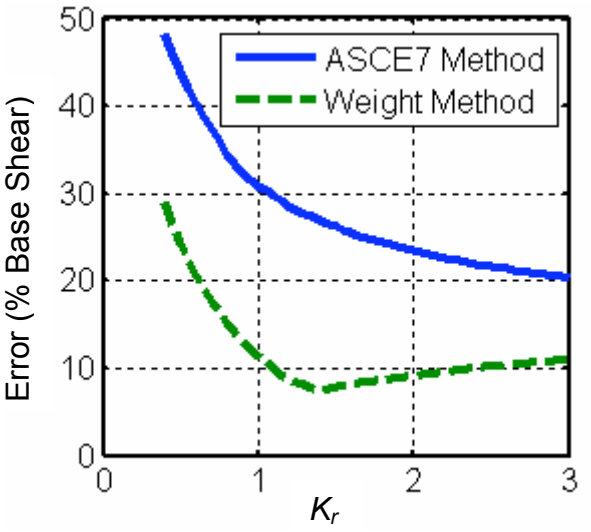


Figure 6. Error envelopes at low K_r values

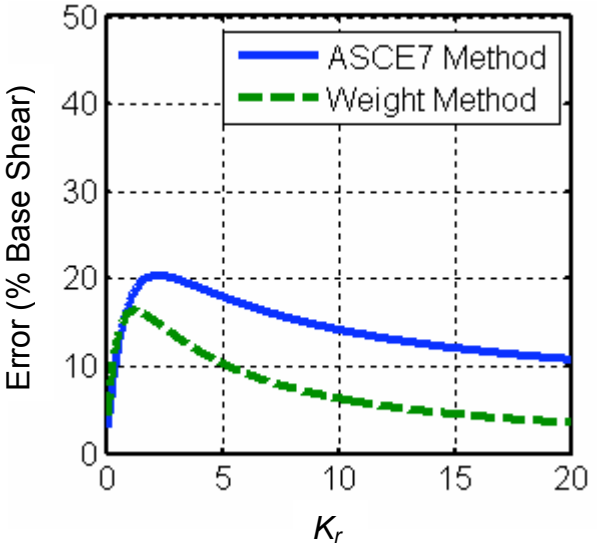


Figure 7. Error envelopes when $K_r > 3$

IMPLICATIONS

In light of the evidence found in these investigations, the Weight method is recommended for use in seismic design of MBS with mezzanines or lean-to attachments when $K_r > 2$, which should be most cases. It is possible that the ASCE 7 method may be improved by including an estimated α in the equation. Future research will investigate this possibility. Both methods give errors of about 20% or less and may be acceptable. If increased accuracy is desired, the Weight method can be used to determine forces for a preliminary design. After a design is in place, the closed-form solutions presented earlier
can be used to determine the first mode shape. This accurate mode shape will determine a better estimate of the story forces, and this process can be repeated until the designer reaches the desired accuracy. It is unlikely, given the general uncertainty level in seismic force determination, that accuracy of this level is necessary, and the Weight method will be sufficient to distribute story forces for design.

It is likely, especially for structures with mezzanines attached to a frame
column, that the second mode could have a significant effect on the internal forces for which the structure must be designed. A simple method to determine if this is the case and then account for it is not readily available; however, a more complicated method of modal response spectrum analysis may be performed. Modal response spectrum analysis may be necessary when $K_r < 2$ as well. Modal response spectrum analysis requires further assumptions about how modes interact, some of which will likely have economic impact on the design of MBS. As an example, when using the square-root-of-sum-of-squares (SRSS) method to combine modal responses, a given response quantity loses its sign (Chopra, 2007). If the response were an internal bending moment, this would render use of the moment gradient, to increase capacity, impossible. This would likely result in increased frame member sizes and a reduced

overall economy. A direct summation of modal responses has the potential to be a better solution for MBS designers. This will be investigated further in future research.

CONCLUSIONS

Common assumptions about seismic forces were investigated. It was shown that in a reasonable worst-case, the second mode could contribute to the base shear response, at a maximum, less than 10% of that which the first mode was capable of contributing. It seems valid that only the first mode's contribution be included when calculating seismic force demands. Since the first mode shape cannot be known until a preliminary structure is designed, two common story force distribution methods were compared with the actual first mode force distribution. Because both methods made assumptions about the mode shape, both produced low errors. The Weight method was found to be generally more accurate throughout a reasonable range of structural parameters and is recommended for use in design. There is room for improvement on the ASCE 7 method which may help make it more accurate. This research will continue with an effort to develop a method to dismiss or account for contribution of the second mode when designing for internal forces. Regardless of whether a mezzanine is considered a floor or not, the results found in this paper are valid as long as the structure can be idealized as a 2-DOF system.

REFERENCES

ASCE (2005), *Minimum Design Loads for Buildings and Other Structures,* American Society of Civil Engineers, New York, New York, USA, 2005;

Bachman, Drake, Johnson, and Murray (2008), *Seismic Design Guide for Metal Building Systems*, International Code Council, Country Club Hills, Illinois, USA, 2008

Chopra, A.K. (2007), *Dynamics of Structures,* 3e., Pearson Prentice Hall, Upper Saddle River, New Jersey, 2007

Uang, C.M., Smith, M.D, and Shoemaker, W.L. (2011), "Earthquake Simulator Testing of Metal Building Systems," *Proceedings*, ASCE Structures Congress, ASCE, 2011

ACKNOWLEDGEMENT

This research was sponsored by MBMA and AISI, with Dr. W. L. Shoemaker as the project manager.

BEHAVIOR OF STEEL PLATE SHEAR WALLS WITH IN-SPAN PLASTIC HINGES

Ronny Purba[1] and Michel Bruneau[2]

[1]Graduate Research Assistant, Department of Civil, Structural, and Environmental Engineering, University at Buffalo, 241 Ketter Hall, Buffalo, NY 14260; Phone: (716) 645-4373; E-mail: rpurba@buffalo.edu
[2]Professor, Dept. of Civil, Structural, and Environmental Engineering, University at Buffalo, 130 Ketter Hall, Buffalo, NY 14260; Phone: (716) 645-3398; E-mail: bruneau@buffalo.edu

ABSTRACT

Research was conducted to investigate the seismic behavior of steel plate shear walls with in-span plastic hinges. Results show that the development of in-span plastic hinges has detrimental impacts on the behavior of the structure through inducing: (1) significant vertical and residual deformations on the HBEs (i.e. shakedown phenomenon); (2) only partial yielding of the infill plates; (3) lower global plastic strength compared to the values predicted by code equations; and (4) total HBE rotations greater than 0.03 radians after the structure was pushed cyclically up to a maximum lateral drift of 3%. Nonlinear time history analyses also demonstrated that the severity of the ground excitations accentuated the shakedown phenomenon.

INTRODUCTION

There have been numerous experimental and analytical studies investigating the behavior of unstiffened Steel Plate Shear Walls (SPSW) in the past thirty years. An extensive summary of that research has been presented in Sabelli and Bruneau (2007). Much of that research has focused on designing and modeling of the SPSW web plates, analysis methods, and validation of satisfactory cyclic inelastic and seismic performance. Few have focused on alternative ways to analyze and design SPSW horizontal and vertical boundary elements (HBEs and VBEs). Xue and Lu (1994) suggested means to reduce demand on VBEs, including connecting the infill panel to only the HBEs. Berman and Bruneau (2008) developed an analytical procedure to obtain correct forces in the VBEs. Lopez-Garcia and Bruneau (2006) and Qu *et al.* (2008) investigated possible inadequate performance of HBEs, building on the work of Vian and Bruneau (2005).

This paper presents the results of an analytical investigation on the seismic behavior of steel plate shear walls having HBEs designed to have different plastic collapse mechanisms. In the first SPSW, formation of in-span plastic hinges on HBEs is possible, whereas in the second SPSW, plastic hinges can only occur at the ends of HBEs. Results and observations from pushover analyses and time-history analyses are used to assess the relative performance of the two SPSWs.

STRUCTURE DESCRIPTION & ANALYTICAL MODEL DEVELOPMENT

As a case study to investigate the possible significance of in-span HBE plastic hinges, a three-story single-bay SPSW was selected. Bay width and typical story height were arbitrarily chosen equal to 20 and 10 ft, respectively, resulting in an infill plate aspect ratio of 2.0. It was also assumed that the structure is located on Class D soil in downtown San Francisco, California and designed for an office building. Total weight of the structure W_t is 1085 kips, distributed as 352 kips on the first two stories and 381 kips on the roof. The total base shear V resisted by the structure was 176 kips, distributed as lateral loads along the height of the building of 92 kips, 56 kips, and 28 kips from the third to the first floor. Two design procedures were applied to design the boundary elements: (1) the Indirect Capacity Design approach (AISC 2010) and (2) the capacity design approach which combines the procedure proposed by Vian and Bruneau (2005) for HBEs and that proposed by Berman and Bruneau (2008) for VBEs. The resulting sizes of VBEs and HBEs obtained by the two different design procedures are compared in Figure 1. For SPSW designed by the capacity approach (SPSW-CD), all the HBE demand-capacity ratios exceed 0.98, except one at 0.95. For SPSW designed by the indirect capacity approach (SPSW-ID), the HBE ratios varied from 0.88 to 0.99; but this slight difference from the second SPSW case will not violate the conclusions reached by this study as will be shown later.

To investigate the behavior of both SPSW-ID and SPSW-CD, two analytical models were developed in SAP2000 program: (1) a strip model for monotonic pushover analysis and (2) a dual strip model for cyclic pushover analysis and time history analyses. In this study, twelve strips were provided at every floor to model the infill plates of the two 3-story SPSWs. The *Axial-P Hinge* (set to exhibit correct hysteretic tension-only behavior, per Purba and Bruneau 2010) was chosen to define the inelastic behavior of the strips. The *Fiber P-M2-M3 Hinge* was chosen to define plastic hinges in the VBEs and HBEs, which automatically accounts for the interaction between the axial loads and moments that can occur in the HBEs and VBEs.

NONLINEAR STATIC ANALYSIS (PUSHOVER ANALYSIS)

A monotonic pushover analysis was conducted for both SPSW-ID and SPSW-CD until each structure reached a 4% lateral drift. At 4% drift, the base shears are 311 and 477 kips for the respective structures; for comparison, their respective theoretical

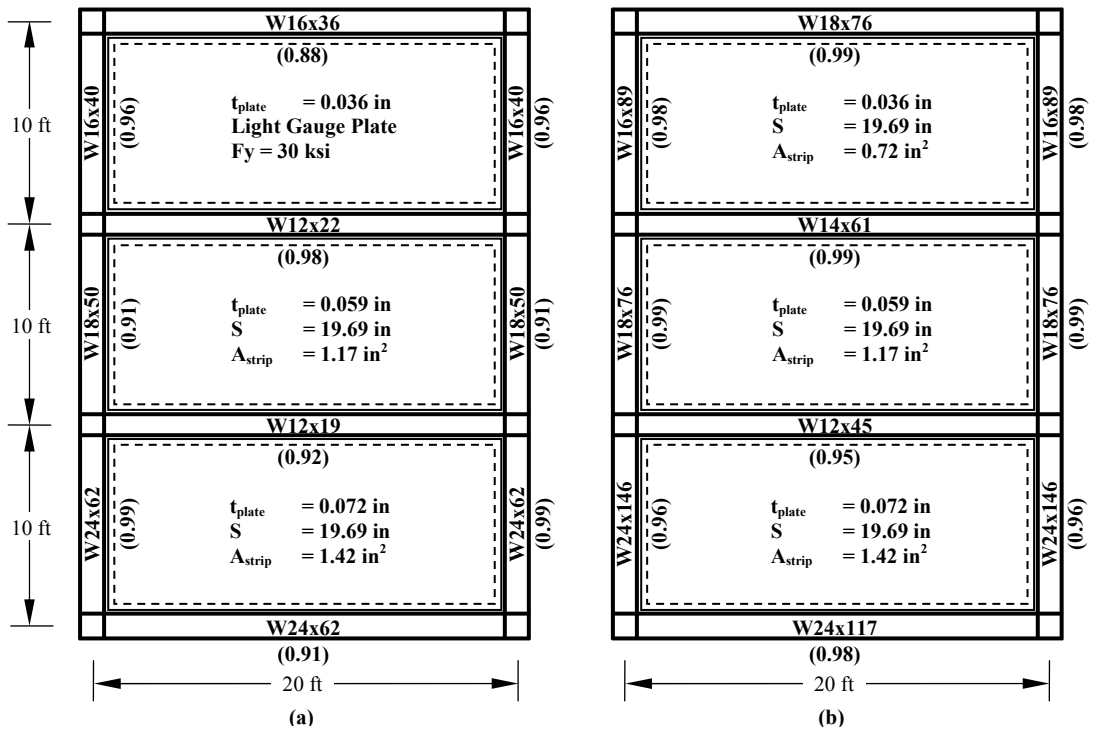


Figure 1. VBE and HBE Sizes (a) SPSW-ID; (b) SPSW-CD

values are 351 and 488 kips, obtained using the plastic analysis equations for uniform plastic collapse mechanism (Berman and Bruneau 2003). For SPSW-CD, the two values are in a good agreement with only a 2.3% difference. However for SPSW-ID, the theoretical base shear is 13% more than obtained from the monotonic pushover analysis. This because SPSW-ID did not follow the uniform plastic collapse sway-mechanism but rather consists of a 'sway' and 'beam' combined mechanism. Four in-span plastic hinges have developed on the HBEs of SPSW-ID and significant vertical deformations were observed along the HBEs spans of SPSW-ID.

In a seismic excitation environment, when a structure experiences cyclic loading, plastic hinging along an HBE span could lead to an unbounded progressively increasing deformation. This detrimental impact on a structure is called a "shakedown phenomenon". To investigate whether this phenomenon develops in the HBEs of SPSW-ID and SPSW-CD, and whether it may detrimentally affect structural performance, cyclic pushover analysis was conducted. A progressively increasing cyclic displacement history of up to 3% drift (in increment of 0.5%) was applied to the top floor of the structure for this purpose.

Figure 2(a) shows the plastic hinge and strip yielding distributions on SPSW-ID. When the structure experienced +1% lateral drift, a total of four plastic hinges (1 partial plastification and 3 fully plastic) occurred at the HBE ends; and somewhat the same distributions occurred at the reversed excursion of −1% lateral drift. In addition, three strips (the right-leaning or left-leaning strips for the positive or negative direction, respectively) on the second and the third floor remained elastic and only two strips on the first floor had yielded. Though more strips yielded as the

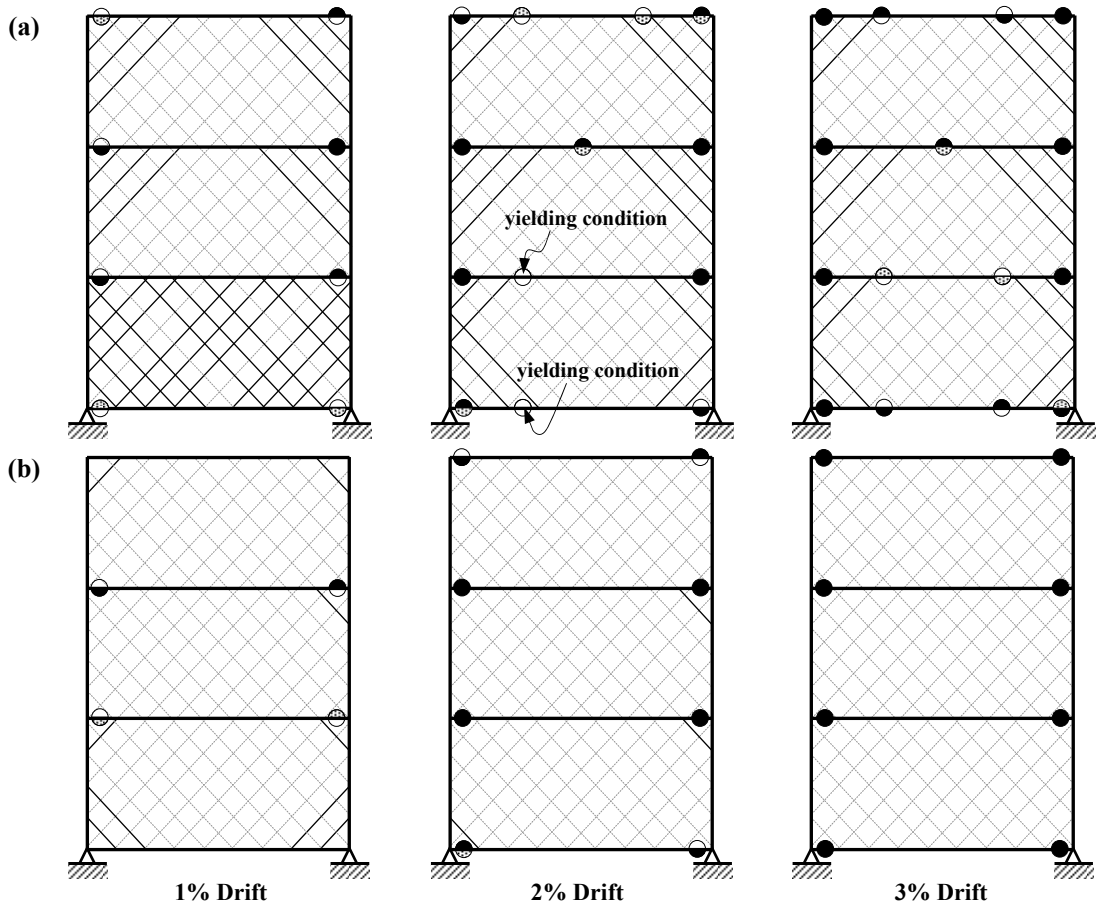


Figure 2. Plastic Hinge and Strip Yielding Distributions on (a) SPSW-ID; (b) SPSW-CD

pushover displacement increased, some strips remained elastic. Moreover for the plastic hinge distribution, beyond the plastic hinges that occurred at the HBE ends, three locations of in-span plastic hinges were also observed on HBE2 and HBE3 at the end of 2% drift cycle; and the yielding condition occurred along the span of HBE0 and HBE1. At the end of the 3% drift cyclic, in-span plastic hinges on the HBEs occurred at 4 locations for both positive and negative drift excursions. In contrast with SPSW-CD [presented in Figure 2(b)], most of the strips had yielded at the end of the 1% drift cycle and only four right-leaning strips and five left-leaning

strips in total had remained elastic. All strips have completely yielded at the end of the 3% drift cycle. In addition, all plastic hinges have developed at the HBE ends of SPSW-CD and no in-span plastic hinge developed.

A most significant phenomenon observed is the HBE vertical downward deformation of SPSW-ID, progressively increasing and of significant magnitude as the lateral drift increased, as one example is shown in Figure 3. This figure compares vertical displacement history at the mid-span of the top HBE for both SPSWs. The backbone-displacement slope (i.e., displacement at maximum drift) of SPSW-ID is stiffer than that of SPSW-CD. This implies that the HBE vertical downward displacement for SPSW-ID increases faster than that for SPSW-CD. In other words, the shakedown phenomenon due to cyclic pushover displacement detrimentally affects the structural performance of SPSW-ID. The same trend was also exhibited with the residual displacements (i.e., displacement when the structure returns to its original position at 0% drift). Moreover, note that the shakedown phenomenon on SPSW-ID would be even worse if a smaller W-section had been used for the top HBE such that its demand-to-capacity ratio was closer to 1.0; recall that a value of 0.88 (as shown in Figure 1) was obtained for that top HBE in the SPSW-ID case, compared to the corresponding 0.99 value at the top HBE of SPSW-CD. If anything, this discrepancy reinforces the conclusions reached by this case study.

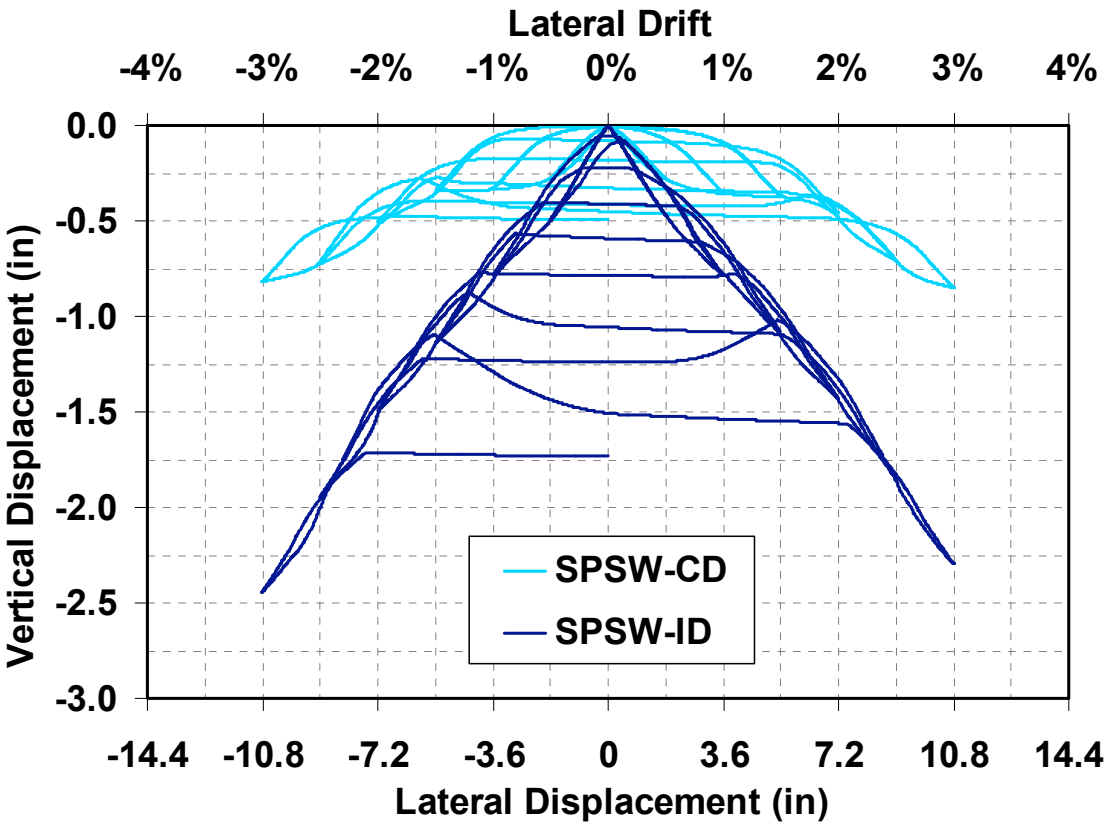


Figure 3. History of HBE3 Vertical Displacement (Cyclic Pushover)

Another approach that can be used to examine the behavior of the two SPSWs is by comparing the moment-rotation hysteresis of their HBEs, as done in Figure 4, which plots the normalized moment-rotation hysteresis of HBE2 (as an example) obtained during the cyclic pushover displacements. Interestingly, the moment-resisting ends of the HBEs of SPSW-ID developed a cross-section rotation greater than 0.03 radians after the structure was pushed cyclically up to a maximum lateral drift of 3%. Such a significantly high cyclic rotation demand would be difficult to achieve using the type of moment resisting connections used in SPSW (the AISC 2010 Seismic Specifications only require that Ordinary-type connections be used in SPSW). In fact, it might also be difficult to achieve with special moment resisting frame (SMRF) beam-to-column connections approved by AISC 2010, which are experimentally verified to perform well up to +/–0.04 radians total rotations, or +/–0.03 radians plastic rotations. By comparison for SPSW-CD, all HBE total rotations obtained were less than or equal to 0.03 radians under the same cyclic pushover displacements up to 3% drift.

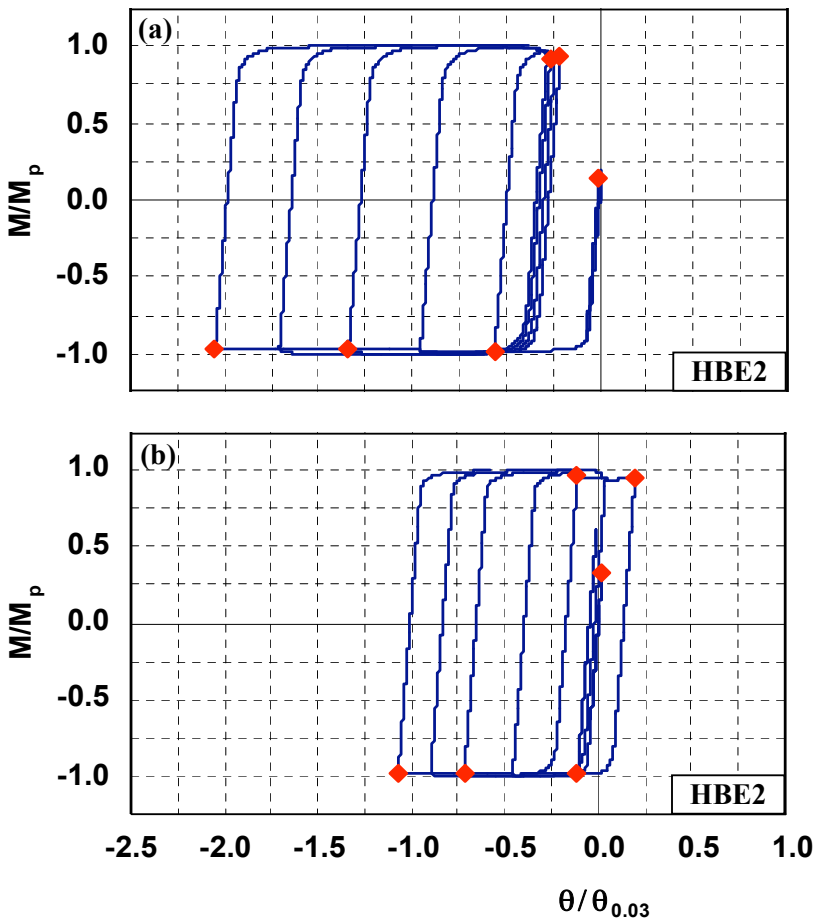


Figure 4. Normalized Moment Rotation Hysteresis at HBE Left End for (a) SPSW-ID; (b) SPSW-CD

NONLINEAR TIME HISTORY ANALYSIS

While several key seismic behaviors of steel plate shear walls having HBEs designed to have different plastic collapse mechanisms have been discovered through the incrementally cyclic pushover analysis, conducting nonlinear time history analysis remains necessary to investigate whether those previous results would be replicated during earthquakes excitations and whether additional seismic behaviors for the aforementioned SPSW systems would emerge as a consequence of the random nature of earthquake records. Three synthetic time histories of ground acceleration were generated for this purpose

The nonlinear time history results show that the shakedown phenomenon is still observed, with maximum and residual vertical deformations more apparent on SPSW-ID than on SPSW-CD. HBE3 vertical downward displacement for SPSW-ID increased faster than that for SPSW-CD as the lateral drift increased. For example, when SPSW-CD reached a lateral drift of 1% for the first time, the largest HBE3 vertical displacement at the same drift for SPSW-ID was 2.25 larger; and became 4 times larger as the ground excitation increased and caused a 2% lateral drift on both structures.

The nonlinear time history analyses were then extended to investigate the performance of both SPSWs under the more severe Maximum Considered Earthquake (MCE). It was observed that as the severity of the synthetic ground motions increased (consequently generating higher lateral drifts on both SPSWs), HBE vertical deformations of SPSW-ID especially at the top two floors significantly increased compared to the corresponding magnitudes in the DBE case. By comparison for SPSW-CD, only minor changes of HBE vertical deformations occurred. Hence, when formation of in-span plastic hinges on HBEs is possible, such as in the case of SPSW-ID, the more severe the ground excitations, the worse the shakedown phenomenon.

CONCLUSIONS

An analytical investigation on the seismic behavior of steel plate shear walls having boundary elements designed by two different philosophies was conducted. It was demonstrated that plastification along HBE spans (i.e., in SPSW-ID) has detrimental impacts on the behavior of the structure. Nonlinear time history analysis also demonstrated that the severity of the ground excitations accentuated the shakedown phenomenon on SPSW-ID, while this was not the case for SPSW-CD. These conclusions on the behavior of the SPSW-ID are equally applicable to SPSWs designed by any method for which in-span hinges is not explicitly prevented.

ACKNOWLEDGMENTS

This work was supported primarily by the George E. Brown, Jr. Network for Earthquake Engineering Simulation (NEES) Program of the National Science Foundation under NSF NEESR Award Number CMMI-0830294. However, any

opinions, findings, conclusions, and recommendations presented in this paper are those of the writers and do not necessarily reflect the views of the sponsors.

REFERENCES

AISC. (2010). "Seismic Provisions for Structural Steel Buildings." ANSI/AISC 341-10, American Institute of Steel Construction, Inc., Chicago, Illinois.

Berman, J. W., and Bruneau, M. (2003). "Plastic Analysis and Design of Steel Plate Shear Walls." *Journal of Structural Engineering*, ASCE, Vol. 129, No. 11, pp. 1448-1456.

Berman, J. W., and Bruneau, M. (2008). "Capacity Design of Vertical Boundary Elements in Steel Plate Shear Walls." *Engineering Journal*, AISC, First Quarter, pp. 57-71.

Lopez-Garcia, D., and Bruneau, M. (2006). "Seismic Behavior of Intermediate Beams in Steel Plate Shear Walls." *Proceeding, 8th U.S. National Conf. on Earthquake Engineering*, San Francisco, Paper No. 1089.

Purba, R., and Bruneau, M. (2010). "Impact of Horizontal Boundary Elements Design on Seismic Behavior of Steel Plate Shear Walls." *Tech. Rep. MCEER-10-0007*, Multidisciplinary Center for Earthquake Engineering Research, State University of New York at Buffalo, Buffalo, New York.

Qu, B., Bruneau, M., Lin, C.H., and Tsai, K.C. (2008). "Testing of Full Scale Two-story Steel Plate Shear Walls with Reduced Beam Section Connections and Composite Floors." *Journal of Structural Engineering*, ASCE, Vol. 134, No. 3, pp. 364-373.

Sabelli, R., and Bruneau, M. (2007). "Steel Plate Shear Walls (AISC Design Guide)", American Institute of Steel Construction, Inc., Chicago, Illinois, 144 p.

Vian, D., and Bruneau, M. (2005). "Steel plate shear walls for seismic design and retrofit of building structures." *Tech. Rep. MCEER-05-0010*, Multidisciplinary Center for Earthquake Engineering Research, State University of New York at Buffalo, Buffalo, New York.

Xue, M., and Lu, L-W. (1994) "Interaction of Infilled Steel Shear Wall Panels with Surrounding Frame Members." *Proceedings, 1994 Annual Task Group Technical Session, Structural Stability Research Council*: reports on current research activities: June 20, 1994, Lehigh University, Bethlehem, PA.

Recent Experimental Researches on Steel Plate Shear Walls in NCREE

Chao-Hsien Li[1], Jing-Tang Chang[2], Keh-Chyuan Tsai[3] and Chih-Han Lin[4]

[1]Assistant Research Fellow, National Center for Research on Earthquake Engineering, No. 200, Sec. 3, Xinhai Rd., Taipei 10668, Taiwan, R.O.C., E-mail: chli@ncree.org, Tel: +886+2+6630-0897.
[2]Former Graduate Student, Department of Civil Engineering, National Taiwan University, No. 1, Sec. 4, Roosevelt Rd., Taipei 10668, Taiwan, R.O.C., E-mail: r96521232@ntu.edu.tw.
[3]Professor, Department of Civil Engineering, National Taiwan University, No. 1, Sec. 4, Roosevelt Rd., Taipei 10668, Taiwan, R.O.C., E-mail: kctsai@ntu.edu.tw, Tel: +886+2+3366-4318.
[4]Assistant Research Fellow, National Center for Research on Earthquake Engineering, No. 200, Sec. 3, Xinhai Rd., Taipei 10668, Taiwan, R.O.C., E-mail: hanklin@ncree.org, Tel: +886+2+6630-0884.

ABSTRACT

This paper describes the recent experimental researches on the steel plate shear wall (SPSW) at National Center for Research on Earthquake Engineering (NCREE). In addition, the design implications learned from the test results are presented. In 2007, the cyclic tests of four full-scale two-story narrow SPSWs confirm that the yielding of the first story column can be confined in the bottom of the column when the proposed capacity design principle is followed. Test results also suggest that, when the column hinging is allowed at a location slightly above the column base, the column size can be cost-effectively reduced without comprising the seismic performance of the SPSW. In 2009, the cyclic test of a reduced scaled coupled SPSW (C-SPSW) substructure was conducted at NCREE. The specimen was the 2/5-scaled substructure of the lowest two-and-half-story of a 6-story C-SPSW prototype building. The C-SPSW specimen consisted of two SPSWs connected together by the coupling beams. In addition to a constant vertical force representing the gravity load effects, cyclic increasing displacements and the associated overturning moments were applied at the boundary of the specimen using the Multi-Axial Testing System (MATS) in NCREE. Test results suggest that the proposed design method, which aims to limit the hinging of the bottom column within the bottom quarter column height, could be a choice of design in the practice. The test results confirm that the effect of the coupling beams in reducing the axial forces in the inner boundary columns. The relationship between the coupling beam rotation and the story drift is explored based on the test data. Test results suggest that the cyclic responses of the C-SPSW specimen can be satisfactorily predicted using the general purposes frame response software incorporating the strip model.

INTRODUCTION

Steel plate shear wall (SPSW) has seen increased usage in North America and Asia in recent years. An SPSW is composed of a structural frame and infill steel plates. The beams and columns surrounding the infill plates are named boundary beams and boundary columns, respectively. SPSW can effectively resist horizontal earthquake forces by allowing the development of diagonal tension field action after the infill plates buckle in shear. The input energy is then dissipated through the cyclic yielding of the infill plates in tension. The boundary elements in an SPSW must to be designed to anchor the plastic tension field action of the infill plates. Recently, many researches (Vian and Bruneau, 2005; Berman and Bruneau, 2008; Qu and Bruneau, 2010) focused on the capacity designs for the boundary elements. In 2007, the objective of the cyclic tests of four 2-story narrow SPSWs at National Center for Research on Earthquake Engineering (NCREE) was to verify the capacity design method for the boundary column proposed by Tsai *et al*. (2010). The test results confirm the effectiveness of Tsai *et al.*'s method in limiting the plastic hinge formation on the boundary column at the column base.

The infilling the steel plate into the structural frame would conflict with the architectural demand for the doorways. In a tall and slender SPSW, the significant overturning moments will result in high axial forces in the boundary columns. Moreover, the tall SPSWs likely behave in the flexure-dominated deformation mode under the lateral forces. It would cause the steel plates in the top stories of the wall to fail in developing the plastic tension field action. The coupled steel plate shear wall (C-SPSW) is considered as a solution to the application of SPSW in the high-rise buildings. In order to investigate the seismic behavior and design of C-SPSW, cyclic test of a recued-scaled C-SPSW substructure was conducted at NCREE in 2009 using the brand-new Multi-Axial Testing System (MATS) facility. In addition, a new design philosophy of boundary column was examined based on the test results of the C-SPSW.

CYCLIC TESTS OF FOUR TWO-STORY NARROW SPSWS

Column capacity design philosophy. The main objective of this experiment is to verify the effectiveness of the column capacity design proposed by Tsai *et al*. (2010). The objective of the design method was to limit the hinging of the column to the column base. Figure 1 illustrates the philosophy of the proposed method. The action on the boundary elements of an SPSW subjected to lateral forces can be considered as the superposition of two parts. One part is only due to frame sway (see Figure 1a-left) while the other is due to panel forces (see Figure 1a-middle). For properly portioned SPSWs, the infill plates would develop the plastic tension field prior to the yielding of the columns. The yield panel forces acting on the boundary elements can be considered as distributed loads with a tension field angle α (AISC, 2005a) from the vertical. The horizontal yield panel force acting on the 1st story columns is denoted as ω_{ch1}.

The top and bottom halves of Figure 1a demonstrate two types of the bending moment distribution patterns on the compressed column. The bending moment from

the frame sway action can be assumed as linearly distributed (Figure 1a-left). The quadratic- distributed moment (Figure 1a-middle) can be estimated by assuming that the column has fixed ends and the column is subjected to a distributed load ω_{ch1}. If the column strength is sufficient to resist enough swaying moment, as shown in the right top of Figure 1a, the maximum superposed moment will locate at the bottom end, which implies that the plastic hinge will form at the bottom end (Figure 1b-top). Tsai *et al.* (2010) derived the equation for the column moment demand based on this kind of moment distribution (right top of Figure 1a). If the column is smaller, as shown in the bottom half of Figure 1, the plastic hinge would form above the bottom end.

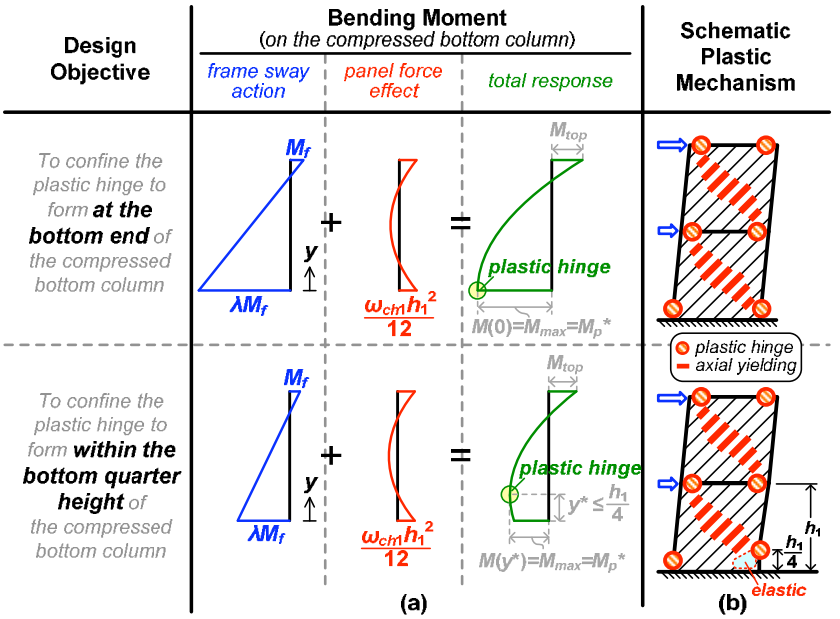


Figure 1. Philosophies of the design methods for the bottom column of SPSW.

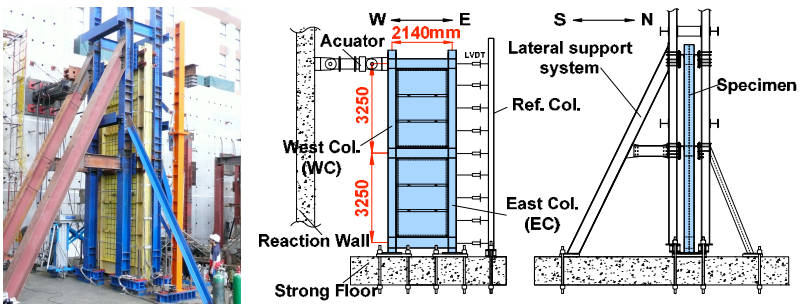


Figure 2. Test setup of cyclic tests of four 2-story narrow SPSWs.

Experimental program. Four 2-story 2.14-meter wide by 6.5-meter tall narrow SPSWs were cyclically tested to a 5% rad. roof drift at NCREE. All four specimens had the same center-to-center line dimensions. All the infill steel plates were 2.6 mm thick low yield strength (LYS) steel with a measured yield stress, f_{yp} = 195MPa. All boundary elements were made of A572GR50 steel. The key differences in the

specimens were the size of the boundary elements and the use of restrainers. The aspect ratio of the infill plates ranged from 0.62 to 0.64, which was less than the lower limit (0.8) specified by 2005 AISC seismic provisions (AISC 2005a). Figure 2 shows the test setup. Increasing cyclic horizontal displacements were applied on the top level of the specimens through two actuators.

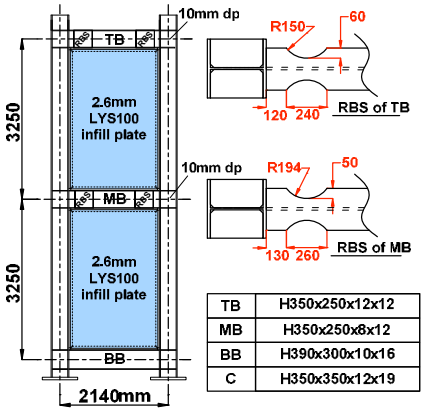


Figure 3. Details of Specimen N.

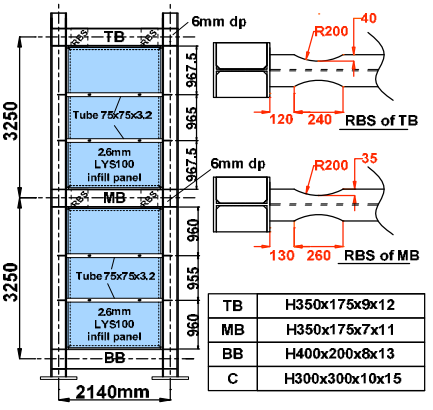


Figure 4. Details of Specimen RS.

This paper focuses on the cyclic performances of three of the four specimens. The details of the specimens and the sizes of the boundary elements are provided in Figures 3 and 4. Specimens N and S are typical unstiffened SPSWs; Specimen RS is a restrained SPSW (R-SPSW) (Tsai *et al*., 2010). The boundary elements are classified into four categories and abbreviated as: the top beam (TB), the middle beam (MB), the bottom beam (BB) and the column (C). All beam-to-column connections are welded moment connections. Specimen N was normal, named from the fact that the column complied with the proposed capacity design method (Tsai *et al*., 2010). The boundary elements in Specimen S were smaller than those in Specimen N. The column in Specimen S did not satisfy the proposed capacity design method. Specimen RS was identical to Specimen S except it adopted two pairs of restrainers for each story. As the restrainers can reduce the horizontal panel force effect on the boundary column, the boundary columns in Specimen RS conformed to the proposed capacity design method (Tsai *et al*., 2010). Figure 5 shows the predicted plastic mechanism of the three specimens based on the proposed capacity design method. As the boundary column strength in Specimen S was insufficient, it was expected that a plastic hinge would form within the column height.

Experimental results and learned implications. Figure 6 shows the lateral force versus story drift relationships of Specimens N, RS and S. In general, all specimens remained elastic before a drift of 0.3%. The boundary elements slightly yielded at this stage. Plastic hinges on the boundary elements were observed at the boundary element ends at a roof drift level of about 1.0% radian. As the roof drifts exceeded 2.5% radians, flange or web local buckling occurred gradually at the plastic hinge zones. Nevertheless, the load-carrying capacity did not decrease significantly.

Figure 7 shows the overall views of the specimens after the tests. Based on the flaking of the whitewashes, the locations of the plastic hinges agree with the

predictions shown in Figure 5. As shown in Figure 8, the plastic hinges developed at the first story column bottom ends can be recognized from the flaking of the whitewashes. Two types of plastic hinges can be observed in the columns. One is the plastic hinge developed when the column is compressed. This kind of plastic hinge can be observed on the column web shown in the photo (Figure 8c) as a ring shape. This is due to the occurrence of web local buckling at the center of the ring. The other type of plastic zone develops when the column is tensioned. In this case, uniform web yielding would be evident as shown in the photo (Figure 8c) at the column bottom end. As there is no plastic hinge zone forming within the column height for Specimens N and RS, these two types of plastic zones overlapped at the column bottom ends (Figures 8a and 8b). On the other hand, in Specimen S, the ring-shape zone was evidently above the column bottom end where uniform yielding zone developed (Figure 8c). The distance from the bottom end to the ring center is about two times the column depth. It clearly indicated that, in Specimen S, the plastic hinges formed away from the bottom ends when the columns were compressed.

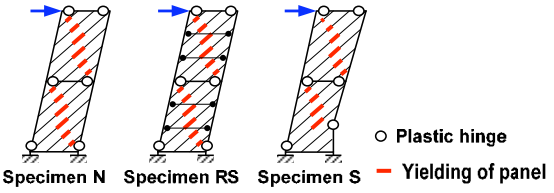


Figure 5. Predicated plastic mechanism.

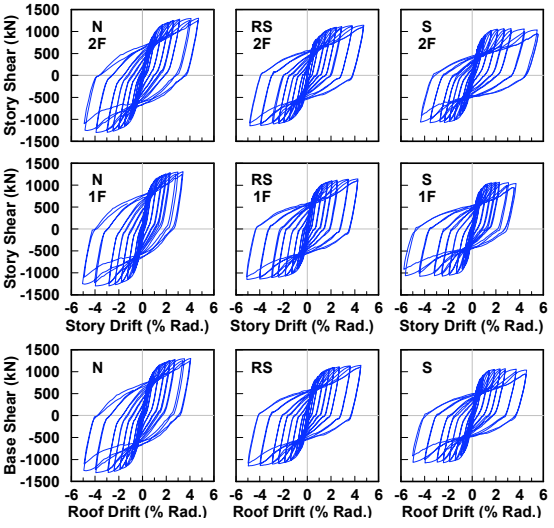
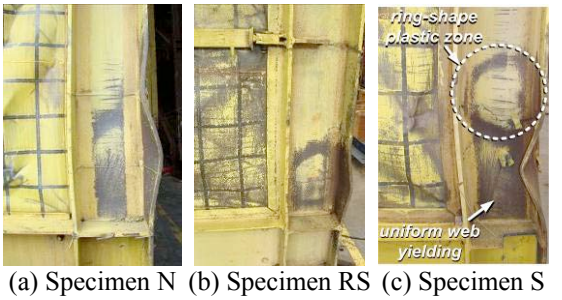


Figure 6. F-D relationships.



(a) Specimen N (b) Specimen RS (c) Specimen S

Figure 7. Specimens after tests.



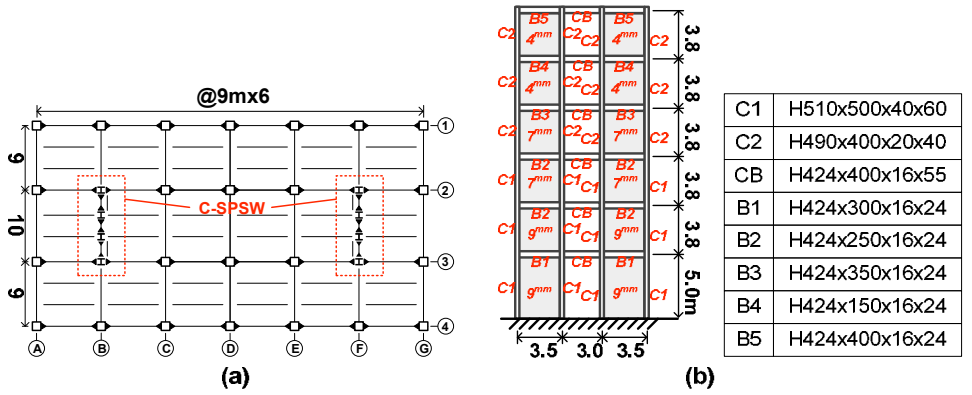
(a) Specimen N (b) Specimen RS (c) Specimen S

Figure 8. Plastic zones on the columns.

Test results confirm that the proposed capacity design is effective in limiting the plastic hinge formation to the column base. However, the cyclic responses shown in Figure 5 indicate that Specimen S possessed satisfactory ductility and load carrying capacity. This suggests that the cyclic performance of an SPSW might not be significantly deteriorated when it has plastic hinges slightly above the column bases. To achieve a more economical SPSW, a slight under-design for the column as illustrated in the case of Specimen S should be acceptable.

CYCLIC TEST OF A REDUCED-SCALE C-SPSW SUBSTRUCTURE

Specimen design. A prototype 6-story coupled steel plate shear wall (C-SPSW) building (see Figure 9) was designed based on the model U.S. standards (AISC, 2005a and 2005b). The site is located at the east zone of the Chiayi City in Taiwan. A 2-D strip model (Thorburn *et al*., 1983) for the C-SPSW was developed using the structural analysis program SAP2000 to check that the infill plates and the other frame elements remain elastic under the code prescribed LRFD load combinations (AISC 2005b). The seismic load was calculated according to Taiwan seismic building code (ABRI, 2002).



C1	H510x500x40x60
C2	H490x400x20x40
CB	H424x400x16x55
B1	H424x300x16x24
B2	H424x250x16x24
B3	H424x350x16x24
B4	H424x150x16x24
B5	H424x400x16x24

Figure 9 (a) Floor plan and (b) elevation of the prototype C-SPSW building.

The bottom boundary column of the prototype 6-story C-SPSW was selected based on a new column capacity design philosophy (Chang, 2009): the plastic hinge on the bottom column is allowed to form above the bottom end but shall be limited within the bottom quarter column height as shown in the bottom half of Figure 1. This design philosophy would result in a more economical design results than the previously proposed design method (Tsai *et al.*, 2010), which limits the plastic hinge formation at the column base. The coupling beams of the 6-story C-SPSW prototype were designed as shear links. By extending the current provisions (AISC 2005a) for the link beam of the eccentrically braced frame (EBF) to the design of the coupling beams, the coupling beam section was selected in accordance with the relationship $e < 1.6M_p / V_p$, where M_p and V_p are the plastic flexural and shear strength of the coupling beam, respectively.

Using the 6-story C-SPSW prototype as a basis, a 40% scale specimen was constructed as the bottom 10.5-m high substructure of the original C-SPSW. The region of the substructure contains the lowest two and half stories of the original structure (shown in Figure 10-left). The infill plates were 3.5-mm thick low yield strength (LYS) steel with a measured yield stress f_{yp} = 220MPa. All the boundary elements and coupling beams were made of A572GR50 steel. The design results of the test specimen are shown in Figure 11. The Reduced Beam Section (RBS) was employed at the ends of the boundary beams. The spacing of the stiffener plates in the coupling beam webs was determined based on the rotational demands of the coupling beams predicted from a finite element analysis. A shell model of the 2/5-scaled C-SPSW specimens was developed using the commercially available

software ABAQUS/Standard. A nonlinear pushover analysis up to a 5% rad. roof drift was conducted to obtain the rotational demands of the coupling wall.

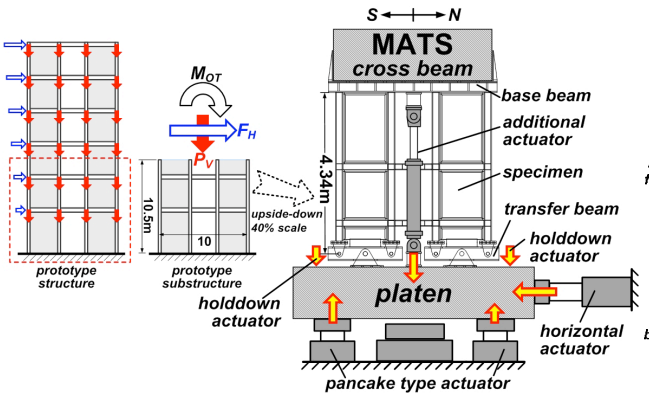


Figure 10: Test setup of cyclic test of reduced-scaled C-SPSW substructure

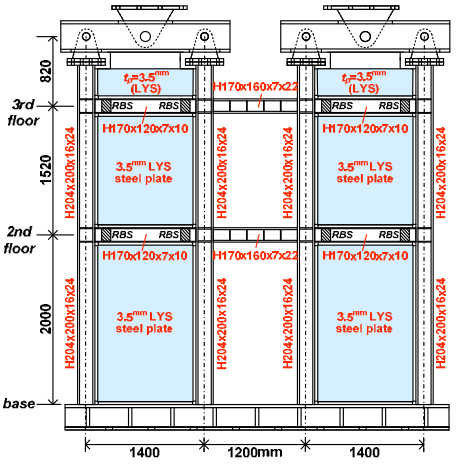


Figure 11: Schematic of the C-SPSW substructure specimen

Experimental Program. The specimen was tested using the Multi-Axial Testing System (MATS) at the NCREE. In order to simulate the effects of the upper substructure acting on the bottom two-and-half story substructure, as illustrated in Figure 10, the specimen was subjected to the cyclic lateral forces, F_H, the cyclic overturning moments, M_{OT}, and a constant 1400 kN vertical force, P_V, which represents the gravity load. The specimen was set upside down in the MATS. The base beam of the specimen was mounted on the cross beam of MATS. The top boundary of each SPSW was connected with a transfer beam. The column top ends were pin-connected with the transfer beam ends; and the top steel plate was welded to the transfer beam using the fishplate connection. The mid-span of the transfer beam was pin-supported on the platen. A lateral support system was constructed on the platen and the reaction frame (A-frame) of MATS.

The actuator system applied forces on the platen. Two horizontal actuators were employed to apply the lateral displacement on the specimen through the platen. Two cycles of 0.1%, 0.2%, 0.3%, 0.5%, 0.75%, 1.0%, 1.5%, 2.0%, 3.0%, 4.0% and 5.0% rad. roof drifts were imposed sequentially on the specimen. The vertical actuators can be classified into 3 categories: (1) two rows of vertical pancake type actuators pushing the bottom of the platen. The difference in the applied forces between the two rows of actuators induced the overturning moment effects on the platen; (2) two built-in hold down actuators which were mounted on the A-frame and pushing the top face of the platen; and (3) two additional actuators which were anchored between the platen and the cross beam. The two additional actuators provided a constant 1960 kN vertical compressive force on the platen. It should be noticed that the pancake type actuators must be always in contact with the platen in compression. The hold down actuators and additional actuators provided vertical compressive forces on the platen to insure the six pancake type actuators were always in compression.

The resultant forces of these vertical actuators applied a constant vertical force (P_V = 1400 kN). The relationship between the resultant moment M_{OT} of these vertical actuators and the lateral force F_H applied by horizontal actuators is: M_{OT} = F_H × (2.51 m). The relationship is calculated based on the inverted triangle vertical distribution of the lateral forces, which was determined from the current Taiwan's seismic code (ABRI, 2002).

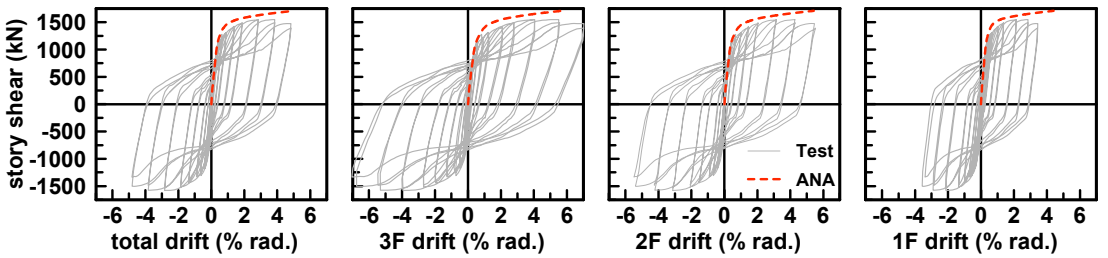


Figure 12: Force versus displacement relationships.

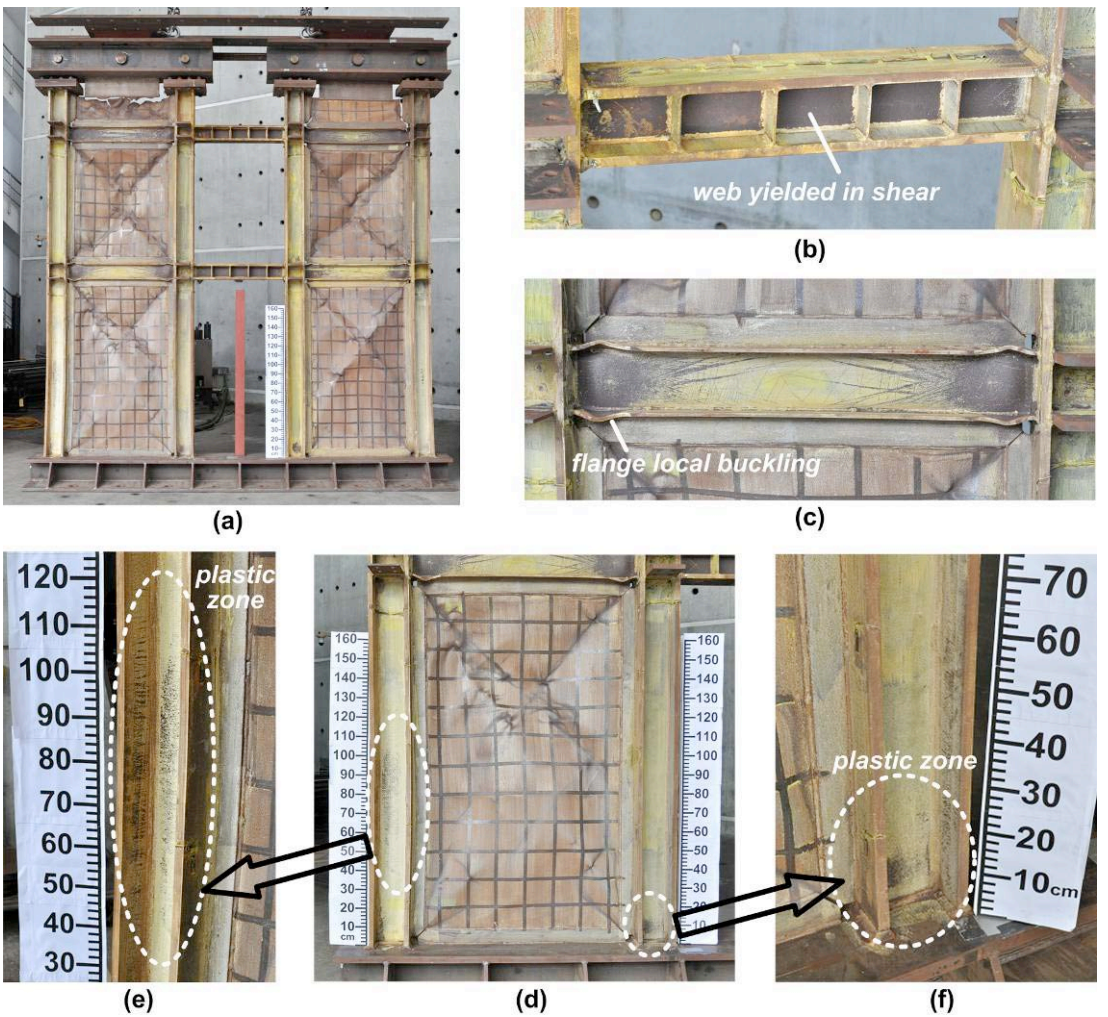


Figure 13: Deformed shapes of the specimen after test: (a) overall; (b) the 3rd floor coupling beam; (c) the 2nd floor boundary beam; (d) the 1st story of the southern SPSW; the plastic zones on the (e) outer and (f) inner bottom columns.

Test results and design implications. Figure 12 illustrates the force versus displacement relationship of the specimen. The C-SPSW specimen exhibited an excellently ductile behavior and dissipated significant amount of hysteresis energy during the cyclic loading test. The lateral and vertical load-carrying capacities did not notably deteriorate when the overall drift of the specimen reached 5% rad. An unanticipated fracture occurred at the early stage of the test. The weld between the fishplate and the transfer beam at the 3rd story of the southern SPSW were totally torn off at 1% rad. roof drift. However, that fracture did not significantly deteriorate the load-carrying capacity of the specimen. Thus, the test went on until the two cycles of 5% rad. roof drift had been completed.

After the test, as shown in Figure 13a, the flaking of the whitewashes on the specimen showed that the specimen had developed the plastic mechanism. The coupling beams developed shear plastic hinges (Figure 13b). The flexural plastic hinges formed at the ends of the boundary beams (Figure 13c) and near the column bases (Figures 13d, 13e and 13f).

Figure 13d shows the flaking of the whitewashes on the bottom (first story) columns of the northern SPSW after the test. As shown in Figure 13e, the plastic zone on the outer bottom column spread over a range from 40 to 100mm measured from the column base. On the other hand, the plastic zone on the inner bottom column concentrated at the column base (Figure 13f). The plastic zone on the outer column was wider than that on the inner column. In addition, the plastic zone on the outer column was located at a higher position than that on the inner column. The difference in the distribution of the plastic zone between the outer and inner columns could be attributed to that the axial force in the inner column was smaller than that in the outer column because of the coupling beam effect illustrated in Figure 14. Hence, the reduced flexural strength of the outer column was smaller than that of the inner column.

Figure 15 shows the relative deflections of the first story columns in northern SPSW when the lateral forces approached zero during the first cycle of the various drift levels. As shown in the top right of Figure 15, the relative deflection is defined as the difference between the absolute deflection and the reference line, which is the straight line from the top end to the bottom end of the column. The relative deflection can be utilized to estimate the inward flexural deformation of the column induced by the horizontal tension field forces of the infill plate. The column deflections measured when the lateral forces approaches zero in the various drift levels could represent the residual deflection after the specimen has experienced such level of drift. As shown in Figure 15, it can be found that residual "pull-in" deformations on the outer column were much larger than those on the inner column. This should be attributed to that the axial forces in the outer column were much higher, thus, the flexural strength of the outer column is smaller due to the axial-flexural interaction effect. However, form the Figure 15, it can be found that the maximum residual deflection of the outer column was about 10 mm (= $h_1/200$) after the specimen had suffered a 2.1% rad. first story drift. The 1/200 of the story height could serve as the deflection index limiting the development of large secondary forces in the columns (Ellingwood, 2003). Moreover, the past test (Tsai *et al.*, 2006) has shown that peak story drift of a well-designed SPSW specimen during

the collapse prevention level (2/50 hazard level) earthquake was about 2.0 to 2.5% rad. The test results suggest that, even if the plastic zones on the bottom columns had spread over the bottom half of the column height, the residual "pull-in" column deflection would not cause a significant secondary effect.

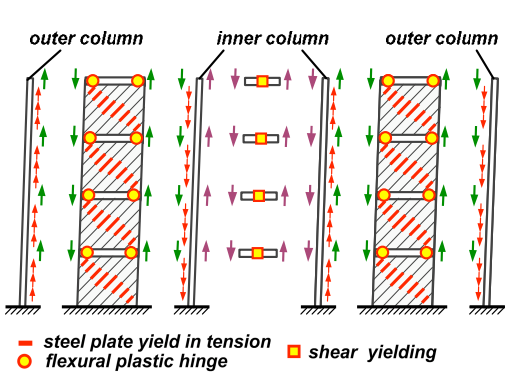


Figure 14: Effects of the coupling beam on reducing the axial forces in the inner boundary columns.

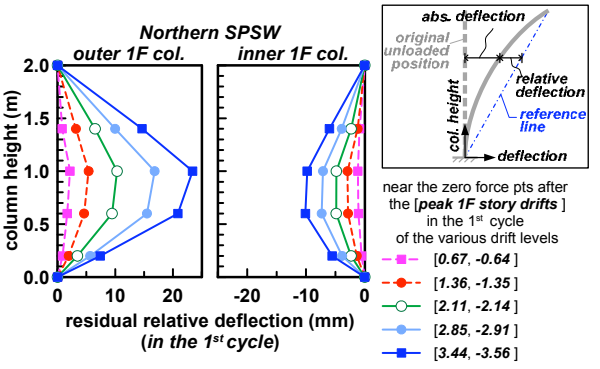


Figure 15: Residual relative deflections of the bottom columns in the northern SPSW in the various drift levels.

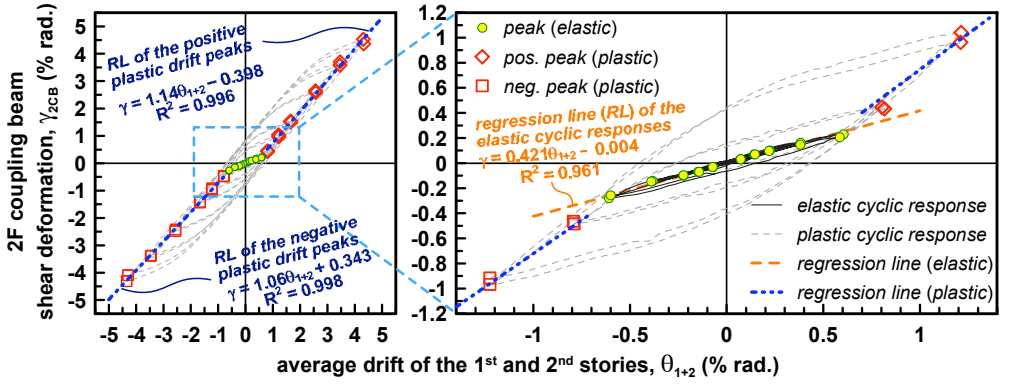


Figure 16: 2F coupling beam shear deformation (γ_{2CB}) versus the average drift (θ_{1+2}) of the 1st and 2nd story relationship.

Figure 16 shows the shear deformation of the second floor (2F) coupling beam, γ_{2CB}, versus the average drift, θ_{1+2}, of the 1st and 2nd story relationship. The slope of the line composed of the data at the various level peak drifts had a sudden change as the story drift reached about 0.75% rad. It indicates that the plastic shear hinge developed at this drift level. From the data at the peak drifts after the shear yielding, it can be found that the plastic shear deformation of coupling beam is close to the inelastic story drift. It suggests that, for seismic design purpose, the plastic rotational demand of the coupling beam at the bottom of a C-SPSW can be estimated as the design story drift. The design of the stiffeners in the coupling beam could be based on the estimated rotational demand.

Simulation. In this research, as shown in figure 17, a strip model (Shishkin *et al.*, 2010) for the C-SPSW specimen was constructed using the nonlinear frame analysis

program PISA3D (Lin *et al.* 2008). The tension field actions of the infill plates at the 1st, 2nd and 3rd story were represented by twelve, eleven and eight truss elements, respectively. The orientation of the tensile strips was determined from the tension field angle prescribed by the modern U.S. building codes (AISC, 2005a). In addition, a diagonal compression strut (Shishkin *et al.*, 2010) was employed to represent the compressive stiffness and strength of each infill plate. The columns were modeled using the PISA3D Fiber Beam-Column element. The boundary beams, coupling beams and the transfer beams were represented by using the PISA3D Beam-Column element. The reduced beam section (RBS) regions were simplified using a prismatic beam segment with the same cross sectional properties as those of the most reduced section. All beam-to-column joints were modeled using rigid end offsets with a rotational spring to representing the flexibility of the panel zone. Special constraints were set to represent the pin-connections between the transfer beams and the boundary columns. The platen in the MATS was modeled by a rigid frame consisting of a rigid beam and two rigid columns representing the half height of the platen. Except the rigid frame presenting the platen was modeled using elastic material, the material properties of the elements representing the infill plates, beams and columns were bilinear, fitting the coupon test results.

Nonlinear pushover analysis up to 5% rad. roof drift was carried out on the strip model. The constant 1400 kN vertical force P_V, the lateral displacement control with a load pattern composing of a horizontal force F_H and a overturning moment, M_{OT}, were applied on the node at the mid-span of the rigid beam representing the platen. Figure 12 shows that the analytical pushover results agree well with the experimental hysteresis loop. Figure 18 shows that the analytical relationship between the shear deformation of the 2F coupling beam and the average story drift of the 1st and 2nd stories quite match the test results.

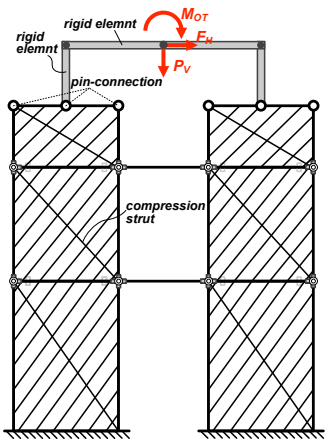


Figure 17: Strip model for the C-SPSW specimen.

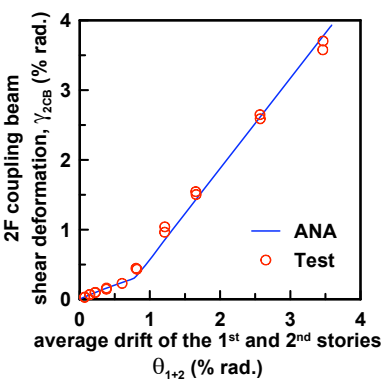


Figure 18: Comparison of experimental and analytical γ_{2CB}-θ_{1+2} relationships.

CONCLUSIONS

The test results of the Specimen S in 2007 and the reduced-scaled C-SPSW specimen in 2009 showed that the plastic hinge formation slightly above the column

base would not result in significant deterioration of strength and ductility. This suggests that the proposed column capacity design, which aims at limiting the plastic hinge on the bottom column within bottom quarter column height, could be a choice of design in the practice. The test results suggest that the rotational demand of the coupling beam at the lowest level of a C-SPSW can be estimated as the design story drift. The strip model can predict the overall and local responses of the C-SPSW specimen very well. Further studies on the seismic design and behaviours of the C-SPSW can be conducted using strip models.

REFERENCE

American Institute of Steel Construction (AISC). (2005a). *Seismic Provisions for Structural Steel,* Chicago*,* Illinois.

American Institute of Steel Construction (AISC). (2005b). *Specification for Structural Steel Buildings,* Chicago, Illinois.

Architectural Building Research Institute (ABRI). (2002). *Seismic Force Requirements for Building Structures,* Taipei, Taiwan.

Berman, J.W and Bruneau, M. (2008). "Capacity Design of Vertical Boundary Elements in Steel Plate Shear Walls." *Engrg. J.,* AISC, 15(1), 55-71.

Chang J.T. (2009). "Seismic Responses of Multi Story Coupled Steel Plate Shear Walls System". *Master Thesis*, Dept. of Civil Engrg., National Taiwan Univ., Taipei, Taiwan. (In Chinese)

Ellingwood, B. (2003). "Specification for Structural Steel Buildings", *Engineering Journal Article*. AISC.

Lin, B.Z., Chuang, M.C. and Tsai, K.C. (2009). "Object-oriented Development and Application of a Nonlinear Structural Analysis Framework." *Advances in Engineering Software,* 40(1), 66-82.

Qu, B. and Bruneau, M. (2010). "Behavior of Vertical Boundary Elements in Steel Plate Shear Walls." *Engrg. J.,* AISC, 17(2), 109-122.

Shishkin, J.J., River, R.G., Grondin, G.Y., (2009). "Analysis of Steel Plate Shear Walls Using the Modified Strip Model." *J. of Struct. Engrg.,* ASCE, 135(11), 1357-1366.

Thorburn, L.J., Kulak, G.L. and Montgomery C.J. (1983). "Analysis of Steel Plate Shear Walls." *Structural Engineering Report No. 107*, Dept. of Civil Engrg., Univ. of Alberta, Edmonton, Alberta, Canada.

Tsai, K.C., Li, C.H., Lin, C.H., Tsai, C.Y. and Yu, Y.J. (2010). "Cyclic Tests of Four Two-Story Narrow Steel Plate Shear Walls. Part 1: Analytical Studies and Specimen Design." *Earthquake Engrg. & Struct. Dyn.,* 39(7), 775-799.

Tsai, K.C., Lin, C.H., Lin, Y.C., Hsieh, W.D and Qu, B. (2006). "Substructural Hybrid Tests of A Full Scale 2-Story Steel Plate Shear Wall." *Technical Report NCREE-06-017*, National Center for Research on Earthquake Engineering, Taipei, Taiwan. (In Chinese)

Vian, D. and Bruneau, M. (2005) "Steel Plate Shear Walls for Seismic Design and Retrofit of Building Structures." *Technical Report MCEER-05-0010,* Multidisciplinary Center for Earthquake Engineering Research, Buffalo, New York.

Design and Testing of Coupled Steel Plate Shear Walls

D.J. Borello[1] and L.A. Fahnestock[2]

[1]Graduate Research Assistant, Department of Civil and Environmental Engineering, University of Illinois at Urbana-Champaign, email: dborello@illinois.edu
[2]Assistant Professor; Department of Civil and Environmental Engineering, University of Illinois at Urbana-Champaign, email: fhnstck@illinois.edu

ABSTRACT

The coupled steel plate shear wall (C-SPSW) system is emerging as a promising configuration for resisting lateral loads in high seismic regions. A C-SPSW is composed of two wall piers, which are special steel plate shear walls (SPSW), joined at the floor levels by coupling beams. The C-SPSW configuration is expected to retain the benefits of the conventional SPSW configuration and provide additional structural efficiency while introducing greater flexibility related to building services and function. However, current provisions do not address analysis and design of C-SPSWs and further research is needed to develop these guidelines. As part of a multi-institution NEESR project on steel plate shear walls, this research explores design procedures for C-SPSW, which build on current provisions for conventional SPSWs. These design procedures are evaluated in the context of a six-story prototype structure. The response of the prototype structure under static loading is studied using numerical models to investigate behavior and performance and to evaluate design procedures. To further study C-SPSW behavior and to validate the design procedures, a large-scale subassembly is being developed for laboratory testing. The preliminary experimental setup and specimen design are described here.

INTRODUCTION

Steel plate shear walls (SPW) are a robust and economical lateral force resisting system in seismic regions. A SPW is comprised of a steel frame (with either flexible or rigid beam-to-column connections) with steel infill web plates as shown in Figure 1a. The frame columns and beams are known as vertical boundary elements (VBE) and horizontal boundary elements (HBE) respectively. Commonly the steel web plate is slender and unstiffened, providing negligible compressive resistance (Sabelli and Bruneau 2006). Lateral force is resisted by developing diagonal tension in the web plate post-buckling. The boundary elements anchor the diagonal tension field,

enabling the web plate to yield. The web plate yielding mechanisms dissipates a significant amount of energy and provides excellent ductility.

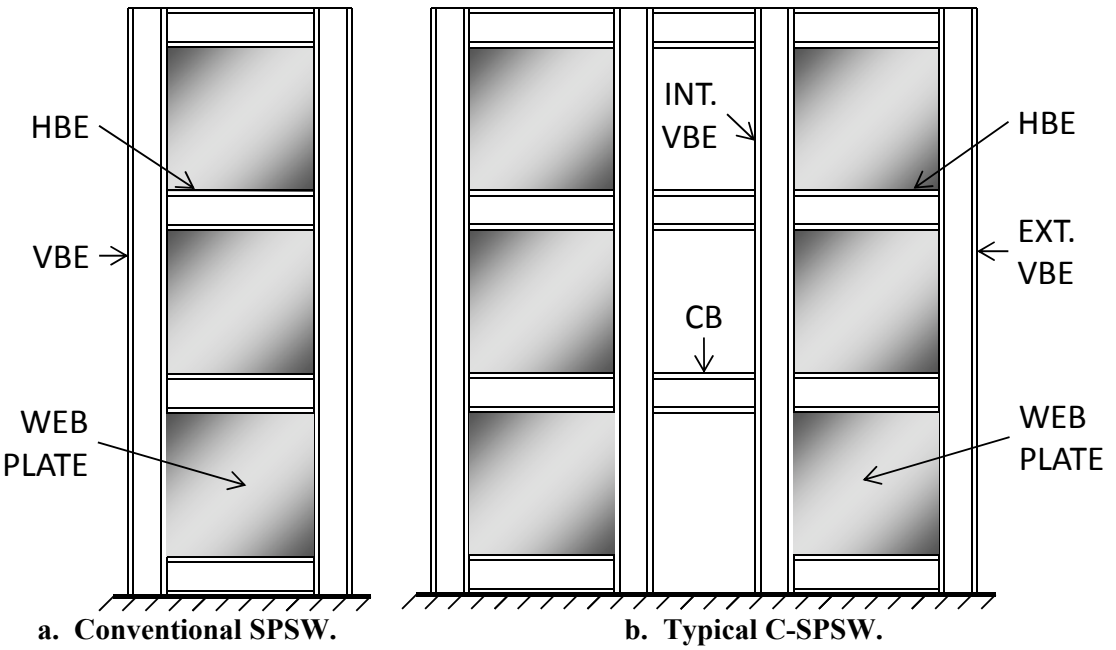


Figure 1. Steel plate shear walls.

The 2005 AISC *Seismic Provisions for Structural Steel Buildings* (AISC 2005) and the 2005 ASCE 7-05 *Minimum Design Loads for Buildings and Other Structures* (ASCE 2005) introduced provisions for Special Steel Plate Shear Walls (SPSW). In a SPSW the boundary elements are connected by moment connections and the web plate is unstiffened and slender. The boundary elements are sized based on a capacity design methodology to remain elastic under full yielding of the web plates. The resultant of the web plate tension on the boundary elements is assumed to act at an angle α, derived based on elastic strain energy (Thorburn et al. 1983).

In a typical building layout, it is not uncommon for the bay width of the gravity columns to be over 10 m and the story height to be as small as 4 m. However, the *Seismic Provisions* limit a SPSW panel length-to-height ratio to a maximum of 2.5 (AISC 2005). Therefore the designer may choose to place two SPSWs within a single bay. The present research explores the behavior of Coupled Special Steel Plate Shear Walls (C-SPSW). A C-SPSW system is comprised of two SPSWs linked by coupling beams (CB) at the floor level as shown in Figure 1b. The C-SPSW system is expected to maintain many of the benefits of the conventional SPSW system while providing additional efficiency, energy dissipation and architectural flexibility.

Limited research has been conducted on the design, behavior and analysis of C-SPSW systems. As part of a multi-institution NEESR project on steel plate shear

walls, C-SPSW behavior is explored. A preliminary design methodology is introduced which is consistent with the existing SPSW provisions. Several six-story prototype buildings are designed to validate the methodology. The prototype buildings are analyzed under static push-over loading conditions. In order to further explore the behavior of C-SPSWs, two large-scale specimens will be tested in the NEES MUST-SIM facility at the University of Illinois at Urbana-Champaign. These specimens will consist of the lower three stories of a six-story prototype building. The loading and boundary conditions applied to the lower three-story subassembly will be based on the analysis of the six-story prototypes.

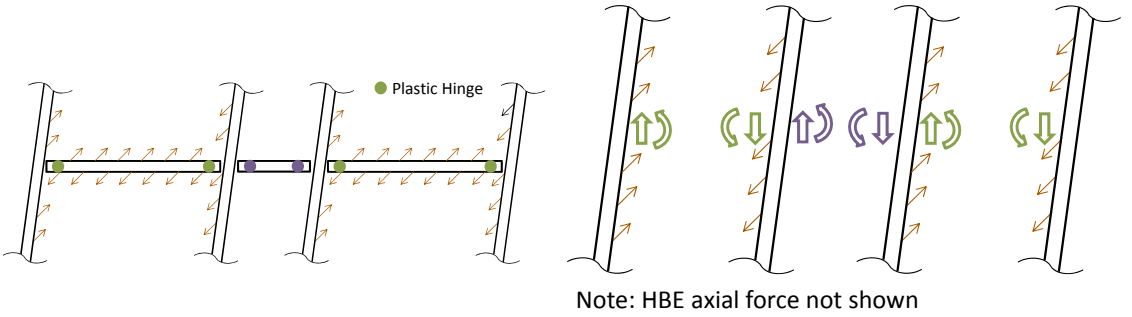
PRELIMINARY DESIGN METHODOLOGY

A preliminary design methodology was developed for C-SPSW systems based on the existing SPSW provisions, which proportion the SPSW at the plastic strength level, assuming that the web plates have completely yielded in tension. The boundary elements are then designed based on the capacity of the web plates. This capacity design of the boundary elements can lead to a surrounding moment frame with significant lateral resistance. Therefore an elastic analysis is performed to determine the proportion of the story shear that is resisted by the moment frame (Sabelli and Bruneau 2006). The web plates are then sized to resist the remaining portion of the story shear. In a C-SPSW system, a larger portion of the lateral load is resisted by frame action due to the coupling beams. Therefore, compared to conventional SPSWs, a smaller portion of the story shear is resisted by the web plates, reducing their required thickness.

The HBEs in a SPSW are permitted to develop hinges at their ends; however they are to remain elastic within the span in order to anchor the web plates. At the design strength level, the HBEs are subjected to the imbalance caused by the tension in the web plates above and below. Since the web plates are thinner in the C-SPSW system than the conventional SPSW system, the capacity design requirements are reduced, allowing lighter HBEs to be selected.

In a SPSW, the vertical boundary elements are sized to resist the yielding of the web plates as well as hinging of the HBE ends as shown in Figure 2a. Since a conventional SPSW is symmetrical, both VBEs are identical. However, in a C-SPSW, the four VBEs can be grouped into two categories; internal and external VBEs (indicated on Figure 1b). In both VBEs of a conventional SPSW and the external VBEs of a C-SPSW, the axial demand consists of the vertical component of the web plate tension and the reactions from the HBEs, assuming plastic hinges have developed at their ends. However, for the internal VBEs in a C-SPSW, the shears developed in the CBs partially negate this axial force, as shown in Figure 2b (HBE

axial force not shown). For consistency with the capacity design and ultimate strength methodology employed for the conventional SPSW system, the CBs in the C-SPSW system are assumed to also develop plastic hinges at their ends.



a. Plastic loads. **b. Free-body diagram of VBEs.**

Figure 2. Plastic strength mechanism.

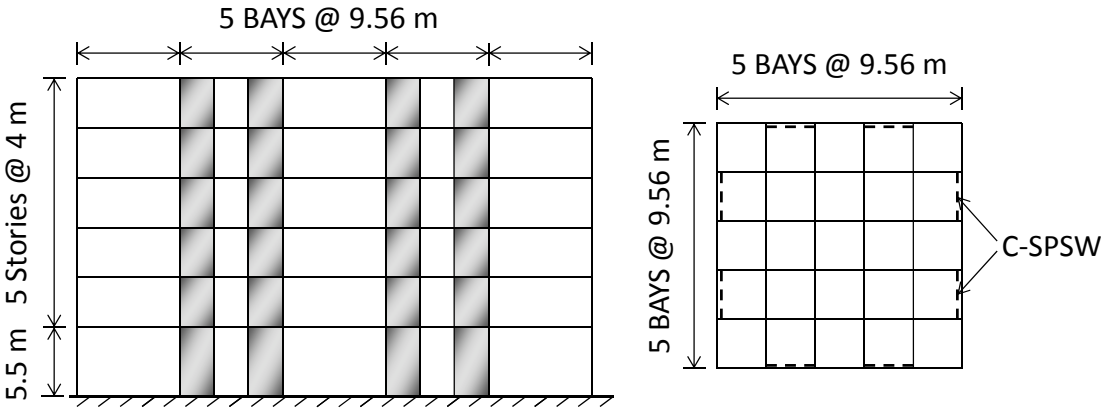
The shears and moments in the VBEs can be estimated by considering each story individually. The web plate tension component in the horizontal direction provides a distributed load between the ends of each segment. Where an HBE connects to a VBE, moment demands on the VBE above and below the connection are assumed to be equal to half of the plastic flexural strength of the HBE. For the internal VBEs of the C-SPSW system, moment from the CBs can be applied in a similar manner (Figure 2b). The moments from the coupling beams are additive to the HBE moments, increasing the shear and moment demands on the VBEs. However, the axial load reduction in the VBEs that occurs due to the CBs has a more significant effect and often internal VBEs are lighter weight than the external VBEs.

For preliminary purposes, the coupling beams were sized based on the size of the HBEs. Since the design procedure is based on plastic strength calculations, the CBs were selected based on their plastic moment strength compared to the HBEs. Further research is warranted to develop CB design procedures to achieve the desired performance.

PROTOTYPE DESIGNS

To validate the preliminary design methodology, three prototype six-story buildings were designed. The geometry of the prototype building was based on the nine-story SAC prototype buildings presented in FEMA-355C (FEMA 2000). Due to force limitations for future experimental testing, the top three stories of the nine-story SAC building were truncated. The basement was replaced with a fixed base at the ground level. The bay width was slightly increased from 9.15 m to 9.56 m to match discrete laboratory pier spacing. The elevation and floor plan of the prototype building are

shown in Figure 3. The gravity loads and story masses from the original prototype buildings were used unmodified ($1.0x10^6$ kg for the first story and $9.9x10^5$ kg for the remaining stories).



a. Elevation **b. Plan**

Figure 3. Prototype building layout.

The prototype structures were configured with four sets of C-SPSWs (8 walls total) along the perimeter in each direction (Figure 3). The shape of the design response spectrum provided in ASCE 7 was used to determine the design loads (ASCE 2005). However, since the SAC ground motions (Somerville et al. 1997) will be used for future nonlinear analysis, the spectral ordinates from FEMA-355C (FEMA 2000) were used. According to ASCE 7, the prototype building's approximate fundamental period is 0.55 sec. The design response spectrum is shown in Figure 4. The design loads were determined using the ASCE 7 Equivalent Lateral Force Procedure. The roughly inverted triangular load profile is shown in Figure 5.

The prototype buildings were designed with three different coupling beam sizes. The coupling beams were selected to have 100%, 200% and 400% of the plastic capacity (i.e., plastic section modulus) of the HBEs at each story (denoted CB/HBE). The VBEs were selected from the W24 family (610 mm nominal depth); the HBEs were selected from the W18 family (460 mm nominal depth). For the two lower CB/HBE ratios the CBs were selected from the W18 family; for the remaining design they were selected from the W24 family. With the selected geometry, the first story of the building violates the panel aspect ratio limit (AISC 2005); therefore a rectangular HSS restrainer was added (Tsai et al. 2010). The prototype with 200% HBE/CB ratio is summarized in Table 1. Column splices occur at mid-height of the story.

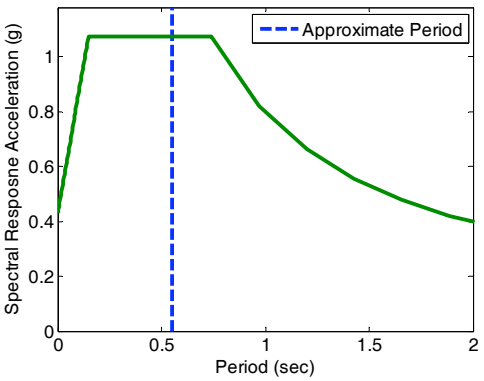


Figure 4. Design response spectrum.

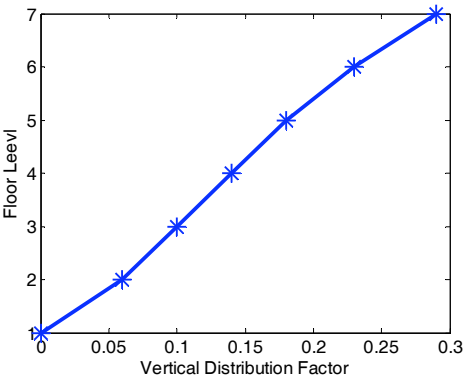


Figure 5. Lateral force distribution.

Table 1. Prototype Design based on 200% CB/HBE.

Story/Level	Height	t_w	VBE_{EXT}	VBE_{INT}	HBE	CB
	m	*mm*				
7	25.3				W18X40	W18X86
6	21.3	1.59	W24X94	W24X131	W18X40	W18X86
5	17.4	1.59	W24X94	W24X131	W18X40	W18X86
4	13.4	1.59	W24X162	W24X146	W18X50	W18X97
3	9.4	2.66	W24X162	W24X146	W18X50	W18X97
2	5.5	3.18	W24X370	W24X229	W18X50	W18X97
1	0.0	3.18	W24X370	W24X229	W18X211	

During design, a strip model (Berman and Bruneau 2003) of the system was constructed in SAP2000 (*SAP2000* 2009) to determine the proportion of the story shear resisted by the web plates and to calculate deflections based on the ASCE 7 approximate amplified elastic deflection method (ASCE 2005). The strength-based designs satisfied the deflection check.

NONLINEAR ANALYSIS

To validate design performance, the prototype buildings were modeled using OpenSees (*OpenSees* 2010). Strip models were used for the walls, with the web plates represented by 15 elastic-perfectly plastic truss elements oriented at an angle α, which is based on the tension field behavior. The boundary elements were nonlinear beam-column elements with fiber sections based on the OpenSees Steel02 constitutive model. The member depths were represented by rigid offsets. The coupling beam constitutive models were calibrated based on link tests at Portland State University (Dusicka and Lewis 2010). The lateral load was evenly distributed between the four beam-column joints on each floor. The gravity load was initially

applied followed by incrementally increasing lateral load. A leaning column that carried the tributary gravity load of the C-SPSW was also included to appropriately capture the destabilizing effects of gravity-only columns. A corotational coordinate transformation was used to capture geometric nonlinearities.

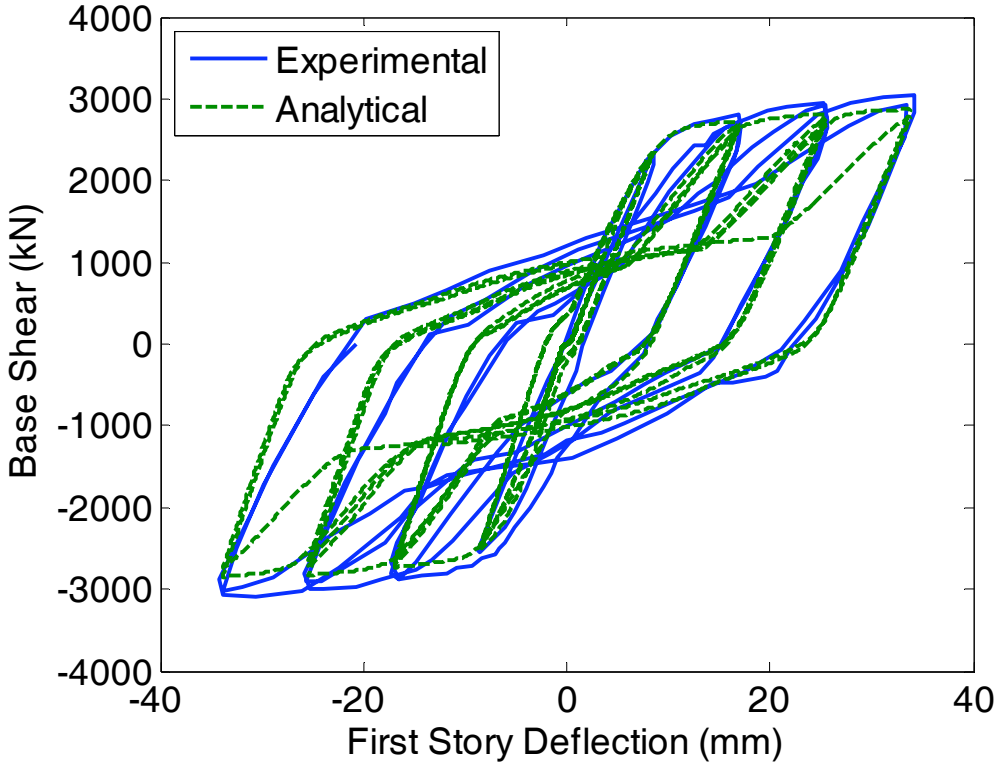


Figure 6. Comparison of Driver (1997) experimental and analytical simulations.

The SPSW test that was conducted at the University of Alberta (Driver et al. 1997) was used to validate the modeling assumptions. Base shear versus first story deflection for the experimental and analytical simulations is shown in Figure 6. The strip model closely traces the experimental response. Therefore the strip model was deemed sufficiently accurate for evaluating global system response.

The prototype buildings were subjected to pushover analyses based on the Equivalent Lateral Force load distribution (Figure 5). The base shear normalized by the design load versus the roof drift is presented in Figure 7. The global response is characterized by an initial linear region followed by yielding and strain hardening. All three designs exhibit a similar stiffness; however the higher CB/HBE designs had higher yield strength. This indicates that some of the benefits of the coupling are not accounted for in the design process.

The story drift at 2% roof drift for the prototypes is shown in Figure 8. For the 100% CB/HBE design, the maximum story drift occurs at the fifth floor level. However, the 200% and 400% CB/HBE design achieves their maximum story drift at the fourth and third floor levels respectively. The response of the 400% CB/HBE design is the most uniform.

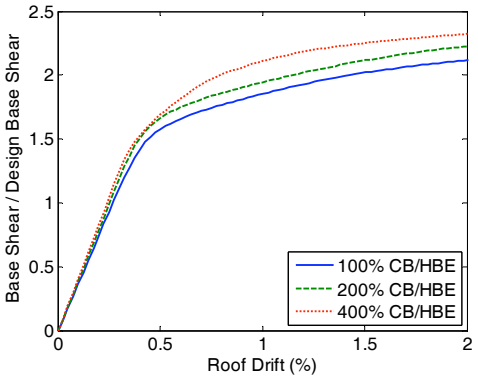


Figure 7. Bases shear versus roof drift of prototype designs.

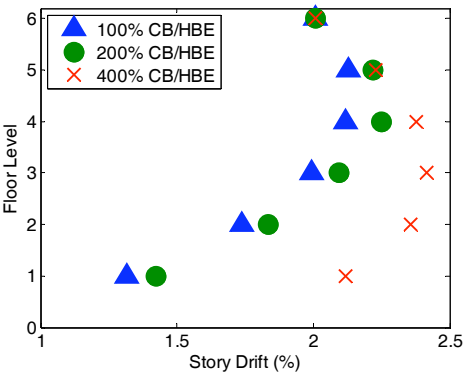


Figure 8. Story drift profiles.

To assess the level of coupled behavior, the degree of coupling (Canadian Standards Association 1994) was calculated as the ratio of the overturning moment resisted by the couple formed by the axial force in each wall pier to the total overturning moment (Figure 9),

$$DC = \frac{M_{OT}}{M_{TOTAL}} = \frac{M_{OT}}{M_{OT} + \Sigma M_{WALL}}.$$

The degree of coupling (DC) is shown in Figure 10 versus roof drift. The degree of coupling is initially constant since the system is initially elastic. In the 100% CB/HBE prototype the DC drops as the CBs begin to yield, increasing the relative stiffness of the individual wall piers to the coupling beams. However, as the CBs yield, the DC once again levels off. The other two prototypes experience an initial increase in the DC as the individual piers yield, lowering their relative stiffness. As the CBs then begin to yield, the DC once again becomes constant.

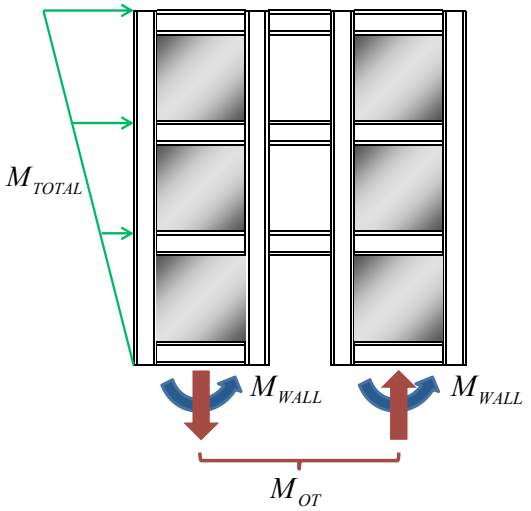


Figure 9. Illustration of Degree of Coupling

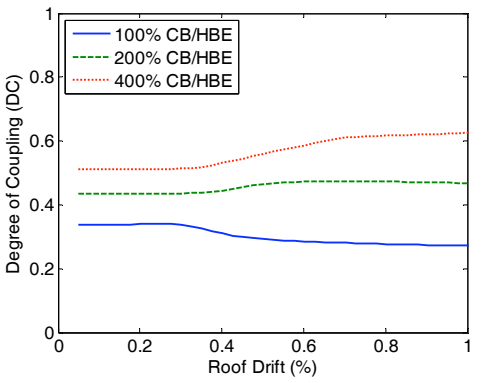


Figure 10. Degree of coupling versus roof drift of prototype designs.

EXPERIMENTAL SETUP AND TEST SPECIMENS

To further explore the behavior of C-SPSW system, two specimens will be tested in the NEES MUST-SIM facility at the University of Illinois at Urbana-Champaign. Each wall pier will be loaded by a Loading and Boundary Condition box (LBCB). Each LBCB is able to impose six degrees-of-freedom in load, displacement or mixed-mode control.

The maximum distance between the strong floor and the LBCB platen is approximately 6 m. Two LBCBs will be placed in the closest position; the distance between the centroids of the loading platens is approximately 2.7 m. The VBE base plates and bottom HBE will be bolted into a 50 mm thick plate that will be pretensioned to the strong floor. A similar connection at the top of the specimen will be used with an adapter plate between the specimen and the LBCB platen.

Each test specimen will be a three-story subassembly of a six-story prototype frame described above. Based on geometric constraints, the specimens will be constructed at approximately half-scale (0.43 scale). Since the two LBCBs may artificially constrain the top coupling beam, it will be excluded. The geometry of the test setup is shown in Figure 11.

The VBEs of the prototype are assumed to be braced at each story (provided by the lateral force resisting system in the perpendicular direction). The specimen will be tied back to the strong wall at each VBE-to-HBE connection to replicate this design assumption and to prevent global out-of-plane instability.

The control algorithms will be developed based on the behavior of the analytical strip model described above. The displacements and loads at the top of the third story (i.e., at the top of the subassembly) for each wall pier under a pushover loading protocol will be condensed down to six degrees-of-freedom. The relationship between these demands will be analyzed and simplified mathematical expressions developed to establish a control algorithm. These simplified controls will then be expanded to allow for an arbitrary loading plan. The control algorithms will be validated on an analytical model of the three story subassembly. The global and local behavior of the bottom three stories of the six-story model will be compared to the response of the subassembly model under the proposed control algorithms. The control algorithms will be further vetted in the MUST-SIM small-scale laboratory using rubber specimens.

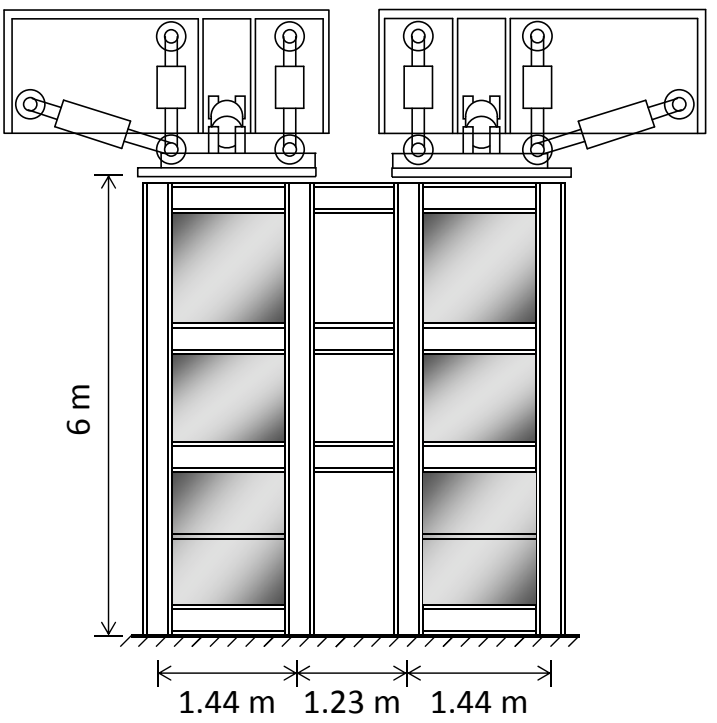


Figure 11. Elevation of experimental configuration.

The specimens will be instrumented with strain gages to capture boundary element and web plate local behavior. Linear displacement transducers will be used to record global displacements and to provide control feedback. To capture more localized response of the specimen, with focus on the infill plates, a Nikon Digital Motion Measurement (DMM) system, which uses light emitting diode targets on the

specimen, will be used. Additionally, a Nikon handheld laser scanner will be used to capture high resolution deformed geometry of the specimens at intervals throughout testing. In particular, this will allow accurate determination of the buckled shape of the web plates.

CONCLUSIONS

Coupling of special steel plate shear walls (SPSWs) is a logical choice in many configurations. The literature does not adequately explore the design and behavior of a coupled special steel plate shear wall system (C-SPSW). A preliminary design methodology was presented which remains consistent with the current design methodology for SPSWs. The design methodology is validated by designing three six-story prototype structures. These structures are studied analytically under push-over loading conditions. The three structures demonstrated similar initial stiffness with a slight correlation between degree of coupling and yield strength (i.e., strength increases as degree of coupling increases). Increasing the degree of coupling shifted the floor with the highest story drift downward.

To further study the behavior of the C-SPSW system, three-story experimental specimens will be used. These specimens represent the lower three stories of the six-story prototype buildings at approximately half-scale. Control algorithms will be developed to replicate the response of the lower three stories of a six-story building. The layout of the experimental tests and instrumentation are presented.

Analyzing the C-SPSW system with time-history analysis will provide additional understanding to the underlying mechanisms. These results will be used to confirm that the design assumptions are valid. Completion of the experimental testing will be used to validate the modeling assumptions and provide confidence in the analytical results. Ultimately, the analytical and experimental results will lead to design recommendations and allow for widespread application of the C-SPSW system.

ACKNOWLEDGEMENTS

This material is based upon work supported by the National Science Foundation under Grant No. (CMMI-0830294) as part of the George E. Brown, Jr. Network for Earthquake Engineering Simulation and by the American Institute of Steel Construction. The authors thank collaborators at the University of Washington, Assistant Professor Jeffrey Berman, Associate Professor Laura Lowes and graduate students Patricia Clayton, Mohammad Malakoutian and David Webster, for their contributions to this research. Any opinions, findings, and conclusions expressed in

this material are those of the authors and do not necessarily reflect the views of those acknowledged here.

REFERENCES

AISC. (2005). *AISC 341-05 Seismic Provisions for Structural Steel Buildings*. American Institute of Steel Construction, Chicago, IL.

ASCE. (2005). *Minimum Design Loads for Buildings And Other Structures: SEI/ASCE 7-05*. American Society of Civil Engineers.

Berman, J., and Bruneau, M. (2003). "Plastic Analysis and Design of Steel Plate Shear Walls." *Journal of Structural Engineering*, 129(11), 1448-1456.

Canadian Standards Association. (1994). *Design of Concrete Structures (A23.3)*. Canadian Portland Cement Association, Ontario, Canada.

Driver, R. G., Kulak, G. L., Kennedy, D. J. L., and Elwi, A. E. (1997). *Seismic Behavior of Steel Plate Shear Walls*. Structural Engineering Report No. 215, University of Alberta.

Dusicka, P., and Lewis, G. (2010). *Investigation of Replaceable Sacrificial Steel Links*. Portland State University.

FEMA. (2000). "FEMA 355 State of the Art Report on Systems Performance of Steel Moment Frames Subject to Earthquake Ground Shaking." *Rep. No. FEMA-355C, Federal Emergency Management Agency, Washington, DC*.

OpenSees. (2010). Open System for Earthquake Engineering Simulation, University of California, Berkeley, CA.

Sabelli, R., and Bruneau, M. (2006). *AISC Design Guide 20 - Steel Plate Shear Walls*. American Institute of Steel Construction.

SAP2000. (2009). Computers and Structures Inc., Berkeley, CA.

Somerville, P., Smith, N., Punyamurthula, S., and Sun, J. (1997). "Development of ground motion time histories for phase 2 of the FEMA/SAC steel project." *Report No. SAC/BD-97*, 4.

Thorburn, L. J., Kulak, G. L., Montgomery, C. J., and Engineering, U. O. A. D. O. C. (1983). *Analysis of steel plate shear walls*. Dept. of Civil Engineering, University of Alberta.

Tsai, K., Li, C., Lin, C., Tsai, C., and Yu, Y. (2010). "Cyclic tests of four two-story narrow steel plate shear walls - Part 1: Analytical studies and specimen design." *Earthquake Engineering & Structural Dynamics*, 39(7), 775-799.

Seismic Design and Analysis of Self-Centering Steel Plate Shear Walls

By Patricia M. Clayton[1], Daniel M. Dowden[2], Ronny Purba[3], Jeffrey W. Berman[4], Laura N. Lowes[5], Michel Bruneau[6]

ABSTRACT:

An innovative Self-Centering Steel Plate Shear Wall (SC-SPSW) system is proposed. It relies on post-tensioned (PT) beam-to-column connections that allow beams to rock about their flanges and provide system re-centering capabilities. A design procedure for the SC-SPSW system, developed based on a performance based design (PBD) approach, is presented, followed by analytical results for a prototype SC-SPSW building designed using this PBD approach, and subjected to a suite of ground motions simulating three different seismic hazard levels. The results of the nonlinear response history analyses show the proposed SC-SPSW design procedure to adequately achieve the desired enhanced performance objectives. Concepts of capacity design principle are integrated in the above approach, to prevent in-span plastic hinges of the beam considering reduced moment capacity due to the presence of axial and shear forces and to ensure that PT reinforcement remain elastic, among other things. To facilitate understanding of the behavior and design of an SC-SPSW system, the moment, shear and axial force distribution along the length of a boundary beam are established based on first principles. Closed form formulations describing the moment, shear and axial force beam diagrams are developed based on component capacity design approach and are used in the performance-based system design approach.

Keywords: Self-centering; Rocking connection; Steel plate; Shear wall; Earthquake engineering

[1] Research Assistant, Dept. of Civil and Environmental Engineering, University of Washington, Seattle, WA 98195-2700; PH: (206)910-0929; Email: claytp@u.washington.edu

[2] Research Assistant, Dept. of Civil, Structural and Environmental Engineering, University at Buffalo, Buffalo, NY 14260; PH:; Email: dmdowden@buffalo.edu

[3] Research Assistant, Dept. of Civil, Structural and Environmental Engineering, University at Buffalo, Buffalo, NY 14260; PH: (716) 645-4373; Email: rpurba@buffalo.edu

[4] Assistant Professor, Dept. of Civil and Environmental Engineering, University of Washington, Seattle, WA 98195-2700; PH: (206)616-3530; E-mail: jwberman@u.washington.edu

[5] Associate Professor, Dept. of Civil and Environmental Engineering, University of Washington, Seattle, WA 98195-2700; PH: (206)685-2563; E-mail: lowes@u.washington.edu

[6] Professor, Dept. of Civil, Structural and Environmental Engineering, University at Buffalo, Buffalo, NY 14260; PH: (716) 645-3398; Email: bruneau@buffalo.edu

INTRODUCTION

Steel plate shear wall (SPSW) systems are frames having steel plates (a.k.a. webs) connected between their beams and columns (Sabelli and Bruneau, 2007). During severe earthquakes, the unstiffened plates of ductile SPSWs buckle in shear and yield by developing a diagonal tension field, together with plastic hinging of the beams at their ends. While SPSW systems are desirable for their significant stiffness, strength, and energy dissipation, strategies to eliminate residual drifts and to localize structural damage only in easily replaceable structural elements are desirable in SPSWs (as in other systems). In moment resisting frames, use of post-tension (PT) rocking moment connections was analytically and experimentally investigated to provide frame self-centering capability and to limit hysteretic damage to replaceable energy dissipating elements during earthquakes (e.g., Ricles *et al.* 2001, Christopoulos *et al.* 2002; Garlock *et al.* 2005; Rojas *et al.* 2005; to name a few). Building on this idea, this paper investigates the potential of achieving Self-Centering Steel Plate Shear Walls (SC-SPSW) by using similar post-tensioned rocking beam connections. In this proposed system, the SC-SPSW web plate is the replaceable energy dissipation element, and beam-plastic hinging is eliminated. The system combines the advantages of high lateral stiffness, a substantial energy dissipation capacity, and self-centering capability, at the expense of additional challenges to understanding the flow of forces within the structure compared to conventional SPSW (themselves, more complex than moment frames).

The objective of this paper is to provide insights on SC-SPSW's beam and system fundamental behavior, through free-body-diagrams of individual beams and non-linear response history dynamic analyses of multistory frames. This is done by developing equations for the moment, shear and axial force diagrams along the HBE from a capacity design approach based on yielding of the SPSW web plate, showing the respective contribution of each factor to the total demand. These closed-form solutions are then integrated into a design procedure proposed to aid in the selection of PT reinforcement area and HBE sizing to prevent in-span plastic hinging of the beam, to keep PT reinforcement elastic at a specified target drift, and to select an adequate initial PT force. Lastly, a performance-based design procedure for the SC-SPSW system is proposed that incorporates this fundamental behavior knowledge and component capacity design method with response-based performance objectives. The seismic response of a prototype SC-SPSW designed using the proposed design procedure was evaluated using non-linear response history dynamic analyses.

BASIC PRINCIPLES OF SELF-CENTERING SPSW SYSTEMS

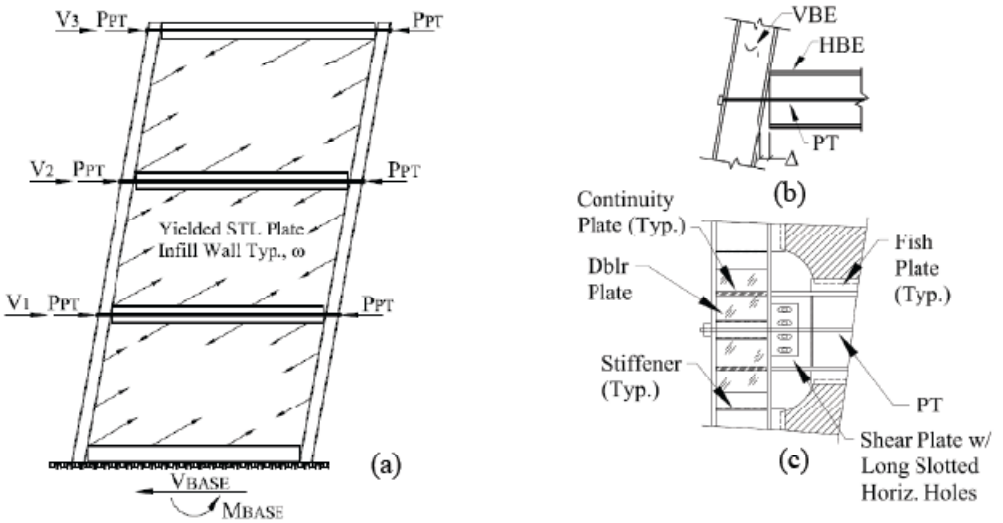


Fig. 1. SC-SPSW: (a) Yield Mechanism; (b) rocking joint; (c) rocking detail

Fig. 1a shows the free-body-diagram (FBD) of a SC-SPSW frame, where HBE is the horizontal boundary element, VBE is the vertical boundary element, P_{PT} is the post-tension (PT) axial compression force applied to the HBE, V_i is the externally applied lateral forces at story i due to applied seismic forces, and ω is the diagonal tension yield force per unit length developed by the steel web plates (Sabelli and Bruneau 2007, Berman and Bruneau 2008).

A SC-SPSW differs from a conventional SPSW in that HBE-to-VBE rigid moment connections in a conventional SPSW are replaced by PT rocking moment connections. This allows a joint gap opening to form between the VBE and HBE interface about a rocking point (i.e. connection decompression), leading to a PT elongation, this being the self-centering mechanism (shown schematically in Fig. 1b). One possible rocking detail configuration is shown in Fig. 1c. The PT boundary frame is designed to essentially remain elastic and hysteretic energy dissipation is intended to be provided by the web plate only. The total hysteretic response of a SC-SPSW is provided by the combined elastic response of the PT boundary frame and the inelastic energy dissipation of the web plate.

FREE-BODY-FORCE DIAGARAM

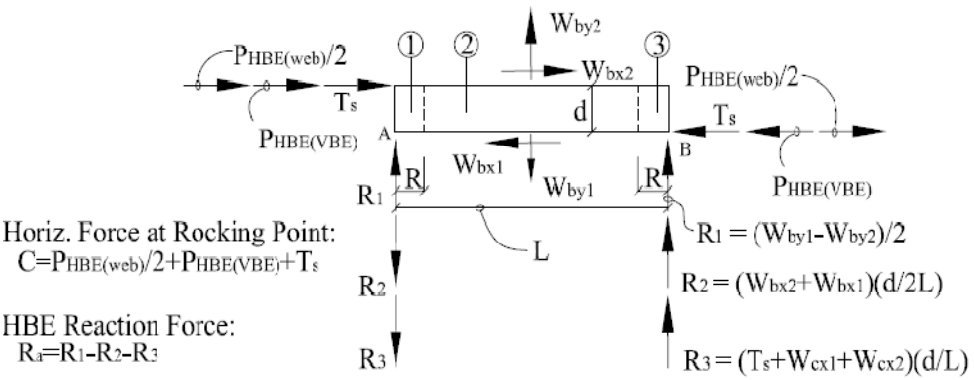


Fig. 2. Force Resultant FBD of HBE

Fig. 2 shows the FBD of an HBE and VBE element located at an intermediate floor level of a SC-SPSW frame once the web plate has fully yielded and the connection has decompressed for a rightward drift, where W_{bx1}, W_{bx2} and W_{by1}, W_{by2} are respectively the horizontal and vertical force resultants along the length of the HBE, W_{cx1},W_{cx2} and W_{cy1}, W_{cy2} are respectively the horizontal and vertical force resultants along the height of the VBE, subscripts *1* and *2* respectively denote the level below and above the HBE, L is the HBE span length, d is the HBE depth and R is the length of the web plate corner cut-out at each end of the HBE provided to accommodate the HBE-to-VBE joint rocking connection detailing and to reduce the potential for corner tear out of the web plate due to high localized web plate strain effects during opening of the rocking joint connection.

The horizontal forces at the rocking point $P_{HBE(web)}$, $P_{HBE(VBE)}$ and T_s shown on Fig. 2 are the reactions due to the story shear contribution due to the web plate, horizontal component of web plate yield forces acting along the VBE and PT tension force calculated as follows:

$$P_{HBE(web)} = W_{bx1} - W_{bx2} = \frac{1}{2}(t_1 - t_2)F_{yp}(L - 2R)\sin(2\alpha) \tag{1}$$

$$P_{HBE(VBE)} = W_{cx1} + W_{cx2} = (\omega_{cx1} + \omega_{cx2})\left(\frac{h}{2} - \frac{d}{2} - R\right) \tag{2}$$

$$T_s = T_o + \frac{A_{PT}E_{PT}}{L_{PT}}\left(\Delta_{drift} - \Delta_{loss}\right) \tag{3}$$

where t_1 and t_2 are the web plate thicknesses below and above the HBE respectively, α is the angle of inclination of the diagonal tension field from the vertical axis, F_{yp} is the web plate yield stress, h is the story height, T_o is the initial PT force applied at the time of construction of the SPSW system, A_{PT}, E_{PT} and L_{PT} are the sectional area, modulus of elasticity and length of PT provided. Additionally, Δ_{drift} is the total drift induced elongation of the PT when the SC-SPSW joint connections open due to rocking action at the HBE-to-VBE joints during building drift and Δ_{loss} is the PT relaxation due to HBE axial shortening calculated as:

$$\Delta_{drift} = 2\left(\phi_{drift}\frac{d}{2}\right) = \phi_{drift}d \tag{4}$$

$$\Delta_{loss} = \frac{P_{HBE(VBE)}}{k_b + k_{PT}} + \left(\frac{k_{PT}}{k_b + k_{PT}}\right)\Delta_{drift} \tag{5}$$

where ϕ_{drift} is the relative joint rotation, k_b and k_{PT} are the axial stiffness (i.e. AE/L) of the HBE and PT elements respectively. Note that for use with multistory frames, the additional lateral story shear force at each HBE level due to multi-story PT frame stiffness (i.e. VBE's fighting beam growth) would have to be considered for preciseness in calculating the HBE demands (Kim and Christopoulos 2009).

Development of HBE Moments

The moment distribution to be used in the design of an HBE of a SC-SPSW can be determined from the FBD of Fig. 2 by taking moment equilibrium at three locations identified where x is any distance from point A leading to:

$$M_1 = \frac{Cd}{2} + R_a x \tag{6}$$

$$M_2 = R_a x + C\frac{d}{2} + \left(W_{by2} - W_{by1}\right)\left(\frac{x-R}{2}\right) + \left(W_{bx2} + W_{bx2}\right)\frac{d}{2} \tag{7}$$

$$M_3 = R_a x + C\frac{d}{2} + \left(W_{by2} - W_{by1}\right)\left(x - \frac{L}{2}\right) + \left(W_{bx2} + W_{bx1}\right)\frac{d}{2} \tag{8}$$

It is instructive to plot the moment distribution along the length of an HBE for a SC-SPSW frame. For illustrative purposes only, to avoid abstract complexities in keeping the problem parametric, all results here are presented in terms of an example. This example considers a W18x HBE with a clear span of 5.74 m (226 inches) and a story height of 3.89 m (153 inches) of a single bay frame. The SPSW web plates consists of 14 Gauge (1.83 mm) and 18 Gauge (1.77 mm) thicknesses below and above the HBE respectively with a corner cut-out radius of 254 mm (10 inches). Area of PT steel was arbitrarily chosen to produce a maximum moment of 60% of the full HBE plastic moment capacity at the end span of the HBE for an arbitrary 2% lateral drift, with a T_o of 30% of the assumed yield strength of the PT. A yield stress of 207 MPa (30 ksi) was assumed for the web plates, an ultimate yield stress of 1034 MPa (150 ksi) was assumed for the PT reinforcement and ASTM A572 (F_y = 345 MPa) steel was used for the boundary frame. After providing substitution of all applicable defined parameters into Eqns. (6) to (8), the resulting moment equations will each yield five distinct components which are separated and plotted on Fig. 3a with the composite moment diagram plotted in Fig. 3b.

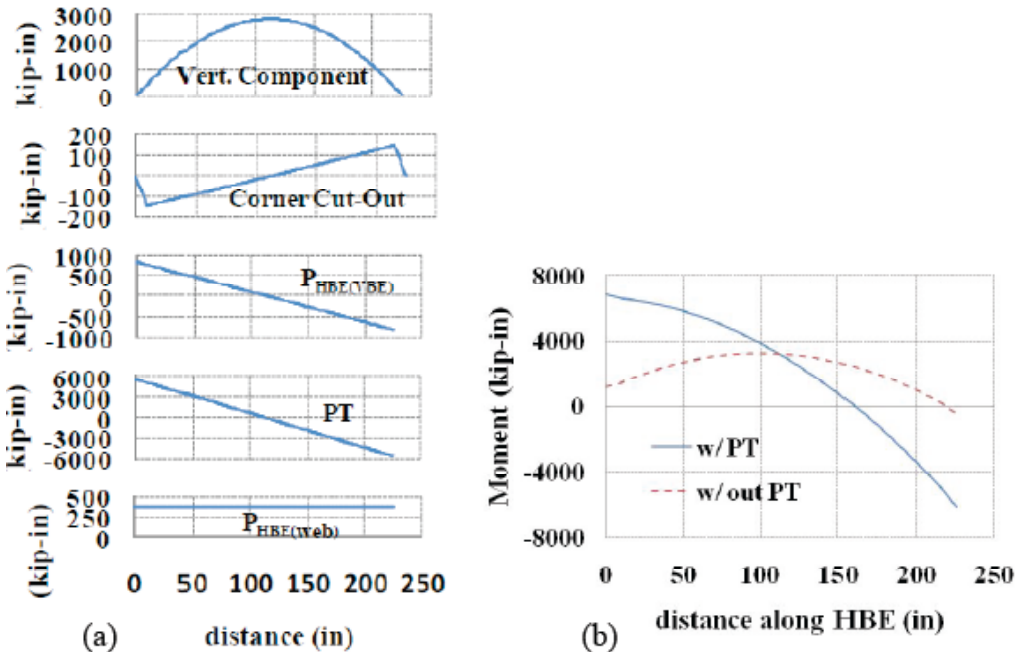


Fig. 3. (a) HBE Moment Components (b) Composite Moment Diagram

It is observed from the moment diagrams that the horizontal reactions at the rocking point will always generate double curvature moments at the ends of the HBE. Additionally, the moment diagrams are of identical shape, only the moment magnitudes are different. The contribution to the HBE moment from the VBE horizontal reaction at the rocking point, will always be additive to the HBE moment produced by the PT component. Without the PT, it can be seen that the maximum moment occurs close to the HBE mid-span, which is not desirable for reasons described later. Therefore, in addition to acting as a self-centering mechanism, the PT forces can be designed to shift the point of maximum moment towards the ends of the HBE (although at the cost of increased HBE moment demand).

Development of HBE Shears and Axial Forces

The shear distribution to be used in the design of an HBE incorporating self-centering components can be determined using the same free-body-diagrams developed earlier for the HBE moments. As a result, for the same 3 zones defined previously in terms of ω defined earlier follows:

$$V_1 = R_a = \frac{(\omega_{by1} - \omega_{by2})(L-2R)}{2} - \frac{(\omega_{bx2} + \omega_{bx1})(L-2R)}{2L}d - (\omega_{cx1} + \omega_{cx2})\left(\frac{h}{2} + \frac{d}{2} - R\right)\left(\frac{d}{L}\right) - T_s\left(\frac{d}{L}\right) \quad (9)$$

$$V_2 = R_a - (\omega_{by1} - \omega_{by2})(x-R) \quad (10)$$

$$V_3 = R_a - (\omega_{by1} - \omega_{by2})(L-2R) \quad (11)$$

Similarly, for axial forces over each of the three zones:

$$P_1 = C = \frac{(\omega_{bx1} - \omega_{bx2})(L-2R)}{2} + (\omega_{cx1} + \omega_{cx1})\left(\frac{h}{2} - \frac{d}{2} - R\right) + T_s \quad (12)$$

$$P_2 = C - (\omega_{bx1} - \omega_{bx2})(x-R) \quad (13)$$

$$P_3 = C - (\omega_{bx1} - \omega_{bx2})(L-2R) \quad (14)$$

DESIGN CONSIDERATION OF SELF-CENTERING CONNECTION

The above understanding of behavior and closed-form solutions also serve to aid in the selection of PT reinforcement area and HBE sizing to force the maximum HBE moment to be at its ends, to prevent in-span plastic hinging and account for moment-axial-shear interaction in the HBE, to keep PT reinforcement elastic, to select an adequate initial PT force, and to account for PT losses due to HBE axial shortening.

Knowing that PT force influences HBE moment distribution (Fig. 3), it is proposed here to design for the smallest PT force needed to shift the point of maximum moment to occur at the HBE ends. One should recognize that the moment distribution including a PT force contribution will vary depending on the magnitude of drift. For SC-SPSW systems to have a comparable performance with conventional SPSWs (e.g.,Park *et al.* 2007; Qu and Bruneau, 2009), it is proposed here that the PT reinforcement be designed to remain elastic at least up to 4% drift to maintain its self-centering capability. In addition to the above requirement, it is proposed that SC-SPSW be designed such that the total PT force that shifts the point of maximum moment to the HBE ends is reached at the target drift. This is proposed to avoid the formation of plastic hinges along the HBE span which can detrimentally impact the behavior of SPSW (Purba and Bruneau 2010).

Building on the system behavior and performance objectives presented above, the following design procedure for SC-SPSW HBE-to-VBE connection is proposed.

1. Select initial boundary elements sizes and web plate thickness (of many possible approaches, this could be done by designing a conventional SPSW, although other approaches are acceptable too).
2. Design the self-centering connection with the least PT forces that would result in the maximum moment occurring at the HBE ends at the target drift.
3. Select post-tension to ensure that the PT reinforcement remain elastic at least up to 4% drift.
4. Select the initial PT force applied to the self-centering connection.
5. Select the least cross sectional areas of PT reinforcement that satisfy the previous conditions.
6. Consider the effect of PT on reducing the HBE plastic moment as well as the effect of PT losses due to axial shortening to assess the adequacy of the HBE.
7. Iterate as needed to reduce the HBE size, ensuring that the HBE moment capacity reduced due to axial and shear forces remains adequate.

PERFORMANCE-BASED DESIGN OF SYSTEM

The fundamental system behavior and HBE-to-VBE design procedure previously described can be incorporated into a design procedure for the overall SC-SPSW system. For design of the system, a performance-based design approach has been developed to achieve the following structural performance objectives:

1. *No connection decompression under wind or gravity loading.* The decompression moment, M_d, of the PT connection ($M_d=T_o\ d/2$, where d and T_o were defined previously) should be designed to be greater than the HBE end-moments induced under wind or gravity loading.
2. *System recenters and no repair required under frequent earthquake demands* (i.e. the demand representing the 50% probability of exceedence in 50 year earthquake [50/50]). Recentering is assessed using a residual drift limit of 0.2%, corresponding to out-of-plumb limits in construction. The no repair limit state is assessed using a peak story drift limit of 0.5%, the median drift at which web plate repair is required in conventional SPSW experimental studies (Baldvins et al. 2010).

3. *System recenters and only web plate repair required under design earthquake demands* (i.e. approximated here as the demand representing the 10% probability of exceedence in 50 year earthquake [10/50]). The web plate may have significant yielding; however, the boundary frame and PT elements should remain elastic and the system should recenter. The damaged web plate can be replaced relatively quickly and simply, resulting in a more rapid return to occupancy following an earthquake (Qu et al. 2008). The story drift at this hazard level should be less than the 2% code-based drift limit for design level earthquakes.
4. *Collapse prevention for the maximum credible earthquake* (i.e. the demand representing the 2% probability of exceedence in 50 year earthquake [2/50]). Residual drifts and minor frame yielding may occur; however, soft story mechanisms and significant PT and frame yielding should be avoided. A target drift limit of this performance objective was assumed to be 4%, based on engineering judgment and the drift at which significant strength loss was observed in conventional SPSW experimental studies (Baldvins et al. 2010).

The following performance-based design procedure, as shown in Fig**.** 4, was developed to meet the previously described performance objectives.

1. Make initial assumptions about SC-SPSW geometry and number of walls in the building.
2. Determine the seismic loads and lateral load distribution. Here a modified load distribution as developed by Chao et al. (2007) was used to account for higher-mode effects, as SC-SPSWs and other self-centering PT systems (Garlock 2003) designed using typical code-based load distributions have exhibited larger drift demands and damage in the upper stories due to these higher-mode effects.
3. Design the web plates to remain elastic under 50% in 50 year loads.
4. Design the PT connection to have sufficient stiffness to ensure recentering under the influence of P-Delta effects.
5. Capacity design the PT and HBE to remain elastic and prevent in-span hinging at 4% drift according to the procedure previously described.
6. Capacity design the VBE to remain elastic up to 5% drift (Berman and Bruneau 2008).
7. Check that design meets code-based drift limits and that the required amount of PT can fit reasonably within the depth of the HBE.
8. Iterate as needed until a final design is converged upon.

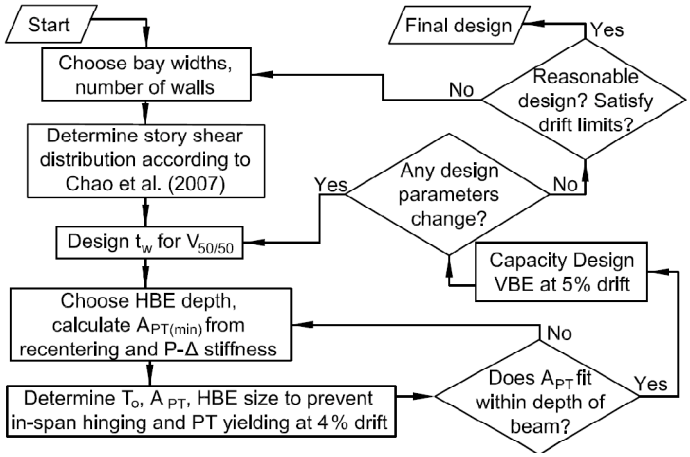


Fig. 4: SC-SPSW performance-based design procedure

A prototype 3-story SC-SPSW was designed according the proposed system design procedure. The 3-story building has story heights of 3.96m (13ft) with plan dimensions, loading, and seismic masses equivalent to those of the 3-story SAC building. The building was assumed to be on soil of Site Class D with spectral response parameters compatible with the ground motions developed for the Los Angeles, California location in the SAC project (Gupta and Krawinkler 1999). The prototype building was designed to have six 4.57m (15ft) wide bays of SC-SPSW in each direction of the building. The web plates were designed using available thicknesses of ASTM A36 steel, and the PT was designed using ½" diameter, Grade 270, seven-wire strand with a cross sectional area of 98.7mm^2 (0.153in^2) and a yield stress of 1689MPa (245ksi). Table 1shows the resulting prototype SC-SPSW design.

Table 1: 3-story prototype SC-SPSW design parameters

Story	Web Plate Thickness (mm)	HBE size	VBE size	# of PT strands	Initial PT force, T_o (kN)
1	7.94	W24x229	W14x605	16	231
2	6.35	W30x211	W14x605	12	503
3	4.18	W14x302	W14x605	32	467

NONLINEAR RESPONSE HISTORY ANALYSES

To assess the adequacy of the proposed performance-based design procedure, a numerical model of the prototype SC-SPSW was subjected to a suite of ground motions representing the seismic hazard levels considered in the design, and the response of the structure was evaluated. The numerical model was developed in OpenSees (Mazzoni et al. 2006). The steel web plates were modeled using the tension strip method consisting of a series of tension-only truss elements oriented in the direction of the diagonal tension-field. The plate material had a yield stress of R_yF_y, where F_y was 248MPa (36ksi) and R_y was 1.3 to account for the ratio of expected to nominal yield strength of A36 plate steel (AISC 2005a).

A PT connection model was developed to allow the HBE to rock about its flanges and cause PT elongation and to allow for shear load transfer without inhibiting the rocking action. The PT connection model (Berman et al. 2010) consisted of (1) stiff horizontal compression-only springs located at the HBE flanges to allow for decompression of the flanges at gap opening, (2) compression-only diagonal springs to transfer shear forces while allowing for gap opening and rotation, and (3) rigid link elements connecting the end of the HBE to the connection springs to ensure that the end of the HBE in contact with the VBE remains planar and is orthogonal to the HBE's longitudinal axis at that point. The tension only truss elements used for the PT elements were connected to the VBEs and were placed within the depth of the HBE.

The boundary frame elements were modeled using nonlinear beam-column elements with fiber cross-sections. The fibers were modeled using the Giuffre-Menegotto-Pinto material model, with an effective yield stress of 345MPa (50ksi), a rounded yield surface to help with numerical convergence, and 2% strain hardening. P-Delta columns were placed symmetrically on each side of the wall to simulate the gravity loads that would contribute to P-Delta effects on the wall. Seismic masses were lumped at the HBE-to-VBE connections, and damping was modeled using Rayleigh damping of 2% in the first and third modes. The earthquake ground motion records used in the nonlinear dynamic analyses were those developed for the SAC project for the Los Angeles site, with 20 ground motions for each seismic hazard level considered in the design procedure (50/50, 10/50, and 2/50).

The response parameters that were evaluated during the dynamic analyses were the peak story drift, $\theta_{s,max}$; the peak residual story drift, $\theta_{resid,max}$; and the HBE and VBE damage value, D_{HBE} and D_{VBE}, respectively, as evaluated by the interaction equation per Eqn. H1-1 (AISC 2005b), where a damage value of one indicates combined axial-flexural hinging. The median and 84th percentile responses for these parameters are shown for each seismic hazard level in **Table** 2.

Table 2: Response parameter values for prototype SC-SPSW

Response Parameter	50% in 50 yr		10% in 50 yr		2% in 50 yr	
	Median	84th percentile	Median	84th percentile	Median	84th percentile
$\theta_{s,max}$(%)	0.40	0.61	0.54	0.84	1.16	1.86
$\theta_{resid,max}$(%)	0.002	0.002	0.002	0.002	0.002	0.002
D_{HBE}	0.52	0.63	0.59	0.71	0.74	0.84
D_{VBE}	0.37	0.53	0.43	0.56	0.66	0.74

The results in **Table** 2 show that the SC-SPSW was able to recenter ($\theta_{resid,max} < 0.02\%$) at the 50% and 10% in 50 year hazard levels (Performance Obj. 2 and 3), and had no frame yielding (D_{HBE} and $D_{VBE} < 1.0$) at the 2% in 50 year hazard level (Performance Obj. 4). The prototype SC-SPSW had peak story drifts less than the 2% code-based drift limits at the 10% in 50 year hazard level (Performance Obj. 3), and the model had story drifts less than the 0.5% no web plate repair drift limit under the 50% in 50 year earthquake at the median level (Performance Obj. 2). Also, as the peak story drifts are well below the 4% target drift assumed in the PT design at the 2% in 50 year hazard level, there were no instances of PT yielding in any of the models at this hazard level (Performance Obj. 4). From all of these results, it is shown that the proposed performance-based system design procedure is capable of producing SC-SPSWs that can meet the intended performance objectives.

CONCLUSIONS

Fundamental behavior of a SC-SPSW was presented, in terms of closed form equations for moment, shear, and axial forces along the HBE. These formulations and development of the free-body-diagrams presented, not only provide insight on the behavior of a SC-SPSW system, but also provide a means to inform design. On the basis of that knowledge, a proposed HBE and PT connection design procedure based on a capacity design approach was formulated. Additionally, a SC-SPSW system design procedure was presented based on proposed structural performance targets and capacity design of the HBE and PT connection components using the previously described methods. The results of a series of nonlinear response history analyses on a prototype SC-SPSW designed according to the proposed performance-based method indicate that the system is capable of achieving the proposed performance objectives at three different seismic hazard levels. The findings presented indicate that SC-SPSW systems could be a viable alternative to traditional lateral force resisting systems. Future research is needed to further validate this system, including experimental work to investigate its behavior and self-centering characteristics.

REFERENCES

AISC (2005). *Seismic Provisions for Structural Steel Buildings*, *ANSI/AISC 341-05*. American Institute of Steel Construction, Chicago, IL.

AISC (2005). *Specification for Structural Steel Buildings*, *ANSI/AISC 341-05*. American Institute of Steel Construction, Chicago, IL.

Baldvins, N., Berman, J.W., Lowes, L.N., and Janes, T. (2010). "Development of damage prediction models for steel plate shear walls." *Earthquake Spectra*, (submitted).

Berman, J, Lowes, L., Bruneau, M., Fahnstock, L., Tsai, K.C., (2010). "An Overview of NEESR-SG: Smart and Resilient Steel Walls for Reducing Earthquake Impacts," Joint 9th US and 10th Canadian Conference on Earthquake Engineering, Toronto, Canada, July 2010.

Berman, J. Bruneau, M., (2008). "Capacity Design of Vertical Boundary Elements in Steel Plate Shear Walls." *Engineering Journal*, First Quarter 57-71

Chao, S.-H., Goel, S.C., and Lee, S.-S. (2007). "A seismic design lateral force distribution based on inelastic state of structures." *Earthquake Spectra*, 23(3), 547-569.

Christopoulos, C., Filiatrault, A., Folz, B. (2002). "Seismic response of self-centering hysteretic SDOF systems." *Earthquake Engineering and Structural Dynamics,* 31:1131-1150 (DOI: 10.1002/eqe.152)

Christopoulos, C., Filiatrault, A., Uang, C.M., Folz, B. (2002). "Posttensioned Energy Dissipating Connections for Moment-Resisting Steel Frame." *ASCE J. Struct. Eng.*, 128(9), 1111-1120

Garlock, M., Ricles J., Sause R., (2005). "Experimental Studies of Full-Scale Posttensioned Steel Connections." *ASCE J. Struct. Eng.*, 131(3), 438-448

Garlock, M. (2003). "Design, Analysis, and Experimental Behavior of Seismic Resistant Post-Tensioned Steel Moment Frames." PhD Thesis, Department of Civil and Environmental Engineering, Lehigh University.

Gupta, A. and Krawinkler, H. (1999). Seismic Demands for Performance Evaluation of Steel Moment Resisting Frame Structures, *Report No. 132*, John A. Blume Earthquake Engineering Center, Stanford University, Stanford, CA.

Kim, H.-J., Christopoulos, C. (2009). "Seismic design procedure and seismic response of post-tensioned self-centering steel frames." *Earthquake Engineering and Structural Dynamics*, Vol. 38, pp 355-376

Mazzoni, S. McKenna, F., Scott, M.H., and Fenves, G.L. (2006). *Open System for Earthquake Engineering Simulation User Command-Language Manual—OpenSees Version 1.7.3*. Pacific Earthquake Engineering Research Center, University of California Berkeley, Berkeley, CA.

Purba, R., and Bruneau, M. (2010). "Impact of Horizontal Boundary Elements Design on Seismic Behavior of Steel Plate Shear Walls." *Tech. Rep. MCEER-10-0007*, Multidisciplinary Center for Earthquake Engineering Research, State University of New York at Buffalo, Buffalo, New York.

Park, H. G., Kwack, J. H., Jeon, S. W., Kim, W. K., and Choi, I. R. (2007). "Framed steel plate wall behavior under cyclic lateral loading." J. Struct. Eng., 133(3), 378–388.

Ricles J., Sause R., Peng, S., Lu, L., (2002). "Experimental Evaluation of Earthquake Resistant Posttensioned Steel Connections." *ASCE J. Struct. Eng.*, 128(7) 850-859

Rojas, P., Ricles, J., Sause, R., (2005). "Seismic Performance of Post-tensioned Steel Moment Resisting Frames With Friction Devices.", *ASCE J. Struct. Eng.*, 131(4), 529-540

Sabelli, R., Bruneau, M., (2007). "Steel Plate Shear Walls." *AISC Steel Design Guide 20*, American Institute of Steel Construction, Inc., Chicago, Ill.

Qu, B., Bruneau, M., Lin, C.H., and Tsai, K.C. (2008). "Testing of Full Scale Two-story Steel Plate Shear Walls with Reduced Beam Section Connections and Composite Floors." Journal of Structural Engineering, ASCE, Vol. 134, No. 3, pp. 364-373

Modular Construction of Steel Plate Shear Walls for Low and Moderate Seismic Regions

Robert G. Driver[1] and Hassan Moghimi[2]

[1]Professor, Department of Civil and Environmental Engineering, University of Alberta, Edmonton, AB, Canada, T6G 2W2; email: rdriver@ualberta.ca
[2]PhD Candidate, Department of Civil and Environmental Engineering, University of Alberta, Edmonton, AB, Canada, T6G 2W2; email: moghimi@ualberta.ca

Abstract

Steel plate shear walls are generally considered to be economical only in high seismic regions, primarily because the high levels of ductility and resilience under cyclic loading have been demonstrated almost exclusively by tests on walls that contain expensive detailing at the beam-to-column connections. However, the lower demands on seismic load resisting systems in low and moderate seismic regions may permit the use of far more economical fabrication options. The use of modular construction methods is one option for reducing the costs associated with fabrication and erection. Modular components with repetitive fabrication processes can be produced in the shop and assembled in the field by bolts, eliminating the need for field welding entirely. This paper describes several potential modular options and discusses their advantages and disadvantages in terms of economics and constructability. The performance of one of these concepts (with different means of meeting capacity design requirements) is evaluated using detailed finite element models.

Introduction

Although steel plate shear walls (SPSW) are gradually gaining prominence within the structural engineering community as a viable seismic load resisting system for buildings, they are generally considered to be economical only in high seismic regions. This is primarily because the high levels of ductility and resilience under cyclic loading that make them so desirable in these regions have been demonstrated almost exclusively by tests on walls that contain expensive detailing at the beam-to-column connections. However, the lower demands on seismic load resisting systems in low and moderate seismic regions may permit the use of more economical fabrication options that have yet to be validated in terms of reliability and performance.

One option for reducing costs in the fabrication and erection of steel plate shear walls is the use of modular construction. As buildings normally have a constant story height and bay width over their height, modular components with repetitive fabrication processes can be produced in the shop and assembled in the field economically. When the field erection is carried out 100% by bolting the component modules together, cost-effective and very rapid assembly is possible.

However, the resulting assembled modular shear wall has several distinct differences from most of the walls that have been tested in the laboratory, and the performance of these walls requires verification. As such, a research investigation has been initiated at the University of Alberta to assess the potential of modular steel plate shear walls for general use in low and moderate seismic regions. This paper describes several potential modular options and discusses their advantages and disadvantages. Some results of detailed finite element analyses of these walls are presented that indicate that good performance can be expected in low and moderate seismic regions, despite significantly reduced fabrication and erection costs. A laboratory test to confirm the performance will be carried out in the next phase of the research.

Modular construction of SPSWs

Most steel plate shear wall research has been conducted with the primary aim of maximizing ductility and robustness under severe cyclic loading, without any explicit consideration of fabrication and erection costs. This has resulted in onerous capacity design rules in current codes and standards, such as CSA Standard S16-09 (CSA 2009) and AISC 341-05 (AISC 2005), for achieving a ductility-related force modification factor, $R_d = 5.0$ (Type D Plate Wall in S16) and $R = 8$ (Special Plate Shear Wall in AISC 341). The current provisions in S16-09 for achieving $R_d = 2.0$ (Type LD Plate Wall) state that the requirements for $R_d = 5.0$ must be met, with certain relaxations. These provisions were not developed independently for the $R_d = 2.0$ case. It is anticipated that simple and relatively inexpensive detailing can be used in steel plate shear walls and still achieve $R_d = 2.0$ due to the nature of the system itself.

In this paper, three concepts for steel plate shear walls are considered that are designed specifically to minimize in-place cost. The main characteristics that distinguish these concepts from conventional steel plate shear walls are that the beam-to-column connections are simple shear connections and that they constitute modular systems that require no field welding. Double web angle beam-to-column connections are assumed, although other types of simple and semi-rigid connections, including Tee connections, end-plate/header-plate connections, seated beam connections, etc., constitute reasonable alternatives that could be selected based on fabricator preference and cost.

All concepts considered allow construction of shear walls with relatively wide bays without the need for unconventional shipping arrangements. The infill plates in all concepts are spliced with single-sided lap plates. The arrangement of the infill plate splices can be changed based on ease of erection. All bolts are intended to be pre-tensioned to avoid slip at design loads.

Concept 1

Figure 1 shows modular steel plate shear wall Concept 1. This concept is intended to minimize the piece sizes that need to be handled in the field and may have applications in small projects or rehabilitation work. It is repetitive in nature and attempts to maximize the number of similar pieces. The figure shows double web angle connections for which the angles are connected to the columns in the shop (by bolting or welding), and then in the field the beams are connected to the angles by bolts. The fish plates are welded to the column and beam centerlines in the shop, and

then after assembling the frame in the field, the infill plates are bolted to the fish plates. Although the infill plates are connected to the surrounding frame via fish plates, in order to reduce the number of bolts other means of connection could be acceptable.

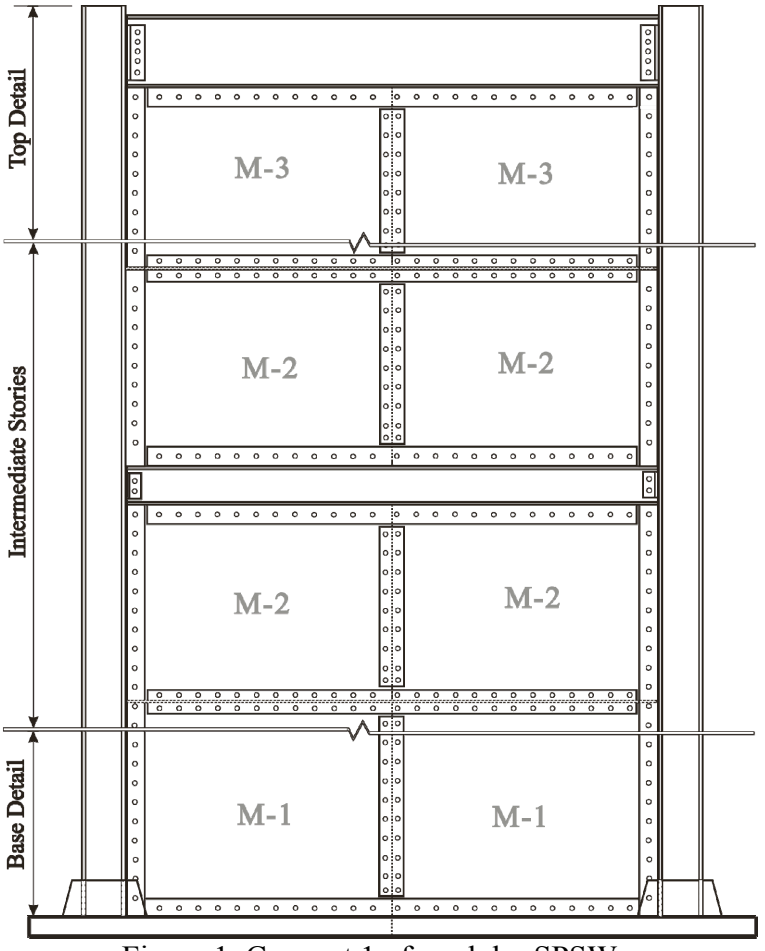


Figure 1. Concept 1 of modular SPSWs.

This concept consists of modular infill plates with only three module types: base module (modules M-1), top module (modules M-3), and intermediate story modules (modules M-2). As long as the heights of the intermediate stories and the associated beam depths are consistent, all modules M-2 will be identical. The field assembly and erection of numerous infill plate pieces may increase construction time in comparison with other concepts.

Since plastic hinges occur at the column bases, stiffener plates at both sides of the columns are provided to increase the ductility of this region. However, to keep the shear at the hinge location as low as possible, the height of the plates should be limited.

If the gravity-load induced axial compression in the infill is significant, it could be alleviated by a planned construction sequence. For instance, delay in the installation of some infill plate splices allows the columns of the system to shorten due to gravity loads prior to fixing of the splice plates (Seilie and Hooper 2005).

Concept 2

While Concept 1 is intended to minimize the piece sizes that need to be handled in the field, Concept 2 is intended to minimize the number of pieces by maximizing shop assembly. Figure 2(a) shows an elevation view of this system and the locations of each module have been demarcated by dashed lines. Figure 2(b) shows a detail of two complete modules after assembly. Again, this concept is repetitive in nature and attempts to maximize the number of similar pieces. In this concept, the larger modules, as compared to Concept 1, necessitate shear connections of the beams to the columns in the shop, and it has been assumed that fish plates are unnecessary under shop conditions. Due to the nature of this concept, moment resisting beam-to-column connections can be exercised as well.

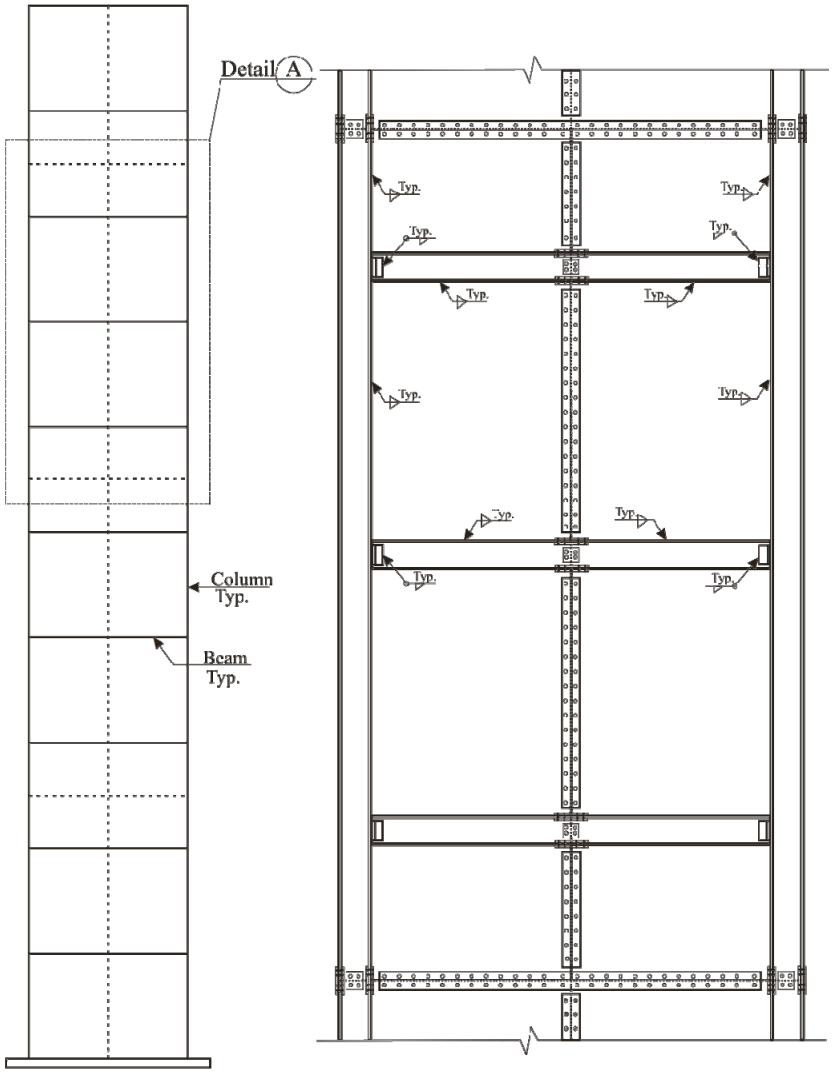


Figure 2. Concept 2 of modular SPSWs:
(a) Overview of SPSW concept; (b) Assembled modules of the system.

The modules of Concept 2 are shown in Figure 2 as being three stories in height (assumed to be the maximum practical size for shipping and lifting) and one-half bay wide, permitting this concept to be used for bays up to twice the maximum shipping load width. Usually there is no specific limitation on the shipping length. Shipping widths within 3.5 m are acceptable in most cases, while widths over 3.7 m require special permits and/or escorts in most jurisdictions, even if the site access permits oversize loads (Wong 2010).

One of the advantages of this system is its speed of construction. Each module has sufficient out-of-plane stiffness during construction and consists of a three-story tier. A potential disadvantage is that the vertical splice may create significant erection and plumbing challenges. Some measures may need to be exercised to alleviate the gravity-load induced axial compression in the infill plates, which can delay the development of tension-field action in the system.

Concept 3

Concept 3, depicted in Figure 3, consists of three module types: base module (module M-1), top module (module M-3), and intermediate story modules (modules M-2). The objective is to provide modules of a single story in height (mid-story to mid-story), with effectively no limit to the bay width imposed by shipping concerns. As long as the heights of the intermediate stories and the associated beam depths are consistent, all modules M-2 will be identical. In modules M-1 and M-3, the infill plate is welded to the base plate and the top beam, respectively, in the shop. In module M-2, the infill plate on both side of the intermediate beam is welded to the beam's flanges in the shop, which eliminates the need for horizontal fish plates.

Fish plates are welded to the column flanges in the shop and shear wall modules are connected to these fish plates on site by bolts. Lap splices are used to connect the modules to each other. Column splices are provided at every third story (aligned with the adjacent module boundary).

Two potential beam-to-column connection details have been shown in Figure 3 (Concepts 3a and 3b). In Concept 3a, a continuous fish plate is used, and at each connection, both beam flanges on one side of the web are coped and a single angle connection is added to the other side of the beam's web, as shown in Figure 4(a). In Concept 3b, the fish plate is terminated at the intersection with each beam and a conventional simple or semi-rigid beam-to-column connection, such as a double angle connection, is used (Figure 4(b)).

If the gravity-load induced axial compression in the infill is significant, it could be treated as explained for Concept 1.

A disadvantage of this system is the lack of out-of-plane stiffness of the modules during handling. These modules consist of large infill plates, with free edges equal to a half-story height, which needs some consideration regarding design and/or erection of the system. One option is to provide temporary perimeter stiffening to the infill plates to facilitate handling until final installation of the panel is completed. Each panel should be planned and detailed to mitigate this construction issue.

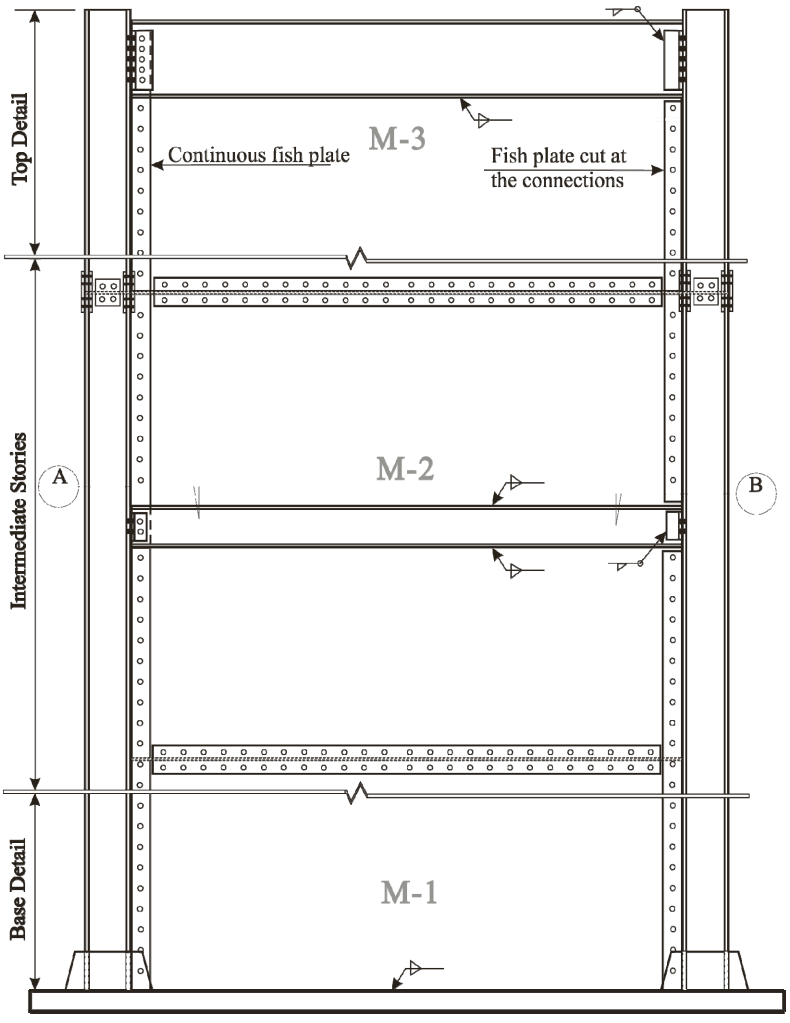


Figure 3. Concept 3 of modular SPSWs.

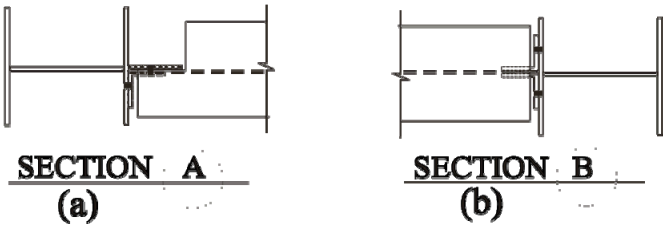


Figure 4. Beam-to-column connection methods:
(a) Details for Concept 3a; (b) Details for Concept 3b.

Numerical studies

The numerical studies presented in this section represent part of the planning process for a laboratory test of a two-story modular steel plate shear wall that will provide evidence of the performance that can be expected from such a system. As such, the dimensions used are

approximately representative of a half-size wall. Due to the nature of numerical analysis, however, this is not expected to impact conclusions arising from these studies about expected overall shear wall performance. Discussions with steel industry personnel have led to the conclusion that Concept 3 is the most promising in terms of practicality and economics and it forms the basis of the numerical investigation.

Based on previous large scale tests (Dastfan and Driver 2010), it has been found that lap-spliced infill plates in combination with high-strength pretensioned bolts (the bolts are designed for bearing and pretensioned to meet the requirement (e.g., CSA 2009) that all bolts resisting cyclic loading should be pretensioned high-strength bolts) provide lateral performance similar to a continuous infill plate. As a result, the performances of the three concepts discussed in the previous section are expected to be similar to each other, as well as similar to a SPSW with shear beam-to-column connections and continuous infill plates (i.e., no splices). In this study, the base model shown in Figure 5 has been selected to obtain the expected performance of a shear wall without splices. The columns are W250×115 sections, the intermediate beam is a W250×58 section, and the top beam is a W460×67 section. Infill plates have 4.8 mm thickness. All the material properties for the columns, beams, and infill plates are selected from the test by Driver et al. (1997). Both infill plates have a yield stress of 340 MPa.

The commercial general-purpose finite element code ABAQUS is selected to model the wall. All components of the wall are modelled using four-node shell elements with reduced integration (S4R element). Material and geometric nonlinearities are both considered. The von Mises yield criterion, along with the kinematic hardening rule is used. The numerical model has been verified by Moghimi and Driver (2010).

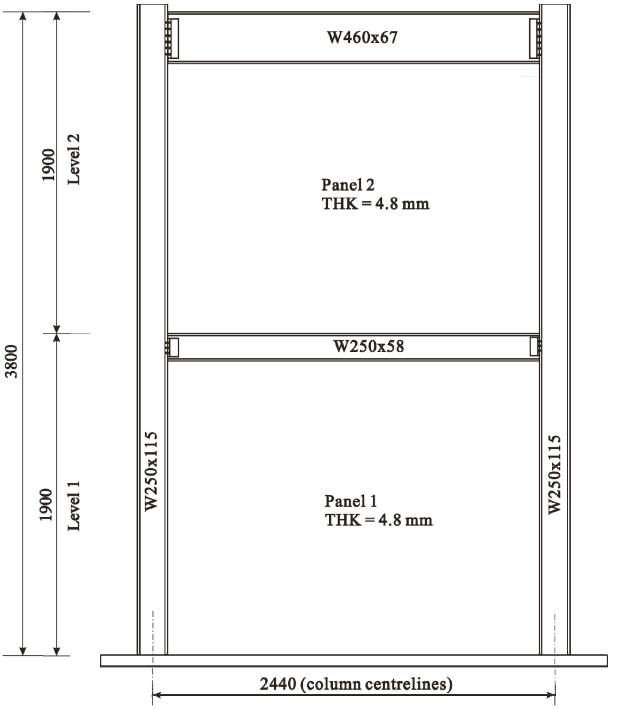


Figure 5. Elevation of base model for numerical studies.

The numerical model of Concept 3 is the same as Figure 5, but with a 2 mm horizontal slit at the mid-height of the first story (the critical story) and with a single-sided lap splice plate connecting the adjacent parts of the infill plate, as depicted in Figure 3. Each side of the splice plate is connected to the adjacent infill plate by bolts (the holes are not modeled and the bolts are modeled with connector constraint at the center of each bolt).

In order to deal with the problem in capacity design related to using infill plates that are thicker than theoretically needed for strength, resulting in large demands on the boundary members, two methods of "weakening" the plate are investigated. In the first, shown conceptually in Figure 6, an intermittent connection is provided at the horizontal infill plate splice to focus the tension field into "bands" that accelerate yielding of the infill plate and therefore reduce the demand on the boundary members (particularly the columns). The total length of the three splices in the model is about half of the width of the infill plate. The second method uses a continuous splice and circular holes are cut into the infill plate in a regular diagonal pattern, as described by Purba and Bruneau (2009). In the model, 14 holes of 200 mm diameter and 17 holes of the same diameter are used in the first and second story infill plates, respectively.

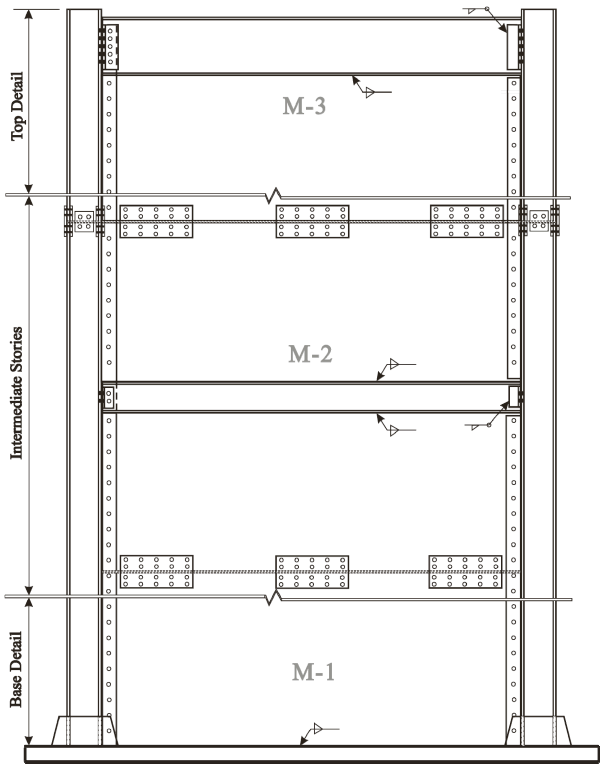


Figure 6. Concept 3 SPSW with intermittent splices.

Each wall is loaded under a monotonically increasing lateral force at each of the two stories. Figure 7 shows the story shear versus story deflection pushover curve for the first panel of each wall. There is little difference between the curves for the base model and the continuous splice.

Figures 8(a), (b), (c), and (d) show the effective plastic strain distributions in the four walls at a lateral deformation of 70 mm for the intermediate beam. Although modular SPSWs are not

intended for high-ductile applications, this lateral deformation is well beyond the target displacement for $R_d = 5.0$. (The target displacement evaluation methods based on design codes and standards represent a mean target displacement value for the design earthquake, and there is considerable scatter about the mean. Thus, ASCE 41-06 (2007) requires that the system be evaluated for a control-node displacement range of zero to 150 % of the target displacement.)

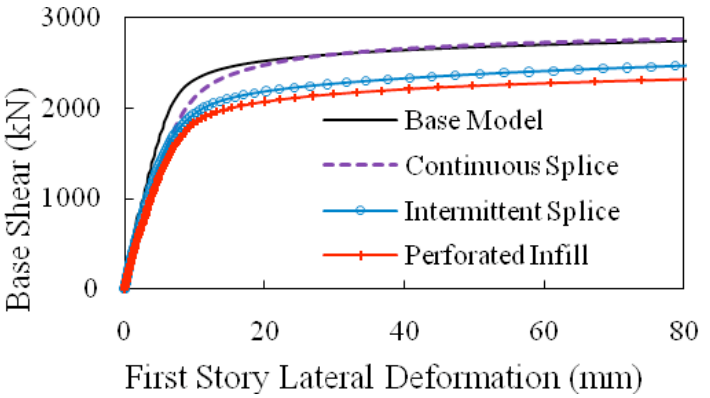


Figure 7. Story shear vs. story deflection of Panel 1.

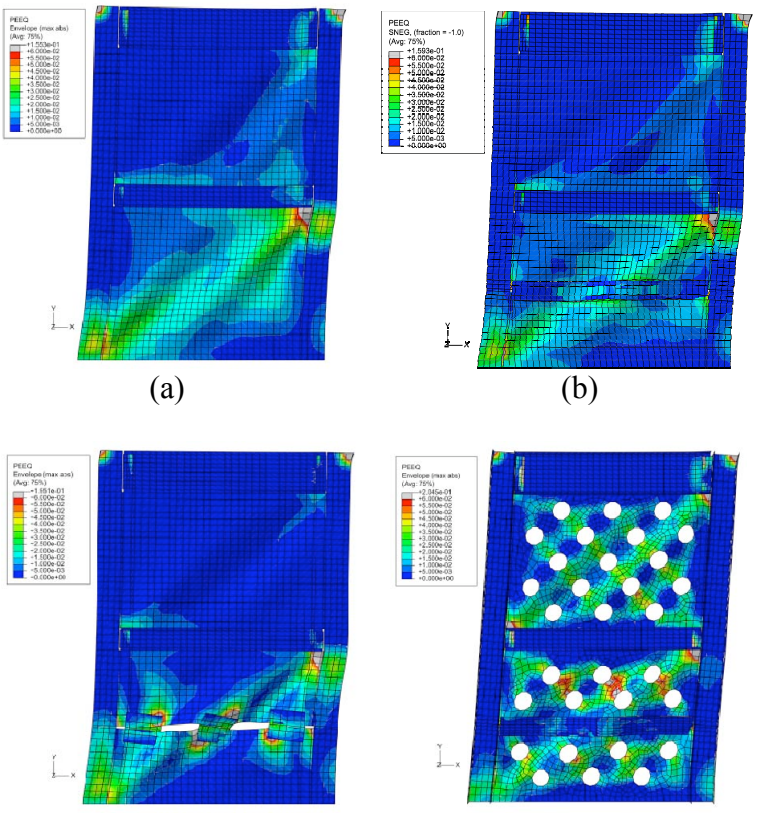


Figure 8. Effective plastic strain distribution: (a) Base model; (b) Continuous splice; (c) Intermittent splice; (d) Perforated infill.

From Figure 8 it can be seen that at a deformation of about 150 % of the target displacement for $R_d = 5.0$, there is a high strain concentration for the Intermittent Splice case (at the splice locations) and the Perforated Infill case (between the holes), while both the Base Model and the Continuous Splice case appear to provide reliable performance even at a very high level of lateral deformation. It can also be seen that the Perforated Infill case imposes a high demand on the first story shear connections, which is the result of the increased effect of frame action in this system, as explained later.

Previous research has shown that most SPSW systems have a high shear resistance, which in many cases leads to thinner infill plates than the minimum practical thickness for handling and welding. Using plates thicker than required for strength imposes increased force demands on the columns. Thus, an important issue for any new SPSW system is the amount of force demand (axial load, shear, and moment) on the columns. Figure 9(a) shows the horizontal component of the total force applied by the infill plate to the first story of the right column versus the first-story lateral deformation, and Figure 9(b) shows the associated vertical component of the force applied to the column by the infill plate. The figures show that the perforated infill plate is most effective in reducing the forces applied to the columns by the infill plate, but these forces do not represent the total demand on the columns.

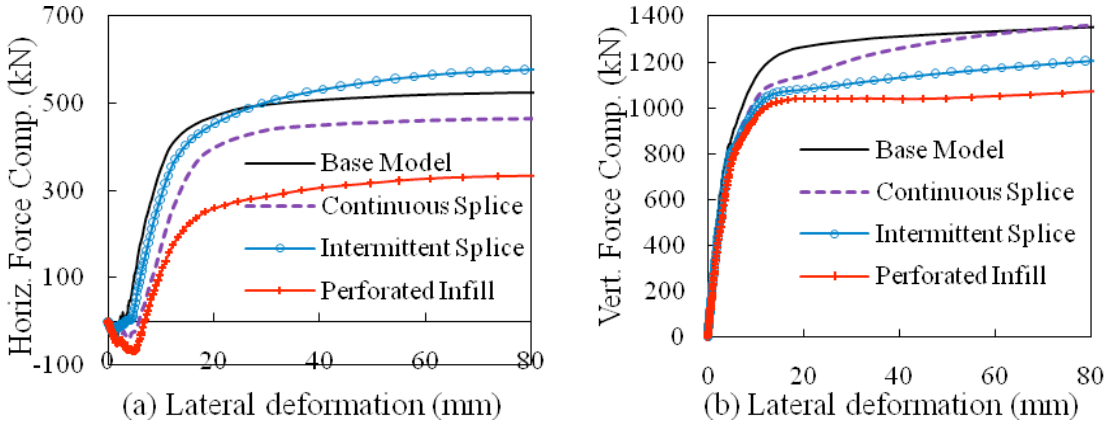


Figure 9. Force demands on the first story of the right column from the infill plate: (a) Horizontal force component; (b) Vertical force component.

Figures 10(a) and (b) show the total internal shear and axial compression demands, respectively, on the right column bases. These figures depict the actual demands on the columns from both the infill plate and frame action, and the columns are designed for these internal forces. Although Figure 9(a) shows that the force demand on the right column from the infill plate is smaller for the Perforated Infill case than for the other walls, Figure 10(a) indicates that the total shear demand on the column base (and also the moment demand) is actually higher at lateral deformations greater than about 35 mm. The reason for this apparent paradox is attributed to the augmented effect of frame action in the Perforated Infill case, which prevents a reduction in the total demand on the columns despite the fact that the perforated infill plate itself imposes a smaller demand. Further investigation is required to characterize this phenomenon.

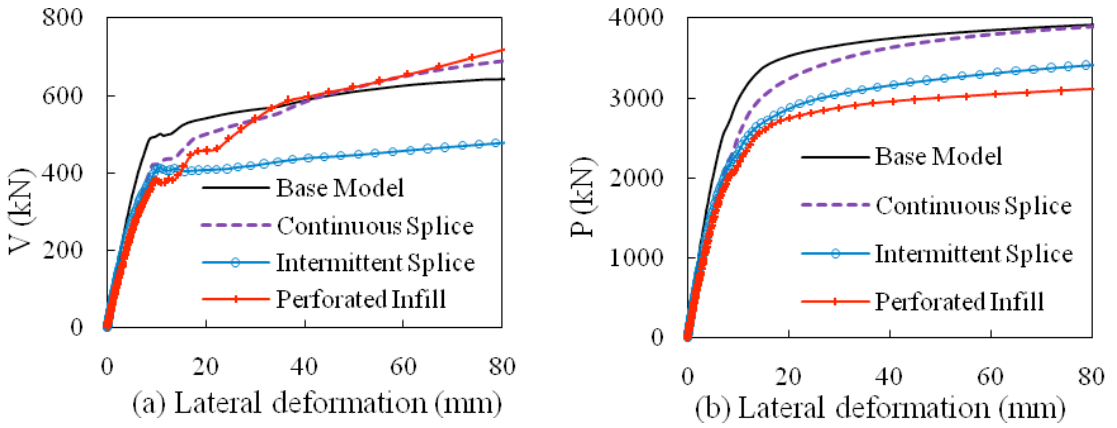


Figure 10. Total force demands on the right column base: (a) Shear force; (b) Axial compression.

Of the three modular cases evaluated in the numerical investigation, the one with the continuous splice showed the best overall pushover performance in terms of lateral shear strength, more uniform stress and plastic strain distributions, and possibly a lower P-delta effect. Also, it has been found that simple shear beam-to-column connections do not eliminate the frame action of the SPSW system, although they reduce its effect in comparison with rigid beam-to-column connections.

Conclusion

This paper provides some ideas related to the potential use of modular construction for SPSW systems in low and moderate seismic regions. The pros and cons of each system are discussed in terms of constructability and explicit consideration of fabrication and erection costs. Also, the inelastic pushover performance has been evaluated for the most promising modular concept. Concept 3, with a continuous infill plate splice, shows reliable performance but with higher forces applied by the infill plate to the columns in comparison with using intermittent infill plate splices or perforated infill plates. Meanwhile, both the Intermittent Splice case and the Perforated Infill case show some signs of infill plate tearing at large deformations. Although the simple beam-to-column connections reduce the frame action, they provide more rotational freedom in the connections and prevent the formation of plastic hinges in the columns near these joints at the design loads.

Acknowledgements

The authors acknowledge several valuable discussions with key members of the steel fabrication industry, with significant contributions to the concepts discussed in this paper provided by Richard Vincent and Alfred Wong. Funding for this research was provided by the G.J. Jackson Fellowship from the Steel Structures Education Foundation, the Alberta Ingenuity Fund from the Alberta Heritage Foundation, the Honorary Izaak Walton Killam Scholarship and Dorothy J. Killam Memorial Graduate Prize from the University of Alberta, and the Graduate Scholarship in Civil Engineering from the Canadian Society for Civil Engineering—Edmonton Section. This support is gratefully acknowledged.

References

AISC. (2005). *Seismic Provisions for Structural Steel Buildings. ANSI/AISC 341-05*, American Institute of Steel Construction, Inc., Chicago, IL.

ASCE. (2007). *Seismic Rehabilitation of Existing Buildings. ASCE/SEI 41-06*, American Society of Civil Engineers, New York, NY.

CSA. (2009). *CAN/CSA S16-09, Design of Steel Structures*, Canadian Standards Association, Mississauga, Ontario.

Dastfan, M. and Driver, R.G. (2010) "Large Scale Test of a Modular Steel Plate Shear Wall with PEC columns." Proc., *9th US National and 10th Canadian Conference on Earthquake Engineering: Reaching Beyond Borders*, July 25-29, Toronto, Ontario.

Driver, R.G., Kulak, G.L., Kennedy, D.J.L., and Elwi, A.E. (1997). "Seismic behaviour of steel plate shear walls." Structural Engineering Report 215, Department of Civil and Environmental Engineering, University of Alberta, Edmonton, Alberta.

Moghimi, H. and Driver, R.G. (2010). "Computational analysis of steel plate shear walls under accidental blast loading." Proc., *2nd Specialty Conference on Disaster Mitigation*, Winnipeg, Manitoba.

Purba, R. and Bruneau, M. (2009). "Finite-element investigation and design recommendations for perforated steel plate shear walls." *Journal of Structural Engineering*, 135(11), 1367-1376.

Seilie, I. F., and Hooper, J. D. (2005). "Steel plate shear walls: Practical design and construction." *Modern Steel Construction*, 45(4), 37-43.

Wong, A.F. (2010). Private communication.

Nonlinear Dynamic Analysis of Structures Using Modal Superposition

K. K. F. Wong[1]

[1]Engineering Laboratory, National Institute of Standards and Technology, MS 7302, 100 Bureau Dr., Bldg. 226, Room B-264, Gaithersburg, MD 20899-7302, USA; PH (301) 975-6361; FAX (301) 975-4032; email: kfwong@nist.gov

ABSTRACT

A fast nonlinear dynamic analysis algorithm is proposed based on modal superposition of structural response incorporating both material and geometric nonlinearities. Because linear modal superposition has found great acceptance in performance-based seismic engineering, it is here extended to the nonlinear domain by using the force analogy method to address material nonlinearity, where the stiffness force is computed by a change in displacement instead of using the traditional way of changing stiffness. Geometric nonlinearity is incorporated into the analysis using stability functions. State space method is used to explicitly calculate the dynamic responses of each modal single-degree-of-freedom system. Through the combination of force analogy method, stability functions, state space method, and modal superposition, numerical simulations are performed and results are demonstrated to be both accurate and efficient.

INTRODUCTION

Buildings constructed in seismic regions are subjected to earthquake activity and are required to be designed such that their seismic capacity must exceed the corresponding seismic demand with sufficient ductility. While design codes and standards have been developed to establish the seismic capacity in design, estimating the seismic demand in nonlinear structures has always been a challenging task mainly because of the lack of accurate scientific computing tools. Since the time when Newmark (1959) began studying the linear response history analysis for studying seismic effects on civil engineering structures, the development of current seismic design procedures relying on this type of linear analysis technique has advanced significantly because of its fundamental simplicity in the calculation procedure. However, while linear dynamic analysis is so popular, it has a shortcoming because all structures are designed with the anticipation that they will behave nonlinearly when a major earthquake occurs.

Significant research works have been attempted to extend the linear dynamic analysis to the nonlinear domain (e.g., Liu 2003 and 2005, Au and Yan 2008), but presently nonlinear dynamic analysis techniques are employed in seismic design only in some special occasions, mainly because the analysis itself is a time-consuming process. Current nonlinear dynamic numerical algorithms require significant computation time to update the stiffness matrix to accommodate for nonlinearity in structures. In addition, many simulations need to be considered due to the uncertainties in earthquake ground motions. Even though nonlinear response history analysis is

believed to be the most accurate method of computing the seismic demand, it requires a huge computational effort, making the analysis impractical in the design process. Therefore, a fast analysis method with high accuracy in predicting the maximum seismic demand is needed, yet the development of such a nonlinear dynamic analysis algorithm remains a challenge without deeper understanding of the theory of nonlinear structural analysis and dynamics.

In this research, linear dynamic analysis based on modal superposition is extended to analyze structural responses in the nonlinear domain – known here as the Nonlinear Modal Analysis (NMA). While the force analogy method is a simple nonlinear analysis tool based on initial stiffness that treats material nonlinearity as an equivalent force, the state space method is a dynamic algorithm that can perform time-stepping calculations explicitly to progress the effects of the equivalent force on structural responses to the next time step. Although some results through the combination of these methods have been published (Yang et al. 2004, Zhao and Wong 2006, Zhang et al. 2007, Chao and Loh 2007), none of these works studied the nonlinear structural responses in the modal coordinate system. In addition, it is the intent of this research to develop a rigorous approach for treating geometric nonlinearity in dynamic analysis through the use of stability functions as the closed-form solution. Accuracy and efficiency are demonstrated through applying the algorithm on an example 10-story frame by comparing output results with existing commercial software packages including Perform-3D and SAP2000.

FORCE ANALOGY METHOD

The detailed derivation of the force analogy method has been presented in Wong and Yang (1999). Consider a moment-resisting frame with n degrees of freedom (DOFs) and m plastic hinge locations (PHLs), let the total displacement $\mathbf{x}(t)$ at each DOF be represented as the summation of the elastic displacement $\mathbf{x}'(t)$ and the inelastic displacement $\mathbf{x}''(t)$:

$$\mathbf{x}(t) = \mathbf{x}'(t) + \mathbf{x}''(t) \tag{1}$$

Similarly, let the total moment $\mathbf{m}(t)$ at the PHLs of a moment-resisting frame be separated into elastic moment $\mathbf{m}'(t)$ and inelastic moment $\mathbf{m}''(t)$:

$$\mathbf{m}(t) = \mathbf{m}'(t) + \mathbf{m}''(t) \tag{2}$$

The displacements in Eq. (1) and the moments in Eq. (2) are related by the equations:

$$\mathbf{m}'(t) = \mathbf{K}'(t)^T \mathbf{x}'(t) \quad , \qquad \mathbf{m}''(t) = -\left[\mathbf{K}''(t) - \mathbf{K}'(t)^T \mathbf{K}(t)^{-1} \mathbf{K}'(t)\right] \boldsymbol{\Theta}''(t) \tag{3}$$

where $\boldsymbol{\Theta}''(t)$ is the plastic rotation at the PHLs, $\mathbf{K}(t)$ is the $n \times n$ global stiffness matrix, $\mathbf{K}'(t)$ is the $n \times m$ stiffness matrix that relates the plastic rotations at the PHLs and the forces at the DOFs, and $\mathbf{K}''(t)$ is the $m \times m$ stiffness matrix that relates the plastic rotations with the corresponding moments at the PHLs. These stiffness matrices are functions of time when geometric nonlinearity with varying axial load is incorporated in the dynamic analysis, and they can be formed by assembling the individual element stiffness matrices in the appropriate DOFs and PHLs. For the ith

column member of the structure with plastic hinges at both ends, the axially-loaded element stiffness matrices related to shear and bending can be written as:

$$\mathbf{K}_i(t) = \left[\begin{array}{cc:cc} s'EI/L^3 & \bar{s}EI/L^2 & -s'EI/L^3 & \bar{s}EI/L^2 \\ \bar{s}EI/L^2 & sEI/L & -\bar{s}EI/L^2 & scEI/L \\ \hdashline -s'EI/L^3 & -\bar{s}EI/L^2 & s'EI/L^3 & -\bar{s}EI/L^2 \\ \bar{s}EI/L^2 & scEI/L & -\bar{s}EI/L^2 & sEI/L \end{array}\right]$$

$$\mathbf{K}_i'(t)^T = \left[\begin{array}{cc:cc} \bar{s}EI/L^2 & sEI/L & -\bar{s}EI/L^2 & scEI/L \\ \bar{s}EI/L^2 & scEI/L & -\bar{s}EI/L^2 & sEI/L \end{array}\right] \qquad \mathbf{K}_i''(t) = \left[\begin{array}{cc} sEI/L & scEI/L \\ scEI/L & sEI/L \end{array}\right]$$

where

$$s = \frac{\lambda(\sin\lambda - \lambda\cos\lambda)}{2 - 2\cos\lambda - \lambda\sin\lambda} \qquad c = \frac{\lambda - \sin\lambda}{\sin\lambda - \lambda\cos\lambda}$$

$$\bar{s} = s + sc = s(1+c) = \frac{\lambda^2(1-\cos\lambda)}{2 - 2\cos\lambda - \lambda\sin\lambda} \qquad s' = 2\bar{s} - \lambda^2 = \frac{\lambda^3\sin\lambda}{2 - 2\cos\lambda - \lambda\sin\lambda}$$

$\lambda = (P(t)/EI)^{0.5} \times L$, $P(t)$ is the time-varying axial compressive force in the column which causes the stiffness matrices to be also time-varying, and E, I, and L are the elastic modulus, moment of inertia, and length of the column member, respectively. The relationship between plastic rotation $\mathbf{\Theta}''(t)$ and inelastic displacement $\mathbf{x}''(t)$ is:

$$\mathbf{x}''(t) = \mathbf{K}(t)^{-1}\mathbf{K}'(t)\mathbf{\Theta}''(t) \tag{4}$$

Substituting Eq. (3) into Eq. (2) and making use of Eqs. (1) and (4), then rearranging the terms gives the governing equation of the force analogy method:

$$\mathbf{m}(t) + \mathbf{K}''(t)\mathbf{\Theta}''(t) = \mathbf{K}'(t)^T\mathbf{x}(t) \tag{5}$$

NONLINEAR MODAL ANALYSIS

When the force analogy method is used, the stiffness force is calculated by multiplying the global stiffness matrix $\mathbf{K}(t)$ with the elastic displacement $\mathbf{x}'(t)$. For an n-DOF system with plastic hinges at both ends of each member subjected to earthquake ground motion, the equation of motion can therefore be written as

$$\mathbf{M}\ddot{\mathbf{x}}(t) + \mathbf{C}\dot{\mathbf{x}}(t) + \mathbf{K}(t)\mathbf{x}'(t) = -\mathbf{M}\ddot{\mathbf{g}}(t) + \mathbf{F}_h(t) \tag{6}$$

where $\mathbf{M}$ is the $n \times n$ mass matrix, $\mathbf{C}$ is the $n \times n$ damping matrix, $\dot{\mathbf{x}}(t)$ is the $n \times 1$ velocity vector at each DOF, $\ddot{\mathbf{x}}(t)$ is the $n \times 1$ acceleration vector at each DOF, $\ddot{\mathbf{g}}(t)$ is the $n \times 1$ ground acceleration vector corresponding to each DOF, and $\mathbf{F}_h(t)$ is an $n \times 1$ force vector that takes into consideration the geometric nonlinearity of the entire structure (i.e., the P-Δ effect), such as the force imposed on the structure using a P-Δ column. In two-dimensional modeling, this force is related to the displacement of the structure, and it can be computed by the formula $\mathbf{F}_h(t) = \mathbf{K}_h\mathbf{x}(t)$, where $\mathbf{K}_h$ is the $n \times n$ stiffness matrix computed using the column heights and axial gravity forces of the

P-Δ column members. Note that the *P*-δ effect has been included in $\mathbf{K}(t)$.

Let $\mathbf{K}(t) = \mathbf{K}_o - \mathbf{K}_G(t)$, where $\mathbf{K}_o$ represents the initial stiffness due to gravity load only, and $\mathbf{K}_G(t)$ represents the change in stiffness due to the variation of axial forces while subjected to the earthquake ground motion. Now replacing the elastic displacement $\mathbf{x}'(t)$ in Eq. (6) by the difference of total displacement $\mathbf{x}(t)$ and inelastic displacement $\mathbf{x}''(t)$ that is rewritten using Eq. (1), it follows that

$$\mathbf{M}\ddot{\mathbf{x}}(t) + \mathbf{C}\dot{\mathbf{x}}(t) + \mathbf{K}_o\mathbf{x}(t) = -\mathbf{M}\ddot{\mathbf{g}}(t) + \mathbf{K}_h\mathbf{x}(t) - \mathbf{K}_G(t)\mathbf{x}(t) + \mathbf{K}(t)\mathbf{x}''(t) \tag{7}$$

Following a similar procedure for the treatment of *P*-Δ effects discussed in Wilson (2002), define $\mathbf{K}_e = \mathbf{K}_o - \mathbf{K}_h$, where $\mathbf{K}_e$ represents the elastic stiffness of the structure. Now substituting Eq. (4) into Eq. (7) gives

$$\mathbf{M}\ddot{\mathbf{x}}(t) + \mathbf{C}\dot{\mathbf{x}}(t) + \mathbf{K}_e\mathbf{x}(t) = -\mathbf{M}\ddot{\mathbf{g}}(t) - \mathbf{K}_G(t)\mathbf{x}(t) + \mathbf{K}'(t)\mathbf{\Theta}''(t) \tag{8}$$

Let the modal displacement response $\vec{\mathbf{q}}(t)$ be the $r \times 1$ vector of the form

$$\mathbf{x}(t) = \mathbf{\Phi}\vec{\mathbf{q}}(t) = \begin{bmatrix}\boldsymbol{\varphi}_1 & \boldsymbol{\varphi}_2 & \cdots & \boldsymbol{\varphi}_r\end{bmatrix}\begin{bmatrix}\vec{q}_1(t) & \vec{q}_2(t) & \cdots & \vec{q}_r(t)\end{bmatrix}^T \tag{9}$$

where $\mathbf{\Phi}$ is the $n \times r$ modal matrix – a collection of the first *r* mode shapes $\boldsymbol{\varphi}_i$ in column form, and *r* is the number of modes to be considered in the analysis, where $r \le n$. Differentiating the modal displacement $\vec{\mathbf{q}}(t)$ with respect to time gives the modal velocity $\dot{\vec{\mathbf{q}}}(t)$, and differentiating it once again with respect to time gives the modal acceleration $\ddot{\vec{\mathbf{q}}}(t)$. Now substituting Eq. (9) into Eq. (8):

$$\mathbf{M}\mathbf{\Phi}\ddot{\vec{\mathbf{q}}}(t) + \mathbf{C}\mathbf{\Phi}\dot{\vec{\mathbf{q}}}(t) + \mathbf{K}_e\mathbf{\Phi}\vec{\mathbf{q}}(t) = -\mathbf{M}\ddot{\mathbf{g}}(t) - \mathbf{K}_G(t)\mathbf{x}(t) + \mathbf{K}'(t)\mathbf{\Theta}''(t) \tag{10}$$

Pre-multiplying Eq. (10) by $\mathbf{\Phi}^T$, it follows that

$$\begin{aligned}\mathbf{\Phi}^T\mathbf{M}\mathbf{\Phi}\ddot{\vec{\mathbf{q}}}(t) + \mathbf{\Phi}^T\mathbf{C}\mathbf{\Phi}\dot{\vec{\mathbf{q}}}(t) + \mathbf{\Phi}^T\mathbf{K}_e\mathbf{\Phi}\vec{\mathbf{q}}(t) \\ = -\mathbf{\Phi}^T\mathbf{M}\ddot{\mathbf{g}}(t) - \mathbf{\Phi}^T\mathbf{K}_G(t)\mathbf{x}(t) + \mathbf{\Phi}^T\mathbf{K}'(t)\mathbf{\Theta}''(t)\end{aligned} \tag{11}$$

While assuming that the damping matrix $\mathbf{C}$ exhibits proportional damping property, let $\vec{\mathbf{M}} = \mathbf{\Phi}^T\mathbf{M}\mathbf{\Phi}$, $\vec{\mathbf{C}} = \mathbf{\Phi}^T\mathbf{C}\mathbf{\Phi}$, and $\vec{\mathbf{K}} = \mathbf{\Phi}^T\mathbf{K}\mathbf{\Phi}$ be the diagonal modal mass, modal damping, and modal stiffness matrices, respectively. This gives *r* modal equations:

$$\vec{m}_i\ddot{\vec{q}}_i(t) + \vec{c}_i\dot{\vec{q}}_i(t) + \vec{k}_i\vec{q}_i(t) = -\boldsymbol{\varphi}_i^T\mathbf{M}\ddot{\mathbf{g}}(t) - \boldsymbol{\varphi}_i^T\mathbf{K}_G(t)\mathbf{x}(t) + \boldsymbol{\varphi}_i^T\mathbf{K}'(t)\mathbf{\Theta}''(t) \quad i = 1,...,r \tag{12}$$

where $\vec{m}_i$, $\vec{c}_i$, and $\vec{k}_i$ are the *i*th modal mass, damping, and stiffness, respectively.

STATE SPACE METHOD

For all *r* modes given in Eq. (12), let the three terms on the right hand side of the equation be treated as the equivalent modal forces:

$$\vec{m}_i\vec{a}_i(t) = \boldsymbol{\varphi}_i^T\mathbf{M}\ddot{\mathbf{g}}(t) \quad i = 1,...,r \tag{13}$$

$$\vec{f}_{mi}(t) = \boldsymbol{\varphi}_i^T\mathbf{K}'(t)\mathbf{\Theta}''(t) \quad i = 1,...,r \tag{14}$$

$$\vec{f}_{Gi}(t) = \boldsymbol{\varphi}_i^T\mathbf{K}_G(t)\mathbf{x}(t) \quad i = 1,...,r \tag{15}$$

where $\vec{a}_i(t)$ is the modal ground acceleration, $\vec{f}_{mi}(t)$ is the equivalent modal force due to material nonlinearity, and $\vec{f}_{Gi}(t)$ is the equivalent modal force due to geometric nonlinearity. Representing each modal equation in Eq. (12) in the state space form:

$$\dot{\vec{\mathbf{z}}}_i(t) = \mathbf{A}_i\vec{\mathbf{z}}_i(t) + \mathbf{G}_i\vec{f}_{mi}(t) - \mathbf{G}_i\vec{f}_{Gi}(t) + \mathbf{H}_i\vec{a}_i(t) \quad i = 1,...,r \tag{16}$$

where

$$\vec{\mathbf{z}}_i(t) = \begin{Bmatrix} \vec{q}_i(t) \\ \dot{\vec{q}}_i(t) \end{Bmatrix}, \quad \mathbf{A}_i = \begin{bmatrix} 0 & 1 \\ -\omega_i^2 & -2\zeta_i\omega_i \end{bmatrix}, \quad \mathbf{G}_i = \begin{bmatrix} 0 \\ 1/\vec{m}_i \end{bmatrix}, \quad \mathbf{H}_i = \begin{bmatrix} 0 \\ -1 \end{bmatrix}$$

and ω_i and ζ_i are the natural frequency and damping ratio of the *i*th mode, respectively.

The solution to the first order linear differential equation given in Eq. (16) is

$$\vec{\mathbf{z}}_i(t) = \mathbf{e}^{\mathbf{A}_i(t-t_0)}\vec{\mathbf{z}}_i(t_0) + \mathbf{e}^{\mathbf{A}_i t}\int_{t_0}^{t}\mathbf{e}^{-\mathbf{A}_i s}\left[\mathbf{G}_i\vec{f}_{mi}(s) - \mathbf{G}_i\vec{f}_{Gi}(s) + \mathbf{H}_i\vec{a}_i(s)\right]ds \quad i = 1,...,r \tag{17}$$

where t_0 is the initial time of integration. The state transition matrix $\mathbf{e}^{\mathbf{A}_i t}$ of a SDOF system is

$$\mathbf{e}^{\mathbf{A}_i t} = e^{-\zeta_i\omega_i t}\begin{bmatrix} \cos\omega_{di}t + \dfrac{\zeta_i}{\sqrt{1-\zeta_i^2}}\sin\omega_{di}t & \dfrac{1}{\omega_i\sqrt{1-\zeta_i^2}}\sin\omega_{di}t \\ -\dfrac{\omega_i}{\sqrt{1-\zeta_i^2}}\sin\omega_{di}t & \cos\omega_{di}t - \dfrac{\zeta_i}{\sqrt{1-\zeta_i^2}}\sin\omega_{di}t \end{bmatrix}$$

and ω_{di} is the damped natural frequency of the *i*th mode computed by the formula $\omega_{di} = \omega_i(1-\zeta_i^2)^{0.5}$. Define $t_{k+1} = t$, $t_k = t_0$, and $\Delta t = t - t_0$, it follows that Eq. (17) can be discretized and integrated as

$$\vec{\mathbf{z}}_{k+1}^{(i)} = \mathbf{F}_d^{(i)}\vec{\mathbf{z}}_k^{(i)} + \mathbf{G}_d^{(i)}\vec{f}_{mk}^{(i)} - \mathbf{G}_d^{(i)}\vec{f}_{Gk}^{(i)} + \mathbf{H}_d^{(i)}\vec{a}_k^{(i)} \quad i = 1,...,r \tag{18}$$

where

$$\mathbf{F}_d^{(i)} = \mathbf{e}^{\mathbf{A}_i\Delta t} \quad , \quad \mathbf{G}_d^{(i)} = \mathbf{e}^{\mathbf{A}_i\Delta t}\mathbf{G}_i\Delta t \quad , \quad \mathbf{H}_d^{(i)} = \mathbf{e}^{\mathbf{A}_i\Delta t}\mathbf{H}_i\Delta t$$

$\vec{\mathbf{z}}_k^{(i)}$, $\vec{f}_{mk}^{(i)}$, $\vec{f}_{Gk}^{(i)}$, and $\vec{a}_k^{(i)}$ are the discretized forms of $\vec{\mathbf{z}}_i(t)$, $\vec{f}_{mi}(t)$, $\vec{f}_{Gi}(t)$, and $\vec{a}_i(t)$, respectively, and the superscript *i* in parenthesis denotes the calculation is based on the *i*th mode. Once the modal displacement and velocity responses embedded in $\vec{\mathbf{z}}_k^{(i)}$ are obtained, the modal relative acceleration response can be calculated using Eq. (12):

$$\ddot{\vec{q}}_k^{(i)} = \vec{f}_{mk}^{(i)}/\vec{m}_i - \vec{f}_{Gk}^{(i)}/\vec{m}_i - \vec{a}_k^{(i)} - \vec{c}_i\dot{\vec{q}}_k^{(i)}/\vec{m}_i - \vec{k}_i\vec{q}_k^{(i)}/\vec{m}_i \quad i = 1,...,r \tag{19}$$

The absolute acceleration of the *i*th mode, $\ddot{\vec{q}}_{a,k}^{(i)}$, can be calculated by summing the relative acceleration in Eq. (19) with the modal ground acceleration defined in Eq. (13):

$$\ddot{\vec{q}}_{a,k}^{(i)} = \ddot{\vec{q}}_k^{(i)} + \vec{a}_k^{(i)} \quad i = 1,...,r \tag{20}$$

Finally, the absolute acceleration of the structure $\ddot{\mathbf{y}}(t)$, or $\ddot{\mathbf{y}}_k$ in discretized form, is computed as:

$$\ddot{\mathbf{y}}_k = \ddot{\mathbf{x}}_k + \ddot{\mathbf{g}}_k = \mathbf{\Phi}\ddot{\mathbf{q}}_k + \mathbf{\Phi}\vec{\mathbf{a}}_k = \mathbf{\Phi}\ddot{\mathbf{q}}_{a,k} = \mathbf{\Phi}\left[\ddot{q}_{a,k}^{(1)} \quad \ddot{q}_{a,k}^{(2)} \quad \cdots \quad \ddot{q}_{a,k}^{(r)}\right]^T \tag{21}$$

Figure 1 shows the flowchart of the proposed calculation procedure for performing the nonlinear response history analysis. Note that nonlinearity causes coupling between modes, as shown in Figure 1. Therefore, all r modes are required to be run simultaneously in order to perform modal combination at each time step.

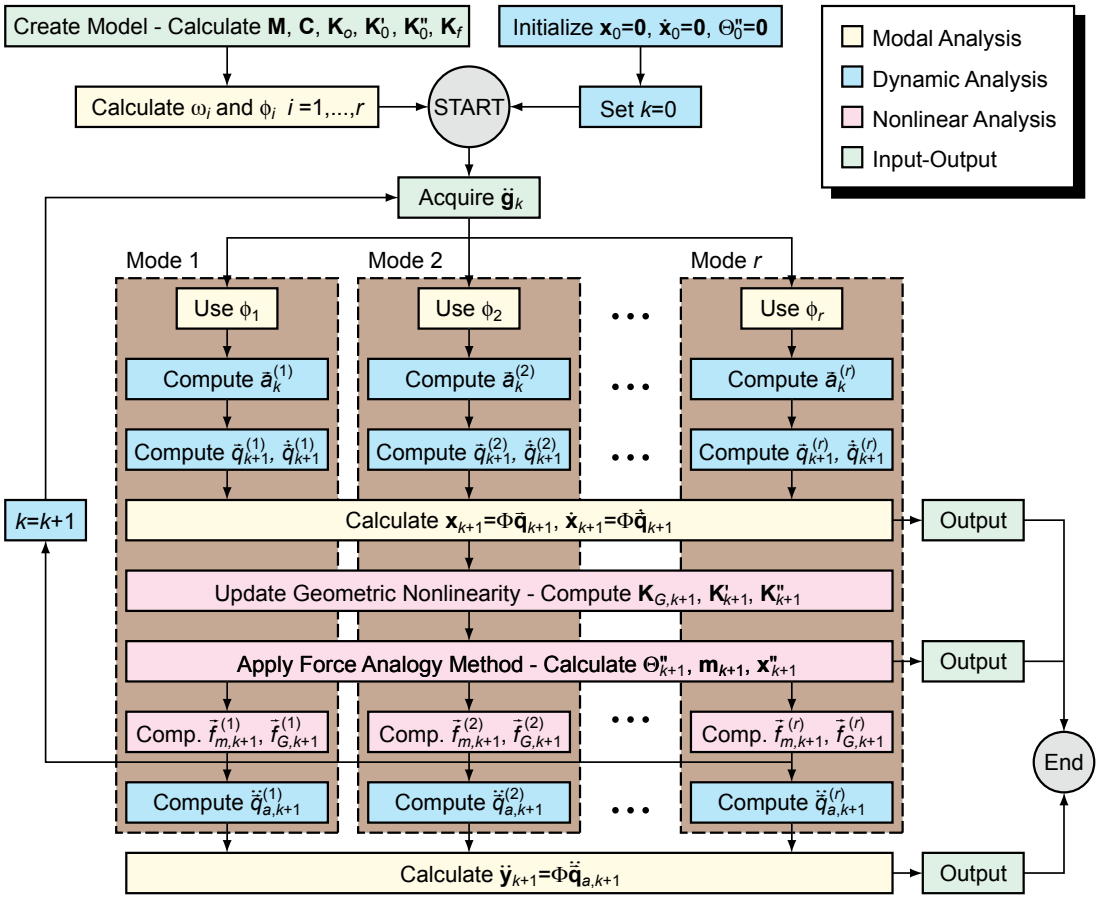
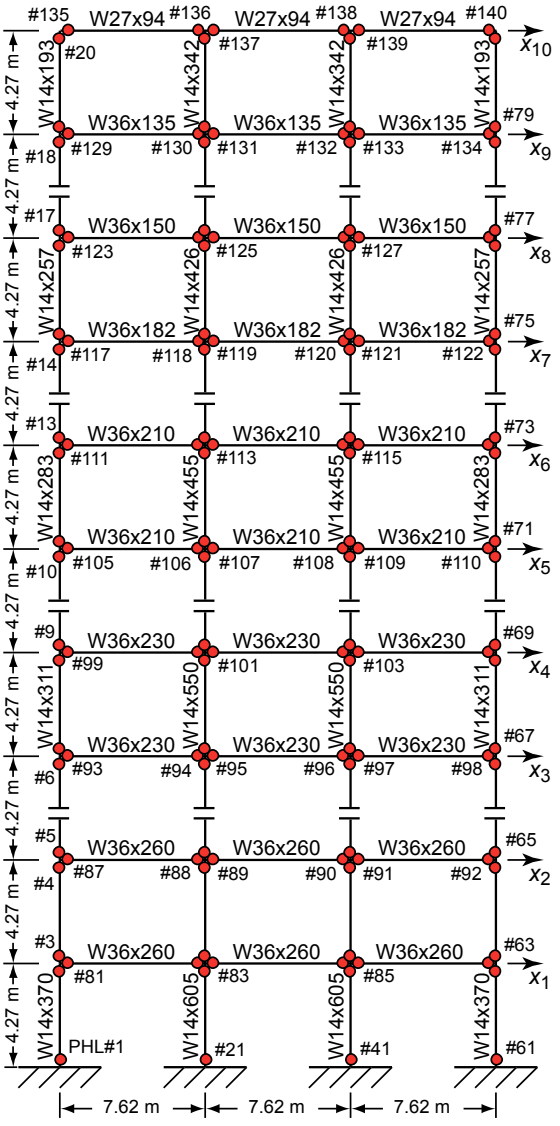


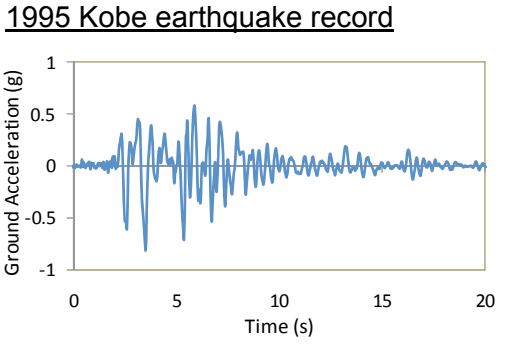
Figure 1. Flowchart for deriving the fully nonlinear response history analysis.

NUMERICAL SIMULATION

Consider a 10-story moment-resisting steel frame as shown in Figure 2. Let the mass be 218.9 Mg on each floor. This gives 10 elastic periods of vibration based on $\mathbf{K}_e$ as summarized in the figure. The damping is assumed to be 3% in all modes for the purpose of this study, even though larger damping ratio may be used in the higher modes which can be easily adjusted in any modal analysis that uses modal coordinates as the mathematical representation. A total of 140 PHLs as shown in Figure 2 are used in the analysis, all of which are assumed to exhibit elastic-plastic behavior with

moment capacity $m_c = \sigma_Y Z$, where $\sigma_Y = 248.2$ MPa is the yield stress of steel, and Z is the plastic section modulus of the member. All beams are subjected to a 21.89 kN/m uniform gravity load, while interaction between axial force and moment capacity is ignored in the columns. Gravity loads of 5,978 kN are applied on each floor of the *P*-Δ column to simulate the geometric nonlinearity of the global structure.





Mass: 218.9 Mg per floor

Dead Load: 21.89 kN/m per beam

P-Δ Column: 5,978 kN per floor

Mode	Period (s)	Damping
1	1.546	3%
2	0.559	3%
3	0.339	3%
4	0.237	3%
5	0.181	3%
6	0.148	3%
7	0.123	3%
8	0.105	3%
9	0.094	3%
10	0.082	3%

Figure 2. Ten-story moment-resisting steel frame model with earthquake record.

To demonstrate the accuracy and efficiency of the current NMA algorithm, the NMA structural responses using all 10 modes subjected to the 1995 Kobe earthquake ground motion as shown in Figure 2 are compared to those obtained using Perform-3D (P3D) and SAP2000 (SAP). Since no interaction between axial force and moment capacity is assumed in this study, only moment hinges are used to model all the PHLs for both beams and columns in P3D. Nonlinear link elements are used to model the plastic hinges in SAP, since the computation will be very time-consuming if the plastic hinges in the beam element are explicitly modeled in the

program. The global displacement, velocity, and absolute acceleration responses at the selected floors between various analysis methods are compared in Figures 3, 4, and 5, respectively. The local plastic rotations at selected beam and column PHLs using both NMA and P3D are also compared in Figure 6. Table 1 summarizes the computation time of each analysis method.

Table 1. Computing time of various programs of fully nonlinear dynamic analysis.

	NMA	P3D	SAP-DI	NMA(v)
Computing Time* (1.0 × Kobe)	107 s	78 s	940 s	19 s
Computing Time* (1.3 × Kobe)	109 s	85 s	1,146 s	22 s

* Based on 32-bit desktop computer with 2.4 GHz Intel processor and 3 GB RAM.

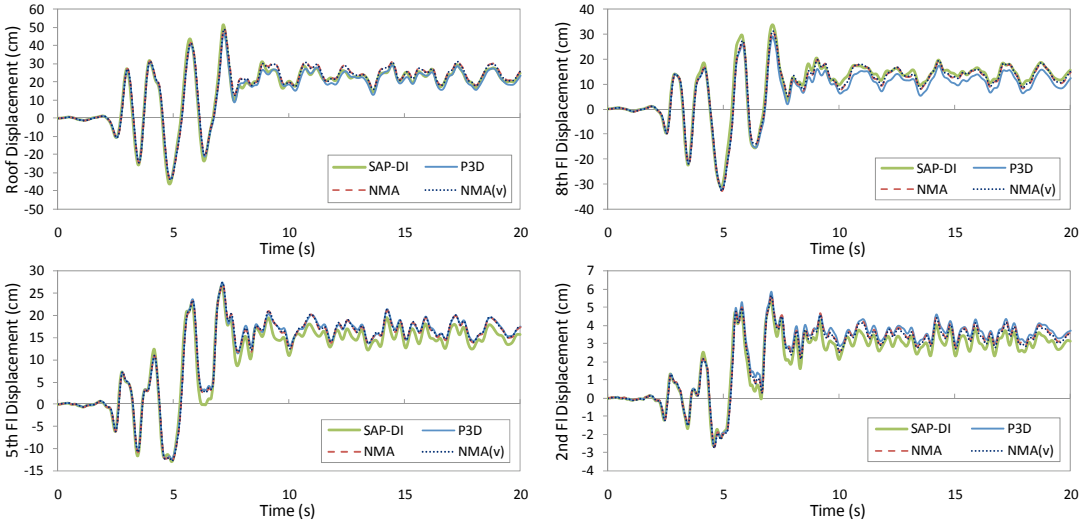


Figure 3. Comparison of displacement responses at selected floors due to 1.0 × Kobe.

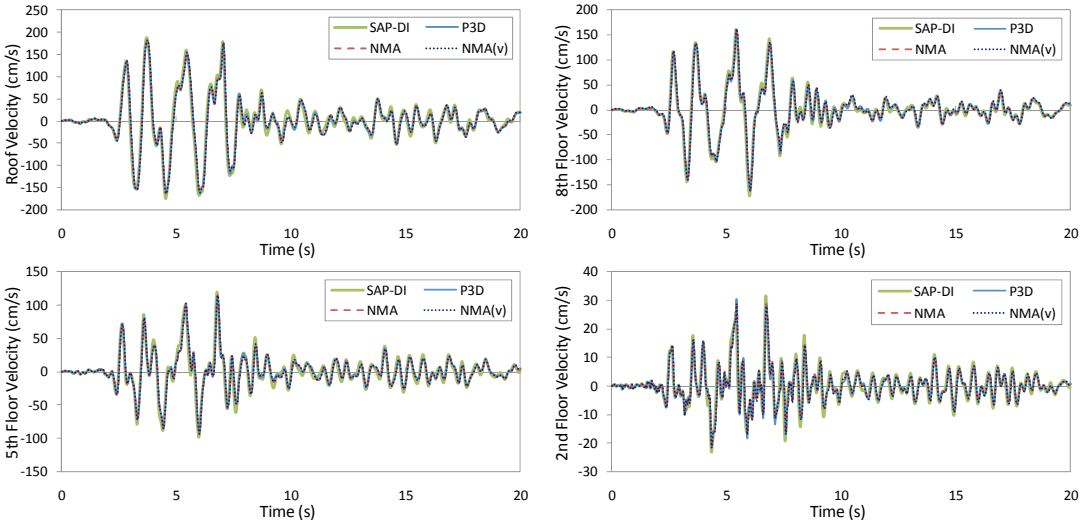


Figure 4. Comparison of velocity responses at selected floors due to 1.0 × Kobe.

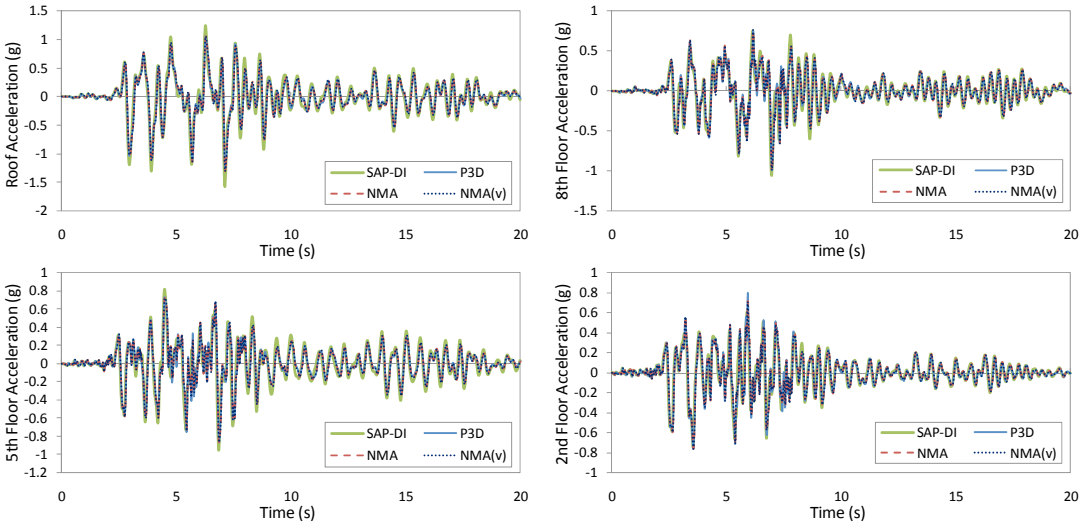


Figure 5. Comparison of acceleration responses at selected floors due to 1.0 × Kobe.

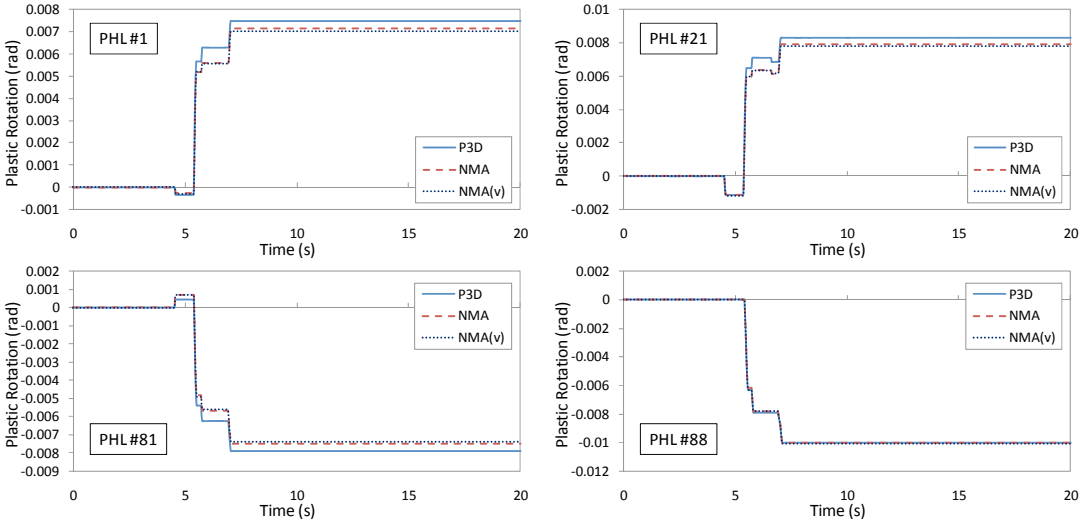


Figure 6. Comparison of plastic rotation at selected PHLs due to 1.0 × Kobe.

Comparison of Table 1 suggests that the computation using the NMA algorithm is quite time-consuming when the change in stiffness for $\mathbf{K}_G(t)$ matrix is updated at every time step. Since the elastic stiffness matrix $\mathbf{K}_e$ has already taken into consideration the local *P*-δ effects due to gravity loads and also the global *P*-Δ effects due to both gravity and earthquake loads in the proposed algorithm, it is sensible to consider another case of NMA where no update is performed (i.e., set $\mathbf{K}_G(t) = \mathbf{0}$), denoted here as NMA(ν). This gives $\vec{f}_{Gi}(t) = 0$ for all modes according to Eq. (15), which eliminates the need to update the local *P*-δ effects due to earthquake loads. Results using NMA(ν) are also shown in Figures 3 to 6 and Table 1 for comparisons.

Figures 3 to 6 show that results from both NMA (i.e., full update) and NMA(ν) (i.e., no update) compare well with other methods of analysis, demonstrating the accuracy and efficiency of the proposed NMA algorithms. It is therefore quite motivating to study the structural responses with greater nonlinear effects, such as at a

limit state of near collapse, by magnifying the ground motion. At this collapse prevention limit state, significant geometric nonlinearity comes into play, which may cause greater differences in the results between NMA and NMA(ν). Similarly, greater material nonlinearity is expected for larger earthquake while causing soft stories in the structure to become more apparent, which can give an indication as to whether the structure is properly designed according to the modern building code.

By subjecting the 10-story frame to the 1995 Kobe earthquake ground motion (all shown in Figure 2) with an amplification factor of 1.3, the global displacement, velocity, and absolute acceleration responses between various analysis methods are compared in Figures 7, 8, and 9, respectively. The local plastic rotations at selected beam and column PHLs using both NMA and P3D are compared and shown in Figure 10. In addition, the computation time of each analysis method due to the Kobe earthquake record with an amplification factor of 1.3 has been summarized in Table 1.

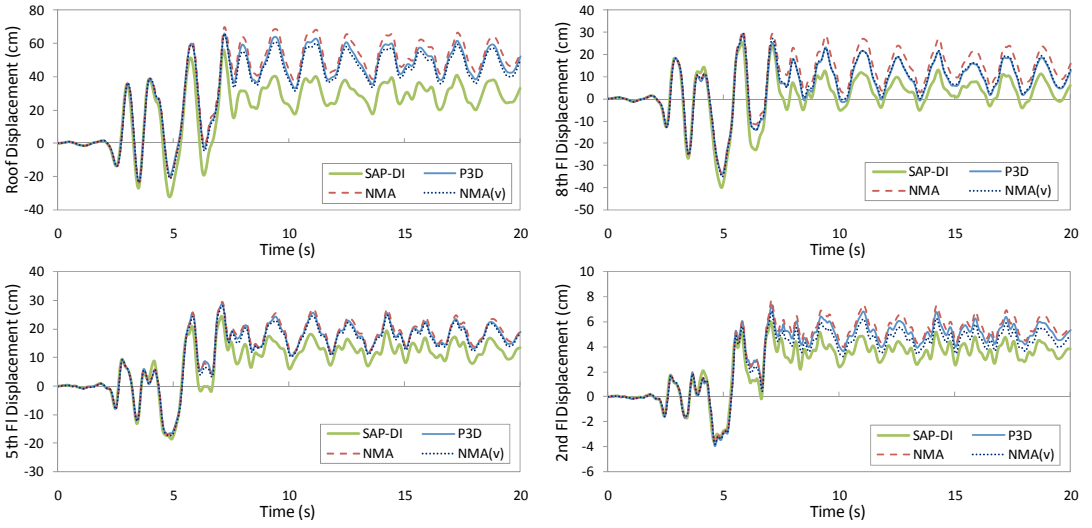


Figure 7. Comparison of displacement responses at selected floors due to 1.3 × Kobe.

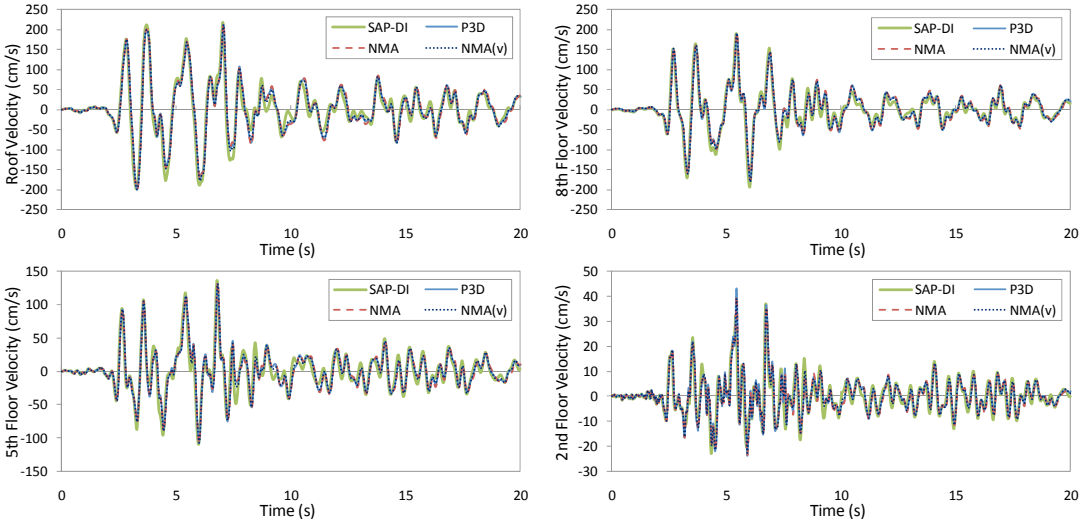


Figure 8. Comparison of velocity responses at selected floors due to 1.3 × Kobe.

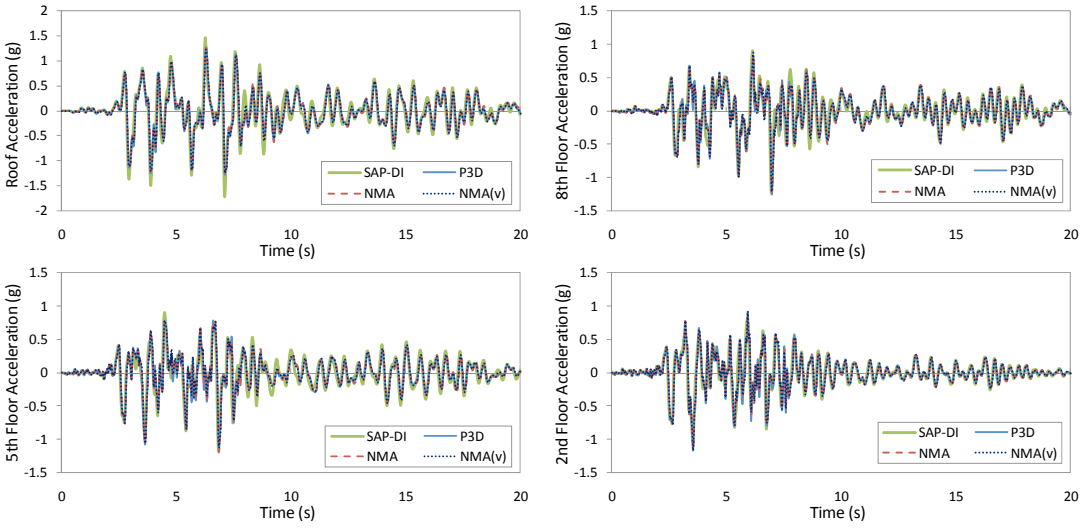


Figure 9. Comparison of acceleration responses at selected floors due to 1.3 × Kobe.

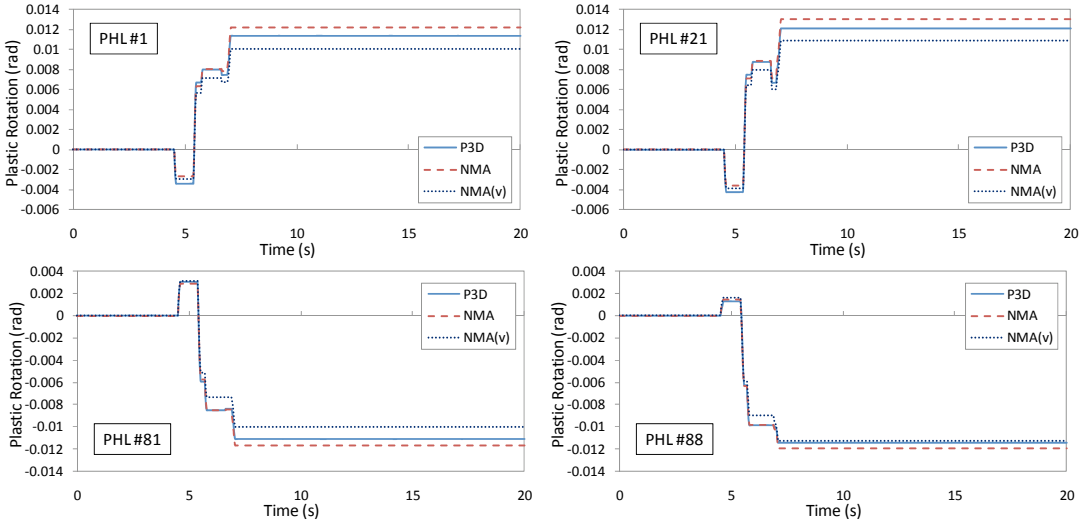


Figure 10. Comparison of plastic rotation at selected PHLs due to 1.3 × Kobe.

Comparison of results in Figures 7 to 10 again demonstrates the accuracy and efficiency of the proposed NMA algorithms. In particular, NMA(v) results seem to be very close to the NMA results and those from Perform-3D, indicating that updating the time-varying nonlinear stiffness matrices due to geometric nonlinearity may not be an important concern in performing nonlinear response history analysis. However, further study, particularly using taller structural models loaded up to near collapse, is necessary to prove this point.

CONCLUSIONS

A nonlinear dynamic analysis algorithm for computing the dynamic response of structures subjected to earthquake excitation based on modal superposition was presented. This algorithm combined the force analogy method, state space method, and

stability functions while transforming the analysis into the modal coordinates. Although modal coupling occurs because of the material and geometric nonlinearities in the analysis, this coupling is decomposed back into each mode using equivalent modal forces. By using the proposed algorithm, numerically simulated results were compared with those obtained from Perform-3D and SAP2000, and excellent agreement was obtained. These results demonstrate that the proposed algorithm has the potential of becoming a useful scientific computing tool that contains high accuracy and efficiency. More importantly, it has the potential of expanding the scope of nonlinear response spectra analysis that may have a greater impact on seismic design.

DISCLAIMER

Certain commercial software may be identified in this paper in order to specify the analytical procedure adequately. Such identification is not intended to imply recommendation or endorsement by the National Institute of Standards and Technology (NIST), nor is it intended to imply that the software identified are necessarily the best available for the purpose.

REFERENCES

Au, F. T. K. and Yan, Z. H. (2008). "Dynamic analysis of frames with material and geometric nonlinearities based on semi-rigid technique." *International Journal of Structural Stability and Dynamics*, 8(3), 415-438.

Chao, S. H. and Loh, C. H. (2007). "Inelastic response analysis of reinforced concrete structures using modified force analogy method." *Earthquake Engineering and Structural Dynamics*, 36(12), 1659-1683.

Liu, J. L. (2003). "Exact solution for dynamic response of multi-degree-of-freedom bilinear hysteretic systems." *Journal of Engineering Mechanics*, ASCE, 129(11), 1342-1350.

Liu, J. L. (2005). "Exact solution of nonlinear hysteretic responses using complex mode superposition method and its application to base-isolated structures." *Journal of Engineering Mechanics*, ASCE, 131(3), 282-289.

Newmark, N. M. (1959). "A method of computation for structural dynamics." *Journal of Engineering Mechanics Division*, ASCE, 85, 67-94.

Wilson E. (2002). *Three-Dimensional Static and Dynamic Analysis of Structures - A Physical Approach with Emphasis on Earthquake Engineering*, 3rd Edition, Computer and Structures Inc., Berkeley, CA.

Wong, K. K. F. and Yang, R. (1999). "Inelastic dynamic response of structures using force analogy method." *Journal of Engineering Mechanics*, ASCE, 125(10), 1190-1199.

Yang, R., Wong, K. K. F., and Pan, T. C. (2004). "Predictive inelastic state control of modern structures during earthquakes." *Journal of Structural Control and Health Monitoring*, 11(4), 291-309.

Zhang, X., Wong, K. K. F., and Wang, Y. (2007). "Performance assessment of moment resisting frames during earthquakes based on force analogy method." *Engineering Structures*, 29(10), 2792-2802.

Zhao, D. F. and Wong, K. K. F. (2006). "New approach for seismic nonlinear analysis of inelastic framed structures." *Journal of Engineering Mechanics*, ASCE, 132(9), 959-966.

Use of Nonlinear Analysis in the Context of the ASCE 7 Seismic Load Provisions

Finley A. Charney[1]

[1]Virginia Tech, Department of Civil and Environmental Engineering, 200 Patton Hall, Blacksburg, Virginia, 24061; PH (540) 231-1444; email: fcharney@vt.edu

ABSTRACT

This paper describes the use of nonlinear analysis within the context of the ASCE 7 seismic load provisions. The methods of analysis that are discussed include P-Delta analysis, nonlinear static analysis, and nonlinear dynamic analysis. All methods of analysis are discussed at the systems (entire structure) level. The use of nonlinear static analysis to perform sub-system evaluation is also described. Also provided in the paper is an assessment of the adequacy of the current analysis techniques in the context of advances that have been made in computational power and analysis capabilities over the last 40 years. Recommendations for improvements in the ASCE 7 analysis procedures are provided at the end of the paper.

INTRODUCTION

The use of nonlinear analysis is becoming more common in structural earthquake engineering, even though ASCE 7 (ASCE, 2010) does not require any form of nonlinear analysis for "traditional" buildings that do not incorporate seismic isolation or passive energy systems. Nonlinear dynamic response history analysis is permitted for traditional systems, and requirements for performing such analysis are provided in Chapter 16 of the ASCE 7. When used, nonlinear dynamic analysis is performed on the system level, meaning that the entire structure is analyzed, and the analysis forms the basis for deciding if the design is acceptable. Currently, the main use of nonlinear dynamic analysis is to assess the performance of buildings that do not satisfy height limits, or for which values of R, C_d, and Ω_o are not provided.

ASCE 7 does not list nonlinear static pushover analysis as permitted method, and for that reason, it does not provide any requirements for performing such analysis. ASCE 41 (ASCE, 2007) allows pushover analysis under certain circumstances, and provides requirements for performing such analysis. Presumably, these procedures, where applicable, could be used in association with ASCE 7 if approved by the local building official, and if independently reviewed by a panel of experts.

While ASCE 7 does not permit nonlinear static analysis as the basis of system design and evaluation, there are cases where limited forms of such analysis would be useful. Examples of such analysis include assessment of weak story irregularities, computing story β factors in P-Delta analysis, and computation of story strength after removal of components as required for redundancy factor (ρ) evaluation. These uses for nonlinear static analysis are described later in this paper.

It is essential that P-Delta effects (a nonlinear effect in itself) be included in all seismic analysis. Currently, ASCE 7 is set up such that linear analysis should not directly include P-Delta effects. Instead, such effects are evaluated through the use of displacement and force magnifiers that are computed on the basis of the results of first order static analysis. This method is seriously flawed because it does not capture the effects of residual inelastic deformations, and it is these deformations that lead to dynamic instability and collapse of some structures.

In the remainder of this paper the above issues are addressed in some detail, starting with P-Delta analysis, moving next to nonlinear static analysis, and finally, nonlinear dynamic analysis.

P-DELTA ANALYSIS

Section 12.7.3 of ASCE 7 requires that P-Delta effects be included in structural modeling, but this is inconsistent with Eqn. 12.8-16 because the stability ratio, θ, determined from this equation should be based on displacements that do not include P-Delta effects. Eqn. 12.8-16 is as follows:

$$\theta = \frac{P_x \Delta I_e}{V_x h_{sx} C_d}$$

It is important to recognize that the stability ratio θ is simply the ratio of the "Geometric Stiffness" of the story (P_x/h_{sx}) to the "Elastic Stiffness" of the story ($V_x C_d / \Delta I_e$), and that when properly computed, θ is independent of the value of C_d and I_e.

If P-Delta effects are included in the analysis, it is permitted to divide the value of θ determined from equation 12.8-16 by the quantity (1- θ). This avoids the potential problem of including P-Delta effects twice in the same analysis. A more rational approach would be to run the analysis twice, once without P-Delta effects and once with P-Delta, and compute the stability ratio for each story as follows:

$$\theta = 1 - \frac{\Delta_o}{\Delta_f}$$

where Δ_o is the story drift computed without P-Delta, and Δ_f is the drift from the analysis which includes P-Delta effects. Where P-Delta effects are included in the analysis, member forces and displacements need not be multiplied by the quantity 1/(1- θ) because this effect is already included.

The stability ratio θ is not permitted to exceed $0.5/\beta C_d$, where β is "the ratio of shear demand to the shear capacity" of the story under consideration. Thus, β is the inverse of the over-strength of the story. Taking β as 1.0 is usually conservative,

but doing so may lead to situations where the limit on θ is exceeded. Unfortunately, the determination of β is not straightforward, even for simple systems such as moment resisting frames.

Consider, for example, the frame shown in Figure 1. If the columns are stronger than the girders, the story mechanism and the computed story strength shown in Part (a) of the figure may be used. For weak column - strong beam systems, the mechanism and computed strength indicated in part (b) of the figure is applicable. Both of the equations shown in Figure 1 come from the commentary of the AISC Seismic Provisions (AISC, 2005). Mechanism (a) is reasonable for special moment frames, but may not be applicable to ordinary or intermediate moment frames where the columns might be weaker than the beams. Some might argue that mechanism (a) is not viable because it cannot occur unless hinges form at mid-height of the columns above and below the level where the girder hinges form. This hinge formation is not possible for strong column systems. The use of nonlinear static analysis to determine story strength and the story β factor is discussed later in this paper.

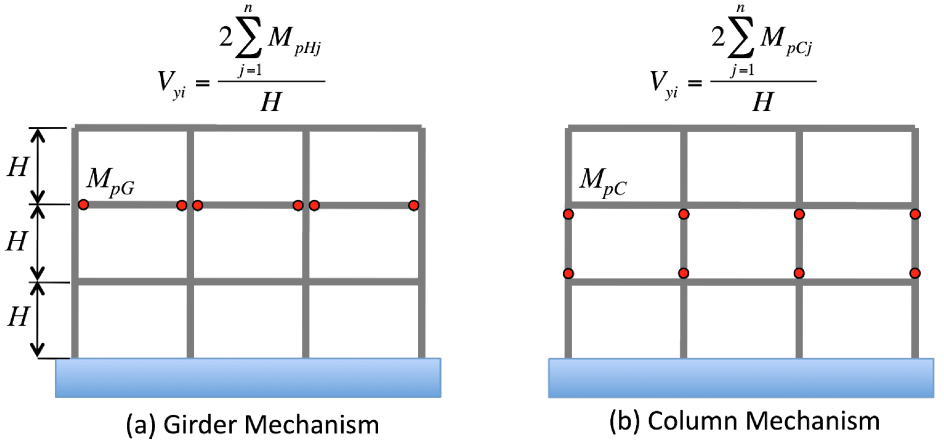


Figure 1. Computing Story Capacity for P-Delta Effects

The stability ratio computed by Eqn. 12.8-16 is a reasonable measure of the sensitivity of elastic structures to P-Delta effects. However, modification of member forces and displacements by the quantity 1/(1- θ) is not reasonable, particularly when θ exceeds 0.1. This is because inelastic dynamic response of systems with larger values of θ tend to have large residual deformations, and these deformations, which are not included in linear analysis, may eventually result in dynamic instability and collapse.

This problem is well known (e.g Gupta and Krawinkler, 2000), and several attempts have been made to modify ASCE 7 to provide more rational methods to assess the significance of P-Delta effects. One approach which was not approved for ASCE 7-10 is described in Part 1 of the *2009 NEHRP Recommended Seismic Provisions* (FEMA, 2010). This procedure establishes the upper limit on θ as 0.1, unless a nonlinear pushover analysis indicates that the post-yield slope of the

pushover curve is continuously positive up to the Target Displacement as defined by ASCE 41 (ASCE, 2007). The pushover analysis should include P-Delta effects, and must include degradation of strength. Alternatively, values of θ in excess of 0.1 may be allowed if it is demonstrated that the system complies with the requirements of nonlinear dynamic analysis as stipulated in Chapter 16 of ASCE 7. Peer review is required for either method of analysis.

NONLINEAR STATIC ANALYSIS

Nonlinear static analysis is not a "permitted" method of analysis in Table 12.6-1 of ASCE 7, and therefore cannot be used as the basis for designing the entire structural system. However, there are cases where nonlinear static analysis would be useful within the context of an ASCE 7 analysis and design:

1. *Determination of the presence of Lateral Strength-Weak Story or Lateral Strength– Extreme Weak Story irregularities*. Such irregularities are evaluated on the basis of the ratio of the lateral strength of two adjacent stories. If the strength of the lower story is less than 80 percent of the strength of the upper story the Weak Story irregularity exists, and if the strength of the lower story is less than 65% of the strength of the upper story, an Extreme Weak Story irregularity exists.

2. *Determination of the redundancy factor, ρ.* For certain situations this factor is evaluated by determining if the story strength is reduced by more than 33% when a key component of that story (e.g. a brace) is removed from the system. This approach is demonstrated in a redundancy factor example prepared by Charney (2010).

3. *Computation of the factor β which is used to determine the upper limit on the computed story stability ratios, θ associated with P-Delta analysis.* The β factor is the ratio of the factored seismic demand to the story capacity.

4. *Determination of the horizontal seismic load effect with overstrength, E_{mh}.* Generally, this factor is taken as $\Omega_o Q_e$, but an exception states that E_{mh} need not be taken as greater than the maximum force that can develop in the element as determined from a rational plastic mechanism analysis or nonlinear analysis utilizing realistic expected values of material strengths.

For items 1 and 3 above, analysis could be as simple as that shown in Figure 2, where a limited pushover analysis is used to determine the strength of a story of a moment frame. For item 2 a full three dimensional nonlinear static analysis analysis would be required. It might be possible to establish substructure models for item 4, but the larger models developed for items 1 through 3 could be utilized. Relatively simple force-deformation relationships (not including strength degradation) could be used for each of the situations because all that is required from the analysis is the computation of story strength.

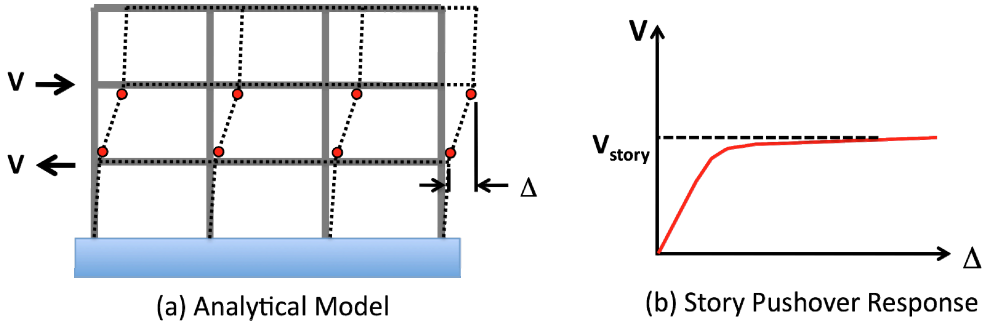


Figure 2. Using Pushover Analysis to Determine Story Strength

While not a required part of an ASCE 7 evaluation, several other aspects of the system performance could be developed using nonlinear static analysis. These include the following:

1. More realistic assessment of the potential for dynamic instability by using a nonlinear static pushover analysis to determine if the post-yield slope of the pushover curve is positive up to the target displacement.

2. Assessing the system compliance with strong column – weak beam requirements of ACI 318 and ANSI/AISC 341.

3. Visualization of the sequence of yielding, assessment of system over strength, and assessment of overall system ductility.

The above three points would require a more detailed model than required for the code compliance assessments listed earlier.

NONLINEAR DYNAMIC RESPONSE HISTORY ANALYSIS

Nonlinear Response History Analysis is generally used when the structure being designed does not adhere to the system limitation requirements of Table 12.2-1 of ASCE 7, or when the system is not listed in the table. The authority to circumvent Table 12.2-1 is provided in Section 12.2.1. The most common use of NHRA is in association with the design of tall buildings, wherein the structural system exceeds the height limitations of Table 12.2-1, or where a hybrid system, such as an outriggered core-wall is used. The Chapter 16 guidelines for performing the analysis define the basic requirements in terms of selecting and scaling of ground motions, modeling criteria, determination of design values for member forces and deformations, and acceptance criteria. However, these requirements are lacking in detail, and should be supplemented with a variety of guidelines that have been published, including those produced by the Structural Engineers Association of Northern California (SEAONC, 2007), the Los Angeles Tall Buildings Council (LATBC, 2008), the Council for Tall Buildings and Urban Habitat (CTUBH, 2008),

FEMA (2009), the Pacific Earthquake Engineering Research Center (PEER, 2010), and the National Institute for Standards and Technology (NIST, 2010).

While nonlinear dynamic analysis is generally regarded as the best method of analysis available, there are a number of barriers to a broad acceptance in the design community. These barriers include the lack of a comprehensive design basis that makes direct use of the analysis, concerns (real or perceived) about the complexity of the analysis, a general lack of training in dynamic response history analysis and in nonlinear analysis, and the necessity to select and scale aground motions for the analysis.

The placement of the linear and nonlinear dynamic analysis procedures in a separate chapter (Chapter 16) is also a barrier to acceptance. In the author's opinion the ground motion selection and scaling aspects of Chapter 16 should be moved into Chapter 11, and the analysis procedures should be moved into Chapter 12. This would generate the impression that linear dynamic and nonlinear dynamic analyses are simply two tiers of a hierarchy of increasingly sophisticated (and presumably increasingly accurate) methods of analysis.

While it would be effective, the above recommendation retains the rest of Chapter 12, which is seriously outdated. A better approach would be to completely rewrite Chapter 12 in terms of a comprehensive approach that utilizes both linear and nonlinear analysis in rational ways. The next section of this paper provides an outline for such an approach.

NONLINEAR ANALYSIS IN FUTURE EDITIONS OF ASCE 7

The current edition of ASCE 7 [ASCE 7-10] has evolved primarily from the ATC 3-06 *Tentative Provisions for the Development of Seismic Regulations for Buildings* (ATC, 1976). This document was published in 1978, before personal computers were generally available, and before nonlinear static or dynamic analysis was practical outside of a research environment. With the exception of the nonlinear dynamic analysis procedures that are provided in Chapter 16 of ASCE 7-10, code provisions for performing analysis for new buildings have remained relatively stagnant since 1978. Given that ASCE 7 will not be updated until 2016 and adopted until 2018, forty years could pass without any significant changes to the required analysis procedures in ASCE 7.

In the same 40 years, very significant advances will have been made in computer capacity and availability, and nonlinear static and nonlinear dynamic response history analysis will be available through number of commercially available programs. While not entirely automatic, the programs simplify some of the more tedious tasks associated with nonlinear modeling, even going so far as to provide "standard" force-deformations relationships that comply with ASCE 41. As mentioned earlier, there are several detailed sets of recommendations for performing nonlinear dynamic analysis, including those provided by Chapter 16 of ASCE 7-10.

Given all the advances over the past 40 years, one can wonder why the seismic provisions have not caught up. In the Author's opinion, part of the problem is that advanced analysis procedures are basically incompatible with the current analysis philosophy, which is based on two-dimensional linear procedures and a variety of ad-hoc corrections to account inelastic behavior, three-dimensional behavior, and dynamic response. Thus, the only way to remedy the situation is to start with a clean slate, and develop an analysis procedure that is consistent with modern technology, and with the principles of performance based design. The basic tenants of the new analysis method should be as follows:

1. The Equivalent Lateral Force method would be used only for preliminary analysis.

2. All analysis should be performed in three dimensions.

3. Diaphragms should be modeled as semi rigid.

4. All final analysis should directly incorporate P-Delta effects, and the sensitivity to such effects should be based on a comparison of results with and without P-Delta effects included.

5. The analytical model should be developed such that, at the minimum, a nonlinear static pushover analysis can be performed. The pushover model would be used to evaluate weak story irregularities, determine system redundancy factors, establish system and component overstrength requirements, assess the compliance with strong column - weak beam requirements, assess the likelihood of dynamic instability associated with P-Delta effects, and determine (in association with other factors) the required final level of analysis.

6. Based on the results of (5) above, the final analysis should be either a linear or nonlinear dynamic response history analysis. Analysis would be based on standardized suites of ground motions, scaled appropriately.

7. Accidental torsion should be included by adjustment of the center of mass of the floor diaphragms.

8. All analysis should include simultaneous application of the ground motions in two orthogonal directions.

9. Acceptance criteria for deformation should be based on shear-strain based damage measures, wherein such strains are monitored at the corners of the building. Acceptance would be based on mean response for both linear and non linear analysis, but nonlinear analysis results would be studied in sufficient detail to determine if outliers pose a significant risk.

A key aspect of the requirements would come in point (5) above where the decision is made whether or not to perform a nonlinear dynamic analysis. This decision could be based on a number of factors, including occupancy category, sensitivity to P-Delta effects, sensitivity to torsional response, type of hysteretic behavior, and use of seismic isolation or passive energy systems. Linear dynamic analysis would most likely be used for the majority of structures. Tola (2010) has shown that linear response history analysis is a very effective replacement for the equivalent lateral force method and the modal response spectrum methods of analysis.

There are numerous advantages to the above approach, and among the most significant is that inelastic behavior is explicitly investigated for all structures. The use of linear response history analysis as the "basic" method would be beneficial because analysts would use such procedures to develop expertise in performing response history analysis, and this would be very useful preparation for those circumstances where nonlinear dynamic analysis would be required. The required inelastic modeling of all structures would also provide useful experience in those cases that nonlinear dynamic analysis is ultimately required. An additional benefit of the above approach would be the direct incorporation of performance based design principles, and unification with the methods of analysis that are used to assess the performance of existing buildings.

REFERENCES

AISC (2005). *Seismic Provisions for Structural Steel Buildings* (ANSI/ASCE 341-05), American Institute of Steel Construction, Chicago, Illinois.

ASCE (2007). *Seismic Rehabilitation of Existing Buildings* (ASCE 41-06), American Society of Civil Engineers, Reston, Virginia.

ASCE (2010). *Minimum Design Loads for Buildings and Other Structures* (ASCE 7-10), American Society of Civil Engineers, Reston, Virginia.

ATC (1976). *Tentative Provisions for the Development of Seismic Regulations for Buildings*, Applied Technology Council, Redwood City, California.

Charney, F.A. (2010). *Seismic Loads: Guide to the Seismic Load Provisions of ASCE 7-10*, ASCE Press, American Society of Civil Engineers, Reston Virginia.

CTUBH (2008). *Recommendations for the Seismic Design of Tall Buildings*, Council on Tall Buildings and Urban Habitat, Chicago, Illinois.

Deierlein, Gregory G., Reinhorn, Andrei M., and Willford, Michael R. (2010). "Nonlinear structural analysis for seismic design," NEHRP Seismic Design Technical Brief No. 4, National Institute of Standards and Technology, Gaithersburg, MD, NIST GCR 10-917-5.

FEMA (2009). *Recommended Seismic Provisions for New Buildings and Other Structures* (FEMA P-750), Federal Emergency Management Agency, Washington, D.C.

Gupta and Krawinkler (2000). "Dynamic P-Delta Effects for Flexible Inelastic Steel Structures", *Journal of Structural Engineering*, 126(1):145-154.

LATBC (2008*). An Alternative Procedure for Seismic Analysis and Design of Tall Buildings Located in the Los Angeles Region*, Los Angeles Tall Building Structural Design Council, Los Angeles, California.

PEER (2010). *Modeling and Acceptance Criteria for Seismic Design and Analysis of Tall Buildings* (PEER/ATC 72-1), Pacific Earthquake Engineering Research Center, Richmond California.

SEAONC (2007). *Recommended Administrative Bulletin on the Seismic Design and Review of Tall Buildings Using Non-Prescriptive Procedures*, Structural Engineers Association of Northern California, San Francisco, California.

Tola, Adrian (2010). *Assessment of the ASCE 7-10 Procedures for Performing Linear Response History Analysis of Structures*, M.S. Thesis, Department of Civil and Environmental Engineering, Virginia Tech, Blacksburg, Virginia.

SEISMIC RETROFIT OF PRE-NORTHRIDGE STEEL MOMENT FRAME BUILDING USING NONLINEAR STATIC ANALYSIS PER ASCE 41-06

Methee Chiewanichakorn[1], Luis Toranzo[2] and Aaron Reynolds[3]

[1]*KPFF* Consulting Engineers, 6080 Center Dr., Suite 300, Los Angeles, CA 90045, U.S.A., PH (310) 665-1536; FAX (310) 665-9070: email: mchiewanichakorn@kpff-la.com
[2]*KPFF* Consulting Engineers, 6080 Center Dr., Suite 300, Los Angeles, CA 90045, U.S.A., PH (310) 665-1536; FAX (310) 665-9070: email: ltoranzo@kpff-la.com
[1]*KPFF* Consulting Engineers, 6080 Center Dr., Suite 300, Los Angeles, CA 90045, U.S.A., PH (310) 665-1536; FAX (310) 665-9070: email: areynolds@kpff-la.com

ABSTRACT

The need to perform cost-effective seismic rehabilitation of essential facilities has made the use of nonlinear analysis techniques an attractive option. The estimation of seismic demands on structures requires explicit consideration of the structural inelastic behavior. Therefore, nonlinear procedures such as pushover analyses are inevitably going to be more widely used.

This paper presents a case study of a 10-story Pre-Northridge steel moment frame hospital building in California that was analyzed using nonlinear pushover analysis approach. Nonlinear force-deformation relationships and acceptance criteria of primary structural components were modeled in accordance to ASCE 41-06 and supplemented by experimental component testing results. Given the nature of steel moment frame buildings constructed during this era, existing connections are highly susceptible to damages during a major earthquake which could lead to an unfavorable failure mechanism. Based on nonlinear pushover analysis results, potential structural deficiencies will be identified and different rehabilitation methods will be presented. Besides, the comparisons of retrofit scopes between conventional and nonlinear methods will be highlighted.

Finally and most importantly, this paper also addresses some challenges found by the authors in the implementation of nonlinear pushover analysis in seismic retrofit application, as well as recommendations from practitioner perspectives.

INTRODUCTION AND BACKGROUND

This paper covers the process followed to improve the seismic performance of an existing non conforming hospital building in Southern California, so that it meets the requirements of current California seismic regulations. Back in 1994 Senate Bill 1953 (SB 1953) was passed as an amendment to the Alfred E. Alquist Hospital Seismic Safety Act of 1983 (Alquist Act), which was enacted to emphasize that essential facilities such as hospitals should remain operational after an earthquake.

The provisions of SB 1953 were developed to regulate the seismic performance of numerous existing, mostly pre-1973 buildings, which were not addressed by the original Alquist Act. SB 1953 established that hospital owners must conduct seismic evaluations on all pre-1973 hospital buildings providing critical care services, and implement seismic rehabilitations if needed.

The purpose of the paper is to examine the effectiveness and benefits of a nonlinear static procedure for the seismic analysis and retrofit design of an existing steel moment frame building. This subject building is on one of the mid-rise hospital buildings located in San Diego, California. The building was constructed in the early 70's using a steel moment frame as lateral system, with Pre-Northridge moment connections, and it is a non-compliant building per 2007 CBC (ICC 2007).

In order to meet the code requirements, the building was analyzed and will be retrofitted based on the results from nonlinear pushover analysis. By implementing this advanced analysis approach, the building's seismic performance was better understood and led to a more efficiently use of retrofit methods. The basis of the seismic analysis and design process is Chapter 34A of 2007 California Building Code (CBC), which in turn, references ASCE 41-06 *Seismic Rehabilitation of Existing Buildings* (ASCE 2007) with some modifications.

BUILDING DESCRIPTIONS

The subject building, a hospital building in San Diego, California, was constructed in 1973 and is a non-conforming building as defined in SB 1953. The building has eight stories above grade, with a roof-top mechanical penthouse. The building has a rectangular shape, measuring approximately 110 feet by 100 feet. The construction consists of light-weight and normal-weight concrete filled metal deck over wide flange steel girder system. The foundation system consists of isolated spread footing below all columns. The lateral force resisting system consists of steel moment frames. Figure 1 shows a three-dimensional view of the building and Figure 2 shows a typical East-West elevation of the building.

This building has two unique structural characteristics. Firstly, this building has a total of 10 moment frame columns and all of them would be subjected to bi-axial bending actions under seismic forces. Secondly, weld filler materials used at the moment connections were low-notch tough type, i.e., E70-T4 electrodes, which is non-compliance to the current code.

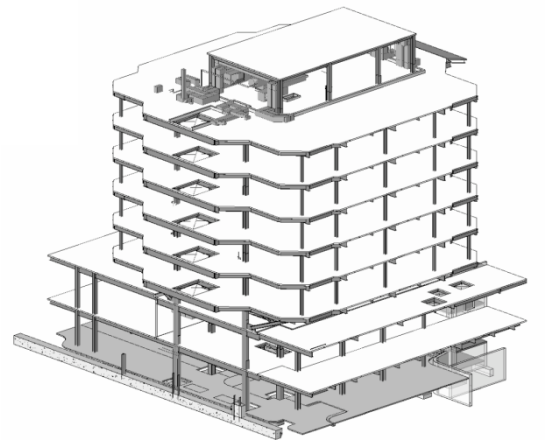


Figure 1. Three-dimensional view of the building

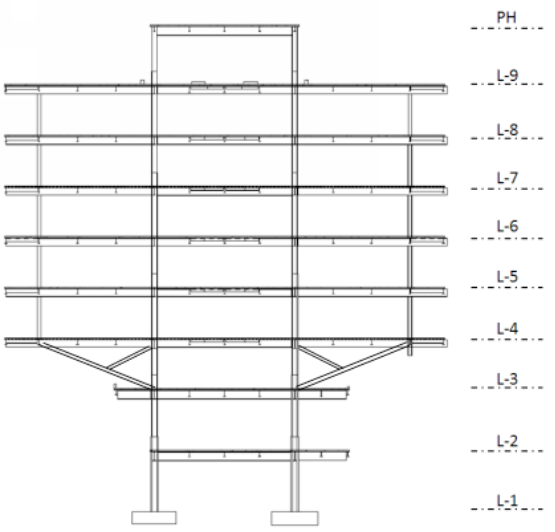


Figure 2. Typical East-West elevation of the building

ANALYTICAL MODELS

Geometrical Modeling

In the analytical model, only the primary lateral force resisting system (LFRS) of this building, steel moment frames, were modeled using Perform-3D (CSI 2006). Beams and columns were modeled using frame elements. Diaphragms were explicitly modeled using four-noded quadrilateral elements. Seismic masses were proportionally distributed on the diaphragm as nodal masses. The supports below each column were modeled as fixed base which mimics the condition of the proposed retrofitted foundation. Figure 3 shows a three-dimensional analytical model created in Perform-3D.

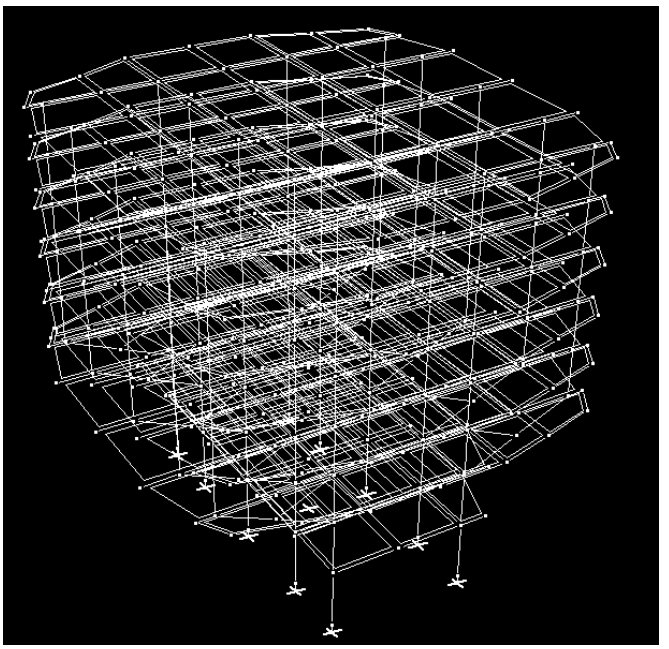


Figure 3. PERFORM-3D nonlinear model

Material Modeling

Material properties, based on a material testing program conducted for this project, were used to derive the non-linear backbone curves for plastic hinge behavior of steel beams and columns. In this project, the non-linear backbone curves given in ASCE 41-06 were implemented in the analysis for existing and retrofitted (i.e., welded top and bottom haunches) conditions. With the presence of the low-notch tough welds in the existing moment connection, cyclic test results are required by 2007 CBC to statistically substantiate the non-linear backbone curves used in the analysis. Experimental testing will be described later in this paper.

Diaphragms were modeled elastically as they were expected to remain elastic. During the course of analysis, if the diaphragm demands exceed the diaphragm capacity, inelastic materials would be used to capture the actual diaphragm behavior and force distributions.

In order to achieve the performance-based design objectives, inelastic behavior of each component had to be limited to the target building performance level which translated to the so-called acceptance criteria. "Life Safety" is the target building performance level of the retrofitted building and the associated acceptance criteria of each structural component are recommended by ASCE 41-06.

Column Bi-axial Bending Effects

As previously mentioned, the lateral-force resisting system of this building is provided by spatial steel moment frames with moment connected beam framing into both the strong- and weak-axes of the wide-flange columns. The purpose of this supplemental study is to show that the presence of a statically loaded transverse beam

in a bi-axial moment connection has a small effect on the cyclic behavior of a strong-axis and weak-axis moment connection.

The detailed analyses were performed by Professor Chia-Ming Uang his student at University of California, San Diego, using the general purpose finite element analysis software ABAQUS. The model simulate the moment connection with W24 beams in both directions, with the proposed retrofitted scopes, i.e., welded top and bottom haunches (FEMA 2000) and welded cover plate to strengthen the column weak-axis. Figure 4 shows the ABAQUS model of the retrofitted bi-axial moment connection.

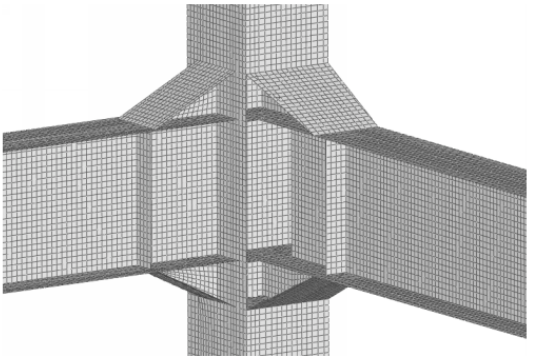
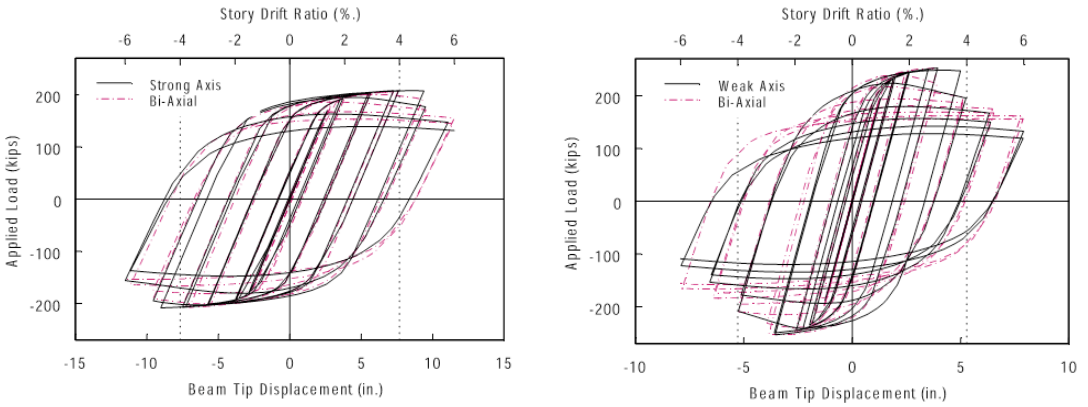


Figure 4. ABAQUS model of bi-axial moment connection

The cyclic loading protocol per AISC Seismic Provisions (AISC 2005) was imposed to the investigated beam end to simulate the story drift while the transverse beam was loaded statically to its expected plastic moment capacity. Figure 5a concludes that the global response of uni-axial bending and bi-axial bending is very similar when beam was cyclically loaded about the column strong-axis. Similar conclusion can be drawn for the beam cyclically loaded about the column weak-axis as shown in Figure 5b.

From this study, the bi-axial bending effect was not considered in the derivation of non-linear backbone relationship in the beam plastic hinges.



(a) Strong-axis bending **(b) Weak-axis bending**

Figure 5. Comparisons of hysteresis curves

Gravity and Lateral Load Modeling

Gravity loads and vertical component of seismic forces were applied as nodal and element loads on the primary lateral force resisting system. Self-weight of walls, beams and columns were included as part of gravity loads.

A fundamental mode lateral load pattern was used as recommended in ASCE 41-06. Fundamental mode load pattern is a vertical distribution proportional to the shape of the fundamental mode in the direction under consideration.

EXPERIMENTAL COMPONENT TESTING

The component testing is intended to serve two purposes in this project. Firstly, to validate the performance of moment connection with the presence of low-notch tough welds in the existing conditions. Secondly, to substantiate the non-linear modeling parameters and acceptance criteria of the retrofitted moment connections, as indicated in ASCE 41-06 that the non-linear modeling parameters and acceptance criteria can be derived using the experimentally obtained cyclic response characteristic of the subassembly.

The test specimens would closely represent the typical beam-to-connection connections in strong- and weak-axis of the building given that: (1) beam depth to column depth ratios will be essentially the same as those in the actual building, and (2) materials used for construction of the specimens will be representative of those used in the actual building.

A total of six specimens will be tested at the University of California at San Diego. All specimens represent the retrofitted condition using welded top and bottom haunches. Four specimens represent the beam bending about the column strong-axis and two specimens represent the beam bending about the column weak-axis.

The test set up shown in Figure 6 shows the vertical displacement δ_{act}, which is the control variable. The applied load will be monitored using a load cell, attached to the actuator. Each test specimen would be instrumented to measure the response quantities necessary to develop the non-linear backbone curves and acceptance criteria. The test specimens would be subjected to fully, reversed cyclic loading at increasing displacement levels in accordance with the loading protocol specified in the AISC Seismic Provisions (AISC 2005). Results for the specimens will be normalized to nominal strength and average backbone curves will be calculated. Design parameters and acceptance criteria will be developed based on the procedures outlined in Section 2.8.3 of ASCE 41-06 Supplement No.1.

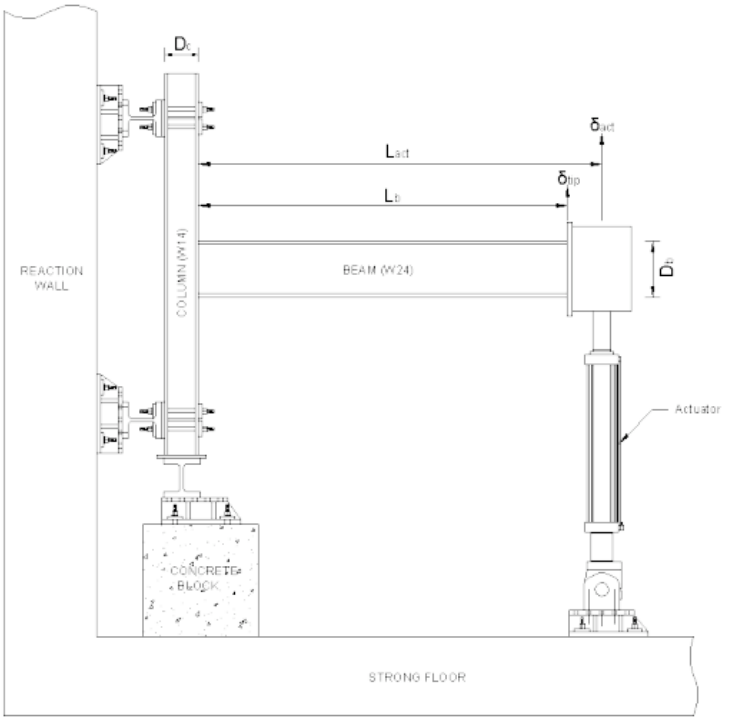


Figure 6. Experimental test set up at UCSD

RESULTS AND DISCUSSIONS

Overall Structural Performance and Mechanisms

Non-linear response of the building before and after retrofit can be illustrated in Figure 7 that compares the pushover curves of existing and retrofitted buildings in East/West and North/South directions. The solid lines represent the retrofitted condition while the dash lines represent the existing condition. It is clear that the overall structural responses are greatly improved after the building has been retrofitted both in strength and ductility.

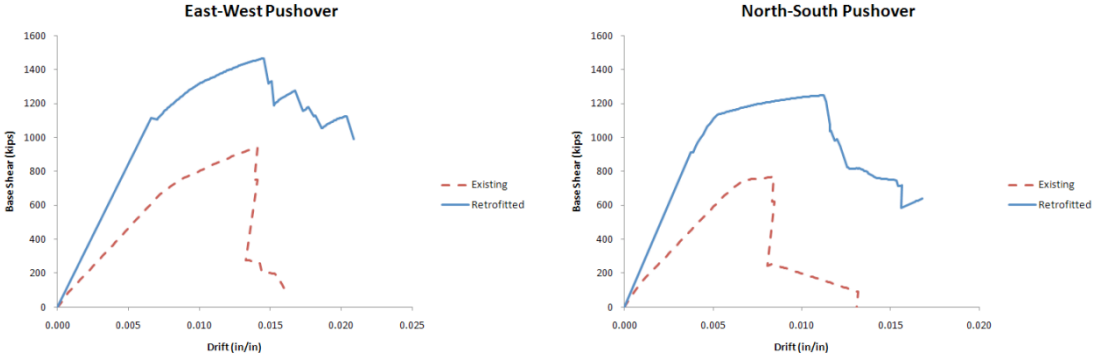


Figure 7. Pushover curves for existing and retrofitted structure

There are two main structural deficiencies of the existing building. Those are a soft-story and excessive inter-story drifts in the lower floors.

For soft-story mechanism, plastic hinges were formed in the columns between the 1st and 3rd floors. Figures 8a and 9a illustrate the soft-story mechanism of the existing building in the East/West and North/South direction, respectively. The red dots indicate the locations of potential plastic hinges. Soft-story mechanism is undesirable because of limited ductility which could lead to a potential loss of vertical load carrying ability. This explains an abrupt drop in the pushover curve of the existing building in Figure 7. As soon as the soft-story mechanism was developed, the structure loses the vertical load carrying capacity which will eventually lead to a structural collapse.

At the same time, excessive inter-story drifts at the lower floors, as shown in Figures 8a and 8b, would adversely increase P-Delta effects on the columns and eventually exacerbate the soft-story mechanism to develop much earlier.

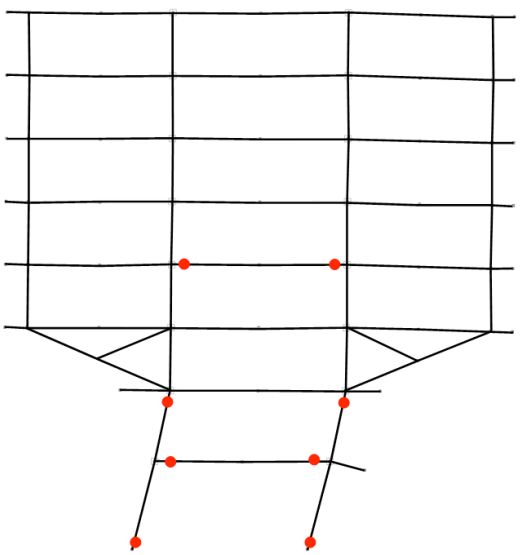


Figure 8a. Existing Structure (E/W)

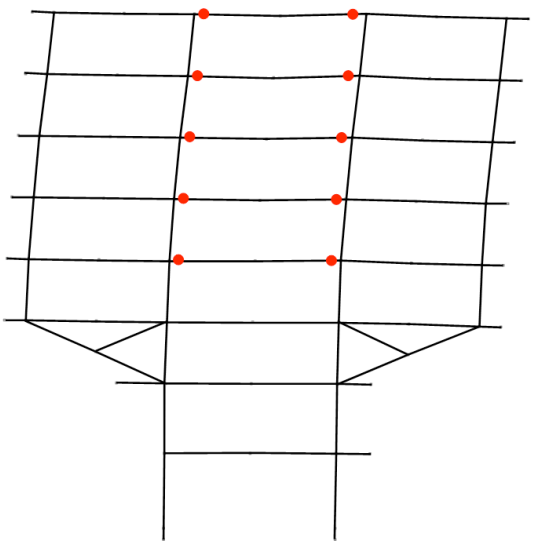


Figure 8b. Retrofitted Structure (E/W)

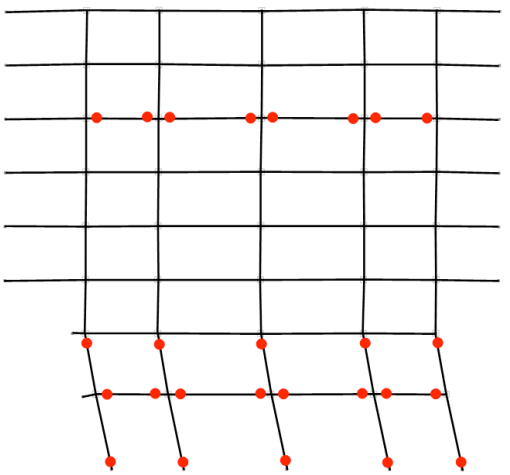


Figure 9a. Existing Structure (N/S)

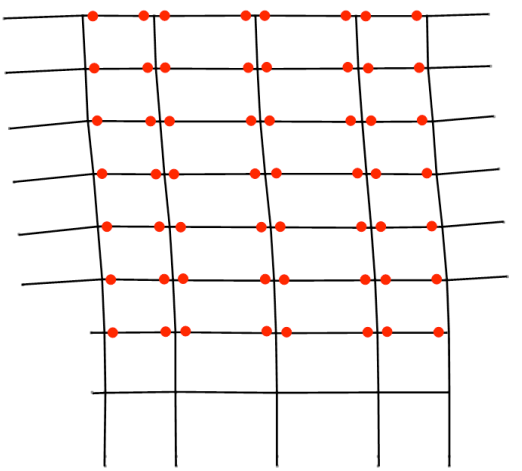


Figure 9b. Retrofitted Structure (N/S)

However, the building exhibits totally different building mechanism after retrofit work has been implemented. As indicated in Figures 8b and9b, strong column-weak beam mechanism would be achieved using the retrofit methods described later in this paper. Plastic hinges form in the beams which is desirable and in turn yields the greater system ductility.

Seismic Retrofit Methods

Based on nonlinear analysis results, several retrofit methods were investigated to achieve the target structural performance level and the preferred building mechanism, more importantly, with minimal disruptions to the functionality of the building. Figures 10b and 11b graphically illustrate the retrofit scopes of this building.

For the mitigation of soft-story mechanisms, all ten columns that are part of lateral-force resisting system were strengthening using welded cover plates. These additional plates were to increase strength and stiffness. Added strength would prolong the formation of column plastic hinges and subsequently force a beam hinging mechanism. Additional stiffness is intended to reduce inter-story drifts, hence minimize the demands induced by P-Delta effects.

To accommodate the expected inelastic drift, the plastic hinges in the beams (with Pre-Northridge moment connections) must be developed within the beam span, remote from the face of the column. This behavior could be obtained by locally stiffening and strengthening type fully restrained moment connections. In this project, welded top and bottom haunches will be implemented at several locations throughout the building. With this type of connection, the inelastic action (plastic hinges) will be forced to take place away from the column face, where its performance is less dependent on the material and workmanship of the welded joint. In the case where only bottom haunch can be installed, the replacement of the existing welds with the conforming welds will be part of the retrofit scopes.

Another mean to minimize inter-story drifts is to impose a fixed condition at the base of building. The capacity of existing spread footings was neglected and new mat foundation was proposed to provide fixity at the base of columns. Column base plate strengthening was proposed accordingly.

Although this building has concrete filled metal deck over wide flange steel girder system, they are lack of headed studs. Therefore, new welded head studs will be installed along the moment frame beams at every floor as part of the retrofit scopes. They were designed to have adequate shear capacity to transfer inertia forces from the diaphragm to the lateral-force resisting system.

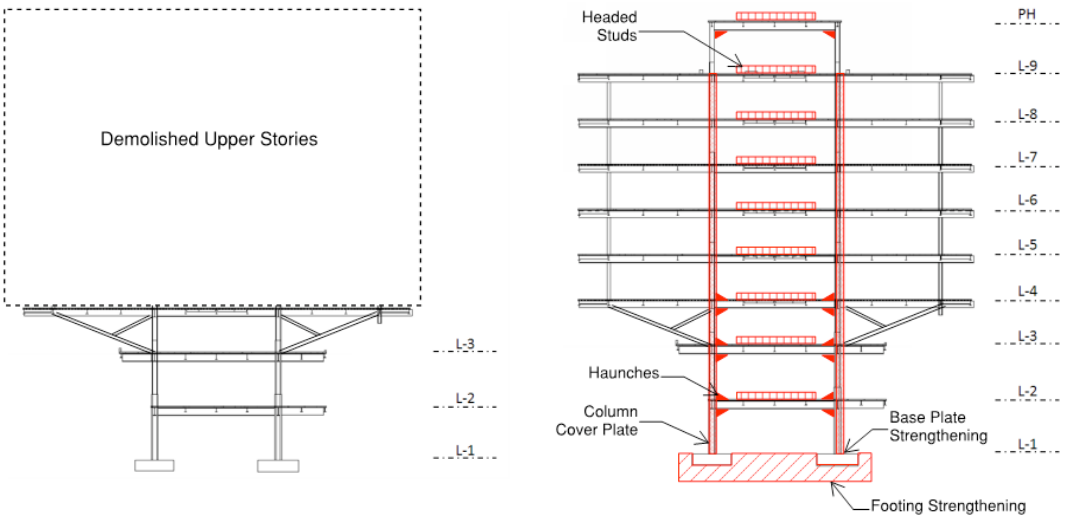
Benefits of Nonlinear-based versus Conventional-based Retrofit Scopes

One of the major benefits for using nonlinear pushover analysis in seismic retrofit projects is an understanding of the possible building mechanisms and strategically modification of the structure to clearly achieve a favorable mechanism. Consequently, retrofit of unnecessary areas and missing retrofit of critical areas can be avoided. Scopes of retrofit based on conventional approach or Linear Dynamic

Procedure (LDP) can be drastically reduced when Nonlinear Static Procedure (NSP) is implemented.

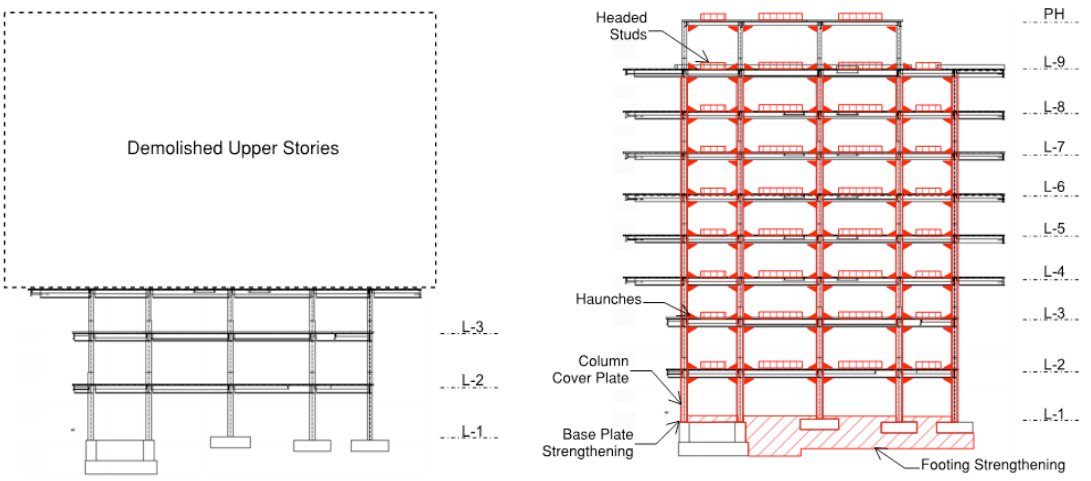
Figures 10 and 11 show the comparison between the retrofit scopes based on conventional versus non-linear approach for East/West and North/South moment frame, respectively. Based on the conventional approach, the demolition of the upper stories (4th to Penthouse) was previously proposed. Based on the non-linear approach, the building owner can save the upper floors with some localized retrofit works.

As the scope of retrofit reduced, overall construction cost also significantly decreased. In addition, construction process can be incrementally performed in phases. Consequently, the disruption of hospital operations can be greatly minimized during the construction.



(a) Conventional Approach (b) Nonlinear Approach

Figure 10. Nonlinear versus conventional E/W frame retrofit



(a) Conventional Approach (b) Nonlinear Approach

Figure 11. Nonlinear versus conventional N/S frame retrofit

SOME RETROFIT DESIGN CHALLENGES

As mentioned previously, a major goal of the proposed retrofit is to implement it with minimal disruptions to the operations and functionality of the building. This constrain was the condition that led to the major project design challenges, which are described below.

- The required strengthening of the foundation created the two most challenging aspects of the project. First, the new mat foundation will have to be built below six existing spread footings using underpinning method and tied back to the two existing wall footings. Second, all foundation work will have to be performed below the slab-on-grade using tunneling and mining approaches. This solution had been driven by the amount of disruptions in the first floor lobby area above and the infection control aspects of the operating hospital if the foundation work ought to be done from above the slab-on-grade.
- The presence of major electrical and mechanical equipment on the 4th floor and penthouse, forced the development of alternate retrofit details for those regions, although, not in all cases it was possible to develop such alternate details, creating coordination challenges for the other disciplines involved in the project. These challenges, therefore, had to be resolved by the entire design team.

CONCLUSIONS

This paper presents a seismic retrofit case study of a hospital building in Southern California. The structure was analyzed and the seismic retrofit designed using both non-linear and conventional approaches. In addition, experimental component testing was included as part of the process such that the designer can abandon excessively conservatisms embedded in the design standard/code. The final

retrofit strategies were proposed based on the non-linear pushover analysis results and the retrofit methods were discussed in details.

Having a better understanding of the structural performance and failure mechanism, thanks to the nonlinear based analysis, helped to better address the key structural deficiencies of the building. As a result, less invasive and more effective retrofit strategy can be implemented. Most importantly, cost saving can be maximized while the disruption of hospital operations can be significantly minimized during the construction.

The graphical comparisons of the retrofit scopes attests how much saving may be put on the owners by implementing nonlinear analysis over the conventional analysis method.

Finally, this paper presents some design challenges that the authors faced during the design development phase and some viable workaround solutions.

ACKNOWLEDGEMENT

The authors would like to thank Professor Chia-Ming Uang and Mr. Dong-Won Kim for assisting on the column bi-axial effect study and for conducting an upcoming component testing at University of California, San Diego.

REFERENCES

AISC (2005). “Seismic Provisions for Structural Steel Buildings”, *ANSI/AISC 341-05 w/ Supplement No.1*, Chicago, Illinois.

American Society of Civil Engineering (2007). "Seismic Rehabilitation of Existing Buildings", *ASCE/SEI 41-06 w/ Supplement No.1*, Reston, Virginia.

International Code Council (ICC) (2007). “2007 California Building Code”, California Code of Regulations, Title 24, Part 2, Volume 2, California Building Standards Commission, Sacramento, California.

Federal Emergency Management Agency (2000). "Recommended Seismic Evaluation and Upgrade Criteria for Existing Welded Steel Moment-Frame Building", *FEMA 351*.

Computer & Structures Inc. (CSI) (2006). “PERFORM-3D Nonlinear Analysis and Performance Assessment for 3D Structures – User Guide", *Version 4*, Berkeley, California.

Seismic Vulnerability Assessments of Marine Structures Using Non-Linear Static Analysis Procedures

Edward. H. Stehmeyer III, P.E., M. A.S.C.E.[1]

[1]Collins Engineers, Inc., 1180 Sam Rittenberg Boulevard, Suite 105, Charleston, SC 29407; PH (843)763-1576; email: estehmeyer@collinsengr.com.

ABSTRACT

As part of maintenance and future planning for marine structures, a condition assessment and load rating are traditionally performed every 2 to 5 years, depending on the use and importance of the structure. Traditionally, the load rating of these structures only considers the "day-to-day" vertical service loading. As a greater understanding of the inherent, seismic hazards present in areas of the United States with marine infrastructure including those on the east and west coasts, vulnerability studies of existing structures are becoming more common. These studies estimate the expected behavior of the structure under a variety of loading conditions. This assessment helps determine if the facility needs to be repaired, given its current condition, or upgraded for changes in operational loading or use. This paper will demonstrate the implementation of non-linear static analysis techniques for assessing the vulnerability of existing marine infrastructure. In particular, the effects of concrete pile deterioration and concrete pile-to-pile cap connectivity on the service and lateral/seismic resistance of a typical pile supported marine structure is presented. The impact of considering the current condition state of the structure throughout the analysis will be emphasized.

INTRODUCTION

The importance of marine infrastructure is often overlooked by the public; however, its usefulness following a natural disaster, such as an earthquake can be immeasurable. The recent damage at the Port of Port-au-Prince, Haiti following a 7.0 magnitude earthquake demonstrated the potential for serious damage to a vital rescue and aid transportation point. As a result, owners of marine infrastructure have begun to seriously consider incorporating seismic vulnerability studies into their routine structural condition inspection and assessments. This paper will highlight the seismic assessment process for a marine structure as it progresses from preliminary drawing review to performing a comprehensive condition survey, followed by a service and seismic lateral loading analysis to determine the displacement capacity. The importance of considering the current structural condition of the substructure elements and the proper modeling of their connection to the superstructure are emphasized as they relate to the service and seismic resistance of the facility.

SEISMIC VULNERABILITY ASSESSMENT PROCESS

The seismic vulnerability assessment of any type of structure involves several common phases. In general, it includes (1) a Preliminary Drawing Review, (2) a Structural Condition Investigation, (3) a Service Load Assessment, and (4) a Seismic Load Assessment. The goal of these studies is to develop a comprehensive condition assessment of the structure that identifies deficiencies that affect the service loading capabilities of the structure as well as identify the vulnerability of the structure to seismic loading. The unique portion of the assessment phase for marine infrastructure is the above water and underwater structural condition assessment that have to be performed as part of phase 2. The following serves to briefly describe the key elements in each phase.

PRELIMINARY DRAWING REVIEW

Conducting a preliminary drawing review is the best preparation for conducting an efficient field investigation. The focus of this review should not only be on the general layout of the structure, but also on the critical structural details that support service and seismic loading. This will establish a checklist of items that need to be verified in the field to determine the as-built construction of the structure.

STRUCTURAL CONDITION INVESTIGATION

For many marine structures, the condition investigation will involve above-water and below-water investigations to document the structure's existing condition. Often the normal deterioration of a structure in a marine environment can limit the structure's capacity for both service and seismic loading. Deterioration in the form of concrete cracks and spalls or corroded steel elements could potentially cause weak links in the structural system. The product of the condition investigation is a report detailing the extent of deterioration throughout the facility and the potential impacts of these defects on the overall performance of the structure.

SERVICE LOAD ASSESSMENT

The service load assessment is typically performed only when significant deterioration is noted or when the intended use of the facility changes. This assessment will provide the owner with a service load capacity for the structure based on its existing condition. In addition, recommended repairs as necessary to meet or exceed the current service loading demands will be included. Often, these deficiency repairs should be made even if a seismic assessment is not being performed.

SEISMIC LOAD ASSESSMENT

The seismic load assessment of a marine structure traditionally considers either the existing condition or the repaired condition of the structure based on the findings of the Service Load Assessment. The appropriate regional seismic hazard is

applied to the structural model and the displacement capacity of the elements is compared to the displacement demand of the seismic hazard. This is referred to as performance based design and assessment which has been adopted for the design of new bridges (Caltrans 2010, SCDOT 2008) and for pier and wharf structures (MOTEMS 2010).

EXAMPLE MARINE STRUCTURE

A typical concrete wharf structure that was constructed in 1974 was chosen to demonstrate the service load and lateral/seismic assessment process of a marine structure. The structure consists of a grid of prestressed concrete piles supporting reinforced concrete pile caps that run in the transverse direction and a reinforced concrete deck structure that spans between caps in the longitudinal direction. The wharf measures 677 feet long by approximately 64 feet wide. The structure is also surrounded by adjacent structures on all sides. A typical section of the demonstration structure is shown in Figure 1. The wharf has a mixed operational use including storage and berthing for vessels. The distance from the deck to the channel bottom varies from 14 feet on the inboard side to 56 feet on the outboard side at mean-low water.

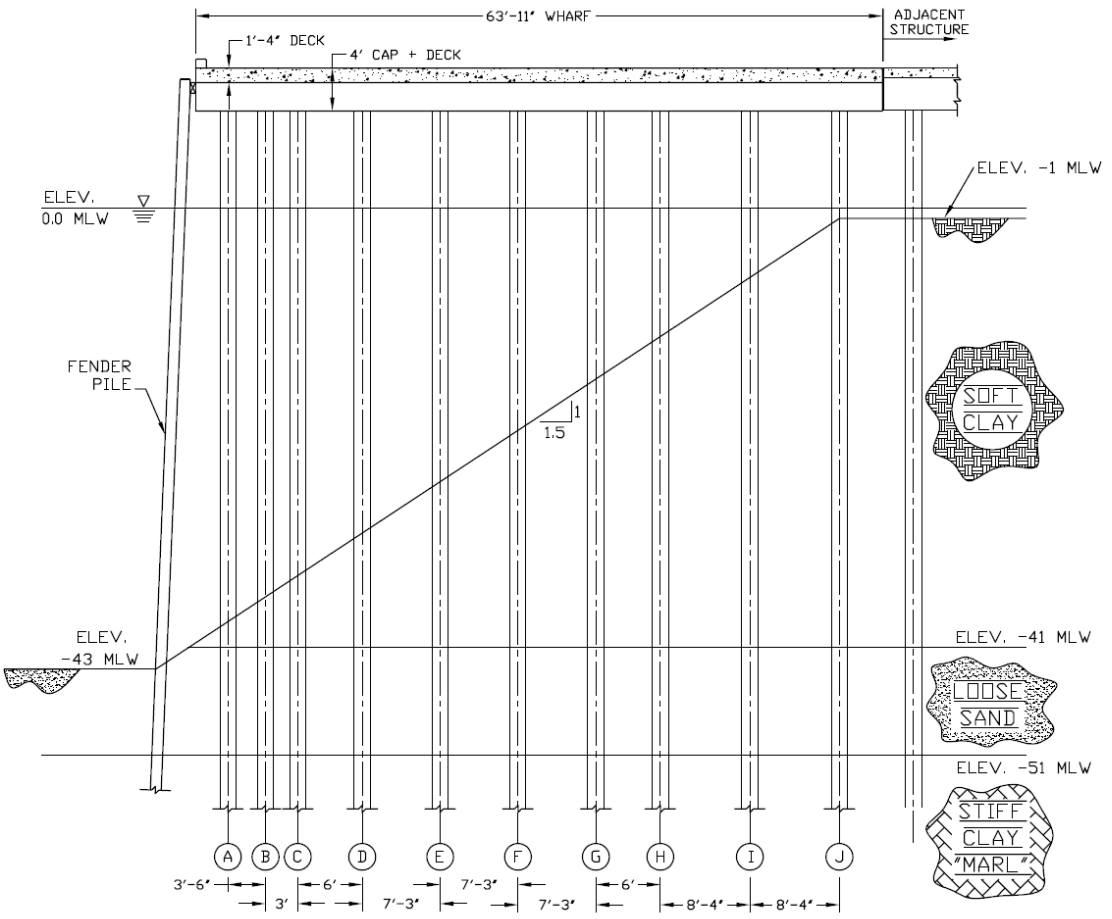


Figure 1: Example Wharf Structure Typical Section

The existing plumb piles in this structure measure 18 in. square and are 83 feet long based on an existing design drawing review. The longitudinal reinforcing consists of 16 - 7/16 in. 250 ksi prestressing strands in a square pattern. Shear reinforcement and confinement are provided from 40 ksi number 5 gage steel wire, spaced at 3 in. over the first and last 4 feet of the pile, and 6 in. spaces through the remaining pile length. The compressive strength of the concrete was f'_c = 5,000 psi, as was common based on the time period when the facility was constructed (MOTEMS 2010). The effective prestress force in the strands was set equal to $P_s = 0.7 \times f_{pu} \times A_{ps}$. This calculation results in an effective prestressing force of 18.9 kips per strand, including losses. The original design plans show that the top of the piles were connected to the pile cap using 4 in. of embeddedment into the pile cap and 4 – number 8 rebar dowels with 18 inches of embedment into the cap. The original pile cross section is shown in Figure 2.

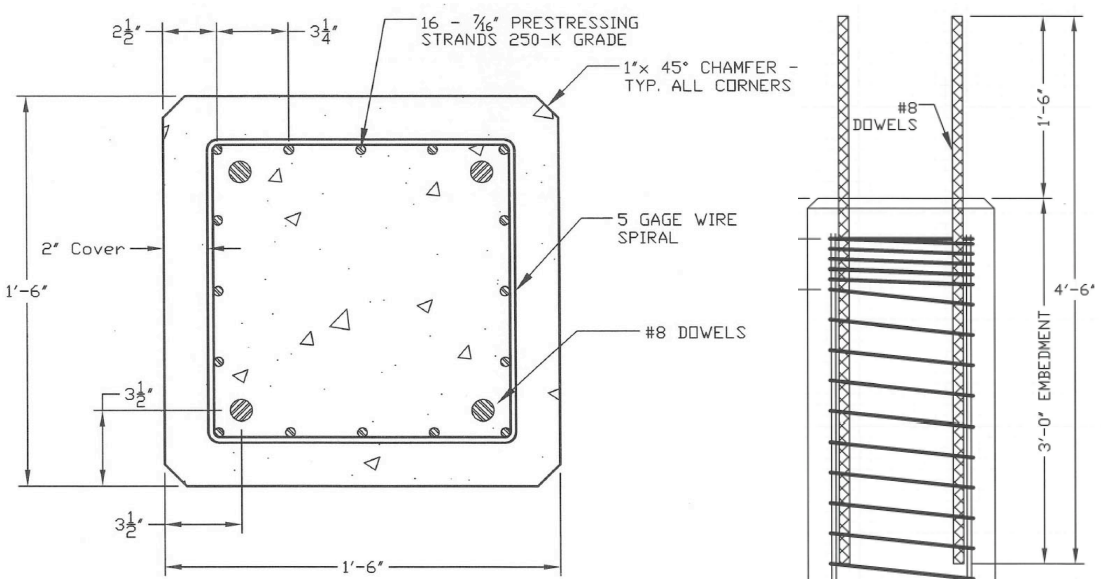


Figure 2: Original Prestressed Concrete Pile Section & Top Connection

EFFECT OF PILE CONDITION ON SERVICE AND SEISMIC CAPACITY

In order to demonstrate the importance of considering the structure's existing condition state in service load and seismic assessments, a moment-curvature analysis is performed. The structural capacity of a single prestressed concrete pile supporting the example marine structure is analyzed in 5 different condition states. Namely, the "original section" model considers the section with no defects, while the remaining models consider typical defects observed in marine structures. In particular, the "side spall" model considers the loss of the cover concrete on one side of the section, and the "side spall with LOS" model considers a single sided cover spall and loss of section (LOS) of the exposed prestressing strands. It should be noted that since the area of 5 prestressing strands are reduced, the effective prestress in each of the strands in the section were increased or decreased based on a proportional stiffness

approach. The "corner spall" model considers a corner spall defect in the pile section and the "cover spall" model considers complete loss of the cover concrete in the section analysis. This cover spall can be thought of as either an extensive impending spall where the concrete is not bonded well to the core, or as the condition of a severely damaged pile where significant deformation of the element has already taken place. Refer to Figure 3 for views of the 5 different pile sections used in this study.

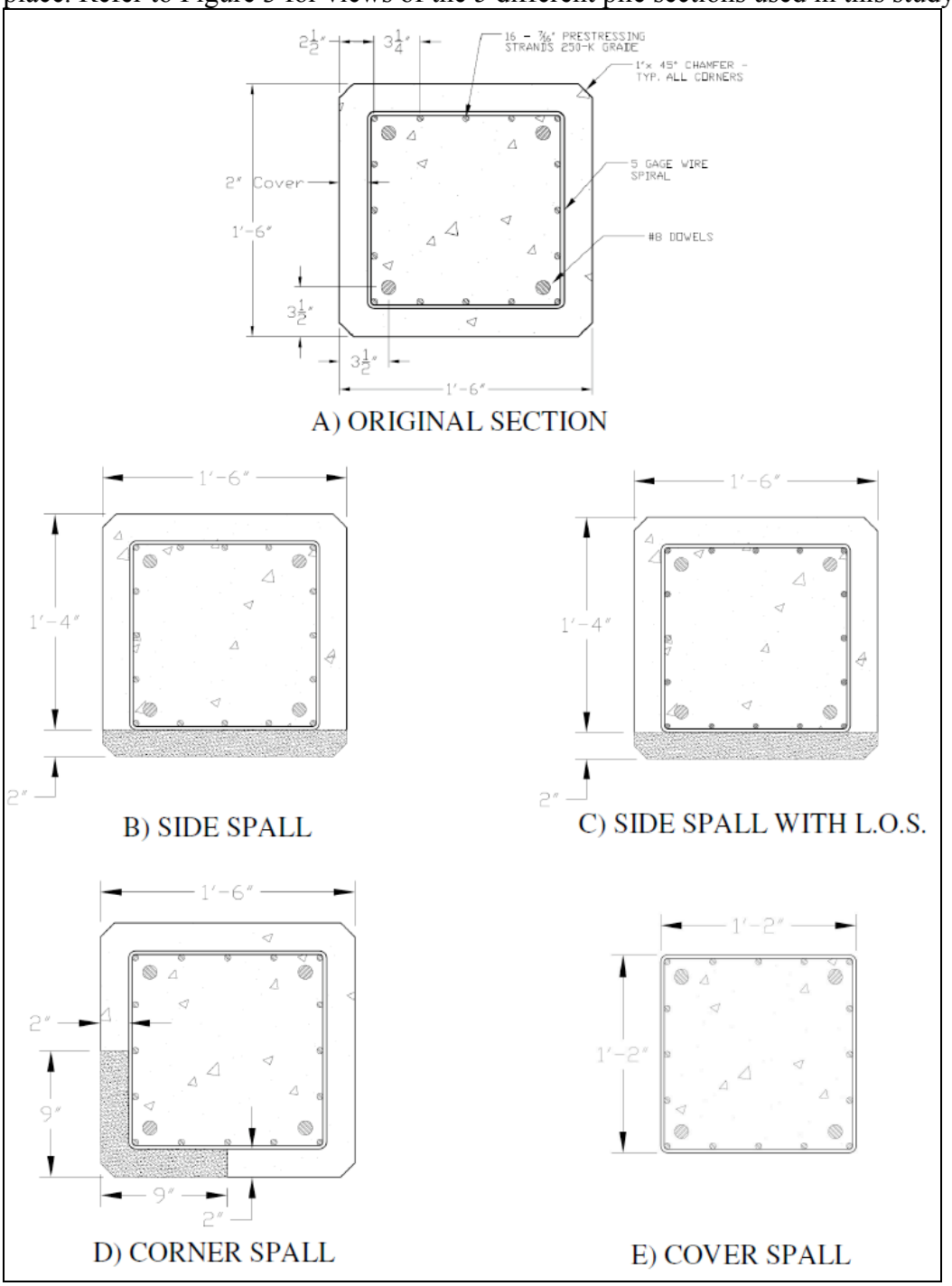
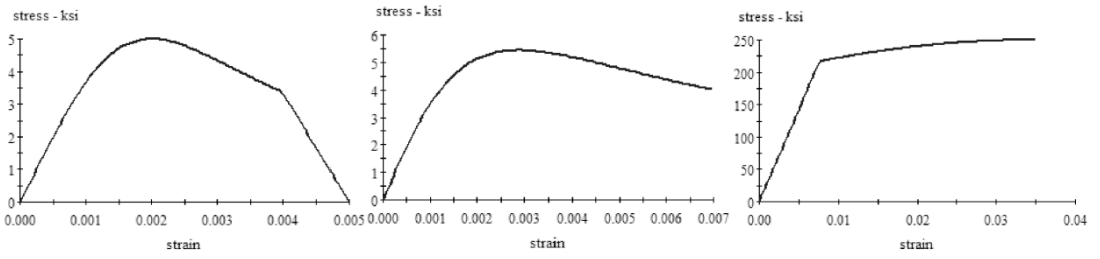


Figure 3: Various PS Concrete Pile Sections Used in the Cross Section Analysis

MOMENT-CURVATURE ANALYSIS

For each cross section case, the moment curvature and axial-moment interaction curves are developed using the software XTRACT (Imbsen 2005). This analysis includes non-linear material models and widely recognized properties and limits for concrete and prestressing (Caltrans 2010, SCDOT 2008, MOTEMS 2010).

A Mander unconfined concrete model was implemented for the concrete outside of the core of the pile while a confined concrete model was used for the inner core (Mander and Priestly 1988). Since the shear reinforcing is modeled through confinement in the pile core, the only other material needed for the model is the prestressing steel. The prestressing strands were modeled using a prestressed steel material model with properties consistent with 250 ksi strand material (Caltrans 2010, SCDOT 2008, MOTEMS 2010). The effective prestress identified previously was also included in the cross sectional analysis. The stress strain curves for the material models are depicted in Figure 4.



A) Unconfined Concrete B) Confined Concrete C) Prestressing Strand

Figure 4: Non-Linear Material Models for the Prestressed Concrete Pile

The original section and cover spall sections were only run for a single direction of moment loading since the section is symmetrical. The defects used in the other cross sections cause an asymmetric condition about the primary x-x axis, therefore moment curvature analyses were performed for positive and negative bending about the x-x axis and the y-y axis.

The results of the cross section analysis revealed several interesting observations as shown in Figures 5 and 6. Since the deteriorated sections are not symmetric about the primary bending axes, different values of effective yield moment, effective yield curvature, and transformed moment of inertia are realized. The cover spall moment curvature behavior is similar to a normally reinforced concrete section since it does not have any unconfined concrete in compression that eventually spalls off. Similar performance of the side spall sections was observed when the moment caused compression on the side where the cover concrete had spalled off. As expected, when the moment was applied to the side opposite of the identified defects, the moment curvature behavior is close to that of the original section. In addition, bending about the minor axis typically exhibited closer behavior

to the original section since the compressive area in both positive and negative bending was only slightly reduced by the defect.

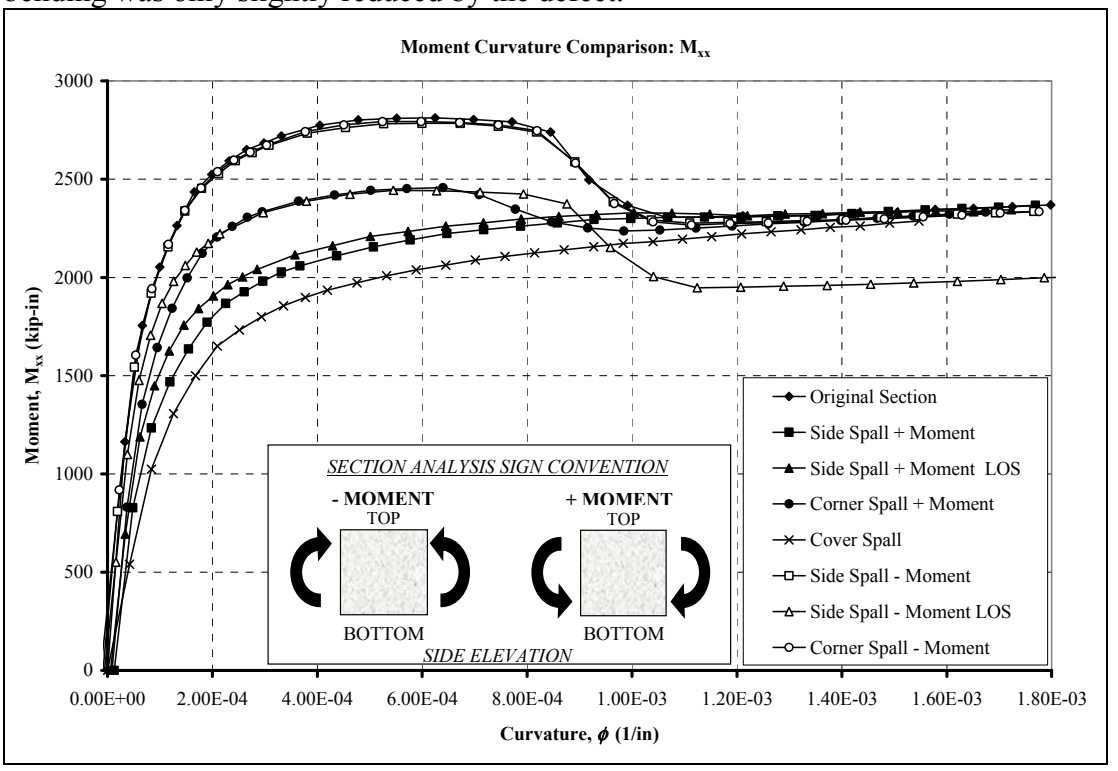


Figure 5: Moment - Curvature Comparison for Moment about the X-Axis

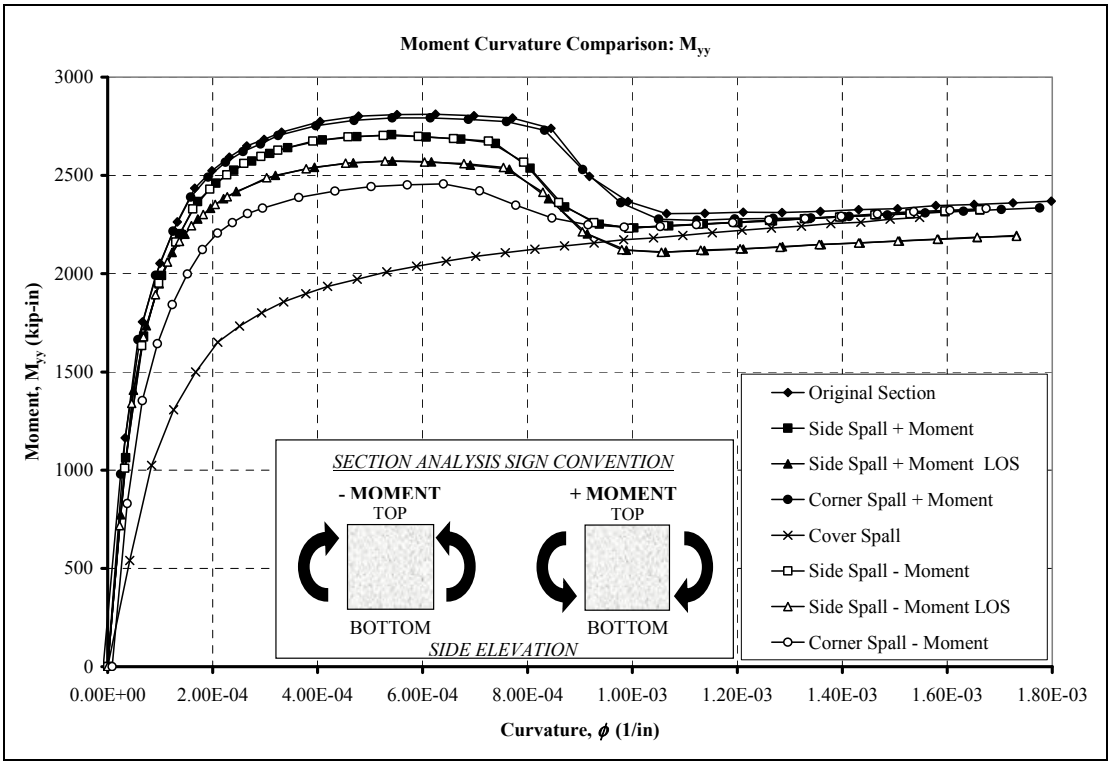


Figure 6: Moment - Curvature Comparison for Moment about the Y-Axis

The cross section "Side Spall with LOS" exhibits a similar shape to the original section; however, the overall performance was lower for a moment applied causing tension in the strands with a loss of section. The resulting effective cross section properties for each section are illustrated in Table 1.

Table 1: Effective Cross Section Properties

Cross Section	Area, A_g (in^2)	Total Area of Steel, A_{pst} (in^2)	Trans. Moment of Inertia, I_{tx} (in4)	Trans. Moment of Inertia, I_{ty} (in4)	Eff. Yield Moment, M_{ye} (kip-in)	Eff. Yield Curvature, f_{ye} (1/in)	Curvature Ductility
Original	324	1.728	9879	9879	2766	0.000188	9.55
Side Spall +M	288	1.728	7486	8917	2192	0.000227	7.812
Side Spall -M	288	1.728	7486	8917	2733	0.00018	9.81
Side Spall +M with LOS	288	1.593	7363	8833	2218	0.00018	9.572
Side Spall +M with LOS	288	1.593	7363	8833	2341	0.000134	13.92
Corner Spall +M	292	1.728	8502	8502	2365	0.000174	9.597
Corner Spall -M	292	1.728	8502	8502	2740	0.00018	9.88
Cover Spall	196	1.728	4347	4347	2003	0.000254	6.08

The axial-moment interaction of each section was also calculated considering code reductions for strength (ACI 2005). In each case, the overall capacity of the section was reduced by the identified deficiencies. The curve typically shifts inward on the side of the graph corresponding to moment causing compression on the side missing cover concrete. In addition, the largest difference in overall capacity was seen in the cover spall section with a 45% reduction in maximum moment capacity compared to an 18% to 22% reduction for the other sections. It is important to realize that these defects not only reduce the strength of the member, but they also reduce the stiffness and overall ductility of the member.

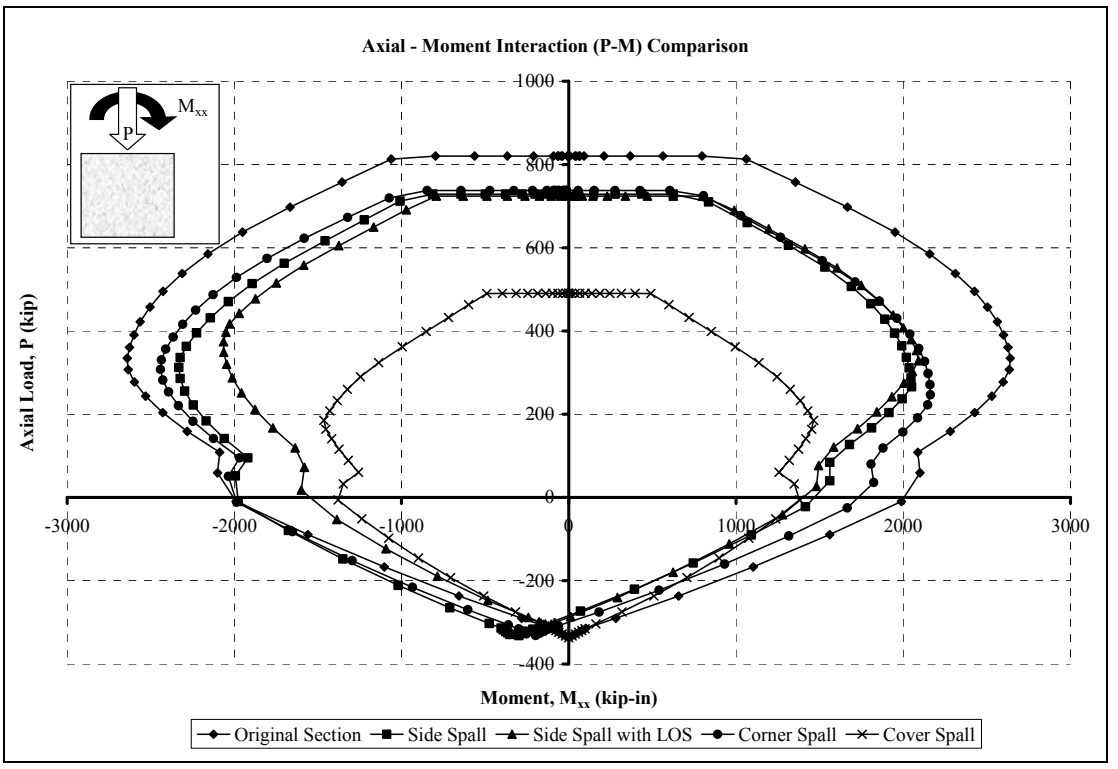


Figure 7: Axial - Moment Interaction Comparison for Moment about the X-Axis

EFFECT OF PILE-TO-PIILE CAP CONNECTION ON SEISMIC CAPACITY

The pile to pile cap connection plays an important role in the lateral and seismic resistance of a moment frame marine structure. These structures, while typically flexible, rely on frame action to resist seismic excitations. The frame action requires the piles to endure moment and shear loading along their length with various moment distributions based on the pile top to pile cap connection condition. As part of the seismic vulnerability assessment of the example structure, the effectiveness of the pile top connection is considered.

PILE-TO-PILE CAP CONNECTION MODEL

The dowels extending into the pile cap are #8 rebar which will not fully develop the original pile section moment capacity at the connection. In addition, this size of reinforcement would require an embedment length of 29 in. in the 4,000 psi compressive strength concrete cap (ACI 2005). Since only 18 in. of embedment is provided, a partial fixity condition exists and the reinforcement will only be able to develop 62% (18/29) of the rebar yield stress. The limiting moment capacity, M_{LIM} is calculated using the limiting steel stress. The pile-to-pile cap connection is modeled as an elasto-plastic Moment-Curvature hinge at the connection of the pile to the pile cap. The first leg of the curve represents the section stiffness up to the limiting moment. The cracked section moment of inertia is used to determine the limiting curvature value. The hinge is incorporated in a global finite element model of the wharf to determine the non-linear pushover capacity of the pile bent.

SUPPORTING SOIL MODEL

The soil chosen for this study is a typical soil profile found in the harbor region of Charleston, South Carolina. The upper 40 feet of the soil column consists of soft, organic clay. Below this clay layer, a 10 foot thick loose sand layer was identified. These upper layers are supported by stiff clay that is locally referred to as "marl". The soil profile was modeled in the software program L-Pile (Ensoft 2010) to obtain the non-linear "p-y" curves for the soil over the height of the soil column. It should be noted that as the channel bottom deepens along the bent, the soft clay layer springs are re-calculated at the appropriate depths. For the purposes of this study, the soil profile is assumed to be parallel along the width of the wharf and consistent along the length of the wharf. Table 2 illustrates the layer thickness, soil properties, and corresponding non-linear spring models used to represent the soil.

Table 2: Soil Properties and Corresponding p-y Models

Soil Type	Thick-ness (ft)	Eff. Unit Weight, γ' (pcf)	Cohe-sion, c (psf)	Friction Angle, ϕ (Deg.)	Lateral Subgrade Modulus, k (pci)	Strain Factor, ε_{50}	p-y Model
Soft Clay	40	46	250	0	30	0.02	Matlock (1970)
Loose Sand	10	56	N/A	30	20	N/A	API Sand (1987)
Stiff Clay	>85	56	2500	0	1000	0.005	Stiff Clay w/ F.W.

NON-LINEAR PUSHOVER ANALYSIS – PILE CAP FIXITY STUDY

In order to assess the impact of pile-to-pile cap fixity on the lateral performance of the wharf bent, a 2-D finite element structural model is developed using SAP2000 (CSI 2010) as shown in Figure 8. Four different models were developed for this study. They include variations of fixity between the pile and pile cap from fully fixed, to fully pinned at the top. The effects of partial fixity are also modeled by an elasto-plastic hinge for the doweled connection into the cap. Two models are developed using this technique with hinge properties consistent with the limited development length and one that considers the dowels to be fully developed for comparison purposes. The model also incorporates the non-linear moment curvature hinge behavior of the original pile section along its length using the SAP2000 section designer. A pushover analysis was performed by incrementally pushing the models to the left and right up to 48 in. of displacement. The models also had the tributary seismic weight applied during the analysis.

The results of the non-linear pushover analysis are presented in Figure 9. It can be seen that the pile-to-pile-cap connection model plays a significant role in the overall capacity of the bent. As expected the fixed and pinned top case bound the responses of the bent with the partial fixity lying between. It is interesting to note

that the limited, partial fixity case represents a decrease of 24% from the fully fixed case and a decrease of 6% from the fully developed rebar model. No significant differences were noted between pushing to the right versus the left for this structure.

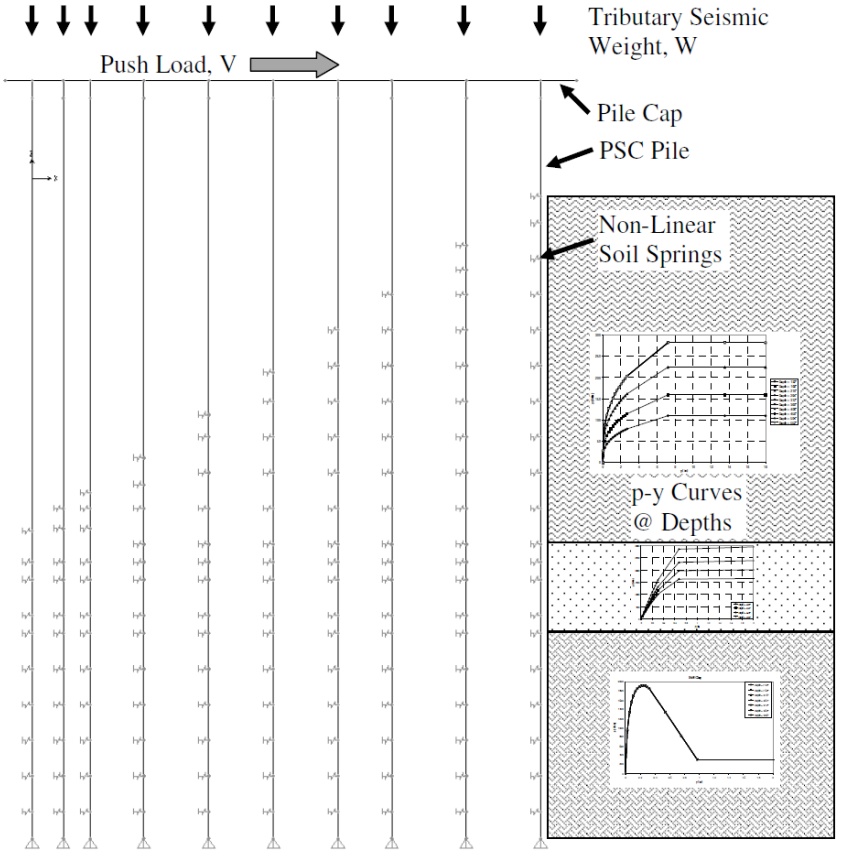


Figure 8: Finite Element Structure Model with Soil Springs

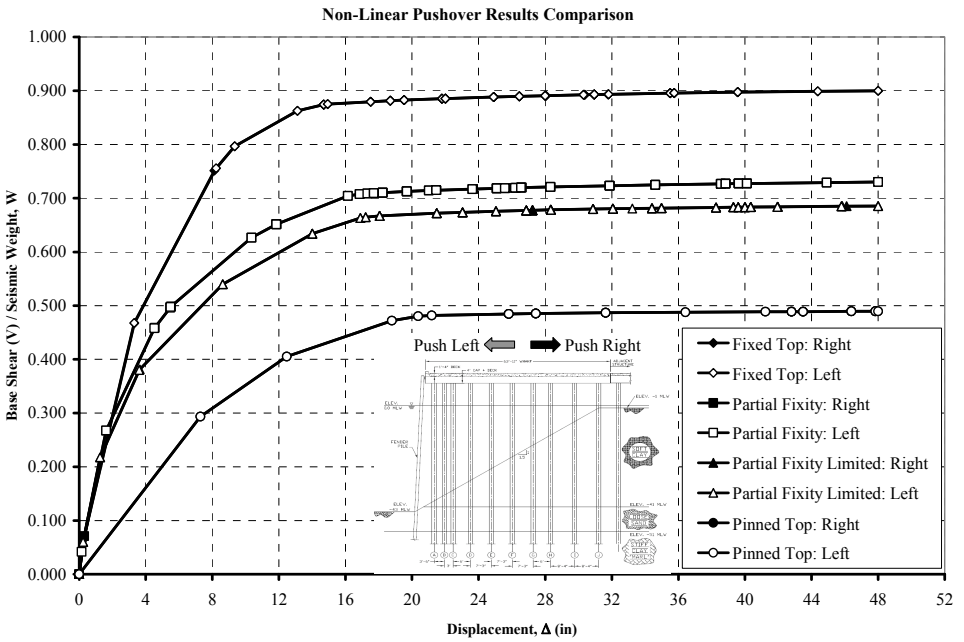


Figure 9: Non-Linear Pushover Comparison for Pile-to-Pile Cap Fixity Study

CONCLUSIONS

This paper briefly described the typical phases associated with a service and seismic condition assessment of marine structures. An example marine structure was then analyzed using non-linear procedures to emphasize the importance of evaluating the structure considering its existing condition including defects such as spalls and rebar or prestressing strand loss of section. The chosen defects vary in severity and were shown to decrease the maximum moment capacity of the selected pile by between 18% to 45%. The defects location also played a crucial role in the decrease in section capacity. In particular, if moment loading causes compression where a concrete spall defect is located, the decrease is larger than if the moment causes tension in the concrete spall area. The study also found that the proper modeling of the pile-to-pile cap fixity in the global structural model has a significant impact on the lateral / seismic capacity of the structure achieved through a non-linear pushover analysis. The use of fully fixed pile top to cap connection is not always applicable, and assuming a fully pinned connection, may be overly conservative. This study demonstrated a technique for incorporating partial fixity that more accurately represents the expected seismic capacity of the pile bent. Combining the results of a thorough structural condition investigation and the proper use of these non-linear analysis techniques, the expected seismic vulnerability of marine structures can be achieved and updated as the structure's intended use or condition changes.

REFERENCES

American Concrete Institute (ACI). (2005). *Building Code Requirements for Structural Concrete (ACI 318-05) and Commentary (ACI 318R-05)*, Farmington Hills, Michigan.

Computers and Structures, Inc (CSI). (2010) SAP2000 Integrated Software for Structural Analysis and Design – Users Manual version 14.2.2, Berkeley, California.

California Department of Transportation (CALTRANS). (2010). *Seismic Design Criteria Version 1.6*, Sacramento, California.

Imbsen Software Systems. (2005). *Cross Sectional Structural Analysis of Components (XTRACT) ver. 3.0.4. – User Manual*, Sacramento, California.

Ensoft Inc. (2010). *A Program for the Analysis of Piles and Drilled Shafts Under Lateral Loads (L-Pile) V5.0 – User & Technical Manual*, Austin, Texas.

Mander, J.B., Priestly, M.J.N. (1988). "Observed stress-strain behavior of confined concrete." *Journal of Structural Engineering*, ASCE, 114(8), 1827-1849.

MOTEMS. (2010). *Marine Oil Terminal Engineering and Maintenance Standard (MOTEMS),* codified as Chapter 31F (Marine Oil Terminals), Title 24, *California Building Code*, Sacramento, California.

South Carolina Department of Transportation (SCDOT). (2008). *Seismic Design Specifications for Highway Bridges*, Columbia, South Carolina.

Seismic Design of a 15 Story Hospital Using Viscous Wall Dampers

James Newell, Ph.D., P.E.[1], Jay Love, S.E.[2], Mark Sinclair, S.E.[3],
Yu-Ning Chen, P.E.[4], and Amarnath Kasalanati, Ph.D., P.E.[5]

[1]Presenter, Degenkolb Engineers, 707 SW Washington St, Suite 600, Portland, OR 97205; PH (503) 223-9932; FAX (503) 242-1780; email: jnewell@degenkolb.com
[2]Degenkolb Engineers, 1300 Clay St., Suite 900, Oakland, CA 94612; PH (510) 272-9040; FAX (510) 272-9526; email: rjlove@degenkolb.com
[3]Degenkolb Engineers, 1300 Clay St., Suite 900, Oakland, CA 94612; (510) 272-9040; FAX (510) 272-9526; email: msinclair@degenkolb.com
[4]Degenkolb Engineers, 1300 Clay St., Suite 900, Oakland, CA 94612; PH (510) 272-9040; FAX (510) 272-9526; email: ynchen@degenkolb.com
[5]Dynamic Isolation Systems, Inc., 885 Denmark Dr, Suite 101, McCarran, NV 89434; PH (925) 283-1166; FAX (775) 359-3985; email: akasalanati@dis-inc.com

ABSTRACT

In order to aid in post-earthquake response and recovery efforts, hospitals and other critical structures must remain operational after a design level seismic event. Protective systems (base-isolation and supplemental damping) provide a means to reliably and economically achieve improved structural and nonstructural performance. Viscous wall dampers (VWDs), originally developed in Japan, will be used in this first U.S. application to provide supplemental damping and enable a new 15 story hospital in San Francisco, California to achieve stringent performance goals. This paper introduces the innovative VWD devices, describes the results of full-scale prototype testing, summarizes VWD properties, and explains modeling techniques for implementation in nonlinear response history analysis. By using VWDs in this hospital application, the overall steel weight was reduced by an amount that more than offset the installed cost of the VWD devices and a unique lateral system was designed that will enable improved structural performance, when compared with traditional systems. Also, floor accelerations in the upper floors of the building were significantly decreased, thereby reducing the costs associated with nonstructural bracing, especially for the central utilities plant located on the top floor.

INTRODUCTION

Viscous Wall Dampers originated in Japan, where they have been used for more than 20 years and in over 100 projects. VWDs consist of a stiffened steel tank filled with viscous "fluid" and one or more steel vanes that extend into the tank of viscous fluid. The VWD tank connects to a girder within a steel moment resisting frame line at one level and the vane assembly connects to the girder at the level above (see

Figure 1). Interstory drift and interstory velocity result in in-plane movement of the vane within the tank. Viscous shearing of the fluid relative to the tank wall and vane provides damping and energy dissipation.

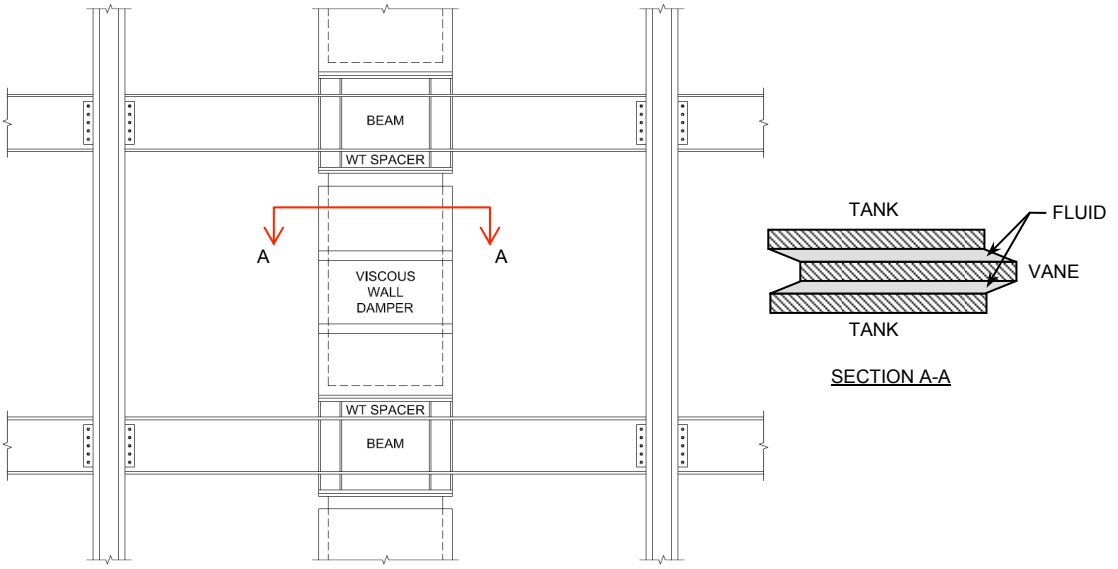


Figure 1. Typical VWD framing elevation.

Hospitals are critical to post-disaster response and recovery efforts. Lessons from past earthquakes have shown that while structural seismic performance has improved something as small as a sprinkler piping leak in an operating room can put a hospital out of commission until repairs are made. This damage to nonstructural components is typically sensitive to floor accelerations. One way to reduce the magnitude of floor accelerations, and reduce the corresponding damage, is with the use of protective systems (i.e. base isolation, or supplemental damping). The Structural Engineer, Architect, and Owner of a new hospital to be located in San Francisco, California, only 11 km from the San Andreas Fault, opted to use innovative viscous wall damper technology to help achieve stringent structural and nonstructural performance goals.

The new hospital (see Figure 2) is 15 stories above grade, with two below-grade levels for parking. Levels P3 through Level 4 occupy the entire site, which measures 385 ft by 275 ft. The building plan area reduces at Levels 5 and 6, and reduces again at Levels 7 through 14 to form the nursing tower. The building roof is up to approximately 250 ft above sloping grade. Level 15 includes an exterior roof with air handling units and in interior central utilities plant. Cooling towers, additional air handling units and emergency generators are located on the Level 16 roof. The lateral force resisting system above grade consists of steel moment resisting frames with 153 supplemental VWDs, provided by Dynamic Isolation Systems, Inc.

This project represents the first U.S. application of these devices, which were originally developed in Japan, and therefore project-specific prototype testing was

conducted in order to characterize VWD wind and seismic performance, determine appropriate device properties for use in nonlinear response history analysis (NRHA), and satisfy building code requirements.

Use of viscous wall dampers having displacement, velocity, cyclic-history and temperature dependent force-deformation properties necessitated the use of NRHA for design. A VWD modeling approach was developed to capture the displacement and velocity dependence, and cyclic-history and temperature dependent properties are considered using an upper and lower bound numerical damper properties analysis approach. The use of advanced analysis techniques allowed the design team to integrate this new VWD technology into this unique structure and ensure that the building seismic performance objectives will be achieved.



Figure 2. Architectural rendering of hospital building.

VISCOUS WALL DAMPER DEVICES

Each VWD consists of a narrow steel tank connected to the lower floor, an inner steel plate (vane) connected to the upper floor, and a viscous fluid in the small gap between the tank and vane plates. During seismic excitation, relative floor movement causes the vane to move through the viscous fluid. The damping force from the shearing action of the fluid is dependent on the displacement and velocity of this relative motion. Wall dampers are used as a passive energy dissipation system to

reduce seismic accelerations and interstory drifts, as well as reduce wind-induced vibration.

VWDs can also be constructed with two vanes. In the case of the double-vane damper there are three plates that form the tank. A double-vane VWD gives twice the damping force with only a small increase in plan size (i.e. thickness of the VWD).

The viscous fluid used for wall dampers is a non-toxic, odorless, transparent fluid with a viscosity of about 90,000 poise at 30°C (95°F). The device can be made to fit typical openings in a building. Dampers with widths of 6 ft to 20 ft and heights of 6 ft to 14 ft (with spacers) have been used in buildings. The force of the damper is approximately proportional to the effective area of the vane.

VWDs operate at atmospheric pressure and do not have seals that require maintenance throughout the service life of the device, unlike other types of viscous dampers. Other than periodic inspection and inspection after a seismic event, VWDs are a maintenance-free system.

When used in steel framed buildings, the VWD tank and vane are typically field bolted to T-stubs that have been welded to the damper bay beams in the shop. Large diameter high-strength bolts are used to transfer damper overturning forces to adjacent structural framing and a series of pretensioned high-strength bolts are used to prevent slip between the steel T-stub and VWD tank and vane components. T-stubs are used to account for variations in the clear distance between framing members, while maintaining a consistent VWD height to minimize device production costs. Other connection configurations are possible when needed to satisfy unique project requirements.

PROTOTYPE TESTING

As part of rigorous regulatory agency review for this first U.S. project utilizing VWDs, project-specific full-scale testing of the devices was required to establish expected wind and seismic performance and determine appropriate properties for modeling the devices in PERFORM-3D (CSI, 2006). Prototype tests on a series of dampers were performed at the University of California, San Diego's Caltrans Seismic Response Modification Device Test Facility. One 7 ft wide by 12 ft tall double vane prototype specimen ready for testing is shown in Figure 3. The dampers were tested to a variety of displacements and velocities (sinusoidal and earthquake motion) in single and bi-directional loading conditions.

Chapter 18 of ASCE 7-05 (ASCE, 2006) requires a series of sinusoidal cyclic prototype tests at the maximum earthquake device displacement to establish device performance. ASCE 7-05 also specifies a 15% tolerance limit on various damper properties, depending on whether the device is displacement- and/or velocity-dependent, compared with the average value from the code prescribed five fully

reversed cycles. VWDs are both displacement- and velocity-dependent and therefore must satisfy the cycle variation tolerance for force at zero displacement (F_0), force at maximum device displacement (F @ D_{max}), effective stiffness (K_{eff}), and area of hysteresis loop (E_{loop}). These parameters are illustrated for typical VWD load-deformation response in Figure 4.

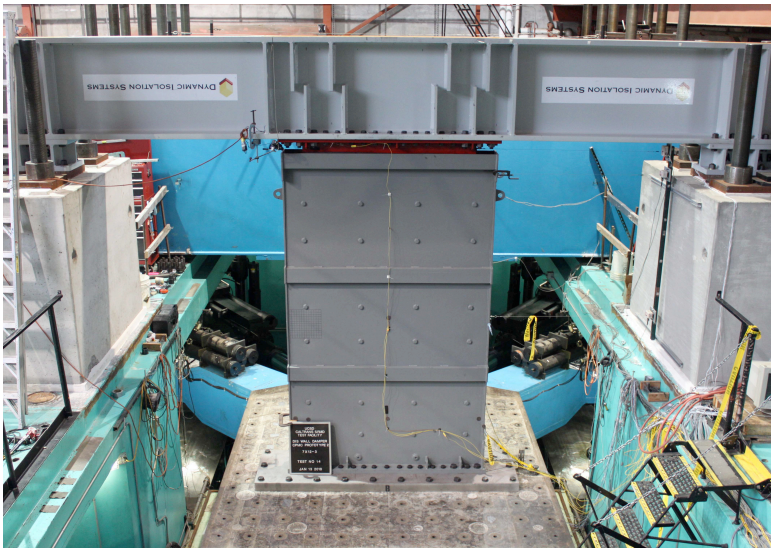


Figure 3. Prototype VWD 7 ft by 12 ft test specimen.

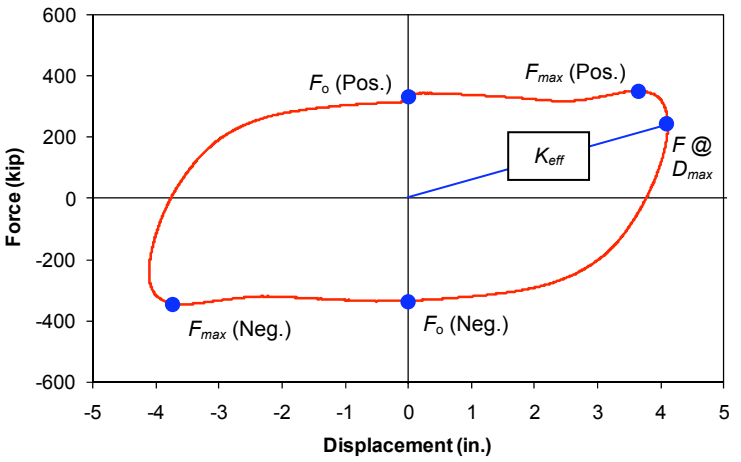
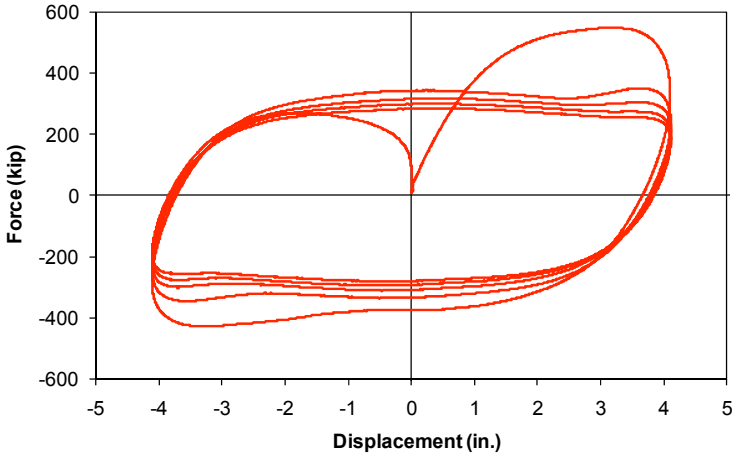


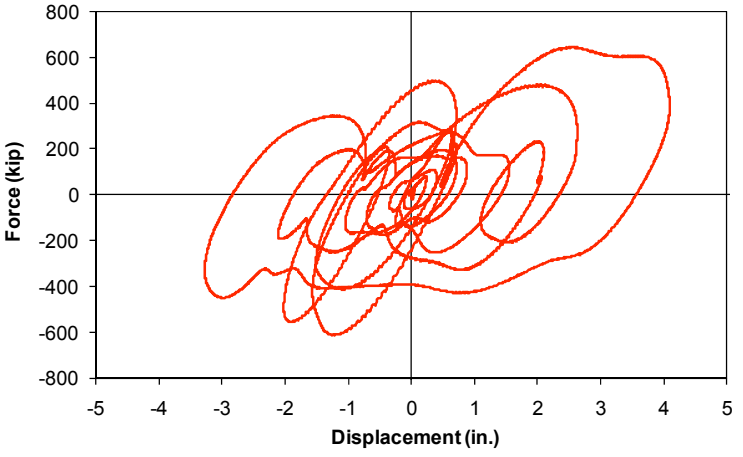
Figure 4. VWD property definitions.

Additional cyclic and simulated earthquake testing was conducted to enable the design team to characterize expected device performance, provide data to establish device damping and stiffness properties, and for calibration of numerical models. A design level earthquake test was performed at the beginning and end of each day of testing and results from these tests were used to demonstrate that damper properties

did not degrade with repeated cycles, even after approximately 20 tests at design to maximum considered earthquake level displacement. Figure 5 shows typical load-deformation response for cyclic and simulated earthquake tests. The larger first-cycle force observed in Figure 5(a) will be discussed in the damper property modification factor section below.



(a) Cyclic test



(b) Earthquake test

Figure 5. Typical load vs. deformation response.

ASCE 7-05 damper prototype testing requirements also prescribe subjecting the device to a wind test of not less than 2000 continuous fully reversed cycles of wind loading at displacement amplitudes expected in the design wind storm. A wind engineering consultant was retained to help establish this expected wind displacement. Building wind displacements are made up of a static component, quasi-static component oscillating at approximately 10 times the building natural frequency, and a dynamic component oscillating at approximately the building natural frequency. The results of previous wind tunnel testing of a model of the building combined with the building dynamic properties were used to characterize the

building response during a 100-year wind event. This building response data was used to develop a realistic wind test loading sequence consisting of the following steps: 1) Apply static displacement offset, 2) Apply simultaneous combination of quasi-static and dynamic cycles in both the in-plane and out-of-plane directions (Figure 6 shows an example of one quasi-static displacement cycle with the superimposed dynamic cycles), and 3) Remove static displacement offset.

Figure 7 shows the load-deformation response for one typical quasi-static cycle of the wind testing sequence. Note that the static displacement offset has been removed from the plotted data. Five iterations of 1000 dynamic wind load cycles were conducted back-to-back with no significant drop in damper properties. Wind test results also confirmed a significant level of damping is provided by the VWDs, even for small amplitude wind-induced displacements.

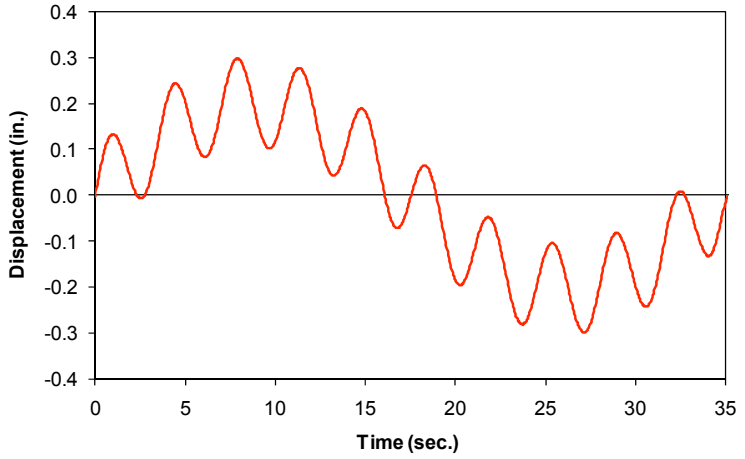


Figure 6. Typical cycle of wind test displacement protocol.

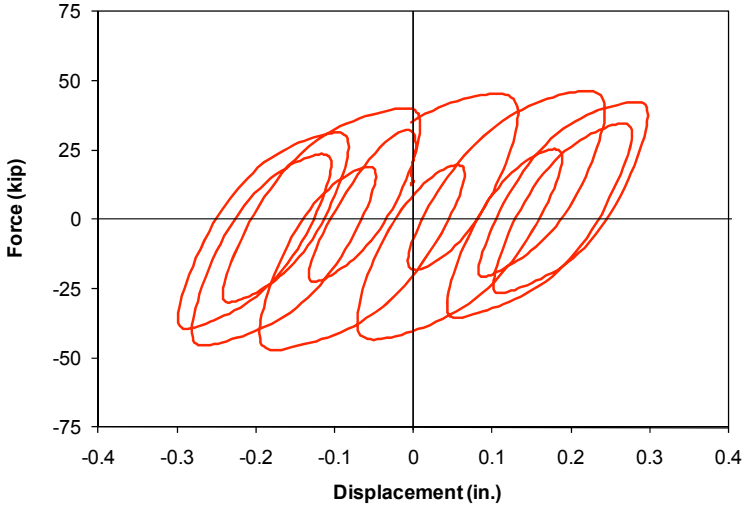


Figure 7. Typical wind test load vs. deformation response.

Damper production testing is also required by ASCE 7-05 Chapter 18 prior to installation of damping devices in a building. Production testing is intended to verify that the force-velocity-displacement characteristics of the actual devices fall within the allowable range assumed in design of the structure. Simulated production tests were conducted on prototype dampers to establish benchmark data for use in actual production testing.

DAMPER PROPERTIES AND MODELING

Based on the results of project specific testing and previous testing in Japan, VWD properties and a modeling scheme were developed for implementation in nonlinear response history analysis using the computer software package PERFORM-3D.

Damper Model

The damper model consists of a linear spring in series with a nonlinear damper (Maxwell Model). This damper model was implemented with the PERFORM-3D viscous bar element made up of a fluid damper and linear elastic bar component. The damper force versus velocity relationship was represented by Equation 1 and an additional force cap.

$$F = CV^{\alpha} \qquad \text{(Eq. 1)}$$

where: C = damping coefficient, F = damper force, V = damper velocity, α = damper velocity exponent. The damper velocity exponent ($\alpha = 0.7$) was selected based on empirical Japanese practice and fit of the damper model to prototype test data. PERFORM-3D implements a multi-linear discretization of the Equation 1 force versus velocity relationship. The additional force cap was based on observations from testing.

The compound viscous bar element (dashpot and linear elastic spring) was located at story mid-height and is connected to the beam above and below with rigid vane and tank elements. Interstory drift causes relative displacement between the two damper nodes and activates the viscous bar element. A portion of a typical frame with dampers is shown in Figure 8.

Stiffness of the VWD vane and tank components was included in the dashpot-spring damper model properties that were determined based on the results of prototype testing. Therefore, the component properties of the elastic vane and tank elements (Column, Steel Type, Nonstandard Section) in the PERFORM-3D model were considered to be essentially rigid.

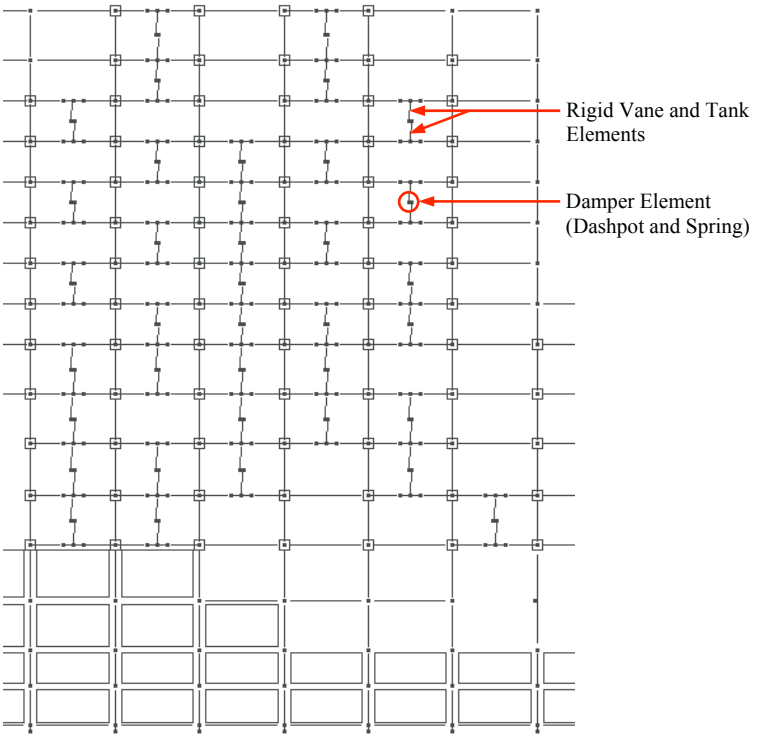


Figure 8. PERFORM-3D model typical damper bays.

Damper Properties

The load-deformation response of VWDs is temperature, displacement, velocity, and cyclic-history dependent. Temperature and cyclic-history dependence are accounted for by use of the property modification factors discussed in the next section. Figures 9 and 10 show the displacement and velocity dependence of the VWD load-deformation response for representative cyclic prototype tests. In general, VWD forces tend to increase for larger displacement amplitudes and larger velocities.

Fluid damper and linear elastic bar component properties, for use in PERFORM-3D, were determined with an iterative process based on prototype test results and a simple PERFORM-3D model of the prototype specimens. Results from PERFORM-3D simulation of a test was compared to prototype test results to determine damper properties that provided the best match over a range of different displacement amplitudes and velocities. This data was also examined to verify that damper properties used in the overall building model satisfied project-specific design criteria requirements for the match between prototype test and numerical simulation results.

Damper Property Modification Factors

In order to appropriately account for the expected range of building response due to variation in damper properties due to first-cycle effect, temperature variation, aging, and specification tolerance an upper and lower bound damper properties analysis scheme was adopted. The force-based nominal damper properties determined from prototype testing were modified by an upper bound or lower bound damper property

modification factor and two analysis cases were completed. Displacement based demands were typically controlled by analysis with lower bound damper properties and force based demands by upper bound damper property analysis.

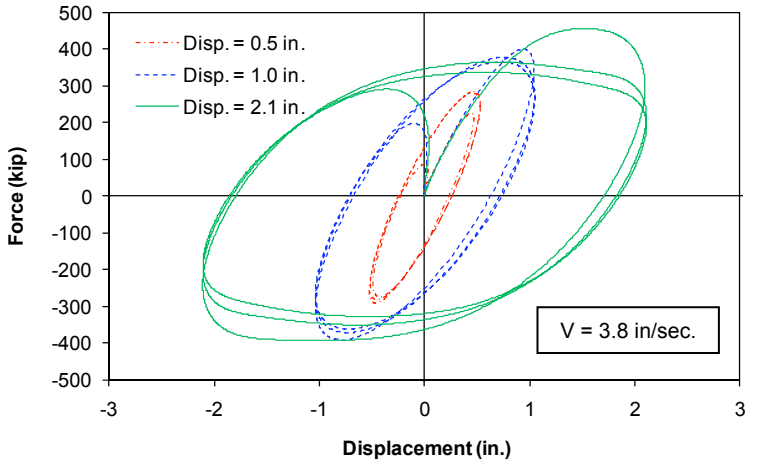


Figure 9. Typical displacement dependent cyclic load vs. deformation response.

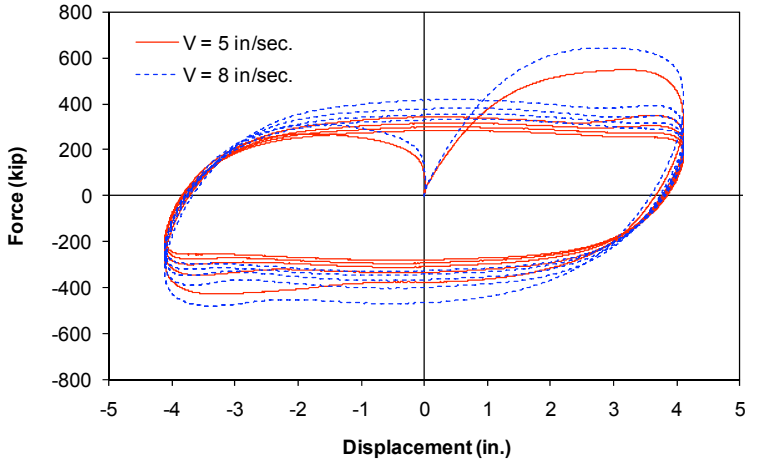


Figure 10. Typical velocity dependent cyclic load vs. deformation response.

As observed in Figures 5(a), 9, and 10, VWDs typically exhibit a higher force capacity on the first excursion to large displacements (cyclic-history dependence). This phenomenon is not captured by the damper model implemented in PERFORM-3D and is referred to as the first-cycle effect. A first-cycle effect upper bound damper property modification factor (>1.0) is used to ensure the structure is adequately designed for the increased force demand resulting from the first-cycle effect. To establish the appropriate values for first-cycle factors maximum positive and maximum negative force data from prototype testing was compared with maximum values from PERFORM-3D simulation of the tests. The maximum value

of the test force divided by PERFOM-3D simulation force was used to establish the first-cycle factor for a given damper size and earthquake demand level.

Table 1 provides a summary of upper and lower bound damper property modification factors. The first-cycle factor was established as described above and other factors were established based on Japanese experience with past projects, or in the case of the individual damper specification tolerance factor based on ASCE 7-05 requirements.

Table 1. Property modification factors.

System Modification Factors (λ)	Upper Bound Property Multiplier (λ_{max})	Lower Bound Property Multiplier (λ_{min})
First Cycle Effect, λ_{1st}	1.55 to 1.82	1.0
Temperature, λ_{temp}	1.05	0.87
Aging, λ_{aging}	1.05	0.95
Specification Tolerance, $\lambda_{spec,a}$ (average of all dampers)	1.1	0.9
Specification Tolerance, $\lambda_{spec,i}$ (individual dampers)	1.15	0.85

ADDITIONAL DESIGN CONSIDERATIONS

Damper bay beams are expected to form a plastic hinge near the column face, but should remain elastic at the damper face. Beams can be initially sized based on the expected moment demand from the VWDs considering upper bound damper properties.

The presence of VWDs in moment frame bays alters the typically assumed inflection point location at mid-span of the beam under lateral loading. The VWD applies a large moment at the center of the damper bay beam that is only partially out-of-phase with moment frame action. The decrease in assumed inflection point location due to VWDs may result in a clear span to depth ratio less than the prequalification limits for beam-to-column moment frame connections specified in AISC 358-05s1 (AISC, 2005) and project-specific moment frame connection testing may be required.

To limit column and foundation overturning forces, dampers are often offset in a checkerboard pattern instead of a single stack up the height of the building. While this is effective at reducing overturning forces, special consideration must be given to the drag members needed to transfer seismic forces between adjacent offset dampers. The ductility of beam sections that are efficient as flexural members is often significantly reduced for combined compressive and flexural loading (Newell, 2008). Stockier sections may provide improved ductility and increased axial load capacity.

In addition to improved structural performance, use of protective systems, such as VWDs, reduces seismically induced building floor accelerations when compared to more traditional seismic force resisting systems. This reduction in floor acceleration demands can result in better performance of nonstructural components (i.e. less damage) and reduced construction costs associated with nonstructural bracing. NRHA results can be used to determine floor acceleration values for use in calculation of nonstructural component horizontal seismic design forces, instead of using the default equation in ASCE 7. For this hospital, roof level nonstructural component seismic design forces were reduced by approximately 30%. This will result in a significant savings in the cost of nonstructural bracing, especially since the central utilities plant will be located near the hospital roof level.

SUMMARY

The first U.S. implementation of Viscous Wall Dampers has been designed for a hospital located in San Francisco, California. VWDs were selected for this project because they will provide a reliable, maintenance-free, cost-effective protective system to ensure stringent performance goals are achieved. The use of supplemental damping will reduce seismic induced floor acceleration demands, reduce nonstructural bracing costs, and reduce potential nonstructural damage after an earthquake.

Full-scale VWD prototype testing was conducted per the requirements of Chapter 18 of ASCE 7-05, to establish expected wind and seismic performance and determine appropriate properties for nonlinear response history analysis with PERFORM-3D. VWDs were modeled with a viscous bar element consisting of a fluid damper and linear elastic bar components. An analysis approach considering upper and lower bound damper properties was adopted to appropriately consider the expected range of building response resulting from potential variability in VWD properties.

REFERENCES

American Institute of Steel Construction (AISC). (2005). *Prequalified Connections for Special and Intermediate Steel Moment Frames for Seismic Applications including Supplement No. 1, AISC 358-05s1*, Chicago, IL.

American Society of Civil Engineers (ASCE). (2006). *Minimum Design Loads for Buildings and Other Structures, ASCE/SEI 7-05,* Reston, VA.

Computers and Structures Inc. (CSI). (2006). "PERFORM-3D Nonlinear Analysis and Performance Assessment for 3D Structures Users Guide." Berkeley, CA.

Newell, J. (2008). "Cyclic Behavior and Design of Steel Columns Subjected to Large Drift." PhD Dissertation, University of California San Diego, La Jolla, CA.

SEISMIC ANALYSIS AND REHABILITATION OF A 15 STORY PRE-NORTHRIDGE STEEL MOMENT RESISTING FRAME BUILDING

Timothy Graf, S.E.[1]; James O. Malley, S.E.[2]; Mark Sinclair, S.E.[3]; James Newell, Ph.D., P.E.[4]; Colin Blaney, S.E.[5]; Moisey Fraynt, P.E.[6]; Chia-Ming Uang, Ph.D.[7]; Tamer Ahmed, P.E.[8]

[1]Presenter, Degenkolb Engineers, 707 SW Washington St, Suite 600, Portland, OR 97205; PH (503) 223-9932; FAX (503) 242-1780; email: tgraf@degenkolb.com
[2]Degenkolb Engineers, 235 Montgomery St, Suite 500, San Francisco, CA 94104; PH (415) 392-6952; FAX (415) 544-0782; email: malley@degenkolb.com
[3]Degenkolb Engineers, 235 Montgomery St, Suite 500, San Francisco, CA 94104; PH (415) 392-6952; FAX (415) 544-0783; email: msinclair@degenkolb.com
[4]Degenkolb Engineers, 707 SW Washington St, Suite 600, Portland, OR 97205; PH (503) 223-9932; FAX (503) 242-1780; email: jnewell@degenkolb.com
[5]Crosby Group, 2200 Bridge Parkway, Suite 104, Redwood City, CA 94065; PH (650) 367-8100; FAX (650) 598-0277; email: colin@crosbygroup.com
[6]Fluor Enterprises, 4140 Dublin Boulevard, Suite 300, Dublin, CA 94568; PH (925) 307-1200; FAX (925) 307-1439
[7]University of California, San Diego, Dept. of Structural Engineering, 9500 Gilman Drive, MC 0085, La Jolla, CA 92093-0085; PH (858) 534-9880; FAX (858) 534-6373; email: cmu@ucsd.edu
[8]State of California, Department of General Services, 707 3rd St, Suite 3-305, MS #502, West Sacramento, CA 95605; PH (916) 376-1661; FAX (916) 376-1641; email: Tamer.Ahmed@dgs.ca.gov

ABSTRACT

This paper summarizes the seismic analysis and rehabilitation design of a fifteen story steel moment resisting frame building in Oakland, California, less than five miles from the Hayward Fault. The building was constructed with connection details that were found to be vulnerable to fracture in the 1994 Northridge earthquake.

Previous testing of the existing connections indicated that the welded connections were highly vulnerable to fracture, and consequently the building presented a risk to life safety in the event of a major earthquake. Seismic strengthening to meet the State of California Guidelines for the Seismic Retrofit of State Buildings Risk Level III resulted in a requirement to reduce the story drifts to 1.5% in a 475-year return period event.

After considering several retrofitting schemes including connection strengthening, BRBF's and seismic isolation, a scheme that included strengthening sixty percent of the existing pre-Northridge moment frame connections and adding viscous dampers was selected.

Since the existing moment connections had performed so poorly in previous testing, and because the size of the members in this building exceeded those that had been previously tested, a series of four full-scale tests were performed to confirm the validity of the connection upgrade design.

Two phases of advanced analysis techniques were performed in the rehabilitation design; a study phase with multi-mode two-dimensional nonlinear pushover analyses along with single-degree-of-freedom nonlinear dynamic time-history analyses; and a working drawings phase with nonlinear response history analyses of building frames to refine the scheme and perform member checks.

The extra steps taken beyond typical engineering practices were intended to provide better assurance that the project's performance goals would be met during the design basis seismic event.

INTRODUCTION

Building Description

The Caltrans District 4 Office Building, located in the downtown section of Oakland, California, is a 15-story steel moment frame structure designed to meet the 1988 Uniform Building Code and constructed in 1991. The building has one basement level, a first story lobby/public space level, four levels of above grade parking, and ten stories of office space. The building is rectangular in plan with a large atrium above the parking levels.

Moment Frame Vulnerability

Caltrans structural engineers were very aware of the damage caused to steel moment frames by the Northridge earthquake and so a brief study was commissioned that identified the building as Risk Level V, as defined in the Guidelines for the Seismic Retrofit of State Buildings (Guidelines, 1994, Rev. April, 2001). In accordance with the state guidelines, the building needed to be seismically upgraded to meet Risk Level III. The Guidelines include a table that attempts to categorize potential levels of building performance and associated risk. The description for levels III and V are presented below:

	Risk Level III	**Risk Level V**
Building:	Minor structural damage: repairable. Moderate non-structural damage: extensive repair.	Substantial structural damage: partial collapse likely: repair may not be cost-effective. Extensive non-structural
Risk to Life:	Minor	Substantial
Systems:	Disruption of systems for days to months	Total disruption of systems: repair may not be cost-effective
Occupancy:	Return within weeks, with minor disruptions	Totally vacated during repairs

The project design criteria were written to incorporate the recommendations of both FEMA 351 and 356 in order to meet the state guidelines. The state guidelines were interpreted to result in the following expected performance:

- A significant number of connection fractures may occur for DBE design earthquake; however, local collapse of framing is not expected.
- Repair of the lateral system (e.g. existing moment frame connections) may be required to restore the building to Risk Level III.
- After the DBE, a complete lateral system will still exist that should have sufficient capacity to permit occupancy of the building within weeks, while detailed inspection and any required repair of the lateral system is performed, or continues.
- FEMA 351 was used as the basis for design to establish Risk Level III drift limits. Structural life safety drift limits were established using 75% of the collapse prevention limits in FEMA 351. Appendix A was used to determine the expected variability of the drift response for the MCE and to calculate a project specific Demand Variability Factor.
- FEMA 356 life safety limits were used to establish column plastic hinge deformation limits.

SEISMIC GROUND MOTION DESIGN CRITERIA

Site-specific response spectra were developed for this site to represent the Design Base Earthquake (DBE, BSE-1) and the Maximum Considered Earthquake (MCE, BSE-2), in accordance with FEMA 356. These spectra were based upon deterministic considerations of both the San Andreas and Hayward faults and represent anticipated earthquakes of Richter magnitude 7.0 and 7.25. The site-specific response spectra are shown in Figure 1.

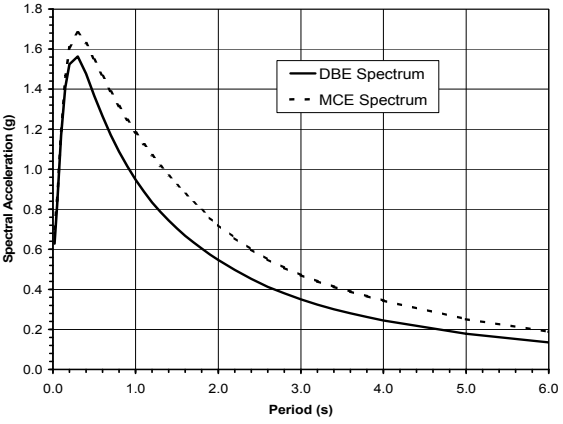


Figure 1. Project Design Response Spectra

Seven pairs of time-histories for use in the nonlinear response history analysis were also developed and scaled in accordance with FEMA 351 requirements. Directivity effects were not considered since the building is oriented approximately 45 degrees to the Hayward fault.

SELECTED RETROFIT SCHEME

The retrofit scheme was designed in two phases, a study phase and a working drawings phase. Four strengthening schemes were developed during the study phase of the project: an all-connection-strengthening scheme, a connection-strengthening-plus-dampers scheme, a buckling restrained brace scheme, and a base isolation scheme. Each scheme was designed to meet the design criteria and the schemes were compared on the basis of construction cost and associated "soft" costs such as construction phasing, long-term and short-term staff relocation and other facility down time. Items also considered long-term architectural impacts to the building as well as projected cost for repair after a significant seismic event.

DESCRIPTION OF SELECTED SCHEME

The retrofit scheme chosen by the owner was the connection-strengthening-plus-dampers scheme. The transverse frames are shown in Figure 2; the configuration is similar in the longitudinal direction.

The particulars of the scheme are as follows:

- Connection upgrades and dampers have been placed at the same locations to minimize number of work locations.
- Maximum practical damper sizes have been used to reduce number of work locations.
- The damper layout avoids interference with major points of entry and interior building flow.
- Of 1218 existing moment-resisting connections in building, 746 connections were strengthened (60% of connections).
- 228 dampers have been added at perimeter locations only, ranging from 225k to 670k dampers with $\alpha = 0.4$, and C ranging from 80 k $(\text{sec/in})^{0.4}$ to 240 k $(\text{sec/in})^{0.4}$.

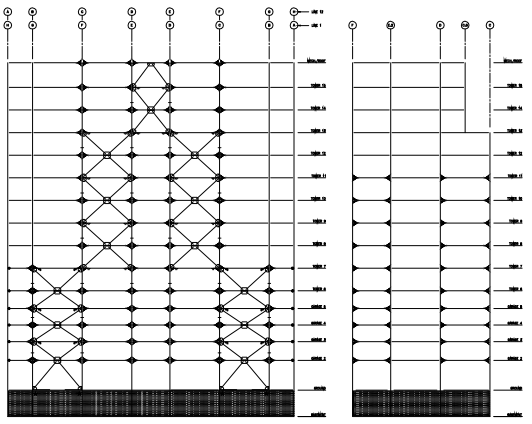


Figure 2. Transverse strengthening scheme for exterior and interior frames.

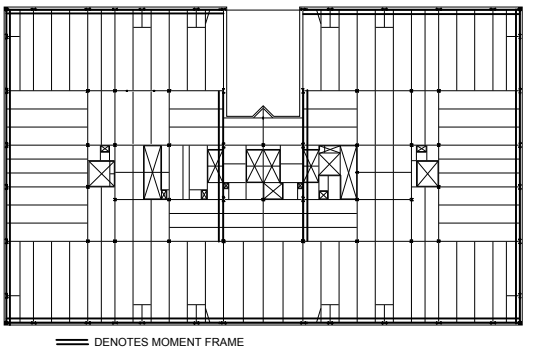


Figure 3. Typical Floor Plan.

CONNECTION TEST PROGRAM

FEMA 351 presented a series of pre-qualified data for existing beam to column configurations strengthened by various means. However, due to the large column sizes found within the existing building, none of the details could be specified and utilized within the building without supplemental testing. A series of alternative types of strengthening schemes were considered for upgrading the existing joints. These included the welded bottom haunch (WBH), the welded top and bottom haunch (WTBH) and the bolted bracket modification (BB).

The first test specimen was the welded bottom haunch and rib plates at the top. This detail with similar parameters had been tested previously under the SAC joint Venture and NIST/AISC testing programs. The SAC tested connections showed good response; however this specimen experienced an abrupt fracture through the column during the first negative excursion at approximately 2% drift. Subsequent finite element analysis (FEA) demonstrated the large strain demands that occur at the top flange weld, which led to the specimen fracture.

The second test specimen was the welded top and bottom haunch and is shown in Figure 4. Similar procedures were developed for the top and bottom haunch and used to size all members and connections. Pre-test FEA was also conducted for both specimens to better connection behavior. This specimen performed quite well, achieving 5% drift before a fracture occurred in the beam flange due to low cycle fatigue. Figure 5 shows the hysteretic loops for this specimen.

The third test specimen incorporated a series of four cast steel bolted brackets. This connection could have potentially eliminated field welding in the retrofit, leading to significant cost savings through avoiding the need for welding precautions in an occupied building. These brackets are a proprietary element that had been extensively tested on smaller sizes in previous research, and have been implemented on a number of projects for both post-earthquake repair and seismic retrofits. Note the member sizes in this building are substantially larger than what has been previously studied for this connection type. The specimen performed without incident through the 3% drift cycles. During the first half cycle to 4% drift, one of the column high strength bolts fractured in tension. Shortly the remaining column bolts and the existing beam to column flange weld all fractured suddenly. This fracture then propagated through the column web connection. No distress was noted in the bolted brackets.

The double welded haunch connection was chosen to retrofit the connections. A final test was conducted utilizing the double welded haunch on one side of the column and stiffened gusset plates on the other side. These gusset plates are being tested to simulate conditions where the dampers are connected to the existing moment frame. Finite element analyses on this connection have indicated that the most significant demands on this connection result from the member going through the building drifts (as opposed to the direct forces generated by the damper elements themselves).

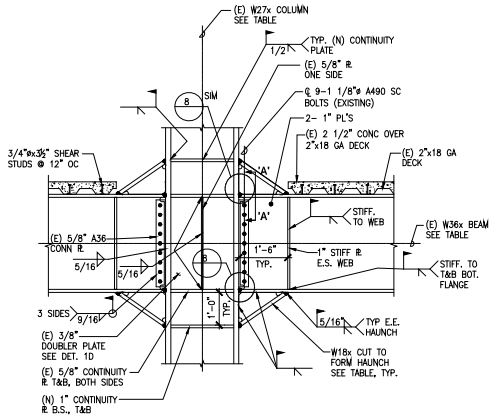


Figure 4: WTBH Detail

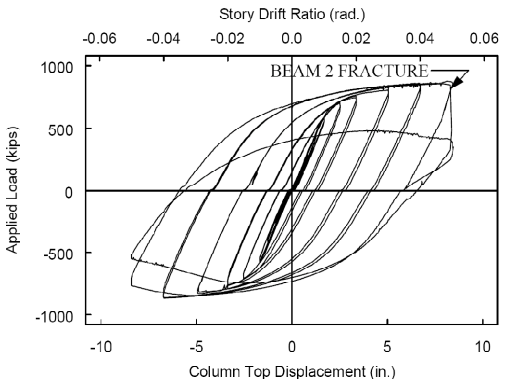


Figure 5. WTBH Test Hysteretic Loops

ANALYSIS TECHNIQUES

Two types of analysis were used on the project. A simplified analysis was performed during the initial study phase of the project based on the Equivalent Linearization Procedure (FEMA 440, 2004), and nonlinear dynamic response-history analysis (NRHA) was performed during the working drawings phase. Separate analysis programs were used for each type of analysis, SAP 2000, and PERFORM-3D.

Study Phase Analysis

The simplified analysis performed during the study phase of the project utilized SAP 2000 models, and a mixture of nonlinear static pushover analysis, spreadsheets, and nonlinear dynamic response-history analysis (NRHA) of single-degree-of-freedom (SDOF) models.

A pushover was performed of the selected retrofit scheme for the first three modes in each horizontal direction. Initial estimates of the target displacement for each mode were established using the Equivalent Linearization Procedure described in FEMA 440 Chapter 6. The displacement reducing effect of the added dampers was estimated using an iterative spreadsheet based procedure. The added damping was calculated using the pushover load vector, the displaced shape of the building at the target displacement, the damper sizes and distribution, and the building effective period. The target displacement of each mode was then reduced by the corresponding displacement reduction factor ("B-factor"), adopted from FEMA 450.

Once the scheme was finalized an additional check was performed on the target displacement of the first mode, the primary contributor to drift in the building. The pushover curve from the first mode pushover was idealized to a SDOF model, with nonlinear spring and damper elements that represent the behavior of the both the new and existing building structural components. NRHA was performed to confirm the target displacement of that mode, which was approximately 10% less than that calculated using FEMA 440.

In the final step, the pushover analysis results for each mode are combined in a statistical manner (CQC) to determine the overall performance of the retrofitted building.

Working Drawings Phase Analysis

In the working drawings phase of the project two two-dimensional models were constructed in PERFORM-3D, one for each direction of moment frames. Gravity columns were included in both models for secondary effects. Rigid diaphragms were assumed.

The moment frames are built with compound elements comprised of elastic frame elements with discrete inelastic hinges.

Beam elements used an inelastic moment-rotation hinge for strengthened connections or an inelastic fiber section for the existing connections. A fiber section is comprised of axial-only fibers assigned locations along a vertical axis. Each fiber is then assigned a chosen inelastic material property. The cross section will act inelastically in tension, compression, and bending but is considered to remain elastic in shear. The existing connection fiber is comprised of three different types of fibers: one fiber representing the top flange, one fiber representing the bottom flange, and one fiber for each of the bolts in the shear tab – shown in Figure 6.

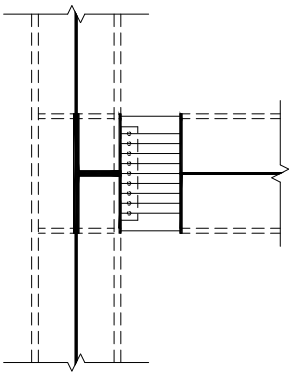


Figure 6. Graphical representation of beam connection fiber model.

Using the fiber elements allows the existing connection model to closely mimic tested behavior. The key aspects of using the fiber section to model the existing connection are that the fiber model captures:

- The top and bottom flanges fracturing at different moments, both which are significantly below the expected moment strength of the beam.
- The effect of the prying action that occurs on the bolts in the shear tab, and the individual fracture of each shear tab bolt at the expected bolt ultimate strength.

Other aspects of the mode include:

- Column elements utilize inelastic axial moment interaction (PMM) hinges.
- Column splices are included in the model as nodes.
- The basement walls remain elastic and are modeled as elastic shear wall elements.
- The base of the model consists of inelastic soil springs with properties developed from force-deflection curves provided by the geotechnical engineer.
- The dampers are modeled using an elastic bar and an inelastic damper element.
- Floor diaphragms were checked separately using inertia forces determined from the analyses.

Two-dimensional frame analyses were used for both phases of the analysis since the building has been found to be torsionally very regular. Torsion was accounted for in the design of the retrofit scheme by increasing drifts computed from the two-dimensional analyses by a factor determined from a linear response spectrum analysis of the full 3D SAP model including the dampers.

CONNECTION MODEL VALIDATION

To validate the existing fiber connection model, the existing connection test specimen was modeled and subjected to the same loading protocol as the original connection testing (Kim and Stojadinovic 2003). The correlation between the model and the test specimen is shown in Figure 7.

The slab was not included in the existing test specimen or in the fiber model. The potential contribution to the connection flexural strength is relatively small and the effect was not expected to substantially change the analysis results.

The fiber model revealed that a second type of slab interaction occurs with the steel frame. Post-fracture lengthening of the bay occurs due to the diagonal length between beam flanges in compression exceeding the original clear length of the bay during each drift excursion. This mechanism, which is shown in Figure 8, could result in overall frame lengthening of several inches over the dimension of the building. This behavior is not observed in subassemblage connection tests as the beam is unrestrained, and so no additional lateral resistance is generated. In the initial version PERFORM-3D model, very large axial loads were generated in the beam due to the slab, which was modeled as a rigid diaphragm. In the building, the axial loads would be limited by the slab strength, which is limited by tensile yielding of the reinforcement and bearing of the slab concrete against the column flanges, and by the capacity of the shear studs. Since there was no test data available to validate the strength and stiffness characteristics of this mechanism the effect was removed from the PERFORM-3D model by releasing the axial load in the beams. This slab-beam coupling mechanism would not have generated sufficient resistance to substantially alter the evaluation of the building or the scope of the subsequent strengthening scheme; however, it might improve the outcome in other more marginal cases. Further research is required to more clearly understand this behavior.

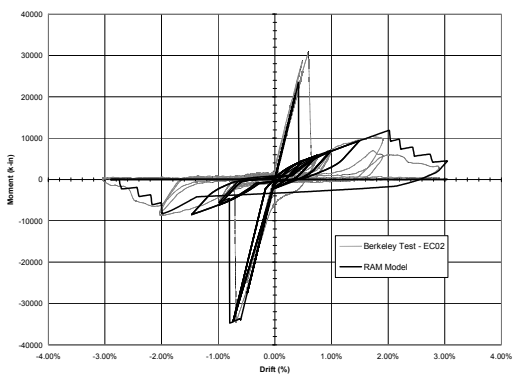


Figure 7. Connection fiber model compared to test results.

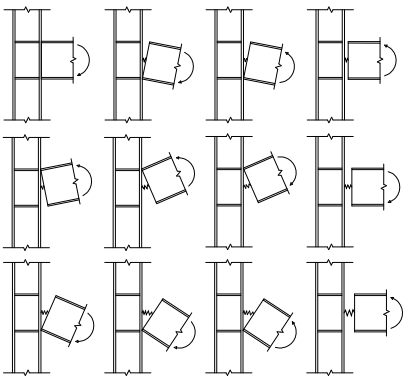


Figure 8. Ratcheting effect observed in connection test model

ANALYSIS RESULTS

Study Phase Analysis Results

The displacement and drift results from the study phase analysis are shown in Figure 9. The distribution of connection strengthening and dampers obtained using this analysis was relatively uniform throughout the height of the building – approximately 60% of connections at each floor with dampers distributed up the height of the building.

The pushover curves for the first three modes in the transverse direction are shown in Figure 10 together with the equivalent viscous damping computed for that mode. The higher modes were in general elastically performing, and were much more heavily damped than the first mode.

The pushover analyses performed in SAP2000 were not able to capture the fracture events due to the high degree of nonlinearity in the connection behavior and the large number of fracture events that occur near simultaneously. Consequently, the existing connections were modeled with only the residual post-fracture hysteretic characteristics of the connection. Although this was a conservative assumption, this resulted in a significant variation in the computed drift profile when the results were subsequently compared to those from NRHA in the working drawings phase of the project, see Figure 11.

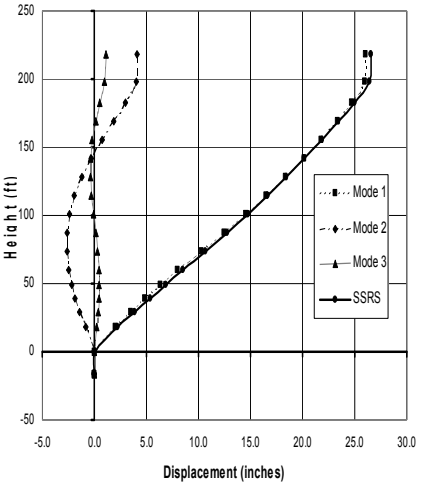


Figure 9. Study phase analysis displacement and drift results.

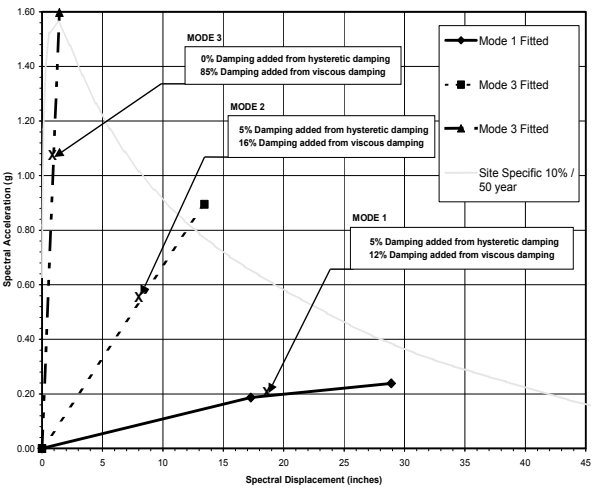


Figure 10. Capacity spectrum results for study phase analysis.

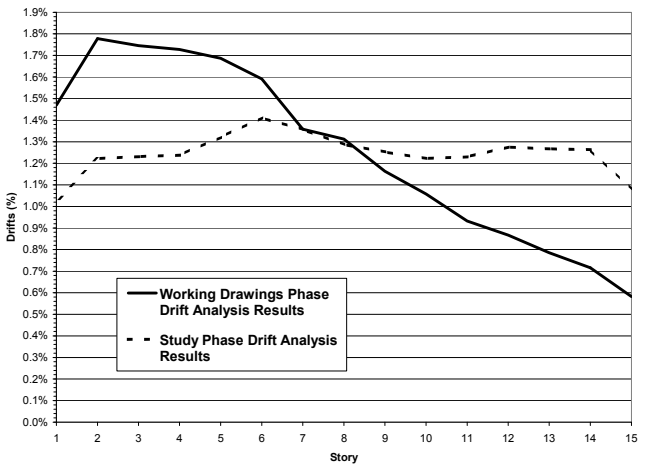


Figure 11. Study Phase and Working Phase Average Drift Comparison

Working Drawings Analysis Results

The drift performance of the building is shown in Figure 12. Results for three conditions are shown, (1) the existing structure with fracturing connections, (2) the structure with all connections fixed – representing either an all-connection strengthening scheme or the performance where fracture of the connections does not occur, and (3) the structure with the selected retrofit scheme consisting of dampers and 60% connection strengthening. The results shown are the average of the maximum drift response from each time-history analysis.

In the NRHA of the building in the existing condition, connection fractures were observed to propagate from the bottom of the building upward, resulting in high drift demands in the lower portion of the building compared to the upper portion (Figure 13). Beams with existing connections in the upper portion of the building retained a significant portion of their original stiffness by reverting to a "pin-fixed" condition following fracture of both bottom flanges within one beam span.

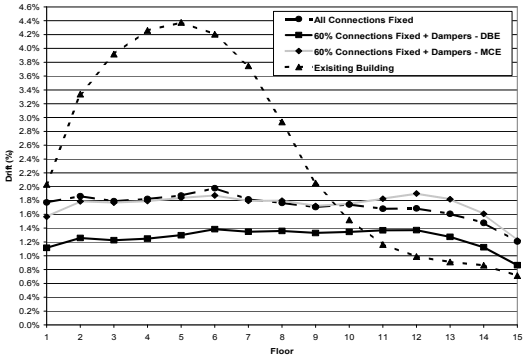


Figure 12. Average drift results for all existing connections, all connections fixed, and 60% connections fixed plus dampers (DBE/MCE).

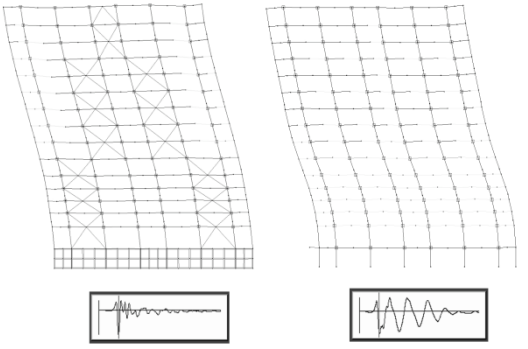


Figure 13. Comparison of retrofitted building (left) versus existing building (right) displaced shape at same time in same ground motion.

CONCLUSIONS

The Caltrans District 4 Office Building is a steel moment resisting frame building with connections similar to those that fractured in the 1994 Northridge, California earthquake. After studying various schemes, a combination of moment connection retrofits and the addition of viscous dampers was chosen to meet the performance goals established by the State of California.

The type of rapid weld fracture observed in the existing connection test specimens (Kim and Stojadinovic 2003) has typically not been observed in other moment frame connection tests. The reasons for this behavior have not been fully understood but may be related to the deep column sections present in the test specimens. The drift performance of the Caltrans building with existing connections modeled clearly shows that this condition, if it exists for all connections in the building, presents a significant risk to life safety for the building occupants.

Deep columns were commonly used in high-rise steel frame construction prior to 1994 due to the stiffness advantage that they represent. If connections of this type perform in a similarly brittle fashion then buildings using this connection type may be less safe than would otherwise be assumed. Further research is needed to more completely understand this condition.

However, as shown through the project's testing program, the connections of deep column moment frames can be successfully retrofitted to prevent fracture of the connection and develop plastic hinges within the frame beams.

The simplified analysis used to estimate the performance of the proposed retrofit scheme was reasonably successful in estimating the overall extent of strengthening work required to achieve the desire performance. However, the simplified analysis substantially underestimated the drift in the lower stories and overestimated the drift in the upper stories. This resulted in a substantial revision to the damper and connection strengthening scheme configuration based on the initial response from the PERFORM-3D response history analysis.

Nonlinear response history analyses were successfully completed using PERFORM-3D to verify the performance of the existing and retrofitted structure. Highly nonlinear existing connection behavior was successfully captured using a fiber model. The computer model of the building produces a connection failure pattern observed in 1994 Northridge earthquake, with primarily bottom flange fractures observed at existing connections. The hysteresis of the existing connection closely matches the test data.

The extra steps taken beyond typical engineering practices were intended to provide better assurance that the project's performance goals would be met during the design basis seismic event.

ACKNOWLEDGEMENTS

Funding for this project was provided by the California Department of General Services.

REFERENCES

ABS Consulting, 2003. *Seismic Evaluation of CALTRANS District 4 Headquarter 111 Grand Avenue Oakland, California*, ABS Consulting, Inc., EQE Structural Engineers Division, Oakland, CA.

Blaney, C.P.; M. Fraynt; C. M. Uang; J. D. Newell and T. A. Ahmed, *Experimental and Analytical Evaluation of Project-Specific Rehabilitated Steel Moment Connections for a 15-Story Building*, Proceedings 100th Anniversary Earthquake Conference Commemorating the 1906 San Francisco Earthquake, 2006.

Chopra, A. K. and R. K. Goel, *A modal pushover analysis procedure for estimating seismic demands for buildings,* Earthquake Engineering & Structural Dynamics, Vol. 31, no. 3, pp. 561-582, Mar. 2002.

Computers and Structures, Inc., *SAP2000 v.8 Analysis Reference Manual*, 2002.

Federal Emergency Management Agency, July 2000 *Recommended Seismic Evaluation and Upgrade Criteria for Existing Welded Steel Moment-Frame Buildings*, FEMA 351. Washington, D.C.

Federal Emergency Management Agency. November 2000. Prestandard and Commentary for the Seismic Rehabilitation of Buildings, FEMA 356. Washington, D.C.

Federal Emergency Management Agency, 2004 *Improvement of Nonlinear Static Seismic Analysis Procedures*, FEMA 440. Washington, D.C.

Federal Emergency Management Agency, *2003 NEHRP Recommended Provisions for Seismic Regulations for New Buildings and Other Structures*, FEMA 450. Washington, D.C.

Graham H. Powell Inc and RAM International LLC., *RAM PERFORM-3D v2.0 User Guide*, 2000.

Kim, T. and B. Stojadinovic, *Physical and Numerical Performance Evaluation of Steel Moment Resisting Frames,* Pacific Earthquake Engineering Research Center, August 2003.

Newell, J. and C.M. Uang, 2005. *Cyclic Testing of Steel Moment Connections for the Caltrans District 4 Office Building Seismic Upgrade*, Report No. SSRP-05/03, Department of Structural Engineering, University of California, San Diego.

State of California, Real Estate Services Division, *Guidelines for the Seismic Retrofit of State Buildings*, 1994, Rev. April 2001.

Yu, K.; J. Heintz and C. Poland, *Assessment of Nonlinear Static Analysis Procedures for Seismic Evaluation of Building Structures,* Proceedings U.S.-Japan Joint Workshop and Third Grantees Meeting, U.S.-Japan Cooperative Research on Urban Earthquake Disaster Mitigation, 15-16 August 2001, University of Washington, Seattle, Washington; pp. 431-450, 2001.

"The Bowls Project" – A Prototype for Full Scale Testing as an Alternate Approval Process for Small Scale Base-Isolated Structures

Gordon Wray, S.E.[1], Mark Sinclair, S.E.[2], Michael H. Ramage[3]

[1]Degenkolb Engineers, 300 Frank H. Ogawa Plaza, Suite 450, Oakland CA 94610; PH (510) 272-9040; FAX (510) 262-9526; email: gwray@degenkolb.com
[2]Degenkolb Engineers, 235 Montgomery Street, Suite 500, San Francisco CA 94104; PH (415) 392-6952; FAX (415) 544-0783; email: msinclair@degenkolb.com
[3]Department of Architecture, University of Cambridge, 1 Scroope Terrace Cambridge CB2 1PX; PH +44 (0) 1223 760 121; FAX +44 (0) 1223 332 960; email: mhr29@cam.ac.uk

ABSTRACT

The Bowls Project in San Francisco, California was synthesis of music, history, architecture, and engineering inspired by ancient Babylonian clay bowls. The structure is a base-isolated pair of intersecting masonry domes using the Mediterranean system of tile-vaulting.

Construction of the domes as an unreinforced masonry structure would not be permitted by the San Francisco Department of Building Inspection if not for an alternate means of compliance through a base-isolated design. The typical ASCE 7-05 approval process for base-isolated structures is expensive and time-consuming – the review cost alone would have exceeded the entire budget for this small project.

The Department of Building Inspections recognized the seismic protection that base-isolation would provide to the domes and agreed to permit the design using full scale testing of the completed structure to validate design properties of the isolation system. This not only made the project feasible, it allowed the schedule to move from conception to completion in only 2 months.

The isolators use a Ball-N-Cone design by Worksafe Technologies. Upon completion of the masonry dome construction on the isolated plinth, the structure was pulled to maximum displacement and released in a series of "snap back" tests in orthogonal directions. The plinth and the top of the dome were monitored with accelerometers to capture the acceleration time history in free vibration. The data was used to confirm the maximum acceleration of the plinth, the damping ratio, fundamental period, and hysteretic behavior of the isolation system.

This method to verify isolation system properties satisfies the intent of ASCE 7-05 by providing engineers with the design properties and surpasses the intent by providing these properties under actual load conditions. Future applications could provide artists, architects, and engineers the ability to build innovative, efficient structures in high seismic areas with the assurance that structure performs as intended.

INTRODUCTION

The Bowls Project is an interactive sound sculpture/immersive performance installation created by interdisciplinary artist Jewlia Eisenberg and architectural designer Michael Ramage. The Bowls Project takes place within a stunning masterwork of ancient-meets-modern design: two intersecting vaulted masonry domes. The Bowls Project is inspired by texts drawn from Babylonian demon bowls, women's amulets common from 300-700 CE in the area now known as Iraq. These demon bowls were inscribed with a householder's secrets and desires and then buried upside-down under the doorway to protect her home. Demon bowl inscriptions are about secrets of the home: love and sensuality; angels and demons; and the trials and joys of daily life. They explore domestic secrets in unexpected ways, suggesting a spirit-rich world that is strange and inspiring.

The form of The Bowls Project draws on the shape of the Babylonian ceramics, using two intersecting domes of different sizes to create a larger performance space and a smaller intimate contemplative space. The profile of the domes grows out of the static structural analysis, giving a compression-only form under dead load.

Creating the space using the materials and methods that Michael and Jewlia envisioned was not without its obstacles. The team had an ambitious, one-of-a-kind project to complete on a very aggressive schedule. The San Francisco Building Code does not allow the new construction of un-reinforced masonry structures. Degenkolb Engineers was added to the project team in order to engineer a system that would meet the intent of the building code, by providing a life-safe structural system. The City granted a construction permit to the project through an alternate means of compliance, which allowed for full scale testing of the completed building and base isolated system. The conventional process for approving base-isolated systems typically involves months of prototype testing and peer review. Full scale testing of base isolated structures is normally impossible, or extremely impractical due to the large forces required to displace a full scale building. The scale of The Bowls project provided a unique opportunity to apply an isolation system design usually reserved for sensitive equipment on a larger-than-normal scale without being too large to render full scale testing impractical. The successful completion of this project opens doors to full scale testing opportunities of similar sized projects, including single family residences, large equipment and other future art projects.



Figure 1. The Bowls Project.

THE BOWLS PROJECT

The tile-vaulted dome has roots in medieval Mediterranean cultures and was revisited by the 19th-century architect and engineer Raphael Guastavino, who brought the technique to the United States, eventually building over 1000 structures with this technique[12]. Tile vaulting relies on fast-setting gypsum mortar and thin tiles to build elegant structural spans with a minimum of formwork. The structures typically work in compression only, and are used with great architectural and structural expression in the works of Antoni Gaudi and others in the Barcelona region. Tile-vaulting can be applied and adapted for contemporary architecture, where there is a benefit to using ancient techniques with new materials. A number of buildings using tile vaulting have been recently completed where structural form, minimal material, and constructability were paramount concerns. These include The Pines Calyx and Crossway House in Kent, England, and the Mapungubwe Interpretive Centre in South Africa. Because the structures are designed for compressive loads, tile-vaulted structures are not typical in earthquake regions. The Bowls Project was the first application of a novel hybrid tile-vault, using geotextile for reinforcing between the layers of masonry.

Tile-vaults are built in multiple layers of thin tiles with a thick (~1/2") mortar bed between the layers. Usually the vaults are in layers of three or more tiles to give enough thickness to withstand asymmetric loads. The Bowls Project domes are constructed from autoclaved aerated concrete (AAC) tiles reinforced with geotextile

for earthquake safety. AAC is lightweight foamed concrete that is easy to cut, has minimal environmental impact, and works well with the tile vaulting technique due to its surface roughness. The minimum compressive strength of AAC is low (580 psi), but the stresses in the domes, due to their large contact area, are an order of magnitude lower, with a maximum of 23 psi. The dome construction incorporates a geogrid (Tensar TriAx 160) embedded in the mortar layers. The geogrid, typically used for reinforcing road-beds, adds a level of omni-directional tensile properties to the composite through a mechanical bond between the mortar and masonry. Ongoing research at Cambridge University is quantifying the improvements possible so that tile-vaulted structures can be safely built in areas with moderate earthquake risk. Because the geogrid is only effective for moderate earthquakes, and is currently experimental, the additional base isolated plinth was required in San Francisco.

Understanding and quantifying the forces in the masonry domes relies on thrust-line analysis[3] and applying an equivalent static loading for dynamic earthquake analysis[4]. By tilting the interactive thrust-line model (Figure 2), the amount by which the thrustline escapes the geometry can be calculated. The distance of the thrust line from the geometry, the thrust value and lune element size are used to calculate the additional performance envelope given by the geotextile. The graphic analysis is conservative -- it assumes that the thrust line returns to the centerline of the masonry at the supports, which with reinforcing isn't necessary. Just as the thrust line can (and does) exit the masonry geometry throughout the span, it can do so at the base. Choosing a thrust line that is shifted to the left in the counter-clockwise rotated EQ model would result in drastically lower tensile forces where the thrust line exits the masonry.

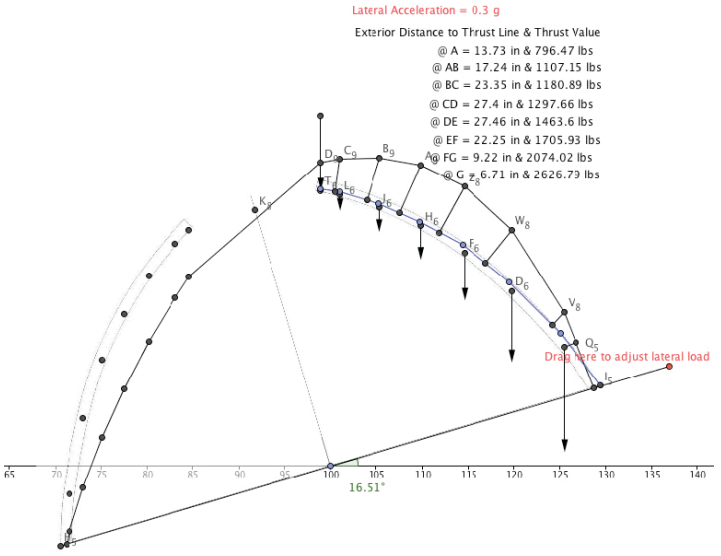


Figure 2. Example Output of Thrust Line Analysis for Seismic Loading

The vaulted masonry domes were supported by a steel and wood plinth connected to the supporting structure by 30 Ball-N-Cone seismic isolators. The weight of the

domes was supported by 1-1/8" plywood spanning to 2x8 joists at 16" o.c.. Additional blocking was provided around the perimeter of the domes. The joists were hung from wood nailers on top of W6 steel beams. The W6 steel beams were centered at 6'-6" in each direction forming a four bay by five bay platform measuring 26' x 32'-6" to the outer framing. The lateral inertial force of the masonry (and the static thrust from the vault) was transferred to the plywood diaphragm through plywood rings cut to fit the inner and outer diameters of the walls. The diaphragm was screwed to the 2x nailers and the nailers were bolted to the top flange of the W6 beams.

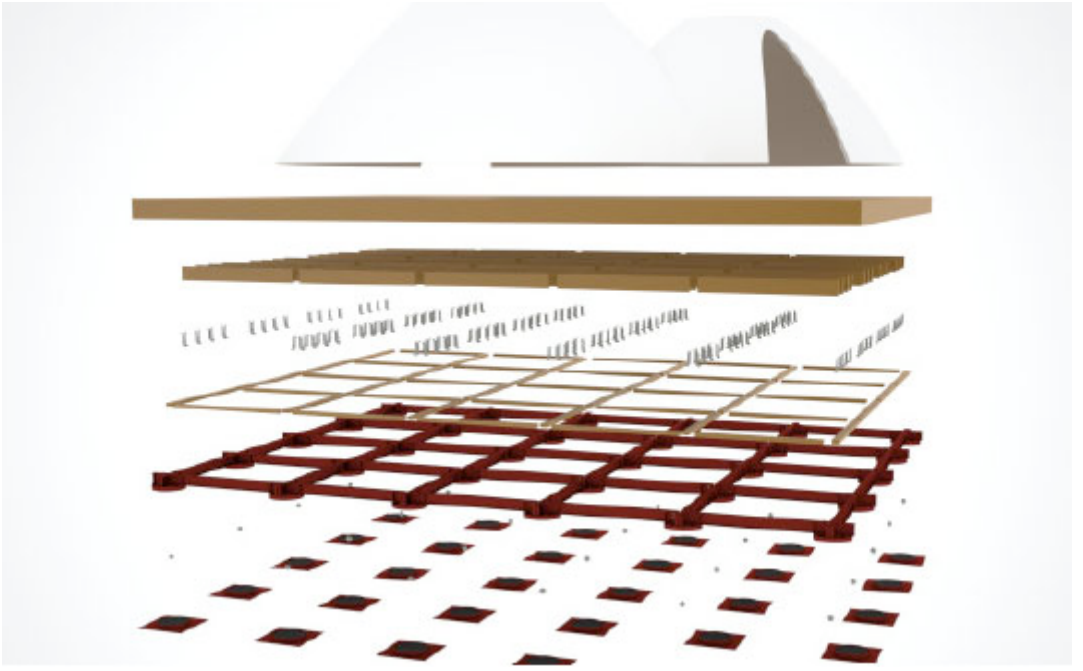


Figure 3. 3-D Rendering of Plinth Construction.

An isolator was located at each beam intersection. The isolator surface was formed from 5/8" steel plate, which was pressed into the specified shape required by design. Perimeter rings provided stability to the curved plates as well as a lip to limit displacement of the ball bearing. The top plates were welded directly to the beam intersections. The bottom plates were welded to ¼" steel plates and arranged and leveled on site. Since The Bowls Project was constructed as a temporary installation, ease of construction, demolition, and reuse were primary design considerations of the plinth. The steel elements were designed as bolted modules to be assembled in the field. P-Δ loading at the maximum isolator displacement was considered in the design of the framing and connections.

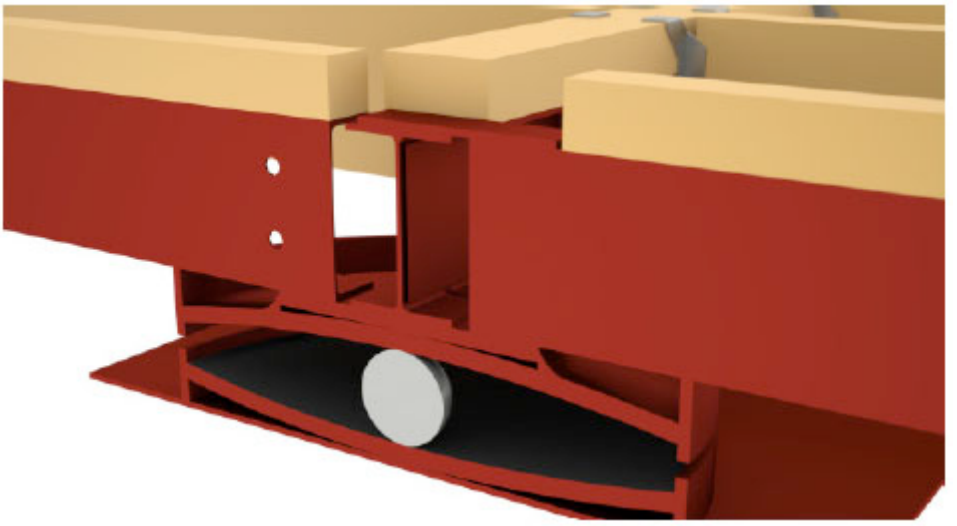


Figure 4. 3-D Section through Isolator.

The seismic isolators use a design derived from the Ball-N-Cone isolator by WorkSafe Technologies. A 3-1/2" diameter steel ball bearing is located between two concave plates. In a seismic event, the top plate displaces relative to the bottom plate, causing the ball to roll along both surfaces. The initial stiffness is a function of the weight divided by the effective pendulum length, *l*, which is equal to two times the difference in the radius of the concave plate and the ball diameter. Near the perimeter of the plate, a constant restoring force is provided by a constant slope which meets the curved surface at a tangent. A steel ring around the edge of each plate provides a lip to limit displacement; however the isolators were designed to meet the displacement demand of the MCE earthquake in San Francisco. The interface of the steel ball bearing to the steel plate provides very little rolling friction resistance and subsequently very little damping. Neoprene liners were applied to the surface of each plate to increase the rolling friction resulting in greater damping.

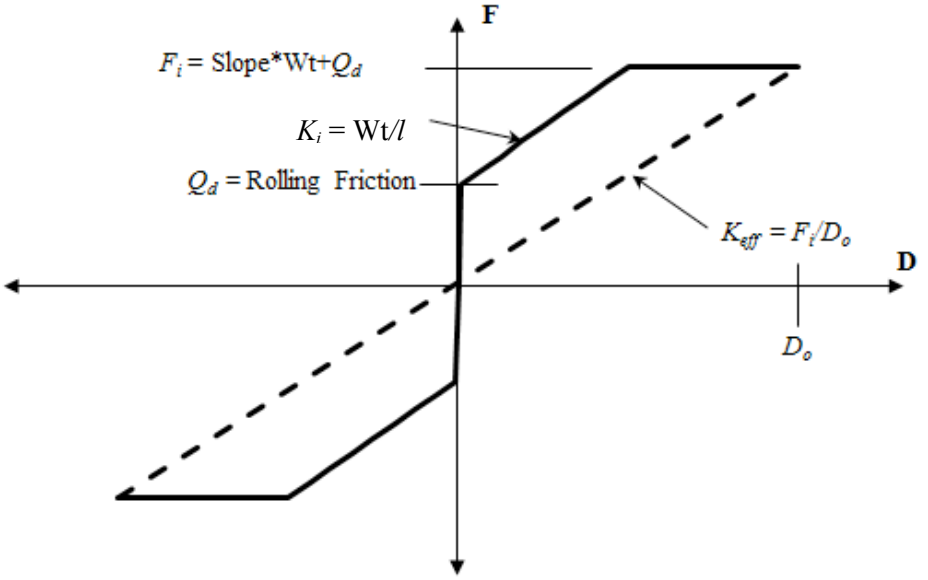


Figure 5. Theoretical force-deformation behavior of Ball-N-Cone isolator.

The method of fabricating the isolators was unique to The Bowls Project. Flat 5/8" circular steel plates were pressed into the required shape, which proved to be much more cost effective than machining.

CODE BASED DESIGN AND APPROVAL PROCESS FOR BASE ISOLATED BUILDINGS

ASCE 7-05 permits isolated structures to be designed using the Equivalent Lateral Force, Response Spectrum, or Response History Procedure. Most designs in the United States use the Response History Procedure based on a suite of ground motion pairs and a nonlinear analytical model to capture the dynamic response of the isolation system.

The Equivalent Lateral Force Procedure is limited to regularly-configured low-rise structures with low seismicity, and firm soil. In addition, the isolation system must have an effective period less than 3 seconds, adequate period separation from superstructure, adequate restoring force and be capable of accommodate the displacement demands from the maximum capable earthquake (Reference ASCE 7-05, Section 17.4.1 for limitations of Equivalent Lateral Force Procedure)

The Equivalent Lateral Procedure is an iterative process based on equivalent linear isolator properties, effective (or secant) stiffness damping. The 1-second spectral acceleration is a known quantity from the site. Isolator Displacement (D_D or D_M) is a function of effective stiffness and damping, which are functions of an initially assumed displacement. The process confirms isolator displacement and yields the Isolated Base Shear, V_b (which is used in one of the minimum base shear requirements for dynamic procedures). The Equivalent Lateral Procedure was used to determine the maximum displacement and isolated base shear for The Bowls project. These quantities were confirmed through full scale testing.

ASCE 7-05 enforces the Design Review and Testing requirements of 17.7 and 17.8 regardless of analysis procedure selection. An argument could be made to waive the Design Review requirements for simple projects that are designed using the Equivalent Lateral Procedure.

The ASCE 7-05 process for Design Review of isolated structures begins with the selection of an independent peer review team. This team is tasked with

a. Review of site specific seismic criteria, including the development of site specific-spectra and ground motion histories,
b. Review of preliminary design, including determination of total design displacement, total maximum displacement, and lateral force level,
c. Overview of prototype testing,
d. Review of the final design of the entire structural system, and all supporting analyses,
e. Review of the isolation system quality control testing program.

The intent of the code-based Design Review and Testing program is to prove the effectiveness of the seismic isolation system and the superstructure design under the dynamic loads that could result in the event of a major earthquake. The design team for the Bowls Project did not have the time or financial resources to engage a peer review team and complete testing prior to construction.

The San Francisco Department of Building Inspections saw the value provided by full scale testing as an alternate means to meet the intent of the code. The design team provided criteria for a series of "Snap-Back" tests in which the plinth was pulled sideways, away from its stable resting position, and then released. The test results were compared against the theoretical results in order to validate isolation system properties and the acceptability of the masonry superstructure to resist the seismic forces transferred through the system. These forces were calculated (and proved) to be on the order of 1/6 the force that would be seen in an equivalent fixed base structure.

In addition to testing all of the components of the isolation system the full scale testing also generates lateral loads within the supported dome superstructure. This was particularly important in this case because the dome construction was not an approved structural system. The testing therefore validated the structural integrity of the dome at the same time as the performance of the isolation system. This approach is not possible in a fixed base design because it would be necessary to confirm that the dome can accommodate the required ductility demands in addition to resisting the required lateral forces.

The lateral forces generated in the dome superstructure were approximately 0.1g. While this was slightly less than the computed design earthquake acceleration of 0.13g the results were judged to be acceptable based on the absence of any observable damage following several tests.

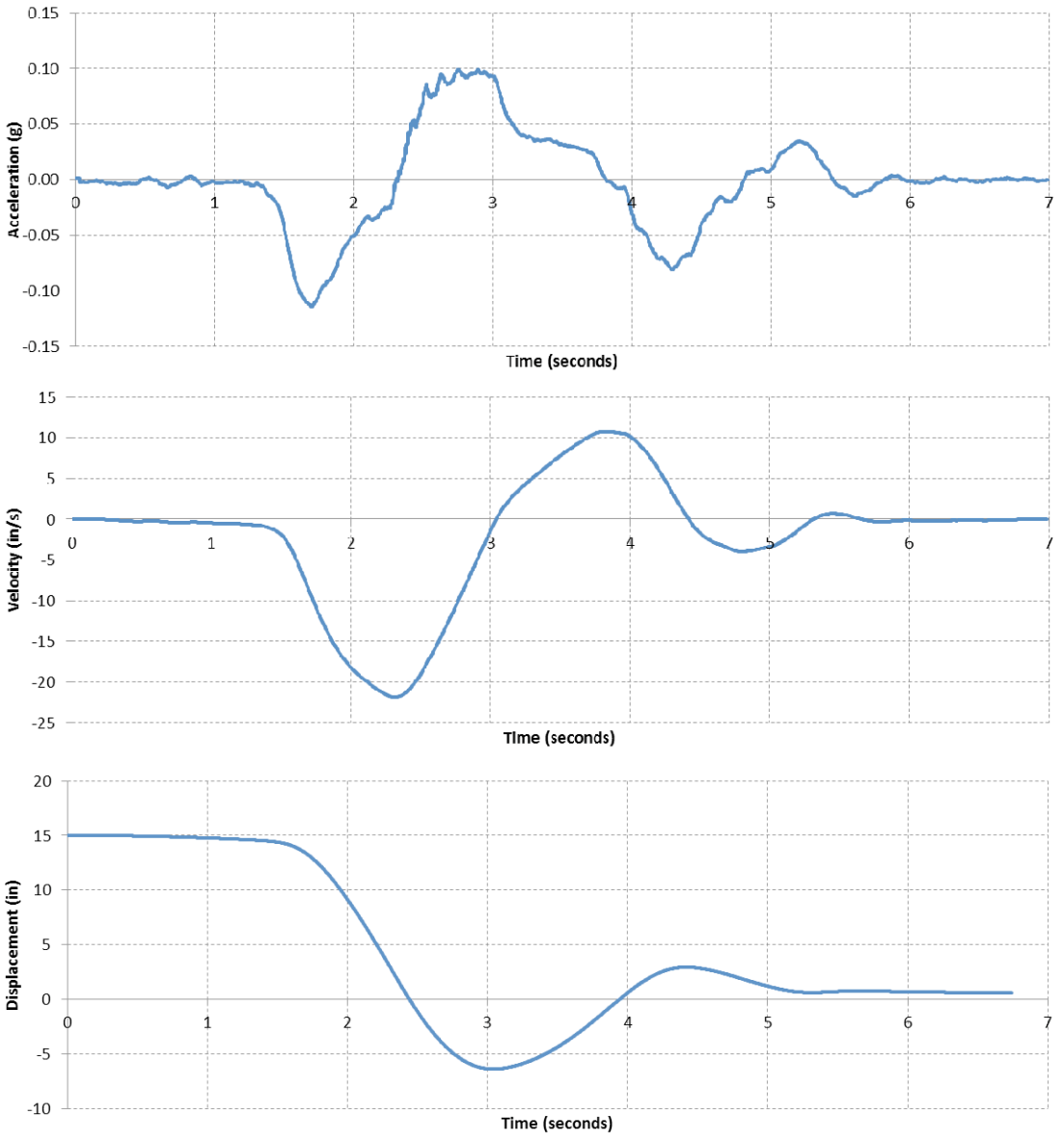


Figure 6. Snap-Back Test Results

The rubber liner in the isolators provided a significant amount of damping, which limited the number of cycles in a snap-back test. The isolation system damping values were estimated using the logarithmic decay of the recorded displacement trace. Because the damping value is relatively high, the trace decays quickly. Using 15" initial displacement, the first half cycle measured 6.4", and the first full cycle measured 2.9" on the return. These values result in about 25% effective damping.

The hysteresis loop computed using the target isolation properties is shown overlaid on the test hysteresis loop in the following figure. The results are very close to the originally assumed effective stiffness.

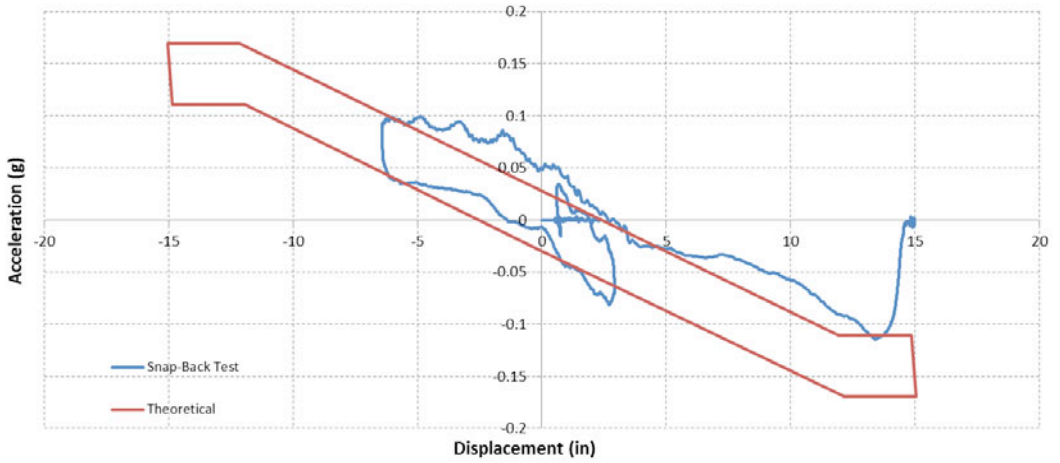


Figure 7. Snap-Back Hysteresis

In order to justify the cyclic performance of the isolators, dynamic test results were achieved by repeated cycling of a segment of the plinth back and forth under human power. The forced cyclic response maintained about 15" maximum displacement per cycle. The uncertainty of the input force (in opposite directions from either side of the plinth) distorts the fullness of the acceleration-displacement loops, consequently making the damping ratio difficult to quantify, The average theoretical result, with no initial acceleration, has been plotted for reference. The average of the dynamic loops closely traces the average theoretical properties although the individual loops may be distorted from the input force. Despite the nuances from the low-tech test method, the results indicate that the isolators would perform acceptably under dynamic earthquake loading.

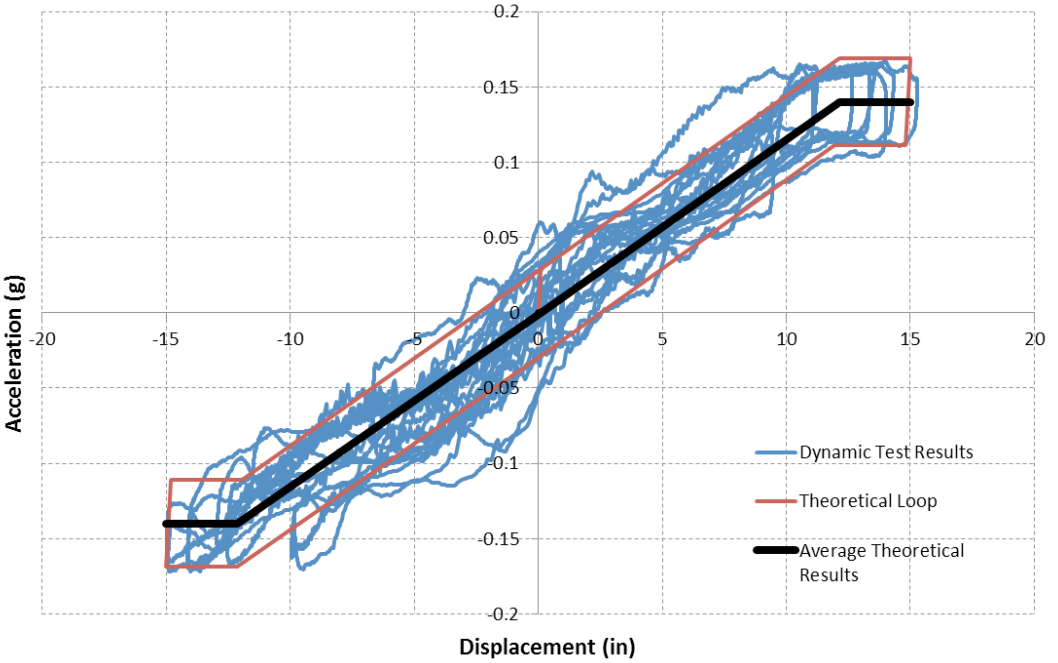


Figure 8. Isolation System Hysteresis under Dynamic Loading

FULL SCALE TESTING ALTERNATIVE

The Full Scale Testing Alternative must meet the intent of ASCE 7-05 in order to demonstrate effective functioning of the seismic isolation system and stability of the superstructure and supporting platform under the dynamic loads that could result in the event of a major earthquake. ASCE 7-05 requires testing as a means to establish and validate the deformation characteristics and damping values of the isolated system. The full scale testing alternative focuses on the validation of the design using knowledge of base-isolation principles and consistency in fabrication to establish isolator properties.

The limits defined by the Equivalent Lateral Procedure establish expected upper bound force and displacement under lateral loads. Regardless of design procedure, in the current practice of design in the United States, engineers forgo the "prototype" tests and jump straight to system design with the confidence that isolators can be fabricated to meet design parameters. Prototype testing in the laboratory is used as a means to confirm the adequacy of a design.

The proposed Full Scale Testing Alternative pushes the validation of design properties to the final stage of construction. In addition to the code acceptance criteria, care should be taken to include project specific performance criteria for the superstructure. Project size, required testing loads, and ability to provide safety to all persons involved in the test are pertinent considerations for the use of Full Scale Testing.

ASCE 7-05 establishes acceptability criteria in section 17.8.4. Using this section, the following conditions must be satisfied:

1. The force-deflection plots for all tests specified in Section 17.8.2 have a positive incremental force-resisting capacity
2. For each increment of test displacement specified in Section 17.8.2.2, and for each vertical load case specified in Section 17.8.2.2,
    a. For each test specimen, the difference between the effective stiffness at each of the three cycles of test and the average value of effective stiffness is no greater than 15 percent.
    b. For each cycle of test, the difference between effective stiffness of the two test specimens of a common type and size of the isolator unit and average effective stiffness is no greater than 15 percent.
3. For each specimen, there is no greater than a 20 percent change in the initial effective stiffness over the cycles specified in item 4 of Section 17.8.2.2.
4. For each specimen, there is no greater than a 20 percent decrease in the initial effective damping over the cycles specified in item 4 of Section 17.8.2.2.
5. All specimens of vertical-load-carrying elements of the isolation system remain stable where tested in accordance with Section 17.8.2.5.

For the Bowls Project, the test procedure required two "snap-back" tests in each principle direction at full displacement. Since the system was tested as a whole, comparative tests between individual specimens were not required. The acceptance criteria for the isolation system were modified from ASCE 7-05 as follows:

1. Loop has positive incremental stiffness in each direction. *[Similar to Item 1 above]*
2. For the tests in each direction, K_{eff} at each displacement cycle above 3" shall be within 15% of the average value for the two tests. *[Similar to Item 2a above]*
3. The value of K_{eff} at the cycles closest to D_d and D_m during the 4th test shall be within 15% of the value in the first test.
4. The effective damping, beta, at the cycles closest to D_d and D_m during the 4th test shall be within 15% of the value in the first test.
5. All isolators shall be stable during each test, no delamination of liners observed, or jamming or deformation of the ball bearings.

In addition to the isolation system acceptance criteria, project specific acceptance criteria for The Bowls Project were the following:

1. No collapse of masonry, global or local.
2. No cracks greater than 1/8" following the test.
3. Hairlines cracks shall be repaired following completion of the test sequence.
4. From the recorded test hysteresis loop demonstrate that the isolator stiffness and damping characteristics match the values used in the calculations, specifically:

K_d	>=0.63 k/in	for test displacement closest to D_d=7.7"
K_m	>=0.39 k/in	for test displacement closest to D_m =15.6"
β_d	>=23%	for test displacement closest to D_d =7.7"
β_m	>=19%	for test displacement closest to D_m =15.6"

   The acceptability values may be adjusted to match actual test displacements.
5. The plinth acceleration must exceed 0.13g, the code minimum base shear determined for the isolation system in these calculations for the design earthquake.

The isolation system proved to have a very high damping level, sufficient to prevent the snap-back tests from achieving the larger displacements listed above. However, the testing did confirm that the isolation system met the requirements for the design level earthquake displacements following adjustment of the target properties for the actual test displacement. The cyclic testing was used to validate the isolator properties for the maximum capable earthquake displacements.

CONCLUSIONS

The unconventional structural system of The Bowls Project necessitated use of base-isolation as a protective system, and the scale of the project allowed an unconventional testing method. A conventional structural system or a building more massive than The Bowls would have rendered base isolation unnecessary and/or full-scale in-place testing impractical. The combination of high seismicity, vaulted masonry construction, design team creativity and local jurisdiction cooperation provided a unique opportunity for innovation.

The application of full-scale testing as an alternative to testing individual (or pairs) or isolators allows smaller scale isolation projects to be viable. Time and budget constraints for conventional approval of an isolated system for The Bowls Project would have never allowed the project to get off the ground. The process in itself is similar to the current design-practice, where isolators are tested in order to verify assumed properties, instead of to establish design properties.

This approach appears to have great potential to improve the adoption rate for small isolated structures, particularly when alternate structural systems are used.

REFERENCES

American Society of Civil Engineers (ASCE). (2005) *Minimum Design Loads for Buildings and Other Structures (ASCE 7-05)*.

Block, P., Ciblac, T., and Ochsendorf, J.A. (2005). "Real-Time Limit Analysis of Vaulted Masonry Buildings." *Computers and Structures*

Block, P., DeJong, M. and Ochsendorf, J.A. (2006) "As Hangs the Flexible Line: Equilibrium of Masonry Arches." *Nexus Network Journal*, 2006-10-08, Birkhauser, 1590-5896

Collins, George R. (1968). "The Transfer of Thin Masonry Vaulting from Spain to America." *Journal of the Society of Architectural Historians,* October, 177

Ochsendorf, J.A. (2010). *Guastavino Vaulting: The Art of Structural Tile*. Princeton Architectural Press

WorkSafe Technologies (2010). "Modeling the Performance of a Ball-in-Cone Isolation System"

Seismic Isolation: Applications of WorkSafe Technologies Ball-N-Cone Isolator

A. M. Nacamuli[1] and K. M. Sinclair[2]

[1]Degenkolb Engineers, 235 Montgomery Street, Suite 500, San Francisco, CA 94104; PH (415) 392-6952; FAX (415) 544-0783; email: nacamuli@degenkolb.com
[2]Degenkolb Engineers, 235 Montgomery Street, Suite 500, San Francisco, CA 94104; PH (415) 392-6952; FAX (415) 544-0783; email: msinclair@degenkolb.com

ABSTRACT

The WorkSafe ISO-Base planks, Isolated Raised Access Floor and Isolated Equipment Platform take a new approach to protection of building contents in seismic areas by implementing isolation technology. Seismic isolation has been in use since the 1970s to protect buildings and other large structures from earthquake shaking in seismically active areas around the world. Seismic isolation technology works by decoupling the isolated component from the ground, essentially allowing the ground to move underneath the component without transmitting the damaging accelerations above the plane of isolation. WorkSafe Technologies owns the patents on the Ball-N-Cone isolation technology, which uses a steel dish and ball bearing to provide seismic isolation and has developed systems for isolating individual cabinets as well as entire access floors. The technology has now been extended to include large isolated platforms, suitable for large heavy items such as equipment, art installations and potentially light framed residential construction. The patented Ball-N-Cone isolators are well suited to the lighter vertical loads associated with building contents compared to those present in larger building and bridge structures. The WorkSafe ISO-Base planks are unique in applying isolation technology to individual server cabinets, or rows of cabinets. The Isolated Raised Access Floor (IRAF) applies the same isolation technology, but to an entire access floor by moving the isolation plane to the base of the access floor pedestals. The benefits of using isolation as opposed to conventional bracing are two-fold – critical equipment is protected against damaging earthquake accelerations and facility managers do not have to deal with installing traditional bracing, with the associated concrete drilling and relatively heavy construction in the sensitive data center environment. The Isolated Equipment Platform extends the use of the Ball-N-Cone isolator to heavier components such as large pieces of equipment, art installations and potentially light framed construction. This paper presents several case studies on the applications of equipment isolation and the benefits it provides.

INTRODUCTION

Traditional fixed base building structures and their contents are prone to significant damage when subjected to the high horizontal accelerations from large earthquakes. The seismic performance of typical fixed based buildings designed in accordance with current building codes assumes nonlinear response of the building's lateral force resisting system as codified in the response modification coefficient (R).

Furthermore, floor accelerations of a fixed base structure can be significantly higher than the input earthquake horizontal ground acceleration. This amplification of the earthquake horizontal accelerations up the height of a building is included in building codes for the design of the structure as well as the anchorage of contents. Fragile contents such as computers, servers, data storage systems, networking equipment, pharmaceutical filling equipment, and museum contents are especially susceptible to damage when subjected to high lateral accelerations.

Damage to the building structure can be reduced or eliminated by designing the structure to remain nearly elastic when subjected to the design level earthquake ground shaking. However, this will generally increase the accelerations that the building contents will be subjected to. Other alternatives to reducing damage to the structure include energy dissipation systems or a capacity design approach. Both of these methods will still result in relatively high lateral accelerations on building contents. The only method to significantly reduce damage to the building structure and its contents is to base isolate the entire building.

Seismic isolation has been in use since the 1970s to protect buildings and other large structures from earthquake shaking in seismically active areas around the world. Base isolation decouples the building from the earthquake horizontal accelerations, significantly reducing lateral demands on the structure and contents. However, building a new base isolated facility is not always possible and retrofitting an existing structure with base isolation is prohibitively expensive, except for rare cases. With WorkSafe Technologies Ball-N-Cone isolation products there is now an alternative to isolating the entire structure.

WorkSafe ISO-Base planks, Isolated Raised Access Floor and Isolated Equipment Platform take a new approach to protection of building contents in seismic areas by implementing isolation technology.

WorkSafe Technologies owns the patents on the Ball-N-Cone isolation technology, which uses a steel dish and ball bearing to provide seismic isolation and has developed systems for isolating individual cabinets as well as entire access floors. The technology has now been extended to include large isolated platforms, suitable for large heavy items such as equipment, art installations and potentially light framed low-rise construction. The patented Ball-N-Cone isolators are well suited to the lighter vertical loads associated with building contents and lightweight structures compared to those present in larger building and bridge structures.

The WorkSafe ISO-Base platforms are unique in applying isolation technology to individual server cabinets, or rows of cabinets. The Isolated Raised Access Floor (IRAF) applies the same isolation technology, but to an entire access floor by moving the isolation plane to the base of the access floor pedestals. The benefits of using isolation as opposed to conventional bracing are two-fold – critical equipment is protected against damaging earthquake accelerations and facility managers do not have to deal with installing traditional bracing, with the associated concrete drilling

and relatively heavy construction in the sensitive data center environment. The Isolated Equipment Platform extends the use of the Ball-N-Cone isolator to heavier components such as large pieces of equipment, art installations and potentially light framed construction.

FUNDAMENTALS OF BASE ISOLATION

The concept of base isolation is to decouple the structure from the horizontal components of the earthquake ground motion by creating an isolation plane. The isolation plane is created by introducing a structural system that has a relatively low lateral stiffness between the structure to be isolated and the foundation or supporting elements. The low lateral stiffness of the isolation system gives the isolated structure a fundamental frequency that is lower than both the fixed base structure and the earthquake ground motion frequencies with the most damaging accelerations. The isolated structure responds primarily in the first mode, which consists of lateral displacement of the isolation system, and the structure above remains almost rigid. Figure 1 shows a comparison of the idealized response of an isolated and fixed base structure to earthquake ground shaking.

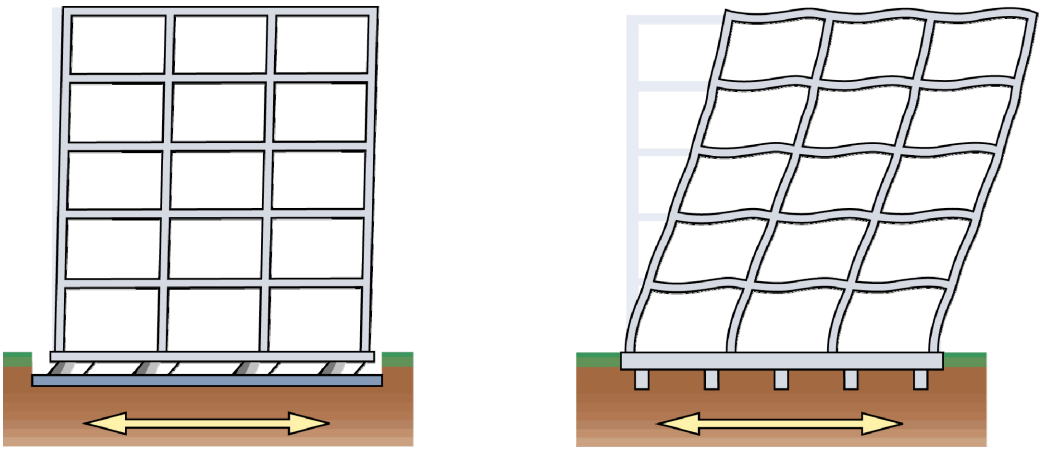


Figure 1. Comparison of Response Between Isolated and Fixed Base Structure

The benefit of base isolation is that the horizontal accelerations on the structure and components above the isolation plane are significantly reduced when compared with a fixed base structure, as much as 5 to 10 times, depending on the application. An additional benefit is that the elements above the isolation plane can be easily designed to remain elastic due to the significant reduction in horizontal accelerations, which greatly reduces or eliminates damage to the structure and contents.

BALL-N-CONE ISOLATOR

There are two basic types of isolation systems that are routinely used for the base isolation of buildings and bridges: elastomeric bearings and sliders. The Ball-N-Cone

isolator represents a third type of isolation system and uses a ball bearing sandwiched between two steel dishes. The typical Ball-N-Cone isolator used in the ISO-Base planks is shown in Figure 2.

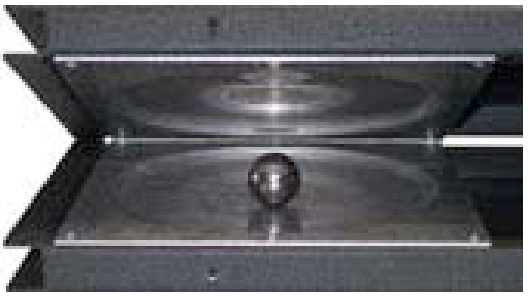


Figure 2. Ball-N-Cone Isolator (ISO-Base Plank)

The isolator consists of a 1.5-inch diameter hardened steel ball bearing and two 8-inch diameter steel dishes. Larger isolators have also been manufactured and tested. The isolator functions by the top and bottom dishes moving relative to each other by rolling of the steel ball bearing. The profile of the steel dish consists of mainly a cone with a slope of approximately 1:10 (rise to run) connected by a small radius transition at the center, as shown in Figure 3. The lateral displacement capacity of a Ball-N-Cone isolator is approximately two times the radius of a dish.

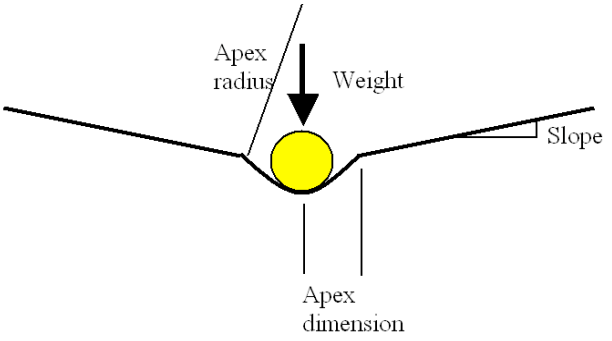


Figure 3. Idealized Profile of Ball-N-Cone Isolator

The vertical load carrying capacity of a Ball-N-Cone isolator is typically limited by the strength of the dish or its supporting elements. The ball bearings, which are typically hardened to Rockwell 59C, have a very high strength and are not the limiting factor. For a typical ISO-Base plank the maximum load is on the order of 1,000 pounds. If the dish is adequately supported an increase in the vertical load results in the ball bearing penetrating the surface of the dish, creating a small indentation. When the isolator displaces laterally the ball tracks through the dish, leaving an indication of its path.

The structural properties of a system using Ball-N-Cone isolators is a function of the apex radius (R), the slope of the dish (S) and the weight on the ball bearing (W). The initial stiffness is a function of the weight and radius, Ki = W/(2R). Once the ball moves out of the apex of the dish, which is relatively small, the system has a constant restoring force, which is a function of the slope of the dish and the weight on the ball bearing, Fr = SW. The low slope (0.1) of a typical Ball-N-Cone limits the lateral accelerations that can be transmitted above the isolation plane to approximately 10% of gravity, which is significantly lower than a typical fixed base system. Because the system has a nonlinear elastic force-deformation curve the period of the system depends only on the slope of the dish and the displacement demand. For a standard ISO-Base plank, which has a slope of approximately 0.1 and a diameter of 8-inches, the period at maximum displacement, calculated using the secant stiffness, is approximately 2.9 seconds.

Unlike sliding isolators or lead-rubber bearings the Ball-N-Cone isolator exhibits very low damping. System damping is primarily due to rolling friction between the ball bearing and the steel dishes. Because the vertical loads are typically limited to a low value, the resulting rolling friction is also low resulting in system damping on the order of 1-2%. For applications with vertical loads less than 500 pounds per isolator, a polymer liner can be bonded to the two dishes. The polymer liner increases rolling friction and as a result leads to an increase in system damping.

APPLICATIONS OF BALL-N-CONE ISOLATION

Ball-N-Cone isolators are best suited for applications with relatively low axial loads (less than 15,000 pounds) due to the practical limitations of component availability and system design. These applications include protection of data center components, such as computer racks, network storage racks and associated equipment, entire data centers (by isolating the floor) and large components such as pharmaceutical fill-finish equipment and art installations. Future applications include light framed construction, such as single family residential. The following sections describe the range of applications of Ball-N-Cone isolators.

ISO-Base Seismic Isolation Planks for Computer Racks

The first wide spread use of Ball-N-Cone isolators is in WorkSafe Technologies ISO-Base seismic isolation planks for computer racks typically found in data centers. The benefits of base isolating computer racks is three fold; first, the equipment is protected from the high lateral accelerations that a fixed base rack would be subjected to, second, the horizontal forces that the supporting structure (typically a raised access floor) are subjected to are reduced, and third, cumbersome mechanical anchors are eliminated, providing increased flexibility to data center managers.

A typical ISO-Base plank assembly used to isolate a single rack is shown in Figure 4. Each plank consists of two dishes interconnected be small steel tubes. Two create an isolation platform for one computer rack two planks are placed on the floor face up,

followed by four ball bearings with two additional planks on top facing down. The two adjacent top and bottom planks are interconnected with bolted steel tubes.



Figure 4. Typical Isolation Platform for Computer Rack using ISO-Base Planks

The modular nature of the system allows the isolated platform to grow, such that an entire row of racks can be isolated, as shown in Figure 5.



Figure 5. ISO-Base Planks Assembled into Rows

As discussed previously, the standard ISO-Base planks are fitted with 8-inch diameter dishes, which means that the lateral displacement capacity of the system is 8-inches. Eight inches of lateral displacement capacity for a system with low damping results in full protection for earthquakes with a one second spectral acceleration of 30% of gravity or less. To improve the seismic performance of the system, polymer liners can be bonded to the dishes. This enhancement provides full protection for earthquakes with a one second spectral acceleration of approximately 45% of gravity. This provides full protection for most locations except for areas in high seismic regions, such as coastal California. To best determine the performance of an ISO-Base installation a structural engineer should perform a site specific analysis taking in to consideration the following items: seismicity, including near-field effects, height of installation in a building, lateral system of the building, soil conditions at the site, rack weights and configuration.

Based on testing conducted at the University of British Columbia, should isolator lock-up occur, the performance of the rack is equivalent to a fixed based rack. The result is that the ISO-Base planks provide full protection for all but the rarest earthquakes. To address the potential life-safety hazard associated with toppling of the racks, several additional enhancements have been developed. These include ball bearing restraints, which prevent the balls from rolling out of the dishes and limit straps, which prevent the top and bottom planks from separating. These elements are shown in Figures 6 and 7.

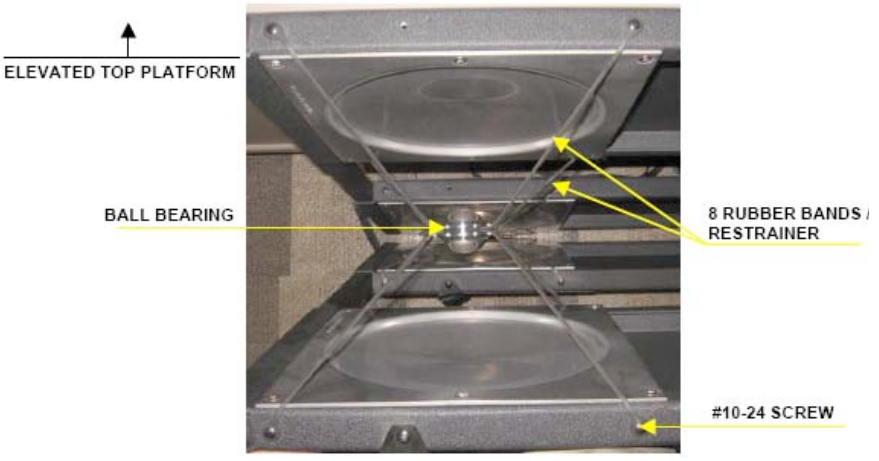


Figure 6. Ball Bearing Restraints

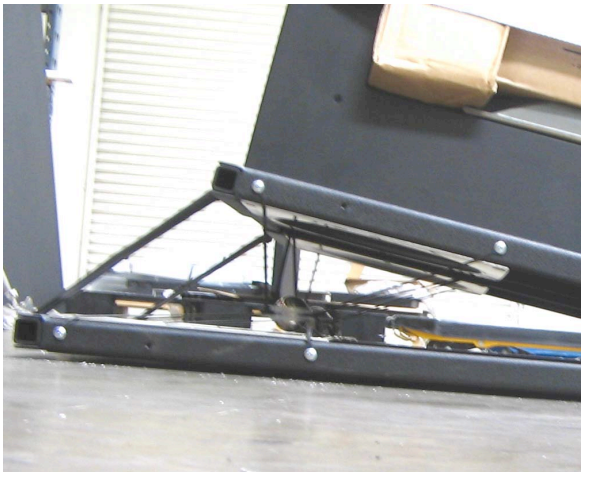


Figure 7. Limit Straps

Testing has shown that no mechanical connections are required between the bottom planks and supporting structure, even for the case of isolator lock-up. The computer racks are typically secured to the top plank with nylon straps, which have been shown through testing to be adequate to keep the racks in place on the top plank. The ease of installation is ideal for data center managers as it allows full protection of the racks without permanent anchoring typically associated with mechanical anchoring,

providing a flexible solution for seismic solution. To provide even more flexibility and earthquake protection an isolated raised access floor has been developed. The isolated access floor can be designed for any seismic hazard level and allows for complete flexibility in the arrangement of data center components.

Isolated Raised Access Floor

The Isolated Raised Access Floor has been developed to provide data center owners with maximum seismic protection and complete flexibility in data center configuration. By moving the isolation plane to the bottom of the raised floor pedestals, data center owners are free to configure their cabinets in any manner they desire. Furthermore, there is no need to move the racks on and off ISO-Base planks or deal with complicated fixed base anchorage. The Isolated Raised Access Floor is suitable for both new and existing construction; it can easily replace an existing raised access floor with a few simple modifications to allow for floor lateral displacement. The floor has been designed to use standard 24-inch square raised access floor tiles, allowing existing data center owners to reuse components from their current floor. Figure 8 shows an image of the structural system of the Isolated Raised Access Floor.



Figure 8. Isolated Raised Access Floor Structural System

The design features modular bolted construction allowing for ease of on-site installation. The Ball-N-Cone isolators are larger than those used in the ISO-Base planks, allowing for higher axial loads and larger lateral displacement capacity. The floor can be designed to have pedestal spacing of four to six feet, allowing the system to work within an existing facility. A typical cross section through the Isolated Raised Access Floor is shown in Figure 9.

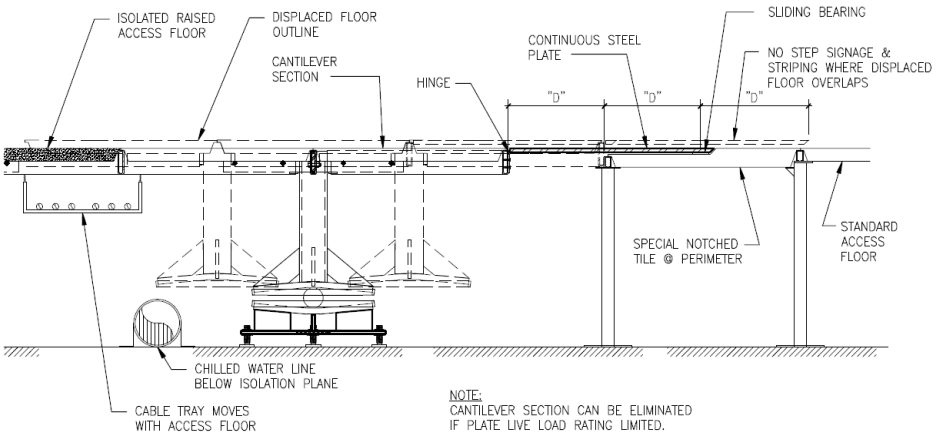


Figure 9. Typical Isolated Raised Access Floor Cross Section

As shown in the section, data and power cables can be suspended from the bottom of the access floor and large chilled water pipes can be located between the isolated pedestals. The Ball-N-Cone isolators sit on leveling feet allowing for leveling of the floor system.

The Isolated Raised Access Floor has been tested on the shake table at the University of British Columbia and its performance has been validated. Currently the floor can be designed to have a lateral displacement capacity of up to 18 inches. If the seismic demands exceed this displacement capacity, for example a data center located near the top of a flexible building in a high seismic area, the floor can be designed to include viscous dampers to reduce the displacement demands. The dampers can be installed around the perimeter of the floor below the space typically reserved for CRAC units.

Isolated Equipment Platforms

Isolated Equipment Platforms take the concept of the ISO-Base planks and Isolated Raised Access Floor and extend it to a more general case. Isolated Equipment Platforms can be used for the seismic protection of a wide range of components, from complex pharmaceutical fill-finish lines composed of multiple individual components to fragile art installations. Similar to the isolated floor, the equipment platforms can be designed with a displacement capacity of up to 18 inches. Vertical loads can be upwards of 15,000 pounds per isolator, which typically use a 3.5-inch diameter high strength ball bearing. The design of the isolated platforms is tailored to meet the specific needs of the application.

For one application two platforms were designed and constructed to seismically isolate two pharmaceutical fill-finish lines. Based on business interruption analysis it was determined that the filling lines were critical to operations and that damage to the equipment was not acceptable. Isolation platforms were the perfect solution – providing the desired protection and easily adaptable to the existing construction.

The platforms limit the lateral accelerations on the equipment to less than 15% of gravity and are recessed into a slab depression to avoid changes in manufacturing operations. Figure 10 shows a photo of one of the partially completed platforms in the slab depression during installation.

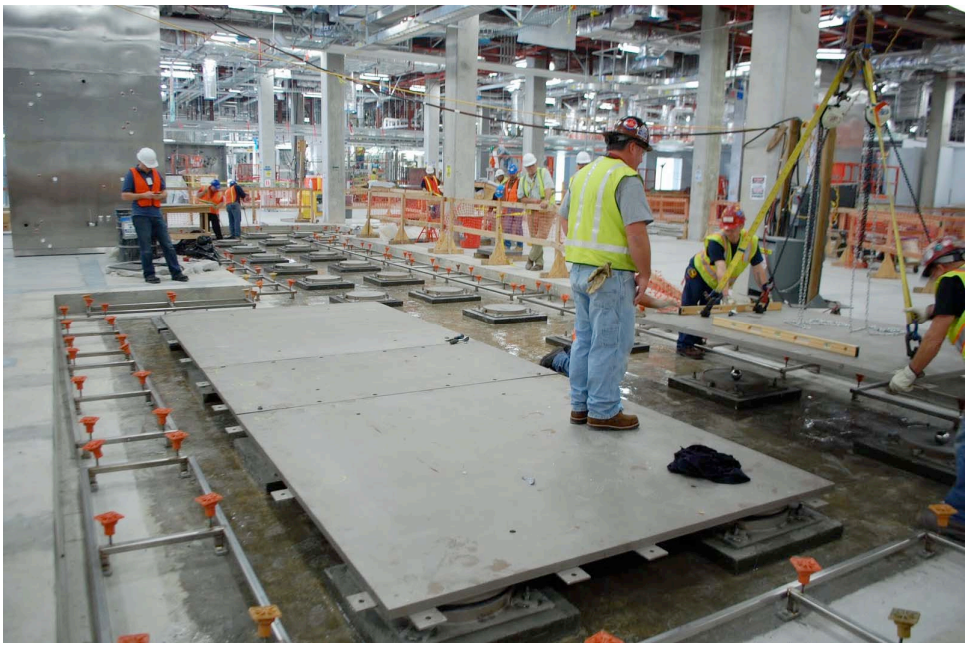


Figure 10. Partially Completed Isolation Platform

To minimize the depth of the slab depression, the platform was designed using a 1.5-inch thick top plate as the primary structural element. The top dishes of the Ball-N-Cone isolators were attached directly to the bottom of the plate in the shop by welding. The bottom isolators were field installed using leveling nuts, grout, oversized holes with welded plate washers and adhesive anchors. To minimize installation time, the platform was constructed with all bolted connections, allowing one platform to be installed in a single day (base dishes were already in place). The location and relative elevation of every dish attached to the top plate was surveyed during fabrication so that the base dishes could be accurately located in the field to minimize any field modifications. Out of 32 isolators on one line, only two isolators required minor adjustments in elevation.

The installation of the isolated platforms in a pharmaceutical clean room environment represents the strictest of criteria. The platform could not interfere with the manufacturing operations, the materials had to meet strict cleanliness requirements, which required the use of AIS 304L stainless steel for all platform components, except for the ball bearings, which were made from hardened AISI 440C stainless steel, the slab depression had to be water tight, yet allow movement of the platform in a seismic event.

A simpler application of the isolated platform is the system designed and constructed for The Bowls project in San Francisco, California. The project consists of the base isolation of a temporary art installation, which is composed of unreinforced masonry domes. Because the domes could be occupied by visitors, the installation had to meet the requirements of the building code. The team came up with the innovative solution of base isolating the domes and then conducting a full scale test for the building department. The Bowls project, which is described in detail in another paper submitted for this conference, uses similar isolators connected by a modular steel frame of wide flange beams. The platform is then created by infill wood joists topped with plywood. The steel frame and isolators is shown in Figure 11 and the final completed project in Figure 12.

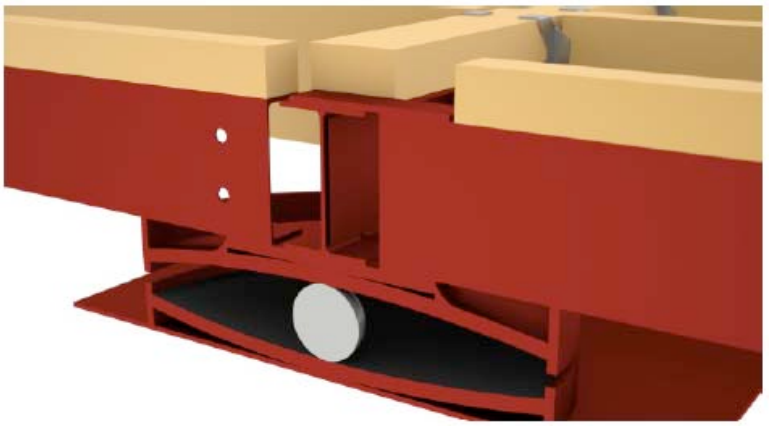


Figure 11. Section Through Isolator and Steel Frame



Figure 12. The Bowls Project

One unique feature of both the pharmaceutical installation and the Bowls project is that they could both be relatively easily tested to demonstrate that the design meets the performance objective, providing further assurance to both owners and building officials that the system provides the protection intended.

FUTURE APPLICATIONS

Given the relatively low cost of Ball-N-Cone isolators and the ease with which they can be configured into a variety of structural systems there are many opportunities for their use in seismic protection. One area that the system could easily be extended to is low-rise light-framed construction, such as residential. The Ball-N-Cone isolators are ideal for supporting the relatively low vertical loads associated with this type of construction and the cost per isolator is very affordable. The application of Ball-N-Cone isolators is well suited to high-end residential or for any owner who is looking for improved protection compared to standard construction.

CONCLUSIONS

WorkSafe Technologies Ball-N-Cone isolators provide a simple, effective, and low cost alternative to traditional base isolation systems. The Ball-N-Cone isolators are best suited for applications with relatively low vertical loads, such as nonstructural components or low-rise light-framed construction. Currently the technology has been applied for the protection of computer racks, entire data centers, and for large equipment and even fragile art installations. There are numerous other applications that the technology can be extended too in the future.

Probabilistic and Deterministic Seismic Soil Structure Interaction Analyses for the Lotung Quarter-Scale Containment Model

D.W. Eggers[1], S. Bolourchi[2], F. Ostadan[3]

[1]Simpson Gumpertz & Heger Inc., 41 Seyon Street, Building 1, Suite 500, Waltham, MA 02453; PH (781) 907-9265; email: dweggers@sgh.com
[2]Simpson Gumpertz & Heger Inc., 41 Seyon Street, Building 1, Suite 500, Waltham, MA 02453; PH (781) 907-9253; email: sbolourchi@sgh.com
[3]Bechtel National, Inc., 50 Beale Street, San Francisco, CA 94119; PH (415) 768-3734; email: fostadan@bechtel.com

ABSTRACT

The seismic responses for nuclear facilities are required to consider soil-structure interaction (SSI) effects. The upcoming revision of ASCE 4 establishes a goal of developing seismic responses with an 80% probability of non-exceedance. It is important to ensure the widely used deterministic analysis results to be in an 80th-percentile level response or higher as compared to the probabilistic analysis.

The SSI analysis of the Lotung quarter-scale containment model is repeated using the probabilistic method using the computer program SASSI2000. The experimental Lotung results are used to evaluate the merits of the probabilistic approach and to make an assessment of the 80th-percentile responses with the responses obtained from recoded motion.

The analysis is subsequently repeated at three sites with different soil depths and with modifications to the input parameters to observe their effects on the probabilistic analyses. Probabilistic analysis considers the variation of soil properties, layer thicknesses, and structural parameters. For all cases, a comparison of the seismic loads and in-structure response spectra (ISRS) at the 80th-percentile level is made with the envelope of three deterministic SSI analyses, demonstrating that the deterministic method envelopes the probabilistic ISRS, but probabilistic structural forces may exceed the deterministic. This paper further examines the effects of Monte Carlo and Latin Hypercube sampling methods and of the number of samples on the accuracy of results for the probabilistic analyses.

INTRODUCTION

The seismic responses for nuclear facilities are required to consider dynamic soil-structure interaction (SSI) effects. SSI effects are typically considered by the use of computer programs such as SASSI or CLASSI and account for the behavior of the free field soil, modeled building structures, and the interaction of these components. The upcoming revision to ASCE 4 establishes a goal of developing seismic responses with approximately an 80% probability of non-exceedance for the given mean input motion. The mean input motion is typically developed using probabilistic site

response analyses. The same techniques used for probabilistic site response analyses can be expanded to SSI analyses or even combined into joint probabilistic analyses. Use of probabilistic SSI analyses can provide the required output with 80% probability of non-exceedance along with significant additional data on sensitivity of results to input variations. The recommended probabilistic SSI analysis is a robust method that can be integrated in the probabilistic site response analysis for development of the design motion, and also used for probabilistic risk assessment (PRA) for the structure and its components.

While probabilistic methodologies provide many benefits, they are not widely used due in part to the computational expense in performing the analyses. SASSI analyses calculate impedances in the frequency domain and are computationally expensive to run for large models, particularly for large embedded structures in soft soil, where wave-passage requirements demand the use of refined models. To reduce the computational expense, the response is calculated directly only at user-selected frequencies, and the intermediate frequency responses are calculated using an interpolation technique. The use of interpolation techniques requires additional effort on the part of the engineer to ensure that the analyses produce accurate results.

The deterministic methodology presented in ASCE 4 is intended to achieve the same goal of 80% probability of non-exceedance for the same mean input motion. Deterministic analyses consider uncertainties through variations in the soil profile to produce a lower-bound, mean, and upper-bound profile with a minimum soil shear modulus coefficient of variation of 0.5. The results of the three deterministic analyses are enveloped. Additional uncertainty is accounted for in the calculation of in-structure response spectra (ISRS) by broadening the results by ±15%. It is important to ensure the widely used deterministic analysis results in an 80th-percentile-level response or higher as compared to the probabilistic analysis.

In the following sections, this paper presents deterministic and probabilistic analyses of the Lotung experiment using SASSI2000 for three different soil sites: one site consistent with the Lotung experiment data, one deep-soil site, and one shallow-soil site. In each case, the enveloped deterministic responses are compared to probabilistic 80th-percentile responses to determine if the deterministic responses meet the intent of ASCE 4. For the shallow-soil site, the effect of probabilistic sampling methods and sample size are examined to determine their effect on the accuracy of the probabilistic results.

LOTUNG EXPERIMENT MODEL DESCRIPTION

The Lotung experiment was conducted by the Electric Power Research Institute (EPRI), Taiwan Power Company (TPC), and U.S. Nuclear Regulatory Commission (US NRC) in Lotung, Taiwan (EPRI 1987). The experiment considered a quarter-scale containment model (Figure 1) constructed with reinforced concrete cylinder containment walls 1 ft thick and 50 ft high. The structure is embedded 15 ft into the soil, with a 3 ft thick flat base slab and a 4 ft thick flat roof slab, and the structure supports a steam generator. Motions in the structure and at adjacent free field locations were recorded for the experiment. This structural model was selected for use in all analyses used in this paper because of the availability of recorded data to evaluate the results.

The SASSI2000 User's Manual provides a SASSI analysis considering a model of the Lotung Experiment using the recorded site motions and comparing the analyses results to the in-structure recorded motions as part of the program validation (Ostadan 2007). The SSI model is a half model with a plane of symmetry (Figure 2). The below-grade walls are modeled with thin-shell elements and the base slab is modeled with 3-D solid elements. The above-grade containment structure is modeled with a lumped mass stick model connected to the subsurface walls by rigid links. The internal steam generator and support structures are modeled with beams and lumped masses. The fixed-base containment structure has modes around 10.8 Hz and above 30 Hz, and the steam generator has modes around 5.5 Hz, 10.5 Hz, 15 to 20 Hz, and above 30 Hz. For use in the analyses presented herein, ISRS will be examined at the base slab (Node 178), top of the containment structure (Node 311), base of the steam generator (Node 300), and the top of the steam generator (Node 302); and structural shear force examined at the containment structure stick just above grade (Beam 1). All analyses are performed for vertically propagating shear waves excited in the Y-direction of motion using the direct method for calculation of impedances.

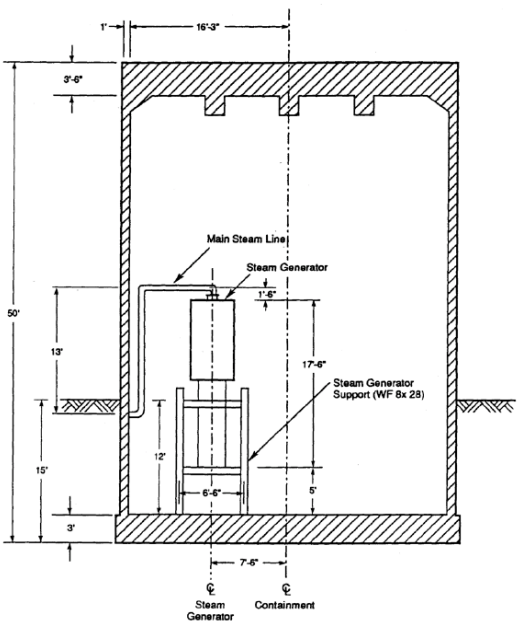


Figure 1. Vertical section of Lotung experiment.

DETERMINISTIC METHODOLOGY

The deterministic analyses follow the guidelines of ASCE 4 including variation of soil shear modulus by one standard deviation but not less than a coefficient of variation of 0.5 and considering no structural variation. Three soil profiles are considered, a lower-bound, mean, and upper-bound soil cases. Typically, the same soil layering was used in all three profiles. For the shallow soil profile, the deterministic analysis was performed, including variation in soil layer thicknesses to account for the significant effect these thicknesses play on the responses for shallow soil sites. The results of the three deterministic soil cases are enveloped, and the ISRS are broadened by 15% frequency shift at all frequencies. No peak clipping is performed.

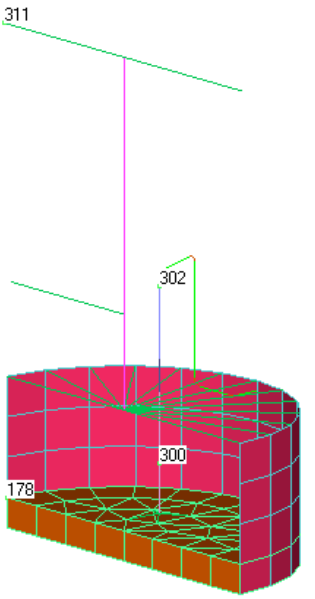


Figure 2. Lotung SSI model.

PROBABILISTIC STRUCTURAL VARIATION

For probabilistic analyses, the structural properties are varied. The mean and probabilistic distributions used are based on "Methodology for Developing Seismic Fragilities" (EPRI 1994), with the exception of steel damping where a lower mean value was used to avoid unconservative results compared to the deterministic analyses. Concrete elastic modulus, concrete material damping, steel elastic modulus, and steel damping are modeled with truncated lognormal distributions using the parameters indicated in Table 1. The variations used are similar to those proposed by ASCE 4.

Table 1. Probabilistic Structural Properties.

		Probabilistic		
	Deterministic	Mean	Cv (Used)	Cv (ASCE 4)
Concrete Elastic Modulus	518,400 ksf	518,400 ksf	0.32	0.35
Concrete Damping	4%	3%	0.5	0.4
Steel Elastic Modulus	2,088,000 ksf	2,088,000 ksf	0.32	0.35
Steel Damping	2%	2%	0.5	0.4
Structural Mass Coefficient	100%	100%	5%	–

SOIL SITES

Lotung site- The Lotung soil site was developed based on the geotechnical properties. The soil consists of 154 ft of soil over a linear elastic half space with shear wave velocities of 3,000 ft/s. Uncertainties in the soil profile included variation in shear-wave velocity, strain-dependent shear modulus degradation and damping curves, and layer thicknesses. Low-strain shear wave velocity was varied with a coefficient of variation of 0.2 with a lognormal distribution truncated at two standard deviations; thickness considered a beta distribution within ±20% variation bounds; and strain-dependent property curves considered a logarithmic variation based on a model by Darendeli (2001). Shear wave velocities of adjacent layers were correlated based on a model by Toro (1995), resulting in interlayer correlations between 0.55 and 0.7. Furthermore, a correlation of –0.7 was imposed between G/Go values and damping curves and 0.7 between G/Go and shear wave velocity. Sixty soil profiles were developed using the Latin Hypercube sampling method. Each of the sixty soil profiles were subjected to the ground-surface motion recorded at the Lotung site using an equivalent linear site response analysis performed using P-SHAKE to calculate the strain-compatible soil profiles for use in

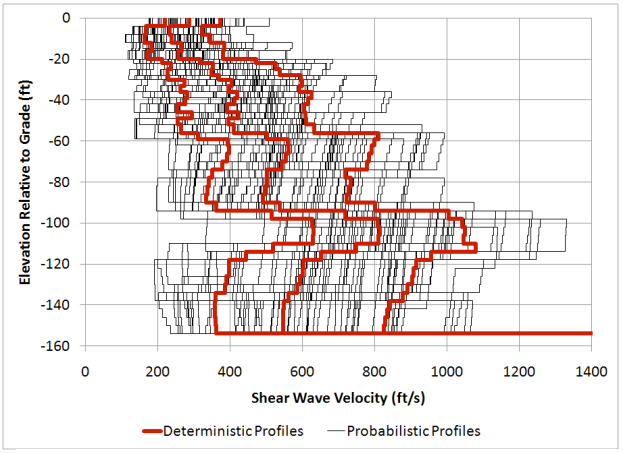


Figure 3. Lotung soil site Vs

SASSI analyses. The shear wave velocity profile of all sixty profiles plus the three deterministic profiles are shown in Figure 3.

Deep soil site- A deep soil site consists of 524 ft of soil modeled using ninety-five layers over a soil half space. Mean strain compatible shear modulus was varied with truncated lognormal distribution with a coefficient of variation Cv = 0.5 truncated at 3 Cv. The mean soil damping was varied with truncated normal distribution considering the calculated a standard of deviation of each soil layer and truncated at three standard deviations. A correlation coefficient of –1.0 was applied between the shear wave velocity coefficient and the damping deviation applied to each soil case. A correlation coefficient of 1.0 was applied between the shear wave velocities of all soil layers. Sixty soil profiles were developed using the Latin Hypercube sampling method. The shear wave velocity profile of all sixty profiles plus the three deterministic profiles are shown in Figure 4.

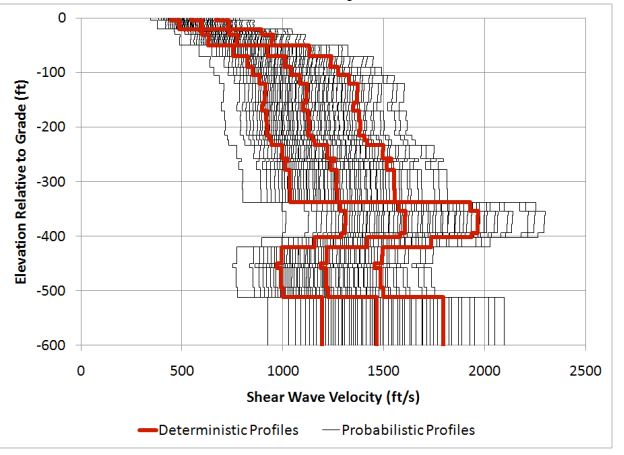


Figure 4. Deep soil site Vs

Shallow soil site- The shallow soil site consists of between 40 and 48 ft of soil over hard rock. The soil consists of three layers, an upper layer of relatively soft soil (Layer A), a lower layer of stiffer soil (Layer B), and a layer of clay (Layer C) over a stiff rock. Soil profile uncertainties considered variation in shear-wave velocity, strain-dependent shear modulus degradation and damping curves, and layer thicknesses. Variation of layer thicknesses considered uniform distributions for total depth to rock, Layer A, and Layer B with thickness of Layer C calculated from the other three parameters. Low-strain shear moduli were varied based on the layer coefficient of variation with a lognormal distribution truncated at three standard deviations. Variation of layer thicknesses considered uniform distributions for total depth to rock, Layer A, and Layer B with thickness of Layer C calculated from the other three parameters. Strain-dependent dynamic property curves considered a logarithmic variation similar to that used for the Lotung site. All soil properties were considered uncorrelated. Sixty low-strain soil profiles were developed using the Latin Hypercube sampling method.

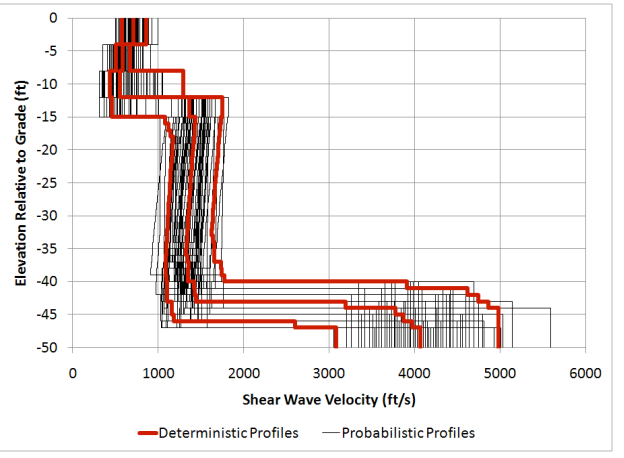


Figure 5. Shallow soil site Vs

Each of the sixty soil profiles were subjected to the PSHA rock outcrop motion in an equivalent linear site response analysis performed using SHAKE91 to calculate the strain-compatible soil profiles for use in SASSI analyses and the ground-surface motions. The shear wave velocity profile of all sixty profiles plus the three deterministic profiles are shown in Figure 5. The mean ground surface response spectra (GMRS) was calculated from the sixty profiles.

SASSI ANALYSES

Each analysis case was performed in SASSI2000 using the direct method for determining foundation impedances. The input motion for the Lotung site analyses was the recorded site ground motion for the Lotung experiment. The deep soil site input motions closely resemble a RG 1.60 response spectra scaled to 0.13 g. The shallow site input motions is a time history matched to the calculated site GMRS described above.

Three sets of analyses were run for each soil case. First, a set of three deterministic analyses were run, and the analyses enveloped to calculate the deterministic responses. Second, a set of sixty structural models were developed using the Latin Hypercube sampling method and the structural variations described above. The sixty structural models were randomly paired with the sixty strain-compatible soil profiles without replacement. The results of these analyses were processed to determine the 80th-percentile response by taking the twelfth-highest response value from the sixty cases. Third, additional sixty probabilistic analyses were performed using the deterministic base structure without variation and the sixty strain-compatible soil profiles. These sets are identified as deterministic, probabilistic, and probabilistic soil, respectively.

RESULTS

Lotung site- Comparisons of the Lotung experiment input motions and recorded ISRS to the probabilistic and broadened deterministic ISRS are shown in Figure 6. The calculated ISRS demonstrate that the motion at the base is well represented by the probabilistic responses. At the top of the containment structure, the probabilistic ISRS are near or exceed the recorded motions, and exceed the recorded motions by a large margin between 2 and 5 Hz. At the top of steam generator, the probabilistic ISRS provide close match with the recorded motions with a conservative response around 2.5 Hz. These results demonstrate that the probabilistic ISRS provide a conservative match to the recorded motions. Comparisons of the probabilistic ISRS with the broadened deterministic envelope ISRS shown in Figure 6 also show that the deterministic envelope is similar to, or greater than, the probabilistic response. The probabilistic structural variation causes a slight reduction and broadening of the spectra peak around 5.5 Hz at the top of the steam generator.

Comparisons of the probabilistic shear force with the deterministic shear force (Table 2) show that the probabilistic forces are enveloped by the deterministic results. The structural variation increases the response slightly.

Deep site- Comparisons of probabilistic ISRS with and without structural variation with the deterministic envelope and the broadened deterministic envelope ISRS are shown in Figure 7. Deterministic and probabilistic ISRS are similar at the base and top of the containment structure, indicating that both methods produce similar SSI responses. At the base and top of the steam generator, the ISRS is greatly amplified because the peak of the containment structure ISRS aligns with the natural frequency of the steam generator. For the steam generator, the deterministic ISRS is similar to the probabilistic response without structural variation. However, when the structural variation is included, the peak reduces and the spectra widens. This reduction and broadening occurs due to the variation in structural frequency and the resulting shifting in peak response. Regardless of whether structural variation is included, the deterministic envelope provides a reasonable, conservative response compared to the 80th-percentile probabilistic ISRS. The broadened envelope provides adequate broadening to envelope the probabilistic response.

Comparisons of the probabilistic and deterministic shear forces also show that the forces obtained from the probabilistic result including structural variation exceed the deterministic result slightly.

Shallow site- Comparisons of probabilistic ISRS with the deterministic envelope and the broadened deterministic envelope ISRS were examined and shown with additional sampling technique study curves (Figure 8). In nearly all cases, the deterministic envelope is similar to, or greater than, the probabilistic ISRS. The probabilistic peak response exceeds the deterministic over a narrow frequency range at the top of containment and top of steam generator. The broadened envelope provides adequate broadening to cover the structural variations.

Comparisons of the probabilistic and deterministic shear force demands show that the forces obtained from the probabilistic demands including structural variation exceed the deterministic demands by 17%. The 80th-percentile case has concrete damping of 1.2% and a mass adjustment factor of 1.03%. The damping value of 1.2% is very low and while appropriate for inclusion in probabilistic analyses to calculate response spectra, this value is lower than would be consistent for elements stressed to near their design strengths. Higher levels of damping may be justified but are not further examined herein. Excluding structural variation, the probabilistic shear demands exceed the deterministic by only 7%.

Table 2. Shear Force.

Shear (kips)	Lotung	Deep	Shallow
Deterministic Envelope	122	139	229
Probabilistic with No Structural Variation	113	139	244
Probabilistic with Structural Variation	118	143	269

EXAMINATION OF SAMPLING TECHNIQUES

All previously examined probabilistic analyses were performed considering the Latin Hypercube sampling method and sixty samples. This methodology was selected to

be consistent with current practice for sampling to obtain the mean input motions. Proposed ASCE 4 recommends at least thirty-two samples using either Monte Carlo or Latin Hypercube sampling. To examine the sampling effect, two thousand Monte Carlo analyses were performed using the same techniques as discussed above for the shallow soil site with structural variation. The 80th-percentile results from these two thousand analyses form the baseline against which other analyses are evaluated. The same analysis was performed using the Latin Hypercube sampling method with sets of sixty and thirty-two samples.

To evaluate the accuracy of the sixty-sample Monte Carlo analyses, one hundred sets of sixty results were randomly sampled, and the 80th-percentile response was calculated from each. These mean and standard deviation of these 80th-percentile ISRS were calculated at the top of containment and top of steam generator for comparison to the deterministic and baseline results (Figure 8). At all locations, the deterministic results envelop the probabilistic results, and the two thousand samples are closer to the deterministic envelope than was the sixty-sample case previously discussed. The mean of the one hundred samples is nearly identical to the baseline, and the standard of deviation is less than 7% of the mean value at each frequency for ISRS at the top of the containment structure and less than of the mean value at each frequency for ISRS at the top of the steam generator. Six of the one hundred cases at the top of the containment and twenty cases at the steam generator have spectral values more than 10% below the baseline any given frequency. The same technique was repeated with one hundred samples of thirty-two cases. The mean of these cases is also very similar to the baseline. At the top of the containment structure, the standard deviation is just under 10% of the mean with nineteen samples more than 10% below the baseline. At the top of the steam generator the standard deviation is just under 18% of the mean with thirty samples more than 10% below the baseline. Therefore, for this analysis, there is at least an 80% confidence that a Monte Carlo sampling of sixty cases is not more than 10% below the probabilistic ISRS, and this confidence reduces to 70% for a Monte Carlo sampling of thirty-two cases.

The comparison of the thirty-two- and sixty-sample Latin Hypercube cases demonstrates nearly identical ISRS to the two thousand Monte Carlo spectra except over a narrow frequency range (Figure 8). In this range, the sixty-sample case is within 87% of the baseline, and the thirty-two-sample case is within 79%. These results may be low due to failure of the small sample size to adequately represent the full subspace of probabilistic cases for the large number of variables. However, additional study is required to determine the cause of the discrepancy and how to improve the probabilistic results for analyses with relatively small sample sizes.

CONCLUSIONS AND RECOMMENDATIONS

This paper examined probabilistic and deterministic analyses of the Lotung experiment model considering probabilistic variation in soil profiles and structural properties. The deterministic analysis ISRS without peak clipping envelop the 80th-percentile probabilistic responses with minor exceptions. Where the probabilistic results exceed the deterministic results, they do so only by a small percentage and over narrow frequency ranges. Structural variation in the probabilistic analyses

typically reduces the peak value and broadens ISRS near structural frequencies. The effects of structural variation are adequately covered by the deterministic ±15% ISRS broadening.

Probabilistically determined force demands have been shown to exceed deterministic demands in some cases. Inclusion of structural variation increases probabilistic demands.

The study of probabilistic sampling methods demonstrated that increased sample sizes significantly improve accuracy of and confidence in the probabilistic responses. Care should be taken to avoid sampling bias through review of sampling or improved sampling techniques such as Latin Hypercube. Additional research is required to better define sampling required to accurately represent the probabilistic response with large number of variables and relatively small sample sizes and how to identify potentially unconservative probabilistic sampling.

REFERENCES

American Society of Civil Engineers (ASCE). (1999). "Seismic Analysis of Safety-Related Nuclear Structures and Commentary." ASCE 4-98, Reston, VA.

Darendeli, M.B. (2001). "Development of a New Family of Normalized Modulus Reduction and Material Damping Curves." Ph.D. Dissertation. University of Texas, Austin, TX.

Electric Power Research Institute (EPRI) (1994). "Methodology for Developing Seismic Fragilities." *Final Report TR-103959*. Electric Power Research Institute (EPRI), Palo Alto, CA.

Ostadan, F. (2007). SASSI2000 User's Manual, "A System for Analysis of Soil-Structure Interaction," Version 3.

Proceedings: EPRI/NRC/TPC (EPRI) (1987). "Workshop on Seismic Soil-Structure Interaction Analysis Techniques Using Data from Lotung." Taiwan, NP-6145, prepared by Electric Power Research Institute, Palo Alto, CA, Dec. 1987.

Toro, G.R. (1995). "Probabilistic Models of Site Velocity Profiles for Generic and Site-Specific Ground-Motion Amplification Studies." Brookhaven National Laboratory, Upton, NY.

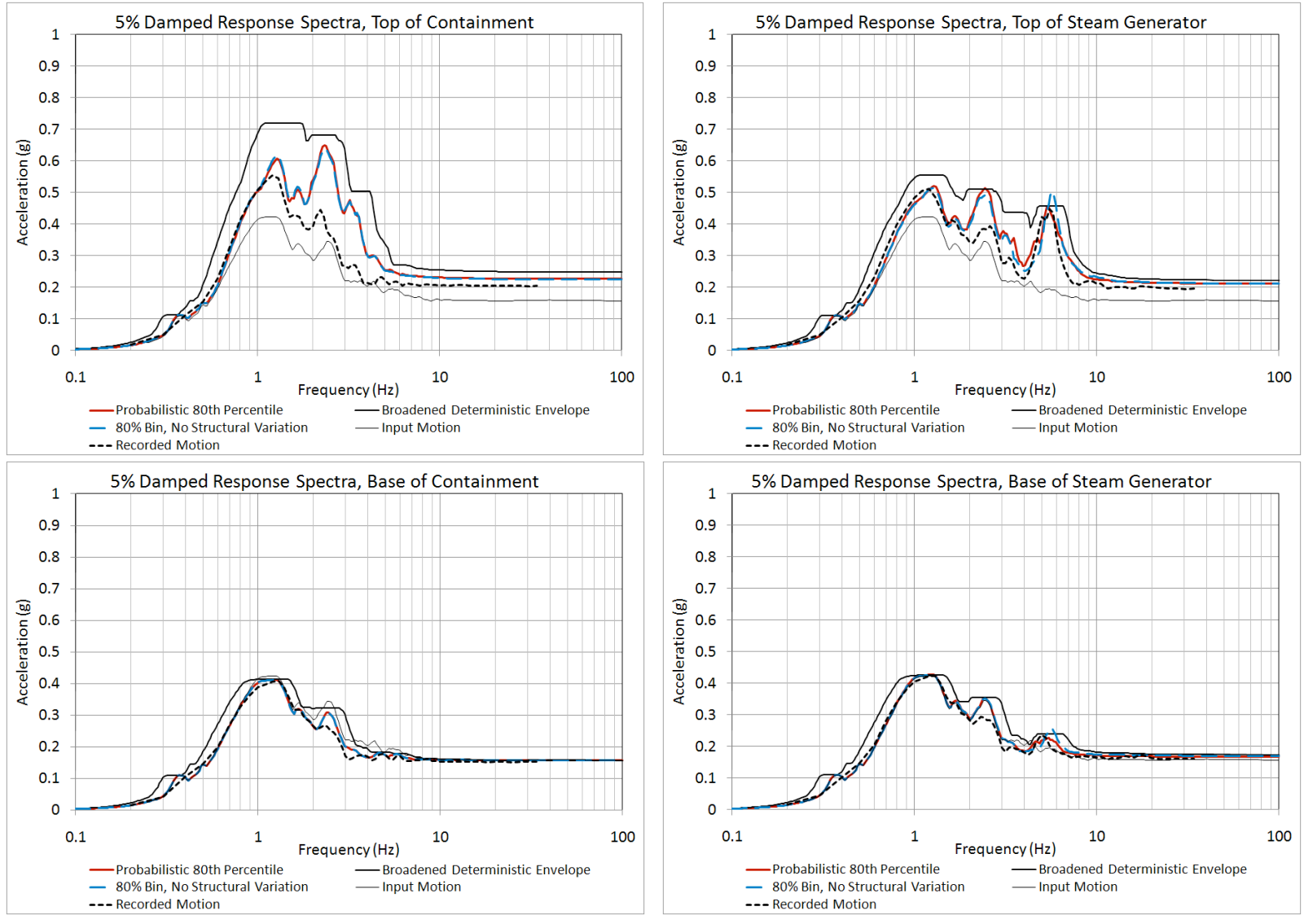


Figure 6. 5% Damped Response Spectra forLotung Soil Profiles: Comparison of Deterministic and Probabilistic Responses.

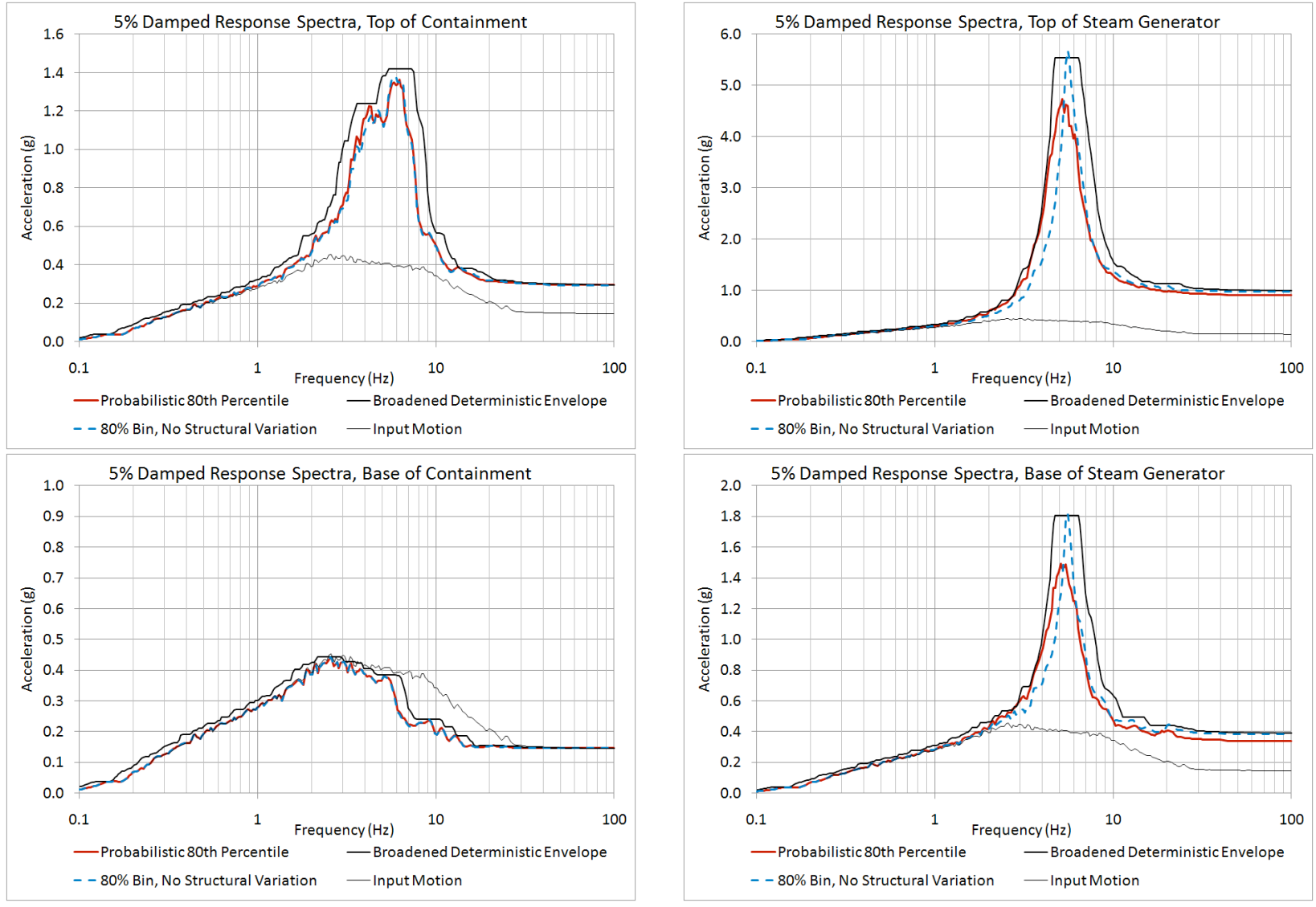


Figure 7. 5% Damped Response Spectra for Deep Soil Profiles: Comparison of Deterministic and Probabilistic Responses.

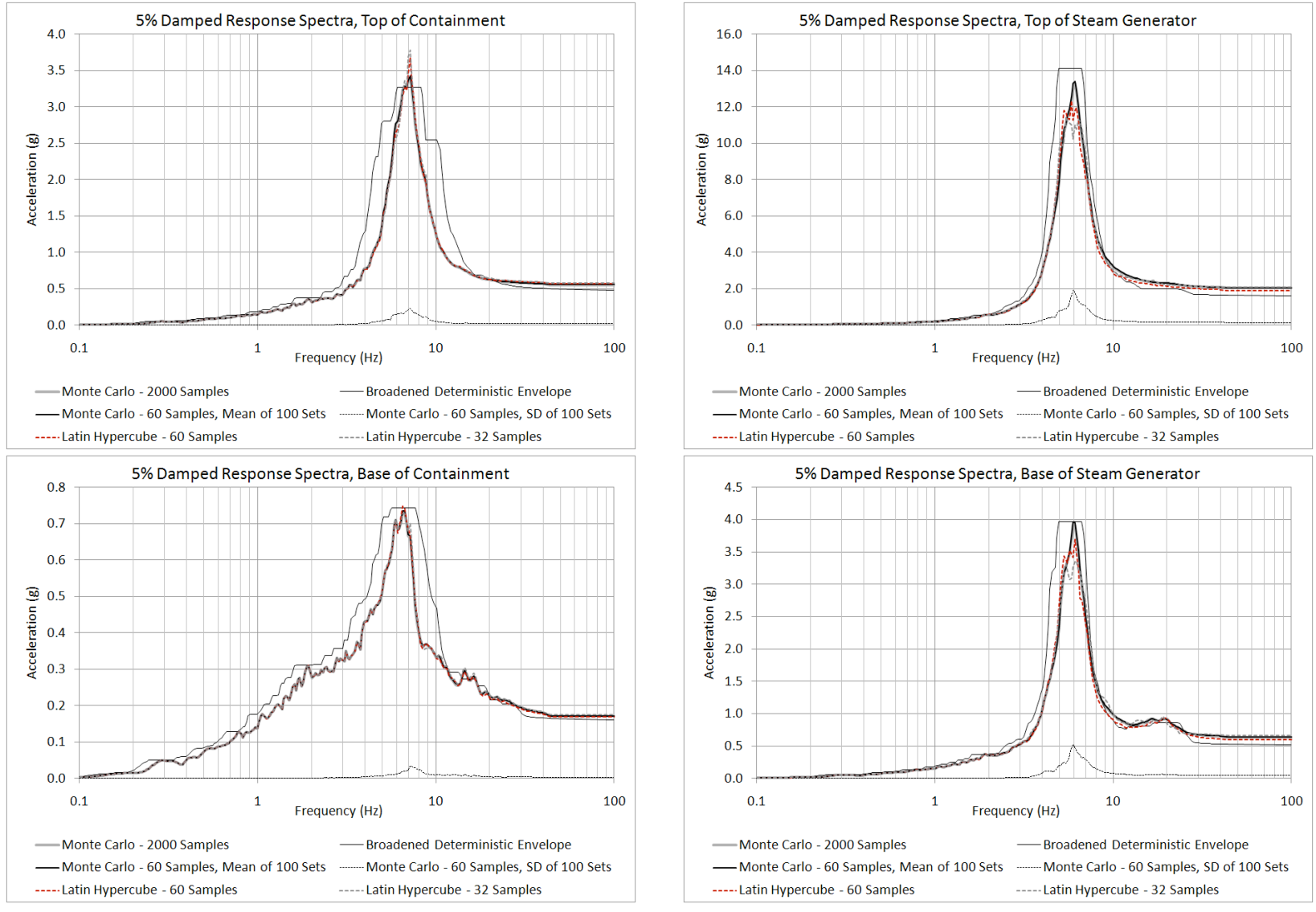


Figure 8. 5% Damped Response Spectra for Shallow Soil Profiles: Comparison of Probabilistic Methods.

Seismic Isolation of Safety-Related Nuclear Structures

A. S. Whittaker[1], Y.-N. Huang, R. L. Mayes[3] and R. P. Kennedy[4]

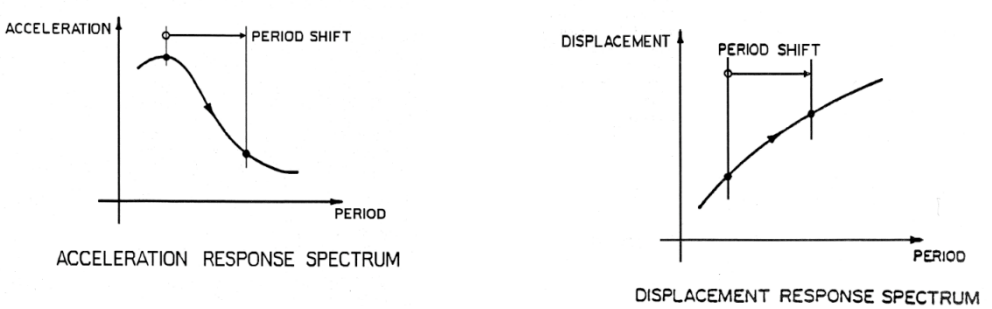
[1]University of Buffalo, State University of New York, Red Jacket Quadrangle, Buffalo, NY, 14261; Ph: 1-716-645-4364; email: awhittak@buffalo.edu
[2]National Taiwan University, No. 1., Sec. 4, Roosevelt Road, Taipei, 106, Taiwan; Ph: 886-2-23623356; email: yinnantw@yahoo.com
[3]Simpson, Gumpertz and Heger, 1 Market St, San Francisco, CA, 94105; Ph: 1-415-495-3700; email: rlmayes@sgh.com
[4]RPK Structural Mechanics Consulting Inc, 28625 Mountain Meadow Rd, Escondido, CA 92026; Ph: 1-760-751-3510; email: bob@rpkstruct.com

ABSTRACT

The forthcoming update of ASCE 4 includes expanded provisions for analysis, design of seismically isolated nuclear structures and testing of seismic isolation bearings. The paper describes the provisions and their technical basis. The analysis and design provisions are consistent with the ASCE 43-05 performance objectives for nuclear structures, namely, 1) 1% probability of unacceptable performance for 100% Design Basis Earthquake (DBE) shaking, and 2) 10% probability of unacceptable performance for 150% DBE shaking.

INTRODUCTION

The implementation of a seismic isolation system at the base of a safety-related nuclear structure will serve to substantially reduce inertial forces on the superstructure and substructure as indicated in Figure 1. The increase in displacements shown in Figure 1 is accommodated by-and-large by the seismic isolators that are proportioned to support high axial loads at large lateral displacements as required by the draft Standard.



a. inertial forces b. displacements

Figure 1. Impact of seismic isolation on inertial forces and displacements

Figure 2 illustrates one of the benefits of seismic isolation, namely, a sharp reduction in spectral demand: increasing the fundamental period from 0.1 second (conventional

construction) to 2+ seconds (isolated construction) reduces the spectral demand by a factor of more than 10. The 5% damped spectrum presented in the figure is the design basis earthquake spectrum for the site of a nuclear power plant on rock in the Eastern United States.

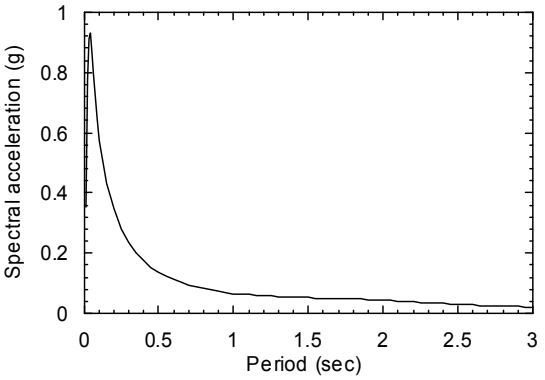


Figure 2. Design basis earthquake spectrum for a rock site in the EUS

The Provisions are written for three types of seismic isolator: low-damping and lead-rubber elastomeric bearings and Friction Pendulum™ sliding bearings. No other types of isolators are considered appropriate for nuclear structures.

Low-damping (LD) elastomeric bearings are composed of alternating layers of natural rubber and steel, and can be modeled as viscoelastic components. The shear modulus of the rubber ranges between 60 psi and 120 psi. The equivalent viscous damping is between 2 and 4% of critical. Lead-rubber (LR) elastomeric bearings are constructed similarly to low-damping rubber bearings but include a central lead core to dissipate earthquake-induced energy. The hysteresis loop for the LR bearing is bilinear per Figure 3 and defined by a zero-displacement force intercept, $Q_d W$, and a second-slope stiffness, K_d, where W is the supported weight.

Sliding bearings with restoring force provided by gravity have the hysteresis loop of Figure 3. In the Friction Pendulum™ (FP) family of bearings, the second-slope stiffness is equal to the supported weight divided by the radius of curvature of the sliding surface.

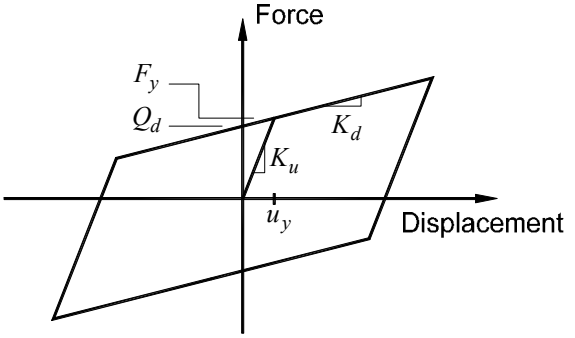


Figure 3. Mechanical properties of LR and FP bearings

The performance expectations of Section 1.3 of ASCE-43 (ASCE 2005) form the basis of the provisions in the seismic isolation section (7.7) of the draft ASCE Standard 4: 1) 1% probability of unacceptable performance for 100% DBE shaking, and 2) 10% probability of unacceptable performance for 150% DBE. More stringent criteria may be imposed by regulatory agencies, including the US Nuclear Regulatory Commission (USNRC), who require a plant-level HCLPF of 1% for 167% design basis shaking, noting that the plant-level HCLPF may not be dictated by a failure sequence involving seismic isolators (USNRC 2007, 2010).

Three performance statements for achieving the two performance objectives of ASCE-43 were assumed in the writing of Section 7.7 of the draft Standard, namely, 1) individual isolators shall suffer no damage in design earthquake shaking, 2) the probability of the isolated nuclear structure impacting surrounding structure (moat) for 100% (150%) design earthquake shaking is 1% (10%) or less, and 3) individual isolators sustain gravity and earthquake-induced axial loads at 90th percentile lateral displacements consistent with 150% design earthquake shaking. Performance statement 1 will be realized by production testing of each isolator supplied to a project for 80%-ile DBE displacements and co-existing gravity and earthquake-induced axial forces. Analysis can be used in support of performance statement 2 provided that the isolators are modeled correctly and the ground motion representations are reasonable. Performance statement 3 can be realized by prototype testing of a limited number of isolators for mean displacements and co-existing axial forces consistent with 150% of the design earthquake, noting that an isolation system is composed of 10s to 100s of isolators and that failure of the isolation system would have to involve the simultaneous failure of a significant percentage of the isolators in the system.

Diaphragms are required above and below the isolation system. In the draft Standard, the diaphragms above and below the isolation system are identified as basemat and foundation, respectively. These diaphragms are required to be stiff in the horizontal plane to effectively engage all of the seismic isolators in the seismic-force-resisting system. The basemat and foundation must be stiff out-of-plane to engage all isolators in the gravity load resisting system.

Constantinou et al. (2007) and Naeim and Kelly (1999) provide information on LD, LR and FP seismic isolators. Huang et al. (2008, 2009, 2010) provide data and information in support of the isolation of nuclear structures and the proposed isolation provisions in the Standard. Constantinou et al. (1999, 2007), Thompson et al. (2000) and Morgan and Whittaker (2001) provide the data used by Huang et al. (2009) to characterize the impact of variations in isolator material properties on the displacement response of seismic isolation systems.

GENERAL DESIGN REQUIREMENTS

Environmental and Operating Conditions

Best-estimate mechanical properties for the isolator units are used for DBE analysis. Analysis has been performed by Huang et al. (2009) to estimate displacements for LD, LR and FP bearing isolation systems at representative sites across the United States for DBE and 150% DBE shaking. These analyses considered variability in both the seismic input (i.e., a distribution in spectral demand; see Huang et al. 2009) and the mechanical properties of the isolation system. Factors were developed to relate the median design displacement in the isolation system in DBE shaking to a displacement with 1% probability of exceedance in DBE shaking and a 10% probability of exceedance in 150% DBE shaking. The greatest variability considered for isolator properties was ±20% from the best-estimate values with 95% probability.

Wind Loads

Lateral forces in seismic isolators under design wind loads should be a) less than the zero-displacement force intercept for a bilinear isolation system such as the lead-rubber bearing and sliding bearing per Figure 3, and b) small for low-damping rubber bearings.

Isolator Inspection and Replacement

Although isolators should likely not need to be replaced after DBE or 150% DBE shaking, the design of the structural framing system must provide for access to the isolators for periodic and post-earthquake inspection and possible replacement. Periodic inspection is required because seismic isolation has not been used for nuclear structures in the United States at the time of this writing. The isolators, isolation system, framing above and below the isolators and secondary systems crossing the isolation interface should be inspected after significant earthquake shaking. Components that are damaged should be replaced or repaired.

Spare isolators of each type used in the isolation system should be stored on-site and tested at 10-year intervals to build further confidence in the technology amongst structural engineers implementing isolators in nuclear structures. This requirement may be deleted if the isolators being implemented in a safety-related nuclear structure have a long track record of good seismic performance and no significant change in material properties with time.

Isolator Performance

Vertical load resistance

The vertical loads used to check the stability of an isolator should be calculated using the maximum positive and minimum negative values of a) dead load, b) live load, and

c) earthquake load associated with 80%-ile DBE shaking at the 80%-ile level and 150% DBE shaking.

No isolator damage is permitted for DBE displacements and forces calculated at the 80%-ile level. Isolator damage is permitted for 150% DBE shaking provided that it does not compromise the required vertical load resistance of the isolation system.

Minimum lateral restoring force

The restoring-force requirement is intended to limit residual displacement as a result of an earthquake, so that the isolated structure will survive aftershocks and future earthquakes. The rule is identical to that in ASCE 7 (ASCE 2010) for isolated buildings and other structures.

Basemat and Foundation Designs

The plan dimensions of foundations for nuclear islands are generally large. Vertical deflection of the basemat and/or settlement of the foundation below a small part of the isolation system will lead to a redistribution of gravity loads to the isolators that is generally undesirable. The basemat and the foundation should be sufficiently stiff in the vertical direction to engage all isolators in resisting gravity load effects. To provide a redundant gravity load resisting system, the basemat should be designed to span over one or more isolators in event of local settlement under an isolator.

DYNAMIC ANALYSIS

Response-history Analysis

General

Two procedures may be used for the analysis of seismically isolated nuclear structures. Each procedure is assumed to result in displacements in DBE shaking at the 80+%-ile level. Displacements in seismic isolators are calculated by time-stop as the vector sum of the two orthogonal horizontal displacements.

Time-domain analysis

The use of peak maximum values of isolator and superstructure response from analysis using three sets of three-component ground motions and three soil columns is assumed to meet the 80%-ile non-exceedance probability for DBE shaking.

Alternate calculations may be performed using 11+ sets of three-component ground motions and three soil columns (a minimum of 33 sets of calculations) to estimate the dispersion in the isolator and superstructure responses and thus the 80%-ile non-exceedance values.

Multi-step analysis

The horizontal and vertical envelope spectra at the foundation of the isolated structure calculated by frequency-domain analysis is assumed to represent 80%-ile spectral demands.

Three-component sets of ground motion time-series that are matched to these spectra are assumed to be 80%-ile ground motions. If less than five sets of ground motions are used for analysis, 80%-ile responses shall be taken as the peak maximum responses. If five or more sets of ground motions are used for analysis, 80%-ile responses may be taken as mean maximum responses.

Mathematical Modeling

Isolation system

The isolators shall be modeled using proven mathematical models with design parameters that have been validated by full-scale dynamic testing. Each isolator should be included in the mathematical model of the seismically isolated structure. The mathematical models of the isolators should account for changes in isolator properties associated with large-amplitude earthquake shaking (e.g., Kalpakidis et al. 2010).

For time-domain analysis, nonlinear models are required for lead-rubber and sliding bearings. Linear models are permitted for low-damping rubber bearings provided the computed shear strains for 150% design basis earthquake shaking are smaller than that associated with the onset of strain stiffening in the elastomer.

For frequency-domain analysis, equivalent linear properties shall be used for the isolators. The calculation of the equivalent properties should conform to the procedures of ASCE 7 for linear elastic analysis of seismically isolated structures. Multiple iterations may be required to validate the choice of isolator secant stiffness and equivalent viscous damping.

Superstructure

The superstructure can be modeled using elastic properties unless inelastic response is anticipated in components of the isolated superstructure at the level of shaking being considered. Simplified, validated elastic models of the isolated superstructure may be used for the purpose of calculating isolator displacements and floor accelerations if the superstructure remains elastic for the level of shaking considered.

Displacements and Forces for Design

Seismic Isolators

Values of the 80%-ile design displacement and the 80%-ile total design displacement from the response analysis for DBE shaking shall be calculated and reported for a)

establishing the scope of the isolator testing program, b) final design of the isolation system, and c) designing and detailing the seismic joints and the SSCs crossing the isolation interface.

Huang et al. (2009) showed that displacement demands (and thus transmitted forces) associated with 10% probability of exceedance (PE) in 150% DBE shaking are greater than those associated with 1% PE in DBE shaking. Accordingly, the connections of the isolators to the substructure and superstructure shall be designed to resist the forces associated with the 10% PE displacement for 150% of DBE shaking to ensure that inelastic action is confined to the isolators.

Seismic Joints

A performance objective for seismically isolated structures is the high probability of avoidance of impact with adjacent built and geo-structures. The width of a seismic joint that separates a seismically isolated structure from adjacent structures shall have a PE in 150% DBE shaking of 10% or less. The width of the joint shall be taken as 3 times the 80%-ile total design displacement if analysis is not performed for 150% DBE shaking. If analysis is performed for a distribution of ground shaking consistent with 150% of the intensity of the DBE, the width of the seismic joint shall be associated with a 10-% probability of exceedance.

SSCs Above the Isolation Interface

The design of the superstructure, systems and components above the isolation interface shall be based on the results of response-history analysis for DBE shaking and use the same procedures and standards adopted for non-isolated nuclear structures.

SSCs Below the Isolation Interface

The design of substructure, systems and components below the isolation interface shall be based on the results of response-history analysis for DBE shaking and use the same procedures and standards adopted for non-isolated nuclear structures. Systems and components bridging the isolation interface shall not be damaged or lose function in DBE shaking (1% PE). The probability of damage or loss of function in 150% DBE shaking shall be 10-%.

DESIGN REVIEW

A peer review of the design of an isolated nuclear structure should follow the requirements of the draft Standard for non-isolated structures and also address those aspects of the design and specification related to the seismic isolators, isolation system, and SSCs that cross the isolation interface.

Review of the design and analysis of the isolation system and design review of the isolator-testing program is mandated by the draft Standard because 1) the

consequences of isolator failure could be catastrophic, and 2) isolator design and fabrication technology is evolving rapidly and may be based on technologies unfamiliar to many design professionals.

The draft Standard requires that a team of registered design professionals perform the design review. The peer review team should be independent of the design team and other project contractors. The review team should include individuals with special expertise in one or more aspects of the design, analysis, testing and implementation of seismic isolation systems.

TESTING OF PROTOTYPE AND PRODUCTION ISOLATORS

General

The draft Standard describes the two types of tests to be performed on seismic isolators: 1) prototype, and 2) production. Prototype bearing tests are performed on a small number of isolators of each type planned for use in the isolation system. These tests are conducted prior to isolator production for the project. The purpose of the tests is to ensure that the isolators perform as anticipated by the design team for DBE and 150% DBE shaking. Production (or quality control) tests are performed on each isolator fabricated for a project. The production-testing program is less onerous than the prototype-testing program: dynamic tests are not required and the peak test displacement is that computed for the DBE.

Prototype Testing

Test specimens

Two isolators of each type and size in the isolation system are fabricated for prototype testing. This requirement is identical to that for building structures per ASCE 7.

Record

The minimum data to be recorded in a prototype test should enable the calculation of axial force, axial displacement, horizontal force and horizontal displacement histories, and the generation for force-displacement hysteresis loops. A sampling rate of 200 Hz is sufficient to resolve the response of isolators that are tested at frequencies of between 0.5 Hz and 0.01 Hz.

Sequence and cycles

The draft Standard specifies a minimum sequence of tests for prototype isolators. Other tests may be specified on a project-specific basis, including tests to compute vertical stiffness. ASCE 7 (ASCE 2010) and the AASHTO Guide Specification for Seismic Isolation Design (AASHTO 2010) include tests for isolators in buildings and

bridges, respectively. The number of cycles of loading is conservatively based on the data of Warn and Whittaker (2004).

Test specimen adequacy

The acceptance criteria used for prototype bearing tests should be consistent with the assumptions made for the design of the seismic isolators and seismic isolation system, and must therefore be developed on a project-by-project basis. Basic acceptance criteria for the three prototype tests are provided in the draft Standard for inclusion in the prototype-isolator acceptance criteria developed by the engineer of record. Sample criteria can be found in ASCE 7 (ASCE 2010) and the AASHTO Guide Specification for Seismic Isolation Design (AASHTO 2010).

Production Testing

Test specimens

Each production isolator shall be tested.

Sequence and cycles

Project-specific acceptance criteria will generally be developed for the production testing of isolators. For each type and size of bearing, shearing force-lateral displacement relationships should range between limits specified by the engineer of record. A minimum vertical stiffness for each type and size of isolator should be specified. The reader is referred to ASCE 7 (ASCE 2010) and the AASHTO Guide Specification for Seismic Isolation Design (AASHTO 2010) for additional information.

Test specimen adequacy

The acceptance criteria used for production bearing tests should be consistent with the assumptions made for the design of the seismic isolators and seismic isolation system, and must therefore be developed on a project-by-project basis. An acceptance criterion for production testing is provided in this section for inclusion in the production-isolator acceptance criteria developed by the engineer of record.

REFERENCES

American Association of State Highway and Transportation Officials (AASHTO). (2010). "Guide specification for seismic isolation design." Washington, D.C.

American Society of Civil Engineers (ASCE). (2005). "Seismic design criteria for structures, systems, and components in nuclear facilities." *ASCE/SEI 43-05*, ASCE, Reston, VA.

American Society of Civil Engineers (ASCE). (2010). "Minimum design loads for buildings and other structures." *ASCE/SEI 7-10*, ASCE, Reston, VA.

Constantinou, M. C., Tsopelas, P., Kasalanati, A., and Wolff, E. D. (1999). "Property modification factors for seismic isolation bearings." *MCEER-99-0012*, State University of New York, Buffalo, NY.

Constantinou, M. C., Whittaker, A. S., Kalpakidis, Y., Fenz, D. M., and Warn, G. P. (2007) "Performance of seismic isolation hardware under service and seismic loading." *MCEER-07-0012*, State University of New York, Buffalo, NY.

Federal Emergency Management Agency (FEMA). (2010). "NEHRP recommended provisions for seismic regulations for new buildings and other structures." *FEMA 750-1/2009 Edition (Provisions) and 750-2/2010 Edition (Commentary)*, FEMA, Washington, D.C.

Huang, Y.-N., Whittaker, A. S., and Luco, N. (2008). "Performance assessment of conventional and base-isolated nuclear power plants for earthquake and blast loadings." *MCEER-08-0019*, State University of New York, Buffalo, NY.

Huang, Y.-N, Whittaker, A. S., Kennedy, R. P. and Mayes, R. L. (2009). "Assessment of base-isolated nuclear structures for design and beyond-design basis earthquake shaking." *MCEER-09-0008*, State University of New York, Buffalo, NY.

Huang, Y.-N., Whittaker, A. S. and Luco, N. (2010). "Seismic performance assessment of base-isolated safety-related nuclear structures." *Earthquake Engineering and Structural Dynamics*, Vol. 39, No. 13, pp. 1421-1442.

Kalpakidis, I. V. and Constantinou, M. C., (2010). "Principles of scaling and similarity for testing of lead-rubber bearings." *Earthquake Engineering and Structural Dynamics*, Vol. 39, No. 13, pp. 1551-1568.

Kalpakidis, I. V., Constantinou, M. C., and Whittaker, A. S. (2010). "Modeling strength degradation in lead-rubber bearings under earthquake shaking." *Earthquake Engineering and Structural Dynamics*, Vol. 39, No. 13, pp. 1533-1549.

Morgan, T., Whittaker, A. S. and Thompson, A.C. (2001). "Cyclic behavior of high-damping rubber bearings." *Proceedings*, Fifth World Congress on Joints, Bearings and Seismic Systems for Concrete Structures, American Concrete Institute, Rome, Italy.

Naeim, F., and Kelly, J. M. (1999). *Design of seismic isolated structures: from theory to practice*, John Wiley, NY.

Thompson, A., Whittaker, A. S., Fenves, G. L. and Mahin, S. A. (2000). "Property modification factors for elastomeric bearings. " *Proceedings*, Twelfth World Conference on Earthquake Engineering, Auckland, New Zealand.

United States Nuclear Regulatory Commission (USNRC). (2007). "Evaluation of the seismic design criteria in ASCE/SEI Standard 43-05 for application to nuclear power plants." *NUREG/CR-6926*, Washington DC.

United States Nuclear Regulatory Commission (USNRC). (2010). "Interim staff guidance on implementation of probabilistic risk assessment-based seismic margin analysis for new reactors." *DC/COL-ISG-20*, Washington DC.

Warn, G. and Whittaker, A. S. (2004). "Performance estimates in seismically isolated bridges." *Engineering Structures*, Vol. 26, No. 9, pp. 1261-1278.

SITE RESPONSE ANALYSES

C. J. Costantino[1], T. W. Houston[1] and M. C. Costantino[1]

[1]C. J. Costantino and Associates 4 Rockingham Road, Spring Valley, New York 10977, PH. (845) 354-2602, FAX (845) 362-8161; email: carl@cjcassoc.com

ABSTRACT

The subject of development of site specific performance-based design motion and its application to soil-structure interaction (SSI) analyses has been discussed in a number of guidance documents developed for both the Nuclear Regulatory Commission (USNRC) and Department of Energy (USDOE). NRC's Regulatory Guide 1.208 and upgrade to Sections 2.5.2, 3.7.1, 3.7.2 and 3.7.3 of NRC's Standard Review Plan (NUREG-0800) and DOE Standards (DOE Std 1020-94) have emphasized probabilistic approaches to development of seismic hazard and site response. These procedures are now used to estimate seismic response of critical facilities for design and evaluation purposes.

Chapter 2 of the new revision of ASCE 4 attempts to captures all significant changes to the recommended site response analysis procedures with the goal of providing an industry consensus on this process. This paper summarizes the interpretation of the regulations and guides, and the industry agreement on the details of the development and application of the ground motion for SSI analysis. The objective of the recommended methodologies is to maintain consistency from development of the design motion from site response analysis to its application to SSI analysis and evaluation of results. Consistent use of soil property data and input motions developed based on the recommendations in Chapter 2 of ASCE4 for application to SSI analyses described in Chapter 5.

Issues currently being emphasized in probabilistic site response analyses include (a) development of Foundation Input Response Spectra (FIRS) to be used as input to deterministic SSI analyses, (b) development of appropriate description of nonlinear soil properties to accommodate the incorporation of nonlinear behavior in the site response evaluation, and (c) consideration of layer-to-layer velocity correlation models in the column realizations

INTRODUCTION

With the introduction and acceptance of the probabilistic procedures for seismic analyses of SSC's described in ASCE 43-05, a number of modifications have been introduced into the design and evaluation process for critical facilities. Using the procedures for site response evaluation that are described in NUREG/CR-6728 and 6769, the development of surface design ground motions to be used for facility design were modified to incorporate probabilistic concepts, including the potential strong

influences of site response on these estimates. The issues described in this summary are primarily concerned with issues of site response only and do not consider other aspects of seismic hazard development. The primary presumption made is that a Probabilistic Seismic Hazard Assessment (PSHA) is available at the top of hard rock (velocity of about 9200 fps) and the remaining issue is to estimate the potential impact of the site specific configuration on the corresponding PSHA at the ground surface.

Most critical facilities being constructed in the USA (particularly in the EUS) are sited on or in relatively soft soils or rocks. Local site-specific conditions must therefore be considered. It is presumed that a significant site investigation program is conducted so as to characterize geotechnical and geophysical properties for the entire site column from hard rock to the ground surface. Unfortunately, for deep soil sites, this is not always the case. Depths to which adequate geophysical data and (relatively) undisturbed samples can be obtained are usually severely limited. One purpose of the probabilistic study is to attempt to incorporate this uncertainty in site data into the evaluation as well as the impact of normal variability in geotechnical and geophysical properties that occurs at all sites.

In addition to these limitations on determining the data required to define the entire site column from hard rock to the ground surface, the results of the probabilistic site response analyses must be put into a form that is suitable for incorporation into the deterministic process that is used to assess soil-structure interaction (SSI) effects. This process is currently defined in relatively subjective terms and much more work needs to be conducted to ensure that the current recommendations for target performance goals are attained for systems of interest.

In the descriptions presented herein as well as in Chapter 2 of ASCE4, it is presumed that the seismic input motions at the rock outcrop are defined in terms of a given UHRS defined at the appropriate return period. The input rock UHRS is defined for a given characteristic event determined from deaggregation of the seismic hazard at the site. Spectral site amplification for this input is then used to define the corresponding surface motions. If the hazard indicates that two spectra have significant contributions at low and high spectral frequencies (to be discussed later), then two or more rock characteristic events can be used to determine site amplification factors. This process is referred to as Method 2 in NUREG/CR-6728. The most accurate method of determining surface motions is to perform the entire site response calculation for every source contribution to the hazard. This is referred to as Method 4 in the document but has the disadvantage of being computationally intensive. Approximations to reducing the extent of computations (Bazzuro & Cornell, 2004) can be used, leading to Method 3 of the site response assessment.

PROCEDURES FOR FIRS DEVELOPMENT

The process currently recommended for determining near-surface ground motions to be used for SSI analysis lead to the development of Foundation Input Response

Spectra (FIRS) in the free-field at the depth of the foundation. The process is aimed at determining the mean estimate of the spectra as noted in Figure 1. The use of the mean foundation spectra ensures that the reduction in motions at depth in any one realization of the site response does not overly dominate the calculated input motions to the building.

Unfortunately, two different methods are currently accepted in NRC's Interim Staff Guidance (ISG) document to develop FIRS as noted in Figure 2, One method (so-called BNL approach) uses the definition of the foundation outcrop motion as a geologic outcrop wherein the section of the soil column above the foundation depth is removed from the profile. Using the input outcrop rock motions at depth, two separate sets of column responses need to be performed, one for the full column to the ground surface, and one stopping at the foundation depth. This process correctly incorporates the fact that the mass of the layers above the foundation is properly captured.

In the second approach (the NEI approach), an approximate outcrop motion is calculated from the convolutions by using the incoming wave solutions. However, although simpler, the process does not correctly account for the mass effect and the results for each realization are different since the surface layers are different for each realization. It should be noted that in place of the FIRS, a mean in-column motion can be developed at depth and this is the same for each of the two FIRS definitions. This mean in-column motion also satisfies the requirement of smoothing the dip in the motions at depth so that no one large decrease can dominate the calculations.

The FIRS or in-column spectra are then determined at the mean (Best Estimate, BE), minus one-sigma (lower bound, LB) and plus one-sigma (upper bound, UB) levels. Corresponding BE, LB and UB soil columns are also determined from the realizations used in the site response. It is typical to use at least 60 soil columns to get reasonable estimates of the UB and LB responses. An example of amplification factors are shown in Figure 4 for two input characteristic rock spectra at a low frequency (1-2.5 hz) and high frequency (5-10 hz) motions from the PSHA. These spectral shapes are then scaled to the target rock UHRS and used as input to the soil columns. The envelope of each set of amplification factors is then used to determine the surface and FIRS spectra. The FIRS (or in-column motions) are then used deterministically to determine SSI motions for the BE, LB and UB profiles. The envelope of the corresponding surface motions must be shown to exceed the surface PSHA. Otherwise inputs must be suitably scaled to ensure that the SSI inputs are adequate. It should be noted that the same process (BNL or NEI) must be used for the site response and SSI calculations.

An example of FIRS calculations for a variable site profile of Figure 5 (incorporating velocity inversions in the profiles) is shown in Figure 6 in which FIRS motions were developed at a variety of depths in thee profile. As can be noted, the FIRS calculations are exceedingly sensitive to the profile.

NONLINEAR SOIL PROPERTY DESCRIPTIONS

The issue of selection of nonlinear properties for foundation materials is obviously a serious consideration in the determination of site response. These properties are typically defined in terms of strain dependent modulus reduction and hysteretic damping properties used in the equivalent linear analysis methodology used in the one-dimensional analysis process used in the various site response codes (SHAKE, RASCAL, CARES) often used in these calculations. Examples of these properties are shown in Figures 7 and 8 for different soils. The recommendations presented in thee EPRI93 guidelines are often referred to, although their applications to a particular soil material must be shown to be appropriate. Unfortunately, for many site profiles, these properties are often unavailable, particularly for depths below about 125' due to difficulties in obtaining even reasonably undisturbed samples to bring to the laboratory.

The approximations used to define these properties often lead to the use of large values of uncertainty than appears warranted. The larger the uncertainty, the broader the computed surface amplification tends to become. Unfortunately, the amplification functions also tend to decrease in magnitude, not the most conservative of result desired. It is probably more appropriate to use more base case profiles based on the few samples typically available with smaller uncertainty parameters.

LAYER-TO-LAYER CORRELATIONS

An issue that is becoming of more interest recently is the layer-to-layer correlation models used to develop individual velocity and damping properties for each soil layer of the computational site profile. There are several approaches that can be used to develop these multiple realizations. One method can use the assumption that the layers are fully correlated; that is, if one layer is randomly selected to be at a given fractile (either stiff or soft of the BE velocity profile), all layers can be chosen to be at the same fractile. The selected velocities of each realization have the same shape of the BE profile. The selection minimizes layer-to-layer variability but its appropriateness to arrive at a reasonable estimate of the mean site amplification may still be appropriate.

Another simple-minded approach is to assume that the selected velocity for each computational layer is fully uncorrelated. Thus, two adjacent computational layers, which may be part of the same material zone of the profile, could have widely different velocities, leading to what appears to be a more unreasonable assumption. The larger swings in velocities would also be expected to lower site response since the alternate velocities add computational damping to the system.

Recently, the Toro model has been used at a number of sites where in layer-to-layer variability is assumed to decrease with depth. This model is based on the extensive velocity data available at the Savannah River site. This site is a deep soil site of essentially silty sands and may be appropriate for application to similar sites.

However, most sites are not similar to SRS and its application needs to be shown to be appropriate.

Figure 9 presents a plot of velocity profiles for a given site based on the fully correlated model. Figure 10 presents plots of the velocity realizations for a Toro model assumption while Figure 11 presents a similar plot of a fully uncorrelated set of realizations. The amplification functions generated from these three different models are shown in Figure 12. As may be noted, above about 1 Hz, the fully correlated model yields the highest response, while the fully uncorrelated model, as expected, is significantly lower. The Toro model falls somewhere in between. The conclusion clearly indicates that more effort needs to be expended to define appropriateness of the selected correlation model used in the analyses.

CONCLUSIONS

This paper has intended to present some of the interesting issues that have developed in recent years with the advent of probabilistic site response approaches, particularly when coupled with deterministic SSI analyses. One of the most important developments that has been noted is the important coupling that needs to be maintained between geotechnical/geophysical and structural analysts and reviewers. It is essential that these different analyses be conducted in a consistent methodology.

References

ASCE (2005) "Seismic Design Criteria for Structures, Systems, and Components in Nuclear Facilities," ASCE/SEI 43-05, American Society of Civil Engineers

Bazzuro, P. and C.A. Cornell (2004) "Nonlinear Soil-Site Effects in Probabilistic Seismic-Hazard Analysis," Bulletin, Seismological Society of America 94, 6, 2110-2123

Costantino, C.J., (2008) "Consistent Site Response - SSI Calculations", BNL Report N6112-051208 Rev. 1, Dec.

Costantino, C.J., C.A Miller, and E. Heymsfield, (2000) "CARES (Computer Analysis for Rapid Evaluation of Structures)", ver. 1.3, Costantino, Miller and Associates

Cramer, C.H. (2003) "Site-Specific Seismic Hazard Analysis That Is Completely Probabilistic Bulletin, Seismological Society of America, 93, 1841-1846, 2003.

Idriss, I.M., and H.B. Seed (1968), "Seismic Response of Horizontal Soil Layers", Journal of the Soil Mechanics and Foundations Division, ASCE, 94, 1003-1031, 1968

McGuire, R.K., W.J. Silva, and C.J. Costantino, (2001)."Technical Basis for Revision of Regulatory Guidance on Design Ground Motions: Hazard- and Risk-Consistent Ground Motion Spectra Guidelines", NUREG/CR-6728, U.S. Nuclear Regulatory Commission

McGuire, R.K., W.J. Silva, and C.J. Costantino (2002) "Technical Basis for Revision of Regulatory Guidance on Design Ground Motions: Development of Hazard- and Risk-Consistent Seismic Spectra for Two Sites," NUREG/CR-6769, U.S. Nuclear Regulatory Commission, 2002

McGuire, R.K., (2004) "Seismic Hazard and Risk Analysis", Monograph MNO-10, Earthquake Engineering Research Institute Oakland, CA, 2004

Schnabel, P.B., J. Lysmer, H. B. Seed, (1972) "SHAKE, A Computer Program for Earthquake Response Analysis of Horizontally Layered Sites", Report EERC 72-12, University of California, Berkeley

Silva, W.J., N.A. Abrahamson, G. Toro, and C. Costantino, (1997) "Description and Validation of the Stochastic Ground Motion Model", Unpublished Report Prepared for the Brookhaven National Laboratory, 1997

Silva, W., (1989) "Site Dependent Specification of Strong Ground Motion" in Dynamic Soil Property and Site Characterization, Proceedings of the Workshop sponsored by NSF and EPRI, Palo Alto, CA,

Silva, W.J., and K. Lee, (1987) "WES RASCAL Code for Synthesizing Earthquake Ground Motions", State-of-the-Art for Assessing Earthquake Hazards in the United States, Report 24. U.S. Corps of Engineers, Waterways Experiment Station, Miscellaneous Paper S-73-1

Stokoe, Kenneth H, and K, Hwang, M. Darendeli, N. K. J. Lee, (1995) "Correlation Study of Nonlinear Dynamic Soil Properties", Savannah River Site, Aiken, South Carolina, Rev. 0, File No. SRS-FR-CDP-95, University of Texas at Austin, Department of Civil Engineering

Toro, G.R., (1997), "Probabilistic Models of Shear Wave Velocity Profiles at the Savannah River Site", Aiken, SC, Final Report to WSRC, April

USDOE Standard, (1994) "Natural Phenomena Hazards Design and Evaluation Criteria for Department of Energy Facilities", DOE-STD-1020-94, Washington DC

USNRC (2007) "NUREG-0800 Standard Review Plan"

USNRC (2007) "A Performance-Based Approach to Define the Site-Specific Earthquake Ground Motion," Regulatory Guide 1.208

USNRC (2009) "Interim Staff Guidance On Ensuring Hazard Consistent Seismic Input for Site Response and Soil Structure Interaction Analyses"

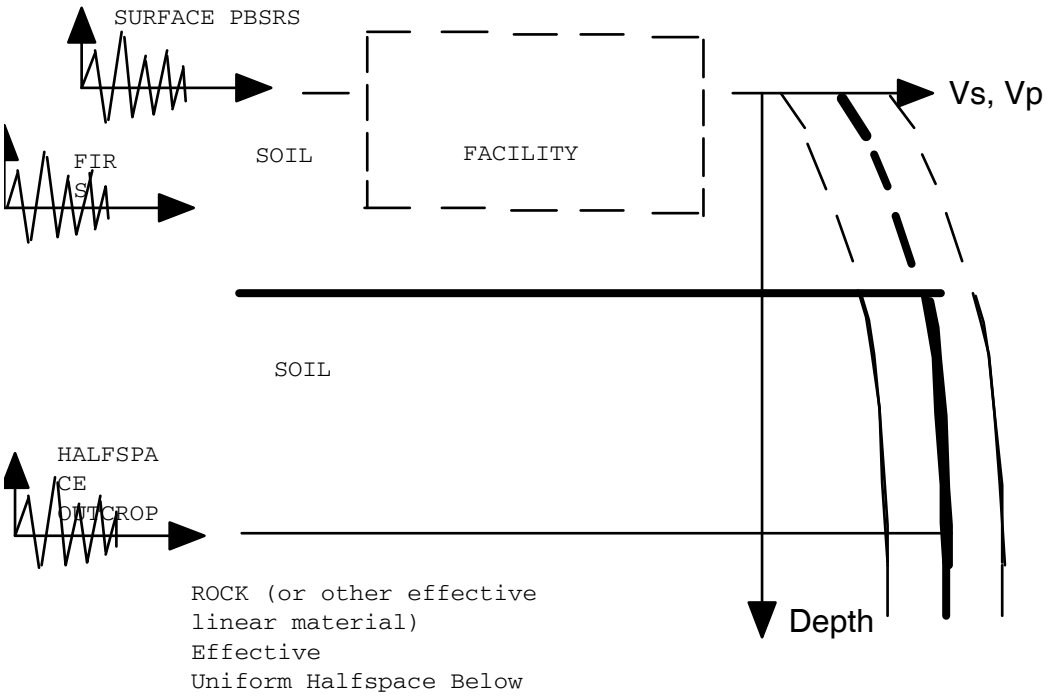


FIGURE 1 SITE SPECIFIC SSI ANALYSES EMBEDDED FACILITY

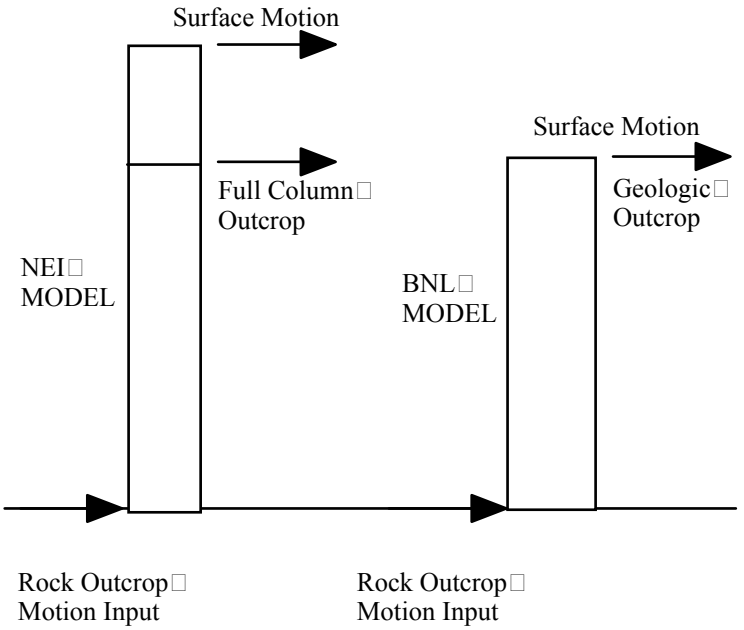


FIGURE 2 OUTCROP DEFINITIONS FOR FIRS

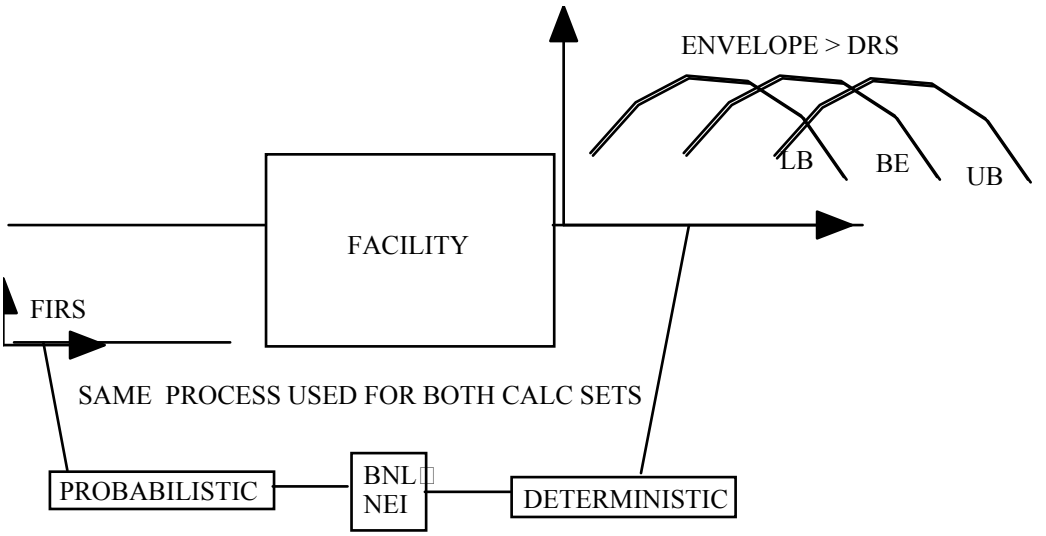


FIGURE 3 1D RESPONSE PROCEDURE FOR
PROB. & DETERM. CALCULATIONS

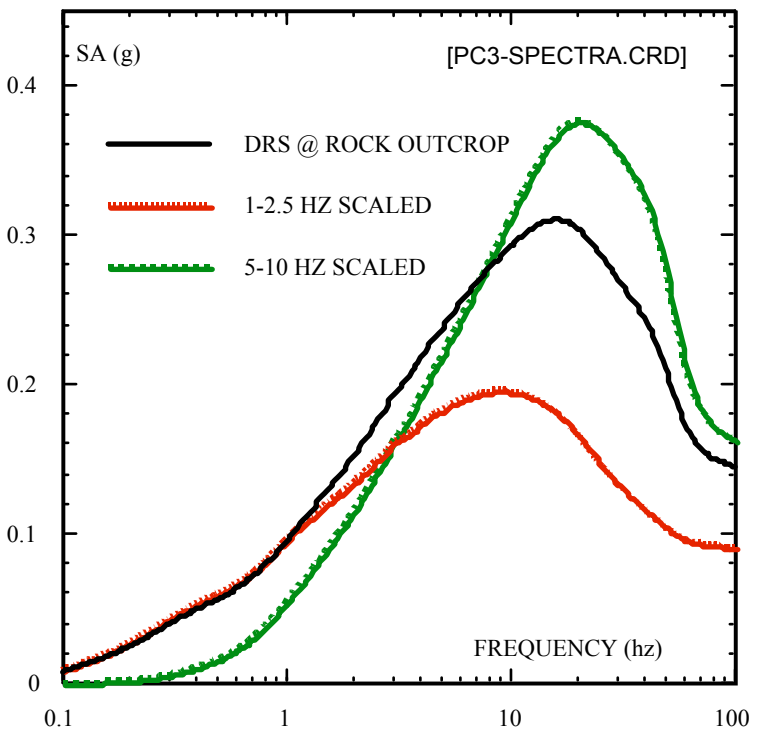


FIGURE 4 PC3 OUTCROP DRS AT BEDROCK

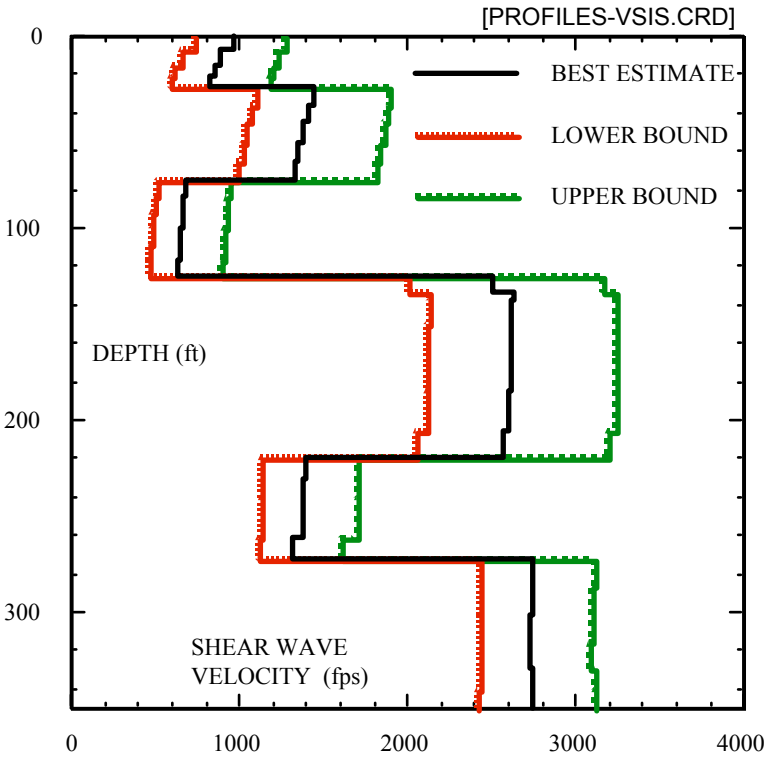


FIGURE 5 INPUT VELOCITY PROFILES
MEDIAN, ± ONE SIGMA TARGETS

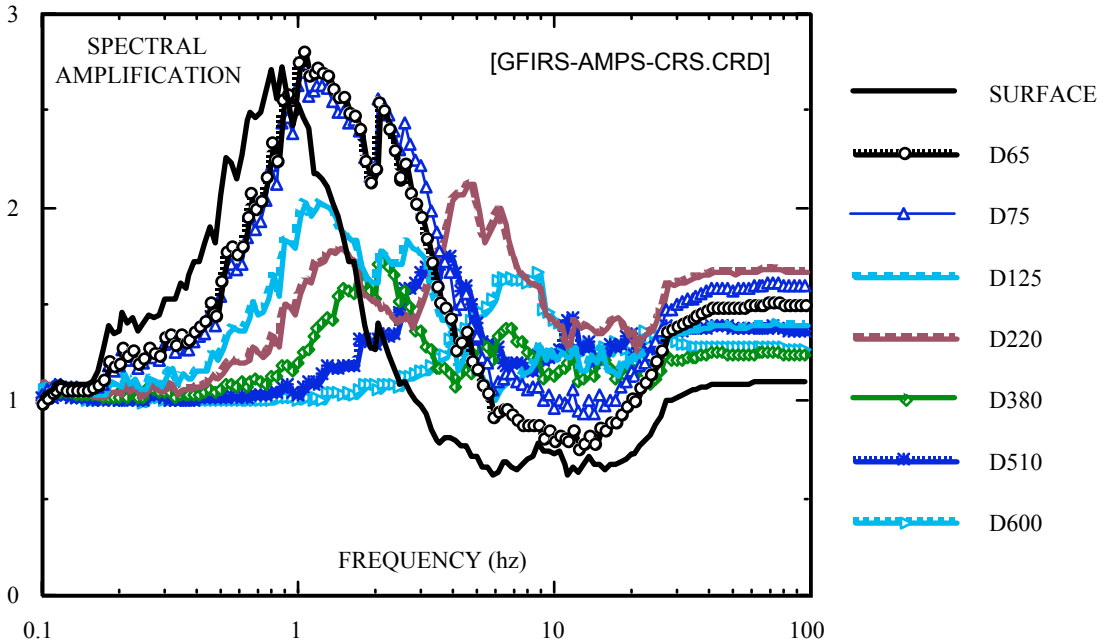


FIGURE 6 FIRS SPECTRAL AMPLIFICATION FUNCTIONS
BNL GEOLOGIC OUTCROP DEFINITION

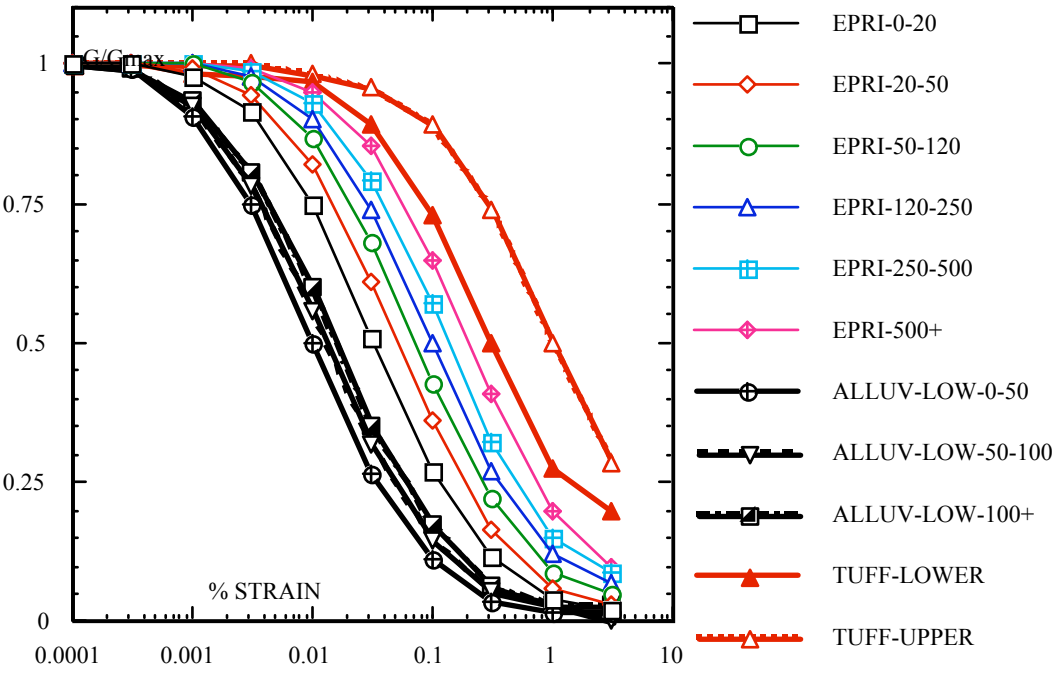


FIGURE 8 G/Gmax DEGRADATION MODELS

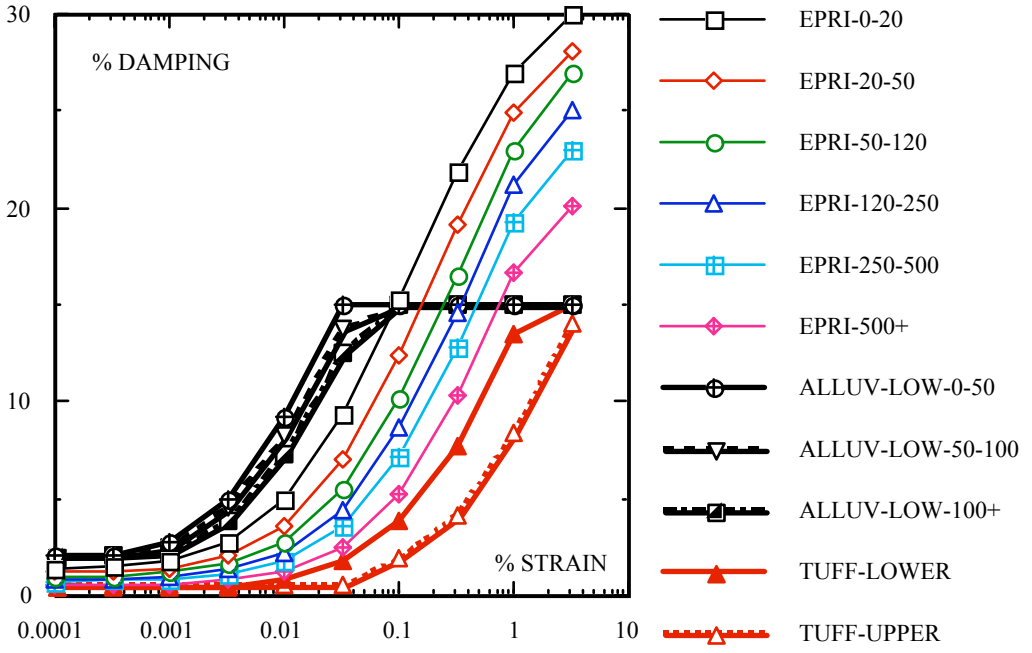


FIGURE 7 HYSTERETIC DAMPING MODELS

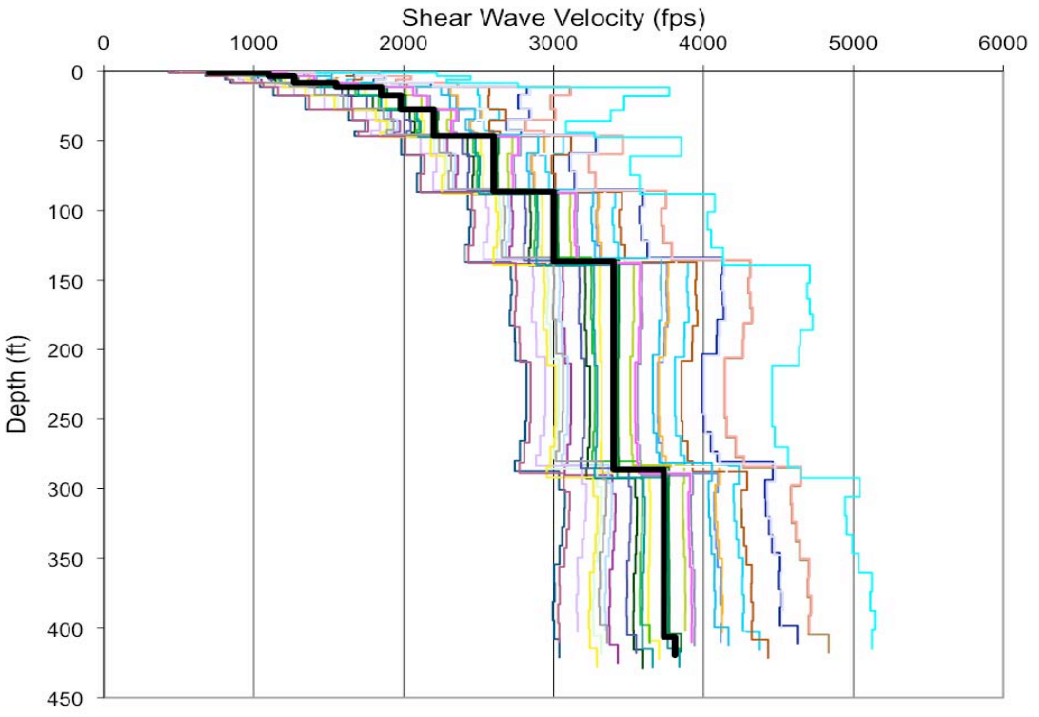


FIGURE 9 PROFILE REALIZATIONS – FULLY CORRELATED

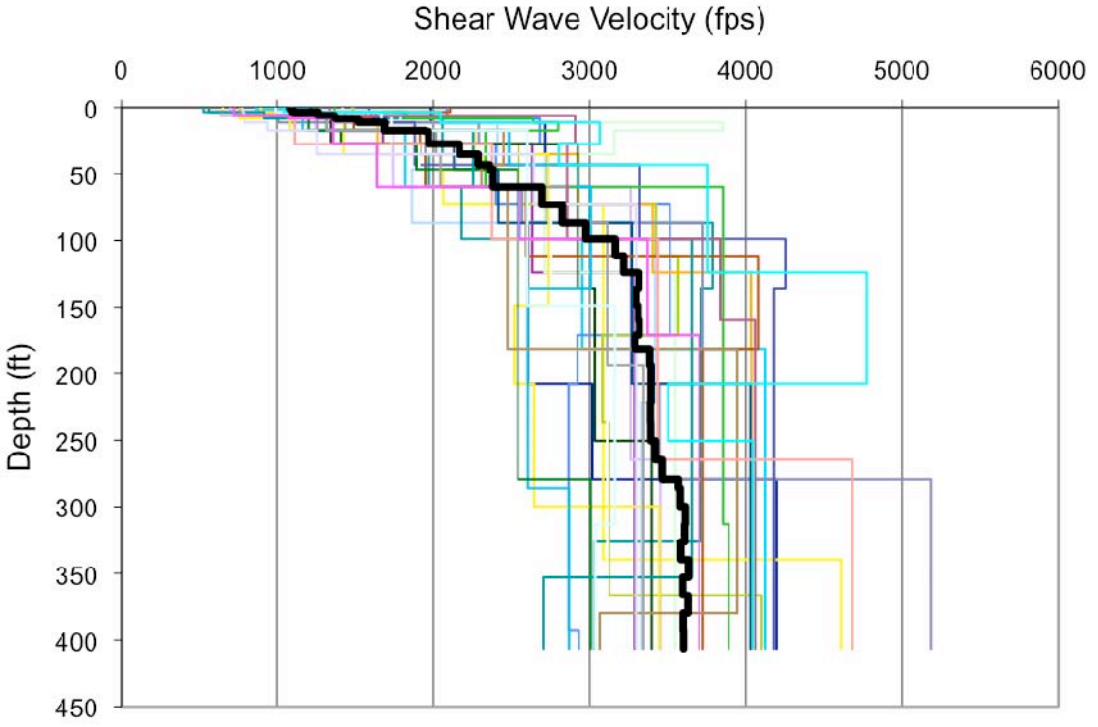


FIGURE 10 PROFILE REALIZATIONS – TORO CORRELATION

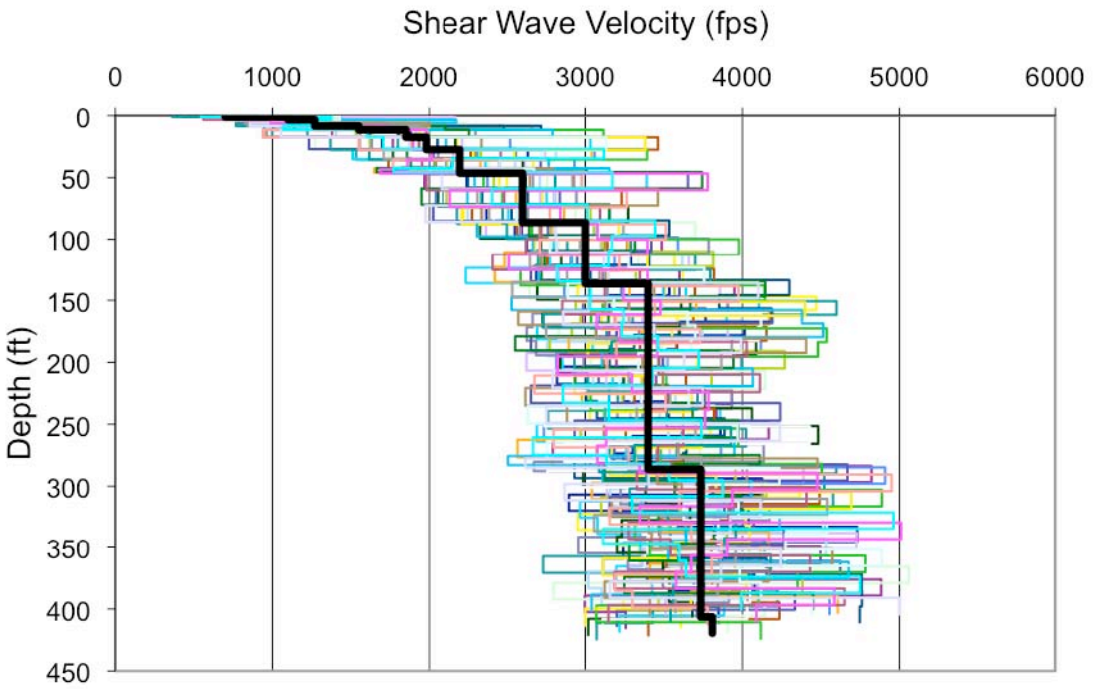


FIGURE 11 – PROFILE REALIZATIONS – FULLY UNCORRELATED

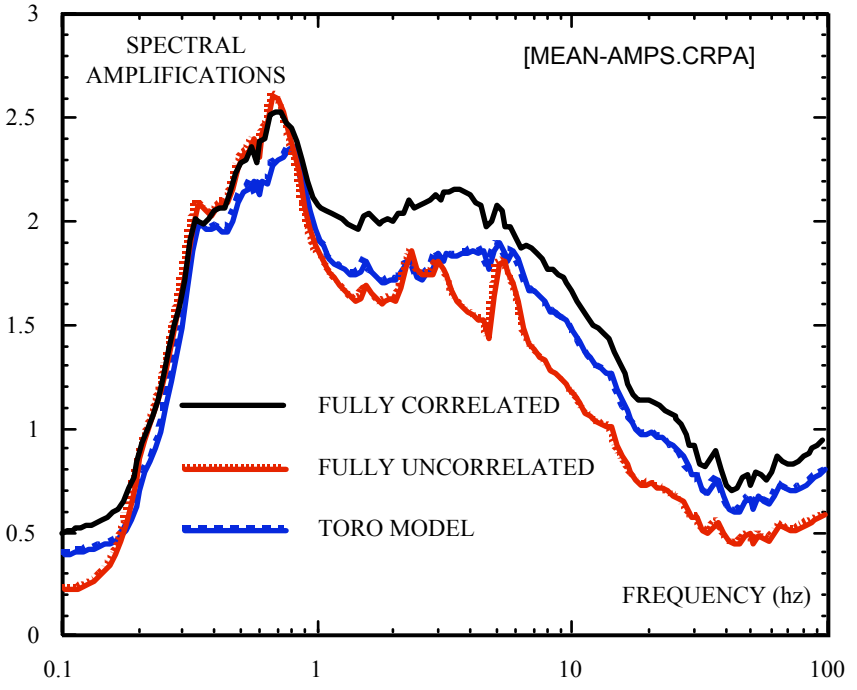


FIGURE 12 MEAN SITE AMPLIFICATIONS

Simple Shear Connections – Not So Simple

Erik Anders Nelson, PE, SE[1]

[1] Structures Workshop, Inc. One Richmond Sq, Suite 147N, Providence, RI 02906; PH (401) 383-8988; FAX (401) 351-8788; email: ean@structuresworkshop.com

ABSTRACT

This article addresses engineering, detailing, and erection of shear connections which represent 95% of the connections on every steel project. While they are often unfairly regarded as simple, they are rarely simple. Shear connection are complex due to the many different types of connections, number of limit states to check, as well as geometry and erection complexity. This article will compare and rate the various methods the Engineer of Record (EOR) uses to provide shear demands. In addition, common types of shear connections will be presented and discussed. Shear connections are rarely controlled simply by the number and capacity of the bolts, and this paper will examine all limit states and discuss what to look out for during shop drawing review.

1.0 Introduction

There has been an ongoing debate as to the responsibility for the design of steel connections for building projects. As a result, different practices are used in design office varying across the country. For instance, on the west coast, the connections are often fully designed by be EOR as part of the construction documentations. Whereas, on the East coast, the connection design criteria and requirements are specified on the construction documents, but the final design is delegated to a licensed professional engineer (often hired by the fabricator) in the state of jurisdiction.

The author has the rather unique experience of seeing both sides of the issue of connections design, first as an EOR designing buildings, specifying connection criteria and checking the shop drawings for conformance. And now for the past three years the author has worked for fabricators to design connections based on the requirements specified by the EOR. It through seeing this issue from both sides, that the author has an appreciation for the importance of the proper attention to shear connection design.

The 2010 edition of the AISC Code of Standard Practice outlines three options for the responsibility of the connection design. It presents a new (albeit already established and widely used) third option where by the EOR delegates the connection design to a professional engineer hired by the fabricator. This article is not a review of these options, but rather a presentation of the various practices used by the EOR to specify the shear connection requirements as seen by the author in review of hundreds of Construction Documents. It is the hope that through the presentation of these practices, it becomes clear that this new third option should become the industry standard for all connections including simple shear connections.

2.0 Why Every Shear Connection Must be Checked

Most often, at least on the East Coast, the steel connection design is relegated to the fabricator and the EOR provides demand criteria and typical details for the design of the connections. The fabricator either has an in house engineer or hires a connection engineer to design the connections (typically the shear, moment and bracing connections). .

However, in some cases the EOR does not always require the shear connections to be designed by an engineer, only the moment and bracing connections. This is a mistake in the opinion of this author. While shear connections are perceived as simple, they often are not. Take for instance the most common type of shear connection - the beam-to-beam connection, which is actually pretty complicated. As is commonly known, all beam-to-beam shear connections have a top cope, which can make the design tricky. In addition, the cope varies based on the size of the

girder – so it is not uncommon for the same size beams with the same type of connection material (shear tabs, bolts, etc) will have very different capacities. For example, a W12x14 framing into a W16x31 has a very different capacity than a W12x14 framing into a W12x53 even if the shear connection is identical, see Figure 1.

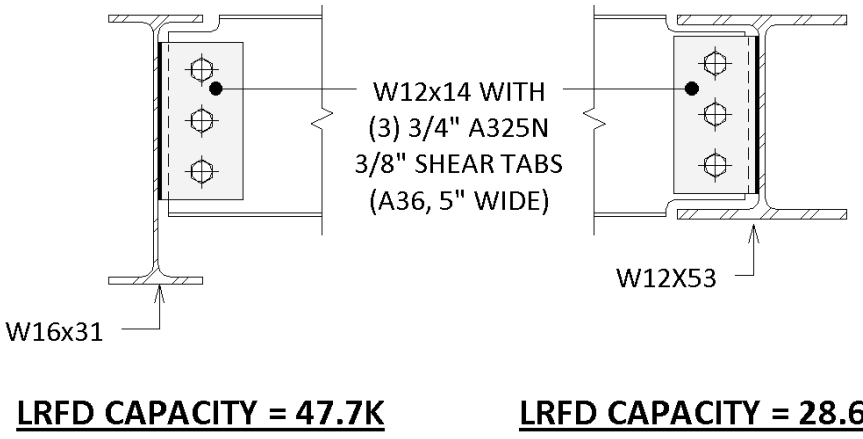


Figure 1. W12x14 beams with same Connection but different Shear Capacity

Not only is the W12x14 double coped when framed into the W12x53, but the copes are larger (both deeper and wider due to the thicker and wider girder flange) in comparison with the W12x14 framing into the W16x31. The reduced section due to the large copes significantly decreases the shear capacity of the connection by nearly half. Often times shear connections are not controlled by the bolt shear capacity (especially light beams with double angle shear connections). They may be controlled by bolt bearing, shear rupture of the web, block shear capacity of the web or coped section capacity. In the following sections we will explore the various ways the engineer of record specifies shear demands in addition to clarifying the different shear connection types.

3.0 EOR Methods of Supplying Shear Demand on Drawings

There are a variety of methods that are used by engineers to provide the fabricator the shear demands for the design of shear connections, and based the author's experience, some are good and some should be avoided.

3.1 **Method 1**: Provide Actual Shears on Each Beam on the Plans

This method is when the EOR provides the actual shear on the plans for every beam. This provides a uniform reliability in all of the members and the most accurate and efficient connections result.

Advantages	**Disadvantages**
Results in Least Expensive / Most Efficient Connections	Most work for EOR but can be automated. EOR does not and will not get paid for this work.
Most Reliable Shear Demands and Fewest RFIs from Fabricator	Can sometimes lead to very small connections that make the beam appear oversized (for example having only 2 bolts within a W30 looks strange even if it works)
Lower and More accurate bids from Fabricator	
OVERALL GRADE: A	

3.2 **Method 2**: Provide a Table of Shear Values

This is method can work but it may be overly conservative for some beams on the project if done improperly. The table on the left is too simplistic and greatly overestimates the shear demand on lighter sections. For example, a W18x35 will have the same demand as a W18x76. The author derived the right table based on the plastic modulus of the beam and studied each connection type and number of bolts required. The right table is a good one and feels free to use it on your project if appropriate. You can select the ASD or LRFD method, it really doesn't matter to a connection engineer and it doesn't affect the connection.

.

Beam Size	Required Shear Capacity, ASD / LRFD
W8	20 k / 30 k
W10	30 k / 45 k
W12	40 k / 60 k
W14	50 k / 75 k
W16	70 k / 105 k
W18	90 k / 135 k
W21	110 k / 165 k
W24	130 k / 195 k

Beam Sizes	Required Shear Capacity ASD / LRFD
W8x10-18 W10x12-15	10 k / 15 k
W8x21-28 W10x17-26 W12x14-19	20 k / 30 k
W8x31+ W10x30-45 W12x22-30 W14x22-30	30 k / 45 k
W10x49+ W12x35-58 W14x34-48 W16x26-40	40 k / 60 k
W12x65+ W14x53-61 W16x45-57 W18x35-55 W21x44-50	50 k / 75 k
W14x68+ W16x67+ W18x60-71 W21x55-62	70 k / 105 k
W18x76+ W21x68-73 W24x62-68	90 k / 135 k
W21x83+ W24x76-94 W27x84-94 W30x99	110 k / 165 k
W?? x100+	See Plans

Advantages	**Disadvantages**
Simple for EOR to add to General Notes	If table is not properly derived, it can lead to over (e.g. short infill beams) or under (e.g. transfer beams) designed connections depending on the framing condition.
More Reliable Shear Demands than providing demands based on AISC maximum uniform load tables (Method 3 in the next section)	EOR will need to verify chart on the very rare occasion the actual shear is higher.
Less RFIs from Fabricator	Connections are generally conservative and not cost effective
Less Cluttered Framing Plans compared to providing all the shears on the framing plans (Method 1 in the previous section)	
OVERALL GRADE: VARIES FROM 'F' (Left Chart) TO 'B' (Right Chart)	

3.3 **Method 3**: Shear demands based on Length of Beam

This is a very common method. It is provided in many different forms on the general notes but it is always based on the ***maximum total uniform load tables*** in the AISC manual. These tables are based on the moment capacity of the beam in which the max uniform load is "backed out" and the shear is determined. So these tables are based on the following: $M=wL^2/8$ and since $V=wL/2$, then $M=VL/4$ or $V=M/(L/4)$. Paradoxically, the longer the beam - the smaller the shear demands. Therefore, beams will have to be designed close to their flexural capacity for a connection to be reasonable. Figure 2 clearly describes the absurdity of this method. The shorter member requires much larger bolts and tabs, in addition to the welded doubler plate to meet the demand.

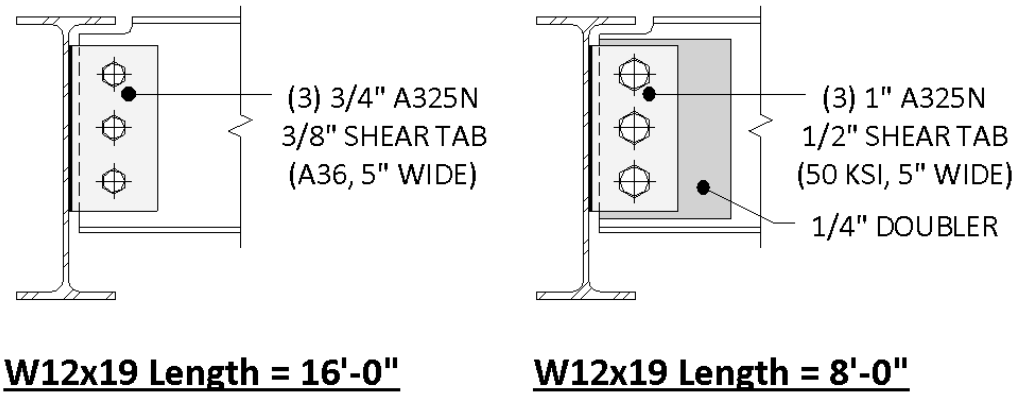


Figure 2. W12x19 (8ft Long) and W12x19 (16ft long)

For composite beams, the EOR will add a multiplier of anywhere between 1.5 and 2.3 on top of this shear to account for the increased moment capacity due to composite action with the concrete slab. For cantilevers, the EOR should be careful because this method is inappropriate, since the maximum total uniform load tables are based on simple span and cantilevers are usually not governed by strength.

For the EOR, this is the simplest method, just a quick note on the drawing. The EOR knows that as long as the beam works in bending (often from their analysis model), the shear connection will work. So the connection is designed for the maximum load it can support. This is often very conservative and inapproiate. It is a very costly method for the owner and fabricator and always leads to larger connections than necessary.

Advantages	Disadvantages
Simple for EOR to add to General Notes	Often leads to overly conservative and costly connections
	Least reliable since it is often a general criteria, broadly applied to most (if not all) conditions on the project.
	Short beams and composite beams often unnecessarily require doubler plates and/or web extension plates
	Many RFIs will result to verify shears
	Fabricator can lose money on a project because of unforeseen connection costs
	This method is derived for simple span members that are governed by flexure only. Beams that are governed by deflection, vibration, or overly designed are severely penalized.
OVERALL GRADE: F	

4.0 Types and Capacity of Shear Connections

4.1 Type 1: Beam to Beam Connections

Generally beam–to-beam connections have at least a top cope. Therefore, the capacities are difficult to calculate (cope section, block shear, etc). These are the most common connection on a project, yet they are often deemed as insignificant and "simple". This is not the case.

Another complexity is when double angles are required on a project. If all the bolts are shared on each side of the girder web, an erection bolt (or other aid) must be added to the connection to be able to build and meet OSHA requirements. This can lead to problems with fit up and erection sequencing.

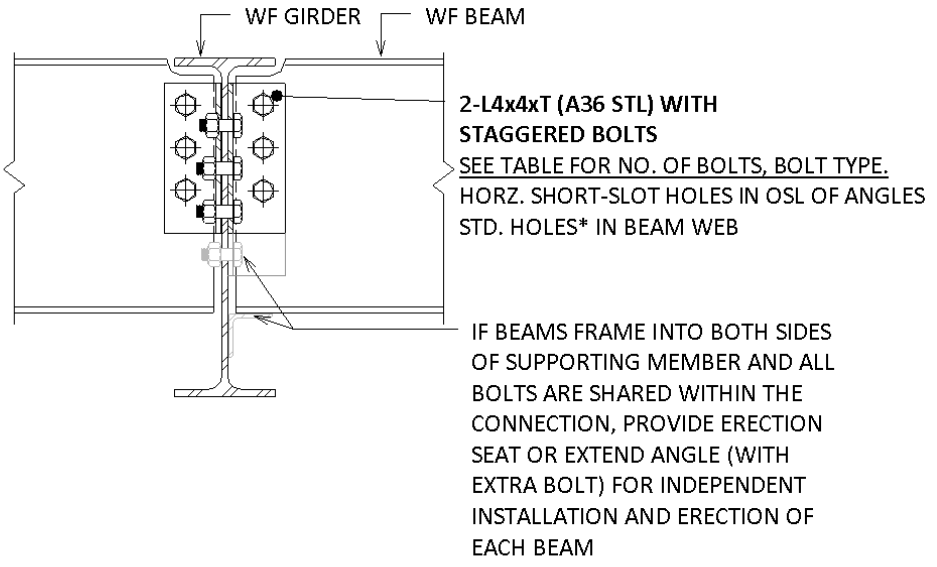


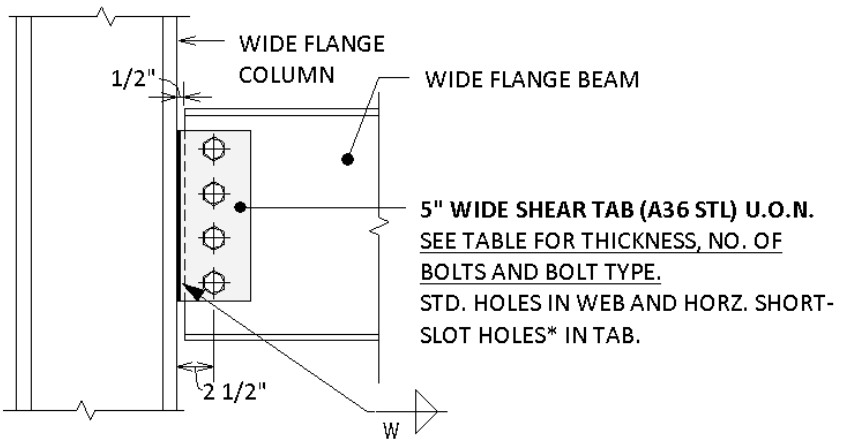
Figure 3. Double Angles can be a Problem

The EOR may not realize this, but when requiring the use of double angles for beam-girder connections, it is forcing the detailer to add erection bolts and often to extend the connection angles. In addition, it may affect the erection sequence and force the erector to place the floor beams in a specific sequence. For example, in the case where beams of different depths frame on either side of a girder and share bolts, the deeper beam may have to be erected before the shallower beam on the opposite side of the girder web (so the lower bolts can serve as the erection aid). This can cause delays. A clever detailer will stagger the angles on each side of the same beam web such that either beam can be erected first, but these angles may not fit due to the greater web clearance height required.

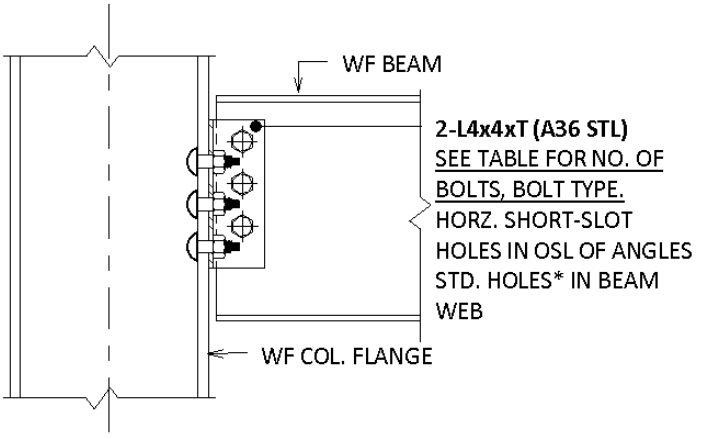
An example of inefficient use of connection material is the use of double angles to connect light beams with thin webs. Using 5/16" thick angle legs on each side of a beam web when the web is only a quarter inch is wasteful, yet very common. Furthermore, for beams with weights less than 30plf, it is not the connection angles that control the capacity; it is usually the web in block shear, coped section, or shear rupture (or bolt shear). Therefore, it is the author's opinion that the EOR should allow the fabricator the freedom to use shear tabs for these reasons. Please note, the bolts in Figure 3 do not need to be staggered for 4" angle legs. If not staggered, this connection will be easier to erect if the shop installs the bolts to the beam web such that the orientation of the tail end of the bolts never meet (spiral pattern in plan).

4.2 Type 2: Beam to Column Flange Connections

The simplest connection for an erector to a column flange is a shear tab as shown in Figure 4.



BEAM TO WF COL FLANGE SHEAR TAB



WF BEAM TO WF COL FLANGE USING DOUBLE ANGLES, BOLTED - BOLTED, STAGGERED

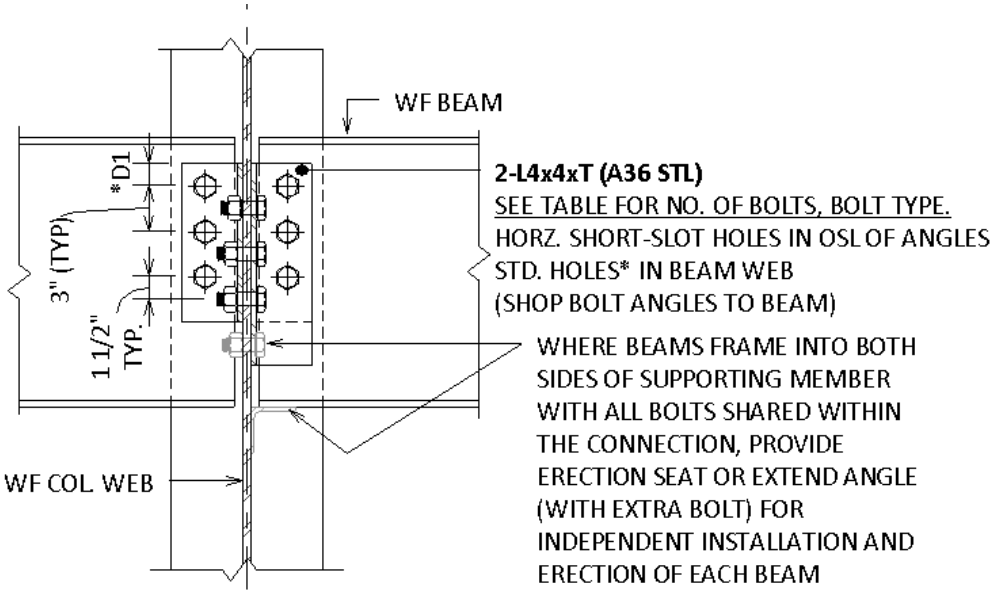
Figure 4. Connections to Column Flange I

If double angles are used, it may be important to stagger the bolts in this configuration. For the erector to have access to the tails of the column bolts using the TC bolt gun, the tails will always be facing out. This could cause interference with the shop installed bolts on the beam when two tails are on the same side of the beam web. Therefore, the author stronger recommends shear double angle shear connections to column flanges have staggered bolts.

4.3 Type 3: Beam to Column Web Connections

Double angles are best for beam-to-column web connections. Erectors that like the use of TC bolts in the field do not like shear tabs since the column flange interferes with the bolt gun.

Bla bla



WF BEAM TO WF COL WEB USING DOUBLE ANGLES, BOLTED - BOLTED, STAGGERED

5.0 Key Takeaways for EOR

- If the EOR is not designing all the shear connections, then require calculations by a PE registered in the state of the project for all connections, including shear connections, to be submitted for approval (similar to all connections). Do not put a table indicating the number of bolts only without checking every limit state of every connection.
- Try to add shears to the plans (method 1) or provide good table (method 2) – do not use note about the uniform load table method (method 3).
- Do not require double angles when shear tabs work
- Let the fabricator and/or fabricator's engineer select the type of shear connection. Shear tabs are generally preferred for beam-to-beam and beam-to-column flange connections.
- It is more efficient and cost effective for the fabricator to hire or staff an engineer to design connections specific to their shop and erection standards and practices (e.g. shop bolted, staggered bolts for double angle connections, shop standards for connection material...).

Designing and Detailing Welded Skewed T-Joints

T. Green[1] and T. Schlafly[2]

[1]Wiss, Janney, Elstner Associates, Inc., 2751 Prosperity Avenue, Fairfax, VA 22031; PH (703) 641-4601, FAX (703) 641-8822; email: tgreen@wje.com
[2]American Institute of Steel Construction, Inc., One East Wacker Drive, Suite 700, Chicago, IL 60601-1802; PH (312) 670-2400, FAX (312) 670-5403; email: schlafly@aisc.org

ABSTRACT

In the last 20 years, computer aided drafting and analysis software has allowed steel structure geometries to become more complicated. As the steel structure geometries become more complicated, the use of skewed t-joints for both tubular and nontubular connections has become more common. The American Welding Society Structural Welding Code - Steel (AWS D1.1) provides design and detailing requirements for skewed t-joints. Depending on the skewed t-joint geometry, designers are required to define the required weld leg or effective throat size. However, many designers are unaware of the AWS D1.1 skewed t-joint requirements and apply typical 90 degree fillet weld details to skewed connections. Contradiction between these 90 degree and skewed details in combination with the variety of AWS D1.1 prequalified joint configurations can lead to confusion and fabrication inefficiencies. AWS D1.1 design and detailing requirements for skewed t-joints are summarized and discussed.

INTRODUCTION

AWS D1.1 Annex K defines a t-joint as "a joint between two members located approximately at right angles to each other in the form of a T." A skewed t-joint, as the name suggests, is a joint where the two members may not form a right angle (see Figures 1 and 2). Skewed t-joints can be used to connect tubular as well as nontubular members. While some of the details discussed here may apply to the heel and toe of tubular skewed joints, tubular joints have many more topics to consider that are not discussed here. In the last 20 years, steel structure geometries have become more complicated, and therefore, the use of skewed t-joints has become more common.

Skewed t-joint welds typically consist of fillet welds or partial joint penetration (PJP) groove welds. Skewed t-joint geometric variables include dihedral angle, leg and throat dimensions, z-loss, groove angle and root opening. The dihedral angle (Ψ) is the angle at which the two surfaces meet - this angle will be acute or obtuse depending on the side of the connection being considered. Leg (b) and throat (t) dimensions define the weld geometry while z-loss accounts for potential lack of fusion and slag inclusions at the root of small included angle welds (i.e. welds on the acute side of a joint). The groove angle, which is used in PJP groove welds, is the angle between the two base metal faces at the weld. The root opening is the distance,

or gap, between the two surfaces at the weld root. The gap between the parts at the toe of the weld is not given a name in normal welding terminology but it is a critical variable used in selecting the appropriate weld joint detail in skewed t-joints. In Annex B, it is referred to as a root gap relative to the obtuse fillet type weld. Again, the purpose of this paper is to raise awareness and discuss AWS D1.1 skewed t-joint requirements.

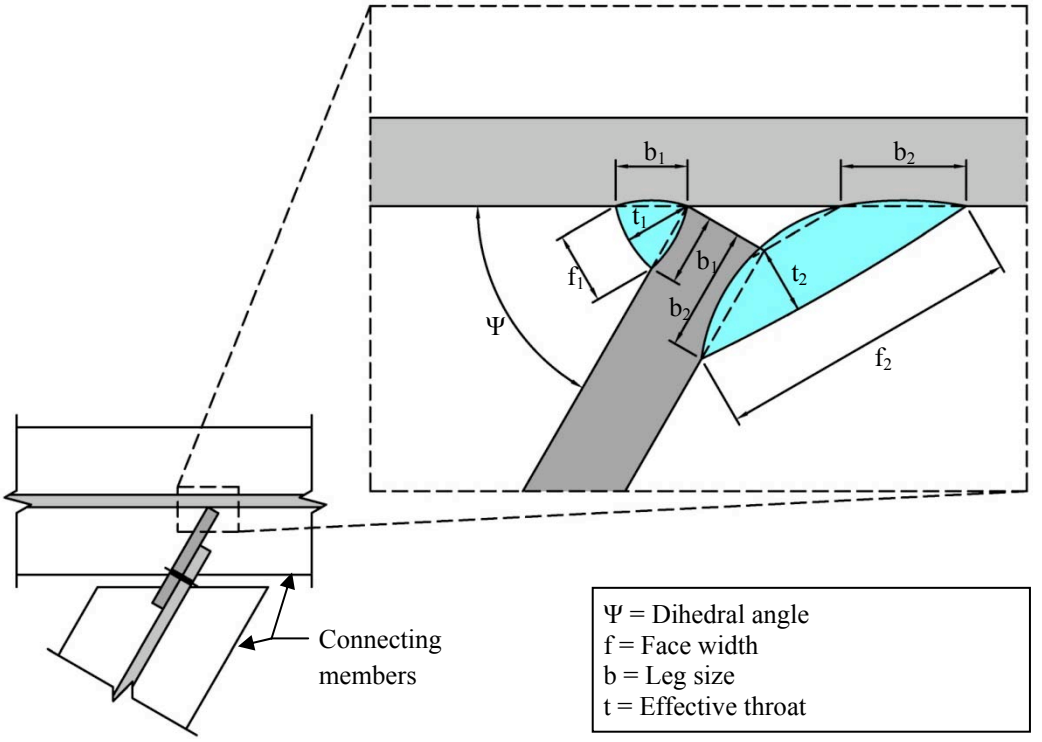


Figure 1. Skewed single plate connection with square edge.

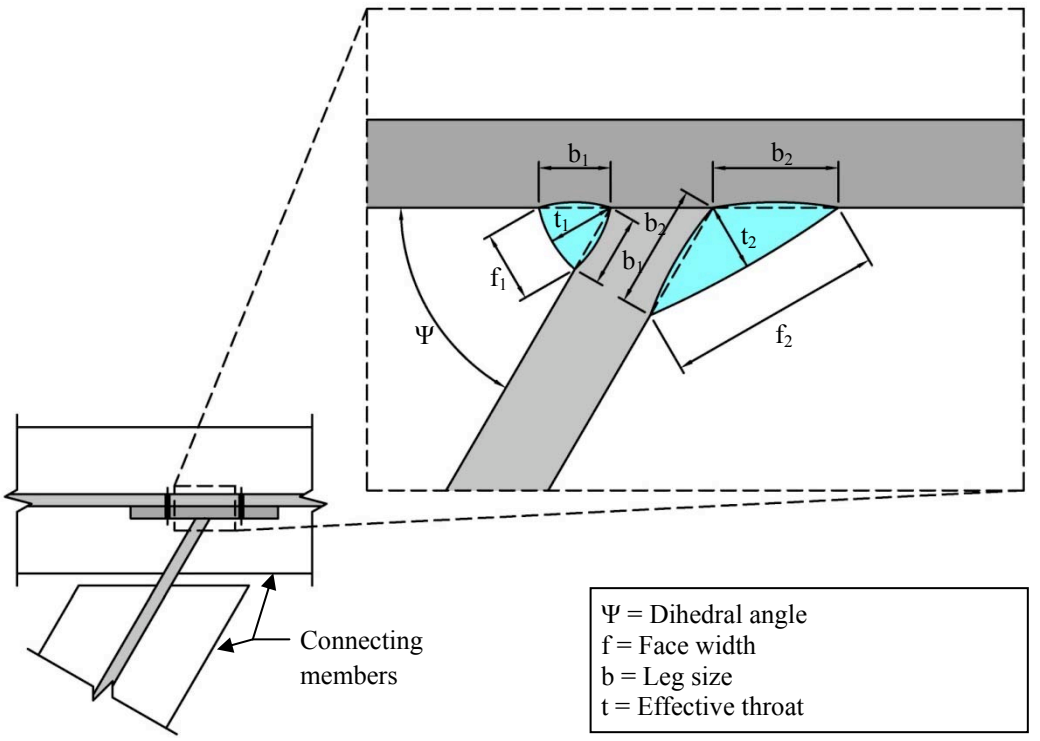


Figure 2. Skewed shear end-plate connection with beveled edge.

AWS REQUIREMENTS

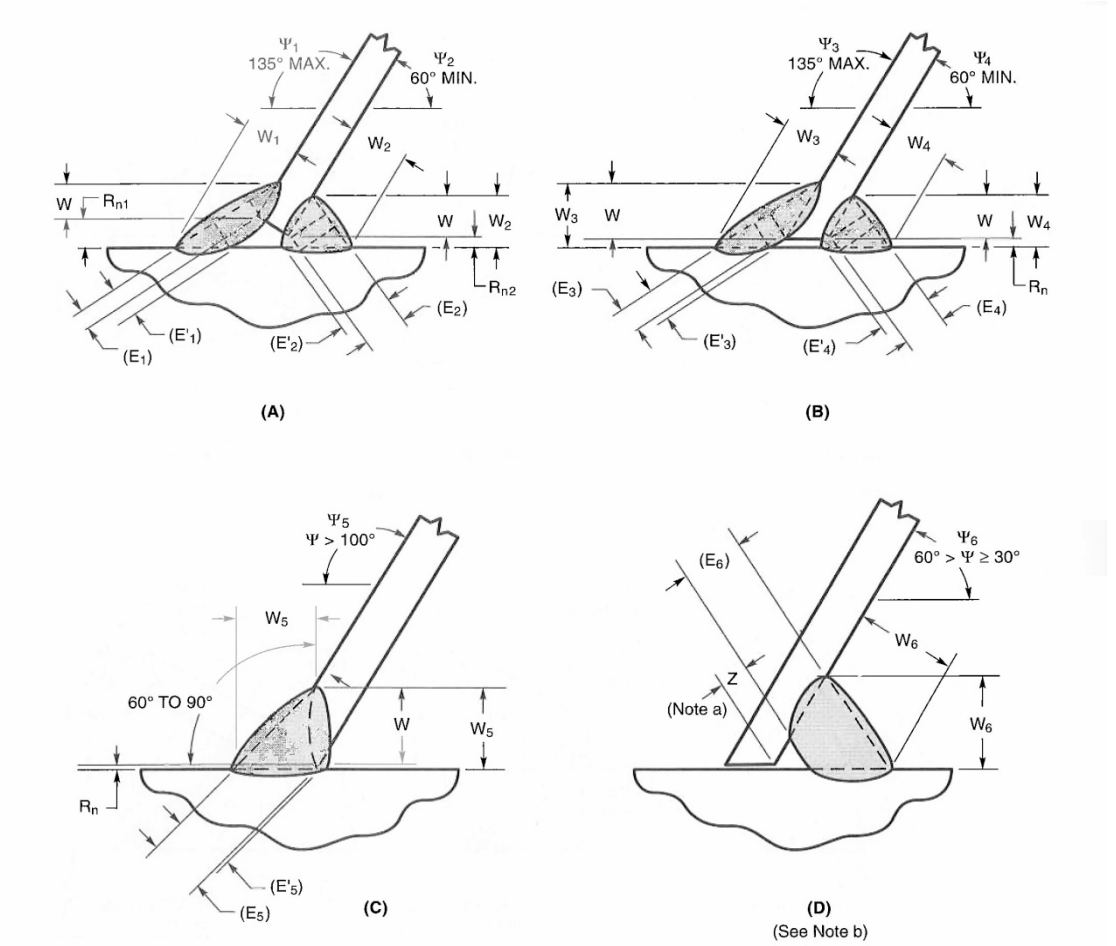
Previous Codes. In 1980, fillet welds could be used in skewed t-joints having dihedral angles between 60 and 135 degrees. For dihedral angles smaller than 60 degrees, the joint was considered a PJP groove weld. In 1985, Note Q2 was added to the prequalified PJP groove weld figures indicating that "the member orientation may be changed provided that groove dimensions are maintained as specified." In the 1998 code, skewed t-joint design and prequalification requirements similar to the 2010 requirements were incorporated.

2010 Code. Skewed t-joint requirements are defined in Clause 2 - *Design of Welded Connections*, Clause 3 - *Prequalification of WPSs* and Annex B. For clarity, Clause 2 includes information related to applied stresses, allowable stresses and joint configurations for both tubular and nontubular members subject to static and cyclic loads. Clause 3 defines important variables that must be satisfied for a welded joint to be considered prequalified. Prequalified joints, in general, utilize materials and joint configurations that have a long history of good performance. Annex B Table B.1 helps geometrically convert 90 degree fillet weld leg size to skewed fillet weld leg size. Table 10-13 in the American Institute of Steel Construction (AISC) Manual of Steel Construction also provides design guidance for these welds.

The following provides a summary of several current skewed t-joint requirements:

1. Design Drawings
    a. Provide fillet weld leg size for surfaces meeting at 80 to 100 degrees.

   b. Provide weld effective throat size for surfaces meeting at less than 80 degrees and greater than 100 degrees.
2. Shop Drawings
   a. Provide fillet weld leg size for surfaces meeting at 80 to 100 degrees.
   b. Provide weld leg size, including z-loss and additional weld to account for the gap between the parts, for surfaces meeting at less than 80 degrees and greater than 100 degrees.
3. Calculation of Effective Throat and Leg Size
   a. Fillet welds at surfaces meeting at 80 to 100 degrees - effective throat is the shortest distance between the root and weld face of a 90 degree diagrammatic weld (Annex A). The effects of the 10 degree skew are neglected in accordance with AWS Clause 2.
   b. Fillet welds at surfaces meeting at 60 to 80 or greater than 100 degrees - effective throat is calculated based on leg size and dihedral angle. Leg size is calculated based on the root or face opening and effective throat (Annex B).
   c. Fillet welds at surfaces meeting at 30 to 60 degrees - effective throat is calculated based on leg size and dihedral angle. Leg size is calculated based on root opening, effective throat and z-loss (Annex B and Table 2.2)
   d. Fillet welds at surfaces meeting at less than 30 degrees - these welds are typically not considered to be effective in transmitting applied forces (some tubular joints are an exception). This can present problems in some geometries that are driven by architectural demands.
4. Prequalified Joint Details
   a. AWS Figure 3.11 (Figure 3) provides four different prequalified joint details. Details A, B and D depict fillet weld details fused to the side of the skewed part while Detail C depicts a weld fused to the edge of the skewed part. Note that the plate in Detail A is not beveled while the plate in Detail B is beveled parallel to the main member. In Detail C, the plate is beveled 60 to 90 degrees to the main member. Detail D is shown beveled parallel to the main member but this is irrelevant to the weld and unnecessary. Also note that Detail D represents a one-sided fillet weld for dihedral angles between 30 and 60 degrees.



[a] Detail (D). Apply Z loss dimension of Table 2.2 to determine effective throat.
[b] Detail (D) shall not be prequalified for under 30°. For welder qualifications, see Table 4.10.

Notes:
1. (E_n), (E'_n) = Effective throats dependent on magnitude of root opening (R_n) (see 5.22.1). (n) represents 1 through 5.
2. t = thickness of thinner part
3. Not prequalified for GMAW-S or GTAW.

Figure 3. AWS D1.1 2010 Figure 3.11 illustrating prequalified skewed t-joint details for nontubular applications.

EXAMPLES

Example 1. An engineer has a skewed t-joint with an acute dihedral angle (Ψ) equal to 60 degrees. The equivalent 90 degree fillet weld size (b) is 0.25 inches on both sides of the part. Note that the designer would show the effective throat on the contract drawings (0.707*0.25 inches=0.177 inches or, when rounded up, 3/16 inch).

The fabricator can utilize Figure 3.11 Details A, B or C. Since no end preparation is typically more cost effective than installing a bevel at the end of the plate, the fabricator selects Detail A with no root opening. Note that for most applications, the weld toe gap on the obtuse side needs to be equal to or less than 5/16 inch to comply with AWS D1.1 fit-up requirements. Using Annex B, the equivalent acute side skewed leg dimension (b) is equal to 0.71*0.25 inches=0.178 inches. Rounding up to a practical dimension, the acute side skewed leg dimension is equal to

3/16 inch. For the obtuse side, the equivalent skewed leg dimension is equal to 1.23*0.25 inches=0.308 inches. Again, rounding up to a practical dimension, the obtuse side skewed leg dimension is equal to 5/16 inch. Note that the opening or gap at the weld toe must be added to the 5/16 inch leg dimension. On the shop drawings, the fabricator would provide a 3/16 inch dimension on the acute side fillet weld and 5/16 inch plus the weld toe gap dimension on the obtuse side fillet weld.

For this example, both the designer and fabricator illustrate fillet welds but the dimensions shown on the contract and shop drawings are different. While the joints are equivalent from a structural performance perspective, modifications between contract and shop drawings should be clear to the designer and fabricator.

Example 2. An engineer has a skewed t-joint with an acute dihedral angle (Ψ) equal to 45 degrees. The equivalent 90 degree fillet weld size (b) is 0.25 inches. Again, note that the designer would show the effective throat on the contract drawings (0.707*0.25 inches=0.177 inches, or when rounded up, 3/16 inch).

The fabricator can utilize Figure 3.11 Details C or D but given the desire to avoid one sided fillets where possible, elects to use Detail C with no root opening. Due to groove angle limitations, the end of the plate must be beveled an additional 15 degrees to provide a 60 degree groove angle. Since there is only one PJP groove weld instead of two fillet welds, the total effective throat must be equal to 3/8 inch. On the shop drawings, the fabricator would provide a 3/8 inch PJP groove weld with a 60 degree root opening.

For this example, the designer specified fillet welds and the fabricator produced a PJP groove weld. Again, while the joints are equivalent from a structural performance perspective, modifications between contract and shop drawings should be clear to the designer and fabricator.

In addition, note that many of the existing prequalified, single bevel, PJP groove welds require groove angles equal to 45 degrees with minimum root face dimensions equal to or greater than 1/8 inch (see joint designation BTC-P4 in AWS D1.1 Figure 3.3 for reference). Comparing the example skewed joint with joint BTC-P4, the 45 degree groove angle (prior to beveling) for the skewed joint is not acceptable based on Detail C in Figure 3.11 even though a 45 degree bevel is acceptable for BTC-P4. In addition, no minimum root face dimension is required on Detail C in Figure 3.11 which contradicts the 1/8 inch minimum root face allowed for joint BTC-P4.

POTENTIAL AREAS FOR CONFUSION AND INEFFICIENCY

Weld symbol. In most structural drawings, designers provide a design load at each connection and reference typical connection details. Assuming that the typical details illustrate 90 degree, welded, single plate or end-plate connections, the fillet weld leg size would be provided for a range of plate lengths - typically 1/4 to 3/8 inch. For skewed t-joints between 80 and 100 degrees, these typical details are clear and work well.

However, when the two surfaces meet at less than 80 or greater than 100 degrees, a fillet weld symbol (with the required leg size) does not always adequately portray the required weld. For these welds, the detailer will typically select one of the AWS prequalified welds in Figure 3.11, design the connection, and produce shop drawings to be approved by the designer. Note that as part of this process, the fabricator may have to modify the fillet welds to PJP groove welds. In order to make sure that designers and engineers both understand that skewed t-joints are slightly different than typical fillet weld joints, a unique weld symbol clearly indicating whether the leg or throat dimension is given may be useful.

Drawing requirements. For skewed t-joints, fillet weld effective throat information is provided on the contract drawings and leg size is provided on shop drawings. For designers, lack of knowledge related to this requirement can lead to confusion. For example, if the contract drawings indicate that the size of a particular fillet weld is 1/4 inch for a 60 degree skewed t-joint, the fabricator assumes that the 1/4 inch dimension is the effective throat, not the fillet weld leg size. The fabricator converts the 1/4 inch effective throat value back into a 90 degree leg size and uses Annex B to determine the required skewed fillet weld leg dimension. The skewed fillet weld leg dimension is then provided on the shop drawing.

If the fabricator incorrectly assumed that the contract drawings specified a 90 degree fillet weld with 1/4 inch leg size, they could use Annex B to convert directly to the required skewed fillet weld leg size. However, this would result in the installed weld being smaller than the required weld which might reduce the overall strength of the connection. Knowledge of the information required on contract and shop drawings is critical to producing a safe, cost-effective structure.

Joint details. The prequalified skewed t-joint details include numerous variables which provide designers and fabricators with the flexibility to use geometries that produce the most reliable, cost-effective joint. However, there are several variables in the prequalified details that can cause confusion.

First, Details A and B define maximum and minimum dihedral angles (135 and 60 degrees, respectively). It is not clear why the dihedral angle does not range from 60 to 120 degrees or 45 to 135 degrees. Second, Detail C allows a PJP groove

weld to be installed at dihedral angles greater than 100 degrees. However, it also requires that the groove angle be greater than 60 degrees which would require beveling of the plate for all dihedral angles less than 60 degrees. Since previous codes allowed PJP groove weld configurations to be modified provided the groove dimensions were maintained and current prequalified, single bevel PJP groove welds allow for groove angles equal to 45 degrees, the 60 degree groove angle limitation may lead to additional joint preparation resulting increased overall cost.

Finally, Annex B is intended to facilitate designer and fabricator conversion from 90 degree fillet weld leg size to skewed fillet weld leg size. Annex B Table B.1 includes conversion information for dihedral angles from 60 to 135 degrees. Since Detail D in Figure 3.11 allows acute side fillet welds with dihedral angles as small as 30 degrees, is unclear why the conversion values in Annex B are limited to 60 to 135 degrees. In addition, a new table in Annex B that converts the required effective throat value directly to the skewed leg dimension may also be useful to the fabricator.

POTENTIAL CLARIFICATIONS

The following provides a brief summary of potential clarifications that may result in more efficient, safe, and cost-effective skewed t-joints.

1. Weld Symbol - Clarify fillet or PJP groove weld symbols so that weld type is clear to the designer and fabricator.
2. Design Requirements - Clarify fillet and PJP groove weld size designations so that effective throat or skewed leg dimensions are clear to designers and fabricators. Part of this effort may be to publicize the information required on the contract drawing to designers.
3. Joint Details - For Details A and B, clarify the two dihedral angles shown on each drawing. For Detail C, allow groove angles less than 60 degrees to be used particularly when being used in combination with a root opening. In all details, clarify joint angle requirements and permit less restriction on dihedral angle. In Annex B, include dihedral angles from 30 to 150 degrees. In addition, consider adding a new table to Annex B that will convert the designer's effective throat information to the fabricator's skewed leg size information.

PERMISSIONS

AWS D1.1 2010 Figure 3.11 and the definition of a t-joint were reproduced with the written authorization of AWS.

SUMMARY

Skewed t-joints have a long history of good performance and their use is increasing as the geometry of our steel buildings becomes more complex. The information presented in this paper is intended to clarify skewed t-joint design and

fabrication requirements while highlighting several topics that may have proven slightly confusing to designers and fabricators. The potential clarifications suggested above are for general consideration in order to produce more efficient, safe, and cost-effective skewed t-joints.

REFERENCES

American Institute of Steel Construction (AISC) (2005), Steel Construction Manual, Thirteenth Edition, Chicago, IL.

American Welding Society (AWS) (2010), Structural Welding Code, D1.1, Miami, FL.

Kloiber, L. (2004). "Orthogonal and Skewed Shear Connections Design and Detailing Requirements." NASCC Conference Proceedings, AISC, March 24-27.

Kloiber, L. and Thornton, W. A. (2001), "Design of Skewed Connections." Engineering Journal, AISC, 38(3), 140-147.

Miller, D.K. (2006). "Welding Considerations for Designers and Fabricators." Modern Steel Construction, AISC, February, 37-42.

Miller, D.K. (2002). "Designing Fillet Welds for Skewed T-joints-Part 1." Welding Innovation, The James F. Lincoln Arc Welding Foundation, 19(1). 7-11.

Schlafly, T. and Erickson, J. (2007). "Saying What You Mean." Modern Steel Construction, AISC, July, 55-59.

Thornton, W. and Kloiber, L. (1999). "Connections for Skewed Beams." Modern Steel Construction, AISC, May, 19-26.

Finite Element Analyses of Super Composite Column and Its Connections For Ping An International Financial Center Tower

Authors: Dennis C.K. Poon[1], Ling-en Hsiao[2], Zhu Yi[3], Steve Zuo[4], Steve Pacitto[5], Torsten Gottlebe[6], Jianhai Liang[7]

[1] P.E., Managing Principal, Thornton Tomasetti, Inc., dpoon@thorntontomasetti.com

[2] PhD, Senior Principal, Thornton Tomasetti, Inc., lhsiao@thorntontomasetti.com

[3] MSSE, Senior Principal, Thornton Tomasetti, Inc., yzhu@thorntontomasetti.com

[4] P.E., Senior Associate, Thornton Tomasetti, Inc., szuo@thorntontomasetti.com

[5] Principal, Thornton Tomasetti, Inc., spacitto@thorntontomasetti.com

[6] Associate, Thornton Tomasetti, Inc., tgottlebe@thorntontomasetti.com

[7] PhD, Project Engineer, Thornton Tomasetti, Inc., jliang@thorntontomasetti.com

Thornton Tomasetti, Inc., 51 Madison Ave, New York NY 10010, Tel: 917-661-7800

ABSTRACT

This paper presents the design, and the examination of ductile structural behavior through finite element analyses, of super composite columns and their connections to the outriggers, double belt trusses, and mega bracing members of the Ping An International Financial Center Tower in Shenzhen, China. When completed, this 660m-tall structure will be the tallest building in China and the second tallest building in the world.

Many complicated steel connections were analyzed and designed. Finite element analyses were performed on the super column, outriggers, double belt trusses, and mega bracing connections to evaluate the performance of the as-designed connections under 100 year wind forces and three levels of seismic action: frequent earthquake, moderate earthquake and severe earthquake.

This paper also briefly presents the design of the steel connections; describes the ABAQUS finite element analyses model; presents the major results of the finite element analyses; and evaluates the performance of the connections based on the analysis results.

PROJECT DESCRIPTION

The 660-meter tall Ping An Tower is sited on lot B116-0040 in the central business district of the Futian district of Shenzhen, China. Within its 115 stories, Ping An Tower contains mainly Class A office space, with some retail stores, entertainment venues, conference centers and trading areas (See Figure 1). The complex also includes an 11-story podium housing deluxe retail stores, offices, dining and lobby space. Beneath the tower and podium a five story deep basement mainly contains retail stores and parking. Occupying a total site area of about 12,000 m^2, the Ping An Tower has a total gross floor area (GFA) of approximately 462,000 m^2.



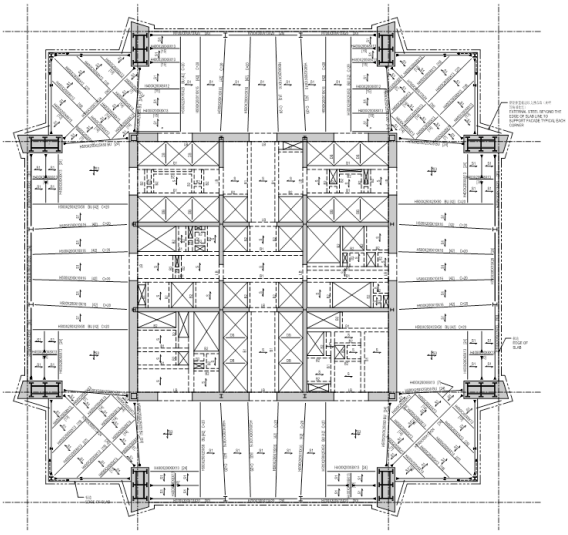




Figure 1 – Ping An Tower Site Plan, Typical Floor Plan and 3D Rendering (courtesy of KPF)

STRUCTURAL SYSTEM

The tower floor plate is typically square in plan with recessed corners. Floors reduce in size at upper levels. The tower primary lateral force resisting system

consists of a hybrid concrete core linked by steel outrigger trusses at four levels to eight super composite perimeter columns. The tower secondary lateral system consists of a mega frame with super columns, belt trusses and diagonal braces on each face, working together through chevron braces wrapping around the corners. While the hybrid concrete core, super columns, and outrigger trusses can be designed to resist the lateral forces by themselves, the perimeter mega frame and chevron braces improve lateral system redundancy and help decrease deflections.

The hybrid concrete core starts as a 32m by 32m square with 1.5m thick flange walls and 0.8m thick web walls. At upper floors, wall thicknesses decrease. At the top, flange walls are 0.5m thick and web walls are 0.4m thick. Steel shape columns embedded at wall corners and intersections increase core stiffness and ductility.

The super columns are approximately rectangular in plan, with corners shaped to suit the architecture. The super columns start as 6.0m by 3.2m and reduce in size with height to a minimum of 2.9m by 1.4m at the top. Steel built-up columns are also embedded in the super columns to reduce column sizes and increase column ductility. The steel ratio of the columns is 6% at the bottom and 4% at the top.

The tower is divided into nine stacked zones separated by MEP/refuge floors. Two-story tall steel outrigger trusses at the MEP/refuge floors above zones 1, 3, 5, and 6 connect the core and the super columns. The outriggers also help to increase system ductility and decrease story drift. A steel belt truss is located at every MEP/refuge zone. The belt truss, together with diagonal braces and super columns, forms the secondary lateral force resisting system. Mega bracing around each corner of the building increases mega frame integrity and stiffness. Complicated connections occur at refuge floors where outrigger trusses, belt trusses, and mega braces are connected to the super columns. Figure 2 shows the tower lateral force resisting system.

Tower gravity load on every floor is shared by the core, super columns and much smaller gravity columns. The gravity forces in the gravity columns are collected by belt trusses at the MEP/refuge floors and transferred to the super columns. This load path not only reduces the accumulated gravity forces taken by the gravity columns, but also helps to reduce tensile forces in the super columns due to lateral loads. At the top of each zone, gravity columns are connected to the bottom of belt trusses with vertically slotted connections to release potential stresses due to creep, shrinkage and differential movements.

SUPER COMPOSITE COLUMN MODEL

Due to the very large scale of the Ping An Tower super columns and their critical role in both the tower lateral force resisting system and gravity system, their behavior is very important to overall tower performance. The super columns must have adequate strength to sustain the applied loads, adequate stiffness to control

tower drift and adequate ductility to prevent tower brittle failure under extreme conditions. This paper will concentrate on super composite column ductility analysis.

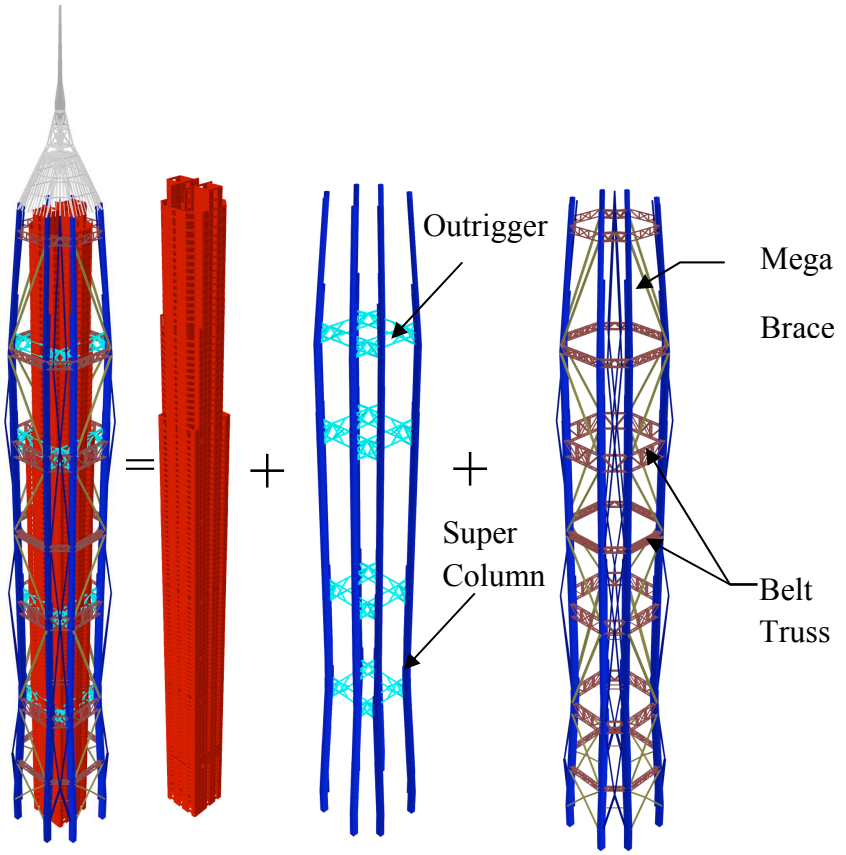
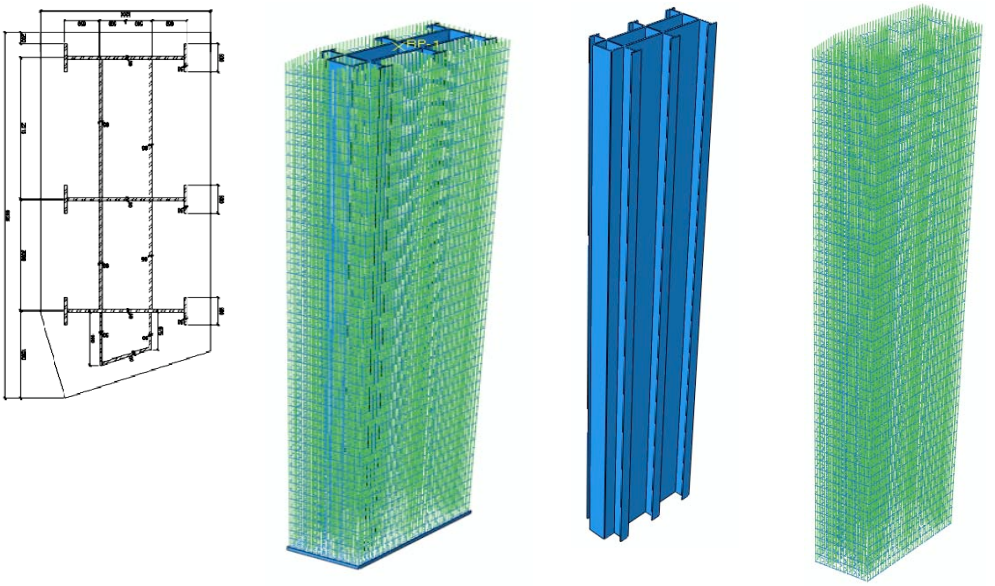


Figure 2. Lateral Force Resisting System = Core + Outriggers + Perimeter Braced Mega Frame

Super composite column ductility analysis was performed using the commercial finite analysis software ABAQUS Version 6.9 (Dassault Systemes, 2009). The load was applied using the displacement-control method. The super column of the podium zone at the bottom of the tower was modeled. From a buckling analysis, equivalent length of the modeled column is about 25m. Overall column plan dimensions were about 6.5m by 3.2m. The model included column concrete, embedded steel shapes and plates, and typical longitudinal reinforcing steel and stirrups (Figure 3). The model considered material nonlinear behavior to follow the specifications of the China Building Codes (GB50010-2002, 2002).

Concrete in the super composite column was modeled with solid elements. The concrete is China grade C70 with design compressive strength of 31.8 MPa (GB50010-2002, 2002). Concrete stress-strain curves were derived from the China concrete code as shown in Figure 4. Nonlinear concrete behavior was modeled using the versatile “Damaged Plastic Model” module of ABAQUS.

Embedded steel was also modeled with solid elements, while both longitudinal and stirrup reinforcement was modeled as truss elements. Both the steel shape and the regular steel reinforcement bars were "embedded" in the concrete by forcing the two parts to have the same displacements at common nodes. Steel materials were modeled as ideally elastic-plastic with no material strengthening beyond yielding.



a. Column Cross Section (rebar not shown) b. Composite Column Model c. Embedded Steel Section d. Rebar Cage

Figure 3. Perspective View of the Super Column Model

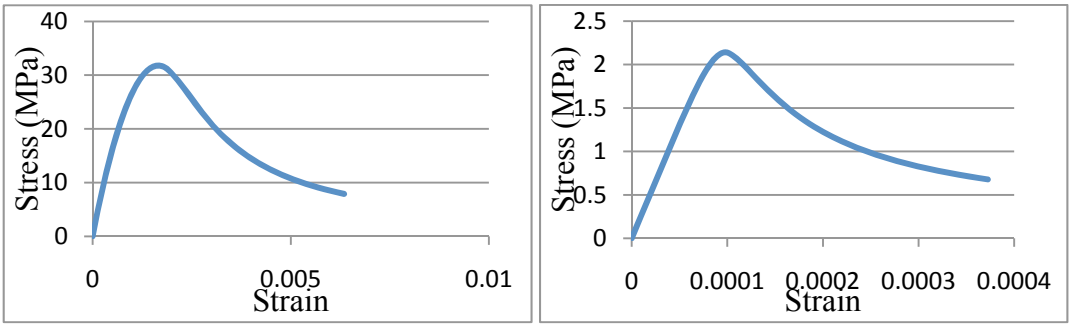


Figure 4.a Concrete Compressive σ-ε Curve Figure4.b Concrete Tensile σ-ε Curve

SUPER COMPOSITE COLUMN ANALYSES RESULTS

The super composite column analyses demonstrated that the column has satisfactory ductile performance. As an example, Figure 5 shows the moment – rotation of the super composite column with respect to the weak axis. The curve shows that the super composite column is able to develop significant displacement

after the capacity of the column is reached. When rotation of the column reaches 0.03 radian, the member still has about 85% of the maximum capacity. And the capacity of the member decreases gradually with no abrupt drop. Therefore, no brittle failure is expected.

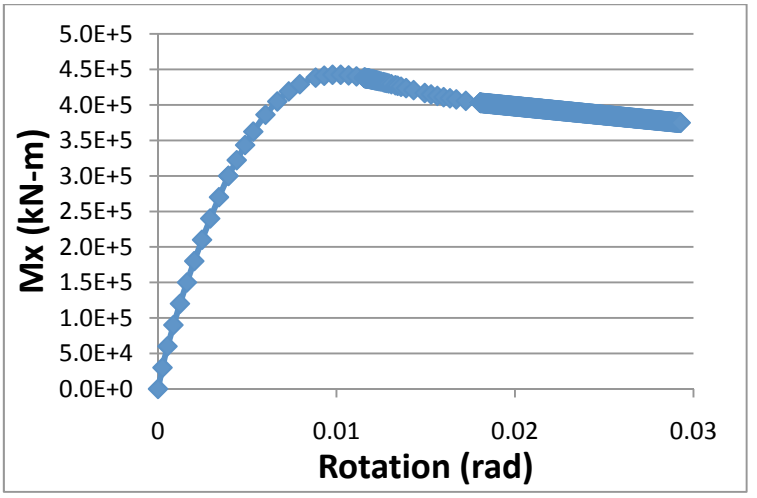


Figure 5. M-Φ Curve of the Super Composite Column with Respect to the Weak Axis

Figure 6 shows the stress contours of the steel shape and the longitudinal reinforcement at the ultimate stage. At the ultimate stage, both the embedded steel shape and the longitudinal reinforcement start to yield. The yielding of the steel helps to dissipate energy and therefore helps provide a ductile design of the super composite column.

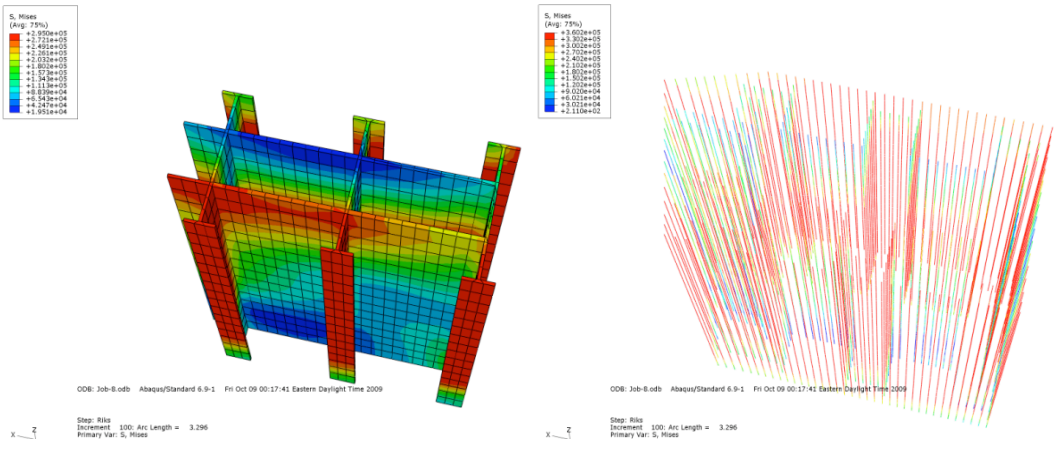


Figure 6 Stress Contour of the Steel Shape and the Longitudinal Reinforcement (The stress is in MPa. The red color steel shape stress contour indicates 295MPa, while for longitudinal reinforcement the red stress contour indicates 360MPa.)

CONNECTION DESIGN AND FINITE ELEMENT MODEL

Tower structural performance depends on good connection performance. The complex building structure results in complex loading conditions at connections, especially those super column connections where outrigger trusses, belt trusses, and mega diagonal braces all frame in.

The building is not located in a severe seismic area. The peak ground seismic acceleration of the area with a return period of 50 years and 10% probability of being exceeded is 0.10g (the Response Modification Coefficient as used in the International Building Code does not apply in the China building code) (GB50011-2001, 2008). However, tower seismic design was considered critical due to the significance of this landmark building and the huge potential impact of any failure on the surrounding community. A mandatory expert panel formed by the Chinese Bureau of Construction consulted with the designers and approved project-specific seismic design criteria.

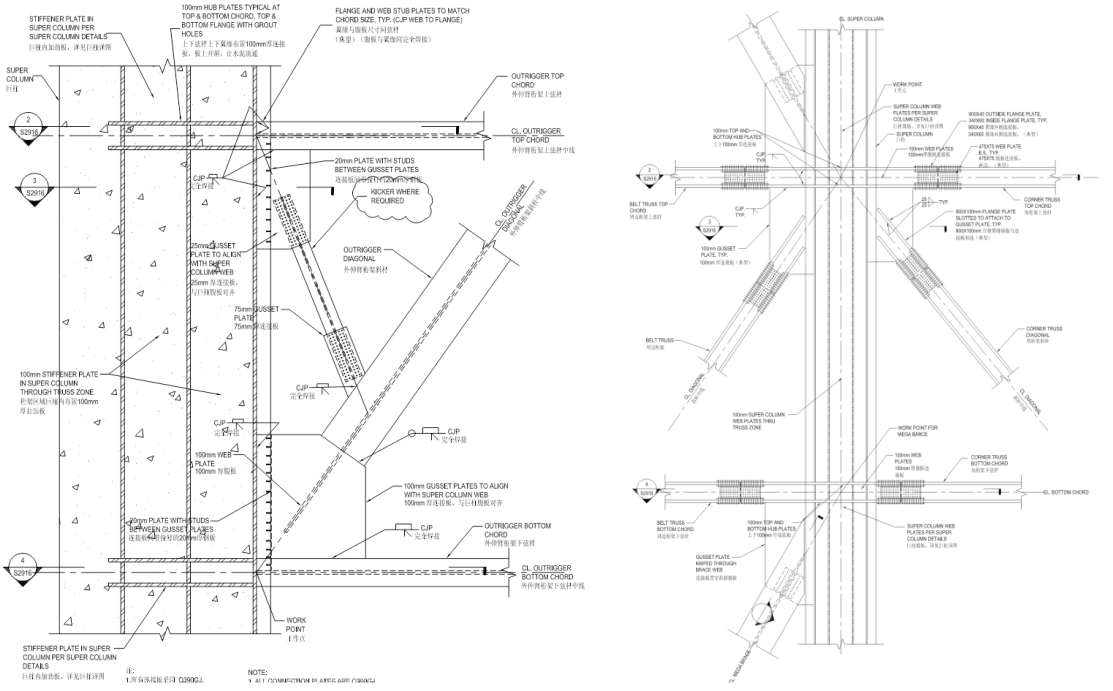
Seismic design criteria of the connections between the super composite columns and the trusses aimed at connection performance at three seismic levels:

a) Connections should remain elastic under gravity and wind load combinations.
b) Connections should remain elastic under Frequent Earthquake load (63% probability of being exceeded in 50 years) combinations.
c) Connections should remain elastic under combinations with gravity and Medium/Moderate Earthquake loads (10% probability of being exceeded in 50 years). Considering the way members are designed, this means connection capacities should be higher than those of the members.
d) Connections can yield, but should not fail under combinations with gravity and Severe Earthquake loads (2~3% probability of being exceeded in 50 years).
e) Conservatively assume that the embedded steel must take all connection loads because local congestion from reinforcing bars, steel shapes and plates, gusset plates and stiffeners means concrete quality at the column joint zone cannot be satisfactorily controlled.

Since China building codes have prescriptive requirements related to strength design only under the Frequent Earthquake level, finite element analyses (FEA) were used to evaluate performance of the connections under Medium and Severe Earthquake loads. As an example, this paper presents the modeling process and analytical results of a connection including a super composite column (SC), an outrigger truss (RT), a double belt trusses (DBT) including one interior truss and one exterior truss, and two diagonal mega braces (MB). Design details of the connection are shown in Figure 7.

The finite element analyses were performed with ABAQUS. In addition to the above-mentioned assumptions, it was assumed that welds and bolts will not fail before connection elements, so they were not specifically modeled. This assumption is consistent with the usual design strategy that welds and bolts have capacities at least equal to the capacities of the members connected. The finite element models

also conservatively ignore any contribution by typical reinforcing bars since many of them are potentially subject to being interrupted at the joint by steel connection plates.



Connection between SC and RT Connection between SC, DBT, and MB

Figure 7. Design Detail of the Connection between SC, RT, DBT, and MB

Figure 8 shows the finite element model of the connection. All steel members are modeled with solid elements. The outrigger trusses are made of China Q460GJ steel with yield strength of 395 MPa. The embedded steel shape in the super composite column, the belt trusses, and the diagonal mega braces are made of China Q345GJ steel with yield strength of 295 MPa. And the gusset plates are made of China Q390GJ steel with yield strength of 330 MPa. Young's Modulus of all steel is 2.06 X10^5MPa. The steel material is modeled as ideally elastic-plastic with no strengthening beyond yielding.

All gravity loads, wind loads and seismic loads are considered in combinations in the analyses. Member forces applied to the connection model were extracted from the tower ETABS model based on both time-history analyses and China code spectrum analyses.

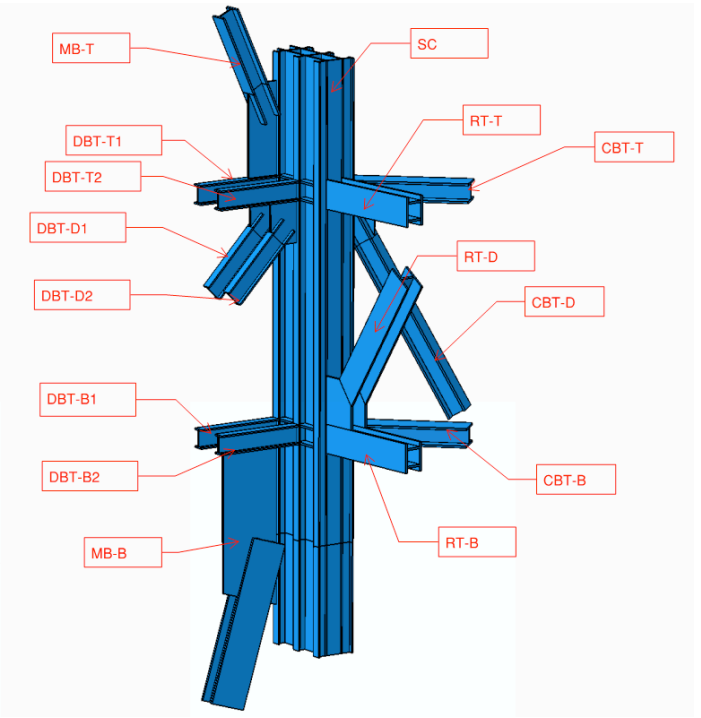


Figure 8. Finite Element Model of the Connection

CONNECTION ANALYSES RESULTS

Connection analyses were performed using member forces under load combinations with Frequent Earthquake, Medium/Moderate Earthquake, and Severe Earthquake forces. Since stress in the connection was expected to be lower than material yield stress under the Frequent Earthquake load combination, linear analyses were performed for this seismic level. Connections were designed to remain elastic under Medium Earthquake load combinations, but nonlinear analyses were performed for both Medium Earthquake and Severe Earthquake load combinations. Maximum stresses in components were evaluated using their respective material strengths and the Von Mises yield criterion.

Maximum stress under the Frequent Earthquake load combination is located at the local point where the bottom chord of the outrigger truss frames into the super column. While the maximum stress is around 340 MPa, this localized high stress spot can be eliminated by rounding of sharp corners. Other than at localized stress concentrations, maximum stress in most members is lower than 250 MPa. Therefore, the connection is elastic under the Frequent Earthquake load combination.

The Medium Earthquake ground acceleration used is about three times that of the Frequent Earthquake. However, gravity and wind loadings do not change. Other than localized stress concentration, maximum stresses in all components are lower than yield so the connection is still elastic under Medium Earthquake load combinations.

The Severe Earthquake ground acceleration used is about twice that of the Medium Earthquake or six times that of the Frequent Earthquake. However, the Severe Earthquake is an extreme load case so load factors in load combinations including it can be taken as 1.0. As a result, the overall design forces of members under Severe Earthquake load combinations are not necessary much higher than those of Medium Earthquake load combinations, especially where member design is mainly controlled by gravity loads and wind loads.

Under Severe Earthquake load combinations most member maximum stresses do not exceed 260 MPa. However, the connection components start to yield at the outrigger diagonal member, at top and bottom outrigger chords framing into the super column, and at the flange of the super column. Since the steel material was defined as ideally elastic-plastic, maximum stress tops at 395 MPa and yielding does not penetrate the whole section of the members. Hence the connection will still be able to take more load. There are also some localized stress concentrations reaching 395 MPa at concave corners where members intersect with the gusset plates. These hot spots could be eliminated by optimized detail design. Figure 9 shows an example stress contour of the connection under the controlling Severe Earthquake load combination.

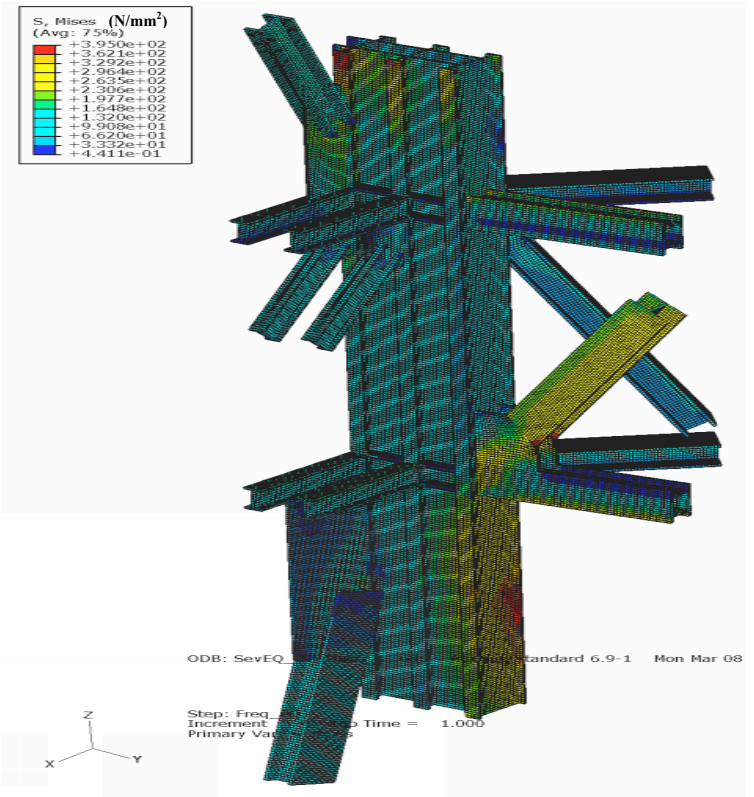


Figure 9. Stress Contour of the Connection under Severe Earthquake Load Combination (The red color stress contour indicates that stress exceeds yield of the specific material.)

CONCLUSION

Due to the super-tall nature of the Ping An Tower, performance of the super composite columns and related connections under extreme load cases is of great interest as fundamental to the overall performance of the 660m tall tower. To evaluate stress levels and ductility of the super columns, related connections and embedded steel shapes, detailed finite element analyses were performed under load combinations considering three levels of seismic loading.

Analysis results indicate that the super column is able to develop significant displacement before failure, with only a moderate decrease in capacity beyond yielding. Therefore it is concluded that the super column has a satisfactory level of ductility. Under Frequent and Medium Earthquake load combinations maximum stresses from the connection studies are less than the material yield point. Under Severe Earthquake load combinations the connection reaches yield at various places, but still has additional available capacity before failure, which is satisfactory. These analyses demonstrate that the Ping An Tower design meets performance criteria established in conjunction with the project expert review panel.

ACKNOWLEDGEMENT

We would like to thank Mr. Leonard Martin Joseph, P.E., S.E., Senior Vice President of Thornton Tomasetti, Inc, for enhancing this paper through his thoughtful suggestions.

PROJECT DESIGN TEAM CREDITS

Client: Ping An Insurance (Group) Company of China, Ltd.

Architect: Kohn Pedersen Fox Associates

Structural Engineer: Thornton Tomasetti Inc.

MEP Engineer: J. Roger Preston Group

Local Design Institute: China Construction (Shenzhen) Design International

REFERENCE

- Dassault Systemes. (2009). *ABAQUS 6.9 Documentation.*
- GB50010-2002. (2002). Code for Design of Concrete Structures, Ministry of Housing and Urban-Rural Development of People's Republic of China
- GB50011-2001. (2008). *Code for Seismic Design of Buildings*, Ministry of Housing and Urban-Rural Development of People's Republic of China.

Steel Detailing Practices: Using Global Variation to Envision Innovation

K. Simonen, RA, SE[1]

[1]Department of Architecture, University of Washington, P.O. Box 355720 Seattle, WA 98195-5720; PH (206) 685-7282; email:ksimonen@uw.edu

ABSTRACT

While architecture, engineering and construction continue to become more globally integrated, significant regional differences in practice continue. This paper explores the regional differences in structural steel detailing. There is significant global variation in who typically takes responsibility for the detailing (both for structural strength and for specifics of fabrication) of steel connections. Interviews with over thirty professionals (architects, engineers, fabricators and others) with expertise in ten countries and three regions of the US were completed to characterize four distinct methods of designing and detailing steel connections for construction.

Case studies of three practices are presented to demonstrate established practices in which the distinction between engineer and fabricator is reduced or eliminated, explore the challenges and opportunities of the practice methods, provide examples for engineers, detailers and fabricators considering adaptation of their roles in an evolving market and present a framework for challenging basic assumptions and exploring alternate methods of project delivery.

INTRODUCTION

While architecture, engineering and construction continue to become a more global industry, significant regional differences in practice continue. These cultural and procedural differences impact both the social character and technical work processes between architects, engineers and builders. This paper explores the regional differences in structural steel design and fabrication processes and explores the potential use of regional variation as models for local innovation. Particular attention is paid to the interface between design and construction teams during the creation of fabrication (shop) drawings.

There is broad support for the idea that more effective collaboration is needed to improve building practice (CURT 2004, Smith and Tardif 2009). Currently much work is being done to develop new contractual agreements to promote a more collaborative practice (AIA 2007, Sakal 2005). The changes to responsibilities and processes needed to improve collaboration also require study (Dossick 2008). Participants are often reluctant to change fearing either increase risk (scope) or reduce responsibility (fee) without a clear understanding of the potential benefits of the altered work process (Allen et al. 2005). Often unaware of the wide variety of practice models successfully in use, people can be skeptical of changing methods to which they have become accustomed to (Moore 2002).

With limited understanding of differing processes, innovation happens based on individual intuition or unique local conditions. Understanding of the implications and value of innovation is essential for a more comprehensive transformation of the

industry. The established regional differences in the practice of steel detailing provide a unique opportunity to systematically compare differing established work processes and identify unique conditions. This paper summarizes key findings presented elsewhere (Simonen, 2010) and presents developed case studies of unique global practices and speculates on if and how these methods can be models innovation.

BACKGROUND

Expectations have been that advances in digital design, analysis and manufacturing capabilities will facilitate effective collaboration and the creation of more integrated buildings designs (CURT 2005, AIA 2006, Smith and Tardif 2009). However, the reality of practice is still far from this idealized concept. The limited interoperability of digital platforms most often results in transfer of little more than basic geometry. Multiple models are built for multiple needs such as design, analysis, representation, fabrication and construction usually resulting in a 'loosely coupled network' rather than a single master model (Dossick 2008). The tools of collaboration may have changed (3D digital models vs. 2D paper drawings) but without a culture of collaboration, using a digital model will not guarantee a collaborative or integrated practice.

The use of 3D digital modeling is prevalent in all phases of steel design and construction. In nearly all cases the structural engineering analysis model (e.g., ETABS, and SAP2000) is different than the representation model used for communication (e.g. REVIT, ArchiCAD, or AutoCAD) and is different again from the detailing model that defines detailed geometry for fabrication (e.g. Tekla or SDS2). Significant effort is being expended to enable interoperability between these formats, however the author has found it common that assumptions critical for one model render the model data inaccurate from another's perspective. For example, engineers create multiple analytic models of structures that must represent structural behavior of elements (lateral system, floor system etc) but are often abstractions of physical reality to optimize modeling effort and accurately predict structural performance. In addition, engineering judgment and approximations lead to simplified structural performance models, which efficiently represent complex and slightly varied physical conditions accurately enough to reflect structural performance but not accurately enough for construction.

Historically, steel fabricators had in house drafters creating the fabrication drawings. Over the past 20 years most steel detailers (at least in Australia and the US) have become independent consultants working under contract to different fabricators.

RESEARCH METHOD

This research was completed primarily through interviews with structural engineers, architects, steel fabricators/detailers, and other industry experts with experience working in ten countries and three regions of the US. Initial interviews were supplemented with follow up interviews with engineers and fabricators to develop more detailed case studies of unique practice conditions. These discussions focused on specifics of individual practices within the context of regional standards and the following questions were addressed in the interviews: What is the most effective way to integrate fabrication and design expertise? Are there unique regional conditions that

make one practice method superior to others? Who is motivated/empowered to initiate change? How is the balance between efficiency and performance maintained? How are risks and rewards allocated?

GLOBAL VARIABILITY IN ROLES & RESPONSIBILITIES

The design and construction of the structural components of a steel building typically require input from a wide number of contributors including the perspectives of the client (developer and end users), the design team (architects and engineers) and the builders (fabricators, erectors, general contractors). The roles and responsibilities at the beginning and end of projects are most consistent throughout global practice. There is significant variety in who takes responsibility for specific portions of the work during the detailing (both for structural strength and for specifics of fabrication) of steel connections. Summaries, described in more depth elsewhere (Simonen, 2010), of the primary characteristics of the identified methods are as follows:

Method 1: Steel fabricator's engineer configures and sizes entire steel structure

In this method, the structural steel subcontractor is responsible for design and detailing of the structural system. This method is common for industrial buildings (e.g. portal frame sheds) worldwide. However, with an increase in design-build contracts in the UK, companies have expanded their services to include more complex/architecturally significant projects. The UK design standards (BCSA 2007) include this as one of the three standard levels of service provided by a fabricator (in addition to methods 2 & 3 described below).

In some instances a consulting design engineer participates in the schematic design, configuration and coordination of the structure. When preliminary configuration (e.g. column locations and beam depths) is established, the project is bid to steel subcontractors who subsequently perform the final calculations, sizing members as well as connections. In these instances the consulting design engineer helps to establish any unique performance criteria that the project should be built to.

Method 2: Steel fabricator's engineer designs and details connections

In this process method, the design engineer establishes performance standards, sizes the members and determines the connection loads and delegates the design and detailing of connections to the fabricator. Typically the connection loads are either scheduled based on member sizes or with forces noted explicitly on the plans. The fabricator selects and configures the connection type typically using standardized connection methods. The fabricator's engineer prepares structural calculations and finalizes the connection design (number of bolts, size of plates and welds etc). This is what would be considered 'East Coast' style in the US.

Although similar in general description, the UK and US practices have significant differences. UK design standards (BCSA 2007) are explicit in assigning engineering responsibility to the fabricator. The design engineer is expected to deliver a clearly defined project scope to the fabricator. US design standards (AISC 2005) explicitly maintain that the design engineer retains full responsibility for the design and assume that assessment of the connection design and capacity takes place during the shop drawing review phase. Interviews with engineers with experience in both the US and

UK confirmed that there is significantly more design work done during shop drawing production in the US than in the UK. Typical European methods were described as similar to the UK with some regional variability.

Method 3: Structural engineer designs and details connections

In this process method the engineer prepares prescriptive connection details: specifying the sizes of plates, bolts and welds etc of details. Often, 'typical' details are developed that cover a range of member sizes with variables developed in a schedule. The fabricator must extrapolate from these details to determine the exact configuration of each detail and develop the fabrication and assembly drawings.

The structural engineer of record prepares the calculations to verify connection details, capacity and ultimate performance. If fabricators propose alternate methods, the engineer must review and approve the change. This may inhibit the fabricator from proposing alternate methods given the risk of being rejected. This method is common in the Western US, Australia and New Zealand.

Method 4: Structural engineer designs, details and creates steel shop drawings

In this process method the engineer completes a comprehensive design of the details including the creation of the fabrication drawings. The fabrication model (all interviewed utilized Tekla) is a database driven model that can be used to drive digitally controlled fabrication equipment. Thus fabrication drawings, rather than more schematic representation drawings, can then be priced and produced by competing fabricating shops. The engineer takes responsibility for the structural performance, geometric configuration and constructability of the structure. This method is the norm in Finland. A British engineer with experience in Hungary noted that there too the engineers develop full details often building up sections from welded plates as rolled sections are not easily available.

CHALLENGING ASSUMPTIONS

The initial assumptions of both the author and early interviewees were that the origins of the differences in work processes would be traced to seismic/non-seismic technical requirements and Germanic/Anglo cultural differences. However, as the interview pool expanded, interesting contradictions to the preliminary justifications emerged.

Outside of the US, there does not seem to be a relationship between the detailing system and the seismicity of the region. It seems likely that differences have more to do with the power structure and technical sophistication of the steel industries in select regions than on cultural engineering practices. In areas such as the UK, Germany and Eastern US where structural steel industries originated in the 1800's, the major steel suppliers developed proprietary member capacities and details (Gillette 1980, BCSA 2006). The manufacturers led the way to adoption of what was then an innovative and new structural system. In areas farther from steel manufacturing plants local fabricators imported steel shapes and it seems likely that the local structural engineer had the dominant technical expertise needed to develop the details. The Finnish steel industry developed primarily after World War II. Within that community there are a limited number of structural engineers and fabricators. Perhaps in select regions the

engineers developed the expertise in fabrication detailing out of necessity.

INNOVATION CASE STUDIES

In the course of the research three unique industry practices were identified: a unique region, Finland; unique expansion of scope by fabricators in the UK; and an innovative architect/owner in Australia. What follows is a description of and commentary upon these case studies.

Finland: unique region

Knowledge of the unique conditions in Finland was the spark that initiated this research. The author worked in a structural engineering firm in Finland in the 1990's where the structural and reinforcing steel shop drawings were all produced in house. Eliminating a step in the conventional US documentation process (bypassing 'construction documents' and going straight to 'shop drawings') appeared efficient and practical. As noted above, initial speculation that this was a European and/or German method was found not to be true but rather that Finland appears to have independently developed distinct process differences.

A Finnish engineer, Ragnar Wessman (interviewed November 24, 2009), has led the development of one of three-dimensional detailing program, Tekla. The program had originally been developed for structural engineers using the 'Finnish method' however the actual creation of the details does not change significantly when using other practice methods. He found the wide global variation in work practices and typical details was surprising and could not attribute this variation to anything other than 'happenstance in history'. He noted that historically the Finnish fabrication shops have been set up to be flexible and willing to fabricate whatever is designed. The relatively late development of structural steel in Finland along with the smaller market (when compared to the UK or Eastern US) may have made flexibility a necessity for an emerging steel industry. Wessman noted that in order to do good detailing, one must obey certain rules. While these rules are not that complex, applying them correctly does require a good understanding of fabrication and construction methods. He foresees greatest opportunity in exploring the links between subcontractors, contractors and operators in enabling more efficient delivery and operation of integrated facilities.

Timo Koivisto (interviewed January 12, 2010) a fabricator with experience in the UK and Finland noted that Finnish engineers have an intense culture of efficiency, optimizing individual member sizes to lower overall weight. The two main steel fabricators in Finland do work across Europe and take on additional detailing responsibilities when working outside of Finland. Antti Pekkala (interviewed December 15, 2010), a practicing structural engineer, confirmed that engineers take significant pride in reducing the overall weight of their structures and noted that this 'efficiency training' was done in the workplace not in University. He also noted that given the scale of the country, standards and reputations are easily communicated which could account for the effectiveness of the method.

Engineers with experience in this method expressed confidence that the 'rules' of detailing appropriately for fabrication/construction are not difficult to learn. They identified that the most important requirements is for the person in charge of detailing for fabrication to maintain adequate dimensional control. Some interviewed questioned

whether this method would be applicable outside of Finland with a larger and more diverse group of engineers and fabricators.

UK: fabricators expanding role

British steel subcontractors are expanding their services to offer comprehensive engineering for projects beyond the simple industrial portal sheds they have been engineering since the 1970's. Steve Mason (interviewed Nov 24, 2010), the technical director at a UK steel subcontractor, noted that the scope of their engineering responsibility can vary from conventional Method 2 to Method 1. Expanding their scope to develop full engineering designs enables them to improve their market share and 'keep (their) structural engineers motivated and committed'. He acknowledged that consulting engineers are better suited to spend long periods of time iterating through design development but felt that integrated design build typically resulted in lower weight/lower cost structures. In great part the services they provide are dictated by the demands of the client looking to shift risk and take advantage of a competitive market.

Richard Shuttleworth (interviewed December 15, 2010) is a practicing structural engineer who has worked in both methods 1 and 2. He noted that the primary driver for adopting Method 1 is coming from institutional clients looking to reduce risk and identify costs up front. In response, builders are putting together fixed price bids before the construction documents are complete. In these instances design teams put together schematic documents and specifications that the contractor uses to price and complete. Given the competitive nature of the UK steel industry, it is his opinion that the steel suppliers must be very aggressive in reducing material and detailing costs in order to achieve economically viable results. When asked about the challenge of balancing performance and efficiency he reflected that consulting engineers often deliver designs that provide flexibility and redundancy to support commonly occurring (but not guaranteed) irregularities (e.g. providing torsional stiffness to support potential cladding loads). Consulting engineers contracted to the architect are more likely to integrate these conditions into the design but specifying criteria for others to meet can be more challenging. Shuttleworth noted that developer clients are more likely to keep the structural engineering consultant as prime engineer (method 2) as developers have a better understanding of project risk and would like to maintain more control over the process.

AU: architect as innovator

Project Services is a unique consulting firm in Brisbane Australia. Established in 1992 as an AEC firm with public as shareholder it is expected to be commercially viable and support and lead the AEC industry. Tom Fussell (interviewed December 1, 2009) is the executive director and chief architect and is looking to enact change in a 'measured' way. Conventional practice in Australia is similar to the Western US/method 3 noted above. In 2001 Project Services purchased ArchiCAD and a 'pre-Autodesk' version of Revit and began integrating 3D BIM into their design process. The North Lakes Police Station project (CRCCI, 2009) was selected to test the generation of integrated interdisciplinary 3D models to be shared with the contractor for construction. Project Services hired BDS Group (now BDS Viracon) to create fabrication ready contract documents for the structural steel using Tekla. For portions of the design work a detailer co-located with the structural engineering team to create the model and collaboratively resolve design and constructability issues. The Tekla model was exported

and integrated into the architectural model and shop drawings were issued directly from the architectural/engineering team.

This is similar to the Finnish model/Method 3 except that the detailing expertise is not integrated into the structural engineering practice but rather brought in as a consultant. Independent steel detailing companies can use global labor pools to create cost-effective labor-intensive models and have developed methods to adapt to the varying standards of different steel fabricators. In this instance the architect/structural engineer took on added responsibility and risk by hiring the steel detailer directly in order to develop a more integrated proposal. The architect noted that this required the design team to take greater care in checking dimensional coordination than typical. Given the lack of CNC capabilities of local fabricators, traditional printed shop drawings were used to direct the work.

The end result of the process used by Project Services is very similar to the Finnish model. However, utilizing consultant detailers minimizes concerns about design engineers understanding and ability to detail for construction because the team integrated standard industry knowledge and expertise. Given Project Services unique role as an industry leader, they were willing to take on added risk to explore potential larger scale benefits and were able to alter the project fees to reflect this reorganization. This is similar to design assist and IPD methods currently being tested in the US.

CHALLENGES

Although the goal of improving quality and efficiency can be easily supported, empowering and motivating effective change can be elusive. While collaboration between structural engineers and detailers and/or expanding one disciplines roles to encompass the others may be effective at reducing time, cost and translational errors, structural engineers and steel detailers are rarely in a position to shape the contract or redistribute resources as both are subcontracted out by disciplinary 'primes'. In order to implement innovative methods, leadership must often come from owners with the ability to redistribute fees, risk and responsibility.

Multiple interviews included interesting discussions about the varying methods of establishing professional responsibility and the legal and building code structures that provide unique constraints. Even as international codes such as the IBC and Eurocode develop, individual jurisdictions execute and implement generalized requirements with unique local requirements.

CONCLUSIONS

The roles and responsibilities with regard to steel design, detailing and fabrication is an important area of the building process currently in a stage of significant flux. Regional variability in industry expertise and standards is significant and must be considered when proposing innovations in work processes and project delivery methods. As the industry actively explores improving the design process and product, there is a strong need for both qualitative understanding and quantitative assessment of different processes and their results. Having established different regional work processes provides a unique opportunity for quantitative research comparing performance

measures of costs, time, error etc. among regions to better understand the relative merits of different processes.

The case studies presented here are qualitative assessments of different practices. With a more comprehensive quantitative study, interesting comparisons could be made on effectiveness of collaboration and work processes and differences in structural efficiency and performance and construction cost, errors and time. Additional information about the successes and challenges of different processes would be valuable for professionals looking to evaluate options and establish what work processes should be optimum given an individual projects demands and constraints.

ACKNOWLEDGEMENTS

The author would like to thank the many professionals (only a small portion of whom are identified above) who participated in the interviews and whose time and interest made this research possible. Their diverse experience and insightful input provided significant valuable information and the seeds for future research beyond the scope of this project. They are greatly appreciated.

Allen, R. K., B. Becerik, et al. (2005). Promise and Barriers to Technology Enabled and Open Project Team Collaboration. *Journal of Professional Issues in Engineering Education & Practice* 131(4): 301-311.

American Institute of Architects, C. o. I. P. (2006). *Report on Integrated Practice.* C. McEntee, N. Strong, A. Sido and M. Allison. Washington, D.C., American Institute of Architects.

American Institute of Architects (AIA) 2007. *Integrated Project Delivery: A Guide Version 1.*

American Institute of Steel Construction (AISC) 2005. *Code of Standard Practice for Steel Buildings and Bridges.* Chicago: AISC.

Australian Institute of Steel Detailing 2009. www.aisd.com.au/professional_declaration.html.

Ashcraft, D. 2004. Specifying Structural Steel Connection Design. In Blandford, G. (ed.), *Building on the Past: Securing the Future Proceedings of the Structures Congress 2004*. CD-ROM, ASCE.

British Constructional Steelwork Association Ltd. (BCSA) 2006. *A Century of Steel Construction, 1906-2006*. London: BCSA.

British Constructional Steelwork Association Ltd. (BCSA) 2007. *National Structural Steelwork Specification for Building Construction 5th Edition*. London: BCSA.

Cairns, I., Cocciardi, P. & Dallas, S. 2009. Streamlining the supply chain-Industry Best Practice for steel structure coordination. *Steel Australia.* June 2008, pp 28-29.

Cooperative Research Center for Construction Innovation (CRCCI), 2009. *National Guidelines for Digital Modeling: Case Studies.* Brisbane: Icon.

CURT (2004). *Collaboration, Integrated Information and the Project Lifecycle in Building Design, Construction and Operation* Cincinnati, OH, Construction Users Roundtable

CURT (2005). *Optimizing the Construction Process: An Implementation Strategy*, Construction Users Roundtable.

Dossick, C., Neff, G. & Juan, H. 2008. Analyzing the Ramifications of Building Information Technologies for Collaboration in Architecture, Engineering and

Construction. *Proceedings from the 12th International Conference on Computing in Civil and Building Engineering, Beijing*, China 16-18 October 2009.

Gillette, L. 1980. *The First 60 years: The American Institute of Steel Construction, Inc 1921-1980*. Chicago, AISC.

Harman, D 1995. Structural Steel Connection Design Responsibility. In Sanayei, M. (ed.), *Restructuring: America and Beyond; Proceedings of the Structures Congress XIII, Boston, 2-5 April 1995. New York: ACSE.*

Isbell, J.E.1995. Connection Design – Shared Effort, Single Responsibility. In Sanayei, M. (ed.), *Restructuring: America and Beyond; Proceedings of the Structures Congress XIII, Boston, 2-5 April 1995. New York: ACSE.*

Moore, G. A. 2002. *Crossing the Chasm: Marketing and Selling High-Tech Products to Mainstream Customers*. New York, Harper Business Essentials.

Muir, Larry 2004. *Communication of Structural Steel Connection Design Information. In Blandford, G. (ed.), Building on the Past: Securing the Future Proceedings of the Structures Congress 2004. CD-ROM, ASCE.*

Sakal, M. 2005. Project Alliancing: A relational Contracting Mechanism for Dynamic Projects. *Lean Construction Journal* Vol 2 #1 April 2007 pp. 67-79.

Simonen, K. 2010. Steel detailing and collaboration: A global perspective. *Structures and Architecture. Proceedings of the First International Conference on Structures and Architecture, ICSA 2010*. London: Taylor & Francis Group.

Smith, D. K. and M. Tardif (2009). *Building Information Modeling: A Strategic Implementation Guide for Architects, Engineers, Constructors, and Real Estate Asset Managers*. Hoboken, New Jersey, John Wiley & Sons, Inc.

Out-of-Plane Stability of Buckling-Restrained Braces

Tsuyoshi Hikino[1], Taichiro Okazaki[2], Kouichi Kajiwara[3], and Masayoshi Nakashima[4]

[1] Steel Structures Engineering Division, Nippon Steel Engineering Co. Ltd. (formerly NIED); email: hikino.tsuyoshi@nsc-eng.co.jp
[2] Faculty and Graduate School of Engineering, Hokkaido University, Japan; (formerly NIED); email: tokazaki@eng.hokudai.ac.jp
[3] National Research Institute for Earth Science and Disaster Prevention, Japan; email: kaji@bosai.go.jp
[4] Disaster Prevention Research Institute, Kyoto University, Japan; email: nakashima@archi.kyoto-u.ac.jp

ABSTRACT

Large-scale shake table tests were performed to examine the out-of-plane stability of buckling-restrained braces (BRBs). Two specimens were subjected repeatedly to a near-fault ground motion with increasing magnitude. The test specimens comprised a single-bay, single-story steel frame and a pair of BRBs placed in a chevron arrangement. The chevron braced frame specimens were not braced at the point of intersection in the beam, and was therefore susceptible to out-of-plane instability. Standard BRBs were used in the first specimen, while unique BRBs with a flexible segment at each end of the steel core were used in the second specimen. A simple stability model predicted the BRBs in the second specimen to fail due to out-of-plane buckling at a force smaller than the yielding strength of the steel core. The first specimen exhibited excellent ductility during the shake table tests, while the second specimen developed noticeable out-of-plane deformation. Observations from the tested are described along with design implications.

INTRODUCTION

Buckling-restrained braces (BRBs) refer to a class of axially loaded members that achieve stable hysteretic behavior under both tension and compression (AISC 2005b; Uang and Nakashima 2004). BRBs have been used extensively in Japanese building structures since the 1980's as a performance enhancement device that dissipates seismic energy while maintaining the rest of the structure damage-free (Wada et al. 2004). On the other hand, the US practice has incorporated BRBs into a new class of concentrically braced frames (CBFs), named buckling-restrained braced frames (BRBFs) which exhibits excellent ductility (AISC 2005b).

Previous studies by Inoue et al. (2001) and Black et al. (2004), among others, established a design procedure to preclude flexural buckling of the BRB, local buckling of the steel core, or instability of the bracing element outside of the buckling-restraining system. The stable and predictable cyclic behavior of BRBs has been demonstrated by numerous tests (e.g., Saeki et al. 1995; Black et al. 2004). Meanwhile, Tembata et al. (2004) and Takeuchi et al. (2004) noted that BRBs with a flat-plate steel core require special attention to avoid out-of-plane instability. Such BRBs include relatively flexible segments between the end of the steel casing (of the buckling-restraining system that contain mortar) and the termination of stiffened segment. Because the flat plate is generally oriented parallel to the plane of the frame and parallel to the gusset plates for fabrication and constructability considerations, BRBs with a flat-pate steel core may be

usceptible to out-of-plane instability. This instability issue pertains primarily to BRBs placed in a chevron arrangement (or "inverted-V" arrangement).

Previously, Tembata et al. (2004) and Kinoshita et al. (2007) derived a comprehensive set of analytical solutions to the out-of-plane stability problem of BRBs, and validated the solutions against static, cyclic loading tests. Further, Kinoshita et al. (2008) performed a combined computational and experimental study to evaluate the rotational stiffness of standard BRB bracing connections in Japan. Experiments by Takeuchi et al. (2004) demonstrated how flexible bracing connections can trigger instability of BRBs.

A research project was conducted to further examine the stability requirements for BRBs subjected to dynamic loading and to examine how the BRBs may behave after the instability occurs. This paper defines the stability problem, describes analytical solutions to a mathematical stability model, and reports a large-scale shake-table test program. Findings and observations are described, followed by a discussion of practical implications.

STABILITY MODEL

The following four assumptions are introduced to derive an analytical expression for the out-of-plane buckling strength of BRBs placed in a chevron arrangement as shown in Fig. 1(a).

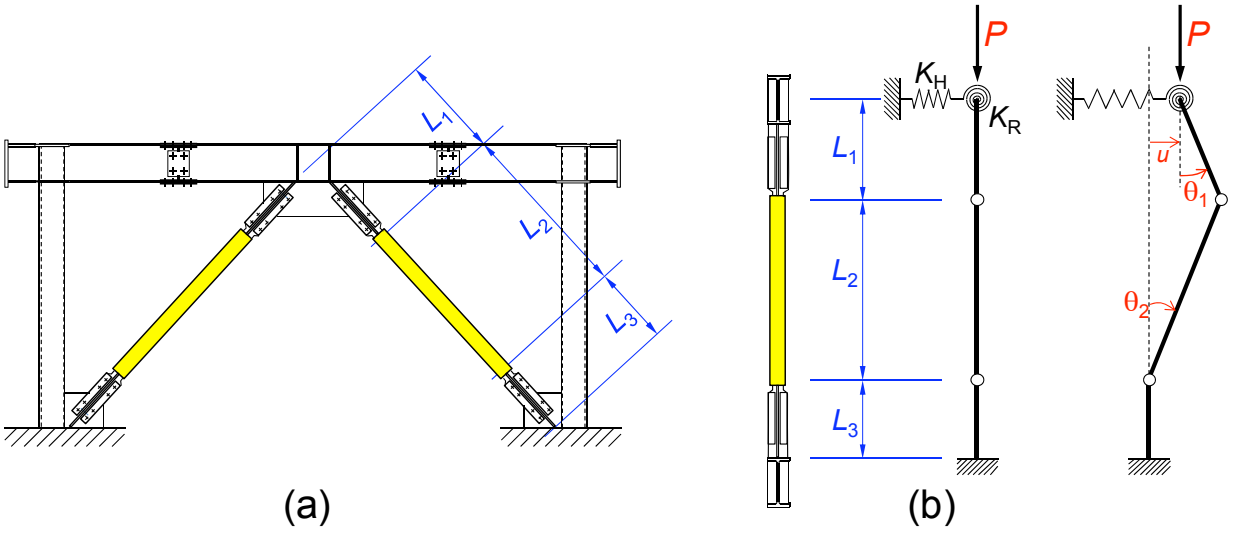


Fig. 1 Out-of-plane stability model: (a) chevron brace; (b) first-order buckling model.

1) The bracing member includes short segments which are flexible against out-of-plane rotation. The flexible segments are located at each end of the steel core, between the end of the steel casing and the termination of stiffened segment.
2) Yielding occurs only in the steel core while the segment outside of the BRB, the bracing connection, or the beam remains elastic. Distortion of the gusset plates and the beam section is negligibly small compared to out-of-plane rotation in the steel core.
3) The BRB is adequately designed such that flexural buckling of the BRB or local buckling of the steel core does not control the strength of the BRB.
4) Initial imperfection and out-of-plane drift is negligibly small.

Fig. 1(b) shows a first-order buckling model of the BRB based on the above assumptions, which is composed of rigid elements, internal hinges, and elastic end restrains. The internal

hinges are placed at the ends of the steel core. The top end of the system is the point of intersection of the BRBs which typically coincides with the centroid axis of the beam. The bottom of the system is assumed to be rigid because the bottom represents the brace-beam-column node that is well braced for translation and rotation. Initial imperfection is neglected.

It is noted that engineers may choose a different detail for the gusset plate connections, in which case assumption (2) may not be valid, and the buckling model shown in Fig. 1(c) may be adequate. The model may be viewed as a simplification of the elastic-perfectly plastic model proposed by Tembata et al. (2004) and Kinoshita et al. (2007), whose model considered elastic deformation of the gusset plates and BRB, and thus assumptions (2) and (3) do not apply. Tembata et al. and Kinoshita et al. justified assumption (1) only under the idealization that the steel core is an elastic-perfectly plastic material, and only when the BRB is subjected to a compressive force equal to the yield strength of the steel core.

The spring constants K_H and K_R may be evaluated based on the flexural and torsional stiffness of the beam and properties of lateral braces acting at the point of intersection. Fig. 2 shows all possible buckling modes. While three displacement parameters are shown (θ_1, θ_2, and u), the modes are defined in terms of two independent parameters. The critical loads, P_1 to P_3, corresponding to the first three modes are derived as follows.

$$P_1 = K_H \cdot L_2 \quad P_2 = \frac{K_R + K_H \cdot L_1^{\,2}}{L_1} \quad P_3 = \frac{K_R}{L_1} \qquad (1a-c)$$

Because $P_2 > P_3$ for $K_H \cdot L_1 > 0$, mode 2 never governs. The critical load, P_4, corresponding to mode 4 is determined as the smaller solution to the following quadratic equation.

$$(P - P_1)(P - P_3) - P \cdot \left(\frac{L_1}{L_2} P_1\right) = 0 \qquad (2)$$

The above equation suggests that mode 4 always governs and that mode 4 is a combination of modes 1 and 3. Denoting the solution to Equation (2) as P_{cr}, the buckling mode may be expressed as follows.

$$\frac{\theta_1}{\theta_2} = \frac{P_1}{P_3 - P_{cr} + \frac{L_1}{L_2} P_1} = \frac{P_1 - P_{cr}}{\frac{L_1}{L_2} P_1}, \quad \frac{u}{L_1 \theta_1} = \frac{P_{cr}}{P_1 - P_{cr}} \qquad (3a, b)$$

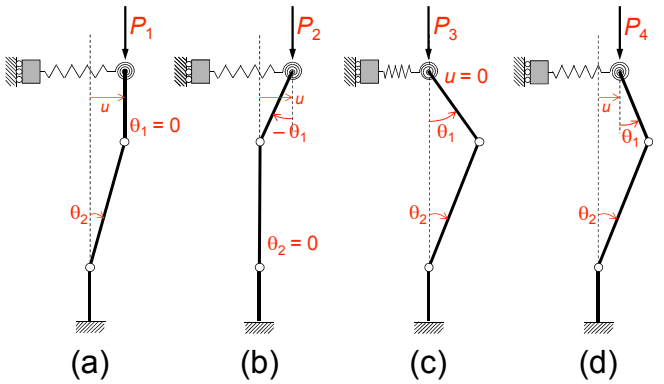


Fig. 2 Buckling modes: (a) to (d) indicate modes 1 to 4.

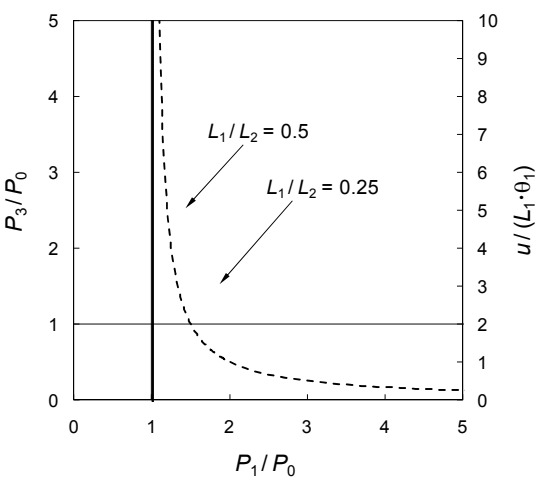


Fig. 3 Condition to achieve $P_{cr} = P_0$

Fig. 3 plots the combinations of P_1 and P_3 to achieve a fixed critical load $P_{cr} = P_0$. The domain in the P_1– P_3 space above the curve and opposite the origin defines the safe domain where the buckling strength is greater than P_0, and thus out-of-plane buckling of the BRB may be avoided. The curves are plotted for $L_1/L_2 = 0.25$ and 0.5. The case $L_1/L_2 = 0.25$ may represent BRBs with compact bracing connections, while $L_1/L_2 = 0.5$ may represent BRBs with larger bracing connections that uses bolted splices. The value P_3/P_0 approaches $(1 + L_1/L_2)$ as P_1/P_0 tends to infinity and P_1/P_0 approaches unity as P_3/P_0 tends to infinity. BRBs proportioned with larger bracing connections and shorter steel-core length requires somewhat larger restraints. The broken line in Fig. 3 indicates the transition of mode shape $u/(L_1 \cdot \theta_1)$ as a function of the P_1, given $P_{cr} = P_0$. Mode 1 ($\theta_1 = 0$) dominates when P_3 is significantly greater than P_1 and thus $P_{cr} \approx P_1$, and mode 3 ($u = 0$, $u = L_1 \cdot \theta_1$) dominates when P_1 is significantly greater than P_3 and thus $P_{cr} \approx P_3$.

TEST PLAN

Two braced-frame specimens were subjected to a series of strong earthquake ground motions to examine whether the out-of-plane buckling load of BRBs can be predicted based on the analytical solutions described above, and to examine how the system behavior may be affected by instability of BRBs. The tests were conducted at E-Defense, a three-dimensional, large-scale earthquake testing facility operated the National Research Institute for Earth Science and Disaster Prevention of Japan.

Specimens

As shown in Fig. 4(a), the specimens comprised a built-up wide-flange beam, two cold-formed square-tube columns, and a pair of BRBs. The 4.15-m span and 2.25-m height correspond to a 70%-scale building structure. After Specimen 1 was tested, the BRBs were replaced by a new pair of BRBs to prepare Specimen 2. The standard through-diaphragm detail (Nakashima et al. 1998) was used to achieve rigid beam-to-column connections. The bracing connections adopted a common Japanese detail that welds the fin plates (stiffener plates oriented perpendicular to the gusset plate) to the beam or column. The columns were rigidly connected to large base beams which were, in turn, fixed to the shake table. Table 1 lists the Japanese Industry Standards (JIS) designation and measured mechanical properties for each material used to fabricate the specimen. The specified minimum yield strength is 235, 295, and 325 MPa, respectively, for SN400, BCR295, and SM490 steel.

At the top side of the specimen, each end of the beam was connected to the test-bed system (described later) through a pin-ended load cell. The specimen was laterally braced along the columns and beam at discrete locations indicated in Fig. 4(a). No bracing was provided at the middle segment of the beam to intentionally reduce the torsional and translational restraint at the intersection point of the BRBs.

The two specimens were nominally identical except for the BRBs. As shown in Fig. 4(b) and (c), the BRBs used a 74 × 12 mm plate for the steel core and a square 125 ×125 × 2.3 mm steel tube casing filled with mortar for the buckling-restraining system. Unlike most standard BRB products, no capping steel plate was placed at either ends of the casing. The key difference between the two BRBs was the embedment length of the stiffened segment inside the buckling-restraining casing. While Specimen 1 used a standard embedment in current Japanese practice (110 mm as indicated in Fig. 4(b)), Specimen 2 used a shorter embedment length (30 mm).

Because out-of-plane restraint of the BRB is developed by bearing between the stiffened segment and mortar, and the steel core itself possesses little out-of-plane stiffness, the shorter embedment length in Specimen 2 was expected to promote out-of-plane stability of the specimen.

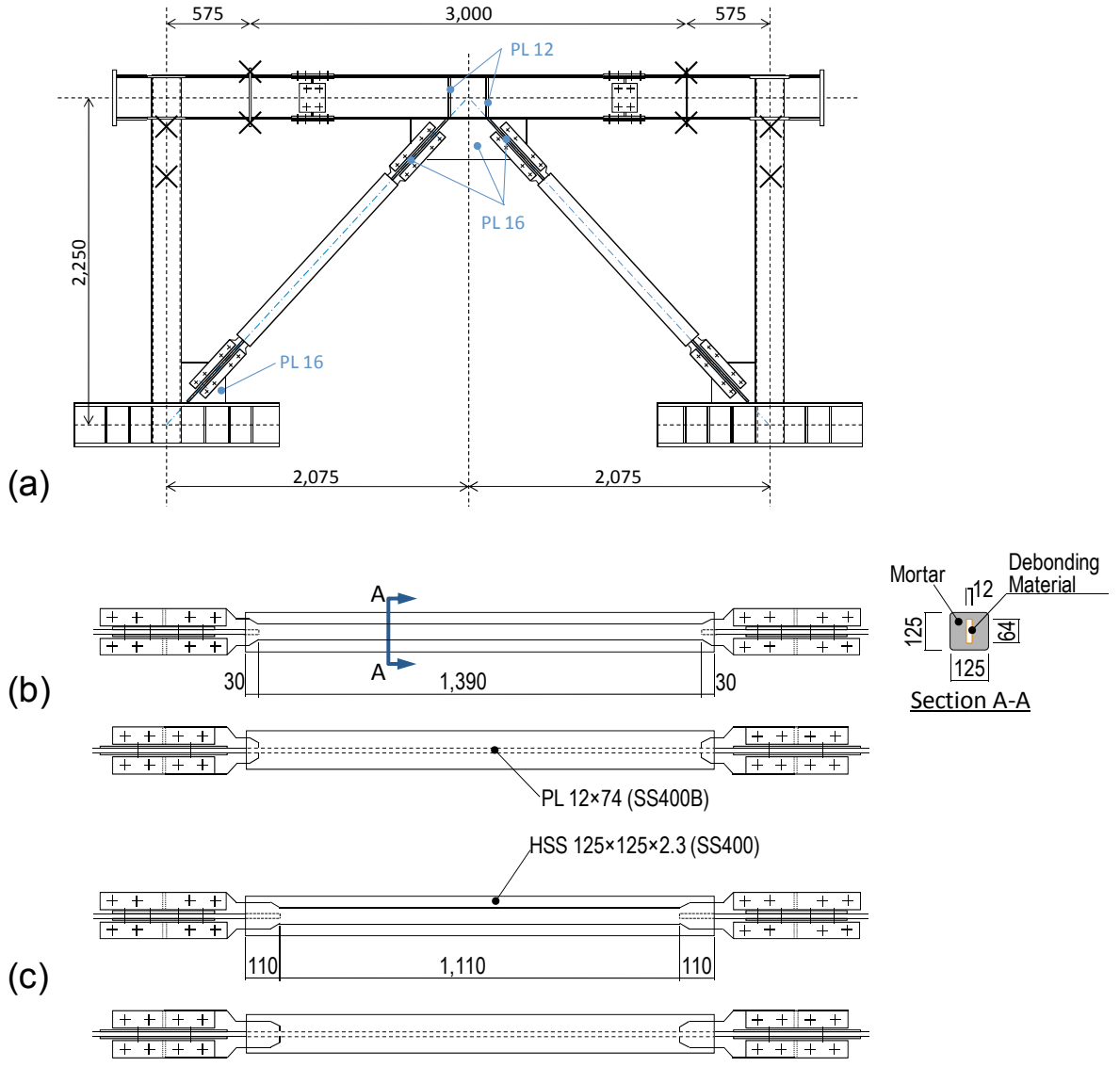


Fig. 4 Test specimen: (a) elevation and out-of-plane bracing points; (b) BRBs in Specimen 1; and (c) BRBs in Specimen 2.

Table 1 Material properties

Material	JIS designation	Yield strength (MPa)	Tensile strength (MPa)	Elongation (%)
Steel core (12 mm)	SN400B	297	421	35
Beam flange (9 mm)	SN400B	327	456	27
Beam web (6 mm)	SN400B	376	472	29
Column (9 mm)	BCR295	434	518	19
Gusset plate (12 mm)	SM490A	315	441	32

In other words, assumption (1) of the stability model in Fig. 1 was valid for Specimen 2 but not for Specimen 1.

A simple, rigid-plastic analysis using the measured material properties estimated the lateral strength of the specimen to be 798 kN, and suggested that the BRBs and underlying moment frame provide 58 and 42%, respectively, of the lateral strength.

Stability Design Check

The elastic stiffness of the beam between bracing points B and C determine the spring constants K_H and K_R shown in Fig. 1(b). Assuming that the beam is simply supported at the bracing points B and C and at the beam-to-column connections (A and D) and neglecting the stiffness added by the gusset plate, K_H = 5,530 kN/m and K_R = 330 kN·m/rad. From Fig. 4, L_1 = 1.39 m and L_2 = 0.83 m. Consequently, from Equations (1) and (2), P_1 = 4,590 kN, P_3 = 238 kN, and P_4 = 88 kN. While P_1 is substantially larger than the yield strength of the steel core based on the measured yield strength, P_y = 263 kN, P_3 and P_4 are smaller than P_y. Therefore, the instability model predicted Specimen 2 to experience substantial out-of-plane buckling and predicted that mode 3 would dominate over mode 1.

The *AISC Seismic Provisions* (2005b) require both flanges of the beam to be braced at the point of intersection of bracing unless the beam provides the required brace horizontal strength, P_{br}, and stiffness, β, defined as follows:

$$P_{br} = 0.01 P_r \tag{4}$$

$$\beta = \frac{1}{0.75}\left(\frac{8P_r}{L_b}\right) \tag{5}$$

In the above equations, P_r = required compressive strength of the BRB, L_b = the distance between the bracing point and point of intersection of the BRBs, and 0.75 is the resistance factor. The required translational stiffness according to Equation (5) is β = 19 kN/cm. Consequently, because K_H is nearly three times β, the *AISC Seismic Provisions* do not require lateral bracing at the middle of the beam.

Test Bed

The specimens were subjected to ground shaking at the E-Defense facility using the "test bed" system developed by Takeuchi et al. (2008). The test beds are multi-purpose devices that supply horizontal mass to the specimen while adding minimal lateral force resistance. As shown in Fig. 5, a pair of test beds was used for this program, one at each side of the loading plane of the specimen. At the base, the test bed was connected to the shaking table through a set of linear bearings which produced minimal friction (the friction coefficient was estimated as 0.0033 by Takeuchi et al. (2008)) for motion in the loading plane, and which restrained out-of-plane motion. At the top, the test bed was connected to each end of the specimen, with a load cell placed in the load path. The two test beds and additional test rigs supplied a combined 69.4 ton mass to the specimen. The test bed was also used to anchor the out-of-plane bracing indicated in Fig. 4(a). Consequently, the test beds were arranged to permit planar motion of the planar specimen.

Test Procedure

As mentioned above, the dimensions of the specimen was 70%-scale of typical building structures. The scaling rules for the shake table test are summarized in Table 2, where λ indicates the inverse of the dimension scaling factor for dimensions. In this case, λ = 1/0.7 = 1.41. Time

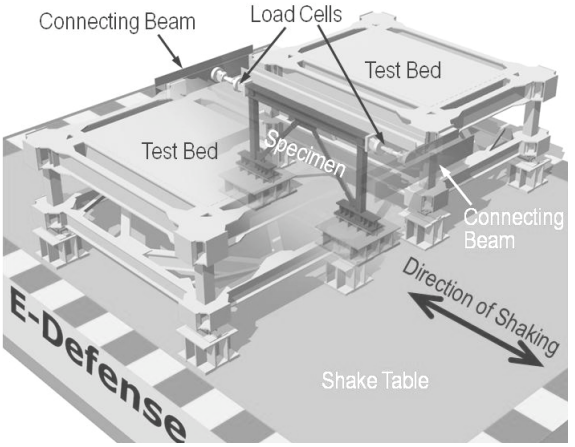


Fig. 5 Specimen and test-bed system

Table 2 Scaling rule

Parameters	Scaling Factor	
Dimension	$1/\lambda$	0.7
Mass	$1/\lambda$	0.7
Acceleration	$1/\lambda$	0.7
Time	1	1
(Inertia) Force	$1/\lambda^2$	0.5
Velocity	$1/\lambda$	0.7
Stress	1	1

and stress are not scaled.

The East-West component of the JR Takatori motion was introduced in the direction parallel to the primary plane of the specimen. The JR Takatori motion is a strong motion record from the 1995 Kobe earthquake, measured immediately adjacent to the fault. The EW component is characterized by a peak acceleration of 6.6 m/s^2 and strong velocity pulses. Fig. 6(a) shows the acceleration history of the motion while Fig. 6(b) shows the response acceleration spectrum obtained for 2 to 10% of critical damping (h = 0.02 to 0.1). The spectral response for h = 0.05 was between 17 and 23 m/s^2 for periods between 0.15 and 0.4 seconds. The natural vibration period of the specimen was predicted as 0.2 sec. After adjusting for the scaling factors, the JR Takatori motion was three times as large as the design basis earthquake in the Japanese design code. The shake table tests were conducted by introducing the motion repeatedly with increasing intensity. Table 3 lists the target excitation levels. Specimen 1 was tested with nine excitations, targeting between 14 and 120% of the JR Takatori EW motion. Specimen 2 was tested with seven excitations, targeting between 14 and 150% of the JR Takatori EW motion, with the 28% motion introduced twice.

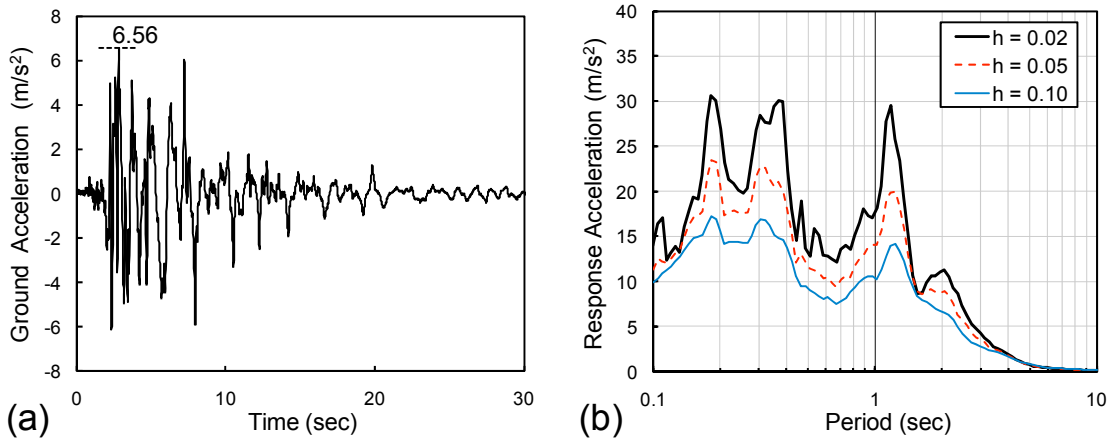


Fig. 6 JR Takatori EW motion: (a) ground acceleration history; and (b) response spectra.

Table 3 Excitation levels

Target Level	Specimen 1		Specimen 2	
	Max. acc. (m/s^2)	Averaged RSA (m/s^2)	Max. acc. (m/s^2)	Averaged RSA (m/s^2)
14%	1.21	4.8	1.16	4.6
21%	1.54	6.6	—	—
28%	1.99	8.6	2.06 / 2.09	9.0 / 9.2
42%	3.45	16	—	—
56%	4.40	20	—	—
70%	4.43	20	4.48	20
84%	5.58	25	—	—
100%	6.78	30	6.77	30
120%	7.98	35	8.40	38
150%	—	—	10.2	46

Instrumentation

The load cells were used to evaluate the story shear. Displacement transducers were used to monitor the story drift and the out-of-plane deformation of the beam and BRBs. The force distributions in the beam, columns, and BRBs were evaluated based on strain gauges placed at selected sections of the beam and columns. Elongation of the BRB steel core was measured from the change in relative distance between the end of steel casing and connection region of the BRB. Data was collected at a rate of 1,000 Hz. All data was passed through a low-pass filter to eliminate frequency content above 50 Hz.

RESULTS

Based on unidirectional white noise excitation, the natural vibration period was determined as 0.18 sec for Specimen 1 and 0.19 sec for Specimen 2. The vibration period of the specimens was equivalent to that of a single or two story building.

Table 3 lists the maximum measured acceleration of the shake table. The table also lists the response spectral acceleration averaged over a period of 0.17 to 0.2 seconds, evaluated from the measured table motion and assuming a damping ratio h = 0.02. The corresponding values from the JR Takatori EW motion (i.e., target 100% motion) were 6.56 m/s^2 and 29 m/s^2, respectively. Therefore, the listed values indicate that the table motion was accurately amplified according to the targets.

Both specimens exhibited very similar response up to the 70% motion. Fig. 7 shows the story shear versus story drift response of the two specimens under the 100 and 120% motions. Specimen 1 exhibited very stable and ductile behavior even under the largest 120% motion, developing a maximum drift ratio of 0.013 radians and leaving a residual drift ratio smaller than 0.001 radians. Minimal yielding was observed in the framing members after testing of Specimen 1 was completed. On the other hand, Specimen 2 experienced substantial degradation in elastic stiffness during motions 100% and larger, recording a maximum drift ratio of 0.015 radians during the 100% motion and 0.03 radians during the 120% motion.

Fig. 8 shows the maximum drift and residual drift measured from each motion. The figure indicates very similar response of the two specimens under motions up to 70%. Motions larger than 100% caused minimal damage to Specimen 1 but severe damage to Specimen 2.

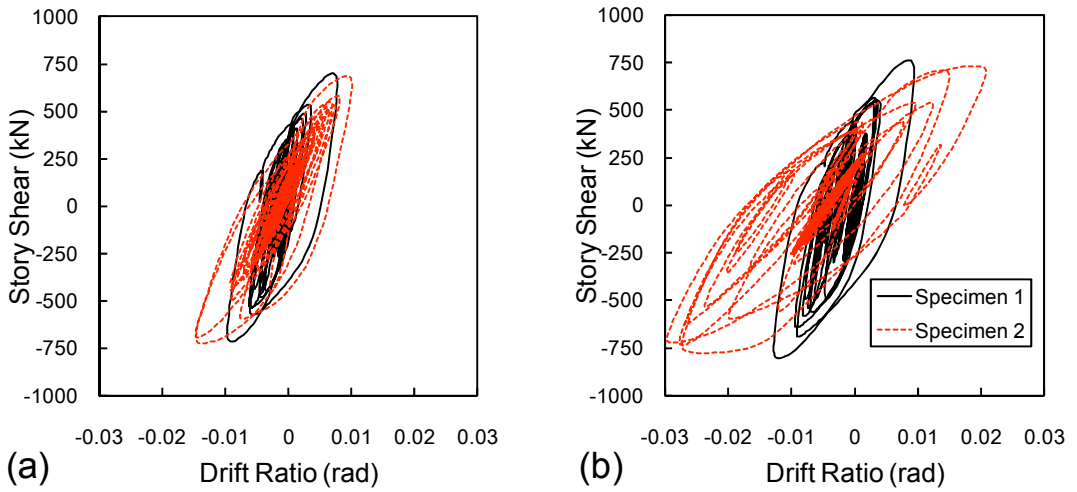


Fig. 7 Frame response at: (a) 100% motion; and (b) 120% motion.

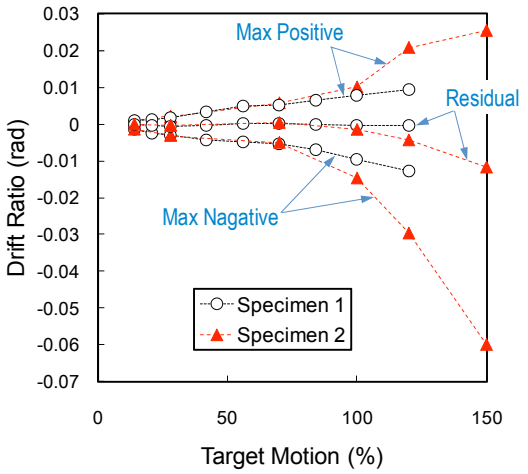


Fig. 8 Maximum drift and residual drift from each motion

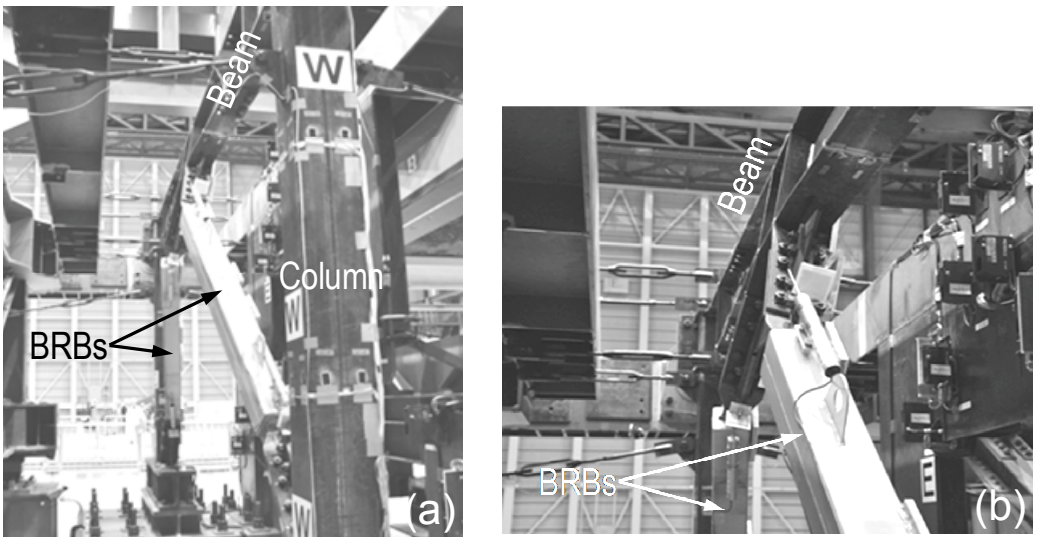


Fig. 9 Specimen 2 after 120% motion: (a) side view; and (b) close-up view.

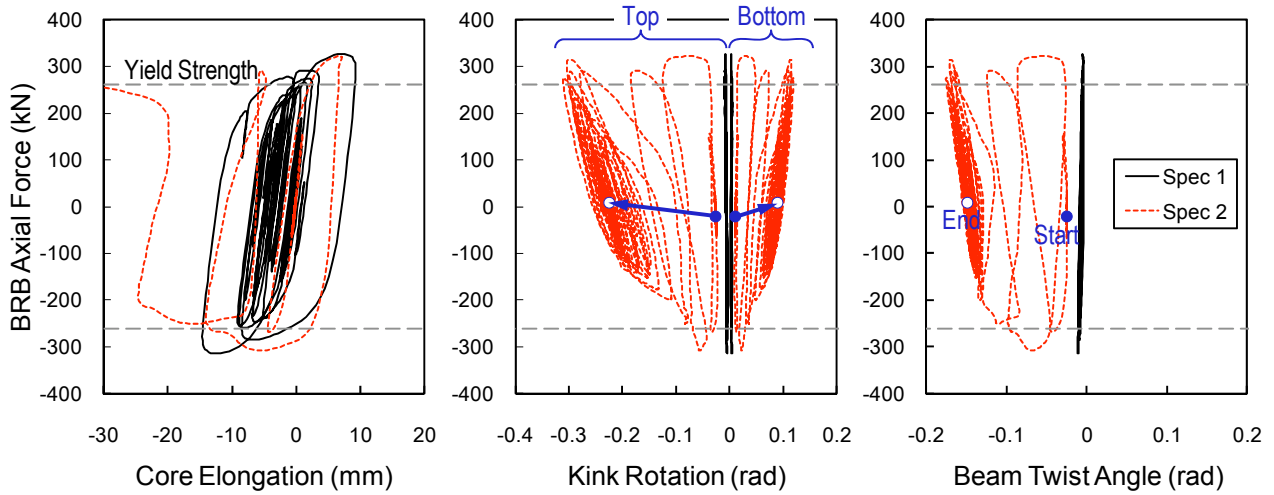


Fig. 10 BRB response at 100% motion: (a) BRB elongation; (b) BRB kink rotation; and (c) beam twist angle.

While the 150% motion produced extremely large drift ratios between -0.06 and 0.025 radians, the residual drift ratio after this motion was fairly small at 0.012 radians. The large deformation history did not cause collapse of Specimen 2. It is noted that P-Delta effects were not incorporated in the tests.

Fig. 9 shows photographs of Specimen 2 taken after the 120% motion. Fig. 9(a) views the elevation of the specimen from an angle. Kinking deformation is seen at the top and bottom ends of both BRBs, between the bolted gusset plate connection and steel casing. The kink rotation angle is notably larger at the top end of the BRB than at the bottom end, and the direction of kink rotation is opposite between the top and bottom. Fig. 9(b) is a close-up view of the middle portion of the beam where the top ends of the two BRBs connect to the beam. The close-up view indicates that the kinking deformation of the BRBs is accompanied by twisting of the beam between the two braced sections. The deformation seen in the photos agrees with the buckling mode illustrated in Fig. 2(c). As predicted by the analytical model, instability of Specimen 2 was promoted by lack of bracing of the beam at the work point of the two BRBs, and the lack of out-of-plane rotational stiffness at both ends of the BRBs.

Fig. 10 compares the BRB performance during the 100% motion, plotting the elongation of the BRB steel core, kink rotation at the top and bottom ends of the BRB, and twist angle of the beam immediately above the BRB, respectively, against the BRB axial force. The response is taken from the BRB placed on the closer side as viewed in Fig. 9. The direction of measured rotation is consistent with the visual observation in Fig. 9. The broken horizontal lines indicate the yield strength of the BRB steel core, P_y, based on the measured yield strength. The maximum tensile and compressive force was 1.25 and 1.20P_y, respectively, for Specimen 1 and 1.23 and 1.18P_y, respectively, for Specimen 2. The BRBs tested in this program exhibited similar behavior in tension and compression, although the BRBs in Specimen 2 were affected by instability and severe distortion of the frame during large motion.

Specimen 1 exhibited very stable cyclic behavior, with the BRB developing steadily larger forces with larger elongation, little kink rotation in the BRBs, and minimal twisting of the beam. Specimen 2 was able to exceed the yield strength. However, it could not effectively develop the full strength of the BRB due to instability of the system. Fig. 10(b) indicates that the kinking rotation at the top and bottom ends of the BRB formed in opposite directions, and the

rotation at the top end was twice the rotation at the bottom. Residual kinking rotation was present after the 84% motion. The 100% motion caused a very large residual rotation of 0.2 radians at the top and 0.1 radians at the bottom. Fig. 10(c) indicates that the kinking rotation of the BRB was accompanied by very severe twisting of the beam.

The occurrence of out-of-plane buckling was predicted by the first-order buckling model in Fig. 1(b). However, the BRB was able to sustain a much large force than predicted by the model. The study is continued by the authors to identify the reason for this discrepancy between predicted and measured BRB strength.

CONLUSIONS

A series of large-scale shake table tests were conducted to examine out-of-plane instability of BRBs. Two chevron braced-frame specimens were repeatedly subjected to the JR Takatori EW motion with increasing amplification. Both specimens implemented oddities from the Japanese practice to promote instability of the specimen: no lateral bracing was provided at the middle of the beam where two BRBs connected to the beam; and no steel cap was provided at the end of the steel casing. In addition, the BRBs in Specimen 2 had an unusually short embedment length of the stiffened segment into the steel casing. Key findings are summarized in the following.

1) Specimen 1 exhibited excellent performance despite the above mentioned measures to promote instability of the BRBs. After nine excitations from 14 to 120% motions, Specimen 1 was left with negligible residual drift. Even under the largest 120% motion, the specimen experienced minimal yielding in the framing members.
2) Specimen 2 was intentionally designed to exhibit out-of-plane instability of BRBs. This specimen exhibited excellent behavior until instability of the system led to severe kinking deformation at both ends of the BRBs, which was accompanied by severe twisting of the beam intersecting the top ends of the BRBs. Due to distortion of the BRBs and the beam, Specimen 2 was unable to develop the full strength of the BRBs during the 100, 120, and 150% motions.
3) Despite the severe out-of-plane distortion of the system and stiffness reduction, Specimen 2 exhibited minimal strength degradation at a very large drift of 0.06 rad. At the end of the test, no fracture was observed at the bracing connections.
4) The severe frame distortion observed in Specimen 2 would compromise serviceability of the structure and replacement of the BRBs following a seismic event. Therefore, out-of-plane instability of BRBs should be prevented. The first-order buckling model presented in this study offers a conservative estimate of the condition that causes the instability.

ACKNOWLEDGEMENTS

The project presented in this study was funded by the National Research Institute for Earth Science and Disaster Prevention of Japan. Mr. Naomiki Suzuki and Dr. Makoto Ohsaki provided guidance to the overall project and specimen design. The authors thank Dr. Toru Takeuchi and Dr. Yuji Koetaka for sharing their views and latest research findings. Ms. Sachi Furukawa, Mr. Ryo Umehara, and Mr. Xuchuan Lin helped processing the data. The steel frame components were fabricated by Sakamoto Industrial Iron Works Co. Maekawa Co., Ltd. managed specimen fabrication and construction of the test setup. Special thanks are extended to

the administrative and technical staff at E-Defense, officially named the Hyogo Earthquake Engineering Research Center. The opinions expressed in this paper are those of the authors and do not necessarily reflect the views of the individuals and organizations mentioned above.

REFERENCES

American Institute of Steel Construction, Inc. (AISC). (2005a). *Seismic Provisions for Structural Steel Buildings*. ANSI/AISC Standard 341-05. AISC, Chicago, Illinois.

American Institute of Steel Construction, Inc. (AISC). (2005b). *Specification for Structural Steel Buildings*. ANSI/AISC Standard 360-05. AISC, Chicago, Illinois.

American Society of Civil Engineers (ASCE). (2005). *Minimum Design Loads for Buildings and Other Structures*. ASCE/SEI 7-05. ASCE, Reston, Virginia.

Black, C.J., Makris, N., and Aiken, I.D. (2004). "Component testing, seismic evaluation and characterization of buckling-restrained braces." *Journal of Structural Engineering*, ASCE, 130(6), 880-894.

Inoue, K., Sawaizumi, S., and Higashibata, Y. (2001). "Stiffening requirements for unbounded braces encased in concrete panels." *Journal of Structural Engineering*, ASCE, 127(6), 712-719.

Kinoshita, T., Koetaka, Y., Inoue, K., and Iitani, K. (2008). "Out-of-plane stiffness and yield strength of cruciform connection for buckling-restrained brace." *Journal of Structural and Construction Engineering*, Architectural Institute of Japan, 632, 1865-1873.

Nakashima, M., Suita, K., Morisako, K., and Maruoka, Y. (1998). "Tests of welded beam-column subassemblies. I: Global behavior." *Journal of Structural Engineering*, ASCE, 124(11), 1236-1244.

Saeki, E., Maeda, Y., Nakamura, H., Midorikawa, M., and Wada, A. (1995). "Experimental study on practical-scale unbounded braces." *Journal of Structural and Construction Engineering*, Architectural Institute of Japan, 476, 149-158.

Takeuchi, T., Yamada, S., Kitagawa, M., Suzuki, K., and Wada, A. (2004). "Stability of buckling-restrained braces affected by the out-of-plane stiffness of the joint element." *Journal of Structural and Construction Engineering*, Architectural Institute of Japan, 575, 121-128.

Takeuchi, T., Kasai, K., Midorikawa, M., Matsuoka, Y., Asakawa, T., Kubodera, I., Kurokawa, Y., Kishiki, S., and Ando, H. (2008). "Shaking table test using E-Defense multipurpose test bed." *14th World Conference on Earthquake Engineering*, Beijing, China, October 12-17, 2008.

Tembata, H., Koetaka, Y., and Inoue, K. (2004). "Out-of-plane buckling load of buckling-restrained braces including brace joints." *Journal of Structural and Construction Engineering*, Architectural Institute of Japan, 581, 127-134.

Uang, C.-M. and Nakashima, M. (2004). "Steel buckling-restrained braced frames." *Earthquake Engineering from Engineering Seismology to Performance Based Engineering*, Chapter 16, Y. Bozorgnia and V.V. Bertero (eds.), CRC Press, Boca Raton, Florida.

Wada, A., Huang, Y., and Bertero, V.V. (2004). "Innovative strategies in earthquake engineering." *Earthquake Engineering from Engineering Seismology to Performance Based Engineering*, Chapter 10, Y. Bozorgnia and V.V. Bertero (eds.), CRC Press, Boca Raton, Florida.

Dynamic Response of a Steel Concentrically Braced Frame

Taichiro Okazaki[1], Dimitrios G. Lignos[2], Tsuyoshi Hikino[3], and Kouichi Kajiwara[4]

[1] Faculty and Graduate School of Engineering, Hokkaido University, Japan; (formerly NIED); email: tokazaki@eng.hokudai.ac.jp
[2] Department of Civil and Applied Mechanics, McGill University, dimitrios.lignos@mcgill.ca
[3] Steel Structures Engineering Division, Nippon Steel Engineering Co. Ltd. (formerly NIED); email: hikino.tsuyoshi@nsc-eng.co.jp
[4] National Research Institute for Earth Science and Disaster Prevention, Japan; email: kaji@bosai.go.jp

ABSTRACT

Large-scale shake table tests were conducted to examine the dynamic response of steel concentrically braced frames. The specimen was a single-bay, single-story frame with a pair of square-tube braces placed in a chevron arrangement. The gusset plates connecting the brace to the framing elements were provided with an elliptical clearance to permit free out-of-plane rotation. The specimen was subjected repeatedly to unidirectional ground motion with increasing magnitude until the braces fractured. The test results demonstrated excellent performance of the gusset plate connections. The specimen response was reproduced by a numerical model using fiber elements. This model was able to predict the occurrence of brace fracture and post-fracture behavior of the frame. Observations from the shake table tests and aspects of the numerical analysis are reported in this paper.

INTRODUCTION

Concentrically-braced frames (CBFs) are an efficient structural system to achieve the lateral stiffness and strength required by modern seismic design provisions. The design rules in the *AISC Seismic Provisions for Structural Steel Buildings* (AISC 2005b) are based on an extensive body of research conducted since the 1970's (Popov et al. 1976; Astaneh-Asl et al. 1986; Nakashima and Wakabayashi 1993), which suggest that the seismic performance of axially loaded members degrade with the width-to-thickness and slenderness of the brace. Recent tests by Uriz and Mahin (2004), Lehman et al. (2008), and Roeder and Lehman (2009) indicate that secondary bending in the framing members caused by frame deformation can significantly affect bracing connections. Based on such observations, Lehman et al. (2008) developed a design procedure that promotes compact and thin gusset plates. While much improvement has been made in the design and detailing of CBFs, evaluating the behavior of CBFs under severe ground motions remains a challenging problem due to their complex nonlinear behavior following brace buckling and ultimately fracture.

This paper describes a research program that involved shake table tests of a large-scale braced frame specimen. The test results were used to evaluate the accuracy and reliability of state-of-the-art nonlinear analysis. The experimental and analytical study was used to examine the dynamic behavior of CBFs detailed according to the most recent recommendations.

TEST PLAN

A single story, single span, chevron-braced (or "inverted V-braced") frame specimen was subjected to a series of strong earthquake ground motions. The tests were conducted at E-Defense, a three-dimensional, large-scale earthquake testing facility maintained and operated by the National Research Institute for Earth Science and Disaster Prevention of Japan.

Specimens

Fig. 1 shows an elevation view of the braced-frame specimen. The 4.15-m span and 2.25-m height correspond to 70%-scale of a typical building structure. The braces were arranged to frame into the beam and column in an angle close to 45 degrees. The beam was rigidly connected to the columns. This frame comprised a built-up wide-flange beam (d = 300, b_f = 150, t_w = 6.5, t_f = 9 mm), two cold-formed square-tube columns (d = b = 200, t = 9 mm), and a pair of square tubular braces (d = b = 75, t = 3.2 mm) connected to the beam-to-column joints through 4.5-mm gusset plates. Table 1 lists the Japanese Industry Standards (JIS) designation and measured mechanical properties for each material used to fabricate the specimen. The specified minimum yield strength is 245, 235, 295, and 245 MPa, respectively, for STKR400, SN400, BCR295, and SS400 steel. The table also indicates the measured yield strength established from tension coupon tests. The measured yield strength for the beam and columns and tubular braces was 50% stronger than the specified minimum value. Interestingly, the measured yield strength for the gusset plate, 204 MPa, did not meet the specified minimum value of 245 MPa.

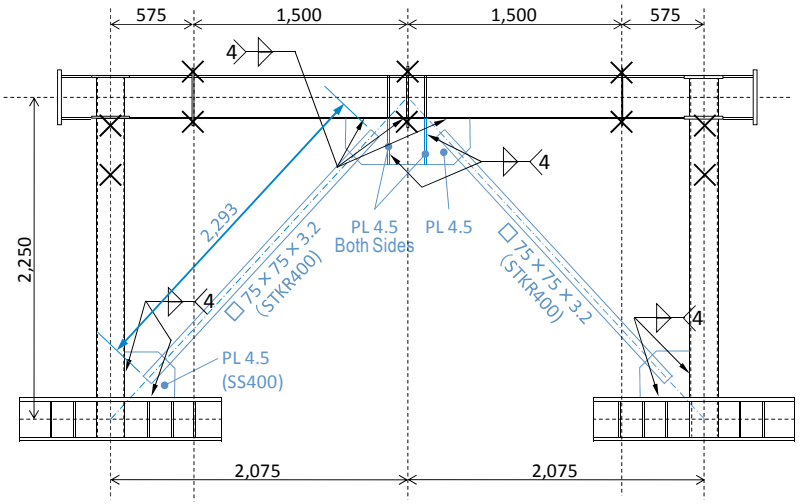


Figure 1. Test specimen and out-of-plane bracing points

Table 1. Material Properties

Material	JIS designation	Yield Strength (MPa)	Tensile Strength (MPa)	Elongation (%)
Brace	STKR400	383	452	36
Beam flange (9 mm)	SN400B	327	456	27
Beam web (6 mm)	SN400B	376	472	29
Column (9 mm)	BCR295	434	518	19
Gusset plate (4.5 mm)	SS400	204	291	54

The standard through-diaphragm detail (Nakashima et al. 2000) was used to achieve rigid beam-to-column connections. The gusset plate at the bracing connections was detailed according to the elliptical clearance rule proposed by Lehman et al. (2008). The gusset plate at the top end of the braces, between the braces and beam, was further provided with a pair of vertical stiffener plates to control interaction between the two braces. The columns were rigidly connected to large base beams which were, in turn, fixed to the shake table. At the top side of the specimen, each end of the beam was connected to the test-bed system described later. The specimen was laterally braced along the columns and beam at the discrete locations indicated in Fig. 1.

Compliance to Code Requirements

The tubular braces had a width-to-thickness ratio of b/t = 19.4 and member slenderness ratio of L/r = 103, where the member length L is the diagonal distance between beam-to-column nodes. The b/t ratio slightly violates the seismically compact limit of $0.64(E/F_y)^{1/2}$ = 18.5,while the L/r ratio is within the limit of $4(E/F_y)^{1/2}$ = 116 specified for Special CBFs per the *AISC Seismic Provisions*. The member slenderness ratio based on the length L measured between the elliptical fold lines was L/r = 91. The nominal strength based on the *AISC Specification for Structural Steel Buildings* (AISC 2005) was $0.658^{(Fe/Fy)}F_y$ = 143 kN for L/r = 103 and 161 kN for L/r = 91, using F_y = 245 kN.

Per the *AISC Seismic Provisions*, the bracing connections were detailed to develop the required tensile and compressive strength of the tubular braces. The elliptical clearance rule proposed by Lehman et al. (2008) was adopted for sizing the gusset plates.

Test Bed

The specimens were subjected to ground shaking at the E-Defense facility using the "test bed" system developed by Takeuchi et al. (2008). The test beds are multi-purpose devices that supply horizontal mass to the specimen while adding minimal lateral force resistance. As shown in Fig. 2, a pair of test beds was used for this program, one at each side of the loading plane of the specimen. At the base, the test bed was connected to the shaking table through a set of linear bearings which produced minimal friction (friction coefficient was estimated as 0.0033 by Takeuchi et al. (2008)) for motion in the loading plane, and which restrained out-of-plane motion. At the top, the test bed was connected to each end of the specimen, with a load cell placed in the load path. The two test beds and additional test rigs supplied a combined 69.4 ton mass to the

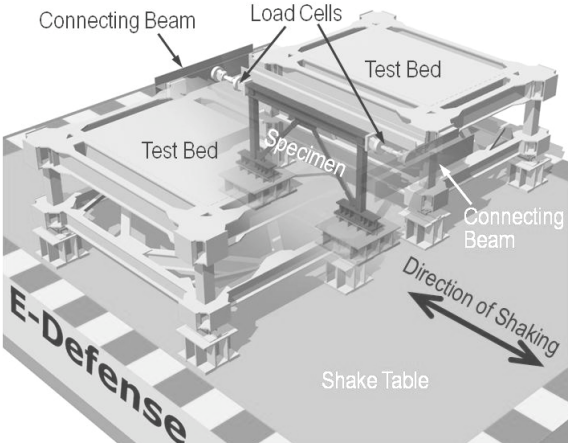


Figure 2. Specimen and test-bed system

specimen. The test bed was also used to anchor the out-of-plane bracing indicated in Fig. 1. Consequently, the test beds were arranged to permit planar motion of the planar specimen. The test-bed system has been used previously in a similar fashion for two experimental programs (Takeuchi et al. 2008; Ma et al. 2010).

Test Procedure

The East-West component of the JR Takatori motion (Nakamura et al. 1996) was introduced in the direction parallel to the primary plane of the specimen. The JR Takatori motion is a strong motion record from the 1995 Kobe earthquake, measured immediately adjacent to the fault. The EW component is characterized by a peak acceleration of 6.6 m/s^2 and strong velocity pulses. Fig. 3(a) shows the acceleration history of the motion while Fig. 3(b) shows the response acceleration spectrum obtained for 2% of critical damping (h = 0.02). The shake table tests were conducted by introducing the Takatori EW motion seven times, with target amplification level increasing from 10, 12, 14, 28, 28 (second time), to 42, and finally 70%. Fig. 3(b) also shows the acceleration response spectra constructed from the measured table motion assuming h = 0.02. The targeted amplification was achieved over a wide range of periods between 0.1 and 3 seconds, although the 70% motion exceeded the target in the short period range between 0.1 and 0.5 sec.

The load cells mentioned above were used to evaluate the story shear. Displacement transducers were used to monitor the story drift and the out-of-plane deformation of the beam and braces. The force distributions in the beam, columns, and braces were evaluated based on strain gauges placed at selected sections of the beam and columns. Elongation of the braces was measured based on the relative distance between the ends of tubular brace. Data was collected at a rate of 1,000 Hz. All data was passed through a low-pass filter to eliminate frequency content above 50 Hz.

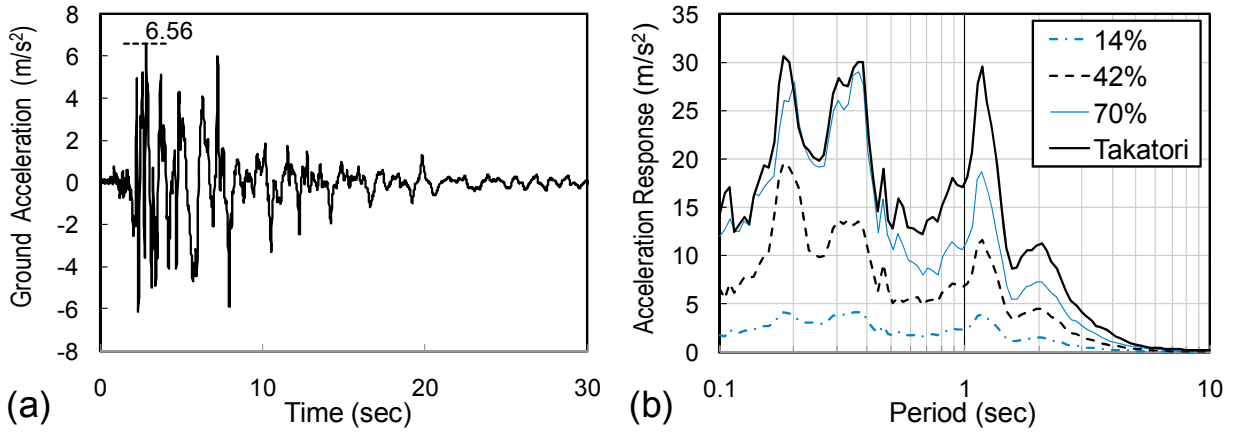


Figure 3. Ground motion: (a) JR Takatori EW acceleration history; and (b) response spectra for h = 0.02.

RESULTS

Global Behavior

Based on unidirectional white noise excitation, the natural vibration period was determined as 0.21 sec. The vibration period of the specimens was equivalent to that of a single or two story building.

Fig. 4 shows the story shear versus story drift response measured for the three tests using

the 28, 42, and 70% Takatori EW motions. The figure indicates that the structure remained elastic during the 28% motion, but some inelasticity occurred during the 42% motion. The response from the 70% motion plotted in Fig. 4(c) indicates that the stiffness of the system suddenly reduced after experiencing two and one-half drift cycles of -0.015 to +0.01 rad. During these drift cycles, the strength of the system dipped notably at rather small drifts.

Brace Performance

Fig. 5 shows the axial force (tension taken as positive) versus elongation relationship measured from a brace for the 28, 42, and 70% motions. The horizontal lines indicate the tensile yield strength and compressive strength of the brace member. The compressive strength was computed based on the measured yield strength, the AISC design equation, and a slenderness ratio L/r = 91. It is noted that beyond the deformation range where the beam yielded near the connections to the columns, the accuracy of brace force estimation based on strain gauge measurements is eroded. Nonetheless, Fig. 5 clearly illustrates the key characteristics of buckling

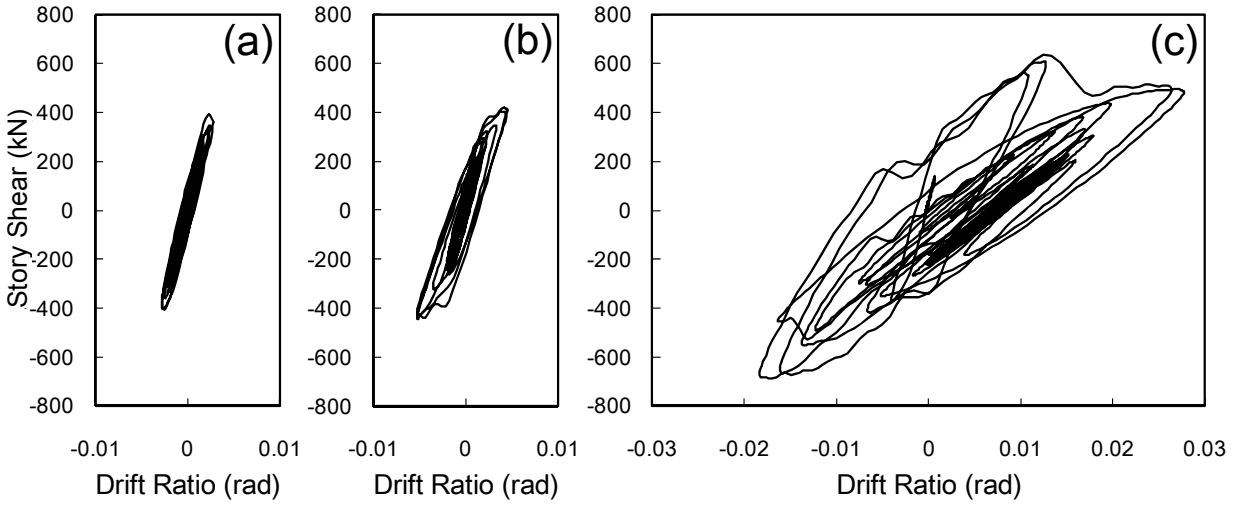


Figure. 4 Frame response at: (a) 28%; (b) 42%; and (c) 70% motion.

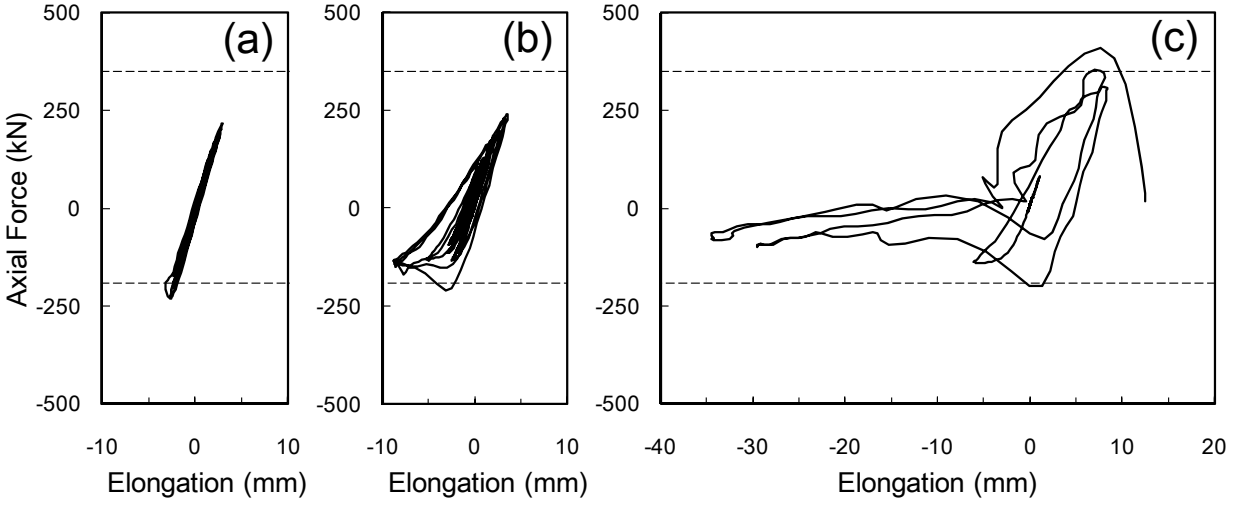


Figure. 5 Brace axial response at: (a) 28%; (b) 42%; and (c) 70% motion.

brace behavior. While the compressive force exceeded the estimated buckling strength during the 28% motion, no sign of instability was observed at this stage. A clear indication of buckling and degradation in compressive strength was observed from the 42% motion. No sign of residual deformation was visible in the brace member after the 42% motion test. During the 70% motion, the brace shown in Fig. 5(c) fractured after experiencing two and one-half loading cycles of -30 to 10 mm (1% contraction and 0.25% extension). The other brace fractured similarly shortly afterwards. The drift ratio of the specimen was smaller than 0.02 rad. when the fracture occurred. After both braces fractured, the underlying moment frame developed a story drift ratio approaching 0.03 rad.

Fig. 6 shows photographs of the specimen taken after the 70% motion test was completed. Fig. 6(a) shows the fractured brace. Both braces fractured near mid-length of the member. Indication of local buckling and ductile tearing was evident near the fractured section. Figs. 6(b) and (c) demonstrate that the gusset plates, either at the column base or at the middle of the beam, folded nicely along the elliptical clearance. No discernable damage was observed at the bracing connections, suggesting that the performance of the bracing connections was excellent.

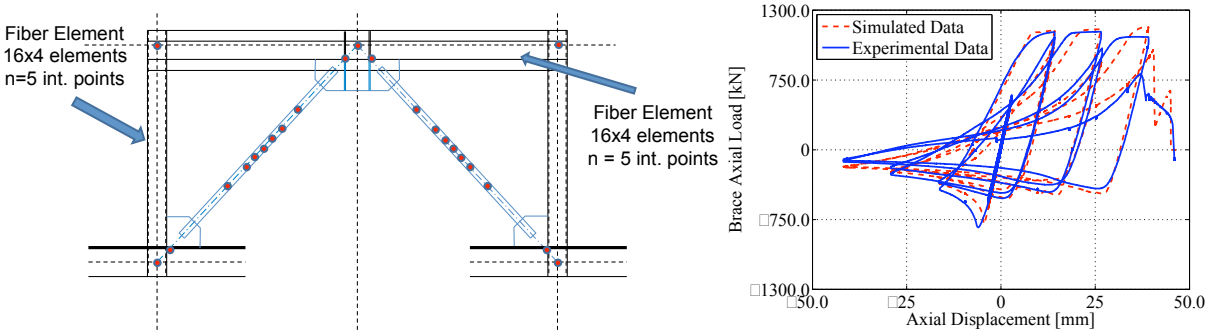


Figure. 6 Specimen after 70% motion: (a) gusset plate at the column base; (b) gusset plate at the beam; and (c) fractured brace.

NUMERICAL SIMULATION

A numerical model of the specimen was constructed in the OpenSees platform (Mazzoni et al. 2009) using fiber elements. Figure 7a illustrates the analytical model of the test specimen. The geometry of the test specimen was modeled based on centerline dimensions, i.e. panel zones were not considered since they behaved elastically during the shaking table tests. To simulate inertia forces a leaning column was used that was connected with an axially rigid rod to the frame model. Since large P-Delta effects were not applied to the test specimen due to the sliding masses, only small P-delta effects were considered in the analysis. Corotational transformation was utilized. Steel beams and columns were modeled with fiber elements (16x4 elements) with five integration points along the length of each steel component. The brace members of the test specimen were modeled with a center node and an application of initial imperfection in accordance with the techniques summarized in Uriz et al. (2008) and Chen and Mahin (2008) in order to simulate overall buckling of the brace. The integration points along the brace element were based on Gauss-Lobatto quadrature rule (two integration points at the element ends). The material properties used for all steel components of the test specimen were

the ones previously summarized in Table 1. Three percent mass proportional damping was assumed at the first mode period of the test frame (T_1=0.20sec) since it was a single degree of freedom system. The 3% damping is justified based on the fact that friction damping due to sliding of the seismic masses was not simulated in the analytical model. Cumulative damage effects from phase to phase were considered in the numerical simulation since the scaled Takatori motions were analyzed sequentially. Further, the analytical model of the test frame incorporated fracture of the steel braces that can initiate according to a rain-flow-counting rule. The fracture model was calibrated against previous quasi-static experimental data on tubular steel braces by Fell et al. (2009). These steel brace components had similar slenderness ratios (L/r_y = 80, D/t =16) with the steel braces of the test specimen. An example of calibration of the fatigue model is shown in Figure 7b, including modeling of fracture at the center of the brace. a

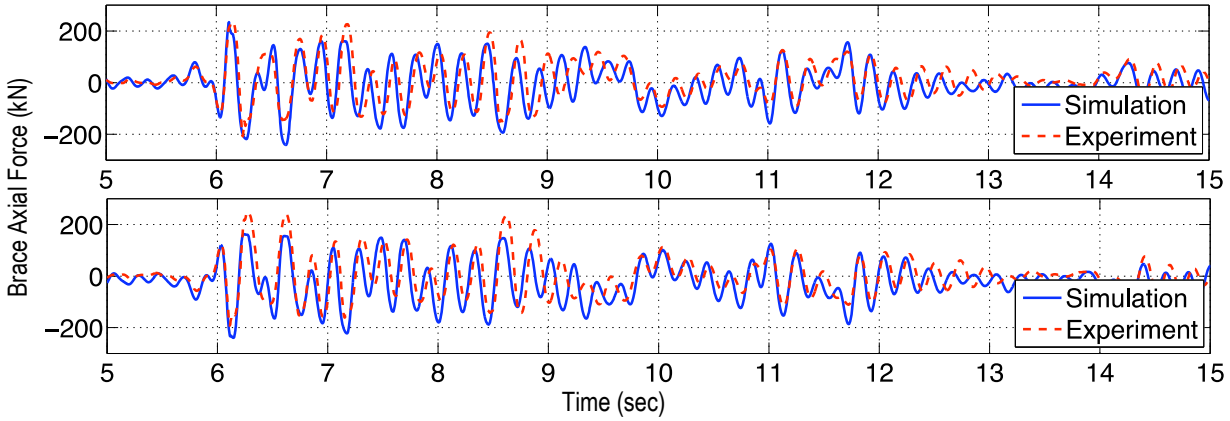


(a) Test specimen (b) fatigue model calibration

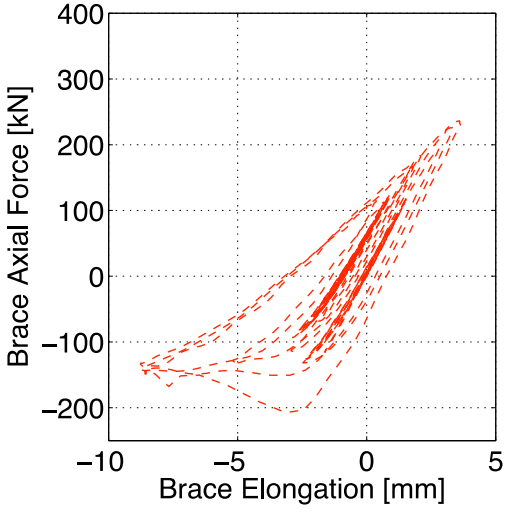
Figure 7. Modeling scheme

Figure 8a shows the axial force distribution history of the two braces of the test specimen for the 42% JR Takatori record. The force distribution of the braces is predicted fairly accurately prior to fracture. The same can be seen from Figures 8b and 8c that compare the recorded simulated brace force versus elongation with the simulated one for the same ground motion intensity. The base shear versus story drift ratio for the 42% motion is shown is Figure 8d. The base shear is normalized with respect to the total seismic weight of the test specimen. The figure superimposing the simulated response over the experimental response indicates that the global response is traced fairly accurately, indicating that the numerical model of the test specimen is reliable.

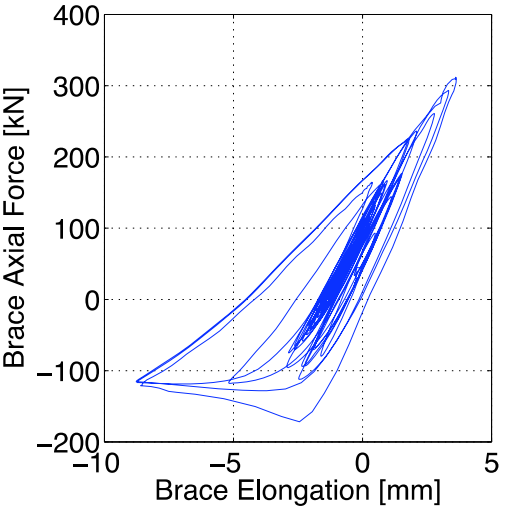
During the 70% motion, the two braces fractured. This resulted to a loss of lateral stiffness of the test specimen. However, the numerical model is able to simulate the loss of stiffness due to fracture of the braces since fracture is accurately traced for both braces. This can be seen in Figure 8e that shows a comparison of the simulated versus recorded normalized base shear versus story drift ratio of the test specimen. The model was able to predict the post-fracture behavior of the frame after the occurrence of brace fracture. This can be seen in Figure 9 that shows the base shear history of the test specimen as predicted by the numerical model compared to the experimental data. The phase difference between simulated and experimental results after the first 9 seconds of the ground motion is attributed to the fact that the predicted fracture time of the second brace occurred about 2 seconds earlier than in the experiment as can be seen from the same figure.



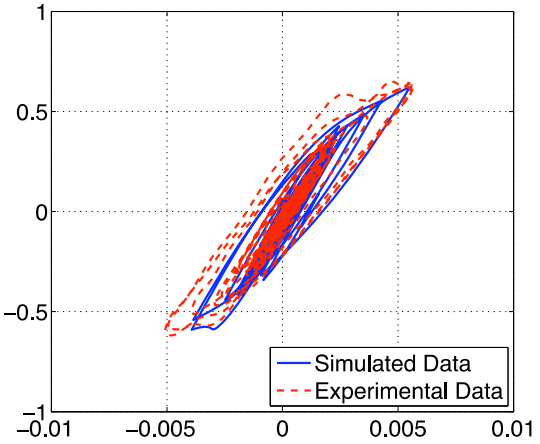
(a) Brace force history during 42% of JR Takori motion



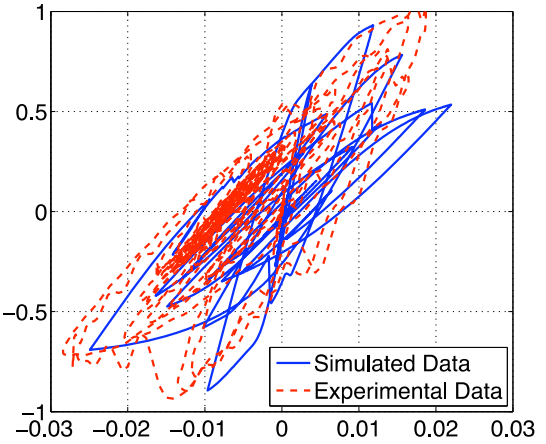
(b) Experimental data (42% JR Takatori)



(c) Simulated data (42% JR Takatori)



(d) 42% JR Takatori Motion



(e) 70% JR Takatori Motion

Figure 8. Comparison of experimental vs analytical results (42% and 70% JR Takatori)

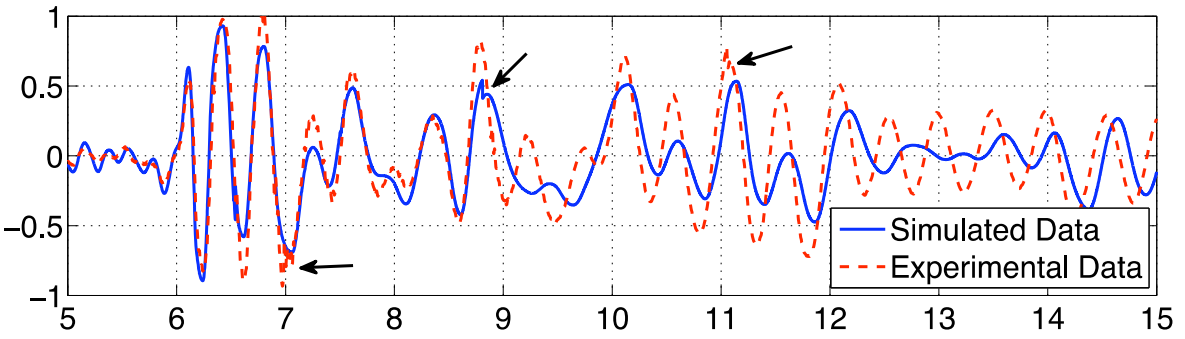


Figure 9. Normalized base shear history of the test specimen during 70% JR Takatori record; comparison between simulated and experimental results

CONCLUSIONS

A series of large-scale shake table tests were conducted. The specimen was a 70%-scale, single-bay, single-story moment resisting frame with a pair of square tube braces placed in a chevron arrangement. The braces had a width-to-thickness ratio of 19.4 and member slenderness ratio of 103, where the brace length was taken as the diagonal distance between beam-to-column nodes. The width-to-thickness ratio was slightly greater than the seismically compact limit per the AISC Seismic Provisions. The gusset plates connecting the brace to the framing elements were provided with an elliptical clearance to permit free out-of-plane rotation. The specimen was subjected to a number of unidirectional ground motions with increasing intensity. During the final excitation, both braces experienced large inelastic loading cycles, and subsequently fractured in the middle at a drift ratio smaller than 0.02 rad. After the brace fractured, the underlying moment frame developed a story drift approaching 0.03 rad. After all tests were completed, no discernable damage was observed at the bracing connections.

A numerical model was constructed using fiber elements and incorporating fracture that can initiate according to a rain-flow-count rule calibrated against previous experimental data. The story drift, story shear, brace elongation, and force distribution recorded from the shake table tests was traced fairly accurately by the numerical model. The model was able to predict the occurrence of brace fracture and subsequent behavior of the frame.

ACKNOWLEDGEMENTS

The project was funded by the National Research Institute for Earth Science and Disaster Prevention of Japan. Sachi Furukawa, Ryo Umehara, and Xuchuan Lin helped processing the data. Special thanks are extended to the administrative and technical staff at E-Defense, officially named the Hyogo Earthquake Engineering Research Center. Dr. Chui-Hsin Chen and Professor Steve Mahin at the University of California, Berkeley, kindly shared information on their numerical models. The opinions expressed in this paper are those of the authors and do not necessarily reflect the views of the individuals and organizations mentioned above.

REFERENCES

American Institute of Steel Construction, Inc. (AISC). (2005a). Seismic Provisions for Structural

Steel Buildings. ANSI/AISC Standard 341-05. AISC, Chicago, Illinois.
American Institute of Steel Construction, Inc. (AISC). (2005b). Specification for Structural Steel Buildings. ANSI/AISC Standard 360-05. AISC, Chicago, Illinois.
American Society of Civil Engineers (ASCE). (2005). Minimum Design Loads for Buildings and Other Structures. ASCE/SEI 7-05. ASCE, Reston, Virginia.
Astaneh-Asl, A., Goel, S.C, and Hanson, R.D. (1986). "Earthquake-resistant design of double angle bracing." Engineering Journal, AISC, 23(4), 133-147.
Black, R.G., Wenger, W.A., and Popov, E.P. "Inelastic buckling of steel struts under cyclic load reversals." *Report No. UCB/EERC-80-40*, Earthquake Engineering Research Center, Berkeley, California.
Fell, B.V., Kanvinde, A.M., Deierlein, G.G., and Myers, A.T. (2009), "Experimental investigation of inelastic cyclic buckling and fracture of steel braces," Journal of Structural Engineering, ASCE, 135(1), 19-32.
Lehman, D.E., Roeder, C.W., Herman, .D, Johnson, S., and Kotulka, B. (2008). "Improved seismic performance of gusset plate connections." Journal of Structural Engineering, ASCE, 134(6), 890-901.
Ma, X., Deierlein, G., Eatherton, M., Krawinkler, H., Hajjar, J., Takeuchi, T., Kasai, K., Midorikawa, M., and Hikino, T. (2010). "Large-scale shaking table tests of steel braced frame with controlled rocking and energy dissipating fuses." 9th U.S. National and 10th Canadian Conference on Earthquake Engineering, Paper No. 1681, Toronto, Quebec, Canada, July 25-29, 2010.
Mazzoni, S., McKenna, F., Scott, M.H., Fenves, G.L. (2009). Open System for Earthquake Engineering Simulation User Command-Language Manual. <http://opensees.berkeley.edu/OpenSees/manuals/usermanual/index.html> (March 28, 2009), Pacific Earthquake Engineering Research Center, Berkeley, California.
Nakamura, Y., Uehan, F., and Inoue, H. (1996). "Waveform and its analysis of the 1995 Hyogo-ken-Nanubu Earthquake II." *JR Earthquake Information No. 23d*, UrEDAS R&D Promotion Department, Railway Technical Research Institute, Tokyo, Japan.
Nakashima, M. and Wakabayashi, M. (1992). "Analysis and design of steel braces and braced frames in building structures." Chapter in: Stability and Ductility of Steel Structures under Cyclic Loading, Edited by Fukumoto, Y. and Lee, G. CRC Press.
Nakashima, M., Roeder, C.W., and Maruoka, Y. (2000). "Steel moment frames for earthquakes in United States and Japan." Journal of Structural Engineering, ASCE, 126(8), 861-868.
Roeder, C.W. and Lehman, D.E. (2009). "Performance and behavior of gusset plate connections." North American Steel Construction Conference, Phoenix, Arizona, April 1-4, 2009.
Takeuchi, T., Kasai, K., Midorikawa, M., Matsuoka, Y., Asakawa, T., Kubodera, I., Kurokawa, Y., Kishiki, S., and Ando, H. (2008). "Shaking table test using E-Defense multipurpose test bed." *14th World Conference on Earthquake Engineering*, Beijing, China, October 12-17, 2008.
Uriz, P. and Mahin, S.A. (2004). "Seismic performance assessment of concentrically braced steel frames." 13th World Conference on Earthquake Engineering, Vancouver, British Columbia, Canada, August 1-6, 2004, Paper No. 1639.
Uriz, P., Filippou, F.C., and Mahin, S.A. (2008). "Model for cyclic inelastic buckling of steel braces." Journal of Structural Engineering, ASCE, 134(4), 619-628.

Self-Centering Buckling-Restrained Braces for Advanced Seismic Performance

David J. Miller[1], Larry A. Fahnestock[1], and Matthew R. Eatherton[2]

[1]Department of Civil and Environmental Engineering, University of Illinois at Urbana-Champaign, 205 N. Matthews Avenue, Urbana, IL 61801

[2]Department of Civil and Environmental Engineering, Virginia Tech, 200 Patton Hall, Blacksburg, VA 24061

ABSTRACT

Although conventional earthquake-resisting structural systems provide adequate life safety when properly designed, they rely on significant structural damage to dissipate the seismic energy. This structural damage and the residual drift that may result from the inelastic response can make a building difficult, if not financially unreasonable, to repair after an earthquake. As a result, development of systems that return to their initial position (i.e., "self-center") following an earthquake and minimize structural damage is a crucial need. This research aims to address this need by creating an innovative self-centering brace for advanced seismic performance.

In the present study, the seismic behavior and performance of self-centering buckling-restrained braces (SC-BRBs) is investigated. A SC-BRB consists of a typical BRB component, which provides energy dissipation, and pre-tensioned superelastic NiTi shape memory alloy (SMA) rods, which provide self-centering. The SMA rods are attached to the BRB portion of the brace using a set of concentric tubes and free-floating end plates that cause the SMA rods to elongate when the brace is in both tension and compression. Half-scale SC-BRBs are designed and fabricated for experimental validation. To characterize hysteretic response, the braces are subjected to a cyclic loading protocol adapted from the AISC Seismic Provisions for Structural Steel Buildings. The results of the experiments are used to validate a SC-BRB numerical model, which is used to conduct further parametric studies of SC-BRB behavior and to perform system studies of concentrically-braced frames with SC-BRBs.

INTRODUCTION

Although conventional earthquake-resisting structural systems, such as moment-resisting frames (MRFs) and concentrically-braced frames (CBFs), are generally deemed to provide adequate seismic safety, they depend on significant structural damage to survive strong ground shaking. Thus, protection against economic loss is not guaranteed owing to repair costs and associated business downtime. Distributed inelastic response in structural members and residual drift are two critical issues that can make a building difficult, if not financially unreasonable, to repair after an earthquake. As a result, development of systems that return to their initial position (i.e., self-center) following an earthquake and minimize structural damage is needed.

This research aims to address this need through investigation of an innovative self-centering brace for advanced seismic performance.

BACKGROUND

Two important topics provide context to the development of the present research: the buckling-restrained brace (BRB) and structural self-centering (SC).

Buckling-Restrained Braces: The BRB is a robust structural component with excellent hysteretic behavior. In the last few years, steel CBFs with BRBs, commonly called buckling-restrained braced frames (BRBFs), have been used extensively in the U.S. since the first application in the Plant and Environmental Sciences Building on the campus of the University of California at Davis (Clark et al. 2000). A BRB has two basic components: a steel core element that carries the entire brace axial force, and a restraining exterior element that prevents the core from buckling in compression allowing it to yield in both tension and compression. The restraining element is typically a concrete filled steel tube, and the steel core is not bonded to the concrete. BRBs have stable, predictable hysteretic behavior and provide significant energy dissipation and large ductility capacity.

BRBFs have been adopted rapidly since they offer significantly better performance than traditional steel CBFs, they are easier to design, and there is little to no additional effort required in construction. Although BRBFs address one of the critical requirements of high performance earthquake-resistant structural systems (i.e., they offer robust performance and concentrate structural damage in distinct locations that can be easily accessed for repair while preventing structural damage elsewhere), they are still susceptible to residual drift. Thus, although the BRB concept offers advantages over traditional steel braces, the lack of self-centering is still a shortcoming.

Self-Centering Systems: Self-centering (SC) earthquake-resisting structural systems, which have the ability to dissipate energy and also return to their original position after ground shaking, are a relatively new and promising concept for seismic design. SC system approaches can be grouped broadly into three categories: 1) systems with horizontal post-tensioned (PT) steel elements (bars or strands) that develop flexural gap opening at specified connections when lateral load is applied; 2) rocking systems, with or without vertical post-tensioned steel elements, that allow uplift at the base of the structure when lateral load is applied; and 3) braced-frame systems with SC braces that return to their initial length after undergoing shortening and elongation due to lateral load.

SC braces offer a significant advantage over the first two classes of SC systems since they lack the challenges associated with connection to the gravity system and transfer of inertial forces. SC braces can be substituted for conventional braces and the remainder of the braced frame system does not need to change. Recently, a SC brace was developed using PT high-strain-capacity aramid-fiber tendons to clamp the brace together (Christopoulos et al. 2008b, Tremblay et al. 2008). Inner and outer steel tubes are configured such that self-centering forces are produced when both tensile and compressive deformations are imposed on the brace. Energy dissipation is

introduced using friction pads clamped together with tensioned bolts. Several studies (e.g., Dolce and Cardone 2006, Zhu and Zhang 2008) have also considered SC braces using shape memory alloys (SMA) elements, both to create the self-centering force and to dissipate energy.

SMAs possess unique characteristics that are particularly suited to application in high-performance earthquake-resisting systems. The distinctive SMA characteristic that is most valuable for such applications is typically called "superelasticity" referring to the fact that very large strains (up to 10%) can be recovered elastically upon the removal of load. The superelastic region exhibits a stress plateau after a phase transition from austenite to martensite, which researchers have noted could be used to limit the forces transferred to other parts of the structure and concentrate deformation in the SMA (McCormick et al. 2007). As described below, this research takes advantage of the superelasticity of SMA to develop a brace with deformation capacity well beyond what even a large earthquake could require.

SELF-CENTERING BUCKLING-RESTRAINED BRACE BEHAVIOR

The self-centering buckling restrained brace (SC-BRB), shown in Figure 1, uses the widely accepted BRB concept as the energy dissipating mechanism and pre-tensioned NiTi SMA rods to create the self-centering force. The SC-BRB is a brace that can be substituted for a conventional steel brace or a buckling-restrained brace without changing the rest of the structure. It does not require any unusual detailing, or construction methods, but instead could be easily implemented using current design and construction practice. Unlike PT moment frame or rocking braced frame systems, there are no additional challenges associated with accommodating connection gap-opening or rocking displacement and interfacing the lateral-load-resisting frames with the gravity system and the rigid floor diaphragms.

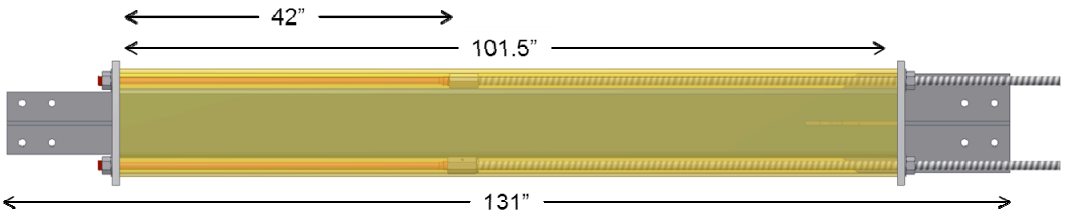


Figure 1 – SC-BRB with dimensions for a half-scale specimen

SC-BRB Components: The SC-BRB configuration is shown in Figure 2 and consists of the following key components:

1) The BRB core is a continuous steel element from the bolted connection at one end to the bolted connection at the other end. As the brace deforms, the core yields in tension or compression and dissipates energy.
2) The inner tube is nominally unstressed and provides buckling restraint for the BRB core. Grout is placed between the inner tube and the BRB steel core, with a bond break and small gap provided between the core and the grout to allow for uninhibited movement of the steel core.

3) The middle tube is welded to the left end of the BRB core and remains fixed with respect to the left end bolted connection.
4) The outer tube is welded to the right end of the BRB core and remains fixed with respect to the right end bolted connection.
5) Anchorage plates at each end have cross shaped slots through which the BRB core passes. The anchorage plates are not connected to the BRB core or to the tubes.
6) SMA rods are post-tensioned, clamping the anchorage plates against the middle and outer tubes and creating an initial compression in these two tubes.

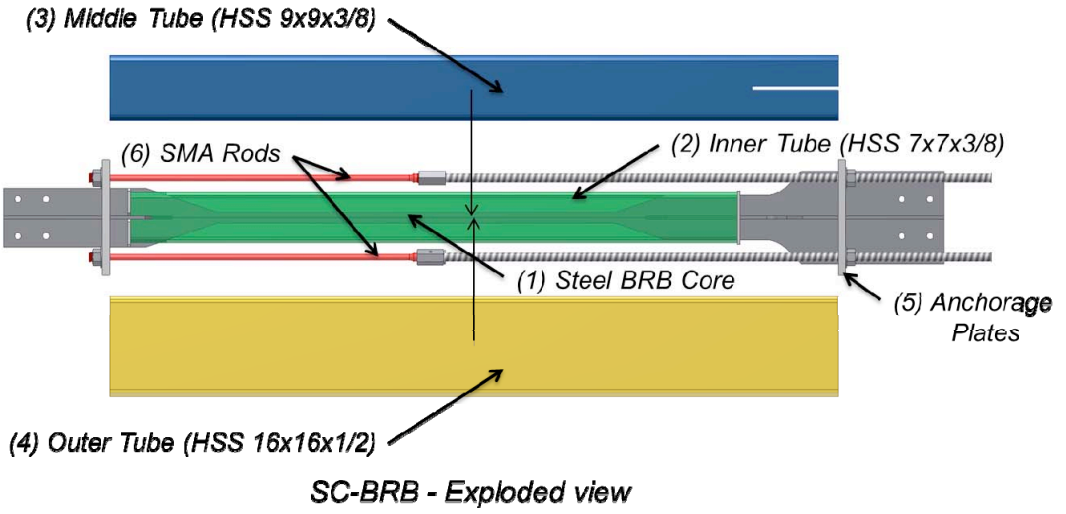


Figure 2 – SC-BRB components

The middle and outer tubes act as struts that push the anchorage plates apart as the brace deforms. As shown in Figure 3, both compression and tension brace forces cause the anchorage plates to move apart, resulting in additional SMA elongation and increasing self-centering force. The BRB core dissipates energy as it yields in tension and compression. The SMA pretension is selected to overcome the BRB yield force, including strain hardening, and thus produces self-centering.

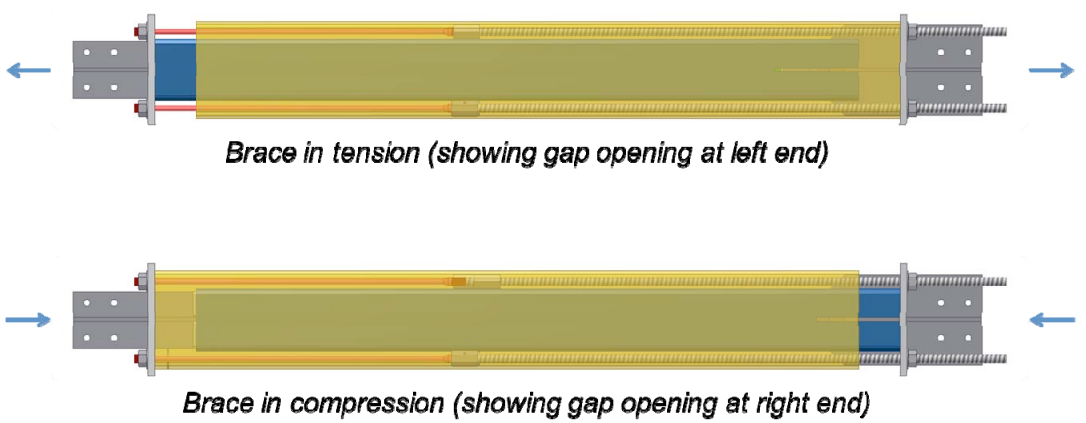


Figure 3 - SC-BRB functionality

SC-BRB DESIGN AND NUMERICAL MODELING

Preliminary analyses were conducted to examine the validity of the proposed brace. A prototype building was chosen to match a five-story BRBF design example (SEAOC/ICC 2006). Proportioning and detailing were carried out using a preliminary capacity design methodology, which will be examined and refined as the research continues. The initial design and detailing suggest that the SC-BRB can be reasonably proportioned and constructed for the design loads and geometry of this prototype building.

A numerical model was created in OpenSees (Mazzoni et al. 2009) to predict the response of the SC-BRB that was designed for the prototype building described above. The model uses gap elements to represent the contact between the tubes and the anchorage plates. The model is assembled in stages to allow for the pretensioning of the SMA (Figure 4).

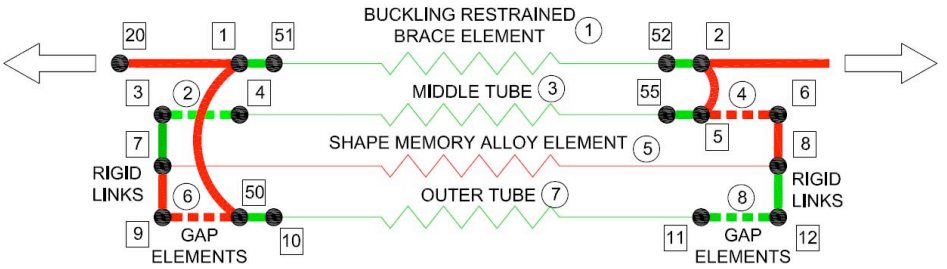


Figure 4 - Preliminary numerical model of the SC-BRB

The results of the preliminary analysis are shown in Figure 5 and Figure 6. Figure 5 illustrates the contribution of the BRB and SMA elements individually, whereas Figure 6 shows the total hysteretic response of the brace. At the end of the loading history, the brace is predicted to experience only a trivial amount of residual deformation.

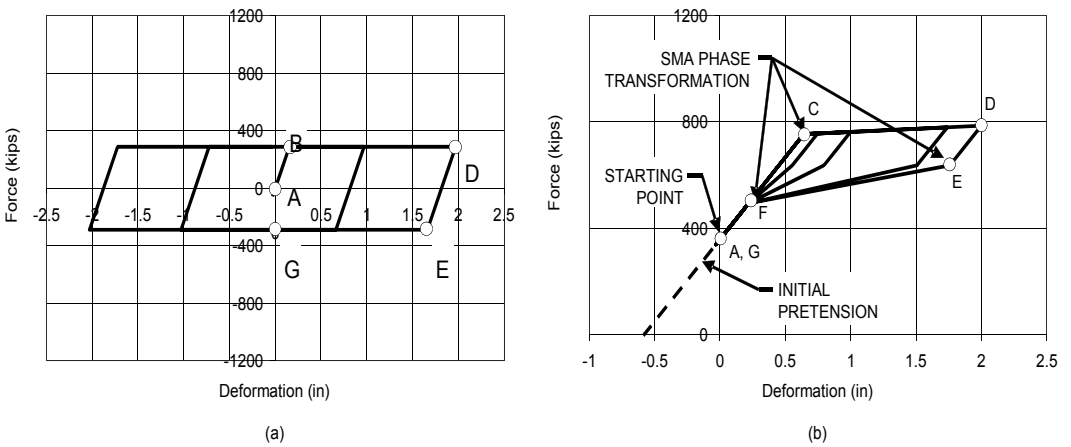


Figure 5 – Numerical simulation results demonstrating component response: (a) BRB; (b) SMA

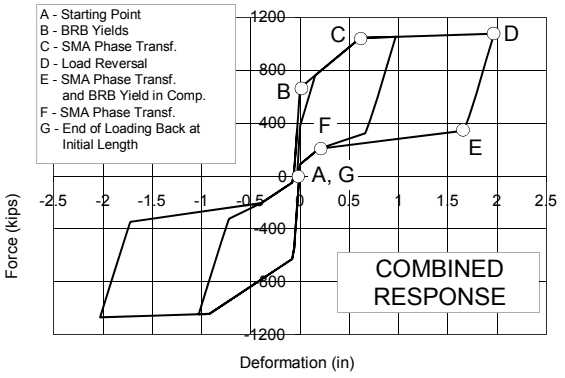


Figure 6 – Total SC-BRB response from numerical simulation

MATERIAL TESTING

A series of quasi-static cyclic tensile tests was performed on four sample specimens of NiTi SMA to measure the following mechanical properties (ASTM International 2008) of the bars that will be used in the SC-BRB:

1) Lower Plateau Strength – the value of stress at 2.5% strain during unloading
2) Upper Plateau Strength – the value of stress at 3% strain during initial loading
3) Residual Elongation – difference between strain at a stress of 7.0 MPa during loading and unloading
4) Uniform Elongation – elongation when maximum force is reached just before necking or fracture

Prior to testing, each bar was heat treated to achieve superelastic behavior in the SMA. The two variables studied in these tests were the length of time of the heat treatment and sequence of machining and heat treatment. The details of machining and heat treatment for each specimen are summarized below. All tests were performed using a 600-kip MTS uniaxial hydraulic testing frame.

Table 1 - Summary of SMA specimen heat treatment

Specimen	Time (min.)	Temp (°C)	Before/After Machining
1	30	375	Before
2	30 + 30	375	Before
3	90	375	After
4	60	375	After

Specimen Fabrication: The test specimens were proportioned according to ASTM E8 (ASTM International 2009), and had identical gage lengths and diameters. Specimens 1 and 2 were heat treated prior to machining, and specimens 3 and 4 were

heat treated after machining. Additionally, specimens 3 and 4 were threaded after heat treatment to ensure that the heat would not affect the thread dimensions. The fabrication details of each specimen are summarized in Table 1.

Loading Protocol: The specimens were tested using increasing strain cycles of 0.5%, 1.0%, 2.0%, 3.0%, 4.0%, 5.0%, and 6.0%. Figure 7 shows the loading protocol used for the test, a modified version of the testing protocol used by DesRoches et al. (2004).

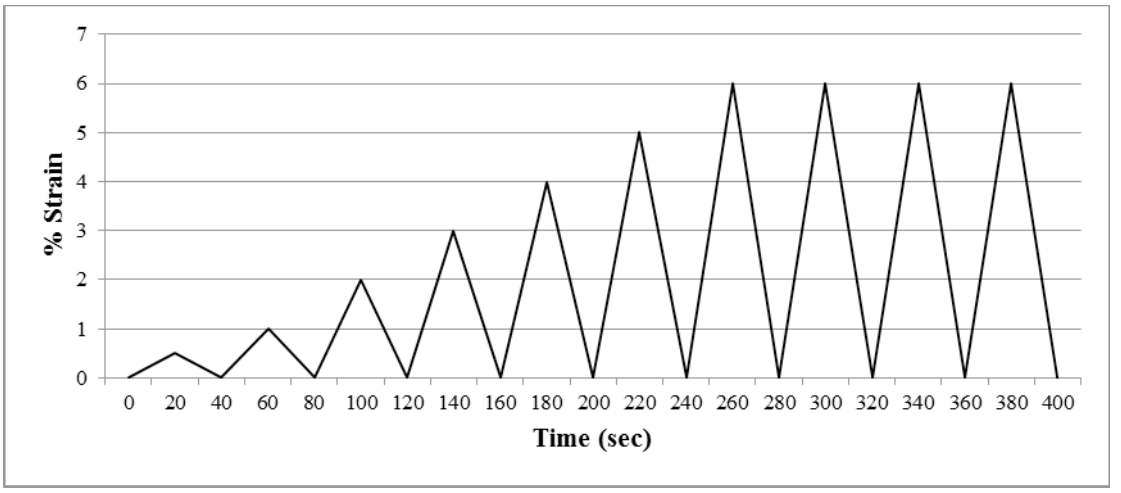


Figure 7 - Loading protocol used for cyclic testing of NiTi shape memory alloy bars

Tensile Test Results: The stress-strain curves from each specimen are presented in Figure 8 through Figure 11. Figure 8 shows that Specimen #1 had much larger residual deformation than representative tests from prior SMA research (Desroches et al. 2004) with a residual strain of approximately 3.5% after the fourth 6% cycle. Further investigation into the heat treatment process was performed by the manufacturer of the bar, and it was determined that the heat treatment performed by the manufacturer was insufficient. Therefore, the stock material for the second specimen was heat treated for an additional 30 minutes at 375° C prior to machining.

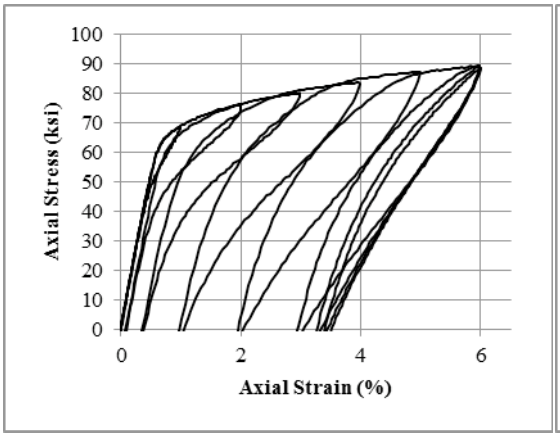


Figure 8 –Stress-strain curve for 0.75 in. diameter SMA bar (Specimen #1)

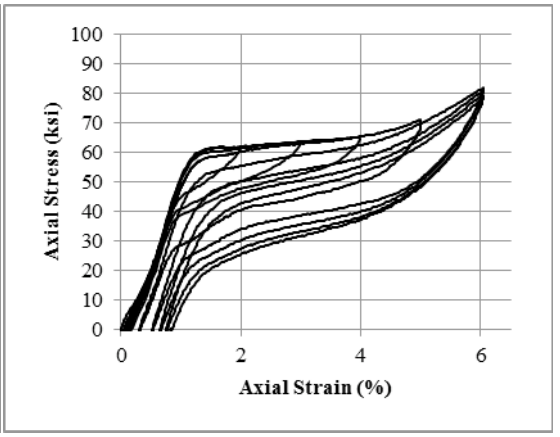


Figure 9 –Stress-strain curve for 0.75 in. diameter SMA bar (Specimen #2)

The initial cycles of testing on Specimen #2 show very little residual strain in the bar (Figure 9). After the 4% cycle, the residual elongation was only 0.20%, much lower than the 1.06% seen at the same point in the testing of Specimen #1. After the final 6% cycle, the residual elongation was 0.87%, a value much closer to reported values from prior studies (Desroches et al. 2004). There was a notable increase in the residual elongation after unloading the bar from the 5% cycle, and there was a drop in the upper plateau strength in subsequent cycles.

The initial cycles of testing on Specimen #3 show very little residual strain in the bar (Figure 10). After the 4% cycle, the residual elongation was only 0.01%, much lower than the 0.20% seen at the same point in the testing of Specimen #2. After the final 6% cycle, the residual elongation was 0.29%, a value less than that measured in the testing of Specimen #2. There was a notable increase in the residual elongation after unloading the bar from the 5% cycle, and there was a drop in the upper plateau strength in subsequent cycles. The upper and lower plateau strengths for Specimen #3 were considerably lower than those for Specimen #2.

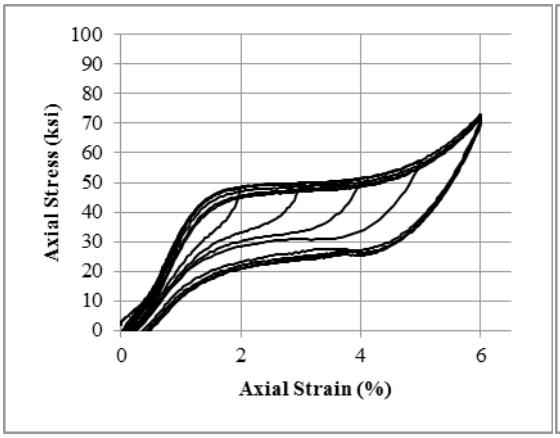


Figure 10 –Stress-strain curve for 0.75 in. diameter SMA bar (Specimen #3)

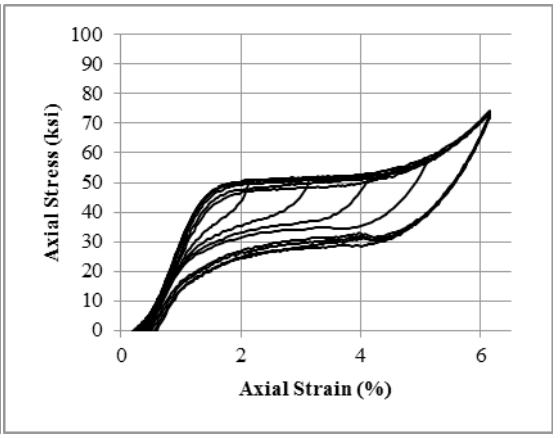


Figure 11 –Stress-strain curve for 0.75 in. diameter SMA bar (Specimen #4)

After the 4% cycle for Specimen #4 (Figure 11), the residual elongation was only 0.10%, which is higher than the 0.014% seen at the same point in the testing of Specimen #3, but lower than the 0.18% seen at the same point in the testing of Specimen #2. After the final 6% cycle, the residual elongation was 0.35%, a value that was the smallest of the four tests. Again, there was a notable increase in the residual elongation after unloading the bar from the 5% cycle, as well as a drop in the upper plateau strength in subsequent cycles. The upper and lower plateau strengths for Specimen #4 are greater than those for Specimen #3, but still considerably lower than those for Specimen #2. Table 2 summarizes the mechanical properties of all specimens tested.

Table 2 – Mechanical properties of SMA bars

Specimen	1	2	3	4
Lower Plateau Strength (ksi)	66.7	52.5	36.9	38.6
Upper Plateau Strength (ksi)	81.1	63.5	49.5	51.1
Residual Elongation (%)	6.26	0.87	0.54	0.35
Uniform Elongation (%)	9.44	6.99	6.87	9.01

CONCLUSIONS

Heat treating the bars for 60 minutes after machining resulted in the smallest amount of residual elongation. Additionally, machining the bars prior to heat treatment was easier. Strength decreased as heat treatment time increased. Since the SMA provides self-centering in the SC-BRB, control of residual elongation is very important. As a result, it is preferable to reduce the residual elongation even if it means that strength is reduced slightly. The results of the tensile tests also show that the superelastic SMA bars exhibit very little residual elongation when the maximum strain is 5% or lower. Therefore, the length of the bars in the final brace design was chosen to limit the overall strain in the SMA to less than 5%.

CONTINUING RESEARCH

Half-scale SC-BRB specimens will be tested at the University of Illinois using a 600-kip MTS uniaxial servo-controlled testing frame. The proposed loading protocol shown in Figure 12 is a modified version of the qualifying cyclic tests of BRBs given in the AISC *Seismic Provisions* (AISC 2005).

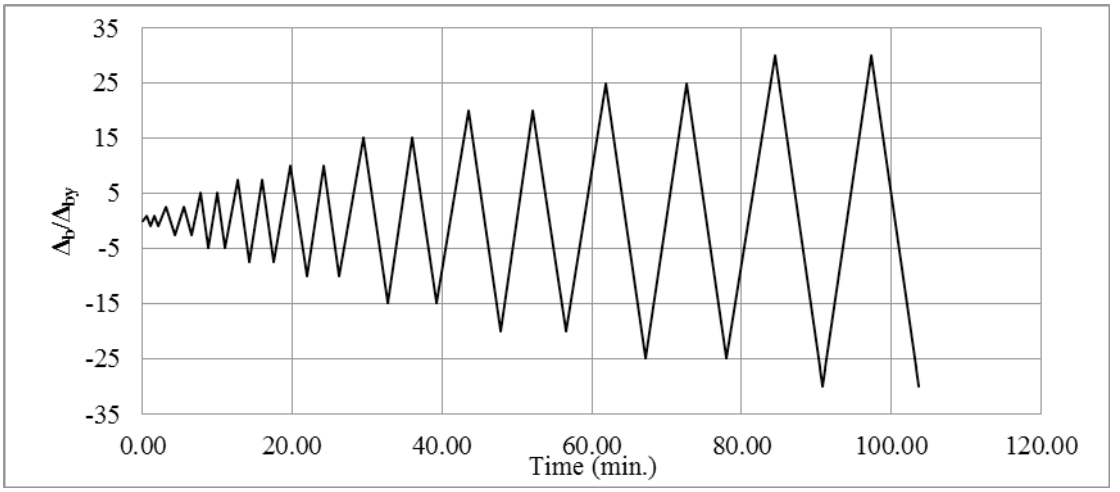


Figure 12 – Planned testing protocol for SC-BRBs

The tests will measure the performance of each brace and compare the effect of the relative pretension force to the brace core capacity. Data collected from the experimental studies will be used to validate and refine the brace numerical model,

which will be used for nonlinear dynamic system analyses. Ultimately, the results from the experimental and numerical studies will be used to develop design, detailing, and modeling guidelines for self-centering buckling-restrained braced frames.

ACKNOWLEDGEMENTS

This study is supported by the National Science Foundation through the Hazard Mitigation and Structural Engineering Program (Grant No. CMMI-0856555). The authors would like to thank SAES Smart Materials for advice on machining and heat treating the SMA, and the Newmark Structural Engineering Laboratory staff for assistance with fabrication and testing. Opinions, findings, and conclusions expressed in this paper are those of the authors and do not necessarily reflect the views of those acknowledged here.

REFERENCES

American Institute of Steel Construction (AISC). (2005). *Seismic Provisions for Structural Steel Buildings,* American Institute of Steel Construction, Inc., Chicago, Ill.

ASTM Standard E8, 2009. "Standard Test Methods for Tension Testing of Metallic Materials," ASTM International, West Conshohocken, PA, 2009, DOI: 10.1520/E0008_E0008M-09, www.astm.org

ASTM Standard F2516, 2008, "Standard Test Method for Tension Testing of Nickel-Titanium Superelastic Materials," ASTM International, Conshohocken, PA, 2008, www.astm.org

Christopoulos, C., Tremblay, R., Erochko, J., Choi, H. (2008a). "Response of 2-d and 3-d buildings incorporating buckling-restrained and self-centering bracing systems." *Proc., Annual Conference of the Canadian Society for Civil Engineering 2008 - "Partnership for Innovation", June 10, 2008 - June 13,* Canadian Society for Civil Engineering, , 2162-2171.

Christopoulos, C., Tremblay, R., Kim, H. -., Lacerte, M. (2008b). "Self-Centering Energy Dissipative Bracing System for the Seismic Resistance of Structures: Development and Validation." *J. Struct. Eng.,* 134(1), 96-107.

Clark, P., Kasai, K., Aiken, I. D., Kimura, I. (2000). "Evaluation of design methodologies for structures incorporating steel unbonded braces for energy dissipation." *Proc., Proceedings, 12th World Conference on Earthquake Engineering,* Upper Hut, New Zealand.

Desroches, R., McCormick, J., Delemont, M. (2004). "Cyclic Properties of Superelastic Shape Memory Alloy Wires and Bars." *J. Struct. Eng.,* 130(1), 38-46.

Dolce, M., and Cardone, D. (2006). "Theoretical and Experimental Studies for the Application of Shape Memory Alloys in Civil Engineering." *J Eng Mater Technol Trans ASME,* 128(3), 302-311.

Mazzoni, S., McKenna, F., Scott, M. H., Fenves, G. L. (2009). "Open system for earthquake engineering simulation user command-language manual." <http://opensees.berkeley.edu/OpenSees/manuals/usermanual/> (08/31/2009).

McCormick, J., Tyber, J., DesRoches, R., Gall, K., Maier, H. J. (2007). "Structural Engineering with NiTi. II: Mechanical Behavior and Scaling." *J. Eng. Mech.,* 133(9), 1019-1029.

Merritt, S., Uang, C. M., Benzoni, G. (2003). *Subassemblage Testing of Star Seismic Buckling-Restrained Braces,* University of California, San Diego, La Jolla, CA.

Structural Engineers Association of California, and International Code Council (SEAOC/ICC). (2006). *2006 IBC Structuralseismic Design Manual,* Structural Engineers Association of California, Sacramento, Calif.

Tremblay, R., Lacerte, M., Christopoulos, C. (2008). "Seismic Response of Multistory Buildings with Self-Centering Energy Dissipative Steel Braces." *J. Struct. Eng.,* 134(1), 108-120.

Zhu, S., and Zhang, Y. (2008). "Seismic Analysis of Concentrically Braced Frame Systems with Self-Centering Friction Damping Braces." *J. Struct. Eng.,* 134(1), 121-131.

A Celebration of Structure as Architecture - The Cathedral of Christ the Light

Mark Sarkisian[1], Peter Lee[2], Eric Long[2]

[1] PE, SE, Director, Skidmore Owings & Merrill LLP, San Francisco, CA
[2] PE, SE, Associate Director, Skidmore Owings & Merrill LLP, San Francisco, CA

ABSTRACT

The Cathedral of Christ the Light is an artistic celebration of modest and common building materials used to transform a site on the north end of Lake Merritt in Oakland California. The structure uses the most advanced geometric and scientific approaches to created a building that satisfied the Diocese of Oakland's need to construct a new cathedral with the service life of at least 300 years; a request that was not unexpected considering the venerable cathedrals of the Catholic Church that have survived for centuries. The project site exists only 4.6 km from the Hayward Fault, one of the most active seismic faults in the world, making the request substantially more challenging. Ground motions expected at the site could result in an earthquake of magnitude 7.0 or more on the Richter Scale.

The approach to design embodies lightness (both visually and structurally) and luminosity, hence its name, The Cathedral of Christ the Light. The structure is defined by sacred geometries and designed for lightness by using seismic isolation to manage ground motions and reduce the demand on the superstructure during an earthquake. It is the light that transforms the structure and its material throughout the day creating what the cathedral's lead architect and SOM Design Partner Craig Hartman calls a space of "ephemeral lightness" with a "primordial connection to the earth." In developing the design, Hartman thought that "the cathedral must be in the architectural language of our time. The Catholic Church has historically applied the most advanced architectural thinking to create architecture that illuminates, inspires and ennobles the human spirit."

The cathedral incorporates a highly innovative use of natural, yet ordinary, materials with an ethos of sustainability. Glued-laminated timber from sustainable forests, exposed reinforced concrete using replacement slag and fly ash, recycled high-strength steel, aluminum, and glass create the symbolic form.

The 1,350-seat cathedral, located on the northern edge of Lake Merritt, is the centerpiece



Figure 1. The Cathedral of Christ the Light

of a 224,000-square-foot complex with a complement of facilities that includes a mausoleum, a conference center, administrative offices, bishop and clergy residences, a bookstore, a café, and community-serving ministries. A landscaped public plaza, accessible from all directions, firmly links the center with the city's commercial downtown and surrounding neighborhoods. As a whole, the structure honors its religious and civic obligations to both the Catholic Diocese and the city of Oakland.

SACRED GEOMETRY

Vesica Piscis, or "vessel of the fish," is important to early Christian symbolism and the language of sacred geometry. Formed of two interpenetrating circles of the same diameter, the shape represents the fusion and reconciliation of opposites. These interpenetrating circles are related to one another through the square roots of 2, 3, and 5, the first three digits of the Fibonacci Sequence (other than unity). The height and width of the shape resulting from the intersecting circles are related by the square root of 3. Thus, the height or the longitudinal length of the Cathedral is equal to the diameter times the square root of 3 or 1.73205, and the width or the transverse length of the Cathedral is equal to the longitudinal length divided by the square root of 3. The geometric and mathematical applications of the resulting shape are the same as those commonly occurring in nature and in the order of the universe itself.

The vesica piscis conceived in plan is translated three dimensionally into the Cathedral's superstructure. Two intersecting spheres define the interior volume, while creating truncated vesici at the Alpha (beginning and the first letter of the Greek alphabet) and Omega (ending/everlasting and the last letter of the Greek alphabet) Windows. The architecturally exposed reinforced concrete reliquary walls used to create both the inside and outside of the structure are formed by overlapping circles with the same radii, simply offset in plan. The interior spherically-defined volume supported on the inside face of the reliquary wall is enclosed with a conical form supported on the outside face of the reliquary wall. The conical form, if continued to its apex, would close, but is instead truncated symbolically referring to the Cathedral's openness to the sky and, by extension, the heavens.

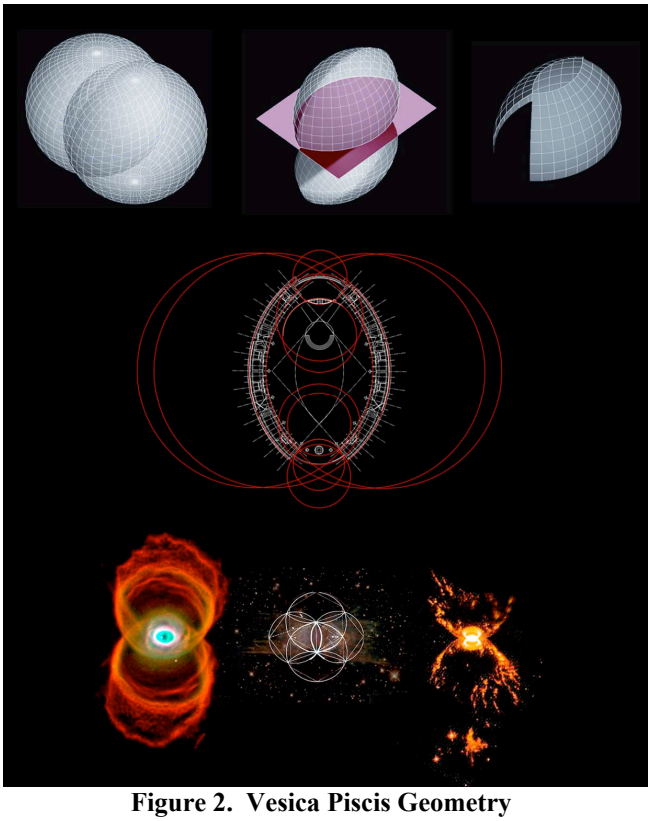


Figure 2. Vesica Piscis Geometry

DELICACY OF STRUCTURE

Drawing on the tradition of light as a scared phenomenon, Design Partner Craig Hartman envisioned the Cathedral to transform throughout the day as changing patterns of light interacted with the structure. In order to accommodate both the design concept and the potential seismic motion caused by nearby faults, a delicate structure was required to enable the play of light within the sanctuary and manage ground motions reduce the demand on the superstore during an earthquake. The main Cathedral superstructure consists of a hybrid structural system composed of reinforced concrete, pre-fabricated glued-laminated wood timber members, high-strength structural steel rods paired with glued-laminated wood compression struts, and a steel friction-pendulum seismic base isolation system.

Curved, tapered glued-laminated wood timber rib members form the framework of the sanctuary superstructure. A total of 724 closely spaced glued-laminated timber "louver" members interconnect and provide lateral bracing for inner rib members. The louvers also serve an integral role in the casting of natural daylight into the Sanctuary space. Louver orientation and widths change over the height of the structure. Louvers are wider with steeper angles near the base and narrower with flatter angles near the top. Light reflects off of the upper louver surfaces and illuminates lower surfaces of neighboring louvers. The size of the louvers directly corresponds to the structural demand in forming the inner shell of the sanctuary. Other than nighttime events, the Cathedral is lit entirely with natural daylight.

Inner curved rib members are 10-3/4 inches wide and vary from 30 inches deep at the base to 19-5/8 inches deep at the top connection to the oculus roof framing. These ribs form a spherical shape in plan and section. Exterior sloping straight glued-laminated outer rib members 10-3/4 inches wide and 15 inches deep form a conical shape in plan and are aligned on a radial geometry with inner ribs. A total of 13 sets of inner and outer vertical glued-laminated ribs form each half of the superstructure. Gravity loads are resisted by a total of 52 vertical glued-laminated wood timber elements.

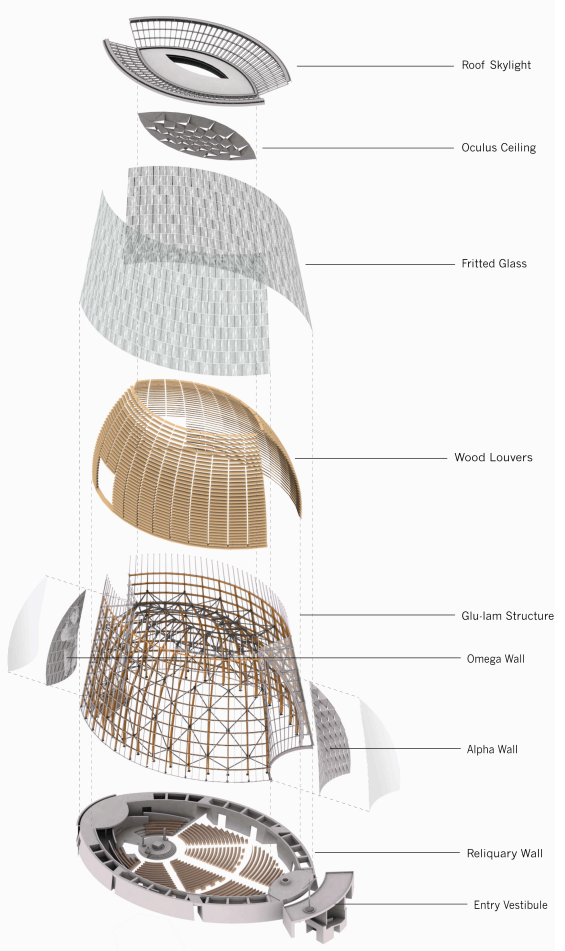


Figure 3. Model of main Cathedral showing primary superstructure elements

High-strength steel rods and tapering, turned glued-laminated wood struts interconnect the inner and outer ribs forming a hybrid steel-timber braced frame structure, which provides stability under both vertical and horizontal loading. Steel rods are designed to resist both wind and seismic forces. A total of 224 steel rods and 104 glued-laminated wood timber compression struts provide redundancy and reserve ductile capacity in the lateral load resisting system. The high-strength steel rods and glued-laminated wood struts are connected to the glued-laminated wood ribs with hidden steel knife plates and steel dowels from the backside of the ribs.

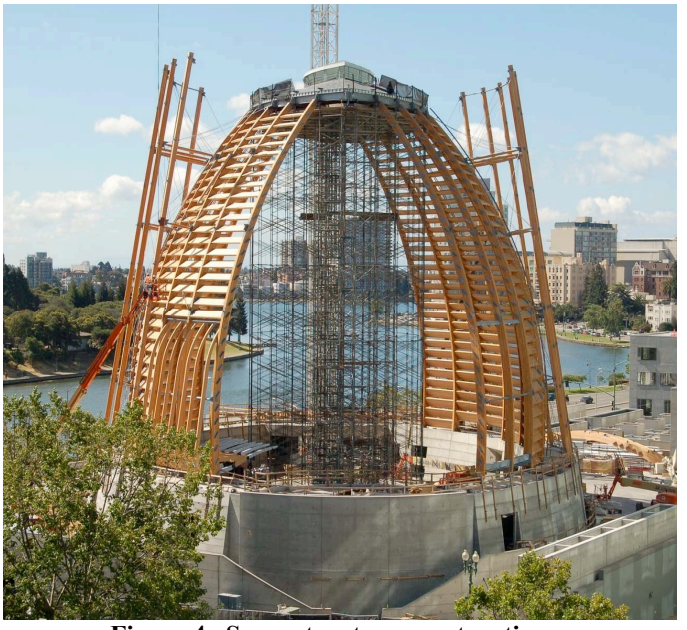


Figure 4. Superstructure construction



Figure 5. Interior View from altar looking south

Symmetric about the longitudinal centerline axis of the sanctuary, two sets of inner and outer ribs support the oculus roof structure comprised of structural steel framing and metal roof deck. In addition, the steel framing acts as a compression ring and diaphragm interconnecting the hybrid steel-timber braced frame elements from all sides of the Cathedral at the roof elevation.

Horizontal tubular steel members provide lateral bracing for exterior outer ribs and provide support for the exterior wall system. Structural steel and steel pin / bolted connections are used to connect primary structural members. Tubular structural steel framing is also used to support the north, “omega”, and south, “alpha”, end walls of the main Cathedral. These glazed end walls are supported by the roof compression ring, end glue laminated timber ribs, and reliquary wall reinforced concrete elements. All hybrid frame timber and steel elements and their connections are shop welded and hot-dipped galvanized allowing for field bolted erection.

The superstructure system of timber and structural steel is supported by 14 in. thick cast-in-place ductile reinforced-concrete reliquary walls. The architecturally exposed concrete reliquary walls extend 15 ft above the sanctuary floor and provide both gravity and lateral load support for the superstructure above. The walls are curved in plan and slope in section, and they contain highly articulate openings or "carvings" for doorways into side chapels, speakers, niches, and other programmatic elements. The reliquary walls were constructed with high density overlay plywood formwork and self-consolidating concrete, allowing for the natural formed finish to serve as the permanent architectural appearance. The base of the reliquary walls are interconnected by a horizontal two-way 12 in. thick reinforced-concrete diaphragm slab at the sanctuary floor. The top of the reliquary walls are interconnected by reinforced-concrete framing beams and slabs providing support for the 4-inch diameter steel pin connections to the glued-laminated wood timber ribs above.

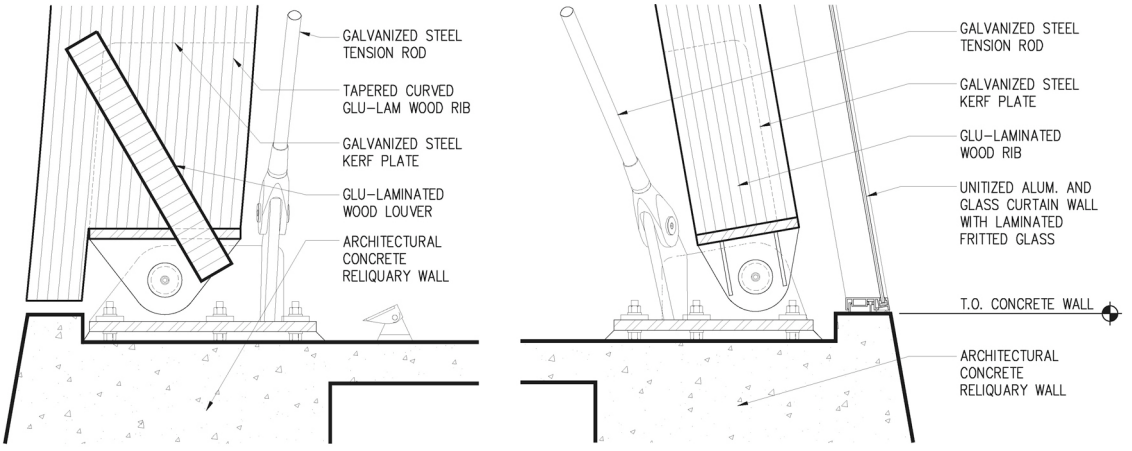


Figure 6. Detail of interior timber louvered wall and exterior glazed wall at base



Figure 7. Reliquary wall formwork construction and finished wall

BASE ISOLATION SYSTEM

The reliquary walls and sanctuary floor diaphragm are supported by a steel friction pendulum seismic base-isolation system provided by Earthquake Protection Systems, Inc., of Vallejo, California. Twenty isolators are located directly beneath the reliquary walls with 16 additional isolators located beneath the sanctuary diaphragm floor slab for a total of 36 isolation bearings provided throughout. The double concave friction pendulum-type isolation bearings provide 30 in. of displacement capacity under the expected maximum capable earthquake (MCE) events.

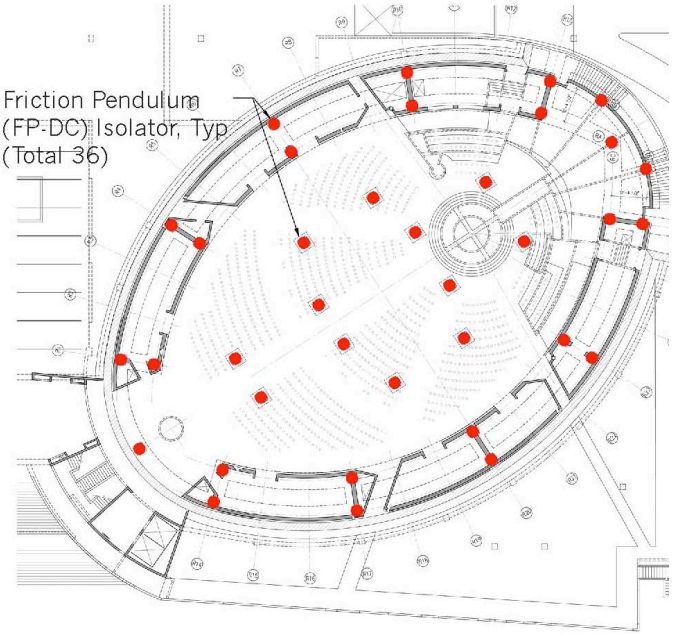


Figure 8. Level 1 Plan / Isolator Layout

The typical steel bearing assembly is 47 inches square in plan and 12.5 inches high. A bounded dynamic non-linear analysis to capture extremes of seismic performance is undertaken for analysis and design. Bounds of sliding friction are established based on a range of expected vertical loading conditions defining the seismic isolation system design properties. The analysis is then "bounded" by the lower bound friction (4.7%) to calculate maximum displacement demands under MCE, and by the upper bound friction (7.7%) to calculate maximum force demands under DBE. From analysis modeling, bearing design criteria was then established for both prototype and production bearing testing for typical bearing types. Weighted average values of friction are then established for both lower and upper bound coefficients of friction. A free body diagram (Fenz & Constantinou, 2006) of the articulated slider on the upper concave surface in the deformed configuration at horizontal displacement illustrates equilibrium in both the horizontal and vertical directions including the eccentric effects of both gravity and lateral overturning loads.

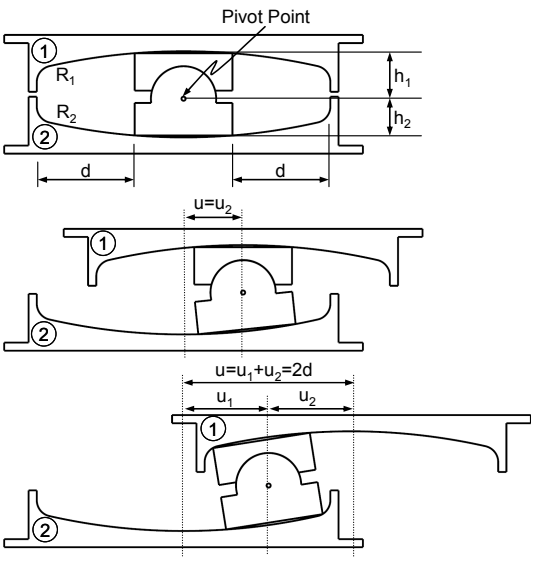


Figure 9. Section through isolator at Various stages of motion (Fenz & Constantinou, 2006)

The substructure below the seismic isolation system consists of a series of 12 in. thick ductile reinforced-concrete bearing walls located below the sanctuary within the mausoleum and under the perimeter reliquary wall supports. These walls extend to a 5 ft thick reinforced-concrete mat slab and perimeter basement wall foundation. The top of the mausoleum walls as well as the walls located directly below the sanctuary reliquary walls are interconnected with a continuous 6 in. thick reinforced-concrete diaphragm. This diaphragm is located directly below the isolation plane. The cellular structure of the mausoleum has an integral role in supporting the isolation plane.

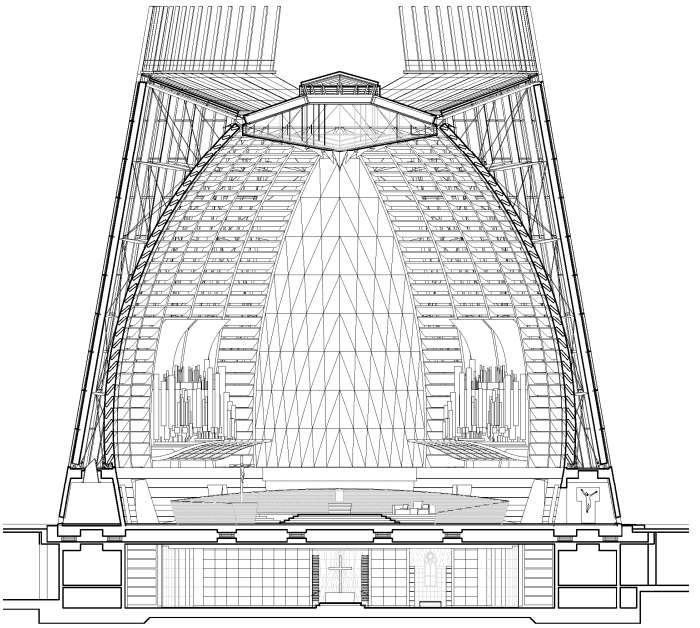


Figure 10. Transverse section through main Cathedral superstructure and substructure

EXTERIOR ENCLOSURE

The exterior envelope is defined by 2 custom designed enclosure systems. The primary system consists of 1,028 shop-fabricated unitized curtain wall panels. Each panel is a parallelogram frame and contains two layers of ¼" clear glass, laminated together with a 0.030 PVB translucent interlayer. A custom designed ceramic frit coating is baked on the inner surface of the layer of glass. This translucent frit coating modulates daylight within and captures the natural shifting of light throughout the day. The panels are nominally 10'-3" in height and vary in width from bottom to top based on the conical geometry of the outer exterior wall surface. The extruded aluminum mullions extend past the top of the enclosure to give a sense of verticality to the tapering conical form. The expressed mullions are clad in stainless steel. Multiple glass assemblies were reviewed in the design phases. Laminated glass was selected for increased acoustic performance. Each unitized curtainwall panel is supported from a tubular steel structural subframe. The unitized system frames and joinery are designed and sized to accommodate seismic movement and return to their original position without damage after a seismic event.

The South and North enclosure walls are named the "Alpha" wall and "Omega" wall respectively. The variable plan dimension from base to top and the segmented curved jamb conditions resulted in a design of varying sizes of triangular shaped clear laminated glass. The triangular glass lites are supported with stainless steel point fittings with universal joints to accommodate the geometrical

configuration. Triangular aluminum panels mounted on the interior side form the petal-shaped Alpha Window, which diffuses light above the Cathedral's entrance. The Omega Window rises behind the altar. Mounted on the interior side of the Omega wall enclosure are triangular aluminum panels perforated with 94,000 laser-cut holes. As points of light shine through the holes in varying levels of brightness, a 58-foot-tall image of Christ is visible from the sanctuary interior. The image is displayed in varying levels of contrast as light naturally shifts from bright sunlight, to overcast shadows, and to interior lighting at night.



Figure 11: Interior view of Omega Wall

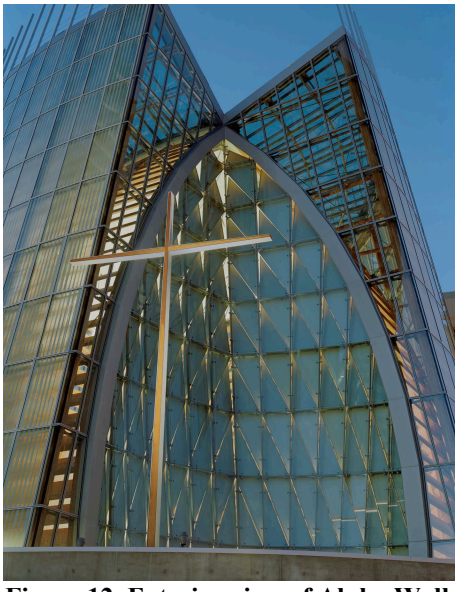


Figure 12. Exterior view of Alpha Wall

LONGEVITY AND DURABILITY OF GLUED-LAMINATED TIMBER

While wood is an important unifying architectural, structural and spiritual design element of the Cathedral structure and space, consideration of its use as a primary structural element in the Cathedral's glued-laminated superstructure was of tantamount importance with respect to the Oakland Diocese's desired long-term performance objectives of the Cathedral.

Longevity and durability design considerations in the use of glued-laminated wood timber for the project included historical development and state-of-the-art standards and codes, durability and exposure to ultraviolet light, effects of temperature and relative humidity, fire resistance, structural design factors dependent on conditions of use, wood species, structural redundancy, protective treatments, as well as, monitoring and long-term maintenance issues. Glued-laminated wood timber construction has had a long history of successful and economical implementation in the design of structures with significant advancements made in the design, production and fabrication technology over the last 30 years.

It is expected that the glued-laminated wood timber construction will see no detrimental effects as a result of exposure to ultraviolet light other than a natural darkening in the color of the wood material over time. Wood timber's natural cellular

structure of lignin and cellulose fibers make it an excellent insulating material that is also highly resistant against acids, alkali, salts and most other chemical substances.

Although the main Cathedral volume is enclosed by weather-tight exterior walls and roof system, fluctuation of air temperature and relative humidity will vary depending on the level of insulating materials, infiltration, thermal mass, ventilation, and type of heating and air conditioning systems employed. Within the main Cathedral volume, for an average sustained peak ambient air temperature of 80 deg F and a relative humidity range of 60 to 65 percent, wood will reach equilibrium at a wood moisture content of 11.7 percent. This is well below a 20 percent threshold of potential formation of decay, and therefore, there will be no impact on the primary glued-laminated wood members. The dimensional stability of wood is considered detrimental only when affected by large ranges and variations of both temperature and relative humidity that are sustained for longer periods of time under service conditions. For a controlled environment within the main Cathedral volume that allows the glued-laminated wood timber to reach equilibrium at a wood moisture content of 8 to 12 percent and peak extreme variations in the range of 4 to 6 percent, it is expected that the dimensional stability of the glued-laminated wood timber construction will be sufficiently maintained without adverse conditions.

The glued-laminated heavy timber construction is inherently resistant to fire due to the natural structure and insulating properties of wood. Under fire load, the charring of the exterior surface of wood acts to create an insulating layer that protects the core of the structural element and can achieve a minimum One Hour Fire Resistive Timber Construction fire rating.

The large majority of glued-laminated wood timber construction in the United States is typically comprised of various softwood species. Douglas Fir was selected as the most appropriate for the project because of its production availability on the West Coast, economical considerations, strength, stability, consistency and natural architectural appearance.

The reliability of wood timber structures and their connections rely on proven design standards and methods which include “condition of use” design factors that account for short-term and long-term load duration, volume, curvature, and beam/column stability.

SEISMICITY

Because the cathedral features a bracing system that relies on steel tension—which under the 2001 CBC’s prescriptive code for an occupied structure in Zone 4 would have limited the height of the church to just 65 ft.—the building had to be considered an “undefined” structure under the 2001 CBC. This meant that the design team had to provide rigorous proof that the structure has the strength and ductility to resist some of the strongest potential ground motions in the world. It was an unavoidable challenge because the tension members were critical to the design, providing a three-dimensional tie between the inner curved glued-laminated members and the outer straight glued-laminated members. These members maximize structural efficiency and provide superior performance even when subjected to the most severe seismic motion.

To prove the structural performance of this system, the design team utilized advanced computer modeling techniques to capture the behavior of seismic isolation combined with the glued-laminated superstructure interconnected with pre-stressed high-strength steel rods and timber compression struts supported on a base of reinforced-concrete reliquary wall and sanctuary floor structure. In addition, additional nonlinear analysis modeling was used to assess the unique structure's ability to resist strength and ductility demands beyond the maximum-considered earthquake levels.

To develop the cathedral's the complex superstructure, a full 3-dimensional nonlinear structural analysis model was developed using the SAP2000 computer analysis program, manufactured by Computers & Structures, Inc., in Berkeley, California. For final analysis, the base-isolated superstructure and the substructure were modeled separately using tri-directional response history analysis. Additionally, both isolated superstructure and substructure models were analyzed and designed to meet minimum 2001 CBC equivalent static provisions.

Two levels of site-specific probabilistic earthquake hazard ground motion criteria—consistent with CBC requirements—were provided by the project geotechnical engineer, Treadwell & Rollo, Inc. The seismic performance objectives were defined for both the 2001 CBC's "design basis earthquake" (DBE) and the "maximum capable earthquake" (MCE) levels of ground shaking. The lower bound DBE is defined as an event with a 10 percent chance of exceedance in 50 years based on a 475 year return period with a peak ground acceleration of 0.683g. The upper bound MCE is defined as an event with 10 percent chance of exceedance in 100 years based on a 972 year return period with a peak ground acceleration of 0.827g.

These performance objectives were used to further define expected levels of performance with expected levels of seismic ground motions. In consideration of the important design aspects of the cathedral—including the location of the site in close proximity to two so-called "near faults," the uniqueness of the design of the superstructure, and the use of a seismic isolation system to achieve enhanced seismic performance objectives—the design team took particular care in the development of site-specific spectra with input from the seismic isolation peer review panel for the project with an emphasis on state-of-the-art ground motion criteria which addressed proximity to near-faults, directivity effects, depth to rock, as well as, vertical ground accelerations.

Near-fault and directivity effects were incorporated in the development of horizontal fault normal, fault parallel and fault average site-specific response spectra at both the DBE and MCE levels. For both the DBE and MCE levels, a suite of seven pairs of horizontal fault normal and fault parallel acceleration time history ground motions were "matched" to the site-specific horizontal fault normal and fault parallel response spectra. It should be noted that the use of fault normal and fault parallel site-specific response spectra to address fault directivity and other near-fault directionality issues is not addressed explicitly by the 2001 CBC. The 2001 CBC assumes that site-specific spectra is independent of fault directionality and provides near-fault factors based on proximity to faults.

Because vertical site-specific response spectra were also required for this project under the 2001 CBC, a suite of seven vertical acceleration time history ground

motions were generated by the geotechnical consultant, Treadwell & Rollo, Inc. The vertical acceleration records were also scaled to match the site-specific vertical response spectra at both the DBE and MCE levels.

The non-linear dynamic time history analyses for the main cathedral superstructure was undertaken using methodologies from a 2003 study, "Earthquake Probabilities in the San Francisco Bay Region: 2002–2031," that was developed by the Working Group on California Earthquake Probabilities, a comprehensive analysis lead by the U.S. Geological Survey and involving input from a broad group of geologists, seismologists, and other earth scientists representing government, academia, and the private sector. For the North Hayward Fault segment, in particular, the seismic source segments and slip rates were considered. The spectrally matched DBE and MCE fault normal and fault parallel ground motion response histories were rotated and applied with respect to the primary transverse and longitudinal axis of main cathedral.

ENHANCED SEISMIC PERFORMANCE

For the main Cathedral superstructure, the owner elected to provide "enhanced" seismic performance objectives. An "enhanced" seismic performance objective provides better performance, or lower risk, than minimum "life-safety," or "collapse prevention" objectives of the CBC. This enhanced seismic performance is achieved by employing a seismic base isolation system and limiting the response of superstructure and substructure elements to achieve elastic behavior under the DBE with negligible structural damage, and, essentially elastic behavior under the MCE with minimal structural damage. To ensure elastic behavior under the DBE with negligible structural damage, the isolated superstructure was designed using maximum force demands calculated based on maximum stiffness (upper bound friction) of the isolation system and R_I=1. The superstructure drift was limited to $0.010/R_I = 0.01$ vs. a CBC limit of $0.020/R_I = 0.02$. To ensure essentially elastic behavior under the MCE, ductility demands were limited to be less than 1.0 and the superstructure drift was limited to $0.020/R_I = 0.02$.

Non-structural components and exterior wall elements are designed and detailed to accommodate the MCE movement without damage or permanent deformation. Nonstructural exterior wall, roof enclosure and interior components were designed for the DBE and MCE force levels, including peak horizontal and vertical accelerations to a life-safety criterion where limited component damage without failure may be expected.

WIND

Under the CBC's design wind loads, the base-isolated main cathedral superstructure is expected to provide stability to resist wind loading and to provide sufficient stiffness—and minimum friction—to resist maximum resultant wind loads at the base of the structure to resist potential sliding of the superstructure at the seismic isolation plane.

In considering the effects of wind, the site was modeled including a 1,200 ft. radius environment with 285 pressure taps to assess the exterior wall cladding pressures. Pedestrian level wind tunnel studies were also conducted along with an estimation of the base resultant forces that included base shears, overturning moments, base torques, load case combinations, and the dynamic effects of wind gusts. Rowan Williams Davies & Irwin Inc., of Guelph, Ontario, performed wind tunnel tests that among other factors, examined a 50-year fastest-mile wind speed of 70 mi/h.

SUMMARY

The cathedral honors the devotion and craftsmanship that unifies the world's great religious landmarks, using advanced technologies to achieve a luminous and evocative architecture with modest materials while minimizing the building's ecological footprint. The thermal mass of the cathedral's base—made of resource-conserving slag and fly-ash concrete—helps to efficiently heat and cool the occupied, lower strata of the interior volume. The Diocese challenged the design team to create a building for the ages. Through the highly innovative use of renewable materials and advanced seismic techniques, including base isolation, the structure has been designed to withstand a 1,000-year earthquake while using minimal energy and natural resources. As a result, the Cathedral of Christ the Light will endure for centuries rather than decades.



Figure 13. The Cathedral of Christ the Light

REFERENCES

California Building Standards Commission. (2001). *2001 California building code*, Sacramento, California.

Fenz, D. Constantinou, M. (2006). "Behavior of double concave friction pendulum bearing", *Earthquake Engineering and Structural Dynamics*, Vol. 35(11), 1403-1424.

International Conference of Building Officials (ICBO). (1997). *Uniform building code*, Whittier, California.

Performance-based Seismic Evaluation of Ping An International Finance Center

Authors: Dennis C.K. Poon[1], Ling-en Hsiao[2], Yi Zhu[3], Steven Pacitto[4], Steve Zuo[5] Torsten Gottlebe[6], Rohit Srikonda[7]

[1]PE., Managing Principal, Thornton Tomasetti, Inc., dpoon@thorntontomasetti.com
[2]Senior Principal, Thornton Tomasetti, Inc., lhsiao@thorntontomasetti.com
[3]MSSE., Principal, Thornton Tomasetti, Inc., yzhu@thorntontomasetti.com
[4]PE., Principal, Thornton Tomasetti, Inc., spacitto@thorntontomasetti.com
[5]PE.,Vice President, Thornton Tomasetti, Inc., szuo@thorntontomasetti.com
[6]Associate, Thornton Tomasetti, Inc., tgottlebe@thorntontomasetti.com
[7]MSCE, Senior Engineer Thornton Tomasetti, Inc., rsrikonda@thorntontomasetti.com

Thornton Tomasetti, Inc., 51 Madison Ave, New York NY 10010, Tel: 917-661-7800

ABSTRACT

This paper discusses the analysis procedure adopted for performance evaluation of Ping An International Finance Center in Shenzhen, China. Upon completion, the 115 story tower 660 meters tall will become the world's second tallest building and tallest building in China. The selected structural system consists of a composite concrete core, seven exterior double layer belt trusses, four sets of steel outriggers, eight super columns and super diagonal braces between super columns.

Given the scale and importance of this building, a rather sophisticated evaluation of seismic performance during a rare earthquake (2% probability in 50 years or 2475 year return period) was performed. Two synthetic and five recorded ground motions were selected for the nonlinear time-history analysis. These ground motions were scaled to meet the provisions in China Seismic Code; BG50011-2008. The performance levels for immediate occupancy, life safety and collapse prevention were set based on ASCE 41-06 "Seismic Rehabilitation of Existing Buildings" (2006). Complex 3D computer models with geometric and material nonlinearities were generated for nonlinear dynamic time-history analyses.

The detailed performance assessments of main structural elements such as coupling beams, core walls, super columns, outriggers, belt-trusses and super-diagonal braces are presented in this paper.

Introduction

Located in Shenzhen, Peoples' Republic of China, the Ping An International Finance Center Tower will become the world's second tallest building and the tallest in China, at 660 meters. This building is a 115 story office tower consisting of offices, support facilities, a conference center, retail and parking. The building has a total gross floor area of 385,000 square meters plus a basement area of 77,000 square meters. The project also includes a steel-framed 11-story podium with high-end shopping arcades, restaurants and roof-top cafes.



Figure 1, Rendering of Ping An Tower (Courtesy of KPF)

Structural System

The selected structural system consists of a reinforced composite concrete core with steel outriggers connecting to eight composite super-columns at four levels as shown in Figure 3.

The exterior frame is composed of seven double layer belt trusses located at the mechanical and refuge floors as shown in Figure 2: Main Lateral Force Resisting System and Figure 4: Belt Truss. The exterior belt trusses are connect to a super diagonal at each exterior face of the building.

Core wall thicknesses range from 1500mm at the base to 400mm at the top. Super column plan dimensions range from 6.0m by 3.2m at the base to 2.9m by 1.4m at the top. The main lateral force resisting system is designed for a 100 year return period wind (Strength limit state) and 50 year return period wind (Serviceability limit state) based on wind loads determined by wind tunnel testing done by RWDI, Ontario, Canada. Based on the current China Seismic Code (GB50011-2008), the Tower will be designed for different performance goals under three levels of seismic hazard:

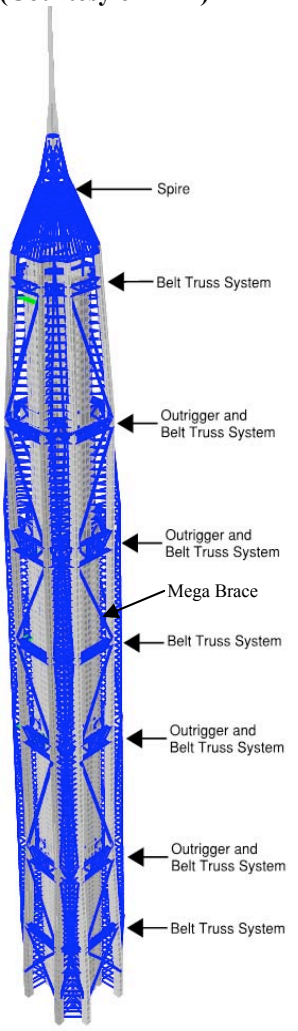


Figure 2: Main Lateral Force Resisting System

- Elastic Stage I: “No damage” under Frequent Earthquake (63% probability of exceedance in 50 years).
- Elastic Stage/Plastic II: “Minor Damage, but Repairable” under Moderate Earthquake (10% probability of exceedance in 50 years).
- Plastic Stage: “No Collapse” under Severe Earthquake (2% probability of exceedance in 50 years).

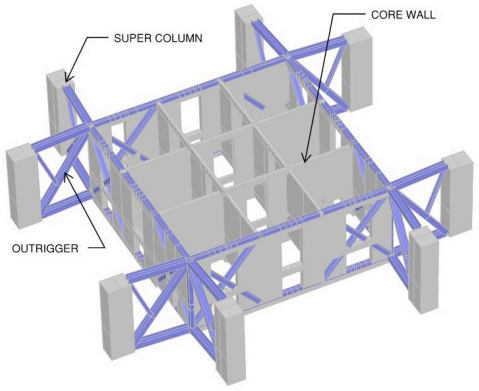


Figure 3: Outrigger, Super Column & Core Wall

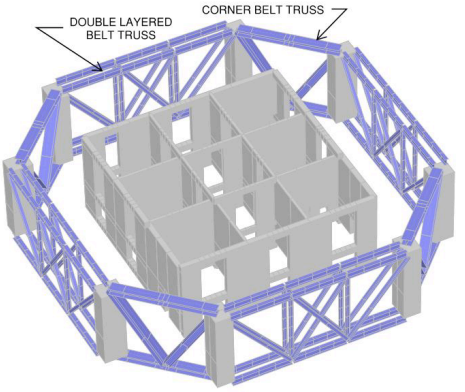


Figure 4: Belt Truss

Seismic Evaluation Process

During the design development phase of the project, while the building was being designed for 50 year (for serviceability checks), 100 year wind (times 1.4 load factor for strength check) and frequent and moderate earthquakes, a seismic evaluation process was started to study the behavior of various structural members under a severe earthquake.

The objective of this performance based seismic evaluation was to verify the inter-story drift demand of the structure, shear demand in the core and performance of link beams, core wall, super column, belt truss, outrigger and super diagonals under a severe earthquake. For this purpose, a three dimensional direct integration nonlinear time-history analysis was performed in PERFORM 3D software.

Analytical Model

Complex analytical models with detailed material and geometric nonlinearities (P-Δ effects) were generated in PERFORM-3D; a CSI Product. The modeling parameters for nonlinear response were in accordance with ASCE 41. Material characteristics were based on the China Building Code. All of the elements that are part of the main lateral force resisting system were modeled. Core wall elements and super columns were modeled as wall fiber elements. Outriggers were defined as frame elements with nonlinear fibers. Strains in these fibers can be monitored at any time-step of the analysis to evaluate member performance. Coupling

beams were modeled as frame elements with plastic hinges at both ends. Nonlinear behavior of these plastic hinges was defined using moment-curvature curves obtained from XTRACT (Imbsen). Belt trusses, chevron braces, mega braces and moment frame beams seen in Figure 5 were assumed to remain elastic. For each set of ground motions, these elements were checked to verify the assumption.

The seismic weight was calculated as $W = D_{exp} + L_{exp}$, where, D_{exp} and L_{exp} are realistic expected dead and anticipated realistic live loads (50% of total live load), respectively. Floor mass was assigned as a lumped mass and torsional mass on each floor diaphragm.

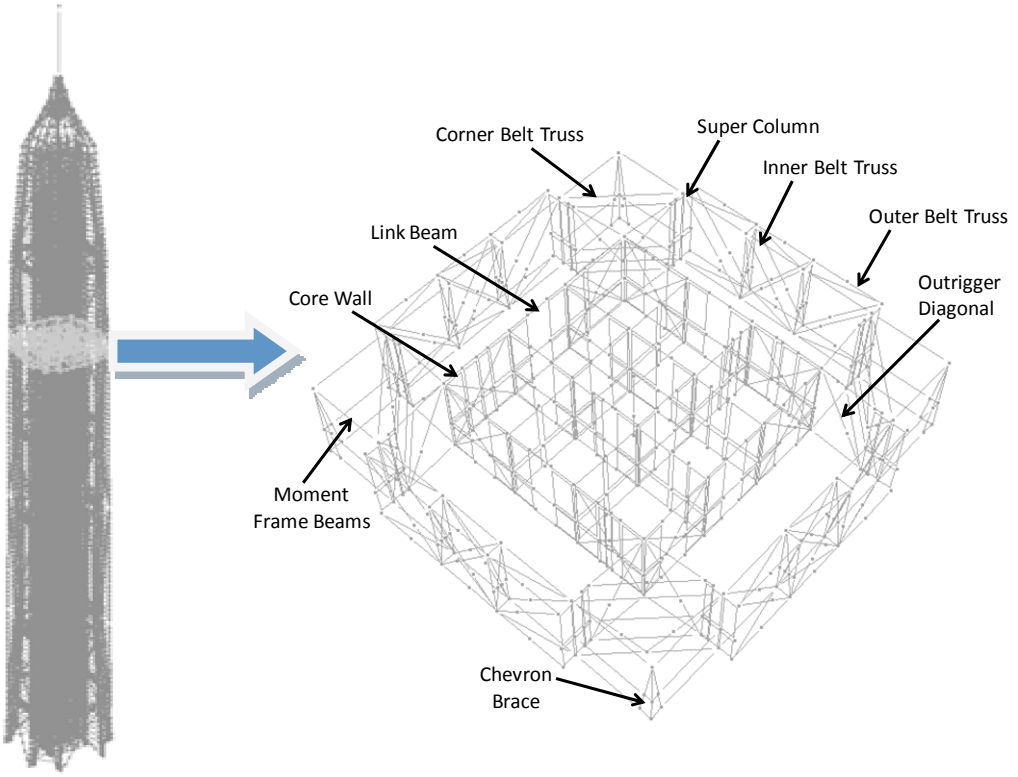


Figure 5: Analytical Model in PERFORM-3D

Damping

A key aspect of seismic behavior is the flow of energy as it is transformed from base input motions to tower movements, structural deformations and absorption as damping. Time history modeling with material nonlinearity can determine energy stored and absorbed by the structural frame. In addition, some

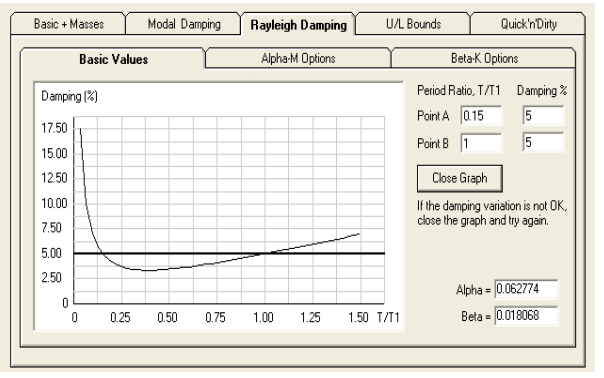


Figure 6: Rayleigh Damping

energy dissipation in a structure occurs through behaviors of various non-structural and structural components that are not explicitly modeled. To reflect energy dissipation not explicitly modeled, Rayleigh damping is specified for the structure as shown in Figure 6: Rayleigh Damping. The damping ratio for the more dominant periods of the structure is between 3.5% and 5%.

Selection of Ground Motions

Nonlinear time history analysis requires that earthquake records be used as input. Records were selected to reflect geological conditions at the site, and then scaled. Based on the China Seismic Code, three requirements should be met by the selected ground motions after scaling:

a. The lowest base shear shall be higher than 65% of China Seismic Design Code (GB50011) spectrum base shear for severe earthquake level.
b. The average base shear shall be higher than 80% of China Seismic Design Code (GB50011) spectrum base shear for severe earthquake level
c. Peak ground acceleration in major direction cannot be lower than 220 gal (cm/sec2).

Two synthesized and five recorded sets of time history curves equivalent to the severe earthquake hazard were selected satisfying the criteria above. Each set consisted of three time histories: two horizontal and one vertical.

Analysis Directions

For each of the seven sets of ground motions a major and minor component was identified. Analysis was performed by applying 100% of the major component motion along the X direction, 85% of the minor component along the Y direction and 65% of the vertical component along the Z direction. The analysis was repeated while applying 100% of the major component along the Y direction, 85% of the minor component along the X direction and 65% of the vertical component along the Z direction. A total of 14 analyses were run on this structure to evaluate the global and member performance.

Analysis Results

Gravity load was first applied to the structure to cause initial stressing of the members and then the nonlinear time history analysis was performed. The results obtained from the nonlinear direct integration time history analysis enabled us to understand global structural behavior as well as behavior of individual members during a severe earthquake. It identified any locations that should be strengthened during the design development stage of this project. A summary of maximum roof displacements, roof drifts and interstory drifts is shown in Table 1: Summary of Maximum Roof Displacements, Roof Drifts & Interstory Drift.

Table 1: Summary of Maximum Roof Displacements, Roof Drifts & Interstory Drift

Earthquake	Maximum Roof Displacement (m)	Maximum Roof Drift/H	Maximum Inter-story drift/h
L7552	1.4	1/386	1/232
L7555	1.4	1/386	1/227
US256	1.27	1/425	1/254
US335	0.89	1/607	1/213
US640	0.8	1/675	1/318
US689	0.74	1/730	1/304
US787	1.36	1/397	1/235

Maximum interstory drift of story height/213 is seen for the US335 ground motion. Since maximum allowable interstory drift according to the China Code is height/100, the interstory drifts are within the code prescribed limits.

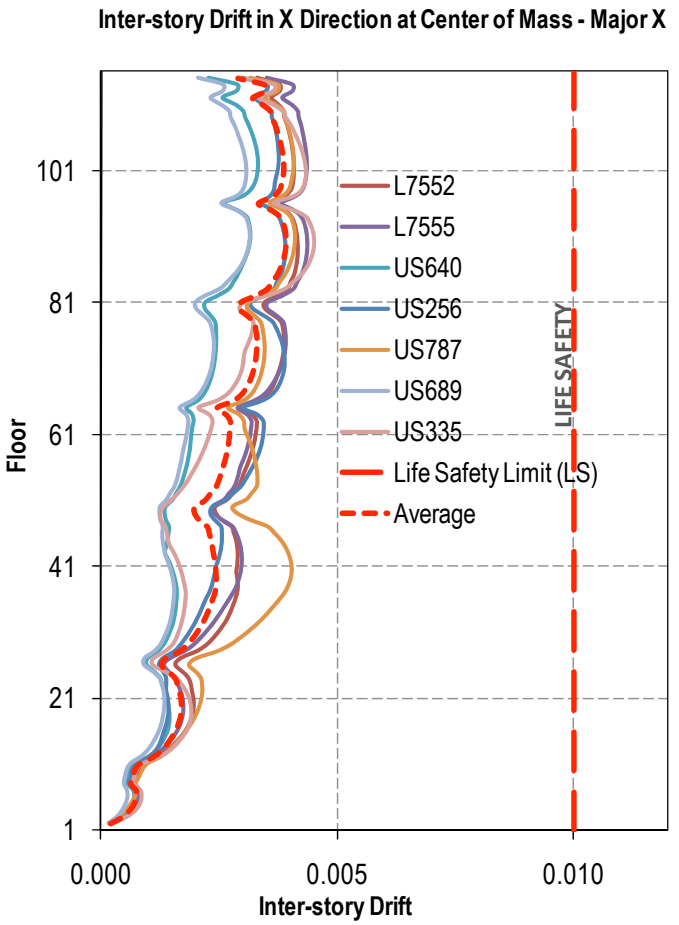


Figure 7: Maximum Inter-Story Drift

Plastic end rotations in the link beams were monitered and the link beams were categorized based on three performance levels; Immediate Occupancy(IO), Life Safety(LS) and Collapse Prevention(CP) as defined within ASCE 41.

Figure 8: Link Beam Performance based on ASCE 41 shows the percentage of link beams exceeding a particular performance level for each of the seven ground motions. It is seen that only 2% of link beams exceed the life safety performance level for one of the sets of ground motions (US787) while all other link beams perform within the life safety performance level or better.

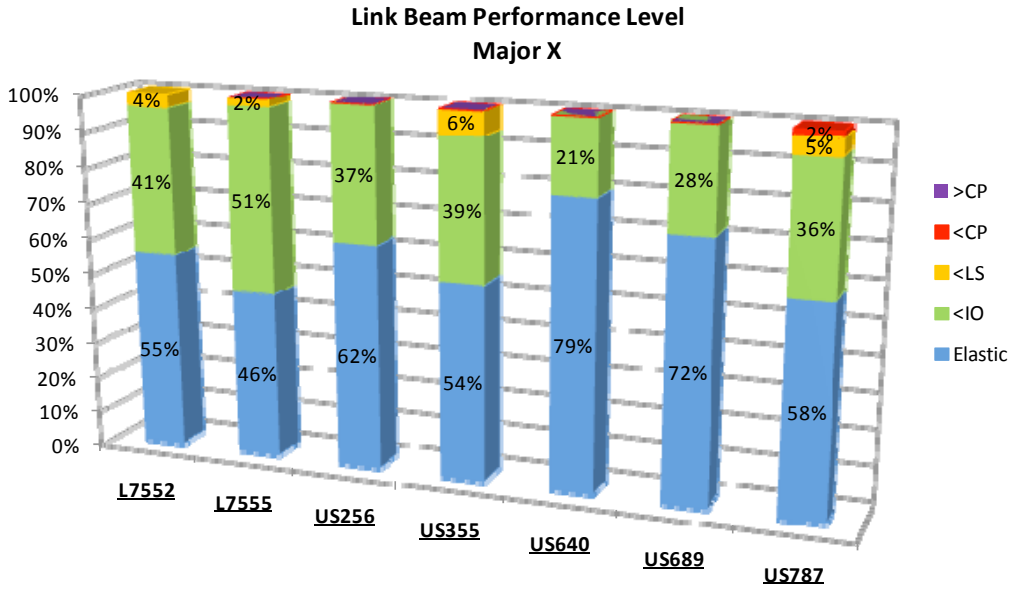


Figure 8: Link Beam Performance based on ASCE 41

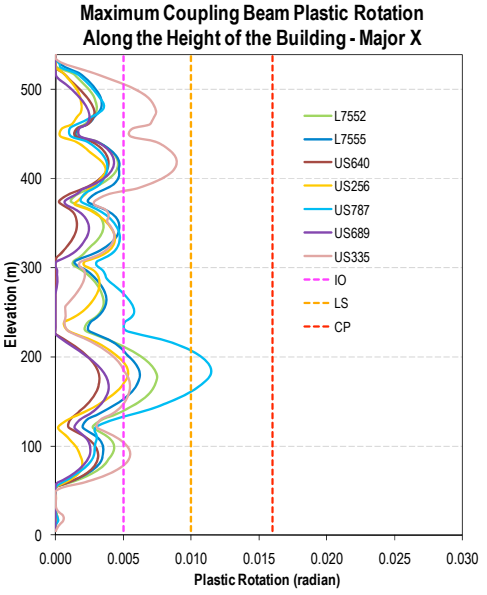


Figure 9: Maximum Link Beam Rotation

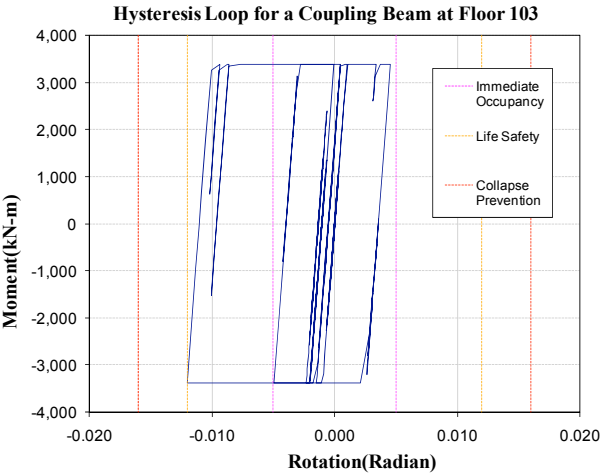


Figure 10: Hysteresis Loop for Link Beam

Figure 9 shows the maximum plastic rotations in the link beams located at different elevations of the building. Figure 10 shows the hysteresis loop for a link beam at floor 103 for the US335 ground motion. This shows the cyclic end rotations in the link beam and the ability of the link beams to dissipate energy hysteretically while undergoing plastic deformations as the building is subjected to ground acceleration. Appropriate link beam detailing can provide stable and reliable

hysteretic energy dissipation through this mechanism while limiting the plastic rotations such that link beams perform within the Life Safety performance level.

Strains in the core wall were monitored for all seven sets of ground motions. As shown in Figure 11, compressive strains in the core wall do not exceed the elastic material behavior limit for concrete. Figure 12 shows the tensile strains in the core wall along the height of the building. The presence of tensile strain exceeding the cracking limit indicates that some cracking of concrete occurs in the upper stories of the building but there is no yielding of steel rebar in the core wall.

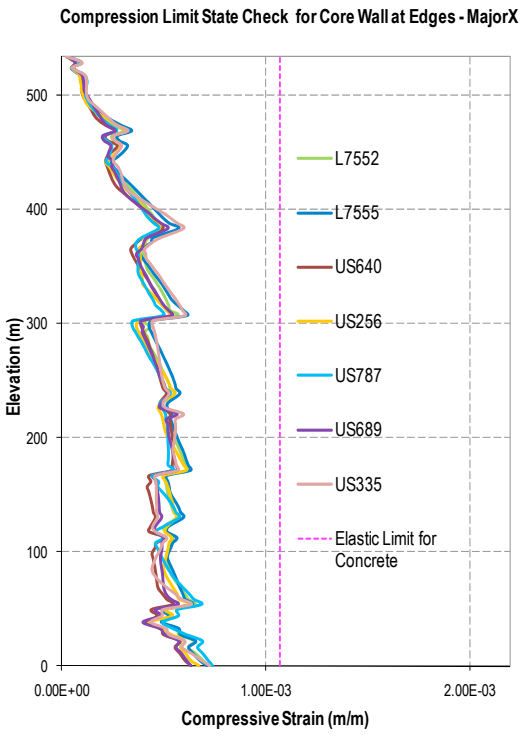


Figure 11: Compressive Strains in the Core Wall

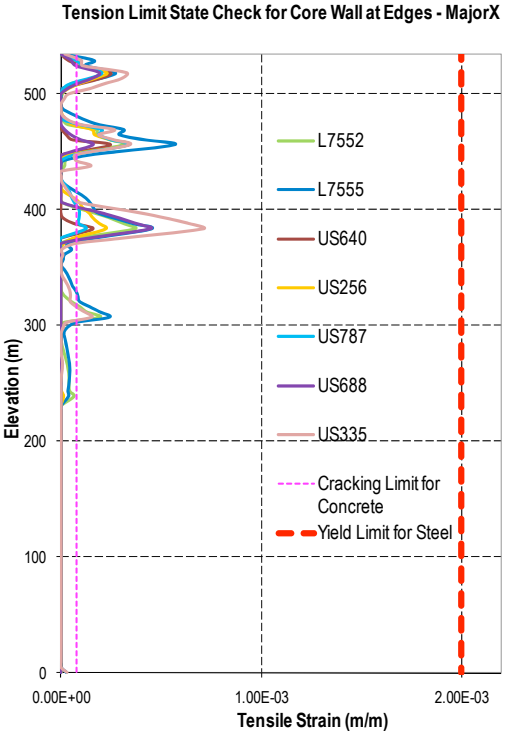


Figure 12: Tensile Strains in the Core Wall

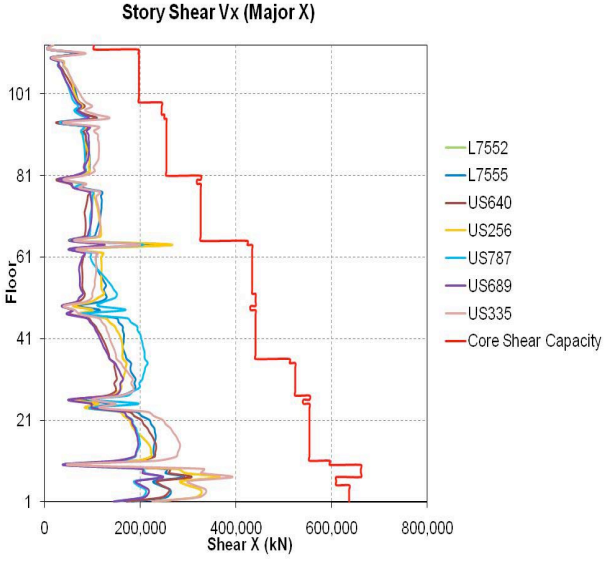


Figure 13, Core Shear Capacity Check

Shear force in the core wall from the nonlinear time-history analysis was checked against shear capacity of the core wall as calculated per the China Code. Figure 13 shows the shear demand in the core does not exceed the shear capacity of the core wall.

Similarly, the strains in the super columns were monitored for all seven sets of ground motions. Figures 14 and 15 show peak strains at the regions where outriggers connect the core wall and super columns.

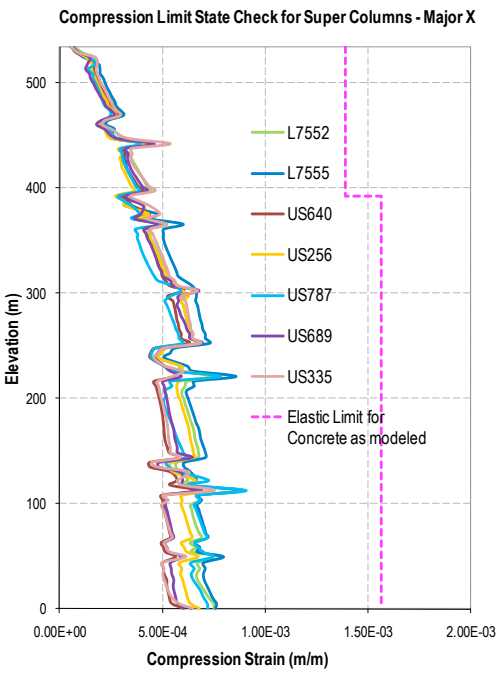


Figure 14: Compressive Strains in Super Column

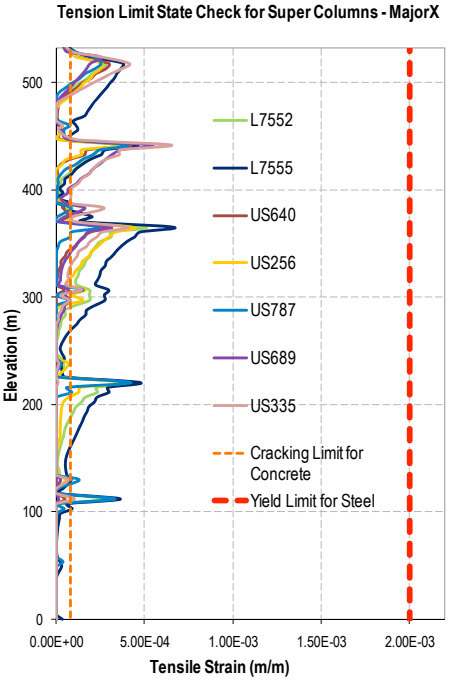
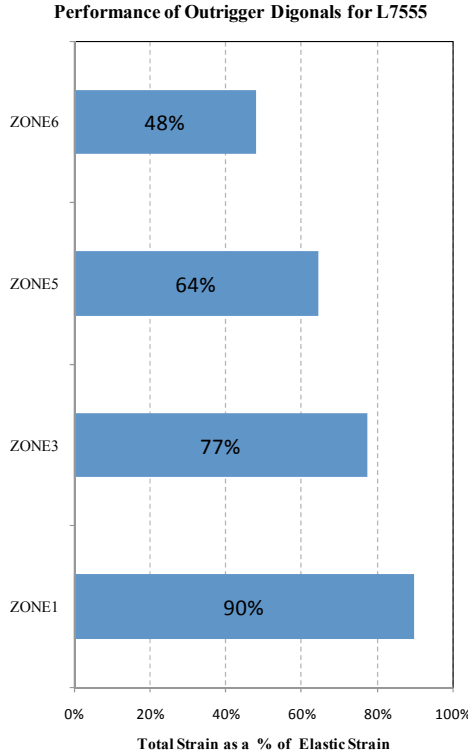


Figure 15: Tensile Strain in Super Column



Performance of outrigger diagonals was evaluated by monitoring the strains. As shown in figure 16, none of outriggers experience inelastic deformations. For L7555 ground motion, maximum strain in the outrigger diagonal was noted to be 90% at, the lowest-most outrigger level.

Forces in the belt truss and super diagonal member obtained from the nonlinear time-history analysis were used to calculate the stress ratio based on the strength limit state check per the China Code. Figures 17 and 18 show the maximum stress ratios in the belt truss and super diagonals for L7555. All the members behaved satisfactorily for the strength limit state check for all seven ground motions.

Figure 16: Performance of Outrigger Diagonals

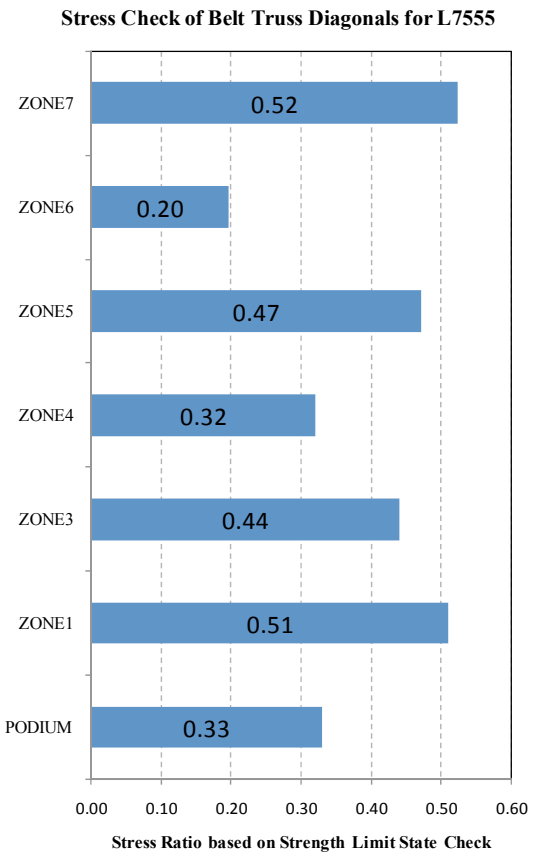


Figure 17, Stress Check of Belt Truss Diagonals

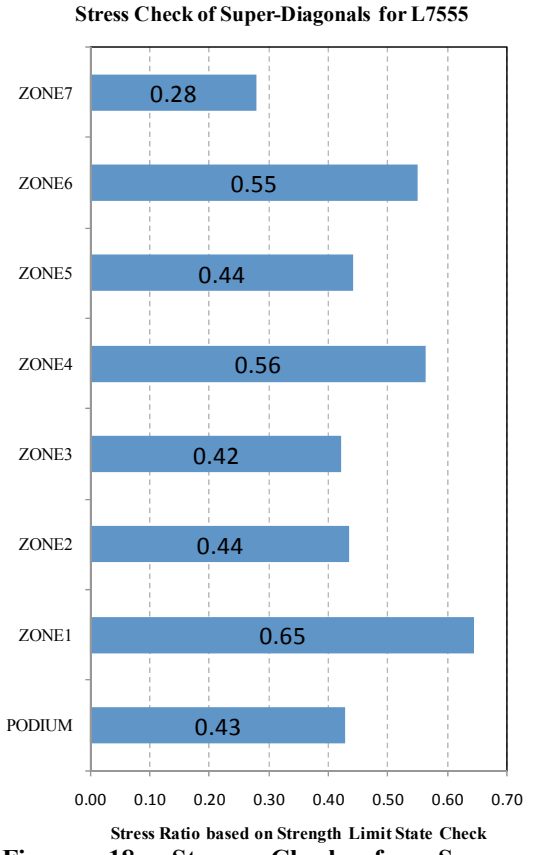


Figure 18, Stress Check for Super Diagonals

Conclusion

Performance-based seismic evaluation of Ping An International Finance Center aided the design team in obtaining approval of the seismic design from the national panel of experts. Complex analytical models were used to study structural behavior under the severe earthquake level (a rare event with 2% probability of exceedance in 50 years). The analytical results provided the design team with very useful information on building performance that helps provide the desired level of safety within an economical building design.

ACKNOWLEDGEMENT

We would like to thank Mr. Leonard Martin Joseph, P.E., S.E., Principal of Thornton Tomasetti, Inc, and CT Tam, Senior Associate of Thornton Tomasetti for comments and assistance during design of the structure as well as for enhancing this paper through his thoughtful suggestions.

PROJECT DESIGN TEAM CREDITS

Client: Ping An Insurance (Group) Company of China, Ltd.

Architect: Kohn Pedersen Fox Associates

Structural Engineer: Thornton Tomasetti Inc.

MEP Engineer: J. Roger Preston Group

Local Design Institute: China Construction (Shenzhen) Design International

Wind Engineering Consultant: Rowan Williams Davies and Irwin Inc. (*RWDI*)

Mr. I. Paul Lew, P.E., R.A., Senior Vice President, Thornton Tomasetti
Mr. Jianhai Liang, Ph.D., Project Engineer, Thornton Tomasetti

References:

- ASCE-41 (2006), *Seismic Rehabilitation of Existing Buildings*, American Society of Civil Engineers, Structural Engineering Institute, Reston VA.
- CECS 160 (2004), *General Rule for Performance Based Seismic Design of Building,* Ministry of Housing and Urban-Rural Development of People's Republic of China.
- GB50009 (2006), *Load Code for the Design of Building Structures,* Ministry of Housing and Urban-Rural Development of People's Republic of China.
- GB50011 (2008), *Code For Seismic Design of Buildings,* Ministry of Housing and Urban-Rural Development of People's Republic of China.
- Perform 3D (2008), *Nonlinear Analysis and Performance Assessment for 3D Structures*, Computers and Structures, Inc. Berkeley California.
- XTRACT (2002), *Cross Section Analysis Program for Structural Engineers v.2.6*, Imbsen Software Systems, Sacramento CA.

Enhanced Seismic Design of the New San Bernardino Court

M. Sarkisian[1], P. Lee[2], L. Hu[3] and C. Doo[4]

[1]PE, SE, M.ASCE, Director, mark.sarkisian@som.com; [2]PE, SE, M.ASCE, Associate Director, peter.lee@som.com; [3]PE, Associate, lindsay.hu@som.com; [4]PE, SE, chung-soo.doo@som.com; Skidmore, Owings & Merrill LLP, San Francisco, CA 94111; PH (415) 981-1555; FAX (415) 398-3214.

ABSTRACT

This paper presents an overview of the "Enhanced" seismic design of the New San Bernardino Court facility. Designed for the Judicial Council of California under the jurisdiction of the Administrative Office of the Courts, the state-of-the-art Superior Court facility will be located in the City of San Bernardino, California – a region of high seismicity in close proximity to active earthquake faults. The 12-story structure with one below grade level was designed to meet "Enhanced" seismic performance objectives of the 2006 California Trial Court Facility Standards in accordance with the 2007 California Building Code. The final design features a cost-effective steel-framed superstructure with special moment-resisting frames and supplementary viscous damping devices supported on a triple-concave friction pendulum seismic isolation system. This paper focuses on the overall progression of the final design from early design phases through final construction documents. This includes architectural design development, site-specific seismic hazard evaluation, structural system options considered, as well as, seismic risk assessment and life-cycle cost analysis to help inform decision making and system selection.

INTRODUCTION

This paper describes the seismic design procedure used for the New San Bernardino Court building. The seismic performance objective for this building is to provide "Enhanced" seismic performance objective of the California Trial Court Facilities Standards (AOC, 2006) using the 2007 California Building Code (CBC) and ASCE/SEI 7-05 requirements in response to project site-specific seismic hazard and ground motion criteria resulting in approximately two times greater than CBC minimum building code requirements. The lateral force resisting superstructure system (LFRS) consists of steel special moment-resisting frames (SMRF) with viscous damping devices (VDD) supported on a seismic isolation system. The SMRF are sized and designed with the strength requirements under Design Earthquake (DE) criteria while beam and column SMRF elements are prequalified per AISC 358-05. VDDs are provided to control horizontal displacement of the superstructure, rotational demands at SMRF connections and vertical column uplift demands at the isolation plane. The VDDs are designed to strength requirements under the Maximum Considered Earthquake (MCE). The seismic isolation system, including the frame members used for the stability of the isolation system at the isolation plane, was designed for displacement demand and strength requirements under the MCE.

The structural response was estimated through a series of nonlinear response-history analyses using a suite of 7-pairs of bi-directional time-history records developed based on the site-specific seismic hazard analysis results. The design of the fully CBC compliant steel framed ductile superstructure, supplemented by a fluid viscous damping system and supported by the isolation system provides an "Enhanced" seismic performance objective which minimizes damage to structural elements, non-structural components, and building contents under expected maximum peak earthquake ground motions. While minimizing potential business interruption and loss of use, the "Enhanced" seismic design seeks to protect the functionality, long-term investment and sustainability of the critical courthouse facility.



Figure 1. 3D Building Rendering

BUILDING DESCRIPTION

The New San Bernardino Court building, a state-of-the-art 36-courtroom facility, is comprised of approximately 400,000 square feet of administrative, clerk, jury, security operations, holding and building support spaces. The 12-story above grade structure includes an interconnected low-rise 3-story podium and one below grade detention level allowing vehicular access on the sloping site. The architectural exterior wall system consists typically of a combination of precast wall panel and glazed curtain wall system.

Superstructure Gravity Framing. The gravity composite steel-framed structure consists typically of a 3¼-inch lightweight concrete fill over a 3-inch 20-gauge metal deck slab. A typical podium level structural framing plan is shown in Figure 2. Composite steel floor framing at mechanical, roof penthouse, Level 1 and below grade levels consists of 4½-inch normal weight concrete fill over a 3-inch 18-gauge metal deck slabs. The typical story height of 16 feet accommodates the typical courtroom floors with clear ceiling heights of 12 feet. The story height of 17 feet at first floor and below grade level accommodates holding access, parking and general administration. The roof/penthouse mechanical level has a story height of typically 20 feet 6 inches to accommodate the mechanical systems.

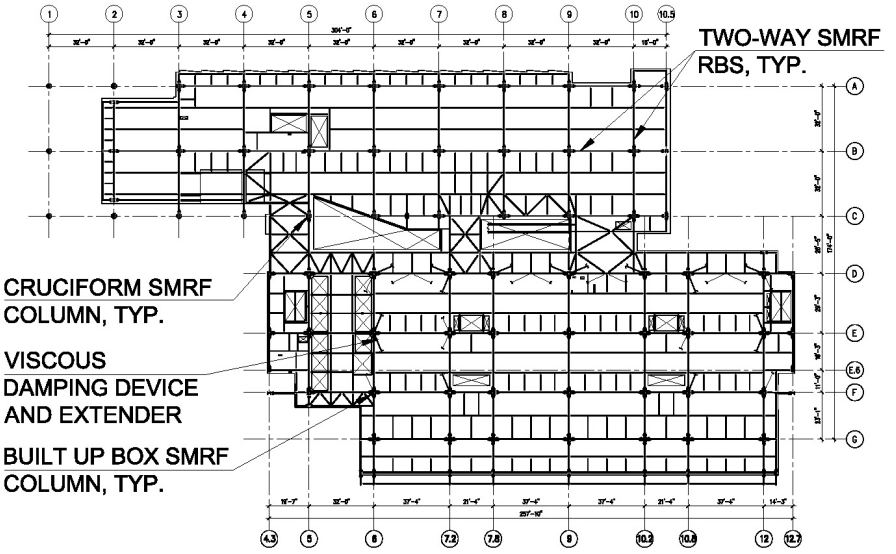


Figure 2. Typical Framing Plan at Podium Level 3

Superstructure Lateral Frame. The lateral force resisting system features a steel-framed superstructure with two-way special moment-resisting frames on essentially all frame lines in each direction utilizing both steel WF cruciform and built-up Box column with 184 distributed supplementary viscous damping devices (VDD) with extender brace elements supported on an energy dissipating seismic isolation system above the lowest mat foundation level. The VDD brace elements have a 440-kip design force with a +/- 5-inch stroke capacity. Pre-qualified steel moment frame connections include reduced-beam section ductile detailing. The uppermost two levels of the building have only two-way special moment-resisting frames to allow for future flexibility in future courtroom and office administration planning. A typical frame elevation in the transverse (N-S) direction is shown in Figure 3.

Seismic Isolation System. The seismic isolation bearing system, as manufactured by Earthquake Protection Systems, Vallejo, CA, consists of 69 Triple Concave-Friction Pendulum (TC-FP) bearings located above the base mat foundation. The TC-FP isolation bearing system will accommodate up to 42 inches of lateral movement at the seismic isolation plane and perimeter moat walls. The TC-FP bearings transfer gravity and lateral forces to the supporting foundation subgrade via reinforced concrete pedestals and mat foundation slab system. The isolation plane was carefully selected at below the lowest occupied level and at perimeter building perimeter conditions to minimize number of building utilities and service elements required to be detailed to accommodate movements across the seismic isolation plane. Locating the isolation plane above the mat foundation required approximately 55,000 sq ft of additional steel framing at the lowest building level.

Courthouse Security. Additionally, the design of the building superstructure incorporates physical security measures to further protect the facility and its

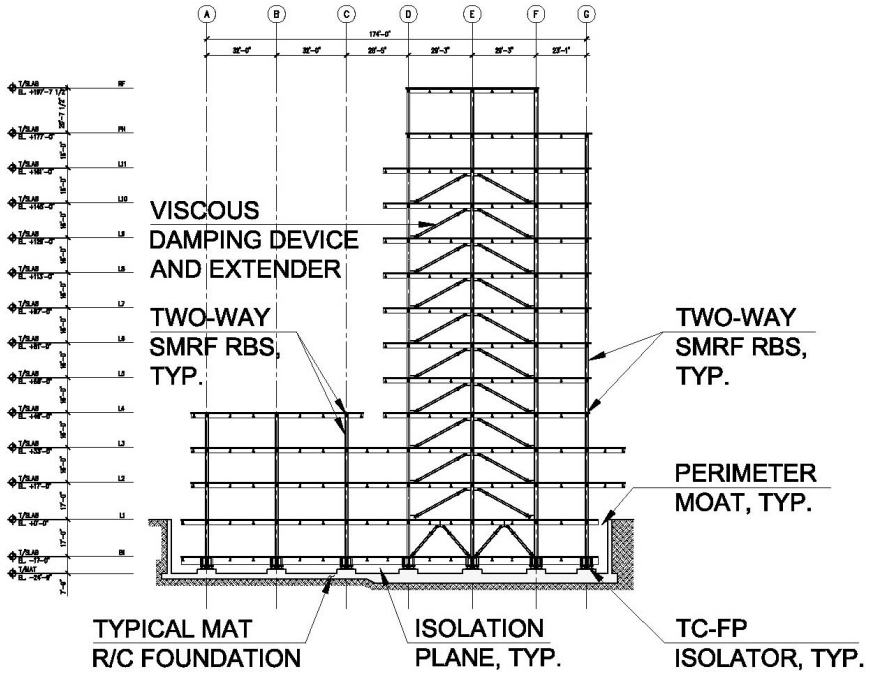


Figure 3. Typical Frame Elevation (N-S Trans Dir)

inhabitants to provide for courthouse security consistent with AOC (2006) requirements to provide security and blast resistant mitigation strategies. Redundant perimeter two-way moment frames at the grade level are designed to reduce the potential for progressive collapse. Interior columns in uncontrolled areas not subject to progressive collapse design are encased to provide hardening, as well as, blast resistant soffit framing slabs at exterior overhangs are provided. Other measures include perimeter building setbacks at grade, bollards protection and blast resistant exterior wall systems.

SEISMIC HAZARD

The facility is located southeast of the intersection of West 3rd Street and North Arrowhead Avenue in the City of San Bernardino, California, in close proximity to active earthquake faults including the San Jacinto (3.9 km), the San Andreas (9.1 km) and the Cucamonga (16.1 km) as shown in Figure 4. At a depth of about 20 feet and below, the site soil consists of dense to very dense sandy layers. The site is classified as "D" based on the measured shear-wave velocity (V_{s30}) of ranging between approximately 1,060 ft/sec and 1,530 ft/sec. The seismic design response spectra was prepared (GeoPentech, 2009) based on the CBC "mapped" USGS 2002; and the site-specific seismic design response spectra was developed based on the seismic hazard analysis and Chapter 21 of ASCE 7-05. The Maximum Considered Earthquake

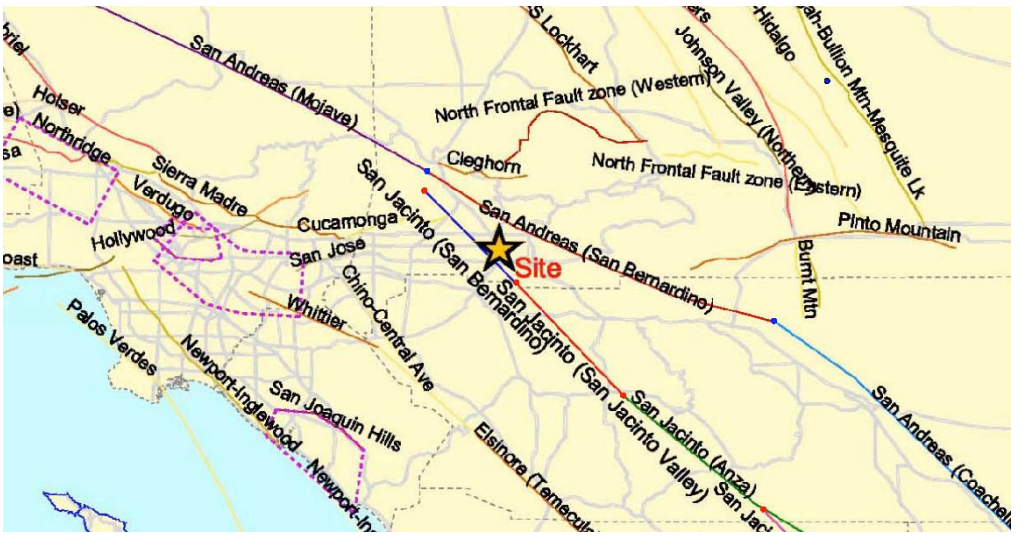


Figure 4. Seismic Source Map (GeoPentech, 2009)

(MCE) are developed based on the lesser of the deterministic 84th percentile "geomean" response spectra (5% damping) without directivity effects associated with the San Andreas Fault (M 7.8) and San Jacinto Fault (M 7.4) and the probabilistic seismic hazard analysis (PSHA) reflecting multiple-segment rupture scenarios corresponding to an average return period of 2,475 years (2% exceedance probability in 50 years). The PSHA reflects the "geomean" NGA attenuation relationships, as well as, near fault directivity effects to provide the Fault Parallel (FP), Fault Normal (FN) and vertical components of ground motion. Figure 5 presents the comparison between the CBC "mapped" and site-specific MCE response spectra including design response parameters. The site-specific spectra for Design Earthquake (DE) is calculated as 2/3 of MCE spectra. When the fault-normal component of spectra is

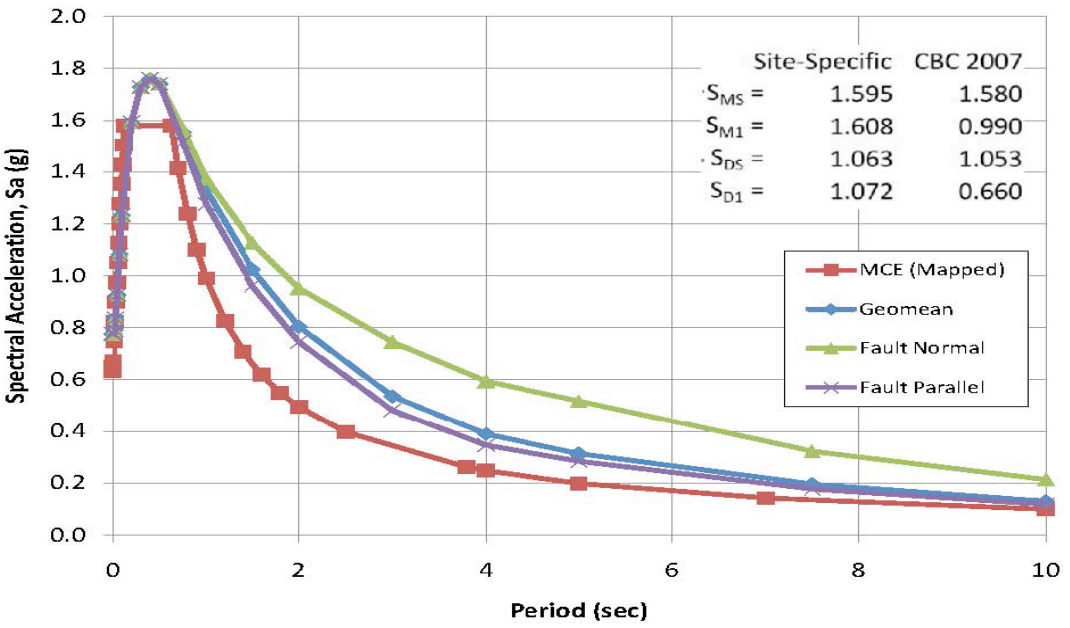


Figure 5. MCE (CBC) vs. Site-Specific Response Spectra (GeoPentech)

compared to the mapped spectra, the site-specific response spectral acceleration is estimated almost 40%, 100% and 2.6 times higher than the corresponding mapped values at 1-second, 2-second and at 5-second period respectively. Due to the AOC "Enhanced" seismic performance objectives, the adoption of the site-specific spectra, without reduction per CBC / ASCE 7-05 provisions, represented a significant design challenge. For the response-history analysis, based on the site-specific spectra, seven time-history records were selected considering the fault rates, magnitude and distance with scaled matching at the period range of interest of 0.2*T to 1.5*T (T is the natural period of the structure) for a fixed base building as required in Chapter 16 of ASCE 7-05. These ground-motion response time histories were further adjusted for the final period of interest of $0.5*T_D$ to $1.25*T_M$ (T_D and T_M are the effective period at Design Displacement and Maximum Displacement) as required for seismically isolated structure provisions of Chapter 17 (ASCE 7-05) based on final selected isolation system properties.

SEISMIC PERFORMANCE CRITERIA

The building is designed to achieve "Enhanced" seismic performance objectives of the California Trial Court Facility Standards (AOC, 2006) based on the governing site-specific seismic hazard and ground motion criteria, as noted above, designed to 2007 California Building Code (CBC) requirements. As shown in Figures 6 and 7,

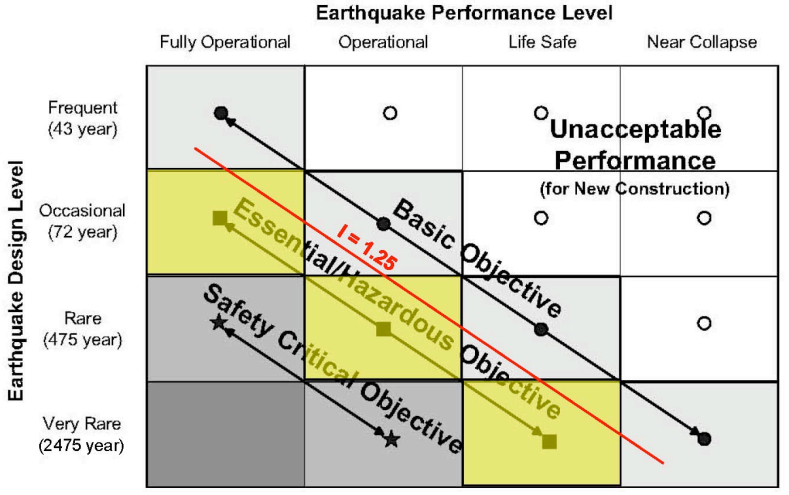


Figure 6. Seismic Performance Objectives (SEAOC, 1999)

this implied that the minimum seismic performance objectives of the building were now required to be higher than the "Basic Objective" earthquake performance objectives of the CBC as illustrated in SEAOC Blue Book (1999) and FEMA 356 (FEMA, 2000) provisions. With these "Enhanced" seismic performance objectives, it is expected that the structure may experience minor to moderate inelastic demands allowing economical repairs, while damage to non-structural components, contents, as well as, potential loss of functionality and business interruption is expected to be significantly reduced.

Nonstructural Performance Levels	Structural Performance Levels and Ranges					
	S-1 Immediate Occupancy	**S-2** Damage Control Range	**S-3** Life Safety	**S-4** Limited Safety Range	**S-5** Collapse Prevention	**S-6** Not Considered
N-A Operational	1-A Operational	2-A	Not recommended	Not recommended	Not recommended	Not recommended
N-B Immediate Occupancy	1-B Immediate Occupancy	2-B	3-B	Not recommended	Not recommended	Not recommended
N-C Life Safety	1-C	2-C	3-C Life Safety	4-C	5-C	6-C
N-D Hazards Reduced	Not recommended	2-D	3-D	4-D	5-D	6-D
N-E Not Considered	Not recommended	Not recommended	Not recommended	4-E	5-E Collapse Prevention	No rehabilitation

Figure 7. Seismic Performance Objectives (FEMA, 2000)

STRUCTURAL SYSTEM OPTIONS

CBC "Mapped" Ground Motion Baseline Options. During Schematic Design and Design Development phases, the several levels of seismic performance objectives and corresponding lateral force-resisting system options were investigated in consideration of both first construction and long-term life-cycle costs. Serving as a baseline for relative cost and performance evaluations, CBC "mapped" ground motion LFRS options were developed based on CBC seismic importance factors of I=1.0, 1.25 and 1.5. Structural systems considered included steel special moment resisting frames (SMRF), dual systems with steel buckling-restrained braced frames (BRBF), special reinforced concrete moment frames, and dual systems with special reinforced concrete shear walls.

Site-Specific Ground Motion "Enhanced" Options. Using site-specific ground motion criteria, LFRS options were developed for "Enhanced" seismic performance objectives (I=1.25) only. Additionally, for "Enhanced" systems, reinforced concrete systems were not further considered based on least cost evaluations. Technologies considered for "Enhanced" seismic performance included seismic base-isolation systems for both elastomeric (Lead Rubber Bearing) and sliding (Triple Concave-Friction Pendulum System) bearings, as well as, superstructure frame energy dissipation systems including viscous damping devices (VDD), BRBFs and SOM patented Pin Fuse Frames. "Fixed-Base" structural system options considered included steel SMRFs dual systems with BRBFs in comparison with supplementary VDDs. These "Fixed-Base" options were further expanded by introducing the seismically "Isolated" systems to achieve "Enhanced" performance objectives. Based on evaluations with very large lateral displacement and overturning demands at the isolation plane, the Triple Concave-Friction Pendulum (TC-FP) bearings were considered as a more economical seismic isolation system considering extreme project site-specific ground motion criteria.

SEISMIC RISK ASSESSMENT AND LIFE-CYCLE COST ANALYSIS

Seismic risk assessment and long-term life-cycle cost analyses were performed on Design Development options to compare the relative seismic performance and cost of potential structural systems under consideration. The results were used to further help inform structural system selection decision making consistent with Life-Cycle Cost Analysis objectives as prescribed in the California Trial Court Facilities Standards (AOC, 2006). Based on HAZUS (FEMA) seismic risk assessment methodologies using a large range of earthquake ground motion return periods, nonlinear analyses and project specific damage fragility parameters were utilized to estimate building damage – including structural and nonstructural components, contents loss and business interruption – over a 25 year building lifetime (Certus/SOM, 2009). Performance of structural system options was compared with the mean annual loss that is expected in the fixed base structure ("baseline" option). The reduction in expected losses in the "Enhanced" system options was compared with the added initial investment. The analysis results, an approximate 19% Return on Investment with a Cost/Benefit ratio of 8, indicated that mean annual losses are expected to be significantly less for the "Enhanced" scheme with the seismic isolation system compared to the additional initial investment for the seismic isolation system and related costs. Throughout the risk assessment and LCCA, the additional initial costs of the complete base-isolated system were justified in terms of reducing potential future losses in earthquakes through improved performance, while implementing the "Enhanced" system within original projected budgets.

SELECTED LATERAL FORCE-RESISTING SYSTEM

Superstructure SMRF and VDDs. The final selected LFRS consists of steel SMRFs on essentially all frame lines in each direction at each level with 184 distributed superstructure VDDs supported on an energy dissipating seismic isolation system. The steel SMRFs consist typically of WF beam/girder two-way moment-connected to box and cruciform columns, as well as, rolled W14 columns in conformance with prequalification connection criteria of AISC 341-05 (AISC, 2005). The viscous damper and extender brace elements are located at each level with typically 8 damper elements in each frame direction, integrated with standard courtroom layouts and supporting areas, were utilized to control lateral drift are shown in Figures 2 and 3. The viscous damper devices are located at the top of each damper extender brace element in both chevron (Figure 8) and single diagonal configurations.

Seismic Isolation System and Isolation Plane. The superstructure is supported by the seismic isolation system above the horizontal isolation plane located directly above the mat foundation over entire building podium and tower footprint. The isolation system is comprised of 69 TC-FP isolation bearing units located at each column. Typical detail of the TC-FP isolation bearing at interior condition is shown in Figure 9. Units are located approximately 4'-0" below the top of slab and placed on concrete pedestals to allow access for utilities, construction, maintenance, testing and inspection. The total clearance from the underside of the metal deck to the top of

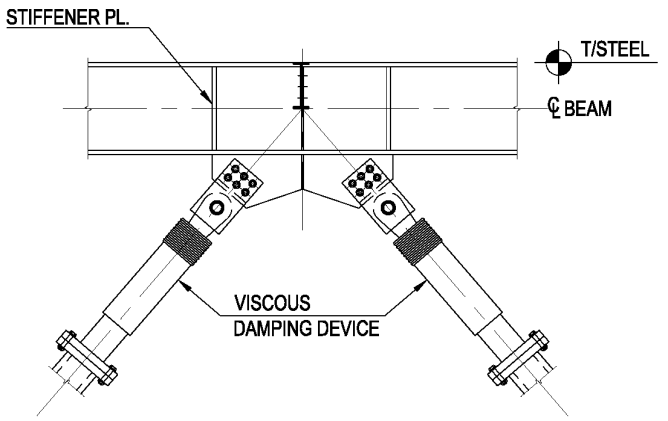


Figure 8. Typical Viscous Damper Frame Detail

mat is approximately 6'-0". Cantilevered retaining walls are provided at building moat wall conditions. The perimeter moat, which allows for free-seismic movement of the isolated superstructure, is provided with a clear distance of 42 inches as shown in Figure 10. At lower level vehicular access conditions, a reinforced concrete slab and/or steel closure plate cover the moat space making up the seismic joint assembly and allowing for functionality under relative seismic movements of the isolated superstructure.

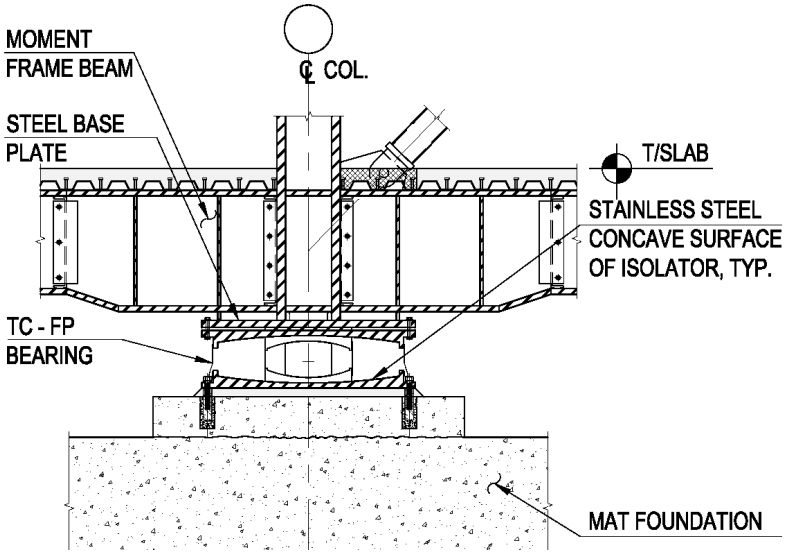


Figure 9. Typical TC-FP Isolator Detail at Mat Foundation

To maintain stability during lateral movement of the isolation system, structural steel framing elements and connections at the isolation plane are designed to remain elastic under MCE level ground motion response design criteria. Moment-connected girders to columns at the isolation plane were designed considering gravity and overturning axial loads, additional moments developed from the P-Δ effects, horizontal shear due to the friction at isolator surfaces, as well as, the restoring force equilibrium. The concrete pedestals which support the isolator units are designed for the MCE level ground motion responses and the additional moment due to P-Δ effects, axial loads and the horizontal shear. The reinforced concrete mat foundation was designed for

the DE level structural response with R_I = 1 and also evaluated for punching shear requirements including the additional strength demands to maintain stability under MCE level responses.

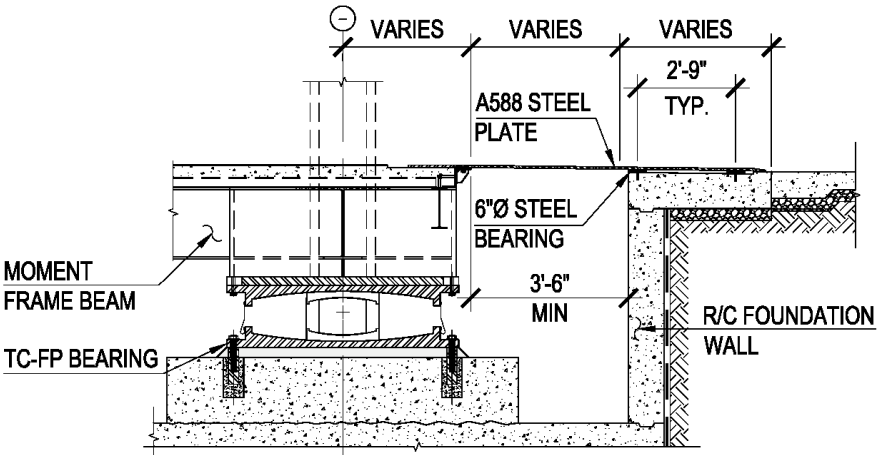


Figure 10. Typical TC-FP Isolator Detail at Lower Level Perimeter Moat

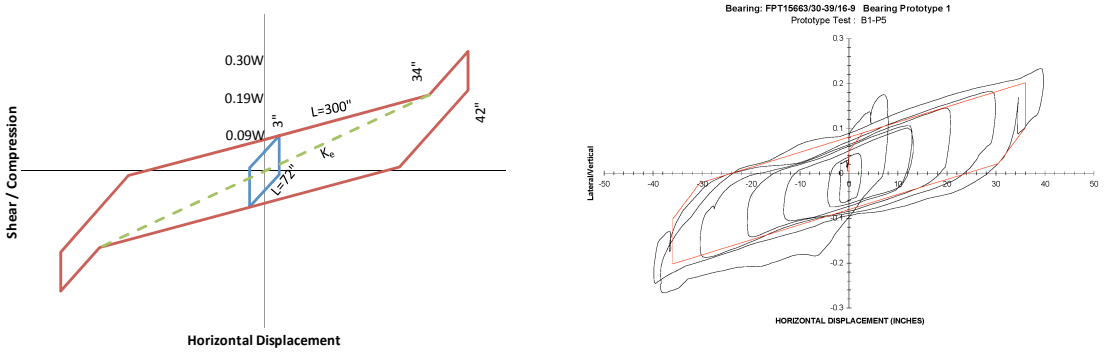
STRUCTURAL ANALYSIS AND DESIGN

Nonlinear Analysis Modeling. The ETABS computer program was used to prepare 3D analysis models of the building. All pertinent stiffness of structural members, mass and gravity loads were included in the models. The beams and columns were modeled as elastic frame elements. The composite floor decks were modeled as one-way deck elements and rigid diaphragms were applied to them. Seven sets of time-history ground motions were used in the nonlinear response-history analyses performed while accounting for nonlinearity in the damper elements of the superstructure, the seismic isolators and capture uplift on seismic isolators where occurs. The analysis cases included the bounded properties of the seismic isolator friction coefficients and the viscous damping devices in order to capture the governing structural responses as prescribed by ASCE 7-05 Ch. 17 & 18. The analyses with DE ground motion sets were used to calculate design lateral forces and displacements of the lateral-force resisting systems above the seismic isolation plane. The structural elements in the superstructure were designed to remain essentially elastic. The MCE ground motion sets were used for the analyses to calculate the total maximum displacement, D_{TM}, of the isolation system, the vertical displacement and the stability demands of each isolator, as well as, to estimate maximum damper axial force and displacement demands.

Viscous Damping Devices. The VDDs have a velocity exponent (α) of 0.5, a damping constant (C) of 150 kip-(sec/in)$^{\alpha}$, a maximum stroke of ± 5 inch and a maximum design force capacity of 440-kip. The structural analyses included the bounded analysis of (± 15%) the upper and lower bound damper properties. The VDD elements are modeled using nonlinear damper elements in ETABS. The damping devices were designed to have displacement and design force capacities for MCE level demands. The connections and components, including the damper

extenders, transferring the damper forces to the structural members were designed to develop the capacity of the VDDs. Since the damper forces are substantially out-of-phase with elastic forces, they do not significantly increase loading on the structural members.

Isolation Bearing System (TC-FP). Analysis modeling of each bearing was developed on the basis of assumed mechanical properties of the TC-FP bearings as provided by bearing manufacturer, EPS, with target nominal properties as shown in Figure 11(a), as later verified by prototype testing, Figure 11(b)



(a) Nominal Bearing Properties

(b) Prototype Bearing Tests (EPS)

Figure 11. TC-FP Isolation System Bearing Properties

The effective radii (L) of the outer and inner concave surfaces are 300 and 72 inches, respectively. The friction coefficients of Breakaway, Target, Lower Bound (LB) and Upper Bound (UB) are 5.0%, 9.0%, 7.5% and 10.5%, respectively. UB and LB properties included adjustments for potential aging and contamination effects. EPS (2010) confirmed analysis parameters based on the results of prototype bearing testing as conducted during the CD design phase under direction of SOM and Design Review panel. Modeling of TC-FP is based on the equivalent bilinear model to represent the breakaway friction coefficients of inner and outer surfaces. Equivalent bilinear modeling of TC-FP represents the actual hysteretic behavior without significant loss of accuracy. The TC-FP mechanical properties are averaged based on the global behavior of entire building, as well as, in establishing prototype testing acceptance criteria. The TC-FP was idealized using a combination of isolator2 link element and gap/hook elements of ETABS program. The isolator2 link elements are used to model the equivalent bilinear model to represent the breakaway friction coefficient of inner and outer surfaces. The gap/hook elements are used to model later stage stiffening effects of isolator. The structural analyses included the bounded analysis the upper and lower bound friction coefficients to determine maximum force and displacement demands.

Isolation Plane Framing. The isolation plane seismic force resisting system consists of all the structural elements between the top of the isolators and below the top of

basement floor slab. The elements in this plane was designed to have a capacity for 100% of the required seismic story shear under DE with $R_I = 1.0$. When the elements are required to have a strength for the stability, which are the girders and columns directly connected to the isolator, the elements are designed to have a capacity for 100% of the required seismic story shear under MCE with $R_I = 1.0$, including secondary moments developed from the large lateral displacement of the isolator.

Superstructure Frame. The superstructure, defined as the structural system above the top of the basement floor slab, consists of steel SMRFs with supplementary VDDs with the SMRF beams and columns assembled with fully ductile prequalified connections per AISC 358-05. The members were designed to the structural responses under DE events with $R_I = 2.0$. Additionally, the superstructure members were evaluated per FEMA 356 to meet the structural Life Safety seismic performance criteria and estimated SMRF connection rotational demands under MCE level events. Based on the series of nonlinear response-history analyses, the maximum average drift ratios are about 1.4% under DE level ground motions and about 1.7% under MCE level ground motions.

DISCUSSION AND CONCLUSIONS

The seismic isolation system was an appropriate design strategy for the courthouse to limit earthquake damage and to protect facility function. Since the building is located in a region of very high seismicity and is subject to particularly strong ground motions, the large seismic demands posed a challenge for the design of seismically isolated structure in terms of the displacement capacity of the isolation system and the strength capacity of the superstructure while attempting to achieve AOC "Enhanced" seismic performance objectives.

The viscous damping devices were used to supplement isolation system damping and to reduce the displacement demand. As a result of the installation of supplementary dampers at the superstructure in line with SMRF system, it was able to reduce the interstory drifts and isolator vertical, as well as, horizontal displacement demands. By reducing drifts, the rotational demands on the SMRF beam-column connections were also reduced to an essentially elastic level.

The lateral force resisting system utilizes both seismic isolation and viscous damping systems along with fully ductile prescribed LFRS system. The resulting system achieves an "Enhanced" seismic performance level by protecting the structural elements, non-structural components, and building contents against damage, as well as, loss of use under expected severe demands of MCE ground motions. It is also considered that the "Enhanced" seismic design provides a sustainable low-carbon footprint with significant benefits on the environment while protecting the long-term investment and continued use of the critical courthouse facility.

ACKNOWLEDEMENT

The authors gratefully acknowledge the support of the Judicial Council of California, and the Administrative Office of the Courts (AOC) during the design development of this project. Additionally, AOC project oversight was provided by Afshar Jalalian, and, CBC Design Review was provided by Robert Bachman (Chair), Professor Michael Constantinou, and Dr. Norman Abrahamson. Contributions are gratefully acknowledged.

REFERENCES

Administrative Office of the Courts (AOC). (2006). *California Trial Court Facilities Standards*, San Francisco, California

American Institute of Steel Construction (2005). ANSI/AISC 341-05, *Specification for Structural Steel Buildings*, Chicago, Illinois

American Society of Civil Engineers (2006). ASCE/SEI 41-06, *Seismic Rehabilitation of Existing Buildings*, Reston Virginia

American Society of Civil Engineers (2007). ASCE/SEI 7-05, *Minimum Design Loads for Buildings and Other Structures*, Reston Virginia

California Building Standards Commission (2007). *2007 California Building Code,* California Code of Regulations, Title 24, Part 2, Volume 2 of 2, Sacramento, California

Certus Consulting, Inc. (2009). *Seismic Risk Assessment Report, California Administrative Office of the Courts, New San Bernardino Court Facility*, Oakland, California

Earthquake Protection Systems (2010), *Real Time Prototype Bearing Test Report for the FPT15663/30-39/16-9 and FPT15656/24-39/10-6 Triple Pendulum Bearings for San Bernardino Court Protect*, Vallejo, California

Federal Emergency Management Agency (2000). FEMA 356, *Prestandard and Commentary for the Seismic Rehabilitation of Buildings*, Washington, D.C.

GeoPentech (2009). *Geotechnical Investigation New San Bernardino Courthouse*, Santa Ana, California

Structural Engineers Association of California (SEAOC). (1999). *Recommended Lateral Force Requirements and Commentary*, Seventh Edition, Sacramento, California

Seismic Retrofit of a Higher-Education Building Using Advanced Analysis to Optimize Use of Existing Building Components

Devon Lumbard, P.E.[1], James Newell, Ph.D., P.E.[2], Qi-Song "Kent" Yu, Ph.D., S.E.[3], and James O. Malley, S.E.[4]

[1]Presenter, Degenkolb Engineers, 707 SW Washington St, Suite 600, Portland, OR 97205; PH (503) 223-9932; FAX (503) 242-1780; email: dlumbard@degenkolb.com
[2]Degenkolb Engineers, 707 SW Washington St, Suite 600, Portland, OR 97205; PH (503) 223-9932; FAX (503) 242-1780; email: jnewell@degenkolb.com
[3]Degenkolb Engineers, 707 SW Washington St, Suite 600, Portland, OR 97205; PH (503) 223-9932; FAX (503) 242-1780; email: kyu@degenkolb.com
[4]Degenkolb Engineers, 235 Montgomery St, Suite 500, San Francisco, CA 94104; PH (415) 392-6952; FAX (415) 544-0782; email: malley@degenkolb.com

ABSTRACT

This paper summarizes the case study of a four-story building with three additional levels below grade in the Pacific Northwest of the U.S. consisting primarily of precast and cast-in-place concrete elements. The lateral force resisting system consists of eight reinforced concrete shear wall towers located around the perimeter of the building and four shear walls down the centerline of the building. The building was analyzed and a retrofit scheme was developed using both linear and nonlinear static analysis procedures conforming to the requirements of ASCE 31 and 41. The retrofit scheme had to meet a number of criteria set forth by the owner. The retrofit had to visually promote the owner's commitment to seismic safety while embodying sustainability. The building had to remain occupied and operational while the retrofit construction took place; which required noise, dust and vibration be minimized. The HVAC system also had to remain in operation while it was modernized. To satisfy these constraints, the retrofit employed a mostly exterior strengthening scheme that included large horizontal steel trusses and steel collectors in order to engage previously unused exterior tower walls. Four strips of new roof over the existing roofs were added to confine the existing gypsum concrete roofs and provide support for a new HVAC system. Collectively, the retrofit scheme was a tailored solution which optimized use of the existing structural elements while providing the owner with an economical retrofit which is expected to meet or exceed the established performance goals.

INTRODUCTION

Facility managers and government representatives are becoming increasingly aware of the life-safety risk posed by older buildings not designed and constructed to meet the requirements of current building codes. This problem is compounded in geographic areas where the understanding of seismicity has evolved in recent years

and is now understood to represent an increased risk. In response to this risk, a university located in the Pacific Northwest of the United States has undertaken a program to improve the seismic safety of their campus facilities. The state's legislature, also wishing to support and promote the goals of seismic safety, employed a matching funds program to help promote seismic safety in the local community.

One such example of this combined state and university objective to improve the seismic safety of existing buildings is a pre-1975 non-ductile concrete building used for a large portion of the university's science and technology lab space. The building houses teaching and research laboratories for chemistry, biology, physics, environmental engineering, and structural engineering. A preliminary Tier 1 seismic evaluation per ASCE 31 (ASCE, 2003) indicated several Life-Safety concerns; and subsequent Tier 2 and Tier 3 evaluations indicated retrofit strengthening would be required for the building to achieve the desired seismic performance of the Basic Safety Objective including Life-Safety performance in the BSE-1 (the Design Basis Earthquake with a 10% probability of exceedance in 50 years) and Collapse Prevention in the BSE-2 (the Maximum Considered Earthquake with a 2% probability of exceedance in 50 years) per ASCE 41 (ASCE, 2006).

Additionally, both the state and the university wanted to use the renovation of this building to demonstrate their commitment to promoting seismic safety and sustainability statewide. This project also served to showcase their commitment to attracting top-notch faculty, students and support research and workforce development for their healthcare, advanced manufacturing and high-technology industries.

However, the strengthening had to be carefully coordinated out of respect for the occupants and uses of the building. The laboratories for the various university departments contain active research that cannot be interrupted or compromised. Furthermore, the university could ill afford to lose precious classroom space inside the building as that was already scarce. Therefore, because the building would need to remain occupied and operational, any construction work to seismically strengthen and modernize the building would need to be carefully coordinated to minimize noise, vibration, and dust. Furthermore, the HVAC system would need to remain online for the full duration of construction to support the research and teaching functions.

BUILDING DESCRIPTION

The building was constructed in 1970 and has four stories above grade, with three levels below grade; with two levels containing offices and labs and a third level for mechanical and HVAC systems. The building is rectangular in plan, and has dimensions of 280 feet by 146 feet at most of the levels (see Figure 1). At the fourth and roof levels, the plan steps back to 208 feet by 146 feet in plan (see Figure 2).

Story heights are approximately 18 feet for the mechanical level, 12 feet for the two lower levels, and 13 feet 9 inches for the levels above grade (see Figure 3).

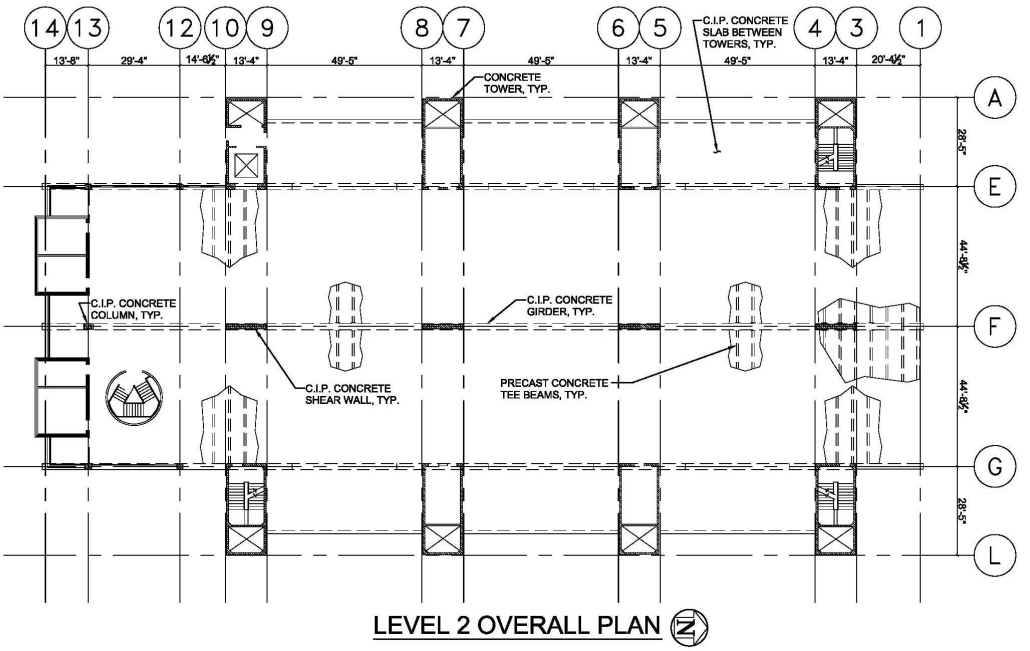


Figure 1. Typical floor plan

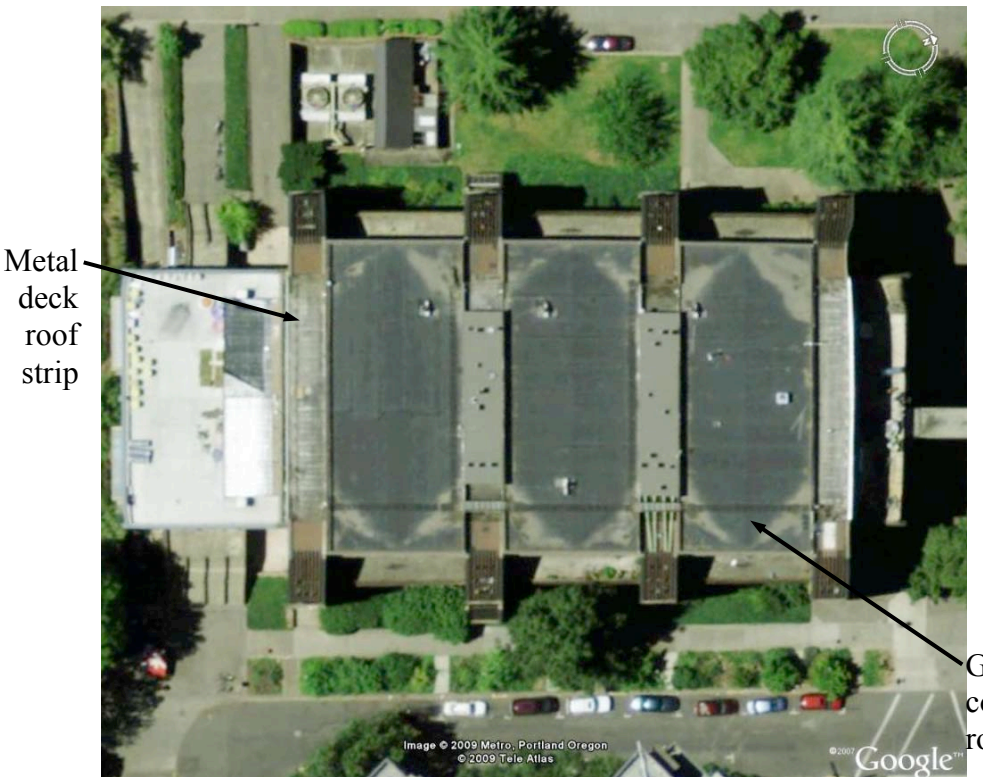


Figure 2. Roof view (Google, 2007)

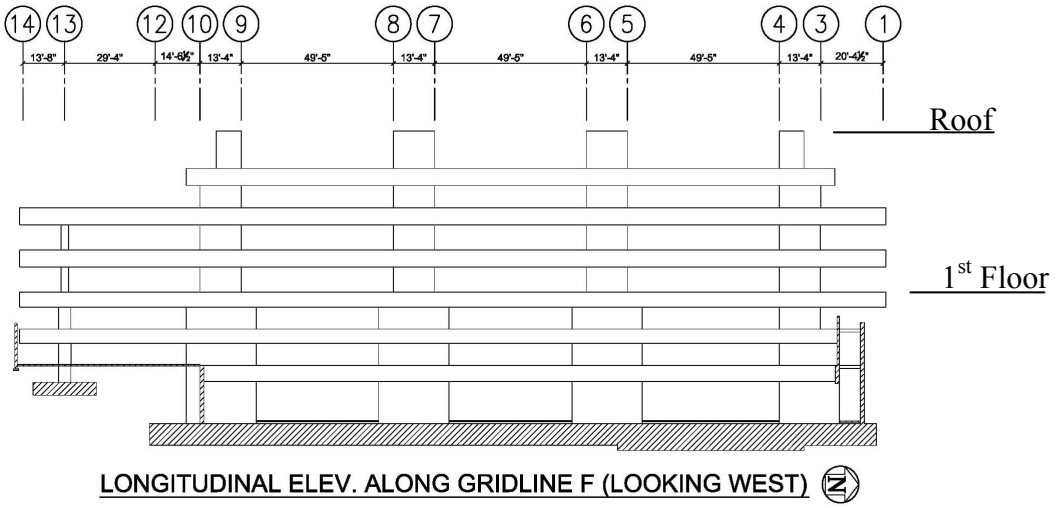


Figure 3. Elevation along gridline F

The gravity-load-resisting system consists primarily of precast and cast-in-place (CIP) concrete elements. There are eight stair and elevator cores in the building (four on both the east and west sides), all consisting of reinforced concrete bearing walls. There are also four large shear walls situated along the centerline of the building along gridline F (see Figure 1 for gridlines). The stair towers are founded on four-foot-thick concrete footings, and the centerline walls are founded on a seven-foot-thick strip footing. The foundation walls surround the levels below grade and do not have a strip footing, but span between the adjacent tower footings.

The majority of the roof consists of two inch thick gypsum concrete over form board, supported by open-web steel joists. The steel joists span in the east-west direction to wide flange girders. These girders span between the reinforced concrete bearing walls at the building centerline and between the towers on the sides of the building. Small strips of the roof consist of a metal deck supported by open web steel joists spanning in the east-west direction between the towers and the centerline walls. These strips are three feet lower in elevation than the gypsum concrete roof areas. A portion of the metal deck roof supports a penthouse with miscellaneous mechanical equipment.

The floors consist of precast tee sections, with a minimum three-inch reinforced topping slab, spanning east-west to cast-in-place and precast girders. The girders are cast in place along gridline F and span to concrete bearing walls at the building centerline. The girders along gridlines E and G consist of both cast in place and precast portions. The cast in place portion is cast integrally with the interior face of the tower wall and cantilever from the tower. These cantilevered girders support a precast middle portion between the towers. Between the towers on the east and west sides of each floor are one-way concrete slabs spanning between the precast girders and edge beams.

The lateral force-resisting system of the building consists of the gypsum concrete and metal deck diaphragms of the roof, reinforced concrete topping slabs and one-way slabs at the floors, and reinforced concrete shear walls around the eight stair and elevator cores, as well as down the centerline of the building. The tower walls are eight inches thick. The walls on the north and south sides of the towers are mostly solid; however, the walls on the east and west sides of the tower on the interior side have many openings for doorways. The centerline walls are eighteen inches thick. Below the first level, the perimeter retaining walls substantially increase the amount of shear wall in both directions. However, due to floor penetrations for the building ventilation system, the basement wall on the north side of the building is not effectively connected to the rest of the diaphragm.

COMPUTER MODEL AND MODELING ASSUMPTIONS

The computer modeling for the building was carried out in two phases. First, a linear static model was utilized to gain a quick preliminary understanding of the building behavior. This provided the design team with an understanding of the cost of the structural retrofit portion of the project and therefore an approximation of how much money remained for modernization of the architectural and MEP systems so that these disciplines could plan their portion of the project. A nonlinear static analysis was then utilized to improve the understanding of the building behavior and reduce the scope of required strengthening. This improved understanding of building performance and reduced strengthening allowed the project team to save approximately $1.4M in construction costs while also reducing the corresponding construction impact on the occupants of the building.

The computer program ETABS (CSI, 2008) was used to perform the linear static analysis of the building. The tower walls, centerline walls, basement walls and lower level diaphragms were modeled with shell elements as seen in Figure 4 and all major openings from doorways and duct penetrations were included. The girders along the centerline of the building were modeled with frame elements along centerline dimensions. Cracked section properties were used for flexural stiffness for all concrete elements. The bases of all the walls were fixed. The seismic demands were based on site-specific response spectra provided by the geotechnical engineer, and all seismic loads, including horizontal accidental torsion, were applied at the center of rigidity for the fixed diaphragms and distributed point loads for the shell modeled diaphragms.

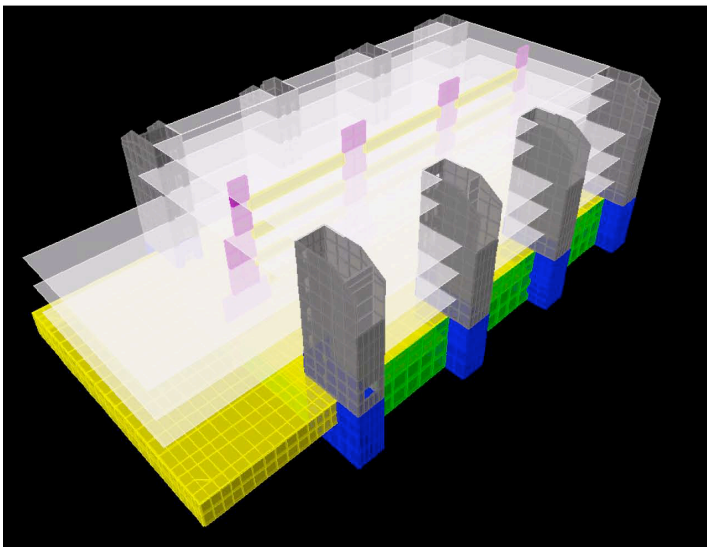


Figure 4. Linear static model

The computer program ETABS was also used to perform the nonlinear static analysis of the building. The nonlinear model required the centerline walls and tower walls be modeled with frame elements in order to capture their inelastic shear and flexure performance. Each centerline wall was simply modeled with a vertical frame element. However, the tower posed a more interesting challenge. The nonlinear tower model needed to capture the composite flexural action of the tower as well as the potential yielding of the portion of the tower wall above the doorways on the interior faces of the towers.

To accomplish this, each tower was divided into four discrete elements to enable modeling the tower section with vertical line elements. The four vertical line elements were connected with horizontal rigid link elements at each floor level and at the roof, except at the doorway penetrations in the towers. At these penetrations, the horizontal element was a frame element with section properties to represent the wall (and integral beam) between the door penetrations. Geometric section properties for each of the vertical elements and for each story were determined using the computer program RC-Section (Pikaso, 1994).

The tower shell element model from the linear static analysis was used to calibrate the tower line element model global stiffness in the N-S and E-W directions. These models are shown in Figure 5. Equivalent stiffness was achieved by modifying the line element tower plan dimensions. The story displacements for the shell element and calibrated line element models were compared.

The use of the four separate vertical frame elements to model the towers required a modified approach to capture the flexural plastic hinging of the composite tower sections. Equivalent axial plastic hinges were defined based on the chord reinforcing steel axial capacity and moment arm of the tower section tension-compression couple between the corresponding vertical frame elements. The axial hinges were defined as

tension only hinges because the area of concrete in compression had adequate capacity to remain elastic. Different axial hinge properties were defined for the N-S and E-W directions to account for the different moment arms of the tension-compression couple in the two directions.

Shear hinges were modeled in the tower vertical line elements at mid-height of each story. The shear areas of these elements included only the section of wall parallel to the direction of loading (i.e., neglecting the perpendicular leg of the L shape). Shear hinges were also modeled at midspan of the horizontal elements over the tower doorways. The capacity of these shear hinges was calculated based on the portion of the tower wall over the door and CIP beam along gridlines E and G. Proper activation of tower plastic hinges was verified before incorporating the towers into the overall building model.

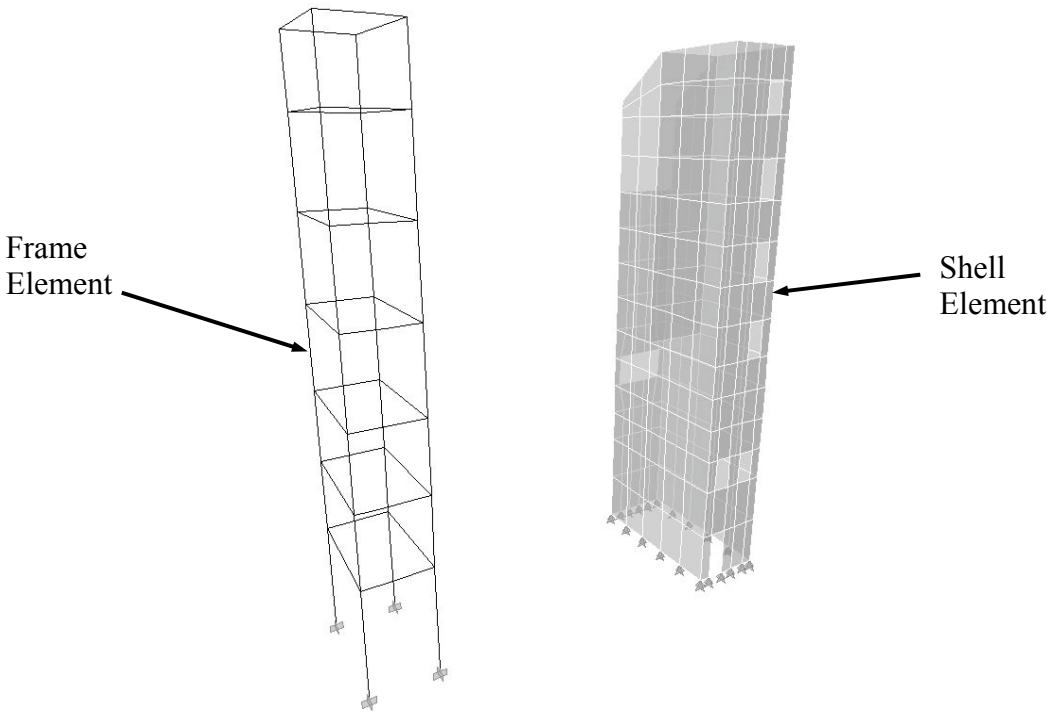


Figure 5. Comparison between frame model and shell model of tower

BUIDING EVALUATION RESULTS

The linear static analysis indicated that the as-built configuration of the building did not allow for the transfer of force to all of the existing walls. In the north-south direction, the exterior walls of the towers were unable to resist north-south seismic loads since the towers extended beyond the diaphragms. This significantly overstressed the walls along the centerline of the building and the interior face of the towers where penetrations for doorways into the towers drastically reduced the available wall. In the east-west direction, no collector was present to drag load into

the tower walls along gridlines 3 and 10. Therefore, it was determined that either these load paths would need to be created or additional walls would need to be added.

Both options were considered. Ultimately, the option to extend the floor diaphragms and add wall collectors along gridlines 3 and 10 were chosen because it would result in less impact to the occupants of the building during construction and the usability of floor plans. However, even with this retrofit approach, the elastic analysis still indicated that the walls were potentially overstressed. Even with the diaphragms extended to the outside face of the tower walls, some of the centerline shear walls and interior face tower walls were overstressed in shear at the lower levels. Additionally, even with the tower collectors, the tower walls were also overstressed in flexure and shear. Therefore, given that only some of the shear walls were overstressed in the north-south direction, and the tower walls were not significantly overstressed in the east-west direction based on the linear static analysis, it was felt that a nonlinear static analysis would verify that the shear walls would be adequate with only minor infilling of existing penetrations.

As shown in Figures 6 and 7, the nonlinear static analysis indeed showed the retrofitted building could satisfy both the Life Safety performance objective at the BSE-1 target displacement and the Collapse Prevention performance objective at the BSE-2 target displacement. In the north-south direction, the building could reach the Life Safety performance objective at the BSE-1 target displacement with shear yielding in only some of the walls. The building could reach the Collapse Prevention performance objective at the BSE-2 target displacement before the building formed the governing mechanism of shear yielding above the basement walls, as seen in Figure 8. In the east-west direction, the building could reach the BSE-1 level performance objective with some initial flexural yielding of the towers followed by shear yielding after the BSE-2 level target displacement was reached as seen in Figure 9.

Even with the use of advanced analysis, there were several deficiencies that required remediation. In particular, at the roof, while the gypsum was reinforced with weld wire fabric, there was a lack of shear connection between the gypsum concrete diaphragm and the steel girders in the north-south direction. Furthermore, the connections of the steel girders in the north-south direction to the centerline walls and tower walls were insufficient to resist the cross-tie loads for the roof. Finally, the open web steel joists were insufficient to resist the cross-tie loads for the roof in the east-west direction.

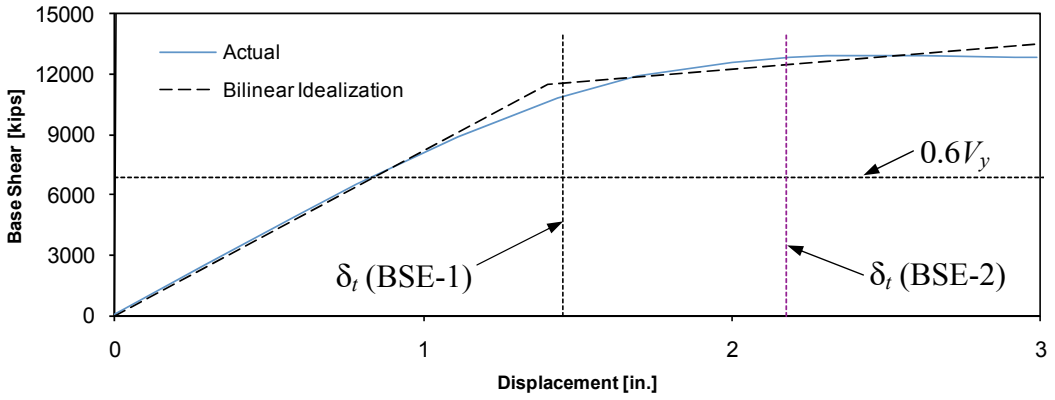


Figure 6. Typical pushover response (push to north)

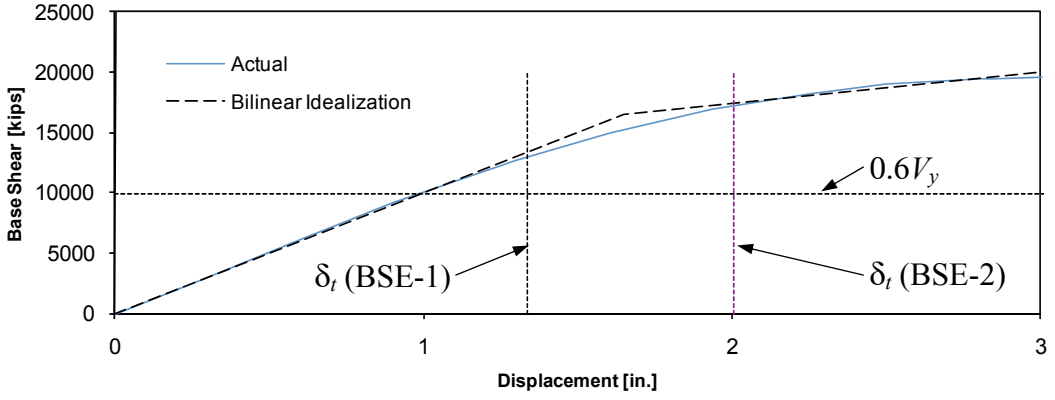


Figure 7. Typical pushover response (push to west)

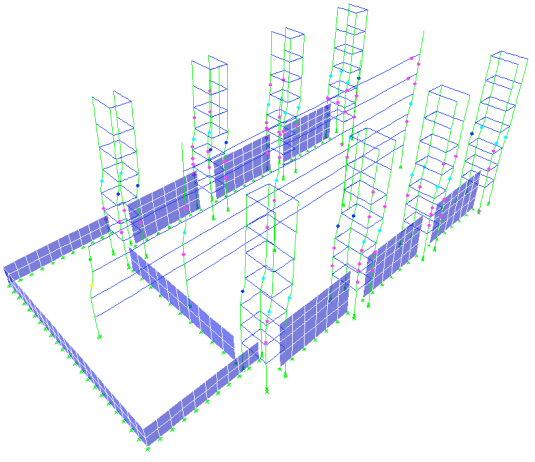


Figure 8. Typical pushover response (push to the north)

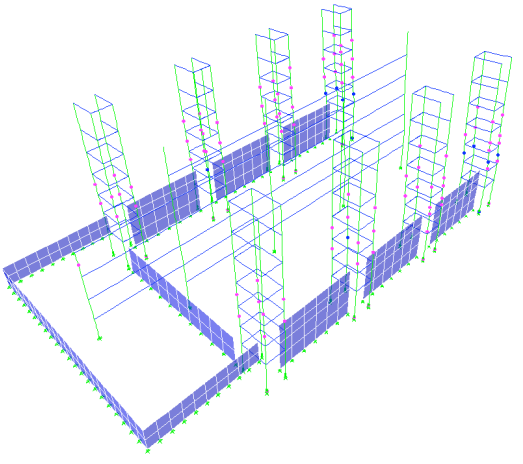


Figure 9. Typical pushover response (push to the west)

SPECIFIC DEFICIENCIES AND RETROFIT SOLUTIONS

While the replacement of the roof was a possible solution to the deficiencies in load path and cross-ties, the impact to the occupants would have been extensive. Alternatively, the fact that the metal deck strips of roof between the towers was lower than the gypsum concrete roof was used to good effect in adding new concrete over metal deck strips of roof over each of the existing metal deck roof strips. This new strip of roof was supported by new steel girders spanning from the interior corners of the towers at gridlines E and G to the walls along gridline F. The new roof was connected to the existing open web steel joists at the sides of the gypsum concrete roofs, transferring the east-west seismic loads from the gypsum concrete into the concrete strip and, ultimately, to the tower walls through the new steel girders. The new roof strips also served as beams to confine the gypsum concrete roofs through bearing in the north-south direction and transferring the seismic loads to the centerline walls along gridline F and the interior walls of the towers along gridlines E and G. Also, the new steel girders that support the roof strips between gridlines 5 to 6 and 7 to 8 served to support raised mechanical platforms which contained new mechanical equipment for the building, part of the modernization of the HVAC systems.

As previously mentioned, the tower walls along gridlines 3 and 10 were capable of resisting the lateral loads of the building as there were no collectors for these walls in the original design. Therefore, vertical steel plates were bolted to the outside face of the concrete tower walls and behind the brick facade as the brick was removed and replaced. These vertical plates were spliced with horizontal plates inside the building which were through-bolted to the precast tee beam that spans in the east-west direction between gridline F and either E or G. These horizontal plates were recessed into the 3” topping slab on top of the precast tee beams, the topping slab was then repaired flush with the surrounding floor so as not to interfere with the use of the floor.

The remediation of one of the main seismic deficiencies of the building involved the need to increase the amount of shear wall in the north-south direction. The centerline shear walls were inadequate when simply combined with only the interior face of the tower walls given the numerous door openings in these walls. The exterior face of the tower walls needed to be engaged, and the diaphragm needed to be extended to these walls for this to occur. While extending the floor slabs out to the outside face of the towers was considered, it was not attractive due to the high cost and impact to the occupants from the associated construction. Therefore, a horizontal steel truss solution was developed that would be less costly and faster to construct, would have much less impact on the building occupants, and would integrate with the aesthetic look the architect was designing for the modernized building. The trusses, some measuring as much as 17 by 50 feet, were designed to be fabricated off-site, trucked in, and then lifted into place as one complete unit. The connections to the edge beams and the sides of the towers were designed to receive the trusses as the trusses were

slid into place by a crane. The brick was repaired around these connections giving a clean, modern look to the trusses and the building as shown in Figure 10.



Figure 10. East elevation showing exterior trusses

CONCLUSIONS

Through the use of nonlinear static analysis and creative problem-solving, a seismic retrofit for the building was designed to achieve the desired seismic performance using primarily the existing structural components. The addition of new structural elements was kept to a minimum, and most of the work involved strengthening connections and utilizing existing structural framing. The new elements that were added served multiple purposes, beyond the basic seismic structural purposes. The new roof, while strengthening the roof diaphragm, also supported the new mechanical equipment that was part of the modernization of the research labs. Placing the new equipment and associated ductwork on the roof allowed the existing equipment and ductwork in the basement to remain operational for the continued use of the lab spaces while most the rest of the construction project progressed. The horizontal trusses, while capturing the exterior tower walls for lateral resistance, also featured prominently in the architect's modernization of the overall appearance of the building.

Central to all of the seismic strengthening work was the theme of minimizing the impact to the occupants; the important research in the science facility was conducted and student lessons continued uninterrupted during construction. This was accomplished through keeping as much of the construction work outside the building

as possible and modifying the envelope of the building as little as possible; thus minimizing the dust, vibration, and noise inside the building during construction.

Ultimately, the approach taken to analyze and strengthen the building satisfied the university and state's goals for this project. The new building stands as a prominent example of the university and state's desire to promote seismic safety and sustainability. Accordingly, the building has already hosted a tour for representatives from nearly 20 Pacific Rim countries, which was organized by the U.S. State Department, World Affairs Council, for the purpose of showcasing the state's commitment. Additionally, the building has been featured by National Geographic in a filmed segment focusing on the state's proactive steps to implement seismic safety and sustainability. On a local level, through a presentation to the student chapter of ASCE, the building has recently served the engineering students of the university as an example of a seismic retrofit project. This project also will continue to serve as a teaching example for future engineering classes.

REFERENCES

American Society of Civil Engineers (ASCE). (2003). *Seismic Evaluation of Existing Buildings,* ASCE/SEI 31, Reston, Va.

American Society of Civil Engineers (ASCE). (2006). *Seismic Rehabilitation of Existing Buildings,* ASCE/SEI 41, Reston, Va.

Computers and Structures, Inc. (2008), ETABS (Version 9), Berkeley, Ca.

Google (2007), Google Earth (Version 6), Mountain View, Ca.

Pikaso Software Inc. (1994), RcSection (Version 1.3), Ottawa, Ontario, Canada.

Impact of I-35W Bridge Failure on State Transportation Agency Bridge Inspection and Evaluation Programs

S. Alampalli[1] and K.C. Rehm[2]

[1]Director, Structures Evaluation Services Bureau, New York State Department of Transportation, Albany, NY 12232; PH (518) 457-5498; FAX (518) 457-6945; email: salampalli@dot.state.ny.us
[2]Engineering Program Manager - Bridges and Structures, Hydrology and Hydraulics, American Association of State Highway and Transportation Officials, 602 Idlewood Drive, Mount Juliet, TN 37122; PH: (859) 433-9623; email: krehm@aashto.org

ABSTRACT

The unfortunate collapse of the I-35W Bridge in Minneapolis, Minnesota in August 2007 has brought bridge safety to the forefront of the public. The immediate reaction to the incident was focused on highway bridge inspection and evaluation practices, especially related to inspection and evaluation of gusset plates on truss bridges. There were several directives from federal and state authorities to address these issues in the short-term and long-term. The short-term directives were to address the inspection and evaluation of gusset plates on truss bridges similar to the collapsed I-35W bridge. For the long-term, Congress and the bridge industry have focused on reviewing current practices in bridge inspection and bridge management, identifying gaps and issues with current practices and policies that can be improved in the future, and providing methodologies to effectively utilize available limited resources using risk based methodologies. This paper will discuss these issues from the owners' perspective based on the authors' involvement and experience in working with state and other transportation agencies on such issues.

INTRODUCTION

The deck truss of the eight-lane I-35W Highway Bridge over the Mississippi River in Minneapolis, MN collapsed on August 1st of 2007 causing 13 deaths and 145 injuries (see Figure 1). The detailed studies by the National Transportation Safety Board (NTSB) attributed the collapse to inadequate load capacity of a gusset plate that failed under a combination of substantial increase in the weight of the bridge due to previous modifications and the traffic and concentrated construction loads on the bridge on the day of the collapse (National 2008). The gusset plate was under-designed and did not have adequate load capacity. But before this was made clear, the immediate focus of the owners and regulating agencies had been on inspection and evaluation aspects and possible improvements.

As a reaction to any failure, the immediate focus of bridge owners and the government (both federal and local) is to assure the public that these types of bridges in their jurisdiction are safe and take appropriate actions to avoid such failures in the future. This involved identification of all such structures, initial quick visual

inspections, followed by detailed inspections and evaluations as more and more information became available. Issues were resolved by incorporating appropriate policies and initiating research required to make the programs better in the long-term.

This paper briefly discusses the major studies conducted after I-35W Bridge collapse to prevent such failures in the future with emphasis on efforts by the New York State Department of Transportation (NYSDOT) and the American Association of State Highway and Transportation Officials (AASHTO).



Figure 1. I-35W Bridge Failure (Courtesy: Minnesota DOT Web site)

MAJOR STUDIES AND OUTCOMES

This section briefly describes some of the efforts by NTSB, Government Accountability Office (GAO), American Society of Civil Engineers (ASCE), AASHTO, and Federal Highway Administration (FHWA) in the bridge inspection and evaluation area.

NTSB Study. NTSB has investigated the I-35W failure to determine the probable cause of the accident and made recommendations to prevent similar failures from occurring in the future. Based on their study, NTSB identified five safety issues in the investigation (National 2008): 1) Insufficient quality control procedures by the bridge design firm for designing bridges and insufficient federal and state procedures for reviewing and approving bridge design plans and calculations. 2) Lack of guidance for bridge owners in regard to the placement of construction loads on bridges during repair or maintenance activities. 3) Exclusion of gusset plates in bridge load rating calculations. 4) Lack of inspection guidance for condition of gusset plate distortion. 5) Inadequate use of technologies for accurately assessing the condition of gusset plates on deck truss bridges. NTSB made several recommendations to FHWA and AASHTO and urged them to take action on these safety recommendations in order to prevent failures in the future.

GAO Study. After the I-35W Bridge collapse, the GAO prepared a report to Congressional Committees on the U.S. Department of Transportation's ability to prioritize resources for bridges (United 2008). The Highway Bridge Program (HBP) is considered one of the primary sources of federal funding for bridges and this study examined the use and effectiveness of this funding based on the review of program documents, bridge data analysis, and meetings with transportation officials in states that have high levels of HBP funding and large bridge inventories. The report concluded that the current HBP program, while generally helping to improve bridge conditions (see Figure 2), does not have goals and performance measures that align with federal funding. The report also found no-ties between the HBP funding and bridge performance and lack of data to ascertain the effectiveness of HBP. The report made several recommendations to improve the focus, performance, and sustainability of the HBP.

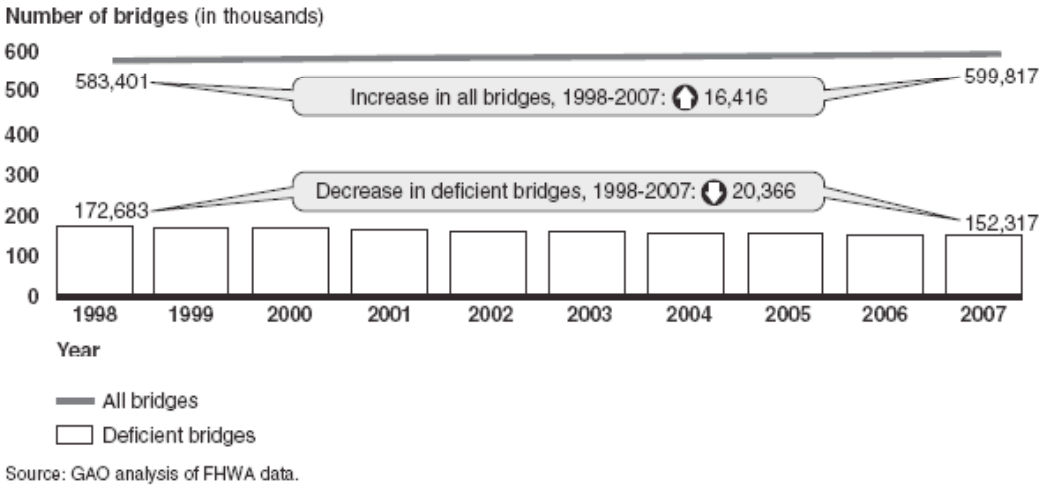


Figure 2. Trends in Numbers of Bridges and Deficient Bridges, 1998 through 2007 (Source: GAO-08-1043, Page 26)

Structural Engineering Institute (SEI) of ASCE. There were several non-government efforts on identifying the gaps in bridge inspection and management practices. One such effort was initiated by SEI. SEI formed a joint ad-hoc group with members from SEI and AASHTO. (Authors of this paper were part of this ad-hoc group.) This group discussed bridge inspection and rating methods and practices used to ensure the safety of highway bridges in the United States. The group concluded that, in general, the current National Bridge Inspection Standards (NBIS) and programs developed to address those standards have adequate policies and procedures in place to ensure public safety (White Paper 2009). The group also concluded that the current system can be improved and identified gaps and needs to improve bridge safety and ensure uniformity, consistency, and reliability of bridge inspections nationwide. Four of these are listed here: 1) A more rational, risk-based approach considering factors such as the design, details, materials, age, and loading of specific bridges to determine the appropriate inspection intervals for bridges as opposed to a set 24 month cycle. 2) New and more assertive types of quality control and assurance, such as performance testing of inspectors that could be used to encourage consistency

of inspections. 3) Close collaboration between those responsible for maintenance and repair of a bridge and those responsible for bridge inspection. 4) Accurate definitions of terms such as structurally deficient, functionally obsolete, and fracture critical to make public perception of bridge safety consistent with the facts.

AASHTO. AASHTO, representing all state transportation agencies, provided the required information and data to investigators of all the above studies, as well as providing information to the public and to politicians through testimonies and hearings. They also collected, as needed, information from all the states through questionnaires and surveys.

NTSB made several recommendations to AASHTO regarding bridge inspection and management issues (National 2008); and AASHTO took appropriate actions as noted below.

H-08-21: Revise AASHTO Manual for Bridge Evaluation (MBE) to include guidance for conducting load ratings on new bridges before they are placed in-service: AASHTO Subcommittee on Bridges and Structures (SCOBS), at their annual meeting, approved changes to the MBE which includes language that further clarifies the purpose of load rating. The new language includes information stating that as-built construction and shop drawings should be used rather than design drawings to calculate load ratings, and emphasizes that load ratings should be reviewed and updated if necessary during every inspection cycle. These updates to the MBE are available as an Interim as of January of 2010 (Manual 2010).

H-08-22: Modify the guidance and procedures in MBE to include evaluating the capacity of gusset plates as part of the load rating calculations performed for non-load-path-redundant steel truss bridges: The AASHTO SCOBS approved changes to the MBE that outlined inspection methods of gusset plates and connections as well as methods for load rating of gusset plates. Also included in the updates to the MBE is reference to the FHWA memorandum addressing guidance on load rating of gusset plates. These updates to the MBE are available as an Interim as of January of 2010 (Manual 2010).

H-08-23: When the findings of the FHWA/AASHTO joint study on gusset plates become available, update the MBE: Upon completion of the NCHRP Project 12-84, "Guidelines for the Load and Resistance Factor Design and Rating of Riveted and Bolted, and Welded Gusset-Plate Connections for Steel Bridges," AASHTO will review and consider incorporating appropriate recommendations from this study into AASHTO specifications as soon as practical.

H-08-25: Include gusset plates as a commonly recognized structural element (CoRe) and develop guidance for bridge owners in tracking and responding to potentially damaging conditions in gusset plates, such as corrosion and distortion; and revise the AASHTO Guide for Commonly Recognized (CoRe) Structural Elements to incorporate the new information: The CoRe document (Guide 2010) was amended with an Interim, and now includes gusset plates.

In addition to the response to the NTSB recommendations, AASHTO has also recognized the need for a better, easier to use document outlining Element Level Bridge Inspection Practices. In 2010, a new Guide Manual for Bridge Element Inspection (Guide 2011) was developed and accepted by SCOBS. This manual will supersede the *CoRe* Manual in the future and will be available in print in January

2011. The new element guidelines will also be incorporated into the PONTIS bridge management software in 2011.

FHWA. The immediate efforts of Federal Highways was for their division offices to offer support to the states during the mandated immediate inspections and to provide communication channels from the federal government. The FHWA Office of Bridge Technology also worked closely with AASHTO participating in immediate conference calls with all the states to discuss reactions to the collapse.

Also in response to the I-35 W Bridge collapse, on January 15th 2008, FHWA issued Technical Advisory 5140.29 "Load-carrying Capacity Considerations of Gusset Plates in Non-load-path-redundant Steel Truss Bridges" giving guidance for load rating of gusset plates. Since then, webinars and support have been given to the states to enact these methods.

After NTSB completed their investigations the following recommendations were made to FHWA concerning bridge inspection and management.

H-08-18: Require that bridge owners assess the truss bridges in their inventories to identify locations where visual inspections may not detect gusset plate corrosion and where, therefore, appropriate nondestructive evaluation technologies should be used to assess gusset plate condition: The FHWA concurred with this recommendation to supplement visual inspection with appropriate nondestructive evaluation methods to more thoroughly assess gusset plate condition as necessary. The FHWA evaluated feasible alternatives for nondestructive evaluation of locations where visual inspections may not detect gusset plate corrosion. FHWA also cooperated and collaborated with AASHTO and bridge owners to study options that are practical and could be effectively put into practice in compliance with this recommendation and NBIS. These findings are now being shared with the states.

H-08-19: Modify the approved bridge inspector training as follows: (1) update the National Highway Institute training courses to address inspection techniques and conditions specific to gusset plates, emphasizing issues associated with gusset plate distortion as well as the use of nondestructive evaluation at locations where visual inspections may be inadequate to assess and quantify such conditions as section loss due to corrosion; and, (2) at a minimum, include revisions to reference material, such as the Bridge Inspector's Reference Manual, and address any newly developed gusset plate condition ratings in the American Association of State Highway and Transportation Officials commonly recognized (CoRe) structural elements: The FHWA has begun the process of updating and revising the inspection training courses offered through the National Highway Institute and other reference documents, such as the Bridge Inspector's Reference Manual, to emphasize inspection issues associated with gusset plates, including corrosion and distortion.

National Highway Bridge Reconstruction and Inspection Act of 2008 (S. 3338): After the I-35W Bridge failure, a legislation at the national level was proposed in the previous Congress to authorize additional funding to improve bridge infrastructure condition. The legislation proposed strengthening bridge inspection standards, adopting a risk-based prioritization process for certain bridge rehabilitation and replacement projects, required that states develop 5-year performance plans for bridge

inspections and for the rehabilitation or replacement of deficient bridges, and required states to develop and implement a bridge management system. The proposed legislation had several implications on the bridge inspection and evaluation program, but was never acted upon.

STATE EFFORTS

The immediate reaction of most states has been to check their inventories for number, location, and condition of bridges similar to I-35W (i.e. deck truss bridges) to review their condition and to provide this data to the public. Most of these structures were inspected as soon as possible with their load ratings reviewed. As the details of the failure and gusset plate issues surfaced, the policies governing the construction loads, including gusset plates in detailed bridge inspections, and inspection procedures were reviewed with appropriate changes made to assure safety and adhere to mandates. New York State experience is given below. It is the authors' opinion that similar actions might have been taken in other states, but exact actions might vary depending on the structure of the State Transportation agencies, local practices, bridge ownerships, etc.

NY State Efforts. (Annual 2008 and 2009) In response to the tragic collapse of the I-35W Bridge in Minneapolis on August 1, 2007, the Governor of New York State established a Task Force, chaired by the NYSDOT Executive Deputy Commissioner and comprised of participants from the New York State Department of Transportation, New York State Thruway Authority, New York State Bridge Authority, and the Metropolitan Transportation Authority. The Task Force was directed to determine whether bridges in New York State of similar design and type as the I-35W bridge continued to be safe to use, to review the State's bridge inspection standards and procedures, and to report back to the Governor in 30 days.

There are 49 deck truss highway bridges in New York State. Of the 49, twenty are State-owned, 12 are locally owned, 15 are owned by authorities, and 2 are highway bridges owned by railroads. All 49 bridges had visual inspections completed by August 31, 2007. Detailed, hands-on inspections were also completed on each of these bridges by October 17, 2007. The visual inspections and the more detailed inspections found that these structures are safe and the current inspection protocols are adequate to ensure the safety of the traveling public. The Task Force concluded that all the public highway bridge owners are meeting or exceeding the standards for bridge inspection and safety assurance that were established by NYSDOT pursuant to Federal regulations, 23 CFR Part 650, and Article 9 of the Highway Law as amended by the State's Graber Law -- Chapter 781 of the Laws of 1988.

Two reports summarizing Task Force activities were prepared and submitted to the Governor: an initial report issued on August 31, 2007 and a final report issued on November 30, 2007. These reports (New York 2007a and 2007b) may be viewed on the Department's Website at www.nysdot.gov/bridgedata.

Following the National Transportation Safety Board recommendations and a related Federal directive, all the truss bridges were screened to ensure that the gusset plates had been adequately designed. An implementation plan was developed to achieve this result with specific guidance and direction developed and issued for

reviewing the adequacy of existing bridge gusset plates in accordance with FHWA's Technical Advisory. The Department developed software for analysis of gusset plate capacity and also organized a training session on the use of the developed software and associated methodology. All of the 132 truss bridges identified as meeting the criteria outlined in the Federal Advisory were analyzed to ensure that the gusset plates had been adequately designed. These efforts found no design related deficiencies. At the same time, these efforts revealed some deterioration related deficiencies in about 10 of the bridges and these were addressed through repairs, postings, or closure of the bridges.

Due to public awareness and interest in bridge data, a website (www.nysdot.gov/bridgedata) was created with the latest bridge inspection and condition data that is updated periodically. This website also gives relevant information on bridge condition definitions, the bridge inspection program, and bridge statistics.

A research project is also in progress to document quantitatively the variability of condition scores associated with the New York State Bridge Inspection Program, suggesting improvements to policy and procedures and areas requiring further training, if needed, to reduce the variability and improve the reliability/consistency of the program. The project is expected to be completed in 2011.

SUMMARY

The unfortunate collapse of the I-35W Bridge, similar to other past bridge failures, brought bridge safety to the forefront of public attention. Several studies were conducted by public and private agencies to review the failure and take steps to avoid such failures in the future. Connections have always been included as part of the primary members, but generally were designed to be stronger than the primary members. Thus, they normally do not control the design and hence, were not included in most load rating analyses. These will be included by the owners in the future load rating analyses as they could be a controlling factor when deterioration affects them. Considerable research is on-going on the use of advanced technologies for bridge health monitoring and risk based evaluations that may be incorporated into practice in the coming decade.

ACKNOWLEDGEMENTS

Authors thank Linda Banks for proof reading this paper. The views expressed in this paper are those of the authors and not necessarily of the organizations they represent.

REFERENCES

Annual Report on Bridge Management and Inspection Programs: State Fiscal Year 2007-08. (2008). New York State Department of Transportation, Albany, NY.

Annual Report on Bridge Management and Inspection Programs: State Fiscal Year 2008-09. (2009). New York State Department of Transportation, Albany, NY.

Guide Manual for Bridge Element Inspection, 1st Edition. (2011). American Association of State Highway and Transportation Officials, Washington, D.C.

Guide for Commonly Recognized Structural Elements with 2010 Interim Revisions. (2010). American Association of State Highway and Transportation Officials, Washington, D.C.

Manual for Bridge Evaluation, 1st Edition with 2010 Interim Revisions. (2010). American Association of State Highway and Transportation Officials, Washington, D.C.

National Transportation Safety Board (NTSB). (2008). Collapse of I-35W Highway Bridge, Minneapolis, Minnesota, August 1, 2007. Highway Accident Report, , NTSB/HAR-08/03, Washington, D.C.

New York State Bridge Task Force Report to the Governor, Status of Bridge Review. (2007a). New York State Department of Transportation, Albany, NY, August 31, 2007.

New York State Bridge Task Force, Final Report to the Governor, Completion of Bridge Review. (2007b). New York State Department of Transportation, Albany, NY, November 30, 2007

United States Government Accountability Office (GAO) Report to Congressional Committees. (2008). Highway Bridge Program: Clearer Goals and Performance Measures Needed for a More Focused and Sustainable Program, GAO-08-1043.

"White Paper on Bridge Inspection and Rating." (2009). ASCE/SEI-AASHTO Ad Hoc Group on Bridge Inspection, Rating, Rehabilitation, and Replacement, Journal of Bridge Engineering, ASCE, 14(1).

Simple Check for Yielding in Truss Bridge Gusset Plate Connections

J.W. Berman[1], B.S. Wang[2], A. Olson[3], C.W. Roeder[4], D.E. Lehman[5],

[1]Assistant Professor, Department of Civil and Environmental Engineering, University of Washington, Seattle, WA 98195, jwberman@u.washington.edu
[2]Research Assistant, Department of Civil and Environmental Engineering, University of Washington, Seattle, WA 98195
[3]Research Assistant, Department of Civil and Environmental Engineering, University of Washington, Seattle, WA 98195
[5]Professor, Department of Civil and Environmental Engineering, University of Washington, Seattle, WA 98195, roeder@u.washington.edu
[5]Associate Professor, Department of Civil and Environmental Engineering, University of Washington, Seattle, WA 98195, lehman@u.washington.edu

ABSTRACT

The failure of a large steel truss bridge in Minnesota has been, in part, attributed to overstressed and buckled gusset plates. This catastrophic event signaled concerns of the potential for a similar overstressed state in gusset plates in steel truss bridges across the county. To provide guidance to bridge engineers, the Federal Highway Administration released FHWA Bridge Design Guidance No. 1 Load Rating Evaluation of Gusset Plates in Truss Bridges; however, the somewhat complex evaluation methods make rapid assessment costly for DOTs. A study supported by the Washington State Department of Transportation and FHWA has developed a procedure for rapid and reliable evaluation of the state of gusset plates, including the maximum stresses and likelihood of yielding. The development utilized a parametric study of several gusset plate configurations performed using advanced nonlinear finite element analysis. Parameters such as plate thickness, yield stress, and load distribution were considered for actual gusset plate connections from bridges primarily in Washington State. The selected gusset connections also had different geometries to ensure the resulting evaluation approach is sufficiently broad in applicability. The new approach should enable bridge engineers to more expediently evaluate the capacity of gusset plates, allowing gusset plates with near critical demand-to-capacity ratios to be identified for further, more refined analysis or retrofit. The paper and presentation will detail the analyses and resulting rapid gusset plate evaluation procedure.

INTRODUCTION

A Federal Highway Administration report (Ocel and Wright 2008) has demonstrated that several of the gusset plates on the collapsed I-35 Mississippi River Bridge in Minneapolis were significantly over stressed and has identified the inelastic buckling of one of the plates in particular as a likely cause of the collapse. Thus, there is an urgent need to evaluate the safety of gusset plates on such bridges across the county. In response, FHWA has released *Load Rating Guidance and Examples for Bolted and Riveted Gusset Plates in Truss Bridges* (FHWA Guide, FHWA 2009) which provides Departments of Transportation (DOTs) with guidance for gusset plate evaluation. In addition to checking the resistance of fasteners, the recommended approach includes four plate checks: compressive buckling, tension, shear and block shear. The shear check requires point-in-time truss element loads (denoted concurrent loads) for consistent estimation of the shear stress rather than envelope loads, which can make the check cumbersome

and time consuming. While it is important that gusset plates be evaluated, the number of truss bridges that have failed relative to the total number of truss bridges in service suggests that the number of over stressed gusset plates on steel truss bridges throughout the U.S. is small. Thus, a rapid evaluation procedure that is appropriately conservative but can be easily and cost-effectively applied is warranted. The procedure should identify gusset plates that are highly stressed and warrant more detailed investigation while quickly demonstrating that many others are not of concern.

This paper describes analytical research that develops a rapid procedure to identify highly stressed gusset plates, denoted the Triage Evaluation Procedure (TEP). In the process of this development, extensive nonlinear analyses are performed which show the relationships between the TEP, the procedure in the FHWA Guide, and expected gusset plate performance. Three bridges in the Washington State Department of Transportation (WSDOT) inventory were selected for this research, each with different geometries and gusset plate configurations. Global analysis of each bridge was performed to establish realistic gusset plate loads and load distributions. Results of the global bridge analyses were used to select gusset plate geometries from each bridge for high resolution finite element analysis. Finite element (FE) models of the three selected gusset plates and the suspect gusset from the I-35 bridge were developed and used to study the onset of yielding, the interactions of gusset plate stresses generated from loads in the truss elements, and gusset buckling. For each gusset plate model several analyses were conducted with different gusset plate thicknesses and load distributions to clearly establish initiation of yielding and buckling

BRIDGE AND GUSSET PLATE DESCRIPTIONS

Elevations and photographs of the three bridges from the WSDOT inventory selected for use in this research are shown in Fig. 1. Two are deck truss bridges that cantilever off inner piers and have simply supported drop-in trusses in the middle (BR 31-36 and BR 101-217) and one is a simply supported through truss (BR 90-134N). Open circles in Fig. 1 indicate locations where hinges were included in the trusses via large pins to allow the center portions of the deck trusses to remain simply supported and to allow for thermal movements. Each bridge carries two lanes of traffic, with BR 90-134N carrying two lanes that travel in the same direction. The bridge shop drawings are dated 1930 for BR 101-217, 1949 for BR 90-134N, and 1950 for BR 31-36.

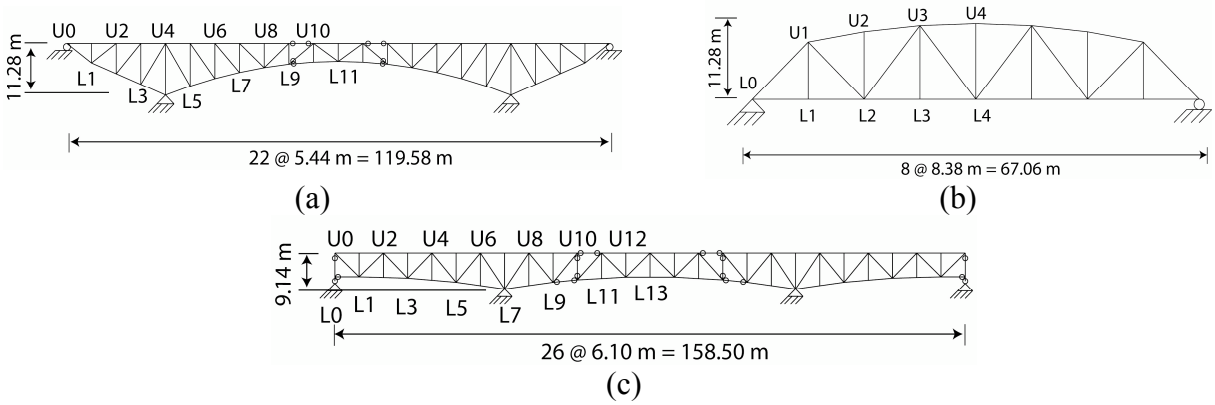


Figure 1. Elevation schematics and photographs of WSDOT bridges: (a) BR 101-217, (b) BR 90-134N, (c) BR 31-36.

Global two-dimensional analysis of each truss was performed for dead load and the HS-20 live loads (AASHTO Manual for Bridge Evaluation, AASHTO 2008) to identify gussets with high stresses and unique geometry for detailed FE modeling. Tension and compression Whitmore stresses for all members connected at a joint were used as indicators of gussets with relatively high stresses**.** One gusset plate connection from each bridge described above was selected for detailed.

Each selected joint is shown in Fig. 2. Joint L5 from BR 101-217 (Fig. 2a) is a lower chord connection with 9.5 mm (3/8 in.) thick gusset plates positioned between the back-to-back channels and the diagonal and vertical members pass between the gusset plates with the vertical member extending through to the bottom flange of the chord. The steel is specified as "Structural O.H. Steel", which for the purposes of this research was taken to have a specified yield stress of 207 MPa (30 ksi). Joint L9 from BR 31-36 (Fig. 2b) has two 13 mm (1/2 in.) thick gusset plates that are riveted to the outer faces of the truss members. This connection is at a hinge location in the truss and has a zero force chord member attached (L9-L10) with a large pin along where secondary plates increase the bearing strength of the pin hole for construction loads. All steel for this bridge was specified as A7 with a specified yield stress of 228 MPa (33 ksi)**.** Joint L2 from BR 90-134N (Fig. 2c) has two 13 mm (1/2 in.) thick gusset plates located on the outer faces of the members that were specified as silicon steel, for which a specified yield stress of 310 MPa (45 ksi) is assumed. The gusset also serves as a chord splice, where the splice is offset from the midpoint of the gusset, with the connection for Chord L2-L4 being longer. Joint U10 from the I-35 Bridge in Minneapolis (Fig. 2d) was also considered, since it serves as a baseline and comparison to other analytical studies. It is described in detail in Ocel and Wright (2008).

The selected gusset plates provide considerable variation in geometry and gusset plate layout as may be encountered in practice. The distribution of load between members attached to the gusset plates and the thickness of the gusset plates were additional parameters considered in the analytical research.

A suite of load distributions was considered because of the wide variability in dynamic bridge loading and necessity that loads satisfy equilibrium in FE analysis. These variations evaluated their impact on the stress distribution, occurrence of yielding, and buckling capacity of the gusset plates. The load distributions for the gusset plates from the three WSDOT bridges were determined by moving an HS-20 live load over the bridge in the global analyses and factoring the results to be consistent with the Load Factored Rating (LFR) Operating Rating Level per AASHTO (2008), including impact.

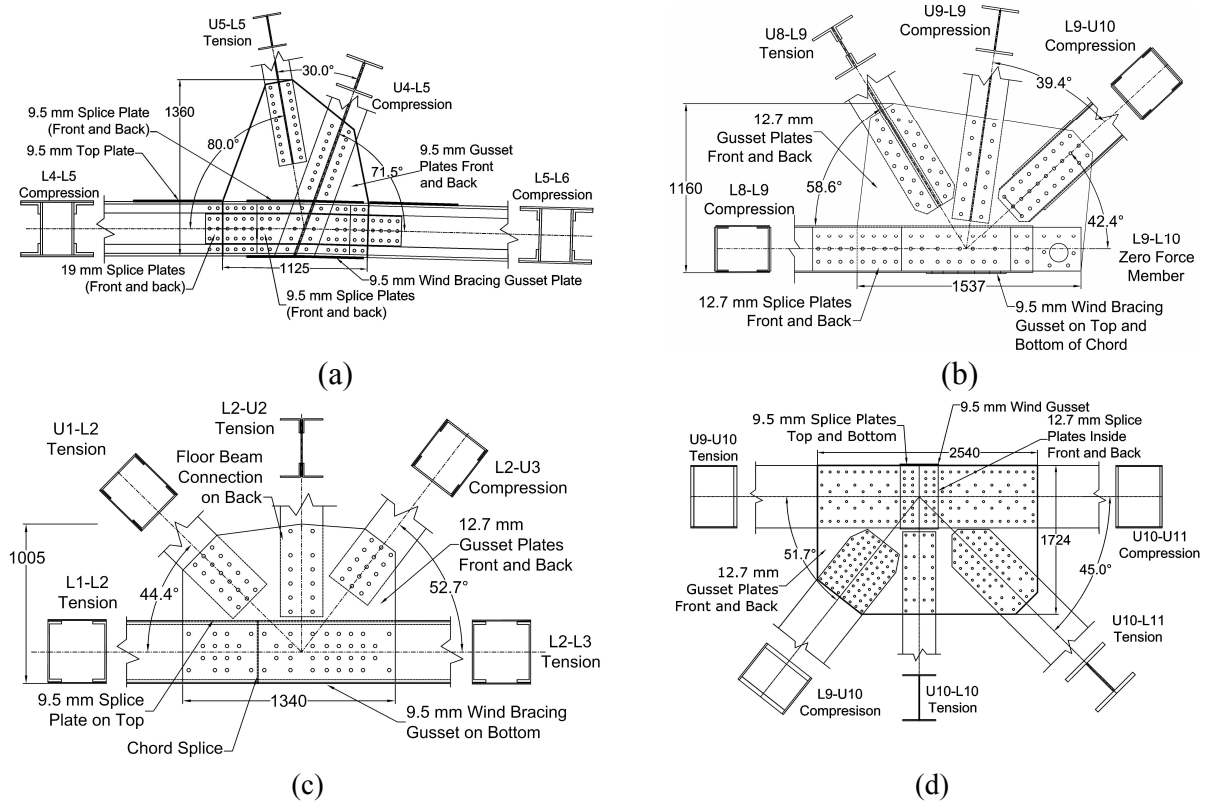


Figure 2. Selected gusset plate connections for detailed evaluation: (a) Joint L5 BR 101-217, (b) Joint L9 BR 31-36, (c) Joint L2 BR 90-134N, and (d) Joint U10 I-35.

FE MODELS

Detailed FE models of each connection were developed using the ANSYS software package (ANSYS 2008) as shown in Fig. 3 for Joint U10 of the I-35 Bridge. All models had similar features except as noted in this discussion. Four-noded reduced integration shell elements were used to model the gusset plates, splices, wind bracing plates and truss members in the vicinity of the gusset plates, as shown in Fig. 3. A mesh refinement study found that a 25 mm (1 in.) average element edge length was adequate and produced similar stress distributions and stress magnitudes at key points as models with smaller mesh sizes. At a distance of twice the member depth, *d*, from the gusset edge the truss members were transitioned to beam elements. A plane-sections-remain-plane master-slave constraint was applied at this transition. The beam elements ended at adjacent panel points where all degrees of freedom except translation in the member's axial direction were restrained. Loads were applied in the axial direction of the members at these adjacent panel points. Restraint was provided against out-of-plane gusset displacement at the locations where wind bracing and/or floor beams connected to the gusset. Gusset L2 of Bridge 90-134N had a floor beam attached to it via a riveted web angle connection. In this case, floor beam loads were applied to the modeled connection at the rivet line of the floor beam web. The web angles were modeled completely and were riveted to the inner gusset plate of the joint.

All rivets were modeled as rigid fasteners. Translational degrees of freedom of nodes at rivet locations were constrained to be equal for members and gussets plates. Contact or gap elements were not used at the surfaces to simplify the modeling process and minimize computational time. This leads to conservative estimates of the gusset plate buckling load, since contact between

plates and members provides additional buckling restraint. All gusset plate and splice plate steel was modeled as bilinear kinematic hardening materials that had an initial modulus of 200 GPa (29,000 ksi) and 3% strain hardening. The strain hardening was found by linearizing the stress-strain results from tests on the I-35 Bridge gusset plate material reported in Ocel and Wright (2008). All shell and beam elements modeling truss members were assigned elastic material properties so that their nonlinear response would not influence the gusset plate response.

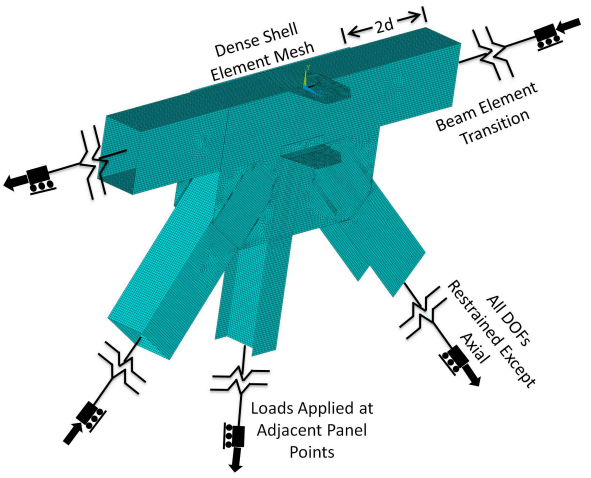


Figure 3. Finite element mesh for Joint U10 I-35 shown with schematic of typical boundary conditions.

DEVELOPMENT OF THE TRIAGE EVALUATION PROCEDURE

Based on the progression of gusset plate yielding described in Berman et al. (2011), the onset of yielding in a gusset plate is defined here to be when 0.5% of the gusset plate area has Von Mises stress above the yield stress of the material. It is important to note that this clearly does not constitute gusset plate failure; however, it is a stress state that may be of concern for bridge owners, since they would not want to exceed this stress too many times in the bridge's life. As a result, bridge engineers would require further investigation of a gusset plate which exceeded this stress state when it occurs under service loading.

To predict the onset of gusset plate yielding the interactions of the stresses generated from the connected truss members must be considered. Fig. 4 illustrates how the stresses from the two diagonal members connected to a gusset plate may interfere with each other. Here, a simple method for combining stresses is developed. While more complex and accurate methods may be possible and are the focus of future research by the authors, the objective of the current endeavor is to develop a conservative, simple and straightforward process for evaluating gusset plates for the onset of yielding.

The Whitmore method conservatively predicts the maximum uniaxial stresses in the gusset at the end of a riveted member connection, which are denoted σ_{11} and σ_{22} in Fig. 5. The TEP conservatively assumes these uniaxial stresses to be principle stresses. The most adverse condition occurs when these stresses for different members are orthogonal to each other and opposite in sign. When these conditions occur, the two dimensional Von Mises yield criterion can be used to demonstrate that yielding occurs when the Whitmore stress at the end of a member, σ_{11}, exceeds $\sigma_y/\sqrt{3}$, where σ_y is the yield stress of the gusset plate (Berman et a. 2011).

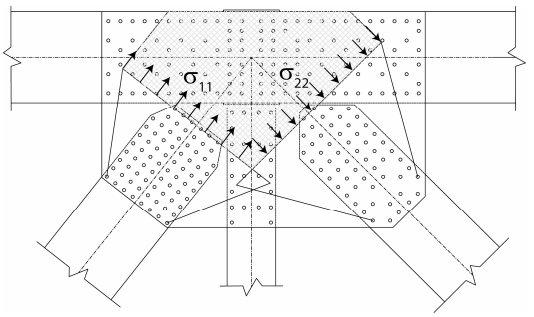


Figure 5. Interference of stresses in truss bridge gusset plates.

COMPARISON OF THE TEP AND FHWA GUIDE PROCEDURE

For each analysis that did not exhibit elastic buckling (typically gusset plates above 3.2 mm (1/8 in.) thick) the truss member loads at the point in the analysis where 0.5% of the gusset plate is yielding was recorded. Those loads were then used to compute the values shown in Table 1, which include the maximum uniaxial stress on the Whitmore section (considering all members) and the maximum gross shear stress (considering multiple shear sections), the latter calculated per the approach in the FHWA Guide. The values shown are for the gusset plates at their actual thicknesses and are shown for only one load distribution, although similar results were observed for other thicknesses and load distributions where elastic buckling did not occur. For Joint L5 of BR 101-217 no shear stress is shown because both possible shear lines pass through either a chord or vertical hanger since the chord is continuous through the gusset and the vertical hanger goes completely through the gusset to the bottom of the chord as shown in Fig. 2. The stresses shown Table 1 demonstrate that in all cases the maximum uniaxial stress on the Whitmore section and maximum shear stress are both below yield and in some cases are as much as 40% below yield when the onset of gusset plate yielding occurs. This result clearly shows that both the shear stress and Whitmore stress evaluations in the FHWA Guide do not identify the onset of gusset plate yielding. This result is not surprising since: (i) the shear stress evaluation assumes full shear yielding over the entire selected shear section, and (ii) yielding along the entire Whitmore width at the end of a truss member implies that the critical stresses are uniaxial and are not influenced by the stresses generated by other members, which was shown above to not be the case.

Table 1. Maximum shear and Whitmore stresses per the FHWA Guide at the onset of significant gusset plate yielding for Load Distribution Case 1.

	Gusset L5 BR 101-217		Gusset L9 BR 31-36		Gusset L2 BR 90-134N		Gusset U10 I-35 Bridge	
	τ_{max} (MPa)	$\sigma_{w,max}$ (MPa)	τ_{max} (MPa)	$\sigma_{w,max}$ (MPa)	τ_{max} (MPa)	$\sigma_{w,max}$ (MPa)	τ_{max} (MPa)	$\sigma_{w,max}$ (MPa)
1	107	133	85	140	101	262	148	237
F_y	207		228		310		345	
$F_y/\sqrt{3}$	119		132		179		199	

Examining the maximum uniaxial stresses along the Whitmore section at yield shown in Table 1, indicates that in all cases, it is greater than $F_y/\sqrt{3}$. Therefore, the proposed yielding check in the TEP is conservative with respect to indicating gusset plate yielding. The TEP

yielding check is a single stress check is made that accounts for the worst possible stress interactions without considering stresses at multiple sections and eliminating the need for concurrent point-in-time loads. The proposed yielding check is significantly faster to employ than the checks in the FHWA guide and should save DOTs considerable resources.

IMPLEMENTATION OF THE TRIAGE EVALUATION PROCEDURE

Here, the TEP and procedure from the FHWA Guide are used to evaluate various gusset plates, including those on the selected WSDOT bridges and Joint U10 of the I-35 Bridge. The fasteners are not evaluated since the focus of the TEP is to identify gusset plates that may be yielding and/or buckling. However, an evaluation of fastener capacity would be necessary as part of a complete joint evaluation. Further, a compression buckling check has been developed for the TEP but is not presented here for brevity (see Berman et al. 2011 for complete details).

Three loading conditions were considered for Joint U10 of the I-35 Bridge: (i) the loads denoted Step 2 in Ocel and Wright (2008), which are an estimate of the forces at the joint due to the dead loads when the bridge first opened for service, (ii) the loads denoted Step 3 in Ocel and Wright (2008), which are an estimate of the forces at the joint due to the dead loads after modifications were made to the bridge in 1999 and (iii) the estimated loads at the time of collapse as given in Ocel and Wright (2008). Table 3 shows demand-to-capacity ratios (DC ratios) for these three loading conditions for Joint U10, where the demand is the maximum Whitmore stress in the gusset considering all members and the capacity is $F_y/\sqrt{3}$ per the TEP. As shown in Table 2 the DC ratio is 1.04 for the Step 2 loading, which indicates this gusset plate was likely to be yielding under only dead loads when the bridge opened for service. With the addition of the construction and traffic loads estimated to be on the bridge at the time of collapse the DC ratio climbs to 1.42 for the TEP. Yielding of the gusset plates at both load levels has indeed been confirmed by finite element analyses conducted as part of this research and by those conducted by Ocel and Wright (2008). DC ratios are also shown for the limit states in the FHWA Guide with resistance factors per the LRFR procedure. For the three loading conditions the horizontal shear governed the capacity of the gusset plate with the factor Ω taken as 0.74 (see the FHWA Guide), resulting in DC ratios above 1.0 for both Step 3 and 4 loads. The values indicate the TEP is conservative relative to FHWA Guide.

Table 2. Capacity-to-demand ratios for Joint U10 of I-35 for Load Steps 2, 3, and 4 from Ocel and Wright (2008).

	Step 2 (Dead Loads 1965)	Step 3 (Dead Loads 1999)	Step 4 (Loads at Collapse)
Triage	0.96	0.78	0.70
FHWA Guide	1.02	0.83	0.78

Rating factors for legal loads for all joints were calculated for the three WSDOT bridges per the AASHTO Manual for Bridge Evaluation (AASHTO 2008) using the HS-20 live load as the legal load and assuming unknown average daily truck traffic. Rating factors (RFs) were calculated per LRFR using factored loads for the Service II load combination for the TEP and the Strength I load combination for procedure from the FHWA Guide and are shown in Tables 3, 4, and 5 for BR 90-134N, BR 31-36 and BR 101-217, respectively. The Service II load combination was selected for the TEP because the yielding check derived is not a failure mode,

but rather indicates the onset of yielding. In all cases, gusset plate yielding governed in the TEP over gusset plate buckling. Comparing the RFs from the TEP and FHWA procedure indicates that the TEP is conservative for all gussets considered.

Table 3. Rating factors for BR 90-134N gusset plates from the proposed Triage Evaluation Procedure with Service II loads and the approach in the FHWA Guide with Strength I loads.

	Joint Identification			
	U1	U3	L2	L4
Triage RF	2.33	1.41	2.20	2.00
FHWA RF	3.51	4.09	2.59	2.75

Table 4. Rating factors for BR 31-36 gusset plates from the proposed Triage Evaluation Procedure with Service II loads and the approach in the FHWA Guide with Strength I loads.

	Joint Identification						
	U2	U4	U6	U8	U10	U11	U13
Triage RF	1.02	2.81	1.95	1.84	5.24	1.08	2.61
FHWA RF	1.24	2.83	2.19	1.90	5.44	1.49	4.85
	Joint Identification						
	L1	L3	L5	L7	L9	L10	L12
Triage RF	1.13	1.82	2.10	3.75	0.78	2.48	1.50
FHWA RF	1.23	1.96	2.12	5.32	0.95	3.14	1.95

Table 5. Rating factors for BR 101-217 gusset plates from the proposed Triage Evaluation Procedure with Service II loads and the approach in the FHWA Guide with Strength I loads.

	Joint Identification								
	U2	U3	U4	U5	U6	U7	U9	U10	
Triage RF	0.93	1.07	1.92	1.68	2.14	1.50	1.15	2.38	
FHWA RF	1.35	1.55	2.47	2.29	2.79	2.02	2.86	2.94	
	Joint Identification								
	L1	L2	L3	L5	L6	L7	L8	L9	L11
Triage RF	1.83	2.25	0.98	1.50	1.74	1.25	1.31	1.24	2.40
FHWA RF	1.84	2.56	1.78	2.47	2.34	2.79	2.53	2.25	3.39

As shown in the tables only a few gusset plates have RFs less than 1.0 from the TEP and will require further investigation. This demonstrates that the procedure is not overly conservative when checked against Service II loads. No joints on BR 90-134N have an RF less than 1.0. On BR 31-36 only Joint L9 has an RF less than 1.0 from the TEP, and also has an RF less than 1.0 from the FHWA Guide procedures. This joint has stresses at Whitmore sections that approximate the assumptions used in the derivation of the yield check for the TEP, i.e., there are Whitmore stresses that are nearly orthogonal, equal in magnitude and opposite in sign. Therefore, this joint would require further investigation and may indeed be yielding under Service II loads. BR 101-217, has two joints, U2 and L3, with RF's less than 1.0 from the TEP and serves as an example

of the limitations of both the TEP and the FHWA procedure. Examining Joint L3 reveals that the RF from the TEP is governed by stresses at the Whitmore sections of the compression chords, which are milled-to-bear. Thus, if these chords are verified to still be bearing against each other they may be neglected and this joint will have an RF greater than 1.0. The RF values all demonstrate that the TEP is conservative relative to the FHWA Guide.

CONCLUSIONS

The currently recommended FHWA procedures for gusset plate evaluation may not identify all gusset plates in steel truss bridges that may be yielding under service loads. Analysis results indicate that a complex interaction of stresses is generated in gusset plates by connecting members and that this interaction can initiate gusset plate yielding when the uniaxial stresses on Whitmore sections associated with those connecting members are well below yield. A conservative and considerably simpler process for identifying gusset plates that may be yielding was developed and is recommended for identifying gusset plates that may need more detailed evaluation.

ACKNOWLEDGEMENTS

This work was supported in part by the Washington State Department of Transportation and the Federal Highway Administration. However, any opinions, findings, conclusions, and recommendations presented in this paper are those of the authors and do not necessarily reflect the views of the sponsors. The authors would like to specifically thank Washington State Bridge Preservation Engineer Harvey Coffman and Load Rating Engineer Mohamad Al-Salman for their invaluable contributions to this research.

REFERENCES

AASHTO (2008), Manual for Bridge Evaluation, 1st Edition, American Association of State Highway and Transportation Officials.

AISC (2002). Specifications for Structural Steel Buildings, American Institute of Steel Construction.

Berman, JW, Wang, BS, Olson, A, Roeder, CW, and Lehman, DL (2011). “Rapid Assessment of Gusset Plate Safety in Steel Truss Bridges” Journal of Bridge Engineering, (In revew).

FHWA (2009). Load Rating Guidance and Examples for Bolted and Riveted Gusset Plates in Truss Bridges. Publication No. FHWA-IF-09-014, Federal Highway Administration.

Ocel, J.M. and Wright, W.J. (2008). Finite Element Modeling of I-35 Bridge Collapse, Final Report, Turner-Fairbank Highway Research Center Report, Federal Highway Administration.

Lessons Learned from the Utah Experience: Suggestions for Implementing a Structural License and Practice Act in Your State

Author
Barry Kay Arnold, P.E., S.E., SECB *(**barrya@arwengineers.com**) has a Master of Science Degree from Utah State University. He is a Vice President at ARW Engineers in Ogden, Utah. Barry is a Past President of the Structural Engineers Association of Utah (SEAU) and serves as SEAU's Delegate to the National Council of Structural Engineers Associations (NCSEA). He is a member of the NCSEA Licensing Committee and the NCSEA Board of Directors.*

Abstract
Wading through the mechanics of writing a bill and getting support for structural licensing and practice acts can appear to be an overwhelming, difficult, and time-consuming experience. Working through the political process can especially be a challenge if you are unfamiliar with the motivating factors and back-room negotiations that typically influence a legislative decision. However, a number of Structural Engineers Associations (SEAs) have successfully worked through the legislative process and effectively lobbied for structural licensing and practice acts. Learning from their experience will provide you with the essential background information that you need to ensure success as you move forward toward structural licensing and practice acts in your state.

Because the specific methods of changing the licensing laws will vary from state to state, this session will focus on general topics that each state should have in common. Specifically, this session will include important information about establishing a firm foundation of support, emphasizing the reasons for a practice act, creating a vision that will motivate and inspire, developing strategies for success, presenting talking points that will have impact, and explaining why structural licensing and practice acts are essential. Additional topics will include understanding your legislators and actually writing the bill.

Discussion
Because a change in current licensing laws will be required to incorporate structural licensing and practice acts in most states, a review and understanding of the process and terms are beneficial. This paper provides any SEA and/or SEI Chapter that is pursuing structural licensing and practice acts some insight into the legislative and internal process to help create a winning strategy that will ultimately lead to success and better protection for the public.

The Three Components of the Bill to Change the Licensing Law

Structural Licensing

Structural licensing is a means of defining the credentials an individual must have in order to use the title, "structural engineer." Once these requirements are codified in each state's licensing laws, the term "structural engineer" will be protected such that only those engineers who have met them will be allowed to use it. This is called a title act; it does not create any restriction on the practice of structural engineering by other engineers, but does define the education, experience, and examination requirements of those using the title "structural engineer."

Practice Act

A practice act defines the types of buildings and structures that a structural engineer, as defined by the title act, must be responsible for designing. Restrictions based on structure size, height, use, occupancy, and proximity to high-risk regions are common.

Transition Clause (Grandfathering)

The transition clause, or Grandfathering as it has been called in the past, allows currently licensed and qualified professional engineers the opportunity to continue practicing structural engineering without conforming to the revised examination, education, and/or experience requirements defined in the title act. This is an important component of the process of changing the licensing laws and must be included when a change is made to the law. The purpose of the transition clause is to avoid restricting any existing business or individual from practicing in an area of engineering they have previously practiced in.

Writing the Bill to Change the Licensing Law

Writing the proposed changes to the current licensing laws may appear daunting, but it need not be. In fact, it is a simple process when it includes input from the division responsible for professional licensing and a legislative analyst. It involves taking the existing licensing language and adding to it or deleting portions from it.

Title Act Language

An example of a title act might look like this:

> Each applicant for licensure as a professional structural engineer shall meet the requirements for licensure as a professional engineer and:
>
> (a) submit an application in a form prescribed by the division;
>
> (b) pay a fee determined by the department under Section XX-XX-XX;
>
> (c) provide satisfactory evidence of good moral character;
>
> (d) have graduated and received an earned bachelors or masters degree from an engineering program meeting criteria established by rule by the division in collaboration with the board;

(e) have successfully completed three years of licensed professional engineering experience established by rule by the division in collaboration with the board;
(f) have successfully passed examinations established by rule by the division in collaboration with the board;
(g) meet with the board or representative of the division upon request for the purpose of evaluating the applicant's qualification for licensure.

Item (d) is the education requirement. Item (e) is the experience requirement. Item (f) is the examination requirement. The examination, that has been "established by rule," and in this case, is the NCEES 16-hour structural exam.

The specific examination requirement is generally contained in the rules and not in the law so that a change in the type of allowed examinations can be made by the licensing board and will not require legislative action.

In the above example, the Structural Engineering license (SE) is a post-Professional Engineer (PE) credential. This is a stance recommended by ASCE/SEI. Some states have opted instead to have SE applicants take either the PE exam or the SE exam, but not both.

Practice Act Language

An example of a portion of a practice act might look like this:

"Professional structural engineering or the practice of structural engineering" means a service or creative work in the following areas, and may be further defined by rule by the division in collaboration with the board:
(a) providing structural engineering services for significant structures including:
(i) buildings and other structures representing a substantial hazard to human life, which include:
(A) buildings and other structures whose primary occupancy is public assembly with an occupant load greater than 300;
(B) buildings and other structures with elementary school, secondary school or day care facilities with an occupant load greater than 250;
(C) buildings and other structures with an occupant load greater than 500 for colleges or adult education facilities;
(D) health care facilities with an occupant load of 50 or more resident patients, but not having surgery or emergency treatment facilities;
(E) jails and detention facilities with a gross area greater than 3000 square feet; or

(F) an occupancy with an occupant load greater than 5,000;

(ii) buildings and other structures designated as essential facilities, including:

(A) hospitals and other health care facilities having surgery or emergency treatment facilities with a gross area greater than 3000 square feet;

(B) fire, rescue and police stations and emergency vehicle garages with a mean height greater than 24 feet, or a gross area greater than 5000 square feet;

(C) designated earthquake, hurricane, or other emergency shelters with a gross area greater than 3000 square feet;

(D) designated emergency preparedness, communication, and operation centers and other buildings required for emergency response with a mean height more than 24 feet, or a gross area greater than 5000 square feet;

(E) power-generating stations and other public utility facilities required as emergency backup facilities with a gross area greater than 3000 square feet;

(F) structures with a mean height more than 24 feet, or a gross area greater than 5000 square feet containing highly toxic materials as defined by the division by rule, where the quantity of the material exceeds the maximum allowable quantities set by the division by rule;

(G) aviation control towers, air traffic control centers and emergency aircraft hangars at commercial service and cargo air services airports as defined by the Federal Aviation Administration with a mean height greater than 35 feet, or a gross area greater than 20,000 square feet; and,

(iii) buildings and other structures requiring special consideration, including:

(A) structures or buildings that are:

(I) normally occupied by human beings; and

(II) five stories or more in height; or

(III) that have an average roof height more than 60 feet above the average ground level measured at the perimeter of the structure;

(B) all buildings over 60,000 aggregate gross square feet in area; and

(b) includes the definition of professional engineering or the practice of engineering provided in Subsection (X).

In the above example specific restrictions are defined regarding which categories of structures must be designed by a licensed structural engineer based on building size and height, occupancy, and use. Additional categories could include building use, high wind speed zones, high snow loads, seismic site class, and problematic soil conditions like liquefaction or expansive clays.

Transition Clause Language

An example of a transition clause might look like this:

(f) have successfully passed examinations established by rule by the division in collaboration with the board, *except that prior to (DATE), an applicant for licensure may submit a signed affidavit in a form prescribed by the division stating that the applicant is currently engaged in the practice of structural engineering;*

The above portion of the transition clause is intended to be incorporated as part of the title act section (f) described above. The text in italics specifically defines the exception to the proposed rule for professional engineers desiring to utilize the transition clause to acquire the title of structural engineer in lieu of taking an additional examination.

It is important to understand that the title act, practice act, and transition clause noted above are intended to be examples only and are not intended to be viewed as guidelines or recommendations endorsed by any national organization.

Keep in mind that the wording of the proposed changes is important. All words have a legal definition(s) that may differ from the common usage or ordinary dictionary definition of the word. Watch for words with double or multiple meanings to avoid ambiguity.

Although the initial process of writing the title act, practice act, and transition clause may be completed by a structural licensing committee within the SEA, it is imperative that the proposed changes be circulated to all organizations that may have an interest in the matter. The process should be open and fair and sincerely consider all input and recommendations from any source. The benefit of having a variety of organizations provide input is to minimize the possibility of having unintended consequences. Contractors, building owners, architects, and engineering organizations can provide a variety of valuable perspectives, useful assistance, and insights.

It is imperative throughout the bill-writing process that you are willing to negotiate, compromise, and acquiesce. As with all bills that go through the legislative process, the single best way to get your bill defeated is to be inflexible. On the other hand, the single best way to get your bill passed is to be willing to give and take a little.

Getting the Public Relations Machine Rolling

Many structural engineers tend to avoid publicity and take a back row seat behind the owner, contractor and architect when a project on which they have worked is in the limelight. That type of passive behavior is unproductive when you are trying to get a bill for structural licensing and practice acts passed. Because many structural engineers are seldom seen in the spotlight, it is likely that some of your legislators and the general public may not fully understand the important role that structural engineers play in protecting their health, safety and welfare.

It is imperative that structural engineers raise awareness about the structural engineering profession and the potential problems and hazards that the public faces because of unqualified individuals attempting to perform structural design.

Populate Boards and Committees

There are a variety of boards, organizations, or committees to which the media and your legislators turn for advice and recommendations. It would be beneficial if members of the local SEA and/or SEI Chapter populated those groups to offer advice and provide a voice from the structural engineer's perspective.

Does a representative from your SEA/SEI regularly attend your state's licensing board meetings? Is there a structural engineer on the licensing board? Does your state have other appointed advisory boards to which they turn for advice? A structural engineer should volunteer to sit on every board that may be consulted by the legislature while debating the issue of structural licensing and practice acts to provide input and clarify the motivation and reasons behind the bill.

There are a variety of local engineering-related associations such as ASCE and ACEC that have boards and committees that may support changes to the current laws. Members of the SEA should volunteer to be involved in those organizations to keep them abreast of developments and progress, and to be a conduit for information and input back to the SEA/SEI.

Increase Awareness of What Structural Engineers Do for the Public

Journalists from local television stations, magazines and newspapers are always looking for interviews and articles of local interest and concern. Publishing an opinion piece or appearing on television is a great opportunity to increase the public's awareness about structural engineering. If it is appropriate, emphasize what structural engineers do and what sets them apart from other branches of engineering.

Remember that the media are looking for local interest stories that will grab the public's attention and provide useful information that they can use and from which

they can benefit. When you discuss or write on a topic for the media, keep this question in mind: "What is in it for their viewers, listeners, or readers?" That is the question they are asking themselves, and it will ultimately be a deciding factor in whether you are published or interviewed.

To be of use to the general public, any interview that is given or article that is written should use non-technical language, such that it is void of jargon, and should emphasize why the public should be concerned about the topic.

A sample of article titles that may be of interest to the public and media include:

- Why Did My Neighbor's House Fall Down? (after a hurricane, earthquake, or snow storm)
- Is My House Safe Against Earthquakes?
- Things to Consider When Building in Earthquake Country.
- What to Look for Before You Buy a House in Hurricane Country.
- How Much Snow is Too Much Snow on My House?
- The Hurricane is Gone, but the Damage Remains – What You Can Do to Prevent This from Happening Next Time

The White Paper and the One-Pager

Writing a white paper is a good starting point to help the SEA/SEI Structural Licensing Committee members collect their thoughts and firm up their positions regarding structural licensing and practice acts. A white paper is generally three to five pages in length and emphasizes the reasons for structural licensing and practice acts.

A white paper is good, but a one-pager is even better. A one-pager is, as the name suggests, one side of one sheet of paper. The one-pager is a concise summary of the contents of the white paper. The one-pager should be easy to read and have bullet points to emphasize important aspects of structural licensing and practice acts. The one-pager is a great way to introduce the public, legislators, and media to the topic of Structural Licensing and Practice Acts.

The value of a well crafted one-pager is that it is likely to be read, while the lengthier white paper will generally *not* be read in its entirety. A sample one-pager is included at the end of this paper.

Making the Case for Structural Licensing and Practice Acts

From the national arena there has been a variety of investigations and studies that have highlighted the problem of member failure, building collapse, and–in some cases–death as a result of an engineer practicing outside the area of his or her competence. As informative as those cases are, it is more beneficial to document similar problems within your state. Making the problem more of a local concern and issue carries more weight and impact with the legislature and media than to highlight the problems with poor-quality structural design nationally.

Know Who May Resist SE Licensure

As obvious as the need for structural licensing and practice acts are for many, there are those who are wholly unaware of the magnitude of the problem of licensed engineers practicing outside the areas of their competence and the potential life-threatening consequences that may result. States that require a plan check review before issuing a building permit have firsthand knowledge about the magnitude of the problem. Many contractors, owners, architects, insurance companies, and fabricators and manufacturers of products used on structures are also keenly aware of the magnitude of the problem and its consequences. Unfortunately, there are those in the legislature and within some engineering organizations who choose to turn a blind eye to the situation, preferring to wait and "count the bodies" before they are willing to do something about it.

Some of the groups that have had, in the past, some concern about structural licensing and practice acts include:

- The National Society of Professional Engineers (NSPE) and its state-level affiliates. They prefer to have engineers unrestricted and left to decide for themselves what work they are competent to perform. Unfortunately, some engineers who may not be competent to perform structural engineering genuinely believe that they are competent to do this work.
- Commercial Contractors. They are concerned about having to pay higher fees for structural engineering services and higher building costs. This is only speculation and is not the intent for a SE licensing act.
- Residential Contractors. They are concerned that if a residential building is designed correctly by a knowledgeable structural engineer that the cost of a home will go up and may cause a potential home buyer not to build. This is only speculation and is not the intent for a SE licensing act.
- Some Engineers. Some engineers are concerned about the low pass rate on the NCEES structural exam and a lack of adequate resources for preparing for it. There are several courses available to prepare engineers to pass the structural engineering exam requirement.

Common questions, accusations, and misconceptions that surround structural licensing and practice acts include:

- "Won't buildings cost more?" No, buildings should not cost more. The code establishes the minimum requirements for a safe building. This bill makes sure that certain structures comply with the code by requiring them to be designed by those who have the appropriate education and experience, and who have passed a structural exam.
- "PEs and SEs, aren't they all the same?" Experience, education and examination separate and differentiate SEs from PEs.
- "Are we currently having a problem?" Although, as noted above, the problem of engineers practicing outside the areas of their competence is a real danger and threat to the public, there are some who are unaware of it. It is important to emphasize that we would rather take action now than "count bodies" later.

- "Ethics shouldn't be legislated." We are not trying to legislate ethics; this is about protecting the public - like drivers' licenses, speed limits and seat belt laws.
- "Aren't all professional engineers intelligent and capable?" Sure, but this is about having engineers demonstrate their knowledge and understanding of structures by passing the requisite examination. History is full of people that were intelligent and capable but—knowingly or otherwise—did not work for the public good.

Some people, including engineers and legislators, may never understand the importance of structural licensing and practice acts as a means of protecting the health, safety, and welfare of the public. Ignorance and ego will be unfortunate obstacles, but they are not insurmountable. Patience and a desire to educate others are virtues that will be invaluable throughout the process.

Generating Support

There are a variety of organizations and individuals that support structural licensing and practice acts. They include:

- National Council of Structural Engineers Associations (NCSEA)
- American Society of Civil Engineers (ASCE)
- Structural Engineering Institute (SEI)
- Council of American Structural Engineers (CASE)
- Local chapters of ACEC
- Some local chapters of the American Institute of Architects (AIA)
- Building officials and those who perform structural plan reviews
- The state Division of Professional Licensing (or equivalent)

All of these organizations should be informed about the proposed changes to the licensing laws and be given the opportunity to offer input and advice.

All members of the SEA/SEI Chapters and the supporting organizations should be kept fully informed about the progress and changes that may be made to the proposed changes to the licensing laws. The SEA/SEI's membership will appreciate monthly newsletter articles or emails that keep them fully informed. Some of the groups listed above may find it more advantageous to receive frequent emails.

When the proposed changes to the licensing laws are being debated in the legislature, it is advantageous to have the legislators receive email from their constituents declaring support for the bill. Declaring support is not always as clear-cut as it seems. Legislators must receive email, or other forms of communication, clearly noting that the sender "supports the bill as it is currently written." Emails that state, "I support the proposed bill …….. but suggest the following changes….." or "I agree with structural licensing and practice acts in principle but would request the following changes…" are viewed as non-support of the bill and will be counterproductive.

Emails and letters sent to legislators should be short, direct, and to the point to ensure that they are read. Lengthy correspondence is often not read by busy legislators. The first few paragraphs should be short, perhaps no more than two to five sentences in length, and should explicitly declare support for the bill. The correspondence should be cordial and avoid name-calling, fault-finding, and digging up past disagreements. A paragraph or two highlighting why you support the bill would be appropriate and acceptable.

It is important, but not critical, to have support emails from across the state, because most Legislators will not read or be swayed by any correspondence unless it is from their actual constituents. This does not mean that a person sending an email to every legislator is ineffective or useless, but it means that such a tactic is not as effective as every legislator receiving correspondence from their own constituents.

Working with Your Legislatures

Most states have a brief outline published or posted online that spells out the legislative process. Some states require a bill to go through an interim committee and/or legislative analyst review, receive a fiscal note, be reviewed by a Senate committee, be read and be voted on twice in the Senate, be reviewed by a House committee, and finally be read and voted on twice in the House. The process can be lengthy, catching the uninformed off-guard. It is a good idea to have a firm grasp on how the legislative process works in your state.

In addition, it is important to know something about the state leadership in the House and Senate. The leadership typically has the power to stall or throw out any bill that they deem of low importance or that they do not support.

It is also important to know something of the quality and character of the legislators with whom you are dealing. When asked by a legislator why the SEA of Utah was pursuing this course of action, I stated: “We’re proposing this bill on its own merits - because it’s the right thing to do.” To that, the legislator responded: “We don’t pass bills based on their merits or principle. Right has nothing to do with the decisions that are made.” Did he misspeak? Maybe. Was he right? Unfortunately, yes. A state’s legislature has many pressing and important problems to deal with and usually has a limited time frame within which to complete their work. What seems right and necessary to you may not be important to particular legislators based on the overall scope of the many issues that they face.

Working with a Legislator

Most states have information online about each legislator. Often the information includes a resume, the district that he or she represents, background information, committee assignments, contact information and past successful legislation. It is important to have as much information as you can about every legislator so that you can decide which one(s) to approach about sponsoring the bill.

Factors that influence the effectiveness of a legislator include, but are not necessarily limited to:

- Whether he/she belongs to the majority or minority party.
- His/her relationship with the Senate and House leadership.
- His/her longevity; senior legislators are generally more effective than freshmen.

Once you choose a legislator and that person accepts the responsibility of sponsoring the bill in either the Senate or House, he/she can assist you in choosing a legislator to co-sponsor the bill in the other legislative branch. It is important to review the credentials of all the legislators before asking one to sponsor the bill. Those who are eager to sponsor it may not be the best choice for getting it through the legislative process.

Legislators are good people who believe strongly in what they are doing and the notion that they are making a positive difference in the world. They also have to worry about getting re-elected. Because of that, no legislator wants to sponsor a bill that may fail because it could be bad for their campaign and image.

Important considerations that a legislator may entertain before agreeing to sponsor the bill may include:

- Will the bill result in a cost to the state? (The legislator will not want to increase taxes. Generally, the fiscal note for a bill on structural licensing and practice acts will be zero or very small.)
- Will the bill result in a cost to their constituents? (No.)
- Does the bill restrict or adversely affect existing businesses? (No. The transition clause ensures that the Bill will not affect existing businesses.)

Do not be afraid to interview your legislators to determine their level of commitment to the bill and assess their ability to assist you in seeing it successfully through the legislative process. This is probably the most important part of the whole effort – choose the sponsors carefully.

Once the sponsors have been selected, it is vital to educate them and help them fully to understand the reasons and purpose behind the bill. Your legislator must stand alone on the floor to speak in support of the bill and answer any questions that arise. It is important to make sure that they are well–prepared for this task.

When the Bill is being reviewed in committee or discussed on the floor, it is important to have the one-pager readily available and distribute it to every legislator so that they can read the main points of the Bill and perhaps gain a greater understanding of the importance of structural licensing and practice acts.

Closure

Licensing structural engineers separately and establishing a practice act will raise the bar for structural engineers above that of a Professional Engineer. However, we

should keep in mind that the purpose of structural licensing is not to create a group of elitist snobs. An open process and clear purpose will demonstrate our willingness to work with all interested parties and our desire to create a better future for our profession. The push toward structural licensing and practice acts in all states should be viewed for what it is: an expression of our desire to serve the public better and fulfill our ethical obligation to hold paramount the safety, health, and welfare of the public.

A Structural Practice Act for the State of Utah

IN A NUTSHELL

- Need for greater public safety in the structural design of significant buildings and structures
- Those presently qualified and competent to practice structural engineering as defined will remain qualified to do so
- Six month window for transitioning professionals to apply for S.E. licensing
- Administration changes for DOPL are minimal

PROPOSED STRUCTURAL LICENSE ACT FOR UTAH

The current Utah law concerning the practice of structural engineering does not define which structures or buildings require structural design other than to suggest that they are complex.

A proposal by the Structural Engineers Association of Utah (SEAU) would better define the practice of structural design by explicitly stating which buildings and structures would be considered not only complex, but also of sufficient importance to warrant the added expertise of structural engineers.

The International Building Code (IBC) classifies structures according to their occupancy with the intent of requiring increased care in the design of certain buildings. Hospitals, schools, and structures housing large numbers of occupants are deemed important and the code requirements for their structural design are consequently elevated.

These structures are among those defined in the proposed structural practice act for Utah.

Why Is A Structural Practice Act Necessary?

With the adoption of the 2006 International Building Code, Utah is leading the way in public safety. There is an increasing complexity requiring higher levels of competence and experience for structural design of significant structures

Reasons for improving structural practice:

- *Education Requirements:* Bachelor of Science degree requirements have steadily decreased from 140 to 150 semester hours to as little as 124 hours.
- *Complex Codes:* Structural engineering design and building code requirements have become increasingly complex
- *Computerization:* Use of advanced software by less competent engineers to design structures
- *Hidden Problems in Existing Buildings:* Many potential problems will only be evident when an earthquake or design snow load is applied
- *Plan Checking:* Many jurisdictions do not have the resources to perform sufficient structural plan reviews. Reliance on the "engineers stamp" does not always assure quality performance
- *Insurance Costs:* Poor design and construction can affect many different insurance policies
- *Cost Effective Design:* A structure can be designed which may be safe and meets the building code, yet is not the most cost effective structural solution

How Will the Current Practice of Structural Engineering Change?

Those presently qualified and competent in the areas defined by the act will continue to be able to practice structural engineering. If not presently licensed as an SE in Utah, they will submit application to DOPL for review together with an affidavit attesting to their competence and experience.

How Will It Be Implemented?

Beginning July 1, 2008, those professional engineers not holding a valid S.E. license in Utah and desiring to be transitioned will have six months to make application to the Division of Occupational and Professional Licensing (DOPL).

After January 1, 2009 licensing as a S.E. in Utah will follow the requirements presently established by the state and administered by the DOPL.

Benefits

- Increased public safety for the structural design of significant buildings and structures
- Clearly defines the responsibilities for the practice of structural engineering
- Maintains and improves upon the standards established by the state of Utah for the practice of structural engineering and the qualifications of license holders.

SEAU online
The Web Site of the Structural Engineers Association of Utah
www.seau.org

Contact info: *BKA, Co-Chair SEAU Licensing committee: (801) 782-XXXX: barrya@XXXXXXXXXX.com;*
KC, Co-Chair SEAU Licensing committee: (801) 466-XXXX: kelly@XXXXXXXXXX.com
BW, President, Structural Engineers Assoc. of Utah: (801)-553-XXXX; barryw@XXXXXXX.net

The New 16-Hour NCEES Structural Exam – How we got here

E. T. Huston P. E., S.E., MASCE[1] and T. L. Miller P. E.[2]
[1]Smith & Huston, Inc. Consulting Engineers, Vice President, 8618 Roosevelt Way NE, Seattle, WA 98115-3041; PH (206) 448-8448; FAX (206) 728-2872; email: huston@smithhustoninc.com
[2]National Council 0f Examiners for Engineering and Surveying, Po Box 1686, Clemson, SC 29633-1686; PH (800) 250-3196; FAX (864) 654-6033; email: tmiller@ncees.org

ABSTRACT

In April 2011, National Council 0f Examiners for Engineering and Surveying (NCEES) will begin offering a new 16-hour Structural Examination to replace the Structural I and Structural II examinations. This new exam will also replace the state specific seismic structural examinations currently offered by California, Oregon, and Washington.

The first half of this paper will focus on how and why the changes were made, including discussion of how different states use the current structural examinations, difficulties in mobility of structural licenses, the NCEES Structural Task Force, the NCEES Professional Activities and Knowledges Survey for the new 16-hour Structural Examination, and the new Test Specification.

The second half of this paper will discuss the format of the new 16-hour Structural Examination, the new 16-hour Structural Examination writing committee, and how the new 16-hour Structural Examination is graded.

INTRODUCTION

The first administration of the new 16-hour Structural Examination which replaces the Structural I and Structural II examinations was April 8-9, 2011. This paper will discuss the history of structural examinations in the United States and its Territories, the reasons for the change from the Structural I and Structural II examinations to the new 16-hour Structural Examination, and the process of the change.

HISTORY OF NATIONAL STRUCTURAL LICENSURE

The states of California, Illinois and Washington wrote state specific structural engineering examinations in the later half of the twentieth century. Illinois suggested that the National Council of Examiners for Engineering and Surveying (NCEES) write a national exam and that Illinois would use that exam rather than continue to write a state specific exam. In 1986 NCEES offered the first Structural I Examination (SE I) as the first day of a 2 day exam. In 1986 NCEES offered the first Structural II Examination (SE II) to complete sixteen hours of examination. In 1993, at Illinois request, NCEES added seismic content to the afternoon portion of the Structural II Examination.

In 1932 California passed a Structural Engineer title authority act. This was the year before the 1933 Long Beach Earthquake. After the 1933 Long Beach Earthquake the Field Act was passed to require a Structural Engineer for schools. Modifications to this act added a requirement that a Structural Engineer be engaged to design a hospital. California subsequently started writing state specific structural engineering examinations.

The structural engineering examination in Washington was first offered in 1950 following the 1949 Olympia Earthquake. This examination was initially an 8-hour exam. In 1963 it was changed to a 16-hour exam

In 1986 California, Hawaii, Oregon and Washington cooperated in writing the 16-hour Western States Examination. Idaho and Nevada subsequently joined this exam. In 1993 Hawaii, Oregon and Nevada left the Western States exam and went to the NCEES SE I and SE II exams because NCEES had added seismic content to the afternoon problems on the SE II Exam. Washington left the Western States Exam in 1998.

STRUCTURAL EXAMINATION USEAGE AND MOBILITY

As shown in Table 1, after 1998 different U.S. states and territories have granted structural licenses using a variety of examinations.

Table 1. U.S. States and Territories Which Used 16-Hour Licensing Examinations

STATE OR TERRITORY	EXAMINATIONS USED
Arizona	SE I + SE II
California	SE II + CA SE III
Guam	SE I + SE II
Hawaii	SE I + SE II or Civil/Structural + SE II
Idaho	SE I + SE II
Illinois	SE I + SE II
Louisiana	SE I + SE II
Nebraska	SE I + SE II
Nevada	SE I + SE II
Northern Mariana Islands	SE I + SE II
Oregon	SE II + WA/OR SE III
Utah	SE I + SE II
Washington	SE II + WA/OR SE III

Forty-seven states and territories offered the NCEES SE I, but thirty-four of them did not require the SE II exam. The forty-seven states and territories include the 13 states and territories listed in Table 1. Some of these thirty-four states and territories which did not require the SE II exam offered the SE I so that engineers in their jurisdiction could apply for comity in other jurisdictions. Other jurisdictions offered the SE I in lieu of another PE exam, such as the civil exam with the structural module.

California, Guam, Idaho, Nevada, Oregon, Utah and Washington required a PE license prior to allowing candidates to sit for the structural examinations.

These various permutations of examination usage made comity and mobility difficult. For example, recently licensed structural engineers from Oregon, Washington, and in some cases, recently licensed structural engineers from California or Hawaii would have to take the NCEES SE I examination to obtain a license in Illinois. Similarly, licensed structural engineers from Arizona, Guam, Idaho, Illinois, Louisiana, Nebraska, Nevada, the Northern Mariana Islands and Utah would have to travel to California, Oregon or Washington to take one of the two state specific seismic examinations. Candidates from other states and territories would have to take both the SE II and one of the two state specific seismic examinations to become licensed in any of the states or territories listed in Table 1.

THE NCEES STRUCTURAL EXAMINATION TASK FORCE

In 2006 NCEES established a Structural Examination Task Force to address these examination, comity and mobility issues. The Task Force developed three recommendations.

The first recommendation was that it is desirable and appropriate to have a single 16-hour structural engineering examination that would be accepted by all jurisdictions listed in Table 1 and other jurisdictions that might currently be using the NCEES SE I examination as a stand alone licensing exam.

Illinois pointed out to the Task force that the SE I was always intended to be the breadth portion of a 16-hour breadth-depth examination. Using the SE I examination as a stand alone licensing exam, had the effect of licensing structural engineers without a depth portion of the licensing examination.

At the end of the last century, there were three legacy codes used to design building structures in the United States. Usage of these legacy codes was on a regional basis as shown in Figure 1. By the time that the NCEES Structural Examination Task Force was created, the International Building Code (IBC) was the single dominate building code for the United States as shown in Figure 2.

The IBC used the new United States Geologic Survey seismic maps. These maps showed that even with low to moderate seismicity, sites with poor soil conditions in most states and territories qualify as Seismic Design Category D. Structures designed for sites in Seismic Design Category D generally have to be designed using “Special” seismic force resisting systems; such as Special Reinforced Concrete Moment Frames; Special Reinforced Masonry Shear Walls; or Special Steel Concentric Braced Frames. Design of these “Special” systems triggers an additional body of knowledge which includes the AISC Seismic standards; all of Chapter 21 of ACI 318; the high seismic portions of the “Building Code Requirements and Specification for Masonry Structures”; and the high seismic portions of the NDS “Special Design Provisions for Wind and Seismic”. The use of this high seismic body of knowledge in many more U.S. states and territories meant that it was

appropriate that structural engineers in more states and territories be examined on these high seismic systems. Further, to maximize licensing mobility and protect life safety, structural engineers should be examined on these high seismic systems since even if they do not have sites which qualify as Seismic Design Category D in their home state or territory; they are likely to encounter such sites when they seek comity in other states and territories.

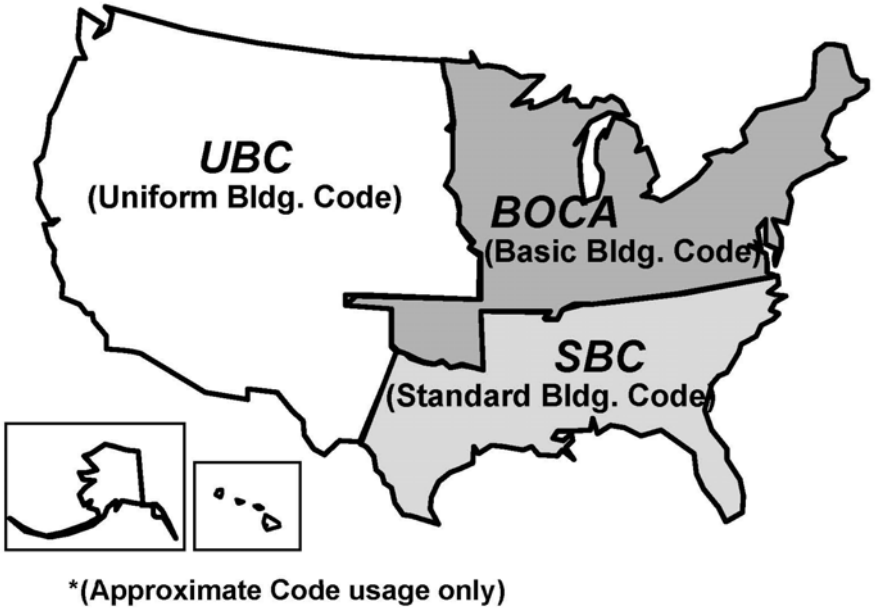


Figure 1. Building code usage under the legacy codes

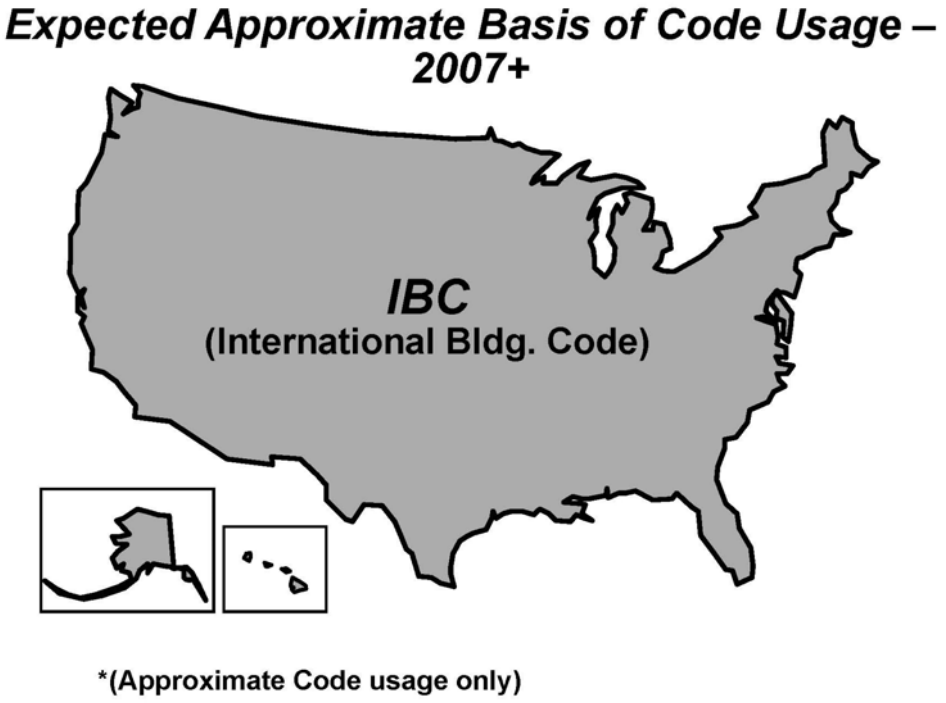


Figure 2 Building code usage in 2010 and beyond

The second recommendation was that moving to a structural engineering examination based on the IBC triggered the need for a new structural Professional Activities and Knowledges Study (PAKS). NCEES conducts a PAKS for all of the examinations that it writes. PAKS are generally conducted on a six to nine year cycle. The Task Force concluded that while a new structural PAKS was not yet required for the SE I and SE II examinations based on timing, it was required based on the major changes in design created by adoption of the IBC as the reference code for building structural design.

The third recommendation concerned specific format suggestions for the new 16-hour structural engineering examination. These suggestions included ways to address the breadth/depth requirements and ways to group the knowledges and abilities for the new structural examination. These will be addressed below in the section titled "FORMAT OF THE NEW 16-HOUR STRUCTURAL EXAMINATION".

PROFESSIONAL ACTIVITIES AND KNOWLEDGES SURVEY

NCEES established a committee to create the Professional Activities and Knowledges Study for the new 16-hour structural examination. The structural PAKS committee membership included members of the Structural Engineering Task Force; representatives from all 16-hour structural examination jurisdictions; representatives from the Civil/Structural exam module; representatives from the existing SE I and SE II examinations committee; representatives from the Structural Engineering Institute (SEI); and representatives from the National Council of Structural Engineering Associations (NCSEA).

The structural PAKS committee created a survey with fifty-five abilities, one hundred fifty-six knowledges and seventeen codes and standards. Abilities include the development of concepts, calculations and drawings. Knowledges include design of specific elements and systems.

The structural PAKS was administered as an on-line survey. News about the survey was distributed to all licensed structural engineers in the states and territories listed in Table 1; all licensed structural engineers on mailing lists obtained from NCEES Member Boards; practicing structural engineers on mailing lists obtained from SEI and NCSEA; and through articles appeared in professional engineering journals and NCEES member board newsletters. Recipients of postcard announcements and the articles also requested that structural engineers inform their colleagues (non-members of SEI and NCESEA) about the survey and urge them to participate in the on-line survey.

A total of 1,019 structural engineers completed the survey. This was considered to be quite a robust response, compared to the response on other NCEES examination PAKS. The respondents represented almost all of the U.S. states and territories. The majority of respondents were licensed professional engineers, currently practicing structural engineering, who devoted more than 75% of their

current work time to hands-on structural engineering. Most of the respondents worked in private consulting practice.

Of the respondents who were licensed structural engineers in the states and territories listed in Table 1, the number of respondents ranged from four who were licensed to practice in the Northern Mariana Islands to two hundred fifty-five who were licensed to practice in California. As Figure 3 shows, no state or territory dominated the survey.

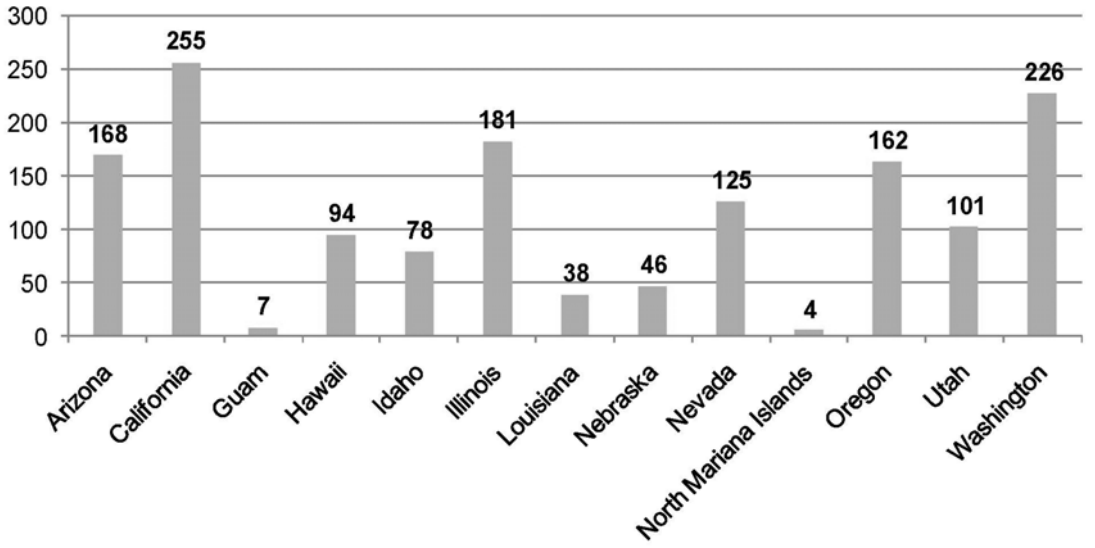


Figure 3. States of respondent licensure

In general, as Figure 4 shows, there was an even distribution of number of years of practice of the respondents, with the exception of a slight increase by the respondents who reported that they had been practicing between six and ten years. Since this is near the point in a structural engineers career where they would sit for the licensing examination, this slight increase was viewed as a positive outcome.

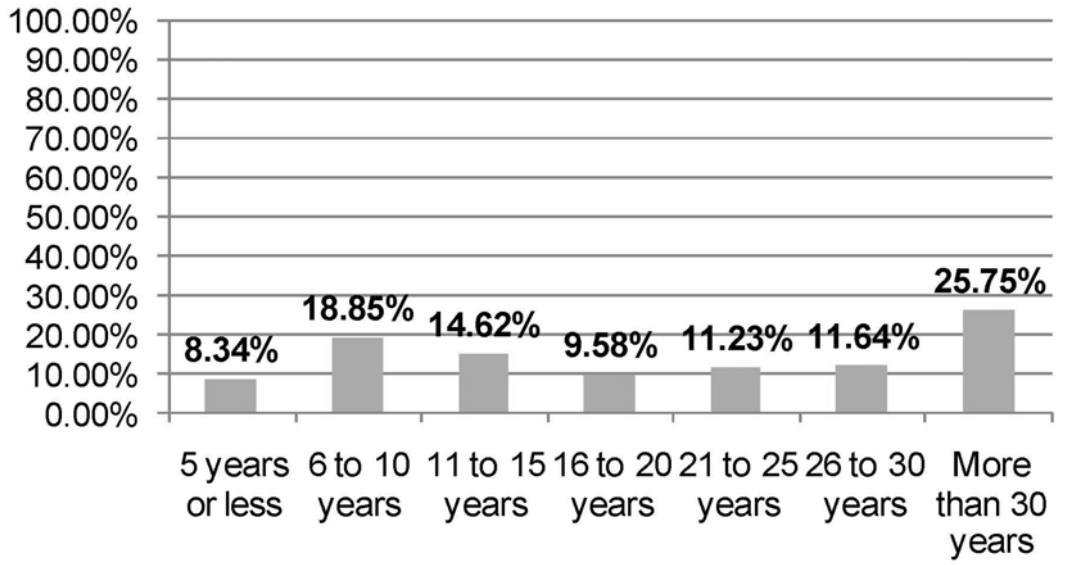


Figure 4 Survey respondents' years of practice

Fifty-three of the fifty-five professional activities on the survey achieved high importance ratings. The respondents indicated that the survey covered the important professional activities adequately to well.

One hundred thirty-two of the one hundred fifty-six knowledges on the survey achieved high importance ratings. Respondents indicated that the survey covered the important knowledges adequately to well.

Eight of the seventeen codes and standards on the survey achieved high importance ratings.

The NCEES Structural Professional Activities and Knowledges Survey conducted in 2008 and 2009 asked the profession specific questions about the importance of knowledge of design for systems of moderate seismicity versus systems the importance of knowledge of design for systems of high seismicity. All of the high seismic systems achieved high importance ratings. This result did not change when the survey responses were sorted by states with high seismicity versus states with moderate to low seismicity. Thus the profession clearly stated that it was essential that candidates for structural licensure be examined on these "Special" systems. This result was notably different from the previous PAKS and reflects the changes brought about by adoption of the IBC and the new seismic maps. The PAKS also gave high importance ratings to the design for high wind forces.

TEST SPECIFICATION

Once the PAKS results were analyzed, NCEES established a committee to create the Test Specification for the new 16-hour structural examination. The Structural Test Specification Committee membership added one new member to the structural PAKS Committee.

Based on the results of the PAKS a test specification was created for each component of each module of the new 16-hour structural examination. These components are described in the next section. Each ability or knowledge on the PAKS had a numeric importance rating of 1 to 5. The test specification reflects all abilities and knowledges which achieved an aggregate importance rating higher than 2.6.

The new Test Specification is presented in four parts, one for each component of each module of the new 16-hour structural examination. The Test Specification is available as a free download on the NCEES web site at **www.ncees.org**.

FORMAT OF THE NEW 16-HOUR STRUCTURAL EXAMINATION

The new 16-hour Structural Examination consists of two 8-hour components both of which include breadth and depth modules. The components contain integrated design, analysis and detailing questions. NCEES has been very clear that no single portion of the exam is a sufficient stand-alone exam for any purpose.

Component one examines candidates on the "Analysis and Design for Gravity Forces and Incidental Lateral Forces from soil, ice, etc." It contains a 4-hour multiple choice problem module which is administered in the morning. There are forty questions in this multiple choice module. The multiple choice module is comprised of both building and bridge questions.

Component one also contains a 4 hours objectively scored (essay) problem module which is administered in the afternoon. The afternoon module of component one will have a building track and a bridge track. The building track will contain four 1-hour building problems. The bridge track will contain two 1-hour and one 2-hour bridge problems. Candidates must declare whether they are going to attempt the building track or the bridge track in the afternoon when they register for the examination.

Component two examines candidates on the "Analysis and Design for Lateral Forces – High Wind and High Seismic." It contains a 4-hour multiple choice problem module which will be administered in the morning. There are forty questions in this multiple choice module. The multiple choice module is comprised of both building and bridge questions.

Component two also contains a 4 hour objectively scored problem module which will be administered in the afternoon. The afternoon module of component two will have a building track and a bridge track. The building track will contain four 1-hour building problems. The building problems will include at least two problems in Seismic Design Category D or above and at least one wind problem with wind speeds of 110 mph or higher. The bridge track will contain two 1-hour and one 2-hour bridge problems. Candidates must declare whether they are going to attempt the building track or the bridge track in the afternoon when they register for the examination. They must select the same track, buildings or bridges on both components.

PASSING THE NEW 16-HOUR STRUCTURAL EXAMINATION

Each 8-hour component of the exam may be taken on consecutive days in the same exam administration, or each component may be taken in separate exam administrations. Candidates must achieve an acceptable result on both vertical and lateral components to pass the exam.

If a candidate does not achieve an acceptable result on one of the two 8-hour components, that 8-hour component can be retaken. Due to the changing nature of the design codes, some states or territories may impose a limit of five years during which the candidate must achieve an acceptable result on the second 8-hour component. If the candidate does not achieve an acceptable result on the second 8-hour component within five years, the first 8-hour component (on which the candidate had previously achieved an acceptable result) must be retaken.

NCEES has prepared a sample questions and solutions book for the new 16-hour Structural Examination. It can be ordered online.

NEW 16-HOUR STRUCTURAL EXAMINATION WRITING COMMITTEE

The NCEES structural committee whic h writes the new 16-hour Structural Examination is comprised of subject matter experts who can legally practice as structural engineers in the jurisdiction in which they have been licensed. In general, for the thirteen states and territories which are listed in Table 1, these subject matter experts have passed a sixteen-hour structural exam. Subject matter experts from other states or territories may have only passed an eight-hour licensing exam. Nonetheless, they can legally practice in their jurisdiction. This same guideline was adopted by the Structural Engineer's Certification Board (SECB) when it set it's guidelines for acceptance of applicants.

In some cases, subject matter experts also serve on standards development organizations or code advisory committees.

With the increased emphasis on high wind and high seismic forces, new committee members have been recruited from regions of the country where design for these forces is common practice.

GRADING THE NEW 16-HOUR STRUCTURAL EXAMINATION

The multiple choice sections of both m odules are machine scored. Statistics of each problem are examined for anomalies and problems which appear to have anomalous results are given an additional review by subject matter experts prior to the release of scores.

The objectively scored portions of both modules are graded in workshop scoring sessions. Teams of graders who are subject matter experts and who can legally practice as structural engineers in the jurisdiction they are licensed in are assembled, trained, and certified. Each candidate's solution to a given problem is graded by at least two graders on the team. In fairness to the candidates, the training and certification process is robust.

CONCLUSION

The new 16-hour Structural Examination which replaces the Structural I and Structural II examinations has been developed through a robust process which included direct input by the structural engineering profession through the NCEES Structural Professional Activities and Knowledges Study. The test specification was based on activities, knowledges and codes which the profession rated to be of high importance in the PAKS. These include lateral design of high seismic and high wind systems.

The new 16-hour Structural Examination will protect public safety of structures and promote mobility of licensure throughout the United States and its Territories. As Boards of Registration understand the increased seismic risk in their jurisdiction, it is anticipated that the use of the new 16-hour structural exam will expand to more of these jurisdictions.

REFERENCES

American Forest & Paper Association (AF&PA) (2008). *Special Design Provisions for Wind & Seismic* Washington, DC

American Concrete Institute (ACI) (2008). *Building Code Requirements for Structural Concrete (ACI 318-08) and Commentary,* Farmington Hills, MI

American Institute of Steel Construction Inc. (AISC) (2006). "*Seismic Design Manual,* Chicago, IL

Masonry Standards Joint Committee (MSJC) (2008) *Building Code Requirements and Specification for Masonry Structures,* Boulder, CO

International Code Council (ICC). (2006). International *Building Code,* County Club Hills, IL

Masonry Standards Joint Committee (2008) *Building Code Requirements and Specification for Masonry Structures,* Boulder, CO

The Intentionality of Design

By Jon A. Schmidt, PE, SECB, M.ASCE[1]

[1]Aviation & Facilities Group, Burns & McDonnell, P.O. Box 419173, Kansas City, MO 64141-6173; PH (816) 822-3373; FAX (816) 822-3415; email: jschmid@burnsmcd.com

ABSTRACT

Science is widely perceived as an especially systematic approach to knowing; engineering could be conceived as an especially systematic approach to willing. In science, although the will is implicitly involved, the intellect is primary, because the goal is ideal—additional "objective" knowledge. In engineering, although the intellect is implicitly involved, the will is primary, because the goal is pragmatic—some "subjective" outcome, which is often selected by a manager or client, rather than the engineer. Furthermore, engineering problems are rarely well-defined; uncertainties and resource constraints dictate that they be conceptualized and solved heuristically. As a result, different engineers will follow different design procedures and develop different models, none of which is uniquely "correct." Because tradeoffs are always necessary, engineering decision-making—and human behavior in general—is more intentional than rational. Recognizing this can help today's society to engage engineers more explicitly in addressing the many challenges that it faces, technological and otherwise.

INTRODUCTION

What is engineering? At first glance, it appears that engineers would simply be those who operate engines. However, in other languages—such as French, German, or Spanish—the word for "engineer" starts with the letter I, not the letter E. This reflects the etymological fact that "engineers" are fundamentally people who exercise *ingenuity*.

The classic definition of engineering reflects this somewhat. It is attributed to Thomas Tredgold and dates to the 1828 charter of the Institution of Civil Engineers in Great Britain. It says, "Engineering is the art of directing the great sources of power in nature for the use and convenience of man." This certainly sounds important and impressive, but the problem is that it does not really capture what engineers do on a daily basis. Few would seriously claim that their professional activities constitute "directing the great sources of power in nature."

There is another definition, specific to structural engineering, which is perhaps less familiar and has been attributed to various individuals. It is so pithy, and has been

repeated so often, that apparently no one really knows for sure who originally uttered it. The earliest documented instance was in a structural analysis textbook (Brown 1967): "The art of moulding materials we do not really understand into shapes we cannot really analyze, so as to withstand forces we cannot really assess, in such a way that the public does not really suspect." This seems much closer to the mark.

One of the interesting things about both of these definitions of engineering is that, contrary to popular usage, neither refers to it as a *science*. Instead, both refer to it as an *art*. What is the difference? The dictionary (*Merriam-Webster's*, 1993) provides three relevant definitions of science:

- "a department of systematized knowledge as an object of study;"
- "a system of knowledge covering general truths or the operation of general laws;" and
- "principles and procedures for the systematic pursuit of knowledge."

Notice the one word that is common to all three: knowledge. Apparently science is all about knowledge. Is engineering all about knowledge? In light of these definitions, is engineering a science? Should engineers also call themselves scientists?

What about the definition of art? Once again, the dictionary (*Merriam-Webster's*, 1993) provides three definitions that are potentially relevant:

- "skill acquired by experience, study, or observation;"
- "an occupation requiring knowledge or skill;" and
- "the conscious use of skill and creative imagination."

Once again, notice the one word that is common to all three: skill. Apparently art is all about skill. Is engineering all about skill? In light of these definitions, is engineering an art? Should engineers also call themselves artists? Do engineers perceive what they do for a living as "the conscious use of skill and creative imagination"? Is that how non-engineers typically perceive what engineers do for a living?

KNOWING AND WILLING

To explore this distinction a bit further, consider that science primarily has to do with *knowing*, while art primarily has to do with *willing*—that is, making conscious decisions that may or may not have a rational justification. In particular, just as science is widely perceived as an especially systematic approach to knowing, so engineering could be conceived as an especially systematic approach to willing.

This becomes evident if we simply compare the scientific and engineering methods. Scientists observe natural phenomena, propose hypotheses in an effort to explain them, and conduct careful experiments to test their theories. Although the will is

implicitly involved, the *intellect* is primary, because the goal is ideal: additional knowledge that is supposed to be objective.

By contrast, as Koen (2003, 2010) has long been arguing, engineers use "state-of-the-art heuristics to create the best change in an uncertain situation within the available resources." Note that this definition of the engineering method invokes the "state of the *art*," not the "state of the *science*," and explicitly acknowledges that engineering is a *creative* activity. Although the intellect is implicitly involved, the *will* is primary, because the goal is pragmatic: some outcome that is usually subjective. Knowledge serves mainly as a necessary but insufficient means to that contingent end—"the best change," which is usually not something that is up to the engineer to determine.

In fact, as Goldman (1991) has observed, engineering is a captive enterprise. For one thing, it is widely—and wrongly—perceived as nothing more than *applied* science. In addition, the practice of engineering has been limited in terms of what problems engineers are allowed to address and what solutions are considered acceptable. The autonomy of the profession is restricted by the need for someone to retain an engineer before he or she can undertake a specific project. Engineers rarely have the opportunity to influence the process that leads a manager or client to decide that a certain product or facility is necessary or desirable. Furthermore, a variety of constraints are imposed on engineering designs by others as a result of aesthetic, functional, or other considerations, which are often non-technical.

These two types of captivity—one intellectual, the other social—are not separate, but interdependent; the first anchors the second, which in turn reinforces the legitimacy of the first. Goldman's thesis was (and still is) that technology and innovation are generally dominated by market-driven value assessments, rather than by technical knowledge. Even when managers or clients are engineers by training, the decisions that they make inevitably reflect the agendas and priorities of the organizations that they serve—not necessarily the capabilities and limitations of the engineers whom they supervise or retain. As a result, engineering tends to be *instrumental* in nature; it is exploited by non-engineers to achieve their own objectives, which may be quite arbitrary. In other words, the willfulness of engineering is both enabled and restricted by the willfulness of the institutions that appropriate it.

This has significant ethical implications. Mitcham (2009) has argued that engineering is "philosophically inadequate" because it does not have an integral ideal that is "good in itself" and well-embedded in its curriculum and practice. Physicians pursue health and lawyers seek justice, but engineers solve whatever design problems are presented to them and leave the use (or misuse) of the resulting technology up to others. Although they are explicitly charged with holding paramount the safety and welfare of the public, engineers are not especially well-qualified to determine exactly what satisfies that obligation.

Goldberg (2009) has responded to this assessment. His view is that Mitcham is properly differentiating occupations that are ethically simple vs. ethically complex,

based on whether serving the client's interests will align naturally and consistently with serving the interests of society as a whole. In this sense, engineering is clearly ethically complex, because it can be utilized for malevolent purposes; and even when this is not the case, the uncertainties involved are such that good intentions can still lead to unfortunate consequences.

HEURISTICS AND DESIGN PROCEDURES

In fact, Koen (2003) holds that heuristics are central to engineering practice—and everything else, for that matter. A heuristic is "anything that provides a plausible aid or direction in the solution of a problem but is in the final analysis unjustified, incapable of justification, and potentially fallible." Familiar examples include rules of thumb and factors of safety. Why is the stress at 2% strain considered to be the yield strength? Why are most structural designs based on this particular value? Why do engineers typically divide it by something like 1.67 in order to determine a member's capacity to resist service loads? The short answer to all of these questions is: Because it usually works. There is no timeless truth waiting to be discovered here, something embedded within the essence of reality.

With this in mind, Goldman (1984, 1990, 2004) has pointed out that science is supposed to be concerned with necessity, certainty, universality, abstractness, and theory. It seeks objective knowledge of timeless truth that is based on reality, for the purpose of intellectual contemplation and understanding. By contrast, engineering is characterized by contingency, probability, particularity, concreteness, and practice. Engineers rely on subjective know-how and historical opinions that are derived from experience, with the goal of willful action and use. Heuristics cannot be "proven" in the absolute sense, but their utilization is legitimately warranted, frequently on the grounds of successful past implementation.

In fact, each individual engineer has a unique collection of relevant heuristics at his or her disposal, along with "meta-heuristics" for selecting which heuristics are most appropriate in a given set of circumstances. When these are combined to facilitate converting a client's technical and non-technical requirements into a viable solution that adequately accounts for the unknowns and satisfies all applicable constraints, they constitute what Addis (1990) calls a design procedure. This is analogous to a hypothesis in the scientific method; however, a design procedure does not lead inevitably to a particular outcome. In fact, Addis notes "that it is possible to produce very similar structural designs using different design procedures and that similar design procedures can lead to significantly different structures—there is no logical connection between the two."

Most design procedures include the development of mathematical *models* that are supposed to capture the important aspects of reality. The engineer’s challenge is to ascertain what those features are and what assumptions and simplifications can safely be incorporated in order to keep everything manageable, while still yielding a meaningful assessment of likely performance. As de Vries (2010) has observed, two

common strategies are abstraction and idealization. Abstraction involves neglecting certain aspects of reality in order to gain a better understanding of the remaining aspects. Idealization involves replacing a complicated aspect of reality with a simplified version.

Fundamentally, models are approximate representations that serve as epistemic tools (Boon and Knuuttila 2009)—they help engineers learn about the parameters of a design problem and evaluate possible solutions. Although analysis of a model is usually straightforward, conforming to fundamental principles derived from *science*, its initial construction and subsequent adjustment require "the conscious use of skill and creative imagination"—which, as you may recall, is one of the dictionary definitions of *art* (*Merriam-Webster's*, 1993).

ENGINEERING INTENTIONALITY

The bottom line here is that engineering is not deterministic; it routinely requires setting priorities and selecting the best way forward from among multiple options when there is no one "right" answer (Addis 1997). Consequently, attempts to apply a theory of *rationality* to engineering are probably misguided (e.g., Kroes et al. 2009); *intentionality* seems like a more appropriate concept. Take the example of a bridge. Is there a single optimal span for a particular location? You can make an argument for the one across the Golden Gate. But the reality is that there is a staggering array of variables that influence what will ultimately be constructed. For example:

- What kind of traffic will the bridge carry—cars, trucks, or trains?
- What type of bridge will it be—suspension, cable-stayed, or box girder?
- What primary material will be used—wood, steel, or concrete?

Tradeoffs are inevitable, and not just for technical reasons—there are often budget constraints, legal restrictions, or political considerations that come into play. As Goldman (2010) has discussed, these kinds of tradeoffs—both technical and non-technical—are at the heart of the design process, and therefore constitute the essence of engineering intentionality.

In the end, how does a bridge designer settle on the final form of the structure? There is no rigid and inerrant formula that will provide the "proper" outcome. This is the challenge that engineers face—they routinely have to make and justify seemingly arbitrary decisions with an understanding of the situation that is incomplete, at best. The contrast here is really between deduction and induction. *Deduction* reaches conclusions that are absolutely certain, because they contain no new information that was not already present in the premises; accepting the premises requires accepting the conclusion. *Induction* reaches conclusions that are *not* certain, because they *do* contain new information; the argument has to add something to the premises.

With this in mind, which approach do engineers most commonly employ? Consider the question this way: Is every design a foregone conclusion, derived deductively

from the specified criteria and other project requirements? Of course not! Engineering is clearly an *inductive* activity—it requires the addition of information along the pathway from thought to thing, or from concept to completion. In other words, engineers are *information creators*. In fact, one definition of information is "the actualization of one possibility to the exclusion of others" (Dembski 1997)—which is exactly what engineering is all about.

There is no law of nature or mathematics that dictates a particular design. There are constraints, to be sure. There are decisions made by others that limit the engineer's options. In the end, though, the engineer makes certain choices; and another, equally competent engineer might well go in a different direction. Each designer has a singular point of view that informs how he or she "sees" a problem and its (potential) solution. Certain concepts, especially within a particular discipline, are familiar to all; but each individual also develops and refines a certain amount of technical intuition through professional experiences—"tacit" knowledge that is difficult to capture and communicate to others.

As a consequence of all this, two models of the same system can both be "correct," yet yield different results. The advantage that an engineer has over a scientist is the ability not only to adjust the model to represent reality better, but also to adjust *reality* to suit the model better—yet another example of engineering practice being more of an art than a science. This is especially true for unconventional projects that go beyond standard designs and details, requiring the engineer to develop *custom* designs and details using first principles. In such cases, it is often the model that dictates reality, rather than the other way around.

In this way, engineering practice involves reinterpreting an inductive situation to facilitate deductive analysis. Once the model is set up, the results follow inexorably; but setting up the model is the real work of the engineer. In other words, engineering includes problem *definition*, not just problem solution. Engineers have to convert all of the relevant design criteria—which are often dictated by clients, codes, and other authorities—into the "language," so to speak, of engineering.

And as in the case of natural language translation, the formulation of engineering problems and their solutions is inherently indeterminate. They tend to be ill-structured (Simon 1973) or even "wicked" (Rittel and Webber 1969). Consequently, design—in fact, all human behavior—is not ultimately governed by *reasons*, but by *motives*. Although common usage treats these two terms as virtually synonymous, the prevalence of the first one in both ordinary and philosophical discourse reflects an ancient prejudice—going all the way back to Plato—that subordinates action to contemplation; that is, willing to knowing.

CONCLUSION

As members of the profession that exemplifies willing, engineers should strive to resist and reverse this tendency. For example, although it is common in many

fields—including engineering—to perceive a "gap between theory and practice," Addis (1990) advocates abandoning this widespread notion in favor of an alternative classification: engineering *science* vs. engineering *design*. The essential difference between these two activities is not in the types of *knowledge* that they employ, but rather in their distinct *purposes*—further understanding and explaining the natural world vs. efficiently producing useful artifacts in a context of uncertainty.

The outcomes of engineering are rarely black and white, right or wrong. Managers and clients give engineers their problems and expect them to solve them, even though there are no *objective* solutions—there are simply too many parameters and too many criteria. They depend on engineers to exercise good *judgment*, grounded in their formal education and honed by their subsequent experience. As Vick (2002) wrote, "The novice begins with data and ends with a number; the expert begins with knowledge and ends with understanding."

There is a widespread perception that engineers are little more than number crunchers. This is not only inaccurate, it is *dangerous*. Data and numbers are meaningless—unless and until they are *properly* interpreted by someone who *knows* where they came from and *understands* what they mean.

With this in mind, consider the motion made by Florman (1997): "I propose that we take the time to think about who we are, as citizens living in a 'technological society,' and—for engineers—as the profession most essential to the well-being of that society." After all: Is there any situation in human existence that is *not* subject to uncertainty and resource constraints? Or that does *not* require the use of successful heuristics? Or that does *not* demand willing, as well as knowing? It is precisely when there is more than one path to follow that it is possible and desirable to exercise *wisdom*.

This being the case, in light of their training and temperament, engineers are uniquely suited to help society wrestle with the many challenges that it faces—not only in the technological realm, but across all aspects of human existence.

REFERENCES

Addis, W. (1990). *Structural engineering: The nature of theory and design*. New York: Ellis Horwood.

Addis, W. (1997). "Free will and determinism in the conception of structures." *Journal of the International Association for Shell and Spatial Structures*, 38(2), 83-89.

Boon, M. and Knuuttila, T. (2009). "Models as epistemic tools in engineering sciences." In *Philosophy of technology and engineering sciences*, ed. Anthonie Meijers, 693-726. Amsterdam: Elsevier.

Brown, E. H. (1967). *Structural analysis volume I*. New York, NY: John Wiley & Sons.

Dembski, W. A. (1997). "Intelligent design as a theory of information." *Perspectives on science and Christian faith*, 49(3), 180-191.

de Vries, M. J. (2010). "Engineering science as a 'discipline of the particular'? Types of generalization in engineering sciences." In *Philosophy and engineering: An emerging agenda*, ed. Ibo van de Poel and David E. Goldberg. Dordrecht: Springer.

Florman, S. C. (1996). *The introspective engineer*. New York: St. Martin's Griffin.

Goldberg, D. G. (2009). "Is engineering philosophically weak? A linguistic & institutional analysis." *16th Biennial Conference*, Society for Philosophy and Technology.

Goldman, S. L. (1984). "The *techne* of philosophy and the philosophy of technology." *Research in Philosophy & Technology*, 7, 115-144.

Goldman, S. L. (1990). "Philosophy, engineering, and western culture." In *Broad and narrow interpretations of philosophy of technology*, ed. Paul T. Durbin, 125-152. Netherlands: Kluwer Academic Publishers.

Goldman, S. L. (1991). "The social captivity of engineering." In *Critical perspectives on nonacademic science and engineering*, ed. Paul T. Durbin, 121-145. Bethlehem, PA: Lehigh University Press.

Goldman, S. L. (2004). "Why we need a philosophy of engineering: A work in progress." *Interdisciplinary Science Reviews*, 29(2), 163-176.

Goldman, S. L. (2010). "Beyond satisficing: Design, trade offs and the rationality of engineering." *2010 Forum on Philosophy, Engineering & Technology.*

Koen, B. V. (2003). *Discussion of the method: Conducting the engineer's approach to problem solving*. New York: Oxford University Press.

Koen, B. V. (2010). "Debunking contemporary myths about engineering." *2010 Forum on Philosophy, Engineering & Technology*.

Kroes, P., Franssen, M., and Bucciarelli, L. (2009). "Rationality in design." In *Philosophy of technology and engineering sciences*, ed. Anthonie Meijers, 564-600. Amsterdam: Elsevier.

Merriam-Webster's collegiate dictionary, 10th ed. (1993). Springfield, MA: Merriam-Webster.

Mitcham, C. (2009). "A philosophical inadequacy of engineering." *The Monist*, 92(3), 339-356.

Rittel, H. W. J. and Webber, M. M. (1969). "Dilemmas in a general theory of planning." *Panel on Policy Sciences, American Association for the Advancement of Science*, 4.

Simon, H. (1973). "The structure of ill-structured problems." *Artificial intelligence*, 4, 181-201.

Vick, S. G. (2002). *Degrees of belief: Subjective probability and engineering judgment*. Reston, VA: American Society of Civil Engineers.

Philosophy of Structural Building Codes

William M. Bulleit[1], Dave K. Adams[2]

[1]Professor and Chair, Department of Civil and Environmental Engineering, Michigan Tech, 1400 Townsend Dr., Houghton, MI, 49931-1295; PH (906) 487-2853; FAX (906) 487-2943; email: wmbullei@mtu.edu

[2]Structural Engineer, Lane Engineers, Inc., 979 N. Blackstone Street, Tulare, CA 93274; PH (559) 688-5263; FAX (559) 688-8893; email: davea@laneengineers.com

ABSTRACT

Structural building codes serve a number of purposes, but the primary one is to provide minimum standards of design that protect human health and safety. Codes have grown more complicated over the past 25 years primarily by providing increasing numbers of explicit provisions for the design of most structural members. Explicit provisions appear to be a good way to encode design knowledge, but too many of them will make the code difficult to decode. Encoding and decoding of design knowledge is best performed by a combination of implicit and explicit provisions providing general design principles and optimizing the number of explicit provisions in order to minimize the noise in the encoding/decoding process.

INTRODUCTION

The authority of building codes is granted by a common appeal to public safety. These codes are identified as minimum standards to safeguard the health, safety, property, and welfare of the public, which seems like a reasonable foundation upon which to build a set of regulations or to formulate a philosophy of how the public can best be served and protected. Building codes contain both explicit and implicit directives that identify minimum standards of building performance with which engineers must comply in structural design. Viewed from an information theory perspective (Pierce 1980), the provisions in a building code are an encoding of some portion of the design knowledge space. The designer's job is then to decode this encoded design knowledge.

Viewed this way, it is apparent that enhancements to a building code can come from doing a better job at encoding the design knowledge, enhancing the decoding process, or a combination of the two. Arguments for simplification of the building code often seem to be arguments to reduce the portion of the design knowledge space that is encoded, or just to do a better job encoding the portion of the design knowledge space that has been chosen (Hess 2009). Of course, another option is to enhance the decoding process by educating engineers better. However, no matter how well

engineers are educated, the decoding will be a personal process that will guarantee, in some cases, different interpretations of the building code directives.

It seems appropriate at this point to list some of the goals of building codes. The list is loosely ordered by relative importance of the goals, and some of the goals are not mutually exclusive.

- Define minimum standards
- Document legal requirements
- Enhance safety
- Protect property
- Assist engineers
- Assist code officials
- Enhance consistency across designs
- Reduce uncertainty
- Maintain heuristics

All of these goals are best met when the encoding and decoding processes are as optimal as possible. This paper considers some of the forms that the encoding takes, how it might be possible to encode in a way that reduces noise, and how the decoding process might be enhanced.

ENCODING DESIGN KNOWLEDGE

One form of design knowledge encoding is the use of explicit and implicit requirements; both kinds are necessary in order to meet the overall goal of safety. Building officials charged with enforcing the regulations often do not possess adequate training to interpret the appropriate response to an implicit code requirement, whereas they are generally suited to enforce explicit directives. Implicit requirements permit a range of solutions based on the engineer's experience and creativity, whereas explicit instructions allow limited or no leeway.

An example of an explicit requirement is that an anchorage of a concrete wall to a roof diaphragm must be able to carry 200 pounds per linear foot (plf) for allowable stress design under seismic load combinations (ICC 2006, Section 1604.8.2). Thus, if a minimum anchorage force of 200 plf is required, then 190 plf is insufficient and would be in violation of the building code. An example of an implicit criterion (ICC 2006, Section 1604.4) is that structural systems must provide a complete load path capable of transferring all loads from their point of origin to the load-resisting elements (e.g., walls and roof diaphragms). The implicit requirement for a complete load path, however, would allow an engineer to design a system based on actual loads (possibly less than 200 plf) and select components that are better suited for smaller loads, yet retain the characteristics of ductility so important in seismic design. The engineer is thus allowed broader latitude with which to judge the performance of a specific structure. From an informational standpoint, explicit requirements would appear to encode the design knowledge with less noise than do implicit requirements,

where noise here means that the requirement can be interpreted in more and varied ways.

Over the years, codes have become more explicit, and implicit instructions are often overshadowed. Granted, implicit directives are more difficult to enforce, but a greater amount of explicit requirements does not necessarily lead to safer structures. It is often difficult to decide how heavily to weigh the importance of these two elements (Shapiro, 1997; Coeckelbergh, 2006). If building codes are too explicit, innovation can be hampered and engineers may be viewed as simply instruction-following technicians (Coeckelbergh, 2006). Furthermore, as the number of explicit requirements increase, so does the noise in the code. If codes are too implicit, then proper enforcement of construction requirements for safe structures can be difficult to perform and the likelihood of a structural failure may be increased (Elms, 1999).

Many engineers argue that modern building codes do not adequately achieve a balance, typically tilting too far in the direction of prescription, as the ever-increasing thickness of the printed code documents suggests (Hess, 2009). The intent of the code often gets lost as it grows in size, and explicit provisions that were simple at one time become more complicated, which reduces the effectiveness of the code, increases noise, and stifles innovation and creativity on the part of responsible designers. Codes that are too complicated (often overly explicit) make it difficult for a designer to know how many of the requirements must be met to justify a specific design. So although explicit requirements may at first make for a better encoding, using a large number of explicit requirements that are strongly interconnected will make the decoding process more difficult. Codes that are too simple (overly implicit) can cause a similar decoding problem, except in this case the question is what should be used that is not specified to justify the design (Addis 1990). In summary, in the overly explicit case, the engineer will have difficulty determining what the code writers had in mind; and in the overly implicit case, the engineer will have to choose directly from the design knowledge space without help from the code writers.

In ASCE 7 (ASCE 2010), there are now three ways to approach designs: strength procedures, allowable stress procedures, and performance-based procedures. The designer is even allowed to choose among these procedures for different members in the same structure. In other words, there are three fairly explicit requirements that are strongly connected because different procedures can be used for different parts of a structure and for different load combinations (ASCE 2010). These provisions make the overall result implicit since the engineer has the discretion to choose among the three procedures.

However, the provision allowing choice among the three procedures presents a problem for an engineer who has a good understanding of these procedures: Is it safe to optimize a structure by choosing among the three procedures for various elements? Under most conditions, building codes are member–based, meaning that if you designed each member to the minimum standards throughout the structure, it could possibly behave in ways that are not safe due to system effects. This limitation is true

for designs performed within a single procedure, and thus may be magnified if the designer could design each member by choosing the smallest outcome from the three procedures for each element in a structure. The safety question does not have an answer in this case, so a knowledgeable engineer would be unlikely to blend the procedures in a single structure. An engineer with less understanding of the background of these procedures could, if time and money permitted, attempt the type of optimization described above. Allowing selection among the three procedures increases the noise in the code and increases uncertainty about the safety of structures designed under these provisions.

Other explicit requirements are heuristics. A heuristic is, to quote Koen (2003), "anything that provides a plausible aid or direction in the solution of a problem, but is in the final analysis unjustified, incapable of justification, and potentially fallible." Koen would argue that all provisions in a building code are heuristics, but some provisions appear to be more heuristic that others. An example from ACI 318 (ACI 2008) is the procedure for determining the effective flange width of reinforced concrete T-beams, which has been in use for over 90 years (Chen et al. 2007). This design procedure is a crude but effective way to deal with shear lag, thus a heuristic for shear lag design. Heuristics of this type are common in building codes, have a history of adequate performance, and allow engineers to solve problems in fairly simple, consistent ways across a range of designs.

Brenner (2007) discusses the manner in which a code can change when a relatively simple heuristic is replaced with a more rigorous approach. The AASHTO LRFD provisions (AASHTO 2007) for determining the live load distribution factor for bridge stringers changed from a simple heuristic in terms of one parameter, the stringer spacing, to a formula with up to eight parameters. Is the new, more complicated heuristic really worth the additional time required to use it? Is the previous, much simpler formula still adequate? Was the simpler heuristic a minimum standard? If so, why is the new one necessary? The encoding of the design knowledge has become noisier and decoding has become more difficult. The value of the change for the design engineer is unknown.

DECODING ENCODED DESIGN KNOWLEDGE

Decoding building codes has become increasingly more difficult over the past 25 years or so. Part of the difficulty is due to the significant increase in the size of the codes and the number of provisions contained within them, particularly ones that direct the engineer down a range of possible paths depending on certain criteria related to the structure and the load. Examples include seismic design and wind design, and criteria like that described above for design procedures that allow the engineer to choose between and even mix and match a few provisions. As stated previously, in an overly explicit code, the engineer has difficulty determining what the code writers had in mind; and in the overly implicit code, the engineer must

choose directly from the design knowledge space without help from the code writers. Erring too much in either direction increases the noise in the code.

The length of building codes has increased significantly. Considering ASCE 7, the size of the code has grown as follows: 1988, 94 pages; 1993, 134 pages; 1995, 214 pages; 1998, 330 pages; 2002, 376 pages; 2005, 388 pages; and 2010, 608 pages. Even accounting for the fact that some of these page changes are due to font size, the code has grown significantly. Over the 25-year period from 1983 to 2008, ACI 318, combining code and commentary, grew from 266 pages to 436 pages. This growth is not nearly as explosive as that for ASCE 7, but is still significant. Writing nearly twenty years ago about design codes, Galambos (1992) stated: "In the opinion of this writer, the present generation of codes has probably reached the limit of tolerable bulk and complexity. More of this complication will make the codes a modern dinosaur. Future design codes should concentrate on providing general principles and deemphasize detailed requirements." The present code structures are generally complicated encodings that force an engineer into a difficult decoding process. Complicated code structures can increase the chance of human error (Galambos 1992).

So what kinds of encodings would make the building codes more readily decoded? If we consider the list of goals for these documents, then clearly the code must provide minimum standards. Present codes seem to go beyond minimum standards, although the term 'minimum standard' is "in the eye of the beholder." For example, an engineer in Alaska once wanted to know why shear wall design could not be simplified, and in the same breath asked why a portion of the walls perpendicular to the shear wall at its ends could not be used as part of the chord members of the shear wall to make it an I-section.

Minimum standards do not necessarily provide the most economical design, and in most cases will not provide it. Building codes should be minimum standards; designing to more rigorous standards in order to make a structure more economical and/or innovative is beyond the minimum. Codes should assist engineers in their designs and assist code officials in making sure that designs are safe. Assisting engineers beyond the minimum standards is outside the code. Certainly it might be in a commentary, but that itself is outside the code. Assisting code officials and the other goals of design codes would seem to be best performed by making a code as explicit as possible, but an explicit code can itself cause confusion and increase noise in the decoding process.

Design codes should be just explicit enough to define minimum standards, which should assist both engineers and code officials. Most existing codes imply that the procedures in the code are the exclusive way to design that type of structural member. The change described above for live load distribution in stringer bridges would seem to be an unnecessary change, at least as far as minimum standards go. The old simple heuristic had been working well for years, and unless the new formula is a necessary

change from a safety standpoint, it should not be replaced. The new one would be appropriate in a commentary, but seems inappropriate as a requirement.

BALANCING ACT

Engineers who call for building code simplification are often calling for a reduction in explicit provisions in the code and, consequently, a smaller and less complicated document. A simplified code with essentially no explicit provisions may also prove to be inadequate, because engineers would need to depend on their own resources, which would likely decrease design consistency and increase uncertainty in the safety of structures. A balance needs to be found that reduces the noise in the code to its minimum. There will never be zero noise, because design of a structure is an individual process, and each engineer's interpretation of the code provisions will be potentially different (Bucciarelli 2003).

Perhaps there is a better way to blend explicit requirements with implicit provisions so that codes do not become increasingly burdensome, and yet the intent is clear enough to meet the goals of design codes and permit innovative approaches to solving structural engineering problems. An approach to future code updates that might serve society and the engineering profession better would reduce explicit provisions and expand on implicit directions in the code and include a commentary that gives suggestions to an engineer for achieving the stated goals, including suggested explicit provisions. For instance, the design code could consist of a *specification* that is mostly implicit, but may include longstanding, simple heuristics; a *commentary* that gives suggestions about how the specification could be met, including more complicated explicit provisions; and a *supplement* that includes aids for designs prepared in accordance with the commentary methods. The specification could be written such that use of the commentary techniques would lead to a deemed-to-comply design. This approach would not reduce the information available to an engineer, but would make it clear that most of the presently explicit procedures are suggested for use, rather than required. It would be up to the engineer to choose the design method that will best meet the implicit requirements in the specification.

CONCLUSION

Structural building codes have become increasingly more complicated over the past 25 years. Although at first it might appear that adding more explicit design requirements will make for better and safer designs, there is reason to believe that codes that are overly explicit reduce safety. Codes are an encoding of the design knowledge space, and overly explicit requirements increase the noise in the code, making decoding more difficult for the engineer. Overly implicit codes would also cause noise, but present codes are clearly not too implicit. An ideal code would minimize the noise in the encoding/decoding process by finding a balance between explicit and implicit requirements.

REFERENCES

AASHTO (2007) *AASHTO LRFD Bridge Design Specification, 4th Ed.,* American Association of State Highway and Transportation Officials, Washington, D.C.

ACI (2010) *Building Code Requirements for Structural Concrete (ACI 318)*, American Concrete Institute, Farmington Hills, MI.

Addis, W. (1990). *Structural Engineering: The Nature of Theory and Design,* Ellis Horwood, Ltd., Chichester, England.

ASCE (2010) *Minimum Design Loads for Buildings and Other Structures (ASCE 7-10),* American Society of Civil Engineers, Reston, VA.

Brenner, B. R. (2007) *Don't Throw This Away!: The Civil Engineering Life,* American Society of Civil Engineers, Reston, VA.

Bucciarelli, L. L. (2003) *Engineering Philosophy*, Delft University Press, Delft, The Netherlands.

Chen, S. S., Aref, A. J., Chiewanichakorn, M., and Ahn, I.-S. (2007) "Proposed effective flange width criteria for composite bridge girders," *Journal of Bridge Engineering,* ASCE, 12(3): 325-338.

Coeckelbergh, M. (2006). "Regulation or responsibility? Autonomy, moral imagination, and engineering." *Science, Technology, and Human Values,* 31(3), 237-260.

Elms, D. (1999). "Achieving structural safety: theoretical considerations." *Structural Safety,* 21, 311-333.

Galambos, T. V. (1992) "Design Codes." *Engineering Safety*, David Blockley, Ed., McGraw-Hill Book Co., London, UK, pp. 47-71.

Hess, R. L. (2009). "Does the building code need simplification?" *STRUCTURE*, 16(10), 7.

ICC (2006). *International Building Code (IBC)*. International Code Council (ICC), Country Club Hills, IL.

Koen, B. V. (2003) *Discussion of the Method: Conducting the Engineer's Approach to Problem Solving,* Oxford University Press, New York, NY.

Pierce, J. R. (1980) *An Introduction to Information Theory: Symbols, Signals and Noise,* Dover Publications, Inc., New York, NY.

Shapiro, S. (1997). "Degrees of freedom: Interaction of standards of practice and engineering judgment." *Science, Technology, and Human Values*, 22(3), 286-316.

What does it mean to be sustainable?

Tonatiuh Rodriguez-Nikl[1]

[1]M.ASCE., Ph.D., P.E., Oregon State University, School of Civil and Construction Engineering, 220 Owen Hall, Corvallis, OR, 97331. Email: rodrigto@engr.orst.edu, Phone: (541)737-2057, Fax: (541)737-3052

Abstract

Most engineers today have heard of sustainability, but there are probably few who would feel comfortable defining what it means. Even well-intentioned and well-read practitioners struggle with a useful definition of sustainability. Depending on who is asked topics that fall under the umbrella of sustainability can include green materials, energy independence, pervious pavement, the heat island effect, health of local waterways, social justice, etc. The scope of topics is extremely broad and can create a lack of focus that is a barrier to making progress on technical issues and communicating an effective message about sustainability.

In civil engineering, perhaps the two viewpoints on sustainability most commonly offered are a quote from the Brundtland Commission: "meeting the needs of the present without compromising the ability of future generations to meet their own needs" and the Triple Bottom Line of people, planet, and profit. These and other approaches contribute to our understanding of sustainability, sometimes from radically different points of view. In this paper the different approaches are discussed. Commonalities and differences are noted and a generalized framework of sustainability is developed. This framework can serve as a guide to analyzing some of the more popular topics in the discourse surrounding sustainability as related to civil engineering, to determine which do not fall within the scope of sustainability, which are the most important, and where we as technical practitioners should be focusing our efforts. Ultimately, the goal of this paper is to help engineers actively discuss and answer these questions for themselves.

Introduction

The word "sustainability" has gained significant popularity in recent years. It has become a common concept both in everyday life and in the profession. The American Society of Civil Engineers (ASCE) has released books on the topic (ASCE 2004, Kestner et al. 2010) and its leadership considers this a central topic. In January 2010 ASCE convened five roundtables in Washington, D.C. One of these was centered on the theme of promoting "sustainability and resilience in infrastructure to protect the natural environment and withstand natural and man-made hazards" (Powell 2010). Sustainable development even appears in the First Cannon of the ASCE Code of Ethics as "the process of applying natural, human, and economic resources to enhance

the safety, welfare, and quality of life for all of society while maintaining the availability of the remaining natural resources."

Despite the popularity of sustainability, or perhaps because of it, there is still considerable skepticism surrounding the idea. Paul Jowitt (2004), former president of the Institution of Civil Engineers and a proponent of sustainable development wrote that "the problem with sustainability and sustainable development is not a lack of definitions – there are very many. It is easy to see why some are so skeptical." Certainly there are many disingenuous misuses of the term for purposes of blatant marketing with no underlying substance. A similar although perhaps unintentional misuse is equating sustainability with being "green" (environmentally less invasive) as in the phrase "our project was sustainable because we reduced noise, reduced construction waste, and used recycled materials." More troubling is the seeming preponderance of well-intentioned technical presentations and articles that use "sustainability" superficially without providing the audience or the reader a clear idea of what it really means. While this may simply be done in the interest of space and time, not through ignorance, the proliferation of superficial and different uses of "sustainability" carries the danger of making the term practically meaningless.

In no way should these arguments and examples be taken as reason to dismiss sustainability out of hand. The motivations for promoting sustainability are based on significant and important considerations. At stake is whether it is possible to maintain the social benefits provided by the recent centuries of industrialization in the face of the detrimental impacts that have accompanied such development. As civil engineers – entrusted with designing, building, and maintaining much of the physical infrastructure that supports modern society – we are intimately bound to this question. In addition to the social benefit it might bring, our work contributes in a negative way to pressing global challenges such as climate change and natural resource depletion. How important or pressing these issues are is out of the scope of this paper, but whatever the final verdict, the questions are of significant consequence and merit serious, careful, and rational consideration.

This paper is an attempt to respond to the skepticism that often surrounds the mention of "sustainability" by providing a theoretical framework that captures its essential features and allows for meaningful and rational dialogue. The ultimate hope for this framework is that it be useful for making well informed decisions by providing a clear way to think about the relevant issues involved. Thus, although this topic is necessarily broad and theoretical, the motivation is practical: enabling the profession to identify the most important problems and to find the most effective solutions to those problems.

In the remainder of the paper the more common definitions of sustainability are reviewed, the theoretical framework is proposed and discussed, and finally the question posed in the title of the paper is answered and a list of questions is provided to help determine whether something can genuinely be called sustainable.

Common Definitions of Sustainability

Within the civil engineering profession there are two definitions almost invariably offered for "sustainability". One is often referred to as the "Brundtland Definition" and stated as "meeting the needs of the present without compromising the ability of future generations to meet their own needs". The other common definition is the "Triple Bottom Line", which defines sustainability as the intersection of social needs, economic needs, and environmental needs. It is sometimes referred to as "People-Planet-Profit" or the "Three Pillars of Sustainability". With no further elaboration both definitions are overly general and vague and admit a variety of competing interpretations. These definitions sound good at first glance but become difficult to use as decision criteria when attempting to analyze a concrete scenario. For instance, when applying the first definition, what exactly is a "need"? When applying the second, how little weight can be given to any of the three factors (people, planet, and profit) while still being considered "sustainable"? To understand these questions better, it is important to reflect briefly on the context surrounding each of them.

The Brundtland Definition arose in 1987 in a report of the United Nations World Commission on Environment and Development (WCED 1987). It became known as the Brundtland Report because of its chair, Gro Harlem Brundtland of Norway. The report provides a rich vision of the problems and solutions surrounding their definition of sustainable development, addressing such issues as population, food security, ecosystems, energy, industry, and urban environments. It calls for responsible economic growth as a means of eliminating poverty. An extended quotation provides a more honest interpretation of the intentions of the report: "Sustainable development is development that meets the needs of the present without compromising the ability of future generations to meet their own needs. It contains within it two key concepts: the concept of 'needs', in particular the essential needs of the world's poor, to which overriding priority should be given; and the idea of limitations imposed by the state of technology and social organization on the environment's ability to meet present and future needs." It is interesting that these issues are often ignored or contradicted by people who use the shorter version of the passage.

The Triple Bottom Line (TBL) was coined in 1994 by John Elkington of the British consultant firm SustainAbility (Elkington 2004). The intent of the term was to present ideas such as those of the Brundtland Report to the business world. Elkington (1998, ch. 4) identifies the traditional accounting framework in which one (1) identifies what counts as capital (physical, financial, etc.), (2) accounts for this capital, (3) identifies relevant issues of concern (e.g., profit/loss and balance sheets as well as long term financial issues), (4) conducts audits to determine the performance in these areas, and (5) reports these results to the appropriate audience (e.g., stockholders). This same framework is then adapted to environmental and social issues. As Elkington clarifies, environmental accounting is more than just "counting the trees and trying to put a price tag on the lumber they represent"; it is important to capture the "underlying natural wealth". Environmental capital includes global resources such as natural resources, but because TBL speaks to individual firms, the scope of interest is

only with those resources affected by the firm. Similarly, while social capital represents broad issues as public health, education, social friction, and society's wealth-creation potential, the scope of interest is with those issues that the firm affects directly. These are issues such as "community relations, product safety, training and education initiatives, sponsorship, charitable donations of money and time, and employment of disadvantaged groups." While identifying the need for measurable metrics for environmental and social issues, Elkington admits that this is an area in which much work is needed.

Before proceeding to the new proposal one more topic is discussed because of its popularity in the building industry. LEED (Leadership in Energy and Environmental Design) is an increasingly popular approach to sustainability in buildings. In part because of its success for buildings it is being piloted for neighborhoods and similar approaches are being developed by others for infrastructure (ASCE 2010, Greenroads 2010). LEED identifies the following areas of concern: sustainable sites, water efficiency, energy & atmosphere, materials & resources, indoor environmental quality, and locations & linkages. In addition to these are awareness & education, innovation in design, and regionally important issues. LEED establishes basic design requirements in those areas and suggests optional improvements. Each of the optional improvements can earn points and a minimum number of points is required. Additional points can be earned to obtain higher certifications.

Some themes run through all these frameworks; others through just one or two. Environmental issues are paramount and social issues are at least addressed by all three. All three focus on a long-term future and expect at least maintenance of the status-quo during this term. The proposals differ in geographical scale; the Brundtland definition is global while TBL is applied at the scale of an individual business and LEED is applied at the level of an individual facility. The Brundtland definition focuses on the poor and demands a marked improvement in their situation; the other two do not discuss issues of poverty. LEED has a detailed measurement system not found in the other two.

Proposed Framework

A generalized framework is now proposed to capture concisely the important aspects of these and other definitions to provide a generalized notion of sustainability and a way of evaluating new developments, be they theoretical and broad or technical solutions to specific problems. A dictionary definition of "sustainable" provides a suitable starting point. The Oxford English Dictionary defines it as "capable of being maintained at a certain rate or level". Other definitions are similar. One can construct a graphical interpretation of this definition as shown in Figure 1 on the following page. The vertical axis in this figure represents Quality, a term that will be used here in a general sense to refer to how good something is. It can refer to the financial standing of a firm, the functionality of a car, the reliability of a bridge, or the level of social inequality in a society. The horizontal axis represents time t and Quality is represented as the function $Q(t)$. The quantity t_f represents a time threshold beyond

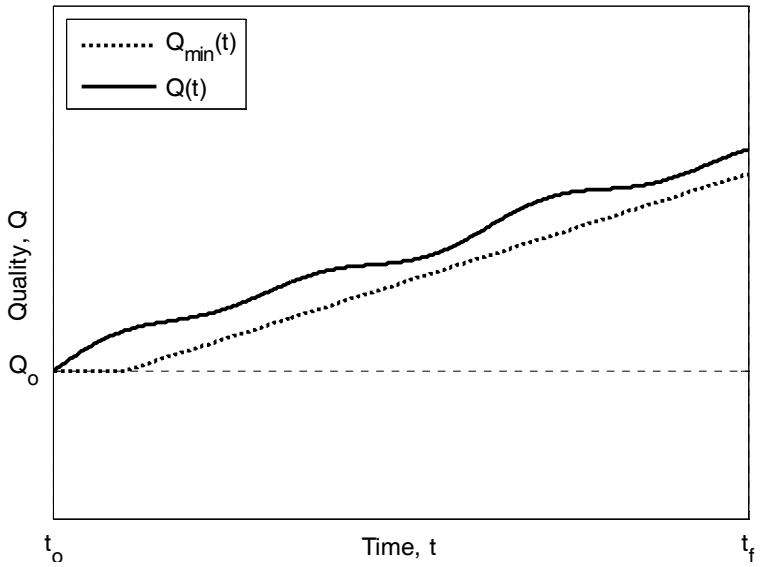


Figure 1. Graphical representation of proposed sustainability framework.

which we are no longer concerned. A function $Q_{min}(t)$ is defined to determine the limit below which $Q(t)$ cannot drop. With this framework it is possible to define sustainability in mathematical terms. A process is said to be sustainable if

$$Q(t) \geq Q_{\min}(t) \forall t \in [t_o, t_f].$$

This idea will be illustrated in an example that is intentionally simple, but that is familiar to structural engineers and provides a springboard for talking about more general ideas. While this example does not capture the whole of what people mean when they say "sustainability", a term that tends to be attached to global problems at long time scales, it will lead directly to a generalized framework.

Consider a reinforced concrete bridge in a seismic region with cold winters. Once the bridge is in service, the primary concerns are earthquakes, freeze-thaw, and chloride ion penetration from de-icing salts. The seismic robustness of the bridge is measured by its reliability index β, which is related to the probability of exceeding a defined damage state in an earthquake. With no maintenance and mitigation plan the reliability index of the bridge might decrease in time as shown by the solid line in Figure 2 on the following page. The pristine bridge has a relatively high reliability index but after a certain initiation time, rebar corrosion begins and the reliability index decreases indefinitely, at some point dropping below β_{min}, the lower limit. In this case, applying the definition above, we can say that the seismic robustness of the bridge as measured by its reliability index is not sustainable over its intended service life. With a maintenance and mitigation plan in place, the reliability index of the bridge might progress as shown by the dashed line. The plan is to use cathodic protection to delay the initiation time. At a later time the bridge is retrofitted to make up for the steel rebar lost to oxidation. This does not stop further loss of rebar but does increase the strength sufficiently for the bridge's reliability index to remain above the required

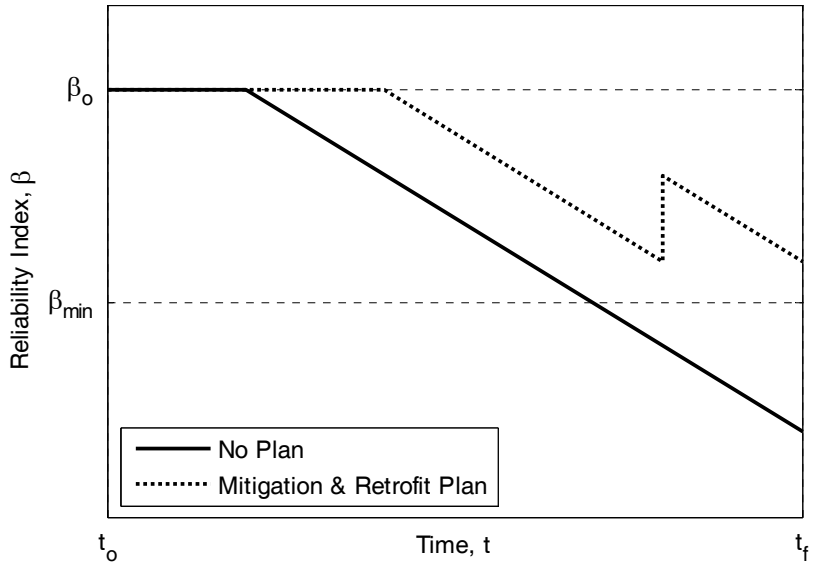


Figure 2. Reliability index of a bridge with and without mitigation and retrofit plans

minimum before the end of it service life. In this case we can say that the seismic robustness of the bridge as measured by its reliability index is sustainable over its intended service life. The following important issues are observed in this example:

1) There is a salient topic of concern, in this case the seismic robustness of the bridge.
2) The seismic robustness is measured by a numerical metric, the reliability index.
3) Some of the parameters are determined a-priori, namely t_f (the service life) and β_{min} (the minimum allowable reliability index).
4) The evolution of the reliability index is affected by natural laws (e.g., corrosion, weather, and seismicity) that are beyond the control of any individual.
5) The evolution of reliability index with time is also affected by the chosen maintenance and rehabilitation plan.
6) Once the maintenance and rehabilitation plan is chosen and the natural laws understood, the evolution of reliability index is determined by our physical models.
7) The predicted and required performance are compared to determine whether the seismic robustness is sustainable.

These seven steps can be generalized as follows:

1) Clearly identify the issues pertinent to the problem at hand.
2) Establish a method of assessing the Quality of these features. These are preferably numerical metrics.
3) Determine the performance requirements in the form of the minimum level of Quality $Q_{min}(t)$ and the time horizon t_f. Depending on the scenario these re-

quirements are determined by the engineer, the individual, the political system, etc.
4) Identify the natural laws that will govern $Q(t)$, i.e., the evolution of the features identified in step 1.
5) Determine the policies that will also govern $Q(t)$.
6) Determine the evolution of $Q(t)$ given the natural laws and processes.
7) Compare the predicted Quality to the required minimum level $Q_{min}(t)$.

Discussion

To illustrate how this framework can be applied, in the remainder of this section it is used to discuss the three common visions of sustainability presented above. Using the framework in the context of sustainable development not just as discussed in the Brundtland Report but including additional developments as summarized by Brandon and Lombardi (2011), we observe the following:

1) Human development is a complex issue that depends on such different factors such as standard of living, education, and public health among many others. One of the main tasks of the Brundtland report is to identify the relevant issues and describe them in detail. Despite the age of the document its findings are still relevant today.
2) The Brundtland report discusses the metrics used to measure these relevant issues. Others have attempted to establish a single summary metric to help in measuring changes in development. One such example is the human development index (HDI), which depends on more fundamental metrics such as gross domestic product, literacy rate and infant mortality.
3) The time horizon (t_f) and the development goals $Q_{min}(t)$ are issues subject to intense debate, but it is possible to establish them. Regarding t_f the Brundtland Report speaks of elimination of poverty in the time span of "several generations". Researchers have suggested 500 years (Hansen 2007) to 1000 years (MacKay 2008, 157) as suitable time scales.
4) The issues identified in step 1 are governed by laws and models from a wide variety of disciplines that include economics, public health, and climate science, to name a few.
5) The course of human development is affected by public policies at all geographical scales. The intention of the field of sustainable development is to influence policies to make the goals in step 1 more easily attainable.
6) Although the analysis might prove too complex, in theory predictions of the evolution of human development could now be made. Given the complexity of the problem and the number of assumptions that must be made, many analyses should be made to establish lower and upper bounds and our level of certainty in the predictions.
7) Having obtained predictions and measures of uncertainty, it would be possible to gauge whether the development goals could be reached. Because the answer depends on the social sciences, whose predictive abilities are not as accurate as those in the natural sciences, this is a difficult step.

As shown in this brief analysis, efforts in sustainable development are complex, perhaps too complex to obtain meaningful answer, but these efforts do address all the areas that have been identified as relevant. In contrast, when the Brundtland definition is decontextualized and reduced to simply "meeting the needs of the present without compromising the ability of future generations to meet their own needs", the relevant features are no longer clearly identified. Reference is made to the needs of the present and future generations, but what these needs are is not elaborated further. Because the needs are not identified it is impossible to assess their Quality in any objective way; anybody is able to provide their own definition of needs to suit their own agendas. Because Quality cannot be assessed, it is impossible to establish useful limits, or to identify evolutionary processes, even in theory.

A similar story can be told for the Triple Bottom Line (TBL). The detailed description provided by Elkington (1998) addresses the seven points identified by the framework proposed in this paper, although it is admitted that environmental and social accounting are areas in need of development. However, if one makes the simple claim that sustainability means accounting for economic, social, and environmental considerations, this removes any chance at a rational analysis. Interpretations can differ wildly, from taking the point of view of a business to being global in scale and political in scope with radical social justice and environmentalist goals. With a vague definition and a range of interpretations this wide, it is again not possible to develop a meaningful way of assessing Quality nor of determining the evolution of the economic, social, and environmental considerations.

Applying the proposed framework to LEED we observe the following:

1) The overarching goals of the LEED program are "improving performance" in "energy savings, water efficiency, CO_2 emissions reduction, improved indoor environmental quality, and stewardship of resources and sensitivity to their impacts" (USGBC 2010). These are typical of goals proposed by the green building community. There are no specific targets such as reducing CO_2 emissions by 30% in 50 years. The goal is simply to "improve performance".
2) LEED has a detailed measurement scheme. It is intended for use during design to influence the decisions of the design team. There is at present no requirement for long term performance measurement or modeling. Thus this score does not directly relate to the goals above. The items that are scored are practices that may (or may not) result in positive changes with regard to the stated goals. There are concerns that LEED certified buildings fail to perform as per the LEED program goals (Scofield 2009). While additional research is still needed this is an important concern.
3) There is no time horizon defined by LEED and while there are clearly defined point thresholds for different levels of certification, there are no defined minimum levels of Quality. This is due to the indirect relation between the goals and the measurement scheme. The only information that can be gathered by their requirement to "improve performance" is that $Q(t) > Q(0)$, i.e., that is that the performance be marginally better in some undefined time frame.

4) The knowledge does exist for determining the environmental impact of the building in the areas identified in the first bullet. Public and commercial life cycle inventories (databases) are available and software programs exist to calculate the impacts of a building project though its design life.
5) LEED makes no provisions for building operation, maintenance, or adaptability to the future. The typical LEED certified building will be operated in the same way as any conventional building.
6) Life cycle assessment (LCA) is a well established technique for determining the impacts in any given project through time (see e.g., ISO 2006). By using LCA one would be able to determine the performance of conventional and LEED certified buildings according to the goals stated in bullet 1. At present LEED is considering including LCA. It is too early to tell how it will be included or what changes this might bring.
7) It is not possible to use the LEED framework to determine whether a project can be called sustainable or not. This is due to two fundamental limitations: the vague statement of overarching goals and the disconnect between these goals and the system of measurement.

This analysis reveals that the point system offered by LEED is not a metric of sustainability. Although it may be a useful metric of something else, achieving LEED certification for a building provides no guarantee of performance that can be classified as sustainable.

What Does It Mean To Be Sustainable? The answer to this question follows from the structure of the proposed framework: (1) issues of concern are identified, (2) metrics are developed, (3) desired performance through time is determined, (4-5) forces governing the evolution of these issues are identified, (6) the evolution is modeled with sufficient accuracy, and (7) it is determined whether the predicted performance meets the desired performance.

While identification of an issue may be a matter of opinion, the choice should be defensible. Why are the chosen issues important? Why should these issues take precedence over all others? This is the most important step since without it it is not clear what question is being answered, if the proposed question is relevant, or even if a question is being answered. This step is also often ignored and people seem to assume that others share their views, creating a major source of miscommunication. This is a source of the ambiguity mentioned in the introduction between the many uses of "sustainability".

An important consideration that must be made when defining the issue of concern is the geographical scale of the issue; is it local like a bridge, a firm, or a building; is it regional like a watershed or the heat island effect in an urban area; is it national like calls for energy independence; or is it global like climate change? As in the example above, it is possible to refer to the sustainability of the bridge, as measured by its reliability index, under seismic loading and a particular de-icing and maintenance plan. Yet this does not capture what most people mean when using the stand-alone term

"sustainable". If this term is to be given the importance of a stand-alone term it should carry with it grandiose assumptions; it should refer to issues that are global in scale and relevant over long time spans. These issues would be those that affect the whole of humanity and its ability to at least maintain a level of development near what we have achieved so far. These are issues such as those discussed in the Brundtland Report.

Only an evolving process can be called sustainable. Something unchanging is tautologically sustainable. Thus, a technological innovation cannot be called sustainable without understanding the ways in which it will be used and applied, i.e., the ways in which it will effect change and be changed. A single building cannot be sustainable, but it can be an example of methods that when applied over a wide sector of society can contribute to sustainable urban development.

How well we can predict an evolving process depends on our knowledge about the natural forces that govern it as well as the influential practices within human control, e.g., public policies, standard industry practices, maintenance procedures, etc. The human-controlled practices must match the scale of the issues of interest. For instance, a new "green" (environmentally less invasive) material may use large amounts of recycled materials and result in significant reductions in CO_2 emissions, but if the availability of those materials is limited to small geographical regions, if the mechanical properties of that material limit its use to a few special applications, or if practices in the construction industry are such that they cannot produce or use the material extensively, then the impact of that innovation will be negligible. This material cannot fall under the banner of sustainability because its influence does not match the global, long term scale of resource depletion and climate change that would have made use of recycled materials and reduction of CO_2 emissions worthwhile goals to pursue.

Once the issues, the proper evaluation metrics, and the natural and human forces affecting those issues are identified, the evolution of the issues can be predicted. The nature of the analysis may look vastly different depending on the field of study, but because the problems are multidisciplinary and large (both spatially and temporally) most analyses will have in common the need to consider complex systems and significant uncertainty. Engineers may not be accustomed to considering such matters. Rodriguez-Nikl and Brown (2011) offer guidance for conducting such analyses.

In considering the distant future, it is important to determine the discount rate that accounts for the tendency for people to discount risks in the future, i.e., to fear a risk today more than the same risk in the future. It has been argued that when considering long term decisions that the smallest possible discount rate should be used (Brandon and Lombardi 2011, 47-49; Weitzman 1998). It can be shown that introducing even a very small discount rate can result in drastically different conclusions about the future, e.g., without a discount rate one may predict a net degradation whereas with even a small discount rate one may predict net modest improvement. For this reason,

it is suggested not to use a discount rate when making predictions about the distant future.

Once this analysis is conducted to satisfaction, determining whether a course of action is sustainable is a simple matter of determining whether the predicted performance of the issues of concern is within the stated limits. *For something to be sustainable means that it is a globally relevant and significant process that can be maintained within stated limits over long time scales*. If a claim of sustainability is being made the following questions need to be satisfactorily addressed:

1) Are the issues of concern clearly identified, well argued for, and global in scope?
2) Have appropriate metrics been developed for analyzing these issues? Are the chosen metrics directly relevant to the issues of concern?
3) Are appropriate limits chosen for these metrics? Is the time horizon long enough?
4) How well are natural laws understood? What does this imply about the uncertainty in our analyses?
5) Are human practices that influence the issues of concern well understood and defined? Do these practices allow for action at the same global scale as the issues of concern?
6) Is the evolution of these issues known with sufficient accuracy and certainty?
7) Is the predicted performance within the stated limits?

If one is a potential user of a technology and wants to determine whether that technology can honestly be called sustainable, if one wishes to invent a new technology that can honestly be called sustainable, or if one simply wants to evaluate their personal practices at home with regard to sustainability, this list of questions will help guide one's thinking to allow action consistent with one's values.

Summary

The aim of this paper is to present a comprehensive general definition of sustainability that can bring clarity to contemporary discussions and provide a way of assessing proposed solutions for the pressing problems of the day. The more common paradigms for sustainability are first presented. These are the Brundtland definition: "meeting the needs of the present without compromising the ability of future generations to meet their own needs" and the Triple Bottom Line of people, planet, and profit. LEED is also discussed because of its popularity in the building industry. Following this a general theoretical framework of sustainability is proposed for discussing the issues involved and a list of questions is provided to help determine whether something can genuinely be called sustainable.

References

ASCE (2004). Sustainable Engineering Practice: An Introduction, Reston, VA.

ASCE (2010). "ILC Works to Help Develop Sustainability Rating System", ASCE News, May, 35(5).

Brandon, P.S., and Lombardi, P. (2011). Evaluating Sustainable Development in the Built Environment, second edition, Wiley-Blackwell.

Elkington, John (1998). Cannibals with forks: The triple bottom line of 21st century business, New Society Publishers, Stony Creek CT.

Elkington, John (2004). Enter the Triple Bottom Line, in Adrian Henriques and Julie Richardson (ed), The triple bottom line: does it all add up?, Earthscan, Sterling, VA.

Greenroads (2010). Greenroads rating system v1.0, www.greenroads.us.

Hansen J. et al. (2007). "Climate change and trace gases", Phil. Trans. R. Soc. 365, 1925-1954.

ISO (2006). Environmental management – Life cycle assessment – Principles and framework, ISO 14040, International Organization for Standardization, Switzerland.

Jowitt, P.W. (2004). "Sustainability and the formation of the civil engineer", Proceedings of the institution of civil engineers, I57(ES2) 79-88.

Kestner, D.M., Goupil J., and Lorenz, E., editors (2010). Sustainability guidelines for the structural engineer, ASCE, Reston, VA.

MacKay, D.J.C. (2008). Sustainable Energy – without the hot air, UIT, Cambridge, England.

Powell, A.E., (2010). "The Infrastructure Roundtables: Seeking Solutions to an American Crisis", Civil Engineering, ASCE, April, 42-103.

Rodriguez-Nikl, T. and Brown, C.B. (2011). "Sustainability: Complexity, Regulations, Decision", ICVRAM/ISUMA 2011, ASCE, April 11-13, Hyattsville, MD.

Scofield (2009). "Do LEED-certified buildings save energy? Not really…", Energy and Buildings, 41, 1386-1390.

USGBC (2010). "What LEED Is", online at <<http://www.usgbc.org/DisplayPage.aspx?CMSPageID=1988>> as of 7 Jan 2011.

Weitzman, M.L. (1998). "Why the far distant future should be discounted at its lowest possible rate", J. Environmental Economics and Management 36, 201-208.

WCED (1987). Our Common Future, Report of the World Commission on Environment and development, United Nations.

Connection Details - Practicing Engineers and the Code

C. Wilcox[1], S.E., B. Nuttall[2], S.E., and T. Barnett[3], S.E.

[1]Vice President, MWH Americas Inc., Walnut Creek, CA 94596; email: craig.j.wilcox@us.mwhglobal.com
[2]Associate Professor, Architectural Engineering Department, California Polytechnic State University, San Luis Obispo, CA 93407; email: bnuttall@calpoly.edu
[3]Partner, Hanson Professional Services Inc., Rockford, IL 61108; email: tbarnett@hanson-inc.com

ABSTRACT

There is widespread concern among practicing engineers that the clarity and usability of the building codes have radically diminished as the size and complexity of the codes have increased. One tool for assessing the ability of practicing engineers to consistently and reliably implement the code is the use of Trial Design Problems. The Trial Design Problem process consists of (a) developing a common engineering problem, (b) enlisting practicing engineers to complete the engineering problem using the code, (c) evaluating the engineering solutions submitted by practicing engineers, and (d) conveying the results of the problems to the engineering community and code development committees.

The Design Practices Committee has recently completed evaluating two different Design Problems. One design problem was for the application of ACI 318 Appendix D cracked concrete anchor bolt design. The second problem was the analysis and detailing specification of Wall-to-Roof anchorage in masonry construction intended to be per ACI 530-08. These problems have exhibited and proved that new code sections are routinely misinterpreted or not applied by practicing engineers. The application of these important and more recently instituted code sections has proved to be a subject that can cause confusion and misapplication as will be evidenced in the session. A movement is in progress to encourage greater collaboration between Code writing authors, and application and interpretation of code sections by the practicing engineers. The purpose of this session is to present the results of these trial problems and encourage further collaboration to advance the practice of structural engineering as it relates to code interpretation and design of elements and components. The objective is to improve clarity regarding current issues in the profession such as application of code sections, the complexity of codes and their detailed application. Presentations will introduce these topics, allowing time for comments, questions, and further discussion with members of the audience in attendance.

INTRODUCTION

Is the code written for practicing design engineers or for researchers? Are practicing design engineers able to keep up with the fast pace of code changes? Is the code

being properly and consistently applied in practice? With the introduction of a national building code (IBC), there has been growing concern among practicing engineers that the complexity of the code has significantly increased while the clarity and usability of the code has radically diminished. This paper describes the activities being performed by the Design Practices Committee of the Structural Engineering Institute (SEI) to evaluate the impact of code complexity on the practice of structural engineering by soliciting solutions to Trial Design Problems.

Trial Design Problems – Two Trial Design Problems were recently completed that quantitatively evaluated the effectiveness of the ACI 318 Appendix D, ACI 530-08 and ASCE 7-05 codes in producing reliable, safe and consistent engineering design applications. The results of the Trial Design Problems presented in this paper quantitatively demonstrate that unnecessarily complex code provisions result in less reliable, less safe and less consistent design practices.

In general, Trial Design Problems are intended to:

1. Investigate how practicing engineers interpret and apply current code provisions.
2. Investigate the consistency of engineering judgment of practicing engineers.
3. Promote dialog and continuing education among practicing engineers.
4. Identify and promote needed improvements in the code requirements.

The Trial Design Problem process consists of:

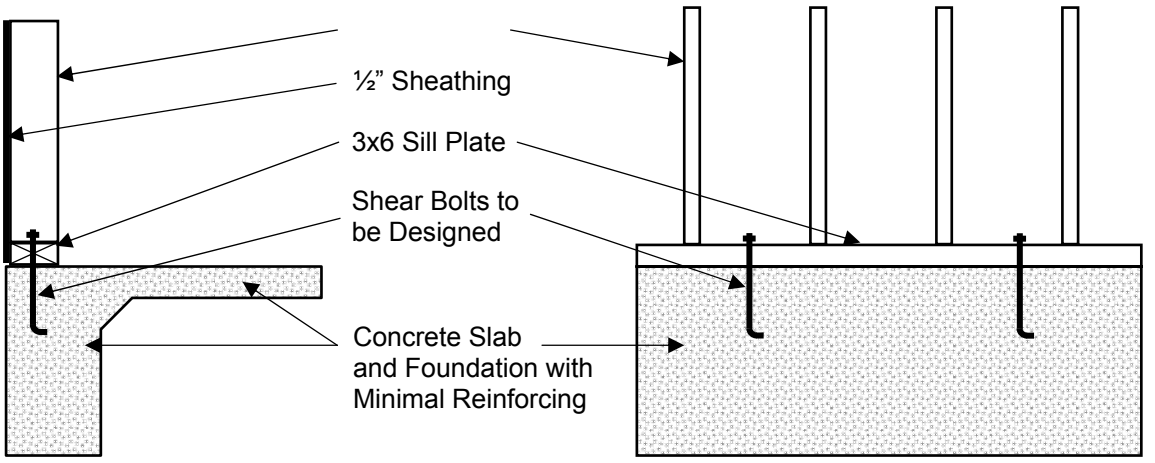
1. Developing a problem based on code provisions,
2. Enlisting practicing engineers to complete the engineering problem,
3. Evaluating the engineering solutions submitted by practicing engineers, and
4. Conveying the results of the problems to the engineering community and code development committees.

Trial Design Problem #1 - ACI 318 Appendix D

You are designing a new wood framed residence located in San Diego, California. You have already determined the lateral forces on the wood shear walls and that the house is classified as Seismic Design Category D. You have also determined that you will be using a 3x sill plate of pressure treated Hem Fir lumber and 2,500 psi normal weight concrete for the slab and foundation. The maximum in-plane shear force on the wood shear walls is as follows:

υ_{wind} = 600 plf ultimate / 420 plf allowable
$\upsilon_{earthquake}$ = 500 plf ultimate / 350 plf allowable

Design the shear anchor bolts connecting the 3x wood sill plate of the shear wall to the cast-in-place reinforced concrete foundation.



SOLUTION - ANCHOR DESIGN PROBLEM 2009

Time to Complete: **Way, way, way too much time.**

Bolt Type: ***Cast-in-Place 'J' Bolt***
(e.g. cast-in-place 'J' bolt, post-installed expansion anchor, etc.)

Bolt Grade / Material: ***A307***
(e.g. A307, etc.)

Bolt Capacity Sources: ***ACI Appendix D, NDS***
(e.g. IBC Bolt Capacity Tables, ACI Appendix D, NDS, Bolt Vendor Information, etc.)

Bolt Diameter: ***5/8" diameter***

Bolt Embedment: ***7"***

Bolt Spacing: ***48"***

Solution

ACI Shear Anchor Design (ACI D.4.1)

- $\phi V_n \geq V_{ua}$ (Eq. D-1)
- ϕV_n equals lesser of ϕV_{sa} or ϕV_{cb} or ϕV_{cp}

Steel Strength of Anchor in Shear (ACI D.6.1)

- Use 5/8" diameter A307 Hooked Anchor Bolts
- $V_{sa} = n0.6A_{se,v}f_{uta}$ (ACI Eq. D-20)
    - $A_{se} = 0.226in^2$ (Threads considered)
    - $f_{uta} = 58{,}000psi$ (A307)

- $V_{sa} = (1)(0.6)(0.226in^2)(58{,}000\,psi) = 7{,}860lbs$
- $\phi V_{sa} = (0.65)(7{,}860lbs) = 5{,}110lbs$
    - $\phi = 0.65$ (ACI D.4.4)

Concrete Breakout Strength in Shear (ACI D6.2)

- $V_{cb} = 2\frac{A_{Vc}}{A_{Vco}}\psi_{ed,V}\psi_{c,V}\psi_{h,V}V_b$ (ACI Eq. D-21 & D.6.2.1.c)
    - $A_{Vc} = A_{Vco} = 4.5(c_{a1})^2 = 4.5(2.5")^2 = 28.1in^2$
        - $c_{a1} = 2.5"$
    - $\psi_{ed,V} = 1.0$ (ACI D.6.2.1.c)
    - $\psi_{c,V} = 1.0$ (ACI D.6.2.7)
    - $\psi_{h,V} = 1.0$ (ACI D.6.2.8)
    - $V_b = \left(7\left(\frac{l_e}{d_a}\right)^{0.2}\sqrt{d_a}\right)\lambda\sqrt{f_c'}(c_{a1})^{1.5}$ (ACI Eq. D-24)
        - $l_e = h_{ef} = 6"$
        - $d_a = 0.625"$
        - $\lambda = 1.0$
    - $V_b = \left(7\left(\frac{6"}{0.625"}\right)^{0.2}\sqrt{0.625"}\right)1.0\sqrt{2{,}500\,psi}(2.5")^{1.5} = 1{,}710lbs$

- $V_{cb} = (2)\left(\frac{28.1in^2}{28.1in^2}\right)(1.0)(1.0)(1.0)(1{,}710lbs) = 3{,}420lbs$
- $\phi V_{cb} = (0.70)(3{,}420lbs) = 2{,}390lbs$
    - $\phi = 0.70$ (ACI D.4.4)

Concrete Pryout Strength (ACI D.6.3)

- $V_{cp} = k_{cp}N_{cb}$ (ACI Eq. D-30)
    - $k_{cp} = 2.0$
        - $h_{ef} = 6.0" > 2.5"$
    - $N_{cb} = \frac{A_{Nc}}{A_{Nco}}\psi_{ed,N}\psi_{c,N}\psi_{cp,N}N_b$
        - $A_{Nc} = (c_{a1} + 1.5h_{ef})(2\times 1.5h_{ef})$ (ACI Fig. Rd.5.2.1)
        - $A_{Nc} = (2.5"+1.5(6.0"))((2)(1.5)(6.0"))=207in^2$
        - $A_{Nco} = 9h_{ef}^2 = (9)(6.0")^2 = 324in^2$
        - $\psi_{ed,N} = 0.7 + 0.3\frac{c_{a,\min}}{1.5h_{ef}}$ (ACI Eq. D-11 for $c_{a,min}<1.5h_{ef}$)

- $\psi_{ed,N} = 0.7 + 0.3\dfrac{2.5"}{1.5(6.0")} = 0.78$
- $\psi_{c,N} = 1.0$ (ACI D.5.2.6)
- $\psi_{cp,N} = 1.0$ (ACI D.5.2.7)
- $N_b = k_c\lambda\sqrt{f_c'}h_{ef}^{1.5} = (24)(1.0)(\sqrt{2500\,psi})(6.0)^{1.5} = 17{,}636lbs$

  - $N_{cb} = \dfrac{207in^2}{324in^2}(0.78)(1.0)(1.0)(17{,}636lbs) = 8{,}790lbs$

- $V_{cp} = (2.0)(8{,}790lbs) = 17{,}580lbs$
- $\phi V_{cp} = (0.70)(17{,}580lbs) = 12{,}310lbs$
  - $\phi = 0.70$ (ACI D.4.4)

Wood Sill Plate (NDS)

- $Z' = ZC_DC_MC_tC_gC_\Delta C_{eg}C_{di}C_{tn}$
  - $Z = 1{,}170lbs$ (NDS Table 11E)
  - $C_D = 1.6$, $C_M = 1.0$, $C_t = 1.0$, $C_g = 1.0$, $C_\Delta = 1.0$, $C_{eg} = 1.0$, $C_{di} = 1.0$, $C_{tn} = 1.0$
- $Z' = (1{,}170lbs)(1.6) = 1{,}870lbs$

Wind Design

- Concrete
  - $\phi V_n = \phi V_{cb} = 2{,}410lbs$
  - $V_u = 600\,plf$
  - $Spacing = \dfrac{2{,}410lbs}{600\,plf} = 4.0\,ft$
- Wood
  - $Z' = 1{,}870lbs$
  - $V = 420\,plf$
  - $Spacing = \dfrac{1{,}870lbs}{420\,plf} = 4.5\,ft$

Earthquake Design

- Concrete
  - $0.75\phi V_n = 0.75(2{,}410lbs) = 1{,}810lbs$
  - $V_u = 500\,plf$
  - $Spacing = \dfrac{1{,}810lbs}{500\,plf} = 3.6\,ft$ (Governs Design, Use 32" o.c.)
- Wood
  - $Z' = 1{,}870lbs$
  - $V = 350\,plf$

- $Spacing = \frac{1{,}870 lbs}{350 plf} = 5.3 ft$

Final Selection

- Use 5/8" diameter cast-in-place hooked anchor bolts with 7" embedment spaced at 32" on center.

The Design Practices Committee of the Structural Engineering Institute recently completed the above Trial Design Problem related to the application of ACI 318 Appendix D with an anchor bolt problem for wood frame construction. The quantitative analysis of the Trial Design Problem solutions indicated serious concerns with the ability of practicing engineers to reliably and efficiently implement several provisions of the ACI 318 Appendix D procedures including:

- Significant variation in the application of Appendix D sections, variable values and variation in the interpretation of NDS sections and values. Specifically values for the seismic capacity of the anchor bolts in the concrete varied from a low of 521# to a high of 41,800#.
- Experience is essential as engineers with less than 5 years experience consisted of only 11% of respondents and one utilized only off the shelf software to complete the solution and did not check the wood capacity.
- Selection of Appendix D as the governing code for the concrete portion was made only 61% of the time even though ACI 318 Appendix D was referenced right on the problem statement.
- Short embedment depths for the 5/8" diameter anchors were selected many times that shows a lack understanding of the behavior of materials to keep connections ductile and not have brittle shear failures of the concrete. Over 60% of the embedments specified were 6 inches or less.

Recommendations going forward indicate efforts can be made to increase engineer's awareness to ductile behavior of anchorage into concrete construction. Increase professional development seminars, and increase training. Considering the Trial Design Problem results, training should include various options for working through practical examples of ACI 318 Appendix D problems, including the use of software.

The demographics of the participants were as follows:

Highest Educational Degree	28% Bachelors	50% Masters	22% Unknown	
Years Experience	11% 0-4 Years	38% 5-10 Years	28% 11-20 Years	0% 21+ Years
Professional License	17% EIT Only	61% PE	17% SE	
States	33% Virginia	11% Minnesota	56% Other	

Experience is Essential - This is the first lesson learned (or reinforced) from the trial design solutions. Education alone is not adequate to ensure practicing engineers are able to safely and consistently design elements of structures. As an example, the concrete capacity from the published solution was 2.41 kips. The answer submitted by engineers with less than 5 years experience varied from 1.5 kips to 3.5 kips. While having experience certainly did not eliminate all errors, having at least 5 years of experience seemed to give engineers enough judgment to recognize unreasonable answers that were grossly incorrect. As a result of the large variation in results for those with less than 5 years of experience, findings for subsequent portions of the assessment were based on data gathered from those engineers with 5+ years of experience.

Use of ACI 318 Appendix D to solve for the concrete strength vs. Not solving for this at all or using IBC – Over 60% of the submitted solutions used the ACI 318 Appendix D Method to solve for the concretes wind and seismic capacity.

Degree of Difficulty on arriving at the solution - The average time to complete the analysis was approximately 2 hours.

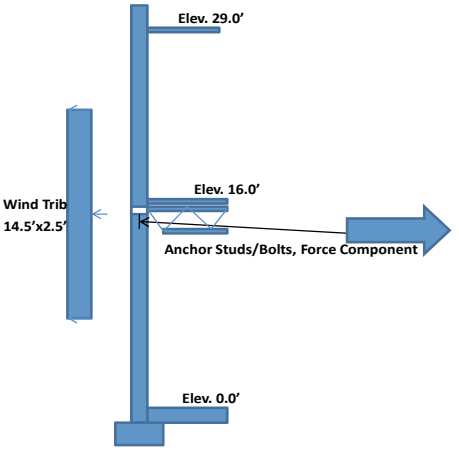
Recommendations – The results of this problem indicate that efforts should be made to:

1. Increase engineer's awareness of the ACI 318 Appendix D Design Procedures. These efforts could include: (a) increased referencing to ACI 318 in the IBC and ASCE 7 code requirements, (b) increased exposure in ASCE 7 professional development seminars.

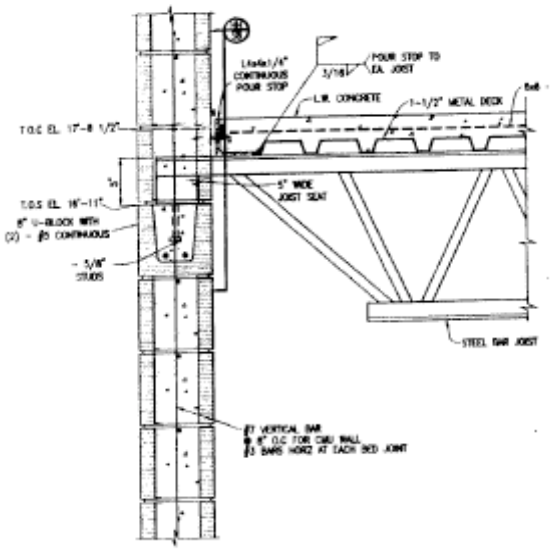
2. Increase training in and education in both younger engineers and among experienced senior engineers (10+ year's experience). The training should include ACI 318 Appendix D anchorage problem solutions for both concrete and steel elements and include applicable software solutions.

Trial Design Problem #2 – Wall to 2nd Floor Anchorage in Masonry Construction per ACI 530-08

You are designing a new concrete block masonry wall Fire Station in New Orleans, Louisiana that is approximately 100'x100' in plan and in a flat urban area. You need to determine the component wind lateral out-of-plane wall force based on the Code required 150 mph basic wind speed. The second floor open web joist framing will be anchored to the grouted 8-inch, f'm = 2000 psi reinforced concrete block masonry wall at joist pockets every 2.5' feet on center. The tributary height contributing to the 2nd floor wind out of plane load is 14.5 feet so the out of plane wind load area is 2.5' x 14.5' to be attached to the floor framing. The Roof is at elevation 29 feet as shown in the wall section below.



WALL SECTION



DETAIL AT SECOND FLOOR

Determine the wind out-of-plane lateral force (leeward side) and the proposed number of 5/8-inch diameter anchors connecting the joist bearing plate to the masonry wall for the force. The governing Building Codes are IBC 2009, ASCE 7-05 and ACI 530-08.

Solution

Time to Complete: **Averaged about 2 hours**
Wind Resultant Force Component: ***2016#***

Anchor Type, Grade, Material: ***Cast-in-Place Headed Stud (Nelson Stud), ASTM A108***
(e.g. Headed Anchor Stud, cast-in-place 'J' bolt, post-installed expansion anchor, A307 Anchor Bolt, etc.)
Anchor Capacity Sources: ***ACI 530-08/ASCE 7-05***
(e.g. Code, Bolt Vendor Information, etc.)
Number of 5/8" diameter anchors per attachment: **2 @ *5/8" diameter***
Bolt Embedment and Spacing: ***7"embedment and 8 inch spacing***

Solution

Wind Resultant Force Component for lateral out-of plane load.
ASCE 7-05 Wind Components (ASCE 7-05 6.4.2.2)

- $p_{net} = \lambda K_{zt} I p_{net30}$ (EQ 6-2)
- In the City of New Orleans, Exposure B, Urban Area, $\lambda = 1.0$ for Urban Area
- Topographic Factor K_{zt} for the flat site is 1.0
- Fire station is an Occupancy Category IV structure per ASCE 7-05 Table 1-1
- Importance Factor per ASCE 7-05 Table 6-1 for Category IV in Hurricane Prone regions is 1.15
- End Wall Zone 5 used as 10% of the building length is = 100' (0.10) = 10'
- Tributary Wind Area on each joist anchor location component = 2.5'x14.5'= 36 ft^2
- p_{net30} from ASCE 7-05, Figure 6-3, Components and Cladding, Wall, End Zone 5, Greater than 20ft^2 but less than 50ft^2,
  Straight line Interpolate between the value for 20ft^2 of 50.5 psf and 50ft^2 of 45.7 psf for 36 ft^2.
- (50.5 psf – 45.7 psf) / 50ft^2 – 20ft^2 = 4.8 psf/ft^2
- (4.8 psf/ft^2) (36ft^2 -20ft^2 / 50ft^2 – 20ft^2) = 2.56 psf
- p_{net30} = 45.7 psf + 2.56 psf = 48.26 psf
- p_{net} =1.0 (1.0) (1.15) 48.26psf = 56 psf
- Wind Resultant Force Component = 56 psf (36ft^2) = 2016 #

ACI 530-08 Shear Design (ACI 2.1.4.3)

- Use 5/8" diameter A307 Headed Anchor Bolts
- L_{bc} = 7.625/2 = 3.81" which is governed by half the thickness of the 8" inch thick CMU wall
- $A_{pv} = \pi L_{bc}^2 / 2 = \pi 3.81^2 / 2$ = 22.8 sq. in.
- $A_{pt} = \pi L_{bc}^2 = \pi 3.81^2$ = 45.6 sq. in
- B_v is the lesser of $B_{vb} = 1.25\ A_{pv} \sqrt{f'm}$ (Eq. 2-6)

  -or-

  $B_{vc} = 350\ \sqrt[4]{f'mA_b}$ (Eq. 2-7)

  -or-

  $B_{vpry} = 2.0\ B_{ab} = 2.5\ A_{pt} \sqrt{f'm}$ (Eq. 2-8)

  -or-

  $B_{vs} = 0.36\ A_b f_y$ (Eq. 2-9)
- $B_{vb} = 1.25\ A_{pv} \sqrt{f'm}$ = 1.25 (22.8) $\sqrt{2000}$ = 1275# <u>GOVERNS</u>

- $B_{vc} = 350\ \sqrt[4]{(2000 psi)(0.31 in2)} = 1746\#$
- $B_{vpry} = 2.0\ B_{ab} = 2.5\ A_{pt}\ \sqrt{f'm} = 2.5\ (45.6)\ \sqrt{2000} = 5100\#$
- $B_{vs} = 0.36\ (0.31)\ 30{,}000 = 3350\ \#$
- B_{vb} Masonry breakout controls
- Check overlap if bolts spaced at 8 inches on center.
  $A_{pv} = 22.8 + 8"x3.81" = 53.2$ sq. in.
  $B_{vb} = 1.25\ (53.2)\ \sqrt{2000} = 2974\#$ OK
- Number of 5/8" diameter Anchors Needed = 2016# / 1275# per anchor = 1.6 anchors

Final Selection
- Use (2) 5/8" diameter cast-in-place headed anchor bolts located in the center of the wall with 7" embedment spaced at 8" on center (one anchor each cell, 12 bolt diameters on center for the anchors.)

The demographics of the 27 participants were as follows:

Highest Educational Degree	63% Bachelors	37% Masters	0% Unknown	
Years Experience	18.5% 0-4 Years	37% 5-10 Years	18.5% 11-20 Years	26% 21+ Years
Professional License	26% EIT Only	74% PE	26% SE	
States	44% Virginia	11% Oregon	7.5% each NC, WI, GA	22.5% Others

Experience is Essential - This is the first lesson learned (or reinforced) from the trial design solutions. Education and number of years of experience alone are not adequate to ensure practicing engineers are able to safely and consistently design buildings. As examples, 4 participants arrived at only needing one 5/8" diameter anchor to secure this connection. Typically the answer of needing only one anchor bolt was arrived at due to a low wind force resultant and not checking for wind forces at the edge of the structure where the force can be higher. The answers submitted by engineers with less than 5 years experience varied from 1 kips to 2 kips for the wind force resultant on the detail. However even very experienced engineers arrived at wind force demands as low as 500 pounds. While having experience certainly did not eliminate all errors, having at least 5 years of experience seemed to give engineers more judgment to recognize unreasonable answers that were incorrect. Additionally the use of only one anchor is very impractical and can be irresponsible. The use of only one anchor will most likely result in an eccentric loading condition between the joist and the anchor that can result in unaccounted for torsion and failure of the anchor when loaded.

Central vs. End Wall Zone Wind Force – 55% of the submitted solutions did not calculate the end wall zone wind force component. Given the simplicity of the

problem and the fact that many of the engineers that submitted solutions were from regions of the Atlantic or Gulf Coast, it is interesting to observe the omission of the End Wall Wind Zones from the calculations.

Revision of ACI 530-05 to ACI 530-08 Section 2.1.4.3.2 - The determination of correct number of anchors changed from 4 to 2 by using the newer ACI 530-08 code section 2.1.4.3.2 as opposed to the previous version in ACI 530-05. The change in the code away from linear interpolation once 12 diameter edge distance was not achieved resulted in a significant change in the calculations and results. Most all respondents stated they used the ACI 530-08 code. However, one respondent stated they were using the ACI 530-08 code but upon examination of the submitted calculations they had actually used the ACI 530-05 section and arrived at the need for the 4 anchors instead of only 2. The practicality of 4 anchors in this type of detail would almost be prohibitive.

Bolt/Anchor Embedment – 52% of respondents have an anchor embedment of 4 inches or less. Further 22% of respondents had an embedment depth of only 2.5 inches. This shallow embedment does not allow for much if any ductility in the anchorages performance and can lead to a more brittle failure of the anchorage. This was not recognized by the respondents ion their solutions by upsizing the anchor embedment depths. With only a 2.5 inch embedment often times the bearing plates for such anchorage require the use of leveling grout that could truly jeopardize the true embedment in the masonry.

Headed Shear Stud Usage as opposed to Anchor Bolts – 22% of respondents utilized headed anchor studs that would need to be welded to the bearing plate above prior to either wet setting these bearing plates and anchors or carefully prepositioning and grouting around and underneath. The recognition that the placement of the prewelded headed shear studs to the underside of the bearing plates and then the difficulty of placing this in the grouted cell was assumed to take place by the other 78% of respondents and their use of cast in place anchor bolts. This observation by the majority of participants is encouraging. However having 22% of the respondents not recognize this also indicates more experience and judgment would be beneficial in the applications of the right materials for the right application.

Recommendations – The results of this problem indicate that efforts should be made to:

1. Increase engineers awareness of the ASCE 7 wind load requirements for end zones especially. These efforts can include increased exposure to ASCE 7 wind loading professional development seminars.

2. Increase engineer's awareness of the AVI 530-08 procedures. These efforts could include: (a) increased referencing to ACI 530–08 Section 2.1.4.2.2.1 in ASCE 7 code requirements, (b) increased exposure in ACI 530-08 and ASCE 7 professional development seminars.

3. Increase training in practical detailing of connections for constructability and ductility. Often this training is best done in offices where experienced engineers can mentor junior engineers to avoid the lessons learned over the years. The training should include the various options and consequences for detailing critical connections in alternative ways. A good quality control program instituted by senior engineers reviewing junior engineers work can also yield these benefits from a training manner.

Conclusions

An evaluation of the data presented in the trial design problems leads to the following conclusions:

Trial Design Problems – Trial design problems are an important tool in assessing the ability of practicing design engineers to safely and consistently apply the code provisions. We encourage code committees to consider expanding the use of this tool in assessing the efficacy of future code changes.

Experience Matters – The trial design problem results clearly indicate that engineers with at least 5 years of experience produce much safer and more consistent designs. Perhaps increased experience requirements for licensure should be considered with more emphasis on pre-licensure mentorship.

Code Complexity and Safety – The perceived accuracy of complex codes is overshadowed by a significant increase in errors. The trial design problems quantitatively demonstrate that complex codes, such as the current ASCE 7-05 wind provisions, and few years of experience produce results that are less accurate, less consistent and less safe. We applaud the efforts of ASCE 7 and ACI 530 for revising the codes sections to determine anchorage in a more reasonable manner. When this problem was solved using the ACI 530-05 code an impractical four 5/8" diameter anchors were needed to provide adequate anchorage. ASCE and ACI are consciously developing better provisions that reduce design errors and increase building safety, while decreasing the amount of time needed for design.

Code Committees need Practicing Engineers – Practicing design engineers must be adequately represented on code committees to insure that codes do not become unnecessarily complex.

Moderator
Craig Wilcox, PE, SE, LEED AP, Vice President, MWH Americas Inc.
2121 California Blvd, Suite 600, Walnut Creek, CA 94549
Tel: 925-627-4554 / Fax: 925-627-4501 / Email: craig.wilcox@mwhglobal.com

Organizing/Sponsoring Committee
BPAD Design Practices

Using Failure Case Studies to Teach Reinforced Concrete Design

Norbert Delatte, M.ASCE[1]

[1]Professor and Interim Chair, Civil & Environmental Engineering Department, Stilwell Hall Room SH 121, Euclid Avenue at East 24th Street, Cleveland State University, Cleveland, Ohio 44115, Tel: 216-687-9259, Fax: 216-687-5395
Email: n.delatte@csuohio.edu

ABSTRACT

The study of failures, particularly in a design course, can help teach students how to ensure the satisfactory performance of buildings and bridges. Some of the shear design provisions in the current ACI 318 Building Code can be traced back to two collapses of Air Force warehouses in the mid-1950s. Three building collapses in the 1970s and 1980s showed the importance of punching shear. There is also much to be learned from reinforced concrete building performance under extreme conditions, such as the terrorist attacks on the Oklahoma City Murrah Building and the Pentagon (9/11). Another classic case is the collapse of a major section of the Ronan Point apartment towers in the UK in 1968, illustrating the need to properly tie precast building elements together. The relatively recent collapse of the Laval, Quebec concrete bridge abutments in Canada shows the importance of providing continuity of reinforcement.

INTRODUCTION

The study of failures, particularly in a design course, can help teach students how to ensure the satisfactory performance of buildings and bridges. A number of failure case studies have been developed for use in courses teaching reinforced concrete design, as outlined in the book "Beyond Failure." These include failures in the construction process and in formwork, such as the collapse of the Willow Island Cooling Tower. Some of the shear design provisions in the current ACI 318 Building Code can be traced back to two collapses of Air Force warehouses in the mid-1950s. Three building collapses in the 1970s and 1980s showed the importance of punching shear. These were the 2000 Commonwealth Avenue collapse in Massachusetts, the Skyline Plaza/ Bailey's Crossroads collapse in Virginia, and the Harbour Cay Condominium collapse in Florida. The latter two were investigated by the National Bureau of Standards, NBS (now the National Institute of Standards and Technology, NIST). There is also much to be learned from reinforced concrete building performance under extreme conditions, such as the terrorist attacks on the Oklahoma City Murrah Building and the Pentagon (9/11). Another classic case is the collapse of a major section of the Ronan Point apartment towers in the UK in 1968, illustrating the need to properly tie precast building elements together. The relatively recent collapse of the Laval, Quebec concrete bridge abutments in Canada shows the importance of providing continuity of reinforcement. This case study also offers the

opportunity to illustrate the application of strut and tie models to the analysis of complex reinforced concrete structures.

In the U.S., a typical first course in Design of Reinforced Concrete Structures (such as CVE 422 at Cleveland State University) focuses on basic theory and design of reinforced concrete structures according to the American Concrete Institute (ACI) 318-08 (ACI 2008) code. Often the course is taught using a textbook based on that standard, such as Wight and MacGregor (2009). In most cases, only about half of the textbook material is covered in an introductory course, although some universities offer a subsequent advanced course on topics such as torsion, slender columns, plastic design, yield line theory, and so forth.

For the past two years the course at Cleveland State University has included a number of failure case studies selected to illustrate the behavior of reinforced concrete structures and members. In addition to the course text (Wight and MacGregor, 2009) and code (ACI 2008), the course included excerpts from Chapter 5 (Reinforced Concrete Structures) of the book *Beyond Failure* (Delatte, 2008).

CONCRETE MATERIALS AND CONSTRUCTION

Although construction methods are not the focus of the CVE 422 course, the designer is also responsible for construction specifications, and an understanding of material behavior and construction practices is of considerable value.

One case study of this type is the collapse of the Willow Island Cooling Tower at Willow Island, West Virginia, on April 27, 1978. Because this collapse case study focuses on concrete strength and formwork practices, it is more of a construction case study and is found in Chapter 9 (Construction Materials) of *Beyond Failure* (Delatte, 2008). This case study is not covered in the CVE 422, because the same principles are addressed in the 2000 Commonwealth Avenue collapse case study, which will be discussed shortly.

SHEAR MECHANISMS AND FAILURES

Shear in reinforced concrete can be a complex subject for students to grasp. First of all, the flow of forces can be difficult to envision. Second, while the need to use stirrup reinforcement to enhance shear strength is straightforward, the need to provide minimum stirrups when the calculated forces show that they aren't necessary is not so obvious.

The roof collapses of the Air Force Warehouses at Wilkins Air Force Depot in Shelby, Ohio, on August 17, 1955, and at Robins Air Force Base near Macon, Georgia, on September 5, 1956, are often used to show the need for minimum stirrup reinforcement (e.g. p. 234 of Wight and MacGregor, 2009). These collapses are generally attributed to combined load, shrinkage, and thermal effects. In each case,

400 foot lengths of roof girders functioned as single units due to defective expansion joints (pp. 130 – 133, Delatte, 2008).

Three case studies illustrate the collapse of buildings under construction due to punching shear and similar mechanisms. The first of the three was the January 25, 1971 collapse of the 2000 Commonwealth Avenue apartment building under construction in Boston. Four workers were killed in this collapse. The project was characterized by an almost total lack of construction control and inspection. The floor plan and the extent of collapse are shown in figure 1.

This building used flat plate construction. A plate is a slab of uniform thickness supported on columns. This is a very economical type of construction for short spans and light loads because formwork is very simple and the absence of beams reduces the floor-to-floor height (p. 606, Wight and MacGregor, 2009). However, the problem with the system is that it is subject to two-way or punching shear of the slabs, which can be a brittle failure mechanism. Despite the importance of this failure mechanism, textbooks often suggest that the material not be covered in an introductory course but be deferred to an advanced course.

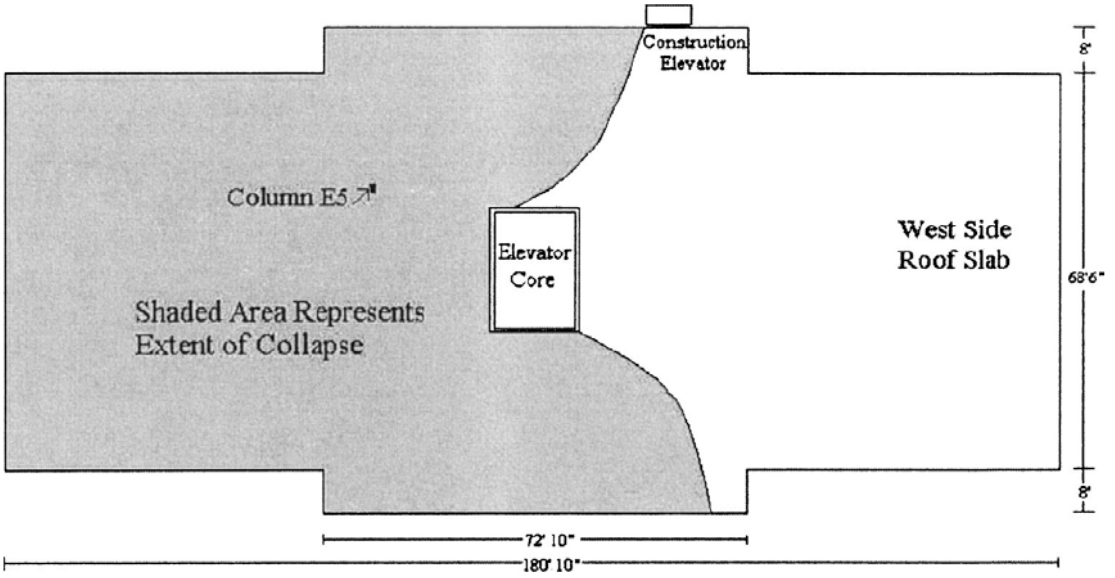


Figure 1: Collapsed Section of 2000 Commonwealth Avenue (King and Delatte, 2004, Delatte, 2008)

The punching shear mechanism is illustrated in figure 2. The slab breaks away and the column "punches" through the slab. The resistance to punching shear depends on the strength of the concrete, the effective depth of the slab, and the perimeter of the failure plane around the column. Clearly, the loads applied to the slab and the removal of shoring under the slab are also important. In the collapse at 2000 Commonwealth Avenue, the strength of the concrete was low and strength

development was impaired by cold weather. Some of the reinforcement was improperly placed and poorly developed. The roof slab of the building held heavy mechanical equipment, and there was evidence that shoring had been removed prematurely. Details are provided in King and Delatte (2004) and Delatte (2008). The City of Boston published a detailed report (Granger et al., 1971).

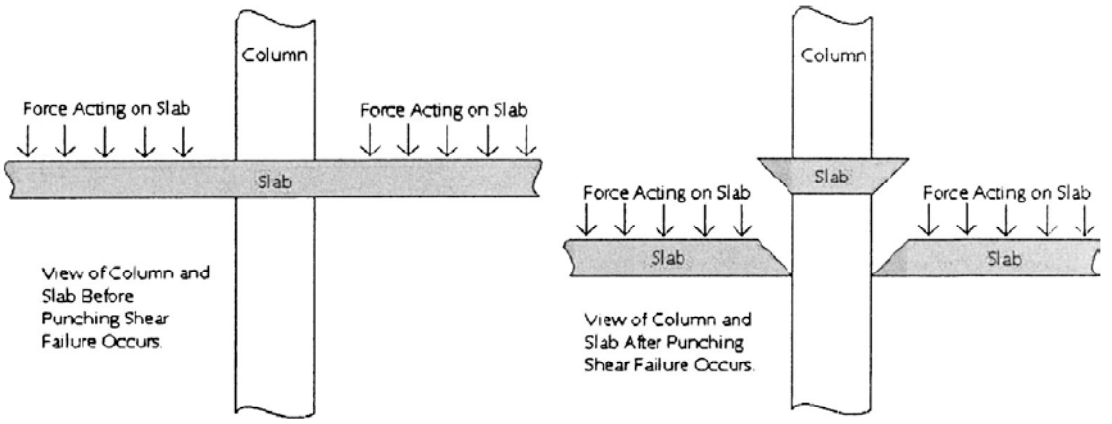


Figure 2: Punching shear failure mechanism (King and Delatte, 2004, Delatte, 2008)

Only a few years after the 2000 Commonwealth Avenue collapse, a similar collapse occurred at Skyline Plaza, Bailey's Crossroads, Virginia. On March 2, 1973, a section of the apartment building under construction collapsed to the ground. The collapsed structure is shown in figures 3 and 4. This collapse was investigated by the National Bureau of Standards (NBS) which is now the National Institute of Standards and Technology (NIST) (Leyendecker and Fattal, 1977, Carino et al., 1983).

Once again, punching shear was the culprit. An entire section of the building collapsed to the ground, so that the structure looked like two separate buildings (figure 4). The rate of construction was approximately one floor per week, but in cold weather (e.g. March) rate of concrete strength gain was severely retarded. NBS used the maturity method to estimate that the compressive concrete strength was only about 1,000 – 1,500 psi at the time of the collapse. The investigation also found that the collapse occurred while shoring was being removed several floors below a fresh concrete placement. The NBS published a full report on their investigation (Leyendecker and Fattal, 1977, Carino et al., 1983).

The third punching shear case study was the collapse of the Harbour Cay Condominium on March 27, 1981 in Cocoa Beach, Florida. Eleven workers were killed and 23 were injured. The condominium was five stories tall, with shoring at all levels (figure 5). When the forms were removed, the structure collapsed completely with all floors pancaking to the ground (figure 6).



Figure 3: Skyline Plaza/ Bailey's Crossroads Collapse, (Delatte, 2008, photo courtesy Nick Carino of NIST)

Figure 6 shows an important clue to the collapse. The column standing up shows a telltale sign of punching shear where the slab used to be attached to the column. This collapse was also investigated by the NBS (Lew et al., 1981, Lew et al., 1982).

The investigation found that the slabs were considerably thinner than the ACI minimum typically used for deflection control. Moreover, the reinforcing steel had been placed too low in the slab because chairs of the wrong height had been used, which made the effective depth of the slab too small. The column sizes were too small. In addition to causing the problem of column reinforcement congestion and poor consolidation of concrete, this meant that the perimeter around the columns to resist punching shear was too small. The concrete, however, had been of adequate strength.

This failure was due to design error. Critical calculations had never been performed, including those for slab minimum thickness and for punching shear.



Figure 4: Skyline Plaza/ Bailey's Crossroads Collapse, (Delatte, 2008, photo courtesy Nick Carino of NIST)



Figure 5: Harbour Cay Condominium before Collapse, (Delatte, 2008, photo courtesy Nick Carino of NIST)



Figure 6: Harbour Cay Condominium Collapse, (Delatte, 2008, photo courtesy Nick Carino of NIST)

PERFORMANCE UNDER EXTREME CONDITIONS

One early case study of concrete building performance under extreme conditions was the partial collapse of the Ronan Point apartment tower in London, U.K., on the morning of May 16, 1968. Ronan Point was 22 stories tall and was built using a system of precast panels fastened together. As the occupant of one apartment lit a stove to brew her morning tea, leaking gas exploded and blew out an exterior load-bearing wall. An entire corner of the building collapsed to the ground, killing four. Subsequent investigations showed that the connections between the panels were very poorly constructed (figure 7). A very light explosion was able to cause a disproportionate collapse of the structure. This case study led to changes in building codes to improve structural integrity and robustness. The U.K. government published a thorough investigative report (Griffiths et al. 1968).

In recent years, reinforced concrete structures have been tested under extreme events, including terrorist attacks. These include the bombing of the Oklahoma City Murrah Federal Building on April 19, 1995, and the attack on the Pentagon on September 11, 2001. Although neither building was designed for this type of event, there are lessons to be learned by contrasting the performance of the two structures.

By pretty much any criterion the Murrah Federal Building performed poorly. Approximately half of the floor plan was destroyed and 169 people were killed. A detailed analysis is provided by Hinman and Hammond (1997).

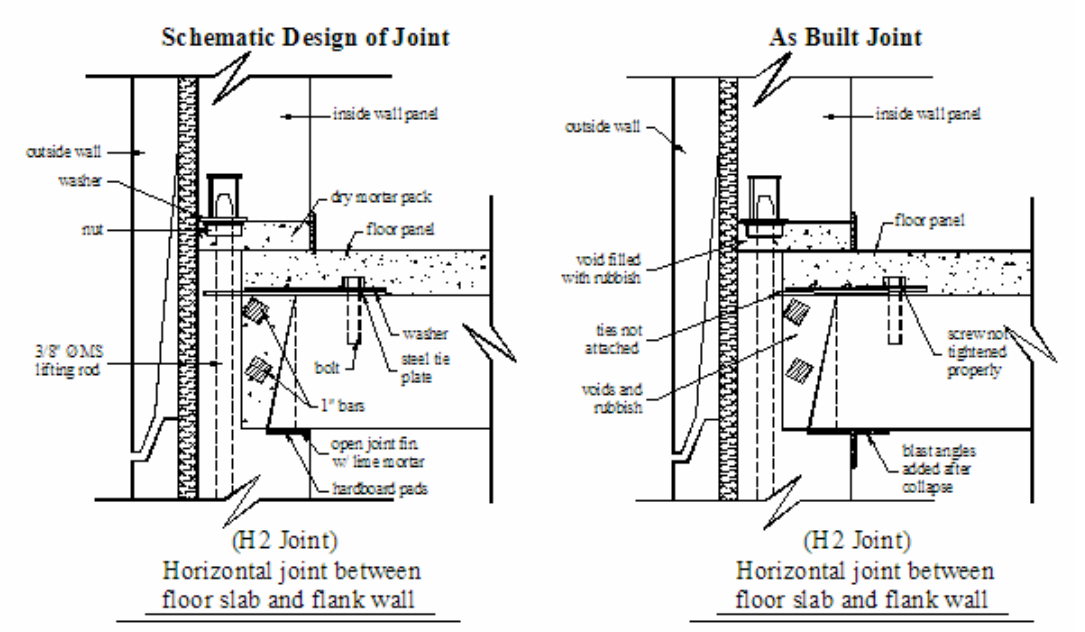


Figure 7: Ronan Point connection (Pearson and Delatte, 2005, Delatte, 2008)

Once a critical column was shattered, the continuity of the structure was severely disrupted. Floor slabs were blasted upwards and shattered, and then fell downward and pancaked to the ground.

On the other hand, the performance of the Pentagon to the September 11, 2001 attack is generally considered to be very good. The building had been constructed during World War II, and the original design concept called for it to store records after the war, so it was designed for high floor live loads of 150 psf. Circular columns with spiral reinforcement were used, and beam bottom reinforcement was continuous through the columns. The building was also in the process of being renovated to improve safety against blast.

As a result, the collapse of the building was localized to the immediate area of the aircraft impact, and the damage did not spread disproportionately. Columns continued to carry loads even though severely bent. A comprehensive building performance report has been published (Pentagon 2003).

CONTINUITY OF REINFORCEMENT AND STRUT-AND-TIE MODELS

Although collapses of structures in service without an immediate, obvious triggering cause are rare, one such case was the failure of the Autoroute 19 de la Concorde Overpass in Laval, Quebec, on September 30, 2006. This bridge collapse killed five people and injured six.

The bridge consisted of parallel prestressed concrete box beams resting on cast-in-place concrete cantilevers extending out from the abutments. The supports doubled

as expansion joints, and were subjected to unpredictable tension forces from the expansion and contraction of the bridge.

The cantilever supports relied on a complex reinforcement detail to transfer bearing forces to the top bars of the cantilevers through stirrups. However, the tops of the stirrups were placed slightly below the top reinforcement, leaving a horizontal plane of weakness. The support peeled away along that plane of weakness.

This case study offers the opportunity to illustrate the use of strut-and-tie models in design and analysis of reinforced concrete structures. The provincial government of Quebec published a lengthy report, with versions in both French and English (Commission 2007).

SUMMARY AND CONCLUSIONS

The case for the inclusion of case studies in engineering courses, particularly design courses, has been made elsewhere – for example, in Chapter 1 of Delatte (2008). There are a number of case studies, as outlined in this paper that could be used in a reinforced concrete design course. More information on these cases and others may be found in the references cited below, in Delatte (2008), and in the failure case studies project web site http://matdl.org/failurecases/ (Delatte, 2011).

Obviously, too much of a good thing can quickly become too much. The author uses five case studies in the CVE 422 Reinforced Concrete Design course. These are the Air Force Warehouses, 2000 Commonwealth Avenue, Skyline Plaza/ Bailey's Crossroads, Harbour Cay Condominium, and the Laval Quebec Bridge collapse.

ACKNOWLEDGEMENTS

This work was sponsored by the grant "Implementation and Assessment of Failure Case Studies in the Engineering Curriculum," National Science Foundation Project DUE-0919487, $ 500,000, August 1, 2009 – July 31, 2013. Opinions expressed are solely those of the authors and not of the National Science Foundation.

REFERENCES

ACI 318-08 *Building Code Requirements for Structural Concrete and Commentary,* American Concrete Institute

Carino, N. J., Woodward, K. A., Leyendecker, E. V., and Fattal, S. G. (1983) "A Review of the Skyline Plaza Collapse." *Concrete International*, American Concrete Institute, pp. 35 – 42, July 1983, reprinted in ACI 1989.

Commission of Inquiry into the Collapse of a Portion of the de la Concorde Overpass: October 3, 2006 – October 15, 2007 (2007), *Report*, Government of Quebec, Canada. Available online at http://www.cevc.gouv.qc.ca/UserFiles/File/Rapport/report_eng.pdf

Delatte, Norbert J., (2009) *Beyond Failure: Forensic Case Studies for Civil Engineers*, ASCE Press.

Delatte (2010) web site "Failure Case Studies: Civil Engineering and Engineering Mechanics" http://matdl.org/failurecases/

Granger, R. O., Peirce, J. W., Protze, H. G., Tobin, J. J., and Lally, F. J. (1971), *The Building Collapse at 2000 Commonwealth Avenue, Boston, Massachusetts, on January 25, 1971,* Report of the Mayor's Investigating Commission, The City of Boston, Massachusetts.

Griffiths, H., Pugsley, A. G., and Saunders, O. (1968). "Report of the inquiry into the collapse of flats at Ronan Point, Canning Town." Her Majesty's Stationery Office, London.

Hinman, E.E., and Hammond, D.J. (1997) *Lessons from the Oklahoma City Bombing: Defensive Design Techniques,* ASCE Press.

King, Suzanne, and Norbert Delatte, "Collapse of 2000 Commonwealth Avenue: A Punching Shear Case Study," ASCE Journal of Performance of Constructed Facilities, pp. 54 – 61, Vol. 18, No. 1, February 2004.

Lew, H. S., Carino, N. J., Fattal, S. G., and Batts, M.E. (1981) "Investigation of Construction Failure of Harbour Cay Condominium in Cocoa Beach, Florida," Publication No. NBSIR 81-2374, National Bureau of Standards, Washington D.C. (NTIS PB-82 117 409)

Lew, H. S., Carino, N. J., and Fattal, S. G. (1982) "Cause of the Condominium Collapse in Cocoa Beach, Florida." Concrete International, American Concrete Institute, August 1982.

Leyendecker, E. V., and Fattal, S. G. (1977) "Investigation of the Skyline Plaza Collapse in Fairfax Count, Virginia," *Building Science Series* No. 94, National Bureau of Standards, Washington, D.C.

Pearson, C. and Delatte, N. (2005) "The Ronan Point Apartment Tower Collapse and its Effect on Building Codes," ASCE Journal of Performance of Constructed Facilities, Volume 19, Number 2, pp. 172 – 177, May 2005.

The Pentagon Building Performance Study Team (2003), *The Pentagon Building Performance Report,* ASCE Press.

Wight, J.K., and MacGregor, J.G., *Reinforced Concrete: Mechanics and Design,* 5th Edition, 2009.

Lessons Learned through the Development of an Undergraduate Course on Civil Engineering Failures

K.A. Salyards, P.E., Ph.D.[1]

[1]Department of Civil and Environmental Engineering, Bucknell University, 302 Dana Engineering, Lewisburg, PA 17837; PH (570) 577-1757; FAX (570) 577-3415; email: kas046@bucknell.edu

Abstract

A new undergraduate course was developed to introduce civil engineering students to the field of forensic engineering and foster an awareness of how engineers can and should learn from failures. Several other individuals and engineering departments have made commendable efforts to integrate information about specific failure cases within civil engineering courses while others have developed graduate-level courses designed to teach the students to become forensic engineers. This undergraduate course was designed to fit somewhere in between. The goals were two-fold: to improve the general knowledge base of historic and common failure modes and to introduce the field of forensic engineering and what it requires in an effort to encourage continued education in the field. The development of such a course was difficult for a number of reasons including the vast scope of the field, the scarce supply of teaching materials, and the disparity between the level of student knowledge at an undergraduate level and that required to fully understand an engineering failure. This paper describes the educational objectives and resources utilized in the preparation of the course, the variety of teaching methods and techniques undertaken during the course of the semester, and the successful components of the course as well as the difficulties and challenges encountered. Several considerations and suggestions are presented for others in the development of similar courses and recommendations for improving future offerings of this course are also presented.

Introduction

Numerous engineering educators, practitioners, and professional organizations have long recognized the need for integration of engineering failures into civil engineering curriculums. Methods for accomplishing this and the benefits of such integration have been the subject of professional discussion over the past two decades (Bosela 1993, Rendon-Herrero 1993, Delatte 1997, Delatte and Rens 2002, Reynolds 2003, Parfitt 2006, Prevatt 2010). In support of these needs, the Committee on Education of the Technical Council of Forensic Engineering, ASCE, continues to study engineering curricula (Rens et al. 2000) and develop and distribute educational resources including workshops for faculty on teaching with failure case studies.

Several approaches for integrating engineering failures into a civil engineering curriculum are possible depending on the needs of the individual department or college. In most cases, it is not viable to add another core course to a curriculum that is already full. Integration of short failure case studies into other required courses, such as mechanics, soil mechanics, structural design, or senior capstone courses is perhaps the best alternative (Delatte and Rens 2002). These case studies can be used to reinforce technical concepts while providing an opportunity for discussion of engineering ethics and professional development. The details for individual case studies are now available through several sources, including ASCE's Journal of Performance of Constructed Facilities and manuscripts (Delatte 2009, Frost 1995).

This approach integrating failure case studies into a variety of engineering courses has the advantage that it can be undertaken by almost any instructor. This approach can evolve over time as the instructor examines individual case studies and develops instructional activities to accompany each case study and technical concept. The level of expertise of the instructor will influence the level of detail with which the case study can be presented, but an in-depth analysis is not often required if the goal is to simply reinforce basic engineering concepts and introduce the concept of learning from failures. It is believed that this approach is even more effective if failure case studies are consistently incorporated across the curriculum.

A review of this approach has identified the instructor's lack of time to research and prepare case studies as the main obstacle impeding more widespread application (Delatte and Rens 2002). However, numerous sources are available for historic case studies (Nicastro 1996) and improvement in this area continues through the periodic publication of case studies in journals, news articles, internet sites (Delatte 2008, Parfitt 2009), and new books (Delatte 2009). These sources provide instructors with the pertinent information and references, while removing the difficulty associated with uncovering potentially confidential information.

Another approach, albeit rare, involves the development of an upper-level elective or graduate-level course in failure analysis and forensic engineering. Survey results (Delatte and Rens 2002) indicate that less than 10% of universities offer such a course. The availability of an instructor with sufficient practical engineering or failure investigation experience is rare. Many of these courses rely on support and involvement from external industry professionals involved in forensic work. In addition, these courses are primarily offered at the graduate level minimizing the likelihood that undergraduate students would be able to enroll because of prerequisites. Despite the appropriateness and success of such courses at the graduate level, the infrequent availability and preclusion of undergraduate enrollment falls short in realizing the learning opportunities available from engineering failures.

Although both of these approaches have been effective in expanding the awareness and educational perspectives of their target audiences, there seems to be a void in between. Integration of failure case studies into the curriculum reinforces technical

concepts and exposes students to select engineering failures but it doesn't directly address the field of forensic engineering. A stand-alone graduate-level course is likely to encompass both aspects, but the availability is limited by both instructor expertise and prerequisite requirements. The development of an undergraduate course to encompass both a review of a variety of case studies and the lessons learned from them as well as an introduction to the field of forensic engineering is described herein.

Motivation for Course Development

The motivation for the development of an elective course in building failures is multi-faceted and influenced by the educational environment at Bucknell University. Bucknell University is a private, liberal arts university in central Pennsylvania with 3600 undergraduate students. Approximately 900 students are enrolled in the College of Engineering with 170 in the Department of Civil and Environmental Engineering (CEE). As a predominately undergraduate university, the students do not have access to many graduate-level courses and the rural location also limits the involvement of local practitioners and professional organizations. The combination of both factors precludes the educational approach of a stand-alone course in forensic engineering.

The student population also influenced the development of the course. Less than 30% of all applicants are accepted into the CEE program yielding a selective student population and a large number of graduating students subsequently enter graduate degree programs. The student population is generally strong academically and the majority of students have broad interests in the field of civil engineering. Both undergraduate research and graduate-level education are strongly encouraged. Alumni of the department are frequently employed in non-traditional engineering positions, as exhibited by numerous working in the forensic engineering profession. Exposure to a variety of alternative career paths within civil engineering including forensic engineering is fitting for all students, especially those with an inclination for non-traditional careers.

Bucknell's civil engineering curriculum requires core courses in the traditional areas of civil engineering: geotechnical, water resources, environmental, structural, and transportation. Electives are offered in each of the subdisciplines as well as construction. This breadth of required courses coupled with the small size of the student body allows for few electives which require significant background. To populate an elective, it must be sufficiently broad to attract students interested in a variety of subdisciplines and not require advanced coursework in any one particular discipline. An elective focusing on engineering failures therefore must be sufficiently broad, while requiring a solid base in engineering fundamentals. For this reason, the course registration was restricted to fifteen engineering students in their senior year.

From the author's perspective with education and experience in architectural engineering, an introduction to building and architectural systems, building science and construction issues as they relate to building failures was also desirable. It is also

the author's opinion that an introduction to the field of forensic engineering is valuable to encourage further education and specialization.

Resources Utilized

In the preliminary stage of course development, references describing both approaches were consulted. Delatte and Rens (2002) proposed a variety of methods for utilizing case studies within the context of required engineering courses including topic introductions, class discussions, example problems, and group or individual projects. General case study approaches (Pietroforte 1998, Russell and McCullouch 1990) and individual accounts of case studies used in a specific course (Delatte 1997, Sutterer 2003) were referenced. Case histories from a variety of sources were reviewed (Delatte 2008, Delatte 2009). Publications describing the organization of stand-alone forensic engineering courses were also consulted (Delatte and Rens 2002, Ratay 2005, Wang 2005, Parfitt 2006).

Learning Outcomes and Objectives

Based on the motivations and references discussed above, a course in civil engineering failures and forensic engineering was developed for its first offering in the spring semester of 2009. The overall learning outcomes for the first offering of the course were:

1. To improve the general knowledge base of historic engineering failures, common failure modes and the lessons learned from them.
2. To introduce and encourage continued education in the field of forensic engineering or related fields

To achieve these general learning outcomes, the following learning objectives were established. "At the conclusion of the course, students will be able to:

1. Demonstrate an awareness of a variety of civil engineering failure case studies
2. Summarize the technical, ethical and professional issues involved in a variety of failure case studies incorporating structural, serviceability, building envelope, transportation, geotechnical and environmental issues
3. Describe the typical stages involved in the forensic engineering process for civil engineering and describe some of the investigative methods and tools available including non-destructive evaluation
4. Compose a proposal for forensic engineering services, a final written report, and present an oral summation of your findings
5. Recognize the limits of your knowledge; identify and locate the appropriate sources for the information sought; and utilize the information in a suitable manner
6. Develop improved observation skills and recognize possible indicators of issues that may warrant further investigation
7. Perform as an effective contributing member of an investigative or research-oriented team"

Course Details

To gauge the appropriateness of the course development and preparation, a survey was distributed to determine the incoming awareness of engineering failures and the student expectations for the course. The results clearly indicated that the students' awareness of both historic and current engineering failures was nearly nonexistent. Even such prominent cases as the Kansas City Hyatt Regency collapse were not universally recognized. In light of this revelation, the course was modified to incorporate more case history presentations by both instructor and students. The topics introduced in the class included:

- Case histories
- Forensic engineering process
- Contract language and legal issues
- Common failure types and related investigative techniques
    - Building envelope failures
    - Material deterioration and maintenance
    - Structural failure
- Historic preservation
- Accident reconstruction
- Ethics in engineering practice

The class met three hours a week with an additional weekly two hour lab period. The hourly meetings were typically utilized for traditional lecture, instructor case history presentations, and class discussions. The lab period was reserved for student presentations on assigned case histories, guest speakers, and class discussions.

Teaching techniques

To address a range of learning styles, several educational approaches were incorporated.

Traditional Classroom Lecture
The traditional classroom lecture was utilized to introduce new material and provide the pertinent technical information required for comprehension. In this manner, the material was structured in a logical manner and related discussions were directed. This approach was most suitable for topics such as the forensic engineering process and contract language and legal issues. Questions were designed and utilized to stimulate individual thinking and prompt short class discussions. Shorter periods of traditional lecture were used to counteract the typically negative implications of a passive audience.

Guest lectures
To emphasize forensic engineering as a possible career path, practicing professionals were invited to participate in the course as guest presenters throughout the semester. The practitioners offered a personal perspective and firsthand experience with current

industry practices, recent investigation case studies, and represent the diversity of opportunities involved in some type of forensic investigation. During the first offering of this course, practitioners from the following firms offered a guest lecture:

- Simpson Gumpertz & Heger, Inc. (SGH)
- Thornton-Tomasetti, Inc.
- Masonry Preservation Services, Inc. (MPS)
- Architectural Testing
- ENVIRON International Corporation

In addition, practitioners from Wiss, Janney, Elstner Associates, Inc. (WJE) have presented on the field of forensic engineering as part of the senior capstone course in the semester following the first offering of this course.

Class discussions – current issues

Each week, a class discussion was planned to incorporate relatively recent failures, articles, or investigations of interest to the students. Students were required to contribute articles or topics in preparation for these weekly discussions. Topics were wide ranging, including the controlled demolition of a local smoke stack tower, the failure of wood roof trusses under construction at a local site, legal issues relating to engineering failures as posed in NCSEA's Structure magazine, review of both media coverage and forensic reports of the recent I-35 Minneapolis Bridge collapse, and ethical dilemmas relating to engineering failures as posed in the "A Question of Ethics" section of ASCE News.

Simulated Client Interaction - Proposal

To improve observation skills and professional writing, a mid-semester assignment was developed incorporating the façade condition assessment of a campus building. The University had previously completed an investigation for the restoration of an aging masonry façade exhibiting significant cracking at certain locations. The assignment required the students to visually examine the façade, research material and construction details, and prepare a proposal for engineering services for the project. This required research into non-destructive testing methods and possible underlying causes of the deterioration. The results of the University's condition assessment were discussed and the façade restoration was completed during the summer following this course offering.

Individual research report

Because of the diversity of student interest within the class, a final individual research report was incorporated for which each student selected an appropriate topic that was of interest to him/her. The research report was to be a synopsis and evaluation of a category or type of failure written in the form of a technical note. Examples of selected topics included fire damage investigation, failure modes of asphalt, accident reconstruction techniques, glass and glazing problems, and wood truss failure modes. This assignment promoted individual research, professional writing, and the summary and evaluation of information.

Case history presentations

The benefits of examining historic engineering failures and analyzing the details of the case are widely acknowledged. To introduce the principle of learning from failure, several noteworthy and detailed case histories were presented by the instructor or guest speakers. Examples included the Kansas City Hyatt, Citicorp Headquarters, John Hancock Tower, and L'Ambiance Plaza. The details of the construction, failure, and key players in each history were presented using all available sources, including figures, photographs, video, and reports. The ensuing investigation details and conclusions were presented along with the resulting legal consequences and industry changes, if applicable. Each case history presentation was followed with a discussion period about noteworthy details of each case, including ethical dilemmas, investigation techniques, and relevance of the case to current industry practices.

After several case history presentations by the instructor or guest speakers, the format of the presentation shifted slightly to engage the students after the basic facts of the construction and failure were presented. The students were prompted to analyze the given information and identify evidence to be gathered, tests to be performed, and potential causes of the failure. After a short discussion, the details of the investigation and likely cause of failure were unveiled. This approach forced the students to play an active role in the case history presentation and begin to develop their observation and analysis skills.

Student case history research presentations

To facilitate the introduction of a significant number of case histories, student groups were assigned a case history to research, summarize, and present every other week. Each thirty minute presentation was to be accompanied by a single 8 ½ x 11 synopsis handout highlighting critical details in a poster-like format. The student groups were required to reference several reliable sources and identify any conflicting reports or conclusions. These assignments provided opportunity for furthering research skills, improving team interaction, and enhancing both oral and graphic communication skills. Each student was also required to review every presentation for thoroughness of the case history and clarity of the presentation. Questions were posed to each team and they were responsible for further research if required.

After several weeks of weekly presentations, an additional component was incorporated into the case history presentations. Each group was required to develop a visual aid of the failure mode to supplement their presentation. The visual aid could be in the form of a physical model or a graphical animation. The goal of this assignment was to further the understanding of the case history and promote forms of communication beyond the traditional powerpoint presentation.

Course Assessment

For the first offering of the course, the student response was quite positive. Despite an 8:00 time period and a course restricted to second-semester seniors, fifteen students

enrolled, filling the course. The students were engaged by the wide variety of topics introduced and were particularly interested in the case histories. A survey, identical to that which was distributed on the first day of class, was also administered at the end of the class to gauge the effect that the course had on engineering failure awareness. The results indicated that the students were significantly more aware of engineering failures, even those not specifically addressed during the course. It is also noteworthy that two of the fifteen students are currently employed by one of the firms volunteering as guest speakers. Both students continued their education in a graduate program and are now employed in the building performance sector of the firm.

Several components were identified by both the students and instructor as particularly successful. The student case history research presentations were the most highly ranked component by the students. They enjoyed discovering the details of each case history and rather than passively absorbing the material. The inclusion of a physical model or animation component was also identified as a particularly effective tool in understanding the failure mode. In addition to the goal of educating the students about engineering failures and the lessons to be learned from each case history, the students were excited about the vast improvement in their presentation skills. After graduation, several students emailed back about positive feedback they had received from their employers about their presentation skills that they attributed to this course.

The second most highly ranked component of the course was the presentations made by industry professionals. As expected, the speakers were able to bring a different perspective and personal experience to a variety of topics. The guest speakers also elaborated on the industry and offered advice for those interested in entering the field of forensic engineering. Other highlights of the course noted by the students was the inclusion of Engineering Disaster videos to complement and illustrate case histories and the fortuitously timed field trip to watch the controlled demolition of a local smoke stack tower.

The development and delivery of this course for the first time was not without a fair number of challenges and frustrations. One of the main challenges for the course was the organization. The broad scope of the field and struggling to incorporate topics of interest for the diverse student population impacted the organization as it seemed to jump from topic to topic without consistently smooth transitions. The students perceived the difficulty in achieving an effective organization of the course and identified this as one of the weakest points of the course. This difficulty was compounded with the challenge of the timely scheduling of guest speakers to relate to recent topics. This struggle is not limited to this course and has been experienced by other instructors organizing and scheduling guest speakers.

A related challenge was the availability of industry professional able to travel to central Pennsylvania to offer a presentation. Unfortunately, the rural nature of Bucknell's location is unfavorable for effective participation of practitioners.

As the instructor, the most significant difficulty experienced was the level of supporting information necessary to bring undergraduate students to a level where a failure could be understood and discussed. Civil engineering students are rarely exposed to important details of construction, such as flashing location, material selection, joints, etc., through coursework. For example, a discussion of water infiltration in cavity wall construction or façade preservation requires a working knowledge of these subjects. It was difficult to foresee when additional material was required and to effectively prepare and plan accordingly. For the first offering of the course, this required a significant amount of time and probably factored into review comments that the organization of the course could be improved.

Summary

As expected for the development of a new course, several challenges were encountered in both the planning and delivery of the course. These difficulties, along with several successful components of the course, have focused the strategy for improving the course before its next offering. The author has begun to narrow the scope of the course to improve its organization and continues to gather additional case histories to expand upon this successful component. Support from practicing professionals continues to be garnered. Because it is likely to be several years before the course is offered again, the author endeavors to improve and expand the incorporation of short engineering failure case studies in core civil engineering undergraduate courses to raise the awareness and interest of forensic engineering as a potential career path. Case studies have been incorporated into the other courses taught by the author including Statics, Mechanics of Materials, and Design of Concrete Structures and the instructional activities are being shared with colleagues throughout the College of Engineering. The development and initial delivery of this course in engineering failures has not only enhanced the educational experience of the students enrolled in the course, but has also initiated an increased awareness and motivation for a broader integration of failures and the lessons learned into the civil engineering curriculum.

References

Bosela, P. (1993). "Failure of Engineered Facilities: Academia Responds to the Challenge." *J. of Constructed Facilities,* ASCE, 7(2), 140-144.

Delatte, N. (1997). "Failure Case Studies and Ethics in Engineering Mechanics Courses." *J. of Professional Issues in Engineering Education Practice,* ASCE, 123(3), 111-116.

Delatte, N. and Rens, K. (2000). "Forensics and Case Studies in Civil Engineering Education: State of the Art." *J. of Constructed Facilities,* ASCE, 16(3), 98-109.

Delatte, N. "Failures and Ethics Case Studies Project." *NSDL Materials Pathway.* 8 Aug. 2008. Web. Accessed Nov. 2010. <http://matdl.org/failurcases/>

Delatte, N. (2009). *Beyond Failure: Forensic Case Studies for Civil Engineers,* ASCE Press, Reston, VA.

Nicastro, D.H. (1996). "Annotated Bibliography of Forensic Engineering." *J. of Performance of Constructed Facilities,* 10(1), 2-4.

Parfitt, M.K. (2006). "Learning From Failure: Teaching a Course on Building Performance and Forensic Techniques." *Proc. 4th Forensic Engineering Congress,* ASCE, 353-363.

Parfitt, M.K. "Failures Wiki: Building, Architectural and Civil Engineering Failures and Forensic Practices." *Wikispaces.* Oct. 2009. Web. Accessed Dec. 2010. <http://failures.wikispaces.com>

Pietroforte, R. (1998). "Civil Engineering Education Through Case Studies of Failures." *J. of Performance of Constructed Facilities,* 12(2), 51-55.

Prevatt, D. (2010). "On the Job versus Graduate School Training of Forensic Engineers – An Instructor and Professional Engineer's View." *J. of Performance of Constructed Facilities,* ASCE, 24(1), 78-86.

Ratay, R. (2005). "A Course in Forensic Structural Engineering." *Proc. 2005 Forensic Engineering Symposium,* ASCE, 5 pgs.

Rendon-Herrero, O. (1993). "Including Failure Case Studies in Civil Engineering Courses." *J. of Constructed Facilities,* ASCE, 7(3), 181-185.

Rens, K., Rendon-Herrero, O. and Clark, M. (2000). "Failure of Constructed Facilities in Civil Engineering Curricula." *J. of Performance of Constructed Facilities,* ASCE, 14(1), 27-37.

Reynolds, C. (2003). "Rewriting the Curriculum: A Review and Proposal of Forensic Engineering Coursework in U.S. Universities." *Proc. 3rd Forensic Engineering Congress,* ASCE, 307-319.

Russell, J.S. and McCullouch, B.G. (1990). "Civil Engineering Education: Case Study Approach." *J. of Professional Issues in Engineering Education and Practice,* 116(2), 164-174.

Shepherd, R. and Frost, J.D., eds. (1995). *Failures in Civil Engineering: Structural, Foundation, and Geoenvironmental Case Studies,* ASCE, Reston, VA.

Sutterer, K.G. (2003). "Service Learning and Forensic Engineering in Soil Mechanics." *Proc. 3rd Forensic Engineering Congress,* ASCE, Reston, VA, 297-306.

Wang, S. (2005). "Lessons Learned from Civil Engineering Failures." *Proc. 2005 Forensic Engineering Symposium,* ASCE, 12 pgs.

Using the Hyatt Regency Skywalk Collapse Case Study in Engineering Education.

John W. Lawson[1] S.E. M.ASCE & Pamalee A. Brady[2] P.E. M.ASCE

[1]Department of Architectural Engineering, California Polytechnic State University, San Luis Obispo, CA 93407; PH (805) 756-7123; email: jwlawson@calpoly.edu
[2]Department of Architectural Engineering, California Polytechnic State University, San Luis Obispo, CA 93407; PH (805) 756-6167; email: pbrady@calpoly.edu

ABSTRACT

To this day, the 1981 skywalk collapse in the Kansas City Hyatt Regency resulted in the worst loss of life from a structural engineering mistake in United States history. While many important engineering lessons can be drawn from this disaster, it is just as important to recognize the broader lessons learned in the design and construction process as a whole that can be successfully brought into the classroom. Numerous organizations have undertaken the task of envisioning how engineering education can meet the demands of the future. ABET's baccalaureate degree accreditation criteria, ASCE's Body of Knowledge and Body of Knowledge 2 as well as the National Academy of Engineering have documented the need to change engineering education from its historical focus on technical content knowledge to include greater emphasis on professional issues and to integrate engineering practice into education. To this end teaching methods such as project based learning, active learning and the use of case studies are being explored to address these broader learning outcomes while actively engaging students. Because of the attraction students have in extraordinary events, the Hyatt disaster provides an ideal backdrop to introduce many of the professional issues needed to broaden the undergraduates' learning experience. This paper discusses the use of the Hyatt Regency skywalk collapse in design coursework with specific application to third and fourth year civil and architectural engineering student learning. Besides the traditional concepts of load flow analysis and member design, broader concepts relating to professional roles and responsibilities, design team interplay, the design process, the construction process and professional practice ethics are emphasized.

INTRODUCTION

Today's engineering graduates face a world more complex than ever before. Their engineering profession is being challenged by both technical complexities and societal complexities. Historically, engineering education has primarily focused on technical content to provide a strong theoretical foundation for future practicing engineers. Learning to *apply* their technical knowledge as well as *experiencing* the professional and societal issues was relegated to their early years of employment under the guidance of a mentor or watchful supervisor.

In a similar fashion, other professionals in the construction industry had apprentice and journeymen approaches to teach the broader professional issues on the job. However, in today's fast-paced society, with increasing job complexity and competing priorities for limited time, there has been less fostering within the engineering profession and more relying upon skills acquired during college education. The expectation has become that engineering graduates must be well prepared to meet the new challenges of not only heightened technical complexity but also escalating professional complexity.

As engineering students begin their career path, they are facing challenges of competing and conflicting demands. Exciting and dramatic projects must be economically feasible; durable materials must be sustainable, and more daring structures must be at the same time safer. Under this backdrop, the engineering office is often expected to meet unrealistic deadlines, for lower fees, while maintaining a high level of quality control to ensure human safety, health, and welfare. These professional and technical challenges require engineering students to be adept in interdisciplinary and teamwork skills, have refined communication skills, appreciate responsibility and accountability, and embark on lifelong learning. It has been well established that the education of the future engineer must incorporate these professional issues in the classroom as well as into the early years of employment to face these challenges (ASCE Body of Knowledge Committee, 2008).

The Kansas City Hyatt Regency skywalk collapse has at its heart non-technical issues of communication, interdisciplinary teamwork, and ethical challenges; and provides an excellent tool as a case study to engage students while teaching these boarder professional issues. This paper is not meant to educate the reader of the events that led up to and followed the disaster; but instead demonstrate the usefulness of this using this tragedy as a platform to engage engineering students and introduce broad professional issues into the classroom.

LEARNING OBJECTIVES

It is now widely accepted that the incorporation of both technical and professional issues is necessary in an undergraduate engineering education. The National Academy of Engineering (2005) and ABET's accreditation criteria (ABET, 2010) emphasize this objective, yet the need for integrating professional issues into the classroom is clearest in the ASCE's report *Civil Engineering Body of Knowledge for the 21st Century: Preparing the Civil Engineer for the Future* (ASCE Body of Knowledge Committee, 2008).

The objective of ASCE's Body of Knowledge report is to provide a guide to reform education and pre-licensure experience to shape the civil engineer of the future. The vision of the civil engineer in year 2025 is seen as being quite different from the past due to society's dramatic globalization with the complexities of sustainability demands, risk management, and the larger number of interested parties in a particular project. ASCE's Body of Knowledge report identifies the knowledge, skills and

attitudes necessary to enter the practice of civil engineering at the professional level, through education and early experience. It is ASCE's hope that engineering curricula and pre-licensing experience will change over time towards this model. And indeed, ABET education accreditation and National Council of Examiners for Engineering and Surveying (NCEES) engineering licensing criteria are working together with ASCE's Body of Knowledge for an integrated process towards licensing.

ASCE's Body of Knowledge guidelines contain the traditional instructional objectives in foundational and technical outcomes. These basics broadly include work in math and sciences, experimentation and problem solving. What have been more difficult to incorporate in existing curricula are the nine professional issue outcomes identified. Figure 1 lists the desired professional outcomes and their respective level of achievement to be reached upon completing an *undergraduate* education in civil engineering (on a scale of 6). In the ASCE's outcomes rubric it is interesting to note that none of the professional outcomes are assigned to the master's degree education process. The master's degree is recommended to focus exclusively on technical experimentation, problem solving and area specialization.

Level	*Professional Outcome*
4	Communication
2	Public Policy
2	Business and Public Administration
3	Globalization
3	Leadership
3	Teamwork
2	Attitudes
3	Lifelong Learning
4	Professional and Ethical Responsibility

Figure 1. ASCE's Body of Knowledge Professional Issue Outcomes at the Undergraduate Level

The level of outcome achievement is tied to the cognitive domain of Bloom's Taxonomy. The two highest professional issues on this cognitive achievement scale are Communication and Professional and Ethical Responsibility. While some educators may simply regard communications as being satisfied by their institution's general breadth requirements in speech or writing, the intent is far more extensive. Undergraduates are expected to understand communication issues *within* the professional practice, including graphic presentation, construction drawings, computer models, hand sketches, verbal instructions, technical and non-technical writing. Reinforcement of these professional issue outcomes are also addressed in ABET's *a-k* criteria for baccalaureate engineering degree programs. Criteria *f, g* and *h* specifically address: an understanding of professional and ethical responsibility, an ability to communicate effectively and the broad education necessary to understand the impact of engineering solutions in a global and societal context, respectively.

PROFESSIONAL ISSUES IN THE HYATT REGENCY COLLAPSE

The Kansas City Hyatt Regency skywalk collapse is a uniquely suited case study to engage and educate students in the more important professional outcomes desired by the Body of Knowledge. The two most significant professional issues identified by ASCE's Body of Knowledge are communications and professional ethics and responsibilities, both of which are spotlighted in the collapse.

The major issue at the heart of the Hyatt Regency disaster is the breakdown of communications (Banset, 1989). There was a failure for the structural engineer to clearly communicate his intent to the steel fabricator his role or responsibility in the design of the critical rod-to-beam connection. In addition, the failure of this connection was traced back to an inadequate design that was not properly communicated graphically in the construction documents or verbally in subsequent phone calls between the two disciplines.

The ambiguous communication between the structural engineer and the steel fabricator was identified in Missouri's Administrative Hearing as a major factor in the disaster (Deutsch, 1985). The Commission report states that the structural engineer "bears the burden of communicating his intent to the contractor and *assumes the risk* of confusion or noncommunication." The report also states, "…the burden and responsibility for clear communication lies with the engineer who assumes the risk of ambiguity in his design drawings."

In line with another learning outcome is the understanding of professional responsibility and its ethical implementation by the Hyatt's structural engineer. Despite making assurances to the owner and architect of doing so, the structural engineer never ran calculations on the flawed connection. In addition, the structural engineer and the steel fabricator did not properly coordinate their responsibilities in the connection design; and in their rush to complete the job, the critical shop drawings never got a proper review despite the engineer's review stamp. Valuable opportunities exist in such a teachable case study to highlight important professional issues in communications, professional responsibilities, professional ethics, and interdisciplinary teamwork.

TEACHING TECHNIQUES

Case studies lend themselves as a powerful tool for contextual learning of professional issues. These are real-life stories with characters, a setting, a plot with a struggle, and an outcome; and when presented in story form, students are immersed briefly into a chain of unfolding events with an underlying professional context. Weaving factual information into an emotional story has been shown to develop better comprehension and long-term memorization [Abrahamson, 1998; Haven, 2007]. In addition, a deeper emotional connection is made allowing the students to personally experience and internalize engineering judgment dilemmas and ethical decisions. This is very difficult to achieve in the classroom through any other method of instruction.

When case study events are presented in chronological order with a surprise ending, teaching tends to take an inductive approach rather than a traditional deductive style. Instead of first describing how mistakes were made along the way in the Hyatt disaster, an inductive approach reveals the disaster and then encourages the students to determine the cause by sifting through the facts. In general, the inductive approach first gives students the reason why they need to learn the material and then challenges them to make logical sense of a complex problem. This problem-solving skill is imperative to the success of life-long learning. The inductive approach to student learning is supported by the best research on learning currently available (Prince, 2006).

Another powerful teaching technique well-suited for the Hyatt Regency case study is the use of project-based active learning strategies. This is a dynamic approach to teaching with a high level of student engagement and participation. Research indicates that students are more likely to retain the knowledge gained through this approach than through traditional lecture-centered or textbook-centered learning. In addition, students develop confidence and self-direction as they move through both team-based and independent work. There are various approaches to implementing active learning strategies in conjunction with inductive learning and storytelling, and a few approaches considered by the authors will now be discussed.

HYATT REGENCY COLLAPSE CASE STUDY APPROACHES

Various approaches are available to introduce case studies to students. One author's approach to introducing the Hyatt Regency case study lesson involves only one or two days of class time. The students are first introduced to a "hypothetical" hotel project as an in-class exercise where the instructor challenges them to develop engineering ideas to span elevated walkways across a 120-ft wide atrium space. Students break into small groups and develop schematic design solutions for two stacked, visually floating, walkways across the atrium space. During the exercise, the instructor plays the role of the architect guiding and challenging students to make the walkways thin and visually floating. This is an excellent time to provide an overview of the entire design process from the developer's original concept to the completed construction drawings as the students experience a portion of this process. Additionally, the professional roles and responsibilities of the developer, architect and structural engineer are discussed in this context.

At the conclusion of the groups' schematic design exercise, the instructor compares and contrasts the different approaches developed. While some design solution differences may simply be a matter of different perspectives, other differences could be attributed to intentionally ambiguous communications from the instructor. An important lesson in clear communications and the pitfalls of inappropriate assumptions can be taught here, foreshadowing later parts of the case study.

It is at this point that the instructor explains that this exercise is actually based on a real design problem, and then unveils the *as-designed* solution with three pairs of continuous suspended rods supporting both stacked walkways. Once it is revealed that this is a real project, the instructor can engage the students further using the

actual setting and participants' names to begin to tell the story. The as-designed solution is discussed in general and contrasted with the student designs, and it is of some benefit to encourage the students to mentally adopt the as-design solution as reasonably appropriate.

Using the power of storytelling the instructor can slowly unveil the story with plot twists and emotional surprises providing drama, but importantly allowing the instructor to control the student's experience and to introduce key points in communication failures, ethical dilemmas, professional roles and responsibilities. The revelation that the adopted design detail led to 114 deaths provides an emotional attachment as the students search for causes. The process provides students with a self-motivated inductive learning approach.

Similar to an actual investigation, the instructor slowly reveals more information being learned of the collapse. Using an important active learning approach, students are periodically polled with a show of hands or electronic clickers to observe opinion shift as to perceived fault. Using the following hypothetical series of discoveries, the instructor gradually introduces many professional issues while students critically think of responsibilities and ethical challenges:

> *Investigation discovery #1:* The hanger rods pulled through the inadequately designed box beam flanges.
> *Teachable moment:* Basic technical design concepts may be introduced. Graphic communication methods of drawings and details are introduced.
> *Students' general opinion:* The structural engineer is at fault.
>
> *Investigation discovery #2:* The steel fabricator revised the single continuous rod design to a design using two separate rods, thus doubling the load on the failed box beam connection.
> *Teachable moment:* The roles and responsibilities of the engineer and fabricator are compared and contrasted.
> *Students' general opinion:* Fault has shifted towards the steel fabricator.
>
> *Investigation discovery #3:* The steel fabricator explains that the single rod design is impractical to build, as it requires a fully threaded rod design and mid-length nut assembly.
> *Teachable moment:* The issue of constructability is introduced and whose responsibility it is.
> *Students' general opinion:* Class split between the engineer and fabricator as to fault.
>
> *Investigation discovery #4:* The steel fabricator's shop drawings indicate the revised connection was communicated to the engineer who reviewed it and stamped his approval.
> *Teachable moment:* Introduction of the purpose of steel shop drawings, with roles and responsibilities of the involved disciplines.

Students' general opinion: Fault has shifted back to the structural engineer.

Investigation discovery #5: The engineer says he doesn't "approve" shop drawings but only provides a cursory review as indicated on the stamp.
Teachable moment: Ambiguous communications of responsibility and expectations are a major factor in this disaster. Additionally, the introduction of fast-track projects and this delivery mode's rushed nature are discussed.
Students' general opinion: Class becomes split as to fault assignment.

Investigation discovery #6: The steel fabricator's detailer and the architect testify that they had undocumented phone calls with the engineer regarding the connection revision, and that they were assured by the engineer that it was safe. Engineer admits to some of the phone calls, but denies assuming responsibility for the connection.
Teachable moment: Communications need to be clear and documented to avoid ambiguity and accountability.
Students' general opinion: Fault shifts more towards the engineer again.

Investigation discovery #7: During construction, a 2700 square foot portion of the atrium collapsed due to a poor connection, alarming the owner. The engineer assured the owner that every atrium detail would be checked for safety. Despite being compensated for checking the atrium again and writing a letter to the architect assuring safety of the suspended walkways, a review commission determined that engineering calculations of the box-beam and connection were never made.
Teachable moment: Ethical behavior serves an important purpose.
Students' general opinion: The engineer is at fault.

Additional hypothetical scenarios for discussion:

What if the steel fabricator dumped over 500 pages of shop drawings on the engineer for immediate review?

What if it was standard practice for the steel fabricator to complete the design of typical connections?

What if the engineer strongly suggested to the architect it would be safer to support the walkways with columns instead of suspended rods?

As this case study is presented with unfolding drama, students are immersed into different situations that challenge their perceptions and attitudes. This experiential approach can instill professional ethics very successfully, and gives the students the practice of making difficult judgments before beginning their careers. With both intellectual and emotional engagement, students are in a valuable learning environment to introduce ASCE's and NSPE's Code of Ethics and to introduce other

professional learning outcomes in communications, interdisciplinary teamwork, roles and responsibilities, and leadership.

Student response to the introduction of case studies has been overwhelmingly positive. During the exercises and discussions, student engagement is very apparent with insightful questions and full attention throughout the classroom.

Another instructor takes a different approach using the Hyatt walkway collapse within a professional issues module that is a part of a broad quarter-long design problem. The objectives of the module are to discuss an engineer's professional responsibilities and the relationship of these responsibilities to society; to discuss various engineering ethics codes; to identify the need for an ethics code; to emphasize the importance of communication – both written and verbal; and, within a setting – the Hyatt walkway collapse – identify ethical concerns, describe what action should be taken and discuss the ethical basis for these actions. The case works well within the context of a design project wherein the students are progressing from conceptual design through final design and developing a calculation package and set of construction documents. The lessons require limited class time but make use of asynchronous discussions conducted through a website.

The instructor begins the module by conducting an assessment of the students' understanding of what distinguishes engineering as a profession, what is an engineer's responsibility and to whom is an engineer responsible; and what if any is the distinction between professional ethics and personal ethics? The instructor then begins a discussion of the assessment topics along with an introduction to the steps to licensure as a professional engineer and structural engineer, the latter of which always elicits much student inquiry. The responsibility of engineers to the society as well as the public trust placed in the profession to establish standards of conduct and to enforce those standards highlights the importance of professional ethical tenets beyond personal opinions. The ASCE and NSPE codes of ethics are introduced along with some history of their development. A brief PowerPoint presentation is used to open the story of the Hyatt Regency design and construction – a project much larger but similar to the one they are undertaking. The context of practice in the 1980s is presented; the roles of individuals are described. The story is set in motion. The walkway collapse is not yet discussed.

The students are then divided into four teams; each team is assigned four technical papers (Gillum, 2000; Luth, 2000; Moncarz, 2000; Pfatteicher, 2000) for reading and discussion within their teams. Each team is given a list of questions for discussion on the technical / human / organizational / socio-cultural aspects of the case. Sample questions from each of these four areas follow:

> *Technical:* Describe the features of the critical detail that failed in the walkway collapse.
> *Human factors:* As an entry level engineer what steps will you take when new situations arise in a design project that you have not faced before? How

will you convey your knowledge and understanding and what you don't yet understand?
Organizational: What is the responsibility of the Engineer of record?
Socio-cultural: What do you believe should be the responsibility of building departments for projects such as the Hyatt Regency Hotel? How can building departments provide the level of review appropriate for such a project?

The students are also required to submit a question that they think should be answered regarding each aspect of the case.

Over a period of approximately two weeks the students answer the questions and undertake an asynchronous discussion with one another in the four areas via an electronic discussion board. During this period they are engaged in the structural detailing of a multi-story building in the classroom. The final task of the assignment is to compile a summary presentation of the team's perspective of what can be learned from these events. A post assessment on professional ethics follows sometime later in the term.

Student responses in the asynchronous discussion for each aspect of the case are evaluated based on their depth of inquiry and reflection of the reading. A team score is assigned. Some responses provided by students to posed questions include:

"[in new modes of delivery and contractual arrangements] early delineation of responsibilities should stimulate cooperation and communication."

"One thing that [is mentioned] that I have not considered is being open to everyone and letting them know that you are not completely familiar with the problem, this can help with avoiding any mishaps and it also reaffirms the team aspect of a project."

"…this situation shows that more structured communication between parties was necessary to avoid problems."

Suggested questions by students include:

"How can the lack of communication and ineffective collaboration between the design and construction professionals that characterized this project be prevented in the future?"

"…about having an onsite engineer…what should an onsite engineer be looking for and checking during construction?"

The concluding student PowerPoint presentation and final professional engineering ethics quiz administered following the case study module indicate that students develop a keen awareness of the responsibilities embodied in engineering practice. Future assessments will include a student survey evaluating the contribution of case

studies to both technical and ethics learning. The survey was developed by faculty at Cleveland State University for evaluating individual course learning with respect to ABET's *a-k* criteria as well as the impact of case studies, along with other course elements, in contributing to student interest in the course material.

OTHER APPROACHES

The two presented approaches are those most familiar to the authors. A myriad of other approaches are possible to achieve the similar learning objectives. The use of active learning strategies enhances student engagement and material retention, and should be strongly considered. Another such approach with strong potential is to have each student assume the role of a Kansas City Star newspaper reporter and write an article with the intended audience being the general public. This exercise challenges students to research complex events and then disseminate them into basic concepts and translate technical terminology into lay terms. Student then exchange the proposed articles with each other and then take on the role of newspaper editor for a peer review. To enhance the active learning and engagement, the articles are formatted similar to newspaper with multiple column formatting, headline, photograph, several figures, and notable quotes. With a restrictive word count it will be impossible for students to have a comprehensive discussion; thus students are challenged to prioritize the relevant information from the public's perspective, and to be as succinct as possible.

A similar role playing approach places the students into the uncomfortable position of representing Hyatt Hotels. In this exercise, students assume the role of Hyatt's public relations officer who must write a letter to the disaster survivors explaining what was determined to be the cause of the collapse. This style of letter will be quite different than a newspaper article in its demeanor. The use of analogies is strongly encouraged to help relate the mechanics of the collapse with everyday concepts the intended audience is familiar with. Another important aspect of this exercise is students' selection of language and disposition when communicating with survivors who are still healing physically and mentally from their experience. Students are challenged to be transparent and open, yet to experience the underlying fear of a disgraced corporate image and potential liability. These are real professional conflicts that occur in an engineering office, and the ethical implications of different courses of action can be discussed.

Another approach which has been shown to be very successful is the implementation of a mock trial or public inquiry (Jennings, 2000). Students form teams to research the disaster, form opinions, and then support or even argue their findings to the rest of the class. This student-based learning approach encourages students to be inquisitive about the roles, responsibilities, and priorities of the engineering profession. In addition, student-based learning as opposed to teacher-imparted learning fosters student self-discovery, an important trait for lifelong learning. These outcomes are core professional issues desired by ASCE's Body of Knowledge and ABET. An additional benefit of this approach is that student-based learning has less

reliance on the instructor's practical experience, thus making this case study approach more acceptable to the entire faculty. Detailed descriptions of the events from various perspectives are widely available for students to draw upon, especially five articles published in the Journal of Performance of Constructed Facilities (Gillum, 2000; Luth, 2000; Moncarz, 2000; Pfatteicher, 2000; Rubin, 1987).

Using approaches that involve teamwork, communications within a group, communications to lay people, and self-directed discovery creates an experiential learning environment that is similar to the engineer's practice environment. These approaches not only allow students to experience some of the professional issues in a design office, but also allow students to possibly connect with how these professional issues affected the initiation of the Hyatt Regency disaster.

CONCLUSION

Traditional classroom assignments involve a hypothetical situation with a single solution or obvious best answer. The engineering profession is far more complex with competing priorities, numerous uncertainties, and several feasible solutions, all subjected to various human factors such as communication, risk adversity, and our ability to work with others constructively. The vision of the future engineer has embraced the need to educate towards these professional issues for the benefit of the profession and society.

Using case studies, active learning techniques, and student-based approaches are powerful tools educators use to engage students and introduce professional issues. The Hyatt Regency skywalk collapse is well suited to assist educators towards the outcomes desired for the future engineer. Whether the instructor has practitioner experience or is more comfortable in academia, different approaches are available to match the instructor's level of involvement and past experiences.

It is especially rewarding as instructors to witness increased levels of student engagement and excitement while students learn an important chapter of our profession's past and interlacing the more mundane professional issues into the subject matter. Others are encouraged to find other significant events and engaging teaching approaches to reach the same outcomes.

REFERENCES

ABET (2010). *Criteria for Accrediting Engineering Programs,* Engineering Accreditation Commission, ABET, Inc., 111 Market Place, Suite 1050, Baltimore, MD 21202, http://www.abet.org/.

Abrahamson, C. (1998). "Storytelling as a Pedagogical Tool in Higher Education," *Education,* Vol. 118.

ASCE Body of Knowledge Committee. (2008). *Civil Engineering Body of Knowledge for the 21st Century: Preparing the Civil Engineer for the Future, 2nd Edition,* Reston, VA; http://www.asce.org/raisethebar.

Banset, E. and Parsons, G. (1989). "Communications Failure in Hyatt Regency Disaster," *Journal of Professional Issues in Engineering,* Vol. 115, No. 3. ASCE, Reston, VA.

Deutsch, J. (1985). "Report of the Administrative Hearing Commission, State of Missouri." *Case No. AR-84-0239,* Missouri Board of Architects, Professional Engineers, and Land Surveyors vs. Daniel M. Duncan, Jack D. Gillum, and G.C.E. Int., Inc., Jefferson City, Mo.

Gillum, J. (2000). "The Engineer of Record and Design Responsibility," *Journal of Performance of Constructed Facilities,* Vol. 14, No. 2. ASCE, Reston, VA.

Haven, K. (2007). *Story Proof: The Science behind the Startling Power of Story,* Libraries Unlimited, Westport, CT.

Jennings, A. and Mackinnon, P. (2000). "Case for Undergraduate Study of Disasters," *Journal of Performance of Constructed Facilities,* Vol. 14, No. 1. ASCE, Reston, VA.

Luth, G. (2000). "Chronology and Context of the Hyatt Regency Collapse," *Journal of Performance of Constructed Facilities,* Vol. 14, No. 2. ASCE, Reston, VA.

Moncarz, P. and Taylor, R. (2000). "Engineering Process Failure – Hyatt Walkway Collapse," *Journal of Performance of Constructed Facilities,* Vol. 14, No. 2. ASCE, Reston, VA.

National Academy of Engineering. (2005). *Educating the Engineer of 2020: Adapting Engineering Education to the New Century,* National Academies of Sciences, Washington, DC.

Pfatteicher, S. (2000). "'The Hyatt Horror': Failure and Responsibility in American Engineering," *Journal of Performance of Constructed Facilities,* Vol. 14, No. 2. ASCE, Reston, VA.

Prince, M. J., and Felder, R. M., 2006. "Inductive Teaching and Learning Methods: Definitions, Comparisons, and Research Bases," *Journal of Engineering Education,* Vol. 95.

Rubin, R. and Banick, L. (1987). "The Hyatt Regency Decision: One View," *Journal of Performance of Constructed Facilities,* Vol. 1, No. 3. ASCE, Reston, VA.

Use of Failure Case Studies in a Construction Planning and Estimating Course

P. A. Bosela[1] and N. J. Delatte[2]

[1]Department of Civil and Environmental Engineering, Cleveland State University, 2121 Euclid Avenue, SH 121, Cleveland, Ohio, 44115-2214; PH (216) 687-2597; FAX (216) 687-5395; email: p.bosela@csuohio.edu
[2]Department of Civil and Environmental Engineering, Cleveland State University, 2121 Euclid Avenue, SH 108, Cleveland, Ohio, 44115-2214; PH (216) 687-9259; FAX (216) 687-5395; email: n.delatte@csuohio.edu

Abstract

Reasons for including failure case studies within the undergraduate engineering curriculum have been made by various authors. Specific cases have been integrated into the syllabi of engineering mechanics, structural analysis, and structural design courses. The case studies used are typically catastrophic structural failures, where failure can be defined as a structural collapse, often with significant loss of life.

Many civil engineering undergraduate programs include a course in construction planning and management. The American Society of Civil Engineers (ASCE) Civil Engineering Body of Knowledge (BOK) for the 21th Century, Second Edition emphasizes a need for Civil Engineers to understand not only the technical areas of analysis and design, but also more of the project management issues that enable a project to go from design to fruition. Hence, it is likely that more programs will include construction management courses.

This paper deals with the integration of failure case studies into a construction planning and estimating course. In addition to structural failures, this course looks at the definition of "failure" from an engineering/construction perspective. It explains that failure includes the inability of an engineered facility to perform as designed. It further opines that failure to be constructed within reasonable time and budgetary constraints falls within the definition of failure. While most students may have the pre-conceived notion that failures are only caused by design deficiencies and perhaps natural hazards, the examples used in this course emphasize how many failures are caused by deficiencies in the design and/or construction process itself.

In addition to the use of more typical and catastrophic failure case studies, such as the Hyatt Regency Walkway Collapse (Kansas City, Missouri), and the L'Ambiance Plaza Collapse (Bridgeport, Connecticut), the course makes extensive use of the Montreal Olympic Facility design and construction to demonstrate how deficiencies in the design and construction process can lead to extreme constructability issues and exorbitant cost overruns.

The author also shows how the inclusion of the case studies addresses some of the more difficult areas to address in the Accreditation Board for Engineering and Technology (ABET) evaluation criteria, such as the understanding of the impact of civil and environmental engineering solutions in a global and social context.

Introduction

Reasons for including failure case studies within the undergraduate engineering curriculum have been made by various authors (Baer 1996; Carper 2000, Carpet et al 2008; Delatte 1997; Delatte 2000; Delatte and Rens 2002, Jennings and Mackinnon 2000; Pietroforte 1998; Rendon-Herrero 1993a). Barriers to using failure case studies in civil engineering courses were identified (Rendon-Herrero 1993a) as a lack of readily available case study information and an already overcrowded undergraduate curriculum built around ABET requirements (Rendon-Herrero 1993a). Although stand alone courses which deal with forensic engineering have also been developed (Bosela 1993) most are either senior elective or graduate level courses. One of the major factors identified is offering such courses as required undergraduate courses is the constraints already placed on the undergraduate program by the Accreditation Board for Engineering and Technology (ABET) and other general university requirements. Since that time, engineering failures and forensic engineering have received considerable attention, via publications such as the ASCE Journal of Performance of Constructed Facilities, and ASCE Forensic Congresses with published proceedings (Rens 1997; Rens et al 2000c; Bosela et al 2003; Bosela and Delatte 2006; Chen et al 2009). Case materials have been developed (Delatte et al 2007; Delatte et al 2008a,b; Delatte et al 2010) case study websites (Delatte et al 2008b; Delatte et al 2010; Parfitt 2010; Rens et al 2000a,b,c), text books (Delatte 2010; Shepherd and Frost 1995), and failure vignettes (Zickle 2000) etc., to enable faculty members to more easily include failure case studies in their undergraduate courses. Workshops have been held to assist faculty members in incorporating lessons learned from failure case studies into their courses (Delatte et al 2007). Typically, specific cases have been integrated into the syllabi of engineering mechanics, structural analysis, structural design, and geotechnical engineering courses (Delatte et al 2010). The case studies used generally fall into the classification of "engineering disasters", such as catastrophic structural failures, where such failure may result in a significant loss of life. In some cases, students have worked on an existing failure case as part of a class project (Rendon-Herrero 1993b; Sutterer 2003).

Many civil engineering undergraduate programs include a course in construction planning and management. The American Society of Civil Engineers (ASCE) Body of Knowledge (BOK) 2nd Edition (2008) emphasizes a need for Civil Engineers to understand not only the technical areas of analysis and design, but also more of the construction and project management issues (BOK Outcome 13) that enable a project to go from design to fruition. Hence, it is likely that more civil engineering programs will include construction management courses in their curricula.

Cleveland State University offers an ABET accredited undergraduate program in Civil Engineering, which includes the course CVE 403 Construction Planning & Principles of Estimating. It is a required three semester credit hour course, offered during the final semester of the senior year. The basic course objectives are as follows:

- basic understanding of construction procedures, equipment and details
- understand the roles and responsibilities of design and construction professional, and how they interact to construct a project
- show how probable cost of construction projects can be estimated

- show how he/she can best use systematic construction tools for improving project estimates, management procedures, & early identification of potential problems
- show how to use a detailed project schedule for project control
- provide an understanding of legal and professional practice issues related to the construction industry
- use lessons learned from failures to illustrate various professional practice issues, such as design responsibilities, importance of licensure & lifelong learning, etc.

In addition, ABET and the ASCE Body of Knowledge (BOK) include additional broader outcomes, such as

- *understand the principles of ethical behavior & society-serving role of practicing engineers* (BOK Outcome 24)
- *are motivated to continue their professional growth through graduate education and/or professional development* (BOK Outcome 23)
- *contemporary issues and historical perspectives* (BOK Outcome 11)

Over a period of time, the author modified what had been a traditional, broad-based construction management course, integrating lessons learned from failures throughout the course.

Although this course does use some case studies of structural failures, such as the Hyatt Regency Walkway, Kansas City, Missouri, Collapse, and the L'Ambiance Plaza, Hartford, Connecticut Collapse during construction, it also looks at the definition of "failure" from an engineering/construction perspective. It explains that failure includes the inability of an engineered facility to perform as designed. It further explains how failure to be constructed within reasonable time and budgetary constraints falls within the definition of failure. While most students may have the pre-conceived notion that failures are only caused by design deficiencies and perhaps natural hazards, the examples used in this course emphasize how many failures are caused by deficiencies in the design and/or construction process itself. This course makes extensive use of the Montreal Olympic Facility design and construction to demonstrate how deficiencies in the design and construction process can lead to extreme constructability problems and exorbitant cost overruns. An overview of the Montreal Olympic Case Study is presented at the very beginning of the course, and it is re-visited many times when specific management and estimating functions are later being discussed.

Montreal Olympic Complex

The Montreal Olympic complex consisted of a main stadium, velodrome, roads, walkways, practice fields, an Olympic Village housing facility, and other structures and landscaping, which were constructed for the 1976 Summer Olympics, held in Montreal, Quebec, Canada, commencing on July 4, 1976. It was nicknamed the "Big O", due to its name and the shape of the stadium, but it later became known as "The Big Owe" and "The Big Woe" (CBC 1999; CBC News 2006). Planning began in 1970, and preliminary estimates prepared at that time indicated a projected cost for the entire complex of $836 million dollars, including a projected cost for the main stadium of $40 million dollars. The final costs in 1976 were $1.5 billion dollars, with $120 million for the main stadium. In addition to the cost overruns, there were considerable time overruns, which meant that the complex was almost not completed in

time for the Olympics, and some of the final activities were still on-going at the time the Olympics started, and major components originally planned such as the retractable roof were not begun until after the Olympics (Neil 1979).

The original "owner" was the City of Montreal, Quebec, who contracted with architect Roger Taillibert to design the Olympic Park, including the Olympic Stadium and velodrome (Auf der Maur 1976). Mr. Taillibert lived and conducted business in Paris, France. Both the velodrome and Olympic stadium were relatively unusual, unique artistic creations. The Velodrome was comprised of three arches supported by abutments. It was designed to have the appearance of a cycling helmet. The Olympic Stadium was another ultramodern design which resembled an elliptical sea shell with a handle. The original design also included a retractable fabric roof, which was subsequently deleted for cost savings.

The contract for the Velodrome construction was awarded to Prime Contractor Charles Drunceau with a $12 million bid, based on half complete plans, and construction began in 1973. The City of Montreal had also promised to host the 1974 World Cycling Championship in the Velodrome, resulting in a very tight and unrealistic critical path. Soil problems due to low bearing capacity and the high loads on the abutments resulted in substantial time delays and cost overruns for the foundation work. A new foreign project engineer was hired and a new critical path schedule was developed. Due to the time constraints, most of the construction contracts were cost plus, rather than low bid fixed cost contracts. There were also a number of labor problems, such as tasks taking too long, strikes, overtime, and extra equipment, which themselves added about $12 million to the project cost. The deadline could not be met, and a temporary facility had to be constructed for the World Cycling Championships. The final cost for the 7,000 seat Velodrome was approximately $70 million, compared to a $60 million cost for a 60,000 seat domed stadium in Seattle, Washington, USA at the same time.

The Olympic Stadium design was extremely complex. The structure consisted of epoxy connected precast post-tensioned concrete ribs, which were connected to a hollow ring at the top. No more than two ribs were identical. This construction procedure (epoxy-glued, post-tensioned structural members) had been used in Europe, but not in North America. It was extremely difficult to align the ribs to perform the post-tensioning and make the connections. Scaffold could not be used, since it would restrict access. Hence numerous cranes had to be used to secure each rib. There was a slow and expensive learning curve for the contractor to become even somewhat proficient. All of which greatly extended the construction time, pushing much of the post-tensioning to the winter months, when water freezing in the post-tensioning tubes further increased the construction difficulty. The final cost for the Stadium was approximately $13,000 per seat, compared to approximately $2,400 per seat for the Superdome in New Orleans, Louisiana, USA constructed at approximately the same time.

The Main Road Viaduct also had a relatively high construction cost due to its design. Although the main road was straight, the Viaduct had a complex design, with curved faces and outstretched legs. The curved surfaces resulted in the in-ability to use standard, re-usable formwork. Whereas convention formwork would have cost approximately $27 per square foot,

the formwork cost for the Viaduct was approximately $400 per square foot. Hence, the final cost of the Viaduct was approximately $14 million, versus a projected cost of only $5 million if a conventional design would have been used.

During the construction of the Olympic Complex the cost and time overruns were spiraling out of control, and it became apparent that the City of Montreal was unable to complete the project, which would have been an embarrassment to not only the city, but to Canada. Hence, the Province of Quebec took over and completed the project. Labor problems remained rampant, as the fixed deadline and absence of no-strike agreements created an atmosphere of labor strikes, slowdowns, and sabotage. Eventually the Province of Quebec issued the ultimatum that either the construction workers get on with the work or the project would be cancelled, and the Olympic games would need to be held elsewhere. Following the ultimatum, productivity did increase, and the project was eventually completed.

The Montreal Olympic Village also experienced considerable problems and irregularities. Originally it was to provide low-cost housing units after the Olympics, and the federal government was going to provide 95 % of the clearance cost and 75 % of the construction cost. The deadline for bids for a developer was March 1, 1974, but in January of 1974 Joseph Zappia visited France and claimed to be the developer. At the bid deadline, none of the 53 bidders heard anything, and Joseph Zappia was chosen behind the scene. The developer went to French architect Andre Manangoy because he liked his design of condos at Bai des Anges, France. The design was ill-suited for Montreal's cold winters, and the Federal government chose not to provide the funding due to the elaborate design which was not comparable to low-cost housing. Zarolega received a generous cost-plus contract without a "not-to-exceed" clause. The "plus" was 12 % on the first $30 million, and 6 % on anything above. Zarolega estimated that the project would not exceed $45 million. Concerns about the potential cost led to the government committee hiring of a consultant for a second opinion. He predicted a project cost of $55-$58 million, with a possible $10 million overtime bill. Despite the second opinion, they went with the Zarolega estimate. A number of problems occurred during the construction, including outrageous sub-contracts, dangerous construction techniques, poor coordination, and theft. A new consultant was brought in to manage the construction. The actual cost for the Olympic Village was approximately $70 million.

There are a number of technical, procedural, and ethical issues that contributed to the problems experienced by the Montreal Olympics project (Neil 1979) including the following:

Extreme Time Constraints

There was an unrealistic deadline for the project. An additional two years would have been much more reasonable for the design and construction. The City of Montreal was so late with design documents that most work packages could not be bid. Instead, most of the contracts were negotiated.

Unrealistic Project Schedule

Project scheduling was forced to fit extremely tight deadlines. Hence the critical paths were much too optimistic, and did not allow for any normal problems which occur in all construction projects. The critical paths included a multitude of simultaneous activities, without considering

their negative impact on the productivity of each. Hence, almost everything took much longer because of the conflicts. A proper construction schedule is based upon normal crews and construction activity durations, so that individual activities on a critical path can be intelligently expedited, or "crashed", to prudently compensate for project delays while minimizing increased costs. The unrealistic nature of the schedules made it impossible to intelligently crash selected activities. The schedules were abandoned and everything became a daily crash.

Unusual design, one-of-a-kind components

As mentioned previously, it was extremely difficult and labor intensive to construct the stadium with the pre-cast, post-tensioned, epoxy connected ribs of varying sizes. The required use of one-of-a-kind, single-use formwork for the curved surfaces of the viaduct also resulted in increased costs.

Crowded Work Space

The time constraints and schedule compression resulted in even more simultaneous activities, and an extremely crowed work space. At one point, there were 80 different cranes trying to operate in the stadium. This resulted in cranes waiting for other cranes to finish their lifts, and crews standing around waiting for their turn. Doubling of the amount of cranes used on the job substantially increased the equipment cost, but only increased the productivity 25 %.

Shortage of Resources

Due to the size of the project, there was a shortage of local resources. Labor, material and equipment had to be brought in from other areas. This resulted in additional transportation costs. It also resulted in poorer quality labor, as well as non-local labor not having the same sense of "civic pride" as regular Montreal residents.

Organization and Relationship

The original client was the City of Montreal, which did not have the expertise and experience to manage a job of that magnitude. A change in client occurred when the Province of Quebec was forced to step in and assume that role. Although the change was necessary, additional difficulties, such as communication problems, typically occur when the major constituents change during a project.

In addition, the relationship of the design professionals hindered prompt communication. The design and engineering was done in France, and converted from metric to English units by Canadian engineers.

The client, architect, design engineers and project management did not function as a team. The architect was unwilling to consider value engineering ("Experts Slam the Olympic Structures of Montreal" 1976). He was primarily interested in the artistic value of his design, without consideration of any cost saving suggestions from the other parties, including the design engineers.

Weather

The weather contributed to the problems, particularly since weather protection and heating was needed, especially for the concrete work and installation of the post-tensioning tendons. The project delays pushed much of that work into the winter months.

Ethical Aspects

There were a number of ethical aspects brought out in this case, including the experience necessary for undertaking such a project, team goals and responsibilities, public safety (including the safety of workers when simultaneous work is being done in crowded conditions), as well as awarding of contracts (especially for the Olympic Village).

After the 1976 Olympics, the Olympic Stadium saga continued. The roof and tower are completed, but the retractable Kevlar roof failed (Wikipedia 2008), an "indestructible" Teflon roof also collapsed (CBC News 1999) and a fiberglass panel roof installed later suffered a partial collapse (Merron 2008).

Lessons Learned

In conclusion, the Montreal Olympics Complex is an excellent example of a failure, based upon the excessive cost overruns, attributable to the following:

- inadequate time available and improper project scheduling
- constructability issues
- organizational structure
- ethics

Based upon that experience, the following is a recipe for a construction cost/time failure:

1. Insufficient time
2. Unusual construction
3. Unrealistic critical path
4. Lack of experience/expertise
5. Lack of team approach (Every man for himself)
6. Constructibility issues
7. Shortage of resources
8. Poor organizational structure/communications
9. Lack of ethics (including lack of transparency of procedures)

Hyatt Regency Walkway

The Hyatt Regency Walkway Collapse is well known, and hence the details of the case will only have a cursory discussion in this paper. Suspended walkways supported by long threaded steel rods were used in a lobby/atrium of the hotel in Kansas City, Missouri, USA. The second floor walkways were suspended from the beams of the 4th floor walkways. The hotel had been completed the previous year, and on July 17, 1981, while between 1,500 and 2,000 people were attending a dance in the atrium, the walkways collapsed, killing 114 people (Carper

2001). The story most often told is that a blatant error was made in the design of the walkways, which resulted in them being extremely under-designed, causing the collapse. Detailed analysis of the structural system (Moncarz and Taylor 2000) showed that the connection was near failure at dead load only. However, the connection was never actually designed (Luth 2000). Hence, the failure should be classified as a process failure (Moncarz and Taylor 2000). In the classroom, our discussion goes beyond the inadequacy of the connection, and looks at the organization and procedural issues which led to the collapse, including the convoluted project delivery system, ethical issues (Pfatteicher 2000) and the roles and responsibilities of the engineer-of-record, steel fabricator and erector, particularly regarding the connection details, and whether those responsibilities can be contractually assigned to other parties. Detailed discussions of this case study are readily available in the literature (Delatte 2009), including a paper by the engineer-of-record (Gillum 2000).

L'AMBIANCE PLAZA – (1987)

This was a sixteen story apartment building in Bridgeport, Connecticut, USA, which was being constructed using the lift-slab method. when it suddenly collapsed, killing 28 construction workers. There were multiple theories on the cause of the collapse, including failures of the lifting mechanisms (shearhead collar deformation allowing a lifting rod to slip out (Scribner and Culver 1988, Culver 2002, McGuire 1992), rolling out of the wedges temporarily supporting the slabs (Cuoco et al 1992), foundation movement, improper design of floor slab post-tensioning tendons (Poston et al 1991), and general instability of the structure during construction (Moncarz et al 1992). These theories were never fully resolved due to a controversial mediated settlement of claims (Felsen, M. D. 1989). Details of this case study are available in the literature (Heger 1991; Martin and Delatte 2000).

This tragedy led to the development of guidelines for lift-slab construction , as well as perhaps the demise of lift-slab construction, which had an enviable safety record. It also illustrated how a convoluted project delivery system can make it unclear on who has the prime responsibility for structural safety. Students may understand the engineer-of-records responsibility for the completed structure, but they are typically unfamiliar with the lift-slab construction method and the engineer's responsibilities during construction. This is a particularly interesting case study for the students, as the engineer-of-record has supplied the author with his personal perspective (O'Kon 1993), including how he dealt with the tragedy and the controversial mediated settlement. It also graphically illustrates the relative instability of many structures during construction, lack of redundant load paths, and the need for temporary bracing. Following this tragedy, guidelines for lift-slab construction were developed (Zallen and Peraza 2003).

Assessment of Construction Planning and Estimating Course

An assessment of this course was done over a three year period, using survey forms and focus groups (Delatte et al 2008a,b; Delatte et al 2010). On a scale of 1-5, with 5 being strongly agree, the course received the following average scores:

Year	2007	2008
Understanding of professional and ethical responsibilities	4.75	4.88
Impact of engineering solutions in a global and societal context	3.75	4.38
Recognition of the need for, and an ability to engage in life-long learning	4.25	4.63
Knowledge of contemporary issues	4.0	4.0

Conclusion

Engineering failures are often the result of poor organization and process. This course effectively uses failure case studies, including failures as defined by extreme cost and time overruns, to address some of the required outcomes which are traditionally more difficult to quantify in most technical courses, particularly with respect to project management, professional and ethical responsibilities, and their impact.

References:

Auf der Maur, N. (1976). "The Billion-Dollar Game : Jean Drapeau and the 1976 Olympics." James Lorimer & Company, Toronto.

Baer, R. J. (1996). "Guest editorial (Are civil engineering graduates adequately informed on failure? A practitioner's view)." *Journal of Performance of Constructed Facilities*, 10(2), 46.

Bosela, P.A. (1993), "Failure of engineered facilities: Academia responds to the challenge." *Journal of Performance of Constructed Facilities*, ASCE, New York, NY, 7(2), 140-144.

Bosela, P. A., Delatte, N. J., and Rens, K. L. eds., (2003). *Forensic Engineering, Proceedings of the Third Congress*, ASCE, Reston, VA.

Bosela, P. A. and Delatte, N. J. (2006). *Forensic Engineering, Proceedings of the 4th Congress*, ASCE, Reston, VA.

Carper, K. L. (2000), "Lessons from failures: case studies as an integral component of the civil engineering curriculum." *Civil and structural engineering education in the 21st century*, Southampton, UK.

Carper, K. (2001), *Why Buildings Fail,* National Council of Architectural Registration Boards, Washington, D.C., pp. 44 - 48 and 66 – 71.

Carper, K. L., Delatte, N. J., and Bosela, P. A. (2008). "Status of forensic engineering education in the United States, *Proc., Fourth Int. Conf. on Forensic Engineering – from Failure to Understanding,* ICE, London, UK

CBC News (1999). "The Big Woe." <http://archives.cbc.ca/sports/olympics/topics/1316-7926/ >(January 22, 1999)

CBC News (2006). "Quebec's Big Owe Stadium Debt is Over." <http://www.cbc.ca/canada/montreal/story/2006/12/19/qc-olympicstadium.html> (September 30, 2008).

Chen, S., Diaz de Leon, A., Dolhon, A. M, Drerup, M. J., and Parfitt, M. K. , eds. (2009). *Forensic Engineering 2009: Pathology of the Built Environment, Proceedings of the Fifth Congress on Forensic Engineering*, ASCE, Reston, VA.

(2008). *Civil Engineering Body of Knowledge for the 21st Century*, Second Edition, ASCE, Reston, VA.

Culver, C. G. (2002), Discussion of "Another Look at the L'Ambiance Plaza Collapse), Journal of Performance of Constructed Facilities, February, Vol. 16, No. 1.
Cuoco, D., D. Peraza and Scarangello, T. Z. (1992). "Investigation of the L'Ambiance Plaza Building Collapse," Journal of Performance of Constructed Facilities, ASCE, Vol. 6, No.4, pp. 211-231.

Delatte, N. J. (1997), "Integrating failure case studies and engineering ethics in fundamental engineering mechanics courses," Journal *of Professional Issues in Engineering Education and Practice*, 123 (3) 111-116.
Delatte, N. J. (2000). "Using failure case studies in civil engineering education." *Forensic Engineering, Proceeding of the Second Congress*, K. L. Rens, O. Rendon-Herrero, and P. A. Bosela, eds., ASCE, Reston, VA, 430-440.

Delatte, N.J. and Rens, K. L. (2002), "Forensics and case studies in civil engineering education: State of the art." *Journal of Performance of Constructed Facilities*, ASCE, Reston, VA, 16(3), 98-109.

Delatte, N. J., Bosela, P. A., Rens, K. , Carper, K., and Sutterer, K. (2007) *"*Findings from Workshops on Failure Case Studies in the Civil Engineering and Engineering Mechanics Curriculum*," Proceedings of the 2007 American Society for Engineering Education Annual Conference & Exposition,* Honolulu, Hawaii, June 24 – 27, 2007.

Delatte, N. J. Bosela, P.,A., Sutton, R., Beasley, W., and Bagaka's, J. (2008). "Assessing the Impact of Case Studies on the Civil Engineering and Engineering Mechanics Curriculum, Phase II", *Proceedings of the 2008 American Society for Engineering Education Annual Conference & Exposition,* Pittsburgh, Pennsylvania, June 2008.

Delatte, N. J., Bosela, P. A., Sutton, R., and Bagakas, J. (2008). ***"****Implementing Forensics and Failures in the Civil Engineering Curriculum"*, *Proceedings of the Fourth International Conference on Forensic Engineering – From Failure to Understanding*, London, UK, December 2, 2008., p585-594.

Delatte, N. J. (2009). Beyond Failure, Forensic Case Studies for Civil Engineers, ASCE Press, Reston, VA.

Delatte, N. J., Roberts, M., Ralston, P., Brady, P., Zoghi, M., Hagerty, D. J., and Yu, X. (2010). "Implementation and Assessment of Case Studies in the Engineering Curriculum." *Proc., 2010 American Society for Engineering Education Annual Conf. & Exposition,* Louisville, Kentucky, June 2010.

"Experts Slam the Olympic Structures of Montreal." (1976). Civil Engineering, ASCE, December, 1976, 50-54.

Felsen, M. D. (1989), "Mediation that Worked: Role of OSHA in L'Ambiance Plaza Settlement," Journal of Performance of Constructed Facilities, ASCE, Vol. 3, No.4, pp. 212-217.

Fotheringham, Allan (1999). "The Woes of the Olympics Began in Montreal." *Maclean's,* 112(6).

Gillum, J. D. (2000). "The engineer of record and design responsibility." *Journal of Performance of Constructed Facilities*, 14(2), 67-70.

Government of Quebec. (2004). "History of the Olympic Park." <http://www.rio.gouv.qc.ca/pub/parc/historique_po.jsp> (September 29, 2008).

Heger, F.J., (1991), "Public Safety Issues in Collapse of L'Ambiance Plaza." Journal of Performance of Constructed Facilities, ASCE, Vol. 5, No.2, pp. 92-112.

Hendrick, Ricia S. (1989). "Defying Gravity in Montreal." *Elevator World,* 37(5), 13.

Jennings, A., and Mackinnon, P. (2000). "Case for undergraduate study of disasters." *Journal of Performance of Constructed Facilities*, 14(1), 38-41.

Kidd, B. (1992). "The Culture Wars of the Montreal Olympics." *International Review for the Sociology of Sport,* 27, 151

Luth, G. P. (2000). "Chronology and context of the Hyatt Regency collapse." *Journal of Performance of Constructed Facilities*, 14(2), 51-61.

Martin, R., and Delatte, N. (2000). "Another Look at the L'Ambiance Plaza Collapse," ASCE Journal of Performance of Constructed Facilities, 14(4), 160-165.

McGuire, W. (1992), "Comments on L'Ambiance Plaza Lifting Collar/Shearheads," *Journal of Performance of Constructed Facilities*, ASCE, Vol. 6, No.2, pp. 78-95.

Merron, Jeff. (2008). "Olympic Stadium Disaster Timeline."*ESPN.* <http://espn.go.com/mlb/s/2003/0422/1542317.html> (September 24, 2008).

Moncarz, P. D., and Taylor, R. K. (2000). "Engineering process faiure-Hyatt Walkway collapse." *Journal of Performance of Constructed Facilities*. (12(2), 46-50.

Moncarz, P. D., Hooley, R., Osteraas, J. D., and Lahnert, R. J. (1992), "Analysis of Stability of L'Ambiance Plaza Lift-Slab Towers," *Journal of Performance of Constructed Facilities*, ASCE, Vol. 6, No.4, pp. 232-245.

Neil, James. (1979). "Construction Cost Estimating Concepts and their Applications." Texas A&M University.

O'kon, J. (1991) "Professional Survival after a Tragedy", ASCE Annual Civil Engineering Convention & Exposition, Orlando, Florida, October 21-24, 1991.

PBs Online. (2000-2001). "Olympic Stadium." <http://www.pbs.org/wgbh/buildingbig/wonder/structure/olympic_stadium.html> (September 24, 2008).

Parfitt, M. K. (2010). "Failures Wiki – Building, Architectural and Civil Engineering Failures and Forensic Practices." <http://failures.wikispaces.com/> (June 22, 2010)

Pfatteicher, S. K. A. (2000). "The Hyatt horror: Failure and responsibility in American engineering." *Journal of Performance of Constructed Facilities*, 14(2), 62-66.

Pietroforte, R. (1998). "Civil Engineering Education through case studies of failures", *Journal of Performance of Constructed Facilities*, ASCE, New York, NY, 12(2), 51-55.

Poston, R., Feldmann, G. C., and Suarez, M. G. (1991), "Evaluation of L'Ambiance Plaza Post-tensioned Floor Slabs," Journal of Performance of Constructed Facilities, ASCE, Vol. 5, No.2, pp. 75-91.

Rendon-Herrero, O. (1993a). "Too many failures: what can education do?", *Journal of Performance of Constructed Facilities*, ASCE, New York, NY, 7(2), 133-139.

Rendon-Herrero, O. (1993b). "Including failure case studies in civil engineering courses." *Journal of Performance of Constructed Facilities*, ASCE, New York, NY, 7(3), 181-185.

Rens, K. L., ed. (1997). *Forensic engineering*, *Proceedings of the First* Congress, ASCE, New York.

Rens, K.L., Rendon-Herrero, O., and Clark, M. J. (2000), "Failure of constructed facilities in the civil engineering curriculum." *Journal of Performance of Constructed Facilities,* ASCE, Reston, VA, 15(1), 27-37.

Rens, K. ., Clark, M. J., and Knott, A. W. (2000a). "A failure analysis case study information disseminator." *Journal of Performance of Constructed Facilities*, 4(3), 127-131.

Rens, K.L., Clark, M. J. and Knott, A. W. (2000b) "Development of an internet failure information disseminator for professors." *Forensic Engineering*, *Proceedings of the Second* Congress, K. L. Rens, O. Rendon-Herrero, and P. A. Bosela, eds., ASCE, Reston, VA.

Rens, K. L., Rendon-Herrero, O. and Bosela, P. A., eds. (2000c). *Forensic Engineering*, *Proceedings of the Second Congress*, ASCE, Reston, VA.

Scribner, C.F. and C.G. Culver (1988), "Investigation of the Collapse of L'Ambiance Plaza," Journal of Performance of Constructed Facilities, ASCE, Vol. 2, No.2, pp. 58-79.

Shepherd, R. and Frost, J. D., eds. (1995). *Failures in civil engineering: structural, foundation and Geoenvironmental case studies*. Committee on Education, Technical Council on Forensic Engineering, ASCE, New York, NY.

Sutterer, K.G. (2003), "Service learning and forensic engineering in Soil Mechanics", *Forensic Engineering, Proceedings of the Third Congress*, P. A. Bosela and N. J. Delatte, eds., ASCE, Reston, VA, 297-306.

Wikipedia (2008). "Olympic Stadium (Montreal)." <http://en.wikipedia.org/wiki/Olympic_Stadium_(Montreal)> (September 29, 2008).

Zallen, R. M., and Peraza, D. P. (2003). "Engineering Considerations for Lift-Slab Construction," ASCE.

Zickel, L. L. (2000). "Failure vignettes for teachers." *Forensic Engineering, Proceedings of 2nd Congress*, K. L. Rens, O. Rendon-Herrero, and P. A. Bosela eds., ASCE, Reston, VA, 421-429.



Figure 1 Montreal Olympic Stadium Model (Photo from Ken Carper)

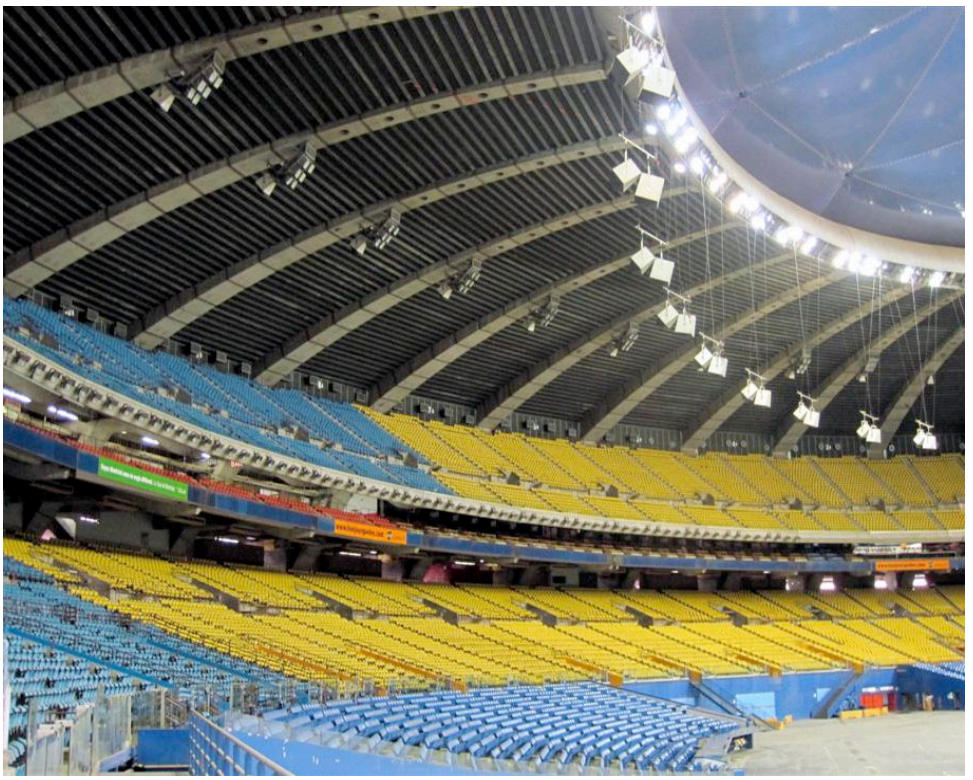


Figure 2 Interior View of Stadium (Photo from Ken Carper)



Figure 3 The Kansas City Hyatt Regency atrium walkways (Photo from NBS/NIST)

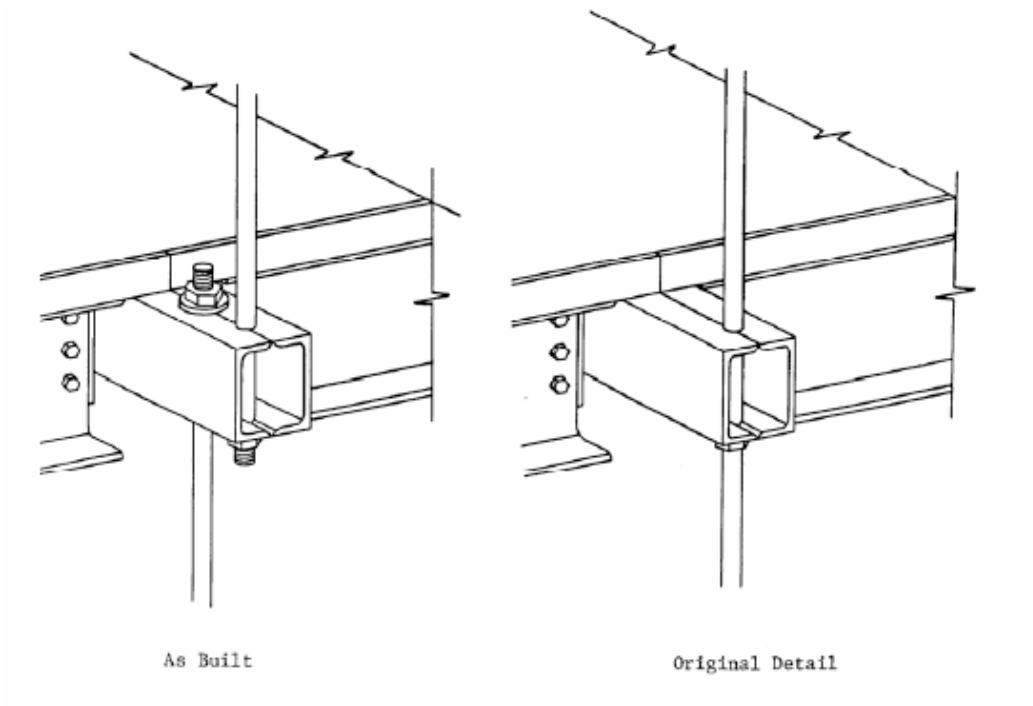


Figure 4 Original and As Built Details of the Hyatt Regency Walkway (Figure from NBS/NIST)



Figure 5 L'Ambiance Plaza under construction. (Photos from NBS/NIST)



Figure 6 L' Ambiance Plaza after collapse (Photos from NBS/NIST)

Engineered Biobased Composites for Construction: Material Development, Multiscale Modeling, and Long-Term Durability

W.V. Srubar III, LEED® AP[1] and S.L. Billington, Ph.D.[2]

[1]John A. Blume Earthquake Engineering Center, Department of Civil and Environmental Engineering, Stanford University, Building 540, MC: 3037, Stanford, CA 94305; PH (650) 723-4150; FAX (650) 725-9755; email: wsrubar@stanford.edu
[2]Yang and Yamazaki Environment and Energy Building, Department of Civil and Environmental Engineering, Stanford University, 473 Via Ortega, Room 285A, Stanford, CA 94305-4020; PH (650) 723-4125; FAX (650) 723-7514; email: billington@stanford.edu

ABSTRACT

Fully biodegradable composite materials fabricated using natural fiber reinforcements and biopolymeric matrices derived from poly(β-hydroxybutyrate) (PHB) and PHB-*co*-poly(β-hydroxyvalerate) (PHBV), are being investigated as potential alternatives to traditional residential construction materials. The materials are envisioned to be rapidly renewable by using biogas from their anaerobic biodegradation as the feedstock for microbial production of the biopolymer and using plant-based materials for composite reinforcement and fillers. These biobased composites are being engineered to satisfy acceptable stiffness, strength, ductility, and in-service durability performance criteria while maintaining the propensity for rapid out-of-service anaerobic biodegradation. In this paper a brief overview of research on material development, mechanical properties, and multiscale modeling, as well as moisture absorption and long-term durability of PHBV-wood fiber filled composites with and without fiber treatments is given. This research is an interdisciplinary collaboration between structural, environmental, and chemical engineers.

INTRODUCTION

Holistic characterizations of solid waste streams in the United States have attributed 40% (96 million tons) of all landfilled debris to building-related construction and demolition (C&D) activities (EPA 2008); typical residential construction materials, including wood, plastic, and drywall, constitute 45% (43.2 million tons) of landfilled C&D material waste (EPA 1998). Traditional residential construction materials seemingly possess a cradle-to-grave lifecycle and ostensibly lie recalcitrant in landfills, due to the predominantly idle rates of biodegradation.

Through the transformation of material lifecycles using a cradle-to-cradle design methodology which harnesses the power of naturally occurring bioprocesses, rapidly renewable, fully biodegradable composite materials fabricated using natural fibers as reinforcement in matrices derived from poly(β-hydroxybutyrate) (PHB), a

microbially synthesized biopolymer, and PHB-*co*-poly(β-hydroxyvalerate) (PHBV), a copolymer blend, are being investigated as potential alternatives to traditional residential construction materials in both structural and non-structural applications. As shown in Figure 1, the construction biomaterials are envisioned to be rapidly renewable by a) utilizing methane biogas captured from anaerobic degradation and biotransformation of the material as the carbon-based feedstock for microbial production of PHB and b) using plant-based materials for composite reinforcement.

Laboratory-scale research has investigated the mechanical characterization (Alvarez 2003, Luo 1999, Avella 2007), thermal stability (Li 2007), and water absorption behavior (Alvarez 2003, Alam 2006) of various natural fibers in matrices derived from starch, polyhydroxyalkanoates (PHB, PHBV), polylactides (PLA, PGA), soy-based resins, and other biorenewable resources. Potential applications of these materials range from automotive parts, interior trims and finishes, furniture, decking, fencing, and, of particular interest, both temporary and permanent building components (Humphreys 2003).

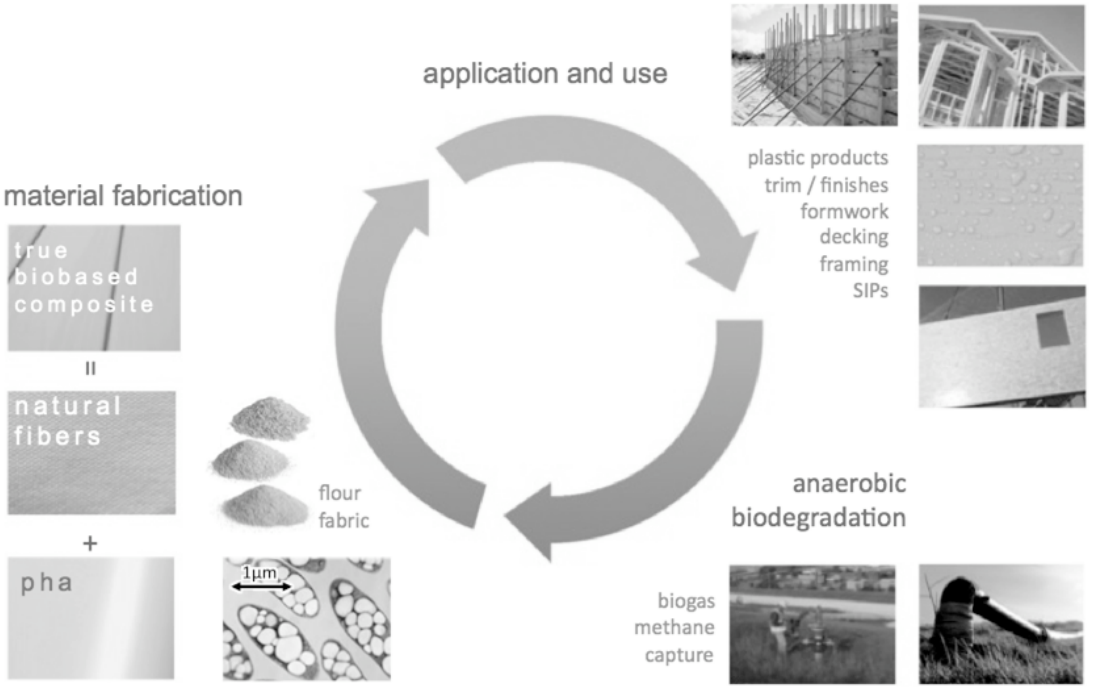


Figure 1. Envisioned closed-loop life-cycle for PHB-based composite materials

Material properties achieved by PHB-based composites are comparable to dimensional lumber (Christian 2009) and are being engineered to satisfy acceptable stiffness, strength, ductility, and in-service material durability performance criteria (low moisture absorption, thermal stability, UV resistance) while maintaining the propensity for rapid anaerobic biodegradation. To the authors' knowledge, no studies have comprehensively characterized a class of materials from a holistic composite systems engineering approach wherein the benefits of fiber reinforcements or fillers and interfacial modifications for increased in-service mechanical performance and durability are balanced with tradeoff effects of out-of-service biodegradation.

Material Durability. While biobased materials have demonstrated adequate initial mechanical properties for specific target applications, long-term durability concerns exist due to the inherent differences in morphology and chemical composition of natural fibers and PHB-based biopolymers. The hydrophilicity of the fibers, hydrophobicity of the matrix, and corresponding differences in surface energies of the two phases have been shown to decrease material stiffness and exacerbate water uptake in high humidity environments. Water absorption leads to fiber swelling, dimensional instability, matrix cracking, mass loss, susceptibility to fungal attack, and biodeterioration. To address fiber-matrix incompatibility concerns, various modification techniques have traditionally been employed to improve both the moisture resistance and mechanical performance of biobased composites.

For this preliminary study, engineered biobased composite specimens of PHBV and a reinforcing filler of natural, lignocellulosic oak wood flour (OWF) were fabricated using an extrusion-injection molding process. Degradation studies have shown that PHB-based polymers biodegrade more rapidly than other biopolymers (such as cellulose acetate and soybean oil-based resins) (Morse 2009); furthermore, it has been shown that the gaseous products of the anaerobic biodegradation of PHBV consist primarily of carbon dioxide and methane, the latter of which can be captured and used as a closed-loop carbon source for the production of new PHBV. OWF was selected as a lignocellulosic filler to: 1) utilize a waste material byproduct from commercial wood manufacturing and agricultural processes; 2) improve the mechanical stiffness of the matrix material; and 3) reduce the overall cost of the composite.

Mechanical and water absorption properties are being characterized as a function of wood fiber loading by volume percent. The effects of a silane coupling agent fiber treatment and a maleic anhydride matrix grafting technique are under investigation and are being correlated with the morphology of the altered fiber-matrix interface using scanning electron microscopy (SEM). Experimental results are being correlated with theoretical predictive models with consideration given to the phenomenological effects of the employed fiber-matrix interfacial compatibilization techniques. In addition, the effect of the modifications on both moisture absorption and anaerobic biodegradation are being studied. An overview of selected research results from this project is presented herein.

MATERIAL DEVELOPMENT AND METHODS

Materials. PHBV (ENMAT^{TM} Y1000P, Tianan Biological Materials Company, Zhejiang, China) was used as the matrix material and was measured to have a density of 1.21 g/cm^3. Prior to composite processing, the PHBV was dried in a 50°C oven for a minimum of 12 hours to remove moisture. OWF (2037-Oak, American Wood Fibers, Wisconsin, USA) was used as the natural fiber filler. Based on a sieve analysis and volumetric measurements, the OWF had a 20 mesh wood flour particle size <841μm and an apparent (bulk) density of 0.44 g/cm^3. Measurements using optical microscopy confirmed an average fiber aspect ratio (l/d) of 3.6. The OWF was preconditioned in an oven overnight at a temperature of 100°C prior to compound

extrusion. For the silanation and maleic anhydride reactive extrusion, trimethoxy-(octadecyl)silane ($C_{21}H_{46}O_3Si$), maleic anhydride (2.5-Furandione, $C_4H_2O_3$); dicumyl peroxide (bis(1-methyl-1-phenylethyl) peroxide, $C_{18}H_{22}O_2$), and phenolphthalein were obtained from Sigma-Aldrich.

Fiber-Matrix Compatibilization. The effects of a silane coupling agent and a maleic anhydride grafting technique were investigated for improving fiber-matrix compatibilization. For the silane treatment, a vapor deposition technique using foil-lined dessicators was employed to ensure silane was sufficiently chemisorbed onto the OWF particles. At the end of the thermochemical treatment, 1g samples of OWF were extracted from the bottom of the dessicator and tested with a drop of distilled water from a pipette to verify the hydrophobicity of the treated fibers. Maleic anhydride was grafted onto the PHBV polymer chains via a reactive extrusion technique using a Brabender Plasti-Corder single-screw extruder. A dry blend of PHBV pellets, maleic anhdride, and dicumyl peroxide (10% and 0.75% of PHBV by weight, respectively) was fed through the main hopper. The reactive extrusion was performed at a melt temperature of 160°C and an extruder screw speed of 20 rpm, which corresponded to a residence time of 150 seconds. The graft percentage of MA-grafted PHBV (mPHBV) in the extracted material was found to be 0.8% via an acid-base titration technique using phenolphthalein as an indicator.

Composite Processing. To investigate the effects of various fiber treatments, four families of PHBV/OWF composites were processed. These included pure PHBV/untreated OWF composites (P), pure PHBV/silanated OWF composites (PS), 1% mPHBV/untreated OWF composites (1M), and 2% mPHBV/untreated OWF composites (2M). The 1% mPHBV nomenclature indicates that 1% of the PHBV used in the composite was modified with maleic anhydride with the balance being unmodified PHBV. Each family of composite mixture formulations was reinforced with varying amounts of OWF. Target fiber loadings ranged from 0-40% in 10% increments by weight percent of filler.

Master batches of composite mixtures were fabricated by compound extrusion using an American Leistritz ZSE-18HP twin-screw extruder set at a processing temperature of 165°C and a main screw speed of 190 rpm. The extruded composite was fed from the die into a cooling water bath and immediately pelletized into uniformly sized pellets, using a Scheer Bay BT-25 pelletizer. Prior to injection molding, the compounded pellets were dried in an oven at 40°C for 12 hours. After oven-drying, ASTM standard specimens for testing of tensile (D638) mechanical properties as well as 3-mm-thick 50-mm-diameter disc specimens were prepared using an Arburg 320A injection-molding machine. Complete details on all materials and fabrication methods are reported in (Srubar 2011a).

Uniaxial Tension. The cross-sectional geometry (width, thickness) was measured on all samples. The densities of the PHBV/OWF composites were measured by immersion of oven-dry samples in water according to ASTM D792 and calculated based on Archimedes' Principle. ASTM D3171 was used to determine the constituent

content of fiber-reinforced polymeric composites with chloroform as the solvent. The existence of soluble organics in the pure OWF was found to be negligible. Although not reported herein, microscopy has been used to investigate filler morphology, fiber-matrix interfacial adhesion, and particle dispersion, and differential scanning calorimeter was performed to determine the thermal properties of the polymer composites (i.e., crystallization, melting, and glass transition temperatures).

Tensile specimens were tested according to ASTM D638 using an MTS 858 tabletop machine with a 13.5 kN capacity. Modulus of elasticity, ultimate strength, maximum elongation, and Poisson's ratio for the specimens were determined. The longitudinal and transverse strains were measured using a 50 mm gage length extensometer and a strain gage, respectively. Three specimens were tested for each variable.

For the sorption testing, disc samples were equilibrated in an oven at 70°C for 36 hours until a constant weight was achieved. Water sorption experiments were performed in a sealed room-temperature water immersion basin as per ASTM D570. Composite specimens were periodically removed from the water basin, bound surface moisture was carefully removed, and weights as well as radial and through-thickness dimension measurements were recorded to obtain both time-dependent mass gain and coefficients of hygroexpansion.

SELECTED EXPERIMENTAL RESULTS

Composite and Filler Density. The densities of the PHBV/OWF composites resulted in an increase in composite density from 1.21 g/cm^3 for the neat PHBV to 1.22-1.30 g/cm^3 dependent upon fiber loading. The experimental determination of filler density in the composite yielded an average value of 1.44 g/cm^3 whereas the overall density of preprocessed natural oak wood ranges from 0.32-0.72 g/cm^3 due to its tubular microstructure and porous anatomy (Clemons 2005). Similar results in terms of increased densities in both injection-molded and extruded wood flour composites have been reported in the literature (Anderson 2007) and are primarily due to the compressibility of wood flour particles. During processing, the wood flour fibers are exposed to elevated pressures, which results in the collapse of the wood fiber cell walls. Substantiating this phenomenon, the density of wood cell walls is well documented to be 1.40-1.60 g/cm^3 contingent upon the wood specie (Clemons 2005).

Uniaxial Tension Response. The uniaxial tension stress-strain response of representative samples of pure PHBV and PHBV/untreated OWF composites are shown in Figure 2. The modulus of elasticity calculated as the initial slope of the stress-strain relationship increased with increases in fiber loading. Initial stiffness increased neat PHBV stiffness from 3800±102 MPa to 4820±180 MPa for a 40% fiber loading. As the filler-matrix bond is expected to be weak, the increase in stiffness is attributed to the increase in the quantity of nucleation sites due to the added surface area of wood fibers in the reinforcement phase. These nucleation sites promote ubiquitous crystalline spherulite formation, which results in an overall increase in polymer crystallinity and, correspondingly, an overall increase in

composite stiffness. The increase in stiffness is expected to plateau with the addition of more OWF due to limitations related to the packing density of wood flour particles with an aspect ratio of 3.6. This plateau is apparent in Figure 3 where the effect of fiber loading on modulus of elasticity is shown.

In contrast, the addition of OWF systematically decreases the ultimate tensile strength of the composites as well as the elongation to break (Figure 2). The tensile strength of neat PHBV decreased from 34.8±0.7 MPa to 21.4±1.8 MPa with a fiber loading of 40%. This corresponds to an average strength decrease of 3.4 MPa with every 5% OWF added by volume. The decrease in tensile strength can be quantifiably predicted under the assumption of no interfacial adhesion between particle and matrix. The wood flour filler simply displaces matrix material; thus, the tensile strength is only dependent upon the tensile strength and volume fraction of PHBV (Srubar 2011a).

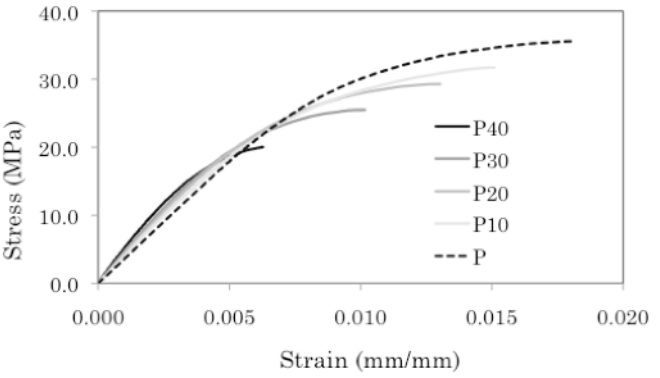


Figure 2. Effect of fiber loading on stress-strain behavior of PHBV/untreated OWF composites.

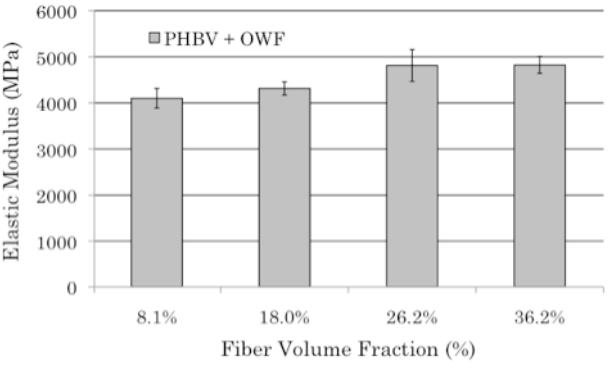


Figure 3. Effect of fiber loading on the tensile elastic modulus of PHBV/untreated OWF composites.

For all untreated and treated families of PHBV/OWF composites, the same increase in composite stiffness and decreases in strength and elongation to break were observed as the amount of filler increased. Initial comparisons between the effects of modification techniques on the material properties show that both fiber and matrix treatments do improve mechanical performance. Complete results of the effects and mechanisms governing interfacial improvements are reported in (Srubar 2011b).

Water Absorption Behavior. Figure 4 shows the water uptake behavior of PHBV/untreated OWF composites. An increase of fiber loading corresponds to an increase in water uptake as expected and as shown in other water absorption studies with natural fiber composites (Wang 2006). As can be seen in Figure 4, PHBV is primarily hydrophobic; the slight gain in moisture mass is the result of polymer plasticization and relaxation. The marked difference between the slopes of the 20% (shallow) and 40% (steep) composites suggest a volume fraction threshold that relates to the packing density of fibers in the composite. Percolation thresholds for ellipsoidal particulate fillers with an aspect ratio of 3.6 are being investigated for applicability to the moisture absorption behavior of PHBV/OWF composites.

Preliminary results also indicate that the modification techniques were not effective in reducing overall equilibrium moisture contents (Figure 5) particularly in the case of the silane treatment. It is believed that this is due, primarily, to the processing damage incurred during the injection-molding of the composites, where wood flour particles have collapsed due to elevated temperatures and pressures. The vapor deposition of silane onto fiber surfaces was a preprocessing technique and the collapse of the cell walls during processing would expose untreated fiber surfaces creating preferential pathways for water to enter the wood fibers. In addition, the low graft percent of maleated PHBV does not significantly affect the water absorption behavior in low volume fraction composites. Maleation improves fiber wettability and dispersion; however, in low filler fraction composites, good dispersion of particles can occur in untreated composites since there are appreciably fewer particles to disperse.

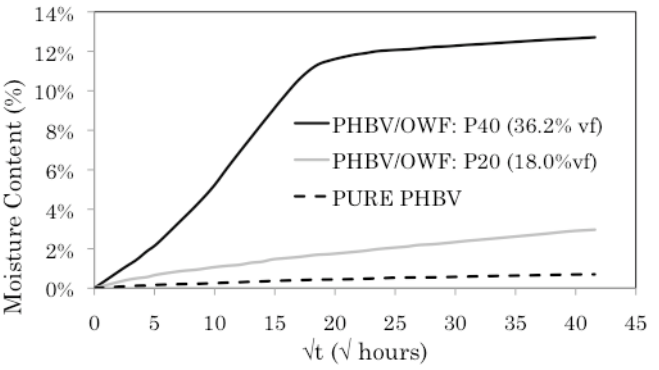


Figure 4. Water sorption of neat PHBV and PHBV reinforced with 20% and 40% OWF.

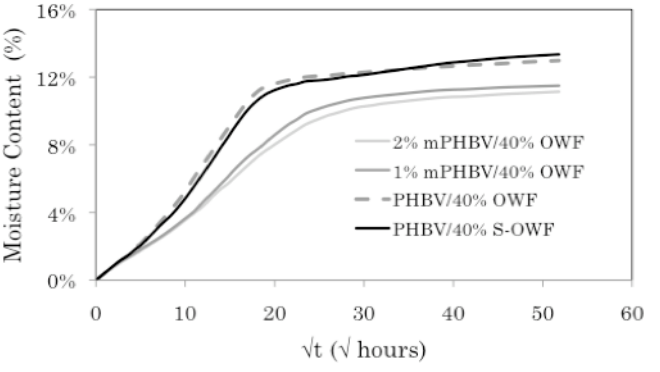


Figure 5. Water uptake profiles of four families of composites: untreated, silanated OWF, and 1% and 2% maleated PHBV.

However, there is noticeable impedance induced in the retardation of the rate of water absorption with high fiber loadings (Figure 5), especially by the maleic anhydride-treated polymer composites. As previously noted, maleation of the polymer improves fiber wettability, which corresponds to better fiber dispersion. The increase in fiber dispersion increases the hygrophobicity of the bulk composite by providing polymer-rich coatings on individual fibers. This phenomenon would explain the slight decrease in rate of water absorption coupled with the gradual inclination toward the same ultimate equilibrium moisture content as the untreated fiber samples.

PRELIMINARY MODELING

Experimental data obtained from fundamental tensile tests can be compared with the most commonly used theoretical models for initial composite stiffness. The Halpin-Tsai and Tsai-Pagano equations were developed to predict the global tensile modulus

of aligned short wood fiber reinforced biopolymeric composites using the micromechanical properties of the individual fiber and matrix phase constituents. Using experimentally determined parameters, this micromechanical modeling approach has been used previously in initial stiffness predictions of PHBV/wood flour composites (see Singh 2007).

Figure 6 shows the comparison of modulus of elasticity values determined experimentally with the initial composite stiffness predictions of the Halpin-Tsai / Tsai-Pagano Model for each of the four families of composites. As can be seen in the figure, the model provides a good estimation of composite stiffness for PHBV/untreated OWF, while it does not capture the enhanced improvement exhibited by the silanated and maleic anhydride treated families of PHBV/OWF composites.

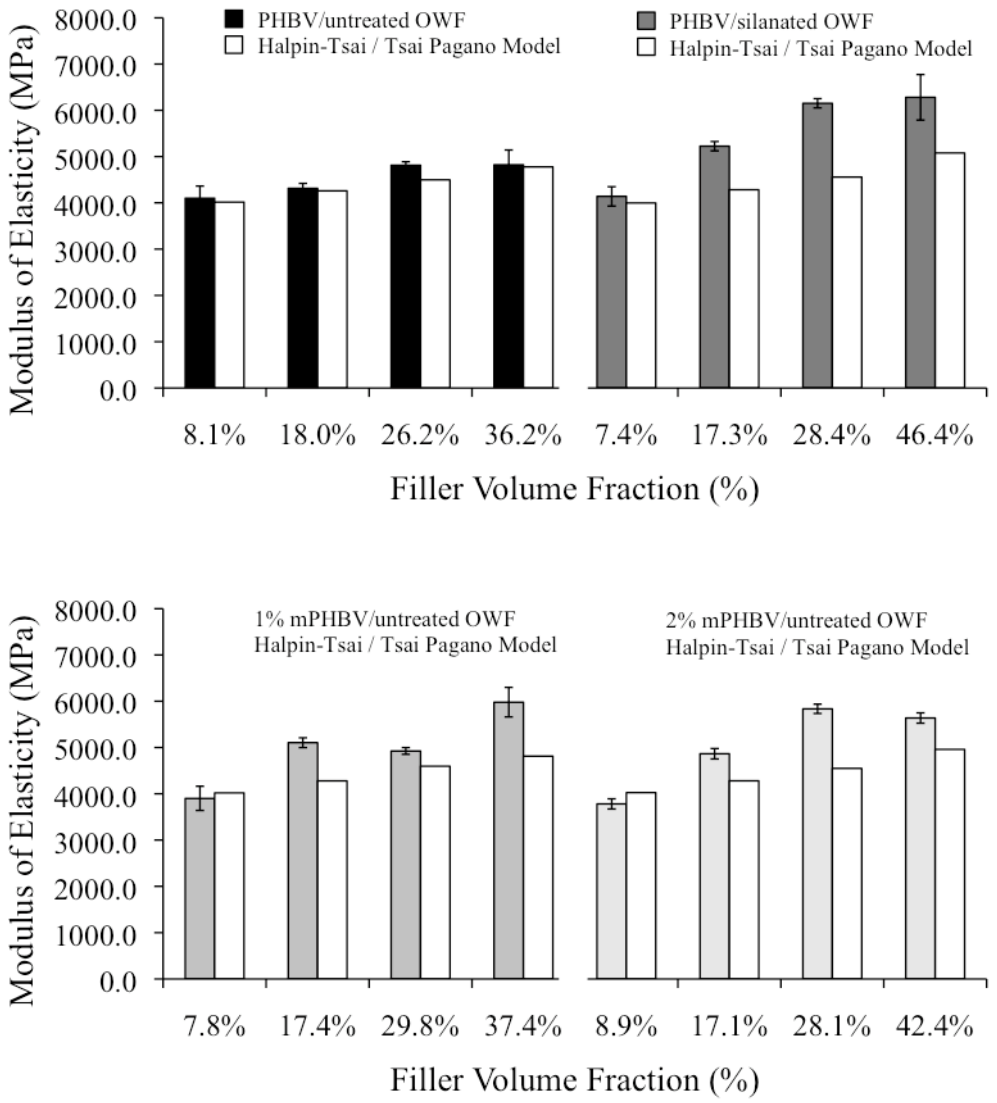


Figure 6. Comparison of experimental results with a micromechanical model for composite stiffness.

The inabilities of the model to provide a good estimation for the treated composites is attributed to its failure to incorporate improved fiber wettability and dispersion and the corresponding fundamental changes in crystalline matrix morphology that occur during processing. Current research investigations include further refinement and development of new models that account for these treatment-induced morphological changes in the matrix microstructure.

CONCLUSIONS

The introduction of OWF filler into PHBV led to increasing stiffness and decreasing strength with increasing filler content. The increased stiffness with increasing filler content is attributed to increased available fiber surface area and therefore nucleation sites for crystalline structure formation in the polymer matrix. This argument is further supported by an embrittlement of the composite and the reduction in elongation to break of tensile test data. Additional characterization techniques to support this conclusion are ongoing. In plain PHBV/untreated OWF composites, tensile strength can be predicted by considering only the matrix tensile strength and matrix filler fraction, indicating no interfacial adhesion between filler and matrix and, correspondingly, no contribution of tensile strength from the particulate filler.

The compatibilization techniques did not have a significant impact on reducing overall equilibrium moisture contents but did reduce the rate of moisture uptake relative to the composites with untreated wood fiber filler. In the case of the silane pre-treatment of the filler, it is believed (and confirmed through SEM imaging (Srubar 2011b)) that during extrusion and injection-molding, the wood fiber particles collapsed, exposing untreated fiber surfaces and thus creating preferential pathways for water to enter the wood filler. Untreated PHBV/OWF composite stiffness can be predicted with the conventional Halpin-Tsai / Tsai-Pagano Model; however, the model fails to account for alterations in the material microstructure induced by the employed chemical compatibilization techniques.

Acknowledgments. This research has been funded primarily by the National Science Foundation through CMMI Grant 0900325 with partial support from the California Environmental Protection Agency, Department of Toxic Substances Control under grant No. 07T3451. The results presented herein represent the views of the authors and not necessarily those of the sponsors. The collaboration with Prof. J. Greene at CalState Chico as well as Dr. Srikanth Pilla for the fabrication of test specimens is gratefully acknowledged.

REFERENCES

Alam, M. K. and Kahn, M. A. (2006). "Comparative Study of Water Absorption Behavior in Biopol and Jute-Reinforced Biopol Composite Using Neutron Radiography Technique," *J of Reinf Plastics and Comp*, 25, 1179-1187.

Alvarez, V., Ruscekaite, A., and Vazquez, A. (2003). "Mechanical Properties and Water Absorption Behavior of Composites Made from a Biodegradable Matrix and Alkaline-Treated Sisal Fibers." *J of Comp Mat*, 37, 1575-1588.

Anderson, S. P. (2007) "Wood Fiber Reinforced Bacterial Biocomposites," Masters Thesis, Washington State University.

Avella, M., Bogoeva-Gaceva, G., Buzarovska, A., Errico, M. E., Gentile, G., and Grozdanov, A. (2007). "PHBV-Based Biocomposites Reinforced with Kenaf Fibers." *J of App Poly Sci*, 104, 3192-3200.

Christian, S. and Billington, S. L. (2009). "Sustainable Biocomposites for Construction," *ACMA Composites & Polycom Conference*, Tampa, FL.

Clemons, C. and Caufield, D. F. (2005). "Wood Flour" in *Functional Fillers for Plastics*, Xanthos, M., Ed., Wiley-VCH Verlag GmbH & Co KGaA.

Environmental Protection Agency (EPA). (1998). "Characterization of Building-Related Construction and Demolition Debris in the United States," Waste and Management Research, www.epa.gov.

EPA. (2008). "Recover Your Resources Reduce, Reuse, and Recycle Construction and Demolition Materials at Land Revitalization Projects," EPA-560-F-08-242, www.epa.gov.

Humphreys, M. (2003). "The Use of Polymer Composites in Construction," Queensland University of Technology.

Luo, S. and Netravali, A. N. (1999). "Interfacial and Mechanical Properties of Environment-Friendly Green Composites Made From Pineapple Fibers and Poly(hydroxybutyrate-co-valerate) Resin." *J of Mat Sci*, 34, 3709-3719.

Li, X., Tabil, L. G., and Panigrahi, S. (2007). "Chemical Treatments of Natural Fibers for Use in Natural Fiber-Reinforced Composites." *J Polym Environ*, 15, 25-33.

Morse, M. (2009) "Anaerobic Biodegradation of Biocomposites for the Building Industry," Ph.D. Dissertation, Stanford University.

Singh, S. and Mohanty, A. (2007). Wood Fiber Reinforced Bacterial Bioplastic Composites, *Comp Sci and Tech*, 67, 1753-1763.

Srubar, W.V. and S.L. Billington (2011a). "Engineered Biobased Composites-Tensile Properties and Water Absorption Behavior," *ACMA Composites & Polycom Conference*, Ft. Lauderdale, FL.

Srubar III, W.V., Pilla, S., Wright, Z., Ryan, C., Frank, C. and Billington, S. L. (2011b). "Mechanisms and Impact of Fiber-Matrix Compatibilization Techniques on the Material Characterization of PHBV/Oak Wood Flour Engineered Biobased Composites," Manuscript submitted to *Comp Sci and Tech*.

Wang, W., Sain, M. and Cooper, P. A. (2006)."Study of Moisture Absorption in Natural Fiber Plastic Composites," *Comp Sci and Tech*, 66, 379-386.

An Evaluation of Anchorage Systems for Fiber-Reinforced Polymer (FRP) Laminates Bonded to Reinforced Concrete Elements

S.V. Grelle[1] and L.H. Sneed[2]

[1]Graduate Research Assistant, Department of Civil, Architectural & Environmental Engineering, Missouri University of Science and Technology (Missouri S&T), 1401 N. Pine St., 219 Butler-Carlton Hall, Rolla, MO 65409-6510; PH (636) 236-1897; FAX (573) 341-4729; email: stephen.grelle@mail.mst.edu
[2]Assistant Professor of Civil Engineering, Department of Civil, Architectural & Environmental Engineering, Missouri S&T, 1401 N. Pine St., 327 Butler-Carlton Hall, Rolla, MO 65409-6510; PH (573) 341-4553; FAX (573) 341-4729; email: sneedlh@mst.edu

ABSTRACT

Many studies have shown that fiber-reinforced polymer (FRP) laminates are an effective alternative for structural retrofit and repair of insufficiently reinforced concrete members; however, achieving the full tensile capacity of the externally bonded FRP is often very difficult. This is especially true when FRP is used on elements where there is inadequate length to develop the full tensile strength of the FRP laminate, leading to premature debonding failure. Anchorage systems attempt to mechanically restrain the FRP or improve the FRP-to-concrete bond, thus reducing the length required to develop its full design strength. Many types of anchorage systems have been tested by different investigators, but mixed and inconclusive results have been presented. Additionally, no evidence exists to show that one particular type of anchorage system is completely effective in developing the full tensile strength of FRP. The lack of conclusive results is exacerbated by the absence of a consistent testing procedure for evaluating anchorage strength and a system for categorizing the purpose of the anchorage system, despite the current design guide's recommendation that anchorage testing should precede the strengthening of a structure with FRP. An overview of previously tested anchorage systems is presented along with applicable testing procedures from existing literature. The limitations of each anchorage system are mentioned with respect to specific structural strengthening applications. The existing anchorages are then categorized according to their specific application to FRP anchorage, and the applicability of testing procedures to each anchorage category is discussed. Finally, the need for systematic testing is discussed and potential research topics are explored.

INTRODUCTION

For the past several decades, strengthening of reinforced concrete (RC) elements with fiber-reinforced polymer (FRP) composites has been studied as an effective method of structural retrofit and repair of insufficient members. FRP has become an

attractive construction material for these purposes due to its high strength-to-weight ratio, corrosion resistance, and ease of installation. Despite the extremely high strength of FRP composites, specifically those bonded externally to RC members, premature failure modes and difficulties in detailing often prevent the design strength, which is a function of the rupture strength of FRP, from being reached. To solve this problem, various anchorage systems have been devised and tested in an attempt to allow the strength of the FRP to approach its ultimate capacity.

Performance of anchorages becomes critical in the design of FRP strengthening systems because the improved strength due to the anchorage still may not be high enough to develop the full tensile strength of FRP. Therefore, failure modes are most often anchorage failure, FRP rupture due to local stress concentrations imposed by the anchorage, or FRP debonding. Because FRP rupture and debonding are sudden and brittle, a thorough understanding of the behavior and strength of anchorage is crucial for designing a safe, reliable structure.

While a wide variety of anchorage systems have been created and tested, the process of choosing an anchorage system for a specific strengthening application is often difficult due to the difference in behavior and lack of categorization with respect to application or purpose. To date, all anchorage systems have been grouped together in the single category of "FRP anchorage" or a similar term, even though different systems are not entirely interchangeable. Therefore, categorization of anchorage purposes will be useful for designers and for the scholarly exchange of information.

Because of the critical nature of FRP anchorage performance, current design guidelines require that a proposed anchorage system be heavily scrutinized under representative physical testing. Test procedures that have been published recently by scholars, however, have limited applicability. Further, while test data for a specific type of anchorage system may be available, the data may not be relevant to a different application depending on the usage of that particular system.

This paper presents a review of existing anchorage systems and focuses on their physical characteristics, role as a part of an FRP strengthening system, and applications. Existing types of anchorage systems are briefly discussed, categorized according to strengthening application, and related to an applicable testing procedure. Finally, the need for further research and consistent testing procedures is discussed.

CHARACTERISTICS OF FRP ANCHORAGE SYSTEMS

FRP anchorage systems for strengthening RC members are typically fabricated from the following materials: metal, usually steel and sometimes aluminum; carbon fibers, glass fibers, or other composite materials; a modification of the original concrete surface; or a combination of the three. For laboratory purposes, the use of metal anchorages is an attractive option because innovative devices can be easily fabricated by non-specialized personnel. Additionally, they can be designed to fail in a ductile manner, whereas FRP failure is usually sudden and brittle. For many applications of

FRP strengthening, however, corrosion is a major concern, and the use of a steel anchorage system is not an option. Anchorage devices made from carbon fiber-reinforced polymer (CFRP) or glass fiber-reinforced polymer (GFRP) are attractive because they can be integrated seamlessly with the overall FRP strengthening system and do not have the potential for galvanic corrosion. A disadvantage to using FRP or other composite anchorage systems is that the geometry of the devices can be limited unless advanced production techniques are used.

Current design guidelines for FRP anchorage systems can be found in *ACI 440.2R-08*, "Guide for the Design and Construction of Externally Bonded FRP Systems for Strengthening Concrete Structures." Recommendations and guidelines for anchorage systems found in this document, however, are limited at best. Although the guide states that any proposed method of anchorage should be "heavily scrutinized" or evaluated through "representative physical testing," it does not specify types of testing procedures that are considered adequate. The document also states that an anchorage system's ability to restrain FRP "is believed to result from their ability to resist tensile normal stresses rather than enhancing interfacial shear capacity." While this statement is true for many types of anchorages, there are many more that do not rely on resisting the tensile normal forces.

It is worth noting that many FRP strengthening systems are constructed without the need for anchorage systems because sufficient space exists for the FRP design strength to be developed along an "active bond length" over which the majority of the bond stress is maintained. While this bond length can be considered a form of anchorage, the depth and complexity of determining this "active bond length" warrants much discussion and is beyond the scope of this paper.

CATEGORIZATION OF FRP ANCHORAGE SYSTEMS

The purpose of anchorage systems is to allow the FRP strengthening system to reach a higher design strength by accomplishing one or more of the following: (I) preventing or delaying a premature debonding failure by resisting tensile normal forces; (II) reducing the in-plane development length required to achieve a specified design strength by transferring load from the FRP to the anchorage via shear; or (III) transferring the force in the FRP laminate to another structural component where no development length is available. For the remainder of this paper, anchorages serving these purposes will be categorized as Type I, Type II, and Type III anchorages and are described in the following paragraphs.

Type I. Type I anchorages are often used at the termination of FRP sheets or plates, or sometimes throughout their entire length, to resist tensile forces normal to the plane of the FRP. An example condition is when the soffit of a beam is strengthened in flexure with FRP, and either plate-end debonding or intermediate flexural or flexural-shear crack induced (collectively referred to as I.C.) debonding is a concern. In this case, a Type I system is installed over/though the FRP to resist the normal forces as shown in Figure 1 and achieve a higher design strength. (For a thorough

description of FRP failure modes, the reader is referred to Teng et. al., 2002).

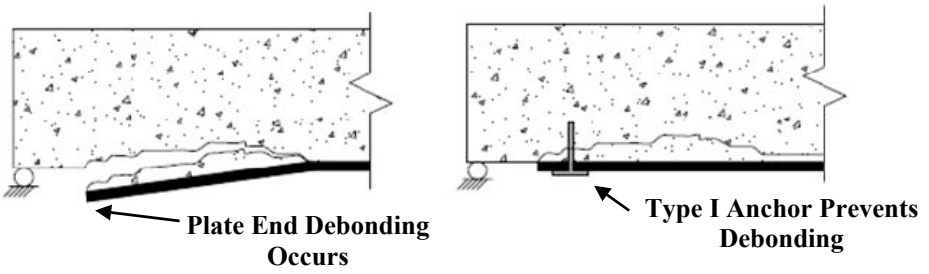


Figure 1: Type I Anchorage

Type II. Type II anchorages are used where insufficient space exists due to geometric conditions to allow the FRP to be developed to reach a specified design strength. In a Type II system, load is transferred in shear via bond between the FRP and anchorage system. This is distinguished from Type I anchorage because Type II anchorages do not include a mechanism to restrain plate-end or I.C. debonding. An example of this is a T-beam where an FRP U-Wrap (described later) is used for shear strengthening as seen in Figure 2. In this case, the beam flange requires the FRP to be terminated and prevents it from being fully developed. The installation of a Type II anchor in this situation would bond the end of the U-Wrap to the anchorage system and would result in a higher strength due to the increased bond transfer.

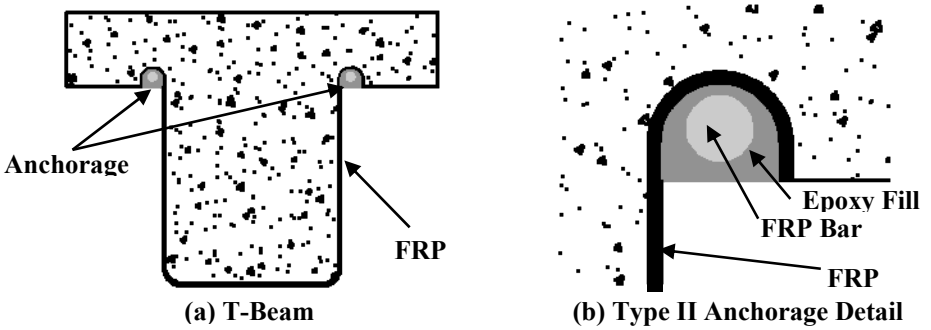


Figure 2: Example of Type II Anchorage on T-Beam

Type III. Type III anchorages are used in situations where the location of maximum FRP stress lies at sheet or plate end or near a change in direction in the fiber direction, such as the interface between two structural members. An example of this is vertical FRP strips installed on a concrete or masonry shear wall to increase flexural resistance. While Type III anchorages may include characteristics of Type I and Type II anchorages, Type III anchorages present a special and difficult challenge in that the FRP strengthening system can be considered to have no strength before their inclusion. While some Type III anchorages may have some debonding-preventing characteristics, they differ from Type I anchorages in that they must transfer the entire force in the FRP to another structural element instead of simply resisting the debonding normal force. Type III anchorages differ from Type II anchorages in that the demand on a Type II anchorage is less since some of the force is transferred along a "bonded length." Type III anchors do not benefit from a "bonded length."

Table 1: Summary and Categorization of Anchorage Systems

Type	System/Device	Study	Independent Anchorage Test?	Test Type	FRP Strengthening Application
I	Transverse Wrapping	Khan & Ayub 2010	No	-	Flexure of rectangular RC beams
		Pan et al. 2010	No	-	Flexure of rectangular RC beams
		Orton 2007	Yes	I, II	Flexure of RC beams with height transition
		Zhuo et. al 2009	No	-	Prestressed FRP strap
		Sadeghian et al. 2010	No	-	Flexure of eccentrically loaded RC columns
		Antonopoulos & Triantafillou 2003	No	-	Flexure and shear of RC beam-column joints
	90° Anchor Spike	Piyong et al. 2003	Yes	III	Flexure of RC slab with prestressed flexural FRP reinforcement
		Li & Chua 2009	No	-	Flexure of RC beam-column and beam-wall joints
		Orton 2007	Yes	I, II	Flexure of RC beams with height transition
		Sami et al. 2010	Yes	I, II & III	Representative testing only
		Teng et al. 2001	No	-	Flexure in RC cantilever slab
		Kim & Smith 2010	No	-	Analytical anchor model only
		Eshwar et al. 2003	Yes	III	Flexure of RC beams with curved soffits
I & II	FRP Strips	Ortega 2009	No	-	Shear in RC and PC girders
		Donchev & Nabi 2010	No	-	Flexure of RC slabs
		Antonopoulos & Triantafillou 2003	No	-	Flexure and shear of RC beam-column joints
	Steel/FRP Plates	Ortega 2009	No	-	Shear in RC and PC girders
		Ceroni et al. 2008	Yes	I, II	Representative testing only
	FRP Sandwich Plate	Ortega 2009	No	-	Shear in RC and PC girders
	Bolted U-Anchor/Angle	Nagy-György et al. 2005	No	-	Flexure and axial loads in RC shear walls
	After-Joint Plate	Ceroni et al. 2008	Yes	I, II	Representative testing only
	Steel Angle	Antonopoulos & Triantafillou 2003	No	-	Flexure and shear of RC beam-column joints
II	Type II U-Anchor	Beigay et al. 2010	No	-	In- and out-of-plane flexure in masonry shear wall
		Micelli et al. 2002	No	-	Shear in RC T-beams
		Khalifa et al. 1999	No	-	Shear in RC T-beams
		Ceroni et al. 2008	Yes	I, II	Representative testing only
	Longitudinal Chase	Kalfat & Al-Mahaidi 2010	Yes	I, II	Representative testing only
	Type II 180° Anchor Spike	Kim & Smith 2010	No	-	Analytical anchor model only
III	Type III 180° Anchor Spike	Sadone et al. 2010	Yes	I, II	Representative testing only
		Prota et al. 2005	No	-	Flexure/shear and axial loads in RC columns
	Bolted Angle	Foo et al. 2001	No	-	Flexure in RC shear wall
		Hall et al. 2002	Yes	I, II	Flexure in masonry shear wall
		Hiotakis 2004	No	-	Flexure in RC shear wall
		Hwang et al. 2004	No	-	Flexure in RC shear wall
	CHS Anchor	Hiotakis 2004	No	-	Flexure in RC shear wall
	Plate Angle/Pipe	Hall et al. 2002	Yes	I, II	Flexure in masonry shear wall
	Type III U-Anchor	Beigay et al. 2010	No	-	Flexure in masonry shear wall
		Teng et al. 2001	No	-	Flexure in RC cantilever slab

EXISTING FRP ANCHORAGE SYSTEM TYPES

A wide variety of innovative anchorage systems have been used for structural strengthening applications or have been subjected to representative physical testing. Different anchorage system types are described and categorized in the sections that follow. Studies from the literature that use each system type are presented in Table 1.

Anchor Spikes. Anchor spikes are strands of bundled fibers that have one end embedded in the composite matrix and the other end embedded in the concrete below or adjacent to the FRP sheet being anchored. Anchor spikes made from CFRP, GFRP, or steel have been reported in the literature. Anchor spikes fall into all three anchorage categories. 90º anchor spikes, which fall into the Type I category, are embedded in a hole drilled into the concrete substrate and through the FRP sheet. Their means of force transfer is primarily through resisting the tensile normal forces associated with debonding. 180º anchor spikes can be considered Type II or Type III depending on the strengthening application. When a 180º anchor spike is inserted through the flange of a T-beam and bonded directly to an FRP stirrup, it is being used as a Type II anchor. If a 180º anchor spike is used to anchor an FRP sheet on a cantilever beam at the point of maximum moment, it is being used as a Type III anchor. Types of anchor spikes are shown in Figure 3.

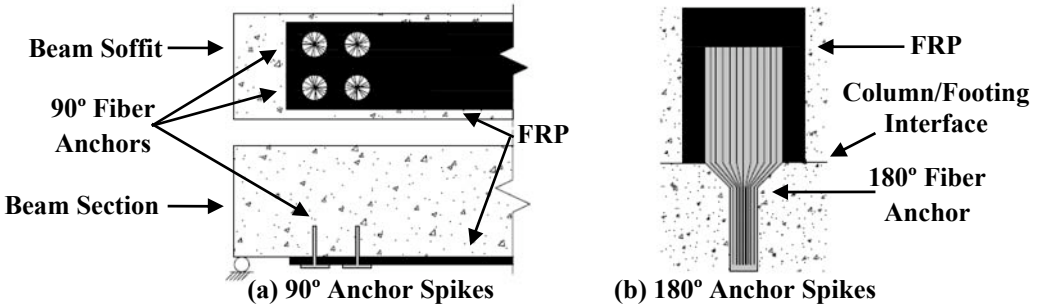


Figure 3: Types of Anchor Spikes

Transverse Wrapping. Transverse wrapping of flexural FRP reinforcement with shear or confining reinforcement, commonly referred to as a "U-Wrap", is an effective way to increase the debonding strain of the flexural FRP reinforcement. While detailed studies of the anchorage mechanics of transverse wrapping have been minimal, several studies have shown that they are an effective anchorage system. In fact, *ACI 440.2R-08* notes an improvement "of up to 30% increase in debonding strains has been observed." While transverse wrapping is typically not prestressed, a study by Zhuo et al. (2009) demonstrated a prestressed FRP strap that has potential for use as a transverse wrapping anchorage system.

FRP Strips. Anchoring at the sheet end with perpendicular strips of FRP is another method of anchorage. While this may seem similar to transverse wrapping, it can be distinguished because the strips do not provide a confinement effect. Because of this, the FRP strip anchorage must be loaded out-of-plane, or in other words, loaded in a direction other than that of the fibers, leading to an inefficient force transfer mechanism. While this type of anchorage has not been shown to be as effective as

other types, its major advantage is that the anchorage and strengthening materials are the same, allowing for easy construction and eliminating the potential for corrosion.

U-Anchors. U-Anchors increase the capacity of an FRP strengthening system by increasing the bonded area of FRP-to-concrete. U-Anchors are installed by cutting a groove into the concrete surface perpendicular to the FRP fiber direction at or near the end of an FRP sheet. The FRP sheet is then pressed into the groove and the remainder of the groove filled with polymer (see Figure 4). Increase in area is attributed to the FRP bond to the walls of the groove. In some cases, an FRP or steel rod is placed into the groove, although the inclusion of the rod serves only to ease the installation procedure and does not provide an increase in anchoring strength. Thus, inclusion of a rod in a U-Anchor groove is not necessary (Khalifa et al. 1999). U-Anchors have been used in Type II and Type III applications.

Longitudinal Chase. A study by Kalfat and Al-Mahaidi (2010) involved a "Longitudinal Chase" anchorage system, which is similar in behavior to a U-Anchor. Instead of anchoring the FRP sheet in a transverse groove at or near the plate end, a groove is cut in the concrete longitudinally, or in the fiber direction of the FRP, and filled with polymer (Figure 4). The inclusion of a bar in the groove is optional as its inclusion does not contribute to the strength of the anchorage system. Because FRP failure is rarely through the polymer matrix, the increased bond surface area provided by the walls of the chase allows for more force transfer along the length of the FRP.

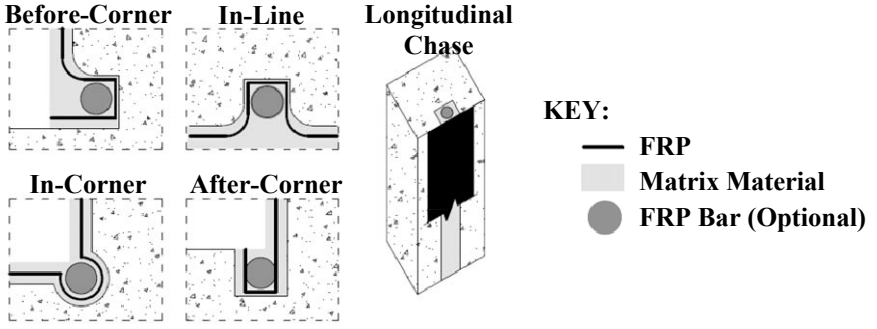


Figure 4: U-Anchors and Longitudinal Chase

Steel and FRP Plates. Steel and FRP plates have been used for several applications of FRP anchorage. The plates are usually placed at or near the FRP sheet end and bonded to the FRP. The plates are then either glued, or more often, bolted to the concrete surface. While the presence of the plates may help prevent debonding of the FRP sheet by resisting the normal debonding forces, their primary mode of load transfer is via shear between the plate and FRP. Therefore, plated anchorage devices can be considered to have both Type I and Type II anchorage properties. Detailing of plated anchorage systems varies widely in literature and often varies widely within a given study. Ortega (2009) studied plated anchorage systems used to anchor FRP U-Wraps on RC and PC T-beams at the web/flange interface. Plated devices included a continuous plate that spanned the length of the beam with bolts around the FRP U-Wrap strips, discontinuous plates that were bolted around the FRP strips, and plates that sandwich the FRP to transfer load in double shear. Ceroni et al. (2008) compared several glued and bolted plated anchorage systems through representative testing. In

this study, plates were used before and after a 90º joint for comparative purposes.

Steel Angles/Pipes. Steel angles have been used for FRP anchorage at 90º joints. Typically, the FRP is laid around the joint, the angle bonded to the FRP in the joint, and the angle bolted to the concrete either through or around the FRP sheet. Steel angles behave in a Type I & II manner and also can be used as a Type III anchorage system. Nagy-György et al. (2005) used a combination of a bolted angle and a U-Anchor in a Type III application. Despite wide use of steel angles as an FRP anchorage device, premature FRP failures due to local stress concentrations at the angle corner have resulted in limitations for their use.

Because of local stress concentrations developed in the FRP resulting from their steel angle anchorage devices, Hall et al. (2002) and Hiotakis (2004) developed similar alternative devices, both of which were used in Type III applications. The device used by Hall et al. involved a plate that was bolted to concrete after a 90º joint. Under this plate, a rounded angle or a quarter-section of pipe was placed immediately adjacent to the joint so that the FRP would lay tangent to the pipe or angle and cause the plate to bend as a cantilever about the line of the bolts. By placing the rounded angle or quarter-pipe at the joint, the stress concentrations are reduced. The system developed by Hiotakis, referred to as a "Cylindrical Hollow Section (CHS) Anchorage", involves a pipe or bar placed in the 90º joint with the pipe or bar anchored directly to the concrete using one of several bolt configurations. The Hiotakis system is currently protected by a U.S. patent. Detailing of the anchor bolts for this anchorage device must be carefully monitored to ensure they are not installed in the plastic hinge region of a member. This is an important consideration since Appendix D of *ACI 318-08* specifically excludes anchors in plastic hinge regions, and anchors qualified through *ACI 355.2-07* do not anticipate the level of crack widths typically developed in plastic hinge regions.

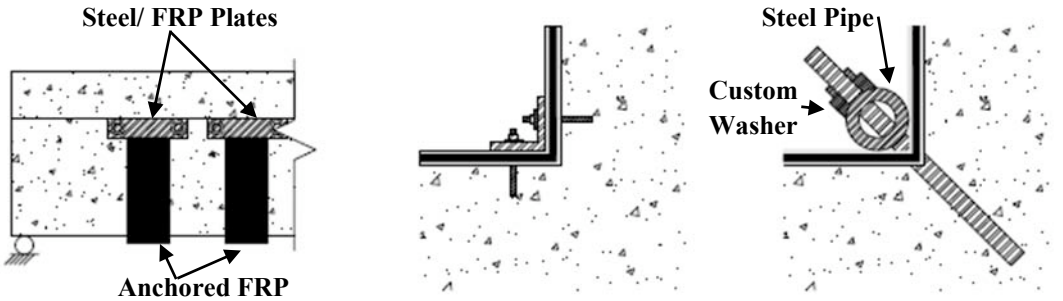


Figure 5: Plates, Angles, and CHS Anchorages

TESTING PROCEDURES FOR ANCHORAGE SYSTEMS

Most studies involving FRP anchorage systems involved tests that were one component of a larger strengthening system study, as indicated in Table 1. Also noted in the table are details about the FRP strengthening application studied. While these types of tests are very useful in demonstrating application-specific performances of these anchorage systems, the data they provide are difficult to use for design purposes

because of the complex variables that affect their response. As previously mentioned, *ACI 440.2R-08* requires that sufficient representative testing be performed before an anchorage system is used in field applications. Very little representative testing has been reported in literature, however, and most of the testing procedures reported have a limited range of applicability. Thus, the need exists for systematic, representative testing procedures based on the anchorage category. Further, these procedures should include enough applicable variables so that conclusions for design can be reached.

Type I and Type II anchorages should have similar testing procedures. With proper test design, the procedure may be duplicated for both monotonic or fatigue loadings. Testing procedures appropriate for Type I and Type II anchorages have been developed and reported by Hall et al. (2002), Teng et al. (2001), Ceroni et al. (2008), Kalfat & Al-Mahaidi (2010), Sadone et al. (2010), and Sami et al. (2010). Test procedures in Hall et al. (2002), Ceroni et al. (2008), and Sami et al. (2010) use double-sided specimens, which are attractive for use because of their initial loading symmetry. It is worth noting that while these tests have a simple design and testing procedure, they require that two sets of anchorages are tested to obtain one test result. Additionally, this testing procedure may tend to underestimate the ultimate strength of the anchorage in question. The test must be stopped when symmetry is lost in the test setup, which does not necessarily correspond to anchorage failure. Orton (2007) performed representative testing of Type I and Type II anchorages, but because the specimen construction and loading were designed to replicate a specific strengthening application, the data may not be applicable to other applications of the same type of anchorage.

Type III anchorage testing procedures can be similar to Type I and Type II procedures with the exception that the FRP-to-concrete bonded length between the anchorage and applied load must be zero. Any bonded length will transfer load to the bonded concrete, which will lead to an overestimation of the strength of the anchorage. Again, with proper test design the procedure may be duplicated for both monotonic or fatigue loadings. Very few representative testing procedures exist in literature for Type III anchorages. Studies by Eshwar et al. (2003) and Piyong et al. (2003) involving pullout tests for GFRP anchor spikes would be appropriate for Type III anchorage testing only if it is known that the bond between anchor spike and the anchored FRP is adequate.

CONCLUSION

Anchorage systems in existing literature have certainly shown that their presence can contribute significantly to the overall strength of an FRP strengthening system. Additionally, in the case of a Type III anchor, their presence is essential. Due to the limited amount of existing test results from independent anchorage tests, however, design of FRP strengthening systems containing anchorage systems becomes rather difficult. Therefore, it is recommended that future research establish a large database of simple anchorage tests, the results of which can be compared and correlated among large-scale FRP strengthening systems. While the many different applications of

anchorage systems each present their own challenges and limitations, the existence of a large database of simple test results will surely aid the development of new and improved anchorage systems and assist in the creation of design guidelines.

For example, data for Type I and Type II anchorages can be easily obtained through the creation of simple shear tests or a double-lap shear test. Important variables for Type I and Type II tests include, but are not limited to, bonded length of FRP to concrete between the anchorage and applied load, number of sheets anchored, applied load magnitude, width of FRP plate or sheet anchored, concrete substrate properties, and various other anchorage system-specific parameters that are dependent on anchorage design and detailing. Data from these tests could then be related to a control specimen with no anchorage system and compared to existing bond strength models to determine the strength enhancement resulting from the presence of the anchorage. Finally, results could be used to predict the strength of an FRP system used for large-scale strengthening, and the results used to prepare design guidelines.

Due to the nature of Type III anchorage systems, which do not benefit from a "bonded length" ahead of the anchorage system, a simple "pull-out" type test will suffice to obtain preliminary data. An example specimen for a Type III system test involves a concrete block onto which the anchorage system is installed. The FRP is then attached to the anchorage system and/or the concrete surface and an external force is applied to the FRP normal to the concrete surface. This creates a very simple test, and the only variables not involving anchorage detailing or concrete substrate properties would include applied load and number of sheets anchored. The results from this type of test would be immensely useful in determining a design strength for an FRP system needing Type III anchorage systems, although it must be noted that detailing at the joint is critical and should be evaluated further using representative testing of the entire FRP strengthening system.

REFERENCES

ACI Committee 318. (2008). "Building Code Requirements for Structural Concrete (ACI 318-08) and Commentary." American Concrete Institute (ACI), Farmington Hills, MI.

ACI Committee 355. (2007). "Qualification of Post-Installed Mechanical Anchors in Concrete and Commentary (*ACI 355.2-07)*." American Concrete Institute, Farmington Hills, MI.

ACI Committee 440. (2008). "Guide for the Design and Construction of Externally Bonded FRP Systems for Strengthening Concrete Structures (*ACI 440.2R-08)*," American Concrete Institute, Farmington Hills, MI.

Antonopoulos, C.P. and Triantafillou, T.C. (2003). "Experimental Investigation of FRP-Strengthened RC Beam-Column Joints," *Journal of Composites for Construction*, 7(1), 39-49.

Beigay, M., Young, D.T. and Gergely, J. "An Improved Composite Anchoring System," *QuakeWrap*, <http://www.quakewrap.com/frp%20papers/An-Improved-Composite-Anchoring-System.pdf>(7 Nov. 2010).

Brosens, K. and Van Gemert, D. (2001). "Anchorage of Externally Bonded Reinforcements Subjected to Combined Shear/Bending Action." *FRP Composites in Civil Engineering: Proceedings of the International Conference on FRP Composites in Civil Engineering*, 12-15 Dec. 2001, Hong Kong, China, 589.

Ceroni, F., Pecce, M., Matthys S. and Taerwe, L. (2008). "Debonding Strength and Anchorage Devices For Reinforced Concrete Elements Strengthened with FRP Sheets." *Composites: Part B*, 39, 429-441.

Donchev, T. and Nabi, P. (2010). "Non-Bolted Anchorage Systems for CFRP Laminates Applied for Strengthening of RC Slabs." *Proceedings of the 5th International Conference on FRP Composites in Civil Engineering*, CICE, 27-29 Sept. 2010, Beijing, China.

Eshwar, N., Ibell, T. and Nanni, A. (2003). "CFRP Strengthening of Concrete Bridges with Curved Soffits," *Proceedings of International Conference on Structural Faults and Repairs,* 1-3 July 2003, London, England.

Foo, S., Naumoski, N. and Cheung, M. (2001). "Research and Application of Seismic Retrofit Technologies in Canada." *RPS/AES/Technology Directorate*, Public Works & Government Services Canada, Hull, Quebec, Canada.

Galal, K. and Mofidi, A. (2009). "Strengthening RC Beams in Flexure Using New Hybrid FRP Sheet/Ductile Anchor System." *Journal of Composites for Construction*, ASCE, 13(3), 217-225.

Hall, J.D., Schuman, P.M. and Hamilton III, H.R. (2002). "Ductile Anchorage for Connecting FRP Strengthening of Under-Reinforced Masonry Buildings." *Journal of Composites for Construction*, 6(1), 3-10.

Hiotakis, S. (2004). "Repair and Strengthening of Reinforced Concrete Shear Walls for Earthquake Resistance Using Externally Bonded Carbon Fibre Sheets and a Novel Anchor System." MS Thesis, Carleton University, Ottawa, Ontario, Canada.

Hwang, S-J., Tu, Y-S., Yeh, Y-H. and Chiou, T-C. (2004). "Reinforced Concrete Partition Walls Retrofitted with Carbon Fiber Reinforced Polymer." *ANCER Annual Meeting: Networking of Young Earthquake Engineering Researchers and Professionals,* ANCER, 2004.

Kalfat, R. and Al-Mahaidi, R. (2010). "Investigation Into Bond Behaviour of a New CFRP Anchorage System for Concrete Utilising a Mechanically Strengthened Substrate." *Composite Structures*, 92(11), 2738-2746.

Khalifa, A., Alkhrdaji, T., Nanni, A. and Lansburg, S. (1999). "Anchorage of Surface Mounted FRP Reinforcement." *Concrete International: Design and Construction*, 21(10), 49-54.

Khan, A.A.R. and Ayub, T. (2010). "Effectiveness of U-Shaped CFRP Wraps as End Anchorages in Predominant Flexure and Shear Region." *Proceedings of the 5th International Conference on FRP Composites in Civil Engineering*, CICE, 27-29 Sept. 2010, Beijing, China.

Kim, S.J. and Smith, S.T. (2010). "Pullout Strength Models for FRP Anchors in Uncracked Concrete." *Journal of Composites for Construction*, ASCE, 14(4), 406-414.

Li, B. and Grace Chua, H.Y. (2009). "Rapid Repair of Earthquake Damaged RC

Interior Beam-Wide Column Joints and Beam-Wall Joints using FRP Composites." *Key Engineering Materials*, Vols. 400-402, 491-499.

Micelli, F., Annaiah, R.H. and Nanni, A. (2002). "Strengthening of Short Shear Span Reinforced Concrete T Joists with Fiber-Reinforced Plastic Composites." *Journal of Composites for Construction*, 6(4), 264-271.

Nagy-György, T., Moşoarcă, M., Stoian, V., Gergely, J. and Dan, D. (2005). "Retrofit of Reinforced Concrete Shear Walls With CFRP Composites." *Keep Concrete Attractive: Proceedings of the fib Symposium*, Hungarian Group of *fib*, 23-25 May 2005, Budapest, Hungary.

Ortega, C. (2009). "Anchorage and Bond Characteristics of Externally Bonded FRP Laminates Used for Shear Strengthening of RC and PC Girders," MS Thesis, Missouri University of Science and Technology, Rolla, MO, 232 pp.

Orton, S.L. (2007). "Development of a CFRP System to Provide Continuity in Existing Reinforced Concrete Buildings Vulnerable to Progressive Collapse." PhD Dissertation, University of Texas at Austin, Austin, Texas.

Pan, J., Leung, C.K.Y., and Luo, M. (2010). "Effect of Multiple Secondary Cracks on FRP Debonding From the Substrate of Reinforced Concrete Beams." *Construction and Building Materials*, 24(12), 2507-2516.

Piyong, Y., Silva, P.F. and Nanni, A. (2003). "Flexural Strengthening of Concrete Slabs by a Three-stage Prestressing FRP System Enhanced with the Presence of GFRP Anchor Spikes." *Proceedings of the International Conference Composites in Construction (CCC2003),* 239-244.

Prota, A., Manfredi, G., Balsamo, A., Nanni, A. and Cosenza, E. (2005). "Innovative Technique for Seismic Upgrade of RC Square Columns." *7th International Symposium on Fiber Reinforced Polymer for Reinforced Concrete Structures (FRPRCS-7)*, ACI, Kansas City, MO, Nov. 2005.

Sadeghian, P., Rahai, A.R. and Ehsani, M.R. (2010). "Experimental Study of Rectangular RC Columns Strengthened with CFRP Composites Under Eccentric Loading." *Journal of Composites for Construction*, ASCE, 14(4), 443-450.

Sadone, R., Quiertant, M., Chataigner, S., Mercier, J. and Ferrier, E. (2010). "Behaviour of an Innovative End-Anchored Externally Bonded CFRP Strengthening System Under Low Cycle Fatigue." *Proceedings of the 5th International Conference on FRP Composites in Civil Engineering*, CICE, 27-29 Sept. 2010, Beijing, China.

Sami, Q., Ferrier, E., Michel, L., Si-Larbi, A. and Hamelin, P. (2010). "Experimental Investigation of CF Anchorage System Used for Seismic Retrofitting of RC Columns." *Proceedings of the 5th International Conference on FRP Composites in Civil Engineering*, CICE, 27-29 Sept. 2010, Beijing, China.

Teng, J.G., Cao, S.Y. and Lam, L. (2001). "Behaviour of GFRP-Strengthened RC Cantilever Slabs." *Construction and Building Materials,* 15(7), 339-349.

Teng, J.G., Chen, J.F., Smith, S.T. and Lam, L. (2002). *FRP-Strengthened RC Structures.* John Wiley & Sons, Ltd., West Sussex, England.

Zhuo, J., Wang, F. and Li, T. (2009). "Application of FRP Strap in an Innovative Prestressed Method." *Journal of Materials in Civil Engineering*, ASCE, 21(4), 176-180.

Analysis of RC Structures with Carbon-Nanofiber Concrete

T Ravi S Mullapudi[1], and Ashraf Ayoub[2]

[1]PhD Candidate, University of Houston, Department of Civil and Environmental Engineering, W103 Engineering Building 2, Houston, TX 77204, Tel: (281) 217-3936 Fax: 713-743-4260, tsmullapudi@uh.edu
[2]Associate Professor, University of Houston, Department of Civil and Environmental Engineering, N107 Engineering Building 1, Houston, TX 77204-4003, Tel: 713-743-4285, Fax: 713-743-4260, asayoub@uh.edu

ABSTRACT

Concrete has been used as the major construction material for many years in the field of civil engineering because of its high compressive strength and constructability. In order to restrict the growth of micro cracks, Carbon-Nanofibers (CNF's) were added to the concrete mix. The concentration of CNF in concrete mix also yields higher strength and ductility. Uniaxial compression tests on CNF concrete were conducted to find the best CNF concentration. To evaluate the performance of CNF concrete, experiments were conducted at the University of Houston (UH) and an inelastic non-linear fiber beam element with bending, shear and axial force interaction for the analysis of reinforced concrete structures was developed and evaluated to correlate with the experimental results.

INTRODUCTION

The use of carbon nanofiber composites began with the discovery of carbon nanotubes in the late 1980s (Lau and Hui 2002). Carbon nanotubes are over 100 times stronger than steel and only one-sixth of the weight in addition to its high thermal and electrical conductivities (Lau and Hui 2002). These properties make carbon nanotubes extremely attractive for engineering materials.

Since the 1990s, researchers have been adding carbon nanofibers (CNF) to cement paste (containing no aggregate), mortar (containing fine aggregate) and concrete (containing fine and coarse aggregate) (Chung 2000). The addition of CNF to cement-based materials has many advantageous mechanical and electrical properties including increased strength, ductility and conductivity (Chen and Chung 1993, Li et al. 2004, Li et al 2006, Li et al 2007). The most difficult issue during CNF concrete production is dispersion of the CNF. Well dispersed CNF results in uniform calcium-silicate-hydrate (CSH) gel formation, which improves the structural and electrical properties of the concrete (Chung 2005). It was discovered that CNF disperse better in Self-Consolidated Concrete (SCC) (Gao et al 2009). A carbon nanofiber self-consolidating reinforced concrete (CNFSCRC) column was built and tested under a reversed cyclic load (Howser 2010).

SHEAR-BASED FIBER ELEMENT FORMULATION

Shear-based fiber beam element with Timoshenko type displacement and force formulations were proved accurate in simulating the behavior of columns (Mullapudi and Ayoub 2010). So here the same approach was used for the analysis of Carbon-nanofiber reinforced concrete columns. Monotonic and cyclic constitutive relationships were modified based on the uni-axial stress strain relations derived by Gao et al (2009).

Axial force N; shear force V and section moment M (Fig. 1 b) are derived from the known kinematic variables axial strain ε_x, shear strain γ_{xy} and section rotation β (Fig. 1 a) as described by Mullapudi and Ayoub (2010).

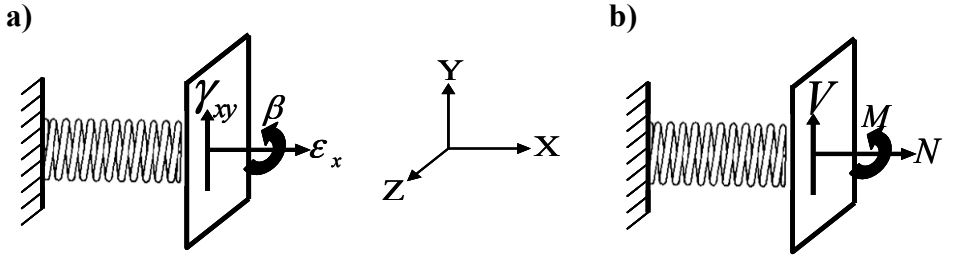


Fig. 1 (a) Section Deformations and (b) Section Forces

ORTHOGONAL STRESS STATE DETERMINATION

COMPRESSION-COMPRESSION REGION

Current research uses the Vecchio's (1992) simplified version of Kupfer et al. (1969) biaxial compression strength equation. The concrete compressive strength increase in the lateral direction depends on the confining stress in the orthogonal direction. Strength enhancement and increase in ductility are dependent on the biaxial compressive stresses. Concrete in compression exhibits lateral expansion and increase in Poison ratio. An upper limit of 0.5 has been considered for Poison ratio.

TENSION-COMPRESSION REGION

In this case, the uniaxial strain of concrete $\bar{\varepsilon}_1$ in principal direction 1 is in tension, and the uniaxial strain $\bar{\varepsilon}_2$ of concrete in principal direction 2 is in compression. Due to this condition, the uniaxial concrete stress σ_1 in direction 1 is calculated from $\bar{\varepsilon}_1$, and is not a function of the perpendicular concrete strain $\bar{\varepsilon}_2$. The compressive strength in direction 2, σ_2 will soften due to tension in the orthogonal direction. Hsu and Zhu (2002) derived a softening equation in the tension-compression region, which is implemented in the current model (Fig. 2). Based on panel testing as proposed by Hsu et al. (1995), Belarbi and Hsu (1995) also developed

a similar expression based on the softened concrete constitutive laws. The lateral tensile stress reduces the compressive strength in the orthogonal direction. The equation for compressive strength reduction factor proposed by Hsu and Zhu (2002) is:

$$\zeta = \left(\frac{5.8}{\sqrt{f_c^{'}(MPa)}} \le 0.9 \right) \left(\frac{1}{\sqrt{1+400\bar{\varepsilon}_1}} \right) \left(1 - \frac{|\alpha_{r1}|}{24^{\circ}} \right), \qquad (1)$$

The softening coefficient ζ value is limited to 0.9 because the uni-axial concrete compressive strength $f_c^{'}$ is calculated from standard cylinder tests, while from the panel experiments at the University of Houston, it was observed that concrete strength does not reach $f_c^{'}$; the reasons for this are due to size effect, loading rate, and shape factor, which have a significant effect on concrete compressive strength $f_c^{'}$. The ultimate stress in the orthogonal direction is therefore $\zeta f_c^{'}$ at a softened strain $\zeta\varepsilon_0$ (Fig. 2), where ζ is the softening coefficient and α_{r1} is the deviation angle in degrees. This is the difference between the applied stress angle α_1 and the rotating angle α_r; $\bar{\varepsilon}_1$ represents the lateral tensile strain while ε_0 is the concrete strain at peak compressive strength $f_c^{'}$, and $\zeta f_c^{'}$ is the softened concrete compressive strength.

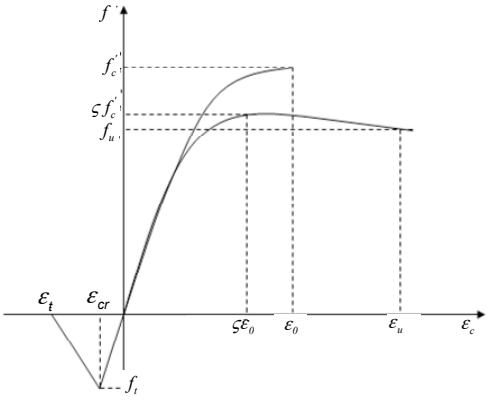


Fig. 2 Stress-Strain curve with softening

TENSION-TENSION REGION

In the current model, tensile strength is not affected by its orthogonal compressive or tensile stresses. Always the tensile strength is equal to the uniaxial tensile strength at cracking and tension stiffening is considered only after cracking.

ORTHOTROPY WITH UNIAXIAL STRESS STATE

The concrete model is simplified with plane stress orthotropic assumption. The model has perpendicular planes of elastic symmetry 1 and 2 with the local principal axes normal to these planes of symmetry.

The stresses in the orthogonal directions are:

$$\sigma = D_{LO}\varepsilon \tag{2}$$

where σ is the local stress vector, ε is the local strain vector and D_{lo} is the local material stiffness matrix in the principal direction (Chen 1976).

RC structures are considered orthotropic materials with axes oriented at an angel θ between the principal and x-axes. The rotational matrix R is introduced as:

$$R = \begin{bmatrix} \cos^2\theta & \sin^2\theta & \cos\theta\sin\theta \\ \sin^2\theta & \cos^2\theta & -\cos\theta\sin\theta \\ -2\cos\theta\sin\theta & 2\cos\theta\sin\theta & \cos^2\theta - \sin^2\theta \end{bmatrix} \tag{3}$$

The orthotropic stiffness matrix in global direction D_{gl} is:

$$D_{gl} = R^T D_{lo} R \tag{4}$$

The sectional stiffness $K_{Section}$ can be formulated by coupling the axial, shear and bending terms in $D_{gl.}$

STIRRUP CONSIDERATION

Transverse strains are internal variables determined by imposing equilibrium at each fiber between concrete and vertical steel stirrups. Transverse strains are not known in advance and due to the non-linear behavior of the concrete and steel, an iterative procedure is needed to satisfy the equilibrium in the transverse direction (Fig. 3), following the procedure proposed by Petrangeli et al. (1999).

$$\sigma^i_{y,c} A^i_{y,c} + \sigma^i_{y,s} A^i_{y,s} = 0 \tag{5}$$

where $\sigma^i_{y,c}$, $\sigma^i_{y,s}$ are concrete and steel stresses in the transverse direction at fiber i, and $A^i_{y,c}$, $A^i_{y,s}$ represents the areas of concrete and steel in the transverse direction at fiber *i*.

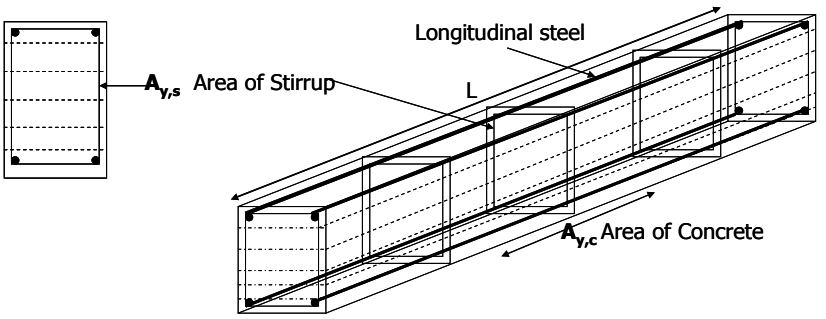


Fig. 3 Fiber element with stirrup

STIFFNESS AND FORCE RESULTANTS

The total stiffness of the section is the sum of concrete and steel stiffness, and is evaluated as follows.

$$K_{Section} = \sum_{1}^{nC} (K_{Section})_C + \sum_{1}^{nS} (K_{Section})_S \quad (6)$$

where the subscripts C, S denotes the parameters related to concrete and steel respectively, nC and nS are the number of concrete and steel fibers in the section and $K_{Section}$ is the section stiffness.

The total force of the section is the sum of concrete and steel forces in the respective direction, and is evaluated as

$$F_{Section} = \sum_{1}^{nC} (F_{Section})_C + \sum_{1}^{nS} (F_{Section})_S \quad (7)$$

where $F_{Section}$ is the section force.

CORRELATIONS WITH EXPERIMENT

SIMULATION OF ABOUTAHA ET AL. (1999) COLUMN SC3

The model was calibrated to simulate the behavior of a half scale cantilever frame column (Column SC3) tested by Aboutaha et al. (1999) at the University of Texas. The column has a length-depth ratio of 2.67.

The width of the specimen is 914.4 mm (36 in.), and its depth is 457.2 mm (18 in.). The longitudinal reinforcement consists of two layers of eight No.8 bars, uniformly spaced along each side of the width of the column with a concrete cover of 38 mm (1.5 inches). No. 3 steel stirrups are provided with a spacing of 406.4 mm (16 inches). The column is tested without axial loads.

A concrete compressive strength of f_c' = 21.9 MPa (3.2 ksi) was used to analyze the reinforced concrete column. A yield stress of longitudinal and transverse reinforcement of f_y = 434 MPa (63.0 ksi) and f_y = 400 MPa (68.0 ksi), respectively, was used in the analysis. The Young's modulus of concrete and steel are E_c = 21900 MPa (3200 ksi) and E_s = 200,000 MPa (29,000 ksi) respectively.

Column SC3 was the control specimen and was tested under cyclic uni-axial bending along the weak axis. The currently developed shear model was used to simulate the experimental cyclic force-displacement response, as shown in Fig. 4 and Fig. 5. The flexural element (Fig. 4) overestimated the shear capacity and did not

capture the pinching behavior well, but the shear element (Fig. 5) estimated well the energy dissipation and shear capacity. Column SC3 was reinforced with a very small amount of transverse steel (0.096%), and because of this small confinement, the transverse steel yielded early, and pinching occurred, which resulted in shear degradation.

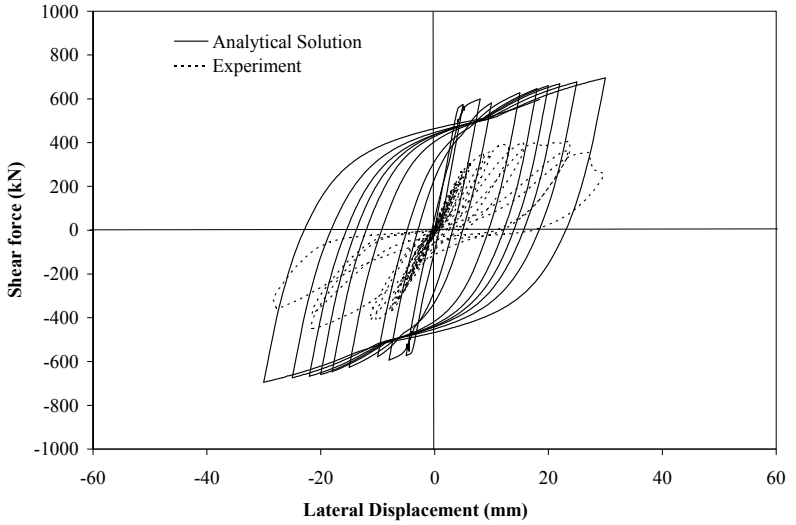


Fig. 4 Cyclic shear force displacement comparison with experiment and flexural element

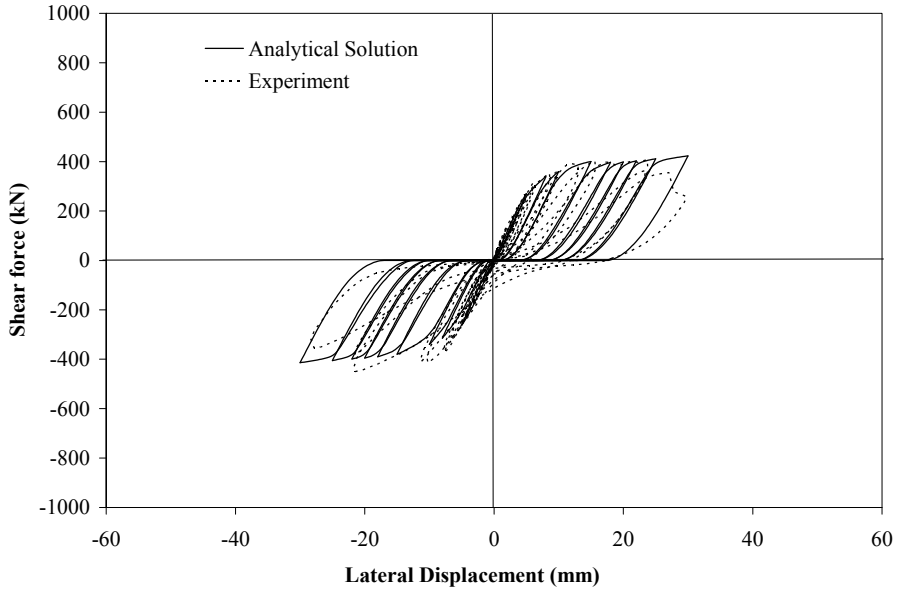


Fig. 5 Cyclic shear force displacement comparison with experiment and shear element

SIMULATION OF XIAO AND MARTIROSSYAN (1998) COLUMN HC4-8L 16-T6-0.2P

As shown in Table 1, six mixtures of Self Consolidated Concrete (SCC) were studied by Gao et al (2009) and used for the analysis of the column tested by Xiao and Martirossyan (1998) at the University of Southern California, Los Angeles. The binder weight is the total weight of cement and CNF. CNFSCC07-LO, CNFSCC10-LO, CNFSCC15-LO, CNFSCC20-LO and CNFSCC25-LO denote self-consolidating concrete containing the CNF PR-19- XT-LHT-OX in amounts of 0.7%, 1.0%, 1.5%, 2.0% and 2.5% by volume of binder, respectively.

The peak compressive strength varies as follows (Table 2): CNFSCC10-LO > CNFSCC15-LO > SCC > CNFSCC07-LO > CNFSCC25-LO > CNFSCC20 -LO and is increased 21.4% compared to plain SCC when the CNF concentration is 1.0%. This indicates the threshold of the concentration is around 1.0% and gives higher energy dissipation.

Table 1 Mixing proportions

Mix	Carbon nanofiber (vol% binder)	Water (kg m^{-3} concrete)	Cement (kg m^{-3} concrete)	Coarse aggregate (kg m^{-3} concrete)	Fine aggregate (kg m^{-3} concrete)	High-range water reducer (fl.oz./cw)	Antifoam (fl.oz./cw)
SCC	0	191	480	901	1005	11	0
CNFSCC07-LO	0.7	191	478	902	1008	7	11
CNFSCC10-LO	1	191	478	902	1008	11	11
CNFSCC15-LO	1.5	191	478	902	1008	19	11
CNFSCC20-LO	2	191	478	902	1008	23	11
CNFSCC25-LO	2.5	191	478	902	1008	35	11

Table 2 Carbon-nanofiber concrete destructive properties

Concrete	Strength MPa	Peak strain ε_0
SCC	45.5	0.0017
CNFSCC07-LO	44.7	0.0018
CNFSCC10-LO	55.2	0.0025
CNFSCC15-LO	51.2	0.0023
CNFSCC20-LO	43.8	0.0022
CNFSCC25-LO	44.3	0.0023

An axial load of 1068 kN (240 kip) was applied constantly on the column. Rotations were fixed at the column bottom and top so that the column deformed anti-symmetrically with respect to the mid-height under combined axial and lateral loading. In the numerical analysis, the column was divided into several finite elements until convergence was achieved. Column HC4-8L16-T6-0.2P had low shear reinforcement ($\rho_s = 1.63\%$), and was analyzed under monotonic uni-axial bending.

The width of the column section is 254 mm (10 in.), and its depth is also 254 mm (10 inches). The longitudinal reinforcement consists of eight No. 16 (15.9 mm (0.63-inch) diameter) bars, uniformly spaced along the perimeter, with a clear cover of 13 mm (0.51 inches). No. 6 (6.4 mm, 0.25-inch diameter) steel stirrups are provided with a spacing of 51 mm (2 inches).

Concrete compressive strengths and concrete strains at peak strength were taken from the test results of Gao et al (2009) which are given in Table 2. The ultimate strain of concrete was taken same for all types of mixtures for this example but actually the ultimate strain will be higher for the concrete with CNF. A yield stress f_y = 510 and 449 MPa (74 and 65.12 ksi) is being used for the longitudinal and transverse reinforcements. Young's modulus of concrete and steel are E_c = 45,500 MPa (6600 ksi) and E_s = 200,000 MPa (29,000 ksi), respectively.

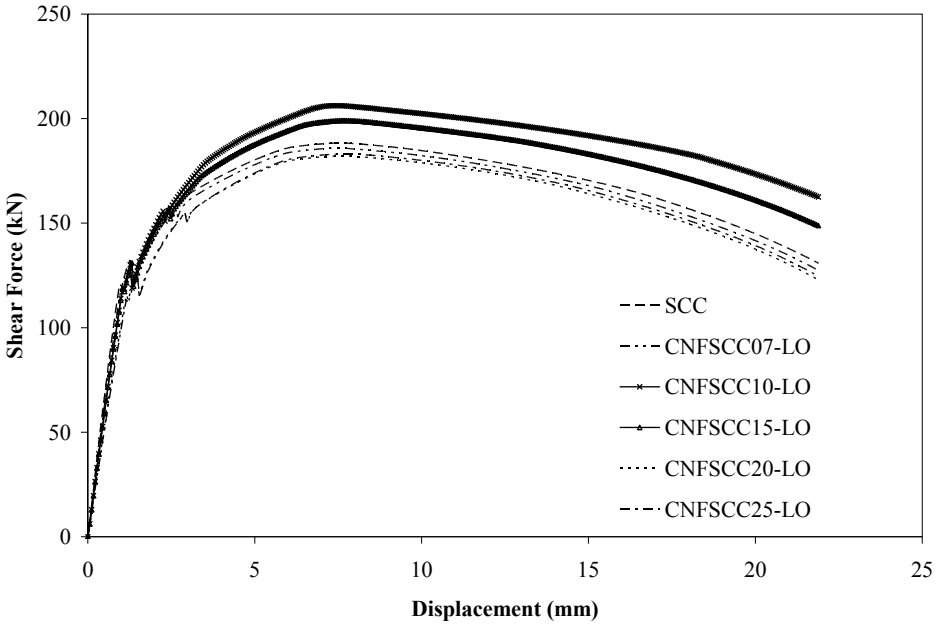


Fig. 6 Load-displacement relation of CNF with different mixtures

As shown in Fig. 6, the shear resistance of the column is in order of CNFSCC10-LO > CNFSCC15-LO > SCC > CNFSCC07-LO > CNFSCC25-LO > CNFSCC20 –LO. Shear resistance was increased 9% compared to plain SCC when the CNF concentration is 1.0%. Longitudinal and transverse reinforcement yielded early for the column made up of SCC compared to the column made up of CNFSCC10-LO. The column failed in shear after core degradation of the concrete.

CONCLUSIONS

This work represents a new approach to the numerical analysis of structures made up of non-linear carbon- nanofiber (CNF) concrete. A Fiber beam element was developed to analyze the CNF structure with the incorporation of mechanisms of shear deformation and strength. The emphasis of the paper is on the evaluation of the

effect of orthotropic model parameters to account for shear sensitive structures and the action of transverse reinforcement. The section deformations are determined from the strain state using the classical plane section hypothesis. The proposed model is able to capture the interaction between axial, flexural, and shear responses. The results of a numerical correlation with the experimental results of a bridge pier section show that the model is able to capture the shear failure and provides reasonable results.

REFERENCES

Aboutaha, R.S., Engelhardt, M.D., Jirsa, J.O., and Kreger, M.E., 1999, "Rehabilitation of Shear Critical Concrete Columns by Use of Rectangular Steel Jackets," *ACI Structural Journal*, V. 96, No.1, Jan.-Feb., pp.68-78.

Belarbi, A. and Hsu, T.T.C. "Constitutive Laws of Softened Concrete in BiaxialTension-Compression", *Structural Journal, American Concrete Institute*, Vol 92, No 5, 1995, pp.562-573.

Chen, W.F. "Plasticity in reinforced concrete". MCGraw-Hill Book Co.,New Yourk, N.Y, 1976

Chen, Pu-Woei, and Chung, D. D. L. "Concrete reinforced with up to 0.2 vol% of short carbon fibres." *Composites,*Vol. 24, No. 1, 1993, pp.33-52.

Chung, D. D. L. "Cement-matrix composites for smart structures." *Smart Materials and Structures,*Vol. 9, No. 4, 2000, pp.389-401.

Chung, D. D. L. "Dispersion of Short Fibers in Cement." *Journal of Materials in Civil Engineering*, ASCE,Vol. 17, No. 4, 2005, pp.379-383.

Gao, D., Strum, M. and Mo, Y. L., "Electrical resistance of carbon-nanofiber concrete." *Smart Materials and Structures,*Vol. 18, No. 9, 2009, pp.1-7.

Howser, R., "Behavior Of Steel Fibers and Carbon Nanofibers In Shear-Critical Reinforced Concrete Columns", *MS Thesis*, Department of Civil Engineering, University of Houston, 2010.

Hsu, T.T.C., Zhu R.R.H, "Softend Membrane Model for Reinforce Concrete Elements in Shear", *Structural Journal, American Concrete Institute* , Vol 92, No 5, 2002, pp.460-469.

Hsu, T.T.C., Belarbi, A., and Pang, X., "A Universal Panel Tester, Testing and Evaluation" *Journal, American Society for Testing and Materials*, Vol 23, No 1, 1995, pp.41-49.

Kupfer, H. B., Hildorf, H. K., and Rusch, H.. "Behavior of concrete under biaxial stresses." *ACI J.*, Vol. 66, No. 8, 1969, pp.656–666.

Lau, K. and Hui, D., "The revolutionary creation of new advanced materials--carbon nanotube composites." *Composites: Part B,*Vol. 33, No. 4, 2002, pp.263-277.

Li, H., Xiao, H., Yuan, J. and Ou, J., "Microstructure of cement mortar with nano-particles." *Composites Part B: Engineering*, Vol. 35, No. 2, 2004, pp.185-189.

Li, H., Zhang, M. and Ou, J., "Abrasion resistance on concrete containing nano-particles for pavement." *Wear*, Vol. 260, No. 11-12, 2006, pp.1262-1266.

Li, H., Zhang, M. and Ou, J., "Flexural fatigue performance of concrete containing nano-particles for pavement." *International Journal of Fatigue*, Vol. 29, No. 7, 2007, pp.1292-1301.

Mullapudi, T.R.S., Ayoub, A., "Modeling of the Seismic Behavior of Shear-Critical Reinforced Concrete Columns", *Journal of Engineering Structures*, Vol. 32, No.11, 2010, pp. 3601-15.

Petrangeli, M.; Pinto, P. E.; and Ciampi, V., "Fiber Element for Cyclic Bending and Shear of R/C Structures, Part I: Theory," *Journal of Engineering Mechanics*, ASCE, Vol. 125, No. 9, Sept.1999, pp. 994-1001.

Pyrograf Products, Inc. 2009 *www.pyrografproducts.com*

Vecchio, F.J. "Finite element modeling of concrete expansion and confinement." *J. Struct. Engg*, ASCE, Vol. 118, No. 9, September 1992, pp. 2390-2405.

Xiao, Y., and Martirossyan, A., 1998, "Seismic Performance of High-Strength Concrete Columns," *Journal of Structural Engineering*, ASCE, Vol. 124, No. 3, pp. 241-251.

Experimental and Analytical Studies of Hospital Piping Assemblies Subjected to Seismic Loading

Arash E. Zaghi[1], E. "Manos" Maragakis [2], Ahmad Itani[3], and Elliott Goodwin[4]

[1] Department of Civil and Environmental Engineering, University of Nevada, Reno, MS 0258, Reno, NV 89557-0258; PH (775) 327-5323; FAX (775) 784-4466; email: esmailiz@unr.edu
[2] College Engineering, University of Nevada, Reno, MS 0258, Reno, NV 89557-0258; PH (775) 784-6937; FAX (775) 784-1390; email: maragaki@unr.edu
[3] Department of Civil and Environmental Engineering, University of Nevada, Reno, MS 0258, Reno, NV 89557-0258; PH (775) 784-4379; FAX (775) 784-4466; email: itani@unr.edu
[4] PeopleSpaces Design Group, Inc, 901 Jefferson Street, No. 104, Oakland, CA 94607; PH (925) 413-6896; email: elliott.goodwin@gmail.com

ABSTRACT

Post-earthquake functionality of essential facilities, like hospitals, relies heavily on operation of its nonstructural components such as piping systems, fire suppressors, elevators, and medical equipments. This paper presents the findings from experiments performed on welded and threaded hospital piping subassemblies, with and without cable braces, subjected to various intensities of equivalent inter-story drift. The subassemblies were tested between a stationary frame and a biaxial shake table with an input motion compatible with ICC-ES AC156. A simplified computational model was developed in SAP2000 and calibrated with the experimental data. The model was used to investigate the dynamic characteristics of the piping subassemblies. The effective stiffness of the cable bracing system was found from the computational model to be approximately 10% of full stiffness due to initial looseness that typically exists in piping bracings.

INTRODUCTION

In recent earthquakes, nonstructural components of hospitals and medical facilities have suffered severe damage, consequently interrupting the functionality of these facilities (OSHPD 2010). The 1971 San Fernando Earthquake caused excessive damage to many hospitals and medical facilities, which led to evacuation of four of the eleven damaged medical facilities in the area (Wasilewski 1998). Due to this unacceptable performance, the State of California passed the Hospital Seismic Safety Act in 1973, which requires medical facilities to remain operational after earthquake events.

The costs of repair and replacement of non-residential buildings after the Northridge earthquake was $6.3 billion, with only $1.1 billion due to structural damage (Kircher 2003). Immediately after this earthquake, 88% of the hospital beds in the damaged area (13 hospitals) had to be evacuated because of nonstructural damage such as elevator failure, water damage, etc. (Ayres and Phillips 1998). Hospitals built in accordance with the 1973 Hospital Act were successful in resisting structural damage. However, damage to nonstructural components (plumbing, ceiling systems, etc.) in post 1973 construction was still extensive, emphasizing the urgent need to better understand the general seismic behavior of these systems and specifically that of piping systems.

In an earthquake, inadequately or improperly restrained piping systems may suffer damage as a result of large differential movement of the system or from impacts with adjacent structural and nonstructural components. Several entities have provided seismic restraining guidelines and design provisions for piping systems and other nonstructural components: the National Fire Protection Association has had seismic restraint guidelines since 1939 (NFPA 2007); the Seismology Committee of the Structural Engineers Association of California (SEAOC) has published seismic restraint guidelines for fire sprinkler piping since 1959 (SEAOC Blue Book 2006); and the Sheet Metal Industry Fund of Los Angeles published the Guidelines for Seismic Restraint of Mechanical Systems in 1976 (SMACNA 2008) to restrict the movement of piping systems. As one of the most recent efforts, American Lifeline Alliance, a partnership between the Federal Emergency Management Agency (FEMA) and the American Society of Civil Engineers (ASCE), has published Seismic Design and Retrofit of Piping Systems (ALA 2002).

This paper presents the results of a series of experimental and analytical studies of typical hospital piping assemblies that was conducted at the Large Scale Structure Laboratory of the University of Nevada, Reno. Based on the results of these experiments, a simplified computational model was developed as part of this study using SAP2000 finite element analysis packages (CSI 2009).

EXPERIMENTAL INVESTIGATION

Welded and threaded piping assemblies were subjected to a series of simulated ground motions using a biaxial shake table at the *NEES Equipment Site* at the University of Nevada, Reno. These experiments were conducted on piping systems with and without seismic cable restrainers.

Test Setup. The piping assemblies were comprised of two water heaters, one heat exchanger, three riser branches, and horizontal runs. The assembly was fixed on the shake table and hung from, or restrained to, a stationary frame that was attached to the laboratory floor (Fig. 1a and 1b). The piping assemblies were tested under horizontal seismic excitations, allowing investigation of the response of the piping systems to the imposed inter-story drifts expected to occur between adjacent floors of a multistory building. This test setup was capable of imposing realistic differential inter-story displacements on the piping assembly; however, since the frame used to suspend the piping assembly was fixed on the lab floor, the accelerations were not representative of actual field responses in which the floors supporting a piping system also respond to the ground excitation. A computational model was developed to study the response characteristics of the piping assembly and their importance on the assembly's response to realistic inter-story drifts. This model was calibrated using the experimental results.

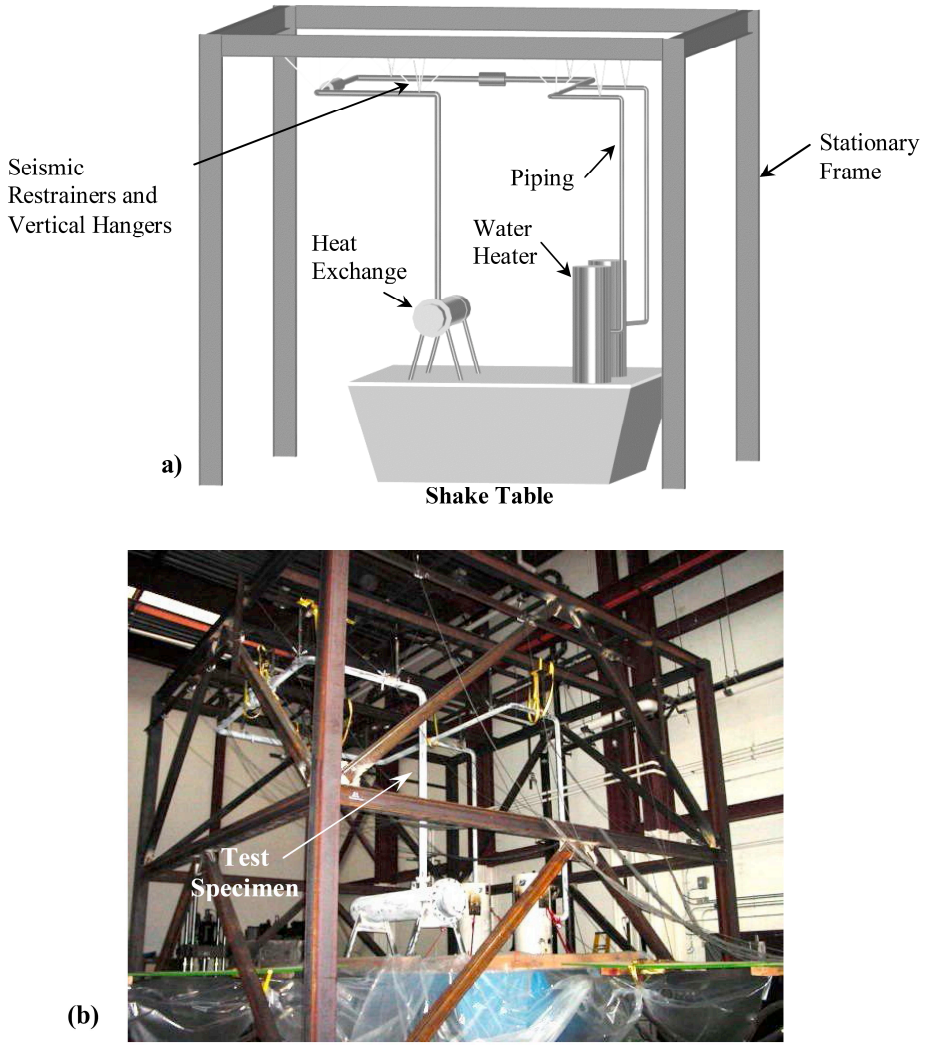
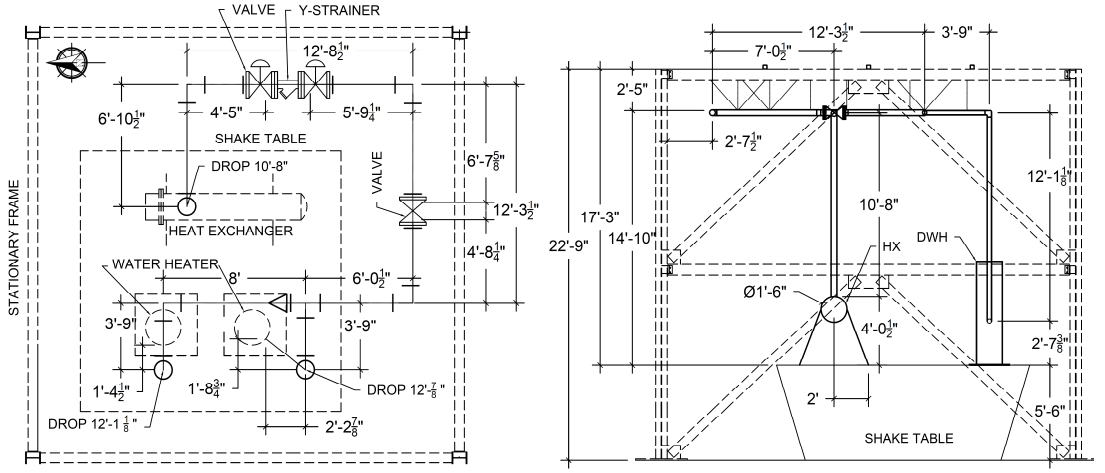


Figure 2. Experimental Setup a) Schematic of the Setup, b) Final Setup.

Piping Assembly Test Specimens. In consultation with California Office of Statewide Health Planning and Development (OSHPD) engineers, a partial system of hospital piping was selected to resemble a piping configuration used in the University of California, Davis Medical Center. The system was slightly modified to accommodate the dimensions and geometrical restrictions of the shake table. The system was tested with welded and threaded connections in separate test specimens with the same geometry, valves, and bracing layout.

Figures 2 and 3 show the plan and elevation view of the piping layout and major components. The piping assembly was made up of 3" and 4" schedule 40 ASTM A53 grade-B black steel pipe with outer diameter and thickness of 3.5 in and 4.5 in, and 0.216 in and 0.237 in, respectively. The specimen included a heat exchanger and two water heaters that were attached to the shake table. The water heaters were connected to the 3" pipes through four-bolt flanged connections. The heat exchanger and all valves were connected to the 4" pipes through eight-bolt flanged connections. A combination of one y-strainer (61 lbs) between two gate valves (83 lbs/valve) and a separate check valve (80lbs) were installed on the horizontal run.



(a) **(b)**

Figure 2. a) Plan View of Piping Subassembly, b) Elevation View of Piping Subassembly.

In the welded assemblies, all fittings, including the flanges and elbows, were made of forged steel. The fittings on the threaded assemblies were made of cast iron. The pipes with threaded joints were secured with enough torque to engage all of the threads in the fitting. The pipes were filled with water under hydrostatic pressure prior to the experiment to account for the additional mass of water and to detect any leakage in the system.

Hangers and Seismic Restraining. Each of the two test assemblies (threaded and welded) was tested with and without seismic restraining. Cable restrainers were used as seismic bracings as shown in Figure 3. Cable restrainers were originally designed to restrain displacements of isolated systems, but they have shown to be a preferred pipe restrainer system because of their effectiveness and ease of installation (Manson

2009). The restrainer cables used in the test setup were made of ⅛-in diameter galvanized 7 x 19 (number of strands x wires per strand) aircraft grade steel with a specified minimum break strength of 1700 lb. The vertical hanger rods were of two sizes: ⅝-in diameter all-thread rod for supporting the 4" pipe, and ½-in diameter all-thread rod for supporting the 3" pipe. The vertical hanger rods were braced laterally along their length with a 1⅝-in square, 12-gauge strut to prevent buckling of the hanger rods.

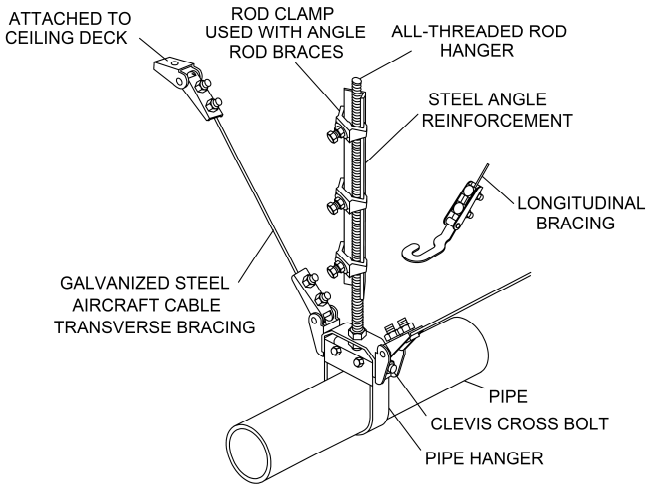


Figure 3. Seismic Bracing Details.

Of a total of eleven vertical support points, seven were used to attach cable restrainers and four were used only as hanger points. Two of the seven restraining points had cable restrainers in both the longitudinal and lateral directions. Figure 4 shows the bracing layout. In this figure, the letter "H" designates a point of vertical support (hanger) and the letter "B" tags a seismic restraining point. For unrestrained piping assemblies, all of the cable restrainers, the strut braces around the hanger rods, and the cross bolts in clevises (shown in Fig. 3) were removed to reflect the unbraced condition of piping systems seen in the field.

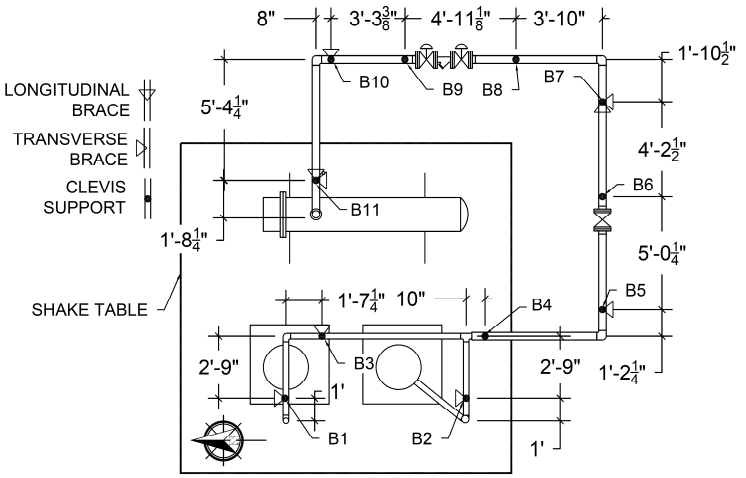
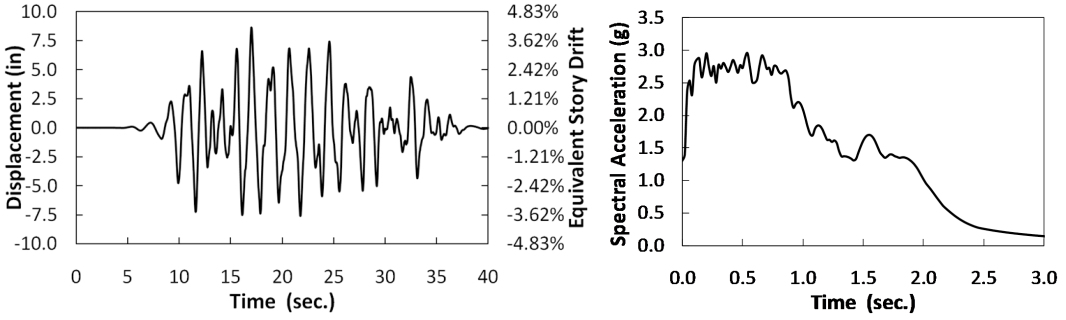


Figure 4. Bracing Layout.

Table Input Motion. The ICC-ES AC156 testing protocol (ICC Evaluation Service, Inc. 2007) was considered after consulting OSHPD engineers. The program SIMQKE (Gasparini 1976) was used to generate a synthetic table input motion compatible with the requirements of AC156 assuming conservative values that are typical of Seismic Design Category D. The peak acceleration and peak displacement of the full scale motion were 1.31g and 8.65 in, respectively. The achieved table motion is shown in Fig. 5a and the 5% damped pseudo-acceleration spectrum of the achieved motion is plotted in Fig. 5b. This input motion subjected the specimen to an equivalent maximum inter-story drift of 4.3%.

Each experimental model was subjected to increasing intensities of the input motion. These excitations were applied independently along each of the main axes, referred to as N-S, E-W. Biaxial excitation was also applied along 45° with respect to these axes (Goodwin et al., 2005).



(a) **(b)**

Figure 5. a) Achieved Shake Table Motion, b) Spectral Acc. of the Table Motion

EXPERIMENTAL RESULTS

Dynamic Properties. Prior to the experiments, the models were subjected to sine sweep excitation in order to identify the dynamic characteristics of the system. The average of acceleration transfer functions between table and the pipe at each of the four corners of the piping assembly was used to identify the frequencies of the first three modes of vibration of each model.

Table 1 presents the frequencies of the four models. Higher frequency values of the braced system as compared to the corresponding values of the unbraced system are due to the effect of added stiffness of the cable restrainers. Dynamic characteristics of the welded and threaded system were comparable and indicated that the rigidity of the threaded connections was similar to that of welded joints.

Table 1. Frequencies of the Piping Subassembly Model.

Subassembly Type	Frequency (Hz)		
	1st Mode	2nd Mode	3rd Mode
Welded Braced	2.98	4.56	6.51
Threaded Braced	2.76	4.1	6.17
Welded Unbraced	1.63	2.61	3.66
Threaded Unbraced	1.61	2.33	3.86

Measured Data. An arrangement of different instruments was installed on the test assembly to measure its seismic response. Figure 6 shows the four representative points of measured responses. The measured displacements (or drifts) are denoted as Δ_1, Δ_2, Δ_3, and Δ_4, and the accelerations are denoted as Acc_1 and Acc_2. Drifts were calculated by dividing the measured displacements by the clear distance between table and stationary frame.

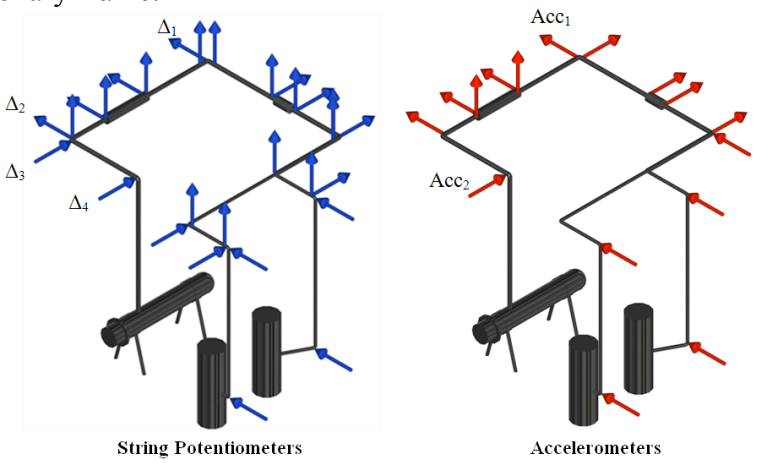


Figure 5. Instrumentation Configuration

Figures 6a and 6b show the maximum measured accelerations, Acc_1 and Acc_2, versus the corresponding maximum drifts, Δ_1 and Δ_4, in progressive biaxial motions of the welded assembly. Figure 11a shows that the maximum accelerations in E-W direction increased by increasing drifts. In contrast with E-W direction, the accelerations in N-S direction stopped increasing for drifts larger than approximately 2.5% as displayed in Fig. 11b, implying the piping assembly yielded thereafter. These figures also reveal that the accelerations of restrained and unrestrained systems are comparable.

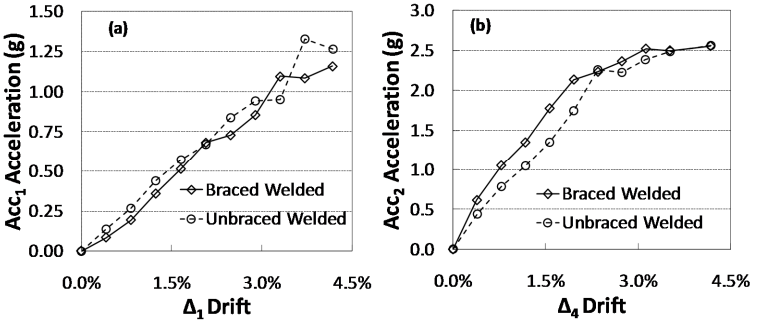


Figure 5. Acceleration Response versus Drift

In Fig. 7, Δ_4 in the restrained welded assembly is compared with the corresponding value of the threaded one at 70% IM that the system was still elastic. Responses of the systems were essentially similar, indicating that the type of fittings (threaded or welded) did not change the dynamic response of the piping system.

Figures 8a and 8b display Δ_1 and Δ_4 displacement histories of the welded assembly at 70% IM. The displacements of the unrestrained system were significantly larger than those of the restrained system. This observation signifies that seismic

restraining is necessary when the displacement of piping systems may impose damage to other adjacent components by impacting them.

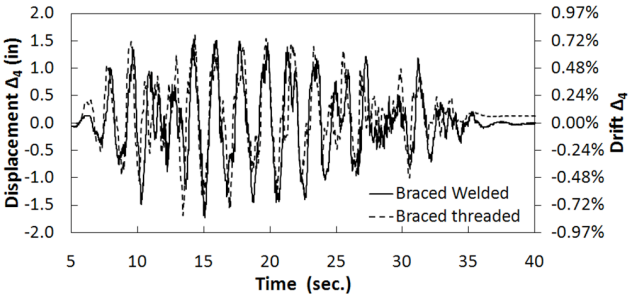


Figure 7. Comparison of Welded and Threaded Systems at 70% MI

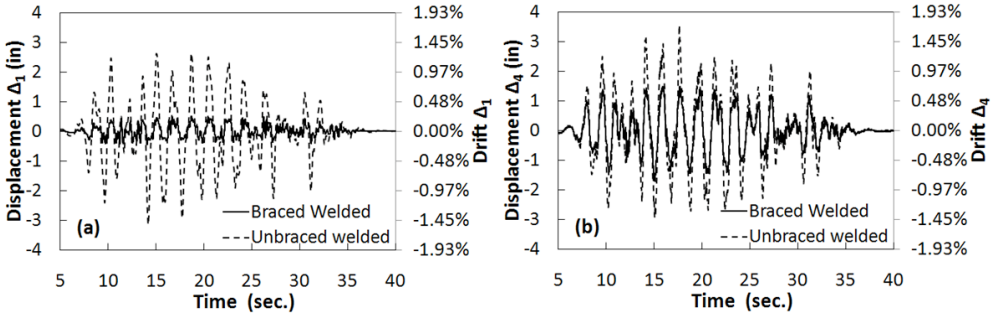


Figure 8. Comparison of Responses of Braced and Unbraced Systems at 70% MI

COMPUTATIONAL MODEL OF THE SPECIMENS

The purpose of the computational modeling was to develop a simplified method that can be employed in the design procedure of piping systems. The experimental data was used to calibrate the response of the seismic cable restrainers and validate the computational model.

Development of a Simplified Computational Model. The SAP2000 software (CSI 2009) was utilized for computational modeling. Pipes were modeled as linear elastic frame elements with gross pipe section properties. The mass of water inside the pipes was included in the model as additional distributed massed on the pipe members. The connections of the pipes to the heat exchanger and heaters were assumed rigid in all directions except rotationally about the longitudinal axis of these equipments. Joint areas were not explicitly modeled. The achieved table motion was defined as the support displacement history in the direction of shaking.

Preliminary analyses showed that if full stiffness of the cable restrainers is used, the computed response and dynamic properties are very different from the experimental results. The main reason was found to be the flexibility of the clamps and clevises and the initial slack in the cables. This initial slack in the restrainers was also discussed by Hoehler et al. (2009). To better represent the initial conditions of the seismic restrainers in the model, an equivalent effective axial stiffness was used for the cables. To keep the model simple, any sophisticated elements such as gaps or nonlinear links were not used.

Figure 9 shows the expected load-displacement relationship of an elastic system with an initial looseness. This figure shows that the maximum "effective" stiffness increases when displacement increases. The effective stiffness should be adjusted for the anticipated or target displacements.

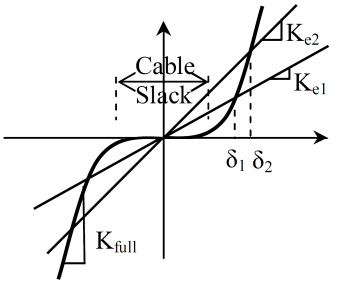


Figure 9. Effective Stiffness of Cable Restrainers Due to Looseness

By matching the dynamic properties of the computational model and the experimental specimen at 50% IM, the effective stiffness of the cable restrainers was discovered to be 1/10 of the gross section of the cables to account for the initial slack. By using 10% of full stiffness of the cable restrainers, frequencies of the first three modes of vibration for the restrained assemblies were calculated as 3.21 Hz, 4.15 Hz, and 6.02 Hz, respectively. The calculated frequencies for the unrestrained system were 1.81 Hz, 2.43 Hz, and 3.36 Hz for the first three modes.

Figures 10a, b compare the computational and experimental Δ_2 displacements for the restrained and unrestrained welded assemblies under 50% IM. The error differences between the analytical and computational displacement results are less than 10%. This is acceptable considering the simplicity of the analytical model.

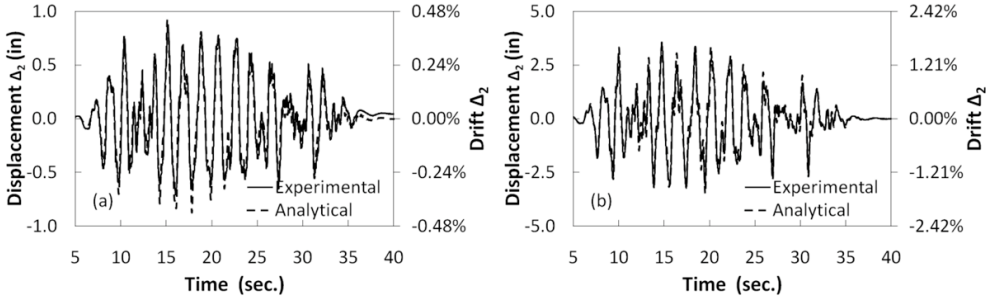


Figure 10. Δ2 under E-W 50% IM, a) Braced Welded System, b) Unbraced Welded System

Kinematic and Dynamic Responses. A piping system installed between two floors of a building is essentially a dynamic system that is subjected to differential support excitation during an earthquake. Figure 11 shows a mass-spring simplified SDOF model of the test assembly. In this model, K_p is the total lateral stiffness of the vertical pipe risers, and K_r is the total lateral stiffness of seismic restrainers that attach the piping to the stationary frame. The dynamic influence vector can be found from the partitioned stiffness matrix of the mass-spring system, according to the methodology described in Chopra (2007). The dynamic influence vector of the piping system is:

$$\iota = \left[\frac{K_p}{K_p + K_r} \quad \frac{K_r}{K_p + K_r} \right] \tag{1}$$

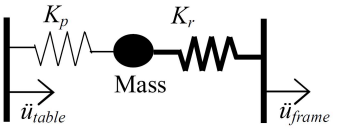


Figure 11. Equivalent Mass-Spring Model

The effective acceleration will be obtained by multiplying the dynamic influence vector by the support excitation vector. Accordingly, the effective inertial force is:

$$P_{eff} = \frac{m}{K_p + K_r}\left(K_p \ddot{u}_{table} + K_r \ddot{u}_{frame}\right) \tag{2}$$

In Equation 2, $\ddot{u}_{table}$ and $\ddot{u}_{frame}$ are the acceleration histories of the shake table and the supporting frame, respectively. The stationary frame was fixed in all experiments, and the test assembly was excited only through movement of the shake table; therefore, the second portion of Eq. 2 can be discarded. For such a system, the dynamic influence coefficient is the ratio of the pipe stiffness to the summation of stiffnesses of the pipes and restrainers. For the restrained assemblies this coefficient was about 0.25, which implies that the mass sensed 25% of table accelerations and displacements.

Response of a system under multiple support excitations is comprised of kinematic and dynamic effects (Chopra, 2007) as shown in Eq. 3; in this equation, ι is the influence vector as introduced in Eq. 1, u_g is the support displacement vector, and u is the dynamic response. The kinematic response is static deformations due to the imposed differential support displacements.

$$u_{total} = \iota u_g + u \tag{3}$$

The computational model was used to study the significance of the inertial effects shown in Eq. 2 on the total response of the piping system. To accomplish this, all the masses were removed from the model, and the model was subjected to 50% IM biaxial table motion and 100% IM biaxial roof motion to produce 2.17% inter-story drift in each direction. Response of the massless system (kinematic response) was compared to dynamic response, which was calculated by subtracting the kinematic response from the response of the system with real masses and subjected to the same support excitations.

Figure 12a, b shows the dynamic and kinematic portions of Δ_2 and Δ_3. For these points, the maximum dynamic responses were approximately 10% and 30% of the kinematic responses, respectively. Measured data show that the dynamic effects are insignificant compared to the kinematic deformations experienced by the tested restrained piping system. Therefore, for a similar piping system running between the adjacent floors of a building, the displacements imposed to the system due to the differential floor motions is larger than the dynamic responses. This conclusion may not apply to the piping systems that primarily run horizontally beneath the floors, or to systems composed of large diameter pipes that mobilize large inertial loads. Furthermore, considering the small spacing used between the restrainers in the test assembly, real piping systems with larger spacing between restrainers may experience large inertial forces.

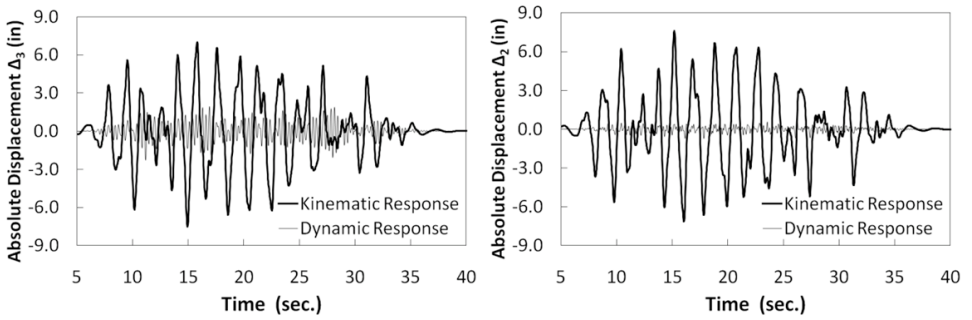


Figure 12. Analytical Dynamic and Kinematic Responses under 50% IM Table and 100% IM Roof Biaxial Motion

SUMMARY AND CONCLUSIONS

The objective of this research was to identify dynamic characteristics of typical hospital piping assemblies by subjecting them to different levels of dynamic inter-story drifts. One of the assemblies used welded connections whereas the other used threaded connections. The piping assemblies were hung from a stationary frame that was installed outside the table on the laboratory floor. The assemblies were tested using a synthetic input motion. Both assemblies were tested with and without cable seismic restrainers. Subsequent to the experimental studies, a simplified computational model was developed in SAP2000 to better understand the effects of different parameters on the response of the system.

The following observations and conclusions are drawn from the presented experimental and computational studies; however, designers should be mindful of the differences between the boundary conditions of the test assembly and piping systems supported by building floors.

- The seismic restrainers did not have a major effect on the acceleration response of the piping assemblies, though they were effective in limiting displacement responses.
- The flexural rigidities of the threaded and the welded joints were comparable.
- Due to the inherent slack of the cable restrainers, their effective stiffness was found to be one-tenth of the full stiffness.
- The kinematic response of the system comprised less than 23% of the total response. It showed that the dynamic response of a similar piping assembly could be insignificant compared to other structural systems due to the small associated masses.

ACKNOWLEDGEMENTS

This study was funded by the Multidisciplinary Center for Earthquake Engineering Research (MCEER) through a grant from the Earthquake Engineering Research Centers Program of the National Science Foundation (NSF) under NSF award number EEC- 9701471. Assistance from Dr. Patrick Laplace and Mr. Paul Lucas of the UNR Large Scale Structures Lab during the assembly and testing is appreciated.

REFERENCES

American Lifeline Alliance. (2002). *Seismic Design and Retrofit of Piping Systems*, www.americanlifelinesalliance.org

Applied Technology Council (ATC). (2008) *Reducing the Risk of Nonstructural Earthquake Damage*, *Report No. ATC-69,* Redwood City, CA.

Ayres, J. M., Phillips, R. J. (1998). Water Damage in Hospitals Resulting from the Northridge Earthquake, *ASHRAE Trans.*, Vol. 104, Part 1, American Society of Heating, Refrigerating and Air-Conditioning Engineers, Atlanta, Georgia.

California Seismic Safety Commission. (2001). *Hospital Seismic Safety Findings and Recommendations,* Sacramento, California.

Chopra, A. K. (2006). *Dynamics of Structures (3rd Ed.)*, Prentice Hall, New Jersey.

FEMA 412. (2002). *Installing Seismic Restraints for Mechanical Equipment*, prepared by the Vibration Isolation and Seismic Control Manufacturers Association for the Federal Emergency Management Agency, Washington, D.C.

Gasparini, D. A., and Vanmarcke, E. H. (1976). *Simulated Earthquake Motions Compatible with Prescribed Response Spectra, Publication No. R76-4,* Massachusetts Institute of Technology, Cambridge, Massachusetts.

Goodwin, E., Maragakis, M., Itani, A. and Luo, S. (2005). *Experimental Evaluation of the Seismic Performance of Hospital Piping Subassemblies, Report No. CCEER-05-5*, Center for Civil Engineering Earthquake Research, Department of Civil Engineering, University of Nevada, Reno, Nevada.

Hoehler, M. S., Panagiotou, M., Restrepo, J. I., Silva, J. F., Floriani, L., Bourgund, U., Gassnerd, H. (2009). Performance of Suspended Pipes and Their Anchorages during Shake Table Testing of a Seven-Story Building, *Earthquake Spectra* **25**, 71–91.

ICC. (2006a). *International Building Code,* International Code Council, Washington, D.C.

ICC-ES AC 156. (2007). *Acceptance Criteria for Seismic Qualification by Shake-Table Testing of Nonstructural Components and Systems,* International Code Council Evaluation Service, Whittier, California.

Kircher, C. A. (2003). It Makes Dollars and Sense to Improve Nonstructural System Performance. *ATC-29-2 Proceedings of Seminar on Seismic Design, Performance, and Retrofit of Nonstructural Components in Critical Facilities*.

Mason Industries. (2009). *Seismic Restraint Guidelines for Suspended Piping, Ductwork and Electrical System,* Smithtown, New York

NFPA. (2007). *Standard for Installation of Sprinkler Systems. 2007 Edition (NFPA 13)*, National Fire Protection Association, Quincy, Massachusetts.

OSHPD (2010). *California Senate Health Committee Hearing on Hospital Seismic Safety,* The Office of Statewide Health Planning and Development, Sacramento, CA

SMACNA. (2008). *The Seismic Restraint Manual: Guidelines for Mechanical Systems, 3rd edition*, ANSI/SMACNA 001-2008, Washington, D.C.

Wasilweski, R. J. (1998). Seismic Restraints for Piping Systems, *ASHRAE Trans.*, Vol. 104, Part 1, American Society of Heating, Refrigerating and Air-Conditioning Engineers, Atlanta, Georgia.

Design of a Test-Bed Structure for Shake Table Simulation of the Seismic Performance of Nonstructural Systems

Siavash Soroushian[1],ManosMaragakis[2], Ahmad Itani[3], Gokhan Pekcan[4], and Arash E. Zaghi[5]

[1]Department of Civil and Environmental Engineering, University of Nevada, Reno, MS 0258, Reno, NV 89557-0258; PH (775) 762-0966; FAX (775) 784-1390; email: siyavashs@yahoo.com
[2] Department of Civil and Environmental Engineering, University of Nevada, Reno, MS 0258, Reno, NV 89557-0258; PH (775) 784-6937; FAX (775) 784-1390; email: maragaki@unr.edu
[3]Department of Civil and Environmental Engineering, University of Nevada, Reno, MS 0258, Reno, NV 89557-0258; PH (775) 784-4379; FAX (775) 784-4466; email: itani@unr.edu
[4]Department of Civil and Environmental Engineering, University of Nevada, Reno, MS 0258, Reno, NV 89557-0258; PH (775) 784-4512; FAX (775) 784-1390; email: pekcan@unr.edu
[5]Department of Civil and Environmental Engineering, University of Nevada, Reno, MS 0258, Reno, NV 89557-0258; PH (775) 200-6687; FAX (775) 784-1390; email: esmailiz@unr.edu

ABSTRACT

As part of the project entitled "*NEESR-GC: Simulation of the Seismic Performance of Nonstructural System,*" a series of system-level full-scale experiments of ceilings-piping-partition systems will be conducted at the University of Nevada, Reno NEES Site. This project is aimed at understanding the seismic response of these systems and their interaction with each other and the parent structure. A two-story, two-bay steel braced frame spanning across three biaxial shake tables was designed as a Test-Bed structure to simulate a variety of dynamic environments. After introducing the design considerations of the Test-Bed structure within this paper, the method proposed to develop the shake table drive motions is explained. To obtain the drive motion, a transfer function (TF) was formulated for a multi-support dynamic system under differential support excitation and combined with a TF previously developed for target floor acceleration of a generic structure. A suitable high-pass filter was suggested to limit exerted demands on the shake tables.

1. Introduction

After an earthquake, the functionality of an essential facility, such as a hospital, relies heavily on the functionality of its nonstructural components, such as piping systems, fire suppression systems, elevators, and other equipment. In recent earthquakes, nonstructural components of hospitals and medical facilities have suffered severe damage, which consequently interrupted the functionality of these facilities (OSHPD, 2010). The 1971 San Fernando Earthquake caused excessive damage to many hospitals and medical facilities, which led to evacuation of four of the eleven damaged medical facilities in the area (Wasilweski, 1998). Due to this unacceptable performance, the State of California passed the Hospital Seismic Safety Act in 1973, requiring medical facilities to remain operational after earthquake events.

The repair and replacement costs of nonresidential buildings after the Northridge earthquake were $6.3 billion, with only $1.1 billion of the total in structural damage (Kircher, 2003). Immediately after this earthquake, 88% of the occupants of the hospital beds in the damaged area (13 hospitals) had to be evacuated as a result of nonstructural damage such as water damage, elevator failure, etc. (Ayres et al., 1998). Hospitals built in accordance with the 1973 Hospital Act, however, were successful in resisting structural damage. Nevertheless, nonstructural damage (plumbing, ceiling systems, etc.) in post 1973 construction was, and still is, extensive after strong seismic activities. This shows an urgent need to better understand the seismic behavior of nonstructural systems.

Extensive systematic experimental data is required as a supplement to previous experience to improve available nonstructural design provisions. Several studies have been conducted on the seismic response of nonstructural subassemblies and their components as early as 1980s on ceiling tiles and piping systems (ANCO, 1983; Hoehler et al., 2009; ATC, 2007); however, the understanding on the system-level response of these subassemblies is significantly limited necessitating the design of large-scale experiments on complete systems (Zaghi, 2010).

As a part of the NEESR Grand Challenge project "*Simulation of the Seismic Performance of Nonstructural Systems*," a large scale Test-Bed structure is constructed to conduct system-level experiments of full-scale, complex, nonstructural systems. The NEES earthquake simulator (three biaxial shake tables) at the Large Scale Structure Laboratory of University of Nevada, Reno will be used to subject the Test-Bed structure and nested nonstructural systems to desired levels of dynamic excitations.

Nonstructural components can be divided into two categories in terms of seismic performance: 1) acceleration sensitive elements such as ceiling and horizontal pipe runs; and 2) drift sensitive components, including partition and riser pipes. The Test-Bed structure is designed in a way that it can subject the nested subassemblies to large accelerations as well as large inter-story drifts.

Before describing the methodology used for the development of the shake table input motion, a brief review of the NEESR Grand Challenge is presented, followed by the design philosophy and provisions of the proposed Test-Bed structure.

2.NEESR Nonstructural Grand Challenge Project

The Grand Challenge Project entitled "Simulation of the Seismic Performance of Nonstructural Systems"(http://www.nees-nonstructural.org) integrates multidisciplinary system-level studies that develop, for the first time, the simulation capabilities and implementation process for enhancing the seismic performance of ceiling-piping-partition (CPP) nonstructural systems. This project is led by the University of Nevada, Reno in collaboration with the Consortium of Universities for Research in Earthquake Engineering (CUREE), Cornell University, Georgia Institute of Technology, North Carolina Agricultural and Technical State University, North Carolina State University, Rutherford & Chekene, State University of New York at Buffalo, and University of California, San Diego. In the first experimental phase of the project, a comprehensive testing program is using the University at Buffalo and the University of Nevada, Reno NEES Equipment Sites to conduct full-scale subsystem and system-level experiments, respectively. The main objective of the subsystem level test series is to characterize the seismic performance of CPP systems and to provide the input for the design and execution of system-level experiments at the University of Nevada, Reno. This paper reports on design considerations and characteristics of UNR Test-Bed structure.

3.Test-Bed Structure Design Philosophy

To achieve the objectives of system-level experimental investigation, several key requirements were identified, particularly with respect to the design of the Test-Bed structure. During the experiments, it will be utmost importance to simulate experimentally and to capture the various types of interactions that will take place among the subassemblies and the parent Test-Bed structure. Moreover, the Test-Bed structure should allow investigators to study the effects of structural yielding on the response of the subassemblies. A discussion of the performance design concepts were utilized in the design of the Test-Bed structure with the provisions follows.

A two-story, two-bay (61ft-long, 12ft-wide, 24ft-high) Test-Bed structure was designed. The dimensions are typical of spans and story heights in multi-story buildings and allow for the installation of full height partition walls as well as large ceiling areas. The longitudinal and transverse views of the frame are presented in Figure1.

Nonstructural components can be divided into two categories in terms of seismic response: 1) acceleration sensitive elements such as ceiling, horizontal pipe runs, and sprinkler heads, and 2) drift sensitive components, including partition and riser pipes. To study both categories, two designs were considered for the Test-Bed structure by implementing two sets of bracing systems. Elastic braces restrained against buckling, used to achieve large floor accelerations, and buckling resistant braces (BRBs), used to produce large inter-story drifts.

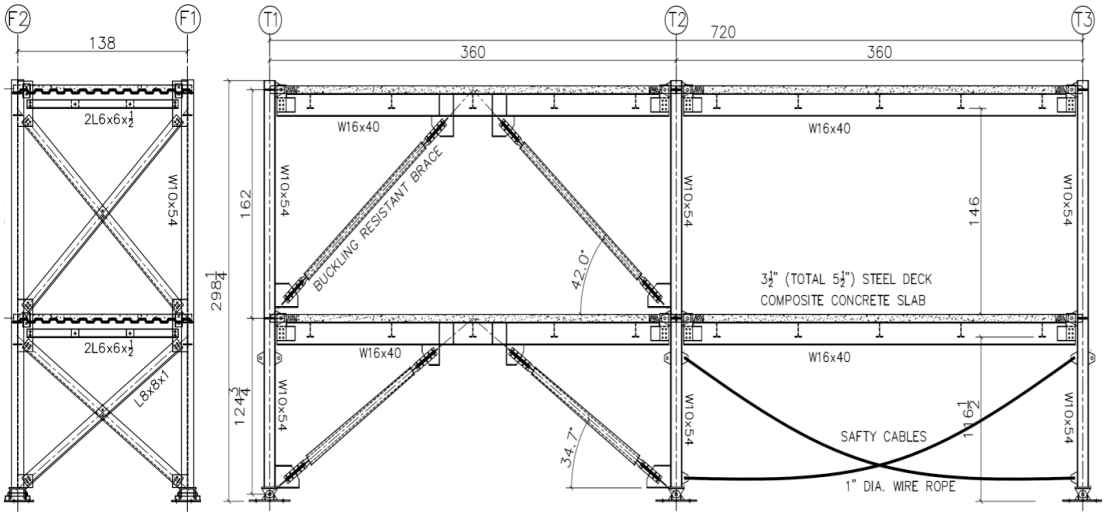


Figure 1: Longitudinal and Transverse Views of the Test-Bed Structure

Although the Test-Bed structure is a two-story frame, it may represent any two adjacent floors of a multi-story building (for instance, the $(j+1)^{th}$ and $(j+2)^{th}$floors) aspresented in Figure 2. This can be achieved by generating table acceleration that gives the first and second floor of Test-Bed structure motions most similar to $(j+1)^{th}$ and $(j+2)^{th}$floor motions of that multi-story building.

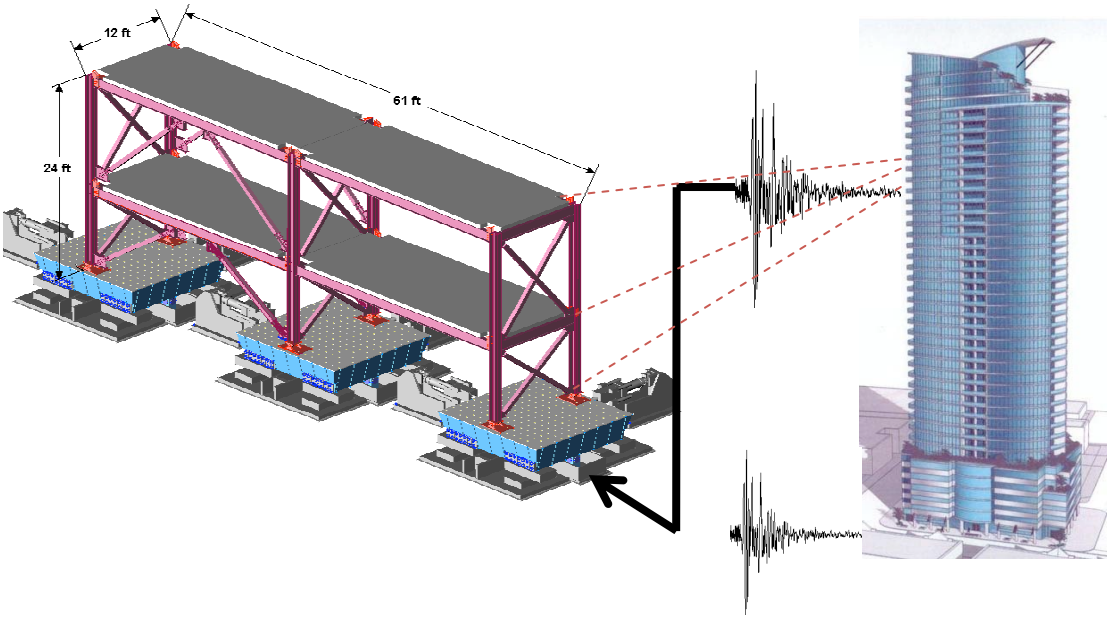


Figure2: Test-Bed Structure on Shake Tables and Two Adjacent Floors of Tall Building Concept

To understand the effects of the nonstructural subassemblies on the seismic response of structures (specifically stiffness, lateral strength, and added damping) structural dynamic characteristics of the Test-Bed structure should be well known,

predictable, and controllable. The Test-Bed structure was designed with 'frictionless' tight-fit hinges in order to avoid any possible deviation of the physical responses from that of numerical models. The column-base and beam-column connections were pinned, minimizing the rotational fixity. The lateral stiffness and strength of the frame is provided by a set of eight brace members that are installed in a chevron configuration. This design methodology allows yielding to take place in predefined members (BRB braces).

The Test-Bed structure is planned to be used for multiple experiments, and therefore, should remain linear-elastic during the shake table testing. Utilization of the buckling restrained members as lateral resisting members enables the Test-Bed structure to be used a number of times after replacement of the yielded braces. Furthermore, to allow for a safe assembly and disassembly of the structure, each floor is divided into two prefabricated 5.5-in thick steel deck concrete composite slabs panels that were built off-site and will be shipped to the laboratory. These floor panels as well as other structural members can be stored in a small area before and after the test.

4. Target Performance of the Test-Bed

Taking the limitations of the shake table into consideration, the Test-Bed was designed to reach the target inter-story drift and peak floor acceleration without exceeding the hydraulic system restraints. The target performances of linear and nonlinear Test-Bed structures are separately discussed in this section.

The test bed is designed for longitudinal excitation. Therefore, the transverse bracing system of the Test-Bed structure was significantly overdesigned to ensure that the longitudinal dynamic modes dominate vibration of the frame.

4.1Nonlinear Test-Bed

This setup was designed to achieve large inter-story drifts similar to that of nonlinear frame structure. This setup was aimed at the evaluation of drift sensitive subassemblies such as in-plane partitions, pipe risers, and riser ducts. Design target of the nonlinear Test-Bed was to achieve an inter-story drift larger than 3% on both stories.

The nonlinear BRBs were designed for 20kips yield force and stiffness of 70kips/in and 59kips/in in the first and second floors, respectively. On each floor 31kips of additional was provided using low profile lead baskets bolted to the floor to provide required inertial forces. The natural period of the structure was calculated as 0.43sec and the effective period of the structure at 3% drift was found to be 1.21sec.

4.2 Linear Test-Bed

This setup was designed to investigate acceleration sensitive subassemblies including ceilings, sprinkler piping, and out-of-plane partitions. The linear Test-Bed was designed to simulate linear or stiff structures in which large floor acceleration is expected. The target peak floor acceleration (PFA) was larger than 2.0g on both

floors.

Because conventional braces required a large cross-section area for local or global buckling requirements, buckling restrained elastic braces were used for the linear structure. This large area increases the elastic stiffness of the structure and as a consequence significantly reduces the effective periods. Although a high frequency Test-Bed experiences large floor accelerations, its period does not fall within the range of practical structures. To avoid yielding of the brace members in the linear structure, strength of the brace members was increased by using higher-grade steel for the brace cores to control the lateral stiffness. The linear BRBs were designed for a yield force of 60kips and stiffnesses of 186 kips/in and 176kips/in in the first and second floors, respectively. An additional mass of 7kips was provided on the first floor and 3.5kips on the second floor to achieve the target period. The natural period of the structure was found to be 0.19sec.

It should be mentioned that the Test-Bed structure may be designed to achieve other performance limits in accordance with the purpose of the experiment.

5. Development of the Shake Table Input Motion

It is evident that if a ground acceleration is used as the shake table input motion, the Test-Bed structure will simulate the response of a two-story building supported on the ground.However, the Test-Bed structure is meant to simulate the floor response of any multistory building: a method was developed as part of this project to allow simulation of floor acceleration responses of multistory buildingsby using the Test-Bed structure.The theory of a reduced-order earthquake demand assessment that is presented in detail by Taghavi and Miranda(2005) was adopted. The absolute acceleration transfer function (TF) was obtained by superposition of modal TFs. This TF was multiplied by the inverse of a TF for the Test-Bed structure that was formulated with theeffect of multi-support excitationin mind.To satisfy the displacement and velocity limitations of the shake-tables, a high-pass filter was added to TF of the system. This method is described in detail in this section.

5.1 Description of Generic Buildings

The dynamic characteristicsof multistory buildings are approximated (Taghavi and Miranda, 2005) by using an equivalent continuum model consisting of a flexural cantilever beam and a shear cantilever beam deforming in bending and shear, respectively (Fig. 3). These flexural and shear cantilever beams were assumed to undergo the same lateral deformation. Under a horizontal acceleration at the base, response of this continuum system can be expressed by the following partial differential equation(Taghavi and Miranda, 2005):

$$\rho(x)\frac{\partial^2 u(x,t)}{\partial(t^2)}+c(x)\frac{\partial^2 u(x,t)}{\partial(t)}+\frac{1}{H^4}\frac{\partial^2}{\partial x^2}\left[EI(x)\frac{\partial^2 u(x,t)}{\partial x^2}\right]-\frac{1}{H^2}\frac{\partial}{\partial x}\left[GA(x)\frac{\partial u(x,t)}{\partial x}\right]=-\rho(x)\frac{\partial^2 u_g(t)}{\partial t^2} \quad (1)$$

where $\rho(x)$ is mass per unit height, $u(x,t)$ is the displacement at normalized height $x$at time t(x variesbetween zero, at the base of the building, and one, at the roof level), H

is the total height of the building,*c(x)* is damping coefficient per unit height,*EI(x)* is flexural rigidity of the flexural beam along the height,*GA(x)* is shear rigidity of the shear beam and $u_g(t)$is the ground displacement at time *t*.

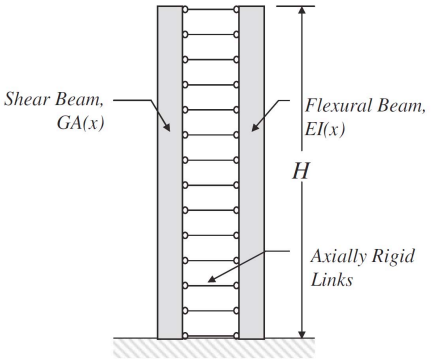


Figure3: GenericModel to Estimate Dynamic Properties of Multi-Story Buildings (Taghavi and Miranda, 2005)

By solving Eq.(1), the shape of the mode of vibration corresponding to the i^{th} mode, normalized to unity at *x=1* is found by:

$$\phi_i(x)=\frac{\sin(\gamma_i x)-\gamma_i\left(\gamma_i^2+\alpha_o^2\right)^{-\frac{1}{2}}\sinh\left(x\sqrt{\gamma_i^2+\alpha_o^2}\right)+\eta_i\left[\cosh\left(x\sqrt{\gamma_i^2+\alpha_o^2}\right)-\cos(\gamma_i x)\right]}{\sin(\gamma_i)-\gamma_i\left(\gamma_i^2+\alpha_o^2\right)^{-\frac{1}{2}}\sinh\left(\sqrt{\gamma_i^2+\alpha_o^2}\right)+\eta_i\left[\cosh\left(\sqrt{\gamma_i^2+\alpha_o^2}\right)-\cos(\gamma_i)\right]} \quad (2)$$

where,

$$\eta_i=\frac{\gamma_i^2\sin(\gamma_i)+\gamma_i\sqrt{\gamma_i^2+\alpha_o^2}\sinh\left(\sqrt{\gamma_i^2+\alpha_o^2}\right)}{\gamma_i^2\cos(\gamma_i)+\left(\gamma_i^2+\alpha_o^2\right)\sinh\left(\sqrt{\gamma_i^2+\alpha_o^2}\right)} \quad (3)$$

In Eq. (2), γ_i is obtained from the solution of the characteristic equation shown as Eq. (4):

$$2+\left[2+\frac{\alpha_o^4}{\gamma_i^2\left(\gamma_i^2+\alpha_o^2\right)}\right]\cos(\gamma_i)\cosh\left(\sqrt{\gamma_i^2+\alpha_o^2}\right)+\left[\frac{\alpha_o^2}{\gamma_i\left(\gamma_i^2+\alpha_o^2\right)}\right]\sin(\gamma_i)\sinh\left(\sqrt{\gamma_i^2+\alpha_o^2}\right)=0 \quad (4)$$

The dimensionless parameter α_o in Eq. (2) controls the degree of participation of overall flexural and overall shear deformations in the genericmodel of multistory buildings. A value of α_o equal to zero represents a pure flexural and a value larger than 30corresponds to a shear dominated deformation for a building. In these equations *i* represent the mode number.

For a continuum model with uniformly distributed mass, themodal participation factor of the i^{th} mode of vibration is given by:

$$\Gamma_i = \frac{\int_0^1 \phi_i(x)dx}{\int_0^1 \phi_i^2(x)dx} \tag{5}$$

Eqs. (2) and (5) were implemented to generate the TF for the absolute acceleration of q^{th} floor of generic building.A method that is discussed in detail in Maddaloni et al.(2010)was utilized to obtain theTFshown in Eq. (6):

$$H_q(\omega) = \sum_{im=1}^{k} \frac{-\left(2i\omega\xi_{im}\omega_{im} + \omega_{im}^2\right)}{\omega_{im}^2 - \omega^2 + 2i\omega\xi_{im}\omega_{im}} \phi_{im,q}\Gamma_{im} \tag{6}$$

Where ω_{im}^2 , Γ_{im} and ξ_{im} are the circular frequency,modal participation factor, and damping ratio of im^{th} mode of generic building, respectively.Only the first $k$significant modes were participated in this derivation. In this equation, $\phi_{im,q}$ corresponds to the value of the im^{th} mode in the q^{th} floor of the building.

5.2 Development of a TF for the Absolute Floor Accelerationof the Test-Bed Structure

The Test-Bed structure is supported on three shake tables.Each shake table respondsslightly different to the drive motion as can be explained by servo-valve control basics. The following formulation for a dynamic system with multiple support excitations wasextended to include the support degrees of freedom (DOFs) in the system TF equations. The matrix form of the equation of motion for the Test-Bed Structure with two dynamic DOFs and three support DOFs can be written as (Chopra AK, 2001)

$$\begin{bmatrix} {}_{2x2}M_{ss} & 0 \\ 0 & {}_{3x3}M_{tt} \end{bmatrix} \begin{bmatrix} {}_{2x1}\ddot{u}_s^t \\ {}_{3x1}\ddot{u}_t \end{bmatrix} + \begin{bmatrix} {}_{2x2}C_{ss} & {}_{2x3}C_{st} \\ {}_{3x2}C_{ts} & {}_{3x3}C_{tt} \end{bmatrix} \begin{bmatrix} {}_{2x1}\dot{u}_s^t \\ {}_{3x1}\dot{u}_t \end{bmatrix} + \begin{bmatrix} {}_{2x2}K_{ss} & {}_{2x3}K_{st} \\ {}_{3x2}K_{ts} & {}_{3x3}K_{tt} \end{bmatrix} \begin{bmatrix} {}_{2x1}u_s^t \\ {}_{1x3}u_t \end{bmatrix} = \begin{bmatrix} 0 \\ {}_{3x1}p_t(t) \end{bmatrix} \tag{7}$$

The total displacements include contributions from dynamic and static displacements as:

$$\begin{bmatrix} {}_{2x1}u_s^t \\ {}_{3x1}u_t \end{bmatrix} = \begin{bmatrix} {}_{2x1}u_s^s \\ {}_{3x1}u_t \end{bmatrix} + \begin{bmatrix} {}_{2x1}u_s \\ 0 \end{bmatrix} \tag{8}$$

Where[M], [C], [K] are the mass, stiffness, and viscous damping matrices, respectively. The vectors [$\ddot{u}$], [$\dot{u}$], [u] are the acceleration, velocity, and displacement, respectively.The superscripts t and s stand for the total and static responses, accordingly. The subscripts t and s are related to the shake table's and the structure's responses, respectively. The $P_t(t)$ is the table force vector.

Equation (7) can be reduced to Eq. (9) after satisfying static equilibrium.

$$_{2x2}M_{ss\ 2x1}\ddot{u}_s(t)+{}_{2x2}C_{ss\ 2x1}\dot{u}_s(t)+{}_{2x2}K_{ss\ 2x1}u_s(t)=-{}_{2x2}M_{ss\ 2x3}\iota_{3x1}\ddot{u}_t(t) \quad (9)$$

Where $_{2x3}\iota=_{2x2}K_{ss}^{-1}{}_{2x3}K_{st}$ describes the influence of support displacements (or accelerations) on structure displacement (or acceleration) at dynamic DOFs.

Dynamic response of the structure may be decomposed in modal coordinates, $q_i(t)$, that $u(t)=\phi_i q_i(t)$ and ϕ_i is the i^{th} mass-normalized mode shape.Assuming that response is composed of harmonic functions, Eq. (9)can be transformed to Eq. (10) infrequency domain:

$$-\omega^2 q_i(\omega)+2i\omega\xi_i\omega_i q_i(\omega)+\omega_i^2 q_i(\omega)=-{}_{1x2}\Gamma_{i\ 2x3}\iota_{3x1}\ddot{u}_t(\omega) \quad (10)$$

where $\left(\phi_i^T K_{ss}\phi_i\right)/M_{ss,i}^*=\omega_i^2$ is the circular frequency and $\left(C_{ss,i}^*/M_{ss,i}^*\right)/2\,\omega_i=\xi_i$ is the damping ratio of i^{th} mode of vibration.

The absolute acceleration response vector, $\ddot{u}_s^t$, for the Test-Bed structure with two horizontal dynamic DOFs is the summation of the relative acceleration vector and the influence of table acceleration:

$$_{2x1}\ddot{u}_s^t(\omega)=\sum_{i=1}^{2}-\omega^2{}_{2x1}\phi_i q(\omega)_i+{}_{2x3}\iota_{3x1}\ddot{u}_t(\omega) \quad (11)$$

Equation (11) was pre-multiplied by $\left({}_{1x2}\phi_i^T{}_{2x2}M_{ss}\right)=-{}_{1x2}\Gamma_i$ and combined with Eq. (10) to obtain:

$$_{1x2}\phi_i^T{}_{2x2}M_{ss\ 2x1}\ddot{u}_s^t(\omega)=\frac{-\left(2i\omega\xi_i\omega_i+\omega_i^2\right)}{\omega_i^2-\omega^2+2i\omega\xi_i\omega_i}{}_{1x2}\Gamma_{i\ 2x3}\iota_{3x1}\ddot{u}_t(\omega) \quad (12)$$

The mode shape is mass normalized, $\Phi^T M=\Phi^{-1}$, thus Eq. (12) can be manipulated to achieve the absolute acceleration of the j^{th} floor of the Test-Bed structureas:

$$\ddot{u}_s^t(\omega)_j=\left[\sum_{i=1}^{2}\frac{-\left(2i\omega\xi_i\omega_i+\omega_i^2\right)}{\omega_i^2-\omega^2+2i\omega\xi_i\omega_i}\phi_{i,j\ 1x3}\kappa_i\right]_{3x1}\ddot{u}_t(\omega) \quad (13)$$

The term shown in the bracket is a TF that relates the accelerations of shake tables to the absolute floor acceleration of the Test-Bed. The TF that relates motion of the n^{th} shake tableto the acceleration of the j^{th}floor is defined by Eq. (14).

$$H_{sn,j}(\omega)=\frac{\ddot{u}_s^t(\omega)_j}{\ddot{u}_t(\omega)_n}=\sum_{i=1}^{2}\frac{-\left(2i\omega\xi_i\omega_i+\omega_i^2\right)}{\omega_i^2-\omega^2+2i\omega\xi_i\omega_i}\phi_{i,j}\kappa_{i,n} \quad (14)$$

In this equation, parameter $\kappa_{i,n} = \left(_{1x2}\Gamma_{i\ 2x3}\iota\right)_n$ is a measure of the participation of n^{th} table on the absolute acceleration of the j^{th} floor in i^{th} mode of vibration. As was mentioned earlier, the achieved table motions may be different from the drive motion (or target motion) due to several factors including the servo valve's dynamic response, the compressibility of the actuator fluid, oil leakage through the actuator seals, and the influence of the mass and stiffness of the test specimen(Maddaloni et al., 2010). The achieved and target shake table motions are assumed to be related through a transfer function H_{tn} for the n^{th} shake table. The TF that relates acceleration of the j^{th} floor to the drive motion can be obtained from the summation of the multiplication of structure TFs, as shown in Eq. (14), with H_{tn}. Figure 4 shows the structure-table dynamic system.

$$H_j(\omega) = \sum_{n=1}^{3} H_{tn}(\omega) \cdot H_{sn,j}(\omega) \tag{15}$$

or

$$H_j(\omega) = \sum_{n=1}^{3} H_{tn} \cdot \left[\sum_{i=1}^{2} \frac{-\left(2i\omega\xi_i\omega_i + \omega_i^2\right)}{\omega_i^2 - \omega^2 + 2i\omega\xi_i\omega_i} \phi_{i,j}\kappa_{i,n} \right] \tag{16}$$

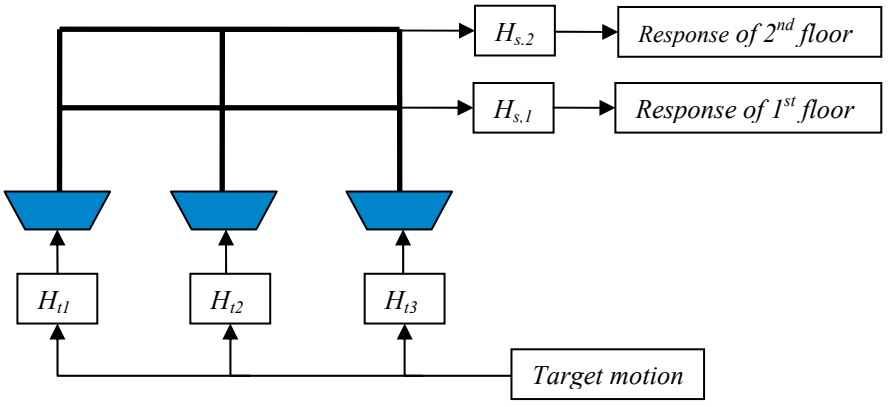


Figure4: Structure-Table Dynamic System

5.3 Development of Shake Table Drive Motion

The Test-Bed structure should simulate the specific floor responses of any target building. Floor response of a multistory building subjected to a ground motion, $\ddot{u}_g(\omega)$, can be obtained by using the TF presented as Eq.(6).

The drive motion of the shake tablesto achieve the target floor motion can be generatedby multiplication of the inverse of the TF of the Test-Bedshake table system shown in Fig. (4) and can express as:

$$\ddot{u}_{Drive}(\omega) = H_q(\omega) \,.\, H_j(\omega)^{-1} \,.\, \ddot{u}_g(\omega) \tag{17}$$

Or in its expanded form:

$$\ddot{u}_{Drive}(\omega) = \frac{\sum_{im=1}^{k} \dfrac{-\left(2i\omega\xi_{im}\omega_{im} + \omega_{im}^2\right)}{\omega_{im}^2 - \omega^2 + 2i\omega\xi_{im}\omega_{im}} \phi_{im,q}}{\sum_{n=1}^{3} H_{tn} \cdot \left[\sum_{i=1}^{2} \dfrac{-\left(2i\omega\xi_i\omega_i + \omega_i^2\right)}{\omega_i^2 - \omega^2 + 2i\omega\xi_i\omega_i} \phi_{i,j}\kappa_{i,n} \right]} \ddot{u}_g(\omega) \tag{18}$$

Expression of $\ddot{u}_{Drive}(\omega)$ in the time domain gives the time history ofthe drive motion of the shake tables. A suitable high-pass filter may be needed to insure thatthe demands on the shake tables are within acceptable limitsto permit continued use. This method allows for the simulation of floor accelerations of any type of structural system subjected to any set of ground motions.

This work will be continued to develop a similar formulation that can be used for simulation of the inter-story drifts of the generic building. A simplified method will be used to account for the structural nonlinearities.

6. Summary and Conclusions

A reusable Test-Bed structure was developed for shake table investigations of nonstructural systems. The Test-Bed structure simulates two adjacent floors of a multistory building. This two-story, two-bay frame can accommodate full-scale subassemblies and subject them to large drifts and/or accelerations. The design of this frame allows for reusing the Test-Bed.

The drive motion of the shake tables was obtained in order to achieve a target floor motion. This target floor motion was obtained from analysis of a continuum dynamic system representing a generic multistory building, offering a notable versatility to simulate floor acceleration of any type of structure. Nonlinearities will be included in this formulation in the extension of this study.

7. Acknowledgements

This material is based upon work supported by the National Science Foundation under Grant No. 0721399. Any opinions, findings, conclusions or recommendations expressed in this document are those of the investigators and do not necessarily reflect the views of the NSF. The input provided by the Practice Committee of the NEES Nonstructural Project, composed of W. Holmes (Chair), D. Allen, D. Alvarez, and R. Fleming; by the Advisory Board, composed of R. Bachman (Chair), S. Eder, R. Kirchner, E. Miranda, W. Petak, S. Rose and C. Tokas; and by the other members of the Experimental Group, A, Filiatrault, G. Mosqueda, A. Reinhorn, and J. T. Hutchinson, has been crucial for the completion of this research. The authors are grateful to Yajima USA Ltd. for the cooperation during construction of the Test-Bed structure.

References

ANCO Engineers, Inc. (1983). "Seismic Hazard Assessment of Nonstructural Ceiling Components Phase I," *NSF grant CEE-8114155, ANCO Engineers, Inc.,* Culver City, CA.

ATC.(2007). "FEMA 461-Interim protocols for determining seismic performance characteristics of structural and nonstructural components through laboratory testing," Redwood City, CA.

Ayres, J.M., Phillips, R.J. (1998)."Water Damage in Hospitals Resulting from the Northridge Earthquake," *ASHRAE Trans.*, Vol. 104, Part 1, American Society of Heating, Refrigerating and Air-Conditioning Engineers, Atlanta, Georgia.

Chopra A. K. (2001). "*Dynamics of Structures, Theory and Applications to Earthquake Engineering (2nd edn)*".Prentice-Hall: Upper Saddle River, NJ.

Hoehler, M. S., Panagiotou, M., Restrepo, Silva, J. F., Floriani, L., Bourgund, U., and Gassner, H. (2009). "Performance of Suspended Pipes and Their Anchorages During Shake Table Testing of a Seven-Story Building," *Earthquake Spectra* 25, 71.

Kircher, C. A. (2003), "It Makes Dollars and Sense to Improve Nonstructural System Performance." *ATC-29-2 Proceedings of Seminar on Seismic Design, Performance, and Retrofit of Nonstructural Components in Critical Facilities*.

Maddaloni G, RyuP.K, ReinhornA.M. (2010). "Simulation of floor response spectra in shake table experiments," *Earthquake Engineering and Structural Dynamics* DOI:10.1002/eqe.1035.

Miranda E, Taghavi S. (2005a). "Approximate floor acceleration demands in multistory buildings. I: Formulation".*Journal of Structural Engineering* 131(2): 203–211.

OSHPD.(2010). "California Senate Health Committee Hearing on Hospital Seismic Safety," *The Office of Statewide Health Planning and Development*, Sacramento, CA.

Wasilweski, R.J.(1998). "Seismic Restraints for Piping Systems," *ASHRAE Trans*., Vol. 104, Part 1, American Society of Heating, Refrigerating and Air-Conditioning Engineers, Atlanta, Georgia.

Zaghi, A. E., Maragakis, E. M., Itani, A., and Goodwin, E. (2010) (In Press)."Experimental and Analytical Studies of Hospital Piping Subassemblies Subjected to Seismic Loading," *Earthquake Spectra*, EERI

Seismic Performance Evaluation of Highway N High-Voltage Substation

Dongming Yan[1], Genda Chen[2] and Dennis Bouse[3]

[1] Center for Infrastructure Engineering Studies, Department of Civil, Environmental and Architectural Engineering, Missouri University of Science & Technology, Rolla, MO, E-mail: yando@mst.edu, Phone: (573) 341-6699

[2] Center for Infrastructure Engineering Studies, Department of Civil, Environmental and Architectural Engineering, Missouri University of Science & Technology, Rolla, MO, E-mail: gchen@mst.edu

[3] Civil and Structural Design Division, Ameren Corporate, 1901 Chouteau Avenue, St. Louis, MO, E-mail: DBouse@ameren.com

ABSTRACT

In this study, 38/ 34kV Highway N Substation, St. Charles County, Missouri was analyzed with a finite element model (FEM) for its vulnerability during earthquake excitations. Every component of the substation was modeled with due considerations of mass density, stiffness and geometries. Based on the FEM, modal analysis was conducted to identify the natural frequencies of structures along with their corresponding mass participation factors. In response spectrum analysis, the dynamic responses of main components such as 'rigid' buses and switches were evaluated. In time-history analysis, both site-specific synthetic ground motion and spectrum compatible ground motion were considered. The numerical results under both ground motions were compared and the magnitude and location of the maximum moments in each case were identified.

1 INTRODUCTION

In recent years, strong earthquakes have occurred in urban areas. They often lead to devastating damage of constructed facilities, such as lifeline systems, gas and water distribution systems, power transmission systems and communication networks, threatening the safety and security of citizens and impacting regional economy. For example, the El Salvador Earthquake that occurred on January 13, 2001, Japan, caused nationwide damage to the electric power system (Konagai, 2001). To minimize losses such as these, shortly after an earthquake, damaged substations must be repaired and resumed to full operation. Typical damages were observed in transformers, bushings, interrupters, connectors, radiators, circuit breakers, surge arresters and capacitor banks. This highlights the need to identify and strengthen the critical components of these systems so that their functionality during future earthquakes is ensured. A power substation is comprised of interconnected components including transformers, bushings, disconnect switches, interrupters, connectors, circuit breakers, surge arresters, etc.. Some

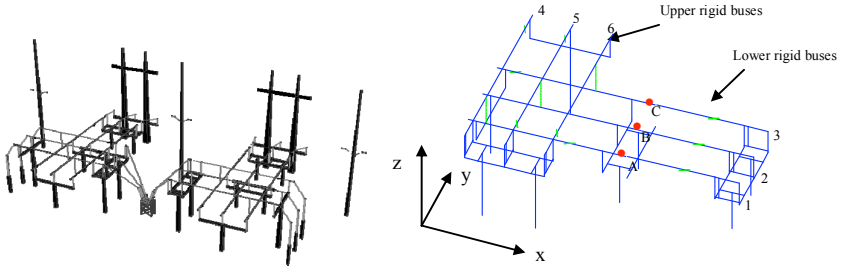
components of power substations such as porcelain insulators and bushings were quite susceptible to earthquakes and easily broken due to strong shaking. These equipment items are usually connected to each other through conductor buses or flexible cables. In the event of earthquakes, these connections may induce dynamic interaction among the items. Previous studies (Kiureghian and Sackman et al., 1999; Kiureghian and Hong, 2000) have indicated that the dynamic characteristics may have contributed significantly to the damage of power substations. However, design guidelines or analysis methods that account for this interaction effect are currently unavailable.

The objective of this paper is to evaluate the seismic performance of various components of the Highway N Substation with FEM, using a site-specific design response spectrum or a synthesized ground motions for the region.

2 FEM ANALYSIS

2.1 FEM Modeling

The SAP2000 finite element code was used to develop a model of the 138kV side of the power substation. The FEM of the main parts of the substation includes steel support structures, porcelain bushings, rigid bus, dampers, and cables, as shown in **Figure 1a**. ain focus of the analysis was to determine the seismic response of the 138kV rigid bus assembly. In particular, the goal was to obtain the 138kV disconnect switch seismic response (**Figure 1b**). The upper rigid buses (4, 5, and 6) are oriented in 90° with the lower rigid buses (1, 2, and 3). The sliding mechanisms such as sleeves in the rigid bus and the electric switches were modeled by constraining two sets of nodes at the two sides of each sliding mechanism except for their slippage along the centerline of a rigid bus and a switch arm. The 'rigid' bus and disconnect switch components in the FEM model, which is one of the critical parts of the power substation, were validated with a full scale shake table test on three Turner Electric's TMX switches (Chen, 2009).



(a) Full model (b) Partial model

Figure 1 FEM of the substation

2.2 Modal Analysis

The modal analysis of the Highway N rigid bus assembly structure wasconducted to determine the natural frequencies and mode shapes of the structure and evaluate its responses under dynamic loading. In general, the

dynamic responses of the structure are governed by a number of the lowest vibration modes.

How many modes of vibration must be included in analysis is a practical question. In building design, the accumulated modal participation mass factor (MPMF) in each horizontal direction must exceed 90%. For complex 3-D structures, it is often difficult to achieve that level of mass participation in all directions. In this study, an effort was made to include an accumulated MPMF of over 90% in each horizontal direction (X and Y directions in Figure 3). To this end, a total of 40 modes are specified in the initial analysis of the structure to ensure satisfied accuracy of the first 20 vibration mode characteristics.

The natural frequencies of the first 20 modes with modal mass-participant factors are listed in Table 1 along with a brief description of each dominant motion and its respective MPMF. Here, the significant modes are defined as those with an MPMR of 2% or higher in any single direction.

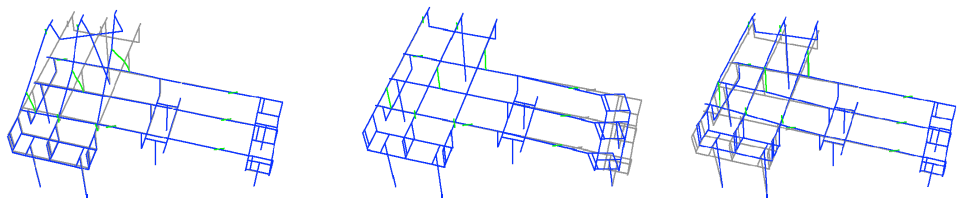
Table 1 Frequencies, periods and mass participating factors

Mode No.	Period (sec)	Frequency (Hz)	Modal mass participation factor (%)						Description
			UX	UY	UZ	RX	RY	RZ	
1	0.826	1.21	**7.5**	**1.6**	0.0	0.3	**4.3**	**11.9**	**UX+RY+RZ**
2	0.784	1.28	**25.7**	0.0	0.1	0.1	**3.5**	**18.0**	**UX+RY+RZ**
3	0.719	1.39	0.3	**44.5**	0.0	**12.2**	0.1	0.3	**UY+RX**
4	0.615	1.63	**32.5**	0.0	0.0	0.0	**12.6**	**4.7**	**UX+RY+RZ**
5	0.484	2.07	0.0	0.5	0.0	0.1	0.0	0.1	
6	0.410	2.44	0.0	0.3	0.0	0.0	0.0	0.2	
7	0.322	3.10	0.0	**32.3**	0.0	**3.6**	0.0	**34.1**	**UY+ RZ**
8	0.305	3.28	0.2	0.0	0.0	0.0	0.0	**2.1**	**RZ**
9	0.286	3.49	**25.3**	0.0	0.2	0.2	**3.2**	**17.4**	**UX+RY+RZ**
10	0.270	3.71	**1.1**	0.1	0.0	0.1	0.0	**2.0**	**RZ**
11	0.243	4.12	0.0	**12.6**	0.0	**1.3**	0.0	**1.9**	**UY+RZ**
12	0.233	4.29	0.4	0.0	0.0	0.0	0.0	0.3	
13	0.213	4.70	0.2	0.0	0.0	0.0	0.0	0.4	
14	0.204	4.90	0.0	**2.4**	0.1	0.2	0.0	0.0	**UY**
15	0.188	5.31	0.0	**4.3**	0.0	0.2	0.0	0.3	**UY**
16	0.180	5.55	0.0	0.1	0.1	0.1	0.0	0.0	
17	0.159	6.31	0.0	0.1	0.1	0.2	0.0	0.8	
18	0.147	6.79	0.3	0.0	**6.6**	**6.3**	0.3	0.2	**UZ+RX**
19	0.144	6.96	0.9	0.0	0.4	0.4	**3.6**	0.7	**RY**
20	0.141	7.08	0.3	0.0	**2.0**	**1.8**	0.4	0.2	**UZ+RX**
Total	-	-	94.7	99.0	9.6	27.3	28.1	95.6	

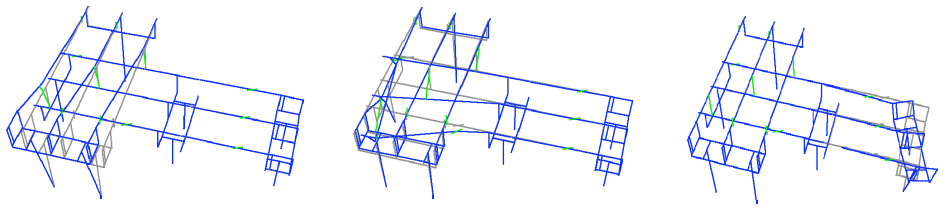
In Table 1, UX, UY, and UZ represent the translational motions along X, Y, and Z axes while RX, RY, and RZ, denote the rotational motions about X, Y, and Z axes, respectively. The MPMF value provides a measure of how important a particular mode of vibration is for the overall response to the acceleration loads in

each of the three global directions though a small MPMF value could correspond to a significant local vibration mode. It helps ensure a significant and required number of vibration modes are included in the seismic response analysis. Table 1 indicates that the accumulated MPMF exceeds 90% in X and Y directions as well as in rotational motions about the vertical axis. The MPMF in vertical direction is low since the critical components, rigid buses, participating in various vibration are relatively light in comparison with vertical members. The fact that a less mass participation is observed in the vertical direction is likely attributable to the presence of flexible cables in the model, where some of them vibrate independently of the remaining structure.

The first 6 mode shapes of vibration are presented in **Figure** 2. Most modes correspond to the coupled motion in X and Y directions. This observation indicates that the structure is flexible in the X and Y direction. Indeed, the fundamental period of 0.826s mainly corresponds to the X movement of the tall part of the structure together with the slight Y movement and the rotation around Y and Z, as shown in **Figure** 2(a).



(a) Mode No. 1 (b) Mode No. 2 (c) Mode No. 3



(d) Mode No. 4 (e) Mode No. 5 (f) Mode No. 6

Figure 2 Mode shapes of the FEM

Figure 2(b) shows the second mode of vibration in the X direction at a period of 0.784 sec. The shape of the 3rd mode is shown in Figure 4(c); it mainly corresponds to the Y motion. The shapes of the 4^{th} mode and 9^{th} mode primarily correspond to the X motion while Modes 7, 11, 14 and 15 mainly correspond to the Y motion. Basically, the first 11 modes dominate the horizontal vibration of the substation structure. These modes are mainly related to the motion of the supports in the structure. After the 11^{th} mode, more and more rigid bus begins to participate in the motion. That is why the mass participant factors are relatively small for the several last vibration modes.

2.3 Response Spectrum Analysis

2.3.1 Response spectrum

Surface exploration at the project site was reported by Geotechnology (2004). Based on the soil condition, the project site was classified as Class D (IBC, 2003). In this case, the design spectral response accelerations (S_{DS} & S_{D1}) were calculated using the procedures outlined in Section 1615 of the 2003 IBC. The spectral parameters used for estimation of the ground accelerations at short period (S_{DS}) and at one second period (S_{D1}) were determined based on the site condition. The design spectrum was governed by S_{DS} = 0.45g, S_{D1} = 0.15g and T_0 = 0.1 sec.

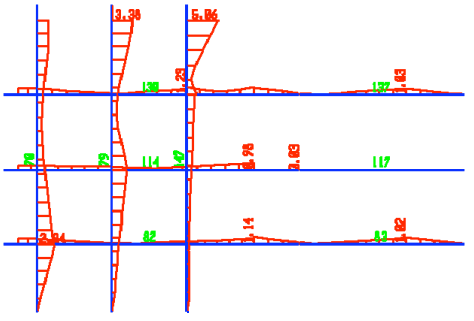
2.3.2 FEM analysis

The FEM of the substation's 138kV side rigid bus assembly was analyzed under the design earthquake described by the response spectrum. The maximum relative velocity and displacement obtained at the three key points at lower rigid buses, as indicated in **Figure 1** (b) are listed in Table 2. The maximum relative displacements are approximately 2.24 in.

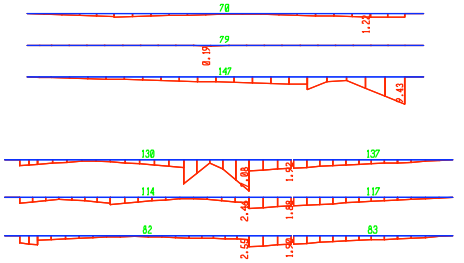
Table 2 Relative acceleration, velocity and displacement

Location	Relative velocity (in/sec)	Relative displacement (in)
A	15.3	2.24
B	15.2	2.22
C	15.3	2.23

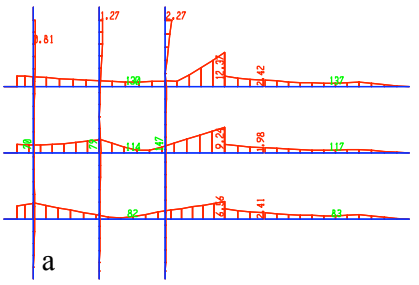
The flexural moment distributed along the six main buses are presented in **Figure 3**(a, b) are due to the earthquake excitation in X direction while **Figure 3**(c, d) result from the excitation in Y direction. It is evidenced that the maximum out-of-plane moment occurred in lower main buses (1, 2, and 3) as a result of the Y-directional earthquake. The maximum in-plane moment occurs in upper main buses (4, 5, and 6) due to the X-directional earthquake.



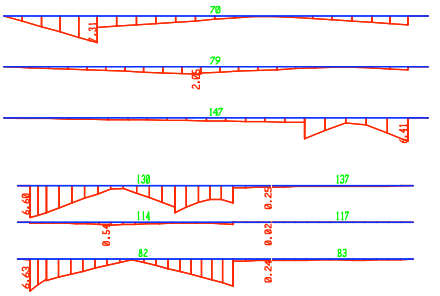
(a) Out-of-plane moment about vertical axis under X-directional earthquake



(b) In-plane moment about horizontal axis under the X-directional earthquake



c)) Out-of-plane moment about vertical axis under the Y-directional earthquake



(d) In-plane moment under horizontal axis due to Y-directional earthquake

Figure 3 Moment distribution along main buses

Each main bus has at least one vibration absorber and a cable constraint between two levels of switch structures. It can be seen from Figure 3 that the maximum moment in various buses varies. The absolute maximum moment among all the buses occurs in bus #3. It is noted that the larger value of vertical and transverse moments does not necessarily happen in the same direction. This observation can be seen in **Table 3**. The maximum moment in bus 3 reaches about 12.4 kip-in out of plan due to the Y-directional earthquake. It is also observed that both the 30% and the square-root-of-the-sum-of-the-squared load combination rules give higher moments due to the combined effect of directional earthquake components.

Table 3 Maximum moment in each bus (kip-in)

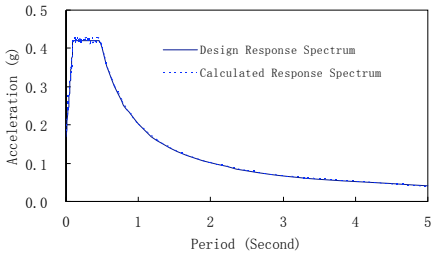
Earthquake component	Moment	Bus #1	Bus #2	Bus #3	Bus #4	Bus #5	Bus #6
X	In-plane	1.14	0.98	1.23	2.84	3.38	5.06
	Out-of-plane	2.55	2.46	7.08	1.22	0.19	**9.43**
Y	In-plane	6.56	9.25	**12.4**	0.81	1.27	2.27
	Out-of-plane	6.63	0.54	6.60	7.31	2.05	6.41
X + 30%Y	In-plane	3.11	3.76	4.94	3.08	3.76	5.74
	Out-of-plane	4.54	2.62	9.06	3.41	0.81	**11.4**
30%X + Y	In-plane	6.90	9.54	**12.7**	1.66	2.28	3.79
	Out-of-plane	7.40	1.28	8.72	7.68	2.11	9.24
$\sqrt{X^2+Y^2}$	In-plane	6.66	9.30	**12.4**	2.95	3.61	5.55
	Out-of-plane	7.10	2.52	9.68	7.41	2.06	**11.4**

2.4 Time History Analysis

Two methods were employed to generate synthetic ground motions in this study. The first method is for the ground motions compatible with the design response spectrum as specified in the 2003 IBC. The second one is for site-specific ground motions generated with the point source model.

2.4.1 Spectrum compatible ground motions

Ground motions were generated to ensure their acceleration response spectrum compatible with that in **Figure 4**, taken from the 2003 IBC. First, 10 synthetic ground motions were generated to match the spectral accelerations, S_{DS} and S_{D1}. Their response spectra were then evaluated and compared with the design acceleration spectrum. The best matched spectrum is selected as illustrated **Figure 4** along with the design spectrum. Its corresponding time history is presented in **Figure 5**. It is observed from **Figure 4 and Figure 5** that the synthetic ground motion results in a response spectrum that matches well with the design spectrum.



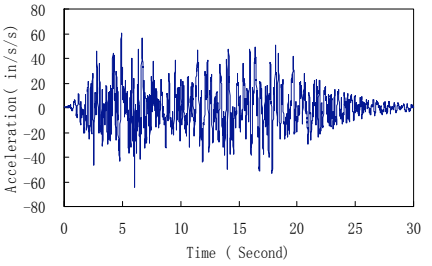
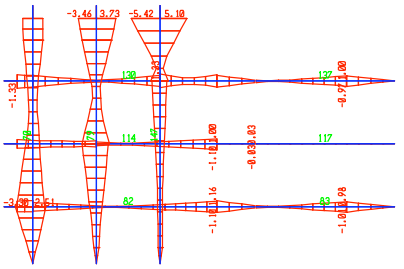
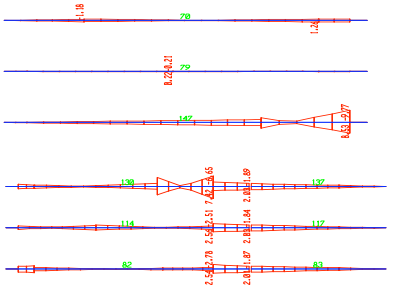


Figure 4 Response spectrum **Figure 5 Synthetic ground motion**

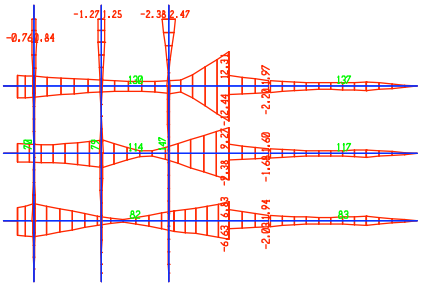
Time history analysis was also conducted with the FEM of the substation. Modal damping taken in this study was 0.05. The maximum moment is distributed along each bus as shown in Figure 6 for out-of-plane and in-plane moments in X direction (a and b) and Y direction (c and d), respectively.



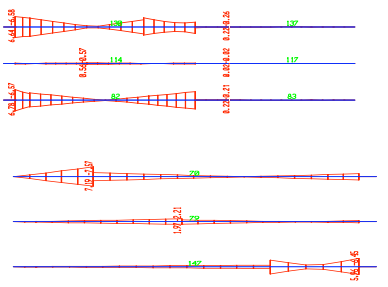
(a)Out-of-plane moment about the vertical axis



(b)In-plane moment about the horizontal axis



(c) Out of plane moment about the vertical axis



(d) In-plane moment around the horizontal axis

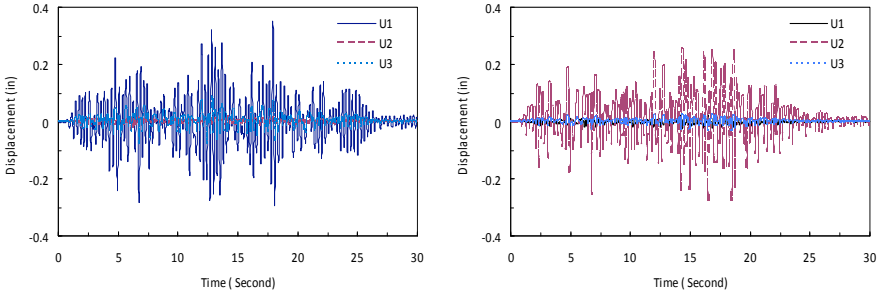
Figure 6 Moment envelop of main buses

The maximum moments along each bus due to individual component earthquakes and their combination are summarized in **Table 4.** The absolute maximum moments due to X- and Y-directional earthquakes are 9.77 kip-in and 12.4 kip-in, respectively. They occur in bus #6 and bus #3. Both the magnitude and location of the absolute moments well correspond to those from response spectrum analysis.

Table 4 Maximum moment in each bus (kip-in)

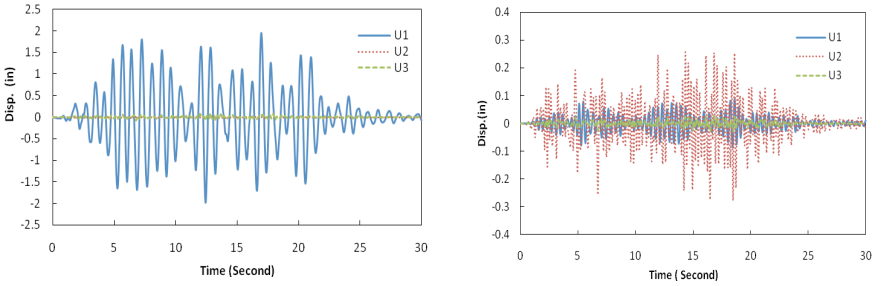
Earth**quake component**	**Moment**	**Bus #1**	**Bus #2**	**Bus #3**	**Bus #4**	**Bus #5**	**Bus #6**
X	In-plane	1.16	1.10	1.33	3.30	3.73	5.42
	Out-of-plane	2.78	2.56	7.42	1.26	0.22	**9.77**
Y	In-plane	6.83	9.38	**12.4**	0.84	1.27	2.47
	Out-of-plane	6.78	0.57	6.64	7.57	2.21	6.45
X + 30%Y	In-plane	3.21	3.91	5.06	3.55	4.11	6.16
	Out-of-plane	4.81	2.73	9.41	3.53	0.88	**11.7**
30%X + Y	In-plane	7.18	9.71	**12.8**	1.83	2.39	4.10
	Out-of-plane	7.61	1.34	8.87	7.95	2.28	9.38
$\sqrt{X^2+Y^2}$	In-plane	6.93	9.44	**12.5**	3.41	3.94	5.96
	Out-of-plane	7.33	2.62	9.96	7.67	2.22	**11.7**

The three-directional time history responses at joint "A" are presented in Figure 7 due to ground motions in X- and Y-direction, respectively. Since the main bus #1 with joint A is oriented along the X direction, the displacement at joint A (-X and +X sides) is the largest in the X- and Y-direction under the X- and Y-directional earthquakes, respectively. Note that U1, U2, and U3 in **Figures 7** and **8** represent the axiald is placement and the transverse displacements both in horizontal and vertical directions.



(a)Ground motion in X-direction (b) Ground motion in Y-direction

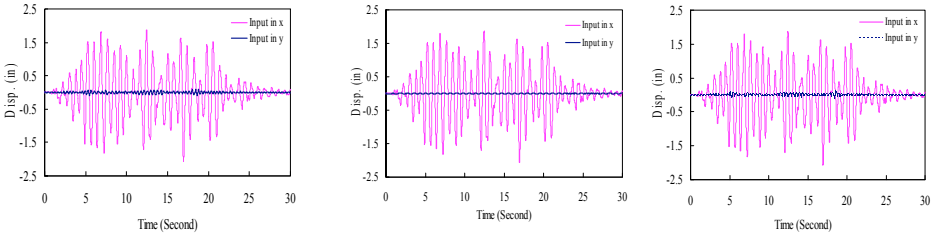
Figure 7 Displacement time histories at joint A (-X side) underground motions



(a)Ground motion in X-direction (b) Ground motion in Y direction

Figure 8 Displacement time histories at joint A (+X side) underground motions

The relative displacements at three slip joints (A, B, and C) are presented in **Figure 9** as the difference between the motions on two sides of each joint. It can be seen from the figure that the maximum relative displacement reaches 1.86 inches, which is slightly less than that obtained from the response spectrum analysis. The dominant excitation is in the X- direction and the influence of the excitation from Y direction can be neglected.



(a) Slip joint A (b) Slip joint B (c) Slip joint C

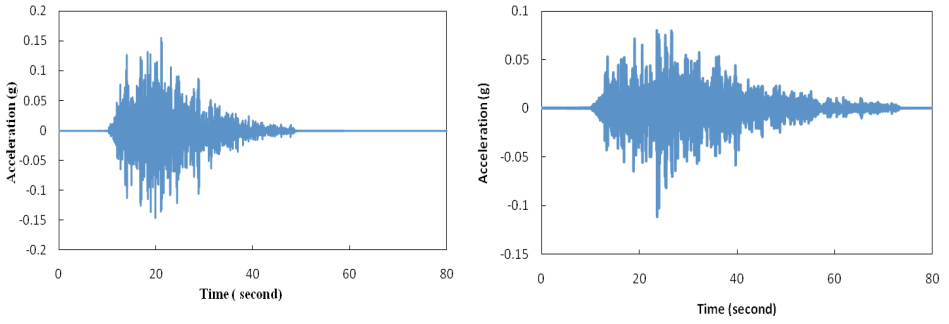
Figure 9 Open-and-close of the switches underground motions

2.5 Site-specific synthetic ground motion

The epicenter distance and the earthquake magnitude were selected for the synthesis of a site-specific ground motion. To match their spectral accelerations with S_{DS} & S_{D1}, several synthetic rock motions with a pair of distance and magnitude were first generated using the Boore's SMSIM method for the project site. A soil profile was then created using the boring log data reported by Geotechnology (2004), and the mean shear wave velocities (V_{sm}) of upper deposits (Karadeniz, 2007). Finally, site-specific response analyses were conducted with the SHAKE2000 software and the response spectra were examined to see how well they matched the design spectral accelerations, taken from the 2003 IBC. An appropriate rock motion was determined from the "best match" of these data.

For the project site located on the south side of the Old Highway "N" and east of the intersection with Highway K, the simulated rock motions predicted by the Boore SMSIM procedure were as follows: (1) M7.5 earthquake at a distance of 240 km, and (2) M7 earthquake at a distance of 100 km. These events result in

spectral accelerations of approximately 0.416g at 0.14 second and approximately 0.024g at 1 second periods. The time history of the ground motions induced by both earthquakes is depicted in **Figure 10.**



(a) M7.0 earthquake at 100 kim distance(b) M7.5 earthquake at 240 km distance

Figure 10 Synthetic ground motions at the project site

The maximum moments under one component and a combined action of two components of ground motions are presented in **Table 5** under an M7 earthquake at 100 km and in **Table 6** under an M7.5 earthquake at 240 km. In comparison with **Table 4**, **Tables 5** and **6** indicate that the maximum moment of the structure under the site specific ground motion is significantly smaller than that under the spectrum-compatible ground motion. This is attributed to different characteristics in the synthetic ground motions. The site specific ground motion depends upon the local geologic condition while the spectrum compatible ground motion was generated by following the design response spectrum that was developed based on the probabilistic seismic risk analysis.

Table 5 Maximum moment under an M7.0 earthquake at 100 km distance (kip-in)

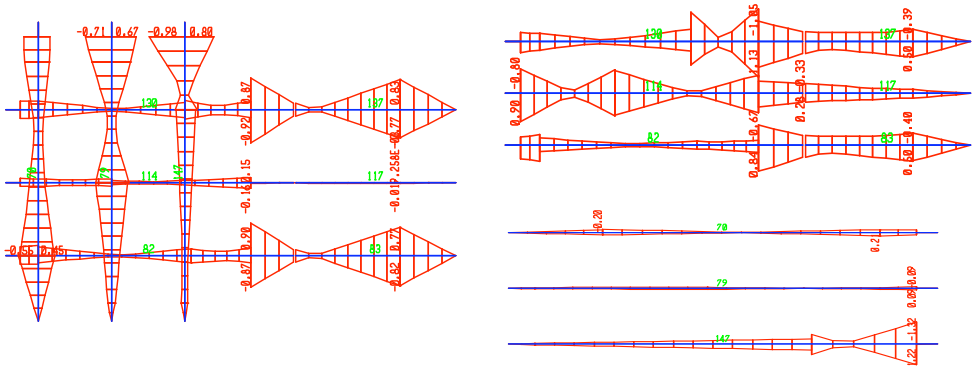
Earthquake component	Moment	Bus #1	Bus #2	Bus #3	Bus #4	Bus #5	Bus #6
X	In-plane	0.99	0.08	1.0	0.73	0.58	0.49
	Out-of-plane	0.53	0.78	0.65	0.13	0.08	1.07
Y	In-plane	0.64	0.94	1.23	0.1	0.11	0.24
	Out-of-plane	0.63	0.29	0.66	0.82	0.23	0.55
X + 30%Y	In-plane	1.18	0.36	1.37	0.76	0.61	0.56
	Out-of-plane	0.72	0.87	0.85	0.38	0.15	1.24
30%X + Y	In-plane	0.94	0.96	1.53	0.32	0.28	0.39
	Out-of-plane	0.79	0.52	0.86	0.86	0.25	0.87
$\sqrt{X^2+Y^2}$	In-plane	1.18	0.94	1.59	0.74	0.59	0.55
	Out-of-plane	0.82	0.83	0.93	0.83	0.24	1.20

Table 6 Maximum moment under an M7.5 earthquake at 240 km distance (kip-in)

Earthquake component	Moment	Bus #1	Bus #2	Bus #3	Bus #4	Bus #5	Bus #6
X	In-plane	0.90	0.18	0.92	0.55	0.71	0.98

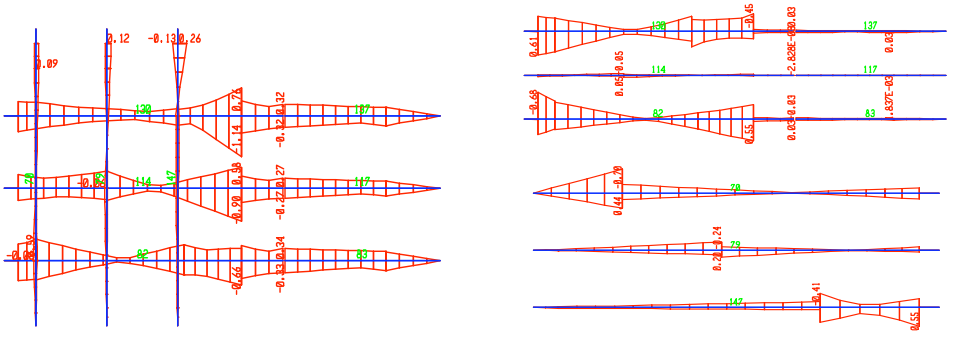
	Out-of-plane	0.84	0.90	1.13	0.21	0.09	1.32
Y	In-plane	0.66	0.90	1.14	0.09	0.12	0.27
	Out-of-plane	0.68	0.05	0.61	0.70	0.24	0.55
X + 30%Y	In-plane	1.10	0.45	1.26	0.58	0.75	1.06
	Out-of-plane	1.04	0.92	1.31	0.42	0.16	1.49
30%X + Y	In-plane	0.93	0.95	1.42	0.26	0.33	0.56
	Out-of-plane	0.93	0.32	0.95	0.76	0.27	0.95
$\sqrt{X^2+Y^2}$	In-plane	1.12	0.92	1.46	0.56	0.72	1.02
	Out-of-plane	1.08	0.90	1.28	0.73	0.26	1.43

Both the out-of-plane and the in-plane moment distributions along all main buses are shown in **Figures 11** and **12** under X-component and Y-component of the M7.5 earthquake, respectively. Their distribution is similar to that under the spectrum compatible ground motion.



(a) Out-of-plane moment (b) In-plane moment

Figure 11 Moment envelope under X-component of the M7.5 earthquake



(a) Out-of-plane moment (b) In-plane moment

Figure 12 Moment envelope under Y-component of the M7.5 earthquake

3 CONCLUDING REMARKS

1. The three-dimensional responses of the electric substation structure are evident. Most of the vibration modes are coupled together. The dynamic characteristics (frequency and mode shapes) of the structure indicate that the rigid bus-stayed structure is flexible in both horizontal directions.

2. The 20 significant modes of vibration up to 7.08 Hz include more than 90% mass participations in both horizontal directions.
3. Based on the time history analysis with synthetic ground motions, the maximum moment is approximately 12.44 kip-in, comparable to that obtained from the response spectrum analysis. The maximum relative displacement at the slip joints is 1.86 inches, 17% lower than the result from the response spectrum analysis. This conclusion mainly results from the fact that the response spectrum analysis loses the phase information among various responses, thus amplifying the relative motion.

ACKNOWLEDGEMENT

Financial support to complete this study was in part provided by Ameren and by the Center for Transportation Infrastructure and Safety at Missouri University of Science and Technology. The assistances from Dr. Kazi R. Karim on the establishment of the initial FEM model and Drs. Jianbo Li and David Rogers on ground motion generations are highly appreciated.

REFERENCES

1. KazuoKonagai, Nelson E. Pulido and Teturou Yamamoto et al. “The journal 13, 2001 off the coast of EL Salvador Earthquake,” Earthquake Engineering Committee, Japan Society of Civil Engineers, August, 2001.
2. Genda Chen, Dongming Yan, Zuocai Wang, et al. Numerical and Experimental Study on Seismic Vulnerability of the Highway N Substation. Final Report: NUTC R213&R228, October 2009.
3. Armen Der Kiureghian, Jerome L. Sackman and Kee-Jeung Hong. “Interaction in interconnected electrical substation equipment subjected to earthquake ground motions,” Report No. PEER 1999/01, Submitted to Pacific Gas & Electric Co., San Francisco, California. February, 1999.
4. Armen Der Kiureghian, Kee-Jeung Hong and Jerome L. Sackman. “Further studies on seismic interaction in interconnected electrical substation equipment,” Report No. PEER 2000/01, Pacific Earthquake Engineering Research Center, College of Engineering, University of California, Berkeley, November, 1999.
5. Junho Song, Armen Der Kiureghian and Jerome L. Sackman. “Seismic response and reliability of electrical substation equipment and system,” Report No. PEER 2005/16, Pacific Earthquake Engineering Research Center, College of Engineering, University of California, Berkeley, April, 2006.
6. Geotechnology Inc. “Subsurface exploration highway ‘N’ substation in O’Fallon, Missouri,” Report-IN/739001SE, 2004.
7. International Code Council. *International Building Code (IBC)*, Section 1615, p.322-307, 2003.
8. D. Karadeniz. “Pilot program to assess seismic hazards of the Granite City, Monks Mound, and Columbia Bottom Quadrangles, St. Louis Metropolitan Area, Missouri and Illinois,” Ph.D. at Missouri University of Science and Technology, unpublished, 2007.

Performance Indicators for Structures and Infrastructures

Dan M. Frangopol[1] and Duygu Saydam[2]

[1] Professor and the Fazlur R. Khan Endowed Chair of Structural Engineering and Architecture, Department of Civil and Environmental Engineering, ATLSS Engineering Research Center, Lehigh University, 117 ATLSS Dr., Bethlehem, PA 18015-4729, USA, PH (610) 758-6103; FAX (610) 768-4115; email: dan.frangopol@lehigh.edu (Corresponding author)
[2] Graduate Research Assistant, Department of Civil and Environmental Eng., ATLSS Engineering Research Center, Lehigh University, 117 ATLSS Dr., Bethlehem, PA 18015-4729, USA, PH (610) 758-6270; FAX (610) 738-5553; email: dus207@lehigh.edu

ABSTRACT

Design, assessment and prediction of the performance of structures and infrastructures based on component analysis have been the conventional methodologies enforced by the specifications. Nevertheless, system-based performance indicators can provide more efficiency and dependability in performance-based design, assessment, and prediction of structures and infrastructures. The objective of this paper is to provide a general overview of performance indicators applicable to civil structures and infrastructures. Definitions and formulations of selected performance indicators are presented. Information on what level (section, component, system, system of systems) these indicators are useful is provided. Interaction between life-cycle cost and lifetime performance is presented.

INTRODUCTION

Civil infrastructural systems are subjected to deterioration in strength and performance due to the aggressive environmental conditions (e.g., corrosion) and aging of the materials they are composed of. Therefore, the safety of these systems is highly affected by this deterioration. In order to avoid the consequences of structural failures, maintenance programs are carried out by the responsible authorities. It is necessary to predict the life-cycle performance of these systems accurately to establish a rational maintenance program. However, difficulties arise in prediction of life-cycle performance because of the complexity and high uncertainty in loading and deterioration processes. Consequently, it is essential to use proper indicators to evaluate the structural performance in a quantitative manner.

So far, many researchers focused on quantifying structural performance with deterministic and probabilistic indicators such as safety factor and reliability index, respectively. National design codes take uncertainty into account by including specific factors in the computation of structural resistance and load. However, the prediction of structural performance under deterioration may require the use of several performance indicators. For example, system reliability index is an adequate

measure for quantifying the safety of a structure with respect to ultimate limit states, but system redundancy index is required to evaluate the availability of warning before final failure. Moreover, performance indicators related to damage tolerance of structures, such as vulnerability and robustness are essential to consider for structures under deterioration and local damage together with the indicators related to ultimate limit states. To provide a desired safety level of structures, the values of performance indicators under consideration shouldn't down-cross required threshold levels. On the other hand, life-cycle cost of structures is another measure which decision makers have to balance with the performance indicators. Nevertheless, it is evident that evaluating structural performance requires considering multiple indicators simultaneously. The purpose of this paper is to review several structural performance indicators used to evaluate the performance of civil structural and infrastructural systems. The formulation of these indices and several associated references are presented. Information on what level (section, component, system, system of systems) these indicators are useful is provided. Background of balancing cost and performance is also briefly indicated.

LIMIT STATES IN PERFORMANCE QUANTIFICATION

Performance evaluation of cross-sections, members, parts of structures, and overall structures is based on limit states defining the failure domain under specific loading conditions. The limit states defining the failure modes of components are included in design codes. For instance, AASHTO LRFD Bridge Design Specifications (2007), regardless of type and analysis used, requires that

$$\sum \eta_i \gamma_i Q_i \le \phi R_n \tag{1}$$

is satisfied for all specified load effects and combinations, where Q_i is the load effect, R_n is the nominal strength, γ_i is load factor, ϕ_i is resistance factor and η_i is load modifier. Eq. (1) applies to all strength limit states, service limit states and fatigue and fracture limit states. The factors multiplying the load effects and nominal strength exist to ensure a predefined safety level of the component. However, if the purpose is to evaluate the performance of an existing structure or design with respect to different target performance levels, the equation defining limit states must be in the pure form. A general representation of limit states which is used in reliability analysis in terms of a performance function $g(\mathbf{X})$ can be expressed as

$$g(\mathbf{X}) = g(X_1, X_2, ..., X_n) = 0 \tag{2}$$

where $\mathbf{X} = (X_1, X_2, \ldots, X_n)$ is a vector of random variables of the system, and the performance function $g(\mathbf{X})$ determines the state of the system as $[g(\mathbf{X}) > 0]$ = "Safe state", and $[g(\mathbf{X}) < 0]$ = "Failure state".

LEVELS OF PERFORMANCE QUANTIFICATION

In regard to the purpose and type of analysis, structural performance can be quantified at cross-section level, member (component) level, overall structure (system) level, and group of structures (system of systems) level. The strength of a component under different loading conditions can be expressed in terms of the capacity of its most critical section when stability problems are not accounted for. Under consideration of stability problems, the performance is quantified at component level. In most of the current building design codes, strength requirements are based on component strength. Although this kind of approach may ensure an adequate level of safety of components, it lacks the information about the interaction between the components and overall performance of the whole structure. However, performance at system level is of concern in performance-based design. Structural reliability theory offers a rational framework for quantification of system performance by also including the uncertainties both in the resistance and the load effects. Overall system performance for a limit state can be evaluated by assuming that the system limit state is series or parallel or series-parallel combination of component limit states (Ditlevsen and Bjerager, 1986; Hendawi and Frangopol, 1994). The domain Ω, representing the violation of system limit state can be expressed in terms of component limit states as (Ang and Tang 1984):

(a) for series system $\Omega \equiv \bigcup_{k=1}^{n} \{g_k(X) < 0\}$

(b) for parallel system $\Omega \equiv \bigcap_{k=1}^{n} \{g_k(X) < 0\}$

(c) for series-parallel system $\Omega \equiv \bigcup_{k=1}^{n} \bigcap_{j=1}^{c_n} \{g_{k,j}(X) < 0\}$

where c_n is the number of components in the n-th cut set.

The performance of a system which consists of a number of subsystems depends not only on the performance of the subsystems but also on the interaction of these subsystems. An example of a system of systems is a highway bridge network, where each bridge is a system itself and interacts with the other bridges for the performance of whole network by means of traffic flow.

DEFINITIONS OF COMMON PERFORMANCE INDICATORS

Safety factor. The simplest deterministic interpretation of the safety factor, when there is a linear relationship between the load and the stress produced by the load, is

$$SF = \frac{\sigma_u}{\sigma_{all}} \tag{3}$$

where SF represents the safety factor, σ_u is the maximum usable stress which can be either the yield stress or the ultimate stress, and σ_{all} is the allowable stress which is usually defined in structural design codes.

The most common use of safety factor is design at section and component levels. Allowable stress design is based on the concept that the maximum stress in a cross-section or a component shall not exceed a certain allowable stress under normal service conditions (AISC, 2005). The limiting stress, which can be yield stress or stress at instability or fracture, is divided by a safety factor to provide the allowable stress. The safety factor is used to provide a design margin over the theoretical design capacity to allow for consideration of uncertainty due to any components of the design process including calculations, material strengths, and manufacture quality.

Load and resistance factors. Load and resistance factor design is based on the ultimate strength of critical member sections or the load carrying capacity of members (Ellingwood et al., 1980). In Load and Resistance Factor Design (LRFD), the resistances R and the load effects Q are usually considered as statistically independent random variables. If the resistance R is greater than the load effect Q, a margin of safety exists. On the other hand, since resistance and load effect are random variables, there is a probability that resistance is smaller than load effect. This probability is related to the overlap area of the frequency distributions of the resistance and load effect and their dispersions (AISC, 2005). Figure 1 illustrates the probability density functions (PDFs) of the resistance and load effect. In this figure $E(Q)$ and $E(R)$ represent the mean values of load effect and resistance, respectively.

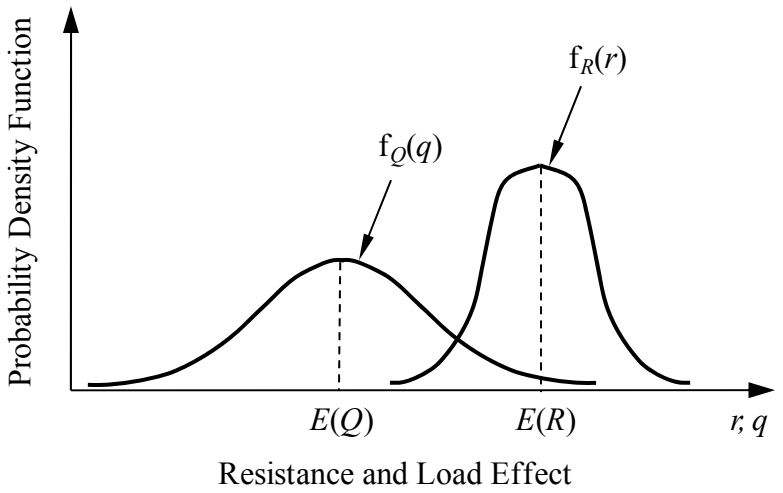


Figure 1 – Probability density functions of resistance and load effect

Load and resistance factors are used for design at section and component levels. LRFD suggests the use of resistance factor and partial load factors to account for the uncertainty in the resistance and the load effect. The partial load factor approach was originally developed during 1960s for reinforced concrete structures. It gives the opportunity for live and wind loads to have greater partial load factors than the dead load due to the fact that live loads and wind loads have greater uncertainty. The condition of safety with respect to the occurrence of failure mode i including the reduced resistance and factored loads using resistance and partial load factors can be written as

$$\phi_i R_i \geq \gamma_{Di} Q_{Di} + \gamma_{Li} Q_{Li} + \ldots \tag{4}$$

where R is the member resistance, ϕ_i is the resistance factor, Q_D and Q_L are the dead and live load effects, and γ_D and γ_L are the partial load factors associated with the dead and live load, respectively.

Probability of failure. The stochastic nature of the structural resistance and the load effects can be described by their probability density functions. The probability of failure of any section, component or system is defined as the probability of occurrence of the event that resistance is smaller than the load effects and can be evaluated by solving the following convolution integral:

$$P_f = P(g \leq 0) = \int_0^\infty F_R(s) f_Q(s) ds \tag{5}$$

where g is the performance function, R is the resistance in a certain failure mode, Q is the load effect in the same failure mode, F_R is the cumulative distribution function of R, and f_Q is the probability density function of the load effect Q.

Probability of failure is the basis for most probabilistic performance indicators. It is used at all levels (section, component, system, system of systems). In many cases, it is impossible or very demanding to evaluate P_f by analytical methods. Therefore, numerical methods such as Monte Carlo Simulations are used.

Reliability index. The reliability of a structure can be expressed in terms of either probability of failure or its corresponding reliability index. As a measure of reliability, reliability index can be defined as the shortest distance from the origin to the limit state surface in the standard normal space. For normally distributed independent variables reliability index can be calculated as

$$\beta = \frac{E(R) - E(Q)}{\sqrt{\sigma^2(R) + \sigma^2(Q)}} \tag{6}$$

where β indicates the reliability index, $E(R)$ and $E(Q)$ are the mean values of the resistance and load effect, and $\sigma(R)$ and $\sigma(Q)$ are the standard deviations of the resistance and load effect, respectively. For more complex problems, first and second order reliability methods (FORM and SORM) which approximately provide the reliability index by searching the most probable point on the failure surface (g_j=0), are the most common methods to compute reliability index. The probability of failure and reliability index are approximately related to each other as follows

$$P_f = 1 - \Phi(\beta) \tag{7}$$

where $\Phi(.)$ indicates the standard normal distribution function.

Cumulative time probability of failure. The probability of failure within a certain period of time is called cumulative time probability of failure. The basic approach considers only one random variable, the time at which the component or system fails. Cumulative time probability of failure up to time t_f can be calculated as (Frangopol and Okasha, 2008)

$$F(t_f) = P(T \le t_f) = \int_0^{t_f} f(u)du \tag{8}$$

where $F(t_f)$ is the area under the probability density function $f(u)$ of the time to failure to the left of t_f. Cumulative time probability of failure is a time-dependent performance indicator.

Survivor function. Survivor function is the probability that a component or system survives until time t. It is equal to the reliability function, which is the probability that a component or system is still functioning at time t. Survivor function is the complement of the cumulative time probability of failure and can be expressed as

$$S(t) = 1 - F(t) = P(T > t) = \int_{t_f}^{\infty} f(u)du \tag{9}$$

where $F(t_f)$ is the area under the probability density function $f(u)$ of the time to failure to the left of t_f. Survivor function is a time-dependent performance indicator.

Hazard function. Hazard function is a measure of risk associated with an item at time t. It is also known as hazard rate or failure rate. Hazard function also can be defined as the conditional probability of failure in a time interval $t+dt$, given that a component has survived until time t (Ramakumar, 1993). Hazard function is the ratio of probability density function to the survivor function and can be expressed as

$$h(t) = \frac{f(t)}{S(t)} \tag{10}$$

where $h(t)$ indicates the hazard function, $f(t)$ and $S(t)$ represent the probability density function and survivor function, respectively. Hazard function is a time-dependent performance indicator.

Redundancy. There are several definitions and indicators for structural redundancy in the literature. A measure of redundancy, in the context of availability of warning before system failure, was proposed by Frangopol and Curley (1987) as

$$RI_1 = \frac{P_{f(dmg)} - P_{f(sys)}}{P_{f(sys)}} \tag{11}$$

where $P_{f(dmg)}$ is the probability of damage occurrence to the system, and $P_{f(sys)}$ is the probability of system failure.

A measure of redundancy, as the availability of alternative load path after sudden local damage, was proposed by Frangopol and Curley (1987) as

$$RI_2 = \frac{\beta_{intact}}{\beta_{intact} - \beta_{damaged}} \tag{12}$$

where β_{intact} is the reliability index of the intact system and $\beta_{damaged}$ is the reliability index of the damaged system.

Redundancy is a system performance measure. However, it is also applicable at the section and component levels as a measure of warning with respect to failure. AASHTO LRFD Bridge Design Specifications (2007) considers redundancy in bridge structures based on the study of Frangopol and Nakib (1991). The load modifier η_i in Eq. (1), which accounts for redundancy level, is based on the redundancy definition in Frangopol and Nakib (1991). Application of redundancy concept to deteriorating structures can be found in Okasha and Frangopol (2009, 2010a).

Vulnerability and damage tolerance. In structural engineering, vulnerability is one of the key measures used to capture the essential feature of damage tolerant structures. A probabilistic measure of vulnerability was proposed by Lind (1995), defined as the ratio of the failure probability of the damaged system to the failure probability of the undamaged system

$$V = \frac{P(r_d, Q)}{P(r_0, Q)} \tag{13}$$

where r_d indicates a particular damaged state, r_0 indicates a pristine system state, Q is the prospective loading, $P(r_d, Q)$ represents the probability of failure of the system in the damaged state, $P(r_0, Q)$ represents the probability of failure of the system in the pristine state, and V refers to vulnerability of the system in state r_d for prospective loading Q. The value of vulnerability is 1.0 if the probabilities of failure of the damaged and intact systems are the same. Lind (1995) also defined the damage tolerance of a structure as the reciprocal of vulnerability. Vulnerability and damage tolerance are system performance indicators.

Risk. The most common formulation of risk in engineering is multiplication of probability of occurrence by the consequences of an event. Direct risk is the one associated with the damage occurrence itself while indirect risk is associated with the system failure as a result of the damage. Direct and indirect risks are formulated as (Baker et al., 2006)

$$R_{Dir} = \int_x \int_y C_{Dir} f_{D|E}(y \mid x) f_E(x) dy dx \tag{14}$$

$$R_{Indir} = \int_x \int_y C_{Indir} P(F \mid D = y) f_{D|E}(y \mid x) f_E(x) dy dx \tag{15}$$

where C_{Dir} and C_{Indir} are the direct and indirect consequences, and $f_Z(z)$ is used to denote the probability density function of a random variable Z. E, D and F represent the hazard occurrence, damage occurrence, and system failure, respectively. These integrals can be computed with numerical integration or Monte Carlo Simulation. Risk is applicable at component and system levels as well as system of systems level.

Robustness. Robustness is one of the key measures in the field of progressive collapse and damage tolerant structures. Although robustness is recognized as a desirable property in structures and systems, there is not a widely accepted theory on robust structures. Maes *et al*. (2006) defined robustness of a system as

$$R = \min_i \frac{P_{s0}}{P_{si}} \tag{16}$$

where P_{s0} is the system failure probability of the undamaged system, and P_{si} is the system failure probability assuming one impaired member i.

Baker *et al*. (2008) state a robust system to be one where indirect risks do not contribute significantly to the total system risk. An index of robustness is proposed as

$$I_{Rob} = \frac{R_{Dir}}{R_{Dir} + R_{Ind}} \tag{17}$$

where I_{Rob} is the index of robustness, and R_{Dir} and R_{Ind} are the direct and indirect risks, respectively. This index varies between 0 and 1.0 with larger values representing a larger robustness. Additional robustness indicators are indicated in Biondini and Frangopol (2010), Biondini et al. (2008), Ghosn and Frangopol (2007) , and Ghosn et al. (2010). Robustness is a system performance indicator.

Resilience. Bruneau et al. (2003) defined resilience as the ability of the system to reduce the chances of a shock, to absorb a shock if it occurs (abrupt reduction of performance), and to recover quickly after a shock (re-establish normal performance). According to their definition, a resilient system exhibits (a) reduced failure probabilities, (b) reduced consequences from failures in terms of lives lost, damage, and negative economic and social consequences, and (c) reduced time to recovery. The analytical definition of resilience is based on the concept of functionality, also called “serviceability” or “quality of infrastructure” (Bruneau et al. 2003; Cimellaro et al. 2010). Then, resilience is defined as the integral of the functionality in time as

$$R = \int_{t_0}^{t_h} Q(t) dt \tag{18}$$

where t_0 is the time at which the extreme event occurs, and t_h is the investigated time horizon. Resilience is a system performance indicator. Resilience is also applied to

system of systems such as highway bridge networks. Application of resilience concept to highway bridge networks can be found in Bocchini and Frangopol (2011), Frangopol and Bocchini (2011).

Life-cycle cost. One of the most important measures in evaluation of structural performance is life-cycle cost. The proper allocation of resources can be achieved by minimizing the total cost while keeping structural safety at a desired level. The expected total cost during the lifetime of a structure can be expressed as (Frangopol et al., 1997)

$$C_{ET} = C_T + C_{PM} + C_{INS} + C_{REP} + C_F \tag{19}$$

where C_T is the initial cost, C_{PM} is the expected cost of routine maintenance cost, C_{INS} is the expected cost of inspections, C_{REP} is the expected cost of repair, and C_F is expected failure cost.

BALANCING COST AND PERFORMANCE

Life-cycle cost and performance level of a structure are two conflicting criteria that should be balanced. Significant amount of research has been done in the area of optimum planning for life-cycle management of civil structures and infrastructures (Chang and Shinozuka, 1996; Ang and De Leon, 1997; Frangopol et al. 1997, 2001; Ang et al. 1998; Estes and Frangopol, 1999; Frangopol and Kong, 2001; Okasha and Frangopol, 2010b).

The interaction between the components of life-cycle cost and initial performance level (i.e., reliability index) is qualitatively illustrated in Figure 2. Higher performance levels require higher initial cost. However, if the initial performance level is high, failure cost, preventive maintenance cost and repair cost are lower.

CONCLUSIONS

In this paper, common performance indicators for civil structures and infrastructures are presented. Some indicators are used to define performance at cross-section and component levels while others are used to quantify performance of systems and groups of systems.

The matter of which indicators should be considered depends on the priorities and objectives of the decision makers. In most design processes, the main purpose is minimizing the life-cycle cost while maintaining safety at an acceptable level. If time-dependent analysis is required, time-dependent indices such as cumulative probability of failure, survivor function, hazard function or cumulative hazard function may be essential. Furthermore, structures are subjected to damage and deterioration during their lifetime. In this case, not only basic safety measures such as reliability index but also the measures related to damage tolerance of structures such as vulnerability, redundancy, and robustness may be beneficial.

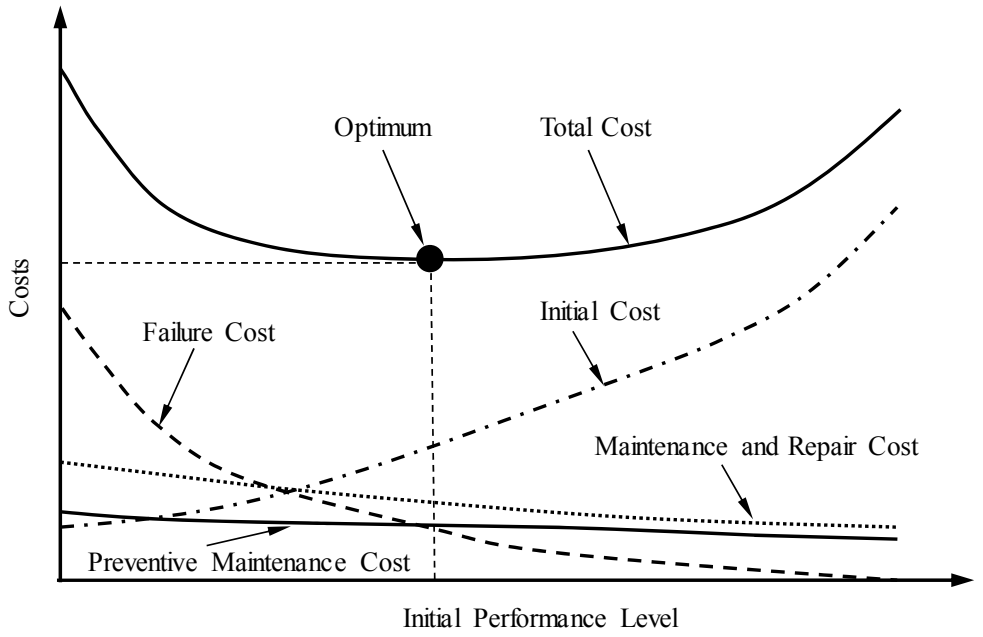


Figure 2 – Interaction between costs and initial performance level

The performance indicators for civil structures and infrastructures are not limited to those mentioned in this paper. More effort should be placed on determination of performance indicators and their use in risk communication and optimal decision making under uncertainty.

ACKNOWLEDGMENTS

The support from (a) the National Science Foundation through grants CMS-0638728 and CMS-0639428, (b) the Commonwealth of Pennsylvania, Department of Community and Economic Development, through the Pennsylvania Infrastructure Technology Alliance (PITA), (c) the U.S. Federal Highway Administration Cooperative Agreement Award DTFH61-07-H-00040, and (d) the U.S. Office of Naval Research Contract Number N00014-08-1-0188 is gratefully acknowledged. The opinions and conclusions presented in this paper are those of the authors and do not necessarily reflect the views of the sponsoring organizations.

REFERENCES

American Institute of Steel Construction (AISC). (2005). *Steel Construction Manual*, Thirteenth Edition, Chicago, IL.

American Association of State Highway and Transportation Officials (AASHTO). (2007). *LRFD Bridge Design Specifications*, AASHTO 4th Ed., Washington, D.C.

Ang, A. H-S., and De Leon, D. (1997). "Target reliability for structural design based on minimum expected life-cycle cost." *Reliability and optimization of structural systems*, D. M. Frangopol, R. B. Corotis, and R. Rackwitz, eds., Pergamon, New York, 71–83.

Ang, A. H-S., Lee, J-C., and Pires, J. A. (1998). "Cost-effectiveness evaluation of design criteria." *Optimal performance of civil infrastructure systems*, D. M. Frangopol, ed., ASCE, Reston, Va., 1–16.

Ang, A. H.-S. and Tang, W. H. (1984), "Probability concepts in engineering planning and design." Vol. II, John Wiley & Sons.

Baker, J. W., Schubert, M., Faber, M. H. (2006). "On the Assessment of Robustness." *Structural Safety*, Elsevier, 30, 253-267.

Biondini, F., and Frangopol, D. M. (2010). "Structural robustness and redundancy of deteriorating concrete bridges." *Proceedings of the Fifth International Conference on Bridge Maintenance, Safety, and Management,* IABMAS2010, Philadelphia, USA, July 11-15, 2010; in *Bridge Maintenance, Safety, Management, Health Monitoring and Optimization*, D.M. Frangopol, R. Sause, and C.S. Kusko, eds., CRC Press/Balkema, Taylor & Francis Group plc, London, 487, and full paper on CD-ROM, Taylor & Francis Group plc, London, 2473-2480.

Biondini, F., Frangopol, D.M., and Restelli, S. (2008). "On structural robustness, redundancy and static indeterminacy." *Proceedings of the ASCE Structures Congress,* Vancouver, Canada, April 24-26, 2008; in *Structures 2008: Crossing Borders,* ASCE, 2008, 10 pages on CD-ROM.

Bocchini, P., and Frangopol, D. M., (2011). "Optimal resilience- and cost-based post-disaster intervention prioritization for bridges along a highway segment", *Journal of Bridge Engineering*, ASCE, doi: 10.1061/(ASCE)BE.1943-5592.0000201.

Bruneau, M., Chang, S. E., Eguchi, R. T., Lee, G. C., O'Rourke, T. D., Reinhorn, A. M., Shinozuka, M., Tierney, K., Wallace, W., and Winterfelt, D. V. (2003). "A framework to quantitatively assess and enhance the seismic resilience of communities." *Earthquake Spectra*, EERI, 19(4), 733-752.

Chang, S. E., and Shinozuka, M. (1996). "Life-cycle cost analysis with natural hazard risk." *J. Infrastruct. Syst.*, 2(3), 118–126.

Cimellaro, G. P., Reinhorn, A. M., and Bruneau, M. (2010). "Seismic resilience of a hospital system." *Structure and Infrastructure Engineering*, Taylor and Francis, 6(1), 127-144.

Ditlevsen. O and Bjerager. P. (1986), "Methods of structural systems reliability." *Structural Safety*, Elsevier, 3(3-4), 195-229.

Ellingwood, B., Galambos, T. V., MacGregor, J. G., and Cornell, C. A. (1980). "Development of a probability-based load criterion for American National Standard A58." *NBS Special Publication 577*, U.S. Dept of Commerce, Washington, D.C.

Estes, A.C. and Frangopol, D. M., (1999). "Repair optimization of highway bridges using system reliability approach", *Journal of Structural Engineering*, ASCE, 125(7), 766-775.

Frangopol, D. M., and Bocchini, P. (2011). "Resilience as optimization criterion for the rehabilitation of bridges belonging to a transportation network subject to earthquake." *Proceedings of the 2011 Structures Congress*, ASCE, Las Vegas, NV, USA, April 14-16, 2011.

Frangopol, D. M. and Curley, J. P. (1987). "Effects of Damage and Redundancy on Structural Reliability." *Journal of Structural Engineering*, ASCE, 113(7), 1533-1549.

Frangopol, D. M., Kong, J. S., and Gharaibeh, E. S. (2001). "Reliabilitybased life-cycle management of highway bridges." *J. Comput. Civ. Eng.*, 15(1), 27–34.

Frangopol, D. M., Lin, K-Y., and Estes, A. C., (1997). "Life-cycle cost design of deteriorating structures", *J. Struct. Eng.*, ASCE, 123(10), 1390–1401.

Frangopol, D. M. and Nakib, R. (1991). "Redundancy in Highway Bridges." *Engineering Journal*, American Institute of Steel Construction, Chicago, IL, 28(1), 45-50.

Frangopol, D. M. and Okasha, N. M. (2008). "Life-Cycle Performance and Redundancy of Structures." *Proc. 6th International Probabilistic Workshop*, Darmstadt, Germany.

Ghosn, M., and Frangopol, D. M. (2007). "Structural redundancy and robustness measures and their use in assessment and design." *Proceedings of the Tenth International Conference on Applications of Statistics and Probability in Civil Engineering,* ICASP 10, Tokyo, Japan., July 31-August 3, 2007; in *Applications of Statistics and Probability in Civil Engineering*, Kanda, J., Takada, T., and Furuta, H., eds., Taylor & Francis Group plc., London, 2007, 181-182, and full 7 page paper on CD-ROM

Ghosn, M., Moses, F, and Frangopol, D. M. (2010). "Redundancy and robustness of highway bridge superstructures and substructures." *Structure and Infrastructure Engineering*, Taylor & Francis, 6(1-2), 257-278,

Hendawi. S., and Frangopol, D. M. (1994). "System reliability and redundancy in structural design and evaluation." *Structural Safety*, Elsevier, 16(1-2), 47-71.

Kong, J. S. and Frangopol, D. M. (2004). "Cost-Reliability Interaction in Life-Cycle Cost Optimization of Deteriorating Structures." *Journal of Structural Engineering*, ASCE, 130(11), 1704–1712.

Lind, N. C. (1994). "A Measure of Vulnerability and Damage Tolerance." *Reliability Engineering and System Safety*, Elsevier, 43(1), 1-6.

Maes, M. A., Fritzson, K. E., Glowienka, S. (2006). "Structural Robustness in the Light of Risk and Consequence Analysis." *Structural Engineering International*, IABSE, 16(2), 101-107.

Okasha, N. M. and Frangopol, D. M. (2009). "Lifetime-Oriented Multi-Objective Optimization of Structural Maintenance Considering System Reliability, Redundancy and Life-Cycle Cost using GA." *Structural Safety*, Elsevier, 31(6), 460-474.

Okasha, N. M. and Frangopol, D. M. (2010a). "Time-Variant Redundancy of Structural Systems." *Structure and Infrastructure Engineering*, Taylor & Francis, 6(1-2), 279-301.

Okasha, N. M. and Frangopol, D. M. (2010b). "Novel approach for multi-criteria optimization of life-cycle preventive and essential maintenance of deteriorating structures." *J. of Str. Engineering*, ASCE, 136(8), 1009-1022.

Ramakumar, R. (1993). *Engineering Reliability: Fundamentals and Applications*, Prentice Hall, New Jersey.

Performance Indicators for Offshore Wind Farms

A. Longabard[1], G. Tsiatas[2] and L. Manuel[3]

[1]Grad Student, Dept. of Civil and Env. Engineering, Univ. of Rhode Island.
[2]Professor, Dept. of Civil and Env. Engineering, Univ. of Rhode Island
[3]Professor, Civil, Architectural and Env. Engineering, Univ. of Texas at Austin

ABSTRACT

The drive for alternative energy sources has resulted in many proposals for offshore wind farms in the United Sates. Offshore wind turbines are subject to harsh environmental conditions including but not limited to simultaneous action of extreme wind and wave loading as well as hurricanes. From a structural reliability point of view, there are several failure mechanisms of a wind turbine such as blade or other component fatigue, tower local or global buckling and foundation failure such as sliding. In addition, there are several mechanical components and a control mechanism that could be studied from a traditional reliability point of view. Given the complexity of the problem which involves a combination of structural and electromechanical systems, an approach based on annual power generation is considered here to evaluate the performance of offshore wind farms.

INTRODUCTION

In recent years, the desire for renewable (green) energy resources has increased dramatically. One such source of green energy is wind. Harnessing the power of wind has been documented to ancient times. Those early beginnings used wind as a direct source of power to provide mechanical work. In the modern era, the need for electrical energy has resulted in the development of numerous wind turbine schemes designed for that purpose. Despite unlimited, yet intermittently available, wind resources, wind turbines, like all electrical power-producing devices, require maintenance and suffer failures from time to time. Wind turbines have the additional complication in that they need to be located near the best sources of wind. Often times, these locations are difficult to approach (for maintenance) depending upon the weather and time of year. To further exacerbate the situation, failures frequently occur during times of inclement weather and harsh seasons. For wind to become a desirable major source of energy, its cost must prove reasonable compared to other sources.

There have been many studies related to the reliability of offshore wind turbines (Sorensen and Toft, 2010, Agarwal and Manuel, 2009). Structural reliability has been a key consideration. However, reliability cannot be isolated from performance

of mechanical components, control mechanisms, etc. Eventually, in order to make a comparison between wind turbine power generation and other types of power generation, a cost-benefit analysis needs to be undertaken to provide a solid rationale for its implementation. The benefits associated with wind energy could be a function of factors including net power generated, cost of net power generation, reduction of direct greenhouse gas emissions, overall carbon footprint, reduction in fossil fuel dependence, etc. It could in general be a combination of factors with varying weights assigned to the individual benefits.

If the various benefits are to be related to power generation, their evaluation is most appropriately associated with performance indicators deemed relevant to power generation. Performance indicators for wind turbines could include gross available power at a specified location, structural performance of the individual components or the entire system, net available power at a specified location, net cost of power, etc. Some indicators that have been suggested have targets such as "reduce installation costs by 20% by 2020," or "wind energy production forecast with less than 3% uncertainty by 2020."

An exact assignment of a single performance index that may be used for all wind farms is not easily attainable, but a generalized relation or index can be developed that is usable across a wide range of potential wind farm locations. In the present study, a procedure for the determination of the performance of wind farm total net annual output is investigated.

WIND TURBINE SYSTEMS AND SUBSYSTEMS

To account for the performance of a wind turbine, one needs to be familiar with its main components which include the foundation, the tower structure, the nacelle, and the rotor. Each of these components is made up of many subcomponents and their design can differ radically depending upon the size of the turbine, its operating environment, and what the designer considers the ideal turbine configuration given the constraints of the individual project.

For offshore wind turbines, the design of the foundation and support structure could be one of several alternative types including gravity, pilings, guy wires, tension legs, ballast stabilization, and suction-based anchors. The choice of specific foundation depends upon the water depth at the wind farm and the geology of the sea floor. Very limited evidence of foundation failures has been found during the research of existing systems. It is possible that experience from the offshore oil and gas technology can be of benefit in this regard. However, given that we have had no experience to date in locating wind turbines offshore in the United States on either the East or West coasts, it is not possible to make definitive conclusions regarding foundation performance. Experience with European offshore wind turbines has offered far greater data in this regard, but both the metocean and the seabed conditions in Europe are quite different from that on either coast of the United States.

The tower structure of a wind turbine is typically made of rolled, tubular steel. It might be expected that the corrosive effects related to seawater would be of considerable concern. However, given adequate inspection and the experience with performance coatings associated with oil and gas platforms, corrosion is of a lesser concern than other factors associated with the long-term operation of the wind turbine as a complete system.

The nacelle and the rotor are the two most complex systems in a wind turbine. The complexity of the nacelle is due its housing of the majority of the subsystems required for the operation of the wind turbine, including power generation and control systems (mechanical, hydraulic, and electrical). The major subsystems include the transmission, generator, brake, and the yaw/pitch/stall controller and actuators. The transmission subsystem varies substantially depending upon the design selected. Its purpose is to convert the rotation rate of the shaft from the rotor to the speed necessary for the generator to convert rotational energy into electrical energy. Two principal designs for the transmission are direct-drive (i.e. gearbox-free) and conventional gearbox-based or indirect-drive. Direct-drive transmissions may have higher initial costs but may lead to lower maintenance costs. There is a trend towards direct-drive systems for offshore applications due to reduced maintenance needs.

The brake system for a wind turbine is comprised of a mechanical friction brake and a hydraulic system that stops the turbine blades during maintenance and overhaul. A braking system is also used in the yaw mechanism to maintain nacelle position. In addition to these two braking systems, there are controllers for yaw as well as blade pitch/stall. Yaw control rotates the turbine directly into the wind in order to generate maximum power.

Typically, four yaw sensors monitor the wind direction and activate the yaw motors to face the prevailing wind. A four-point bearing connects the nacelle to the tower. The yaw mechanism turns the blades 90 degrees from prevailing winds under high winds to reduce stresses on internal components and to avoid over-speed conditions. If a grid failure were to occur in conjunction with an extreme wind event—which is a likely scenario—the yaw control system will become inactive. The loss of yaw control could increase the likelihood of damage/failure in the case of an extreme wind event.

The rotor portion of the wind turbine consists of the turbine blades, the hub at which the roots of the blades are connected, and individual blade pitching systems, if present in the particular design. The wind turbine blades experience the most complex, dynamic loading of the entire wind turbine system. In addition to experiencing rapid changes in wind direction and speed as well as wind shear, turbine blades may be susceptible to icing conditions, lightning, severe weather conditions, and debris impact. The structure of the blade is typically made up of an ‘internal beam’ which may be jointed in the case of blade pitching designs. The internal beam is designed such that it withstands the major portion of the dynamic loading (bending and torsion) of the blade. The materials employed in its manufacture vary widely depending upon size and manufacturer. Some of the largest blades consist of steel spars with composite outer sections and aeroshells. Some blades consist primarily of

composite materials. Regardless of design, the composite portions of blades are subjected to harsh environments of wind, salt spray, and constant ultraviolet exposure that can degrade the strength, creep resistance, toughness, and adhesive properties of the composite material that may ultimately lead to failure of the turbine blade.

ECONOMY OF OFFSHORE WIND

From an economic standpoint, wind energy is a sensible energy source as the primary source of such power generation results from a non-expendable natural resource. Wind does not suffer from erratic commodity prices unlike every other source of energy with the exception of solar energy. For this reason alone, continued exploration into the development of more efficient and resilient wind turbines is important as the need for energy continues to rise as the population of the world grows. Significant investment is required for any power generation project. Its selection is based upon net power generation as a function of cost. Expansion of wind as a major source of energy necessitates a continued drive toward reduction of cost. For wind, these costs include initial construction expenses, regular and unscheduled maintenance and repairs, as well as decommissioning at the end of the design life. The two components that experience the greatest dynamic loads are also the two most expensive components, i.e., the gearbox and turbine blades; they account for about 13% and 16%, respectively, of initial costs. A couple of cost factors for offshore wind farms that should not be overlooked are hose related to ‘grid connection’ and ‘feed-in rates’ since distances from land to these offshore facilities can be great.

Maintenance can be divided into two subsets, preventative and corrective. Preventative maintenance is composed of calendar-based, regular interval maintenance as well as condition-based maintenance that is a function of the state of a component at specific points in time. Corrective maintenance consists of planned and unplanned maintenance. Planned maintenance deals with maintenance as a result of an observed condition while unplanned maintenance deals with unexpected failures.

The availability of power from an offshore wind farm is a complicated issue of conflicting parameters. On one hand, a location with high constant wind energy density is desired for greatest consistent net energy production. However, a site with high wind energy density will also likely experience greater sea states and wind gusts. These conditions will require robust designs capable of withstanding high loads which can lead to increasing design, construction, and installation costs. Such conditions can also complicate maintenance procedures which will likely increase in frequency. As an alternative, additional wind data for offshore locations could be collected to determine the most ideal location for a wind farm (a location with sufficiently high consistent wind energy density without excessively severe sea states or gusts). The determination of such a perfect location would likely take a great deal of time and, thus, increase initial design costs. Also, a search for this perfect location could reduce the number of available wind farm locations to a degree at which point

the overall power goals for offshore wind may not be achieved. Furthermore, the likelihood of the perfect location coinciding with major traffic lanes, endangered wildlife habitats, or points of recreational/visual interest could increase as well. It seems that a delicate balance of low cost, robustness, high efficiency, low maintenance, and versatility must be achieved in order for offshore wind to become a viable option for energy production.

FAILURE MODES OF WIND TURBINES

The components of a wind turbine including the blades, tower, foundation, and mechanical elements can exhibit various structural failure modes. These can include fatigue of blades or foundation components, local buckling in the tower assembly, and foundation failure such as sliding or anchorage failure. However, failures are not just structural. Other failure modes include material failure, electrical failure, mechanical failure, output inaccuracy, and electrical insulation failure. These conditions can reduce energy output and render a project uneconomical. Typical root causes of failure include mechanical overload, vibration fatigue, and corrosion.

Failures that have been observed in the past and up to the present day suggest that the working environment for a wind turbine is very complex and not completely understood yet. Or, at the very least, it has not been fully accounted for in the design and manufacture of the units themselves. The various systems within a turbine are interconnected. If a sub-system or a component within a system fails to perform properly (e.g., due to excessive blade flexure), it may lead to catastrophic failure of the entire wind turbine. The environment (and the resulting load spectra) in which each wind farm operates is undeniably site-specific. Therefore, it may be necessary to modify the design of each turbine individually thus incurring additional design and manufacturing costs that would not be required if one robust design could meet the demands of most situations.

For large-scale offshore wind farms to become a reality in the United States, these hurdles faced by existing wind farms must be overcome. Cost-effective electricity will require efficiently designed, inexpensive, robust structures requiring minimal maintenance and downtime.

STATISTICAL RELIABILITY OF WIND FARM TOTAL NET ANNUAL OUTPUT

An offshore wind farm is a complex system with many inter-related variables which makes reliability evaluations difficult. There have been several reliability studies of specific limit states such as tower bending or foundation failure. Since cost is always critical for new energy-producing plants, cost-benefit studies have also been undertaken to investigate their economic viability. Ultimately, regardless of the factors chosen to determine the performance of a wind turbine or an entire offshore wind farm, this is a complex system of dependent variables. Generalized means of

defining and evaluating relevant parameters may be the only way to critique performance and compare potential wind farm locations versus other means of power generation. The parameters chosen for comparison depend upon the goal of the particular study. The study may be focused on structural behavior, maintenance activity, output power, cost of net power generation, or a combination of these. It may also be concerned with the survivability of a single component or group of components with respect to different design/build schemes and particular siting factors.

Given the high variability of wind and the dependence on other factors that affect overall net power generation over specified periods of time, developing a means of assessing the reliability of power output from a statistical standpoint could prove beneficial. Output power is dependent upon air density, area swept by the turbine blades, wind velocity, and the power coefficient (related to Betz Law). Other factors that may be affected by the inflow wind include power generation losses (the difference between gross and net power output), availability of the wind turbine to produce power due to planned or unplanned maintenance, frequency of occurrence of storms that force the entire wind farm to cease operation or stagnant conditions in which power generation is not feasible, as well as aerodynamic effects caused by the geometry of the wind farm itself (referred to as wake effects). Selection of a location for a wind farm is not arbitrary. Detailed studies of the wind are typically performed to determine not only the feasibility of a wind farm, but the ideal design of the turbines as well as the geometric layout of the farm itself.

Internal losses of a wind turbine may be a function of the rotational speed of the turbine blades. Such losses might result from friction in components including bearing, gears, and rotating portions of the generator. Other internal losses may be independent of rotational speed and might occur in stationary portions of the generator and subsystems of the wind turbine that utilize output power of the turbine to function. Availability of the turbine associated with planned and unplanned maintenance and repair is somewhat predictable. Planned maintenance is scheduled ahead of time with fairly certain downtime; unplanned events are not predictable. However, for a given design, historical maintenance records can be used to predict an approximate percentage of downtime for a given year. Severe storm and stagnation periods typically follow weather patterns that repeat on a fairly predictable basis at least from the standpoint of predicting approximate yearly downtime as a result of such events. Finally, a factor that may pose a lot of uncertainty is the wake effect. Many times, wind turbines are situated such that they are staggered with respect to prevailing winds. However, significant winds can occur outside of the prevailing direction. It is likely impossible to totally negate the effect of the wake. Continued research into this phenomenon with respect to its effects on wind turbines, both structurally and on power output, will assist in predicting power output and downtime. It may be reasonable to assume that a wake will affect power output (in a nonlinear fashion) from the leading row of turbines to the trailing rows.

Gross output power for a single wind turbine as a function of air density (ρ), rotor sweep diameter (d), hub-height air velocity or wind speed (v), and power coefficient (c_p), is as follows:

$$\dot{W}_{gross} = \frac{\pi}{8}\rho d^2 v^3 c_p \tag{1}$$

Taking into account losses (l_i) that are dependent upon rotational speed and those that are independent of rotational speed (L_i), turbine availability due to planned and unplanned maintenance (a_i), wake effect (ω_i), severe storm and stagnation period (z), and the layout of the farm into rows (r) and columns (n), the net power generation for a wind farm can be expressed as follows:

$$\dot{W}_{net} = zn \cdot \sum_{i=1}^{r} a_i \omega_i \left[l_i \dot{W}_{gross} - L_i \right] \tag{2}$$

The hub-height wind speed is typically assumed to follow a Weibull distribution curve. The equation describing the Weibull probability density function (pdf) is the following:

$$f(v) = \frac{k}{\lambda}\left(\frac{v}{\lambda}\right)^{k-1} \cdot e^{-\left(\frac{v}{\lambda}\right)^k} \tag{3}$$

The actual net work or energy output for a power generation system is the area under a curve of instantaneous net power as a function of time. Using the pdf for the hub-height wind speed, the gross output can be expressed as follows:

$$W_{gross} = \dot{W}_{gross} \cdot \Delta t \tag{4}$$

where $\Delta t = f(v)dv \cdot (1\ year)$ for an entire year of net generation.

Combining the previously defined equations for $\dot{W}_{net}$, $f(v)$, and W_{gross} (i.e., Eqs. 2, 3, and 4), an expression for net output can be found as follows:

$$W_{net} = \frac{\pi}{8} k \left(\frac{1}{\lambda}\right)^k \rho d^2 zn(1\ year) \cdot \sum_{i=1}^{r} a_i \omega_i \int_{v_{cut-in}}^{v_{cut-out}} \left(l_i v^3 c_p - L_i'\right) v^{k-1} e^{\left(\frac{v}{\lambda}\right)^k} dv \tag{5}$$

where $L_i' = \frac{8}{\pi} \frac{L_i}{\rho d^2}$

The goal of the statistical analysis is to determine the probability that certain specified event(s) will occur. In this case, the objective is to estimate the probability that the actual annual net output will meet the design value (W_{design}). Thus, the resulting reliability function is as follows:

$$\frac{\pi}{8} k \left(\frac{1}{\lambda}\right)^k \rho d^2 zn(1\ year) \cdot \sum_{i=1}^{r} a_i \omega_i \int_{v_{cut-in}}^{v_{cut-out}} \left(l_i v^3 c_p - L_i'\right) v^{k-1} e^{\left(\frac{v}{\lambda}\right)^k} dv - W_{des} \tag{6}$$

This function is made up of two parts, the resistance (capacity) and the load (demand). The annual output energy capacity of the wind turbine is the first term in Eq. (6) while the power demand is the second term, W_{design}. All the random variables that appear in Eq. (6) can be transformed into standard normal random variables using either their probability distributions or their first two marginal statistical moments and correlation coefficients, if applicable for correlated variables. Using the Hasofer-Lind First-Order Reliability Method (FORM) algorithm (Melchers, 1999; Nowak and Collins, 2000), a reliability index (or performance indicator) associated with Eq. (6) can be evaluated. This can be used as a relative means to assess the power generation performance of a wind farm.

CONCLUSION

A general reliability function describing the probability of net available energy meeting a prescribed design value was developed. Thorough examination and determination of second-order statistics (mean, standard deviation, and correlation coefficients) for each random variable in the function will allow for estimates of the probability that specific wind farm schemes composed of particular wind turbine designs can meet imposed demands. This measure of probability should prove to be a better means of characterization of wind farm output compared to the customary use of rated power in conjunction with a fixed reduction factor. The proposed probability method takes into account all variations that are present in the entire energy generation process for a wind farm and ultimately leads to estimates of the

likelihood of meeting the proposed value (W_{design}) set by the developer of the wind farm.

Future efforts may include examination of existing wind farms and turbine designs to estimate desired statistics for the variables defined herein. These statistical values can be used in turn to obtain statistical estimates of net wind farm output. Subsequently, a probability distribution function of output values can be generated and compared against actual output values of a wind farm over several periods of time as a means of verification and validation of this concept.

REFERENCES

Agarwal, P., and Manuel, L. (2009) "Modeling Nonlinear Irregular Waves in Reliability Studies for Offshore Wind Turbines," *Proceedings of the 28th International Conference on Ocean, Offshore and Arctic Engineering (OMAE2009)*, Honolulu, Hawaii.

Melchers, R.E. (1999) *Structural Reliability Analysis and Prediction*, John Wiley & Sons, 2nd Edition, 1999.

Nowak, A. S. and Collins, K. (2000) *Reliability of Structures*, McGraw-Hill New York.

Sorensen, J.D., and Toft, H.S. (2010) "Probabilistic Design of Wind Turbines." *Energies*, 3(2), 241-257.

Marine Hydrokinetic Energy Generation Systems and Their Performance Indicators

H. S. Tang[1] and S. Skraatz[2]

[1]Dept. of Civil Eng., City College, City Univ. of New York, 138th st. and Convent Ave., New York, NY 10031; (212) 650-8006; htang@ccny.cuny.edu (corresponding author)
[2]Dept. of Civil Eng., City College, City Univ. of New York, 138th st. and Convent Ave., New York, NY 10031; (212) 650-7000, ext. 13736; skraatz00@ccny.cuny.edu

ABSTRACT

As an important clean and renewable energy, tidal energy is attracting more and more attention, and various plan and projects are being made worldwide to generate power. First, this paper discusses the current status of tidal power generation, and then describes Marine Hydrokinetic (MHK) energy turbines and related facilities. Then, the paper proposes performance indicators of the power generation systems in aspects of their power output estimate and reliability.

INTRODUCTION

According to a recent survey, the global energy consumption in 2007 is 11103 million tons of oil equivalence, and this consumption consists of 35.6% oil, 23.8% natural gas, 28.6% coal, 5.6% nuclear power, and 6.4% hydroelectricity, with 88% of it coming from fossil fuels (IEA, 2007; Rourke et al., 2010). The heavy dependence on fossil energy now results in an unprecedented consequence that challenges the whole world; at the current rate of exploitation, this type of energy is expected to be exhausted in a near future. Even more, burning of fossil fuels produces CO_2 and has led to the greenhouse effect, which results in global warming and climate change (US NREL, 2005).

In recent years, more and more attention has been shifted to clean and renewable energy, and various plans and pilot projects have been developed to move away from using fossil fuels as the primary source of energy generation. Tidal energy is a clean and renewable energy, and it is able to provide a significant amount of energy. A study completed in 1999 by the Marine Oversight Committee of the British House of Commons concluded: “if 1/10 of 1% of the energy in the world’s oceans could be converted into electricity; it would supply the world energy demand five times over.”

At present about 5% of the UK's electricity comes from renewable energy resources. With a plan to produce 20% of its total energy from renewable resources by 2020, which corresponds to about 35% of its electricity demand, the UK is exploring to increase generation of renewable energy from tidal sources (DTI, 2003; Xia et al., 2010). The Korean government plans to increase investment on alternative energy sources in the country's energy spending from current 1.4 percent to 5 percent by 2011 (Lee and Yoo, 2009). New Jersey State has set goals to achieve 20% renewable energy generation by 2020 and considers tidal energy as an important part of it. It is estimated that if only 1% of the New Jersey shoreline is utilized for tidal energy production, it could contribute an estimated 500 MW or more power based on presently available technology during the next 2-3 years, while adding over $1 Billion to the New Jersey economy in the next decade (NJDOT 2010). The first tidal energy site in New Jersey received its Waterfront Development Permit from the NJ Department of Environmental Protection (NJDEP) on January 14, 2010.

Tidal energy consists of potential and kinetic components. Accordingly tidal power facilities are categorized into two types: tidal barrages and tidal current turbines, which use the potential and kinetic energy of the tides, respectively (Lemonis & Cutler, 2004). A tidal barrage is typically a dam, built across a bay or estuary that experiences a tidal range in excess of 5 m, and electricity generation from it employs the same principles as hydroelectric generation, except that tidal currents flow in both directions (IET, 2007). Tidal barrage is the main form in tidal energy generation at the early stage in its development. Currently, there are four such power plants in operation in the world. The four plants are La Rance, France, built in 1960's, Jangxia Creek, east China sea, constructed about the same time, Kislaya Guba power facility, Russia, also built in 1960, and Annapolistidal generation, Canada, finished in 1980's. Technology of electricity generation using tidal barrages has become mature and reliable. However, in consideration of cost and environmental impact, it is now a trend to utilize Marine Hydrokinetic (MHK) energy and tidal current turbines in tidal power generation. Currently the technology of MHK energy power generation is still in its infancy, and various problems are involved and need investigation. Reviews for tidal power generation can be found in Khan et al., (2009) and Rourke et al. (2010).

This paper deals with MHK energy generation and facilities and discusses related performance indicators.

MHK ENERGY, TURBINES, AND SUPPOERTING STRUCTURES

Marine Hydrokinetic (MHK) energy comes various motions of coastal ocean waters. MHK energy of a current can be evaluated using the per square meter transient kinetic energy flux F as follows (e.g., Carballo, 2009):

$$F = \frac{1}{2}\rho V^3 \tag{1}$$

where ρ is the density of water and V is the transient depth-averaged velocity. With the seawater density of 1030 kg/m^3, it is known from this formula that the kinetic energy flux is about 515 W/m^2 at V=1 m/s and 4120W/m^2 at V=2 m/s. This indicates that water current contains a large amount of energy that increases rapidly with its velocity.

In power generation using MHK energy, the energy flux will be transformed into electricity by current power generation systems (Fig. 1). A simple current power generation system consists of four parts: 1) a turbine, 2) a gear box, 3) an electricity generator, and 4) a supporting system. Parts 1), 2), and 3) of the system are mounted to the supporting structure 4). Flowing water turns the turbine by propelling its blades, the gear box transfers the rotation of the turbine into motion of the generator, and the generator transforms the energy of its mechanical motion into electricity, which is transmitted to land through cables.

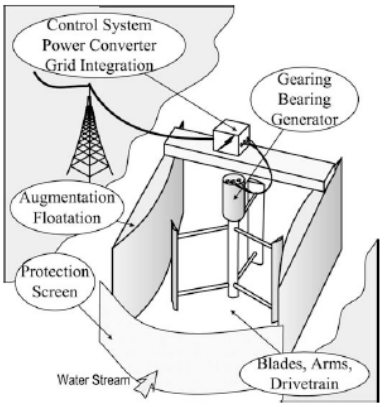
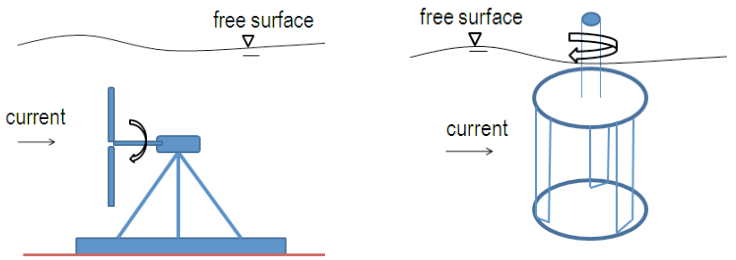


Figure 1. Schematic representation of power generation using MHK energy (from Khan et al., 2009).



(a) (b)

Figure 2. Categories of MHK energy turbines. a) Horizontal axis turbines. b) Vertical axis turbines.

Turbines using MHK energy fall primarily into two categories: vertical and horizontal axis turbines (Khan et al., 2009), as illustrated in Fig. 2. Horizontal axis turbines are common in tidal energy converters and are very similar to modern day

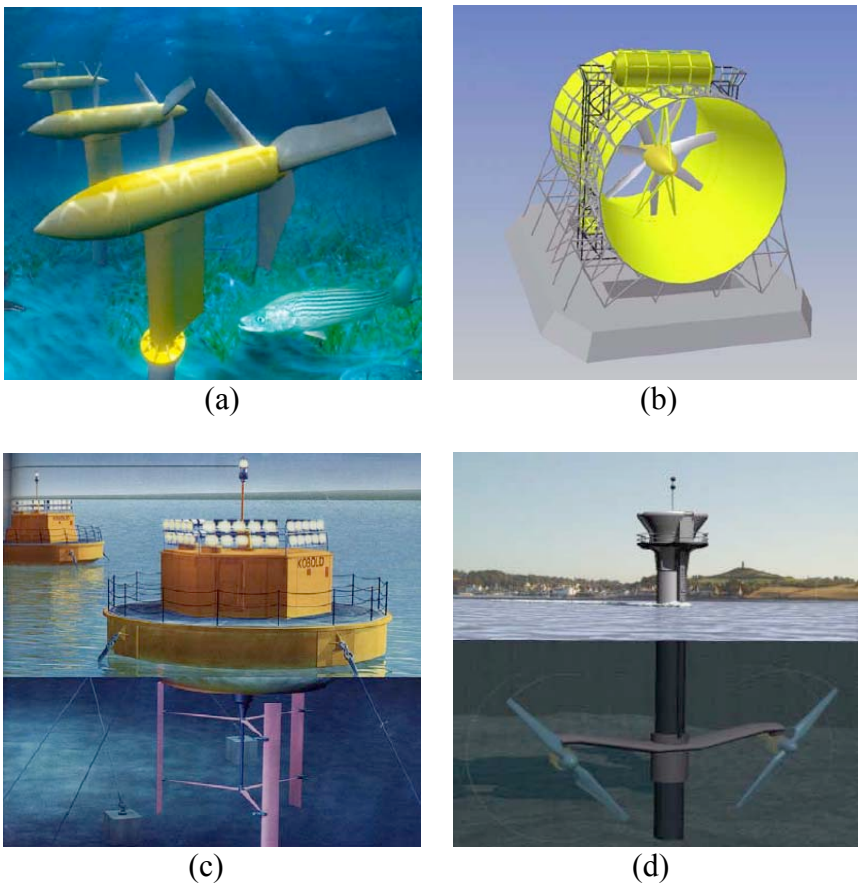


Figure 3. Examples of tidal current turbines (from Bedard, 2005; Rourke et al., 2010). (a) Free flow turbine. (b) Lunar energy tidal turbine. (c) Kobold turbine. (d) Marine current turbine.

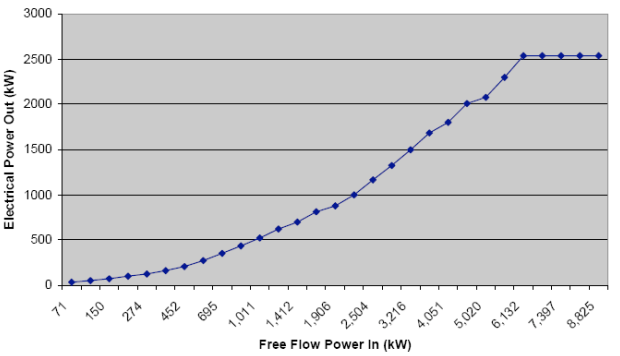


Figure 4. Power curve of Marine current turbine (from Bedard, 2005).

wind turbines from concept and design point of view. MHK turbines can be either mounted on the structures at seabed or floating structures floating in water. The floating structures are usually moored to the seafloor using chains or wires. Fig. 3 presents examples of several actually designed MHK turbines. Various investigations have been made to characterize the efficiency of the turbines (e.g., Bedard, 2005), and Fig. 4 presents the efficiency for one of such MHK energy turbines.

From Eq. (1) it is known that kinetic energy flux from a fluid flow is proportional to the cube of the stream velocity of the flow. Therefore, in order to increase the available MHK energy flux, it is crucial to obtain a large flow velocity. For this purpose, augmentation channels are proposed for MHK turbines (Setoguchi et al., 2004; Ponta and Jacovkis 2008). Fig. 5 presents an augmentation channel supporting a floating water current turbine. A simple channel may consist of a single nozzle or cylinder or straight path. In a hybrid design, all the three options may be incorporated in one unit. A survey shows that around one-third of the horizontal axis turbines are considered for such arrangements, and almost half of vertical turbines are planned with some form of augmentation (Khan et al., 2009).

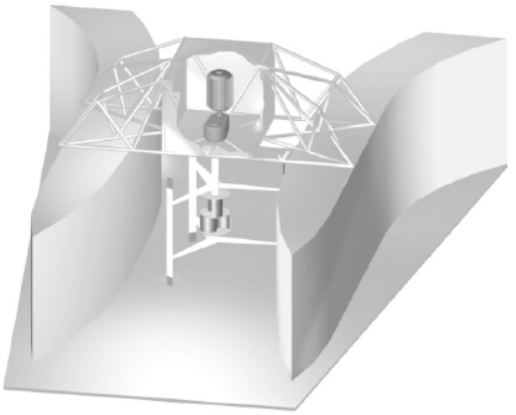


Figure 5. A designed and tested argumentation channel for a floating MHK turbine (from Ponta and Jacovkis, 2008).

PERFORMANCE INDICTORS

It requires a significant amount of historical data and effort to develop a realistic velocity process for a geographic site. Consider a site with an annual tide current velocity history as shown in Fig. 6. Frequently, for a tide power generation device, there is a cut in and cut out velocity. The device stops working at a current velocity lower than the cut in velocity or higher than the cut out velocity. The output power P of such device can be expressed as follows:

$$P = \begin{cases} \frac{\eta}{8}\pi\rho V^3 D^2, & V_{ci} \le |V| \le V_{co} \\ 0, & otherwise, \end{cases}, \tag{2}$$

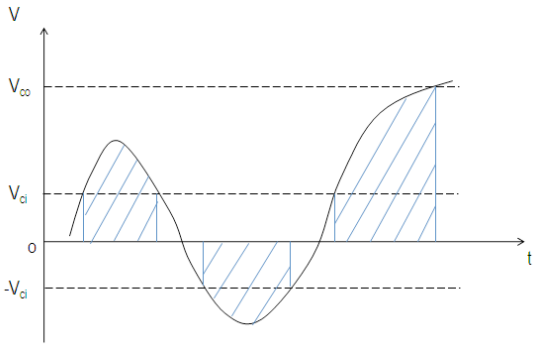


Figure 6. Current velocity history. The shadow area indicates MHK energy available for a turbine to generate power.

where D is the diameter of the blades η is the efficiency coefficient of the turbine, and V_{ci} and V_{co} are respectively the cut in and cut out velocity. The annual average output of the device $\overline{P}$ reads as

$$\overline{P} = \frac{\eta\pi\rho D^2}{2T}\int_0^T |\hat{V}|^3 \, dt, \tag{3a}$$

$$\hat{V} = \begin{cases} V, & V_{ci} \le |V| \le V_{co} \\ 0, & otherwise, \end{cases} \tag{3b}$$

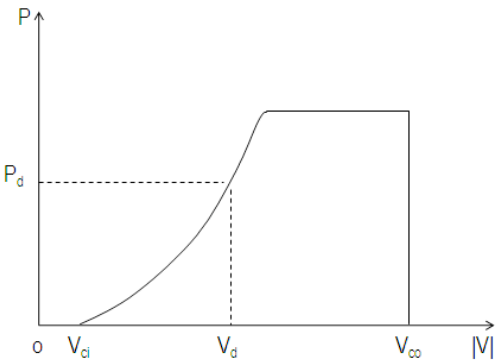


Figure 7. Power curve of MHK energy generation system. P_d is the designed minimum power output of the system, and V_d is the corresponding current velocity.

where T is one year duration or 3.1536×10^7 s. In view of the cut in and cut out velocity and other specifications, the power curve of a MHK energy generation system can be modeled as that shown in Fig. 7 (Bedard, 2005; Karki et al, 2006).

Suppose the velocity of a selected site at a time follows a probability distribution function f as shown in Fig. 8. Unlike wind power generation (Karki et al., 2006), two directions rather than one direction of flow are considered. At a given time at this site, the probability that a current is available for a MHK energy generation system to produce designed power output P_d will be

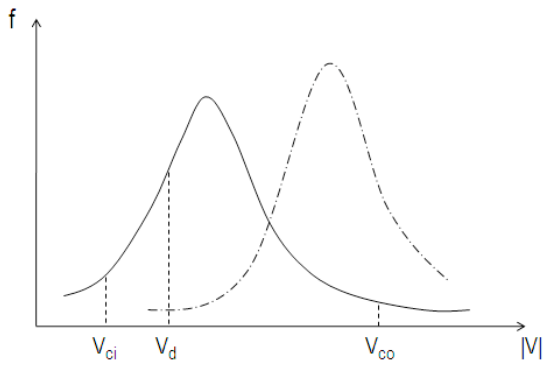


Figure 8. Probability distribution function of current velocity.

$$p_c = p(V_d \le |V| \le V_{co}) = \int_{V_{ci}}^{V_d} f d|V|, \tag{4}$$

and the probability that the system cannot generate the designed power output will be

$$p_{nc} = p(|V| < V_d \cup |V| > V_{co}) = 1 - p(V_d \le |V| \le V_{co}). \tag{5}$$

Let the probability that the turbine, the gear box, the generator, and the supporting structure of a MHK energy generation system be at working states be p_t, p_b, p_g, and p_s, respectively. Since all of these components are subject to impact of water and air flows, the probability if they are at working states will be related to the categories of hurricane classes. Hurricanes are classified into five categories as shown in Table 1, and the observations of damages on structures due to them have been found (ORACLE ThinkQuest, 2011).

Let index i denote the categories of hurricane 0, 1, 2, 3, 4, and 5, and the probability of occurrence of them are p_h^i. Assume the probability that the turbine, gear box, the generator, and the supporting system are working under the condition of hurricane p_h^i is respectively p_t^i, p_b^i, p_g^i, and p_s^i. Then, according to the theorem of total

probability, the probability for the turbine at working condition is (Ang and Tang, 2007)

Table 1 Hurricane category and its wind speed, storm surge height, and air pressure (from ORACLE ThinkQuest, 2011).

Category	Wind Speed	Surge Height	Central Pressure
0 – No hurricanes	<74 mph	<4 feet	> 28.94 in
1 - Minimal	74 - 95 mph	4- 5 feet	>28.94 in
2 - Moderate	96 - 110 mph	6 - 8 feet	28.50 - 28.91 in
3 - Extensive	111 - 130 mph	9 - 12 feet	27.91 - 28.47 in
4 - Extreme	131 - 155 mph	13 - 18 feet	27.17 - 27.88 in
5 - Catastrophic	>155 mph	>18 feet	< 27.17 in

$$p_t = \sum_{i=0}^{5} p_t^i \cdot p_h^i , \quad p_b = \sum_{i=0}^{5} p_b^i \cdot p_h^i , \quad p_g = \sum_{i=0}^{5} p_g^i \cdot p_h^i , \quad p_s = \sum_{i=0}^{5} p_s^i \cdot p_h^i . \tag{6}$$

Then, the probability for a single MHK energy generation system to output designed power at the given time will be

$$p_o = p(P > P_d) = p_d \cdot p_t \cdot p_b \cdot p_g \cdot p_s . \tag{7}$$

In Eqs. (6) and (7), the probability p_d, p_h^i, p_t^i, p_b^i, p_g^i, and p_s^i will be evaluated on the basis of information on manufacture, constructions, weather and current conditions at the sites.

Suppose that there are N MHK energy generation devices at a tide site and each of them is independent of each other, then the number of the devices that are producing the minimum required power output follows the binomial distribution (Ang and Tang, 2007). The probability of at least M ($M \leq N$) of them work at a given time is

$$p_N = \sum_{n=M}^{N} \binom{N}{n} p_o^{\,n} (1 - p_o)^{N-n} . \tag{8}$$

Eqs. (2) and (3) are performance indictors on power output of MHK energy generation systems, and Eqs. (7) and (8) are those on reliability of them.

CONCLUDING REMARKS

Tidal energy is now becoming a significant energy source for our society, and power generation using MHK energy has become a trend in its research and development. Although many technologies in hydro and wind power generation are potentially available for tidal power generation, many new problems are involved and investigations on new technologies are necessary. For instance, a crucial issue will be the estimate of reliability of tidal power systems including their individual components under conditions of normal tides as well as hurricanes at different categories, that is, the probability that involves in Eq. (7). How to make a robust electricity generators and circuits immersed in water? How to construct supporting system that can survive huge repeated hydrodynamic impact including that in thunderstorms and last long time? In addition, the impact of tidal energy generation on environments and ecological systems will be another crucial issue in its commercialization.

ACKNOLEDGEMENT

This work is supported by NJDOT and UTRC. The valuable input from R. Bason and Dr. T. Wang is acknowledged.

REFERENCES

Ang, Alfredo H-S. and Tang, Wilson H. (2007). *Probability Concepts in Engineering (Emphasis on Applications to Civil and Environmental Engineering)*, Wiley.

Bedard, R. (2005). "Survey and characterization tidal in stream energy conversion (TISEC) devices". *EPRI-TP-004 NA*.

Carballo, R., Iglesias, G., and Castro, A. (2009). "Numerical model evaluation of tidal stream energy resources in the Rı´a de Muros (NW Spain)". *Renewable Energy*, 34, 1517–1524.

DTI. (2003) "Energy White Paper: Our Energy Future-Creating a Low Carbon Economy. Department of Trade and Industry, London.

IEA. (2007). "World Energy Outlook 2007", International Energy Agency.

IET. (2007). "I. Tidal power". Institute of Engineering and Technology.

Karki, R., Hu, P., and Billinton, R. (2006). "A simplified wind power generation model for reliability evaluation". *IEEE Trans*. *Energy Conversion*, 21, 533-540.

Khan, M.J., Bhuyan, G., Iqbal, M.T., and Quaicoe, J.E. (2009). "Hydrokinetic energy conversion systems and assessment of horizontal and vertical axis turbines for river and tidal applications: A technology status review". *Applied Energy*, 86, 1823–1835.

Lee, J. S. and Yoo, S. H. (2009). Measuring the environmental costs of tidal power plant construction: A choice experiment study. Energy Policy, 37, 5069–5074.

Lemonis, G. and Cutler, J. C. (2004). "Wave and tidal energy conversion". In: *Encyclopedia of Energy*. New York: Elsevier; 2004. 385–396.

NJDOT. (2010). "Potential tidal power for New Jersey". *Program Project 2010-15*, Bureau of Research, New Jersey Department of Transportation.

ORACLE ThinkQuest. (2011). http://library.thinkquest.org/C001472/en/hurricanes/scales.content.html

Ponta, F.L. and Jacovkis, P.M. (2008). "Marine-current power generation by diffuser-augmented floating hydro-turbines". *Renewable Energy*, 33, 665–673.

Rourke, F. O., Boyle, F., and Reynolds, A. (2010). "Tidal energy update 2009". *Applied Energy*, 87, 398–409.

Setoguchi, T., Shiomi, N., and Kaneko, K. (2004). "Development of two-way diffuser for fluid energy conversion system". *Renewable Energy*, 29, 1757–1771.

US NREL. (2005). "Climate change technology program, technology options: for the near and long term". *DOE/PI-0002*.

Xia, J. Q., Falconer, R. A., Lin, B. L. (2010). "Impact of different tidal renewable energy projects on the hydrodynamic processes in the Severn Estuary, UK", *Ocean Modelling*. 32, 86-104.

Design Loads for Transmission Towers under Skewed Wind Loading

T.G. Mara[1] and T.C.E. Ho[2]

[1]A.M. ASCE, Boundary Layer Wind Tunnel Laboratory, Department of Civil & Environmental Engineering, University of Western Ontario, London, Ontario, Canada, N6A 5B9; PH (519) 661-3338; FAX (519) 661-3339; email: tmara3@uwo.ca

[2]Director, Boundary Layer Wind Tunnel Laboratory, University of Western Ontario, London, Ontario, Canada, N6A 5B9; PH (519) 661-3338; FAX (519) 661-3339; email: ericho@blwtl.uwo.ca

ABSTRACT

Transmission tower networks, consisting of lattice support towers and conductor cables, play an important role in the infrastructure system of many countries throughout the world. Lattice support towers are typically comprised of two different components: the vertical tower body and the horizontal conductor support cross-arms. Much research has been directed towards the evaluation of aerodynamic coefficients of the compact lattice form typical of the vertical tower body sections of transmission towers, which now can often be calculated (based on solidity ratio) to an acceptable accuracy. However, the horizontal lattice form of the conductor support cross-arms have not been studied in depth. In this paper, results from wind tunnel tests on a typical conductor support cross-arm are used to show that the aerodynamics of these types of horizontal lattice sections are not as easily predicted as those for vertical lattice sections. The results from the wind tunnel tests are compared to the values calculated through the use of *ASCE Manual No. 74: Guidelines for Electrical Transmission Line Structural Loading*, and reasons for these discrepancies are discussed. This comparison is used to illustrate two examples where *Manual No. 74* may or may not provide a conservative design estimate for tower and line loading at skewed wind directions, depending on the relative contributions of the cross-arm and tower body sections to the total wind loads. This is attributed to the underestimation of the wind loads on the cross-arms at skewed wind directions. Examples are used to show that the ratio of cross-arm area to total structure area is important for the consideration of the design wind direction. In light of the emphasis on efficiency in the world of transmission tower design, recommendations towards an improved evaluation of cross-arm force coefficients are provided.

INTRODUCTION

Power distribution companies across the globe rely on transmission networks comprised of lattice towers and conductor cables in order to transmit and distribute electricity. Many of these networks exist across the United States and are highly visible; it is rare to drive for much longer than half an hour without spotting such a system. In order to compile and disseminate a combination of research, accepted

practice, and general knowledge on the subject of transmission lines, the American Society of Civil Engineers (ASCE) maintains the *ASCE Manuals and Reports on Engineering Practice No. 74: Guidelines for Electrical Transmission Line Structural Loading* (for brevity, herein referred to as Manual No. 74), which is currently in its 3rd edition (ASCE, 2010). While Manual No. 74 itself is not an official code, the provisions and methodology for the calculation of structural loading are compatible with *ASCE-7 Minimum Design Loads for Buildings and Other Structures* (ASCE, 2010b). Some of the important facets of transmission tower and line design that Manual No. 74 addresses are: advice on weather related loads (including ice accretion); information on design loads for various failure mechanisms; and suggestions of force coefficients for 3-D lattice frames and conductor cables.

In order to facilitate discussion of the various wind loads on the tower-line system this paper adopts the terminology used in Manual No. 74, for which a diagram is shown in Figure 1. As in Manual No. 74, a longitudinal force is any force which acts parallel to the conductor cables, while a transverse force is any force which acts perpendicular to the conductor cables. For skewed winds ($0° < \Psi < 180°$), both a longitudinal and transverse force will exist for the tower, while only a transverse force exists for the conductors (assuming a line angle of 0°).

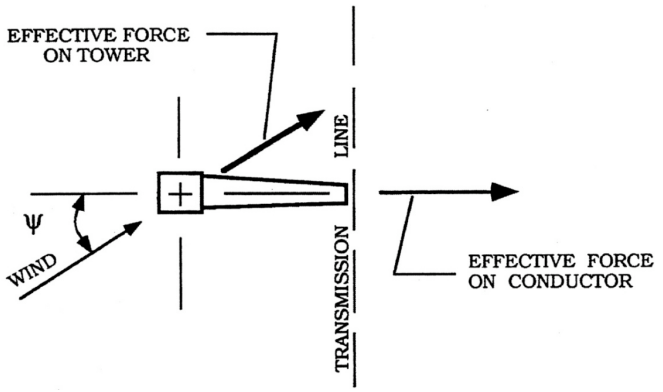


Figure 1. Sign convention in ASCE Manual No. 74 (ASCE, 2010)

For the calculation of the longitudinal and transverse forces on the tower due to wind loading, basic geometric and aerodynamic information must be known about the tower. This information includes the force coefficients of the longitudinal and transverse faces, C_{fl} and C_{ft}, and the solid areas of the longitudinal and transverse faces, A_{ml} and A_{mt}. The force coefficients are calculated based on solidity ratio, which is the ratio of solid area to total enclosed area; this relationship is tabulated in Manual No. 74. The evaluation and use of force coefficients is developed further in the following section. In addition to the aerodynamic and geometric information, the calculation of the forces includes the design wind speed, V, and the yaw angle of the wind, Ψ, as well as additional constants accounting for topographic effects, unit conversion and exposure.

The focus of the remainder of this paper is on the evaluation of the aerodynamic force coefficients, specifically for cross-arm geometries, and how wind tunnel experiments recently performed at the Boundary Layer Wind Tunnel

Laboratory resulted in aerodynamic behaviour which differs significantly from that proposed by Manual No. 74. The intent of the paper is to identify cases where cross-arm geometry may result in wind loads not adequately specified in Manual No. 74.

FORCE COEFFICIENT DEVELOPMENT

Early investigations into the force coefficients of lattice sections were primarily directed at assessing the wind loads on bridge trusses and girders (e.g., Biggs, 1954; Pagon, 1958). At the time of these experiments, it was generally accepted that a relationship existed between the drag coefficient and the solidity ratio, and the results in these studies supported that notion. Although the conclusions drawn from experiments directed at the above trusses answered questions regarding the force coefficients for 2-dimensional (2-D) lattice frames, they were not applicable to 3-D lattice frames. This is due to the presence of shielding (sometimes called interference), which is the effect of members on the leeward face of the frame being shielded from the wind flow by those on the windward face. This effect led to significant differences between the 2-D results mentioned above and realistic wind loads on 3-D trusses or frames, and was the focus of investigation in numerous studies (e.g., Jacobs, 1978; Georgiou and Vickery, 1979; Whitbread, 1979; Kopp et al., 2010). The effects of turbulence intensity has been investigated in many studies as well (e.g., Sykes, 1991; Carril Jr. et al, 2003; Mara, 2007), all which suggest that the level of turbulence intensity is negligible over the range explored in the experiments for the calculation of mean aerodynamic coefficients.

A relationship between force coefficient and solidity ratio is presented in Manual No. 74 (ASCE, 2010), which follows closely with that given by Bayar (1986) resulting from wind tunnel experiments on 3-D lattice frames. Each of these relationships are plotted in Figure 2. The experimental drag coefficients developed from the wind tunnel tests on the cross-arm section (Mara, 2007) described in the following sections are also plotted for yaw angles 0° and 90°.

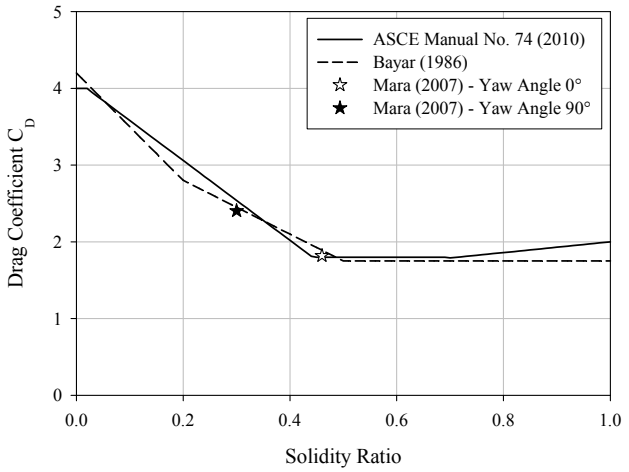


Figure 2. Manual No. 74 and experimental drag coefficients vs. solidity ratio

As shown in Figure 2, it can be seen that the provisions in Manual No. 74 (ASCE, 2010) provide excellent estimates of the force (drag) coefficient at each of these 'normal' yaw angles (0° and 90°). However, in the case of cross-arm type sections of towers, the evaluation of the drag coefficient at skewed yaw angles is cumbersome, primarily due to the calculation of the projected and total enclosed areas. Manual No. 74 circumvents this problem by considering only the solidities and areas of each face and applying a wind pressure which reduces at skewed angles. This is a convenient method, as the calculation of projected area at skewed wind directions is an extremely tedious task due the geometry of lattices sections. This calculation is further complicated if it is being carried out for a section similar to that of a cross-arm, which is comprised of many members which are not at right angles to one another. Thus, the evaluation and interpretation of the conventional drag coefficient becomes confusing as the value of projected area may change considerably over a change in yaw angle of 10°. The amount of projected area is also highly dependent on individual member design.

While the force coefficient provisions in Manual No. 74 provide good estimates at 'normal' wind directions, the prototype parameters required to use the provisions are complicated to assess, as described in the above paragraph. In addition, the force coefficient data are only provided for 3-D frames which are square or triangular in plan, a category into which a cross-arm certainly does not fall. Thus, the following questions pertaining to cross-arm aerodynamics are raised, of which the answers are obtained through experimental investigation:

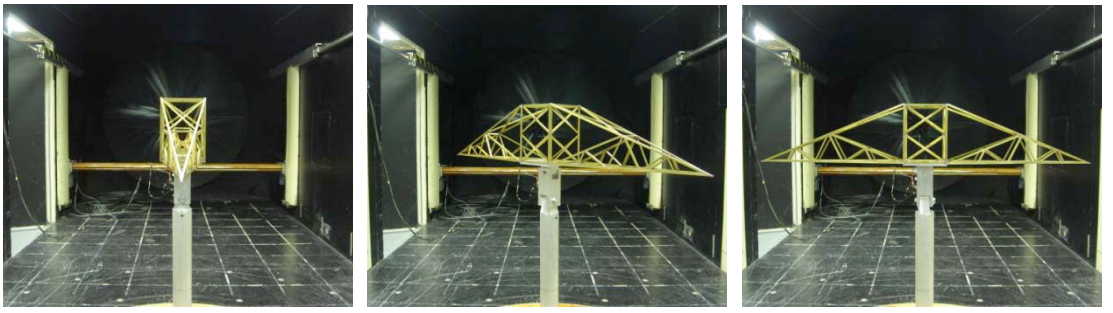
- How applicable are the force coefficients provided in Manual No. 74 at describing the aerodynamics of unique sections such as cross-arms?
- If a discrepancy does exist, are the provisions conservative?
- What will be the effect on the total structure if the wind loading contribution from the cross-arm increases?

Due to the paucity of investigations into the aerodynamic force coefficients of transmission tower cross-arm sections, a reduced-scale wind tunnel testing programme was conceived which would provide estimates of the aerodynamic force coefficients of the cross-arm section for a full range of wind directions. The results from this series of wind tunnel tests, as well as the applicability to design considerations for transmission tower structures, are described in the remainder of this paper.

WIND TUNNEL EXPERIMENT

In order to evaluate the aerodynamics of a realistic cross-arm design, the wind tunnel tests were carried out on a model based on the cross-arm of a Manitoba Hydro Type A HVDC guyed transmission tower. The cross-arm was modelled at a scale of 1:10 and was constructed from angled brass sections; all members were soldered and rigid. The model was then mounted on a strut in order to elevate the model outside of the boundary layer, and measurements of the mean drag forces on the cross-arm were carried out for wind directions at 10° intervals. The wind load accumulated on the strut alone was treated as a tare subtraction from the overall measurement of base

forces. Measurements were averaged over a sampling time of 90 seconds, and the experiments exhibited a repeatability within 1%. All tests were carried out under steady-state flow conditions at a wind speed of 7.6 m/s and a longitudinal turbulence intensity of approximately 7%, which are consistent with testing parameters used in past experiments (e.g., Sykes, 1981; Bayar, 1986; Carril Jr. et al, 2003). Hotwire measurements were used to measure profiles of the speed and turbulence intensity at various positions across the test section, and no abnormalities in flow conditions existed over the area of the model. All wind tunnel tests were conducted in Tunnel I at the Boundary Layer Wind Tunnel Laboratory at the University of Western Ontario and are described in detail by Mara (2007). The cross-arm model is shown mounted in the wind tunnel in Figure 3 at a) a yaw angle of 0°; b) a yaw angle of 45°; and c) a yaw angle of 90°.



a) b) c)

Figure 3. Cross-arm model shown in wind tunnel at a) 0°, b) 45° and c) 90°

The overall drag force on the model was measured using a robust balance located at the base of the strut, which was necessary to support the weight of the model. The measurement of the overall drag force can be decomposed into its vector components, which correspond to the longitudinal and transverse forces that the presence of the cross-arm would add to the tower-line system. The experimental results are presented in terms of $C_D A_p$, which is obtained by rearranging the basic drag force equation

$$F_D = \frac{1}{2}\rho V^2 C_D A_p \tag{1}$$

where F_D is the measured drag force, ρ is air density, V is the mean wind speed used in the experiment, C_D is the drag coefficient of the section, and A_p is the amount of projected member area. This approach is analogous to the effective projected area (EPA) approach to wind design used in ANSI/TIA 222-G (ANSI, 2006), and facilitates the comparison of different yaw angles as the change in area is inherently included in the comparative values of $C_D A_p$. It also provides an accessible comparison to the provisions in Manual No. 74, which are carried out later in the paper.

The experimental values are plotted in terms of $C_D A_p$ at each yaw angle for the overall drag force, the longitudinal force, and the transverse force in Figure 4. It should be noted the that overall force is not simply the sum of the forces in the longitudinal and transverse directions, rather it is the vector sum. It is interesting to

see that the experimental data shows a maximum transverse force occurring at 40°, although due to the resolution of the yaw increments the true maximum may occur at +/- 5° from this angle.

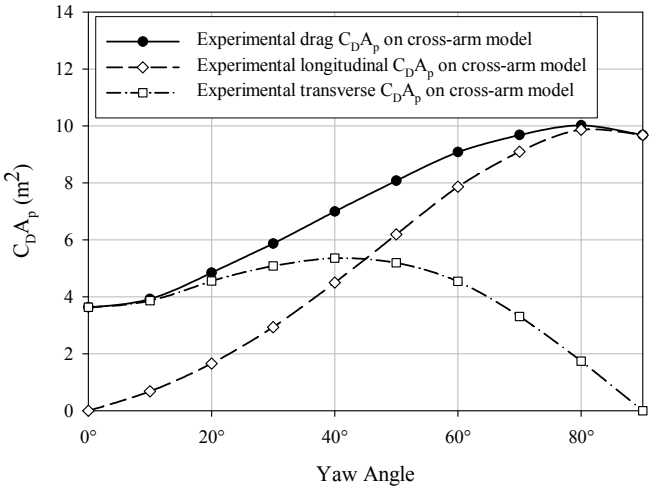


Figure 4. Experimental C_DA_p on cross-arm model

COMPARISON OF EXPERIMENTAL DATA TO ASCE MANUAL NO. 74

ASCE Manual No. 74 approaches the calculation of longitudinal and transverse forces on a transmission tower structure in an orthogonal fashion. In other words, for skewed wind directions the methodology assumes that there are components of the resultant wind which pass through the longitudinal face-plane and transverse face-plane of the structure, which result in longitudinal and transverse forces on the tower-line system. The equations taken from Manual No. 74 are shown in Equations (2) and (3), in which F_l and F_t are the longitudinal and transverse forces, respectively, and where Ψ is the yaw angle measured clockwise from the transverse axis of the tower. That is, when $\Psi = 0°$, the transverse wind load is theoretically at a maximum and the longitudinal wind load is 0. This results in a large transverse force, as the conductors accumulate the greatest amount of wind loading at this orientation, and is often viewed as a design case. Due to this fact, the comparison between Manual No. 74 and experimental data is focussed on forces in the transverse direction. The remainder of the terms are constants accounting for various features (e.g., exposure, wind speed) and correspond to full scale conditions. Thus, they are not discussed in any of the comparisons made.

$$F_l = \gamma_w Q K_z V^2 G_t \sin\Psi \, C_{fl} A_{ml} \tag{2}$$

$$F_t = \gamma_w Q K_z V^2 G_t \cos\Psi \, C_{ft} A_{mt} \tag{3}$$

In order to compare experimental values to those calculated using Manual No. 74, the terms which are not constants were extracted from (3). Thus, the transverse C_DA_p measured in the wind tunnel tests can be compared to the term ($\cos\Psi \, C_{ft} A_{mt}$),

in which C_{ft} and A_{mt} correspond to the cross-arm geometry. These data are plotted in Figure 5, and it is shown that the yaw angle which results in the maximum force differs significantly between the experimental results and that predicted by Manual No. 74. It is noteworthy to mention that the previous edition of Manual No. 74 (ASCE, 1991) included an additional equation for the calculation of the resultant force on tower components, which is based on an IEC standard (IEC, 1988). Equation (4) shows the transverse component of this resultant force, the calculation of which uses characteristics of both the transverse and longitudinal faces. In this case, the term $\{(1 + 0.2sin^2(2\Psi))(A_{mt}C_{ft}cos^2\Psi + A_{ml}C_{fl}sin^2\Psi)(\cos\Psi)\}$ can be considered analogous to $C_D A_p$. It can be seen that the relationship in (4) provides a much better description of the transverse force on the structure, however it is acknowledged that results have been compared for a single cross-arm design only. While the magnitude difference is likely due to complex member aerodynamics, the shape of the curve is likely to be similar for cross-arm type frames.

$$F_t = \gamma_w Q K_z V^2 G_t (1 + 0.2sin^2(2\Psi))(A_{mt}C_{ft}cos^2\Psi + A_{ml}C_{fl}sin^2\Psi)(\cos\Psi) \quad (4)$$

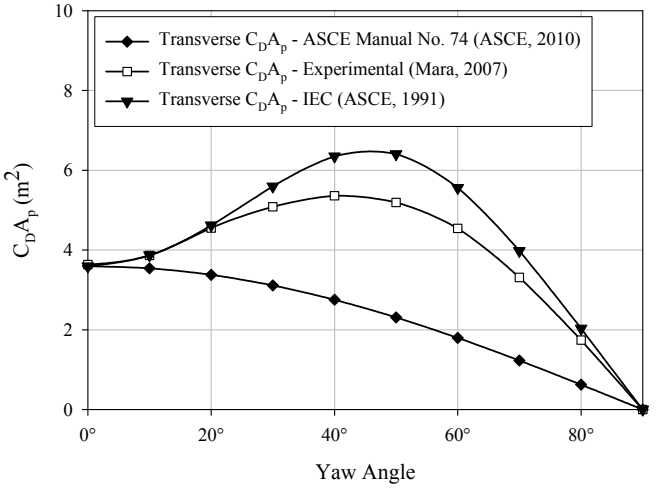


Figure 5. Manual No. 74 vs. experimental transverse $C_D A_p$ on cross-arm section

In Figure 6 an 'overage factor' is introduced, which describes how much greater the transverse wind load on the cross-arm is when calculated using the wind tunnel data than that calculated using Manual No. 74. The overage factor is based on the data presented in Figure 5, and will be used in combination with Manual No. 74 calculations in the following section. It should also be noted that no overage factor is calculated for a yaw angle of 90°, as no transverse force theoretically exists for this wind direction.

IMPLICATIONS ON OVERALL TOWER WIND LOADING

When considering the design case for part of a transmission tower network, it is important to address every part of the system which accumulates wind load. While the results presented in the previous section discussed the wind load on the cross-arm

only, the following sections apply those results and put them into context of an entire tower structure in order to assess the importance of the load contributions from the cross-arm. As shown in Figure 5, the complicated geometry of the cross-arm section will result in a transverse force greater than that calculated using Manual No. 74. It is worth mentioning that due to the fact that the cross-arm features are often located near the top of the tower, they will experience a greater wind load than most of the tower body section. This also plays a role in the ratio of loading, and is accounted for in the current results, but is beyond the scope of discussion in this paper.

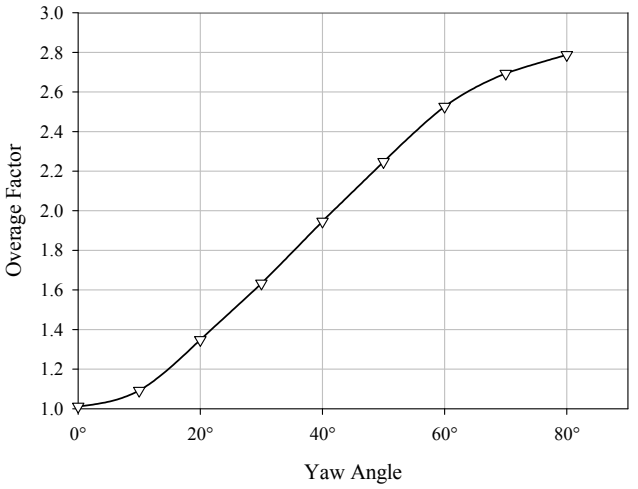


Figure 6. Overage factor for transverse $C_D A_p$ with yaw angle

In order to assess the importance of the increased wind forces on the cross-arm to the wind loading on the entire tower, the design of the full Manitoba Hydro Type A guyed tower (the same tower design on which the cross-arm is based) was considered. The geometry was used with the methodology in Manual No. 74 to calculate the expected transverse forces on the entire tower, which are shown in Figure 7a. The forces are shown in kips in order to maintain consistent units with Manual No. 74. Figures 7a and 7b include 4 tower configurations: no cross-arm (this is theoretical, and provides a base for comparison); a single cross-arm (which corresponds to the design of the Manitoba Hydro tower); 2 cross-arms; and 3 cross-arms. A range of yaw angles from 0° to 50° was selected for the plots in order to focus on the differences at the most important wind directions for the transverse force. It is shown that although the transverse force increases over low yaw angles, each curve exhibits a similar shape, which illustrates the additive behaviour of Manual No. 74.

Figure 7b shows the expected wind loads based on the aerodynamic behaviour obtained from the wind tunnel tests. Here the contribution of the cross-arm section is determined from the Manual No. 74 calculation augmented by the overage factors shown in Figure 6. The difference in the form of the curves when compared to Figure 7a illustrates the importance of the cross-arm wind loads in the overall tower loads, particularly for cases where the tower has more than one cross-arm.

Figure 8 shows the ratio of the expected transverse force to the original transverse force calculated using Manual No. 74. While Figure 8a plots the entire range of yaw angles, Figure 8b is provided in order to observe the ratios at the low end of the range of yaw angles. It is worth mentioning that although the ratios seem high at large yaw angles, these forces are not as important in the calculation of the transverse force on the structure due to the skewed direction of the wind.

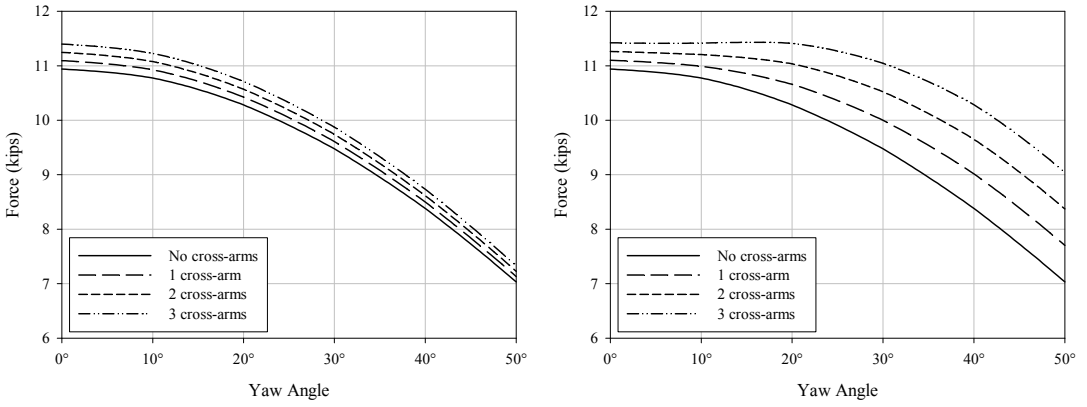


Figure 7. Transverse force on tower for a) Manual No. 74 and b) augmented with wind tunnel data for cross-arm aerodynamics

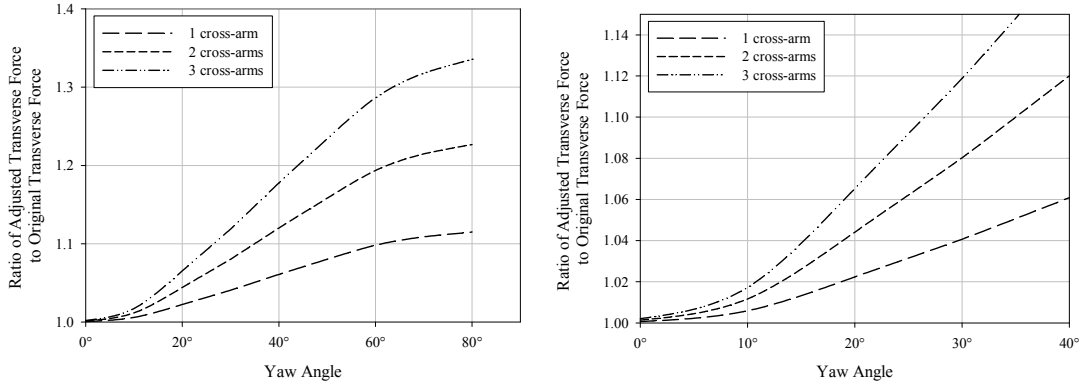


Figure 8. Effect of using wind tunnel test data in transverse force calculation

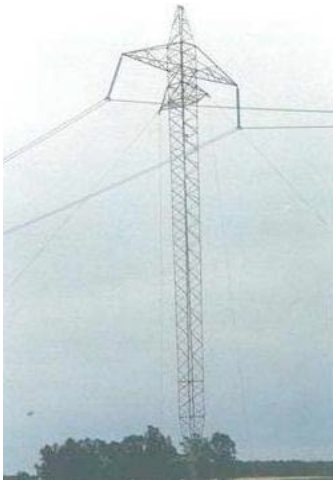
In addition to the wind forces on the tower structure, the wind forces on the conductors contribute a significant amount to wind load on the tower-line system. The wind force on the conductor (or ground wire) is calculated per Equation (5), where F is the transverse force on the wire. It is worth noting that the wind forces on the wires resolve to transverse forces only, with the exception of cases where a line angle exists between towers (see ASCE (2010) for further discussion).

$$F = \gamma_w Q K_z K_{zt} V^2 G_w \cos^2 \Psi \, C_f A \tag{5}$$

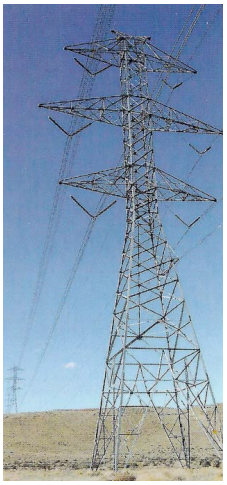
The addition of the wind loads on the lines will also reduce the importance of the increases in loading from the cross-arm on the overall wind loading of the structure. Of importance is the fact that the wind loads on the conductors reduce with yaw angle proportional to $\cos^2 \Psi$, while the wind loads on the structure only reduce with yaw angle proportional to $\cos \Psi$. Examination of various design cases is ongoing, with the outcome expected to provide a quantitative range of the reduction. While worth mentioning, the work in this paper is focused on the tower loads only.

INFLUENCE OF UNIQUE TOWER DESIGN

There are many conditions which contribute to the style and design of transmission tower used in particular situation. These include the transmission capacity of the network, available surrounding land and topographic features, to name a few. These factors often result in a wide variety of transmission tower designs used in practice, which are tailored to the exact demands of the loading situation at hand. For example, towers may be self-supported or supported by guy wires. The example design used in this paper to develop the methodology was a guyed tower (see Figure 9a), and was characterized by a relatively small ratio of cross-arm area to total area as it had a single, small cross-arm. Shorter, bulkier self-supported towers (see Figure 9b) are also common, and possess much higher cross-arm area to total area ratios. While the effects of the approach taken in this paper has not been applied to this type of tower, it is expected that the increases observed in the transverse force at skewed wind directions would be more severe.



a) (Horr et al., 2004)



b) (ASCE, 2010)

Figure 9. Examples of two different transmission tower designs

CONCLUSIONS AND RECOMMENDATIONS

The third edition of *ASCE Manual No. 74: Guidelines for Electrical Transmission Line Structural Loading* is an important contribution to the field of transmission tower design. The work carried out in this paper combines the findings

from a series of wind tunnel tests with the Manual No. 74 approach for the calculation of transverse wind forces on a lattice transmission tower. A comparison of the aerodynamic behaviour of the cross-arm was carried out between the Manual No. 74 calculation and the wind tunnel tests over a range of yaw angles, and it was found that the maximum force on the cross-arm occurs at a yaw angle of approximately 40°, rather than the yaw angle of 0° suggested by Manual No. 74. The IEC method (IEC, 1988) of calculating resultant force (Equation 4) was also compared to the experimental work, and was shown to provide a better relationship of transverse force with yaw angle for the cross-arm in question. The impact of the increased wind forces on the cross-arm component were considered in the calculation of the transverse wind force on the entire structure, and it was found that the impact is not significant for a small ratio of cross-arm member area to total area. However, the impact increases as this ratio grows, and for some towers may result in a design case which does not correspond a yaw angle of 0° (pure transverse loading). Winds occurring at this direction are assumed by Manual No. 74 to be the governing case. Work is currently being carried out to quantify this effect, and will hopefully result in a set of generic specifications which would assist in identifying if a particular structure is susceptible to the mentioned increases in transverse wind load.

With regards to force coefficients, the conclusion can be drawn that the orthogonal method used for the calculation of the longitudinal and transverse forces as specified in Manual No. 74 are likely appropriate for typical vertical portions of lattice transmission towers, but may underestimate the wind loads on cross-arm portions at skewed wind directions. This is attributed to the complex geometry of the cross-arm section, which results aerodynamic and geometric parameters varying significantly with yaw angle. While the method in Manual No. 74 for the calculation of longitudinal and transverse forces is convenient (as only the wind pressure changes with yaw angle), the approach fails to properly account for accumulated wind load on cross-arm type sections due to complicated aerodynamic features. The IEC method suggested in previous editions of Manual No. 74 appears to capture the correct shape of increased loading due to skewed winds for the cross-arm, although it is slightly conservative in magnitude. Wind tunnel testing is likely the most accessible method to study these features, and therefore further investigation into the aerodynamic behaviour at skewed winds for sections which are characterized by unbalanced aspect ratios (e.g., cross-arm, bridge) is recommended. When approaching the wind load calculations for sections such as these, current provisions for typical 3-D lattice frames appear to be inadequate.

ACKNOWLEDGEMENTS

The authors would like to thank Manitoba Hydro, the Natural Sciences and Engineering Research Council of Canada (NSERC), CEA Technologies Inc. (CEATI), and the Institute for Catastrophic Loss Reduction (ICLR) for providing financial support towards the wind tunnel testing component of this work.

REFERENCES

American National Standards Institute/Telecommunications Industry Association (ANSI/TIA) (2006). *Structural Standard for Antenna Supporting Structures and Antennas*. ANSI/TIA Standard 222-G, Arlington, VA.

American Society of Civil Engineers (ASCE) (2010b). *ASCE-7 Minimum Design Loads for Buildings and Other Structures*. ASCE, New York.

ASCE (1991). "Guidelines for Electrical Transmission Line Structural Loading, Second Edition." *ASCE Manuals and Reports on Engineering Practice No. 74*. ASCE, New York, NY.

ASCE (2010). "Guidelines for Electrical Transmission Line Structural Loading, Third Edition." *ASCE Manuals and Reports on Engineering Practice No. 74*. ASCE, Reston, VA.

Bayar, D.C. (1986). "Drag coefficients of latticed towers." *J. Struct. Eng.*, 112, 417-430.

Biggs, J.M. (1954). "Wind loads on truss bridges." *Trans. of the ASCE*, 1, 879-898.

Carril Jr., C.F., Isyumov, N., and Brasil, R.M.L.R.F. (2003). "Experimental study of the wind forces on rectangular lattices communication towers with antennas." *J. Wind Eng. Ind. Aerodyn.*, 91, 1007-1022.

Georgiou, P.N., and Vickery, B.J. (1979). "Wind loads on building frames", in: *Proceedings of the 5th International Conference on Wind Engineering*, Fort Collins, CO, USA.

Horr, A.M., Yibulayin, A., and Disney, P. (2004). "Nonlinear spectral dynamic analysis of guyed towers. Part II: Manitoba towers case study." *Can. J. Civ. Eng.*, 31, 1061-1076.

International Electrotechnical Commission (IEC) (1988). "Loading and Strength of Overhead Transmission Lines (in draft form)", International Electrotechnical Commission, Technical Committee 11, Working Group 08, Geneva, Switzerland.

Jacobs, B.E.A. (1978). "Determination of shielding factors for multiple frame structures", in: *Proceedings of the 3rd Colloquium on Wind Engineering*, Aachen, Germany.

Kopp, G.A., Galsworthy, J.K., and Oh, J.H. (2010). "Horizontal wind loads on open-frame, low-rise buildings." *J. Struct. Eng.*, 136, 98-105.

Mara, T.G. (2007). "The effects of multi-directional winds on lattice sections." M.E.Sc. Thesis, University of Western Ontario.

Mara, T.G., Galsworthy, J.K., and Savory, E. (2010). "Assessment of vertical wind loads on lattice framework with application to thunderstorm winds." *Wind Struct*. 13, 413-431.

Pagon, W.W. (1958). "Wind forces on structures – plate girders and trusses.", *J. Struct. Div.*, 84, 1-27.

Sykes, D.M. (1981). "Lattice frames in turbulent airflow." *J. Wind Eng. Ind. Aerodyn.*, 7, 203-214.

Whitbread, R.E. (1979). "The influence of shielding on the wind forces experienced by arrays of lattice frames", in: *Proceedings of the 5th International Conference on Wind Engineering*, Fort Collins, CO, USA.

NEW APPROACHES IN FIXING TECHNOLOGY: APPROVALS FOLLOW DESIGN GUIDES, SHOWN BY EXAMPLE OF ANCHOR CHANNELS

Matthias Roik[1]

[1]Halfen GmbH, Department Research and Development, Liebigstrasse 14, D-40764 Langenfeld; Germany; PH +49 (0)2173-970-485; email:matthias.roik@halfen.de

ABSTRACT

Connections between steel and concrete were not yet covered by codes until 2009.
A European Technical Specification was published in 06/2009 with the aim to provide design rules for anchorages to concrete. This work of the European committee CEN TC 250, published as prCENTS 1992-4, led to a European Technical Approval (ETA) for anchor channels.
Following the technical approach, a *fib* design guide was developed. This design guide will be published approx. in 2010 and gives design rules for several fixing methods such as dowels, headed studs and also anchor channels. This *fib* design guide will present the basis for a future international approval for anchor channels. This approval will be issued approximately in 2010/2011.

In the present state of the art, technical approvals basing on test results only confirm a defined amount of applications with definite boundary conditions. A building product (here: a fixing construction) can only be used in accordance to these regulations. Diverging from the boundary conditions of the technical approval means using a non licensed product e.g. to infringe the approval.
With a design guide which describes the general application of a product, a universal calculation becomes possible without constraints towards boundary conditions.
A technical approval then "only" proves the applicability of the design rule and the suitability of the product to this documented state of technique.
It should be a clear aim of the holders of approvals to support the efforts obtaining design guides and standards to document the technical state of the art which then can be incorporated into technical approvals.

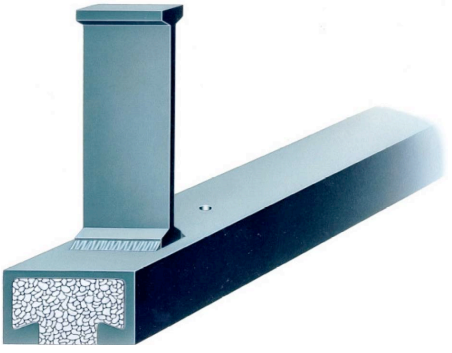
This paper gives an overview of these new methods of calculating the resistance of fixing constructions, in this case: anchor channels. The practicality of these formulas on the products is stated by an adequate approval. The design rules are explained and the experimental results are illustrated.

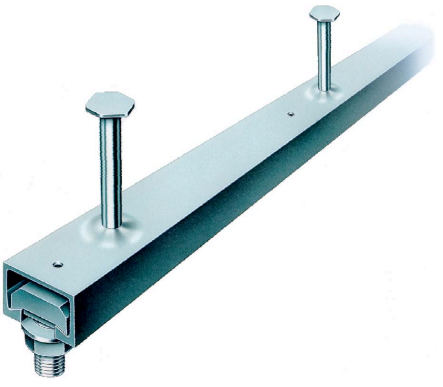
INTRODUCTION

The design of fixing constructions was not yet covered by codes. All results concerning the resistance of a fixing were gained by tests, which had to be provided by the supplier.
The preliminary release of the technical specification prCEN/TS 1992-4 (CEN, 2009) enables the calculation of a fixing construction's resistance. In this technical specification fixings with headed fasteners, post installed fasteners as mechanical and chemical systems, and anchor channels are covered.
In the following, the technical regulations for anchor channels are introduced and their contents are compared. The focus lies on the possibility of calculating all significant parameters which influence the load bearing of an anchor channel to gain a flexible and variable fixing method to concrete constructions which guarantees the required safety and reliability.

ANCHOR CHANNELS AND THEIR APPLICATION

Cast-in channels consist of a C-profile with at least two anchors attached to the back of the profile. Corrosion protection is achieved by galvanization or the use of stainless steel.





Figures 1 and 2: anchor channels with welded I-anchor and with riveted round anchor

The channels are equipped with anchors either made of a cut I-profile, fig. 1, or round anchors, shown in fig. 2. The round anchors are riveted or welded to the back of the channel. I-anchors can be welded on in longitudinal or transversal direction.
Before casting the concrete, the channels are fixed onto the formwork. After curing of the concrete and striking the formwork, the foam filling inside the channel is removed and the channel is ready for installation of the fixtures. Hammerhead or hookhead bolts with associated nuts and washers are supplied for the fixing of any structural element.
Using anchor channels, a flexible and multi-functional fixing method is accomplished.
In the following, the development of the design methods is shown.

In the wake of this approvals became more and more specific permitting a growing number of applications.

REGULATIONS

Anchor channels were not produced and planned according to harmonised standards. Due to this, a technical approval is to be achieved, in which the design resistances and the boundary conditions for the use of such building products are defined.

GERMAN NATIONAL APPROVAL

The national approval for anchor channels valid for Germany is based on test results only. The first examinations of the load bearing behaviour of anchor channels which led to the technical approval started in 1965. Large series of tests were performed. Not only was the selection of different types of anchor channels examined but also a large variety of applications. All tests were performed on channels cast into concrete with precisely specified geometrical boundary conditions. Edge distances as well as member thicknesses were defined as minimum values, see fig. 3.

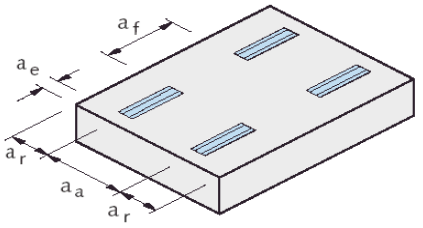
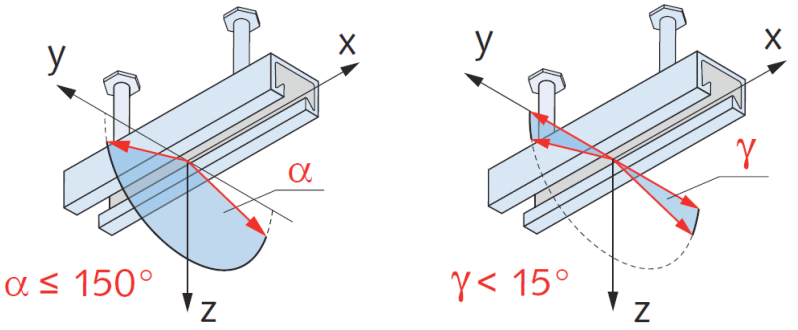


Figure 3: Definition of geometrical boundary conditions

The large variety of load directions and load application made it difficult to find an universal model to describe the bearing behaviour of anchor channels. As an easy to handle method to regard the direction of the applied load two areas of load direction were defined. Loads were differentiated between tension and shear loads. The range of shear was defined from 90° to 75°, relating to the axis of the bolts, see fig. 5. The rest of the load range was considered as tension, figure 4. Both load ranges were tested under different boundary conditions such as varying concrete strength or varying geometries i.e. edge distances, member thicknesses etc.



Figures 4 and 5: Load range Tension" and load range "Shear"

The achieved loads were statistically evaluated and - after taking into account the adequate global safety factor – given in the technical approval (DIBt, 1976) as a table for maximum permissible load.

As a consequence only the considered geometrical combinations could be fixed in the German national approval. As no statements are made regarding the general bearing behaviour, this approval cannot give values for applications where those boundary conditions are not maintained. Diverging from these boundary conditions means to infringe this technical approval.

TECHNICAL PROGRESS

In the last decades, the technical basis for the design of fixing constructions was developed. Based on test results, universally valid equations were derived to describe the bearing behaviour.
Especially the research work on concrete cone failure led to a universally valid calculation method which could be adapted to manifold applications. By these approaches the geometrical conditions, the material properties and the individual bearing behaviour of diverse fixing can be considered in the calculation of the resistance.
The sum of these approaches are published by the European Committee for Standardisation, CEN, in a technical specification.
Up to now this specification has the status of a preliminary standard and is incorporated in the Eurocode series as prCEN/TS 1992-4 (CEN, 2009). It is also published in Germany as DINspec 1021 (DIN, 2009).
This technical specification (TS) contains chapters for general applications, headed fasteners, post installed fasteners as mechanical and chemical systems and for anchor channels.

Failure modes. For a universally valid calculation method, the knowledge about all possible failure modes is required.
Subdivided into tension and shear as well as into steel and concrete failure modes, figures 6 to 7 show the observed failure modes.

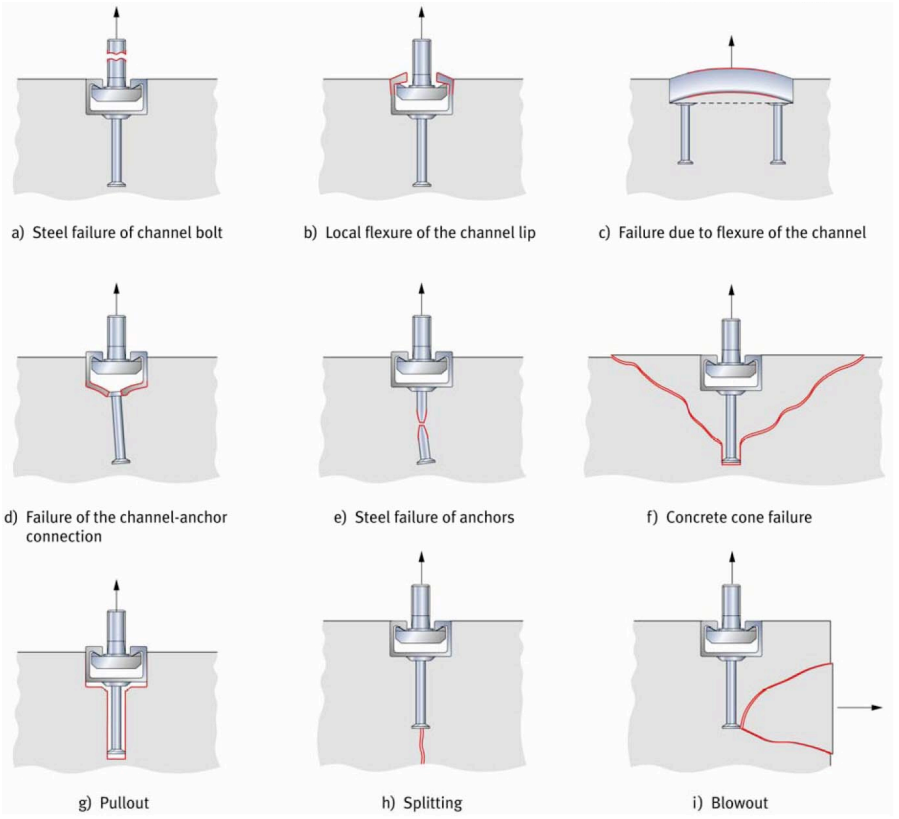


Figure 6: Failure modes of anchor channels due to tension load

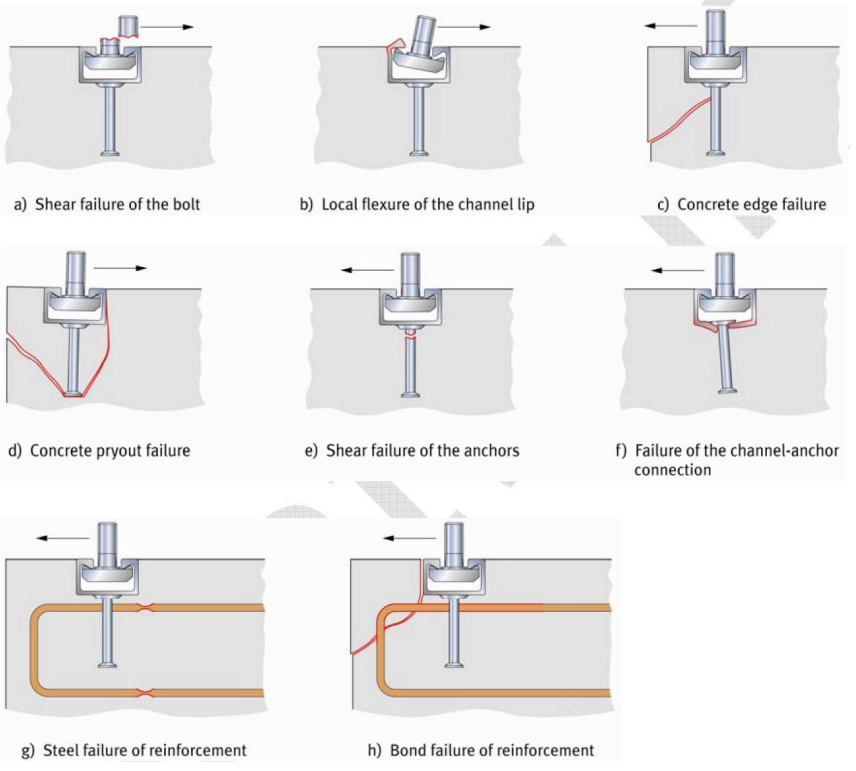
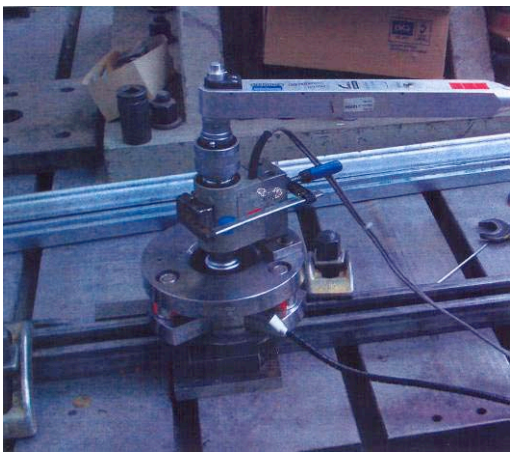


Figure 7: Failure modes of anchor channels due to shear load

Each failure mode was observed and evaluated individually. An enormous effort of experimental work was provided to figure out the decisive parameters which influence the bearing behaviour.
In the following figures some test setups and failure modes are shown. The pictures are taken from variouss tests, arranged

Steel failure. The steel failure modes due to tension and shear have to be examined to determine the characteristic resistance of the bolt, the channel profile and the anchor. In various installation tests, tensile as well as shear tests and pull out tests, the failure modes were examined. Exemplary see fig. 8 and 9 which show the test setup for installation tests.



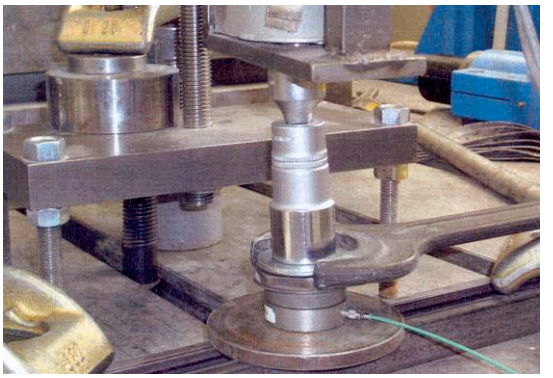
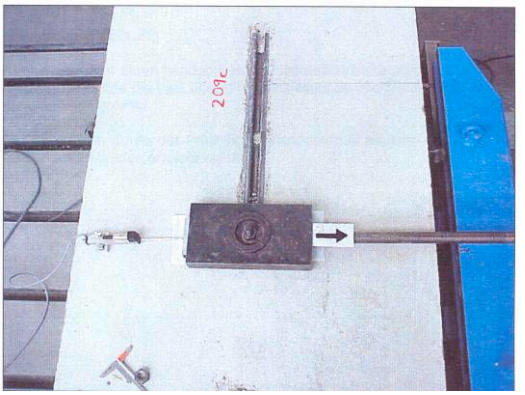


Fig 8 and 9: Test setups for evaluating tension forces due to installation

Concrete failure. Some test setups and results are shown in the following figures, fig. 10 to 13. The possible failure modes e.g. concrete cone breakout, blow out, pry out or edge failure had to be investigated by taking into account the specific characteristics of the fixture, here: anchor channel.
It is assumed, that the channel profile distributes attached loads into the anchors which introduce the loads into the concrete.



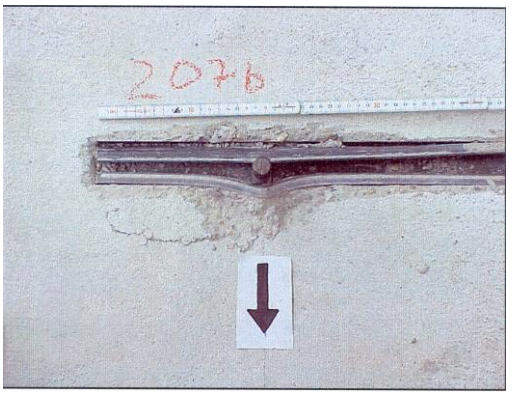
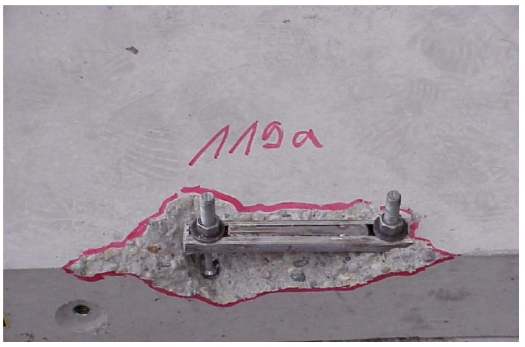


Fig 10 and 11: Test setup and failure mode for shear failure without edge influence



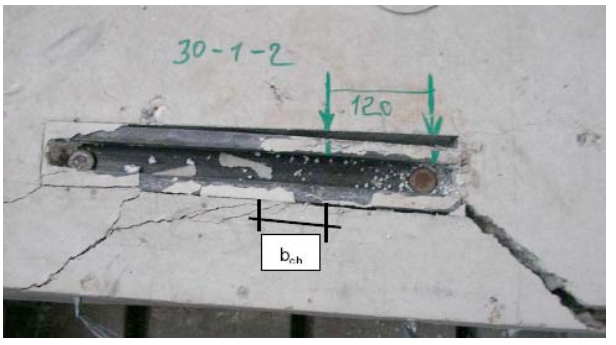
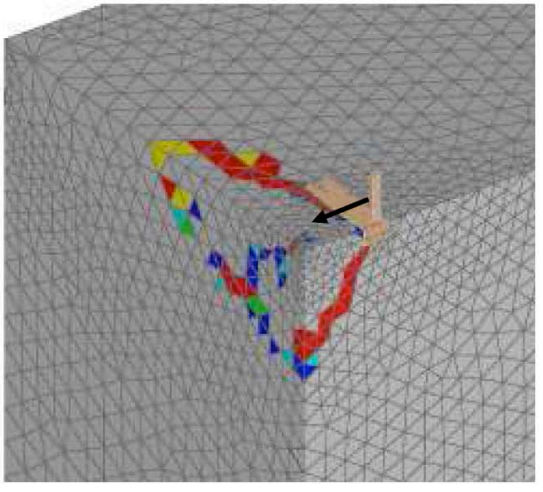


Fig. 12 and 13: Concrete breakout failure due to tension and shear for channels close to an edge

Additionally, results from numerical investigations were taken into account to interpret basic effects of the bearing behaviour.



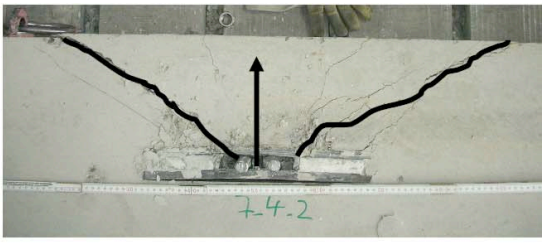


Fig. 14 and 15: Numerical Investigation and comparison to test results (Schmid, 2010)

Alternatively to specific tests, some basic parameters were adopted from similar bearing constructions, mostly from headed studs. For example the concrete breakout failure mode is equivalent for anchor channels and for headed studs. The basic resistance can be calculated by the CC-method with supplemental consideration of the channel profile which crosses the concrete breakout cone: The channel might disrupt the flow of the stress in the concrete and introduce splitting forces by reducing the deformation due to creep and shrinkage. In this case, an additional factor is introduced which takes this effect into account:

$$N_{u,c}^{0} = N_{u,c}^{0}(headed\ stud) \cdot \alpha_{ch,N} = 15{,}5 \cdot h_{ef}^{1,5} \cdot f_{cc}^{0,5} \cdot \alpha_{ch,N}$$

with :

$$\alpha_{ch,N} = (h_{ef}\ /180)^{0,15} \leq 1{,}0$$

The factor $\alpha_{ch,N}$ is derived from additional tests.

This example shows how universally valid parameters can be adjusted by specific factors.

For each possible failure mode, a numerical verification is required. It must be stated that the design action does not exceed the design value of the resistance:
$E_d \leq R_d$

The adequate resistance has to be specified for the product. Some resistances may be calculated, some have to be evaluated by tests. It is task of the applicant for a technical approval to attest the necessary resistances of his product e.g. fixing construction.

Safety concept. The design resistances according to the above mentioned failure modes are calculated basing on the European system for partial safety factors.
The partial safety factors from EN 1990 apply (CEN, 2002).

$$\mathrm{E_d} = \sum \gamma_{\mathrm{G}} \cdot \mathrm{G_k} + \gamma_{\mathrm{Q,1}} \cdot \mathrm{Q_{k,1}} + \sum_{\mathrm{i>1}} \gamma_{\mathrm{Q,i}} \cdot \psi_{\mathrm{0,i}} \cdot \mathrm{Q_{k,i}}$$

γ_{G} = partial safety factor for permanent actions (γ_{G}=1,35)
γ_{Q} = partial safety factor for variable actions (γ_{Q}=1,5)
$\mathrm{G_k}$ = characteristic value of the permanent actions
$\mathrm{Q_{k,1}}$ = characteristic value of the largest variable action
$\mathrm{Q_{k,i}}$ = characteristic value for further variable actions
ψ_0 = combination factor for variable actions

EUROPEAN APPROVAL

Approval concept. An official guidance document is required to obtain an European Approval (ETA). For product groups, a so called ETAG - European Technical Approval Guideline - is to be developed by a European Approval Body.
For single building products, such as anchor channels, a leaner guideline, the CUAP - Common Understanding of Assessment Procedure -, is sufficient. This guidance document which specifies the required testing procedures was published in 2004 (DIBt, 2004).
A final report – the Evaluation Report – states the adduced test results and the properties of the product.
These documents - the documentation of the Technical Design Rules, the Approval Guideline and the Evaluation Report - lead to a European Technical Approval which is issued by the European Organisation for Technical Approvals, EOTA.
This ETA is valid in all European EOTA-member states, which are up to now 27 European states.
It is valid for 5 years and enables the owner to "CE-mark" the approved products.

Up to now, two German manufacturers have received an ETA for anchor channels (EOTA, 2009-1) and (EOTA, 2009-2).

INTERNATIONAL APPROVAL

Approval concept. The concept for applying for an International Approval is similar to the before described European concept.
The International Codes, or I-Codes, are published by the International Code Council and fifty states and the District of Columbia have adopted the I-Codes at the state or jurisdictional level.
For fixing constructions and here for anchor channels the concerning technical regulation can be found in the *fib* design guide for Anchorages to Concrete, which has reached the final draft status and is to be published in 2011 (fib, 2010).
This design guide covers fixing constructions by various dowel systems, headed anchors, post installed reinforcing bars and anchor channels.

Based on this regulation, the so called Acceptance Criteria are developed by the ICC-ES (International Code Council – Evaluation Service). These Acceptance Criteria define the required properties the product should provide. Also the testing procedure and the evaluation method are determined.

Fig 16 shows the complete test program. The program is composed to verify the resistances according to the before mentioned failure modes.

TABLE 4.1 -- TEST PROGRAM FOR ANCHOR CHANNELS FOR USE IN UNCRACKED AND CRACKED CONCRETE

Test no.	Test ref.	Test description	f_c	Δw	Minimum No. of tests	Channel	Anchor	Material	Channel bolt	
									d_s	strength
[-]	Section in Annex A	[-]	psi [N/mm²]	inch [mm]	[-]	[-]	[-]	[-]	inch [mm]	[-]
Steel failure under tension load										
1	7.3	channel / anchor	-	-	5[1]	all	all	all	max	max
2	7.3	bending of channel lips, pull-out of channel bolt	-	-	5[1]	all	all	all	see Section 7.3.2	
3	7.3	screw head	-	-	5	see Section 7.3.2	-	all	see Section 7.3.2	
4	7.4	bending strength of the channel[2]	low	0						
		$s=s_{max}$, inch [mm]			5	all	max	all	max	max
		$s<s_{max}$, inch [mm][3]			5	all	max	all	max	max
5	7.5	torque tests[4]	-	-	5	all	max	all	all	all
Concrete failure under tension load										
6	7.6	splitting failure due to installation[5] $c_a = c_{a,min}$ $s=s_{min}$, $h=h_{min}$	low	0	5	all	see Section 7.6.2			
7	7.7	Splitting failure under load $c_{a1} = c_{a2} = c_{cr,sp}$; $s_{cr,sp}$	low	0	4	all	see Section 7.7.2		max	max
Steel failure under shear load										
8	7.8	failure of anchor, failure of connection between anchor and channel, local rupture of channel lips[6],	low	0	5[1]	all	see Section 7.8.2	all	max	max
9	7.9	Interaction for combined tension and shear loads[7]	low	0	5[1]	See Section 7.9.2				
Concrete failure under shear load										
10	7.10	Concrete edge failure[8] $c_a = c_{a,min}$, $= s = s_{max}$	low	0	5	see Section 7.10.2			max	max
Seismic tests										
11	7.11	Seismic tension	low	0,5	5	all	all	all	see Section 7.11.2	
12	7.12	Seismic shear	low	0,5	5	all	all	all	see Section 7.12.2	

[1]If the coefficient of variation of the failure loads is $V \leq 5$ percent, the number of tests can be reduced to $n = 3$.

[2]Tests are only necessary if restraint of channels embedded in concrete shall be taken into account ($\alpha_r > 4$).

[3]The tests shall only be performed if the conditions in Section 7.4.2.1 of this annex apply.

Fig 16: Test program for anchor channels (ICC-ES, 2010)

The test program assures the determination of each characteristic resistance which is needed for each specific verification.
All test results will be gathered in an evaluation report that states the specific value for each resistance that is needed.

It becomes possible to verify the resistance of a fixture with anchor channels according to the fib design guide.

CONCLUSION

The technical progress especially on the field o anchorages to concrete improved enormously in the last decade. The number of publications grew continuously so that a verified scientific basement could be gained.
A large amount of research work was incorporated into norms and regulations. Provided by institutes and manufacturers a profound technical background and knowledge could get gathered and compressed into technical papers such as design guides and regulations. These technical specifications enables the user to provide a "realistic" design of a fixing construction, as the influencing parameters such as various boundary conditions - concrete strength, edge distance, member thickness, anchor distances and interaction tension /shear – are considered.
Applications basing on these regulations, such as European Technical Approvals (ETA) or ICC Approvals therefore represent technically the "state of the art". It should be a clear aim of the holders of approvals to support the efforts obtaining design guides and standards to document the technical state of the art which then can be incorporated into technical approvals.

REFERENCES

CEN, European Organisation for Standardisation (2002). "Basis of Structural Design", EN 1990, Brussels

CEN, European Organisation for Standardisation (2009). "Design of Fastenings for Use in Concrete", published as: prCEN/TS 1992-4-1:2009, Brussels

DIBt, Deutsches Institut für Bautechnik (1976). Approval Z-21.4-34 for HALFEN anchor channels HTA, 02.08.2007, first issued 1976, Berlin

DIBt, Deutsches Institut für Bautechnik (2004). "Common Understanding of Assessment Procedure", CUAP, Berlin

DIN, Deutsches Institut für Normung, (2009). "Design of fastenings for use in concrete", DIN spec 1021

EOTA, European Organisation for Technical Approvals (2009-1). "European Technical Approval for Jordahl anchor channel JTA", ETA-09/0338 from 15.02.2010

EOTA, European Organisation for Technical Approvals (2009-2). "European Technical Approval for HALFEN anchor channel HTA", ETA-09/0339 from 15.02.2010

fib, federation international du béton, (2010). "Design of fastenings in concrete" - Design guide – Parts 1 to 5, final draft June 2010; to be published 2011, Lausanne

ICC-ES, ICC Evaluation Service (2010), "Proposed Acceptance Criteria for Anchor Channels in Concrete Elements", Whittier, California 90601

Schmid, Klaus (2010). "Behaviour and design of fastenings at the edge with anchor reinforcement under shear loads towards the edge", Doctor Thesis, Universität Stuttgart, (in German)

Design of Sports Lighting Support Structures – Will Your Structures Perform to Expectation?

Brian R. Reese, P.E., C.W.I, M.ASCE[1]

[1] Vice President Northeast Region, ReliaPOLE Inspection Services Co., 22955 Tomball Parkway, Suite 24, Tomball, TX 77375; Chairman TIA TR-14.7 Engineering Subcommittee; PH (281) 259-7000; FAX (281) 754-4166; email: breese@polesafety.com

ABSTRACT

For many years, tubular steel poles have been utilized in various industries. A popular support structure for the sports lighting industry due to their strength, reliability, and ease of installation, the steel pole has served the industry well. The industry has steel pole installations that have been in service upward of fifty years. However, in recent years, there have been numerous failures of sports lighting structures. While manufacturing, installation, and maintenance issues have contributed to these failures, design issues have also contributed. Careful attention to the design requirements for these structures will prolong their lifespan and ensure public safety.

As with any steel support structure, consistent application of a design standard is critical. Historically, the sports lighting industry has not utilized a consistent standard for the design of its support structures. Some pole structures are purchased to meet a recognized structural code with appropriate load and strength safety factors and others are sold as general "commercial" design. Design issues include improper factors of safety, inadequate base plate design, insufficient anchor bolts, improper application of wind and wind coefficients, undersized welds, improper material specifications, and ignoring fatigue issues. Standardizing the design process will improve the safety of these structures and reduce confusion during the procurement process.

This article will present current methods used to design sports lighting structures to the AASHTO *Standard Specifications for Structural Supports for Highway Signs, Luminaries, and Traffic Signals*, 5th Edition, 2009. The document is specifically for pole structures, specifies factor of safety, addresses fatigue issues, and addresses wind induced vibration issues.

INTRODUCTION

Tubular steel poles are a popular support structure in many industries. Poles have been utilized as support structures in the sports lighting, utility, transportation, and communications industries for many decades. Combining a long history of reliable performance, competitive pricing, and ease of use and installation, steel poles are the sports lighting industry's preferred support structure and have performed admirably at some of America's most popular sporting venues. A typical installation of sports lighting poles can be seen in Figure 1 below. However, in recent years, there have been numerous failures of sports lighting structures across the country. In some cases, the property damage has been significant. As with America's other aging infrastructure, the cost of ignoring this issue can be significant to public safety and welfare. While manufacturing, installation, and maintenance issues have contributed to these failures, design issues have also played a role. Careful attention to the design requirements for sports lighting pole structures will prolong their lifespan and ensure public safety.



Figure 1. Typical sports lighting pole installation

STEEL POLES

Steel poles in the sports lighting industry can be anchor based, direct burial, or stub based. AASHTO *Standard Specifications for Structural Supports for Highway Signs, Luminaires, and Traffic Signals*, Fifth Edition, 2009, defines a pole as a vertical

support that is long, relatively slender, and generally rounded or multisided (Specifications, 2009). Anchor based poles are supported with anchor bolts embedded into a concrete foundation. Direct burial structures are embedded into the soil. Stub based poles are flanged to a pipe section that is also directly embedded into the soil. Typically galvanized and in some cases weathering steel, steel poles are pressed in polygonal shapes or comprised of round cross sections. Polygonal pole shells are longseamed (vertical weld along pole axis joining pole half-shells) via submerged arc welding (SAW) techniques and round tapered poles are longseamed via SAW or electric resistance welding (ERW) methods. In most cases for structural efficiency, the structures taper over their height to a smaller tip diameter at the top. Steel sports lighting poles are typically fabricated with high strength steel plate and range in height from 55 ft to 150 ft. The structures can be designed to support as little as four lighting fixtures or as many as dozens of fixtures. A standard sport lighting pole and its components can be seen in Figure 2 below.

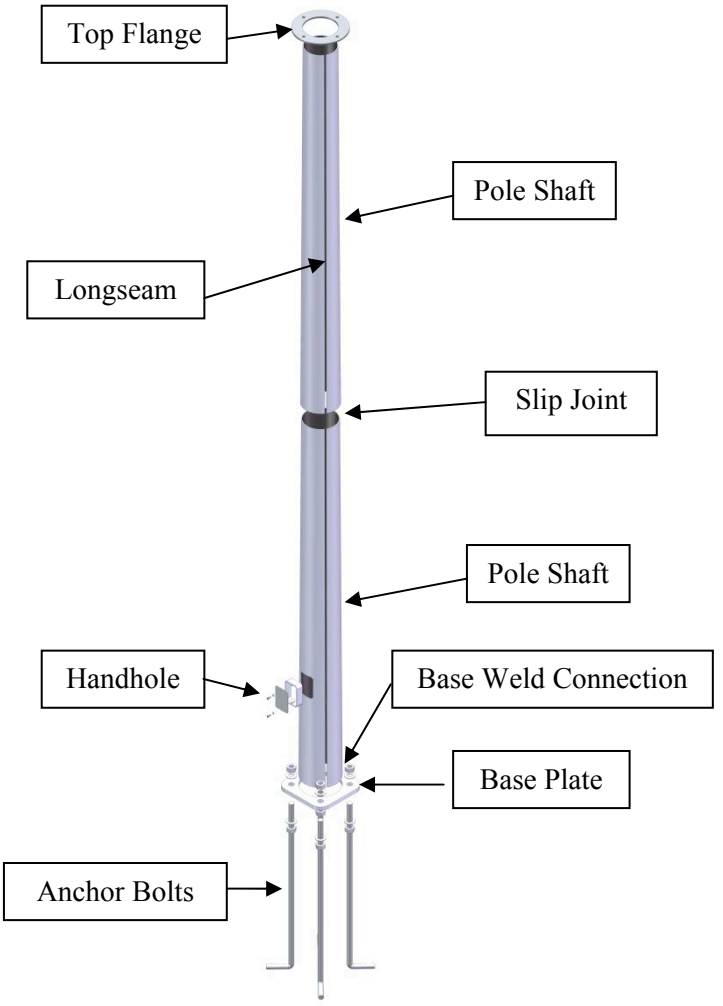


Figure 2. Sports lighting pole structure components

Pole collapses in the sports lighting industry, while an infrequent occurrence, have increased in occurrence and have made news in recent years. With their proximity to areas where the public gathers for sporting events, there is a significant potential for loss of life and injury. Collapses of sports lighting poles are shown in Figure 3.



Figure 3. Sports lighting pole collapses

LACK OF DESIGN CONSISTENCY

Historically, the sports lighting industry has not utilized a consistent standard for the design of its support structures. There has been significant latitude on design techniques for sports lighting poles causing confusion with owners, designers, and those procuring light support structures. Typically, the supporting pole structures are packaged with the light fixtures and provided as a component of the lighting system by the supplier. Unlike other industries where the support structures are purchased by a knowledgeable owner directly from the pole manufacturer, owners of sports lighting poles are typically not active in the specifications development or procurement process and are downstream in the supply chain. As a result, owners have had very little input into the specifications and design processes for their sports lighting pole structures.

Some pole structures today are purchased to meet a recognized structural code with appropriate load and strength safety factors and others are sold as general "commercial" design. Design issues include improper factors of safety, inadequate base plate design, insufficient anchor bolts, improper application of wind and wind coefficients, undersized welds, improper material specifications, and ignoring fatigue issues. These issues have resulted in drastic differences in pole structure design and quality depending on the supplier. As with any steel support structure, consistent application of a design standard is critical. Standardizing the design process will

improve the safety of these structures, reduce confusion during the procurement process, and ensure the longevity of the structure.

AASHTO STANDARD SPECIFICATIONS

AASHTO's *Standard Specifications for Structural Supports for Highway Signs, Luminaires, and Traffic Signals*, Fifth Edition, (Specifications, 2009) are applicable to the structural design of supports for highway signs, luminaires, and traffic signals. The document is intended to serve as a standard and guide for the design, fabrication, and erection of these types of structures. As the only available standard to address the design of luminaire support structures, the Specifications should be utilized for the design of sports lighting poles. The Specifications state in Article 1.4.2 that structural supports for luminaires include typical lighting poles, pole top-mounted luminaire poles, and high-level poles (Specifications, 2009). Commentary C1.4.2 further defines high-level lighting poles as structures normally in heights from 55 ft (17 m) to 150 ft (46 m) or more, usually supporting four (4) to twelve (12) luminaires and used to illuminate large areas (Specifications, 2009). This definition clearly covers the application of sports lighting pole structures.

The Specifications were the result of National Cooperative Highway Research Program Project (NCHRP) 17-10 and the corresponding NCHRP Report 411 (1998) and replace the previous 2001 version of the AASHTO Standard Specifications (2001). Note that the Specifications are only the minimum requirements necessary to provide for public safety. The owner in conjunction with the designer may require the pole design be greater than the minimum requirements as established in the Specifications.

POLE LOADING

Section 3 of the Specifications specifies the minimum requirements for loads and forces, the limits of their application, and load combinations that are used for the design of lighting pole structures. Criteria for dead load, live load, ice load, and wind load is addressed.

Dead load - consists of the weight of the pole, lights, support baskets or arms, and any other appurtenances. Temporary loads applied during maintenance should also be considered (Article 3.5, Specifications 2009).

Live load – consists of a single load of 500 lb (2200 N) distributed over 2 ft (0.6 m) transversely to the member used for design of members for walkways and platforms. This load represents the weight of a person and equipment during servicing of the structure and is only applied to members of walkways and service platforms (Article 3.6, Specifications 2009).

Ice load – consists of a load of 3.0 psf (145 Pa) applied around the surfaces of the pole and luminaires. The map in Figure 4 below from the Specifications shows where ice loading should be considered in the United States (Figure 3-1, Specifications, 2009). The loading is based on a 0.60 in (15 mm) radial thickness of ice at a unit weight of 60 pcf (960 kg/m^3) applied uniformly over the exposed surface (Article 3.7 and Commentary C3.7, Specifications, 2009).

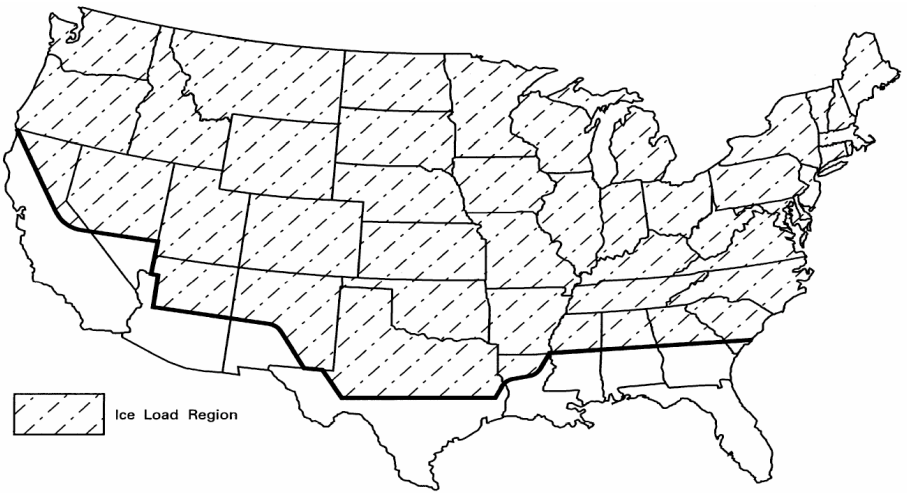


Figure 4. Ice Load Map (Figure 3-1 from *Standard Specifications for Structural Supports for Highway Signs, Luminaires, and Traffic Signals*, 2009, by the American Association of State Highway and Transportation Officials, Washington D.C. Used by permission.)

Wind load – the pressure of the wind acting horizontally on the pole, lights, support baskets or arms, and any other appurtenances corresponding to the appropriate 50-yr mean recurrence interval basic wind speed and the appropriate wind importance factor, I_r (Article 3.8, Specifications, 2009). Wind load is defined in terms of 3-s gust wind speeds instead of the fastest-mile wind speed utilized in the previous version of the Specifications (2001). A 3-s gust wind speed is defined as the average wind speed measured over an interval of three (3) seconds. The country map of 3-s wind speeds is included below in Figure 5 with permission of ASCE.

The design wind pressure calculation is based on fundamental fluid-flow theory and formulations presented in ASCE 7-95, *Minimum Design Loads for Buildings and Other Structures* (1995), and is computed as follows:

$$P_z = 0.00256\, K_z\, G\, V^2\, I_r\, C_d \quad \text{(psf)} \qquad \text{(Equation 3-1, Specifications, 2009)}$$

$$P_z = 0.613\, K_z\, G\, V^2\, I_r\, C_d \quad \text{(Pa)} \qquad \text{(Equation 3-1, Specifications, 2009)}$$

The height and exposure factor, K_z, is related to height and is determined from Table 3-5 in the Specifications or calculated by equation C3-1. The gust effect factor, G, is a minimum of 1.14. Previous versions of the Specifications addressed wind sensitivity by incorporating an increased gust coefficient of 1.3. This gust coefficient corresponded to a gust effect factor of 1.69 = (1.3)(1.3) for use with fastest-mile wind speeds. The fastest-mile gust coefficient of 1.3 is converted to a 3-s gust coefficient by multiplying the gust coefficient of 1.3 by the ratio of the fastest-mile wind speed to the 3-s gust wind speed. The corresponding gust effect factor, G, is then found by squaring the 3-s gust coefficient (Commentary C3.8.5, Specifications 2009). The basic wind speed, V, is determined from the ASCE wind map in Figure 5 below (Figures 3.2 a and b, ASCE 7-05) associated with a height of 33 ft (10 m) for open terrain and associated with a 50-yr mean recurrence interval (annual probability of two percent that the wind speeds will be met or exceeded). The wind importance factor, I_r is determined from Table 3-2 in the Specifications and is selected based on the specified design life of the structure. For a 50-yr recurrence interval, I_r is 1.00.

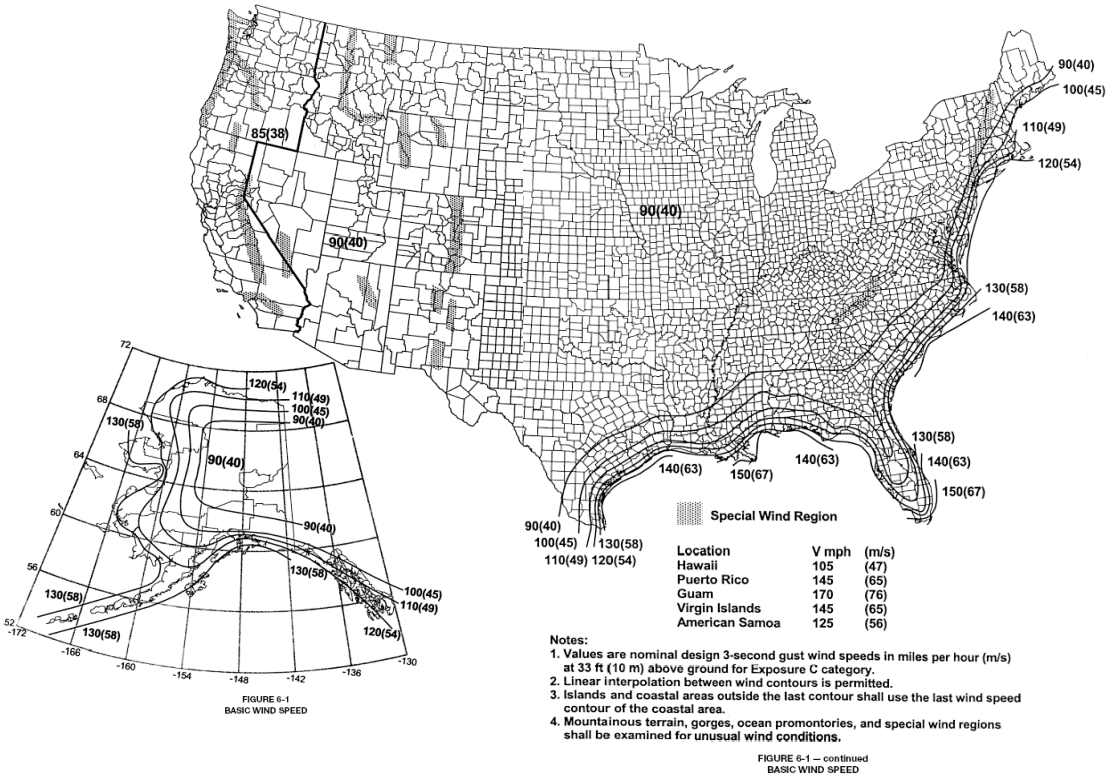


Figure 5. Basic Wind Speed Map in mph (m/s) - Figure 3-2 from ASCE 7-05
(with permission from ASCE)

The wind drag coefficient, C_d, is determined from Table 3-6 of the Specifications. For a pole structure, C_d will depend on the number of flats (shape) of the pole, the ratio of corner radius to radius of inscribed circle, and the wind speed. For attachments such as luminaires, the drag coefficient is typically provided by the light fixture supplier in terms of effective projected area (EPA), which is the drag coefficient multiplied by the projected area. If the EPA is provided, the drag coefficient is taken as 1.0.

Group loading combinations are addressed specifically in Article 3.4 of the Specifications. Each individual load is to be combined into group load combinations as shown in Table 1 below (Table 3-1, Specifications, 2009). Each part of the structure shall be designed for the combination producing the maximum load effect using allowable stresses increased as indicated for the group load.

Group Load	Load Combination	Percentage of Allowable Stress[a]
I	*DL*	100
II	*DL* + *W*	133
III	*DL* + *Ice* + ½(*W*)[b]	133
IV	Fatigue	[c]

[a] Percentages of allowable stress are applicable for the allowable stress design method. No load reduction factors shall be applied in conjunction with these increased allowable stresses.

[b] *W* shall be computed based on the wind pressure. A minimum value of 1200 Pa (25 psf) shall be used for *W* in Group III.

[c] See Section 11 for fatigue loads and stress range limits.

[d] See Article 3.6 regarding application of live load.

Table 1. Group Load Combinations (Table 3-1 from *Standard Specifications for Structural Supports for Highway Signs, Luminaires, and Traffic Signals*, 2009, by the American Association of State Highway and Transportation Officials, Washington D.C. Used by permission.)

POLE DESIGN

Section 4 of the Specifications describes methods of analysis for the structural design of poles. Although the engineering community has been trending to Load and Resistance Factor Design, (LRFD, AISC 1994), the Specifications follow an allowable stress design, (ASD, AISC 1989) approach for design. ASD is based on elastic stress calculations where the strength of the member is divided by a factor of

safety. The allowable stress value is compared to actual calculated stresses in the member and structure. For pole structures, Article 4.8 of the Specifications require second-order effects be accounted for in the design. Secondary bending moments caused by the axial load should be accounted for by an approximate simplified method in Article 4.8.1 or a more exact method where the member is analyzed considering the actual deflected shape of the structure in Article 4.8.2 (Specifications, 2009).

Section 5 specifies design provisions for steel poles. Article 5.5 addresses local buckling and the classification of steel sections as compact, non-compact, or slender element sections. For a section to qualify as compact or non-compact, the width-thickness ratios of compression elements must not exceed the applicable corresponding values given in Table 5-1 of the Specifications. For design, Table 5-3 provides the allowable bending stress, F_b, for tubular members. Pole structures subjected to axial compression, bending moment, shear, and torsion should satisfy the following requirement from Article 5.12.1:

$$\frac{f_a}{0.6F_y} + \frac{f_b}{C_A F_b} + (f_v / F_v)^2 \leq 1.0 \qquad \text{(Equation 5-16, Specifications, 2009)}$$

Equation 5-16 may be increased by 1/3 for load combination Groups II and III involving wind. C_A is calculated in accordance with Article 4.8.1 to estimate second-order effects or is 1.0 if the more exact method of 4.8.2 is utilized (Specifications, 2009).

Per Article 5.14 of the Specifications, the minimum thickness of material used for main supporting members shall be 3/16 in (4.76 mm). Telescoping slip joint field splices should be detailed such that the minimum length shall be 1.5 times the inside diameter of the female pole section. All welding design should be per the latest edition of the American Welding Society *Structural Welding Code D1.1* (2010). Article 5.15 states that full-penetration groove welds shall be used for pole and arms sections joined by circumferential welds. Longitudinal seam welds for pole and arms sections shall have 60% minimum penetration expect within 6 in (150 mm) of circumferential welds where the weld shall be full-penetration and in slip joint areas where it shall be full-penetration the length of the slip joint plus 6 in (150 mm).

BASE PLATE AND ANCHOR BOLT DESIGN

The Specifications state in Article 5.14.2 that the pole base plate thickness should be considered in the design of the structure and that the thickness of unstiffened base plates should be equal to or greater than the nominal diameter of the connection bolt. In steel poles, the flexibility of this joint can greatly contribute to the reduced fatigue strength of this connection. While the Specifications do not provide detailed

guidance on base plate design techniques, it is recommended that careful consideration be given to the design of the pole base plate connection so that premature failure of this joint due to design, fatigue, or manufacturing issues does not occur. The pole shaft to base plate weld connection should be a full-penetration groove weld (CJP) or socket-type joint with two fillet welds per Article 5.15.3 as shown below in cutaway Figures 6 and 7. The CJP connection base plate is butted against the pole shaft and consists of a groove weld with 100% complete weld penetration and reinforcing fillet weld. The socket connection base plate sleeves over the pole wall and is welded with double fillet welds. For base plate materials per Article 5.4, all steels greater than 1/2 in (13 mm) in thickness that are main carrying load members shall meet the current Charpy V-Notch impact requirements in AASHTO *Standard Specifications for Highway Bridges*, 17th Edition (2002).

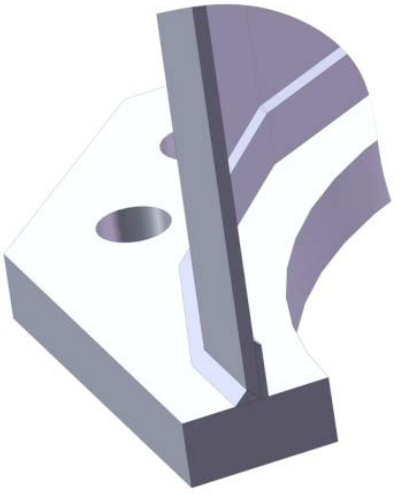


Figure 6. Pole base complete penetration groove weld joint (CJP)



Figure 7. Pole base socket weld joint

Article 5.17 addresses anchor bolt connections and provides minimum requirements for the design of steel anchor bolts used to transmit loads in the critical connection from the pole to the foundation. The Specifications require cast-in-place anchor bolts be used conforming to the requirements of ASTM F1554 (2007) or hooked smooth bars with a yield strength not exceeding 55 ksi (380 MPa). Headed anchor bolts are preferred to reduce the possibility of pull-out. To reduce susceptibility to corrosion and fatigue, for a design life of 50 years, a minimum of six (6) anchor bolts should be considered at the base plate connection (C5.17.3, Specifications, 2009). This is not widely practiced by designers and pole manufacturers in the industry today. For a

single anchor bolt subjected to combined tension and shear, the following equation shall be satisfied:

$$(f_v / F_v)^2 + (f_t / F_T)^2 \leq 1.0 \qquad \text{(Equation 5-24, Specifications, 2009)}$$

For a single anchor bolt subjected to combined compression and shear, the following equation shall be satisfied:

$$(f_v / F_v)^2 + (f_c / F_C)^2 \leq 1.0 \qquad \text{(Equation 5-25, Specifications, 2009)}$$

Equations 5-24 and 5-25 may be increased by 1/3 for load combination Groups II and III. If the clear distance between the bottom of the bottom leveling nut and the top of concrete is less than the nominal anchor bolt diameter, bending in the anchor bolt from shear forces or torsion may be ignored. If the clear distance exceeds one bolt diameter, bending of the anchor shall be considered per Article 5.17.4.3 (Specifications, 2009).

SERVICEABILITY REQUIREMENTS

Horizontal deflection limits for poles are defined in Section 10, specifically Article 10.4.2 in the Specifications. According to the Commentary in C10.4, deflection limits serve two purposes: 1) Provide for an aesthetically pleasing structure under dead load; and 2) Provide adequate structural stiffness that will result in acceptable serviceability performance (Specifications, 2009). Limits for Group I load combinations (dead load only) include a deflection limit of 2.5% of the structure height and 0.35 in/ft (30 mm/m) slope. For pole structures under Group II load combination (dead load and wind load), deflection should be limited to 15% of the structure height. The 15% deflection limitation for Group II load combination is not a serviceability requirement, but it constitutes a safeguard against the design of highly flexible structures. While serviceability may be more critical for certain types of traffic structures than sports lighting poles, the owner and designer should understand the ramifications of overly flexible structures and the resulting fatigue consequences.

FATIGUE

Fatigue is damage resulting in fracture caused by stress fluctuations due to cyclic loading. The fatigue and premature failure of structures has cost lives and industry billions of dollars. Specifically for pole structures, fatigue can be very detrimental to the long term performance of the structure and can risk public safety. Sports lighting poles are exposed to several wind phenomena that can produce cyclic loads. The resulting vibrations can be significant and can shorten the lifespan of the pole. A pole structure is especially susceptible to vortex shedding and natural wind gusts; the amplitude of vibration and resulting stress ranges are increased by the low levels of

stiffness and damping possessed by a flexible pole structure (C11.7, Specifications, 2009). As tall, slender, cantilevered structures with no base connection redundancy, this phenomenon should be acknowledged by owners and considered carefully by the sports lighting pole designer.

Section 11 of the Specifications requires fatigue design for high-level, high-mast lighting structures. To avoid large-amplitude vibrations and to preclude the development of fatigue cracks at the base connection of a pole structure, sports lighting poles should be designed to resist limit state equivalent static wind loads acting separately per Article 11.7. These loads should be used to calculate nominal stress ranges near the fatigue-sensitive base connection of the pole and deflections for service limits described in Article 11.8. Stresses due to these loads on all components of the pole should be limited to satisfy the requirements of their respective detail categories within the constant-amplitude fatigue limits (CAFL) provided in Article 11.9 (Specifications, 2009). The basis of the pole fatigue design provisions in the Specifications is the National Cooperative Highway Research Program Project Report 412 (1998).

Fatigue importance factors are introduced in Article 11.6 of the Specifications to adjust the level of structural reliability of a pole structure. The fatigue importance factor, I_F, accounts for risk of hazard and should be applied to the limit state wind load effects specified in Article 11.7. The Commentary of the Specifications in C11.6 recommends this value be determined by the owner. In the case of sports lighting structures, the owner should be generally aware of these provisions and determine this in conjunction with the advice of the pole designer. The Commentary in C11.6 also states that high-mast structures (without mitigation devices) in excess of 100 ft may be classified as Fatigue Category 1. Typically, sports lighting poles present a high hazard in the event of failure and as a result should be designed to resist wind loading and vibration phenomena. Based on Section 11.0 and Table 11-1 in the Specifications, the fatigue importance factor, $I_{F,}$ is 1.0 for cantilevered lighting pole structures for both vortex shedding and natural wind gusts (Specifications, 2009). The importance categories and fatigue importance factors in the Specifications are from NCHRP Reports 469 (2002) and 494 (2003).

VORTEX SHEDDING

The shedding of vortices on alternate sides of a pole exposed to wind may result in oscillations in a plane normal to the direction of wind flow as shown below in Figure 8. This phenomenon is commonly seen with tubular steel poles.

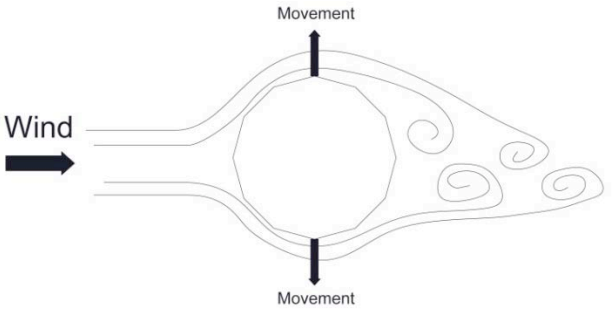


Figure 8. Vortex shedding phenomenon

NCHRP Report 469 (2002) shows that poles with tapers exceeding 0.14 in/ft (0.0117 m/m) can experience vortex shedding. A taper of 0.14 in/ft (0.0117 m/m) is very common for a sports lighting pole. According to the Commentary in C11.7.2 of the Specifications, tapered poles can experience vortex shedding in second or third mode vibrations which can lead to fatigue problems. Per Article 11.7.2, high-level, high-mast lighting structures should be designed to resist vortex shedding-induced loads for critical wind velocities less than approximately 45 mph (20 m/s). The critical wind velocity, V_c, in mph at which vortex shedding lock-in can occur may be calculated by the Strouhal relationship as follows for circular sections:

$V_c = 0.68\,(f_n\, d / S_n)$ (mph) $V_c = f_n\, d / S_n$ (m/s) (Eq. 11-2, Specifications, 2009)

For multisided sections:

$V_c = 0.68\,(f_n\, b / S_n)$ (mph) $V_c = f_n\, b / S_n$ (m/s) (Eq. 11-3, Specifications, 2009)

where f_n is the natural frequency of the structure in cycles per second; d and b are the diameter and flat-to-flat width of the pole shaft for circular or multi-sided sections (ft, m), respectively; and S_n is the Strouhal number (0.18 for circular sections or 0.15 for polygonal sections). For tapered poles, d and b are the average diameter and width (Specifications, 2009).

Article 11.7.2 designates the equivalent static pressure range to be used for the design of vortex shedding-induced loads for poles as follows:

$P_{VS} = (0.00256\, V_C^2\, C_d\, I_F)/2\beta$ (psf) (Equation 11-4, Specifications, 2009)

$P_{VS} = (0.613\, V_C^2\, C_d\, I_F)/2\beta$ (Pa) (Equation 11-4, Specifications, 2009)

where V_c is mph (m/s); C_d is the drag coefficient as specified in Section 3 which is based on the critical wind velocity V_c; and β is the damping ratio, which may be

estimated as 0.005. The equivalent static pressure, P_{vs}, is to be applied transversely (horizontal direction) to pole structures (Specifications, 2009).

NATURAL WIND GUST

Natural wind gusts are basic wind phenomena that are variable in velocity and direction and can induce vibrations in pole structures. This is also a fairly common phenomenon with pole structures. Per Article 11.7.3, steel poles should be designed to resist an equivalent static natural wind gust pressure range of:

$$P_{NW} = 5.2\ C_d\ I_F \quad \text{(psf)} \qquad \text{(Equation 11-5, Specifications, 2009)}$$

$$P_{NW} = 250\ C_d\ I_F \quad \text{(Pa)} \qquad \text{(Equation 11-5, Specifications, 2009)}$$

where C_d is the appropriate drag coefficient based on the yearly mean wind velocity of 11.2 mph (5 m/s) specified in Section 3 of the Specifications. The natural wind gust pressure range should be applied in the horizontal direction to all exposed areas and should consider the application of gusts for any direction of wind. The Specifications allow the owner to modify the natural wind gust pressure if there are more detailed wind records available.

FATIGUE RESISTANCE

Constant-amplitude fatigue limits (CAFL) are the nominal stress ranges below which a particular fatigue detail can withstand an infinite number of repetitions without fatigue failure. Typical fatigue sensitive connections in steel poles are the base plate to shaft weld connection and the slip joint previously shown in Figures 6, 7, and 2, respectively. Fatigue details and corresponding stress categories are specified in Table 11-2 and illustrated in Figure 11-1 of the Specifications for use by the designer. Allowable CAFL's are specified in the Specifications Article 11.9, Table 11-3 (Specifications, 2009). For steel pole base connections (Figures 6 and 7), the Stress Category and corresponding CAFL is as follows:

CJP groove weld ➡ *Stress Category E'* ➡ *CAFL = 2.6 ksi (18 MPa)*

Socket weld ➡ *Stress Category E'* ➡ *CAFL = 2.6 ksi (18 MPa)*

Table 11-2 of the Specifications, footnote j, states that fillet welds for socket connections shall be unequal leg welds, with the long leg of the fillet weld along the column. The termination of the longer weld leg should contact the pole shaft's surface at approximately a 30° angle.

For pole slip joints (Figure 2), where the telescoping overlap is greater than or equal to 1.5 diameters, the Stress Category and corresponding CAFL is as follows:

Slip joint ➡ *Stress Category B* ➡ *CAFL = 16 ksi (110 MPa)*

Note that the wind loads from Article 11.7 should be utilized to compute the fatigue stress range.

CONCLUSION

Active involvement of the owner, communication with the pole designer, and professional responsibility is crucial to the accurate structural design of steel poles for sports lighting applications. Standardizing the design process will improve the safety of these structures and reduce confusion during the procurement process. The owner should ensure the following:

1. Hire an experienced professional engineer (P.E.) to develop the technical specification for the procurement process for the pole structures
2. Require the poles be designed to AASHTO *Standard Specifications for Structural Supports for Highway Signs, Luminaries, and Traffic Signals*, 5th Edition, 2009 (Specifications, 2009)
3. If the poles are being procured packaged with the lights and electrical components, know who is fabricating the pole structures
4. Require a P.E. certification of pole and foundation designs provided prior to shipping and installation of the structures
5. Have a third party review the pole and foundation designs
6. Maintain all project records including specifications, site specific soils information, P.E. documentation, and the pole fabricator's drawings

The AASHTO *Standard Specifications for Structural Supports for Highway Signs, Luminaries, and Traffic Signals* (Specifications, 2009) discussed in this paper is specifically for pole structures and specifies factor of safety, addresses fatigue issues, addresses wind induced vibration issues, and other design requirements. With longevity and proven performance in the traffic industry, the owner who specifies this document as a design standard will have sports lighting pole structures that will perform satisfactorily and safely for many years.

REFERENCES

American Association of State Highway and Transportation Officials (AASHTO). (2009). *Standard Specifications for Structural Supports for Highway Signs, Luminaires, and Traffic Signals*, Fifth Edition, Washington, D.C.

American Association of State Highway and Transportation Officials (AASHTO). (2001). *Standard Specifications for Structural Supports for Highway Signs, Luminaires, and Traffic Signals*, Fourth Edition, Washington, D.C.

American Association of State Highway and Transportation Officials (AASHTO). (2002). *Standard Specifications for Highway Bridges*, 17th Edition, HB-17, Washington, D.C.

American Institute of Steel Construction (AISC) (1994). *Manual of Steel Construction – Load and Resistance Factor Design*, Second Edition, Chicago, IL.

American Institute of Steel Construction (AISC) (1989). *Manual of Steel Construction – Allowable Stress Design*, Ninth Edition, Chicago, IL.

American Society of Civil Engineers (ASCE). (2005). Standard 7-05, *Minimum Design Loads for Buildings and Other Structures*, Reston, VA.

American Society of Civil Engineers (ASCE). (1995). Standard 7-95, *Minimum Design Loads for Buildings and Other Structures*, Reston, VA.

American Welding Society (AWS). (2010). AWS D1.1/D1.1M-2010, *Structural Welding Code – Steel*, Miami, FL.

ASTM International (ASTM). (2007). Standard F1554-07a, *Standard Specification for Anchor Bolts, Steel, 36, 55, and 105-ksi Yield Strength,* West Conshohocken, PA.

Dexter. R., and M. Ricker. (2002). *Fatigue-Resistant Design of Cantilever Signal, Sign, and Light Supports,* NCHRP Report 469, Transportation Research Board, National Research Council, Washington, D.C.

Fouad, F.H., E.A. Calvert, and E. Nunez. (1998). *Structural Supports for Highway Signs, Luminaires, and Traffic Signals*, NCHRP Report 411, Transportation Research Board, National Research Council, Washington, D.C.

Fouad, F., et al. (2003). *Structural Supports for Highway Signs, Luminaires, and Traffic Signals*, NCHRP Report 494, Transportation Research Board, National Research Council, Washington, D.C.

Kaczinski, M.R., R. J. Dexter, D. Freytag, and J.P. Van Dien. (1998). *Fatigue Resistant Design of Cantilevered Signal, Sign, and Light Supports*, NCHRP Report 412, Transportation Research Board, National Research Council, Washington, D.C.

FIGURE AND PHOTOGRAPH CREDITS

Figure 4 and Table 1 is from *Standard Specifications for Structural Supports for Highway Signs, Luminaires, and Traffic Signals*, 2009, by the American Association of State Highway and Transportation Officials, Washington D.C. Used by permission.

Figure 5 is used with permission from ASCE

All other Figures and Photographs provided by author.

Parametric Investigation of Seismic Interaction between Precast Concrete Cladding Systems and Moment Resisting Frames

Andrew Baird[1], Riccardo Diaferia[2], Alessandro Palermo[3] and Stefano Pampanin[4]

[1]PhD Candidate, Dept. of Civil and Natural Resources Engineering, University of Canterbury, P.O. Box 4800, Christchurch 8140, New Zealand; PH (+64) 27-6961791; email: andrew.baird@pg.canterbury.ac.nz
[2]Master Student, Dept. of Civil Engineering, Politecnico di Milano, Campus Leonardo, Milano, Italy; PH (+39) 328-3934441; email: rikdia@hotmail.it
[3]Senior Lecturer, Dept. of Civil and Natural Resources Engineering, University of Canterbury, P.O. Box 4800, Christchurch, 8140 New Zealand; PH (+64) 21-2370407; email: alessandro.palermo@canterbury.ac.nz
[4]Associate Professor, Dept. of Civil and Natural Resources Engineering, University of Canterbury, P.O. Box 4800, Christchurch 8140, New Zealand; PH (+64) 21-2370407; email: stefano.pampanin@canterbury.ac.nz

ABSTRACT

This paper presents the results of a preliminary numerical investigation into the interaction between precast concrete cladding systems and moment resisting frames. Macro-scale models of cladding systems are implemented in existing lumped plasticity models for moment resisting frames. Different failure mechanisms and various configurations are considered in order to show the effect of the entire cladding system upon a structure's seismic behavior. Several parameters are varied in order to establish their associated influence on the overall structural response. Results show that it is clearly more advantageous to have a failure mechanism governed by the connection than one governed by either the panel or the frame.

An experimental program is now underway building on what has been learnt from the parametric investigation. The authors intend to continue the research to successively develop improved or innovative low-damage cladding-moment resisting frame systems. They also aim to produce simple design tools that provide easy inclusion of the seismic effects of cladding-frame interaction.

INTRODUCTION

The response of non-structural components can significantly affect the functionality of a building after an earthquake, even when the structural members are left undamaged. The poor performance of non-structural components or secondary structural elements in past earthquakes has led to buildings being left unoccupied, resulting in substantial economic losses due to business interruption. Furthermore, damage to non-structural components, such as that shown in Figure 1, can pose a serious risk to the safety of people inside and outside the building (Charleson, 2008). Recent earthquakes in L'Aquila, Italy (6 April 2009), Concepcion, Chile (27 February 2010) and Darfield, New Zealand (4 September 2010) have further highlighted the severe impact that damage to non-structural elements can have upon the overall recovery effort.

In order to develop and propose practical and efficient solutions that reduce the risk of damage to non-structural components it is necessary to understand how they interact with a structure. In addition, determining which parameters most influence this interaction is essential so that all possible damage and/or failure mechanisms are identified.

This paper presents the preliminary results of a numerical study on the interaction between a precast concrete cladding panel attached to a reinforced concrete moment resisting frame. This is achieved using static push-over and cyclic push-pull analyses of a lumped plasticity model representing an interior single-storey, single bay of a multi-storey building. In order to understand the different possible damage and failure mechanisms several parameters of the systems are varied. The results also confirmed the sensitivity of the systems' behavior to such changes.



Figure 1: Example of cladding failures

BACKGROUND

Precast concrete panels are widely used around the world as an exterior cladding for multi-storey buildings. Such cladding can be considered as non load bearing wall systems which are designed primarily to transfer their self-weight and out-of-plane (wind and earthquake) lateral loads to the supporting building structure. The contribution of the cladding system to the lateral stiffness of the building is often ignored in the structural design. However, experimental investigations on newly designed buildings have shown that claddings can contribute significantly to the lateral stiffness of the structure and that the panels can be subjected to significant in-plane forces (Goodno et al., 1988) which might cause unexpected structural failure. In order to avoid this unintended interaction, it is possible to isolate cladding panels, as shown by research using autoclaved lightweight aerated concrete (ALC) panels. ALC panels can be connected using sliding and rotating connections, as shown in Figure 2, such that they contribute very little to the stiffness and strength of the overall structure, even under a very large inter-storey drifts of 0.04 radians (Okazaki et al., 2007).

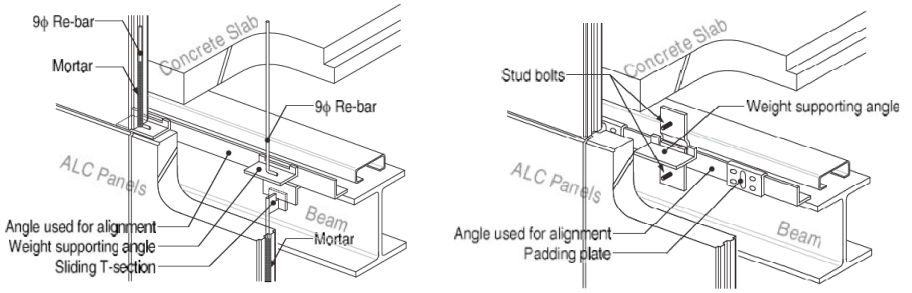


Figure 2: Sliding panel (left) and rotating panel (right), (Okazaki et al., 2007)

Complete isolation with the structural system does however mean that the cladding is simply a dead weight. Consequently, investigations have been carried out into ways in which the structure can profit from having cladding panels attached. If the additional stiffness and strength that cladding panels provide is utilized during design then a savings up to 25% in the volume of steel used in the structure can be achieved (De Matteis, 2005).

Cladding panels can also be used to provide passive control for the seismic behavior of buildings with the use of energy dissipative connections. Results show that energy dissipative cladding connections like that shown in Figure 3 could provide the total hysteretic energy required of the structural system (Pinelli et al., 1995).

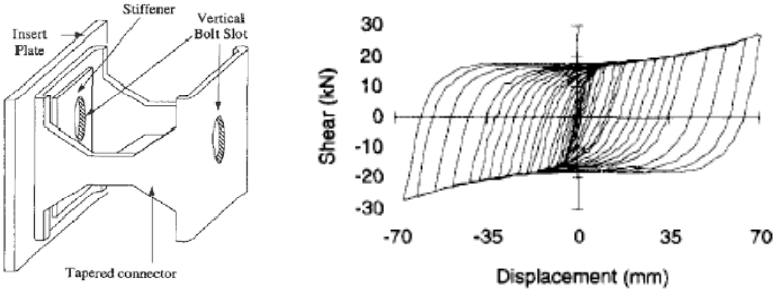


Figure 3: Advanced energy dissipating connection (left) and hysteretic loop (right), (Pinelli et al., 1995)

The main emphasis of research on cladding systems to date is on detailed research into isolated façade technology. This therefore leaves open the question of whether benefits found can be applied should some parameter be slightly different. This paper aims to help in providing a way to broaden the results of such research so it can be applied to a range of similar façade technology.

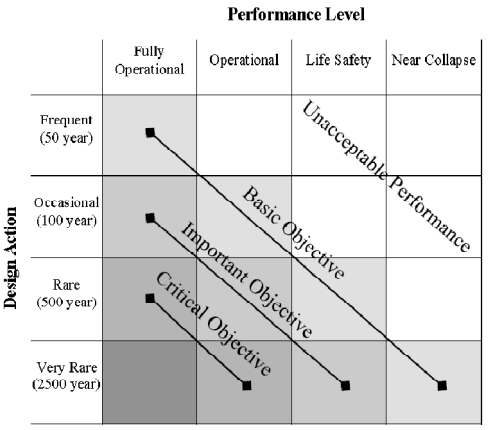
PERFORMANCE-BASED DESIGN and FAILURE MECHANISMS

Design for seismic resistance has been undergoing a critical reappraisal in recent years, with the emphasis changing from ‘strength’ to ‘performance’. For most of the past 80 years (the period over which specific design calculations for seismic resistance have been required by codes) strength and performance have been considered to be synonymous (Priestley, 2000). However now, performance based engineering has become a standard norm for research, development and practice of earthquake engineering, particularly after the 1994 Northridge and 1995 Kobe earthquakes (Okazaki et al., 2007). The primary function of performance-based seismic design is the ability to achieve, through analytical tools, a building design that will reliably perform in a prescribed manner under one or more seismic hazard conditions. The performance,

or condition of the building as a whole, is typically expressed through qualitative terms, intended to be meaningful to the general public. These terms use general terminology and concepts describing the status of the facility (i.e. Fully Operational, Operational, Life Safety and Near Collapse) but should also be associated and linked to appropriate technically-sound engineering terms and parameters. These performance-based design criteria are applicable to both structural and non-structural elements. Table 1 provides descriptions of the damage associated with three performance levels for two façade elements.

Table 1: Suggested performance levels (FEMA 356, 2000) and seismic design performance matrix (SEAOC Vision 2000 Committee, 1995)

	PERFORMANCE LEVEL		
Element	**Collapse Prevention**	**Life Safety**	**Immediate Occupancy**
Precast Concrete Panels	Some connection failure but no elements dislodged.	Local crushing, spalling at connections, but no gross failure.	Minor working at connections, crack width <1.5mm
Cladding	Severe damage to connections and cladding. Many panels loosened.	Severe distortion in connections. Distributed cracking, bending, crushing and spalling of claddings	Connections yield; minor cracks (<1.5 mm width) or bending in cladding.



Seismic Performance and Failure Mechanisms for Façade Systems

In assessing the overall performance of a building, traditional design methods tend to consider the structural and the non-structural systems separately. When the behavior of the bare structure is affected by the interaction with the façade, e.g. additional stiffening and hysteretic damping, then it becomes more appropriate to assess the performance of the combined system rather than the systems separately. Both of these approaches are depicted below in Figure 4 using a simplified chain diagram.

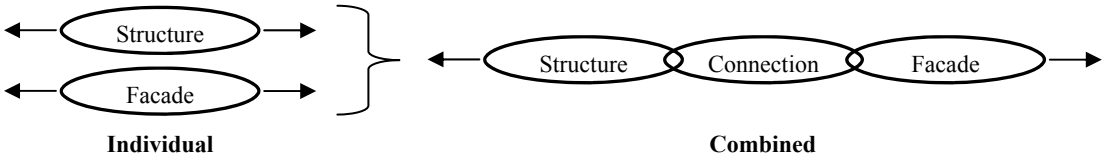


Figure 4: Simplified diagram for structure-façade system of a building

When a combined system approach is taken, capacity design principles can be used to define a number of different scenarios of failure, as depicted in Figure 6. Assuming that the cladding system is comprised of a structural frame member, a connector body and cladding panel, linked together with strong and stiff attachments, as shown in Figure 5, then the problem can be simplified in order to determine where failure is most likely to occur. An advanced performance-based design would thus target the most desirable hierarchy of strength and sequence of events of the overall system.

If the in-plane strength of the cladding panel is greater than that of the connector body, then the connector body (weakest link of the chain) is expected to govern the

overall cladding failure mechanism. Conversely, if the connector body is stronger than the panel, then failure is governed by the panel strength which becomes this time the weakest link of the chain. For the above two scenarios it is assumed that the attachment of the connector body is stronger than both the cladding and the connector body itself. Despite the simplicity of these design principles, errors have been made in the past where the attachment ends up being the weakest link in the system. When the attachment governs the failure then the risk of falling panels is very high. From herein the connector body is referred to as the 'connection'.

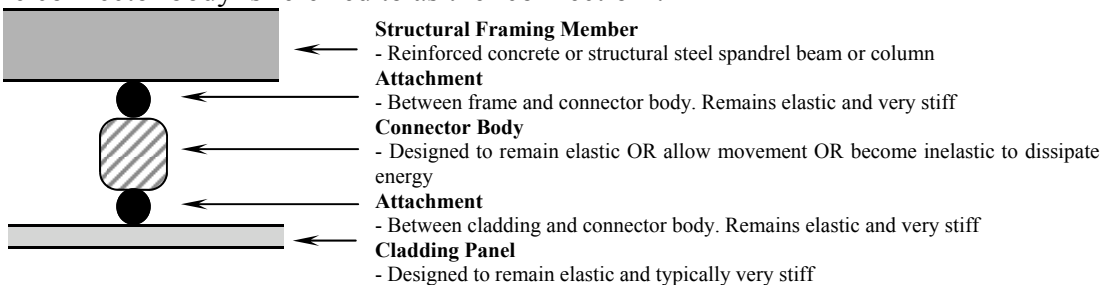


Figure 5: Structure – cladding system (Cohen, 1993)

There is also the highly undesirable case where the panel, connector and attachments are stronger than the frame member and failure occurs in structural members due to local interaction. This scenario is only possible if concrete panels might be adopted and designed with the intention to behave as a structural wall.

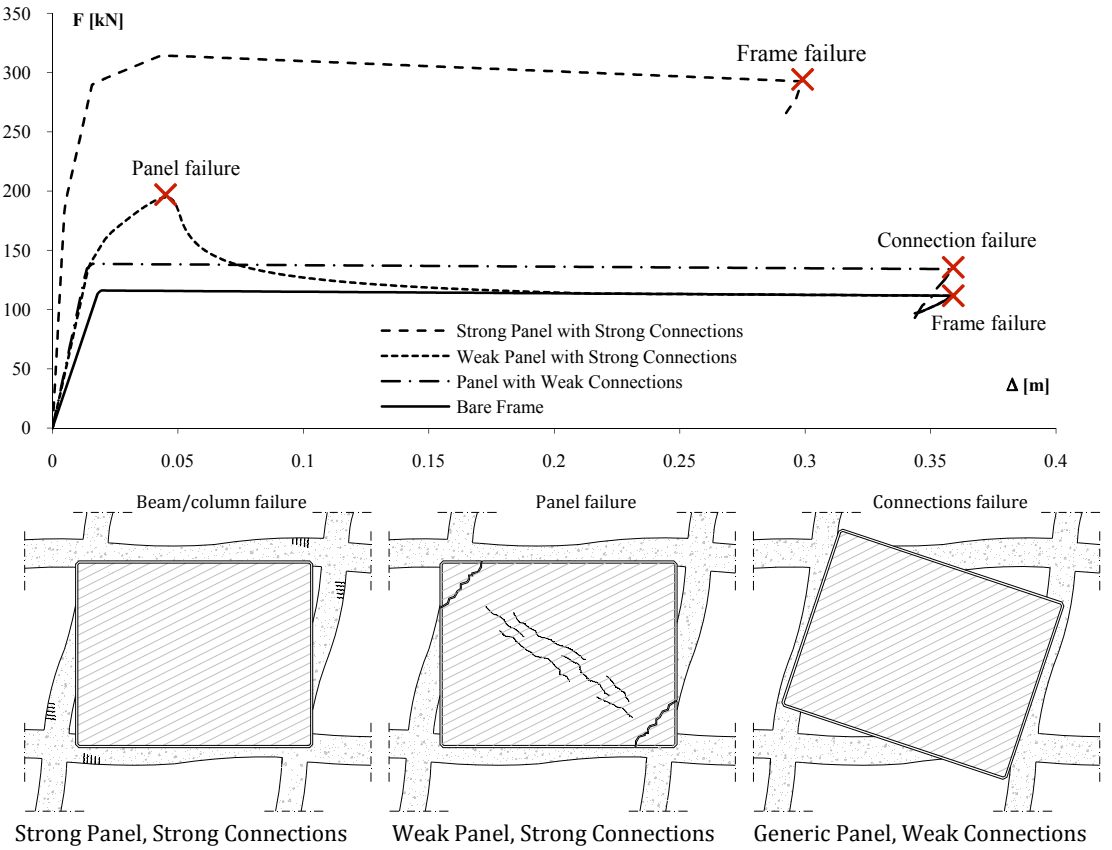


Figure 6: Different failure mechanisms and push-over behaviour of precast panels attached to a frame system

NUMERICAL INVESTIGATION

The numerical investigation has been considered using a monolithic single bay, singly storey reinforced concrete frame with the presence of a single precast concrete cladding panel. The setup is based on a corresponding experimental program that is currently undergoing considering cladding typologies and various cladding panel/connection configurations. The frame is designed in accordance with capacity design principles and the cladding system is designed considering the drift limits at Serviceability Limit State (SLS) and at Ultimate Limit State (ULS).

The numerical investigation only considers a single panel and all openings in the panels are herein neglected. The model has been implemented using the program RUAUMOKO (Carr, 2004), based on a lumped plasticity model, with the beams and columns represented by elastic elements with inelastic behavior concentrated in plastic hinge regions (Giberson model) and defined by the moment curvature hysteresis rule 'Modified Takeda' (Otani, 1974).

The cladding panel is connected either vertically on the beams or horizontally on the columns. The behavior of the connections is based on experimental testing of several connections used to support precast concrete cladding (McMullin et al., 2004). The panel and connections are modeled with appropriate hysteretic rules which vary case by case. The aim of the numerical investigation is to carry out a sensitivity analysis of the parameters which affect the behavior of the facade-structure system. This will be achieved through a parametric analysis. At the same time, different failure mechanisms of the facade-structure system will be explored.

The investigation is separated into two parts, distinguished by failure mechanism. The first part covers the cases where failure of the cladding connections governs the behavior of the system. The second section covers the cases where the failure of the cladding panel or the frame governs.

Part 1: Connection Governing Model

The connection governing model has been designed such that yielding of the cladding connection occurs prior to yielding of either the cladding panel or the frame. The connection yield displacement was based on a drift chosen between the range of SLS and ULS. For this example the value used for the yielding drift is 0.3%. Considering commercial connections available, the strength and stiffness of the connections was chosen to satisfy this predetermined limit.

The panel element has four connections; two bearing connections and two tie-back connections. The bearing connections are located on the lower half of the panel and are intended to transfer the self weight of the panel to the structure. The tie-back connections are located on the top half and are intended to deform under in-plane loading whilst providing out-of-plane support. Each connection is modeled by a spring member with horizontal and vertical stiffness. For the bearing connections, the connector elements in both horizontal and vertical directions are assumed to be very stiff and very strong. The tie-back connections have lower stiffness and yield strength so these govern the force that the cladding can carry. The model and force displacement behavior are shown in Figure 7.

The tie-back connections are modeled with an elasto-plastic hysteresis rule or bi-linear with slackness (representing a slotted connection, which is typically used to also accommodate thermal variations). The use of a perfectly plastic model with no strain hardening is a simplification that is judged reasonable based on the behavior of experimental cladding connector testing (McMullin et al., 2004).

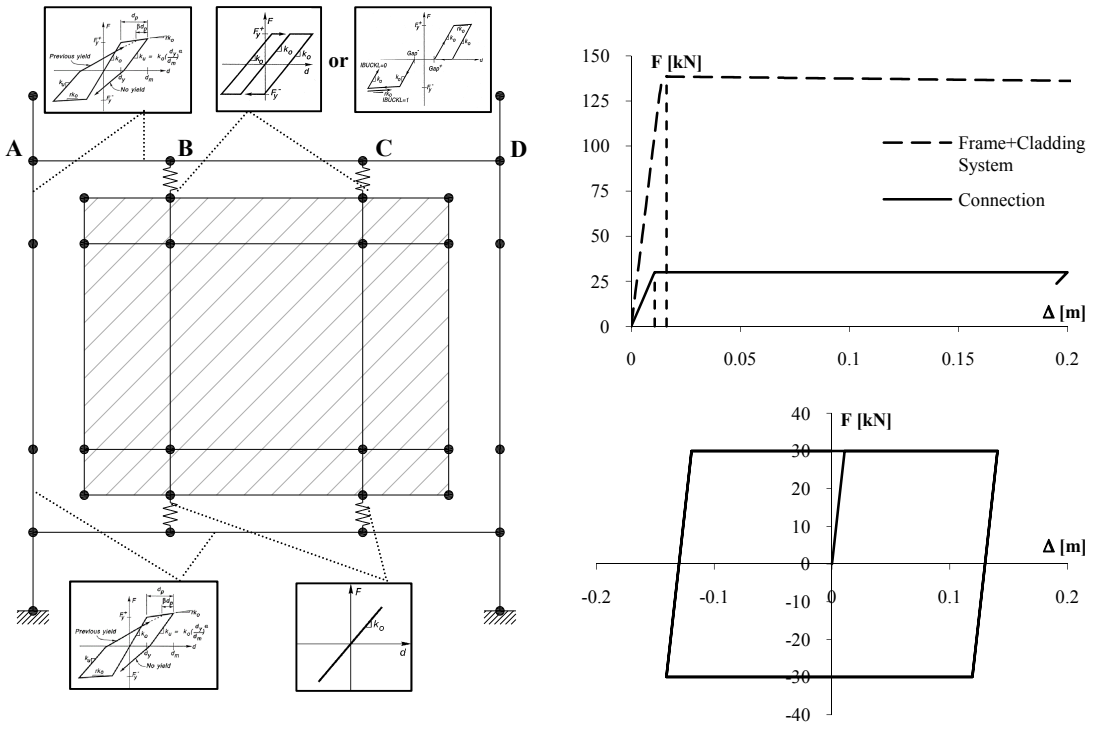


Figure 7: Connection governing model with force displacement behavior

Since the tie-back connections are significantly weaker and less stiff than the bearing connections, the bearing connections are modeled as elastic. The tie-back connections can also not carry sufficient force for the panel to ever yield, thus the panel is assumed to remain elastic and is represented by an elastic 'quadrilateral' element, as shown in Figure 7 (left), which does not consider post-yielding effects.

Part 2: Panel/Frame Governing Model

If the cladding connection is assumed to be strong, then the failure mechanism is not governed by the connection but rather by either the panel or the frame. When this is the case it is essential that the panel is modeled with an appropriate non-linear behavior. Diagonal springs representing the compressive struts are herein used as typically done for infill panels. The model and force displacement behavior is shown in Figure 7.

The hysteretic behavior of the diagonal struts is modeled using the Crisafulli hysteresis rule, extensively validated to model stiffness and strength degradation in masonry infill panels (Crisafulli, 1997). The implementation of this rule requires several parameters which are based largely on experimental data. The most critical parameter dictating the behavior of the strut is the compressive strength. This does not represent the standard compressive stress of the concrete but rather of the strut. Hence it should take into account the inclination of the strut and expected mode of failure (Crisafulli, 1997). Accordingly, without experimental data to verify the accuracy for a panel of the particular geometry and reinforcement used, the accuracy of this parameter is, at this stage, likely to be limited. However, it has been assumed that panel failure consists of crushing of the concrete where the strut bottlenecks into where the panel connection is located and values have been used that correspond to such behavior (Brown et al., 2006). Even so, the compressive strength is varied as part of the investigation in order to appreciate the different behavior expected of different strength panels. The model does not take into account possible shear failure mechanism in the joint induced by the panel.

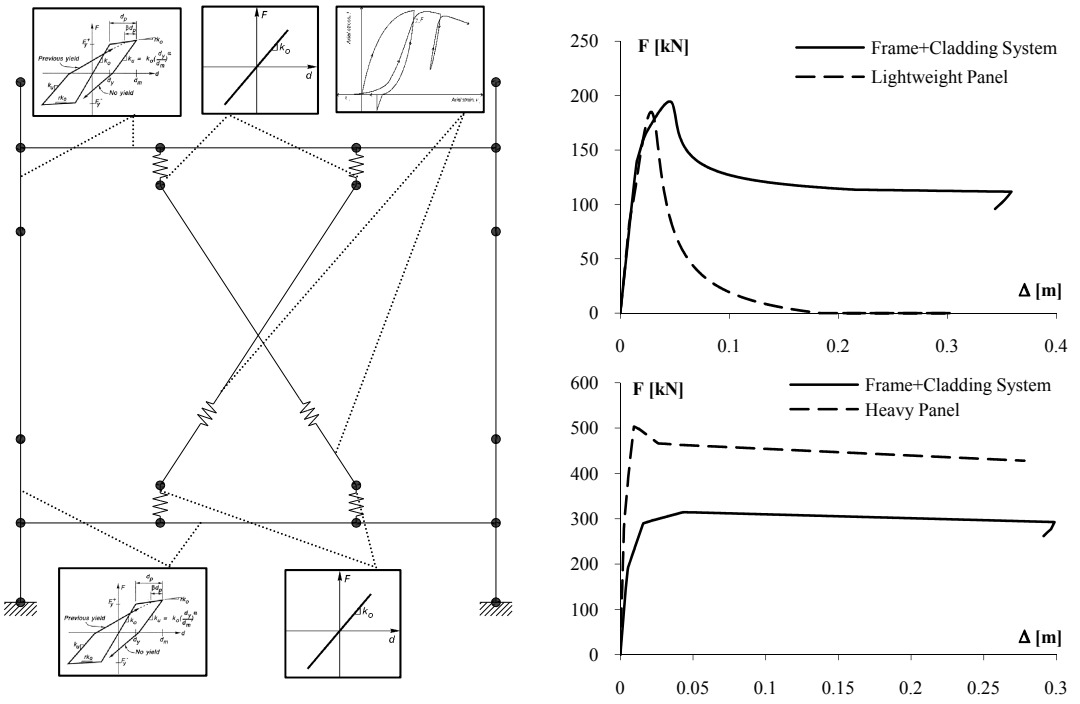


Figure 8: Panel/frame governing model with force-displacement behavior

PARAMETRIC ANALYSIS

In order to understand the effect that various parameters have upon the behavior and performance of cladding panels under in-plane seismic loading, a multi-parametric analysis has been conducted. The parameters to be varied are based primarily on modifications to typical commercial connections. The analyses consist of push-over and push-pull displacement controlled tests where a monotonic displacement is applied at the top of the column. The push-over analyses aim to reveal the yielding and failure characteristics of both individual components and of the system as a whole. The push-pull analyses are performed at repeating cycles of 4% drift in order to provide additional information on the hysteretic behavior.

As mentioned in the previous section, the parametric analysis is separated into two groups; those cases where the connection failure governs the interaction between the panel and the frame and the cases where either failure of the panel or frame governs. This means that not all variables are considered in each part of the analyses but only those that are deemed appropriate, e.g. modifying the panel strength is not seen as important when the connection failure governs. Furthermore, modularity of cladding, i.e. panels' configuration, is not considered for sake of brevity.

The following parameters are to be varied:

- Frame height to span ratio (1:1, 1:1.5, 1:2)
- Connection configuration (beam vs. column)
- Connection behavior (fixed vs. slotted)
- Panel type (and strength)

Part 1: Connection Governing Analyses

The fixed variables for these analyses are the panel type and bearing connection behavior. The panel type is a concrete panel that covers the entire frame bay and is reinforced with steel mesh. Both the panel and the bearing connections are assumed to be stiff and elastic.

Results

Shown in Figure 9 are force-displacement plots of the push-over and push-pull analysis results. These particular plots are for a frame ratio of 1:1 with fixed beam connections. The general shape of these plots is similar for all analyses where connection failure governs. The frames base shear and deflection at yield for all of the analyses conducted can be seen in Table 2 in order to compare the results.

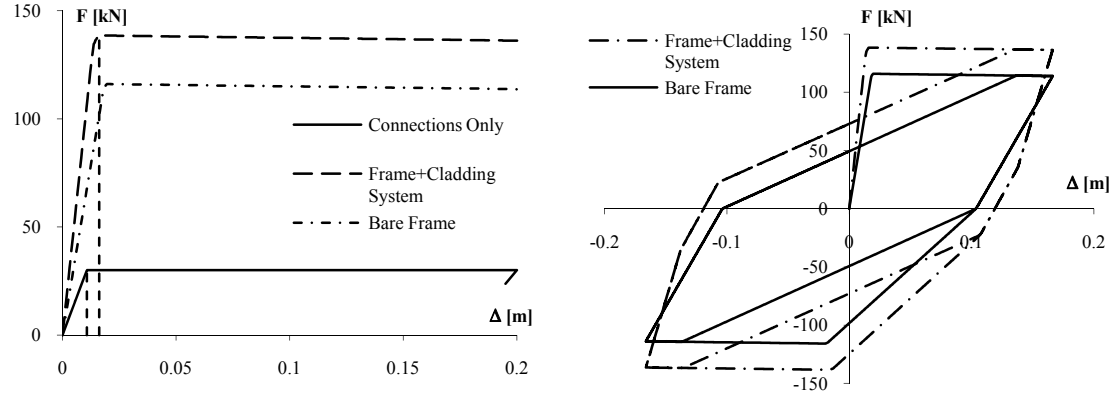


Figure 9: Force-displacement analyses for connection governing cases

Table 2: Parametric results for push-over analyses of connection governing cases

			Beam Connections		Column Connection	
	Frame Ratio	Bare Frame	Fixed	Slotted	Fixed	Slotted
Base Shear at Yield	1:1	115.8 kN	129.3 kN (+11.7%)	129.2 kN (+11.6%)	138.3 kN (+19.4%)	138.3 kN (+19.4%)
	1:1.5	115.8 kN	129.4 kN (+11.7%)	129.3 kN (+11.7%)	138.4 kN (+19.5%)	138.3 kN (+19.4%)
	1:2	115.8 kN	129.4 kN (+11.7%)	129.4 kN (+11.7%)	138.4 kN (+19.5%)	138.4 kN (+19.5%)
Frame Deflection at Yield	1:1	0.020 m	0.021 m (+5.0%)	0.033 m (+65.0%)	0.016 m (-20.0%)	0.020 m (+0.0%)
	1:1.5	0.025 m	0.024 m (-4.0%)	0.033 m (+32.0%)	0.017 m (-32.0%)	0.020 m (-20.0%)
	1:2	0.030 m	0.029 m (-3.4%)	0.033 m (+10.0%)	0.019 m (-36.6%)	0.020 m (-33.0%)

The changing level of damping of the system as well as individual elements is shown in Figure 10 for increasing levels of ductility. The four lines show the damping of the bare frame, the frame-cladding system and the contribution from each component to the system.

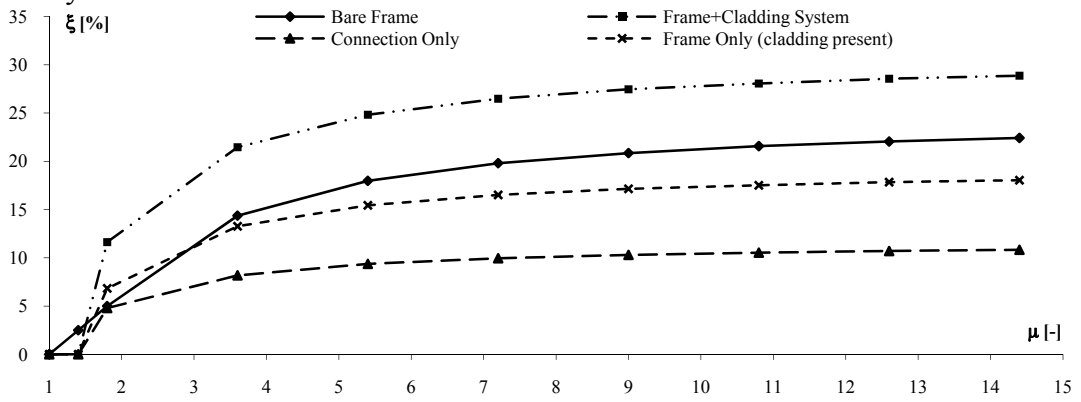


Figure 10: Damping vs. ductility for connection governing cases

Member demand envelopes along one of the beams are shown for a frame ratio of 1:1 with fixed beam connections. Again, the general shape of these plots is similar for all analyses where connection failure governs; so the full results have been tabulated in Table 3 for comparison purposes. The values in the table represent the largest moment and shear force in the beam or column at the cladding panel connection.

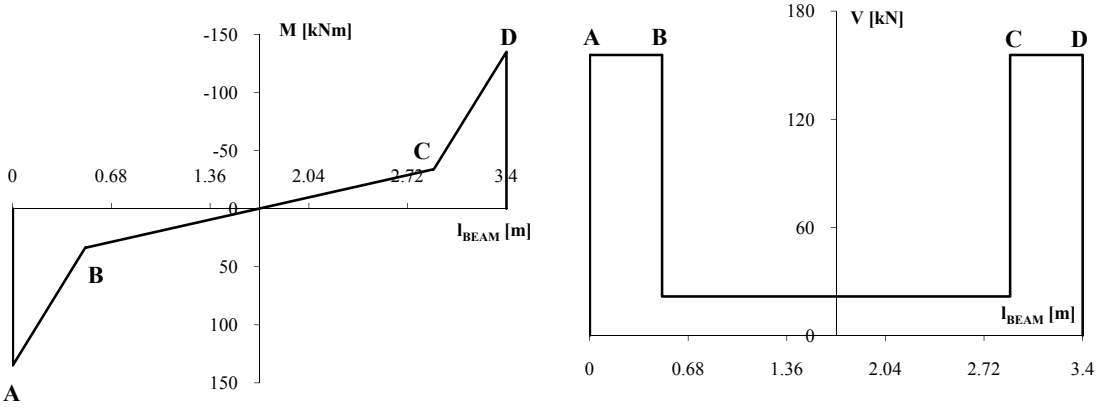


Figure 11: Moment/shear envelope for connection governing cases (refer to Figure 7 (left), where B and C are locations of panel connections)

Table 3: Full results for moment/shear envelope

Beam Connection	Bare Frame		Fixed		Slotted	
Frame Ratio	M	V	M	V	M	V
1:1	85.2 kNm	71.0 kN	-69.5 %	-69.4 %	-68.8 %	-68.7 %
1:1.5	102.4 kNm	46.5 kN	-70.9 %	-70.8 %	-70.6 %	-70.5 %
1:2	110.8 kNm	34.5 kN	-71.8 %	-71.6 %	-71.7 %	-71.6 %
Column Connection	Bare Frame		Fixed		Slotted	
Frame Ratio	M	V	M	V	M	V
1:1	58.8 kNm	57.9 kN	-13.1 %	-13.3 %	-6.0 %	-6.6 %
1:1.5	58.7 kNm	57.9 kN	-14.7 %	-14.2 %	-9.4 %	-9.5 %
1:2	58.5 kNm	57.9 kN	-15.0 %	-14.2 %	-12.1 %	-12.3 %

Part 2: Panel/Frame Governing Analyses

For these analyses the connections are assumed to be infinitely stiff and to remain elastic. This assumption is valid for cladding panels of low strength, however, for higher strength panels, the force transmitted through the connections becomes very large and as such would be unrealistic if a typical cladding connection is used. This case would be applicable to a panel that is fixed in place with grouted connections or intended to behave similarly to a shear wall. The connection configuration is varied in the same way as part 1. The panel strength is varied from a low strength, typical of aerated concrete, up to a high concrete strength (from 4 MPa to 30 MPa). The 'medium' strength panel represents the failure transition point from panel failure to frame failure. The frame's height to span ratio is kept fixed.

Results

Shown in Figure 12 are force-displacement plots of the push-over and push-pull analysis results. These particular plots are for a frame ratio of 1:1 with fixed beam connections. The general shape of these plots is similar for all analyses where panel/frame failure governs. The frames base shear and deflection at yield for all of the analyses can be seen in Table 4 in order to compare the results and failure mechanism.

The push-over plot in Figure 12 (left) shows the different behavior of the three different panel strengths particularly the change in failure mechanism. The low strength panel fails before the frame so the overall resistance provided by the system returns to that provided by the frame alone. The theoretical medium strength panel shows the same behavior as the high strength panel up to yielding. If the panel is weaker than this failure transition strength then it exhibits the same behavior as the low strength panel, decaying back to the frame strength. However, if the panel is stronger it results in the beam yielding in flexure at the connection point and eventually leads to failure of the beam at this point.

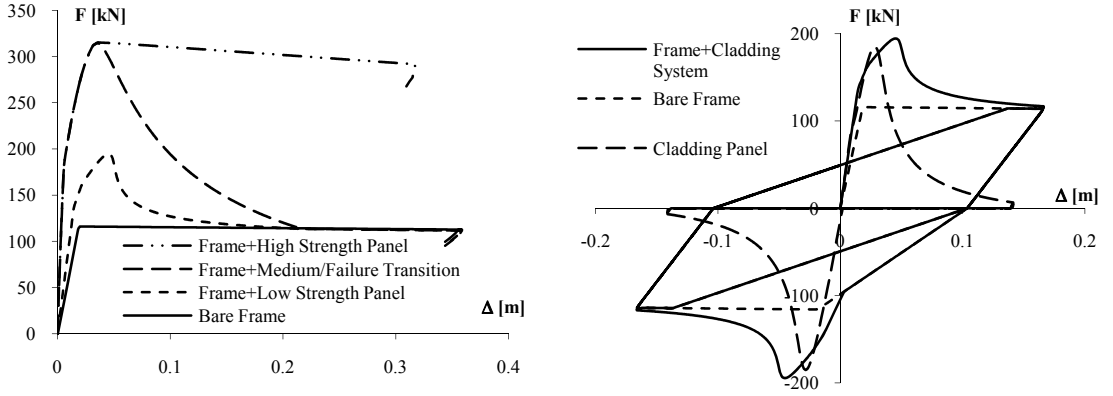


Figure 12: Force-displacement analyses for panel/frame governing cases

The push-pull analyses can only be conducted for cases where the frame does not fail, i.e. panel failure. As shown in Figure 12 (right) after one cycle in either direction, once the compressive strut representing the panel is effectively destroyed then the behavior returns to that of the bare frame.

When the panel is attached to the column the failure mechanism was found to always be in the panel however this result is not very realistic because of the large shear forces in the column. Since the model herein adopted does not take into account shear failure in the structural elements this failure mechanism is likely being missed.

Table 4: Parametric results for push-over analyses of panel/frame governing cases

		Bare Frame	Low strength	Medium strength Failure transition	High strength
Fixed beam connections	Base shear at yield	116.1 kN	194.6 kN (+67.6%)	314.8 kN (+171.1%)	314.8 kN (+171.1%)
	Frame deflection at yield	0.020 m	0.045 m (+128.3%)	0.036 m (+83.0%)	0.044 m (+127.4%)
	Failure mechanism	STRUCTURE	PANEL	PANEL/STRUCTURE	STRUCTURE
Fixed column connections	Base shear at yield	116.1 kN	186.5 kN (+60.6%)	300.2 kN (+158.6%)	662.2 kN (+470.4%)
	Frame deflection at yield	0.020 m	0.024 m (+20.0%)	0.045 m (+132.0%)	0.062 m (+216.8)%
	Failure mechanism	STRUCTURE	PANEL	PANEL	PANEL

CONCLUSIONS

The results show that there is an increase in strength of at least 10-20% for all systems when the influence of cladding panels is taken into account. This contribution is greater when panels are attached to the columns rather than to the beams because the beams deflect more and activate the connections later. There is also an increase in hysteretic damping for all systems. Frame height to span ratio does not affect the yield force of the system greatly however, increasing it does allow for a higher

deflection/drift of the system at yield. When both panel and connections are strong the capacity of the system is increased but the ductility is decreased. The model limits the additional hysteretic damping provided by the panel crushing to one cycle, when in reality the panel would still be dissipative, but this dissipation is not reliable.

It is apparent that it is more advantageous to have and thus design for a connection governed failure mechanism than a failure mechanism which is governed by either the panel or the frame. Connection governed failure allows greater damping, strength and stiffness over many cycles. However this assumes that the tie-back connections are designed to accommodate a large level of ductility. Also in terms of the cost and ease of repairs; the substitution of failed connections is seen to be more favorable than having to replace entire damaged panels.

To improve the analyses, the consideration of shear failure in the beams, columns and beam-column joint is vital. It is also worth considering other typologies of connections with different behavior, e.g. non-ductile.

REFERENCES

Brown, M.D., Sankovich, C.L., Bayrak, O., and Jirsa, J.O. (2006). "Behavior and Efficiency of Bottle-Shaped Struts". *ACI Structural Journal*, 103(3), 348-355.

Carr, A. (2004). "Ruaumoko Programme for Inelastic Dynamic Analysis - User Manual". Department of Civil Engineering, University of Canterbury.

Charleson, A. (2008). "Seismic Design for Architects: Outwitting the Quake." *Architectural Press*.

Cohen, J.M. (1993). "Feasibility of two-level seismic retrofit using an energy dissipating cladding system". *Cladding Research Institute*.

Crisafulli, F.J. (1997). "Seismic Behaviour of Reinforced Concrete Structures with Masonry Infills". Ph.D. Thesis, University of Canterbury.

De Matteis, G. (2005). "Effect of Lightweight Cladding Panels on the Seismic Performance of Moment Resisting Steel Frames". *Engineering Structures, 27* (11)

FEMA 356. (2000). "Prestandard and Commentary for the Seismic Rehabilitation of Building". FEMA.

Goodno, B.J., Meyyappa, M., and Nagarajaiah, S. (1988). "A Refined Model for Precast Cladding and Connections". *Proceedings, 9th World Conference in Earthquake Engineering*, Tokyo, Japan, pp. 195-200.

McMullin, K., Wong, Y., Choi, C. and Chan, K. (2004). "Seismic performance thresholds of precast concrete cladding connections". *13th World Conference on Earthquake Engineering*, Vancouver, Canada

Okazaki, T., Nakashima, M., Suita, K., & Matusmiya, T. (2007). "Interaction between Cladding and Structural Frame Observed in a Full-Scale Steel Building Test". *Earthquake Engineering & Structural Dynamics , 36* (1)

Otani, S., Sake, A. (1974). "A Computer Program for Inelastic Response of R/C Frames to Earthquakes". Report UILU-ENG-74-2029, Civil Engineering Studies, Univ. Of Illinois at Urbana-Champaign.

Pinelli, J.P., Craig, J. I., & Goodno, B. J. (1995). "Energy-Based Seismic Design of Ductile Cladding Systems". *Journal of Structural Engineering, 121*(3)

Priestley, M.J.N. (2000). "Performance Based Seismic Design". *12th World Conference on Earthquake Engineering*, Auckland, New Zealand

SEAOC Vision 2000 Committee. (1995). Performance-based seismic engineering. Sacramento, California: Structural Engineers Associate of California.

Evaluation of Fatigue Resistance of Multi-sided Sign and Traffic Signal Structures

Y.C. Park[1], S. Roy[2], R. Sause[3] and J.W. Fisher[4]

[1]ATLSS Center, Lehigh University, 117 ATLSS Drive, Bethlehem, PA 18015-4729; PH (610) 758-3498; FAX (610) 758-5553; email: ycp206@lehigh.edu
[2]ATLSS Center, Lehigh University, 117 ATLSS Drive, Bethlehem, PA 18015-4729; PH (610) 758-5822; FAX (610) 758-5553; email: sor3@lehigh.edu
[3]ATLSS Center, Lehigh University, 117 ATLSS Drive, Bethlehem, PA 18015-4729; PH (610) 758-3565; FAX (610) 758-5553; email: rs0c@lehigh.edu
[4]ATLSS Center, Lehigh University, 117 ATLSS Drive, Bethlehem, PA 18015-4729; PH (610) 758-5537; FAX (610) 758-5553; email: jwf2@lehigh.edu

ABSTRACT

Over the past two decades fatigue failure of cantilevered highway sign and traffic signal structures are increasingly being reported around the United States, primarily due to wind induced oscillations. For aesthetic reasons many of these structures are built with multisided tubular sections with sharp corners. Fatigue performance of fillet-welded tube-to-end plate connections in multi-sided sign/signal structures were evaluated by laboratory testing and parametric finite element analyses (FEA). Seven full size galvanized sign/signal structure specimens having eight sided cross section were fatigue tested under constant amplitude loading simulating wind induced aero-elastic galloping oscillation. Fatigue cracking in multi-sided sections mostly initiate at the bend corners of tube-to-end plate welded connection, and may appear early in service. Flexibility of the end plate, the number of sides, and the corner bend radius are the important parameters that affect fatigue resistance of multi-sided tubular structures. The existing specification does not address the effects of the connection geometry on their fatigue design. The experimental and analytical studies established the fatigue design provisions of tube-to-end plate connections in multi-sided sign and signal structures.

INTRODUCTION

Background. Over the past two decades, fatigue cracking in cantilever sign, luminaire, and traffic signal structures are increasingly being reported around the United States. These structures, built with thin-walled hollow shapes of circular or multisided cross section, are extremely flexible with a typical fundamental natural frequency on the order of 1.0 Hz and damping usually less than 1% of critical. As a result, they are often subjected to large amplitude and long duration vibrations owing to wind induced aero-elastic effects such as galloping and vortex shedding, in addition to aerodynamic vibrations due to natural gusts and truck induced gusts, which impart fatigue damage to the various welded connections in these structures.

Fatigue cracking in these structures has mostly occurred at the tube-to-end plate connections at the mast-arm and pole bases. The primary load carrying mechanism in these thin tubular structures is through in-plane membrane stresses. At the tube-to-end plate connection, the membrane stress is augmented by large out-of-plane bending stress through the thickness of the tube that arises to maintain compatibility of deformations between the tube and the end plate. This geometric stress coupled with conditions inherent to a welded connection (Roy et al. 2008), and precipitates fatigue cracking at the weld toe on the tube wall.

For aesthetic and fabrication reasons the sign and traffic signal structures are often built with multisided tubular sections with sharp corners. The fatigue resistance of these connections is further affected by the geometric stress concentration at the bend corners. Fatigue cracking may appear early in service at the bend corner. The multi-sided tube-to-end plate connections mostly employ a socket connection, where the tube is inserted into a matching through-thickness hole in the end plate, and a fillet weld is deposited around the perimeter between the tube wall and the end plate.

Previous research and specification. The only previous research on multi-sided specimens was conducted at the University of Minnesota (UM) (Ocel et al. 2006) on twenty full size sign and traffic signal structures specimens having eight sided cross section. In sixteen specimens comprising pole and mast-arm assembly, eight poles employed socket connections having 8 mm ($^5/_{16}$ in) thick tubes and 32 mm ($1^1/_4$ in) thick end plates. The outer flat-to-flat distance of the sections in poles and mast-arms were 328 mm (12.9 in) and 272 mm (10.7 in), respectively. Remaining four specimens only consisted poles with outer flat-to-flat distance of 328 mm (12.9 in) and 64 mm ($2^1/_2$ in) thick end plate. Two of these specimens had 8 mm ($^5/_{16}$ in) thick tubes, and the other two had 5 mm ($^3/_{16}$ in) thick tubes. A bend radius of 22 mm ($^7/_8$ in) was specified for all specimens. Static tests on these specimens showed presence of higher stress concentration at the weld toe in bend corners compared to the weld toe on the flat side. The cracking at the tube-to-end plate connection was found at the toe or the root of fillet-welds initiating at the bends. The weld toe cracking of tube-to-end plate connections with 32 mm ($1^1/_4$ in) end plate exhibited a fatigue resistance much less than AASHTO fatigue Category E′, which is defined as the fatigue resistance of this detail in the existing AASHTO specifications. The specimens with thicker end plate exhibited a fatigue resistance between Category E′ and D.

Ocel (2006) also conducted parametric studies involving the geometric parameters of a tube-to-end plate connection in multisided section such as, number of sides, corner bend radius, tube diameter (outer flat-to-flat distance), tube thickness, end plate thickness and number of anchor bolts. These studies indicated that the geometric stress concentration increased with fewer anchor bolts, sharper bends, and proximity of a bend to an anchor bolt. Although the experimental results provided valuable insight into the behavior of the multisided sections, their use for designing the structures is limited. Use of thin end plates and discrete fasteners are the primary reasons for increased geometric stresses and poor fatigue performance of tube-to-end plate connections. As the test results showed, using a thicker end plate is the most cost-effective means of improving fatigue resistance of these connections (Roy et al. 2008). Moreover, in view of the uncertainty in defining the accurate wind load

spectra for designing these structures, and the possibility that these structures may experience more than 100 million cycles of wind induced oscillations in their design life time of 25 years, infinite life design of the structures is rational and mandatory. The UM study, however, did not investigate the infinite life fatigue performance of multi-sided tube-to-end plate connections.

The fatigue design guidelines in the existing *AASHTO Standard Specification for Structural Supports for Highway Signs, Luminaries, and Traffic Signals,* were developed based on limited fatigue test results of socket connections in round tubes and anchor rods, and were extrapolated from the provisions for: the attachment details in the AASHTO LRFD Bridge Design Specifications; the tubular structure details in AWS D1.1; and similar structural details in the Eurocode. These provisions do not consider the out-of-plane deformation associated with the connection geometry and do not make any distinction in fatigue performance of welded connections having round and multi-sided sections.

Current study. To address the deficiencies of the existing specification, fatigue performance of multi-sided tube-to-end plate welded connection was evaluated under the National Cooperative Highway Research Program (NCHRP) Project 10-70: Cost Effective Connection Details for Highway Sign, Luminaire and Traffic Signal Structures, at the ATLSS Engineering Research Center, Lehigh University. Fatigue performance of the subject structures was evaluated in full scale specimens in both finite and infinite life regimes. The effects of multi-sided section geometry on fatigue performance of subject structures were also evaluated by parametric finite element analyses (FEA).

EXPERIMENTAL STUDIES

Specimen design. When the testing under NCHRP Project 10-70 was initiated, the only fatigue test data available for multi-sided signal and pole structures were conducted at the University of Minnesota (UM) (Ocel et al. 2006). A full scale specimen, identified as Type VII, representing a multi-sided sign and traffic signal structure was designed to provide bases for comparison with the previous test results, as well as with the structures having circular cross sections that were tested under this project. An eight sided cross section was decided similar to the UM study, but with a bend radius of 25 mm (1 in). The bend radius of UM study was 22 mm ($^{7}/_{8}$ in). The bend radius was increased as it was realized that a radius as sharp as the previous test specimens will cause severe stress concentration and poor fatigue performance. The bend radius of 25 mm (1 in) was chosen somewhat arbitrarily such that it was not too large compared to the previous test specimens to confound the effects of all the geometric changes on the fatigue test results, and also to satisfy the limitations of available tooling with most fabricators.

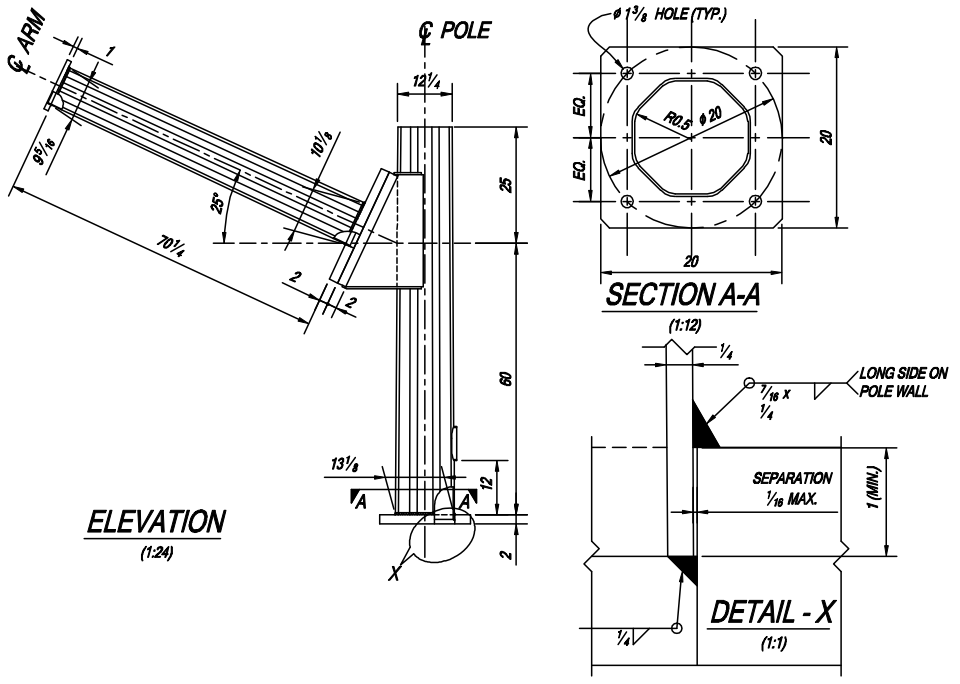


Figure 1. Details of Specimen (units in inches, 1 inch=25.4 mm)

Seven Type VII specimens were fatigue tested. These specimens employed fillet-welded tube-to-end plate connections in the pole and the mast-arm. The outer flat-to-flat dimensions of the poles and the mast-arms were respectively 330 mm (13 in) and 254 mm (10 in). An end plate of 51 mm (2 in) thickness was also provided at the pole and mast-arm bases. Although a bend radius of 25 mm (1 in) was specified, the as-received specimens had a bend radius of about 13 mm (0.5 in). The details of this specimen are shown in Figure 1.

Prior to testing, a three dimensional (3D) finite element analysis (FEA) of the specimen was conducted. The FE model was developed as the specimen was designed and included all the features of the as-built specimen. The FEA results, in terms of maximum principal stress contour, are shown in Figure 2 demonstrating the behavior of the multi-sided tube-to-end plate connections in the mast-arm and the pole. A sharp stress concentration is noted at the weld toes on the tube in bend corner. The cut-away view also shows the reverse bending at the welded connection. The predicted finite life for both mast-arm and pole was determined based on the local stress approach for tubular joints suggested in the *Det Norske Veritas (DNV) Recommended Practice DNV-RP-C203: Fatigue Design of Offshore Steel Structures*. The constant amplitude fatigue threshold (CAFT) was estimated by the notch stress based analytical approach implemented by Roy and Fisher (2005), which was determined for the mast-arm as 20 MPa (2.9 ksi).



Figure 2. Result of sub-model analysis of specimen Type VII

Fatigue test results. Fatigue testing of the specimens was conducted under constant amplitude sinusoidal fatigue loading. Minimum stress and stress range were the two design stress variables considered for the fatigue tests. The specimens were tested under a high level of minimum stress, representing the dead load effects from the overhanging weights of the signs and signal attachments. The applied nominal minimum tensile stress was 105 MPa (15.3 ksi) at the weld toe on the tube in the middle of flat side of the mast-arm tube-to-end plate connection.

Three specimens were fatigue tested to determine the finite life fatigue performance in this specimen. The remaining four specimens were fatigue tested to determine CAFT of the tube-to-end plate connection.

Specimens VII-1, VII-2 and VII-3 were tested at 83 MPa (12 ksi) nominal stress range at the section of mast-arm tube-to-end plate weld toe and experienced fatigue cracking in the mast-arm tube-to-end plate weld toe. Specimens VII-4 and VII-5 were tested under a nominal stress range of 31 MPa (4.5 ksi), the CAFT of AASHTO Category E, at the tube-to-end plate fillet-weld toe on the tube at the mast-arm base and experienced fatigue cracking in the mast-arm. In view of the result of VII-4 and VII-5, it was decided to fatigue test specimens VII-6 and VII-7 at a nominal stress range of 18 MPa (2.6 ksi), corresponding to the CAFT of AASHTO Category E′, at the tube-to-end plate weld toe on the tube at the mast-arm base. In VII-7, a small crack was detected at one of the outermost bend corners on the tension face at a very early age of 70,000 cycles. However, this crack did not demonstrate any significant growth since. Fatigue testing of specimens VII-6 and VII-7 was run-out at the stress range corresponding to the CAFT of Category E′. The testing stress range was raised to the stress range corresponding to the CAFT of Category E which is 31 MPa (4.5 ksi). Testing of specimen VII-6 was again run-out, without further fatigue cracking from the other welded details. Specimen VII-7, however, experienced fatigue cracking in the mast-arm. Specimen VII-6 experienced fatigue cracking in the

mast-arm when re-tested at an elevated stress range of 48 MPa (7.0 ksi) at the tube-to-end plate fillet-weld toe on the tube at the mast-arm base.

All Type VII specimens developed fatigue cracking in the mast-arm at the tube-to-end plate fillet-weld toe on the tube at the mast-arm base (Figure 3). These cracks initiated at the at the bend corners on the tension face at an early age due to high stress concentration, precipitated by sharp bend radius (~13 mm (0.5 in)) and were detected very early into the fatigue tests. The cracks then progressed through the thickness and grew as a through thickness crack on two fronts. Specimens VII-1, VII-2 and VII-3 also experienced similar fatigue crack growth at the tube-to-end plate fillet-weld at the pole base. The stress range at the pole base was 46 MPa (6.6 ksi), which corresponds to the stress range of 83 MPa (12 ksi) at mast-arm.

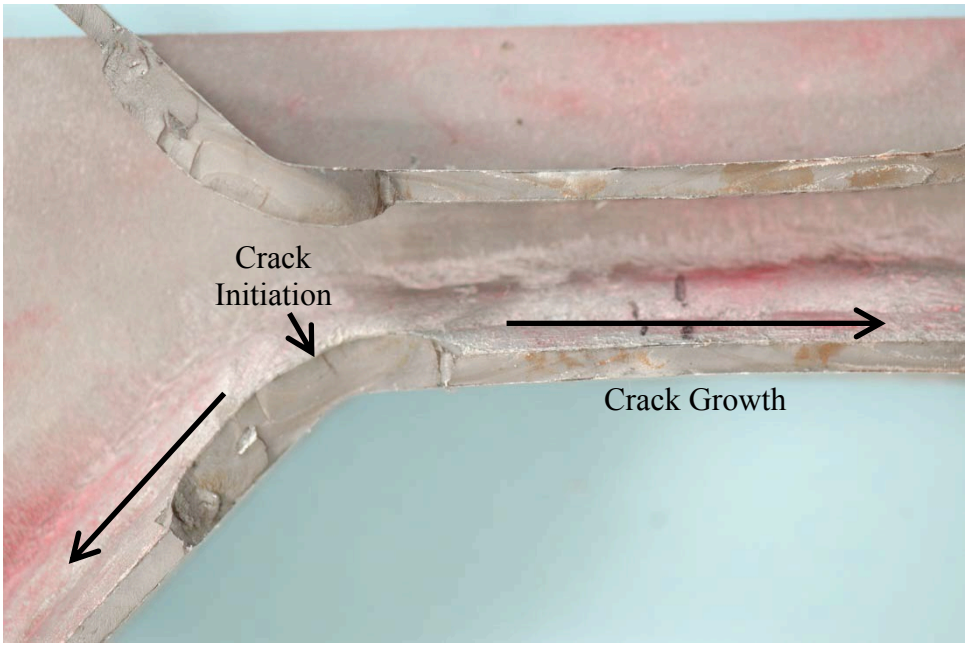


Figure 3. Facture surface of specimen VII-1 mast-arm

After failure of mast-arms in specimens VII-4, VII-5, VII-6, and VII-7, fatigue testing of the poles in these specimens were continued with a special replacement mast-arm. The pole base in specimen VII-6 and VII-7 was tested at a nominal stress range of 10 MPa (1.4 ksi), which corresponds to a nominal stress range of 18 MPa (2.6 ksi) at the mast-arm tube-to-end plate weld toe section. The specimens did not develop a crack at the stress range until the stress cycle reached to 20×10^6 cycles. The pole base specimens VII-4, VII-5, VII-6, and VII-7 were tested at a nominal stress range of 18 MPa (2.6 ksi), which corresponded to a nominal stress range of 31 MPa (4.5 ksi) at the mast-arm base. The specimens also did not crack at the stress range. The specimens VII-6 and VII-7 re-tested at an elevated stress range of 27 MPa (3.9 ksi), which corresponds to a nominal stress range of 48 MPa (7.0 ksi) in the mast-arm, at the pole base. The fatigue crack initiated at the pole base in specimen VII-6, but the test was terminated after 15.4×10^6 cycles due to the fatigue cracking at the handhole. The fatigue crack also initiated at the pole base in specimen

VII-7 and failed at the stress range. The poles in specimens VII-4 and VII-5 were re-tested at an elevated nominal stress range of 31 MPa (4.5 ksi), corresponding to the CAFT of AASHTO Category E. In specimen VII-4, test terminated after 1.2×10^6 cycles due to the fatigue cracking at handhole. The pole base of specimen VII-5 developed a fatigue crack at the tube-to-end plate weld toe on the tube.

DISCUSSION OF FATIGUE TEST RESULTS

Presentation of results. The S-N plot of the fatigue test results of specimen Type VII having multi-sided cross section are shown in Figure 4, along with the fatigue design curves from the AASHTO LRFD Bridge Design Specification. The fatigue test results are plotted against the corresponding nominal stresses, which were computed based on the section properties at the cracked section. The plotted fatigue lives correspond to a crack length of half the tube diameter (outer flat-to-flat distance) at the critical section – 127 mm (5 in) for mast-arm and 165 mm (6 ½ in) for pole – which were defined as a fatigue failure criteria.

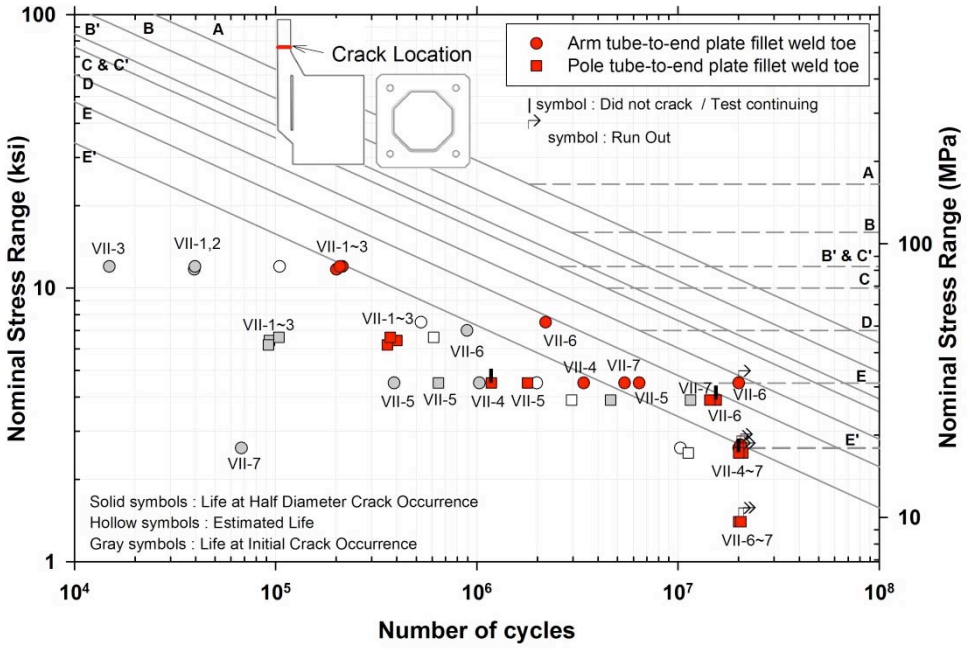


Figure 4. Fatigue test results for specimen Type VII

Evaluation of fatigue performance. The fillet-welded tube-to-end plate connections in the mast-arms demonstrated a fatigue resistance of AASHTO Category E′ corresponding to a crack length of 127 mm (5 in). These cracks initiated at the outermost bend corner on the tension face and were detected very early into the fatigue tests. Once the cracks developed out of the corner bends into the flat face, the crack propagation rate reduced.

The fillet welded tube-to-end plate connections in poles also exhibited early cracking at the outermost bend corners on the tension face and demonstrated similar crack propagation behavior. Due to higher geometric stress concentration in the pole

compared to the mast-arm, these details demonstrated a fatigue resistance less than Category E′ corresponding to a crack length of 165 mm (6 ½ in).

None of the type VII specimens developed fatigue cracks when tested at or below a stress range of 18 MPa (2.6 ksi), the CAFT of AASHTO fatigue Category E′. It appears that the CAFT of the multi-side tube-to-end plate fillet-welded connection for this specimen geometry is 18 MPa (2.6 ksi). The analytically predicted CAFT for this detail was 20 MPa (2.9 ksi).

PARAMETRIC EVALUATION OF MULTI-SIDED TUBE-TO-END PLATE CONNECTIONS

Behavior of multi-sided tube-to-end plate connections. As discussed earlier, fatigue cracking at the tube-to-end plate connections precipitate due to the out-of-plane bending stress in the tube wall that develop to maintain compatibility between the tube and the plate, irrespective of the tube cross section. To determine the reasons for high stress concentration at the bend corners of multi-sided tubes, FE models for round and multi-sided tube-to-end plate connection were analyzed. The diameter (outer flat-to-flat distance in multi-sided sections) and the thickness of tubes were 254 mm (10 in) and 5 mm (0.179 in) respectively. The end plates were 51 mm (2 in) thick and fastened with four bolts on a bolt circle of 584 mm (23 in). The normal stresses in the longitudinal (meridional) direction and the deflection in the radial direction as obtained from FEA are compared between an eight-sided and a round tube around the perimeter at the tube-to-end plate fillet-welded connection (Figure 5). Both tubes were analyzed for identical condition. The longitudinal stresses were obtained at the section $0.1\sqrt{(rt)}$ ahead of the weld toe on the tension side, where r and t are respectively the radius and thickness of the tubular member (DNV 2005). The stress profiles show that higher stress occurred at the bend corner of multi-sided tube compared to the stress in the round tube at the same circumferential position. The stress in the multi-sided tube then decreased compared to the stress in the round tube, as the circumferential position moved towards the center of flat side. The behavior could be interpreted as the bend corner behaving as a stiffener to the flat face. Since this stiffening effect would disappear as the multi-sided section approaches round, it is obvious that the stiffening effect and the resulting stress concentration are functions of the cross-sectional geometry of multi-sided tube.

Overview of parametric studies. The effect of geometric parameters of a multi-sided section on the fatigue performance of a tube-to-end plate connection was evaluated parametrically based on elastic FEA of 3D models. The models for parametric studies consisted of a tube and an end plate with fillet-welded connection. The maximum stress at the section $0.1\sqrt{(rt)}$ ahead of the weld toe on the tube wall was considered as a fatigue critical stress, and was used as the basis for comparison. The geometric parameters considered for the study was the tube diameter (outer flat-to-flat distance), the tube thickness, the bend radius, and the number of sides. Total 102 FE models were analyzed considering different combinations of the geometric parameters. The outer flat-to-flat distance and the thickness of a tube were varied from 254 mm (10 in) to 610 mm (24 in) and 5 mm (0.179 in) to 13 mm (0.5 in), respectively. The thickness of the end plate was kept constant at 51 mm (2 in). The

number of sides was varied from 8 to 20, and bend radius was varied from 13 mm (0.5 in) to 152 mm (6 in). All models were analyzed such as to produce the same nominal stress at the critical section. The FEA were conducted using the commercially available software ABAQUS (Dassault Systèmes. 2010). Twenty node iso-parametric quadratic elements with reduced integration (C3D20R) were used.

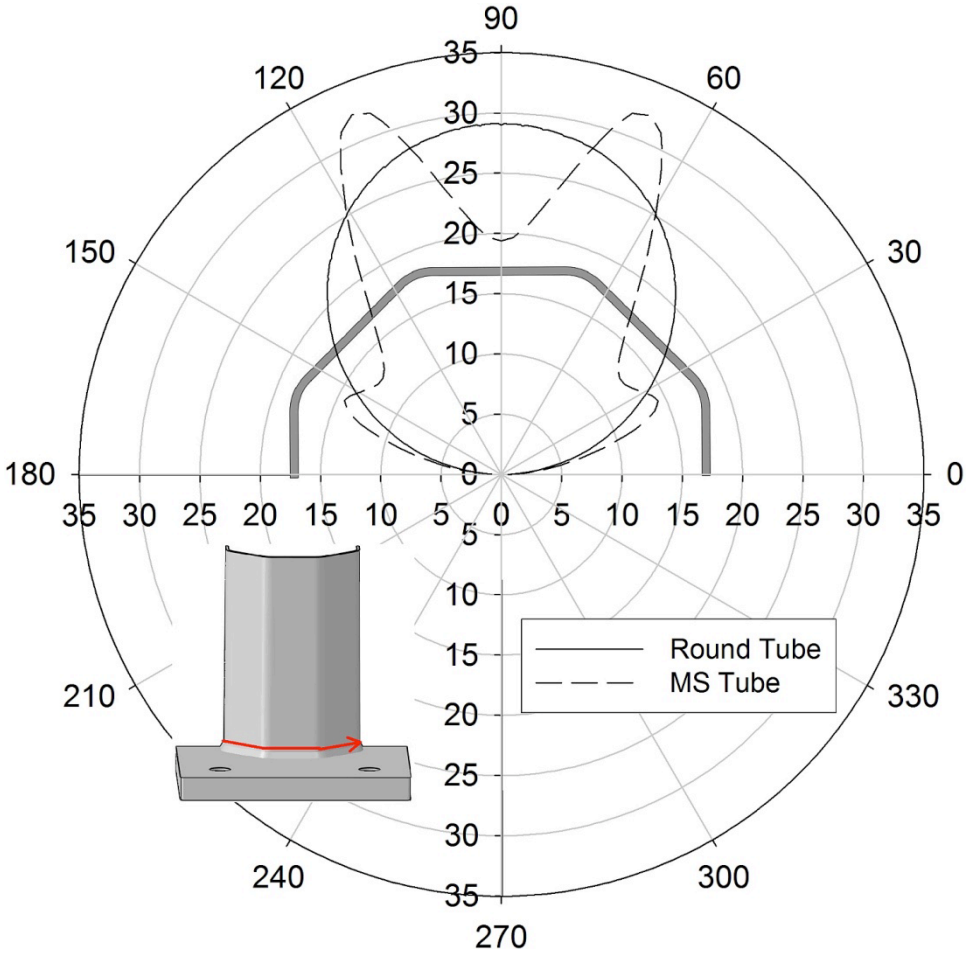


Figure 5. Comparison of longitudinal stress distribution between round and multi-sided tube-to-end plate connections

Discussion of findings. The parametric study results of the multi-sided tube-to-end plate fillet-welded connection are presented in Figure 6 (*a*) and (*b*), as an example. The effects of bend radius and number of sides on the stress concentration are presented as ratio of stress concentrations in a multi-sided tube and a round tube having the same cross-sectional dimensions. The results show that the stress concentration ratios decrease as bend radius and number of sides increase, and stress concentrations approach to that of round tube-to-end plate connections.

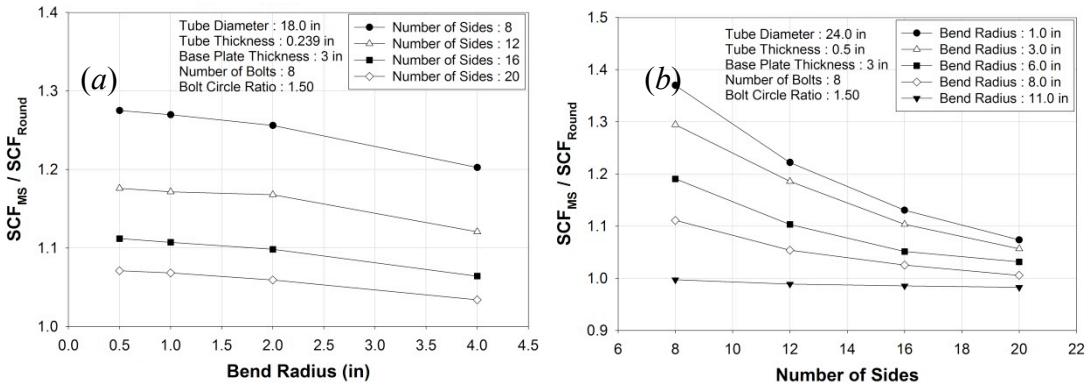


Figure 6. Typical parametric study results : (*a*) effect of bend radius; (*b*) effect of number of sides

To define the combined effect of bend radius and number of sides, a "roundness" factor was defined that quantifies the closeness of a multi-sided section to a round section.

$$\text{Roundness} = \frac{\cos(\frac{\pi}{N_S})}{1-\frac{r_b}{R_i}\left[1-\cos(\frac{\pi}{N_S})\right]}$$

The definition consists of three factors — the inside bend radius (r_b), the radius of inside inscribed circle (R_i), and the number of sides (N_S). The factor was determined by dividing the distance from the center of tube to the inside face of bend corner with the inscribed radius of inside face of multi-sided tube section. The factor can vary from 0.5 to 1.0, where 0.5 indicates three-sided tube with zero bend radius and 1.0 is represents a perfectly round tube. For a given number of sides, the length of flat face will reduce with increasing bend radius, and the shape will approach to that of a round tube. On the other hand, with increasing number of sides the shape of a multi-sided tube will approach to round tube, even with a sharp bend radius. Fouad et al. (1999) proposed a "roundness" factor, defined as the ratio of the inside bend radius to the inscribed radius of the multi-sided tube, which varied from 0 to 1, where 0 denoted the perfectly sharp corner and 1 denoted the perfectly round tube. However, this definition did not include the effect of number of sides, one of the primary and independent geometric parameter, and as such was incomplete. For a eight sided tube, the roundness factor as obtained from the above equation is greater than 0.923, which is the value of roundness for zero bend radius.

Figure 7 shows the variation in ratio of stress concentrations with respect to the roundness. The stress concentration ratios decreased with higher roundness and approached 1.0 for a perfectly round section. However, the ratios are clearly grouped by different outer flat-to-flat distance of a tube, and a small variation caused by variation in tube thickness is evident within each group. It is apparent that the stress concentration ratio is a function of the tube flat-to-flat distance, and the variation with respect to roundness factor for each tube flat-to-flat distance exhibits similar trend. The results also demonstrated that for a tube with a larger flat-to-flat distance, the

roundness should be increased to reduce stress concentration. This can be achieved by increasing number of sides and/or increasing bend radius.

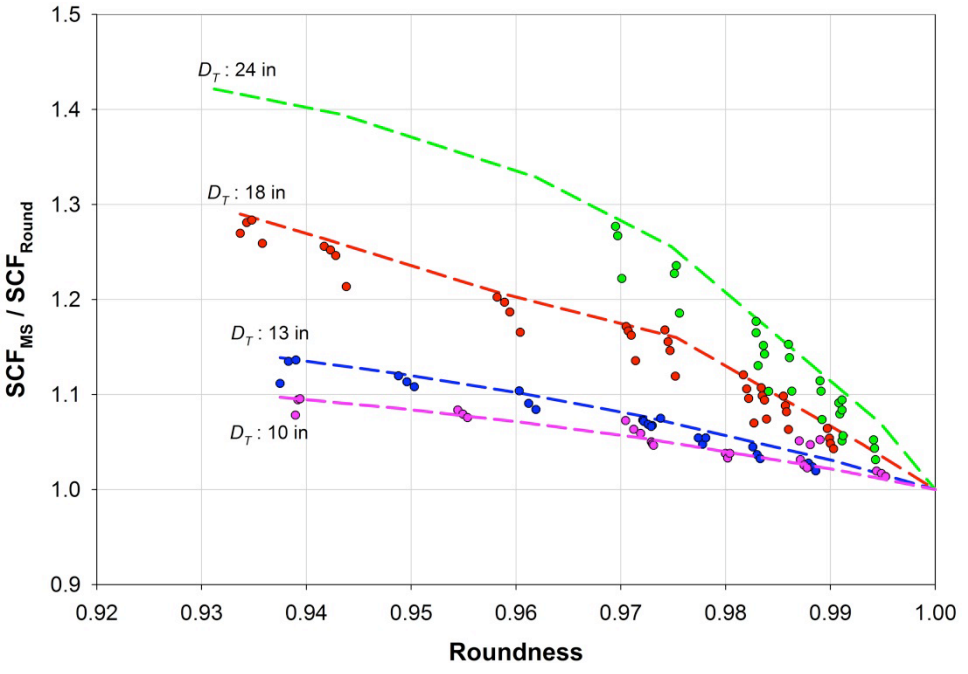


Figure 7. Parametric study results: stress concentration ratio verse roundness

CONCLUSIONS

The experimental studies established the fatigue resistance of multi-sided tube-to-end plate fillet-welded connections, against fatigue cracking at fillet-weld toe on the tube, as AASHTO Category E′ both in the finite and infinite life regimes. Fatigue cracking in multisided tube-to-transverse plate connections initiated at the bend corners and progressed towards the flat face in between the corners. Experimental and analytical research showed existence of high stress concentration at the bend corners, which caused crack initiation very early during the fatigue tests in eight sided tubes with sharper bend radius. The local stress and notch stress approach provided reasonable lower bound estimates of fatigue performance in finite life and infinite life regimes respectively. The parametric studies demonstrated that compared to a round tube of similar size, welded connections in multi-sided tubes with lower roundness exhibited significantly less fatigue resistance. Increasing number of sides and/or increasing the internal bend radius can improve fatigue performance of multisided sections. The fatigue design provision in the current AASHTO specification should be revised to reflect the effects of connection geometry on their fatigue resistance.

ACKNOWLEDGEMENTS

The research reported herein was performed under NCHRP Project 10-70 by the ATLSS Engineering Research Center, Lehigh University. This work is sponsored

by AASHTO, in cooperation with FHWA, and is administered by NCHRP. The research results presented and the opinions and conclusions expressed or implied are those of the authors and are not of AASHTO, or FHWA, or the individual states participating in the NCHRP, or the project administrators TRB and NRC.

The authors acknowledge the valuable contributions of other members of the research team: Dr. Ben Yen, Dr. Eric Kaufmann, Mr. Reilly W. Thompson, Mr. Nirab Manandhar, and the support staff of the ATLSS Engineering Research Center and the Fritz Engineering Laboratory at Lehigh University. Special thanks are due to: the members of the NCHRP project panel for their valuable guidance; to the fabricators of the test specimens Millerbernd Manufacturing Company of South Winsted, Minnesota for their generous support.

REFERENCES

Dassault Systèmes. (2010). Abaqus 6.10: Analysis User's Manual. Providence, RI: Dassault Systèmes Simulia Corp.

Det Norske Veritas. (2005). *Recommended Practice DNV-RP-C203 : Fatigue Design of Offshore Steel Structures,* Høvik.

Fouad, F.H., Calvert, E. A., and Nunes, E. (1999). *NCHRP Report 411: Structural Supports for Highway Signs, Luminaries, and Traffic Signals.* Transportation Research Board, National Research Council, Washington, D.C.,

Ocel, J. M. (2006). "The Behavior of Thin Hollow Structural Section (HSS) to Plate Connections." *Ph.D. Dissertation*, University of Minnesota.

Roy, S., and Fisher J. W. (2005). "Enhancing Fatigue Strength by Ultrasonic Impact Treatment." *International Journal of Steel Structures,* 5(3), 241-252.

Roy, S. Park, Y.C., Sause, R., and Fisher, J.W. (2008). "Evaluating Fatigue Lives of Highway Signs, Signals and High Level Lighting Structures." *In Proc. IABSE Annual Meetings and Congress*, Chicago.

Use of Empirical Constitutive Properties to Develop a Resistance Function for Reinforced Masonry

R. S. Browning[1] and J. S. Davidson[2]

[1]Robert S. Browning, E.I., A.M.ASCE, Research Civil Engineer, Geotechnical and Structures Laboratory, U.S. Army Engineer Research and Development Center
3909 Halls Ferry Road, CEERD-GS-M, Bldg 5008, Vicksburg, MS 39180-6199
PH (601) 634-5228; email: Robert.S.Browning@usace.army.mil
[2]James S. Davidson, Associate Professor, Department of Civil Engineering, Auburn University, 238 Harbert Engineering Center, Auburn, AL 36849
PH (334) 844-8777; email: Jim.Davidson@auburn.edu

ABSTRACT

The current practices used in blast design for reinforced masonry are largely based on single-degree-of-freedom analyses. These analyses use a resistance function, i.e., a load-deflection response, to define the behavior of the structural system (in this case, a wall). This paper presents an improved method for determining the resistance function for reinforced masonry walls. The new approach is capable of more accurately capturing the true behavior of a reinforced masonry wall loaded out-of-plane. The improved method is compared to current blast design practices and test data.

INTRODUCTION

Reinforced masonry (RM) is commonly used for exterior wall applications when the walls must be designed to resist an external explosive load. For infill applications, RM walls are typically non-loadbearing since the vertical loads are carried by a steel or reinforced concrete frame. RM is very effective at resisting both accidental explosions and intentional terrorist attacks. This is mostly due to the fact that when RM is fully grouted, it has a significant amount of mass that supplies an inertial resistance force. However, designers can only rely on this inertial resistance if the wall is adequately reinforced to allow it to sustain very large strains and deflections.

Typical blast design for RM uses the single-degree-of-freedom (SDOF) approach, which usually relies on a bilinear, linear-elastic-perfectly-plastic resistance function. Some references on blast design ignore the guidance provided by ACI 530/530.1 (ACI Committee 530 2008) and simply use the procedures for reinforced concrete to develop the resistance function. Most blast design standards, such as the Unified Facilities Criteria (UFC) 3-340-02 (Department of Defense 2008), are being updated to adopt the RM design procedures outlined by ACI 530/530.1. However, the resistance function will still be bilinear, and therefore, cannot properly describe the deflection at which cracking of the masonry or yielding of the reinforcement occurs.

Also, because it is assumed to behave plastically under large deflection, the design procedure does not account for any additional resistance due to strain hardening nor does it identify the deflection at which the ultimate capacity is reached. This paper describes the development of a resistance function for RM that includes these regions of behavior and also predicts the ultimate allowable deflection. The resistance function is based on empirical constitutive properties for the masonry and the steel reinforcement. The empirical relations are used in a user-developed numerical routine to calculate the complete nonlinear moment-curvature relation for an RM section. The moment-curvature relation is then used to calculate a nonlinear resistance function using a numerical implementation of the moment-area method. The resulting resistance function is compared to that obtained using the bilinear approach.

APPROACH

Previously, Browning et al. (submitted 2010) analyzed the flexural response of an RM wall using a numerical implementation of the moment-area method (Gere and Timoshenko 1997). The procedure used a piecewise-linear moment-curvature definition to calculate the resistance function, i.e., the load-deflection response, of the wall. The results of the analysis from Browning et al. showed that this approach was conservative in terms of both ultimate capacity and allowable deflection. This procedure also provided a more robust and fundamental definition of resistance because it explicitly defined the load-deflection values at which cracking, reinforcement yielding, and masonry crushing occurred; this is in direct contrast to the current approach taken by UFC 3-340-02, which cannot correctly identify any of these values.

The approach taken here was to build on the previous work by Browning et al. and to incorporate more robust constitutive properties for the masonry and reinforcing steel. The properties of reinforcing steel have been understood for quite some time, and equations defining the complete stress-strain response for reinforcing bars can be found in various textbooks. Accurate definitions of the complete stress-strain response for concrete masonry are less abundant, but a thorough search provided a set of equations that appear to perform quite well. By implementing these constitutive definitions into the procedure for calculating the resistance function, a more accurate definition of strength and ductility should be obtained.

CONSTITUTIVE PROPERTIES FOR STEEL

In constructing the algorithm to calculate the moment-curvature response, two options were used for defining the constitutive properties for the steel reinforcement. The first option uses a generic set of equations taken from Naaman (2004), a textbook on prestressed concrete design. The second option allows the user to define an engineering stress-strain curve for the steel.

Naaman's constitutive definition for the steel separates the stress-strain curve into three segments: a linear-elastic segment up to yield, a yield plateau up to strain hardening, and a strain hardening segment up to failure. The three segments are defined as follows.

$$\sigma_s = E_s \varepsilon_s \qquad \text{for} \quad 0 \le \varepsilon_s \le \varepsilon_y \tag{1}$$

$$\sigma_s = f_y \qquad \text{for} \quad \varepsilon_y \le \varepsilon_s \le \varepsilon_{sh} \tag{2}$$

$$\sigma_s = f_y + E_{sh}\left(\varepsilon_s - \varepsilon_{sh}\right)\left\{1 - \frac{E_{sh}\left(\varepsilon_s - \varepsilon_{sh}\right)}{4\left(f_{su} - f_y\right)}\right\} \qquad \text{for} \quad \varepsilon_{sh} < \varepsilon_s \tag{3}$$

where σ_s and ε_s are the stress and strain in the steel, E_s is the modulus of elasticity, f_y is the yield stress, ε_{sh} is the strain at the onset of strain hardening, E_{sh} is the modulus at the onset of strain hardening, f_{su} is the ultimate stress achieved during strain hardening, and ε_{su} is the strain corresponding to f_{su}. Using the regression equations from Naaman's textbook to calculate the undefined parameters, the resulting stress-strain definition for a Grade 60 reinforcing bar is shown in Figure 1. Also shown in Figure 1 is the stress-strain data from Browning et al. for an ASTM A 615 Grade 60 steel. The yield stress for the tested material is approximately 33% higher than that used for design; but, if the modulus of toughness is calculated by integrating these curves with respect to strain, then the strain-energy density is found to only differ by 1.5%. The strain-energy density values were compared at a strain value of 10.5%, which was the ultimate strain of the test specimen. This shows that the prediction provides a reasonable and conservative estimate for many applications. However, using a lower yield stress is not necessarily conservative in situations where reaction forces are being calculated for the purpose of designing connections. Therefore, the designer must ensure that the constitutive properties are appropriate for the problem at hand.

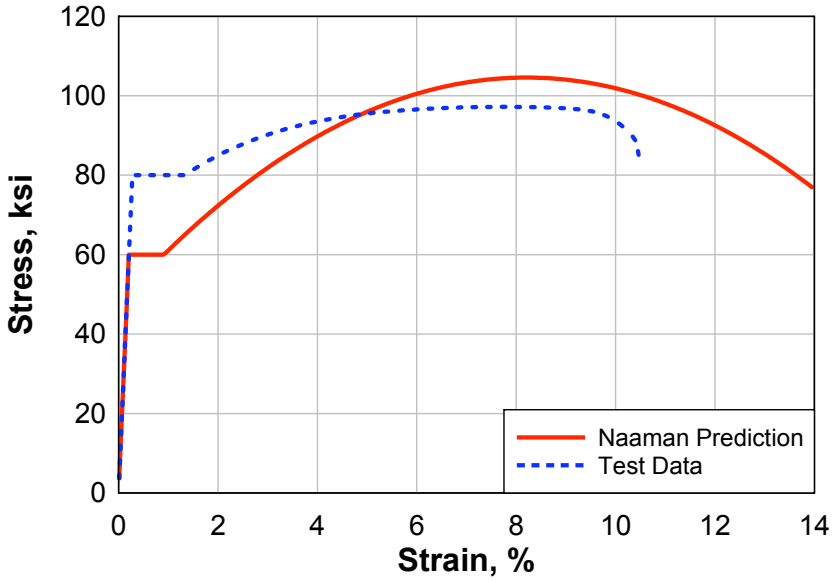


Figure 1. Predicted stress-strain curve for Grade 60 reinforcing bar.

CONSTITUTIVE PROPERTIES FOR MASONRY

The constitutive properties for masonry were taken from a paper by Hart et al. (1989). This work was conducted to complement the work done by the Technical Coordinating Committee for Masonry Research (TCCMAR) U.S.-Japan Coordinated Program for Masonry Research. Hart et al. developed two analytical models for defining the stress-strain behavior of confined and unconfined concrete masonry. The first model was known as the Acceptable Fit model, and the second was known as the Best Fit model. The Acceptable Fit model was intended to be very simple and user-friendly for designers. The Best Fit model was intended to provide a more accurate definition of the behavior at the cost of more complexity. Because this effort is focused on implementing the equations into an automated software program, the more robust Best Fit model was used.

The Best Fit model separates the stress-strain response of concrete masonry into two regions: the rising branch and the falling branch, as shown in Figure 2. The rising branch is described by a second-degree polynomial of the form

$$\sigma_m = A\varepsilon_m^{\,2} + B\varepsilon_m \tag{4}$$

where σ_m is the stress in the masonry, ε_m is the strain in the masonry, and A and B are shape parameters.

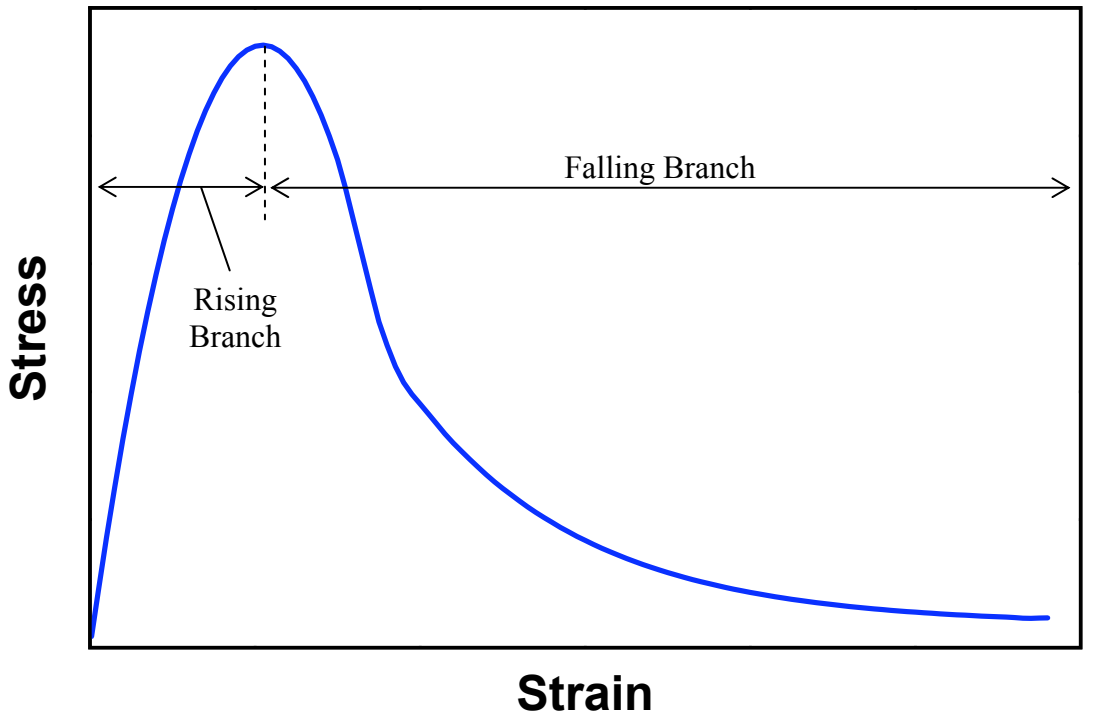


Figure 2. Typical stress-strain behavior of concrete masonry.

Hart et al. show that the rising branch equation can be written in terms of one shape parameter and two material parameters by defining a new parameter C as A/f'_m, where f'_m is the unconfined compressive strength of the masonry, and by applying the boundary condition $\sigma_m = f'_m$ at $\varepsilon_m = \varepsilon_u$, where ε_u is the strain at ultimate strength. This allows Eq. (4) to be rewritten as

$$\sigma_m = f'_m \left\{ C\varepsilon_m{}^2 + \left[\left(1/\varepsilon_u \right) - C\varepsilon_u \right] \varepsilon_m \right\} \tag{5}$$

The falling branch is defined by an exponential function of the form

$$\sigma_m = B + Ce^{(-E\varepsilon_m)} \tag{6}$$

Hart et al. rewrote Eq. (6) by applying the same boundary condition as before and by defining a new parameter D as B/f'_m. The new form of the equation then becomes

$$\sigma_m = f'_m \left\{ D + [1 - D] e^{(-E(\varepsilon_m - \varepsilon_u))} \right\} \tag{7}$$

This allows the full range of behavior to be defined by three shape parameters (C, D, and E) and two material parameters (f'_m and ε_u). Hart et al. then fit the curves to experimental data to obtain the shape parameters. For this effort, Hart et al.'s shape parameters were used, but in practice, the parameters could be recalculated if more precise experimental data were available.

CALCULATION OF MOMENT-CURVATURE RESPONSE

A complete explanation of the classical approach for calculating a moment-curvature response for RM is provided by Browning et al. (submitted 2010). The classical approach provides a simple piecewise-linear plot such as that shown in Figure 3. This approach can be used to develop a nonlinear resistance function, but it does not account for strain hardening of the steel or the nonlinear behavior of the masonry. Therefore, a more robust method is needed.

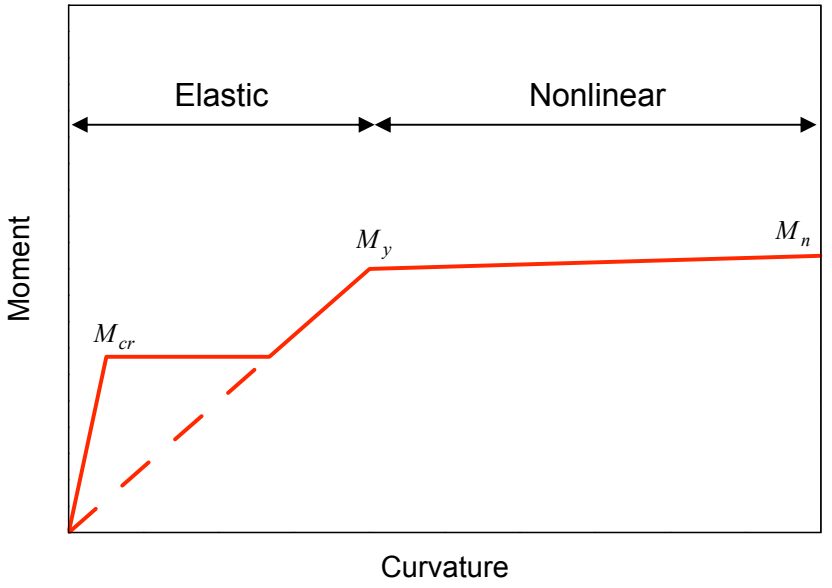


Figure 3. Piecewise-linear moment-curvature definition for reinforced masonry.

The method used to calculate the moment-curvature response is sometimes referred to as a fiber analysis or a sectional analysis. This procedure discretizes the cross section of the wall or beam in question into a large number of layers, or fibers, that can be analyzed individually. A strain profile is then applied, which is assumed to remain linear throughout the entire response. From the strain profile, the strain is known in each fiber; then, the stress can be calculated using the appropriate constitutive relations. Once the stress in each fiber is known, the forces in each fiber can be used to calculate the bending moment on the section. The curvature is calculated based on the current value of the strain. This gives a moment-curvature point, and then a new strain profile is applied to obtain another point. This process is repeated until a limiting factor, such as ultimate stress or strain, is reached. The accuracy of this process depends on the number of fibers. Therefore, it is not a practical option for hand calculations but is easily handled by the computational power offered by a normal desktop computer.

The moment-curvature definition was developed using input data from Browning et al. The input data was taken from what was referred to as the static calibrated prediction. The input parameters for calculating the moment-curvature response, as well as the resistance function, are summarized in Table 1. The stress-strain curve for the steel was taken from the test data shown in Figure 1. The resulting moment-curvature response is shown in Figure 4 along with the piecewise-linear approach previously used by Browning et al. Note that the response is essentially the same while the curvature is small, which is only natural since the simplified methods are most accurate for small strains.

Table 1. Parameters for moment-curvature and resistance function calculation.

Material Property	Definition	Input Value
f'_m, psi (kPa)	Unconfined compressive strength of masonry	4,670 (32,199)
f_r, psi (kPa)	Modulus of rupture of masonry	163 (1124)
ε_{mu}, in./in. (cm/cm)	Maximum usable compressive strain of masonry	0.0025 (0.0025)
f_y, ksi (MPa)	Yield stress of reinforcement	80 (552)
E_s, ksi (MPa)	Modulus of elasticity of reinforcement	29,000 (199,948)
b, in. (cm)	Width of cross section	144 (366)
h, in. (cm)	Thickness of cross section	7.625 (19.37)
d, in. (cm)	Depth of reinforcement	3.8125 (9.68)
A_s, in.^{2} (cm^2)	Area of reinforcement	1.24 (8.00)
L, in. (cm)	Clear span	112 (284)

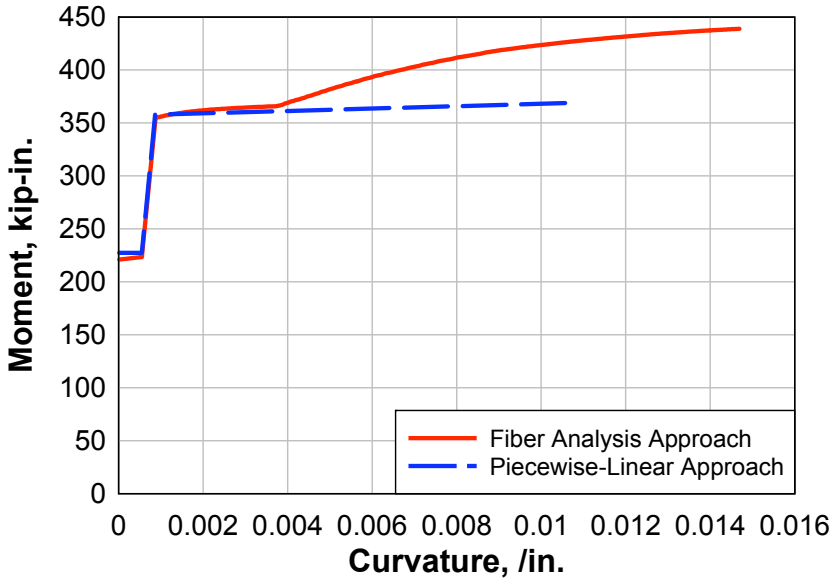


Figure 4. Moment-curvature plots.

CALCULATION OF THE RESISTANCE FUNCTION

The resistance function is simply a plot of load vs. deflection for a given structural element. In the case of a simply supported masonry wall, the deflection of interest is at midspan. In the past, Biggs (1964) showed a simple way to determine the linear-elastic-perfectly-plastic resistance function using a few fundamental equations. More recently, Browning et al. showed that an arbitrary nonlinear resistance function can be easily produced using a numerical implementation of the moment-area method. This method is currently applied only to a simply supported beam/wall, but the method is applicable to any set of boundary conditions.

The resistance function developed by the method described here is shown in Figure 5 along with that corresponding to the piecewise-linear approach. Also shown is the resistance function currently used by UFC 3-340-02 (Department of Defense 2008), which superseded the tri-service manual TM 5-1300 (U.S. Army et al. 1990). Lastly, the test data used by Browning et al. is also shown in Figure 5. These test data are more thoroughly described in the Air Force Research Laboratory report by Salim et al. (pending publication 2011). All of these cases represent the same wall loaded at a quasi-static rate; dynamic increase factors were therefore not included in the resistance function calculations.

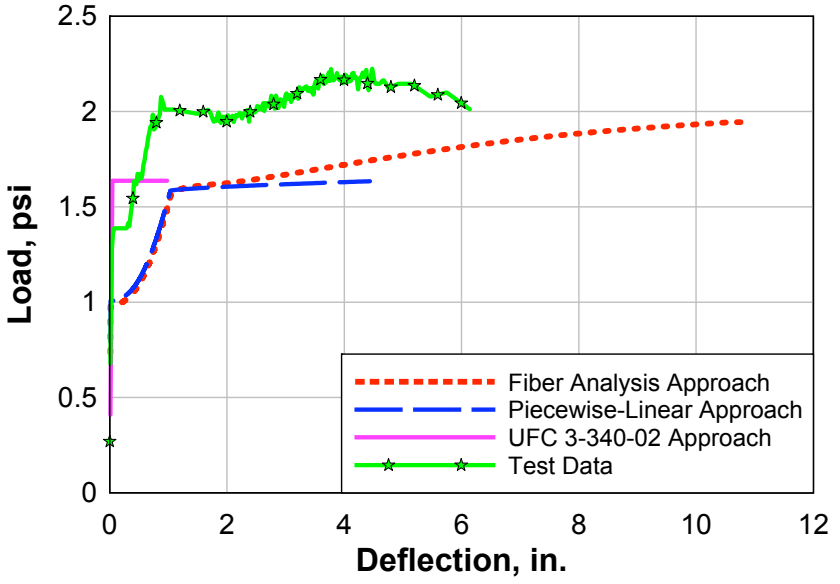


Figure 5. Resistance function plots.

Figure 5 shows that the UFC 3-340-02 approach is conservative in terms of ultimate deflection but does not correctly depict the overall behavior. For a case where deflections were required to be kept very small, it is conceivable that the UFC approach could become non-conservative if the cracking strength of the wall was significantly lower than expected. For this reason, it is proposed that a more robust definition of resistance should be used so that the actual behavior of the wall is adequately simulated.

Figure 5 also shows that there is a significant difference between the ultimate deflections predicted by the piecewise-linear method and the fiber analysis. This difference is simply due to the fact that the fiber analysis allowed the calculation to be carried out to a larger ultimate strain in the masonry. Therefore, this approach may raise more questions than answers, such as: which one is correct? This question is not an easy one to answer and is often problem dependent. However, one observation is that at deflections on the order of 6 in. (which is where the test specimen failed), the moments caused by P-delta effects from self-weight become quite significant. Further study is needed to determine if this is true, but the hypothesis is that the fiber analysis is more correct. However, the fiber analysis needs to be modified to account for P-delta effects when the resistance function is calculated. This would reduce the failure deflection, which would likely correlate better with test results.

SUMMARY AND CONCLUSIONS

A more robust method for defining the flexural resistance of RM walls was presented. The method makes use of more advanced constitutive properties than are historically used for SDOF analyses for blast resistant design. The advanced constitutive properties were used to develop a nonlinear moment-curvature definition using a fiber analysis. A numerical implementation of the moment-area method was then used to convert the moment-curvature response into a resistance function.

This method was compared to a previous approach taken by Browning et al. that made use of a simple piecewise-linear moment-curvature definition. The two approaches match well during small to medium deflections. However, there are significant differences in the ultimate deflection and noticeable difference in ultimate capacity. The reason for these differences is due to the ultimate strain used in the calculation, but the most appropriate method for calculating ultimate deflection is still being studied. It is hypothesized that P-delta effects must be included to accurately predict the failure deflection and capacity.

This method and the previous method by Browning et al. were also compared to the linear-elastic-perfectly-plastic approach taken by UFC 3-340-02. The UFC approach did not capture the true behavior of the wall, i.e., it cannot define the point at which cracking of the masonry or yielding of the reinforcement occurs. It was also shown that it could be non-conservative in special cases where deflections are critical.

REFERENCES

ACI Committee 530 (2008). “Building Code Requirements and Specification for Masonry Structures (ACI 530/530.1-08),” American Concrete Institute, Farmington Hills, MI.

Biggs, J. M. (1964). *Introduction to Structural Dynamics*, McGraw-Hill Book Company, New York, NY.

Browning, R. S., Hoemann, J. M., and Davidson, J. S. (submitted 2010). “Large-Deflection Response of Fully Grouted Reinforced Masonry Walls to Static and Dynamic Out-of-Plane Pressure,” Submitted for review for Special Publication by the American Concrete Institute organized by ACI Committee 370.

Department of Defense (2008). "Structures to Resist the Effects of Accidental Explosions," Unified Facilities Criteria (UFC) 3-340-02, Whole Building Design Guide, http://dod.wbdg.org/ (accessed Feb. 2010).

Gere, J. M., and Timoshenko, S. P. (1997). *Mechanics of Materials – 4th Edition*, PWS Publishing Company, Boston, MA.

Hart, G. C., Sajjad, N., Kingsley, G. R., and Noland, J. L. (1989). "Analytical Models for the Stress-Strain Behavior of Confined and Unconfined Concrete Masonry," Presented at the 5th Canadian Masonry Symposium, Vancouver, BC.

Naaman, A. E. (2004). *Prestressed Concrete Analysis and Design: Fundamentals – 2nd Edition*, Techno Press 3000, Ann Arbor, MI.

Salim, H., Saucier, A., Bell, B., Hoemann, J., Bewick, B., Davidson, J., and Shull, J. (pending publication in 2011). "Experimental Evaluation of Full-Scale NCMA Walls under Uniform Pressure using Vacuum," draft of Air Force Research Laboratory Report.

U.S. Army, U.S. Navy, and U.S. Air Force (1990). "Structures to Resist the Effects of Accidental Explosions," Army TM 5-1300, NAVFAC P-397, AFR 88-22.

Permission to publish was granted by the Director, Geotechnical and Structures Laboratory.

Material Characterization of Fiber Reinforced Concrete for Improved Blast Performance

W. F. Heard[1,2], P. K. Basu[2], N. Nordendale[2], J. Hoemann[1]

[1]U.S. Army Engineer Research and Development Center, 3909 Halls Ferry Road, Vicksburg, MS, 39180, USA, PH: (601) 634-2616, William.F.Heard@usace.army.mil
[2]Vanderbilt University, Department of Civil and Environmental Engineering, VU Station B 351831, 2301 Vanderbilt Place, Nashville, TN 37235, USA, PH: (615) 322-2697, p.k.basu@vanderbilt.edu

Abstract

The U.S. Army Engineer Research and Development Center (ERDC) is currently conducting material research on advanced cementitious composites with randomly distributed fiber reinforcement. The successes of the research are well documented, and unconfined compressive strengths on the order of 200 MPa are not uncommon. However, as with most cementitious materials, these materials exhibit a brittle tensile failure response. To improve the material's response to blast and ballistic loads, the tensile capacity must first be quantified and subsequently enhanced. This paper presents findings of three laboratory experimental series conducted to characterize, quantify, and enhance the tensile failure response of a new rapid-set, field-curable geopolymer concrete that offers distinct advantages over other cementitious composites.

Individual fiber, single fiber pull-out, and direct uniaxial tension experiments were conducted for a geopolymer concrete capable of achieving 44 MPa in 24 hours, and 62 MPa in 28 days in ambient temperatures with no additional curing requirements. Three fiber types were examined at various embedment lengths in the matrix. Load versus displacement curves are presented for each type of fiber, as well as the mechanical properties of the fiber itself. Direct tension samples were cast with each type of fiber at 2% by volume in the matrix and tested in a direct uniaxial experiment. The corresponding load versus displacement responses are presented and discussed. Key steps are identified for ongoing research to optimize the fiber matrix interaction, thus maximizing ductility for enhanced material response to tensile forces.

Introduction

A mission of the Geotechnical and Structures Laboratory of the ERDC is to provide innovative engineering and scientific solutions to protect the U.S. warfighter and

critical facilities. Recent shifts toward nontraditional threats and tactics from terrorists have presented new challenges to providing force protection for U.S. troops in foreign theaters of operation. In typical operations, a significant threat to the U.S. warfighter was direct and indirect fire weapons such as mortars, artillery, shoulder-fired rockets, suicide bombings, and small-arms fire. Physical protection for the warfighter was traditionally provided by hardened structures, large soil-filled revetment walls or concrete barriers or, simply put, mass.

Although a proven protective solution, the typical approach is often not practical or desirable, as it requires significant time, manpower, equipment, and other valuable resources. Furthermore, constructing massive concrete structures with limited, or at best, poor quality, in situ construction materials often results in having to transport better quality raw material from neighboring countries or from the United States. This presents many logistical challenges and is often not cost effective. Additionally, U.S. troops operating in close-engagement conditions such as contingency outposts and outside-the-wire construction or repair operations are often left vulnerable to terrorist attacks. In this typical scenario, the warfighter may occupy an area for very short periods of time—typically hours or days, rather than months or years—until the task is completed. Hardened structures and massive walls or barriers are not practical for such conditions.

Given this, recent Army research programs are focused on developing high performance concrete (HPC) mixtures and lightweight, rapidly deployable protective structures. A goal of the research thrust is to develop protective options that depend more on system ductility or enhanced material properties to provide protection from blast and weapon fragmentation, rather than mass alone (O'Neil et al. 2004). Examples of such research programs include the "Modular Protective System for Future Force Assets" (MPS) and "Defeat of Emerging Adaptive Threats" (DEFEAT). For the MPS program, a primary objective was to develop a lightweight structure that could be rapidly constructed and positioned without heavy equipment or significant manpower while providing the required level of protection from specific threats (Nelson et al. 2008). The lightweight structure was clad with multiple layers of thin HPC panels that were prefabricated at a U.S. manufacturing facility and shipped into theater. The panels were developed to provide protection from blast and weapon fragmentation at a considerably reduced thickness than that required by a more traditional concrete mixture, thus reducing mass. Full-scale field experiments validated the prototype and showed initial success of the approach. To build on this success, a component of the DEFEAT program investigated further development of a similar HPC mixture, as well as a more thorough multiscale material property characterization effort to better understand and improve similar cementitious composites. This paper

will present the initial results from unique laboratory experiments conducted on a specific cementitious composite that offers distinctive benefits, different from current HPC mixes. The cementitious composite discussed in this paper may serve as a material option for providing physical protection to the U.S. warfighter.

High Performance Concrete

The term "HPC" typically refers to a concrete that satisfies certain criteria that conventional concrete cannot. Examples of such criteria may be strength, durability, toughness, increased structural capacity, or even resistance to environmental influences (Zia et al. 1997). With respect to force protection, a HPC is typically distinguished as a concrete mixture with a very small maximum particle size, randomly distributed short fiber reinforcement, and high compressive strength.

Researchers focused on attaining high compressive strength as the criterion for achieving improved ballistic resistance. Some studies (Borvik et al. 2007) reported that an increase in compressive strength may result in improved ballistic resistance; however, it was often noted that an increase in compressive strength did not necessarily produce a comparable increase in such resistance. For example, one penetration study (Borvik et al. 2007) with a conical-nose projectile against a 100-mm-thick concrete slab showed that increasing the compressive strength from 41.4 MPa to 116.7 MPa resulted in only a 20% increase in ballistic limit. Similarly, increasing the compressive strength of a second concrete mixture from 84.4 MPa to 196.6 MPa also increased the ballistic limit by the same 20%. The ballistic limit is defined as the average of the fastest impact velocity without producing perforation and the slowest impact velocity producing complete perforation. Thus, a higher ballistic limit is advantageous and beneficial in mitigating weapon fragmentation. Other studies showed that the benefits might be less than 20% (Hanchak et al. 1992).

Pursuing a higher ballistic limit, ERDC researchers demonstrated substantial progress in producing a HPC that has a compressive strength in excess of 200 MPa. For this specific mixture, the high compressive strength was achieved by dense particle packing, a very low water-to-cement ratio, high-range water-reducing admixtures, and specific curing conditions at elevated temperatures (O'Neil 2008). A typical curing regimen would include 7 days at 22°C and 100% humidity, followed by submersion in a water bath at 85°C for 4 days and then drying in an oven at 85°C for 2 days (Williams et al. 2009). Though these techniques successfully achieved a very high compressive strength, data showed that the HPC tends to be quite brittle and has very limited tensile capacity. While conventional concrete has a tensile capacity that is normally 10% to 15% of the compressive strength, the specific HPC developed at

ERDC has a tensile capacity that is approximately 4% to 5% of the compressive strength (Williams et al. 2009). Current ERDC research programs are investigating and improving this aspect of the HPC mixture (Li et al. 2010).

Ductility is another important material property for protection against forces caused by blast and impact effects. In general, an increase in material ductility increases material toughness, or energy dissipation potential. This is an important attribute for a material resisting severe loading, such as blast load. In a high compressive strength HPC with a brittle matrix, ductility is achieved through an optimized selection of fiber reinforcement. It should be noted that randomly distributed short fibers are the preferred method for HPC reinforcement because conventional continuous reinforcement is not practical for thin panels, especially for applications stated in the preceding section. Since the brittle matrix has very low tensile strength, appropriate fibers must be selected to successfully bridge the crack openings. If this process is properly engineered and optimized, additional energy is consumed as the fiber partially pulls out of the matrix before arresting the crack, causing another crack to repeat the process. In order for this progressive cracking condition to exist, a balanced design between the fiber, matrix and interface is required. This quantitative link between material properties and material microstructures (i.e., fiber, matrix, and interface) is termed "micromechanics" (Li 1992). Researchers at the University of Michigan successfully developed and implemented this approach.

The purpose of the research discussed herein was to investigate and enhance an alternative high-early-strength cementitious material offering a simplified mixing and curing procedure capable of being produced by a soldier in the field. Such a material would retain some of the benefits of a high compressive strength HPC, while offering a more versatile casting and curing process achievable in an austere environment. To better understand the inherent material properties and enhanced ductility, laboratory experiments were developed to apply the micromechanics approach toward optimal material performance. Relevant mechanical properties were obtained for three fibers, as well as their bonding properties with the matrix. Finally, direct uniaxial tension tests were developed and conducted to quantify the tensile properties of the matrix with and without coarse aggregate, and the matrix reinforced with these three fiber types.

Description of Material

Matrix

The primary focus was on a geopolymer cement as a HPC material option for use by the U.S. warfighter. The term "geopolymer" was coined by Davidovits to describe materials stemming from his research on inorganic polymers; it refers to a broad class of synthetic alkali aluminosilicate materials (Davidovits 1991, Tempest et al. 2009). Specifically, when an aluminosilicate powder reacts with a highly alkaline silicate or hydroxide solution, a synthetic alkali aluminosilicate, or "geopolymer," is formed. Depending on its constituent raw materials, a geopolymer can possess many desirable properties, such as high compressive strength, high early strength, fire resistance, low thermal conductivity, and fast or slow setting characteristics. Therefore, the key to realizing the desirable material properties hinges strongly on the source of the aluminosilicate and the activating agent (Duxson et al. 2007).

Fly ash is an example of an aluminosilicate powder that may be used to produce a geopolymer cement. This is an industrial waste product that is generated from burning pulverized coal in power stations. Most engineers are familiar with fly ash as a mineral admixture in portland cement concrete. However, because of aluminosilicate content and easy availability, the material has generated research interest as a component for geopolymer cements. Whether low calcium (Class F) or high calcium (Class C), most fly ashes generated from modern furnaces contain 50% to 85% aluminosilicate glass (Hewlett 1998, Mehta and Monteiro 2006). The benefits of using an industrial waste product that "poses a major solid waste disposal problem in the United States and Canada" (Helmuth 1987) to produce geopolymer cements to protect the U.S. warfighter, as an alternative to portland cement produced by an industry identified as "one of the most important users of carbon-based fuels as a source of heat energy," are obvious (Hewlett 1998).

For producing this type of geopolymer cement, a Class C fly ash was combined with an alkali metal salt of citric acid. No hydraulic or portland cement was used in the mix. A chemical retarder and a superplasticizer were added to slow the reaction and to improve workability, respectively. All components of the resulting cementitious product can be premixed and stored with a 3-year shelf life, requiring only the addition of water to initiate the reaction when desired. This geopolymer cement is capable of achieving 44 MPa in 24 hours, 55 MPa in 7 days, and 62 MPa in 28 days in ambient temperatures ranging from 12^{o} to 44^{o}C. These rapid strength gains in ambient temperatures are an advantage not typical among other HPC mixes.

Aggregate

A crushed limestone aggregate with maximum particle size of 6.35 mm was included in the geopolymer cement. The grain-size distribution of the aggregate is shown in Figure 1. Coarse aggregates are typically not used in HPC mixtures. The bond between the paste and aggregate is a source of weakness that can be detrimental to the HPC. Aggregate mineralogy and surface texture affect the bond between the paste and aggregate, and studies showed that surface texture may also affect the modulus of elasticity. Moreover, surface texture and surface area per unit volume of the aggregate can affect tensile strength (Zia et al. 1997). Another study showed that aggregate mineralogy significantly influenced compressive strength and elastic moduli for concretes with strengths ranging from 85 MPa to 105 MPa. However, of the aggregates investigated, crushed limestone produced the best results. Although aggregates may have deleterious effects on HPC material response to an applied load, they offer significant benefits to the mixture, such as improved workability, dimensional stability, and significant cost savings (Mehta and Monteiro 2006). Therefore, to observe the influence of the aggregate on material response to unconfined compression, direct uniaxial tension, and packing density, samples were also cast with 74% of the aggregates removed, leaving only aggregates smaller than 1.2 mm (passing No. 16 sieve) in the mixture. This grain size distribution will be referred to as “Gradation B.”

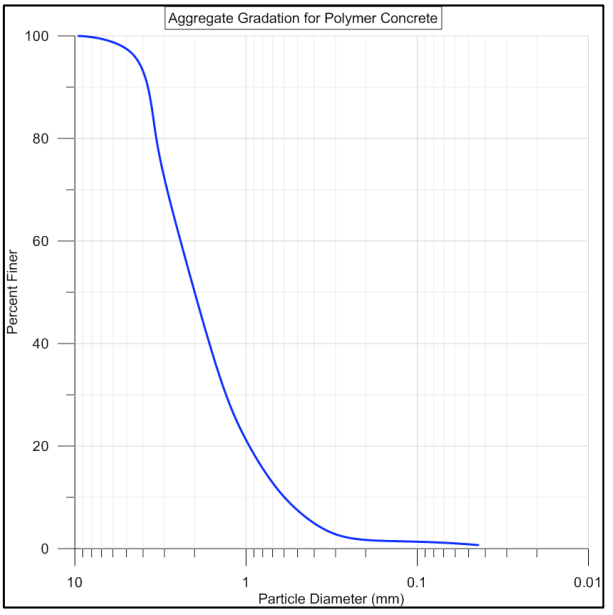


Figure 1. Grain-size distribution of aggregate used in the geopolymer concrete.

Fibers

Several fibers were evaluated for use in the geopolymer concrete. The initial findings are presented for three of the fibers that were tested: a crimped steel fiber (STC), a crimped monofilament polypropylene fiber (PPC), and a bundled monofilament polypropylene fiber (PPH) (all shown in Figure 2). The STC fiber is a continuously deformed low-carbon steel fiber approximately 38 mm long. The PPC is a continuously deformed polypropylene fiber 49 mm long. The PPH fiber is approximately 41 mm long, consisting of several monofilament polypropylene fibers bundled by two larger diameter helical monofilament fibers. A literature review on the use of various fiber reinforced cements (FRC) suggested that 2% by volume is the upper limit of fiber volume content for mixing without special processing techniques or additional admixtures to improve workability and dispersion. This limit was adequately confirmed after several unsuccessful attempts to exceed this limit in the laboratory, regardless of the fiber type used in the batch.

According to Li (1997), FRCs can be considered under three groups based on their fiber volume content. Low fiber volume contents (<1%) are typically used only for plastic shrinkage crack control with very little strength enhancement. Medium fiber volume contents (1%–2%) are often used to supplement main reinforcing steel and offer good workability for use as a cast-in-place or precast FRC without special processing requirements. High fiber volume content (>2%) can offer exceptional mechanical properties such as improved fracture toughness and enhanced ductility, and some may demonstrate strain hardening. However, to ensure proper dispersion, high fiber volume content FRCs are burdened by inordinate processing requirements, thus limiting their use in the field. Therefore, obtaining the benefits of a high volume fiber content FRC with a fiber content not exceeding 2% would, by definition, categorize the material as a HPC. Furthermore, since the stated purpose of this research was to investigate, and potentially enhance, geopolymer concrete as a field-cast and cured HPC for use by a soldier, maintaining a simple mixing and casting process with common tools is considered to be of paramount importance.

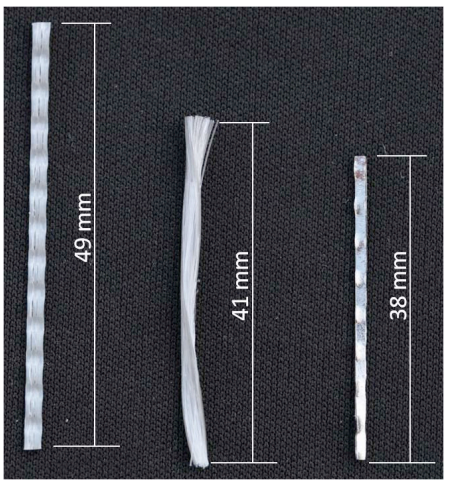


Figure 2. PPC (left), PPH (middle), and STC (right) fibers.

Casting

All samples cast for the experiments described below follow the same mixing and curing procedures. The dry ingredients, consisting of fly ash, activator, chemical retarder, superplasticizer, and aggregate, were stirred to ensure a thorough mixing of the components. Water was added to the components and stirred for 3 minutes, 30 seconds with a common hand-held 12.7-mm drill with a paddle bit. The mixture was then cast into the appropriate mold and vibrated on a platform for 2 minutes and then cured at ambient temperatures. If fibers were included in the mixture, the same procedure was used, but fibers were introduced into the mixture after 2 minutes of mixing. The yield of a typical batch was approximately 1.2×10^{-2} m^3. For samples cast without aggregates larger than 1.2 mm, the only adjustment was a slight reduction in the amount of water to maintain consistency of the mixture and to account for water absorbed by the aggregate. When the aggregate was removed from the mixture, the yield was approximately 7.6×10^{-3} m^3. Figure 3 shows an example of a small batch being mixed in a 20-liter bucket. For larger batches, a mortar mixer was used.



Figure 3. Mixing a small batch of the geopolymer concrete.

Description of Experiments

Three sets of experiments were conducted to quantify tensile properties of the fiber, matrix, and interfacial bond. First, individual fiber tests were conducted to establish the tensile strength of an individual fiber under a displacement-controlled quasi-static load. Secondly, for fiber pull-out tests, single fibers were embedded in the matrix at different embedment lengths and angles of inclination to the direction of the applied load. The single fiber pull-out experiments were conducted to establish the load versus displacement relationship and to determine the pull-out response to a quasi-static load. The third experimental set was designed to capture the response of a fiber reinforced coupon subjected to a quasi-static direct uniaxial tensile load. Each experimental setup is described below.

Individual Fiber

Figure 4 shows the individual fiber experiment. Testing was conducted on an Instron Electropuls universal testing machine (UTM) with a 2-KN load cell. A closed-loop setup with a displacement rate control of 2.54 mm per minute was provided by a built-in linear variable displacement transducer (LVDT). For the PPH fiber, the sample ends were set in resin and cured for 24 hours. This prevented slippage between the fiber and the grips and ensured that all of the bundled fibers were engaged, thus identifying the load capacity of the fiber independent of the bond. However, the STC fiber was gripped directly, as was the PPC fiber. This was justified by the location and mode of failure observed in the fibers.

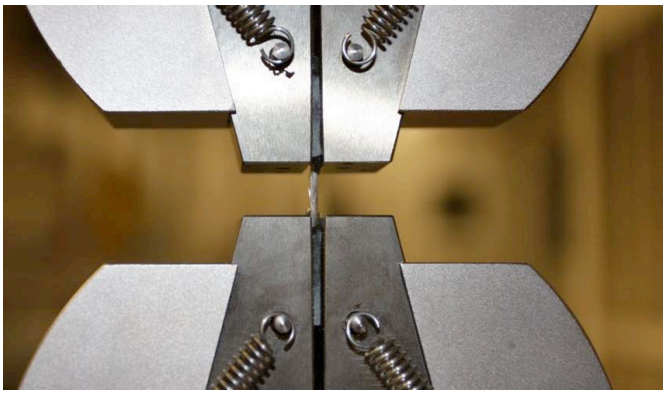


Figure 4. Testing a PPH fiber.

Single Fiber Pull-Out

A single fiber pull-out experiment was conducted to determine the bond capacity between the matrix and the fibers. These tests were also conducted on the Instron

Electropuls UTM with a 2-KN load cell and a displacement rate control of 0.254 mm per minute. When the total displacement had reached 5.08 mm, the rate was increased to 2.54 mm per minute. The rate was increased to significantly reduce the amount of time required for each test and was not expected to influence the load displacement relationship. Various lengths of PPH, PPC, and STC fibers were embedded in the matrix. Single fiber pull-out tests were conducted for each fiber with various embedment lengths. Figure 5 shows the specially designed mold (to position the fiber at the desired angle and embedment depth) and a sample being tested in the single fiber pull-out experiment.

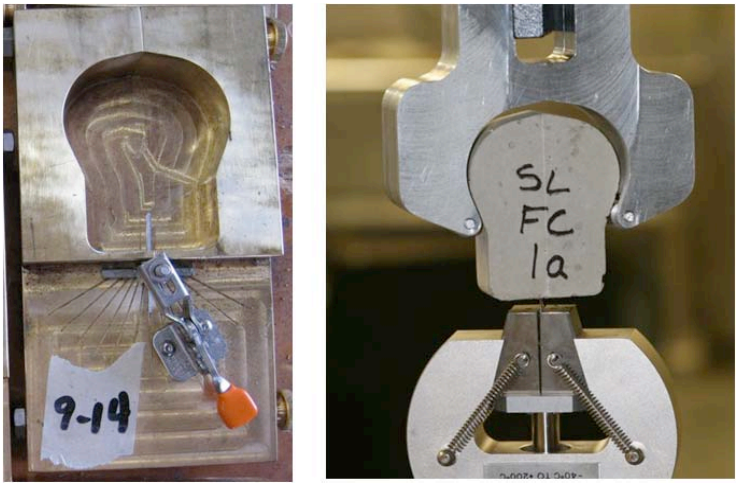


Figure 5. Fiber ready for casting and sample tested in single fiber pull-out experiment.

Direct Uniaxial Tension

In the literature, there appears to be no consensus on the recommend procedure for testing concrete in direct uniaxial tension. Some researchers have attempted a uniform sample geometry with various epoxy bonded end designs to transfer the load to the sample through the grips of the UTM. However, this approach requires tedious sample preparation and allows the potential for slippage due to inadequate strength of epoxy. More importantly, this method tends to induce significant clamping forces on the sample area held within the grips of the testing equipment. An alternative approach is to use a variation in sample geometry near the ends to enable load transfer through friction. With this approach, stress concentrations are developed at any abrupt change in sample geometry. However, the sample geometry can be designed to minimize this effect. The Japan Society of Civil Engineers has adopted a recommended procedure for testing HPC under direct uniaxial tension employing this method (Yokota et al. 2007). This procedure formed the impetus for conducting the direct tension experiments on the geopolymer concrete specimens. The sample geom-

etry used in the study is shown in Figure 6. Tests were conducted on an MTS 810 testing machine with a 98-KN load cell. The loading machine head was monitored with a built-in LVDT to maintain a displacement rate of 0.5 mm per minute throughout testing. Head displacement was recorded in addition to measurements obtained using two external LVDTs. The external LVDTs were Honeywell Model S5 with a ±5-mm stroke and were mounted on the sides of the sample slightly above the tapered region. The sample rate for the exterior LVDTs was 20 Hz, or one sample every 0.05 second.

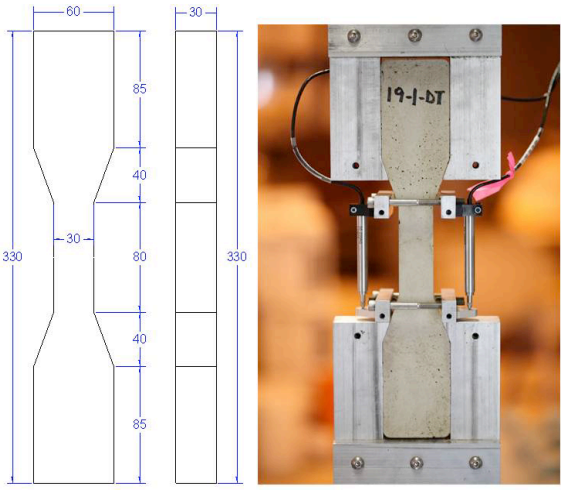


Figure 6. Direct tension dimensions and test configuration.

Results

Figure 7 shows the results of the individual fiber and the single fiber pull-out experiments for a given embedment of L/4 for each fiber where L is the fiber length. In this figure, a dashed line represents the load-displacement relationship for the individual fiber alone. In other words, a dashed line is a fiber's response to a load that is independent of bond; therefore, these results are from the individual fiber (IF) tests. Similarly, a solid line represents the load-displacement plot, or slip capacity, of a single fiber when 25% of the fiber length (L/4) was embedded in the matrix representing the results from the single fiber pull-out (SFPO) test. Since the length, surface area, and surface geometry were different for all three fibers, maintaining an L/4 embedment allows for a relative comparison of the effectiveness of these variables and their contribution to the energy dissipated when the fiber pulls out of the matrix.

In Figure 7, no IF result is shown for the STC fiber. This lack of data resulted from the combined effect of surface geometry and mechanical properties of the low carbon steel in the STC fiber leading to a bond capacity far exceeding the fiber's tensile load capacity. Essentially, the fiber failed in tension prior to bond failure for any fiber embedment length exceeding 6 mm, or L/6, when the load was applied along the axis

of the fiber. As the angle between the direction of the applied load and fiber axis was increased to a maximum of 45 degrees, a combination of fiber yielding and matrix spalling was observed, but the bond never failed. Recalling that more energy is dissipated by fiber pulling out of the matrix than fiber yielding, the above behavior is not a desirable scenario for composite material ductility.

Other notable aspects of the results shown in Figure 7 are the ratio between peak load of the IF curve and SFPO curve for each fiber type, as well as the area under the curve, or total work expended in pulling out each fiber. It is not the value of the peak load that is important; rather, the relative contribution of the two values for a particular fiber indicates the energy dissipation potential in the pull-out test. For example, the ratio of peak loads for the PPH fiber is approximately 3.0, whereas the PPC fiber has a ratio of approximately 2.0. On the other hand, the STC fiber has a ratio of 1.0. Clearly, a higher value of this ratio would indicate better potential for bond failure at a given embedment length, rather than fiber failure. Similar data were generated for different embedment lengths and angles, but only the results for the L/4 embedment at 0 degrees are shown here. These plots provide insight to the potential material ductility manifested in the direct uniaxial tension test for different fiber parameters but with a constant percent volume in the matrix.

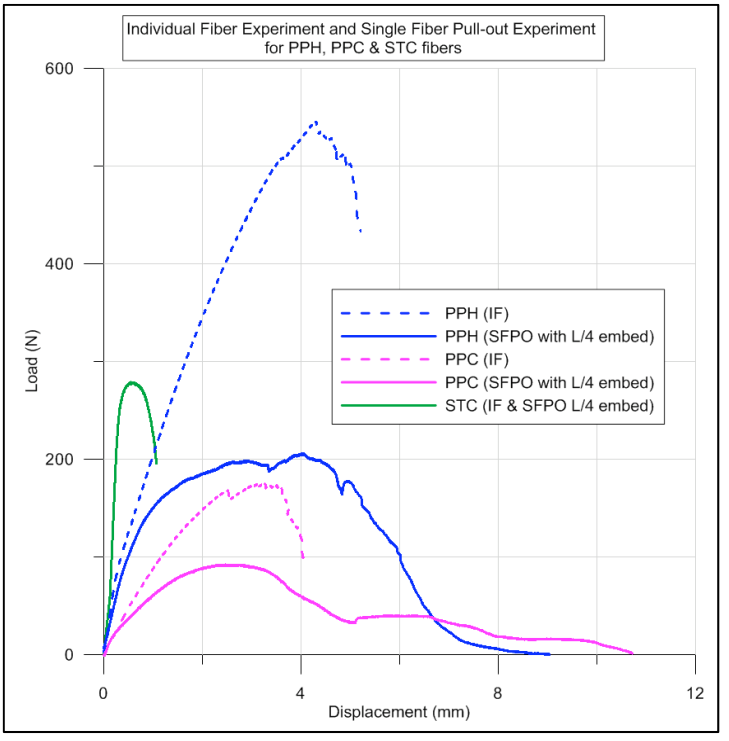


Figure 7. Results of the individual fiber and single fiber pull-out experiments for all three fibers.

Figure 8 shows two typical examples of cross sections of direct tension samples cast with the aggregate gradations shown in Figure 1. Several tests were conducted on these direct tension samples; however, the results are inconclusive because the external LVDTs indicated that the applied load to the samples cast with aggregate gradation B was eccentric. This eccentricity led to a lower initial cracking tensile load in the direct uniaxial tension test, which is inconsistent with an increase in compressive strength for the batch. Therefore, these tests will be repeated in the near future. However, the photos in Figure 8 are useful to observe typical aggregate volume and distribution as well as voids generated during the casting process.

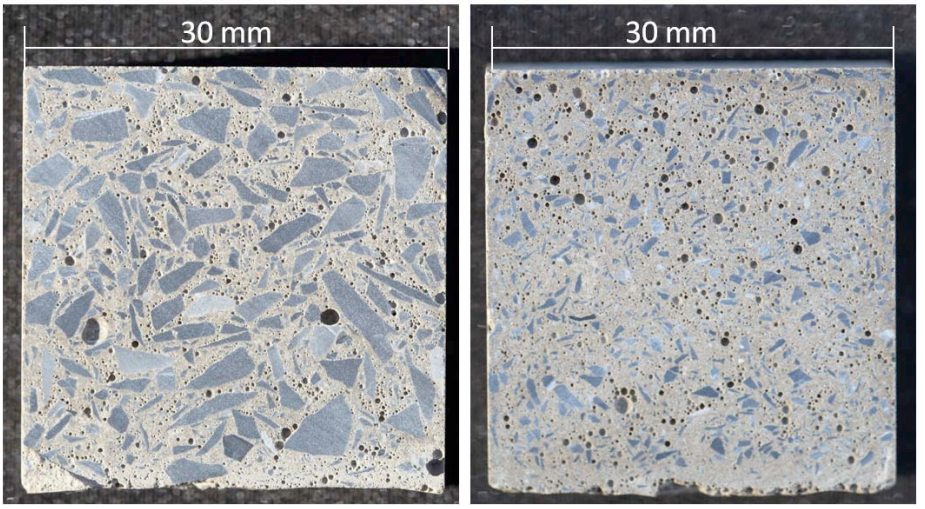


Figure 8. Typical aggregate gradation (left), Gradation "B"- maximum particle larger than 1.2 mm removed (right).

Results from the direct uniaxial tension experiments are shown in Figure 9. During the casting process, a minimum of three cylinders were cast for each batch of geopolymer concrete. These 4-in.-diameter by 8-in.-high cylinders were tested according to American Society for Testing and Materials (ASTM) C39 (2005) to monitor compressive strength of the mixture at the same time the direct tension samples were tested.

Table 1 shows values for the compressive strengths along with key values taken from all direct tension tests. Data shown in the table were obtained from a minimum number of four direct tension samples for each fiber type with the exception of the PPC fiber. For the PPC fiber, data were obtained from only three samples. As seen from the data, this batch encountered some inconsistencies with a very low compressive strength and, as a result, a low initial tensile cracking load of the matrix was obtained. This was most likely due to an error during mixing of the particular batch. This fact should be kept in mind when comparing results for the PPC fiber with

the PPH fiber. Additional testing with the PPC fiber is needed for more conclusive data. As anticipated, the direct tension samples cast with the STC fibers experienced less ductility and toughness than the samples cast with the PPH and PPC fibers. To verify adequate fiber distribution, several direct tension samples cast with the STC fiber were cut through the cross section. Examples of these photos are shown in Figure 10.

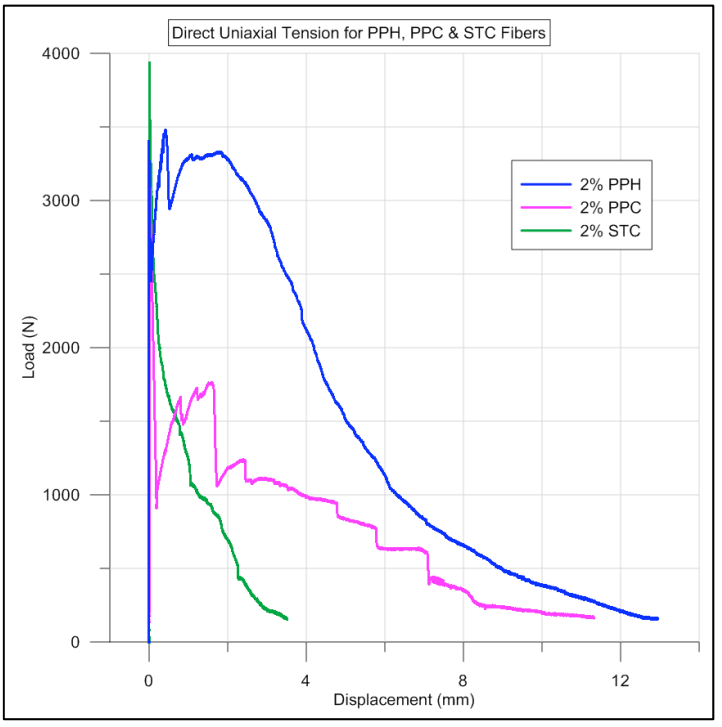


Figure 9. Direct uniaxial tension test results for all three fiber reinforcements at 2% by volume in the mixture.

Table 1. Results from the direct uniaxial tension experiments.

Sample	Wt. avg. (gm)	P_M avg. (N)	P_M std. dev. (N)	P_F avg. (N)	P_F std. dev. (N)	F'c avg. (MPa)	F'c std. dev. (MPa)
PPH	0.045	3588	180	3277	228	50.4	2.4
PPC	0.027	1987	1028	1505	495	30.0	4.9
STC	0.154	4273	471	-	-	46.9	2.7
NF_A	n/a	3114	222	n/a	n/a	49.1	2.9
NF_B	n/a	-	-	n/a	n/a	60.1	2.9

Table notes:
Wt. avg. – average weight of a single fiber
P_M avg – average load (N) at first cracking of the matrix
P_M std – standard deviation of P_M
P_F avg – average maximum load (N) carried by 2% fiber volume after initial crack

P_F std – standard deviation of P_F
F'c avg – average compressive strength (MPa) for a given batch
F'c std – standard deviation of F'c
NF_A – samples cast with no fibers with aggregate gradation A
NF_B – samples cast with no fibers with aggregate gradation B

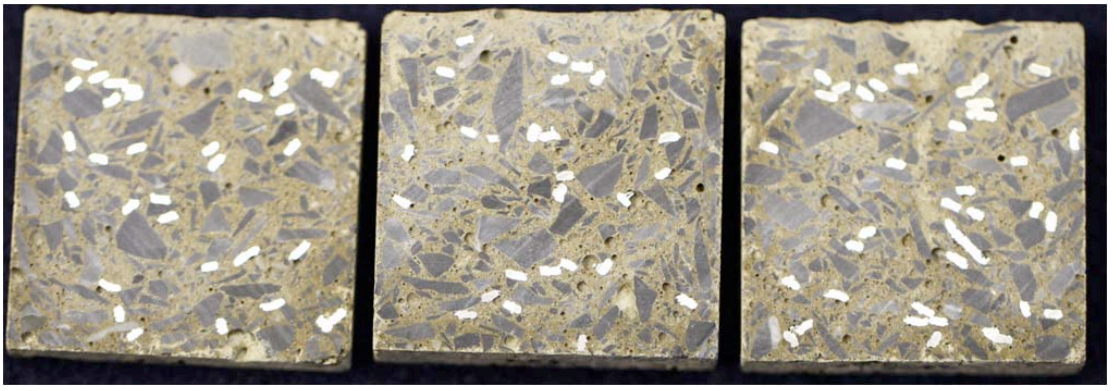


Figure 10. Cross sections taken from direct tension samples cast with the STC fiber.

Conclusions

The geopolymer concrete achieved early high compressive strengths without the aid of special curing environments or techniques. Mixing and casting was a very simple procedure that was accomplished with common tools. Incorporating aggregates improved workability and significantly increased the yield. Additional testing is required to fully understand the impact of the aggregate on the mechanical properties of the geopolymer concrete. The STC fiber had a very strong mechanical bond with the matrix, but low yield and ultimate strengths; as a result, the fiber did not pull out of the matrix. This resulted in low ductility and toughness for samples cast with the STC fiber and tested in the direct uniaxial tension experiment. The PPH and PPC fibers did not break, but were pulled out of the matrix in the single fiber pull-out experiment. This resulted in an increase in toughness and ductility of the direct tension samples compared with the STC fiber samples. Some of the direct tension samples cast with the PPH fiber experienced work-hardening after initial cracking of the matrix. Fracture toughness of the matrix should be determined experimentally, and further improvement of the geopolymer cement could result in additional work-hardening.

This paper represents initial findings of ongoing research on a geopolymer concrete. All three types of experiments were conducted with quasi-static loads. Though these experiments serve as an indicator of material performance under quasi-static tensile loads, response to dynamic loads may be entirely different. Bond between the matrix

and the PPH and PPC fibers demonstrated sensitivity to the loading rate when the quasi-static load rate was increased by a factor of 10 in the single fiber pull-out experiment. This is evidence that further testing is required.

References

American Society for Testing and Materials, (2005). Designation C 39-05. "Standard test method for compressive strength of concrete specimens."

Borvik, T, Gjorv, O.E., and Langseth, M., (June 2007). "Ballistic Perforation resistance of high-strength concrete slabs." *Concrete International*, pp. 45-50.

Davidovits, J., (1991). "Geopolymers Inorganic polymeric new materials." *Journal of Thermal Analysis and Calorimetry*, Vol. 37, 1633-1656.

Duxson, P., Fernandez-Jimenez, A., Provis, J.L., Lukey, G.C., Palomo, A., and Deventer, J.S.J., (2007). "Geopolymer technology: the current state of the art." *Journal of Materials Science*, 42, pp 2917-2933.

Hanchak, S.J., Forrestal, M.J., Young, E.R., and Ehrgott, J.Q., (1992). "Perforation of concrete slabs with 48 MPa (7 ksi) and 140 MPa (20 ksi) unconfined compressive strengths." *International Journal of Impact Engineering*, V. 12, No. 1, pp. 1-7.

Helmuth, R., (1987). "Fly ash in cement and concrete." Portland Cement Association, Skokie, IL.

Hewlett, P.C., (1998). "Lea's chemistry of cement and concrete." 4th edition, Elsevier Butterworth Heinemann, Burlington, MA.

Li, V.C., (1992). "Performance driven design of fiber reinforced cementitious composites." http://ace-mrl.engin.umich.edu/NewFiles/publications/performance_driven_design_92.pdf, Ann Arbor, MI.

Li, V.C., (1997). "Engineered cementitious composites (ECC)–Tailored composites through micromechanical modeling." http://ace-mrl.engin.umich.edu/NewFiles/publications/csce_tailoredecc_98.pdf (Jan. 5, 2011).

Li, V.C., Stults, M., Ranade, R., Heard, W.F., Rushing, T.S., and Roth, M.R., (2010). "Development of high-strength high-ductility concrete." *ERDC/GSL Technical Report* (in preparation), Vicksburg, MS.

Mehta, P.K., and Monteiro, P.J.M., (2006). "Concrete microstructure, properties and materials." 3rd edition, McGraw-Hill, New York, NY.

Nelson, D.H., Heard, W.F., Roth, M.J., and Slawson, T.R., (Dec 2008). "Development of a novel, lightweight, protective structure to resist impulsive, dynamic loads." *U.S. Army Science Conference*, Orlando, FL.

O'Neil, E.F., III, (Dec 2008). "On engineering the microstructure of high-performance concretes to improve strength, rheology, toughness, and frangibility." *Doctoral Dissertation,* Northwestern University, Evanston, IL.

O'Neil, E.F., III, Cummins, T.K., Durst, B.P., Kinnebrew, P.G., Boone, R.N., and Torres, R.X., (Dec 2004). "Development of very-high-strength and high-performance concrete materials for improvement of barriers against blast and projectile penetration." *U.S. Army Science Conference,* Orlando, FL.

Tempest, B., Sanusi, O. Gergely, J. Ogunro, V., and Weggel, D., (2009). "Compressive strength and embodied energy optimization of fly ash based geopolymer concrete." *World of Coal Ash Conference*, Lexington, KY.

Williams, E.M., Graham, S.S., Reed, P.A., and Rushing, T.S. (July 2009). "Laboratory characterization of Cor-Tuf concrete with and without steel fibers." *ERDC/GSL TR-09-22*, Vicksburg, Ms.

Yokota, H., Rokugo, K., and Sakata, N. (2007). JSCE Recommendations for design and construction of high performance reinforced composite with multiple fine cracks." Japan Society of Civil Engineers, Tokyo, Japan.

Zia, P. Ahmad, S., and Liming, M., (1997), "High-performance concretes a state-of-art report (1984-1994)." *FHWA-RD-97-030*, U.S. Department of Transportation.

Permission to publish was granted by Director, Geotechnical and Structures Laboratory.

The Evaluation of Pre-stressed Pre-cast Panels Subjected to Blast

A. Billek[1] and S. Marjanishvili[2]

[1]Hinman Consulting Engineers, One Bush Street, Suite 510, San Francisco, CA 94104; PH (415) 621-4423; email: abillek@hce.com; [2]email: shalva@hce.com

Abstract

In this paper we present a comparative study of precast prestressed concrete façade panel analysis using single degree of freedom (SDOF) and finite element methodologies. LS-Dyna was used to develop the finite element formulation. The goal of the study is to identify simple, easy and economical analytical procedure to determine the reaction loads for the precast panels. This study was motivated by a real project, with the requirements dictated by UFC 4-010-01 *DoD Minimum Antiterrorism Standards for Buildings*. The reaction forces obtained from the two analysis methods are juxtaposed and the differences are discussed. This paper presents a summary of our findings, conclusions and recommendations.

Introduction

The following paper presents a case study of the evaluation of architectural precast prestressed concrete façade wall panels subjected to blast as designed for a three-story military office building. The goal of the study is to identify simple, easy and economical analytical procedure to determine the reaction loads for detailed connection design using different analysis methods. In this study we have compared the results of single degree of freedom analysis with the results obtained using nonlinear finite element methodology. Our study is based on a real project which was completed in 2010. This paper summarizes our findings and conclusions. The goal of the design project was to analyze and design the precast façade panels for a Low Level of Protection to comply with the UFC 4-010-01 requirements. Each precast panel, measuring approximately 50ft by 10ft, is comprised of both prestressed and non-prestressed concrete regions and blast resistant glazing. Our study assumed all panel designs were complete to conventional and extreme loadings (including air-blast)were complete and focuses on the differences in the reaction forces between the two methods of analysis. Figure 1 below shows a plan and elevation view of the building with the location of the elevation circled on plan and the typical panel shaded.

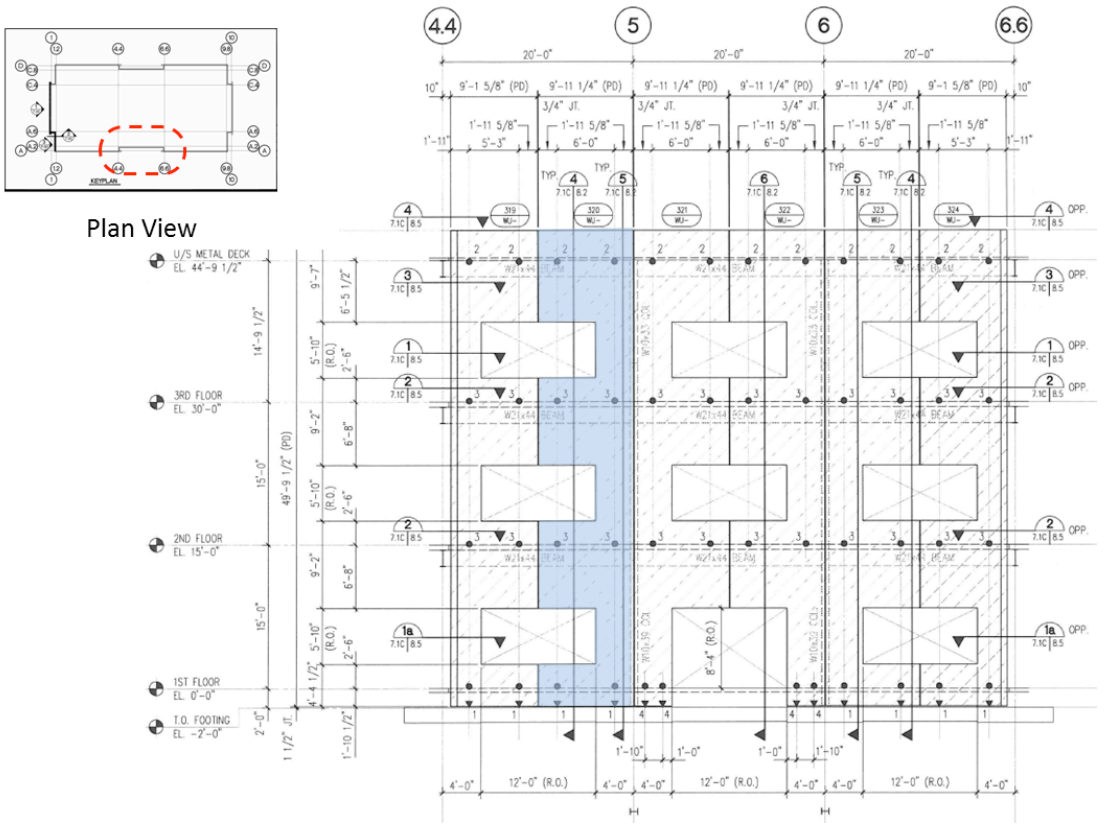


Figure 1 – Plan and Elevation View of Precast Prestressed Concrete Façade Panels

Overview of Study

The precast wall panels analyzed in this paper make up the façade of a three-story mixed-use military office building. The building, rectangular in plan, is three stories tall and clad with full-height precast prestressed concrete façade panels with fenestrations. Each panel, ranging in width from 9 to 13ft, is supported by eight lateral support points, two at each floor level. The gravity load was resisted by bearing at the ground level. The clear story height was 15ft with the exception of the roof slab which sloped for drainage. Without considering the specific connection details, there were three distinct panel types; panels without windows, panels with windows centered within the width and panels with windows adjacent to one edge of the panel

Although multiple panel types with different geometry and connection details were present, this paper will focus on what we consider to be the most complex panel type on the facade, the E-type panel, as shown in Figure 2 below. The E-type panel is primarily comprised of three different structural sections; prestressed reinforced concrete section along the height of the panel, mild reinforced concrete section between window fenestrations and blast resistant glazing at each story. The prestressed reinforced concrete section is composed of both (5) 1/2" oversized 270k prestressing strands and welded wire fabric (WWF) mild reinforcement both placed

at the mid-depth of the panel. The window spandrels account for the non-prestressed section of the façade and are reinforced with WWF at mid-depth. Between both reinforcement schemes, WWF is present at every cross-section along the panel height which provides continuous reinforcement throughout the panel. Lastly, the panel design assumes that all fenestrations will be fitted with blast resistant glazing capable of resisting the blast load without failure. The overall section depth for the panel is 8" but a ¾" reveal exists both vertically and horizontally such that the structural section depth was considered to be 7-¼".

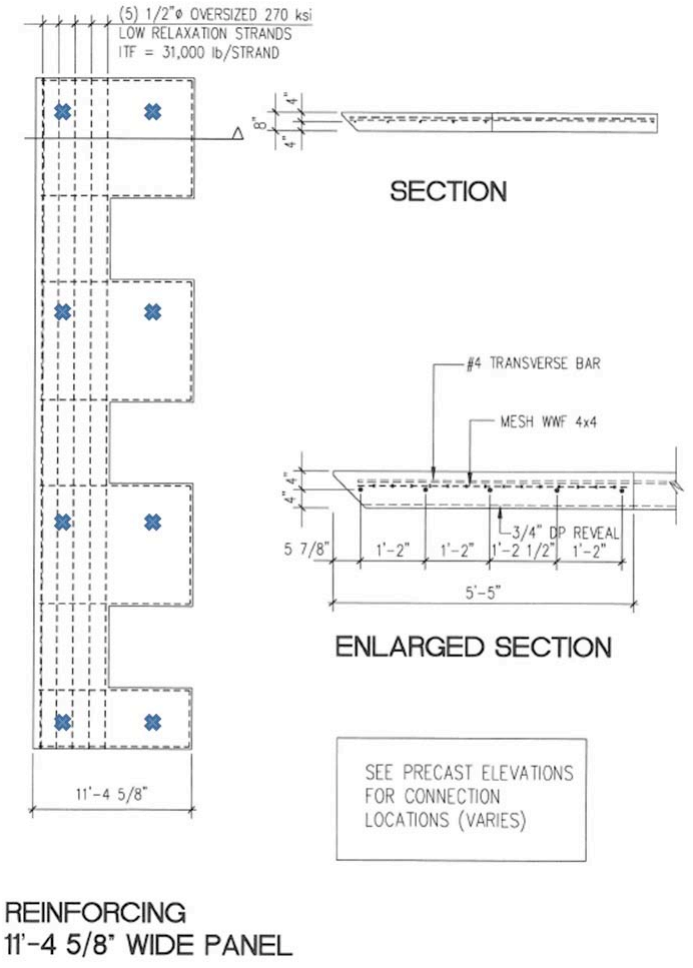


Figure 2 – Typical Prestressed Precast E-Type Panels

Because the building meets the required standoffs as stated by the UFC, there are two basic design threats to consider. The UFC requires that inhabited buildings which meet all conventional standoffs be designed for a W1 threat at a standoff of no greater than 148ft and a W2 threat no greater than 82ft. Based on threat and standoff location alone, it is not possible to predict which scenario will govern the design. We have completed analyses for both threats.

Approach

Based on the geometric complexity of the prestressed panels, our main concern was to determine an analysis procedure that would address both the material properties of prestressed concrete and the geometry of the façade panels. As we proceeded through the study, we experimented with multiple analysis methods to evaluate the performance of the panels. This case study will contrast the results obtained from the following two analyses:

- Single Degree of Freedom Analysis (SDOF)
- Finite Element Analysis using LS-DYNA

SDOF Analysis

The first analysis we used to develop the response quantities of interest was an SDOF system model. SDOF modeling is the most typical analysis methodology used in industry as it's the simplest solution technique available to obtain the nonlinear response of a dynamically loaded element. For single span elements and geometrically simple components, the SDOF solution can provide accurate results without requiring far reaching assumptions. However when using a SDOF procedure to model a complex component such as our façade panel, we will need to verify that our analysis assumptions develop a model which reflects the actual structure as closely as possible.

The continuous façade panel was divided into three independent SDOF models. Each model was assigned end restraints which matched the curvature of the deflected shape under a uniform lateral load. Therefore, the SDOF model corresponding to the first and third stories was analyzed as fix-pin and the second story façade model was analyzed as fix-fix. Solutions for these three systems can be obtained independently using the SDOF procedure (as highlighted by Biggs) and the overall results for the whole panel can be determined post-analysis. To determine the reaction forces, we can sum up the end forces from the three SDOF models and obtain the support reactions. Figure 3 below shows how a typical façade panel is divided into three SDOF analysis models.

In order to create any SDOF model, a load resistance path must be determined and quantified. Although our façade panel may seem to have one primary load path apparent, there are many different ways our support reactions can be loaded. Our SDOF model assumes the primary lateral load path between supports will be the continuous prestressed section which extends the full height of the panel (See Figure 2). Additional structural concrete present at the window spandrels is not account for in the SDOF resistance function but it is considered as additional mass in the system.

In order to determine the stiffness of the prestressed section, we followed the equations for prestressed concrete given by UFC 3-340-02, *Structures to Resist the Effects of Accidental Explosions*. Our SDOF model considered both the prestress and mild steel within the section when computing the moment capacity. Our resistance

function assumes elastic-perfectly plastic behavior at yield. Dynamic increase factors were considered for materials when appropriate to account for the increased strength due to high strain rate loading. For prestressing steel, a dynamic increase factor of 1 was used since prestressed steel is not expected to increase in strength at high strain rates.

We have used a number of different assumptions in order to model prestressed panels using the SDOF methodology. Without comparative analysis, it is difficult to determine how our assumptions will affect our response quantities of interest. It is important to remember that the SDOF method has reduced our complex load path, continuous beam structure into three simple, independent SDOF models. We will compare our SDOF analysis with the FEA methodology to determine the validity of our assumptions.

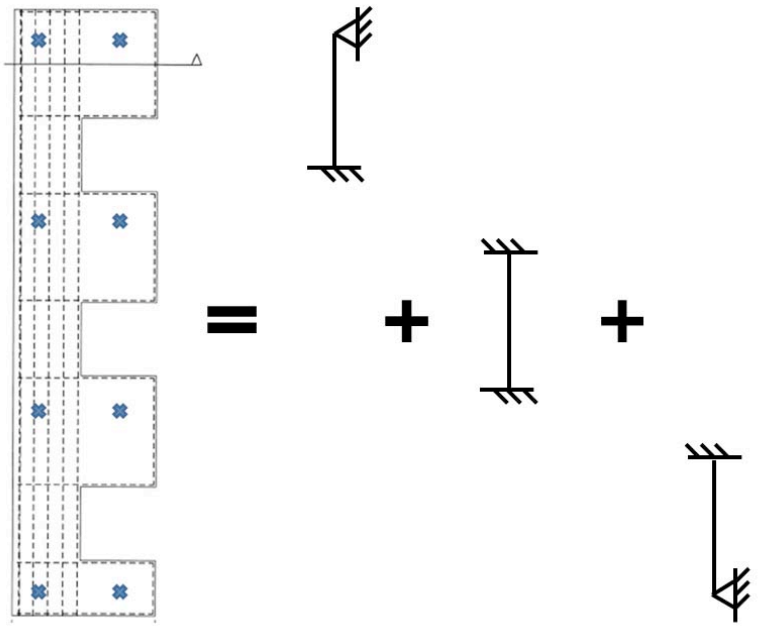


Figure 3 – SDOF System Model

SDOF Results

Figure 4 below shows the displacement time history response of each SDOF model and the reaction forces at each slab level. The reaction forces drawn on the façade panel are the total force to be resisted at the support level based on the aggregate reaction forces from the three independent SDOF models. Because the SDOF methodology lumped all the resistance to a single load path and assumed single end supports, it is unclear how to distribute the reaction loads to supports at the same slab level. A simple distribution of the reaction forces at particular slab level would be to

assume that each support takes half of the load. Depending on the level of accuracy required, this approach may be acceptable however it is clear from the geometry of the panel and the relative stiffness of all the structural elements present that the true force distribution is quite complex.

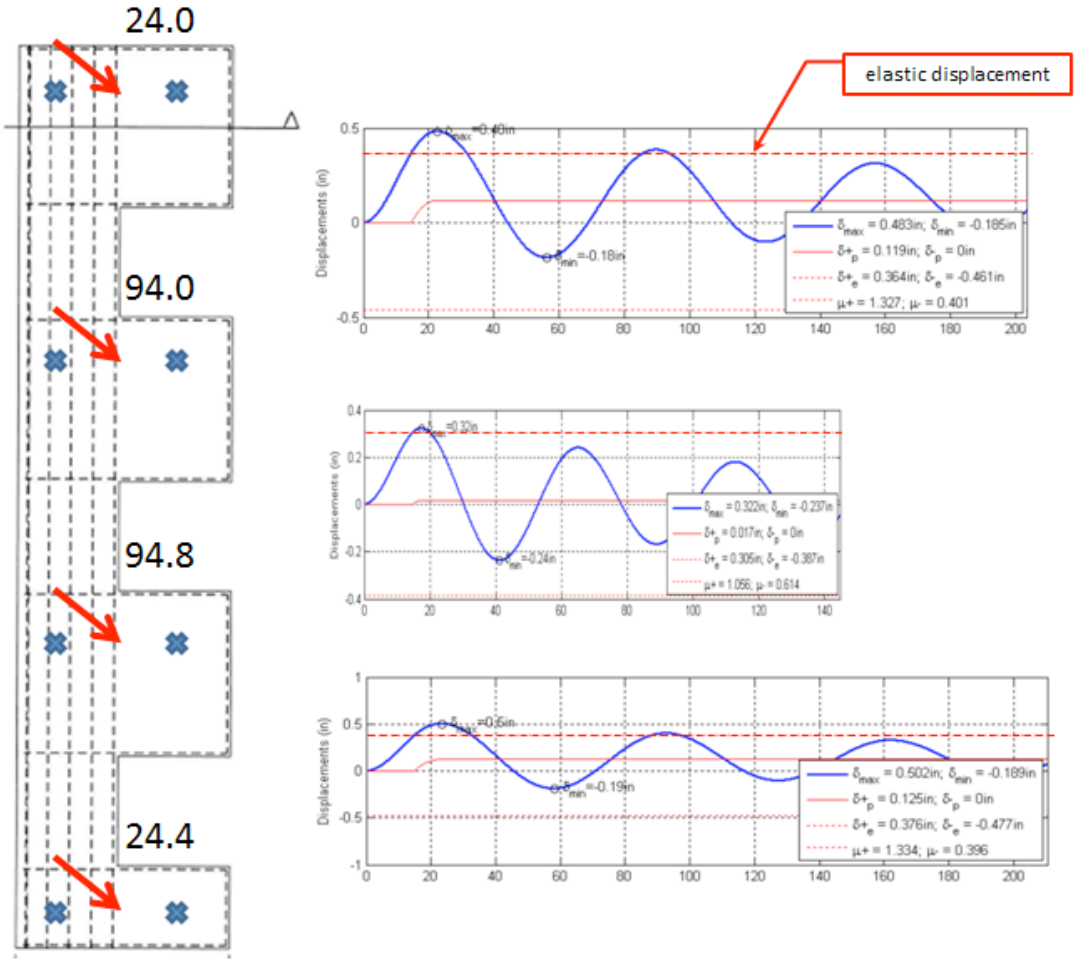


Figure 4 – SDOF Reaction Forces (units = kips)

Considering the displacement time history response plot for each SDOF model (see Figure 4), we can see that each model has yielded because the maximum displacement exceeds the elastic displacement, as indicated by the thick dotted lines on each

plot. The yielding of each SDOF model is significant to the development of the reaction forces. Because our SDOF model assumes elastic perfectly plastic behavior, yielding implies that the peak reaction forces are no longer governed by the dynamic response of the system but rather the equivalent static capacity. Therefore, although the reaction loads presented in Figure 4 were computed using a dynamic solution methodology, the same results could have been obtained by computing a static plastic hinge capacity calculation and accepting the maximum reaction.

Finite Element Analysis

To capture the effects of the precast panel geometry, we have developed a finite element model of the panel. A computer program, LS-DYNA was used to analyze the precast panel in question. Below is a list of our assumptions.

The façade was modeled using Belytschko-Tsay shell elements. Shell elements were assigned material type 103P, mat_anisotropic_plastic, and were used to model the concrete as elastic perfectly plastic. All plasticity parameters were based on the moment capacity equations of TM5-1300 (UFC 3-340-02) regarding prestressed concrete materials. By using this material type, our model is based on a "smeared" plasticity approach where the effort was made to capture the global nonlinear behavior of the section. To compute the yield stress for the material model, the moment capacity developed using UFC 3-340-02 was divided by the gross plastic modulus of the section.

Both the continuous prestressed concrete section and the non-prestressed concrete window spandrels were developed with different material properties using the same plasticity material. Nodes between both prestressed and non-prestressed sections were constrained with respect to displacement and rotation such that shear and moment forces can transfer through the panel.

Because the windows are expected to resist the blast loads without failure and are expected to distribute all blast loads over the entire duration, all window glazing was modeled as material type 101, mat_elastic, the elastic material type. Window glazing was connected to the façade panels at the window corners such that the nodal displacements were constrained and shear forces were transferred but relative rotation between the two materials was not captured.

LS-Dyna Results

Figure 5 below shows the peak reaction forces for our finite element analysis. The eight graphs plotted to the right of the façade model represent the reaction force time history at the eight lateral support points of the panel. The peak inbound reaction force is noted in black.

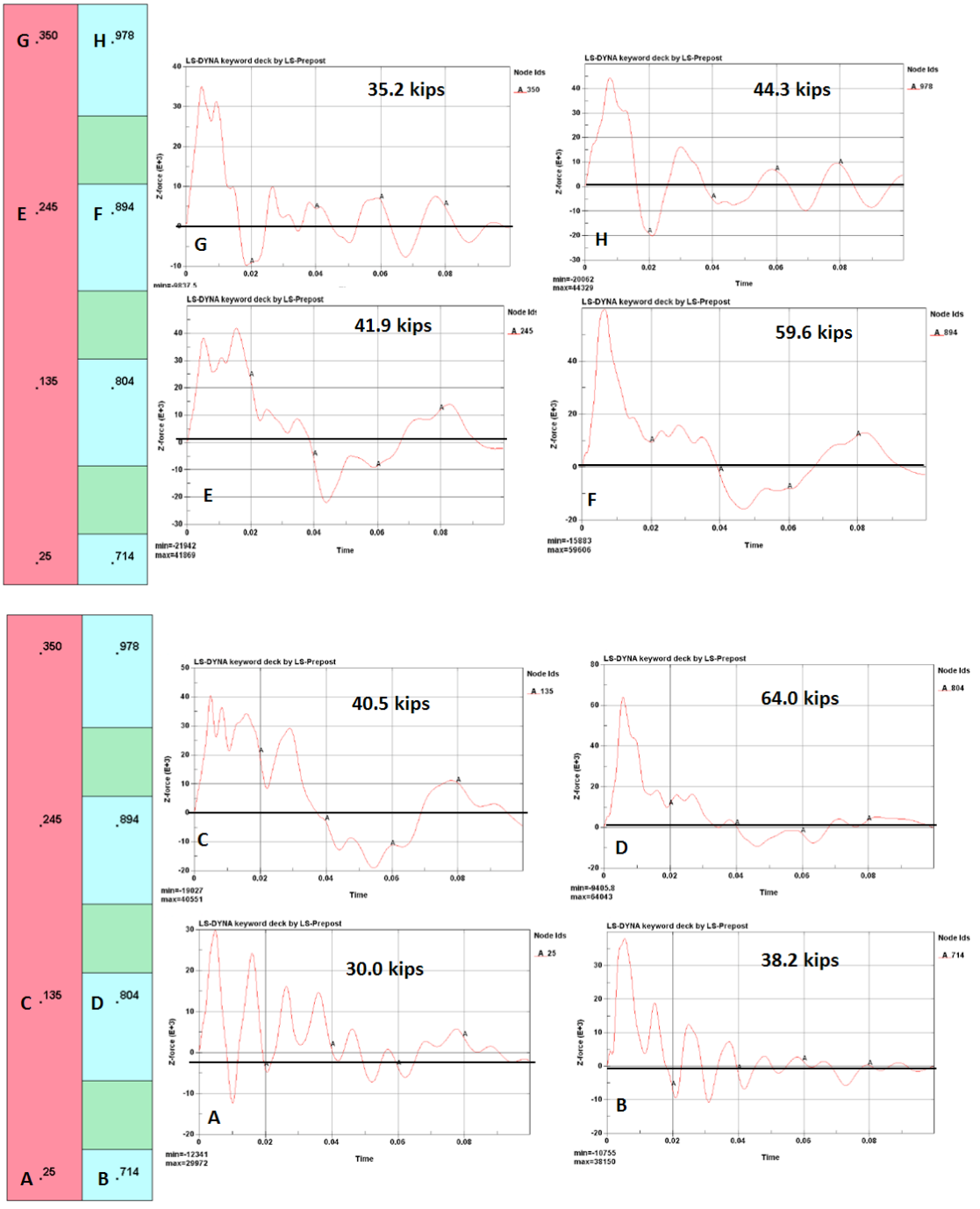


Figure 5 – LS-DYNA Reaction Force Time Histories.
Peak inbound reaction forces are noted.

Comparison of Analysis Results

Figure 6 below shows the reaction forces computed for both the SDOF and FEA methodology.

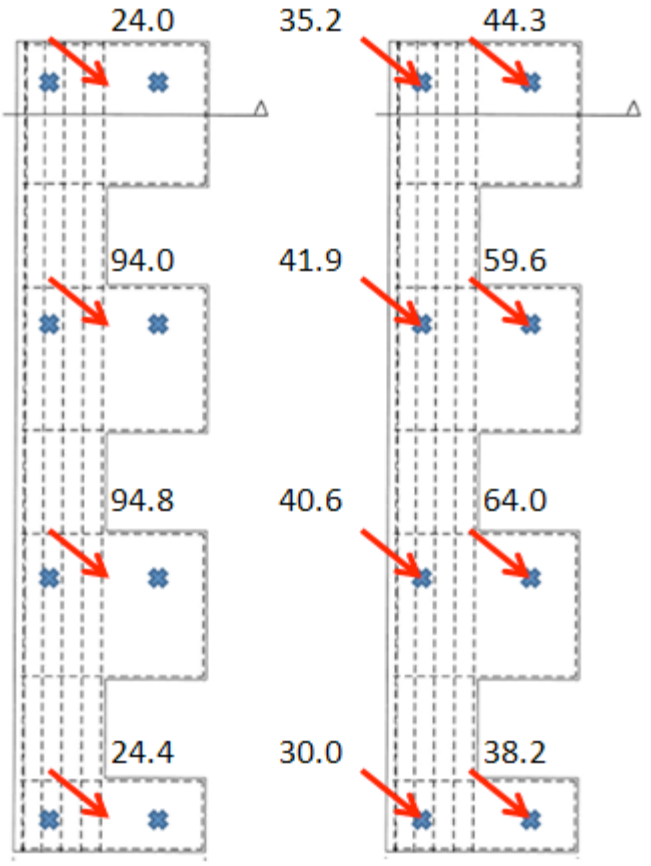


Figure 6 – SDOF (left) vs. FEA (left) peak inbound reaction forces (units = kips)

Side by Side comparison of the reaction forces developed using the SDOF method and the FEA method show that the reaction forces under FEA were larger than the SDOF results. Our results also show that FEA reaction forces were different for reaction connections at the same support level. Most interestingly, the FEA model shows that the inbound forces on the right side of the panel (where the fenestrations are) have the highest reaction forces, which are higher than the reaction forces for the left side prestress supports at the same level.

Conclusion

In this study we have used two methods of analysis for evaluation of the precast panels. The first analysis method used an SDOF system model which divided the façade panel into three SDOF models and aggregated the results to determine the

reaction forces. The SDOF analysis resulted in an equivalent static approximation of the support reaction forces that provided the total load at each slab level but not the distribution of force between individual supports. Our second analysis developed a FE model to verify and possibly improve our SDOF analysis results by accounting for the geometric complexities of the panel. Contrary to our original thought that SDOF analysis would yield conservative reactions, the FE model resulted in higher reaction forces by developing multiple horizontal and vertical load paths. These load paths are apparent in our results because the difference in magnitude of the reaction forces is considerable for each analysis methodology.

One possible explanation for the difference in the support reactions is due to the number of load paths available. The reactions developed using the SDOF model were based on the prestressed section properties assuming no other alternate load path was developed. In contrast, the FE analysis developed different reaction forces by allowing load carrying mechanisms to form organically thereby assuming no particular load path. Another explanation for the higher reaction forces can be attributed to the interaction effects between the different parts of the panel with various resistance and relative stiffness (see Figure 3), which are captured by the FE analysis but missed in SDOF.

Recommendations

Based on the limited study we have conducted during this project, the following recommendations are made:

1. Peak dynamic forces from FE analysis are larger than SDOF reactions. To obtain maximum reaction forces for panels with complex geometry, FE analysis of façade panels should be completed.
2. Peak dynamic forces in FE analysis are present for a short period of time and it may be overly conservative to design connections assuming peak reaction forces are static.
3. Currently there is no definitive approach to connection design to the effects of highly impulsive loading. Therefore a series of physical testing should be conducted to gain essential knowledge about connection behavior for very short duration loads.

References

1. United Facilities Criteria (UFC) (5 December 2008). UFC 3-340-02 *Structures to Resist the Effects of Accidental Explosions*
2. United Facilities Criteria (UFC) (8 October 2003). UFC 4-010-01 *DoD Minimum Antiterrorism Standards for Buildings*
3. United States Army Corps of Engineers, Protective Design Center (PDC) (7 January 2008). PDC-TR 06-08 *Single Degree of Freedom Structural Response Limits for Antiterrorism Design*
4. Biggs, J. M. (1964). *Introduction to Structural Dynamics*, McGraw Hill Book Company, New York.

Development of Design Recommendations for Edge-Bolted Laminated Glass

D. Duke[1] and B. T. Bewick[2], T. Casey[3] and S. R. Misko

[1]Daniel Duke, Ph.D., P.E., M.ASCE, Staff Engineer, Southern Research Institute
757 Tom Martin Drive, Birmingham, AL 35211
PH (205) 410-9603; email: DanDuke@SouthernResearch.org
[2]Bryan T. Bewick, Ph.D., Research Civil Engineer, Air Force Research Laboratory
139 Barnes Drive, Suite 2, Tyndall AFB, FL 32403
PH (850) 283-3605; email: Bryan.Bewick@tyndall.af.mil
[3]Tony Casey, MSME, Mechanical Engineer, Southern Research Institute
757 Tom Martin Drive, Birmingham, AL 35211
PH (205) 581-2370; email: casey@SouthernResearch.org
[4]Samuel R. Misko, BSEE, Instrumentation Engineer, Air Force Research Laboratory
104 Research Rd, Bldg 9742, Tyndall AFB, FL 32403
PH (850) 283-3605; email: samuel.misko.ctr@tyndall.af.mil

ABSTRACT

This paper presents the results of testing and analytical developments sponsored by the U.S. Department of State to provide recommendations for support connection design of through-edge bolted laminated glass. Design equations are presented that capture the capacity of the through-bolted laminate material in reaction to in-plane membrane induced loading. A simple analytical treatment of edge-clamping and tear-out resistance forces is presented. Specific recommendations for bolt pre-load and gasket characteristics are presented. Test data are presented to support the validity of the calculations and recommendations. The various tests were executed by the Force Protection Branch of the Air Force Research Laboratory (AFRL) at Tyndall Air Force Base, Florida and Southern Research Institute in Birmingham, Alabama.

INTRODUCTION

The current research is a continuation of efforts to support developments of the U.S. Department of State focused on new and innovative ways to retrofit facilities for improved safety against physical threats resulting from blast, ballistic, and forced-entry attacks. Considerable effort has been directed toward evaluation and design recommendations for connecting laminated glass to framing members in window and curtain wall retrofit systems. Global failure of laminated glass subjected to high-energy, short-duration blast loading most often results from glass edge support failure. Edge support failure results from displacement induced loss of glass edge bite or insufficient in-plane membrane resistance at the glass-frame interface. The primary

objective of the present investigation is to develop detailed guidelines for the evaluation and design of through-bolted, edge supported laminated glass. Edge confirmations are sought that will fully utilize the strength and ductility of laminates in the post-cracked-glass phase of blast shock wave resistance. Simply said, the goal is that the connection not be the weak link in the global laminated glass response. This research involves static, high strain rate, and high load rate testing to support the development and validation of design equations and guidelines.

BACKGROUND

The current investigation as described in Duke et al. (2009) focuses on window retrofit systems wherein laminated glass is connected to framing systems using through-bolted edge connections. The retrofit systems currently under investigation may be subjected to extreme blast loading. Many of the systems are designed with allowance for very large displacements and rotations. Movement of the support and framing systems allows and sometimes induces glass edge conditions that are well outside the realm of classical blast window design. While the glass displacements and edge deformations are extremely high, the glass edge must be supported in a way such that the glass panels are restrained against free flight into the building. An example of one of the retrofit concepts is shown in Browning et al. (2009). The through-bolted connection shown in Figure 1 is a concept being pursued for supporting the laminated glass edge. A typical connection is made up of gasket material with pressure bars that press the gasket material against the glass. The bolts are preloaded against the pressure bar, causing gasket compression. The primary technical goal of the current investigation is to provide a connection design that will support the full capacity of the laminated glass panel. An architectural concern is the width of the connection and the associated interference with visual sight lines.

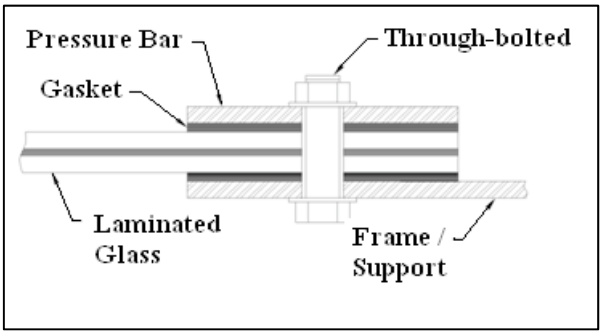


Figure 1. Typical through-bolted edge connection.

Glass panel and support frame displacements and deformations combine to yield both in-plane and bending loads along the edges of the laminated glass. As the edge of the glass is recessed between the support and the pressure bar (Figure 1), the impact of the through-holes on bending capacity of the glass edge at the connection is assumed to be small. However, the presence of holes at the through-bolted connection results in classical bolted connection tensile stress risers at and between the holes

when the laminated glass is subjected to in-plane loading. The stress risers can reduce the capacity of the connection to the point that full in-plane capacity of the laminate is not developed. Thus, while global evaluation of the glass is outside of the scope of the current investigation, the connection may become the weak link in the global response of the laminated glass.

Blast load induced glass panel and support displacements typically result in cracking throughout the glass layers early in the response of the system. The post-crack response of the laminated glass is primarily characterized by the laminate material with glass fragments remaining attached. A common assumption is that the post-crack behavior is dominated by laminate material acting as a membrane with the glass providing mass only. In terms of in-plane loading this may be a valid assumption. However, the post-cracked bending resistance of laminated glass is likely very different than that of a simple membrane. The membrane assumption is integral to one aspect of the current research in that it matches the effort to understand the capacity of the edge support relative to in-plane membrane loading. Thus, the current research is focused on characterizing the in-plane capacity of through-bolted edge supported laminated glass panels.

The discussion that follows summarizes previous results, reports new findings and describes planned efforts.

SUMMARY OF PREVIOUS RESULTS

Duke et al. (2009) presented test results aimed at characterizing the in-plane pull-out capacity of a common laminate material. The test setup is shown in Figure 2. Tests were conducted with variations in bolt spacing and edge distances. Failures at or between the bolts were observed that match classical bolted connection results for in-plane tensile loading. Shown in Figure 3 from left to right are classic V-notch failure, pure shear/pull-out, and hole-to-hole net area tension failure.

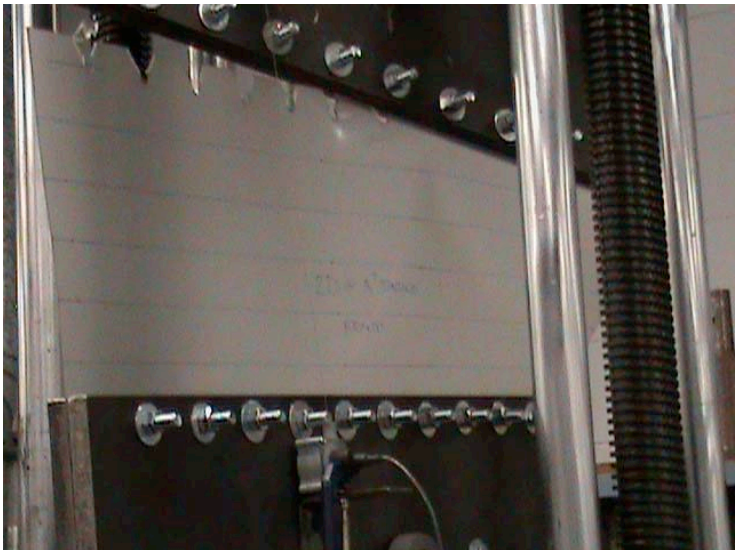


Figure 2. Static component level testing of laminate.

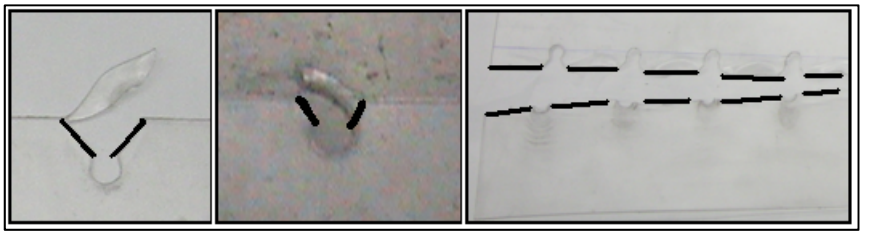


Figure 3. Laminate edge failure mechanisms.

Simple equations based on classical mechanics were developed to predict the edge capacity of the laminate material. Figure 4 shows the key geometric parameters used to evaluate the edge capacity. As seen above, failure is either V-notch / tear-out at the bolts or net area tension failure between the bolts. The V-notch / tear-out resistance is predicted by Equation 1

$$R_n = \frac{2\left(e - \frac{d}{4}\right)tF_u Tan\theta}{s} \qquad \text{Eq. 1}$$

where Rn has units of force per unit length, t is the laminate thickness, Fu is the ultimate tensile strength of the laminate, and s is the center-to-center bolt spacing dimension. The bolt-to-bolt net area tension failure capacity is calculated from

$$R_n = \frac{(s-d)tF_u}{s} \qquad \text{Eq. 2}$$

The (s - d) term in Equation 2 is the net distance between the bolt holes. The minimum value from Equations 1 and 2 is taken as the capacity of the laminate.

Test results confirm that the capacity prediction shown above provides reasonable and conservative values for the edge capacity of the laminate material. Additional tests have been performed that were aimed at capturing other key aspects of through-edge bolted connections. Specifically, a series of drop hammer tests was conducted where various make-ups of laminated glass panels were supported by a rigid frame and subjected to impact loading. The results supported the predictions represented by Equations 1 and 2 above. There were also clear indications that a more fundamental understanding of the connection characteristics would serve to clarify interpretation of the drop hammer results. Thus, a series of tests described below was executed.

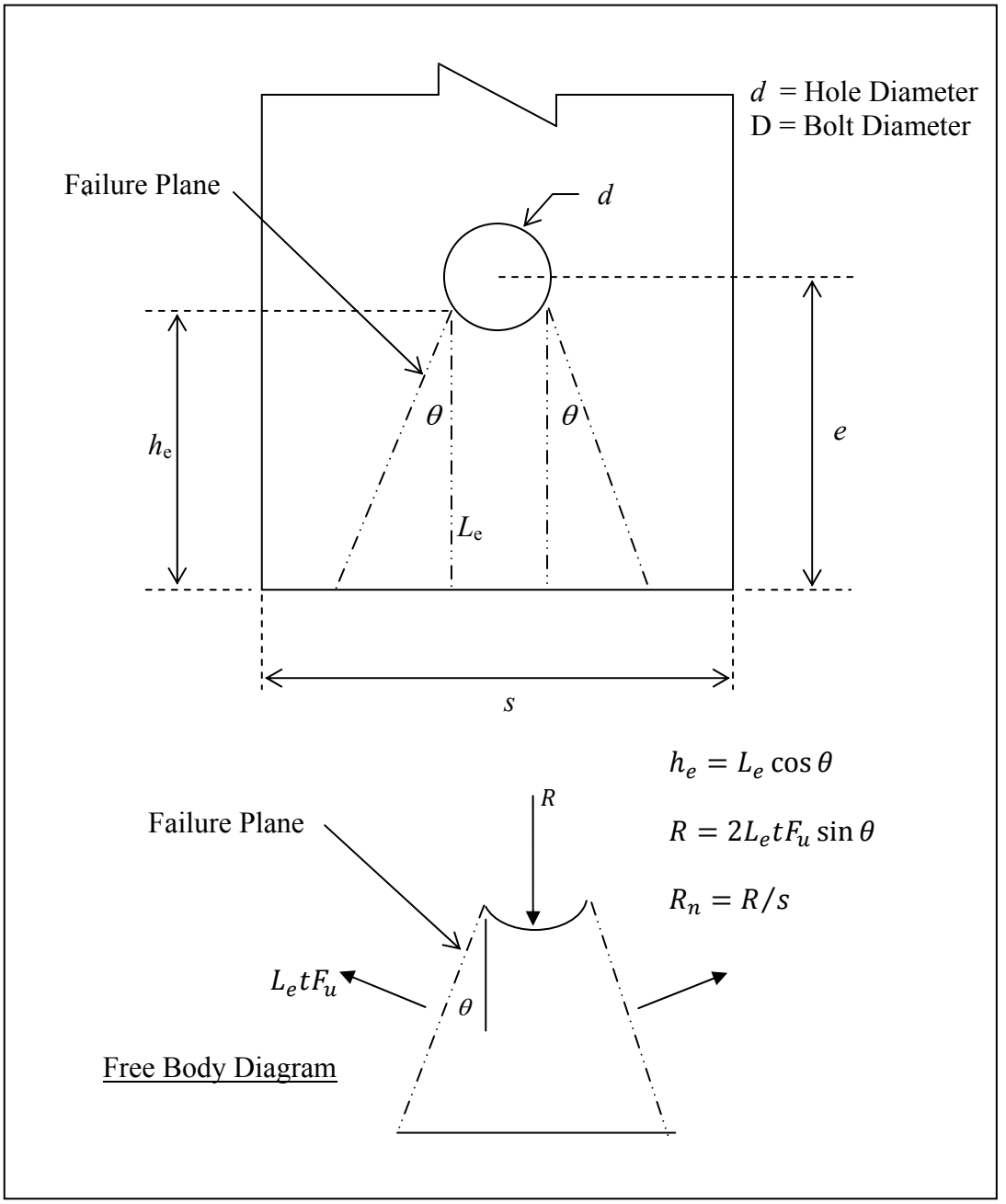


Figure 4. Classical solution parameters.

PULL-OUT TESTS

In-plane pull-out resistance for the inner layer (laminate) of through-edge bolted laminated glass is presented above. Further testing was conducted at AFRL to help clarify some of the results from previous tests. While a fundamental part of edge pull-out resistance is characterized by the laminate capacity, other factors contribute to edge capacity. Those factors include shear forces between the glass and the gaskets in the form of either simple friction or cracked glass "digging" into the gasket material. The shear forces between the gasket and cracked glass is considered as an effective friction. A second factor relates to the added strength resulting from glass remaining attached to the laminate in a post-cracked configuration. The test setup in Figure 5 was designed to help capture the effects of some of the factors described above. In the test setup laminated glass is held between fixture plates and gaskets with through-bolts. For the current set of tests the bolt spacing and edge distance were held constant. Load cells were used in some of the tests to capture bolt pre-tension so that bolt preload and bolt torque could be correlated. Very large edge distances were used at the upper edge of the glass specimens so that edge failure would be predictably seen at the bottom edge. As part of the core investigation, the bolted connection at the bottom has either through-holes in the laminated glass panel or the glass panel was slotted from the center of the bolt hole locations to the bottom glass edge as shown in Figure 6.

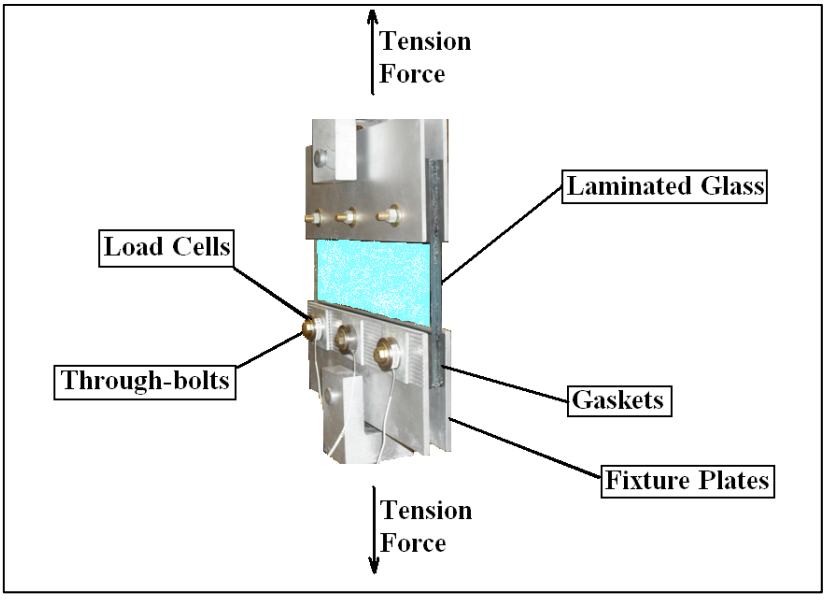


Figure 5. Pull test setup.

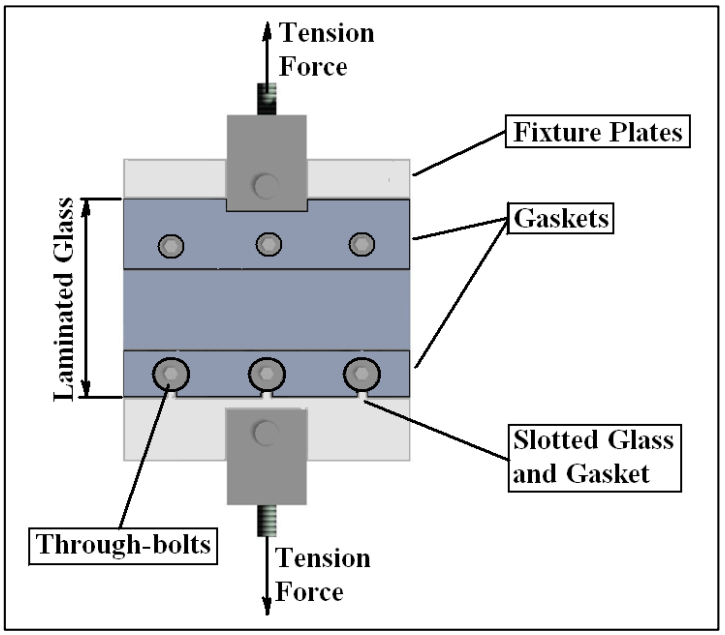


Figure 6. Slotted glass setup.

Bolt preload.

A practical issue associated with bolted connections where tension preload is important is how to assure that the bolts are installed with the proper range of preload. In classical structural applications various methods are available to control preload including the turn-of-the nut method and load indicator washers. In the window and glass curtain wall industry bolt torque measurement is often the preferred method. All of the methods have advantages and disadvantages under the best of conditions. In the current research where gasket material and laminated glass are in the stack of bolted layers, there are additional concerns over proper bolt preload. In an effort to quantify bolt preloads in this context, bolt tension forces were measured using load cells. Corresponding bolt torques were also measured. Figure 7 shows a plot of preload versus torque. A semi-empirical formula that is widely used to estimate bolt torque versus preload is $T=0.2FD$ where T (in-lb) is torque, F (lbf) is preload bolt tension and D (in) is the bolt diameter. The data in Figure 7 provides reasonable correlation with the classical formula and thereby supports the notion of using the formula to estimate compressive forces in the gasket.

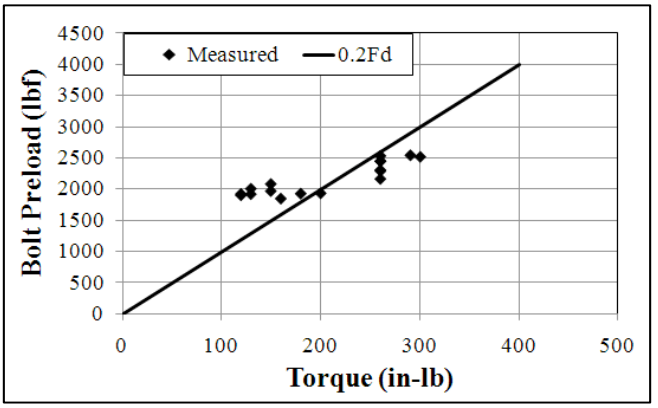


Figure 7. Bolt preload versus torque.

Effective friction.

More testing is planned to characterize the segmented strengthening effect of fragments of glass remaining attached to the laminate in a post-cracked configuration. However, the primary focus of this discussion relates to the effective friction associated with the interaction between the glass and the gasket material. As indicated above several test specimens were used that have slotted holes at the edge. The goal for this portion of the test was to quantify the effective friction versus clamping force (bolt preload) for smooth and cracked glass. The slots allow pullout without engagement between the bolts and the inside edge of the bolt holes. That is, the goal is to obtain friction only with the understanding that the structural capacity of the laminate inner layer is quantified using Equations 1 and 2 above.

Pull-out tests were conducted using the setup shown in Figures 5 and 6 above. Table 1 lists the geometrical characteristics of the specimens. The bolts at the bottom (slotted) edge were pre-loaded using torque values (or in some cases load-cell measurements in conjunction with torque values as in Figure 7 above). The pull-out tension force was measured for each specimen. Table 2 summarizes those results for the slotted specimens. Note that in all but one case the glass layers cracked early in the loading. This is likely due to the bolts bearing on inside edge of the holes near the top edge of the glass. In the one case where the glass did not crack, the effective friction force corresponds to the case of smooth glass on gasket material. Using the classical preload estimate from 0.2FD the effective preload force is calculated to be 4200 lbf. Given two surfaces of contact, the effective coulomb friction value is 0.3. While one data point should not be considered statistically defensible, it is worth noting that 0.3 is considerably lower than values in the literature for similar materials.

Figure 8 provides a plot of the pull-out force versus the average bolt torque. A plot of effective friction versus gasket compression force (bolt pre-load) would yield a plot with a similar shape. An immediate point to take from the shape of the curve is the fact that the linear curve fit does not pass through zero force at zero torque. The fact that at least some preload is present and the glass is cracked combine to yield a

gasket to cracked glass interface that is far different than that of simple coulomb friction. The digging in effect clearly contributes to the complexity of the problem of predicting edge capacity. Observations made during the test indicate that the cracked glass does not simply slide on the gasket. There is actually surface shaving and cutting of the gasket by the glass at the crack locations. It is suggested that in the presence of gasket compression forces, the cracked glass edges function much like teeth that dig into the gasket.

A second point to take from Figure 8 is that an increase in torque correlates to an increase in pull-out force, there is not a one-to-one relationship. Approximately 80 percent of the maximum pullout resistance was developed with 500 in-lb torque as compared with 1500 in-lb. In addition, there is concern over the sensitivity of laminated glass to cracking during the installation and bolt pre-loading process. These points suggest that there is a practical limit to value of increasing torque to increase pullout resistance.

Laminated glass make-up	0.25 in. Heat Strengthened 0.18 in DuPont SentryGard 0.25 in. Heat Strengthened
Overall dimensions	18 in. wide, ~12 in. high
Bolt size	0.5 in.
Bolt spacing	6.0 in.
Edge distance	1.5 in. (3d)
Gasket material	EPDM, Durometer 60, Shore A
Gasket width	3.0 in.

Table 1. Specimen characteristics.

Example.

Practical application of the results from Figure 8 involves obtaining an effective friction value based on torque. Bolt pre-load values may be summed to obtain to gasket compression force. The effective friction value is used with the pullout force to obtain an effective coefficient of friction. In an effort to generalize the results, it may be useful to convert the forces to forces per unit area. An example corresponding to an average bolt torque of 600 in-lb from Figure 8 is summarized in Table 3 below. For the example in Table 3 the shear force per area is calculated to be 78.1 psi. The range of values for all the cracked slotted glass is 52.1 to 97.6 psi.

Bolt Torque1	Bolt Torque2	Bolt Torque3	Average Torque (in-lb)	Pull-out (lbf)	Glass not cracked
180	120	120	140	2572	X
130	130	200	153	5542	
160	150	150	153	6202	
260	260	260	260	8777	
260	260	260	260	7399	
300	290	260	283	7944	
192	192	312	232	8143	
240	348	360	316	6203	
240	396	432	356	5332	
600	600	600	600	8784	
830	830	830	830	9991	
750	800	750	767	9472	
1390	1494	1330	1405	10580	
1440	1480	1546	1489	9970	
1480	1480	1480	1480	8755	

Table 2. Pull-out force versus torque.

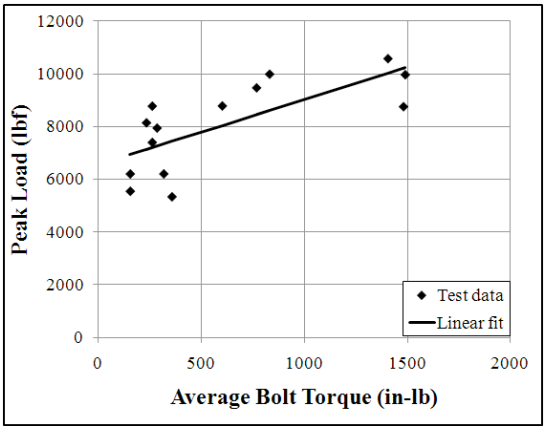


Figure 8. Pull-out force versus torque - slotted edge.

Torque (in-lb)	600
Pull-out force (lbf)	8000
Bolt pre-load (lbf from 0.2Fd)	6000
Gasket compression force (lbf)	18000
Effective friction coefficient	.222
Net gasket area (in^2)	51.2
Shear force per area (psi)	78.1
Compression force per area (psi)	352

Table 3. Pull-out force versus torque.

Application of the values in the previous paragraph along with the predictions from Equations 1 and 2 results in an estimate of edge capacity based on in-plane resistance of the laminate plus effective friction associated with cracked glass interaction with compressed gasket material. Using the test specimen bolt hole size, bolt spacing and edge distance as an example, the edge capacity calculated from Equations 1 and 2 yields a laminate edge capacity of 150 lb/in (Fu = 4000 psi, θ = 25º, d = 0.625 in). Using the values from Table 3 the effective friction force is 444 lb/in. The sum capacity is 594 lb/in. A basic goal of the current development is that the edge pull-out capacity be large enough to develop the full strength of the inner layer acting as a membrane. For this example the membrane strength is calculated as 720 lb/in. The 594 lb/in value obtained here falls short of the membrane strength of the laminate by 17.5 percent.

OBSERVATIONS AND RECOMMENDATIONS

Note that while the capacity obtained in the example above falls short of the goal capacity, there are some additional points that should be highlighted.

1. The pull-out resistance obtained here is under ideal in-plane loading. In reality, while the edge loading may be dominated by pull-out, there is generally a component of bending or shear at the edge of the glass near the support. The localized interaction between the glass and gasket material and the associated digging in effect is very likely more severe than indicated by the pull-out test results presented above. Moving forward, the results of this investigation will be used along with the drop hammer test data referred to above to help quantify the full effect of connection racking, and high strain rate effects.
2. Until further test results are obtained and reduced it is suggested that the results from Equations 1 and 2 are suitable for use with a simple adjustment for strain rate effects.
3. Given specific cases involving materials and conditions listed above, the data in Figure 8 is suitable for use in design conditions.
4. Application of the test results presented above to other glass types must be executed with caution. Heat strengthened glass crack patterns are typically

random in shape but somewhat uniformly distributed and spaced at less than one inch apart. The crack patterns for annealed glass are such that there may be relatively large areas of un-cracked glass. The possible absence of cracks at the gasket interface could reduce the digging in effect thus minimizing the effective friction. Alternatively, fully tempered glass most often exhibits crack spacing that is smaller than heat strengthened glass of the same thickness. Given that point, the effective friction is anticipated to be higher for fully tempered glass.

5. Pressure between cracked glass and the gasket material induces a digging in effect. Bolt pre-load is used to compress the gasket material. There is concern over relaxation (compression set) of the gasket material that may serve to diminish the pressure with time. Investigation and / or testing to clarify this issue should follow.

SUMMARY AND CONCLUSIONS

Results of various analytical and experimental efforts have been presented that address pull-out resistance of through-edge bolted laminated glass. Specific design recommendations have been provided along with suggestions for further testing

REFERENCES

Duke, D., Bewick, B. T., Browning, R. S., and Casey, T. (2009). "Edge Capacity of Through-Bolted Laminated Glass", presented at 80th Shock & Vibration Symposium, San Diego, CA, U.S. Air Force report AFRL-RX-TY-TP-2010-0022.

Browning, R. S., Duke, D., and, Bewick, B. T. (2009). "Testing and Analysis of a Retrofit System for Windows Subjected to Blast Loads", presented at 80th Shock & Vibration Symposium, San Diego, CA, U.S. Air Force report AFRL-RX-TY-TP-2010-0016.

Design and Testing of Cable Catchment Systems for Historic Window Blast Protection

Seda Dogruel[1], M.S. and Caroline Field[2], M.S., P.E.

[1]Hinman Consulting Engineers, Inc., One Bush Street, Suite 510, San Francisco, CA 94104; PH (415) 621-4423; FAX (415) 621-4447; email: sdogruel@hce.com

[2]Hinman Consulting Engineers, Inc., One Bush Street, Suite 510, San Francisco, CA 94104; PH (415) 621-4423; FAX (415) 621-4447; email: cfield@hce.com

ABSTRACT

The Federal government mandates blast protection for all of its facilities, which can be particularly challenging for existing buildings, especially those of historic interest. The blast protection of historic façades is one of the most challenging aspects since historic window structures offer little blast resistance and it is critical to preserve the existing aesthetic. As a solution to this issue, Hinman Consulting Engineers, Inc. (Hinman) investigated the potential application of a window cable catchment system as a means of cost-effective blast protection.

This paper discusses the unique design features and analytical modeling of the cable system on exterior windows to resist potential external blast threats. The cable catchment system consists of steel cables installed behind glass panes and anchored into the structural system above and below each window. A three-dimensional finite element (FE) model was developed to investigate the performance of the window catchment system. This analytical model was then validated by the results of shock tube tests sponsored by the General Services Administration (GSA). Finally, the key parameters of interest in the performance of different cable system configurations including the interaction between cables and glass panels, details of the system configuration, and the reliability of the system are outlined. The results of this study show that the cable systems demonstrate considerable potential to provide efficient blast protection for existing window systems.

INTRODUCTION

Windows are an important aesthetic consideration for historic buildings and their blast mitigation presents both challenges and the opportunity to apply innovative mitigation technologies. Other than providing sufficient blast protection, low cost and feasibility are the other major objectives of the blast engineer in the design of mitigating solutions. However, in addition to historic and blast considerations, there are often other design objectives that must be integrated in to the design solution, for example, energy performance, daylighting, and window operability. These are project specific and provide additional challenges for developing an appropriate mitigation system.

WINDOW MITIGATION OPTIONS FOR BLAST PROTECTION

In general, window replacement and window retaining/retrofit are the two major mitigation approaches for upgrading existing historical windows to provide the required blast protection level. *Window replacement* requires the replacement of the entire window system, which may have a significant impact on the appearance and authenticity of the historic building. The argument for replacing existing windows is usually based on the energy efficiency and replacement of deteriorating window materials. However, replacement of the entire window of a historic building may not be cost effective due to historic replication workmanship requirements and the likely requirement for supporting structure strengthening. Accordingly, this mitigation approach is generally not a desirable upgrade option for historic buildings.

Applicable *window retaining and retrofit* approaches may consist of the following: (1) Application of anti-shatter security films, (2) Secondary interior window installment, (3) Glazing replacement, and (4) Catchment or debris mitigating systems.

(1) Application of anti-shatter security film is one of the most common methods of upgrading existing windows for blast mitigation. The easiest and fastest way of applying anti-shatter film is to use day-light film, which bonds directly to the glass without any attachment to the mullions or window frame. Wet-glazed film or high-strength anchored film are other means of anti-shatter film applications; wet-glazed film requires removal of the pane from its frame for installation (resulting in more labor cost); anchored film can be problematic with operable windows and transfers load in to the framing elements, which will likely necessitate strengthening of the supporting frame. While anti-shatter film does hold glass fragments together, it also fails as a single pane, which could result in more serious occupant injuries (Bogosian and Avanessian, 2002).

(2) Providing a secondary interior window (*i.e.,* storm window) behind the existing is another common retrofit option for historic windows, because it does not require strengthening of existing mullions and window frame. However, most systems are not operable, which limits natural ventilation opportunities and can lead to maintenance issues. In addition, a secondary window will impart significant anchorage forces on the existing supporting structure, which will need to be evaluated. This system will provide a higher level of protection than window film only and is relatively easy to install, however the upfront cost is likely to be higher. In addition, the interior aesthetic will be significantly affected by this addition.

(3) Replacement of the existing glazing is another retrofit solution when the mullions, window frame, and structural members have adequate capacity to resist the loads transferred from the new glass. For historic windows, this option is usually not preferable as a standalone solution due to its high installment and labor cost and lack of measurements for the load bearing capacity of existing window elements at in-situ conditions.

(4) Catchment or debris-mitigating systems consist of the application of advanced systems such as blast curtains, shades, blinds, and cable catchment systems. Blast curtains, shades, and blinds sufficiently increase the blast protection level when they are used in conjunction with anti-shatter film application or laminated glass replacement. One serious shortcoming of these upgrade solutions is that they are intended to remain secured or shut at all times to be effective, limiting access to the operable windows. Additionally, they may significantly impact the aesthetics and reduce the energy efficiency of the building by degrading the amount of light that can pass through the window. Another solution, the installment of cable catchment systems behind the existing windows in conjunction with window film or glass replacement, catches and limits glass debris from entering protected areas. In combination with energy absorbing spring anchorage systems they can limit the load transferred in to the existing structure and are easy to install and cost efficient. They also allow access to open windows and are relatively unobtrusive from an aesthetic perspective.

The cable catchment system is discussed in detail in the following sections with its recent application to two historic building modernization projects. Additional information on the other window retrofit options is provided in Lin *et al*. (2004), GSA's Technical Preservation Guideline on Upgrading Historic Building Windows (Alderson, 2009).

DESCRIPTION OF CABLE CATCHMENT SYSTEMS

The presented cable catchment system was developed by Glasslock Inc. and is composed of three major components: (1) High-strength cables, (2) Aluminum track; and (3) Patented spring system and is shown in Figure 1. Rather than strengthening the façade, this system is expected to provide the level of protection required for the building by capturing the glass (which is preferably filmed or laminated) exiting the window frame during a blast event, while at the same time maintaining the historic sashes, keeping the window operable, and minimizing reaction forces on the existing structure. Because of their ease of installation and low maintenance requirements, these systems are cost-effective systems to achieve blast protection in renovation projects with budget restrictions, the desire for operable windows, and the concern of historic preservation.

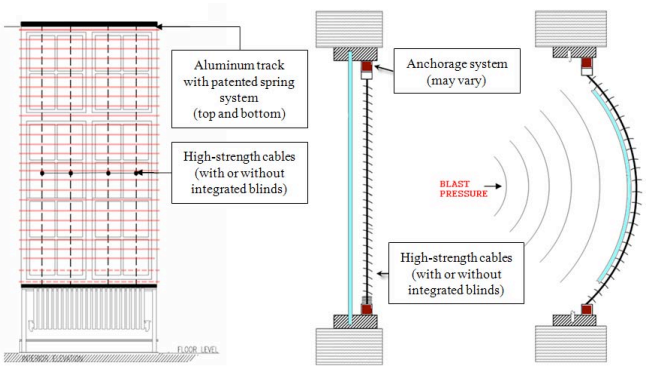


Figure 1. Illustration of Cable Catchment System

PROJECT APPLICATIONS

The cable catchment system has been used on several commercial buildings and the blast protection it provides has been recognized for large pane systems (Crawford, Lan et al., 2006). Hinman has investigated the application of this system on a couple of recent Federal historic renovation projects.

The presented renovation projects, *Project 1* and *Project 2*, involve the retrofit of existing operable wood frame windows to meet a medium level of protection under a 4 psi and 28 psi-ms blast load as defined in the *ISC Security Design Criteria for New Federal Office Buildings and Major Modernization Projects* (ISC, 2004). The following criteria contributed to the decision to opt for a cable catchment solution:

(1) Operability: Having minimum number of cables for the ease of window operation by the building occupants

(2) Blast protection and energy requirements: Meeting the intended blast design criteria and energy efficiency performance requirements

(3) Budget restrictions: Avoiding labor intensive installment and anchorage details

(4) Minimize aesthetic impact and retain historic character

For *Project 1,* it was decided to retain the existing window frames, sashes, and muntins but to upgrade the existing glass to a 1/4-inch laminated glass with 0.030-inch PVB (Polyvinyl butyral) interlayer that is more durable and provides more energy efficiency than the existing 1/4-inch monolithic glass. Although replacement of glass costs more than the secure daylight film application, laminated glass does not need maintenance, so there are minimal life-cycle costs compared to a daylight film application. *Project 2*, has a target for lead Platinum, so the glass needed to be upgraded to an IGU to meet for energy performance requirements. Due to deterioration of the existing sash and the fact that the sash needs to be re-profiled to accommodate an IGU, it was more cost effective to replace the existing sash and glass together. To keep the IGU thickness to a minimum, the preferred glass layup was 1/8-inch tempered glass pane, ¼-inch air gap, and a ¼-inch laminated glass with 30-mil PVB interlayer, however, a thicker glass layup comprising double ¼-inch laminated glass panes (with 30-mil PVB interlayer) separated with 1/4-inch air gap was also considered as a replacement option due to concerns regarding the unpredictable nature of the tempered glass fragmentation.

As the cable catchment system is a newly-developed system and its design depends on the project specific conditions, a blast design approach, analytical procedures, as well as physical testing program had to be developed to validate its performance for their proposed applications.

First, Hinman developed numerical models using the nonlinear dynamic simulation software LS-DYNA version 971 (Livermore Software Technology Corporation, 2007) to simulate the behavior of the cable catchment systems. Next, a series of shock-tube explosive tests of the cable catchment system were conducted at the testing facility of Baker Engineering and Risk Consultants, Inc. in San Antonio, Texas. The objective of the testing program was to validate the performance of the system to meet the design requirements defined in "*ISC Security Design Criteria for*

New Federal Office Buildings and Major Modernization Projects" (ISC, 2004). These tests consisted of several full-scale window system configurations with or without integrated blinds. Following the tests, the FE models were refined and validated using the physical explosive test data.

PRELIMINARY FINITE ELEMENT ANALYSIS

Details of FE Model

To investigate the feasibility of the proposed cable catchment system manufactured by Glasslock Inc. for the selected two renovation projects, *Project 1* and *Project 2*, preliminary FE analysis was performed. The finite element model consisted of the glass, cables, and springs. The wooden window frame and sashes were not included in the model as the mechanical behavior and failure mode of wood are strongly dependent on the wood material properties, aging conditions, and moisture content, which are difficult to model accurately with FE analysis. Since it was expected that the wood frame and putty would be weaker than the glass and would not restrain the glass in reality, it was predicted that excluding it from the model would not affect the results. Aluminum channels housing the springs at the head and sill were also not included in the model, therefore, any energy absorption through plastic deformation was neglected for a conservative approach. Additionally, the spring ends were modeled with fixed connections to the supporting structure, assuming that the connections would have higher capacity than the catchment system.

The initial FE models developed based on the GlassLock catchment system proposed for the glazing blast retrofit of *Project 1* and *Project 2* are shown in Figure 2 and Figure 3 and in Figure 4 and Figure 5, respectively. Window glazing layups and vision openings of each glass lite are summarized in Table 2 and Table 3. Due to aesthetic and operability considerations for *Project 1*, only one cable per pane was desired even though this was unlikely to be effective. It was anticipated that non-uniform blast loading and aerodynamic effects would cause the glass panes to rotate around the cables in reality. Due to energy and historic considerations for *Project 2*, an IGU unit was desired with a tempered outer layer, so there were concerns regarding the tempered fragments entering the protected space. However, tempered glass (*i.e.,* outer pane of the IGU) was not included in the FE models, since tempered glass fragmentation could not be captured in the FE analysis.

In LS-DYNA, MAT_LAMINATED_GLASS (Material#32) was employed to model laminated glass with a PVB interlayer. This material model allows different material properties for the glass and PVB materials. When the force in the glass layer reaches the yield limit, the glass fails and the PVB remains as the element contacting the cable and resisting the blast load. The cables (7x19 pre-formed stainless steel aircraft cable with a reported 1760 lbs breaking strength) were modeled with MAT_PLASTIC_KINEMATIC (Material#3). This material model includes the yielding and plastic hardening of cable elements. MAT_SPRING_ELASTIC (Material#S1) was employed to model the springs, which remain elastic throughout the simulation. For accurate analysis, mesh studies involving shell and beam elements were performed through uniform mesh refinement. A robust and computationally

efficient automated contact algorithm between the cables and the glazing was also included in the model. The material properties used for the components of the cable catchment system are listed in Table 3. Detailed information about the material models used can be found in the LS-DYNA Keyword User's Manual (Livermore Software Technology Corporation, 2007).

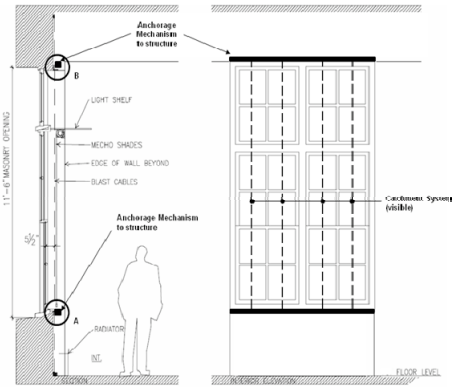


Figure 2. Project 1: Preliminary Cable Catchment System

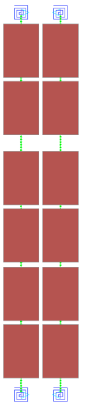


Figure 3. Project 1: Preliminary FE Model

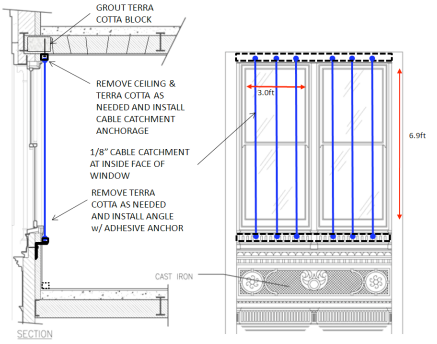


Figure 4. Project 2: Preliminary Cable Catchment System

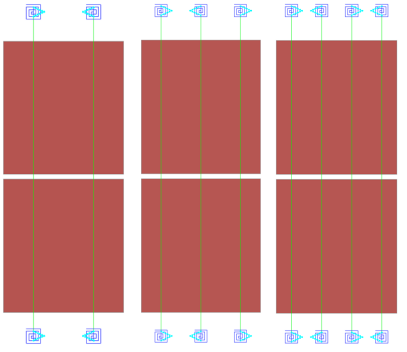


Figure 5. Project 2: Preliminary FE Model with 2, 3, and 4 Cables Across Each Glass Pane

Table 1. Window Details for Project 1 and Project 2

Window Details	
Project 1	
Glass layup	1/4-inch laminated glass with 30-mil PVB interlayer.
Vision opening	14 inches wide by 19 inches high
Configuration	12 glass panes externally glazed with putty
Project 2	
Glass layup – Option 1	Tempered IGU: 1/8-inch tempered glass pane, ¼-inch air gap, and a 1/4-inch laminated glass with 30-mil PVB interlayer
Glass layup – Option 2	Double Laminated: 1/4-inch laminated glass panes (with 30-mil PVB interlayer) separated with 1/4-inch air gap
Vision opening	36 inches wide by 40 inches high
Configuration	2 glass panes externally glazed and held in place with silicone and wooden stops

Table 2. Glazing Properties

Glazing	
Glazing mass density (lb-ms^2/in^4)	
¼" Laminated Glass (Inner pane)	217 (1)
Tempered IGU	243 (2)
Total inner pane thickness (in)	0.260 (3)
PVB thickness (in)	0.030
PVB Young's modulus (ksi)	50
PVB Yield stress (psi)	3000
PVB Plastic strain at failure (%)	250
Glass Young's modulus (ksi)	10000
Glass Poisson's ratio	0.220
Glass Yield stress (psi)	14610

Table 3. Cable Properties

Cable (7x19 Stainless Steel Cable)	
Cable diameter (in)	0.104
Cable mass density (lb-ms^2/in^4)	736
Cable Young's modulus (ksi)	1690
Cable yield stress (ksi)	210
Cable plastic strain at failure (%)	35
Cable Poisson's ratio	0.300
Cable yield strength (lbs)	1760

1-Single pane mass density for the material model of laminated glass
2-Only 25% of the tempered glass mass included for tempered IGU in Project 2
3-Nominal thickness of ¼-inch laminated glass

Results of Preliminary Finite Element Analysis for Project 1:

Results from the preliminary FE parametric studies showed that 1/4-inch laminated annealed glass with 0.030-inch PVB retrofitted with single 1/8-inch stainless steel cables was predicted to perform to a GSA Condition 3b for 4 psi and 28 psi-ms dynamic blast loading. The maximum predicted tension reached by the cable was 1724 lbs, which is less than the reported capacity of 1760 lbs. The maximum inward cable deflection was predicted to be 31 inches. Given the desire and space for only a single cable per pane and the concern that uneven loading or aerodynamic instability effects would have on the pane angle, simulations that considered the angle of impact effects were performed for the system. These simulations showed that the cables were not capable of catching the 1-degree rotated glass panels that were propelled inwards by the blast load, because the panes rotated around and slipped through the cables. It was, therefore, predicted that integrated blast blinds would be required for the window retrofit of *Project 1*.

Results of Preliminary Finite Element Analysis for Project 2:

The preliminary FE analysis showed that the following systems were predicted to perform to a GSA Condition 3b for 4 psi and 28 psi-ms dynamic blast loading: (1) System with double ¼" laminated glass and three cables across each pane, and (2) System with tempered IGU and three cables across each pane (assuming tempered glass was contained). FE simulations of these two systems indicated that the maximum tension force reached by the cable was within the axial force capacity of the cable. For both of the systems, the maximum inward cable deflection was predicted to be less than 25 inches. The system with double laminated glass predicted a lower tensile cable force than the tempered IGU which was attributed to the increased period of the system due to the additional mass of the glass. The FE simulations demonstrated that the inner glass pane of the tempered IGU was not significantly wrapping around the cables, which was expected to result in small openings for the fragments of the outer tempered glass pane to enter inward and land on the floor. Therefore, physical testing

of the system with tempered IGU was required due to its unpredictable fragmentation progress and cable response. Based on the promising results of the double laminated glass and three cables across each pane, additional FE simulations were run for a two cable system as a backup and it was predicted that that the cable forces were slightly exceeding the allowable limits. These results indicated that a double laminated glass layup with three cables would be required for the window retrofit of *Project 2*.

FULL-SCALE TESTING PROGRAM

There were three primary objectives of the testing program as follows:

(1) Evaluate the performance of the cable catchment system (whether they meet the GSA Performance Condition 3b for a 4 psi and 28 psi-ms blast load)

(2) Establish the failure limit-states for the system

(3) Validate the FE model against the test data for system performance

Hinman developed the test plans for each project based on the results of the preliminary FE analysis to achieve the above objectives. For each project, the testing program consisted of eight-shock tube tests that were conducted in accordance with the "*Standard Test Method of Windows and Glazing Systems Subject to Dynamic Overpressure Loadings*" dated January 1, 2003 (U.S. General Service Administration, 2003).

The window system specimen that represents the typical triple-hung wood-framed operable historic windows of *Project 1* and the typical double-hung poplar wood-framed operable historic windows of *Project 2* are shown in Figure 6 and Figure 7, respectively. For each project, eight identical specimens were built and during each test, one specimen was mounted in an enclosed steel reaction structure with the cable catchment system configuration to be tested. For *Project 1*, the preferred system with one cable per pane was tested first and then the backup systems with blinds followed, whereas for *Project 2,* the preferred tempered system with three-cables was tested first and then the double laminated systems followed.

It is important to note that since it was not possible to place a load cell on the cable, dynamic load cells were located on the anchorage bolts used to attach the aluminum track of the cable catchment system to the steel reaction frame as shown in Figure 8. This was to provide data on the reaction forces to be resisted by the anchor bolts.



(a) Historically replicated, triple-hung window specimen in steel reaction structure

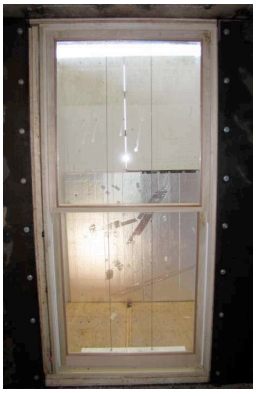


(b) Test specimen



(c) Blast blinds secured at the top of the aluminum cable catchment box

Figure 6. Test Details for Project 1



(a) Window specimen mounted in steel reaction structure



(b) Test specimen



(c) Glazing stops at unprotected side (Test with reversed orientation of window)

Figure 7. Test Details for Project 2



Figure 8. Load Cell Locations

Major Findings for Project 1

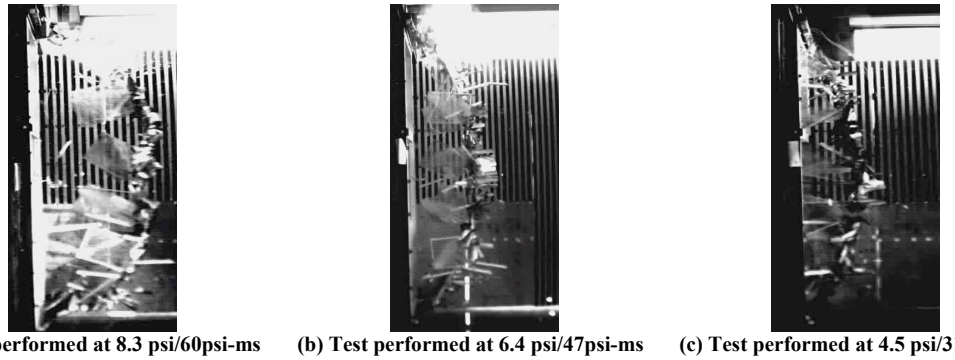
The wood sashes remained in place during the tests, but both the glass and small muntins exited the frame, as expected. It was noted that there was significant rotation of the panes due to less stiffness in the center of the sash compared with the edge, which resulted in the panes rotating rather than wrapping around the cables. The single cable per pane cable catchment system without blinds subjected to 4 psi and 28 psi-ms blast load did not meet the GSA Condition 3b requirement due to significant wood debris from the wooden muntins. Since the cable catchment system alone was not effective for this application, blast blinds were introduced into the system. The addition of blinds met the performance requirements, mitigating most of the wood and

glass debris from the window, although some small wood debris exited the system, but the velocity and mass would be unlikely to cause significant injuries.

The introduction of blinds would make it more difficult to open the windows; therefore, tests were performed raising the blinds to a third of the way up and only 8 inches up, respectively, to allow the building occupants direct access to open the windows. The former did not meet the performance criterion due to both glass and wood debris escaping the system. The latter constrained the glass, but small fragments of wood debris were in evidence on the witness panel. However, these were very small pieces with little mass. Video snap-shots showing the maximum inward displacement of cables for selected tests that were performed in an attempt to determine the failure load of the system are included in Figure 10. Based on these tests, the failure load was estimated to be around 7 psi and 50 psi-ms.



Figure 9. Project 1: Integrated Blast-blind Cable Catchment System with Blinds Secured at the Top of the Aluminum Cable Catchment Box at Sill (4 psi and 30 psi-ms)



(a) Test performed at 8.3 psi/60psi-ms 45" max. inward cable displacement

(b) Test performed at 6.4 psi/47psi-ms 36" max. inward cable displacement

(c) Test performed at 4.5 psi/31psi-ms 30" max. inward cable displacement

Figure 10. Side View Shots from Tests of Project 1

Major Findings for Project 2

During all tests for *Project 2*, the top edge of the bottom sash with glass and stops exited the frame, but the top sash remained in place. This illustrated that the wooden frame and glass had significant resistance to the blast load and glass did not exit the sash, as had been anticipated.

The response of the window system consisting of two cables per glass pane with the double laminated glass layup is shown in Figure 11. Video snap-shots showing the maximum inward displacement of cables for these tests are also included in Figure 12. Overall, the test results of *Project 2* showed that there were two major sources of

debris: (1) Wood debris from the wood window frame, window stops, and sashes entering into the protected area, and (2) Glass debris from the tempered outer glass pane, escaping from the cable catchment system and perforating the witness panel. At the design blast loads, the top window sash remained in the frame and was not propelled into the protected area, but the sash stops spalled and made it to the witness panel, causing some wood debris. Given that only one pane exited the window frame, the cable catchment system did not have to restrain the entire window system; however, in reality, in-situ conditions could cause the existing system to be weaker and then the cable system would see more load. Consequently, the preferred solution was the double laminated IGU and it was suggested to maintain three cables per pane, which was later verified using the validated FE analysis as documented in the section below.

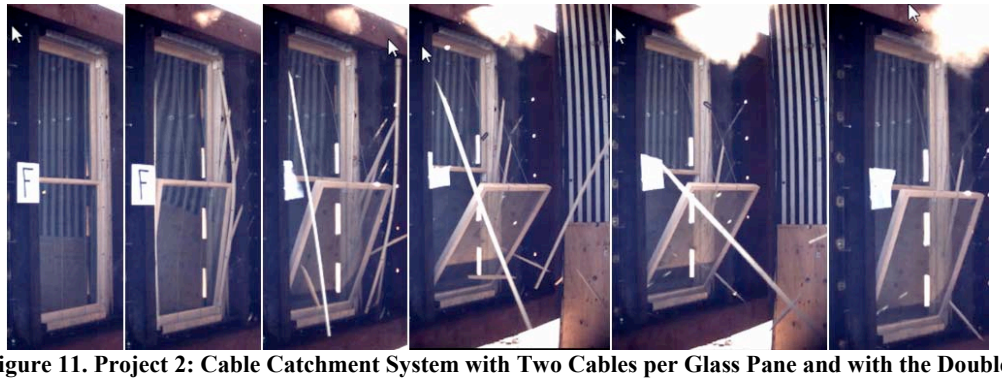
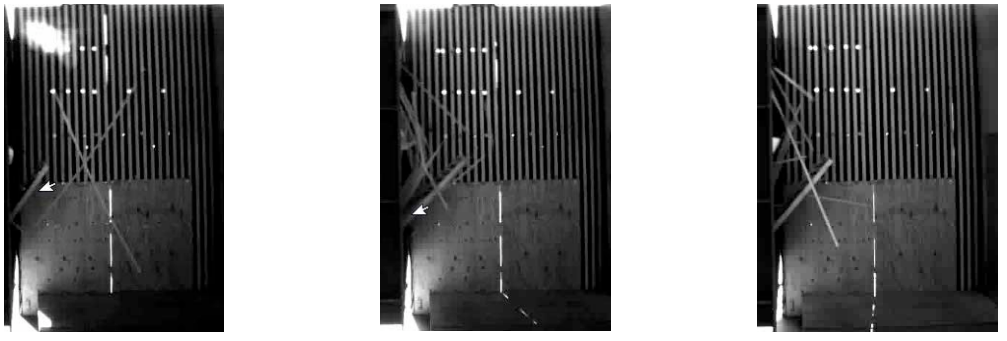


Figure 11. Project 2: Cable Catchment System with Two Cables per Glass Pane and with the Double Laminated Glass Layup (4.1 psi & 30 psi-ms)



(a) Test performed at 4.1 psi/30 psi-ms 20" max. inward cable displacement

(b) Test performed at 9.3 psi/62 psi-ms

(c) Test performed at 6.4 psi/49 psi-ms 16" max. inward cable displacement

Figure 12. Side View Shots from Tests of Project 2

VALIDATION AND EVALUATION OF TEST RESULTS

Following the tests, the FE models were calibrated to match the observed test results by varying the following items:

Glass: For *Project 1*, the physical tests confirmed that the individual panes exhibited several degrees of rotation before hitting the cables due to the discrepancy in stiffness between the center and edges of the window frame. This initial rotation was incorporated in to the FE model. The physical tests of the double-hung window of *Project 2* showed that the top sash remained in the window frame and did not engage

with the cable. Therefore, for validation purposes, the top glass pane was removed from the FE model.

Blinds: For *Project 1*, the physical tests confirmed that aluminum blinds would be required in addition to the single cable per pane. Therefore, 2-inch wide aluminum (6063-T6) blast blinds were included in the FE model using material model MAT_PLASTIC_KINEMATIC (Material#3). This material model includes yielding and plastic hardening, with limited energy absorption capacity through plastic deformation.

Sash weight: For *Project 2*, the preliminary FE model only included glass weight. However, tests showed that glass panes remained in the wood sashes. Therefore, the measured weight of the tested sashes was incorporated in to the modified FE model to account for this additional mass. Nodes of the glass edges were coupled with *CONSTRAINED_NODAL_RIGID_BODY in the FE model to account for the pane sashes that kept the inner and outer panes of the IGU together during the test.

Aerodynamic resistance: Gravity and damping were included in the FE model to account for aerodynamic drag forces that were experienced during the physical testing. Damping was adjusted to 1% and applied to the cables, glass, and blinds.

The FE model of *Project 1* was modified based on the collected data from the three tests for the integrated blind cable system with two cables per pane. The first two tests provided information on the cable yielding and failure limit states as they determined the performance of the system subject to high blast loads (*i.e.,* test performed at 8.3psi & 59psi-ms and test performed at 6.4psi & 47psi-ms). The third test performed at 4.5 psi/31 psi-ms was selected for validation purposes as it determined the performance of cable catchment system for the required blast design criteria.

For *Project 2*, the FE model was refined with the available data from the tests of the double laminated window system with two cables per pane. The main objective of the validation study was to reproduce the overall physical response of the system observed during the two tests (*i.e.,* test performed at 6.4 psi & 49 psi-ms and test performed at 9.3 psi & 62 psi-ms), in which the system was subjected to high blast loads and cable failure was observed. Next, the performance of the cable catchment system was determined when subjected to the explosive load (*i.e.,* 4 psi and 28 psi-ms) in Test F, with the assumption that the bottom sash would fully engage with the cable catchment assembly. Finally, the analysis was re-run assuming both sashes disengaged to conservatively account for potentially weaker windows.

Results of Finite Element Analysis

The refined FE simulations of the window system in *Project 1* and *Project 2* captured at different time states during the non-linear dynamic analysis are illustrated in Figure 13 and Figure 14, respectively. Results of FE simulations for *Project 1* shown in Figure 15 and Figure 17, indicate that all cable forces were within the allowable limits with a maximum cable force of 1390 lbs (Figure 15a) with a maximum inward cable displacement of 26.5 inches (Figure 15b). Additionally, FE simulation results for *Project 2* showed that all cable forces were within the allowable limits with the maximum cable force and the maximum inward displacement of 1445 lbs (Figure 16a

and Figure 18) and 22 inches (Figure 16b), respectively. Additional FE analysis, where the pressure impulse combinations were iterated to find the failure load of the systems in Project 1 (integrated blind cable system with single cable per pane) and in Project 2 (double laminated system with two cables per pane with the assumption that only the bottom sash disengage) also confirmed the results observed during the physical tests. These results predicted that cable catchment systems fail at approximately 7 psi and 50 psi-ms and 5.5 psi and 38.5 psi-ms, for *Project 1* and *Project 2*, respectively.

The FE analysis that explored the performance of the two-cable system for *Project* 2 when both the top and bottom sashes exit the frame to provide a conservative prediction in the event of a weaker existing window system, indicated that the cable force exceeds the allowable limits with a maximum value of 1930 lbs and therefore 3 cables per pane were recommended.

Comparisons between actual test results and the FE analysis predictions for *Project 1* and *Project 2* are summarized in Table 4 and Table 5, respectively. Given the modeling difficulties, such as the geometric imperfections, unknown initial positions, and boundary conditions, the differences in results for the FE simulations compared to actual collected data appear to be relatively insignificant and to err towards conservatism for the response of the cable by predicting larger cable forces. Overall, the results of the FE simulations showed good correlation with the physical tests, even though the wood component was not included in the analysis.

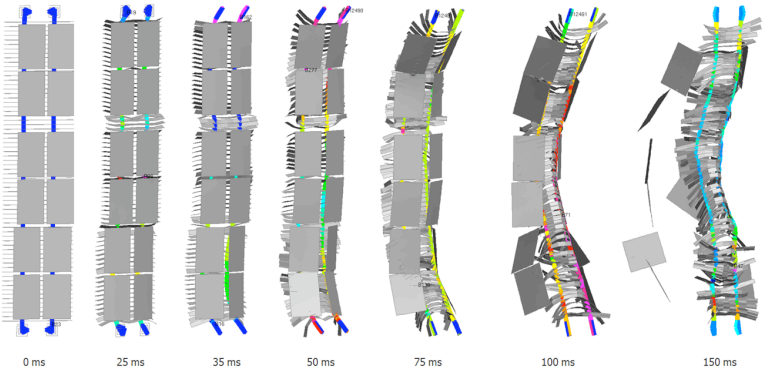


Figure 13. Project 1: Integrated Blast-blind Cable Catchment System Subjected to Nominal 4 psi and 28psi-msec with FE Model Results Captured at Different Time States

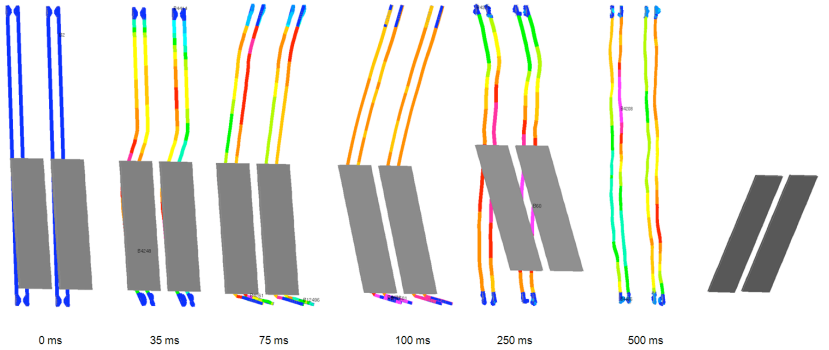
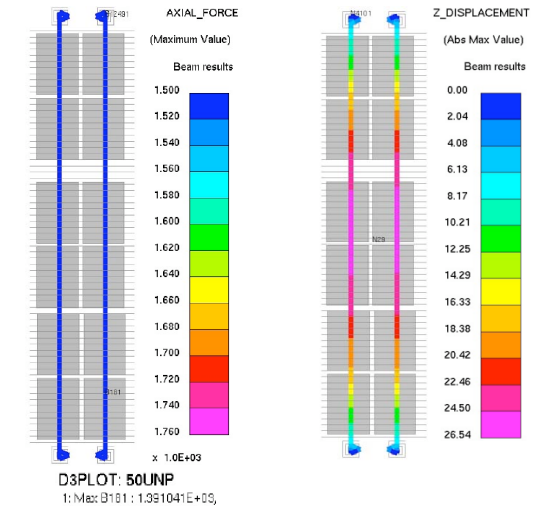
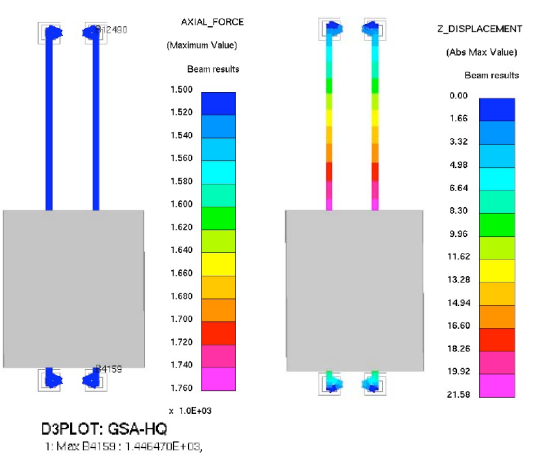


Figure 14. Project 2: Cable Catchment System of Two Cables per Glass Pane and Double Laminated Glass Layup Subjected to 4.1 psi and 30psi-msec with FE Model Results Captured at Different Time States



(a) Cable axial force (b) Cable Displacement

Figure 15. Project 1: Integrated Blast-Blind Cable Catchment System (4 psi and 28psi-msec)



(a) Cable axial force (b) Cable displacement

Figure 16. Project 2: Cable Catchment System of Two Cables per Glass Pane and Double Laminated Glass Layup (4 psi and 28psi-msec)

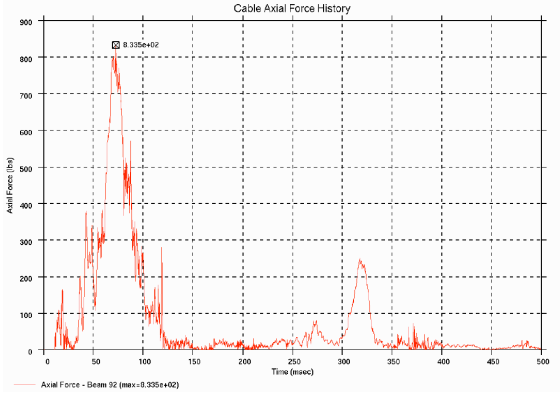


Figure 17. Project 1: Typical Axial Force in the Cables for the Integrated Blast-blind Cable Catchment System (4 psi and 28psi-msec)

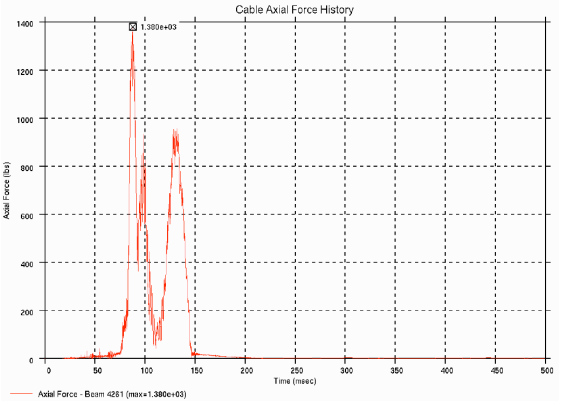


Figure 18. Project 2: Typical Axial Force In The Cables for the Window Catchment System (4 psi and 28psi-msec)

Table 4. Project 1: Integrated Blast-blind Cable Catchment System

Test performed at 8.3psi & 59psi-ms	Physical test	FE Analysis
Peak axial force in cables (lbs)	1170 at anchor	>1760 (1)
Maximum inward deflection of cables (in)	~45	42
Test performed at 6.4psi & 47psi-ms	Physical test	FE Analysis
Peak axial force in cables (lbs)	680 at anchor	1760 (2)
Maximum inward deflection of cables (in)	36	33
Test performed at 4.5 psi & 31 psi-ms	Physical test	FE Analysis
Peak axial force in cables (lbs)	465 at anchor	1390
Maximum inward deflection of cables (in)	30	27

1-Exceeding breakage limit of the cable
2-Observation on the limited portion of the cables, indicating localized failure mode

Table 5. Project 2: Cable Catchment System of Two Cables per Glass Pane with the Double Laminated Glass

Test performed at 6.4 psi & 49 psi-ms	Physical test	FE Analysis	
Peak axial force in cables (lbs)	1714 at anchor	>1760[1]	
Maximum inward deflection of cables (in)	~20	21	
Test performed at 9.3 psi & 62 psi-ms	**Physical test**	**FE Analysis**	
Peak axial force in cables (lbs)	1898 at anchor	>1760[1]	
Maximum inward deflection of cables (in)	N/A [2]	23	
Test performed at 4.1 psi & 30 psi-ms	**Physical test**	**FE Analysis (w/ bottom sash)**	**FE Analysis (w/ bottom & top sashes)**
Peak axial force in cables (lbs)	114 at anchor [3]	1445	>1760 [1]
Maximum inward deflection of cables (in)	16	22 [4]	23

1-Exceeding breakage limit of the cable
2-Not available from sidewall video due to failure of cables
3-Readings from load cells located on the anchor bolts (not reflecting the exact cable load)
4-Full engagement to cable from bottom sash

CONCLUSIONS AND RECOMMENDATIONS

In this paper, the application of cable catchment systems to historic windows as a blast mitigation option was reviewed based on the results of both physical tests and FE simulations and the following was observed:

(1) For large pane windows with a minimum of two cables, the cable catchment system alone is effective at mitigating glass debris from entering the protected space and provides access to open windows and minimal aesthetic impact.

(2) For large windows with small panes and muntins (*Project 1*), significant wood debris from the muntins is to be expected, therefore blast blinds in conjunction with the cable catchment system are recommended to reduce this hazard. It is possible to allow the blinds to be raised slightly to allow access to open windows, but the height depends on the pane size and configuration.

(3) For single glazed systems either laminated glass or filmed glass is recommended in conjunction with the cable catchment system. Where IGUs are required for energy reasons, a double laminated IGU is recommended to reduce potential glass debris from the exterior pane.

(4) The performance of the cable catchment system showed high dependency on the historic window details, such as window stops, locks, and putty conditions. Physical test results indicated that glass panes cannot be released from the wood frame and fully engage with the cable catchment system when they are externally glazed windows with a window stop inside. Therefore, for historic window upgrades, it is important to carefully assess the existing conditions and detailing of the existing windows. The most favorable preconditions consist of interior putty and no interior window stops.

Overall, test results showed that the cable catchment system performed well and provided a promising blast mitigation solution while preserving the historic nature of the building and meeting window operability and low maintenance needs.

In addition, Hinman developed FE models of project-specific cable catchment systems and validated the accuracy of the simulation model against test data. In general, FE analysis was shown to be a cost-effective means of predicting the overall system response, especially when wood fragments are less of a concern. Considering the budget and time constraints of renovation projects, and the limited feasibility of repeated testing and instrumentation capabilities, validated FE models in combination with the measured data from complementary physical tests showed the potential to offer options for reducing the need of configuration-specific physical tests. The validation of FE analysis performed will serve as a base for future studies and provide a computational platform for the optimization of catchment system configurations prior to prototype production and the investigation of new retrofit strategies.

ACKNOWLEDGMENTS

The work presented in this paper was supported by the U.S. General Service Administration (GSA). The tests discussed were conducted by Baker Engineering and Risk Consultants, Inc. in San Antonia, Texas. The authors wish to thank Mr. Willie Hirano of GSA and Mr. Brian Frest of GlassLock, Inc. for their review and guidance during the program, as well as in the course of the preparation of this paper.

REFERENCES

Alderson, C. (2009). "Technical Preservation Guidelines - Upgrading Historic Windows." Center for Historic Buildings, Office of the Chief Architect, Public Buildings Service, U.S. General Services Administration.

Bogosian, D. and Avanessian, H. D. (2002). To Film Or Not To Film: Effects Of Anti-Shatter Film On Blunt Trauma Lethality From Tempered Glass. 17th International Symposium on the Military Aspects of Blast and Shock. Las Vegas, NV.

Crawford, J., Lan, S. and Dunn, B. W. (2006). Cable Catcher Systems for Improving Blast Resistance of Glazing Facades. 19th Military Aspects of Blast and Shock Symposium, Alberta, Canada.

ISC (2004). Security Design Criteria for New Federal Office Buildings and Major Modernization Projects, dated September 29, 2004.

Lin, L. H., Hinman, E., Stone, H. F. and Roberts, A. M. (2004). "Survey of Window Retrofit Solutions for Blast Mitigation." Journal of Performance of Constructed Facilities 18(2): 86-94.

Livermore Software Technology Corporation (2007). LS-DYNA Keyword User's Manual, Version 971. Livermore, CA.

Livermore Software Technology Corporation (2007). LS-DYNA Software Version 971. Livermore, CA.

U.S. General Service Administration (2003). Standard Test Method of Windows and Glazing Systems Subject to Dynamic Overpressure Loadings.

Testing and Analytical Evaluation of Doors

Michael J. Lowak, Jay S. Idriss, and James W. Wesevich

Baker Engineering and Risk Consultants.3330 Oakwell Court, Suite 100, San Antonio, Texas 78218-3024; PH: (210) 824-5960; E-mail: MLowak@BakerRisk.com, JIdriss@BakerRisk.com, and JWesevich@BakerRisk.com

ABSTRACT

The application of blast resistant design principles has become more prevalent for buildings due to risk of accidental industrial explosions and terrorist attack. This has precipitated to more attention to exterior doors subjected to blast loadings, including the publication of ASTM F2247-043 "Standard Test Method for Metal Doors Used in Blast Resistant Applications (Equivalent Static Load Method)". However, the evaluation of doors subject to blast loadings lags significantly compared to the documented analytical tools and methodologies for other structural components, as well as windows. This paper lists and compares several techniques for evaluating doors subject to blast loadings, including testing and analytical approaches.

A recent research program has generated static and dynamic shock tube test results for various low-range hollow metal door types. The static data was used to develop single-degree-of-freedom models which were used to predict the door response for several dynamic tests. The comparison of the analytical predictions and test data provides a basis to adjust the dynamic model to better predict the response of the subject door. The results of the effort may allow blast designers to utilize existing static data for commercial doors to develop reasonable dynamic models for blast evaluations.

INTRODUCTION

Over the last two decades, buildings are more apt to include blast design to limit damage from either accidental explosions or terrorist bomb attacks. The response of doors to blast loads has received less attention than other building components, simply because they have been typically addressed by the architects since historically are not part of the primary resisting structural system and do not represent a major percentage of the building exterior such as glazing and other cladding systems. However, as blast resistant building design became more common, the response of blast doors has become a higher priority because doors do exist in every building and they represent the means of ingress and egress to the building for occupants and rescuers. Deaths resulting from failed doors from accidental explosions have also been documented. The early lack of focus on doors in the blast resistant design of buildings has led to a situation where well documented methodologies for predicting the response of doors to blast loads lags behind methodologies for other building components. In fact, most available blast related data for doors is limited to doors specifically designed for blast resistance by a handful of specialized door manufacturers. Therefore, research in this area was deemed necessary.

This paper provides background on available blast response data on doors, discusses various methods of evaluating doors for applied blast loads, and summarizes a recently completed research project aimed at developing a methodology more accurately predict the response of doors to applied blast loads. The research effort was performed by Baker Engineering and Risk Consultants, Inc. (BakerRisk) under a contract with the National Institute of Building Sciences and under the direction and funding by the US Army Corps of Engineers, Protective Design Center. The research effort was focused on determining the effectiveness of using load-deflection data from uniform static tests of doors as input into single-degree-of-freedom (SDOF) analysis models for the prediction of door response. The research program also focused on doors likely to be used in government buildings that were not specifically designed for blast resistance.

EVALUATION METHODOLOGIES FOR DOOR RESPONSE TO BLAST LOADS

The common methodologies used to evaluate doors for response to blast loads includes a full spectrum of analytical and testing methodologies similar that of other building components. The difference is that lack of research in this area and the nature of door construction provide for a higher level of uncertainty in analytical prediction of door response compared to other building components that have been studied in numerous previous research programs.

Analytical Methodologies

Doors have been evaluated for response to blast loads by the more common approaches used for other building components, including static equivalent design, SDOF, multiple-degree-of-freedom (MDOF), and finite element analysis (FEA) modeling techniques. Each of these methods are reasonable means of analysis, but the complexity of door construction, door panel support conditions, and interaction of the door panel and door frame require the analyst to make various structural interaction and response limit assumptions that can affect the model results significantly.

The static equivalent method is a convenient analytical tool for determining if a building component meets a given response criteria for a given blast load. Comparisons of the component's natural period of vibration to the load duration allows determination of a dynamic load factor for a given response limit. The static capacity of the component is then compared to the equivalent static load based on the dynamic load factor and peak blast pressure. Determination of the natural period and load capacity of door panels can be a complex task if done by analytical means, as hollow-metal doors may exhibit partial composite action between its member make-ups and support conditions lead to complex two-way plate responses. It is also difficult to take into account potential support movement with regards to the door frame in the static equivalent load analysis. In addition, door rebound response can only be considered in an uncoupled evaluation with an assumed rebound load.

SDOF and MDOF methods of analysis are possibly better means of determining response of structural components as they can predict both inbound and rebound response of the component. MDOF methods can also account for interaction between various components. However, like the static equivalent approach, the SDOF and MDOF methods depend on the definition of the resistance and deflection characteristics of the component being analyzed.

FEA analysis of doors may provide the best method of predicting response of doors to blast loads assuming a pure first principal analytical approach, but this depends on the complexity of material and geometric modeling and the accuracy of the contact algorithms between the door hardware, panel and frame. A FEA model that clearly defines all individual parts of the door, each spot weld, door hardware, and possible bonding to filler materials should predict response well if the contact is also modeled well. However, it is not always practical to build such a detailed model for each hollow metal door product.

Test Methodologies

Testing of doors in support of blast resistant applications can be provided by several means. Static and dynamic uniform pressure tests can be performed to validate analytical model assumptions for all analytical approaches. Dynamic testing can be used to prove performance of a door design for a specific blast loading. Note that in all testing, tests may be valid only for the support conditions used in the tests. Because doors may be installed in a variety of wall types, the stiffness of the door frame or connections to the building and the level of support provided can vary significantly depending on details.

Static testing of doors can provide good load-deflection data for use in analytical models, but cannot be used singularly to prove performance of a door for a specified blast load. With that said, doors must be tested in both the seated and unseated direction to determine response data for each direction, including when concerned with blast loading in one direction but with defined rebound requirements. In summary, static testing alone cannot be used to support door response to blast loadings. Another limitation of static data is that the data will not provide indications of dynamic strength increases that are typically observed for dynamically loaded members.

Dynamic testing of doors can provide proof of performance for a given door design and installation at a specified load on its own. However, a single dynamic door test cannot be used to prove performance when variables exist between test conditions and installation conditions

without some form of analytical proof that the variability does not affect door response. Therefore, it is inefficient to use dynamic testing alone to prove door response to a range of blast loads or a multitude of installation conditions.

Combined Analytical and Testing Methodologies

Using test data to validate analytical models is a very effective means to gain confidence in an analytical model that can be used for multiple door installation conditions. Static and dynamic test data can be used to validate analytical models. The more structural response information gathered in the test the better support provided for assumptions made in the models. However, even a simple static load test with no more than a "passed" response characterization can be used to support assumptions.

Static testing can be used to determine the load-deflection characteristics of a door, which provides all the data necessary to confidently use the static equivalent load analysis methodology. ASTM F 2247-03[1] provides direct guidance in testing of doors to gather the necessary door response information to determine a static equivalent load and provides the necessary analytical equations and information to do so.

Typically, validation of dynamic analytical models (SDOF, MDOF, and FEA models) is performed by comparing model predictions to observed responses in dynamic tests. In this manner, the model is assumed to be properly accounting for the most important response mechanisms in the components being evaluated. By testing numerous doors to various loading conditions to vary observed responses and to account for different natural period-to-load-duration ratios, the models can be validated for use for a large range of blast loads, or door response levels.

RESEARCH PROGRAM

The research program discussed in this paper specifically focuses on the use of static testing to develop load deflection curves that can be converted to SDOF properties for a door. The program also included dynamic testing to provide a means of validating the SDOF models developed and to determine if adjustment of the data from static testing was warranted to account for dynamic strength increases. This combination of static testing and dynamic testing is intended to determine if using SDOF models created using load-deflection information from static testing is an acceptable door evaluation methodology.

The research program included a literature search to gather information on commercially available doors, including design details, existing static test data and existing dynamic test data. After evaluation of the gathered information, a test plan was developed that included static and

[1] ASTM F2247 – 04, *Standard Test Method for Metal Doors Used in Blast Resistant Applications (Equivalent Static Load Method)*, 2004.

dynamic testing of selected doors. The static test data was used to create analytical models and the dynamic test data was used for comparison to analytical model predictions.

Literature Survey

The literature survey gathered publically available data on hollow metal doors available from a variety of manufacturers. The data collected included typical door details and static test data, as well as additional references for the evaluation of doors for applied static loads.

Door detail information included details of the door panel internal components, door frame details, and door frame anchorage details from several door manufacturers. Comparison of these details indicated that doors from different manufacturers use different details for doors having the same general description. These differences may significantly affect performance of the doors in their analysis. For example, there can be differences in stiffener section properties, door skin connection details, and locations of reinforcement. Figure 1 through Figure 4 show typical construction of doors from four door vendors.

Figure 5 shows a comparison of the reinforcement present in the door lock insertion areas for some typical doors. Note that while some degree of reinforcement is present in all the systems, the reinforcement approach used is often times different depending on manufacturer and model, and may result in different localized stiffness characteristics during their deflection.

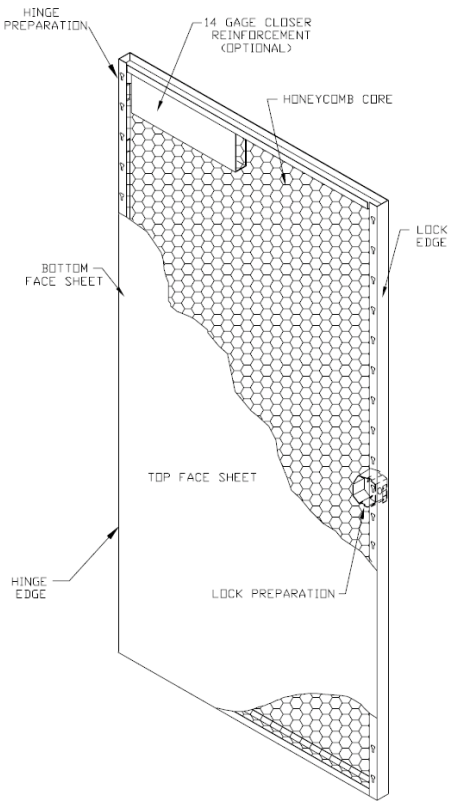


Figure 1. Ceco Regent or Omega Door – With Honeycomb Core

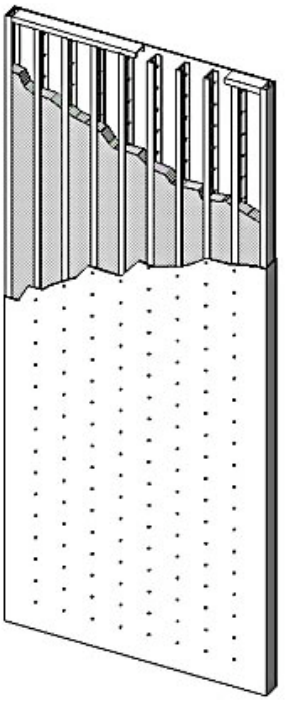


Figure 2. Forderer Vertically Stiffened Door Panel

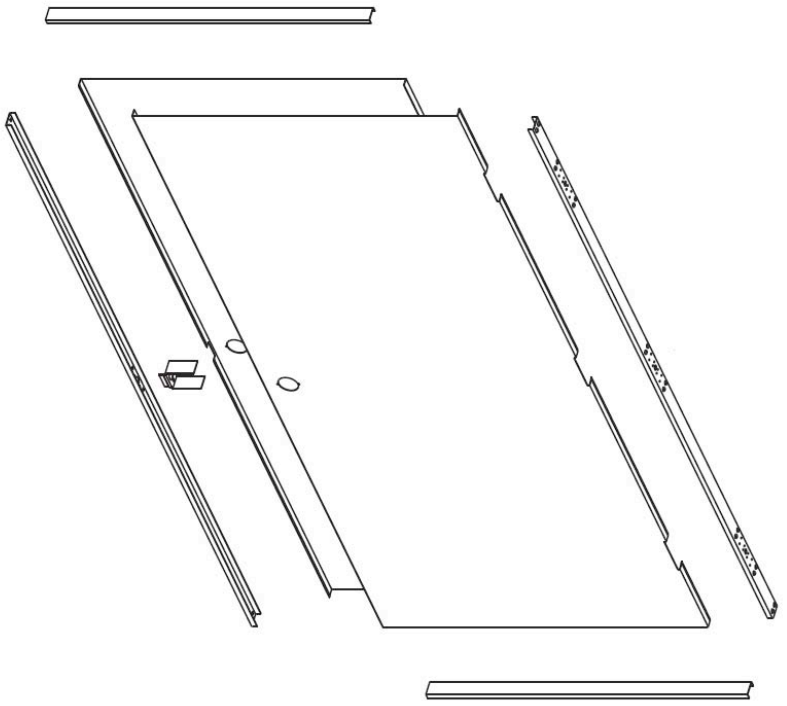


Figure 3. Republic DL Series Door Components

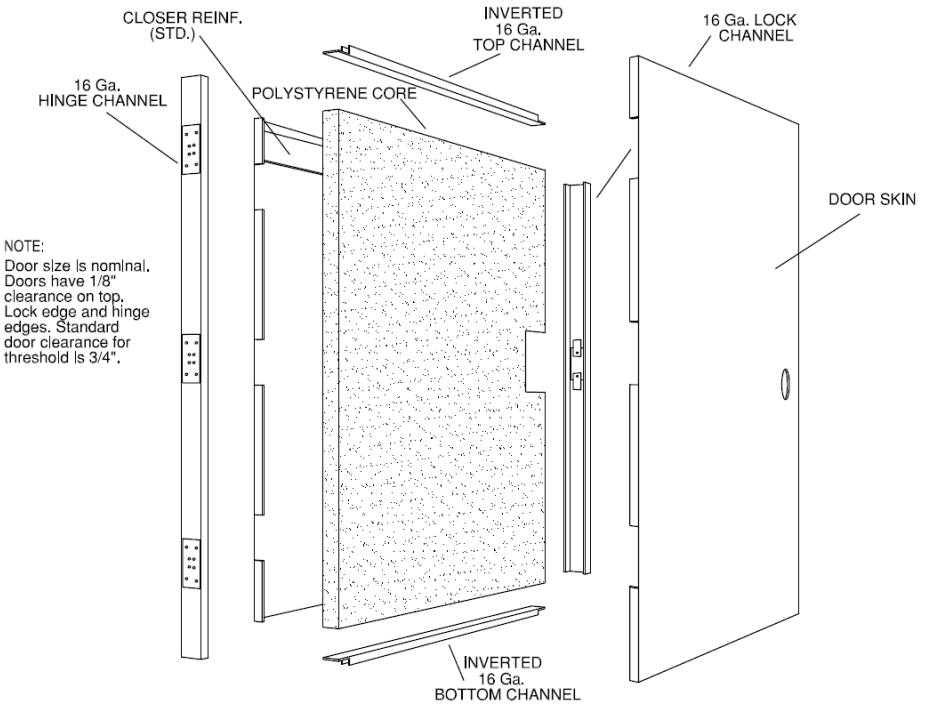


Figure 4. Deansteel Standard Door Construction

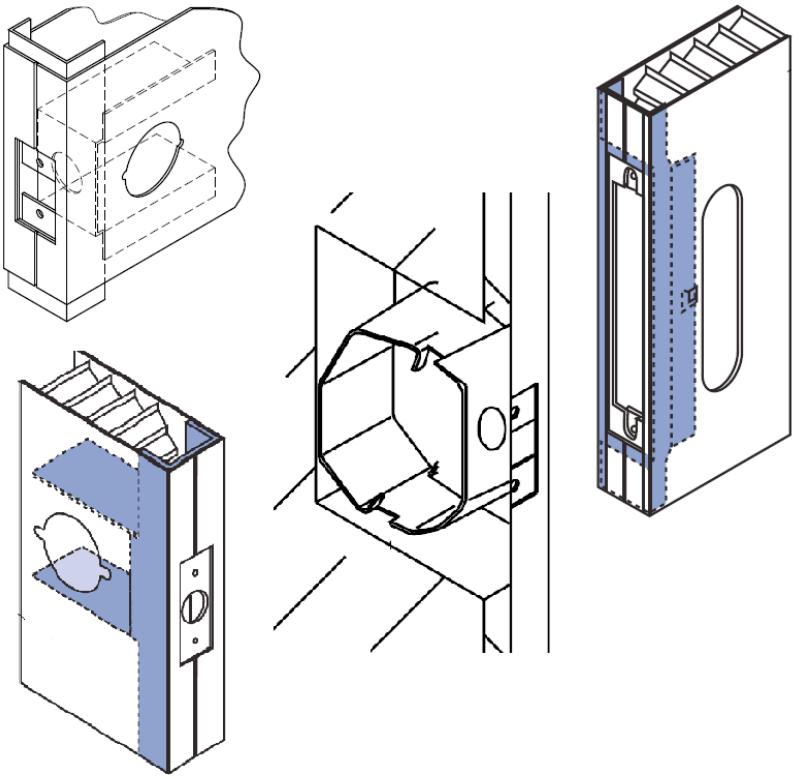


Figure 5. Comparison of Door Latch Reinforcement Systems (Clockwise from left: Deansteel, Republic Cylindrical, Ceco, Republic Mortise)

Most manufacturers provide some static capacity information for their doors, typically a design pressure rating. These ratings vary from manufacturer to manufacturer for similar door types as would be expected to the variability in internal reinforcement observed in the door details. Examples hurricane pressure ratings for selected doors are provided in Table 1 and Table 2.

Table 1. Typical Hurricane-Resistant Doors Manufactured by Ceco

Model Series	Design Pressure	Maximum Opening Size	Glazing	Panel Gauge	Frame Gauge	Frame Construction[1]
Regent	± 60 psf	3'-0" x 7'-0"	N/A	18	16	KD or Weld
Omega	± 60 psf	3'-0" x 7'-0"	1/4" Polycarb	18	16	KD or Weld
	± 60 psf	3'-0" x 7'-0"	Laminated	18	16	KD or Weld
	±70 psf	3'-0" x 7'-0"	N/A	18	16	KD or Weld
Legion	± 60 psf	3'-0" x 8'-0"	N/A	18	16	KD or Weld
Ultra	± 60 psf	3'-0" x 8'-0"	1/4" Polycarb	18	16	KD or Weld
	± 60 psf	3'-0" x 8'-0"	Laminated	18	16	KD or Weld
	± 70 psf	4'-0" x 8'-0"	N/A	16	16	KD or Weld
Medallion	± 60 psf	4'-0" x 8'-0"	1/4" Polycarb	16	16	KD or Weld
	± 60 psf	4'-0" x 8'-0"	Laminated	16	16	KD or Weld
	±70 psf	8'-0" x 8'-0"	N/A	16	16	KD or Weld
	±60 psf	8'-0" x 8'-0"	1/4" Polycarb	16	16	KD or Weld
	±60 psf	8'-0" x 8'-0"	Laminated	16	16	KD or Weld
	±70 psf	8'-0" x 8'-0"	N/A	16	16	KD or Weld
	± 60 psf	8'-0" x 8'-0"	1/4" Polycarb	16	16	KD or Weld
	± 60 psf	8'-0" x 8'-0"	Laminated	16	16	KD or Weld

[1]KD: Knock-Down frame provided in three pieces for field assembly. Weld: One piece factory-welded frame.

Table 2. Typical Hurricane Resistant Doors Manufactured by Republic

Model Series	Design Pressure	Maximum Opening Size	Panel Gauge	Frame Gauge	Frame Construction[1]
DL Series (HC, Poly, Steel Stiffened Core)	± 114 psf	3'-0" x 7'-0"	18	16	KD or Weld
DL Series (HC, Poly, Steel Stiffened Core)	± 100 psf	3'-0" x 8'-0"	18	16	KD or Weld
DL & DM Series 2, 4 & 6 Panel Doors (Poly Core)	± 80 psf	3-'0" x 7'-0"	18	16	KD or Weld
DL Series (HC, Poly, Steel Stiffened Core)	± 75 psf	4-'0" x 8'-0"	18	16	KD or Weld
DL Series (Honeycomb)	± 60 psf	4'-0" x 8'-0"	16	16	KD or Weld
DL Series (Honeycomb)	± 50 psf	12'8" x 10'4" Storefront	18	16	Weld
DL Series (HC, Poly, Steel Stiffened Core)	± 90 psf	6-'0" x 7'-0"	18	16	KD or Weld
DL Series (HC, Poly, Steel Stiffened Core)	± 80 psf	6'-0" x 8'-0"	18	16	KD or Weld
DL Series (HC, Poly, Steel Stiffened Core)	± 60 psf	8'-0" x 8'-0"	18	16	KD or Weld
DL Series (Honeycomb)	± 60 psf	8'-0" x 8'-0"	16	16	KD or Weld
DL Series (Honeycomb)	± 70 psf	8'-0" x 8'-0"	16	16	KD or Weld

[1]KD: Knock-Down frame provided in three pieces for field assembly. Weld: One piece factory-welded frame.

Static data from tests that include load-deflection information was very limited in the public domain. In fact, the only data from ASTM F2247 found was for doors specifically designed for blast resistance and thus not applicable to the study. Significantly more manufacturer test data is available in the public domain provided in accordance with ASTM E-330, which is a standard used to determine structural performance by using a uniform static air pressure differential across the panel. This method is primarily intended to simulate positive and negative pressures sustained by structural components under wind loading, the results of which are not directly applicable to blast resistance. However, the results of such testing do provide a range of static test loads to which the tested doors in this study should be subjected.

Additional static test results of doors found in open literature follow other test standards and guidelines, or follow very generic test descriptions. For example, some data is available for door systems tested under FEMA 361 criteria, which specifies the design of safe rooms to resist wind loads.[2] This set of criteria borrows heavily from ICC-500[3] and ASCE 7-05[4]. Other test results are simply presented as load-deflection measurements, with no duration or load cycle information given. Figure 6 shows an example of such results, defined simply as a "surface load

[2] FEMA 361, Design and Construction Guidance for Community Safe Rooms, Second Edition, August, 2008.

[3] ICC-500, ICC/NSSA Standard for the Design and Construction of Storm Shelters, August, 2008.

[4] ASCE 7-05, Minimum Design Loads for Buildings and Other Structures, 2005

test." These results may not be comparable to results from the above testing standards or ASTM testing specifications such as F2247 or E330.

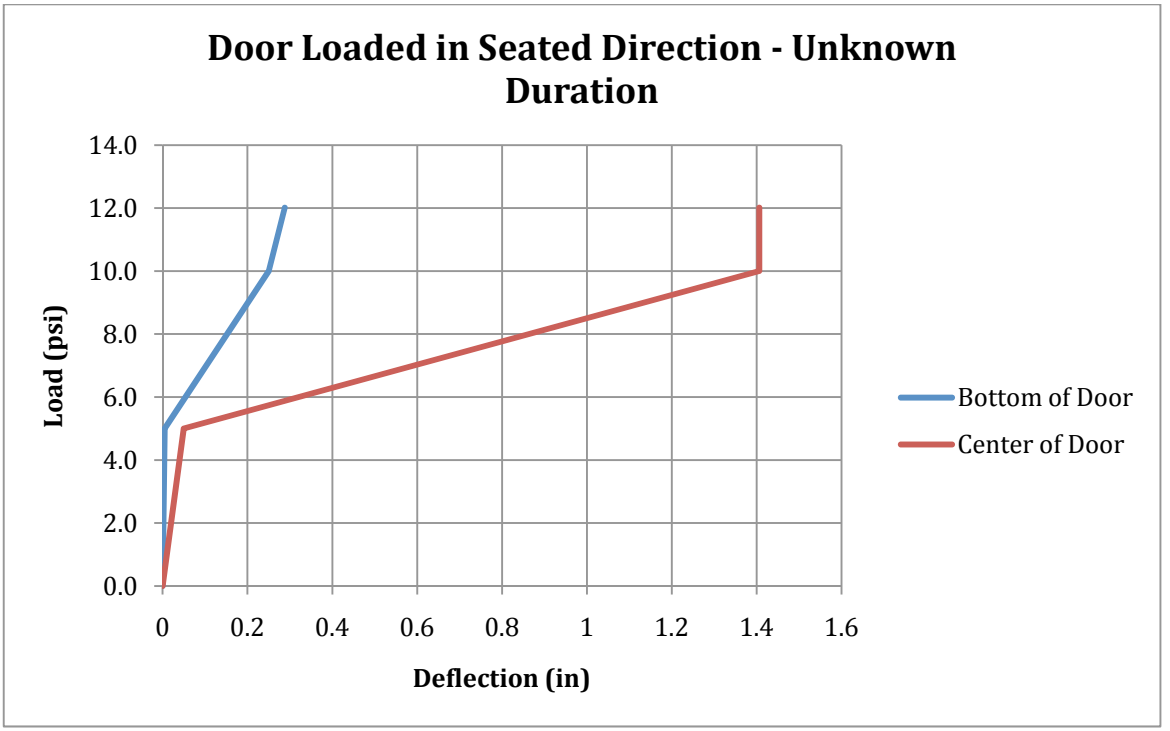


Figure 6. Composite Steel-Polystyrene Core Door Static Test Results

Dynamic test data available in open literature was also very limited. The only data available for non-blast resistant doors was available previous research performed by BakerRisk (formerly, Wilfred Baker Engineering).[5,6,7]. This data was limited to 18ga and 20 ga. hollow metal doors test to low pressure long duration blast loads, which was not directly related to the door types and blast loads of interest for this study. However, the data was useful in aiding in the selection of door for use in the test program. A summary plot of the prior BakerRisk door test information is provided in Figure 7. Note that the test was performed prior to the writing of ASTM F 2247 and used slightly different door response criteria. The door responses were correlated to ASTM F 2247 response level descriptions for presentation of the data in Figure **7**.

[5] Lowak, Michael J., *Testing of Hollow Metal Doors*, BakerRisk Internal Research, July 2006.

[6] Swofford, Jason L., Peterson, Jeff P., and Baker, Quentin A., *Test Program for Dynamic Response of Conventional Hollow Metal Doors*, Wilfred Baker Engineering Project No. 829-003, May 1998.

[7] Bogosian, David D. and Lowak, Michael J., *Retrofit Design for Conventional Hollow Metal Doors*, BakerRisk Project No. 01-760-325-08.

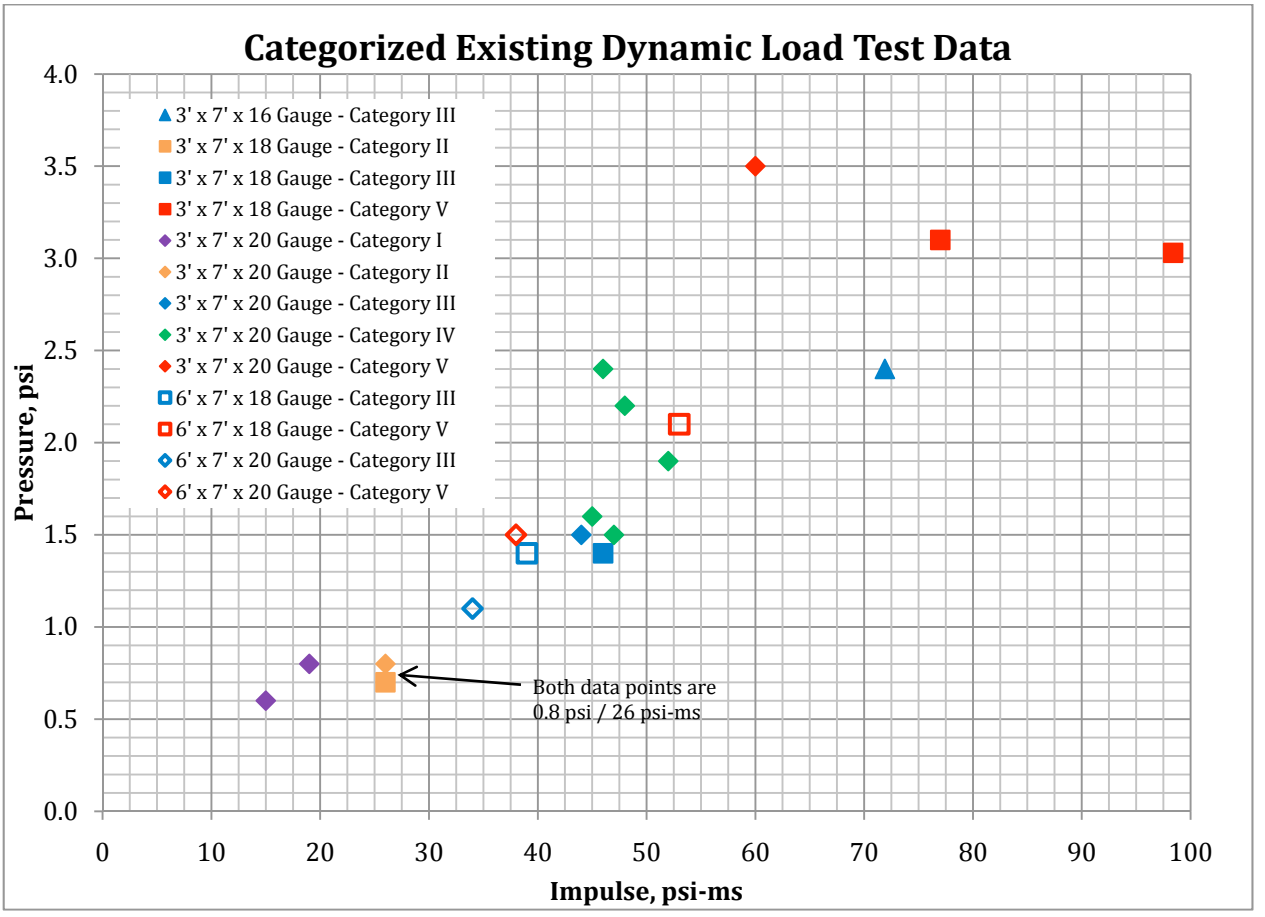


Figure 7 – Categorized Existing Dynamic Load Test Data

TEST PLAN AND PROCEDURES

A test plan was developed to provide a data set to evaluate the use of resistance functions obtained from static tests on doors to predict the dynamic response of those doors using SDOF analysis. The information obtained from the literature search was used to focus the test plan on the testing of doors suitable for use in government facilities for the protection against the minimum blast loads specified for antiterrorism protection. The test plan consists of the test approach and subsequent validation of the static test method according to dynamic shock tube testing. Door configurations for the initial testing were selected in coordination with the PDC. The initial proposed test matrix is defined and discussion related to the door configurations is included.

The static and dynamic test apparatus, data collection, and documentation are described, as well as response characterization for both static and dynamic test results. Frame configuration is addressed, along with the feasibility of numerical methods for use in the development of resistance-deflection functions for doors.

Test Approach

BakerRisk developed a progressive test approach in conjunction with the PDC, in which three series of tests were performed and the results of each test series were used to determine the tests conducted in subsequent test series. Additionally, test loads for the dynamic tests were developed from static tests performed in accordance with a modified approach to Procedure B outlined in ASTM F2247 as well as the commonly specified dynamic design loads for antiterrorism projects.

In contrast with the procedure outlined in the ASTM test specification, the BakerRisk test method does not predefine the maximum static test load for each specimen. Each specimen was tested to its ultimate (failure) resistance. As the original Procedure B calls for no less than four approximately equal increments of load application based on a pre-determined maximum test load, the increments used were calculated according to the postulated capacity of the door, which were based on the door's static load rating and existing test data.

Upon completion of the static test and development of the resistance-deflection curve based on the empirical data for each specimen, the natural period of the primary mode of response for each door was calculated according to the procedure outlined in the Annex of ASTM F2247. This approach provides all necessary data available from the ASTM test approach for determining static equivalent loads for given blast threats. The resistance-deflection curve was used in an SDOF model to prepare P-I (pressure-impulse) diagrams for the doors for each of the defined response categories. The design response limits used to develop the P-I curves are based on observed deflections in the static tests that relate to elastic limit, loss of support at the door frame stop, the deflection just prior to complete loss of support by the frame or other failure event, and latch failure in the unseating direction. These P-I curves were used to determine dynamic test loads expected to cause a specific door response for use in the latter stages of the test program.

Based on the existing data, blast loading interests of the PDC, and knowledge of doors typically used in government buildings a test matrix was developed. This test matrix along with the selected test approach provided resistance deflection relationships for two types of doors from the static tests. The dynamic tests provided a data set for validating SDOF model predictions using the resistance-deflection curves from the static tests. Additionally, they could serve to validate the basis and rationale of the equivalent load determination method outlined in the Annex of ASTM F2247.

Test Matrix

The door test matrix is provided in Table 3. Again, the matrix was conducted in three phases, with each phase of matrix development defining eight tests in the matrix. The conclusions of all completed tasks were considered in development of the subsequent tests.

The doors selected for use in the test program were a 16 ga. polystyrene core door and a 14 ga. vertically stiffened door. These doors were selected in a concerted effort with the PDC, with consideration of commonality, variation in fabrication details, and feasibility of the doors providing the blast resistance required for antiterrorism protection. The 16 ga. polystyrene core door represents a readily available standard door and the 14 ga. vertically stiffened door represents the most robust of typical conventional metal doors on the market. Note that although the 14 ga. door is a standard design for most manufacturers, it is considered a special order door.

The doors identified for use in the project were purchased from Deansteel Manufacturing, Inc. in San Antonio, Texas. Deansteel manufactures a full line of conventional steel doors, marine fire doors and several blast rated doors. Their conventional doors are of similar design and value to other door manufacturers identified in the literature search effort.

The 16 ga. polystyrene core doors are fabricated from galvanized materials and include reinforcements for door closers, and are prepared for 4 ½-inch hinges and mortise locks. The doors are provided in 5 ¾ inch deep cold-rolled 16 ga. door frames. The frames are welded at the head-to-jamb interface and prepared for bolt-in installation with four 3/8-inch diameter bolts. Door hardware includes PBB, Inc. standard weight 4 ½-inch ball bearing (BB) non-removable pin (NRP) hinges and Dorma Grade 1 mortise locksets (ML9956LTM) with lever handles.

The 14 ga. vertically stiffened doors are stiffened with cold-rolled steel hat members and includes reinforcements for door closers and are prepared for 4 ½-inch hinges and a mortise lock. The doors are provided in 14 ga frames identical in detail to the 16 ga. frame for the polystyrene doors, and have identical hinges and locksets.

Table 3. Test Matrix

Test No.	Method	Door Panel Type	Load
1	Static, Seated	16 ga. with Polystyrene Core	Increasing load to failure of door
2	Static, Unseated	16 ga. with Polystyrene Core	
3	Static, Seated	14 ga. Vertically Stiffened	
4	Static, Unseated	14 ga. Vertically Stiffened	
5	Dynamic	16 ga. with Polystyrene Core	5.8 psi, 31 psi-msec
6	Dynamic	16 ga. with Polystyrene Core	4.8 psi, 41 psi-msec
7	Dynamic	14 ga. Vertically Stiffened	5.8 psi, 31 psi-msec
8	Dynamic	14 ga. Vertically Stiffened	4.8 psi, 41 psi-msec
9	Static, Seated	16 ga. with Polystyrene Core, Mounted in Wood Studs	Increasing load to failure of door
10	Static, Seated	16 ga. with Polystyrene Core, Stiffened Frame	
11	Static, Seated	14 ga. Vertically Stiffened, Stiffened Frame	
12	Static, Seated	14 ga. Vertically Stiffened, Mounted in Wood Stud	
13	Dynamic	14 ga. Vertically Stiffened, Mounted in Wood Stud	4.8 psi, 41 psi-msec
14	Dynamic	16 ga. with Polystyrene Core Mounted in Wood Studs	4.8 psi, 41 psi-msec
15	Dynamic	16 ga. with Polystyrene Core, Stiffened Frame	4.8 psi, 41 psi-msec
16	Dynamic	14 ga. Vertically Stiffened, Stiffened Frame	4.8 psi, 41 psi-msec
17	Dynamic	16 ga. with Polystyrene Core	12.6 psi, 78 psi-msec
18	Dynamic	16 ga. with Polystyrene Core	
19	Dynamic	16 ga. with Polystyrene Core	
20	Dynamic	14 ga. Vertically Stiffened	12.6 psi, 78 psi-msec
21	Dynamic	14 ga. Vertically Stiffened	
22	Dynamic	14 ga. Vertically Stiffened	
23	Dynamic	16 ga. with Polystyrene Core, Mounted in Wood Studs	5.8 psi, 31 psi-msec
24	Dynamic	14 ga. Vertically Stiffened, Mounted in Wood Studs	5.8 psi, 31 psi-msec

Static Testing Apparatus

The static tests were performed in a test apparatus similar to the required fixture outlined in ASTM F2247. Figure 8, adopted from the ASTM document, show horizontal and vertical section views of the membrane system used to apply a uniform static load on the test specimen, for seated direction tests. The BakerRisk static test apparatus uses modular bladders within a rigid box in place of the sealed box and membrane shown in the ASTM apparatus. The bladders are designed to take the shape of the confined space within the apparatus with the test specimen forming one side of the space. The apparatus uses the same support fixture for doors that are dynamically tested in the BakerRisk shock tube. The use of the same reaction structure provides very consistent installation and support of specimens between the two test methods. A photograph of the static test apparatus with the bladders inflated against a clear test sample is provided in Figure 9.

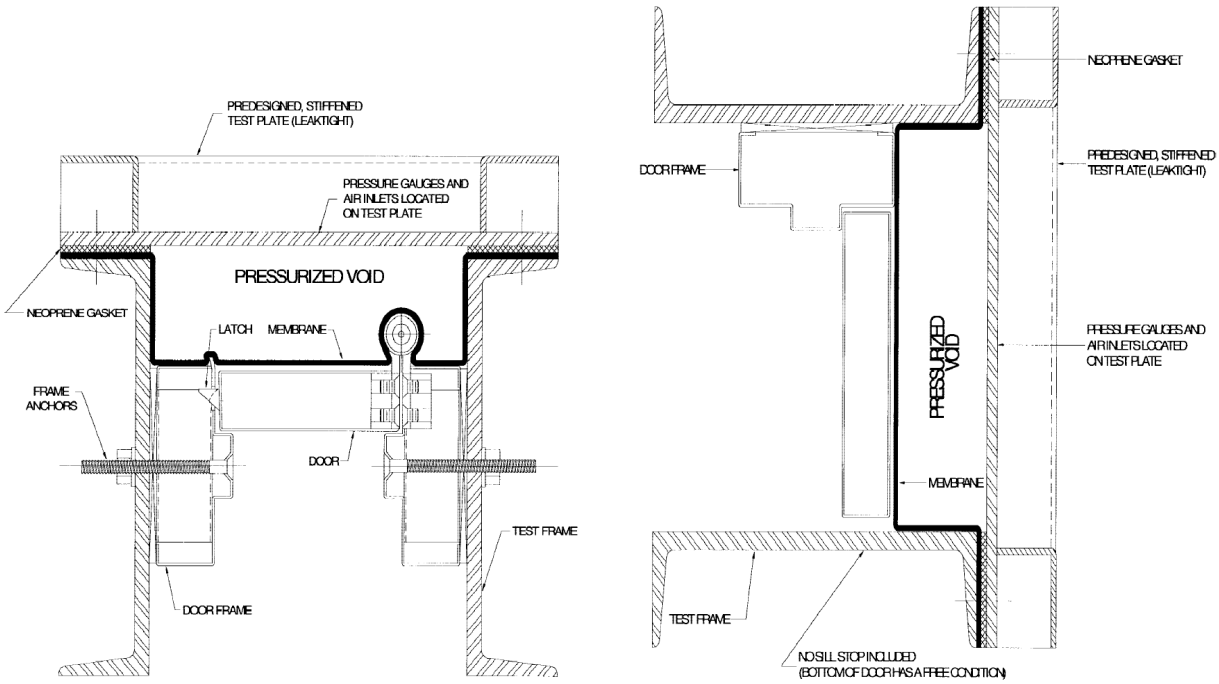


Figure 8 – Section Views, Seated Load Case



Figure 9. Photograph of the BakerRisk Static Test Apparatus

Dynamic Testing Apparatus

All dynamic tests in this test program were performed in the BakerRisk shock tube. Although the BakerRisk shock tube is capable of testing up to a 10-foot by 10-foot square test specimen, the 8-foot by 8-foot section was used in its normal configuration for the dynamic tests. A photograph of the BakerRisk shock tube is shown in Figure 10. For this test program, the target end of the shock tube was fitted with a test frame with a variable sized door opening.



Figure 10. BakerRisk Shock Tube

Instrumentation, Data Collection, and Test Documentation

Each dynamic test was instrumented with three airblast pressure transducers measuring the blast load applied to the test specimen and one airblast pressure transducer measuring pressure that may be present on the back side of the test specimen. All data from the blast transducers were electronically recorded at a sampling rate of 500 kHz or faster. These data were plotted as pressure-time histories and included in the test report.

High-speed video was used to record the response of the door system from two view angles oblique to the blast direction. A digital video camera was used to record each test, in addition to the high-speed video cameras. The digital video camera was also used to record the post-test state of the each test specimen, and to document the location of any debris generated during the test.

For both static and dynamic tests, still photography was used to document the test in both pre-test and post-test states.

The pressure and deflection measurements for each static test were documented for use in the test report in accordance with Section 13 of ASTM F2247.

Response Characterization Improvements

For informational purposes, although ASTM F2247 defines four categories of door blast response, there exists slightly modified performance categories defined by the BakerRisk Petroleum and Chemical Processing Industry Technology Cooperative (PCPITC), now the Explosion Research Cooperative (ERC). These ERC categories consist of expanded definitions of the four ASTM categories, and will be included in the future draft of a new standard test method for blast resistant doors being developed by ASTM subcommittee F12.10. The categories for response characterization are shown in Table 4.

Table 4. Expanded Performance Categories

Response	Description
Category I: No Damage	The door panel and all other components of the door must remain in the elastic response range. Analytical design limits for this response category are a ductility ratio of 1. Additionally, the analysis must include an evaluation that demonstrates that all parts of the door can support the door panel to its maximum capacity.
Category II: Limited Damage	The door panel may experience limited plastic deformation, but must be shown to remain in the frame in both the inbound blast direction and in rebound. All hardware must be evaluated and proven capable of supporting the door panel to its ultimate capacity. An evaluation of door shortening must be performed to ensure that shortening of the door panel due to deflection does not cause loss of bearing on the doorstop or pullout of the lock bolt from the frame. The design limit on the door panel is 5 degrees of support rotation. The panel shortening evaluation includes effects of doorpost deformation, if applicable, and rounded corners of bent plate frames and door skins. The total loss of panel/stop or latch bolt/plate engagement is limited to one-half of that provided under normal installation tolerances.
Category III: Non-Catastrophic Failure	The door panel must remain in the frame and remain a barrier to prevent blast load propagation through the door opening. The door panel may be severely deformed and may be inoperable. The design limit on the door panel is 8 degrees of support rotation. An evaluation related to loss of support due to door panel and post deformation must show that the total loss of engagement is less than the engagement provided, minus the dimensions of any corner radii.
Category IV: Failure without Debris Hazard	The door panel may be severely deformed, with openings between the panel and door frame allowed, but the door panel must remain affixed to the door frame. This level of response is difficult to predict analytically, due to the many influencing factors of response once a door panel deflects to the point where bearing supports or latch bolt engagement is lost. Also, simple analytical methods such as single-degree-of-freedom models assuming elastic/perfectly-plastic response do not predict large deformation well. Testing is the best methodology to predict this level of response.

These performance categories were used for both static and dynamic tests. Note that a category is not included to characterize blow-out failure. For this test program, characterization of this type of failure is not necessary, as door panel response occurring after total separation from the frame falls above the ultimate resistance of a door system.

Both inbound and rebound response of the door systems are considered by default in the dynamic tests. In the static tests, considerations were made for both inbound and rebound response by the testing of the door specimens in both the seated and unseated directions, respectively.

Frame Connection Configurations

Frame connections, such as the attachment of the door frame to the test fixture, followed normal installation details as close as possible to be representative of those normally employed for

anchorage to steel substrates. The effects of minor differences in shimming for rough openings in door frame openings in typical construction practices are not expected to play a significant role in the applicability of the test results to real-world blast response of the door systems, if proper manufacturer connection specifications are adhered to in construction.

Deviation from ASTM F2247-03 Test Specification Methodology

A deviation was made from Procedure B of the ASTM specification regarding the static testing in this program. The maximum static test load was not predefined. The load increments were calculated according to a postulated capacity of the doors for selection of incremental load steps, but ultimately the doors were tested to failure. During setup and testing two other deviations from the ASTM recommended approach were made. These are described in the following paragraphs.

A deviation from the ASTM suggested approach was made with regard to the suggested data instrumentation locations for the door specimens in both the seated and unseated directions. The locations of the BakerRisk test apparatus deflection instrumentation are shown in Figure 11, superimposed on the ASTM suggested locations. These measurement location adjustments were made based upon previous observations of door deformation under blast loading. The resistance-deflection curves created in this study use the deflection gathered at mid-span of the door panel, rather than at the bottom edge. Test observations indicate that the panel jamb may lose frame engagement, prior to development of full panel resistance. This point is best for predicting door performance, as the door panel behaves as a two-way plate with maximum deflection at the mid-point, except in the vertically stiffened case where the point of maximum deflection shifts to the bottom of the panel after it is pushed past the frame stop and the resistance continues to be provided by load transfer through the stiffeners.

The ASTM approach requires checking for door operability after each load step. BakerRisk did not perform these checks. The purpose of these static checks was to determine the ultimate load capacity of the doors. If a door operability check resulted in a non-operable result, such that a door latch opens but would not re-latch, the test could not continue and the ultimate resistance could not be determined. Therefore, BakerRisk did not operate the latches once a test was started.

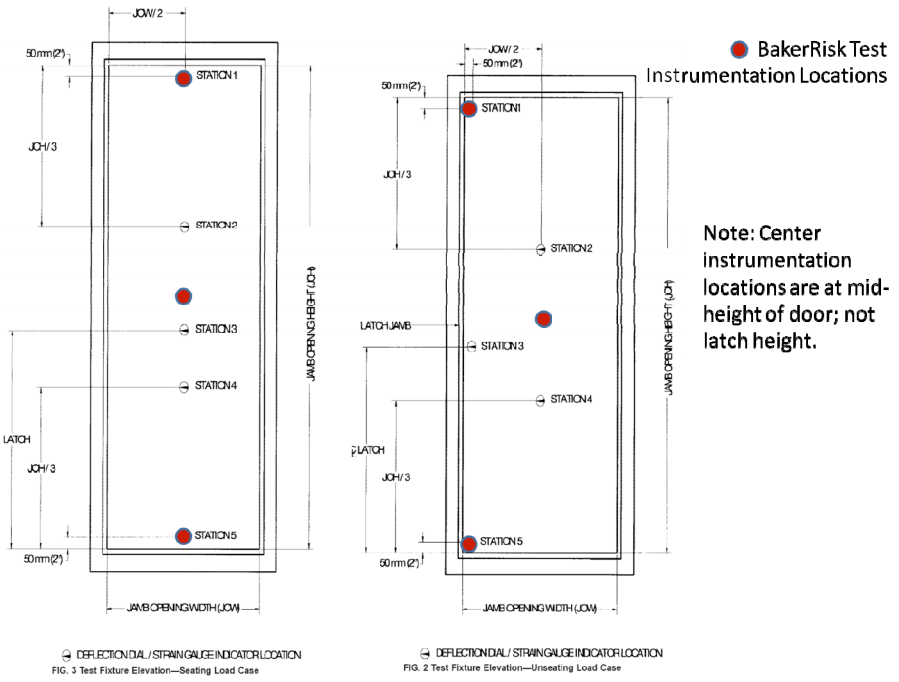


Figure 11. BakerRisk Test Instrumentation Locations: Seated (Left) and Unseated (Right)

TEST RESULTS

The results of all three tests are reported in the following sections grouped by each test series. Conclusions drawn from each test series that were used in the development of the follow-on test series are discussed with the results. Sub-sets of data are grouped in the analysis section based on door type for side by side comparisons.

Static Test Results

The all static tests were conducted in the BakerRisk static test apparatus. Results of each test are summarized in Table 5. For door type and installation details, see the test matrix in Table 3. Sample recorded data and resulting resistance deflection curves for sample seated and unseated static tests are provided in Figure 12 and Figure 13. Post-test photographs for these same tests are provided in Figure 14 and Figure 15.

Table 5. ASTM F2247-03 Damage Category Ratings – Static Testing

Test Number	Load Increment	Increment Load (psi)	Category[1]
1	1	0.4	I
	2	0.8	II
	3	1.2	II / III
	4	1.6	III
	Failure	3.5	IV
2	1	0.3	I
	2	0.6	II
	3	0.9	II / III
	Failure	1.2	IV
3	1	1.0	II
	2	2.0	III
	Failure	2.8	IV
4	1	0.3	II
	2	0.6	II / III
	3	0.9	II / III
	4	1.2	III
	Failure	1.5	IV
9	1	0.7	II
	2	1.4	II
	3	2.1	II
	Failure	2.4	IV
10	1	0.8	II
	2	1.6	II
	3	2.4	II/III
	4	3.2	II/III
	5	4.1	III
	Failure	5.2	IV
11	1	0.7	II
	2	1.4	II
	3	2.1	II/III
	4	2.8	II/III
	5	3.5	II/III
	6	4.2	III
	7[3]	5.0	III
	Failure	5.6	IV
12	1	0.8	II
	2	1.6	II
	3[3]	2.4	II
	Failure	3.3	IV

[1]Differentiation between ASTM F2247 Categories II and III based upon door operability was not made; testing door operability between load cycles is not practical. Distinctions between Categories II and III are made based upon visual observation of damage during testing.

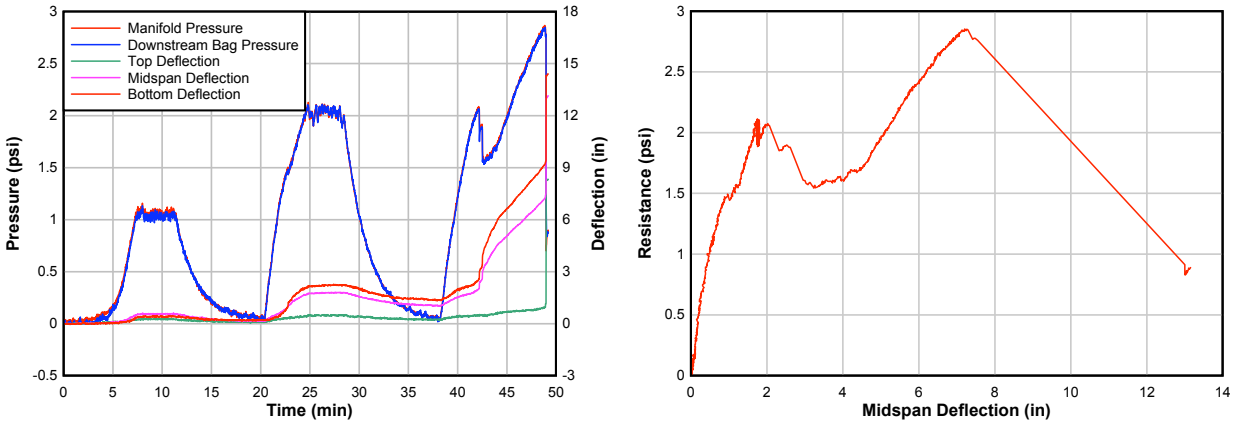


Figure 12. Seated Pressure and Deflection vs. Time and Resistance-Deflection Function

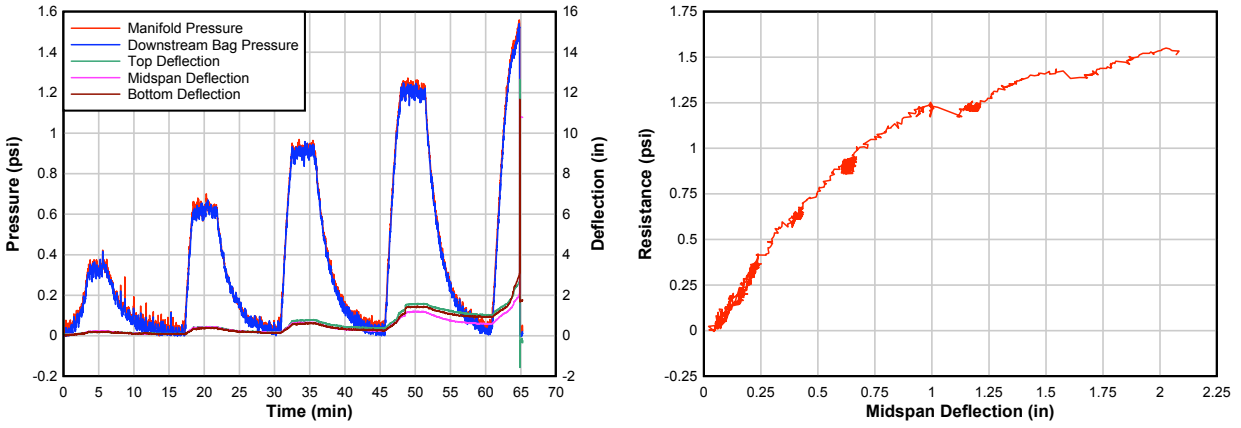


Figure 13. Unseated Pressure and Deflection vs. Time and Resistance-Deflection Function



Figure 14. Test 3: Post-Test Photographs

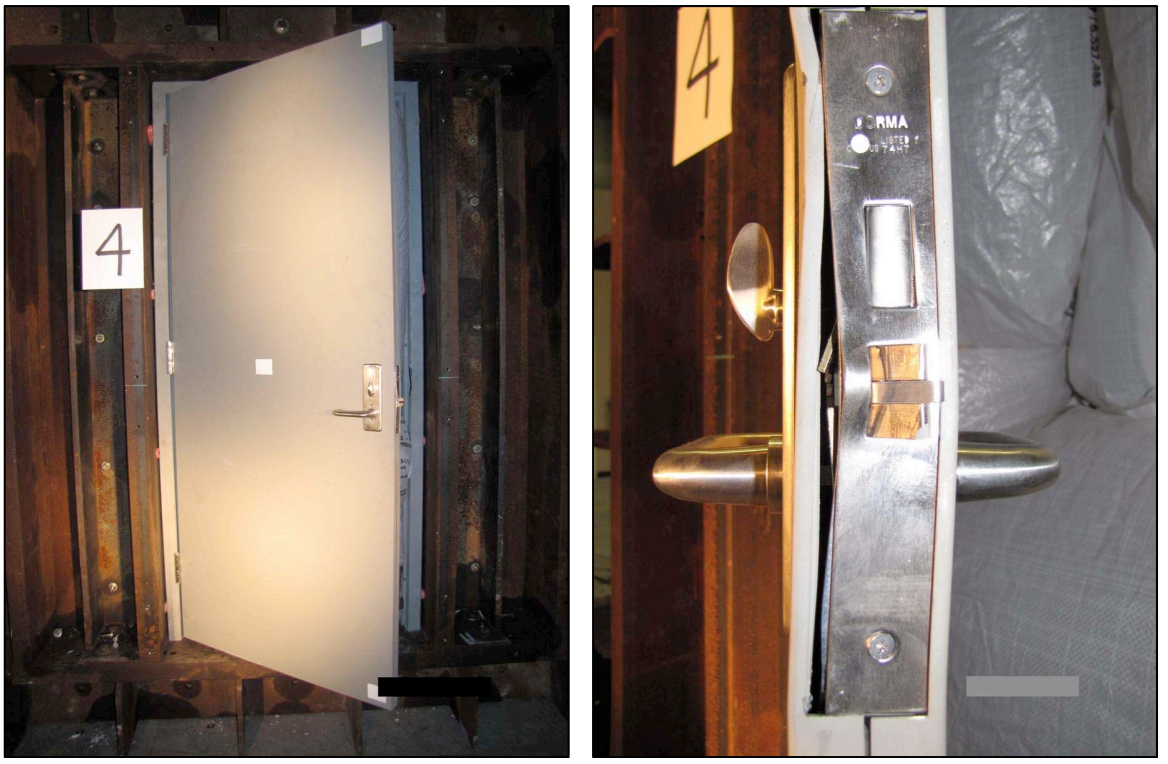


Figure 15. Test 4: Post-Test Photographs

Dynamic Test Results

Dynamic tests were conducted using the BakerRisk Shock Tube. All tests of doors were performed in the seated direction. The dynamic test loads used in each test were selected based on the test matrix prepared for the test program. The ASTM F2247-03 damage category rating results for each dynamic test is shown in Table 6. Note that a shock tube misfire occurred during Test 6. A subsequent test, Test 6A, was performed on the same specimen. Sample post-test photographs are provided in Figure 16 through Figure 19.

Table 6 – ASTM F2247-03 Damage Category Ratings – Dynamic Testing

Test Number	Load (psi / psi-ms)	Door Panel Type	Category[1]
5	6.3 / 34	16 ga. with Polystyrene Core	II
6	3.6 / 33	16 ga. with Polystyrene Core	II
6A	4.4 / 39	16 ga. with Polystyrene Core	III
7	6.2 / 30	14 ga. Vertically Stiffened	I
8	5.2 / 41	14 ga. Vertically Stiffened	I
13	4.8 / 41	14 ga. Vertically Stiffened - Wood	V
14	4.9 / 38	16 ga. Polystyrene Core - Wood	V
15	4.9 / 39	16 ga. Polystyrene Core – Stiffened Frame	III[2]
16	4.9 / 38	14 ga. Vertically Stiffened – Stiffened Frame	III[2]
17	12.0 / 77	16 ga. with Polystyrene Core	V
18	9.1 / 58	16 ga. with Polystyrene Core	III
19	10.9 / 79	16 ga. with Polystyrene Core	IV
20	13.7 / 96	14 ga. Vertically Stiffened	IV
21	14.7 / 112	14 ga. Vertically Stiffened	IV
22	10.1 / 63	14 ga. Vertically Stiffened	III
23	5.6 / 27	16 ga. with Polystyrene Core Mounted in Wood Studs	II
24	5.2 / 27	14 ga. Vertically Stiffened Mounted in Wood Studs	II

[1]ASTM equivalent static test methodology category rating, applied to dynamic test results.

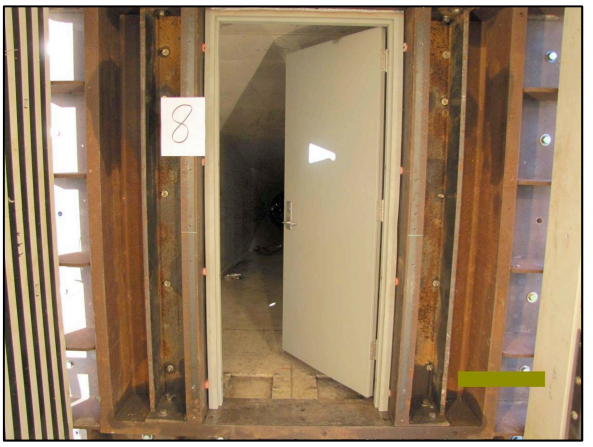


Figure 16. Test 8: Post-Test Overall View



Figure 17. Test 8: Post-Test Frame View



Figure 18. Test 20: Post-Test Overall View



Figure 19. Test 20: Post-Test View of Door Pushed Past the Stop

POST-TEST ANALYSIS

Using the resistance-deflection curves obtained from the static tests of the first series, SDOF and two degree of freedom (2DOF) models were created. The PDC tool SBEDS was used for SDOF modeling, while the BakerRisk proprietary ISADS tool was used to model both the frame and panel components as a 2DOF system. The second degree of freedom in the analysis was developed by loading a static finite element frame model with a unit load and obtaining the peak elastic deflection. The displacement criterion used was a frame sway limit of H/50.

While the displacement-time history phasing of door opening during rebound matched closely for most tests, it did not match for Test 6A, for which the frame may have been slightly deformed from the earlier misfire in Test 6. Models were executed with both the measured applied loads from the tests (Table 7) and equivalent right-triangular loads (Table 8) and the results are similar.

Table 7 SDOF and 2DOF Preliminary Modeling Results Summary (Measured Loads)

Door Type	Load (psi / psi-ms)	Component	Analysis Type	Tool	Inbound defl. (in)	Rebound defl. (in)	Ductility
16GA Unstiffened (Test 5)	6.3 / 34	Door Panel	SDOF	SBEDS	2.86	N/A	1.43
		Door Panel	2DOF	ISADS	2.00	N/A	1.09
		Frame			0.37	N/A	10.95
		Door Panel	SDOF - with rebound	SBEDS	2.23	> 1.52 (opens[1])	0.99
		Door Panel	2DOF - with rebound	ISADS	2.00	> 1.52 (opens[1])	1.00
		Frame			0.35	0	10.5
14GA Stiffened (Test 7)	6.2 / 20	Door Panel	SDOF	SBEDS	2.08	N/A	1.44
		Door Panel	2DOF	ISADS	2.10	N/A	1.22
		Frame			0.02	N/A	0.85
		Door Panel	SDOF - with rebound	SBEDS	2.08	0.03 (no open[2])	1.44
		Door Panel	2DOF - with rebound	ISADS	2.15	0.96 (no open[2])	1.23
		Frame			0.02	N/A	0.83
16GA Unstiffened (Test 6A)	4.4 / 39	Door Panel	SDOF - with rebound	SBEDS	2.33	> 1.52 (opens[3])	1.16
16GA Unstiffened (Test 6)	3.6 / 33	Door Panel	2DOF - with rebound	ISADS	1.85	2.52 (opens[1])	1.01
		Frame			0.24	0	7.2

[1]Confirmed with hi-speed video.

[2]Door opened in the test.

[3]Door pushed through frame in test.

Table 8. SDOF and 2DOF Preliminary Modeling Results Summary (Equivalent Right-Triangular Loads)

Door Type	Load (psi / psi-ms)	Component	Analysis Type	Tool	Inbound defl. (in)	Rebound defl. (in)	Ductility
16GA Unstiffened (Test 5)	6.3 / 34	Door Panel	SDOF	SBEDS	2.37	N/A	1.19
		Door Panel	2DOF	ISADS	1.85	N/A	1.01
		Frame			0.24	N/A	7.28
		Door Panel	SDOF - with rebound	SBEDS	2.23	> 1.52 (opens[1])	1.18
		Door Panel	2DOF - with rebound	ISADS	1.85	> 1.52 (opens[1])	1.01
		Frame			0.24	0	7.20
14GA Stiffened (Test 7)	6.2 / 20	Door Panel	SDOF	SBEDS	2.2	N/A	1.52
		Door Panel	2DOF	ISADS	2.21	N/A	1.26
		Frame			0.02	N/A	0.79
		Door Panel	SDOF - with rebound	SBEDS	2.04	0.25 (no open[2])	1.41
		Door Panel	2DOF - with rebound	ISADS	2.21	1.18 (no open[2])	1.26
		Frame			0.02	N/A	0.78
16GA Unstiffened (Test 6A)	4.4 / 39	Door Panel	SDOF - with rebound	SBEDS	2.43	> 1.52 (opens[3])	1.21
16GA Unstiffened (Test 6)	3.6 / 33	Door Panel	2DOF - with rebound	ISADS	1.85	2.19 (opens[1])	1.01
		Frame			0.28	0	8.38

[1]Confirmed with hi-speed video and time matches.

[2]Door opened in the test.

[3]Door pushed through frame in test.

RECOMMENDED ANALYTICAL MODELING METHODOLOGY

The paramount goal of this study was to establish a methodology to utilize static test data gathered in accordance with ASTM F2247-03 for the development of SDOF resistance functions for hollow metal doors. This section presents analytical pressure-impulse (P-i) diagrams created from SDOF analysis using the ASTM F2247-03 static resistance functions obtained from this program. The diagrams presented provide conservative estimates of damage level, based on the available test data. Recommendations for use and applicability of static door test data for assessment of dynamic response are given.

SDOF Parameters

Using the load-mass factors for a 3-sided simply supported 2-way plate, SDOF models can be created for doors with both unstiffened and vertically stiffened panels. The resistance-deflection curves obtained in this program were curve-fit for use in the SBEDS software for inbound and rebound response.

Care must be taken to examine the response output for post-yield response in rebound so that subsequent response is disregarded. For example, Figure 20 shows a sample SBEDS input page representing a model of the 16GA door in Test 5 of this program. Note that the maximum ductility ratio computed by the SBEDS input sheet is shown for the rebound phase, which is technically incorrect. The peak positive displacement is 2.2 inches, which is approximately 10% over yield, representing a ductility ratio of 1.1. Examining the SDOF response output shown in Figure 21, the door reached rebound yield deflection (-1.5 inches) at 31 ms, which occurs earlier in time than the peak rebound response shown in the model.

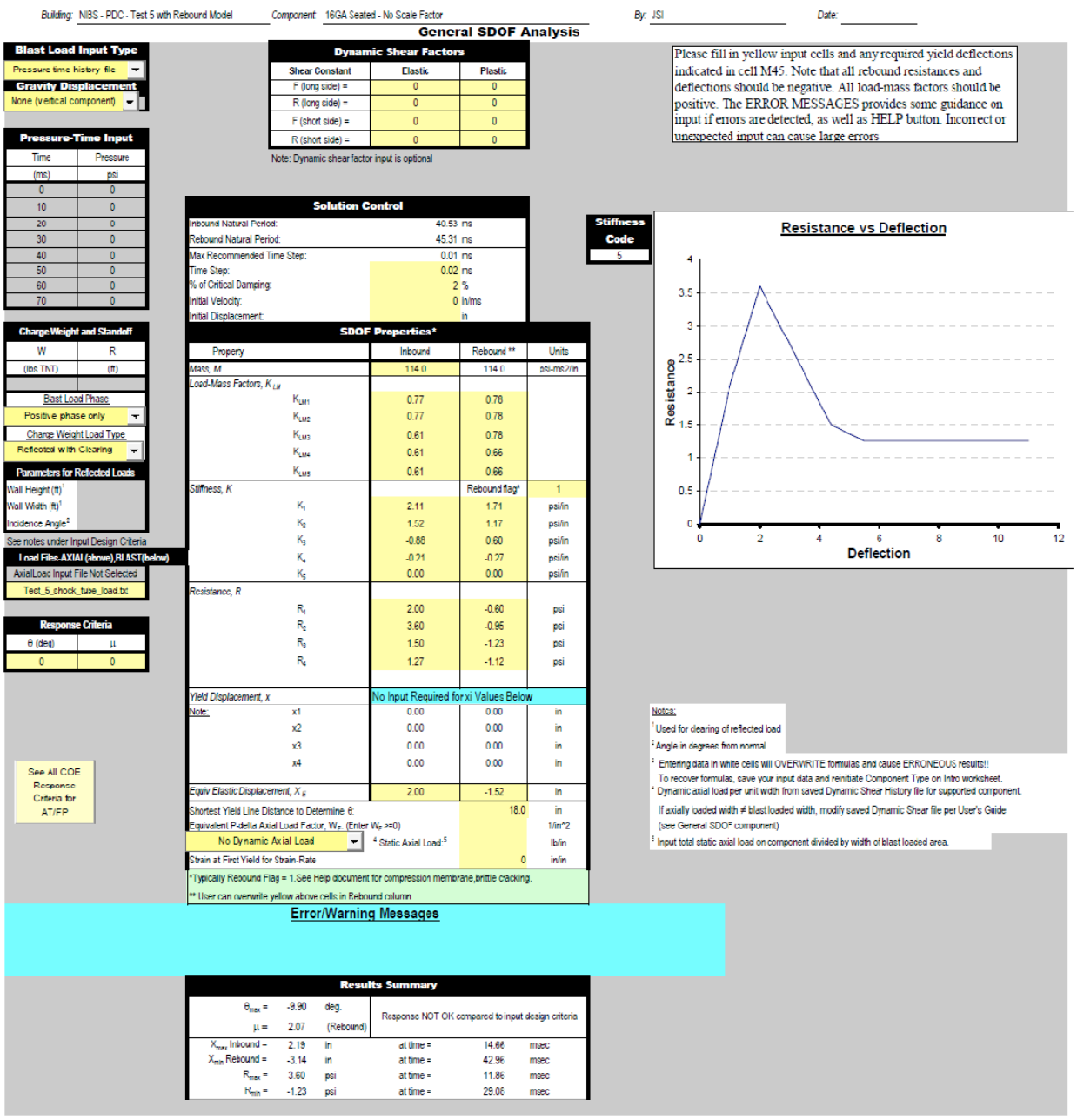


Figure 20. SBEDS Input Sheet (Test 5)

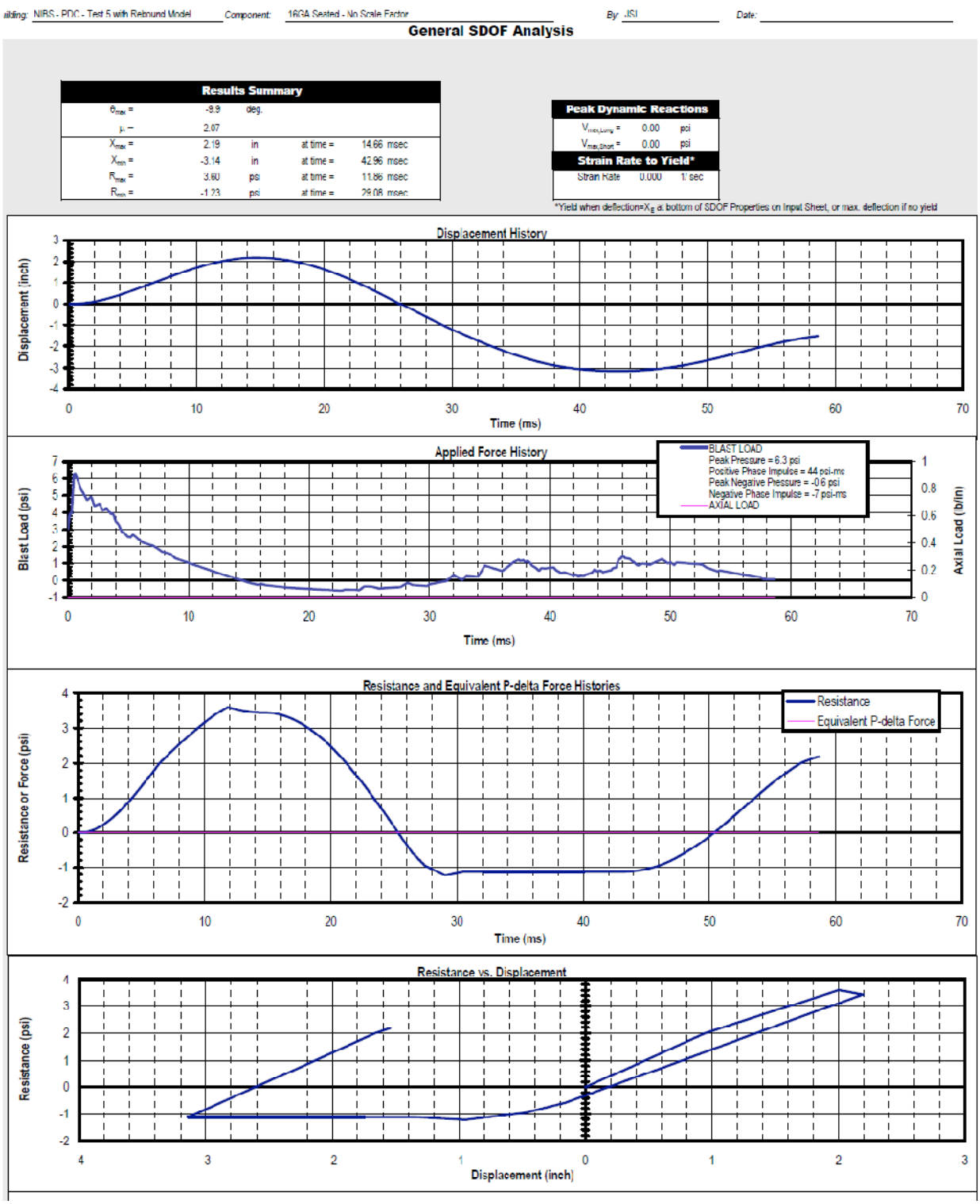


Figure 21. SBEDS Output Sheet (Test 5)

16GA Doors with Polystyrene Cores

The static resistance deflection curves obtained from the first test series were used to model the dynamic behavior of the 16GA polystyrene core doors using SDOF methods. A comparison of these analytical results with the test data is shown in Table 9.

Table 9 – 16GA Polystyrene Core Door Test and Analytical Data Comparison

Test	Observed Panel Response		Calculated Panel Response	
	Qualitative	Measured	Ductility	Time to Peak
5	Rebounded open at 36ms	None	1.1	Rebounded open at 31ms
6	Rebounded open at 30ms	None	1.0	Rebounded open at 33ms
6A[1]	Panel pushed past stop at 24ms	N/A	1.2	Pushed past stop at 49ms
17	Door panel and frame detached from test fixture; panel pushed past stop at 10ms	N/A	7.0	Pushed past stop at 7ms
18	Panel pushed past stop at 6ms, rebounded, then opened	5/8" Perm. at Midspan	3.1	Pushed past stop at 8ms
19	Panel lodged in frame; first peak of bottom of panel response at 32ms, second at 66ms	3.25" Perm. At Midspan	3.9	First and second peak at 32ms and 66ms[2]

[1]Test 6A was a retest due to a shock-tube misfire in Test 6. As a result, the frame had already undergone slight permanent deformation, which provided a stiffer support for Test 6A. This phenomenon is reflection in both the experimental and analytical results.

[2]The peak response of the bottom of the door panel and the mid-height, mid-span of the door panel may not be necessarily in phase.

The analytical results, using the static resistance deflection curves, agree very closely with the observed experimental results without the use of any increase factors applied to obtain the dynamic response. P-i diagrams representing the ASTM F2247-03 static door damage categories are shown in Figure **22**. These diagrams are based on the analytical models. Test data points from this program are plotted on the diagram independently.

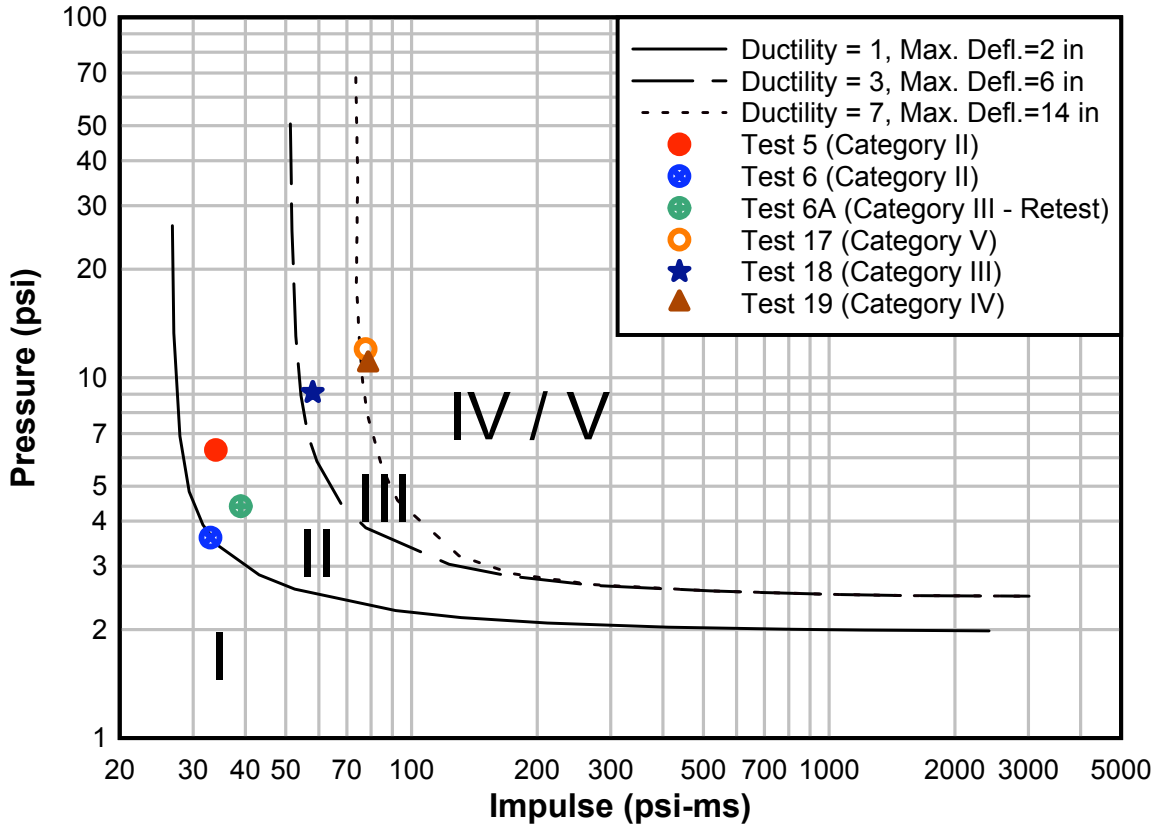


Figure 22 – 16GA Polystyrene Core Door Damage Levels

14GA Doors with Vertically Stiffened Panels

The static resistance deflection curves obtained from the first test series were used to model the dynamic behavior of the 14GA doors with vertically stiffened panels using SDOF methods. Again, the analytical results agree very closely with observed experimental results. While inbound response agrees well, the SDOF models tend to under predict the rebound response. A comparison of these analytical results with the test data is shown in Table 10.

Again, the analytical models were used to create P-i diagrams of the ASTM F2247-03 damage levels, as shown in Figure 23. Test data from this program is overlaid on the chart. The data point representing Test 22 appears in the Category III region, while observed test results dictate a Category II (permanently deformed but operable) rating. Note that the door frame flexed significantly in this test, thus reducing the likelihood of latch damage and further door panel damage.

Table 10. 14GA Vertically Stiffened Panel Door Test and Analytical Data Comparison

Test	Observed Panel Response		Calculated Panel Response	
	Qualitative	Measured	Ductility	Time to Peak
7	Rebounded open at 40ms	1/4" Perm. at Midspan	1.2	Did not rebound open, but peak rebound occurred at 40ms
8	Rebounded open at 40ms	1/2" Perm. at Midspan	2.0	Did not rebound open, but peak rebound occurred at 53ms
20	Panel pushed past stop at 20ms and two frame bolts failed in shear	3.8125” Perm. At Midspan	5.4	Pushed past stop at 22ms
21	Panel pushed through frame at 14ms, five frame bolts failed in shear, and the door frame partially came out of the test fixture	N/A	7.1	Pushed past stop at 18ms
22	Panel stayed closed, exhibited permanent deformation, and frame flexed significantly	5/8" Perm. at Midspan	4.0	Stayed closed

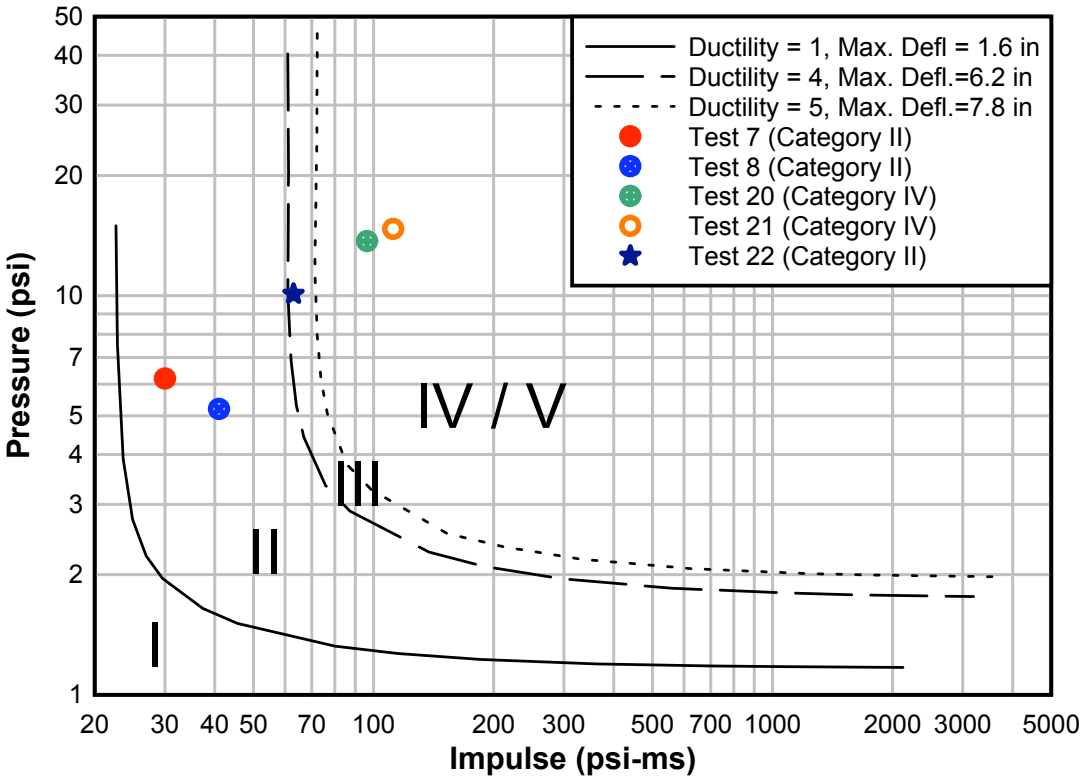


Figure 23. 14GA Vertically Stiffened Panel Door Damage Levels

Rigid Door Frames

Two dynamic tests were conducted with stiffened door frames, representing frames made rigid by grouting during construction (Tests 15 and 16). Although rigid door frames may increase door panel resistance, they decrease the chance of operability, post-blast. The permanent deformation of the door panels was decreased by 88% for the 16GA doors and by 40% for the 14GA doors when using rigid frames. However, both doors rebounded open and were rendered inoperable by latch failure. In door tests without rigid frames, the frame twist and flex, allowing door latches to often disengage with minimal or no damage. Due to the rigidity of the door frames in Tests 15 and 16, the latches failed when the door panels rebounded.

For the reasons above, and with the absence of further dynamic test data for rigid frame doors, shifting of the damage level P-i diagrams to represent increased door panel resistance when using rigid frames is not recommended. The two rigid frame test data points will currently fall within the Category II region of the respective charts, although their responses can be technically characterized as Category III due to latch damage during rebound response resulting in inoperability. Operability is the only parameter which defines the threshold between these two categories, and these categories are intended for use in categorizing static tests which do not subject doors to rebound. The Category III response in these two tests characterized by rebound latch damage is not equivalent to Category III response observed in a case where inoperability is the result of inbound latch damage and door panel push-through. Therefore, it is determined that the use of these diagrams for rigid door frame systems is conservative.

Applicability of ASTM F2247-03 Static Test Data to Dynamic Results

It is evident that the static resistance-deflection functions obtained in this test program provide relatively accurate SDOF models for dynamic behavior of hollow metal door systems. It is logical to assume that FEA models can be validated to produce similar static test results and then used for dynamic analysis. However, there are several aspects of the ASTM standard which this study deems unnecessary for the applicability of static test results to dynamic models.

The ASTM standard calls for subdividing the test load into segmented peaks, and maintaining these peak pressures for a period of no less than three minutes, while unloading the specimen completely to measure permanent deformation after each loading period. However, without a check for operability after each loading period, the permanent deformation data is of no use for damage categorization. Checking and observing for operability may compromise the test results by disturbing a deformed and latched specimen. Furthermore, loading the specimen in segments is unnecessary, as the speed in which the load is applied, even if done in a continuously increasing trend to failure, is still much too slow to induce any possible dynamic effects. Lastly, the repeated cyclic loading may induce failure of internal welds or other structural failure which may not occur at the same deflection during continuously increasing load or dynamic load. It is for these reasons that BakerRisk recommends a continuously increasing load to failure.

Other Concerns

Throughout the test program, the results indicated that variables in frame stiffness and anchorage can play a major role in the response of the doors both under static and dynamic loading. Therefore it is important to consider these door support details when evaluating doors.

ASCE 7-10 Changes to Flood Load Provisions

William L. Coulbourne, P.E. M.ASCE

Director, Wind and Flood Hazard Mitigation, Applied Technology Council, 19266 Coastal Highway, Unit 4, #19, Rehoboth Beach, DE, 703-850-2891 (cell), 302-227-7652 (fax), email: bcoulbourne@atcouncil.org

ABSTRACT

The flood loads that are covered in Chapter 5 of ASCE 7-10 have not changed in any substantive way since ASCE 7-05. The same flood forces are discussed with formulas exactly as they were in ASCE 7-05. The issue for the designer using the flood standard is in trying to understand the unknowns inherent in the formulas so they can make good decisions about how to apply the formulas to real problems.

The paper will describe the issues that designers must consider for each of the flood forces delineated in ASCE 7-10 and where continued work needs to be done to improve the understanding we have about the magnitudes of flood loads. The paper will also offer guidance on the magnitude of the load factors used in strength and allowable stress design situations.

INTRODUCTION

The ASCE 7 flood load provisions we use today have not changed significantly since the ASCE7-02 version. Nevertheless, it appears that many designers are not familiar with the provisions and how they should be applied. The results of the last several coastal flood events suggests we continue to ignore or improperly apply flood forces to building designs, again especially at the coastlines, and the results of significant damage somewhat support that conclusion.

There are many unknowns about flood conditions and forces. For example, as a profession we know little about the magnitude and direction of flood velocity during a design event, especially at coastal locations. Also, while some work has been done on determining floodborne debris forces, we still have low confidence in our method for calculating these forces.

CURRENT ASCE 7-05 FLOOD LOAD REQUIREMENTS

Hydrostatic loads

Hydrostatic loads are caused by standing water and include horizontal loads such as those against a basement wall or vertical loads on immersed objects (buoyancy). The application of hydrostatic loads has not changed over many years since fluid mechanics principles were developed.

The formula for lateral hydrostatic force (lb/ft) is:

$f = 1/2\gamma d^2$ where γ is the unit weight of water (lb/ft^3) and d is the depth (ft) of standing water (or stillwater if coastal wave conditions exist). Figure 1 illustrates the concept of hydrostatic loads and uses d_s as the depth of stillwater. The force is applied normal to the surface at a point 2/3 below the water surface. The unit weight of water can vary from 62.4 lb/ft^3 for fresh water to 64.0 lb/ft^3 for salt water.

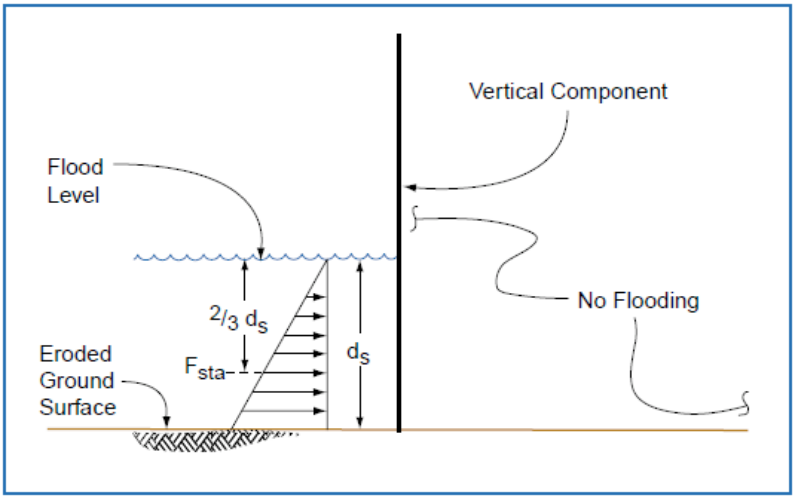


Figure 1. Hydrostatic load diagram

The nuance related to hydrostatic forces for flooded buildings is that there is a floodplain requirement that building foundations in floodplain locations have flood vents in the walls to reduce unbalanced hydrostatic pressure. So while the principles of water pressure against vertical or horizontal surfaces still applies, the application of these loads has been purposely modified by requiring flood openings in walls. An issue that arises frequently is one where standing water will be on both sides of a wall but will be at unequal depths, thus presenting an unbalanced hydrostatic force.

Hydrostatic loads can also act vertically, primarily as buoyancy loads. These loads must be counterbalanced by either the weight of the object or by some attachment of the object to a counterbalancing weight such as a concrete foundation. The formula for buoyancy forces is:

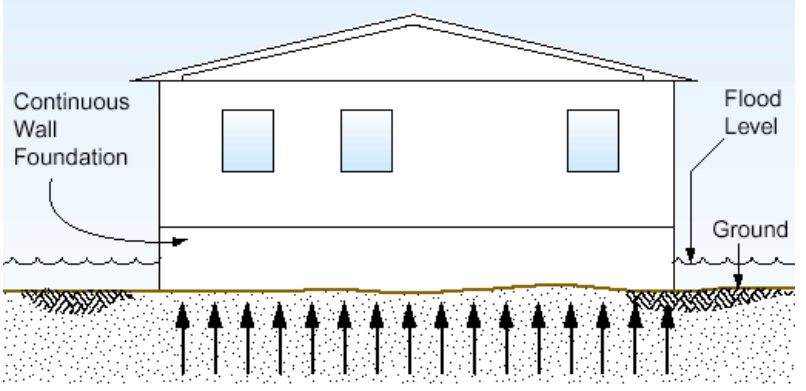


Figure 2. Buoyancy under building

$F = \gamma * volumedisplaced$ where γ is the unit weight of water and the volume displaced is the volume of building, tank, or pool that displaces the water. Figure 2 illustrates the concept of buoyancy. Objects submerged under water also weigh less than they would if not submerged -- by the buoyancy force F (weight of the displaced water) as written above.

Hydrodynamic loads

Hydrodynamic loads are those caused by moving water. The primary flood parameter needed to determine these loads is the velocity of the moving water. In riverine flood conditions where flow is confined to a streambed or channel, our ability to calculate velocity is determined by the relationship between quantity of flow (cfs) and area (sf) of a cross-section used to carry the flow, and the results are frequently provided in a Flood Insurance Study (FIS).

The actual hydrodynamic force depends on the shape of the object water is flowing around. This shape is defined by a drag coefficient. Drag coefficients are provided in fluid mechanics texts or in the Coastal Construction Manual (CCM). The Commentary in ASCE 7-10 suggests using a drag coefficient C_d = 1.25 unless better information is available. The C_d factor usually only varies between 1.0 and 2.0 in any case.

Section 5.4.3 of ASCE 7-10 states that hydrodynamic loads should be calculated by basic principles of fluid mechanics. However, the Standard does allow hydrodynamic loads to be converted to equivalent hydrostatic loads in cases where velocities are less than 10 fps.

The Commentary provides guidance for estimating lower and upper velocity bounds for coastal areas. In coastal areas, velocities are much less certain so the depth of water is used either as a proxy (in areas that are some distance from the flood source) ($V = d \div s$) or to help determine velocity using the wave celerity (in areas that are closer to the flood source) ($V = \sqrt{gd}$).

The result for hydrodynamic force using either the equivalent head method or the equation below is fundamentally the same. If the flow was 8 fps and the water depth was 5 ft, the hydrodynamic force calculated by converting the velocity flow into head and treating it as a hydrostatic force is 387.58 lb/ft. The formula for hydrodynamic force when the velocity is greater than 10 fps is:

$f_{dyn} = 1/2 C_d \rho V^2 d$ where C_d is the drag coefficient, ρ is the mass density of water, V is the velocity and d_s is the depth of water. The unit hydrodynamic force for the example above using this formula is 388 lb/ft (nearly identical to the previous answer). The force f is assumed to act at mid-depth of the water.

Wave loads

Wave loads presented in ASCE 7-10 have formulas to determine loads for both piles and solid walls. The magnitude of the loads is primarily a function of the square of the wave height (which is assumed equal to a depth-limited value of 0.78 x d_s). The formula for breaking wave forces on a pile is:

$F_{brkp} = 1/2\gamma C_d D H_b^2$ where C_d is the drag coefficient for the pile, D is the pile diameter in feet, and H_b is the breaking wave height. C_d is 1.75 for round piles and 2.25 for square piles. F_{brkp} acts at the stillwater elevation.

Wave loads on solid walls is provided for two cases: one case where the water is on one side of the wall only and one case where water is on both sides of the wall by using wall openings to equalize the hydrostatic pressure. The formula accounts for both hydrostatic and dynamic pressures and is shown here as Figure 3 (Figure 5.4-1 in ASCE 7-10). The formula for the condition of water on one side of a wall is:

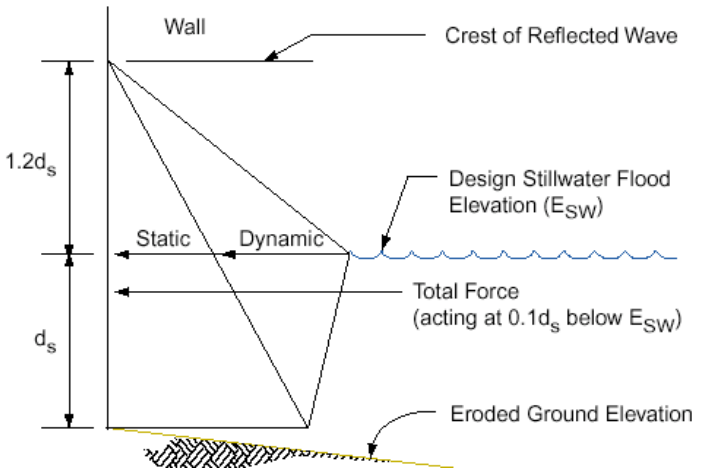


Figure 3. Pressure distribution for wave loads on wall

$F = 1.1 C_p \gamma d^2 + 2.4 \gamma d^2$ where C_p is a dynamic pressure coefficient that is based on the risk category for the structure and d is the stillwater depth. The force F is a unit force per length of wall and acts at the stillwater elevation.

Wave loads on walls where there is water on both sides is determined by the formula:

$F = 1.1 C_p \gamma d^2 + 1.9 \gamma d^2$

The formulas assume that the waves are normal to the walls. If the waves break on the walls at an angle, the forces are reduced by the square of the sin of the incident angle calculated by: $F_{oi} = F \sin^2 \alpha$ where ά is the incident angle and F is the normal force on the wall as determined from above for water on one side or both sides of the wall.

Debris impact loads

Debris impact loads are caused by objects propelled by the water into the structure. These loads are difficult to quantify, and the damage is difficult to predict. ASCE 7-10 has limited information in the body of the standard; most useful information is in the commentary where there is no requirement for users to comply with the design suggestions and no requirement for the Authority Having Jurisdiction to mandate the calculation procedure.

Significant laboratory work has been done in recent years attempting to improve the approach to determining debris loads. It is reasonable to assume that debris striking a structure is a dynamic impulse and is affected by the stiffness of the structure, the material properties of the structure, the velocity of the debris, and the orientation of

the structure component being struck with the debris. In the commentary, the formula for determining the debris force is:

$$F_i = \pi W V C_i C_o C_D C_B R_{\max} / 2g\Delta t$$

This formula requires a substantial amount of designer understanding of the flood debris damage mechanism in order to make accurate assumptions regarding the many coefficients in this formula. There is substantial explanation of the parameters in the ASCE 7-10 Chapter 5 Commentary.

There have been significant variations on how to handle debris impact loads in several documents published by FEMA. The method suggested in the 2000 version of the CCM had contact time of debris with the structure in tenths of seconds. Note in the formula above, that the magnitude of Δt will significantly influence the result given it is in the denominator. FEMA P646 *Guidelines for Design of Structures for Vertical Evacuation from Tsunamis* devotes an appendix to the discussion of impact loads and concludes that an equation that is in the form of constant-stiffness has greater reliability and less variability than an equation that uses Δt. However, one form can be converted to the other, and designers may choose the form to use, depending on whether they have better knowledge regarding impact duration or structure stiffness.

Flood Load Combinations

Chapter 2 in ASCE 7-10 includes flood loads (F_a) as one of the loads that combine with wind and is included for either riverine or coastal flooding conditions. The ASCE 7-10 Commentary for Chapter 2 describes how the load factors were developed but it does not describe what how individual flood loads [hydrostatic (F_{sta}), hydrodynamic (F_{dyn}), breaking waves on piles (F_{brkp}), and debris impact (F_i)] should be combined to yield F_a – the maximum of all flood loads that are applicable or some combination of flood loads that do or can occur simultaneously.

The only reference that discusses the combination of flood loads to use for F_a is the CCM (FEMA 55). In the 2000 version, the guidance for flooding in V Zones was to use the largest of breaking wave loads or hydrodynamic loads and then add debris impact loads to a critical structural element (such as a corner pile or column) and the sum of the largest loads should be used in global overturning or sliding investigations as F_a.

This guidance has still caused confusion so it is being modified again in the new edition of CCM, and may be included in the ASCE 7-15 revision for flood loads. The revised guidance will be published in an upcoming revision to the CCM and will suggest that F_a for global forces be the largest of F_{brkp} or F_{dyn} on the front row of piles + F_{dyn} for all the other piles, and for forces on any one pile, F_a should be the sum of the largest of F_{brkp} or F_{dyn} + F_i. One of the appropriate flood load combinations will be F_a and then must be multiplied by a load factor for use in the appropriate load combination cases.

FLOOD LOAD UNKNOWNS

One of the reasons why the flood load factors used in the load combinations are so large is the uncertainty inherent in flood design. The issues that are important to determining flood load magnitudes yet for which we know little include:

- Velocity: wave celerity is used as the way to determine wave and water velocity yet there is little known research in this area and values for velocity have low confidence
- Wave heights: the assumption in coastal flooding is that waves are depth limited, thus the water depth determines the wave height. The breaker index used to relate wave height to stillwater depth (0.78) is conservative, and lower values may be justified in some cases. Small changes in depth caused by erosion can then change the depth, thus increasing the waves, and this process is constantly changing over the life of a storm.
- Debris impact: the resulting impact to the structure when debris strikes is based on mathematical simulation and testing of debris but in water conditions different than actual wave conditions.

These unknowns – velocity, wave heights and debris impacts are those physical phenomena that largely determine the magnitude of our flood forces and thus the robustness of our flood design and because we know so little about them, a load factor of 2.0 (for strength design) is applied to these loads, increasing the magnitude and the robustness even more.

CCM REVISIONS

Four significant changes will be occurring in the 2011 CCM update:

1. Hydrodynamic load calculations will be made simpler by using just one equation for those loads irrespective of the velocity of the water. This will eliminate some confusion about how to treat these loads while not changing the magnitudes of the results.
2. Debris impact load calculations will also be revised. The current equation shown above for debris loads and that is provided in the ASCE 7-10 Commentary will be changed to:
   $F_i = WVC_D C_B C_{str}$ where C_{str} is a structure coefficient that accounts for structure responses based on construction materials, the suggested time of impact of the debris is 0.03 seconds and default values for other coefficients provided in ASCE 7-10 will be used. The value of C_{str} varies: 0.2 for timber piles or masonry columns, 0.4 for concrete piles or concrete or steel moment-resisting frames, and 0.8 for reinforced concrete walls.

   A comparison of results using the two debris load methods in this paper show that for a timber pile building, with a 1000 lb object as debris, with velocity of 5 fps based on water depth of 5 ft and blockage and importance coefficients of

1.0, F_i using the current formula in ASCE 7-10 equals 1041 lb. F_i using the revised CCM formula equals 1000 lb.

3. Flood load combinations that are required to develop Fa used in the load combinations of ASCE 7-10 Chapter 2 will be made much clearer. This discussion will still not be part of the standard; it will require consideration for the next revision of ASCE 7.

4. An additional flood load will be discussed for the first time in the CCM and this load occurs when the building frame is lower than the top of breaking waves. The load is called wave slam and is important to understand when analyzing damage to buildings. The form of the equation is similar to hydrodynamic loads where a wave slam coefficient is used instead of a drag coefficient.

CONCLUSIONS

The flood damage that has been caused to buildings after the severe flood events of the last 10 years has created an important and urgent need to do a more thorough analysis of flood loads and their effects on buildings in an effort to reduce flood-related losses.

Several aspects of flood design as currently provided in ASCE 7-10 will be changing in the current update of FEMA's CCM due to be published in 2011. Revisions to ASCE 7 flood provisions, likely similar to those in CCM, will be the first significant changes since 2002.

REFERENCES

American Society of Civil Engineers, ASCE 7-10 *Minimum Design Loads for Buildings and Other Structures*, Reston, VA, 2010

American Society of Civil Engineers, ASCE 7-05 *Minimum Design Loads for Buildings and Other Structures*, Reston, VA, 2006

Federal Emergency Management Agency, FEMA 55 *Coastal Construction Manual*, Washington, DC, 2000

Federal Emergency Management Agency, FEMA P646 *Guidelines for Design of Structures for Vertical Evacuation from Tsunamis*, Washington, DC, 2008

ASCE Standard 7-10 Dead and Live Loads

Harry B. Thomas, P.E., M.ASCE[1]

[1]Consulting Engineer, 2617 Geyerwood Court, Grove City, Ohio 43123; PH (614) 875-5240; FAX (614) 875-4178; email: harrybthomas@msn.com

ABSTRACT

The new edition of ASCE 7, ASCE 7-10 *Minimum Design Loads for Buildings and Other Structures*, contains new, revised and updated provisions for dead and live loads to be used for structural design since the previous edition, ASCE 7-05, was published five years before. The provisions of this Standard, adopted by reference by building codes across the nation, impact the structural design of nearly every building in the country, and are used by all who are responsible for these designs.

New material has been introduced which provide for the live load requirements for structures not previously covered in prior editions, specifically for helipads and screen enclosures.

Revisions to the live load requirements for balconies and decks, roofs, and vehicle barrier systems have been made which better define the nature of live loads acting on these particular occupancy areas or structural elements.

There has also been a revision to the live load reduction provisions for structural members in one- and two-family dwellings supporting more than one floor load.

The rationale for the new live load provisions and for the substantial technical revisions to previous live load requirements are presented, relating the discussions and comments by committee members during the five-year balloting period since the previous Standard was published in 2005, and incorporating guidance from the Commentary to the Standard where this helps to clarify some of the new or revised loading requirements.

NEW LIVE LOAD PROVISIONS

Helipad. Load requirements for helipads, defined as structural surfaces that are used for landing, taking off, taxiing, and parking of helicopters, are introduced into the ASCE 7 Standard for the first time. In building codes and other references, different terminology may be used when describing helipads, e.g., heliports, helistops, but the distinctions between these are not relevant to the structural loading issue addressed in the Standard.

The uniform load requirement of 60 psf (2.87 kN/m^2) is a minimum to ensure a degree of substantial construction, but may be lowered to 40 psf (1.92 kN/m^2) where the design basis helicopter has a maximum take-off weight of 3,000 lbs (13.35

kN) or less. The uniform load requirement may not be reduced based on influence area loaded.

Concentrated loads, intended to cover the primary helicopter load and which shall not be concurrent with the uniform load, must also be investigated in the event they produce a greater load effect on the structural members under consideration. Two single concentrated loads (representing the helicopter's two main landing gear, whether skid type or wheeled type, intending to account for an impact factor for a hard landing with many kinds of landing gear), 8 ft (2.44 m) apart shall be applied on the landing area, each having a magnitude of 0.75 times the maximum take-off weight of the helicopter. These loads shall be applied over an area of 8 in. by 8 in. (200 mm by 200 mm).

A single concentrated load of 3,000 lbs (13.35 kN), intended to cover maintenance activities similar to the jack load for a parking garage, shall be applied over an area of 4.5 in. by 4.5 in. (114 mm by 114 mm).

The designer should always consider the geometry of the design basis helicopter and be aware that some helicopter configurations, particularly those with rigid landing gear, could result in substantially higher impact factors that should be considered.

Screen Enclosure. Load requirements for screen enclosures, defined as buildings or parts thereof, in whole or in part self-supporting, having walls and roofs of insect or sun screening using fiberglass, aluminum, plastic, or similar lightweight netting material, which enclose an occupancy or use such as outdoor swimming pools, patios or decks, and horticultural and agricultural production facilities, are introduced into the ASCE 7 Standard for the first time.

The uniform load requirement of 5 psf (0.24 kN/m^2) is applied to the roof frame members only, not the screen, and is nonreducible.

A concentrated load of 200 lbs (0.89 kN) is applied to the supporting roof frame members only. This load provides for miscellaneous loads (such as flower pots or similar items) which may be suspended from the frame members.

REVISED LIVE LOAD PROVISIONS

Balconies and Decks. Previous editions of the Standard prescribed the following uniform live loads:

- Balconies not exceeding 100 ft^2 (9.30m^2) on one- and two-family residences . . . . . 60 psf (2.87 kN/m^2)
- Exterior balconies . . . . . 100 psf (4.79 kN/m^2)
- Patio and roof decks. . . . . same as the area served or the type of occupancy accommodated

ASCE 7-10 revises these uniform live loads to:

- Balconies and decks . . . . . 1.5 times the live load for the occupancy served, but need not exceed 100 psf (4.79 kN/m^2)

There was considerable discussion by committee members for the proposal submitted to revise these live loads which were based on a perceived illogical

distinction between deck and exterior balcony live loads. ASCE 7-05 defined an exterior balcony as *an exterior floor projecting from and supported by a structure without additional independent supports*, and defined a deck as *an exterior floor supported on at least two opposing sides by an adjacent structure and/or posts, piers, or other independent supports*.

A view was put forth that there was no engineering justification for having different live loads for different support conditions, if the use is the same. Either the loads are there, or they aren't, and changing how the element is supported doesn't change the loads. If it was felt that cantilevers or prop cantilevers are less redundant than supported structures and, thus, should have a higher live load requirement, then the solution should be dealt with on the resistance side by increasing the factor of safety rather than by increasing the live load.

Accepting the premise that the loads should not differ based on the structural support conditions, the committee considered the question of the appropriate live load. ASCE 7-05 stipulated uniform live loads ranging from 50 psf (2.40 kN/m^2) for decks serving offices to 100 psf (4.79 kN/m^2) for decks serving public rooms and corridors in hotel/multifamily houses and for exterior balconies.

Establishing the live load to be 1.5 times the occupancy served, but not to exceed 100 psf (4.79 kN/m^2) results in the following examples of revised balcony and deck design loads for various defined occupancies:

Occupancy or Use Served (psf/kN/m^2)	Design Live Load (psf/kN/m^2)
Dining rooms and restaurants (100/4.79)	100/4.79
Office buildings, offices (50/2.40)	75/3.59
Residential, one- and two-family (40/1.92)	60/2.87
Residential, private rooms/corridors (40/1.92)	60/2.87
Residential, public rooms/corridors (100/4.79)	100/4.79

Balconies and decks are generally found contiguous to defined occupancy areas which have defined live loads which, in turn, tend to create balcony and deck areas having similar occupancy or use, but which have generally recognized distinctly different loading characteristics. A number of committee member comments raised the issue of balconies and decks being subjected to concentrated live loads from people congregating along the edges of these areas (e.g., for viewing vantage points), and this loading condition is acknowledged by the increase of the live load for the occupancy served, up to the point of satisfying the loading requirement for most assembly occupancies. The addition of a line load along the edge of all balconies and decks to address the concern of balcony and deck occupants tending to congregate at an edge was judged to be slanted to provide extra insurance for balconies and decks which are cantilevered from their support, and this view was rejected based on the concept that loads are not a function of the structural support conditions.

Vehicle Barrier Systems. The point of application of the stipulated horizontal load of 6,000 lb (26.70 kN), applied to a system of components placed near open sides or walls of garage floors or ramps which act as restraints for vehicles, was changed from 1 ft 6 in. (460 mm) above the floor or ramp surface to between 1 ft 6 in. (460 mm) and 2 ft 3 in. (686 mm).

The impetus for this change was the latest vehicle sales data which showed that approximately 50% of the vehicles sold in 2006 were light trucks, vans or SUV's which had front bumper heights well in excess of the 1 ft 6 in. (460 mm) application height above the pavement that previous editions of the Standard required. The revised upper limit of 2 ft 3 in. (686 mm) covers 96% of these vehicles, with the remaining 4% of vehicles having front bumper heights only 2 in. (51 mm) higher.

A direct reference to the AASHTO *LRFD Bridge Design Specifications* has been added for the design of vehicle barrier systems in garages accommodating trucks and buses.

Reduction in Live Loads. The existing criteria for reducing live loads for members supporting two or more floors permitted a reduced live load provided the influence area for such members, $K_{LL}A_T$, was 400 ft^2 (37.16 m^2) or more, and limited the reduction to $L \geq 0.40L_0$, where:

L = reduced design live load per ft^2 (m^2) of area supported by the member
L_0 = unreduced design live load per ft^2 (m^2) of area supported by the member
K_{LL} = live load element factor
A_T = tributary area in ft^2 (m^2)

There was a proposal submitted to modify the live load reduction permitted for such members, requesting an exception to the criteria and offering an alternate formula for this exception:

> EXCEPTION: For structural members in one- and two-family dwellings supporting more than one floor load, the following live load reduction shall be permitted as an alternate to Eq. 4.7-1:
>
> $$L = 0.7 \times (L_{o1} + L_{o2} + \ldots)$$
>
> L_{o1}, L_{o2}, . . . are the unreduced floor live loads applicable to each of multiple supported story levels regardless of tributary area. The reduced floor live load effect, L, shall not be less than that produced by the effect of the largest unreduced floor live load on a given story level acting alone.

This proposal intended to provide a means of accounting for multi-story live load coincidence effects independent from tributary area effects. The concern was felt important for typical light frame dwelling design because tributary areas of individual repetitive members are small (typically much less than 200 ft^2), yet the effects of floor live load coincidence over multiple stories are valid from a probabilistic standpoint irrespective of cumulative floor area served.

The justification for the proposal was based on a study from *Residential Building Loads: Review and Roadmap for Future Progress* which called attention to the fact that live load reductions in ASCE 7 are limited to influence areas greater than 400 ft^2, yet in the design of residential construction, influence areas for individual repetitive framing elements (i.e., studs and joists) are narrow, long, and commonly less than the 400 ft^2 influence area limitation in ASCE 7, even for multi-story loading conditions. In such cases, live load area reductions of ASCE 7 do not apply even though a multi-story live load coincidence effect may be present for influence areas of less than 400 ft^2.

Recent findings indicate that, depending on the level of correlation between live load processes on different stories, the accumulative multi-story nominal design live load may be reduced by a factor of 0.4 to 1.0.

A view was expressed that differences in level of multi-story live load temporal correlation may be dependent on the nature of the residential occupancy. For typical single-family detached dwellings and townhouses of multiple stories, upper stories are often used as sleeping areas whereas the lower story level is used for day-time activity and gathering purposes.

Based on this information, a live load reduction factor of 0.7 was proposed for the alternative live load reduction formula.

Live Load Reduction Restriction. In ASCE 7-05, live load reductions were not permitted for certain categories of occupancies:

4.8.2 Heavy Live Loads. Live loads that exceed 100 lb/ft^2 (4.79 kN/m^2) shall not be reduced.

4.8.4 Special Occupancies. Live loads of 100 lb/ft^2 (4.79 kN/m^2) or less shall not be reduced in public assembly occupancies.

ASCE 7-10 has editorially revised the text (for Section 4.8.4 only) so that these requirements now read:

4.7.3 Heavy Live Loads

Live loads that exceed 100 lb/ft^2 (4.79 kN/m^2) shall not be reduced.

4.7.5 Assembly Uses

Live loads shall not be reduced in assembly areas.

To clarify these restrictions, a footnote "a" was added to some of the listed occupancies in Table 4-1:

[a]Live load reduction for this use is not permitted by Section 4.7 unless specific exceptions apply.

This has not changed any technical requirements from previous editions of ASCE 7, but was added to simplify those occupancies or uses in Table 4-1 which are not allowed to have their live loads reduced. Footnote "a" flags these occupancies where live loads shall not be reduced, even though some of the occupancies may have live loads less than or equal to 100 lbs/ft^2 (4.79kN/m^2) since they are considered to be assembly areas.

Marquees. The occupancy or use defined as "Marquees" has been listed in the Standard extending back to 1945. The term has not been defined in ASCE 7, but has been defined in building codes as a roofed structure that projects into a public right-of-way.

The committee judged that the relationship between a structure and a right-of-way does not control loads that are applied to a structure, and that a marquee should therefore be designed with loads appropriate for a roofed structure. If the arrangement of the structure is such that it would invite additional occupant loading

(e.g., there is a window or door access that might invite loading by spectators of a parade), then balcony loading should be considered for the design.

Based on this view, the occupancy or use defined as "Marquee" was removed from Table 4-1 in the ASCE 7-10 Standard, and its removal is noted and documented in the Commentary.

Roofs. ASCE 7-05 listed an occupancy or use for "Roofs used for promenade purposes" stipulating a loading of 60 psf (2.87kN/m^2). The term "promenade" was considered to be an archaic term not used elsewhere in the Standard or in building codes. "Promenade purposes" is essentially an assembly use and is more clearly identified as such.

Accordingly, Table 4-1 in the ASCE 7-10 Standard no longer lists "Roofs used for promenade purposes" and provides an occupancy or use for "Roofs used for assembly purposes" with an associated uniform live load stipulated to be the same as the occupancy served.

The occupancy or use defined in ASCE 7-05 as "Roofs used for roof gardens or assembly purposes" has been revised to read "Roofs used for roof gardens" with the associated live load remaining unchanged.

Elevators. Elevator impact loads in the ASCE 7-10 Standard have been changed from a direct 100% impact factor to a reference to ASME A17.1. The provisions in ASME A17.1 include the 100% impact factor, along with deflection limits on the applicable elements.

There were some sentiments (one comment being that "going back and forth between standards is driving the designers nuts") against removing the explicit 100% impact provision and instead incorporating the structural requirements for elevators contained in ASME A17.1 directly into ASCE 7-10. However, the committee felt that the requirements in ASME A17.1 were more complex than a mere increase of 100% in elevator loads for impact and that all elements of the structure that are designed to support elevator loads are required by ASME A17.1 to be designed for increased loads. Furthermore, there are limitations on allowable stresses for allowable stress design (and, by implication, increases in load factors for strength design) to be considered. Replicating the requirements of ASME A17.1 for structural design in ASCE 7-10 would necessitate a large amount of text that could be subject to misinterpretation, and that ASME A17.1 should be consulted directly for these requirements.

ERRATA FOR CHAPTER 3, TABLE 3.2-1

In ASCE 7-10, Chapter 3, Dead Loads, Soil Loads, and Hydrostatic Pressure the text and technical provisions remain unchanged from the previous edition. However, in the printing of the new Standard errors to the footnotes in Table 3.2-1 have occurred.

At the bottom of the Table, the footnote designated as "c" should be corrected to read "b"; the footnote designated as "d" should be corrected to read "c"; and the footnote designated as "b" should be corrected to read "d".

CONCLUSIONS

Changing society needs has had an impact on altering live load requirements for buildings. Some occupancies and uses now present did not exist in the past or were not previously recognized.

Helicopters atop buildings, screen enclosures for outdoor living and working areas, increased and changing uses of balconies and decks, new information concerning live load reduction requirements – these have caused engineers to examine and alter the live loads resulting from these activities, and to revise the ASCE 7 Standard accordingly.

The importance of the ASCE 7 Standard cannot be overemphasized. As a document written in mandatory language and produced under consensus procedures, it has been adopted by reference by the nation's building codes. To this end, there is an ongoing effort by the ASCE committee members to continually review the loading requirements of the Standard, revising existing requirements where research has indicated the necessity for doing so, and incorporating new requirements as our understanding of structural loadings and material behavior increases.

Structural failures, while rare, provide engineers with important information concerning the nature of building loads and their application to structures and, coupled with ongoing structural research and changing society needs, dictates continual change to the loading requirements contained in the ASCE 7 Standard.

It is anticipated that the next edition of the Standard will continue the trend of providing vital new and revised information to the nation's structural engineering community.

REFERENCES

American Association of State Highway and Transportation Officials. *AASHTO LRFD Bridge Design Specifications, 4th edition, 2007, with 2008 Interim Revisions.*

American Society of Civil Engineers (ASCE). *ASCE 7-05 Minimum Design Loads For Buildings and Other Structures.*

American Society of Civil Engineers (ASCE). *ASCE 7-10 Minimum Design Loads For Buildings and Other Structures.*

American Society of Mechanical Engineers (ASME). *ASME A17.1 American National Standard Safety Code for Elevators and Escalators, 2007.*

ASCE/SEI (2006). *Residential Building Loads: Review and Roadmap for Future Progress.*

Load Combination Requirements in ASCE Standard 7-10: New Developments

Therese P. McAllister,[1] M. ASCE
Bruce R. Ellingwood,[2] Dist. M. ASCE

Abstract

The fundamental load combination requirements for strength design (or load and resistance factor design) appearing in Section 2.3 of *ASCE Standard 7-10* incorporate major revisions, among them the treatment of self-straining actions, fluid and soil loads, load combinations for extraordinary events, and probability-based load requirements for non-specified loads. The last item is based on suggested reliability levels for the new performance-based design procedures in the Section 1.3.1 Commentary. The Commentary to Section 2 of *ASCE Standard 7-10* presents the technical basis for these changes. Since the basis of the traditional allowable stress design combinations was purely judgmental, the ASD combinations in Section 2.4 have been brought into alignment with the strength combinations in Section 2.3, which have a rational reliability basis.

Introduction

The fundamental load combination requirements for strength design (or load and resistance factor design) appearing in Section 2.3 of *ASCE Standard 7-10* were first implemented in 1982 (Galambos et al., 1982; Ellingwood et al., 1982). These load combinations were developed using modern probabilistic models of structural loads and load combinations, statistical data on load intensities, and structural reliability analysis. They utilize a "principal action – companion action" format, which is based on the notion that the maximum combined load (or load effect) during a service period (commonly taken as 50 years) occurs when one time-varying load attains its maximum value while the remaining time-varying loads are at their frequent (or arbitrary-point-in-time) values. Research has demonstrated conclusively that this model best represents how time-varying loads found in other sections of *ASCE 7* combine on structural members, components and systems (Turkstra and Madsen, 1980).

The new load combination requirements for strength design in *ASCE Standard 7-10* incorporate a number of significant revisions. The self straining force, T, fluid load, F, and soil (lateral earth pressure) load, H, are no longer shown in the basic combinations. The reliability analysis leading to *ASCE 7-05*, Section 2.3.2, was supported by an extensive statistical database on dead, live, snow, wind and earthquake loads. However, the self-straining force, fluid load, and soil load do *not* have the same statistical support as the primary loads. Over the years, they were added to the combinations primarily on the basis of judgment, in order to be responsive to users of *ASCE Standard 7* and the other design documents that refer to *ASCE Standard 7*. The treatment of these loads now is addressed separately in

[1] Research Structural Engineer, Building and Fire Research Laboratory, National Institute of Standards and Technology, Gaithersburg, MD 20899 (therese.mcallister@nist.gov)
[2] The Raymond Allen Jones Chair in Civil Engineering, School of Civil and Environmental Engineering, Georgia Institute of Technology, Atlanta, GA 30332 (ellingwood@gatech.edu)

text following the basic combinations to remain responsive to the needs of the design community and, at the same time, to distinguish load combinations technically supported by engineering principles and observed data from those based on judgment. The wind load factors were revised to accommodate the changes in the wind load criteria. The load combinations for extraordinary events, which formerly appeared in a Commentary section, now appear in the *Standard*, where they serve as a point of reference for codes, standards and guidelines for design against disproportionate collapse, fire and other extreme events. In anticipation of the demands for "beyond-code" design from performance-based engineering and to accommodate design of structural systems for loads that are not included in *ASCE Standard 7*, a new standardized method for calculating load and resistance factors has been provided, along with an extended commentary on its proper application. The load 0.6D in the ASD combinations for counteracting loads now is permitted to be increased to 0.9D in certain instances. Since the basis of the traditional allowable stress design combinations was purely judgmental, the ASD combinations in Section 2.4 have been brought into alignment with the strength combinations, which have a rational reliability basis. Additional guidance on the use of LRFD and ASD methods for structural design is provided in the Commentary. Finally, the Commentary to Section 2 of *ASCE Standard 7-10* has been extensively revised to explain the technical basis for these changes.

The following sections describe the basis for these changes in more detail.

Self-Straining Force

The self-straining force, T, was removed from the basic combinations in Sections 2.3.2 and 2.4.1 and now is treated in Sections 2.3.5 and 2.4.4, respectively, with an extended commentary. The self-straining force covers temperature effects, creep, shrinkage, differential settlement and similar effects. The presence of T in the basic combinations was problematic because its effect depends on the material of construction and conditions of constraint. This load situation is more a potential issue for concrete/masonry than it is for steel. Cracking may relieve the stress in concrete/masonry structures; however, it may be detrimental to the performance and serviceability of structures, such as tanks and containment structures.

Self-straining actions should be calculated based on a realistic assessment of the most probable values rather than the upper bound values. The most probable value is the value that can be expected at any "arbitrary point-in-time".

When self straining loads are combined with dead loads as the principal action, a load factor of 1.2 may be used. However, when self straining loads are considered as a companion load, the load factor may be reduced to no less than 1.0, if it is unlikely that the principal and companion loads will attain their maximum values at the same time.

If only limited data are available to define the magnitude and frequency distribution of the self-straining load, then its value must be estimated carefully. Estimating the uncertainty in the self straining load may be complicated by variability in material stiffness of a member or structure under consideration.

Fluid Loads

Fluid load, *F*, defines structural actions in structural supports, framework, or foundations of a storage tank, vessel, or similar container due to stored liquid products. The fluid load of a product in a storage tank shares characteristics of both dead and live loads. It is similar to a dead load in that its self-weight and hydrostatic loads have a maximum calculated value, and that the magnitude of the actual load may have a relatively small dispersion. However, the fluid load is not permanent. Emptying and filling causes fluctuating forces in the structure, the maximum load may be exceeded by overfilling, and densities of stored products in a specific tank may vary.

The fluid load, F, was removed in the basic load combinations. There are no statistical data on fluid loads that can be used to address its treatment in load combination analysis or to support a particular value of load factor. However, when fluid loads are considered in design, they are included with the same load factor as dead load D in combinations 1 through 5, when additive to other loads, and in combination 7 when it provides resistance to uplift forces. To make it clear that the fluid weight in a tank can be used to resist uplift, F was added to load combination 7 where it will be treated as dead load only when F counteracts earthquake load, E. The mass of the fluid also is included in the inertial effect due to E (see 15.4.3) and the base shear calculations for tanks (15.7). Note that the fluid mass effects on stabilization depend on the degree to which the tank is filled. F is not included in combination 6 because the wind load can be present, whether the tank is full or empty, so the governing load case in combination 6 is when F is zero.

Loads due to Lateral Earth Pressure, Ground Water Pressure and Bulk Materials

Loads due to lateral earth pressure, ground water pressure and pressure of bulk materials, H, were removed from the basic load combinations. Similar to fluid loads, there are no statistical data on H. However, where they are present, they are included in the load combinations as follows:

1. where the effect of H adds to the primary variable load effect, include H with a load factor of 1.6;
2. where the effect of H resists the primary variable load effect, include H with a load factor of 0.9 where the soil load is permanent or a load factor of 0 for all other conditions.

Uncertainties in lateral forces from bulk materials, included in *H*, are higher than those in fluids, particularly when dynamic effects are introduced as the bulk material is set in motion by filling or emptying operations. Accordingly, the load factor for such loads is set equal to 1.6.

Where H acts as a resistance, a factor of 0.9 is suggested if the passive resistance is computed with a conservative bias. The intent is that soil resistance be computed for a deformation limit appropriate for the structure being designed, not at the ultimate passive resistance. Thus an at-rest lateral pressure, as defined in

the technical literature, would be sufficiently conservative. Higher resistances than at-rest lateral pressure are possible, given appropriate soil conditions. Fully passive resistance seldom would be appropriate because the necessary deformations in the soil would cause the structure to be compromised. Furthermore, there is great uncertainty in the nominal value of passive resistance, which would also argue for a lower factor on H.

Load Factors on Wind Loads

ASCE Standard 7-10 contains new wind speed maps in Chapter 26. The wind loads, W, for ordinary buildings and other structures in the previous edition of ASCE Standard 7 were based on mapped 3-s gust wind speeds with a 50-year mean recurrence interval (MRI) [the MRIs were 100 years for critical facilities.] and the load factor applied to the nominal wind load was 1.6. The wind climatology in interior and in hurricane-prone coastal areas of the United States is different, and using the 50-yr MRI as a basis led to differences in facility risk in those areas. ASCE Standard 7-10 now maps the "design-basis" wind speed directly (MRI of 700 years for ordinary buildings; 1700 years for critical facilities), and applies a load factor of 1.0 to the resulting wind load. This approach ensures that the risk is essentially uniform and better aligns the manner in which ASCE 7 treats the wind and earthquake hazards. At the same time, the wind load factor in Section 2.3 was reduced from 1.6 to 1.0 in combinations where it was the principal load to maintain the reliability of the load combinations.

Counteracting Loads in ASD

Beginning with the 1998 edition of ASCE Standard 7, the load factor on the nominal dead load in ASD combinations (7) and (8), which govern counteracting loads, was reduced to 0.6 to achieve consistency between ASD and LRFD. This factored load, 0.6D, has been viewed as problematic and has drawn criticism from segments of the structural engineering community. Ellingwood and Li (2009) have confirmed that this reduction was warranted and necessitated by the large variability in W and E; failure to reduce the gravity load for design (i.e., not using 0.6 D) may lead to inadequate safety in many counteracting load situations. However, in the design of certain non-building structures, foundations and in special reinforced masonry shear walls, adjustments to ASD combinations (6) and (7) may be justified on other grounds. These adjustments are reflected in the Exceptions to the ASD combinations in Section 2.4.1.

The first of these situations is defined by Exception 2 of Section 2.4.1 for non-building industrial facilities, which permits the wind load factor in the counteracting load combination to be modified for foundation design of non-building structures. When wind forces act on a structure, the structural action causing uplift at the structure-foundation interface is less than would be computed from the peak lateral force, due to area-averaging. Accordingly, the wind effects can be reduced when checking global stability and bearing or uplift at the soil-foundation interface. Accordingly, for situations where a foundation element exceeds 1000 ft^2 (93 m^2), on either a vertical or a horizontal plane, W can be replaced with 0.9W in combination (7), excluding anchorage of the structure to the foundation. Exception (2) applies to the design of the foundation and to self-anchored ground-supported tanks. For different reasons, a similar approach is

already provided for seismic actions by ASCE 7-05 Section 12.13.4 and in Section 12.4.2.2, exception 2.

The second of these situations is defined by Exception 3 for Special Reinforced Masonry Walls. This Exception is based upon three factors, all of which yield a conservative design for overturning resistance under the seismic load combination:

1. The basic allowable stress for reinforcing steel is 40% of the specified yield, f_y;
2. The minimum reinforcement required in the vertical direction provides protection against the circumstance where the dead and seismic loads result in a very small demand for tension reinforcement; and
3. The maximum reinforcement limit prevents compression failure under overturning.

Of these three, the low allowable stress in the reinforcing steel is the most significant. Exception 3 will be reconsidered if the allowable stress in tension reinforcement in the standard for design of masonry structures is increased above $0.4f_y$.

Load Combinations for Extraordinary Events

Section 2.5, Load Combinations for Extraordinary Events, provides load combinations for low-probability events such as fire, explosions and vehicular impact. Since the 1995 edition of ASCE Standard 7, Commentary C2.5 has provided a set of load combinations that were derived using a probabilistic basis similar to that used to develop the load combination requirements for ordinary loads in Section 2.3 (Ellingwood and Leyendecker, 1978; Ellingwood and Dusenberry, 2005). In recent years, social and political events have led to an increasing desire on the part of architects and structural engineers, project developers and regulatory authorities to enhance design and construction practices for certain buildings by providing additional structural robustness and to lessen the likelihood of disproportionate collapse if an extreme event were to occur. Several Federal, state and local agencies have adopted policies that require new buildings and structures to be constructed with such enhancements of structural robustness [GSA 2003, DOD 2009]. Concurrently, advances in structural engineering for fire conditions (e.g., AISC 2005 Specification, Appendix 4) raise the prospect that new structural design requirements for fire safety will supplement the existing deemed-to-satisfy provisions in the next several years. To meet these needs, the load combinations for extraordinary events, which formerly appeared in the Commentary, were moved up to Section 2.5 Standard, where they now serve as a point of reference for codes, standards and guidelines for design against disproportionate collapse, fire and other extreme events.

Performance-Based Engineering

Engineers may wish to develop load criteria for strength design that are consistent with the requirements in *ASCE Standard 7* for situations that are not covered explicitly in the *Standard*. They also may wish to consider loading criteria for

special situations, as required by the client in performance-based engineering (PBE) applications, in accordance with Section 1.3.1.3. In addition, groups writing standards and specifications for strength design of structural systems and elements may wish to develop resistance factors that, when used with the load requirements in the *Standard*, permit a stipulated reliability to be achieved. Such load criteria must be developed using a standardized procedure to ensure that the resulting factored design loads/load combinations will lead to target reliabilities (or levels of performance) that can be benchmarked against the common load criteria in Section 2.3.2 and in existing standards and specifications governing strength design for common construction materials. Section 2.3.6 permits, for the first time, the engineer to develop load combinations for strength design through a standardized method that is consistent with the methodology used to develop the basic combinations that appear in Section 2.3.2.

Use of LRFD and ASD Methods

Section 2.1 requires the engineer to use either ASD or LRFD exclusively when designing a structure. This requirement dates back to the introduction of the load combinations for strength design (LRFD) in the 1982 edition of the Standard. The General Commentary in C2.1 notes that an indiscriminate mix of the LRFD and ASD methods is not permitted in structural design, as such an approach may lead to unpredictable structural system performance. The reliability analyses and code calibrations leading to the LRFD load combinations were based on member limit states rather than system limit states.

However, designers of cold-formed steel and open web steel joists often design (or specify) these products using ASD and, at the same time, design the structural steel in the rest of the building or other structure using LRFD. The AISC *Code of Standard Practice* states that cold-formed products and steel joists are not considered to be structural steel. Foundations are also commonly designed using ASD, while strength design is used for the remainder of the structure. Using different design standards in these situations has not been shown to be a problem. Thus, Section 2.1 is intended to permit current industry practice while, at the same time, not permitting LRFD and ASD to be mixed indiscriminately in the design of a structural frame.

Summary

The load combination requirements for strength design in *ASCE Standard 7-10* incorporate a number of major revisions. Changes to the ASD requirements were made for consistency with the probability-based strength design requirements:

- Self-straining force, T, was removed from the basic combinations and now is treated in a separate section, with an extended commentary.

- Wind load factors were revised to accommodate the changes in the wind speed map in Section 26.

- The load 0.6D in the ASD combinations for counteracting loads may be increased to 0.9D in design of certain non-building structures and special reinforced masonry shear walls;

- Load combinations for extraordinary events, formerly in a Commentary section, were moved up to the Standard, as a point of reference for codes, standards and guidelines for design against disproportionate collapse, fire and other extreme events.

- A standardized method for calculating load and resistance factors has been provided, along with an extended commentary on the application of this method.

References

DOD (2009), Design of buildings to resist progressive collapse. *Unified Facilities Criteria (UFC) 4-023-03*, Washington, DC, June, 2009.

Ellingwood B.R. and E.V. Leyendecker (1978). "Approaches for design against progressive collapse." *J. Struct. Div. ASCE* 104(3):413-423.

Ellingwood, B.R., et al (1982). "Probability-based load criteria: load factors and load combinations." *J. Struct. Div. ASCE* 108(5):978-997.

Ellingwood, B. (1998). "Reliability-based performance concept for building construction." in *Structural Engineering Worldwide 1998*, Paper T178-4, Elsevier Science Publishers (CD-ROM).

Ellingwood, B. R. and D.O. Dusenberry 2005. Building design for abnormal loads and progressive collapse. *Computer-aided Civil and Infrastruct. Engrg*. 20(5):194-205.

Ellingwood, B.R. and Y. Li (2009). "Counteracting Structural Loads: Treatment in ASCE Standard 7-05." *J. Struct. Div. ASCE* 135(1):94-97.

GSA (2003), Progressive collapse analysis and design guidelines for new federal office buildings and major modernization projects. General Services Administration, Washington, DC.

Galambos, T. V., et al (1982). "Probability-based load criteria: assessment of current design practice." *J. Struct. Div. ASCE* 108(5):959-977.

Turkstra, C.J. and H.O. Madsen (1980). "Load combinations in codified structural design." J. Struct. Div., 106(12), 2527-2543.

Introduction of Performance Criteria into Chapter 1 of ASCE 7-10

Ronald O. Hamburger, SE, SECB[1]

ABSTRACT

Since its inception, the purpose of the ASCE 7 standard has been to set minimum design loads for buildings and other structures, such that they would provide safe and reliable service. It has never been intended to comprise a complete design standard, deferring for the most part to other industry standards for requirements for determination of strength and detailing. Because reliable seismic performance is as much dependent on structural detailing as it is strength and stiffness, the seismic chapters have also included detailing requirements as a condition of loading determination. The 2010 revisions to Chapter 1 of the standard take a major step towards conversion of the document into a comprehensive design standard with the introduction of a performance-based design alternative. The Performance-based design process is one of setting performance criteria then evaluating the ability of a design, either through testing, simulation or a combination of these, to meet these criteria. As such, design loading, in the conventional sense is not used, but rather design scenarios, which include consideration of inherently uncertain loading events and equally uncertain structural response, must be evaluated. Initially, the performance-based option is likely to see most application in seismic and force-protection design, where it already experiences wide use. However, as engineers become more familiar with this approach and the freedom it provides, it will likely see wider use with satisfaction of performance criteria being the primary objective of design.

INTRODUCTION

U.S. building codes first developed in the late 19th and early 20th century as a means of avoiding large scale life and property loss in urban conflagrations, earthquakes and other disasters. These early codes were developed on an experience-basis, by documenting and codifying procedures and methods that had been observed over time to provide acceptable performance, while prohibiting designs and procedures observed to perform unacceptably. The developers of these early codes recognized that if the codes only permitted design and construction practices validated by past successful experience, there would be no way to permit the use of new design and construction methods and provide for an ability for practice to evolve and modernize. Therefore, since their inception, U.S. building codes have included so-called "alternative means" clauses that specifically permit the use of design and construction methods not specifically prescribed by the code, provided that the proponent for the alternative method could demonstrate to the building official's satisfaction, that the alternative approach would provide equivalent durability, serviceability and protection of the public safety. Since durability, serviceability and protection of the public safety are measures of performance, the use of alternative means eventually came to be known as performance-based design.

In recent years, performance-based design approaches have become increasingly popular and have been used not only to introduce new design methods and construction procedures, but also

[1] Senior Principal, Simpson Gumpertz & Heger Inc. The Landmark @ 1 Market, Suite 600, San Francisco, CA 94105, rohamburger@sgh.com

as a means of designing building types and occupancies not previously considered by the code, designing buildings capable of superior performance, reducing project construction costs, or providing other building attributes not achievable by strict conformance to the code. Performance-based design approaches have seen extensive use in seismic engineering, fire engineering and force-protection engineering.

Present-day approaches to performance-based engineering evolved in the 1990s with the development of the ATC-40 (ATC, 1996) seismic evaluation and retrofit methodology and the FEMA-273/274 *Guidelines and Commentary for Seismic Rehabilitation of Buildings* (ATC, 1997), now revised and standardized as the ASCE 41.06 (SEI, 2006). These procedures form the basis not only for performance-based seismic design but also design to protect against blast and progressive collapse. Figure 1, adopted from the FEMA P-58 (ATC, 2011) report presents the basic performance-based design process. As shown in the figure, the basic steps include 1) confirmation with all parties that the approach is acceptable, 2) selecting the performance project performance objectives, 3) developing an initial design, 4) assessing the design's performance capability, 5) comparing the design's performance capability against the objectives set in the second step, and 6) revision of the design and re-evaluation of its performance capability until the design is demonstrated capable of meeting the performance objectives agreed to by the building official.

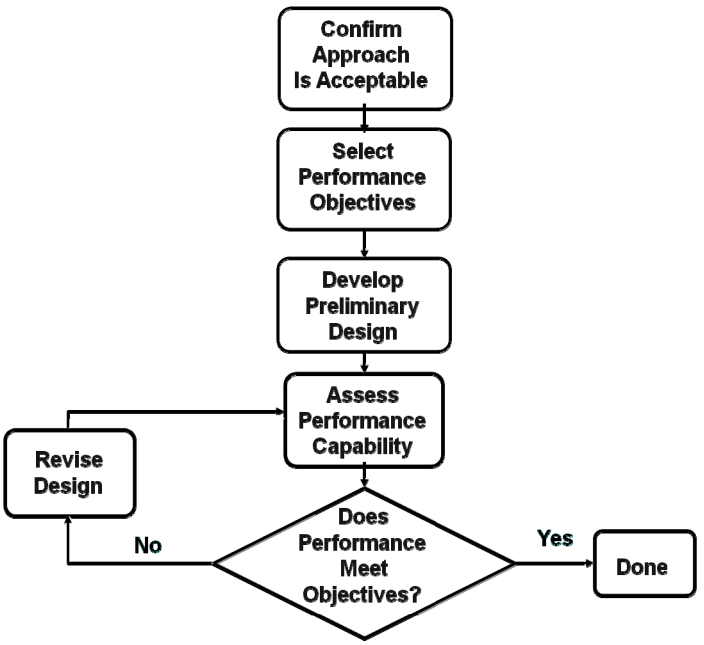


Figure 1 – Performance-based Design Process

For the first time, the 2010 edition of the ASCE 7 loading standard (SEI, 2010) addresses this design process. Chapter 1 of the standard specifies the acceptable procedures to assess a design's performance, and demonstrate that it meets acceptable criteria, while commentary to Chapter 1 describes the performance objectives inherent in buildings conforming to different occupancy categories, renamed in the 2011 edition of the standard as Risk Categories.

PERFORMANCE OBJECTIVES

Performance objectives are quantitative statements of the desired behavior for a design, given that it is subjected to a particular design scenario or event. Classical structural design methods are based on achievement of two performance objectives: 1) a service level state, and 2) a strength level state. Service level behavior is typically expected to preclude damage that would result in strength loss or require repair, while maintaining deflections and vibration at levels that do not impair the structure's use. The strength level state is specified as a means of protecting against structural failure. Service level behavior is expected to be achieved under the routine "point in time" loads that structures will experience on a routine basis throughout their lifetimes. Strength level behavior is targeted to assure that structures have a suitably low probability of incurring loading that would exceed their capacity and trigger failure. Early Allowable Stress Design procedures sought to meet these performance objectives, by requiring design of structures to provide acceptable control of deflections under code-specified loads (the Service level state) and to provide a suitable margin against failure (the Strength level state) through specification of allowable stresses that incorporated a suitable factor of safety. Later, when Load and Resistance Factor design methods were developed, researchers set specific notional reliability targets, or acceptable probabilities of failure, and using statistical methods, developed load and resistance factors to account for the uncertainty inherent in load and strength prediction and to achieve the desired reliability.

For the Service level state, the standard continues to rely on the time-honored methods first introduced with Allowable Stress design procedures. However, for the first time, Commentary to Chapter 1 of ASCE 7-10 sets forward in one location, the strength-level reliability criteria that underpin the Load and Resistance Factor Design method. In parallel with this introduction, Commentary to Chapter 2 of the standard set forth the procedures for development of load and resistance factors to achieve these reliabilities, given quantification of loading and resistance variability in the form of dispersions.

The standard differentiates between reliabilities sought for seismic loading and other sources of loading, such as that from the structure's self weight, occupant (live) loading, snow, wind and thermal effects. Table C1.3.1a of the standard, reproduced below as Table 1 below, specifies desired reliability as a function of the risk associated with failure. Risk of failure is measured in two ways: 1) by a structure's occupancy, and the number of persons that would be put at jeopardy should failure occur; and, 2) by the nature of the failure mode. Three failure mode natures are recognized: 1) gradual and non-progressive; 2) gradual but progressive; and, 3) sudden and progressive. Failures of the first type occur slowly, and are foreshadowed by evidence including visible deformation and cracking that provide warning that failure is impending. Also, such failures tend to be localized and do not result in spread of failure to adjacent elements. The second type of failure occur slowly, as do the first type, but can lead to progression of failure, with more global structural consequences. The third type, are failures that are sudden, and therefore do not provide evidential warnings of their occurrence, and which also progress to more global failures. Progressively more reliable performance (lower probability of failure) is required for each of these various failure types.

Table 1 – Acceptable Reliability for Loading Other than Seismic

	Risk Category			
Basis	**I**	**II**	**III**	**IV**
Failure that is not sudden and does not lead to wide-spread progression of damage	$P_F = 1.25 \times 10^{-4}$/yr $\beta = 2.5$	$P_F = 3.0 \times 10^{-5}$/yr $\beta = 3.0$	$P_F = 1.25 \times 10^{-5}$/yr $\beta = 3.25$	$P_F = 5.0 \times 10^{-6}$/yr $\beta = 3.5$
Failure that is either sudden or leads to wide-spread progression of damage	$P_F = 3.0 \times 10^{-5}$/yr\ $\beta = 3.0$	$P_F = 5.0 \times 10^{-6}$/yr $\beta = 3.5$	$P_F = 2.0 \times 10^{-6}$/yr $\beta = 3.75$	$P_F = 7.0 \times 10^{-7}$/yr $\beta = 4.0$
Failure that is sudden and results in wide spread progression of damage	$P_F = 5.0 \times 10^{-6}$/yr $\beta = 3.5$	$P_F = 7.0 \times 10^{-7}$/yr $\beta = 4.0$	$P_F = 2.5 \times 10^{-7}$/yr $\beta = 4.25$	$P_F = 1.0 \times 10^{-7}$/yr $\beta = 4.5$

The reliability indices are provided for a 50-year service period, while the probabilities of

The Risk Categories referenced in Table 1 (C1.3.1a of ASCE 7-10) serve the same role as the Occupancy Categories contained in earlier editions of the standard. The Committee felt that the term Risk Category more appropriately recognized their role in the design process, i.e., to adjust design conservatism based on the acceptable risk of failure, as reflected in Table C1.3.1a, rather than just the functional use of the structure, as implied by the term Occupancy. In parallel with this change in terminology, the standard deleted the lists of building occupancy types associated with each Risk Category, and instead, defined the categories in broad terms. Risk Category I now includes structures that are typically not habited and whose failure poses little risk to human life. Risk Category II, III and IV structures are habited by progressively greater numbers of persons, or have other attributes, e.g. containment of hazardous materials, or provision of essential service, that could affect the lives of many persons. Commentary to Chapter 1 suggests that Risk Category should be selected based on the number of persons placed at risk, should the structure fail, as represented in Figure C1.1, reproduced as Figure 2, below. Recognizing that these concepts may be uncomfortable to some engineers and building officials, the standard requires that Risk Category not be assigned at a lower value than the corresponding Occupancy Category, specified by the building code.

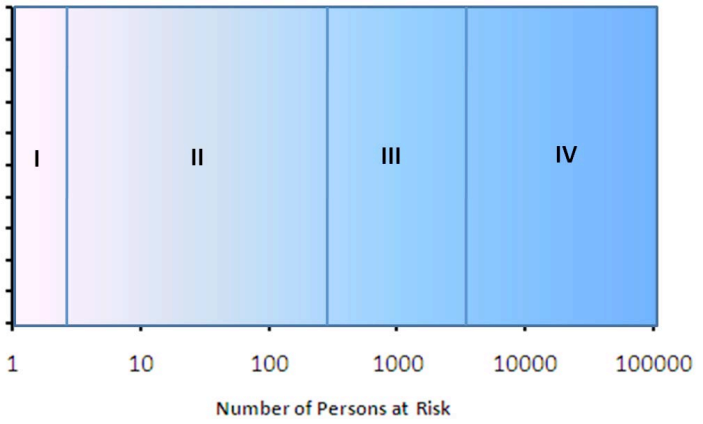


Figure 2 – Risk Category and Persons Placed at Risk (ASCE 7-10, Figure C1.1)

In Table 1 (Table C1.3.1a), the P_F value for each Risk Category and failure mode type is the acceptable annual frequency of failure for a single member or connection, under the specified loading. The term β in the table is the so-called reliability index, which is the number of standard deviations below the mean probable value at which design capacity is set to achieve these annual failure frequencies. The reliability indices are used in the calculation of resistance factors contained in the materials industry design standards, as explained in companion commentary in Chapter 2.

Historically, the profession has accepted much higher risk of seismic-initiated failure than it has for other load types. This is a function of the infrequency of severe seismic events, the severity of the loading when it occurs, the high uncertainty associated with prediction of that loading and the economic impracticality of designing to achieve reliability levels comparable with those that underpin design procedures for other load types. The reliability criteria adopted by the standard for seismic loading are based on those contained in FEMA P-750 (BSSC, 2009). Table C1.3.1b of the standard, reproduced as Table 2 below states these criteria.

Table 2 – Acceptable Earthquake Reliability

Occupancy Category I and II	
Total or partial structural collapse	10% conditioned on the occurrence of Maximum Considered Earthquake shaking
Failure that could result in endangerment of individual lives	25% conditioned on the occurrence of Maximum Considered effects
Occupancy Category III	
Total or partial structural collapse	6% conditioned on the occurrence of Maximum Considered Earthquake shaking
Failure that could result in endangerment of individual lives	15% conditioned on the occurrence of Maximum Considered Earthquake shaking
Occupancy Category IV	
Total or partial structural collapse	3% conditioned on the occurrence of Maximum Considered Earthquake shaking
Failure that could result in endangerment of individual lives	10% conditioned on the occurrence of Maximum Considered Earthquake shaking

For seismic loading, the table distinguishes between failures that could result in endangerment of individual lives, such as failure of anchorage for an architectural element or mechanical equipment item, as opposed to partial or total structural collapse which would place many lives in jeopardy. In all cases, seismic reliability is conditioned on the occurrence of Maximum Considered Earthquake shaking as depicted on national seismic design maps maintained by the United States Geologic Survey. For most regions of the United States, Maximum Considered Earthquake shaking has an annual frequency of exceedance of approximately 4×10^{-4}, adjusted so that the annual probability of partial or total collapse for appropriately configured, ordinary occupancy structures (Risk Category II) does not exceed 2×10^{-4}. This can also be stated as a 1% risk of collapse or partial collapse in 50 years, which as can be seen in comparison with the values in Table 1, is several orders of magnitude higher risk

of failure than is accepted for other load conditions. In regions of high seismic activity, within a few kilometers of major active faults, such as portions of California, the acceptable risk is set higher, with Maximum Considered Earthquake shaking specified based on deterministic events that have return periods of hundreds, as opposed to thousands of years.

PERFORMANCE ASSESSMENT

The standard sets three means of demonstrating that a design is capable of meeting the prescribed performance objectives. Two of these are satisfaction of the prescriptive provisions contained in the standard and the building code. These procedures are now respectively called the Allowable Stress Design Procedures and the Strength Design Procedures. Both procedures are "deemed to comply" means, in that the engineer using these procedures never actually evaluates the design's performance capability, but instead, demonstrates that the design conforms to prescriptive criteria that are deemed capable of providing the desired performance. Using the Allowable Stress Design Procedures, engineers use the load intensities for dead, live and environmental loads specified in later chapters of the standard, combine them in accordance with the Allowable Stress Load Combinations of Section 2.4 of the Standard and assure that the design complies with the appropriate strength and detailing criteria of referenced national design standards. Under the Strength Procedures, engineers use the same load intensities, but combine them using the Strength Load Combinations of Section 2.3 and again assure that their design provide adequate strength and meet the detailing criteria of the referenced national design standards. In addition, using either the Allowable Stress or Strength procedures, engineers must assure that their designs comply with the Serviceability criteria of Section 1.3.2 of the standard.

The third, Performance-based Procedure is specified by Section 1.3.1 which requires demonstration by analysis, or by a combination of analysis and testing, that structures are capable of providing reliability equivalent to that anticipated of structures designed using the Strength Procedures, and described in the section on Performance Objectives, above. Although rigorous methods of structural reliability analysis could be used to satisfy the requirements of this Section, few practicing engineers today have the knowledge and training to employ such methods, and therefore, it is unlikely that such methods will be frequently used. Instead, it is more likely that two other approaches will be adopted. One of these involves the use of Load and Resistance Factor Methods, but in which the engineer develops custom resistance factors based on the unique characteristics of their structural system and the inherent uncertainties. Commentary to Chapter 2 of the standard provides guidance on the implementation of this technique.

The second approach, and the one most likely to be used in the immediate future involves definition of conservative deterministic design scenarios and performing simulations (analyses) of the structure's response to these scenarios to demonstrate conformance with the intended performance. For seismic design, this approach involves selection of suites of ground motion records that represent the Maximum Considered Earthquake shaking intensity, then performing nonlinear response history analysis of the structure to predict its response and qualitatively, a suitable low probability of collapse or partial collapse. For wind design, the scenario event would consist of flashover fires with appropriate estimates of fuel and air flow. For wind design, the scenario events would consist of suitable wind storm simulations.

The standard requires that analytical models used to predict performance be benchmarked against suitable test data. Where national standards specify appropriate test procedures, such as those indicated by AISC 341 (AISC, 2010) for testing of steel moment connections, those must be used. Based on requirements contained in AISI S100-07 (AISI, 2007), analytical modeling parameters and acceptance criteria for simulations must be based on at least three tests. Where the coefficient of variation for parameters obtained from the tests exceeds 15%, additional tests must be performed until either the coefficient of variation is 15% or less, or at least 6 tests have been performed.

The testing and analytical procedures used in performance-based approaches are sophisticated and few building departments have personnel with suitable training to perform meaningful review of the designs and supporting data. Therefore, the standard requires that designs justified by performance-based procedures be subjected to rigorous peer review of the assumptions, underlying test and analytical data, reliability calculations and detailing. Peer review must be performed by knowledgeable engineers and researchers with appropriate experience and knowledge of the structural systems and materials. Peer reviewers must present certification to the building official that they have performed the review and that they concur with its performance capability.

CONCLUSION

The inclusion of performance-based design procedures in the 2010 edition of ASCE 7-10 is an important step in the evolution of the standard. Though a long history of acceptance of performance-based designs by building officials exists, neither the building codes nor their referenced standards have ever attempted to quantify the required performance characteristics for structures nor the procedures used to demonstrate compliance. The ASCE 7-10 standard does both, for the first time publishing quantitative reliability standards that designs should be capable of meeting, and also indicating acceptable procedure for demonstrating compliance.

Much additional work needs to be done in future editions of the standard to improve and enhance these new procedures. In particular, the performance criteria specified in Tables 1 and 2 above focuses on 1) protection of life safety, and 2) structural performance. However, structural design is intended to protect more than life safety, including continued function and operability of some structures, and minimization of repair and replacement costs to acceptable levels. Performance criteria for these other considerations are still needed and should be considered in the development of future editions of the Standard. In addition, the ASCE-7 standard also addresses design of cladding and nonstructural components to resist structural loading. The performance criteria of Tables 1 and 2 should be expanded to better address these building components.

Performance-based design has already become a popular approach for the seismic design of tall and important structures worldwide, as well as design to resist terrorist attach and unanticipated events. In New Zealand and Australia, performance-based design is also commonly used to justify fire/life safety design features of buildings. The introduction of performance-based design procedures into ASCE 7-10 should facilitate the further development of this approach in the U.S. and its spread to a broader range of structure types and design considerations.

REFERENCES

American Iron and Steel Institute (AISI), 2007, *North American Specification for the Design of Cold Formed Steel Structural Members AISI S100-07*, American Iron and Steel Institute, Washington, D.C.

American Institute of Steel Construction (AISC), 2010, *Seismic Provisions for Steel Buildings, AISC 341-10*, American Institute of Steel Construction, Chicago, IL.

Applied Technology Council (ATC), 1996, *Seismic Evaluation and Retrofit of Concrete Buildings, Report ATC-40*, Applied Technology Council, Redwood City, CA

Applied Technology Council (ATC), 1997, *Guidelines and Commentary for Seismic Rehabilitation of Buildings Report FEMA-273/274*, Federal Emergency Management Agency, Washington, D.C.

Applied Technology Council (ATC), 2011, *Seismic Performance Assessment Methodology for Individual Buildings FEMA P-58*, Federal Emergency Management Agency, Washington, D.C.

Building Seismic Safety Council (BSSC), 2009, *NEHRP Recommended Provisions for New Buildings and Structures, FEMA P-750*, Federal Emergency Management Agency, Washington, D.C.

Structural Engineering Institute (SEI), 2006*, Seismic Rehabilitation of Existing Buildings ASCE 41.06*, American Society of Civil Engineers, Reston, VA

Structural Engineering Institute (SEI), 2010*, Minimum Design Loads for Buildings and Other Structures ASCE 7.10*, American Society of Civil Engineers, Reston, VA

ASCE 7-10 Wind Loads

Ronald Cook[1], Larry Griffis[2], Peter Vickery[3], Eric Stafford[4]

[1]Civil and Coastal Engineering, University of Florida, rcook@ce.ufl.edu
[2]Structures Division, Walter P. Moore and Associates, lgriffis@walterpmoore.com
[3]Applied Research Associates, pvickery@ara.com
[4]T. Eric Stafford & Associates, testafford@charter.net

ABSTRACT

ASCE 7-10 "Minimum Design Loads for Buildings and Other Structures" contains several changes regarding wind loads. The major editorial change is a complete reorganization to a multiple-chapter format as done previously for seismic loads with the objective being to make the provisions easier to follow. Technical changes include the introduction of new wind speed maps to be used with a 1.0 load factor for LRFD and a 0.6 load factor for ASD, the reintroduction of Exposure D for water surfaces in hurricane-prone regions, and revised wind-borne debris regions. A new simplified procedure for buildings up to 160 ft has been added based on the provisions for buildings of all heights.

INTRODUCTION

The major changes to the wind load provisions of ASCE 7 introduced in ASCE 7-10 are:

- Reorganization of wind load provisions
- Wind speed maps
- Re-introduction of Exposure D in hurricane-prone regions
- Wind-borne debris region
- Simplified procedure for buildings ≤ 160 ft

This paper presents a general background on the basis for these changes. Thirty other changes related to wind loads were included in ASCE 7-10. The majority of these changes were editorial but some did include technical changes. These include:

- Minimum wind loads
- Improved exposure and roughness examples
- Revisions to low-rise "envelope" method
- Rooftop equipment

REORGANIZATION OF WIND LOAD PROVISIONS

The wind load provisions of Chapter 6 in ASCE 7 have been reorganized into 6 new Chapters. In recent years, there has been much discussion about the layout and presentation of the wind load provisions in ASCE 7. While, ASCE 7-98 did make some improvements to the format (introduction of the 3 Methods), much of the important information was buried deep within the paragraph numbering. In addition, Method 2 Analytical Procedure actually contained several analytical methods embedded within the section (e.g., Buildings of All Heights and Low-rise Buildings). While the provisions were technically correct and properly numbered, understanding and applying the appropriate wind loads could be somewhat cumbersome.

The primary goals of the reorganization effort were to keep the section numbering smaller and to locate major subject areas as distinct chapters. Additionally, it was desired to order the wind provisions in a logical sequence for the general structural design community. Accomplishing these goals led to the creation of 6 distinct chapters and the relocation of the provisions into their most logical new chapter. For example, the provisions for determining MWFRS loads are in separate chapters from Components and Cladding. Additionally, the different methods for determining MWFRS loads are located in the 3 separate chapters – Chapter 27 Directional Procedure (formerly buildings of all heights in Method 2); Chapter 28 Envelope Procedure (formerly low-rise buildings in Method 2); and Chapter 29 Other Structures and Building Appurtenances (formerly embedded in Method 2).

Each chapter was again subdivided into “parts” where deemed appropriate for clarity. For example in Chapter 28 the analytical method for determining wind loads for low-rise buildings is identified as Part 1 and the simplified method for determining wind loads for low-rise buildings is identified as Part 2. Similar subdivisions occur in Chapters 27 and 30.

To ease the transition to the new format and to facilitate improved awareness of the provisions applicable to the various methods, each chapter and parts contain tables that specifically identify and outline the steps and provisions applicable for that respective chapter or part. Table 27.2-1 shown below is an example of one of the outlines presented for Part 1 in Chapter 27.

Table 27.2-1
Steps to Determine MWFRS Wind Loads
Enclosed, Partially Enclosed and Open Buildings of All Heights

Step 1: Determine risk category of building or other structure, see Table 1.4-1
Step 2: Determine the basic wind speed, V, for the applicable risk category, see Figure 26.5-1A, B or C
Step 3: Determine wind load parameters:
- Wind directionality factor, K_d, see Section 26.6 and Table 26.6-1
- Exposure category, see Section 26.7
- Topographic factor, K_{zt}, see Section 26.8 and Table 26.8-1
- Gust Effect Factor, G, see Section 26.9
- Enclosure classification, see Section 26.10
- Internal pressure coefficient, GC_{pi}, see Section 26.11 and Table 26.11-1

Step 4: Determine velocity pressure exposure coefficient, K_z or K_h, see Table 27.3-1
Step 5: Determine velocity pressure q_z or q_h Eq. 27.3-1
Step 6: Determine external pressure coefficient, C_p or C_N
- Fig. 27.4-1 for walls and flat, gable, hip, monoslope or mansard roofs
- Fig. 27.4-2 for domed roofs
- Fig. 27.4-3 for arched roofs
- Fig. 27.4-4 for monoslope roof, open building
- Fig. 27.4-5 for pitched roof, open building
- Fig. 27.4-6 for troughed roof, open building
- Fig. 27.4-7 for along-ridge/valley wind load case for monoslope, pitched or troughed roof, open building

Step 7: Calculate wind pressure, p, on each building surface
- Eq. 27.4-1 for rigid buildings
- Eq. 27.4-2 for flexible buildings
- Eq. 27.4-3 for open buildings

Additionally, a table was added to the commentary that provides a cross-reference of all sections, figures, and tables between ASCE 7-05 and ASCE 7-10. Sections applicable to ASCE 7-05 are shown in the left column in numerical sequence so that users familiar the ASCE 7-05 may easily locate the applicable sections in ASCE 7-10.

WIND SPEED MAPS

Multiple Maps. The decision to move to multiple ultimate, limit state, or strength design wind speed maps to be used in conjunction with a wind load factor of 1.0 for LRFD instead of using a single map coupled with an importance factor and a wind load factor of 1.6 was made because:

- An ultimate or strength based map brings the wind design approach more in line with that used for seismic design in that they both essentially eliminate the use of a 1.0 load factor for strength design.
- The multiple map approach eliminates the inconsistencies in the use of the importance factor that strictly varies with location and between the hurricane and non-hurricane regions.

- The new maps establish uniformity in the return period for the design basis winds, and they more clearly convey that information
- The new maps, by providing the design speeds directly, more clearly inform owners and their consultants about the storm intensities for which their designs are performed.

The hurricane importance factor specified in ANSI A58.1 1982 and ASCE 7-93 was eliminated from the 1995 Edition of ASCE 7 by incorporating it into the wind speed contours. Consequently, at no time since the introduction of ASCE 7-95 have the wind speed contours in the hurricane prone region been representative of a 50 year return period wind speed, although most users erroneously thought this was the case. In the development of the wind speed map used in ASCE 7-98 the Wind Load Task Committee (WLTC) re-visited the hurricane importance factor inherent in the Standard since 1982 primarily because it was recognized that the importance factor varied with location along the coast and using a constant value of 1.05 was not appropriate. This spatially varying factor was incorporated into the map by dividing the 500 year wind speeds by the square root of the load factor, which at the time was expected to be 1.5, not the value of 1.6 that was finally recommended by the load factor committee.

In ASCE 7-10, the approach taken to determine the return periods associated with different occupancy category importance factors began with the premise that the nominal wind load, computed using the methods given in ASCE 7-05, when multiplied by the wind load factor, represents a limit state or strength load. Furthermore, it was assumed that the variability of the wind speed dominates the calculation of the wind load factor. This is an approximation, and depends on the uncertainty in the various components of the wind loading chain (Davenport, 1983). The wind speed uncertainty is combined with uncertainties in pressure coefficient, exposure factor, gust factor and modeling errors. Since these errors combine as sums of squares, and because the uncertainty effect of the wind speed is doubled as it appears in the wind load equation as a pressure, the net result is the wind speed uncertainty contributes in the range of 70% to 80% of the total uncertainty. Regardless of the exact contribution of the wind speed uncertainty to the total uncertainty, the return period for the ultimate, or strength, design point for ASCE 7-10 was determined using the approximation where all the uncertainty was treated through the wind speed variability. Using this approach, the limit state wind load, W_T, is given as:

$$W_T = C_F V_{50}^2 W_{LF} I_v \quad (1)$$

where C_F is a component/structure specific coefficient that includes the effects building height, geometry, terrain, etc. V_{50} is the 50 year return period wind speed, W_{LF} is the wind load factor, and I_v is the occupancy importance factor applied to the wind load. In order to estimate the magnitude of I_H, the committee required that the annual probability of exceeding the limit state wind load in hurricane and non-

hurricane regions be the same. Recalling that the nominal design wind speed in the non-hurricane regions of the United States is associated a 50 year return period, the WLTC sought to determine the return period associated with the wind speed producing the limit state load in a non-hurricane region. As defined in ASCE 7-95 through the present, in the non-hurricane regions of the United States, the ratio of the wind speed for any return period, T, to the 50 year return period wind speed is:

$$V_T / V_{50} = [0.36 + 0.1\ln(12T)] \tag{2}$$

where V_T is wind speed associated with the strength load condition having an annual exceedance probability of $1/T$. This strength load, W_T, for an occupancy Category II structure (I_v=*1*.0) occurs when:

$$W_T = C_F V_T^2 = C_F V_{50}^2 W_{LF} \tag{3}$$

Consequently from (2) and (3), V_T / V_{50} can be represented as an algebraic function in the form:

$$V_T / V_{50} = [0.36 + 0.1\ln(12T)] = \sqrt{W_{LF}} \tag{4}$$

From (4), the return period T associated with the limit state wind speed in non-hurricane regions is for Occupancy Category II structures is:

$$T = 0.00228\exp(10\sqrt{W_{LF}}) \tag{5}$$

Using the wind load factor of 1.6 as is currently specified in ASCE 7-05, from (5) we get T = 709 years~700 years for Occupancy Category II structures. In the case of Occupancy Category I and Occupancy Categories III and IV, W_{LF} in (3), (4) and (5) is replaced with $W_{LF}\, I_v$, yielding return periods of 294 years (rounded to 300) for Occupancy Category I and 1700 years for Occupancy Categories III and IV. The return periods of 294 and 1700 years were computed with the more accurate definition of importance factor obtained from the square of (3) with T= 25 years for Occupancy Category I and 100 years for Occupancy Category III and IV, rather than using the rounded values given in ASCE 7-05 which yield return periods of 309 years and 1780 years. In ASD the wind speed from any of the three maps are used in conjunction with a WLF of 0.6, which is the rounded result of an ASD WLF that is equal to $1/\sqrt{1.6} = 0.623$.

Hurricane Simulation Model Updates. The design wind speeds given in ANSI A58.1 1982 and all versions of ASCE since that time have been comprised of a combination of hurricane and non-hurricane winds. The non-hurricane wind speeds are the same as those that have been in ASCE 7 since 1995 (adjusted to different return periods). The hurricane winds which are derived from a simulation model

differ due to updates in the hurricane modeling. The hurricane wind speeds were developed using the hurricane hazard model described in Vickery et al. (2009b). These hurricane wind speeds are combined with the statistical model for non-hurricane wind speeds given in Peterka and Shahid (1998) to develop maps that consider both hurricane and non-hurricane winds.

The major differences between the simulation models described Vickery et al. (2000a,b) (used to define the design wind speeds in ASCE 7-98 through ASCE 7-05) to those in the current model (Vickery et al., 2009b) are:

- A new intensity model includes ocean mixing to limit hurricane
- A new statistical model for Holland B parameter
- A new filling (storm weakening after landfall) model
- A new wind field model

In addition to changes to the simulation model itself, the new maps were developed using a 100,000 year simulation vs. a 20,000 year simulation for the old map. The maps were developed using predicted wind speeds at 2851 points vs. the 208 points used to develop the old map, resulting in a much more precise representation of the change in contours as one moves inland away from the coast.

The *primary* reason for the reduction in wind speeds produced by the 2009 model compared to those obtained using the previous model is through the modeling of the Holland *B* parameter. The details of Holland *B* parameter are discussed in Holland (1980) as well as Vickery et al. (2010), among others. Figure xx1 shows the impact of changes in *B* on the radial variation of the wind speeds and pressures for a hurricane with constant values of central pressure, radius to maximum wind speed (*RMW*) and translation speed.

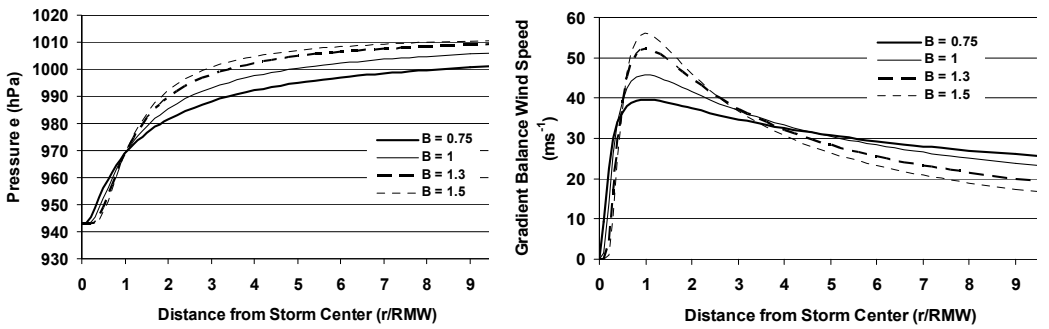


Figure 1 Effect of B on azimuthally averaged radial profiles of wind speed and pressure

Figure 1 shows that as *B* increases, the radial variation of both wind speed and pressure increases, and the maximum wind speed increase. It can be shown that in a stationary hurricane the maximum gradient level wind speed, V_{Gmax}, in a hurricane is proportional to the square root of *B* in the form $V_{G\max} \propto \sqrt{B\Delta p}$ where Δp is the

difference between the low pressure at the center of the hurricane and the high pressure well away from the storm center. With all else equal, in a stationary hurricane, a 10% decrease in either B or Δp corresponds to a 5% decrease in the maximum wind speed in the hurricane, indicating that both variables are important.

As discussed in Vickery and Wadhera (2008), B has statistically significant correlations with RMW (increasing as RMW decreases), latitude (decreasing as latitude increases) and sea surface temperature (SST) (decreasing with decreasing SST). In an attempt to incorporate a relationship between latitude, SST, RMW and B using a single parameter, B over open water, is modeled as:

$$B = 1.7642 - 1.2098\sqrt{A} + \varepsilon \; ; \qquad r^2=0.345,\ \sigma_B = 0.226 \qquad (6)$$

where A is a non-dimensional parameter that incorporates SST, RMW and latitude. In (6) the numerator of A is a function RMW and latitude and the denominator is a function of central pressure and SST. The two most important parameters controlling the behavior of B in (6) are RMW and latitude.

The model for B used in Vickery et al. (2000b) is:

$$B = 1.38 + 0.00184\Delta p - 0.00309\,RMW + \varepsilon \; ; \qquad r^2=0.026,\ \sigma_B = 0.381 \qquad (7)$$

Note that in (7) there is no dependence on latitude and that the r^2 value is much lower and the error term is much higher than in (6). The reduction in r^2 and the associated decrease in the error term, σ_B, plays an important role in the reduction of wind speeds associated with rarer events, as these events are driven by the tails of the input distributions rather than the means.

Whereas Figure 1 shows the importance of B from the viewpoint of a single storm, Figure 2 shows the effect of the new statistical model for B on predicted wind speeds though comparisons of predicted hurricane gust wind speeds at Wilmington, NC and Miami, FL. In the Wilmington case, the use of the new model for B reduces the 100 year return period gust wind speed by 9.4%, and in the Miami case a 6.8% reduction occurs. For a 700 year return period, the reductions are 10.9% and 9.3% for Wilmington and Miami respectively.

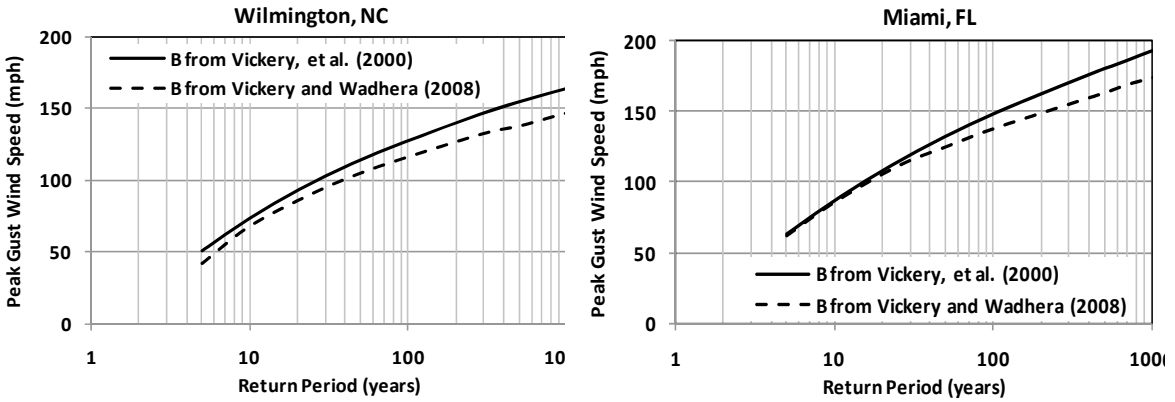


Figure 2. Effect of Holland B modeling on predicted wind speeds

RE-INTRODUCTION OF EXPOSURE D IN HURRICANE PRONE AREAS

One of the more significant differences between the hurricane wind field models used in Vickery et al. (2000a) and Vickery et al. (2009) is in the modeling of the sea surface drag coefficient, C_d. In Vickery et al. (2009) the hurricane wind field model uses a representation of C_d, which reaches a maximum value at mean wind speeds of around 20 m/sec. This treatment of the C_d varies markedly from that used in Vickery et al. (2000a), where C_d increases monotonically with wind speed without limit. The change in the modeling of the C_d is due to the work described in Powell et al. (2003) which indicates that C_d does not continue to increase with increasing wind speed, but reaches a maximum or limiting value. A limiting value of C_d contradicts the findings given in the earlier works of both Powell (1980) and Garrett (1977), but has been supported by other research since 2003. The hurricane wind field model used to develop the ASCE 7-10 wind speeds models the limiting C_d through the use of an upper bound on C_d that varies with distance from the center of the hurricane

Figure 3 presents the water-land gust wind speed ratios derived from the Vickery, et al. (2008) model (near the *RMW*), the ratios derived from the Vickery et al. (2000a) model (also near the *RMW*), and those implied in ASCE 7. The wind speed ratio is defined as the marine gust wind speed divided by the open terrain (defined as z_o=0.03m) gust wind speed. In ASCE 7 this ratio is equal to $\sqrt{K_z}$ evaluated in Exposure D at z=10 m. As indicated in Figure 3, the ratios produced by the new wind model are approximately consistent with the Exposure D ratio. Using model for C_d that does not have a limiting value the wind speed ratio approaches that of Exposure C in ASCE 7 as the wind speed increases, and thus for simplicity Exposure D was eliminated from the hurricane prone coastline in the 1998 Edition of ASCE 7.

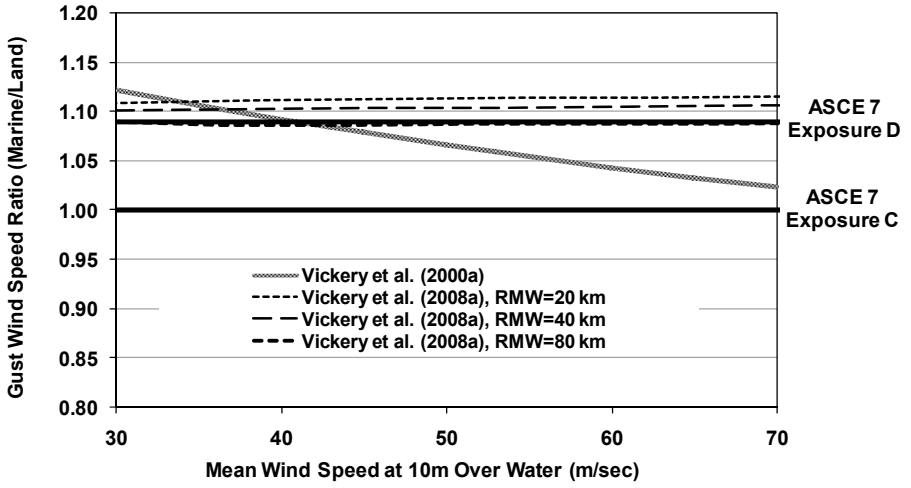


Figure 3. Gust wind speed ratio (Gust wind speed on land divided by gust wind speed over water). A gust wind speed ratio of 1 indicates no reduction in wind speed as wind moves from sea to land (i.e. marine roughness is the same as open terrain).

WIND-BORNE DEBRIS REGIONS

The primary changes to the wind-borne debris provisions in ASCE 7 are to accomplish relative coordination with the new ultimate wind speed maps that are now basis for determining design wind speeds. The language that triggers the Wind-borne Debris Region (WBDR) has been relocated to Section 26.10.3.1. The language is still similar but includes a couple of key changes. The appropriate map for the category of building under consideration is to be used for determining the application of the WBDR requirements. For Risk Category II buildings and Risk Category III buildings except health care facilities, the WBDR triggers are to be based on the wind speed map for Risk Category II buildings, Figure 26.5.1A. For Risk Category IV buildings and Risk Category III health care facilities, the WBDR triggers are to be based on the wind speed map for Category III and IV buildings, figure 26.5.1B. Using the Risk Category III and IV wind speed map does substantially increase the WBDR for these buildings and structures as compared with the provisions of ASCE 7-05 except around Jacksonville, Florida and the "big bend" region of Florida. Using the appropriate risk based map for the appropriate Risk Category provides a means for achieving a more risk consistent approach for defining WBDR, particularly with regards to life safety. The types of buildings and structures included in Risk Category III suggest that life safety is most important for health care facilities. Therefore, the expanded WBDR in Figure 26.5.1B applies to Risk Category III health care facilities.

For Risk Category II buildings, there is a notable change in the geographic area that is now designated as a WBDR. The WBDR contained in the previous editions of ASCE 7 (1998, 2002, and 2005) were based on judgment and essentially applied the region in a strip of the coast along most of the Gulf of Mexico and

Atlantic coast regions where the risk of a direct strike of a Category 3 or larger hurricane was high. The new criteria continue that judgment based definition by including the coastal areas that are approximately consistent with those given in prior editions of ASCE 7 for Risk Category II. A straight translation of the 110 and 120 mph wind speeds from ASCE 7-05 to the 700 year return period maps in ASCE 7-10 would yield triggers of 140 mph and 150 mph respectively. This would have eliminated the WBDR along most the Texas coast and substantially reduce the region in other areas that are considered to be in a WBDR in ASCE 7-05. This is due to the changes in the hurricane simulation model that reduces the magnitude of wind speeds for long return periods. However, while the applicability of the WBDR has essentially been shifted by 10 mph, the applicable region for Risk Category II and Risk Category III buildings excluding health care facilities has be substantially narrowed and eliminated in some places as compared to the regions applicable in ASCE 7-05 and prior editions. Significant reductions in the WBDR occur around Jacksonville, Florida, the Florida panhandle, and along the coast of North Carolina.

SIMPLIFIED PROCEDURE FOR BUILDINGS ≤ 160 FT

New to ASCE 7-10 is a simplified approach for determining design wind pressures applicable to buildings with a mean roof height $h \leq 160$ ft. Design pressures for both roof and wall surfaces are determined directly from a set of tables. The method is based on the same principles that form the basis of the Directional Procedure defined in Chapter 27 Part1 for the MWFRS and Chapter 30 Part 3 for CC.

MWFRS – Chapter 27 Part 2. The method for MWFRS covers two classes of buildings that are a function of building height. In addition to the normal limitations listed in Chapter 27 Section 27.1.2 regarding a regular building and absence of unusual dynamic characteristics, the requirements for each class are stipulated below:

Class 1 Buildings:

1. Enclosed simple diaphragm building (as defined in Section 26.2)
2. $h \leq 60$ ft.
3. $0.2 \leq L/B \leq 5.0$
4. $K_{zt} = 1.0$ with exceptions as defined in Section 27.5.2

Class 2 Buildings:

1. Enclosed simple diaphragm building (as defined in Section 26.2)
2. $60\ ft < h \leq 160$ ft.
3. $0.2 \leq L/B \leq 5.0$
4. $K_{zt} = 1.0$ with exceptions as defined in Section 27.5.2
5. The fundamental natural frequency shall not be less than $75/h$ where h is in feet.

The procedure can be applied for buildings with either rigid or flexible diaphragms as discussed in Section 27.5.4. Net wind pressures for wall and roof surfaces are determined from Tables 27.6-1 and Table 27.6-2 respectively. Tables are presented for all exposures, B, C and D and for wind speeds varying from 110 MPH to 200 MPH. A procedure is also specified for determining pressures for roof parapets (see Figure 27.6-2) and roof overhangs (see Figure 27.6-3). Loads from the tables are applied to the walls and roof simultaneously. The step by step procedure is defined at the front of Chapter 27 Part 2 Table 27.5-1.

An excerpt from Table 27.6-1 for walls is shown below. An excerpt from Table 27.6-2 for roofs is also shown. For roofs, the procedure covers flat, gable, hip, monoslope and mansard roofs as referenced in Table 27.6-2.

For wall pressures determined from Table 27.6-1, two pressures are tabulated for each building height and wind speed. The uppermost row in the table defines p_h which is the roof pressure at the top of the building. The lower row (shown shaded) defines p_0 which is the pressure at the base of the building. A linear variation of pressure between the two is to be used in design as shown at the front of Table 27.6-1. This linear variation has been developed to produce essentially the same story shears and overturning moments as the "exact" values from Part 1 of Chapter 27. It is to be noted that the procedure includes the calculation of the Gust Effect Factor based on conservative assumptions for building frequency and damping. Further details on the derivation of tabulated pressure values can be found in the commentary to ASCE 7-10.

Table 27.6-1
MWFRS Wind Loads – Walls
Exposure B

V(mph)	110			115			120			130			140			160			180			200		
h(ft.), L/B	0.5	1	2	0.5	1	2	0.5	1	2	0.5	1	2	0.5	1	2	0.5	1	2	0.5	1	2	0.5	1	2
160	38.1	37.7	34.1	42.1	41.7	37.8	46.4	45.9	41.7	55.8	55.1	50.2	66.3	65.4	59.7	91.0	89.4	81.8	120.8	118.3	108.5	156.2	152.4	140.0
	25.6	25.4	21.0	28.3	28.1	23.3	31.2	30.9	25.7	37.5	37.1	30.9	44.6	44.0	36.8	61.2	60.1	50.4	81.3	79.6	66.9	105.2	102.6	86.2
150	36.9	36.6	33.0	40.7	40.4	36.5	44.9	44.4	40.3	53.9	53.3	48.5	63.9	63.1	57.6	87.5	86.1	78.9	116.1	113.8	104.5	149.9	146.5	134.7
	25.1	24.9	20.6	27.7	27.5	22.8	30.5	30.2	25.2	36.7	36.2	30.3	43.5	43.0	36.0	59.6	58.6	49.3	79.0	77.4	65.3	102.0	99.7	84.2
140	36.6	35.4	31.9	39.3	39.1	35.3	43.3	42.9	38.9	51.9	51.4	46.7	61.5	60.8	55.5	84.0	82.8	75.9	111.2	109.2	100.4	143.5	140.5	129.3
	24.5	24.4	20.2	27.1	26.9	22.4	29.8	29.6	24.6	35.7	35.4	29.6	42.4	41.9	35.2	57.9	57.0	48.1	76.6	75.2	63.7	98.8	96.7	82.0
130	34.4	34.2	30.8	37.9	37.7	34.0	41.7	41.4	37.4	49.9	49.5	44.9	59.1	58.5	53.3	80.5	79.5	72.8	106.3	104.6	96.2	136.9	134.3	123.8
	24.0	23.9	19.8	26.5	26.3	21.9	29.1	28.9	24.1	34.8	34.5	28.9	41.2	40.8	34.3	56.2	55.4	46.9	74.2	73.0	62.0	95.5	93.7	79.8
120	33.1	33.0	29.6	36.5	36.3	32.7	40.1	39.9	35.9	47.9	47.6	43.1	56.6	56.2	51.0	76.9	76.1	69.6	101.3	99.9	91.8	130.2	128.0	118.0
	23.4	23.3	19.4	25.8	25.7	21.4	28.4	28.2	23.6	33.9	33.7	28.3	40.1	39.7	33.5	54.4	53.8	45.6	71.7	70.7	60.2	92.2	90.6	77.4

Table 27.6-2
MWFRS - Roof
Exposure C

MWFRS – Roof
V = 110–120 mph
h = 15–40 ft.

V (MPH)			110					115					120				
		Load			Zone					Zone					Zone		
h (ft)	Roof Slope	Case	1	2	3	4	5	1	2	3	4	5	1	2	3	4	5
40	Flat < 2:12 (9.46 deg)	1	NA	NA	-29.1	-26.0	-21.3	NA	NA	-31.8	-28.4	-23.3	NA	NA	-34.7	-30.9	-25.3
		2	NA	NA	0.0	0.0	0.0	NA	NA	0.0	0.0	0.0	NA	NA	0.0	0.0	0.0
	3:12 (14.0 deg)	1	-28.6	-19.4	-29.1	-26.0	-21.3	-31.2	-22.5	-31.8	-28.4	-23.3	-34.0	-23.1	-34.7	-30.9	-25.3
		2	4.1	-5.8	0.0	0.0	0.0	4.5	-6.3	0.0	0.0	0.0	4.9	-6.9	0.0	0.0	0.0
	4:12 (18.4 deg)	1	-23.5	-19.0	-29.1	-26.0	-21.3	-25.7	-20.7	-31.8	-28.4	-23.3	-28.0	-22.6	-34.7	-30.9	-25.3
		2	8.1	-8.3	0.0	0.0	0.0	8.9	-9.1	0.0	0.0	0.0	9.7	-9.9	0.0	0.0	0.0
	5:12 (22.6 deg)	1	-18.8	-19.0	-29.1	-26.0	-21.3	-20.6	-20.7	-31.8	-28.4	-23.3	-22.4	-22.6	-34.7	-30.9	-25.3
		2	10.8	-9.1	0.0	0.0	0.0	11.8	-9.9	0.0	0.0	0.0	12.9	-10.8	0.0	0.0	0.0
	6:12 (26.6 deg)	1	-15.1	-19.0	-29.1	-26.0	-21.3	-16.5	-20.7	-31.8	-28.4	-23.3	-18.0	-22.6	-34.7	-30.9	-25.3
		2	12.0	-9.1	0.0	0.0	0.0	13.1	-9.9	0.0	0.0	0.0	14.2	-10.8	0.0	0.0	0.0
	9:12 (36.9 deg)	1	-8.8	-19.0	-29.1	-26.0	-21.3	-9.6	-20.7	-31.8	-28.4	-23.3	-10.4	-22.6	-34.7	-30.9	-25.3
		2	14.3	-9.1	0.0	0.0	0.0	15.6	-9.9	0.0	0.0	0.0	17.0	-10.8	0.0	0.0	0.0
	12:12 (45.0 deg)	1	-4.9	-19.0	-29.1	-26.0	-21.3	-5.4	-20.7	-31.8	-28.4	-23.3	-5.9	-22.6	-34.7	-30.9	-25.3
		2	14.3	-9.1	0.0	0.0	0.0	15.6	-9.9	0.0	0.0	0.0	17.0	-10.8	0.0	0.0	0.0

C&C – Chapter 30 Part 4. The method for CC covers both wall and roof surfaces. Roof and wall pressures for flat, gable, mansard, hip and monoslope roof buildings are covered Table 30.7-2. Tabulated pressures are shown for five zones that include all wall and roof surfaces as shown in the figures in Table 30.7-2. The step by step procedure is defined at the front of Chapter 30 Part 4 in Table 30.7-1.

Table 30.7-2 shows pressure for Exposure C only. However, pressures for all exposures can be determined by applying the Exposure Adjustment Factor shown in a graph within the table. Tabulated values are shown for an effective wind area of 10 sf but reduction factors are shown in graphs part of the table for other effective wind areas. The various factors are applied to the tabulated pressures according to Equation 30.7-1. A procedure is also specified for determining pressures on parapets (refer to Figure 30.7-1) and overhangs (refer to Figure 30.7-2). An excerpt to Table 30.7-2 is shown below.

Table 30.7-1
Components and Cladding
Exposure C

C & C
V = 110-120 mph
h = 15-80 ft.

V (MPH)			110					115					120				
		Load			Zone					Zone					Zone		
h (ft)	Roof Form	Case	1	2	3	4	5	1	2	3	4	5	1	2	3	4	5
80	Flat Roof	1	-50.2	-78.8	-107.5	-34.3	-63.0	-54.9	-86.2	-117.5	-37.5	-68.8	-59.8	-93.8	-127.9	-40.9	-74.9
		2	NA	NA	NA	34.3	34.3	NA	NA	NA	37.5	37.5	NA	NA	NA	40.9	40.9
	Gable Roof	1	-37.5	-63.0	-94.7	-40.7	-63.0	-41.0	-68.8	-103.6	-44.5	-68.8	-44.6	-74.9	-112.8	-48.4	-74.9
	Mansard Roof	2	21.6	21.6	21.6	37.5	34.3	23.6	23.6	23.6	41.0	37.5	25.7	25.7	25.7	44.6	40.9
	Hip Roof	1	-34.3	-59.8	-88.4	-40.7	-63.0	-37.5	-65.3	-96.6	-44.5	-68.8	-40.9	-71.1	-105.2	-48.4	-74.9
		2	21.6	21.6	21.6	37.5	34.3	23.6	23.6	23.6	41.0	37.5	25.7	25.7	25.7	44.6	40.9
	Monoslope Roof	1	-43.9	-56.6	-97.9	-40.7	-63.0	-48.0	-61.9	-107.0	-44.5	-68.8	-52.2	-67.4	-116.5	-48.4	-74.9
		2	18.4	18.4	18.4	37.5	37.5	20.2	20.2	20.2	41.0	41.0	21.9	21.9	21.9	44.6	44.6
70	Flat Roof	1	-48.8	-76.7	-104.5	-33.4	-61.2	-53.4	-83.8	-114.2	-36.5	-66.9	-58.1	-91.2	-124.3	-39.7	-72.8
		2	NA	NA	NA	33.4	33.4	NA	NA	NA	36.5	36.5	NA	NA	NA	39.7	39.7
	Gable Roof	1	-36.5	-61.2	-92.1	-39.6	-61.2	-39.9	-66.9	-100.7	-43.2	-66.9	-43.4	-72.8	-109.6	-47.1	-72.8
	Mansard Roof	2	21.0	21.0	21.0	36.5	33.4	23.0	23.0	23.0	39.9	36.5	25.0	25.0	25.0	43.4	39.7
	Hip Roof	1	-33.4	-58.1	-85.9	-39.6	-61.2	-36.5	-63.5	-93.9	-43.2	-66.9	-39.7	-69.2	-102.3	-47.1	-72.8
		2	21.0	21.0	21.0	36.5	33.4	23.0	23.0	23.0	39.9	36.5	25.0	25.0	25.0	43.4	39.7
	Monoslope Roof	1	-42.7	-55.0	-95.2	-39.6	-61.2	-46.6	-60.1	-104.1	-43.2	-66.9	-50.8	-65.5	-113.3	-47.1	-72.8
		2	17.9	17.9	17.9	36.5	36.5	19.6	19.6	19.6	39.9	39.9	21.3	21.3	21.3	43.4	43.4

OTHER CHANGES

Minimum wind loads. Minimum wind load pressure was increased from 10 psf to 16 psf to account for the change in load factors.

Improved exposure and roughness examples. New figures were added to the commentary to provide examples on how to determine exposure conditions for different roughness conditions around the building

.

Revisions to low-rise "envelope" method. The figure for determining MWFRS exterior pressure coefficients, GC_{pf}, for low-rise buildings was revised to be consistent with that used in ASCE 7-98.

Provisions for roof-top equipment. Provisions have been added to quantify both lateral and vertical wind loads on rooftop equipment.

CONCLUSION

This paper provides a general overview of the major changes to the ASCE 7 wind load provisions in ASCE 7-10. The reorganization and change in the return period of the wind speed maps has made the overall format of the wind load provisions similar to that of the ASCE 7 seismic provisions. Additional information on changes can be found in the ASCE 7-10 Commentary.

REFERENCES

Davenport, A.G. (1983), "The relationship of reliability to wind loading", *J. Wind Eng. Ind. Aerodyn.* **13,** 3-27

Garratt, J.R. (1977), "Review of drag coefficients over oceans and continents", *Mon. Wea. Rev.* **105**, 915–929

Holland, G. J., (1980), "An analytical model of the wind and pressure profiles in hurricanes *Mon. Wea. Rev.* **108**, 1212-1218.

Peterka, J. A. and Shahid, S (1998), "Design Gust Wind Speeds in the United States". *J. Struct. Eng.* **124**, 207-

Powell, M.D. (1980), "Evaluations of Diagnostic Marine Boundary-Layer Models Applied to Hurricanes", *Mon. Wea. Rev.* **108**, 757–766

Powell, M.D., P.J. Vickery, and T.A. Reinhold, (2003) "Reduced drag coefficients for high wind speeds in tropical cyclones", *Nature* **422**, 279-283.

Stafford, T. Eric (2010) "Significant Changes to the Wind Load Provisions of ASCE 7-10, An Illustrated Guide," ASCE Press

Vickery, P.J. and D. Wadhera, (2008), "Statistical Models of the Holland Pressure Profile Parameter and Radius to Maximum Winds of Hurricanes from Flight Level Pressure and H*Wind Data", *J. Appl. Meteor*., **47,** 2497-2517

Vickery, P.J., D. Wadhera, M.D. Powell and Y. Chen, (2009a) "A Hurricane Boundary Layer and Wind Field Model for Use in Engineering Applications", *J. Appl. Meteor*., **48,** 381-405

Vickery, P.J.; D. Wadhera, L.A. Twisdale Jr. and F. M. Lavelle, (2009b). "United States Hurricane Wind Speed Risk and Uncertainty", *J. Struct. Eng*. **135,** 301-320

Vickery, P.J, P.F., Skerlj, A.C. Steckley and L.A. Twisdale, (2000a) "Hurricane wind field model for use in hurricane simulations", *J. Struct. Eng.*, **126,** 1203-1221.

Vickery, P.J., P.F. Skerlj and L.A. Twisdale Jr., (2000b) "Simulation of hurricane risk in the U.S. using an empirical track model," *J. Struct. Eng.*, **126**, 1222-1237

Vickery P.J., D. Wadhera, J. Galsworthy, J. A. Peterka, P.A. Irwin, and L. A. Griffis (2010), "Ultimate wind load design gust wind speeds in the United States for use in ASCE-7", *J. Struct. Eng*., **136**, 613-625

OVERVIEW OF UFC 3-340-02, STRUCTURES TO RESIST THE EFFECTS OF ACCIDENTAL EXPLOSIONS

Author: Patrick F. Acosta, PE, US Army Engineering and Support Center, Huntsville; ATTN: CEHNC-ED-CS-S (Acosta); PO Box 1600; Huntsville, AL 35807-4301; phone 256-895-1661; fax 256-895-1602; e-mail: Patrick.F.Acosta@usace.army.mil.

Abstract

UFC 3-340-02, "Structures to Resist the Effects of Accidental Explosions," was recently approved by the Services. Publication of UFC 3-340-02 represents the culmination of a 5-year, Department of Defense Explosives Safety Board (DDESB) effort to update DoD's mandatory blast design requirements for explosives safety applications, as provided in Army TM 5-1300/NAVFAC P-397/AFR 88-22 (TM 5-1300), revision 1, November 1990. As an unlimited distribution document approved for public release, TM 5-1300 has long provided both government and private sector engineers with an invaluable source of blast effects and loading data and with step-by-step procedures for blast analysis and design. UFC 3-340-02 continues this tradition, using straightforward guidance and examples to illustrate and explain protective construction design requirements.

While based upon TM 5-1300, UFC 3-340-02 incorporates several beneficial changes to the manual's reinforced concrete design requirements. This presentation provides an overview of the more significant of these changes. Anticipated, future revisions and additions to other chapters also are presented and discussed.

UFC 3-340-02 may be downloaded from the Whole Building Design Guide website. For users who have the DPLOT computer program, readable versions of some manual figures also are available through this website. In 2003, the Department of Defense Explosives Safety Board (DDESB) established a Technical Working Group to revise the tri-service blast design manual, "Structures to Resist the Effects of Accidental Explosions," Army Technical Manual 5-1300/NAVFAC P-397/AFR 88-22. As an unlimited distribution document approved for public release, TM 5-1300 provides both government and private sector engineers with an invaluable source of blast effects and loading data and with step-by-step procedures for blast analysis and design.

This paper provides a status update of TWG activities and plans for future work. Emphasis will be given to revisions to chapter 4, "Reinforced Concrete Design." Anticipated revisions and additions to other manual chapters also will be presented and discussed.

Introduction

When US Army Technical Manual 5-1300/NAVFAC P-397/AFR 88-22, "Structures to Resist the Effects of Accidental Explosions" (TM 5-1300) was first published in 1969, it provided

engineers with groundbreaking, quantitative procedures for analyzing and designing structures to withstand non-nuclear blast effects (Department of the Army, 1969) [1]. Based upon the results of numerous explosive test programs and accident investigations, the manual included detailed design procedures and step-by-step design examples to illustrate their application. Since reinforced concrete performs particularly well under intense, short duration blast pressures, the manual emphasized the design of reinforced concrete structural elements.

DDESB in 2001 solicited input from a broad range of TM 5-1300 users on recommended changes, corrections, and additions to the manual. APT Research, Inc., Huntsville, AL, consolidated the resulting comments in a summary report (APT Research, 2002) [3]. In October 2002, Naval Facilities Engineering Service Center (NFESC) submitted supplementary comments (NFESC, 2002) [4].

A wide range of input was received. The blast design community strongly recommended the update of the manual, both to remove outdated criteria and to incorporate research conducted since publication of revision 1. In addition, TM 5-1300 users requested the addition of new guidance on various topics such as the retrofit of existing structures, constructability, and the applicability of computer codes in blast resistant design.

Based upon these comments, DDESB established the Technical Working Group to Update Army Technical Manual 5-1300/NAVFAC P-397/AFR 88-22 (TWG) in March 2003. The TWG provides direction to the revision effort and makes technical decisions related to the manual's content. The TWG charter specifically limits the scope to incorporation of existing procedures and products; no new research will be funded. Mr. Bill Zehrt, DDESB, serves as TWG chair.

At the June 2003 organizational meeting, TWG members reviewed recent advances in blast resistant design meriting inclusion in Revision 2. A wide range of areas were considered including blast load prediction and modeling, analytical methods, design procedures, retrofit of existing structures, and innovative blast resistant materials. Per the TWG charter, discussions centered on items that were sufficiently developed to allow their incorporation without additional research.

In addition, the TWG-funded studies to evaluate reinforced concrete research and test data published since the development of revision 1. When warranted, draft revisions to chapter 4 requirements were prepared for TWG consideration.

At the June 2006 TWG meeting, USAESCH was tasked with developing a draft final interim UFC that incorporates both the foregoing changes and other updates approved at the meeting, including the revision of outdated references in chapter 4 to satisfy current code requirements (ACI, 1983) [6] and (ACI, 2008) [7]. Draft final revisions to the manual then were developed and disseminated, first through 2006 DoD Explosives Safety Seminar papers (Woodson and Zehrt, 2006) [8] and (Zehrt, Woodson and Beck, 2006) [9], next through draft final mark-ups to TWG members. Since that time, TWG comments have been resolved and incorporated in chapter 4.

Chapter 4 Revision Highlights

Due to the extent of chapter 4 revisions, it is not feasible to discuss each change in this paper. Instead, we will illustrate the scope of the changes by providing portions of the pending revision 2 guidance in four manual sections: Section 4-13.2. Dynamic Increase Factor; Section 4-22. Design of Non-Laced Reinforced Slabs – Introduction; Section 4-55. Prediction of Concrete Spalling; and Section 4-66.3.1. Single Leg Stirrups.

4-13.2. Dynamic Increase Factor

The dynamic increase factor, DIF, is equal to the ratio of the dynamic stress to the static stress, e.g., f_{dy}/f_y, f_{du}/f_u and f'_{dc}/f'_c. The DIF depends upon the rate of strain of the element, increasing as the strain rate increases. The design curves for the DIF for the unconfined compressive strength of concrete are given in Figure 4-9 for $2{,}500 < f'_c < 5{,}000$ psi and in Figures 4-9a and 4-9b for $f'_c = 6{,}000$ psi. Test values for the DIF in tension (before cracking) also are given on Figures 4-9a and 4-9b. The DIF design curves for the yield and ultimate stresses of ASTM A 615 Grade 40, Grade 60 and Grade 75 reinforcing steel are given in Figure 4-10. Grade 40 steel is not permitted in new protective construction. Thus, Grade 40 data are provided for comparative purposes and for use in evaluating existing construction. The curves were derived from test data having a maximum strain rate of 300 in./in./sec. for concrete and 100 in./in./sec. for steel. Values taken from these design curves are conservative estimates of DIF and safe for design purposes.

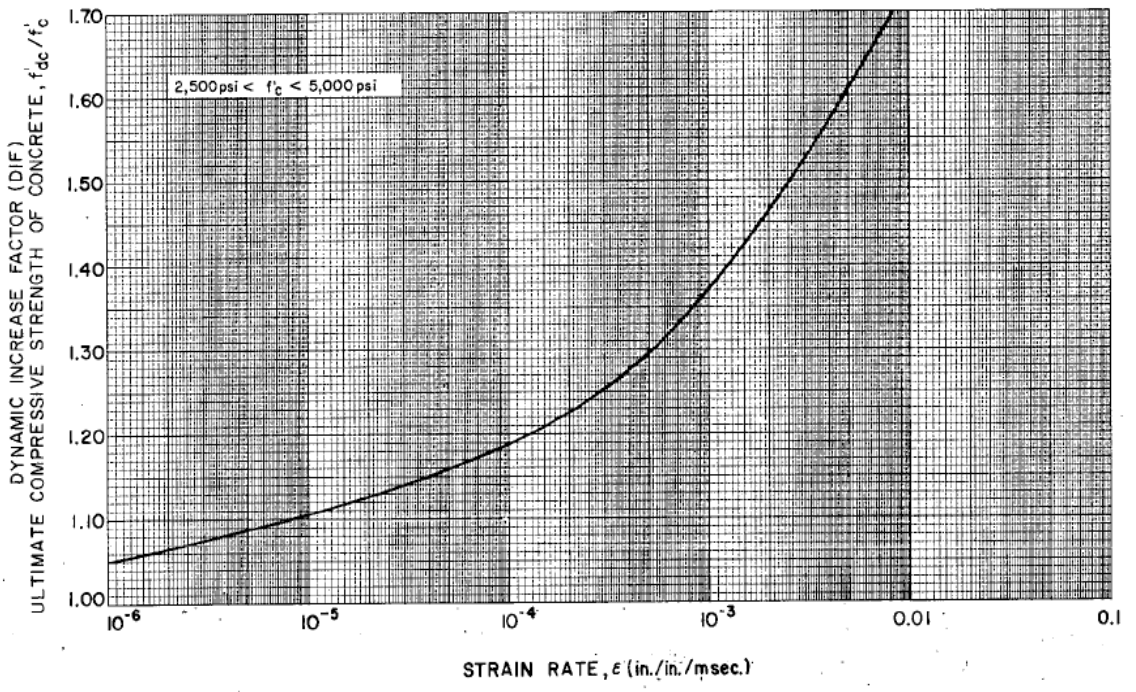


Figure 4-9 Design curve for DIF for ultimate compressive strength of concrete ($2{,}500$ psi $< f'_c < 5{,}000$ psi)

Figure 4-9a Design Curves for *DIFs* for Ultimate Compressive and Tensile Strengths of Concrete (f'_c = 6,000 psi) in Semi-Log Format

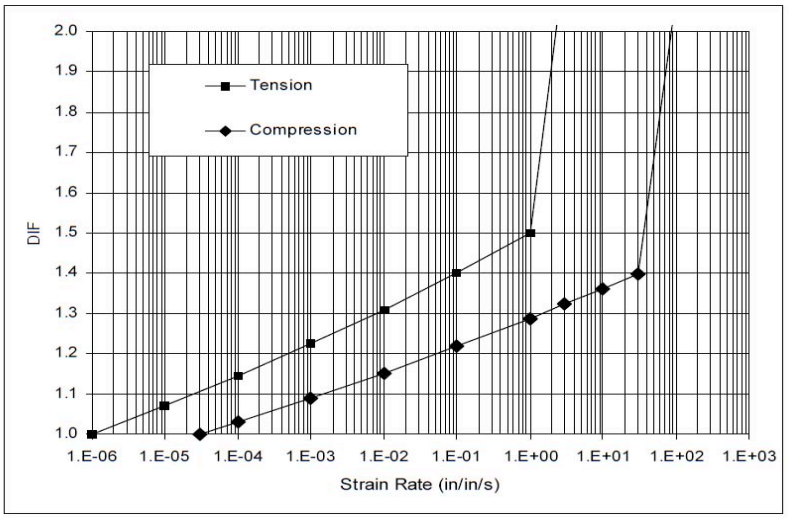


Figure 4-9b – Design Curves for *DIFs* for Ultimate Compressive and Tensile Strengths of Concrete (f'_c = 6,000 psi) in Log-Log Format

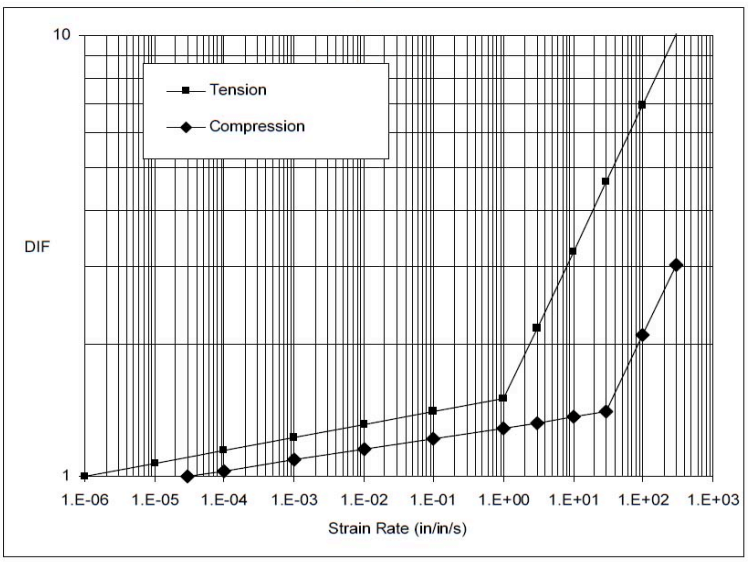
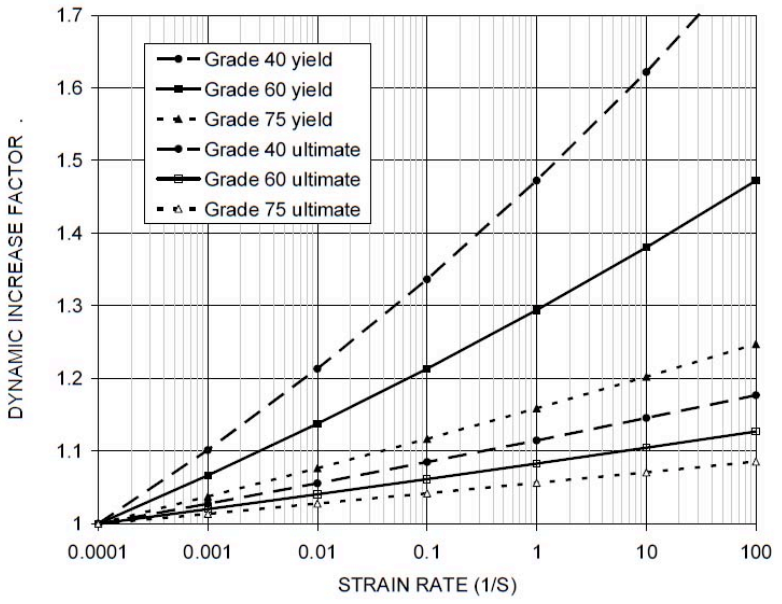


Figure 4-10 Design Curves for *DIFs* for Yield and Ultimate Stresses of ASTM A 615 Grade 40, Grade 60, and Grade 75 Reinforcing Steel



Section 4-22. Design of Non-Laced Reinforced Slabs - Introduction

Conventional reinforced concrete elements are for the purpose of this manual, members without lacing. These non-laced elements make up the bulk of protective concrete construction. They are generally used to withstand the blast and fragment effects associated with the far design range but may also be designed to resist the effects associated with the close-in design range. Non-laced elements may be designed to attain small or large deflections depending upon the protection requirements of the acceptor system.

A non-laced element designed for far range effects may attain deflections corresponding to support rotations up to 2 degrees under flexural action. Single leg stirrups are not required to attain this deflection. However, shear reinforcement is required if the shear capacity of the concrete is not sufficient to develop the ultimate flexural strength.

Type A, Type B, or Type C single leg stirrups, as defined in section 4-66.3, must be provided when a non-laced element is designed to resist close-in effects. The shear reinforcement must be provided to prevent local punching shear failure. When the explosive charge is located at scaled distances less than 1.0, Type C single leg stirrups or lacing must be employed. For scaled

distances greater than 1.0 but less than 3.0, single leg stirrups must be provided, while for scaled distances greater than 3.0, shear reinforcement should be used only if required by analysis.

Type A stirrups may be used only if concrete spalling is prevented and the scaled distance is greater than 1.0. If these requirements are satisfied, a slab with Type A stirrups may attain deflections corresponding to support rotations up to 2 degrees under flexural action.

A slab with Type B or Type C stirrups may attain deflections corresponding to support rotations of up to 12 degrees. While Type B stirrups may be used only if the scaled distance is greater than 1.0, Type C stirrups are allowed as long as the minimum separation distance requirements of section 2-14.2.1 are satisfied. It should be emphasized that the Section 2-14.2.1 separation distances are the minimum clear distance from the surface of the charge to the surface of the element. The normal scaled distances R_A (center of charge to surface of barrier) corresponding to these minimum clear separation distances are equal to approximately 0.25 ft/lb$^{1/3}$.

A type I and II cross-section provides the ultimate moment capacity and mass to resist motion for elements designed for 2 and 6 degrees support rotation, respectively. If spalling occurs then a type III cross-section would be available. In addition, a non-laced element designed for small deflections in the close-in design range is not reusable and, therefore, cannot sustain multiple incidents.

A non-laced reinforced element may be designed to attain large deflections, that is, deflections corresponding to incipient failure. These increased deflections are possible only if the element has sufficient lateral restraint to develop in-plane forces. The element may be designed for both the close-in end far design range. A type III cross-section provides the ultimate moment capacity and mass to resist motion.

4-55. Prediction of Concrete Spalling

As previously explained, direct spalling is due to a compression wave traveling through a concrete element, reaching the back face and being reflected as a tension wave. Spalling occurs when the tension is greater than the tensile strength of the concrete.

Many spall tests have been conducted on the configuration shown in Figure 4-65, where a cylindrical charge, cased or bare, is oriented side-on at a stand-off distance from a wall slab and oriented end-on in contact with the ground. Tested variations to this configuration include non-cylindrical charge shapes, charges off the ground, and charges in contact with the slab. Test data for all of these cases have been compiled and analyzed and are plotted in Figure 4-65a. The test data in this figure are reported in terms of the observed severity of spall, i.e., as either no spall, spall (no breach), or breach. Threshold spall and breach curves are plotted as approximate upper bounds to the spall and breach data points, respectively and may be used in design. The spall threshold curve is given by Equation 4-178:

$$\frac{h}{R} = \frac{1}{a + b\Psi^{2.5} + c\Psi^{0.5}} \qquad 4\text{-}178$$

where: h = concrete thickness (ft.)
R = Range from slab face to charge center of gravity (ft.)
a = -0.02511
b = 0.01004
c = 0.13613
Ψ = spall parameter (equations 4-180a and 4-180b)

The breach threshold curve is given by Equation 4-179:

$$\frac{h}{R} = \frac{1}{a + b\Psi + c\Psi^2} \qquad 4\text{-}179$$

where: h = concrete thickness (ft.)
R = range from slab face to charge center of gravity (ft.)
a = 0.028205
b = 0.144308
c = 0.049265
Ψ = spall parameter (Equations 4-180a and 4-180b)

The spall parameter for noncontact charges is given by Equation 4-180a:

$$\Psi = R^{0.926} f'_c{}^{0.266} W_{adj}{}^{-0.353} \left(\frac{W_{adj}}{W_{adj} + W_c} \right)^{0.333} \qquad 4\text{-}180a$$

Equation 4-180b gives the spall parameter for contact charges:

$$\Psi = 0.527 R^{0.972} f'_c{}^{0.308} W_{adj}{}^{-0.341} \qquad 4\text{-}180b$$

where: Ψ = spall parameter
R = range from slab face to center of charge (ft.)
f'_c = concrete compressive strength (psi)
W_{adj} = adjusted charge weight (lb)
W_c = steel casing weight (lb)

The spall parameter equations have limits of $0.5 \leq \Psi \leq 14$. The adjusted charge weight, W_{adj}, is the weight of a hemispherical surface charge that applies an equal explosive impulse at the target to that of the actual charge (see Figure 4-65) and is given by Equation 4-181a:

$$W_{adj} = B_f C_f W \qquad 4\text{-}181a$$

where: W_{adj} = adjusted charge weight (lb)
B_f = burst configuration factor = 1.0 for surface bursts, 0.5 for free air bursts
W = equivalent TNT charge weight (lb)
C_f = cylindrical charge factor given by equations 4-181b and 4-181c:

$$C_f = 1 + 2\left(\frac{LD}{\pi(3LD^2/16)^{0.667}} - 1\right)\left(1 - \frac{R}{2W^{0.333}}\right); \text{L > D and R/W}^{0.333} < 2.0 \qquad \text{4-181b}$$

$C_f = 1.0$; all other cases 4-181c

where: L = charge length [ft]
D = charge diameter [ft]
R = range from slab face to charge center of gravity [ft]
W = equivalent TNT charge mass [lb]

The burst configuration factor, B_f, is used to correct to a surface burst condition, such as the ground in Figure 4-65. The charge shape factor, C_f, is used to correct to a hemispherical charge geometry in the case of close-in cylindrical charges oriented side-on to the slab. These corrections are applicable to both standoff and contact charges. It should be considered in design that when the munition position is variable, a contact burst may not be worst-case. The spall effect for cased charges can be greatest at a small standoff, particularly for heavy casings.

The test data range listed in Table 4-15a for each parameter shows that the data spans a wide range of subscale and full-scale tests. Although subscale tests predominate in the data base, the applicability of Figure 4-65a to large full-scale weapons is enhanced by the fact that concrete strain rate effects are accounted for in the Ψ term.

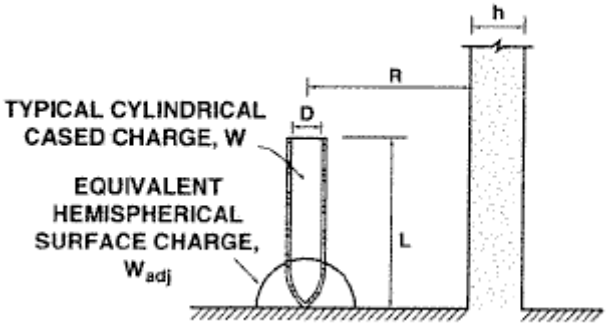


Figure 4-65 Typical geometry for spall predictions

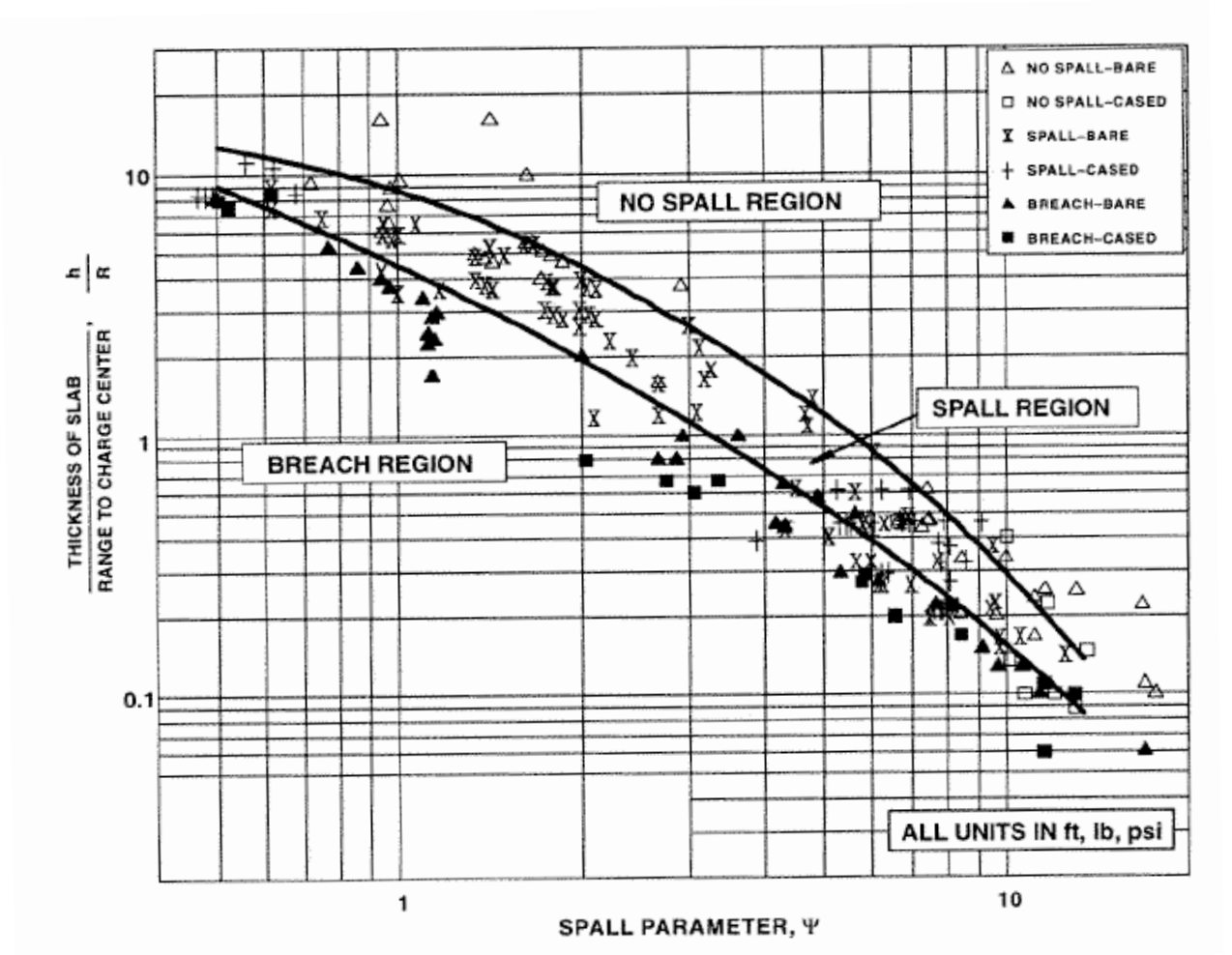


Figure 4-65a Threshold spall and breach curves for slabs subject to high-explosive bursts in air (standoff and contact charges, cased and bare)

Table 4-15a Parametric ranges for spall prediction

Parameter	Max.	Min.	Avg.	
R, in.	360	0.1	21.0	
Charge Weight, W, lb.		2299	0.03	24.4
Case length, in.		60.0	0.80	8.8
Case diameter, in.	18.0	0.80	4.0	
Case thickness, in.	0.62	0.00	0.05	
[1]$R/W^{1/3}$, $in/lb^{1/3}$		12.1	0.008	0.70
Concrete thickness, T, in.		84.0	2.00	9.23
f'_c, psi	13815	1535	5067	
Rebar spacing, S, in.	11.8	1.25	7.16	
Reinf. Ratio, ρ	0.025	0.0005	0.0054	

[1] Per section 4-32, the minimum allowable design value for $R/W^{1/3}$ is approximately 0.25 $ft/lb^{1/3}$.

4-66.3. Elements Reinforced with Single Leg Stirrups

4-66.3.1. Single Leg Stirrups

A single leg stirrup consists of a straight bar with a hook at each end. Minimum bar bend requirements for single leg stirrups depend upon both the design support rotation and the scaled distance of the charge from the element, as follows:

1. Type A – Single leg stirrup with a 90-degree hook on one end and a 135-degree hook on the other end. Type A stirrups may be used only if the scaled distance from the center of the charge to the element is greater than 1.0 $ft/lb^{1/3}$, the design support rotation is 2-degrees or less, and concrete spalling is prevented in accordance with section 4-55. Placement requirements for Type A stirrups are summarized in Figure 4-101. For elements designed for blast loading on one-face only, the 90-degree leg shall be placed on the blast face. For elements designed for blast loading on either face, the 90-degree leg shall be alternated between each face.

2. Type B – Single leg stirrup with 135-degree hooks on both ends. Type B stirrups may be used only if the scaled distance from the center of the charge to the element is greater than 1.0 $ft/lb^{1/3}$. Type B stirrups are acceptable for all protection categories and thus, may be used for design support rotations up to 12-degrees.

3. Type C – Single leg stirrup with 180-degree hooks on each end. Type C stirrups may be used for all charge separation distances allowed by this manual. Type C stirrups also are acceptable for all protection categories and thus, may be used for design support rotations up to 12-degrees.

Hooks shall conform to the ACI 318 Building Code. At any particular section of an element, the longitudinal flexural reinforcement is placed to the interior of the transverse reinforcement and the stirrups are bent around the transverse reinforcement (Fig. 4-101).

The required quantity of single leg stirrups is calculated in the same manner as lacing. It is a function of the element's flexural capacity while the size of rebar used is a function of the required area and spacing of the stirrups. The maximum and minimum size of stirrup bars are No. 8 and No. 3, respectively, while the spacing between stirrups is limited to a maximum of d/2 or $d_c/2$ for type I and type II or III cross-sections, respectively.

The preferable placement of single-leg stirrups is at every flexural bar intersection. However, the transverse flexural reinforcement does not have to be tied at every intersection with a longitudinal bar. A grid system may be established whereby alternate bar intersections in one or both directions are tied within a distance not greater than 2 feet. The choice of the three possible schemes depends upon the quantity of flexural reinforcement, the spacing of the flexural bars and the thickness of the concrete element. For thick, lightly reinforced elements, stirrups may be furnished at alternate bar intersections, whereas for thin and/or heavily reinforced elements, stirrups will be required at every bar intersection. For those sites where large stirrups are required at every flexural bar intersection, the bar size used may be reduced by furnishing two stirrups at each flexural bar intersection. In this situation, a stirrup is provided at each side of longitudinal bar.

Single leg stirrups must be distributed throughout an element. Unlike shear reinforcement in conventionally loaded elements, the stirrups cannot be reduced in regions of low shear stress. The size of the stirrups is determined for the high stress areas and, because of the non-uniformity of the blast loads associated with close-in detonations, this size stirrup is placed across the span length to distribute the loads. For two-way elements, diagonal tension stresses must he resisted in two directions. The size of stirrup determined for each direction is placed to the same extent as the lacing shown in Figure 4-92. However, the distribution does not apply for cantilever elements since they are one-way elements requiring only one stirrup size which is uniformly distributed throughout.

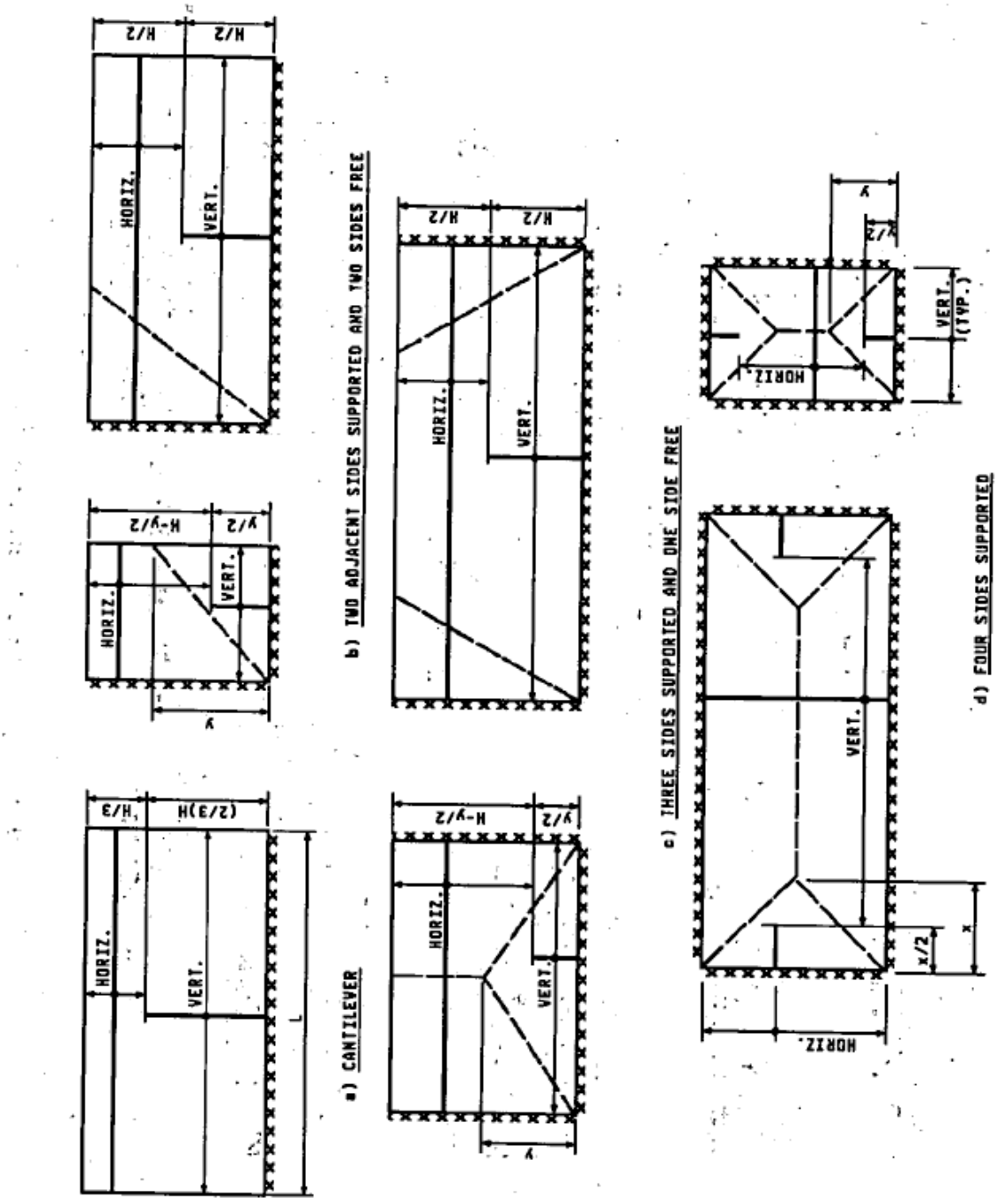
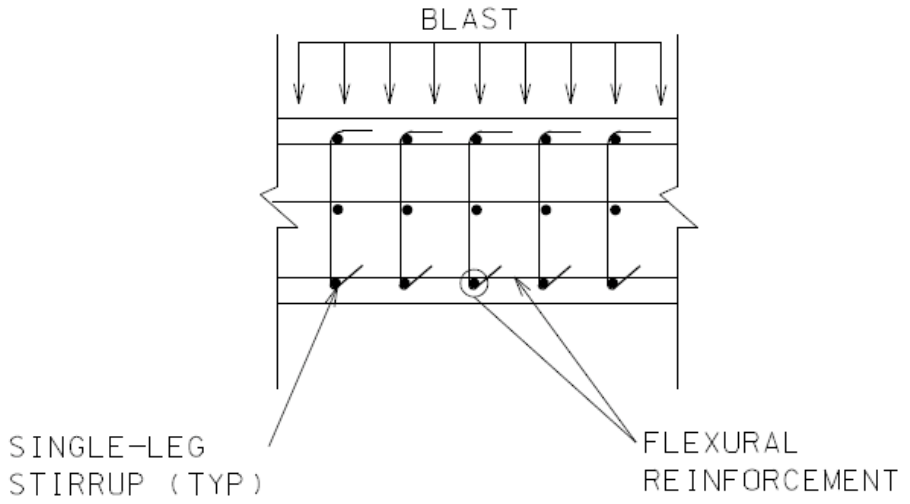


Figure 4-92 Typical locations of continuous and discontinuous lacing



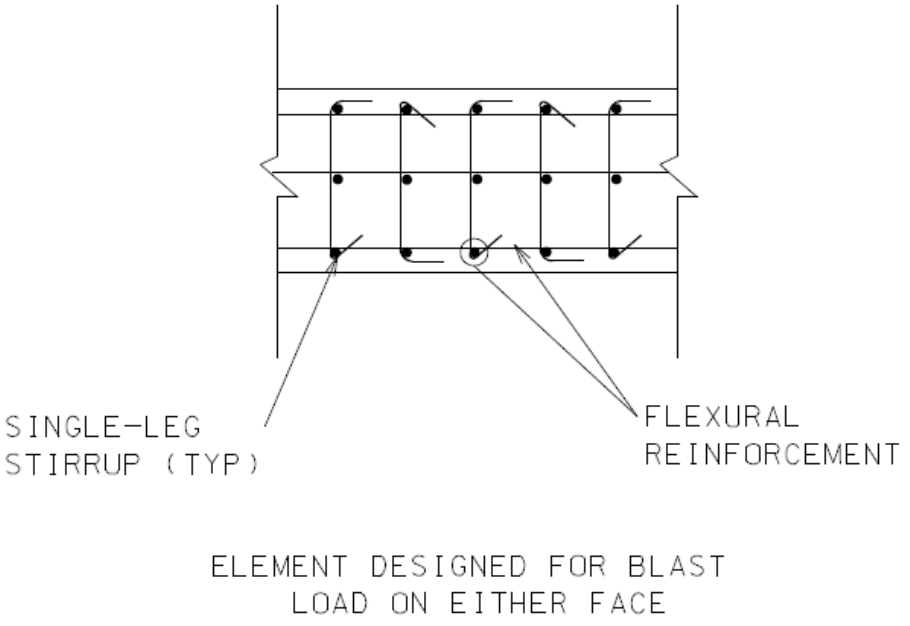


Figure 4-101 Placement requirements for Type A single-leg stirrups.

Future Work

Future TM 5-1300 TWG tasks will focus on two areas. First, we will continue to update and expand the content of TM 5-1300. We anticipate that this work will include the revision of the gas pressure calculation procedure for partial containment cells (Bogosian & Zehrt, 1998) [10], (Tancreto & Zehrt, 1998) [11] and (Hager, Doolittle and Needham, 2006) [12]; the update and expansion of structural steel and masonry design guidance; and the addition of new guidance on innovative materials and retrofit of existing structures. Second, we will support both JUM development and the corresponding revision of TM 5-1300 to provide guidance specific to explosives safety applications.

Conclusions and Recommendations

Since its initial publication in 1969, Army TM 5-1300/NAVFAC P-397/AFR 88-22 (TM 5-1300, 1969) [1] has provided uniquely practical and intuitively straightforward procedures for analyzing and designing blast resistant structures. With its unlimited distribution, TM 5-1300 is the blast design manual of choice of both government explosives safety experts and private A-E firms throughout the world.

The September 11, 2001 terrorist attacks on the United States underscore the need for up-to-date, blast design guidance. To obtain maximum benefit from recent research advances, pertinent data must be disseminated quickly to the blast design community in an open distribution document. Whenever possible, guidance should be written so it can be understood and applied by a veteran structural designer with little or no blast experience.

Although the interim TM 5-1300 UFC chapter 4 revision will provide updated guidance in several key areas, additional revisions and supplementary coverage of new, innovative systems and materials are sorely needed. Future TWG work will concentrate on developing and disseminating this guidance, either in a future TM 5-1300 revision or in the proposed Joint Use Manual for the explosives safety, hardened structures, and AT/FP communities.

References

1. Departments of the Army, the Navy, and the Air Force (1969), *Structures to Resist the Effects of Accidental Explosions*, Army Technical Manual No. 5-1300, Navy Publication NAVFAC P-397, and Air Force Manual AFM 88-22, Washington, DC.

2. Departments of the Army, the Navy, and the Air Force (1990), *Structures to Resist the Effects of Accidental Explosions*, Army Technical Manual No. 5-1300, Navy Publication NAVFAC P-397, and Air Force Manual AFM 88-22, Revision 1, Washington, DC.

3. APT Research, Inc. (2002), "Final Report TM 5-1300 Comments and Suggested Revisions," Huntsville, AL.

4. Naval Facilities Engineering Service Center (NFESC) (2002), "Proposed Revisions Army TM 5-1300 Navy NAVFAC P-397, Air Force AFR 88-22 Structures to Resist the Effects of Accidental Explosions," Port Hueneme, CA.

5. The Departments of the Army, Air Force, and Navy and the Defense Special Weapons Agency (1998), *Design and Analysis of Hardened Structures to Conventional Weapon Effects*, UFC 3-340-01 (formerly Army TM 5-855-1, Air Force AFPAM 32-1147(I), Navy NAVFAC P-1080, DSWA DAHSCEWMAN-97), Washington, DC.

6. American Concrete Institute (1983), *Building Code Requirements for Reinforced Concrete (ACI 318-83)*, Detroit, MI.

7. American Concrete Institute (2008), *Building Code Requirements for Structural Concrete (ACI 318-08) and Commentary (ACI 318R-08)*, Detroit, MI.

8. Woodson, S. C. and Zehrt, W. H., Jr., "Investigation of Army TM 5-1300/NAVFAC P-397/AFR 88-22 Diagonal Tension Requirements at Low Scaled Distances," Thirty-Second DOD Explosives Safety Seminar Proceedings, Philadelphia, PA, August 2006.

9. Zehrt, W. H., Jr., Woodson, S. C., and Beck, D. C., "Investigation of Army TM 5-1300/NAVFAC P-397/AFR 88-22 Bar Bend Requirements for Single Leg Stirrups used as Diagonal Tension Reinforcement," Thirty-Second DOD Explosives Safety Seminar Proceedings, Philadelphia, PA, August 2006.

10. Bogosian, D. D. and Zehrt, W. H., Jr. (1998), "Assessment of Analytical Methods Used to Predict the Structural Response of 12-inch Concrete Substantial Dividing Walls to Blast Loading," presented at 28th DoD Explosives Safety Seminar, Orlando, FL.

11. Tancreto, J. E. and Zehrt, W. H., Jr. (1998), "Design for Internal Quasi-Static Pressures from Partially Contained Explosions," presented at 28th DoD Explosives Safety Seminar, Orlando, FL.

12. Hager, K., Doolittle, C. and Needham, C. (2006), “Proposed Gas Pressure Rise-Time Model for TM 5-1300 <March 2006 Draft>,” Technical Report TR-2273-SHR, Naval Facilities Engineering Service Center, Port Hueneme, CA.

Design of Windows for Blast Loading – Moving Forward

D. Duke[1], J. S. Shull[2], and R. S. Browning[3]

[1]Daniel Duke, Ph.D., P.E., Staff Engineer, Southern Research Institute
757 Tom Martin Drive, Birmingham, AL 35211
PH (205) 410-9603; email: DanDuke@SouthernResearch.org
[2]Jonathan S. Shull, P.E., Structural Engineer, Black & Veatch
6601 College Park Boulevard, Overland Park, KS 66211
PH (816) 808-7766; email: ShullJS@BV.com
[3]Robert S. Browning, E.I., A.M.ASCE, Research Civil Engineer, Geotechnical and Structures Laboratory, U.S. Army Engineer Research and Development Center
3909 Halls Ferry Road, CEERD-GS-M, Bldg 5008, Vicksburg, MS 39180-6199
PH (601) 634-5228; email: Robert.S.Browning@usace.army.mil

ABSTRACT

This paper presents a brief overview of historical and current practices for the design of windows and glass curtain walls subjected to short-duration, high-energy loading from blast shock waves. General discussion is provided that describes typical treatment of force-displacement relationships, boundary conditions, pre- and post-cracked behavior of laminated glass, and failure criterion. Various practical examples from design projects are presented that demonstrate limitations or misapplications of methods that are often used in blast engineering. Developments from parallel research are cited to highlight some of the current deficiencies.

CLASSICAL METHODS

High-energy load events associated with accidental and intentional explosions present serious threats to the physical safety of building occupants in countless private, commercial, and government facilities around the world. In particular, there continue to be very real threats of terrorist attacks against U.S. assets globally. The threats often take the form of high-energy, short-duration blast-induced forces applied to the exterior of buildings. As part of the façade of a building, windows and glass curtain walls most often serve as weak points in the protection of personnel against explosion events. Failure of windows often results in physical harm or death of occupants. "In the 1996 Khobar Towers Bombing for example, approximately 80 – 90% of injuries were caused by flying glass." (HazL, 2004).

Major testing, research, and development efforts over decades have focused on design of windows to protect against blast loading. Several references offer insight into many of the technical aspects of window design including ASCE (1999), GANA (2010), HazL (2004) and WINGARD (2005). As is typical of structural applications, the design process involves load prediction, physical model definition,

mathematical solution, response evaluation, failure criteria assessment, and design of support system.

In the context of this paper, reference to classical methods may include classical analytical developments and empirical methods where physical test data or finite element analysis results are used to characterize various aspects of the problem. The discussion that follows highlights selected topics related to classical approaches to the evaluation of windows and glass curtain walls for blast application. An exhaustive treatment of the issue is well beyond the scope of this paper.

Load prediction.

Blast loads are obtained from information regarding explosive charge type, mass, and position relative to the impacted structure. Predictive methods typically result in pressure versus time load curves similar to those shown in Figure 1. The curved line is the result of an exponential-form curve fit of experimental data which is rooted in developments by Friedlander (1946). As represented by the curve, the pressure wave typically exhibits a very short (almost instantaneous) rise time to a peak pressure. The pressure is initially positive against exposed surfaces (positive phase) followed by a negative pressure pulling away from the surface (negative phase). The peak positive pressure is typically several times larger than the largest negative pressure. Accordingly, the pressure wave may often be idealized by a simple linear load curve as shown in Figure 1. The linear curve is in the shape of triangular pulse with a zero rise time. The area under the triangular pulse is typically set equal to the area under the positive phase portion of the Friedlander curve. Both forms are often used in blast engineering with the linear shape being particularly suited for the application of classical methods (Biggs, 1964).

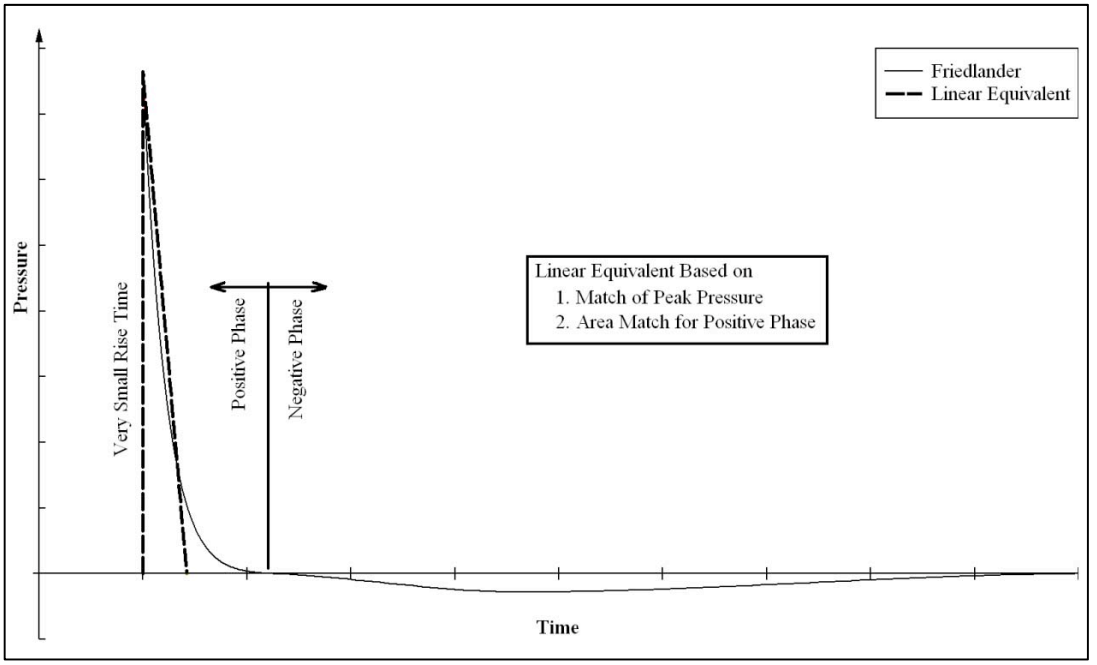


Figure 1. Pressure versus time curve.

Physical model definition.

Characteristics that are considered in historical and current modeling tools include the following.

1. Glass Characteristics. The response of glass is generally treated as linearly elastic up to a stress level corresponding to brittle cracking. Glass cracking varies in stress and crack pattern depending on glass type (annealed, heat strengthened, tempered, etc.). Glass generally exhibits a relatively large range of maximum stress versus probability of failure. Low failure probabilities are typically used in the selection of glass while higher glass failure probabilities (yielding higher reaction predictions) are used in the design of the glass support framing.

2. Glass Makeup. Glass "make-up" is used to describe the combination of glass and other components that serve as the "glass" portion of a window. The glass make-ups vary depending on specific application and performance requirements. Glass make-ups can include combinations of monolithic glass plates, intermediate air spaces, laminated glass panels, shatter resistant films, and ballistic resistant layers. Laminate inner layers, shatter resistant films, and ballistic layers are typically modeled as linearly elastic or linearly elastic perfectly plastic materials. Air spaces are often treated as gaps with closed volumes of air. The closed volume of air effectively serves as a nonlinear spring between inner and outer panes of glass.

3. Boundary Conditions. Figure 2 depicts the two classes of boundary conditions that are most often used in current practice. In the pre-cracked configuration, the edge is held against translation normal to the plane of the glass. Thus, the glass edge is allowed to translate toward the support edge. This assumption is consistent with that included in Moore (1980), which serves as a key reference in much of the mathematical modeling of the glass. The post-cracked stage of the glass response (non-monolithic) is assumed to be dominated by membrane action of inner layers or films. The post-crack membrane edge condition has the glass edge restrained against movement toward the support edge. The implied assumption is that in-plane reactive forces develop between the laminate or film and the supporting frame through some form of friction, bonding, or mechanical attachment.

   The supports are assumed to be dynamically rigid as related to glass response calculations. Limits on support displacement and rotation are typically imposed with an aim toward maintaining a safe overlap between the edge of the glass and the edge of the support (glass bite).

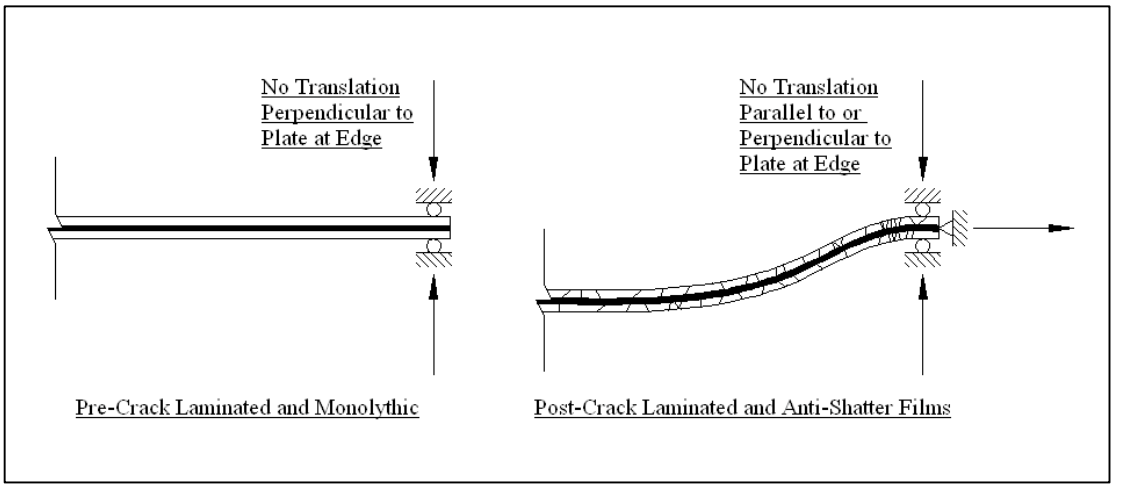


Figure 2. Glass edge boundary conditions.

4. Force – Displacement Relationships. In the context of classical blast engineering applications, resistance functions are developed to represent the response of structural components to load. Figure 3 shows various resistance functions for a simple laminated glass make-up. As seen in Figure 3, the HazL Analytical curve and the WINGARD Default curve yield very similar results. The most pronounced differences lie in the following:

    a. Probability of glass failure and associated glass cracking stress.
    b. Single-step glass cracking versus two-step glass cracking.
    c. Prediction of yield stress in the laminate.

    Various other issues may influence the shape of the resistance function including limitations on maximum glass deflection plus stress or strain limits for laminates, films, and ballistic materials.

    Referring again to Figure 3, the HazL Empirical curve shows significantly higher resistance capacity in the post-crack phase of the response compared with the analytical model results. This observation matches results from research related to edge capacity of through-bolted glass (Duke et al., 2009). It is proposed that the increase in resistance is associated with the post-crack interaction between the glass and the laminate. In the analytical model results presented in Figure 3, the post-cracked glass is assumed to contribute mass with no stiffness to the laminate membrane. In reality, the post-crack piecewise continuous attachment of glass fragments to the laminate interlayer provides increased bending and in-plane stiffnesses that are not accounted for in the current classical analytical models.

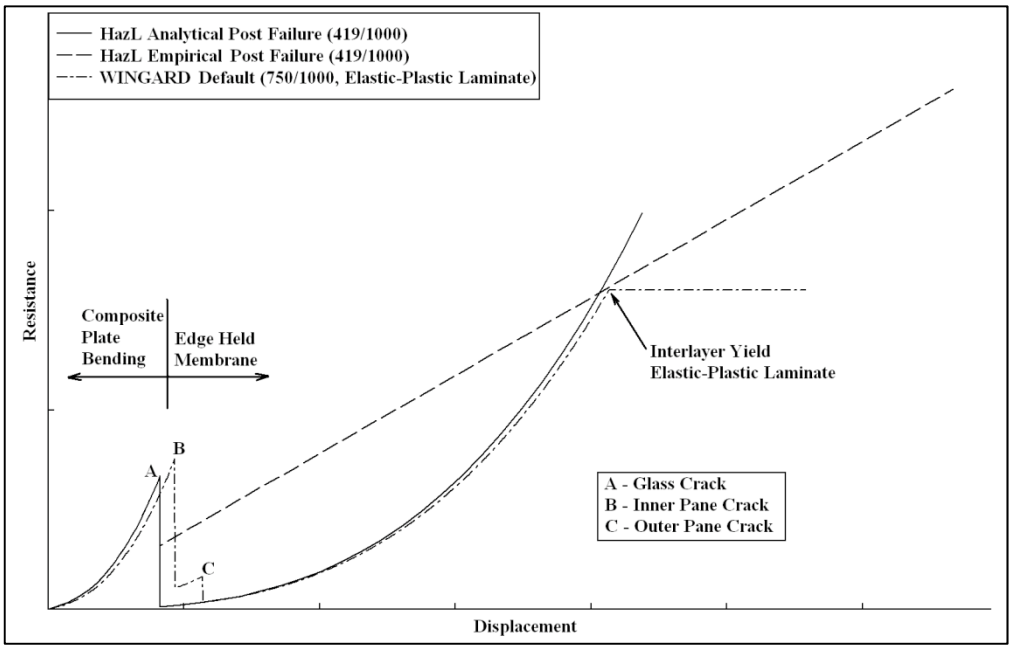


Figure 3. Glass resistance function.

Mathematical solution.

In general, load applications similar to Figure 1 along with force-displacement relationships similar to Figure 3 combine to yield nonlinear transient dynamic problems. In the simplest form, the problem may be treated using a classical equivalent static load method. In most cases, however, the dynamic nature of the problem mandates application of single-degree-of-freedom (SDOF) numerical solution techniques similar to those discussed by Biggs (1964). The solutions typically yield a displacement as the primary result with stresses and reactions as secondary. If predicted glass deflections indicate separation of the pane from the support, projectile dynamics calculations are typically performed to predict the flight paths of fragments.

Response evaluation.

1. Displacements. The displacement prediction resulting from the mathematical solution represents the maximum displacement in the glass panes (at the center of the panel). Assuring that the glass remains attached to the frame is most often essential to a suitable design. In addition to stress and strain evaluations for the various layers of the glass make-up, the bite is evaluated relative to the displaced shape of the glass. A common practice for bite evaluation is represented in Figure 4. The primary concern is that the edge of the glass remains engaged with the support. As the glass deflects, the glass edge moves toward the edge of the support, and the bite dimension decreases. For small glass displacements, the bite reduction is small. However, many blast window designs exhibit very large displacements where the bite can be

compromised. As indicated in Figure 4, the overall glass length is assumed to be unchanged (no in-plane membrane strain).

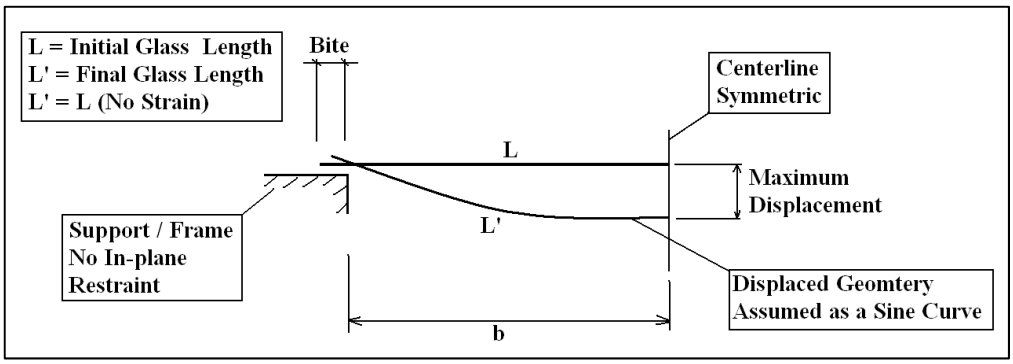


Figure 4. Bite evaluation.

2. Stresses and Strains. Pre-crack stresses are often evaluated using methods similar to Moore (1980) wherein laminated panes are treated as monolithic glass. A lamination factor is often used to account for the lower stiffness of laminated glass. Post-crack stresses are obtained from classical membrane developments where the edge is assumed to be pinned but held against in-plane translation (true pin – not a roller).

3. Reactions. Edge reactions are determined by using simple equations from dynamics and/or force displacement relationships. Given that SDOF models are typically used, the edge shear reactions are represented by a total force as a function of time. The total force is typically distributed around the glass edges using results from small displacement plate theory, which is historically considered accurate for displacements up to approximately one-half the plate thickness. Note that in the context of blast window design, the displacements are most often much higher than one-half the plate thickness. In-plane reactions may be obtained from the post-cracked membrane model described above. Note that boundary conditions integral to the pre-cracked plate model do not include allowance for in-plane reactions at the supported edge.

Failure criteria.

Various limits are imposed that influence component level responses including glass stress and glass deflection. Either may be used to trigger glass cracking. Limits on predicted laminate and film membrane strains are also imposed that prevent. The limits which are based on a percentage of strain to material failure typically represent very large global strains that may be unrealistic when evaluated in light of the post-cracked glass behavior discussed below. Global failure of a glass pane results from either failure of all layers in a pane or loss of bite at the edge of the glass. The actual definition of failure associated with the response of windows to blast loading most often falls into the following categories.

1. No glass breakage predicted. Glass remains attached to the frame.

2. Glass cracks but remains attached to the frame. A limited number of glass shards may travel some distance into the building.

3. Global failure. Glass panes separate from the frame and travel into the building. Categories are defined that effectively scale the violence with which the glass travels into the building (GANA, 2010).

4. Window travelling away from the building. The window separating from the frame and falling away from the building may occur due to some combination of timing of the negative phase, dynamic rebound of window, and weaker restraint at the support in the outward direction.

Design of support system.

Predicted dynamic reactions are typically reported in terms of force versus time. The dynamic reaction curves are most often used as input for the evaluation of connections and framing members. In the case of reactive (flexible) support systems, dynamic methods similar to those indicated above for the glass are used to predict dynamic responses. An embedded assumption is that the support response and the glass response are dynamically uncoupled. Limits on frame deflections are typically imposed that serve to support many assumptions made in the window analysis developments. Note that blast events most often result in high strain-rate responses of structural components. Accordingly, some increased effective strength is often allowed for selected materials.

FINITE ELEMENT METHODS

The finite element method has been a viable tool for decades in structural engineering and, specifically, nonlinear transient dynamic applications. Proper application of the methods to windows and curtain wall systems requires the following:

1. Understanding the physical characteristics of the actual structures.
2. Understanding the nature of blast load events and the general response of structural components.
3. Understanding nonlinear dynamic applications of the principles from engineering mechanics.
4. Understanding finite element methods in the context of nonlinear transient applications.

Viable finite element solutions to blast window and curtain wall applications fit into two major categories. First are high fidelity models that require large amounts of memory, large computers, and/or excessive computational time. Modeling and post-processing requirements may be unwieldy. The glass make-up may, for example, be modeled using several layers of solid elements that by their nature drive

up the model size. This class of solution is particularly useful for research and development efforts but is simply not practical for production design applications.

The second category of models compares with those used by Browning et al. (2009) and Duke (2005). Beam, shell, contact, weld, and solid elements are used to capture the essence of the physical characteristics of the structure. This type of model is suitable for practical design applications in that they execute quickly on a personal computer. Most of the key aspects of the system response may be captured including glass response, edge loading, component stresses, dynamic reactions, and displacement of reactive supports. This class of finite element model has repeatedly been shown to provide reasonable predictions of blast response and can be particularly useful in guiding the development, design, and evaluation process. As with the high-fidelity models, this type of model can be very useful in support of research and development efforts related to dynamic response of structures.

A primary limitation of plate-element-level finite element models for windows and curtain walls relates to the element formulations available for laminated glass. As an example, LS-DYNA (2006) has a laminated glass model that includes polymer layers and glass layers. As the predicted glass stresses exceed an input failure stress, the glass stiffness is removed from the element. In effect, the post-cracked stiffness of the laminated glass is primarily that of the internal polymer layer acting as a membrane. This characteristic matches a basic assumption included in the classical approach discussed above. As indicated above, the reality is that the post-cracked behavior of laminated glass panes is most often much different from that of a simple membrane.

A second concern regarding plate-element-level models relates to the experience and technical knowledge of the analyst. In general terms, blast engineering requires specialized abilities and experience for proper application of any of the available tools (SDOF, experimental, empirical and finite element). However, issues related to model design including selection of element type, element formulations, material models, mesh refinement and integration schemes cause yet another level of technical requirements for proper use of plate-element-level finite element models.

TECHNICAL CHALLENGES

As suggested by the discussion above, there are several areas where it is challenging to execute technically sound investigations using the current methods. As an example, Figure 5 shows representative cross sections for glass to mullion attachment for a curtain wall design at a government office building in the United States. The aluminum extrusions serve as the frame members for the glass. In the context of the actual project, some of the extrusions are primary and span floor to floor vertically. Other frame members are secondary and span between the primary verticals. In the case shown, the glass make-up includes a laminated inner pane with a monolithic outer pane separated by a closed air space. The inner pane is attached to the frame at the inside edge with structural silicone. The outer edge is covered by a non-structural snap cover. Screw chases are included in the extruded shapes to provide for mullion to mullion connection, typically using shear blocks.

Eccentric loading.

Note that while the middle image in Figure 5 amplifies the possibility of eccentric loading on the mullions, reality may be much worse. As an example, glass may only be on one side of the frame member. The glass span dimensions and resulting edge loadings are most often different on either side of the frame. The fact that the structural silicone attachment is at the inside edge only results in eccentric resistance to in-plane forces in the glass. The eccentric loading conditions cause torsional rotation of the mullions and edge bending of the glass that is often not considered using classical methods. Both responses may contribute to additional glass stresses and possible compromise of bite retention.

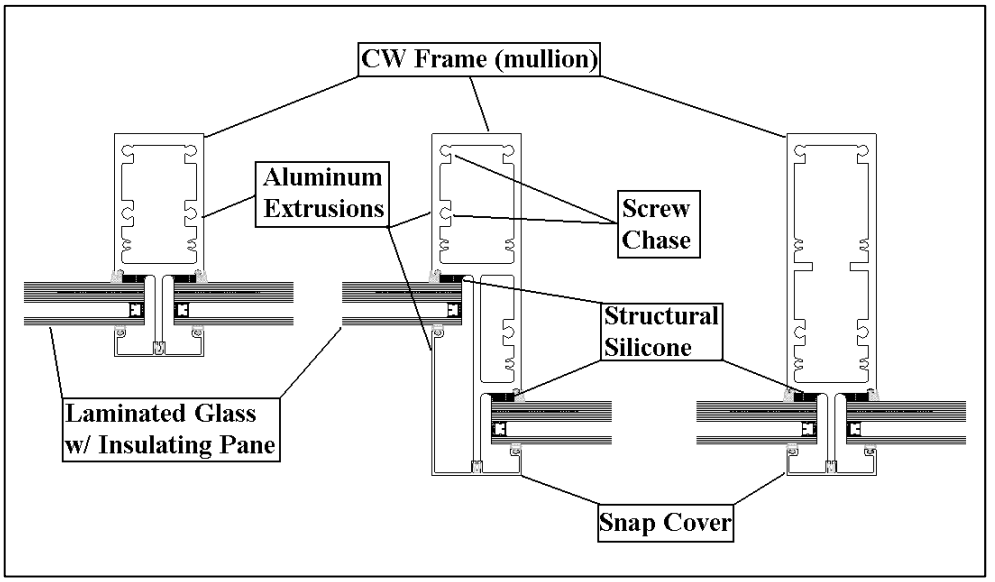


Figure 5. Curtain wall frame.

Reactive structures.

Reactive structures are structures that exhibit significant displacements during a load event. The reactive nature of the mullions is a consideration. As the mullions undergo translations and torsional rotations, the actual reactions at the edge of the glass may be significantly reduced. The effectively softer supports likely improve the performance of the glass in reference to the rigid support assumption integral to the classical methods. Considerable efficiencies may be gained by taking advantage of energy absorbing characteristics of highly reactive structures. Duke (2005) developed mathematical models of structural connections that allow very large frame movements. The allowance for large frame movements was integral to solving an otherwise very challenging blast design problem.

Another issue related to reactions and reactive structures is in-plane load prediction. Given that the post-cracked membrane model in the classical approach includes a rigid boundary assumption, the in-plane reactions are often over-estimated. This point is supported by finite element calculations and anecdotal evidence from

various curtain wall test results. Direct application of the predicted in-plane reactions to the frame members often results in overly conservative designs for the frame members.

Multiple examples exist where supports and frame members exhibit movements that allow large edge translations and rotations while providing appropriate levels of life safety. In all cases, evaluation of the system requires dynamic modeling where the support system response is included as part of a fully coupled dynamic analysis.

Glass to frame interface.

Figure 5 above shows a structural silicon bond between the inside edge of the glass and the frame. Use of structural silicone, glazing tapes, gaskets with adhesive bonds, through bolted connections, deep rebate at the edge, mechanically attached films, etc. can greatly enhance the capacity of glass in blast events. The classical assumption regarding development of in-plane membrane forces at the supports is based on the notion that the membrane is rigidly held against in-plane translations. The actual connection characteristics may allow responses that are significantly different from the rigidly held assumption.

As an example, structural silicone acts as a relatively soft spring and will allow considerable in-plane movement before failure. The rigidly held assumption often results in in-plane forces that are predicted to fail the silicone. The soft spring action of the silicone serves to relieve some of the in-plane edge loading to the point where the forces in the silicone are acceptable. In parallel to this observation is the reality that the soft silicone may allow larger global deflections and, therefore, more reduction in bite than anticipated.

Another issue relates to glass edge movements allowed in structural silicone connections like in Figure 5 and in dry-glazed configurations similar to Figure 6. Figure 6 represents dry-glazed systems that are widely used in the curtain wall industry. In the case of the single sided structural silicone connection, the softness of the silicone or the possible failure of the silicone associated with shear and uplift allows movement of the glass edge perpendicular to and away from the plane of the support, which is contrary to the boundary condition assumptions in the classical method development (see Figure 2). A similar observation may be made in reference to Figure 6 where the extruded outer bulb gasket is most often chosen to be particularly soft so as to facilitate sealing against air and water leakage. There is concern that the movement indicated above may significantly impact preservation of glass bite and edge reaction distribution. The absence of significant two-sided clamping and associated friction is in conflict with the deeply-rebated-edge assumption integral to the classical post-cracked membrane model.

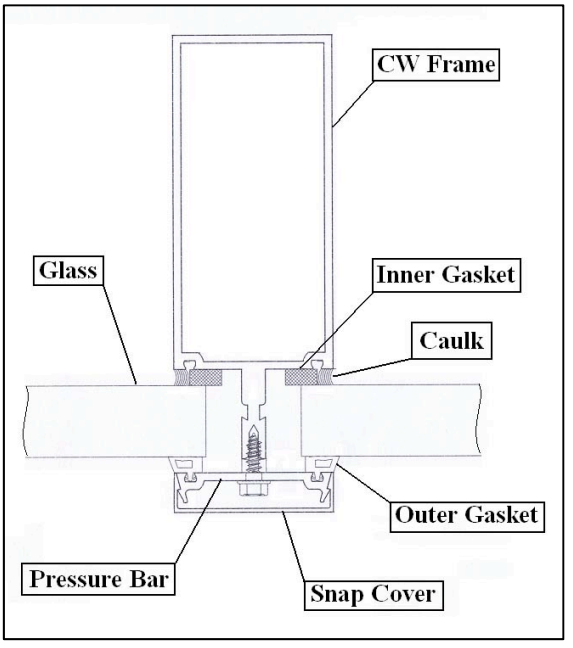


Figure 6. Dry-glazed curtain wall.

Post-cracked behavior of laminate glass.

Considerable evidence indicates that the post-crack behavior of laminated glass is not generally consistent with the pure membrane assumption integral to both classical methods and some finite element approaches. In the post-cracked configuration, large areas of cracked glass remain bonded to the laminate. The result is piecewise continuous stiffening of the laminate by the bonded glass pieces. The stiffening effect may help to explain the higher resistance represented by the empirical data in Figure 3. The stiffening impacts both in-plane and bending characteristics of post-cracked glass.

A second issue relates to treatment of large strains in the laminate material. Inner layer (laminate) materials that are often used in laminated glass make-ups for blast applications exhibit very high post-yield strains before failure (200 – 500 percent). It is common to limit post-crack membrane strains to similar levels. Results of research by Duke et al. (2009) demonstrated that the post-cracked global stains to failure are often much lower than typically assumed.

PRACTICAL CHALLENGE

In practice, window and glass curtain wall designers are faced with the challenge of providing designs that balance life safety and cost effectiveness. It is appropriate that designers provide defensible qualification of the supplied systems. The classical methods discussed above represent decades of testing, development, and evaluation that yield good results within the parameters of the development. Careful review of the discussion above along with more extensive study of the classical methods currently in wide use reveals several limitations or misapplications

of the methods. However, in many cases, the only tools available are the classical methods. Project design review and approval requirements often mandate use of the classical methods. Alternatives include simplified methods that may lead to overdesign and unwarranted cost. Project execution schedules often limit the practicality of testing programs and finite element modeling efforts. Execution of modeling and testing programs to qualify standard designs, particularly as related to windows, is reasonable. However, the glass curtain wall industry offers a much larger challenge in terms of the number of possible configurations. In addition, as new materials or material application concepts are developed, tools are needed that speed the feasibility evaluation process so that the efforts to develop viable designs may be expedited. In summary, the tools currently available for use in a production environment are limited in scope and applicability and thus need extensive enhancement.

MOVING FORWARD

The technical and practical challenges listed above are beyond the capability of current tools. While widely used classical analytical methods have been developed to a significant level of technical sophistication and maturity, they are not suitable to address many of the technical challenges listed above. Empirical methods should continue to be used where test programs and data are available. Test programs should be included in any development to tune modeling assumptions and to provide verification for mathematical models. However, addressing the full spectrum of issues and configurations would require a major test program. The technical flexibility found in finite element modeling techniques is generally suited to address most of the technical challenges. A primary exception relates to material models for post-cracked laminated glass. The greatest downfall in using finite element methods lies in user experience and knowledge requirements and modeling, execution, and post-processing time.

Efforts moving forward should support the primary goals of balancing life safety with cost efficient designs that can be developed within the time constraints of typical design and build projects. New design tools should be developed that are technically well founded and provide practical results both in terms of communication of results and of constructability of the window and curtain wall systems. Tools moving forward should facilitate development of new material applications and design concepts.

The technical and practical challenges warrant a fresh approach to carefully designed engineering level models that merge classical approaches with advanced finite element methods. Practical, productive, and time efficient engineering models have been developed that provide “engineer friendly” user interfaces with classical and finite element calculations executed automatically. The finite element analyses are effectively transparent to the users in that modeling and post-processing are automated within the software system. Many of the key aspects of the design process are rooted in classical methods with the embedded finite element processes focused on analyses that are outside the range of classical methods. As an example, PENCURV+ is a software package that uses the Lagrangian finite element code EPIC

to perform more robust penetration analyses. Information regarding PENCURV+ can be found on the web site for the U.S. Army Corps of Engineers Protective Design Center; PENCURV+ is provided by the U.S. Army Engineer Research and Development Center.

It is proposed that a development similar to that done for PENCURV+ is warranted. The challenges for such a development are in many ways different from those faced by the developers of PENCURV+, but the success of embedding finite element methods into such a program validates the proposed approach. By embedding well designed parametrically driven finite element models within a window and curtain wall evaluation and design program, the result should be a practical tool that can better address the complex technical issues without requiring the user to be a finite element expert.

SUMMARY AND CONCLUSIONS

Selected topics were discussed that address general approaches to window and glass curtain wall design. Key deficiencies in current methods were discussed. A summary of key points includes the following:

- The development and application of classical and empirical methods over a period of decades represents tools and methods that are very effective within the context of assumed geometries and boundary conditions.
- Many applications encountered by practicing designers involve conditions that are outside the boundaries for appropriate application of the current classical and empirical methods.
- The technical depth and breadth of finite element methods offers proper treatment of many of the technical challenges.
- Practical concerns over modeling time, execution, and post-processing most often reduce the effectiveness of finite element methods in their current form.
- A proposed approach is presented that marries classical, empirical, and finite element methods to provide a practical approach to addressing many of the technical challenges.
- In all cases, test programs should be executed that, as a minimum, provide verification data for any models, methods, and analytical tools that are developed.

ACKNOWLEDGEMENT

The authors would like to acknowledge Mr. Steve Lofton. Mr. Lofton was a research structural engineer at the US Army Engineer Research and Development Center in Vicksburg, Mississippi. He dedicated most of his career to the development of blast resistant windows. Mr. Lofton was a key contributor to the vision of this paper but unexpectedly passed away in 2010. The authors dedicate this paper to Mr. Steve Lofton with hopes that it will contribute to continued progress in the field he loved and helped develop.

REFERENCES

ASCE (1999). American Society of Civil Engineers. *Structural Design for Physical Security: State of the Practice,* Reston, VA.

Biggs, J. M. (1964). *Introduction to Structural Dynamics,* McGraw-Hill Book Company, New York, NY.

Browning, R. S., Duke, D., and, Bewick, B. T. (2009). "Testing and Analysis of a Retrofit System for Windows Subjected to Blast Loads", presented at 80th Shock & Vibration Symposium, San Diego, CA, US Air Force report AFRL-RX-TY-TP-2010-0016.

Duke, D. (2005). *USSCB – Windows: Blast Analysis*, report issued to BauTech, Inc. Pelham, AL.

Duke, D., Bewick, B. T., Browning, R. S., and Casey, T. (2009). "Edge Capacity of Through-Bolted Laminated Glass", presented at 80th Shock & Vibration Symposium, San Diego, CA, US Air Force report AFRL-RX-TY-TP-2010-0022.

Friedlander, F. G. (1946). "The Diffraction of Sound Pulses. I. Diffraction by a Semi-infinite Plate", *Proceedings of the Royal Society A*, London, 186, 322-344.

GANA (2010). Glass Association of North America and Protective Glazing Council International. *Protective Glazing Manual*, Topeka, Kansas.

HazL (2004). HazL - Window Fragment Hazard Level Analysis, Version 1.2, Help Files. U.S. Army Corps of Engineers, Engineer Research and Development Center, Vicksburg, MS, July 2004.

LS-SYNA (2006). *LS-DYNA Theory Manual*, Livermore Scientific Technology Corporation, Livermore, CA.

Moore, D. M. (1980). *Proposed Method for Determining the Thickness of Glass in Solar Collector Plates*, Jet Propulsion Laboratory, Pasadena, CA.

PENCURV+ V1.5. Penetration into Multilayered Curvilinear Geologic Materials in 3D Space, U.S. Army Corps of Engineers, Protective Design Center, https://pdc.usace.army.mil/software/pencurv/.

WINGARD (2005). WINGARD – Window Glazing Analysis Response & Design, Technical Manual, U.S. General Services Administration, Washington, DC, (prepared by Applied Research Associates, Vicksburg, MS)

Design Guidelines for Post-Installed Mechanical Anchors in Concrete Subjected to Impact Loads

Daniel Gavahi, MS[1] and Sharon Gallant, MS, SE[2]

[1]Hinman Consulting Engineers, Inc, 1 Bush Street, Suite 510, San Francisco, CA 94104; PH (415) 621-4423; email: dgavahi@hce.com
[2]Hinman Consulting Engineers, Inc, 1 Bush Street, Suite 510, San Francisco, CA 94104; PH (415) 621-4423; email: sgallant@hce.com

ABSTRACT

Current United States design provisions for post-installed mechanical anchors are typically tailored toward conventional static and dynamic load regimes, such as seismic and wind loads. In fact, the dynamic behavior of post-installed anchors in reinforced concrete is primarily based on seismic loading effects. Yet, dynamic loads that produce extremely short duration impact, such as air-blast, are not addressed in design criteria, including anchorage to concrete. Usually this is not an issue as most structures are not designed to withstand these forces; however, when blast applications are considered, there is no clear method to determine how these anchors will perform. With little research on the behavior of anchor bolts under impact loads, in comparison to other long term cyclical loadings, properly designing concrete anchorage to meet these demands is difficult.

INTRODUCTION

The International Building Code (IBC) is the design code commonly used for structures in the U.S. In building design of concrete construction, the IBC makes reference to the American Concrete Institute (ACI) 318 manual. ACI 318 provides design procedures and standards for the majority of structural components, including anchorage to concrete. The design of concrete anchorage can actually be very difficult when a blast-resistant design is warranted.

In consideration of air-blast loading effects, structures are designed to withstand a high magnitude, short duration load that linearly decays within milliseconds. Unfortunately, this type of load is not addressed in the design procedures of ACI 318 Appendix D that provides a design methodology for conventional static and dynamic loads. When this approach has been tested on anchors under impact loads, research frequently shows that this method may be overconservative. Therefore, this paper attempts to provide design guidelines for post-installed mechanical anchors that may be utilized in future construction where blast design is required.

IMPACT VS. CONVENTIONAL DYNAMIC LOADS

Impact loads do not behave in the same manner as conventional dynamic loads (i.e., seismic). A typical impact load (Figure 1) initially starts at a high magnitude force or

pressure and linearly decays quickly, on the order of milliseconds. This loading type affects structures locally to the explosive event where large inelastic deformations are expected. Additionally, increase in material strengths are expected due to high loading rates.

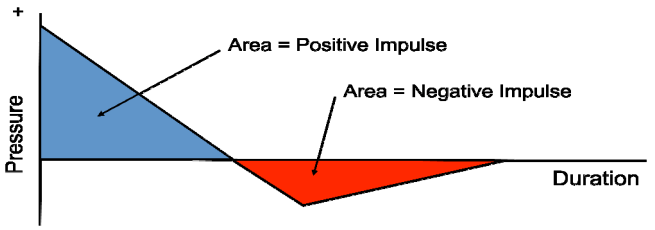


Figure 1. Typical Impact Load Curve

Conversely, conventional dynamic loads (Figure 2) have much longer durations and usually generate less energy demand than impacts. These dynamic loads are cyclic in nature, while impact loads have a positive loading phase in one direction and a negative suction in the other direction. For seismic loads, structures are loaded on a global scale, and rarely affect local components. As this loading is much slower than impacts, there are no increases in material strengths.

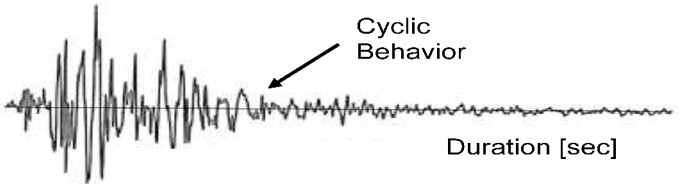


Figure 2. Conventional Dynamic Load (Loma Prieta Time History Adapted from *Chopra 2001*)

ACI 318 APPENDIX D

ACI 318 Appendix D provides a design procedure for structural anchors in concrete that "transmit structural loads related to strength, stability, or life safety" (ACI 318) based on the Concrete Capacity Design (CCD) method (*Fuchs, Eligehausen, Breen 1995*). First introduced in ACI 318-02, it was not implemented until IBC 2003 was released. IBC 2003 required the use of Appendix D if the designer was working with one of the following scenarios: (1) any anchors resisting seismic forces; and (2) post-installed anchors installed in hardened concrete. Dynamic loads that are predominately high cyclic fatigue or impact are outside the scope of Appendix D.

Per Appendix D, anchors are evaluated for failure mechanisms most commonly associated with them under tensile and shear forces. When post-installed anchors are to be used, they must be qualified in accordance with ACI 355.2 (*Qualification of Post-Installed Mechanical Anchors in Concrete and Commentary*). ACI 355.2 presents the methodology to determine the reported post-installed anchor capacities for concrete breakout, pull-out, and shear under both static and seismic loads. The

failure modes designed for in ACI 318 Appendix D are provided below with brief descriptions:

- Tension Failure Modes
  - Steel Rupture: When the external tensile load exceeds the ultimate capacity of the steel, it is expected that the steel will rupture. The maximum capacity of the steel is calculated from the stressed cross-sectional area and the tensile strength of steel.

    This mode of failure is typically a ductile failure mode, where the steel anchor, after it has yielded, is likely to undergo a period of strain hardening and be capable of withstanding further stress and strain.

  - Pull-Out: Pull-out failure is usually associated with expansion anchors. As expansion anchors further expand into the concrete, it creates local deformations in the concrete around the drilled hole, generating a force due to the radial expansion pressure. The failure pull-out load is proportional to the expansion force via the frictional coefficient between the steel and concrete. The pull-out mechanism is at a load level in which the anchor is unable to develop follow-up expansion with a brittle failure occurring.

    This failure mode is considered brittle because once the frictional resistance developed by the concrete and steel is lost, failure immediately occurs.

  - Concrete Cone Breakout: Anchors subjected to conventional loads are likely to fail under concrete cone breakout. This failure mechanism is exhibited when the full tensile capacity of the concrete is exceeded. This mode is characterized by the formation of a 30° to 40° conical fracture to the surface. Edge distance, embedment depth, and concrete compressive strength affect this failure mode.

    Concrete cone breakout is also a brittle failure mode. The failure of the concrete will tend to follow a linear elastic stress-strain curve initially, but as there is no clearly defined yield point of the material, it will fail unexpectedly.

- Shear Failure Modes
  - Steel Failure: This failure mechanism is exhibited when the edge distance and embedment depth of the anchor is sufficient to prevent concrete and pry-out failure. It is indicative of the shear capacity of the steel material. If ductile steel is used, relatively large anchor deformation can be developed.

  - Concrete Edge Failure: Anchors located near a free edge are likely to fail from concrete fracture before the shear capacity of the steel is

reached. The fracture in the concrete originates at the point of bearing and radiates to the free surface. This is another example of a brittle failure mode.

- Pryout Failure: When limited embedment depth is provided, anchors loaded in shear may rotate and produce a pry-out fracture. A pry-out fracture is when the primary fracture surface develops behind the point of load application. Edge distance does not affect this failure mode.

As previously stated, post-installed anchors to be used in hardened concrete are required to follow design protocols established in ACI 318, Appendix D. Post-installed anchors are comprised of both mechanical and adhesive anchors. Since adhesive anchors are excluded from the scope of Appendix D, they have been excluded from this discussion.

Post-installed mechanical anchors typically consist of expansion and undercut anchors. Provided is a brief description of these anchors:

- Expansion Anchors: Expansions anchors can be divided into two groups: (1) torque-controlled; and (2) displacement-controlled.

  Torque-controlled anchors transfer external forces through friction and mechanical interlock to the deformed concrete. When torque is introduced upon installation, it generates a pre-stressing force in the bolt and clamps the item being fastened against the concrete surface. As the anchor is loaded beyond the pre-stressing force, the expansion sleeve further expands generating the necessary additional friction to resist the applied load. Figure 3 shows several examples of torque-controlled expansion anchors, including their load-transfer mechanism.

  Displacement-controlled anchors (Figure 4) are secured through the expansion of the sleeve as controlled by the axial displacement of the plug within the sleeve. These expansion anchors transfer external loads into the base material through friction, and to a lesser degree, mechanical interlock. Additionally, displacement-controlled anchors initially generate a greater expansion force than their torque-controlled counterparts; however, as external load is introduced, subsequent expansion does not increase the resistance force.

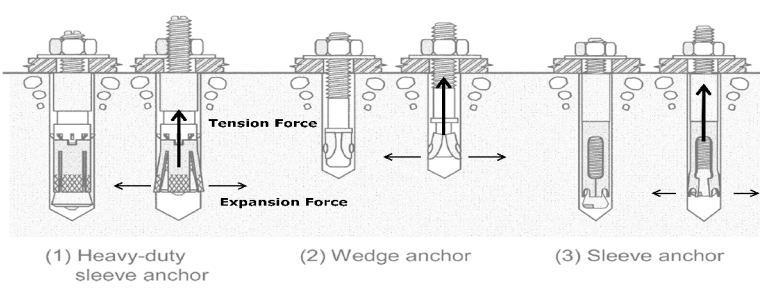


Figure 3. Torque-Controlled Expansion Anchors (Adapted from *ACI 355.2 - 07*)

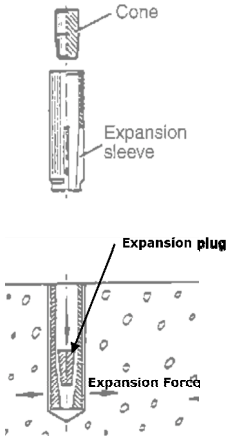


Figure 4. Displacement-Controlled Anchor (Adapted from *Eligehausen, Mallée, Rehm* (1997))

- Undercut Anchors: These anchors transfer external forces by developing a mechanical interlock between the anchor and concrete. Unlike expansion anchors, undercut anchors are installed in a two step process. The first step is to create the undercut in the concrete using an undercutting tool. This process is crucial in developing the maximum capacity of the bolt, as the anchor will bear on the concrete. The second step is to insert the undercut anchor and apply the appropriate torque to develop a bearing pressure that properly clamps the bolt in place, as shown in Figure 5.

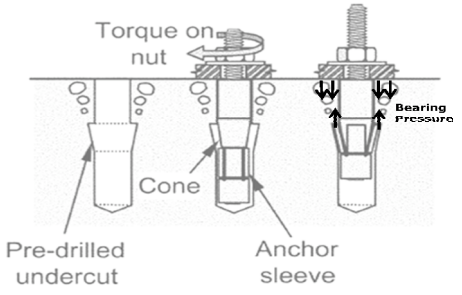


Figure 5. Undercut Anchor (Adapted from *ACI 355.2-07*)

RESEARCH REVIEW

Several studies have been conducted on the tensile and shear capacity of post-installed mechanical anchors under static and seismic loads, but few studies have been done for high strain rate dynamic behavior that are typical of impact loads. Research on this material includes the following: *D. M. Collins, R. E. Klinger, and D. Polyzois* (1989), *Hilti and R.E. Klinger* (1995), *D. Schuler* (1997), *P. Hunziker* (1999), *M. Rodriguez, D. Lotze, J. H. Gross, Y. G. Zhang, R. E. Klinger, and H.I. Graves, III* (2001), *H. Salim, R. Dinan, J. Shull, and P.T. Townsend* (2005), and *G. Mitchell, M. Tolnai, V. Gokani, R. Picon, S. Yang, R.E. Klinger, and E. B. Williamson* (2006).

Collins (1989) and *Rodriguez* (2001) tested anchors with loading rise times of approximately 250 msec. At this loading rate, the load is still relatively slow

compared to impact loads, and anchors behave approximately equivalent as under static conditions. *Hunziker* (1999) tested anchors with load duration rates of roughly 35 msec, and found that torque-controlled expansion and undercut anchors could resist impact loads with torque-controlled expansion anchors resisting more than 4 times the European static capacity. *Salim* (2005) looked at several anchoring systems at various loads. Of these, *Salim* (2005) showed that torque-controlled expansion anchors loaded with relatively short rise times could resist up to 20% more than the U.S. static capacity. Ultimately, all studies showed that displacement-controlled expansion anchors performed unfavorably and should not be considered for applications where impact loads are possible.

Experimental data has shown that as loading rate increases, tensile capacity of expansion anchors and undercut anchors increase also. This increase in capacity is referred to as the Dynamic Increase Factor (DIF). The DIF is equal to the ratio of dynamic stress to static stress of an element, and increases as the strain rate increases. Many Hilti anchors in Europe have been tested under impact loads and allowable shock capacities have been reported, as well as appropriate DIF for expansion and undercut anchors. Assuming that anchors are allowed to undergo plastic deformations and are to be replaced, Hilti states that expansion anchors and undercut anchors can have a DIF of 1.7 and 2.7 respectively, compared to DIBt (Deutsches Institut für Bautechnik)-approved static resistance. Much like the International Code Council (ICC) Evaluation Service in the U.S., the DIBt is the German approval body that evaluates construction products.

ANCHORS SUBJECTED TO IMPACT LOADINGS

The design approach presented attempts to incorporate Appendix D with recommended guidelines derived from research. Further, recommendations are based on the assumption that bolts have manufacturer's minimum embedment depth and edge distances greater than or equal to 150% of the embedment depth. Unless noted, all commentary and design requirements specified in ACI 318 Appendix D are to be used in conjunction with the approach shown.

GENERAL RECOMMENDATIONS

Displacement-controlled expansion anchors are not to be used as testing has shown that these systems do not meet or exceed the static capacity when subjected to an impact load.

In accordance with ACI 318, anchor capacities are lowered and design loads are increased with the use of Strength Reduction Factors, ϕ, and Load Increase Factors, respectively. In doing so, uncertainties in the material and loading are accounted for in the analysis. For blast loading, the resultant force on anchors of a connection is explicitly determined based on the inelastic, non-linear dynamic response of the member being connected to its ultimate flexural capacity. It is therefore

recommended that given the nature of the loading, the Load Increase Factor for blast is assumed equal to 1.0 because it is at an ultimate load level.

Material uncertainties are accounted for inherently in design equations per ACI 318 Appendix D through ψ factors that modify anchor capacities due to anchor location and material properties, etc. Also, the behavior of steel is well documented and easily predictable. Moreover, concrete behaves in a brittle manner under shear and tensile rupture and does not have a well defined yield point.

It is recommended that strength reduction factors are eliminated as this is not a strength design, but rather an ultimate load design. Dynamic increase factors are to be introduced based on material overstrengths and testing results for anchor failure modes due to the nature of this loading type.

DESIGN REQUIREMENTS FOR TENSILE LOADING

ACI 318 Appendix D provides design guidelines to determine the capacity of anchors at failure for steel rupture, concrete pull-out, and concrete cone breakout. Along with recommendations for impact design, Appendix D equations have been provided for comparison.

Steel Rupture: The nominal steel strength of a single anchor or group of anchors is given in ACI 318 Appendix D equation D-3 as $N_{sa} = nA_{se,N}f_{uta}$, where n is the number of anchors in the group, $A_{se,N}$ is the effective cross-sectional area of a single anchor in tension, and f_{uta} shall not be taken greater than the smaller of $1.9\boldsymbol{f_{ya}}$ and 125,000 psi.

Research has shown that anchors subjected to an impact load will have an increase in capacity. As this is a ductile failure mode, it is recommended that deformations enter the plastic region of the steel constitutive model. Therefore, the steel rupture capacity may be multiplied by a DIF.

The recommended DIF is taken from the Hilti European dynamic design manual for anchors. The use of a DIF assumes that the anchor undergoes plastic deformations and will be replaced after an impact event. The steel strength is determined in the same fashion as is given in ACI 318 Appendix D; therefore the following DIF's are to be used:

- Torque-Controlled Expansion Anchors: 1.7
- Undercut Anchors: 2.7

Steel Pull-Out: The nominal pullout strength of a single anchor in tension from Appendix D shall not exceed $N_{pn} = \psi_{c,P}N_p$ where $\psi_{c,P}$ is the modification factor for an anchor located in a region where no cracking is present at service load levels, and N_p is the pullout tensile strength based on the 5 percent fractile of tests evaluated according to ACI 355.2.

Testing has shown that under impact loads, steel pull-out is most common. While pull-out is considered a brittle failure mode, DIF values may still be formulated from the experimental failure impact loads. In comparison with U.S. testing standards, the European Technical Approvals (ETA) provide lower capacities for steel pull-out in cracked concrete. Capacities, not including partial safety factors, conservatively appear to be 65% lower than their U.S. counterparts. For this reason, the recommended values from Hilti of 1.7 and 2.7 for expansion anchors and undercut anchors, respectively, have been factored to reflect this trend.

For pull-out design of anchors, it is recommended to use the prescribed equation in ACI 318 with the inclusion of the following DIF's:

- Torque-Controlled Expansion Anchors: 1.1
- Undercut Anchors: 1.8

Concrete Breakout Strength: The nominal concrete breakout strength of a single anchor or group of anchors in tension from Appendix D is determined from the following equations:

$$N_{cb} = \frac{A_{Nc}}{A_{Nco}} \psi_{ed,N} \psi_{c,N} \psi_{cp,N} N_b \text{ (single anchor)}$$

$$N_{cb} = \frac{A_{Nc}}{A_{Nco}} \psi_{ec,N} \psi_{ed,N} \psi_{c,N} \psi_{cp,N} N_b \text{ (group of anchors)}$$

where A_{nc} is the projected concrete failure area of a single anchor or group of anchors, A_{nco} is the projected concrete failure area of a single anchor with an edge distance equal to or greater than 50% greater than the embedment depth, N_b is the basic concrete breakout strength derived from testing of a single anchor in tension in cracked concrete, and $\psi_{ec,N}$, $\psi_{ed,N}$, $\psi_{c,N}$, $\psi_{cp,N}$ are modification factors as prescribed in ACI 318.

The behavior of anchors under a concrete cone breakout failure mode due to impact loads was not tested. Further, as this is a brittle failure mode, material overstrengths are not expected. Upon further testing, no recommendation can be made for a dynamic increase factor.

Interestingly, the ETA specifies larger anchor spacing and edge distances than the ICC criteria do. At this point, no recommendation is provided for these distances, as well as for this failure mechanism. Further research is required on this topic to provide insight on this matter.

DESIGN REQUIREMENTS FOR SHEAR LOADING

The following section is a recommendation for the design of post-installed mechanical anchors in shear.

Steel Shear Strength: The nominal steel strength of a single anchor or group of anchors is given in ACI 318 Appendix D as $V_{sa} = nA_{se,V} f_{uta}$ where n is the number of

anchors in the group, $A_{se,V}$ is the effective cross-sectional area of a single anchor in shear, and f_{uta} shall not be taken greater than the smaller of $1.9\boldsymbol{f_{ya}}$ and 125,000 psi.

It is recommended that the steel shear capacity use the DIF's proposed for steel rupture. The shear strength for this mode is to be increased by 1.7 or 2.7 for torque-controlled expansion anchors or undercut anchors, respectively.

Concrete Breakout Strength: The nominal concrete breakout strength of a single anchor or group of anchors in tension from Appendix D is determined from the following equations:

$$V_{cb} = \frac{A_{vc}}{A_{vco}} \psi_{ed,V} \psi_{c,V} \psi_{h,V} V_b \text{ (single anchor)}$$

$$V_{cbg} = \frac{A_{vc}}{A_{vco}} \psi_{ec,V} \psi_{ed,V} \psi_{c,V} \psi_{h,V} V_b \text{ (group of anchors)}$$

where A_{vc} is the projected area of the failure surface on the side of the concrete member at its edge, A_{Vco} is the projected area for a single anchor in a deep member with a distance from edges equal or greater 50% greater than the critical edge distance, and $\psi_{ec,V}\psi_{ed,V}\psi_{c,V}\psi_{h,V}$ are modification factors given in ACI 318.

Much like concrete breakout in tension, this is a brittle failure mode and does not warrant increasing the capacity with the use of a DIF.

Steel Pryout: The nominal pryout strength of a single anchor in tension from Appendix D shall not exceed $V_{cp} = k_{cp} N_{cb}$ where k_{cp} is the modification factor for the effect of embedment depth, and N_{cb} is the nominal concrete breakout strength.

No recommendations for DIF are provided for this design as this is a brittle failure mode and research on this topic is sparse.

RECOMMENDATIONS

In the process of developing design guidelines for impact loads on post-installed mechanical anchors, it is apparent that more research is needed on the topic. Furthermore, it appears that the state of practice in Europe on this subject is further ahead than the United States, as testing standards have already been developed in the area. Presented below are items that require more investigation or need to be developed on the topic.

Loading Rate: In the studies reviewed that focused on impact testing of anchors, only few had rise times that were comparable to impact loadings. It is imperative that research be conducted with loads that have time durations with a maximum time of 100 msec to better understand the behavior of post-installed mechanical anchors.

Anchor Properties: Research shows that anchor diameters and embedment depths will have an effect on the anchor's behavior under impact loads. Consequently, the

DIF is expected to not be a single value for just one type of bolt or failure mode. Further investigations could potentially develop trends in capacities and properties, which could be incorporated into future designs.

Anchor Layout: Anchors were tested with large edge distances, which likely led to the dominant failure mode of pull-out. As the anchor edge distance starts decreasing, it is assumed that concrete cone breakout may occur. Testing is needed considering anchors with reduced edge distances. Also, it appears that research did not evaluate the effect impact loads had on anchor groups. Testing of groups of anchors is necessary to fill in the gaps of knowledge on this topic.

Shear Capacity: With little experimental data on the topic, it was very difficult to develop design guidelines for shear. It is predicted that post-installed mechanical anchors, not located near concrete edges, will fail by pryout as anchors will displace horizontally from the initial load and begin to rotate causing this failure mechanism.

Anchor Evaluation Testing: It is important that manufacturers in the United States work with academia and industry to develop testing standards for post-installed mechanical anchors. At a minimum, anchors should be tested to failure to determine prominent failure mechanisms and maximum loads and impulses. This would allow designers to specify anchors that could withstand the energy demands for a given impact.

As an example of a current testing standard for impact, AC Laboratory Spiez Report 9710 (Schuler 1997) provides a testing method to evaluate the pull-out probability and slip behavior in cracked concrete for civil defense installations in Switzerland. Anchors are placed in concrete blocks to manufacturer's standards and loaded twice with impact loads. Slip movements are measured after each load and reported, as well as whether the anchor completely pulled out of the block. These responses are compared to an acceptable pull probability and slip displacement.

CONCLUSION

U.S. design of concrete post-installed mechanical anchors is based on procedures and standards given in ACI 318 Appendix D. For structures that are not subjected to impact forces, the use of Appendix D is appropriate as loads on elements are of a static or conventional dynamic nature. However, Appendix D does not account for impact loads causing a dilemma for designers.

While only a few studies have been done on the topic, design recommendations for impact applications have been provided herein and include:

- Displacement-controlled anchors are not to be used

- Resultant forces on anchors are considered as ultimate loads. For that reason, Strength Reduction Factors are to be eliminated and Load Increase Factors equal 1.0

- Failure loads prescribed in ACI 318 for steel rupture in tension, as well as steel failure in shear may be increased with DIF's specified for torque-controlled expansion anchors and undercut anchors as they are ductile failure modes.

- Failure load prescribed in ACI 318 for pull-out may be increased with DIF's specified for torque-controlled expansion anchors and undercut anchors due to experimental testing

In order for U.S. design to become more efficient and lead the way on this topic, further research is required that would investigate the following: (1) loading rate; (2) anchor properties; (3) anchor layout; and (4) shear capacity. Above all else, it is absolutely necessary that manufacturers work with industry and acadamia to determine a method to qualify post-installed mechanical anchors for impact loads.

REFERENCES

American Concrete Insitute (ACI). (2007). *ACI 355.2-07 Qualification of Post-Installed Mechanical Anchors in Concrete and Commentary*, Farmington Hills, Michigan.

American Concrete Insitute (ACI). (2008). *Building Code Requirements for Structural Concrete (ACI 318-08) and Commentary*, Farmington Hills, Michigan.

Centre Scientifique et Technique du Bâtiment. *European Technical Approval ETA-99/0009.* Champs sur Marne, France, 2008.

Centre Scientifique et Technique du Bâtiment. *European Technical Approval ETA-02/0042.* Champs sur Marne, France, 2008.

Chopra, A. K. *Dynamics of Structures*. 2nd Edition. Upper Saddle River, New Jersey: Prentice-Hall, 2001.

Collins, D. M., Klinger, R. E., and Polyzois, D. *Load-Deflection Behavior of Cast-In-Place and Retrofit Concrete Anchors Subjected to Static, Fatigue, and Impact Tensile Loads*. Research Report 1126-1. The University of Texas at Austin, 1989.

Deutsches Institut für Bautechnik. *European Technical Approval ETA-98/0001*. Berlin, Germany, 2009.

Eligehausen, R., Mallée, R., and Rehm,G. *Befestigungstechnik.* Betonkalender 1997, Part II, Ernst and Sohn, 1997.

Eligehausen, R., Mallée, R., and Silva, J. *Anchorage in Concrete Construction.* Berlin, Germany: Ernst & Sohn, 2006.

Fuchs, W., Eligehausen, R., and Breen, J. "Concrete Capacity Design (CCD) Approach for Fastening to Concrete" *ACI Structural Journal.* January-February 1995: 73-94.

Hilti Corporation. (1995). *Hilti HSL Metric Expansion Anchor Dynamic Performance*. Tulsa, Oklahoma.

Hilti Corporation. (2003). *Dynamic Design for Anchors*. Principality of Liechtenstein.

Hilti Corporation. (2008). *North American Product Technical Guide*, Tulsa, Oklahoma.

Hunziker, P. "Shock Testing of Concrete Anchor Bolts for Shock Resistant Applications in Protective Structures." *3rd International Conference on Shock and Impact Loads on Structures.* Singapore, 1999.

International Code Council (ICC). (2006). *International Building Code*, Country Club Hills, Illinois.

Mitchell, G., Strahota, M. T., Gokani, V., Picón, R., Yang, S., Klinger, R. E., and Williamson, E.B. *Design of Retrofit Vehicular Barriers Using Mechanical Anchors*. CTR Techincal Report 0-4823-CT-1. The University of Texas at Austin, 2006.

Rodriguez, M., Lotze, D., Gross, J.H., Zhang, Y.-G., Klinger, R.E., and Graves, H.L. "Dynamic Behavior of Tensile Anchors to Concrete." *ACI Structural Journal.* July-August 2001: 511-524.

Salim.H., Dinan, R., Shull, J., and Townsend, P.T. "Shock Load Capacity of Concrete Expansion Anchoring Systems in Uncracked Concrete." *ASCE Journal of Structural Engineering.* August 2005: 1206-1215.

Schuler, D. *Fundamentals of Shock Testing Anchors.* Report ACLS 9710. Wintherthur, Switzerland. Defence Procurement Agency, 1997.

U.S. Army Corp of Engineers. *UFC 3-340-02 Structures to Resist the Effects of Accidental Explosions*. December 5, 2008.

Zhang, Y. *Dynamic Behavior of Multiple-Anchor Connections in Cracked Concrete*. Diss. The University of Texas at Austin, 1997.

Analysis Techniques for Terrorist Risk Assessment and Mitigation of Bridges

A. M. Coughlin[1], P.E., M.ASCE

[1]Hinman Consulting Engineers, One Bush Street Suite 510, San Francisco, CA 94104; PH (415) 621-4423; FAX (415) 621-4447; email: acoughlin@hce.com

ABSTRACT

In 2003, the Blue Ribbon Panel on Bridge and Tunnel Security issued its recommendations for risk assessment and mitigation of bridges and tunnels. The report gives general guidelines to help decision makers improve the security of bridges and tunnels. However, the actual implementation can be highly dependent on the methods used to carry out the assessment. Variability in risk assessments may prevent limited funding from going to projects where it is needed most. The factors that determine the relative risk of a bridge include: Occurrence – the likelihood of an event taking place, whether intentional or unintentional; Vulnerability – the consequences of an event; and Importance – the tangible and intangible value of the asset. The product of weighted scores for each of these factors determines the relative level of risk.

A real life example of risk assessment is presented with special attention paid toward the calculation of the weighted score for vulnerability. The threats listed in the Blue Ribbon Panel report were used to determine the consequences of various terrorist tactics of a real-life group of movable bridges over a waterway used for shipping. Potential consequences of attack included damage to bridge, downtime of bridge and waterway, human casualties, and collateral damage to surrounding area. Conventional blast resistant engineering methodology, more commonly used on buildings, was used where applicable and compared to high fidelity modeling. The damage expected on each component in the bridge was used to estimate the vulnerability scores.

The Blue Ribbon Panel report discusses possible mitigation measures and how to prioritize their implementation. Mitigation measures usually focus on reducing either occurrence, though deterrence measures, or vulnerability, through hardening or increasing standoff. Both types of mitigation measures are applied to these real life examples as a model of how bridge owners can most effectively reduce terrorist risk on their assets.

INTRODUCTION AND BACKGROUND

Terrorist actions in recent decades have prompted a global response to mitigate these threats. While terrorist attacks can often be prevented through intelligence, border security, blocking funding sources, and other measures, the last line of defense against terrorist plots on critical targets is physical and operational security. Bridges represent a significant number of attractive targets to terrorists, partly due to their high number of users, importance to local economies, and

relatively easy access to key structural components. In the months following the September 11, 2001 attacks, U.S. officials warned of specific intelligence that high profile bridges in San Francisco were potential next targets. Mitigation efforts were quickly put in place over the next years (San Jose Mercury News 2003). To better allocate terrorist threat mitigation funds, decision makers rely on terrorist risk assessments to identify critical assets, key vulnerabilities, consequences, and countermeasures. Procedures for these assessments have been proposed by SIAC (2002) and others.

In 2003 the Blue Ribbon Panel on Bridge and Tunnel Security issued its recommendations for the protection of U.S. bridges and tunnels (FHWA 2003). Within their seven overarching recommendations were two related to the technical implementation of risk assessment procedures, including:

- *Technical Expertise* – to "engineer" security solutions with the necessary engineering expertise.
- *Research, Development, and Implementation* – To use existing engineering tools and develop new tools to implement consistent standards.

In light of these technical recommendations this paper investigates several established analysis methods and seeks to determine when each method should be used within the time and budgetary constraints of terrorist risk assessments addressing anywhere from several to several hundred bridges at once. As the Blue Ribbon Panel pointed out, the U.S. transportation infrastructure network "is fractionated and regulated by multiple jurisdictions at state, federal, and sometimes local levels" (FHWA 2003). It is clear that a consistent set of threat scenarios and performance objectives should be used by all who are tasked with quantifying the vulnerability on a particular bridge. This paper proposes that a consistent set of analysis *methods* is also critical to terrorist risk assessments that can be useful on a large scale.

TERRORIST RISK ASSESSMENTS

Terrorist risk assessments have been modeled after procedures originally developed for seismic hazard mitigation. They seek to identify assets that have high risk of losses occurring from terrorist attack. It should be noted that terrorist risks are some of the many risks that bridges face and mitigation monies should be allocated considering other natural and manmade hazards.

An important step in a terrorist risk assessment is to identify critical assets. The criticality of these assets is not only due to their critical function, but also to their likelihood of becoming a terrorist target. As Williamson and Winget (2005) point out, terrorist goals vary based on the specific goals of their organization but have most commonly focused on attacks that have high visibility and media coverage, target iconic or critical assets, make political statements or obtain publicity for their cause, cause fear, damage economies, and more. Terrorists would therefore be more likely to target bridges whose destruction would accomplish many of these goals.

Once critical assets have been identified a risk assessment can be conducted, often involving the calculation of risk scores with the following equation (Blue Ribbon Panel 2003):

$$R = \sum (O_i V_i) \times I \quad (1)$$

where

R = Risk score

O = Occurrence: a factor representing the likelihood of a specific terrorist threat

V = Vulnerability: a factor representing the consequences to an asset given a specific threat occurs

I = Importance: a factor representing the socioeconomic value of an asset and its function

i = each threat under consideration

The "occurrence" and "vulnerability" factors are calculated for each specific threat and their product is summed for all threats considered. Potential terrorist threats to bridges include: explosives, ranging from hand-carried explosives to larger explosives delivered by car, truck, or watercraft; cutting devices such as torches, saws, or small explosives; fire which can result in weakening and/or failure of key structural elements; impact by vehicles or watercraft; and, in the case of moveable bridges, sabotage of machinery to disrupt normal operation.

Bridges with a high risk score may be chosen to receive mitigation strategies to reduce risk. Mitigation strategies are prioritized in order of their benefit to cost ratio, where benefit is measured as the reduction in risk score. Mitigation strategies typically seek to deter, deny, detect, and defend, which are explained in Table 1.

Table 1. Examples of Mitigation Strategies

Mitigation Strategy	Goal
Deter	Make target less attractive for potential attacks
Deny	Prevent access to vulnerable locations
Detect	Identify threats and monitor suspicious activity
Defend	Design elements to limit damage from terrorist attacks

Improved response can be considered another mitigation strategy. Well implemented emergency response plans geared toward attending to injured people, providing temporary alternative transportation routes, clearing wreckage, and mobilizing repair crews reduce consequences and should not be overlooked as terrorist risk mitigation strategies.

ANALYSIS TECHNIQUES

The task of conducting terrorist risk assessments for U.S. bridges is often shared between government agencies at the federal, state, and local levels and private consultants experienced bridge design, blast analysis, and physical security. The assessments are often first carried out on a national level to identify critical assets and earmark mitigation funds on a national level. Then, as mitigation funds are made available to bridge owners, more in-depth risk assessments are carried out. The diversity of personnel who may be tasked with a risk assessment will undoubtedly

result in a diversity of methods to conduct the assessments. Assessments to calculate vulnerability may be very detailed, considering many different threats and locations, or very broad, dealing with only specific bridge attributes, such as bridge type, span lengths, number of spans, average daily traffic, etc. This depends on the number of bridges assessed and the time and funding allocated.

Analysis techniques used to calculate vulnerability may include one or more of the following:

- *Visual Observation* – vulnerabilities are identified by an experienced professional and engineering judgment is used to determine likely consequences.
- *Single Degree-of-Freedom (SDOF) Analysis* – individual structural elements are modeled using a lumped mass-spring approximation according to Biggs (1964) often with empirically derived blast pressure-time histories.
- *Finite Element Modeling (FEM)* – multiple response modes are modeled to calculate the response of all or part of the bridge structural system.
- *Coupled Finite Element Modeling* – Computational fluid dynamics (CFD) are used to model the blast wave as it interacts with the structure.

Each method has distinct advantages and disadvantages and all depend, to some extent, on empirical data. As shown in Figure 1, increased accuracy has the tradeoff of taking increased time and cost. In risk assessments of multiple bridges there is rarely time or budget available for finite element modeling. These methods are more often used when a known threat is being considered on a single high profile asset.

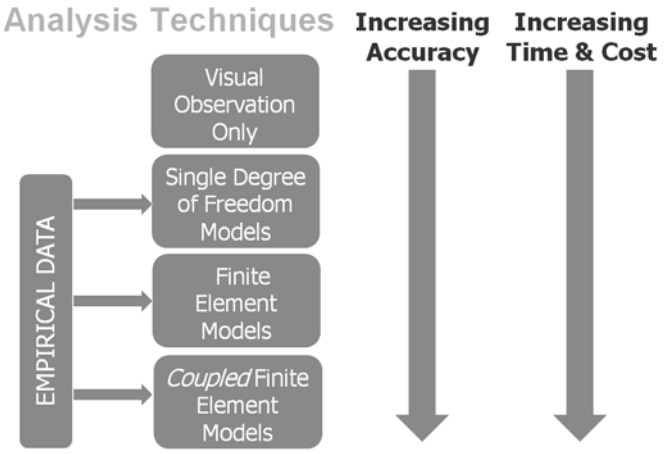


Figure 1. Accuracy, Time, and Cost of Analysis Techniques

SDOF blast analysis has many advantages over simple visual observation without the computational cost of FEM. Commonly used for blast analysis of buildings, SDOF methods are well established and have been validated by an abundance of testing that dates back to the 1940's. Element damage has been separated into superficial, repairable, unrepairable, heavy and blowout based on support rotations and ductilities (UFC 3-040-02 2008). SDOF methods are typically limited to individual elements with standard support conditions where explosive weight and standoff are within the limits of empirical pressure and impulse charts.

Many cases in bridge blast analysis are outside the scope of SDOF methods and require alternative methods.

A useful tool for the analysis of structural elements to blast loads is a Pressure-Impulse (PI) diagram. Calculated with SDOF methods, PI diagrams can be constructed for specific elements with curves predicting the expected damage for blast pressure and impulse combinations. Since a PI diagram is a property of a structure, it can be used to quickly calculate response for many charge weight and standoff distance combinations. An Excel® based tool for construction of PI diagrams is the Component Explosive Damage Assessment Workbook (CEDAW), which is distributed by the U.S. Army Corps of Engineers Protective Design Center (Oswald 2005).

Analytical methods are supplemented by empirical data, especially when close-in blast analysis is required. Localized response becomes more prevalent when scaled distance of an explosive is less than 0.4 $m/kg^{0.33}$ (1 $ft/lb^{0.33}$). Concrete breach prediction curves have been published (UFC 3-340-01 2002), though there is a significant lack of information regarding steel local response. Despite their inherent limitations, breach prediction curves can be used to find crater diameter on a bridge deck or determine the amount of local damage on a concrete pier or abutment. This is especially important since large bridge members, such as primary girders and piers, may not experience flexural or shear failure from a blast but could be severely compromised due to local damage at a critical location. More information about blast effects on bridge piers, including design guidance, is available in *Blast-Resistant Highway Bridges: Design and Detailing Guidelines* (Williamson et al. 2010).

Damage from non-blast threats such as cutting devices, fire, and vehicle impact also have a variety of analysis methods that can be used, though discussion of them is outside the scope of this paper.

POST-EVENT STABILITY ANALYSIS

Progressive collapse analysis following damage to bridge members is important to consider when calculating vulnerability scores for specific terrorist threats. The stability of a bridge following the failure of one or more of its primary members is a function of many things, such as structural redundancy, overstrength of adjacent members, and alternate load paths. Progressive collapse analysis takes the damaged state as initial conditions and finds the structure's ability to transfer forces through alternate load paths. It can be done statically or dynamically with linear or nonlinear member response. The analysis must be repeated for each damage scenario and can be extremely time consuming. In circumstances where full progressive collapse analysis is not feasible, energy balance methods can be used. A conservative assumption , that a structure will collapse once all primary load paths have been removed, can be used to predict progressive collapse if analysis of the structural system is not feasible within the time and budget constraints of a risk assessment.

A measure of a structure's ability to sustain local damage without global collapse is called robustness. Many researchers have embarked on finding methods to quantify robustness. Cavaco et al. proposed a calculation that is applicable to nearly any structure and cause of damage, given as:

$$R_d = \int_{d=0}^{d=1} f(x)dx \tag{2}$$

where R_d is the robustness index (between 0 and 1), d is the amount of damage (0 = no damage, 1 = complete damage), and f is failure (0 = no failure, 1 = total failure). If a small amount of damage, d, results in a large amount of failure, f, the structure will have a very low robustness index. Conversely, if the structure sustains failure at the same rate it sustains damage it will have a higher robustness index (Cavaco et al. 2010). Calculation of robustness index theoretically considers damage resulting from any manmade or natural threat; though in actual practice a finite number of threat scenarios would be considered. Given the number scenarios needed for consideration, simplified methods of analysis are ideally suited for robustness index calculation.

CHOICE OF ANALYSIS TECHNIQUE

Ideally a comprehensive risk assessment of all bridges within a country would be undertaken with a consistent set of analysis methods. However some assessments warrant more in-depth methods and in others it is sufficient to use quicker, simplified methods. Choice of analysis technique for bridge risk assessments depends on:

- Number of bridges in study
- Structural complexity of each bridge
- Type of threats being considered
- Time and budget constraints

When the analysis methods used to calculate vulnerability scores are inconsistent for bridges in the same risk assessment, the results may be skewed and mitigation funds may be withheld from where they are needed most. A case study is used to demonstrate how analysis techniques may be applied to a real-life risk assessment.

CASE STUDY

A group of twelve bridges crossing an inland waterway in a major U.S. city were chosen to receive federal funds to assess the risk of a variety of threats, both natural and manmade. The terrorist risk portion of the assessment was delegated to experts in that field. Details of these bridges are omitted for security reasons. Some of the bridges served critical local and regional transportation routes and heavy economic losses were anticipated if the waterway was blocked. Because of deadlines to use funds the task of calculating the risk scores for the bridges was divided between three consultants, each taking four bridges. This author was tasked with finding the terrorist vulnerability for four moveable bascule bridges serving city streets. The bridges consisted of tapered girders which rotated around a trunnion on each side of the waterway. Steel stringers and girders supported decks of either concrete or open-grate steel. One of the bridges is shown in Figure 2 open with a barge passing beneath it. The threat scenarios considered were taken from the Blue

Ribbon Panel Report (FHWA 2003) and included four sizes of explosives – delivered by hand, passenger car, truck, and barge – and an incendiary threat, not discussed in this paper.



Figure 2. Moveable Bascule Girder Bridge from Case Study

The assessment assumed that each threat was delivered at the location most effective in damaging the bridge threat locations were only considered if they were accessible by the delivery method. For the vulnerability assessment, calculations were done independent of the likelihood of occurrence. It was decided that PI diagrams were an ideal tool because of the ease of analysis for the entire bridge system. Using SDOF methods, PI diagrams were developed for all bridge framing members based on limit states of superficial, repairable, unrepairable, and heavy damage, and blowout taken from U.S. Army Corps of Engineers Protective Design Center, *Single-Degree-of-Freedom Structural Response Limits for Antiterrorism Design* (2008). In some cases the member capacity was reduced based on its connection capacity. The PI diagrams were mapped to their location on the bridge and blast pressures were calculated for the specified location of the threat using a script in Matlab. The bascule girders, typically nonprismatic members, were analyzed using SDOF properties calculated based on first principles (Clough and Penzien 1993). Figure 3 shows the result for an example case and Figure 4 shows a schematic of one of the bascule girders analyzed. The analysis was repeated until the worst case was found for each threat scenario.

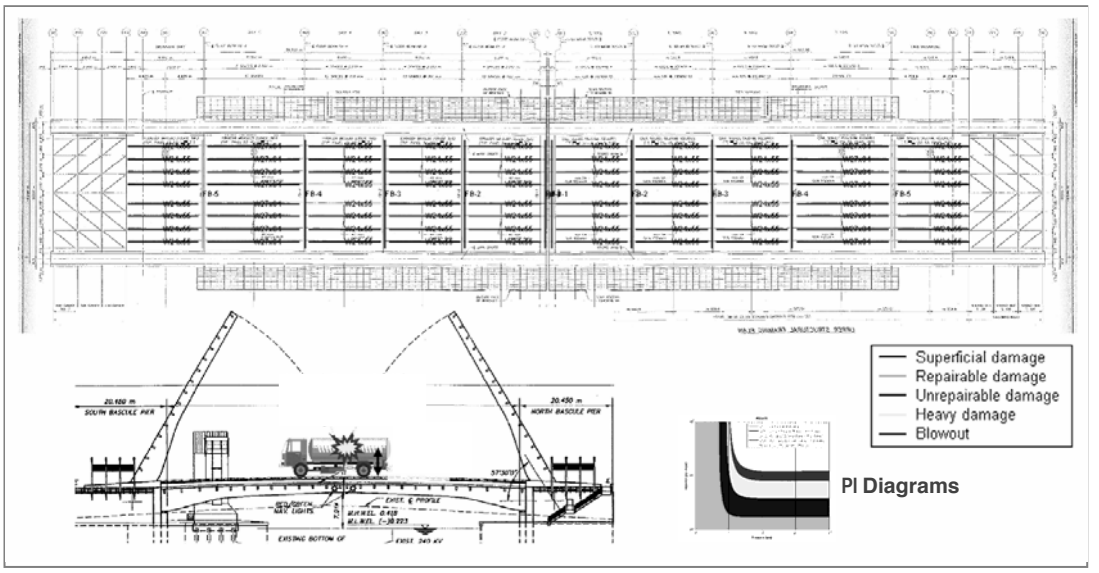


Figure 3. PI Diagram Analysis of Bascule Girder Bridge

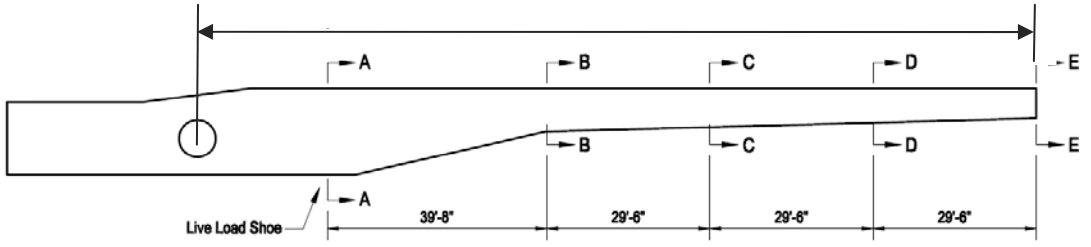


Figure 4. Bascule Girder Schematic

Local effects of blast were found with empirical curves for concrete breach taken from UFC 3-040-1 (2002) and for steel breach taken from FM5-250 (Headquarters Department of the Army 1992). Though these methods may oversimplify a highly variable and complicated phenomenon, they were considered adequate for the scope of the assessment. Based on the damaged condition of the bridge following the blast event, it was assumed that the members experiencing heavy damage and those members supported by them would collapse. Based on the local damage calculated from empirical curves, the residual capacity of the main girders was checked to determine if it could sustain the loads from the AASHTO Extreme Event II load combination, 1.25DC + 0.5LL (Ghosn 2003).

Some aspects of vulnerability, conversely, could be calculated without using analytical methods. If the equipment used to open and close the bridge was disabled, the barge traffic in the waterway would be disrupted. On several bridges, the operating machinery was protected by a concrete wall and on others it was exposed. Without calculation, it was determined that a package sized threat could destroy the operating machinery and disable the bridge until it could be repaired or replaced.

These vulnerability scores were used to calculate risk score for the four bascule bridges and the risk scores were combined with those from the other eight bridges. It was found, however, that the three consultants hired to conduct the risk

assessments used vastly different methods, such that comparison of mitigation options was difficult. Such variance in methods due to lack of guidance from funding agencies may have resulted in mitigation funds going to less critical projects.

SUMMARY OF RECOMMENDATIONS

In some aspects of bridge engineering over-standardization limits engineers from finding creative new solutions to design challenges. In bridge terrorist risk assessments, however, a degree of standardization is necessary so risk scores can be compared and mitigation funds can be properly allocated. The Blue Ribbon Panel made important steps toward standardization of risk assessments (FHWA 2003), but better further guidance is necessary in the areas of:

- Threat definition – Credible threats (both explosive and other threats) for bridges of varying importance should be adopted and provided on an as-needed basis to professionals performing risk assessments. Williamson and Winget have proposed threat definitions that should be considered by federal agencies for standardized risk assessments (2005). Where intelligence suggests a specific threat exists at a certain bridge, that threat should be added those considered.
- Analysis methods – Analysis should be in accordance with blast industry standards – including SDOF analysis, PI diagrams, empirical curves for local damage, etc. More advanced methods should be required in cases outside the scope of these methods.
- Levels of performance – Response of bridges to defined threats should be quantified and benchmark vulnerability scores based on metrics like downtime, repair cost, casualties, and disruption to local economy should be provided.

Many of the above recommendations follow current standards for federal buildings where anti-terrorist design and risk assessment is more established. Though risk assessment and mitigation of bridges can be more complicated than buildings there is no reason similar standards cannot be implemented for transportation assets to protect the nation's critical infrastructure.

REFERENCES

"Anti-Terrorist Security Network Almost Done on Bay Area Bridges and Tunnels," The San Jose Mercury News, March 25, 2003.

Biggs, J.M. (1964). *Introduction to Structural Dynamics*, McGraw Hill, New York.

Cavaco, E.S., Neves, L.A.C., Casas, J.R., Huespe, A.H. (2010). "A framework for robustness assessment in the context of corroded RC structures," *Proceedings of the Fifth International Conference on Bridge Maintenance, Safety and Management*, Philadelphia.

Clough, R.W., Penzien, J. (1993). *Dynamics of Structures, 2nd Ed.,* McGraw Hill, New York.

Federal Highway Administration (FHWA). (2003). "Recommendations for bridge and tunnel security." Rep. Prepared by the Blue Ribbon Panel on Bridge and Tunnel Security for AASHTO Transportation Security Task Force.

Ghosn, M., Moses, F., Wang, J. (2003) *Design of highway bridges for extreme events*, NCHRP Report 489, Transportation Research Board, Washington D.C.

Headquarters Department of the Army. (1992) *Explosives and Demolitions*, FM5-250, Washington D.C.

Oswald, C.J. (2005). *Component Explosive Damage Assessment Workbook (CEDAW) Methodology Manual V1.0,* Baker Engineering and Risk Consultants, Inc. <https://pdc.usace.army.mil/software/cedaw/help/cedaw_final_report.pdf>, (December 30, 2010)

Science Applications International Corporation (SIAC). (2002). "A Guide to Highway Vulnerability Assessment for Critical Asset Identification and Protection." *Prepared for the American Association of State Highway and Transportation Officials' Security Task Force*.

Unified Facilities Criteria (UFC) 3-340-01. (2002). *Design and Analysis of Hardened Structures to Conventional Weapon Effects (FOUO)*, Limited Distribution.

Unified Facilities Criteria (UFC) 3-340-02. (2008). *Structures to Resist the Effects of Accidental Explosions*, < http://www.wbdg.org/ccb/DOD/UFC/ufc_3_340_02.pdf> (October 25, 2010).

United States Army Corps of Engineers Protective Design Center. (2008). *Single-Degree-of-Freedom Structural Response Limits for Antiterrorism Design*, PDC TR-06-08, Omaha.

Williamson, E.B. et al. (2010). *Blast-Resistant Highway Bridges: Design and Detailing Guidelines*, NCHRP Report 645, Transportation Research Board, Washington D.C.

Williamson, E.B., and Winget, D.G. (2005). "Risk Management and Design of Critical Bridges for Terrorist Attacks." *J. of Bridge Engrg*., ASCE, 10(1), 96-106.

Case Study of Bridge and Tunnel TVAs: Since the Blue Ribbon Panel Recommendations for Bridge and Tunnel Security Were Issued

Joseph M. Englot[1]

[1] PE, MASCE, BSCE, MSCE, HNTB Corporation, 5 Penn Plaza, 6th Floor, New York, NY, 10001-1810; PH (212) 594-9717; FAX (212) 947-4030; email: jenglot@hntb.com

ABSTRACT

As an original member of the Blue Ribbon Panel (BRP) that developed the "Recommendations for Bridge and Tunnel Security" published in September 2003 by the Federal Highway Administration and AASHTO the author reviews the use of this and other subsequent homeland security related risk assessment guidelines in practice by sharing observations on how threat and vulnerability assessment (TVA) of existing bridges has evolved and where it may be going. The paper focuses on the original objectives of the BRP recommendations, how they align with the latest National Infrastructure Protection Plans for the Transportation Sector, how well their application has worked in practice, whether they assist DOTs and other agencies in obtaining DHS grant funding for security related projects, their application to rail bridges and tunnels, and why they are an essential part in the decision making process for implementing security improvements and countermeasures for bridges and tunnels. This will be discussed in the context of a case study.

Since the BRP recommendations were issued best practices for TVAs conducted by some state DOTs have given way to simplified decision tables for risk equations and risk values used with electronic spread sheets that can be used to sort security mitigation costs for critical bridges using cost-benefit factors. The prioritized mitigation projects for existing bridges are then included in the rehabilitation project scope for each bridge when they are contracted out based upon the DOT's state-of-good-repair program. Many states, however, have not yet embraced the BRP recommendations based upon the judgment that funds for repairing deficient bridges are their first priority and they will not deal with security related issues until those needs are addressed. Independent of the availability of funds to repair or secure bridges in a given state or agency, there is a need to prioritize the criticality of the bridge and tunnel inventory because whether a bridge fails due to deterioration, an accident, natural hazards, or intentional attack, the owner should know where the first dollar of funding should be spent, be it for repair of deficiencies or for hazard reduction.

BACKGROUND

Blue Ribbon Panel. Following the September 11, 2001 terrorist attacks, the Federal Highway Administration (FHWA) and the American Association of State Highway and Transportation Officials (AASHTO) jointly sponsored a panel of bridge and tunnel experts from professional practice, academia, federal and state agencies, and

toll authorities to assess the vulnerability of bridges and tunnels to the actions of terrorists and other hazards and to develop and recommend strategies and practices to reduce the likelihood of catastrophic structural damage possibly resulting in human casualties, economic losses, and socio-political damage on a national, regional, and local level. The Blue Ribbon Panel on Bridge and Tunnel Security (BRP) published "Recommendations for Bridge and Tunnel Security" in September 2003.

A significant part of the recommendations of the BRP was the use of a risk based approach to guide planning, design, and engineering recommendations to increase security and reduce the vulnerability of bridges and tunnels in a cost effective way. The risk based approach consisted of two tiers, the first being a prioritization of the large number of bridge and tunnel assets by their criticality or importance, and the second being a risk equation similar to ones previously used for natural hazards such as the assessment of seismic risk to bridges and subsequently recommended in FEMA 426 for risk assessment of building facilities.

NIPP. Another major disaster that has influenced the risk assessment of bridges and tunnels was Hurricane Katrina which occurred in August of 2004. After the experiences with emergency response in the aftermath of the event the Department of Homeland Security (DHS), which included FEMA, developed a National Infrastructure Protection Plan (NIPP) that embraced the multi-hazard approach to the planning, risk assessment, emergency preparedness, and mitigation of all hazards to our nation's critical infrastructure, including acts of terrorism. This meant that whether a disaster or extreme event affecting critical infrastructure is caused by a natural event, a manmade accident, or an act of terrorism, the emergency preparedness activities, system resiliency objectives, and recovery operations for critical infrastructure will be similar if not the same. Subsequent to the NIPP being published in 2006, DHS published the Transportation Systems Critical Infrastructure and Key Resources Sector-Specific Plan as input to the National Infrastructure Protection Plan in May 2007. This plan specifically covers the nation's highway infrastructure of which bridges and tunnels are a major subset.

The transportation sector's security goals and objectives are consistent with the goals outlined in the President's National Strategy for Homeland Security and the joint DHS and DOT National Strategy for Transportation Security (NSTS). The three major goals and objectives focus on:

1. Prevent and deter acts of terrorism using or against the transportation system.
2. Enhance resilience of the U.S. transportation system.
3. Improve the cost-effective use of resources for transportation security.

All three on these goals are in harmony with the threat and vulnerability assessment methodology recommended by the BRP. This will be demonstrated further in the body of the text.

TVA METHODOLOGY

Importance of Risk Based Approach. The importance of the TVA methodology cannot be overemphasized. Terrorism and disasters, whether natural or manmade, cannot be treated the way codified engineering design criteria for bridges and tunnels is treated because they represent extreme events of low probability but of high consequence. We could never by any stretch of the imagination afford to protect all of our bridge and tunnel assets to the same level against these extreme events, hence the need for a methodology to allow asset owners, transportation officials, and engineers to selectively identify and evaluate the cost effectiveness of mitigations that are affordable and justified by a rational risk-based procedure.

Basic Risk Equation. The risk equations are adequately covered in the BRP recommendations.

CASE STUDY

Scope. The scope of the case study project was to first provide assistance to the New Jersey Office of Homeland Security and Preparedness Critical Infrastructure Unit (NJ OHS&P) and the New Jersey Department of Transportation (NJDOT) in validating an existing Vulnerability Assessment of Highway Structures and provide a recommended prioritization of bridges and tunnels including freight and passenger rail as well as highway bridge and tunnel assets. This was followed by conducting a threat assessment, a vulnerability assessment, an impact assessment, and a countermeasures needs assessment for the State's top 50 bridge assets. The study was performed by HNTB Corporation with Weidlinger Associates Incorporated.

PRIORITIZATION METHODOLOGY

Tier 1 Prioritization. The original screening conducted by NJDOT followed AASHTO's guide, "A Guide to Highway Vulnerability Assessment for Critical Asset Identification and Protection" (May 2002). The formula prescribed in this guide consists of 14 separate categories in which to rate the facility under evaluation. Each category has a designated point value; some categories have varying values (up to 5 point maximum) while other categories have a maximum value of one. The maximum score for each facility is 43 points. A higher point total implies a facility with a higher vulnerability. It should be noted that the rating system is subjective requiring an expert panel type of decision to establish point values and does not lend itself to prioritizing the thousands of bridges that a typical state DOT has to deal with. A tier 1 methodology that lends itself to sorting by computer spreadsheets is required to meet this need.

Revised Tier 1 Screening Methodology. The revised first tier screening methodology was based upon the following considerations:

1. Reflected the mission of NJ DOT and DHS
2. Reflected a multi-hazard approach

3. Reflected the resiliency of the transportation network
4. Measured cost of the recovery period to the economy by transportation delay
5. Measured impacts to transportation on multi-modal basis

In the process only five of the 14 attributes in the previous tier 1 prioritization methodology aligned with these considerations and were retained. A new metric for the purposes of validating the results produced by the previous screening effort was proposed. Realizing that one of the primary functions of the NJDOT system is to transport people and goods, this new metric serves to quantify the volume of people and goods that are delayed in transport if the given bridge or tunnel is lost or otherwise unavailable for use. In particular, the following four factors are considered important in identifying the most critical bridges:

1. Volume of transport units carried by the bridge each day under full operation.
2. The number of days the bridge would be unavailable for use if it were to be lost in a damaging event of any type.
3. The time delay incurred by each transport unit due to the detour around the closed bridge. This is assumed to be a function of the bridge detour length and the assumed speed that vehicles would use on the detour route.
4. A fourth factor is included to account for the increased importance or criticality of those bridges that serve as designated emergency evacuation routes.

In any state transportation network, the bridges and tunnels are the critical choke points in the system because they cross geographic features that limit other means of access. For the purpose of the screening criteria developed for this project, resiliency is reflected in the availability and length of a viable detour if a bridge or tunnel is knocked out of service by a catastrophic event. The length of detour for each highway bridge is listed in the SI&A database and was used in the calculation of delay due to the need to rely on that detour until the bridge that is lost is restored to service. The assumption made is that the additional detour length traveled will be at a lower than normal speed adding to the delay. This is due to the fact that local roads will likely be used to access the bridge or tunnel detour which may also be of a lower traffic volume capacity than the normal route.

The screening process also included passenger rail and freight rail tunnels and bridges, which required information on passenger or freight volumes be obtained or generated for those assets. In addition, the presence of express buses or HOV lanes are not reflected in the SI&A database for highway bridges and had to be added. In that case, estimates of average daily number of express buses and passengers were added to the volumes for the bridges or tunnels. In the case of detours for passenger rail bridges, it was assumed that passengers will be transported between the train stations at either end of the lost bridge or tunnel by bus. An equivalent detour length was computed adding equivalent time for transfer of passengers to and from a bus.

For freight rail movement of goods, the system is less resilient. If a freight rail bridge is lost for a period of time, it was assumed that the freight trains will have to be detoured to another available freight rail line. Since many old fright rail lines have been abandoned there are relatively few alternative paths left to move rail freight.

If any bridge or tunnel suffers a catastrophic loss, an assumption was made about the length of time it takes to reconstruct the bridge or tunnel. This was based

upon actual data when available for the reconstruction of bridges lost to disasters and assumptions made for repair and recovery of tunnels. This time element for recovery was a major factor in the delay calculation and was a function of the bridges longest span length. This is because construction schedules show that the longer the bridge span the longer it takes to fabricate and erect the bridge.

Another critical factor that tests the resiliency of a transportation network in times of disaster is the ability of the system to evacuate large populations when storms or hurricanes threaten to flood coastal and waterfront communities. Because the designated coastal evacuation routes become critical in such an emergency, the bridges on those routes are even more critical. For this reason the screening criteria applied a factor to increase the criticality of bridges on coastal evacuation routes across the board.

Due to the high volume of bridges and data included in the first phase, the decision was made to base the screening values entirely on available Structural Inventory & Appraisal (SI&A) data provided by NJDOT and other agencies in a spreadsheet format.

New Tier 1 Metric. The formulation of the metric for quantifying the volume of people and goods impacted is as follows:

$$\mathbf{PDTU = [TVTU \times DD \times TDD] \times ER} \qquad \text{(Basic Equation)}$$

Where:

PDTU = Potential delay of transport units (in unit-hours).

TVTU = Total volume of transport units (in units/day, see item 1. above).

DD = Days of downtime when bridge or tunnel is not functional (in days, see item 2. above).

TDD = Time delay due to detour (in hours, see item 3. above).

ER = Importance factor for bridges that are designated evacuation routes. This is a multiplier (1.2 was used) to increase the importance of those facilities that are intended for use during emergencies.

Volume of Transport Units. The Total Volume of Transport Units (TVTU) is a direct manipulation of the SI&A Average Daily Traffic (ADT) data. Since ADT includes truck volume, and Average Daily Truck Traffic (ADTT) is given as a percentage, the percentage of trucks was deducted from the ADT. The following conversions were used to convert various vehicles to Transport Units in this project:

1 automobile (1.2 avg. passengers) = 1 Transport Unit

1 truck = 2 Transport Units

1 railroad passenger = 0.83 Transport Units

1 rail hopper car = 4 trucks = 8 Transport Units

100 Tons (rail freight) = 8 Transport Units

1 cargo container = 1 truck = 2 Transport Units

The numbers and ratios used were determined from a literature search of studies of highway user costs due to construction delays in several states, parameters obtained from the New Jersey DOT Manual of Highway User Costs, and published data from the Iowa Department of Transportation on equivalent units of freight volumes transported by truck, rail, and barge.

Days of Downtime. Based upon an examination of actual bridge collapses and reconstruction periods, and in the absence of such information, the construction schedules for design-build bridge projects, Days of Downtime (DD) was based upon an empirical formula that reflects a best fit to the following data points:

Bridge Constructed (or Reconstructed)	Max Span[1]	Recovery Period
MacArthur Maze Bridge, Oakland, CA	100 ft.	1 month
I 35 Bridge, Minneapolis, MN	500 ft.	13 months
New Tacoma Narrows Bridge, Tacoma, WA	1,500 ft.	42 months

Table 1

The equations[1] for the Maximum Span Length Factor and Days of Down Time (DD) are shown here and plotted in Figure 1:

$$\textbf{Max Span Length Factor (months)} = 7.0E\text{-}6(\text{Max Span})^2 + 0.0168(\text{Max Span})$$

$$\textbf{DD} = 30(\text{Max Span Length Factor})$$

Time Delay Due To Detour. The Time Delay due to Detour (TDD) parameter is the product of two multipliers:

County Multiplier
Detour Multiplier

These two multipliers are based on the location of the bridge that best characterizes the impact of downtime to users. The dimensionless County Multiplier was taken from the Roadway Congestion Index (RCI) from Mobility and the Cost of Congestion in New Jersey – 2003 Update – Appendix II. It adjusts the detour travel time based upon the traffic congestion in each county. The Detour Multiplier is based on the SI&A detour length data divided by a reduced detour speed of travel while traversing the detour to yield the detour travel time.

Evacuation Route. The Evacuation Route (ER) multiplier is an additional weighting that considers the importance of a structure with regards to evacuation routes. This value was not taken from SI&A data, but was determined from county evacuation routes. For any structure found on an evacuation route, a factor of 1.2 was used. For all other structures, the value of the multiplier was taken as 1.0.

Master Ranked List of All State Bridges. The prioritization methodology was used to rank all bridges and tunnels in the state as shown in Figure 2 for state bridge project planning purposes. The information for all 6,600 state bridges was sorted by county and bridge owner and distributed by NJ OHSP to their state wide emergency preparedness task force representatives consisting of county prosecutors and emergency management officers of state transportation agencies who own and operated the assets. A template of the sorted information is shown in Figure 3.

[1] Note: The equations are based upon the NBIS SI&A database which is in units of feet.

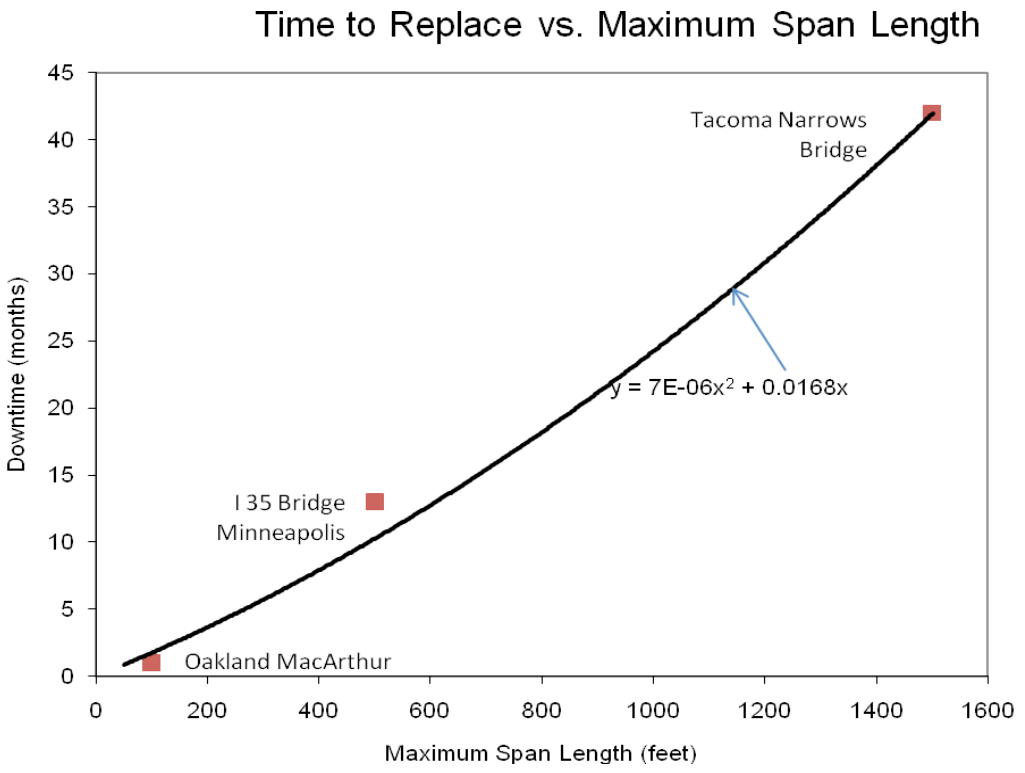


Figure 1

Tier 1 Prioritization Results.

Bridge Characteristics	Percent	Number
State Gov't. Owned Bridges	24%	12 / 50
Evacuation Routes	70%	35 / 50
ADTT exceeding 10,000	34%	17 / 50
ADT exceeding 100,000 (w/o trucks)	38%	19 / 50
12 or more months of recovery time	24%	12 / 50
Passenger Rail Tunnels	10%	5 / 50
Passenger Rail Bridges	8%	4 / 50
Rank of Top 3 Freight Rail Bridges	Ranked 52, 110, 145 (In top 2 percentile of all 6,600 bridges in state)	

Table 2 - Results for Top 50 Bridges & Tunnels – All Owners

Bridge Characteristics	Percent	Number
Moved into Top 50 w Revised Screening Methodology	44%	22 / 50
Evacuation Routes	70%	35 / 50
No detour available	8%	4 / 50
ADTT exceeding 10,000	36%	18 / 50
ADT exceeding 100,000 (w/o trucks)	44%	22 / 50
3 or more months of recovery time	26%	13 / 50

Table 3 - Results for Top 50 Bridges - State, County, Local Government Owned

RANKED LIST OF STATE WIDE BRIDGES AND TUNNELS - ALL OWNERS												
RANK	BRIDGE OR TUNNEL NAME	MAX. SPAN LENGTH	DD	COUNTY MULTIPLIER	DETOUR MULTIPLIER	TDD	ER	TOTAL MULTIPLIER	ADT	ADTT	TVTU	PDTU
1												
2												
3												
4												
5												
.												
.												
.												
48												
49												
50												

Figure 2 – Confidential Prioritization of All Bridges and Tunnels in State

AGENCY: (State Routes, County, or other owner) **REPORT GENERATED ON:** (YR.MO.DY TIME)

STRUCTURES: (Number of bridges)

Note: Potential casualty estimates only apply to bridges carrying vehicular traffic (i.e. not rail bridges or tunnels).

BRIDGE NAME	ID NUMBER	ROUTE	TOTAL RANKING	STATE RANKING	ADT	ADTT	DOWN TIME	DETOUR LENGTH	POTENTIAL CASUALTIES	ECONOMIC IMPACT

Figure 3 – Confidential List of All Bridges Sorted by County and Owner

The information will be used for:

- Use to Determine the criticality of every bridge in the county asset inventory for emergency planning purposes, business continuity planning, and insurance purposes
- Constitutes a "Risk Based" assessment for DHS/TSA federal grant distribution
- Use to develop security/hazard mitigation budget and the order of priority for spending funds
- Use as tool for prioritizing investing of funds for state-of-good-repair for bridges

TVA METHODOLOGY

Sorting Methodology. After identifying the top 50 critical bridges in the NJDOT-owned inventory by the tier 1 prioritization, individual second tier threat and vulnerability assessments (TVAs) were first be conducted on the most critical bridges that represent bridge types or categories. The most critical bridges are those with the highest V values in the R=OVI equation. This means they represent the highest values for expected damage, expected down time, and expected casualties. This is based primarily upon the length of the longest span that could potentially collapse in a hazard or attack, and whether the feature crossed by the bridge is water or land. It is assumed that for the same span length, a bridge constructed over water will be more expensive, will take longer to reconstruct, and will likely have more casualties than a bridge constructed over land. This judgment was validated later since both the longest span over water and longest span over land were selected for an individual TVA. In addition, the types of threats for bridges over land or over water are different in that bridges over land are not exposed to water vessel threats. The database has an additional parameter that reflects the crossing of navigable waterways.

In general the planned methodology for conducting the initial set of representative TVAs was as follows:

1. Sort top 50 bridges by Structure Type
2. Sort by Feature Crossed
3. Conduct one detailed TVA risk analysis per combination (example: Type A over water and Type A over land)
4. Develop Specific Threats
5. Assess Vulnerabilities and Consequences
6. Develop Preliminary Mitigations

Selecting Representative or Key Bridges. After sorting the bridges, map views and satellite photo views from available internet web pages were utilized to examine the representative bridges of each type with the longest spans to confirm their suitability for a detailed TVA. This information was helpful in planning the individual site visits and confirming that existing bridge plans and inspection reports for the structures were consistent.

An individual detailed TVA was conducted for each representative bridge type. This required collection of bridge plans and previous inspection reports. The methodology utilizes the equation R= O x V x I, where the "I" value was based upon the prioritization performed in the step above. The following steps were performed:

1. Perform an on-site assessment of the bridge spans documenting the accessibility, existing level of protective security, and assess target attractiveness and capability of the aggressor. These form the basis of the "O" values.
2. Perform an engineering assessment to determine the impact of each type of threat or hazard to the structures, looking at critical elements that could be attacked. For each type of attack or hazard determine the consequence of that attack (downtime, casualties, and cost to recover the facility after an attack). These will be the basis for the "V" values. The

engineering assessment included an analysis of the structure as detailed below:

a) Perform Blast Analysis using conventional software (Also available through US Army Corps of Engineers Protective Design Center https://pdc.usace.army.mil/ or other source.)

b) Assess structural damage severity from fuel tanker or vessel fire and vehicle or vessel collision if applicable.

c) Perform Progressive Collapse Analysis to assess if damage is local or will lead to collapse.

d) Assess potential for scour or storm surge damage.

3. Adjacent infrastructure that may either increase target attractiveness, or may increase hazards present due to an adjacent independent attack or accident was also assessed and noted. Items of note included the navigable waterway, maritime facilities, ports for large ships, and fuel storage facilities.

4. A pre-mitigation risk assessment was performed to calculate the severity of each potential threat to each critical bridge element (compute sum of R values). The most likely and significant threats were prioritized.

Countermeasure Assessment for Key Bridges. Once the pre-mitigation risks were computed for the bridge facility, effective mitigation measures or countermeasure projects were conceived for each ranked threat starting from the top ranked threat and working downward. The mitigation measures include any measure that reduces one or more of the occurrence or vulnerability attribute values, which are: access for attacks, level of security, attractiveness of target, expected damage, expected downtime, or expected casualties. Capability of the aggressor is not considered because it is usually outside of the control of the facility owner. This can typically only be changed by federal, state, or local law enforcement practices and anti-terror intelligence. Following is a list of categories of countermeasures that are considered:

1. Increase Security Presence (increase security patrols)
2. Establish Secure Perimeter (physical barriers and secure access control)
3. Surveillance, Intrusion Detection & Enforcement
4. Create Standoff Distance (install crash rated barriers, fender systems)
5. Add design Redundancy (modify structure to create additional load paths)
6. Harden/Strengthen Structural Elements (install shields, armor, reinforcing)
7. Develop An Accelerated Response And Recovery Plan (Emergency response plans)

Each mitigation category listed above will either reduce the Occurrence risk values or the Vulnerability risk values. Creating standoff distance actually reduces both since access for attack is reduced, as well as expected damage since the effects of air blast will be lessened, resulting in less damage. The revised risk values were discussed with NJ DOT Officials and law enforcement representatives at a workshop held on March 30, 2007. The values were subsequently modified to reflect the consensus of the workshop attendees.

Construction and Operating Cost Estimating. The following steps were completed to assess the effectiveness and cost-benefit of each mitigation measure:

1. Prepare a conceptual plan or design for the mitigation.
2. Re-analyze the structural effects of the mitigation for standoff, redundancy, and structural hardening mitigations.
3. Estimate the cost (initial and O&M).
4. Re-calculate the mitigated risk value for the threat on the structure.
5. Calculate the reduction in total risk for the entire facility for the mitigation measure.
6. For each mitigation measure, plot reduction in facility risk value (vertical axis) versus cost (horizontal axis). A log-log scale is best. This helps to identify the most effective mitigation measures for the dollars spent on them, for the structure in question. Priority points will plot in upper left quadrant (i.e. highest vertical axis value and lower horizontal axis value).

The last step (6.) above is used to prioritize the mitigation measures to be implemented based upon the available security capital budget and operating budget for each facility and the entire NJDOT program. The plot results for all mitigations for the seven representative bridges are shown in Figure 4.

Extrapolation Methodology for Remaining Top 50 Bridges. Once the seven representative bridges' threat and vulnerability assessments were complete, the results were extrapolated to the remaining 43 bridges of the NJDOT top 50. The seven representative bridges were selected based on two primary characteristics: structure type and feature crossed. Based on these two characteristics, each of the remaining 43 bridges was associated with one of the seven representative bridges.

CONCLUSIONS AND RECOMMENDATIONS

Recommended General Uses for the Assessment Results. The full assessment results, for both representative and extrapolated bridges, will be useful for programming and distributing resources for security projects. For each bridge all of the mitigations, their descriptions, aerial photos, and the cost estimates were formatted in Excel spread sheets and can be sorted by county, by mitigation type, or by cost benefit ratio. By sorting the results in various ways, projects can be developed and grouped by value, by type, or by bridge. While most threat and hazard mitigations will require further design development, the estimate costs can be used to incorporate security improvements in upcoming rehabilitation contracts for critical bridges.

Usefulness of Bridge and Tunnel Prioritization. The ability to prioritize all the bridges and tunnels in the state based upon their criticality to the transportation network is essential for long range transportation planning, for emergency planning purposes, for business continuity planning, and for targeting the most critical assets for state of good repair and bridge rehabilitation funding as well. It also constitutes a "Risk Based" assessment for DHS/TSA federal grant distribution.

State DOTs can utilize Homeland Security funding through Urban Area Security Initiative (UASI) grants and Regional Transit Working Group (RTSWG) grants to

cover their planning costs to conduct both prioritization and threat assessment and mitigation studies so they can develop short term and long term strategies to improve the resiliency of their transportation networks, both for highway and rail systems.

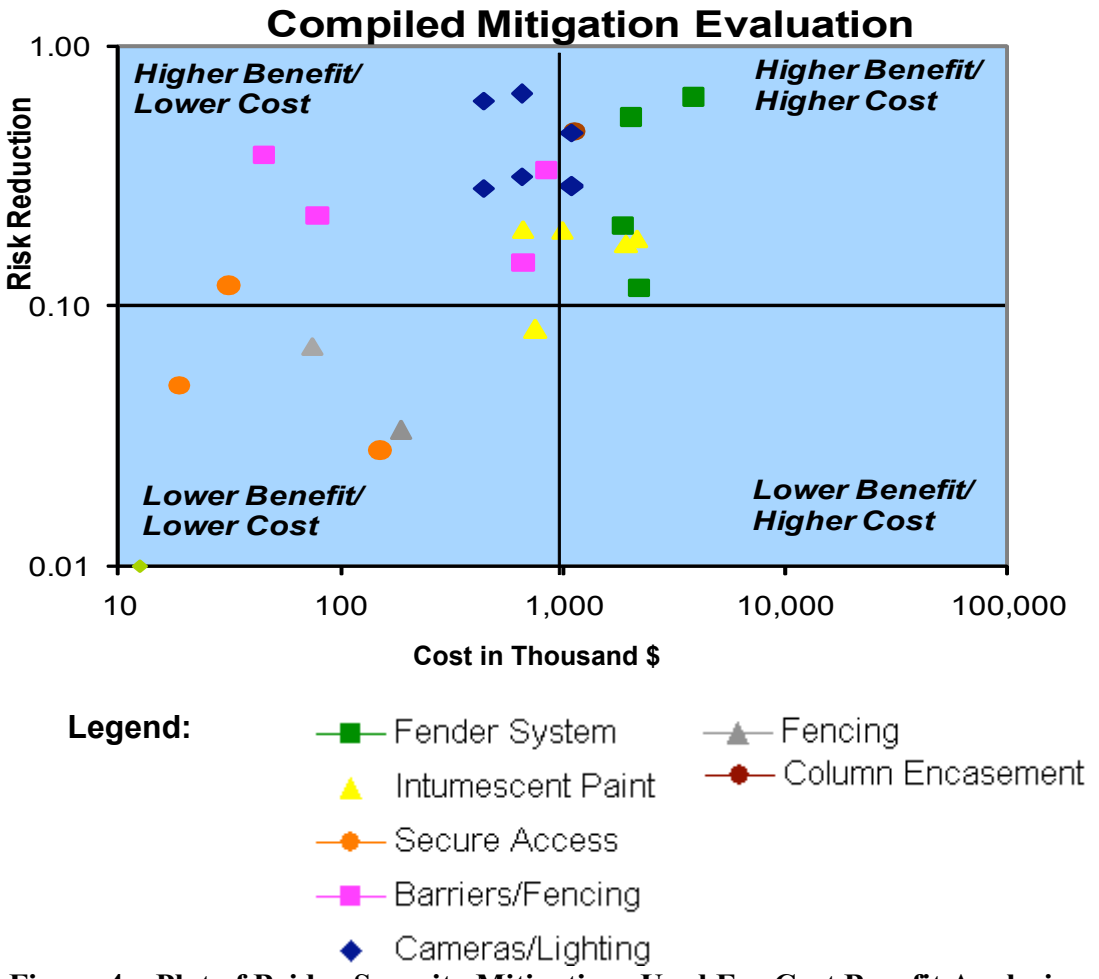


Figure 4 – Plot of Bridge Security Mitigations Used For Cost Benefit Analysis

REFERENCES

"Recommendations for Bridge and Tunnel Security" published by the Federal Highway Administration and AASHTO, September 2003

"A Guide to Highway Vulnerability Assessment for Critical Asset Identification and Protection" published by AASHTO Security Task Force, May 2002

"National Infrastructure Protection Plans for the Transportation Sector" published by the Department of Homeland Security, 2007

Blast Amelioration Systems: Effect of Topological Parameters on Performance of Layered Metallic-Lattice Sandwich Panels

John Przywara[1] and Kapil Khandelwal[2]

[1]Undergraduate Student, Department of Civil Engineering and Geological Sciences, University of Notre Dame, Notre Dame, IN – 46556; email: jprzywar@nd.edu
[2]Assistant Professor, Department of Civil Engineering and Geological Sciences, University of Notre Dame, Notre Dame, IN – 46556; email: kapil.khandelwal@nd.edu

ABSTRACT

In recent times, the use of sandwich panels as sacrificial claddings in the blast/impact protection of structural systems has been the subject of much investigation. Popular sandwich panels systems include core consisting of regular metallic-lattice and metallic-foams. These systems have been proven to be beneficial when used as sacrificial claddings because of their propensity to sustain large deformations and plastic energy dissipation. This allows the panels systems to absorb more energy than a single metallic plate consisting of the same mass. In case of metallic-lattice cores, energy absorption capacity depends on the topological structure and the optimal topology for these cores is not yet established. In this study the effect of topological parameters on the performance of sandwich panel systems with metallic-lattice cores is investigated. Nonlinear finite element analyses of cladding systems with different core topologies are carried out to investigate the effect of core parameters on their performance. The simulation results shows that the performance of the sandwich panel systems is highly influenced the topological parameters.

INTRODUCTION

Sandwich panels (Figure 1) are a popular system that can be used for blast and impact amelioration. In the past, numerous studies have been conducted regarding the use of sandwich panels in blast or impact protection. Many of these studies have focused on investigating different structural topologies that can be implemented within these panels. As a result, a number of different core topologies that can be used in applications are available. Available topologies can be subdivided into three distinct groups: truss, folded plate (corrugated), and honeycomb cores.

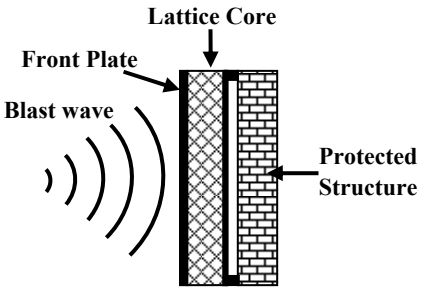


Figure 1. Sandwich Panels for Sacrificial Cladding Systems

Commonly included among the truss topologies are tetrahedral trusses, pyramidal trusses, kagome trusses, octet trusses, and woven trusses. Y-frame, triangular, and diamond shapes generally make up the group of folded plate cores. Finally, the honeycomb cores include square, triangular, and hexagonal honeycomb shapes. Early studies Zhenyu and Hutchinson (2004a) and Zhenyu and Hutchinson (2004b) investigated pyramidal truss, triangular folded plate, and square honeycomb core topologies. These studies investigated the cores behavior under statically applied uniformly distributed pressure, the plastic energy dissipation under quasi-static loading, and the front and back face deflections due to uniform impulse loading. Sandwich panels with triangular folded plate cores and diamond honeycomb cores subjected to different loading directions were investigated by Valdevit et al. (2004). McShane et al. (2007) compared sandwich panels comprised of pyramidal truss and square honeycomb cores subjected to quasi-static and impulsive loading via both experimental testing and finite element simulations. Cote et al. (2006) investigated sandwich panels comprised of triangular folded plate and diamond honeycomb cores for their compressive, transverse shear, and longitudinal shear responses via both experiments and finite element simulations. Vaziri and Hutchinson (2007) investigated air shocks on sandwich panels with square honeycomb and triangular folded plate cores via finite element analyses that subjected the cores to uniform pressure loads and uniform prescribed velocity loads. More recent studies have focused on Y-frame and triangular folded plate core topologies. For instance, Tilbrook et al. (2007) conducted experimental and two-dimensional finite element analyses of the aforementioned topologies. Rubino et al. (2009a) and Rubino et al. (2009b) produced two studies in conjunction with one another to analyze these topologies with experimental and finite element analyses.

The above studies utilized a variety of loading conditions, specimen dimensions, and boundary conditions. Therefore, it is not possible to rationally compare and evaluate the performance of various core topologies. To this end, this study investigates the performance of standardized sandwich panel system with various core topologies using finite element simulations. In particular, the performance of popular core topologies including honeycomb and folded plate cores are compared under the specified blast loading conditions. The effect of front plate thickness, which is considered to be an important topology parameter, on the system performance is evaluated.

FINITE ELEMENT MODELING OF CLADDING SYSTEMS

Three-dimensional finite element simulations of sandwich panels with different core topologies subjected to representative blast loading is conducted using finite element program LS-DYNA (Hallquist 2010). The sandwich panels are modeled using fully integrated Hughes-Liu using shell elements. The shell formulation accounts for finite deformations and 5 mm × 5 mm element sizes are used to account for local strain gradients and to accurately capture the panel response. All elements were initially created with thickness, t = 0.3 mm, however, some of the finite element analyses involved changing component thickness to investigate the

effect of plate thickness on the panel performance. The modeling process including constitutive model selection and the setup of the loading and the boundary conditions are described in the following sections.

MATERIAL PROPERTIES

The material properties used are those corresponding to AISI 304 stainless steel. Steel constitutive behavior is represented by a rate dependent piecewise linear J_2 plasticity material model MAT24 in LS-DYNA. The steel is modeled with the following parameters: relative density, ρ = 7900 kg/m^3; Young's modulus, E = 210 GPa; and yield strength, σ_y = 210 MPa. Strain rates effects are included to accurately capture steel plastic flow under high strain rates. Experimental data from (Rubino et al. 2009a) is used in this investigation. The experimental data includes stress-strain curves for quasi-static strain rate ($\dot{\varepsilon} = 10^{-3}$ s^{-1}) and for several dynamic strain rates ($\dot{\varepsilon} = 1$ s^{-1}, $\dot{\varepsilon} = 10^{2}$ s^{-1}, $\dot{\varepsilon} = 10^{3}$ s^{-1}, and $\dot{\varepsilon} = 10^{4}$ s^{-1}). Figure 2 shows the measured stress-strain data for different strain rates obtained from (Rubino et al. 2009a) and used in this study.

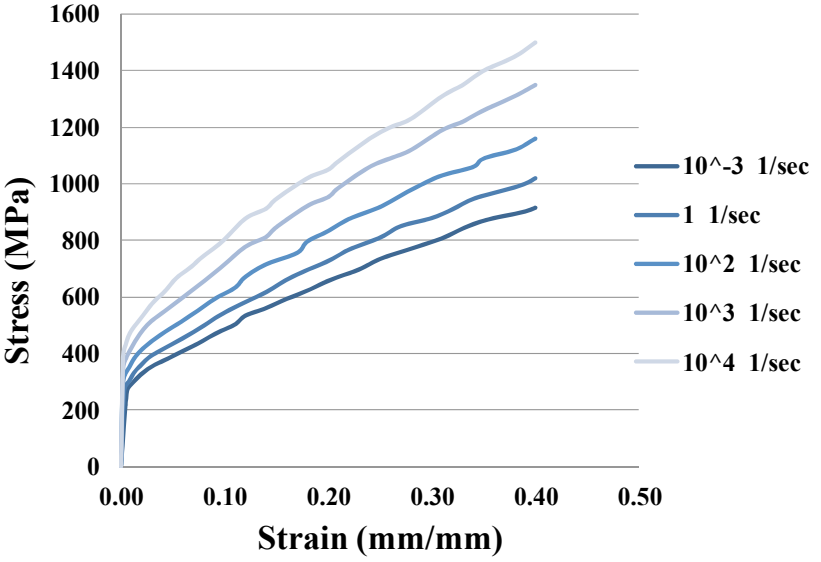


Figure 2. Stress vs. strain for different strain rates (Rubino et al. 2009a)

MODELING OF BLAST LOADING

The panels are subjected to blast loading as described in this section. This loading can be considered as a representation of actual blast loads that can be experienced by these panel systems. In case of blast loading, the pressure that is exerted on a particular point in space from an explosive blast in the air is dependent on the linear distance that the point is from the center of the blast as well as the magnitude of the blast. A popular model for defining blast pressure is given by the modified Friedlander equation (Baker 1973) and is given by Eq. 1:

$$p(t) = p_o + p_{\max}(1 - \frac{t}{t_d})^{-\frac{bt}{t_d}} \qquad (1)$$

where $p(t)$ is the pressure at time t, p_o is the initial air pressure, p_{max} is the peak overpressure from the blast, t_d is the positive pressure phase duration, and b is a parameter to describe the decay of the curve. An idealized plot of the blast pressure vs. time response as modeled by the Friedlander equation is presented in Figure 3.

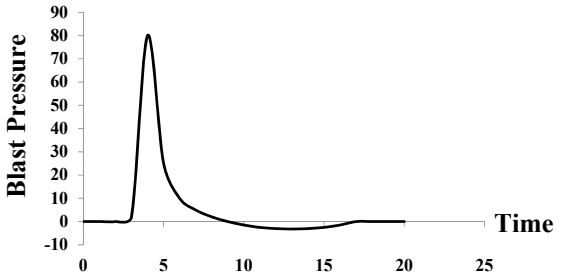


Figure 3. Idealized blast pressure vs. time response of an air blast as modeled by the Friedlander equation

The peak overpressure occurs at the time known as the arrival time, t_a. Additionally, functions that represent the parameters for this pressure vs. time response are typically given in terms of the scaled distance, Z. The scaled distance is the relationship between the distance, d, from the center of a charge of TNT and the mass, W, of the TNT and is given by (2):

$$Z = \frac{d}{\sqrt[3]{W}} \qquad (2)$$

To obtain more realistic blast pressures, Kingery and Bulmash (1984) produced curves of fit to represent the parameters of the pressure vs. time response obtained from experimental data determined on study of blast waves. These curves are deemed appropriate for any scaled distance of less than 40 m/kg$^{1/3}$. The blast pressure vs. time parameters represented by the curves include the scaled time of arrival, peak overpressure, scaled positive phase duration, scaled positive phase impulse, reflected pressure, reflected impulse, and shock front velocity. The data for the curves for these parameters are implemented within the computer model CONWEP, a program utilized by the military in studies of blast impacts on vehicles and structures (Hyde 1988). The CONWEP equations are also available in LS-DYNA, where the user input the coordinates of the blast center and the mass of TNT used to create the blast in order to model the data for the blast wave at any desired point in space.

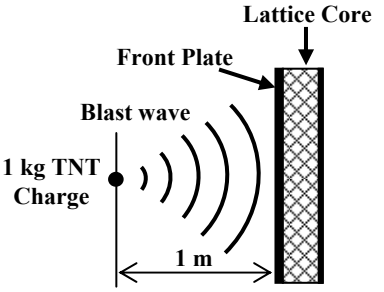


Figure 4. Sandwich Panels - Loading

For this study, the CONWEP blast model in LS-DYNA is used to represent the pressure on the front plate of the sandwich panel created by a blast of size 1 kg of TNT. The front face of the panels is placed at an angle of 90° to the center

of the blast, with the centroid of the face placed at a distance of 1 m away from the center of the blast (Figure 4). Since all sandwich panels modeled have the same front face dimensions, the same loading is applied on each model. This eliminated the effect of various type of dynamic loads utilized in previous studies, and any differences in the responses of the sandwich panels are due to the physical properties of the sandwich panels themselves.

CORE SELECTION

The topological properties of sandwich panel models are selected based on those used in recent studies. In all, six different types of core topologies are modeled, including the three most common types of folded plate topologies as well as the three most common types of honeycomb topologies. The folded plate cores used are the triangular folded plate, the diamond folded plate, and the Y-frame folded plate, while the honeycomb cores used are the square honeycomb, the triangular honeycomb, and the hexagonal honeycomb. Figure 5a shows folded plate core topologies, while Figure 5b shows honeycomb core topologies used in this study.

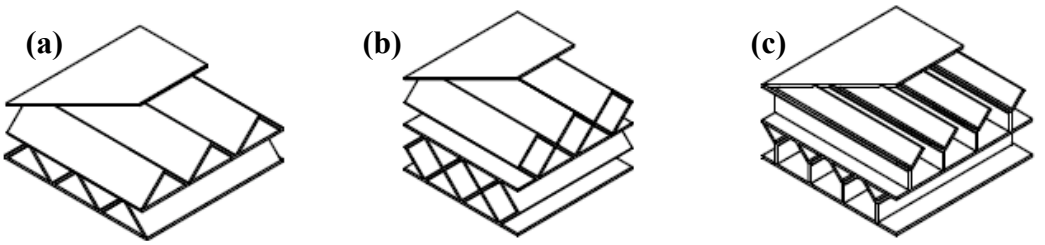


Figure 5a. (a) Triangular folded plate, (b) diamond folded plate, and (c) Y-frame folded plate core topologies used in finite element simulations

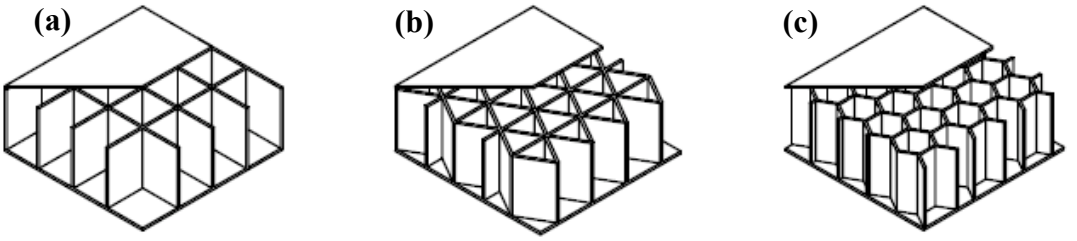


Figure 5b. (a) Square honeycomb, (b) triangular honeycomb, and (c) hexagonal honeycomb core topologies used in finite element simulations

All cores models are designed with a constant area density to ensure that same amount of extra loading per unit area is added to a structure. Furthermore, all cores modeled are .5 m in length and .5 m in width, with varying thickness and varying interior dimensions so as to create cores with constant area densities. Contact and impact between the sandwich panel components is modeling using the CONACT_AUTOMATIC_SINGLE_SURFACE card in LSDYNA.

BOUNDARY CONDITIONS

The manner in which sacrificial claddings can be used in a structure significantly impacts the boundary conditions. For the sake of computation time, the sandwich panels created for finite element analysis represent a 0.5 m by 0.5 m panel section. Actual sacrificial cladding added to a building may be significantly larger in area than this, so this fact is taken into consideration when determining boundary conditions for these models. These claddings can be attached to structures in one of the two ways. In the first scenario, the cladding can be attached by connectors with some clear distance between the face of the structure and the cladding. The second scenario consist of a cladding that it is flush against the face of the structure and thus not allow any clear distance between the two. Both scenarios are considered in this study, and appropriate boundary conditions and performance criteria for these scenarios are selected. In the first scenario, the boundary conditions are chosen to be clamped along the edges of the front and back plates of the sandwich panel and are referred to as the "clamped" boundary condition. For the second scenario, the boundary conditions are chosen to be fixed along the entire back plate and constrained along the edges of the front plate and is referred to as the "fixed" boundary condition.

MODEL LIMITATIONS AND ASSUMPTIONS

Even though the rates effects are accounted for in the constitutive modeling of steel, the actual fracture of the material is not considered. The material model only accounts for the strain dependent plasticity, however, other modes of behavior including brittle fracture is not modeled. Boundary conditions and loading are considered to be representative of that present in real applications.

SIMULATION RESULTS

A series of finite element simulations are conducted with clamped boundary conditions to analyze the effect of varying front plate thickness on a variety of sandwich panels. Core topologies included in these analyses are the triangular folded plate, the diamond folded plate, the Y-frame folded plate, the square honeycomb, the triangular honeycomb, and the hexagonal honeycomb cores. The performance criteria that are investigated include: (a) the front and the back plate deflection, (b) reaction forces at the clamped edges, and (c) the plastic energy dissipation. In addition, finite element simulations on triangular folded plate core topologies with fixed boundary conditions are conducted to investigate the effect of boundary condition.

SANDWICH PANELS - CLAMPED BOUNDARY CONDITIONS

Sandwich panels with different core topologies performed differently for finite element simulations conducted using clamped boundary conditions and varying front plate thickness. For each type of core topology, front plate thicknesses of 0.3 mm, 0.5 mm, 0.8 mm, 1.0 mm, and 1.2 mm are used in the simulations.

Figure 6 shows front plate deformation for all core topologies with varying front plate thickness. For all types of core topologies, the front plate displacements decreased as the front plate thickness increased. However, these displacements decreased at a lesser rate for higher front plate thicknesses. The honeycomb cores experienced less deformation than the folded plate cores, with all of the honeycomb cores performing almost exactly the same. The deformation in the folded plate cores was significantly higher than any of the honeycomb cores, with deformation for certain folded plate cores being in excess of 35 mm greater than any of the honeycomb cores. There were some differences in the front plate deformation for all of the folded plate cores. The Y-frame folded plate cores experienced the least deformation for all front plate thicknesses, while the diamond folded plate core experienced less deformation than the triangular folded plate core for front plate thickness of .3 mm but greater deformation for all over front plate thicknesses.

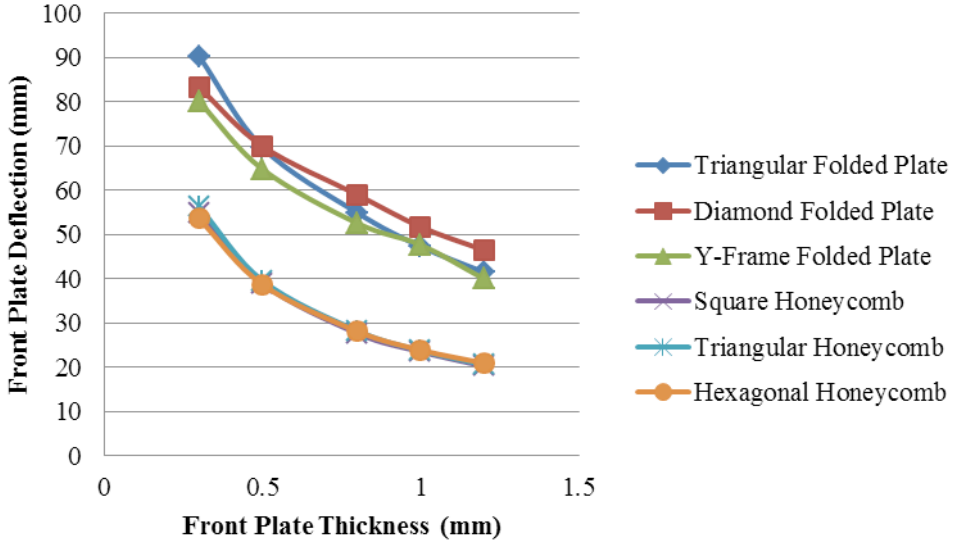


Figure 6. Front Plate Displacement vs. Front Plate Thickness for Sandwich Panels with Clamped Boundary Conditions for Different Core Topologies

Figure 7 summarizes the results of the back plate deformation with varying front plate thickness for all of the cores simulated. The back plate displacements also decreased with increased front plate thickness. However, the honeycomb cores decreased at an almost linear rate while the folded plate cores decreased less and less as the front plate thickness increased. For the honeycomb cores with the smallest front plate thicknesses, the triangular honeycomb core deformed the most and the square honeycomb core deformed the least. For the thicker front plates, the hexagonal honeycomb cores deformed the most and the triangular honeycomb cores deformed the least. The folded plate cores experienced significantly less deformation than the honeycomb cores. For the smallest front plate thickness, the back plate in the diamond folded plate core did deflect almost as much as the honeycomb cores. However, the back plate deformation was almost nonexistent for the diamond and Y-frame folded plate cores with thicker front plates.

Figure 8 shows the variation of the plastic energy dissipation with varying front plate thickness for the honeycomb and the folded plate cores. The plastic energy dissipation decreases with increased front plate thickness, indicating that more blast energy is reflected when a thicker plate is used. The folded plate core topologies all had higher plastic dissipation, with the diamond folded plate cores having the highest amount of dissipation.

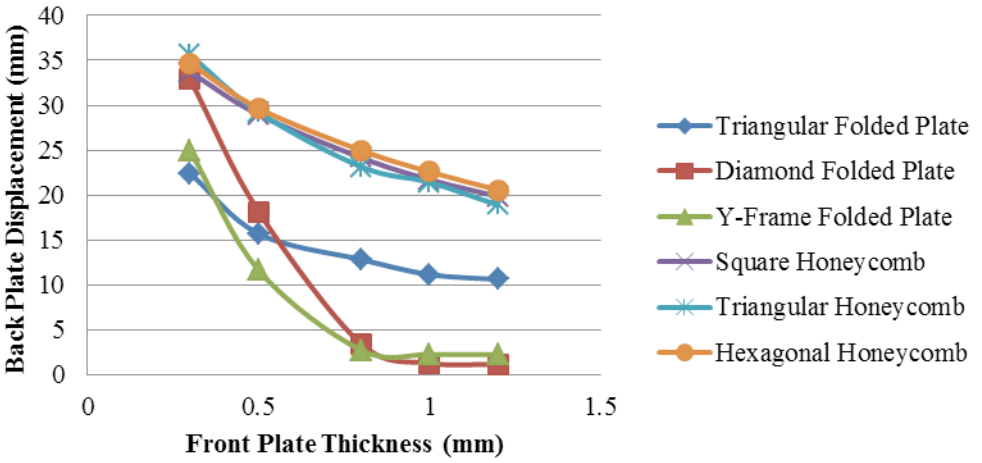


Figure 7. Back plate displacement vs. front plate thickness for sandwich panels with clamped boundary conditions for different core topologies

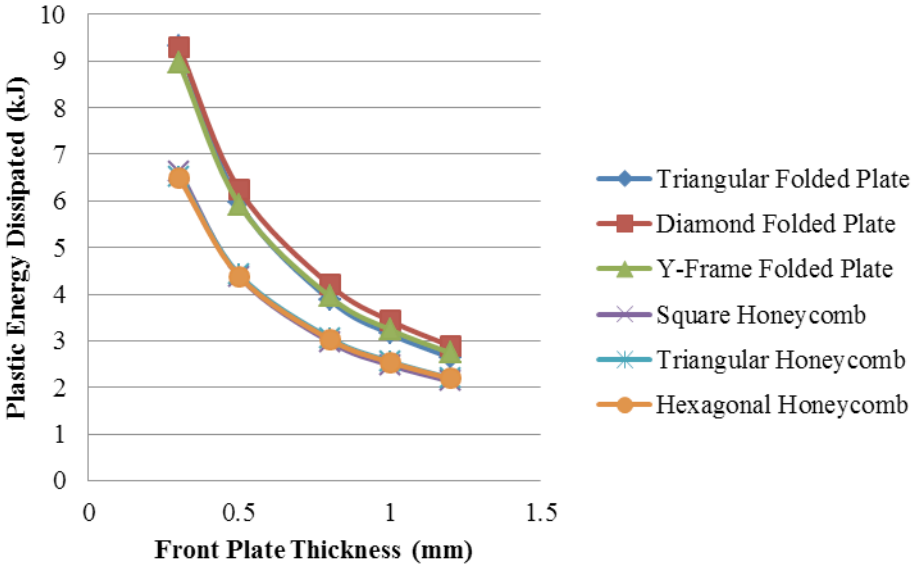


Figure 8. Plastic energy dissipated vs. front plate thickness for sandwich panels with clamped boundary conditions for different core topologies

Figure 9 shows the variation of reaction forces with varying front plate thickness. The maximum reaction forces for the folded plate core topologies gradually decreased linearly with increased front plate thickness, while the maximum

reaction forces for the honeycomb core topologies either remained the same or increased. For the thinnest front plates, the triangular and Y-frame folded plate topologies experienced the highest reaction forces, and, for the thicker front plates, all core topologies experienced a similar amount of reaction force with some variance.

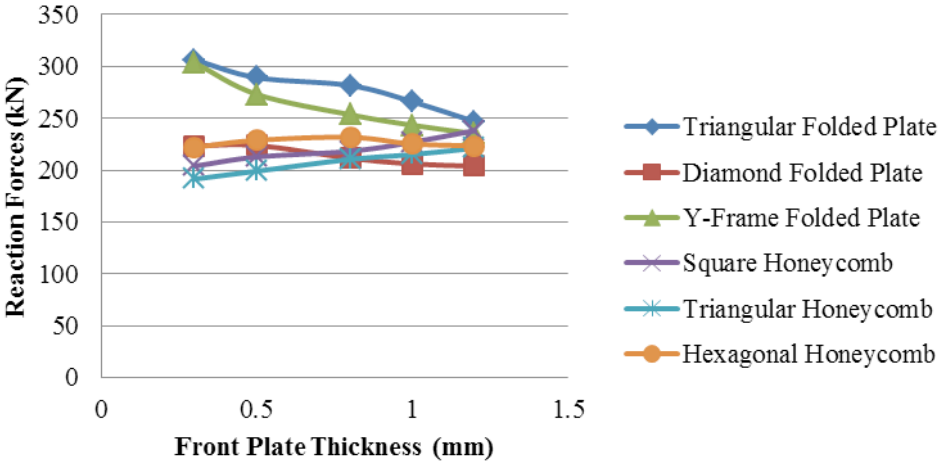


Figure 9. Maximum reaction forces vs. front plate thickness for sandwich panels with clamped boundary conditions for different core topologies

EFFECT OF BOUNDARY CONDITION

Effect of clamped and fixed boundary condition is investigated on the triangular folded plate topology. The clamped boundary condition allowed for the two-way bending of the entire sandwich panel, while the fixed boundary condition allowed the sandwich panel to crush upon itself. With clamped boundary conditions, at large deformations, the areas of the highest strain occurred at the peaks of the two inner-most triangular folded plates that make up the interior core (Figure 10). The magnitude of the strain at a majority of these locations did not exceed the maximum specified plastic strain of 0.4. However, for a front plate thickness of 0.3 mm, the magnitude of the strain did exceed this value immediately next to the clamped edge of the front plate along the triangular folded plate core.

The triangular folded plate core is also simulated with fixed boundary conditions for varying front plate thickness. In this case, at high deformations, the entire sandwich panels crushed. The final deformed shape of the crushed core had very little void space. For increased front plate thickness, the uniform deformation was even more pronounced, and the final deformed shape contains even less void space. Figure 10 shows the final deformed shape of the triangular folded plate core with fixed boundary conditions and front plate thickness of 1.2 mm.

There are several noticeable differences between the boundary conditions. The first difference was the fact that the fixed boundary condition allows for the deformation response of the sandwich panel to be purely the result of the crushing of the core. This was in stark contrast to the clamped boundary condition, which allowed for a significant amount of bending. Additionally, excessive strains were not

generated with the fixed boundary condition. While the clamped boundary condition simulations for triangular folded plate cores had plastic strains that exceeded the limit of 0.4 when the front plate thickness was 0.3 mm and 0.5 mm thick, the fixed boundary condition simulations have strains that did not even come close to approaching this limit.

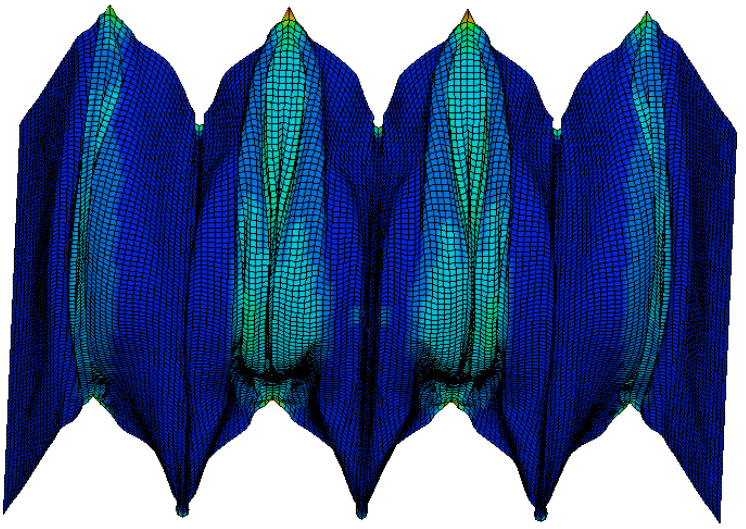


Figure 10. Core deformation of a sandwich panel with a triangular folded plate core and clamped boundary conditions (higher strains are indicated by warmer colors)

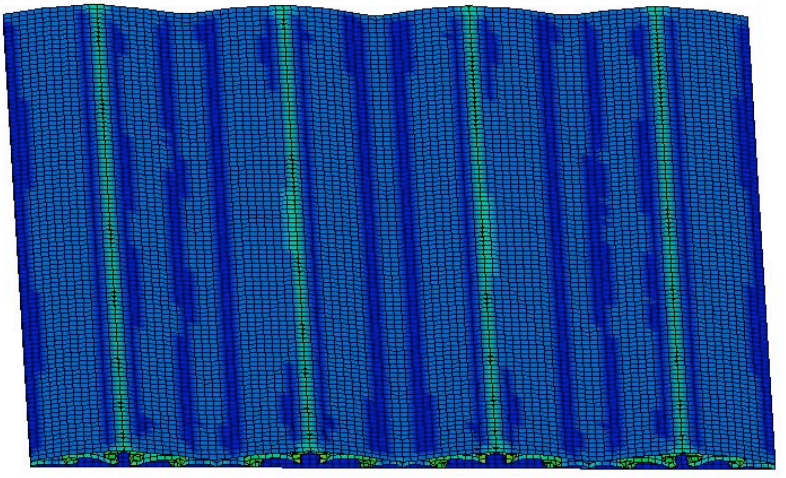


Figure 11: Final deformed shape of a triangular folded plate core sandwich panel with fixed boundary conditions and front plate thickness of 1.2 mm

OBSERVATIONS AND CONCLUSIONS

Following are the important conclusions that can be drawn from the limited simulations carried out under this study:

1. Honeycomb cores have lower front plate displacement because they had many more support locations than the folded plate cores, which increase their stiffness. However, the back plate displacement is large as compared to folded plate cores as the deformation is mode is a bending mode.
2. The folded plate cores, with lower core stiffness, had much greater deformation than the honeycomb cores and deforms in a core crushing mode. However, most of the deformation is concentrated in the cores with reduced back plate displacements as compared to honeycomb cores. As a result, these panels can absorb/dissipate more energy as compared to honeycomb cores.
3. Plastic energy absorption increases with a decrease in front plate thickness for all core topologies considered.

ACKNOWLEDGEMENTS

The presented work was supported by the University of Notre Dame. Any opinions, findings, conclusions, and recommendations expressed in this paper are those of the authors and do not necessarily reflect the views of the sponsors.

REFERENCES

Baker, W. E. (1973). *Explosions in air*, University of Texas Press, Austin, TX.

Cote, F., Deshpande, V. S., Fleck, N. A., and Evans, A. G. (2006). "The compressive and shear responses of corrugated and diamond lattice materials." *International Journal of Solids and Structures*, 43(20), 6220-6242.

Hallquist, J. (2010). "LS-DYNA." Livermore Software Technology Corp., Livermore, CA.

Hyde, D. (1988). "Guide for microcomputer programs CONWEP and FUNPRO – applications of TM 5-855-1." U.S. Army Waterways Experimental Station, Vicksburg, MS.

Kingery, C. N., and Bulmash, G. (1984). "Airblast parameters from TNT spherical air burst and hemispherical surface burst ", Aberdeen Proving Ground, U.S. Army BRL., MD.

McShane, G. J., Deshpande, V. S., and Fleck, N. A. (2007). "The underwater blast resistance of metallic sandwich beams with prismatic lattice cores." *Transactions of the ASME. Journal of Applied Mechanics*, 74(2), 352-64.

Rubino, V., Deshpande, V. S., and Fleck, N. A. (2009a). "The dynamic response of clamped rectangular Y-frame and corrugated core sandwich plates." *European Journal of Mechanics, A/Solids*, 28(1), 14-24.

Rubino, V., Deshpande, V. S., and Fleck, N. A. (2009b). "The three-point bending of Y-frame and corrugated core sandwich beams." *International Journal of Mechanical Sciences*, 52(3), 485-494.

Tilbrook, M. T., Radford, D. D., Deshpande, V. S., and Fleck, N. A. (2007). "Dynamic crushing of sandwich panels with prismatic lattice cores." *International Journal of Solids and Structures*, 44(18-19), 6101-23.

Valdevit, L., Hutchinson, J. W., and Evans, A. G. (2004). "Structurally optimized sandwich panels with prismatic cores." *International Journal of Solids and Structures*, 41(18-19), 5105-5124.

Vaziri, A., and Hutchinson, J. W. (2007). "Metal sandwich plates subject to intense air shocks." *International Journal of Solids and Structures*, 44(6), 2021-2035.

Zhenyu, X., and Hutchinson, J. W. (2004a). "A comparative study of impulse-resistant metal sandwich plates." *International Journal of Impact Engineering*, 30(10), 1283-305.

Zhenyu, X., and Hutchinson, J. W. (2004b). "Constitutive model for quasi-static deformation of metallic sandwich cores." *International Journal for Numerical Methods in Engineering*, 61(13), 2205-38.

Damage Size Prediction of Reinforced Concrete Slabs under Blast Loads using Artificial Neural Networks

Ahmed Ibrahim[1], Hani Salim[2], and Ian Flood[3]

[1]Department of Civil Engineering and Construction, Bradley University, 206 Jobst Hall, Peoria, IL, 61625, Ph. (309) 677-2780, email: aibrahim@bradley.edu
[2]Department of Civil and Environmental Engineering, University of Missouri, E2509 Lafferre Hall, Columbia, MO, 65211, Ph. (573) 884-6761, salimh@missouri.edu
[3]School of Building Construction, University of Florida, Gainesville, FL 32611, Ph. (352) 273-1159, email: flood@ufl.edu

ABSTRACT

There are a few related researches that provide well-defined models to predict the damage size under close-in explosions. This paper presents a prediction of the damage size experienced by reinforced concrete (RC) slabs subjected to close-in detonations using numerical data and a neural network–based model. To train and validate the artificial neural network (ANN), a data base is developed through a series of measurements of the damage diameter (crater/spalling) size induced in reinforced concrete two-way slabs under blast loads. The data was obtained by performing various simulations using the dynamic explicit finite element code LS-DYNA. The principle parameters controlling the breaching size are charge weight, standoff distance, and slab thickness, which were used to develop the ANN training input data set. The trained and validated neural network was used to develop an ANN model capable of predicting the breach size of concrete slabs under close-in detonations.

INTRODUCTION

The damage level in reinforced concrete (RC) slabs is a function of spalling/cratering the slab will suffer under the near-field detonations. The numerical analysis of this study was conducted using the explicit dynamic software LS-DYNA, which can model the blast load propagation towards concrete structures and the slab response to these types of impulsive loads. The blast load definition and properties are introduced in the following section. Also, a review of the up-to-date research regarding reinforced concrete slabs under blast loads is summarized next.

BLAST LOADS

Blast loads are considered one of the extreme loads affecting structures, and even a small amount of blast can produce severe localized damage to the structure skeleton.

In some cases this localized severe damage can potentially progress to global collapse of the entire structure. An explosion starts when a highly explosive material is detonated forming a detonation wave in the material which is pressurized up to 27,580 N/m^2 and temperatures in the range of 4,700° k. This hot gas is expanded, as a rapid release of energy occurs. A shock front moving at supersonic velocity is formed in front of this gas and is called blast wave. This wave propagates outward in all directions from the detonation center. The front of the wave is called the shock front which travels faster than the speed of sound. The pressure of the wave front is called the incident pressure, or overpressure. The flow of the air mass behind the shock results in an outward movement of air and debris which is known as the dynamic pressure. This dynamic pressure depends on the incident pressure, air density, and the explosive material.

BLAST LOADS ON RC SLABS

The study of the structural and material response of RC slabs under blast loads are conducted either by experiments or numerical simulations. However experiments are difficult to be done in full scale and are also costly to perform. In addition to that, the other important factor is the difficulty of measuring the various parameters in the field for close-in detonations where the instrument is often destroyed and the failure process is difficult to document. Therefore, numerical solutions are considered an attractive approach to evaluate reinforced concrete slabs response to explosions.

Cimo (2007) performed background information related to loads caused by blasts and analytical modeling options, as well as a literature review of related research findings. AUTODYN was selected to conduct this modeling. A study to determine the most appropriate constitutive models considering the dynamic material properties was subsequently conducted. This resulted in the selection of four constitutive models for the four materials incorporated in the modeling: air, TNT, concrete, and steel. A mesh sensitivity analysis was also performed to determine the optimum element size to be used, considering the conflicting interests of increased accuracy and decreased processing speed and memory availability with smaller elements. For Cimo's analysis, AUTODYN results were compared against results generated using the semi-empirically based program called ConWep, as well as hand calculations, which also served as a general validation of the accuracy of the program. The results of the constitutive model studies and mesh sensitivity analyses were incorporated in developing a model of a cross-section of a two-lane bridge, where the performance of the cross-section when subjected to a blast below deck was investigated. Within the bridge cross-section investigation, it was determined that the movement of the shock front and its interaction with the structure was greatly influenced by the girder location. Due to the reflected waves generated in confined corners, the pressure in the deck close to the girders was increased and caused this to be the highest area of stress within the deck.

Nago et al. (2007) estimated that blast loading typically produces very high strain rate ranges of 10^2 to 10^4 s^{-1} rather than the ordinary static strain rates of 10^{-6} to 10^{-5} s^{-1}. At high strain rates, the dynamic mechanical properties of the structure may be different from the mechanical properties under static loading. It is reported that the

yield stress of mild steel could be doubled when the strain rate changes from 10^{-3} to 10^{3} s^{-1}.

The effect of explosives on civil bridges was studied by Pelton (1993). It has been suggested that main load carrying members of all bridge structures can be classified into three categories based on the level of damage the bridge might experience and its post-blast load carrying capacity.

Wu et al. (2009) investigated the blast resistance of ultra–high performance fiber reinforced concrete (UHPRC) and FRP-retrofitted concrete slabs against normal concrete slabs as control specimens. The pressure and displacement were recorded at the middle point of the slab and the results were compared with TM5-1300. Wu et al. (2009) added the CFRP to the compression face of the slabs which increased the ductility and the blast resistance as well. The UHPFC samples suffered the least damage between all the specimens.

Mosalam et al. (2001) conducted a computational model using the finite element method to study the nonlinear transient behavior of reinforced concrete slab subjected to blast loading and retrofitted with CFRP composites. The model was used to investigate the effect of loading duration and the effect of the CFRP on the slabs damage accumulations. The study showed that using CFRP prevents the total failure of the slab systems against the cracking and crushing of the as-built slabs. The load carrying capacity of the retrofitted slabs was increased by 200%. Retrofitting the two way slab systems by CFRP limited the spread of yielding in the steel reinforcement.

The basis of a procedure to estimate the explosive charge weight and stand-off distance to impose certain levels of damage on RC structures was conducted by Silva et al. (2009). A series of experiments were also showed to confirm its applicability for assessing the blast resistance capacity of RC slabs. Test results showed that the procedure was accurate in predicting the explosive charge weight and stand-off distance to impose a given damage level on the tested RC slabs. This main conclusion was derived because a reasonable agreement was observed between the damage levels selected for assessment and the damage levels observed during testing.

In the next section, the details of the finite element modeling and the geometry for the studied RC slabs are presented. The material models for concrete and conventional steel are presented.

FINITE ELEMENT MODELING

The numerical simulations were conducted using LS-DYNA 971 (2009) code, which is common finite element analysis software for modeling non-linear mechanics of structures, fluids, and their interaction. LS-DYNA is based on explicit numerical methods, for problems associated with large deformation, and blast load wave propagation. The RC slabs under consideration were designed according to the ultimate strength limit states using the ACI 318-08 building code. The details of the material models and finite element mesh are discussed in the next section.

MODELING GEOMETRY

The slab model represents a two way square slab system of a span of 3.05 m (10ft). The geometric model of the slab system used in these simulations is shown in Fig.1. Concrete was meshed using Lagrangian 8-node solid hexahedron elements with one point of integration and the conventional steel were modeled using the 3-D beam elements. Perfect bond was assumed between concrete and all the embedded steel. With the slab loaded by blast, both the steel and concrete is expected to experience large deformations, causing plastic strains and buckling of the rebars. When widespread element erosion in the model is observed, it was concluded that cracking and spalling of concrete is present. To track the element erosions as the blast event progressed, a damage-based erosion function was implemented to delete the elements which reached a plastic strain of 0.005 for concrete and 0.15 for the steel.

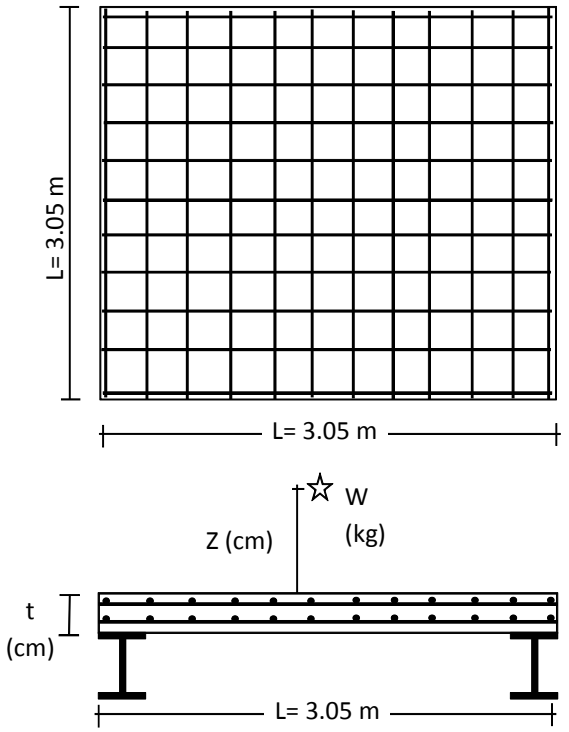


Figure 1. Plan and section elevation of the studied slab.

BLAST LOAD MODELING

In this simulation, the load is imparted on the RC slab by defining the blast function. The load defines an air-blast function for the application of pressure loads due to explosives (LSDYNA, 2009). This option calculates the pressure values when used with the LOAD_SEGMENT command, and these segments normals point toward the charge. The maximum predicted reflected pressure using the procedure in TM5-1300

is compared to the values obtained from LS-DYNA. The calculated pressure from LS-DYNA was measured at the nearest element to the ignition point which is considered as a reflected pressure.

ANN ANALYSIS

Neural networks are computing devices that process information in a manner similar to that of the central nervous system (Flood et al., 1990). In this section, the prediction of the damage size in two way RC slabs subjected to free air blast loads is introduced using an existing ANN code developed by Flood et al. (1994). The prediction for the damage size depends on many parameters, which are discussed in detail later. The study was conducted using the numerical dynamic hydrocode LS-DYNA to develop the training data set. Experimental results were first used to verify the numerical modeling using LS-DYNA first (Ibrahim, 2010, Ibrahim et al., 2011).

The ANN approach is a fast engineering tool that provides a direct mapping of results based on the required inputs. ANN can solve problems from a limited data set to a huge number of variables in an extreme rapid way; capturing nonlinearities in the model with sufficient training data (Flood et al., 1994). Also the ANN is very tolerant to errors in the input data set. The ANN can produce reasonable solutions for problems that have incomplete data set. The ANN consists of three main steps, the input variables, the output variables, and the processing stage. At the same time, the ANN have many shortcomings of its own, most notably, and the results of inexact solutions. Such issues should be solved before the ANN is generalized to every problem (Flood et al., 1994).

The configuration of the ANN consists of parallel processors called neurons or cells, connected to some circuit, the neurons outline is considered individually as trivial functions but in the network itself they can be used to solve very complex problems. These problems varied from the evaluation of production rates in construction process (Karshenain et al., 1992) to the prediction of tower-guy pretension (Issa et al., 1992).

NUMERICAL SIMULATION AND ANN VALIDATION

The goal for this study is to generate an accurate and efficient neural network model which is capable of modifying the limitations of existing methods for predicting the damage size of RC slabs subjected to blast loads. The idea behind using the ANN is that it fits a surface to a set of observations of the performance of the real system. The benefits of using the neural network is it could be trained to find a very good predicted model of damage size.

The three layer feed forward system ANN method was implemented in a RGIN (1992) code with an incremental learning pattern (Flood et al., 1994). The ANN code RGIN represents the data using radial-Gaussian functions. The radial-Gaussian functions represent the hidden neuron part of the feed forward system to calibrate the data points. When a hidden neuron is added to the ANN, a radial-Gaussian automatically added into the system to capture the data point with the

largest error, and then is used to determine the position, amplitude, and spread of the radial-Gaussian function that reduces the residual errors as much as possible.

After the numerical model was set up, the simulations were performed by LS-DYNA. A study was conducted to verify that the data parameters cover a wide range of various damage cases including the spalling, breaching, and no damage cases. The independent variables were the charge weight (kg-TNT), the standoff distance (cm), and the slab thickness (cm). The damage was recorded in terms of three different values; D1, D2, and D3 as described in Figure 2. Some cases exhibited a whole punching failure and others exhibited spalling from one side, while some exhibited spalling and cratering from both sides of the slab. A total of 125 RC slab simulations were performed in this study (Ibrahim et al, 2011).

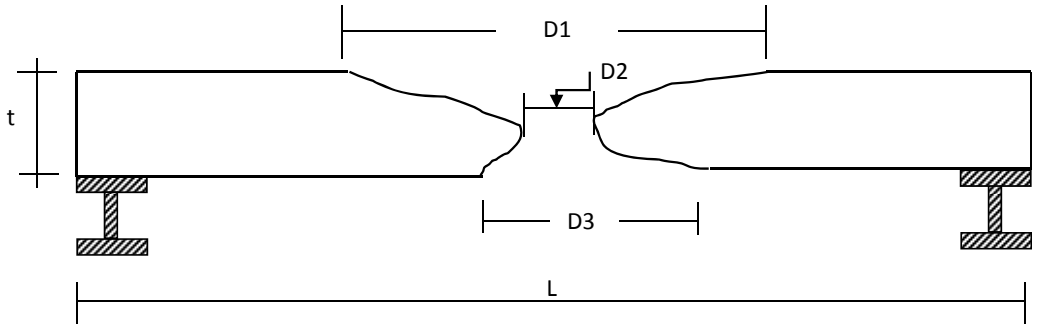


Figure 2. Cross section of slab showing the dependent variables D1, D2, and D3.

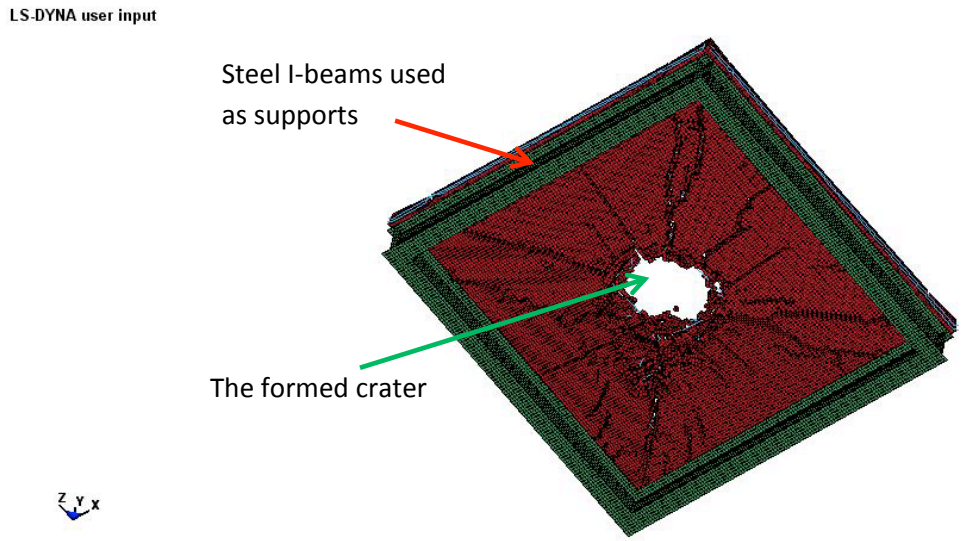


Figure 3. Punching failure mode of one of the tested slabs (bottom view).

The response of one of the slab cases is shown in Fig. 3, which shows the failure as pure shear punching due to the high explosive effect with a small standoff distance. It can be seen that the failure is a typical one as the there is a crater at the middle of the slab and there are many cracks or yield lines expanding towards the corners of the slab.

Figure 4 shows a scatter plot of numerical simulation results for all 125 simulations versus the ANN predicted damage size model for 25 Gaussian points. It is shown in Figure 4 that using 25 Gaussian points does give good results and using the ANN model and the error in the prediction of D1, D2. And D3 was reasonably accepted. The scatter of the ANN and the numerical results were closer to the 45° line when 100 Gaussian points were used to train the neural network. This indicates that the numerical results follow reasonable trends and thus can be fed into the ANN to generate accurate and precise models to predict the damage size for concrete slabs.

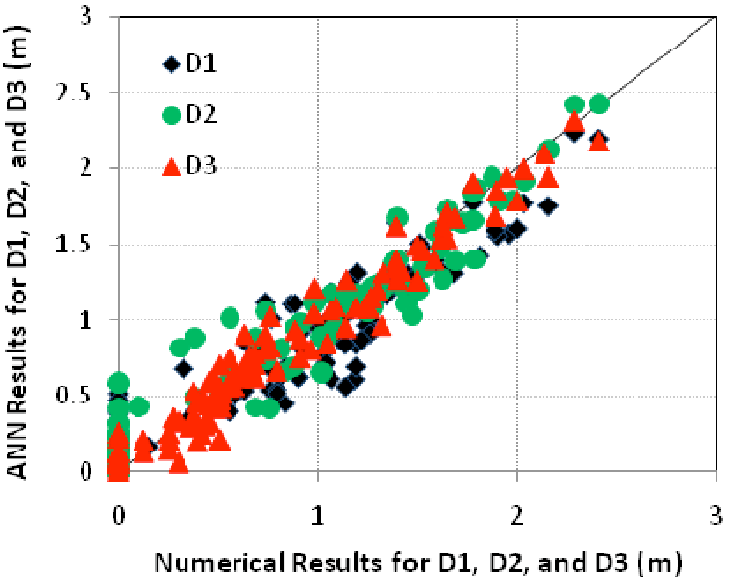


Figure 4. Correlation of ANN and the numerical results for damage size D1, D2, and D3 using 25 Gaussian points.

CONCLUSIONS

The spalling and cratering of reinforced concrete slabs under blast loading was studied in this paper based on a model-based simulation. The two-way reinforced concrete slabs were simulated and verified using the nonlinear explicit dynamic code LS-DYNA. The key parameters of the numerical simulations were the charge weight, the standoff distance, and the slab thickness, which led to 125 simulation experiments. The damage (cratering/spalling) of the concrete slabs were traced and mapped. The study showed that the damage varied between cases with no failure to the formation of large craters. The results of the numerical simulations were fed into a high accuracy Artificial Neural Network (ANN) to predict and estimate the damage size experienced by an RC slab under close-in detonations. A comparison between the ANN results and the numerical simulations were conducted, which showed a good correlation. The damage model can be used to perform post-blast global dynamic response assessment of structural systems resulting from the local damage. Additional research is recommended to include other parameters that could influence the damage size, such as steel reinforcement ratio, concrete compressive strength, etc.

REFERENCES

ACI 318-08, Building Code Requirements for Structural Concrete and commentary, Farmington Hills, MI.

Cimo, R. (2007). *Analytical Modeling to Predict Bridge Performance under Blast Loading*.

Flood, I., and Kartam, N., (1994). "Neural Network in Civil Engineering; Principles and Understanding." *Journal of Computing in Engineering*, *ASCE*, 8(2), 131-148

Flood, I., Bewick, B., Dinan, R., and Salim, H. (2009). "Modeling Blast Wave Propagation using Artificial Neural Network Methods." *Advanced Engineering Informatics*, 23, 418-423

Ibrahim, A. (2010). *Assessment of Prestressed Reinforced Box Girder Bridges under Blast Loads*, Ph.D. Dissertation, University of Missouri, Columbia, MO 65211, USA.

Ibrahim, A., Salim, H., and Flood, I. (2011). "Damage Prediction Model for RC Slabs under Near-Field Blasts." *International Journal of Protective Structures, submitted 2011(submitted).*

Issa, R., Fletcher, D., and Cade, R. (1992). "Predicting Tower Guy Pretension using a Neural Network." *Proc., 8th Conf. in Civil Engrg. and Geographic Information Systems*, ASCE, New York, N.Y., 1074-1081.

Karshenain, S., and Xin, F. (1992). "Application of Neural Networks in Earth Moving Equipment Production Estimating." *Proc., 8th Conf. in Civil Engrg. and Geographic Information Systems*, ASCE, New York, N.Y., 841-847.

Livermore Software Technology Corporation, LS-DYNA. (2009). Nonlinear Dynamic Analysis of Structures. Version 971, Livermore, California

Mosalam, M.K., and Mosallam, A.S. (2001). "Nonlinear Transient Analysis of Reinforced Concrete Slabs Subjected to Blast Loading and Retrofitted with CFRP Composites." *Composites and Structures*, Part B 32, 623-636.

Ngo, T., Mendis, P., M. & Mak, S. (2007). "High Strain Rate Behavior of Concrete Cylinders Subjected to Uniaxial Compressive Impact Loading." *Proc of 18th Australasian Conference on the Mechanics of Structures and Materials*, Perth, Australia.

Pelton, J.F. (1993). "Bridge Inspections in Bosnia-Operation Grapple." *The Royal Engineering Journal*, 10(2).

Silva, P.F., Binggeng, and Lu. (2009). "Blast Resistance Capacity of Reinforced Concrete Slabs." *Journal of Structural Engineering, ASCE*, 135(6).

Wu C., Oehlers, D.J., Rebentrost, J., Leach, J., and Whittaker, A.S. (2009). Blast testing of Ultra-High Performance Fiber and FRP-Retrofitted Concrete Slabs." *Engineering Structures*, 31, 2060-2069.

Blast Test of Full-Size Wall Barriers Reinforced with Enamel-Coated Steel Rebar

Dongming Yan[1], Genda Chen[1], Jason Baird[1], Huawei Yin[1] and Mike Koenigstein[2]
[1.] Missouri University of Science and Technology, Rolla, MO, 65401, USA
[2.] ProPerma Engineered Coating, Rolla, MO, 65401, USA

Abstract:

A type of enamel coating that contain hydraulically reactive calcium silicates have been developed to improve the performance and service life of steel used as reinforcement in concrete structures. To demonstrate the effect of enamel coating on the mechanical performance of concrete structures subject to blast loading, two wall barriers with identical dimensions, which were often used to keep the terrorism attack (such as car bomb attack) away from critical buildings, were fabricated and tested in a military base. One of the wall barriers was reinforced with coated rebar and the other with regular rebar. Four equivalent TNT weights, 4 lbs, 10 lbs, 30 lbs and 45 lbs explosive were applied to observe the deformation, cracking and failure mode of the two barrier walls. Generally, the test results indicate that the barrier wall reinforced with enamel coated rebar has much better integrity than that with regular rebar: fewer cracks on the front and back faces of the wall, more stress transferred to the steel rebar, and mitigated catastrophic failure of the wall. The new coating can be of great value in increasing the performance and the service life of defense-critical infrastructure.

1. Introduction

Steel reinforced concrete has been widely used as construction material in buildings and civil infrastructures. The structural condition at the concrete-steel interface is a significant factor in the design and maintenance of constructed facilities. In the past decades, researchers have been seeking effective approaches to enhancing the corrosion resistance of reinforcement and the bond strength between rebar and substrate concrete. To reduce the potential for corrosion in concrete reinforcement, one of the solutions is to coat the concrete with different materials, such as CS compound (Moon et al., 2007), elastomeric surface coatings (Seneviratne et al., 2000) and geopolymer (Zhang et al., 2010) to increase the resistance for chloride penetration, freezing-thawing and carbonation processes.

A direct and practical way to increase the corrosion resistance of steel reinforcement is to coat the steel with corrosion-inhibiting materials: both organic and inorganic. Organic materials include epoxy (Kobayashi and Takewaka, 1984) and modified

resin (Selvaraj et al., 2009) while inorganic materials include galvanizing metal (Kayali and Yeomans, 2000) and phosphate conversion coatings (Jalili et al., 2009). However, studies of evaluating epoxy-coated rebar performance in field conditions by Virginia, Florida, and Oregon Departments of Transportation concluded that epoxy-coated rebar corroded at a faster rate than uncoated rebar due to moisture trapped underneath breached epoxy coatings (Sagues et al., 1994; Brown and Weyers, 2003). The use of epoxy coated rebar requires 20% longer development length because of a reduction in the pullout strength of the rebar in concrete (Kayali and Yeomans, 2000). Kayali and Yeomans (2000) also observed that galvanized steel seemed to have negligible effects on bond strength with concrete. Jalili et al. (2009) concluded that the bond strength between Zn-Ca phosphate coated rebar and concrete is 74% higher than that between uncoated rebar and concrete. In recent years, vitreous enamels have been introduced to increase the corrosion resistance of steel reinforcing bars and their bond strength with concrete (Day et al., 2006; Hackler et al., 2006). They are yet to be systematically characterized for bond and corrosion enhancements in various civil engineering applications.

In this study, pure enamel and enamel mixture with chemically reactive calcium silicate (CS) were applied to improve the bond strength at mortar-steel interfaces. They are characterized with barrier wall subjected to blast loading. The effects of enamel coating on blast resistance performance are studied experimentally. The work presented in this paper constitutes part of a collaborative research program involving comprehensive studies on corrosion resistance, chemical composition optimization, coating process design, and concrete-rebar interface behavior of enamel coatings.

2. Specimen preparation and test setup

2.1. Design and Fabrication

In this study, the military concrete barrier walls used in Iraq were considered as prototype structures to be tested under blast loads. These barriers have been used to protect crucial infrastructure from car-bomb attacks.

Two full-scale barrier walls were tested in this study, each approximately 6 feet tall, 4 feet wide and 6 inches thick. The base of the barrier walls is 4 feet in square and 12 inches thick. Four PVC pipes were embedded in the base of each barrier, which can be used to facilitate the anchoring of the barrier into ground as needed. Each wall is reinforced with #5 vertical reinforcement and #3 transverse stirrups, both at 6 inches spacing. The clear concrete cover on all sides of wall is one inch.

2.2. Material Properties

The materials used in barrier tests include concrete and steel reinforcing bars. The steel bars in one wall were coated by Properma Engineered Coatings, St. Louis, MO, with reactive enamels. Those in the other barrier wall were uncoated for comparison.

At the time of casting each barrier wall, 6 concrete cylinders were cast and used to determine concrete compressive strength. After 28 days of curing, the compressive strength of the concrete is 44 MPa with a standard deviation of 1.38 MPa; the Modulus of Elasticity is 31.5 GPa with a standard deviation of 827 MPa. The yield stress of the rebar is 490 MPa and the ultimate strength is 619MPa. The average strain at yield stress is 0.42%.

2.3. Test plan and procedure

The full-scale barrier specimens were constructed and cured in the laboratory and then transported to the test site at Fort Leonard Wood. Steel formworks were used for the casting of barrier walls and bases. Steel formworks were placed on the plywood that was laid on the Highbay Structures Laboratory floor. The rebar steel cage for the wall base was first made and placed inside the steel formwork. The vertical reinforcement of walls was then inserted into the base steel cage. Standard 90° hooks detailed according to ACI 318-08 (2008) were utilized to provide an appropriate development length for transverse tie bars. All vertical reinforcement was straight and was placed toward the bottom of the wall base with one inch of concrete cover. The base and the wall of each specimen were cast separately at two different times. After three days of base casting, the barrier wall was cast. During the wall casting, six concrete cylinders were also cast for the determination of concrete compressive strengths. After another week, the formworks were disassembled with the finished wall.

A total of 12 multi-purpose strain gauges manufactured by Vishay Company were installed on vertical reinforcing bars as detailed in an inset of Figure 8. Six of them were installed at mid- height and the other six at the very bottom of the wall. At each location (mid-height or bottom), four strain gauges were installed in the front side rebar near explosives and two in the back side rebar away from explosives. They have a grid resistance of 120.0±0.5% Ohms. From two gauges in the front and back rebar, the moment at the location of strain gauges may be evaluated. Additionally, six accelerometers were installed on each barrier wall as indicated in Figure 1 during testing.

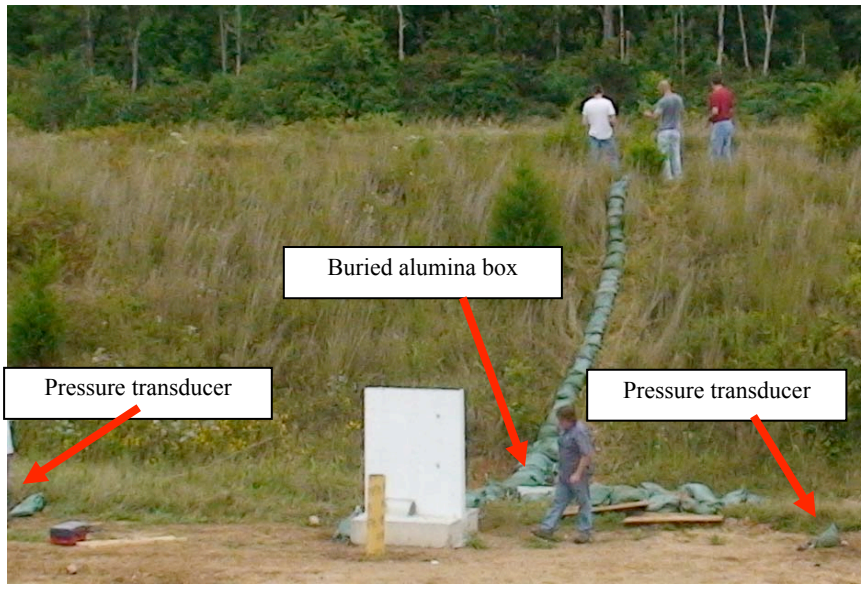


Figure 1 Test site

Each wall was installed with two coaxial cable crack sensors that were embedded into the two grooves preset on the near face of the wall (near explosives). Prior to blast, a connection cable was connected to each coaxial cable sensor for reading during and after each explosion. To protect the connector from blast damage, the connection cable was embedded near the top surface of the wall base and covered by a steel angle.

The full-scale barrier walls were tested at FLW. Several data acquisition systems were utilized during each blast test. To acquire strain, pressure and acceleration data, two Synergy data recorders were used. A sampling rate of 20 kHz was used for the Synergy Box data recorders. For the crack sensors, a Digital TDR Oscilloscope was used along with a pulse generator, which is used for dynamic measurements. However, measurements were taken from both sensors during each blast test. A laptop was used to configure and record data from the Synergy Box data recorders.

Explosion creates a very harsh environment for sensors, instruments, and connection wires. For protection purposes, the Digital TDR Oscilloscope and the pulse generator were placed in an alumina box, as shown in Figure 1. The box was situated in a nearby ditch and covered with sandbags. Most part of the connection cable between the Oscilloscope and the cable sensor were buried into the ground and covered with sandbags, as illustrated in Figure 1.

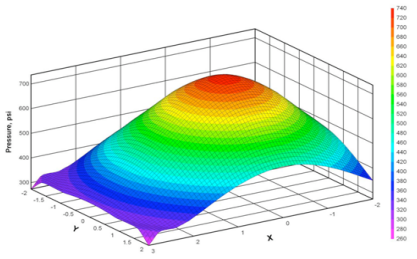
All wires of strain gauges embedded in each wall were led to one side of the wall. To protect them from the effects of blast pressure and its induced debris impact, the strain gauge wirings will then be guided through a steel angle attached to the wall base, and embedded underground together with two strain conditioners.

Coaxial cable sensors were connected to extension cables at the bottom of each wall. For protection purposes, the connectors were covered by steel angles and the extension cables were embedded near top surface of the wall base, which were then covered with sandbags as shown in Figure 1.

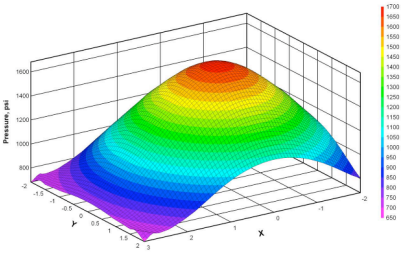
Each wall was tested with 4 lbs, 10 lbs, 30 lbs charge weights with 4ft standoff distance from the center of the wall. After that, all instrumentations were removed and the wall was subjected to one additional charge of 45 lbs placed right above the wall base.

Four different charges were considered for blast testing of each barrier wall. Charge weight is always specified in TNT (Trinitrotoluene) equivalence. The TNT equivalence factor is defined as the ratio of the mass specific energy of the explosive compound to the mass specific energy of TNT (4520 kJ/kg). An alternative approach makes use of two conversion factors, depending on whether the peak overpressure or impulse is to be matched (Mays and Smith, 1995).

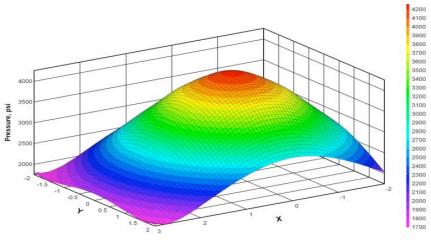
The specific charge weights were determined from a simple analysis with the software COMWEP. The pressure distribution each blast causes along the wall is shown in Figure 2. It can be seen from the figure that the pressure reaches its maximum at the center of the wall and decays rapidly away from the wall center. As the charge weight increases from 4 lbs to 45 lbs, the peak pressure at the center of the wall varies from 736 psi to 19,370 psi, which will cause significantly different damages to the wall.



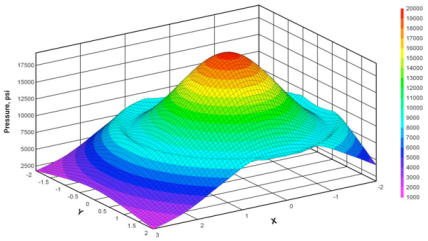
(a) Charge weight: 4 pounds TNT



(b) Charge weight: 10 pounds TNT



(c) Charge weight: 30 pounds TNT



(d) Charge weight: 45 pounds TNT

Figure 2 Pressure distribution: standoff distance of 4 ft

The first charge was made up of 4-pound pentolite cast boosters, resulting in a TNT equivalent charge of 4.4 lbs (with a TNT equivalence of 1.1). For convenience, this event is hereafter referred to as the 4-pound blast. The second charge was made up of 4-pound pentolite cast boosters and a 0.25 lbs pentolite cast booster, resulting in a total TNT equivalent charge weight of 10.2 lbs. This event is hereafter referred to as the 10 lb blast. The third charge was made up of 33-pound ANFO (with a TNT equivalence of 0.83) and 2-pound pentolite cast boosters, resulting in a total TNT equivalent charge weight of 30 lbs. The fourth charge was made up with a TNT equivalence of 45 lbs.

After the completion of each blast, a thorough inspection of each wall was performed. Cracks were marked on the tested wall and their patterns were documented. Any additional visible damage to the wall and its supporting base were also recorded. Based on various measurements, the overall performance of the tested wall can be assessed. It is noted that, due to a measurement limit of 70g, the acceleration data collected during various blasts was distorted and thus not used in the following analysis.

3. Test data and analysis

Two types of spalling can occur in concrete during a blast load — direct spalling and scabbing (TM 5-1300, 1990). Direct spalling of a concrete element is the result of a tension failure of concrete that is caused by the shock pressures of an impinging blast wave as it is being transmitted through the element.

Concrete elements subjected to a close-in blast are generally accelerating before or soon after spalling takes place. This accelerated motion of the element in turn accelerates spalled fragments. The velocities of these fragments can be as high as several hundred feet per second. These fragments can be a real hazard to human occupants, causing casualties in an explosion event.

Scabbing of a concrete element is the result of a tension failure of concrete that is normal to its free surface and is associated with large deflections. In the later stages of the ductile response mode of a reinforced concrete element, extremely large deflections are developed producing large strains in the flexural reinforcement and, consequently severe cracking and/or crushing of the concrete perpendicular to the free surfaces (TM 5-1300, 1990). Since the tension and compression strains are highest at the surface and since the shear reinforcement in the later stages of deflection confines the core concrete, damage to the cover concrete is more severe than damage to the core. After the applied blast load is over, the element is in a stage of deceleration at these large deflections (TM 5-1300, 1990). Therefore, the velocities of scabbed fragments, which are equal to the velocity of the element at θ =

5° (start of scabbing), are lower than the velocities of direct spalling fragments. However, the velocities of scabbed fragments may also be on the order of several hundred feet per second.

3.1. Pressure transducer measurements

Three pressure transducers were placed 18 ft away from the center of the charge and pointed directly at the charge, as illustrated in Figure 1. Although pressure can be measured directly on each wall, pressure transducers mounted on the wall may receive both incipient and reflected shock waves, making post-test data interpretation a challenge. In addition to the high likelihood of being damaged, it would be difficult to keep the transducer mounting apparatus steady during blast tests. As such, the pressure data acquired directly from the wall face may not be credible.

The measured pressure pulses under a 4-, 10-, and 30-pound charge are presented in Figure 3. It can be clearly observed that they are all in single pulse with various intensities and times of arrival. The difference in arrival time is attributed to various sizes of the charges used during tests. The 4-pound TNT equivalent was a cylindrical charge of 8 inches diameter and 10 inches length; 10-pound TNT equivalent was a cubic charge of 12 inches on each side; and the 30-pound TNT equivalent was a rectangular cube with 16 inches long, 12 inches high and 12 inches deep.

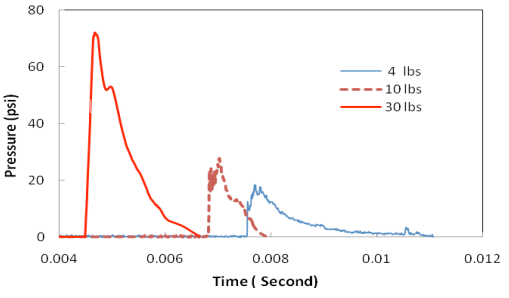


Figure 3 Measured pressures with various charge weights

For comparison with the measured pressure data, the reflected pressure from a spherical free-air burst of a charge of 4, 10, and 30 lbs, placed 4 ft above the ground, was simulated at the locations of two transducers with the A.T. Blast computer software developed by Applied Research Associates, Inc. For realistic simulations, the finite dimension of each charge was taken into account in various simulations. The peak pressure, time of arrival and positive duration of simulated pressure pulses are compared with those in Table 2. Clearly, these parameters are in good agreement.

Since the calculated pressure pulses agree with their corresponding measurements, the pressure pulses and impulses at the face of the wall can be obtained from the A.T. Blast computer software. In various simulations, each wall was considered as a

simply-supported structure. Ammonium nitrate fuel oil (ANFO) of different charge weights was placed 4 feet away from the wall. The pressure pulse and impulse parameters for each of the different charge weights are presented in Table 2.

Table 1 Calculated versus measured pressure pulses at the location of transducers

Charge weight (lb)	Calculated pressure pulse		Measured pressure pulse	
	Peak pressure (psi)	Time of arrival (msec)	Peak pressure (psi)	Time of arrival (msec)
4	18.9	9.04	18.1	7.79
10	31.6	7.80	25.0	6.98
30	69.4	5.97	71.6	4.64

3.2. Observations on barrier wall faces after blast tests

To facilitate the understanding of the structural behavior of two barrier walls under blast loading, cracks after each shock were examined carefully. The crack often becomes visible when its width is greater than 0.02 millimeter (7.8×10^{-4} in). Visible cracks were marked with a black marker on the tested walls as shown in Figures 4 and 5 for the walls reinforced with uncoated and enamel coated steel bars, respectively. Note that no concrete spalling was observed on both walls.



(a) 4 lbs charge (b) 10 lbs charge (c) 30 lbs charge

Figure 4 Barrier walls with uncoated rebar after each blast: front face

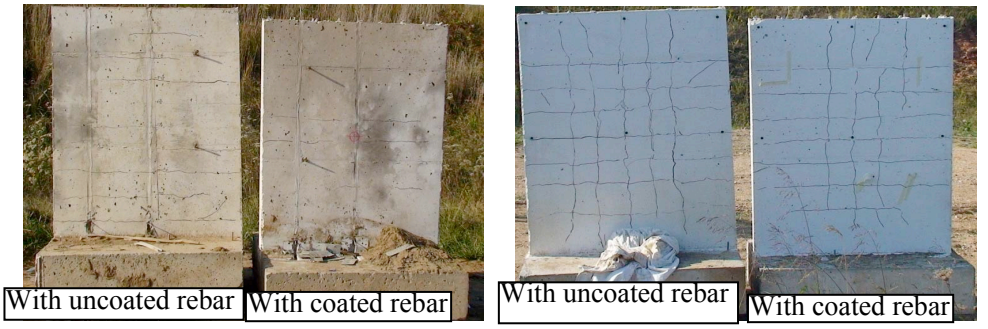


(a) 4 lbs charge (b) 10 lbs charge (c) 30 lbs charge

Figure 5 Barrier walls with enamel coated rebar after each blast: front face

As indicated in Figures 4 and 5, no cracks were observed on the front face of both walls after the first test with a 4-pound charge weight. After the second test with a 10-pound charge weight, despite several dents on the front face, no cracks were visible. After the third test with a 30-pound charge, visible cracks were clearly observed on the front face. Similarly, no visible cracks were observed on the back face of both walls after the blast test with a 10-pound charge weight. Note that cracks basically follow the pattern of steel reinforcement grids in the walls.

For a better comparison, tested walls are presented side by side in Figure 6. It is clearly observed from the figure that more visible cracks occurred on the front face of the wall reinforced with uncoated rebar. The difference in the extent and pattern of cracks between the two test walls is likely due to the use of enamel coating. As the shock front is engaged with a concrete wall and generates compressive stress on the concrete in contact, the concrete on the front face of the wall and on the shock front is locally subjected to bending as the stiffness of the front reinforcement grid suddenly changes, potentially causing concrete crack. The use of enamel coating on steel reinforcement stimulates a stronger bond between the concrete and steel, and thus a less stiffness change around the shock front. It results in fewer cracks, particularly on the upper portion of the wall. In this case, steel reinforcement is subjected to increased stress as will be discussed later.



(a)Front faces (b) Back faces

Figure 6 Crack distributions on the faces of barrier walls after three blasts

Figure 6 also indicates that a few more cracks appear to have occurred on the lower portion of each wall. This likely results from the global flexural behavior of a cantilevered wall as the shock wave continues to spread on the front face of the wall.

Similarly, the crack patterns on the back face of the two walls are compared in Figure 6(b). Like the front face, the back face of the wall experienced more visible cracks when the wall is reinforced with uncoated rebar. The difference in the extent and pattern of cracks between the two test walls is likely attributed to the use of enamel coating. With a stronger bond between concrete and enamel-coated rebar, the cracked concrete can still attach to the rebar firmly with no or few longitudinal microcracks developed along the rebar. As such, the locally cracked concrete can work better with the rebar to make the concrete-rebar system stiffer and more difficult to bend as the compressive wave propagates through the reinforcement grid on the back face. This effect is translated into fewer cracks on the back face of the wall.

After the fourth blast test with a 45-pound charge, the barrier wall reinforced with uncoated rebar was completely destroyed as shown in Figure 7(a), leaving the back half of the wall base behind only. The steel cage in the front half of the base was disassembled. The damaged barrier wall reinforced with enamel coated rebar is shown in Figure 7(b). Although the concrete of the wall completely disappeared, the enamel coated rebar on the back side of the wall remained anchored into the base in bent shape. In comparison with Figure 7(a), the remaining rebar in Figure 7(b) implied that the rebar bond with concrete was stronger when coated with enamel coating. Additionally, the rebar cage in the front half of the wall base remained intact with some loose concrete pieces stick to the exposed rebar, indicating strong bond between them as well.

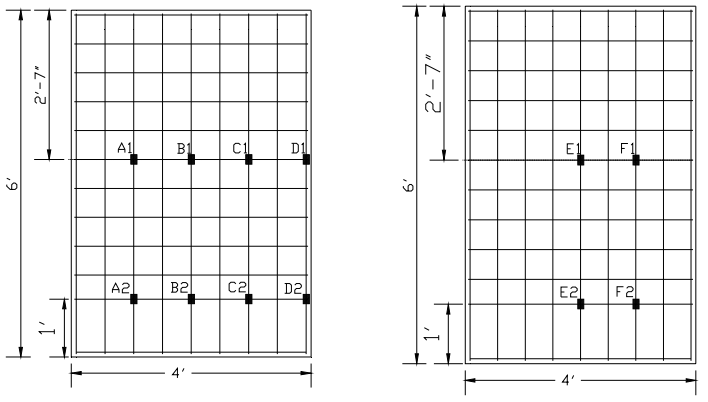


(a) With uncoated rebar (b) With coated rebar

Figure 7 Damaged walls after four blast tests

3.3. Strain gauge data

The 12 strain gauges instrumented on each wall are designated in Figure 8. For the wall reinforced with uncoated rebar, 5 of them were malfunctional due to casting and transportation of the wall and preparation (groove cutting) of the wall test. For the wall reinforced with enamel coated rebar, 4 of them were damaged prior to testing. The strain data taken under a blast load of 4-pound charge are presented in Figure 9 and Figure 10 for the walls reinforced with uncoated and coated rebar, respectively.



(a) Front side (b) Back side

Figure 8 Locations and designations of strain gauges

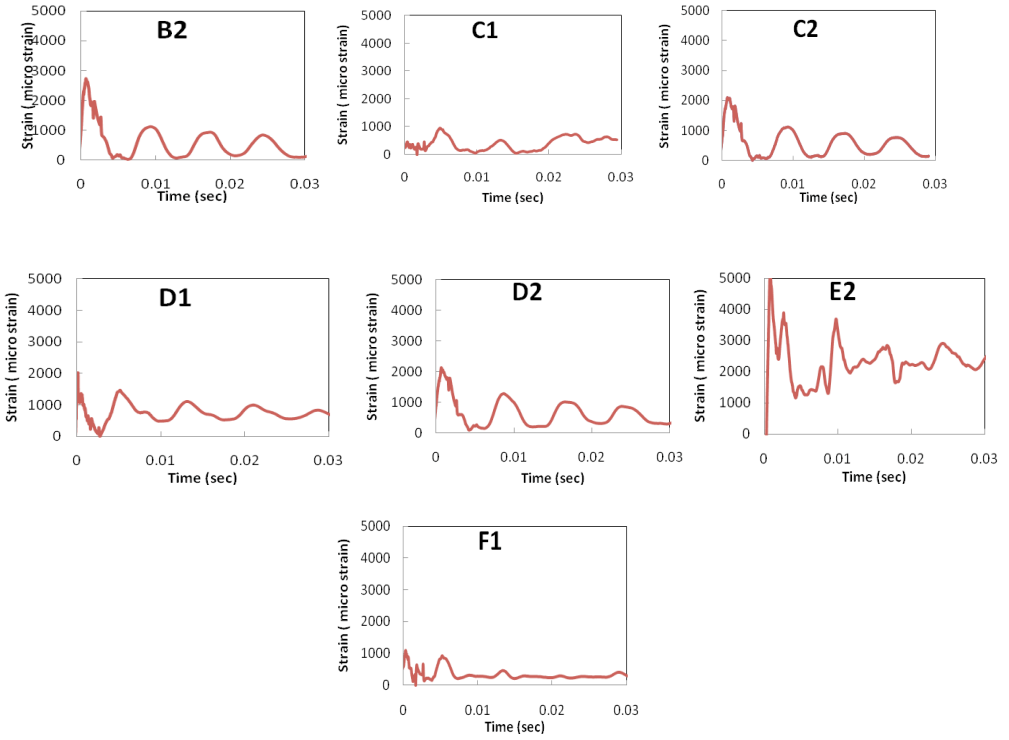


Figure 9 Strain data from the barrier wall with uncoated rebar

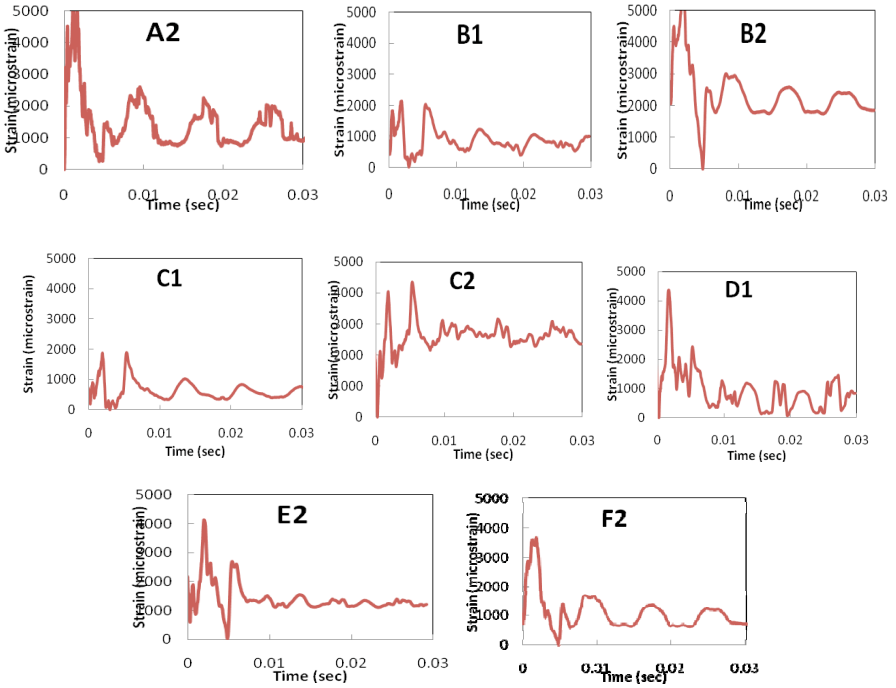


Figure 10 Strain data from the barrier wall with enamel coated rebar

The strain time histories as shown in Figures 9 and 10 are very consistent in terms of locations of peaks. For example, the locations of the first 4 peaks from B2, C2 and D2 are very close. This ensures the reliability of the experimental data. It can also be seen from Figures 10 and 11 that the tensile strains measured from the enamel coated rebar are higher than those from the corresponding uncoated rebar at the middle height of the walls. These results verify the conclusion drawn from the observations on crack patterns that the enamel coated rebar has stronger bond with concrete and, under blast loads, experiences larger strain transferred from concrete.

Consider a barrier wall as a uniform cantilevered beam with consistent mass. The fundamental period of vibration can be estimated to be 0.11 sec, which is over 20 times longer than the positive duration of all blast-induced pressure pulses. Therefore, the propagation of shock waves dominates the deformation and cracking of the barrier wall.

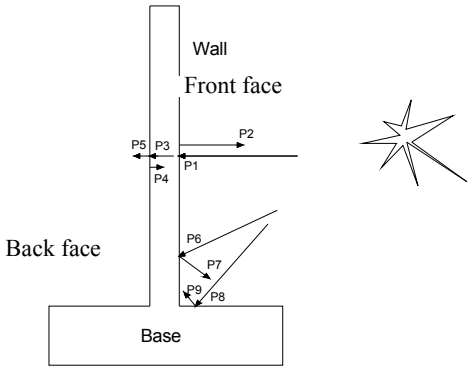


Figure 11 Illustration of pressure wave propagation

Generally, the peak strains at the bottom of the front face (e.g., C2, D2) are larger than that in the mid-height (e.g., C1, D1). Cracks can be found on both front face and back face. This can be illustrated in Figure 12. When the sock is induced from detonation of an adjacent explosive, pressure wave (P1) will reach the front face first, where a reflection wave P2 will be produced. The interaction of left-going wave P1 and right-going wave P2 leads a tension wave on the front face, thus, the front surface may experience a tension stress at some moments and tension cracks will occur there. Besides the reflection wave P2, part of wave P1 will also transmit through the wall, arriving at back face, reflection wave P4 and transmission wave P5 will be produced at the back face. The interaction of waves P3, P4 and P5 will produce tension pressure on the back face. The pressure in the mid-height of the wall is directly caused by pressure P1 and its reflection P2. For the bottom of the wall, in addition to the action of direct wave P6 and its reflection P7, the reflection wave (P9) of the wave P8 on the base will also have vital impact on the bottom part of the wall. The combination of these waves at the bottom may cause much larger deformation at the bottom part of the wall than that in the mid-height. Large cracks were observed at the wall-base corner. This assures that the waves on the base and their reflections have significant effect on the overall behavior of the barriers. More detailed theory about the wave propagation can be found in text books (Paul, 1996).

4. Concluding Remarks

This study has led to the following observations:

- From the typical failure modes of the barrier walls subject to 30 lbs charge, it can be inferred that the enamel coating can enable the adjacent concrete hold the rebar more rightly, inducing less slippage and thus resulting in less cracks on the front face of the wall.

- The results from the strains of steel bar obtained from embedded strain gauges show that the more stress was transferred into the steel rebar with stronger bonding. As a result, larger strains were found in the enamel coated rebar, improving the integrity of the whole structure.
- The failure mode of walls under 45lbs charge clearly indicates the improvement effect of enamel coating on the bonding between steel bars and concrete. This further confirms the conclusions drew from previous report about the mechanical bonding effect on the overall behavior of reinforced structures.
- Future studies shall be directed to investigate a new enamel formulation with improved corrosion resistance, characterize the development length of steel fibers in concrete, and develop the constitutive law of fiber-reinforced concrete in tension and compression.

5. REFERENCES

Baker, W.E. (1983), *Explosion Hazards and Evaluation*, Elsevier Scientific Publishing Company, New York, NY.

Day D.C., Weiss C.A., Malone P., and Hackler C.L. (2006), "*Innovative Method of Bonding Portland Cement Concrete to Steel Using a Porcelain Interface*," Materials Science and Technology (MS&T) Conference Proceedings, The American Ceramic Society, Westerville, OH.

Hackler, C., Koenigstein M., and Malone P. (2006), "*The Use of Porcelain Enamel Coatings on Reinforcing Steel to Enhance the Bond to Concrete and Steel Surfaces*," Materials Science and Technology (MS&T) Conference Proceedings, The American Ceramic Society, Westerville, OH.

Manahan, M.P. and Siewert, T. A. (2006), "*The History of Instrumented Impact Testing, STP 1476 Pendulum Impact Machines: Procedures and Specimens*," American Society for Testing Materials.

Paul W. Cooper. *Explosives Engineering*, Wiley-VCH, New York, 1996.

Zhu, X., Dou H., Ban Z., Liu Y., and He J. (2007), Surface and Coatings Technology 201.

Modeling and Testing of Laminated Window Systems under Blast Loading

B. Lusk[1], H. Salim[2], K. Perry[1], M. Nawar[2], W.C. Wedding[1], S. Kiger[2], and A. Ibrahim[3]

[1]Department of Mining Engineering, 234-D Mining and Mineral Resources Building, University of Kentucky, Lexington, KY, 40506-0107, USA
[2]Department of Civil Engineering, E2509 Lafferre Hall, University of Missouri, Columbia, MO 65211-2200, USA
[3]Civil Engineering and Construction Department, 206 Jobst Hall, Bradley University Peoria, IL, 61625, USA

ABSTRACT

Dynamic modeling and field testing of full-scale window systems using a shock tube are presented in this paper. The modeling includes numerical simulations using LS-DYNA. The dynamic response in terms of the center deflection as well as the dynamic reactions around the window frame is measured and compared to the modeling results. In addition to the positive phase of the blast loading, the response of the window system to negative phase is also investigated. The modeled dynamic deflections and reactions correlated well within the first few peaks of the measured response of the window systems. The results of this study can be used to improve the existing methods for predicting the dynamic response of windows under blast and to provide affordable design recommendations.

INTRODUCTION

Design of civilian structures to resist blast loading has received much attention over the past several years. The behavior of glazing is of particular interest since it is estimated that the majority of injuries from blasts result from airborne glass fragments from glazing (Hinman, 1995). Upon failure due to a blast, sharp fragments of glass can be propelled into a building, resulting in the injury or death of occupants (Norville and Conrath, 2001 and 2006).

In recent years, blast design of window and curtain wall systems made benefit of conventional materials and systems through the use of laminated glass that is properly attached to a window frame and mullion system. To counter the effects of flaws in annealed glass, tempered and/or heat-strengthened glass, which exhibit high compressive residual stresses at the surface of the glass (Amstock, 1997), are often used for blast resistance applications. Laminated glazing is generally fabricated from two or more layers of tempered/heat-strengthened glass with an elastic material between each two layers. Over short durations and at low strains, this interlayer can be treated as a linear elastic material with a Poisson's ratio approaching 0.5 and

stiffness obtained from shear modulus using solid mechanics equations (Wei and Dharani, 2005). The elastic interlayer layer allows the glazing to undergo large deformations, and thus resulting in large dynamic reactions around the edges of the window frame. In addition, insulated laminated architectural glazing systems, which may include an annealed glass layer separated from the laminated glass with an air gap, can provide added blast resistance through the creation of a "sacrificial" layer. These layers are also used to meet other design criteria such as thermal and sound insulations.

The large-deflection response of the glazing system under blast loads generates dynamic reaction parallel and perpendicular to the plane of the glazing. The dynamic reactions are transmitted to the supporting mullion and/or structural frame. This paper present a numerical simulation and field testing program aimed at evaluating the dynamic response of laminated windows, including dynamic reactions, under blast loads as well as comparison of models to measured data for dynamic reactions at the connections.

MODELING

The numerical modeling is performed in this paper using the commercial code LS-DYNA (2009), which is commonly utilized by the blast research community. The glass layers and interlayer polymer are modeled as separate layers within single composite elements using the LS-DYNA material model 32 "MAT-_LAMINATED_GLASS". This material model uses multiple through-thickness integration points to account for multiple layers of glass and polymer within a single shell element, Chung et al. (2010). The glass layers are modeled by isotropic hardening plasticity with failure based on exceeding a specified level of plastic strain. Neither the entire element nor the entire sub-layer is deleted at this specified level of plastic strain but there is a redistribution of internal stress to the remaining glass and polymer sub-layers. This polymer sub-layer material which the glass is bonded is assumed to stretch plastically without failure. Each integration point is flagged with a zero if the layer is glass and with a one if the layer is polymer, LS-DYNA user's manual (2009). The input data for glass layers includes the mass density, Young's modulus, Poisson's ratio, yield stress and plastic strain at failure. The input data for polymer layer includes Young's modulus, Poisson's ratio, yield stress and plastic hardening modulus.

VERIFICATION USING FIELD EXPERIMENTS

Three laminated window systems were tested in the field using a full-scale shock tube (Figure 1). The laminated windows were 1.22 m wide × 1.68 m high. The three windows were made up of 3 layers of glazing and an aluminum frame. Table 1 shows the relevant information of the three windows evaluated in this study, and Figure 2 shows one of the window samples inserted in the test frame before and after test. The measured pressure and impulse are shown in Table 1, and sample gage readings during the shock tube tests of one of the windows is shown in Figure 3.

The pressure-time history recorded from the field experiments was used as the input loading function to the LS-DYNA model, which accounted for all positive and

negative loading phases. The center deflection of the glazing and dynamic reactions transmitted to the aluminum frame are recorded during the experiments and are compared to the numerical modeling results.

The numerical dynamic responses of the windows are compared to field results as shown in Figures 4. The plastic strains contours predicted using the numerical model are compared to glazing failure profile observed in the experiment for window sample #1 as shown in Figure 5. The numerical predictions correlate closely with the field results.



Figure 1. Shock tube.

Table 1. Field Data of Window Systems.

Window Sample #	Laminated Pane Constituents			Measured Average Blast Loading		
	Outer Layer (blast side)	Interlayer	Inner Layer	Pressure (kPa)	Impulse (kPa-msec)	Positive Phase Duration (msec)
1	3.2 mm Annealed	1.0 mm Uvekol-A	3.2 mm Annealed	29	152	30
2	3.2 mm HS*	1.5 mm Uvekol-S	3.2 mm HS*	49	308	59
3	6.4 mm Annealed	1.0 mm Uvekol-A	6.4 mm Annealed	55	306	54

*HS = High Strength

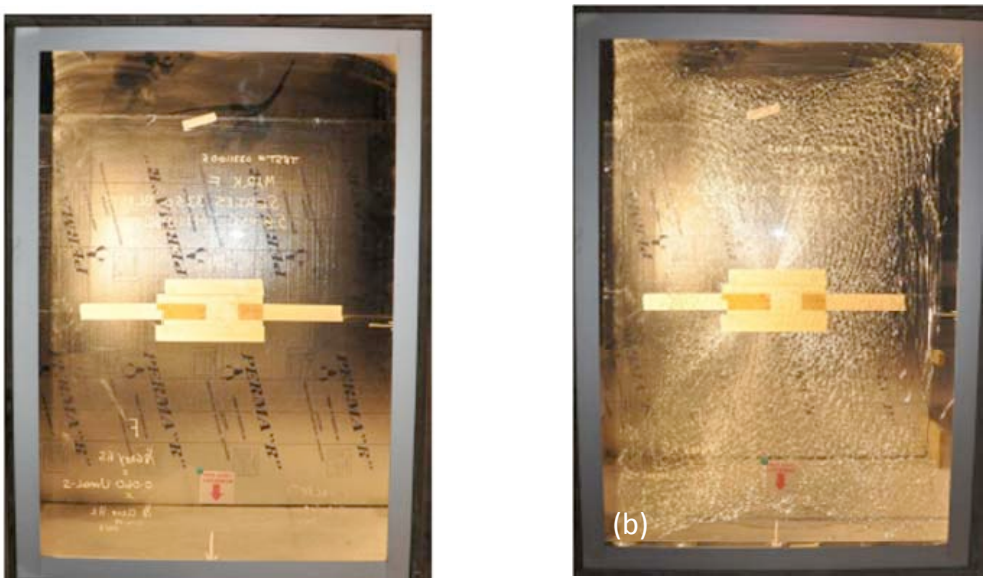


Figure 2. Window sample: (a) before test; (b) after test.

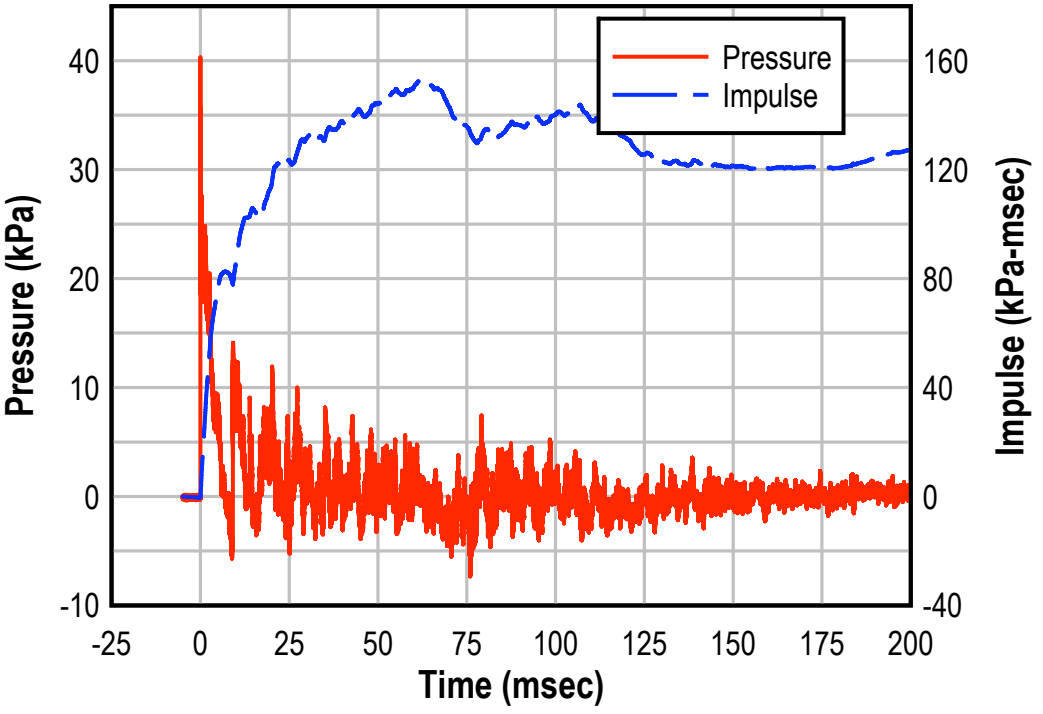


Figure 3. Sample pressure-time history.

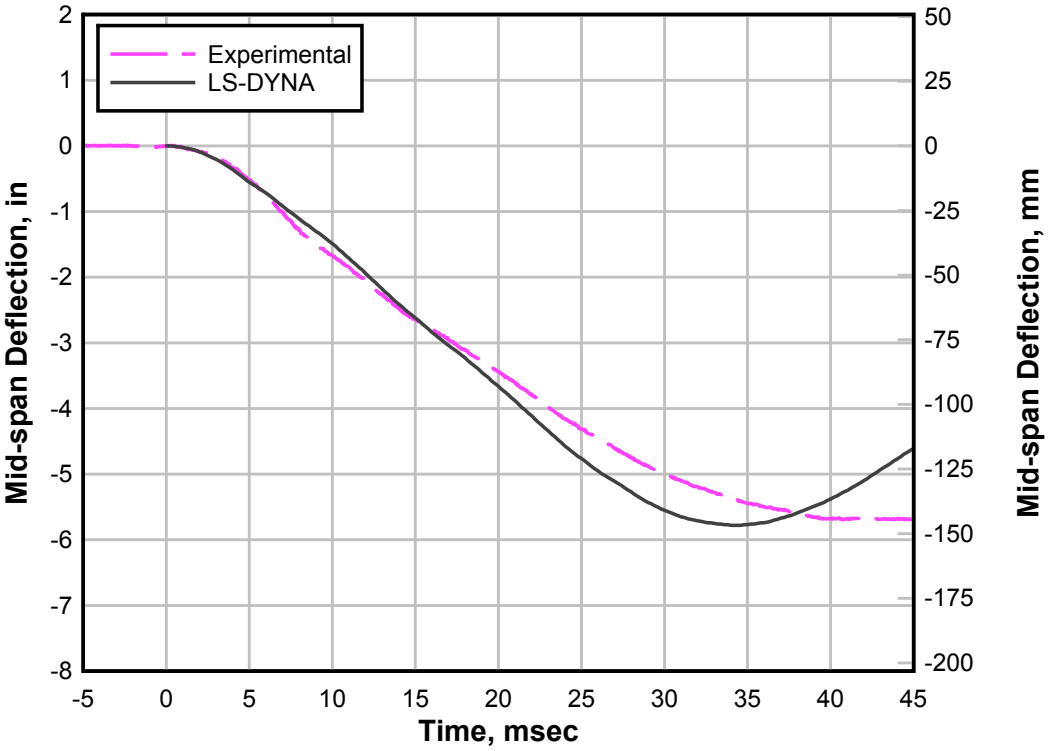


Figure 4. Center deflection comparison for window system #1.

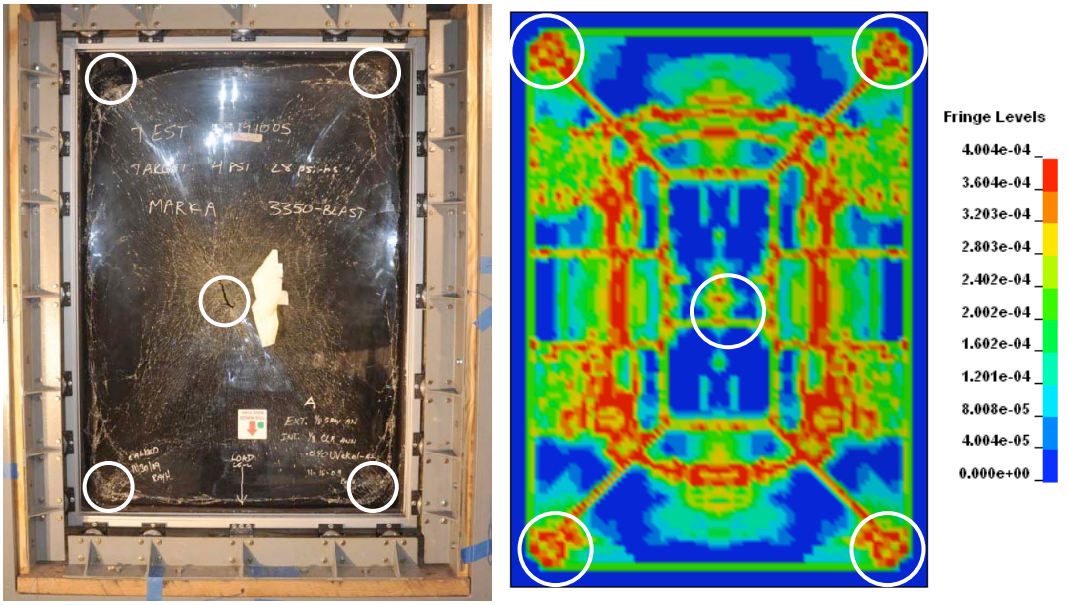


Figure 5. Plastic strains (right) showing predicted failure (left) shown in experiment for window #1.

The dynamic response prediction of window samples 2 and 3, including the dynamic reactions along the aluminum window frames are shown in Figures 6 - 9. The dynamic deflection prediction for window sample 2 matches closely the first two peaks field response, while the results deviate after 40 milliseconds as shown in Figure 6. On the other hand, the dynamic response prediction of window sample 3 matches closely the field response for the first three peaks as shown in Figure 7.

The dynamic reactions for both windows along the vertical (long) edges of the aluminum frames are shown in Figures 8 and 9. The dynamic reactions shown are the ones perpendicular to the plane of the window, i.e., along the blast wave direction. In general, the dynamic reaction predicted by the numerical model matched closely the field dynamic reactions recorded during the blast event. The dynamic reactions for window sample 2 are shown in Figure 8, while the results for window sample 3 are shown in Figure 9. Similar results were also observed for the dynamic reactions along the horizontal (short) edges of the aluminum window frame.

The predicted and measured dynamic reactions can be used to evaluate the existing united facilities criteria (UFC) requirement, which specifies that the loading transmitted to the supporting structure of a laminated window to be eight times the glazing resistance determined by the ASTM standards (ASTM, 2003, 2004, and 2007). Additional numerical modeling and field testing results can be used to develop a probabilistic value for the dynamic reactions experienced by the supporting structure. Alternatively, closed-form solutions of the resistance function of the glazing system can be incorporated into a single degree of freedom (SDOF) dynamic model to calculate analytically the dynamic reactions for a specific window system and blast loading.

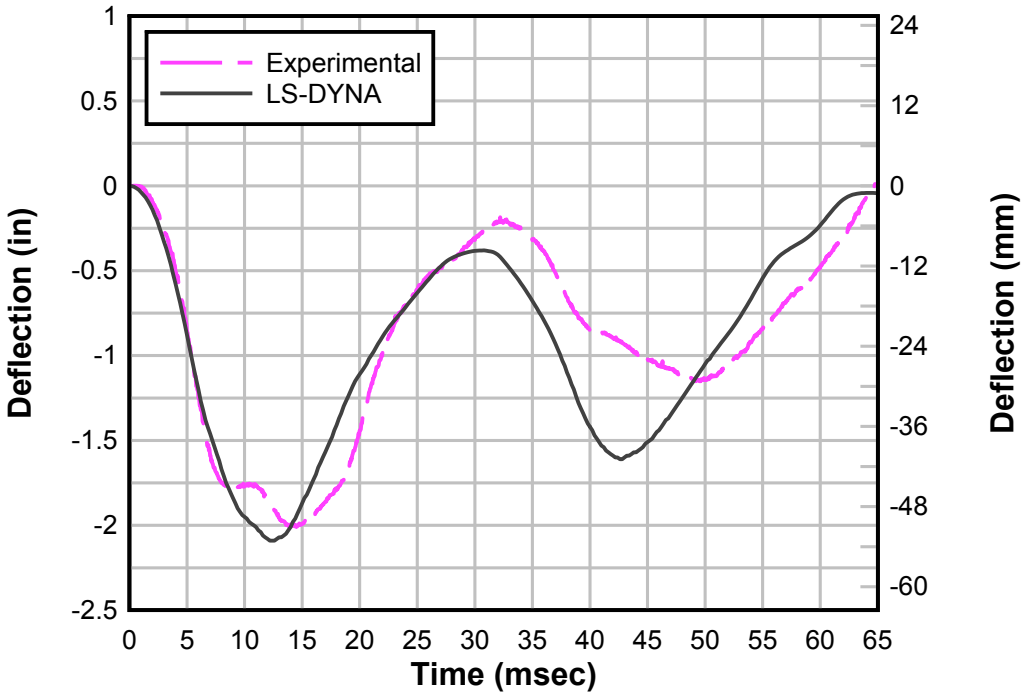


Figure 6. Center deflection comparison for window system #2.

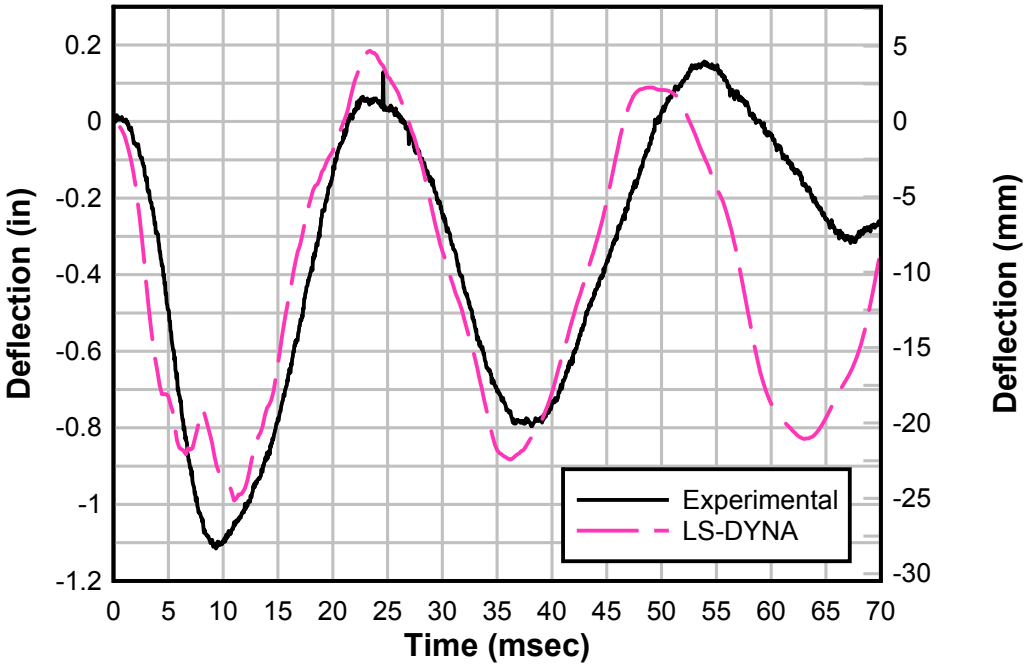


Figure 7. Center deflection comparison for window system #3.

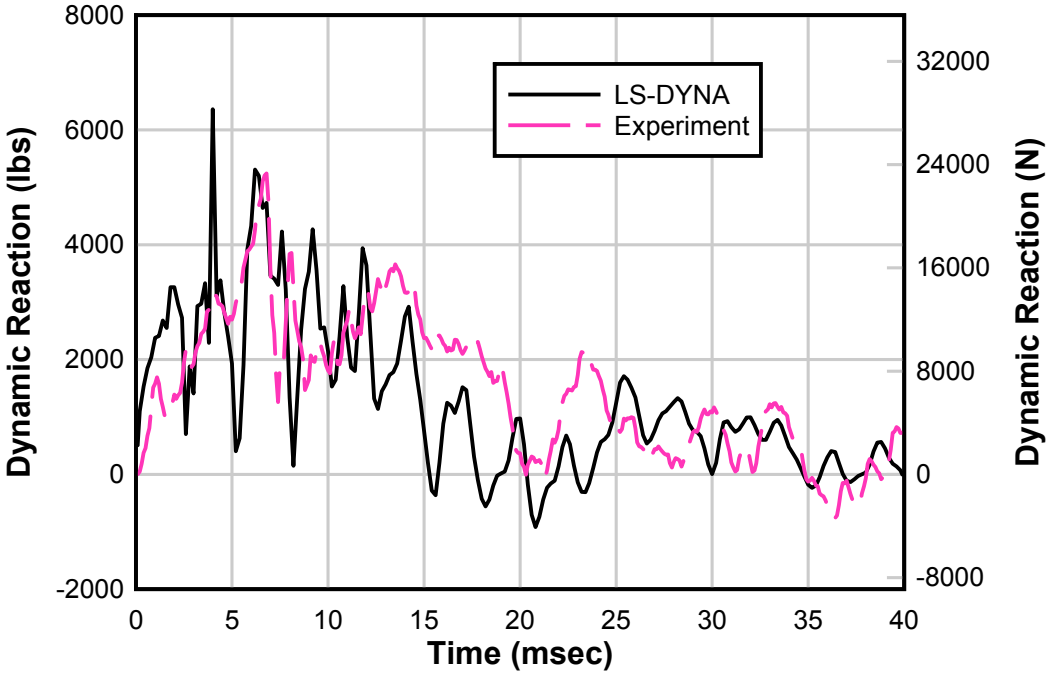


Figure 8. Total dynamic reaction acting on long edge of aluminum frame for window sample #2.

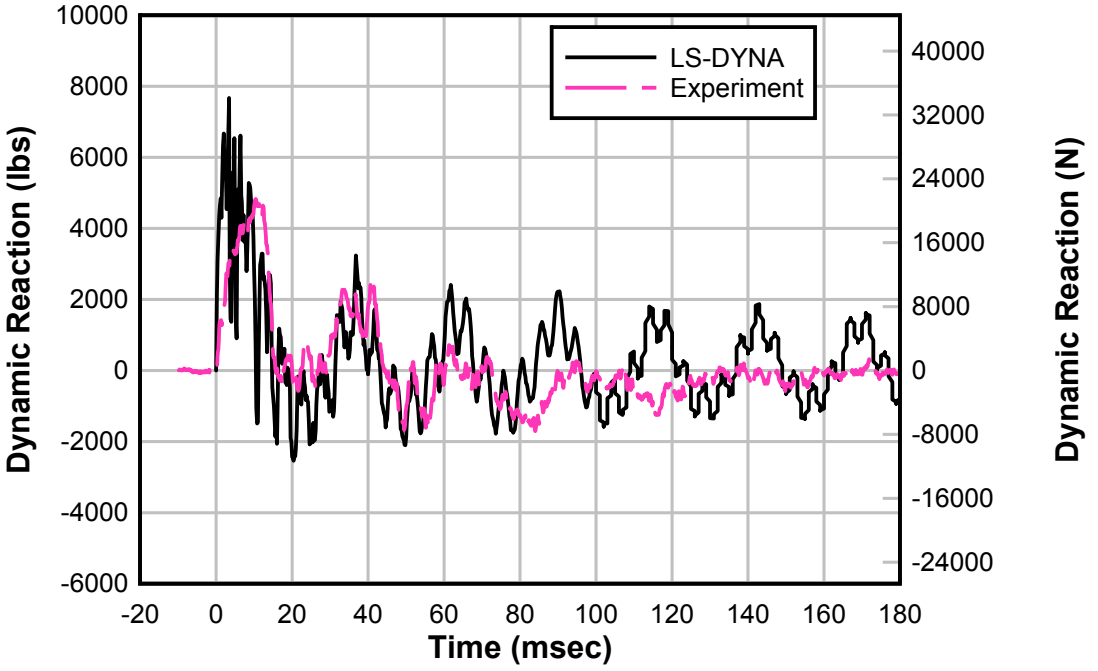


Figure 9. Total dynamic reaction acting on long edge of aluminum frame for window sample #3.

SUMMARY

Numerical modeling was used to predict the dynamic response of the window systems and were verified using field tests under blast loading performed using a full-scale shock tube. The numerical simulations using LSDYNA predicted well the dynamic response and total dynamic reactions. The results of this study can be extended to develop engineering-level analytical models for the design of window systems and their supporting structures. The measured dynamic response from the shock-tube experiment, in terms of the center deflection, compared relatively well with the numerical models developed in this paper for all three windows. In addition, the measured total dynamic reactions perpendicular to the window compared well with the numerical models.

It is recommended that additional numerical modeling supported by field testing be performed to develop a probabilistic factor, similar to the recommended by the UFC for predicting the dynamic reactions for blast design of the supporting system of laminated glazing. Since the static resistance and the mechanical properties of the materials that makeup the window system are the most important inputs to the analytical and numerical models, it is recommended that material, component, and full-scale static testing of various window systems be performed.

ACKNOWLEDGEMENT

The authors acknowledge the financial support and technical advice provided by Mr. Gantt Miller, Kurtis Suellentrop, and Larry Frost of Winco Window Company, St. Louis, MO, USA.

REFERENCES

Amstock, J. (1997). *Glass in construction.* New York: McGraw Hill.

ASTM. (2007). *ASTM E 1300 - 07 Standard practice for determining load resistance of glass in buildings.* West Conshohocken, PA: ASTM International.

ASTM. (2004). *ASTM F 1642 - 04 Standard test method for glazing and glazing systems subject to air-blast loading.* West Conshohocken, PA: ASTM International.

ASTM. (2003). *ASTM F 2248 - 03 Standard practice for specifying an equivalent 3-second duration design loading for blast resistant glazing fabricated with laminated glass.* West Conshohocken, PA: ASTM International.

Chung, J.H., Consolazio, G.R., Dinan, R.J. and Rinehart, S.A. (2010). "Finite-Element Analysis of Fluid-Structure Interaction in a Blast-Resistant Window System" *Journal of structural Engineering, Vol. 136, No. 3.*

Hinman, E. (1995). "Lessons from ground zero." *American Society for Industrial Security: Security Managemen*t, October 1995, 26–35.

Livermore Software Technology Corporation. (2009). LS-DYNA KEYWORD USER'S MANUAL, Version 971, May 2009.

Norville, H., and Conrath, J. (2006). "Blast-resistant glazing design". *Journal of Architectural Engineering,* 12 (3), 129-136.

Norville, S., and Conrath, E. J. (2001). "Considerations for blast-resistant glazing design." *J. Archit. Eng.*, 7(3), 80–86.

Unified Facilities Criteria (2007). *UFC 3-010-01: DOD Minimum Antiterrorism Standards for Buildings.* U.S. Army Corps of Engineers, Department of Defense.

Wei, J., and Dharani, L.R. (2005). "Fracture mechanics of laminated glass subject to blast loading." *Theoretical and Applied Fracture Mechanics,* 44(2), 157-167.

Attaching Tower Cranes to Buildings in New York City

Dan Eschenasy, P.E., M.ASCE
Chief Structural Engineer
New York City Buildings Department
deschenasy@buildings.nyc.gov

Abstract.

The paper presents an overview of the issues related to the application of tower crane loads to buildings under construction. Intended for the structural engineers who design these buildings, it provides a primer on the derivation of these loads by the crane installation designers. Based on a review of tower cranes installations designs executed in New York City, the author finds that the attachments at the top of the structure can develop horizontal loads of same order of magnitude as the wind loads used for the base building design. Interaction and responsibility between crane and building engineers is examined. The building designers are better suited to evaluate the effects on the main lateral load resisting system. The crane installation designers need to use more consistency and clarity when presenting the loads for evaluation by the engineers of record.

Introduction. Following two major accidents in New York City, the Buildings Department embarked in a massive revision of its crane approval and inspections processes. The Department has engaged a consortium of engineering companies led by CTL Group, to help in the evaluation of crane procedures as well as of other categories of construction operations where it was experiencing problems (concrete, support of excavation). This process, called High Risk Construction Operations (HRCO) , lasted three years. For the crane section of the project CTL Group selected Crane Tech Solutions (CTS) whose principals Manfred Kohler and Frank Hegan have vast experience in the domain.

Most of the HRCO findings have been made public as the proposed changes in code or operations were discussed with the industry. This author participated in the discussions that CTL and CTS experts had with the New York City engineering consulting industry. The proposal that the structural engineers of record be required to approve the loads imposed on the structure met with significant resistance. Following these discussions and relatively independent of the HRCO effort, the

author examined several crane installation projects focusing on the loads exerted by the tower cranes on the building structure.

At the time the designs under review were prepared, the NYC Building's Crane and Derick approval process required two distinct engineering submittals. The first submittal, required to permit a crane model to operate in the city, includes general structural calculations, description of safety features, etc. Specific calculations are to be submitted for the actual installation at a specific site of any approved model. These designs formed the subject of the author's review. This review focused on methods and engineering responsibility for verifying the capacity of the building to sustain loads induced by the attachment of a tower crane.

Engineers of Record for the Building and for the Crane Installation. The design of the building structure is the responsibility of its structural engineer of record [(B)EOR], who at the time of the design is not aware of the specific methods that will be selected for the erection of the building. The design of the building is based on code prescribed loads and load combinations. These derive their maximums values from the effects of extreme natural events. For the New York City area, most tall building designs are controlled by the wind load.

At some point in the construction management phase, a tower crane solution is selected and an engineer with expertise in tower cranes, designs an installation system. The tower crane installation design includes selection of type of crane, positioning of crane, positioning of the tower attachment, design of tower foundation. This crane installation engineer [(C)EOR], bases the calculations on loads provided by crane manufacturers together with loads specified in building codes or national standards. The load combinations are not always sanctioned by building codes. Crane in service loads loads do not usually account for the possibility of accidents. Excessive loads are avoided by means of mechanical and electrical controls as well as operator training. Human errors play a much larger role in the life of cranes than of buildings'. Human factors are minimized by adherence to the engineer's project specific instructions as well as to the manufacturer's general instructions.

After they reach certain heights, tower cranes cannot stand alone and need to be supported laterally. Such support is most commonly obtained by attaching the tower to the buildings under construction. A collar is set around the tower and tied to the building structure with several steel beams (ties) that are intended to transferonly horizontal loads to the building. The ties need to be positioned in a manner that blocks any horizontal movement of the tower. As the tower advances in height, new collars and ties are installed. The spacing of the collars is limited by the structural characteristics of the tower given the anticipated usage demand and wind speed. The collar also needs to be placed such that it meets a tower horizontal frame. Each new collar addition creates a different structural system, a new loading configuration that needs to be resisted by the building.

The building designed by the (B)EOR under one set of loads is subjected to horizontal loads for which it was not designed. These special new loads are the result of decisions by the (C)EOR whose purpose is to minimize the number of collar (as

the collar installation is a complicated operation). The intensity of these new loads is calculated by the (C)EOR based on manufacturer data and specific local conditions.

Which engineer has the responsibility to verify that the building under construction can safely sustain these loads? Which engineer is in better position to make this evaluation?

General Model of Engineering Responsibility. As a result of various building code provisions a model for engineering responsibility has developed for cases when buildings are subjected to loads for which they were not specifically designed. For example, when the floor of an existing building is subjected to a new set of loads, an engineer representing the tenant introducing these loads needs to verify that these are within the original approved design rating. When the loads exceed this rating, the tenant 's engineer has the obligation to verify that any affected part of the structure can safely sustain the load. Any necessary structural changes to the existing building have to be accepted by the building owner. This owner makes his decision based the advice of his own engineering consultants, usually the engineers of record of the original structure. Discussions between the two sets of engineers ensue.

The building department expects a licensed engineer to demonstrate the adequacy and places entire responsibility on this engineer without regard of who commissioned the evaluation. In fact, this engineer is expected to have performed a due diligence inspection to assess any degradation of the original design condition of the structure.

Crane Loads and the Building Design Process. There are some specific conditions related to supported tower cranes: both sets of engineers work for the same owner, some engineering consultants are covered liability insurance policies that prevent them to perform designs of construction related installations, the officially structural design documents list only the vertical loads related to building occupancy. As the construction is in progress some materials might not have reached their full strength, some installations or connections might not have been completed, results of some inspections might not be available.

There is no dispute as to the responsibility of the (C)EOR to design any local strengthening at and around the attachment points of the crane to the building, but is the (C)EOR in the best position to certify the general capacity of the building to safely resist the crane loads?

Ideally, the crane loads should be specified early so as to be included in the original structural design. This is rarely the case, as final decisions on the erection methods are made at later points. At this point to avoid a costly complete recalculation of the building one tries to first to verify the loads by comparing them to the original design loads.

To perform such lateral load comparison, the (C)EOR can only examine the building’s structural drawings, but these include only the general parameters used in the wind design (exposure, importance factors, etc.). Without collaboration with the

(B)EOR, the (C)EOR has no simple way of knowing what were the actual horizontal loads used in the design of the structure.

Up till recently, in NYC there was only scant collaboration by these two different engineers. The Buildings Department is in the process to require (B)EORs to collaborate in assessments of crane loads effects. Changes in design responsibility will affect also the responsibility for inspection of the execution of the specific construction details present in the crane installation drawings. To be part of the process, engineers involved in high rise design need some basic understanding of crane loads.

Primer on the Derivation of Loads. Structural engineers of tall buildings need to have a basic understanding of the crane effects on buildings. The following paragraphs provide some simplified explanations.

When the crane is not in service (does not lift any load) the weight and resulting moment of the boom is not fully balanced by the moment produced by the counter weight. The resulting unbalanced moment is a dead weight type of load and tends to rotate the tower towards the counterweights. The essential variation in this load would be the result of an improper installation of the counter weights. (Location or actual weight).

When the crane is in operation, the moment produced by the weight of the jib and the weight being lifted might not be entirely balanced by the counterweight moment. The maximum size of this unbalanced moment is determined by the capacity of the crane for a given the type and orientation of the boom. This is a construction live load. One needs to add to this the effect of the slewing moment, an horizontal moment produced by the rotation and braking of the crane. The calculated load could be exceeded by an over loading of the crane combined with a malfunctioning of the embedded safety stops. The specified load might be exceeded during the site load test when this is performed following manufacturer's instruction to use a 10% overload.

Even in the absence of air movement, flexibility due to the unsupported height of the tower or due to the jib configuration can induce second order effects that affect stability of the crane.

Wind effects are a major concern for the stability of cranes. As crane are allowed to lift loads only when winds are below 30 or 35 mph, the pressure at this wind speed and the related effects are added to the “in operation” loads. During operations, the jib might need to take any position so both wind along and perpendicular to the jib need to be considered. The center of application of the wind loads on the jib is determined by its angle to the vertical. The effects of the wind perpendicular to the jib, a larger exposed area, will produce forces and moments in a plane perpendicular to the “in service” overturning moment that acts in plane with the jib.

Effects of stronger winds are combined with effects of “out of service” loads. Crane out of operation are allowed to weathervane so only wind along the jib needs to be considered. Of course for locations where the presence of adjoining structures

(including other cranes) can determine weathervaning. The jib might need to be raised in a certain position to avoid obstructions or weathervaning might not be possible at all. In such cases one needs to consider the position of the resultant of wind forces or even the effect of wind perpendicular to the jib.

In most cases manufacturers recommend removal of some intermediate ties for wind speeds over 65mph (usually the one before last tie). This has the effect of improving the structural behavior of the tower, but also of increasing the load transmitted to the building by the top tie.

It results from that several loading cases are possible.

- Crane without load, no wind included
- Crane at maximum load, no wind included.
- Crane in operation with the wind along and wind across jib.
- Crane out of operation with all braces inplace and wind up to 65 mph. (or at whatever wind speed some ties might have to be removed)
- Crane at maximum wind load with or without any ties removed.

In principle all these load combinations need to be considered for each collar configuration, but some the combinations producing low load demands can be discounted by inspection.

PROJECT		1			2		3				4	5			
Bldg, floor height		9.67			8.7		9.7				9.2	12			
Building Length/Width		2.00			1.29		1.28				1.30	2.37			
Crane Model		Potain MR415			Potain MR295B		FFC M440D				Favco STD 1500	PECCO SN-169			
Boom Length (ft)		164			98		180				181	140			
Tower height (ft)		395.5			369.5		472.5				311.5	357.67			
Tower Section (ft)		10			10		8.67				10	6.5			
No of Collars		3			2		4				1 (and floor wedge)	4			
Collar Spacing (ft)		120, 99, 96.5			112.5, 113		98.5, 90, 91, 100				175.5	82, 64, 69			
Tower height above last tie (ft)		79.5			154		93				136	74			
Tie:		#1	#2	#3	#1	#2	#1	#2	#3	#4	#1	#1	#2	#3	#4
max load **IN** service (kips)	P1	86	84.17	71	93	76	104	97	97	83	116	45	50	47	39
	N2	86	61	52	16	13	102	95	95	82	76	24	26	25	21
	P2	62	16	14	69	57	51	48	48	41	75	41	46	43	35
max load **OUT** service (kips)	P1	136.19	152.79	112	162	164	158	153	153	122	172	108	115	114	81
	N2	135	111	81	27	27	156	152	152	120	111	45	48	47	34
	P2	110	41	30	114	116	78	76	76	60	56	105	111	111	79
Base Moment (ft.k)		7160			2320		8285				7741	0			
Base Shear (k)		58.5			63		76				59	19			
Axial Load (k)		355			379		685				543	248			
Attached To		slab conc. 4000 psi			slab conc. 4000 psi		slab conc. 4000 psi				slab conc. 4000 psi	steel frame			
Floor Reinforcement		(C)EOR			(C)EOR		(C)EOR				(B)EOR	(C)EOR			
Engineer Approval		(C)EOR			(C)EOR		(B)EOR				(B)EOR	(C)EOR			
Notes							Second crane is attached to building. No crane release pre-hurricane.				Crane tower within podium, wedged at 4th fl. Wedge release pre-hurricane.	Tie release before winds of 60 mph.			
IN Service Wind (mph)		30			45		35				30	30			
OUT of Service Wind (mph)		94			94		90				83.3	60, 75			

Table 1. Crane and Tie Load Data

Supported Tower Crane -Observations on the current practice in New York City. Several crane installation designs were reviewed Although not random, and

clearly not encompassing all possible cases, the selection provided a good representation of the crane installation design practice as it was evolving under stricter regulation.

All designs required the cranes to be installed outside the main building tower, but in several cases the tower crane was placed inside the low rise podium. The buildings reviewed were relatively symmetric, but their length to width ratios differed significantly. Also, the presence and configuration of setbacks was different for each building. The structural framing systems encountered were steel, concrete and steel frame with concrete shear walls. In one case an existing 16 stories building was altered by the addition of 16 more floors. Here, the tower crane ties were attached directly to the main vertical steel truss core. Data obtained from installation drawings on five of these crane projects is presented in Table 1.

The usual attachment to the structure uses three ties, two of which converge towards to a point in the building's structure. The values P1 represent loads in the first tie and are the loads used for the design of the ties. The values N2 and P2 represent the loads at the point of convergence and do no describe the actual load in the ties. The highest value loads (P1 or the combination of P2 and N2) are used to design the reinforcement at the attachment point. The drawings present separately the In Service and Out of Service loads at each floor. There is no indication as from what particular load combination they were extracted. We found that in fact they are the envelope value of maximum forces. In each of the projects reviewed, the (C)EOR calculated the values P1, P2 and N2 and performed the related calculations related to transfer loads from the collar to the building. The collar loads were sometimes calculated by the (C)EOR and sometimes provided by the crane manufacturer. This resulted in inconsistencies on the wind speed used to evaluate the loads. The manufacturers use full code wind pressures to design the cranes, while the (C)EORs take advantage of the provisions of reduction factors recommended in ASCE 37 *Design Loads on Structures During Construction.* This discrepancy seems justifiable as crane designs need to provide for many years of operation are while the attachment to one particular structure is unlikely to exceed one, two years. The based wind load needs be from NYC Building Code and, as required, it is modified according to applicable provisions from ASCE 7 *Minimum Design Loads for Buildings and other Structures.* At the time when the installation projects were prepared, both ASCE 7 and the NYC Building Code were being modified. This resulted in additional discrepancies.

Structural Capacity of Building and Reinforcement. For all the cases observed, the tie loads at their attachment points exceeded the capacity of the surrounding slab. In addition, these loads overstressed the structural elements in their path towards the main lateral resisting system. All installation projects examined included drawings depicting some local reinforcements. In almost every case, these drawings were prepared by the (C)EOR. The information available on the building structural drawings (slab and beam sizes, type of material, etc) was sufficient to allow a proper verification and design. In some cases, conservative (C)EORs designed the

reinforcement without bothering to verify if the original building structural design was sufficient. The use of the envelope reaction forces (as listed in table) at each tie connection point was adequately conservative. For all practical purposes, we did not see any need to require verification or even acceptance by (B)EOR of the local reinforcement. Coordination was the only potential issue (e.g. to insure that the additional rebars are installed).

All projects reviewed have an engineer's statement certifying the building's main structural system's capacity to carry the tower crane loads. There is no record on how this evaluation was effectuated. When the (B)EORs offered their acceptance, this was based on the loads P1, P2, N2 shown on the crane installation drawings. One can safely assume the (B)EOR has, at a minimum compared these loads to the loads used for the basic structure. In fact, the inspection should compare the resultant of P1, P2 and N2. Admittedly, this combination of envelope values would be over conservative as the actual loads are the loads at the collar and the moments generated by these as they are transferred to the main lateral resisting system.

The (C)EOR knows the loads at the collar, but does not know the loads used for the design of the building. The (C)EOR does not even know if the building was design using wind loads were obtained from wind tunnel studies. Is this acceptance by the (C)EOR, the result of a detailed effort or just based on general considerations?

It is true that for many attached tower cranes operating in New York City, the out of service loads are larger than the in service loads and that this difference is a consequence of the difference between the in and out of service wind speeds. It is also true that the wind load on a tower crane is a fraction of the wind used to design the building. But one does not know in what general situation the preceding considerations can be applied, as buildings and crane configurations, crane payloads and attachments to buildings are extraordinarily diverse.

Maximum Forces Exerted by Crane on Collars (kips)					
PROJECT	1	2	3	4	5
Building Exposure Type by ASCE-7	by manufacturer	by manufacturer	by manufacturer	Exposure A	Exposure B
Collar Level #4 (k)	-	-	107 (x2)	-	61.6
Collar Level #3 (k)	107	-	135	-	86.5
Collar Level #2 (k)	146	143	135	-	86.3
Collar Level #1 (k)	127	141	139	119.6	80.9
Cummulated Floor Wind Shear at Collar Level					
Floor at Tie #4 (k)	-	-	221	-	84
Floor at Tie #3 (k)	75	-	575	-	200
Floor at Tie #2 (k)	290	344	888	-	309
Floor at Tie #1 (k)	589	591	1326	490	434

Table 2. Forces at Collar vs Wind Design Loads

Simplified Verification. A comparison was performed between the loads at the collar and code imposed wind loads. See Table 2.

The values of the loads at the collar, shown in Table 2, were obtained from the calculation notes submitted to the department. These values underestimate the

crane load on the main lateral resiting system as the effect of the transfer of crane forces to the frame is not accounted for.

The wind shear for the (enclosed) building, cummulated from top down, was evaluated using the base code wind speed and ASCE 7 provisions. The evaluation used architectural renderings of the envelope of each building. The cumulative wind shear was calculated both along and across the building. The tabulated value is the lower of the two. In short, the loads that presumably created the weaker building lateral system were compared to the loads on the collar. Obviously, when the two sets of loads are comparable in intensity, detailed evaluations should follow.

It is evident that the difference is smallest at the top-most collar, although the load at this top collar is not always the smallest. The weakness at this level is due to the fact that the top-most floors are designed for compounded shear values smaller than the lower floor. Even in the few examples shown in Table 2 one can observe the some problems. For building (1), the load at the top collar is higher than the cumulative wind shear. This is due to the fact that the building had a penthouse tower with a smaller footprint. Building (3) is served by two cranes and their added out of service load of 214 kips is within 5% of the wind shear. In fact, the wind affects both the crane and building frame, so one would need to add to the crane loads, the wind effect on the unenclosed building (cummulated from top to that level). This can reach about 20-30% of the enclosed building load. Such addition would make building (5) suspect also.

This simple verification confirms that buildings need an attentive evaluation for horizontal crane loads. The lateral force support systems at the top of buildings are more sensitive and in some cases detailed structural calculations are required as load comparisons cannot suffice. Such calculations are most effective when performed by (B)EORs as they possess complete information on the design capacity.

Other Observations.

Clarification of the responsibility of various engineers needs to reflect the method and stages of erection and field inspection. There are differences between the erection of cast in place concrete and some steel structures where the lateral force resisting system might not always need keep pace with the floor installation. The situation is even more critical for steel buildings with concrete shear walls as the walls are always poured at later stages.

We could not identify tunnel laboratories that have performed tunnel wind tests on cranes. It is not evident that results of such tests will lead to reductions in loads at collars. Similarly, in our discussion with major laboratories, we could not find any example of wind tunnel tests on buildings under construction (unenclosed). Research in this area is necessary.

When loads are provided by manufacturers, they should state explicitly what what terrain condition was considered and if they include the case when the one before last tie is removed.

Experts preparing design standards should examine and specify the load combinations to be used with in service and out of service crane loads. It seems that

there is a high probability that the in service loads are reached during the life of every crane installation.

Conclusions.

Engineering evaluation of capacity of the building to carry crane loads is absolutely necessary. While evaluation of local effects by (C)EORs seems to be standard procedure, evaluation of the lateral structural system seems to use approximations that might not be sufficiently reliable, especially for the levels close to the top of the building. Crane and building engineers need to collaborate in this system evaluation, with (B)EOR taking the lead.

The author thanks David Adler for his contribution in collecting and preparing the data.

Bibliography.

ASCE/SEI 37-02, "*Design loads on structures during construction*" , ASCE , Reston Va.

ASCE/SEI 7-05, "*Minimum design loads for buildings and other structures*", ASCE, 2005, Reston, VA

Boggs D.W., and Peterka J.A., "Wind speeds for design of temporary structures" *Proceedings of the ASCE 10th Structures Congress*, San Antonio, Texas, 1992, pp. 800- 803, ASCE, 1993, New York

Mohammadi J. and Heydari A.Z., "Seismic and Wind Load Considerations for Temporary Structures", *Practice Periodical on Structural Design and Construction*, August 2008, pp. 128-133 @ASCE

Shapiro H.I., Shapiro, J.P., and Shapiro, L.K. *Crane and Derricks*, 3rd ed. McGraw-Hill, 1999, New York

Smith, S., and Coreley W.G., *High Risk Construction Oversight Study*, New York City Buildings Department, 2009
http://www.nyc.gov/html/dob/downloads/pdf/hrco_report.pdf

Collapse of the I-280 Maumee River Bridge Launching Gantry in Toledo Ohio

Paul E. Kassabian, P.E., M.ASCE[1], Michael McCall, P.E., M.ASCE[2],
Donald O. Dusenberry, P.E., F.ASCE[3], William P. Konicki, P.E., M.ASCE[4]

On 16 February 2004, one of two identical launching gantries used for the parallel construction of the approach viaducts for the I-280 Maumee River Bridge crossing collapsed. The collapse killed four workers and injured four others.

Each launching gantry consisted of two overhead steel trusses and a central lower steel-box-girder underbridge. The trusses spanned between adjacent piers and supported precast concrete segments for post-tensioning. Once a concrete span was post-tensioned, the trusses were moved forward across the newly completed span and the underbridge, which was advanced before the subsequent span. The process was then repeated.

Simpson Gumpertz & Heger Inc. (SGH) was on site after the collapse to observe and record the debris in place and as it was removed. SGH also had access to the second, essentially identical, launching gantry in its position on the approach viaduct.

From review of the two launching gantries and construction records, it was clear that modifications were made to the method and extent of anchoring the gantries to the new bridge.

The results of our analysis indicated that the failure to install prestressed rods at the stools supporting the rear legs of the gantry trusses meant there was insufficient resistance to movement when the underbridge was reversed backwards into a pier.

This paper presents our investigation of possible failure sequences and their correlation to the facts observed on site.

1. INTRODUCTION

On 16 February 2004 at 2:22 p.m., one of two self-launching gantries used to construct the approach viaducts of the I-280 Maumee River Bridge collapsed. The collapse occurred on the south side of the Maumee River during parallel construction

[1] Senior Staff II – Structures, Simpson Gumpertz & Heger Inc, 41 Seyon Street, Waltham, MA, 02453; PH (781) 907-9000; email: pekassabian@sgh.com (corresponding author)
[2] Associate Principal, Simpson Gumpertz & Heger Inc, 41 Seyon Street, Waltham, MA, 02453; PH (781) 907-9000; email: mmmccall@sgh.com
[3] Senior Principal, Simpson Gumpertz & Heger Inc, 41 Seyon Street, Waltham, MA, 02453; PH (781) 907-9000; email: dodusenberry@sgh.com
[4] Senior Principal, Simpson Gumpertz & Heger Inc, 41 Seyon Street, Waltham, MA, 02453; PH (781) 907-9000; email: wpkonicki@sgh.com

of both the northbound and southbound approach viaducts. The collapsed launching gantry was on the northbound approach viaduct and was referred to as "LG2" for Launching Gantry No. 2. The adjacent launching gantry on the southbound approach was LG1. See Photo 1. The collapse of LG2 killed four construction workers and injured four others.

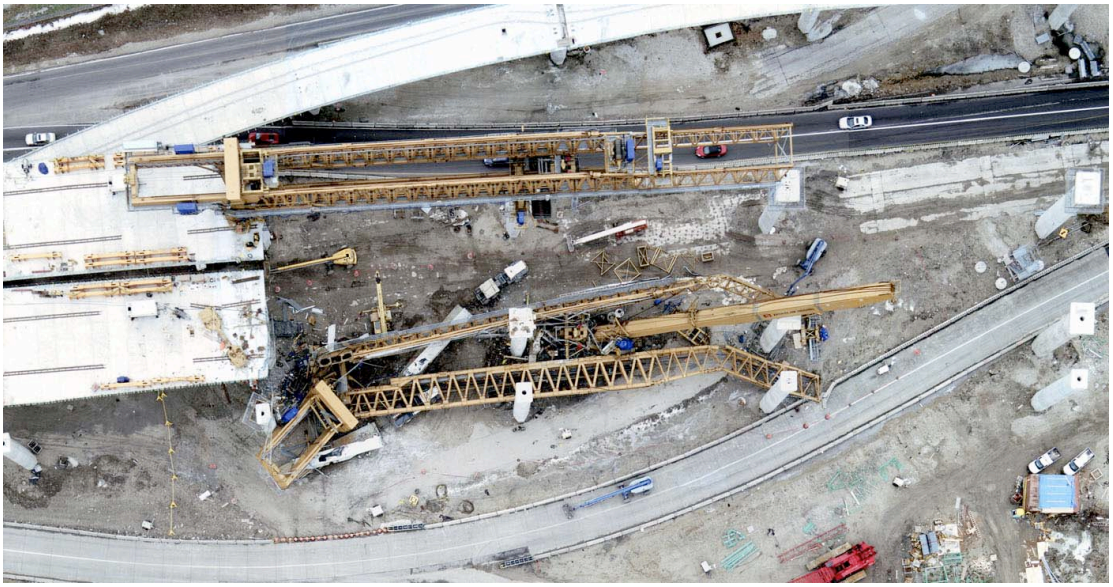


Photo 1. Overhead photo of the launching gantries after the collapse of LG2. (North is to the right of the image.)

2. THE PROJECT

2.1 The Bridge and Parties Involved

The I-280 Maumee River Bridge in Toledo, Ohio, is a cable-stayed bridge with two 612.5 ft spans either side of a single concrete pylon located in the middle of the Maumee River. Carrying three lanes of traffic in each direction, the bridge is a fixed high-level continuous passage for Route I-280 that was previously routed across the Craig Memorial Bridge, a bascule bridge that frequently caused traffic delays from regular opening for ship passage (Bonzon, 2008). The bridge was named the "Veterans' Glass City Skyway" to honor military veterans and the region's glass-manufacturing heritage.

The approach viaducts consist of precast post-tensioned concrete segmental box-girder spans initially set into place by the launching gantries using the span-by-span method.

The bridge design was by FIGG of Denver, Colorado. The General Contractor was Fru-Con (the contractor) of Saint Louis, Missouri. The designer and supplier of the launching gantries was Paolo de Nicola (the manufacturer) of Padova, Italy.

2.2 Launching Gantry Layout and Operating Procedure

The manufacturer custom-designed and built the two launching gantries for this project based on designs and sequencing used on other completed bridge projects. Each launching gantry consisted of two overhead steel trusses that supported the precast concrete segments from above. The trusses spanned between rear legs positioned at the end of the previously completed span and front legs that sat on the next pier (called the central pier herein). The rear legs rested on stools that had flat bases and spherical bearings at the top, to accommodate variations in level and beam-like rotations of the rear end of the trusses. The stools were to be anchored to the bridge with four post-tensioned (PT) rods each, to prevent movement. The front legs of the trusses were posts pinned at the top and bottom, thereby offering no resistance to longitudinal forces in the trusses.

A steel box-girder underbridge was positioned over the subsequent span and acted as a temporary bridge to allow the launching gantry to travel forward once post-tensioning of a span was complete. See Figure 1. It was advanced by mechanisms on the trusses that moved the underbridge forward while it was suspended from the cantilevering portion of the trusses. The rear legs of the underbridge rested on the central concrete pier, and were affixed to the forward top face of this pier with horizontal post-tensioned anchor rods that protrude forward. The manufacturer's Safe Operating Procedure stated that the underbridge must be reversed to bring the rear legs into contact with the forward face of the pier, and that the operator needed to move the underbridge slowly and follow signals. Subsequently, spacers were to be inserted between the pier and the underbridge rear bracket.

The forward legs of the underbridge were pinned at the top and bottom, thereby offering no resistance to longitudinal forces in the underbridge.

The seats for the legs of the trusses and the underbridge could be shimmed to achieve leveling of these components.

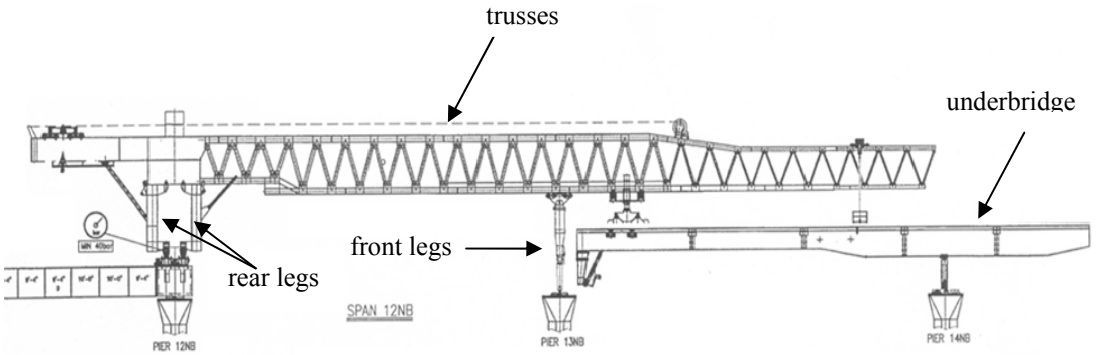


Figure 1. Layout of launching gantry and underbridge before collapse

2.3 Operating Stage at Collapse

By 16 February 2004, the contractor had completed eleven of the thirty spans of the approach viaduct on the south side of the river. Both launching gantries were positioned over the twelfth northbound and southbound spans, between Piers 12 and 13. The underbridge of LG1 was under the main trusses between Piers 12 and 13. The underbridge of LG2 was in the process of being launched to the subsequent span, between Piers 13 and 14.

At the time of collapse, the underbridge had been moved forward into the next span, but was being reversed toward the north side of Pier 13 for attachment to the forward face of that pier.

Photo 2 shows the north side of Pier 13 after the collapse. The horizontal anchor rods and the spacers were already in place. The operator of the underbridge at the time of the collapse stated in an interview that he tried to get the underbridge as tight as possible against the face of the pier to aid with subsequent stressing of the horizontal anchor bolts at the rear of the underbridge.

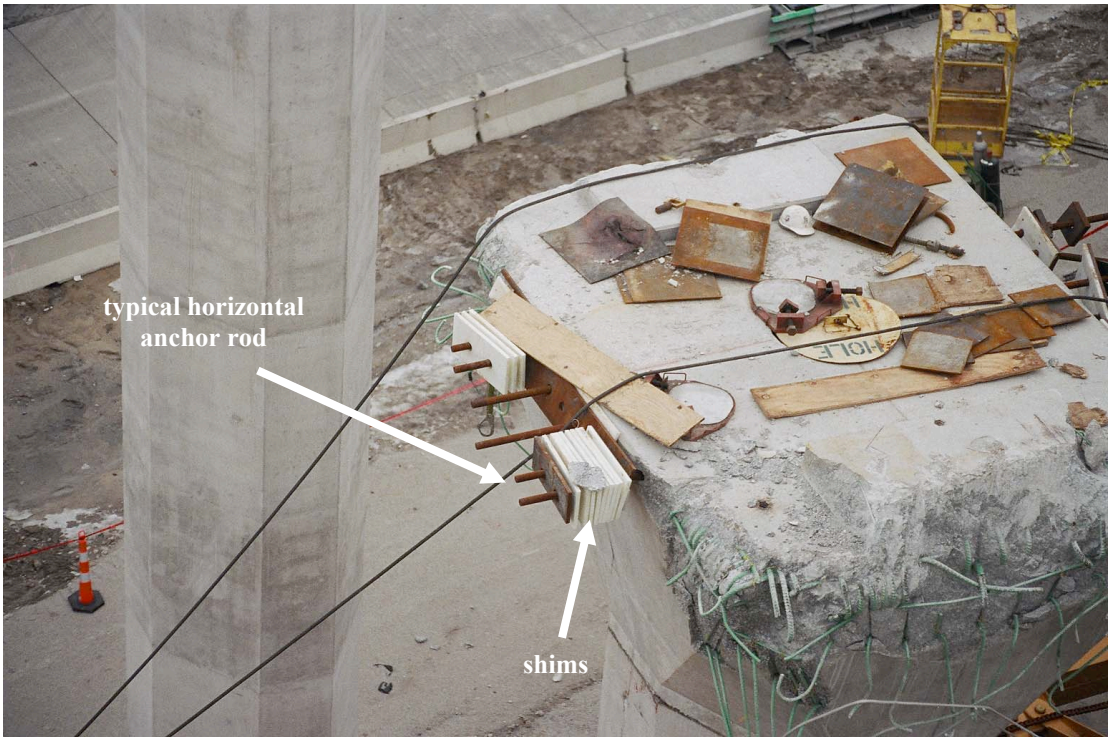


Photo 2. North side of Pier 13NB after the collapse. (North is to the left of the image.)

3. INVESTIGATION

The attorneys for the manufacturer retained SGH to investigate the failure. SGH was on site almost continuously from 23 February to 24 March 2004 while debris was removed. During this time, we monitored activities at the site and in the storage

areas. We observed, photographed, and measured debris in place and as it was removed. SGH was also on site during April and May 2004 for concrete core extractions from a pier and during the download of software and data from the Program Logic Controller (PLC), which was the device that controlled the mechanisms of the trusses and underbridge. SGH analyzed LG2 for its weight, strength, and stability using information based on the manufacturer's Safe Operating Procedure, facts from our site investigations, and operating procedures reportedly used at the time of the accident.

Some information that proved important in our review of failure scenarios is provided below.

3.1 Rear Legs

The manufacturer's Safe Operating Procedure stated the rear legs of each launching gantry must be prestressed to the bridge deck using the four PT rods before launching the underbridge.

From interview reports with the construction workers after the collapse, it seems that the PT rods were not installed before the movement sequence that was underway at the time of the collapse. During our investigation, we verified that the rods were not installed at the stools for the rear legs of LG2. This was based on both the existing condition of LG1, which did not have PT rods (Photo 3), and the rear-leg location for LG2 having (a) not enough holes in the deck to receive the rods and (b) no rods in the inserts and no damaged threads in the inserts (Photo 4).

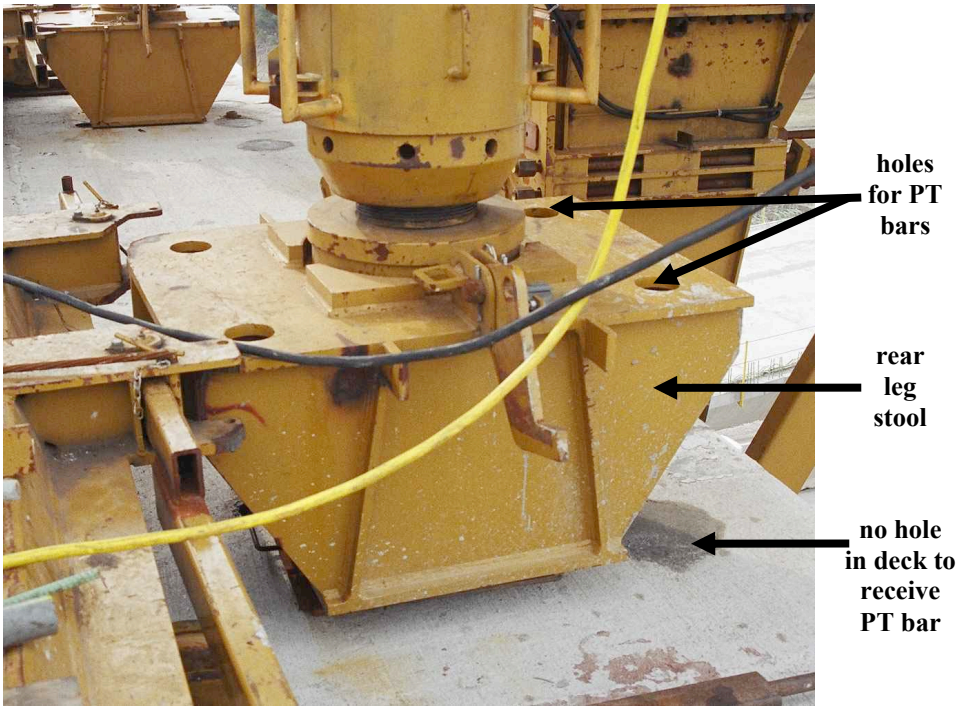


Photo 3. Rear leg supports for LG1.



Photo 4. Rear leg area for LG2. Deck inserts are adjacent to the square shims near the edge of the deck. (North is to the left of the image.)

3.2 Front Legs

The manufacturer's Safe Operating Procedure stated the front legs are to be plumb. We learned that the plumbness of the front legs was being determined primarily by workers using a 4 ft long carpenter's spirit level. From recorded interviews, the accuracy of this plumbness was variously quoted from 1/8 in 4 ft to 4°.

3.3 Plan Curve

To accommodate plan curvature of the bridge, the front legs of the gantry needed to be moved laterally ("sideshifted"). The Safe Operating Procedure stated that a stress-relieving sequence was required at the rear legs after this sideshifting, to relieve the induced horizontal forces at the rear legs of the trusses. The procedure involved the sequential raising and lowering of individual leg components of the four-legged rear-leg structural system. Testimony revealed that this stress-relief procedure did not take place.

3.4 Water in the Underbridge

There were reports that water could collect in the underbridges. We inspected the underbridge of LG1 and observed water trapped between the partial height transverse diaphragms. This water likely leaked in from coped areas in the top flange plate. The water caused staining of the interior plate.

We also noted similar staining from our inspection in the storage yard of the underbridge of the collapsed LG2. See Photo 5. Based on the staining, we believe that the additional weight of water to the underbridge was approximately 0.6% of the total underbridge weight.



Photo 5. Water in the underbridge and staining indicating typical water level.

4. FAILURE SCENARIOS

We reviewed a number of failure scenarios that we developed based on comments from those involved and on our site observations. We correlated our reviews and analyses of these scenarios with our site observations and measurements in developing our final opinions on the most probable cause of the collapse.

4.1 Improper Function of the Controller

Each launching gantry has a PLC that has software to connect the operator's controls to the mechanical system of the gantries. There were reports of programming problems or discrepancies between the PLCs of the two launching gantries. The PLC for LG2 was obtained and the downloaded software was made available for review. No significant difference in the software of the controllers was found.

4.2 Structural Failure

We created an analytical model of the launching gantry to determine forces at various stages of the operation. The analytical load cases for the launching gantry model included the following:

a) The sequence if the manufacturer's Safe Operating Procedure had been followed.

b) The sequence, as described above, that we believe was undertaken by the contractor.

c) The above sequence including the effect of the underbridge possibly positioned at full launch extension with water load.

Five key components of the steel structural system of LG2 were fractured after the collapse. We evaluated the adequacy of each of these under the demands resulting from the load cases listed above. A metallurgist expert also examined the fracture surfaces and found no anomalies that would indicate material weakness or metal fatigue.

In each case, we determined that the steel component should not have yielded or fractured under the operating loads. Further, all applied stresses that we calculated were well below the allowable stresses used in the design of the gantries. Hence, it did not appear that structural failure induced the collapse.

4.3 Overall Structural Instability

The moving components of the gantries – the trusses and the underbridge – were to be sequentially anchored to and released from the bridge structures. They were propelled forward by mechanisms that push or pull against the bridge. At the same time, they rested partially on legs that did not transmit longitudinal forces between the gantry structures and the bridge. Under these circumstances, there existed potential that positioning operations could induce instabilities in the gantry structures.

4.3.1 Underbridge Launch

A witness said he observed the underbridge moving north during the process of the collapse. Gouges, scrapes, and the final resting places of the trusses and the underbridge confirm that the entire gantry structure moved north during collapse.

One scenario we investigated to evaluate the reasons for this movement was the possibility that the underbridge, with added water, when moved to its full extent in the north direction on the cantilever of the trusses, caused overall instability of the structure by lifting the rear legs of the trusses. For this analysis, we reduced the beneficial weight of the gantry (the weight that causes an increased downward reaction at the rear legs) and increased the detrimental weight of the underbridge by 10% (far greater than the additional water weight listed above).

This analysis revealed that the underbridge, at its full extent in the north direction, would not cause uplift at the rear legs.

Marks on the underbridge soffit confirm that the underbridge was not positioned too far forward at the time of the collapse. Scrapes and gouges show that the initial impact location of the underbridge with the concrete pier corresponds to the position to which the underbridge would fall if the rear legs of the underbridge had been positioned at the face of the central pier and both the trusses and the underbridge moved forward together from their pre-collapse location. See Photo 6.



Photo 6. Underbridge soffit with initial impact location visible to the north of the bolted splice with scraping from subsequent sliding down damaged edge of concrete pier. (North is to the left of the image.)

4.4 Horizontal Anchor Rods not Damaged

As seen in Photo 2 above, the horizontal anchor rods on the north side of Pier 13 were not damaged even though reports indicated that the rear legs of the underbridge had been moved rearward over the anchor rods at the start of collapse. We needed to understand how the underbridge could fall away from these anchor rods without damaging them if, indeed, the rear legs of the underbridge were against the spacers at the face of the pier.

During our site visits to the storage yard, we observed that the underbridge rear-leg holes that received the anchor rods had been enlarged by burning away portions of steel plates, apparently to make positioning the underbridge easier. From our site measurements and geometric analysis, we determined that the anchor rods were likely positioned near the center of the opening (shown as a white circle for scale in Photo 7 below). In this position, the rear legs of the underbridge would not have contacted the anchor rods during the collapse if the movement of the underbridge followed that of the trusses from which it was suspended, assuming the trusses first moved principally forward (moving the underbridge off the anchor bolts) and then downward as controlled by the northward tilting of the two-pinned front legs of the trusses.



Photo 7. The rear legs of LG2 underbridge on their side with a close-up showing burnt-out divider plate and a white circle representing the scale of an anchor rod.

4.5 Movement of Rear Legs of Trusses

If the rear-leg assembly of the trusses was not prestressed to the concrete deck in accordance with the manufacturer's Safe Operating Procedure, then there were several sliding and tipping interfaces at which movement could start. In addition, the actual loads on the rear legs were dependent on the following:

1) The existing slope of the deck. This provided lateral force in the south direction at the rear legs.

2) The incline of the front legs. This is unknown but likely was no further than 4° to the vertical based on worker interviews. Northward tilt would provide northerly-acting force on the rear legs.

3) The extent of transverse motion at the front legs. There was some transverse motion induced at the front legs to allow for the plan curvature of the bridge. We calculated the expected amount based on the road geometry and we correlated this estimate with observations of the positioning of the sideshifting mechanism of LG2 after the collapse. Because there was no stress relief at the rear legs (this process requires prestressing of the PT anchor bars), the transverse motion likely imposed longitudinal forces on the rear legs, in the northerly direction on one leg/stool and in the southerly direction on the other.

4) The coefficient of friction between possible slip surfaces. We used a lower, middle, and upper-bound range based on a literature review and correlated these values with site tests of the actual slip surfaces (to account for site grease and dirt, etc.).

5) Location of shims under the legs. It is possible that shims placed eccentrically under the rear legs of the trusses could contribute to tipping or

sliding. Since the actual position of shims could not be determined after the collapse, we reviewed both an offset and a centered position for the shims.

We studied the sensitivity of the stability response to the variables listed above, and found that the incline of the front legs and transverse motion of trusses with respect to the front legs had the greatest effect. We used these variables as the axes of stability charts, and plotted the influence of the other factors. We analyzed the results for tipping and slipping of the various rear-leg-stool interfaces and plotted these as bounding regions.

We determined that with the PT rods for the rear legs missing, the launching gantry could still have been unstable even if normal procedures were followed. However, we also determined that overall instability of unanchored rear-leg stools was effectively ensured if the front legs were out of plumb by 4° or if the underbridge was reversed into the pier with substantial force, thereby inducing a reactive forward force to the rear-leg stools. A sample plot for this latter scenario is provided below.

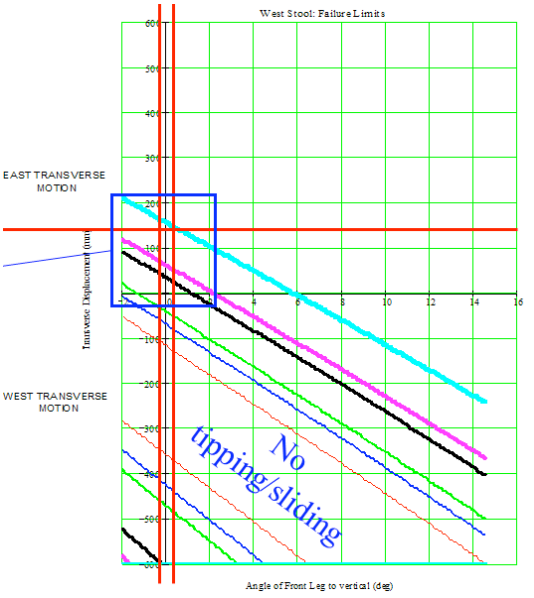


Image 3. Sample plot of bounding zones for west rear leg without prestress and force from reversing underbridge.

In addition, our calculations showed that if the manufacturer's Safe Operating Procedure had been followed completely (i.e., PT bars installed at rear-leg stools, front legs within vertical tolerance, etc.), then the overall gantry would have been stable.

5. CONCLUSION AND DISCUSSION OF LESSONS LEARNED

Most collapse investigations must address potentially-contributing conditions that cannot be determined exactly after the accident. In this case, certain facts were clear from our site observations and others were less certain. However, by bounding the unknown variables, we showed that this collapse occurred principally because the

movement of the underbridge was reversed into the forward face of the central pier while the required anchors for the rear legs of the trusses were missing.

From a construction-safety perspective, probably the most important lesson to be learned from this disaster is that well-developed construction procedures, based on rigorous considerations of structural stability and performance of complex equipment such as large cranes and gantries, should not be violated without careful consideration of the consequences. In this case, it seems that the contractor misunderstood that the PT bars stabilized the entire gantry against unrestrained longitudinal movement, rather than functioning simply as "hold-down" devices. In fact, the PT bars were part of an interrelated, multi-component structural system for operating the gantries in a way required to build a new bridge that had significant horizontal curvature. The sideshifting of the trusses to accommodate this curvature resulted in changes to vertical and horizontal forces in the individual rear legs and stools, and the bridge slope potentially caused longitudinal forces, as did moving and seating the underbridge. These behaviors might not be intuitively apparent without in-depth evaluations. The elimination of these anchors, which were critical to the resistance of longitudinal forces, and the failure to relieve locked-in horizontal forces after sideshifting caused instability due to sliding and overturning of the rear-leg stools when the underbridge was reversed back into the central pier. The movement of the stools inevitably resulted in the global instability and collapse of the entire gantry system, as the two-pinned front legs of the trusses tilted forward.

6. AFTERWORD

Following its investigation, the federal Occupational Safety and Health Administration (OSHA) initially cited the contractor, resulting in a fine of $280,000 (i.e., the maximum fine of $70,000 for each of four cited safety violations related to the failure to anchor the rear-leg stools) (OSHA, 2005). OSHA subsequently reached a settlement with the contractor and released a Safety and Health Information Bulletin highlighting "the hazards associated with deviating from the manufacturers [*sic*] guidelines on the use of overhead launching gantry cranes" (OSHA, 2006).

Following additional operational problems with a modified version of LG1, and at the insistence of the Ohio Department of Transportation, the contractor abandoned the self-launching gantry system and completed the construction of the approach spans using alternate methods. The I-280 Veterans' Glass City Skyway bridge opened to traffic on 24 June 2007, approximately twenty-two months after the original accelerated-construction-completion date.

7. REFERENCES

Bonzon, W.S. (2008). "Toledo's I-280 Veterans' Glass City Skyway: A Precast Concrete Landmark Bridge." *ASCE 2008 Structures Congress*, Vancouver, Canada.

OSHA (2005) Region5 News Release: 05-851-Chi dated May 26, 2005, "OSHA, Fru-Con, Settle Citations Issued Following Maumee River Bridge Collapse."

OSHA (2006) Overhead Launching Gantry Crane Safety and Health Information Bulleting. SHIB 05-01-2006.

Vulnerability Assessments of Structural Frames for Critical Facilities

William L. Coulbourne, P.E. M.ASCE

Director, Wind and Flood Hazard Mitigation, Applied Technology Council, 19266 Coastal Highway, Unit 4, #19, Rehoboth Beach, DE 19971, (703) 850-2891, FAX (302) 227-7652, email: bcoulbourne@atcouncil.org

ABSTRACT

There currently is no peer reviewed or broadly accepted protocols for conducting vulnerability assessments on the structural frame of buildings. This lack of protocols and lack of uniformity in vulnerability assessments is particularly important when the building is located in an area that might be subject to a natural hazard event such as a hurricane, a tornado, an earthquake or a flood. The design firm conducting the assessment is required to determine what might constitute a vulnerability based on their knowledge of the building, the hazard, or the owner's stated operational intent during or after any or all of these potential hazards.

The vulnerability of the structural frame of a critical facility (or any other building) depends on:

- Age (which influences the codes and standards that were available at the time of design)
- Quality of design and construction
- Type of construction (wood, concrete, steel, masonry or combinations of these and other materials)
- Risk to the structural frame from events such as an earthquake, a hurricane or a tornado, or from a man-made hazard such as a bomb blast
- Number and extent of past modifications to the building
- Deterioration (corrosion decay, termite damage)

These issues are crucial in understanding how vulnerable any particular building is to an unexpected load (i.e. hurricane or bomb) or to an expected load but one that has not ever occurred or not occurred recently. These issues are very important for the vulnerability assessment team to understand before they can state with some confidence that the building that is being assessed can be expected to perform in some stated manner when future catastrophic events might occur.

This paper will explore what a vulnerability assessment protocol for the structural frame should include, how a standardized protocol would be helpful to both the engineering profession and the building owners, and how such a protocol might reduce potential liability and misunderstandings with owners or future building buyers if a "standardized gage" could be developed that would give an owner a comparative basis for understanding the condition of the subject building vs. the condition of others within the use type (critical facilities) or construction type (wood, concrete, steel, etc.).

THE NEED FOR A STANDARDIZED PROTOCOL

There is currently no standardized method for evaluating existing buildings that are subject to high winds. This lack of a standardized evaluation method requires engineering professionals to create a method for evaluating an existing building each time a building evaluation is needed. When this is done on a project-by-project basis, there is no assurance that the evaluation method will adequately communicate how the building will perform during a high wind event, and there is no consistency between evaluations and approaches.

Most buildings that might be evaluated for performance during a high wind event are likely to be used for health care (such as nursing homes, hospitals, assisted living centers), shelters (for hurricane or tornado evacuations), government (including emergency operations centers, police and fire stations), or large or tall buildings used for hotels or office occupancies that are being sold or converted to different uses. New buildings must be designed to current building codes which for the types of structures mentioned also include being designed for wind loads in accordance with ASCE 7 (with some of these buildings being modeled and tested in a wind tunnel). Existing buildings can be modeled and pressures determined by wind tunnel testing, but in order to determine a building response to the wind, some method of analysis of the existing structure and building envelope still is necessary.

A protocol does exist for conducting evaluations of buildings for seismic hazards (ATC 14, FEMA 310) and this protocol provides the user with a "script" to follow for conducting an evaluation and the owner can be assured that the methodology used for the evaluation has been peer reviewed and tested by experts in the engineering discipline most appropriate for the hazard. This same peer-reviewed methodology needs to be created for high winds.

In many cases, the expected performance of a building in a high wind event is determined by comparing the building construction to the requirements of the current building code. Given the building code defines a minimum set of criteria, this evaluation standard is frequently inadequate to determine more precisely the expected performance of any particular building. Some residential and commercial buildings built prescriptively in accordance with the code might perform closer to expected because there is often little extra load capacity in these types of buildings given their use and the prescriptive nature of the codes. For larger, more structurally robust buildings, the comparison of high wind pressures to the capacity of the building is not a sufficient measure of expected performance. The development of the wind design standard currently in use (ASCE 7 *Minimum Design Loads for buildings and Other Structures*) over the last 15-20 years has seen significant changes occur in the way we determine wind pressures on buildings. These changes have modified our wind design practice substantially and these changes should have improved the performance of our buildings as well.

WHAT SHOULD BE INCLUDED IN AN ASSESSMENT?

Owner Performance Requirements

The starting point for a vulnerability analysis of the structural frame should be the owner's performance expectations. These expectations will vary with defined building use and importance to the community for service during a high wind event. The International Code Council (ICC) has a 2009 Performance Code for Buildings and Facilities with a suggested matrix of damage levels for various performance groups and for a series of event magnitudes (re-created from the 2009 ICC Performance Code as Table 1). The damage levels are defined as mild, moderate, high, and severe and each of these levels is defined in the code. The performance groups are the same as the occupancy groups in ASCE 7 (now called risk groups). The magnitude of the event is defined as small, medium, large and very large and the Mean Recurrence Intervals (MRI) for these various levels for various loads (both ordinary loads such as live and dead loads and extraordinary loads such as explosions or natural hazard loads) is presented in Chapter 5 of the code titled Stability and shown below as Table 2.

Table 1. Expected Performance Levels (per 2009 ICC Performance Code)

		Increasing Level of Performance → Performance Groups			
↓	Event Magnitude	Performance Group I	Performance Group II	Performance Group III	Performance Group IV
	Small	Moderate	Mild	Mild	Mild
	Medium	High	Moderate	Mild	Mild
	Large	Severe	High	Moderate	Mild
	Very Large	Severe	Severe	High	Moderate

Table 2. MRI for Various Event Magnitudes

Event Magnitude	MRI (yrs.) for Environmental Loads of Various Event Magnitudes					
	Flood	Wind	Snow	Earthquake	Ice	Rain
Small	100	50	25	25	25	25
Medium	500	75	30	72	50	50
Large	As determined	100	50	475	100	100
Very large	As determined	125	100	2475	200	100

The robustness of the building design will be largely governed by the types of events that are expected and by the magnitude of the event determined from the MRI. The wind event magnitudes used in the ICC Performance Code are highlighted in Table 2. It should be noted that the very large event of 125 years MRI does not approximate the ultimate wind speeds in ASCE 7-10. The ultimate wind speeds in ASCE 7-10

represent 1700 year MRI for critical facilities and depending on building locations, have a range of speeds from 120 mph to 200 mph. The discrepancy between these event magnitudes must be discussed by the owner and the design team.

Building Performance Expectation

The predicted building performance during a high wind event is a function of:

- Age
- Quality/robustness of design
- Quality of construction
- Building materials
- Building code used for construction
- MRI used for design
- Condition
- Types and/or number of changes to the building over the building life

The expectation of performance for these attributes could be assumed to follow linearly from assumed damage if built today under the current IBC. For any attribute likely to increase performance, an addition would be added to a base score, for any attribute likely to decrease the performance a subtraction would be taken from a base score.

The building age and code used for construction can sometimes be used interchangeably except when no building code has been enforced. Significant building code changes related to wind design occurred approximately in 1960, 1978, 1987, 1995, and 2000 with the initial publication of the International Building Code (IBC). Prior to the 1980s, the model codes used the same uplift pressure throughout the roof area with no uplift pressure increase for perimeters and corners. Uplift pressures on overhangs were not considered by model codes until the 1990s. Building age could be assumed to affect performance approximately the same the building code changes would affect performance. The base building age and building code reference could be taken as the year 2000.

Building materials can be used as a proxy for performance if sufficient detail is included about the many ways various materials perform in high wind events. The materials used in the structural frame listed below are in increasing order of likely damage from a high wind event:

1. reinforced concrete
2. reinforced masonry
3. prestressed or post-tensioned concrete (if tendons fully grouted or attached)
4. precast concrete (if connections to other load path elements are strong)
5. steel moment or braced frame
6. light gage metal frame
7. wood
8. unreinforced masonry

In addition to the primary frame, an important component for wind design is the lateral bracing system and the bracing systems below are in approximate order of increasingly likely damage to the bracing:

1. concrete moment frame
2. steel moment frame
3. reinforced concrete shear walls
4. steel bracing (cross-bracing)
5. wood shear walls
6. unreinforced masonry shear walls (infill walls)

The MRI used in the design is another way to determine robustness. The longer the return period used in design, the better the building is expected to perform under small magnitude, frequent events, and the greater damage is expected from the larger, less frequent event. The difficulty is determining what the design MRI actually is. If new wind speed maps from ASCE 7-10 are used, the MRI will be clear since these maps are based on ultimate speeds and the MRI is noted on the map appropriate to the risk category of the building. For buildings built to other versions of ASCE 7, it is possible to assume an MRI based on the wind speed used and the building type. For buildings designed using building codes prior to the use of the ASCE 7 wind load standard, the conservative approach is to assume a design MRI of 50 years.

The actual condition of the building will have a significant affect on how the building performs in a high wind event. Old, but well maintained buildings with little evidence of material deterioration or corrosion in connections will perform better than a newer building with substantial amounts of deterioration or corrosion in important elements of the building. Condition could be rated on a continuum from poor to excellent as long as descriptions along the continuum were defined. These definitions are shown in Table 3 and might be:

Table 3. Definition of Building Conditions

Building Condition	Definition
Poor	Significant deterioration in materials and/or connections. Stress cracks might be evident in materials.
Fair	Deterioration evident in either materials or connections such that strength is affected. Condition of the building is such that retrofitting is required to recover strength.
Average	Condition represents normal wear and tear on the building materials and connections. Some deterioration and/or corrosion are evident in the structural elements.
Excellent	Materials are practically new in condition with no evidence of deterioration, corrosion, loss of strength or gaps in either the vertical or horizontal load paths.

The type and number of additions or changes that have been made to the building is an indicator of possible discontinuities between structural frames and buildings built to different standards over the years. Although a thorough analysis must be made of the effect of the additions to the overall performance, some aspects of newer additions can be beneficial to performance. For instance, a critical part of an operation may now occupy the addition, so expected performance for that operation is not improved with the addition. The older part of the building now may be considered sacrificial, and while this could affect insurance losses for a building, it might very well improve operational stability during and after a high wind event.

Another important affect on the building performance desired is the difference in building use now compared to the time of original construction. A building built originally for a critical function will more likely have a structural frame designed for more severe loading, especially if built within the last 15-20 years. A building built for a commercial use will not be as likely to be robust enough to resist the higher expected loads for a critical facility and will be more likely to require some level of retrofitting in order to resist the expected loads and meet the expected performance.

The Gap Analysis

A gap analysis must be completed that looks at the differences between the owner's expectations and the expected performance of the building during the wind events defined. Only after this analysis can we make reasonable assumptions about the impact to the owner from the design event. This analysis also may provide the owner with important information about the reality of his expectations if the gaps between required and expected performance is very large and costly to mitigate. This analysis might very well help discover alternatives to mitigation that would positively improve the performance while not completely eliminating damage.

DEVELOPING A COMPARATIVE BASIS

The greatest advantage of having a methodology for evaluating existing buildings for a high wind event is that when all buildings in a portfolio are subjected to the same methodology, the owner will be able to easily determine the relative condition and expected performance of each building compared to the other buildings. This comparative analysis will make it easier to determine which building assets need the most capital improvement funds, which services might need to be relocated to other, better performing buildings, or which services need to either be moved to another site or discontinued as is, since the required performance for that building and those services can not economically be achieved within the configuration of space in the owner's portfolio.

Even with a methodology in place, there must be a way developed to be able to compare properties. For each building, the expected damage level before mitigation would have to be determined. Those damage states would be mild, moderate, high and severe. In order to achieve the required performance level, the extent of building refurbishment must be determined and thus the cost for bringing the building into the

expected range of damage such that the performance level can be achieved. The comparison could thus be developed looking at expected performance, expected damage without mitigation, and the cost to repair to reduce the damage to the level considered acceptable to meet the required performance.

Example

A building built in 1988 is located in Charleston, SC and is to be purchased by the local government as a judicial center. The building is four stories tall, is located in an Exposure B wind environment, the structural frame is steel with an exterior of concrete panels. The roof is flat with a roof deck of reinforced concrete on a metal deck. All windows are vulnerable to windborne debris. The building condition is considered good; there was some roof damage experienced during the 1989 Hurricane Hugo event. The design wind speed for Risk Category III buildings in ASCE 7-10 is 157 mph at a MRI of 1700 years or 114 mph at a MRI of 100 years. The building is shown as Figure 1.



Figure 1. Example Building in SC

The vulnerability assessment would provide a screening mechanism to determine how much further the analysis needed to go before a conclusion could be reached about the possible purchase of this building for its intended use as a judicial center. Each of the screening steps would be assessed against the "norm" where the 2000 IBC is used as the code standard and the construction from 2000 used as the building standard when the construction was specifically for a critical facility.

Table 4. Vulnerability Screening Matrix

Evaluation Metric	Comparison to norm									
1.Design MRI	25	50	75	100	125	500	700	1000	1700	2000
2.Age	1960		1978		1987		1995		2000	
3.Building materials	WD	URM	LGS	STL	PC-PTC		RM		RC	
4.Building code year	1960		1978		1987		1995		2000	
5.Condition	Poor		Fair			Average			Excellent	
6.Number of changes	Many		Some			Few			None	

Table 4 is a possible vulnerability screening matrix for the example building. The elements that apply to this example building are highlighted. The matrix for all six

metrics is in a continuum of "worst to best" along the rows. Since the design considered wind speeds for a 100-year MRI and the building age and building code used in design are more than a decade older than the assumed "norm" of the year 2000, this suggests a steel frame building possibly susceptible to some wind damage. Given the age, the steel frame type and the vulnerability of the building envelope to breakage from windborne debris, this suggests further analysis would be required to sort out the details of possible structural frame failure that could be caused by high winds. It is assumed in this existing building that most if not all of the structural frame is covered over with finish materials and is not accessible for inspection without some level of destructive testing.

There are many aspects to the detailed analysis and any vulnerability assessment protocol must provide some direction on what types of structural details to investigate and what the findings will suggest in terms of likely performance. Those structural details would include but not be limited to:

- roof-to-wall connection strength to determine uplift resistance
- roof deck and roof framing uplift resistance (see Smith 2011 paper on roof covering and assembly vulnerability assessment issues)
- window and door glazing resistance to windborne debris
- exterior wall resistance to both in-plane and out-of-plane bending from wind loads and to windborne debris
- structural frame resistance to lateral loads if exterior walls do not provide this resistance
- stiffness of roof and floor diaphragms

The Gap Analysis

After conducting a screening analysis for building vulnerability to high winds, the owner and the design team need to conduct a "gap analysis" of the desired performance and the likely performance based on the screening and decide the most appropriate next steps.

In the example above, if the performance group is Group III (a critical facility use) and the event magnitude is very large (greater than a 100-year MRI wind event), then the expected damage is **High.** The design team knows that the design event for this type of facility should be the ultimate wind event or the 1700-year MRI event. Given the actual design, the team must evaluate the differences in expected loads/pressures vs. the expected actual resistances in connections, stresses and windborne debris resistance. Using this gap information, the design team then must develop a set of retrofitting strategies that would reduce the vulnerability of the structural frame so that the expected performance level could be achieved when the design event occurred.

BENEFITS OF "STANDARDIZED" APPROACH

Make Building Comparisons Meaningful

A standard approach to the problem of conducting vulnerability assessments on critical facilities is that no matter where the facility is, no matter what the possible hazards are and no matter what the construction type or the condition of the building, design professionals, lenders, insurance agents, and owners would all be able to assess and compare one facility to another when those facilities had been evaluated using the same methodology. The terminology in the reports, the techniques used for assessment, the comparative results of required mitigation and the way the owners articulated performance criteria would all be substantially the same, aiding in a much clearer comparison of various facilities.

Reduce Liability

Using a peer-reviewed methodology for determining high wind vulnerability to critical facilities would potentially reduce the structural engineer's exposure and liability. When the professional uses a methodology they 'made up' based on sound technical information but which together constitutes a procedure that has not been industry tested, the potential liability increases because the procedure has been developed by the lone practitioner.

There is a building inspection methodology adopted by ASTM (ASTM E-2018-08) that provides a standardized basis for conducting building inspections. This ASTM standard does not go very far into how the inspection should be conducted. The stated use of the standard is to obtain a baseline Property Condition Assessment (PCA) using a walk-through survey and reporting on that baseline condition using a report developed by the consultant. A review of architectural or engineering drawings of a building is not a requirement for the consultant under this ASTM standard. The PCA is focused on observable deficiencies and the report is to focus on the deficiency and the recommended remedy. It is generally considered out of scope to prepare calculations to determine a systems adequacy with any specific design requirement.

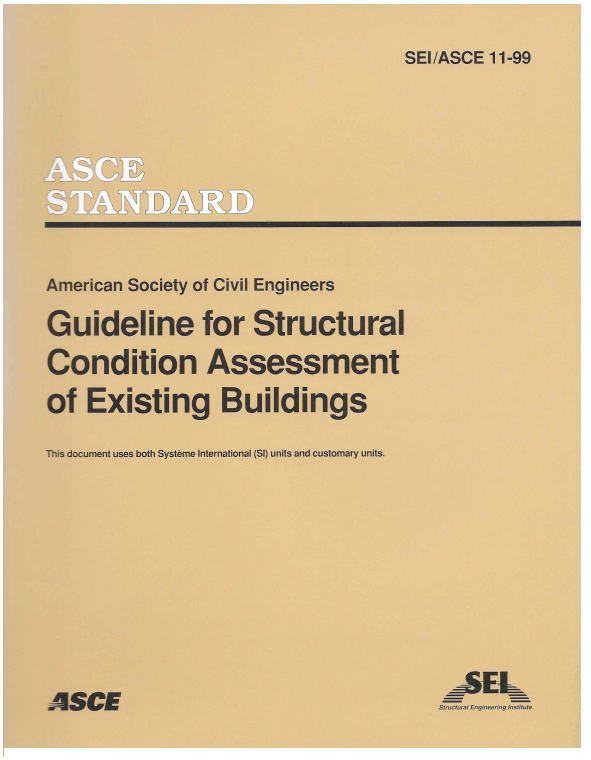


Figure 2. Cover of SEI/ASCE 11-99

SEI/ASCE 11-99 is a Structural Condition Assessment standard supported and published by the Structural

Engineering Institute of ASCE (cover shown as Figure 2). This standard focuses on the structural condition of the building and includes buildings constructed of concrete, steel, masonry and wood or a combination of these materials. The recommended assessment procedure includes a review of the available documentation on the building including drawings and specifications if available, conducting the site inspection, and performing an analysis of the structural elements of the building that compares the expected loads developed if the performance criteria are met with the expected resistance of the structural elements.

Included in the structural analysis is an investigation of the vertical and lateral load paths and the capacity of the elements of those paths to resist the loads expected when the performance level is met. There are preliminary and detailed assessment procedures included but both cover the review of documents, the inspection and the analysis of information – the only difference is in the level of detail required for each assessment step.

There is no specific requirement that the assessment process include the effects of high winds on the building. The procedure for the detailed assessment specifically discusses developing performance criteria that could include drift and deflection limitations which somewhat address issues caused by high winds. The balance of the standard deals with assessment techniques and issues relevant specifically to the various materials that are covered.

Conclusion - Develop an ASCE Standard

This author recommends that ASCE support the development of a standard for the evaluation of critical facilities subject to high winds. The development of such a standard would be viewed by the industry of building assessment professionals as one without bias. It would be a peer reviewed document from the nation's leading experts in various wind engineering issues and building design practices. It would have credibility with courts, insurance and real estate professionals and with the practice of structural engineering.

REFERENCES

American Society of Civil Engineers, ASCE 11-99, *Guideline for Structural Condition Assessment of Existing Buildings*, Reston, VA, 2000

American Society of Civil Engineers, ASCE 7-10, *Minimum Design Loads for Buildings and Other Structures*, Reston, VA, 2010

American Society of Testing Materials, ASTM E 2018-99, *Standard Guide for Property Condition Assessments: Baseline Property Condition Assessment Process*, West Conshohocken, PA, 1999

Applied Technology Council, ATC 14, *Evaluating the Seismic Resistance of Existing Buildings*, Redwood City, CA, 1987

Applied Technology Council, Structural Engineers Association of Washington, *SEAW Commentary on wind code provisions*, SEAW/ATC 60, Redwood City, CA, 2004

International Code Council, *ICC Performance Code for Buildings and Facilities*, Country Club Hills, IL, 2009

Federal Emergency Management Agency, FEMA 310, *Handbook for the Seismic Evaluation of Buildings – A Prestandard*, Washington, DC, 1998

Federal Emergency Management Agency, FEMA 424, *Design Guide for Improving School Safety in Earthquakes, Floods, and High Winds*, Washington, DC, 2004

Federal Emergency Management Agency, FEMA 543, *Design Guide for Improving Critical Facility Safety from Flooding and High Winds*, Washington, DC, 2006

Federal Emergency Management Agency, FEMA 577, *Design Guide for Improving Hospital Safety in Earthquakes, Floods and High Winds*, Washington, DC, 2007

Wind Vulnerability Assessment of Roof Systems and Rooftop Equipment for Critical Facilities: A Preliminary Protocol for Design Professionals

Thomas L. Smith, AIA, RRC[1]

[1]TLSmith Consulting Inc., 16681 Boswell Road, Rockton, IL 61072; PH (815) 629-2455; email: tlsmith@hughes.net

ABSTRACT

This paper presents a preliminary protocol for assessing the wind vulnerability of roof systems and rooftop equipment on critical facilities. Such facilities include emergency operations centers, fire and police stations, hospitals, jails, nursing homes, power plants, schools, water supply and treatment plants, and other buildings that are essential for the delivery of vital services or protection of a community.

Roof systems and rooftop equipment are key building elements that are frequently damaged during high winds. Leakage from damaged roofs or rooftop equipment has interrupted numerous facility operations, and many critical facilities have been forced to evacuate due to roof leakage. By identifying wind vulnerabilities, mitigation efforts can be undertaken to avoid future damage and disruption of services. The preliminary protocol can be used by design professionals to systematically guide their assessment of these building elements.

INTRODUCTION

A design firm conducting a wind vulnerability assessment on a critical facility is tasked to determine what might constitute a vulnerability based on their knowledge of the building elements, the wind hazard, and the building owner's stated operational intent during and/or after a wind event. However, currently there is no comprehensive peer-reviewed or broadly accepted protocol for conducting such an assessment. Guidance provided by a quality vulnerability assessment protocol would assist design professionals with their assessment work and enhance their understanding of the expected wind and wind-driven rain resistance. Findings from vulnerability assessments can also be used by entities awarding grants for mitigating existing building deficiencies. By better understanding vulnerabilities, the effectiveness of funded mitigation measures can be improved.

If the assessment identifies deficiencies, they can be prioritized and scheduled for remediation. Mitigating deficiencies avoids costly wind damage and interruption of needed services provided by critical facilities. FEMA P-424, 543 and 577 recommend performing a vulnerability assessment on all critical facilities that are older than 5 years. If the facility is located in a hurricane-prone region (as defined in

ASCE 7), the assessment is recommended regardless of building age. These publications note that it is particularly important to perform assessments on facilities located in hurricane-prone and tornado-prone regions.

Mitigation efforts can be very ineffective if they do not address all items that are likely to fail. Therefore, to help ensure that all significant vulnerabilities with respect to wind, wind-borne debris (missiles) and wind-driven rain are identified, the assessment should include the structural system and the entire building envelope. For facilities located in hurricane-prone regions, ramifications of interruption of municipal utilities should also be evaluated. FEMA P-424, 543 and 577 provide a general checklist for performing assessments, and they provide examples of common vulnerabilities. Coulbourne (2011) and Beers (2011) provide further guidance on vulnerability assessments of structural and glazing systems. Development of additional guidance for assessing non-load-bearing walls and wall coverings is needed.

If a building owner has several facilities (such as a school district or large hospital complex), budget constraints may prohibit timely evaluation of all of the facilities. In this case, FEMA P-424 recommends prioritizing facility evaluation, based on the owner's needs and perceived vulnerabilities of the facilities.

Roof systems and rooftop equipment are key building elements that are frequently damaged during high winds (see Figure 1). The wind vulnerability of these elements depends on a variety of factors, including adequacy of their design and installation, and material degradation over time. The following is a preliminary protocol for conducting wind vulnerability assessments of roof systems and rooftop equipment.



Figure 1: The roof membrane on this new police station became detached shortly before the station was to be occupied. The station is located in the Midwest. It was damaged by winds that were well below the design wind speed. A vulnerability assessment has the potential to find problems so that they can be corrected before damage and interruption occurs.

GENERAL

Professional judgment: Accurately assessing the wind resistance of existing roof systems and rooftop equipment is very difficult (in part due to lack of a comprehensive protocol and a severe lack of field test methods). Accordingly, good professional judgment is vital for a quality assessment. The design professional(s) performing the assessment should be experienced with the type of roof system(s) on the building being evaluated.

Building owner's performance expectations: As a starting point for the assessment, a discussion should be held with the building owner to determine their expectations regarding desired building performance. See Coulbourne (2011) for further discussion. As part of the discussion with the owner, also discuss limitations of a vulnerability assessment (see DATA ANALYSIS AND REPORTING).

General guideline: ASCE 30 is a general guideline for assessing the condition of building envelopes. It includes information on professional service agreements, assessment procedures, evaluation of findings, and reporting. It is recommended that the design professional(s) performing the assessment be familiar with this guideline.

Level of assessment: This preliminary protocol identifies two levels of assessment. For some buildings, a Level 1 assessment will be sufficient. For other buildings, both a Level 1 and a Level 2 assessment should be performed. The elements of these two levels of investigation and the need for a Level 2 assessment are as follows:

- **Level 1:** This assessment consists of the following: 1) review of the historical file (i.e., as-built drawings and specifications, submittals, previous leakage and repair reports), 2) discussion with building owner personnel who are familiar with the roof to determine if it is leaking and to obtain historical information that is not in the file, 3) perform a field investigation and 4) provide a report. (Note: Normally a report is prepared prior to beginning a Level 2 assessment. However, an initial verbal report may be given on Level 1 findings. Written findings can subsequently be included in a final report that addresses both Level 1 and 2.

  This assessment should address the general condition of the roof and rooftop equipment (i.e., remaining service life). For guidance in making this assessment, see CIB/RILEM (2003) and Smith (2001). If the roof is leaking, refer to ASTM D 7053 for determining and evaluating the cause of the leakage. If the Level 1 assessment reveals that the roof is at or near the end of its useful service life, it should be scheduled for reroofing. See FEMA P-424, 543 and 577 for reroofing recommendations.

  The Level 1 assessment should also address wind resistance as discussed in the SPECIFIC RECOMMENDATIONS section below.

- **Level 2:** If the Level 1 assessment reveals that the roof has several more years of useful service life, then a Level 2 assessment is recommended for those buildings located where the basic wind speed is greater than 120 miles per hour (mph).[1] However, many of these building owners will be unable to afford a Level 2 assessment. Although all critical facilities are valuable assets, some are more critical than others. For example, a hospital is a more valuable asset than is a clinic. For the very important buildings, funding a Level 2 assessment is prudent because a Level 2 investigation will provide a more accurate vulnerability assessment.

  A Level 2 assessment consists of the following: 1) perform field uplift testing (for those systems where a test method exists), 2) perform destructive observations and 3) provide a report. For those systems that have insulation below the roof covering, a nondestructive evaluation (NDE) to check for moisture is also recommended. In some instances, it is prudent to perform the NDE as part of the Level 1 assessment. For further information about NDE, see Smith (2001). In addition to the techniques discussed in that publication, electronic vector mapping is also available.

  The purpose of the Level 2 assessment is to validate wind-resistance information provided by the as-built drawings and specifications and submittals, or to obtain wind-resistance information when documents are not available.

SPECIFIC RECOMMENDATIONS

The following items are recommended as part of the Level 1 assessment:

- Design uplift pressures: Determine what design uplift pressures the existing roof system was designed for. If this information is not identified on the drawings, specifications, or the submittals, check to see if a roof membrane manufacturer's warranty was issued. If so, check with the warrantor to see if they have this information. If not, find out what building code or standard would have likely been used to determine the original design uplift pressures and then calculate the field, perimeter and corner loads in accordance with that code or standard. Also calculate the design loads based on the current edition of ASCE 7 and compare the original design loads with current loads.[2] (Note: As part of the structural vulnerability assessment, the original and current design loads for the roof deck and deck support framing should also be determined.)

- Roof system uplift resistance: Check the drawings, specifications, submittals or warranty to determine if an uplift resistance rating was specified (e.g., FM 1-60).

[1] The 120-mph basic wind speed is based on ASCE 7-10, Risk Category III and IV buildings. If ASCE 7-05 or an earlier version is used, the equivalent wind speed trigger is 90 mph.
[2] If the building is in a hurricane-prone region, FEMA P424, 543 and 577 recommend using 1.0 for the directionality factor for the roof system.

If so, compare that rating with the rating that would be required based on current design loads. If the original rating is significantly less than what would be currently required, the existing system will need to be enhanced (if possible) or replaced, or the system will present a residual risk of failure. (Note: As part of the structural vulnerability assessment, the resistance of the roof deck and deck support framing should also be determined and compared with current criteria.) Also, if FM *Loss Prevention Data Sheet 1-29* was used to adjust fastener or adhesive ribbon spacings at corners and the perimeter, be aware that prior to the 2006 revision of 1-29, a safety factor of 1.5 was used. In 2006, the safety factor in the corners and perimeter was increased to 2 so that it would match the safety factor of 2 that had been used in the field of the roof.

If the drawings, specifications, or submittals reference a test method, check to see if there have been significant changes to the test method that would negatively affect the uplift test results. For example, if the existing roof system is a mechanically attached single-ply system that was installed around 1990, and the submittals indicate that it had an FM 1-60 rating, then the system was tested on a 5' x 9' apparatus. However in 1993, the test method was revised to require a 12' x 24' apparatus for most mechanically attached single-plies. The apparatus size was changed because it was determined that the smaller frame typically over-estimated the load capacity of the system.

Also check to see if the test method that was originally used is what is currently recommended. For example, metal roof systems can be tested in accordance with UL 580 or ASTM E 1592. ASTM E 1592 is generally recommended because it gives a better representation of the system's uplift resistance. Another example pertains to asphalt shingles, which can be tested in accordance with ASTM D 3161 or by a method referenced in ASTM D 7158. The method referenced in D 7158 is the current state of the practice, and is believed to provide a better representation of shingle wind resistance.

- Nailers and equipment curbs: Check the drawings and specifications to determine if attachment criteria were given for nailers that occur below edge flashings and copings, and for rooftop equipment curbs and stands. If so, determine if the specified attachment is sufficient to resist current uplift loads (and over-turning loads for curbs and stands), using a safety factor of three (as recommended in FEMA P4-24, 543 and 577).[3] (Field assessment of nailers, curbs and stands is addressed in the Level 2 recommendations below.)

- General field assessment: As part of the field investigation, visually observe the roof for signs of distress and detachment, such as tented fasteners and large blisters. Walk the entire perimeter of the roof (make two trips if the width of the perimeter zone exceeds 8'). Also walk the field of the roof at intervals not

[3] Although a safety factor of 2 is typically used for roof systems, a safety factor of 3 is recommended for edge flashings, copings, nailers and curbs because of wind loading uncertainties and the relative importance of these elements and consequences of their failure.

exceeding approximately 20'. With each "footfall," be sensitive to a change in softness of the substrate, which could indicate wet insulation or displaced materials. Also be sensitive to indications of lack of attachment of adhered roof membranes and insulation boards.

- Field assessment of mechanically attached single-ply membranes: Spot check fastener row spacing and spacing of fasteners along the rows. This can be accomplished in a number of ways: 1) by using a magnetic or electronic stud finder, 2) by looking for dust or debris at fastener plate depressions, 3) by feeling or lightly scrubbing the surface of the membrane over the fastener line. Spot checks should be made at each corner,[4] at the perimeter and in the field of the roof. Also spot check for fastener plate bending by feeling the membrane at plate locations. Normally it is sufficient to check plate bending at just the corner areas. Where plate bending checks are made, also carefully observed the membrane in the vicinity of the plate and the nearby seam. Look for fatigue-induced holes, cracks or tears.

  If the deck is steel, check to see if the fastener rows are perpendicular to the deck ribs. If the rows are parallel to the ribs, the decking may be susceptible to blow-off (see FEMA P-424, 543 and 577 for discussion).

- Field assessment of edge flashings and copings: For shop-fabricated units, check to see if the vertical flange is cleated. (For copings, check both vertical flanges.) If the vertical flange is face-fastened, check the fastener type and spacing. If the flange is not adequately face-fastened or if it is not cleated, the edge flashing or coping is quite susceptible to blow-off. Also, grab the bottom of the vertical flange with both hands and try to rotate the flange.[5] On copings, try to rotate both the inner and outer flanges. Perform this rotation test at each side of each corner,[6] and at a few locations along the perimeter. Weak edge flashings and copings will be easily detected by an experienced investigator. However, an edge flashing or coping may be very resistant to rotation and give the impression that it possess adequate wind resistance, when in fact it may not. A field test method (other than hand manipulation) to provide a more definitive evaluation of resistance does not currently exist.

  For pre-engineered edge flashings and copings, check to see if submittal data indicates wind resistance information. (Note: A safety factor of three is recommended for edge flashings and copings). To the extent possible, check to see if the units were installed in accordance with the submittal data. In addition, perform the above rotation tests.

---

[4] If the building has several roofs, it is usually not necessary to check all corners. Also, if the building is outside of hurricane-prone regions, usually it is sufficient to check the corner(s) that faces the prevailing wind direction.

[5] Appropriate safety precautions should be taken when performing rotation tests.

[6] See footnote 4.

For shop-fabricated and pre-engineered edge flashings, check to see if the horizontal flange was placed over the membrane and then stripped-in, rather than placed underneath the membrane. When the horizontal flange is underneath the membrane, it is unable to clamp the edge of the membrane, thereby making the membrane susceptible to lifting and peeling.

- Field assessment of gutters: Visually check the gutter to see if there is a mechanical connection or interlock between the gutter and gutter bracket. If the gutter is not connected or is inadequately connected to the brackets, the gutter is susceptible to blow-off. Also perform rotation tests as described above. For some tests, place a hand on either side of a bracket. For other tests, place both hands mid-way between two brackets. A field test method (other than hand manipulation) to provide a more definitive evaluation of resistance does not currently exist. Also evaluate gutter load path. The uplift and rotational wind load exerted on the gutter will be transferred to the wall, nailers or deck, depending upon the bracket design and attachment. A safety factor of three is recommended for gutters.

- Field assessment of parapet base flashings: For fully adhered base flashings, visually check for detachment. Also check for detachment by spot-slapping with the palm of the hand. For mechanically attached base flashings spot check fastener locations using one of the techniques described above for locating mechanically attached single-ply membrane fasteners. Also, if the base flashing is mechanically attached, but the membrane is fully adhered at the roof, ballooning of the base flashing has high potential to cause lifting and peeling of the roof membrane (as shown in Figure 1). Check to see if the base flashing is applied directly to brick. If so, the base flashing is likely inadequately attached due to the surface irregularity (i.e., lack of planar flatness) that is often associated with the roof-side of brick parapets). Regardless of base flashing type or attachment method, when performing checks, check each corner[7] area and check a few locations along the perimeter.

- Field assessment of ballasted single-plies: If the building is not in a hurricane-prone region and it has a single-ply membrane that is ballasted with aggregate, pavers or cementitious-coated insulation boards, check to see if the system (including parapet height) complies with ANSI/SPRI RP-4.

- Aggregate and lightweight paver surfacing in hurricane-prone regions: If the building has aggregate surfacing, lightweight pavers (i.e. those weighing less than 22 psf), or cementitious-coated insulation boards, FEMA P-424, 543 and 577 recommend replacing the roof system.

- Missile resistance: If the building is located in a hurricane-prone region, check to see if the roof system includes a secondary membrane that will avoid water

[7] ibid

leakage into the building in the event the roof membrane is punctured by missiles. If as-built drawings or submittals are not available, a test cut should be taken to determine roof system composition. Note: If the roof is sprayed polyurethane foam and of the thickness recommended in FEMA P-424, 543 and 577, or the roof is surfaced with concrete pavers weighing a minimum of 22 pounds per square foot (psf), then the foam itself or the pavers should provide adequate protection.

- Field assessment of drainage: If the building is located in a hurricane-prone region and the building has primary through-wall scuppers or roof drains, evaluate the potential for the scuppers or drains to become blocked by leaves, tree limbs and other wind-borne debris. See FEMA P-424 for guidance. Also refer to Sections 8.2 Roof Drainage and 8.3 Design Rain Loads in ASCE 7.

  Check to verify that secondary drainage is provided for all roof areas that have parapets or edge flashings on raised curbs.

- Field assessment of rooftop equipment:

  - Fans, HVAC units, relief air hoods and condensers: Check attachment of the equipment to the curb or stand. FEMA P-424, 543 and 577 provide attachment guidance. Note: Do not assume the dead load of the equipment is sufficient to resist the wind load. If wind resistance is only provided by the equipment dead load, perform wind uplift and over-turning load and resistance calculations to determine if the dead load is sufficient to resist the current wind load. As a qualitative evaluation, push and lift up on equipment. Equipment with weak or no attachment may be detected by an experienced investigator. However, equipment may be very resistant to movement and give the impression that it possess adequate wind resistance, when in fact it may not.

  - Fan cowlings: Where the basic wind speed is greater than 120 mph, check to see if the manufacturer specifically engineered the cowling attachment to resist the current design wind load, or check to see if the cowling has strap or cable tie-downs.

  - Exposed ductwork: Evaluate the wind resistance of the ducts and check to see if the ductwork is mechanically attached to supports that are anchored to the roof deck. Also, as a qualitative evaluation, push and lift up on the ductwork. Ductwork with weak or no attachment may be detected by an experienced investigator. However, ductwork equipment may be very resistant to movement and give the impression that it possess adequate wind resistance, when in fact it may not.

  - Flexible connectors between ducts and fans: Check the connectors for cracks or tears (which can allow water infiltration). If the building is located in a

hurricane-prone region, the flexible connectors may be susceptible to missile damage. See FEMA P-424 for guidance.

- Vibration isolators: If vibration isolators are used to support equipment, check to see if the isolators provide uplift resistance, or check to see if cables or straps are present to provide wind resistance.

- Boiler and exhaust stacks: Check adequacy and tautness of guy-wires. If guy-wires do not exist, check the stack's wind resistance.

- Equipment access panels and doors: Check adequacy of attachment. See FEMA P-424, 543 and 577 for guidance.

- Sheet metal hoods on HVAC units: Check adequacy of attachment. See FEMA P-424 for guidance.

- Natural gas and condensate drain lines: Where the basic wind speed is greater than 120 mph, check adequacy of attachment. See FEMA P-424 for guidance.

- Equipment screens: If screens occur around equipment, check adequacy of attachment.

- Antenna (communication mast): Check mast strength and adequacy of attachment. Also, if satellite dishes are mounted on the mast, try to determine if the mast was designed for the additional wind load that is transferred to the mast. See ANSI/TIA-222-G for guidance.

- Satellite dishes: Check adequacy of attachment. If wind resistance is provided by ballast (e.g., CMU or concrete pavers), perform calculations to verify the ballast is sufficient. In hurricane-prone regions, FEMA P-424, 543 and 577 recommend that dishes be mechanically anchored rather than ballasted.

- Lightning protection system (LPS): Spot check conductor connectors to verify that 1) the prongs engage the conductor, 2) the connectors are still anchored and 3) the connectors are approximately 3' on center. Also spot check the air terminals to verify that they are anchored. Where the roof is more that 100' above grade or if the building is in a hurricane-prone region where the basic wind speed is 135 mph[8] or greater, special attachment is recommended. See FEMA P-424, 543 and 577 for guidance.

The following items are recommended as part of the Level 2 assessment:

[8] The 135 mph basic wind speed is based on ASCE 7-10, Risk Category III and IV buildings. If ASCE 7-05 or an earlier version is used, the equivalent trigger is 100 mph.

- Uplift resistance testing: Field uplift testing in accordance with ASTM E 907 is recommended for built-up, modified bitumen[9] and fully adhered single-ply roof systems. It is recommended that a test be performed at each corner[10] area, at perimeter locations, and at least one test in the field of the roof. Note: This test method is not capable of evaluating the uplift resistance of the roof deck.

- Test cuts at leakage areas: If there has been a history of roof leakage, take 2' x 2' minimum test cuts down to the deck in the leakage area(s) to assess deck integrity. The number of cuts will depend upon several factors, including deck type, leakage history and extent of wet insulation. Where possible, the underside of the deck in the leakage area(s) should also be evaluated. Note: If the roof system is warranted, notify the warrantor before taking the cuts and have the repair performed by a roofing contractor authorized by the warrantor.

- Test cuts to evaluate deck attachment: Except for concrete decks, take 2' x 2' minimum test cuts down to the deck to check deck attachment. It is recommended that a cut be taken at each corner[11] area, at perimeter locations, and at least one cut in the field of the roof. See the note above regarding warrantor notification and repair.

- Destructive observations of nailers: To verify or determine the attachment of nailers that occur below edge flashings or copings, remove lengths of edge flashing or coping (which are typically 8' or 10' long) and membrane material so that the nailer fasteners can be observed. Remove at least two fasteners per length of edge flashing or coping to determine fastener type and length (embedment). It is recommended that one length of edge flashing or coping be removed at each corner[12] area, and at a few locations along the perimeter. See the note above regarding warrantor notification and repair.

- Destructive observation of equipment curbs and stands: To verify or determine the attachment of equipment curbs and stands, remove the base flashing / pitch pocket. See the note above regarding warrantor notification and repair. Note: Destructive observation of curbs or stands is relatively expensive. Considering that curb or stand failure is relatively rare,[13] this effort is typically reserved for those facilities that are particularly important and/or where the basic wind speed is very high.

DATA ANALYSIS AND REPORTING

[9] ASTM E 907 is not suitable for a modified bitumen system mechanically attached just at the seams.
[10] See footnote 4.
[11] Ibid.
[12] Ibid.
[13] Rare failure of curbs and stands may in part be due to weak connections between the equipment and the curb or stand. As more attention is given to attachment of the equipment, curb or stand failure may become more common, and hence suggest the importance of performing destructive observations to determine curb or stand resistance.

After completing a review of the historical file, performing calculations and the field investigation(s), the collected data need to be analyzed in the context of the building owner's expectation regarding desired building performance. Although unlikely, the analysis may reveal that no remedial work is required to meet the desired building performance. The analysis may reveal the need for relatively minor enhancements, or it may reveal the need to reroof. With all three scenarios, there may be acceptable residual risk that is deemed by the building owner to be too expensive to correct.

In reporting the Level 1 and 2 findings and analysis to the building owner, it is important to discuss limitations of the vulnerability assessment (see ASCE 30 for further discussion). As previously noted, a more accurate assessment will be provided by a Level 2 investigation. However, even with a comprehensive Level 2 investigation, the true vulnerability of the roof and rooftop equipment will not be known until actually tested by a real wind event. The assessment limitations are due in part to the severe lack of field test methods, and the fact that field testing and various field checks are performed at discrete locations. These tests and checks provide data on conditions and wind resistance at areas that were tested or checked. However, there is always the potential for an undetected anomaly that can lead to water infiltration. Accordingly, it is prudent for owners of critical facilities to have contingency plans in the event that leakage occurs. For example, if roof leakage begins to occur at a given location in a hospital, a pre-event plan should be available to the staff in that area that directs where their department should be relocated within the facility. A pre-event plan should also be available for evacuating the entire facility.

The report should recommend that the roof and rooftop equipment have a routine visual inspection at least once a year by persons knowledgeable of the type of roof system(s) on the building. FEMA P-424, 543 and 577 also recommend a special inspection following unusually high winds (such as a thunderstorm with wind speeds of 70 mph peak gust or greater).

If the vulnerability assessment reveals the need to reroof or strengthen attachment of rooftop equipment, see the guidance provided in FEMA P-424, 543 and 577 for guidance.

CONCLUSIONS

This paper presents a useful protocol for design professionals. It obviously needs to be expanded to address special considerations and guidance pertaining to a variety of systems, such as asphalt shingles, metal panels, slate, tile, vegetative roofs and photovoltaic panels. Additional specificity is also needed regarding the number of tests and field checks to be taken, and additional specificity is needed for various types of field checking.

There is need for a comprehensive protocol for the vulnerability assessment of the structural system, the entire building envelope and ramifications of interruptions of municipal utilities. This paper along with the papers by Coulbourne (2011) and Beers (2011) lay the foundation for the development of such a protocol.

REFERENCES

American Society of Civil Engineers, ASCE 7-10, *Minimum Design Loads for Buildings and Other Structures*, 2010.

American Society of Civil Engineers, ASCE 30-00, *Guideline for Condition Assessment of the Building Envelope*, 2000.

ASTM International, ASTM E 907-96, *Standard Test Method for Field Testing Uplift Resistance of Adhered Membrane Roof Systems*, 2004.

ASTM International, ASTM D 7053-07, *Standard Guide for Determining and Evaluating Causes of Water Leakage of Low-Sloped Roofs*, 2007.

Beers, P.E., (2011). "Wind Risk Assessments for Cladding and Glazing Systems in Critical Facilities." ASCE 2011 Structures Congress, Las Vegas, NV.

CIB/RILEM Joint Committee on Roofing Materials and Systems, *Condition Assessment of Roofs*, 2003. Available online: www.rilem.net/reports.php

Coulbourne, W.L., (2011). "Vulnerability Assessments of Structural Frames for Critical Facilities." ASCE 2011 Structures Congress, Las Vegas, NV.

Federal Emergency Management Agency, FEMA P-424, *Design Guide for Improving School Safety in Earthquakes, Floods, and High Winds*, 2011.

Federal Emergency Management Agency, FEMA 543, *Design Guide for Improving Critical Facility Safety from Flooding and High Winds*, 2007.

Federal Emergency Management Agency, FEMA 577, *Design Guide for Improving Hospital Safety in Earthquakes, Floods, and High Winds*, 2007.

Single Ply Roofing Industry, ANSI/SPRI RP-4, *Wind Design Standard for Ballasted Single-ply Roofing Systems*, 2008. Available on line: www.spri.org

Smith, T.L., (2001). National Council of Architectural Registration Boards, *Low-Slope Roofing II*.

Telecommunications Industry Association, ANSI/TIA 222G (Addendum 2), *Structural Standard for Antenna Supporting Structures and Antennas*, December 2009.

Wind Risk Assessments for Cladding and Glazing in Critical Facilities

Paul E. Beers[1]

[1]Managing Member, Glazing Consultants International, LLC, 2460 Metrocentre Boulevard, West Palm Beach, FL 33407; PH (561) 689-0055; FAX (561) 689-0052; email: pbeers@glazingconsultants.com

ABSTRACT

One of the most vulnerable areas for critical facilities in severe windstorms is the exterior building envelope. Loss of roofing, cladding or glazing exposes building occupants to life safety risks and renders facilities inoperable at the time they are most needed. Engineers, Architects and Building Professionals are in need of guidelines for how to assess building envelopes to predict performance during severe windstorms and identify required upgrades.

This paper outlines the necessary steps for assessing severe windstorm threats to cladding and glazing on existing critical facilities. This outline includes developing appropriate design criteria for wind pressure, windborne debris and water infiltration, as the code mandated minimum may not be enough, depending upon the location and use of the facility. A staged analysis approach is presented to allow the user to determine the condition of existing cladding and glazing. An initial assessment would include a review of project documents and a visual survey. Higher level assessments include field testing and destructive analysis.

The included methodology for assessing and analyzing various cladding and glazing systems provides the reader with guidance for make a determination about the resistance of components and overall systems in severe windstorms. The assessment can then be used to identify needed upgrades and plan for safe operations during severe windstorms.

INTRODUCTION

There is a long history of documented failures of cladding and glazing during severe windstorms such as hurricanes and tornadoes. Following Hurricane Alicia in 1982, there was heavy damage to cladding and glazing in high rise buildings in downtown Houston, TX (ASCE 1985). Hurricane Andrew in South Florida in 1992 (ASCE 1993) damaged many exterior facades of commercial buildings, including hospitals and shelters. Tornadoes in Atlanta in 2000 (Dewan) caused glass breakage in high rise buildings downtown. There was extensive glass breakage in some commercial buildings in downtown areas of Miami and Fort Lauderdale following Hurricane Wilma in 2005 (Pasch). Houston had a repeat of glass breakage in downtown high rises during Hurricane Ike in 2006 (Vega), 34 years after the damage from Hurricane Alicia in 1982. Figures 1 and 2 show examples of the damage.



Figure 1. Hurricane Andrew Damage.

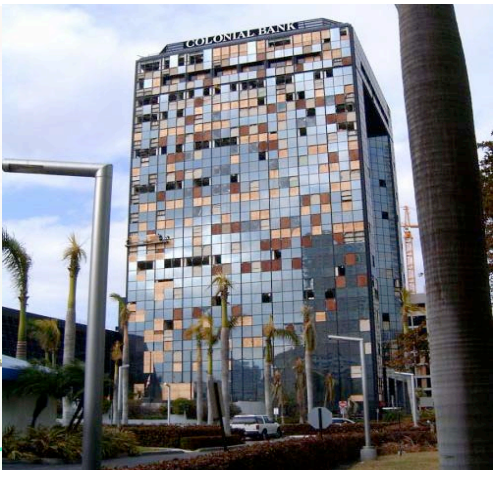


Figure 2. Hurricane Wilma Damage.

Much has been done to improve building façade performance during hurricanes and tornadoes since Hurricanes Alicia and Andrew. Building codes have been improved to design for higher wind loads and to account for windborne debris. In South Florida, buildings constructed after 1995 utilized improved code requirements and have demonstrated improved performance capabilities. Other hurricane prone areas in the United States also have adopted improved standards for wind loads and windborne debris resistance after they were included as part of the International Building Code in 2000.

Many existing critical facilities have upgraded their facades for improved performance in severe wind storms. Mitigation grant funding has provided for hurricane protection of facades at critical facilities including hospitals, shelters, schools, courthouses and public safety facilities. These upgrades typically included

the installation of code compliant storm shutters or replacement of glazing with missile impact resistant systems. Or, as was done at Miami Children's Hospital in 2004 (FEMA), an entire new façade was installed over the existing one.

While the technology exists to improve façade performance during severe windstorms, there is an information void when it comes to determining the ability of existing components to perform during these events. Facility owners need to be able to develop appropriate design criteria for the importance and use of the facility, assess existing facades, predict performance in future wind events, and be able to determine which systems and components need retrofit or replacement.

A staged approach can be used to assess windstorm threats to facades. This includes determining the original design criteria of existing systems, documenting their current condition and performance, and developing appropriate design criteria to utilize in making judgments about their windstorm resistance. After determining the appropriate design criteria, staged levels of assessment can be performed to determine construction types and field conditions, from which a judgment about performance in future windstorms can be developed.

DESIGN CRITERIA

Prior to an assessment, appropriate design criteria must be developed. Sometimes it is provided by the building owner, other times it must be developed by the designer or assessor. Design criteria for building façade assessment includes wind loads, windborne debris resistance and water leakage resistance.

For wind loads and debris resistance, requirements of the local building code in force at the time of the assessment can be used. However, it must be noted that building codes are minimum standards. The stated purpose of building codes "is to establish the minimum requirements to safeguard the public health, safety and general welfare" (Florida Building Code). More often than not, the common practice is to design to meet the code and no effort is made to exceed the code requirements. In addition, some building codes do not have criteria for water leakage resistance.

Critical facilities have uses that differ from structures in the typical building stock. They often need to remain fully functional throughout a severe windstorm event or be ready for use immediately after the storm passes. Some critical facilities, such as hospitals, house critically ill patients during storms. Others, such as shelters and emergency response facilities house people throughout a severe windstorm and must have functioning utilities and infrastructure (Vickery) (Lee) (Emanuel).

For critical facilities, it may be desirous to use design criteria that exceeds minimum building code standards (Beers). The following needs to be considered for enhanced design criteria:

Wind loads: Wind loads are usually developed by following the requirements of ASCE 7, which contains an enhancement factor for "important" facilities. Wind loads in ASCE are based upon wind speed maps and return periods defined as mean recurrence intervals (MRI). ASCE 7 uses a 100-year MRI as a baseline for important buildings, meaning the associated wind loads are based upon the probability of exceeding the wind speed during a 100-year period. Since some severe windstorms can exceed the 100-year MRI, the designer may elect to select a higher MRI, say 300 or 500 years, which would increase the wind loads for the building when using ASCE 7. Although ASCE 7 contains a procedure for determining design wind speeds at a given geographical location for MRI other than 100 years, this procedure does not include consideration of hurricane winds. In hurricane regions a computer modeling technique must be employed to determine wind speeds associated with a specific MRI at a given geographical location.

Another approach is to utilize site specific computer modeling and select a return period that is appropriate for the intended use of the facility (Minor).

Windborne debris design criteria typically uses code mandated missile impacts and cyclic pressure loading or ASTM requirements (ASTM E 1886 and ASTM E 1996). The ASTM standards also have enhanced requirements for important facilities. However, for some sites with a high potential for windborne debris or a use that requires a fail-safe design, higher levels of missile impacts may be appropriate.

For windborne debris, ASTM E1996 provides missile impact requirements for important facilities. However, it may be appropriate to exceed the recommended requirements. A recommendation for higher missile weights and speeds must be developed by the designer as part of the assessment process. The environment around the building must be reviewed to determine the potential for windborne debris in a severe windstorm. Potential debris can be generated from within the building and surrounding site itself, or from adjacent structures, landscaping and site conditions.

The age, condition and construction of adjacent structures must be assessed. If they were not built to newer building codes that include missile impact requirements, the potential for windborne debris is greater. If they contain known

elements of windborne debris, such as gravel or tile roofs, there is high potential for debris. Site conditions, such as vegetation, signage and temporary structures can also be potential debris generators.

It should also be noted that some buildings may be on sites with a low potential for debris, such as campuses of buildings built under recent code requirements, or a high rise structure with no other high rises around it. In those cases, the minimum requirements of the applicable building code may suffice.

Selection of appropriate windborne debris design criteria should be based upon guidance from codes and standards and by considering the site conditions. There often is precedence for what was done with other facilities and standards that can be referenced to determine the appropriate design missile. The pressure cycle portion of the design criteria is directly tied to wind load, so enhanced wind loads are factored in.

Industry standards are used for water leakage design criteria (AAMA/WDMA/CSA). Typically assemblies are tested at 15 to 20 percent of design load using ASTM E 331 for laboratory tests and ASTM E 1105 for field tests. Some projects specify higher loads.

ASSESSMENTS

To evaluate building façade and glazing components resistance to severe windstorms, the assessment team must possess several qualifications. The team must have extensive experience with the systems that are being analyzed including design and testing of such systems. A working knowledge of relevant codes and standards is also required. Assessment teams must also have experience evaluating windstorm damage. Because some parts of the analysis of existing building façade and glazing components will require professional judgment, experience and knowledge is critical for developing conclusions following the assessment.

This paper will present a three stage process for façade and glazing assessments. Level 1 assessment is a non-invasive analysis that includes gathering information about the original design and service history of the building along with a walk around inspection of façade and glazing components. Level 2 assessment builds upon the information developed during Level 1 and may include testing and destructive analysis. Level 3 assessment consists of theoretical calculations utilizing the information collected during earlier assessment stages.

Level 1: This assessment level includes: 1.) review of the original project documents including plans, specifications, shop drawings, calculations and submittals, if available; 2.) review of service and maintenance records; 3.) interviews with onsite building management and users to determine additional information about the service history; 3.) research of weather records to learn about any severe wind storms that the building has already experienced, and 4.) a visual inspection of façade and glazing components.

Level 2: This assessment level adds to the information collected during Level 1 and includes: 1.) selected disassembly of glazing systems; 2.) destructive analysis of cladding systems; 3.) field water infiltration tests, and 4.) analysis of anchors and fasteners.

Level 3: This assessment level takes the information from Levels 1 and 2 and adds theoretical calculations to determine the wind load resistance of glazing and component systems and anchors and compares them to the target design criteria.

Depending upon the building owner's needs and the assessment fee budget, the assessment can be finalized after any stage. If Level 1 is the only stage conducted, useful information will be developed and may be sufficient for an Owner/Operator decision about retrofit or replacement requirements. In addition, it may be appropriate to end the assessment after Level 1 if it is determined that certain materials are not windstorm resistant, rending further analysis useless. Level 2 can be used to develop additional information if Level 1 data does not provide enough information to make decisions. Level 3 takes the information from Levels 1 and 2 and further analyzes it to provide additional information about the existing systems.

LEVEL 1 ASSESSMENT REQUIRMENTS

Level 1 consists of information gathering about the project history and a non-invasive site inspection. The following needs to be considered:

- Review of plans and specifications: If the original plans, specifications and "as built" drawings still exist, valuable information about materials, manufacturers and construction details can be learned. These documents would also contain information about design criteria at the time of construction.
- Review of shop drawings and submittals: Additional information about construction details, materials, warranties and manufacturers can be discovered. Test reports and calculations may contain structural properties needed for a theoretical analysis.

- Review of service history: Seek out any documents that document storm damage, repairs and maintenance of the system.
- Interview building operators and users: Gain insight about problems such as prior storm damage, ongoing water leakage and air infiltration issues.
- Research weather records: Look for a history of the storms that may have affected the property over its service history
- Site inspection: Perform a walk around visual inspection of the exterior façade and glazing. If storm shutters are present they must be also be inspected. For multi-story buildings, it may be necessary to utilize a lift or swing stage to access upper floor areas. Inspect as much as possible, however, it is not necessary to inspect the entire exterior. All unique conditions should be inspected along with typical conditions on each building elevation.

LEVEL 2 ASSESSMENT REQUIREMENTS

Level 2 consists of additional information gathering to build on the data from Level 1. The following actions may be taken:

- Selected disassembly of glazing systems: This step would be required if shop drawings are not available to determine system design and details or to confirm if the field work was done in accordance with the drawings. Measurements can be taken to develop structural properties for theoretical calculations.
- Destructive analysis of cladding systems: If the materials and construction details cannot be determined during Level 1, destructive analysis may be required to determine needed information to make a judgment about the wind resistance of cladding systems.
- Documentation of storm shutters (if present): If there is no information to identify the storm shutter manufacturer, take measurements of sizes and material profiles. Document anchor materials, details and condition.
- Field water infiltration tests: Water leakage performance can be confirmed with the use of field water infiltration tests. Perform tests at areas that exhibit evidence of water damage using ASTM E 1105. The test simulates the conditions of a wind driven rain storm and can recreate leaks that occur during actual storms. Other tests using a water hose or high water pressure are not reliable and should not be used.
- Analysis of Anchors and Fasteners: Destructive analysis and partial disassembly of glazing systems will also allow for inspection of anchors. Determine the materials, details and condition of anchors. Also document the substrate (type and condition) that the anchors are set into.

LEVEL 3 ASSESSMENT REQUIREMENTS

Level 3 consists of a theoretical analysis of the ability of the cladding and glazing to meet the required loads using data developed during Levels 1 and 2. The following analysis is recommended:

- Develop design criteria: As discussed earlier in this paper, develop current design criteria based upon the building owner's requirements, use of the building, codes and standards requirements, anticipated future environmental conditions, and precedence at other similar projects.
- Document or develop structural properties of materials and components including glazing system framing, glass, cladding materials, cladding support systems and anchors. If the manufacturer can be determined, published data may be available. If not, measure and survey materials and develop structural properties as required.
- Calculate load resistance of existing systems: Perform theoretical calculations for cladding and glazing systems to compare their resistance to the desired design criteria.

DATA ANALYSIS

After the staged investigation is complete, the data must be analyzed and a judgment made about the resistance of existing cladding and glazing systems to severe wind storms. The purpose of the analysis is to determine if the existing cladding and glazing systems are resistant to design criteria developed for possible future storm events, including wind loads, windborne debris resistance and water leakage resistance. Development of needed repairs, retrofits and upgrades are beyond the scope of this paper.

The failure criteria for cladding and glazing systems must be developed by the owner and designer. It is not reasonable to expect there would be no damage during a severe windstorm. More reasonable failure criteria would be that the systems would continue to provide shelter from wind and water during and after a storm event, while protecting building occupants and contents. Damage to cladding and glazing systems is acceptable if they provide the needed protection and can be repaired or replaced on a reasonable schedule after the storm event, not under duress.

CLADDING SYSTEMS

Wind loads, windborne debris resistance and water leakage resistance are the factors that must be evaluated in making a judgment about the ability of cladding systems to perform satisfactorily in severe windstorms. The systems must resist wind loads without catastrophic failure. They must stay on the building and be able to survive impacts from windborne debris without failure. They must not allow water entry into the building

Determination of the wind load resistance of cladding systems can be determined from test reports, if they were submitted as part of the construction documents and are still available for review. Wind load resistance can also be determined by consulting with the original manufacturer if they can be identified or reviewing their published literature. Wind load resistance can also be calculated if no other information is available.

In addition to the cladding system, any support structure, such as metal studs must also be analyzed. Anchors, fasteners and anchor assemblies must be analyzed to assure the system will stay on the building in a severe windstorm.

Cladding materials must also be analyzed for their resistance to windborne debris. Resistance to windborne debris can be determined from test reports or manufacturers literature, if available for review. Theoretical calculations cannot be used to determine the resistance of a system or material to windborne debris. In the absence of test data or manufacturers literature, the assessor may be able to compare the materials and construction of cladding systems to similar tested systems and make a judgment about their windborne debris resistance.

Cladding must not allow water entry into the building during a severe windstorm. Site inspections and field water infiltration tests will provide information about the water resistance of cladding systems.

GLAZING SYSTEMS

Glazing systems must also demonstrate resistance to wind loads and windborne debris and water leakage using current design criteria. Evaluations should include the framing, glass and anchors.

Framing should be evaluated to confirm it will resist the specified wind loads. This can be accomplished by referencing the framing manufacturers test reports if they were part of the submittal package or if they are still available from the

manufacturer or evaluation authorities. It can also be accomplished through theoretical calculations.

Glass should be evaluated for wind loads using ASTM E1300. Glass should also be evaluated for resistance to windborne debris. Theoretical analysis cannot be used to evaluate glazing for compliance with ASTM E 1996. Laboratory testing is the only basis for evaluating for compliance

When attempting to predict performance of glass in existing building in severe windstorms, only laminated glass or glazing that meets the desired wind load requirements of the projects and is protected with compliant storm shutters compliant with ASTM E 1996 should be considered for judgment as being compliant. Ordinary window glass types including annealed, heat strengthened or tempered do not pass missile impact testing and can be deemed as not compliant.

Storm shutters complying with ASTM E 1996 used to protect glazing systems that are deemed to meet the desired wind load requirements for the building provide can be deemed to provide adequate protection. This can only be determined with laboratory testing of shutter systems or with test reports evidencing such testing.

CONCLUSION

Development of appropriate design criteria that meets the projected needs of a facility is based upon importance and use, and may exceed minimum building code requirements. Evaluation of existing systems can be a complex process requiring experience, knowledge and professional judgment by the assessor and design professional. While it may be possible to determine a building was constructed to recent hurricane resistant standards, most often that is not the case. Many buildings do not retain records from construction.

Older buildings that predate recent hurricane resistant codes and standards most likely will not be deemed to meet desired design criteria. Simply identifying the glass type in most instances will provide information indicating that the building will not comply. Additional more sophisticated analysis including invasive inspections and field water infiltration tests may identify further areas of concern.

Although it is beyond the scope of this paper, the information developed during an assessment can be used to design upgrades to existing systems for compliance with enhanced design criteria. The enhanced design criteria in

combination with information developed about the structure can also be used to design compliant replacement systems.

In addition to cladding and glazing, vulnerability assessments of critical facilities should include the structure and roof to encompass the structural frame and entire exterior building envelope. This paper in combination with papers by Colbourne (2011) and Smith (2011) can be used for that purpose.

REFERENCES

AAMA (2008) North American Fenestration Standard, AAMA/WDMA/CSA 101/I.S.2/A440, American Architectural Manufacturers Association, Schaumburg, IL.

ASCE (1985) "Proceedings," *Specialty Conference on Hurricane Alicia: One Year Late*r (Galveston, TX, August 16-17, 1984), ASCE, New York, NY, pp. 151-167.

ASCE (1993) "Proceedings," *Conference on Hurricanes of 1992*, (Miami, December 1-3, 1993), ASCE, New York, NY, pp. 476-485.

ASCE (2005) *Minimum Design Loads for Buildings and Other Structures*, ASCE/SEI 7-05, American Society of Civil Engineers, Reston, VA.

ASTM "E331-00 (2009) Standard Test Method for Water Penetration of Exterior Windows, Skylights, Doors, and Curtain Walls by Uniform Static Air Pressure Difference," *Book of Standards, Volume 04.11*, ASTM, West Conshohocken, PA.

ASTM "E1105-00 (2008) Standard Test Method for Field Determination of Water Penetration of Installed Exterior Windows, Skylights, Doors, and Curtain Walls by Uniform or Cyclic Static Air Pressure Difference," *Book of Standards, Volume 04.11*, ASTM, West Conshohocken, PA

ASTM "E1300 - 09a (2009) Standard Practice for Determining Load Resistance of Glass in Buildings, *Book of Standards, Volume 04.11*," ASTM, West Conshohocken, PA.

ASTM "E1886 - 05 (2005) Standard Test Method for Performance of Exterior Windows, Curtain Walls, Doors, and Impact Protective Systems Impacted by Missile(s) and Exposed to Cyclic Pressure Differentials," *Book of Standards, Volume 04.11*, ASTM, West Conshohocken, PA.

ASTM "E1996 - 09 (2009) Standard Specification for Performance of Exterior Windows, Curtain Walls, Doors, and Impact Protective Systems Impacted by Windborne Debris in Hurricanes," *Book of Standards, Volume 04.11*, ASTM, West Conshohocken, PA.

Beers, P. E. (2008) "Designing Beyond the Code," *US Glass Metal and Glazing*, March issue, pp. 64 -66.

Coulbourne, W.L., (2011). "Vulnerability Assessments of Structural Frames for Critical Facilities," *ASCE 2011 Structures Congress*, Las Vegas, NV.

Dewan, S. and Goodman, B. (2008) "*Tornadoes Tear Through Downtown Atlanta*," New York Times, March 16 issue.

Emanuel, K.A., Ravela, S., Vivant. E. and Risi, C. (2006) "A statistical–deterministic approach to hurricane risk assessment," Bull. Amer. Meteor. Soc., 19, pp. 299-314.

FEMA (2007) "Hospital Haven: Facelift Provides Safe Hurricane Refuge for Young Patients," *Full Mitigation Best Practice Story*, http://www.fema.gov/mitigationbp/bestPracticeDetail.do?mitssId=2525, (November 29, 2007).

Florida Building Code (2004) Florida Building Commission, Department of Community Affairs, Tallahassee, FL.

Lee, K. H. and D.V. Rosowsky (2007) "Synthetic hurricane wind speed records: development of a database for hazard analyses and risk studies," *Natural Hazards Review*, pp. 23-34.

Minor, J.E. (2009) "Glazing Systems to Resist Windstorms on Special Buildings," "*Architectural Glass to Resist Seismic and Extreme Climatic Events*," Chapter 8 (edited by R.A. Behr), Woodhead Publishing Limited, pp. 217-231.

Pasch, R., Blake, E., Cobb, H., and Roberts, D. (2006) "Tropical Cyclone Report Hurricane Wilma, 15-25 October 2005" National Hurricane Center.

Vega, R. and Koke, R (2008) "Wind Effects of Hurricane Ike on Chase Tower in Downtown Houston," *Newsletter of American Association for Wind Engineering*, December issue.

Vickery, P.J., Masters, F.J., Powell, Mark D., and Wadhera, D. (2007) "Hurricane Hazard Modeling: The Past, Present and Future," *Proceedings, Twelfth International Conference on Wind Engineering*, (Cairns, Australia, July 1-6, 2007), Australasian Wind Engineering Society.

A preliminary proposal for a probabilistic Performance-Based Hurricane Engineering framework

Michele Barbato[1], Francesco Petrini[2] and Marcello Ciampoli[2]

[1] Louisiana State University and A&M College, Civil & Env. Eng. Dept., 3531 PFTH, Baton Rouge, LA 70803, USA; email: mbarbato@lsu.edu

[2] Sapienza University of Rome, Struct. & Geotech. Eng. Dept., via Eudossiana 18, 00184, Rome, Italy; email: marcello.ciampoli@uniroma1.it, francesco.petrini@uniroma1.it

ABSTRACT

This paper proposes an innovative fully probabilistic Performance-Based Hurricane Engineering (PBHE) approach for risk assessment and design of structural systems located in hurricane-prone regions. The methodology is based on the Total Probability Theorem and disaggregates the risk assessment analysis into independent elementary components, namely hazard analysis, structural characterization, interaction analysis, structural analysis, damage analysis, and loss analysis. The proposed PBHE methodology accounts for the multi-hazard nature of hurricane events by including the separate effects of, and the interaction among, hurricane wind, flood, windborne debris, and rainfall hazard. A review of existing models with the ability to describe the different sources of hazard is performed, and a consistent vector of intensity measures for hurricane hazard analysis is proposed. The PBHE approach illustrated in this paper represents a first step toward a rational methodology for risk assessment and design of structures subjected to multi-hazard scenarios.

INTRODUCTION

Performance-Based Engineering (PBE) is a general methodology that (1) defines the performance objectives for structural systems during their design life, (2) provides criteria and methods for verifying the achievement of these performance objectives, and (3) offers appropriate methodologies to improve the design of structural systems. In the last two decades, significant research efforts have been devoted to the development of PBE in earthquake engineering (Ellingwood 2001, Porter 2003), and have led, e.g., to the Pacific Earthquake Engineering Research center (PEER) Performance-Based Earthquake Engineering (PBEE) framework (Porter 2003). Several motivations have generated significant interest in the possible development and extension of PBE to other subfields of civil engineering (Augusti and Ciampoli 2008). In particular, Performance-Based Blast Engineering has received considerable attention in the US after the terrorist attacks of September 11, 2001 (Hamburger and Whittaker 2003). Other PBE

examples are Performance-Based Fire Engineering (Rini and Lamont 2008), Performance-Based Tsunami Engineering (Riggs et al. 2008), and Performance-Based Wind Engineering (PBWE) (Augusti and Ciampoli 2006, Petrini 2009, Ciampoli et al. 2009). PBE has been widely recognized as a rational methodology for assessing and mitigating the risk associated with engineering structures and infrastructures subject to natural and man-made hazard. In earthquake engineering, modern design codes are gradually substituting prescriptive approaches with PBEE procedures for the design of new facilities and the retrofit of existing ones (FEMA 1997, ATC 2005). PBEE has been shown to facilitate design and construction of structural systems based on a realistic and reliable assessment of the risk associated with seismic hazard, leading to a more efficient use of resources for construction, maintenance, and retrofit of structures.

The advantages demonstrated by a PBE approach to civil engineering provide a strong motivation to develop a PBE methodology for structures subjected to hurricanes. The need for assessing and improving the resilience of the built environment subjected to hurricane hazard is widely recognized (NSB 2007). Some initial interest in PBE has been expressed in hurricane engineering (Easley 2003), but a complete and rigorous framework is still needed. The development of a Performance-Based Hurricane Engineering (PBHE) methodology presents several additional challenges when compared to other existing PBE methodologies. In contrast with other natural hazard events, in which a single type of hazard is considered, the landfall of a hurricane involves different hazard sources that interact to generate the risk for a given structure. Therefore, hurricanes can be viewed, and must be analyzed, as "multi-hazard" scenarios.

In this paper, the formal extension of the PBE approach is proposed for a fully probabilistic PBHE methodology. A classification of the uncertainties involved in hurricane hazard analysis is proposed, and analytical models of the relevant environmental phenomena generated by hurricane events are briefly described. The paper concludes with suggestions for possible improvement of the hazard description and for further research regarding PBHE.

PBHE FRAMEWORK

In a probabilistic PBE approach, the structural risk is conventionally measured by the probability of exceeding a specified value of a decision variable (*DV*) corresponding to a target performance. Each *DV* is a measurable attribute of a specific structural performance and can be defined in terms of cost/benefit for the users and/or the society (e.g., loss of human lives, economic losses, exceedance of safety/serviceability limit states). A PBE assessment analysis provides a probabilistic description of an appropriate *DV* for different design choices in order to allow a rational decision among different design options.

In order to outline a procedure for PBE assessment analysis of structures subjected to hurricanes, the assessment analysis can be decomposed into the elementary phases which must be carried out in sequence. Perhaps the most

important expected feature of this procedure is the qualitative independence of each phase from the others (i.e., the choice of certain parameters in a given phase is independent from the parameters adopted in previous phases). A widely accepted approach based on this principle is the one proposed by PEER (Porter 2003) and based on the Total Probability Theorem (TPT).

The probabilistic PBHE framework presented in this paper is based on the TPT, similar to the PEER PBEE and the PBWE frameworks. The structural risk is defined in terms of *DV*s as follows

$$G(DV) = \int\int\int\int\int G(DV|DM)\cdot f(DM|EDP)\cdot f(EDP|IM,IP,SP)\cdot f(IP|IM,SP) \cdot f(IM)\cdot f(SP)\cdot dDM\cdot dEDP\cdot \mathrm{d}IM\cdot \mathrm{d}IP\cdot \mathrm{d}SP \quad (1)$$

in which $G(\cdot)$ = complementary cumulative distribution function, and $G(\cdot|\cdot)$ = conditional complementary cumulative distribution function; $f(\cdot)$ = probability density function, and $f(\cdot|\cdot)$ = conditional probability density function; *DM* = damage measure(s) (i.e., parameters describing the physical damage of the structure); *EDP* = engineering demand parameter(s) (i.e., parameters describing the structural response for the performance evaluation); *IM* = intensity measure(s) (i.e., parameters characterizing the environmental hazard); *SP* = structural parameter(s) (i.e., parameters describing the relevant properties of the structural system and non-environmental actions); and *IP* = interaction parameters (i.e., parameters describing the interaction phenomena between environment and structure). In Eq. (1), *IM* and *SP* are assumed as uncorrelated and independent of *IP*, while *IP* is dependent on both *IM* and *SP*. By means of Eq. (1), the problem of risk assessment is disaggregated into the following tasks (see Figure 1): (1) hazard analysis, (2) structural characterization, (3) interaction analysis, (4) structural analysis, (5) damage analysis, and (6) loss analysis. Detailed explanation of steps (1), (4), (5), and (6) can be found in the PBEE literature (e.g., Porter 2003), while steps (2) and (3) have been introduced in PBWE to rigorously model the effects of interaction between the structural system and the environment on the structural response (e.g., aerodynamic effects, see Petrini 2009).

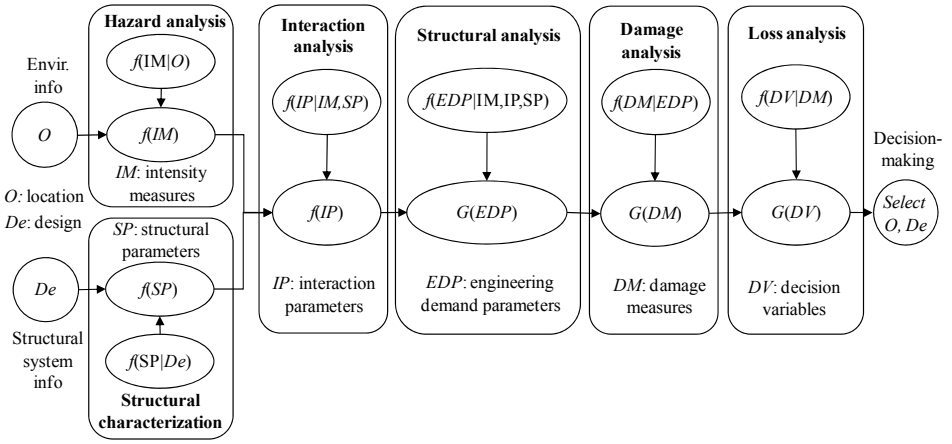


Figure 1. Probabilistic analysis components of the PBHE framework

The remainder of this paper focuses on probabilistic hazard analysis, i.e., on the probabilistic characterization of the *IM*s. This characterization can be done by using the (joint) probability density function *f*(*IM*). The *IM*s are strictly independent on the investigated structure. Thus, the probabilistic information about *IM* should be provided by climatologists, while the engineers have the task of clarifying what information is needed. The proposed point of view is consistent with the state-of-the-art in hurricane hazard and loss modeling, which can be identified with the HAZUS® methodology (FEMA 2007).

CHARACTERIZATION OF UNCERTAINTIES

The PBHE methodology outlined above requires the identification of the uncertainties that characterize the various phases of the assessment analysis. This paper focuses on the hazard for a single structure located in a hurricane-prone region. Three zones can be distinguished (see Figure 2):

- *Environment*, i.e., the space surrounding the structure but sufficiently far from it, where the parameters describing the wind field and other environmental actions (e.g., wind velocity, water level of water bodies surrounding the structure) are not influenced by the presence of the structure itself.
- *Exchange zone*, i.e., the space immediately surrounding the structure, where the structural configuration and the environmental actions are strongly correlated, and the interaction between the structure and the environmental agents, as well as the presence of adjacent structures, cannot be disregarded.
- *Structure*, which includes the original structural system (characterized by a set of uncertain parameters collected in a vector *S*) as well as non-environmental actions and/or elements (characterized by a set of uncertain parameters collected in a vector *A*) that can modify the structure's behavior.

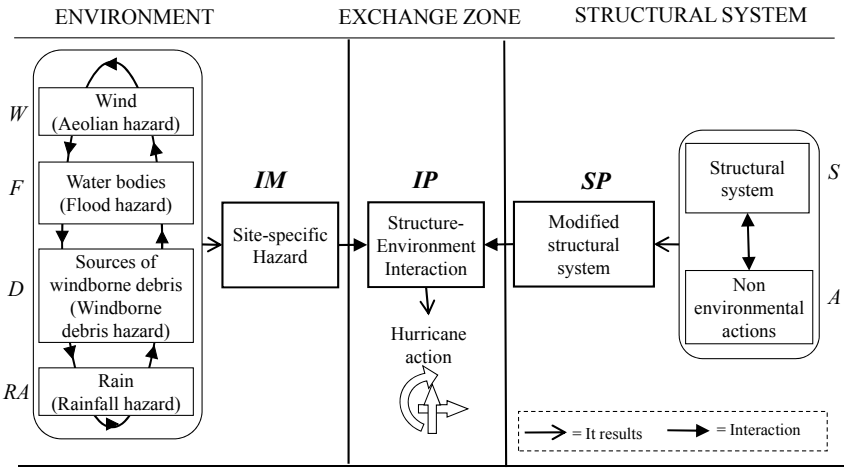


Figure 2. Identification of uncertainties in PBHE

Hereinafter, the uncertain basic parameters of interest describing the environmental actions in the environment zone are collected in the intensity measure vector *IM*; the uncertain basic parameters describing the structural

system and non-environmental actions or devices applied to it are collected in the structural parameter vector *SP*; and the uncertain derived parameters of interest in the exchange zone are collected in the interaction parameter vector *IP* (Figure 2). Examples of *IP*s are aerodynamic and hydrodynamic coefficients, as well as peak factors for stochastic structural response.

Figure 2 shows the different sources of uncertainties corresponding to environment, structure, and exchange zone, and identifies the different hazard sources and their interactions. The environmental hazard due to a hurricane event in a specified geographic region is generated by four main sources of hazard:

- Hurricane strong winds (characterized by the uncertain parameter vector *W*), which can produce wind damage (*aeolian hazard*).
- Water bodies (characterized by the uncertain parameter vector *F*), which can produce flood damage (*flood hazard*).
- Sources of windborne debris (characterized by the uncertain parameter vector *D*), which can produce windborne debris damage (*windborne debris hazard*).
- High rainfall rates (characterized by the uncertain parameter vector *RA*), which can induce flash flooding and direct damage to the interiors of building when the building envelope has been breached (*rainfall hazard*).

In the environment zone, the various sources of hazard usually interact to produce the actual hurricane hazard for a given structure. Typical examples are the interaction between wind and waves in offshore sites and the interaction between storm surge and wind in coastal regions.

A set of uncertain parameters included in vectors *W*, *F*, *D*, and *RA* must be selected in order to describe *IM*. This set must accurately describe all hazard sources and must be as small as possible in order to be both "sufficient" and "efficient" (Luco and Cornell 2007). The same selection operation (from vectors *A* and *S*) is needed to describe *SP*. The PBHE methodology also requires the identification of the vector *IP* of the stochastic parameters governing the interaction between environment and structural system in the exchange zone. The probabilistic description of vectors *IM*, *SP*, and *IP* is needed in order to derive the probabilistic characterization of the hurricane actions on the structural system under study.

INTENSITY MEASURES AND HAZARD ANALYSIS

A selection of the basic parameter vectors *W*, *F*, *D*, and *RA* is needed to generate a comprehensive vector *IM* that can be used for a general hurricane hazard analysis. With regard to the hazard analysis conducted for a specific structure *s* and regarding a specific performance objective *p*, the elements of the general *IM* vector that do not represent a relevant hazard for *s*, and those that have small influence on *p,* can be neglected or treated as deterministic. This selection is performed in order to improve the efficiency of the $IM^{(s,p)}$ (i.e., the vector *IM* specialized for structure *s* and performance *p*) at a negligible loss of sufficiency. For example, the flooding hazard can be neglected in the case of structures that

are located sufficiently far away from water bodies.

The selection of the *IM* parameters strictly depends on the choice of the models used to describe the environmental phenomena related to the various hazards. In general, deterministic models are used, while the key parameters of these models are treated as stochastic variables. In this paper, state-of-the-art models for hurricane-related environmental phenomena are reviewed and the corresponding *IM* components are identified. While the selected *IM* vector depends on the specific models considered, the approach proposed here to identify *IM* is general and can also be applied to different hazard models.

In the following equations, the dependence of a given parameter x from other variables is expressed collecting first the subset of continuous variables independent of the hurricane characteristics, and then the subset of parameters used to characterize the hurricane (i.e., *IM* components). For example, $x = x(\alpha, \beta; \gamma, \delta)$, indicates that x is a function of continuous variables α and β (e.g., distance and time), and of characteristic parameters γ and δ (e.g., hurricane radius of maximum wind and central pressure deficit).

Wind field and aeolian hazard characterization

A model of the wind field associated with a hurricane is needed to characterize the aeolian hazard. In general, two methodologies can be followed to define the hurricane wind field and the corresponding hazard (FEMA 2007):

- The site specific statistics of some fundamental hurricane parameters are obtained and a Monte Carlo approach is used to sample these parameters from the available statistical information. Using these samples, a mathematical representation of the hurricane is adopted and the statistics of parameters needed to describe the hurricane actions are evaluated for the structure of interest at its specific location (Vickery and Twisdale 1995).
- The full track of a hurricane is modeled, from its initiation over the ocean until its final dissipation (Jakobsen and Madsen 2004). Several tracks are statistically simulated. The statistics of the parameters describing the hurricane actions are estimated from the parameters' values in each simulated track for the structure of interest at its specific location.

This study uses the first methodology. The hurricane wind hazard model is subdivided into three components (see Figure 3):

- *Hurricane model*, which provides the wind speed at the gradient height V_G. For a stationary storm, V_G can be obtained as (Vickery et al. 2009)

$$V_G(r;\Delta p_c, RMW, B) = \sqrt{\left(\frac{RMW}{r}\right)^B \cdot B^{-\left(\frac{RMW}{r}\right)^B / \rho_a} + \frac{r^2 \cdot f_c^2}{4}} - \frac{r \cdot f_c}{2} \qquad (2)$$

  in which r = radial distance of the structure to the hurricane storm center, ρ_a = air density, f_c = Coriolis parameter, B = Holland parameter, RMW = radius of maximum wind (defined as the radial distance between the storm center and the maximum wind location), and Δp_c = hurricane central pressure deficit.

- *Boundary layer model*, which provides the mean wind speed U. U can be obtained using one of the existing relations describing its variation inside the atmospheric boundary layer, e.g. (Vickery and Twisdale 1995),

$$U(z,r;\Delta p_c,RMW,B,H^*,z_0)=V_G(r;\Delta p_c,RMW,B)\cdot\left[\frac{ln(z/z_0)}{ln(H^*/z_0)}\right] \quad (3)$$

in which z = height from sea level, z_0 = terrain roughness length, and H^* = atmospheric boundary layer height.

- *Turbulence model*, which provides the gust wind speed V_{gust} for a specified sampling time duration T_0. V_{gust} is commonly expressed as (ESDU 1983)

$$V_{gust}(\tau,z,r;\Delta p_c,RMW,B,H^*,z_0)=U\cdot g(\tau,z,r;U,T_0,u_*) \quad (4)$$

in which τ = averaging time, g = gust factor, and u_* = friction velocity (Vickery et al. 2009).

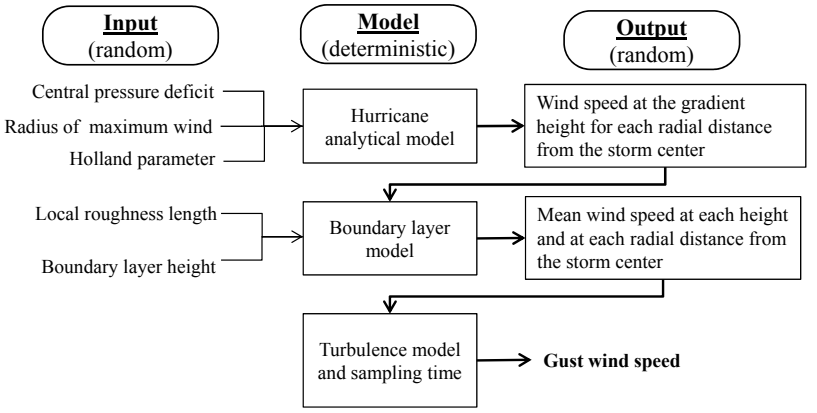


Figure 3. Hurricane wind field characterization and hazard model.

The total hurricane wind speed acting on a structure during a wind gust is equal to the vector sum of V_{gust} given in Eq. (4) and the instantaneous (horizontal) translational speed of the storm V_c. Based on the considered models, the vector W of basic stochastic parameters describing the wind field (Figure 1) becomes

$$W=\left[RMW \quad V_c \quad \Delta p_c \quad B \quad H^* \quad z_0\right]^T \quad (5)$$

where the superscript T denotes the matrix transpose operator.

Flood hazard characterization

The flood hazard due to the presence of water bodies surrounding the considered structure depends on the total water surface elevation with respect to the mean surface, η_{tot}, and on the flooding water velocity, V_{water} (i.e., the value of the component of the water velocity orthogonal to the flooding barriers). These two parameters allow for the computation of the volumetric rate of flow and can be used as synthetic intensity indicators for flood. In this paper, the basic parameters characterizing these indicators are selected as components of the intensity vector F. Three main natural phenomena cause water level increase and contribute to flood hazard: astronomical tide (η_{tide}), waves (η_{wave}), and storm surge

(η_{surge}). The total water surface elevation is the sum of the three contributions at the same instant of time: $\eta_{tot} = \eta_{tide} + \eta_{wave} + \eta_{surge}$. The flooding water velocity V_{water} can be assumed, in first approximation, equal to the highest velocity for each of the three considered phenomena (V_{tide}, V_{wave}, V_{surge} respectively).

The flood hazard due to the astronomical tide can be characterized by the two random variables η_{tide} and V_{tide}, i.e., $F_{tide} = [\eta_{tide} \; V_{tide}]^T$. The individual characterizations of the flood hazard due to waves (parameter vector F_{wave}) and to the storm surge (parameter vector F_{surge}) require more detailed considerations.

The water level, η_{wave}, and the wave celerity, V_{wave}, can be directly related to the water depth, d; the wave height, H; the wave length, L; and the wave period, T. The last three quantities can be obtained by propagating in space and time (Young 1999) the waves corresponding to a wave energy density spectrum (e.g., JONSWAP, Hasselmann et al. 1973) valid for the sea waves as determined by the wind field (i.e., RMW, V_c, Δp_c, and B), as well as by other parameters (Dean and Dalrymple 2004). Due to space constraints, the complete procedure for analysis of flood hazard due to waves is not presented here.

A storm surge is defined as the water surface response to wind-induced surface shear stress and pressure fields (US Army Corps of Engineers 2002). Storm surges can produce considerable short-term increases in water level. Current storm surge models are based on the depth-averaged momentum and continuity equations for steady long waves under the hypothesis of incompressible water (Bode and Hardy 1997). Due to space constraints, the complete procedure for analysis of flood hazard due to storm surge is not presented here.

The vectors F_{wave} and F_{surge} proposed in this paper coincide and are

$$F_{wave} = F_{surge} = \left[RMW \quad V_c \quad \Delta p_c \quad B \quad H^* \quad z_0 \quad d \quad U_{curr} \quad z_b\right]^T \tag{6}$$

in which U_{curr} = current velocity, and z_b = sea bottom friction roughness.

Windborne debris hazard characterization

The main intensity indicators for windborne debris impact hazard are the linear momentum, $M = m_{debris} \cdot u_m$, and the kinetic energy, $E = m_{debris} \cdot u_m^2 / 2$, of the missile at impact, in which m_{debris} = mass of the missile at impact, and u_m = impact velocity of the missile at impact. The proposed procedure for windborne debris hazard analysis is shown in Figure 4. The starting point is the description of the hurricane wind field, which provides some of the input data needed for a debris generation model. The additional data that cannot be derived from the wind field model consists of the density of upwind buildings with respect to the investigated structure, $n_{buildings}$; the properties of the different debris types (m_{debris} = mass of the debris, $C_{D,av}$ = average drag coefficient of the debris, and A_{debris} = reference debris area); and the resistance model for the missile sources. The debris generation model provides the input data for a debris trajectory model (Holmes 2004, Holmes et al. 2006, Baker 2007, Lin et al. 2007). The main goal of a debris trajectory model is the assessment of the wind debris velocity at impact with a

downwind building at a given distance from the debris source. Finally, a debris impact model can be used to determine the probabilistic characterization of impact kinetic energy, impact linear momentum, and number of impacts on the considered structure. The proposed vector D of basic random parameters is

$$D = \left[RMW \quad V_c \quad \Delta p_c \quad B \quad H^* \quad z_0 \quad n_{buildings} \quad C_{D,av} \quad A_{debris} \quad m_{debris} \right]^T \tag{7}$$

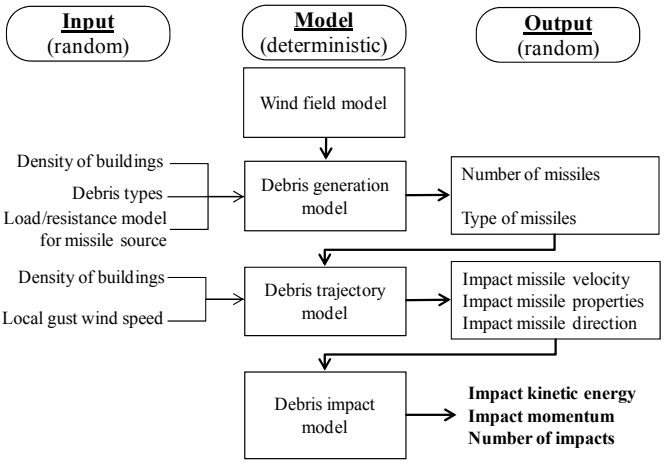


Figure 4. Windborne debris hazard model.

Rainfall hazard characterization

The high rainfall rate associated with hurricane events can induce significant damage to the interior of buildings when the building envelope has been breached (Huang et al. 2001). To the best of the authors' knowledge, no analytical rainfall models are available in the literature heretofore. However, several models based on interpolation of statistical data exist that define the correlation between the rainfall rate and some fundamental hurricane parameters. One of the most widely accepted and used model is the one implemented in HAZUS® (Vickery et al. 2006, FEMA 2007), which is valid for tropical cyclones. The estimates of rainfall rates resulting from this model are successively employed in HAZUS® to estimate the amount of water that enters buildings through broken windows and doors, while these estimates are not used to assess the risk associated with inland flash flooding. Consistent with HAZUS®, this study does not consider inland flash flooding hazard. Due to space constraints, the complete procedure for analysis of rainfall hazard is not presented here. The proposed vector RA of basic random parameters is given by

$$RA = \left[RMW \quad \Delta p_c \quad \mathrm{d}p_c / \mathrm{d}t \right]^T \tag{8}$$

in which $\mathrm{d}p_c/\mathrm{d}t$ = time rate of change in central pressure, and t = time.

PROPOSED INTENSITY MEASURE VECTOR

An analysis of the vectors of basic random parameters describing the different hazard sources associated with a hurricane shows that several parameters are common to different hazards. Therefore, the resulting vector of IM is given by

$$IM = \left[IM_W \quad IM_F \quad IM_D \quad IM_{RA} \right]^T \tag{9}$$

in which

$$\begin{aligned} IM_W &= \left[RMW \quad V_c \quad \Delta p_c \quad B \quad H^* \quad z_0 \right]^T \\ IM_F &= \left[d \quad U_{curr} \quad z_b \quad \eta_{tide} \quad V_{tide} \right]^T \\ IM_D &= \left[n_{buildings} \quad C_{D,av} \quad A_{debris} \quad m_{debris} \right]^T \\ IM_{RA} &= \mathrm{d}p_c / \mathrm{d}t \end{aligned} \tag{10}$$

denote the random parameters needed to describe the hurricane wind hazard, the additional random parameters needed to describe the flood hazard, the additional random parameters needed to describe the windborne debris hazard, and the additional random parameter needed to describe the rainfall hazard, respectively.

CONCLUSION

In this paper, a probabilistic methodology for Performance-Based Hurricane Engineering (PBHE) has been proposed and illustrated. This methodology is based on the Total Probability Theorem and builds on methodologies already developed and used in other civil engineering subfields. The proposed procedure can be used to evaluate the structural risk associated with facilities located in hurricane prone regions. The structural risk is conventionally measured by the probability of exceeding a specified value of a decision variable (*DV*) corresponding to a target performance. Each *DV* is a measurable attribute that represents a specific structural performance and can be defined in terms of the cost and/or benefit for the users and/or the society. The problem of risk assessment is disaggregated into the following basic probabilistic components: (1) hazard analysis, (2) structural characterization, (3) interaction analysis, (4) structural analysis, (5) damage analysis, and (6) loss analysis. This paper presents a review of existing models describing the different sources of hazard associated with a hurricane event. A vector of intensity measures (*IM*) (consistent with the state-of-the-art modeling of hurricane wind, flood, windborne debris, and rainfall hazard) is proposed for hurricane hazard analysis.

This paper presents a general methodology for a performance-oriented design under multi-hazard scenarios, such as the ones determined by hurricanes. The proposed methodology is a first step in this direction with a scope limited to hazard analysis for PBHE. Research is still needed to (1) improve the probabilistic description of the environmental parameters used in hurricane hazard analysis; (2) define sufficient and efficient *IM* vectors for different structures and different geographical regions; (3) develop procedures for interaction analysis, structural analysis, damage analysis, and loss analysis that are appropriate for PBHE; (4) define appropriate performance objectives for hurricane engineering problems; and (5) relate the target performance objectives and the *DV*s obtained using the proposed PBHE methodology with feasible design procedures.

ACKNOWLEDGEMENTS

The authors gratefully acknowledge support of this research by (1) the Louisiana Board of Regents through the Pilot Funding for New Research Program under Award No. NSF(2008)-PFUND-86; (2) the LSU Council on Research through the 2009-2010 Faculty Research Grant Program; (3) the Longwell's Family Foundation through the Fund for Innovation in Engineering Research (FIER) Program; and (4) the Italian Ministry for Education, University and Research – MIUR, which partially financed the Wi-POD Research Project (2008-2010). Fruitful discussions with Dr. Sauro Manenti (Univ. of Pavia) are gratefully acknowledged. Any opinions, findings, conclusions or recommendations expressed in this publication are those of the authors and do not necessarily reflect the views of the sponsors.

REFERENCES

ATC (2005). *Development of Next-Generation Performance-Based Seismic Design Procedures for New and Existing Buildings*, *ATC-58*, Applied Technology Council, Redwood City, CA.

Augusti G., Ciampoli M. (2006). "First steps towards Performance-Based Wind Engineering." *Performance of Wind Exposed Structures: Results of the PERBACCO project*, Firenze University Press, Florence, Italy, 13-20.

Augusti G., Ciampoli M. (2008). "Performance-Based Design in risk assessment and reduction." *Probabilist. Eng. Mech.*, 23, 496-508.

Baker C.J. (2007). "The debris flight equations." *J. Wind Eng. Ind. Aerod.*, 95, 329-353.

Bode L., Hardy A. (1997). "Progress and recent developments in storm surge modeling." *J. Hydraul. Eng.-ASCE*, 12(4), 315-331.

Ciampoli M., Petrini F., Augusti G. (2009). "A procedure for the Performance-Based Wind Engineering." *Proc. ICOSSAR'09*, CRC Press, New York.

Dean R.G., Dalrymple R.A. (2004). *Water Wave Mechanics for Engineers and Scientists*, Advanced Series on Ocean Engineering, Vol. 2, World Scientific, New Jersey.

Easley J.E. (2003). *Development of a Performance-Based Design Approach and Related Loads for Facilities Designated as Essential During a Hurricane Event*, M.S. Thesis, Louisiana State University, Baton Rouge, LA.

Ellingwood B.R. (2001). "Earthquake risk assessment of buildings structures." *Reliab. Eng. Syst. Safe.*, 74, 251-262.

ESDU (1983). *Strong Winds in the Atmospheric Boundary Layer. Part II: Discrete Gust Speeds, Report No. 83045*, www.esdu.com (June 2, 2008).

Federal Emergency Management Agency (FEMA) (1997). *NEHRP Guidelines for the Seismic Rehabilitation of Buildings, Report No. FEMA 273*, prepared by the Applied Technology Council for FEMA, Washington, D.C.

Federal Emergency Management Administration (FEMA) (2007). "Multi-hazard estimation methodology – Hurricane Model. HAZUS-MH-MR4 Technical Manual." *FEMA*, www.fema.gov/plan/prevent/hazus/hz_manuals (February 15, 2010).

Hamburger R.O., Whittaker A.S. (2003). "Considerations in performance-based blast

resistant design of steel structures." *Proc. AISC-SINY Symposium on Resisting Blast and Progressive Collapse*, American Institute of Steel Construction, New York.

Hasselmann K. (1973). "Measurements of wind-wave growth and swell decay during the Joint North Sea Wave Project (JONSWAP)." *Dtsch. Hydrogr. Z. Suppl.*, 12(A8), 1-95.

Holmes J.D. (2004). "Trajectories of spheres in strong winds with application to wind-borne debris." *J. Wind Eng. Ind. Aerod.*, 92, 9-22.

Holmes J.D., Letchford C.W., Lin N. (2006). "Investigations of plate-type windborne debris. II. Computed Trajectories." *J. Wind Eng. Ind. Aerod.*, 94, 21-39.

Huang A., Rosowsky D.V., Sparks P.R. (2001). "Hurricane simulation techniques for the evaluation of wind-speeds and expected insurance losses." *J. Wind Eng. Ind. Aerod.*, 89, 605-617.

Jakobsen F., Madsen H. (2004). "Comparison and further development of parametric tropical cyclone models for storm surge modeling." *J. Wind Eng. Ind. Aerod.*, 95, 375-391.

Lin N., Holmes J.D., Letchford C.W. (2007). "Trajectories of wind-borne debris in horizontal winds and applications to impact testing." *J. Struct. Eng.-ASCE*, 133, 274-282.

Luco N., Cornell C.A. (2007). "Structure-specific scalar intensity measures for near-source and ordinary earthquake ground motions." *Earthq. Spectra*, 23(2), 357-392.

National Science Board (NSB) (2007). *Hurricane Warning: The Critical Need for a National Hurricane Research Initiative*, NSB-06-115, National Science Foundation, Arlington, VA.

Petrini F. (2009). *A Probabilistic Approach to Performance-Based Wind Engineering (PBWE)*, PhD Dissertation, University of Rome "La Sapienza", Rome, Italy.

Porter K.A. (2003). "An Overview of PEER's Performance-Based Engineering methodology." *Proc. ICASP9*, Millpress Rotterdam.

Riggs H.R., Robertson I.N., Cheung K.F., Pawlak G., Young Y.L., Yim S.C.S. (2008). "Experimental simulation of tsunami hazards to buildings and bridges." *Proc. NSF CMMI Engineering Research and Innovation Conference*.

Rini D., Lamont S. (2008). "Performance based structural fire engineering for modern building design." *Proc. 2008 Structures Congress*.

U.S. Army Corps of Engineers (2002). *Coastal Engineering Manual*, U.S. Army Corps of Engineers, http://140.194.76.129/publications/eng-manuals/ (February 15, 2010).

Vickery P.J., Twisdale L.A. (1995). "Wind-field and filling models for hurricane wind-speed predictions." *J. Struct. Eng.-ASCE*, 121(11), 1700-1709.

Vickery P.J., Lin J., Skerlj P.F., Twinsdale L.A., Huang K. (2006). "HAZUS-MH Hurricane model methodology. I: Hurricane hazard, terrain and wind load modeling." *Natural Hazard Review*, 7(2), 82-93.

Vickery P.J., Masters F.J., Powell M.D., Wadhera D. (2009). "Hurricane hazard modelling: The past, present and future." *J. Wind Eng. Ind. Aerod.*, 97(7-8), 392-405.

Young I.R. (1999). *Wind Generated Ocean Waves,* Elsevier Ocean Engineering book series, Oxford, UK.

ASCE 7-10 Changes to Wind Provisions and Our Approach to Forensics

William L. Coulbourne, P.E. M.ASCE[1]
Philip Line, P.E.[2]

[1]Director, Wind and Flood Hazard Mitigation, Applied Technology Council, 19266 Coastal Highway, Unit 4, #19, Rehoboth Beach, DE, 703-850-2891 (cell), 302-227-7652 (fax), bcoulbourne@atcouncil.org
[2]Senior Structural Engineer, URS Corporation, 200 Orchard Ridge Drive, Suite 100, Gaithersburg, MD 20878, 301-548-5156 (work), 301-721-2204 (fax), Philip_line@urscorp.com

ABSTRACT

The net effect of changes incorporated into *ASCE 7-10 Minimum Design Loads for Buildings and Other Structures* for wind design is often described in broad terms. These include use of uniform recurrence intervals for wind speed contours and removal of conservatism in the hurricane prone region. This paper will explore the net effect of changes on calculated wind pressures for specific locations both within the hurricane prone region and outside of the hurricane prone region. Design velocity pressure calculated using ASCE 7-10 and ASCE 7-05 will be compared and implications on relative vulnerabilities of buildings (between those designed under ASCE 7-05 and ASCE 7-10) will be explored.

INTRODUCTION

Wind design in ASCE 7-10 incorporates several major changes for wind design. Among the changes are new wind speed maps, referred to as ultimate wind speed maps in the 2012 International Building Code (IBC), that vary by risk category and incorporate wind speed contours of uniform recurrence interval throughout all geographic regions including hurricane prone regions of the U.S. In addition, revisions to the definition of Exposure D no longer preclude it from being applicable in hurricane prone regions. Coupled with these changes that affect calculation of the nominal load are revised load factors for wind in ASD and LRFD load combinations.

It is recognized that one outcome of all of the changes includes a reduction in design velocity pressure in some hurricane prone regions. Rather than address the changes in broad terms, this paper evaluates the net effect of all of the above changes for specific sites by comparing the design velocity pressure calculated using provisions of ASCE 7-05 and ASCE 7-10. The purpose of the comparison is two-fold: i) to illustrate where differences in calculations occur, and ii) provide insight into the affect of changes on calculated pressures for specific locations and buildings of varying risk category.

Of particular interest, are the reduced design pressures for Risk Category III and IV buildings given the importance of these buildings to our communities both before and after a major wind event such as a tornado or hurricane. While there is not substantial evidence of failure from high winds using the most recent versions of ASCE 7 or the IBC, there is a concern that reducing design wind pressures will potentially lead to high wind failures that otherwise would not have occurred.

DESIGN VELOCITY PRESSURE

For purposes of comparison, the design velocity pressures calculated herein will represent the factored pressures that would result from use of ASD or LRFD load combinations contained in ASCE 7.

ASCE 7-05 Velocity Pressure

$$q_{z05} = 0.00256 K_z K_{zt} K_d V^2 I \qquad \text{(Eq. 1)}$$

where:

q_{z05} = ASCE 7-05 velocity pressure evaluated at mean roof height (psf)
K_z = velocity pressure exposure coefficient
K_{zt} = topographic factor
K_d = wind directionality factor
V = basic wind speed (mph) from ASCE 7-05 maps
I = Importance factor (1.0 for Category II buildings, 1.15 for Category III and IV buildings)

Design velocity pressure for ASD and LRFD are:

ASD: $(1.0)(q_{z05})$ (Eq. 2)
LRFD: $(1.6)(q_{z05})$ (Eq. 3)

where:

1.0 = ASCE 7-05 ASD load factor for wind
1.6 = ASCE 7-05 LRFD load factor for wind

ASCE 7-10 Velocity Pressure

$$q_{z10} = 0.00256 K_z K_{zt} K_d V^2 \qquad \text{(Eq. 4)}$$

where:

q_{z10} = ASCE 7-10 velocity pressure evaluated at mean roof height (psf)
K_z = velocity pressure exposure coefficient
K_{zt} = topographic factor
K_d = wind directionality factor

V = basic wind speed (mph) from ASCE 7-10 maps referred to as ultimate wind speed maps in 2012 IBC.

Design velocity pressure for ASD and LRFD are:

ASD: $(0.6)(q_{z10})$ (Eq. 5)
LRFD: $(1.0)(q_{z10})$ (Eq.6)

where:

0.6 = ASCE 7-10 ASD load factor for wind
1.0 = ASCE 7-10 LRFD load factor for wind

For comparisons in this paper, values for the topographic factor are taken as 1.0 and the wind directionality factor is taken as 0.85. ASCE 7-10 and ASCE 7-05 equations for calculation of the design velocity pressure have a similar form and are easily compared. The effects of changes to the mapped basic wind speed on design velocity pressure are less obvious. To see effects, the above equations are applied to buildings of different risk category in different locations in the U.S.

BUILDING LOCATIONS AND RISK CATEGORY

Design velocity pressures for specific building locations and within building Risk Category II, III and IV are shown in Table 1. All locations are within the hurricane prone region with the exception of Dallas, TX. Wind speeds shown for each location are determined by interpolation where applicable or taken from Tables C26.5-3 and C26.5-6 from the ASCE 7-10 Commentary.

Table 1. Comparison of design velocity pressures based on ASCE 7-10 and ASCE 7-05 (Exposure C, 33 ft mean roof height)[1]

		ASCE 7-10			ASCE 7-05		
Location	Risk Category	Wind Speed (MPH)	ASD Velocity Pressure (psf)	LRFD Velocity Pressure (psf)	Wind Speed (MPH)	ASD Velocity Pressure (psf)	LRFD Velocity Pressure (psf)
Boston, MA	II	128	21.4	35.7	105	24.0	38.4
Va Beach, VA	II	122	19.4	32.4	114	28.3	45.2
Miami, FL	II	170	37.7	62.9	146	46.4	74.2
Galveston, TX	II	150	29.4	49.0	132	37.9	60.7
Dallas, TX	II	115	17.3	28.8	90	17.6	28.2
Boston, MA	III, IV	140	25.6	42.6	105	27.6	44.1
Va Beach, VA	III, IV	132	22.7	37.9	114	32.5	52.0
Miami, FL	III, IV	181	42.8	71.3	146	53.3	85.3
Galveston, TX	III, IV	160	33.4	55.7	132	43.6	69.8
Dallas, TX	III, IV	120	18.8	31.3	90	20.3	32.4

[1] Exposure C at 33' mean roof height assumed for all calculations, $K_z = 1.0$.

Table 2 provides the same information as Table 1 except design velocity pressure in accordance with ASCE 7-10 assumes Exposure D for sites located in hurricane prone regions. Design velocity pressures for ASCE 7-05 are based on assumed Exposure C because Exposure D is not applicable in hurricane prone regions per ASCE 7-05.

Table 2. Comparison of design velocity pressures based on ASCE 7-10 (Exposure D, 33 ft mean roof height)[1] and ASCE 7-05 (Exposure C, 33 ft mean roof height)[2]

		ASCE 7-10			ASCE 7-05		
Location	Risk Category	Wind Speed (MPH)	ASD Velocity Pressure (psf)	LRFD Velocity Pressure (psf)	Wind Speed (MPH)	ASD Velocity Pressure (psf)	LRFD Velocity Pressure (psf)
Boston, MA	II	128	25.2	42.1	105	24.0	38.4
Va Beach, VA	II	122	22.9	38.2	114	28.3	45.2
Miami, FL	II	170	44.5	74.2	146	46.4	74.2
Galveston, TX	II	150	34.7	57.8	132	37.9	60.7
Boston, MA	III, IV	140	30.2	50.3	105	27.6	44.1
Va Beach, VA	III, IV	132	26.8	44.7	114	32.5	52.0
Miami, FL	III, IV	181	50.5	84.1	146	53.3	85.3
Galveston, TX	III, IV	160	39.4	65.7	132	43.6	69.8

[1] Exposure D at 33' mean roof height assumed for ASCE 7-10 calculations, $K_z = 1.18$.
[2] Exposure C at 33' mean roof height assumed for ASCE 7-05 calculations, $K_z = 1.0$.

DESIGN PRESSURE DIFFERENCES

From Tables 1 and 2, the ratio of ASD to LRFD is a constant as would be expected based on the applicable equations. A slight reduction in ASD loads relative to LRFD loads results from the load factor differences between ASCE 7-10 and ASCE 7-05 (e.g. ratio of 0.6 versus 0.625). Table 3 compares the relative increase or decrease in design velocity pressures based on location, building risk category, and exposure. Only design velocity pressures for LRFD are shown based on the prior observation that ASD and LRFD velocity pressures vary by a constant value.

Table 3. Comparison of LRFD design velocity pressures based on ASCE 7-10 and ASCE 7-05

		ASDCE 7-10			ASCE 7-05		Ratio	
Location	Risk Category	Wind Speed (MPH)	[A] Exp C Pressure (psf)[1]	[B] Exp D Pressure (psf)[1]	Wind Speed (MPH)	[C] Velocity Pressure (psf)[2]	[A] / [C]	[B] / [C]
Boston, MA	II	128	35.7	42.1	105	38.4	0.93	1.10
Va Beach, VA	II	122	32.4	38.2	114	45.2	0.72	0.84
Miami, FL	II	170	62.9	74.2	146	74.2	0.85	1.00
Galveston, TX	II	150	49.0	57.8	132	60.7	0.81	0.95

Dallas, TX	II	115	28.8	-	90	28.2	1.02	-
Boston, MA	III, IV	140	42.6	50.3	105	44.1	0.97	1.14
Va Beach, VA	III, IV	132	37.9	44.7	114	52.0	0.73	0.86
Miami, FL	III, IV	181	71.3	84.1	146	85.3	0.84	0.99
Galveston, TX	III, IV	160	55.7	65.7	132	69.8	0.80	0.94
Dallas, TX	III, IV	120	31.3	-	90	32.4	0.97	-

[1] Exposure D at 33' mean roof height assumed for ASCE 7-10 calculations, $K_z = 1.18$.
[2] Exposure C at 33' mean roof height assumed for ASCE 7-05 calculations, $K_z = 1.0$.

One of the expected changes in results due to ultimate maps and the reduced load factor was a reduction generally in the design pressures for Exposure C, especially along the Gulf and southern Atlantic coastlines. For Risk Category III and IV buildings the reader will notice that in every location, the pressures using ASCE 7-05 are higher than the pressures using ASCE 7-10 (i.e. ratio less than 1.0). The inland location, Dallas, TX, show only small differences between ASCE 7-10 and ASCE 7-05 for Risk Category II, III and IV buildings.

As noted, one of the expected changes in the use of ultimate maps and Exposure D is that design wind pressures for buildings built where Exposure D is applicable will be very similar to the design pressures used for Exposure C in ASCE 7-05 (see Table 3, column [B]/[C].. However, where the exposures are the same (Exposure C), the elimination of the importance factor coupled with use of uniform return period ultimate maps does not provide equivalent design pressures. For critical facilities, pressures are as much as 27% lower using ASCE 7-10 vs. ASCE 7-05 (see Table 3, column [A]/[C]). The northeast US and inland US locations are closer in comparative wind pressures than many areas of the hurricane coastlines.

RELATIVE SAFETY - ASCE 7-10 VS. ASCE 7-05

In this paper, only wind speed provision comparisons between two versions of the ASCE 7 standard are made. As shown in Table 3, the provisions of ASCE 7-05 were conservative relative to ASCE 7-10. In many areas of the country, new designs that precisely meet ASCE 7-10 wind loads will be designed with lower wind pressures than similar designs that were done in accordance with ASCE 7-05.

The re-introduction of Exposure D in ASCE 7-10 in hurricane prone regions that are on the water or in areas that would be directly impacted by over water flow of high winds was intended to bring the wind pressures in these areas closer to the pressures developed for Exposure C in ASCE 7-05 given the other changes that were made with wind contours and wind speed changes using higher return period maps. The last column in Table 3 illustrates this point. As indicated, for both Risk Categories II and III and IV, the ratio of Exposure D (ASCE 7-10) pressures to Exposure C (ASCE 7-05) pressures is very nearly 1.0 in the five locations considered with the exception of Virginia Beach, VA. While this ratio will vary some along the hurricane prone

coastline, the inland area of the country can be generally represented by results for Dallas, TX (except for Special Wind Regions).

None of the five locations studied have an ASCE 7-10 wind pressure equal to or greater than the pressures developed using ASCE 7-05. In a few cases, the pressures are nearly 30% lower. The pressures for Risk Category II buildings are equally lower using ASCE 7-10.

CONCLUSIONS

Changes in wind design provisions in ASCE 7-10 appear to produce the greatest differences in design velocity pressure when compared to ASCE 7-05 for areas within the hurricane prone regions. In hurricane prone regions where Exposure D is applicable, design velocity pressures in accordance with ASCE 7-10 are both larger (Boston, MA) and smaller (Virginia Beach, VA) than those determined in accordance with ASCE 7-05. For hurricane prone regions where Exposure D is not applicable under ASCE 7-10, design velocity pressures are smaller by as much as 28 percent than those calculated using ASCE 7-05. Differences in changes in design velocity pressures followed the same trends for Risk Category II and Risk Category III and IV buildings.

The actual reduction in design pressures of course is a location specific issue. As seen in the tables in this paper, some hurricane locations indicate significant differences in pressures between the ASCE 7-05 and the ASCE 7-10 standards and other locations indicate very little difference. Design professionals might investigate the differences in design pressures as they prepare a design for an owner, and discuss the differences with the owner in light of the reduction design pressures obtained using the ASCE 7-10 methodology for locations in the hurricane prone region.

Determination of exposure has always been an important issue in determination of wind pressures, but the reduction in design pressures in the hurricane prone region makes the accurate determination of exposures even more important. With the new Exposure D in ASCE 7-10, it becomes even more important for those conducting post event assessments of building performance to accurately identify the exposure category for each building location. Proper assessment of the exposure category is needed to identify the applicable design loads for the specific building location. The demand to capacity ratio associated with the buildings design can then be determined as a possible performance metric when coupled with knowledge of assumptions for design resistance.

REFERENCES

American Society of Civil Engineers, ASCE 7-05, *Minimum Design Loads for Buildings and Other Structures*, Reston, VA, 2005

American Society of Civil Engineers, ASCE 7-10, *Minimum Design Loads for Buildings and Other Structures*, Reston, VA, 2010

International Code Council., *2012 International Building Code*. Country Club Hills, IL, 2011.

Assessment of Seismic Performance of Structures in 2010 Chile Earthquake through Field Investigation and Case Studies

O. Kwon[1], A.S. Elnashai[2], B. Gencturk[3], S. Kim[4], S. Jeong[5], and J. Dukes[6]

[1] Assistant Professor (os.kwon@utoronto.ca), Department of Civil Engineering, University of Toronto. Toronto, Ontario, Canada.
[2] Professor and Department Head (aelnash@illinois.edu), [3] Graduate Research Assistant (bgenctu2@illinois.edu), Department of Civil and Environmental Engineering, University of Illinois at Urbana-Champaign.
[4] Postdoctoral Researcher (sjkim@engr.uconn.edu), Department of Civil and Environmental Engineering, University of Connecticut.
[5] Assistant Professor (jeong@inha.ac.kr), Department of Architectural Engineering, Inha University, Seoul, Korea.
[6] Graduate Research Assistant (jdukes6@gatech.edu), School of Civil and Environmental Engineering, Georgia Institute of Technology.

ABSTRACT

This paper presents an overview of the damage from the 2010 Chile Earthquake observed by a field reconnaissance team from the Mid-America Earthquake Center. Seismic performances of structures in Santiago, Biobío, and Maule regions in Chile are summarized based on field observations and discussions with researchers and city officials. In addition, post-earthquake analyses of a damaged bridge and a building structure are presented. The analyses are carried out with detailed documentation from the field and the acquired design drawings of the structures. For the building structure, the focus of the analysis is to understand the effect of masonry infill walls on the shear force demand of columns. The analysis results confirm that the infill walls of the building may have caused the damage to columns by increasing the shear force demand. For the bridge structure, the effect of seismic bars on the bridge response is investigated. The seismic bars in the bridge reduce the displacement demand of the superstructure by increasing the energy dissipation capacity of elastomeric bearings.

INTRODUCTION

The Chile Earthquake of February 27, 2010 was the fifth largest earthquake ever recorded in history. The magnitude of the earthquake was 8.8 and it caused damage to at least 370,000 houses and displaced 800,000 people with economic losses of $30 billion (USGS 2010). Despite the large intensity of the earthquake, the number of collapsed structures and the death toll were limited due to the country's modern seismic design code and the strict enforcement of the code. Many researchers from different organizations participated in field investigations after the earthquake to learn how structures designed according to modern seismic code performed in the event of a large earthquake. The research presented in this paper is an overview of the damage observed by a field reconnaissance team from the Mid-America Earthquake (MAE) Center. The regional damage is summarized which includes discussions with

researchers, practitioners, and city officials. In addition, case studies of a damaged building and a bridge are presented to investigate the causes of the damage that were observed in the field. For the case study structures, detailed design drawings were acquired and the damage was documented during the field investigations. For the building structure, the focus of the study is on the effect of masonry infill walls on the seismic demand imposed on the building. For the bridge structure, the effect of seismic bars, which are commonly used in Chile, on the displacement demand of the superstructure is investigated through inelastic time history analyses.

REGIONAL DAMAGE DESCRIPTIONS

Santiago. Santiago is the capital of Chile with a population of 5.2 million. The city is located in Santiago Region, which is one of Chile's 15 administrative divisions. Although the distance from the epicenter of the earthquake to Santiago was 200 miles, the city was close to the rupture area due to the large size of the fault. There were six seismic stations operating in the city during the earthquake event. The peak ground accelerations (PGAs) of the recorded accelerations were in the range of 0.17g to 0.56g for horizontal components and 0.11g to 0.28g for vertical components (Figure 1). Based on 922 responses in community survey system in USGS (Wald and Dewey 2005), the seismic intensity (Modified Mercalli) of the city is determined as VII, which corresponds to very strong shaking and moderate structural damage.

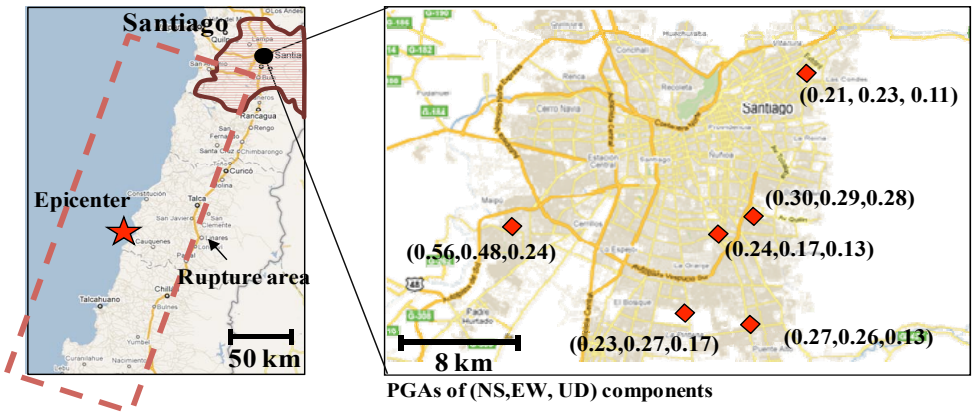


Figure 1. Location of Santiago and recorded PGAs around the city

While most reinforced concrete (RC) buildings in Santiago performed well, suffering only minor damage or even no damage, a limited number of buildings suffered significant damage due to structural deficiencies such as soft stories, horizontal or vertical irregularities, and short-column effects. Several other buildings were damaged due to the failure of bearing walls with proper confinement, as this was not required in the seismic design code. The following is a summary of the observed damage in Santiago.

The building in Figure 2 was used as a hotel. It consists of a tall tower and a low-rise commercial building. The damage shown in the figures are at the connection of the two structures. As it can be observed from the figure, the beams connecting the tall tower and the low-rise building were fractured. It is speculated that the beams were damaged as the tall building vibrated out of phase with the low-rise building,

and that action could have developed large force demand at the connection of the two buildings.

The building in Figure 3 was constructed with load bearing walls covered with masonry cladding. The surface of the bearing walls was chipped such that the cement mortar could develop bond strength between the walls and the masonry cladding. During the earthquake, however, a large portion of the cladding was debonded and fell to the ground, which could have caused injuries or even deaths if people had been near the building at the time of the earthquake. A beam between two vertically slender windows, which separate two large walls, was also damaged. The beam apparently acted as a link (or coupling) beam between the two large walls, and did not have enough shear strength to resist the force demand.

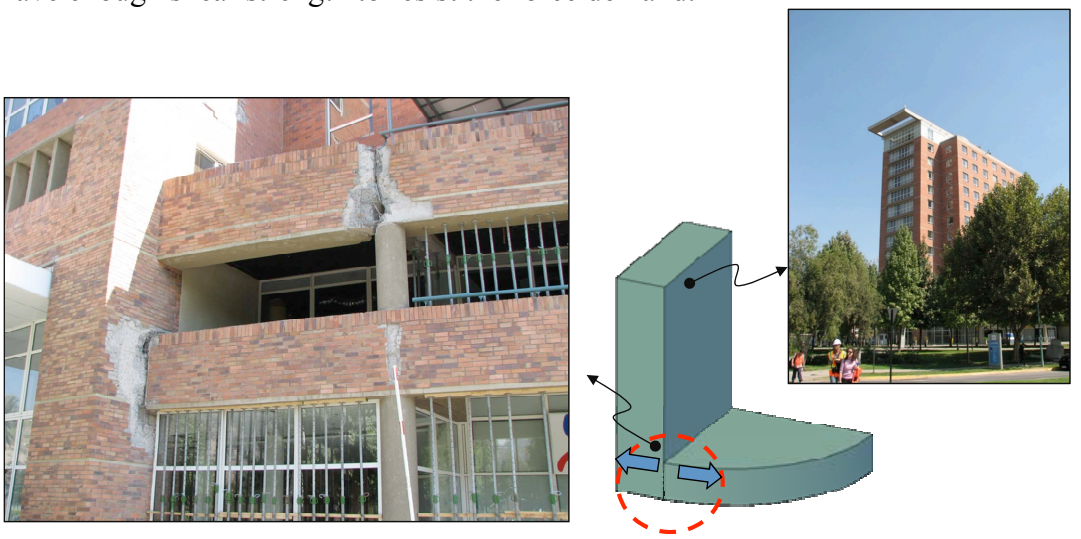


Figure 2. Failure due to vertical irregularity



Figure 3. Collapsed masonry cladding wall and a damaged beam

Biobío Region. The Biobío region is located in the south half of the rupture area as shown in Figure 4. The coseismic slip displacement of Talcahuano and Concepcion area was approximately 3m (Bevis 2010). Main damage to the region was located in the coastal towns of Arauco Province, Talcahuano city, and Dichato town (Figure 4

right). These coastal towns were severely damaged due to tsunami following the earthquake event. The area in Talcahuano Bay inundated with the tsunami is approximately 11km^2 and more than 30,000 people were directly affected by the tsunami (INE 2010).

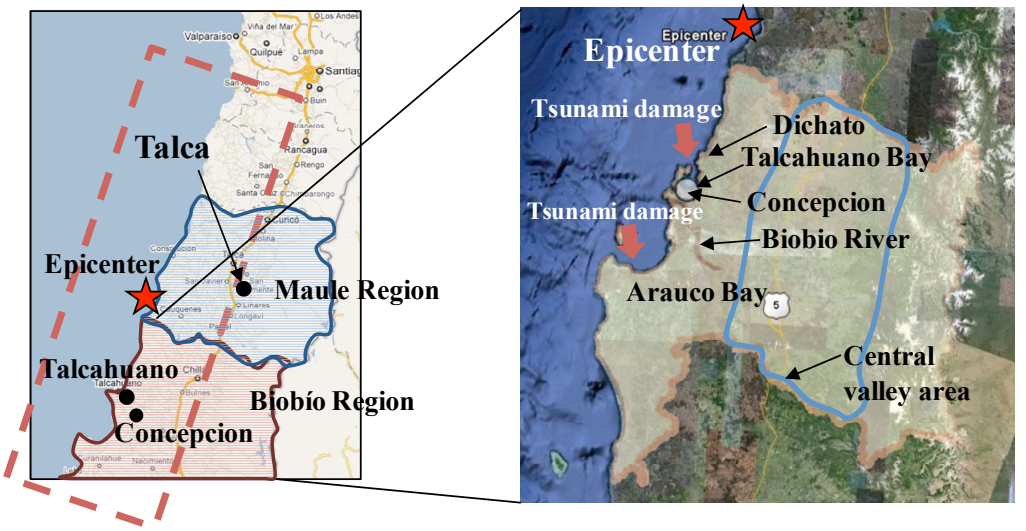


Figure 4. Biobío and Maule Regions (left) and cities in Biobío Region (right)

In Concepcion, several buildings were collapsed and several 15 to 20 story buildings were severely damaged and had to be demolished. Due to the damage to multi-story buildings, several blocks of streets in the downtown of Concepcion were closed at the time of the field investigation. One of the newly constructed buildings was toppled as shown in Figure 5. Interestingly, a nearby building with a similar height remained intact.



Figure 5. Toppled multi-story residential building: Left-illustration of the building before the earthquake, right-toppled building after the earthquake

In the Biobío region, the transportation network suffered only minor damage except a few bridges that were severely damaged or collapsed. Two 2km length bridges collapsed and one 2km length bridge was severely damaged. While the number of failed bridges was small, the failed bridges were the critical links in the regional transportation network, connecting industrial areas to ports. The failure of

these critical bridges resulted in a large economic impact to the area. At the time of the field investigation, around one and a half months after the earthquake event, only 30% of industries were operating in the region due to the difficulty in accessing the facilities in addition to damage to structures and lack of power.

There were failures in critical lifeline networks, such as gas, electricity, water, and waste water. The electricity network was restored most quickly. The gas network was not restored in many areas in the region even after several weeks. As some parts of the network were very old, the vulnerability of the network was high. In general, the central valley area of the Biobío region in Figure 4 was not largely affected by the earthquake except a few of the highway bridges and slopes. The area, however, suffered failures in water irrigation system.

Maule Region. The epicenter of the earthquake was offshore Maule as shown in Figure 4. Talca is the capital of the Maule region with a population of 230,000 and 75,000 houses. The city suffered the largest damage from the earthquake due to its close proximity to the rupture area. In addition, a large portion of buildings in Talca were adobe with negligible seismic resistance. Out of 75,000 houses in Talca, around 15,000 houses were damaged among which around 4,000 were either collapsed or damaged beyond repair. Many of these buildings were 100 to 200 years old. In the historic downtown area, where the majority of buildings were made of adobe, approximately 80% of buildings were damaged and half of the damaged buildings were beyond repair.

There were many new RC or masonry constructions designed according to modern seismic design code. The newly constructed buildings rarely suffered damage. There were only a couple of buildings which had minor architectural damage rather than major structural damage. Timber structures with adobe infill performed relatively well. When interviewed by the field reconnaissance team, the mayor of the city of Talca expressed his concerns that people in the city may rebuild their houses with adobe due to its low construction cost. At the time of the visit, the city did not have a modern design guide for adobe construction.

After the earthquake event, the critical lifeline networks of the city including gas, water, and electricity were damaged. All lifeline networks were recovered in seven to ten days. In the downtown area, recovering from damage took relatively longer as networks were dense in the area. Even though the water network was recovered earlier than the electricity network, due to the lack of electricity, water could not be pumped to higher grounds showing the inter-dependency of the lifeline networks.



Figure 6. Adobe buildings and historic structures

The typical adobe building (left) and the historic structure (right) in Figure 6 exemplify the buildings in downtown area of Talca.

EFFECT ON BRIDGES

Considering the large magnitude and huge rupture area of the earthquake, the damage to bridge structures was not significant. The majority of highways are constructed and maintained by private sectors. These highway networks are as long as 2,200 km in length and have around 2,000 bridges with spans longer than 10 m. Among these bridges, only 1% (8 highway and 12 pedestrian bridges) collapsed due to the earthquake event. Approximately 100 bridges (50 highway and 50 pedestrian) were damaged requiring repairs.

The MAE Center team visited several damaged bridges to understand the failure modes. The most typical bridge damage was due to unseating or displacement of the superstructure, especially for skewed bridges. At one site, it was clearly shown that the bridge designed with a more recent design practice suffered more damage than the bridge constructed with a previous design practice. In the old construction, the integrity of the bridge superstructure was high due to diaphragms connecting the girders. Bridges constructed in recent years often do not have diaphragms. Due to lack of integrity, bridge girders were damaged from the impact of the bridge superstructure to shear keys. In a report from another field investigation team (Yashinsky et al. 2010), it is also stated that the seat-width on bridge bents was not large enough to prevent unseating.

Only a few bridges reportedly had damage at the substructure. It is speculated that as there were not many bridges with integral superstructure-substructure connections, thus the large inertial force from the superstructure was not transferred to the substructure. Instead, the inertial force caused the unseating or large movement of the superstructure, or failure of the shear keys. Most of the investigated bridges had seismic bars, which tied the superstructure to the substructure in order to prevent vertical movement. Based on the design drawings, the seismic bars were embedded such that they can develop enough bond strength. The effect of the seismic bars on the response of the bridge will be discussed later.

CASE STUDIES

After the field investigation, case studies are carried out for one bridge and one building. The main objective of the case studies is to understand the causes of the damage for the building structure and the role of the seismic bars in the bridge structure. Spectrum compatible ground motions are generated using recorded ground motions as seed records. The target response spectra for the sites of the building and the bridge are defined using the attenuation relationships by Zhao et al. (2006) and Campbell and Bozorgnia (2003). For the sake of brevity, only a summary of the observed structural damage, numerical models, and findings from analyses are given in the following. Further details are available in the field investigation report (Elnashai et al. 2010).

Paso Cladio Arrau Bridge

The reference bridge (Paso Cladio Arrau) for this case study has 4-spans and it is 77.5m long. The bridge has three bents each of which consists of 10 piers as shown in Figure 7. As observed in most other bridges in Chile, seismic bars were installed in the bridge. Girders are supported on elastomeric bearings made of neoprene. The bridge has a skew angle of approximately 50 degrees.

The bridge suffered minor damage from the earthquake as shown in Figure 8. The superstructure displaced in the transverse direction, seismic bars yielded and elongated, and the shear keys failed. However, unseating of the superstructure was not observed. Even though the shear keys were damaged, it is speculated that they prevented the unseating of the bridge superstructure. In addition to the shear keys, the seismic bars might have reduced the displacement demands.

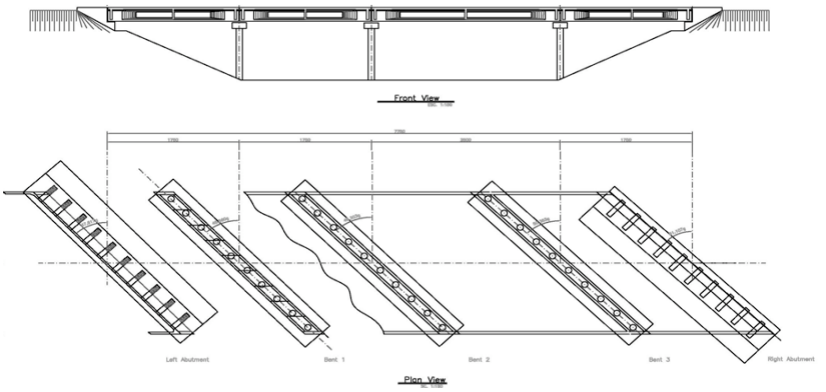


Figure 7. Configuration of bridge bents and abutment



Figure 8. Cracked shear key (left) and yield seismic bars (right)

The 3D model of the bridge was assembled in ZEUS-NL (Elnashai et al., 2010). The stiffness of abutments and hysteretic behavior of the bearings are modeled using lumped springs. The piers, seismic bars, and superstructure are modeled using cubic beam-column elements. Since detailed information on the post-tensioning force of the seismic bars is not available, it is assumed that the seismic bars are post-tensioned up to 30% of the bar's yield stress. The additional normal force to elastomeric bearings due to the post-tensioning is taken into account in the hysteretic behaviour of elastomeric bearings (hysteretic curve in Figure 9). The deck is considered as a rectangular beam having the equivalent section properties of the

girders and the bridge deck. The configuration of the superstructure-substructure connections is illustrated in Figure 9.

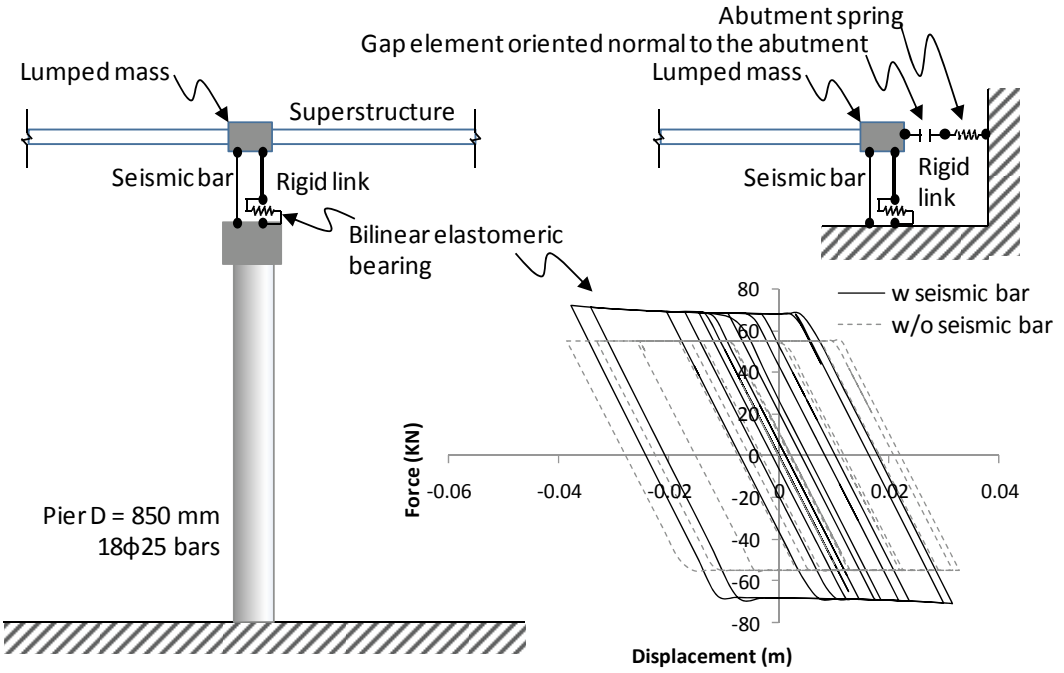


Figure 9. Details of numerical models

Artificially generated ground motions are used for inelastic response history analyses. A total of 18 horizontal components of ground motions are applied in the transverse direction. Two sets of analyses are carried out. In the first set, the seismic bars are included in the numerical model as flexural elements. In addition, the normal force on the elastomeric bearings is increased to take into account the post-tensioning force. It is assumed that the additional normal force on elastomeric bearings due to post-tensioning remains constant throughout the earthquake excitation. For the second set of analyses, all parameters are identical with those in the first set except that the contribution of seismic bars is removed from the model.

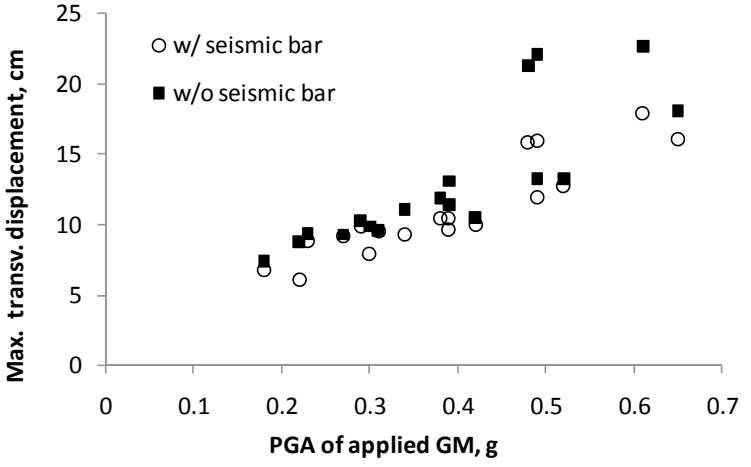


Figure 10. Maximum responses of bridges w/ and w/o seismic bars

Figure 10 compares the maximum transverse displacement for the two analysis cases as a function of PGA of the input ground motion. As it is observed from the figure, the models without seismic bars generally have larger displacement demand, and the same trend is clearly observed as the PGA of the input ground motions increases. This difference is primarily due to increased normal force in elastomeric bearings, which increases the energy dissipation capacity of the bearings.

Odontology Building of the University of Concepcion

This case study aims to explain the observed damage of the Odontology building of the University of Concepcion. The structure was used as the school of dentistry which also included rooms for examination and medical treatment of patients. Due to the requirements of the building occupancy, the reinforced concrete structure has a peculiar configuration. As shown in Figure 11, the structure has 3 regular stories and 3 service stories with approximately half story height that accommodates utility lines. The building has a rectangular shape with 7x5 bays. Structural core-walls are provided at the center of the building to resist the majority of the lateral loads. Except for minor differences in column dimensions of the exterior frames, the structure is symmetrical in both directions. Floors of the building are designed as flat slabs. Masonry infill walls are used at the first floors of the exterior frames. The height of the first story is 3.1 m and the height of the masonry infill walls was measured to be approximately 2.1 m.

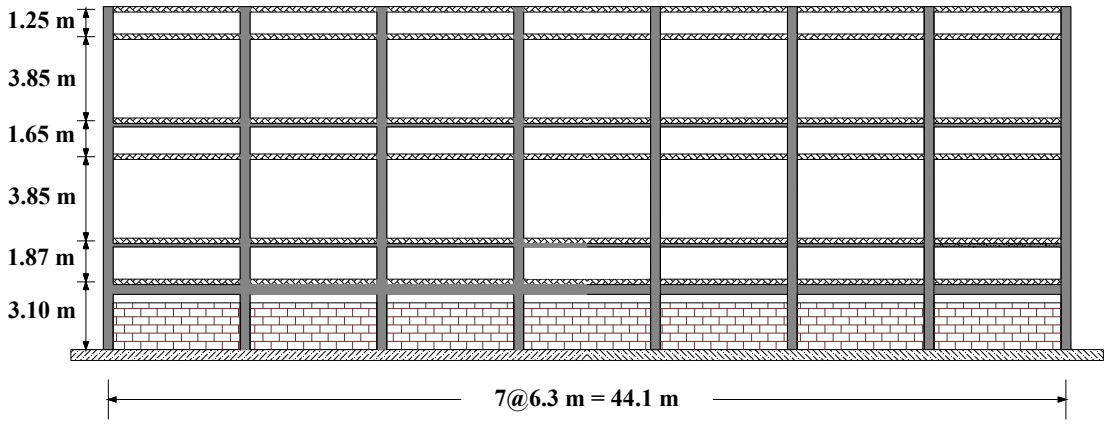


Figure 11. The Odontology building of the University of Concepcion

The earthquake caused interesting damage patterns to the building. The structural damage was confined to columns of the exterior frames. The rest of the observed damage was non-structural: cracking on the partition walls (inside the building) and the diagonal cracks of the masonry infill walls at the exterior frames. The field observations indicated that the combined axial-shear failure at the top of the columns was due to the commonly observed “short-column” effect that results from increased shear demands on a specific portion of the vertical members due to a decrease in the effective length. Some of the damaged columns are shown in Figure

12. In light of the above observations, the 7-bay exterior frame of the building is analyzed to understand the effects of masonry walls on the columns.



Figure 12 Damaged columns of the Odontology building

The fiber-based finite element analysis software ZEUS-NL (Elnashai et al., 2010) is used to model the frame shown in Figure 11. All members except for the masonry infill walls are represented with beam-column elements. The effective flange width of slab is calculated according to ACI 318-08 (ACI 2008). For the flat-slab floors, the portion of the slab that contributes to the frame analysis is determined by using the formulations proposed by Luo and Durrani (1995a, 1995b). The concrete is modeled using the constant confinement model developed by Martinez-Rueda and Elnashai (1997). Steel is modeled with a bilinear elasto-plastic model with kinematic strain hardening. Based on the information on the design drawings, the following material properties are used: a concrete compressive strength of 29.4 MPa, steel yield and ultimate strengths of 411.6 MPa and 617.5 MPa, respectively. In modeling the masonry infill walls, the following assumptions are made: infill walls do not carry any vertical loads and they can be represented with diagonal struts that have horizontal resistance only. The modeling of masonry infill walls follows the approach proposed by Mostafaei and Kabeyasawa (2004). Since the objective of the analysis is to show the effect of masonry infill walls on the response of the structure and observed damage, two building configurations are considered: with and without infill walls. A total of 8 artificially generated ground motions are used for inelastic dynamic time history analysis of the building.

The analysis results indicated that there is a significant reduction in the interstory drift ratio of the first floor, reaching as high as 51%, when the effect of masonry infill walls are considered. In order to explain the shear failures of columns due to the previously described short-column effect, it is required to compute the shear capacity of the columns and compare it against the shear demand imposed during the earthquake. The shear strength of the RC column is calculated according to ACI 318-08 (2008). As an example, the shear capacity and the shear demand on one of the exterior columns is shown in Figure 13. It is observed that the presence of masonry infill walls significantly increase the shear demand on the columns and the shear capacity is exceeded at certain times throughout the analysis.

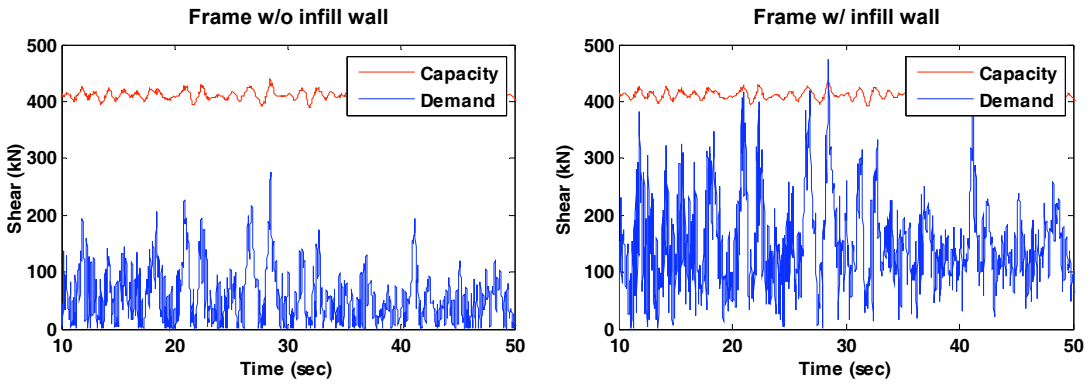


Figure 13 Comparison of shear capacity and demand for column 8

CONCLUSIONS

The seismic performance of structures after the 2010 Chile Earthquake is presented in this paper. Considering the large magnitude of the earthquake, the structures performed very well due to the enforcement of the seismic design code. Some RC buildings in Santiago region were damaged due to insufficient confinement of structural walls. Some others were damaged due to vertical irregularities and/or deficient beam-column connections. In general, damaged buildings were not widely distributed throughout Santiago. In Concepcion, in Biobío region, relatively more buildings were damaged than those in Santiago. It is speculated that it is due to close proximity of the city to the epicenter, or due to local site effects. It was very interesting to observe that a building could collapse while a nearby similar building, supposedly under a similar seismic load, did not suffer major structural damage. It was speculated that the failure of the building was due to a deficiency in the structural system, but more investigation is required to clearly understand the causes of the failure. Talcahuano city in Biobío region suffered significant damage primarily from the tsunami. Most of the damage in Talca in Maule region was due to the failure of adobe structures. Modern buildings in Talca performed very well.

The post-earthquake analysis shows that the seismic bars in bridges may have reduced the displacement demand of bridge superstructures. Since the interaction between seismic bar and elastomeric bearing is not fully considered in the analysis, further study is necessary to generalize this conclusion. The damage to the Odontology building may have resulted from the presence of the masonry infill wall, which can considerably increase the shear force demand imposed on the concrete columns.

ACKNOWLEDGEMENT

The field mission to Chile was sponsored by the Mid-America Earthquake Center, Missouri University of Science and Technology, Georgia Institute of Technology, and National Research Foundation of Korea (KRF-D00644). The MAE Center is an Engineering Research Center funded by the National Science Foundation under cooperative agreement reference EEC 97-01785.

REFERENCES

ACI (2008), *Building Code Requirements for Structural Concrete (ACI 318-08) and Commentary*, American Concrete Institute, Farmington Hills, MI, USA.

Bevis, M. (2010). "Research News." http://researchnews.osu.edu/archive/ chilequakemap.htm. Web accessed on Aug. 15, 2010.

Elnashai, A.S., Gencturk, B., Kwon, O-S., Al Qadi, I., Hashash, Y., Roesler, J., Kim, S-J., Jeong, S-H., Dukes, J. and Valdivia, A. (2010). *The Maule (Chile) Earthquake of February 27, 2010: Consequence Assessment and Case Studies*. Mid-America Earthquake (MAE) Center Report Series, CD-Release 10-04.

Elnashai, A., Papanikolaou, V. and Lee, D. (2010), *ZEUS NL – A system for inelastic analysis of structures, User's Manual*, Mid-America Earthquake (MAE) Center, Department of Civil and Environmental Engineering, University of Illinois at Urbana-Champaign, Urbana, IL.

INE (Instituto Nacional de Estadísticas) (2010). http://www.ine.cl/canales/sala _prensa/noticias/ 2010/marzo/not190310.php. Web accessed on Aug.15, 2010.

Luo, Y. H. and Durrani, A. J. (1995a), "Equivalent beam model for flat-slab buildings. Part I: Interior connection," *ACI Structural Journal*, 92(1), 115–124.

Luo, Y. H. and Durrani, A. J. (1995b), "Equivalent beam model for flat-slab buildings. Part II: Exterior connection," *ACI Structural Journal*, 92(2), 250–257.

Martínez-Rueda, J. E. and Elnashai, A. S. (1997), "Confined Concrete Model under Cyclic Load," *Materials and Structures*, 30(3), 139-147.

Mostafaei, H. and Kabeyasawa, T. (2004), Effect of infill masonry walls on the seismic response of reinforced concrete buildings subjected to the Bam earthquake strong motion: A case study of Bam telephone center, Earthquake Research Institute, University of Tokyo.

USGS (2010*). Magnitude 8.8 - OFFSHORE MAULE, CHILE.* Web page http://earthquake.usgs.gov/earthquakes/eqinthenews/2010/us2010tfan/#details accessed on Dec. 1, 2010.

Wald, D. J., and Dewey, J. W. (2005). "Did You Feel It? Citizens Contribute to Earthquake Science." United States Geological Survey.

Bridge Performance during the 2010 M8.8 Chile Earthquake

P. W. Yen[1], G. D. Chen[2], I. Buckle[3], T. Allen[4], D. Alzamora[5], J. Ger[6], and J. G. Arias[7]

[1] Office of Infrastructure, R&D, Turner-FairBank Highway Research Center, Federal Highway Administration, 6300 Georgetown Pike, McLean, VA 22101; PH (202) 493 -3056; FAX (202) 493-3442; email: wen-huei.yen@dot.gov
[2] Department of Civil, Architectural and Environmental Engineering, Missouri University of Science and Technology, 1400 N. Pine St., Rolla, MO 65409-0030; PH (573) 341-4462; FAX (573) 341-4729; email: gchen@mst.edu
[3] Department of Civil and Environmental Engineering, University of Nevada, Reno, NV 89557; PH (775) 784-1519; email: igbuckle@unr.edu
[4] State Materials Laboratory, Washington State Department of Transportation, P.O. Box 47365, Olympia, WA 98504-7365; PH (360) 709-5450; email: allent@wsdot.wa.gov
[5] Resource Center, Federal Highway Administration, 12300 W. Dakota Ave., Suite 340, Lakewood, CO 80228; PH (720) 963-3214: email: daniel.alzamora@dot.gov
[6] Florida Division, Federal Highway Administration, 545 John Knox Road, Suite 200 Tallahassee, FL 32303; PH (850) 942-9650, email: jeffrey.ger@fhwa.dot.gov
[7] Department of Civil and Environmental Engineering, University of Nevada, Reno, NV 89557-0152; PH (775) 354-6052; FAX (775) 784-1390; email: ariasaco@unr.nevada.edu

ABSTRACT

Field observations and plausible reasons of damaged bridges are presented and their implications to bridge design are discussed. In general, bridge substructures behaved satisfactorily except that a few columns suffered shear failure. Reinforced concrete shear keys served their design purposes, performing well when they functioned as part of the lateral restraint system at the bottom flange of girders. Vertical seismic bars were widely used to restrain the vertical motion of decks and they also performed well. Lateral steel stoppers were also used to provide vertical and lateral restraints on girders but were largely unsuccessful due to their weak connection to capbeams. Many spans of precast, prestressed, discontinuous girder bridges with continuous decks fell from their supports due likely to significant rotation of their superstructure. Other types of bridge damage were related to ground shaking, ground settlement and liquefaction-induced lateral spreading.

INTRODUCTION

The M8.8 offshore Maule earthquake occurred on February 27, 2010, at 3:34 a.m. local time on a thrust fault at the boundary between the Nazca and South

American tectonic plates [USGS, 2010]. The Nazca plate moved down and landward below the South American plate in the subduction zone, resulting in a sudden release of energy accumulated over time. The earthquake epicenter, located at Offshore Maule S35.909 and W72.733, was approximately 335 km SW of Santiago, 105 km NE of Concepcion, and 115 km WSW of Talca, Chile. The depth of the earthquake hypocenter was 35 km. The M8.8 event is the fifth largest earthquake recorded in modern times, followed by 21 aftershocks of magnitude 6.0 or greater by April 26, 2010.

The Chilean geological condition in the Maule region is eerily similar to that in the Northwestern United States such as the states of Washington and Oregon. Many bridges that experienced damage during the 2010 Maule earthquake were designed and constructed following similar practices to what is stipulated by the U.S. seismic codes. Due to the similarities in earthquake environments, bridge design specifications, and construction processes, the observations and findings of bridge performance during the Maule earthquake provided valuable data sets and insights to both the improvement of current bridge design provisions and to the advancement of earthquake engineering.

The February 27, 2010, Chile earthquake and associated tsunami(s) damaged about 200 bridges, including 20 that collapsed. This earthquake provided a unique opportunity to address several bridge design related issues, including (1) the damaging potential of subduction-type ground motions that have multiple pulses, long duration, and possible rotational components; (2) the tsunami effects; (3) the role of transverse diaphragms and their possible elimination for accelerated bridge construction; (4) the effects of the number of joints and joint detail; and (5) the consequences of liquefaction-induced lateral movement and settlement. The following sections will discuss in detail each of these critical issues using example bridges.

SUBDUCTION-TYPE GROUND MOTIONS

The 2010 Chile earthquake generated ground motions with long duration and multiple pulses [Boroschek et al., 2010]. In addition, the earthquake may also have induced significant rotational motions that can be inferred from the patterns of in-plane rotations of bridge superstructures. Figure 1 shows the 32 bridge sites that were visited by the Federal Highway Administration (FHWA) reconnaissance team and highlights in red 7 of them with significant rotations in bridge superstructures. Located near Santiago at relatively stiffer soil deposits, these seven sites are further away from the earthquake epicenter than Constitución and Concepción, but the bridges at these sites exclusively experienced significant rotations. The representative acceleration response spectra at the Hospital Station in Curicó are presented in Figure 2 [Boroschek et al., 2010].

For the bridges with significant rotations, Table 1 lists the name, orientation, skew angle, skew direction, material used in girder, presence of diaphragms, transverse displacement at intermediate bents, and direction of deck rotation. The combination of these parameters will help determine the mechanism of bridge deck rotations. Note that two parallel bridges were inspected at each of sites 1, 2, and 10. At sites 2 and 10, one bridge collapsed and the other bridge suffered minor damage. In Table 1, C denotes a clockwise rotation and C.C. represents a counter clockwise rotation.

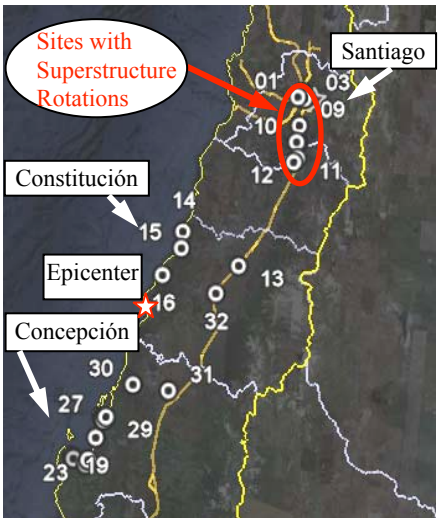


Figure 1. Bridge sites.

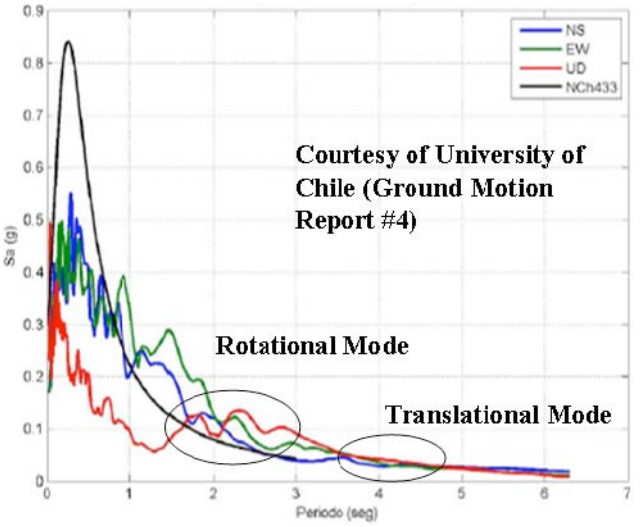


Figure 2. Mode response sensitivity.

Table 1. Bridges with Significant Rotations.

Bridge Characteristics					Movement Pattern	
Site	Name	Orientation	Skew/ Direction	Girder/End Diaphragm	Transverse Movement	Rotation
1a,1b	Miraflores	NE-SW	20°/C.C.	Concrete/No	Negligible	C.
2a	Lo-Echevers	NE-SW	33°/C.C.	Concrete/No	Negligible	C.
5	Matta-Quilicura	E-W	45°/C.C.	Steel/Yes	Negligible	C.
7	Romero	E-W	31°/C.	Concrete/No	Negligible	C.C.
8	Chada	E-W	0°/C.C.	Concrete/No	Negligible	C.C.
10b	Hospital	NW-SE	40°/C.C.	Concrete/No	Significant	C.C.
11	Las Mercedes	NW-SE	≈0°/C.C.	Concrete/No	Negligible	C.C.

The six skewed bridges (1a, 1b, 2a, 5, 7, and 10b in Table 1) rotated about the centroid of the bridge superstructure opposite to their respective skew direction or the direction of rotation from a transverse line perpendicular to the bridge centerline to the abutment back wall of the bridge, regardless of the bridge orientation, the magnitude of the skew angle, and the presence of diaphragms. The straight bridges (8 and 11 in Table 1) also rotated counter clockwise. The fact that all but one bridge experienced negligible transverse displacements indicates the rotation effect was dominant in these bridge superstructures with the acute corners (if skewed) of each bridge moving away from their abutments at both ends.

Considering both the skewed and straight bridges, observations can be made on the overall plausible reasons for bridge deck rotation. Skew of bridges is a significant but not necessarily a decisive factor contributing to bridge rotation. The high sensitivity of the rotational vibration mode of the bridge to ground motion, particularly rotational excitations, could be dominant. The fault directivity effect can play a role in the rotation of bridge superstructures since both straight bridges (8 and 11 in Table 1) are approximately oriented along the E-W direction.

As an example, the 2-span Chada overpass as shown in Figure 3 (a) is discussed in detail. The bridge superstructure was displaced significantly during the earthquake. The transverse offset between the deck and abutment seats ranged from 64 cm to 78

cm. The longitudinal gap between the end of girders and the abutment was up to 9 cm. The bottom flange and web of the exterior precast girder that hit the curtain walls at each abutment failed in shear as seen in Figure 3 (a). The failure of the bottom flange is clearly seen in Figure 3 (b). The two curtain walls at the intermediate bent were both damaged as shown in Figure 3 (c). The bridge experienced strong shaking as indicated by the induced gap around columns, Figure 3 (d). No structural damage was observed in the bridge columns.

When curtain walls at the intermediate bent and two abutments are not engaged, the in-plane motion of the bridge superstructure is governed by the mass of the superstructure, stiffness of seismic bars in round shape, and characteristics of ground motions. The period of the rotational mode of vibration is approximately 70% of the period of the two translational modes that are long due to flexible seismic bars used. In this case, the rotational mode of vibration is more sensitive to ground motions than the translational modes. An insignificant degree of eccentricity between the centers of mass and stiffness that likely existed during the earthquake, given the slumping of the abutment fills and duration of shaking would result in significant rotations even under translational ground motions. Once present, the rotational ground motions can amplify the bridge rotations substantially.



(a) Curtain wall shear failure at abutment



(b) Bottom flange damage



(c) Curtain wall damage at bent



(d) Soil separation from column

Figure 3. Damage to the Chada Bridge.

ROLE OF TRANSVERSE DIAPHRAGMS

The exterior prestressed concrete (PC) girders of the Romero and Chada bridges (7 and 8 in Table 1), which were constructed without diaphragms, experienced out-of-plane block shear failures due to transverse impact loads from shear keys as

illustrated in Figure 4 (a). When partial diaphragms were used between the girders such as in the San Nicholás bridge, the bottom portion of the exterior girder still experienced significant shear cracks as shown in Figure 4 (b). However, with the use of even partial concrete keys between girders as shown in Figure 4 (c), both exterior and interior prestressed concrete girders of the Llacolén bridge suffered no visible damage. This was because the concrete keys provided sufficient lateral restraints on most of the girders, making them work together and share the transverse seismic force. With full diaphragms, the 260-m-long East Ramadillas bridge across the Piteateo River survived the earthquake even though the deck of the bridge was vertically misaligned as a result of liquefaction-induced ground settlements.



(a) Chada bridge with no diaphragms (b) San Nicholás bridge with partial diaphragms



(c) Llacolén bridge with concrete key (d) East Ramadillas bridge with full diaphragm

Figure 4. Damage on exterior prestressed concrete girders.

To illustrate the role of diaphragms, two bridges oriented in the E-W direction at the Independencia/Américo Vespucio site were compared. Built in 2004, the bridge that carries eastbound traffic is a four-span structure with five discontinuous prestressed, precast, girders and a continuous deck. It almost collapsed during the earthquake, experiencing a lateral offset of greater than 0.5 m. The superstructure had steel stoppers but no intermediate or end diaphragms. Both the curtain wall of the abutment and the steel stoppers were significantly damaged. Each stopper was anchored with two bolts that were embedded into the capbeam for a depth of 90 cm.

The westbound bridge is a four-span structure with six discontinuous prestressed precast girders and a continuous deck as shown in Figure 5. Built in 1997, each bent has two flared wall piers. The bridge was designed with both intermediate and end diaphragms, and survived the earthquake with damage limited to concrete shear keys and excessive deformations in the seismic bars. In comparison to the eastbound bridge, the presence of diaphragms seemed to have helped maintain the

structural integrity of the westbound bridge. More importantly, the concrete shear keys likely served their design purpose during the earthquake as opposed to the steel stoppers in the eastbound bridge. For both structures, no visible foundation damage was observed.



(a) Displaced seismic bar (b) Typical flared wall pier (c) Damage of shear keys

Figure 5. Damage to the westbound Independencia Bridge.

TSUNAMI EFFECTS

The 2010 Chile earthquake induced significant tsunami effects on bridges along the coast roads. Two bridges were inspected in detail for combined earthquake and tsunami effects: the Pichibudis bridge and Cardenal Raúl Silva Henŕiquez bridge. The second bridge is a river-crossing multi-span structure that suffered significant damage as discussed below. The nine spans of the SW portion of the bridge are supported on tall, steel pile bents as shown in Figure 6 (a). The legs of these bents are fabricated from 1.5 m diameter tubes with a wall thickness of 14 mm. Their overall height from pile tip to soffit ranges from 44.5 to 51.5 m. The maximum clear height above the water is about 25 m. This portion of the structure appeared to have performed relatively well during the earthquake compared to the NE portion, but suffered local damage at several locations due to tsunami effects. Four major waves were recorded near Constitución with arrival times ranging from 3:50 am to 5:20 am after the mainshock. Wave heights ranged from 6.9 to 11.2 m passing under the superstructure. Nevertheless these waves eroded river sands and gravels from around the piles, Figure 6 (b), to a depth of about 4.5 m, and wave-borne debris punctured a hole in the wall of one of the steel legs as shown in Figure 6 (c) (Courtesy of the Ministerio de Obras Públicas de Chile or MOP).



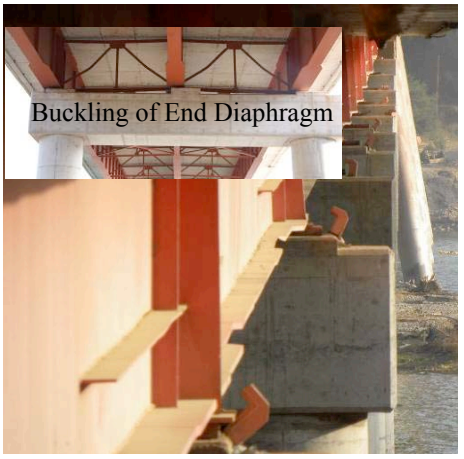
(a) Southern spans and pile bents (b) Erosion of alluvial materials (c) Debris impact

Figure 6. Damage to the Cardenal Raúl Henŕiquez Bridge (MOP).

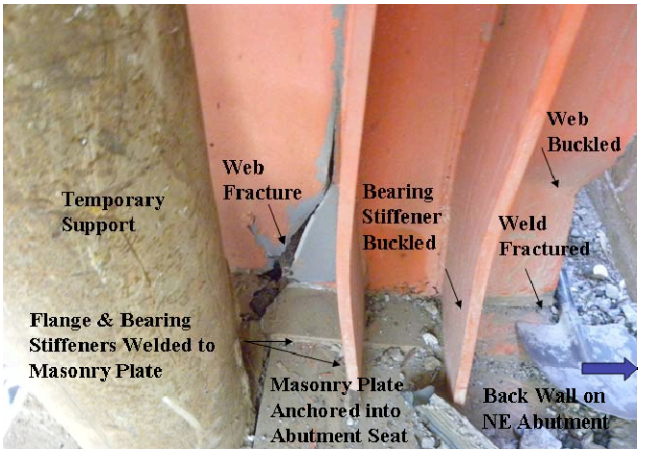
EFFECTS OF THE NUMBER OF JOINTS AND JOINT DETAIL

Built in 2002, the Cardenal Raúl Silva Henŕiquez bridge is a 22-span, steel-girder structure crossing the Maule River near Constitución in the NE-SW direction. It is supported by two seat-type abutments and twenty-one intermediate bents. The first five bents from the NE abutment are supported on two RC columns and drilled shafts. The next six bents are supported on three RC columns and drilled shafts. The following eight bents are steel pile bents with three legs (one vertical and two inclined) with horizontal struts and diagonal braces interconnecting the legs in each bent, as illustrated in Figure 6 (a). The last two bents are supported on three RC columns that rest on footings. The superstructure comprises two continuous segments, each being 11 spans long. Fixed and expansion joints were designed at two abutments and at the middle of the bridge over bent 11, respectively. At each abutment, the bottom flanges of the three girders are welded to masonry plates embedded in the abutment seat. An elastomeric pad is provided over each intermediate bent to permit longitudinal movement. Transverse and vertical movements were restrained by steel stoppers, as shown in Figure 7 (a).

During the earthquake, the NE portion of the bridge moved transversely from west to east as shown in Figure 7 (a). All steel stoppers were deformed and girders were displaced from their elastomeric pads, resulting in the web and flange bending of the exterior girder about its weak axis at the NE abutment, as shown in Figure 7 (d). The transverse diaphragms at the intermediate bents and abutments buckled as shown in Figure 7 (a, c). At the NE abutment, the webs and bottom flanges were fractured in all three steel girders, and both bearing stiffener and web buckled as shown in Figure 7 (b). This type of damage is indicative of large longitudinal loads in the superstructure being attracted to the fixed bearing at the abutment. The weld detail at the abutment transferred the longitudinal loads into a significant bending moment, locally causing stress concentrations in the steel girders at the end of their supporting masonry plates. Note that the weld between the girders and the masonry plate did not fail. As shown in Figure 7 (d), due to severe damage in the web and flange of girders, a steel beam was used to temporarily transfer loads from the flange to the abutment seat bypassing the web of the girders.



(a) Girder offset and cross frame buckling



(b) Girder damage at north abutment





(c) Crossframe buckling (d) Temporary repair at NE abutment

Figure 7. Superstructure damage at the NE portion.

Although similar in connection details, the girders at the SW abutment were subjected to less damage than that at the NE abutment, limited to the buckling of the bearing stiffeners. The reason for this difference is probably due to the fact that the fillet welds connecting the girder flanges and bearing stiffeners to the masonry plates failed during the earthquake and large longitudinal loads were not attracted to this abutment, as shown in Figure 8 (Courtesy of MOP).



(a) The girder end (b) The transverse stiffeners

Figure 8. Damage at the SW abutment (MOP).

LIQUEFACTION-INDUCED LATERAL MOVEMENT AND SETTLEMENT

Liquefaction occurred in 15 out of 32 sites as indicated by surficial features such as sand boils. However, displacement of bridge foundations and columns due to lateral movement occurred only at a few liquefied sites, mainly along the Bio-Bio River. The NE side of the river experienced most of the liquefaction induced slope failures and structural damages. Although liquefied as well, the SW side of the river experienced little or no structural problems due to the flat ground conditions.

The Juan Pablo II Bridge is a crossing link over the Bio Bio River in Concepción and is oriented in the NE-SW direction. Built in 1973, the NE approaches to this bridge are part of an interchange that provides access to the bridge from a river-front highway as shown in Figure 9. In addition to on- and off-ramps, the

interchange comprises a 2-span approach structure, and a 2-span highway overpass as indicated in Figure 9. Each bridge superstructure consists of seven discontinuous prestressed precast girders and a continuous deck. The main river-crossing bridge is a multi-span structure supported on 18 m deep hand excavated caissons. The SW approach, built on elevated fills, suffered no damage.

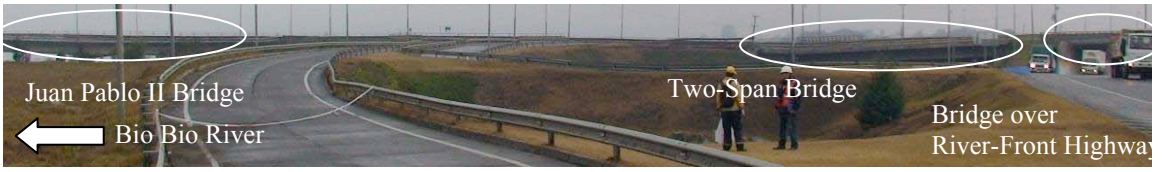
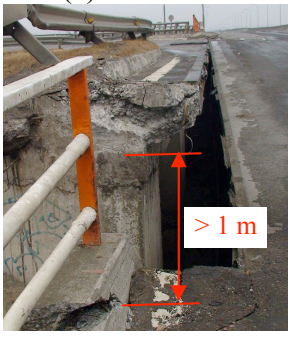


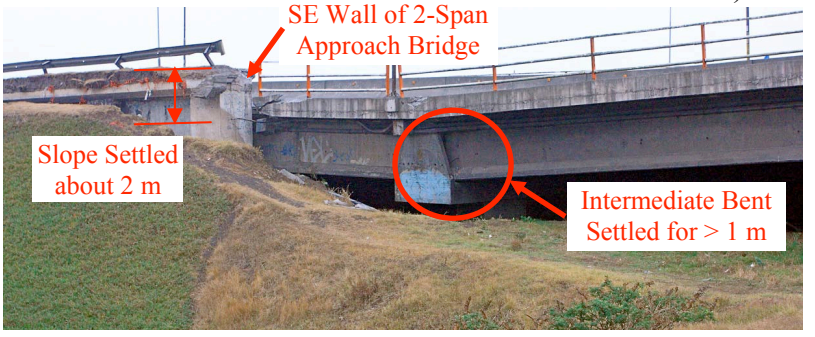
Figure 9 NE approaches to the Juan Pablo II Bridge.

Whereas the river-front overpass was generally undamaged, the 2-span approach structure was damaged both globally and locally at the intermediate bent as shown in Figure 10 and Figure 11. It is clearly seen in Figure 10 that the intermediate bent has settled for over 1 m with respect to the two end bents, leading to a substantial depression in the roadway surface. However, the wall at the SE corner of the approach structure settled little though the surrounding slope settled about 2 m. Supported on drilled shafts, the wall seemed to be newer than the approach structure, probably built with more stringent foundation design requirements together with the NE off-ramp on approach fills that suffered no damage during the earthquake.



(a) Overall settlement of the Juan Pablo II Bridge (facing the Bio Bio River)





(b) SE wall of approach spans (c) Intermediate bent settlement of approach spans

Figure 10 Uneven settlement of the Juan Pablo II Bridge.

As indicated in Figure 11 (a, b), the intermediate bent comprises two rectangular columns which experienced uneven, liquefaction-induced, settlement during the earthquake. The consequential change in stiffness between the two columns shifted the longitudinal seismic force from one to the other column which then failed in

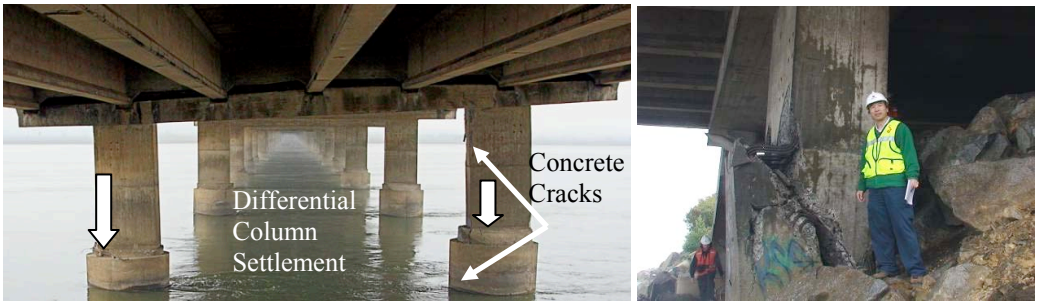
shear as shown in Figure 11 (b). The transverse reinforcement of the failed column was spaced at 46 cm. It is noted that the ground further settled against the undamaged column and the cap-beam above the undamaged column experienced cracking.

The spans of the main bridge also have experienced uneven support settlement as shown in Figure 10 (a), which then tilted the columns and rotated the bridge deck about the centerline of the bridge as seen in Figure 12 (a). In addition, lateral spreading of the NE bank attempted to move the columns of the bent at this position towards the river. But this movement was restrained by the superstructure and the columns were consequently placed in single shear. One failed catastrophically in shear as shown in Figure 12 (b) and the other was seriously damaged. The difference in behavior between the two columns might be due to the uneven settlement and rotation of the bridge deck. The longitudinal movement of the first column (upstream side) was approximately 56 cm at the top of the shear plane and 41 cm at the bottom. While the bridge did not collapse due to severe differential settlements and lateral slope movements, it was seriously damaged and closed to traffic.



(a) Column settlement (cracks on far side) (b) Crushed column due to shear failure

Figure 11. Damage to intermediate bent of approach spans.



(a) Uneven settlement and induced damage (b) Shear failure in upstream column

Figure 12. Damage due to uneven settlement and slope failure.

IMPLICATIONS TO BRIDGE DESIGN

The long-duration and multi-pulse features of the Chile earthquake ground motions can generally affect the inelastic behavior and progressive collapse mechanism of bridges. The rotational component of ground motions is critical to the design of bridges with sensitive rotational modes of vibration. The Chile earthquake-induced tsunami generated significant waves and currents that added both

horizontal and vertical loads on bridges and caused the erosion of soils around the bridge foundations. The additional loads can further stress a bridge that can be damaged by the earthquake, leading to the collapse of the structure. The scour effect on the stability of bridge foundations is a direct threat to the safety of transportation networks as indicated by the past 40 years of bridge operation in the United States. Although scour design provisions are included both in the Chilean and US Bridge Design Specifications, the combined earthquake and scour effects are not considered in design.

Concrete keys on the top of cap-beams can be a good alternative to cross diaphragms between bridge girders to distribute seismic loads among the girders. They can effectively prevent girders from shear failure by reducing the maximum load on individual girders. Such an alternative goes well with an accelerated bridge construction strategy using precast/ prestressed concrete girders. In addition, it provides a new dimension of managing the load path and energy dissipation together with shear keys so that a cost-effective design can be made to ensure that bridge foundations are subjected to little or no damage. A trade-off should be made between the redundancy of a bridge and the number of joints in the bridge superstructure in order to achieve a cost-effective design of the bridge. As the number of joints decreases, the connection detail at the joints becomes more critical in design.

As clearly reminded by the Chile earthquake, liquefaction-induced foundation settlement and lateral movement is one of the main reasons for the brittle shear failure of columns. Appropriate mitigation methods should be adopted in bridge design to minimize the effects of ground and slope failures on bridges.

ACKNOWLEDGMENTS

Financial support for the post-earthquake reconnaissance trip to Chile was mainly provided by the U.S. Federal Highway Administration with Sheila Duwadi serving as point of contact for the U.S. team members. The last author would like to acknowledge the financial support by Earthquake Engineering Research Institute. The findings and opinions expressed in this paper are those of the authors only; they do not necessarily reflect those of the sponsors. Special thanks are due to José Miguel Ortega for his support and coordination with local authorities to make the reconnaissance trip a success, Mauricio Guzmán and Sandra Achurra for their escort and introduction to various bridge sites visited by the reconnaissance team, Alex Union Villarroel for his post-trip assistances, and Rodrigo Oviedo for his participation throughout the reconnaissance trip.

REFERENCES

Boroschek, R., Soto, P., Leon, R., and Comte, D. (2010). "Terremoto Centro Sur Chile – 27 de Febrero de 2010, Informe Preliminar N^{o} 4." *Report No.4*, Universidad de Chile – Depto. Ingenieria Civil, and Depto. De Geofisica, 29 pp.

USGS (2010). "Magnitude 8.8 - offshore Maule, Chile, February 27, 2010." *United States Geological Survey (USGS) Earthquake Hazards Program*, http://earthquake.usgs.gov/earthquakes/eqinthenews/2010/us2010tfan/> (Sept.1, 2010).

PERFORMANCE OF STRUCTURES IN THE JANUARY 2010 M_W 7.0 HAITI EARTHQUAKE

Steven M. Baldridge[1] and Justin D. Marshall[2]

[1]President, Baldridge and Associates Structural Engineering, Inc., 1164 Bishop Street, Suite 600, Honolulu, HI 96813; email: sb@baseengr.com
[2]Assistant Professor, Department of Civil Engineering, 238 Harbert Engineering Center, Auburn University, Auburn, AL 36849; email: jdmarshall@auburn.edu

ABSTRACT

The earthquake that shook the island of Hispaniola on January 12, 2010 devastated Haiti. The resulting damage was widespread due to the construction methods, poor material quality and lack of rigorous design procedures. Post-event reconnaissance has brought to light deficiencies in all these areas. Construction, especially residential, is typically completed by the building owner who may or may not have the necessary skills to design or build safe structures. Very few structures are designed by an engineering professional. The two most common construction materials are masonry block and reinforced concrete. Building response to the ground shaking is demonstrated through damage surveys in downtown Port-au-Prince and Leogane and specific case studies generated through reconnaissance efforts which highlight the infrastructure problems which led to the deadly structural performance.

INTRODUCTION

In the late afternoon of January 12, 2010 an earthquake struck the eastern portion of the island of Hispaniola. The epicenter was located at 18.443°N latitude, 72.571°W longitude, 15 miles southwest of the largest population center in Haiti, Port-au-Prince (USGS, 2010). Several other population centers were also severely affected. According to official estimates reported by the USGS, 222,570 were killed, 300,000 injured and 1.3 million displaced (USGS, 2010). The damage to Haitian infrastructure was severe. The primary port, the power grid and the availability of clean water were nearly completely disabled. The effect from the initial shock was compounded by the significant number and magnitude of aftershocks. People were scared to live in homes that were undamaged or lightly damaged due to the aftershocks and the observed collapses of similar homes. The Haitian people were completely unprepared for this natural hazard.

While the citizens and the infrastructure of Haiti were not ready for a major earthquake, Hispaniola has a history of significant seismicity. The island is on the boundary of the Caribbean and North American tectonic plates. On the western half of the island, two faults capable of producing M_W 7 or greater earthquakes have been identified. The southern section of the east-west fault system in eastern Hispaniola responsible for the recent event has not produced a severe event since 1860. Prior to

that, Port-au-Prince was destroyed in 1751 and 1770 by significant earthquakes thought to be generated by the same fault (USGS, 2010). Due to the long period of inactivity, the government and the citizens of Haiti were not aware of the possibility of significant earthquakes. Haitians are accustomed to significant natural disasters in the form of hurricanes. Four major storms hit the island in 2008. Given the known hurricane hazard, it would be expected that some kind of building code would exist for safety. However, this is not the case. Haiti has no building code, no inspection process, and limited engineering practice.

The most prevalent building type in Haiti, particularly in the Port-au-Prince region, consists of non-engineered, lightly reinforced concrete frame structures with concrete masonry block infill. These low rise buildings are used for single family dwellings and small businesses. Large openings for windows and reduced wall area are very common and contributed to numerous floor collapses, both at the ground level and at singular floor levels above. These building are typically one or two stories, though three or four stories is not uncommon. Floors and roofs are reinforced concrete slabs, typically four to eight inches thick with a single layer of bi-directional reinforcement. Concrete blocks are commonly cast into the slab to minimize the use of concrete. Corrugated steel over a sparse wood or steel truss is also common roof system. Many residences are constructed over a long time period, as the homeowner acquires funds or the family's needs expand. Most are designed and constructed by the owner or a local mason.

When these building types are excited during an earthquake, initially lateral load is resisted by the combination of the reinforced concrete frame and the infill walls. Because the walls are typically not load-bearing their strength capacity is reduced because of a lack of friction development between the masonry units. Due to the lack of reinforcing, the infill walls have no ductility and therefore once cracked become non-structural mass. Following infill cracking, the concrete frame is left as the sole lateral resisting element. Interaction between wall panels and columns results in localized damage, notably in the columns. Lateral capacity of the slender columns was generally insufficient to resist acceleration demands on the structure. P-delta effects ensued, proliferating collapse. Toppling and out of plane failures of wall panels were commonplace and a primary driver many complete structural collapses. Even when they didn't contribute to collapse, these out-of-plane wall failures caused innumerable injuries and deaths.

More detailed presentations of the damage incurred by the earthquake can be found in the many reports from the different reconnaissance teams (Eberhard et al., 2010; EERI, 2010a; EERI 2010b; Fierro and Perry, 2010). The significant damage that occurred was due to the lack of engineering design, substandard and uncontrolled construction, and poor material quality. The lack of resources applied to civil infrastructure and citizen education to prepare for the eventuality of an earthquake are evident in the post-event response. The damage that occurred will be presented in the form of local damage surveys and four case studies. Local surveys completed on the ground in downtown Port-au-Prince and Leogane provide approximations of the percentage of collapsed structures. The surveys were accomplished using photos taken along a route and pre- and post-event satellite imagery to determine the number

of structures in existence prior to the event. The four case studies highlight the different flaws in Haitian buildings.

DAMAGE SURVEYS

The route in downtown Port-au-Prince is shown in Figure 1. The path was rectangular with a long side of 1200 ft and a short side of 350 ft. The Presidential Palace can be seen in the bottom right of Figure 1. The total number of structures along the path was estimated to be 107. Of those structures, 30 were classified as collapsed or severely damaged. The red pushpins show the location of the 30 structures.

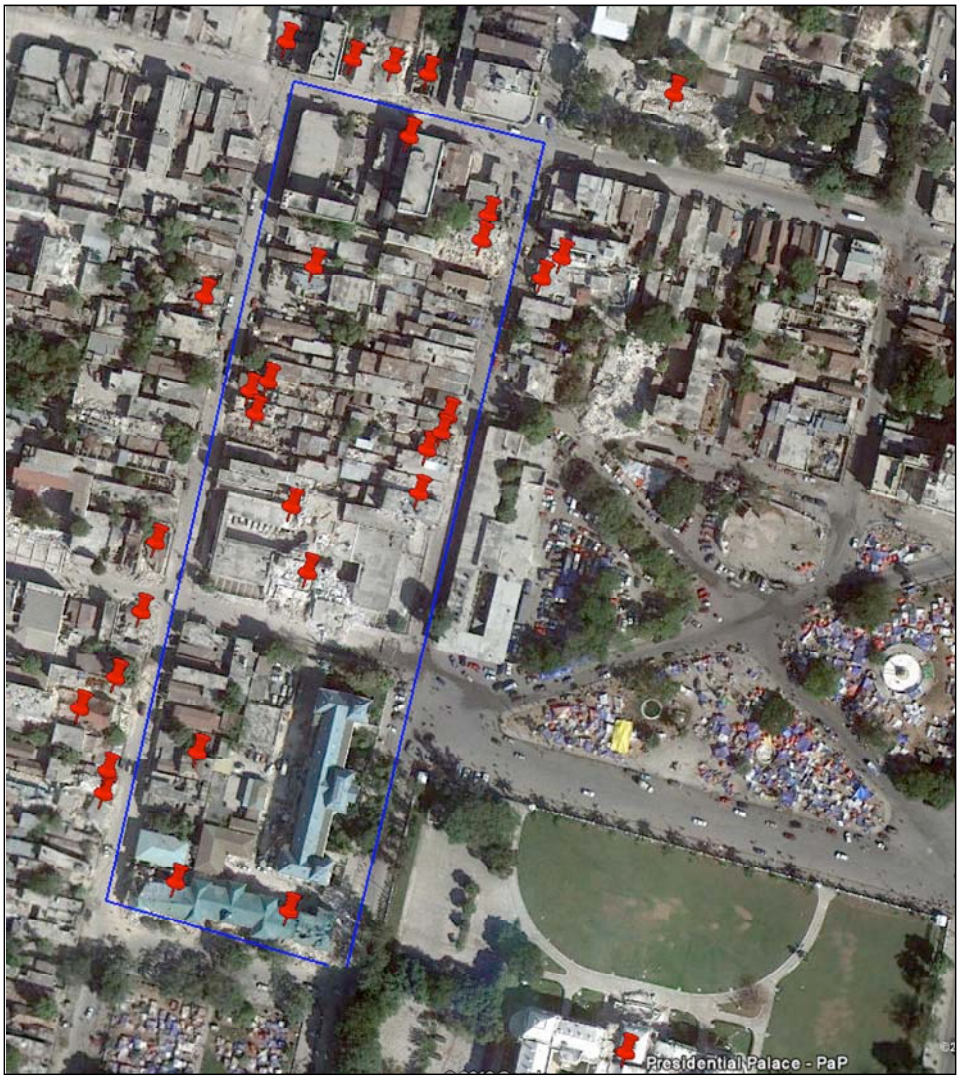


Figure 1 – Damage Survey Route in Downtown Port-au-Prince

A similar survey was completed in Leogane which is 7 miles from the epicenter having a population of approximately 80,000 (CityPopulation, 2010). Due to the epicenter proximity, the percentage of collapsed structures is higher. There could also be differences due to soil conditions which has not been accurately determined. The survey route in Leogane is shown in Figure 2. The route was L-shaped with a long

side of approximately 1200 ft and a short side of 360 ft. The total number of structures was more difficult to estimate due to the amount of damage. Fifty-two total structures were estimated from the photos and overhead imagery. Only four were classified as undamaged. These are shown with green pushpins in Figure 2. The number of collapsed or partially collapsed structures was approximated at 32 which results in a collapse ratio of 68%. This high collapse percentage may be an anomaly. However, compared with reconnaissance in other areas, Leogane was more severely impacted. A residential neighborhood about 4 miles from downtown Leogane experienced significant damage. Although the collapse rate was not as high, a very high percentage of structures were severely damaged.



Figure 2 – Damage Survey Route in Leogane

CASE STUDIES

A series of case studies is presented here to highlight the causes and effects of Haiti's fragile infrastructure. Each case study emphasizes a different flaw in the materials, planning, construction or engineering which resulted in failure.

UNIH UNIVERSITY BUILDING

The UNIH University Building sits alone along Highway 2 about 3.75 miles east of the center of Leogane. This building had not been completed at the time of the earthquake. Prior to the event it was three stories tall with column reinforcing steel protruding from the top deck in preparation for a fourth floor. There did not appear to be any signs of recent construction activity at the site indicating that the project may have stalled. While the concrete frames in each direction of this building were completed for the first three floors, it still suffered catastrophic total collapse. The building was relatively simple and repetitive in plan measuring approximately 61 ft

wide (three 16.5 ft bays with a 5.75 ft cantilever at each end) x 158 ft long (nine 16.25 ft bays with a 5.75 ft cantilever at each end). Measurements were taken of both the concrete and reinforcing steel elements to try to determine the design of the building. The damage was severe enough to expose both the column and beam steel at the lowest level of the building.

The structural floor framing included a grid of 10 in. x 14 in. beams in each direction supporting a 5 in. thick slab. The in. beams were reinforced with three #5 bars top and bottom and #2 stirrups at 9 in. on center. The #5 bars were hooked at the ends of the beam with 90 degree bends and only a 3 in. hook length, substantially shorter than the 10 in. required by ACI. The typical columns were only 10 in. x 10 in. in plan and were estimated to be approximately 12 ft tall. Typical interior column reinforcement included four #5 vertical bars and #2 column ties at 9 in. on center. Typical corner column reinforcement included four #4 vertical bars and #2 column ties at 8 in. on center. In some of the columns, both the vertical and tie reinforcement consisted of smooth bars. Typical column ties had non-seismic 90 degree hooks in lieu of 135 degree hooks required by ACI in seismic regions. The reinforcing steel for both the columns and beams was fairly minimal. The only concrete masonry wall debris observed was on the back (north side) of the building and may have still been a work in progress. An ETABS (CSI, 2007) analysis model of the building indicated that the structural frame would work for gravity loads but would be highly overstressed for lateral seismic loads. The demand-to-capacity ratios assuming 3,000 psi concrete under gravity load only range from 0.64 at the corners to 1.03 at the interior columns. Under lateral loads, the same ratios range from 4.5 at the corners up to 7.3 at the exterior columns on the short side indicating a complete lack of design for lateral loads. Figures 3 and 4 show photos taken during the reconnaissance showing the collapsed structure and the exposed construction details. This case study highlights the fact that for a structure as important as a university building, rigorous design procedures including potential seismic loads was not utilized to ensure safety.

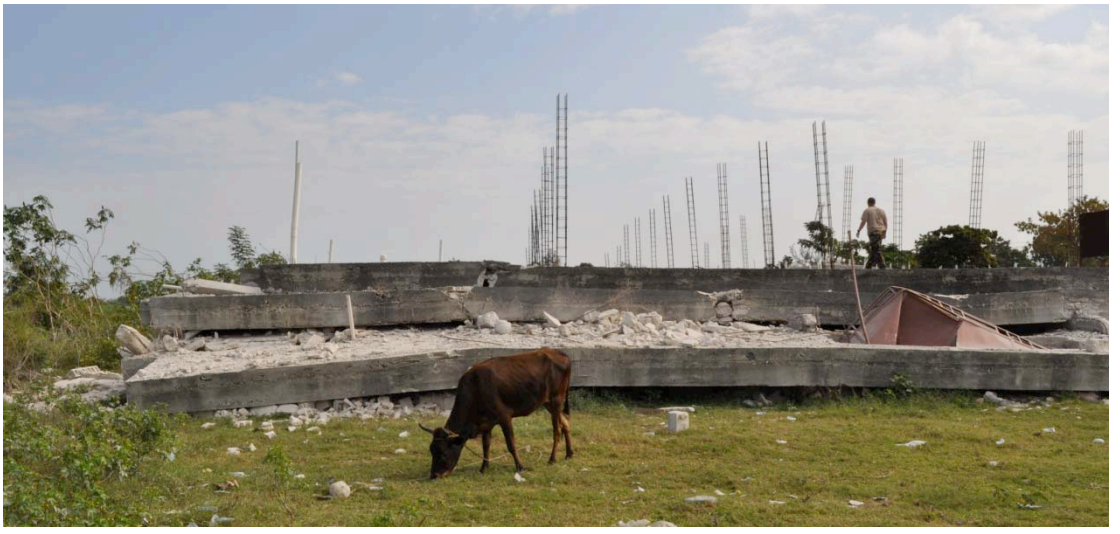


Figure 3 – Pancake Collapse of UNIH Building



Figure 4 – Exposed Connection Details of UNIH Building

"ENGINEERED" SCHOOL BUILDING

There were examples of buildings engineered to U.S. building codes, most noticeably the U.S. Embassy compound which received no permanent damage. The only damage seen in the embassy itself was displaced ceiling tiles and popped rubber seals on a few windows. This would be an example of a building designed and constructed in accordance with the most current and highest level of seismic requirements. Another example of a seismically resistant design is a three-story reinforced concrete frame school building with construction drawings indicating design in accordance with ACI Standard 318-89. The drawings included well detailed frame elevations indicating seismic detailing. The details included tight tie spacing in hinge zones, continuity of beam reinforcing (both top and bottom steel), and code compliant column vertical reinforcing. The drawings also indicated details for isolating CMU partition walls from the concrete frames to ensure ductile behavior and limit masonry cracking. There was however damage in the columns, typically in the middle third, and throughout much of the CMU partition walls. A majority of this damage appeared to be the result of poor quality control in the concrete and masonry materials and lack of inspection needed to ensure conformance to the details specified in the construction documents. Two notable discrepancies were column ties that did not match the seismic ties indicated in the drawings (90 degree versus 135 degree hooks) and CMU partition walls that were not isolated from the frames. Figure 5 shows the damage that occurred which highlights the lack of attention to the details during construction. This study illustrates the need for building officials to ensure the as-built structure conforms to the well-detailed design documents.



Figure 5 – Improper Reinforcing Tie Details

HANDS TOGETHER SCHOOLS

Many buildings in Haiti are combinations of multiple structures of different shapes, roof heights and number of stories. This results from the economic necessity to use existing structures as support for or components of new buildings. This method can be effective and efficient if the appropriate construction details and structural designs are implemented to account for the additional forces on the existing structural elements and dynamic differences between building sections. This could be accomplished through strengthening or by providing seismic expansion joints to allow the two sections to respond at the individual fundamental frequencies. The typical practice in Haiti is to use the wall of an existing structure as a wall for a new structure thereby reducing construction costs. This practice was commonly observed during reconnaissance missions. The post-event detailed structural inspection of eight school sites and one medical clinic run by Hands Together, a nonprofit organization based in the United States, provided multiple examples of this behavior. All of the Hands Together sites are in Cite Soleil.

The St Francois compound, located at 18.5871^{o} north 72.3276^{o} west, is a high school complex. It consists of six buildings, many of which are connected to one or more adjacent structures. A high resolution Google Earth image of the compound is shown in Figure 6. The letters shown in the figure are used to reference the different structures. All the campus buildings are constructed of reinforced concrete frames with masonry infill. Building A is a two-story classroom structure. It experienced very limited damage during the earthquake in the form of masonry wall cracking and damage to the stairway leading to the second story. It is the only structure that is not connected to any other building. Building B is a classroom building. The first two

stories are enclosed while the third floor is a covered patio supported by reinforced concrete columns and a half-height masonry wall. Building B itself experienced some wall cracking. The most significant damage occurred in the stairwell which connects buildings B and D at the second and third story. The damage to the second floor slab is visible from above in Figure 6. Due to the difference in orientation of buildings B and D, the stairwell became the fuse element between the two structures and was severely damaged during the ground motion (See Figure 7).



Figure 6 – Aerial Image of Saint Francois School Compound

Building C, the newest in the complex, is a two-story classroom building. Future expansion upwards is expected as reinforcing cages above the roof slab were installed showing the low level of reinforcing in the frame elements. The building was minimally damaged in the form of cracked masonry around the windows and doors. The only severe damage was at the interface with buildings C and D. Building D is the largest building on the complex. The bottom two stories are enclosed classrooms. The top floor is a covered patio with reinforced concrete columns. It is attached at both ends to the adjacent structures. This was the most seriously damaged building in the complex. It was damaged at both interfaces with adjacent structures. The large difference in plan dimensions resulted in full depth slab cracking at the interface between buildings D and E. Building D also experienced significant cracking of masonry walls and serious damage to the reinforced concrete columns and beams supporting the third floor timber trussed roof. Some of this damage was due to the elimination of every other block just below the slab to allow for lighting into the class rooms. This resulted in early fracture of the single blocks which then transferred the load to other internal walls which also had large voids. Buildings E and F experienced

minimal damage with the exception of the previously mentioned damage at the joint between D and E. Overall, the compound performed well. Had the structures not been linked together or been linked to account for movement, the most significant damage could have been avoided.



Figure 7 – Damage to Stairwell Between Buildings B and D

This case study as well as many other examples of this type of performance are prevalent in Haiti. A medical clinic located in the same region had a single story addition supported on the walls of an existing two-story structure. The single story separated from the two-story structure during the ground shaking, leaving the roof very close to collapse. Sainte Anne's elementary school was another case where the common wall of two different buildings experienced severe cracking due to different plan geometries and an offset in roof height. The practice of building onto existing buildings without considering transfer forces or providing a movement joint resulted in a significant amount of damage. In these cases, it was not fatal, however the repair costs are significantly higher due to the added damage and there are likely cases where this type of behavior was fatal.

PRE-ENGINEERED METAL BUILDINGS

Most industrial or warehouse buildings in Haiti are constructed of long span steel trusses supported on masonry infilled reinforced concrete frame walls. In the United States many of these buildings would be pre-engineered metal buildings (PEMB). Due to the cost and availability of steel in Haiti, they were the exception. The typical construction of PEMBs in Haiti utilized a masonry façade. During reconnaissance efforts, several PEMBs were encountered and the damage to each of them was similar. The masonry façade failed while the primary structural framework was

undamaged. Photos of this failure are shown in Figures 8, 9 and 10. Figures 8 and 9 are pictures of a retail building located across the street from the U.S. Embassy. All five of the front sections detached from the framing although some of them had not fallen. The building is being repaired and the masonry exterior walls are being replaced by insulated metal sheathing. This upgrade will make this structure much more resilient for future events. This out of plane failure of the masonry on the gable end of PEMBs was common on nearly all metal buildings seen during the reconnaissance. Figure 10 shows wind girts attached to a masonry that were damaged during the event by out of plane wall action. The building shown in Figure 10 also experienced the out of plane wall failure on the gable end wall. PEMBs in Haiti did not experience dramatic structural failure with the exception of the warehouse building at the Port-au-Prince port which failed due to significant lateral spreading between the foundations. The consistent failure mechanism of the masonry façade highlights the fact that even with a pre-designed, resilient structural system, not having an engineering professional design all aspects of a structure and including proper detailing for attachment of non-structural components can result in dramatic failure with the potential for significant fatalities.



Figure 8 – Masonry Wall Failure of Retail Metal Building



Figure 9 – Retail Complex Across from U.S. Embassy



Figure 10 – Damaged Wind Girts in Pre-Engineered Metal Building

CONCLUSION

Haitian infrastructure was completely unprepared for the earthquake which struck on January 12, 2010. With rare exception, buildings are not planned, designed or constructed with the necessary detailing to survive significant seismic events. While some buildings may have been designed, the necessary channels are not in place to verify compliance during construction. The damage surveys and case studies presented here highlight many of these deficiencies. In order to avert a disaster of this magnitude in the future, the people of Haiti need to be instructed in the proper

material quality, planning, design and construction of all infrastructure, especially during recovery and rebuilding from this event.

ACKNOWLEDGEMENTS

Numerous individuals and organizations contributed to the work presented in this paper. The reconnaissance efforts were funded by the Earthquake Engineering Research Institute's Learning From Earthquakes program (funded by the National Science Foundation), the Applied Technology Council, and the United States Geologic Service. Invaluable assistance in country was provided by United States Southern Command (SOUTHCOM); the soldiers, marines, sailors and airmen of Joint Task Force Haiti; the U.S. Embassy; and the U.S. Agency for International Development.

REFERENCES

CityPopulation (2010). Retrieved 08/31/10, from http://www.citypopulation.de/Haiti.html

CSI (2007). ETABS User's Guide & Introductory Manual. Berkeley, CA, Computers and Structures, Inc.

Eberhard, M.O., S.M. Baldridge, J.D. Marshall, W. Mooney and G. Rix (2010). The MW 7.0 Haiti Earthquake of January 12, 2010: USGS/EERI Advance Reconnaissance Team: Team Report.

EERI (2010a). Learning From Earthquakes - The Mw 7.0 Haiti Earthquake of January 12, 2010: Report #1. Oakland, CA, Earthquake Engineering Research Institute.

EERI (2010b). Learning From Earthquakes - The Mw 7.0 Haiti Earthquake of January 12, 2010: Report #2. Oakland, CA, Earthquake Engineering Research Institute.

Fierro, E. and C. Perry (2010). Preliminary Reconnnaissance Report - 12 January 2010 Haiti Earthquake.

USGS (2010). "Magnitude 7.0 - Haiti Region." 2010, from http://earthquake.usgs.gov/earthquakes/eqinthenews/2010/us2010rja6/.

February 27, 2010 Chile Earthquake: Preliminary Observations on Structural Performance and Implications for U.S. Building Codes and Standards

John W. Wallace[1]

[1] Ph.D., P.E., M. ASCE, University of California, Los Angeles, Department of Civil & Environmental Engineering, 5731 Boelter Hall, Los Angeles, California, 90095-1593 USA, (PH) (310) 206-7124; FAX (310) 206-2222; email: wallacej@ucla.edu

ABSTRACT

Performance of reinforced concrete buildings in Viña del Mar, Chile following the M7.8 1985 earthquake led to changes to the Uniform Building Code (UBC-94) and the American Concrete Institute Code for design of reinforced concrete buildings (ACI 318-99). In 1996, Chile adopted, with minor modifications, the ACI 318-95 Code. Reinforced concrete buildings are the predominant form of construction in Chile for buildings over four stories. Over the last 10 to 15 years, a construction boom similar to that in the US and other countries resulted in the construction of a substantial number of new buildings. Thus, the Feb. 27, 2010 earthquake provides a unique opportunity to assess the performance of modern reinforced concrete buildings designed using modern codes similar to those used in the US. Preliminary observations on building performance and the potential impact on US codes and practices, particularly with respect to ACI 318 seismic provisions, is presented.

Keywords: Shear wall; Wall; Chile; earthquake, 2010, reconnaissance; damage, code;

1. Introduction

On March 3, 1985, a strong earthquake of surface magnitude 7.8 occurred near the central coast of Chile (EERI, 1986). Approximately 400 modern, reinforced concrete buildings, designed for lateral forces comparable to those used in the highest seismic risk regions of the United States, were subjected to the strong shaking. Reconnaissance reports (EERI, 1986) and subsequent studies (Wallace and Moehle, 1989) indicated that the stiff, shear wall structures constructed in Chile performed extremely well, with little to no apparent damage in the majority of buildings. Later investigations (Wallace and Moehle, 1992, 1993) revealed that although the seismic code requirements (design forces) in Chile were similar to those used for high seismic risk regions in the U.S., detailing requirements were less stringent.

Research following the March 3, 1985 M7.8 earthquake near the central coast of Chile (EERI, 1986; Wallace and Moehle, 1992, 1993) led to significant U. S. code changes for reinforced concrete shear wall buildings in both the Uniform Building Code (Wallace, 1996) and eventually the ACI building Code (Wallace and Orakcal, 2002). Prior code provisions (ACI 318-95) for shear walls, based on simple elastic modeling, were considered easy to use; however, they typically resulted in

excessively conservative assessment of the need for confined boundary regions for most walls. In addition, the required boundary transverse reinforcement typically was required to be extended over a significant height of the wall, which some engineers consider unnecessary. There also were concerns that the procedure lead to excessive flexural over-strength, which could lead to high demands in wall shear, as well as diaphragm and foundation forces.

The UBC-94/97 provisions were developed to address some of the perceived shortcomings of ACI 318-95 (and early versions, since the provisions for shear walls remained essentially the same from ACI 318-83 through ACI 318-95). Provisions in UBC-97 addressed issues for flanged walls and provided a detailed approach for assessing requirements for transverse reinforcement at the boundaries of cantilever walls. Although the provisions for assessing detailing at wall boundaries were quite elaborate, some issues were not addressed, such as the need to check the flexural strength distribution over the height of the wall and detailing requirements for walls that satisfy UBC-97 triggers where no special transverse reinforcement was required. Also, by eliminating the 318-95 approach in UBC-97, there were many cases of irregular walls where the UBC-97 provisions did not apply, yet no design guidance was given.

The ACI 318-99 provisions were introduced to address concerns with ACI 318-95 and UBC-97. The provisions retained the displacement-based approach introduced into UBC-94 but also retained the basic approach of ACI 318-95 to provide an alternative (and simple and familiar) approach, as well as to address cases that do not conform to the geometric limitations and assumptions associated with a displacement-based design approach. To accommodate concerns related to flexural over-strength, changes were introduced to require that wall design for flexure and axial forces be based on section analysis identical to that used for column cross sections. Use of this approach encouraged the engineer to include the entire wall cross section to resist gravity loads and overturning moments rather than concentrating the design resistance in the boundary elements.

In 1996, Chile adopted a new code for design of reinforced concrete buildings based on ACI 318-95 (NCh 433.Of96). The provisions for shear walls are essentially the same as those in ACI 318-95; however, based on the good performance of wall buildings in Viña del Mar in the 1985 earthquake, the Chileans eliminated the ACI 318-95 provisions requiring (in most cases) special transverse reinforcement at wall boundaries to confine the concrete and restrain rebar bucking.

From 1995 through 2010, a construction boom similar to that in the US and other countries resulted in the construction of a substantial number of new buildings designed to the new Chile Code. Over this same period, Chilean engineers were discarding the rather simple and conservative design approaches used to design pre-1985 buildings and introducing design based on computer modeling using programs such as ETABS. The introduction of computer design approaches generally led to the use of fewer and/or thinner walls; building heights were generally increasing from the 10-15 stories common for pre-1985 buildings to 15-25 stories.

Given this history, the Feb. 27, 2010 M_w 8.8 earthquake provides a unique opportunity to assess the performance of modern reinforced concrete buildings designed using modern codes similar to those used in the US. Preliminary

observations (EERI Newsletter) indicate relatively few people lost their life in modern reinforced concrete buildings; however, the degree of damage significantly exceeded that reported following the 1985 earthquake. Preliminary findings are presented in the following sections to assess potential reasons for the observed damage as well as to assess areas where changes are needed to U.S. code requirements.

Recorded Ground Motions

General information related to the intensity of the recorded ground motions in Chile were reported by University of Chile researchers (Boroschek et al, 2010); however, digitized records still have not been released. Therefore, at this time, only general observations are included here.

Plots of recorded ground acceleration and response spectra for Viña del Mar indicate that the peak ground acceleration, duration of shaking, and spectral amplitudes were similar for the 1985 and 2010 earthquakes. It is noted that the spectral displacement demands increase essentially linearly to a peak value of about 15 cm for periods between 0.0 and 1.0 sec, but remain roughly constant for larger periods. This same trend was observed for displacement spectra computed from ground accelerations recorded in the 1985 earthquake. Therefore, spectral displacement demands do not increase for buildings greater than approximately 15 stories, since the cracked fundamental period of buildings in Chile can be approximated as $T_1 = N/15$, where N is the number of stories. Despite the similarities in demands between 1985 and 2010, substantially more damage was observed in Viña del Mar following the 2010 earthquake, particularly in newer buildings.

Displacement spectra for a record obtained in Concepción, Chile are presented in Figure 1. The spectra indicate that spectral displacement demands near the epicenter where significantly greater than recorded in Viña del Mar (represented with an approximately bilinear relation) and that very large demands are observed for periods between 1.5 and 3.0 seconds. Larger displacement demands produce larger local demands (strain, curvature) at critical wall sections, typically near the wall base; one possible reason for observed damage in the large percentage $(\approx 10\%)$ of buildings greater than 10 stories in Concepción.

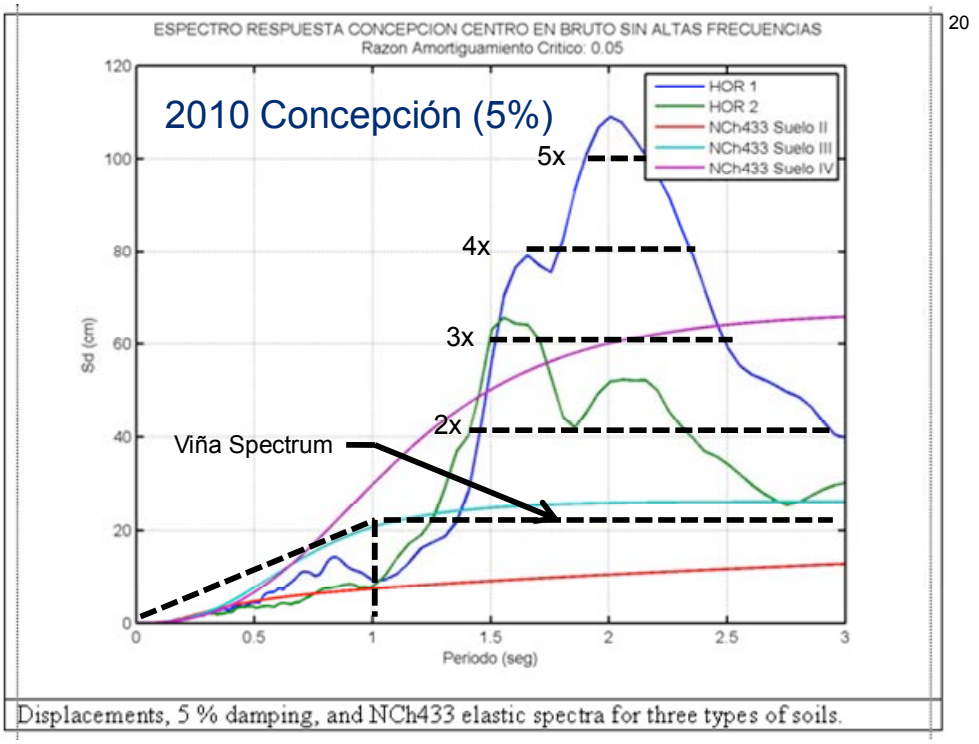


Figure 1 Displacement spectra – Concepción

Typical Construction

A floor plan of a typical pre-1985 Chile building is shown in Figure 2(a). The ratio of wall cross sectional area to building floor plan area $\left(A_w/A_f\right)$ is approximately 3% in each direction (Wood et al, 1987; Wallace and Moehle, 1993). It is also noted that typical wall thicknesses over the first four stories are 20 to 30 cm, with more prominent walls being 30 cm. Very few beams are used. The relatively large ratios of A_w/A_f were identified (Wallace and Moehle, 1992, 1993; Wallace 1994, 1995) as a primary reason for the excellent performance of buildings in the 1985 earthquake. For post-1985 buildings, the ratio of wall cross sectional area to building floor plan area in each direction tends to be considerably less, on the order of 1.0 to 1.5%, because fewer and thinner walls are typically used. As well, the walls are typically arranged with a central corridor in one direction and multiple transverse walls (Figure 2(b)). Wall thickness of 15 to 20cm is common, even for buildings from 10 to 20 stories.

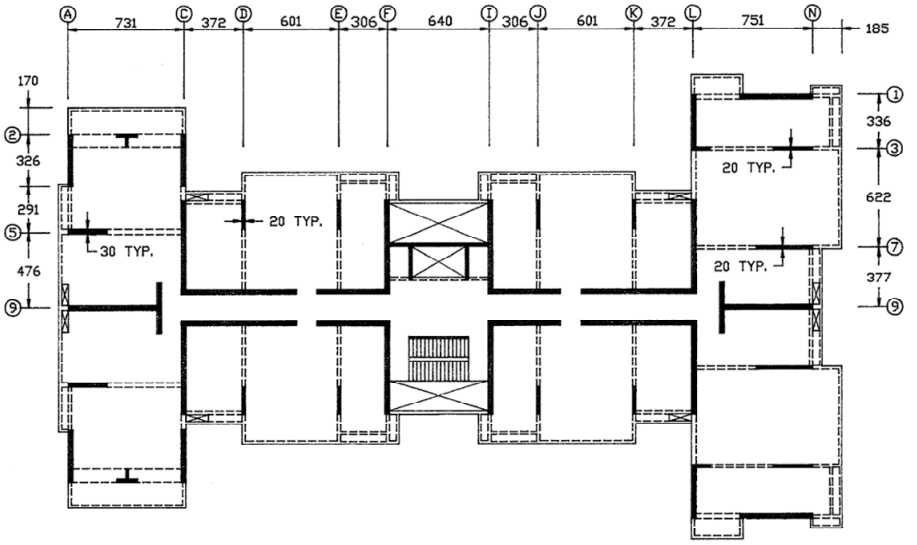


Figure 2(a) Festival Building in Viña del Mar (1978 construction)

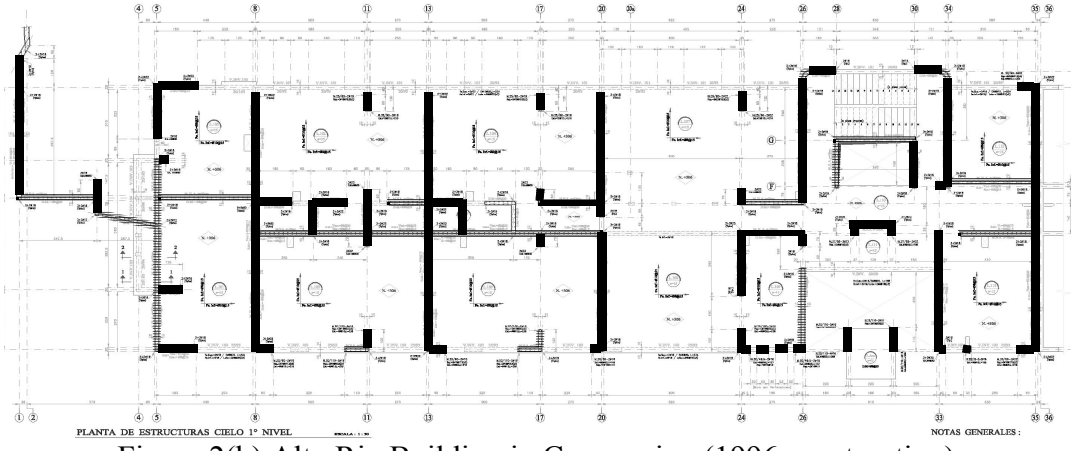


Figure 2(b) Alto Rio Building in Concepcion (1996 construction)

Observed Damage

Widespread and significant damage to shear walls, particularly at or near the ground level, was observed in buildings in Santiago, Viña del Mar, and Concepcion (the major population centers in Chile). Photos of wall damage for four buildings are shown in Figure 3. In general, crushing and spalling of concrete and buckling of vertical reinforcement were observed, often over a large extent of the wall. Typically, the damage was concentrated over a short distance of one to three times the wall thickness, apparently because buckling of vertical bars led to concentration of damage. Closer inspection of the wall boundary region (Figure 4) revealed the relatively large spacing of hoops (20 cm) and horizontal web reinforcement (20 cm), as well as the 90-degree hooks used on hoops (which typically opened due to concrete crushing and/or buckling of vertical reinforcement). In some cases, buckling of the entire wall was observed, presumably from large compression forces acting on relatively thin (15cm) walls. Damage also was common in lintels along corridor walls, sometimes extending over the entire height of the wall, in cap beams, and in corridor slabs.



Figure 3 Typical wall damage in 2010 Chile Earthquake

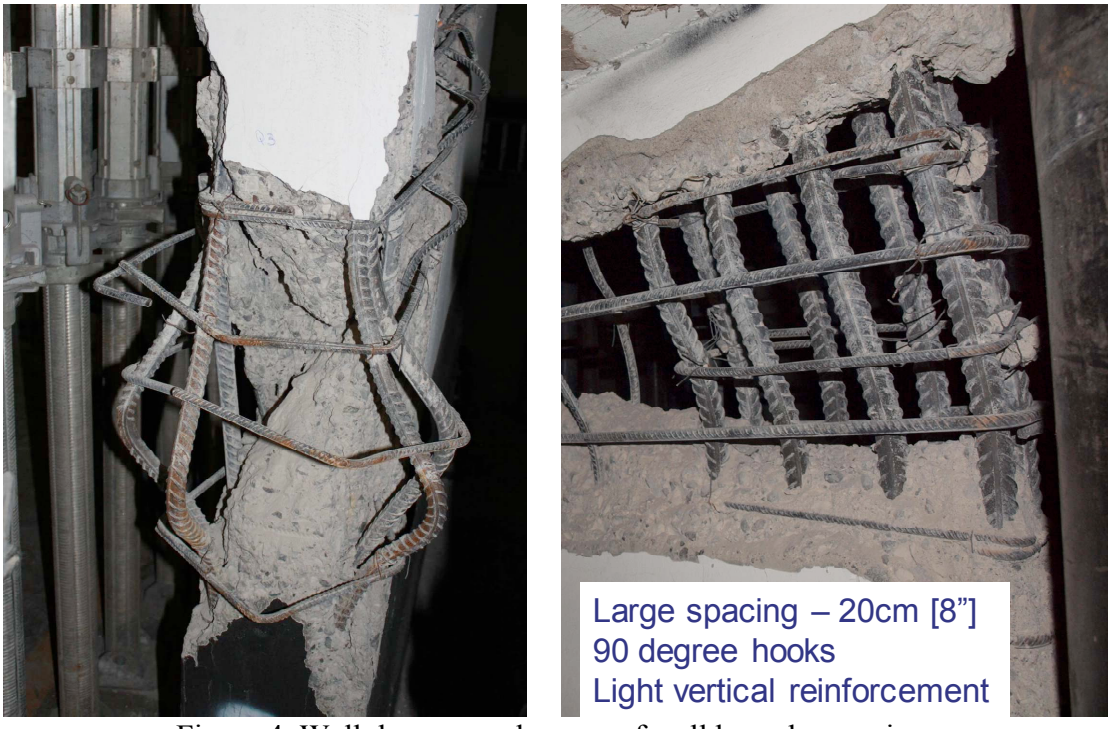


Figure 4 Wall damage – close-up of wall boundary region

ASSESSMENT AND POTENTIAL US CODE ISSUES

A wall damage observed in Chile raises a number of issues that need to be assessed. For example, what role did axial stress, wall configuration, and the lack of well

detailed regions at the wall boundaries play in the degree of damage observed? Are there other important findings that might apply to U.S. buildings and codes? These issues are systematically assessed in the following sections.

The Role of Axial Stress:

Neither the Chilean (NCH 433.OF96) or the ACI code (ACI 318-08) put a limit on the level of axial stress allowed for gravity load or combined gravity and lateral loads. A limit of $P_{gravity} < 0.35P_0$ was incorporated into UBC-94/97. A simple study is conducted to assess the likely level of axial stress in Chilean buildings. Two approaches are considered, one based on tributary area and the other based on ratios of A_w/A_f. For A_w/A_f of 3% in each principal building direction, the unit weight of buildings in Chile is estimated to be 200 kg/m^2 (Wallace and Moehle, 1989), whereas a unit weight of 150 kg/m^2 is estimated for buildings with A_w/A_f of 1%; linear interpolation is used for A_w/A_f ratios between 3 and 1%. Typical values of wall tributary area were found to range between 30 and 42 m^2 based on a review of structural drawings for several buildings constructed around 2005. Results are presented in Figure 5. The results presented in Figure 5 suggest axial load ratios of roughly 12 to 18% in pre-1985 buildings in the range of 10 to 15 stories (A_{trib}=30 m^2 or A_w/A_f = 0.03); however, ratios of 0.3 to 0.5 are computed for newer buildings between 12 and 20 stories (A_{trib}=42 m^2 or A_w/A_f = 0.01). The results suggest that newer buildings, with fewer and thinner walls, and larger tributary area, were subjected to large levels of axial stress due to gravity load. This finding is supported by wall design axial stress ratios obtained from one designer for ten different buildings. The buildings were designed between 2000 and 2006 and the loads include axial stress due to both gravity and lateral earthquake load. The results indicate that axial stress levels range from approximately 20 to 50% with a mean value of about 35%.

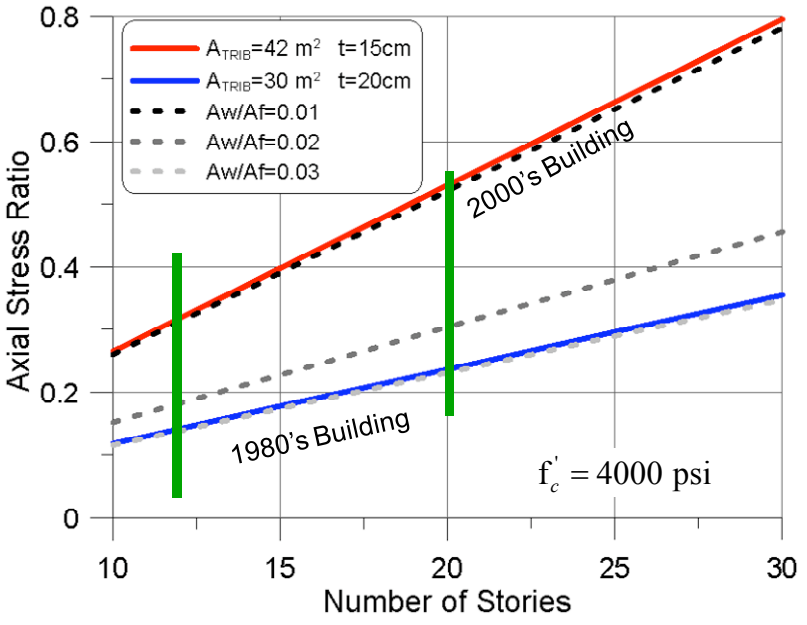


Figure 5 Estimated Wall Axial Stress Ratios

Moment-curvature analysis was used to assess the potential impact of such large axial stress ratios on typical Chilean walls. Using information from a 12-story building in Santiago, moment-curvature relations were calculated for a wall cross section of 7m x 0.15m wit 8-25 mm diameter bars at each wall boundary and 9mm vertical web bars at 20cm spacing. Two levels of axial stress are considered, 0.2 and $0.3A_g f'_c$; ratios of c/l_w, or neutral axis depth to wall length, also are plotted (Figure 6). The relations plotted reveal negative slope beyond the yield curvature (concrete crushing) with relatively low curvature capacity. It is noted that the buckling of vertical bars is not considered in this study. The plot of c/l_w indicates that this ratio is never less than approximately 0.45 for $0.3A_g f'_c$.

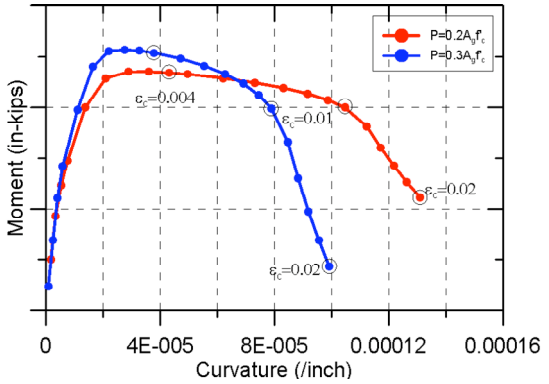


Figure 6(a) Moment - curvature relations

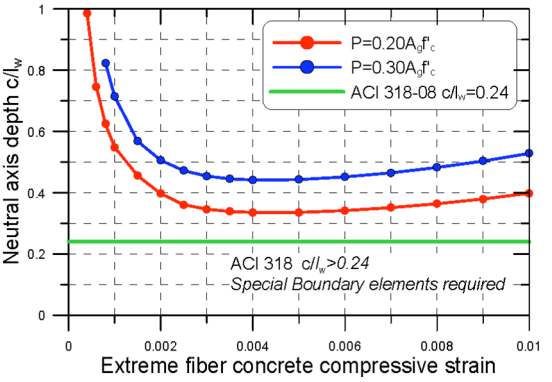


Figure 6(b) Neutral axis depths

ACI 318-99 (and subsequent versions) include a requirement that the design displacement divided by the wall height (δ_u / h_w) cannot be taken less than 0.007. As shown by Wallace and Orakcal (2002), imposing this requirement is equivalent to requiring special transverse reinforcement at wall boundaries for cases where the neutral axis depth exceeds $0.24l_w$. This result is significant because use of special transverse reinforcement at wall boundaries will be required for many U.S. walls in cases where axial stress becomes significant; however, no such provision exists in the Chilean code. Figure 6(b) indicates that ACI 318 (-99 to -08) would require special transverse reinforcement (for the prescribed levels of axial stress considered); therefore, it is likely that substantially improved performance would have resulted if the walls had satisfied ACI requirements.

Although ACI would require special transverse reinforcement at wall boundaries for most walls in Chilean buildings, the question remains whether ACI 318 or ASCE 7 should limit the level of wall axial stress, or like beams, require tension-controlled sections where the reinforcement is required to reach a specified strain level (e.g., 0.005) prior to concrete reaching a compressive strain of 0.003. Another option that could be considered is to required boundary elements to resist all compression (due to axial load and earthquake overturning forces) if a wall is not tension-controlled.

The role of wall configuration

As noted in Figure 2, common floor plans used for buildings in Chile, with long corridor walls in one direction and perpendicular walls in the transverse direction (sometimes referred to as a backbone and rib pattern, or a fishbone pattern), results in

walls with large flanges. Prior research on walls with T-shaped cross-sections has revealed that these walls behave substantially different than rectangular walls with symmetrically placed longitudinal (vertical) reinforcement (Wallace, 1994, 1996; Thomsen and Wallace 1995, 2004). For a wall with a T-shaped cross section, the boundary of the web is typically subjected to large compressive forces; therefore, this region must be well confined to avoid concrete crushing and reinforcement bar buckling. Restraining buckling is particularly challenging, because the bars at the web boundary are subjected to large compressive strains and then very large tensile strains on load reversal.

Load versus displacement results are presented for TW1 (poorly-detailed) and TW2 (well-detailed) in Figure 7. Significant loss in lateral-load capacity was observed for wall TW1 at a little greater than 1% lateral drift when all eight vertical boundary bars and some vertical web bars buckled. In contrast, wall TW2 reached lateral drift ratios in excess of 2.5% before lateral strength degradation initiated. For wall TW2, strength loss resulted due to lateral buckling of the well-confined web boundary, after concrete cover spalled. Because the walls were reduced-scale, the wall thickness was only 4 inches (10 cm); therefore, spalling of the concrete cover resulted in a substantial reduction in the wall thickness.

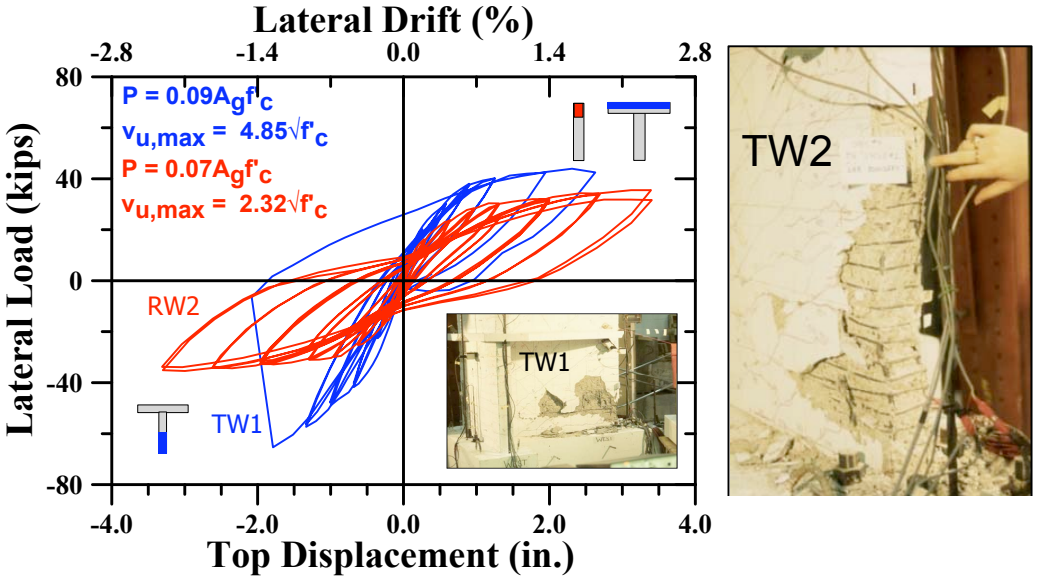


Figure 7 Load-Displacement relations for TW1 and RW2

There was ample evidence of wall damage similar to that observed for TW1 in Chilean buildings following the 2010 earthquake. As well, fracture of web boundary vertical reinforcement also was observed in a number of locations (Figure 8).



(a) Centro Mayor building (b) Alto Rio building

Figure 8 Rebar fracture of web boundaries of T-shaped Walls in Concepción

Displacement-based design provisions and assumptions

Sections 21.6.2 of ACI 318-99 and 21.9.6.2 of ACI 318-08 include provisions that are derived from a displacement-based approach (Wallace and Orakcal, 2002). Embedded in this approach is the assumption that yielding occurs over a specified (plastic hinge) length of $l_w/2$. An examination of wall damage in Chile (Figure 3) suggests that inelastic deformations do not spread out in poorly-detailed walls; therefore, it is important to reassess approach used to develop the ACI 318 provisions.

The model used to develop ACI 318-99 provisions is shown in Figure 7. Given this model, the design displacement $\delta_u(ACI) \equiv \delta_x = C_d \delta_e / I\,(ASCE\ 7)$ is related to local plastic hinge rotation and extreme fiber compressive strain as:

$$\theta_p = \frac{\delta_u}{h_w};\quad \theta_p = \left(\phi_u = \frac{\varepsilon_c}{c}\right)\left(l_p = \frac{l_w}{2}\right) \;\therefore\; \varepsilon_c = 2\left[\frac{\delta_u}{h_w}\right]\left[\frac{c}{l_w}\right] \tag{1}$$

If the compressive strain exceeds a limiting value, typically taken as 0.003, then special transverse reinforcement is required. In ACI 318-99 [see ACI 318-08, Equation 21-8], this approach was rearranged to define a limiting neutral axis depth versus a limiting concrete compressive strain as:

$$c_{\text{limit}} = \frac{0.003 l_w}{2(\delta_u/h_w)} = \frac{l_w}{667(\delta_u/h_w)} \approx \frac{l_w}{600(\delta_u/h_w)} \tag{2}$$

In this approach, it is obvious that the result is sensitive to the value used for the plastic hinge length.

The approach presented by Wallace and Orackal (2002) is modified here to assess the potential impact of variation of the plastic hinge length on the need for special transverse reinforcement at wall boundaries (or SBE, for Special Boundary Elements) for rectangular, symmetrically reinforced walls. Based on observed damage, the plastic hinge length is selected to be a multiple of the wall thickness, i.e., $l_p = \alpha t_w$, where α is taken to be 2, 5 and 8 for poorly, moderately, and well-detailed walls,

respectively. With this modification, the relationship between design displacement, wall geometry, material properties, and extreme fiber concrete compressive strain is:

$$\frac{\delta_u}{h_w} = \varepsilon_{cu}\left(\alpha\frac{t_w}{l_w}\frac{l_w}{c}\right)\left(1-\frac{\alpha}{2}\frac{t_w}{h_w}\right)+\frac{\varepsilon_{sy}}{(1-c/l_w)}\left(\frac{11}{40}\frac{h_w}{l_w}-\alpha\frac{t_w}{l_w}+\alpha^2\frac{t_w}{h_w}\frac{t_w}{l_w}\right) \quad (3)$$

Where t_w is the wall thickness, c is the neutral axis depth, h_w is the wall height, l_w is the wall length, and ε_{sy} is the tensile reinforcement yield strain. The constant 11/40 results based on the assumed distribution of lateral force over the height of the wall (Wallace and Moehle, 1992). In (3), the relationship between the wall neutral axis depth, concrete compressive strain, and drift is computed for various ratios of l_w/t_w and h_w/l_w for the three assumed values of plastic hinge length. For this preliminary study, wall aspect ratio h_w/l_w is set to 3.0 and the ratio of l_w/t_w is set to 15 for U.S. construction and 45 for Chilean construction (because they tend to use thin walls). Concrete compressive strain is set to 0.003; therefore, the results presented in Figure 9 define when special transverse reinforcement would be required at wall boundaries. Results for a plastic hinge length of $l_p = l_w/2$, as implied in current ACI 318-08 provisions, also is included.

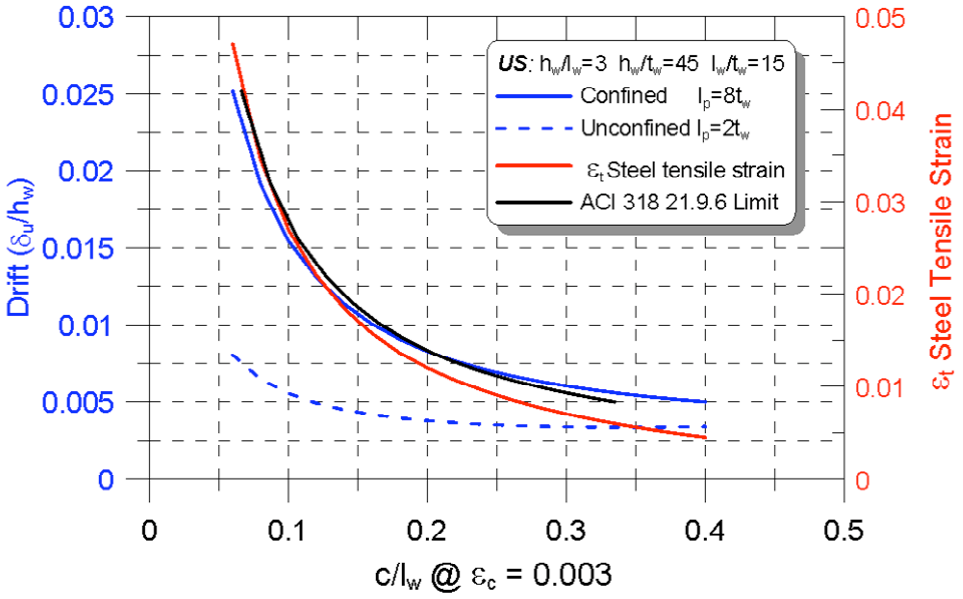


Figure 9(a) Impact of plastic hinge length on SBE – US Construction

The results presented in Figure 9(a) indicate that a use of a plastic hinge length of $l_p = (\alpha = 8)t_w$ is essentially the same as using $l_p = l_w/2$ for typical U.S. construction. In this case, if the drift ratio is 0.01, the neutral axis must exceed $0.15l_w$ before SBE are required. However, for the same neutral axis depth of $0.15l_w$, if inelastic deformations are concentrated over a short height $\left(l_p = (a = 2)t_w\right)$, less than one-half this drift ratio, approximately 0.004, can be tolerated before SBE are required. Results presented in Figure 9(b) reveal that the thinner walls used in Chile are more likely to need SBE and that at least moderate detailing should be provided in all walls.

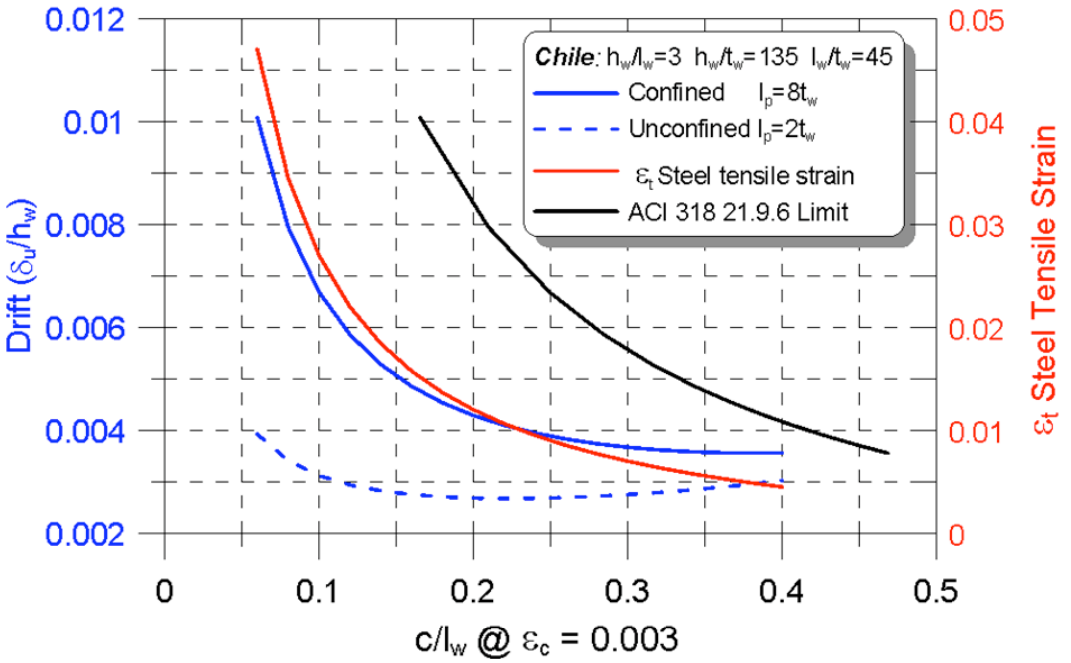


Figure 9(b) Impact of plastic hinge length on SBE – Chilean Construction

Conclusions

The M_w 8.8 earthquake that struck Chile on February 27, 2010 provides a unique opportunity to study the performance of reinforced concrete buildings designed using a modern code based closely on ACI 318-95. Based on reconnaissance efforts and subsequent preliminary studies, a number of issues have been identified to help us understand the observed damage to shear walls in Chile as well as to identify areas where changes to ACI 318-08 may be warranted. Based on this preliminary work, the following observations are noted:

- Spectral displacement demands in Viña del Mar the 1985 and 2010 earthquakes were similar, reach a peak value at a period of about 1 sec, and remain essentially constant for larger periods.
- Pre-1985 buildings in Chile typically performed well because of the large ratios of A_w/A_f, relatively low wall axial stress (typically $0.10 A_g f_c'$), and the relatively low displacement demands.
- Post-1985 buildings, and particularly buildings constructed since 2000, tended to use fewer and/or thinner walls which are likely to produce axial stress ratios in the range of 0.20 to $0.50 A_g f_c'$. Walls with such high axial stress ratios have neutral axis depths exceeding 0.35 to $0.45 l_w$ and low deformation capacity. ACI 318-08 would require special transverse reinforcement at wall boundaries for neutral axis depths exceeding $0.24 l_w$.
- Wall configuration likely played a significant role in the wall damage observed following the 2010 earthquake. Post-2000 buildings in Chile commonly include central corridor walls and multiple transverse walls. Large reinforcement tensile strains accompanied by large concrete compressive strains are expected at web boundaries of walls with T-shaped cross sections. For poorly-detailed web boundaries, sudden loss of lateral strength due to buckling of vertical boundary and web bars has been observed in tests.

- The displacement-based design approach used in ACI 318-99 (and subsequent versions, including ACI 318-08) assumes a plastic hinge length of $l_p = 0.5l_w$. Damage observed following the 2010 earthquake indicates that inelastic deformations concentrate over a much shorter distance in poorly-detailed walls. A reexamination of the ACI 318-08 provisions using a plastic hinge length equal to a multiple of wall thickness $\left(l_p = \alpha t_w;\ \text{with } \alpha = 2, 5, 8\right)$ indicates that use of $\alpha = 8$ is essentially the same as using $l_p = 0.5l_w$, appropriate for well-detailed walls. Use of $\alpha = 2$ reveals that the equation (21-8) used in ACI 318-08 to determine the critical neutral axis depth is not appropriate for poorly-detailed walls, especially for typical Chilean walls because they are much thinner than typical walls in U.S. buildings.

Acknowledgements

The author would like to thank the members of the EERI reconnaissance team for reinforced concrete buildings and our collaborators in Chile: The EERI team: Co-Team Leaders Jack Moehle (UC Berkeley), Rafael Riddell (U Catolica), and Rubén Boroschek (U Chile); Team Members Alvaro Celestino (Degenkolb Engineers), Jeff Dragovich (NIST), Carlos Sempere (Forell/Elsesser). Additional individuals from three Chile universities who contributed generously to the EERI team reconnaissance include: From the Federico Santa Maria Technical University - Professors Patricio Bonelli and Carlos Aguirre, with Arturo Millán; from the Pontificia Universidad Católica de Chile - Professors Juan Carlos De La Llera, Matias Hube, and Carl Lüders, with Vicente Ariztía, Juan Jose Besa, Alvaro Carboni, Claudio Frings, Juan Pablo Herranz, Cristobal Moena, Rodrigo Oviedo, Victor Sandoval, Nicolas Santa Cruz, César Sepúlveda, Benjamin Westenenk; from the Universidad de Chile - Professors María Ofelia Moroni, Leonardo Massone, Rodolfo Saragoni. All of the members listed provided tremendous assistance, especially the students from Pontificia Universidad Católica de Chile and Federico Santa Maria Technical University. Opinions, findings, conclusions, and recommendations in this paper are those of the author, and do not necessarily represent those of the sponsor or others mentioned.

References

ACI Committee 318, "Building Code Requirements for Structural Concrete (ACI 318-08) and Commentary (318R-08)," American Concrete Institute, Farmington Hills, Mich., 2008, 465 pp.

Boroschek R., Soto P., Leon R. "Preliminary Ground Motion Reports: http://www.terremotosuchile.cl/ ," University of Chile, Santiago, Chile.

EERI (1986), "The Chile Earthquake of March 3, 1985," Earthquake Spectra, Vol. 2, No. 2, April 1986.

Thomsen IV, J. H. and Wallace, J. W, "Displacement-Based Design of Slender RC Structural Walls – Experimental Verification, J. Struct. Eng., ASCE, Vol. 130, No. 4, pp 618-630, April 2004.

Wallace, J. W., "Seismic Design of RC Shear Walls; Part I: New Code Format," J. Struct. Eng., ASCE, Vol. 121, No. 1, January 1995, pp.75-87.

Wallace, J. W., "Evaluation of UBC-94 Provisions for Seismic Design of RC Structural Walls," Earthquake Spectra, Vol. 12, No. 2, pp 327 – 348, May 1996.

Wallace JW, Mohle JP, "The 3 March 1985 Chile Earthquake: Structural Requirements for Bearing Wall Buildings," EERI Report No. UCB/EERC-89/5, Earthquake Engineering Research Center, University of California, Berkeley, July 1989.

Wallace, J. W., Moehle, J. P., "Ductility and Detailing Requirements of Bearing Wall Buildings," J. Struct. Eng., ASCE, Vol. 118, No. 6, June 1992, pp.1625-1644.

Wallace, J. W., Moehle, J. P., "An Evaluation of Ductility and Detailing Requirements of Bearing Wall Buildings Using Data from the 3 March 1985 Chile Earthquake," Earthquake Spectra, Vol. 9, No. 1, Feb. 1993, pp.137-156.

Wallace, J. W.; Orakcal, K. (2002), "ACI 318-99 Provisions for Seismic Design of Structural Walls," ACI Structural Journal, Vol. 99, No. 4, American Concrete Institute, pp. 499-508.

Wallace, J. W.; Thomsen IV, J. H., "Seismic Design of RC Shear Walls; Part II: Applications," J. Struct. Eng., ASCE, Vol. 121, No. 1, January 1995, pp.88-101.

Wood SL, Wight JK, Moehle JP, "The 1985 Chile Earthquake, Observations on Earthquake Resistant Construction in Viña del Mar,", Civil Engineering Studies, Structural Research Series No. 532, University of Illinois, Urbana, February 1987.

Uniform Building Code, "International Conference of Building Officials," Whittier, California, (1994; 1997).

Engineering Aspects in Evaluation of Pile Capacity by Dynamic Testing

Mark R. Svinkin, Ph.D., M.ASCE[1]

[1]VIBRACONSULT, 13821 Cedar Road, #205, Cleveland, OH 44118-2376; PH (216) 397-9625; FAX (216) 397-9625; msvinkin@roadrunner.com

ABSTRACT

High strain dynamic pile testing is widely spread in the pile driving industry. Evaluation of pile capacity from field testing is the primary application of the dynamic method, but the accuracy and the area of utilization (soil conditions and pile type) of this method are vague. The application of hardware and software is only partially established because different hardware and software produce substantially diverse pile capacities. Engineering evaluation of pile capacity is not established at all. Statistical analysis of pile capacities is unable to find out applicability of the method to specified site conditions. Uncertainties are available in signal matching technique and comparison of the results of static and dynamic tests. Quality of dynamic measurements together with the software features and the engineering factors affect pile capacity obtained by dynamic testing. Engineering research is needed to ascertain the accuracy and the area of application of high strain dynamic pile testing.

INTRODUCTION

Modern dynamic pile examination in the field or so-called high strain dynamic pile testing (HSDPT) is based on the application of stress wave theory to piles and comprises signal matching technique for computed and measured force and velocity at the pile head. The application of the HSDPT method to driven piles has certain advantages in assessment of the hammer-pile-soil system and in data acquisition during pile driving and restrikes. This method provides verification of hammer performance and energy transferred to a pile, and also evaluation of driving stresses and pile integrity. HSDPT is a significant tool for driveability analysis.

Nevertheless, evaluation of pile capacity at the time of testing is the basic purpose of high-strain dynamic pile testing, but this area of the HSDPT application has some uncertainties and discrepancies (Svinkin, 2004 and 2010).

Dynamic testing is often used to replace static load tests (SLT). Therefore, it is imperative to ascertain the adequacy of HSDPT and SLT. Static methods predict pile capacity as the long term capacity after soil consolidation around the pile is complete. Independently of the time elapsed after driving a test pile, the ratio of pile capacity from static analysis to pile capacity from SLT is used for approximate evaluation of

the reliability of design methods. According to the traditional approach, the main criterion for assessment of pile capacity from HSDPT is the ratio of capacities obtained by dynamic and static tests or vice versa.

In assessment of HSDPT accuracy, the ratio of pile capacities from restrikes to SLT has been considered for various pile types and lengths, soil conditions and time intervals between comparable tests lumped together as shown in Figure 1. Such a mixture of pile capacities depends on a number of factors and confuses the readers. Some papers such as Goble et al. (1980), Denver and Scov (1988), Hannigan (1990), and Likins et al. (1996) have underlined good agreement between dynamic and static tests for all considered piles in spite of ignoring the time between compared tests and specifics of pile types and soil conditions. Other papers, for example, Hannigan and Webster (1987), Paikowsky et al. (1994), Lee et al. (1996), and Liang and Zhou (1997) have revealed considerable over and under estimation of pile capacity by HSDPT.

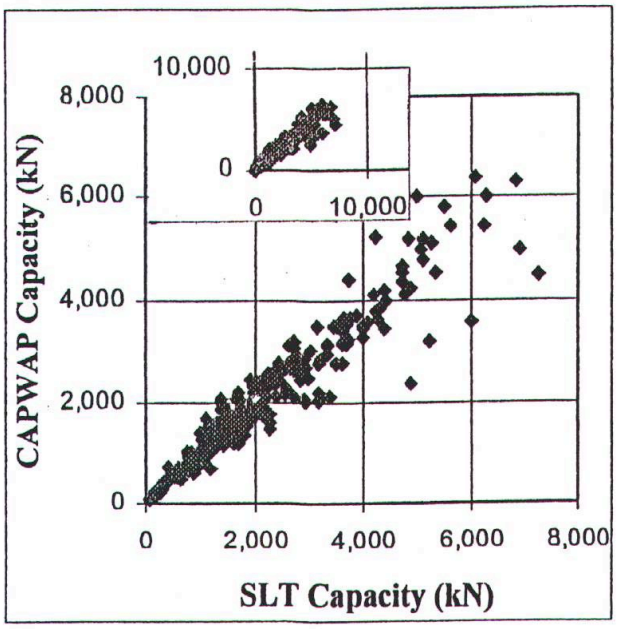


Figure 1. Correlation study of CAPWAP versus SLT. The same results are shown in different scales. Data were modified from Likins and Rausche (2004)

There are three similar but not identical signal matching software: CAPWAP, TNOWAVE, and SIMBAT. These computer programs were made by three companies which use similar dynamic measurements at the pile head, but the programs' procedures are substantially different in signal matching analysis. CAPWAP is the most popular program in USA.

Likins and Rausche (2004) have used CAPWAP analysis for dynamic pile testing and correlated the calculated pile capacities with the results of static load tests. They have summarized the two previous major studies (Goble et al.1980 and Likins et al. 1996) and compiled the results of pile testing from case histories published in the proceedings of six Stress-Wave Conferences. In total, correlation was performed for 303 piles. They have concluded that CAPWAP is generally and statistically conservative and

comparison of CAPWAP results with static load tests on the same piles shows excellent agreement. It seems that these conclusions are inaccurate because they have not presented the whole picture of pile capacity evaluation by HSDPT.

During design and construction of pile foundations, it would be beneficial to know applicability of HSDPT to specific site conditions like soil stratification, pile type and length. The existing publications recommend the use of HSDPT at any construction site. It is very doubtful because any great method has the certain area of applications and restrictions.

A DISTINCTIVE CASE HISTORY

Briaud et al. (2000) have presented a unique distinctive study of static capacity assessment by dynamic methods for three bored piles. This study was chosen toward correlation between the results of dynamic and static tests for two reasons: first, this study presented comprehensive research on determining pile capacity of bored piles by dynamic methods, and second, the research study provides a rare opportunity to compare the pile capacities determined for each of three piles by three companies specialized in the application of dynamic methods to piles: GRL and Associates, Inc., TNO Building and Construction Research, and ESSI – Testconsult. References to static and dynamic pile testing are available in Briaud et al. (2000).

Site and Pile Data

Three bored piles were tested at the two national Geotechnical Experimentation Sites at Texas A&M University. All three piles were planned to be 0.915 m in diameter and varied in length between about 10.7 and 11.7 m. Pile 2 at the sand site was purposely built with defects: mud cake of about 15 mm thick on the side wall, a soft bottom, and a concrete contamination at 5.3 m below the pile head. One more unplanned defect occurred at 5 m below the pile head and resulted in a 45% reduction in area. Pile 4 at the sand site was planned as no-defect pile, but during construction, an unplanned bulging defect resulting in a 10% average increase in diameter between 1.2 and 7.5 m below the pile head. Pile 7 at the clay site was planned and constructed as a perfect pile.

The construction schedule and the testing sequence for each pile are given in Table 1. The piles were constructed by following good drilling and construction practices including desanding of the drilling mud and minimizing slurry stagnation between the end of drilling and the beginning of concreting. Pile 2 at the sand site was an exception. Details of the soil properties at the site and the actual pile shapes are available in Briaud et al. (2000).

Table 1. Construction and Testing Schedule. Data were modified from Briaud et al. (2000)

Pile Number	Soil	Drilling	Concreting	Static Load Test 1	Drop Weight Test	Static Load Test 2
2	sand	11-16-1990	11-19-1990	11-28-1990	12-6-1990	12-8-1990
4	sand	11-19-1990	11-19-1990	11-30-1990	12-7-1990	-
7	clay	11-15-1990	11-15-1990	12-3-1990	12-8-1990	-

Results of Static and Dynamic Pile Tests

There are various criteria to define pile capacity from static load tests. Pile capacities from the load-deformation curves were defined according to the Davisson criterion ($D/120$ + 3.8 mm + PL/AE), and the $D/10$ criterion ($D/10$ + PL/AE). The designations are as follows: D is the diameter of the pile, 3.8 mm is the compression of the pile, P is the load applied, L is the length of the pile, A is the cross section area of the pile, and E is the modulus of the pile material. The values of pile capacities determined from static load tests are shown in Tables 2 for three piles tested.

After static load tests, drop weight tests were performed in 8 days for Pile 2, 7 days for Pile 4, and 5 days for Pile 7. SLT 2 for Pile 2 was made in 2 days after dynamic testing. Three companies, which performed dynamic pile testing, used similar experimental technique in measurement of force-time signals from the strain gages, acceleration-time signals from the accelerometers, and permanent displacements at the pile head for each hammer blow. However, three companies use significantly different software for signal matching of experimental data to determine, not predict, the static capacity and the load-settlement curve. The results of HSDPT and errors in determination of the pile capacity by HSDPT are shown in Tables 2 as well.

Table 2. Comparison of Static Capacity of Piles Determined by Static and Dynamic Tests

Pile No.	Pile Capacity Criterion	SLT Static Capacity kN	CAPWAP		TNOWAVE		SIMBAT	
			Static Capacity kN	Error %	Static Capacity kN	Error %	Static Capacity kN	Error %
2	$D/10$	1068	1300	+22	4900	+359	2100	+97
STL 1	Davisson	472	1300	+175	4900	+938	2100	+345
2	$D/10$	1602	1300	-19	4900	+206	2100	+31
STL 2	Davisson	1112	1300	+17	4900	+341	2100	+89
4	$D/10$	4004	2900	-28	5800	+45	2300	-43
	Davisson	2892	2900	0	5800	+101	2300	-20
7	$D/10$	3025	4250	+40	2850	-6	2500	-17
	Davisson	2491	4250	+71	2850	+14	2500	0

Accuracy of Static Capacity Determined by HSDPT

It is important to clarify what capacity values should be compared. On the one hand Briaud et al. (2000) have preferred the $D/10$ criterion to the Davisson one because the former yields the pile capacity about 1.4 times higher and an average pile head penetration about 7.8 times higher. On the other hand Fellenius (1980) has stated that the Davisson limit has widespread use in conjunction with the wave equation analysis of driven piles.

It seems that the range between the Davisson and D/10 criteria would be appropriate for correct determination of pile capacity from HSDPT. For Pile 2, a comparison was made with the result of SLT 2 because it is obvious that planned and unplanned defects decreased the capacity of Pile 2 at the time of SLT 1. A CAPWAP and TNOWAVE determination of pile capacity is based on a single blow, but an

average of two blows is sometimes used. SIMBAT software employs a series of blows with varying energy to determine pile capacity.

The accuracy of pile capacity calculations by different software on the basis of similar experimental data measured at the pile head are shown in Table 3. It can be seen that CAPWAP provided good results in sand for Pile 2 (+17 & -19) and Pile 4 (0 & -28) but substantially overestimated capacity in clay for Pile 7 (+71 & +40), TNOWAVE largely overestimated capacity in sand for Pile 2 (+341 & +206) and Pile 4 (+101 & +45) but provided good results in clay for Pile 7 (+14 & -6), SIMBAT substantially overestimated capacity in sand for Pile 2 (+89 & +31) and substantially underestimated one at the same site for Pile 4 (-20 & -43) but provided good results in clay for Pile 7 (0 & -17).

Table 3. Evaluation of Static Capacity of Piles Determined by Dynamic Methods

Dynamic Methods	Sand Piles 2& 4 Error (%)	Clay Pile 7 Error (%)
CAPWAP	Good results between Davisson and D/10 for Pile 2: +17 & -19 for Pile 4: 0 & -28	Overestimation +71 & +40
TNOWAVE	Overestimation for Pile 2: +341 & +206 for Pile 4: +101 & +45	Good results between Davisson and D/10 +14 & -6
SIMBAT	Overestimation for Pile 2: +89 & +31 Underestimation for Pile 4: -20 & -43	Good results between Davisson and D/10 0 & -17

Effect of the Time Elapsed between Compared Tests

An assessment of the effect of the time elapsed between compared tests is presented below.

CAPWAP. For Pile 2 with 2 days between dynamic and static test, errors will be almost the same. For Pile 4 with 7 days between static and dynamic test, the capacity from HSDPT will increase within the Davisson and *D*/10 criteria. However, for Pile 7 with 5 days between static and dynamic tests, an increase in the capacity from HSDPT will increase an error.

TNOWAVE. For Piles 2 and 4, the effect of the elapsed time will almost not change the largely overestimated capacity in sand. For Pile 7 with 5 days between static and dynamic tests, an increase in the capacity from HSDPT will move the capacity close to the *D*/10 limit.

SIMBAT. For Pile 2, with 2 days between dynamic and static test, errors will be almost the same. For Pile 4 with 7 days between static and dynamic test, it will be underestimation with less errors. For Pile 7 with 5 days between static and dynamic tests, the capacity from HSDPT will increase within the Davisson and *D*/10 criteria.

One more Distinctive Case History

Similar pile tests were accomplished in California at two sites, but static load test results were known to companies which performed HSDPT before dynamic pile testing was made, Baker et al. (1993). At the Cupertino site, the soil consisted of clay, gravel, and sand layers. Five bored piles with 0.9 m in diameter and 28 or 33 m in length were constructed. Four of them had planned defects. At the San Jose site, the soil profile indicated different layers of clays. Six bored piles with 0.9 m in diameter were constructed. A length of two piles was about 10 m, and four piles had a length between 18.3 and 19.5 m. Some of these piles had planned defects. Details of the soil properties at the site and the actual pile shapes are available in Baker et al. (1993).

Pile capacity from HSDPT were determined by three signal matching techniques and compared with capacity from static load tests. The Davisson criterion was used. For Piles 2 and 4 at the Cupertino site, CAPWAP analysis underestimated the pile capacities on 8 %, TNOWAVE analysis overestimated the pile capacities on 12 %, and SIMBAT analysis overestimated the pile capacities on 16 %. The report concluded that such variation is acceptable for engineering purposes. Nevertheless, a different conclusion was made regarding a comparison of dynamic and static test results obtained for all of the tests when the average value of the three methods yielded overestimation of 61 % and underestimation of 41 %. The range of variation was much greater and less acceptable.

Additional Comments

Two issues considered in Briaud et al. (2000) were discussed in Svinkin and Woods (2009). First, the pile capacity from the CASE method was presented as a function of the pile permanent set or hammer blows per 300 mm (blow count). The lower blow count the higher pile capacity. However, the same blow count can represent much lower pile capacity during easy driving when the much lower energy applied to a pile. It seems that that pile capacity as a function of blow count should be connected with energy value applied to the pile. Second, the CASE method used an average of all blows, and SIMBAT also used a series of blows with varying energy to receive the load-deformation curve. In spite of a similarity of using measured data, the results in determination of pile capacity for the same pile are diverse. For example, the pile capacity of Pile 4 is 2850 kN from CASE method and 2300 kN from SIMBAT. The difference is 24 % only for account of using different signal matching techniques. It means that software features of each method can affect pile capacity determination. Therefore, signal matching software has to be calibrated.

UNCERTAINTY IN HIGH STARIN DYNAMIC PILE TESTING

Limitations of HSDPT

General limitations of high strain dynamic pile testing are presented in Svinkin (2004 and 2010).

HSDPT has limitations in comparison with static load test because the long-term behavior can be represented only approximately over short time dynamic testing is carried out.

HSDPT provides *direct* measurement of data on strain (force) and acceleration (also velocity and/or displacement) at the pile head undergoing a hammer impact force. These data are utilized for *indirect* determination of pile capacity using signal matching procedure.

There are several methods for interpretation of the load-movement of the pile head measured *directly* from SLT. However, there is only one way for verification of pile capacity determined *indirectly* from dynamic pile testing. This capacity is compared with the result of a static load test found in accordance with the Davisson's criterion. The adequacy of static load test and HSDPT has to be confirmed by proper correlation of dynamic testing results.

ASTM D 4945 (1989) states that this test method (dynamic) is not intended to replace Test Method D 1143 (static load test). However, in practice, high-strain dynamic pile testing replaces static load test in violation of ASTM D 4945.

Problems of Signal Matching Technique

The CAPWAP computer program (GRL and Associates, Inc. 1995) is most popular signal matching software, particularly in USA. This program is widely distributed among users of the Pile Driving Analyzer. Comments on CAPWAP are shown below, and similar remarks obviously can be made regarding other signal matching software.

Screwvala (1973) has written that he does not have much confidence in the suggested method for assessment the resistance along the entire length of the pile. Also, he underlined that procedures should be established to identify where non-conservative results can apparently be obtained.

Danziger et al. (1996) performed back analysis of field records of offshore piles driven in calcareous sands and concluded that CAPWAP solutions are not unique. Different sets of soil parameters can produce similar simulated velocities curves at the pile head.

According to Rausche (1986), the match quality in CAPWAP analysis is evaluated by summing the absolute values of the relative differences between the computed and measured pile top variables. For the purpose of match quality determination, the total analyzed time period of variables considered is subdivided into four intervals. There are the overlaps of intervals 2, 3, and 4. Therefore, it can be concluded that values of the pile capacity affect the overall match quality number more than other soil resistance parameters.

Svinkin (2004) emphasized that signal matching is a specific approximation process. It is necessary to point out that the time intervals in signal matching are assigned very conditionally and two questions of the general problem of approximation have not been answered: 1) does the best approximation of a measured curve exist? and 2) is the best approximation determined uniquely? Furthermore, feedback of the pile capacity to the match quality number is an evidence of some uncertainty in determination of pile capacity by signal matching.

Comparison of HSDPT and SLT

As it was mentioned above, the main criterion for assessment of the pile capacity estimated from HSDPT is a ratio of capacities obtained by dynamic and static tests or vice versa. It is necessary to point out that the ratio of HSDPT/SLT or vice versa, taken for arbitrary time between compared tests, is not a verification of dynamic testing results. It is well known that HSDPT yields the real static capacity of piles at the time of testing, Rausche (1985). Besides, the static capacity from SLT is considered as a unique standard for assessment of dynamic testing results. It is a major error. As a matter of fact, pile capacity from SLT is a function of time and the so-called actual static capacity from SLT is not a constant value, Svinkin (2002).

For a general case of assessment of the HSDPT reliability, the ratio of restrikes to SLT results has been considered for various pile types and lengths, soil conditions and time of testing lumped together. Such a mixture has no real meaning. It is not a verification of dynamic testing at restrikes and it is not an assessment of real set-up factor because everything is lumped together without taking into account the time between different tests. Such a comparison of the pile capacities from static load test and dynamic testing is invalid for piles driven in soils with time-dependent properties because the soil properties at the time of dynamic testing do not correspond to the soil properties at the time of static load test, i.e. soil consolidation between two compared tests is taken into account for the latter test and not considered for the former test. As a matter of fact such a comparison uses pile capacity values which are incompatible from the point of verification of dynamic testing (Svinkin and Woods 1998; Svinkin 2000 and 2004).

Effects of Various Factors on Pile Capacity Evaluated by HSDPT

On the one hand previous studies demonstrated numerous cases of good correlation between HSDPT and SLT, but on the other hand there are a number of cases with wrong results of dynamic pile testing. It is necessary to correctly compare the results of dynamic and static pile tests and take into consideration the effects of several factors.

The major part of verification of HSDPT results performed for 303 piles is shown in Figure 1, Likins and Rausche (2004). The same data are displayed in different scales, and the graph in a larger scale demonstrates obvious discrepancies between the results obtained from dynamic and static tests. It means that visual observation of correlation data displayed in a small scale could be misleading.

Various factors can affect the results of HSDPT. It is necessary to consider the effects of soil conditions, the pile type and the pile length, the time between compared tests, the time after pile installation, the sequence of tests, the high blow count, the signal matching technique, and the quality of dynamic records. Besides, the rate of pile capacity change after pile installation should be considered. It was found that the rate of pile capacity change per day decreases with an increase of the elapsed time after EOID and a margin of errors about 10-15 % would be reasonable for a few days after performing the first of two compared tests, Svinkin (2002).

Statistical analysis of pile capacities from HSDPT cannot take into account all factors mentioned above and find out applicability of HSDPT to specified sites. By way of illustration, Svinkin (2002) analyzed pile capacities determined dynamically and statically for 39 piles which are available at FHWA-GRL database. This database was used by Likins et al. (1996) and Likins and Rausche (2004). The elapsed time between compared tests was 1-2 days. For 11 piles (28 %), pile capacities from HSDPT exceeded acceptable margins of 10-15 %. Calculated capacities for 5 among 11 piles had errors from 20 to 25 %. The worst results were obtained in CAPWAP analysis of 6 piles (15%) which were analyzed with errors between 30-54 %. These piles are shown in Table 4. Pile numbers in parentheses are pile numbers from the database. First three piles have underestimated results (30, 42 and 42 %), but other three piles have overestimated pile capacity (31, 54, and 44 %). Obviously, statistical analysis of pile capacities evaluated by CAPWAP was irrelevant for 15-28 % of 39 tested piles analyzed from FHWA database. Comments about the worst obtained results are presented in Svinkin (2002).

Table 4. Comparison Static Capacity of Piles Determined by HSDPT and SLT

Pile			Soil	SLT	Time between SLT & HSDPT	HSDPT		
No.	Description	Length				Time after EOID	Pile Capacity	Error
		m		kN	hours	days	kN	%
2(3)	610 mm PSC 305 mm v. D	20.20	Sand & Clay HWT	3160	+ 24	12	2216	-30
7(48)	762 mm PSC 457 mm v. D	31.10	Sand HWT	6635	+ 48	31	3836	-42
10(51)	762 mm PSC 457 mm v. D	30.02	Sand HWT	6439	+24	26	3751	-42
23(102)	HP 299x79	22.86	Sand & Clay	1664	+5	1	2185	+31
35(169)	CEP 324 mm x 13 mm	21.00	Clay & Silt HWT	788	-24	14	1504	+54
36(170)	CEP 324 mm x 13 mm	17.00	Clay & Silt HWT	712	-24	14	1148	+44

Prediction or Determination of Pile Capacity by HSDPT

The assertions in some publications like "The ability to accurately predict static capacity from dynamic pile testing has resulted in many studies" are incorrect. This is a misleading interpretation of HSDPT which does not have any connection with Class A type prediction defined by Lambe (1973). No in-situ pile test can predict pile capacity as a function of time after pile installation. Only static analysis and wave equation analysis without pile testing are truly predictive methods. It is well known that HSDPT cannot in principle predict pile capacity and only provides determination of pile capacity at the time of testing, Rausche et al. (1985) and Svinkin (2004). Besides, the accuracy of HSDPT is unknown, Svinkin and Woods (1998).

Impact Loads for Dynamic Pile Testing

To properly use HSDPT, it is essential to know the values of impact loads applied to piles during dynamic testing. There are no requirements in existing standards regarding such loads except the common and indistinct condition that the pile capacity be fully mobilized at the time of dynamic pile testing. Svinkin and Woods (2009) proposed an equation to calculate short-duration impact loads for pile testing as a function of the pile capacity, P_u, and the dominant circular natural frequency, ω, of the pile-soil system

$$I = \frac{P_u}{\omega} \tag{1}$$

This new procedure is a step toward increasing the engineering understanding of HSDPT.

CONCLUSIONS

High strain dynamic pile testing is a convenient tool in the pile driving industry, but the actual accuracy and the area of application of this method (pile types and soil conditions), and also the understanding of the results of dynamic pile testing are vague. Previous studies demonstrated numerous cases of good correlation between the results of dynamic pile testing and static load tests. However, there are a number of cases with wrong results of dynamic pile testing. For practical application, it is important to know in advance the accuracy of HSDPT depending on the pile type and soil conditions.

A distinctive case history demonstrates outcomes of application of different hardware and software for dynamic testing of the same piles. For the conditions at the particular testing sites, testing results were various: CAPWAP yielded good results in sand and substantially overestimated pile capacity in clay, TNOWAVE yielded good results in clay and largely overestimated pile capacity in sand, SIMBAT yielded good results in clay and substantially overestimated and underestimated pile capacity in sand. It is difficult to give preference to any one of three methods.

There are uncertainties in high strain dynamic pile testing like limitations of HSDPT, problems of signal matching technique, and difficulties in comparison of HSDPT and SLT. Besides, various factors can affect the results of HSDPT. It is necessary to consider the effects of soil conditions, the pile type and the pile length, the time between compared tests, the time after pile installation, the sequence of tests, the high blow count, the signal matching technique, the quality of dynamic records, and the rate of pile capacity change after pile installation.

Statistical analysis of pile capacities from HSDPT cannot take into account all factors affected pile capacity and find out applicability of HSDPT to specified site conditions. It was demonstrated that statistical analysis of pile capacities evaluated by CAPWAP was irrelevant for assessment of the accuracy of pile capacity determined for 15-28 % of 39 tested piles available in FHWA-GRL database.

There is a need for engineering research and calibration of signal matching techniques to ascertain the accuracy and the area of application of high strain dynamic pile testing.

REFERENCES

ASTM D 4945-89. (1989). *Standard test method for high-strain dynamic testing of piles*. American Society for Testing and Materials.

Baker, C.N., Park, G., Briaud, J.-L., Drumright, E.E., and Mensah, F. (1993). *Drilled shafts for bridge foundations*. *Report No. FHWA-RD-92-004*, Federal Highway Administration, Washington D.C., 335.

Briaud, J.-L., Ballouz, M., and Nasr, G. (2000). "Static capacity prediction by dynamic methods for three bored piles." *Journal of Geotechnical and Geoenvironmental Engineering*, ASCE, New York, Vol. 126, No. 7, 640-649.

Danziger, B.R, Lopes, F.R., Costa, A.M., and Pacheco, M.P. (1996). "A discussion on the uniqueness of CAPWAP-type analysis." *Proceedings of Fifth International Conference on the Application of Stress-Wave Theory to Piles*, F. Townsend, M. Hussein & M. McVay (eds.), Orlando, University of Florida, 394-408.

Denver, H. and Skov, R. (1980). "Investigation of the stress-wave method by instrumented piles." B. Fellenius (ed.), *Proceedings of the Third International Conference on the Application of Stress-Wave Theory to Piles*, 1988, BiTech Publisher, Ottawa, Canada, 613-625.

Fellenius, B.H. (1980). "Analysis of results from routine pile loading tests." *Ground Engineering*, Emap Construct, London, Vol. 13, No. 6, 19-31.

Goble, G.G., Rausche, F., and Likins, G.. (1980). "The analysis of pile driving - A state-of-the-art." *Proceedings of the First International Conference on the Application of Stress-Wave Theory on Piles*, Bredenberg H. (ed.), Stockholm, A.A. Balkema, 131-161.

Hannigan, P.J. (1990). *Dynamic Monitoring and Analysis of Pile Foundation Installations*. A Continuing Education Short Course Text, DFI, Sparta, New Jersey, 69.

Hannigan, P.J. and Webster, S.D. (1987). Comparison of static load test and dynamic pile testing results. *Proceedings of the 2nd International Symposium*, DFI, Luxembourg, May.

Lambe, T.W. (1973). *Predictions in Soil Engineering*. 13th Rankine Lecture.

Lee, W., Lee, I.M., Yoon, S.J., Choi, Y.J. and Kwon, L.H. (1996). Bearing capacity evaluation of the soil-cement injected pile using CAPWAP. F. Townsend, M. Hussein & M. McVay (eds.), *Proceedings of the Fifth International Conference on the Application of Stress-Wave Theory to Piles*, Orlando, University of Florida, 409-419.

Liang, R.Y. and Zhou, U J. "Probability method applied to dynamic pile-driving control." *Journal of Geotechnical Engineering*, ASCE, 1997, Vol. 123, No. 2, 137-144.

Likins, G., Rausche, E F., Thendean, G. and Svinkin, M.R. (1996). "CAPWAP correlation studies." *Proceeding of the Fifth International Conference on the*

Application of Stress-Wave Theory to Piles, F. Townsend, M. Hussein & M. McVay (eds.), Orlando, University of Florida, 447-464.

Likins, G. and Rausche, F. (2004). "Correlation of CAPWAP with static load tests." *Proceeding of the Seventh International Conference on the Application of Stress-Wave Theory to Piles*, The Institution of Engineers Malaysia, 153-165.

Paikowsky, S.G., Regan, J.E., and McDonnell, J.J. (1994). *A simplified field method for capacity evaluation of driven piles*. *Report No. FHWA-RD-94-042*, Federal Highway Administration, Washington D.C.

Rausche, F. (1986). *CAPWAPC™ Principles and Limitations,* GRL and Associates, Inc., Cleveland, Ohio.

Rausche, F., Goble, G.G. and Likins, G. (1985). "Dynamic determination of pile capacity." *Jornal of Geotechnical Engineering*, ASCE, 1985, Vol. 111, No.3, 367-383.

Screwvala, F.N. (1973). "Discussion of 'Soil resistance prediction from pile dynamics' by Rausche et al." *Journal of the Soil Mechanics and Foundation Division*, ASCE, Vol. 99, No. SM5, 412-413.

Svinkin, M.R. (2000). "Time effect in determining pile capacity by dynamic methods." *Proceedings of Sixth International Conference on the Application of Stress-Wave Theory to Piles*, Niyama & Beim (eds), Balkema, Rotterdam, 35-40.

Svinkin, M.R. (2002). "Engineering judgment in determination of pile capacity by dynamic methods." *Deep Foundations 2002, Geotechnical Special Publications No. 116*, ASCE, New York, Vol. 2, 898-914.

Svinkin, M.R. (2004). "Some uncertainties in high-strain dynamic pile testing." *Geotechnical Engineering for Transportation Projects, Geotechnical Special Publication No. 126*, ASCE, New York, Vol. 1, 705-714.

Svinkin, M.R. (2010). "High-strain dynamic pile testing – problems and pitfalls." *Journal of Performance of Constructed Facilities*, ASCE, Vol. 24, No. 2, 99.

Svinkin, M.R. and Woods, R.D. (1998). "Accuracy of determining pile capacity by dynamic methods." *Proceedings of the Seventh International Conference and Exhibition on Piling and Deep Foundations, DFI 98,* Vienna, Austria June 15-17, 1998, Westrade Group Ltd., Rickmansworth, 1.2.1-1.2.8.

Svinkin, M.R. and Woods, R.D. (2009). "Dynamic loads for high-strain dynamic pile", *Proceedings of 17th International Conference on Soil Mechanics and Foundation Engineering*", M. Hamza et al. (Eds.), IOS Press, 1259-1262.

High School Slab on Grade Settlement Evaluation and Permanent Structural Slab Repairs

Aaron R. Lewis[1], Sean M. Homem[2], Michael F. Hughes[3], and Giuliana Zelada-Tumialan[4]

[1]Senior Project Manager, Simpson Gumpertz and Heger Inc., 41 Seyon Street, Waltham, MA 02453; PH (781-907-9325); email: alewis@sgh.com
[2]Staff II – Structures, Simpson Gumpertz and Heger Inc., 41 Seyon Street, Waltham, MA 02453; PH (781-907-9356); email: smhomem@sgh.com
[3]Staff II – Structures, Simpson Gumpertz and Heger Inc., 41 Seyon Street, Waltham, MA 02453; PH (781-907-9269); email: mfhughes@sgh.com
[4]Senior Project Manager, Simpson Gumpertz and Heger Inc., 41 Seyon Street, Waltham, MA 02453; PH (781-907-9290); email: gazelada@sgh.com

ABSTRACT

A low-rise high school building constructed on the site of an existing construction debris landfill included initial site preparation using Deep Dynamic Compaction (DDC) to mitigate potential future settlement of the building's first-floor slab on grade. Within the first six years of building occupancy, the first-floor slab on grade settled up to 6 in. because of consolidation of the landfill. Differential settlement of the first-floor slab relative to the pile-supported building frame caused severe distress to the interior partition walls, buried storm and sanitary drainage systems, interior piping, mechanical and electrical systems, and other finish work.

This paper presents our evaluation of the landfill consolidation effects using precision settlement surveys as well as measurements from vibrating-wire borehole extensometers to model the settlement rates throughout the entire building footprint. The paper also summarizes the final repair design and construction procedures used to mitigate future settlement damage. The cost for repairs completed to date is approximately $10MM.

INTRODUCTION

The existing 195,000 sq ft, low-rise high school building was constructed in the late 1990s over a construction-debris landfill. Subsurface conditions at the site consisted of 5 to 8 ft of imported fill, over 2 to 18 ft of construction debris, over 0 to 12 ft of stiff clay, over 10 to 20 ft of dense glacial till, over bedrock. During the original planning for the new building, the following two options for the first floor slab were considered by the original design team – 1) a structural slab supported on concrete grade beams and steel H-piles and 2) a nonstructural slab supported on structural fill overlying the construction-debris stratum. For both options, the columns for the building frame and the perimeter walls were supported on concrete pile caps and grade beams with steel H-piles driven to rock. Ultimately, the slab on grade

approach was selected because of possible construction cost savings. To reduce the amount of expected slab settlement, the original design team proposed Deep Dynamic Compaction (DDC) to densify the construction debris, to reduce the amount of consolidation, and to drive the top of the construction debris below the lowest estimated groundwater level.



Figure 1. Settlement of Slab Relative to Grade Beam.

Within the first six years of building occupancy (1999 to 2005), the Owner noticed that the first-floor slab on grade was settling significantly. By 2006, settlement varied throughout the building footprint reaching up to 6 in. in some areas. The building had many utility ruptures, cracks in flooring and walls, misaligned doors and frames, glass failures, settlement of the main entry canopies, and a partial collapse of a concrete masonry unit (CMU) wall. Most notably, the slab on grade settled relative to the exterior grade beams around the entire inside face of the perimeter walls (Figure 1). Since the perimeter walls and interior columns supporting the second floor, third floor, and roof were firmly founded below the construction debris and were not settling, the building was subject to significant differential settlement between the first-floor slab and the pile-supported building frame elements.

This paper summarizes the detailed investigations, modeling used to evaluate the settlement, and permanent repairs used to mitigate the settlement issues.

INVESTIGATIONS

We correctly suspected that the cause of the settlement was consolidation of the construction debris. To evaluate the impact of the settlement and the options for repair, we developed an investigative plan to understand the extent of the settlement; to confirm the cause of the settlement; and to determine whether the settlement was ongoing and at what rate. The investigation included precision settlement surveys, soil borings, vibrating-wire borehole extensometers, ground penetrating radar surveys, and periodic visual damage and condition assessments. Each of these investigative elements is discussed in detail below.

Precision Settlement Surveys:

Settlement data is instrumental in developing a predictive settlement model. We engaged a Licensed Land Surveyor to perform annual and, at times, semiannual settlement surveys of the slab on grade. Nine surveys, incorporating 130 settlement monitoring points (SMPs), were performed between 2003 and 2010. The SMPs

were located approximately at the centerline between interior pile caps, where the slab is likely in contact with the settling soil below. We also installed some SMPs on the finished flooring that extended over a portion of the grade beams, which are not settling, to provide an estimate of the initial elevation of the slab immediately after construction and a reference to estimate the total settlement.

The accuracy of the survey is important when planning the time between surveys and the number of rounds; i.e., for slow settlement rates the time between surveys must be long enough to allow the settlement to be measured based on the expected accuracy of the survey. In general, we found that a single survey round was accurate to +/- 1/8 in. at one standard deviation (s). The accuracy of a survey can be improved by increasing the number of rounds (see Equation 1). In our investigation each survey always contained two rounds, which increased the accuracy by 41% when compared with only one round of measurements.

$$\hat{\sigma} = \frac{\sigma}{\sqrt{n}} \qquad \textbf{Equation 1}$$

$n =$ *Number of Rounds*
$\hat{\sigma} =$ *Standard Deviation of Mean*
$\sigma =$ *Standard Deviation of Single Round*

The total slab settlement between 1999 and 2006 is shown in Figure 2. The settlement data shows that the total settlement varies significantly throughout the building.

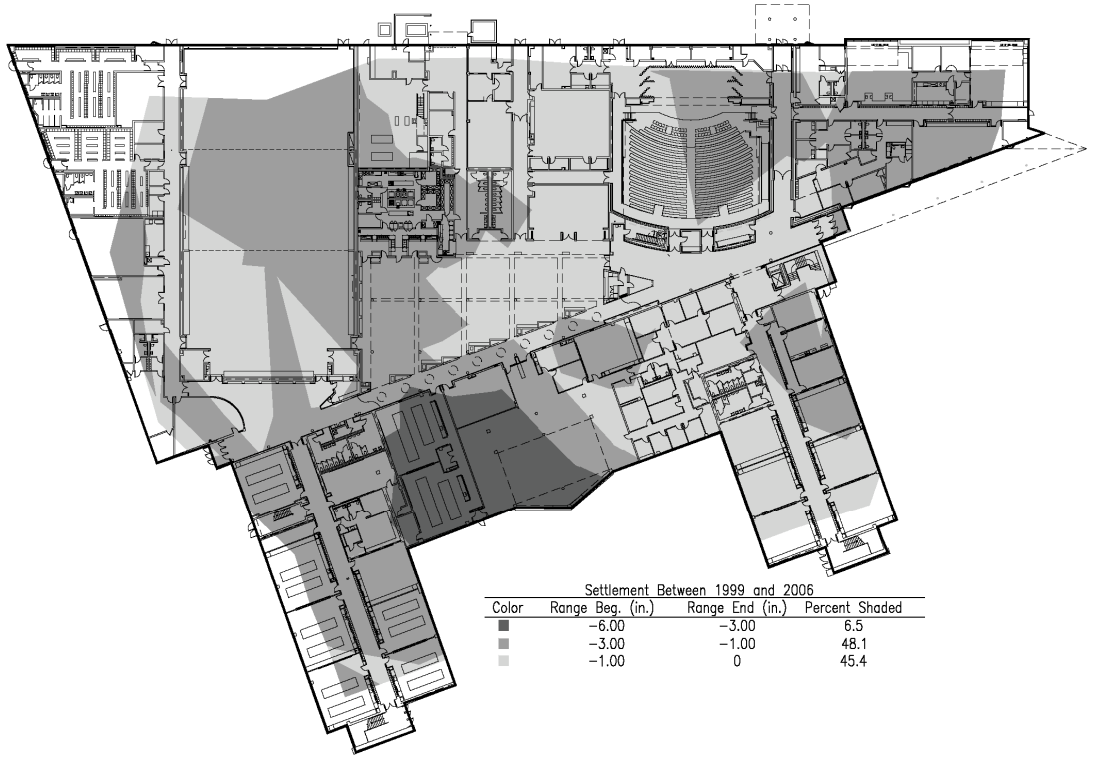


Figure 2. Settlement Between 1999 and 2006.

Soil Borings:

The thickness of the construction-debris stratum is essential to understanding the differences in the settlement magnitudes. Approximately 100 borings and test pits were performed on the site; most were done by others during the original building construction. Several additional borings were performed after the DDC and building construction to confirm the top of the construction-debris stratum.

Vibrating-Wire Borehole Extensometers:

We installed three vibrating-wire borehole extensometers to accurately measure settlement versus time at several discrete points. The extensometers are useful to confirm the settlement model due to their high accuracy (+/- 0.008 in. per the manufacturer); however, the cost to purchase and install each device (+/- $12,000 each in 2005) limits the number that can be economically installed. Each extensometer was installed in a boring and anchored into the construction debris, clay, and glacial-till strata. The glacial-till stratum provided a stable reference.

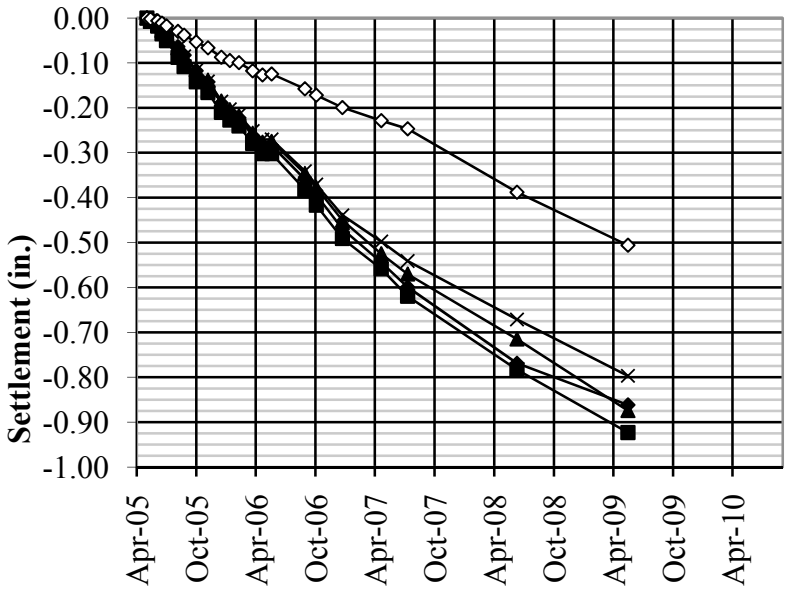


Figure 3. Extensometer Settlement Data.

Vibrating-wire strain gauges provided a direct measurement of the movement of each anchor and were monitored periodically to provide a measure of movement. A plot of the settlement of the anchors versus time for one extensometer is shown in Figure 3. The high accuracy of the extensometer data provides a very accurate confirmation of settlement trends and confirmed the cause of the settlement.

Ground Penetrating Radar:

We performed a ground-penetrating-radar (GPR) survey over the majority of the first floor to search for voids between the slab and the sub-grade. We also performed core holes through the slab to confirm the GPR survey results. The survey confirmed that the slab was generally in contact with the soil at the centerlines between interior pile caps and that regular voids existed near columns and along the perimeter grade beams.

Visual Damage and Condition Assessments

We performed periodic inspections of the building and classified the condition in each building area as Negligible, Slight, Moderate, or Severe based on the criteria given in Boscardin and Cording, 1989.

MECHANISIMS CAUSING SETTLEMENT

The consolidation characteristics of landfills have been compared to the secondary consolidation of organic soils and can be characterized by 1) mechanical compression (bending, crushing, and particle reorientation under self-weight), 2) biological decomposition of organic wastes, 3) physiochemical changes such as oxidation, corrosion, and combustion, and 4) raveling of fines into large voids. (Lukas and Seiler, 1994)

The predictability of the magnitude of consolidation of construction debris landfill sites will be low because of the high variability in the materials. Therefore, monitoring the landfill is the best way to estimate the future consolidation magnitudes. Hossain, Gabr and Barlaz, 2003 indicate that the decomposition will also vary with time.

Methane, carbon dioxide, and oxygen levels are measured at the site. Little landfill gas has been measured, except for high methane levels and low oxygen levels measured across the site in the last year. The settlement data has not reflected any change in settlement rate since the increased landfill gas generation was detected.

Lukas and Seiler, 1994 indicates that the time required for a landfill to become biologically inactive is a function of the climate and the amount of water available, which is required for the decomposition process. The expected duration of the decomposition process is uncertain. In some instances, settlement has been reported to be complete within twenty-five years, and, in others, it has continued for over thirty years with no sign of being complete. In our evaluation, we assumed that the settlement will continue for the entire fifty-year expected service life of the building.

SETTLEMENT MODEL

Evaluation of the survey and extensometer data confirmed that the settlement of the first floor slab on grade is solely and directly related to the consolidation and decomposition of the construction-debris stratum. In order to determine the expected future settlement, we modeled the historic measured settlement based on secondary consolidation theory as outlined in Equation 2 from Bowles, 1996.

Since the thickness of the debris stratum and the settlement magnitudes vary significantly across the building footprint, we separated the building into thirty-six zones based on similar debris thickness, settlement magnitudes, and damage levels. We prepared settlement models for each zone based on the survey measurements of the historic settlement magnitudes, and we back-calculated the C_α value for each zone. Figure 4 shows a sample plot of measured settlement compared to our

$$\Delta H_s = C_\alpha \times H_f \times \log_{10}\frac{t_j}{t_i} \quad \textbf{Equation 2}$$

ΔH_s = Change in Construction Debris Thickness, ft
C_α = Secondary Consolidation Index, unitless
H_f = Original Thickness of Construction – Debris Stratum, ft
t_i = Time from Loading to Beginning Time of Interest, days
t_j = Time from Loading to End Time of Interest, days

settlement model versus time for one building zone. The measured settlement data correlates well with the model.

The back calculated C_α values at this site vary between 0.002 and 0.05 with an average of 0.012. We also performed a further evaluation of the settlement trends using the extensometer data to confirm that the consolidation of construction debris follows the same log-time curve that is the premise of the model.

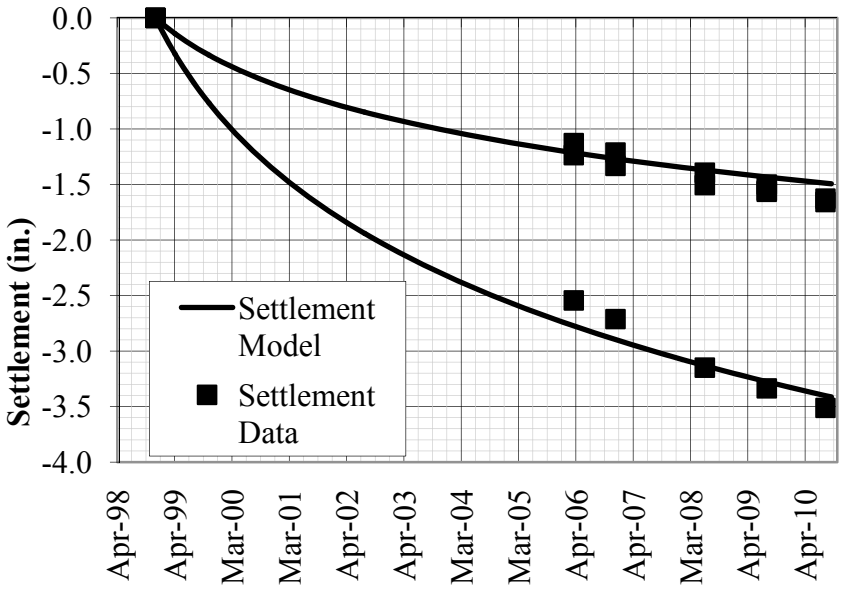


Figure 4. Settlement Model versus Measured Settlement.

We estimated the range of future settlement of the slab on grade as a percentage of the total building area (see Table 1). The settlement magnitude clearly increases with time.

Table 1. Total Settlement versus Time.

Total Settlement	2006 (Actual)	2024 (Estimated)	2049 (Estimated)
0 to 1 in.	45%	14%	10%
1 to 3 in.	48%	46%	42%
3 to 6 in.	7%	40%	48%

DAMAGE MODEL

Total settlement alone is not a true indicator of expected damage as span lengths between the center of a slab panel and the pile caps (providing inadvertent support) vary. For example, a classroom with 2 in. of settlement and a 30 ft span between column pile caps will have significantly more damage than the gymnasium with the same settlement and a 100 ft span. Traditionally the effect of span length on the allowable deflection, or in this case settlement, is handled with a distortion factor. Equation 3 defines the distortion factor.

$$Distortion\ Factor\ (DF) = \frac{Span\ Length\ (in.)}{Settlement\ (in.)} \qquad \textbf{Equation 3}$$

We correlated our calculated distortion factors to damage that we classified by our visual inspections. We found that severe damage corresponds to distortion factors less than 250; moderate damage is between 250 and 350; slight damage is between 350 and 580; and negligible damage is greater than 580. This seems appropriate considering that ACI 318-08 suggests distortion limits of 240 where nonstructural elements are not likely to be damaged and 480 where nonstructural elements need to be protected from damage.

Figure 5 shows the change in distortion factor/damage level in various building zones versus time, where each line represents a zone of the building. Dashed lines represent predicted distortion factors. By 2007, several zones have moderate to severe damage, and by 2025, about half the building service life, we estimate that most of the building will have severe damage if no repairs are performed. It is clear that repairs must be made if the structure is to achieve its fifty-year service life.

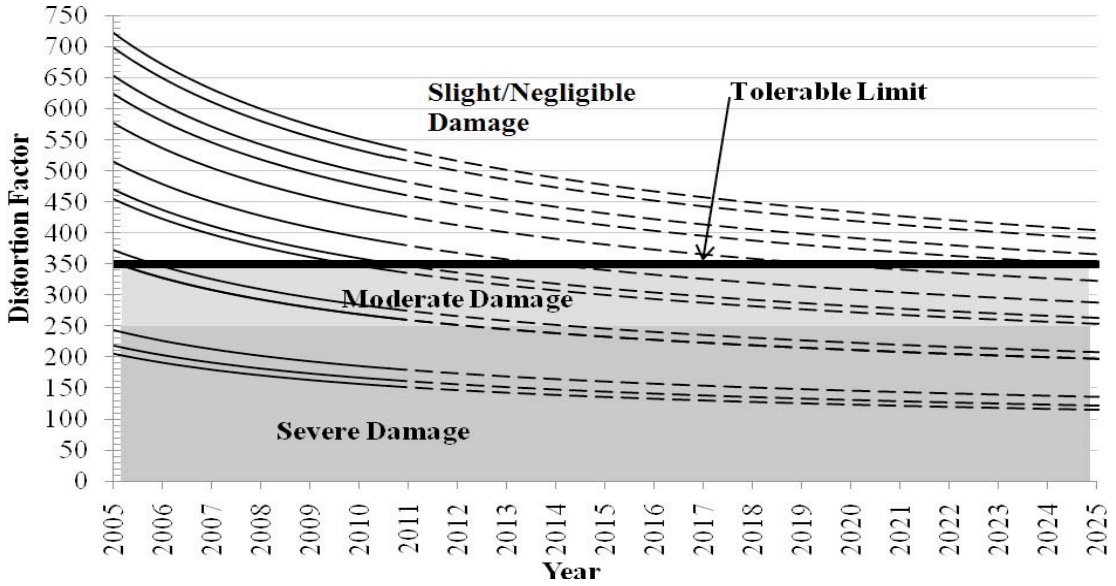


Figure 5. Distortion Factor vs. Time.

PERMANENT SLAB REPAIRS

In many areas of the building, where settlement and damage were greatest, we determined that the only feasible long-term repair option was to replace the existing slab on grade with a new structural slab founded in the stable glacial till and bedrock below the construction-debris. The design of the repairs presented many challenges; the most pertinent are discussed below:

Salvage and Selective Demolition:

Since the building was relatively new, many items were deemed salvageable and required removal, storage, cataloging, and reinstallation during the proposed reconstruction. A detailed review was performed to determine which items could be economically salvaged, including items such as lockers, toilets, sinks, and mechanical equipment. Other items such as casework, doors (mostly because they had been cut many times because of twisting door frames), electrical outlets and below-slab conduit, and ceiling grids could not be economically salvaged.

The existing 6 to 8 in. thick slabs were removed by sawcutting into small sections that were removed by skid-steer loaders equipped with air scrubbers.

Micropile Foundation Support:

We determined that, in many locations, the existing piles and pile caps had sufficient reserve capacity to support the new structural slab. Micropiles were installed for additional support in areas where the piles and pile caps did not have sufficient capacity or because of details associated with the construction phasing. Most of the supplemental micropiles were required in the one-story section where, understandably, lower capacity H-piles were installed during the original construction compared with the three-story section. The micropiles were beneficial over other new foundation options, since they could be installed with a relatively small piece of equipment designed for low-head room installations, see Figure 6.



Figure 6. Micropile Drill Rig.

We used two different types of micropiles with maximum capacities of 60 kips and 240 kips bonded into the glacial till and bedrock, respectively. This allowed the pile lengths to be economized based on design loads. A rotary duplex drilling method was used with a roller bit and internal flush. The use of a roller bit allowed the drill operator to drill through almost all types of debris. Out of forty-seven total micropiles used on the project, only one pile needed

to be abandoned and redrilled. Proper drill flush control was essential, since all drill flush and spoils needed to be controlled and disposed of as contaminated waste due to the landfill. All drill flush was controlled at the surface with a PVC liner attached to a temporary 5 ft long oversized casing. The temporary casing was used to eliminate the risk of losing potentially contaminated drill flush into the uncontaminated fill between the existing geomembrane[1] and the slab.

Each micropile consisted of a 7.625 in. OD steel casing, with a 0.5 in. thick wall, extending 1 ft into the top of the bond zone; with the roller bit advancing approximately 3 in. below the cutting shoe.

For micropiles anchored in the glacial till, the casing was temporarily extended the full depth of the bond zone and withdrawn to the correct elevation during grouting to eliminate the risk of sand infiltrating the drill hole. A No. 14 threaded bar was used as the core reinforcement. These micropiles were tremie grouted with a 75 psi seating pressure applied after casing withdrawal.

For micropiles anchored in bedrock, the cutting shoe was drilled 1 ft into the bedrock and, then, the roller bit was advanced into the bedrock for the required bond length. A No. 28 threaded bar was used as the core reinforcement. Before grouting, the micropiles in bedrock underwent a falling head-watertightness test to determine if there was a significant water loss in the rock socket. If the pile passed the watertightness test, the micropile was tremie grouted. If the hole failed the water test, it was grouted and redrilled at a later date. Static, compression-load tests of a micropile bonded just in the glacial till and another just in bedrock were conducted to confirm the capacities of the two micropile types.

Construction Sequencing and Phasing to Maintain Occupancy:

Detailed construction sequencing was essential, since the Owner was unable to vacate the building during the repairs. To provide a solution that worked, the Owner, School Department, and Design Team worked closely to sequence the work and allow the school to operate with a student, faculty, and staff population of more than 1,000. The design documents provided a detailed sequence to maintain occupancy over four phases that included the following:

- Maintaining electrical room panels that are located on the first floor and that service the occupied upper floors.
- Relocating all electrical conduits located in the floor before slab demolition.
- Installing temporary walkways to maintain pedestrian circulation.
- Underpinning CMU walls surrounding the stair towers while the stair towers remained in operation at the floors above. The demolition of first floor stairway slabs was coordinated to provide appropriate egress.
- Constructing temporary walls and slabs in entryways to maintain circulation.

[1] An existing 60 mil geomembrane liner was located across the entire footprint with an air ventilation system to collect and dispose of any landfill gases.

- Underpinning of corridor walls from one side to maintain circulation and to allow use of adjacent spaces.
- Working second shift hours in areas when the rooms above were occupied during normal hours.
- Relocating essential building equipment in tel/data rooms that could not be shut down while the school was occupied, during summer months.

New Structural Slab:

The new structural slab is a 12 in. thick two-way flat plate with No. 8 reinforcing bars at 6 in. centers, top and bottom, each direction. Because of the irregular support geometry, continuous reinforcement at the top and bottom was used. We prepared a finite element model of the slab using two-dimensional plate elements using an iteratively cracked section analysis to confirm reinforcement requirements and maximum slab deformations.

The slab was supported at the perimeter by doweling into the existing exterior grade beams. Where the interior pile caps had sufficient capacity to support the loads, the new slab was cast against the top of the pile cap's pier. Where the existing pile caps had insufficient capacity, a geo-inclusion material was used to prevent loading the pile caps. Since the slab was doweled into the existing grade beams, shrinkage cracking due to restraint was a concern; therefore, the design required pour strips (Figure 7) around the perimeter to allow a significant portion of the shrinkage in the slab to occur before placement of the pour strips. A shrinkage-reducing admixture (SRA) was used in the concrete mix design to minimize shrinkage. Mortar bar tests in accordance with ASTM C157 were conducted to confirm the SRA dosage and resulting shrinkage. The reduction in shrinkage cracking can reduce the estimated long-term deflection of the slab significantly.



Figure 7. Structural Slab on Grade with Pour Strips.

In our experience and based on published literature, two-way slabs may experience deflections in excess of those calculated using ACI 318-08. In particular, ACI 435R-95, Reapproved 2000 reports that "a number of authors have suggested that the ACI 318 long-term multiplier is too low for application to two-way slab systems and is based on poor correlation between calculated long-term deflections and field measured deflections." In addition, ACI 435R-95 reports that total long-term deflection multipliers could be as much as five times the immediate deflections due to the combined effects of creep, shrinkage, warping, cracking due to restrained early volume change, and cracking due to early construction shoring loads. For

calculation of long-term deflection, we adjusted both the elastic modulus and the creep deflection multiplier considering a time of loading equal to one year, which is approximately equal to the timeframe after placement when we expect the subgrade will settle enough to cause the slab to act as a structural slab. This adjustment will provide a better estimate of the predicted long-term deflections.

Underpinning of Main Corridor, Fire Wall, and Stair Towers:

One of the phasing lines was located along a wall of the main corridor to separate the occupied area from the construction area. The existing corridor wall was constructed of brick masonry with metal stud backup or CMUs. Underpinning of the wall in place required the excavation of underpinning approach pits on the construction side of the wall spaced at about 5 to 7 ft centers and the installation of grout bags to provide temporary support under the wall while the space between the grout bags was excavated for new permanent concrete support elements. The stair tower walls were underpinned using a combination of steel "needle beams" and grout bags (Figure 8).



Figure 8. Underpinning of Stair Tower.

An existing reinforced concrete firewall served as another phasing line. The wall was supported on a spread footing that was also settling and required underpinning. Permanent re-support was provided by coring an oversized hole in the footing and installing the micropile through the footing. Shear rings were provided on the outside of the casing, and the annular space between the casing and the core-hole was filled with non-shrink grout. The micropile used to underpin the footing was also detailed to support the edge of the new slab. A load test of the micropile-to-slab connection was performed to confirm its capacity.

Permanent Sub-Slab Drain Support:

All sub-slab drain lines were hung from the underside of the new structural slab to ensure proper alignment and prevent continued settlement. Lightweight EPS geofoam was used as a backfill material above the utilities to eliminate any downdrag load on the piping due to settlement of the subgrade.

CONSTRUCTION COSTS

Approximately 50,000 sq ft of the first floor slab was repaired between 2007 and 2009. The total construction cost as of 2009 was approximately $10MM, or $200 per

square foot. The unit cost to install the micropiles was approximately $375 per linear foot of pile, which is a significant portion of the total construction cost. We attribute the relatively high cost of micropile installation to the difficult site conditions, obstruction drilling, and work necessary to control the drill spoils.

CONCLUSION

In conclusion, the consolidation of a construction debris landfill can be accurately represented by secondary consolidation theory; to estimate the settlement of a specific landfill, the landfill should be monitored to determine the appropriate site specific secondary consolidation coefficients. Borehole extensometers are one accurate tool that can be used to measure this movement and allow a fairly quick measure of the settlement rate.

Designers should be very cautious when specifying a slab on grade on materials with high secondary consolidation potential; close coordination between the Architect, Structural Engineer, and Geotechnical Engineer is necessary to understand the site constraints and provide a solution to preclude severe distress from consolidation of the underlying soils as repairs can be costly. Repairs to mitigate future settlement and damage by using a new structural slab on piles is not ground-breaking but details to implement the solution in an occupied building can be and require innovation. Close coordination between the Owner and Designer is necessary to provide a repair sequence and a detailed design that can be constructed. During the design, the details and phased approach for dealing with many of the constraints needs to be developed; designers should not rely on a contractor means and methods approach to construction.

REFERENCES

ACI Committee 318. Building Code Requirements for Structural Concrete (ACI 318-08). American Concrete Institute, 2008.

ACI Committee 435. Control of Deflections in Concrete Structures, Report by ACI Committee 435 (ACI 435R-95). American Concrete Institute 2000, Reapproved 2000.

Boscardin, M. D., and E. J. Cording. "Building Response to Excavation-Induced Settlement." ASCE Journal of Geotechnical Engineering 115, no. 1 (1989): 1-21.

Bowles, J. E. Foundation Analysis and Design, 5th Edition. McGraw-Hill, 1996.

Hossain, M. S., M. A. Gabr, and M. A. Barlaz. "Effect of Decomposition and Stress on Creep Compression Index of Municipal Solid Waste in Bioreactor Landfill." Proceedings 12th Panamerican Conference on Soil Mechanics and Geotechnical Engineering. Cambridge, MA: Verlag Glückauf GMBH, 2003. 1435-1440.

Lukas, R. G., and N. H. Seiler. "Settlement of Dynamically Compacted Deposits." Vertical and Horizontal Deformations of Foundations and Embankments, June 1994, Geotechnical Special Publication ed.: 1590-1601.

Loose Mortar-Set Roof Tile Falsehood

Mel Underwood, P.E.[1]

[1]Senior Consultant, Engineering Systems, Inc. (ESI), 9990 S.W. 77th Ave, Suite 325, Miami, FL 33156; PH (786) 301-5491; email: maunderwood@esi-fl.com

ABSTRACT

In south Florida, mortar-set roof tile applications are commonplace. This type of installation, when completed properly, can perform as a durable and long lasting roofing system. A properly installed system includes the tiles having been rigidly affixed to the roofing underlayment by mortar paddies. Problems can arise, for a homeowner experiencing an improper installation, when they discover that the tiles are not rigidly attached and that many individual tiles are loose and easily lifted by hand, during inspection. This is usually discovered sometime after a hurricane event and well after the original installation. Subsequently, the homeowner's insurance company may be called upon during a roof related property loss claim and tasked with determining what, if any, loose roofing tile is categorized as damage due to winds from a presumed and associated storm and/or other causes, unrelated to storm events.

Mortar-set installation of roofing tiles is generally covered by the Concrete and Clay Roof Tile Installation Manual. The mortar paddy is intended to provide the necessary bond between the tile and the roofing underlayment, in order to create resistance against wind uplift forces. Uplift resistances for available properly-installed systems are documented with published values obtained through rigorous testing, which is required prior to a "Notice of Acceptance" (NOA) being issued for each and every roofing system included on the product approval list in Miami-Dade County, Florida. Each approved system has a corresponding NOA that provides documented values, in tabular form, which indicate resistances for an individual tile due to self weight alone, as well as the resistance provided by the "mortar-set fastening/attachment method", which has been documented to provide anywhere from 3 to 5 times additional uplift resistance. This resistance helps to prevent wind forces from removing the tiles from the roof.

The NOA is a valuable resource to aid in determining if/that an existing tile condition, being "loose"/"not bonded" on any particular home, is not automatically or necessarily the result of storm induced wind uplift forces. The fact that the loose tile remains on the roof, in its original position as installed, helps to affirm that the wind forces in question were not large enough to overcome simply the tile's own weight.

BACKGROUND

The purpose of this paper is to help inform the involved parties (homeowner, insurance adjuster, public adjuster, roofing contractor, architect/engineers, etc.) with regard to a mortar-set tile roof and about the history, along with the associated issues, that have been experienced by this type of tile roofing system. There are mortar-set roofing installations which have performed as originally intended and which have withstood tropical storm and hurricane force winds. There are other mortar-set roofing installations which have not performed as intended and this is not necessarily, nor automatically, related to wind storm events.

This paper does not intend to address issues regarding a homeowner who may have been involved in a bad faith claim, may have been wronged by an insurance company, or who may have been provided with a claim payment which was an insufficient amount. This paper does however attempt to address the instance of a homeowner/homeowner's representative who believes and/or has been informed that their mortar-set tile roof exhibits hurricane related wind damages and that the insurance company "owes" them a new roof. This assertion/belief is usually unfounded and/or subscribed to by the homeowner without them having been provided any technical expertise, technical reports or otherwise, which may serve to substantiate the causes of the existing damages/deficiencies. This action, usually occurring years after the subject storm event, may unfairly raise expectations of the homeowner such that they feel that they are entitled to a new roof. This action may also create unwarranted fees for the involved insurance company, fees ultimately passed along at the expense of every homeowner who pays a property insurance premium, especially in Florida.

ROLE OF THE PUBLIC ADJUSTER IN FLORIDA

Homeowners may choose to be represented by a public adjuster in their property loss claim reconciliation. The Florida Association of Public Insurance Adjusters website (FAPIA) defines the role of a public adjuster. This profession is stated to offer, among other services, immediate review of a homeowner's policy, determination of extent of coverage, preparation of details for the property damage, and compilation of necessary documentation. All of this may be performed by the adjuster in order to protect the insured's rights, by handling all associated matters which may be essential with regard to a legitimate loss and claim adjustment.

A public adjuster should be an authority on property loss adjustments and they may be hired by an insured for assistance in adjusting a valid property insurance claim. A public adjuster is employed solely by the insured and they are required to be licensed in Florida (Agent and Agency Services). Public adjusters are required to participate in continuing education and they should act in accordance with their industry's code of ethics, established by the association and governing state agency.

The number of public adjusters ballooned after several hurricanes affected Florida in 2004 and 2005. Numbers increased from approximately 400, to in excess of 2500 (Fred E. Karlinsky et al, 2009). The number of public adjusters in 2010 was stated to be approximately 2500, which decreased from approximately 2900 in 2009 (Public Adjusters [2011-203]).

There are laws and rules which govern the conduct of the citizens of Florida. The current laws are known as the Florida Statutes and they are organized by Titles. Within each title there are chapters, parts and sections. Title XXXVII covers insurance and contains chapters 624 to 651 which are relevant to this paper's topic (The 2010 Florida Statutes). Chapter 626, Insurance Field Representatives and Operations, Part VI, Insurance Adjusters, governs public adjusters and their conduct.

The department within the state of Florida which licenses public adjusters is the Department of Financial Services (DFS) (Public Adjusters [2011-203]). Florida Statutes, Title XXXVII, Chapter 626, Part VI, Section 626.878 Rules; code of ethics, requires that public adjusters shall subscribe to the code of ethics which are specified in the "rules" of the department. In order for a department to "oversee" an entity, such as public adjusters, they need to create and administer "rules" which are similar to laws, but which are created/administered by the department in accordance with Florida statute, Title X, Chapter 120, Administrative Procedure Act (Florida Administrative Code). A "rule" is the department statement of general applicability which implements, interprets, or prescribes law or policy. It also describes procedural or practice requirements of the department. So for example, Rule 69B-220.051, Conduct of Public Adjusters, sets forth the general conduct in matters affecting public adjusters. Rule 69B-220.201, Ethical Requirements, sets forth guidelines to which they are required to conduct themselves. Any and all Florida "rules" are compiled in a document known as the Florida Administrative Code.

A statute of limitations sets a finite timeframe, a legal deadline, after which a property loss claim cannot be legally reopened (Hurricane Losses and the Statute of Limitations). This is covered by Florida Statutes, Title VIII Limitations, Chapter 95 Limitations of Actions; Adverse Possession, Section 95.11 Limitations other than for the recovery of real property. Section 95.11(2)(b) requires that any legal and equitable action sought against a written contract, obligation, or liability be commenced within five years. This includes insurance policy claims against covered losses, as they relate to residential and commercial properties.

Some public adjusters have been attempting to get homeowners to reopen old (previously submitted) claims and/or submit new claims for loss dates that are still within the Florida statute of limitations. Any contractual requirement related to hurricane damage of an insured property from the 2004 hurricane season, which may have gone unclaimed, has expired. The last major hurricane to hit Florida was Hurricane Wilma, an October 2005 storm, and any contractually covered loss-related damages caused by this storm have also passed the 5 year statute limitation.

In 2010 the Florida legislature tried to enact a bill to reduce the statute of limitations to 3 years for new, reopened or additional claims for a subject loss event. This was vetoed by the Governor however and the 5 year Florida limitation currently remains in affect (Public Adjusters [2011-203]).

As statute limitation deadlines approached, public adjusters advertised and solicited that they could get more money for homeowners above and beyond what insurance companies may have already paid. Public adjusters typically required no upfront fees. Very little investment, time-wise or other, would be required on the part of a homeowner to sign on and this has been part of the allure to utilize a public adjuster rather than to pay comparably higher attorney fees by utilizing the legal profession, if legal action was instead pursued. While there may have been valid instances where an insured did not receive appropriate or complete compensation, many reopened claims required insurance companies to expend additional time, monies and resources in an effort to refute the less than "legitimate" losses. Insurance companies have stated that they have paid many, what they feel to be illegitimate claims and/or that they have incurred wasteful costs in an effort to defend and deny those claims. In most cases, the increased costs incurred by the insurance companies have directly affected and have been passed on to homeowners through increased insurance premiums in local and regional markets. Some insurance companies have even gone as far as to no longer write homeowner's policies altogether, in select markets, while others have gone out of business indefinitely and/or completely.

There is a particular property loss category that was frequently pursued by many public adjusters and roofing contractors. This property loss category specifically involved mortar-set tile roof installations. See Figure 1.

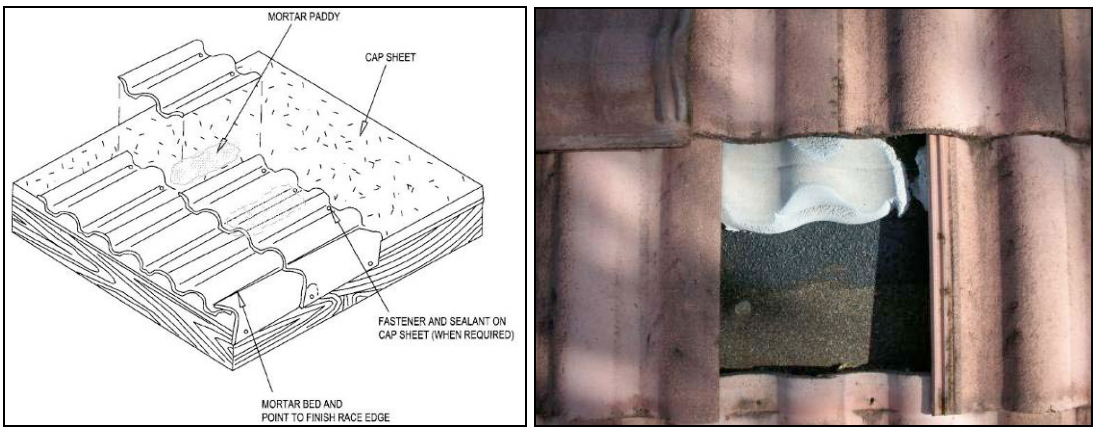


Figure 1 – Mortar paddy application of roof tile with schematic representation (Concrete and Clay Roof Tile Installation Manual, 2005) and an example of an improper mortar paddy installation

The mortar-set tile roofing system was seemingly more frequently misunderstood and subsequently more often submitted/resubmitted to insurance companies as windstorm damage type claims. This is somewhat counterintuitive because, historically speaking, roof related damages have been documented to be the leading cause of building and

residential performance related problems during severe storm/hurricane type wind producing events. One might therefore think that a better understanding of the mortar-set tile roofing system should therefore exist (Hurricane Charley in Florida). Because of the lack of understanding of the mortar-set roofing system issues, combined with misinformation related to this roofing system, this paper has been written with the intent to help educate and inform appropriately involved parties (homeowner, insurance adjuster, public adjuster, roofing contractor, architect/engineers, etc.) with regard to mortar-set tile roofing systems and their history, including associated issues that have been experienced with this particular roofing system over the years.

MORTAR-SET ROOF TILE INSTALLATION TECHNIQUE

Mortar-set application of roofing tile systems is generally covered in the Concrete and Clay Roof Tile Installation Manual. This provides installation guidelines under system #3 included in the manual. These guidelines recommend that the tile is set in a paddy/bed of approved mortar, also currently required to be factory premixed and bagged with Florida Building Code product approval. They recommend that the mortar application occur over a 10 inch minimum length trowel, applied vertically to the underlayment beneath the tile. It states to not apply the mortar under the headlug of a tile, or onto the underlock of an adjacent tile. The mortar is intended to provide the necessary bond between the tile and the roof in order to help resist wind uplift forces. Many of the roof investigations ESI has conducted exhibited improper/inadequate installation methods and techniques which were not in accordance with industry guidelines, industry standards and building code requirements. See Figure 2 for a depiction of tile roof components and associated terminology.

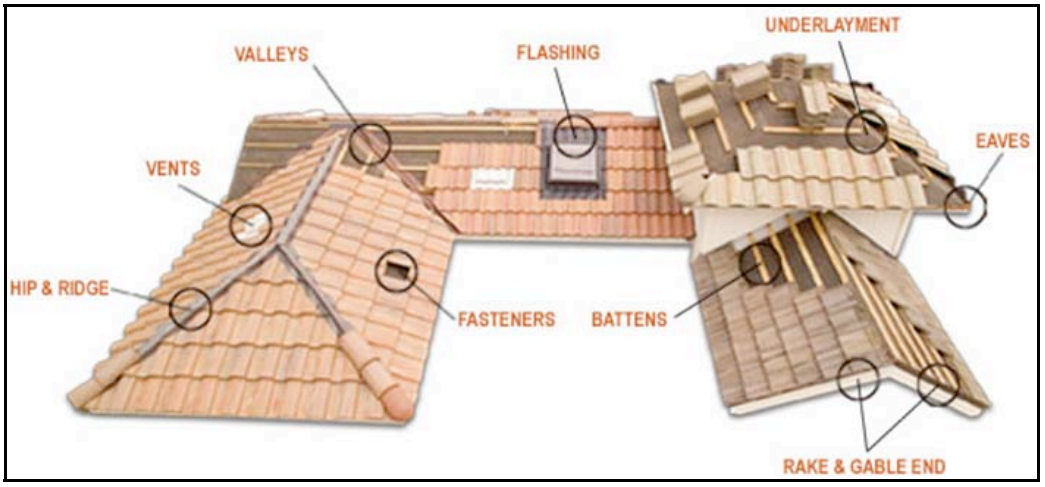


Figure 2 – Tile Roof terminology and schematic diagram courtesy of Boral Roofing (MonierLifetile)

MORTAR-SET ROOF TILE LACK OF BOND WITH MORTAR PADDIES

The first real test and documentation that there was an issue with this installation method, its durability and its usefulness over time became apparent after the 1992 Hurricane Andrew event. It was a known problem that recent tile roof installations had been experiencing bonding problems as early as just after installation, prior to Hurricane Andrew. But this hurricane triggered a widespread awareness of the installation method's shortcomings. Typically the tile covering the roof is intended to stay attached and provide a service life at least equal to the life of the water proofing element of the roofing system, the underlayment. The underlayment is most often some form of rolled roofing material, weighing roughly 90# per square and may be comprised of a modified bitumen material and/or an organic (asphalt impregnated paper) material.

Lack of and/or Loss of bond between the mortar-set "fastening" components has been documented and attributed to several issues. It has been stated that there are more than 30 ways for the mortar-set technique to go wrong and some governmental agencies/reports have even gone as far as to recommend against the use of the mortar-set alternative as a chosen method to secure roof tile (Summary Report Building Performance), (Installing Wind Resistive Tile Roof Covering). Other governmental agencies/reports have similarly recommended the mechanical or the foam-adhesive attachment method as opposed to the mortar-set procedure (Tile Roofing for High-Wind Areas). It has been sufficiently documented that manufacturing processes related to roof tile is much more thoroughly controlled and better overseen as compared to tile roof installation oversight and control on the construction site (Professor Wilson C. Barnes et al, 1994). "Lack of bond", implying that bond was never allowed to occur or never adequately developed, can be produced due to many reasons (poor workmanship, improper mortar mix, mortar drying out before tile applied to roof, overheating of tiles due to sun during installation, inadequate wetting of the tiles prior to installation, inadequate mortar quantity utilized during installation, mortar bed shrinkage upon drying, incorrect location of mortar application under the tile, walking on the roof before tile/mortar bond is properly set, extruded tile manufacture verses tile produced in molds, maintenance activities/footfall, etc.).

As with any specialized field constructed product, a quality installation will produce intended results while a poorly or improperly installed product may not provide intended results. The Florida Building Code (FBC) acknowledges that installation techniques are a major issue and have thus provided safety measures in the form of required inspections which must occur during the time of the installation and prior to the subsequent permit approval process.

MORTAR-SET ROOF TILE CODE REVISIONS AND ADDITIONS RELATED TO THIS SYSTEM'S APPLICATION, FUNCTIONAL IMPROVEMENT AND PUBLIC WELL BEING

The FBC has implemented improvements and safeguards over the years, in the recent past, in order to try and prevent mass building system failures, such as what had been witnessed with mortar-set tile roof installations. In 2005, the improved structural building-envelope provisions within FBC were tested by real life conditions and associated wind events. The data obtained, from the 2005 category 2 wind forces, was believed to be far more valuable, superior and useable than corresponding data that might be obtained through testing under laboratory conditions (Post Hurricane Wilma Progress Assessment). Chapter 9 of the FBC, Residential, Section R905.3 and Chapter 15 of the FBC, Building, Section 1507.3 each state that installation of clay and concrete tile shall follow the recommendations provided in the Concrete and Clay Roof Tile Installation Manual, previously discussed. Also, it should be noted that installation requirements are mandated to be performed in accordance with the Test Protocols Manual of the FBC. More specifically, mortar-set roof tile application requirements are set forth in Roofing Application Standards (RAS) Chapter No. 120, Mortar and Adhesive Set Tile Application.

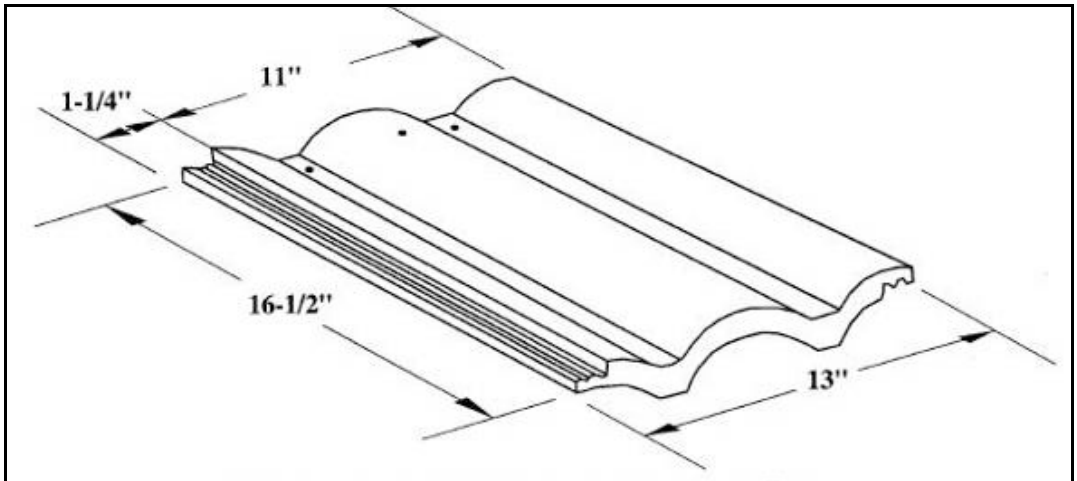
FBC Chapter 15 and Chapter 44, Section R4402.1.4.2.4, each currently require that all newly constructed mortar-set tile roofs shall be static-uplift tested, on a specific percentage of the roof square footage basis, to ensure that an appropriate mortar bond exists, after installation has been completed and prior to construction-building permit finalization. This test procedure and its requirements are thoroughly documented in the Test Protocols Manual of the FBC. More specifically, it is documented in Testing Application Standards (TAS) Chapter No. 106, Standard Procedure for Field Verification of the Bonding of Mortar-Set Tile Systems. This protocol is a quality control test to be utilized for verification of a new product application/installation in order to meet building permit requirements, but it is not, nor was it ever intended to be a test to be utilized on an in-service roof that has experienced a wind event.

FBC Chapter 44, Section R4402.7.8.1.1 currently requires that all roof tile mortar be premixed/prepackaged and contain a corresponding product approval which has also been tested in accordance with TAS 123. Job site mix approvals are also acceptable if they comply with TAS 113 and they are approved by the building officials. Workmanship requirements are discussed in FBC, Residential, Chapter 44, Section R4402.1.2.5 and FBC, Building, Chapter 15, section 1512.2.5.

These and other code related measures have been enacted in order to make an attempt at providing better installation procedures and techniques that are more actively monitored and more tightly controlled for the purpose of protecting the general public's interest, safety and well being.

MIAMI-DADE COUNTY NOTICE OF ACCEPTANCE (NOA) AND ITS USE FOR PURPOSES OF EDUCATING ALL INVOLVED PARTIES ON THE ACTUAL PHYSICS OF TILE PERFORMANCE UNDER WIND LOADING

A very important, yet subtle, point about roof tile storm damage is often overlooked or misunderstood by many. It relates to the physics involved with tile resistance values and wind uplift forces required to detach/remove tile from the roof. These resistance values are documented with published values, obtained through rigorous testing, which is required prior to a "Notice of Acceptance" (NOA) being issued for each and every roofing system to be included in the product approval list in Miami-Dade County, Florida. For discussion purposes, we have included herein tables 3 and 8, which apply to MonierLifetile Corporation's NOA 07-1023.07. This NOA is specifically related to the Vanguard Roll concrete roof tile profile and the associated tables are shown for discussion and clarification purposes. See Figure 3. The product approval is a requirement of FBC, Chapters 15 and 44 – High Velocity Hurricane Zones. ESI references the Miami-Dade County building department NOA materials for each specific roofing system in question, as applicable during an investigation.



MONIER LIFETILE VANGUARD ROLL CONCRETE ROOF TILE

Table 3: Restoring Moments due to Gravity - M_g (ft-lbf)

Tile Profile	2":12"		3":12"		4":12"		5":12"		6":12"		7":12" or greater	
Monier Lifetile	Battens	Direct Deck	Battens	Direct Deck	Battens	Direct Deck	Battens	Direct Deck	Battens	Direct Deck	Battens	Direct Deck
Vanguard Roll Tile	5.30	6.03	5.24	5.97	5.16	5.87	5.05	5.75	4.92	5.60	4.78	5.44

Table 8: Attachment Resistance Expressed as a Moment - M_f (ft-lbf) for Mortar Set Systems

Tile Profile	Tile Application	Attachment Resistance
Monier Lifetile Vanguard Roll Tile	Mortar Set[1]	20.60

Figure 3 – Tile resistance tables from NOA No. 07-1023.07 (Notice of Acceptance)

Homeowners are sometimes convinced by their representatives that because the roof tiles are loose and can be lifted up from the roof surface by hand, during an inspection or routine maintenance, that this must be hurricane/storm related damage. This assessment can be discounted very easily by the table provided in Figure 3. What this table represents is the roof tile's "resistance" to wind uplift forces. Values provided in the table are derived from the tile "self weight" as it rests on a particular roof slope and they are listed in the "Restoring Moments due to Gravity" table of Figure 3. This resistance value for a 5":12" roof slope is 5.75 ft-lbf of resistance provided by the individual tile weight alone and does not include any of the resistance that is provided by the tile's attachment method to the roof (nails, foam adhesive, mortar paddy, etc.).

Next, when comparing the resistance provided by the "mortar-set" attachment method, it is documented that a properly bonded/installed "Vanguard Roll" roof tile will provide 20.6 ft-lbf of additional wind uplift resistance. This resistance helps to prevent the storm/wind forces from uplifting/removing the roof tiles. This is an obvious yet subtle point, but one that is often overlooked or not necessarily understood. The proper bond of the tile to the roof, in this instance, provides more than 3½ times greater resistance to potential wind uplift forces as compared to the tile self weight alone (5.75 from Table 3 and 20.6 from Table 8 in Figure 3).

The most important point that should be taken away from and/or understood by reading this discussion is that the existing tile condition being "loose" and "not bonded" on any particular home is not usually the result of storm forces. This is because of the fact that if the loose tile is still remaining on the roof in its original position, as installed, then the wind forces were not large enough to overcome simply the tiles own self weight. Any storm that is capable of "breaking" the tile-to-mortar-to-roof bond (typically 3 to 5 times greater than the tile self weight resistance for a typical tile profile and even greater for a flat tile profile) is also, by the mere physics of the situation, going to also be capable of then uplifting/removing the unbonded/unadhered tile completely off of the roof. Without any further positive bond or attachment mechanism, the tile self weight resistance is too low to stay on a roof under a wind loading event required to, or being blamed for "breaking the bond" that was or that should have been provided by its mortar attachment to the roof. If the wind was strong enough to remove a 3 to 5 times multiplier (or greater) of units for bond resistance then it could definitely overcome the remaining unbonded tile self weight resistance. See Figure 4.

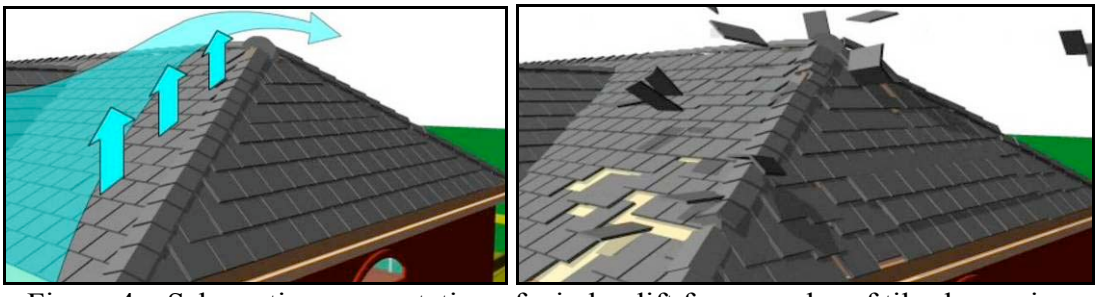


Figure 4 – Schematic representation of wind uplift forces and roof tiles becoming windborne debris (My Safe Florida Home)

This is a key point for any cause and origin analysis as it relates to a roof tile damage/deficiency assessment and decision. This is why ESI can state with confidence in engineering assessment reports what damage is, or is not, related to high winds/hurricane forces depending on each particular case. And it can be backed up with published numbers obtained by unbiased agencies (Miami-Dade County) who have the best interests in mind for the general public, and homeowners, at large.

The fact that a properly bonded tile exhibits a resistance strength which is several times greater than an unbonded/loose/unattached tile has been completely misunderstood/overlooked by many homeowners and/or their representatives. The logic and belief that a loose tile must be related to hurricane winds is shown to be false from this analysis and wind should not be stated as the cause or be associated with unbonded and loose tiles that remain on a roof in their originally installed position. Wind does not turn on and off with the flick of a switch and if wind was responsible for "breaking" the mortar bond, then the tile would also be removed from the roof surface to then most likely become windborne debris, as depicted in Figure 4.

TYPICAL CONDITIONS OBSERVED AND DOCUMENTED IN RELATION TO LEGITIMATELY AFFECTED HURRICANE DAMAGED TILE ROOFS

The FBC states that ASCE 7 shall be utilized for design of wind loads. This design code has documented that certain areas on a roof undergo various degrees of increased wind loading/pressures, according to location and geometry on the roof structure itself. See Figure 5.

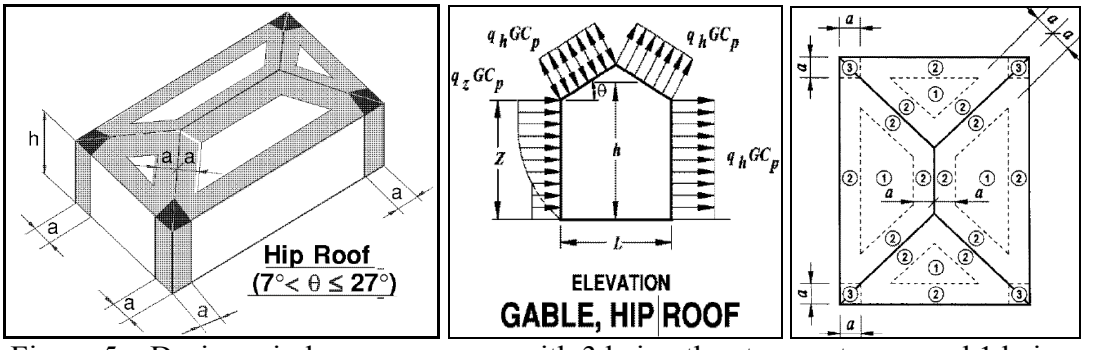


Figure 5 – Design wind pressure zones with 3 being the strongest zone and 1 being the weakest zone (Courtesy of ASCE 7)

This schematic representation shows three locations where wind loads vary in strength. These include (weakest wind zone to strongest wind zone) the field tile, the hips/ridges/perimeter eaves, and the corner eave intersections. Increased wind forces have been witnessed by case studies after storm events along with corresponding tile damage patterns which exhibit greater damages in the higher pressure wind zones and comparatively reduced damages in the lower pressure wind zones. See Figure 6.



Figure 6 – Classical zone 2 roof tile damage pattern from hurricane induced forces (Post Hurricane Wilma Progress Assessment-left, Hurricane Charley in Florida-right)

Ample documentation exists which can be utilized and may aid the homeowner as well as property damage adjusters in assessing possible causes of roof deficiencies and/or damages (Evaluating the condition of Your tile Roof) as well as typical wind related damages expected to be seen in a legitimately wind affected roof loss. Homeowner awareness can be increased by reviewing information provided from the attached reference list at the end of this document.

CONCLUSIONS

The NOA is a valuable resource to aid in determining if/that an existing tile condition, being "loose"/"not bonded" on any particular home, is not automatically or necessarily the result of storm induced wind uplift forces. The fact that the loose tile remains on the roof, in its original position as installed, helps to affirm that the wind forces in question were not large enough to overcome simply the tile's own weight. An existing tile condition being "loose" and "not bonded" on any particular home is not usually the result of storm forces. This is because of the fact that if the loose tile is still remaining on the roof in its original position, as installed, then the wind forces were not large enough to overcome simply the tiles own self weight. Any storm that is capable of "breaking" the mortar bond is also, by the mere physics of the situation, going to be capable of then uplifting the unbonded/unadhered tile, still remaining on the roof to create windborne debris by removing the tiles from the rooftop.

REFERENCES

1. Agent and Agency Services, Florida Department of Financial Services, http://www.myfloridacfo.com/sitePages/agency/sections/AgentAgency.aspx
2. ASCE 7 - Minimum Design Loads for Buildings and Other Structures
3. Concrete and Clay Roof Tile Installation Manual, Fourth Edition, Chicago, 2005, FRSA/TRI 07320/08-05, Florida Roofing, Sheet Metal and Air Conditioning Association, Winter Park, FL, and Tile Roofing Institute, http://www.tileroofing.org/
4. Evaluating the Condition of Your Tile Roof, Hurricane Retrofit Guide, Florida Division of Emergency Management, Bureau of Mitigation, http://www.floridadisaster.org/mitigation/rcmp/HRG/content/roofs/eval_tile.asp
5. Florida Administrative Code, State Library and Archives of Florida, https://www.flrules.org/Help/newHelp.asp#FAC

6. FAPIA, Florida Association of Public Insurance Adjusters, http://www.fapia.net/
7. Florida Building Code, 2004, Florida Department of Community Affairs, Tallahassee, FL, 2005
8. Fred E. Karlinsky and Richard J. Fidei, Florida Still Fine Tuning Public Adjusters, Florida Underwriter Magazine, Nov. 1 – 2009, Department of Financial Services, http://www.myfloridacfo.com/ica/news/Article67.asp http://www.monierlifetile.com/product/products-region.aspx?region=Florida
9. Hurricane Charley in Florida, Mitigation Assessment Team Report, FEMA 488/ April 2005
10. Hurricane Losses and the Statute of Limitations, Jeremy Tyler, Property Insurance Coverage, Law Blog - The Policy Holder Advocates, http://www.propertyinsurancecoveragelaw.com/2010/08/articles/hurricane-katrina/hurricane-losses-and-the-statute-of-limitations/
11. Installing Wind-Resistive Tile Roof Covering, Hurricane Retrofit Guide, Florida Division of Emergency Management, Bureau of Mitigation, http://www.floridadisaster.org/mitigation/rcmp/HRG/content/roofs/install_tile.asp
12. MonierLifetile, Boral Roofing Company, graphic roof terminology schematic,
13. My Safe Florida Home, http://mysafefloridahome.com/, http://www.mysafefloridahome.com/education.asp
14. Notice of Acceptance (NOA) No. 07-1023.07, Vanguard Roll Concrete Roof Tile, Miami Dade Building Code Compliance Office, Product Control Division
15. Post Hurricane Wilma Progress Assessment, April 2006, Miami Dade County, Building Code Compliance Office
16. Professor Wilson C. Barnes, AIA and Professor Jose' D. Mitrani, P.E., The Loss of Bond Between Roof Tiles and Mortar on Pitched Roofs, Technical Publication No. 115, Florida International University 1994, http://www.dca.state.fl.us/fbc/committees/education/educaton_tac/bldg_research_files/1_bldg_research.htm
17. Public Adjusters [2011-203], The Florida Senate, Florida Senate 2010-2011 Interim Work Program, http://www.flsenate.gov/cgibin/View_Page.pl?File=index.html&Directory=Publications/2011/Senate/reports/interim_reports/&Tab=committees&Submenu=2
18. Summary Report Building Performance, 2004 Hurricane Season, FEMA 490/ March 2005
19. The 2010 Florida Statutes, Online Sunshine, http://www.leg.state.fl.us/Statutes/index.cfm?App_mode=Display_Statute&Search_String=&URL=0000-0099/0095/Sections/0095.11.html
20. Tile Roofing for High-Wind Areas, Home Builder's Guide to Coastal Construction, FEMA 499/August 2005 Technical Fact Sheet No. 21

Non-Destructive Examination Techniques of Tubular Steel Pole Sports Lighting Structures

Brian R. Reese, P.E., C.W.I., M.ASCE[1]

[1] Vice President Northeast Region, ReliaPOLE Inspection Services Co., 22955 Tomball Parkway, Suite 24, Tomball, TX 77375; Chairman TIA TR-14.7 Engineering Subcommittee; PH (281) 259-7000; FAX (281) 754-4166; email: breese@polesafety.com

ABSTRACT

For many years, steel poles have been reliable sports lighting support structures. Tubular steel poles have performed admirably at some of America's most popular sporting venues. However, in recent years, there have been numerous failures of sports lighting structures across the country. Planned maintenance and inspection of steel poles including careful attention to the base welded connection will ensure the safety of the structure, prolong their lifespan, and protect the public.

A pole base plate connects the structure via the anchor bolts to the foundation. As the only connection and one that is non-redundant, the structural adequacy and integrity of this connection is crucial to the performance of the pole structure. A failure, if one was to occur at this joint, will in almost all cases be catastrophic resulting in the collapse of the pole.

A crack in a pole base plate weld connection can occur during fabrication, galvanizing, or after loading of the structure. It is imperative that inspections of this connection are carried out by qualified personnel with CWI and non-destructive ASNT credentials.

This article will present current methods used to inspect sports lighting structures from a non-destructive examination standpoint. Specific techniques for non-destructively examining the base weld connection including visual testing, magnetic particle testing, and ultrasonic testing will be discussed.

INTRODUCTION

Tubular steel poles are a popular support structure in many industries. Steel poles have been utilized as support structures in the sports lighting, utility, transportation, and communications industries for many decades. Combining a long history of reliable performance, competitive pricing, and ease of use and installation, steel poles are the sports lighting industry's preferred support structure and have performed admirably at some of America's most popular sporting venues. A typical application and sports lighting pole can be seen in Figures 1 and 2 below. However, in recent years, there have been numerous failures of sports lighting pole structures across the country. The property damage in some cases has been significant. As with America's other aging infrastructure, the cost of ignoring this issue can be significant to public safety and welfare.



Figure 1. Typical sports lighting structure application



Figure 2. Sports lighting pole

STEEL POLES

Steel poles in the sports lighting industry can be anchor based, direct burial, or stub based. Anchor based poles are supported with anchor bolts embedded into a concrete foundation. Direct burial structures are directly embedded into the soil. Stub based poles are flanged to a pipe section that is also directly embedded into the soil. Typically galvanized and in some cases weathering steel, steel poles are pressed in polygonal shapes such as 12-sided, 16-sided, or 18-sided cross sections. Poles may also be provided in round cross sections. Polygonal pole shells are longseamed

(vertical weld along pole axis joining pole half-shells) via submerged arc welding (SAW) techniques and round tapered poles are longseamed via SAW or electric resistance welding (ERW) methods. In most cases, the structures taper over their height to a smaller tip diameter at the top. Entry ports for interior access are welded, reinforced steel frames. Steel poles are typically fabricated with high strength steel plate and range in height from 55 ft to 150 ft. The structures can be designed to support as little as four lighting fixtures or as many as one hundred fixtures. A large percentage of structures are of the steel anchor based variety.

An anchor based pole base plate connects the structure via the anchor bolts to the foundation. More specifically, the base plate attaches the pole shaft structure to the anchors. The connection is facilitated by welding of the members during fabrication at the original manufacturer's facility. As the only connection and one that is non-redundant, the structural adequacy and integrity of this connection is crucial to the performance of the structure. A failure, if one was to occur at this joint, will in almost all cases be catastrophic resulting in the collapse of the pole structure. The connection detail of the pole shaft structure to the base plate can vary depending on the type of pole or the original manufacturer.

Typical pole base details include complete joint penetration groove weld (CJP) and socket style connection as shown below in Figures 3 and 4. The CJP connection base plate is butted against the pole shaft and consists of a groove weld with 100% complete weld penetration and reinforcing fillet weld. In other words, the connection zone is all weld material. This connection style is very popular and is a cost economical method of fabrication for a pole manufacturer. The socket connection base plate sleeves over the pole shaft and is welded with double fillet welds. This connection is also popular due to the fact that a non-destructive examination (NDE) ultrasonic test is not performed on this joint post-fabrication reducing quality assurance costs. While other joints may be possible including stiffeners, the majority of anchor based poles manufactured fall into one of these two base joint categories.

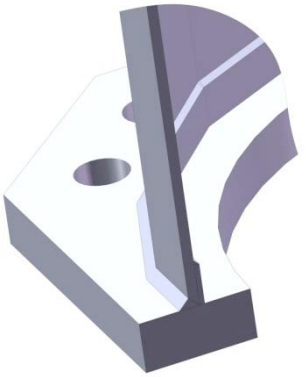


Figure 3. Complete penetration joint (CJP)



Figure 4. Socket joint

FAILURES

Pole collapses in the sports lighting industry, while traditionally an infrequent occurrence, have made news in recent years due to a rash of failures. With their proximity to areas where the public gathers for sporting events, there is a significant potential for loss of life and injury. A typical full height collapse of a sports lighting pole is show in Figure 5.

The recent pole failures have possessed similar characteristics:

1. Toe cracks in the pole structure shaft wall above the base plate weld that propagate along the weld over time causing the pole to collapse full height
2. Thin base plates allowing for excessive movement resulting in fatigue at the base plate/pole wall welded connection
3. Anchor bolt failure



Figure 5: Sports lighting pole failure

Understanding defects and cracks in steel pole structures is critical to establishing a maintenance and NDE program for sports lighting poles. According to the American Welding Society (AWS), a defect is a discontinuity which exceeds the permissible limit of a code (AWS A3.0, 2010). A crack is a fracture type discontinuity characterized by a sharp tip and high ratio of length and width to opening displacement (AWS A3.0, 2010). Cracking occurs in a weld and base metal when the localized stresses at the connection exceed the ultimate strength of the steel material. Left in place without repair, cracks may propagate over time and loading and can be very detrimental to structural adequacy. In addition, cracks greatly reduce the fatigue strength of a member. AWS Structural Welding Code D1.1 does not allow a crack to

be left in the weldment after inspection per Table 6.1, Part 1, regardless of size or location (AWS D1.1, 2008).

While all the contributing issues and their interactions are not yet fully understood, cracks at pole bases can occur due to problems in the following areas:

1. Design – incorrect base plate design resulting in an under-sized base plate and too much joint flexibility.
2. Materials – includes quality of material being joined, yield strength, and brittleness.
3. Production – poor welding quality, lack of pre-heat during welding fabrication, incorrect welding settings in the factory.
4. Quality – poor manufacturing quality control; quality checks at the original manufacturer after fabrication and galvanizing overlooked or incorrectly performed.
5. Galvanizing – cracks due to thermal expansion during the galvanizing process – referred to as 'toe cracks' occurring immediately after galvanizing or delayed.
6. Installation – loose leveling nuts or improper grouting of the base plate which may cause unanticipated stress increase in the weld joint.
7. Fatigue – long term loading effects in combination with any of the above.

In instances where preventative field repairs have been performed on the base plate weld connection, cracks have been found in the pole shaft wall in the toe above the base plate weld at the bend points. This has occurred on multi-sided poles in both complete joint penetration (CJP) groove weld and socket base plate connections. In addition to the base weld, cracks can occur and have been found in the pole longseams, around handhole penetrations (high stress areas), and in the anchor bolts. Field repairs conducted to date show the importance of monitoring and repairing this important connection on an on-going basis.

MAINTENANCE

In many cases in the sports lighting industry there is little to no maintenance of steel pole structures. The structures are typically installed and forgotten. Unfortunately, this issue combined with economic challenges, budget constraints, and manpower has resulted in many structures going virtually unmaintained since installation. Planned maintenance and inspection of steel poles including careful attention to the base welded connection will ensure the safety of the structure, prolong the structure lifespan, and protect the public. Properly maintained, tubular steel poles can safely remain in service well over a half century.

Routine structural maintenance includes the NDE of the base welds and anchors, visually inspecting the pole and its connections, checking the tightness of the anchor hardware, and inspecting the foundation. To ensure the long term performance of a sports lighting pole structure, the maintenance of a pole should be accomplished as follows:

1. Visual inspection (VT)
2. Coating thickness test
3. Magnetic particle test (MT)
4. Ultrasonic test (UT)
5. Structure connections inspection

VISUAL INSPECTION

The first step of a sports lighting steel pole visual inspection (VT) should be identifying the type of pole base weld connection (CJP vs. socket). In addition, the locations of other base welds to be inspected should be located and identified. These welds will include longseam welds if present and reinforcing handhole welds. VT consists of a visual inspection of all welds in the base area of the structure. The goal is to identify any abnormalities in the weld joints to AWS D1.1 Table 6.1 criteria (2008).

Per AWS, the inspector will specifically look for the following (AWS D1.1, 2008) and (AWS B1.10, 2009):

1. Crack – a fracture type discontinuity characterized by a sharp tip and high ratio of length and width to opening displacement. Any crack shall be unacceptable, regardless of size or location.
2. Weld/base-metal fusion – thorough fusion shall exist between adjacent layers of weld metal and between weld metal and base metal.
3. Crater cross section – all crates shall be filled to provide the specified weld size.
4. Weld profile – slightly convex, flat, or slightly convex fillet weld profiles. Groove welds should have minimum face reinforcement; weld finish.
5. Undersized weld – the size of a fillet weld versus drawing requirements.
6. Undercut – a groove melted into the base metal adjacent to the weld toe or weld root and left unfilled by weld metal.
7. Porosity – cavity-type discontinuities formed by gas entrapment during solidification.

VT should be conducted by a Certified Welding Inspector (CWI) or inspector meeting the qualifications as stated in the AWS Structural Welding Code (2008).

While crucial to the overall inspection system, note that VT will only detect surface defects. In almost all cases, this is not sufficient for a thorough inspection and conclusive results of the integrity of the base weld connection.

As can be seen in Figure 6, visual inspection tools required include the following:

1. Fillet weld gauges
2. V-WAC gauge
3. Butt-weld reinforcement gauge
4. Tape measure
5. Ruler
6. Caliper
7. Micrometer
8. Magnifying glass
9. Flashlight
10. Soapstone and marker



Figure 6. Visual inspection tools (Courtesy E. Lair)

COATING THICKNESS TEST

The majority of sports lighting pole structures are hot-dip galvanized per ASTM's Standard A123 *Standard Specification for Zinc (Hot-Dip Galvanized) Coatings on Iron and Steel Products* (2009). As part of the sports lighting pole maintenance program and structure examination, the thickness of the galvanizing coating should be measured and recorded. This will alert the weld inspector to the thickness of coating he will be inspecting while conducting his non-destructive weld examinations (NDE)

and will also serve to alert the owner on the condition and expected lifespan of the coating. Per ASTM A123, the coating thickness for hot-dip galvanized steel plate for common steel pole shaft thicknesses should be around 3.0 to 3.9 mils (ASTM A123, 2009). It is not uncommon to measure a thicker galvanizing coating. Coating thickness can be measured with a paint and coating thickness gauge for steel materials as shown in Figure 7.



Figure 7. Galvanizing coating thickness check

MAGNETIC PARTICLE TESTING

Magnetic particle testing (MT) is conducted by creating a magnetic field in a part and applying iron particles onto the surface of the part. This non-destructive examination is utilized to assess surface and near-surface cracks in welded joints. Typically red iron particles are applied to the joint with a blower while the area is magnetized with a yoke as can be seen in Figure 8. Any defects present in the material hold the magnetic iron particles applied during the test and identify the presence of a crack as shown in Figures 9 and 10. The base weld connection, longseam(s) if present, and reinforcing handhole welds should all be tested with MT. Note that the galvanizing coating and/or paint coating is typically not removed for this process. Experienced MT inspectors will utilize a pie gauge or Castrol strips and MT over the existing coating to verify that the MT exam will be effective over the coating.

MT is a relatively easy and fast inspection method in the field. The test is very effective at locating surface defects. A drawback of this particular NDE exam in the field is wind which has a tendency to blow the iron particle away from the surface being examined. MT should be conducted by an inspector with American Society for Non-Destructive Testing (ASNT) II Certification (SNT-TC-1A, 2006).



Figure 8. Magnetic particle test of pole base weld connection



Figure 9. Base weld crack defect shown holding red powder at weld toe

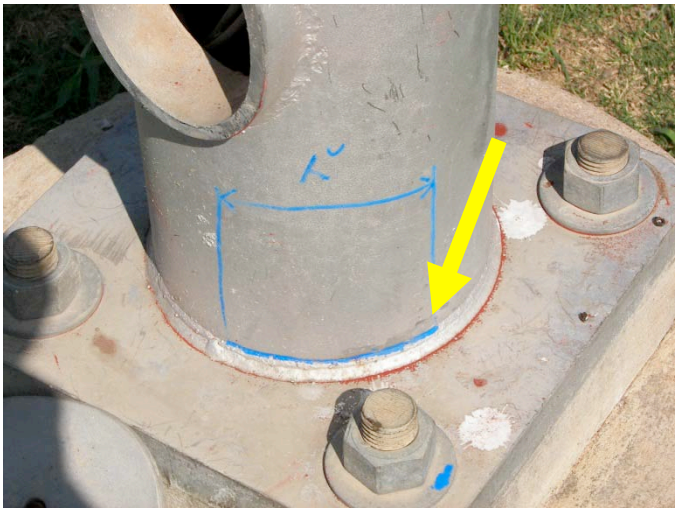


Figure 10. Base weld crack defect marked after MT; also at weld toe

As shown in Figure 11, equipment required for MT includes the following:

1. Yoke
2. Power source
3. Iron particles
4. Particle blower
5. Pie gauge or Castrol strips



Figure 11. Magnetic particle test tools (Courtesy E. Lair)

ULTRASONIC TESTING

Ultrasonic testing uses high frequency sound waves, well above the range of human hearing, to measure geometric and physical properties in materials. The test utilizes ultrasonic waves that are interrupted by any material inconsistency (crack) in the joint and can 'see' through the material (AWS WIT, 2008). UT is not limited to seeing surface defects only. This test is specifically utilized for testing of pole base weld joints that are 100% complete penetration joints (CJP) and for longseam welds. UT of a socket joint will readily show that this joint is not 100% weld material. UT will determine the presence of any defect in a CJP connection or the presence of a defect or lack of penetration in a longseam weld. UT is performed with a transducer and an electric base unit.

Shear waves, or angle beam transducers, are used for weld evaluation because they transmit sound at an angle avoiding the removal of the weld reinforcement. A 70 degree transducer is commonly used. Longitudinal waves or straight beam transducers are used to determine material thickness or the depth of a discontinuity

below the material surface. Shear wave and straight beam can be seen in Figures 12 and 13, respectively.



Figure 12 – UT shear wave



Figure 13 – UT straight beam of anchor bolt

UT is a volumetric test capable of helping the inspector locate the length, lateral location, and depth of the defect (AWS WIT, 2008). However, UT requires more inspector skill and experience for interpreting the results of the examination. It also can be implemented from one side only, not requiring access to the back side of the weldment. UT should also be conducted by an inspector with ASNT Level II Certification (ASNT SNT-TC-1A, 2006).

As shown in Figure 14, equipment required for UT includes the following:

1. Electronic instrument
2. Straight beam transducer
3. Angle beam transducer
4. Transducer couplant
5. Calibration standards
6. Ultrasonic thickness gauge



Figure 14. Ultrasonic test tools (Courtesy E. Lair)

OTHER STRUCTURE CONNECTIONS AND COMPONENTS

The inspector should inspect the pole structure connections. The structure connections include the telescoping slip joints and/or flanged connections. Excessive gaps or movement in the slip joints and loose or missing hardware in flanged connections or light supports should be identified. Any safety climb equipment installed should be visually inspected, also.

The anchor bolt connection hardware should be inspected and checked for tightness. Typically, the full effort of a man on a 4 ft wrench will be sufficient. With structures that have not been maintained, it is common to find loose anchor bolt nuts. In addition, loose anchor nuts are often removed by vandals. Improperly tightened anchor nuts or missing anchor nuts increase the possibility of fatigue related defects. The foundation top, if visible, should be inspected for cracks, spalls, or any other structural issues.

CONCLUSION

It is imperative that sports lighting pole inspections are carried out by qualified personnel with pole engineering experience, CWI credentials, and non-destructive ASNT credentials. It is strongly recommended sports lighting structures are inspected at a two (2) to five (5) year intervals depending upon age, type of structure, condition of the structure, and initial inspection results.

There is certainly much to be learned on this subject by the industry. While there appears to be many contributing factors and variables, careful attention to the following is recommended to prolong the lifespan of sports lighting poles:

1. A maintenance program should be established for sports lighting structures
2. An inspection of sports lighting poles must include NDE of all base welds and anchors
3. Do not relocate or change loading on a sports lighting structure without a complete inspection including NDE
4. Following any significant wind event a comprehensive inspection including NDE should be completed

With increased attention to sport lighting pole maintenance including base weld connection NDE, the owner will prolong the structure lifespan and ensure public safety.

REFERENCES

American Society for Nondestructive Testing. (2006). Recommended Practice No. SNT-TC-1A, *Personnel Qualification and Certification in Nondestructive Testing*, Columbus, OH.

ASTM International (ASTM). (2009). Standard A123/A123M-09, *Standard Specification for Zinc (Hot-Dip Galvanized) Coatings on Iron and Steel Products,* West Conshohocken, PA.

American Welding Society (AWS). (2010). AWS A3.0M/A3.0:2010 *Standard Welding Terms and Definitions*, Miami, FL.

American Welding Society (AWS). (2009). AWS B1/10M/B1.10:2009 *Guide for the Nondestructive Examination of Welds*, Miami, FL.

American Welding Society (AWS). (2008). AWS D1.1/D1.1M: 2008 *Structural Welding Code – Steel*, Miami, FL.

American Welding Society (AWS) Education Department. (2008). *Welding Inspection Technology (WIT)*, Fifth Edition, 2008, Miami, FL.

FIGURE AND PHOTOGRAPH CREDITS

Photographs in Figures 6, 11, 14 are used with permission and provided courtesy of Eddie Lair, Lair Industries, 1125 Waterford Drive, Waxahachie, TX 75167.

All other Figures and Photographs provided by author.

Old Masonry under Seismic Loads: Stiffness Identification and Degradation

T. Zimmermann[1], A. Strauss[2] and R. Wendner[3]

[1] Research Ass. Dipl. Ing. Thomas Zimmermann, University of Natural Resources and Life Sciences, Vienna, Institute for Structural Engineering, zimmermann.thomas@boku.ac.at corresponding author, phone: +43-1-476 54/5265
[2] Assoc. Prof. Dipl. Ing. Dr. habil. Alfred Strauss, University of Natural Resources and Life Sciences, Vienna, Institute for Structural Engineering, alfred.strauss@boku.ac.at
[3] Research Ass. Dipl. Ing. Dr. Roman Wendner, University of Natural Resources and Life Sciences, Vienna, Institute for Structural Engineering, roman.wendner@boku.ac.at

ABSTRACT

The behaviour of masonry under seismic loads has recently become of great interest. New methods for design and analysis, as well as models for resistance, have been developed. The main focus has been on experimental and analytical research for the development of new brick and mortar material whilst the characteristics of old brick material and mortar have been neglected. With the introduction of Eurocode 8 (EC), the behaviour of old masonry structures under seismic load became an interesting topic for architects and engineers. In particular, the available resistance capacity of existing masonry structures is highly relevant to the retrofit and/or improvement of existing buildings.

Deformation energy, or ductile response, is a source for energy dissipation of structures. Since normal levels of internal damping represent only a small portion of energy dissipation, large material deformations such as those required in building components to perform a ductile behaviour, are often associated with cracking and degradation of its stiffness, particularly in masonry structures.

The stiffness identification of masonry walls in an uncracked state is examined by laboratory tests. Further, stiffness degradation due to an imposed pseudo dynamic horizontal load pattern is evaluated. In particular, the wall specimens are distinguished by different mechanical characteristics like old and new brick units, low and high strength bricks and two common brick layouts. Beyond the effect of stiffness degradation in masonry on the inelastic response characteristic parameters for energy dissipation are compared within the varying masonry specimens.

Due to damage propagation, caused by imposed shear load, typical failure states are determined.

The results of a series of laboratory tests are analysed. Resistance and deformation characteristics of masonry under shear are compared to specifications according EC 6.

Keywords: *masonry, seismic resistance, energy dissipation, damping, stiffness degradation, damage*

INTRODUCTION

Masonry has an inelastic, anisotropic and non-homogeneous material behaviour. Old masonry incorporates of brick units and horizontally and vertically oriented mortar interfaces. However, the material properties of bricks and mortar are different and consequently the behaviour of masonry is not elastic even in the range of small deformations and in the uncracked state respectively. Since the introduction of EC 8 in Austria in the year 2009, buildings must correspond with the requirements of this standard.

Masonry is a typical construction material to withstand compression, but shows low shear resistance. Because of this circumstance unreinforced masonry buildings under horizontal became of high interest. The aims of research are (a) to gather mechanical properties and their wide scatter, which is characteristic for old masonry and (b) to obtain appropriate tools for seismic assessment, analysis and retrofit methods.

Structural measures are a combination of both: Conceptional design and design layout of the bearing and non-bearing structure, especially in the case of retrofit. The prior objective is to minimize the earthquake risk and the vulnerability of buildings, Bachmann (2002).

According to EC 8 the design seismic action is an earthquake with a return period of 475 years and a 10 % probability of exceedance in 50 years. Structures should withstand the action without local or global collapse, thus retaining its structural integrity and a residual load bearing capacity after the seismic events – "No-collapse requirement". The structure should also withstand a seismic action having a larger probability of occurrence than the design seismic earthquake. Thereby no damage and/or no associated restriction in usability should occur, where the costs of repair would be disproportionately high in comparison with the costs of the structure itself – "Damage limitation requirement".

Parameters regarding the seismic behaviour, i.e. energy dissipation, are important for the assessment of existing structures and the design of retrofit. Masonry buildings can reduce seismic actions due to non-linear material behaviour. Accordingly design forces are reduced to fulfil equivalence to linear elastic behaviour.

Another point of interest is the actual situation of an existing structure. While new structures remain in an elastic and uncracked state until the first earthquake event occurs, old structures may have certain damage and cracks form prior events.

The main objective of the research presented in this paper is the evaluation of seismic response of old masonry and associated with that stiffness degradation and energy dissipation. Further, mechanical material properties obtained by experiments are compared to recommended characteristics of EC 6 and EC 8.

LABORATORY TESTS

In order to obtain mechanical properties of masonry, laboratory tests were performed. The walls were built using three types of bricks: old bricks, new bricks

and clinker bricks. Lime-cement mortar with compressive strength 2.78 MPa was used. First, three masonry prisms built out of old bricks were tested in vertical compression. The compressive strength f_{kn} = 6.46 MPa and modulus of elasticity of masonry E = 2459 MPa were obtained.

Second, nineteen wall specimens were tested by subjecting them to constant vertical load and cyclic lateral load in order to obtain the lateral resistance, strength and stiffness degradation and displacement and energy dissipation capacity. Two types of brick layout were used for the construction of wall specimens with old bricks, in order to obtain the influence of such layouts on the seismic behaviour of masonry: No.1 (OL1): alternate courses of headers and stretchers and No.2 (OL2): all courses with headers. Only the former was used to construct specimens with new bricks (NL1) and clinker bricks (CL1).

The specimens were 60 cm long, 68 cm high and 29 cm thick if built out of old bricks and 51 cm long, 68 cm high and 25 cm thick if built out of new bricks or clinker bricks, respectively. They were tested as vertical cantilevers and equipped with instruments to measure the displacements and forces. Three different levels of vertical load were used for specimens with old bricks and only one level of vertical load for specimens with new and clinker bricks. A detailed description of the laboratory tests can be found in Zimmermann and Strauss (2010).

On the basis of the observed damage propagation, typical limit states were defined. A prevalent rocking type of behaviour with horizontal cracks in the lower bed joints developed in the initial state. As the imposed displacement amplitude was increased, first vertically to diagonally oriented cracks passing through the bricks in the compressed toes represent the cracking limit state (Index *cr*). The propagation of these cracks lead to the maximum resistance limit state (Index *max*). At ultimate limit state (Index *u*) a diagonal crack, from one corner to the opposite corner, split the wall, which failed in a brittle shear mode. The results of all tests are summarized in Table 1.

Table 1 Test results: lateral load and rotation angle at shear cracking, maximum resistance and ultimate state.

V (kN)	σ_v (MPa)	H_{cr} (kN)	θ_{cr} (%)	H_{max} (kN)	θ_{Hmax} (%)	H_u (kN)	θ_u (%)
Brick layout no. 1 – old bricks							
175	1.02	54.01	0.67	59.75	1.42	43.98	2.13
200	1.17	54.25	0.41	64.10	1.34	54.45	2.05
225	1.32	64.39	0.40	73.61	1.25	44.76	2.17
Brick layout no. 2 – old bricks							
175	1.02	59.24	0.81	68.50	2.29	67.26	2.81
200	1.17	51.03	0.21	61.21	1.05	48.34	1.72
225	1.32	64.32	0.35	76.95	1.24	43.49	1.57
Brick layout no. 1 – new bricks							
175	1.37	50.31	0.91	59.47	2.85	53.97	3.43
Brick layout no. 1 – clinkers							
240	1.88	85.10	3.32	96.52	4.70	72.15	6.03

ELASTIC STIFFNESS

Generally, masonry is an inelastic material. Elastic behaviour can be assumed only in the range of small imposed deflections. For practical use in that state the effective, elastic stiffness K_e of the wall is evaluated as the ratio between a horizontal load H, and the corresponding displacement d:

$$K_e = \frac{H}{d} \tag{1}$$

If we use the theory of elasticity, the displacement d of a simple cantilever wall can be calculated as follows by taking into account bending and shear deformations:

$$d = \frac{H \cdot h^3}{\delta \cdot E \cdot I} + \frac{\kappa \cdot H \cdot h}{G \cdot A} \tag{2}$$

thereby I = moment of inertia of the horizontal cross section of the wall, κ = shear coefficient (κ = 1.2 for rectangular section), δ is a coefficient depending on boundary conditions (δ = 12 when the wall is fixed at both ends and δ = 3 if it is fixed at the bottom and free to rotate on the top – cantilever), h = height of the wall specimen and G = shear modulus.

Hence we can calculate the shear modulus by introducing equation (1) into equation (2) and rearranging:

$$G = \frac{K_e}{\frac{A}{\kappa \cdot h} - \frac{12}{\delta} \cdot \frac{1}{\kappa} \cdot \frac{K_e}{E} \cdot \left(\frac{h}{L}\right)^2} \tag{3}$$

where L = length of the wall. Taking into account the values the effective stiffness K_e at the 2/3rds of the maximum resistance H_{max} and the modulus of elasticity E = 2459 MPa, determined by compression tests, the values of shear modulus G have been obtained. Since (a) experimentally obtained horizontal resistance for both brick layouts are in the same range in the case of old bricks and (b) the brick layout of the walls for compression tests was not the same as either of the two brick layouts for the shear tests, the shear modulus of masonry for both layout types has been estimated as an average value of all tested specimens, yielding G = 546 MPa and G/E = 0.222.

ANALYTICAL INVESTIGATIONS

If we consider an elastic, homogeneous and isotropic material behaviour for the cantilever walls, the principal stress states can be calculated on the basis of the theory of elasticity. Hence we get the principal compressive and tensile strength:

$$\sigma_{c,t} = \sqrt{\left(\frac{\sigma_v}{2}\right)^2 + (b \cdot \tau)^2} \pm \frac{\sigma_v}{2} \tag{4}$$

where σ_v = vertical imposed compression stress, τ = shear stress and b = a parameter which takes into account the wall geometry h/L as well as the shear stress distribution. Equation (4) is affected by the parameter b which according to Magenes and Calvi (1997) can be assumed to be: $b = 1$ for $h/L \leq 1$, $b = h/L$ for $1 < h/L < 1.5$ and $b = 1.5$ for $h/L \geq 1.5$.

If we use the average shear stress $\tau = H/A$ and assume the idealised material behaviour up to the maximum attained horizontal load H_{max} the tensile strength f_{tn} of masonry is equal to the principal stress state σ_t in equation (4):

$$f_{tn} = \sqrt{\left(\frac{\sigma_v}{2}\right)^2 + \left(b \cdot \frac{H_{\max}}{A}\right)^2} - \frac{\sigma_v}{2} \tag{5}$$

where A = area of the horizontal cross section of the wall.

In order to compare experimentally obtained and calculated horizontal loads, a shear strength formulation according to Magenes and Calvi (1997), Tomaževič and Klemenc (1997) and Turnšek and Čačovič (1971) has been used to asses the horizontal resistance:

$$H_{\max} = \frac{f_{tn} \cdot A}{b} \sqrt{\frac{\sigma_v}{f_{tn}} + 1} \tag{6}$$

Table 2 Deviation between calculated and experimentally measured horizontal resistance for old and new bricks and clinkers, using tensile strength from numerical investigations.

V (kN)	σ_v (MPa)	f_{tn} (MPa)	H_{calc} (kN)	H_{exp} (kN)	H_{calc}/H_{exp} -
Brick layout no. 1 – old bricks					
175	1.02	0.12	54.57	59.75	0.91
200	1.17	0.13	60.56	64.10	0.94
225	1.32	0.15	69.08	73.61	0.94
Brick layout no. 2 – old bricks					
175	1.02	0.12	54.57	68.50	0.80
200	1.17	0.13	60.56	61.21	0.99
225	1.32	0.15	69.08	76.95	0.90
Brick layout no. 1 – new bricks					
175	1.37	0.15	45.37	59.47	0.76
Brick layout no. 1 – clinkers					
240	1.88	0.20	61.26	96.53	0.63

The values of tensile strength, obtained by the numerical nonlinear constitutive material model SBETA, have been used in the equation (6) in order to estimate the horizontal resistance. A detailed description of numerical simulation can be found in Zimmermann et.al. (2010).

Table 2 shows the calculated values of horizontal resistance H and their deviations for different vertical loads V.

As can be seen, the analytical approach according to equation (6) and the obtained tensile strength from numerical investigations result in a rather low deviation between the experimental and calculated horizontal loads. Especially for walls with old bricks there is a good agreement. This analytical formulation can be used to estimate the horizontal resistance of unreinforced masonry in a rough but fast way.

Further, more experimental data are necessary to evaluate the behaviour of bricks, mortar as well as their interaction.

ENERGY DISSIPATION AND HYSTERETIC BEHAVIOUR

Energy dissipation capacity has been evaluated on the basis of an experimentally obtained hysteretic relationship between horizontal displacement and horizontal force. It represents one of the important parameters of seismic resistance.

Cumulative input energy E_{inp} is needed to deform the wall according to an imposed deformation. It has been defined as the cumulative work of the horizontal actuator needed to cause a given deformation status. In one cycle of loading (push and pull), ΔE_{inp} is calculated as the area under the hysteretic loop, see Figure 1 a:

$$E_{inp,j} = \sum_{i=1}^{j} \Delta E_{inp,i} \; ; \quad \Delta E_{inp,i} = \int_{(H=0)_i}^{(H=0)_{i+1}} dE_{inp} \tag{7}$$

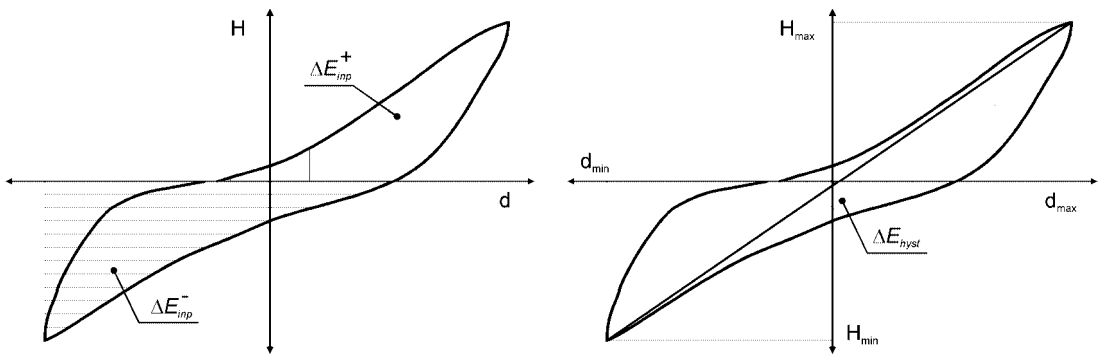
where:

$$dE_{inp} = \begin{cases} 0, & if \quad Hd(d) \le 0 \\ Hd(d), & if \quad Hd(d) > 0 \end{cases}$$

and $d(d)$ = differential displacement increment and H = horizontal force.

The amount of dissipated energy, ΔE_{hyst} in one cycle of loading has been defined as the area of the hysteretic loop between two consecutive maximum deformation states. The cumulative dissipated energy E_{hyst} has been defined as the sum of the dissipated energy of all loading cycles i from the beginning until the end of testing, see Figure 1 b:

$$E_{hyst,j} = \sum_{i=1}^{j} \Delta E_{hyst,i} \; ; \quad \Delta E_{hyst,i} = \int_{(H=0)_i}^{(H=0)_{i+1}} Hd(d) \tag{8}$$



(a) Input energy (b) Dissipated energy

Figure 1 Input energy and dissipated energy during one cycle of loading.

The ratio between the cumulative dissipated energy E_{hyst} and the cumulative input energy E_{inp} can be used as one of the energy dissipation indicators $I_{E,diss}$:

$$I_{E,diss} = \frac{E_{hyst}}{E_{inp}} \tag{9}$$

Another indicator of energy dissipation capacity is the coefficient of equivalent viscous damping ξ, defined as the ratio between the energy dissipated in one cycle of loading and the input potential energy, defined by the displacement amplitude and the lateral load:

$$\xi_i = \frac{\Delta E_{hyst,i}}{2 \cdot \pi \cdot E_{p,i}} \tag{10}$$

where $E_{p,i}$ = input potential energy in the same loading cycle, defined as:

$$E_{p,i} = \frac{1}{4}\left(H_{\max,i} - H_{\min,i}\right) \cdot \left(d_{\max,i} - d_{\min,i}\right) \tag{11}$$

The calculated values of the energy dissipation indicator $I_{E,diss}$ and the coefficient of equivalent viscous damping ξ are summarized in Table 3.

Table 3 Correlation of energy dissipation indicators at characteristic limit states.

Type	cracking limit		maximum resistance		ultimate limit	
	$I_{E,diss-cr}$	ξ_{cr}	$I_{E,diss-max}$	ξ_{max}	$I_{E,diss-u}$	ξ_{u}
OL1	0.32	7.78	0.29	7.69	0.43	39.48
OL2	0.33	8.02	0.29	7.70	0.36	24.22
NL1	0.27	5.85	0.21	5.75	0.26	17.85
CL1	0.20	5.20	0.20	6.65	0.30	32.90

According to Table 3, no significant difference can be observed in the energy dissipation capacity of the different types of brick layouts for the construction of wall specimens with old bricks. On the other hand, the dissipation capacity of the wall specimens with new bricks and clinkers is noticeably lower. Figure 2 shows the progress of equivalent viscous damping over the relative loading cycles (= load cycle *i* with respect to ultimate load cycle) for specimens with old bricks.

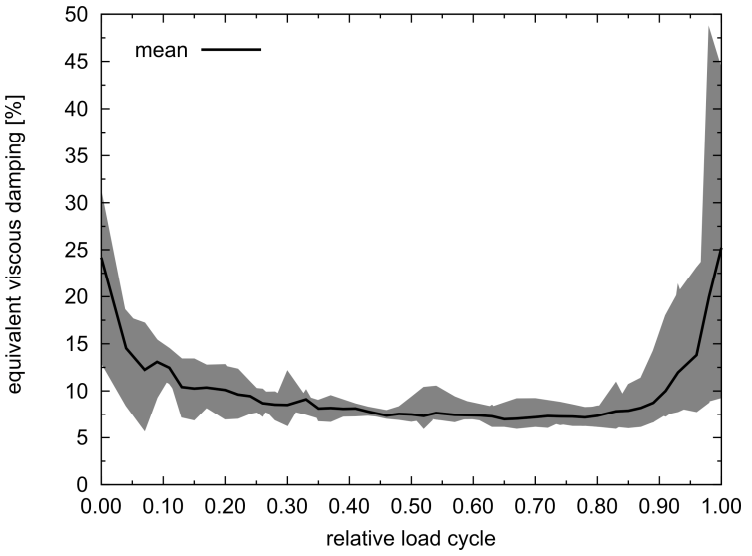


Figure 2 Progress of equivalent viscous damping ξ for old masonry.

DAMAGE PROPAGATION AND STIFFNESS DEGRADATION

When the walls are subjected to repeated pseudo-dynamic load reversals, increasing degree of damage can be described by the damage index I_d, Tomaževič (1999) and Tomaževič et.al. (1999). In accordance with the three characteristic limit states as indicated e.g. in Table 3 the increasing degree of damage or damage state can be described by a damage index. Figure 3 shows these various damage states and an idealised envelope of the horizontal resistance.

The damage index can be divided in the following four types:

- $I_d = 0.00$: Actually this first state represents the elastic state with no damage, the state without any cracking.
- $I_d = 0.25$: The initiation of vertically to diagonally oriented shear cracks, passing through the bricks and mortar joints in the compressed zone. This index defines the cracking limit state.
- $I_d = 0.50$: Due to increasing horizontal deflection, the number of horizontal as well as vertical cracks increases. The cracks appear along mortar joints but also pass through brick units. Generally this crack pattern can be observed at the applied maximum horizontal force.
- $I_d = 1.00$: Again, due to increasing horizontal deflection, the number and width of cracks increase. Thereby also crushing of bricks in the compressed

zone can be observed. Finally there is a collapse of the specimen. This state represents the ultimate limit state.

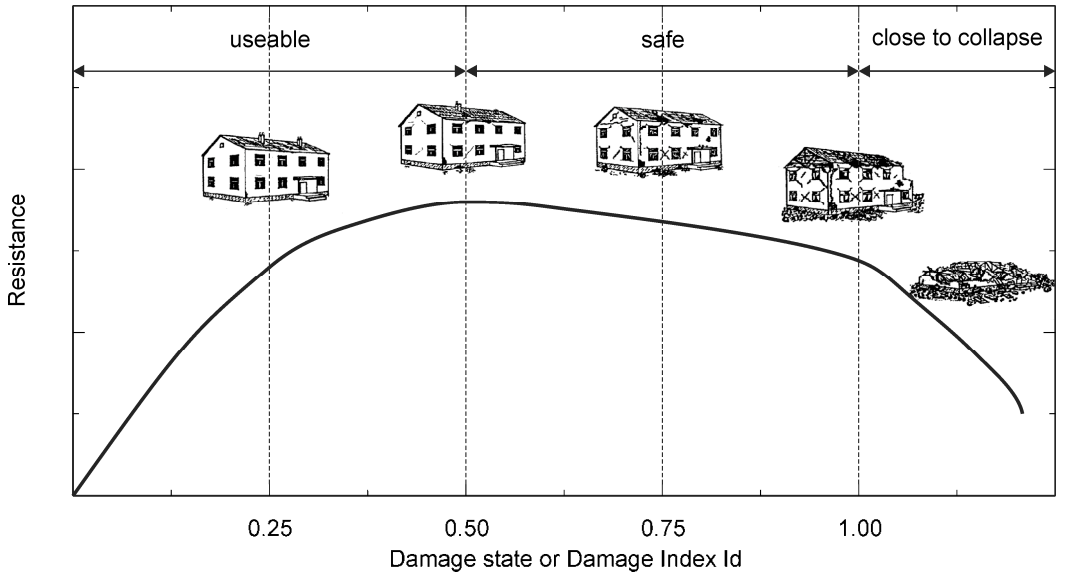


Figure 3 Damage states and envelope of horizontal resistance.

Stiffness degradation occurs, when the walls are subjected to repeated pseudo – dynamic load reversals. Figure 4 shows the stiffness degradation. Thereby the stiffness ratio is plotted with respect to the damage index. In the case of old bricks stiffness degradation is in the same range for both brick layouts. The shape of stiffness degradation can be described by the following simple exponential decay function:

$$\frac{K}{K_e} = e^{-\beta \cdot I_d} \tag{12}$$

where β is the parameter of stiffness degradation which is dependent on the compressive strength. As found out by curve fitting of experimentally obtained degradation curves, β = 4.1 for the masonry walls with old bricks. At the occurrence of the first cracks (I_d = 0.25) and at the state of maximum horizontal force (I_d = 0.50) the stiffness ratio drops down dramatically. Between the last two damage indices rather small stiffness degradation takes place. It is the same phenomenon for all investigated masonry walls.

In the first damage states the plotted equation (12) in Figure 4 a (old bricks) is in good agreement with the average values of obtained experimental data. In later damage states equation (12) it is on the conservative side. A curve fit for masonry walls with new bricks results in β = 4.7, for clinkers the stiffness degradation parameter β = 9.6 (both Figure 4 b). Again, for both masonry walls (new bricks and clinkers) the plotted equation (12) is comparable to an average value in the early damage states and it is on the conservative side for the later damage states.

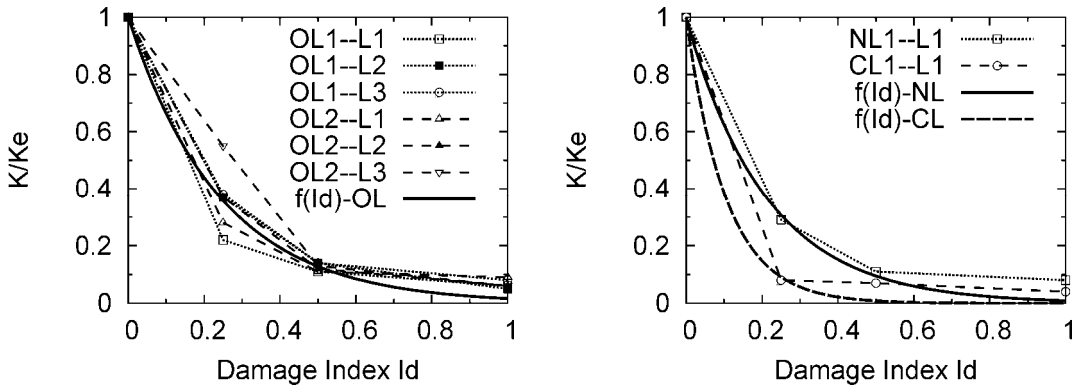


Figure 4 Correlation Correlation between stiffness ratio K/K_e and damage index I_d for (a) old bricks and (b) new bricks and clinkers.

For a seismic assessment of new structures and structures without any damage a stiffness ratio of 1.0 or slightly below can be assumed because they remain in an elastic state. On the other side, for a seismic assessment or a retrofit for old structures the stiffness ratio should be assumed << 1.0, since a cracked state from earlier events can not be excluded.

Figure 5 shows the stiffness degradation with respect to the damage index for various values of compressive strength and decay parameter β.

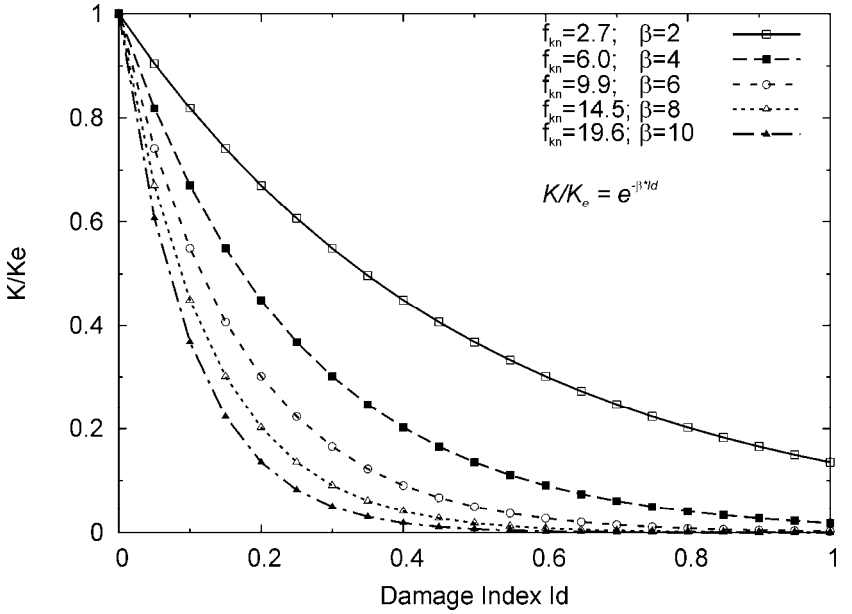


Figure 5 Correlation between stiffness ratio K/K_e and damage index I_d for various compressive strength f_{kn}.

CONCLUSIONS

Typical failure mechanisms of masonry under seismic load can be summarized by the following points:

- *failure due to rocking:* with an increasing horizontal deflection, horizontal joints in the lower part of the specimen fail in tension and the shear load is carried by the masonry part under compression. The final failure occurs by overturning of the specimen and a local failure in compression in the compressed toes of the wall.
- *failure due to sliding:* again, cracks in horizontal joints develop and go along the interface between brick and mortar. This failure type is typical for low vertical compression stress levels.
- *failure in shear:* the crack pattern consists of diagonally oriented cracks, which follow along head and bed joints or pass through brick units. This failure depends on the relative strength between mortar and bricks as well as the strength of the interface.
- *failure in tension:* due to the combination of normal stress and shear stress a inclined principal stress state arises and if the tensile strength of bricks is exceeded, the brick units fail in tension.
- *failure in compression:* mainly for high compression stress levels, but it is also typical for local failure mechanism in the compressed toes of the wall.

Introducing numerical data, in particular the tensile strength, received from Zimmermann et.al. (2010), in analytical investigations results in a good correlation with experimentally obtained data.

Basic mechanical characteristics (modulus of elasticity and shear modulus) have been obtained by experimental testing. The resulting ratio between shear modulus and modulus of elasticity yields $G/E = 0.22$ for masonry walls with old bricks. Thus, the ratio is smaller for the tested walls than the proposed ratio by EC 6 ($G/E = 0.40$). Hence, for numerical simulations this smaller ratio should be considered. The use of $G/E = 0.22$ for numerical simulations is proposed based on isotropic assumptions for masonry. The proposed ratio does not match with the range of the Poisson's ratio for isotropic material. The obtained parameters indicate a rather orthotropic than isotropic material behaviour. In addition, there is the requirement for further investigations and laboratory tests in order to determine deviations between parameters of isotropic and orthotropic material behaviour.

The interaction between deflection and horizontal resistance of shear walls results in a hysteretic relationship. Based on this relation the energy dissipation of each shear wall was analysed based on energy dissipation indicator and equivalent viscous damping ratio. Thereby no significant difference can be observed in the energy dissipation capacity for the construction of wall specimens with old bricks. On the other hand, the dissipation capacity of the wall specimens with new bricks and clinkers is noticeably lower.

Due to repeated pseudo – dynamic load reversals stiffness degradation takes place. For the calculation of the elastic stiffness K_e elastic behaviour of masonry has been assumed until the occurrence of first cracks. The stiffness degradation has been evaluated with respect to a damage index whereby the stiffness is normalized by means of the stiffness ratio. This degradation can be described with a simple exponential decay function. Further a relation between this degradation and the compressive strength of masonry has been obtained. In accordance with a certain

damage state the actual stiffness of masonry should be adjusted according to such a degradation function.

ACKNOWLEDGEMENT

Research results discussed in this conference contribution have been carried out within the European research project SEISMID, supported and financed in cooperation with the Centre for Innovation and Technology (ZIT). We also wish to thank Prof. Miha Tomaževič for his advices and Mr. Uroš Bohinc for his efficient help during testing in the Laboratory of Slovenian National Building and Civil Engineering Institute (ZAG).

REFERENCES

Bachmann, H. (2002): *Erdbebensicherung von Bauwerken*. ISBN: 3-7643-6941-8. Birkhäuserverlag, Basel – Boston – Berlin.

Magnes, G. and Calvi, G.M. (1997): *In-Plane Seismic Response of Brick Masonry*. Earthquake Engineering and Structural Dynamics, 26:1091-1112.

Tomaževič, M. and Klemenc I. (1997): *Seismic behaviour of confined Masonry Walls*. Earthquake Engineering and Structural Dynamics, 26:1059-1071.

Tomaževič, M. (1999): *Correlation between damage and seismic resistance of masonry walls and buildings*. Bernardini, Alberto (ed.): *Seismic damage to masonry buildings*: Proceedings of the International workshop on measures of seismic damage to masonry buildings, Monselice, Padova, Italy, 25-26 June 1998. Rotterdam; Brookfield: A. A. Balkema, 161-167.

Tomaževič, M., Klemenc, I. and Lutman, M. (1999): *Damage as a measure of seismic resistance of masonry structures*. Proceedings of eight Canadian conference on earthquake engineering. Vancouver, 13-16 June, 119-124.

Turnšek, V. and Čačovič, F. (1971): *Some experimental results on the strength of brick masonry walls*. Proceedings of the 2nd International Brick-Masonry Conference. Stoke-on-Trent: British Ceramic Society, 149-156.

Zimmermann, T. and Strauss A. (2010): *Leistungsfähigkeit von alten Ziegelmauerwerk in Bezug auf zyklische Belastung.*. Der Bauingenieur, vol. 85, S2-S9.

Zimmermann, T., Strauss, A. & Bergmeister, K. (2010): *Numerical investigations of historic masonry walls under normal and shear load* – Journal of Construction and Building Materials, 24 (8) 1385-1391.

Standards

Eurocode 6: Design of masonry structures, Part 1-1: *General rules for reinforced and unreinforced masonry structures*, 2006.

Eurocode 8: Design of structures for earthquake resistance, Part 1: *General rules, seismic actions and rules for buildings*, 2005.

"Commonality Test Methodology for Residential Structures in Katrina Canal Breaches Class Action"

Erik L. Nelson, Ph.D., P.E., M.ASCE[1]
Marco A. DeLeon, M.E., P.E., M.ASCE[2]
Gregory G. Schober, M.S., P.E[3]

[1] President, Nelson Architectural Engineers, Inc., 2740 Dallas Parkway Suite 220, Plano, Texas 75093
[2] Branch Director Plano, Nelson Architectural Engineers, Inc., 2740 Dallas Parkway Suite 220, Plano, Texas 75093
[3] Technical Director Mechanical Engineering, Nelson Architectural Engineers, Inc., 2740 Dallas Parkway Suite 220, Plano, Texas 75093

Abstract

The question of commonality of damages was posed in a proposed class of members that was intended to represent the city of New Orleans as a whole. Were patterns of damage common such that they were identifiable by predictive means without individual site assessments? The authors were presented this question in the *Katrina Canal Breaches Consolidated Litigation Levee* with a putative class size of 36 members. Data collection efforts, which involved site specific testing, resulted in detailed class property information such as watermarks; levelness; plumbness; architectural and structural condition; and mechanical, electrical, plumbing (MEP) condition.

Hurricane forces of wind and water and degradation of materials affected structures differently; the extent of subsequent material degradation was related to characteristics unique to each structure (age, design, construction, materials, soil condition, and maintenance). Focusing on flood damages due to canal breaches, predictability was not found due to unknown variables of building height, characteristics, and length of time flood water was present.

The type and degree of damage varied considerably not only in the global putative class but also in the local subclasses, indicating a lack of meaningful subclass boundaries. Damages were not predictive by formula and therefore commonality was not present in the class. The only reliable method of damage assessment due to hurricane related distress is by individual site evaluation. Based on the scientific method, a test methodology is developed for assessing commonality of damages.

Introduction

On August 29, 2005, Hurricane Katrina made landfall between Grand Isle, Louisiana and the mouth of the Mississippi River. At about 8:00 a.m. CDT, Katrina was located 40 miles southeast of New Orleans, and at 10:00 a.m. CDT, Katrina made a second gulf coast landfall near the Mississippi-Louisiana border. The path of this hurricane traveled north to northeast across Louisiana and Mississippi and into Tennessee.

The storm surge associated with Katrina caused the level of Lake Pontchartrain to rise, and the majority of the City of New Orleans was underwater due to rainfall, levee overtopping, and levee breaches. The focus of this paper relates to the damages that occurred due in part to the aforementioned and the influence of wind and other elements during and after the storm event.

The factors that must be present for a class action lawsuit to be certified by the court are numerosity of plaintiffs, commonality of the damages and legal issues of the class, typicality of each class member's claim, adequacy of representation of the class, and viability of the defendant(s) to compensate for the damages (Fed. R. Civ. P. 23(a)). The main purpose of the authors was to establish data for evaluating the validity of the commonality of damages in the class action claim in the *Katrina Canal Breaches Consolidated Litigation*.

Forensic Testing Program

Using the putative class of 36 members (proposed class) located in the City of New Orleans, the cause, origin, and extent of damages from structural, MEP, and architectural standpoints were determined. Following the scientific method, a testing program was developed for the evaluation of the subject structures. Detailed data was collected from each structure using several test methods for the purpose of evaluating damages to the structure. Observed distress, hurricane related or otherwise, and existing conditions were documented and photographed. Data collection and compilation techniques included:

Descriptive Information: The authors developed field-measured floor plans and documented the following information through field observations or review of deposition testimony of proposed class members: structure type: i.e., single-family residential, multi-family residential, commercial, size, number of stories, foundation type, exterior veneer, interior finish, roof type, age, condition of surrounding properties, quality of workmanship, and quality of maintenance prior to/post Katrina.

Elevations: The elevation of each structure relative to the North American Vertical Datum of 1988 (NAVD 88) was determined by a surveying company using a global positioning device. (NAVD 88 is the vertical control datum of orthometric height established for vertical control surveying in the United States.)

Floor levelness: The authors evaluated the levelness of each structure's floor framing by completing a relative elevation survey using an electronic surveying instrument. **Figures 1 and 2** are examples of elevation data.

For comparison purposes within the scope of the forensic testing, the authors classified total floor out-of-levelness less than 3" as minor (**Figure 1**), greater than or equal to 3" and less than 5" as moderate, and greater than or equal to 5" as severe (**Figure 2**). The authors correlated relative elevation data with distress patterns and

determined that the majority of damage was due to long-term differential foundation movement, and was not hurricane related.

Wall plumbness: The authors assessed the plumbness of the exterior or interior walls of the structures. The authors measured the angle of each surface relative to the vertical plane using an electronic plumbness measuring tool.

Using the maximum reading at each structure, for comparison purposes within the scope of the forensic testing, the authors categorized out-of-plumbness readings between 89.5° and 89.1° as minor, between 89.0° and 88.5° as moderate, and severe out-of-plumbness as 88.4° or less.

Based on the plumbness measurements, the authors detected no racking or twist resulting from hurricane winds. Rather, the findings are consistent with long term foundation movement as evidenced by the significant floor out-of-levelness and aged veneer distress.

Watermarks: The authors estimated the maximum flood level within the structures by measuring stains/watermarks left by standing water on interior and exterior finishes including glass window panes, gypsum board, exterior siding, etc. All watermark data were referenced to NAVD 88. The authors found good correlation between watermark data and IPET published data as illustrated in **Figure 3**. (In the Fall of 2005, the U.S. Army Corps of Engineers established the Interagency Performance Evaluation Taskforce (IPET) to provide scientific and engineering answers to questions about the performance of the New Orleans and Southeast Louisiana Hurricane Protection System during Hurricane Katrina. As part of its evaluation, IPET documented flood water elevations throughout New Orleans)

The authors estimated damage to interior finishes using water elevations above finished floor (AFF) based on the IPET high water elevations (IPET, 2006). For comparison purposes within the scope of the forensic testing, damages to interior finishes were categorized as minor for high water levels between 0'-0" and 1'-11" AFF, moderate for high water level between 2'-0" and 5'-11" AFF, and severe for high water level 6'-0" AFF and above.

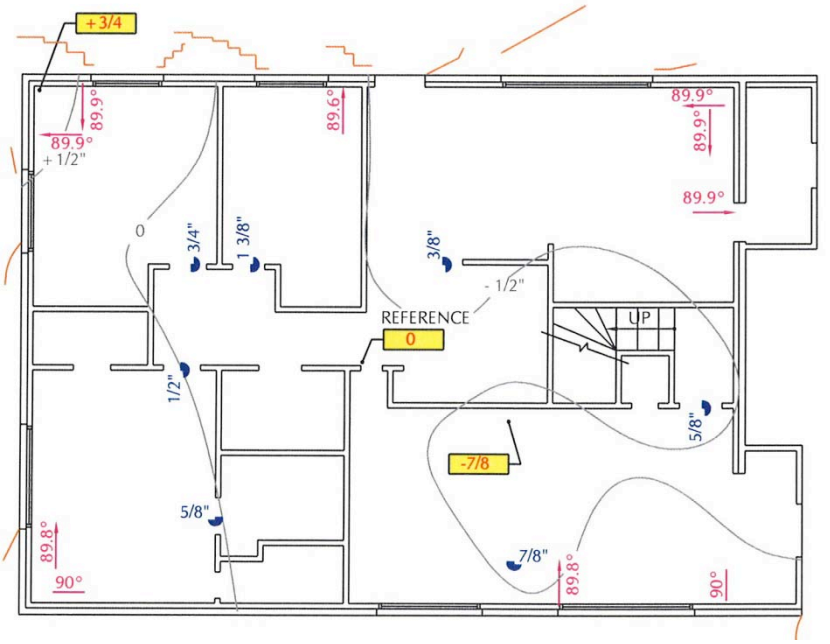


Figure 1: Minor floor total out-of-levelness

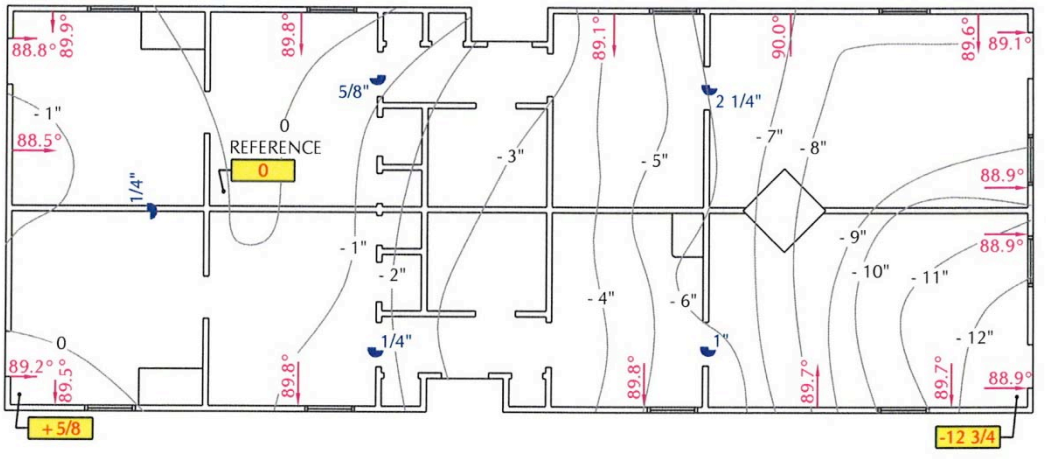


Figure 2: Severe floor total out-of-levelness

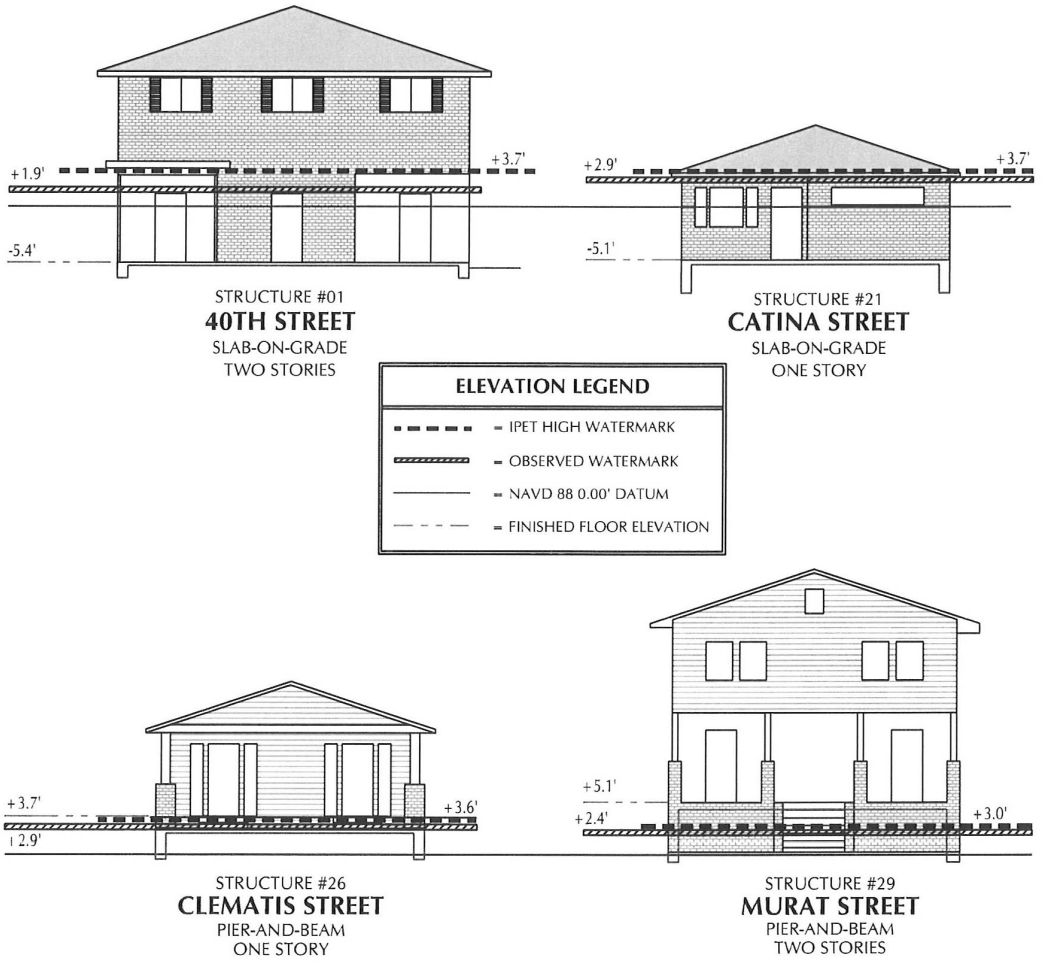


Figure 3: Watermark Data

Distress Mapping: The authors visually identified and mapped distress observed in each structure on a field-developed floor plan. The authors investigated crawl spaces, attics, and roofs as safety and accessibility allowed. For comparison purposes within the scope of the forensic testing, with the exception of window distress, distress was categorized as minor, moderate, or severe based on the percentage of the system impacted. The following types of distress were documented when observed in the subject structures:

- Termite damage: Structural members and veneers impacted by termites.
- Wood deterioration: Structural members and veneers.
- Tilted and/or damaged piers (the pier and beam foundations were typically constructed of brick or concrete masonry units (CMU)): Cracks and/or mortar joint separations and out-of-plumbness, generally due to long-term foundation movement.
- Window damage: Broken glass panes, broken frames/sashes, or missing or boarded-up windows, some likely related to post-storm vandalism.

- Veneer damage: Cracks and/or mortar joint separations on brick veneers, detached and/or missing siding, and cracks on stucco.
- Mechanical equipment damage: Corrosion at heating, ventilating, and air-conditioning (HVAC) equipment and plumbing fixtures and vandalism/theft of components.
- Electrical systems damage: Dislocated weatherheads, electrical service boxes, and electrical conduit; corrosion at receptacles, switches, junction boxes, and cabling; and some vandalism/theft of components.
- Scouring of soils: Loss of soil and exposure of foundation elements.
- Roof damage: Missing shingles, deteriorated and/or damaged roof shingles, rotted and/or exposed roof sheathing, missing, detached or broken ridge tiles, missing, detached or damaged flashing, and detached and/or punctured flat roofing membranes.
- Suspected mold/fungal growth at gypsum board walls and ceilings.

Table 1 is a compilation of damages observed by type.

Table 1: Observed Damages by Type

Damage Type	% of Bldgs w/ Damage	# of Buildings with Similar Damage (0 5 10 15 20 25 30 35)	Proximate Cause: Non-Hurricane	Wind	Flood
Termite	63%	(22)	X		
Wood Rot	77%	(27)	X		
Windows	54%	(19)	X	X	X
Electrical System	51%	(18)	X		X
Scouring of Soils	17%	(6)			X
Roof Damage	71%	(25)		X	
Exterior Veneer	100%	(35)	X	X	
Suspected Mold	20%	(7)			X
Mech. Equipment	57%	(20)	X		X
Tilted Piers	48%[1]	(11 out of 23 pier-and-beam foundations)	X		
Interior Finishes	91%	(32)			X
Floor Out-of-Level	69%	(24)	X		
Wall Out-of-Plumb	91%	(32)	X		

Legend: : Minor Damage : Moderate Damage : Severe Damage : N/A

1 : Calculation based on twenty-three (23) pier-and-beam foundations

Discussion

Hurricane-related damages can be classified by type and cause. Structural damages can be caused by hurricane-applied forces (wind and flowing water). Degradation of architectural building materials can be caused by exposure to wind driven rain, flood water, and wind.

Structural damage is a function of the magnitude of the forces (wind and flowing water) exerted on a structure and a structure's resistance to those forces, also commonly referred to as demand to capacity ratio. Structural damage ($\mathbf{D_s}$) occurs via deformation or failure when the demand to capacity ratio exceeds 1.0. Increasing the applied forces or decreasing the structural resistance increases damages.

Wind damages buildings through velocity-generated pressures (positive and negative) and via debris impact. Flowing water damages structures through dynamic action of storm surge (waves, high velocity flow, scouring, flood-borne debris impact). Riverine (rising water) flooding typically has minimal or no velocity and generally does not lead to structural damage, except in the case of buoyancy.

A particular structure's resistance (**R**) to applied forces (**P**) is determined by its individual and unique characteristics, which include its property topography (its elevation relative to flood levels), age, building design, construction, type and quality of materials, underlying soil properties, pre-existing damage (including termites and wood rot), and maintenance thereof.

The relationship is as follows:

$$D_s \text{ (structural damages)} = f\left[\begin{array}{l} P \text{ (wind, water)} \\ R \text{ (topography, age, design, construction, materials,} \\ \quad \text{soil, pre-existing damage, maintenance)} \end{array}\right]$$

The authors found a wide range of variability in the subject structures' resistances, which resulted in a wide range of variability in damages observed. For example, the structures with pre-existing damage (pre-Hurricane Katrina) such as wood rot and/or termite damage were significantly weaker than structures that were not impacted. No two structures featured identical type, degree, and extent of structural damages.

Degradation of a structure's architectural finishes is a function of exposure to flood water, wind driven rain, and wind forces. A structure's finishes' resistance to water and wind is determined by its unique characteristics, including its property topography, age, height, design, and its material water resistive properties. For example, an increase in the flood water exposure height (**E**) or immersion time (**T**), or a decrease in the building material's water resistance increases the flood damage ($\mathbf{D_f}$) to an individual structure. The relationship for material degradation damages is as follows:

$$D_f \text{ (finish degradation)} = f\begin{bmatrix} E \text{ (water exposure height)} \\ T \text{ (immersion time)} \\ R \text{ (topography, age, height, design, and material water resistance)} \end{bmatrix}$$

As the height of the flood water rises within a structure, more surface area of building materials and electrical and mechanical systems are exposed to water and the damage increases. The flood water height above the structure foundation was a distinct and variable parameter in the flooded structures in New Orleans. The water level varied due to four conditions: subclass basin, topography, type of foundation system and the structures' height, or generally, the number of stories. Flood damages varied from structure to structure and ranged from no flood damage to complete damage to finishes.

Comparative Case Study Examples

Case study comparison examples of several structures by structure type, damage type and cause of damage are presented in this section. The comparisons indicate that individual site assessments are required to evaluate the type and extent of damage, which vary as a function of the hurricane forces and the resistive characteristics of the building.

Example 1 – Variability of Structural Damage: This example illustrates different causes of structural damages at different structures. Structural damage varied at each structure and individual site assessments were necessary to ascertain structural damage and the cause thereof at a specific structure.



Tilted Piers Termite Damage Scour Damage

Figure 4: Structural Damage

At Structure #29, the authors observed several tilted piers, including what appeared to be remedial piers under the floor structure. As the piers tilted, the floor system deflected, causing the superstructure to move. This movement caused distress to architectural finishes as evidenced by plaster cracks and out of square door frames. The tilting of the piers was most likely caused by long-term movement of the subgrade. The maximum riverine type flood water level recorded by IPET was

approximately 2'-1" *below* the finished floor elevation (placing the water level near grade), and unlikely to have caused the tilting of the piers.

Structure #12 featured significant pre-existing (non-hurricane) structural damage caused by termite and wood rot. The extent of the damage was such that large sections of framing members had disintegrated. For example, two ceiling joists had collapsed and several wall top plate sections were near failure. The extent of termite damage at this structure rendered the dwelling structurally compromised and unsafe for habitation.

Structure #6 featured damage in the form of scouring and/or undermining of the wooden piles and concrete grade beams. The IPET observed watermark at this structure was 5'-1" A.F.F. The observed scouring was attributed to flood and/or surge.

Example 2 – Structure #1 (slab-on-grade vs. pier and beam): This second example is a comparative case analysis illustrating different causes of distress based on foundation type. Structures with pier and beam foundations behave differently than structures with slab-on-grade foundations during hurricane and flooding events.

The piers in a pier and beam foundation system transfer the weight of the structure to the load bearing soils. The open pier and beam system allows for fairly unobstructed flow of water during floods (FEMA 2005), but a dangerous condition is created once the flood level reaches the finished floor. In pier and beam construction, the floor system typically consists of lightweight, buoyant wood framing. The combination of buoyancy uplift forces, and possibly wind forces, tends to overstress the piers and the pier to floor connections, potentially resulting in the displacement of piers and/or the entire structure.

In contrast, most of a slab-on-grade foundation lies below grade, so the structure will sustain architectural damage due to flood water at lesser flood elevations than a pier and beam structure. However, slab-on-grade foundations are constructed of concrete and are not as buoyant as lighter structures with pier and beam systems.

A satellite image obtained from Google Earth (Google Earth, 2005) (**Figure 6**) shows the condition of Structure #1, a slab-on-grade structure, and the adjacent structures post Hurricane Katrina (Spring 2006). The image shows that the structure located east of Structure #1 was detached from its foundation and displaced from its original plan position approximately 50' south and 8' east. In addition, the structure had been rotated around its original north-south axis by approximately 45 degrees counter-clockwise. Displacement of the structure and associated damage was the result of flood.

The impact of flood and storm surge was very different for the subject 40th Street structure and the adjacent structure on the east side. While the structure east of Structure #1 was detached from its foundation, displaced, and rotated well beyond its

original as-built condition, Structure #1 remained at its original position without any significant displacement, tilting and/or rotation.

The different behavior of these structures during the storm is most likely the result of the structures' different foundation systems. Structure #1 has a slab-on-grade foundation while the adjacent east structure had a pier and beam foundation. Most likely, upward buoyancy (and possibly lateral water forces due to the proximity to the 17th street canal breach) contributed to the displacement and rotation of the structure east of Structure #1. In addition, improper, failed and/or missing hold-downs at the pier and beam foundation might have contributed to the detachment of the structure from its foundation.

Although the above comparison of substantially different structure responses to flood water forces was not evident at any of the other subject (proposed class) properties, this condition was not isolated and occurred at many other structures as evident by at least nine properties in a three-block area noted to be displaced and/or rotated in plan.



Figure 6: Structure #1 & Adjacent Properties

Example 3 – Structure #5 (two-story) vs. Structure #21 (one-story): The third example is a comparative case illustrating the observed variation and degree of distress between two structures based on the number of floors. On all of the two-story structures, the water level did not reach the second floor (**Figure 3**). Damage consistent with flood was not observed (on the second story of these structures.) Therefore, on a per-living-area basis for a given structure, two-story structures sustained less flood damage than one-story structures.

Conclusions

The study of the 36 class member structures illustrates the varying degrees of damage and uncommon effects related to the wind and water forces from Hurricane Katrina. The causes, types, and extent of damages to one particular structure were not indicative or predictive of causes, types, and extent of damages to another structure.

The cause and effect of damage at each structure depended on the applied hurricane forces and the structure's resistance thereto. Hurricane forces of wind and water and degradation of materials affected structures differently; the extent of subsequent material degradation was related to characteristics unique to each structure.

Based on this analysis, estimates of damages cannot be properly or fairly determined without individual site assessments. A mass assessment of damages without specific site evaluations would be inaccurate because it would not take into account the variability of the applied hurricane forces and the structure-specific resistance characteristics. In this study, each of these variables required site-specific evaluation.

In summary, the authors did not find commonality of type, degree, or extent of damages for the residential structures in the city of New Orleans. Damages were not predictive by formula and therefore, commonality was not present in the class. The cause, type, and degree of damage varied considerably not only in the global putative class, but also within the local subclasses, indicating that the proposed subclass boundaries presented no meaningful divisions.

References

Federal Emergency Management Agency (FEMA), "Reconstruction Guidance Using Hurricane Katrina Surge Inundation and Advisory Base Flood Elevation Maps," November 2005.

Google, Inc., "Google Earth, Version 3.0 (software)," July 2005.

Interagency Performance Evaluation Task Force (IPET)/US Army Corps of Engineers, "Performance Evaluation of the New Orleans and Southeast Louisiana Hurricane Protection System," dated June 1, 2006.

Keith, Edward L., "Performance of Plywood and OSB Sheathing During Hurricanes Andrew and Iniki," Hurricanes of 1992: Lessons Learned and Implications for the Future, Ronald A. Cook and Mehrdad Solanti, Editors, American Society of Civil Engineers, 1994.

Federal Rules of Civil Procedure, "Rule 23. Class Actions," December 1, 2010, available at http://www.law.cornell.edu/rules/frcp/Rule23.htm.

Tendon Failure Investigation and Drying in a Two-Way Unbonded Post-Tensioned Roof Slab

Andrea E. Shear, PE[1], James P. Donnelly[2], PE, SE and Matthew E. Lewis[3], PE

[1]Wiss, Janney, Elstner Associates, Inc., New York, NY; email: ashear@wje.com

[2]Wiss, Janney, Elstner Associates, Inc., Northbrook, IL; email: jdonnelly@wje.com

[3]Wiss, Janney, Elstner Associates, Inc., Bingham Farms, MI; email:mlewis@wje.com

ABSTRACT

Water ingress into unbonded post-tensioning tendons can lead to serious and expensive structural problems. The severity of this condition can be difficult to detect as often there are limited signs of distress until one or more tendons have lost tension as a result of section loss from corrosion. This paper presents a case study illustrating the investigation and the rehabilitation of tendon failures in a two-way, unbonded post-tensioned roof slab. Techniques for identifying deficiencies with the tendons are summarized as well as the proprietary cable drying procedure that was used for tendon rehabilitation. The authors' observations regarding the effectiveness of the tendon drying based upon continued monitoring of the structure are presented.

INTRODUCTION

Post-tensioned concrete structures can provide efficiencies by allowing longer spans between columns and reducing the amount of material required for construction, as compared to conventionally reinforced structures. However, without proper detailing to ensure that water does not enter the tendon sheath, serious and expensive structural problems can result. These issues can be difficult to identify and remediate because they often produce very limited visible signs of distress. Post-tensioning end anchorages in newer structures located in aggressive environments are typically protected by waterproof encapsulation; however, before the late 1980's, end anchorages and intermediate anchorages were left unprotected in the concrete as the tendon movement during stressing and the anchorage geometry made them difficult to protect. Additionally, because the grout used to fill the stressing pockets at the anchorages is often more porous than the surrounding cast-in-place concrete and a cold joint in the concrete is required at intermediate stressing locations, there is often a path for water to reach the interior of the tendon sheath at these locations. Once water has accessed the tendon sheath, there is typically no easy way for it to escape, resulting in corrosion and section loss of the tendon. This paper describes the investigation and remediation of a two-way unbonded post-tensioned concrete roof slab subject to deterioration as a result of water ingress into the tendon sheaths.

STRUCTURE DESCRIPTION

Located in Southeast Michigan and constructed in 1984, the structure is a four story post-tensioned concrete office building with an arched skylight covering a center atrium which divides the interior of the building into east and west halves. As shown in the roof plan in Figure 1, there is an expansion joint, with hollow-core concrete slabs acting as closure elements, dividing each half into north and south sections. The

post-tensioned roof slab is 8 inches thick and spans between columns typically spaced at 30 feet on center in each direction. The post-tensioning strands are ½ inch diameter, 270 ksi, 7-strand low-relaxation tendons that have a parabolic drape profile; they are evenly distributed in the east-west direction and banded in the north-south direction. Each north-south band of tendons typically consists of 14 to 20 individual strands, placed in groups of 2 or 3. There is conventional reinforcing steel in the bottom of the slab at midspan and in the top of the slab over the column lines. At the north and south ends of the building there are conventionally reinforced concrete towers which contain mechanical rooms and elevators, and which are separated from the remainder of the structure by an expansion joint at each end.

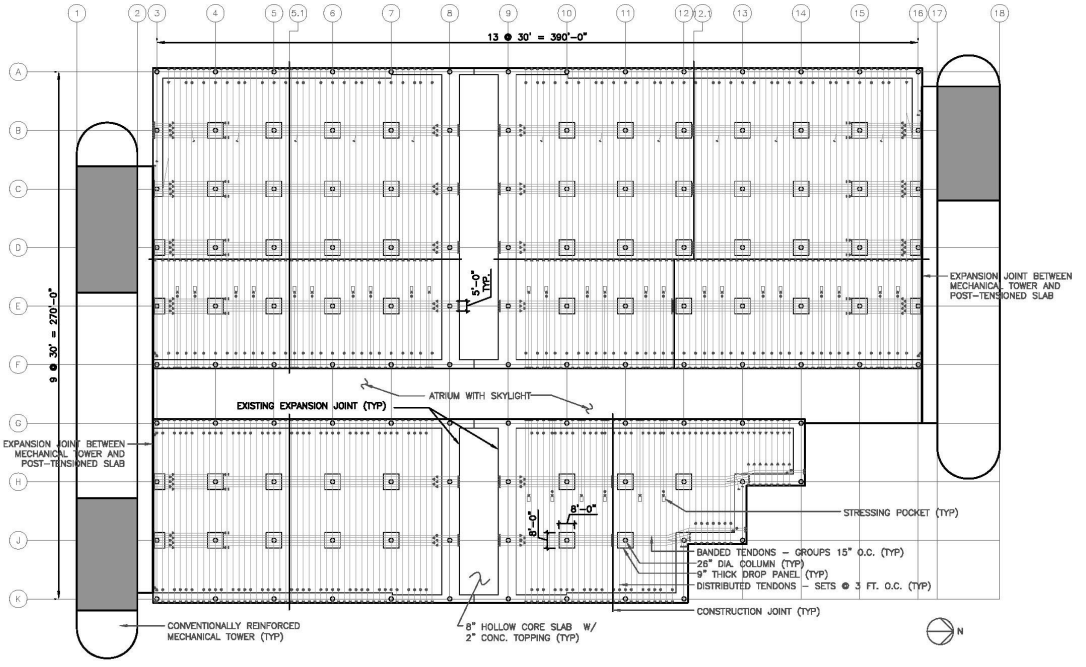


Figure 1. Plan view of roof slab.

In May of 2006, Wiss, Janney, Elstner Associates, Inc. (WJE) was contacted by the Owner of the building as a result of a post-tensioned tendon which had broken during the workday. The sound associated with the sudden release of tension in the tendon was described as being like a gunshot and had scared the building occupants. In investigating the cause of the noise, the onsite building engineers had found two failed tendons protruding from the slab. The Owner required an initial assessment to determine whether the structure remained safe for occupancy, as well as an investigation into the cause of the post-tensioning failures and the extent of tendons affected.

INITIAL INVESTIGATION AND ASSESSMENT

A review of the post-tensioning shop drawings on file at the building showed that the failed tendons were located in a banded tendon line which contained 14 total tendons, with an additional six add-tendons in the end span. A limited inspection was performed on the underside of the structure along the column line with the two known broken tendons to look for evidence of additional breakages or significant

cracking in the concrete at the positive moment regions in the slab, which could be an indication of structural deficiency. While some narrow cracks with water staining were visible in the underside of the slab, they did not appear to be concentrated in positive moment regions, nor did they appear to be widening. Negative moment regions over the tops of the columns, where cracking related to a structural deficiency would likely occur first, were not visible as they were covered with a roof membrane.

Since the discovery of the broken tendons occurred in the springtime, the roof was not expected to be subjected to snow loads in the near future. ADAPT-PT software was used to perform an analysis using the effective frame method to determine whether the structure could safely support the roof dead load and minimum live load with two broken tendons. From this analysis, it was concluded that the structure required only 60 percent of the tendons to safely support the dead load with the code-prescribed load factors. As other evidence of distress was not observed, it was concluded that it was unlikely that eight additional tendons were broken in the affected band of tendons and that the structure was safe for occupancy. Along with those conclusions, it was recommended that the Owner should have a more extensive investigation into the cause and extent of the tendon distress at the building completed prior to the upcoming winter.

DETAILED INVESTIGATION

WJE was authorized to proceed with a detailed investigation of the roof slab post-tensioning system in the summer of 2006. This included a visual survey of the entire underside of the roof slab, removal of two broken tendons from the slab to determine their break location and to allow for inspection of their condition, and investigative openings in selected areas. From discussions with the Owner and onsite building engineers, it was learned that the roofing system had previously leaked over a long period of time, but had been repaired five years earlier. This could have allowed water to reach the roof structure and to subsequently become trapped in the tendon sheaths.

Visual Observations

Access to the slab underside was gained by removing ceiling tiles. While the majority of the slab soffit was visible, some areas were obstructed by large mechanical ducts and hard ceiling finishes, as well as firewall partitions which extended above the ceiling tile. Crack locations were evaluated for patterns which could be indicative of structural distress. Water staining was typically observed along the expansion joints at the center and both ends of the structure, at crack locations, at construction joints, and around drains. Water staining and cracking were generally more severe in the western portion of the roof.

Most of the cracks observed in the slab soffit ran parallel to tendon bands, although some diagonal cracks were observed as well. One additional broken tendon was identified during the investigation; it had erupted through the bottom of the slab and had damaged the sheath of the adjacent tendon.

Tendon Removal

A contractor was engaged to remove two broken tendons from the slab. Tendon removal was accomplished by attaching one end of a come-along to the exposed portion of the broken tendon, wrapping the other end around a column to provide anchorage, and then tightening to exert enough force on the tendon to pull it from the slab. Both extracted tendons, located along different column lines, were found to be broken near midspan, at the low-point of the tendon drape, in the bay adjacent to the expansion joint at the north side of the structure. Observations were made regarding the condition of the strands and the grease along the length of the extracted section of strand. Little or no evidence of emulsification of the grease, corrosion of the tendon, or other evidence of water ingress was found outside of the end bay. Furthermore, almost all the evidence of water in these strands was observed at the low portion of the tendon drape in the end bay. These findings indicated that the source of the water in these tendons was most likely the end anchorages at the slab edge, and that the water ran down the strand to its low spot in the tendon drape, where corrosion and ultimately failure of the strand then occurred.

Investigation Openings

Six locations were selected for inspection openings to further investigate the extent of water in the banded tendons and to identify signs of distress in the distributed tendons. A total of 48 tendons were exposed; these openings were typically located at the midpoints of tendon drapes in end bays or at intermediate anchorages where moisture penetration into the tendon sheaths could have occurred. Portions of the tendon sheaths were removed to allow for visual inspection of the steel wires. Also, each exposed tendon was probed with a screwdriver, which is a commonly used, qualitative test to evaluate whether a post-tensioning tendon is still stressed. If the tip of the screwdriver can be forced between the individual wires, then the tendon has likely failed or has lost a portion of its initial force.

At these openings, almost 40 percent (15 of 38) of the exposed banded tendons were observed to have water trapped in the sheath, 20 percent of which (three of 15) were no longer tensioned. Evidence of corrosion was observed at some of these locations. In the distributed tendons, however, no indications of deterioration or distress were identified.



Figure 2. Exposed tendon which is no longer stressed. Note the grease is emulsified and contains debris, which are indications of water in the tendon sheath.

Summary of Investigation Results

Investigation into the cause of the post-tensioning tendon failures in the roof slab revealed a systematic problem with the banded tendons as water was found in 15 of 38 sheaths opened at the low point in the tendon drape adjacent to the end anchorages. The most likely source of this water was identified to be leakage through the expansion joints between the post-tensioned slab and the conventionally reinforced slabs for the towers located at the north and south ends of the building. Leakage at this joint could have allowed water to enter the tendon sheath through the live end anchorages. Due to the adjacent concrete beam, visual observation of these stressing pockets was very difficult. The observed water staining on the concrete beams and slab soffit at either side of these joints provided evidence of previous water leakage in these areas, but there were no indications of continued water leakage along these joints at the time of the investigation.

In the presence of oxygen, pitting corrosion and stress cracking will occur in tendons which are exposed to moisture. Since only three of the 15 strands identified to have water in their sheaths had failed, it appeared that the level of corrosion was just reaching the point where it would be severe enough to result in tendon failure. Post-tensioning tendons are continually subjected to high stresses (approximately 50 to 65% of their ultimate strength) and have a fairly small cross sectional area. Consequently, it does not require a large amount of section loss to result in full tendon failure.

There was no evidence of water or corrosion at any of the ten locations opened in the distributed tendons. While the distributed tendon openings were made in locations where problems would most likely occur, they were less than 1 foot in length and were made at less than 3 percent of the distributed tendons in the slab. This sample size is too small to draw any statistically significant conclusions as it is possible that moisture or corrosion affected tendons that were not exposed or are located away

from the inspection openings. To date, there is still no evidence of deterioration of the distributed tendons.

REPAIR OPTIONS

Due to the use of the building, the Owner did not have the ability to relocate a significant amount of personnel to perform repairs; therefore, the method of addressing the deterioration would require minimizing disruption of the office space below. Consequently, it was necessary to consider methods that had the potential to minimize future tendon failures in conjunction with monitoring the amount of failed tendons in the structure. The inherent risks associated with tendon failures include physical damage that could occur if tendons erupt out of the slab and reduction in load-carrying capacity; these risks were communicated to the Owner for their consideration regarding the urgency of repairs and tendon rehabilitation. At that time, the locations where the tendons came out of the slab upon failure were all at locations with less than ¼ inch of concrete cover and only very small pieces of concrete debris were dislodged from the roof slab. All the dislodged concrete had been contained by the ceiling tile; therefore, there did not appear to be significant danger to the occupants from falling debris.

Due to the number of failed tendons and the potential for additional tendon failures, the following recommendations were made to the Owner to address the observed tendon distress:

- Conduct inspections of the banded tendons at locations judged to have significant indications of moisture ingress and/or potential distress;
- Perform a rehabilitation program to remove existing moisture from the banded tendon sheaths;
- Repair failed tendons where sufficient tendons have failed within a single band to significantly affect the structural performance;
- Enact a long-term monitoring program for the banded tendons.

Tendon Rehabilitation Program

In order to reduce the probability of future tendon failures, it was recommended that the selected tendon rehabilitation method include the removal of water from the tendon sheaths. Two methods for achieving this were considered: the Post-Tech® PT Cable Drying method offered by Vector Corrosion Technologies and a hydrophobic urethane grout injection system. After consideration of each system, it was recommended that the gas purging method be implemented as the cost per tendon was slightly less and there was less potential for damage to the interior finishes since re-greasing of the tendons would not be performed in the interior environment. The cable drying system involves forcing air at a very low dew point through the tendon sheath over a period of time to draw the existing moisture out of the sheathing.

While initially expensive, this investment had the potential to produce significant savings in construction costs by either eliminating or deferring post-tensioning repairs. Additional cost savings would be realized by avoiding the temporary relocation of personnel required during post-tensioning repairs. The Owner decided that it was worth the added initial cost to rehabilitate the banded tendons in this

manner in order to reduce the risk of failure, due to the disruptive and expensive nature of the post-tensioning repairs.

It should be noted that if tendon corrosion is already in an advanced state, and particularly if stress corrosion cracking exists on the strand, the drying method for tendon rehabilitation may not effectively decrease the probability of tendon failure. Additionally, for projects where only a small number of tendons are affected by moisture or a significant number of those tendons affected by moisture have already failed, it would not be economical to utilize this rehabilitation method to protect a small number of tendons.

Tendon Monitoring Program

While the rehabilitation program was intended to minimize the rate of corrosion, it is not possible to reverse the effects of corrosion or to ensure that the rate of corrosion is stopped completely. To monitor the banded tendons for possible subsequent failures, the installation of an acoustical monitoring system that would detect vibrations resulting from the release of energy during failure, such as that offered by Pure Technologies, was considered but was determined to be cost prohibitive. Acoustic monitoring would have the added benefit of detecting failures in the distributed tendons as well.

As an alternative, bi-annual follow-up inspections, including testing the tension in the tendons with a screwdriver, were recommended to monitor the tendon condition. By regularly observing the tendons, the condition of the roof structure can be monitored to ensure that it remains structurally adequate and that the rate of tendon failures is decreasing as expected.

Post-Tensioning Repairs

Lastly, traditional post-tensioning repairs were recommended for tendon bands identified to contain more than 2 broken tendons. This corresponds to when the maximum tensile stress in the roof slab due to flexure under service loads exceeds 6 times the square root of the compressive stress of concrete (or $6\sqrt{f'_c}$), which is the serviceability criteria for two-way post-tensioned flat slabs according to ACI 318-05. This limitation is intended to prevent cracking in the slab and also accounts for unconservative methods of calculating the moment in the slab at the supports. In our judgment, this provided a reasonable safety factor and also accounted for the uncertainties in the simplistic methods of testing the tension in the tendons, as well as the understanding that there would be some delay associated with engaging a contractor to perform required repair work. As the tension testing was performed at limited areas, it was possible that there were undetected failed tendons, which could have occurred in instances where there might have been significant friction along the tendon length between the test location and the break location.

At the conclusion of the 2006 investigation, it was determined that no post-tensioning repairs were required immediately because no single band had more than two failed tendons. The Owner chose to move forward with the drying operations and construction documents were developed by WJE in early 2007.

ADDITIONAL TENDON FAILURES

In June 2007, prior to initiation of the tendon drying work, an additional tendon failure was reported by the building staff. The tendon failure occurred in a band with two previous failed tendons, bringing the total number of failed tendons in that band to three. This particular tendon failure resulted in a sizable piece of concrete dislodging from the underside of the roof slab and penetrating the ceiling tile. Due to the potential safety hazard of loose concrete falling into the occupied space below, permanent safety netting was designed and installed at locations where tendon failure could result in further dislodged concrete.

The safety nets were constructed with welded wire mesh suspended from steel cables. The cables were looped and clamped at steel eye-bolt anchors embedded into the column drop down panels or, as necessary, into the underside of the roof slab. The nets were installed at select locations along the low point of the draped tendons, where the concrete cover is the thinnest and where all of the previous tendon break outs were observed. As necessary, the nets were cut and lapped to accommodate obstructions within the plenum such as HVAC ducts, plumbing and partition walls.

Another tendon failure was reported by the building staff in July 2007, also located in a band with two previous failed tendons, bringing the total number failed tendons in that band to three. At this location only a small amount of concrete was displaced and was captured in the safety netting.

Because the additional tendon failures in June and July 2007 resulted in bands of tendons with more than two failed tendons, tendon repairs were recommended for those bands. The Owner agreed that the repairs were necessary and, in the interest of minimizing disruption to building tenants, requested that the repairs be performed in conjunction with the tendon drying work. The contractor performing the tendon drying operations (Vector Corrosion Technologies) was also capable of performing the repairs as well. Construction documents for the repair work were developed and the additional work was added to the original tendon drying contract as a change order.

TENDON DRYING AND ADDITIONAL INSPECTION

The tendon drying operations commenced in August 2007, approximately two weeks after completion of the safety netting installation. The scope of work for the tendon drying operations included drying and inspecting all accessible tendons in Bands C, D, E, H, and J between Column Lines 3 and 8; and Bands B, C, D, and E between Column Lines 12.1 and 16 (see Figure 1). These bands contain a total of 184 tendons; however, three tendon groups (nine tendons total) were not accessible for drying or inspection because they were obstructed by HVAC ductwork within the plenum space. The tendon drying operations included chipping an inlet port and drilling an outlet port at the ends of each tendon (see Figures 3 and 4), using specialized equipment to create and force air at a very low dew point through the tendon sheath, and measuring the moisture levels in the air removed from the tendon sheathing until they reached an acceptable level.

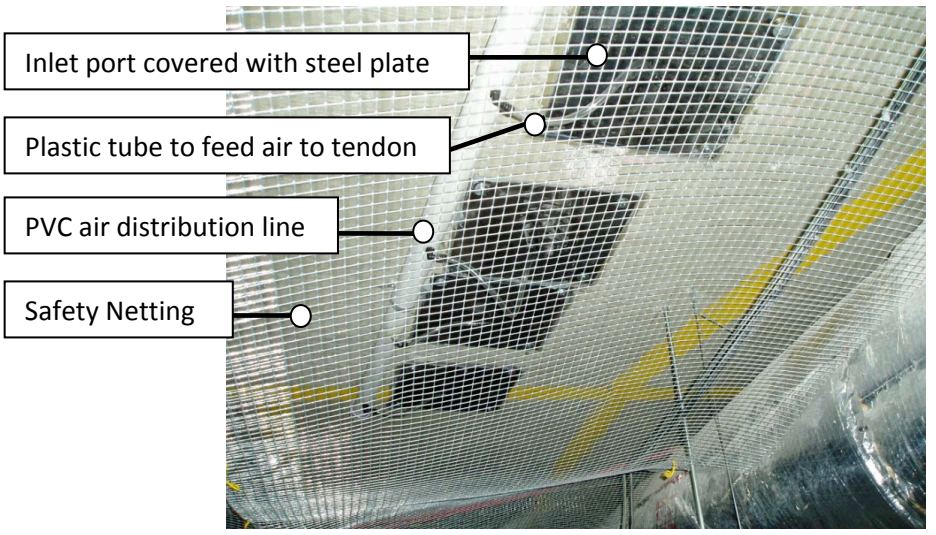


Figure 3. Air inlet ports, also used for tendon inspection, covered with steel plates.

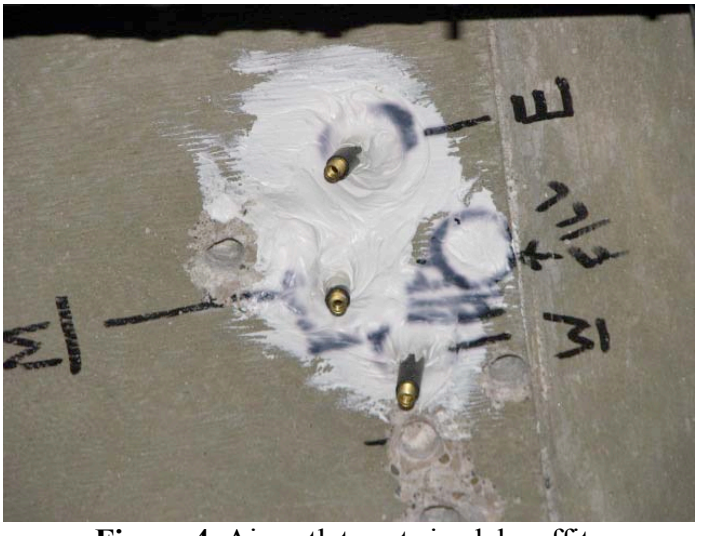


Figure 4. Air outlet ports in slab soffit.

The air inlet ports located in the end bays adjacent to the expansion joints were also used for inspection of the exposed tendons. An initial inspection, consisting of visually observing exposed portions of the tendons and probing the tendons with a screwdriver to assess the presence of tension, was performed at each tendon. A total of eight failed tendons were observed out of the 176 tendons inspected, including the six tendons noted previously which were scheduled to be repaired. Evidence of water and/or corrosion was observed in 55 of the tendons sheaths, or approximately 30 percent of the banded tendons. Each inlet port was then capped with a steel plate anchored and sealed to the underside of the slab after inspection. The cover plates on the inlet ports are removable and continue to be used for bi-annual inspection of the tendon condition.

A plastic air port was installed in the cover plate to serve as the air inlet point. PVC manifolds and plastic tubing were installed as necessary throughout the plenum to supply the dry air to the air inlet ports from the air-drying equipment (see Figure 5), which was located in the mechanical rooms at either end of the building. The

temperature and relative humidity of the air was measured at the outlet ports routinely throughout the drying work. This data was used by the Contractor to determine the moisture content within the tendon sheaths. Testing performed by the Contractor on previous projects had shown that tendons were considered to be sufficiently dry to limit corrosion when the moisture content of the air removed from the sheathing was below 0.3 percent.



Figure 5. Equipment used to manufacture dry air on-site, including a transformer, compressor, and air tank.

All 176 accessible tendons were dried. Initial moisture testing indicated that 38 tendons, or approximately 20 percent, had moisture contents in excess of 0.30 percent prior to drying, with a maximum measured moisture content of 1.43 percent. The time needed to achieve a dry condition for each band of tendons varied from 15 to 47 days, and the drying operations were completed in early November 2007. At the completion of the drying operations, the final reported values included an average moisture content of 0.02 percent with a maximum of 0.09 percent, representing a substantial reduction in the amount of moisture within the tendon sheaths.

MOISTURE TESTING

As there is an intermediate anchorage in the west portion of the structure at Line 12.1, moisture testing was performed on one group of tendons from each band south of the anchorage to assess the need for drying the length of tendons located away from the north side expansion joint, where leakage was identified. The moisture testing method was very similar to the tendon drying, except the inlet ports were drilled (no visual inspection was made) and the air was only forced through the sheath for a short period of time to measure the air content at the outlet port. Of the 12 tendons tested, none had moisture contents in excess of 0.30 percent, indicating a very low probability of corrosion. Since there were no failures observed in this portion of the building either, it was concluded that tendon drying or further investigation was not warranted past the intermediate anchorage at the time.

TENDON REPAIRS

At the two tendon bands where more than two broken tendons were observed, tendon repairs were completed by replacing the deteriorated sections of strand between the end anchorage and an intermediate point where a 'dog-bone' type central stressing splice could be installed beyond the area of strand deterioration. Whenever possible, the length of tendon to be replaced was minimized; however, at a few locations, observations made in the field during the repair work was being performed resulted in longer sections of tendon replacement than originally anticipated. At all tendon repair locations, the repaired tendon was restressed, the new strand and splicing hardware protected, and the slab cross-section restored in a manner consistent with industry standards and PTI recommendations.

The end of one known failed tendon was no longer present in the anchor at the south end of the tendon at Column Line 9. Given the unknown circumstances regarding the release of the tendon end, it was agreed that the entire tendon should be replaced (from Column Line 9 to 16), rather than only the portion that contained the observed failure (from Column Line 14 to 16). This decision was confirmed as frayed (or "birdcaged") sections were observed in the additional portions of the removed tendon.

As necessary, WJE and the Contractor worked together throughout the project to address unique and challenging conditions encountered in the field. Proposed changes to the scope of repairs were reviewed by WJE and the building Owner. In all cases, it was agreed by all parties that the decision to increase the amount of replaced tendons provided a more reliable repair than other alternatives and did not significantly increase the total cost of the repair work. The tendon repairs were completed in January of 2008.

BI-ANNUAL TENDON INSPECTIONS

As of November 2010, six bi-annual follow-up inspections of the 176 accessible tendons were performed to visually observe exposed portions of the tendons and probe the tendons with a screwdriver to assess the presence of tension. Based on the observations, each tendon was assigned a repair priority designation ranging from Priority 5 (good condition) to Priority 1 (repair is required). Individual observations and priority classifications are recorded and compared to those from previous inspections to identify changes in the tendon conditions. In addition to the individual tendon inspections, a limited visual inspection of the underside of the roof slab is performed, including checking the safety nets for dislodged concrete.

Over the nearly three years since the tendon drying and repair work was completed, three additional tendon failures have been observed. Of these failures, only one broke through the underside of the roof slab and all of the dislodged concrete was captured in the safety net. None of these failures were noticed or reported by the building staff. In general, the visible appearance of the exposed portions of the tendons has remained similar between inspections and no additional water or notable increases in corrosion level have been observed. There are currently five failed tendons out of the total of 176 inspected, but no band contains more than one failed tendon; therefore,

no additional repairs have been recommended or performed. Considering that up to six tendon failures were noted within less than a year prior to the tendon rehabilitation and that only three failures were noted in the three years since the Post-Tech® PT Cable Drying was performed by Vector Corrosion, the tendon drying operations were apparently effective at slowing the rate of tendon failures.

CONCLUSIONS

The investigation and rehabilitation of the post-tensioned roof slab was a difficult task as a result of the challenges associated with working in interior, occupied space, in addition to the typical issues associated with unbonded post-tensioning tendon failures. After the completion of the investigation, tendon repair and rehabilitation, and three years of monitoring, the following conclusions can be made based on the work performed:

- A well-planned investigation was critical to the success of the project. In this case, the information gained from removing the broken strands from the slab to locate the break location in combination with visual observations of water staining on the slab soffit was used to determine the optimum locations for inspection openings, and resulted in the identification of a systematic problem of water ingress at the banded tendons.
- Tendon drying using the proprietary Post-Tech® PT Cable Drying system has likely resulted in a good investment for the Owner. While there is no way to tell how many strands would have broken if the drying had not been performed, the rate of tendon breaks has decreased and no additional tendon repairs have been required since the completion of the project.
- Drying of the tendons was successful and efficient in this instance because it resulted in a relatively low impact on the building's occupants and finishes, because the source of the water had already been eliminated, and because there were a significant amount of tendons that had evidence of deterioration which still remained tensioned. Each circumstance should be assessed individually.
- Even after drying is completed, continued monitoring of the tendons is required to ensure that the structure remains in serviceable condition as the effects of corrosion cannot be reversed.
- Decisions regarding the initiation of tendon repairs require an analytical understanding of the applied loads and capacity of the structure as designed, as well as an understanding of what variables exist.
- Tendon failures result in the release of a large amount of energy. Because many failures do not produce significant visible signs of distress, the potential for hazards to the structure's occupants can be easily underestimated. The risks associated with falling concrete or blown out end anchorages on a structure's occupants should be assessed, communicated to the Owner, and mitigated as necessary.

REFERENCES

ACI-ASCE Committee 423, "Tentative Recommendations for Prestressed Concrete Flat Plates," (ACI 423.R-74)(Reaffirmed 1980), ACI JOURNAL, *Proceedings* V.71, No.2, Feb 1974, pp. 61-71. Also *ACI Manual of Concrete Practice*, Part 3.

Saving the Bodie Island Lighthouse: Preservation and rehabilitation challenges in a 140-year old coastal structure

by
Robert A. Bass, P.E., and Jacqueline R. Bass, MHP



Figure 1. Upper levels of Bodie Island Lighthouse
Photo courtesy of Robert A. Bass, Hartrampf, Inc.

Located on Oregon Inlet on the Outer Banks of North Carolina, near the town of Nags Head, is the Bodie Island Light Station, a collection of buildings constructed circa 1872 to serve as an aid to navigation along the dangerous section of the Atlantic coastline known as "The Graveyard of the Atlantic." Listed in the National Register of Historic Places, the Light Station today consists of the historic Lighthouse, Oil House, Light Keeper's Quarters, storage buildings, brick walkways, and a modern Visitor Comfort Station. The Light Station is within the environs of the Cape Hatteras National Seashore, which is maintained by the National Park Service.

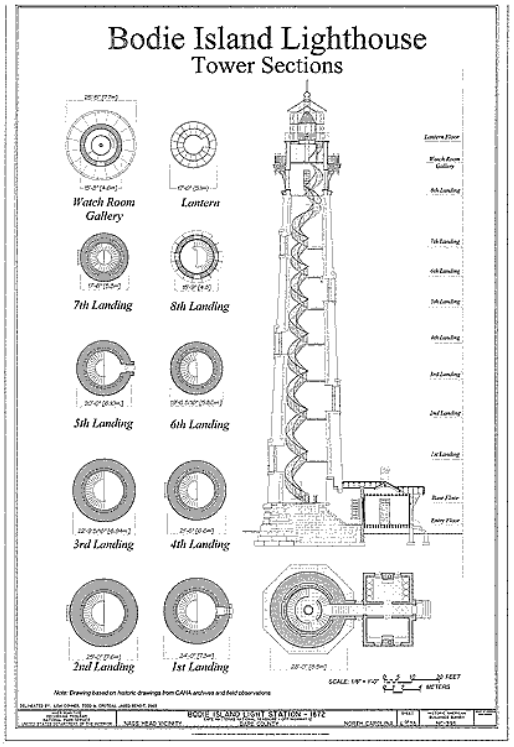


Figure 2. Historic American Building Survey building section and plans
Drawing courtesy of the National Park Service

History of Lighthouse

The existing Lighthouse at Bodie Island is the third built in this vicinity, but it is not on the foundations of either of the first two as they are under water in the Oregon Inlet. The first Lighthouse was constructed by the Lighthouse Board of the United States Treasury Department in 1848, but was replaced ten years later due to defects in the foundation. The foundation had not been designed to accommodate the soils on which the structure was placed, causing it to settle unevenly, leaning nearly a foot out of plumb by 1851. Additionally, the decision was made to upgrade the light apparatus of this Lighthouse. By 1859 a new Tower had been constructed. Whereas the first Tower took nearly 20 years to complete, the second Tower was completed within a year and the old Tower was subsequently razed. Despite efforts to make the second Tower more durable, it did not last as long as the first. In 1861, after North Carolina had seceded from the Union, Confederate forces blew up the Lighthouse – though they salvaged the light – apparently to prevent the Federals from using it as a lookout. The second Lighthouse was left in ruins by the Federal government for the duration of the Civil War because it was felt that the Cape Hatteras light located approximately 50 miles away was adequate to serve the coast at that time.

After the Civil War, normal shipping resumed along the North Carolina coast and by 1867, the number of shipwrecks in the area caused the Lighthouse Board to urge the reconstruction of the Bodie Island Lighthouse. Plans were made to construct the third Lighthouse Tower on a site just north of Oregon Inlet. The decision to build the

Lighthouse on a new location was prompted by the steady advancing of the inlet on the original site.

In 1871, construction of the new Lighthouse began with site preparation, building of storage buildings, workers' quarters, a wharf, and a tramway connecting the wharf to the site. The pit for the Tower foundation was dug, and the foundation was laid. Beams were forged in Baltimore and loaded onto ships bound for Bodie Island. By the late fall the bricks for the Tower were shipped to the site. One year later, in the fall of 1872, the First Order Fresnel lens was installed and the Lighthouse was in operation. A Fresnel lens is a type of lens that was invented in 1822 by French physicist Augustin-Jean Fresnel for use in lighthouses. This type of lens is much thinner than earlier lenses, therefore transmitting more light and allowing lighthouses to be visible over much longer distances. The original Fresnel lens remains in the lighthouse today.

Constructed in the Italianate style, the existing building is made up of three primary elements: the Oil House, consisting of three rooms (including a hall), the connecting hall between the Oil House and the Tower and the Tower. All sections of the building were constructed at the same time. The date carved into the head of the front door is 1871 (per the 1871 construction drawings). Both the Tower and the Oil House have load-bearing masonry wall systems. The Oil House has a wood floor system in the north area and stone on fill in the hall and south room (the Oil Room). The roof structure of the Oil House is wood frame. The stair, landings, and upper rooms of the Tower are cast iron. The exterior finish of the Tower and Oil House is painted brick. The upper exterior of the Tower is cast iron. The Oil House is painted white, and the Tower is painted alternating black and white stripes, consistent with the original exterior markings. The Tower stands 165 feet tall.

Other than substitutions in the fuel source for the lamp and subtle variations in the interior and exterior paint scheme, the Lighthouse remained largely unchanged until 1932, when electricity was introduced to the Tower and the light was converted from a fixed to a flashing light. At this time a generator was installed in the former Oil Room of the Oil House. In 1910, the Lighthouse Board was abolished and the Bureau of Lighthouses was created under the Department of Commerce. The Bureau maintained control of lighthouses until 1939 when they were consolidated with the United States Coast Guard. In 1953, after nearly a century of service, the Coast Guard declared the property surrounding the Light Station as surplus and transferred title to the National Park Service. Except for the Fresnel lens, ownership of which was retained by the Coast Guard, all property associated with the Light Station had been transferred to the National Park Service by 2000. In 2005, the Coast Guard transferred ownership of the Fresnel lens to the National Park Service. However, the Coast Guard continues to use the Lighthouse as a navigational aid and coordinates all maintenance affecting the lens with the National Park Service.

Beyond its obvious age, the historic significance of the Bodie Island Lighthouse is tied to its architectural character as well as its association with maritime, transportation and engineering history in the United States. Until late 2009, when

construction for the preservation and rehabilitation project began, the Lighthouse has continually served as a navigational aid since 1872. As such, the official Period of Significance represents a collective history of the building. Defining this period was important in understanding how to best approach the preservation treatments for the Lighthouse and associated Oil House.

The entire Light Station is a wonderful example of the lighthouse system that was established by the United States during the nineteenth century. It was constructed during a period of building of several such aids along the shores of this country and stands largely unchanged. And it's relevance to United States history extends beyond a regional building type, as there are several sister lighthouses to Bodie Island Lighthouse on the east and west coasts. Two examples of these are Currituck Light in Corolla, North Carolina, located just north of Bodie Island Lighthouse, and Pigeon Point Light in Pigeon Point, California. Such ties contribute to the historic significance of the Bodie Island Lighthouse and the roll it played in the development of maritime history in this country. Furthermore, having witnessed the development of the Outer Banks throughout the twentieth century, while maintaining its pristine environment, the Light Station is a significant part of the North Carolina maritime history and culture.

Project History: The Preservation and Rehabilitation Design Process

The Lighthouse and Oil House had suffered deterioration in their architectural and structural components due to the harsh conditions of their coastal environment and deferred and, in some cases, inappropriate maintenance treatments due to a lack of adequate funding over the years. The exposure of the Lighthouse and Oil House to years of moisture, sand, and salt has had the most significant impact on their condition. As a first step towards preservation and rehabilitation of these buildings, the National Park Service initiated development of a Historic Structure Report (HSR) in 2002. Working with the National Park Service, Hartrampf, Inc. was hired to prepare this report and assembled a team of architects, structural engineers, historic preservation planners, and historians to undertake the physical investigation and historic research. Hartrampf prepared the HSR, as well as the associated Conditions Assessment Report for the buildings, providing information on their history of development and use, physical characteristics, and recommendations for treatment.

Findings of the structural investigation and review of historic documents indicated that substantial repair of the cast iron features on the upper levels of the Lighthouse, as well as replacement of some of the cast iron stair treads was necessary to retain its structural stability and the overall historic integrity of the building. Additionally, repairs to the masonry walls were necessary due to their integral relationship with the cast iron elements. Numerous architectural finishes and features also required repair to preserve them for generations to come.



Figure 3: Missing segments of the cast-iron belt course.
Photo courtesy of Robert A. Bass, Hartrampf, Inc.

In 2002, annual visitation to the Bodie Island Light Station was estimated at around 200,000 people, and the Light Station was open to visitors year round. Despite this level of visitation the public had never been permitted to climb the lighthouse, and visitation inside the building was limited to the interior of the Oil House and to the first level of the Tower. In 2005, due to unsafe conditions from several cast iron features falling from the upper structure, the Oil House and first level of the Tower, and the immediate grounds surrounding the Tower were closed to visitors. Prior to this closing the National Park Service had received numerous requests from visitors to climb the stairs to the top of the Lighthouse, but, due to the documented deficiencies in the cast iron stair system and exterior galleries, it had been deemed unsafe for visitors to do so. Furthermore, continued deterioration was eroding the safety of Park personnel during routine maintenance work on the Lighthouse.

In 2005, funds became available to review the recommendations of the 2002 Historic Structure Report and 2003 Condition Assessment Report to open the Tower to the public. This review became the basis for a multi-year design project to preserve and rehabilitate the Lighthouse and Oil House. This design process involved producing schematic design, design development and construction documents to preserve the remaining historic fabric, rehabilitate the electrical system, introduce a fire suppression system in the Oil House and a fire detection system in the Lighthouse, and, most importantly, rehabilitate the structural systems throughout the Tower to ensure public safety while maintaining the integrity of this important historic resource.

Structural Rehabilitation of Tower

In addition to concerns about public and staff safety, preservation of this historically significant resource was in jeopardy. Coupled with the structural deficiencies of the cast iron features on the upper levels of the Lighthouse, the cast iron stair treads and the masonry walls, the continued loss and damage of their architecturally important features had seriously compromised the integrity of the Light Station.



Figure 4. Bodie Island Lighthouse and Oil House, 2005. *Photo courtesy of Jacqueline R. Bass, Hartrampf, Inc.*

Unique Design Parameters

The location and climate at the Bodie Island Lighthouse presented a number of unique design challenges for all work of this project. The constant humidity and salt air are ideal conditions for moisture problems and rusting of the cast iron. The height of the Lighthouse, combined with its location in the Outer Banks, make it susceptible to high wind loads from hurricanes. The area also has considerable termite activity.

Structurally, the use of cast iron throughout the Lighthouse also presents some unique design considerations. Cast iron is generally not used in modern construction. It is brittle, exhibiting little or no yielding before failure, and it is weak and unpredictable in tension and bending. Different castings also affect its strength and brittleness. The unpredictability of cast iron makes it difficult to accurately determine its load carrying capacity.

Structural System of Lighthouse

The base of the Lighthouse up to approximately 11 feet above grade is comprised of cut granite blocks. The brick Tower walls are approximately six feet thick at the base and taper to approximately two feet thick at the ninth landing. The top of the Lighthouse is constructed of cast and wrought iron elements including belt courses, the Gallery Deck brackets and framing, sheet walls of the Gallery, the Lantern Deck, and the roofing and framing elements of the Lantern. Cast iron is also used in the spiral stairway carriers, stringers, rails and newels, and various window and door frames.

Other dissimilar metals are used in the upper levels of the Lighthouse for various structural and architectural purposes. Bronze was used for window sashes and floor grates at the Lantern Room and door hardware. Brass was used for fittings of the Fresnel lens. The Lantern Room roof is covered in sheet copper, while the underside of the roof is a zinc sheet.



Figure 5: 2007 Detail of Service, Watch and Lantern Levels of Tower
Drawing courtesy of Hartrampf, Inc. and John Milner Associates

Condition Assessment Findings

Many of the original cast iron components of the Lighthouse were in poor condition and presented structural concerns. All the gallery support brackets were in poor condition with cracks present in all sixteen brackets. Two of the belt course segments had fallen with another five presenting significant cracks or broken pieces. Both the Gallery level decking and the cast iron drum walls had cracks which extended through the entire thickness of the plate material. The Lantern window mullions had racked causing numerous panes of glass to crack and fall out. Numerous stair treads were cracked and required replacement. The stair stringers and landings were in good condition and did not need to be replaced.

As part of this project, five alternatives for providing access to the Lighthouse and Oil House by the public were developed for review by the National Park Service. These alternatives were directly related to access by the public to the stairs within the Lighthouse structure. The five alternatives were:

1. No access to the stairs; interpretation from the exterior only.

2. No access to the stairs; access only to the Oil House and the lowest level of the Lighthouse.

3. Limited access to the stairs up to the Watch Level based on existing structural capabilities of the stair system

4. Limited access up to the stairs up to the Watch Level based on management decisions of the Park and strengthening of the structural systems.

5. Unrestricted access to the stai rs up to the Watch Level based on strengthening structural systems.

For alternatives 3, 4, and 5, those allowing access to the Watch Level, there were the related issues of whether to allow visitor access to the Watch Level Gallery and whether to allow them to partially ascend the stairs at that level to view the lens on the Lantern Level. Public access to the Lantern Level will not be allowed in order to protect the Fresnel lens, and public access to the Lantern Level Gallery will not be allowed because the only access to that gallery is either from a ladder from the Watch Level Gallery or through a window at the Lantern Level.

A Value Analysis study was conducted to assure that all viable project alternatives were considered, evaluation factors were sound, solutions were cost effective, an independent opinion was provided, and all project objectives were satisfied by the chosen alternative. One guideline that pervaded the effort was to select alternatives that minimized impacts to the historic resource, kept future options open, and were reversible to the extent practicable. Estimated initial construction costs were available for the Value Analysis team to evaluate and Life Cycle cost estimates based on a 20-

30 year cycle were prepared. The selected preferred alternative was to allow limited public access to the exterior Gallery Deck area and maintain most of the historic fabric. This alternative had an estimated construction cost of $2.9 million.

In spring 2010, during the construction phase of the rehabilitation design, it was discovered that upper level metals were in worse condition than what was apparent during the design phase of work. As a result, several aspects of the design in the construction documents could not be undertaken without further decisions being made on the treatment of these metals.

This phase of the work concentrated on specific cast and wrought iron elements of the upper levels of the Lighthouse, which exhibited more damage and deterioration than was anticipated from the construction documents prepared from assessments conducted seven to eight years ago. Once the multiple layers of paint had been removed, all of the exterior iron showed corrosion to differing degrees. This included the belt courses, the Gallery deck brackets, the Gallery deck, and sheet iron walls of the Gallery.

A structural engineering investigation of the recently exposed conditions at the upper levels of the Lighthouse was conducted, which included a review of the following:

- Identifying any apparent safety issues. These were relayed to the National Park Service and Contractor personnel immediately and later documented for National Park Service records.

- Identifying the structural deficiencies of the 16 Gallery brackets. Each bracket was reviewed. Some of the masonry alongside one of the brackets was removed to expose the bracket to better assess the extent of the damage. Recommendations on repair or replacement were based on maximizing the retention of the historic fabric without compromising the safety of the structure or visiting public using the Gallery walkway above.

- Identifying the structural deficiencies of the belt course segments. Each segment was reviewed. Recommendations on repair or replacement were based on maximizing the retention of the historic fabric without compromising the safety of the structure.

- Identifying the structural deficiencies of the Lantern Walkway sections. Each section was reviewed. Recommendations on repair or replacement were based on maximizing the retention of the historic fabric without compromising the safety of the structure or National Park Service staff utilizing this walkway. This area will not be open to the public and therefore will have different load carrying requirements.

- Identifying the structural deficiencies of the Lantern barrel sections. Each section was reviewed. Recommendations on repair or replacement were

based on maximizing the retention of the historic fabric without compromising the safety of the structure.

- Investigating the cracking of the Lantern level glass to determine, if possible, the cause of this cracking and recommend remedial action.

- Investigating any of structural issues that may become apparent upon inspection of the exposed metal surfaces.

From the cracking pattern of all of the sections mentioned above, the Gallery brackets and walkway deck appeared to be moving outward and down away from the masonry walls of the Lighthouse. The rotation point appeared to be at the bottom of the brackets at the crack through the web just above where they are bolted into the masonry wall. This crack extends through the entire web section of the bracket embedded in the wall and through the backside flange. This weakens any rotational restraint that had kept the brackets vertically plumb.

Each end of the belt course segments are bolted to the Gallery brackets at their base. As the brackets rotate outward they rotate the belt course as well. These rotational forces push the center sections of these segments against the very hard masonry wall below. This has caused many of these sections to crack and break away at the masonry. As the bracket pulls the deck away from the center of the Lighthouse, the bottom of the Gallery level wall is no longer restrained. This would allow movement of the wall and the Lantern level deck above which it supports. This, in turn, could put additional stresses in the Lantern level window mullions. With some of the windows removed, the mullions could have racked in plane and moved enough to cause additional panes to crack.

Another Value Analysis was conducted in summer 2010 to assure that the original goals for opening the Tower up to the public could be met in a cost effective manner while preserving as much historic fabric as possible for future use on the Lighthouse or for remote interpretation. The selected preferred alternative was to support the existing historic metalwork with new structural framing and cabling.

This alternative consisted of adding new structural elements to support the historic fabric and allow the public to visit the Gallery deck. Since more weight would need to be supported, these structural elements may be slightly visible to the eye from the ground, yet not distract from the historic features. The unexpected strength of the masonry walls will be taken advantage of and allow the installation of new steel beams and brackets extending from below the Gallery brackets and below the Gallery deck. The final treatment and priorities to be undertaken are described below:

- Stabilize the Gallery level walls. This will be accomplished by installing cables around the entire wall.
- Stabilize the Lantern level deck. The fascia sections will be replaced.
- Stabilize the Gallery brackets and deck. New structural framing will be installed adjacent to the Gallery brackets, which will support both the brackets

and the decks above. This framing will be anchored into the masonry wall and would incorporate cabling around the entire Tower to provide a tension ring.

- Stabilize the Belt courses. Existing cracked sections will be replaced per the original Rehabilitation project procedures.
- Stabilize the Lantern level by replacing the broken glass panes

A comparison of the preliminary cost estimates for this additional work shows that the selected alternative's initial costs of approximately $400,000 saved more than $1.3 million over more expensive alternatives while providing a greater value to the Park.

At this writing the National Park Service is awaiting funding to complete this additional work and hopes to open the Lighthouse to the public by summer 2011. Through these repairs the public will for the first time gain access to this beautiful historic lighthouse and see the complex designs that went into its construction as it provides a tangible link to the maritime history of the Outer Banks, and an important part of our transportation history in the United States.

Robert A. Bass, P.E. is the President and lead Structural Engineer of Hartrampf, Inc., a multi-discipline architectural, engineering and planning firm located in Atlanta, Georgia. Jacqueline R. Bass, MHP manages the Historic Preservation department at Hartrampf, Inc.

References

Department of the Interior, National Park Service. Bodie Island Lighthouse Historic Structure Report, 2002.

SNOW REMOVAL STRATEGIES OF LIGHTWEIGHT, FLAT ROOF STRUCTURES

Anthony M. Dolhon, P.E., M.ASCE[1] and Rahul Ratakonda A.M.ASCE[2]

[1] Managing Engineer, Exponent, Inc., 420 Lexington Avenue, Suite 1740, New York, New York 10170; Telephone: (212) 895-8134; Facsimile: (212) 895-8199; E-mail: adolhon@exponent.com.
[2] Associate, Exponent, Inc., 420 Lexington Avenue, Suite 1740, New York, New York 10170; Telephone: (212) 895-8101; Facsimile: (212) 895-8199; E-mail: rratakonda@exponent.com.

Abstract

This paper provides guidance to engineers, property owners, property managers, and contractors on the mitigation of damage to lightweight, flat (or low slope) roof structures by snow removal. The objectives are to minimize large deflection, prevent blocked drainage paths, minimize snow-induced ponding, and most importantly, to prevent the collapse of roof structures caused by overload due to snow. The structures most susceptible to overload are lightweight, flat roof, commercial structures, such as "Big Box" stores, warehouses, recreation centers, and shopping malls. These structures commonly have low permissible snow load to dead load ratios making them sensitive to extreme snow loads. In February 2010, there were three successive snowstorms extending from Washington, DC to New York, New York that challenged snow removal efforts. Each storm was a significant event and together in quick succession, these storms caused the collapse of roof structures throughout the region. The collapse of roof structures and the forecast for significant accumulation after the first storm prompted property owners and managers to take precautions to protect their property from damage. Conditions and events motivated the development of these snow removal guidelines to protect against overload. Factors influencing a successful snow removal strategy include the amount of snowfall (i.e., depth of snow, unit weight of snow, and drifting snow), design capacity and condition of the roof structure, potential to exceed the design requirements and/or code specified requirements, size of the roof structure, safety of the snow removal crews, economic aspects of snow removal, etc. This paper considers strategies for snow removal, such as taking no action, removing a uniform depth of snow throughout the roof structure, removing channels of snow from the field of the roof, or a combination. The methodology presented may also be adapted to roof structures undergoing rehabilitation, such as re-roofing.

Introduction

News reports of roof collapses and the forecasts for severe winter weather with significant snowfall accumulation attract the attention of the general public. For building owners, property managers, contractors, and engineers, the challenge of severe winter weather is to protect the life, health, and safety of employees and the public within their buildings and also to mitigate the potential damage and collapse of their buildings.

One particular challenge arose in February 2010. On February 4-6, 9-10, and 24-26, 2010, the Mid-Atlantic region, and in particular Washington, DC; Baltimore, Maryland; Wilmington, Delaware; Philadelphia and Pittsburgh, Pennsylvania; New York, New York; and the surrounding areas experienced three severe winter storms. Significant snowfall accumulation combined with dense wet snow resulted in snow loads that were equal to or greater than the design snow load for many of these areas.

Overload and collapse of lightweight, flat (or low slope) roof structures, such as "Big Box" stores, warehouses, recreation centers, and shopping malls, occurred from snow-induced loading. For example, the weight of snow caused the collapse of the hangar sheltering private jets at Dulles International Airport, Prince William Ice Center in Dale City, Virginia, and a warehouse in California, Maryland.

Other buildings were protected against collapse by the removal of snow from their roofs. Ordinarily, the removal of snow from around drainage devices (i.e., roof drains, scuppers, and gutters) is sufficient to promote positive drainage of snow meltwater; however, the quick succession of the February 2010 storms created new challenges.

The removal of snow from a roof structure, particularly on large roof structures is costly and time consuming. The combination of the amount of roof surface, manpower needed to shovel the roofs, length of time between storms, forecast for additional accumulation before the snow from one storm can be removed or melted, and the assessment of the load reduction (or de-loading) requirements presented many important challenges.

This paper presents the lessons learned from the February 2010 events and various factors considered in snow removal. Guidelines for snow removal are presented in two parts. The first part of the guidelines is the removal of snow to promote positive drainage. The second part of the guidelines is the additional considerations in assessing snow-induced overload.

Winter Storms, February 2010

In February 2010, three severe winter storms tracked across the United States culminating with significant snow accumulation and a state of emergency throughout most of the Mid-Atlantic region. These storms were known for their snow

accumulation and for their rapid succession. News reports nicknamed them "Snowmageddon" and "Snowpocalypse."

The first winter storm came ashore on the West Coast of the United States on February 1, 2010. It tracked across the country from California to the Mid-Atlantic region before moving off the East Coast on February 6, 2010. During the period of February 4-6, 2010, blizzard-like conditions occurred through a large part of the Mid-Atlantic region.

Some places across eastern West Virginia, Maryland, northern Virginia, Washington, DC, Delaware, south-central and southeastern Pennsylvania, and southern New Jersey received approximately 20 to 40 inches of heavy wet snow. The depth of snowfall for the period of February 4-6, 2010, is illustrated in Fig. 1.

The second winter storm formed as an "Alberta Clipper" in Canada on February 7, 2010, before tracking southeast to the Mid-Atlantic region affecting many of the same areas as the first storm before moving off the coast of New England on February 11, 2010. During the period February 9-10, 2010, Washington, DC to Boston received 12 to 40 inches of heavy wet snow. The depth of snowfall for the period of February 9-10, 2010, is illustrated in Fig. 2.

The third winter storm tracked through the Mid-Atlantic and Northeast regions on February 24-26, 2010. The most significant snow accumulation fell across New England, New York, and Pennsylvania with 12 to 24 inches of heavy wet snow with locally as much as 36 inches. The depth of snowfall for the period of February 24-26, 2010, is illustrated in Fig. 3.

Individually and collectively these storms presented challenges to building owners. Among the challenges was whether to remove the snow from their roofs; and if so, how much snow to remove and from where. The economic aspects and the time constraints did not permit the snow to be removed over a prolonged period.

Lightweight, Flat (or Low Slope) Roof Structures

For the purposes of this paper, lightweight structures have generally flat or low slope roofs (i.e., less than 5 degrees), simple-span framing with the roof framing exposed to the occupants below, or concealed by lightweight suspended ceilings. They tend to be large in area with the potential for blowing and drifting snow, particularly at the interface of high/low roofs and alongside penthouses and rooftop units.

The potential for damage and the risk of roof collapse from snow-induced overload varies with the type of roof structure, design loads, conditions, and many other factors. The potential for collapse is not limited solely to the type of construction, but in general lightweight roof structures are more susceptible to collapse than heavyweight structures. This is primarily due to the fact that snow load represents is a large percentage of the total roof load.

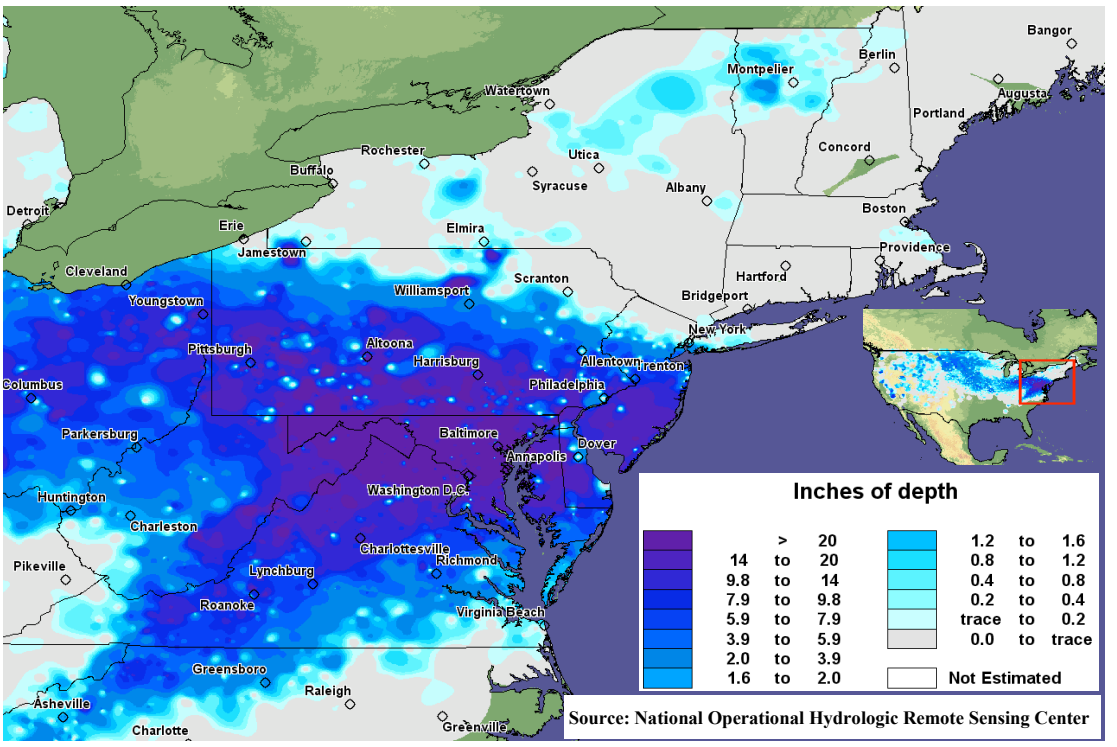


Fig. 1. Depth of Snowfall for the Period February 4-6, 2010

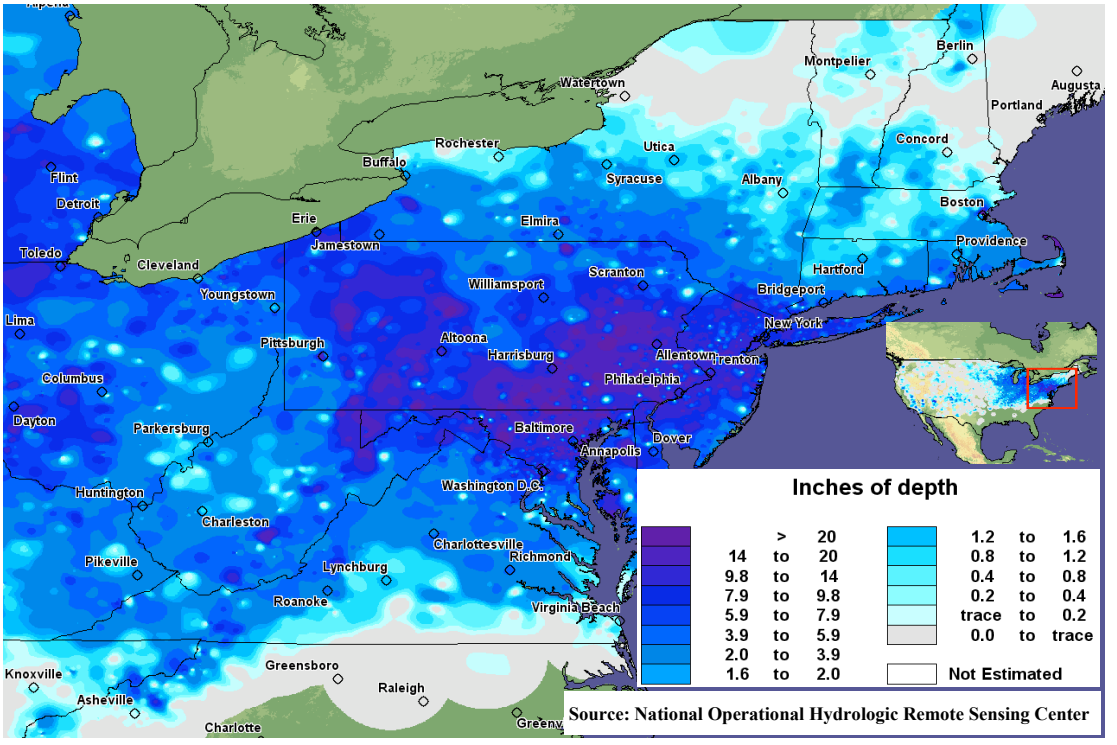


Fig. 2. Depth of Snowfall for the Period February 9-10, 2010

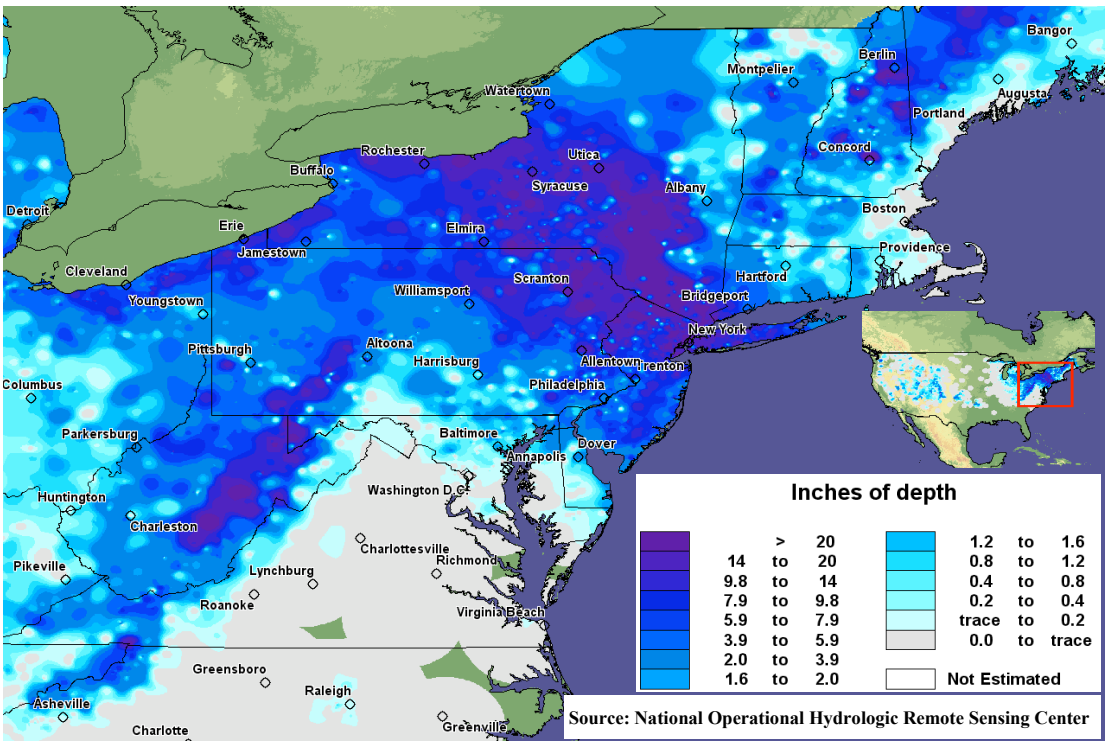


Fig. 3. Depth of Snowfall for the Period February 24-26, 2010

If the design roof snow load on a roof structure is exceeded, the percentage increase in total load would be greater on a lightweight structure than on a heavyweight structure. For example, if a 40 pounds per square foot design roof snow load is exceeded by 20 pounds per square foot for a roof structure having 15 pounds per square foot dead load, the total load increases from 55 pounds per square foot to 75 pounds per square foot, or 36 percent. Whereas, for a 60 pounds per square foot dead load, the total load increases from 100 pounds per square foot to 120 pounds per square foot, or 20 percent.

Guidelines to Promote Positive Roof Drainage

If thawing occurs on snow covered roof structures, but the snowmelt does not drain to the drainage devices or they are blocked by snow and ice, the weight of snow and snow meltwater will not significantly diminish. Therefore, for any snow and ice removal plan to be effective, the roof must be cleared to promote positive drainage. This will also minimize the likelihood of overload.

Diagrams showing the location of snow and ice removal from around drainage devices and drainage channels are illustrated in Figs. 4-5. Guidelines for removing snow and ice from roofs are given below:

1. ***Work Area:*** Provide temporary protection or barricades around areas on the ground where the snow will be dumped or lowered. Do not block fire exits or

exit doors with snow that is removed from the roof or other equipment. Designate work areas and drop zones alongside the building. Provide a secure ladder for access to the roof. Use a front end loader to remove snow accumulation alongside the building that is dropped or lowered from the roof. Distribute snow removal crews within the work area on the roof to avoid localized overload.

2. ***Drainage Devices:*** Locate and remove snow and ice from around drainage devices to promote positive drainage. Use precaution and avoid damaging the roofing membrane or metal roof panels, particularly around drainage devices and also at the base of parapets, rooftop curbs, flashings, etc.

3. ***Drainage Channels:*** Remove snow to create drainage channels as shown in Figs. 6-9. Begin at the drainage device and proceed up slope. Remove the snow from the channels in widths equal to about 5 feet wide to one-third of the column spacing beginning at the mid-span between columns. It is not necessary to remove all of the snow and ice from the field of the roof.

4. ***Means and Methods:*** Remove snow from the roof as it is being cleared. Do not stockpile or relocate snow from one location on the roof to another. Use plastic tip shovels and avoid damage to the roofing membrane or metal roof panels. Avoid using snow blowers, picks, hammers, and other sharp tools to remove snow and ice so as to protect the roof.

Analysis

Promoting positive drainage is an important consideration in overload from snow. Also important are other factors, such as the design snow load versus actual load, snow drifts, snow-induced ponding, existing construction and conditions, economics, etc. As a general rule, failures associated with overload tend to be caused by localized snow load, rather than by uniform loads within the field of the roof.

Design Load: A comparison of the design snow load with the measured snow load or an estimate of the potential (i.e., forecasted snowfall) is the first test for assessing overload. However, design calculations and construction documents that may provide the design snow load may not be readily available. In lieu of the known design snow load, the code specified snow load provides a minimum value to be used for comparison.

The snow load design value for flat roofs, p_f (pounds per square foot) is specified in ASCE 7-10, Section 7.3:

$$p_f = 0.7 C_e \, C_t \, I \, p_g \tag{1}$$

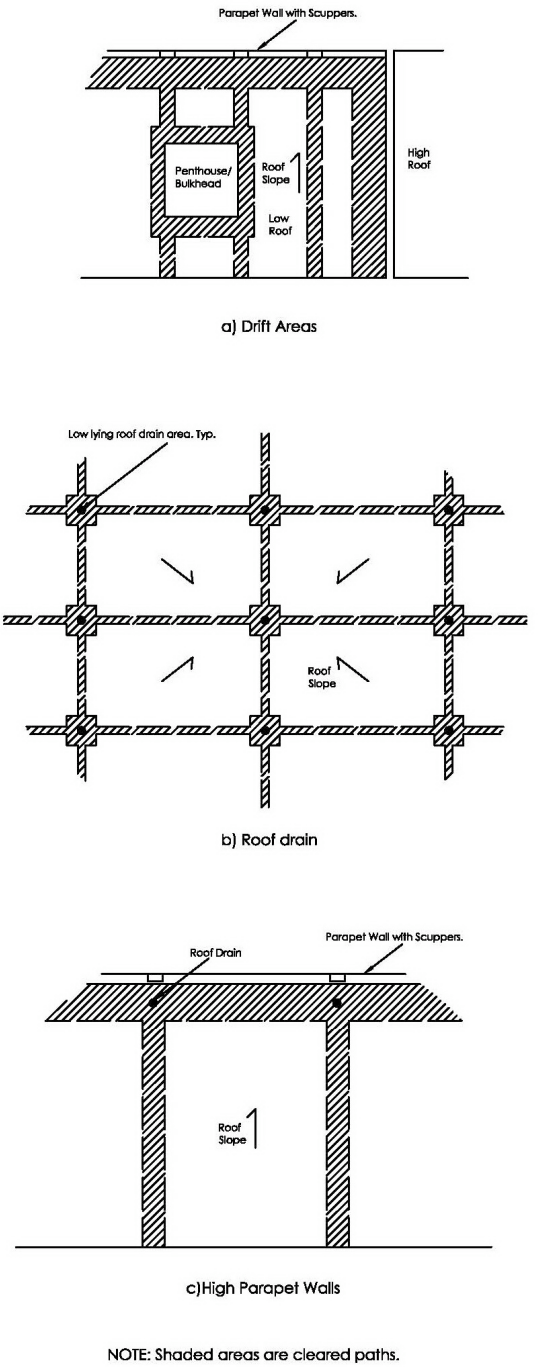
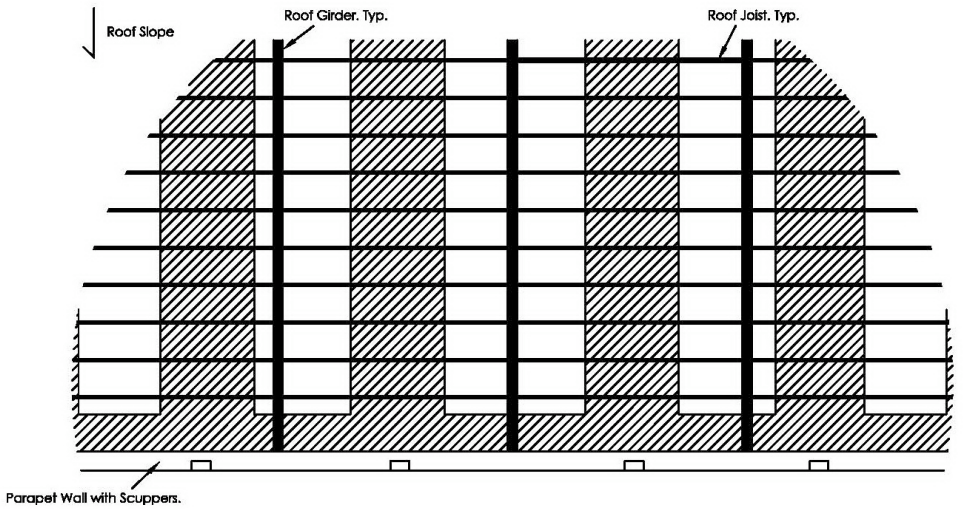
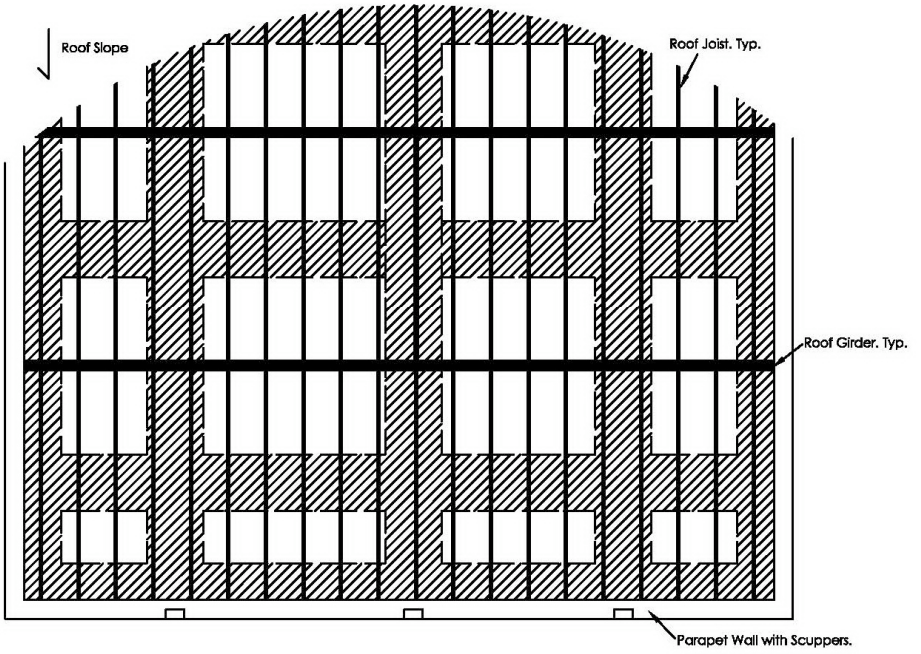


Fig. 4. Snow Removal to Create Drainage Channels



a) Roof Girders perpendicular to Drain Line/Scuppers



b) Roof Girders parallel to Drain Line/Scuppers

NOTE: Shaded areas are cleared paths.

Fig. 5. Snow Removal Patterns Relative to Structural Framing



Fig. 6. Snow Removal in Drainage Channels at Scuppers along High Parapet



Fig. 7. Drainage Channels at Roof Drains (arrows) along Parapet



Fig. 8. Drainage Channels Leading to Roof Drain (arrow)



Fig. 9. Drainage Channels at Scuppers (arrows) along High Parapet

The equation from ASCE-7 acknowledges that the roof snow load is usually less than the ground snow load, because the roof snow load is reduced over time by melting, runoff, and wind between snowfalls. However, the Commentary in ASCE-7 states that a single major storm can generate loads that exceed the amount from this equation. This statement also holds true in the case of two or more large snow events occurring in a short span of time.

Snow Drifts: Snow drifts may form on low roofs at high roof/low roof interfaces, along parapet walls, around penthouses, along snow screens, around rooftop mechanical units, around solar panels, at roof mounted signs, etc. Older structures were generally designed without consideration for snow drift. These may warrant additional snow load reduction.

Condition Survey: Site and condition survey findings may reveal structural distress or indications of distress that warrant additional snow load reduction. For example, joist orientation, displaced sprinkler heads, cracks in drywall, roofing overlays, construction defects, or other construction and conditions may indicate priority areas for snow load reduction.

Snow-Induced Ponding: Snow-induced ponding should be investigated when the with roof slopes less than ¼ inch per foot and also areas around internally drained, mid-span of simple span roof joists, rain-on-snow or snow meltwater, and other low lying areas. Unheated or discontinuous heating of structures as well as cyclic outdoor air temperature (i.e., above and below freezing) may cause thawing of the snow on the roof structure and subsequent refreezing in low lying areas. Exhaust fans and other mechanical equipment on roofs may also generate meltwater. Indicators of roof deflection, such as door binding (i.e., impingement), dropping or sagging suspended ceiling tiles, hanging light fixtures, leaking sprinkler pipes, cracking plaster ceilings and interior partition walls, creaking and crackling noises. These may warrant additional snow load reduction.

Economic Considerations: Economics of snow removal is a challenge for both the building owner/property manager and the snow removal contractor. Factors influencing the cost of snow removal are the uncertainty of the scope of snow removal (i.e., amount of snow and location of snow removal), size of the roof area, limitations on snow removal equipment (i.e., shovels versus snow blowers), the number of people on the roof, severe weather conditions, nighttime and extended hours of work, duration and intensity of forecasted snowfall, hazardous conditions (i.e., slippery surfaces, depth of snow, working at the edge of a roof, etc.), etc.

Additional Snow Removal: In addition to snow removal to promote positive drainage additional snow removal may be warrant to further reduce the snow load at drifts, structural distress, and ponding locations. If additional removal is required, it is not necessary to remove all of the snow throughout the field of the roof. The roof should have sufficient capacity to support a minimum code specified snow load. The additional cost to clear the entire roof is unnecessary. Removal options may include

widening existing drainage channels to accommodate additional snow load reduction. In some situations, unloading continuous beams or cantilevered beams may induce greater stresses in the roof structure than would occur if the entire roof is loaded. Diagrams showing the location of snow and ice removal from drainage channels with structural framing are illustrated in Fig. 5.

Condition survey findings, overload (or the potential for overload), roof deflection, and structural distress may warrant building closure and temporary shoring.

Conclusions

This paper provides two-part guidelines for snow removal. This includes snow removal to promote positive drainage plus additional snow removal for additional load reduction (if necessary).

References

American Society of Civil Engineers (2010). ASCE/SEI 7-10, *"Minimum Design Loads for Buildings and Other Structures."*

National Weather Service. Weather Data February 2010.

Earthquake Hazard Class Mapping by Parcel in Las Vegas Valley

J. N. Louie[1], S. K. Pullammanappallil[2], A. Pancha[2], T. West[2], and W. K. Hellmer[3]

[1]Nevada Seismological Laboratory, Nevada System of Higher Education, MS 0174, University of Nevada, Reno, NV 89557; PH (775) 784-4219; FAX (775) 784-4165; email louie@seismo.unr.edu
[2]Optim Seismic Data Solutions, 200 S. Virginia St. Suite 560, Reno, NV 89501; PH (775) 236-5891; FAX (775) 287-2581; email satish@optimsoftware.com
[3]Clark County Department of Development Services, 4701 W. Russell Rd., Las Vegas, NV 89118; PH (702) 455-8095; email wkh@co.clark.nv.us

ABSTRACT

Clark County, Nevada has completed the Nation's very first effort to map earthquake hazard class systematically through an entire urban area. The map will be used in development and disaster response planning, in addition to its direct use for building code implementation and enforcement. The County and the City of Henderson contracted with the Nevada System of Higher Education to classify about 550 square miles of Las Vegas Valley. The Parcel Map includes more than 10,000 measurements that classify individual parcels on the NEHRP hazard scale. We introduce a "C+" Class for sites with Class B average velocities but soft surface soil. The measured Parcel Map shows a clearly definable C+ to C boundary on the west side of the Valley. The C to D boundary is much more complex. Using the parcel map in computing shaking in the Valley for scenario earthquakes is crucial for obtaining realistic predictions of ground motions. We computed using our "ShakeZoning" process 50 separate earthquake scenarios, yielding estimates of earthquake ground shaking in Las Vegas Valley based on physics and geology rather than on statistics. Despite affecting only the upper 30 m, the Vs30 geotechnical shear-velocity from the Parcel Map shows clear effects on 0.1-Hz to 0.3-Hz shaking predictions.

INTRODUCTION

The Building Code demands that peoples' lives be protected in the event of earthquake shaking. A significant challenge for engineers and urban planners is how to meet the demand for life safety while not making the cost of building impossibly expensive. Two municipalities in southern Nevada, together with the Nevada System of Higher Education, have addressed this challenge with a comprehensive Earthquake Parcel Mapping program. A systematic campaign of ten thousand microzonation measurements across the Las Vegas urban area was the main component of the Parcel Mapping program. With the measurements completed, the partners can now assess the effects that the Parcel Map measurements will have on earthquake ground-shaking predictions, using newly realistic and accurate ShakeZoning procedures.

Motivation and objectives. Construction within the last thirty years has experienced a synergistic evolution of seismic code provisions as structures designed and built to contemporary codes have been "put to the test" by experiencing significant ground motions. One of the most significant recent changes to seismic provisions in the building code involves the addition of the "Seismic Site Class" factor that can modify the intensity of ground motion that a building or structure is required to resist. Current building codes include the 2006 and 2009 IBC, which are largely based upon the design recommendations outlined in ASCE 7-05 and the 2003 NEHRP Provisions. These codes all require that the seismic site class factor must be determined based upon the results of onsite tests and evaluation, or otherwise default to the typically low site class value of "D". In most instances utilizing the default site class value of D produces a conservative design (i.e. over designed). The seismic site class (and several other parameters) are utilized to determine appropriate choices for a structure's Seismic Force-Resisting System and will also impact the requirements for restraint/anchorage of nonstructural elements: mechanical; plumbing; electrical and architectural items. Compliance with all of these requirements directly impacts construction costs; in a general sense more seismic force equates to higher costs.

Having a regional microzonation map that correctly identifies the seismic site class provides a valuable asset to a developing community as it assures that structures can be safely designed to meet building code requirements without experiencing unnecessary additional costs due to the inherent conservatism associated with selecting the default parameter value. Undeveloped areas will take full benefit of this information to plan new construction and developed areas will also benefit when repairs, alterations or additions are performed. The community as a whole will benefit from having an improved knowledge of how local subsurface geology is likely to effect ground motion.

Background. Measurement of shear-wave velocity (Vs) in the shallow subsurface is essential for the estimation of seismic hazard, the development of seismic-hazard maps, and the calibration of recorded ground motion data. The site class measurements are represented by the average shear wave velocity value for the top 100 feet or 30 meters (Vs100-foot or Vs30-meter) as per IBC 2006 Section 1613.5.5. It is an integral to seismic design of structures per the International Building Code and International Residential Code, (IBC) and (IRC) respectively.

Because methods for direct measurement of Vs30 have only recently become cost-effective (Louie, 2001), earthquake-hazard mapping has to date relied upon extrapolation of statistical averages of a few measurements along geological units. Wills et al. (2000) built a microzonation map of all of California from only 500 spot measurements of Vs30. Their database shows that adjacent, nearby measurements can vary widely. Thelen et al. (2006) and Scott et al. (2006) made systematic examinations of the spatial variance of Vs30 from transects of closely spaced measurements stretching across the Los Angeles and Las Vegas urban areas. The velocities would not correlate with any existing soil or geologic mapping, with the standard deviations of the average Vs30 in any unit much larger than the differences in the average between units. These results motivated Clark County and the City of Henderson to embark on a program of comprehensive microzonation measurement.

Earthquake-hazard mapping cannot stop with Vs measurement. The earthquake source, wave-propagation path, and site effects must be combined into a prediction of ground-shaking intensities at a building site, for each of the likely earthquake scenarios that could produce damaging shaking. The USGS ShakeMap tool (Wald et al., 1999) is one of the current, comprehensive means of making scenario computations. ShakeMap is based only on the statistics of relatively sparse recordings of the motions of historical earthquakes. Once shaking levels are predicted from individual scenarios, the scenarios can be combined into a probabilistic seismic hazard map (Frankel et al., 1996).

Our new ShakeZoning procedure for seismic hazard mapping will properly apply the physics of wave propagation through a geologically complex earth. Our Parcel Mapping results in Las Vegas Valley represent a revolution in geotechnical characterization, allowing us to predict wave propagation and shaking amplification across terrain that has been measured to an unprecedented degree of detail. This paper will begin to show the effects of the new Parcel Map on earthquake-hazard assessment in southern Nevada, by providing the map as a ShakeZoning input.

A predecessor to the ShakeZoning concept, the Community Modeling Environment (CME), was developed at the Southern California Earthquake Center (SCEC) under U.S. National Science Foundation Information Technology Research sponsorship. SCEC's CME combines, in part, geologically based 3-d velocity and fault databases, developed as consensus models in the regional geophysical community (e.g., Magistrale et al., 2000), with a seismic-modeling computational engine (e.g., Olsen, 2000).

The purpose of ShakeZoning (known earlier as MA-CME) was initially to provide a community velocity model and seismic modeling environment for Nevada urban areas. Las Vegas is subject to earthquake hazards both from below the local basin, and from earthquake faults up to 200 km away. ShakeZoning computations feed geological and geotechnical results such as the Parcel Map to the E3D code (Larsen et al., 2001) from LLNL for elastic wave-propagation computation. E3D was most recently vetted for ground-shaking prediction at the March 24-25, 2004 Next Generation Attenuation (NGA) Workshop. Such vetting helps to physically and geologically validate ShakeZoning results. Validation is completed by comparing ShakeZoning seismogram output against earthquake recordings.

METHODS

Parcel Mapping. The Nevada System of Higher Education (NSHE) was contracted by Clark County Department of Development Services (CCDDS) and the City of Henderson (CoH) to create a soil classification map based on site-specific shear-wave velocities ("microzonation map") of the urbanized part of the County (Figure 1). NSHE subcontracted Optim SDS to perform this work under their supervision. The areas characterized included: the urbanized and urbanizing areas of Unincorporated Clark County, the urbanized area of the City of Henderson, and portions of the City of Las Vegas within Las Vegas Valley; the proposed Coyote Springs development; the Interstate Highway 15 southern corridor including Jean and Primm; Moapa Valley, Logandale, and Overton; and Laughlin (all shaded on figure

1). An extension of the project to additional urbanized areas of the City of Las Vegas, and to the City of North Las Vegas, is under development.

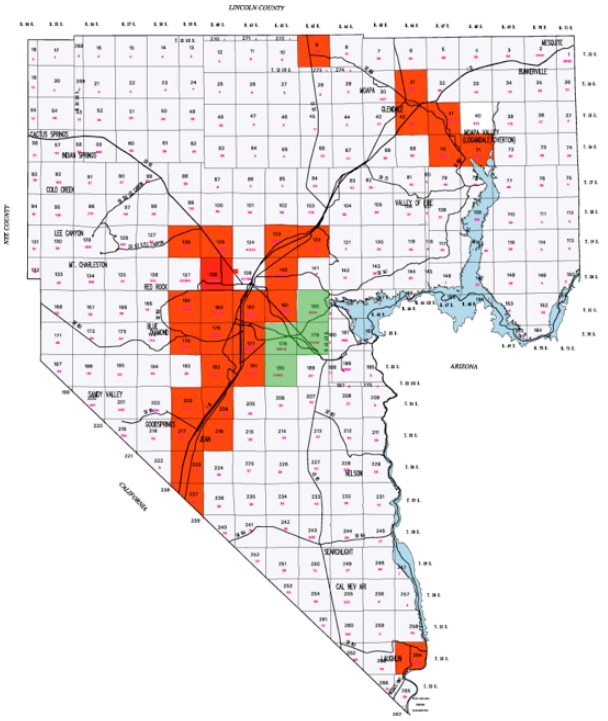


Figure 1. Areas within Clark County mapped for earthquake parcel classification, shaded. CCDDS and the CoH defined the areas mapped.

Optim SDS performed all necessary tasks for completion of the work, including field data acquisition, data processing and reports, working with University personnel to make the products of the work available in a format to be mutually agreed upon during the term of this contract. Optim SDS measured shear velocity as a function of depth at each of the locations using the refraction-microtremor (ReMi) surface array technique. Louie (2001) developed the refraction microtremor technique (commercially available as SeisOpt®ReMi™, © Optim 2001-2010) as a rapid and cost-effective method of measuring Vs30-meter to meet the IBC code (BSSC, 1997), and to derive site conditions. This method has been peer reviewed and blind tested against both borehole measurements and MASW, multi-channel analysis of surface waves (Louie, 2001; Stephenson et al., 2005; Thelen et al., 2006). Refraction microtremor is a volume-averaging surface-wave measurement, averaging velocities where geology is laterally variable, thus providing a more appropriate measure of site effects on earthquake wave propagation than single-point data obtained from downhole logs.

The NEHRP/IBC Site Class is calculated from the measurement results using the equations provided in the 2006 International Building Code book. Section 1613.5.5 of IBC 2006 defines the Vs100-foot vertically averaged shear-wave velocity. Table 1613.5.5 of IBC 2006 defines the NEHRP/IBC site class from the Vs100-foot measurement. Note that even though Vs100-foot values may give you an

average velocity that is Site Class A or B, additional criteria defined in the same section of the IBC 2006 code book must be applied by a geotechnical engineer.

In theory, the accuracy and the resolution of any model is a direct function of the spatial density of the database. In determining the appropriate data density to be used, Optim SDS utilized the Southern Nevada Building Code Amendments as a basis for a data density of one velocity sample per 36 acres. To aid in the capturing of evenly dispersed data, based on 1/36 acres, Optim SDS, CCDDS, and the CoH internally developed a gridded subsection scheme based on the existing book and section projections of Nevada. Site locations typically were reached via street approved vehicles, off highway vehicles (OHV), and hiking, then placed alongside roadways, trails, open fields, or open desert. However, due to limitations imposed by natural terrain, inaccessible areas, large structures, and infrastructure obstructions, the data density across the entire project area varied, rendering the 1/36 acre data density more of a guideline than an absolute standard.

In addition, in several areas, due to proximity to key infrastructure, identified geology of interest, and velocity anomalies discovered in the data set as the project progressed, data density was increased to better define the interpolated modeled surface in those areas. For instance, seismic array locations were intentionally placed with strategic orientation in mind, crossing known faults and fissure zones when possible. In order to maximize the potential to actually cross any subsurface fault or fissure related features, arrays were placed perpendicular to the assumed projected strike when possible.

All seismic array locations were intended to maintain an average test coverage or data density of one array per 36 acres with no less than 1000 feet measured midpoint to midpoint between each array location. The location of the seismic array is further refined from conditions encountered at the proposed location, such as: traffic and other safety and accessibility concerns; private property concerns; ability of the location to fit an array length of 604 feet (up to 2 channels may be omitted from the array under certain circumstances); location of driveways; relative slope and curvature of the array; the availability of parallel noise sources; and avoiding very high energy perpendicular noise sources and artificial underground voids.

Nominally, each site was measured by a linear ReMi array with 24 channels of vertical geophones spaced at 8 meters. Ambient noise microtremor was recorded using standard vertical 4.5 Hz geophones recorded at a rate of two milliseconds for intervals of 30 seconds each. In all, a total of 12 to 20, 30-second recordings were collected for each seismic array. In addition, hammer hits using an 8-pound or 10-pound sledge and strike plate were collected at approximately 15 feet and 30 feet off both ends during normal passive data collection, to increase high frequency energy. This was especially useful in low energy environments, typically rural settings away from traffic and other ambient noise sources.

The noise records were processed using the SeisOpt® ReMi™ software (© Optim, Inc., 2001-2010) that uses the refraction microtremor method (Louie, 2001). processing steps were: 1) create a velocity spectrum (*p-f* image) from the noise data by wavefield transformation; Rayleigh-wave dispersion-curve picking along a ``lowest-velocity envelope" bounding the energy appearing in the p-f image; and 3) interactive shear-wave velocity-profile modeling. The modeling can be subjective and

must be done with constraints: that a minimum number of layers be used to accommodate the observed Rayleigh-wave dispersion; and tests on the necessity and sensitivity of the data to both layer thickness and layer velocity. The resultant model is therefore the simplest to explain the data, following the Occam's Razor principle.

Quality assurance of results begins by plotting of the modeled velocity profiles within each section, to assure consistency. If one model differs from surrounding measurements, or is anomalous given known topographic changes, remodeling of the dispersion curve picks is the first step. An alternate model that is more consistent may be able to be derived. For some data sets, re-analysis of the original data may then occur. This may involve adjustment of picks along indistinct dispersion curves or reconsideration of the curve itself. Consistency of models with adjacent sections is also verified. If there are anomalously high-velocity layers within the upper 100 feet, the reliability of low-frequency dispersion curve picks is examined. In some cases, the accuracy of the dispersion curves at low frequencies is unclear. Again, picks may be adjusted and the dispersion curve at low frequencies is reconsidered. If the site is classified as Class B, the high frequency data are more carefully scrutinized to ensure there is velocity information to determine layers in the upper 20 feet.

"Blind" tests were periodically conducted to test the repeat ability of the data and analysis results. Seismic data were collected using comparable acquisition equipment by engineer James O'Donnell, of Las Vegas, independently at the same location of seismic arrays obtained by Optim SDS. Test locations were spatially dispersed in the map area where data collection was currently occurring. Data acquisition for the two datasets occurred simultaneously. Excerpts of the same ambient noise were therefore recorded by both datasets. Analysis results of the blind test data were compared with those obtained by Optim SDS.

Earthquake Ground-Shaking Prediction. The ShakeZoning tools assemble the available geological and geophysical data sets into a numerical grid for wave-propagation computation, as described by Louie (2008). We develop here an example grid to compute the shaking induced in Las Vegas Valley (LVV) by the June 1992 magnitude 5.5 Little Skull Mountain (LSM) earthquake. Figure 2 shows the location of the tilted grid.

The grid includes two datasets at various scales on Neogene basin thicknesses that are roughly stitched together: 1) Saltus and Jachens's (1995) USGS basin gravity inversions for the Basin and Range, including both sedimentary and Tertiary volcanic basins at 2-km resolution; and 2) the Langenheim et al. (1998) Las Vegas basin model from gravity, refraction, and a few deep wells, at 0.4-km resolution. Figure 3B shows the composite basin-floor model, which sets the LVV basin into its context of the many neighboring basins.

We also incorporate geotechnical data sets, despite their having spacings varying from 0.1 to 0.3 km, and including isolated point measurements. The ShakeZoning tools interpolate all the disparate data sets onto a regular grid, following instructions for how one data set may take precedence over another where they overlap. For the LSM model, three datasets are combined in this way: 1) the regional geologic map controls the default shallow geotechnical Vs30-meter, 250 m/s for basin

sites and 760 m/s for rock sites; 2) the Las Vegas refraction microtremor transect, sites by B. Luke at UNLV, stratigraphy correlated to 1145 wells by W. Taylor of UNLV and G. Wagoner of LLNL, all from Scott et al. (2006); and 3) the raw 10721 Parcel Map measurement results discussed below. Figure 3C shows a geotechnical model developed solely from actual measurements, with no Vs30 prediction.

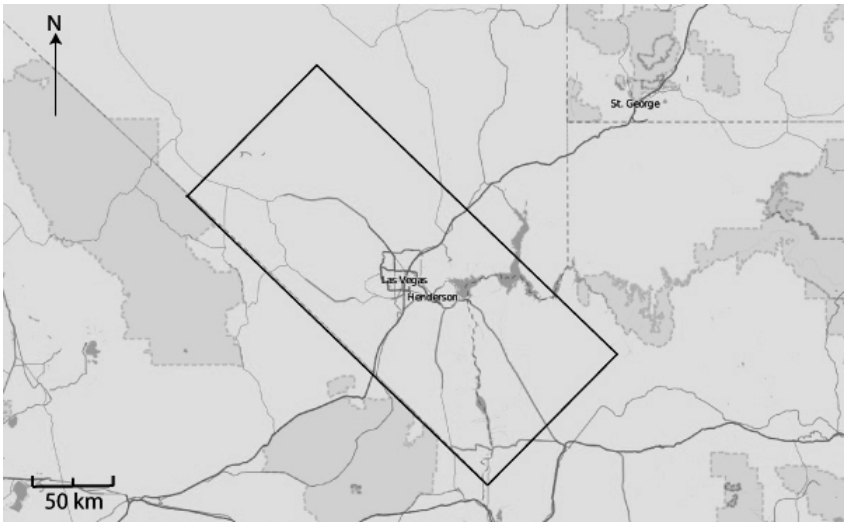


Figure 2. Map of southern Nevada showing the ShakeZoning grid for computing a scenario of the 1992 magnitude 5.5 Little Skull Mountain (LSM) earthquake.

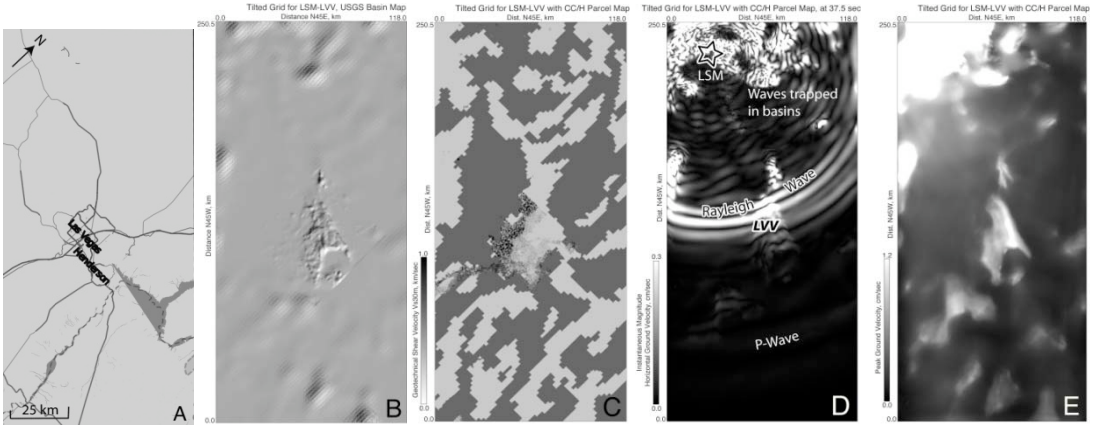


Figure 3. A) Road map on the southeast-tilted LSM ShakeZoning computation grid. B) Shaded-relief map on the grid showing the basement-surface component of the ShakeZoning model. C) Geotechnical shear-velocity map developed from the Clark County and Henderson projects. Higher velocities are shaded darker, with Vs30-meter velocities over 1.0 km/sec black. D) Map snapshot of wave propagation modeled from an LSM scenario, at 37.5 sec after earthquake initiation as Rayleigh waves enter Las Vegas Valley (LVV). E) Peak ground velocity (PGV) map resulting from this 0.1-Hz scenario, with greater shaking as lighter shading. For this scenario white area had greater than 1.2 cm/sec PGV.

We set up the example computation in the ShakeZoning tools to yield 0.1-Hz waves on a 236 NE-SW by 501 NW-SE by 41-node deep grid with a dh=dx=dy=dz

grid spacing of 0.5 km. The grid includes the LSM source zone near its NW end (star in figure 3D). A model of intrinsic seismic attenuation "Q" was developed following Olsen et al. (2003). For this historical earthquake the earthquake source parameters are provided by Smith et al. (2001). Source parameters for scenario earthquakes are derived from the USGS Qfaults database (USGS and CGS, 2010).

Figure 3D shows a snapshot of the wave propagation 37.5 seconds after the origin time of the earthquake. White modes in the basins show intensive horizontal shaking from waves trapped inside the low-velocity basin sediments. After 200 seconds of computed wave propagation on this grid, occupying a quad-core Intel CPU for a few hours, ShakeZoning produces a map showing the peak horizontal ground velocity (PGV) a the surface of the grid. (No topography is included.) Figure 3E shows the PGV map, with the LVV and surrounding basins getting much greater shaking than bedrock areas at similar distances from the earthquake.

RESULTS

Parcel Mapping. ReMi data from a total of 10721 sites were acquired, processed and submitted to CCDDS and the CoH. This represents more than 100% of the total number of seismic lines scheduled to be collected as part of this project. Figure 4 shows the microzonation map generated using ArcGIS and the Vs100-foot values determined from the distribution of seismic arrays. The method of kriging was used to produce this map.

Parallel "blind" tests were conducted at 93 randomly selected sites by O'Donnell. He analyzed and modeled the blind-test data independently of Optim SDS and NSHE. The blind-test Vs100-foot velocities were on average only 0.26% percent higher (5 ft/sec out of an average Vs100-foot of about 2000 ft/sec) than the velocities obtained at the same sites by Optim SDS. This tiny average difference shows that there was no significant systematic bias in the data analysis or modeling procedures. The root-mean-squared (RMS) difference between O'Donnell's blind analyses and Optim SDS's is 4.92% (98 ft/sec RMS difference). Only six of the 93 blind-test sites showed a difference with a magnitude greater than 10%, and the greatest difference was only 13.55%. These results show the consistent high quality of the Parcel Mapping measurements.

Caliche, a calcareous soil cement, is distributed across much of the Las Vegas region. The high-velocity caliche deposition within subsurface layers can result in high velocity layers within the velocity-depth profile, with lower velocity material below: velocity "reversals." An assumption is made that the soil is not varying greatly over the short distances considered, and that the caliche is developing in the same sedimentary layer within the section.

It is to be noted that, based purely on the Vs100-foot value, Site Class B values would be shown in the microzonation map (figure 4). IBC 2006 Section 1613.5.5 states that: "The rock categories, Site Classes A and B, shall not be used if there is more than 10 feet (3048 mm) of soil between the rock surface and the bottom of the spread footing or mat foundation." So, when the values suggest Class B, site-specific consideration should be made (depth of foundation, competency of rock etc.) before deciding whether it is a Site Class B. At most of the higher-velocity sites, our

shear-velocity profiles show more than 10 feet of low-velocity soil at the surface. Accordingly, we are suggesting a Site Class we call "C+" to describe these areas, denoted with dark gray in figure 4.

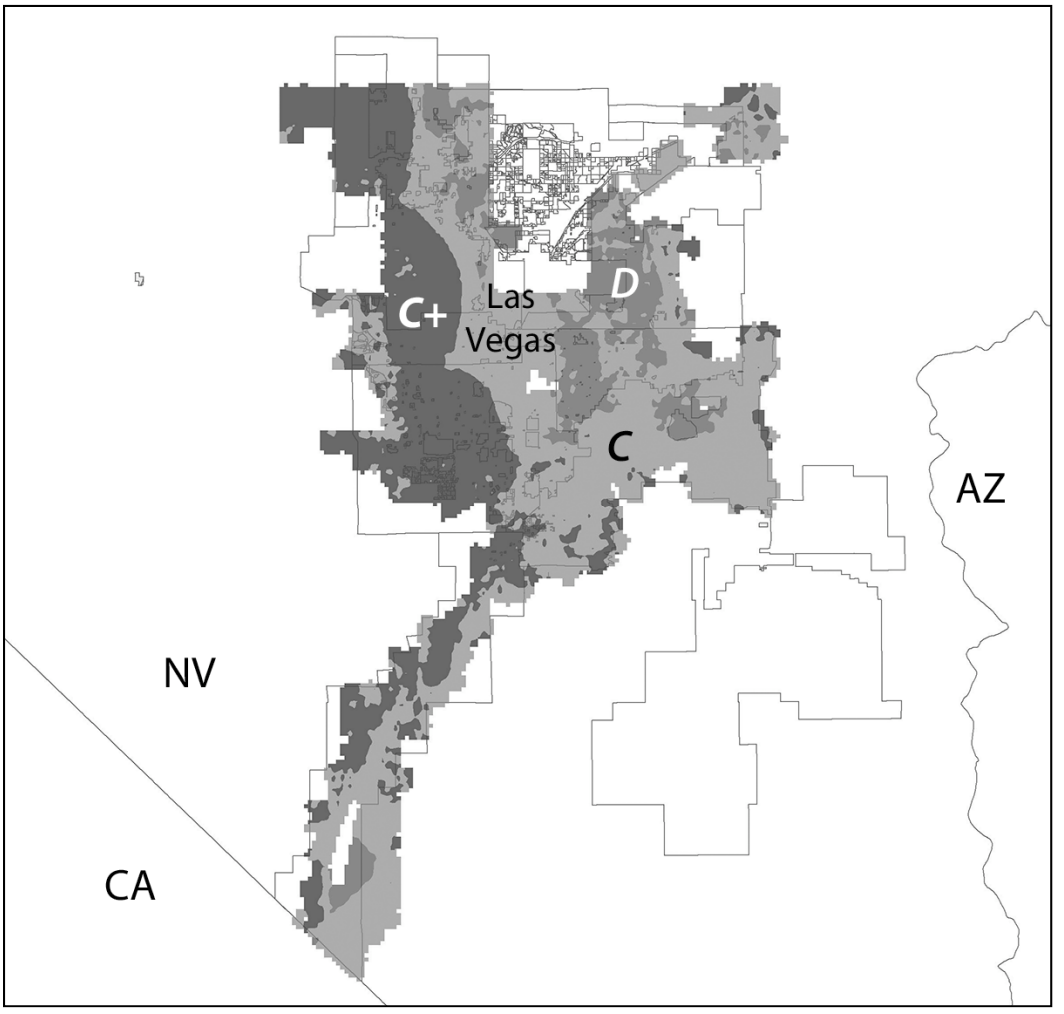


Figure 4. Map showing the IBC seismic zoning results of the Earthquake Parcel Mapping projects sponsored by Clark County and the City of Henderson. Black lines are municipal and state boundaries. The IBC "D" zone is medium gray; the IBC "C" zone is light gray; and the proposed IBC "C+" zone is dark gray.

The measured Parcel Map shows a clearly definable C+ to C boundary on the west side of Las Vegas Valley (dark to light gray in figure 4). The boundary may be associated with the bases of the alluvial fans emanating from the Spring Mountains, where the sediments become finer-grained (Scott et al., 2006). The C to D boundary (light to medium gray) is on the other hand much more complex, and difficult to associate with any known geological features.

Earthquake Ground-Shaking Prediction. The Little Skull Mountain earthquake scenario we show here is one possible example out of the eight additional faults in the USGS Qfaults database (2010) that the USGS National Hazard Maps

(Frankel et al., 1996) rate as probabilistically important to seismic shaking potential in Las Vegas Valley. We use the LSM scenario at 0.1 Hz here to demonstrate the crucial effects the Parcel Map results have on even low-frequency ground shaking in the Valley. Figure 5 shows this effect, unexpectedly strong given that the wavelengths of the 0.1-Hz waves modeled are 100 times larger than the 30-meter depth extent of the Parcel Map measurements.

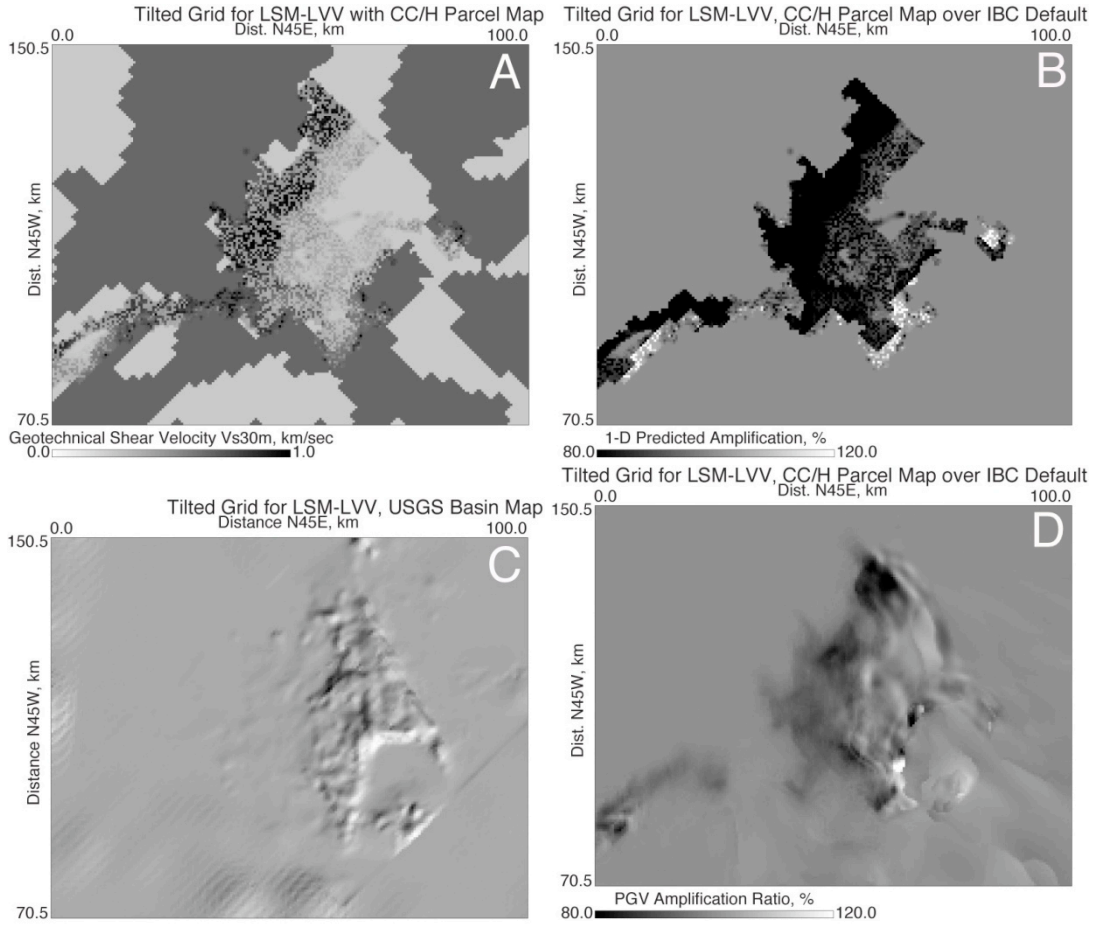


Figure 5. Maps of the Las Vegas Valley (LVV) section of the tilted LSM ShakeZoning scenario grid. A) Default geotechnical map with ~9000 Parcel Mapping Project Vs30-meter measurements included on top of the IBC defaults. B) Shaking amplification expected from the ratios of measured geotechnical velocities over the IBC default velocities, under a simple 1-d model. Amplification of 120% or more is shown as white, and de-amplification to 80% or less is black. C) LVV map showing the basin floor in shaded relief. D) ShakeZoning PGV ratio map comparing the 0.1-Hz results of the LSM scenario, comparing the Parcel Mapping result against the IBC default result. Even at these very low frequencies, 0.1 Hz, where the shallow geotechnical velocities should have minimal effect, comparing the physically correct ShakeZoning computation against the IBC defaults (D) shows surprisingly large and complex patterns of amplification (white) and de-amplification (black), greater than 20%.

At such long wavelengths the effects of the Vs30-meter variations found in the Parcel Map (figure 5A) should be minuscule. The amplifications (white) and de-amplifications (black) are predicted in figure 5B from the measured Vs30 relative to the IBC assumptions only, by the one-dimensional equations in the IBC Code (2006) and in ShakeMaps (Wald et al., 1999). The 1-d amplifications are up to 64% in figure 5B. These amplifications should only appear at much higher frequencies, above 1 Hz. The 0.1-Hz waves should respond mostly to the geologic basin, figure 5C.

However, figure 5D shows 0.1-Hz amplifications, relative to an IBC default geotechnical map, of up to 36%. The 30-meter-deep Parcel Map was the only variant between the two ratioed scenarios. This is from fully 3-d, physically and geologically accurate ShakeZoning computation. Further, the unexpectedly high amplification (white on figure 5D) is not located at either the location of the lowest Parcel Map velocities, nor at the greatest basin depth (nor steepest basin-floor slope). As well, the 64% de-amplifications (black) on the west side of the Valley predicted by the 1-d model in figure 5B are not supported by the realistic 3-d computations. This observation suggests that the current IBC may be too permissive in some higher-velocity areas.

DISCUSSION AND CONCLUSIONS

The Parcel Mapping project was completed successfully for Clark County and the City of Henderson. In all, 10721 individual seismic arrays/lines were assigned, deployed and spatially located in a systematic manner, maximizing the density of the database coverage within urban Clark County. This achievement has put southern Nevada at the forefront of earthquake-hazard mitigation efforts worldwide.

Based on the GIS seismic shear-velocity database developed by NSHE and Optim SDS, the project provides Clark County and the City of Henderson a single shear-wave velocity-based Parcel Map with contoured values corresponding to the site classifications of the IBC and NEHRP definitions for site class. Velocity databases from the CCDDS and the CoH were integrated into a single Vs database and the interpolated velocity map was based on the entire joint database, providing seamless interpolation across the CCDDS and CoH boundaries. This Parcel Map will provide city planners, building officials, design professionals, and researchers alike the opportunity to determine the actual site class value of a particular parcel before a single site-specific investigation is performed.

We show the Parcel Map to be essential for the accurate prediction of earthquake ground shaking across Las Vegas Valley, even at low frequencies that are of interest mostly to the taller buildings in the area. Additional scenario computations are under development, for the eight dangerous earthquake faults in the region, and for higher wave frequencies, up to 1 Hz. The newly accurate ShakeZoning tools developed in this effort will be made available to aid engineers and planners in the region.

REFERENCES

Building Seismic Safety Council, BSSC, (1997). *NEHRP Recommended Provisions for Seismic Regulations for New Buildings and other Structures*, Part1 – Provisions, Federal Emergency Management Agency, Washington D.C., and FEMA 302.

Frankel, A., Mueller, C., T. Barnhard, D. Perkins, E.V. Leyendecker, N. Dickman, S. Hansen, and M. Hopper (1996). *National seismic-hazard maps: documentation, U.S. Geol. Surv. Open-File Rept. 96-352*.

Gvirtzman, Zohar, and John N. Louie, (2010). 2D analysis of earthquake ground motion in Haifa Bay, Israel: *Bull. Seism. Soc. Am., 100*, 733-750, doi: 10.1785/0120090019.

International Building Code, (2006). International Code Council, 679 pages.

Langenheim, V. E., Grow, J., Miller, J. J., Davidson, J. D., and Robison, E., (1998). *Thickness of Cenozoic deposits and location and geometry of the Las Vegas Valley shear zone, Nevada, based on gravity, seismic-reflection, and aeromagnetic data: U. S. Geol. Survey Open-File Report OF 98-0576*, 32 pp.

Larsen, S., Wiley, R., Roberts, P., and House, L., (2001). Next-generation numerical modeling: incorporating elasticity, anisotropy and attenuation: *SEG Expanded Abstracts, 20*, 1218-1221.

Louie, J, N., (2001). Faster, Better: Shear-wave velocity to 100 meters depth from refraction microtremor arrays: *Bull. Seism. Soc. Am., 91*, 347-364.

Louie, John N., 2008, Assembling a Nevada 3-d velocity model: earthquake-wave propagation in the Basin & Range, and seismic shaking predictions for Las Vegas: *SEG Expanded Abstracts, 27*, 2166-2170.

Magistrale, H., S. Day, R. W. Clayton, and R. Graves, (2000). The SCEC Southern California Reference Three-Dimensional Seismic Velocity Model Version 2: *Bull. Seism. Soc. Am., 90*(6B), S65–S76.

Olsen, K. B., (2000). Site amplification in the Los Angeles Basin from three-dimensional modeling of ground motion. *Bull. Seism. Soc. Am., 90*(6B), S77-S94.

Olsen, K. B., S. M. Day, and C. R. Bradley, (2003). Estimation of Q for long-period (>2 sec) waves in the Los Angeles basin: *Bull. Seism. Soc. Am., 93*, 627–638.

Saltus, R. W., and Jachens, R. C., (1995). *Gravity and basin-depth maps of the Basin and Range Province, Western United States: U.S. Geological Survey, Geophysical Investigations Map, Report: GP-1012*, 1 sheet.

Scott, J. B., T. Rasmussen, B. Luke, W. Taylor, J. L. Wagoner, S. B. Smith, and J. N. Louie, (2006). Shallow shear velocity and seismic microzonation of the urban Las Vegas, Nevada basin: *Bull. Seism. Soc. Am., 96*(3), 1055-1067, doi: 10.1785/0120040093.

Smith, Kenneth D., Brune, James N., de Polo, Diane, Savage, Martha K., Anooshehpoor, Rasool, and Sheeham, Anne F., (2001). The 1992 Little Skull Mountain earthquake sequence, southern Nevada Test Site: *Bull. Seism. Soc. Am., 91*, 1595-1606.

Stephenson, W. J., J. N. Louie, S. Pullammanappallil, R. A. Williams, and J. K. Odum, (2005). Blind shear-wave velocity comparison of ReMi and MASW results with boreholes to 200 m in Santa Clara Valley: Implications for earthquake ground motion assessment, *Bull. Seism. Soc. Am., 95*, 2506-2516, doi: 10.1785/0120040240.

Thelen, W. A., M. Clark, C. T. Lopez, C. Loughner, H. Park, J. B. Scott, S. B. Smith, B. Greschke, and J. N. Louie (2006). A transect of 200 shallow shear-velocity profiles across the Los Angeles basin, *Bull. Seism. Soc. Am., 96*, 1055-1067.

U.S. Geological Survey and California Geologic Survey, (2010). *Quaternary fault and fold database for the United States*, accessed 12/20/2010, from USGS web site: http://earthquake.usgs.gov/hazards/qfaults/.

Wald, David J., Vincent. Quitoriano, Tom. H. Heaton, Hiroo. Kanamori, Craig. W. Scrivner, and C. Bruce Worden, (1999). TriNet ``ShakeMaps'': Rapid Generation of Instrumental Ground Motion and Intensity Maps for Earthquakes in Southern California: *Earthquake Spectra, 15,* 537-556.

Wills, C. J., M. D. Petersen, W. A. Bryant, M. S. Reichle, G. J. Saucedo, S. S. Tan, G. C. Taylor, and J. A. Treiman (2000). A site-conditions map for California based on geology and shear wave velocity, *Bull. Seism. Soc. Am., 90*, S187-S208.

Design of the New Mike O'Callaghan Pat Tillman Memorial Bridge at Hoover Dam

David Goodyear, PE, SE, PEng [1]

[1] Chief Bridge Engineer, T. Y. Lin International

Summary

A dramatic new concrete arch joins the setting of the historic Hoover Dam, spanning the Black Canyon between the States of Arizona and Nevada, USA. This 1060 foot (323 m) long arch span is the 4th longest concrete arch in the world, and the longest in the United States. The scale of concrete construction for the bridge is impressive. Four form travelers advanced to the crown of the cast-in-place arch supported by 88 carefully tuned stay cables, while precast segmental construction was used for the tallest precast columns erected to date.

Introduction

A project team of five US government agencies, lead by the Central Federal Lands office of the Federal Highway Administration (CFL-FHWA) collaborated to develop a highway bypass to the existing US93 roadway over the historic Hoover Dam, shown in Fig 1. The existing highway route 93 over the Dam mixed the throng of tourists for whom the Dam is a scenic destination with heavy highway traffic and commercial trucking mixing with pedestrian traffic and crosswalks. The blend of these two created hazard and hardship for both, and served as a bottleneck for commerce along the major north-south route of US93.



Figure 1 (photo by HST)

The Hoover Dam Bypass Project had a decades long history of planning and process. First discussed in the mid 1960's, plans for a highway crossing of the Colorado River were advanced by the US Bureau of Reclamation to address the increasing highway traffic across the top of Hoover Dam. A series of studies ensued, sponsored by several of the project stakeholders throughout the next two decades. In 1997 FHWA Central Federal Lands Division (CFL) became the lead agency for the Project Management Team comprised of the Bureau of Reclamation, Arizona DOT, Nevada DOT, National Park Service and Federal Highway Administration. The project then advanced through the Draft Environmental Impact Statement, Final Environmental Impact Statement and Record of Decision leading to commissioning the project.

General Project Development

A consortium of firms working under the moniker of HST (HDR, Sverdrup, and T.Y. Lin International) teamed with specialty sub-consultants to deliver the design for the 4-mile long bypass project. HDR was the project manager and led the design of the Nevada approaches. Sverdrup (now Jacobs) led the design of the Arizona approaches. T.Y. Lin International led the design of the new Colorado River Bridge.

Bridge Type Screening Process

With the selection of an alignment so close to Hoover Dam, the new bridge would be a prominent feature within the Hoover Dam Historic District, sharing the view-shed with one of the most famous engineering landmarks in the US. The environmental document set a design goal to minimize the height of the new bridge crossing on the horizon, both from the Dam and from a boater's view on Lake Mead. The State Historic Preservation Officers for both Nevada and Arizona – both members of the Design Advisory Panel – emphasized the need to complement and not compete with the architecture of the Dam. The Design Advisory Panel helped establish the mission for the bridge design, which was to "...strive for engineering excellence in the design of today that honors the engineering excellence that went into the Dam in its day" (HDB Design Advisory Panel, 2002).

The typical design approach for a project of this significance would be to conduct a comprehensive type study of all candidate bridge types, carrying design to a level that would permit architectural and economic evaluations of each type. However, since the Hoover Dam Bypass had been studied in one form or another for over 25 years, CFL decided to use previous information developed for prior studies along with new information developed by the design team in an initial Type Screening Process – as a precursor to the type study. This Type Screening process was developed to consider policy-level criteria as a first litmus test on bridge types that should proceed to a more formal type study.



Figure 2 (rendering by TYLI)



Figure 3 (rendering by TYLI)

The Project advanced a full suite of bridge types applicable for a 1000 ft+ span range. Of particular note by all the reviewers was the separation of alternatives. The two most favored options were the natural design choices fitting the site – to span the canyon, or to arch against the canyon walls. The clear spanning suspension option (Fig. 2) was significantly handicapped at the time of this type evaluation in terms of structural vulnerability (time frame was soon after 9/11), first cost and maintenance cost. While being one of the more architecturally alluring options, the suspension span was seen as both the highest life-cycle cost option and the most vulnerable design type, which was a special concern for the Agencies who would soon be maintaining the bridge. As a result of this screening process, the type study proceeded with only deck arch options (Fig. 3).

Type Study

At the time of the type study, detailed geotechnical engineering had just begun. The topography on the Nevada side of the canyon (Fig. 4) included a massive outcropping of rock below the US93 switchback, with a fault line running between this block and the canyon slope behind. Without detailed geotechnical and mapping information, we could not confirm the suitability of the short block as a foundation. Therefore, the type study progressed in parallel with geotechnical exploration assuming either of two different arch spans could be selected; a short span of 1060 ft (323 m) or a longer span of 1325 ft (404 m).

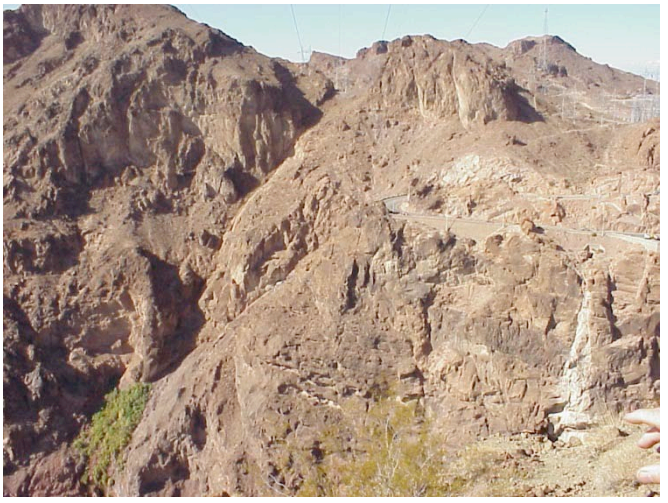


Figure 4 (photo by TYLI)

The family of arch designs (Fig. 5) was reviewed based on architectural and technical criteria. The Design Advisory Panel expressed a desire for simplicity, and rejected any notion of ornamentation or art-decco designs that competed with features on the Dam. Six designs were developed - 3 each for the long and short spans - to the point where general quantities and construction methods could be established for review.



Figure 5

The consensus decision to proceed with the concrete composite alternative was made by the Executive Committee, comprised of the operations chiefs from the 5 Agencies on the Project Management Team.

Major Design Features

The final design is an evolution of engineering considerations, creating a form dictated by efficient resistance to the engineering demands on the structure. Every element of the twin rib framed structure shown in Fig 6 is a product of engineering reasoning.



Figure 6 (rendering by TYLI)

The Arch

At the outset of design the initial seismic hazards evaluation and geophysical analysis of the site led us to believe that earthquake could control the lateral design of the bridge. The twin rib configuration with connecting struts was developed first as a ductile frame for lateral loads, following the successful development of the shear linked tower concept by the Designer for a San Francisco Bay Bridge. A single arch rib would leave no opportunity for tuning stiffness or for providing for frame ductility, whereas twin ribs could provide an excellent means of creating ductile Vierendeel links that could otherwise protect the gravity system of the arch. This ductile frame would allow the concentration of ductility demand in the connecting shear links, rather than in the main arch rib members.

At the time of preliminary design, the current Guide Specification for Seismic Design was in the early stages of development, and the AASHTO design event for the site was a .10g 500 year event. A project specific probabilistic seismic hazards analysis was conducted by AMEC in order to assess the range of ground motion associated with return periods more appropriate for this design. A 1000 year return period was selected (that same return period was later selected by AASHTO for the new Guide Spec), resulting in a design basis PGA of .2g.

Wind was a major environmental loading condition from the outset of design. It played a qualitative role in the type selection, and a key role in design. The unique topography was recognized as a feature requiring special studies. During the preliminary design phase, a site wind study was conducted by West Wind Laboratories to correlate the wind speeds at the bridge site with those at the Las Vegas Airport NOAA station in the valley. With this correlation and a model evaluation of the local terrain effects (Fig. 7), the long term statistics from the Airport were used to develop site wind speeds for design. As a result of this study, the 3 second wind speed was raised



Figure 7

to 56 m/sec, up from the ASCE-7 standard of 40 m/sec. Dynamic studies resulted in a gust loading factor of 2.4 (against mean hourly), which collectively resulted in wind controlling the lateral forces design. Chamfers for the main arch rib were introduced both to control vortex shedding and reduce design-controlling drag forces on the arch. Chamfers were added to the tall columns to control vortex-shedding vibrations observed in the wind tunnel. Wind recordings continued throughout construction, establishing a more complete on-site record. The forecasts produced by West Wind Laboratories based on the NOAA correlation were tested according to the methods of Scanlon based on 4 years of continuous on site record. These records confirmed the accuracy of the initial wind studies conducted with only 6 months of site data.

The 10,000 psi (69 MPa) concrete arch was an efficient element for gravity loads in its final form. There were two aspects of design that favored a twin rib layout instead of the typical single box section for this arch. The first was the seismic framing system noted above. The second was one of practical construction for the open arch section as it cantilevered during construction. A single box would be almost 65 ft (20 m) wide, and weigh approximately 20 kips per ft (292 KN/m). This section size would rule out a precast segmental option. It is for both of these reasons that a twin rib arch framing system was selected (Fig. 8).

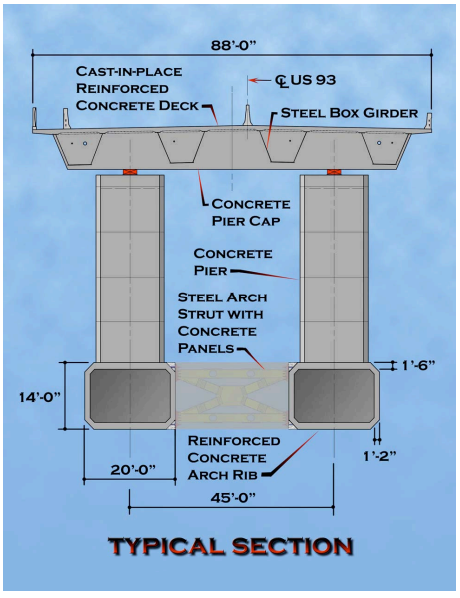


Figure 8

Spandrel Framing

The composite superstructure was selected for speed of erection and to lower weight on the arch. The spacing of spandrels was an extension of the erection concept to erect the bridge using a highline crane system. Above 50 tons, there is a jump in highline cost, so the decision was made to target a 50 ton capacity for major superstructure elements. The span was set in the range that a highline crane could deliver the steel box sections, which resulted in a nominal 120 ft (36.5 m) span. This same span also allows steel girders to be set within the range of most conventional cranes, should an alternative erection system be selected.

One of the many lessons from the smaller Crooked River Arch Bridge in Oregon was that spandrel construction and integral crown construction was very time consuming and expensive. The high rise of the Hoover arch added to the focus on construction of the spandrels, since the height of these columns would exceed what had been built in past segmental structures. Lateral bracing was a system design consideration, affecting the arch, spandrel and approach columns. Bracing for the arch is affected by deck stiffness and continuity conditions in the deck and columns.

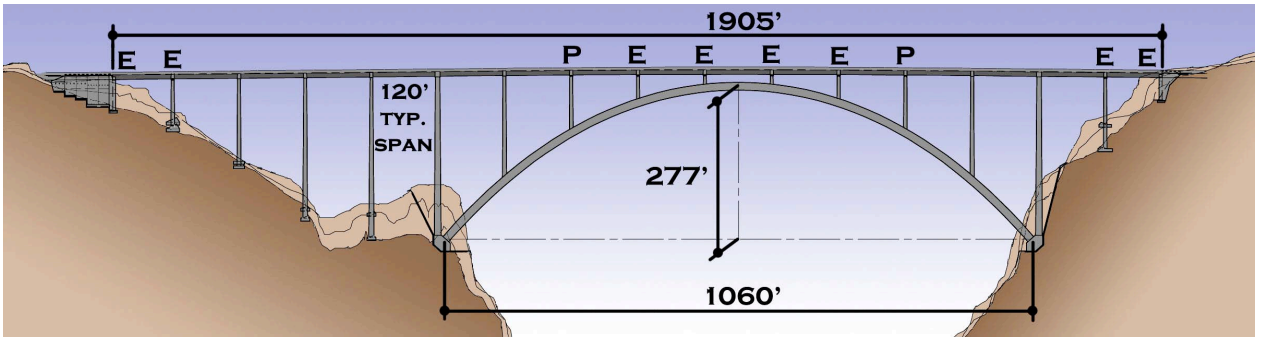


Figure 9

An open arch crown was selected as the best balance for constructability and consistency with the composite deck system. A special consideration for the visual presentation of the short span arch was that the composite steel deck would result in a very abrupt, mechanical looking connection at the crown if an integral crown was selected, due in large part to the high rise of the arch. When studied in either concrete or steel, an integral crown solution for the short span alternatives looked blocky and massive at the crown, and ran counter to the architectural goal of lightness and openness when viewed from Lake Mead. Once selected as an open crown, the statical system included sliding bearings for the short, stiff piers over the arch crown and similar piers near the abutments. This was necessary due to the large secondary moments developed in these piers from creep deflections of the arch. Bearings were also helpful in producing a more even distribution of longitudinal seismic forces among the piers.

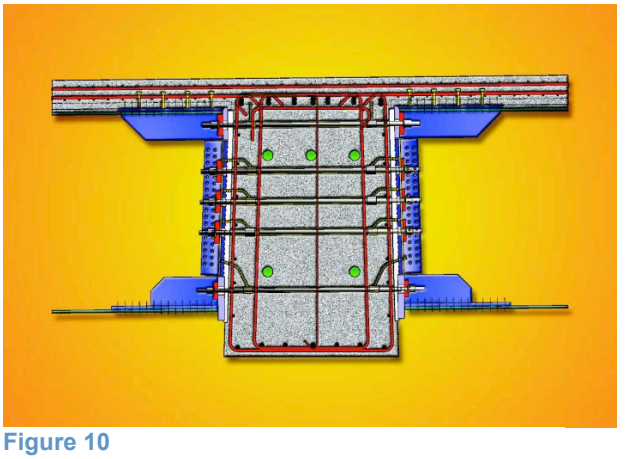


Figure 10

Integral pier caps (Fig. 10) were designed as part of a continuous deck/diaphragm system used for lateral and longitudinal bracing of the columns. Integral concrete pier caps were selected over steel box cap sections to avoid the fracture-critical design and inspection considerations for a steel cap. The integral cap framing was selected to develop the diaphragm action of the deck used to avoid lateral bracing of the spandrel columns and to provide for stability of the flexible columns along station through direct diaphragm action.

Construction Methods

As with any large bridge structure, the dead load design is dominated by the assumptions of a construction scheme. The concrete arch needs little reinforcing for the final closed arch configuration, operating primarily in compression. However prior to closing at the crown, the arch rib is a cantilever box girder. Since post-tensioning has no purpose for the final configuration of the arch, design was based on a conventionally reinforced concrete box for cantilevering conditions. Design for construction was based on allowable stresses in reinforcing

and associated crack controls according to the AASHTO code, eliminating the need for temporary or permanent post-tensioning.

The typical approach in the US is to nominate an erection scheme, but to show it only schematically, and defer responsibility for both the scheme and the details to the contractor. The design management team believed that more informed bids could be developed if there was a more complete erection scheme shown with the plans, even if the contractors elected to use alternative methods. Therefore, the decision was made to show a complete erection scheme for dead load on the plans and allow the contractor to use that scheme or his own.

There are at least two practical erection methods that can be used to erect a cantilevered arch. One is a simple cable-stayed cantilever erection (Fig. 11). The second is the use of temporary stay truss diagonals, erecting the arch, deck and spandrels as a cantilever truss (Fig. 12). In selecting the simple cast-in-place stayed method, we opted for the most conservative method in

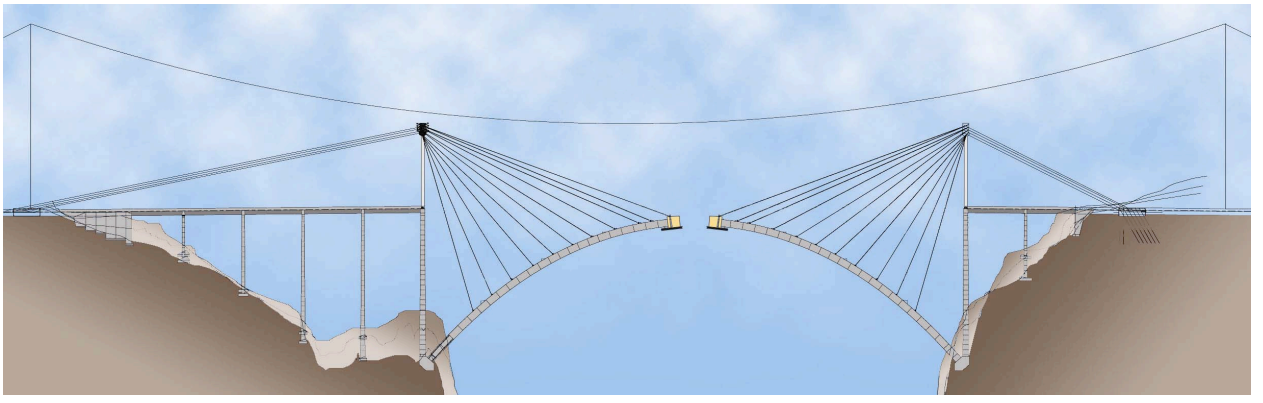


Figure 11

that arch geometry can be controlled and corrected at each step of construction with stays and traveler settings. In addition, this method allows the most flexibility for closing the arch without affecting the geometry of columns and deck (since they are not in place until after closure).

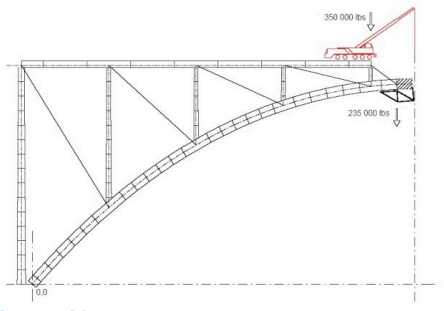


Figure 12

Both precast and cast-in-place methods were permitted for the arch and spandrel columns. The contract was written to allow alternative methods of erection, however both the arch and the columns each were to be of a single type (precast or cast in place) in order to conform to the time dependent assumptions inherent in design. All equipment and ancillary temporary works were also to be designed by the contractor.

Construction

The construction contract was awarded in September of 2004 to Obayashi-PSM, JV, after about a year delay in the funding process. A limited notice to proceed was issued for November, 2004, with full field work beginning in 2005.

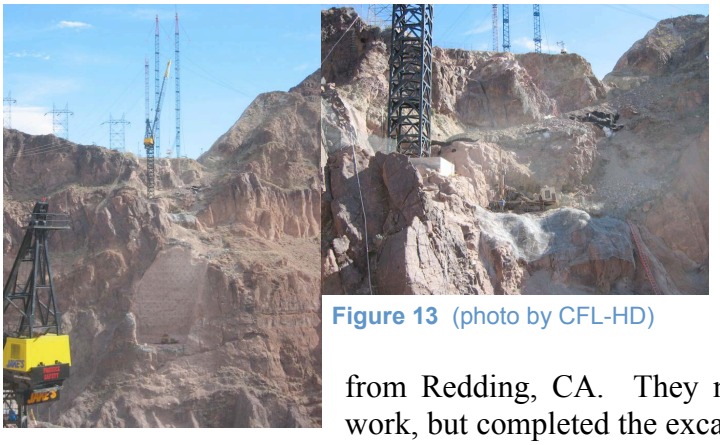


Figure 13 (photo by CFL-HD)

The first challenge for the construction team was creating a foothold for foundation construction (Figs 13, 14). Climbing on the side of the cliff 800 feet over the river below was difficult enough, but excavating (and doing so within the loss limits in the specification) was a considerable challenge. The subcontractor who met this challenge was Ladd Construction from Redding, CA. They not only met the tight schedule for this work, but completed the excavation allowing about half of the rockfall into the river that was permitted.

Initial bridge construction began on site with footing and abutment work, and in the precast yard outside of Boulder City where the contractor set up their own precasting facility and self-performed the precasting. Column sections were trucked to the site as needed for erection, and set into place using both the high-line crane and conventional cranes located at the hairpin in Nevada (Fig. 14, 15).

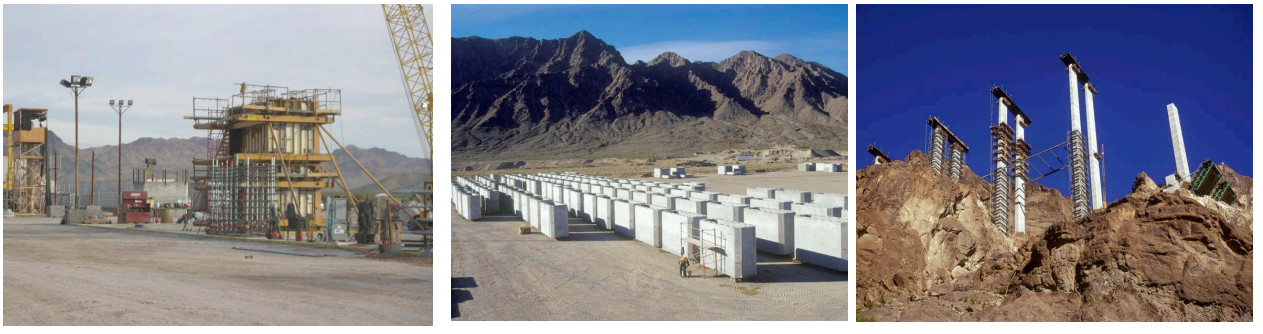


Figure 14 (photo by CFL-HD)



Figure 15 (photo by CFL-HD)

In September, 2006, the high line crane was lost in a strong wind, removing the high line crane from service. The contractor mobilized additional land cranes to continue construction in Nevada, and an S-70 derrick in Arizona (Fig. 16), to both complete approach columns and set approach steel box girders until a new high line could be design, fabricated and erected. Arch Erection was being initiated at the time of the high line crane collapse. The temporary cranes were able to service

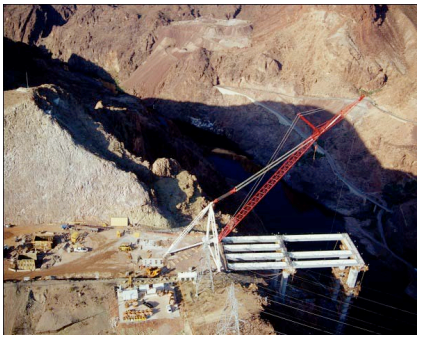


Figure 16 (photo by CFL-HD)

the first few arch segments from the springing, allowing the piece work for the starters and the initial setup of the form travelers to proceed.

Four form traveler headings were used for erection of the arch. Every second arch segment was supported by a temporary stay cable. After erection of the new high line and restarting the main arch erection, the contractor reached a reliable cycle of 2 weeks, and often bested that cycle on segments that did not have a stay cable to install. The arch was closed in August of 2009 within an impressive ¾ inch (19mm) tolerance at closure (Fig. 17).



Figure 17 (photo by CFL-HD)

While the arch construction was the more dramatic effort, construction of the spandrel columns (Fig. 18) and deck structure was just as challenging from a construction standpoint. As the spandrels and deck superstructure are set on the arch, the arch deflects. Staging of the spandrel column erection, column cap construction and box girder placement had to be engineered to achieve final geometry. The contractor was continually monitoring and analyzing the response of the structure as each spandrel column and cap was placed, updating his forecast of geometry throughout the erection process.

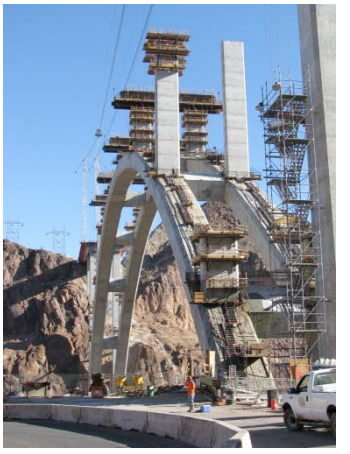


Figure 18 (photo by TYLI)

The assumption during design was that the arch, spandrels and deck would each be completed in series. The contractor decided to complete these tasks in parallel in order to shorten the construction schedule. Deflections were not limited to those from the spandrel columns and caps, but now included the superstructure loads and thermal effects of the steel box girders as they were placed in the partially completed frame. All of this sequence was analyzed in real time by the contractor in the field.



Figure 19 (photo by CFL-HD)

Demobilization of the high line and related temporary works was a project in itself, and had to be completed before final paving and finishing could be completed for the roadway. Bridge construction was essentially completed by August, 2010 (Fig. 19).

The new Colorado River Crossing now frames the view of Black Canyon from Hoover Dam for the coming generations of tourists, and is the cornerstone in a new,

efficient highway system funneling commercial traffic between the States of Nevada and Arizona. The project reflects the skill and determination of the people who built it, all of whom take pride in their accomplishment.

The new bridge has been dedicated as the Mike O'Callaghan Pat Tillman Memorial Bridge in memory of two heroes of the US armed forced from the States of Nevada and Arizona.

CREDITS:

Program Management:	Central Federal Lands Highway Division of FHWA, Dave Zanetell, Project Manager; Bonnie Klamerus, Structures Manager
Construction:	Obayashi/PSM, a Joint Venture, Ken Hirschmugl and Jeff St. John, Construction Management
Design:	T.Y. Lin International w/HDR, David Goodyear, PE SE, Designer and Chief Engineer



(photo by TYLI)

Evaluation of Concrete Shear Strength for FRP Reinforced Beams

M. Zeidan[1], M. A. Barakat[2], Z. Mahmoud[2], A. Khalifa[2]

[1] Civil and Environmental Engineering Department, University of Nevada, Las Vegas, 4505 S. Maryland Parkway, Las Vegas, NV 89154-4015.
[2] Structural Engineering Department, Faculty of Engineering, Alexandria University, Alexandria- 21544, Egypt.

ABSTRACT

In order to expand the use of FRP in new structures, a satisfactory degree of understanding is required for the behavior of members reinforced with FRP rebars. The aim of the current study is to investigate the concrete contribution to shear strength for beams reinforced with FRP longitudinal bars. A review for the available test results for members reinforced with FRP longitudinal bars without shear reinforcement results a database of specimens from different researchers. The available equations for predicting the value of the concrete shear strength for FRP reinforced members were also collected.

An experimental test program was conducted to verify the results for beams with low longitudinal reinforcement ratios. A comparison was made between the experimental results and the shear strengths calculated using the different available equations. Based on the comparison and the experimental program results, the equation adopted by Building Research Institute (BRI)-Japan was found to fit best with the experimental results.

INTRODUCTION

Deterioration of reinforced concrete structures has become a serious problem in the last decades due to the corrosion of steel bars. An alternative type of reinforcement as fiber-reinforced polymers (FRP) is considered to be one of the solutions for the corrosion problem. During the last decade serious efforts were made to use FRP materials in construction industry. Behavior and strength of concrete members depend primarily on the characteristics of concrete and reinforcement. Shear strength of concrete members is influenced by important parameters which significantly affect the design and structural detailing. Extensive studies have been reported for the shear strength of members reinforced with steel; however limited studies were made for shear strength of beams reinforced with FRP. This paper provides a research program conducted to evaluate shear strength of beams reinforced with longitudinal FRP bars without shear reinforcement. The parameters affecting concrete shear strength were carefully selected to fill a gap in the available range of studied parameters available in literature. The design guidelines for concrete members reinforced with FRP bars were also discussed.

RESEARCH SIGNIFICACE

The conducted analytical and experimental investigations concerning the concrete contribution to shear strength of FRP reinforced members, concluded that the shear strength of members reinforced with FRP can be predicted using the proposed equation. This information is valuable for designers and for the development of design guidelines and codes related to concrete structures reinforced with FRP.

EXPERIMENTAL DATA AND DESIGN EQUATIONS

The concrete contribution to shear strength of concrete beams reinforced with FRP bars as longitudinal reinforcement has been evaluated by many researchers as a part of the total shear strength of concrete beams. On the other hand, few researchers tried to evaluate the shear strength of FRP longitudinally reinforced concrete members without web reinforcement. Test results for the studies concerning the concrete shear strength of concrete beams reinforced with FRP bars are reported in this section. Also, equations proposed by different studies and design codes to evaluate the concrete shear strength in this case are presented and compared with the available experimental results and a discussion of the comparison is introduced.

Experimental Data

In order to assess the validity of the equations used to evaluate the concrete shear strength of members reinforced with FRP bars (V_{cf}), a database of 60 specimens was made from collected experimental data. This database is formed of concrete specimens experienced shear failure including concrete beams without stirrups and one-way slabs. These specimens were tested by 13 different researchers (Alkhajardi *et al.* 2001, Duranovic *et al.* 1997, El-Sayed *et al.*2006, Gross *et al.* 2004 Michaluk *et al.* 1998, Nagasaka *et al.* 1993, Razaqpur *et al.* 2004, Tariq and Newhook 2003, Tottori and Wakui 1993, Tureyen and Frosch 2002, Vijay *et al.* 1996, Yost *et al.* 2001 and Zhao *et al.* 1995). The database included specimens having different cross section dimensions, longitudinal reinforcement ratios, concrete strengths and types of reinforcement. The shear span to depth ratio of the specimens included in the database ranged between 1.78 for the shortest beam and 12.5 for the one-way slabs. The longitudinal reinforcement ratios ranged between 0.25% and 3.03% for all specimens. The compressive strength of concretes used for the specimens varied between 23 MPa and 82 MPa. The FRP longitudinal reinforcement used for the specimens was of aramid (AFRP), glass (GFRP) and carbon (GFRP) fibers with modulus of elasticity (E_f) ranging between 38 and 145 GPa.

Available Equations and Design Recommendations

Some of the available equations for evaluating the concrete shear strength of concrete members longitudinally reinforced with FRP bars are presented herein. These equations were proposed by researchers or stated by design recommendations.

Tottori and Wakui (1993) expressed the shear capacity of concrete beams without shear reinforcement V_{cf} as the larger of V_{cf1} and V_{cf2}, given as follows:

$$V_{cf1} = 0.20 (f'_c)^{1/3} (\rho_f^*)^{1/3} (1000/d)^{1/4} \left[0.75 + 1.4/(a/d) \right] bd \qquad \text{(1-a)}$$

$$V_{cf2} = 0.244 (f'_c)^{2/3} (1 + \sqrt{\rho_f^*}) \frac{[1 + 3.33(r/d)]}{[1 + (a/d)^2]} bd \qquad \text{(1-b)}$$

Where $\rho_f^* = \rho_f (E_f / E_s)$

Zhao *et al.* (1995) used the following expression to predict the concrete contribution (V_{cf}):

$$V_{cf} = 0.20 (1 + \beta_p + \beta_d) \left[0.75 + 1.4/(a/d) \right] (f'_c)^{1/3} bd \qquad \text{(2)}$$

Where $\beta_p = (100 \rho_f^*)^{1/2} - 1 \qquad \leq 0.73$

$\beta_d = (1000/d)^{1/4} - 1$

Tureyen and Frosch (2003) proposed a design equation to calculate shear strength provided by concrete for members reinforced by either steel or FRP. Also, this equation was adopted by ACI-440 committee starting from 2006 recommendations. The equation can be expressed as follows:

$$V_{cf} = 0.415 \sqrt{f'_c}\ bc \qquad \text{(3)}$$

Where $c = kd$ = neutral axis depth of cracked transformed section;

$k = \sqrt{2\rho n + (\rho n)^2} - \rho n$;

ρ = longitudinal reinforcement ratio;

$n = E_r / E_c$ = modular ratio;

E_r = modulus of elasticity of reinforcement;

Razaqpur and Isgor (2006) proposed a shear design equation for calculating the shear strength of FRP-reinforced members without stirrups. The equation can be expressed as follows:

$$V_{cf} = 0.035 k_m k_s k_a (1 + k_r) \sqrt{f'_c}\, bd \quad \leq 0.2 k_s \sqrt{f'_c}\, bd \qquad \text{(3)}$$

Where $k_m = \left(\frac{V_F d}{M_F} \right)^{2/3} \qquad k_r = (\rho_f E_f)^{1/3}$

$k_a = 1.0$ for $\frac{M_F}{V_F d} \geq 2.5$,

$= \frac{2.5}{(M_F / V_F d)} \leq 2.5$ for $\frac{M_F}{V_F d} < 2.5$

And $k_s = 1.0$ for $d \le 300\ mm$,

$= \dfrac{750}{450 + d}$ for $d > 300\ mm$

The American Concrete Institute (ACI) guide for the design and construction of concrete members reinforced with FRP bars (ACI 440) proposed an equation on its earlier version (2001 and 2003) to calculate the concrete shear strength as follows:

$$V_{cf} = \frac{\rho_f E_f}{90\beta_1 f_c'} V_c \qquad \le V_c \tag{4}$$

Where V_c is the shear strength calculated according to ACI 318 code for steel reinforced concrete. It can be noticed that for this equation the concrete shear strength is surprisingly inversely proportional to the square root of the concrete compressive strength ($\sqrt{f_c'}$), as V_c is directly proportional to $\sqrt{f_c'}$.

The Japanese Society of Civil Engineers (JSCE) recommendations for design and construction of concrete structures using FRP adopted two different shear design methods for members reinforced longitudinally and transversely with FRP bars.

Method 1: In this method the shear strength of members longitudinally reinforced with FRP bars and without shear reinforcement (V_{cf}) is given by:

$$V_{cf} = \beta_d \beta_p \beta_n f_{vcd} bd / \gamma_b \tag{4}$$

$$f_{vcd} = 0.2(f'_{cd})^{1/3}$$

$$\beta_d = (1000/d)^{1/4} \qquad \le 1.5$$

$$\beta_p = (100\,\rho_f E_f / E_s)^{1/3} \qquad \le 1.5$$

$$\beta_n = 1 + M_o / M_d \qquad for \quad N_d \ge 0$$

$$\beta_n = 1 + 2M_o / M_d \qquad for \quad N_d < 0$$

β_n should be within the limits: $1 \le \beta_n \le 2.0$

where: γ_b is the member safety factor = 1.3

Method 2: In this method, the shear strength of members longitudinally reinforced with FRP bars and without shear reinforcement (V_{cf}) is given by:

$$V_{cf} = \beta_{pEo} \beta_d (f'_{cd})^{1/3} (h - x) b / \gamma_b \tag{7}$$

Where: $\beta_d = (1000/d)^{1/4} \qquad \le \ 1.5$

$$\beta_{pEo} = 0.17\left(\frac{\rho_f E_f}{5000} + 0.66\right) \qquad \le \ 0.28$$

In Japanese Building Research Institute BRI recommendations for design of concrete structures using FRP, the concrete contribution to shear strength (V_{cf}) is given by (as quoted from Sonobe *et al. 1997)*:

$$V_{cf} = 0.08\left[\frac{k_u k'_p (f'_c + 18)}{M/Vd + 0.12}\right] bd \qquad (8)$$

Where: k_u is a correction coefficient = 0.72 for $d \geq 400$ mm
= 1.0 otherwise
k'_p is an equivalent correction coefficient = $0.82\ (100\ \rho_f E_f / E_s)^{0.23}$

EXPERIMENTAL PROGRAM

It was noticed that the available experimental testing data included in the collected database does not include beams with small reinforcement ratio. Among the 60 specimens included in the database, only 2 specimens had reinforcement ratio (ρ_f) less than the balanced reinforcement ratio (ρ_{fbal}). Therefore an experimental test program is conducted to cover this gap .The test program consists of seven beams reinforced with CFRP bars as longitudinal reinforcement, but without stirrups. The specimens were designed to evaluate the shear strength of these concrete beams. The dimensions, details of the test specimens and loading pattern are shown in Figure 1. As shown in the figure, no transverse reinforcement was used within the span of the beams, but only at the overhanging ends in order to improve anchorage.

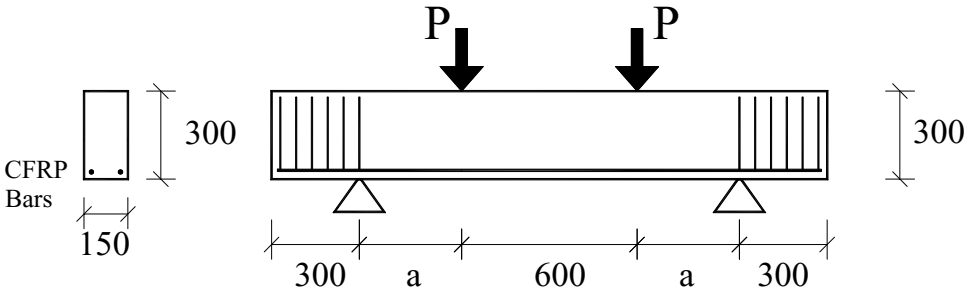


Figure 1. Test specimen details and dimensions.

The tested parameters included in this study were the longitudinal reinforcement ratio, the shear span to depth ratio and the concrete compressive strength. Table 1 presents the dimensions, reinforcement and the considered parameters of each specimen. All the tested beams were simply supported having a rectangular concrete cross section (150×300 mm), an effective depth 280mm, and different spans to match the required shear span to depth ratio (a/d). The beams were designed to have a shear failure prior to flexure failure. CFRP bars of diameter 7.5 mm were used as longitudinal reinforcement for all the tested beams. The modulus of elasticity (Ef) of the used bars was experimentally evaluated to be 148 GPa, while its ultimate strength (ffu) was reported by the manufacturer to be 2840 MPa. In order to investigate the effect of concrete strength, 2 values of fc' were targeted 24 and 48 MPa. The exact concrete strength were determined for each specimen was determined by testing concrete cylinders at the same day of beam testing as shown in Table 1.

Table 1. Dimensions and reinforcement of the tested specimens.

Specimen	*Reinforcement*		f_c' *	*Shear span (a)*	*a/d*
	No. of Bars	(ρ_f) %	*(MPa)*	*(mm)*	
A-I-2.5	1	0.105	24	700	2.5
A-II-1.25	1	0.105	48	350	1.25
A-II-2.5	1	0.105	45	700	2.5
A-II-5.0	1	0.105	49	1400	5.0
B-I-2.5	2	0.210	28	700	2.5
B-II-1.25	2	0.210	54	350	1.25
B-II-2.5	2	0.210	46	700	2.5

* The shown values are the average of the concrete strength for the concrete cylinders tested for each specimen.

Test Setup and Measurements

All the beams were tested up to failure using two concentrated loads 0.6 m apart. The deflection of each tested beam was measured using 3 dial gages one at the mid-span, and one at middle of each shear span. The strains in the longitudinal FRP bars and at the upper surface of the concrete beams were measured at the mid-span using electrical strain gauges. Figure 2 shows the loading setup of the specimens. The load was applied incrementally using hydraulic jack of maximum capacity of 300 kN and was monitored using an electrical load cell. At every load increment the initiation and propagation of cracks were marked; the deflection, concrete strain, reinforcement strain and crack widths were also measured and recorded.

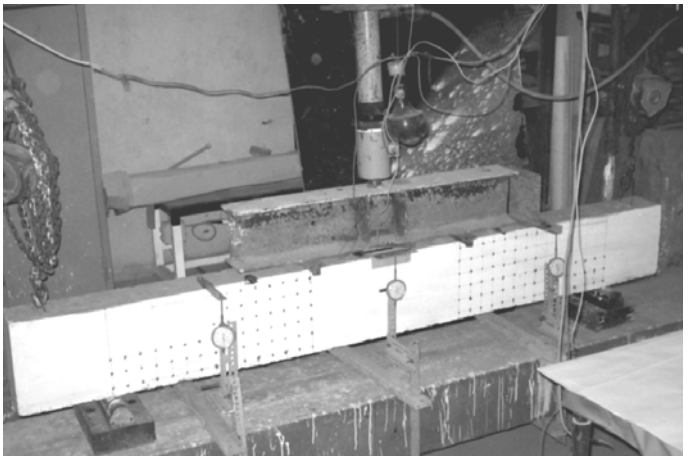


Figure 2. Test setup for the specimens

TEST RESULTS AND ANALYSIS

Table 2 shows the failure loads, and modes of failure for the tested beams in addition to the ratio between the predicted shear strength using BRI equation (Eq.8) and the experimental failure load. For all the tested beams, vertical flexural cracks

were observed in the region of the constant moment at the early stages of loading. With further increase in load, the flexural cracks propagated vertically upwards, and additional cracks were formed in the shear span. All the tested beams failed in shear except specimens A-II-1.25 and B-II-1.25 which have the smallest shear span to depth ratio. Also beam B-I-2.5 unexpectedly failed in flexure. In absence of stirrups, the shear failure of the beams was sudden and no slip of flexural reinforcement was observed during beam testing. Figure 3 shows the failure pattern of the 7 tested beams.

Table 2. Failure loads and cracking loads of the tested specimens.

Specimen	Calculation			Experimental		*Failure Mode*
	$*P_f$ kN	$**P_V$ kN	P_f / P_V	$P_{cracking}$ kN	P_{ult} kN	
A-II-1.25	96.53	64.30	1.50	20.00	92.50	Flexural
A-II-2.5	48.14	32.09	1.50	10.00	22.50	Shear
A-II-5.0	24.15	17.46	1.38	5.00	12.50	Shear
B-II-1.25	157.14	83.41	1.88	17.50	102.50	Flexural
B-II-2.5	74.71	38.77	1.93	8.75	27.50	Shear
A-I-2.5	41.18	21.39	1.93	10.00	22.50	Shear
B-I-2.5	60.18	27.87	2.16	7.50	51.25	Flexural

* The calculated flexural moment capacity.

** The shear strength is calculated using BRI equation (Eq. 8).

Figure 4 shows the relationship between the mid-span and mid-shear span deflections and the load (P) for beam A-II-2.5 which is typical for other beams. On the other hand, Figure 5 shows the relationship between the load (P) and the strain in FRP reinforcement and concrete for specimen B-II-2.5.

Comparison of Design Equations

The values of the concrete shear strength (V_{cf}) were calculated for the 60 specimens included in the database and for the tested beam specimens using the previously mentioned equations (equations 1 to 8). The ratio between the experimental results and the calculated values ($V_{exp.}/V_{calcu.}$) was determined for each specimen using the eight equations. For each equation, the maximum and the minimum values of the ratio ($V_{exp.}/V_{calcu.}$), the mean value of this ratio and its standard deviation are presented in Table 3.

As shown in Table 1, it can be noticed from the mean values of the ratio ($V_{exp.}/V_{calcu.}$), that the available equations used to predict the concrete shear strength generally underestimate this value with different ratios starting from 95% up to 25% of the experimental value. The most underestimating equation is the ACI equation as shown in. The equation is believed to be very conservative and not economic for design purpose. On the other hand, according to Table 3, the values predicted using Razaqpur equation (equation 4) and BRI equation (equation 8) have the best

agreement with the experimental results for the concrete shear strength. However, the BRI equation appears to be simpler and safer than Razaqpur equation. For BRI equation (equation 9), only 17 beams have V_{exp}/V_{calc} less than 1.0 compared to 31 beams for Razaqpur equation (equation 4).

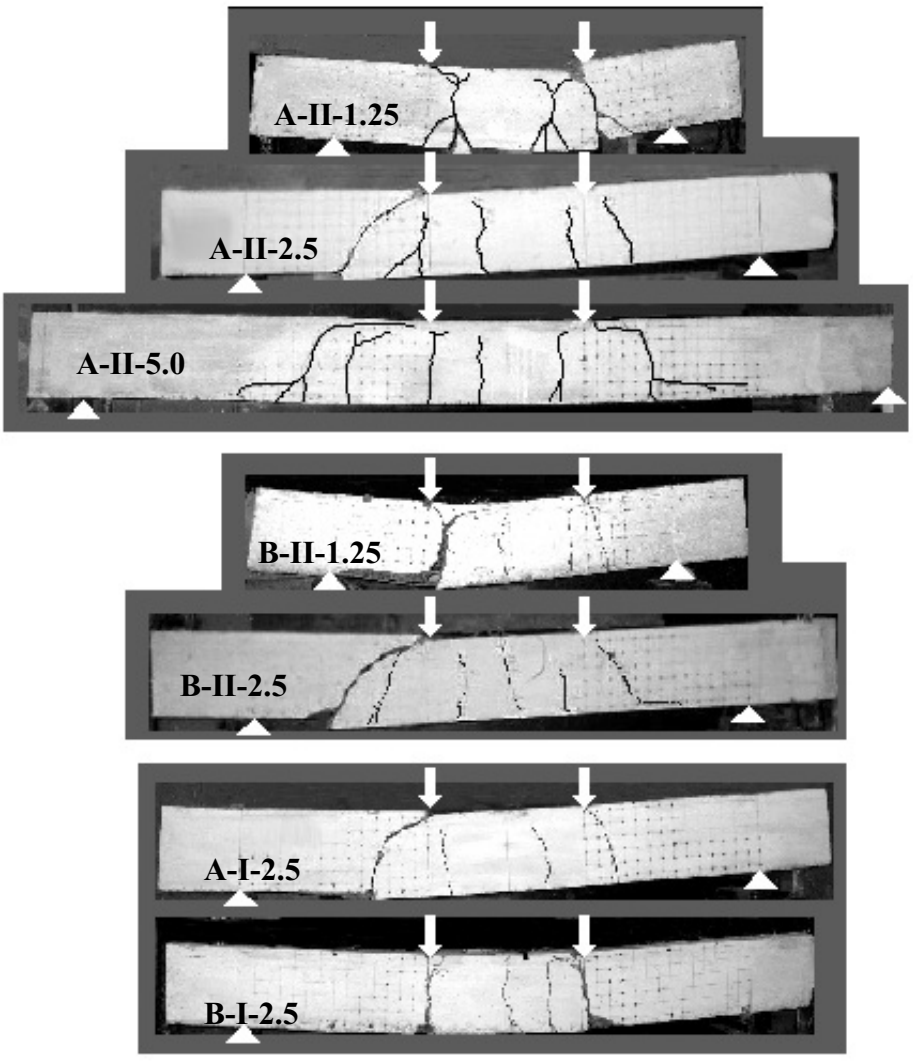


Figure 3. Cracking pattern of the tested beam specimens.

Table 3. Experimental to calculated shear strength.

	Eq.(1) $\frac{V_{exp.}}{V_{Tottori}}$	*Eq.(2)* $\frac{V_{exp.}}{V_{Zhao}}$	*Eq.(3)* $\frac{V_{exp.}}{V_{Tureyen}}$	*Eq.(4)* $\frac{V_{exp.}}{V_{Razaqpur}}$	*Eq.(5)* $\frac{V_{exp.}}{V_{ACI}}$	*Eq.(6)* $\frac{V_{exp.}}{V_{JSCE(1)}}$	*Eq.(7)* $\frac{V_{exp.}}{V_{JSCE(2)}}$	*Eq.(8)* $\frac{V_{exp.}}{V_{BRI}}$
Min.	1.48	0.43	0.79	0.74	1.19	0.51	0.44	0.69
Max.	10.28	2.75	4.95	1.94	12.83	3.80	3.53	2.30
Mean	3.71	1.25	1.97	1.06	4.29	1.52	1.69	1.15
S.D.	1.434	0.388	0.711	0.250	2.255	0.556	0.598	0.270

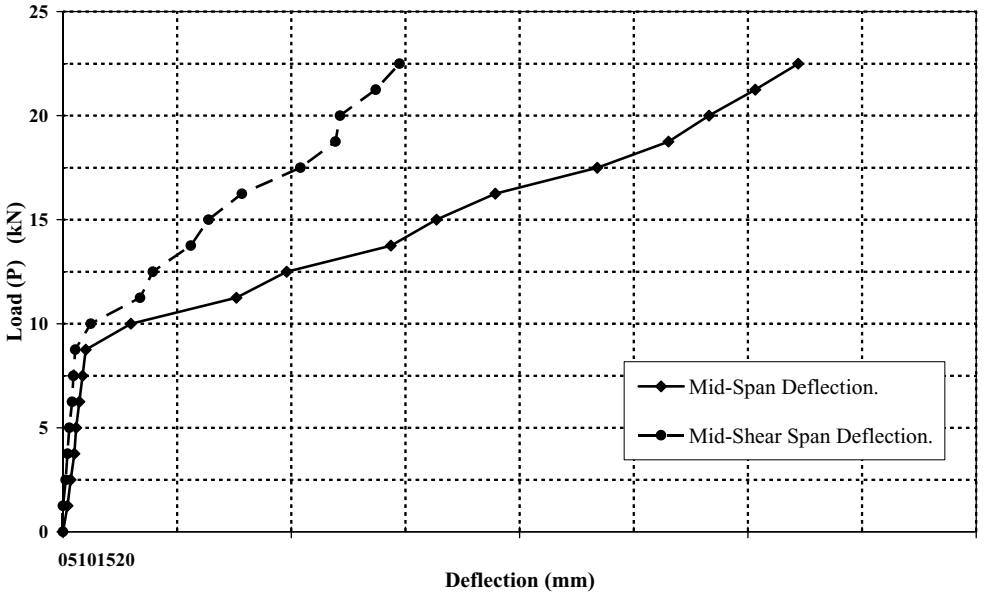


Figure 4. Applied loads versus measured deflections for specimen A-II-2.5.

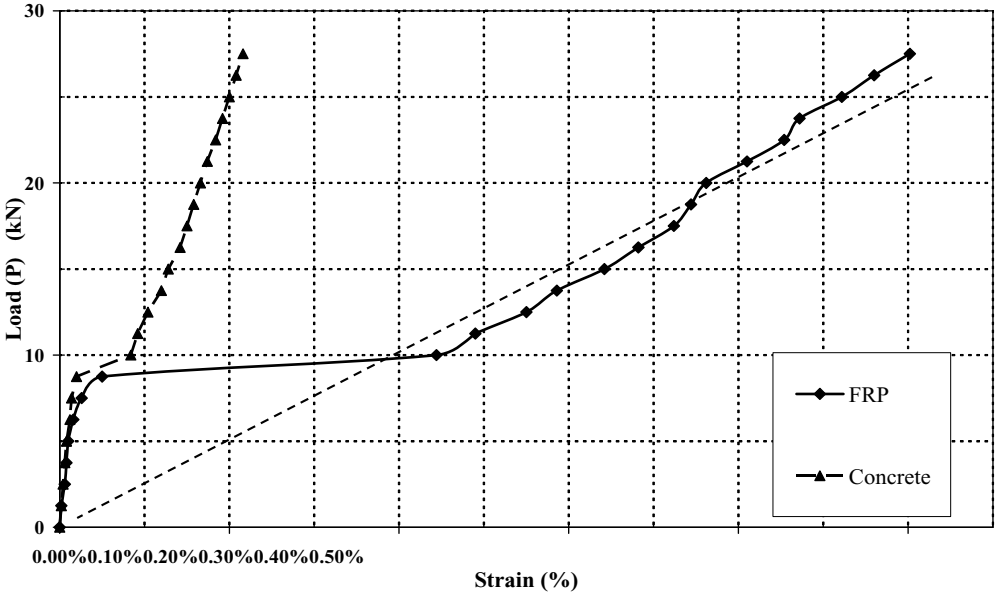


Figure 5. Measured strains in FRP and concrete for specimen B-II-2.5.

CONCLUSIONS

From the available experimental data and the results of the conducted experimental program, the following conclusions can be drawn:

1. The ACI equation for predicting concrete shear strength of members reinforced with FRP longitudinal reinforcement is very conservative.

2. The shear strength of concrete beams reinforced with FRP longitudinal bars is greatly affected by the ratio of $\rho_f / \rho_{f\,bal}$ in addition to concrete strength and the shear span to depth ratio.

3. The Japanese Building Research Institute BRI equation matches well with the available experimental data.

REFERENCES

ACI Committee 318 (2002), "Building Code Requirements for Reinforced Concrete (ACI 318-02) and commentary (ACI 318R-02)," American Concrete Institute, Farmington Hills, MI, 443 p.

ACI Committee 440 (2001), "Guide for the Design and Construction of Concrete Reinforced with FRP Bars (ACI 440.1R-01)," American Concrete Institute, Farmington Hills, MI, 41 p.

ACI Committee 440 (2006), "Guide for the Design and Construction of Concrete Reinforced with FRP Bars (ACI 440.1R-06)," American Concrete Institute, Farmington Hills, MI, 44 p.

Alkhardaji T., Wideman M., Belarbi A. and Nanni A. (2001), "Shear Strength of RC Beams and Slabs," *Composites in Construction*, J. Figueiras, L. Juvandes and R. Faria, eds., A. A. Balkema Publishers, Lisse, Netherlands, pp. 409-414.

Duranovic N., Pilakoutas K. and Waldorn P. (1997), "Tests on Concrete Beams Reinforced with Glass Fibre Reinforced Plastic Bars," Proceeding of the Third International Symposium on Non-Metallic (FRP) Reinforcement for Concrete Structures, Vol. 2, Sapporo, Japan, pp. 479-486.

El-Sayed A.K., El-Salakawy E.F. and Benmokrane B. (2006), "Shear Strength of FRP-Reinforced Concrete Beams without Transverse Reinforcement," *ACI Structural Journal,* Vol. 103, No. 2, pp. 235-243.

Gross S.P., Dinehart D.W., Yost J.R. and Theisz P.M. (2004), "Experimental Tests of High Strength Concrete Beams Reinforced with CFRP Bars," Proceedings of the Fourth International conference on Advanced Composite Materials for Bridge and Structures (ACMBS-IV), Calgary, Alberta, Canada, p.8.

Japanese Society of Civil Engineers JSCE (1997), "Recommendation for Design and Construction of Concrete Structures using Continuous Fiber Reinforcing Materials," Concrete Engineering series 3, Edited by A. Machida, 164 p.

Michaluk R., Rizkalla S.,Tadros G. and Benmokrane B. (1998), "Flexural Behavior of One-Way Concrete Slabs Reinforced by Fiber Reinforced Plastic Reinforcement," *ACI Structural Journal,* Vol. 95, No. 3, pp. 353-365.

Nagasaka T., Fukuyama H. and Tanigaki M. (1993), "Shear Performance of Concrete Beams Reinforced with FRP Stirrups," American Concrete Institute, ACI SP-138, edited by A. Nanni and C.W. Dolan, pp. 789-811.

Razaqpur A.G., Isgor O.B., Greenaway S. and Selley A. (2004), "Concrete Contribution to the Shear Resistance of Fiber Reinforced Polymer Reinforced Concrete Members," *Journal of Composites for Construction*, ASCE, Vol. 8, No. 6, pp. 452-460.

Razaqpur A.G. and Isgor O.B. (2006), "Proposed Shear Design Method for FRP-Reinforced Concrete Members without Stirrups," *ACI Structural Journal,* Vol. 103, No. 4, pp. 93-102.

Sonobe Y., Fukuyama H., Okamoto T., Kani N., Kimura K., Kobayashi K., Masuda Y., Matsuzaki Y., Mochizuki S., Nagasaka T., Shimizu A., Tanano H., Tanigaki M. and Teshigawara M. (1997), "Design Guidelines of FRP Reinforced Concrete Building Structures," *Journal of Composites for Construction*, ASCE, Vol. 1, No. 3, pp. 90-115.

Tariq M. and Newhook J.P. (2003), "Shear Testing of FRP Reinforced Concrete without Transverse Reinforcement," *Proceeding of CSCE 2003-Annual Conference*, Moncton, NB, Canada.

Tottori S., and Wakui H. (1993), "Shear Capacity of RC and PC Beams Using FRP Reinforcement," American Concrete Institute, ACI SP-138, edited by A. Nanni and C.W. Dolan, pp. 615-631

Tureyen K. and Frosch R.J. (2002), "Shear Tests of FRP-Reinforced Concrete Beams without Stirrups," *ACI Structural Journal,* Vol. 99, No. 4, pp. 427-434.

Vijay P.V., Kumar S.V. and GangaRao H.V.S (1996), "Shear and Ductility Behavior of Concrete Beams Reinforced with GFRP Bars," Proceedings of the Second International conference on Advanced Composite Materials for Bridge and Structures (ACMBS-II), Montreal, Québec, pp. 217-226.

Yost J.R., Gross S.P. and Dinehart D.W. (2001), "Shear Strength of Normal Strength Concrete Beams Reinforced with Deformed GFRP Bars," *Journal of Composites for Construction*, ASCE, Vol. 5, No. 4, pp. 263-275.

Zhao w., Maruyama K. and Suzuki H. (1995), "Shear Behavior of Concrete Beams Reinforced by FRP Rods as Longitudinal and Shear Reinforcement," Non-Metallic (FRP) Reinforcement for Concrete Structures, Proceeding of the Second International RILEM Symposium (FRPRCS-2), Edited by L. Taerwe, E & FN SPON, UK, pp. 352-359.

When the Roof Collapses

William T. Bolduc, P.E., S.E., M. ASCE[1]

[1]Keymark Enterprises, LLC, Engineering/Software Development, 6707 Winchester Circle, Boulder, CO 80301; PH (702) 481-0742; FAX (303) 443-9054; email: bbolduc7@gmail.com

ABSTRACT

An overview of the many recent cases of roof collapse and the collapse of other portions of buildings in the United States and Canada is given. This paper discusses many of the recent cases of collapses of buildings or portions of buildings that usually get only local news coverage. In most cases roofs collapse under heavy snow loads, although some also fail under wind or rain loads. Many example cases are given based on information collected from local news coverage and other sources. In most cases, the collapse occurs in ordinary buildings and there are few, if any, serious injuries. In many cases the building gives the occupants some warning of collapse and people escape. One exception to the lack of injuries occurs when a wood deck fails. When a wood deck fails, the deck is usually loaded with people. Surprising, the frequency of collapse may be higher in schools and firehouses. Collapse of a portion of a school or a firehouse is upsetting to the public, even when there are no injuries.

INTRODUCTION

Structural collapse or other significant structural problems rarely occur. Many engineers, architects, and building designers are only exposed to a small number of structural failures during their career. Young engineers and students usually have not experienced any collapses or other failures. They usually have been exposed to information about only a few major structural collapses such as:

- the 1st Tacoma Narrows Bridge (Galloping Gertie) in 1940 as described by Robison
- the walkways at the Hyatt Regency Hotel in Kansas City in 1981 as discussed by Petroski
- the I-35 bridge collapse in Minneapolis as reported by National Transportation Safety Board

Although there is much to learn from these major failures, a better awareness of the more common structural failures adds perspective and importance to the common design, construction, inspection, and maintenance tasks.

SCOPE OF STUDY

The most common type of structural collapse is the collapse of a roof of a building. Although the paper title is: "When the Roof Collapses", the paper includes structural failures of floors, walls, and other structures. Some limits to the scope of the investigation are:

1. Only failures in the United States or Canada were considered. The construction standards, practices, and the building inventory in the United States and Canada are similar. The inclusion of Canada adds to the data of roof collapses due to heavy snow loads.
2. Failures due to severe events that buildings are not expected to resist without damage were excluded. This is to avoid a skew in the data by rare events that buildings are not designed to resist. Damage due to tornados, major hurricanes, major earthquakes, and floods were excluded. No major hurricanes or earthquake occurred during the period studied. Damage due to severe wind storms and heavy snow is included, because almost all buildings are expected to be designed for wind and snow loads (when applicable).
3. Failures due to fire were excluded. In some cases a structural collapse initiates a fire by breaking a gas line or by other means. When it is identified that a structural collapse caused the fire, the case is included.

Collapses that occur during construction were included. Other construction accidents not related to a structural collapse were excluded from this study. Since construction collapses usually occur before all structural elements are completely installed, they are not always considered to be structural failures. These cases are marked with the building age being set to "construction" (const.), so that they can be easily removed when needed in any statistics.

Buildings are not expected to last forever. If they are well maintained they can last for many decades. Structural failures where the age of the building appears to be a significant factor are marked as "old" or "historic". This is a judgment by the author and is usually not based on the knowledge of the actual building age or how well the building was maintained.

SOURCES OF INFORMATION

In most cases the source of information for the listed structural failures is local news media. The main research method used is to perform internet searches of news sites

using keywords related to structural collapse. Often multiple news sites are found for the same structural failure. Nearly all available sources are reviewed. In many cases these sources are no longer available a few weeks after initially posted on the internet. To deal with this problem, searches are performed once or twice a week. Relevant data is copied to local computer files for later review and analysis. Due to the large number of sources, references for all sources are not provided.

When forensic investigation reports are available, they are gathered and reviewed. In most cases, forensic investigation reports are not available to "outside parties". In many cases no professional forensic investigation occurs.

Since the source is most commonly news sites, important details needed to determine the cause of the failure are usually missing. In spite of the lack of detailed information, some summary knowledge is gained by the broad review of a large number of failures. Common problems can be identified. In some cases trends or patterns can be observed.

Some of the best insight into the scope, type, and likely cause of the collapse comes from the review of pictures (and sometimes, video) taken by others at the scene of the collapse. Only a few of the hundreds of pictures could be included in this paper.

One benefit of using open public sources is that the author (and the reader) is completely free to provide commentary without any obligation to the involved parties.

HOW MANY STRUCTURAL FAILURES OCCUR PER YEAR?

How many structural failures occur per year? I was once asked this question by my employer. After some efforts I found no reliable sources to help answer this question. Now, many years later, this paper provides a count of failures in the United States and Canada for the 2010 calendar year. Of course, one can only count what you know. Some failures have likely occurred that did not get any press or media coverage or were missed in the attempt to search for them. Thus, the count provided is a lower bound for a reasonable estimate of the actual number of failures. It seems likely that the actual number of failures is 10 to 50 percent higher than the number that is counted here.

STRUCTURAL FAILURES BEFORE THE 2010 YEAR

The process of recording structural failures started before 2010 began. The search process was inconsistent at first. This allowed the search technique to be perfected. Beginning in December 2009 an attempt was made to capture all available data for the winter snowfall period. It was later extended to capture all available data for the

year of 2010. Table 1 contains the results from this pre 2010 period with a infamous historical structural failure added for perspective.

Table 1. Incomplete record of structural failures before 2010

#	Name	Date	State or Prov.	City or Local	Enviro-ment Type	Bldg Age	Bldg Type	Description	# in-jured	# Dead
1	Boston MA-July 1920-Dance floor collapse-50 dead-Pickwick Club-Boston MA	Jul-20	MA	Boston			Dance Club			50
2	Portable dance floor collapses into swimming pool	Nov-01	NJ	Rochelle Park			portable dance floor			
3	Deck Collapse-Injures Scores-at Casino-Missoullan MT-	Jul-04	MT	Missoullan			deck of small casino		40	
4	Wind storm damages trusses at church construction	Jul-04	TN	Hamilton County	wind	Const.	Church			
5	Verdict-const collapse 1 dead-Truss manufacturer wins trial	Feb-06	MO	New Madrid County		Const.	House	Court Verdict absolves truss manufacturer		1
6	I-35W Bridge Collapse-Minn. MN	Aug-07	MN	Minneaopolis			bridge	major collapse	145	13
7	Jones Auditorium-Muskegon	Jan-08	MI	Muskegon			auditorium			
8	Oklahoma and the Texas Panhandle	Mar-08	OK	panhandle area			multi-bldgs mostly ag			
9	Morin Heights-Bakery Quebec-	Mar-08	Que.	Morin Heights	snow		industrial bakery	wood trusses		2
10	floor collapse at B.C. church concert	Apr-08	BC	Abbots-ford	dancing		church	dancing in-sync		
11	Wall Collapse-Old Bldg-Detroit MI	Apr-08	MI	Detroit		old				
12	Clemens House Chapel	May-08	MO	St. Louis			church			
13	Structural Examination of Woodland WA Airport	May-08	WA	Woodland			hangers	report deemed buildings inadequate and in need of repair or removal		
14	Wall Collapse-1 dead-Manslaughter chage	Jun-08	NY	New York					1	
15	Old Bldg Collapse-Milwaukee WI	Jun-08	WI	Mil-waukee		old				
16	Anaheim-collapseDueToRain	Dec-08	CA	Anaheim	rain		school-retail - Adult Ed.			
17	Gateway Fred Meyer Store	Dec-08	OR	Portland	snow & rain		retail			
18	HighSchoolRoof-OlympiaWA-CauseRoofTrusses-	Dec-08	WA	Olympia	snow		school	roof trusses		

#	Name	Date	State or Prov.	City or Local	Enviro-ment Type	Bldg Age	Bldg Type	Description	# in-jured	# Dead
19	Tampa Int Airport parking garage canopy	Jan-09	FL	Tampa			Public parking garage canapy at Airport			
20	BldgCollapsesContinue	Jan-09	ID	Coeur dAlene						
21	Renter Collect after roof cave-in-Vanvouver BC	Feb-09	BC	Vancouver						
22	BarnCollapse-StLazare	Feb-09	Que.	St. Lazare	snow		barn			
23	Roofs in ruins Kansas	Mar-09	KS	Hutchin-son	snow		Manufac-turing and farm	multiple roofs in south-central and southwestern		
24	Deck collapse and $1 million settlement	May-09	IL	Cary			house deck			
25	Dallas Cowboys Practice Facility	Jun-09	TX	Dallas	wind					
26	1 dead-4 injured-Construction wood truss collapse	Sep-09	GA	Milledge-ville		const.			4	1
27	CMU wall construction collapse kills 14 year old	Oct-09	Ont.	Guelph						1
28	StripStores-Council Bluffs IA	Dec-09	IA	Council Bluffs	snow		retail	strip store complete lose		
29	Store in Des Moines Iowa	Dec-09	IA	Des Moines	snow					
30	School Garage Roof to Collapse-BusGarage	Dec-09	MN	Albany	snow		School bus garage	Wood trusses may have collapse due to missing bracing. See pics and truss design		
31	Wall Collapse-North Dakota State Univ	Dec-09	ND	Fargo						
32	Cattle Feeder Shed - near Omaha	Dec-09	NE	near Omaha			barn			
33	Snow Causes Multiple Roof Collapses	Dec-09	NE	Omaha	snow		commer-cial	multiple roofs		
34	Scaffolding collapse-3 dead	Dec-09	Ont	Toronto		const.				3
35	Ft Lewis Elementary-SalemVA	Dec-09	VA	Salem	snow		school			

STRUCTURAL FAILURES FOR THE 2010 CALENDER YEAR

The process of searching for structural failures continued during the 2010 calendar year. It was expected that rate of failures would drop to a very low rate once the snow stopped falling. Although some decline occurred, a significant rate continued throughout the year. Table 2 shows summary results for 2010.

Table 2 shows that some types of failure occur more frequently and with effects that vary widely. Snow loads on roofs cause the greatest number of building failures, but

relatively few injuries and deaths. It appears that many roof collapses give the occupants warning and allow for escape. Even when an occupant is trapped under the roof, they are often not seriously injured.

Deck, porch, and balcony failures occur less often, but cause far more injuries. Luckily the injuries for deck porch, and balcony failures are usually not life threatening. This high rate of injury for deck, porch, and balcony failure is due to the fact that the weight of people is the major load, so the collapse usually occurs when the deck, porch, or balcony is full of people.

Failures due to rain loads rarely result in injuries. This is because the failure is usually not a complete roof collapse. When a roof failure occurs due to rain loads, it is likely due to poor drainage. Water accumulates on the roof. When the failure begins to occur a hole in the roof membrane develops, and the water on the roof rushes into the building. This unloads the roof structure and stops the collapse from progressing. Thus we get lots of water damage, but almost no injuries.

Collapses during building construction or renovation almost always cause people to fall or construction materials to fall onto people. Thus, construction collapses often have serious injuries and sometimes deaths.

Table 2. Summary results of structural failures for 2010

	# injured	# Dead	# bldg
Snow load on roofs	6	3	146
deck, porch, & balcony	133	1	38
rain load cases	0	0	27
wind load cases	1	2	16
collapse during construction	16	7	21
collapse with only dead load	25	7	94
floor collapse	29	0	6
other	4	0	2
Totals for 2010	214	20	350

Collapses that occur with only dead loads are a mixture of different types. Some occur in older buildings, often with masonry walls. Old buildings that are vacant seem to result in a disproportional number of cases. Lack of proper maintenance can lead to corrosion, decay, or other structural damage.

Some collapses with only dead load are ceiling collapses. These ceiling collapses sometime cause injury. Since there is no design live load for a suspended or other type of ceiling, a ceiling is always holding its full dead load. A construction defect or damage from water leakage will eventually cause a ceiling to collapse.

The third type of collapse with only dead load is a roof collapse with no roof live (snow or wind) load. It is surprising when a building suddenly collapses or sags for no apparent reason. This occurred several times in 2010.

Table 3 contains some selected records from the full list of structural failures recorded in the year 2010. A review of these records can provide a sense for the type of failures that occurred.

Table 3. Selected records of structural failures for 2010

#	Name	Date	State or Prov.	City or Local	Enviro-ment Type	Bldg Age	Bldg Type	Description	# in-jured	# Dead
1	Bookmans And Joann Fabrics	Jan-10	AZ	Flagstaff	snow		retail			
3	Gym Collapse-AZ	Jan-10	AZ	Navajo County	snow		school	steel bar joists		
4	FireStation-Pinetop AZ-	Jan-10	AZ	Pinetop	snow		fire station			
5	Overhang Collapse Traps Teen-BigBear CA	Jan-10	CA	Big Bear	snow		house	porch roof		
7	Rain Causes Roof Collapse In Orange County CA	Jan-10	CA	Orange County	rain		medical offices	partial collapse		
8	Ballroom-Iron Horse Inn	Jan-10	CO	Durango	snow		Ballroo m of hotel			
13	Dietrich Bus Garage	Jan-10	ND	Valley City	snow		Bus Garage	containing school busses		
14	Cover-All Bldg-dairy complex	Jan-10	PA	Crawford County	snow	less than 2 years	barn	fabric covered bldg, one of at least a half dozen of that type to fail in the last eight years.		
16	Fire Station Roof UT	Jan-10	UT	Henrieville	snow		fire station	wood trusses likely a bracing issue		
20	Wash DC-PorchRoofs	Feb-10	DC	Washington	snow		porch of house			
21	Church collapses in NE Wash DC	Feb-10	DC	Washington DC	snow & tree		church			
22	Roof Collapse at Dulles Jet Center	Feb-10	DC	Washington DC	snow		retail Jet Center at airport	several private jets damaged		
25	West Seaford Elementary School collapsed-Delaware	Feb-10	DE	Seaford	snow		school	the collapse occurred at around 4 a.m. in the cafeteria area of the school		
27	Roof collapse starts Fire-Altoona Iowa	Feb-10	IA	Altoona	snow		flat roof at amusem ent park	fire started when high energy wires were pulled out of breaker panel when roof fell		
35	Mom, Daughter Injured In Carport Collapse	Feb-10	MD	Baltimore	snow		carport		2	

#	Name	Date	State or Prov.	City or Local	Enviro-ment Type	Bldg Age	Bldg Type	Description	# in-jured	# Dead
38	Fire station collapses and burns	Feb-10	MD	Dundalk	snow		fire station	roof collapsed & oxygen tanks in ambulances exploded-two paramedic units and two fire engines destroyed		
41	Goats survive MD farm bldg collapse	Feb-10	MD	Indian Springs	snow		barn			
46	Roof collapse-Smithsonian Museum Support Center	Feb-10	MD	Suitland	snow		warehou se			
46	Roof collapse-Smithsonian Museum Support Center	Feb-10	MD	Suitland	snow		warehou se			
47	Firestation-Sykesville MD	Feb-10	MD	Sykesville	snow		fire station	social hall roof collapsed and debris severed a gas line cause fire		
51	Roof of Perkins Lumber-MN	Feb-10	MN	Willmar	snow					
52	Construction Collapse-1 dead 2 injured	Feb-10	NC	Clinton		const.			2	1
53	Private Hanger collapse-Jefferson NC	Feb-10	NC	Jefferson	snow		private hanger	2 airplanes were inside the hangar. One is a total loss and the other is being evaluated		
55	Sysco warehouse in Fargo ND	Feb-10	ND	Fargo	snow		warehou se	100-by-100 foot section of roof collapsed-second roof collapse		
56	Woman Rescued After Awning Collapses-Kittering MD	Feb-10	ND	Kittering	snow		awning	workers free woman who was trapped under awning that collapsed from snow	1	
58	Riverside NJ-man killed in snow collapse	Feb-10	NJ	Riverside	snow		home	roof above the porch collapsed while he was clearing the stairs leading to an upstairs apartment		1
64	Rostraver PA-Ice Rink	Feb-10	PA	30 miles southeast of Pittsburgh	snow			glu-lam arches 100-by-200-foot section of the roof fell		
65	Firestation-Amwell Township PA	Feb-10	PA	Amwell Township	snow		fire station	$1 million of equipment moved from fire department after its roof started to sag		
69	School Bus Garage-Farmington PA	Feb-10	PA	Farmington	snow		School Bus Garage	roof collapsed on 8 school buses in garage-wood trusses		
81	Firestation Washington County PA	Feb-10	PA	Washington County	snow		fire station	snow collapsed part of the roof - fire trucks were temporarily stuck in the building		
89	Blacksburg VA-High school Gym	Feb-10	VA	Blacksburg	snow	30 yr	school	Major collapse of steel trusses. Investigation reports available.		

#	Name	Date	State or Prov.	City or Local	Enviro-ment Type	Bldg Age	Bldg Type	Description	# in-jured	# Dead
91	Firehouse Roof-Falls Church VA	Feb-10	VA	Church	snow		fire station	fire engine, fire truck & medic units inside damaged		
92	Prince William Ice rink collapse VA	Feb-10	VA	Dale City	snow		ice arena	building total loss-Skaters practicing inside evacuated just before collapse		
93	1 dead-Fredericksburg	Feb-10	VA	Fredericks-burg	snow		utility shed	collapse took the life of 76-year-old contractor		1
107	Deck Collapse-7 Injured-St Louis	Mar-10	MO	St Louis			deck	inspector had concerns about the deck months before collapse	7	
111	Stores-Partial Collapse-Harlem NY	Mar-10	NY	Harlem	snow		commerc ial bldg	partial brick wall collapse		
112	Arena Roof-Poteau OK	Mar-10	OK	Poteau	snow		Arena	steel structure destroyed		
119	Canopy at Car Dealership	Mar-10	WV	Beckley	snow		Canopy at Retail	collapsed and damaged a car		
120	Former Car Dealership-Rainelle WV	Mar-10	WV	Rainelle	snow	old 70 yrs	retail	abandoned bldg		
128	Historic Bldg Collapse-Lancaster PA	Apr-10	PA	Lancaster		old his-toric	vacant	5 people have minor injuries because part of building landed on a bus	5	
129	89 MPH Wind Damage	Apr-10	PA	Pittsburg	Wind (89 MPH)		church	high winds damaged the roof of a church & collapse of a wall		
132	Lubbock TX-Roof collapse due to rain	Apr-10	TX	Lubbock	rain	old	college bar "The Nest"	inadequate roof drainage, heavy rains & old age played roles in partial collapse		
137	Wind gust Cause roof collapse-Loveland CO	May-10	CO	Loveland	wind		house	strong winds trigger a roof to collapse at a west Loveland home		
149	Williamstown Theater Roof-Monroe NJ	May-10	NJ	Monroe			Theater	no one was in the building durring the collapse, but a family living in an apartment above had to escape	1	
151	Wind Damage-Henderson Pavillion NV	May-10	NV	Henderson	wind		pavillion	harsh winds ripped through the pavilion's tent, which is fixed over the seating area		
161	Roof Collapse -no loads-retail kids play house	Jun-10	IN	New Castle	no loads		Retail kids fun center	No Loads - Wood truss	1	
167	Building Collapse Kills 1-Kansas City MO-	Jun-10	MO	Kansas City		old	vacant	man on walk near bldg killed		1
177	Earthquake-partial collapse of home	Jun-10	Ont.	Ottawa	minor quake		house	part of fourth-floor roof had collapsed - No other buildings damaged		

#	Name	Date	State or Prov.	City or Local	Enviro-ment Type	Bldg Age	Bldg Type	Description	# in-jured	# Dead
179	Construction Collapse-Wood trusses TN	Jun-10	TN	Louisville		const.		wood trusses		
180	Deck collapse-Fairfax Co VA-	Jun-10	VA	Fairfax Co			deck	10 with minor injuries	10	
182	Parking garage partial collapse	Jun-10	WI	Milwaukee			Public parking garage	Concrete panel fell	3	1
183	Church Roof Collapses-wood trusses	Jul-10	AL	Madison Coounty	no loads		church	a group was playing basketball game in gym and the roof slowly fell down into two pieces. Wood trusses may have collapse due to missing bracing.		
184	1 dead-deck collapse	Jul-10	AL	Hoover			deck of apartment bldg	7 people on the deck when it fell... one died a second person is in critical condition at UAB	1	1
190	Deck collapse-6 injured-Hebron CT	Jul-10	CT	Hebron			deck at house	6 people, including 2-year-old, taken to hospitals with minor injuries after a deck collapsed	6	
192	Library Roof-Hobe Sound FL-Jul2010	Jul-10	FL	Hobe Sound			Public Library	Partial roof collapse - Report available		
195	Rain Partial Roof Collapse-Hobby Lobby-Cartersville GA	Jul-10	GA	Cartersville	rain		retail	partial collapse		
201	Roof collapse-St Paul MN	Jul-10	MN	St Paul			multi-family apartment bldg	collapse while roofing company was replacing shingles		
207	Deck Collapse Danger-OuterBanks NC	Jul-10	NC	OuterBanks			deck			
208	Parking garage collapse at apartment building	Jul-10	NJ	Hackensack			parking garage for large apartment building	18 floors evacuated in apartment bldg		
215	Parking Garage Collapse-Windsor Ont	Jul-10	Ont.	Windsor			concrete parking garage	the asphalt layer on the parking surface contributed to the structure's collapse-punching shear		
230	Church roof collapse	Aug-10	LA	Alexandria			church	appears to be failure of ceiling ties of wood rafter roof		
233	Riding Stable roof const collapse injures 3	Aug-10	MD	Clarksville		const.		wood trusses domino for full length of pole frame bldg	3	
285	Firehouse roof collapses-SantaClara UT	Sep-10	UT	Santa Clara	no loads		fire station	wood truss with only dead load (tile roof)		

#	Name	Date	State or Prov.	City or Local	Enviro-ment Type	Bldg Age	Bldg Type	Description	# in-jured	# Dead
313	Floor collapse while dancing at University party-Dayton OH-Nov2010	Nov-10	OH	Dayton	dancing		rental house	Floor collapse while dancing in-sync		
320	Family Dollar store collapses-4 hurt	Dec-10	IL	Chicago			retail	a portion of the roof collapsed- 4 people inside the Family Dollar store were taken to area hospitals	4	

BUILDING TYPES WITH HIGHER FREQUENCY OF COLLAPSE

Some building types appear to have a higher frequency of collapse. When considering the frequency, the number of collapses for a type of building needs to be compared with the total number of building of the same type. Numerical calculation of this type was not performed but the commonness of a building type was considered as part of the judgment.

Fabric covered building are not very common, but several collapses of this type were noticed. The collapses include both the structural frame support type and the air pressure supported type of fabric covered buildings.

Barns and other agricultural buildings had a large number of roof failures. This is not surprising because these building are commonly built to lower standards and have little review or inspection from building departments.

It is surprising that fire stations appear to have a higher frequency of roof failures. This is concerning since these facilities are needed during time of storms and other emergencies. The newer building codes require that fire stations be designed to higher standards than normal buildings. Most of the fire stations that collapsed in 2010 were likely built before these newer building codes were in effect.

Schools also had a high occurrence of roof failures. From the amount of media coverage of the problems at school buildings, there seems to be greater public concern when structural problems occur in schools compared to other buildings. Even school bus garages, which had a high frequency of collapses, caused public concern.

Houses had a low frequency of collapse when considering the very large number of houses in most communities. It may be useful to educate the public that most houses are safe, even in stormy weather.

In general structures with long clear spans had a higher frequency of collapse than smaller buildings or building with interior walls. This fact may be the major reason

that barns, fire stations, school gymnasiums, and school bus garages all have higher frequencies of collapse.

CONCLUSION

The number of structural failure in the United States has been documented for calendar year 2010. The number counted is 450. Since no count is perfect, the actual number is likely higher. The count is very low compared with the 100 million or higher buildings in the region.

REFERENCES

Robison, R. (1994). "Tacoma Narrows Bridge Collapse." In *When Technology Fails*, edited by Neil Schlager, pp. 18–190. Detroit: Gale Research.

Petroski, H. (1982). *To Engineer Is Human: The Role of Failure in Structural Design* Vintage, New York.

National Transportation Safety Board. 2008. *Collapse of I-35W Highway Bridge, Minneapolis, Minnesota, August 1, 2007*. Highway Accident Report NTSB/HAR-08/03. Washington, DC.

Characterization of High Strength Steel Fiber Reinforced Concrete and Self-Consolidating Concrete Mixtures with Various Steel Volume Fractions for Infrastructures

A. T. Berhe[1] and S. G. Ladkany[2]

[1]Department of Civil and Environmental Engineering, University of Nevada, Las Vegas, 4505 Maryland Parkway, P.O. Box 454015, Las Vegas, NV 89154-4015, USA; PH (702) 895-4135; Fax (702) 895-3936; email: berhea@unlv.nevada.edu,
[2]Department of Civil and Environmental Engineering, University of Nevada, Las Vegas, 4505 Maryland Parkway, P.O. Box 454015, Las Vegas, NV 89154-4015, USA; PH (702) 895-3438; Fax (702) 895-3936; email: samaan@ce.unlv.edu

ABSTRACT: The intent of the study is to incorporate discrete, short, mechanically deformed, small diameter steel fibers into high strength concrete ($f'_c > 69$ MPa) in an attempt to eliminate or reduce the need for steel rebar in concrete construction. This paper presents the rheological properties and behavior of high strength steel fiber reinforced (SFR) / self-consolidating (SFRSC) concrete mixture with different dosages of steel fibers, ranging from zero to 2% by volume in 1% increments. The effect of high range water reducing agent (HRWR) and viscosity modifying agent (VMA) on the fresh properties of SFRC/SCC are studied. Concrete mixtures include fly ash and silica fume. The fresh properties studied are: the flow-ability (spread diameter), the pass-ability (J-Ring and U-Box test) and fill-ability (V-Funnel test). The study shows that, the addition of steel fibers to the mixture results in the reduction of flow-ability, pass-ability, fill-ability and workability, which was mitigated through the adjustment of HRWR and VMA dosage.

1. INTRODUCTION:

The interest to minimize the use of longitudinal and transverse steel reinforcement in the construction of reinforced concrete structures and to reduce the structural weight has triggered the launch of this particular research. In areas such as beam-column joint, two way slab-column joints and heavily loaded columns, where considerable amount of transverse and longitudinal reinforcing steel are normally present, the required quantity of longitudinal reinforcing steel can be reduced greatly and in some cases eliminated if steel-fiber reinforcements coupled with high concrete strength are used. The desirability of high strength concrete is in the overall reduction in the weight of structures, the volume of concrete used in the construction, and the resulting beneficial environmental effects associated with reduction in weight and materials.

This research is the continuation of previous studies conducted at the Civil Engineering Department at University of Nevada, Las Vegas since 1997 (Ahmed, 2001; Ahmed and Ladkany, 2003; Ladkany and et al, 2005). 1% by volume fraction of one inch long steel-fiber and Styrene-Butadiene, rubber based polymer, were added to normal 27.6 MPa (4 ksi) concrete mixture to study the ductility behavior of steel-fiber and polymer concrete mixtures (Ahmed, 2001). High strength steel-fiber mixtures, with 0.3% of steel by volume, were studied for compressive and tensile strength with different combinations of admixtures and cement substitutes (Doli, 2007).

This research is conducted in two phases. In the first phase, results of which are discussed in this paper, the rheological properties of flow-able and/or self-consolidating high strength steel-fiber concrete are presented. The fresh properties of the FRC under consideration are: flow-ability, pass-ability and fill-ability of the mixture with various quantities of steel fibers by volume fraction added to the mixture. The current study investigates the effects of steel fibers and admixtures to the fresh properties of FRC. In addition to the above rheological properties, the research will also investigate the effect of steel fibers on: (a) the mixture's self-consolidating or flow-able behavior, (b) balling effect of the steel-fibers, and (c) the proportioning of water reducing, and viscosity modifying agents to obtain the desirable mixture that meets various ASTM requirements. The admixtures in use are: High Range Water Reducing Agent (HRWR), Viscosity Modifying Agent (VMA), fly ash and silica fume.

The second phase, which is not part of this paper, will deal with the study of shear, flexural and ductility behavior of FRC in relation to thin plates and shell structures.

2. RESEARCH SIGNIFICANCE

The purpose of the research is twofold. First, to observe the fresh properties of FRC mixture and verify if the self-consolidating properties of the mixture can be maintained at different levels of steel-fiber content, 0% to 2% by volume fractions. Second, to study the properties of fresh FRC mixtures at various levels of steel-fiber content with respect to the amount of admixtures, such as HRWR and VMA used. As the steel-fiber content in the concrete mixture increases the need to adjust admixtures dosage and/or w/c ratio becomes necessary.

3. EXPERIMENTAL PROCEDURES

Initially, a control mix, without steel fibers, that meets the fresh properties of self-consolidating concrete, described in section 3.3 below, was established. Maintaining the water-to-cement ratio constant, steel fibers, HRWR and /or VMA were added increasingly to get SCC properties of the FRC mixture. The steel fibers are added in

increments of 1% by volume fraction from 0 to 2%. Therefore, three types of concrete mixtures were studied.

3.1 Raw materials

Coarse and fine aggregates were obtained from a local quarry in Las Vegas, Nevada. Since the application of the concrete mixtures were ultimately to be used for thin plates and shells (about 25.4 mm thick), the size of the coarse aggregate was limited to nominal sizes of 9.53 mm (3/8") and #4. The oven-dry specific gravity and absorption of the coarse aggregate (ASTM C 128-07a) are 2.777 and 0.60%, respectively. Fine aggregate grading, with fineness modulus of 3.03, met the requirements of ASTM C33 grading limitations. The oven-dry specific gravity and absorption of the fine aggregate (ASTM C 128-07a) are 2.785 and 0.64%, respectively. Deleterious substances are substantially below the maximum allowable limits for both coarse and fine aggregates.

The amount of water-to-cement ratio and coarse-to-fine aggregate ratio were adjusted to suite the concrete mixture under consideration. Optimum coarse-to-fine aggregate ratio for FRC was found to be 44% to 56% (724:920 kg/m^3), respectively. The water-to-cement ratio was set at about 0.435 to meet both self consolidating properties and high strength concrete requirements.

ASTM C 150 Type V Portland cement 404 kg/m^3 (25.2 lb/ ft^3), which is widely used in the local area due to its resistance to sulfate and Class F fly ash, at 42.5% by weight of cement, meeting the requirements of ASTM C 618 were used. Silica fume, 7.5% by weight of cement, was also used.

The admixtures used were High Range Water Reducers (HRWR) and Viscosity Modifying Agent (VMA).

ASTM 820-90 Type II Deformed cut sheet carbon steel fibers with equivalent diameter of 0.584 mm (0.023 in) and aspect ratio, l/D, of 47:1 were used. The steel fibers have rectangular cross section of 0.406 x 0.838 x 19.05 mm (0.016 x 0.033 x ¾ in) and specific gravity of 7.85. The tensile strength of steel-fibers ranges between 379 to 763 MPa (55,000 to 111,000 psi).

3.2 Mixing procedures

Preparation of concrete ingredients and procedure of mixing concrete were conducted per ASTM C 192.

The mixer and other tools that came into contact with the concrete were dampened to prevent mixing water fluctuation. Coarse aggregates were mixed for two minutes with 1/3 of the mixing water and steel fibers. Fine aggregates were added to the mixer and

mixed for two minutes with 1/3 of mixing water and steel fibers. Lastly, the silica fume, fly ash and cement were added and mixed for two more minutes with the remaining 1/3 of mixing water and steel fibers. The admixtures, HRWRA and VMA, were added and the content mixed for three minutes followed by three minutes of rest and two more minutes of mixing, for a net mixing time of 14 minutes.

The mixer was stopped while the ingredients were loaded into it, with the exception of water and steel fibers.

3.3 Testing procedures

3.3.1 Flow-ability (slump flow and flow rate test)

The unconfined workability of SCC was measured using slump flow. In the procedure, a standard slump cone (upright or inverted) is filled with concrete and the cone is lifted vertically with no lateral or torsional motion to let the mixture flow. Slump flow is measured by taking the average of two perpendicular diameters of the flow. If the diameters differ by more than 50 mm (2”), the test is invalid and need to be repeated (ASTM C 1611, 2009). Slump is measured from the top of the test cone’s initial position to the top of the spread.

The time elapsed for flow to reach 20 inch diameter from the initial time of test cone lift is defined as the rate of flow (ASTM C 1611, 2009). Target flow rate for SCC is 5 seconds or less (ASTM C09.47, 2009).

3.3.2 Passing ability (J-Ring Test)

A similar set up as slump flow test except a J-Ring, circular ring with 16 #5 deformed bars, see Figure 1, is placed around the perimeter of the test cone before the lift. The J-Ring flow diameter is the average of the two perpendicular diameters measured. The difference between the slump flow and J-Ring flow determines the passing ability of the concrete mixture. A difference of 25 mm (1 in) shows good passing ability and a difference more than 50 mm (2 in) shows poor passing ability (ASTM C 1621,2009).

3.3.3 Filling ability (V-Funnel Test)

A V- shaped funnel, see Figure 2, is filled with concrete mixture, the bottom door is opened and the time passed for the content to clear the apparatus is recorded as V-Funnel flow time (t_v). V-Funnel flow time of 10 seconds or less shows good filling ability (ASTM C09.47, 2009).



Figure 1. J-Ring Apparatus

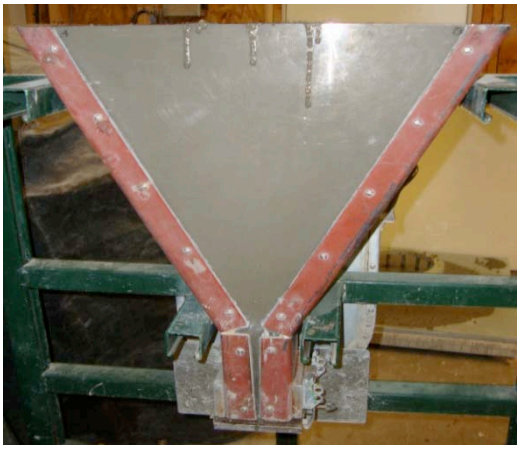


Figure 2. V-Funnel Apparatus

3.3.4 Filling and passing ability (U-Box Test)

A U-shaped box equipped with 3 #4 bars and a sliding door, Figure 3, is filled with the concrete mixture. The sliding door is lifted and the height of the mixture in the two chambers is measured. The difference in height, U-Box filling height, of 304.8 mm (12 in) or less indicates the mixture has good filling and passing ability (ASTM C09.47, 2009).



Figure 3. U-Box Apparatus.

4. RESULTS AND DISCUSSION

4.1 Effects of HRWR Agent on the FRC mixture

HRWR agent is used in our study to reduce the amount of mixing water and hence achieve high concrete compressive strength and to get a self-consolidating or flow-able concrete mixture as well. Table 1 show that the addition of HRWRA increases the slump flow (spread) diameter, slump and the chance of bleeding. The amount of HRWR needed also increases with the increase of steel-fiber content, for similar spread diameter of the mixture.

4.2 Effects of VMA on the FRC mixture

VMA enhances the deformability and uniformity of a mixture. VMA can be used to minimize aggregate piling, segregation and bleeding as the amount of water and/or HRWR in the mixture increases to obtain optimum mixture properties. The main drawback generally is that, VMA slows down the flow of the mixture hence, increasing the time of the flow rate (T_{50}).

Tests were conducted to determine the influence of VMA on the steel-fiber mixtures. An amount of 0.385 kg/m^3 (0.024 lb/ft^3), minimum manufacturer's recommendation, was added to the successful mixtures #1, #4 and #7 in Table 1, having 0%, 1% and 2% of steel volume fractions, respectively. Results in Table 2 show that the VMA shrinks the flow diameter by 15.2 mm (0.6 in) for 0%, 88.9 mm (3.5 in) for 1% and

an increase of 10.2 mm (0.4 in) for 2%. The flow rate (T_{50}) of the mixtures increased by 0, 8 and 5 sec for 0%, 1%, and 2%, respectively. However, bleeding of 12.7 mm (1/2 in) and 15.9 mm (5/8 in) were observed in 0% and 2% steel volume fraction mixtures, which explains the increase in spread diameter and flow rate of the mixtures.

It was concluded that VMA is not needed for mixtures indicated in Table 1, since the flow rate is increased and the slump flow (spread) decreases with some observed bleeding with the addition of VMA.

Table1. Mix dosages and fresh property results kg/m^3 (lb/ft^3)

Mix	HRWR kg (lb)	VMA Kg (lb)	Steel-Fiber % (lb)	Slump Flow mm (in)	Halo mm (in)	SLUMP mm (in)	T_{50} sec
1	0.178 (0.392)	0	0 (0)	759.4 (29.9)	None	279.4 (11)	5
2*	0.196 (0.432)	0	1 (5.00)	793.75 (31.25)	$\leq$ 38.1 (1.5)	279.4 (11)	5
3*	0.181 (0.400)	0	1 (5.00)	762 (30)	$\leq$ 25.4 (1.0)	279.4 (11)	4
4	0.171 (0.376)	0	1 (5.00)	689.1 (27.13)	None	273.05 (10.75)	5
5*	0.174 (0.384)	0	2 (10.00)	641.35 (25.25)	None	266.7 (10.5)	10
6*	0.181 (0.400)	0	2 (10.00)	641.35 (25.25)	None	270.0 (10.63)	12
7	0.189 (0.416)	0	2 (10.00)	673.1 (26.5)	None	270.0 (10.63)	12

* Mix not recommended

Recommended mixtures for 0%, 1% and 2% steel fiber volume fractions are mixture #1, #4 and #7, respectively.

Table 2. Fresh property results of mixtures #1, #4 & #7 with VMA, kg/m^3 (lb/ft^3)

Mix	HRWR kg (lb)	VMA kg (lb)	Steel-Fiber (%) (lb)	Slump Flow mm (in)	Halo mm (in)	SLUMP mm (in)	T_{50} sec
1	0.178 (0.392)	0.011 (0.024)	0 (0)	743.0 (29.25)	0 – 16.0 (0 - 0.63)	276.4 (10.88)	5
4	0.171 (0.376)	0.011 (0.024)	1 (5.00)	603.3 (23.75)	None	266.7 (10.50)	13
7	0.189 (0.416)	0.011 (0.024)	2 (10.00)	682.8 (26.88)	0 – 12.7 (0 - 0.50)	273.1 (10.75)	17

4.3 Effects of Steel Fibers on the FRC mixture

From Table 1 it can be seen that, an addition of 1% steel fibers by volume has very little effect on the fresh properties of the FRC mixture. Fibers are also less noticeable during the mixing and testing process. However, the introduction of steel fibers to the concrete mixture reduces the workability, pass-ability, fill-ability, and flow-ability progressively as the fiber content increases to 2%. With the increase in steel-fiber volume fraction in the mixture, the workability and slump flow decreases but the flow rate and the need for more HRWR increases.

4.4 J-Ring Test Results

Results from J-Ring tests for mixture #1, #4 and #7 are shown in Table 3. The spread diameter differences were an increase of 9.4 mm (0.37 in), decrease of 22.4 mm (0.88 in) and 44.5 mm (1.75 in) for 0%, 1% and 2% steel-fiber volume fraction, respectively. For 0% steel-fiber the ring barrier made no difference. On the other hand, for 1% and 2% the diameter shrank by an amount of less than 50 mm (2 in),

maximum margin that is required for SCC mixture. Therefore, all three mixtures satisfied J-Ring test requirement. In general, the introduction of steel fibers into the mixtures reduces the spread diameter in the J-Ring test.

4.5 V-Funnel Test Results

V-Funnel test results in Table 3 show that, the time needed for a mixture to clear the funnel increased from 8 sec to 18 sec (125%) and 31 sec (287%) for 0%, 1% and 2% steel fiber mixture, respectively. It can be concluded that, the increase in steel-fiber volume fraction in the mixture decreases its fill-ability.

4.6 U-Box Test Results

The results in Table 3 show that the U-Box test requirements for SCC mixture are met for 0% and 1% steel volume fraction mixtures. However, the 2% mixture exhibited 63% higher than the maximum allowable U-Box filling height requirement.

Table 3. J-Ring, V-Funnel and U-Box Test results of mix #1, #4 & #7, kg/m^3 (lb/ft^3)

Mix	HRWR kg (lb)	VMA Kg (lb)	Steel-Fiber (%) (lb)	J-Ring Flow mm (in)	Slump Flow mm (in)	V – Funnel sec	U - Box H_1 - H_2 mm (in)
1	0.178 (0.392)	0	0 (0)	768.4 (30.25)	759.4 (29.9)	8	1.52 (0.06)
4	0.171 (0.376)	0	1 (5.00)	666.8 (26.25)	689.1 (27.13)	18	25.4 (1.00)
7	0.189 (0.416)	0	2 (10.00)	628.7 (24.75)	673.1 (26.5)	31	495.3 19.50

Table 4. Summary of results

Mix	Slump Flow > 482 mm (19 in)	J-Ring Flow ≤ 50 mm (2in)	V – Funnel Flow Time (≤ 5 sec)	U - Box Filling Height ≤ 305mm (12in)
1	Acceptable	Acceptable	Acceptable	Acceptable
4	Acceptable	Acceptable	Not Acceptable	Acceptable
7	Acceptable	Acceptable	Not Acceptable	Not Acceptable

5. CONCLUSION

Preparing SCC or flow-able Steel-fiber concrete is very sensitive and complicated process. Attempting to have high strength concrete, by reducing water-to-cement ratio, in addition to having SCC property makes the process even more complicated and laborious. Table 4 below, summarizes the results of the three mixtures without VMA, in relation to the test conducted and whether the mixture met the SCC requirements. It is shown that Mixture #1, with 0% steel-fiber volume fraction met all the requirements for SCC properties. But the other two mixes, 1% and 2%, fell short in one and two tests each, respectively. Some of the short falls can be remedied by adjusting the HRWRA and/or VMA dosage. If needed the water-to-cement ratio might even be increased to achieve the SCC behavior required, at the expense of concrete compression strength.

From the current experimental study, it can be concluded that, with the increase of steel-fiber volume fraction the required HRWRA increases. Ultimately, VMA and water- to-cement ratio need to be adjusted to get the SCC properties for 1% and 2% steel fiber mixtures.

REFERENCES

Ahmed, A. (2001). *"Characterization of Steel Fiber and/or Polymer Concrete Mixes and Applications to Slender Rectangular and I-Beams".* PhD Thesis, University of Nevada, Las Vegas.

Ahmed, A. and Ladkany, S. (2003). "Effects of Adverse Hot Weather Curing Conditions on Plain and Polymer-Modified Concrete Mixes Used in Foundations and Basements." *Proceedings of the 38th symposium of Engineering Geology and Geotecnical Engineering.* University of Nevada, Reno. 197-201.

American Society for Testing and Materials (ASTM C 1611).(2009). *"Standard Test Method for Slump Flow of Self-Consolidating Concrete".* ASTM International, Conshohocken.

American Society for Testing and Materials (ASTM C09.47).(2009). *"Self-Consolidating Concrete".* ASTM International Sub committee C09.47 on Concrete and Concrete Aggregates.

American Society for Testing and Materials (ASTM C1621).(2009). *"Standard Test Method for Passing Ability of Self-Consolidation Concrete by J-Ring".* ASTM International, Conshohocken.

Doli, V. (2007). *"The Influence of Cementitious Materials and Steel Fiber Reinforcement on the Strength of Self-Consolidating Concrete".* University of Nevada, Las Vegas.

Ladkany, S. and et al (2005). "Mixing performance and strength of steel fiber-reinforced SCC with varing cementitious materials." *SCC 2005 Proceedings.* Center for advanced cement-based materials, Illinois, Chicago. 387-391.

Effect of Different Parameters on the Tensile Strength of Adhesive Anchors

S.E. Robinson[1] and A.M. Said[2]

[1] Civil and Environmental Engineering Department, University of Nevada, Las Vegas, 4505 S. Maryland Parkway, Las Vegas, NV 89154-4015; email: robin165@unlv.nevada.edu

[2] Civil and Environmental Engineering Department, University of Nevada, Las Vegas, 4505 S. Maryland Parkway, Las Vegas, NV 89154-4015; PH (702) 895-2722; FAX (702) 895-3936; email: aly.said@unlv.edu

ABSTRACT

Adhesive-bonded anchors are increasingly adopted as structural fasteners for connections to hardened concrete. The strength of these anchors relies on several factors such as geometric parameters and adhesive bond strength. Due to the complexity of the interaction of these factors, it is difficult to estimate their tensile capacity. Furthermore, these anchors have not yet been incorporated into the design provisions of ACI 318-08. This study aims at estimating the effect of different parameters on the tensile strength of concrete adhesive anchors in uncracked concrete using artificial neural networks (ANNs). The ANN model will be able to capture the complex relationship between the tensile strength of anchors and different parameters.

INTRODUCTION

In many applications, steel structural members are required to be connected to concrete. Accordingly, the use of concrete anchorage systems has increased. Anchors are categorized into two types based on the time of installation. The first type is the cast-in-place anchors, which are installed while concrete is placed. These anchors develop their load capacity through two mechanisms, direct adhesion to concrete along the surface and bearing through anchor surface deformations, a head or a hook. Over the past two decades the knowledge and design of cast-in-place anchors has become well know and established in ACI 318-08 Appendix D (ACI 318-08, 2008). The second anchorage type used is post-installed anchors in which anchors are installed in hardened concrete. This system is, in turn, divided into two categories: mechanical bonded anchors and adhesive anchors. Similar to cast-in place anchors, mechanical anchors develop their strength through the transfer of load to the concrete at the anchor head, while adhesive anchors develop their strength through an adhesive layer that bonds them to concrete along the entire surface (Cook *et al.*, 1998). Post-installed anchors have the versatility to be placed in any desired location after the concrete has hardened, which increases their simplicity and speed of construction. As a result, post-installed anchors are growing in popularity among contractors in the concrete industry especially in retrofitting applications.

Adhesive anchors are post-installed anchors that derive their strength from the chemical compound adhesion to the walls of the hole drilled in concrete and the steel anchor rod. Chemical compounds used include epoxy, cementitious material, polyester resin, and other similar types (ASTM E 488-96, 1996). Typically, the hole diameter is only about 10 to 25 percent larger than the diameter of the reinforcing bar or threaded rod (Cook *et al.*, 1998). Structural adhesives for this type of anchorage are available prepackaged in glass capsules, in dual-cartridge injection systems, or as two-component system requiring user proportioning (Cook *et al.*, 1998).

The difficulty in determining a sensible design approach for adhesive concrete anchors is corroborated by their diverse range of failure modes (Cook *et al.*, 1998). The aim of this paper is to use ANN modeling approach to investigate the effect of various design parameters on the tensile capacity of single adhesive anchors.

MODES OF FAILURE

Given the complexity of the parameters that affect adhesive concrete anchors, it is difficult to develop a universal design equation. The interaction of concrete/adhesive interface in conjunction with the steel/adhesive interface makes it extremely difficult to establish a model that evaluates both failure planes in a small space as such (Zamora *et al.*, 2003). Figure 1 shows different modes of failure for adhesive anchors which may become challenging to distinguish, since they can intermix. There are five typical modes of failure for adhesive anchorage systems as identified by Cook *et al.* (1998), as shown in Figure 1. Adhesive anchors with shallow embedment tend to exhibit the concrete cone pull-out mode. As the anchor embedment depth increases, a combined failure with a bond failure below a shallow concrete cone is usually observed (Cook *et al.*, 1998). The bond failure part can occur at adhesive/concrete or steel/adhesive interfaces and even a mixed mode bond failure maybe observed on different parts of the anchor (Cook *et al.*, 1998; Zamora *et al.*, 2003).

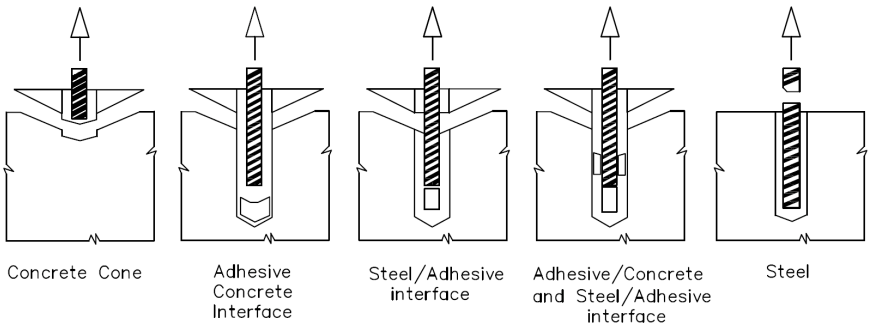


Figure 1. Typical failure modes of adhesive concrete anchors after Cook *et al.* (1998)

CURRENT DESIGN MODELS

For the purpose of comparative analysis, the current design models for adhesive concrete anchors are listed in the following section.

Concrete Cone Models

Concrete cone model was initially proposed by Eligehausen *et al.* (1984). The model is statistically derived based on multiple testing of a single adhesive type and anchors whose ratio of embedment depth to diameter is equal to nine ($h_{ef}/d = 9$). The ultimate predicted strength (N_U) of the anchor depends on the embedment depth and the concrete strength, but does not account for adhesive failure assuming a failure in a concrete cone mode. The model is presented by the following equation:

$$N_U = 0.92 h_{ef}^{\ 2} \sqrt{f_c} \tag{1}$$

where,

N_U = ultimate predicted strength of anchor (N)
h_{ef} = embedment depth (mm.)
f_c = 150 × 300 mm (6 × 12 in.) concrete cylinder compressive strength (MPa)

Uniform Bond Stress Model

The uniform bond stress model, presented in Eq. (3), is dependent on unique bond stress of the adhesive product, the diameter, and embedment length.

$$N_U = \tau \pi d h_{ef} \tag{2}$$

where,

N_U = ultimate predicted strength of anchor (N)
d = anchor diameter (mm)
τ = unique bond stress (MPa)
h_{ef} = embedment depth (mm)

Cook *et al.* (1998) indicate that while using the uniform bond stress model, the anchor diameter is most appropriate to use in Eq. (2) rather than the hole diameter. The bond stress along the embedment length of the anchor (τ) in Eq. (2) can be best represented through the uniform bond stress model, which is very simple to implement (Cook *et al.*, 1998).

Combined Cone/Bond Models

The combined concrete cone and bond stress models were proposed for adhesive anchors by Cook *et al.* (1998) and the Japan Concrete Institute (1994). For deeper embedment, a two term equation proposed by Cook *et al.* (1998) is used to combine the strength of the shallow cone with the bond strength. The cone depth is calculated using Eq. (3), and if it is smaller than the embedment depth, then the combined cone failure and bond failure are calculated in Eq. (5). If the embedment

depth is smaller than the depth of the concrete cone then Eq. (5) is to be used, as it is a concrete cone model as suggested by Eligehausen *et al.* (1984).

$$h_c = \frac{\tau\pi d}{1.84\sqrt{f_c}} \tag{3}$$

$$N_U = 0.92h^2{}_c\sqrt{f_c} + \pi\tau d(h_{ef} - h_c) \tag{4}$$

$$N_U = 0.92h_{ef}{}^2\sqrt{f_c} \tag{5}$$

where,

N_U = ultimate predicted strength of anchor (N)
d = anchor diameter (mm)
τ = unique bond stress (MPa)
h_{ef} = embedment depth (mm)
f_c = 150 × 300 mm concrete cylinder compressive strength (MPa)
h_c = depth of shallow concrete cone (mm)

Two interface bond model

The basis of this design model is differentiating between failure at the adhesive/concrete interface and failure at the steel/adhesive interface. Eq. (6) is appropriate for steel/adhesive interface failure, where the ultimate load depends on the bond stress evaluated at the steel/adhesive interface, the embedment depth, and anchor diameter. Similarly, Eq. (7) is for adhesive/concrete interface failure, where the ultimate load depends on the bond stress evaluated at the concrete/adhesive interface at a low concrete strength, the diameter of the hole, the embedment length, and the ratio of the square root of the concrete strength being considered to the square root of the low strength concrete used to establish τ_0.

$$N_U = \pi\tau dh_{ef} \tag{6}$$

$$N_U = \pi\tau_0 d_0 h_{ef}\Psi_c \tag{7}$$

where,

N_U = ultimate predicted strength of anchor (N)
d = anchor diameter (mm)
d_0 = hole diameter (mm)
τ = unique bond stress (MPa)
τ_0 = bond stress evaluated at hole diameter (MPa)
h_{ef} = embedment depth (mm)
f_c = 150 × 300 mm concrete cylinder compressive strength (MPa)
Ψ_c = 1.0 for products with little or no influence of concrete strength

ARTIFICIAL NEURAL NETWORK APPROACH

Artificial neural networks (ANN) are powerful computational tools inspired by the understanding and abstraction of the structure of biological neurons and the internal operation of the human brain (Haykin, 1994). ANN multi-layer perceptrons (MLP) are used extensively in engineering applications due to their ability to perform nonlinear transformations for functional approximations with given inputs in order to reach desired outputs. The value of neural networks relies in its ability to be trained through adaptive data driven approaches, and therefore the system is able to analyze, learn and capture complex or hidden relationships. MLP networks consist of multiple layers (an input layer, an output layer and one or more hidden layers). Each layer contains a number of processing elements (units) partially or fully connected to units in the consecutive layer. Connections between processing units are initially assigned random numerical values (weights) representing their strength. The main objective in building an artificial neural network-based model is to train specific network architecture to search for an optimum set of weights, for which the trained ANN can predict accurate values of outputs for a given set of inputs from within the range of the training data (Haykin, 1994). While the MLP networks trains the complex array of interconnected data, the training of network is driven by sufficient and relevant data to achieve optimum results. Further investigation of artificial neural networks is outside the scope of this paper. However, more details about how to construct, train and validate MLP networks are available elsewhere (Haykin, 1994; Rumelhart *et al.*, 1986).

EXPERIMENTAL WORLDWIDE DATABASE

Test reports on the behavior of adhesive anchors have been collected from experimental programs in Europe, USA, and Japan. From 36 reports, a database containing the results of 2,878 tests has been established. Currently the adhesive anchor database is maintained for ACI committee 355 by Professor Ronald A. Cook, Department of Civil Engineering, University of Florida, Gainesville. The database contains tensile and shear load testing in uncracked and cracked concrete with single anchors, groups of two anchors, and groups of four anchors. It distinguishes between confined and unconfined tests as well as between tests far from the concrete edge, tests near the concrete edge, and tests with close anchors spacing. Finally, the database differentiates adhesives by manufacturer as well as types such as epoxies, vinylesters, unsaturated polyesters, hybrid adhesives, and inorganic adhesives. Some tests indicate the temperature range at which the adhesive was cured. Currently, the International Code Council Evaluation Service (ICC-ES) AC-308, "Acceptance Criteria for Post-Installed Adhesive Anchors" (2005) along with ASTM E 488, "Standard Test Methods for Strength of Anchors in Concrete and Masonry Elements" (1996) and E 1512, "Standard Test Methods for Testing Bond Performance of Bonded Anchors" (1993) are the testing standards that manufacturers must follow to evaluate their adhesives for commercial use. The dimensions of the geometric properties of the anchorage system are recorded for each test in the concrete anchor database, along with qualitative identification of the failure mode that was observed as well as the quantitative tensile capacity at which the anchorage system failed. However, the tests in the 36 reports (1985-1994) that were used to establish the worldwide database were performed even before the release of the previous

evaluation criteria of ICBO ES AC-58 (1995) and the only available guidelines at that time were for expansion anchors ICBO ES AC-01 (1993). The purpose of the current ICC-ES AC-308, as stated in *Section 1.1* is to establish requirements for different manufactures post-installed adhesive anchors in concrete elements to be recognized in an ICC Evaluation Service, Inc. (2005). This product evaluation methodology allows adhesives from different manufactures to be consistently evaluated. Accordingly, engineers can use a unique bond stress for each product for design purposes.

SELECTION OF DATABASE

The success of establishing an ANN model is dependent on the amount and quality of information provided to train it as stated before. Therefore, the worldwide database was limited to unconfined, single adhesive anchors, far from edge loaded in tension in uncracked concrete with bond failure for the purpose of this study. Furthermore, tests which resulted in the yielding of steel were omitted since these specimens demonstrated sufficient bond between the borehole and adhesive as no bond failure was observed. The database used must be sufficiently large to enable the ANN to fully capture the effect of the considered design parameters on the tensile capacity of single adhesive anchors. The initial geometric and material design parameters that were used to establish and train the ANN were: the diameters of the anchor and the bore hole, the embedment depth of the anchor, the concrete strength and the bond index which is described in the following section. The selected design parameters have all been shown in previous studies and design models to be crucial in estimating the tensile capacity of adhesive anchors (Cook and Konz, 2001). Manufactures are required by the International Code Council Evaluation Service (ICC-ES) AC-308, *Section 2.1.20* "manufacturer's published installation" (2005) to specify the installation of, and condition of the borehole, as well as the curing temperature range at which the adhesive should be applied. Accordingly, the tests selected to train the ANN were in the standard ranges that adhesives would be cured (5°C - 30°C/41°F - 86°F). Previous research by Cook and Konz (2005) shows that inappropriate temperature and conditions of the borehole can have detrimental effects on the performance of the anchorage system, and hence temperatures that were outside the range listed were omitted.

The difficulty of identifying the failure mode is described in more detail by Zamora *et al.* (2003). They indicated that upon inspection of anchor after failure it is extremely difficult to identify if the failure was purely a cone failure, a result of effective adhesive bond, or rather a pull out failure, a result of ineffective adhesive bond (1998). Consequently, it is expected that the classification of the failure mode listed within the worldwide database is subjective nature. While the characteristics of the different failure modes are physically dissimilar yet their combination creates a difficulty in distinguishing a single prevailing mode of failure. For the purpose of this study only explicitly described bond failures were selected for the training the ANN in order to isolate the complex relationship between parameters that affect this mode of failure. Concrete cone failure has already been described by the Concrete Capacity Design (CCD) model by Fuchs *et al.* (1995). In order to properly and accurately train the network, duplicates within the testing data were carefully

eliminated in order to improve the training capability of the network. The duplicates that were found in the database were carefully reduced to a single test data point. If inconsistent values of tensile capacity were found, then the procedure discussed by ASTM E 488 (1996) was followed to eliminate these outliers. The tensile capacities that met the ASTM standard methodology were then averaged and the duplications of these tests were reduced to a single data point representing the general trend observed for that specific anchorage test. Duplicates were deemed to be points with similar geometric parameters (e.g. diameter of anchor, diameter of hole, embedment depth, and concrete strength). However, as discussed in by Cook and Konz (2001) and Meszaros (1999), adhesive bond strengths and consequently the tensile capacity of anchors are manufacturer dependent. Accordingly, tests with identical geometrics parameters yet different adhesive manufactures were not considered as duplicates. The resulting database contained *213* tests from the original worldwide database for training of the ANN model.

ANN MODEL

The ANN model implemented in this study was a single feed-forward back-propagation multi layered perceptron network that utilized a scaled gradient conjugant (SGC) function, contained within MatLAB, Neural Network Toolbox. The network was trained with 80% of the *213* data points while the remaining 20% was used to determine whether the network was appropriately trained and able to capture the relationship between the different input parameters and output. The architecture of the network, shown in Figure 2, was developed with five inputs: diameter of anchor (d), diameter of hole (d_o), embedment depth (h_{ef}), concrete strength (f_c), and an adhesive index, as well as a single output, tensile capacity (N). The inputs and outputs were then normalized to values between 0 and 1, in order for the SGC function to be compatible for training (Rumelhart *et al.*, 1986). To ensure that the operator of the network had no bias of selecting data for training or testing, all datasets were randomized previous to training. Accordingly, inputs were fed to the network through three hidden layers that utilized a tangent sigmoid transfer function. Each layer contained 8 neurons which separated the 5 inputs and output. An epoch or single pass of the data through the network created an error output, between the network's predicted output and desired output. Data is then passed through the network again in order to reduce the error between the network's predicted output and desired output. Subsequently, optimum training results were attained through 2000 epochs.

To train the data more thoroughly, an additional parameter, the adhesive index, was deemed necessary to represents the adhesive bond strength. Examining the ICC AC-308 reveals two main adhesive related issues: product type and anchor diameter. This is evident from ICC-ES AC-308 *Section 2.1.23* (2005), since different anchor diameters must be tested for each adhesive to determine strength of the adhesive at various anchor diameters. The common trend is that larger anchors have higher tensile capacity, but yet lower bond strength. Using these two design principles, the bond index was determined from the uniform bond strength model as suggested by Cook *et al.* (1998) and McVay *et al.* (1996). The bond index was

defined based on ICC-ES AC-308 and assigned as a number between 0 and 1 unique to each adhesive product and diameter size range as outlined by ICC-ES AC-308 and based on the available test data for that product over the diameter size range. A major advantage of the ANN approach is that as new adhesives are tested, their test data can be easily added to the network database.

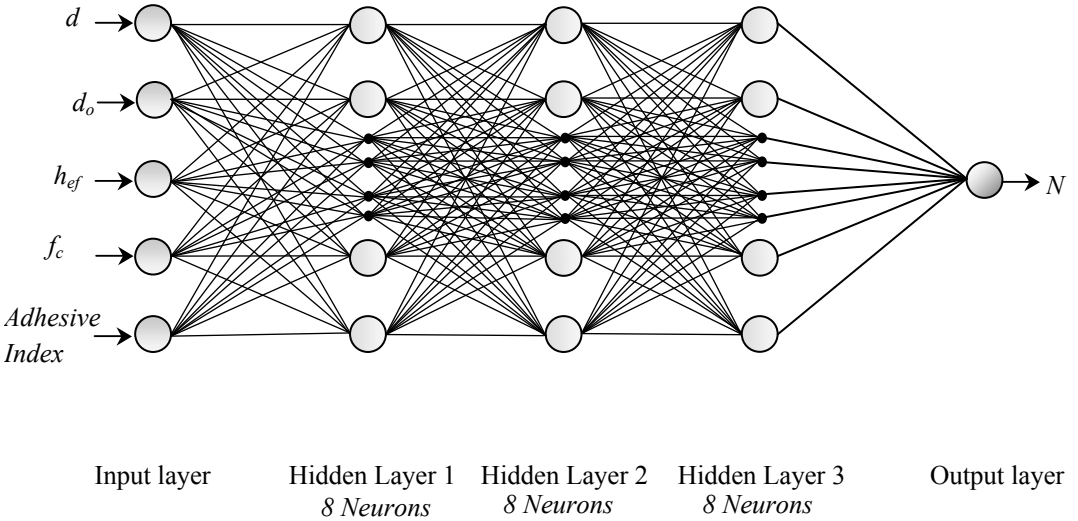


Figure 2. Architecture of the developed artificial neural network model

PARAMETRIC STUDY

Effect of Anchor Diameter on Tensile Capacity

Current ICC-ES AC-308 provisions provide evidence that tensile capacity increases as the anchor diameter increase (ICC-ES AC-308, 2005). This is reasonable since the bond surface area of the anchor ($\pi d h_{ef}$) increases linearly with the anchor diameter increase. Figure 3 displays a plot of the relation between anchor diameter and tensile capacity. It is shown that the increase is not linear despite the linear increase in bond area. Furthermore, as the anchor diameter increases the rate of the tensile capacity increase is reduced as shown in Figure 3.

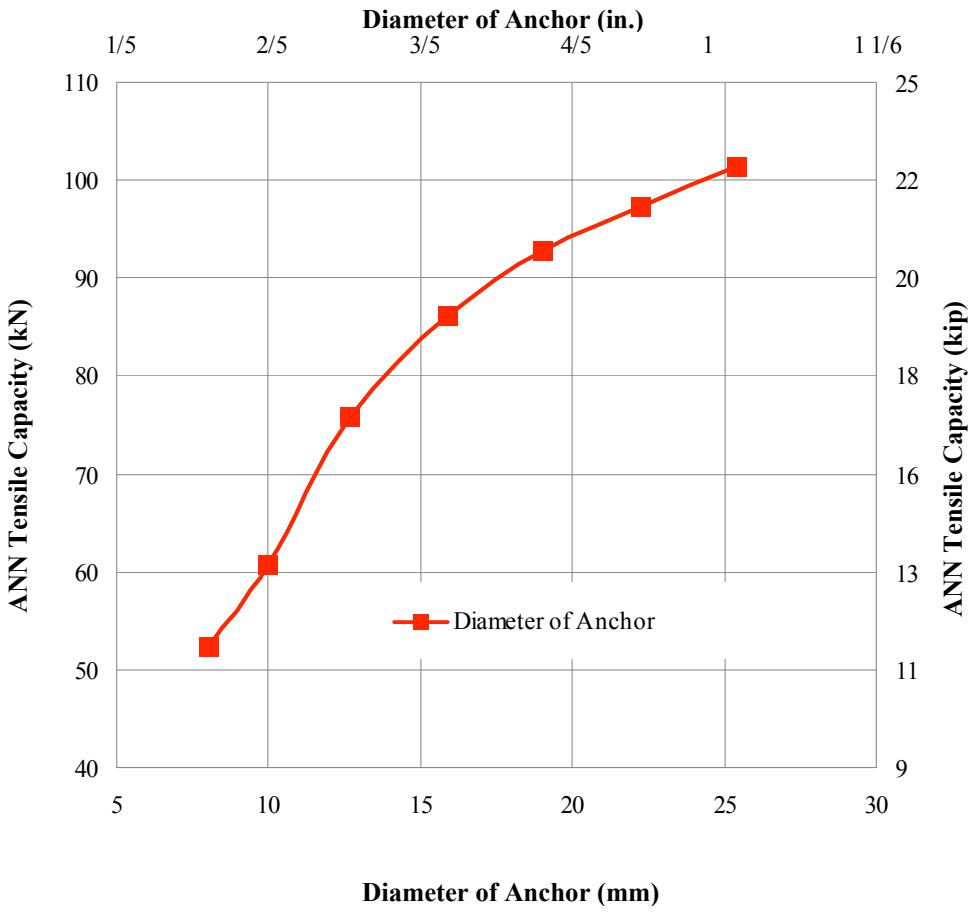


Figure 3. Effect of anchor diameter on tensile adhesive anchor capacity

Effect of Ratio of Anchor to Borehole Diameters on Tensile Capacity

The effect of the borehole diameter with respect to the tensile capacity is difficult to isolate and in many respects impractical since the annular gap is relative to the anchor diameter. Accordingly, the effect of the borehole diameter must be investigated through the borehole to anchor diameter ratio. The general trend from the database reveals typical ratios for borehole to anchor diameters in the range of 1.10 - 1.25 (Cook *et al.*, 1998). Concurrently, the parametric study examines more closely these ratios to determine the effect of this ratio on the tensile capacity of the anchor. The effect of this ratio on tensile capacity was studied for two bolt diameters ½ in. (12 mm) and 1 in. (25.4 mm). As illustrated in Figure 4, the tensile capacity increases with the increase in the borehole/anchor diameters ratio. This indicates that the tensile capacity increases with the increase in annular gap. For the 1 in. (25.4mm) diameter anchor, this increase was observed up to a d_0/d ratio of 1.25, as shown in Figure 4.

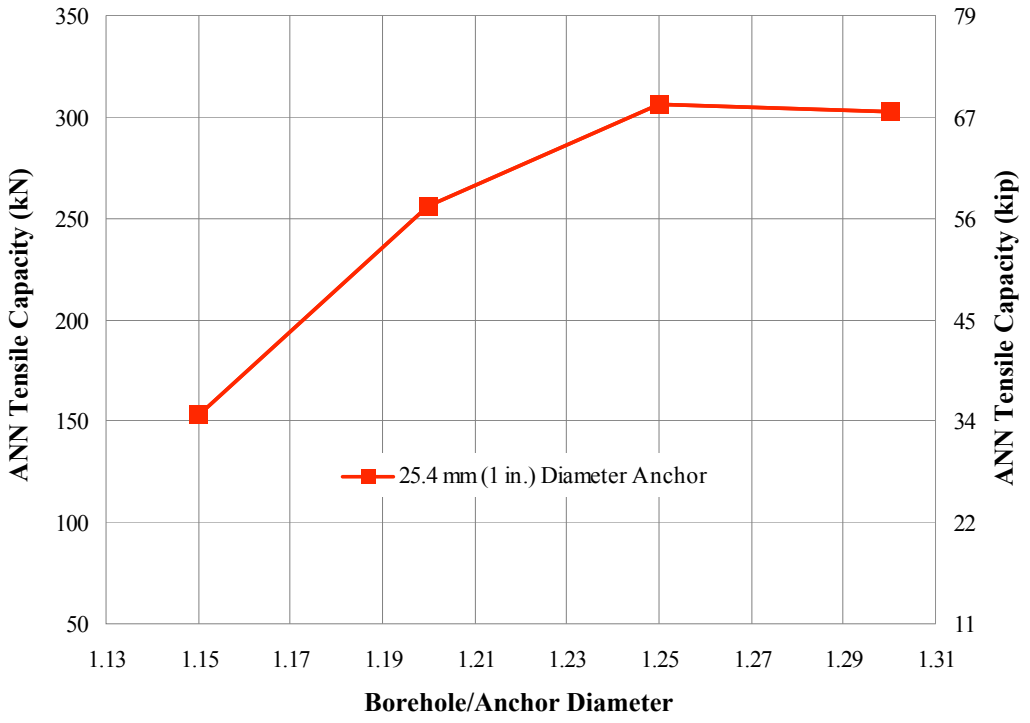


Figure 4. Effect of ratio of anchor diameter and borehole diameter on tensile adhesive anchor capacity (1 in/25.4 mm)

SUMMARY AND CONCLUSION

This study investigated the feasibility of using artificial neural networks as an approach to estimate the effect of several parameters on the tensile capacity of adhesive concrete anchors. The developed model was able to predict the effect of various parameters on the tensile capacity of adhesive anchors. The parametric study showed similar trends to those in the literature on adhesive anchors (ACI Cook *et al.*, 1993 and 1998; McVay *et al.*, 1996) in a quantitative manner. The ANN model can identify the optimum range of use for several parameters. The ANN model once established is readily available to input unique bond stresses that are evaluated for new adhesive products.

ACKNOWLEDGEMENTS

The authors wish to express their sincere appreciation to Dr. Ronald Cook of the University of Florida, ACI Committee 355 member that currently maintains and provided the worldwide database used in this study. Financial support was provided by the Western Alliance to Expand Student Opportunities (WASEO). The support of the Howard R. Hughes College of Engineering at the University of Nevada, Las Vegas is greatly appreciated.

REFERENCES

ACI Committee 318. (2008) "Building Code Requirements for Structural Concrete (ACI 318-08) and Commentary (318R-08)," *American Concrete Institute*, Farmington Hills, Mich., pp. 465.

ASTM E 1512-93. (1993) "Standard Test Methods for Testing Bond Performance of Adhesive-Bonded Anchors," *American Society for Testing and Materials*, West Conshohocken, Pa.

ASTM E 488-96 (1996) "Standard Test Methods for Strength of Anchors in Concrete and Masonry Elements" *American Society for Testing and Materials*, West Conshohocken, Pa.

Cook, R. A, Doerr, G.T., and Klingner, R.E. (1993), "Bond Stress Model for Design of Adhesive Anchors", *ACI Structural Journal*, V. 90, No.5. pp. 514-524.

Cook, R.A. and Konz, R.C. (2001). "Factors influencing Bond Strength of Adhesive Anchors." *ACI Structural Journal,* V 98, No. 1. pp. 76.

Cook, R.A., Kunz, J., Fuchs, W., and Konz, R. (1998). "Behavior and Design of Single Adhesive Anchors under Tensile Load in Uncracked Concrete." *ACI Structural Journal*, V.95. No. 1. pp. 9-26.

Derucher, K.N., Korfiatis, G.P., and Ezeldin, A.S. (1998). Materials for Civil and Highway Engineers, Prentice Hall, Upper Saddle River, N.Y.

Eligehausen, R., Cook, R.A., and, Jőrg, A. (2006). "Behavior and Design of Adhesive Bonded Anchors": *ACI Structural Journal*, V. 103, No. 6. pp. 822-831.

Eligehausen, R., Jőrg, A., Lehr, B., Meszaros, J., and Fuchs, W. (2004) "Tragverhalten und Bemessung von Befestigungen mit Verbunddűbeln unter Zugbenspruchung, Part 1: Einzeldűbel mit groβem Achs-und Randabstand," *Beton und Stahlbetonbau*, V. 99, No. 7. pp. 561-571. (in German)

Eligehausen, R., Mallee, R., and Rehm G. (1984). "Befestigungen mit Verbundankem," Betwonwerk + Fertigteil-Technik, Heft 10, pp. 686-692, Heft 11,pp. 781-785, Heft 12,pp. 825-829.

Fuchs, W., Eligehausen, R., and Breen, J. E. (1995) "Concrete Capacity Design (CCD) Approach for Fastening to Concrete," *ACI Structural Journal*, V.92, No. 1. pp. 73-94.

Haykin, S. (1994) Neural Networks. A Comprehensive Foundation. Macmillan, New York, NY.

ICBO ES AC-01. (1993). "Acceptance Criteria for Expansion Anchors in Concrete and Masonry Elements," International Conference of Building Officials - Evaluation Services. pp. 7.

ICBO ES AC-58. (1995). "Acceptance Criteria for Adhesive Anchors in Concrete and Masonry Elements", International Conference of Building Officials - Evaluation Services, Whittier, Calif.

ICC-ES AC-308. (2005) "Acceptance Criteria for Post-Installed Adhesive Anchor in Concrete," *International Code Council Evaluation Services, Inc.*, Whittier, Calif.

McVay, M., Cook, R.A., and Krishnamurthy, K. (1996). "Pullout Simulation of Post-Installed Chemically Bonded Anchors," *Journal of Structural Engineering*, V. 122. No. 9. pp. 1016-1024.

Meszaros, J., "Tragverhalten von Verbunddubeln im ungerissenen und gerissenen Beton,: Doctoral thesis, University of Stuttgart, Stuttgart, Germany, 1999. (in German)

Ožbolt, J. Li, Y.-J. and Kozar, I. (2001). "Microplane Model for Concrete with Relaxed Kinemactic Constraint*," International Journal of Solids and Structures*, V. 38. pp. 2683-2711.

Post installed Anchor, State of the Art Report, Japan Concrete Institute, 1994 (in Japanese).

Rumelhart, D.E., Hinton, G.E., and William, R.J. (1986), "Learning Internal Representation by Error Propagation", Parallel Distributed Processing, 1, Foundation, MIT Press, Cambridge, MA, 318-362.

Zamora, N.A, Cook, R.A., Konz, R.C., and Consolazio, G.R. (2003) "Behavior and Design of Single, Headed, and Unheaded Grouted Anchors under Tensile Load" *ACI Structural Journal*, V. 100. No. 2. pp. 222-230.

CityCenter Aria Tower – Engineering the Iconic Casino in Las Vegas

Dennis Poon[1], Kim Lin[2], Leonard Joseph[3], Guoyong Fu[4], Allen LaSala[5]

[1]P.E.; Thornton Tomasetti, 51 Madison Avenue, New York, NY 10010;
PH (917) 661-7800; FAX (917) 661-7801; email: dpoon@thorntontomasetti.com
[2]P.E., LEED AP; Thornton Tomasetti, klin@thorntontomasetti.com
[3]P.E., S.E.; Thornton Tomasetti, ljoseph@thorntontomasetti.com
[4]P.E.; Thornton Tomasetti, pfu@thorntontomasetti.com
[5]BSCE; Thornton Tomasetti, alasala@thorntontomasetti.com

ABSTRACT

The Aria Tower is the principal hotel and iconic centerpiece of the MGM Resorts International CityCenter Las Vegas mixed-use complex making its mark on the Nevada skyline. The Aria is designed in an elegant, sophisticated and contemporary architectural style with a floor plan based on interlocking arcs that is distinctly different from the linear, T, Y and X floor plans common to casino hotels. It also has three separate elevator cores with dedicated entry lobbies to provide guests with the experience of entering a smaller, exclusive hotel and avoiding long walks to their rooms. Visual massing of the hotel exterior is minimized by varying the heights of different building areas while fitting over 4 million square feet of hotel/casino spaces in up to 52 stories above ground and two stories below ground within the Federal Aviation Administration (FAA) height limitation of 600 feet. The unusual floor plan, separate cores and varied heights presented unique structural analysis and design challenges. This paper discusses the process and results for structural engineering of the Aria tower, including development of its "Core-Moment Frame" lateral system, its deep foundation interacting with caliche, and its unconventional post-tensioned (PT) slab system applied to a high rise building in a region of moderate seismicity. Guiding the project through turbulent economical times, completing the project on schedule, and achieving the coveted Green Building LEED (The Leadership in Energy and Environmental Design) Gold status were the results of the professionalism, dedication, commitment, and cooperation of the entire Aria Tower ownership, design and construction team.

INTRODUCTION

Aria Tower is the hotel/casino centerpiece of CityCenter, the grand urban development MGM Mirage (now MGM Resorts International) envisioned encompassing entertainment and luxury living within the same complex. That vision was made a reality over the past several years. CityCenter, at the heart of the Las Vegas entertainment district, is on 66 acres bounded by Las Vegas Boulevard, Frank Sinatra Drive along I-15, the existing Monte Carlo Casino and the existing Bellagio Casino to its East, West, South and North respectively. The complex consists of the Aria Tower hotel/casino, the Vdara hotel, the Mandarin Oriental hotel/residence, the

Veer East and Veer West residences, the Crystals shopping mall, a theater, the Harmon Tower and a Central Plant that powers the entire complex. See Figure 1.



Figure 1. Rendering of CityCenter, 2005

Ground breaking of the development took place in the spring of 2005 amid a construction boom in the area. At the peak of its construction, the development employed more than 8,000 trade workers, not counting technical professionals. The project was indisputably a major contributor to the local economy.

Centered within the development complex, the Aria Tower sits nearly 900 feet back from Las Vegas Boulevard. The 600 foot height of the 52 story tower just meets the FAA maximum building height limitation for the site and is one of the tallest buildings in Las Vegas. The tower has a base footprint of 120,000 square feet, with a gross building area of 4.5 million square feet, and a net area of 4.2 million square feet of hotel, casino, and retail spaces.

GEOMETRY AND BUILDING SYSTEM

Aria Tower floor plan geometry is based on two back-to-back overlapping arcs that create four wings merging at a central core area, resembling a butterfly with wings spread. Overall building massing was established considering aesthetics, views, hotel operations and the owner's target mix of hotel rooms and suites, so each of the four wings and the central core are at different heights. See Figure 2. In the upper half of the building, even the story heights vary by wing to create a range of guest room experiences. The West wing drops off progressively from Level 23 to Level 25. At Level 25 the central core stops, creating two independent towers above that point. The North and East wings form a V, with the East Wing terminating in stages from

Level 31 to Level 33 and the North Tower continuing upward. The South Tower stands alone and soars to the maximum height of the building. Tip to tip the Aria Tower floor plan extends 880 feet in the North-South direction and 480 feet in the East-West direction. The central core zone is 310 feet long and 120 feet across at its widest section. All wings are 70 feet wide with lengths varying from 120 feet to 250 feet.

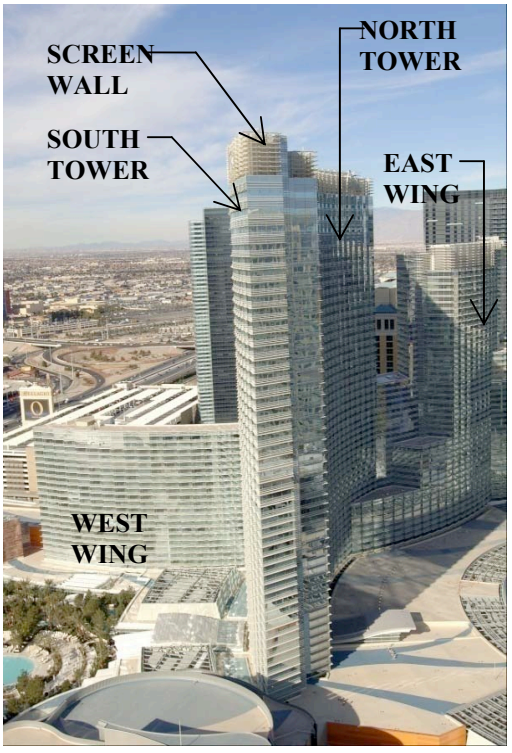


Figure 2. South Aerial View of Aria Tower- Looking North, 2009

Although based on smooth circular arcs, the hotel tower slab edges follow a sawtooth pattern with regular jogs. This edge mates with aluminum and glass façade panels with integral offsets to provide each guest room with an enhanced corner view. The façade articulation also creates exterior elevations that Cesar Pelli of Pelli Clarke Pelli Architects (PCPA) calls a "shimmering world of reflections" that may contain images of adjacent buildings, distant mountains or dramatic Las Vegas lights.

While functionally and aesthetically important, having multiple curved wings of varying heights posed several structural challenges. Wings may try to work separately or together under wind load, and move differently under seismic load. The curved geometry may affect building behavior. Wings of varying heights mean nonuniform mass distribution which can induce torsional effects. To address and minimize these issues, it was essential to establish a lateral system capable of providing stiffness of similar magnitude in every feasible direction to resist lateral forces and achieve the desired occupant comfort level. Additional considerations included building height constraints, usable floor area goals, construction schedules, material sources, bottom line costs, and intricate coordination with adjacent structures. After studying a variety of framing options, a cast-in-place concrete system was selected as most suitable for this application. The Aria Tower was to be a concrete system with shear wall cores, post-tensioned (PT) two way flat plate slabs, and long, narrow concrete perimeter columns aligned with walls between rooms. Completed Aria Tower construction included 250,000 cubic yards of concrete, 8,000 tons of mild steel reinforcement and 1,600 tons of post-tensioned (PT) cables totaling 1,200 miles - enough to nearly encircle the state of Nevada.

ARIA TOWER FOUNDATION

The sub-grade under the Tower consists of moderate to strongly cemented clayey gravel and sandy gravel laced with caliche, or hardened calcium carbonate deposits. The strongly cemented zone extends to a depth of 75 feet below grade, and is underlain by a saturated, under-consolidated, and very soft formation that varies in depth from 50 to 80 feet. Soil excavated for the two story basement would offset only a small fraction of the tower weight, and using a mat under the large tower footprint would result in high compressive stresses in the deep soft soil. The estimated settlement of 12 to 18 inches for a mat foundation was deemed unacceptably large. Therefore a deep foundation system using cast-in-place (CIP) concrete piles was recommended by geotechnical engineer GeoDesign as presented in Table 1.

Building/Location	Location/ Loading Condition	Min. Recommended Shaft Length (ft.)	Estimated Settlement (inches)
Aria Tower	Center Core	100	4
	South Tower	120	5
	North Tower	120	5
	West Wing	100	5
	East Wing	100	4
East Podium	30x90 Grid	70	4
	30x30 Grid	30	3
West Podium	30x30 Grid	50	3

Table 1. Estimated Settlement for Structures Supported on Drilled Shafts

To resist their gravity and overturning forces, the shear wall cores are supported on partial area mats 11 feet thick bearing on 48 inch diameter 8,000 psi concrete piles at least 120 feet long. The actual pile length was determined by field testing to obtain a minimum allowable axial capacity of 4,700 kips. Perimeter tower columns and adjacent podium columns are supported on pile caps bearing on smaller, shorter piles. The first Aria Tower pile was cast in January 2006. When the first Tower mat was cast on June 26, 2006 at the central core, Las Vegas Boulevard was closed from midnight to 8 AM as 550 concrete trucks delivered 5,520 cubic yards as a single pour. The massive concrete mat was continuously monitored for maximum temperature and for temperature differentials as it cured by using thermocouples installed at the top, center, and bottom of mat in six locations.

Upon completion of the Aria Tower and surrounding podium construction, the maximum settlement at tower core was measured at 3 ½ inches, and podium columns located at 70 feet from Tower core settled at 2 ½ inches. The settlements were well below the geotechnical estimates. The site was then locally re-graded to compensate for settlement by matching the as-built finished floor elevations.

LATERAL SYSTEM

Lateral stability of the Tower is provided by ordinary reinforced concrete shear walls located at the central core, at the two junctions where wings meet, and at the stair well on the tip of each wing. Average wall thickness is 24”, with a

maximum thickness of 36" at the central core base. This system was permitted by the governing code based on International Building Code[1] (IBC) 2000 for Seismic Design Category C. Coupling ('link') beams are only 16 inches deep on typical floors to satisfy aesthetic requirements of the ceiling profile transition in elevator lobbies. While such shallow beams can result in excessive flexibility, the cores of this building have long unbroken wall panels that improve stiffness and strength.

ETABS software developed by Computers & Structures, Inc. (CSI) was used to perform lateral analyses. CSI collaborated with TT in modifying, improving, and recalibrating the software throughout the Aria Tower design process to accommodate the unique and complex geometry. The contribution from CSI was invaluable to successful completion of the lateral analyses.

One complication arose in modeling methods. For overall building lateral analysis it is common to treat each floor as a rigid diaphragm. However, that approach had two drawbacks. First, at the time, the rigid diaphragm approach only permitted one diaphragm per plan, so it would incorrectly treat all the nodes at a level as sharing a common slab, even above the separation of wings at Level 25. Second, at every change in core geometry, a rigid diaphragm attempted to redistribute shear through transfer forces that were sudden, unrealistically large and impractical to design for. Consequently a "semi-rigid" diaphragm system was adopted: in-plane rigidity of the diaphragm was based on realistic slab stiffness values. Multiple runs bracketing potential properties for cracked and un-cracked sections and other variations confirmed that the transfer forces were relatively insensitive to the diaphragm values used. Floor plates and perimeter columns were included in the finite element model. As the 2D membrane floor plate elements in the standard semi-rigid model lacked the capacity to properly handle complex mass distribution, further studies concluded that shell element with 6 degrees of freedom was better suited to model the Aria Tower floor plates.

The inclusion of columns and floor plates as shell elements simplified gravity load distribution and building mass applications. It also resulted in through-slab transfer forces with values and distributions along core heights that are realistic, credible and constructible. While creating the comprehensive model required considerable effort, it proved worthwhile for flexibly responding to a continuous stream of requests for feasibility studies due to architectural, interior, and MEP changes. Since tower structural construction led issuance of the core and shell building permit by a year and half, the model offered favorable relief in its expeditious "re-modeling" process.

However, the approach required taking significant precautions as well. The out-of-plane stiffness of shell elements naturally created moment frames from the slab/column gravity system. Moment frame behavior could alter dynamic behavior when linked with the shear wall system. We made it clear that we were not providing a "Dual System", as defined in IBC[1] code, because that would further complicate the analysis and design. From the final model the slab/column frames provided a stiffness

contribution of 12%. This was small enough to have only a minor effect on the building period and on forces taken by the core walls. This justified designing the lateral system under an "Ordinary Shear Wall" classification.

Tower walls also lend lateral stability to the surrounding podium structures, including long span cantilevered east and west canopies, the entire north and east podiums, and part of the south and west Podiums. This was the natural result of avoiding architecturally undesirable seismic separation joints through the active lobby and casino areas and framing podium areas with steel to maximize clear spans and future alteration flexibility. Later versions of the lateral system model included the adjacent podium structures to better simulate podium mass contributions. This also afforded means to extract the resultant lateral forces for podium planning and design. Upon project completion, the mass contribution from the podium was 14% out of a combined total weight of 1.38 million kips. See Figures 3 and 4.

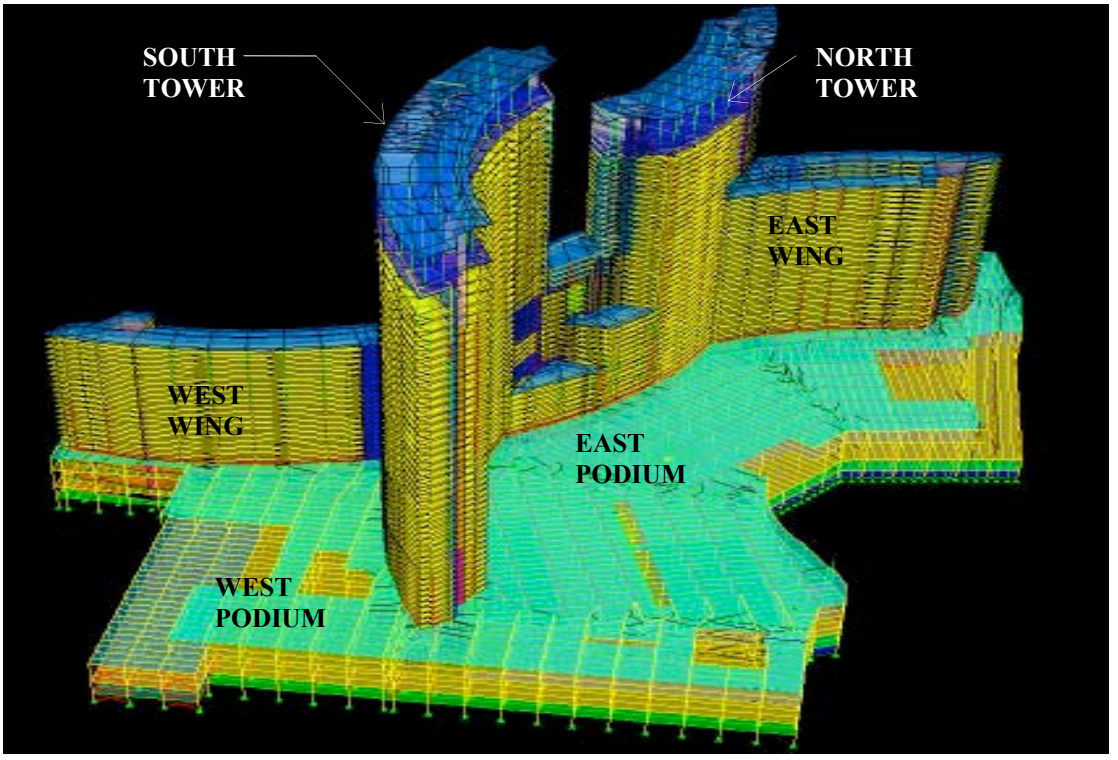


Figure 3. Isometric View of Finite Element ETABS Model of Aria Tower

Wind loads were provided by Rowan Williams Davis & Irwin Inc. (RWDI) based on wind tunnel test results. Recognizing the possibilities for wings to move independently, RWDI determined instantaneous wind forces using a High Frequency Pressure Integration model, where hundreds of pressure taps are monitored in real time. The resulting wind forces were applied at 6 points per floor - one each at the North, South, East, and West wings; and one at each side of the Central Core. To reflect the potential effects on the wings of complex air flows and vortex patterns, RWDI presented a wind load matrix of 170 cases in an assortment of direction and

magnitude combinations. Further combinations with gravity and seismic forces per IBC[1] code resulted in an impressive 200 load cases. So many load combinations applied to a massive finite element model strained the hardware and software built-in limitations, even after software patches and upgrades. To solve this limitation we eventually grouped load cases and analyzed them separately. An EXCEL file was developed to import and sort the results from various grouped analyses and determine the controlling cases. These cases were then applied to the model for final analyses.

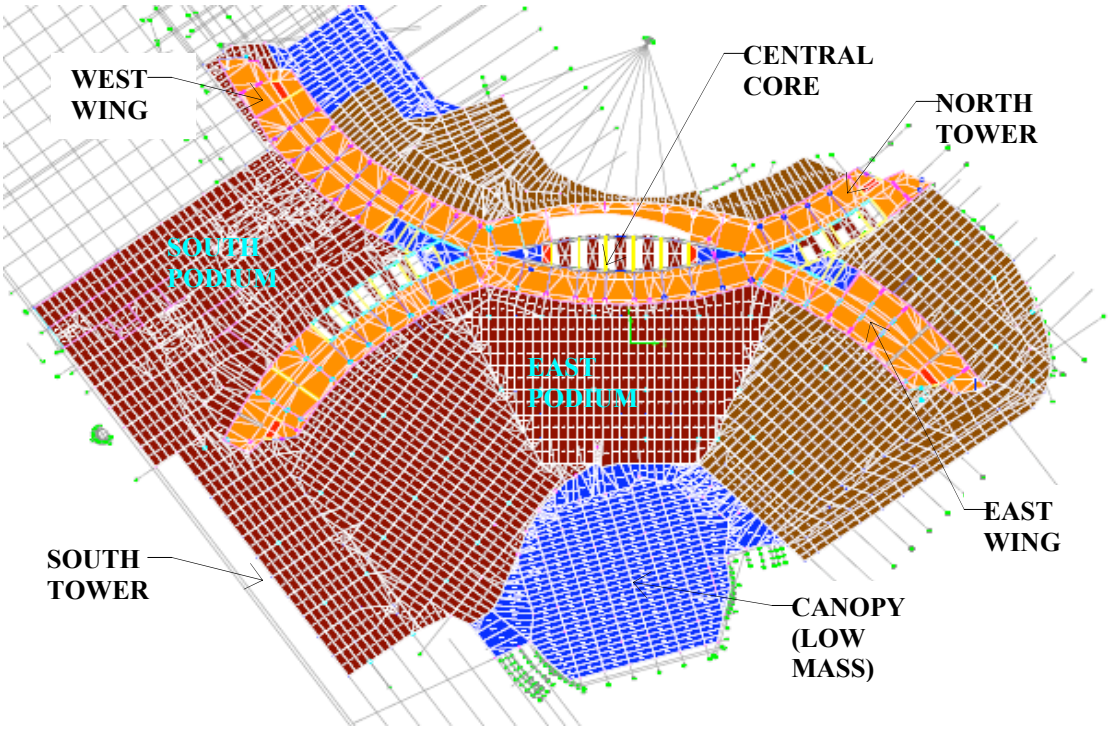


Figure 4. ETABS Model of Aria Tower with Attached Podium at Level 03

Seismic design was based on Modal Response Spectrum Analysis, using a specific response spectrum curve developed by GeoDesign for ground motions with a 2% probability of exceedance in 50 years. To achieve the design objective of balanced performance under seismic behavior, seismic forces were applied at mass centers of each wing along the principal axes of each wing/tower, and were also studied for the combined tower(s). The modal base shear calculated using the Complete Quadratic Combination (CQC) method was scaled up to match the equivalent static base shear. Member stiffness reductions were adjusted based on concrete stress levels from the analyses. The response spectrum and static analyses were then repeated for the new properties and iterated until convergence was reached. The analyses also took into account code-mandated accidental torsion, amplified torsional forces required due to plan irregularity, and amplification from the P-Δ effect.

The lateral system had a first-mode period of 4.62 seconds. Story drifts were well within the code recommended limits of 1.5% and 0.2% of story and building heights under seismic loads and wind load, respectively.

ASTM A1035 MMFX[2] steel was used to ease rebar congestion at critical shear wall end zones. While less ductile than conventional rebar, use of this steel was appropriate in ordinary concrete shear walls with low ductility demand. In addition, the American Concrete Institute[3] (ACI) placed an upper limit of 80 ksi on the yield strength of reinforcing steel, and a variance for higher strength was not granted by the County. As a result, even though the steel has a minimum yield value of 100 ksi, only 80 ksi was used in the design.

GRAVITY SYSTEM

Gravity loads are carried by two-way post-tensioned (PT) slabs supported by columns and shear walls. Exceptions were made at the tower roof, mechanical floors, casino floors, sky villas, and transition floors that have heavy loads, extensive floor openings, and/or interior planning not complete at the time of design. At the exceptional floors, conventionally reinforced two-way flat plate or one-way slab/beam systems were more suitable for their flexibility in responding to structural modifications. To account for the influence of building lateral system deformations on the slab/column frames, all associated gravity frames were designed and checked with appropriate load combinations that included forces from lateral analyses.

PT slabs were first analyzed by using strip models in ADAPT 2D software developed by ADAPT Corporation with the results exporting into its companion 3D finite element ADAPT Modeler for quantity optimization, stress evaluation and slab deflection assessment. See Figure 5. ADAPT Corporation collaborated with TT in modifying, improving and recalibrating their software throughout the tower design process. Their contribution was also invaluable to project completion.

A thickness/maximum span ratio of 1/48 was used per PCI[4] guidelines. While it is common to push for even thinner slabs, a 9 ½ inch thick PT slab was selected for its superior serviceability performance and comparable cost to thinner slabs. Preliminary studies demonstrated that in comparison with thinner slabs, the increase in concrete volume and foundation quantities were offset by savings in total PT and mild steel tonnage.

Neither ACI nor IBC discussed using unbonded PT tendons in resisting seismic force. However, PTI[5] observed that past experiences revealed excellent member performances with unbonded tendons in earthquakes. Hence an unbonded PT system was selected for the project considering the moderate Seismic Design Category C classification, favorable cost and ability to accommodate a tight construction schedule when compared to a bonded tendon system. Sufficient mild steel reinforcement was provided to resist at least 75% of the tensile force for both positive and negative moments at column faces from factored load combinations that included lateral load effects.

Banded tendons were placed in each wing in the transverse (radial) direction, with uniformly distributed tendons running in the longitudinal (circumferential) direction. The choice of tendon orientation addressed a concern that pre-stressing forces are ineffective acting parallel and adjacent to longitudinal stiff shear walls. By running the uniform tendons in this direction, most of the uniform tendons are farther from the shear walls and more effective in providing the desired two way action. Banding tendons in the transverse direction clustered the dead-end anchorages near cross walls and far from the complex and congested reinforcement of the shallow link beams.

The effective post-tensioning force was selected to balance 65% to 75% of the structural dead weight, while the remainder of flexural design moment is resisted by mild steel reinforcement. The design philosophy was to minimize PT based upon coordination with interior design and curtain wall consultants. The interior layout placed structurally undesirable floor penetrations in the vicinity of perimeter columns; the arrays of stud rails provided around these columns to meet punching shear strength requirements further congested areas already teeming with mild steel reinforcement and PT tendons; and the tendons must sweep to avoid openings. At the same time, façade panels with integral offsets at the sawtooth slab edge in front of perimeter columns require many more curtain wall anchorages/embedments, and some intrude into locations reserved for anchorage of banded PT tendons. After extensive cycles of coordination, both façade anchors and PT anchors were fit into the limited space. Minimizing the number of PT tendons alleviated anchorage congestion. In addition, having more than typical mild steel in PT slabs benefited slab ductility, improved redundancy, and provided the ultimate strength needed to resist load combinations including lateral load effects.

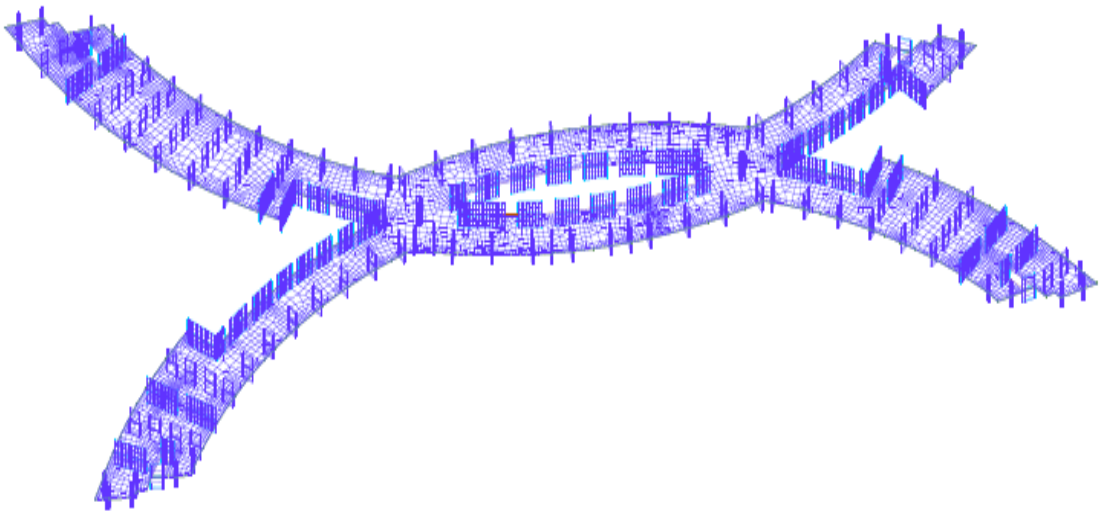


Figure 5. ADAPT 3D Model of Post-Tensioned Floor System

Long concrete structures in general and long PT structures in particular require attention to potential effects from restraint due to shortening. Elastic

shortening from PT precompression, long-term shrinkage and thermal strains must be considered. To address restraint between separate stiff cores, delayed-pour strips were located in the narrow slab 'neck' between the cores. Although the far ends of wings were relatively unrestrained against shortening, the contractor requested that additional pour strips be included in the design to suit concrete pour capacity and construction schedule. See Figure 6. The strips were left open for a minimum of 21 days after cable elongation was approved. These pour strips were critical to minimize the stresses induced by creep and shrinkage of the slabs bounded by stiff vertical elements. All pour strips were designed as simply supported drop-in slabs carried by a cantilevered slab at each side.

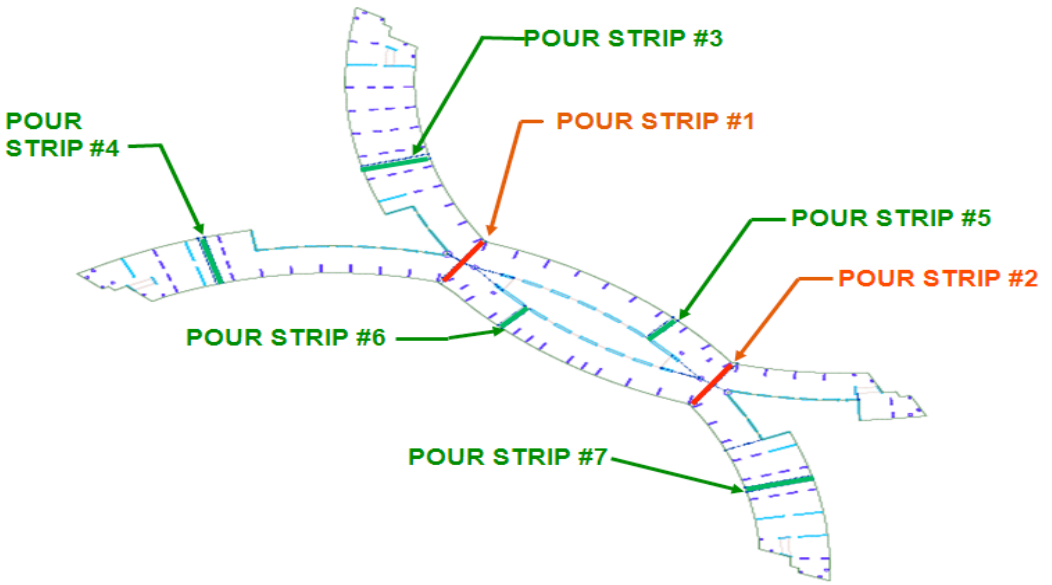


Figure 6. Pour Strip Locations

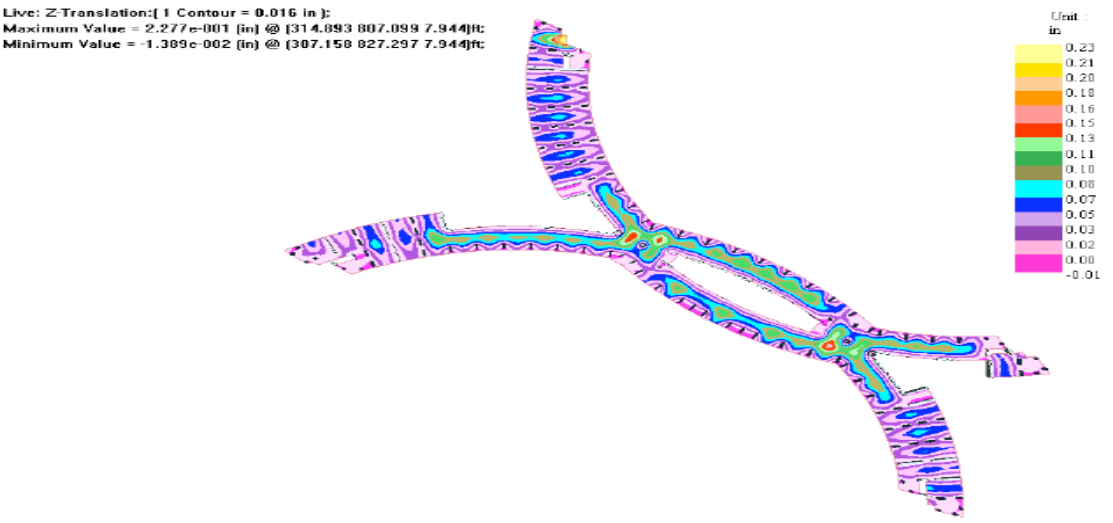


Figure 7. Slab Displacement under Live Load

For curtain wall support and curtain wall joint design it was important to control slab edge live load deflections as well as differential live load deflections between adjacent floors. Relative to adjacent column supports, the PT slab is anticipated to experience only 1/8 inch live load displacement at mid-span along the building perimeter. A maximum live load displacement of 1/4 inch occurs at the tips of 17 foot long cantilevered slabs. See Figure 7. The typical deflection to span ratio of 1/3,500 is well within stringent criteria for sensitive curtain wall installations.

Transfer girders are common occurrences throughout the building to suit different functions at different floors. Deep concrete beams up to two stories in height used as transfer girders were designed in accordance with the ACI[3] "Strut and Tie Model" procedure.

Columns were designed for forces from gravity loads and effects of lateral system deformations through appropriate factored load combinations. Functional changes demanded intricate column geometric shape changes throughout the tower. Columns near wing meeting points change shape numerous times along their height. Transformations that result in a shift in plan center of gravity, which are also common, required careful study for their impacts on column strength and lateral force transfer. At locations where a wing perimeter column above is interrupted by the corridor for a merging wing below, the interrupted column was 'hung' using bonded 150 ksi DYWIDAG pre-stressing thread bars with tightly controlled construction sequences.

SPECIAL FEATURES AND DISCUSSIONS

A tower roof screen wall is one of Aria Tower's distinguishing features. See Figure 2. It serves to conceal building maintenance cranes that facilitate window washing operations. The aluminum fin enclosures complement the reflective glass and aluminum curtain wall panels below. Closely spaced aluminum fins are cantilevered a maximum of 6 feet from back-up alumium frames supported by structural steel tube posts cantilevered up to 36 feet from roof structures. Behind the screen walls, two sets of window washing cranes were designed to operate simultaneously on tracks along the entire length of each tower. The tower cranes with 109 feet booms exert tremendous forces on structural supports in downward, upward, and torsional directions. For smooth crane operation, the deep concrete beams, girders, and pedestals designed to support the tracks were sized to restrict deflection to less than span/1,200 under service loads.

A water wall within the Aria Tower ground floor lobby was only a glimmer of a concept when lower floor construction began: water flowing down thin sheets of glass panels sloped at 7 degrees and suspended from two floors above in a 60 foot high space. To keep structural support as thin as the glass panel and its equally thin frame, a post-tensioned cable system was planned. This required all concrete elements to receive the water wall and associated mechanisms to be tuned to resist

substantial post-tensioning forces and limit deflection to a negligible value to minimize its effect on cable system performance. In 2009, Novum Corporation received the commision to design the water wall by using a stainless steel cable system. This water wall is indubitably one of the highlight features in the tower lobby.

Curved floor plans such as Aria Tower wings often perplex structural designers of post-tensioned systems. Should the tendons be curved or should they run straight? The first impression is that tendons placed along a curve will result in a transverse component perpendicular to the building curvature adding lateral force to the building system. On the contrary, if tendons curve to follow the floor plan curve there should be no net transverse force from the post-tensioning, and precompression stresses from the PT act uniformly. However, if building floor plan and tendons curve differently the force of 27 kips per tendon can have a significant impact on the lateral system and on in-plane forces in the slab itself. It should not be ignored.

Shrinkage and creep effects in tall concrete structures are of significance to building short term and long term serviceability. Differential axial strains on columns and shear walls were of particular interest to Aria Tower curtain wall construction and installation tolerances, as the façade runs along both columns and shear walls. We developed a proprietary program using Visual Basic in EXCEL to estimate cumulative effects based on Model B3 from report ACI 209R-92[6]. The design implemented differential shortening mitigation measures, including optimization of member geometries, reinforcing ratios, and concrete strengths. In addition, floor elevations included compensation at every 5 levels to help mitigate estimated future shrinkage and creep movements.

CONCLUSION

The journey of Aria Tower design and construction started in the spring of 2004, and ended with spectacular fireworks for its Grand Opening ceremony on the 19th of December, 2009. While subsequent events have swirled around CityCenter with drama worthy of Las Vegas, few have paused to reflect on the fact that this LEED Gold Aria Tower is not only iconic and visionary, but a symbol of Las Vegas's future direction: a feat in design, engineering, and construction completed on schedule with few glitches thanks to a successful team effort. Thornton Tomasetti (TT) is proud to have been a part of the design and construction team on a project with such ambitious goals including a vision for the future of Las Vegas, a highly compressed design and construction schedule, and integration with surrounding buildings. This accomplishment entailed collective efforts and a conscientious emphasis on team work and cooperation from all parties involved. Therefore, this article also pays tribute to Udom Hungspruke, project manager of TT, Pelli Clarke Pelli Architects (PCPA) as design architect; HKS Architects as production architect; Perini Construction as General Contractor; and Flack & Kurtz as MEP consultant. We also would like to thank Jonathan Neubauer, MECE, and Corey Guo, P.E. for their technical contributions.

REFERENCES

1. *International Building Code (IBC) 2000*, International Code Council (ICC) Inc., 4051 West Flossmoor Road, Country Club Hills, IL 60478-5795.
2. Ghosh, S.K., "*Application of ASTM A 1035 MMFX Steel Reinforcement in Building Application – An Appraisal*", S.K. Ghosh Associates, Inc, April, 2006.
3. *Building Code Requirements for Structural Concrete (ACI 318-99) and Commentary (ACI 318R-02)*, ACI Committee 318, American Concrete Institute, Farmington Hills, MI, 2002.
4. PCI Manual, 6th Edition. "*PCI design Handbook – Precast and Prestressed Concrete",* Prestressed Concrete Institute (PCI), March, 2004.
5. Alami, B.O., "*Unbonded and Bonded Post-Tensioning Systems in Building Construction – A Design and Performance Review*", Post-Tensioning Institute (PTI) Technical Notes, September, 1994.
6. ACI 209-92., "*Prediction of Creep, Shrinkage, and Temperature effects on Concrete Structures*", American Concrete Institute (ACI) Committee 209, March, 1992.

Implementation of a multiagent-based paradigm for decentralized real-time structural health monitoring

K. Smarsly[1], K. H. Law[1] and D. Hartmann[2]

[1]Stanford University, Department of Civil and Environmental Engineering, 473 Via Ortega, Stanford, CA 94305-4020, USA; email: {smarsly, law}@stanford.edu
[2]Ruhr-University Bochum, Department of Civil and Environmental Engineering, Universitaetsstr. 150, 44780 Bochum, GERMANY; email: hartus@inf.bi.rub.de

ABSTRACT

Engineering structures such as wind turbines require continuous monitoring to ensure structural safety, to reduce the overall maintenance and repair costs and, ultimately, to achieve extended lifetimes and a greater economic viability. For that purpose, an automated SHM system for wind turbines has been developed and installed on a 500 kW wind turbine in Germany. During its operation, temporary malfunctions of the installed sensing units have been observed. These malfunctions, such as temporary sensor breakdowns which are well known from real-time SHM systems, might cause the loss of valuable monitoring data if not detected timely. A multi-agent system, which is capable of self-detecting system malfunctions and notifying the human individuals automatically, has been developed and integrated into the existing SHM system. The SHM system and its subsystem, the multi-agent system, have been in continuous operation since 2009. Since then, various malfunctions have automatically been detected and appropriate actions have been taken in a timely manner. As a result, the malfunctioning of the sensors did not lead to significant data loss, thus enhancing the quality of the SHM system.

INTRODUCTION

Degradation of engineering structures, increasing demands on structural safety and growing maintenance costs are emerging problems that are gaining attention in civil and environmental engineering. Engineering structures require continuous monitoring and frequent inspections in order to reliably assess their performance and safety, to provide timely maintenance support and to increase service life. This paper discusses the development and implementation of a self-managed monitoring system for a wind turbine structure. Wind turbines represent one of the most cost-effective sources of electrical power providing an environmentally friendly energy production. Accordingly, wind energy technology is fostered and large wind energy farms are being built in many countries. The world market for wind turbines has considerably

grown, for example, with approximately 16 GW of new capacity added worldwide in the first half of year 2010 (WWEA 2010).

The necessity of applying innovative structural monitoring systems has been recognized over the past several years. Wind turbine monitoring is considered worthy of substantial investments and supports by governments (BMJ 2009, MIWF 2009). Considerable efforts are currently being undertaken to design SHM systems for wind turbines. Novel sensing technologies and sophisticated monitoring techniques are being developed and applied to wind turbines (Jüngert 2008, Lading *et al.* 2002, Sutherland *et al*. 1994, Rolfes *et al*. 2007). However, robust software platforms designed to facilitate data interrogation, data archiving and automated execution of monitoring tasks have received little attention.

In a previous research project (Hartmann and Höffer 2010), a decentralized real-time SHM system for remote monitoring of wind turbines has been designed, implemented and installed on a 500 kW wind turbine in Germany. The decentralized SHM system integrates different information technologies and provides automated data acquisition, storage and interrogation functionalities. In addition, the SHM system provides remote access to the monitoring data including flexible data visualization and data export mechanisms. During the operation of the SHM system, it has been observed that temporary malfunctions occurred affecting the performance and the reliability of the SHM system. The causes for such malfunctions, well-known from real-time SHM systems, are manifold, e.g. communication problems when using long-distance lines, temporary power blackouts that affect the computer systems or simply hardware problems of the data acquisition units (DAUs) due to extreme weather conditions.

Evidently, if not detected timely the malfunctions might cause the loss of valuable monitoring data. A multi-agent system, which is designed to detect malfunctions automatically and to immediately send out alerts for corrective actions, has been developed and integrated into the existing SHM system. Multi-agent software technology allows creating modular and extensible decentralized systems based on cooperating software agents, which are self-contained computational entities capable of autonomously carrying out monitoring tasks, such as detecting DAU malfunctions, generating alert messages and sending notifications. Each software agent is designed for solving one single task. With a certain degree of flexibility and autonomy, a software agent can decide on its own which actions are appropriate to solve its task and which other cooperative agents are to be requested for assistance to achieve a specific goal. A multi-agent system is scalable and can be easily extended or modified by adding further specialized software agents.

This paper presents a multi-agent system designed for structural health monitoring applications. First, a decentralized real-time SHM system installed on the wind turbine in Germany is described. The design and implementation of the multi-agent system and its integration with the existing SHM system are discussed. Examples are presented to demonstrate the practicability and the reliability of the multi-agent system, which has been in continuous operation since 2009.

A DECENTRALIZED REAL-TIME SHM SYSTEM FOR WIND TURBINES

A decentralized real-time SHM system is designed and prototypically implemented on an Enercon E-40 wind turbine located in Dortmund (Germany) to continuously assess its performance and operational conditions. As shown in Fig. 1, the SHM system consists of a hardware monitoring subsystem M_1 and a software monitoring subsystem M_2. Installed in the observed wind turbine, the hardware subsystem M_1 includes an array of sensors connected to data acquisition units, which are controlled by a computer located on-site in the structure. Remotely connected to the hardware subsystem, the software subsystem M_2 consists of software modules that are designed to autonomously execute crucial monitoring tasks, such as storing and converting the collected data sets. Both subsystems are briefly described in the following.

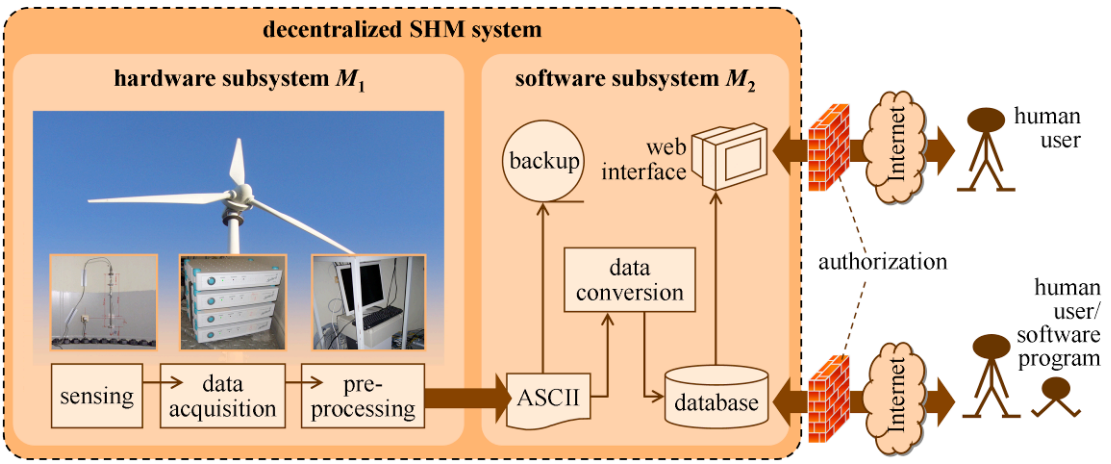


Figure 1. Architecture of the SHM system.

Hardware subsystem

The hardware subsystem M_1 collects structural and environmental data for assessing the conditions of the wind turbine. To this end, the wind turbine is instrumented with sensors that are installed both inside and outside the steel shaft as well as on the foundation of the structure. The sensors are controlled by data acquisition units which are connected to a computer located in the wind turbine.

As shown in Fig. 2, six inductive displacement transducers, type HBM-W5K, are mounted at two different levels inside the shaft. The displacement transducers are complemented by Pt100 resistance temperature detectors to account for temperature influences on the displacement measurements. Additional temperature sensors are placed at two other levels in and outside the wind turbine to measure the temperature gradient of the wind turbine shaft. For the temperature data acquisition, three 4-channel Picotech RTD input modules PT-104 are installed and, through RS232 to USB interface converters, connected to the computer located in the wind turbine.

Six three-dimensional PCB-3713D1FD3G piezoelectric accelerometers, manufactured by PCB Piezotronics, are placed at five levels in the wind turbine shaft. At the foundation of the wind turbine, three single-axis PCB-393B12 piezoelectric

seismic ICP accelerometers are installed. For acquiring wind information, a Metek USA-1 ultrasonic anemometer is mounted on a telescopic mast near the wind turbine. Fig. 2 shows the instrumentation of the wind turbine, exemplarily illustrating the interior of the shaft at the level of 21.3 m as well as the anemometer installed.

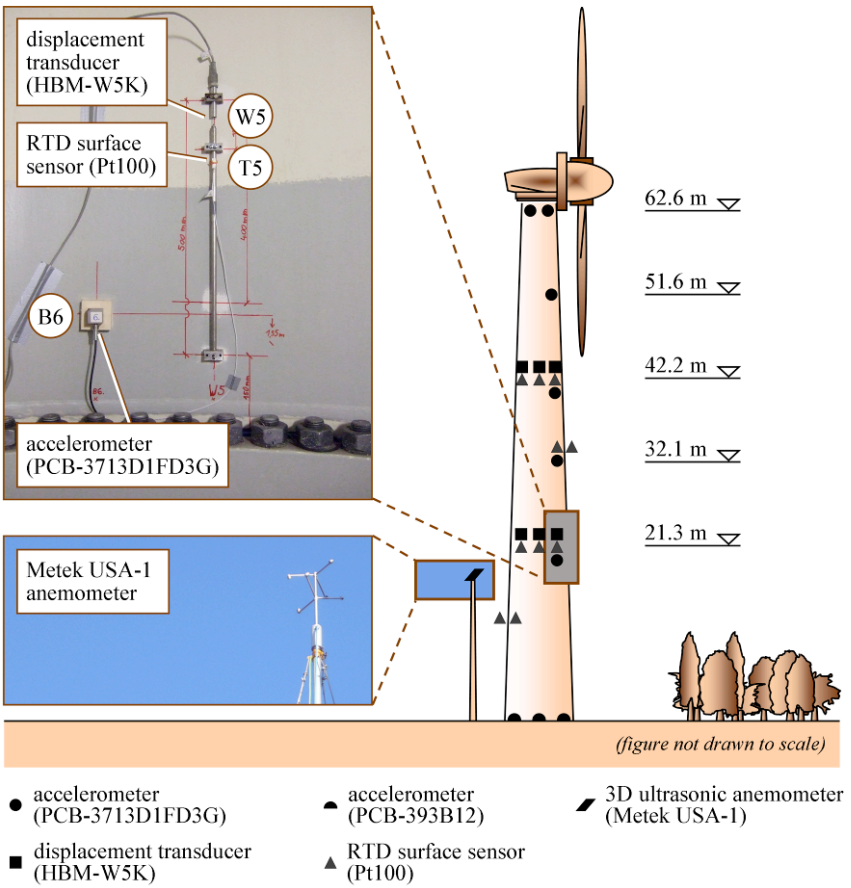


Figure 2. Instrumentation of the wind turbine (hardware subsystem).

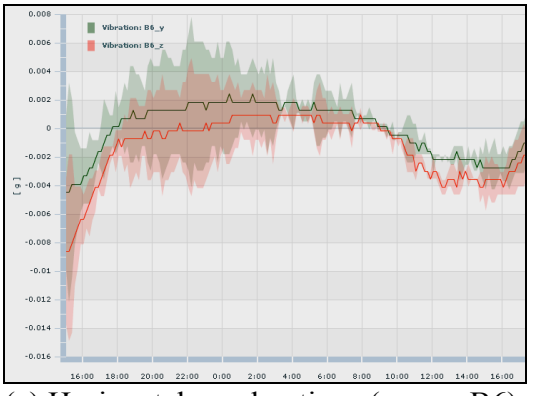
Software subsystem

The data collected and pre-processed by the hardware subsystem M_1 is forwarded to the software subsystem M_2 using a permanently installed DSL connection. The purpose of the software subsystem is to perform data archival and data processing tasks such as condensing, converting and storing of the acquired data sets. Furthermore, the subsystem is design to allow authorized users to remotely access the SHM system independent of their geographical location. The subsystem M_2 comprises (a) server systems for on-line data synchronization, data conversion and data transmission, (b) RAID-based storage systems for periodic backups, and (c) a MySQL database system for persistent data storage. A web-based interface is available for remotely accessing and visualizing the monitoring data.

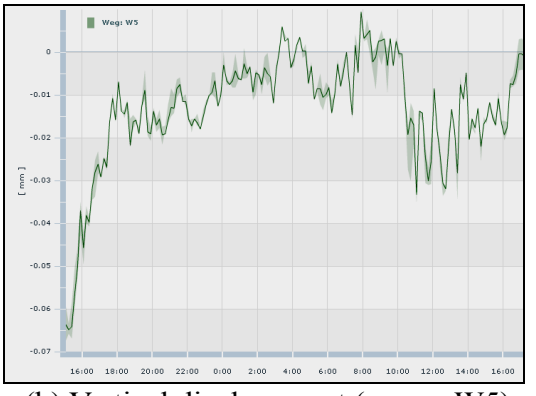
Remote access to the data is provided in two ways: through a web interface and through a direct database connection. The web interface offers GUIs for remotely

visualizing, exporting and analyzing the monitoring data. Through the database connection, the monitoring data can be directly accessed by software applications such as MATLAB and other tools.

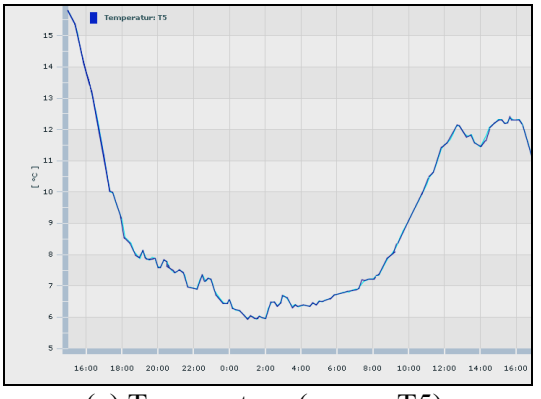
To illustrate the remote access to the SHM system using the web interface, Fig. 3 shows a user's GUI for visualizing wind turbine data, collected on October 22, 2010, in near real-time. In Fig. 3a, a typical acceleration time history is displayed, collected by accelerometer B6 shown in Fig. 2 at the level of 21.3 m. Fig. 3b, 3c and 3d show, respectively, the displacement time histories (collected by sensor W5), temperature data (acquired by displacement transducer T5,) and wind speed (recorded by the anemometer). Besides remotely visualizing the sensor data, the user can analyze the sensor data with embedded functionalities provided by the web interface.



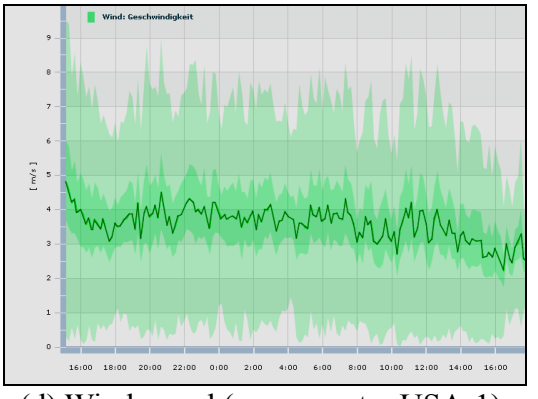
(a) Horizontal accelerations (sensor B6).



(b) Vertical displacement (sensor W5).



(c) Temperature (sensor T5).



(d) Wind speed (anemometer USA-1).

Figure 3. Data sets remotely accessed via the web interface provided by the SHM system (collected on October 22, 2010, during one day).

Malfunctions observed during operation

A typical malfunction of a temperature DAU, observed during operation of the SHM system is elucidated in Fig. 4. As can be seen from Fig. 4, the temperature DAU malfunction is implicitly indicated by anomalies within the data sets collected by the DAUs themselves. A malfunction, or cause for alert, that is characterized by a large number of identical measurements due to an internal system crash of the DAU at time

t_0 is shown in Fig. 4. As a result of the malfunction occured, the DAU cannot record and store the actual temperature measurements. Instead, the last normally collected value (sensed right before the occurrence of the malfunction) is stored repeatedly by the DAU.

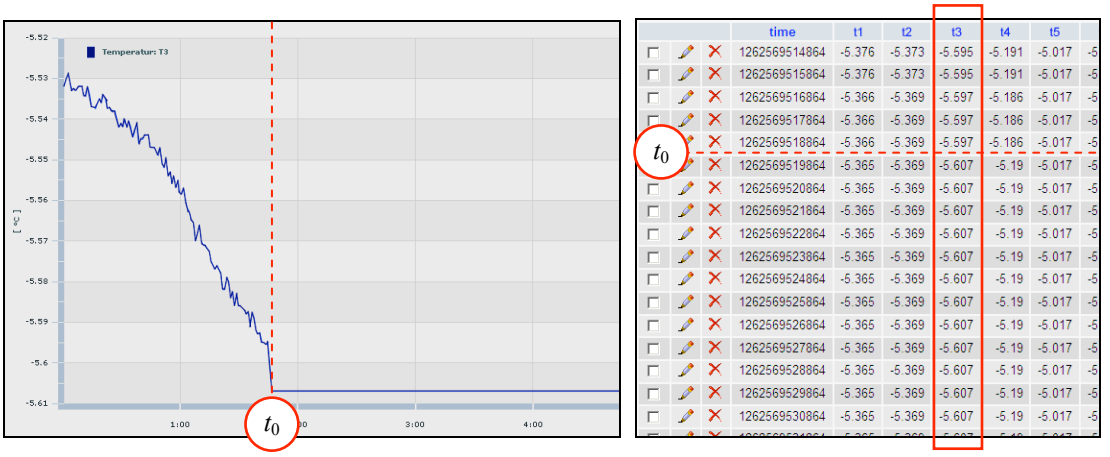


Figure 4. Visual and numerical representation of a DAU malfunction illustrated by temperature sensor T3 through the web interface (left) and the direct database connection (right).

A MULTI-AGENT SYSTEM FOR AUTONOMOUS MALFUNCTION DETECTION

The purpose of the multi-agent system, which is integrated into the SHM system, is to detect malfunctions in the DAUs automatically and to inform the responsible individuals immediately about the defects so that the affected DAUs can be restarted remotely or replaced in a timely manner. The agent-based paradigm has been chosen as a technological basis for the implementation of the self-detection and self-management functions. A software agent can flexibly carry out its autonomous actions and cooperatively communicate and work with other agents. Software agents are characterized by a number of properties (Wooldridge and Jennings 1995):

- **autonomy**: agents operate without any direct intervention by humans and exhibit control over their actions
- **social ability**: agents interact with other agents (and possibly humans) via agent-communication languages
- **reactivity**: agents perceive their environment (for example, the physical world or a SHM system) and respond to the changes that occur in the environment
- **pro-activeness**: agents do not simply act in response to their environment, but they are able to take initiative and to apply goal-directed behavior

The developed multi-agent system comprises a set of collaborating software agents implemented to accomplish the tasks required for malfunction detection. First,

the multi-agent system hosts two special agents, namely the "Agent Management System (AMS) agent" and the "Directory Facilitator (DF) agent". The AMS agent is responsible for the overall management actions, including creating and terminating other agents. The DF agent implements a yellow page service, allowing the agents to advertise their services as well as to look up other agents that offer the services needed to cooperatively accomplish a specific monitoring task. The AMS and DF agents together provide the overall configuration description of the multi-agent system. Furthermore, an "interrogator agent", implemented for analyzing the monitoring data with respect to malfunctions, and a "mail agent" for sending notifications to the responsible individuals are included in the multi-agent system.

Data interrogator agent

The interrogator agent analyzes the sensor data collected by the DAUs to detect malfunctions. As in the example described earlier, one malfunctioning symptom for a temperature DAU can be characterized by a large number of identical measurements. To detect such an anomaly, the interrogator agent at certain time intervals extracts and analyzes the temperature data sets stored in the centralized MySQL database. A set of configuration files (specifying interrogation parameters, database URL, database driver, sensor specification, scheduled interrogation intervals, etc.) is pre-defined in the multi-agent system (Smarsly *et al.* 2010).

The connection to the database being part of the software subsystem M_2 is realized through a programming interface based on the Java Database Connectivity (JDBC). JDBC is an industry standard for database-independent connectivity between Java applications, such as the software agents considered here, and various database systems. The security of database requests and data transmissions are provided by the database system, i.e. the MySQL database, which requires password and username as well as secure drivers to be specified by the agent.

Email notification agent

Upon detecting a malfunction, responsible individuals are immediately notified. On behalf of the interrogator agent, notifications are issued by the mail agent via an agent-based email messaging service in a two-step process. In the first step, the mail agent collects all relevant data from the monitoring system, which is necessary for composing the emails. The mail agent creates the emails using the information about the observed anomaly that are provided by the interrogator agent. Metadata, such as addresses of the recipients or the email server to be used, are acquired for the automated emailing; these metadata are stored in configuration files located in the multi-agent system. In other words, the email content is created based on the anomaly information received from the interrogator agent and the email header is automatically created based on the metadata obtained by the mail agent from the configuration files resided in the multi-agent system. Once the emails are composed, they are sent by the mail agent to the email clients (the individuals responsible for the malfunctioning devices). Secure email messages are ensured by username- and

password-based authentications that the mail agent, like a human user, needs to specify when trying to access the mail server.

Decentralization and extensibility

One distinct advantage of the agent-based approach is that the software system can be easily extended to accommodate additional functions. For example, self-detections of other types of malfunctions (that are not characterized by a large number of identical values) or interrogations of other measurement data (such as acceleration data) can be implemented as additional specialized agents that are integrated into the multi-agent system. Also, damage detection algorithms, such as fast Fourier transforms or autoregressive models, can be included into the multi-agent system as software agents. Software packages, such as MATLAB, can be integrated into the multi-agent system by "wrapping" the particular software package as an agent.

Software agents can be distributed over several computers and geographically situated at different locations. Communications between distributed agents can be carried out through agent messages via computer networks, such as the Internet. Additional agents can be launched remotely to perform specific structural monitoring functions as long as they are registered to the multi-agent system.

To ensure extensibility and interoperability, the multi-agent system is implemented in compliance with the specifications issued by the Foundation for Intelligent Physical Agents (FIPA). FIPA, the IEEE Computer Society standards organization for agents and multi-agent systems, promotes agent-based technology, interoperability of agent applications and the interoperability with other technologies. The FIPA agent communication specifications, for example, ensure a common understanding of two or more communicating agents based on the FIPA Agent Communication Language (ACL) as used for the communication within multi-agent systems (FIPA 2002).

VALIDATION OF THE MULTI-AGENT SYSTEM

The multi-agent system has been integrated into the existing SHM system to monitor the temperature DAUs instrumented on the wind turbine. The SHM system and the multi-agent system are installed at different geographical locations as follows:

- The hardware subsystem M_1 (including sensors, DAUs and on-site computer) is installed with the wind turbine located in Dortmund (Germany).
- The components of the software subsystem M_2, including the MySQL database system, reside on different computers at the Institute for Computational Engineering at the Ruhr-University Bochum (Germany).
- For the validation tests, the multi-agent system is distributively located at different institutes: The interrogator agent and the mail agent for detecting malfunctions and generating alerts are located at Stanford University (USA) while the email server, used by the mail agent at Stanford University, is situated at the Ruhr-University Bochum.

For detection of malfunctions in the temperature DAUs, the interrogator agent scans the collected data sets, based on experience, for 150 consecutive identical values. Fig. 5 shows two malfunctions, detected from the data sets collected by the temperature DAUs in January, 2010 (Fig. 5a), and in July, 2010, (Fig. 5b). These malfunctions are characterized by a large number of identical measurements, which, as a result of a DAU-internal system crash, are repeatedly stored by the DAU instead of regular measurements.

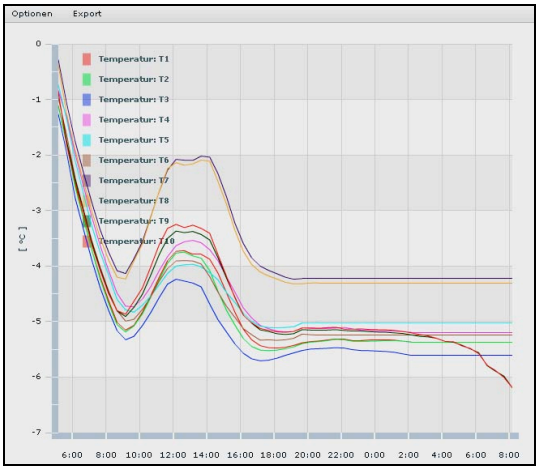
Once a malfunction is detected, the multi-agent system generates an alert to notify the authorized users immediately about the malfunction so that appropriate measures can be taken in order to avoid the loss of valuable monitoring data. In detail, the interrogator agent requests the mail agent to inform the responsible users via email about the malfunction discovered. As a result, the mail agent generates an email to submit it to the recipients as specified in the multi-agent system's configuration files. As shown in Fig. 5c, the email content includes detailed information on the detected malfunction and is generated using the analysis results provided by the interrogator agent. The email header is assembled based on the information taken from the configuration files.

SUMMARY AND CONCLUSIONS

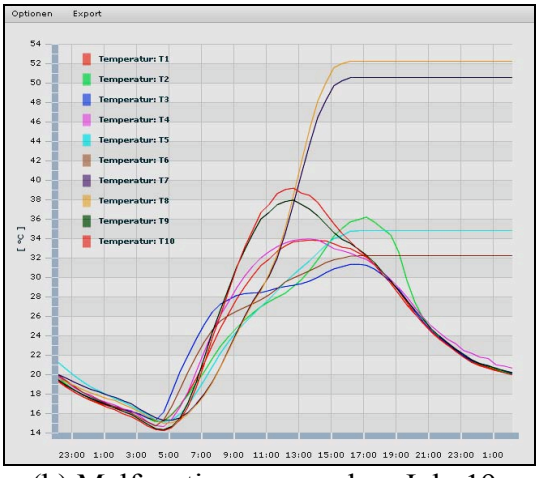
In this paper, a multi-agent system for the autonomous detection of SHM system malfunctions has been presented. The multi-agent system has been integrated into an existing decentralized SHM system for real-time monitoring of a 500 kW wind turbine in Germany. Since its initial deployment in December, 2009, the multi-agent system is in continuous operation and has reliably detected all malfunctions of the temperature data acquisition units of the SHM system[1]. Furthermore, the multi-agent system has immediately notified the technicians by email, whereupon the affected data acquisition units were remotely restarted by the technicians in a timely fashion. Consequently, considerable amounts of valuable sensor data, which could otherwise be lost as in conventional SHM systems, were saved and are available for assessing the performance and operational conditions of the wind turbine.

Due to its adaptability and modularity, the multi-agent system can be easily extended and integrated with other existing SHM systems. Software agents and the multi-agent system can be installed on any computers at any locations away from the SHM system. Treated as software agents, different algorithms for malfunction detection and monitoring functions can easily be added into the multi-agent system. In summary, this research has successfully demonstrated that the multi-agent software paradigm can be advantageously deployed for long-term structural health monitoring practice under real-world conditions.

[1] For long-term operation, the multi-agent system has been installed at the Institute for Computational Engineering in Bochum.



(a) Malfunction occurred on January 3, 2010 (affected sensors: T1, …, T8).



(b) Malfunction occurred on July 19, 2010 (affected sensors: T5, T6, T7, T8).

Von: monitoring@inf.bi.ruhr-uni-bochum.de
An: smarsly@stanford.edu
Betreff: [Generated Email] Wind Turbine Safety Report
Datum: 20.07.2010 03:33:20

This email has autonomously been generated
and was sent by a software agent. Do not reply.

This message is sent by the 'InterrogatorAgent'.
Content:

Analysis properties:
Database driver: com.mysql.jdbc.Driver
Database table: pt104
Number of values observed per sensor: 86400
Number of significant values: 150
Sensors analyzed: t1;t2;t3;t4;t5;t6;t7;t8;t9;t10;

Anomaly detected:
DAU id: pt104
Date: Mon Jul 19 17:57:59 CEST 2010
Sensor: t5
Errornumber: 34.764
(…)

Properties:
IP address: 134.147.216.69
Internet host: tunsql
Hap: tunsql: 1099/JADE
Responsible agent: mailAgent@tunsql:1099/JADE
Agent container: tunsql:1099/JADE
Container state: Ready(4)
Agent platform: tunsql:1099/JADE
Mail host: delta.inf.bi.rub.de
Port: 25
Debugging: true
Protocol: smtp
Sender: monitoring@inf.bi.ruhr-uni-bochum.de
Receivers: 2
Local config file: config\mail.shm

(c) Email notification generated and sent in direct consequence of malfunction (b).

Figure 5. Visual representation of two detected malfunctions and email notification generated and sent by the software agents.

ACKNOWLEDGEMENTS

The authors gratefully acknowledge the financial support of the German Research Foundation (DFG) through the grants SM 281/1-1 and HA 1463/20-1. This research is also partially supported by the National Science Foundation (NSF) through grant CMMI-0824977.

REFERENCES

Foundation for Intelligent Physical Agents – FIPA (2002). SC00061:2002 *FIPA ACL Message Structure Specification*. Alameda, CA, USA.

German Federal Ministry of Justice – BMJ (2009). "*EEG – Gesetz für den Vorrang erneuerbarer Energien*." (BGBl. I S. 2074 and BGBl. I S. 643), Berlin, Germany.

Hartmann, D., and Höffer, R. (2010). "*Lifespan assessment of wind energy converters through system identification (Lebensdauerabschätzung von Windenergieanlagen mit fortlaufend durch Systemidentifikation aktualisierten numerischen Modellen).*" Research project funded by the German Research Foundation (DFG) through the research grant HA 1463/20-1, Ruhr-University Bochum, Bochum, Germany.

Jüngert, A. (2008). "Damage Detection in wind turbine blades using two different acoustic techniques." *The NDT Database & Journal (NDT)*.

Lading, L., McGugan, M., Sendrup, P., Rheinländer, J., and Rusborg, J. (2002). "*Fundamentals for Remote Structural Health Monitoring of Wind Turbine Blades – a Preproject*." Report, Risø National Laboratory, Roskilde, Denmark.

Ministry of Innovation, Science, Research and Technology of the State of North Rhine-Westphalia – MIWF (2009). "*Das Cluster EnergieForschung.NRW*." Report, Düsseldorf, Germany.

Rolfes, R., Zerbst, S., Haake, G., Reetz, J., and Lynch, J.P. (2007). "Integral SHM-System for Offshore Wind Turbines Using Smart Wireless Sensors." *Proceedings of the 6th International Workshop on Structural Health Monitoring*, Stanford, CA, USA.

Smarsly, K., Law, K.H., and Hartmann, D. (2010). "A Multi-Agent-Based Collaborative Framework for a Self-Managing Structural Health Monitoring System." *ASCE Journal of Computing in Civil Engineering* (submitted).

Sutherland, H., Beattie, A., Hansche, B., Musial, W., Alread, J., Johnson, J., and M. Summers (1994). "*The Application of Non-Destructive Techniques to the Testing of a Wind Turbine Blade*." Sandia Report SAND93-1380, Sandia National Laboratories, Albuquerque, NM, USA.

Wooldridge, M., and Jennings, N.R. (1995). "Intelligent Agents: Theory and Practice." *Knowledge Engineering Review*, **10**(2), 115-152.

World Wind Energy Association – WWEA (2010). "*16 Gigawatt of Wind Power added in First Half of 2010*." Press release. [Online]. Available at: http://www.wwindea.org [Accessed October 26, 2010].

Electrical Resistance and Seismic Behavior of Carbon Nanofiber RC Bridge Columns

R. N. Howser[1], H. B. Dhonde[2] and Y. L. Mo[3]

[1]Thomas T.C. Hsu Structural Research Laboratory, Department of Civil and Environmental Engineering, University of Houston, N107 Engineering Building 1, Houston, TX 77002-4003; PH (713) 725-8724; email: rnhowser2@uh.edu
[2]Thomas T.C. Hsu Structural Research Laboratory, Department of Civil and Environmental Engineering, University of Houston, N107 Engineering Building 1, Houston, TX 77002-4003; PH (713) 775-6037; email: hbdhonde@central.uh.edu
[3]Thomas T.C. Hsu Structural Research Laboratory, Department of Civil and Environmental Engineering, University of Houston, N107 Engineering Building 1, Houston, TX 77002-4003; PH (713) 743-4274; email: yilungmo@egr.uh.edu

ABSTRACT

Civil infrastructures are generally a country's most expensive investment, and concrete is the most widely used material in the construction of civil infrastructures. During a structure's service life, concrete ages and deteriorates, leading to substantial loss of structural integrity and potentially resulting in catastrophic disasters such as highway bridge collapses. A solution to prevent such occurrences, is the use of Structural Health Monitoring (SHM) technology for Smart Concrete structures. Smart Concrete is concrete reinforced with Carbon Nanofibers (CNF). CNF concrete has many structural benefits. CNF restricts the growth of micro cracks in addition to yielding higher strength and ductility. Additionally, test results indicate a relationship between electrical resistance and concrete strain. A series of RC columns were built and tested under a reversed cyclic loading using CNF as a SHM device. The SHM device detected and assessed the level of damage in the RC columns, providing a real-time health monitoring system for the structure's overall integrity.

INTRODUCTION

The use of fibers to reinforce brittle materials can be traced back to ancient times when straw was added to mud bricks. The modern development of the use of fibers in construction began in the 1960s with the addition of steel fiber to reinforced concrete structures. This was closely followed by the addition of polymeric fibers, glass fibers and carbon fibers in the 1970s, 80s and 90s, respectively (Li 2002).

Fibers improve brittle materials such as concrete by enhancing tensile strength, ductility and toughness (Shah and Naaman 1976). In concrete, they do this by arresting cracks. The cracking process within concrete begins with the onset of isolated nanocracks. These nanocracks grow together to form localized microcracks, which in turn grow together to form macrocracks. These macrocracks widen to form cracks visible with the naked eye. Fibers arrest these cracks by forming bridges across them. With increasing tensile stress, a bond failure eventually occurs, and the fiber will pull out of the concrete allowing the crack to widen. An ideal concrete in terms of strength, ductility and toughness would include nano, micro and macrofibers; however, this concrete is not currently economically feasible.

Fiber research in concrete construction is an ongoing field and the use of carbon nanofibers (CNF) was examined in this study. The addition of CNF to concrete has many advantageous mechanical and electrical properties. In addition to increased strength and ductility, which is found in all fiber-reinforced concretes, CNF concrete (CNFC) exhibits increased conductivity (Chen and Chung 1993, Li, Xiao, et al. 2004, Li, Zhang and Ou 2006, Li, Zhang and Ou 2007). Because of the tunnel conductivity effect, CNFC exhibits properties necessary for strain monitoring and electromagnetic interference (EMI) shielding. Short-fiber composites were found to be a new class of strain sensor based on the concept of short electrically conducting fiber pull-out that accompanies slight and reversible crack opening. The electrical conductivity of the fibers enables the DC electrical resistivity of the composites to change in response to strain damage or temperature, allowing sensing (Chen and Chung 1996, Chung 1995, Chung 2000, Xiao, et al. 2003). The most difficult issue presented during CNFC production is dispersion of the CNF. Well dispersed CNF results in uniform calcium-silicate-hydrate (CSH) gel formation (Chung 2005). It was discovered that CNF disperses better in self-consolidating concrete (SCC) (Gao, Strum and Mo 2009), so a shear-critical self-consolidating carbon nanofiber concrete (SCCNFC) column was built and tested under a reversed cyclic load. The structural behavior of the column was examined in addition to the self-sensing ability of the SCCNFC. The results were compared to the structural and self-sensing ability of a self-consolidating reinforced concrete (SCRC) specimen that did not contain CNF. It was found that a Smart Concrete containing CNF is capable of self-Structural Health Monitoring.

CARBON NANOFIBER CEMENT-BASED MATERIALS AS A STRAIN SENSOR

The beginning of carbon nanofiber composites began with the discovery of the carbon nanotube (CNT) in the late 1980s (Lau and Hui 2002). CNT are over 100 times stronger than steel and only one-sixth of the weight in addition to demonstrating high thermal and electrical conductivities (Lau and Hui 2002). These properties make CNT extremely attractive for engineering materials.

CNT and carbon nanofibers (CNF) are very similar. CNF consist of grapheme layers arranged as stacks of cones, cups or plates to create a cylindrical nanostructure. CNT consist of grapheme layers wrapped into perfect cylinders. CNF are easier to construct than CNT (Ngo, et al. 2006).

Since the 1990s, researchers have been adding CNF to cement paste (containing no aggregate), mortar (containing fine aggregate) and concrete (containing fine and coarse aggregate) (Chen and Chung 1996, Chung 2000). The addition of CNF to cement-based materials has many advantageous mechanical and electrical properties including increased strength, ductility and conductivity (Chen and Chung 1993, Li, Xiao, et al. 2004, Li, Zhang and Ou 2006, Li, Zhang and Ou 2007).

Strain sensing is a function necessary for smart structures. There are two types of strain sensing, reversible and irreversible. The measurement of irreversible strain allows structural health monitoring, while the sensing of reversible strain permits dynamic load monitoring. Structural health monitoring is the process of implementing a damage detection and characterization strategy for engineering structures. Dynamic load monitoring can detect loads on structures as they are applied and removed in real time. These are important technologies because they gauge the ability of a structure to perform its intended function aging, degradation or disasters. Typically, monitoring reversible strain is more difficult because it can only be

monitored in real time. Additionally, reversible strain tends to be smaller than irreversible strain (Chen and Chung 1996).

Sensing refers to the ability to provide and electrical or optical response to a stress or strain. Chen and Chung (1996) give the following requirements for a structural sensor:

(a) Wide strain/stress range of detection (from small strains up to failure)
(b) Response being reversible upon stimulus removal (necessary for repeated use of the sensor)
(c) Ease of measuring the response (without the need of expensive peripheral equipment)
(d) Presence of the sensor having no bad effect on the structural properties of the structure
(e) Chemical stability and durability
(f) Low cost

Current commonly used sensors include strain gages, optical fibers and piezoelectric sensors, which all suffer from high cost, poor durability and the need for expensive peripheral equipment including electronics and lasers. Because of this, the use of sensors in civil structures is uncommon (Chen and Chung 1996). CNFC could become a better option as a strain sensor because points (a) through (e) are applicable. CNF are currently fairly expensive; however, technology may provide a way to make them more cheaply in the future.

CNFC exhibits properties necessary for reversible strain monitoring and electromagnetic interference (EMI) shielding. Short-fiber composites were found to be a new class of strain sensor based on the concept of short electrically conducting fiber pull-out that accompanies slight and reversible crack opening. For a CNF composite to have strain sensing ability, the fibers must be more conducting than the matrix in which they are embedded, of diameter smaller than the crack length, and well dispersed. Their orientations can be random, and they do not have to touch one another (Chung 1995, Chen and Chung 1996). The electrical conductivity of the fibers enables the DC electrical resistivity of the composites to change in response to strain damage or temperature, allowing sensing (Chen and Chung 1996, Chung 1995, Chung 2000, Xiao, et al. 2003, Gao, Strum and Mo 2009).

DISPERSION OF CARBON NANOFIBERS IN CONCRETE

The most difficult issue presented during CNFC production is dispersion of the CNF. Well dispersed CNF results in uniform calcium-silicate-hydrate (CSH) gel formation, which improves the structural and electrical properties of the concrete (Chung 2005). It was discovered that CNF disperse better in self-consolidating concrete (SCC) (Gao, Strum and Mo 2009). Mixing CNF into SCC creates self-consolidating carbon nanofiber concrete (SCCNFC). Self-consolidating concrete (SCC) is highly flowable, non-segregating concrete that can spread into place, fill the formwork, and encapsulate the reinforcement without any mechanical consolidation (ACI 318 2008).

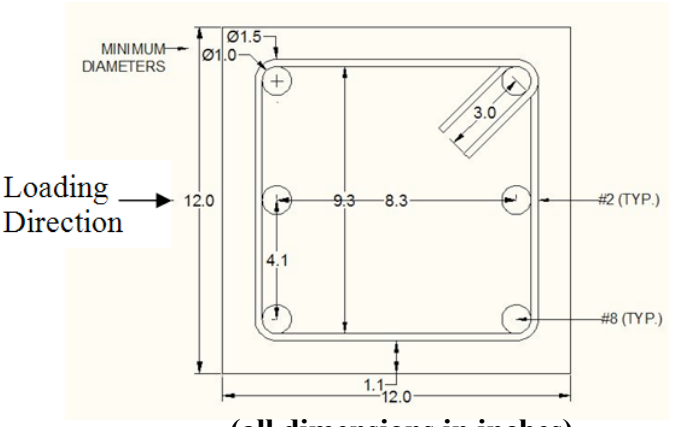
The mixing procedure used for the SCCNFC was used by Gao et al. at the University of Houston (UH) (2009). UH suggested the following procedure:

(a) Blend the CNF, HRWR and enough water to create a homogeneous liquid using laboratory-grade blenderss for three minutes.
(b) Mix the coarse aggregate, sand and cement in a mixer and mix for three minutes.
(c) Add the CNF mixture to the mixer with any additional water.

A SCCNFC column was built and tested under a reversed cyclic load. The structural behavior of the column was examined in addition to the self-sensing ability of the concrete. The results were compared to the structural and self-sensing ability of a SCRC specimens.

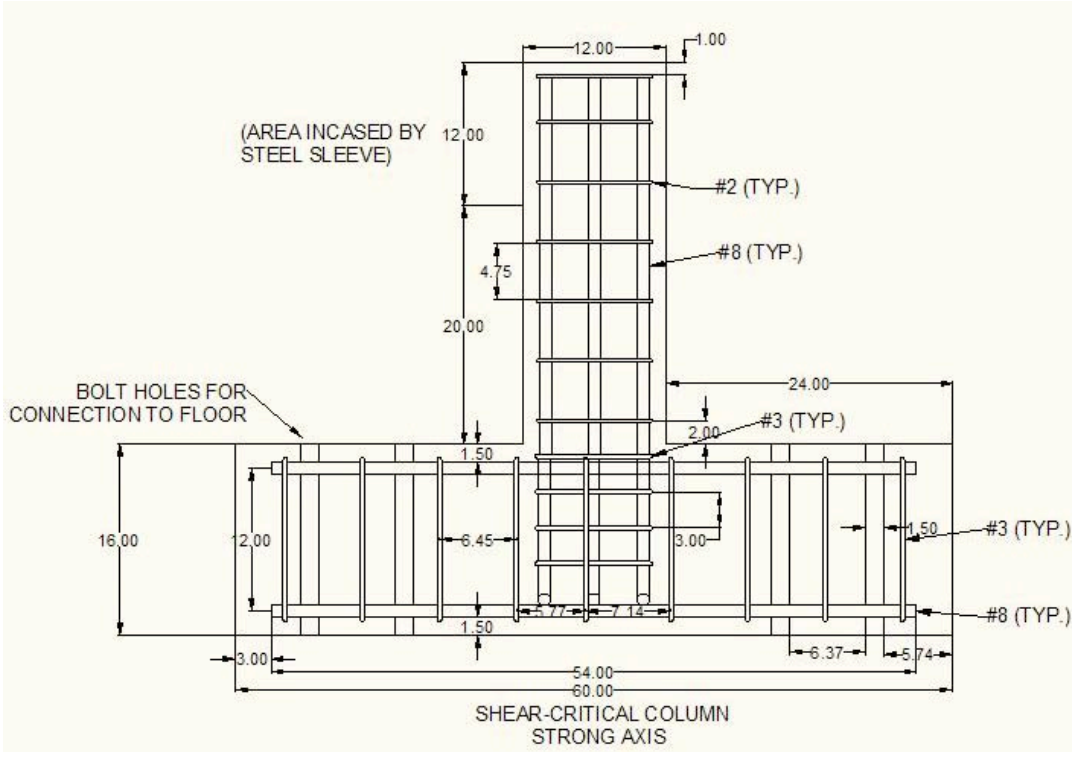
TEST SPECIMENS

Both column cross-sections were 304.8 mm (12 in.) square and contained six #8 rebar (Fig. 1). This percentage of longitudinal steel was 3.27% by volume of concrete. The columns contained #2 stirrups with a spacing of 120.7 mm (4.75 in.) providing transverse reinforcement of 0.287% by volume of concrete. Since the columns were designed to be shear critical, the maximum reinforcement spacing was chosen based on the ACI 318 specifications. The columns were 507 mm (20 in.) in height, which results in an aspect ratio of 1.7. Each of the columns was rigidly connected to similar foundations. See Figs. 2 for the elevation view of the columns and foundations.



(all dimensions in inches)

Fig. 1 Cross-Section of SCRC and SCCNFC Columns



(all dimensions in inches)

Fig. 2 Elevation View of the Strong Axis of the Shear-Critical SCRC and SCCNFC Columns and Foundations

MATERIALS

The properties of the materials used for the mixes were as follows:

(a) Cement: The cement used in all mixtures was ASTM Type III Portland cement.
(b) Fly Ash: Class F fly ash was used for the SCRC mix.
(c) Coarse Aggregate: Crushed limestore with a maximum diameter of ¾" was used in the SCCNFC column. River rock with a maximum diameter of ¾" was used in the SCRC column.
(d) Fine Aggregate: Natural river sand with a fineness modulus of 2.71 was used in all mixes.
(e) High –Range Water Reducer (HRWR): Glenium® 3200HES was used in the SCCNFC column and Glenium® 3400 HES was used in the SCRC. Both chemicals were polycarboxylate admixtures from BASF Chemical Co.
(f) Viscosity Modifying Agent (VMA): RHEOMAC® VMA 450 was used in the specimens and also supplied by BASF Chemical Co.
(g) Carbon Nanofibers: Pyrograf Products, Inc. PR-19-XT-LHT-OX fibers were used in this study. The specific gravity of the fibers was 0.0742. The diameter of the fibers was 149 nm (5.87e-6 in.) and the length was 19 μm (7.48e-4 in.) resulting in an aspect ratio of 128.

MIX PROPORTIONS

Table 1 Mix Proportions in kg/m^3 (lb/yd^3) of Concrete

Material	SCRC Mix	SCCNFC Mix
Cement	446 (752)	457 (771)
Fly Ash (Class F)	299 (504)	-
Fine Aggregate	937 (1580)	898 (1514)
Coarse Aggregate (Limestone)	-	859 (1448)
Coarse Aggregate (River Rock)	491 (827)	-
Water	224 (377)	182 (307)
Glenium® 3400HES	2.81 (4.73)	-
Glenium® 7700HES	-	2.34 (3.94)
REHEOMAC® VMA 450	5.69 (9.59)	-
Carbon Nanofibers	-	3.23 (5.45)

The mix proportions can be seen in Table 1. It was discovered that CNF has an optimal dosage of approximately 1% by volume. In order for CNF to have advantageous properties within concrete, it must be well dispersed. Increased CNF dosages increase concrete properties up to the point where the CNF begin to attract one another and clump. This occurs at dosages higher than 1% by volume (Gao, Strum and Mo 2009).

CONCRETE SENSOR SETUP

One goal of testing the SCCNFC column was to prove that concrete containing CNF can be used as a sensor. The electrical properties of the concrete had to be tested, so wire meshes were constructed and embedded in each of the columns. The wire meshes were made of 12.7 mm (1/2 in.) hardware cloth with 14 gauge copper wire soldered to it. The wire extended outside of the column. Fig. 3 shows one of the wire meshes. The meshes were placed in the column as shown in Fig. 4. The meshes could not touch the rebar in the column because the electrical

properties of the concrete, not the steel, needed to be tested. Fig. 5 shows the installation of the meshes. Fig. 6 shows the wire connected to the mesh protruding from the column.

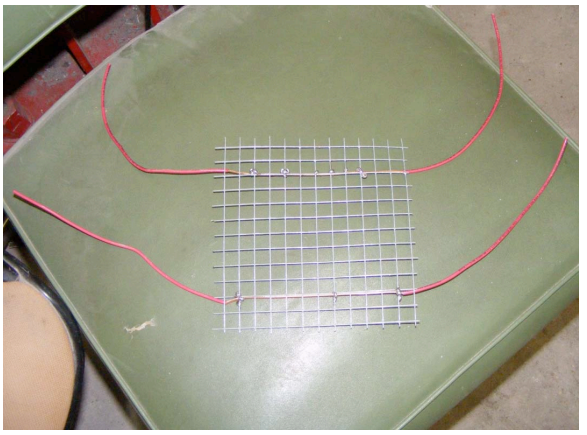


Fig. 3 Wire Mesh

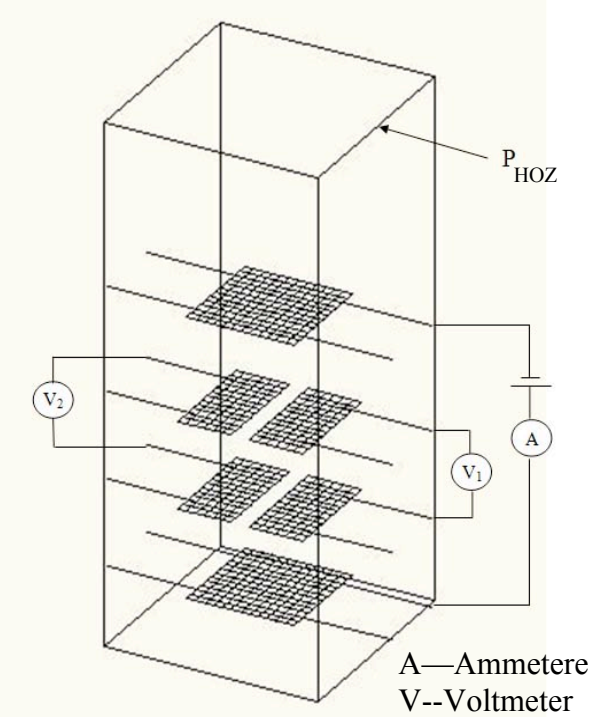


Fig. 4 Wire Mesh Placement Diagram (Four Probe Method)



Fig. 5 Wire Mesh Installation

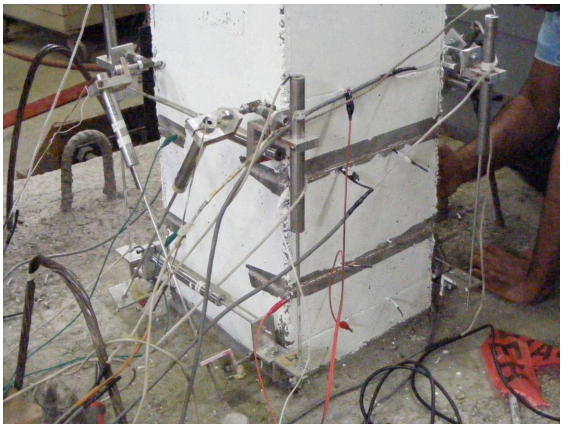


Fig. 6 Wires Connected to Meshes Protruding from Column

To measure the electrical properties of the concrete, the voltage and current were measured using a four-probe method as seen in Fig. 4. A power supply was attached to the top mesh that provided a current of approximately 31 V DC. An ammeter was attached to the bottom mesh and connected back to the power supply to complete a circuit. The current measured by the ammeter was recorded continuously during the tests by hand. Additional voltmeters were attached to the two middle meshes on both the north and south sides of the

column to measure voltage. The voltage readings were also recorded continuously during the tests by hand.

SENSOR SETUP

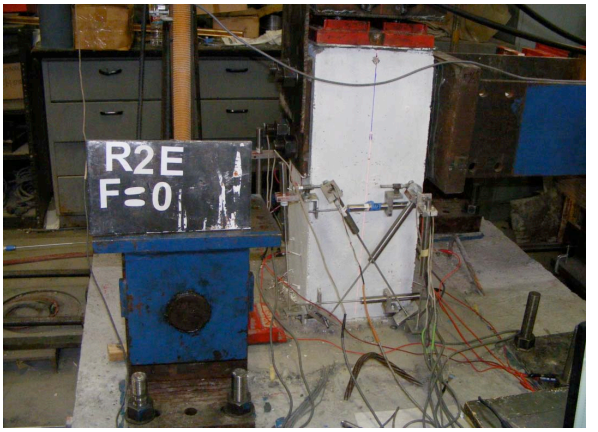


Fig. 7 LVDT Rosette

Linear voltage displacement transducer (LVDT) rosettes were placed on the east and west side of each column to measure the strain in the concrete. Fig. 7 shows one of these LVDT rosettes. LVDTs were placed on the foundation to measure any foundation slippage. Additionally, LVDTs were placed at the top of the column to measure the column displacement. One of these LVDTs was used to control the actuator, Therefore, a closed-loop displacement control was used to test the column more precisely after post-yielding. This was necessary to grasp accurately the ductility of the column after yielding of main flexural rebars occurred. The other LVDT was used to record displacement values. These can be seen in Fig. 11. Data from the LVDTs was continuously monitored and stored by the HBM Spider-8 Data Acquisition System.

TEST SETUP



Fig. 8 Test Setup

During the testing, the columns were subjected to constant vertical axial loading equal to 10% of their axial capacity and horizontal reversed-cyclic loading until failure. Fig. 8 shows the test setup including the horizontal actuator, vertical load jack, support system, column and data acquisition systems. The 649 kN (146 kip) capacity actuator was bolted to a steel beam, which was bolted to a rigid vertical steel frame. Each column was connected to the strong floor by 16-31.75 mm (1.25 in.) diameter all-thread steel rods that went through the foundation. A steel plate was placed around each group of four rods, mortared to the concrete surface and nuts were screwed onto the plates to hold the foundation flush against the strong floor. Additional bracing bolted to the strong floor was placed on the north and south sides of the column's foundation along the loading directions.

The axial loading system consisted of many pieces. When applying the system, first a lead sheet was placed on top of the column, followed by a four-ball roller. A steel plate was placed on top of the roller followed by a jack. A steel beam was put on top of the jack. All-thread rods were connected to the beam and hinges that were connected to the foundation and strong floor. Axial load was applied to the column through adding pressure to the jack.

LOAD PROGRAM

Table 2 Concrete Compressive Strength in MPa (ksi) and Axial Load in kN (kips) for Each Specimen

	SCRC	SCCNFC
f_c MPa (ksi)	49.7 (7.21)	32.7 (4.75)
Axial Load kN (kips)	518 (116)	389 (87.4)
Days of Curing	6	8

The first step of the load program was to apply an axial load that would remain constant during the course of the test. The axial load equaled one-tenth of each of the columns calculated axial capacity. This was calculated using an unfactored interaction diagram. The axial capacity is dependent on the compressive strength of the concrete (f_c), so the axial force varied for each specimen. See Table 2 for the concrete compressive strength and axial load for each of the two columns.

After the axial load was applied, a reversed-cyclic load was added using a 649 kN (146 kip) capacity actuator. The intended load path was to use force control to complete two cycles each of ±89 kN (20 k), two cycles each of ±178 kN (40 k), two cycles each of ±267 kN (60 k). A positive force denotes a push by the actuator while a negative force represents a pull by the actuator. At the point of the yielding of the longitudinal steel, the test would switch to displacement control and complete two cycles each at a displacement ductility of 2, 3, 4, etc. Once failure occurred, the column was pushed in displacement control to try to obtain a descending branch on the load versus displacement curve.

TEST RESULTS

The load path followed for the SCRC column specimen can be seen in Fig. 9 with the first cracks, switch to displacement control and failure marked. The first crack on the south side of the column occurred at -178 kN (-40 k). The first shear crack formed on the column during the first -178 kN (-40 k) cycle at -178 kN (-40 k) on the west side. The column failed in shear and crushing of concrete at 276 kN (62 k). The west side of the column exhibited crushing of the concrete struts with large shear cracks. The east side exhibited local crushing at the actuator connection. The maximum displacement at the top of the column (drift) was 12.7 mm (0.50 in.). Fig. 10 shows the west side of the column after failure. Fig. 11 shows the load versus displacement curve for the test.

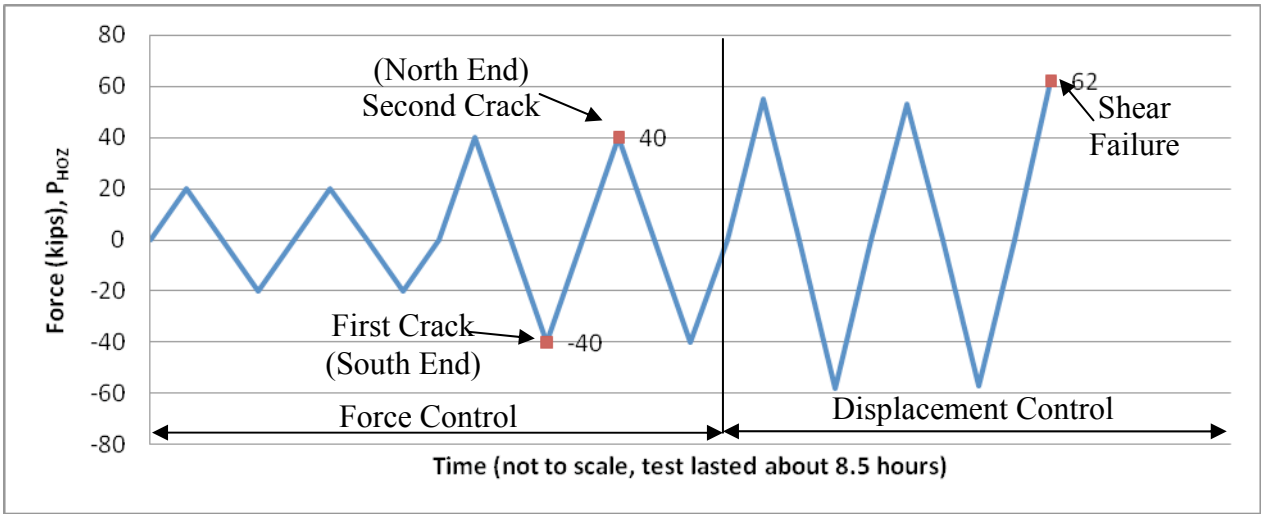


Fig. 9 SCRC Column Load Path

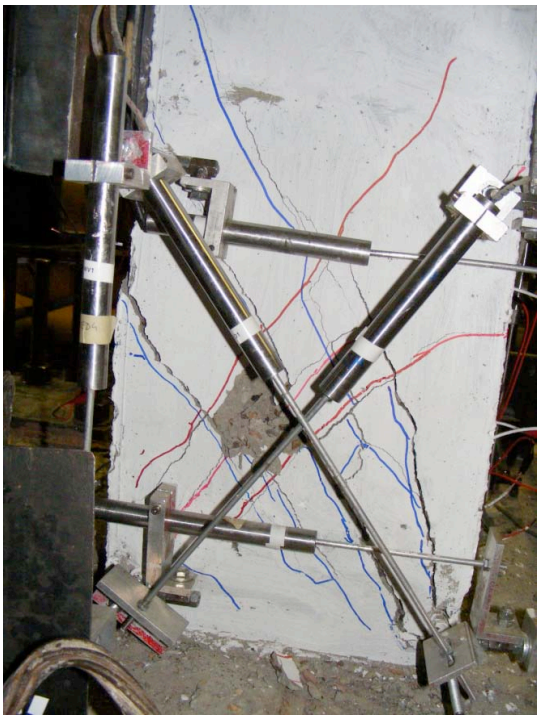


Fig. 10 West Side of SCRC Column After Failure

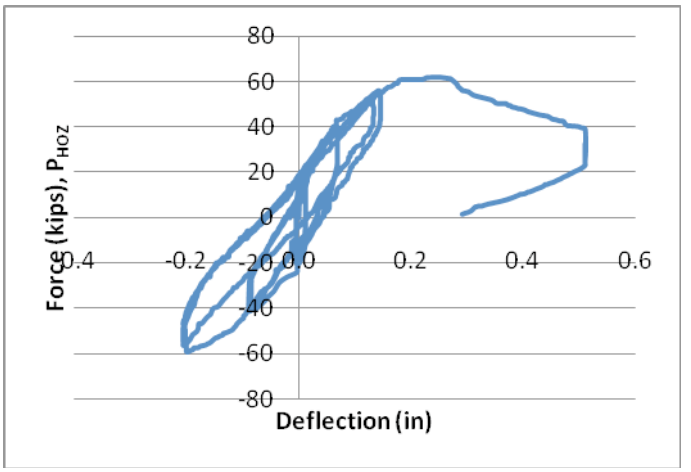


Fig. 11 SCRC Column Force vs. Displacement Curve

The actual load path followed for the SCCNFC column can be seen in Fig. 12. The pump shut down during the test, and the actuator unloaded during the fifth cycle of the test. The pump was turned back on and the test resumed. The first flexural crack formed on the column at 160 kN (36 k) on the east, west and north sides. The second flexural crack formed on the east, west and south sides at a load of -158 kN (-35.6 k). The column failed in the combined modes of shear and concrete crushing at 298 kN (67 k) on the west side of the column. The maximum displacement was 10.16 mm (0.4 in.). Fig. 13 shows the west side of the column after failure. Fig. 14 shows the load versus displacement curve for the test.

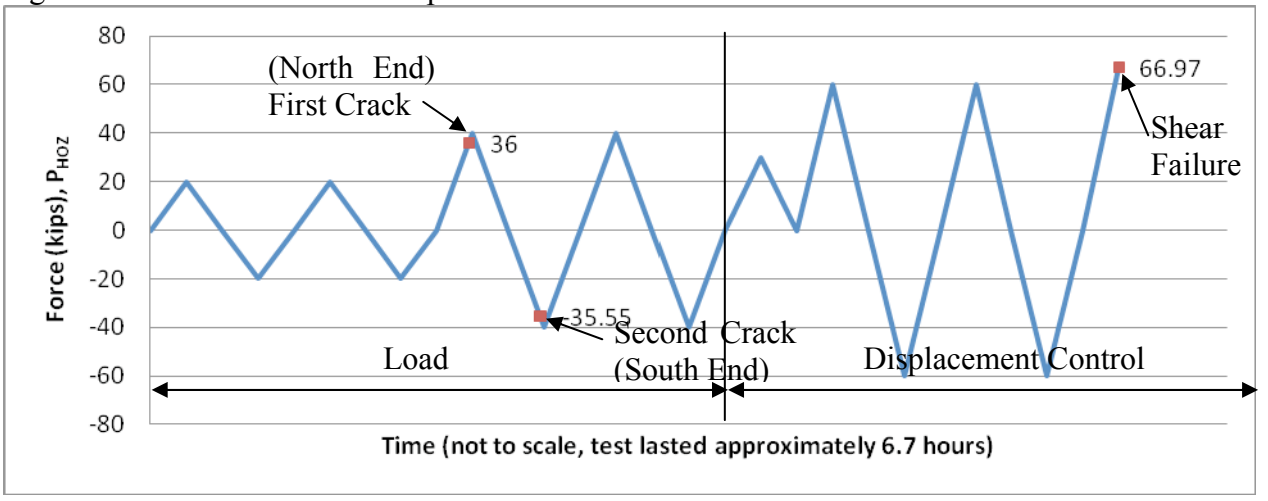


Fig. 12 SCSFC Column Load Path

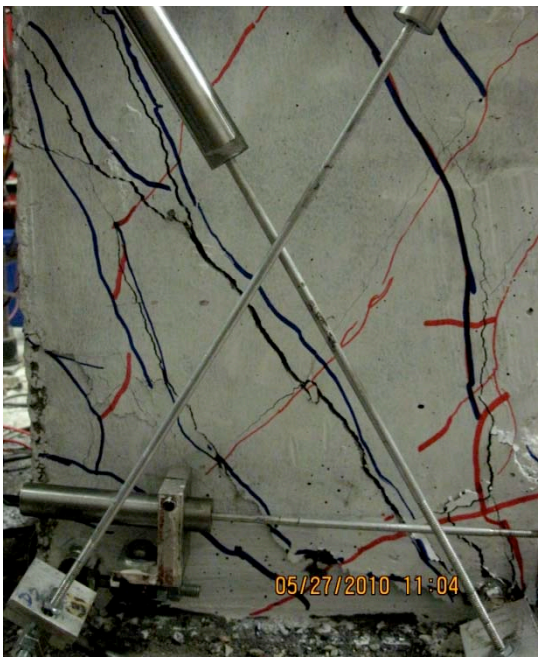


Fig. 13 West Side of SCCNFC Column After Failure

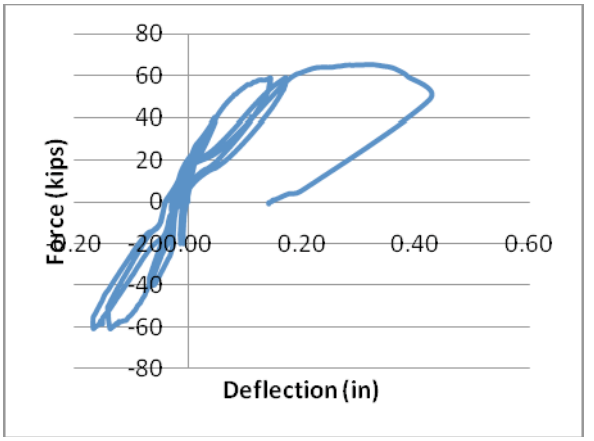


Fig. 14 SCCNFC Column Force vs. Displacement Curve

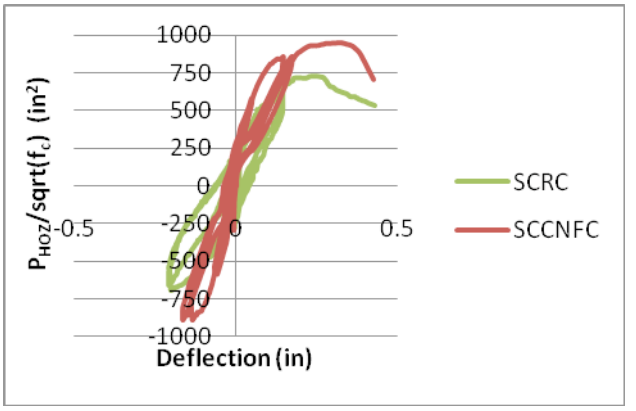


Fig. 15 Force vs. Displacement Curves for all Specimens

COMPARISON OF STRUCTURAL BEHAVIOR OF COLUMNS

Fig. 15 shows a normalized force versus displacement curve for all of the specimens. Since all of the columns had the same dimensions, the horizontal load (P_{HOZ}) was normalized by dividing by the square root of the compressive strength of the concrete. By examining the figure, it is evident that the SCCNFC column failed at higher loads and with larger deflection than the SCRC column. Additionally, the SCCNFC column was much stiffer than the SCRC column and exhibited a higher energy dissipation. A definite yielding of longitudinal steel occurred in both the SCRC and SCCNFC columns. Figs. 10 and 13 show the crack patterns of the SCRC and SCCNFC columns, respectively. The compression struts are easily visible in both the SCRC and SCCNFC columns.

SELF-SENSING ABILITY OF SCCNFC

During each of the column tests, the electrical resistance was determined to check the self-sensing ability of the concrete. To measure the electrical properties of the concrete, the voltage and current were measured as depicted in Fig. 4 using the meshes described. A DC power supply was attached to the top mesh that provided a constant voltage of about 31 V. A voltmeter was attached to the bottom mesh and connected back to the power supply to complete a circuit. The current measured by the ammeter was recorded continuously during the tests. Additional voltmeters were attached to the two middle meshes on both the north and south sides

of the column to measure voltage. The voltage readings were also recorded continuously during the tests. To determine the electrical resistance, Ohm's law was used.

The electrical readings showed a great correlation between the peaks in the applied horizontal force, strain and resistance plots for the SCCNFC column and little correlation between the resistance plots and the force or strain plots for the SCRC column. Fig. 16 shows the relationship between the SCRC column's horizontal force, LVDT strain and electrival resistance versus time on the north side of the column. As shown by the grey vertical lines, there is no relationship between the peaks and valleys in the electrical resistance and the load or strain on the north side of the column.

Fig. 17 shows relationship between the SCCNFC column's horizontal force, LVDT strain and electrical resistance versus time on the north side of column. As shown by the grey vertical lines, there is a very good correlation between the force, strain and resistance. On the north side of the column, the peaks and valleys matched up until the point that the column was greatly damaged.

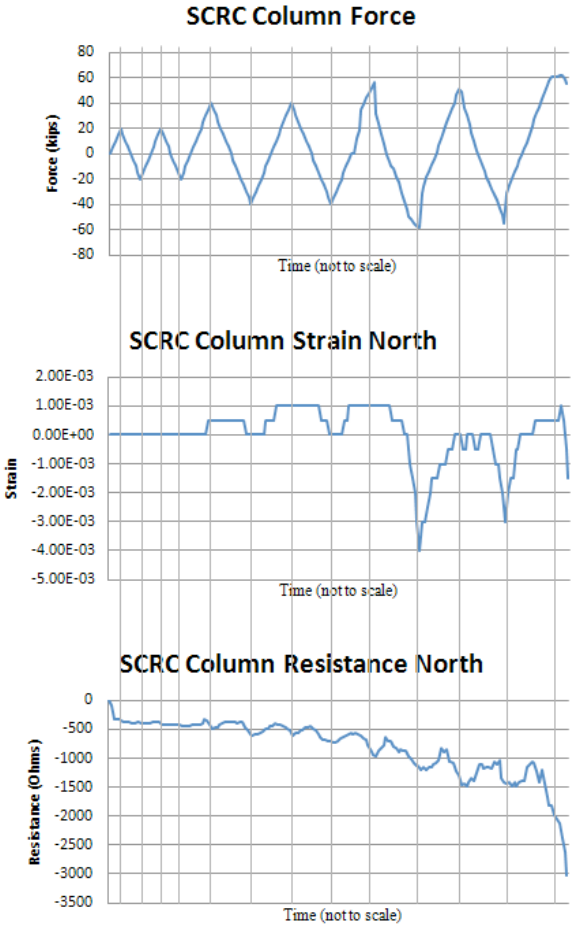


Fig. 16 SCRC Column Comparison of Horizontal Force, LVDT Strain and Electrical Resistance on North Side

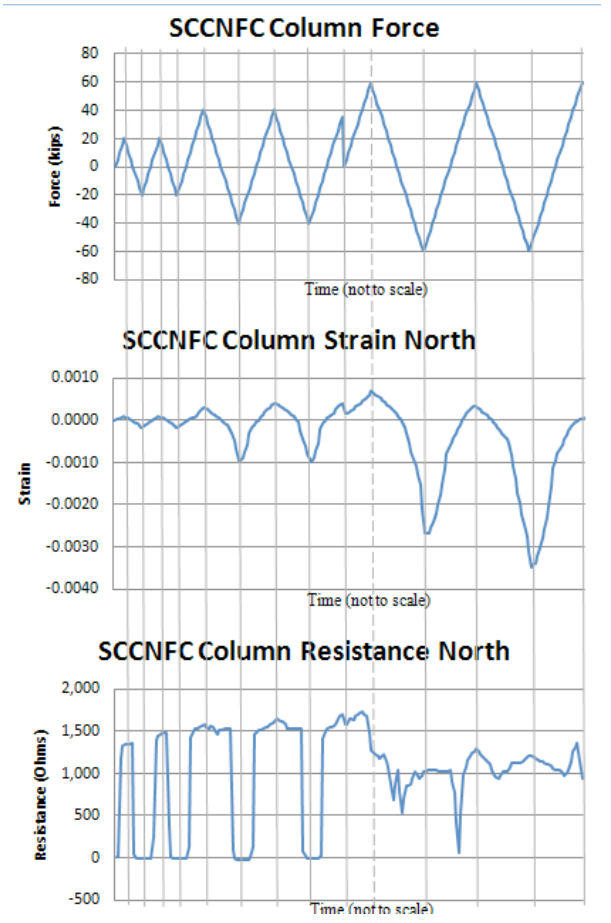


Fig. 17 SCCNFC Column Comparison of Horizontal Force, LVDT Strain and Electrical Resistance on North Side

Because of the strong correlation found between the horizontal force, LVDT strain and electrical resistance verses time graphs for the SCCNFC column, the electrical resistance

variation (ERV) was calculated and compared to the deflection at the top of the column. ERV is the measured electrical resistance minus the initially measured electrical resistance quantity divided by the initially measured electrical resistance. Fig. 18 shows the relationship between the ERV and deflection at the top of the column for the first five cycles of the test. Yielding occurred in the fifth cycle. The envelope shown in Fig. 18 represents the damage in the column measured by the SCCNFC. It is obvious from Fig. 18 that the column shows major damage at approximately a deflection of 2.03 mm (0.08 in.). This corresponds to the steel yielding in the SCCNFC column. This proves that SCCNFC can be used as a type of self-Structural Health Monitoring system.

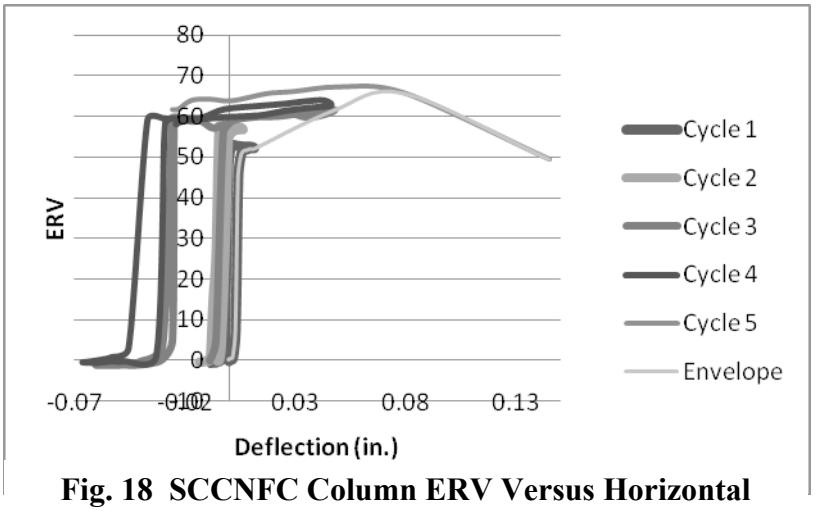


Fig. 18 SCCNFC Column ERV Versus Horizontal Deflection

CONCLUSIONS

Self-consolidating concrete with carbon nanofibers in shear critical columns was investigated and the performance was compared to a conventional self-consolidating reinforced concrete column. This research studied the test results of the two columns tested under reversed-cyclic loads. The columns consist of a traditionally reinforced concrete (SCRC) column that serves as a control specimen and a self-consolidating carbon nanofiber concrete (SCCNFC) column. The objectives of the experiments include studying the structural behavior of the materials and examining the self-sensing abilities of the concretes. The following points detail the research findings and conclusions drawn from those findings:

(1) Highly workable and stable self-consolidation concrete (SCC) can be made from locally available construction materials and can maintain its workability and stability with the addition of fibers. The SCC mixes tested during this research had satisfactory workability and were found suitable for application in short columns. SCC greatly increases the ease of column construction.

(2) The addition of carbon nanofibers (CNF) to concrete increases the strength and ductility of a column.

(3) SCCNFC can be used as a reversible strain sensor. The peaks and valleys in the electrical resistance readings of the concrete match the peaks and valleys of the applied force and the strain in the concrete. The SCRC specimen did not have corresponding strain and electrical resistance values. It was found that concrete structures containing well-dispersed CNF in an appropriate dosage is capable of self-Structural Health Monitoring.

ACKNOWLEDGEMENT

The research study described herein was sponsored by the National Science Foundation under the Award No. EEC-0649163. The opinions expressed in this study are those of the authors and do not necessarily reflect the views of the sponsor.

REFERENCES

ACI 318. *Building Code Requirements for Structural Concrete.* Farmington Hills, Michigan: American Concrete Institute, 2008.

Aoude, Hassan, William D. Cook, and Denis Mitchell. "Behavior of Columns Constructed with Fibers and Self-Consolidating Concrete." *ACI Structural Journal* 106, no. 3 (May-June 2009): 349-357.

Chen, Pu-Woei, and D. D. L. Chung. "Concrete as a new strain/stress sensor." *Composites Part B: Engineering* 27, no. 1 (1996): 11-23.

Chen, Pu-Woei, and D. D. L. Chung. "Concrete reinforced with up to 0.2 vol% of short carbon fibres." *Composites* 24, no. 1 (1993): 33-52.

Chung, D. D. L. "Cement-matrix composites for smart structures." *Smart Materials and Structures* 9, no. 4 (2000): 389-401.

Chung, D. D. L. "Dispersion of Short Fibers in Cement." *Journal of Materials in Civil Engineering, ASCE* 17, no. 4 (2005): 379-383.

Chung, D. D. L. "Strain sensors based on the electrical resistance change accompanying the reversible pull-out of conducting short fibers in a less conducting matrix." *Smart Materials and Structures* 4, no. 1 (1995): 59-61.

Daczko, J. A. "Stability of Self-Consolidating Concrete, Assumed or Ensured?" *Proceedings, First North American Conference on the Design and Use of Self-Consolidating Concrete.* Rosemont, IL, 2002.

Dhonde, Hemant B., Y. L. Mo, Thomas T. C. Hsu, and John Vogel. "Fresh and Hardened Properties of Self-Consolidating Fiber-Reinforced Concrete." *ACI Materials Journal* 104, no. 5 (September 2007): 491-500.

Gaimster, R., and C. Foord. "Self-compacting concrete." *Concrete* 34 (2000): 23-25.

Gao, Di, Mariel Strum, and Y. L. Mo. "Electrical resistance of carbon-nanofiber concrete." *Smart Materials and Structures* 18, no. 9 (2009): 1-7.

Khayat, K. H., C. Hu, and H. Monty. "Stability of Self-Consolidating Concrete, Advantages, and Potential Applications." *Proceedings of First International RILEM Symposium on Self-Compacting Concrete.* Stockholm, Sweden, 1999. 143-152.

Lau, Kin-Tak, and David Hui. "The revolutionary creation of new advanced materials--carbon nanotube composites." *Composites: Part B* 33, no. 4 (2002): 263-277.

Li, Hui, Hui-gang Xiao, Jie Yuan, and Jinping Ou. "Microstructure of cement mortar with nano-particles." *Composites Part B: Engineering* 35, no. 2 (March 2004): 185-189.

Li, Hui, Mao-hua Zhang, and Jin-ping Ou. "Abrasion resistance on concrete containing nano-particles for pavement." *Wear* 260, no. 11-12 (2006): 1262-1266.

Li, Hui, Mao-hua Zhang, and Jin-ping Ou. "Flexural fatigue performance of concrete containing nano-particles for pavement." *International Journal of Fatigue* 29, no. 7 (July 2007): 1292-1301.

Liao, Wen-Cheng, Shih-Ho Chao, Sang-Yeol Park, and Antoine E. Naaman. "Self-Consoldiating High Performance Fiber Reinforced Concrete (SCHPFRC)--Preliminary Investigation." *NSF Program(s): NEES RESEARCH*, 2006.

Narayanan, R., and I. Darwish. "Use of Steel Fibers as Shear Reinforcement." *ACI Structural Journal* 84, no. 3 (1987): 216-277.

Ngo, Quoc, et al. "Characteristics of Aligned Carbon Nanofibers for Interconnect Via Applications." *IEEE Electron Device Letters* 27, no. 4 (April 2006): 221-224.

Okamura, H., and K. Ozawa. "Mix-Design for Self-Compacting Concrete." *Concrete Library of the Japanese Society of Civil Engineers*, 1995: 107-120.

Padmarajaiah, S. K., and A. Ramaswamy. "Comparative Study on Flexural Response of Full and Partial Depth Fiber-Reinforced High-Strength Concrete." *Journal of Materials in Civil Engineering* 14, no. 2 (2002): 130-136.

PCI, TR-6-03. *Interim Guidelines for the Use of Self-Consolidating Concrete in Precast/Prestressed Concrete Institute Member Plants.* Chicago: Precast/Prestressed Concrete Institute, 2003.

Shah, S. P. "Concrete Made with Carbon Nanotube Reinforcement." University of Houston, Houston, 2009.

Shah, S. P., and A. E. Naaman. "Mechanical Properties of Glass and Steel Fiber Reinforced Mortar." *ACI Journal* 73, no. 1 (Jan 1976): 50-53.

Tanaka, K., K. Sato, S. Watanabe, I. Arima, and K. Seunaga. "Development and Utilization of High-Performance Concrete for the Construction of the Akashi Kaikyo Bridge." *High Performance Concrete in Severe Environments, ACI SP-140*, 1993: 25-51.

Xiao, H., C. Lan, X. Ji, and H. Li. "Mechanical and sensing properties of structural materials with nanophase materials." *Pacific Scientific Journal* 5 (2003): 11-17.

Polystyrene-MWCNT based Nanocomposite Multifunctional Strain Sensor: Dynamic Monitoring of Civil Engineering Structures

V. S. M. Vemuru[1], R. K. Srivastava[2], A. Srivastava[3], S. Nagarajaiah[4], P. M. Ajayan[5]

[1]Dept. of Civil and Env. Engrg., Rice University, Houston, TX,svv1@rice.edu
[2]IT- Banaras Hindu University, Varanasi, INDIA, r05bhu@gmail.com
[3]IT-Banaras Hindu University, Varanasi, INDIA, anchalbhu@gmail.com
[4]Dept. of Civil and Env. Engrg., Dept. of Mech. and Mat. Science,Rice University, Houston, TX, satish.nagarajaiah@rice.edu
[5]Dept. of Mech. and Mat. Science, Rice University, Houston, TX, ajayan@rice.edu

ABSTRACT

Structural sensing and dynamic monitoring of critical infrastructure is essential to maintain the ageing critical infrastructure of US. To this end various sensing mechanisms and innovations have been used in the recent past such as strain sensors, accelerometers etc. Measurement of strain gives first hand information about the state of stresses in a structure. The effectiveness of multiwalled carbon nanotube (MWCNT) films as strain sensors has been demonstrated by the authors (Vemuru et al. 2009) and other researchers. In this paper the real time dynamic response of MWCNT polystyrene nanocomposite thin film sensors is studied and experimental results presented of both its dynamic response as well as its response to temperature. Experimental results demonstrate a linear response from the MWCNT nanocomposite. Further electromechanical properties observed are completely reversible and stable. The temperature response of the nanocomposite film is also studied experimentally and results presented. It is demonstrated that the nanocomposite thin films monitors the strain very effectively and can be used as a multifunctional material in civil, mechanical and aerospace applications.

Introduction

Carbon nanotubes (CNTs) first discovered by Ijiima (Iijima 1991) exhibit a remarkable combination of electrical, mechanical and thermal properties ((P. M. Ajayan 1999; Baughman et al. 2002)). The combination of these properties makes CNTs ideal filler materials in nanocomposites. The past decade witnessed large advances in the CNT filler based nanocomposite research. Among the bevy of host polymer matrices it has been observed that hydrocarbon polymers such as polystyrene (PS), polypropylene or polyethylene render the nanocomposites with mechanical properties significantly higher than those of other polymer composites (Fernández-Sánchez et al. 2009).

Schadler et al. (Schadler et al. 1998)observed a shift in the raman peaks in multiwalled carbon nanotube (MWCNT) - epoxy composites when subjected to tensile or compressive loading. Tombler et al. (Tombler et al. 2000) highlight the reversible electromechanical properties of a single walled carbon nanotube (SWCNT) upon deformation using an AFM tip. Semet et al. (Semet et al. 2005) observe a reversible change in the nonlinear conductance of a MWCNT upon being bent longitudinally. Experiments by Jang et al. (Jang et al. 2008) revealed reversible electrical resistance change when individual an MWCNT was strained to a value less than or equal to its elastic limit. Also the change in resistance of the nanotube deformed within its elastic limit corresponds well with the applied strain. All these studies correspond to the piezoresistive characteristics of nanotubes at the nanoscale.

Studies by Dharap et al. (Prasad Dharap et al. 2004) and Li et al. (Z. Li et al. 2004) marked the first attempts done to utilize the piezoelectric properties of CNTs at the nanoscale for strain sensing applications at the macroscale. Using a SWCNT buckypaper they observe a linear change in the voltage response across the film using contact based measurements (electrical measurements using four point probe) (Prasad Dharap et al. 2004) and non contact based measurements (observing a shift in the peak of G band of Raman spectrum) (Z. Li et al. 2004). In both the studies, it was observed that the change in the response observed corresponded with strain linearly. The macroscale strain sensing properties were studied for MWCNTs using MWCNT-buckypaper ((Vemuru et al. 2009; X Li et al. 2008)) and similar behavior was observed.

In this study the mechanical characteristics of multiwalled carbon nanotube PS/MWCNT nanocomposite thin films is studied in detail. The electromechanical response of the nanocomposite thin films under static loading is studied by attaching the film to a brass specimen and subjecting the brass specimen to axial strain in a hydraulic machine for static testing. The electromechanical response of thin film under dynamic loading is studied by attaching the film to a flexible aluminum beam and studying its free vibration response. Finally the electrical response of the film to temperature changes is also studied by attaching the film to Teflon and heating it.

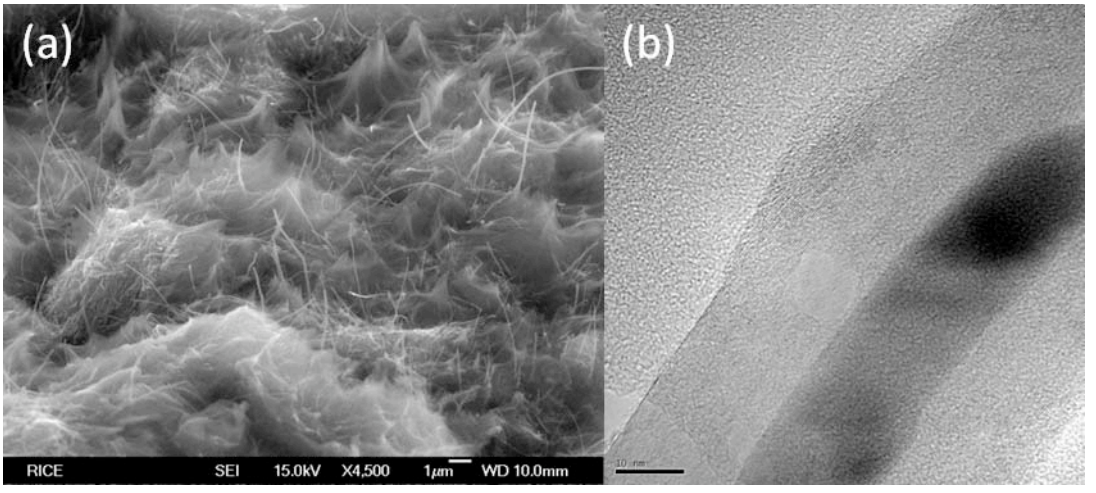


Figure 1: (a) SEM image of PS/MWCNT film (b) TEM image of a MWCNT in the polymer

Preparation of PS/MWCNT nanocomposite films

The purified multiwall carbon nanotubes were prepared by spray pyrolysis method using xylene & ferrocene as a carbon source and catalyst materials respectively. CNTs were functionalized by treating them with a mixture of nitric acid (HNO_3) and sulphuric acid ($H_2 SO_4$) in 3:1 ratio followed by ultrasonication at 42 KHz & stirring at 90^0 C for 3 hrs. To minimize the aggregation of functionalized CNTs in the nanocomposite, they were treated with toluene solution containing a nonionic surfactant, Polyethylene glycol (PEG, Molecular weight is 600), followed by ultrasonication in a sonic bath for 2 hr. The PS used in this work has molecular weight of 100,000. The required amounts of processed CNTs were mixed with PS solution in toluene and the resulting mixture is stirred for 2 hrs resulting in a homogeneous mix. The obtained solutions of composite is taken onto a flat plate and dried at room temperature for about 12 hrs forming

flexible PS/MWCNT composite film. Using the above mentioned technique uniform flexible thin nanocomposite films of 0, 0.5, 1, 3, 5, 6, 8 & 10 wt% CNTs were obtained.

Strain sensing

Experimental Setup

For dynamic loading nanocomposite film was attached to a flexible aluminum beam using vacuum bonding technique. To ensure perfect bonding and subsequent strain transfer the bonding is done using vacuum bonding technique for duration of 12 hours. A four point probe is formed by depositing leads of equal thickness equally spaced on the film by sputter coating technique. Wires are attached to the silver leads using silver epoxy. Electrical measurements from the sample are achieved using a Keithley 2400 sensitive digital source meter (with a measurement precision of ±1 μV or ± 10 pA). The electrical measurements from the nanocomposite film are presented as it is without the use of any analog or digital filters. A strain gage is attached to the same beam for comparison purposes. The aluminum beam is arranged as a cantilever and nanocomposite film and strain sensor are attached close to the support and the tip of the beam is deflected and allowed to vibrate freely. The PS/MWCNT thin film is insulated from the surface of the brass specimen using a thin coat of epoxy. The applied strain to the brass specimen is measured directly using a strain gage attached onto the surface of this insulating epoxy layer on the brass specimen. The strain measurements are performed using National Instruments Bridge module (NI 9237) all strain measurements are taken at a sampling frequency of 2000 Hz.

For static strain measurements, a thin film of PS/MWCNT nanocomposite is attached to a brass specimen (cross section 0.25 inch × 2.0 inch) with epoxy. Electrical contact is attained by depositing silver leads onto the thin film by sputter coating. The brass specimen is subjected to axial load in a hydraulic MTS testing apparatus with a maximum capable load of 100 Kips.

Results and Discussions

Thin film electromechanical characteristics

By applying an input voltage of 0.25 V (the choice of the input voltage is done to ensure that the output current from the nanocomposite film is limited to a value less than 1 mA) the film is subjected to strain by application of mechanical load to the brass specimen to which the film is attached.

The gage factor of the thin film is given by the formula

$$GF = \frac{\frac{\Delta R}{R_o}}{\varepsilon} = \frac{\frac{V}{i_f} - \frac{V}{i_o}}{\varepsilon \times \frac{V}{i_o}} = \frac{i_o - i_f}{\varepsilon \times i_f}$$

Gage factors of PS-MWCNT films at different wt% of CNTs in them can be gauged from figure 2. Using the above formula the gage factor of the 10 %wt PS/MWCNT film is calculated as 1.49. The measured gage factor is less in comparison to the gage factor of commercial strain gages (about 2). However from the response of 6% wt PS/MWCNT film is calculated as 3.28. This observation confirms with earlier literature where researchers have reported that an increase in wt% of CNT fillers leads to reduction of the gage factor of nanocomposite sensors. Table 1 summarizes the gage factors of the PS-MWCNT films with different wt% content of CNTs.

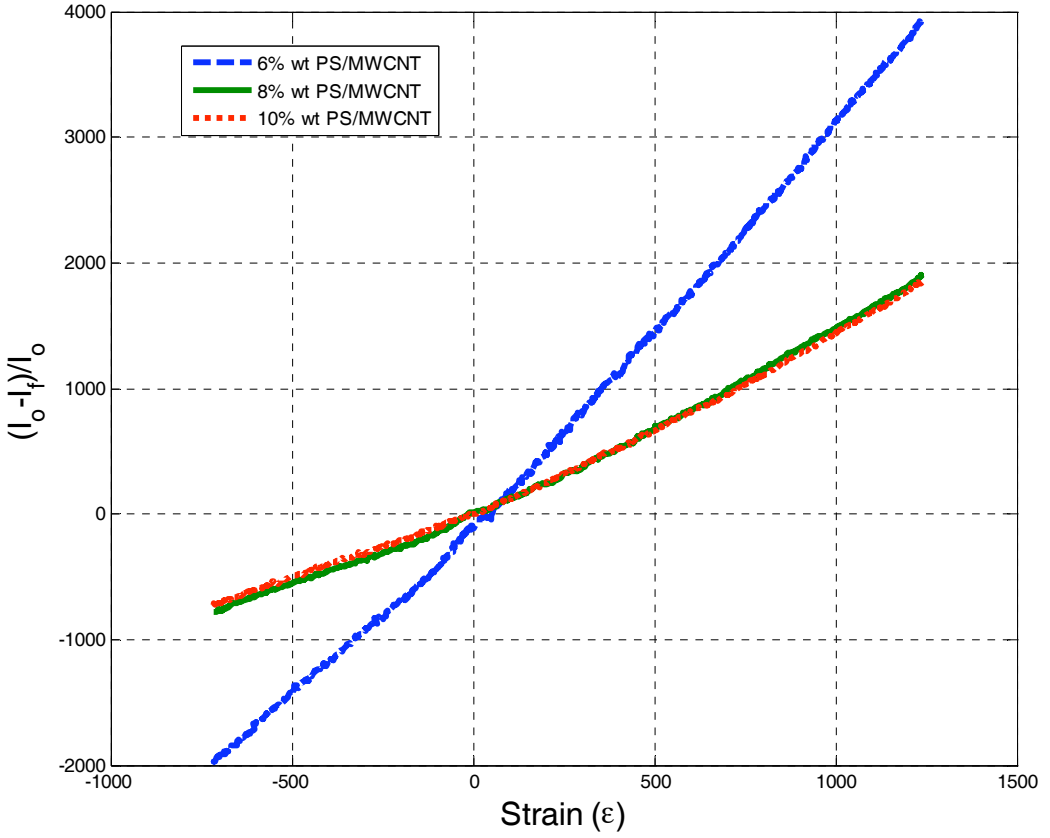


Figure 2: Plot of normalized current response as a function of strain for different % wt content of MWCNTs in the PS-MWCNT nanocomposite films.

CNT wt%	6%	8%	10%
Tension	3.28	1.55	1.49
Compression	2.55	1.04	0.99

Table 1: Gage factors of the PS-MWCNT films with differing % wt of MWCNTs in them for compression and tension

Dynamic Strain Measurement

Several such cycles of free vibrations are recorded and presented in Figure 3. It can be seen that the current response of the sensor is excellent and corresponds closely with the readings obtained from strain gage. The zoomed in superimposed plots of normalized current response and strain readings of different free vibration cycles show in more detail how closely the current response tracks the applied strain. The nanocomposite film further exhibits very good return to pre loading conditions at the end of each set of vibrations. The dynamic strain response characteristics of the nanocomposite film show its potential for SHM.

Temperature Measurement

For temperature measurements nanocomposite film was attached to a Teflon strip using epoxy. The nanocomposite film was heated using a heater and electrical measurements were taken using a four point probe with input voltage of 0.25V as the temperature across the film was varied from 23.5 ^{o}C to 58 ^{o}C and allowed to gradually cool to room temperature. The temperature change across the film is measured using a type K thermocouple in conjunction with a fluke multimeter. The film showed an excellent response to temperature change and the current response as shown in figure 4. It can be seen from the compared normalized response and temperature as the film is heated the change in the resistance of film corresponds clearly with increasing temperature. However the film and the thermocouple exhibit different rates of cooling as can be seen from the way the current responses of the film differs from the temperature decrease of the thermocouple.

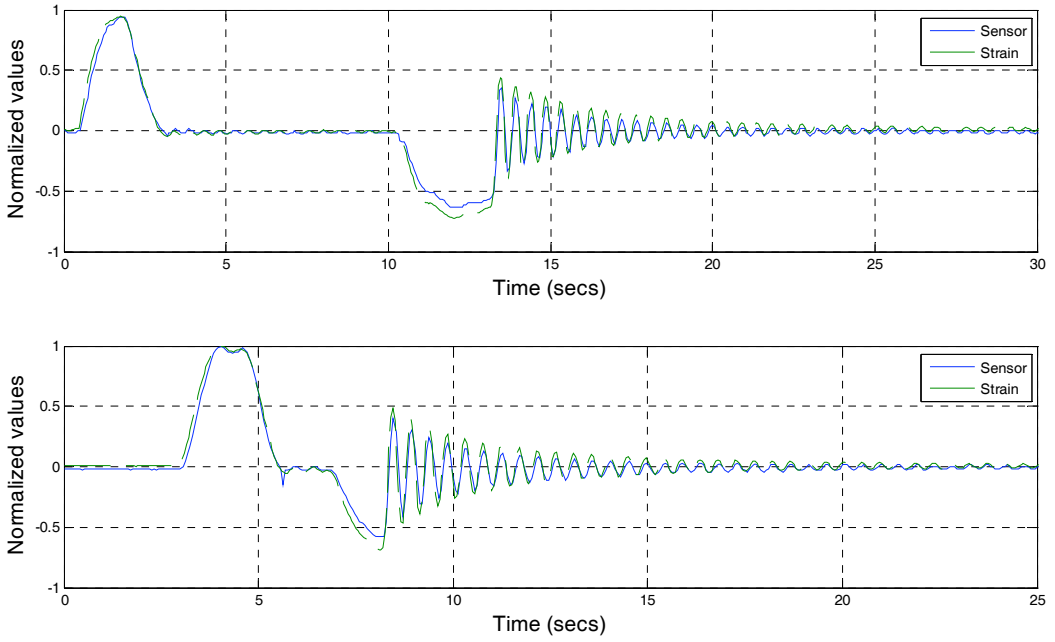


Figure 3: Plot of current response and strain from the free vibration response of a flexible aluminum beam

Conclusions

In this study the electromechanical properties of nanocomposites films made from polystyrene and MWCNTs is thoroughly investigated and the strain sensing behavior of these films is studied in detail. The nanocomposite films show excellent noise free electromechanical response to applied strain both in compression as well as tension. The response of the film was studied under static loading and it corresponded linearly with applied strain. Further the response observed was completely reversible and returned to preloading conditions upon load removal. The sensitivity of the nanocomposite films was studied under different concentrations (by % wt) of MWCNTs in them and it was observed that the increasing concentration of nanotubes led to a reduction in the film sensitivity. The PS-MWCNT films exhibits excellent strain sensing characteristics for both static and dynamic strain measurements and shows great potential for health monitoring

applications. The PS-MWCNT film also exhibit very good sensitivity to temperature changes as is evident from the experimental results.

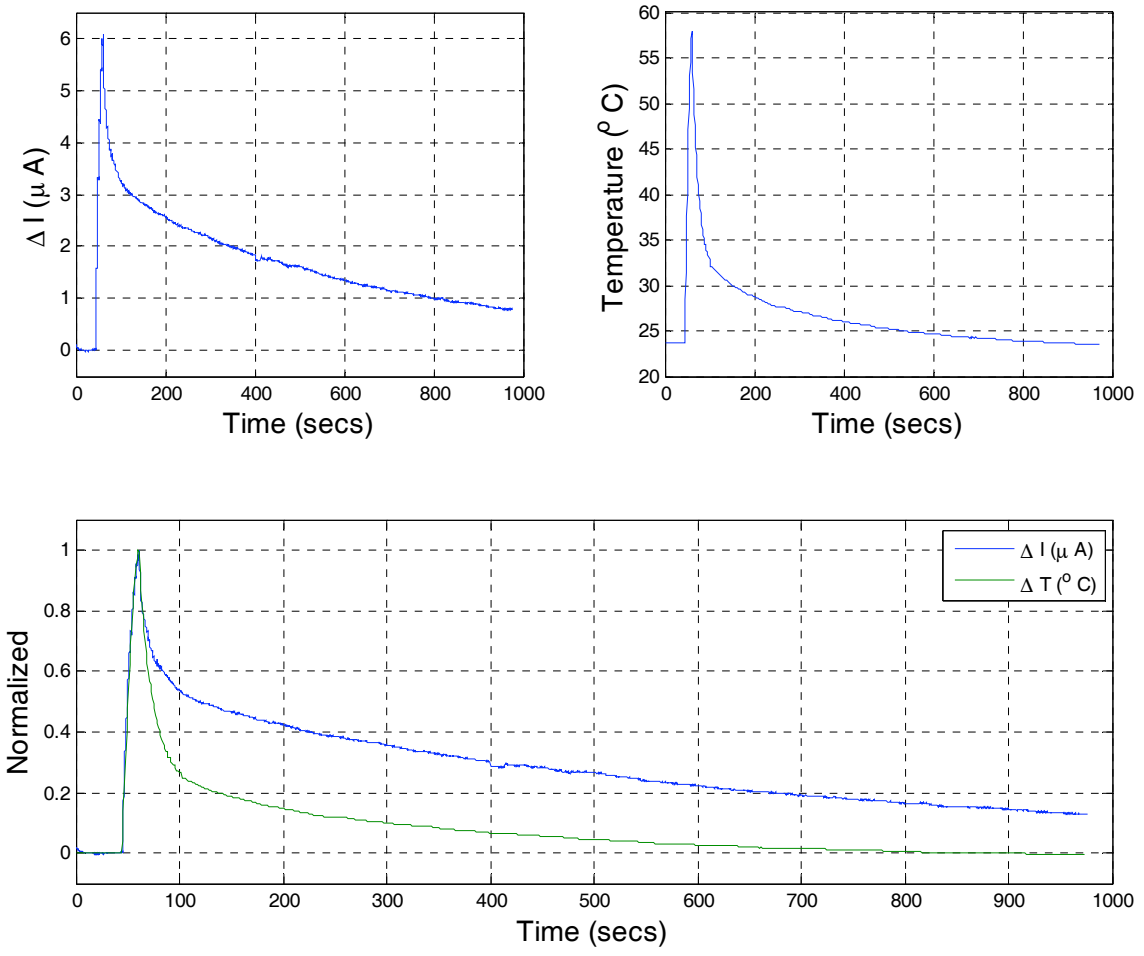


Figure 4: Plot of current response and temperature change across the film as it is heated from 23.5 oC to 58 oC and allowed to gradually cool to room temperature

Acknowledgements

Author RKS acknowledge the financial support from CSIR (SRF: 9/13(0170)/ 2008 –EMRI), New Delhi. Author AS acknowledges the DST and CAS department. Authors VSVM and SN acknowledge supported by fund no. FA8650-05-D-5807 sponsored by the Air Force Research Lab (AFRL) under the Materials and Manufacturing Directorate.

References

1. Vemuru S.M., Wahi R., Nagarajaiah S., and Ajayan P.M. (2009). "Strain sensing using a multiwalled carbon nanotube film," *The Journal of Strain Analysis for Engineering Design*, 44, 555-562.
2. Iijima S. (1991). "Helical microtubules of graphitic carbon," *Nature*, 354(6348), 56-58.
3. Ajayan P.M. (1999) "Nanotubes from Carbon," *Chemical Reviews*, 99(7), 1787-1800.
4. Baughman R.H., Zakhidov A.A., and de Heer W.A. (2002) "Carbon Nanotubes--the Route

Toward Applications," *Science*, 297(5582), 787 -792.
5. Fernández-Sánchez C., Pellicer E., Jiménez-Jorquera C., Lechuga L.M., and Mendoza E. (2009). "Plasma-activated multi-walled carbon nanotube–polystyrene composite substrates for biosensing," *Nanotechnology*, 20(33), 335501.
6. Schadler L.S., Giannaris, S.C. and Ajayan P.M. (1998) "Load transfer in carbon nanotube epoxy composites," *Applied Physics Letters*, 73(26), 3842-3844.
7. Tombler T.W., Zhou C., Alexseyev L., Kong J., Dai H., Liu L., Jayanthi C.S., Tang M., and Wu S., (2000) "Reversible electromechanical characteristics of carbon nanotubes under local-probe manipulation," *Nature*, 405(6788), 769-772.
8. Semet V., Binh V., Guillot D., Teo K., Chhowalla M., Amaratunga G., Milne W., Legagneux P., and Pribat D., (2005) "Reversible electromechanical characteristics of individual multiwall carbon nanotubes," *Applied Physics Letters*, 87(22), 1-3.
9. Jang H., Lee Y., Na H., and Nahm S.H., (2008) "Variation in electrical resistance versus strain of an individual multiwalled carbon nanotube," *Journal of Applied Physics*, 104(11), 114304.
10. Dharap P., Li Z., Nagarajaiah S., and Barrera E.V. (2004) "Nanotube film based on single-wall carbon nanotubes for strain sensing," *Nanotechnology*, 15, 379-382.
11. Li Z., Dharap P., Nagarajaiah S., Barrera E., and Kim J. (2004) "Carbon Nanotube Film Sensors," *Advanced Materials*, 16(7), 640-643.
12. Li X., Levy C., and Elaadil L. (2008) "Multiwalled carbon nanotube film for strain sensing," *Nanotechnology*, 19, 045501.

Long-Term Seismic Performance of RC Bridge Piers in an Aggressive Marine Environment

M. Akiyama[1] and Dan M. Frangopol[2]

[1]Structural Design Laboratory, Department of Civil and Environmental Engineering, Tohoku University, Aramaki-Aza-Aoba 6-6-06, Aoba-Ku, Sendai, Miyagi Prefecture 980-8579, JAPAN; PH +81-22-795-7447; FAX +81-22-795-7448; email: akiyama@civil.tohoku.ac.jp
[2]Department of Civil and Environmental Engineering, ATLSS Engineering Research Center, Lehigh University, 117 ATLSS Drive, Bethlehem, PA 18015-4729, USA; PH (610) 758-6103; FAX (610) 758-4115; email: dan.frangopol@lehigh.edu

ABSTRACT

For structures located in a moderately or highly aggressive environment, multiple environmental and mechanical stressors lead to deterioration of structural performance and, therefore, create maintenance issues. Such deterioration will reduce the service life of structures. The main purpose of this paper is to discuss a methodology previously proposed by the writers for the evaluation of long-term seismic reliability of reinforced concrete (RC) bridge piers in a marine environment and present new results. This methodology consists of three steps: (1) investigate the relationship between material deterioration and structural performance on an experimental basis; (2) consider both the seismic hazard and the hazard associated with marine environment; and (3) perform an analysis of the long-term seismic performance of RC bridge piers in an aggressive marine environment.

INTRODUCTION

Several recent studies deal with the seismic reliability of concrete structures located in earthquake prone regions and aggressive environments (Choe et al. 2008, Coronelli and Gambarova 2004, Ghosh and Padgett 2010, Li et al. 2009, and Simon et al. 2010). However, these studies used a very simple structural model in the evaluation of both seismic capacity and demand. Experimental studies on RC columns with chloride-induced corrosion of steel reinforcement subjected to cyclic loading include: Yamamoto and Kobayashi 2006, Oyado 2007, and Kato et al. 2004, 2005. These studies reported that the numerical model to evaluate the relationship between the load and displacement of corroded RC component needs to consider (a) the reduction of steel bar volumes, (b) cracking of concrete cover due to the expansion of corrosion products, (c) bond degradation between concrete and steel, and (d) non-uniformity of corrosion along the steel bars in RC columns. Since performing the structural analysis only considering the reduced steel rebar cross-section is an oversimplification for evaluating the relationship between load

and displacement of deteriorating RC components, the numerical methods must be improved in order to capture the effect of corrosion on the seismic capacity and demand as reported in previous experimental results. Based on the experimental results of RC specimens with corrosion subjected to cyclic loading, the analytical method to evaluate the relationship between the lateral load and displacement of RC bridge piers and to predict the displacement at the onset of buckling of the longitudinal rebars has to be provided.

For long-term reliability estimation, the steel weight loss $C_w(t)$ at t years after construction is needed. In a marine environment, $C_w(t)$ is affected by many factors such as distance from coastline and wind speed. This study uses the procedure to calculate $C_w(t)$ based on the probabilistic hazard curves associated with airborne chlorides (Akiyama et al. 2009 and 2010a). The effect of differences in marine environment on the long-term reliability could be quantified.

The main purpose of this paper is to discuss a methodology previously proposed by the writers for the evaluation of long-term seismic reliability of reinforced concrete (RC) bridge piers in a marine environment and to present new results.

PROCEDURE TO CALCULATE THE SEISMIC RELIABILITY: A BRIEF REVIEW

Akiyama et al. (2010b) presented the basic equations to estimate the long-term seismic reliability of RC structures in earthquake prone region and a marine environment. This procedure is summarized in this section.

During a given time interval T, the cumulative-time failure probability p_f of a bridge pier subjected to both seismic hazard and hazard associated with airborne chlorides is

$$p_f = 1 - \left(1 - p_{fa}(1)\right) \cdot \left(1 - p_{fa}(2)\right) \cdots \left(1 - p_{fa}(t = T)\right) \tag{1}$$

$$p_{fa}(t) = \int_0^{100} \int_0^{\infty} -\frac{dp_0(\gamma)}{d\gamma} \cdot P\left[D_e \geq C_a \middle| \Gamma = \gamma, C_w = c_w(t)\right] \cdot f\left(c_w(t)\right) d\gamma \, dc_w \tag{2}$$

where $p_0(\gamma)$= the annual probability that the seismic intensity, Γ, at a specific site would exceed a value γ; $P\left[D_e \geq C_a \middle| \Gamma = \gamma, C_w = c_w(t)\right]$ = conditional probability of the seismic demand D_e exceeding the seismic capacity C_a conditioned upon the seismic intensity γ and steel weight loss c_w (t); and $f\left(c_w(t)\right)$ = probabilistic density function, PDF of $c_w(t)$.

RC column with sufficient ties subjected to cyclic loading exhibits ductile behavior and the load-carrying capacity decreases after the onset of buckling of longitudinal rebars. Therefore, the onset of buckling of longitudinal rebars is defined as the ultimate limit state of RC column in the seismic design specification (Japan Road Association 2002). Naito et al. (2010) proposed the displacement ductility evaluation methods of concrete-encased steel columns based on the buckling analysis of longitudinal rebars and concrete-encased steel in plastic hinge. Their model used

in the buckling analysis considered the prevention forces of ties and cover concrete, R_w and R_c, for lateral deformation of longitudinal rebar.

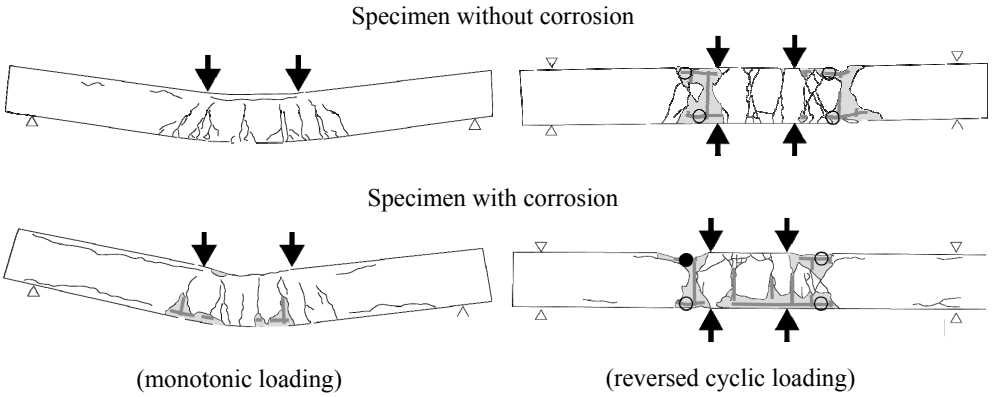


Figure 1. Specimens with and without corrosion after monotonic or cyclic loading (based on information provided by Kobayashi (2006) to the first author)

Kobayashi (2006) investigated the effect of steel corrosion on the seismic capacity and hysteresis loop of RC beams. Figure 1 shows the appearance of RC beams with and without corrosion after monotonic and cyclic loading. Kobayashi (2006) showed that after the cyclic loading, RC beams suffered severe spalling of cover concrete within constant-moment region. This spalling was caused by the steel corrosion products and corrosion cracks that led to debonding between the cover concrete and rebar. From these experimental results of corroded RC component, the expansion of corrosion products could reduce the prevention force R_c. R_c is modified from original equation proposed by Naito et al. (2010) to minimize the differences between computational and experimental displacement (Yamamoto and Kobayashi 2006, Oyado 2007, and Kato et al. 2004 and 2005) at the onset of rebar buckling of corroded RC specimens subjected to cyclic loading. RC bridge pier is modeled as single degree of freedom in nonlinear time history analyses to calculate the seismic demand. Degrading elasto-plastic model (e.g., Takeda model 1970), which could evaluate the nonlinear response behavior of the RC component subjected to cyclic loading, is used as hysteresis rule.

PDF of steel weight loss $c_w(t)$ needs to be calculated in Eqn. (2). Steel weight loss depends on time after construction, hazard associated with airborne chloride, concrete strength and quality, and structural details such as concrete cover and diameter of rebar. Akiyama et al. (2009 and 2010a) presented the procedure to calculate the steel weight loss. Hazard assessment associated with airborne chloride was established based on seismic probabilistic hazard assessment (Kameda and Nojima 1988). The results of hazard assessment associated with airborne chlorides depend on the ratio of sea wind (defined as the percentage of time during one day when the wind is blowing form sea toward land), wind speed in the location analyzed,

and distance from coastline. The probability that C_{air} at a specific site will exceed an assigned value c_{air} is

$$q_s(c_{air}) = \int_0^\infty \int_0^\infty P(C_{air} > c_{air} | u, r) \cdot f_u(u) \cdot f_r(r)\, du dr \quad (3)$$

where $f_u(u)$ and $f_r(r)$ = PDFs of wind speed u and ratio of sea wind r, respectively; and $P(C_{air} > c_{air} | u, r)$ = probability of the event $C_{air} > c_{air}$ given u and r.

LONG-TERM SEISMIC RELIABILITY OF RC BRIDGE PIERS IN A MARINE ENVIRONMENT

The elevation and cross-section of the bridge pier analyzed in this study is shown in Fig. 2. This bridge pier was designed according to the seismic design specification in Japan (Japan Road Association 2002). Specified concrete strength is 24 MPa and concrete cover is 90 mm. In this specification, minimum concrete cover shall be 90 mm and corrosion-resistant coated rebar shall be used, if concrete structure is located in very aggressive marine environment and the distance from coastline is less than 0.1 km.

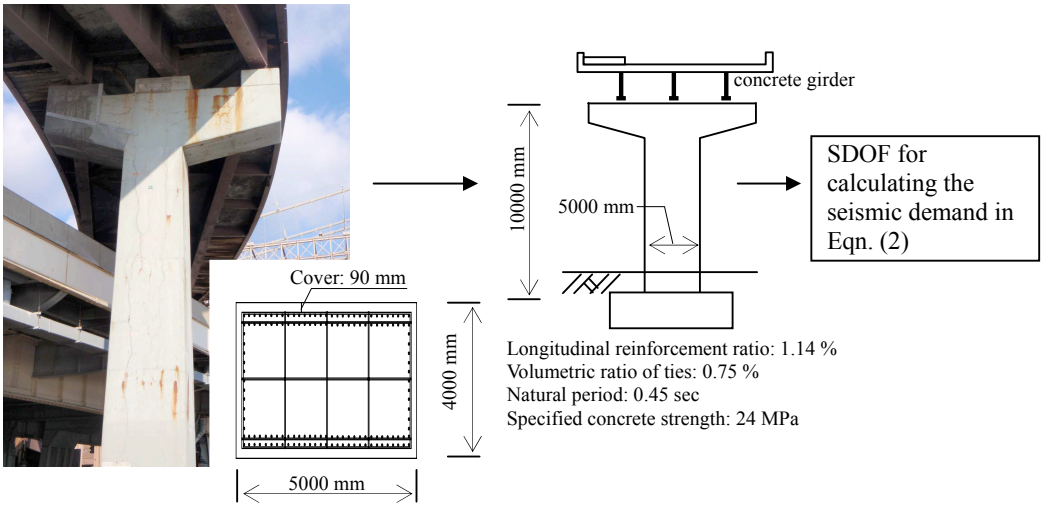


Figure 2. RC bridge pier analyzed

For illustrative purpose, it is assumed that the bridge pier is located in Niigata city and the distance d from coast line is 0.1 km. Seismic hazard curve (National Research Institute for Earth and Disaster Prevention 2010) and hazard curve associated with airborne chloride are shown in Fig. 3. Figure 4 shows the relationship between cumulative-time failure probability and time after construction of RC bridge pier. To examine the effect of corrosion on the failure probability, cumulative-time failure probabilities without deterioration are also shown. As indicated in Fig. 4, concrete cover of 90 mm is not enough to protect the rebar from

airborne chloride attack. This can make the difference between the cumulative-time failure probability associated with both seismic and airborne chloride hazards and that associated with seismic hazard alone. It should be noted that even though the design specification by Japan Road Association (2002) require that coated rebars are used for RC structures in very aggressive marine environment, RC bridge pier shown in Fig. 2 has non-coated rebars.

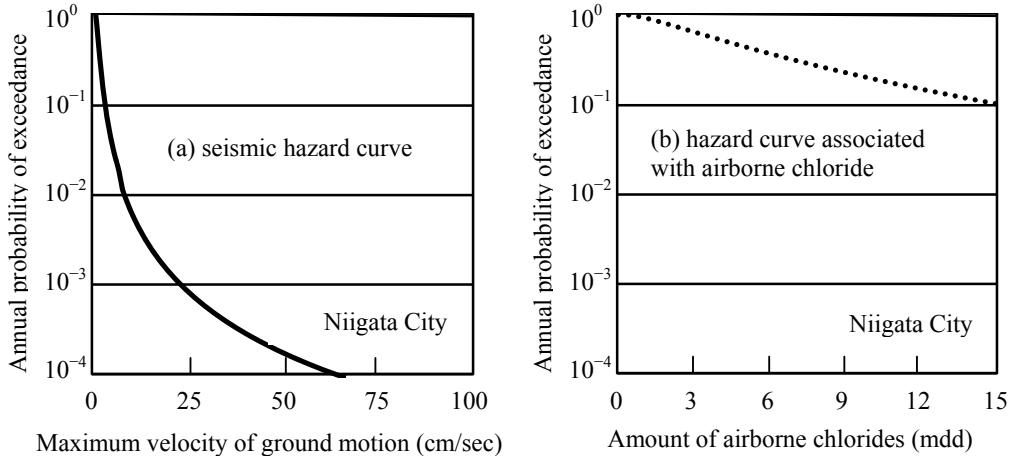


Figure 3. Seismic and airborne chloride hazard curves

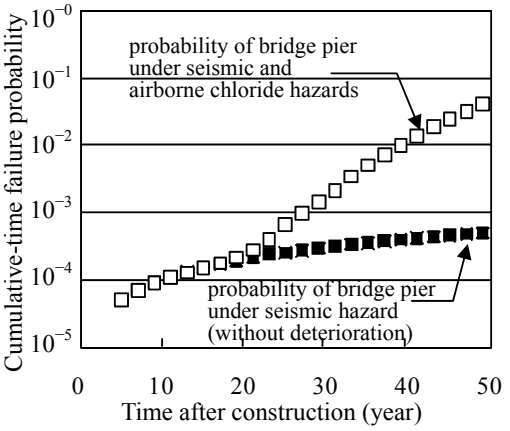


Figure 4. Relationship between time and cumulative-time failure probability

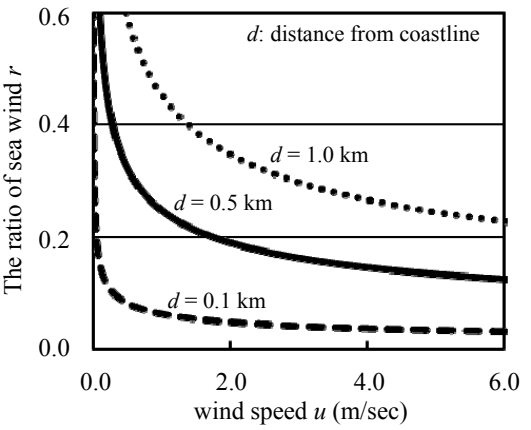


Figure 5. r versus u for several values of d to prevent the deterioration of seismic performance

The difference between the cumulative-time failure probability associated with both seismic and airborne chloride hazards and that associated with seismic hazard alone depends on marine environment. The marine environment required to take into consideration the effect of corrosion on seismic performance is identified using

$$\frac{\beta_{corrosion}}{\beta_{w/o_corrosion}} = \varepsilon_a \tag{4}$$

$$\text{where} \quad \beta_{corrosion} = -\Phi(p_{f2}(u, r, d, T = 50 \text{ years})) \tag{5}$$

$$\beta_{w/o_corrosion} = -\Phi(p_{f1}(T = 50 \text{ years})) \tag{6}$$

$\beta_{corrosion}$ = reliability index associated with probability p_{f2}; $\beta_{w/o_corrosion}$ = reliability index associated with probability p_{f1}; p_{f2} = probability associated with Eqn. (1) considering both seismic and airborne chloride hazards, p_{f1} = probability associated with Eqn. (1) considering seismic hazard alone, Φ = cumulative distribution function of the standard normal variable.

p_{f2} depends on u, r and d used in Eqn. (3). When RC structure is far from coastline, $\beta_{corrosion}$ is almost equal to $\beta_{w/o_corrosion}$. However, when d is less than 1.0 km, the difference between $\beta_{corrosion}$ and $\beta_{w/o_corrosion}$ depends on the combination of the mean values of u and r as shown in Fig. 5. It is assumed in Fig. 5 that (a) bridge pier analyzed has the structural details shown in Fig. 2; and (b) ε_a is 0.90. Since the mean values of u and r in Niigata City are 3.69 m/sec and 0.344, respectively, concrete cover must be larger than 90 mm if d is less than 1.0 km. When the mean values of u and r are provided from meteorological data and the distance from coastline is given, it could be determined from Fig. 5 whether or not the effect of corrosion on the seismic performance is investigated.

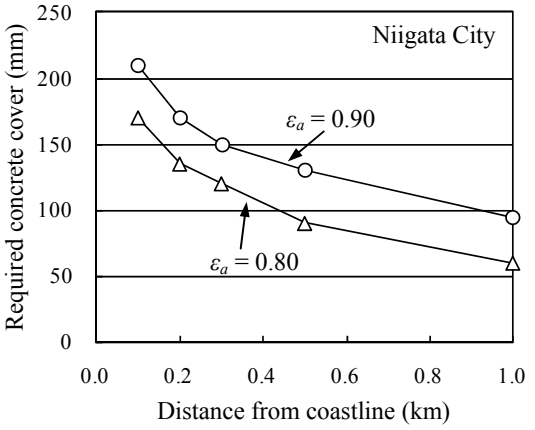


Figure 6. Required concrete cover to prevent the deterioration of seismic performance of RC bridge pier in Niigata City

Figure 6 shows the relationship between distance from coastline and required concrete cover of RC bridge pier in Niigata City to satisfy Eqn. (4) when ε_a is 0.9 or 0.8. In very aggressive environment such as Niigata City, RC components must have an extremely large concrete cover to prevent the deterioration of seismic performance from corrosion. One of the ways to protect RC structures without increasing concrete cover is to use corrosion-resistance coated rebars or stainless rebars. It has been suggested that expected reductions in maintenance and repair costs and the extension of service life can justify their use on a life-cycle cost basis

(e.g., Val and Stewart 2003). Further research is needed on the seismic reliability of RC structures in a marine environment in connection with life-cycle maintenance and optimization (Frangopol and Liu 2007).

CONCLUSIONS

1. For the long-term assessment of RC structures located in a marine environment and earthquake prone regions, the effect of corrosion due to airborne chlorides on the seismic capacity need to be taken into consideration. A computational procedure to integrate the probabilistic hazard associated with airborne chlorides into long-term seismic reliability assessment of RC bridge piers was presented.
2. In very aggressive marine environment, the possible use of corrosion-resistance coated rebars or stainless rebars must be studied based on the life-cycle maintenance and optimization concepts and methods.

REFERENCES

Akiyama M., Frangopol, D. M., and Suzuki M. (2009). "Integration of the effects of airborne chlorides into reliability-based durability design of R/C structures in a marine environment." *Structure and Infrastructure Engineering*, DOI: 10.1080/15732470903363313.

Akiyama, M., Frangopol, D. M., and Yoshida, I. (2010a). "Time-dependent reliability analysis of existing RC structures in a marine environment using hazard associated with airborne chlorides." *Engineering Structures*, 32(11), 3768-3779.

Akiyama, M., Frangopol, D. M, and Matsuzaki, H. (2010b) "Life-cycle reliability of RC bridge piers under seismic and airborne chloride hazards." *Earthquake Engineering and Structural Dynamics*. (submitted for possible publication)

Choe, D. E., Gardoni, P., Rosowsky, D., and Haukaas, T. (2008). "Probabilistic capacity models and seismic fragility estimates for RC columns subject to corrosion." *Reliability Engineering and System Safety*, 93, 383-393.

Coronelli, D., and Gambarova, P. (2004). "Structural assessment of corroded reinforced concrete beam: modeling guidelines." *Journal of Structural Engineering*, ASCE, 130(8), 1214-1224.

Frangopol, D.M., Liu, M. (2007). "Maintenance and management of civil infrastructure based on condition, safety, optimization, and life-cycle cost." *Structure and Infrastructure Engineering*, 3(1), 29–41.

Ghosh, J., and Padgett, JE. (2010). "Aging considerations in the development of time-dependent seismic fragility curves." *Journal of Structural Engineering*, ASCE, doi:10.1061/(ASCE)ST.1943-541X.0000260.

Japan Road Association. (2002). "Design Specification for highway bridges; Part V; Seismic design." *Maruzen*, Japan.

Kameda, H., and Nojima, H. (1988). "Simulation of risk-consistent earthquake motion." *Earthquake Engineering and Structural Dynamics*, 16, 1007-1019.

Kato, E., Iwanami, M., Ito, H., and Yokota, H. (2005). "Influence of rebar corrosion on structural performance of RC column subjected to cyclic loading." *Proceedings of Japan Concrete Institute*, 27(2), 1489-1494. (in Japanese).

Kato, E., Iwanami, M., Yokota, H., Nakamura, K., and Ito, H. (2004). "Influence of rebar corrosion on structural performance of RC beams subject to reversed cyclic loading." *Technical Note of the Port and Airport Research Institute*, 1079. (in Japanese).

Kobayashi, K. (2006). "The seismic behavior of RC member suffering from chloride-induced corrosion," *Proceedings of the second fib Congress*, Paper ID.19-3. Napoli, Italy.

Li, J., Gong, J., and Wang, L. (2009). "Seismic behavior of corrosion-damaged reinforced concrete columns strengthened using combined carbon fiber-reinforced polymer and steel jacket." *Construction and Building Materials*, 23, 2653-2663.

Naito, H., Akiyama, M., and Suzuki, M. (2010). "Ductility evaluation of concrete-encased steel bridge piers subjected to lateral cyclic loading." *Journal of Bridge Engineering*, ASCE. DOI: 10.1061/(ASCE) BE.1943-5592.0000120.

National Research Institute for Earth Science and Disaster Prevention. (2010). *J-SHIS (Japan Seismic Hazard Information Station)*, http://www.j-shis.bosai.go.jp (Nov. 20, 2010).

Oyado, M. (2007). "Mechanical Properties of Corroded Reinforced Concrete Structures." *Ph. D. thesis*, Graduate School of Systems and Information Engineering, Tsukuba University, Japan. (in Japanese).

Simon, J., Bracci, J.M., and Gardoni, P. (2010). "Seismic response and fragility of deteriorated reinforced concrete bridges." *Journal of Structural Engineering*, ASCE, 136(10), 1273-1281.

Takeda, T., Sozen, M., and Nielsen, N. (1970). "Reinforced concrete response to simulated earthquake." *Journal of Structural Engineering*, ASCE, 96(12), 2557-2573.

Yamamoto, T., and Kobayashi, K. (2006). "Report of research project on structural performance of deteriorated concrete structures by JSCE 331 –review of experimental study–." *Proceedings of the International Workshop on Life Cycle Management of Coastal Concrete Structures*, Nagaoka, Japan.

Val, D. V., and Stewart, M. G. (2003). "Life-cycle cost analysis of reinforced concrete structures in marine environments." *Structural Safety*, 25, 343-362.

Probabilistic optimization of the management of corroding RC structures

E. Bastidas-Arteaga[1], F. Schoefs[1] and M. Sánchez-Silva[2]

[1]Research Institute in Civil and Mechanical Engineering, UMR CNRS 6183, University of Nantes, Centrale Nantes. 2, rue de la Houssinière BP 92208 44322 Nantes Cedex 3, France; PH (+33)251125520; email: emilio.bastidas@univ-nantes.fr
[2]Department of Civil and Environmental Engineering. Universidad de los Andes, Bogotá, Colombia

ABSTRACT

This study presents a stochastic method to optimize the inspection of reinforced concrete structures subjected to chloride penetration. The strategy is oriented to find the time interval between two consecutive inspections that (1) minimize the costs of inspection, preventive and corrective repair; and (2) ensure a given level of safety. The optimal interval is therefore determined by using stochastic processes and decision theory. The chloride penetration phenomenon is represented by a Markov chain whose transition matrix is determined from simulations.

INTRODUCTION

Civil infrastructure deteriorates with time mainly as a result of environmental factors. Infrastructure deterioration may be progressive (e.g., as a result of chloride ingress), it may result from sudden events (shocks e.g., earthquakes) or as a combination of both. The cost-efficient design, management and operation of these systems depend, to a large extent, on the assumptions and quality of the deterioration models used for the analysis. Nowadays, design and management of infrastructure must consider economical, social and environmental constrains to reduce environmental impact, optimize resource allocation and decrease waste generation. This new tendency of design and management must also consider all the phenomena which affect the performance of structures. For RC structures, corrosion induced by chloride ingress generates important damage after 10 or 20 years of service (Rosquoet *et al.*, 2006). Consequently, its inspection and maintenance are essential to ensure an optimal level of serviceability and safety during its lifespan.

The purpose of this paper is to develop a method to optimize the intervals of inspection of reinforced concrete structures subjected to chloride penetration. An optimal inspection interval minimizes the costs of inspection, preventive or corrective repair and failure. The method of optimization takes as starting point the work of Sheils *et al.* (2010) and is presented in the following section. Afterwards, the discussion focuses on the estimation of the transition matrices from a comprehensive model of chloride penetration and the cost modeling. Finally, the proposed methodology is illustrated with a numerical example.

STRATEGY OF INSPECTION AND MAINTENANCE

General description. Inspection can be carried out by using destructive and non-destructive methods. This study refers to RC structures subjected to chloride ingress and focuses on inspection/maintenance of major infrastructure such as ports and bridges. The requirements for the strategy of inspection/maintenance were defined within the framework of the European project FUI (2007-2010) MAREO[1] with the collaboration of public agencies, construction companies and research centers. In the strategy of inspection/maintenance considered herein, inspection is undertaken by analyzing the concentration of chlorides at the cover depth on concrete cores (destructive method). Afterwards, depending on inspection results, the repair technique consists of rebuilding the polluted concrete cover. The advantage of the proposed approach is that preventive repair ensures optimal levels of serviceability and safety during the lifespan of the project.

Inspection model. This approach requires that the structure is inspected periodically; i.e., every Δt years. The purpose of these inspections is to establish the real chloride concentration at the cover depth, C. This parameter provides information about the probability of corrosion initiation, and therefore, can be used by the owner/operator to decide if the structure must be repaired or not. The experimental test to determine the chloride profiles is based on the AFREM procedure (RILEM, 2002). Bonnet et al., (2009) found that there are significant differences between "theoretical" and "measured" chloride profiles. To take into account the influence of errors in measurement, the difference between measured $\hat{C}$ and real C values is usually modeled by considering a noise η as follows:

$$\hat{C} = C + \eta \qquad [1]$$

It is supposed herein that the noise is independent of the real chloride concentration because there are several sources of error influencing the results of the inspection. This assumption has been validated from a series of measurements on metallic harbor structures (Schoefs et al. 2009).

Errors in measurement can lead to under or overestimations of chloride content, and consequently, to make erroneous decisions increasing the probability of failure or producing over-costs. From a probabilistic point of view, two measures can be defined to quantify these events:

- Probability of Good Assessment (PGA): determines the probability of detecting an event (crack, defect, concentration, etc.) given that it exists:
$$\text{PGA} = P\left(\hat{C} \geq C_{rep} \middle| \hat{C} \geq C_{rep}\right) \qquad [2]$$
- Probability of Wrong Assessment (PWA): establishes the probability of detecting an event given that it does not exist:
$$\text{PWA} = P\left(\hat{C} \geq C_{rep} \middle| \hat{C} < C_{rep}\right) \qquad [3]$$

[1]. Maintenance and REpair of concrete coastal structures: risk-based Optimization (MAREO) Project

where C_{rep} represents the repair threshold. The equations presented above assume that the noise and the signal follow a normal distribution –i.e. N[μ_η, σ_η] and N[μ_C, σ_C].

Repair model. Chloride penetration into concrete may cause structural failure when no repair is carried out. The repair criterion considers that the polluted concrete is rebuilt when the chloride concentration measured during the inspection reaches a threshold value C_{th}. According to Duracrete (2000), the threshold value C_{th} can be modeled by a normal distribution N[$\mu_{C_{th}}$, $\sigma_{C_{th}}$]. Thus, the probability of corrosion initiation between the inspection intervals can be estimated as:

$$p_f = \Phi\left(\frac{C-\mu_{C_{th}}}{\sigma_{C_{th}}}\right) \quad [4]$$

TRANSITION MATRICES FOR MODELING CHLORIDE INGRESS

A discrete-time Markov process can be used for prediction by knowing the current state of a system. Towards this aim, the space of the variable of interest is discretized into M states. The Markov process is thus used to determine the probability that an event belongs to a state j knowing that in a preceding state it belonged to a state i. This probability, noted as a_{ij}=P(X_{t+1}= j | X_t =i), is called "transition probability". It is considered herein that a_{ij} is independent of t. The transition probabilities can be grouped in a matrix of size M×M called transition matrix **P**. According to the Chapman-Kolmogorov equations, by knowing an initial state, the probabilities of belonging to other states after t transitions, **q**(t), are (Ross, 2004):

$$\mathbf{q}(t) = \mathbf{q}_{ini}\mathbf{P}^t \quad [5]$$

where the vector $\mathbf{q}_{ini}$ contains the probabilities of belonging to the states at an initial time –i.e., t =0. In this study, the variable of interest is the concentration of chlorides at the cover depth, C, which controls corrosion initiation. Therefore, the Markov processes can be used to estimate the probability that C is in a given state at a given time. If it is supposed that after construction t=0 the concentration of chlorides at the cover depth is zero. Consequently, all the concentrations belong to the first state, $\mathbf{q}_{ini}$ becomes $\mathbf{q}_{ini}$=[1, 0, 0, … ,0] and equation [5] provides a vector containing the probabilities of belonging to a state j at time t, **q**(t).

In several applications of Markov chains, the transition matrix is obtained from experimental data or expert judgment. However, given that the rate of chloride ingress into concrete is slow and that chloride ingress is influenced by several parameters (environment, material properties, etc.), it is proposed herein to numerically estimate **q**(t). The following sections will describe the adopted probabilistic model of chloride penetration and the method proposed to estimate the transition matrix.

Chloride ingress model. Chloride ingress into concrete is controlled by a complex interaction between physical and chemical mechanisms that have been commonly modeled as a diffusion phenomenon. However, in this paper a more comprehensive

model is proposed; it considers the interaction between: (1) chloride penetration, (2) diffusion of moisture; and (3) heat transfer. The description of the formulation of the model is beyond the scope of this paper but can be found in Bastidas-Arteaga *et al.*, (2011).

The management of uncertainties considers, first, the random variables presented in Table 1. The criteria for determining the characteristics of the random variables are dicussed in (Bastidas-Arteaga *et al.*, 2011). Taking into account the non-linearity and the complexity of the system of partial differential equations used to model chloride penetration, Monte Carlo simulations and Latin Hypercube sampling are employed herein.

Table 1. Probabilistic parameters of the random variables

Variable	Units	Distribution	Mean	COV
– Reference chloride diffusion coefficient, $D_{c,ref}$	m^2/s	log-normal	$3 \cdot 10^{-11}$	0.20
– Activation energy of the chloride diffusion process, U_c	kJ/mol	beta on [32;44.6]	41.8	0.10
– Aging factor, m		beta on [0;1]	0.15	0.30
– Reference humidity diffusion coefficient, $D_{h,ref}$	m^2/s	log-normal	$3 \cdot 10^{-10}$	0.20
– Parameter representing the ratio $D_{h,min}/D_{h,max}$, α_0		beta on [0.025;0.1]	0.05	0.20
– Parameter characterizing the spread of the drop in D_h, n		beta on [6;16]	11	0.10
– Thermal conductivity of concrete, λ	W/(m°C)	beta on [1.4;3.6]	2.5	0.20
– Specific heat capacity of concrete, c_q	J/(kg°C)	beta on [840;1170]	1000	0.10
– Density of concrete, ρ_c	kg/m^3	Normal	2400	0.04

Estimation of the transition matrix from simulations. Transition matrices are estimated from Monte Carlo simulations of the probabilistic model of chloride penetration. In each simulation, the chloride concentration at cover depth during time is recorded. In all simulations, the frequency of belonging to a given state is determined. Thus, the probability of belonging to a state j at time t is obtained from:

$$\hat{q}_j(t) = \frac{n_o(t)}{N} \qquad [6]$$

where $n_0(t)$ is the number of observations in the state j measured at time t and N is the number of simulations. Table 2 presents the possible states of the system and its corresponding boundaries (minimum and maximum); note that each state corresponds to a chloride concentration C. Taking into account this discretization, Figure 1 shows the variation in time of the probability of belonging to the last state i=10 ($\hat{q}(t)$) obtained from Monte Carlo simulations.

Table 2. States used for discretizing the problem.

State i	1	2	3	4	5	6	7	8	9	10
C minimum (kg/m^3)	0.0	0.4	0.8	1.2	1.6	2.0	2.4	2.8	3.2	3.6
C maximum (kg/m^3)	0.4	0.8	1.2	1.6	2.0	2.4	2.8	3.2	3.6	4.0

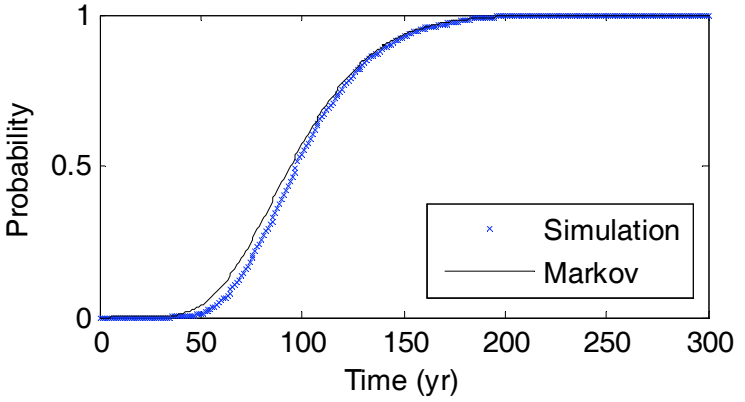


Figure 1. Comparison between the probabilities computed from Monte Carlo simulations and Markov model for the last state.

Once the probabilities $\hat{q}(t)$ have been estimated, several methods can be used to compute the transition probabilities. The major difficulty in the assessment of **P** lies in the number of parameters a_{ij} to estimate. Various studies consider a Markov matrix with two parameters for state (Pappas *et al.*, 2001, Roelfstra *et al.*, 2004). In this case, the transition probabilities can be estimated from a non-linear regression. However, complex stochastic phenomena cannot be modeled by a transition matrix with two transition probabilities per state (Roelfstra *et al.* 2004). To solve this problem, the proposed method searches the values a_{ij} that minimize the difference between the probabilities estimated from simulations and the obtained from the Markov model (equation [5]). Since the kinematics of the time-dependent evolution of each state is similar, there are *M* functions to minimize:

$$\begin{cases} \min_{\mathbf{a}} \max_{\mathbf{F}} \mathbf{F}(\mathbf{a}) = \left(f_1(\mathbf{a}), f_2(\mathbf{a}), \ldots, f_M(\mathbf{a})\right)^T \\ \text{s.c.} \quad a_{ij} \geq 0 \quad \text{et} \quad \sum_{j=0}^{\infty} a_{ij} = 1 \end{cases} \qquad [7]$$

where **a** is a vector containing the transition probabilities (optimization parameters) and:

$$f_j(\mathbf{a}) = \sum_{t=0}^{t_{ana}} \left| \hat{q}_j(t) - q_j(t, \mathbf{a}) \right| \qquad [8]$$

where t_{ana} represents the analysis period used to perform the adjustment. This multi-objective optimization problem has been solved by using the "optimization toolbox" of Matlab©. The selected optimization method minimizes the maximum value of a set of multi-variable functions from an initial value.

COST ANALYSIS

Two kinds of costs are usually considered in cost analysis: *agency* and *user* costs. Agency costs encompass the direct costs incurred by the owner/operator during the life-cycle including initial construction costs and costs associated with inspection,

repair, rehabilitation, replacement and disposal. User costs represent the inconvenience and expenses incurred by users due to traffic disruption such as travel delay costs, ship operating costs and accident costs. According to Thoft-Christensen (2009), user costs should be included in the analysis to formulate a comprehensive strategy of maintenance management of infrastructure. However, given that the information to estimate user costs is hard to establish and find; this work is only based on agency costs.

In this study the direct costs incurred by the agency include only costs associated with maintenance (inspection, preventive repair, corrective repair and failure). The initial construction costs are not included in the analysis because it is assumed that it would be the same for all maintenance alternatives. Since it is not possible to determine the final use of the structure at the end of the life-cycle (deconstruction or demolition), the residual (or salvage) value is also not considered. This study considers costs estimated with standard and intergenerational discounting.

In life-cycle cost analysis, the expected value of the total present value life-cycle cost E[C_T] is computed as:

$$E[C_T] = \sum_{j=0}^{m} E\left[C_j(t)\right] W(t); \text{for } t \le T_t \qquad [9]$$

where m is the total number of interventions carried out within the time interval [0,T_t], $C_j(t)$ is the j^{th} expenditure at time t (for instance in years), T_t is the life-cycle length and $W(t)$ is the weight used to discount $C_j(t)$ to the present value. $C_j(t)$ depends on the properties of the original and repair materials; and on the characteristics of the maintenance strategy (i.e., inspection interval, inspection quality, repair threshold, etc.). The costs of inspection C_I, preventive repair C_{pr} and corrective repair C_{cr} are simply calculated as a fraction of the initial cost of construction C_0 as:

$$C_I = C_0 k_I \qquad [10]$$

$$C_{pr} = C_0 k_{pr} \qquad [11]$$

$$C_{cr} = C_0 k_{cr} \qquad [12]$$

where k_I, k_{pr} and k_{cr} are weights used to compute the costs of inspection, preventive and corrective repair as a fraction of C_0, respectively.In conventional discounting, the standard discount weight can be expressed as:

$$W_s(t) = 1/(1 + r_s)^t \qquad [13]$$

where r_s is the standard discount rate. Sumalia and Walters (2005) and Prager and Shertzer (2006) derived an intergenerational discount weight for computing net benefits from the use of environmental resources. In their formulation, they treat the benefits as accruing to the current generation (at standard discount rates) plus to each of the annual increments of new stakeholders who will have entered the stakeholder population by that future year divided by the generation length, G. Consequently, the intergenerational discounting $W_I(t)$ can be estimated as (Sumalia and Walters, 2005):

$$W_I(t) = W_s(t) + \frac{W_c(t-1)}{(1+r_I)G}\left[\frac{1-\Delta^t}{1-\Delta}\right] \quad [14]$$

where r_I is the intergenerational discount rate computed on an annual basis and $\Delta = (1+r_s)/(1+r_I)$.

NUMERICAL EXAMPLE

Problem description. This example aims to determine an inspection interval that optimizes the maintenance costs of RC structures. Consider a structure placed in a marine environment with temperature ranging from 5 to 25 ºC and with relative humidity between 0.6 and 0.8. The stochastic climate model is described in (Bastidas-Arteaga et al., 2011). The structure is exposed to an average environmental chloride concentration C_{env}=6 kg/m^3. This concentration corresponds to the boundary between high and severe corrosive environments (Weyers, 1994). According Duracrete, (2000), C_{env} is modeled as a stochastic process generated by independent numbers following a log-normal (log-normal noise) with a coefficient of variation of 0.2. To simplify the study, it is assumed that the repair material has the same characteristics that the construction material.

The determination of an optimal inspection interval is very sensitive to the cost models. Therefore, to obtain realistic results, the inspection, preventive repair and corrective repair coefficients (i.e., k_I, k_{pr} and k_{cr}) were defined taking into account the average expenditures for these items incurred by the port of Nantes Saint-Nazaire, France. These coefficients are presented in Table 3 and are used to estimate the costs of inspection, preventive and corrective repair on the basis of an initial construction cost of 1000 units. Given that it is supposed that repair is preventive, there is no failure cost and these coefficients are lower than 1. Whereas the coefficient of preventive repair only considers the cost related to cover rebuilding, the coefficient of corrective repair includes besides the costs of structural strengthening. Table 3 also includes the numerical values used to model inspection and repair.

Table 3. Parameters used in the numerical example

Parameter	value
Noise of the measurement, η, km/m^3	0.30
Standard deviation of noise, σ_η, km/m^3	0.50
Repair threshold, C_{rep}, km/m^3	0.10
Threshold chloride concentration, C_{th}, km/m^3	2.00
Standard deviation of C_{th}, σ_{Cth} , km/m^3	0.40
Initial cost of construction, C_0	1,000
Inspection coefficient, k_I	0.005
Preventive repair coefficient, k_{pr}	0.15
Corrective repair coefficient, k_{cr}	0.30
Discount rate, r_s	5%
Discount rate per generation , r_I	3%
Generation length, G	25 yr
Life-cycle length, T_t	100 yr

Results. To estimate the Markov matrix, the problem is discretized into M = 10 states. The matrix **P** was obtained from 10,000 simulations for a concrete cover of 5cm.

Figure 1 compares the probability of belonging to the state 10 estimated by both simulations and the Markov model. Note that the phenomenon is well represented by the estimated **P**.

Figure 2 presents the expected times to preventive and corrective repair as a function of the length of the inspection interval. These results were obtained from the Markovian approach for a given repair technique to rebuild the concrete cover (formed concrete). As expected, the time to preventive repair, t_{pr}, is lower when the structure is periodically inspected. On the contrary, less inspection implies that the time to corrective repair, t_{cr}, decreases. These times will be used to determine the optimum inspection interval that minimizes costs. To simplify the computation, the results of simulation are adjusted to two analytical functions that will allow us to estimate t_{pr} and t_{cr} in terms of the length of the inspection interval Δt_I (Figure 2).

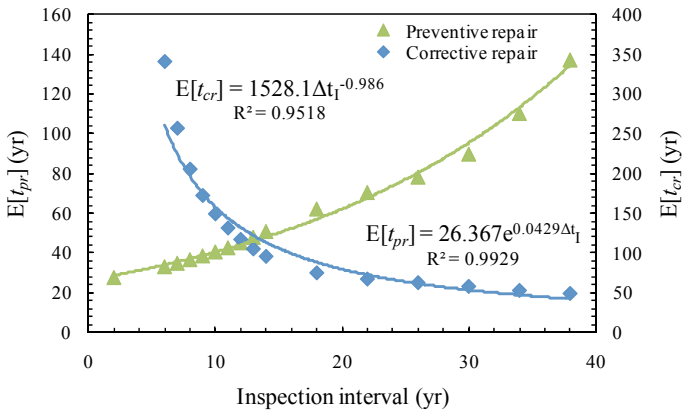


Figure 2. Determination of the expected value of the times to preventive and corrective repair

Figure 3 presents the expected costs for three cases: standard discounting, intergenerational discounting and without discounting. An intergenerational discount rate of r_I = 3% (per generation) was used. The total cost is discriminated into the costs of inspection, preventive and corrective repair. It is observed in all cases that the costs of inspection and preventive repair decrease and the cost of corrective repair increases for larger inspection intervals. This behavior is explained by the fact that when the inspection interval is greater, most inspections detect the component's failure. On the contrary, when the structure is inspected regularly, repair is preventive, and therefore, the corrective repair expenditures diminish.

The results showed that the expected total cost is optimal when the structure is inspected every 20 years for the standard discounting case and every 15 years for the intergenerational case. However, the optimum expected cost is different for all cases because the future flows for the intergenerational and undiscounted cases are important in comparison to the standard case for the life-cycle length T_t. The differences between the optimum inspection intervals imply that the intergenerational and undiscounted cases give more importance to preventive maintenance.

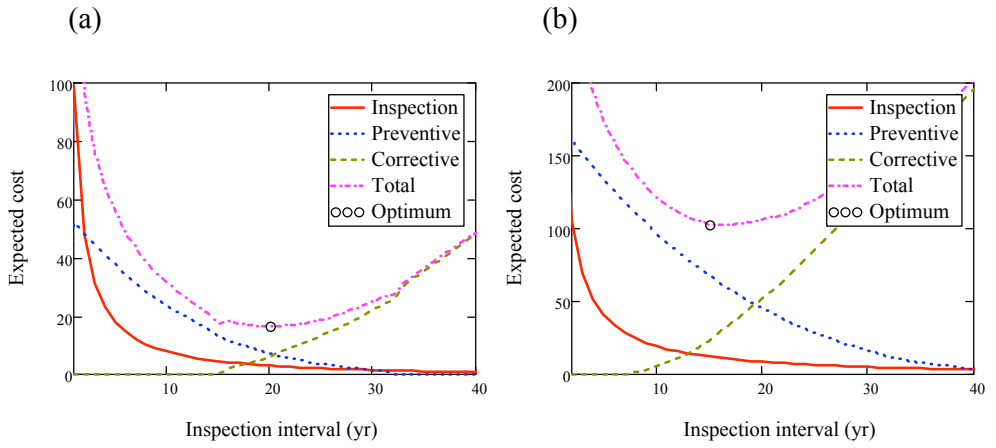


Figure 3. Expected costs for the cases (a) standard and (b) intergenerational discounting

The discount rate per generation can be defined in different ways. For instance Sumalia and Walters (2005) state that the simplest way to fix r_I is to select a value equal to the standard discount rate. It can also be defined from a discussion with the community or it can be used the internal rate of return for educating people to the Ph.D. level in a given country. The influence of this parameter on the length of the optimum inspection interval and on the total expected cost is studied in Table 4. Therefore, for small discount rates per generation, the structure should be inspected more frequently and the total expected cost is larger. On the contrary, when $r_I \rightarrow \infty$, the optimum result converges to the result obtained when intergenerational discounting is neglected.

Table 4. Influence of r_i on the optimum inspection interval and on the total expected costs

r_I (%)	Optimum Δt_I (yr)	Total expected cost
3	15	102.5
5	19	53.8
10	20	26.6
20	20	19.2
∞	20	16.6

CONCLUSIONS

This paper presents a stochastic method for optimizing the inspection/repair of RC structures subjected to chloride penetration. The inspection technique measures the concentration of chlorides at the cover depth. Afterwards, based on the inspection results, the structure is repaired by replacing the polluted concrete with new material. The inspection/maintenance strategy chosen is modeled using decision theory and Markov processes. It is also proposed a methodology for determining the transition matrix from simulations of a chloride penetration model. The proposed method is

illustrated with an example where it is showed that there is an inspection interval that minimizes the costs of inspection, preventive and corrective repair.

ACKNOWLEDGEMENTS

The authors acknowledge financial support of the MAREO project – contact: franck.schoefs@univ-nantes.fr.

REFERENCES

Bastidas-Arteaga E., Chateauneuf A., Sánchez-Silva M., Bressolette P., Schoefs F. (2011). "A comprehensive probabilistic model of chloride ingress in unsaturated concrete." *Engineering Structures*, In pres.

Bonnet S., Schoefs F., Ricardo J., Salta M. (2009). "Effect of error measurement of chloride profiles on reliability assessment." *Proceedings of I.C.O.S.S.A.R.*, Osaka, Japan.

Duracrete, (2000). *Statistical quantification of the variables in the limit state functions*. The European union, BriteEuRam III, contract BRPR-CT95-0132, Project BE95-1347.

Pappas Y.Z., Spanos P.D., Kostopoulos V. (2001). "Markov chains for accumulation of organic and ceramic composites". *Journal of Engineering Mechanics*, vol 127, pp. 915-926.

Prager, M.H. and Shertzer, K.W. (2006). *Remembering the future: A commentary on "Intergenerational discounting: a new intuitive approach"*. Ecological Economics, 60:24-26.

RILEM TC178-TMC, (2002). "Analysis of chloride content in concrete." *Materials and Structures*, v. 35, p. 583-585.

Roelfstra G., Hajdin R., Adey B., Brühwiler E. (2004). "Corrosion evolution in bridge management systems and corrosion-induced deterioration.", *Journal of Bridge Engineering*, vol 9, pp. 268-277.

Ross S.M. (2000). *Introduction to Probability models*, Academic Press.

Schoefs F., Clément A., Nouy A. (2009). "Assessment of spatially dependent ROC curves for inspection of random fields of defects", *Structural Safety*, v. 31, pp. 409-419.

Sheils E., O'Connor A., Breysse D., Schoefs F., Yotte S. (2010). "Development of a two stage inspection process for the assessment of deteriorating infrastructure", *Reliability Engineering and System Safety*, vol. 95, pp. 182-194.

Sumalia, U.R. and Walters, C. (2005). *Intergenerational discounting: a new intuitive approach.* Ecological Economics, 52:135-142.

Thoft-Christensen, P. (2009). *Life-cycle cost-benefit (LCCB) analysis of bridges from a user and social point of view*. Structure and Infrastructure Engineering, 5:49–57.

Weyers R.E. (1994). *Concrete Bridge Protection and Rehabilitation: Chemical and Physical Techniques - Service Life Estimates*. SHRP-S-668.

Structural Risk Evaluation for Offshore Platforms Under Major Accidental Events

Liangsheng Wang[1] Ali Sari[1] Fraser Munro[1]

[1] WS Atkins, 920 Memorial City Way Suite 700, Houston, Texas 77024

Email: liangsheng.wang@atkinsglobal.com (L. Wang)

Email: ali.sari@atkinsglobal.com (A. Sari)

Email: fraser. munro@atkinsglobal.com (F. Munro)

Abstract

A structural risk evaluation methodology is introduced in this paper for the offshore platforms against major hazard events (hurricanes and earthquakes) during the operating life of the platforms. The primary objective is to evaluate the risk level from the major hazard events to identify possible risk reduction solutions. Firstly a non-linear progressive collapse analysis approach is presented to investigate the platform capacity to resist the loads imposed by major hazard events. The structural reliability method is then proposed to estimate the probability of platform failure under major hazard events. The platform failure limit state function is defined in terms of hazard loads and platform capacity. Uncertainties are included in the parameters associated with hazard loads and platform capacity. Finally the platform failure consequence and the probability of platform failure are combined to determine the platform risk associated with the major hazard events. Case studies are presented to illustrate the application of the developed structural risk evaluation approach.

Keywords: Offshore platforms; Structural risk evaluation; Major accidental events

1 INTRODUCTION

Offshore platforms are subjected to major accidental events, such as hurricanes, earthquakes, fires, explosions, dropped objects and vessel impacts, during the operating life of the platforms. Oil production from an offshore platform may be stopped because of a major accident event if the platform or some parts of the platform fail during the accidental event. In 2008 Hurricanes Gustav and Ike resulted in a total of 60 platforms being destroyed and 31 structures with extensive damaged (Kaiser and Yu 2010). The industry's evaluation of recent hurricanes in the Gulf of Mexico indicates that the hurricane 100-year return period event is substantially higher than that presently provided in API RP 2A 21st edition (2008). Thus, the criteria related to a reduced return period during the design phase results in an increase to the operating risk of offshore platforms. A large number (over 100) of fixed offshore platforms has been installed in seismically-active regions all over the world (Asgarian and Agheshlui, 2009). As new regions with the potential for significant seismic activity are now beginning to be developed, methods are needed to assist in the design of the structures which will be placed in those regions. In addition, geological studies have identified the potential for increased seismic activity in regions once believed to be far removed from seismic hazard. Offshore structures within these regions are in need of assessment for earthquake loads or re-assessment for increased earthquake loads. These facts underline the importance of the structural risk evaluation of offshore platforms against major accidental events.

A number of investigators have discussed the structural reliability of platforms subjected to major hazard loadings. Botelho et al. (1994) calculated the failure probability of ST130 "A" platform in the Gulf of Mexico during Hurricane Andrew. Gebara et al. (2000) and Jha et al. (2000) studied the effect of sea floor subsidence on the platform failure probability on three jacket platforms in the North Sea. Heredia-Zavoni et al. (2004) carried out a structural reliability assessment of deck elevations subjected to storm wave loading for fixed platforms in the Bay of Campeche. Dier et al. (2001) developed a reliability analysis methodology for jacket platforms in the North Sea. Ronalds et al. (2003) investigated the structural reliability of a generic caisson under storm overload in the Australian North West Shelf. Park et al. (2010) evaluated the effect of uncertainties of dynamic forces and structural properties on the reliability of the offshore platform using Monte Carlo Simulation (MCS). Nadim and Gudmestad (1994) studied the reliability of an oil production system at the Statfjord Field in the North Sea. However, to date very limited work has been reported on the structural risk evaluation of offshore platforms against major accidental events.

This paper presents a comprehensive structural risk evaluation approach for the offshore fixed platforms against hurricanes and earthquakes. Firstly a non-linear progressive collapse analysis approach is presented to investigate the platform capacity to resist the loads imposed by major hazard events. The structural reliability method is then used to estimate the probability of platform failure under major hazard events. The platform failure limit state function is defined in terms of hazard loads and platform capacity. Uncertainties are included in the parameters associated with hazard loads and platform capacity. The platform failure consequence and the probability of platform failure are combined to determine the platform risk associated with the major hazard events. The risk mitigation measures that could reduce the risks are briefly discussed.

Finally case studies are presented to illustrate the application of the developed structural risk evaluation approach.

2 STRUCTURAL RISK EVALUATION

2.1 Nonlinear Progressive Collapse Analysis

The platform capacity is generally determined from a nonlinear progressive collapse analysis, in which hazard loads are applied progressively until the platform collapses. Nonlinear analysis takes into consideration the non-linear effects of individual component behavior, including non-linear material behavior as well as the non-linear deflection of the structural components and system. Nonlinear progressive collapse analysis also allows the load redistribution from over-utilized members. Platform failure is generally defined as formation of a limiting mechanism in the platform structure or foundation. As the hazard loads are progressively increased during the nonlinear progressive collapse analysis, non-linear events such as member buckling and yielding, joint plasticity, and pile pullout or plunging are monitored, which is used to detect the formation of a limiting mechanism in the structure or foundation.

During a nonlinear progressive collapse analysis, the loadings are generally applied in two steps. The first step consists of the platform's dead weight and topsides loads. In the second step, the hazard loads are ramped up progressively until platform failure is reached. The platform capacity can be characterized in terms of the load factor, which is defined as the ratio of the platform's ultimate hazard load carrying capacity to nominal design load, e.g. 100-year storm lateral loading for hurricane evaluation and 10,000-year seismic loading for earthquake evaluation.

The structural model of a platform consists of the jacket, topsides, piles, foundation, conductors and miscellaneous platform appurtenances, reflecting the platform's as-is condition by accounting for known damage, deterioration and modification based on platform inspection records. The jacket structure is modeled as a space frame, in which tubular beam elements are used to model the jacket structural members. Non-linear joint characteristics are included in the model to check the capacity of each brace-chord intersection at the tubular joints. Jacket appurtenances that are exposed to wave and current loading are included in the model, either explicitly or implicitly by enhancing the hydrodynamic coefficients of the primary jacket members the appurtenances are attached to. All primary members on the topsides structures are included in the structural model to represent the topsides stiffness. The foundation model consists of non-linear beam-column elements to represent the piles with the soil being modeled with non-linear springs which represent the non-linear pile-soil interaction.

2.2 Structural Risk Evaluation

The platform risk is defined as the product of the probability of platform failure (likelihood of failure) and the consequence of failure based on a risk matrix. Risk matrix provides a traceable framework for explicit consideration of the frequency and consequences of hazards. A risk matrix uses a matrix dividing the dimensions of failure probability and consequence into typically 3 to 6 categories. Different operators may

have different risk matrix driven by company policy. Figure 1 presents a risk categorization matrix example. The consequence of platform failure considers life-safety consequence, environmental consequence and business loss/disruption.

Consequence of Failure				
	High	Medium Risk	High Risk	High Risk
	Medium	Low Risk	Medium Risk	High Risk
	Low	Low Risk	Low Risk	Medium Risk
		Low	Medium	High
		Likelihood of Failure		

Figure 1. Risk Matrix Example

The structural reliability analysis is used to estimate the probability of platform failure under major hazard events. During the platform reliability analysis, a platform is modeled in terms of two basic sub-systems: one representing jacket including foundation and the other representing topsides. The platform fails if either the jacket sub-system or the deck sub-system fails. The platform system reliability analysis models the two correlated sub-systems as a system in series.

The limit state function for estimating the failure probability is defined as

$$g(X) = R - S \tag{1}$$

where, R is a random variable describing the platform capacity (resistance) and S is the total hazard load. The uncertainty in the platform capacity considers the variability in the material properties such as yield strength, dimensional tolerances, platform condition and foundation. $g(X)$ defines a failure criterion that is a function of all random variables X. Failure occurs when the load S exceeds the capacity R or when $g(X) < 0$.

With the establishment of a limit state function, the annual probability of failure is defined by the expression:

$$P_f = \int_0^\infty \left(1 - F_S(x)\right) \cdot f_R(x) \cdot dx \tag{2}$$

where, P_f is the annual probability of failure, F_S is the cumulative distribution function (CDF) for the environmental load S, and f_R is the probability density function (PDF) for the capacity R.

The probability of failure can be calculated using the Rackwitz-Fiessler FORM (first order reliability method). In this method, the probability of failure is estimated using first order approximation to the limit state at the design point. Non-normal distribution random variables are transformed to equivalent normal distribution variables. The Newton-type recursive formula is used to iteratively search the most probable point (MPP) of failure in the limit state surface. The probability of failure is calculated as $P_f = \Phi(-\beta)$, where β is reliability index and $\Phi(\cdot)$ is the cumulative distribution function of a standard normal variable.

Risk of failure during an accidental event can be mitigated by a number of methods. All are likely to have significant cost and/or operational impact. Some hurricane mitigation alternative currently being implemented by operators in the Gulf of Mexico include:

- Raising of the deck above the wave crest
- Strengthening of the jacket structure
- Reduction of loading on the structure through the removal of unused wells, boat landings or other appurtenances to the jacket.
- Reduction in platform failure consequence.

2.3 Hurricane Structural Reliability Analysis

The platform failure probability against hurricane events is normally calculated for up to 8 wave approach directions (4 orthogonal directions and 4 diagonal directions). Failure in each direction is treated as a failure element, and the multiple direction failure forms a series system for reliability calculations. For platforms that experience storm waves from a dominant approach direction, probability of failure may be calculated for the dominant direction only.

The limit state function for estimating the failure probability is defined as

$$g(X) = R - S = R - L - W \tag{3}$$

where L is a random variable describing the wave and current load on the platform, and W is wind load on the platform.

By calculating the wave and current loads for a number of storms with different return periods, the wave and current load can be expressed as a function of wave height using regression analysis. The wave and current load characteristics change when the wave crest reaches the bottom of steel of the lowest deck of the topsides. For the regression of wave and current load as a function of wave height, two different functional forms are selected for wave and current load before and after deck inundation. The wave and current load L has the functional form

$$\begin{cases} L = C_1 \cdot H_m^{C_2} & H_m < H_d \\ L = \left[C_1 + C_3\left(H_m - H_d\right)\right] \cdot H_m^{C_2} & H_m \geq H_d \end{cases} \tag{4}$$

where H_d is the maximum wave height which results in a wave crest just hitting the underside of lowest deck of topsides, H_m is a random variable describing the annual

maximum wave height, C_1 is a random variable that characterizes the load uncertainty on the jacket system, C_2 is the exponent in the load-wave height relationship, and C_3 is a random variable that characterizes the uncertainty in the wave-in-deck loads.

For hurricane failure mode the topsides weight might have little effect so the uncertainty in topsides weight was excluded from the reliability calculation in this study. However, in the case that there is significant uncertainty in the topsides weight, the topsides weight should also be considered as a random variable.

2.4 Seismic Structural Reliability Analysis

Modeling of the structure, seismic action input and analysis of a structural dynamic response are three key issues for earthquake assessment. The validity of seismic analysis results depends on not only a proper model of the structure and a high-precision method adopted in the analysis, but also the earthquake loading parameters. In this study, a demand calculation procedure utilizing response spectrum analysis (RSA) has been implemented for the purposes of calculating load demands on the offshore structure. The seismic demand is expressed as maximum base shear force, and the capacity of the structure is expressed in terms of ultimate strength of the platform.

Detailed seismic reliability analysis of an offshore platform is quite involved. The random variables include the resistance of the structural components, the load characteristics, and any other random variable that may influence the performance (Nadim and Gudmestad, 1994). In the present study, a simplified model for the limit state function is assumed as

$$g(X) = R - S = R - \frac{(DD + LL)S_a}{r} \tag{5}$$

where S is the earthquake load in terms of maximum base shear, DD is a random variable describing the total dead load of the offshore platform, LL is a random variable characterizing the reduced live loads, S_a is a random variable that characterizes the design spectral at the fundamental frequency of the platform, and r is the response modification factor estimated utilizing response spectrum analysis.

For seismic failure mode the lateral inertia load had significant effect so the uncertainty in topsides weight was included in the reliability calculation in this study.

3 CASE STUDY

A case study for a 4-leg fixed steel jacket platform is presented to illustrate the application of the developed structural risk evaluation approach. The three-dimensional structural model has been created in USFOS program as shown in Figure 2.

3.1 Hurricane Risk Assessment

The non-linear progressive collapse analyses (pushover analyses) were performed using the USFOS program, resulting in a minimum reserve strength ratio (RSR) of 3.83 when subjected to a 100-year storm wave from platform's diagonal direction. It implies that the platform can resist 3.83 times of the load imposed by the 100-year return period storm. Pushover analyses also showed the collapse of the platform was caused by a

failure mechanism formed within the jacket by brace buckling and yielding. No significant non-linearities were observed in the piles or deck legs.

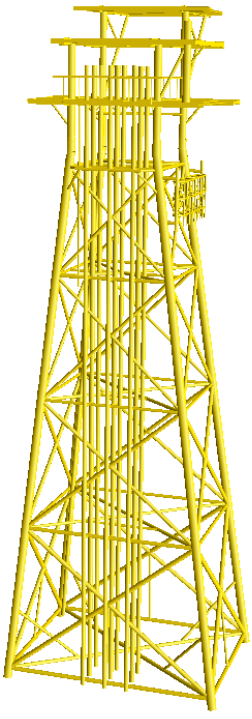


Figure 2. Platform structural model

A metocean study has been carried out using hind-casting techniques to determine the frequency of hurricane events with different magnitudes for the platform location. The significant wave height H_s in storms was fitted using a Weibull distribution. Mean value and standard deviation of H_s are given as

$$\mu_H = \gamma + \eta\Gamma\left(\frac{1}{\beta}+1\right) \tag{6}$$

$$\sigma_H = \eta\sqrt{\Gamma\left(\frac{2}{\beta}+1\right)-\Gamma^2\left(\frac{1}{\beta}+1\right)} \tag{7}$$

where β, η and γ are Weibull distribution parameters: β = 1.1687, η = 2.0970 and γ = 3.8624. The annual probability of exceedance of significant wave height was found by describing the frequency of occurrence of storms as a Poisson process. The annual probability of exceedance of H_s is given as

$$P_e(H) = 1 - \exp\left[-\lambda \exp\left[-\left((H-\gamma)/\eta\right)^{\beta}\right]\right] \tag{8}$$

where λ is a storm rate defined as $\lambda = N_{storms} / T_{hindcast}$, N_{storms} is the number of storms in the hindcast record, and $T_{hindcast}$ is the duration of the hindcast (years).

The regression of maximum wave height H_m as a function of H_s gives $H_m = 1.887 H_s^{0.951}$. Multiple USFOS runs were performed for a number of wave heights to generate wave loads. Coefficients C_1, C_2 and C_3 in Eq. (4) were determined by simultaneously fitting the curve in both regions above and below H_d using the regression method. The regression of wave load to wave height yielded the parametric relationship of wave load as a function of wave height. Relationship between the wave height and wave/current load is plotted in Figure 3.

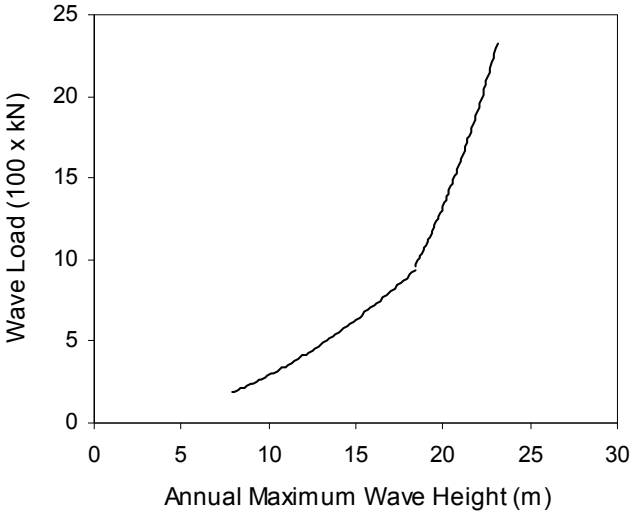


Figure 3. Wave load characteristics

The platform capacity R is assumed to have a lognormal distribution with a coefficient of variation of 0.15 as in PMB report (1996). The coefficient C_1 is assumed as a lognormal random variable with a coefficient of variation of 0.1 as in PMB report (1996). Given the large variability in the wave-in-deck forces, the coefficient C_3 is assumed as a lognormal random variable with a coefficient of variation of 0.35 as recommended by API RP 2A. Table 1 summarizes the random variables used in the reliability analysis and provides a description of the distribution types and coefficients of variation (CoV).

For the platform location, the dominant approach direction of the extreme waves is at the platform's diagonal direction. In this study only the annual failure probability for the diagonal wave direction was considered. The annual probability of platform failure has been calculated using FORM method. The platform has annual probability of failure of 1.438×10^{-4}.

The annual probability of platform failure and the consequence of failure are combined to determine the overall platform risk associated with hurricane hazard based on a risk matrix in Figure 1. The platform has medium failure consequence. The platform has medium likelihood of failure. The risk evaluation indicates that the platform is medium risk for the hurricane hazard.

Random Variable	Distribution	Mean Value	CoV
Platform Capacity, *R* (kips)	Lognormal	4,002	0.15 for jacket 0.20 for foundation
Annual Significant Wave height, *Hs* (ft)	Weibull	per formula (6)	per formula (7)
Coefficient C_1	Lognormal	0.809	0.10
Coefficient C_3	Lognormal	0.033	0.35

Table 1. Random variables for hurricane risk evaluation

3.2 Earthquake Risk Assessment

The design guidelines of the Norwegian Petroleum Directorate require that fixed offshore installations on the Norwegian Continental Shelf should withstand an earthquake event with annual occurrence probability of 10^{-4} (Norwegian Petroleum Directorate, 1992). The annual probability failure for the offshore platform in the platform location is estimated given that the design earthquake with an annual occurrence of 10^{-4} takes place in the field. Table 2 and Figure 4 show the response spectrum of the site specific horizontal motion with 5% damping for the 10^{-4} / year earthquake event.

The non-linear progressive collapse analyses (pushover analyses) were performed using the USFOS program, resulting in a minimum load factor of 8.07 when subjected to a 10^{-4} / year earthquake event. It implies that the platform can resist 8.07 times of the load imposed by the 10^{-4} / year earthquake event.

The calculated fundamental period of the platform is 2.90 seconds and the design spectral response acceleration, at the fundamental period, is 0.097g. A coefficient of variation of 0.30 is assumed for the design spectral response acceleration as shown in Figure 3. The uncertainties of the dead weight and live loads of the structure are considered in the analysis. For design of conventional offshore structures, a normal distribution with a coefficient of variation of 0.13 and 0.14 are recommended for the dead load and the live loads, respectively (Skjong et al. 1995). The uncertainty in the dead load of the offshore platforms is normally considered to be small due to control of weights during design and fabrication. However, the assumed coefficient variation includes uncertainties resulting from the structural analysis in addition to the uncertainty of the load.

Finally, r, the response modification factor is found to be 0.9 by employing the response spectrum analysis. The random variables, mean values and coefficient variables (COV) for the random variables with their statistical distribution functions are summarized in Table 3.

Utilizing FORM method, the annual probability of failure for the platform is found to be 2% given that the 10^{-4} / year earthquake event takes place in the field. The annual probability of platform failure and the consequence of failure are combined to determine the overall platform risk associated with earthquake hazard based on a risk matrix in Figure 1. The platform has medium failure consequence. The platform has medium likelihood of failure. The risk evaluation indicates that the platform is medium risk for the earthquake hazard.

Frequency(Hz)	Sa (g)		COV
	Mean	Stdv	
0.1000	0.0028	0.0011	0.40
0.6366	0.1151	0.0345	0.30
3.3157	0.5997	0.1799	0.30
20.0000	0.5997	0.1199	0.20
40.0000	0.1959	0.0392	0.20

Table 2. Mean response spectrum of horizontal mudline motion

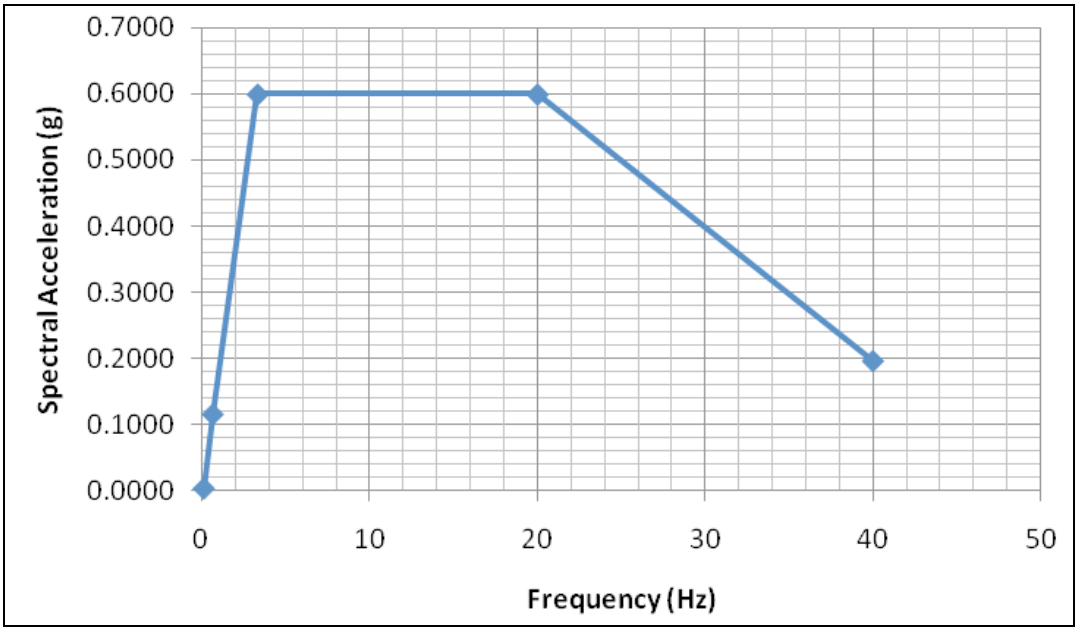


Figure 4. Mean response spectrum of horizontal mudline motion

Random Variable	Distribution	Mean Value	CoV
Capacity, R (kips)	Lognormal	6,109	0.15 for jacket 0.20 for foundation
Spectral Acceleration, Sa (g)	Normal	0.097	0.30
Dead Load, DD (kips)	Normal	6,151	0.13
Reduced Live Load, LL (kips)	Normal	458	0.14

Table 3. Random variables for earthquake risk evaluation

4 CONCLUSION

A comprehensive structural risk evaluation approach has been presented for offshore fixed platforms against major hazard events. Non-linear progressive collapse analysis is used to calculate the platform capacity characterized in terms of the platform's load factor. The probability of platform failure is estimated from the structural reliability analysis. The platform failure consequence and the probability of platform failure are combined to determine the platform risk level associated with the major accidental events. Case studies have illustrated the effectiveness of the developed structural risk evaluation approach. This paper only covers the risk evaluation of hurricanes and earthquakes. The writers are conducting an ongoing research for the development of the risk evaluation approach for other accidental events such as fires and blasts, vessel impacts and dropped objects.

5 REFERENCES

American Petroleum Institute (API) (2005). "Recommended Practice for Planning Designing and Constructing Fixed Offshore Platforms - Working Stress Design." API RP 2A-WSD 21st Edition, Errata and Supplement 2.

Asgarian, B. and Agheshlui, H. (2009). "Reliability-Based Earthquake Design of Jacket-Type Offshore Platforms Considering Pile-Soil-Structure Interaction." American Journal of Applied Sciences, Vol. 6 (4), pp 631-637.

Botelho, D. L. R., and Petrauskas, C. (1994). "A Detailed Study on the Failure Probability of ST130 "A" Platform During the Passage of Hurricane Andrew." OTC7472, 26th Offshore Technology Conference, Houston, Texas.

Dier, A. F., Morandi, A. C., Smith, D., Birkinshaw, M., and Dixon A. (2001). "A Comparison of jacket and jack-up structural reliability." Marine Structures, Vol. 14, pp 507-521.

Gebara, J., Dolan, D., Pawsey, S., Jeanjean, P., and Dahl-Stamnes, K. H. (2000). "Assessment of Offshore Platforms Under Subsidence-Part I: Analysis and Results." Journal of Offshore Mechanics and Arctic Engineering, Vol. 122, pp 260-266.

Heredia-Zavoni, E., Campos, D., and Ramirez, G. (2004). "Reliability Based Assessment of Deck Elevations for Offshore Jacket Platform." Journal of Offshore Mechanics and Arctic Engineering, Vol. 126, pp 331-336.

Jha, A. K., Kiciman, O. K., Gebara, J. M., Stahl, B., and Dahl-Stamnes, K. H. (2000). "Assessment of Offshore Platforms Under Subsidence-Part II: Analysis and Results." Journal of Offshore Mechanics and Arctic Engineering, Vol. 122, pp 267-273.

Kaiser, M. J. and Yu, Y. (2010). "The impact of Hurricanes Gustav and Ike on offshore oil and gas production in the Gulf of Mexico." Applied Energy, Vol. 87, pp 284–297.

Nadim, F. and Gudmestad, O.T. (1994). "Reliability of an Engineering System Under a Strong Earthquake with Application to Offshore Platforms." Structural Safety, Vol. 14, pp 203-217.

Norwegian Petroleum Directorate (1992). "Regulations Concerning Loadbearing Structures in Petroleum Activities." Stavanger, Norway.

Park, M., Kawano, K., Choi, Y. and Koo, W. (2010). "Reliability Response and Reliability Evaluations of an Offshore Platform with Pile-Soil Foundation System due to Wave and Seismic Forces." Proceedings of 2010 International Offshore and Polar Engineering Conference, Beijing, China.

PMB Engineering, Inc. (1996). "Hurricane Andrew Effects on Offshore Platforms," Phase II Joint Industry Project." Final Report, San Francisco, CA.

Ronalds, B. F., Anthony, N. R., Tuty, S., and Fakas, E. (2003). "Structural reliability of monopods under storm overload." Journal of Offshore Mechanics and Arctic Engineering, Vol. 125, pp 114-118.

USFOS Theory Manual (1993). A computer program for progressive collapse analysis of steel offshore structures. SINTEF Report STF71 F88038, Rev. 1993-04-01, Trondheim, Norway.

Skjong, R, Gregersen, E.B., Cramer, E., Croker, A., Hagen, O., Korneliussen, G., Lacasse, Lotsberg, I., Nadim, F., Ronold, K.O. (1995). "Guideline for Offshore Structural Reliability Analysis-General." DNV Report No. 95-2018.

Life Cycle Performance Metrics for Aging and Seismically Vulnerable Bridges

Citlali Tapia[1], Jayadipta Ghosh[2] and Jamie E. Padgett[3]

[1]Undergraduate Research Assistant, Department of Civil and Environmental Engineering, Rice University, 6100 Main Street, MS-318, Houston, TX USA 77005.
[2]Graduate Research Assistant, Department of Civil and Environmental Engineering, Rice University, 6100 Main Street, MS-318, Houston, TX USA 77005.
[3]Assistant Professor, Department of Civil and Environmental Engineering, Rice University, 6100 Main Street, MS-318, Houston, TX USA 77005.

ABSTRACT:

Bridge infrastructure faces both continued aging and deterioration throughout its lifetime, as well as potential exposure to natural hazards such as earthquakes in hazard prone regions. Consequential damage requires increased monetary investments, energy spent on subsequent repair/replacement, as well as carbon dioxide (CO_2) emissions associated with the manufacture/transport of repair materials. This paper will derive and compare estimates of three important metrics associated with the life cycle performance of aging bridges given seismic exposure, namely, life cycle cost, embodied energy and associated CO_2 emissions. A case study is presented for a representative multi-span simply supported (MSSS) concrete girder bridge to evaluate the life cycle sustainability metrics of the corroded bridge system given uncertain performance and repair under lifetime exposure to seismic hazards. The results underscore the importance of capturing the effects of time dependent structural deterioration when conducting life cycle analysis of bridges based on different indicators. The proposed framework is also anticipated to help guide the selection of optimal rehabilitation or retrofit measures for bridge infrastructure based on target sustainability metrics related to life cycle cost, energy usage, and harmful emissions.

1. INTRODUCTION

Within the context of this study, sustainable development is defined as "development which continues to effectively serve public needs despite numerous physical threats to its performance and while promoting limited environmental, social, and economic strains as a result of its existence" (Padgett, Ghosh et al. 2009). This concept is of growing interest within the field of infrastructure and structural engineering due to its potential to promote harmony amongst physical and natural systems. Since infrastructure continues to age and deteriorate throughout its life, and is also exposed to a variety of natural hazards, its degradation or potential damage during natural hazards results in money, energy, and CO_2 expenditures from repairs or replacements performed. These consequences, although not comprehensive in nature, are examples of metrics of the sustainability of built infrastructure.

Quantitative methods of sustainable analyses facilitate engineering sustainable infrastructure by providing engineers with a "more rational decision making [method

by means of]…decisive indicators, trade-offs, and weighting sensitivities" (Sahely, Kennedy et al. 2005). However, most of the measures of sustainability which presently exist for evaluating infrastructure are qualitative (Dorf 2001; Dasgupta and Tam 2005; Jeon and Amekudzi 2005; Litman 2008). Traditional life cycle assessments (LCA) of infrastructure focus on evaluating engineering metrics which have existed for many years and are generally limited to structural performance outcomes (Frangopol 1999; Thoft 2009). By neglecting sustainable metrics such as embodied energy and CO_2 emissions as well as risk from natural hazards such as earthquakes, these LCA methodologies fail to consider factors related to the environmental impacts of the structure throughout its life (Engineers 1999). If the interaction between the structure and environment along with sustainability indicators are taken into account in the process, the life cycle cost (LCC) of the structure will ultimately decrease (Furuta, Katayama et al. 2005; Ugwu, Kumaraswamy et al. 2005).

One aspect of promoting sustainable infrastructure includes the assessment and minimization of energy use, resource depletion, and emissions. This study provides a framework to quantify the life cycle performance of seismically vulnerable aging bridges on the basis of cost, embodied energy expenditure and CO_2 emissions attributed to seismic repairs and replacements. This approach to quantifying bridge infrastructure performance on the basis of non-traditional metrics can help to provide insight into the relationship between natural hazards and infrastructure sustainability, considering uncertainty in exposure, physical performance, and repair action. The results highlight the vulnerable components and likely repair methods that hinder the sustainability of the system and can guide the selection of optimal rehabilitation or replacement measures for bridges.

2. SEISMIC LCA OF SUSTAINABILITY METRICS FOR BRIDGE INFRASTRUCTURE: SCOPE, METHODOLOGY, AND FORMULATION

2.1 *Scope of Study and Estimates of Embodied Energy and CO_2 Emissions*

One definition for embodied energy is "total energy expended for harvesting, transporting, processing, packaging, and installing the (infrastructure) material" (Pearce 2004). Embodied CO_2 emissions of materials is carbon dioxide released which "reflect[s] the specific inputs of ingredients and energy sources and the CO_2 emissions associated with them"(Alcorn 2001). Though several other definitions exist for these terms (Engineers 1999; Alcorn 2003; Venkatarama Reddy 2004; Long 2007; Padgett, Ghosh et al. 2009), there is little variation. Inconsistencies among the various CO_2 and embodied energy coefficients which do exist ensue primarily from the difference in scope of parameters included in the derivations of these coefficients.

Within this study, the life cycle analysis will be defined to include the cost, embodied energy expenditure, and CO_2 emissions from material and labor utilized in different seismic repairs/replacements throughout the life of the aging bridge analyzed. Aging and seismic risk have been integrated in this analysis in order to evaluate the effectiveness of the structure to continue to "serve public needs despite numerous physical threats to its performance" (Padgett, Ghosh et al. 2009)—which is within the boundaries of sustainably built infrastructure. Figure 1 displays the scope

of total embodied energy and CO_2 emission considered in this study. Items not within the red-dashed box are beyond the scope of the current study, but reflect additional contributions to energy and emissions that may be considered in broader life cycle analyses. The total embodied energy expenditure and CO_2 emissions are taken as the sum of the contributions from material and crew. Data required in order to calculate total embodied energy expenditure and CO_2 emissions from labor and material utilized in various seismic repairs/replacements at a specific time during the life of an aging bridge in a seismic zone includes: geometry of bridge, repairs/replacements for bridges exposed to seismic events, quantity of material utilized in repairs, days required to complete repairs, embodied energy/CO_2 emission coefficients for materials and workers.

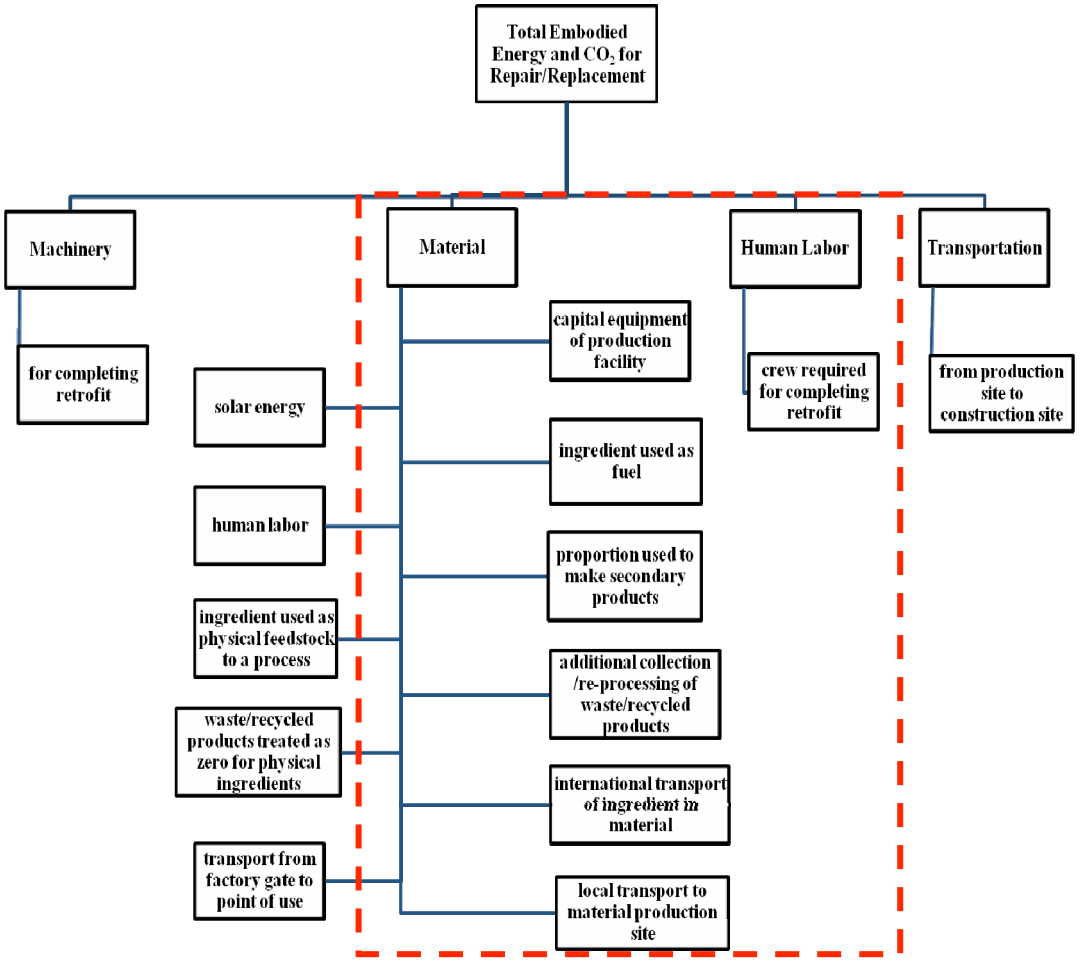


Figure 1: Embodied Energy and CO_2 Emissions Scope of Study

In order to preserve consistency in scope of LCA conducted, the proposed framework utilizes coefficients derived by the Centre for Building Performance Research (CPBR) in collaboration with Building Research Association of New Zealand (BRANZ) (Alcorn 2003) for calculations concerning both embodied energy and embodied CO_2 for construction materials. The metric of embodied energy is measured in units of energy per unit volume (MJ/m^3) and CO_2 coefficients in units of

mass per unit volume (kg/m^3). Table 1 shows values of coefficients for materials used in bridge repair or construction procedures.

Table1: Embodied Energy and CO_2 Coefficients for Materials used in repairs

Material	Embodied energy coefficient MJ/m^3	Embodied CO_2 emission coefficient Kg/m^3
Epoxy (polystyrene)	1401	59.9
Concrete (30MPa)	2762	376
Grout	3496	496
Steel (structural)	245757	9749
Polymer wrap	202650	1030
Stainless steel	613535	44747
Rubber (natural latex)	62100	16478

To increase the scope and accuracy of these sustainability metric estimates, contributions from human labor—which is not accounted for by the CPBR in their coefficient derivations—is included in this study. Although sources from which CO_2 emission coefficients and embodied energy coefficients for human labor are attained are different, the variables required—such as length of work day and age/gender of worker— in order to calculate these coefficients for each worker remain the same. To calculate estimates for labor required to complete seismic repair procedures, the size of the construction crew and number of days required to complete a specific repair are taken from the RS Means Building Construction Cost Data book (RSMeansCo. 2008). For repairs not listed, procedures from similar activities are utilized. Embodied energy and CO_2 emissions corresponding to a crew performing repairs are calculated by multiplying crew size, days required to complete a specific repair, and embodied energy/CO_2 emission of a worker (RSMeansCo. 2008). Total energy expenditure during construction work for an average male adult (18- 30 years old) in an 8 hour work day (1 hour lunch break) is taken to be approximately 5.75 MJ/day per worker (Haggarty, Valencia et al. 1997). Estimation of kilograms of CO_2 emitted per day per worker considers an average adult respiration rate of 16 breaths per minute (Clinics 2005) and grams of CO_2 per breath to be 0.037 grams of CO_2 per breath (Center 1998) per worker. Kilograms of CO_2 emitted is then given by: *(Breaths/minute) * (60 minutes/hour) * (hours/day) * (g CO_2/breath) * (0.001 kg/g) = kg of CO_2/ day per worker*. This results in an approximate 0.28416 kg of CO_2/day emitted per worker. As seen in Figure 1, machinery utilized in repair and transportation to site are not considered in estimate calculations, however future work will integrate these factors.

2.2 *Formulation of Aging Bridge Sustainability LCA*

Recent research developed LCC model based on a non-homogeneous Poisson process (Ghosh and Padgett 2010), which is extended herein to asses life cycle embodied energy and CO_2 emission estimates by integrating the embodied energy and CO_2 emission coefficients discussed in the previous section. This model is specifically

applied to assess the performance of an aging bridge subjected to earthquake exposure, thereby relating lifetime natural hazard performance to metrics of structural sustainability. Given a constant annual earthquake occurrence rate at the bridge site, the annual rate of occurrence of a particular damage state i for a bridge component m at time t can be as a non-homogeneous Poisson process given by $\lambda_{i,m}(t) = \nu P_{i,m}(t)$ where, ν is the constant site specific earthquake occurrence rate and $P_{i,m}(t)$ is the annual probability of exceedance of damage state i for the m^{th} bridge component at time t. Following this assumption, the time between the beginning of exposure of the bridge to earthquakes ($t = 0$), and the occurrence of first failure ($t = \tau$), is an exponentially distributed random variable with the probability density function (PDF), $f_\tau(t)$ given by

$$f_\tau(t) = \lambda_{i,m}(t) e^{-\int_0^t \lambda_{i,m}(t)dt} \tag{1}$$

Additionally, let E_{i,m_t} be defined as the quantity of the sustainability metric in question (embodied energy or CO_2 emissions), corresponding to damage state i to restore the bridge component m to its original full functionality at time *t*.

Assuming the value of the metric in restoring the structure at time *t* is the same as its present day repair metric value— that is $E_{i,m_t} = E_{i,m_0} = E_{i,m}$ — the expected seismic life cycle value for any sustainability metric (LCSM) can be calculated as

$$E\left[SLCSM_{i,m}\right] = \left[\sum_{t=1}^{T} P(E_{i,m_t}).E_{i,m}\right] \tag{2}$$

where $P(E_{i,m_t})$ is the probability of incurring energy expenditure, carbon dioxide emission, or any other metric. $E_{i,m}$ at time t can be replaced by the probability density function of the time elapsed from beginning of exposure to hazard occurrence but in the discrete space. This concept can be further extended to aggregate over *n* distinct damage states and multiple repair strategies using the theorem of total probability to arrive at expected seismic LCSM as

$$E[SLCSM_m] = \sum_{i=1}^{n}\sum_{t=1}^{T}\sum_{j=1}^{J} \lambda_{i,m}(t) e^{-\sum_{t=1}^{t=T}\lambda_{i,m}(t)} P\left(E_{i,m,j}\right)E_{i,m,j} \tag{3}$$

where $P\left(E_{i,m,j}\right)$ is the probability of adopting the j^{th} repair strategy, which has an associated sustainability metric value $E_{i,m,j}$, and J is the total number of viable repair options. In preceding equations, the mean annual rate of failure, $\lambda_{i,m}(t)$, due to occurrence of a particular damage state i can be approximated by the annual probability of damage due to damage state i as (Melchers 1999)

$$\lambda_{i,m}(t) = PA_{i,m}(t) - PA_{i+1,m}(t) \tag{4}$$

where $PA_{i,m}(t)$ is the annual probability of exceedance of damage state i at time t for m^{th} bridge component and is evaluated by convolving the fragility curve with the seismic hazard curve. To estimate probabilities of exceeding different damage states, the use of risk assessment techniques incorporating time dependent bridge fragility curves is employed. Further details on constructing such seismic fragility curves for bridges as well as deterioration mechanisms for bridge components can be found elsewhere (Ghosh and Padgett 2010). To show the effects of deterioration on component vulnerabilities, Figure 2 shows how the fragility curves for moderate damage state for reinforced concrete (RC) columns of the MSSS concrete girder bridge change over time along the service life of the bridge. Parameters of time dependent fragility curves are then used in combination with CO_2 and embodied energy estimates for various seismic repair procedures to arrive at life cycle estimates following the above formulation. Material embodied energy and CO_2 estimates for each repair action including material and labor are adopted as discussed in the previous section.

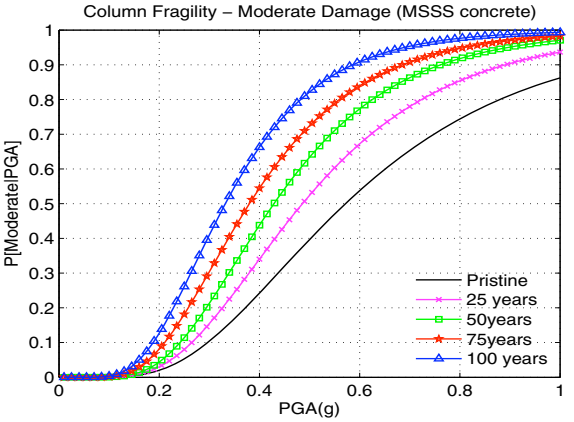


Figure 2: Fragility Curves for Deteriorating Bridge Columns at Different Points in Time Along Service Life

3. CASE STUDY RESULTS AND DISCUSSION

3.1 *Resulting Embodied Energy, Cost, and CO_2 Estimates of Aging Bridge*

The framework is demonstrated with a multi-span simply supported concrete (MSSS Concrete) girder bridge located in Tennessee. Geometry for the bridge is shown in Figure 3 below. This bridge type has been previously identified by researchers (Nielson 2005) as being seismically vulnerable due to inadequate seismic detailing such as poorly confined RC columns, inadequate transverse reinforcement, and 'walking out' of bearings from under the girders during large deformations following seismic events. Additionally, the reinforcing steel in the concrete columns and the bridge bearings are prone to aging and deterioration mechanisms. Such mechanisms include corrosion of reinforcing steel in columns and bearing dowel bars along with increase in stiffness of bearing pads due to thermal oxidation.

The life cycle analysis quantifying total expected value of embodied energy (LCEE) and CO_2 (LCCD) is carried out for both pristine and aging MSSS Concrete bridge models with an assumed 75 year service life. The expected present value of

cost (LCC) is calculated following the method presented in (Ghosh and Padgett 2010) with an assumed discount ratio of 3%. While fragility parameters for the pristine bridge are assumed not to change with time, the aging bridge estimates are performed using the concept of time evolving fragility curves. Life cycle estimates of these three sustainability metrics are quantified for both pristine and deteriorating bridges in order to demonstrate the importance of considering aging within an LCA due to the great parameter underestimations resulting from its negligence.

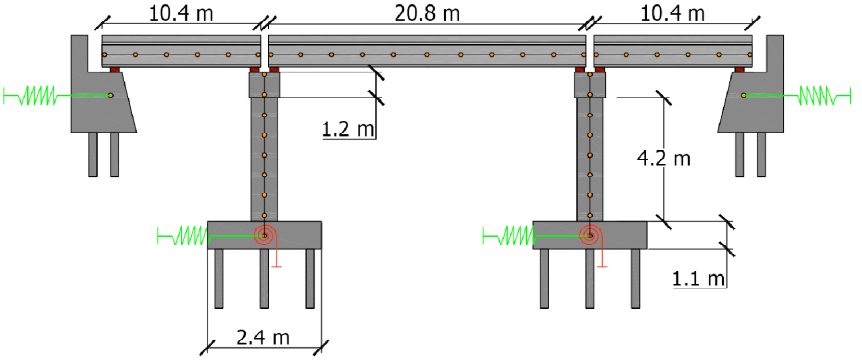
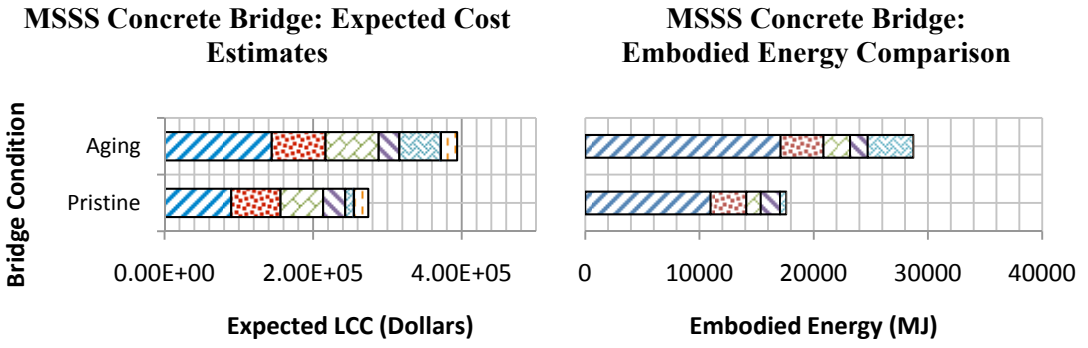


Figure 3: Case Study MSSS Concrete Bridge

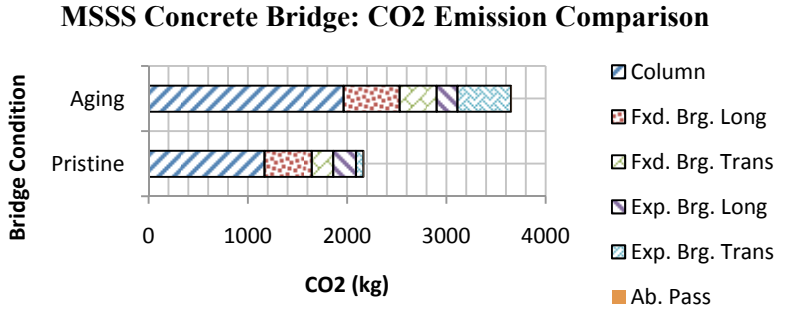
Resulting LCA estimates of cost, embodied energy, and CO_2 for both bridge cases are compared and tabulated in Figures 4 (a) to (c) respectively. Additionally, these figures present the contribution of different bridge components to the life cycle estimate of the three metrics. Columns, fixed longitudinal bearings, and fixed transverse bearings contribute the most to all three metric estimates. To avoid such large contributions from these aging components, priority should be given to retrofit/upgrade the components in order to improve their lateral resistance to damage under seismic loading. Doing so can potentially reduce resulting metric estimates. Figures 4 (a) to (c) demonstrate that neglecting aging/deterioration result in 31% underestimation of life cycle cost, 40% underestimation of embodied energy, and 40% underestimation of CO_2 values throughout the service life of the bridge.. These results underline the importance of incorporating the effects of structural degradation mechanisms into life cycle analyses when quantifying sustainable performance in the face of natural hazards such as earthquakes.

4.2. *Contribution from Repair Procedures to Life Cycle Embodied Energy and CO_2*

The different repair procedures considered within this study have varying relative contributions to both total expected value of seismic life cycle embodied energy and CO_2. Repair procedures which involve major replacements—such as demolishing and replacing a bridge or its column—are anticipated to consume and emit the greatest amount of embodied energy and CO_2 due to the scale of the repairs; however the likelihood of damage occurring requiring these major replacements may not be as large. Contributions from major repair/replacement procedures to total expected value, after integrating fragility, hazard potential, and probability of repair given certain level of damage, are tabulated in Tables 2 below.



4(a) 4(b)



4(c)

Figure 4: (a) Expected LCC Values, (b) Expected LCEE Values, (c) Expected LCCD Values

Table 2: Contribution of Major Repair/Replacement Procedures to Expected Value of Life Cycle Embodied Energy and CO_2 Emissions

Repair Procedure	Bridge Condition	Embodied Energy, MJ (% Contribution)	CO_2, kg (% Contribution)
Column replacement	Pristine	4029 (23%)	538 (25%)
	Aging	5114 (18%)	683 (19%)
Fixed bearing replacement	Pristine	3161 (18%)	485 (22%)
	Aging	3793 (13%)	574 (16%)
Expansion bearing replacement	Pristine	1270 (7%)	220 (10%)
	Aging	2378 (8%)	385 (11%)
Demolish and replace bridge	Pristine	6505 (37%)	869 (40%)
	Aging	14551 (51%)	1943 (53%)

The total embodied energy and CO_2 emissions can be reduced by altering the approach for major repair procedures if viable or mitigating the potential damage to the structure requiring these major repairs. However, due to localized-minor repairs being performed in a more frequent and common manner (as compared to major repairs), improving the sustainability of localized-minor repairs can have a significant

impact on the expected value of these life cycle performance metrics. Localized repair procedures—such as grouting and wrapping—contributing the most to total expected life cycle embodied energy and CO_2 emissions estimates after integrating fragility, hazard potential, and probability of a repair given certain level of damage, are shown in Figure 5 for the aging bridge model. These procedures are the repair methods that most likely hinder the sustainability of the system and should be addressed by using a different alternative to these repairs if possible in order to reduce emissions and energy and hence improve sustainability.

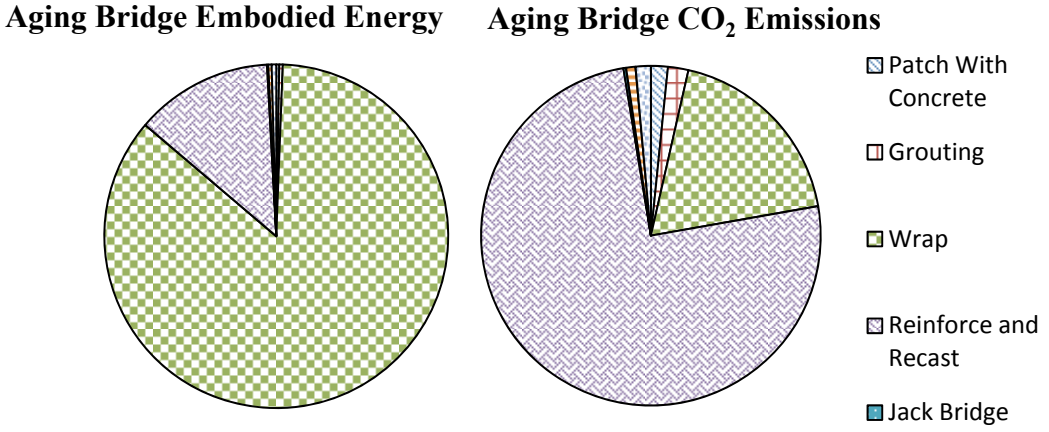


Figure 5: Contribution of Localized Repair Procedures to LCEE and LCCD

4.3 *Testing Sensitivity of Sustainability Metrics to Remaining Service Life*

Sensitivity of total expected embodied energy and CO_2 emission quantities, as well as total expected present values of cost, to remaining service life of a bridge for both aging and pristine models is also assessed. Results are shown in Figures 6 (a) to (c) for all three metrics. The sensitivity results reveal that changes in remaining service life have a considerable effect on all three metric life cycle estimates corresponding to the aging bridge as compared to the pristine bridge. For example, with 25 years of remaining service life, the expected LCC, LCEE, and LCCD for the aging bridge model is 130%, 198% and 216% higher for each metric respectively as compared to the pristine bridge. Additionally as remaining service life of a bridge increases, the expected value of the sustainability metrics also increase as anticipated. Therefore structures with longer service lives may be priorities to upgrade for enhancing long term sustainability.

Even though totals for all sustainability metrics increase for both aging and pristine bridge models as remaining life increases, it is observed that relative difference (percent change) between the two models actually decrease with increasing service life. That is relative difference is greatest at the smallest remaining service life. Results also show that aging affects CO_2 totals the most, followed by embodied energy, and cost. This design or upgrade that mitigates potential deterioration or corrosion susceptibility can have the greatest influence on reducing expected CO_2 emissions. Overall, the relative importance that decision-maker or stakeholders place

upon the sustainability metrics should dictation their weighting in a framework for prioritizing mitigation actions to promote structural sustainability in the face of natural hazards.

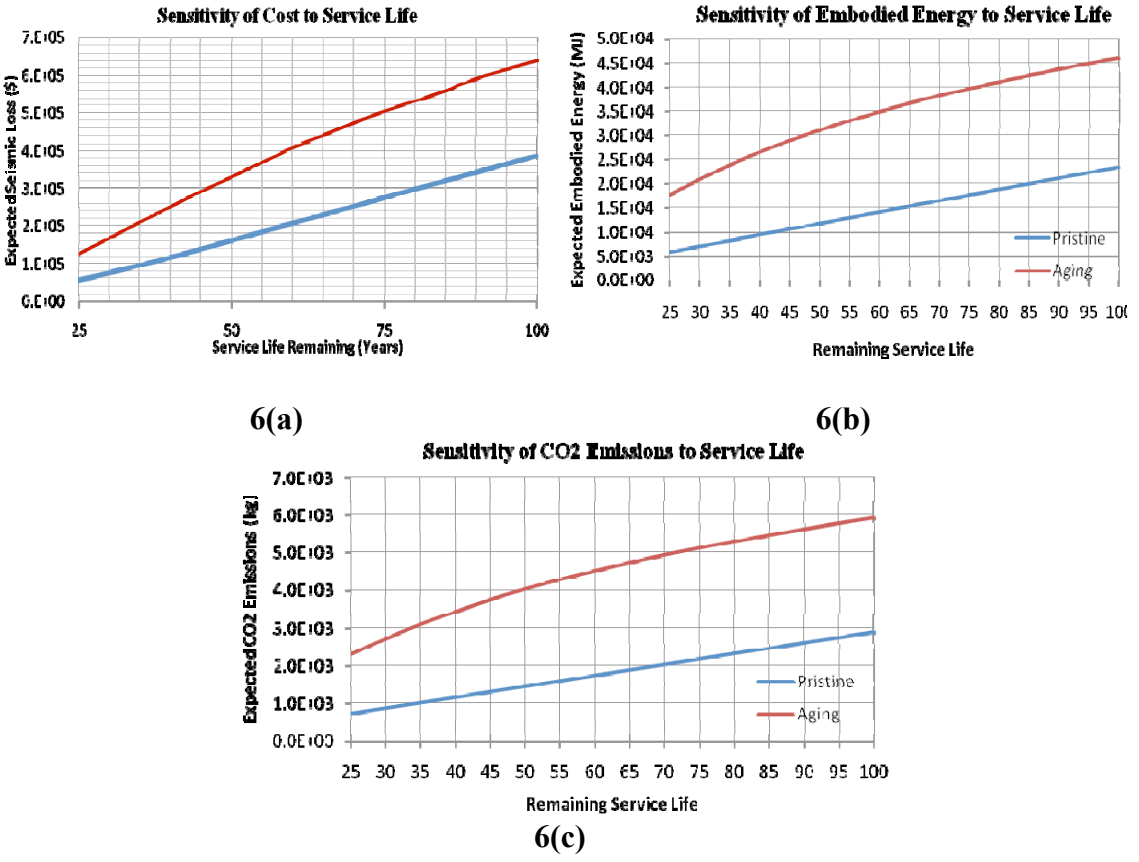


Figure 6: (a) Sensitivity of LCC, (b) Sensitivity of LCEE, (c) Sensitivity of LCCD Estimates

5. CONCLUSIONS

A framework for the estimation of the expected present value of seismic life cycle cost and total expected seismic life cycle embodied energy and carbon dioxide quantities for an aging/deteriorating bridge is presented in this study in order to highlight the critical links between concepts of sustainable engineering and consideration of extreme events. A non-homogeneous Poisson process is adopted in the LCA to capture the effects of aging and deterioration in the seismic life cycle analysis of sustainability metrics. This approach integrates three sustainability metrics—cost, embodied energy, and carbon dioxide—into the life cycle analysis of a structure, two of which (energy and CO_2) are usually disregarded in LCA's for structures exposed to natural hazards. Given increasing environmental challenges and efforts to improve the harmony amongst the built and natural environment, the importance of incorporating and quantifying sustainability metrics beyond cost has become critical.

Through results from the case study on the MSSS Concrete bridge located in Tennessee, it can be seen that taking into account the degradation of a bridge can result in significant differences in the seismic life cycle cost, embodied energy, and CO_2 estimates. Additionally this framework aids in prioritizing bridges which require seismic repairs or replacements based on the sustainability metrics of cost, embodied energy, and CO_2. Although major repair methods contribute the largest percentages to total expected cost, embodied energy, and CO_2, attention should be given to local component repairs due to their higher likelihood or frequency of performance. The findings highlight repair actions for which alternative, more sustainable, methods should be explored as well as vulnerable bridge components for which improving the resistance to damage under seismic loading can significantly affect the resulting cost, emissions or energy expenditures.

Future work will focus on incorporating additional sustainability metrics which extend into other areas of the triple bottom line indicators (environmental, social, and economics), including other phases of a structure's life, as well as extending the boundaries of each metric's totals. Opportunities also exist to explore the discounting of emissions and energy for an equivalent present value analysis of all sustainability metrics, as conducted for the life-cycle cost analysis. Finally, these metrics can be used to directly assess and compare alternative maintenance, design, or retrofit actions for structures exposed to deterioration threats and seismic hazards.

6. ACKNOWLEDGEMENTS

The authors would like to acknowledge the support for this research provided by the National Science Foundation grant CMMI-0928493.

7. REFERENCES

Alcorn, A. (2001). Embodied Energy and CO2 Coefficients for New Zealand Building Materials, Centre for Building Performance Research Report.

Alcorn, A. (2003). Embodied Energy and CO2 Coefficients for New Zealand Building Materials, Centre for Building Performance Research Report.

Center, C. D. I. A. (1998). "Frequently Asked Questions." 2010, from http://cdiac.esd.ornl.gov/pns/faq_othr.html.

Clinics, U. o. I. H. a. (2005). "Health Topics." Vital signs: temperature, pulse, and respiration, 2010, from http://www.uihealthcare.com/topics/generalhealth/ghea4577.html.

Dasgupta, S. and E. K. L. Tam (2005). "Indicators and framework for assessing sustainable infrastructure." Canadian Journal of Civil Engineering **32**: 30-44.

Dorf, R. C. (2001). Technology, Humans, and Society: Toward a Sustainable World.

Engineers, T. I. o. S. (1999). "Building for a Sustainable Future: Construction without Depletion."

Frangopol, D. M. (1999). Life-cycle cost analysis for bridges. Bridge Safety and Reliability. Reston, VA**:** 210- 236.

Furuta, H., H. Katayama, et al. (2005). Effects of Seismic Risk on Life-Cycle Cost Analysis for Bridge Maintenance. Institution of Civil Engineers Fourth

International Conference in Current and Future Trends in Bridge Design**:** 22-33.

Ghosh, J. and J. E. Padgett (2010). "Aging Considerations in the Development of Time-Dependent Seismic Fragility Curves." Journal of Structural Engineering **136**(12): 1497-1511.

Ghosh, J. and J. E. Padgett (2010). "Probabilistic Seismic Loss Assessment of Aging Bridges using a Component Level Cost Estimation Approach." Earthquake Engineering & Structural Dynamics **In Review**.

Haggarty, P., M. E. Valencia, et al. (1997). "Energy Expediture During Heavy Work and its Interaction With Body Weight." British Journal of Nutrition: 359- 373.

Jeon, C. M. and A. Amekudzi (2005). "Addressing sustainability in transportation systems: Definitions, indicators, and metrics." Journal of Infrastructure Systems **11**: 31- 50.

Litman, T. (2008). Sustainable Transportation Indicators: A recommendation program to define a standard set of indicators for sustainable transportation planning. Washington, DC Transportation Research Board.

Long, A. E. (2007). Sustainable Bridges Through Innovative Advances. Joint ICE and TRF Fellows Lecture**:** 3.

Melchers, R. E. (1999). Structural Reliability Analysis and Prediction. John Wiley & Sons Ltd (Import).

Nielson, B. (2005). Analytical fragility curves for highway bridges in moderate seismic zones. Atlanta, Georgia, Georgia Institute of Technology.

Padgett, J. E., J. Ghosh, et al. (2009). Sustainable Infrastructure Systems Subjected to Multiple Threats. 2009 TCLEE Conference. Oakland, CA.

Pearce, A. R. (2004). Rehabilitation as a Strategy to Increase the Sustainability of the Built Environment. School of Civil and Environmental Engineering, Georgia Institute of Technology.

RSMeansCo. (2008). RSMeans Building Construction Cost Data 2009.

Sahely, H. R., C. A. Kennedy, et al. (2005). "Developing sustainability criteria for urban infrastructure systems." Canadian Journal of Civil Engineering(32): 72-85.

Thoft, C. (2009). "Life-cycle cost–benefit (LCCB) analysis of bridges from a user and social point of view." Structure Infrastructure Engineering **5**(1): 49-57.

Ugwu, O. O., M. M. Kumaraswamy, et al. (2005). "Object-Oriented Framework for Durability Assessment and Life Cycle Costing of Highway Bridges." Automatic in Construction **14**: 611- 632.

Venkatarama Reddy, B. V. (2004). "Sustainable Building Technologies." Current Science **87**(7): 899-907.

A Probabilistic Framework for Performance-Based Durability Engineering: Application to Corrosion in Reinforced Concrete

M.M. Flint[1] and S.L. Billington[2]

[1]John A. Blume Earthquake Engineering Center, Department of Civil and Environmental Engineering, Stanford University, Bldg. 540. MC: 3037, Stanford, CA 94305; PH (650) 725-0381; FAX (650) 725-9755; e-mail: flint@stanford.edu
[2]ASCE Associate Member, Associate Professor, Associate Chair, Department of Civil and Environmental Engineering, Stanford University, 473 Via Ortega, Stanford University, Stanford, CA 94305-4020; PH (650) 723-4125; FAX (650) 723-7514; e-mail: billington@stanford.edu

ABSTRACT

A proposed probabilistic framework for performance-based durability engineering is motivated by the successful implementation of the Pacific Earthquake Engineering Research Center's framework for performance-based earthquake engineering. Both approaches combine several stages of analysis linked through a limited set of "pinch point" variables, which allows modeling flexibility. The analysis extends to the computation of information useful to decision makers, and can also provide sensitivity analysis of the modeling stages to be used to direct future research. The major stages, variables, datasets, and models to be used are outlined with corrosion in reinforced concrete as the cause of deterioration.

INTRODUCTION

A durability framework is proposed in accordance with the interest in the engineering community and the SEI-ASCE Technical Council on Life-Cycle Performance, Safety, Reliability and Risk of Structural Systems in the prediction of structural performance over a lifetime of deterioration. Guided by performance-based earthquake engineering (PBEE), the proposed performance-based durability engineering (PBDE) framework has the potential to drive innovation in both research and practice just as the introduction of PBEE's methodology led to improvements in structural analysis and loss estimation. Recently developed models have the ability to predict the onset and propagation of deterioration for a variety of structure types and hazards. Predicting the interaction between traditionally-defined hazards, such as seismic loads, and agents of material or structural degradation is challenging, but new models from research offer great potential in this field. The predictions of performance under deterioration are valuable in themselves and their implementation in a probabilistic framework that provides useful decision information has at this time not been carried out systematically, and is expected to provide increased value.

Background

The Pacific Earthquake Engineering Research (PEER) Center aimed to address uncertainty in structural risk and reliability using a transparent, probabilistic methodology in developing performance-based earthquake engineering. In advancing the PEER framework, researchers and practitioners have succeeded in creating the necessary models and data to evaluate seismic risk in this manner, and to use the results of the framework to make more rational choices in structural design and renovation [1]. While this work is ongoing, analysis tools for nonlinear seismic response and building component fragility curves have been developed and improved through new research and collaboration, after testbed simulations identified parts of the framework with large impact on decision variables. These improvements have reduced some aspects of modeling uncertainty, and have subsequently been incorporated into simplified methods for practicing engineers.

PEER's PBEE methodology is an extension of nuclear risk simulation, linking together the results of four areas of earthquake-related research to allow calculation of recurrence rates at each stage of the analysis [2]. Hazard analysis is used to determine an intensity measure (IM), structural analysis to determine engineering demand parameters (EDP) and damage measures (DM), and risk analysis to predict decision variables such as loss, downtime, and casualties. Each stage of analysis may require complex modeling, but only a few "pinch point" variables are passed between stages, allowing each stage of the analysis to be uncoupled. Uncertainty is incorporated through the intensity measure hazard curve by selection of ground motion "records," through uncertainty in relations between engineering demand parameter (e.g. story drift) and damage measures, as well as through probabilistic loss curves. Convolution of probabilities of exceedence through the PEER equation allows the prediction of rates of exceeding a particular value of a decision variable.

$$\nu_{DV}(DV>dv)=\iiint G_{DV}(DV>dv|DM>dm)dG_{DM}(DM>dm|EDP>edp)dG_{EDP}(EDP>edp|IM>im)d\lambda_{IM}(IM>im)$$

Motivation

The development of a new framework for PBDE is motivated by interest in more explicit consideration of structural durability in design and by the adoption of PBEE in the engineering community. Although probabilistic aspects and modeling stages must differ from those used in PBEE, the methodology of defining analysis "pinch points" where a few variables are passed from one stage of analysis to the next can be used to develop an analogous framework for PBDE.

Structural deterioration due to environmental effects occurs because of a variety of interacting, complex mechanisms. While modeling multiple causes of deterioration is an eventual goal of this research project, the selection of a simpler "testbed" mechanism is necessary to demonstrate the methodology of the proposed framework. The mechanism should be selected on the basis of interest to decision makers due to large losses or safety threats, and to researchers developing deterioration models. Transportation infrastructure offers a class of structures where such deterioration is of interest, and the wide availability of models for steel corrosion in reinforced concrete has led to the selection of this cause of degradation as the testbed mechanism.

Predicting corrosion initiation and propagation in reinforced concrete is very challenging, as is determining effects on structural behavior and reliability. The complexity, need for validation of research models, and large economic losses make this mechanism an important trial case for PBDE.

This paper expands upon a previous outline of the main models, pinch points, and variables required to develop a PBDE framework for chloride-induced corrosion [3]. Four stages of analysis are defined, with reference to existing models to be used in each stage, as well as identification of areas in which more data or models are required. Upon successful demonstration of the utility of the proposed PBDE framework for chloride-induced corrosion in reinforced concrete, the framework will be extended first to other causes of corrosion, such as carbonation, and then to other degradation mechanisms. These might include scour, pounding, or freeze-thaw degradation in concrete and masonry, or degradation mechanisms for other materials, such as rot in timber structures.

Existing Durability and Deterioration Frameworks

Many researchers and practitioners have proposed frameworks for analyzing corrosion-related structural deterioration. These generally divide into three main categories: design criteria for acceptable service-related performance; reliability analysis for serviceability and ultimate limit states; and maintenance optimization.

Design Frameworks

The intent to design structures that satisfy minimum acceptable levels of durability has led to the creation of several codes and frameworks for performance-based design for durability. In addition to US efforts such as the new SEI-ASCE Technical Council on Life-Cycle Performance, Safety, Reliability and Risk of Structural Systems, which intends to develop guidelines for durability, and ACI Life-365 [4], councils and working groups in Europe and Japan have proposed durability frameworks. These include fib's *Bulletin 34 Model Code for Service Life Design* [5], RILEM's DuraCrete model [6], and work by JSCE-331 [7]. These frameworks tend to employ empirical degradation models, and output probabilistic service life predictions. Because they are for the most part designed for use in industry, simplicity tends to be valued over the user's ability to replace parts of the model with their own preferred models. While estimates of service life are valuable, the analysis rarely extends to predicted costs, downtime, or environmental impacts.

Reliability Frameworks

Reliability analyses of corroding structures have been performed by many researchers, including Thoft-Christensen [8], Enright and Frangopol [9], Vu and Stewart [10], and Li and Melchers [11], among others. Many of these assessments have also included sensitivity analysis to identify variables with large impact on the structural reliability, and corrosion rate, steel yield strength, and cover depth have frequently been identified as variables of importance. Spatial correlation of variables such as surface chloride concentration has been found by some studies, e.g. Vu and Stewart [10], to have a large effect on corrosion initiation and reduction in structural

capacity. Previous studies have used several different types of reliability analysis, e.g. FORM and Monte Carlo, and varying characterization of the stochastic variables and definition of end of service-life, but some generalizations about the reliability-based approaches are possible. All results are highly dependent on the models used to predict chloride ingress, corrosion initiation, and corrosion propagation. In some cases, the use of effective Fickian diffusion and assumptions about constant, uniform corrosion rates may lead to inaccuracies in predictions of service life [12, 13]. Additionally, as with the design codes, information on repair costs or observable damage such as crack widths is not always available, and would be helpful to owners and operators.

Maintenance Optimization Methods

Many methods exist for determining optimal repair timing with regard to cost or other constraints such as level of service. Bridge Management Systems (BMS) like Pontis track deterioration of bridge components based on commonly recognized "CoRe" elements. Future deterioration is predicted by component type and environmental conditions using Markov chains [14]. NCHRP Report 590 uses a multi-objective optimization scheme for BMS, and other optimization schemes can become very complex [15]. However, the Markov models used for optimization may not be appropriate for all types of environmental conditions, and the user or decision maker may require information that is not easily accessible from a program like Pontis.

Summary of Existing Methods and Limitations Addressed by this Research

Design, reliability, and maintenance optimization approaches share a few limitations. The main limitation, though not characteristic of every approach, is the difficulty in computing output data that would include a variety of information useful to decision makers. Other limitations are lack of generality due to analysis assumptions and the inability to replace certain models with the analyst's preferred models. Complexity is a limitation of certain frameworks, and is also a limitation of the framework proposed here. The proposed methodology does offer a comprehensive approach, transparency and flexibility in modeling, and clear, practical decision information. Efforts in the PBEE community, such as ATC 58, have used advanced research efforts to develop simpler design approaches, and it is a long term goal of this project to develop a similar simplified version of PBDE. The framework and methodology proposed here is expected to complement other methods for designing durable structures and analyzing the course and effects of deterioration.

PROPOSED PBDE FRAMEWORK

General Description of Phases

The PBDE analysis is broken up into four phases, which pass a limited number of "pinch point" variables to the next phase, shown in Figure 1. This allows the analysis phases to be decoupled, which enhances flexibility in the choice of model for each phase. The first phase, (1) exposure analysis takes information about the location of the site to determine exposure conditions, which might include temperature, humidity, and loads. Variability in these conditions is taken into account by the

computation of exposure "records." Phase (2), deterioration analysis, relates these conditions to structural and material degradation. This phase may require the use of sub-models, or can be modeled in a fully-coupled sense. The damage measures determined by deterioration analysis capture data that can be observed or detected by inspectors, such as crack widths. These damage measures are then related to specific repair actions by repair analysis, phase (3). In phase (4), impact analysis, an inventory of the materials and means required for a specific repair is used to calculate costs, closure or "downtime" for repair, and environmental impacts, through life cycle impact assessment. These impacts, along with safety assessment using system reliability theory, are termed "decision information." At the conclusion of the PBDE assessment, curves of the probability of values of a particular type of decision information are calculated over the time period of analysis, presumably the service life of the structure. These curves can then be used choose maintenance timing, repair schemes, or select an alternative among competing designs.

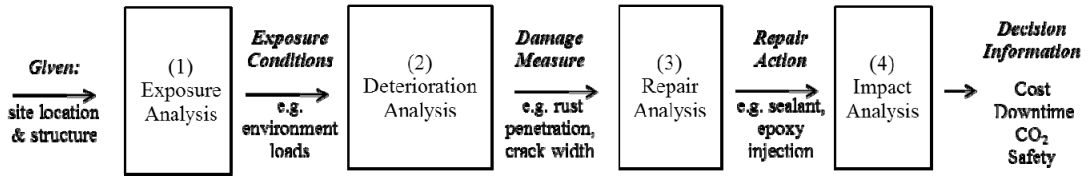


Figure 1: PBDE analysis flow

When chloride-induced corrosion in reinforced concrete is chosen as the deterioration mechanism, it is possible to specify which pinch points will be used in the analysis. Most models for deterioration will require surface chloride concentrations as an environmental condition (EC), as well as information on relative humidity and loading. Practical damage measures (DM) for a corroding structure are chloride ingress, corrosion current, and crack width. Repair actions (RA) include application of sealant, epoxy injection of cracks, removal of concrete cover with sandblasting of corroded rebar, and use of cathodic protection. Impacts of interest would be cost and downtime for maintenance actions, and environmental impacts of the repairs.

Incorporation of Probabilistic Aspects

A major advantage of this framework is the ability to incorporate uncertainty in exposure, similar to how uncertainty in seismic hazard drives PBEE. However, while earthquake occurrence is generally modeled as a Poisson process, the time-varying nature of exposure sources and deterioration requires a different probabilistic treatment. Additionally, the desire to identify particular repair actions for a component, rather than the need for "repair" causes complications. While deterioration is only conditional (in a probabilistic sense) on exposure, and impact is only conditional on repair, the conditioning between exposure, deterioration, and repair is less clear-cut, as the particular repair action and timing will influence future deterioration. A probabilistic framework for probability of exceedence, with substantial similarity to the PEER PBEE equation, has been proposed, but may require implicit repair analysis to avoid some of the aforementioned issues.

$$G_{DI}(DI>di, t)=\iiint G_{DI}(DI>di \mid RA>ra, t)dG_{RA}(R\ ra \mid DM>dm, t)dG_{DM}(DM>dm \mid EC>ec, t)\ dG_{EC}(EC>ec)$$

An alternative approach, widely used in the reliability literature, is to perform Monte Carlo simulation using an input environmental condition "record" and tracking the lifetime deterioration, repair, and decision information for each record. This approach can also accommodate uncertain structural and material parameters, which in other approaches would likely require the use of a response surface or post-analysis adjustment of output curves. The major downside to this approach is the large number of simulations required, which can be very computationally expensive. Alterations to the Monte Carlo method, such as importance sampling, may reduce the amount of computations required. Regardless of the method used to incorporate uncertainty, the end result of the analysis is a distribution of the decision information at all points in time, which can then be collapsed to simpler forms, such as expected values and variances, if desired.

Discretization of Structure

Before analysis can proceed the structure must be discretized into components and sub-components. This discretization is motivated by the need to allow for spatial variation in exposure conditions and material properties at a smaller length-scale and by the recognition that damage measure significance and repair actions vary by component type. For example, crack width limitations are different for concrete decks and bents. Thus at a minimum the structure must be broken down into component types: columns or bents, girders, decks, joints, abutments, and so forth. Choosing the subdivisions based on CoRe elements used in US bridge inspection is a sensible modeling choice. Further spatial subdivision may be performed when necessary. Once the structural discretization is complete the PBDE analysis can commence.

PBDE ANALYSIS PHASES

Phase (1): Exposure Analysis

Exposure conditions are environments (e.g. temperature, humidity, concentrations of chemical species) or loads (e.g. live, earthquake, wind) that cause transient or long-term effects on the structure. The selection of which exposure conditions require modeling is determined by the selected deterioration models, which may require very little (e.g. only surface chloride concentration) or a large quantity of data (e.g. histories of chlorides, temperature, humidity, and loads over the structure lifetime). Thus exposure analysis may be as simple as simulation of random variables based on distributions found in literature or through observation of the site, or may require more complex modeling of the site layout, structural geometry, prevailing wind conditions, and sources of airborne or direct chloride deposition.

There are many sources of these conditions available in the literature, from surveys of existing structures, empirical studies, and analytical models of chloride deposition. Stochastic descriptors for seasonal climatic conditions are generally available from national data sources, such as the National Climatic Data Center [16]. These descriptors can then be used to simulate records of ambient conditions. Surveys and

studies of chloride deposition from marine air, reviewed in Meira, et al. [17], provide ranges of deposition based on wind speed, distance from the coast, and height. While this data may not cover all conditions, it should suffice in many cases. Deposition for deicing salts may be found in research related to the DuraCrete project, among other sources [6]. Research proposed by Lindvall intends to develop analytical models for deposition based on distance from roadway and surface geometry, and could be used in a more complex study if required [18]. It is therefore concluded that current data sources and models will be sufficient to allow for testbed simulation using the PBDE framework for a well-selected site.

Phase (2): Deterioration Analysis

Deterioration analysis for corrosion in reinforced concrete requires simulation of five aspects of corrosion and deterioration, as shown in Figure 2. This simulation may be performed by a single program, such as, among others, DuCOM [19]. Alternately, a series of different models may be used to allow for increased flexibility in modeling all of the interconnected phases of deterioration. Thus, a simple model might track ingress through Fick's second law of diffusion using effective diffusion coefficients and surface chloride concentrations, and predict initiation using a critical chloride concentration or threshold. The resulting corrosion rate might be determined stochastically, and the effects of cracking, bond slip, and other damage mechanisms ignored. This would allow the export of corrosion rate or current and bar area loss as damage measures, as well as the reduction in section structural capacity for impact analysis. This approach has been very frequently used, e.g. by Ting and Nowak [20], and can yield very good results when effective corrosion parameters are available, and conditions are such that a change in conditions or corrosion rates are not anticipated. An example of this might be corrosion in a fully-submerged structure.

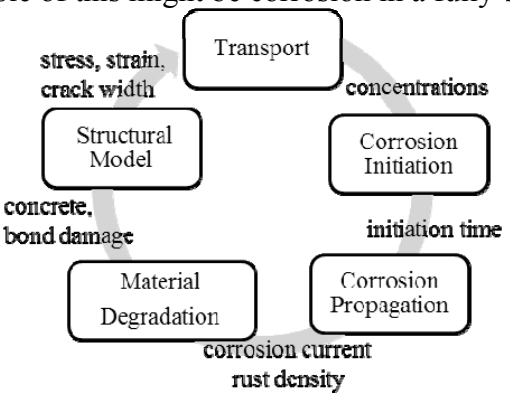


Figure 2: Deterioration Analysis stages

On the other hand, this treatment does not completely capture the phenomenological behavior of corrosion in reinforced concrete, and may not accurately predict damage in cases where exposure and structural geometry is more complex. Thus the most complex treatment would require three-dimensional finite element or finite volume simulation of the structure, with use of coupled partial differential equations governing temperature, moisture, chloride, and oxygen transport, electropotential, stress, and cracking. Such a comprehensive model is available in DuCOM, as previously stated, but sub-models such as that developed by Kemper, et al. for ingress

[21] and Michel, et al. for corrosion propagation [22] might also be adopted for some aspects of the analysis cycle. Cracking due to corrosion propagation has very complex effects on the course of future deterioration, but formulations of transport in cracked media can be used in the finite element method to capture this phenomenon [23]. Use of these complex models requires many input parameters, and may result in issues with convergence and long run-times. This approach is therefore more likely to be used in research and for new structures where simpler methods are not expected to yield accurate results, due to exposure severity or geometric complexity.

When multiple hazards are considered, certain methods of deterioration analysis become more or less attractive. The very complex finite volume and finite element models discussed may not be the ideal models to use when a full suite of nonlinear response histories are required for PBEE assessment using the PEER methodology. In this case fiber models may be a better option, paired with simpler models for chloride ingress and corrosion initiation and propagation. A scenario-specific analysis might allow for the use of the more complex models.

Phase (3): Repair Analysis

Repair analysis uses the observable or detectable damage measures to select a reasonable repair action. Two main methods for choosing a repair action have been proposed: fragility curves like those used in PBEE; and decision or logic trees. Fragility curves have the benefit of incorporating the uncertain relation between damage and repair explicitly. However, because damage states and repair actions do not have a one-to-one mapping (e.g. both large crack widths and detection of a high corrosion current might lead to removal of concrete cover and sandblasting) joint distributions for damage measures and repair actions must be used to avoid "double-counting." This joint behavior will be difficult to model, given the generally slow rate of deterioration and repair and resulting lack of large datasets. Alternately, decision trees make the probabilistic aspects less transparent, but are capable of sorting out the damage measures in such a way that prevents double-counting of the probability of a repair action. While review of existing repair actions chosen through BMS can help populate the logic trees, solicitation of expert opinion from bridge and maintenance inspectors will provide preliminary data for modeling.

Future changes to the AASHTO Bridge Element Inspection Manual will increase the precision of data available on the U.S. national bridge inventory [24]. Inspectors will record both the severity and spatial extent of a certain type of damage, which can then be used to assign probabilities in a logic tree. For example, inspection of a concrete deck would record the presence of cracking, spalls, and efflorescence, their severity, and their quantity. While it will take many years to develop a statistically significant sample of actual damage measures and repair actions, this data source will provide future empirical evidence to complement expert opinion [25].

The separation of damage severity and spatial effects suggests another complication in repair analysis: the "decision" of when the repair takes places, and what components of a set of like components will be repaired. A repair analysis that leads to 93% of the deck surface area being repaired at one time, or bents repaired one at a

time for several years running is insensible. The use of a spatial threshold for repair (e.g. if >80% of a component class is affected, apply the repair to the entire class in that time step) should help to alleviate this problem. This adds a more prescriptive or deterministic aspect to the repair analysis, as the repair timing and extent become less uncertain. However, the practical advantages of the approach are expected to outweigh the potential drawbacks. Additionally, the thresholds could be modeled as stochastic parameters in a Monte Carlo-style simulation, which would reintroduce a suitable level of uncertainty. A repair analysis using a combination of local damage measures, logic trees and spatial thresholds is expected to be the best choice for the form of repair analysis, although other methods of analysis will be studied.

Phase (4): Impact Analysis

Impact analysis is separated into two main categories: those that rely on a repair inventory (cost, downtime, and environmental impacts), and safety or structural reliability, which is computed directly from deterioration analysis. For best results, the repair inventory should be tailored to the particular materials and methods used by the owner or operator. The inventory will be created based on a combination of expert opinion and review of construction documents for actual repairs. It is envisioned that a general inventory will be created, which can then be modified by the analyst to reflect operator preferences.

Each item or process in the inventory (e.g. concrete, sandblasting equipment) must then be linked in unit form to curves for cost, downtime, and environmental impacts. Material costs can be found in, for example, contract cost data provided by state departments of transportation [26], and should reflect variance in bid prices through a probabilistic distribution. Downtime curves are slightly more difficult to obtain, as the aggregation of the time for each unit of repair action (e.g. 1 m^2 of sealant applied) must represent the relative fraction of the total repair time, including setup and breakdown. Preliminary data will again come from review of construction documents. Finally, the methods of life cycle impact assessment (LCIA) are used to analyze the environmental impacts of repair materials and methods. Commercial codes such as SimaPro [27], as well as ongoing research projects [28], link unit inventories of materials and processes to impacts like greenhouse gas emissions, carcinogens, and energy use, and can therefore can be readily linked to output from repair analysis. Uncertainty must also be accommodated in this phase, as, for example, the greenhouse gas emissions of a cement plant or a generator vary by plant and manufacturer. Incorporation of uncertainty in cost, downtime, and environmental impacts given repair action, when convolved with the repair hazard curve, yields the desired exceedence curves for the decision information.

For multihazard analysis structural safety or reliability may be of more interest. As reviewed previously, this field is very well-developed, and many methods exist for computing the probability of "failure," in this case violation of the ultimate limit state. One method is the use of time dependent reliability theory based on upcrossing, as the required time-varying distributions for load and capacity are readily available from the input data for exposure analysis and the output of deterioration analysis. However, this gives only failure from overloading, whereas the probability of failure

from extreme load cases might be of greater interest. Due to the combination of variability in exposure condition/deterioration/repair simulations and in extreme loads (e.g. ground motions, storm surges), this sort of analysis may be better performed using a Monte Carlo approach.

FUTURE WORK

Clearly much work remains to develop and validate the proposed framework. Efforts will first focus on implementing selected deterioration models within the framework, and validating their predictions on controlled laboratory studies of corroding structural members available from literature. Sensitivity analyses will determine which input variables and assumptions have large effects on the accuracy of the predicted deterioration and on decision information. An actual structure will then be selected as a testbed case on the basis of available data for exposure conditions, inspection and maintenance, and knowledge of repair practices. A repair and impact inventory will be developed for this structure, and the decision tree between damage and repair will be developed through review of maintenance records and expert opinion. The PBDE assessment will then be performed using a variety of different models and assumptions to validate the method.

CONCLUSION

A framework for performance-based durability engineering has been proposed after the successful implementation of the PEER Center's performance-based earthquake engineering framework. The approach presented differs from existing frameworks for durability in its use of a sequence of separate analysis stages and "pinch point" variables to provide modeling flexibility. This flexibility allows the assessment of the impact of modeling choices and assumptions, and can provide feedback to researchers. Additionally, the inclusion of impact analysis allows the calculation of decision information useful to owners and operators. Existing models and datasets identified will allow for future testbed simulation to demonstrate how the framework is implemented for archetype structures. It is hoped that the further development of this framework will foster collaboration on new research and design methods, as did the development of performance-based earthquake engineering.

ACKNOWLEDGEMENTS

This research is being conducted under the support of a National Science Foundation Fellowship, a Stanford Graduate Fellowship, and the John A. Blume Earthquake Engineering Center.

REFERENCES

[1] Hamburger, R., "The ATC 58 Project: Development of Next Generation Performance Based Earthquake Engineering Design Criteria for Buildings," Proc. Structures Congress, ASCE.

[2] Deierlein, G., Krawinkler, H., and Cornell, C., "A framework for performance-based earthquake engineering," Proc. Pacific Conference on Earthquake Engineering.
[3] Flint, M., and Billington, S., "Implementation of multiscale models in a probabilistic framework for performance-based durability engineering," Proc. International Workshop on Multiscale and Multiphysics Processes in Geomechanics, R. Borja, ed., Springer.
[4] Thomas, M., and Bentz, E., 2000, "Life-365: Computer program for Predicting the Service Life and Life-Cycle Costs of Reinforced Concrete Exposed to Chlorides," American Concrete Institute.
[5] fib, 2006, "Bulletin 34: Model Code for Service Life Design," fib, Lausanne.
[6] Siemes, T., and Edvardsen, C., "Duracrete: service life design for concrete structures," pp. 1343-1356.
[7] Shimomura, T., Miyazato, S., Yamamoto, T., Kobayashi, K., Sato, T., Saito, S., Kamiharako, A., and Akiyama, M., "Report of Research Project on Structural Performance of Deteriorated Concrete Structures by JSCE-331."
[8] Thoft-Christensen, P., 1998, "Assessment of the reliability profiles for concrete bridges," Engineering Structures, 20(11), pp. 1004-1009.
[9] Enright, M., and Frangopol, D., 1998, "Probabilistic analysis of resistance degradation of reinforced concrete bridge beams under corrosion," Engineering Structures, 20(11), pp. 960-971.
[10] Vu, K. A. T., and Stewart, M. G., 2005, "Predicting the likelihood and extent of reinforced concrete corrosion-induced cracking," Journal of structural engineering, 131, pp. 1681-1689.
[11] Li, C. Q., and Melchers, R. E., 2005, "Time-dependent reliability analysis of corrosion-induced concrete cracking," ACI Structural Journal, 102(4), pp. 543-549.
[12] Angst, U., Elsener, B., Larsen, C., and Vennesland, 2009, "Critical chloride content in reinforced concrete--A review," Cement and Concrete Research, 39(12), pp. 1122-1138.
[13] Melchers, R. E., and Li, C. Q., 2006, "Phenomenological modeling of reinforcement corrosion in marine environments," ACI materials journal, 103(1), pp. 25-32.
[14] Guerre, J., Robert, W., and Fraher, M., 2007, "Framework for Using Pontis Bridge Management System to Support Development of Bridge Programs," Transportation Research Board 86th Annual MeetingWashington, D.C.
[15] Patidar, V., Labi, S., Sinha, K., and Thompson, P., 2007, "Multi-objective optimization for bridge management systems, NCHRP Report 590," Transportation Research Board.
[16] Rutledge, G. K., Alpert, J., and Ebuisaki, W., 2006, "NOMADS: A Climate and Weather Model Archive at the National Oceanic and Atmospheric Adminiatration."
[17] Meira, G., Andrade, C., Padaratz, I., Alonso, C., and Borba Jr, J., 2007, "Chloride penetration into concrete structures in the marine atmosphere zone-Relationship between deposition of chlorides on the wet candle and chlorides accumulated into concrete," Cement and Concrete Composites, 29(9), pp. 667-676.
[18] Lindvall, A., 2007, "Chloride ingress data from field and laboratory exposure-Influence of salinity and temperature," Cement and Concrete Composites, 29(2), pp. 88-93.

[19] Maekawa, K., Ishida, T., and Kishi, T., 2009, Multi-scale modeling of structural concrete, Taylor & Francis Group, New York.
[20] Ting, S., and Nowak, A., 1991, "Effect of reinforcing steel area loss on flexural behavior of reinforced concrete beams," ACI Structural Journal, 88(3), pp. 309-314.
[21] Kemper, M., Timothy, J. J., Kruschwitz, J., and Meschke, G., 2010, "Modeling of Chloride and CO2 transport in intact and cracked concrete in the context of corrosion predictions of RC structures," Computational Modelling of Concrete Structures, N. Bicanic, ed., CRC Press, Rohrmoos, Austria, pp. 503-512.
[22] Michel, A., Geiker, M. R., Stang, H., Olesen, J. F., and Solgaard, A. O. S., 2010, "Numerical modelling of reinforcement corrosion, influence of steel fibres and moisture content on resistivity and corrosion current density," 3rd International PhD Workshop on Modelling the Durability of Reinforced Concrete, R. M. Ferreira, J. Gulikers, and C. Andrade, eds., RILEM, Portugal, pp. 67-74.
[23] Moonen, P., 2009, "Continuous-discontinuous modelling of hygrothermal damage processes in porous media," Ph.D., TU Delft, Delft.
[24] AASHTO, 2010, "Bridge Element Inspection Manual 5," Draft, 5th Ed.
[25] Thompson, P., and Johnson, M., 2005, "Markovian bridge deterioration: developing models from historical data," Structure and Infrastructure Engineering, 1(1), pp. 85-91.
[26] Caltrans, 2009, "2009 Contract Cost Data." State of California, Department of Transportation.
[27] 2007, "SimaPro 7 Live-Cycle Assessment Software," Pre Consultants, Amersfoort, The Netherlands.
[28] Lepech, M., Geiker, M., and Stahng, H., 2011, "Probabilistic Design Framework for sustainable repair & rehabilitation of civil infrastructure," Submitted to fib Symposium, Prague.

A Framework for Performance-Based Engineering in Multi-Hazard Coastal Environments

M. C. McCullough[1] and A. Kareem[2]

[1]NatHaz Modeling Laboratory, Department of Civil Engineering and Geological Sciences, University of Notre Dame, 156 Fitzpatrick Hall, Notre Dame, IN 46545; PH (574) 631-5380; FAX (574) 631-9236; email: mmccull3@nd.edu
[2]NatHaz Modeling Laboratory, Department of Civil Engineering and Geological Sciences, University of Notre Dame, 156 Fitzpatrick Hall, Notre Dame, IN 46545; PH (574) 631-5380; FAX (574) 631-9236; email: kareem@nd.edu

ABSTRACT

The devastation inflicted on civil infrastructure by natural disasters has the potential to result in numerous deaths and huge economic losses. Natural hazards such as hurricanes, earthquakes, floods, and tornadoes have led to extreme property damage and the loss of many lives. While the occurrence of these hazards is beyond our control, novel structural engineering approaches to design and construction have the ability to reduce their consequences. Structures along the coast are particularly susceptible to a variety of natural hazards. Coastal construction practices, however, as they exist today, may not be sufficient to resist their extreme loads. Design and construction in a coastal environment must consider the effects of multiple hazards concurrently rather than focusing on each hazard in isolation. Multi-hazard engineering strategies can be incorporated into design to enhance the inherent resilience and improve the robustness of structures. Current design approaches also lack a probabilistic backbone that can be used to relate specific structural performances with different hazard intensities. Performance-based engineering (PBE) allows for a structure to be designed for specified levels of performance under particular hazard scenarios. Currently, arbitrary importance factors are integrated into design to account for uncertainties in hazards and their loads. In comparison, PBE uses direct analysis procedures to predict the performance of a building under hazard loads over the entire life of the structure. The probabilistic basis of PBE allows future changes in hazard frequencies and intensities due to global climate change to be taken into account. An integration of multi-hazard engineering with PBE promises to significantly improve structural reliability for a wide range of loading scenarios. A possible methodology for assessing response of structures in coastal environments vulnerable to winds, storm surge, tsunamis, and earthquakes is presented.

INTRODUCTION

Structures along the coast are susceptible to several natural hazards, including hurricanes, tsunamis, and earthquakes. Current coastal construction practices, however, may not be sufficient to resist the extreme loads caused by these hazards. Until now, the design of structures has been too focused on treating single hazards in isolation and must be broadened to include the capacity to resist multiple hazards. A

multi-hazard approach takes into account the design strategies for various hazards concurrently within a balanced all-inclusive design (Bruneau 2007; Kafali 2008; Potra and Simiu 2009; Ellingwood et al. 2004; Li and Ellingwood 2009). To further increase the robustness of design and construction in areas vulnerable to several natural hazards, performance-based engineering (PBE) can be combined with multi-hazard engineering. PBE allows for a structure to be designed for specific levels of performance under particular hazard scenarios (FEMA 1997; FEMA 2000; Augusti and Ciampoli 2008; Ellingwood 2008). Therefore, instead of considering code minimums during design and construction for each individual hazard, different levels of structural performance can be achieved based on building function or requirements of building owners. Currently, arbitrary importance factors are integrated into design procedures to account for uncertainties in hazards and their loads (Ellingwood 2008). In comparison, PBE uses direct analysis procedures to predict the performance of a building under multiple hazard scenarios over the entire life of the structure.

Multi-hazard engineering and PBE can be integrated into a framework for the design of structures in coastal areas. The first step in the framework is to define the individual and combined hazards, model the hazards and specific events, and characterize the loads (Thompson and Cardone 1996; Vickery et al. 2000; Jelesnianski et al. 1992; Ellingwood et al. 2004). Monte Carlo based procedures can be used to simulate the independent and combined hazards occurring over the lifetime of the structure (e.g., Shinozuka 1972; Kareem 2008). In this manner, the estimated loads to which a structure will be subjected over its lifetime are determined. Next, the fragility of the structure over a range of loading scenarios is determined. A system fragility analysis is used together with PBE to yield the responses of the structure to the hazards (Kareem 1987; Shinozuka et al. 2000; Wen and Ellingwood 2005). A comprehensive risk-based analysis procedure can then be used to determine whether the responses, which are directly related to the damages, are acceptable over the full range of the different events (e.g., Ellingwood 2008). If the responses are unacceptable, it may be necessary to iterate on the design until the responses over the range of loading scenarios are acceptable.

The probabilistic nature of the method presented herein is particularly important considering the many sources of uncertainty in the analysis. In order to achieve reasonable results and therefore make the proper risk-based decisions, uncertainty in the number of events and their characteristics and intensities, uncertainty in the loads that are acting upon the structures, and uncertainty in the system response must all be considered. In addition, possible changes in the frequency and characteristics of events due to climate change can also be taken into account (Webster et al. 2005; Knutson and Tuleya 2008; Emanuel et al. 2008). Proper consideration of the hazards and consequences, including their uncertainties, within the framework allows resources to be allocated in the most efficient and effective manner. Reduction of overall risk and enhanced robustness without significant increase in cost is the goal of the approach introduced herein.

MULTI-HAZARD ENGINEERING

A multi-hazard engineering approach has the potential to reduce the capacity for dynamic loads to inflict significant damage on structures by considering the

multiple hazards with which a structure may be faced in all aspects of design and construction (Kafali 2008; Ellingwood et al. 2004). Robust design features are chosen such that they enhance performance when considering several individual hazards or the combined loading from two hazards. For the case in which two hazards are present at a site, three types of events must be considered, two hazards occurring individually and events in which both hazards are occurring concurrently. Therefore, the more hazards that are present at a site, the more complicated is their treatment. Fortunately, the analysis and design frameworks for each of the individual hazards are often similar and, therefore, can be combined without much difficulty, as shown in subsequent sections.

Design of coastal structures for hurricanes is inherently a multi-hazard engineering problem. Hurricanes often cause storm surge and waves as well as severe wind. Current methodologies design for each of these hazards independently, without consideration of their combinations. Therefore, the most extreme load conditions may not be considered. Coupling a storm surge model with a hurricane simulation model, however, yields more realistic information on both the flood and wind hazards in a specified area (Huang 1999).

Multi-hazard engineering in its most advanced state will involve the individual and combined modeling of each of the hazards present. Simulations can then be used to fully describe the hazard environment at the site. These models, however, can be computationally expensive and are often not realistic for use when considering large return periods and thus many simulations. At a simpler level, the multi-hazard paradigm can be implemented such that a suite of hazards, both independent and concurrent, are considered and an envelope of the demands induced by the hazards are used for final design. This method, however, can lead to inefficient, and thus suboptimal, designs. HAZUS-MH, developed by the Federal Emergency Management Agency (FEMA), models potential losses from earthquakes, floods, and hurricanes (FEMA 2006a; FEMA 2006b; FEMA 2006c). The ability to estimate impacts from multiple hazards present in a region allows decisions to more easily be made considering allocation of resources and mitigation options.

PERFORMANCE-BASED ENGINEERING

The PBE paradigm has been popular in earthquake engineering and, more recently, it has been extended to blast engineering (ICBO 1997; FEMA 1997; FEMA 2000; FEMA 2004; Hamburger and Whittaker 2003). Although PBE has been informally practiced in wind engineering for decades, its framework is being evaluated for formal adoption. Building codes are intended solely to prevent substantial loss of life or collapse in major hazard events. Therefore, significant damage may be sustained by the structures during events that are considered to have probabilities as high as a 2% annually. While it is not economically practical to design structures to resist the most extreme loads without sustaining damage, the amount of damage sustained for different hazard intensities can be controlled using PBE. Arbitrary safety factors associated with minimum design requirements can be replaced by PBE in an effort to achieve a balance between cost of construction and performance of the structure. PBE necessitates the accurate prediction of response of a structure over a range of natural hazards and intensities that the structure is likely to face over its lifetime. The three main steps of PBE include proper estimation of the hazard(s), evaluation of the vulnerability of the structure to these hazard(s), and

accurate determination of the consequences of the hazard(s) at the system level (Tang et al. 2008). While an understanding of the response of the structural performance at the component level is important, ultimately the system-level behaviors are used as the performance descriptors used to determine the performance levels.

The performance descriptors for individual and concurrent hazards can be chosen such that the performance levels can be set in a straightforward manner. For example, in seismic PBE, interstory drift is often chosen as a performance descriptor (Li and Ellingwood 2007). The probability of exceedance of certain drift ratios are associated with immediate occupancy, life safety, and collapse prevention. Other proposed performance descriptors include flood depth as compared to first floor height of the structure, breach of windows and other openings, and amount of damage to roofing panels. These performance descriptors can then be related to performance levels which are then associated with the hazard intensities.

The quantitative performance descriptors are related to limit states and ultimately qualitative performance levels. The performance levels specified by FEMA (1997) for earthquakes, as mentioned above, are immediate occupancy, life safety, and collapse prevention. Immediate occupancy means limited structural damage has occurred and there is low threat to life safety. Life safety means the structure suffered significant damage but there is low risk of collapse. Collapse prevention means the building is likely to experience partial or total collapse but will continue to carry the gravity load demands for a period of time immediately following the earthquake. While these seismic-based performance levels are a good starting point, additional performance levels are necessary when considering a suite of hazards and their combinations. For example, occupant comfort may be added due to wind/hurricane considerations. Acceptable performance levels are set by the owners and designers for the particular location, type of structure, and use of structure. For example, a lifeline structure, such as a hospital should have immediate occupancy after high intensity, low probability events. The desired performance levels may also be linked to monetary cost. A business may prefer to spend more money up front in the design and construction of the structure rather than risk days or weeks of downtime after high intensity events. The performance levels may be determined by limit states which may be strength related or cost related. This flexibility inherent in PBE is not possible with current code based design.

This paper seeks to extend the probabilistic foundation of PBE to account for multiple hazards present in a coastal environment. Enhancing building design using a PBE approach may increase initial construction costs but long-term savings may easily outweigh the initial investment. In addition, the building owners and occupants are able to choose how the structure will perform over the full range of hazards to which the structure will likely be subjected (Tang et al. 2008). An extension of a PBE framework that considers multiple hazards is outlined below in an effort to show the many advantages of these approaches to engineering design.

DESIGN AND ANALYSIS FRAMEWORK

Figure 1 outlines a proposed framework for performance-based design and analysis of structures in a multi-hazard environment. Each step of this framework is detailed in subsequent sections.

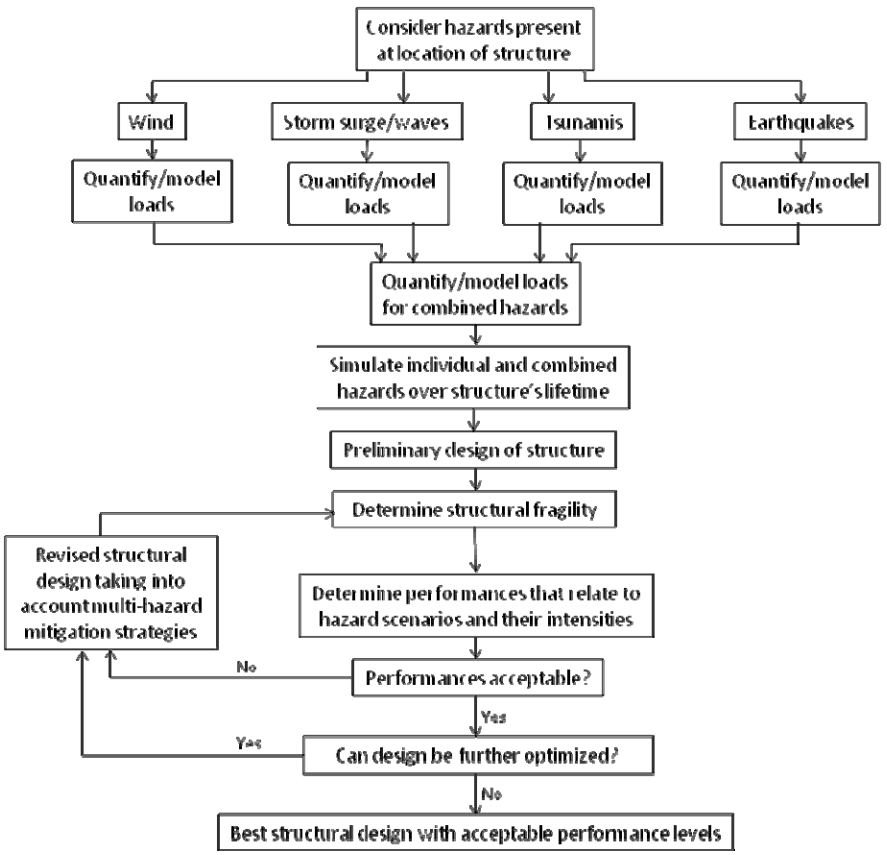


Figure 1. Design and analysis framework for combined multi-hazard engineering and PBE.

Model the hazards present. The risks that are specific to a structure's site are determined and the site is analyzed based on location and previous history. In coastal construction, our focus herein, the natural hazards with which a structure may be faced are narrowed to include storm surge/waves, tsunamis, earthquakes, and wind. Stochastic modeling of the individual and combined loads associated with all hazards present at a location is the important first step. Computationally expensive as well as simplified models are available for the individual as well as the combined loads.

The wind hazard present at a site is often expressed by a maximum wind speed probability distribution that is appropriate for the location, exposure, and elevation of the site. The location determines whether the site is vulnerable to hurricane winds and/or winds associated with extratropical storms. Since our focus is coastal construction, hurricanes are used to determine the extreme wind environment (Thompson and Cardone 1996; Vickery et al. 2000). The modeling of hurricane winds can be complicated depending on how much detail is included. Monte Carlo simulation (MCS) is employed to generate thousands of hurricanes with varying storm sizes, tracks, intensities, and locations to generate probabilities of occurrence of hurricanes in a particular location and the probability distributions of the maximum wind speeds. Historical hurricane data is used to develop probability distributions of the hurricane parameters from which the MCS random variables are drawn (Kafali 2008). Single and multiple point models derived from spectral density functions are used to characterize the fluctuating wind components, which are then combined with the mean wind velocities determined via simulation. Huang et al. (2001) also uses

simulation techniques to characterize the wind environment, but uses more complex wind models derived from previous models by Batts et al. (1980) and Georgiou (1985). The five parameters of focus in this methodology are annual occurrence rate, minimum approach distance, approach angle, central pressure difference, radius of maximum wind speed, and translation velocity (Huang 1999). Once again historical hurricane data is used to develop the probability distributions of the parameters used by MCS. Variations of these parameters in time and correlations between the parameters are also taken into account as the hurricane is moved along its path. For example, central pressure difference is modeled as a Weibull distribution with mean and standard deviation determined for the location of interest. The central pressure difference, however, decreases as the hurricane moves over land. This wind modeling method yields accurate maximum surface wind speeds for a particular site.

Storm surge can be a major source of damage during a hurricane depending on the storm characteristics and the location. Storm surge is water that is forced toward the shore by hurricane winds. Proper modeling of storm surge is important for accurate determination of coastal areas susceptible to flooding. Surge depth, velocity, and duration are the key parameters necessary for complete modeling of storm surge loads. In addition, surface waves superimposed on the storm surge are important since the wave action on a structure can lead to very different loads than those caused by flooding. The primary parameters necessary for modeling hurricane induced storm surge include central pressure difference, storm size, translational velocity of storm, shelf width, bottom slope, and peakedness of storm wind speed distribution (Irish et al. 2008). Some modeling approaches for storm surge make significant simplifications, while other, more complicated, methods take into account all these parameters in significant detail. For example, hurricane inundation can be simulated using the hydrodynamic model ADCIRC (Advanced CIRCulation). ADCIRC is a finite-element, depth integrated model that takes into account storm surge developed due to tides, wind forcing, and ocean wave forcing (Westerink et al. 1992). ADCIRC uses actual wind fields for forcing when available. For predicting storm surge from hypothetical storms, however, simplified wind models are used. ADCIRC does not model the nearshore wave environment. Therefore, ADCIRC can be coupled with the Steady State Spectral Wave (STWAVE) model (Resio 1987) or the Simulating Waves Nearshore (SWAN) model (Booij et al. 1999) to gain a complete understanding of the storm surge and waves present at a site location. In addition, a Pierson-Moskowitz spectrum has been used to determine the waves to be superimposed on the storm surge using the mean wind speed (Kafali 2008). A much simpler method for storm surge prediction has been developed by the National Weather Service and is known as SLOSH (Sea, Lake, and Overland Surges from Hurricanes) (Jelesnianski et al. 1992). SLOSH can estimate storm surge flooding for a given category, forward speed, direction, and location. SLOSH uses simplified parametric wind models to produce surface stresses, which drive the water onto the shore. SLOSH does not include tides, ocean waves, or wind-driven waves. SLOSH may also be coupled with STWAVE or SWAN with some success. In its simplest form, storm surge modeling can be derived from FEMA flood maps associated with the National Flood Insurance Program (NFIP). These flood maps can be used to determine probabilistic flood depths for a structure over its lifetime. The above storm surge/wave modeling methodologies can be used together with ASCE7-05 procedures to quantify the hydrostatic forces from inundation, the hydrodynamic forces from water velocity, the breaking wave forces, and the buoyant forces.

Tsunami forces are similar to those associated with storm surge and can be modeled in much the same way. Hydrostatic, hydrodynamic, and buoyant forces are the cause of most of the destruction from tsunamis. The occurrences of the driving mechanisms for tsunamis, subduction zone earthquakes, sea floor landslides, or volcanic activity, however, are more difficult to predict. The rare occurrence of tsunamis has also hindered development of realistic occurrence and propagation models. Short term tsunami models, however, have been developed by the NOAA Center for Tsunami Research (NCTR) and simulation models are currently being created by a NEES project known as TSUNAMOS at Oregon State University. Inundation forecasts are available through NOAA NCTR based on Method of Splitting Tsunami (MOST) models. MOST is used for the generation of a tsunami by an earthquake, propagation of the tsunami, and subsequent inundation of dry land (Titov and González 1997). MOST is the basis of the Short-term Inundation Forecast for Tsunamis (SIFT) tool, also developed by NCTR. SIFT provides tsunami forecasts quickly and accurately using tsunami propagation simulations after a tsunami generating event has occurred (Gica et al. 2008). SIFT also incorporates data collected by deep water buoys and features site specific inundation forecasts. TSUNAMOS seeks to improve current tsunami models by including 3D breaking waves, improving bathymetric and topographic features in tsunami prone regions, and integrating experimental and full-scale data (NEESR-SG 2007). Once the inundation depths and velocities have been determined via modeling, ASCE7-05 procedures can be used to approximate the forces with which structures will be faced.

Earthquake modeling has been researched extensively over the past several decades. The models available range from very complex to very simple. At the highest levels, stochastic methods are used to generate earthquakes using empirical spectra or spectra based on physical models (Housner and Jennings 1964; O'Connor and Ellingwood 1992; Boore 2003; Kafali 2008). While the earthquake time series generated by the spectra may not resemble actual earthquakes that have occurred or may occur at the site, essential characteristics of the ground motion are captured. An ensemble of seismic acceleration time histories can be used to fully characterize the earthquake environment at the site. Similarly, a suite of actual ground motions at the site or similar sites can be used. At the most simple level, the USGS provides mean yearly rates for combinations of earthquake magnitude and source to site distances that can be related to probable damage states for different types of structures (USGS 2009). These values are also useful when combined with the stochastic and kinematic models. The spectra chosen to generate the time histories are often dependent on the magnitudes and source to site distances associated with different recurrence intervals.

The multi-hazard paradigm necessitates consideration of combined hazard loads. As mentioned above, hurricanes consist of multiple hazards that are directly related to each other. The central pressure difference of the hurricane determines the intensity of the storm, which determines wind speeds as well as potential storm surge depths. Therefore, hurricane wind speeds, storm surge depths, and wave heights should all be modeled together. The difficulty, however, becomes combining models such that they are still computationally efficient. A storm hazard model known as The Arbiter of Storms (TAOS) seeks to achieve this by extending the SLOSH model to include realistic wind estimates and waves (Watson 1995). Tsunamis and earthquakes can also be multi-hazard events. A future goal of the NEES TSUNAMOS simulator is to combine TSUNAMOS with OpenSees, well-known earthquake engineering

software (NEESR-SG 2007). Further development in the combined modeling of hazards is necessary in order to make multi-hazard engineering feasible.

Once models for the individual and combined hazards have been determined and validated it is necessary to simulate random arrival times of the hazards at a site over a structure's lifetime. Figure 2 depicts the potential occurrence of hazards, both combined and individual, over the lifetime of a structure. Simulation procedures not only specify the random arrival times of the events but also their random properties (e.g., Kafali 2008). Event arrivals and intensities of individual hazards can be modeled as a Poisson process (e.g., Huang 1999; Kafali 2008). Then the characteristics of the events once the intensities are known can be specified using MCS. The simulation procedures for event arrivals and characteristics take into account the temporal and spatial uncertainty of the hazards. The characteristics can be simulated from probability density functions associated with the different parameters of the events (Kafali 2008).

The uncertainties associated with global climate change and its potential effects on hurricanes can also be incorporated. Future global warming may cause the sea level to rise and hurricanes to intensify (Webster et al. 2005; Knutson and Tuleya 2008; Emanuel et al. 2008). These possible changes can be taken into account during hazard characterization. For example, mean sea level within ADCIRC can be adjusted for sea level rise (Mousavi et al. 2010). Similarly, adjustments of hurricane intensities can easily be made using simple equations relating sea surface temperature rises and intensity rises (Knutson and Tuleya 2008). Therefore, hazard modeling in a probabilistic framework can easily include predicted changes in overall hazards or specific characteristics of the hazards.

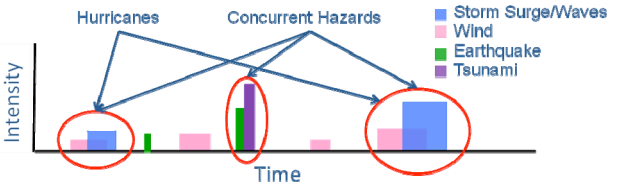


Figure 2. Stochastic modeling of the individual and combined hazards present at a location over the lifetime of the structure.

Determine fragility. Once the hazards have been defined and the loads for all the scenarios are characterized using the tools above, the structural fragilities associated with the range of hazards and intensities are determined. Fragility curves are the result of the combination of the vulnerability of the structure and the hazard loads and are typically assumed as a two-parameter lognormal distribution function. System fragility is the conditional probability that the structural response exceeds a damage state given a hazard intensity. The damage states correspond to defined limit states which are related to the performance levels. For example, a seismic fragility curve may be defined by the exceedance of different interstory drift limit states. Defined limit states (e.g., 1%, 2%, 3% drift ratios) correspond to performance levels such as immediate occupancy, life safety, or collapse prevention. In this manner, system fragility is plotted against the parameters characterizing the natural hazards, i. e., interstory drift, maximum wind speeds, storm surge depth, etc. A variety of empirical and analytical methods can be used to generate fragility curves that range from the very simple to the very complicated. A few of these methods will be discussed below.

One of the most simple, but most attractive, options for fragility analysis involves the use of damage functions already available from FEMA in HAZUS-MH. These damage functions correspond to different building ages, structural types, and exposure categories. They were created through direct comparison between the hazard loads and empirically or analytically derived resistance parameters. The functions are related solely to the intensity of the hazards. Therefore, the full time histories are not necessary for this fragility analysis. For example, the exposure, building age, and structure type would determine which fragility curve would be considered and only the maximum wind speeds would be necessary to determine the damage. Similarly, the source-to-site distance and location would determine the fragility curve to be considered but only the magnitudes of the earthquakes would be necessary to determine the damage. The damage suffered by a structure throughout its lifetime due to the suite of hazards simulated above can be used to estimate the monetary loss over a specific period of time. Determination of whether the extent of damage as well as the losses are acceptable will be explained below. While this approach to fragility analysis is convenient, a number of assumptions are made that can cause the results to be inaccurate.

Empirical fragility curves can also be developed in a straightforward manner as in Shinozuka et al. (2000). This approach, however, is often not possible since damage data must be available for a large number of similar structures affected by the same intensity hazard. This has been possible in seismic fragility analysis because damage to a number of similar structures can be used after a specific event, such as the 1995 Kobe earthquake. The curves are developed by integrating damage state information with the intensity measure (e.g., peak ground acceleration for earthquakes). Several curves can be defined that are associated with different performance levels. This method is not considered further for this framework, however, since we are considering hypothetical hazard scenarios in the future.

Analytical fragility curves may be used when empirical fragility curves cannot be determined (Shinozuka 2000). Generated time histories with specified intensity parameters are used for the hazard loads. These time histories are available via simulations as discussed in the previous section. A finite-element code such as SAP 2000 or ETABS can then be used to simulate the damage due to the different time histories. These damages can then be used to determine the damage states associated with different hazard intensities. Extensions and modifications of this general framework are typically used for the development of fragility curves.

Wen and Ellingwood (2005) use a similar method to assess the vulnerability of structures to different hazards. System response to the generated time histories are determined using single-degree-of-freedom oscillators that represent each mode. Maximum responses due to the different modes are then combined using Square Root Sum of Squares (SRSS). The results from the simplified systems can then be used to develop probabilistic demand curves.

Establish acceptable performance levels. A risk analysis approach is used to determine acceptable damages for different events throughout the lifetime of the structure. Together, the building owner, occupants, and design engineers can determine acceptable probabilities that the structure enters different damage states given a range of load scenarios (Kafali 2008). For example, given a low intensity, high probability scenario the structure should likely undergo no damage. For high intensity, low probability events the structure may undergo moderate to extensive

damage. A cost/benefit analysis couched in a risk based framework is performed to understand the likelihood of specific hazard events as well as potential consequences. Since resources are not endless, it is important to determine how best to design the structure to resist hazards and reduce the consequences with what is available.

Optimization of the design of the structure is performed by iterating through this basic procedure in order to determine the best possible structural design that utilizes the best selection of complementary multi-hazard mitigation strategies. The goal is to minimize risk while still avoiding inefficient and costly construction. Optimization will occur until the acceptable performance levels have been met in the most cost-efficient manner. Optimization may involve changes to the design that are as simple as raising the grade level or adding hurricane straps to the roof or as complicated as adjusting the orientation of the entire structure or considering different structural materials. The final goal of the structural design is a structure that has a total life-cycle cost that is a minimum but the system maintains the specified performance levels during potential hazards. The presentation will include a detailed example of the framework presented here.

CONCLUDING REMARKS

Continued development of coastal areas without consideration of the range of natural hazards, and the benefits and consequences of measures taken to mitigate them, will undoubtedly result in future storm and flood damages, and increased public expenditures for post-storm response and recovery. PBE combined with multi-hazard engineering has the promise to provide a cost-effective and efficient design for a structure subjected to loads from multiple hazards. Multi-hazard mitigation aims to use available resources most effectively to design safe structures that are able to withstand a range of natural hazards. Common practice in design currently considers each hazard separately and combines these designs in a non-optimal manner. The most effective overall solution can be created by considering the portfolio of expected threats to a location and putting together a versatile design. Performance-based engineering offers the optimal framework for creating the best engineering design considering uncertainty in demands and capacities. This paper introduces a basic design framework that combines multi-hazard and performance-based engineering.

REFERENCES

ASCE 7-05 (2005). "Minimum design loads for buildings and other structures." *ASCE/SEI 7-05,* ASCE, Reston, VA.

Augusti, G., and Ciampoli, M. (2008). "Performance-Based Design in risk assessment and reduction." *Probabilistic Engineering Mechanics*, 23, 496-508.

Batts, M. E., Cordes, M. R., Russell, L. R., Shaver, J. R., and Simiu, E. (1980). "Hurricane Wind Speeds in the United States." *NBS Building Science Series 124*, U.S. Department of Commerce, National Bureau of Standards, Washington, D.C.

Booij, N., Ris, R. C., and Holthuijsen, L. H. (1999). "A third-generation wave model for coastal regions, Part I, Model description and validation." *Journal of Geophysical Research,* 104(C4), 7649-7666.

Boore, D. M. (2003). "Simulation of ground motion using the stochastic method." *Pure and Applied Geophysics*, 160, 635-676.

Bruneau, M. (2007). *Symposium on Emerging Developments in Multi-Hazard Engineering,* Steel Institute of New York.

Ellingwood, B. R. (2008). "Structural reliability and performance-based engineering." *Structures and Buildings*, 161, SB4, 199-207.

Ellingwood, B. R., Rosowsky, D. V., Li, Y., and Kim, J. H. (2004). "Fragility Assessment of Light-Frame Wood Construction Subjected to Wind and Earthquake Hazards." *Journal of Structural Engineering*, 130(12), 1921-1930.

Emanuel, K. A., Sundararajan, R., and Williams, J. (2008). "Hurricanes and global warming: results from downscaling IPCC AR3 simulations." *Bulletin of the American Meteorological Society*, 89, 347-367.

Federal Emergency Management Agency (FEMA) (1997). "NEHRP Guidelines for the Seismic Rehabilitation of Buildings." *Report No. FEMA 273,* FEMA, Washington, D.C.

Federal Emergency Management Agency (FEMA) (2000). "NEHRP Recommended Provisions for Seismic Regulations for New Buildings and Other Structures." *Report No. FEMA 368,* FEMA, Washington, D.C.

Federal Emergency Management Agency (FEMA) (2004). "Reference Manual to Mitigate Potential Terrorist Attacks Against Buildings." *Report No. FEMA 426,* FEMA, Washington, D.C.

Federal Emergency Management Agency (FEMA) (2006a). "Multi-hazard loss estimation methodology – hurricane model." *FEMA,* Washington, D.C.

Federal Emergency Management Agency (FEMA) (2006b). "Multi-hazard loss estimation methodology – flood model." *FEMA,* Washington, D.C.

Federal Emergency Management Agency (FEMA) (2006c). "Multi-hazard loss estimation methodology – earthquake model." *FEMA,* Washington, D.C.

Georgiou, P. N. (1985). "Design Wind Speeds in Tropical Cyclone-Prone Regions." *PhD Dissertation, Dept. of Civil Engineering, University of Western Ontario.*

Gica, E., Spillane, M., Titov, V. V., Chamberlin, C., and Newman, J. C. (2008). "Development of the forecast propagation database for NOAA's Short-term Inundation Forecast for Tsunamis (SIFT)." *NOAA Tech. Memo* OAR PMEL-139, 89.

Hamburger, R. O., and Whittaker, A. S. (2003). "Considerations in Performance-Based Blast Resistant Design of Steel Structures." *AISC-SINY Symposium on Resisting Blast and Progressive Collapse,* AISC, New York, NY.

Housner, G., and Jennings, P. C. (1964). "Generation of artificial earthquakes." *ASCE Journal of the Engineering Mechanics Division*, 90, 113-150.

Huang, Z. (1999). "Stochastic models for hurricane hazard analysis." *PhD Dissertation, Civil Engineering, Clemson University.*

Huang, Z., Rosowsky, D. V., and Sparks, P. R. (2001). "Long-term hurricane risk assessment and expected damage to residential structures." *Reliability Engineering and System Safety*, 74, 239-249.

International Conference of Building Officials (ICBO) (1997). *Uniform Building Code*, ICBO, Whittier, CA.

Irish, J. L., Resio, D. T., and Ratcliff, J. J. (2008). "The Influence of Storm Size on Hurricane Surge." *American Meteorological Society,* DOI: 10.1175/2008/JPO3727.1

Jelesnianski, C. P., Chen, J., Shaffer, W. A. (1992). "SLOSH: sea, lake, and overland surges from hurricanes." *National Oceanic and Atmospheric Administration and National Weather Service.* Silver Springs, MD.

Kafali, C. (2008). "System performance under multihazard environment." *PhD Dissertation, Dept. of Civil and Environmental Engineering, Cornell University.*

Kareem, A. (1987). "Structural performance and wind speed damage correlation in Hurricane Alicia." *Journal of Structural Engineering*, 113(11), 2322-2323.

Kareem, A. (2008). "Numerical simulation of wind effects: A probabilistic perspective." *Journal of Wind Engineering and Industrial Aerodynamics*, 96(10-11), 1472-1497.

Knutson, T. R., Tuleya, R. E. (2008). "Tropical cyclones and climate change: revisiting recent studies at GFDL." *Climate extremes and society*, Columbia University Press, New York.

Li, Y., and Ellingwood, B. R. (2007). "Reliability of wood-frame residential construction subjected to earthquakes." *Structural Safety*, 29(4), 294-307.

Li, Y., and Ellingwood, B. R. (2009). "Framework for Multihazard Risk Assessment and Mitigation for Wood-Frame Residential Construction." *Journal of Structural Engineering,* 135(2), 159-168.

Mousavi, M. E., Irish, J. L., Frey, A. E., Olivera, F., and Edge, B. L. (2010). "Global warming and hurricanes: the potential impact of hurricane intensification and sea level rise on coastal flooding." *Climatic Change*, Springer, DOI 10.1007/s10584-009-9790-0.

NEESR-SG (2007). "TSUNAMOS: A Validated, Multi-Scale Tsunami Model for Hybrid Numerical-Experimental Simulation." https://ceprofs.civil.tamu.edu/plynett/TSUNAMOS/index.html.

O'Connor, M. J. and Ellingwood, B. R. (1992). "Site-dependent models of earthquake ground motion." *Earthquake Engineering and Structural Dynamics,* 21, 573-589.

Potra, F. A., and Simiu, E. (2009). "Optimization and Multi-Hazard Structural Design." *Journal of Engineering Mechanics*, 135(12), 1472-1475.

Resio, D. T. (1987). "Shallow-water waves I: theory." *Journal of Waterway, Port, Coastal and Ocean Engineering,* 113(3), 264-281.

Shinozuka, M. (1972). "Monte carlo simulation of structural dynamics." *Computers and Structures*, 2, 855-873.

Shinozuka, M., Feng, M. Q., Lee, J., and Naganuma, T. (2000). "Statistical Analysis of Fragility Curves." *Journal of Engineering Mechanics*, 126(12), 1224-1231.

Tang, M., Castro, E., Pedroni, F., Brzozowski, A., and Ettouney, M. (2008). "Performance-Based Design with Application to Seismic Hazard." *Structure Magazine*, June, 20-22.

Titov, V. V., and González, F. I. (1997). "Implementation and testing of the Method of Splitting Tsunami (MOST) model." *NOAA Tech. Memo.* ERL PMEL-112.

Thompson, E. F., and Cardone, V. J. (1996). "Practical Modeling of Hurricane Surface Wind Fields." *Journal of Waterway, Port, Coastal, and Ocean Engineering*, 122(4), 195-205.

USGS (2009). "2009 Earthquake Probability Mapping." *https://geohazards.usgs.gov/eqprob/2009/*

Vickery, P. J., Skerlj, P. F., Steckley, A. C., and Twisdale, L. A. (2000). "Hurricane Wind Field Model for Use in Hurricane Simulations." *Journal of Structural Engineering*, 126(10), 1203-1221.

Watson, C. C. (1995). "The Arbiter of Storms: a High Resolution, GIS based System for Integrated Storm Hazard Modeling." *National Weather Digest*, 20(2), 2-9.

Webster, P. J., Holland, G. J., Curry, J. A., and Chang, H. R. (2005). "Changes in tropical cyclone number, duration, and intensity in a warming environment." *Science*, 309, 1844-1846.

Wen, Y. K., and Ellingwood, B. R. (2005). "The Role of Fragility Assessment in Consequence-Based Engineering." *Earthquake Spectra,* 21(3), 861-877.

Westerink, J. J., Luettich, A. M., Baptista, A. M., Scheffner, N. W., and Farrar, P. (1992). "Tide and storm surge predictions using finite element model." *Journal of Hydraulic Engineering,* ASCE, 118, 373-390.

Lifetime Seismic Performance of Aging Structural Systems

Fabio Biondini[1], Elena Camnasio[1] and Alessandro Palermo[2]

[1] Department of Structural Engineering, Politecnico di Milano, Piazza L. da Vinci 32, 20133 Milan, Italy; email: biondini@stru.polimi.it; camnasio@stru.polimi.it
[2] Department of Civil and Natural Resources Engineering, University of Canterbury, 8140 Christchurch, New Zealand; email: alessandro.palermo@canterbury.ac.nz

ABSTRACT

The seismic performance of structural systems exposed to aggressive environments has to be considered time-variant. Current capacity design criteria are time-invariant and do not account for the interaction with environmental hazards. In fact, for aging systems the energy-dissipating collapse mode may vary over time due to a reduction of both strength and curvature ductility of critical cross-sections where plastic hinges may occur during a seismic event. In this study the lifetime seismic performance of concrete structures is investigated in both probabilistic and deterministic terms. Static and dynamic non linear analyses are carried out on a three-story concrete frame to evaluate the effects of damage on the time evolution of seismic performance indicators. The results show the important role of a life-cycle approach for both seismic assessment of existing structures and seismic design of new structures.

INTRODUCTION

In seismic design of concrete frame systems a collapse mechanism involving the maximum number of story is required to optimize the seismic performance. The optimal failure mechanism can be selected based on a capacity design with strong columns and weak beams (Pauley and Priestley 1992, CEN-EN 1998-1 2004). This approach is time-invariant and do not account for the interaction with environmental hazards. In fact, for concrete structures the diffusive attack from external aggressive agents, like sulfate and chloride, can take place and lead to deterioration of concrete and corrosion of reinforcement (CEB 1992). Such kind of damage can significantly reduce local strength and ductility and modify, in this way, the failure mechanism (Biondini and Frangopol 2008) and the corresponding seismic performance during the structural lifetime (Biondini *et al.* 2011, Akiyama *et al.* 2011). As a consequence, capacity design criteria should be properly calibrated to consider the severity of environmental exposure and the required structural lifetime (Biondini *et al.* 2008, 2011, Berto *et al.* 2009, Akiyama and Frangopol 2010, Rao *et al.* 2010). The effects of chloride induced corrosion of steel reinforcement on the lifetime seismic performance of concrete structures are investigated in this study. A probabilistic approach is adopted to take into account the uncertainties involved in the diffusion and corrosion processes (Enright and Frangopol 1998, *fib* 2006). The lifetime nonlinear structural analyses are carried out by using a general method for concrete structures in aggressive environments (Biondini *et al.* 2004). Two cross-sections with different shape ratio and reinforcement layout are considered to show that concrete

members designed to have the same initial performance and durability threshold parameters, such as concrete cover and quality of the materials, may exhibit different strength and ductility over time depending on geometrical characteristics of the cross-section (Biondini and Frangopol 2010). The time-variant performance of the critical cross-sections of members is analyzed in terms of bending moment versus curvature relationships. These results are implemented in a structural model based on lumped plasticity beam elements (Carr 2006). Static and dynamic non linear analyses are carried out on a three-story concrete frame to evaluate the effects of damage on the time evolution of seismic performance. The results show that the reduction of strength and ductility of concrete members leads to reduced seismic performance of the structural system and confirm the important role of a life-cycle approach for both seismic assessment of existing structures and seismic design of new structures.

TIME-VARIANT PERFORMANCE OF CONCRETE CROSS-SECTIONS

Case study. Cross-sectional analyses are carried out in order to describe the aging phenomena of concrete elements under chloride diffusive attack. The two cross-sections shown in Figure 1 are considered. These cross-sections have been designed so to have the same resistant bending moment $M_{R0} \cong 620$kNm and curvature ductility $\mu_\chi \cong 20$, by assuming material strengths $f_c = 30$MPa for concrete and $f_s = 430$MPa for steel, strain limits $\varepsilon_{cu} = 0.35\%$ for concrete and $\varepsilon_{su} = 6.00\%$ for steel, and concrete cover $c = 40$mm. The effects of confinement are taken into account by assuming the concrete ultimate strain as a function of the stirrup mechanical ratio ω_w (CEB 1985):

$$\varepsilon_{cu}^{*} = \varepsilon_{cu} + 0.05 \cdot \omega_w$$



Cross-section **1**
8 Φ22mm
Stirrups Φ8/75mm

Cross-section **2**
10 Φ16mm
Stirrups Φ8/75mm

Figure 1. Cross-sections and location of the aggressive agent.

The diffusion process. The cross-sections shown in Figure 1 are exposed to the diffusive attack of chlorides along one side (bottom side in Figure 1). This situation is typical of members placed along the perimeter of buildings with the external surface exposed to aggressive atmosphere. Since most observations indicate that transport of chlorides in concrete is diffusion controlled (Bertolini *et al.* 2003), the diffusive process is described by using the following limit state equation based on Fick's one-dimensional model (*fib* 2006):

$$C(x=c,t)=C_0+(C_{S,\Delta x}-C_0)\cdot\left[1-erf\frac{c-\Delta x}{2\cdot\sqrt{D_{app,C}\cdot t}}\right]=C_{crit}$$

where the actual chloride concentration $C(x = c, t)$ at the depth c of the reinforcing steel at time t is compared to the critical chloride concentration C_{crit} which defines the initiation of the corrosion process; C_0 is the initial chloride content of the concrete, assumed equal zero in the following; Δx is the depth of the convection zone, *i.e.* the concrete layer up to which the process of chloride penetration differs from Fick's model, assumed equal zero in this study; $C_{S,\Delta x}$ is the chloride content at depth Δx and time t; $D_{app,C}$ is the apparent coefficient of chloride diffusion, which is evaluated as follows (*fib* 2006):

$$D_{app,C}=D_{RCM,0}\cdot A(t)$$

where $D_{RCM,0}$ is the chloride migration coefficient, and $A(t)$ is a function considering "aging" according to the following formula (*fib* 2006):

$$A(t)=\left(\frac{t_0}{t}\right)^a$$

where t_0 = 28 days = 0.0767 years is the reference initial time.

The diffusion process is described in probabilistic terms assuming the random variables, distribution type, mean μ and standard deviation σ, listed in Table 1 (*fib* 2006). Based on this model, a probabilistic analysis is carried out by Monte Carlo simulation. The probability density functions (PDFs) of chloride concentration at cover depth c and time steps t = 10, 25, 50 years are shown in Figure 2 with reference to a sample size of 50,000 simulations.

Based on the Fick's limit state equation, the PDF of the initiation time t_i for propagation of steel bar corrosion can also be evaluated as shown in Figure 3 (Enright and Frangopol 1998). A lognormal distribution with mean μ = 9.24 years and standard deviation σ = 4.66 years appears to be a good estimate of the actual distribution for the corrosion initiation time (Figure 3, continuous line).

Table 1. Probability distributions and their parameters (*fib* 2006).

Random Variable	Distribution Type	μ	σ
Concrete cover, c [mm]	Normal (*)	40	8
Aging exponent, a [-]	Beta (b_{min} = 0.0; b_{max} = 1.0) (#)	0.3	0.12
Chloride content at depth Δx, $C_{s,\Delta x}$ [wt.%/c]	Normal (*)	3	$0.3\cdot\mu$
Chloride migration coefficient, $D_{RCM,0}$ [m^2/s]	Normal (*)	$15.8\cdot10^{-12}$	$0.2\cdot\mu$
Critical chloride content, C_{crit} [wt.%/c]	Beta (b_{min} = 0.2; b_{max} = 2.0) (#)	0.6	0.15

(*) Truncated distributions.

(#) b_{min} = lower bound, and b_{max} = upper bound of beta distributions.

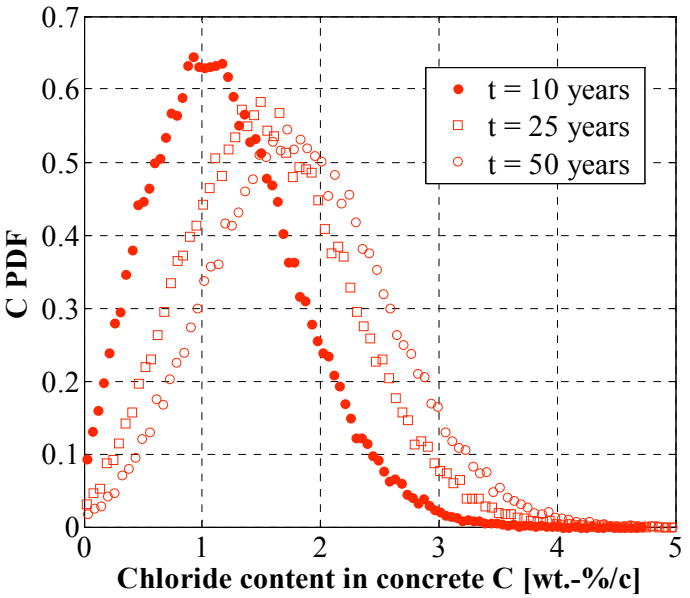


Figure 2. Probability distributions of chloride content in concrete $C(x, t)$ at cover depth $x = c = 40$mm and time steps $t = 10, 25, 50$ years.

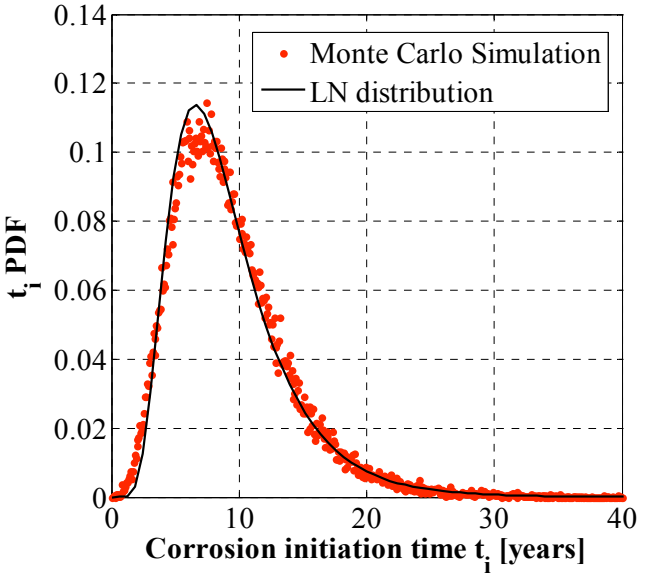


Figure 3. Probability density function of corrosion initiation time t_i.

Damage modeling. The chloride attack induces a corrosion process with reduction of the area of the reinforcing bars. The corrosion penetration P_x is evaluated as follows:

$$P_x = r_{corr} \cdot t_p$$

where r_{corr} is the corrosion rate and $t_p = (t - t_i)$ is the propagation time. Considering uniform corrosion, the reduction in the diameter of a corroding reinforcing bar at time t can be estimated as follows (Berto *et al.* 2009):

$$D(t) = D(0) - P_x .$$

On the basis of correlations between chloride content and corrosion current density in concrete (Bertolini 2003, Liu & Weyers 1998, Thoft-Christensen 1998), a linear relationship between rate of corrosion r_{corr}, in the range 0 to 200μm/year, and chloride content, in the range of 0-3%, is assumed in this study. The time-variant mean value μ of rebar diameter $D(t)$ with respect to the nominal diameter $D(0)$, and the relative coefficient of variation $\delta = \sigma/\mu$, are shown in Figure 4 over a 50 year lifetime.

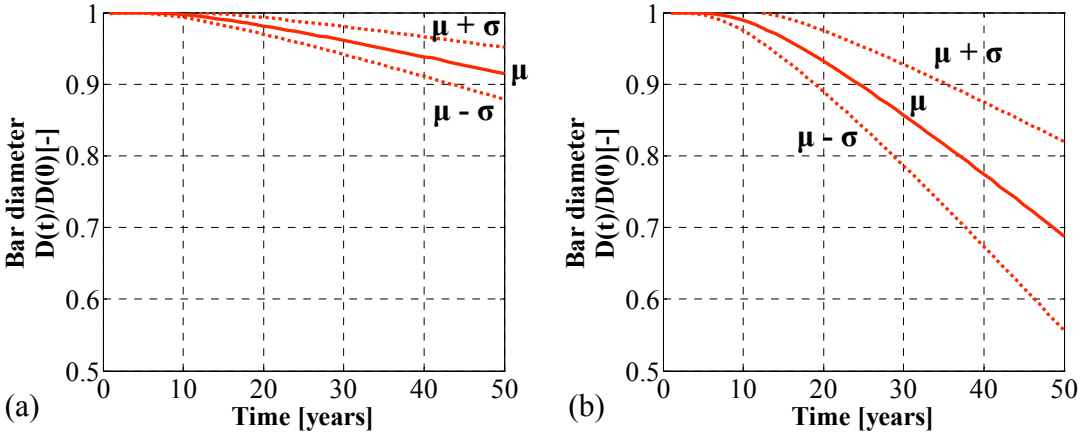


Figure 4. Time evolution of steel bar diameter (a) $D(0)$ = 22mm and (b) $D(0)$ = 16mm: mean (continuous line) and one standard deviation (dotted lines).

Lifetime performance indicators. The time-variant structural performance is evaluated in terms of resistant bending moment $M_R = M_R(t)$ and curvature ductility $\mu_\chi = \mu_\chi(t)$. The performance deterioration is mainly due to the corrosion of the bars closer to the exposed surface. The material strengths f_c and f_y are assumed as lognormally distributed random variables, considering the nominal values as mean values and by assuming 5MPa and 30MPa as standard deviation values for concrete and steel, respectively.

Figures 5 and 6 shows the results of a Monte Carlo simulation in terms of time evolution of the statistical parameters of resistant bending moment $M_R(t)$ and curvature ductility μ_χ, respectively, for the two cross-sections shown in Figure 1. It is noted that cross-section 2 shows a greater reduction in terms of strength than cross-section 1, since the effects of steel reinforcement corrosion are more significant for small bar diameters, as shown in Figure 4.

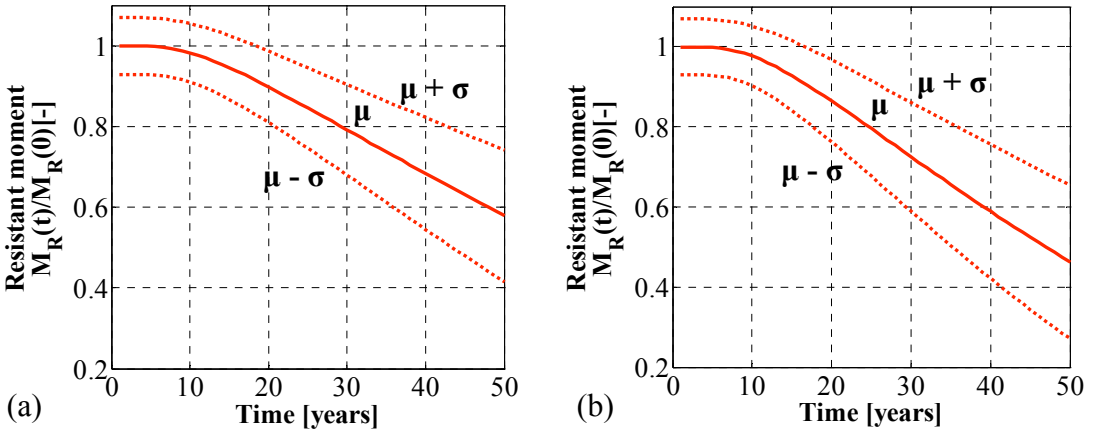


Figure 5. Time evolution of the resistant bending moment $M_R(t)$ of (a) cross-section 1 and (b) cross section 2 (Figure 1): mean μ (continuous line), and standard deviation σ from the mean (dotted lines).

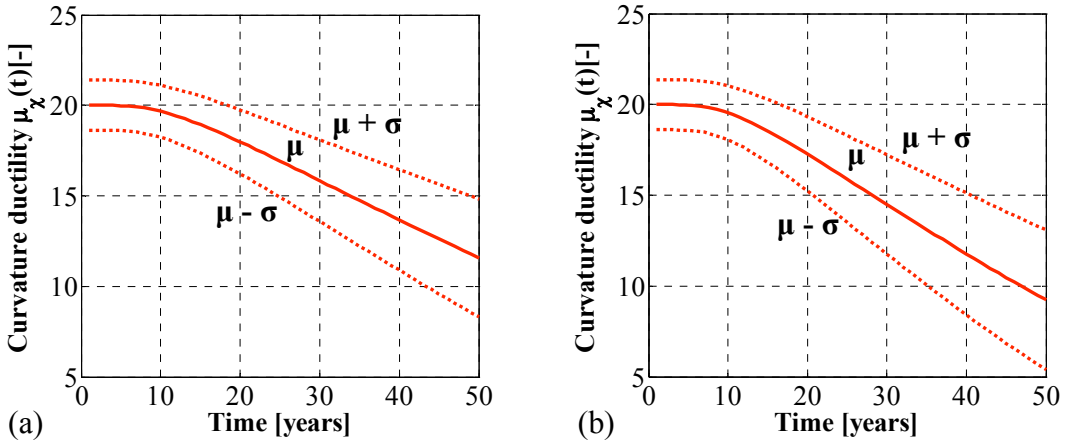


Figure 6. Time evolution of curvature ductility μ_χ of (a) cross-section 1 and (b) cross section 2 (Figure 1): mean μ (continuous line), and standard deviation σ from the mean (dotted lines).

LIFETIME SEISMIC PERFORMANCE OF CONCRETE FRAMES

Case study. The 2D three-story precast concrete frame shown in Figure 7 is considered (Biondini *et al.* 2011). The beams have span l = 8.0m and rectangular section 0.5×0.8m. The columns have inter-story height h = 4.0m. Two different cases are analyzed by considering the two column cross-sections shown in Figure 1. An axial load N_1 = 250kN, due to both dead and live loads, is applied at each story to the columns. Cast-in-situ moment resisting beam-to-column connections are adopted to emulate the structural behavior of monolithic frames. The connections are designed according to capacity design criteria, *i.e.* "strong column-weak beam", by assuming for beams a suitable over-strength ratio γ_c in terms of design resistant bending moments M_{Rd}:

$$\gamma_c = \frac{\left|M_{Rd}^{columns}\right|}{\left|M_{Rd}^{beams}\right|}$$

Two cases are investigated by assuming γ_c = 1.1 and γ_c = 1.3, as suggested by European seismic codes (CEN-EN 1998-1 2004) for structures with low ductility class and high ductility class, respectively. It is assumed that the lifetime material degradation affects the columns only, and that the chloride attack is on the external edge of the columns (Figure 1). The resistant bending moments of the beams are listed in Table 2.

The structure is modeled with elastic beam-type elements and with lumped inelastic rotational springs to simulate the non-linear behavior due to the formation of plastic hinges. For both columns and beams, a linear elastic element with inelastic rotational springs at the ends where formation of plastic hinges is expected, are adopted, as shown in Figure 7.

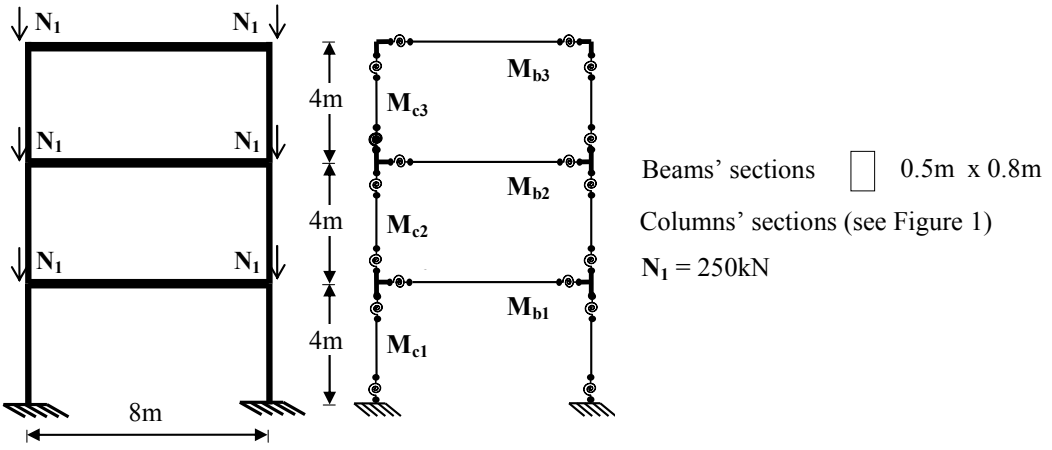


Figure 7. Modeling of the three-storey concrete frame.

Table 2. Resistant bending moments of the beams.

	M_{b1} [kNm]	M_{b2} [kNm]	M_{b3} [kNm]
Low ductility	1127.9	985.6	457.1
High ductility	954.4	834.0	386.8

Lifetime overstrength factor. Based on the reduction of column resistant bending moment $M_R(t)$ shown in Figure 5, the time evolution of the overstrength factor γ_c at the first floor is evaluated in probabilistic terms for both the low ductility and the high ductility frame (Figure 8). A change of collapse mechanism may occur for γ_c < 1, since the capacity design criterion of "strong column-weak beam" no longer holds. With reference to the mean values of the factor γ_c, for the low ductility frame a change of collapse mechanism may occur using both cross-section 1 and cross-section 2 after about 20-30 years of lifetime. For the high ductility frame, the condition γ_c < 1 occurs for cross section 2 only after about 45 years of lifetime.

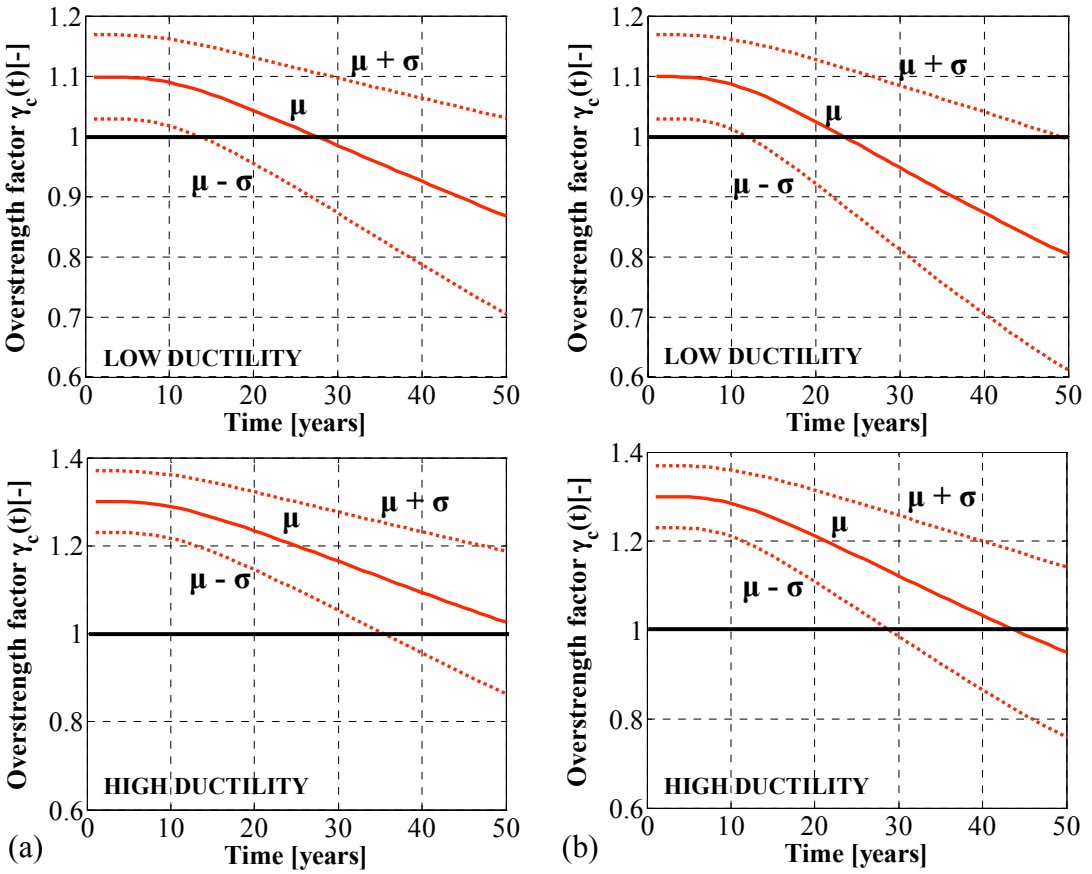


Figure 8. Time evolution of overstrength factor γ_c for low ductility and high ductility frame with (a) cross-section 1 and (b) cross-section 2: mean (continuous line) and one standard deviation from the mean (dotted lines).

Static nonlinear analysis. The lifetime seismic performance of the structural frame system shown in Figure 7 is investigated by static nonlinear analysis. The time-variant performance of the critical cross-sections of members in terms of bending moment versus curvature relationships is implemented in a structural model based on lumped plasticity beam elements (Carr 2006). The analysis is carried out under a linear distribution of horizontal forces by increasing the intensity of the applied loads up to failure. The results obtained for the low ductility frame with column cross-section 1 are discussed in the following. Figure 9 shows these results in terms of total base shear F versus top displacement Δ. A significant reduction of the total base shear strength is obtained over the structural lifetime. Moreover, a significant reduction of the ultimate displacement and hence of the displacement ductility is obtained over time. In fact, as expected, due to the reduction of bending moment capacity of the columns, a change of collapse mechanism occurs moving from a typical "beam sway" to a "column sway" mechanism.

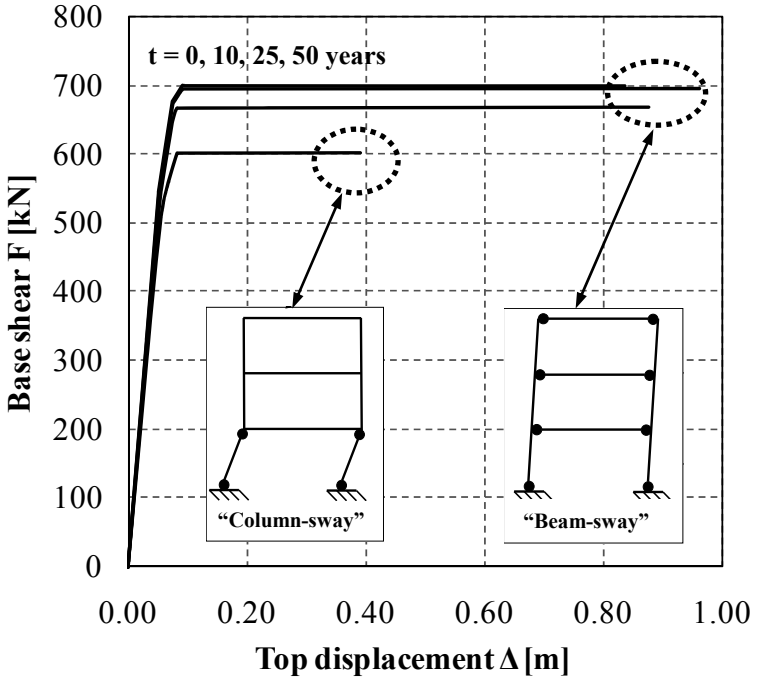


Figure 9. Time evolution of base shear *F* vs. top displacement *Δ*.

Dynamic nonlinear analysis. Time history dynamic nonlinear analyses are carried out for the low ductility frame with column cross-section 1 using the ensemble of ten earthquake records listed in Table 3 (Pampanin *et al.* 2002). These records are scaled to match Eurocode 8 design response spectrum for soil class B and peak ground acceleration PGA = 0.54*g* (CEN-EN 1998-1 2004). Figure 10 shows the lifetime evolution of the mean values of the maximum story displacements and inter-story drifts. The mean values of residual displacements and inter-story drifts after the seismic excitations are listed in Table 4. It is noted that the stiffness and strength reduction at cross-sectional leads to an increase of displacements and drifts over time. This could affects the seismic performance at the damage limit state, with damage of the non-structural elements. On the contrary, story shear forces decrease over time due to the reduced strength of columns, as shown in Figure 11.

Table 3. Characteristics of seismic records (Pampanin *et al.* 2002).

Earthquake record	Year	Station	Soil Type	Scaling Factor	Scaled PGA [g]
Loma Prieta	1989	Hollister Diff. Array	D	2.0	0.54
Loma Prieta	1989	Gilroy Array #7	D	3.0	0.68
Landers	1992	Desert Hot Springs	C	4.1	0.62
Landers	1992	Yermo Fire Station	D	3.3	0.50
Cape Mendocino	1992	Rio Dell Overpass-FF	C	1.8	0.69
Superstition Hills	1987	Plaster City	D	3.3	0.61
Northridge	1994	Canoga Park-Topanga Can	D	1.8	0.64
Northridge	1994	Beverly Hills 14145 Mulhol	C	1.4	0.56
Northridge	1994	N Holliwood-Coldwater Can	C	2.6	0.69
Northridge	1994	Sunland-Mt. Gleason Ave	C	3.3	0.52

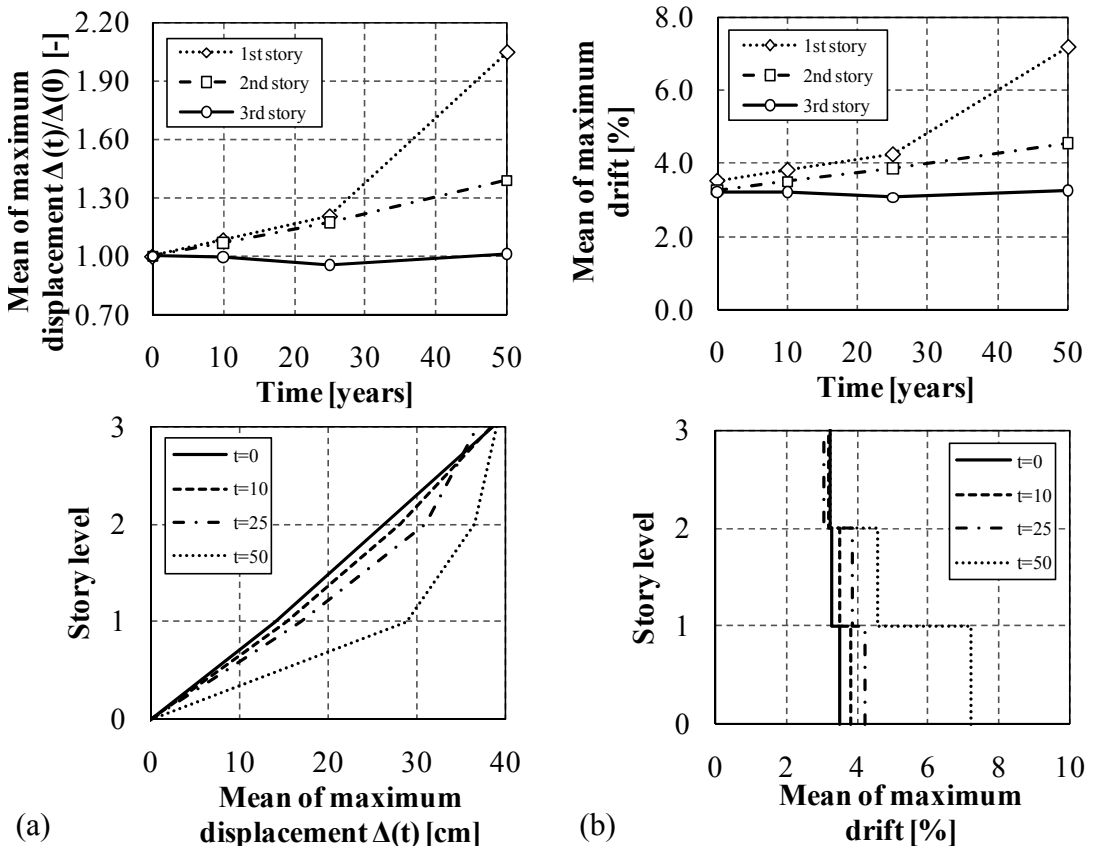


Figure 10. Time evolution of mean values of the (a) maximum displacements of stories and (b) inter-story drift.

Table 4. Mean of residual displacements and inter-story drifts.

Time [years]	Residual displacement [mm]			Residual inter-story drift [%]		
	1st story	2nd story	3rd story	1st story	2nd story	3rd story
***t* = 0**	10	34	90	0.2	0.4	0.7
***t* = 10**	11	34	75	0.3	0.4	0.6
***t* = 25**	20	49	81	0.5	0.6	0.7
***t* = 50**	152	137	134	3.8	1.7	1.1

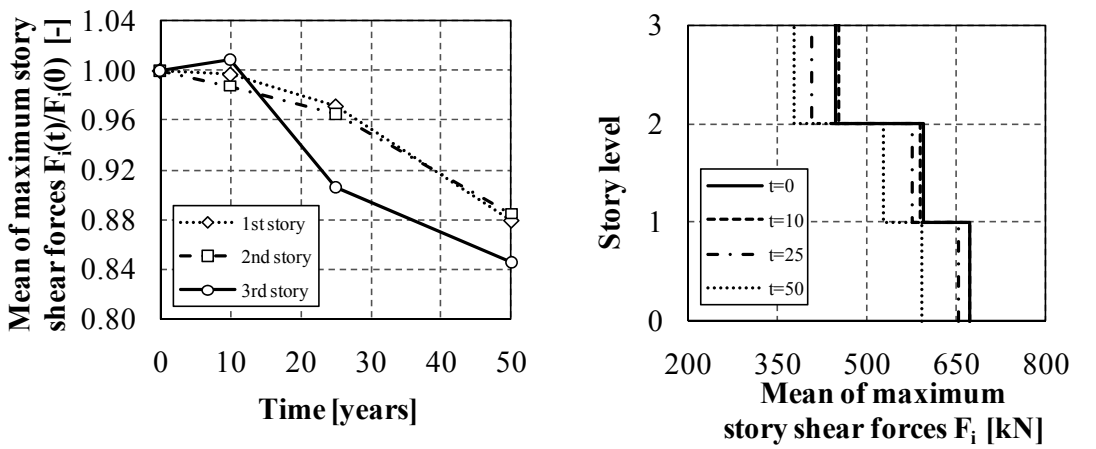


Figure 11. Time evolution of the mean values of the maximum shear forces F_i at each story *i*.

CONCLUSIONS

The effects of chloride induced corrosion of steel reinforcement on the lifetime seismic performance of concrete structures have been investigated. It has been shown that concrete members having the same initial performance and durability threshold parameters, such as concrete cover and quality of the materials, may exhibit different strength and ductility over time depending on geometrical characteristics of the cross-section. Moreover, it has been found that the reduction of stiffness, strength and ductility of concrete members involves a deterioration of the seismic performance of the structural system, with increasing displacement/drift demand and reduction of the seismic capacity over time. These results confirm the importance to take the interaction between seismic and corrosion hazards into account and emphasize the need of a life-cycle approach to seismic assessment of existing structures and seismic design of new structures.

REFERENCES

Akiyama, M., Frangopol, D.M. (2010). On life-cycle reliability under earthquake excitations of corroded reinforced concrete structures. *Second International Symposium on Life-Cycle Civil Engineering (IALCCE2010)*, Taipei, Taiwan, October 27-31, 2010.

Akiyama, M., Matsuzaki, M., Dang, D.H., Suzuki, M. (2011). Reliability-based capacity design for reinforced concrete bridge structures, *Structure and Infrastructure Engineering*, DOI: 10.1080/15732479.2010.507707.

Berto, L., Vitaliani, R., Saetta, A., Simioni, P. (2009). Seismic assessment of existing RC structures affected by degradation phenomena. *Structural Safety*, **31**: 284-297.

Bertolini, L., Elsener, B., Pedeferri, P., Polder, R. (2003). *Corrosion of Steel in Concrete – Prevention, Diagnosis, Repair*. Wiley VCH, Weinheim, Germany.

Biondini, F., Bontempi, F., Frangopol, D.M., and Malerba, P.G. (2004). Cellular automata approach to durability analysis of concrete structures in aggressive environments. Journal of Structural Engineering, ASCE, **130**(11): 1724-1737.

Biondini, F., Frangopol, D.M. (2008). Probabilistic limit analysis and lifetime prediction of concrete structures. *Structure and Infrastructure Engineering*, **4**(5): 399-412.

Biondini, F., Palermo, A., Toniolo, G. (2008). Lifetime Seismic Performance of Precast Reinforced Concrete Industrial Buildings, *First International Symposium on Life-Cycle Structural Engineering* (*IALCCE'08*), Varenna, Lake Como, June 10-14, 2008. In *Life-Cycle Civil Engineering*, Biondini F. and Frangopol D.M. (Eds.), CRC Press, 2008.

Biondini, F., Palermo, A., Toniolo, G. (2011). Seismic performance of concrete structures exposed to corrosion: case studies of low-rise precast buildings. *Structure and Infrastructure Engineering*, Vol. **7**, Nos. 1–2, January-February 2011, 109-119.

Biondini F., Frangopol D.M. (2010). Life-Cycle Performance of Reinforced Concrete Structures Exposed to Aggressive Agents: Design Issues, *SEI-ASCE Structures Congress 2010*, Orlando, FL, USA, May 29-15, 2010.

Carr, A.J. (2006). *RUAUMOKO Program for Inelastic Dynamic Analysis*. Department of Civil Engineering, University of Canterbury, Christchurch, New Zealand.

CEB (1995). *Model Code for Seismic Design of Concrete Structures*, Bulletin **165**.

CEB (1992). *Durable Concrete Structures − Design Guide*, Bulletin **183**.

CEN-EN 1998-1, 2004. *Eurocode 8: Design of Structures for Earthquake Resistance. Part 1: General rules, seismic actions and rules for buildings*. European Committee for Standardization, Brussels.

Enright, M.P., Frangopol, D.M. (1998). Probabilistic analysis of resistance degradation of reinforced concrete bridge beams under corrosion. *Engineering Structures*, **20**(11): 960-971.

fib (2006). *Model Code for Service Life Design*. Bulletin **34**.

Liu, T., Weyers, R.W. (1998). Modeling the dynamic corrosion process in chloride contaminated structures. *Cement and Concrete Research*, **28**(3): 365-379.

Pampanin, S., Christopoulos, C. and Priestley, M.J.N. (2002). *Residual Deformations in the Performance-Based Seismic Assessment of Frame Structures*. IUSS Press, Pavia, Italy.

Paulay, T., Priestley, M.J.N. (1992). *Seismic Design of Reinforced Concrete and Masonry Buildings*. John Wiley & Sons.

Rao, A.S., Lepech, M.D., Kiremidjian A.S., Sun, X.Y. (2010). Time varying risk modeling of deteriorating bridge infrastructure for sustainable infrastructure design. *5th International Conference on Bridge Maintenance, Safety and Management (IABMAS2010)*, Philadelphia, PY, USA, July 11-15, 2010.

Thoft-Christensen, P. (1998). Assessment of the reliability profiles for concrete bridges. *Engineering Structures*, **20**(11): 1004-1009.

The Role of Critical Infrastructure in Community Resilience to Disasters

Scott B. Miles, Ph.D.[1]

[1]Resilience Institute, Department of Environmental Studies, Western Washington University, 516 High St, MS 9085 Bellingham, WA 98225. scott.miles@wwu.edu

ABSTRACT

This paper issues a call to improve the conceptual underpinnings of community resilience to disasters as it relates to critical infrastructure. It is argued that, broadly, infrastructure is the combination of both capital and services. Loss and recovery, and thus resilience, of infrastructure do not make practical sense without consideration of both. Specifically, infrastructure is characterized by its relationship to other infrastructure, agents, possible disruptions, possible interventions, jurisdictions and markets. Based on this and previous development work related to the resilience simulation model ResilUS, the beginnings of a new conceptual model are proposed. The comprehensive nature of the model suggests it is appropriate for planning purposes. The conceptual model provides opportunities for advancing ResilUS, specifically, and infrastructure and community resilience research and planning broadly. It facilitates the creation of a database schema for infrastructure loss and restoration and its impact on indicators of community resilience. Population of this schema will push understanding of community resilience and facilitate the development of better tools for supporting resilience planning.

INTRODUCTION

While resilience is still a contested concept, particularly related to communities and disasters, the contestation suggests perceived utility by a wide range of practitioners and scholars. There are many definitions of resilience. However, whether the topic is psychology, physics, engineering, or disasters, there is essential agreement around the capacity to handle and bounce back from stress – anyhow each of those goals are specifically defined or achieved. For community resilience to disasters (or disruptions in general), critical infrastructure resilience, specifically, is a core issue and arguably, a required capacity for the broader goal. Infrastructure, it is argued here, is the combination of both capitals (physical assets) and services derived from those capitals. Critical infrastructure resilience to disasters has gained considerable attention recently, but the conceptual models of infrastructure, resilience to disasters, and the connection between the two are underdeveloped. Without more robust conceptual models, empirical research, computational modeling, and community resilience capacity building is hindered. As an aside, the debate of what infrastructure is "critical" is not a focus of this paper, though is touched on briefly, and so the adjective is not used further.

Many conceptual models of infrastructure resilience, of the few specific ones in the literature, take a narrow focus. Often the focus is on structural, technical or functional aspects of the system. In doing so, the concept in many instances won't match peoples' needs or expectation for performance of infrastructure in response to disruption as they relate to their livelihoods and well being. Few are likely to consider, for example, that disrupted water infrastructure has been restored if the ruptured pipes are repaired but no potable water comes out of the tap. A telephone company will not bounce back from severed lines, if there is not enough demand for their service after repairs are made. If collapsed transmission towers are replaced but trained SCADA operators are not available to manage electrical distribution, customers probably won't consider their electricity provider as having recovered. A bridge damaged by a particular seismic intensity and built back to a lower seismic design load wouldn't be perceived as resilient to the same or greater hazard by engineers and planners. A final example might be a jurisdiction that ignores population growth needs for increased wastewater treatment capacity or redundancy, resulting in untreated discharge during a large storm event.

These contrived examples intimate that infrastructure and community resilience are influenced, and, as argued in this paper, specifically defined by a wide range of elements. These elements include at minimum the following: 1) the capital it relies on, 2) the services it is expected to provide, 3) the actors involved in its operation and management, 4) the disruptions it is designed for, 5) the resilience interventions that are possible, 6) demand from markets for it, and 7) the capacity of groups with authority over or responsibility for it. By developing a broader and deeper conception of infrastructure a wider range of community resilience interventions are possible.

The paper continues with a description of a conceptual model developed in part by the author to provide a point of departure for this call for the development of better conceptual models. The conceptual model provided the foundations for developing the community resilience simulation model ResilUS. The third section describes a greatly expanded conceptual model based on the ResilUS foundations as an artifact for further discussion and development. The paper concludes by redoubling the call for improved conceptual models of critical infrastructure resilience and a suggestion for future work on the conceptual model presented here, and more broadly.

RESILUS CONCEPTUAL MODEL

The work described here builds upon the conceptual foundations of ResilUS, a prototype simulation model of community resilience to disasters (Miles and Chang, 2011; Miles and Chang, 2007; Miles and Chang, 2006; Miles and Chang, 2003). ResilUS has two distinct versions, with evolution of both the conceptual and computational models. The complete specification (including citations, which are left out due to space constraints) of the first version is detailed in Miles and Chang (2004), the second in Miles and Chang (2006). The proposed conceptual model described in this paper is thus the beginning of a third evolution. It builds on the previous version, while integrating other contributions from the literature. The second version of the ResilUS conceptual model is described briefly to provide contrast with the proposed model and insight into possible elements that can be carried over.

ResilUS represents socio-economic agents – households and businesses – within particular neighborhoods, which are contained within a broader community (Figure 1). ResilUS represents damage and recovery associated with a hazard event to three elements of community capital – economic, human (or, for businesses, individual), and technological, which is limited to buildings and lifelines – transportation network, electrical network, water network and critical facilities.

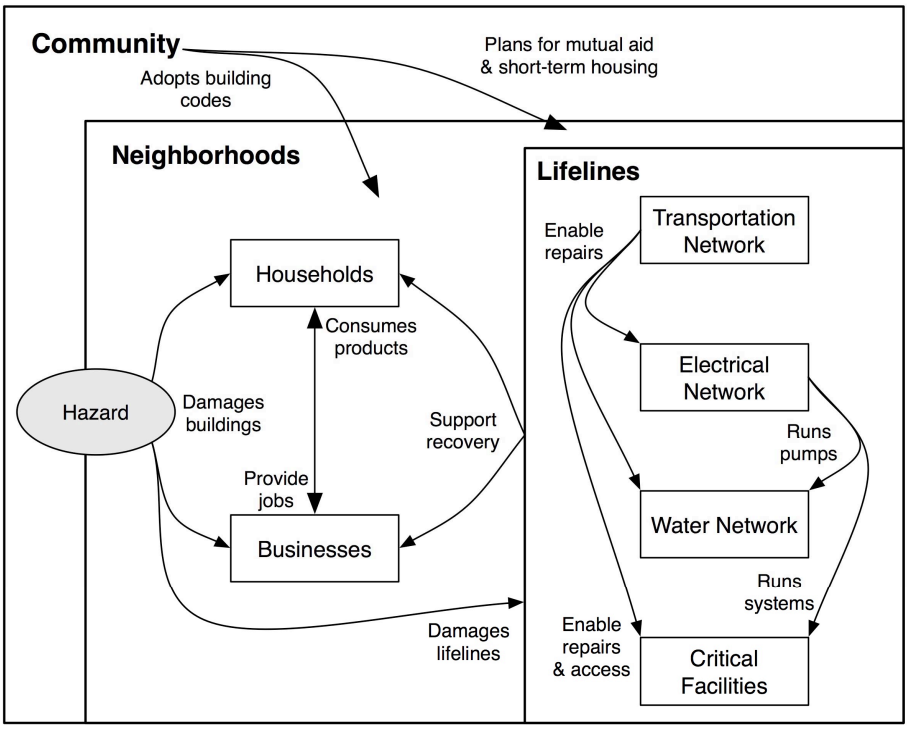


Figure 1. Simplified conceptual model of ResilUS.

ResilUS relies on two generic indicators of resilience – 1) ability to perform and 2) opportunity to perform associated with each hierarchical scale (community, neighborhood, agent). As stated above, the essence of resilience is avoiding loss and achieving recovery resulting from a disruption or hazard event. Figure 2 illustrates these two components of resilience. Resilience, of agents, infrastructure, or communities, is measured in terms of some indicator of performance (e.g., level of service, building stock, income, or gross regional product). A community's capacity to minimize the initial loss is referred to as robustness (Bruneau et al., 2003). As indicated in Figure 2, rapidity – the capacity to recover rapidly – comprises a second important metric of resilience (Bruneau et al., 2003).

Without a disaster, a resilience indicator will have some "normal" path with respect to time (Figure 2, Path A). In the event of a hazard event, the recovery time-path makes a great difference in accumulated loss, cascading effects, and, thus, well being. The indicator level may exceed pre-disruption performance (Path B) due to interventions such as effective recovery planning, mutual aid, or building back better. The indicator level may return to pre-disruption performance (Path C) or permanent losses may be suffered, resulting in a lower equilibrium (Path D). Most importantly, Figure 2 raises

the issue of how recovery is defined. Recovery can be defined based on a comparison between indicator time-paths "with" and "without" disaster or between "before" and "after." The former definition requires modeling what would have happened to the resilience indicator without the disaster; thus, the latter definition is simpler conceptually and computationally. In reality, community recovery is typically characterized by qualitative changes, adaptation, and restructuring, so that conditions don't return to pre-disaster states or merge with a no-disaster time-path. Currently, ResilUS models recovery as a return to pre-disaster conditions or levels (Path C).

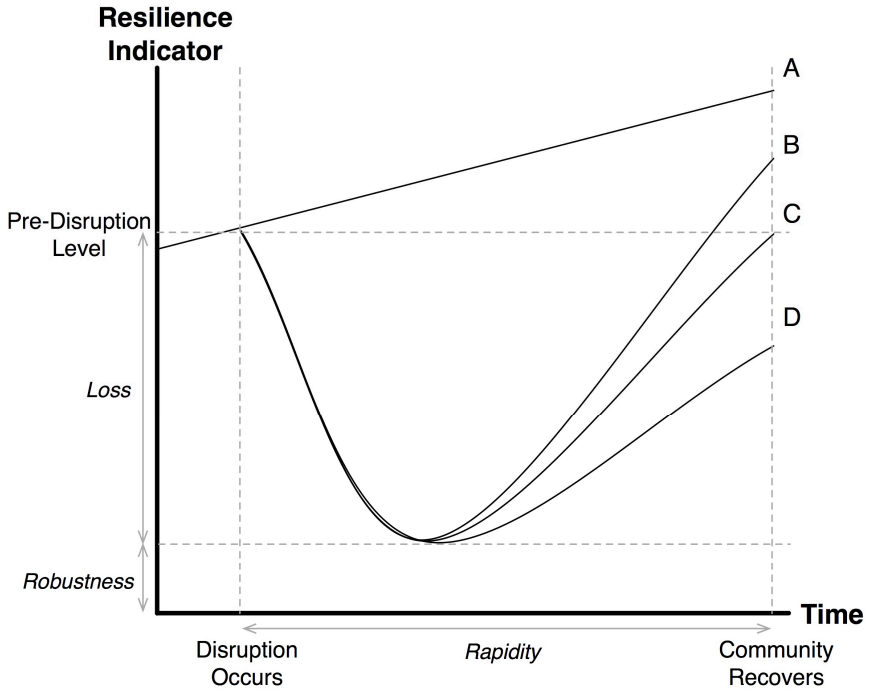


Figure 2. Schematic of community disaster loss and recovery – resilience.

The indicator of the ability to perform for households in ResilUS is represented by household health. Among other variables, health is directly influenced by availability of critical facilities and serviceability of shelter (either their own residence or short-term housing). Shelter serviceability is influenced by residence reconstruction and availability of lifeline services. Reconstruction time is influenced by the size (single-family vs. multi-family) of the respective building in addition to the construction capacity in the community. Reconstruction can only begin after inspections have been completed in the neighborhood, which is influenced by the quality of the preparedness plan, the recovery capacity of the community, and the recovery priority given to the neighborhood. Health influences a household's ability to pay off any incurred debt. ResilUS represents whether a household owns their residence. If they do not, they do not incur debt with respect to any reconstruction loans. The opportunity to perform is represented by employment level in their neighborhood and broader community. Employment influences a household's opportunity to pay off any

incurred debt. Debt is one of the main influences of whether a household is forced to leave their residence, neighborhood or community.

For businesses, the ability to perform is represented by a businesses' capacity to be productive (not necessarily economic productivity or throughput). The service level of a business's physical facility influences this capacity, which is in turn influenced by a combination of reconstruction and service restoration. Reconstruction time is influenced by the complexity or size of the respective facility, in addition to the construction capacity in the community. Again, reconstruction can only begin after inspections have been completed. The ability to perform is also influenced by community-wide health levels of households, the transportation network reconstruction level within the neighborhood, if the business's sector is locally oriented, or throughout the community if the sector is export-oriented. A business's ability to perform influences its ability to pay down incurred debt. Businesses do not incur debt from reconstruction loans if they do not own their facility. The opportunity to perform is represented by the demand for a business's product or services. Recovery of demand is influenced by some proportion of household debt within the respective neighborhood or the entire community, depending on the business's size. Demand influences a business's opportunity to pay down incurred debt, which in turn influences whether the business fails.

Whether an agent (household or business) is able to reconstruct their residence or facility is influenced by their financial resources – the sum of insurance, reconstruction loans, disaster aid in the form of grants, and pre-event savings. If the agent owns their building or facility, the maximum level of financial resources is implicitly related to the value of the building or facility.

Lifelines (infrastructure) are represented as a set of components (technological capital), with each component having attributes of construction age, maintenance level, component type, and degree of structural mitigation. Currently the model conceptually equates service restoration and component reconstruction. The time in which a particular lifeline component is reconstructed is influenced by the particular type of component (e.g., transformer vs. power line) and the infrastructure resources available in the neighborhood. These resources are influenced by the construction capacity in the community, quality of the preparedness plan, quality of mutual aid agreement the recovery capacity of the community, and the neighborhood's priority.

NEW CONCEPTUAL MODEL OF INFRASTRUCTURE AND COMMUNITY RESILIENCE

The previous section's description of the current conceptual model of ResilUS provides a useful starting point for developing a more encompassing, detailed, and integrated representation of the linkages between infrastructure and community resilience associated with disasters and other disruptions. While the proposed conceptual model can serve as a blueprint for improvement of ResilUS, its ultimate value is in spurring additional contributions to it, implementations of it towards an array of effective tools for fostering resilience, and alternatives to it. The proposed model is not fully integrated with many details of the ResilUS model. The contrasts

between the two models are clear, so much as there are conceived, but whether previous elements are carried over is far from settled and is not specifically described.

Figure 3 provides an overview of the proposed conceptual model. It describes general relationships within a community related to four components of resilience – community capital, services, agent well being, and community identity. The model starts on the left depicting the means and progresses to the right as evolving ends. In other words, infrastructure (the combination of capitals and services) is the means to the ends of agent well being and community identity (Monstadt, 2009; Little, 1999).

Capital refers to a stock of assets used to create or obtain additional assets and derive services. This concept applies to many types of assets including financial, ecological and social (Putnam, 2001; Daly, 1997). Community capital refers to any asset, whether corporeal or not, that a community requires for well being and identity (Fey et al., 2006). The classification and distinction of community capital vary in the literature. Here, six types of community capital are proposed for representing community resilience: human, social economic, political, natural, and technological.

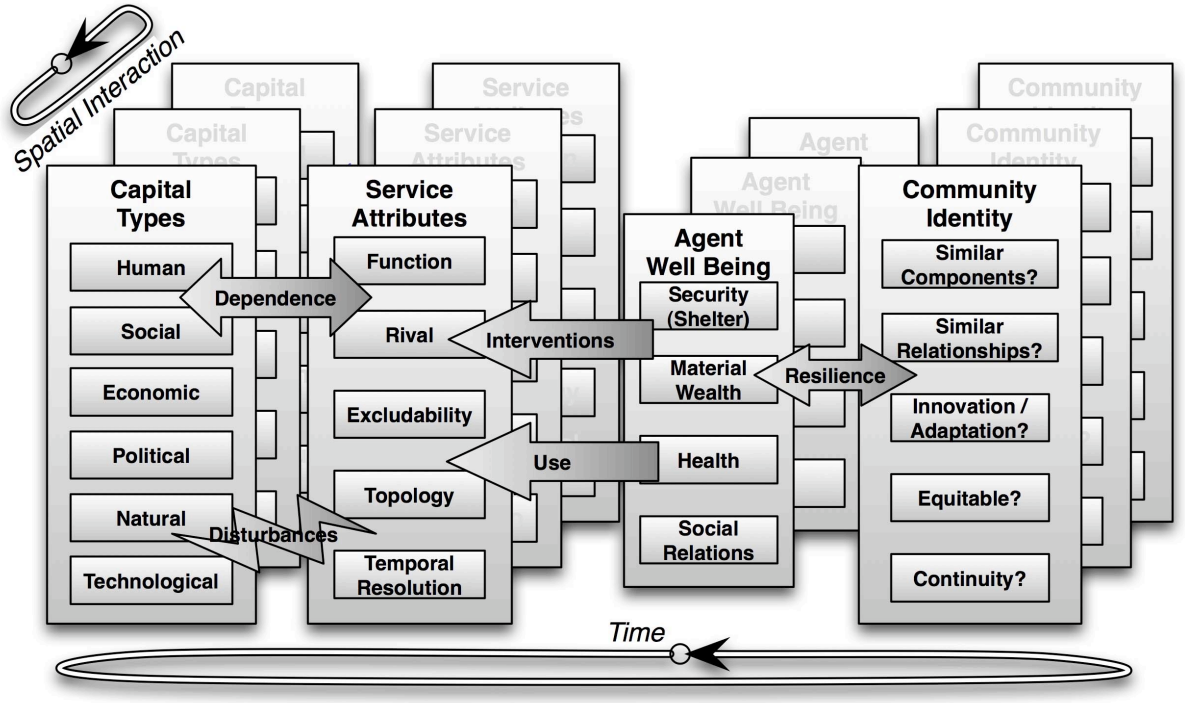


Figure 3. Overview of CRI conceptual model.

Well being and capital are linked by a complex set of relationships with mediating services, which produce waste (Costanza, 2000). The most significant relationships between capitals and community resilience are associated with provision and use of services, and by extension the avoidance of and recovery from disruption of these services. Services are measurable flows or perishable goods provided by or consumed by an agent. Social networks are a set of relationships of varying degree and characteristic to other agents, including markets for businesses. Different services require different types of capital (Olewiler, 2006; Millenium Assessment, 2005;

Olewiler, 2004; de Groot et al., 2002; Costanza et al., 1997). Services have attributes of rivalrousness and excludability, which influence the degree to which they are available to agents (Fisher et al., 2009; Frischman, 2005). Services have a distance from an agent, as well as a topological connection (or not), based on the location of the related capitals and agents (Fisher et al., 2009). Disturbance of services occur in various ways, primarily associated with damage to or loss of some capital (or service requiring that capital) (Beier et al., 2008). Disturbances are events with spatially varying intensity that have the potential to damage capital and/or disrupt services. Various interventions can be taken to protect, maintain, restore and substitute services, though this might manifest at the capital level. Interventions are pre-defined actions, plans, or protocols enacted by an agent. Services that cannot be substituted for are critical services; the capitals required for those services are critical capitals; the pairing of critical services and capital is critical infrastructure (Brand, 2009).

Well-being is associated with agents – individuals to any type of group or organizations. Capitals are accountable stocks that are managed, built, spent, or utilized by an agent. Agents are actors that have some relative degree of power at any scale, for example to use services, provide services, or take interventions. The constituents of well being are material wealth, health, social relations, and freedom (Leemans, 2009). The concept of freedom is provisionally considered out of the scope of this model. Well-being for agents is derived through a complex set of relationships with infrastructure and other agents within their community.

A community is any aggregation of agents that can refer to themselves as "members." This means that community is about identity and that a resilient community is one that can maintain some level of identity with respect to member agents (Pendall et al., 2007; Gillson, 2009). Different sets of conditions (e.g., different locations or topological connections) are associated with different possible states or thresholds between states. Identity is associated with a lack of change or similarity in components and relationships required to derive well being. This can also be extended to issues of equity and continuity. This all exists and occurs within and throughout time and space. It may take time for capital damage to result in any change in community identity; changes in one neighborhood or community may have effects in another neighborhood or community, the magnitude of which likely attenuates with increasing distance and scale.

There are seven proposed object classes (defined elements with attributes and functional capacity) for the conceptual model: agents, capitals, disturbances, interventions, jurisdictions, services, and social networks. These are fundamental, at minimum, to characterize infrastructure and community resilience. The relationships between these seven object classes are illustrated in Figure 4.

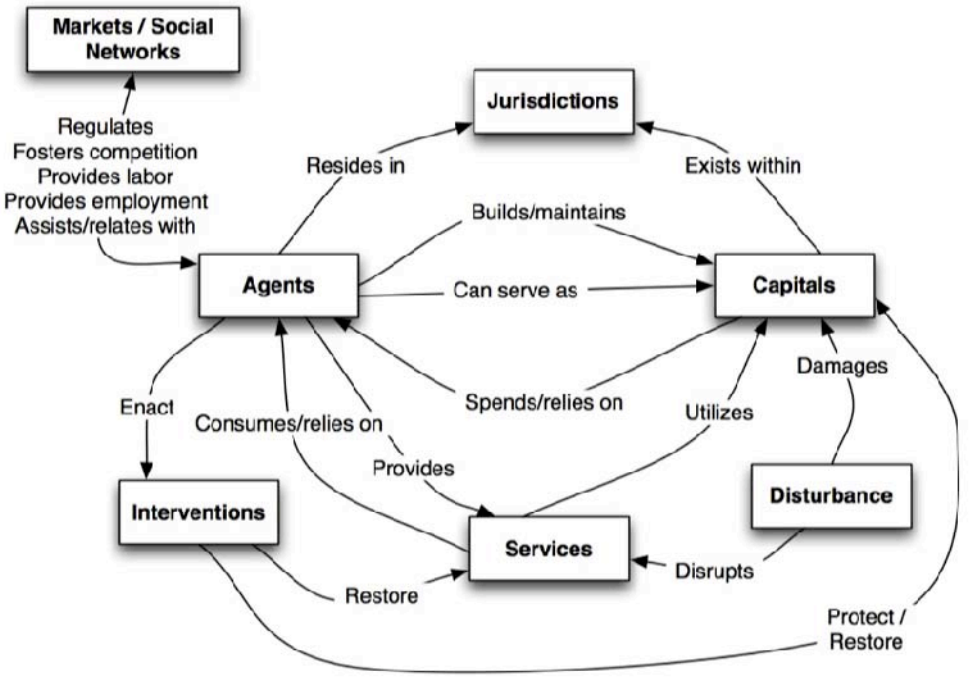


Figure 4. Functional relationships between proposed objects in a new conceptual model of community resilience.

Each object class shares a common set of attributes and actions (functions), which have not been fully specified to date, but will have some similarities with the current ResilUS conceptual model. Sub-classes of each have additional attributes, attribute values, and/or actions that make them distinct (e.g., pipe network vs. fiber optic network). An agent and its resilience is defined by 1) jurisdiction its required capitals and services are contained by, 2) the capital it has or relies on, 3) the services it provides, 4) the services it uses, 5) the markets that demand its services, 6) the possible disturbance it is vulnerable to, and 7) the interventions it can take and how they are implemented. (Jurisdictions are an entity associated with one or more boundaries that governs and/or contains agents.) Similarly, the universe of possible infrastructure types (sub-classes) and its resilience is defined by the logical combinations of the possible jurisdictions, capitals, services, agents, disturbances, and interactions. This topological definition is true for the other objects, as well.

Figure 5 illustrates how agents suffer loss and achieve recovery across both space and time, depending on the condition of community capital and the levels of services they depend on. Agents exist in some location at some point in time with some level of well being (attribute). Agent well being varies with time because of varying levels of required services, which in turn vary based on the conditions of necessary capitals .A disturbance event in a particular location (e.g., a neighborhood) can alter the agent's well being time-space-path because of service loss perhaps related capital damage. Service levels outside of the location are likely to be better, depending on scale effects and distance. This means that some agents may improve their well being by moving locations (either within the community or outside of the community), substituting services, or adapting to a state without those services.

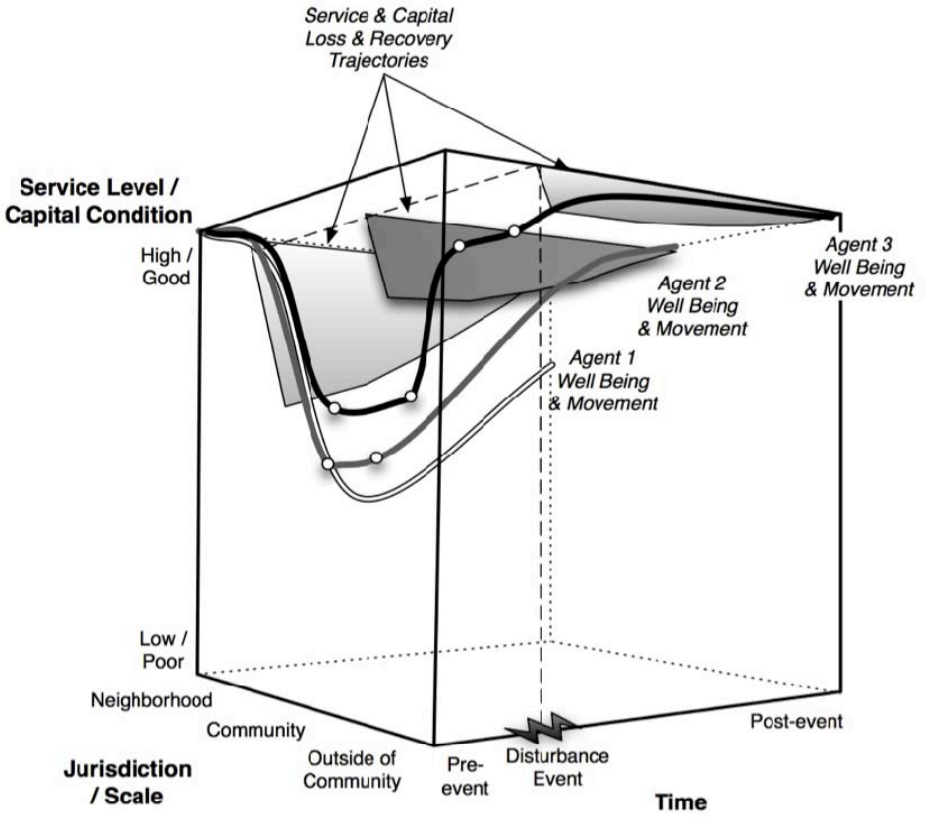


Figure 5. Agent resilience across space and time, as influenced by community capital condition and levels of services. The solid polygons represent resilience time-space-paths for infrastructure (capitals and services), while the lines represent time-space-paths for agents resilience. Points along the time-space-long indicate movement in space.

CONCLUSION

This paper has issued a call for other researchers and practitioners to improve the conceptual underpinnings of community resilience to disasters as this important topic specifically relates to infrastructure. It is argued that, broadly, infrastructure is the combination of both capital and services. Loss and recovery, and thus resilience, of infrastructure do not make practical sense without consideration of both. Infrastructure in the context of community resilience to disasters is defined by the relationship to other infrastructure, agents, possible disruptions, possible interventions, jurisdictions and markets. Based on this and previous work related to ResilUS, the beginnings of a new conceptual model have been proposed.

The comprehensive nature of ResiliUS and the proposed conceptual model make it appropriate for planning and awareness purposes. Many professionals – including emergency managers, but also extending to elected officials, urban planners, and the like – make decisions that intentionally or unintentionally influence community resilience. Yet many are unfamiliar with the research literature on factors that influence resilience. The conceptual model could be used to help educate these

stakeholders about empirical findings from disaster studies (e.g., what types of businesses have the most difficulty recovering from certain infrastructure disruption).

Such a conceptual model is daunting for implementation but can provide significant opportunities for advancing ResilUS, specifically, and infrastructure and community resilience research and planning more broadly. The conceptual model facilitates the creation of a database schema for infrastructure loss and restoration across time and space and its impact on indicators of community resilience. Population of this schema with time-series data collected from various size and types of events by researchers will push our empirical understanding. Analysis of such data will provide valuable insight regarding policies and plans to reduce infrastructure service disruption and the impacts of that loss on communities. It will also facilitate the development of new and better computational tools for supporting resilience planning.

ACKNOWLEDGEMENTS

The work described here is supported by National Science Foundation (Civil, Mechanical and Manufacturing Innovation Program) grant #0927356 and NOAA Award No. NA07NOS4730146. The past work and proposed ideas presented here have been influenced by conversations with many researchers including the following: Alexis Blue, Stephanie Chang, Ron Eguchi, Rebekah Green, CJ Huxford, John Pine, Chris Renschler, and Adam Rose. Many thanks go to them. Of course, the author takes sole responsibility for the content of this paper, any errors or omissions.

REFERENCES

Beier, C.M., Patterson, T.M., Chapin, F. S. (2008) "Ecosystem services and emergent vulnerability in managed ecosystems: A geospatial decision-support tool." *Ecosystems,* 11(6) 923-938.

Brand, F. (2009) "Critical natural capital revisited: Ecological resilience and sustainable development" *Ecological Economics,* 68(3) 605-612.

Bruneau, M., Chang, S.E., Eguchi, R.T., Lee, G.C., O'Rourke, T.D., Reinhorn, A.M., Shinozuka, M., Tierney, K., Wallace, W.A., and von Winterfeldt, D., (2003) "A framework to quantitatively assess and enhance the seismic resilience of communities" *Earthquake Spectra*, 19(4) 733-752.

Costanza, R. (2000) "Social goals and the valuation of ecosystem services" *Ecosystems*, 3(1) 4-10.

Costanza, R. et al. (1997) "The value of the world's ecosystem services and natural capital" *Nature* 387(6630) 253-260.

Daly, H.E. (1997) Beyond Growth. Beacon Press, Boston, MA.

Fisher, B., Turner, R., Morling, P. (2009) "Defining and classifying ecosystem services for decision making" *Ecological Economics,* 68(3) 643-653.

Fey, S., Bregendahl, C. and Flora, C. (2006) "The measurement of community capitals through research" *Online Journal of Rural Research & Policy,* 1, 1-28.

Frischmann, B.M. (2005) "An economic theory of infrastructure and sustainable

infrastructure commons" *Minnesota Law Review,* 89(4) 917–1030.

Gillson, L. (2009) "Landscapes in time and space" *Landscape Ecology,* 24(2) 149-155.

de Groot, R.S., Wilson, M.A., Boumans, R.M.J. (2002) "A typology for the classification, description and valuation of ecosystem functions, goods and services" *Ecological Economics,* 41(3) 393-408.

Leemans, R. (2009) The Millennium Ecosystem Assessment: Securing Interactions between Ecosystems, Ecosystem Services and Human Well-being. Chapter 3: Facing Global Environmental Change, Hexagon Series on Human and Environmental Security and Peace Vol 4. Springer. 53-61.

Little, R.G. (1999) "Educating the infrastructure professional" *Public Works Management & Policy,* 4(2) 93-99.

Miles, S.B. and Chang, S.E. (2011) "ResilUS – A community disaster resilience model" *Journal of Cartography and GIS (CAGIS),* 37(5).

Miles, S.B. and Chang, S.E. (2006) "Modeling community recovery from earthquakes" *Earthquake Spectra,* 22(2) 439-458.

Miles, S. B. and Chang, S. E. (2007) A Simulation Model of Urban Disaster Recovery and Resilience: Implementation for the 1994 Northridge Earthquake, MCEER Technical Report MCEER-07-0014.

Miles, S.B. and Chang, S.E. (2003) Urban Disaster Recovery: A Framework and Simulation Model, MCEER Technical Report 03- 0005.

Monstadt, J. (2009) "Conceptualizing the political ecology of urban infrastructures: insights from technology and urban studies" *Environment and Planning A,* 41(8) 1924-1942

Millennium Ecosystem Assessment (2005) Ecosystems and Human Well-Being: Wetlands and Water Synthesis Synthesis. World Resources Institute, Washington, DC.

Olewiler, N. (2006) "Environmental sustainability for urban areas: The role of natural capital indicators" *Cities*, 23(3), 184-195.

Olewiler, N. (2004).The Value of Natural Capital in Settled Areas of Canada. Published by Ducks Unlimited Canada and the Nature Conservancy of Canada. 36 p.

Pendall, R., Foster, K.A. Cowell, M. (2007) Resilience and Regions: Building Understanding of the Metaphor. Working Paper for the Building Resilient Regions Network. Berkely Institute for Urban and Regional Development. 24 p.

Putnam, R. (2001) Bowling Alone: The Collapse and Revival of American Community, Simon and Schuster, New York.

Resilience Modeling and Simulation of Smart Grids

Min Ouyang[1], Leonardo Dueñas-Osorio[2]

[1]Postdoctoral Fellow, Department of Civil and Environmental Engineering, Rice University, 6100 Main Street, MS-318, TX 77005, United States; email: min.ouyang@rice.edu
[2]Assistant Professor, Department of Civil and Environmental Engineering, Rice University, 6100 Main Street, MS-318,TX 77005,United States; email: leonardo.duenas-osorio@rice.edu

ABSTRACT

This paper proposes a three-stage framework to analyze the smart grid resilience. In each stage, a series of resilience improvement strategies are introduced to realize the smart grids, and appropriate metrics are also identified and then combined to establish an annual resilience metric. Taking the power transmission grid in Harris County, Texas USA as case study, this paper establishes an original power grid model and several smart grid models to compare the effectiveness of resilience improvement strategies in different stages. Results show that the annual resilience of the smart grid with all three-stage improvements increases 0.035% compared to the original grid. Although the improvement is small in magnitude due to the high reliability of real power grids, it may save hundreds of millions of dollars. This framework can provide insights to design resilient smart infrastructure systems and retrofit present ones.

INTRODUCTION

Economic prosperity, national security, and public health and safety cannot be achieved without the continuous reliable operation of electric power grids. The concept of smart grid has been proposed to solve optimization, reliability and resilience problems existing in traditional grids (Roncero 2008; Pothamsetty and Malik 2009; Kothari et al. 2010; Garrity 2008; Suter and Werner 2009). The novel ideas and challenges in the realization of smart grids has attracted multi-disciplinary researchers and led to several technical and strategic studies in the past few years, including visions of the whole smart grid, from generation, to transmission and distribution, implementation and realization of smart grids, and applications of some specific technologies, such as energy storage and smart metering(National Energy Technology Laboratory 2008; Amin 2005; U. S. Department of Energy 2003; U. S. Department of Energy 2008; Lightner and Widergren 2010; Metke and Ekl 2010). Among these studies, there are few contributions on the resilience modeling and simulation of the smart grids, although resilience is an adequate property to describe power grid performance and quality of service under distinct operation conditions, and it synthesizes other concepts such as vulnerability, robustness, reliability, and recoverability.

Regarding the definitions of resilience, they vary by discipline and application. The ecologist Holling (1973) defined resilience at the system level as “a measure of the persistence of systems and of their ability to absorb change and disturbance and still maintain the same relationships between populations or state variables”. The U. S. Department of Homeland Security (2006) conceptualized resilience as “the capacity of an asset, system, or

network to maintain its function during or to recover from a terrorist attack or other incident". Also, the Multidisciplinary Center for Earthquake Engineering Research (MCEER) defined resilience as "the ability of the system to reduce the chances of shock, to absorb a shock if it occurs (abrupt reduction of performance) and to recover quickly after a shock (re-establish normal performance)" (Bruneau et al. 2003). In addition, Vugrin et al. (2010) proposed the definition of system resilience as "Given the occurrence of a particular disruptive event (or set of events), the resilience of a system to that event (or events) is the ability to efficiently reduce both the magnitude and duration of the deviation from targeted system performance levels". To sum up these definitions, resilience includes the aspects of resisting, absorbing and recovering from changing conditions.

To qualitatively or quantitatively analyze system resilience, researchers have proposed different methods. The MCEER proposed a conceptual framework to list three constituent features of a resilient system (Bruneau et al. 2003): low failure probability, low level of impacts, and high speed of recovery. Combining the MCEER's resilience metric, input-output models, and structural fragilities, Reed et al. (2009) introduced a simple methodology to evaluate engineering resilience and interdependency for subsystems of a multi-system networked infrastructure system under extreme natural hazard events. Other studies include Vugrin et al. (2010), who reasoned that system resilience should consider not only systemic impact which was defined as the difference between a targeted system performance level and an actual system performance following a disruptive event, but also the recovery cost.

Among these studies, Bruneau's works and Reed's works did not consider the aspect of recovery cost, and Vugrin's studies ignored the factor of "failure probability". In addition, they all defined the resilience under a specific disruptive event, which does not sufficiently reflect the ability of resisting changing conditions. Based on these existing definitions and studies on resilience, this paper introduces a three-stage resilience analysis framework, where resilience measures the ability of the system to resist, absorb and recover from one or many types of disruptive events, without aiming at a particular disturbance scenario.

The paper firstly introduces the three-stage resilience analysis framework. A series of resilience improvement strategies are proposed to realize smart grids. Then, taking the power transmission network in Harris County, Texas as an example, an original power grid model and several smart grid models are established to compute their resilience and compare the effectiveness of resilience improvement strategies in different stages. Finally, it offers the conclusions from this study and includes directions for future research.

THREE-STAGE RESILIENCE ANALYSIS FRRAMEWORK

This paper defines the resilience as the ability of the system to resist, absorb and recover from one or many types of disruptive events. To propose a framework for the resilience analysis, this section firstly introduces the system performance response process following a disruptive event, as shown in Figure 1. Under normal operation the system performance level is at 100%. However, when an initial failure occurs at point A, the damage propagates and the performance level drops to a certain value I, where 1-I is the maximum impact level. During or after damage propagation, an undesirable system state is detected and recovery resources are dispatched. After a period of recovery time, the system reaches a new steady state performance level at point B, which may be better or worse than its original state.

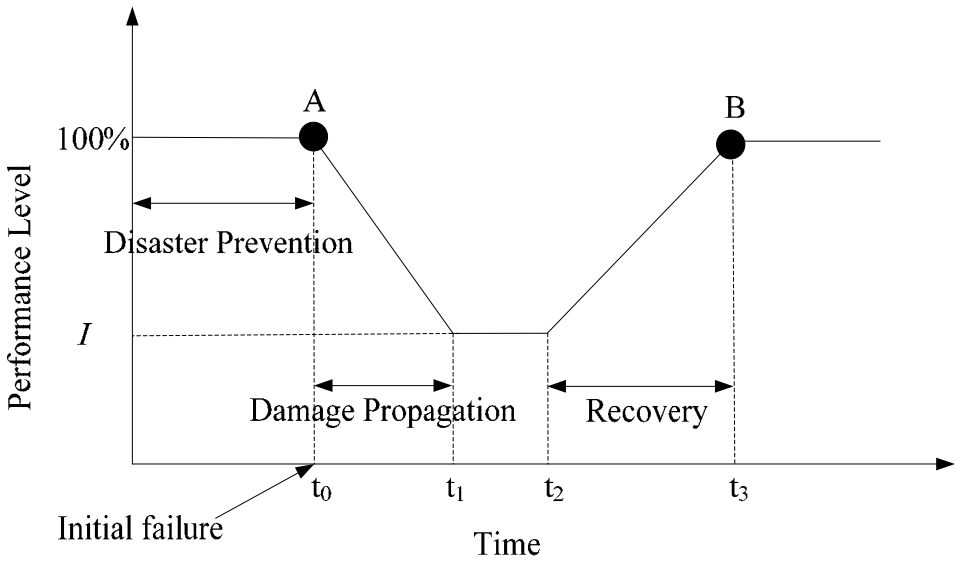


Figure 1: The performance response curve of a system following a disruptive event

Three stages

The performance response process in Figure 1 can be divided into three different stages. The first stage is the disaster prevention stage from the normal operation to the onset of initial failure; the second stage is the damage propagation process after the initial failures; the third stage is the recovery process during which resources are allocated to restore the system. These three stages can respectively reflect the ability of the system to resist, absorb and recover from disruptive events. This ability is just the definition of resilience. Hence, this paper explores resilience in three stages:

The first stage mainly reflects the system's resistant capacity. It is the ability of the system to prevent failures or reduce the initial failure scales (the number of initial failed components). In MCEER's seismic framework (Bruneau et al. 2003), as the seismic occurrence cannot be controlled, resistant capacity is only strengthened through reducing the component failure probabilities, which also means the reduction of initial failure scales. But under some hazard types such as human-related and organization-related failures, their occurrence frequencies can be reduced through various ways. The reduction of the expected hazard frequency also improves the resistant capacity. Hence, instead of the "failure probability" in MCEER's seismic framework, "expected hazard frequency" and "initial failure scales" together describe the resistant capacity and are taken as the resilience indexes in the first stage of the proposed framework.

The second stage mainly reflects the absorptive capacity. It is the degree to which the system can absorb the impact of initial failures and minimize the consequences by themselves. In this stage, the maximum impact level (the value 1-*I* in Figure 1) is used to measure the absorptive capacity and regarded as the resilience index in the second stage.

The third stage mainly reflects the restorative capacity. It is the ability of the system to be repaired quickly and effectively. Recovery time and recovery cost together represent the restoration capacity and characterize the resilience in the third stage.

Resilience improvement strategies

The three system capacities in different stages together determine the system resilience. To improve resilience, this paper identifies a series of strategies per each stage, which are also the ways to realize the smart grids. The main strategies are summarized in Table 1.

Table 1: Main strategies to realize the smart grid per each stage

Stage	Resilience Indexes	Resilience Improvement Strategies
First Stage	Expected hazard frequency; Initial failure scale;	• Identifying and hardening key components • Learning and Improving from previous accidents • Sensing and monitoring in real time and visualizing clearly • Improving decision support platform, staff training, cultures and organizations
Second Stage	Maximum Impact level;	• Adjusting infrastructure topology • Designing redundancy • Self-healing and self-adapting
Third Stage	Recovery time; Recovery cost;	• Improving situational awareness and decision support platform • Increasing available recovery resources • Establishing efficient communication channels and coordination

In the first stage, apart from the listed methods, there are still many other approaches to enhance the resistant capacity, such as adequate training, optimized decision support platforms and several other cultural and organizational factors, which can be all used to realize the smart grids. In the following case study, this paper only considers the random failures. To establish a smart grid model in the first stage, the new system is assumed to have reduced frequency of random failures due to using accident causation methods and adopting real-time monitoring for early warning.

In the second stage, there are also some other approaches to reduce the maximum impact level, but they vary per system type and tend to be more difficult to identify because they often rely upon the ingenuity of people faced with adversity (Vugrin et al. 2010). In the following case study, to establish a smart grid model in the second stage, the new system is supposed to have improved absorptive capacity due to the deployment of energy storages or emergency generators for a proportion of power load substations.

In the following case study, to establish a smart power grid model in the third stage, the new system is supposed to have improved recovery capacity due to improved situational awareness and availability of a decision support platform so that the recovery response is more rapid and the recovery sequences are optimized.

Resilience Metric

Combining the above resilience indexes, this subsection proposes a system-level metric to quantify the resilience. As the expected hazard frequency is one of the resilience indexes,

this paper introduces a time-dependent annual resilience metric. Under a specific disruptive event, the area between the actual performance curve and the targeted performance curve is affected by three resilience indexes: initial failure scales (affecting the maximum impact level 1-*I*), the maximum impact level (1-*I*) and the recovery time. So this paper takes this area (named "impact area" here) as a key parameter in the formulation of the resilience metric.

For a disruptive event with the hazard type h and initial hazard intensity $q^h \in [q_L^h, q_U^h]$, there is a probability distribution $\varphi^h(q^h)$ when events materialize at time t_0. With the amount of recovery resources R, denote the expected restoration curve (performance curve during the recovery process) by $P(t, q^h, R)$ and assume the system is totally restored at time $t_E(q^h, R)$. If the targeted performance curve during the recovery process is represented by $NP(t)$ and the expected hazard frequency is f^h, then the annual impact area (AIA) is expressed as follows:

$$AIA^h(R) = f^h \int_{q_L^h}^{q_U^h} \int_{t=t_0}^{t_E(q^h,R)} (P(t,q^h,R) - NP(t))\varphi(q^h)dtdq^h \tag{2-1}$$

The integral part of the equation (2-1) gives the expected impact area under a disruptive event with any possible intensity q^h, which when weighted by the expected frequency of the failure events f^h leads to the annual impact area. Then, the annual resilience (AR) metric is computed as follow:

$$AR^h(R) = \frac{\int_0^T NP(t)dt - AIA^h(R)}{\int_0^T NP(t)dt} \tag{2-2}$$

Normalizing the difference between the annual targeted performance area (the denominator) and the annual impact area leads to the annual resilience metric. T is the time interval of a year, and its specific value is determined by the unit of t in the performance curve. For example, if t is provided in a daily scale then T=365.

As equations (2-1) and (2-2) include the "recovery cost" (described by R), the expected hazard frequency (f^h) and the "impact area" (affected by the other three resilience indexes), the proposed resilience metric completely integrates the five resilience indexes in Table 1. Additionally, to obtain a global resilience metric under multiple hazard types, main hazard types should be identified so that the global resilience metric $GAR(R)$ is proposed as follows:

$$GAR(R) = \frac{\int_0^T NP(t)dt - \sum_{h=1}^{H} AIA^h(R)}{\int_0^T NP(t)dt} \tag{2-3}$$

Where H is the number of main hazard types. This paper only consider one type of hazards, so H=1 and the equations (2-2) and (2-3) are identical. However, if multiple hazards have been identified and modeled, the proposed framework can also calculate the global resilience according to equation (2-3).

CASE STUDY

This section takes the power transmission grid in Harris County, Texas USA as an

example to simulate its resilience and discuss its resilience improvements. The original power transmission system data is obtained from Platts (Platts 2009). Its geographical representation is shown in Figure 2, while the basic topological and geographical characteristics are illustrated in Table 2. The average degree aligns well with published values of 2.67 for the Western States power grid off the Rocky Mountains (Watts 2004).

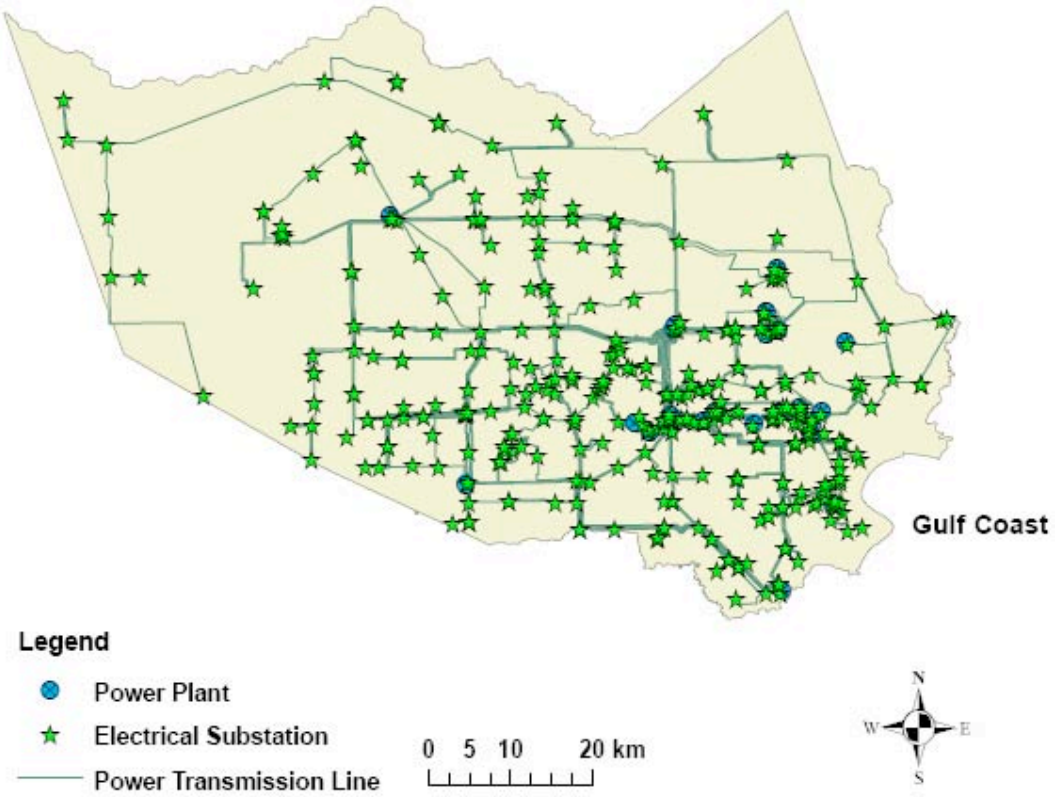


Figure 2: A geographical representation of the power transmission grid in Harris County, Texas

Table 2: Topological and geographical characteristics of the power transmission grid in Harris County, Texas

Number of nodes	Number of links	Average degree	Total edge length
417	551	2.64	2144.5km

Hazard modeling

To illustrate the proposed framework, this paper only considers random failures (h=1). To model random failures, available historical data are used to describe its frequency and the distribution of the hazard intensity (the number of initial failed components). Nationwide historical outage data includes failure records from all hazard types including some infrequent and high-consequences failures, such as hurricane, earthquake, which can cause extensive initial failures. However, due to their relative small frequency, they only slightly affect the distribution of the hazard intensity under random failures. In addition, this paper only considers forced or automatic outages because planned outages are known in advance.

An Institute of Electrical and Electronics Engineers (IEEE) survey of US and Canadian overhead transmission line outages for 230kV (Adler et al 1994) showed that the forced transmission line outage rate for 230kV was 1.25 per 100 kilometers-year (2.0 per 100 miles-year) averaged from 1965 to 1985. Among the 5 901 forced line outages, there were 3 692 (3 692/5 901=0.63) independent failure events and the number of *initial* outage lines in each event is well approximated by a power law with exponent -3.75 (Chen and McCalley 2005). Also, a particular data set recorded by a North American utility over a period of ten years showed that among 8 864 automatic line outages there were 5 227 (5 227/8 864=0.59) independent events, while the number of *initial* outage lines in each event was well approximated by a power law with approximate exponent -3.71 (Dobson and Carreras 2010).

The practical power-law character of the initial failures conflicts with the previous modeling of random failures by only an identical time-dependent failure probability for each component (Dobson et al. 2001; Anghel et al. 2007), which leads to a Poisson distribution of the initial failed components (hazard intensity). Hence, instead of simply using the "time-dependent failure probability", this paper takes the expected hazard frequency (the expected number of failure events per year) and the power-law distribution of initial failed components (hazard intensity) to model random failures.

According to the previous data, given the total transmission line length, the number of forced transmission outage for Harris County per year is computed by multiplying the average failure rate 1.25 per 100 kilometers-year, while the number of independent outage events is determined through a scale factor equal to 0.6. This leads the expected frequency of the "random failures" equals to 19. The distribution of *initial* failure intensity q^1 is assumed to satisfy a power law with exponent -3.7 as follows: $\Pr(q^1 = x) = 0.905x^{-3.7}$, $1 \le x \le 8$, where x is the number of initial failed lines that can lead to cascading outages. The range limitation of x describes the empirical small portion of initial failed components under random failures, and helps excluding the failure events from the infrequent and high-consequences failures subset.

Original grid and smart Grids

To analyze the effectiveness of resilience improvement strategies in each stage, this paper introduces an original power grid model and several smart grid models. To model the power transmission system response under a disruptive event, due to unavailability of power injection and line susceptance data, this paper uses a complex network betweenness model. Betweenness is a proxy for the amount of current passing through network elements, and it is computed as the number of shortest paths that pass through every node when connecting generators with load substations. A disruptive event can cause the failure of some power substations and alter the network topology, which further changes all substation betweenness scores. If a substation betweenness exceeds its maximum capacity defined as the product of its initial betweenness and a tolerance parameter (*tp*), this substation fails operationally. This model has been used to analyze the cascading failure process of many real power transmission grids, such as the North American Power Grid (Kinney et al. 2005), the Italian Electric Power Grid (Crutitti et al. 2004), and the IEEE 118 and 300 bus test systems (Dueñas-Osorio and Vemuru 2009).

To calculate the annual resilience metric, the key is to obtain restoration curves under different hazard intensities q^1 and different amounts of recovery resources R. To mainly discuss the effectiveness of different resilience improvement strategies, this paper doesn't consider the variety of resource types and the dynamic resource mobilization process, so R is simply modeled by a single value as an approximation of the reality. Also, for simplicity, each damaged component is assumed to require one unit of recovery resources. Figure 3 gives the flow chart to simulate the restoration curve $P(t, q^1, R)$ under given q^1 and R. The detailed set of procedures is illustrated as follows:

1. Calculate the initial node loads (betweenenss) and node capacities.
2. Simulate random failures under a given hazard intensity. Determine the number of initial failed component q^1 according to the power-law distribution, then randomly select q^1 lines to be failed and assign each failed line with the repair time, which is the sum of a variable ε satisfying uniform distribution [0, 3h] and a variable η satisfying exponential distribution with mean value 5h (The parameter settings are based on Anghel et al. (2007)). The variable ε describes the traffic time for dispatching resources and η is the time to restore the failed components.
3. Remove the failed components from the network and recalculate the node loads.
4. Find the failed components with loads exceeding their capacities. If failed components exist, assign them with the repair time, which is still assumed to be the sum of ε and η, and then go to step 3; otherwise, go to step 5.
5. Calculate the performance metric (the proportion of normal operating nodes is taken as the metric in this paper), whose value is also the maximum impact level. Mark the time t as t=0, which is the start time of the restoration curve. This paper assumes the damage propagation is instantaneous and ignored due to the rapid power flow. Hence, at the time 0, the performance level sharply decreases to the maximum impact level from the normal performance level.
6. Move forward the time t=t + response time, where response time is the time for failure detections and restoration decisions.
7. Allocate the recovery resources R to the unrestored components according to the recovery sequences (the time order to restore the failed components).
8. Move forward the time t=t+1.
9. Find the restored components with their repair time reaching the set values. If restored components exist, release the recovery resources and reallocate them to unrestored components, and then go to step 10; otherwise, and go to step 8.
10. Reconnect the restored components, and calculate the new network loads. If it leads to new overloaded nodes, cancel the reconnections, go to step 8; otherwise, go to step 11.
11. Get the new network topology, record the simulation time and calculate the performance metric.
12. Assess whether all components have been restored. If it is true, go to step 13; otherwise, go to step 8;
13. Plot the restoration curve under the given hazard intensity.

Repeat the procedures from 1-13 for 500 times to obtain the expected restoration curve under given q^1 and R. Based on the flow chart in Figure 3, some details of the original power

grid model and the smart grid models in each stage are introduced as follows:

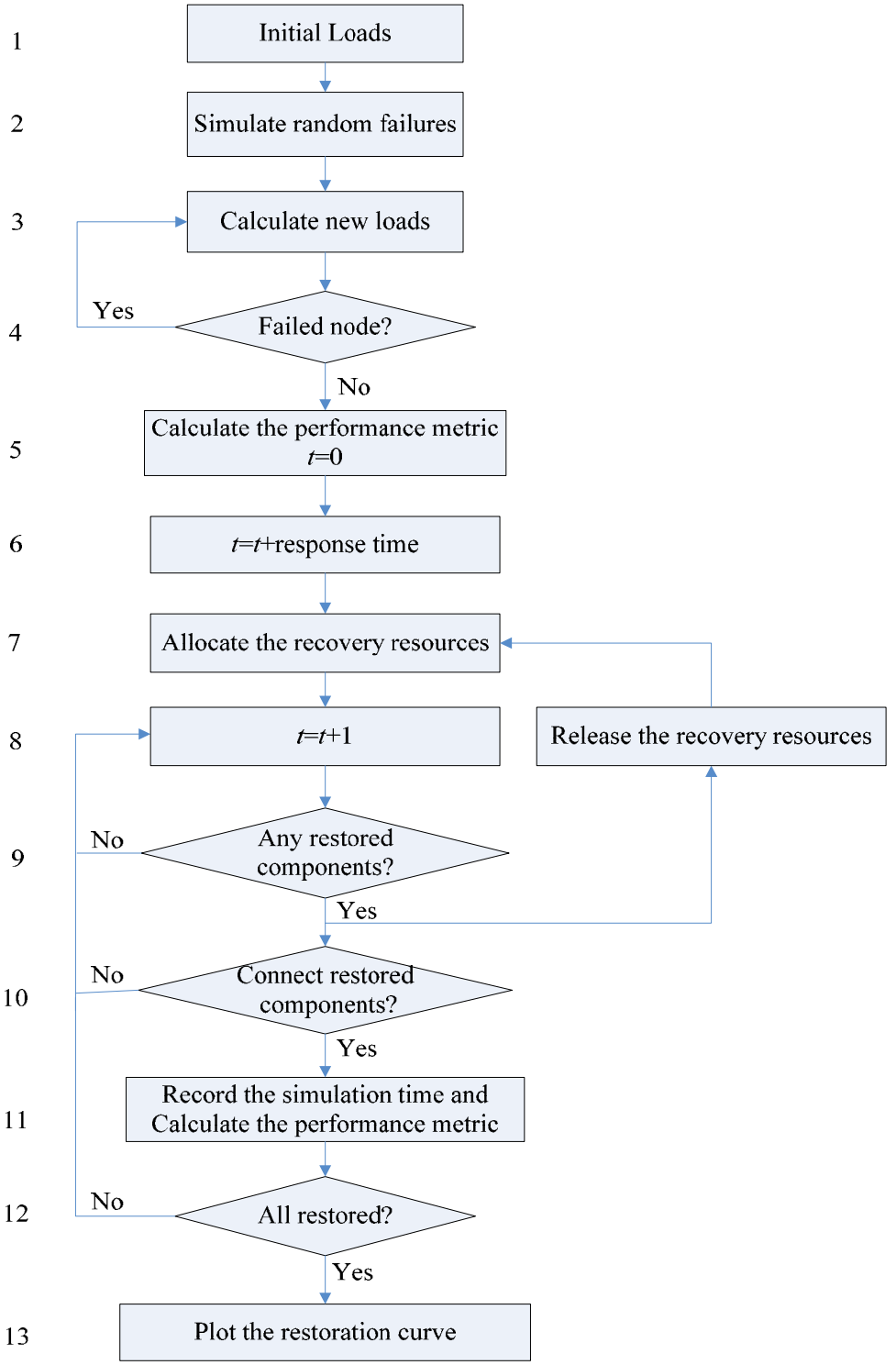


Figure 3: Flow chart to simulate restoration curves

In the first stage, compared with the original power grid, the smart grid has reduced frequency of random failures from 19 to 17.

In the second stage, compared with the original power grid, the smart grid is deployed

with energy storages or emergency generators for 10% critical substations as an approximation of the reality to illustrate the framework. These substations are identified according to their maximum topological degrees, and can still work normally for a period of time (assume 24 hours as an approximation of the reality) after their failures.

In the third stage, compared with the original power grid, the smart grid has shorter recovery response time and better recovery sequences. For the original power grid, the response time is 4h and the recovery sequences are determined randomly. These parameter settings are based on practical experiences from the power companies (Centerpoint Energy 2008). The failures are usually reported by inefficient channels, such as phones by customers. This leads to large delay for failure detections by operators and also incomplete information on all existing failures, which makes the recovery sequences are not optimized and usually based on the time order of the reports of the failures. Hence, this paper models the recovery sequences by random sequences as an approximation of the reality. For the smart grid, the response time is only 1h and the recovery sequences are selected according to the maximum node and link betweenness. The larger the component betweenness, the closer its topological distance (shortest path length) with the generators, and its priority restoration is heightened.

According to above assumptions, this paper considers five system cases to analyze and compare the effectiveness of the offered improvement strategies in different stages. Case 0: the original grid; Case 1: the smart grid with resilience improvement in stage 1. Case 2: the smart grid with resilience improvement in stage 2; Case 3: the smart grid with resilience improvement in stage 3; Case 4: the smart grid with resilience improvement in all three stages.

Simulation Results

This subsection analyzes the annual resilience of five system cases and compares the effectiveness of different resilience improvement strategies.

Restoration curve

For any fixed amount of recovery resources, the restoration curve is simulated under any given hazard intensity. When the amount of recovery resources is 30, Figure 4 shows typical simulation results under 3 initial failed links.

Case 1 enhances the resistant capacity to have reduced frequency of random failures. Its restoration curve is overlapped with the original grid (Case 0). This is because the restoration curve is to aim at the specific disruptive event, and cannot present the effects of the frequency of these events.

Case 2 improves the absorptive capacities to have energy storage units or emergency generators for critical substations (redundancies). Its restoration curve shows the decreased maximum impact level and the enhanced curve during the redundant periods (24 hours or 1 day). After depleting the redundant capacities, its performance level decreases to be the same as that of the original grid.

Case 3 improves the restorative capacity to have rapid recovery responses and better recovery sequences (betweenness-based). The restoration curve clearly shows the effectiveness of prompt responses, components start to be restored after 1 h but it is 4h for the original grid. The effectiveness of better recovery sequences is clearly shown in the Figure.

The recovery speed (the slope of the restoration curve) increases, and the impact area decreases considerably.

Finally, when all three-stage improvement strategies work together (Case 4), the impact area reduces by almost 50% compared with that of the original grid. Adopting better recovery sequences contributes the most to the resilience improvement.

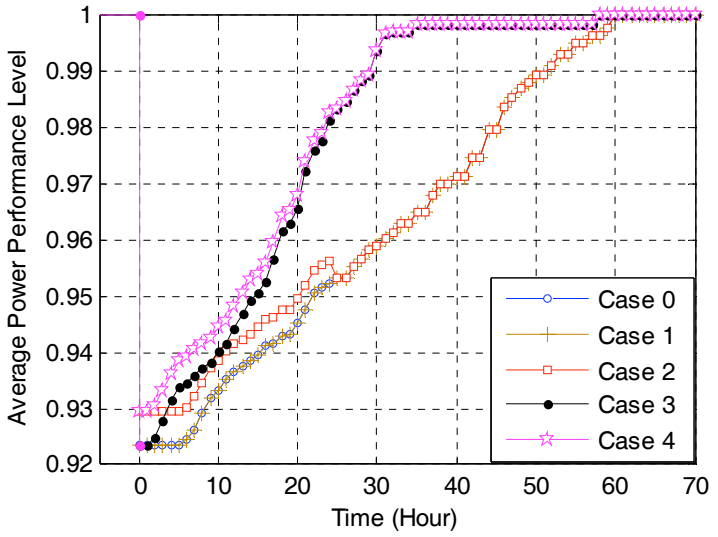


Figure 4: Expected restoration curves under 3 initial failed lines and 30 units of recovery resources.

Annual resilience

For any fixed amount of recovery resources, according to the restoration curves in Figure 4, the impact area is calculated. Further, taking the expected hazard frequency and the distribution of the initial failure intensity into consideration, the annual impact area is computed, and then the annual resilience is calculated according to Equation (2-2). Figure 5 shows the results.

With the increase of the amount of the recovery resources (R), the annual resilience increases for each case, and finally reaches a steady value. Deploying redundancies is the least effective strategy (Case 2) due to the small redundant capacities. Adopting better recovery sequences (betweenness-based sequence) (Case 3) is the most effective strategy, particularly under limited recovery resources. Specially, when the amount of recovery resources is only 10 units, the improvement magnitude (relative to Case 0) of the annual resilience of the system Case 3 is 25 times that of Case 2 and 4.4 times that for Case 1. Under sufficient resources, the improvement magnitude becomes smaller and it is only 2.7 times that for Case 2 and 1.6 times that for Case 1. If taking the cost of different strategies and the budget limitations into consideration, the proposed analysis framework can provide the way to find the most effective strategy to improve the resilience.

When the three-stage improvement strategies work together, the improvement magnitude relative to the original power grid is only 0.035%. It is small, but the saved economic loss may be significant. This is because if substituting the number of normal operating nodes by the number of customers without outage, the annual resilience metric is

tantamount to a power reliability metric used in the industry---the Average Service Availability Index (ASAI), which is the ratio of the total number of customer hours that service was available during a given time period to the total customer hours demanded. The reliability of the U.S. power grid (the total line length of the transmission grid is 300,000km) is 99.97%, and the 0.03% unreliability can cost the economy $150 billion every year (NIST white papers 2010). The length of power transmission grid in Harris County is 2144.5km, according to the length ratio (2144.5/300 000=0.007), small improvements of the annual resilience may still save hundreds of millions of dollars.

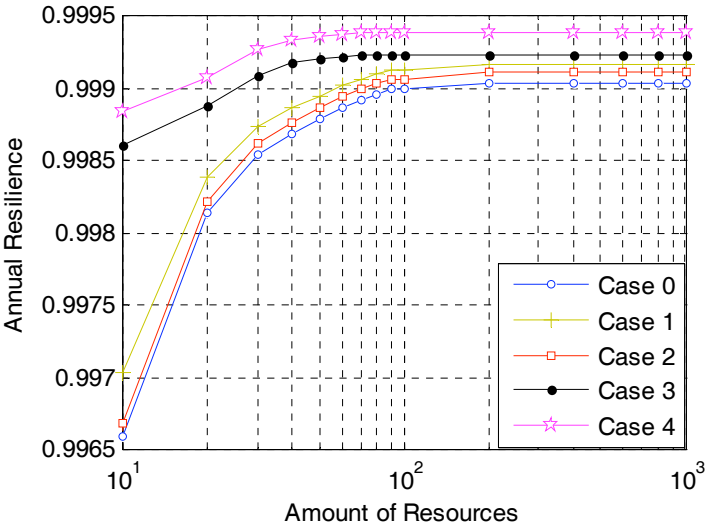


Figure 5: Annual resilience as a function of the amount of recovery resources for different system cases.

CONCLUSIONS

This paper proposes a three-stage framework to analyze the smart grid resilience. Taking the power transmission grid in Harris County, Texas as an example, this paper establishes an original power grid model and several smart grid models to compute their resilience and compare the effectiveness of the improvement strategies in different stages. Results include that under limit availability of recovery resources, adopting better recovery sequences (betweenness-based) is the most effective strategy. Under sufficient availability of recovery resources, reducing failure frequency, deploying with redundancies and rapid recovery response are all effective. The annual resilience of the smart grid with all three-stage improvements increases 0.035% compared to the original grid. The improvement magnitude is small, but it may save hundreds of millions of dollars.

Details in the proposed framework should be studied further and complemented in the future. First, this paper only considers one hazard type, identifying other hazard types, such as hurricane hazards, and then to calculate the global resilience will be the future direction. Second, as there are many performance metrics, such as connectivity, maximum flow and energy served, various resilience metrics can be formulated to reflect system resilience from different aspects. Second, this paper only considers a few resilience improvement strategies

in the case study, while other strategies (mentioned in Table 1) together with their estimated cost can be explored to find the optimum retrofit strategy under limited budget.

ACKNOWLEDGEMENTS

The work presented in this paper has been funded in part by the National Science Foundation through grant CMMI-0748231. The authors also wish to thank Rice University and the Office of Public Safety and Homeland Security of the City of Houston for their support.

REFERENCES

Adler R., Daniel S., Heising C., Lauby M., Ludorf R. and White T. (1994). "An IEEE survey of US and Canadian overhead transmission outages at 230 kV and above". IEEE Transactions on Power Delivery, vol. 9, no. 1, pp. 21 -39 Albert, R., Jeong, H. and Barabasi, A.-L. (2000). Error and attack tolerance of complex networks. Nature 406,378–382.

Amin, S. M. and Wollenberg, B. F. (2005). "Toward a smart grid: power delivery for the 21st century". *IEEE Power and Energy Magazine*, vol. 3, no. 5, pp. 34-41.

Anghel M., Werley K.A. and Motter A.E. (2007). Stochastic model for power grid dynamics. Fortieth Hawaii International conference on system sciences, January 3-6, 2007, Big Island, Hawaii.

Bruneau, M., Chang, S.E., Eguchi, R.T., et al. (2003). "A Framework to Quantitatively Assess and Enhance the Seismic Resilience of Communities". Earthquake Spectra 19(4), 737–738.

Centerpoint Energy. Smart grid demonstration. http://www.centerpointenergy.com/services /electricity/residential/smartmeters/thefuturesmartgrid. 2008.

Chen Q. and McCalley J. D. (2005) "A cluster distribution as a model for estimating higher-order event probabilities in power systems". Probability in the Engineering and Informational Sciences, 19: 489-505, Cambridge University Press.

Crutitti P., Latora V., Marchiori M. (2004). "A topological analysis of the Italian electric power grid". *Physica A*, 338: 92-97.

Dobson I., Carreras B.A., Lynch V. and Newman D.E. An initial model for complex dynamics in electric power system blackouts. 34th Hawaii International Conference on System Sciences, Maui, Hawaii,January 2001.

Dobson I. and Carreras B.A. (2010). Number and propagation of line outages in cascading events in electric power transmission systems. 48th annual allerton coference on communication, control & computing, IL, USA.

Dueñas-Osorio, L. and Vemuru, S. M. (2009). "Cascading failures in complex infrastructure systems." *Structural Safety*, 31, 157-167.

Garrity, T. F. (2008). "Getting smart". IEEE power and energy magazine, vol. 6, no. 2, pp. 38-45.

Holling, C. S. (1973). "Resilience and stability of ecological systems". Annual review of ecology and systematic, 4, 1-23.

Kinney R., Crucitti P. Albert R. and Latora V. (2005) "Modeling cascading failures in the North American power grid". *The European Physical Journal B—Condensed Matter and*

Complex Systems. 46(1): 101-107.

Kothari, D. P., Singh, Pushpendra and Singh, M. (2010). "Smart Grid: Integration of Power and Information Systems". http://www.rimtengg.com/iscet/proceedings/ pdfs/ misc/161.pdf.

Lightner E.M. and Widergren S.E. (2010). An orderly transition to a transformed electricity system. IEEE transactions on smart grid. 1(1): 3-10.

Metke A. R. and Ekl R.L. (2010). Security technology for smart grid networks. 1(1):99-107.

National Energy Technology Laboratory. (2008). "A Vision for the Modern Grid". United States Department of Energy. p.5. http://www.netl.doe.gov/moderngrid/docs/A%20 Vision%20for%20the%20 Modern%20Grid_Final_v1_0.pdf.

NIST (National Institute of Standards and Technology) white paper. (2010). Energy—technologies to enable a smart grid. http://www.nist.gov/tip/wp/upload/energy_wp_ 10_28_10.pdf

Platts. (2009). "Topology of the State of Texas Power Transmission Network". http://www.platts.com/.

Pothamsetty, V. and Malik, S. (2009). "Smart Grid: Leveraging Intelligent Communications to Transform the Power Infrastructure". White paper, CISCO. http://cio.cisco.com/web/about/citizenship/environment/docs/sGrid_wp_c11- 532328. pdf

Reed, D. A., Kapur, K. C. and Christie, R. D. (2009). "Methodology for assessing the resilience of networked infrastructure". IEEE system journal, 3(2): 174-180.

Roncero, J. R. (2008). "Integration is key to Smart Grid management", in *Proc. IET-CIRED Seminar on SmartGrids for Distribution*, June 23-24, 2008, pp. 1–4.

Suter, G., Werner, T. G. (2009). "The distribution control center in a smartgird". *20th International Conference on Electricity Distribution.* Prague, 8-11, June.

U. S. Department of Energy. (2003). "Grid 2030: A national vision for electricity's second 100 years". http://www.ferc.gov/eventcalendar/files/20050608125 055-grid-2030.pdf

U. S. Department of Energy. (2008). "The Smart Grid: An Introduction". Prepared for the US Department of Energy by Litos Strategic Communication. http://www.oe.energy.gov/DocumentsandMedia/DOE_SG_Book_Single_Pages(1).pdf

U.S. Department of Homeland Security. (2006). "National infrastructure protection plan". http://www.dhs.gov/ files/ programes/editorial_0827.shtm.

Vugrin, E.D., Warren, D.E., Ehlen, M.A. and Camphouse, R.C. (2010). "A framework for assessing the resilience of infrastructure and economic systems". in *Sustainable and Resilient Critical Infrastructure Systems:Simulation, Modeling, and Intelligent Engineering*,Kasthurirangan Gopalakrishnan and Srinivas Peeta,eds.,Springer-Verlag, Inc..

Watts, D. J. (2004). The dynamics of networks between order and randomness. *Published by Princeton University Press*, Eighth Printing.

Conceptual and Analytical Differences between Resiliency and Reliability for Seismic Hazards

Ross B. Corotis[1], F.ASCE, NAE, PE

[1]Department of Civil, Environmental and Architectural Engineering, University of Colorado at Boulder, 428 UCB, Boulder, CO 80309-0428; PH (303) 735-0539; FAX (303) 492-7317; email: Corotis@colorado.edu

ABSTRACT

A distinction is made between the reliability of a structural system and its resilience. The former is generally measured probabilistically, evaluated by means of computer algorithms capable of handling multiple failure modes, and forms the basis of design codes. Resilience must incorporate the time history of performance following significant disturbance, include imprecise definitions and evaluations, and reflect the effects of system performance (physical, economic, social and political) on the community served. Reliability analysis, including code calibration, has generally been the purview of structural engineering risk professionals. Resilience, on the other hand, should integrate community input on the degree of inconvenience and time trajectory of recovery, even incorporating concepts of sustainability. Resilience must often use generalized uncertainty, including fuzzy logic, to transform societal goals into metrics, and recognize sensitivity to sources of uncertainty in terms of acceptance of diminished performance. At a minimum, this requires keeping epistemic and aleatory uncertainty separate.

INTRODUCTION

There are many different definitions of resiliency that have become popular within the last few years. A workable one developed five years ago by the U.S. Subcommittee on Disaster Reduction (2005) is as follows:

> "The capacity of a system, community or society potentially exposed to hazards to adapt, by resisting or changing in order to reach and maintain an acceptable level of functioning and structure. This is determined by the degree to which the social system is capable of organizing itself to increase this capacity for learning from past disasters for better future protection and to improve risk reduction measures."

The Subcommittee on Disaster Reduction goes on to say, "Disaster-resilient communities experience minimum disruption to life and economy after a hazard event has passed." A simpler definition of resilience was proposed a year later by the U.S. Department of Homeland Security (2006):

> The capability of an asset, system or network to maintain its function or recover from a terrorist attack or any other incident."

Other definitions of resilience refer to mitigating risk and containing the effects of incidents, including recovery activities and social disruption. Some (San Francisco Planning and Urban Research Association, 2009) even address the issue of the ability of communities to govern after a disaster, including following existing building codes and providing basic infrastructure services, including the ability for people to move about. This last study sets a time goal of weeks for basic services and a few years for a re-established normality.

Resilience will be defined in this paper as the capability of a system to maintain acceptable levels of service in the face of shock, misfortune or significant disturbance, or to recover within an appropriate period of time. This concept is quite distinct from reliability. Reliability is a probabilistically-based measure of the ability of a system to perform its required functions under specified conditions and periods of time.

In order to pursue a quantitative analysis of resilience, it is first necessary to quantify such linguistic terms as *acceptable* service, *appropriate* recovery and *shock*. It is then necessary to move beyond the probabilistic principles that form the basis of reliability analysis and recognize the need to incorporate concepts of generalized uncertainty, including imprecise probabilities and linguistic and fuzzy logic. In addition, assessment of resilience depends on reliability, or functionality *of the system*, and, crucially, focuses on the requirements *of the community served* and the ability to meet these requirements throughout the recovery trajectory. Incorporating the full recovery time history of the community functionalities is an important aspect of resiliency.

Some aspects related to resiliency that are worthy of additional consideration include the development of multiple levels of resilience, related to different degrees of severity of events, and the balance between mitigation and preparedness. Worthy of note is the fact that resiliency encompasses performance in the post-disaster period, while risk and reliability focus on measures such as expected economic loss, mortality and morbidity. Often resilience also incorporates the setting of goals and the development of plans and processes.

At its foundation, the role of infrastructure systems is to enable society to perform its economic, social, cultural, political, mobility, communications and quality of life functions (Tierney et al., 2001; Kahneman and Tversky, 2000). Resiliency must address the capability of systems to provide acceptable levels of service in the face of

impending threats, including extreme events such as earthquakes or other hazards. The understanding of service level resiliencies and impact on community function lays the basis for new decision support methodologies (Corotis, 2007).

STRUCTURAL RELIABILITY

Over the past 40 years the field of structural reliability has matured to the point where efficient computer algorithms are available to evaluate the reliability of structural systems with multiple, correlated failure modes (Bucher and Bourgund, 1990; Der Kiureghian et al, 2006). Concomitantly, design codes have incorporated probabilistically-based load and resistance factor formats based on first and second order reliability methods.

Despite the terminology of strength design and the advancements in seismic engineering of considering modal behavior, current design approach procedures still reduce to member-by-member proportioning without sensitivity of the selected design to failure modes, or certainly their impact on the overall integrity or functionality of the structure. Research on systems analysis and progressive collapse have improved detailing for structural performance (Ellingwood, 2006), but still wanting is direct integral incorporation of the sustainability of the structure in the light of planned and unforeseen loads. Recent research reported by Nishijima and Faber (2009) addresses sustainability in a general engineering decision analysis framework.

RESILIENCE AND RELIABILITY

The concept of structural resilience must be integrated into reliability analysis such that the whole approach to structural seismic design becomes one of the tradeoff of investment in the structure with its sustainability for its intended purpose. Even beyond that, the integrity of the structure in terms of its role in the resilience of the community itself is incorporated in a heuristic fashion (ATC, 1991). Inherent in such an approach is the sensitivity of the performance of the structure to such issues as epistemic uncertainty in the load environment, including low probability high consequence events, and even black swans, or seismic events not directly considered in the design (Taleb, 2010). Even in seismically active regions, current design is based on examining multiple load combinations, and designing each element for its "most critical" combination. Lacking has been the sensitivity of the final design to alternatives, for example unexpected deviations in flood or wind loads on a structure whose final design has been dominated by an assumed earthquake load.

Community resiliency is affected by the performance of coupled infrastructure systems (*Infrastructure Resiliency Guide*, 2007; Teirney and Bruneau, 2007). The basic concept of resiliency is illustrated in Figure 1 (in which the projected trajectory, for the sake of simplicity, is shown as a straight line). For various specific and measurable activities of a community (such as economic production level, access to critical facilities, cultural events and housing starts), the performance will be traced as a function of individual and coupled infrastructure systems along with associated

incidences. As Figure 1 illustrates, each activity will be immediately affected by a particular incident, after which the recovery of the infrastructures and the resiliency of the community will create a unique recovery trajectory. The area below the dashed line and above the actual activity curve represents an integrated measure of activity loss to the community, complicated by the fact that after the recovery the activity level may be higher or lower than the pre-event trajectory. It is clear from this comprehensive approach that the expertise required for deriving resiliency measures needs to be cross-disciplinary, combining engineering theory, mathematical modeling and social/behavioral science aspects (*Critical Thinking: Moving from Infrastructure Protection to Infrastructure Resilience*, 2007). The activity represented in Figure 1 could be economic, but it could also be the level of a utility service.

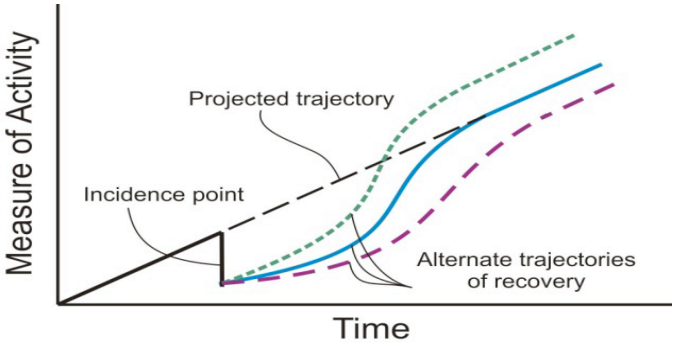


Figure 1. Community activity and recovery over time

Strategies to address resiliency following extraordinary events can be expected to range from constituent system and component upgrades and redundancy provisions, to coupling-decoupling strategies and de-rating actions to ameliorate stress on susceptible infrastructure elements, and even to enhanced situational awareness and preparedness training. Techniques for dealing with events such as shock, misfortune or significant disturbance cannot be limited to the usual approaches to systems reliability or risk assessment. Indeed, such events are often referred to as black swans, and by their very nature are unknowable and therefore unquantifiable in detail. This does not mean, however, that systems and procedures cannot be developed to prepare for and ameliorate losses following such events. As Taleb (2010) in his book specifically on black swans says, "We do not understand the future – but that is not necessarily bad news. We could plan *bearing in mind such limitations*." Even without explicit knowledge of event occurrence probability, forward thinking approaches to system resilience can help to mitigate adverse community impacts.

RESILIENCE AND COMMUNITY INPUT

One of the key differences in developing strategies for resilience in the face of unusual events is the necessity of more extensive incorporation of public involvement and political decision making. Indeed, while there is the need for better communication from the science and engineering community to the broader community, a successful roadmap for investment into more resilient infrastructure

systems requires a much more participatory approach. One of the reasons for this is that people in general behave as if events further into the future are less likely to occur, even if they have the same probability of occurrence as those in the near term (Smithson, 2008). Smithson goes on to point out that, "Professionals, politicians and risk managers must also contend with stakeholder perceptions of uncertainty and the competing interests." Therefore, projects advancing the knowledge of resiliency must be cognizant of this unique dependency between science and society. The situation is well stated by Pidgeon (2008): "Establishing a workable consensus is not merely a matter of educating the public about expert knowledge. Input from the public is valued for its contribution to 'social rationality,' which encompasses matters of preference, culture, values and ethics. Representations can indeed be anchored in probability and consequence, but at times also accommodate culture, context, politics and values [leading to] two-way analytic-deliberative processes." The time has come for a deeper understanding and collaboration between the structural engineering profession and the behavioral and social science discipline in assuming a broader perspective and responsibility for communicating the performance and limitations of the built environment to the public at large, as well as taking a central role in discussions of societal choices and trade-offs (Corotis and Enarson, 2007; Tierney, 2006). Significant advancement in the field of earthquake engineering has recently been developed in this area, including the Great Southern California Shakeout (Wald et al, 2008) and PAGER for the USGS (Porter, 2008).

A challenge for resiliency that must be addressed is that of the possibility of irrational distortion of decision-making when discussing issues of unforeseen hazards. Smithson (2008) points out that, "The core concern is whether risk communication produces (in)appropriate intensification or (in)appropriate attenuation of public risk fears." Even without such distortion, it is important to understand that the rationality understood by technologists is not the same as the rationality that drives political decisions (Corotis, 2005). Furler (2008) notes that political leaders "are focused primarily on managing…in such a way as to ensure the government retains office at the next election." This can be stated even more succinctly: "Politicians sell certainty. Science lives off doubt." (The Economist, 2009).

STRUCTURE RELIABILITY, ROBUSTNESS AND CODE DESIGN

The ASCE Standard (ASCE, 2010) has been a national leader in transforming probabilistic safety concepts into codified form for seismic design. The goal of building codes has been the protection of life safety, by ensuring either the survival of a building or at least a level of performance that promotes life protection and safe evacuation. Codes focus on the performance of individual structures and of life safety, but often do not represent comprehensively community conditions prevailing at the occurrence of earthquakes (or hurricanes, floods, tornadoes, or other natural hazards).

The concept of varying importance of individual structures already exists in codes, but the primary considerations in the selection of an importance category are the potential number of people at risk within the structure, the role of the structure in

disaster response, and the potential for the release of hazardous materials. In the ASCE Standard (ASCE, 2010) the importance category is used for the design of structures to resist earthquakes and other natural hazards, and the concept should be extended to consider the safe evacuation of people from buildings and the effect of continued functioning or non-functioning of the building. Standards and codes currently in use do not take into account the importance of structures with respect to community capacity to withstand the shocks of natural disasters or community vitality in the aftermath of disasters (Ellingwood et al, 1993).

It is also important to understand the relationship of how buildings are actually used, and with what significance for hazard mitigation, emergency preparedness, and disaster response and recovery. Beyond the stated purpose considered in structural design, there are often multiple uses and informal uses throughout a building's history that may greatly alter the impact on a community to damage or loss of a building (Corotis, 2002; Wen, 2001). Loss of a building's instrumental or operational value is self-evident but loss of social or symbolic value also affects the surrounding community. These considerations might, but do not presently, help determine land use planning, siting of buildings, relative safety of buildings implicit in existing building codes, and priorities for retrofitting projects.

The widely accepted approach to structural reliability is based on the methods developed by the Joint Committee on Structural Safety (JCSS, 2008; Faber et al, 2007). In this framework, the direct risk is given by

$$R_D = \sum_{k=1}^{n_{EXP}} \sum_{l=1}^{n_{CSTA}} p(C_l / EX_k) C_D(C_l) p(EX_k) \quad (1)$$

In which $\boldsymbol{R}_D$ is the risk due to direct consequences, n_{EXP} and n_{CSTA} are the number of exposure events and constituent damage states, respectively, $p(C_l/EX_k)$ is the probability of damage to constituent C_l given exposure to hazard event k, and $C_D(C_l)$ is the direct consequence for constituent C_l.

Considerations of resilience must consider the indirect structural risk, which is given by the following formula

$$R_{ID} = \sum_{k=1}^{n_{EXP}} \sum_{l=1}^{n_{CSTA}} \sum_{m=1}^{n_{SSTA}} C_{ID}(S_m, C_D(C_l)) p(S_m / C_l, EX_k) p(C_l / EX_k) p(EX_k) \quad (2)$$

In which n_{SSTA} is the number of different indirect consequence states associated with each constituent, and $C_{ID}(Sm, C_D)$ is the indirect consequence for state Sm for constituent C_l.

ALTERNATIVE MEASURES OF UNCERTAINTY

In the context of resiliency the traditional probabilistic and statistic-based models of likelihood and possibility are not in themselves sufficient to deal with the uncertainty inherent in resilience for shock, misfortune or significant disturbance. Instead, the concepts of generalized uncertainty are necessary (Klir, 2006). The situation at the

heart of resiliency is that theorized by Kasperson (2008): "But where highly complex systems with extensive connectivity and interaction exist …alternative approaches to coping with uncertainty must be found [that include] newer, more holistic and integrative assessment." One of the cornerstones for advancement in resiliency analysis is the further development and application of the principles of generalized uncertainty. Classical probability theory is very powerful and can address many situations in the decision rhetoric, but must be built upon further to address resiliency. When combined with utility theory, probability forms the basis of optimal decision theory, developed over 50 years ago (von Neumann and Morgenstern, 1944) and refined by Haimes (2004).

For practical societal decisions, it has been convenient to distinguish various sources of uncertainty, recognizing that a deeper understanding can be obtained by not combining all sources of uncertainty into one probability measure. For this reason, hazards analysis should distinguish between epistemic and aleatory uncertainty, reflecting such distinctions as inherent randomness, parameter uncertainty, and even model approximations and shortcomings (Corotis, 2003; Ellingwood, 2001). For many sociological applications of uncertainty it has been necessary to extend classical probability theory to fuzzy logic, incorporating linguistic variability. For other cases, the use of subjective probability, which pre-dates frequentist definitions but was out of favor for many decades, is necessary to capture uncertainty (Vick, 2002). Yet these modifications of classical probability theory still often fail to represent the total degree of uncertainty in many practical situations. When converting linguistic information into uncertainty measures, it is necessary to introduced generalized measures, or imprecise probabilities (Klir, 2006).

This introduction of imprecise probabilities allows the use, for instance, of multiple joint distributions when only the marginal distributions of the variables are known from observation. The identification and propagation of sources of uncertainty are necessary to quantify resiliency of structural infrastructure via metrics of community activity, relating the consequences of performance of structures during seismic events. The extrapolation of such approaches as probabilistic methods, fuzzy logic and imprecise probabilities is yet to be fully explored for both generic and real systems in the context of interdependent urban infrastructures' ability to absorb shock, service the community, and restore activity. The characterization of uncertainty in infrastructure resilience metrics is anticipated to be critical.

STRUCTURAL RESILIENCE AS A TIME-VARYING PROCESS

The concept of structural resilience can only be considered comprehensive when characterizing the performance of the structure over time when subjected to unforeseen events. Metrics are needed for the performance of a structure with respect to intended functions under realistic alternative environments (Tao et al, 1995; Wang et al, 1995; Taleb, 2010.

As described in an opening section, structural (as well as community) resilience must be evaluated in a pre-posterior fashion as a time-evolving response to the demands of the environment. In the case of structural function, it is necessary to define the essential functions of buildings, and not just their occupancy for design code purposes. In addition to considering alternate uses as well as possible changes over the lifetime of the structure, it is important to recognize that short and long term objectives of recovery of activities following a disaster are often distinct (Graham, 2007).

Considering the time period following a disaster, the first three days are usually focused on emergency response, and the first week on adding emergency shelter and the beginning of infrastructure service functions. The first month continues the restoration of infrastructure services and provision of shelter, adding oversight of market forces and protection against disease. In the following few months services should be completely restored and businesses returning to normal operation. Also during this period shelter should become of a more long-term nature and extended to commercial enterprises. During the remaining time of that first year the community should look to future resilience, including the adoption of enhanced development plans and procedures. After that, development should implement the plans for resilience and mitigation. This schedule is being developed for earthquake disasters in the United States, and clearly has application for resilience with respect to both natural and intentional hazards.

FUTURE AREAS OF INVESTIGATION

Below are descriptions of three areas where further development of theory is needed to quantify resilience in the face of seismic threats.

- Development of policy innovations that relate the rationalities of political decision making with the low probability, high consequence events associated with seismic hazards and intentional acts of terrorism. Life cycle analysis must be combined with risk perception models incorporating hazards-based social psychology (pertinent references: Slovic, 2000, 2004; Hammel and Corotis, 2007).

- Resiliency-enhancing strategies that create innovative practices for prioritizing a hierarchy of sequential needs for system recovery following an earthquake. Comparison between techniques based on probability/statistics measures and those associated with generalized uncertainty are important (pertinent references: Klir, 2006; McNeill, 2008).

- Quantification of business disruption and economic impacts after service losses due to earthquakes can build on work done by the Applied Technology Council for earthquakes (ATC, 1991), but must be expanded both in terms of regional economic as well as social impacts.

CONCLUSIONS

This brief paper has sought to distinguish structural reliability from resilience. Central differences relate to event modeling, outcome evaluation and uncertainty assessment. More importantly perhaps are the concepts of functionality impact on society, decision making inclusivity, and temporally integrated multiple loss measure.

REFERENCES

ASCE (2010). *Minimum Design Loads for Buildings and Other Structures*, ASCE/SEI 7-10, American Society of Civil Engineers, Reston, Virginia.

(ATC) Applied Technology Council, 1991. Seismic Vulnerability and Impact of Disruption of Lifelines in the Conterminous United States (FEMA 224, ATC-25). Federal Emergency Management Agency, Washington, DC. http://www.fema.gov/plan/prevent/earthquake/pdf/fema-224.pdf [viewed 6 June 2006]

Bucher, C.G. and U. Bourgund (1990). "A Fast and Efficient Response Surface Approach for Structural Reliability Problems," *Structural Safety*, 7(1), 57-66, Elsevier.

Corotis, R.B. (2002). **"**The political realities of life-cycle costing," *Bridge Maintenance, Safety and Management*, J. Casas, D. Frangopol and A. Nowak, Editors, International Center for Numerical Methods in Engineering, Barcelona, Spain.

Corotis, R.B. (2003). "Socially relevant structural safety," *Applications of Statistics and Probability in Civil Engineering*, Millpress, Rotterdam, Netherlands.

Corotis, R.B. (2005). "The Role of Risk Perception in Built Environment Risk Management," in *Safety and Reliability of Engineering Systems and Structures*, G. Augusti, G. Schueller and M. Ciampoli, Editors, Proceedings of the 9th International Conference on Structural Safety and Reliability, , 19-23 June, Rome, Italy.

Corotis, R.B. (2007) "An Overview, History and Context for the Consideration of Risk in the Built Environment," *International Journal of Risk Assessment and Management*, Vol. 7, No. 6/7, 759-772.

Corotis, R. and E. Enarson (2007). "Gender Dimensions of Building Code Disparities in Natural Disasters: A United States Perspective," *Australian Journal of Civil Engineering*, Vol 4, No. 1, 15-26.

Costing Asset Protection: An All Hazards Guide for Transportation Agencies (2009). National Cooperative Highway Research Program (NCHRP) 525, Transportation Research Board, The National Academies, Washington, D.C.

Critical Thinking: Moving from Infrastructure Protection to Infrastructure Resilience (2007). George Mason University School of Law, Critical Infrastructure Protection Program, February.

Department of Homeland Security (2006). National Infrastructure Protection Program. Available at www.fas.org/irp/agency/dhs/nipp.pdf (accessed December 14, 2010).

Der Kiureghian, Armen, T. Haukaas and K. Fujimura (2006). "Structural reliability software at the University of California, Berkeley," *Structural Safety*, 28(1-2), 44-67, Elsevier.

Economist, The (2009). November 28, page 16.

Ellingwood, Bruce (2001). "Acceptable risk bases for design of structures," *Progress in Structural Engineering and Materials,* 3, John Wiley and Sons, Ltd. 170-179.

Ellingwood, Bruce (2006). "Mitigating Risk from Abnormal Loads and Progressive Collapse," ASCE *Journal of Performance of Constructed Facilities*, 20(4), 315-323, ASCE.

Ellingwood, Bruce, Ross Corotis, John Boland and Nicholas Jones (1993). "Assessing Cost of Dam Failure," *Journal of Water Resources Planning and Management*, ASCE, 119(1), 64-81.

Faber, Michael, Marc Maes, Jack Baker, Ton Vrouwenvelder and T. Takada (2007). "Principles of Risk Assessment of Engineered Structures," ICASP10, Tokyo, Japan.

Furler, L. (2008). "Smoke and Mirrors," in *Uncertainty and Risk: Multidisciplinary Perspectives*, G. Bammer and M. Smithson, Eds, Earthscan, Sterling, Virgina, USA, pp 183-193.

Graham, L.T. (2007). "Permanently Failing Organizations? Small Business Recovery after September 11, 2001," *Economic Development Quarterly*, 21, 299-314.

Haimes, Jacov (2004). *Risk Modeling, Assessment, and Management*, Wiley-Interscience, New York, New York, USA.

Hammel, E. and R.B. Corotis (2007). "Multiple-Attribute Aspects for Risk Assessment of Natural Hazards," International Forum on Engineering Decision Making, December, 2007, Port Stephens, Australia.

Infrastructure Resiliency Guide (2007). Department of Defense, Defense Critical Infrastructure Program, Version 1.0, May.

JCSS (2008). Joint Committee on Structural Safety, "Risk Assessment in Engineering: Principles, System Representation and Risk Criteria, JCCS Publisher, 35p, http://www.jcss.ethz.ch/ (accessed August 12, 2010).

Kahneman, D. and A. Tversky (2000). *Choices, Values, and Frames.* Cambridge, UK: Cambridge University Press.

Kasperson, R. (2008). "Coping with Deep Uncertainty: Challenges for Environmental Assessment and Decision-Making," in *Uncertainty and Risk: Multidisciplinary Perspectives*, G. Bammer and M. Smithson, Eds, Earthscan, Sterling, Virgina, USA, pp 337-347.

Klir, G. (2006). *Uncertainty and Information*, Wiley-Interscience, Hoboken, New Jersey, USA.

McNeill, J. B. (2008). *Building Infrastructure Resiliency: Private Sector Investment in Homeland Security*. The Heritage Foundation, Backgrounder No. 2184, September 23.

Nishijima, K. and M.H. Faber (2009). "A Macroeconomic Decision Framework for Sustainable Design and Maintenance Policy Making for Civil Infrastructure," International Forum for Engineering Decision, Hakone, Japan, May.

Porter, K.A. (2008). *Fatality models for PAGER.* SSA 2008 Annual Meeting, Santa Fe, NM, 17 Apr 2008

Subcommittee on Disaster Reduction (2005). *Grand Challenges for Disaster Reduction*, National Science and Technology Council, Committee on Environment and Natural Resources. Available at www.sdr.gov/GrandChallengesSecondPrinting.pdf (accessed December 14, 2010).

Slovic, P. (2004). "Risk as Analysis and Risk as Feelings: Some Thoughts about Affects, Reason, Risk, and Rationality," *Risk Analysis,* Vol. 24, No. 2.

Slovic, P. (2000). *The Perceptions of Risk.* UK and USA: Earthscan Publication Ltd.

Smithson, M. (2008). "The Many Faces and Masks of Uncertainty," in *Uncertainty and Risk: Multidisciplinary Perspectives*, G. Bammer and M. Smithson, Eds, Earthscan, Sterling, Virgina, USA, pp 13-25.

San Francisco Planning and Urban Research Association (2009). "The Resilient City. Part I: Before the Disaster, San Francisco, CA. Available at www.spur.org/publications/library/report/theresilientcity_part1_020109 (accessed December 14, 2010).

Taleb, N. (2010). *Facing the Black Swan: The Impact of the Highly Improbably*, Random House, Melbourne, Australia, 444p.

Tao, Zongwei, R.B. Corotis and J.Hugh Ellis (1995). "Reliability-Based Structural Design with Markov Decision Processes," *Journal of Structural Engineering*, ASCE, Vol. 121, No. 6, 971-980.

Tierney, K.J. (2006). *Facing Hazards and Disasters: Understanding Human Dimensions*, contributing author, National Academy of Sciences Report, National Research Council, Washington, D.C.

Tierney, K., M. Lindell and R. Perry (2001). *Facing the Unexpected: Disaster Preparedness and Response in the United States.* Washington, DC: Joseph Henry Press.

Tierney, K. and M. Bruneau (2007). "Conceptualizing and Measuring Resilience: A key to disaster loss reduction." *TR News,* May-June 2007, 14-18.

Vick, S.G. (2002). *Degrees of Belief*, ASCE Press, Reston, Virginia, USA.

Von Neumann, J. and O. Morgenstern (1944). *Theory of Games and Economic Behavior*, (second edition 1947). Princeton University Press, Princeton, New Jersey.

Wald, D., K.W. Lin, K. Porter, and L. Turner (2008). ShakeCast: automating and improving the use of ShakeMap for post-earthquake decision-making and response. *Earthquake Spectra*, 24 (2), 533-553

Wang, Wei, R.B. Corotis and M.R. Ramirez (1995). "Dominant Failure Modes for Structures with Stochastic Load Processes," *Journal of Engineering Mechanics*, ASCE, Vol. 121, No. 11, 1252-1260.

Wen, Y. K. (2001). "Life Cycle Cost Based Design Against Multiple Hazards," *Maintaining the Safety of Deteriorating Civil Infrastructures*, A. Milamoto and D. Frangopol, editors, Second International Workshop on Life-Cycle Cost Analysis and Design of Civil Infrastructure Systems, Yamaguchi University, Japan, 239-257.

The State of Art of Community Resilience of Physical Infrastructures

G. P. Cimellaro, A. M. ASCE[1], Chris S. Renschler, A. M. ASCE[2], Amy Frazier[2], Lucy A. Arendt[3], A.M. Reinhorn, F. ASCE[4], Michel Bruneau, M. ASCE[4]

[1] Department of Structural & Geotechnical Engineering (DISTR), Politecnico di Torino, room 7, Corso Duca degli Abruzzi 24, 10129 Turin, Italy PH +39 (011) 090 4801 FAX +39 (011) 090 4899, email: gianpaolo.cimellaro@polito.it
[2]Department of Geography, University at Buffalo, The State University of New York, 135 Ketter Hall, Buffalo NY, email: rensch@buffalo.edu
[3]Department of Management | Professional Programs in Business, University of Wisconsin, Green Bay, email: arendtl@uwgb.edu
[4]Department of Civil, Structural & Environmental Engineering, University at Buffalo, The State University of New York, 135 Ketter Hall, Buffalo NY, email: reinhorn@buffalo.edu

ABSTRACT

The concept of Disaster Resilience has received considerable attention in recent years and it is increasingly used as an approach for understanding the dynamics of natural disaster systems. The goal of this paper has two distinct tasks: (i) conduct a literature survey analyzing asset-based approaches for defining and measuring disaster resilience for physical infrastructures that is one of the seven dimensions of the PEOPLES Resilience Framework; (ii) identify the gaps between asset-based approaches and community-scale approaches. It is offered an overview of the models developed in literature to quantify resilience and performances of electric power, water, wastewater and natural gas utilities; communication companies and transportation networks as well as health care facilities. Discussion will be added related to strengths and weakness on how these approaches could facilitate the comparison of alternative resilience options/strategies and measure the speed with which disruptions can be overcome and community functions restored.
A new geographic approach will be introduced to measure community resilience, focusing on spatial, temporal scale of resilience.

INTRODUCTION

Resilience is clearly becoming increasingly important for modern societies as states come to accept that they cannot prevent every risk from being realized, but rather must learn to adapt and manage risks in a way that minimizes impact on human and other systems.
While studies on the disaster resilience of technical systems have been undertaken for quite some time, the societal aspects and the inclusion of various and multiple types of extreme events are new developments. In this regard, countries and states around the world are increasingly debating ways to enhance community resilience. At this time, there is no explicit set of procedures in the existing literature that suggests how to quantify resilience in the context of multiple hazards, how to compare communities with one another in terms of their resilience, or how to determine whether individual communities are moving in the direction of becoming more resilient in the face of various hazards. Considerable research has been accomplished to assess

direct and indirect losses attributable to earthquakes, and to estimate the reduction of these losses as a result of specific actions, policies, or scenarios. However, the notion of resilience suggests a much broader framework than the reduction of monetary losses alone. Equally important, in addition to focusing on the losses produced by multiple hazards, research must also address the ways in which specific pre- and post-event measures and strategies can prevent and contain losses (Bruneau et al, 2003). Resilience (R) is defined as a function indicating the capability to sustain a level of functionality or performance for a given building, bridge, lifeline networks, or community, over a period defined as the control time T_{LC} that is usually decided by owners, or society (usually is the life cycle, life span of the system etc.). Resilience is defined graphically as the normalized shaded area underneath the functionality function of a system, defined as *Q(t)*. *Q(t)* is a non stationary stochastic process and each ensemble is a piecewise continuous function as the one shown in Figure 1 (Cimellaro et al. 2010):

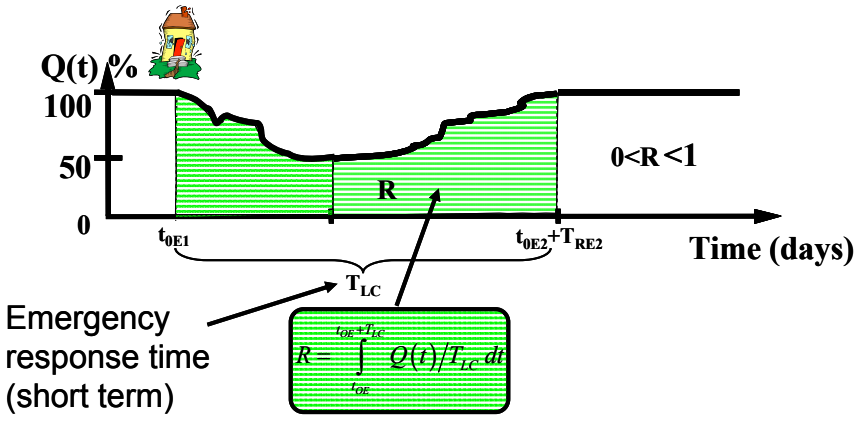


Figure 1 Schematic Representation of Community Resilience

Disaster resilience is often divided between technological units and social systems. On a small scale, when considering critical infrastructures, the focus is mainly on technological aspects. On a greater scale, when considering an entire community, the focus is broadened to include the interplay of multiple systems – human, environmental, and others – which together add up to ensure the functioning of a society. At the community level, the human component is central, because in the case of a major disruptive event, resilience depends first on the actions of people operating at the individual and neighborhood scale. Community resilience also depends heavily on the actions of different levels of government and its agencies at the local and regional scales when a disruptive extreme event occurs.

In order to emphasize the primary role of the human system in community sustainability, the acronym "PEOPLES" have been used This nomenclature highlights both the physical and environmental assets as well as the socio-economic-political/organizational aspects of a particular community. The PEOPLES Resilience Framework is built on and expands previous research at MCEER linking several previously identified resilience dimensions (technical, organizational, societal, and economic) and resilience properties (r4: robustness, redundancy, resourcefulness, and rapidity). PEOPLES incorporates MCEER's widely accepted definitions of service functionality, its components (assets, services, demographics) and the parameters influencing their integrity and resilience.

The PEOPLES Resilience Framework defines components of functionality shown in Figure 2 using a geospatial-temporal distribution within its influence boundaries. Interdependencies

between and among these components are key for determining the resilience of communities. PEOPLES enables the use of various community resilience indices that integrate over space and time the system functionality and services of a community in a landscape setting. In this particular dimension, historical and continuously gathered information through remote sensing and Geographic Information Systems (GIS) will play a major role in assessing the resilience of all integrated systems and feed a predictive resilience model. Resilience can be considered as a dynamic quantity that changes over time and across space. It can be applied to engineering, economic, social, and institutional infrastructures, and it can use various geographic scales. To be able to expand the assessment of resilience to a community and landscape perspective, the PEOPLES Resilience Framework is based on basic community organizational units at a local (neighborhoods, villages, towns or cities) and regional scale (counties/parishes, regions, or states) (see Figure 2).

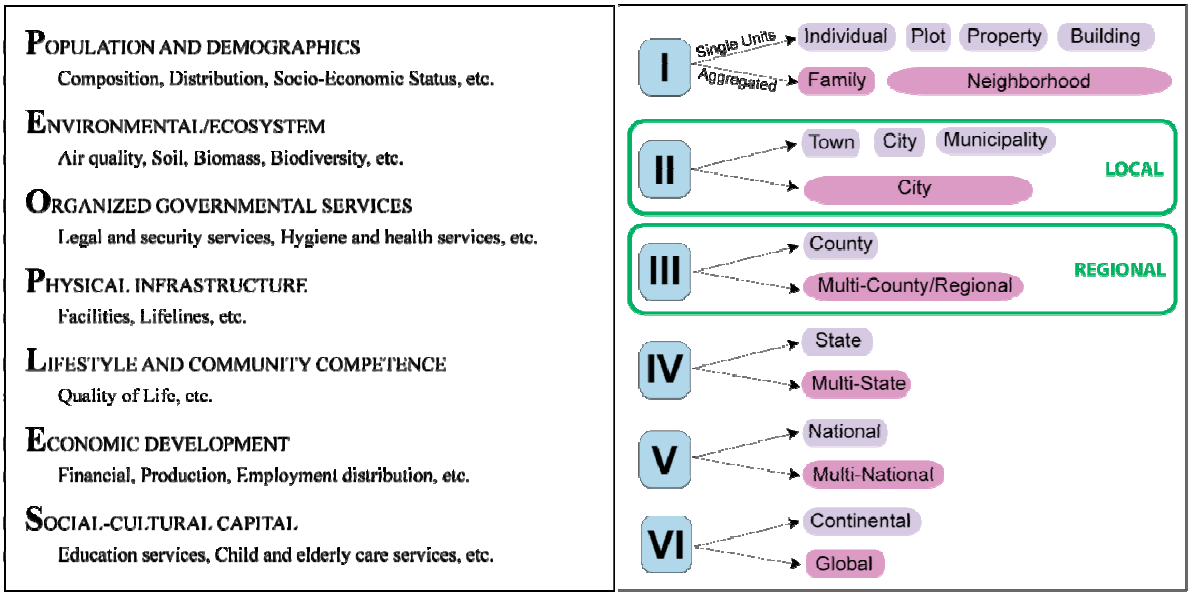


Figure 2 The PEOPLES Resilience Framework and their Geographic Scales

The goal of this paper is to focus only on the physical infrastructure dimension of the PEOPLES framework identifying the different performance measures of the different components.

PHYSICAL INFRASTRUCTURE DIMENSION

The physical infrastructure dimension incorporates both facilities and lifelines. Within the category of facilities, we include housing, commercial facilities, and cultural facilities. Within the category of lifelines, we include food supply, health care, utilities, transportation, and communication networks (Figure 3).

a) Facilities	ii) Health Care
i) Residential	(1) Acute Care
(1) Housing Units	(2) Long-Term Acute Care
(2) Shelters	(3) Primary Care
ii) Commercial	(4) Psychiatric

(1) Distribution Facilities (2) Hotels - Accommodations (3) Manufacturing Facilities (4) Office Buildings iii) Cultural (1) Entertainment Venues (2) Museums (3) Religious Institutions (4) Schools (5) Sports/Recreation Venues **b) Lifelines** i) Communications (1) Internet (2) Phones (3) TV (4) Radio (5) Postal	(5) Specialty iii) Food Supply iv) Utilities (1) Electrical (2) Fuel/Gas/Energy (3) Waste (4) Water v) Transportation (1) Aviation (2) Bridges (3) Highways (4) Railways (5) Transit (6) Vehicles (7) Waterways

Figure 3 List of subcomponents of the PHYSICAL INFRASTRUCTURE dimension of the PEOPLES framework

Eulerian indicators for facilities and lifelines

For residential, commercial and cultural facilities it is possible to use point location indicators such as physical damage indicators and using the analogy with fluid mechanics, these indicators can also be called Eulerian indicators, because they describe the performance of each component at a given location. Some facilities due to their malfunction can also cause indirect damage such as commercial distribution facilities, religious institutions, schools etc. Therefore for these facilities their influence area needs to be considered evaluating the number of users that will not receive service over the total number of users that received service before the extreme event.

When considering residential housing units (1) a good indicator of resilience to extreme events is also the ratio between the vacancy rates for rental housing and the housing stock not rated as substandard or hazardous (Tierney 2009). This indicator is however affected by the damage state of the housing units, so it is representative if all housing units are opportunely retrofitted.

Point location indicators can also be used when considering the other group of physical infrastructures, the lifelines for communication, food supply and utilities lifelines (electric, water, gas etc.). In this case the indicators are defined as percentage of households receiving service at a given location.

Indicators for communication networks

In terms of communication networks, key indicators may include the sufficiency of procedures for communicating with the public and addressing the public's need for accurate information following disasters, adequacy of linkages between official and unofficial information sources, and adequacy of ties between emergency management entities and mass media serving diverse populations (Tierney 2009).

Indicators for health care facilities

In term of health care facilities, a key indicator is the waiting time (WT) that is the time that the patient needs to wait in the hospital before receiving service (Cimellaro et al, 2010b,c). Other models are also available in literature and are summarized in the following table. Further details about key indicators for this dimension can be found in the MCEER report (Cimellaro et al. 2009).

KEY INDICATORS OF THE TRANSPORTATION SYSTEM

Among physical infrastructures special attention should be given to the transportation system. When considering road network in the past, lot of attention has been given to the damage of individual bridge structures, while indicators measuring the performance of the overall transportation system should be considered.

Lagrangian Indicators

Eulerian indicators can be used for lifelines such as water, electric power, natural gas, and telecommunications, where performance can be readily measured by the percentage of households in the study area that have lost lifeline service. However this approach cannot be used for transportation systems, because transportation service is consumed by an individual user across the network, rather than at a point location, therefore using the analogy of fluid mechanics the indices that better describe the performance are the so called lagrangian indicators that describe the performance of a user that move across the network. For example they belong to this group indicators based on the original destination (OD) nodes (e.g. Bocchini and Frangopol, 2011) and on the network connectivity analysis (CA) (Chang and Nojima, 2001).
In term of transportation system there are many key indicators available in literature, therefore it is necessary to distinguish between normal and critical operating conditions. Many indicators can be found describing the performance of the road network in normal operating conditions, while a few can be found to evaluate performances after extreme events as shown in Table 1.

Normal operating condition indicators	Extreme event indicators
Average road user costs	Total length of highway open L (Chang and Nojima, 2001);
Travel time as measure of level of satisfaction	Total distance-based accessibility D (Chang and Nojima, 2001);
Number of fatalities as measure of user risk	Bocchini and Frangopol (2011)
Overhead percentage (fixed costs/total costs) as indicator of road administration's cost-effectiveness	REDARS (Werner et al. 2006)
Roughness (IRI is widely used indicator) related to pave-ment quality, travel cost and user satisfaction	
States of bridges	
Satisfaction with the road system as indicator of road users overall satisfaction	
…	

Table 1 Key indicators divided by normal and critical operating conditions (not exhaustive)

Each of these extreme events indexes is estimated as the ratio of post-earthquake to pre-earthquake conditions and ranges from 0 (system non-functional) to 1 (system fully functional).
Among all it is worthed to focus on the extreme event indicators that are of interest for the PEOPLES framework therefore some of the most relevant and simple to understand are summarized below.

The indicator *L* (Chang and Nojima, 2001) reflects the length *x* of highway in the network that is open to traffic at any point in time *t*, and is defined as a ratio to the pre-earthquake length open $\bar{x}$:

$$L(t) = \frac{x(t)}{\bar{x}} \tag{1}$$

The limit of this indicator is that it is basd only on the extend of damage. A second indicator *D* is based on minimum network travel distances and thus takes into account both the extent and the location of damage. It attempts to measure changes in accessibility at all nodes on the network:

$$D(t) = \frac{f - A(t)}{f - 1} \tag{2}$$

where

$$A(t) = \frac{\sum_i \sum_j d_{i,j}(t)}{\sum_i \sum_j \bar{d}_{i,j}} \qquad 1 \le A \le f \tag{3}$$

with *f*=effective distance multiplier for link closure; *A*=total network accessibility ratio; $d_{i,j}$=minimum travel distance between nodes *i* and *j* on damaged network; $\bar{d}_{i,j}$=minimum travel distance between nodes *i* and *j* on intact network.

Recently Bocchin and Frangopol (2011) developed an index for the functionality of a bridge network. The index is based on the assumption that the time to cover the length of a highway segment is assumed to be the sum of two parts: (i) the time spent on the highway; (ii) the time spent on detour routes. These hypotheses are consequential to the assumption that for every (partially) closed bridge there is at least one possible detour route to bypass the damaged bridge. These detours cause a delay due to the necessity to change the path and to the limited capacity of local routes.

$$Q(t) = 100 \cdot \frac{\Gamma(t) - \Gamma^0}{\Gamma^{100} - \Gamma^0} \tag{4}$$

where

$$\Gamma(t) = \frac{1}{\gamma_t \cdot TTT(t) + \gamma_D \cdot TTD(t)} \tag{5}$$

$TTT(t) = \sum_{i \in I} \sum_{j \in J} f_{ij}(t) \cdot c_{ij}$ is the Total Travel Time; $TTD(t) = \sum_{i \in I} \sum_{j \in J} f_{ij}(t) \cdot d_{ij}$ is the total travel distance; γ_T=is a balancing factor (cost) associated with the time spent by the network users, γ_D=is a similar factor related to length. f_{ij} = is the traffic transiting over the highway segment between nodes *i* and *j*; *i* is the set of nodes of the network and *j* is the subset of nodes connected to node *i*; c_{ij}=is the time required to cover segment *i–j* with traffic flow f (t); d_{ij} =is the length of highway segment *i–j*.

Seismic Risk Analysis for transportation system (REDARS)

Another interesting methodology for measuring the global road network performance after earthquakes is implemented in REDARS (Risks from Earthquake DAmage to Roadway Systems) that is a multi-disciplinary tool for seismic risk analysis (SRA) of highway systems (Werner et al., 2006). Once defined the region of interest the seismic hazard is evaluated and the resulting damage states for each component of the system considering damage extend, type and location. How each component's damage will be repaired, including its repair costs, downtimes, and time-dependent traffic states (i.e., its ability to carry traffic as the repairs proceed over time after the earthquake). Next, REDARS incorporates these traffic states into a highway-network link-node model, in order to form a set of system-states that reflect the extent and spatial distribution of link closures at various times after the earthquake. It applies network analysis procedures to each system-state, in order to estimate how these closures affect system-wide travel times and traffic flows. Finally, REDARS estimates corresponding economic losses and increases in travel times to/from key locations or along key lifeline routes. These steps can be applied for a single earthquake and no uncertainties (deterministic analysis) or for multiple earthquakes and simulations in which uncertainties in earthquake occurrence and in estimates of seismic hazards and component damage are considered (probabilistic analysis).

INTEGRATING FUNCTIONALITIES OF PEOPLES FRAMEWORK

Within the *PEOPLES Resilience Framework,* each dimension and/or service and its indicators or terms of functionality will be represented with a GIS layer of the area of interest (Figure 4). Each dimension of the framework can be represented by a combination of sub-dimensions (or layers), each having spatial-temporal dependent functionalities, each representing a subcomponent. For example the physical infrastructure layer shown in Figure 4 can be subdivided into layers representing the housing, transportation, electric power, water, sewage, communications, etc.
In Figure 4, Q_{HOU} = functionality of the housing units in the community; Q_{TRA}= functionality of the transportation network; Q_{ELE}= functionality of electric power system; Q_{H2O}= functionality of the water system; Q_{COM}= functionality of the communication network; Q_{SEW}= functionality of the sewage system; all terms are function of the location (**r**) and of the time (**t**). This list of functionality terms that is inserted within the physical infrastructure is not exhaustive. Additional terms can be added, such as functionality of schools, dams, fire stations, oil and natural gas systems, emergency centers, etc. For each layer, is possible to define a *resilience index contour map* after integrating the functionality for the control time (T_{LC}) period.

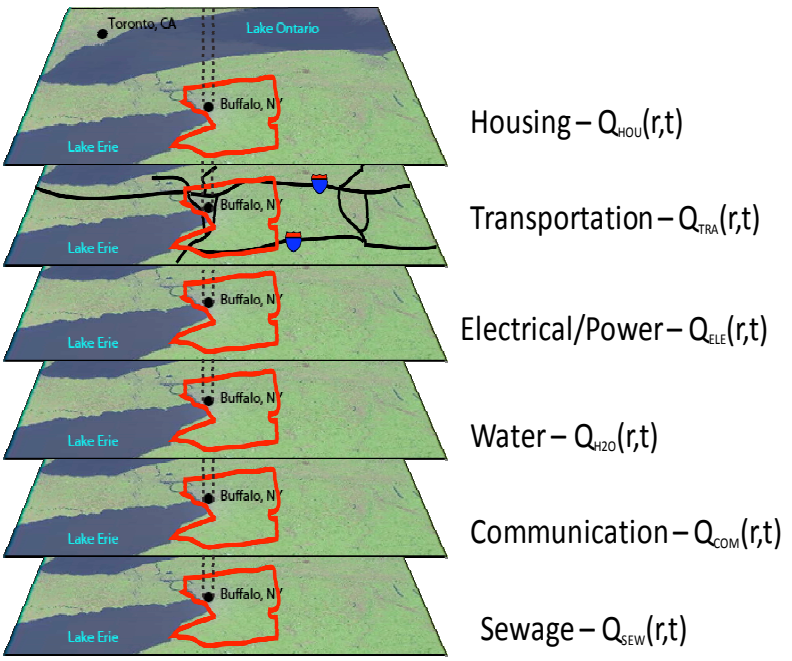


Figure 4 Schematic representation of Physical Infrastructure Functionality Maps

Region of interest

The spatial distribution of functionalities in each dimensional layer is also specific to the area of influence of the network of lifelines that it represents. For example the highway network and the electric grid have different boundaries as well as the areas served by the water system and by the communication system. These areas of influence are not the same for each layer and they can be national, regional or local, dependent on the service provided. Multiple community resilience indices, *Ri*, for each component, i, or a single combined index, R, would be dependent on a defined temporal and geographic size or scale defined by community boundaries. The community will include in its boundaries an entire network, or several networks, but most likely will include only parts of the larger national or regional networks. Therefore in determining resilience, first, the boundaries of the region of interest should be defined. Geographic Information Systems (GIS) are increasingly being used to map vulnerability, and to better understand how various phenomena (hydrological, meteorological, geophysical, social, political and economic) effect human populations. The region of interest is further divided in grid cells and inside each cell, r, a definition of functionality Qi(r,t) at a given time instant, t, is given for each dimension (Figure 5). For example, if the community resilience index of the electric power network has to be calculated for a given region, first the definition of functionality Q_{ELE} needs to be defined, for example as

$$Q_{ELE}(\mathbf{r},t) = \frac{N_{CP}(\mathbf{r},t)}{N_C(\mathbf{r},t)} \quad (1)$$

where N_{CP}=number of households receiving power in the grid cell and N_C= total number of households in the grid cell.

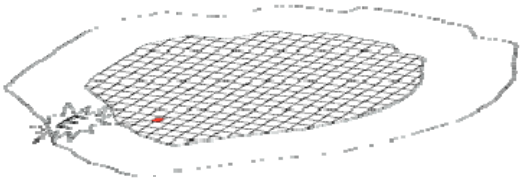


Figure 5 Example of region of interest divided in grid cells

Then, after evaluating the functionality $Q_{ELE}(\mathbf{r},t)$ in each grid cell for the entire period of control, T_{LC}, different ways of representing the data are available.

Resilience maps

At every instant t_0 a given functionality maps $Q_{ELE}(\mathbf{r},t_0)$ (or contour plots) can be plotted over the region of interest. These maps can be used during the entire recovery process, especially in the days immediately after the extreme events and they can be updated on regular basis for example. They can be used to direct resources and personnel toward the zones more affected by the extreme event in the region. At different time periods defined also by the control time, T_{LC}, it is possible integrate the functionality for the given control time and calculate the resilience at each location **r**.

$$R_{ELE}(\mathbf{r}) = \int_{t_{OE}}^{t_{OE}+T_{LC}} Q_{ELE}(\mathbf{r},t)/T_{LC}\,dt \tag{2}$$

Then the resilience indices can be used to develop the resilience maps in the form of contour plots. These maps can be used as information during the entire recovery process, or during any given control period. At the end of the emergency period they give you a status on the level of achieved resiliency of the component/dimension in the aftermath of the extreme event.

Finaly, a global **community resilience index for the specific dimension** (*electric power system* in the example below) can be provided by double integrating over the entire region, r_{LC}, and the control period, T_{LC}..

$$R_{ELE} = \int_{\mathbf{r}_{LC}(t)} R_{ELE}(\mathbf{r})\,dr = \int_{\mathbf{r}_{LC}(t)} \int_{T_{LC}(t)} Q_{ELE}(\mathbf{r},t)/T_{LC}\,dtdr \tag{3}$$

All equations above are presented for the functionality of the electric power network, only, but formulation can be easily extended to all components/dimensions.

Community Resilience indices

When a global resilience index is required to assess the entire community, as a result of all components and dimensions, this index can be obtained using the total functionality $Q_{TOT}(r,t)$, that combines the different dimensions, so the final community resilience index is given by:

$$R = \int_{\mathbf{r}_{LC}(t)} R(\mathbf{r})\,dr = \int_{\mathbf{r}_{LC}(t)} \int_{T_{LC}(t)} Q_{TOT}(\mathbf{r},t)/T_{LC}\,dtdr \quad (4)$$

where Q_{TOT}(r,t) is the global functionality that is a function of time and space and combines all functionality terms considered; r_{LC} is the region of interest that can change with time; t is the time parameter; T_{LC}= control time that can change through the time.

Interdependencies

All resilience dimensions and their respective indices to measure their performances are interdependent (Figure 6).

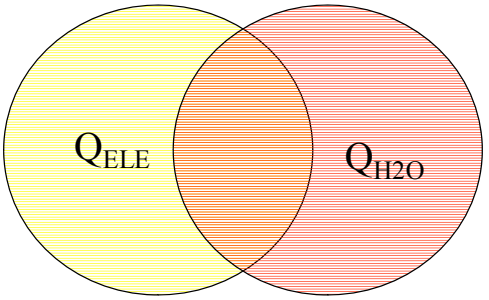


Figure 6 Interdependencies among different functionalities

A simple way of combining different functionalities is using the analogy with the probability axiom of arbitrary events therefore the global definition of functionality is given by

$$Q_{TOT} = \sum_{j=1}^{n} Q_j - \sum_{i=1}^{n}\sum_{j=2}^{n} Q_i Q_J + \sum_{i=1}^{n}\sum_{j=2}^{n}\sum_{k=3}^{n} (Q_i Q_j Q_k) - \ldots + (-1)^{n-1} \sum_{i=1}^{n}\sum_{j=2}^{n}\sum_{k=3}^{n} \ldots\ldots \sum_{l=n-1}^{n} (Q_i Q_j Q_k \ldots Q_l Q_n) \quad (5)$$

It is obvious that not all functionalities might have the same weight; therefore the global functionality can be determined using the mathematical expectation denoted by $E\{Q(\mathbf{r},t)\}$ that is defined by

$$Q_{TOT} = E\{Q(\mathbf{r},t)\} = \sum_{i=1}^{n} p_i(\mathbf{r},t)\,Q_i(\mathbf{r},t) \quad (6)$$

where n is the number of dimensions considered relevant in the functionality, $p_i(r,t)$=priority (probability) factors; Q_i=functionality associated to a given dimension of PEOPLE framework. Notable, for the total system functionality, the number of dimensions can be maximum seven (n=7) as indicated in the PEOPLES framework. However, the same formulation (recurrence formula), with suitable adjustment of the meaning of the indices, applies to the total functionality of a single component/dimension such as the physical infrastructure, or the organizational system, thus allowing to determine the resilience index of just that component/dimension.

The formulation suggested above provides the base for further development of the resilience indices for various locations using a probability framework while considering inherent uncertainties in the systems.

REMARKS AND CONCLUSIONS

The paper conducts a literature survey analyzing asset-based approaches for defining and measuring disaster resilience for physical infrastructures that is one of the seven dimensions of the PEOPLES Resilience Framework. It is offered an overview of the most relevant models developed in literature to quantify resilience and performances of electric power, water, wastewater and natural gas utilities; communication companies and transportation networks as well as health care facilities. A new geographic approach is introduced to measure community resilience, focusing on spatial, temporal scale of resilience. System community resilience measures can provide a very useful tool for mitigation of multiple hazards such as earthquakes and are important for several reasons:

1. They enable comparisons of system conditions across disaster events in different regions.
2. They allow comparisons across scenario disaster events for a single study region, and with a rapid development can be used for pre-event mitigation planning.
3. They may also facilitate discussions of what levels of risk and potential loss are acceptable or unacceptable.
4. They can be used in efficient post-disaster restoration strategies by prioritizing damage repair optimizing system performance.
5. They be implemented for estimating economic impacts for emergency response and recovery planning.

ACKNOWLEDGEMENTS

The research leading to these results has also received funding from the European Community's Seventh Framework Programme - Marie Curie International Reintegration Actions - FP7/2007-2013 under the Grant Agreement n° PIRG06-GA-2009-256316 of the project ICRED - Integrated European Disaster Community Resilience.

REFERENCES

Arcidiacono, V., Cimellaro, G. P., and Reinhorn, A. M. "A software for measuring disaster community resilience according to the PEOPLES methodology." *Proceedings of COMPDYN 2011 - 3rd International Conference in Computational Methods in Structural Dynamics and Earthquake Engineering*, Corfu`, Greece, May 26-28, 2011.

Bocchini, P., and Frangopol, D. (2011). "A stochastic computational framework for the joint transportation network fragility analysis and traffic flow distribution under extreme events " *Probabilistic Engineering Mechanics*, 26(2), 182-193.

Bruneau, M., Chang, S. E., Eguchi, R. T., Lee, G. C., O'Rourke, T. D., M., R. A., Masanobu, S., Kathleen, T., Wallace, W. A., and Winterfeldt, D. v. (2003). "A Framework to Quantitatively Assess and Enhance the Seismic Resilience of Communities." *Earthquake Spectra*, 19(4), 733-752.

Chang, S. E., and Nojima, N. (2001). "Measuring Post-Disaster Transportation System Performance: The 1995 Kobe Earthquake in Comparative Perspective." *Transportation Research Part A: Policy and Practice*, 35(6), 475-494

Chang, S. E., and Shinozuka, M. (2004). "Measuring Improvements in the Disaster Resilience of Communities." *Earthquake Spectra*, 20(3), 739-755.

Cimellaro, G. P., Reinhorn, A. M., and Bruneau, M. (2010a). "Framework for analytical quantification of disaster resilience." *Engineering Structures*, 32(2010), 3639–3649.

Cimellaro, G. P., Reinhorn, A. M., and Bruneau, M. (2010b). "Seismic resilience of a hospital system." *Structure and Infrastructure Engineering*, 6(1-2), 127-144.

Cimellaro, G. P., Reinhorn, A. M., and Bruneau, M. (2010c). "Performance-based metamodel for health care facilities." *Earthquake Engineering & Structural Dynamics*, article first published online: 16 DEC 2010, DOI: 10.1002/eqe.1084.

Cimellaro, G. P., Fumo, C., Reinhorn, A. M., and Bruneau, M. (2009). "Quantification of Seismic Resilience of Health care facilities " *MCEER Technical Report-MCEER-09-0009*, Multidisciplinary Center for Earthquake Engineering Research, Buffalo, NY.

Renschler, C., Frazier, A., Arendt, L., Cimellaro, G. P., Reinhorn, A. M., and Bruneau, M. (2010). "Framework for Defining and Measuring Resilience at the Community Scale: The PEOPLES Resilience Framework." *MCEER Technical Report –MCEER-10-006, pp. 91*, University at Buffalo (SUNY), The State University of New York, Buffalo, New York.

Miles, S., and Chang, S. (2003). "Urban Disaster Recovery: A Framework and Simulation Model." *MCEER-03-0005*, State University of New York, University at Buffalo, Buffalo, NY.

Miles, S., and Chang, S. (2006). "Modeling Community Recovery from Earthquakes." *Earthquake Spectra*, 22(2), 439-458.

Tierney, K. (2009). Disaster response: Research findings and their implications for resilience measures. CARRI Research Report 6. Oak Ridge, TN: Community and Regional Resilience Initiative (CARRI). URL: www.resilientUS.org

Werner, S. D., Taylor, C. E., Cho, S., Lavoie, J.-P., Huyck, C., Eitzel, C., Chung, H., and Eguchi, R. (2006). "REDARS 2 Methodology and Software for Seismic Risk analysis of highway systems." *Technical Report MCEER-06-SP08*, MCEER Multidisciplinary Center Earthquake Engineering Research, Buffalo, NY.

Measuring, Monitoring and Evaluating Post-Disaster Recovery: A Key Element in Understanding Community Resilience

J. S. Bevington[1], A. A. Hill[2], R. A. Davidson[3],
S. E. Chang[4], A. Vicini[1], B. J. Adams[1], R. T. Eguchi[5]

[1]ImageCat, Ltd., Communications House, 63 Woodfield Lane, Ashtead, Surrey, KT21 2BT, United Kingdom; PH +44 1372 278 777; FAX +44 5601 155 791; email: jb@imagecatinc.com / avi@imagecatinc.com / bja@imagecatinc.com
[2]Department of Earth Sciences, The University of Memphis, 1 Johnson Hall, Memphis, TN 38152; PH (901) 678-2589; FAX (901) 678-2178; email: aahill@memphis.edu
[3]Department of Civil and Environmental Engineering, University of Delaware, Newark, DE 19716; PH (302) 831-4952; FAX (302) 831-3640; email: rdavidso@udel.edu
[4]School of Community and Regional Planning, University of British Columbia, 242-1933 West Mall, Vancouver, BC V6T 1Z2, Canada; PH (604) 827-5054; FAX (604)822-6164; email: stephanie.chang@ubc.ca
[5]ImageCat, Inc., 400 Oceangate, Suite 1050; Long Beach, CA 90802; PH (562) 628-1675; FAX (562) 628-1676; email: rte@imagecatinc.com

ABSTRACT

The process of community recovery in the aftermath of a disaster is complex, long lasting, resource intensive, and poorly understood. Insights described here result from an ongoing project that aims to monitor, quantify, and evaluate the process of post-disaster recovery for two events, Hurricane Charley (2004, Charlotte County and Punta Gorda, Florida) and Hurricane Katrina (2005, Harrison County and Biloxi, Mississippi). A mixed-methods approach using statistical data, interviews, and remote sensing-derived data is applied in an effort to understand as well as monitor, measure and evaluate the recovery process and its outcomes. Observations associated with the post-disaster course of moving residents from temporary to transitional, and ultimately permanent housing serves as the focus for this paper. This work represents a discrete portion of a multi-sector project where Economic, Environmental, Housing/Infrastructure, and Social elements of community recovery are explored. Understanding community recovery can inform community resilience-building strategies.

INTRODUCTION

Post-disaster recovery efforts often require many years, enormous resources, and define the character of the affected communities for an extended period of time. Nevertheless, recovery is cited as the most poorly understood phase of the disaster cycle (e.g., Berke and Beatley, 1997; Haas et al., 1977; Mileti, 1999; Olshansky, 2005; Rubin et al., 1985). An improved understanding of recovery could promote recovery planning and community resilience prior to a disaster as well as management following a disaster. An important first step in advancing the

understanding of post-disaster recovery is improving the ability to measure, monitor, and evaluate it. In fact, participants at a meeting of the aid community identified an urgent need for basic and applied research into the long-term recovery process, noting in particular the *lack of a standard, independent and replicable approach by which progress made during the relief and recovery phases can be measured, monitored and evaluated against existing guidelines* (Shelter, 2006). In recent years, supported by organizations including DfiD, ECHO and USAID, aid agencies have devoted considerable effort to developing guidelines for the emergency relief and recovery processes (e.g., Corsellis and Vitale 2004, Sphere 2004. Currently, governments and relief organizations evaluate their programs in an *ad hoc* manner, without a systematic approach or standardized criteria. The goal of this research is to develop a systematic approach for identifying evidence of post-disaster recovery through a unique fusion of multi-source data. In doing so, and by examining the post-disaster landscape over time, one aim of this research is to comment on wider community resilience for several post-hurricane scenarios.

Post-disaster recovery is a complex physical, social, economic, environmental, and political process (Phillips, 2009). Given the importance of recovery, limitations of previous research on it, and new technological opportunities, this project aims to develop innovative methods for systematically and quantitatively measuring, monitoring and evaluating post-disaster recovery through a unique integration of multi-source data. Two study areas support the methodological development, focusing on communities in southwest Florida impacted by 2004 Hurricane Charley, with validation of the method using areas in Mississippi affected by 2005 Hurricane Katrina. The project is producing unique comprehensive recovery datasets, including new remote sensing-based and previously underutilized statistical data, together with interview and expert judgment data. This paper establishes a methodological framework for assessing recovery that complements existing theoretical and practically-based metrics and models, and established recovery assessment techniques. The paper discusses methods that synergistically exploit qualitative and quantitative information, enhancing the value of both and facilitating a deeper understanding of the complex nature of recovery.

Resilience is equally complex, to define, to promote, and to sustain. Gaps exist in the implementation of resiliency concepts within community development and emergency planning activities (Paton and Johnston, 2006). The experiences and realities of long-term recovery can serve as a resource to communities that are attempting to build their internal capacity to absorb or adapt to a disruption or disaster event. This research aims to harness the opportunity to learn from communities who have long-term disaster experience, and so there is much potential to apply recovery lessons to facilitate resilience-building efforts.

New methods for acquiring and analyzing recovery data can provide diverse benefits to those who manage, fund, and study disaster recovery: This can empower communities and provide evidence to support their experiences of the recovery process. It can open a new source of dialogue and discourse that could have practical

repercussions for the creation of resilient communities, for the distribution of aid and resources. It also facilitates theoretical discussions on the potential identification of different types of recovery, dependent on their initial conditions and key decisions post-disaster. Further, by augmenting existing ways of empirically measuring recovery, the project advances the state-of-the-art in post-disaster recovery studies and supports the continuing development of a theory of post-disaster recovery.

This paper demonstrates the development of methods to assess recovery. Described through the use of exemplars that highlight a single sector of recovery - temporary housing – we demonstrate how the recovery can be better understood through the use of multi-source data. We provide an overview of the use of remote sensing and field interviews carried out in one study area. These exemplars provide an insight into how the fusion of diverse information sources are being used in the wider research project to aid evaluation of recovery and resilience.

STUDY EVENTS AND LOCATIONS

Given the complexities of post-disaster recovery, diversity of disaster impacts, and differential rates of recovery, this project includes two study events, Hurricanes Charley and Katrina, two counties, Charlotte County Florida and Harrison County Mississippi, and two municipalities within the study counties, Punta Gorda, Florida (Figure 1) and Biloxi, Mississippi (Figure 2). The purpose of this multiple event and multi-location approach is to mitigate place- and event-specific effects on recovery and to support development of findings that are scale, place and event independent.

Charlotte County and Punta Gorda, Florida

Hurricane Charley made landfall with the eye passing directly over the city of Punta Gorda, Florida at 16:45 EDT on Friday, August 13, 2004. Charley was a fast moving storm that brought 150 mph sustained winds, 8in of rainfall, and a 7 foot storm surge to the study area (Pasch et al., 2005). Charley changed direction and unexpectedly headed toward Punta Gorda, making landfall as a Category 4 storm.

Harrison County and City of Biloxi, Mississippi

Hurricane Katrina made its final Gulf Coast landfall on Monday, August 29, 2005 at the mouth of the Pearl River, close to the Louisiana/Mississippi state boundary, as a Category 3 storm. At landfall, sustained winds of up to 120mph impacted the Mississippi coast including the study area (Faulkner et al. 2007). The storm surge, which ranged from 24-28 feet along the coast, contributed significantly to losses along the Mississippi Gulf Coast (Farris 2007). This surge was complemented by 10-12 inches of rainfall between August 24 and August 30 (Grauman et al. 2005).

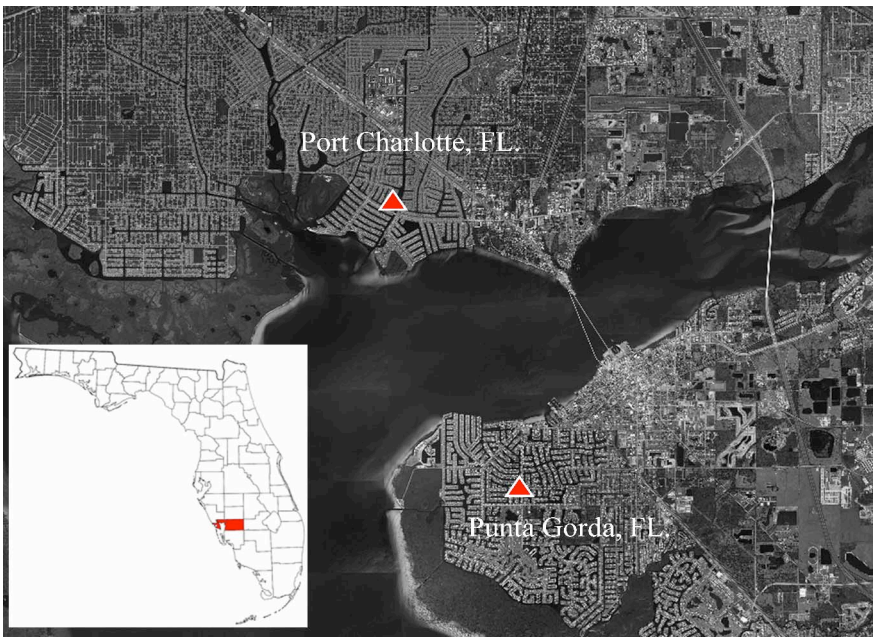


Figure 1. Hurricane Charley study locations, Charlotte County, Florida (imagery courtesy of SWFWMD).



Figure 2. Hurricane Katrina study locations, Harrison County, Mississippi (imagery courtesy of Google Maps)

DATA AND METHODS

A mixed-methods approach fused interviews and survey instruments with statistical data and satellite imagery/aerial photography in order to develop a comprehensive picture of the recovery process operating in our study locations. In the aftermath of a disaster, record keeping and reporting requirements (housing permits for example) are often suspended for a discrete period of time to remove impediments to repair and recovery. By combining diverse and complementary data sources, the aim of this research is to provide self-validating approach to measure and evaluate recovery efforts.

Remote Sensing Imagery

Remotely-sensed images were sourced from several sources for both study areas. For Punta Gorda and Charlotte County, aerial orthophotographs with a spatial resolution of 1 foot were sourced from the Southwest Florida Water Management District (SWFWMD), captured in January of each year, for 2004-2009. These were combined with Quickbird-02 satellite imagery captured before and after Hurricane Charley (23 March 2004, 14 and 19 August 2004), with spatial resolution of 60cm for the pansharpened product. The imagery for the second study site of Mississippi were collected from several state and local agencies for 2005-2008. Field validation information was collected during site visits to Florida and Mississippi in January and October 2010, respectively. This entailed collecting GPS-registered video and photo data (using the VIEWS^{TM} system; ImageCat, Inc. 2010) for every street in the study areas, providing a snap-shot of the recovery progress in each location. Similar VIEWS^{TM} footage had been captured within days of both Hurricane Charley and Katrina, and has been used for validation of much of the image analysis in the wider research project.

Several manual and semi-automated methods were adopted during the project to analyze the multi-temporal remotely-sensed imagery, producing datasets pertaining to *Housing, Environmental* and *Economic* sectors. Much of this work is still in progress at time of publication. However, as an exemplar, this paper provides an overview of the analysis of a large concentration of temporary shelters (*Housing* sector), on Airport Road, 3 miles east of central Punta Gorda.

Analysis of temporary shelters, Punta Gorda FL.

Using the multi-temporal imagery provided by SWFWMD, a presence/absence analysis was performed to quantify the changes in availability of temporary housing. This required the generation of point information for each unit of manufactured housing sited on the lot that the imagery showed to be vacant prior to the storm. Each housing unit (confirmed during field visits as FEMA-supplied trailers) was identified by a point in a GIS, and given attributes indicating its presence or absence in a series of images, acquired at a one year intervals for 2005, 2006 and 2007. As the numbers changed over time as temporary shelters came and went, the presence or absence of

trailers in the imagery was recorded. This also enabled the estimation of the total area used for temporary housing over time, based on the boundaries of the site.

Considering the normal specifications for these types of housing units (FEMA trailers), and allowing for an average capacity of three occupants, it was possible to estimate the occupation of the camp over time. This assumed that the presence of the shelter in the imagery also meant the shelter was occupied.

Field Visit Interview Data

Field work in study locations not only provided key contextual information of study areas and ground validation of remote sensing imagery analysis, but also interviews were carried out to provide experiential data and an opportunity for communities to help explain patterns found in statistical and imagery analysis. Research teams traveled to Port Charlotte and Punta Gorda (Charlotte County, Florida) on two occasions, in August 2009 and in January 2010. The first visit coincided with an *Extreme Makeover* community celebration marking the fifth anniversary of Charley's landfall. This provided an opportunity to interview residents regarding the pace and perceived milestones in the community recovery process. A total of 114 residents shared experiences and opinions of recovery across time and space. Interviews with three agencies and organizations who took the lead in recovery efforts, provided background and overview information as well as facilitating introductions to key individuals/organizations. This information supported the second field visit in January, 2010. During this visit, in-depth interviews were conducted with over two dozen organizations/agencies. These agencies/organizations included city, county and regional scales, as well as spanned housing, emergency management, planning, transportation, infrastructure and housing, economic and social welfare sectors. Similar field reconnaissance, ground validation, and interviewing took place in October 2010 for the Mississippi study area. In this case, city, county and state organizations and agencies were interview targets, with specific focus on the economic, environment and housing sectors. In total three dozen interviews were completed.

OBSERVATIONS AND FINDINGS

Temporary Housing

The image analysis of the concentration of FEMA-provided shelters in Punta Gorda showed that before Hurricane Charley, the site was a vacant, vegetated lot. By January 2005, in an area of 0.287 km^2, 552 housing units had been established in regular blocks containing 6-14 individual units (Figure 3), accounting for an estimated population of 1656. The number of units was reduced to 369 by January 2006 (population = 1107, and to 11 in January 2007 (population = 33; Figure 4). By 2008, all trailers had been removed and the site had been cleared to make way for permanent administrative units, including the new Charlotte County Fire and Emergency Services Center. By the field visit in 2010, there were no traces of the

temporary shelters on the site. Figure 5 shows the transition of part of the site from 2005-07.

Imagery was not available in the time between the storm and January 2005, therefore the exact date that the temporary housing area was established can only be estimated from imagery alone. The limitation of image sampling rate is a common factor when using remotely-sensed data, which can be reduced through the collection of additional images in this interim time period, or through fusion of ancillary datasets.



Figure 3. Presence of Temporary Housing Units in Punta Gorda, January 2005 (imagery courtesy of SWFWMD)

Although this exemplar has been shown to describe the transition of multiple families into and out of temporary shelters, often transitional trailers are situated next to damaged homes and residences. In a wider, multi-temporal study of housing for the whole of Punta Gorda (under review for publication), many trailers were identified on private properties, and stayed *in situ* until repairs or rebuilding was completed. These particular temporary shelters from FEMA have been a useful and identifiable proxy for monitoring transitional populations from remotely-sensed data.

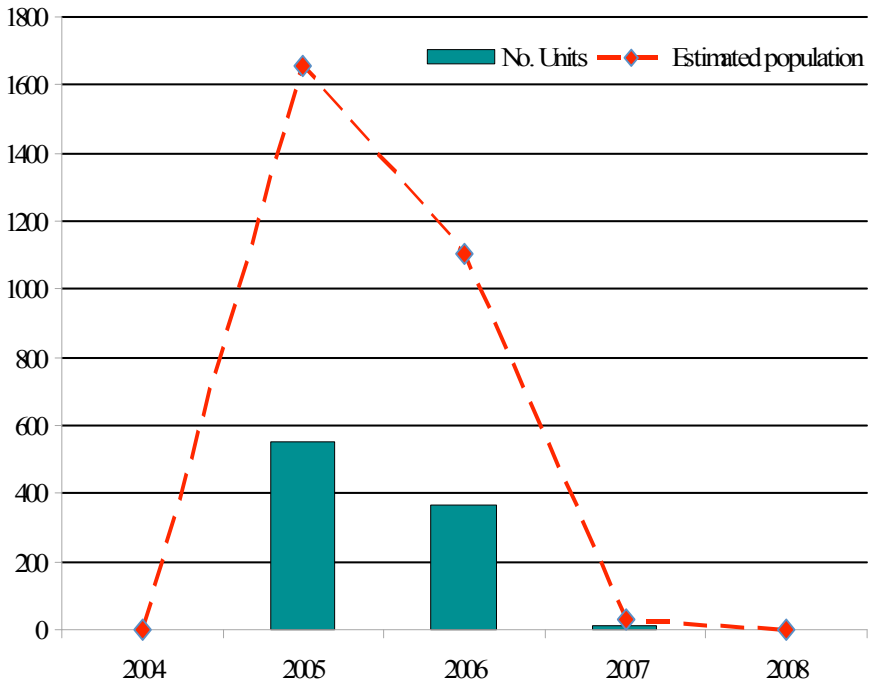


Figure 4. Quantification of temporary housing units in Punta Gorda: 2004-08. All data derived from SWFWMD orthophotographs.

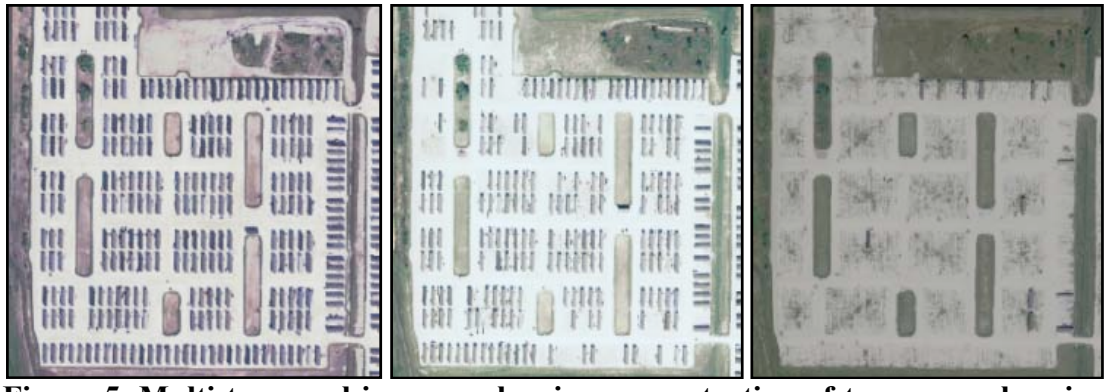


Figure 5. Multi-temporal imagery showing concentration of temporary housing in Punta Gorda. (left-right: 2005, 06, 07). Imagery courtesy of SWFWMD.

During interviews in Florida the topic of FEMA temporary shelters was discussed in all meetings. Travel-trailers and other temporary shelters (whether from FEMA or another source) generally fell into two categories – those situated at or near a resident's original address, and those situated in parks/camps removed from a resident's property. Community non-governmental organizations expressed concern about the consequences of positioning temporary housing parks/camps in a remote location. While a large area was available and utilities were installed expeditiously, residents living in the facility were far removed from aid distribution centers,

employment opportunities, and daycare facilities. The unintended consequences of the remote location were ultimately mitigated by transportation facilities provided to residents of the temporary shelter.

Concerns were expressed to the field teams, not over the timing that temporary shelter was available, but at the length of time that availability extended. Interviewees commented that it was difficult to move families from temporary to permanent housing, and as such, temporary housing units stayed much longer than had originally been envisioned. Without clear limitations on occupancy, abuse of the temporary shelters was described; both in terms of populations impacted by Hurricane Charley, but also by individuals who moved to the area specifically to reside in the temporary housing after the storm. The assumption of full occupancy used in the described remote sensing analysis was valid as there were attempts to remove the trailers as soon as occupants left to avoid informal occupancy of these units. Residents and agencies both stated that in many cases across the city, low-income families ultimately moved away from the community and from the state of Florida.

Similar concerns about temporary housing were expressed in the second study. In Harrison County, MS, residents and agencies both described the need to have a plan for mobile homes to be strictly temporary and not linger and become established as a permanent park or second homes at private addresses. Particularly in areas were zoning requirements are flexible, officials suggested that plans for phasing out temporary housing are critical.

The issue of occupancy and how it changes over time (i.e. the sequence of multiple families in one structure with time), is one example of where the fusion of image analysis with interviews and statistical data can provide a full picture of post-disaster recovery. Analysis of remote sensing data provides valuable data from which to monitor, measure and evaluate post-disaster recovery. When combined with contextual information provided by ancillary documents, key-informant interviews, and surveys of residents, an explanation of the patterns observed through image analysis emerges. Understanding the unintended consequences of decisions, such as the location and functionality of facilities, and how this changes over time, provides a set of lessons learned that can inform future decisions as well as aiding other communities manage their own long-term community recovery in a disaster's aftermath.

CONCLUSIONS

Understanding the ways that community recovery in the aftermath of a disaster unfolds with time, the pace, the decision-making, pitfalls, and lessons learned all combine to provide a unique source of input and validation for the community resilience-building activities that communities engage in. A community (or business or individual) who constructs and maintains resilience will (or should) recover more efficiently, equitably, and sustainably than less resilient places. In that sense, lessons learned regarding recovery can inform resilience building decisions and resilience

measurement criteria. The goal of this paper has been to highlight observations that are potentially generalizable and provide evidence of key elements of resilience. Using exemplars to highlight a unique and multi-source data fusion, the focus has explicitly been on temporary shelter and the intent is that recommendations derived from these observations would be complemented with recommendations related to other sectors of community (economic, environment, infrastructure, and social/demographic sectors).

A. Pre-disaster plans for siting and removing temporary shelters (tents to trailers) enhance community resilience and promote disaster recovery.
B. Pre-disaster plans for repairing/rebuilding low-income housing are critical to ensuring that middle and low income residents are able to return to their communities. A resilient community may or may not be one where demographic shifts result from disaster pressures, but a resilient community recovers in an equitable way when the causes and consequences of such social disruption and change are considered prior to the disaster event.
C. Rental costs and property values fluctuate substantially in the immediate, short-term and long-term aftermath of a disaster; resilient communities identify and address the causes and consequences of such fluctuations.
D. Resilient communities recognize that disasters pose opportunities to address community goals.

ACKNOWLEDGEMENTS

The authors would like to acknowledge all residents and leaders who volunteered to share their recovery experiences with our project team. Field visits and analysis were supported by an enthusiastic team of students and support staff, including Dana Rathfon (U. Delaware), Katie Correll and Mia Murray (U. Memphis), Marleen de Ruiter (U. British Columbia), and Matthew Honey (ImageCat Ltd).

This research is sponsored by a grant from the National Science Foundation (CMMI: 0926142).

REFERENCES

Berke, P. R. and Beatley, T. (1997). "*After the Hurricane: Linking Recovery to Sustainable Development in the Caribbean".* The Johns Hopkins University Press. Baltimore and London. Corsellis and Vitale. (2004). "*Guidelines on Transitional Settlements for Displaced Populations".* OXFAM Publishing, Oxford.

Farris, G. (2007). "The Major Hurricanes of 2005: a Few Facts. Science and the Storms: the USGS Response to the Hurricanes of 2005". *United States Geological Survey Circular 1306*, pp. 12-15. <http://pubs.usgs.gov/circ/1306/>. (December 3, 2008).

Faulkner, W., Barrow, W., Couvillion, B., Conner, W., Randall, L., and Baldwin, M. (2007). "Impacts of Hurricane Katrina on Floodplain Forests of the Pearl River. Science and the Storms: the USGS Response to the Hurricanes of 2005" *United States Geological Survey Circular* 1306, pp. 124-130. <http://pubs.usgs.gov/circ/1306/>. (November 11, 2008).

Graumann, A., Houston, T., Lawrimore, J., Levinson, D., Lott, N., McCown, S., Stephens, S., Wuertz, D. (2005). "Hurricane Katrina: A Climatological Perspective". *National Oceanic and Atmospheric Administration (NOAA): National Hurricane Center,* <http://www.preventionweb.net/english/professional/publications/v.php?id=1539>. (December, 12, 2008).

Haas, J. E., Kates, R. W. and Bowden, M. J. (1977). "*Reconstruction Following Disaster"*. MIT Press, Cambridge. pp. 331.

ImageCat, Inc. (2010) VIEWS™ <http://www.imagecatinc.com/services/proprietary-solutions/views>. (January 8, 2011).

Mileti, D. (1999). "*Disasters by Design: A Reassessment of Natural Hazards in the United States"*. Joseph Henry Press, Washington, D.C.

Olshansky, R. B. (2005). "Toward a Theory of Community Recovery from Disaster: A Review of Existing Literature". *Presented at 1st International Conference of Urban Disaster Reduction, Kobe, Japan*.

Pasch, R., Brown, D., and Blake, E. (2005). "Tropical Cyclone Report: Hurricane Charley: 9-14 August 2004*." National Oceanic and Atmospheric Administration (NOAA): National Hurricane Center,* <http://www.nhc.noaa.gov/2004charley.shtml> (January 5, 2009).Paton, D. and Johnston, D. (2006). "Disaster Resilience: An Integrated Approach". Charles C Thomas Publisher, Ltd., Springfield, IL.

Phillips, B. D. (2009). "Disaster Recovery". CRC Press, New York, NY.

Rubin, C. B. (1985). "The Community Recovery Process in the US after a Major Natural Disaster." *International Journal of Mass Emergencies and Disasters,* pp. 9-28.

Shelter. (2006). "Shelter after Disaster". *Shelter Meeting by the Shelter Centre*. Geneva. 16-17 November 2006.

Sphere Project 2004. Humanitarian Charter and Minimum Standards in Disaster Response, OXFAM Publishing, Oxford.

Resilience as Optimization Criterion for the Rehabilitation of Bridges Belonging to a Transportation Network Subject to Earthquake

Dan M. Frangopol[1] Dist.M.ASCE and Paolo Bocchini[2] M.ASCE

[1]Advanced Technology for Large Structural Systems (ATLSS) Engineering Research Center, Department of Civil and Environmental Engineering, Lehigh University, 117 ATLSS Drive, Bethlehem, PA 18015, USA; PH (610) 758 6103; FAX (610) 758 4115; email: dan.frangopol@lehigh.edu
[2]Advanced Technology for Large Structural Systems (ATLSS) Engineering Research Center, Department of Civil and Environmental Engineering, Lehigh University, 117 ATLSS Drive, Bethlehem, PA 18015, USA; PH (610) 758 3066; FAX (610) 738 5553; email: paolo.bocchini@lehigh.edu

ABSTRACT

This paper deals with the concept of "resilience" and proposes its use as optimization criterion for the rehabilitation of a transportation network subject to earthquake. The most earthquake damage prone components of a transportation network are certainly its bridges; therefore, the proposed approach focuses on bridge rehabilitation interventions.

The design variables of the optimization problem are the application times and durations of the interventions on bridges of the network. These durations are determined by the amount of funding invested on each bridge. Hence, the proposed methodology provides the optimal rehabilitation schedule and cost breakdown for all the bridges of the network.

A numerical application is presented to illustrate the proposed approach and to show its capabilities.

INTRODUCTION

After the occurrence of an extreme event, such as an earthquake, that heavily damages a transportation network, the rehabilitation interventions should be prioritized so that the overall serviceability of the network is restored as soon as possible. In fact, the emergency response and the economic and social recovery of the region affected by the extreme event strongly depend on the condition of the transportation infrastructure. The most used indicator to quantify the promptness and effectiveness of the restoration is resilience (Bruneau *et al*. 2003). This indicator is defined as the integral over time of the serviceability and, therefore, measures the ability to restore quickly the original network performance level (Cimellaro *et al*. 2010).

Bocchini and Frangopol (2011a) proposed a computational framework based on multi-objective optimization for the post-event rehabilitation of bridges along a

highway segment. This paper is an extension of their approach to the case of transportation networks. The two objectives of the optimization are the maximization of the transportation network resilience and the minimization of the total rehabilitation cost. The design variables of the problem are the starting time and the pace of the rehabilitation actions (i.e., damage rehabilitation rates) on the various bridges of the transportation network. Several constraints can be added to the optimization problem. For instance, a maximum total cost can be set, or the number of simultaneous interventions can be limited. Since the two objectives of the optimization are conflicting, the result is not a single solution, but a Pareto optimal set of solutions, among which the decision makers can choose one, based on economic and engineering judgment. The numerical solution of the problem is achieved by means of bi-objective genetic algorithms (Goldberg 1989), which are an optimization tool that does not require a closed form expression of the objective functions to compute the Pareto front (Deb 2001).

The use of this technique for the assisted decision making can drive and significantly enhance the infrastructure recovery process during the critical months that follow the occurrence of an extreme event. A numerical application to a realistic transportation network confirms the effectiveness of the proposed technique. Finally, it should be noted that even if the procedure and the numerical example are presented referring to the case of earthquake damage, the proposed technique is applicable in the case of any other extreme event as well.

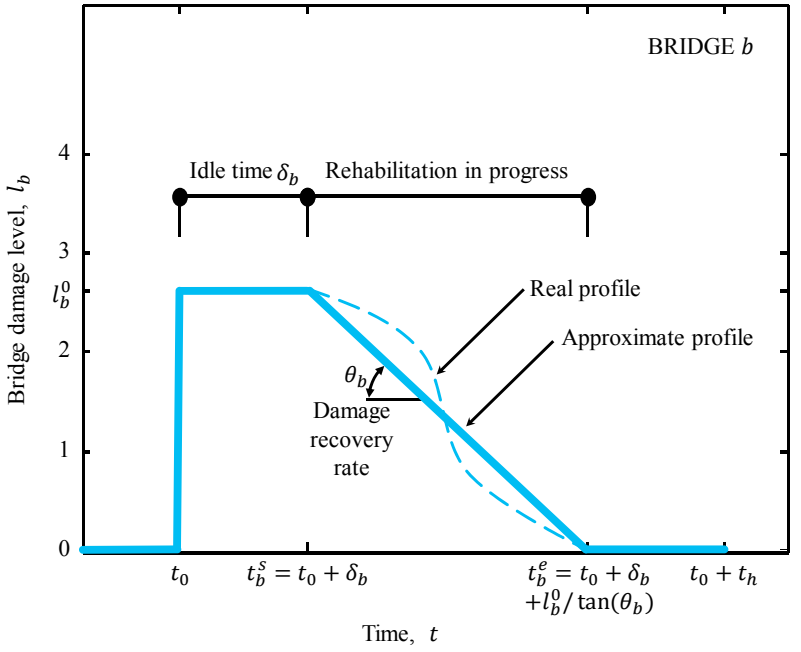


Figure 1. Bridge rehabilitation model and design variables.

BRIDGE REHABILITATION

As already mentioned, the design variables of the problem are associated with the bridge rehabilitation procedure. In particular, for each bridge b they are (i) the idle time δ_b between the occurrence of the extreme event and the beginning of the

rehabilitation activities, and (ii) the damage recovery rate θ_b. In a network with N_B bridges, the number of design variables is $2N_B$. Figure 1 provides a representation of the bridge rehabilitation process and illustrates graphically the meaning of the design variables (i.e., δ_b and θ_b). The real rehabilitation path can have a shape that is very difficult to predict. Therefore, considering also the large amount of uncertainties involved in the problem at hand, the damage recovery is approximated with a linear function.

The bridge damage level $l_b(t)$ affects the functionality of the bridge, in terms of its ability to carry traffic flows. For instance, when the damage level is at least moderate ($l_b \geq 2$), the bridge in unsafe and should be prudentially closed to traffic. Therefore, its functionality is null. The functionality of the bridge is modeled by the variable $q_b(t)$. Table 1 shows that for high damage levels, $q_b = 0$. If the damage is between minor and moderate ($1 \leq l_b < 2$) the bridge can be partially open to traffic, but its capacity should be limited. In fact, opening only some lanes the parts of the structure more affected by damage can be protected and the overall traffic loads can be reduced. This leads to a partial reduction of the bridge functionality (e.g., $q_b = 0.5$). When the rehabilitation activities start on a bridge that has damage in this range (from minor to moderate), additional lanes have to be closed and the bridge is likely to be out of service. If a bridge has only very minor damages ($0 \leq l_b < 1$), the rehabilitation activities require a partial reduction of the traffic flow capacity. However, while the rehabilitation works are not in progress, the bridge is fully open to traffic. Table 1 summarizes the bridge states and the bridge functionality for various damage levels. More accurate value of q_b can be assessed for specific bridges and types of damage.

Table 1. Bridge functionality.

Damage level	Rehabilitation in progress	Bridge state	Functionality q_b
$2 \leq l_b \leq 4$	Yes	Out of service	0
$2 \leq l_b \leq 4$	No	Out of service	0
$1 \leq l_b < 2$	Yes	Out of service	0
$1 \leq l_b < 2$	No	Partially in service	0.5
$0 \leq l_b < 1$	Yes	Partially in service	0.5
$0 \leq l_b < 1$	No	In service	1

TRANSPORTATION NETWORK RESILIENCE ASSESSMENT

A possible analytical definition of resilience is

$$R = \frac{\int_{t_0}^{t_0+t_h} Q(t)\mathrm{d}t}{t_h} \tag{1}$$

where t_0 denotes the instant in which the earthquake occurs, t_h is the investigated time horizon, and $Q(t)$ is an indicator of the "functionality" (or "serviceability") level of the considered infrastructure. In Figure 2 a graphical representation of the meaning of resilience is provided. For a fixed extreme event and time horizon (t_0 and t_h), resilience is the ratio between the shaded area under the functionality (i.e., the integral

at the numerator) and the total area (i.e., $100\% \cdot t_h = t_h$). Figure 2 shows that the functionality can also decrease during the rehabilitation process. In fact, when interventions start on bridges, they often require a temporary reduction of the functionality (e.g., a partial closure of a bridge for the work in progress). The definition of resilience in Eq. (1) takes into account all the effects of this kind.

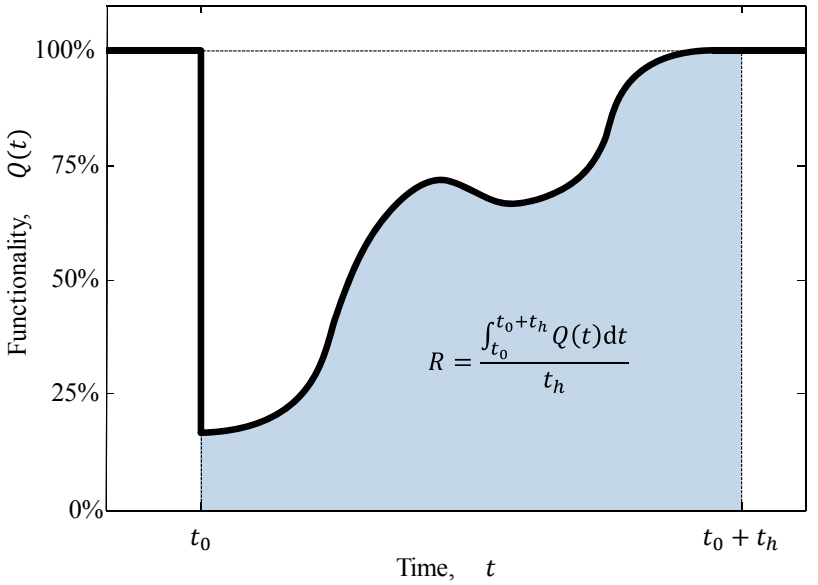


Figure 2. Definition of resilience and relationship with functionality.

Eq. (1) clearly states that the concept of resilience is based on the concept of functionality. For a transportation network, several functionality indicators have been proposed in the literature. In this paper, the performance of the network is measured as a function of the total travel time spent (TTT) and total travel distance covered (TTD) by all the users that start they trip in a predefined time frame (Bocchini and Frangopol 2011a):

$$Q(t) = \frac{\Gamma(t) - \Gamma^0}{\Gamma^{100} - \Gamma^0}\ ; \qquad Q(t)\epsilon[0,1] \subset R \tag{2}$$

$$\Gamma(t) = \frac{1}{\gamma_T \cdot TTT(t) + \gamma_D \cdot TTD(t)}\ ; \qquad \Gamma(t)\epsilon R^+ \tag{3}$$

where γ_T is a balancing factor (cost) associated with the time spent by the network users and measured in min^{-1}; γ_D is a similar factor associated with the distance traveled and measured in km^{-1}; Γ^0 and Γ^{100} are the values attained by the network performance indicator Γ in the special cases when all the bridges are out of service and in service, respectively. The quantities $TTT(t)$ and $TTD(t)$ are computed solving the complete traffic distribution and assignment problem (Bocchini and Frangopol 2011b).

The traffic flow capacity of each highway segment is affected by the functionality of the bridges that carry it, as provided in Table 1. In particular, the following model is used (Bocchini and Frangopol 2011a):

$$c_{ij} = c_{ij}^{e}\left[1 + \alpha\left(\frac{f_{ij}}{f_{ij}^{e}}\right)^{\beta}\right] \tag{4}$$

where c_{ij} is the time spent by a driver to go from node i of the network to node j; c_{ij}^{e} is the time spent to cover the same segment at free flow, considering also the limited capacity of the damaged bridges; f_{ij} is the traffic flow (number of vehicles per hour) on segment i-j; f_{ij}^{e} is the traffic flow capacity of segment i-j, considering the detrimental impact of closed or partially closed bridges; and α and β are parameters of the model. For a more detailed description of the effect of the bridge functionality on the traffic flow, the reader is referred to Bocchini and Frangopol (2011a).

FORMULATION OF THE PROBLEM

The problem is formulated as a bi-objective optimization. The first objective is the maximization of the network resilience over the investigated time horizon. The value of R is provided by Eq. (1), where the network functionality over time is computed through traffic flow analyses. The second objective is the minimization of the total present rehabilitation cost. This cost is a function of the time of rehabilitation (since it considers the discount rate of money) and the damage recovery rate (since a faster rehabilitation requires more resources). The following total present cost model can be adopted (adapted from Bocchini and Frangopol 2011a):

$$C = \sum_{b=1}^{N_B}\left[\int_{t_b^s(\delta_b)}^{t_b^e(\delta_b,\theta_b,l_b^0)} \frac{k_b \cdot \tan(\theta_b)}{(1+r)^t}\,\mathrm{d}t\right] \tag{5}$$

where subscript b runs over the bridges; $t_b^s(\delta_b)$ and $t_b^e(\delta_b, \theta_b, l_b^0)$ are the time at which the rehabilitation starts and ends on bridge b, respectively; k_b is the reference rehabilitation cost of bridge b, which can be assessed as one fourth of its total cost; and r is the annual discount rate of money.

As mentioned previously, the design variables are the idle time before the initiation of the rehabilitation δ_b and the damage recovery rate θ_b, presented in Figure 1. The first set of design variables is subject to the obvious constraint $0 \le \delta_b \le t_h$. The damage recovery rate is assumed to be constrained as well. In fact it is assumed that the recovery rate cannot be pushed by any means beyond a certain limit θ_{max}. Moreover, to exclude too slow interventions from the search domain, since they are certainly non convenient, it is also imposed that $\theta_b \ge \theta_{min}$. A constraint is also imposed on the maximum cost $C \le C_{max}$. Finally, an additional constraint is introduced in this paper. It requires that the number of simultaneous interventions N_{SI} on the bridges of the network never exceeds a prescribed value N_{SImax}. This

constraint reflects the fact that the number of large construction companies that can work in an area (especially an area that experienced an extreme event) is limited. If the maximum number of simultaneous interventions is small (e.g., half of the number of bridges) this constraint limits very significantly the domain of feasible solutions. The formulation of the optimization problem is summarized in Table 2.

Table 2. Problem formulation.

Given:	network topology;
(input)	traffic data;
	road capacities;
	secondary detour routes characteristics;
	bridge locations;
	approximate rehabilitation costs;
	discount rate of money;
	l_b^0 (post-event damage level for bridge b) $\quad \forall\, b = 1,2,\dots,N_B$;
find:	δ_b (idle time for bridge b) $\quad \forall\, b = 1,2,\dots,N$;
(design variables)	θ_b (damage recovery rate for bridge b) $\quad \forall\, b = 1,2,\dots,N_B$;
so that:	$R = maximum$;
(objectives)	$C = minimum$;
subject to:	$0 \le \delta_b \le t_h$, $\quad \forall\, b = 1,2,\dots,N_b$;
(constraints)	$\theta_{min} \le \theta_b \le \theta_{max}$, $\quad \forall\, b = 1,2,\dots,N_b$;
	$C \le C_{max}$;
	$N_{SI}(t) \le N_{SImax}$, $\quad \forall t \in [t_0, t_0 + t_h]$.

The optimization problem is solved using multi-objective genetic algorithms. At the end of the optimization, a Pareto front of solutions is provided. Each of these solutions consists in the values of δ_b and θ_b for all the bridges of the network. Therefore, each solution describes a global rehabilitation plan in terms of schedule of interventions, damage recovery rate and, in turn, cost breakdown among the various bridges. All the Pareto solutions are optimal, meaning that for each one of them it is not possible to find another solution that improves an objective without worsening the other. Decision makers choose the optimal solution that seems the most appropriate for the specific scenario under consideration.

NUMERICAL EXAMPLE

Description of the problem. A bridge network located in the Lehigh Valley, Pennsylvania, is considered for a numerical application. For illustrative purpose, a very rare earthquake with magnitude 7 and hypocenter 10 km deep is assumed to damage the bridges of the network. The value of l_b^0 is computed performing a series of fragility analyses associated with four damage states with the program HAZUS-MH MR4 (DHS 2009) and taking the expected value of the damage (Bocchini and Frangopol 2011b). The location of the epicenter, the transportation network layout, the location of the bridges, and the associated earthquake damages are shown in Figure 3. Nodes 1 and 4 represent the cities of Allentown and Easton, respectively,

while nodes 2 and 6 collect traffic from the northern and southern parts of the city of Bethlehem. Nodes 3 and 5 are highway junctions. Data on the characteristics of the nodes and of the highway segments are provided in Bocchini and Frangopol (2011b). Data associated with bridges and detour routes are collected in Table 3. The detour time is computed based on the detour length provided by the National Bridge Inventory (FHWA 2009). The detour capacity is estimated as 1500 cars/hour for the entire network, depending on the characteristics of the region (medium population density, urban) and the number of lanes of the secondary routes. The representative restoration cost is computed as one fourth of the bridge cost, as provided by the database of HAZUS.

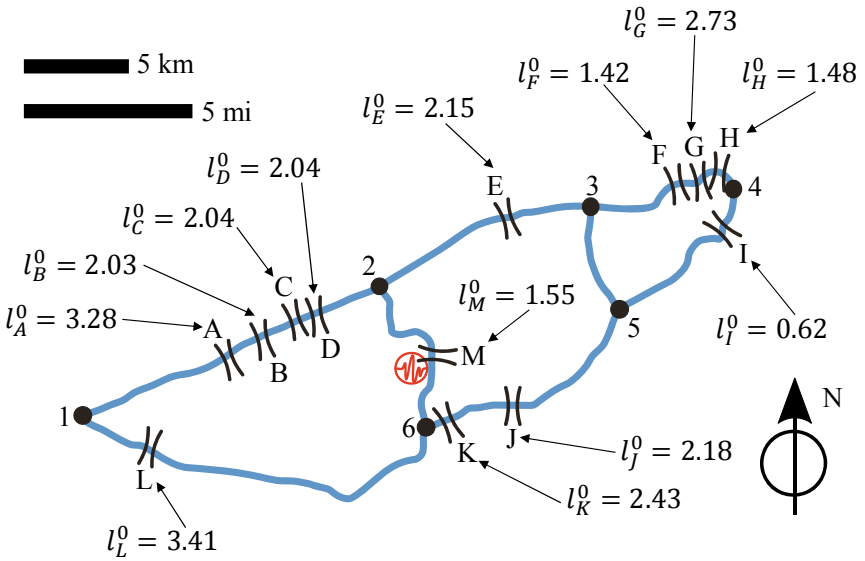


Figure 3. Layout of the network, location of the epicenter, and expected damage levels.

Table 3. Bridge characteristics.

Bridge	Detour time [minutes]	Detour capacity [cars/hour]	k_b [$]
A	12	1500	885,000
B	10	1500	889,000
C	12	1500	1,773,000
D	12	1500	1,345,000
E	26	1500	925,000
F	10	1500	731,000
G	10	1500	1,752,000
H	10	1500	731,000
I	32	1500	1,165,000
J	26	1500	3,873,000
K	16	1500	621,000
L	16	1500	928,000
M	10	1500	4,088,000

The investigated time horizon is 24 months; admissible damage recovery rates are between 0.58 and 5.67 damage recovered per year (equivalent to slopes between 30^o and 80^o in Figure 1); the maximum number of simultaneous interventions is 6; the annual discount rate of money is 5%; the maximum cost of the rehabilitations is \$8,000,000; and the parameters γ_T and γ_D are $2 \cdot 10^{-7}$ min^{-1} and $6.21 \cdot 10^{-8}$ km^{-1}, respectively.

Results of the analysis. In 1896.9 minutes, genetic algorithms running on a personal computer produced in 2006 with a single-core 3.4GHz CPU and 2GB of RAM completed 100 generations made by 400 individuals each. The resulting Pareto front is plotted in Figure 4.

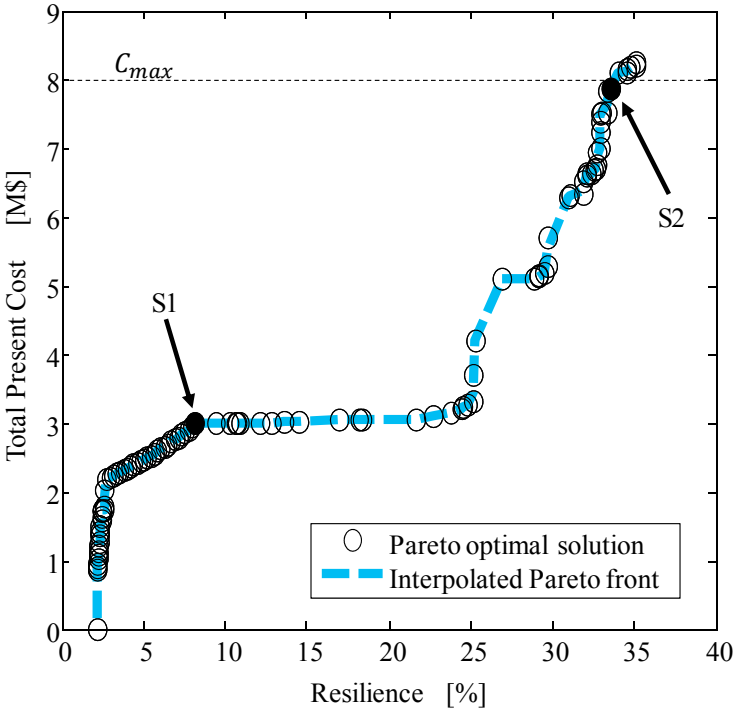


Figure 4. Pareto front of optimal solutions.

The solution indicated in Figure 4 as S1 prescribes interventions only on the critical bridge L, which is heavily damaged and affects the large volume of traffic that departs from and is headed to node 1 (Allentown). For this reason, $\delta_L = 0$, while for all the other bridges $\delta_b = t_h$. This solution is relatively inexpensive (\$2,980,000) because it affects only one bridge, but provides a value of resilience that is very limited (8.2%). The group of solutions on the left of S1 are very similar to S1, but with a slightly larger value of δ_L. Hence, the resilience that they provide is a little lower, but also the cost is lower, due to the annual discount rate of money.

The cost associated with solution S2 in Figure 4 is the closest to C_{max} . Solution S2 prescribes interventions on bridges E and L immediately, on bridge H after approximately 6 months, and on bridge B after one year. Figure 5a shows the rehabilitation schedules and the damage recovery rates (i.e., the design variables)

associated with this solution. Figure 5b presents the time-dependent network functionality. The ratio between the shaded area and the total area is the resilience associated with S2. Even though only four out of 13 damaged bridges are rehabilitated, at the end of the investigated time horizon the functionality of the network is restored to 51.6% of its original value. Figure 5c shows the cumulative cost of the interventions discounted at t_0.

It should be noticed that the strict constraints on the maximum number of simultaneous interventions and on the available funding have determined that none of the optimal solutions allows to completely restore the original network functionality. In a real scenario, this type of analysis should be used for the immediate emergency response after the occurrence of an earthquake. For the complete restoration of an infrastructure network subject to this level of damage, more resources and a longer time horizon must be considered.

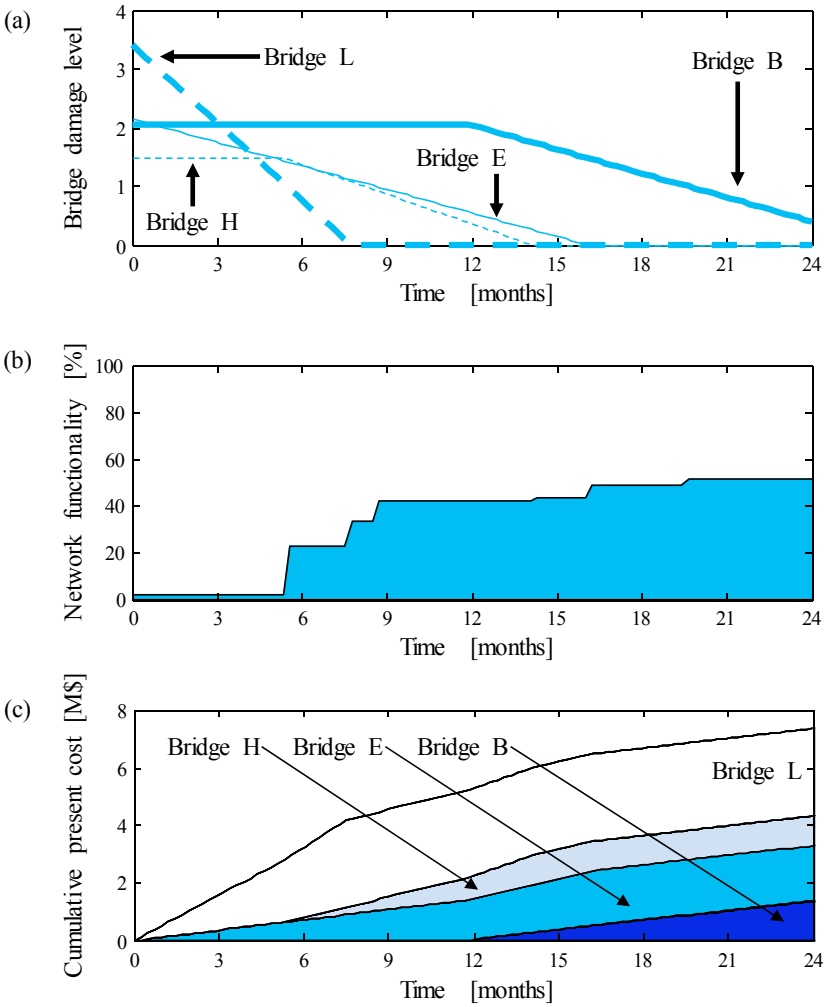


Figure 5. Rehabilitation plan associated with solution S2: (a) schedule of the rehabilitations, damage recovery rates, and damage level profiles for the bridges that are rehabilitated; (b) evolution of the network functionality and resilience (shaded area); (c) cumulative present cost of the rehabilitations.

Discussion of results. The CPU time required by the solution indicates that with any modern computer this type of computation is perfectly feasible, even in the case of complex bridge networks. The computational effort can be further reduced as follows. Approximately 97.5% of the time is used for the repeated solution of the traffic assignment and distribution problem (performed several millions times per run). The proposed procedure already builds a lookup table automatically during its execution (i.e., it stores the results of the network analysis for each bridge configuration that it investigates). This way, every time it is already available, the code retrieves the network functionality associated with a certain bridge configuration, rather than computing it again. Network owners or managers can run the code and make it build the lookup table for the set of most probable bridge configurations. In this way, in case of an extreme event, the execution of the optimization would be extremely fast. Figure 6 shows a dramatic reduction of the CPU time along the generations used by genetic algorithms. Indeed, this reduction is mostly due to the fact that the latest generations could take advantage of a more complete lookup table built along the execution.

The proposed technique automatically identifies the bridges that need to be rehabilitated first and the optimal damage recovery rates (i.e., the best cost breakdown) in order to quickly restore the original network functionality.

The new constraint introduced on the maximum number of simultaneous interventions forces the technique to select only a subset of bridges. For this example, the constraint on N_{SI} turned out to be the one that affected the most the Pareto front. In fact, in the last generation, 39% of the candidate solutions were discarded because they did not satisfy this constraint.

Since the time horizon is short (two years) the effect of the annual discount rate of money is very limited, even if a very high value was selected (5%).

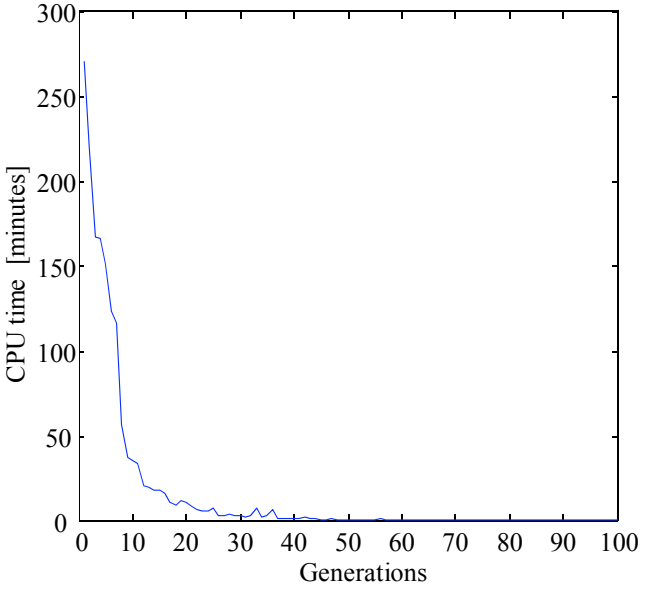


Figure 6. CPU time per generation (single-core PC produced in 2006).

CONCLUDING REMARKS

A methodology has been presented for the use of resilience as optimization criterion for the rehabilitation of bridges belonging to a transportation network subject to earthquake. This methodology provides a Pareto front of schedules and damage recovery rates for the rehabilitation interventions that maximize the network resilience and minimize the cost of interventions. The proposed approach assists decision makers to enhance the disaster management and the recovery of the region.

With respect to other techniques addressing similar issues, the one proposed in this paper extends the applicability to complex transportation networks. This is achieved through the solution of the complete traffic assignment and distribution problem. Moreover, a new constraint on the maximum number of simultaneous interventions has been introduced.

The time required for the analysis depends on the complexity of the network, on the original damage level of the bridges, and on the constraints that are imposed. The presented numerical example shows that the technique is applicable to the investigated network and the CPU time required is kept feasible by the use of genetic algorithms and the lookup table technique (Bocchini and Frangopol 2010a). It is expected that even for more complex bridge networks, the computational effort remains affordable.

AKNOWLEDGMENTS

The support from (a) the National Science Foundation through grant CMS-0639428, (b) the Commonwealth of Pennsylvania, Department of Community and Economic Development, through the Pennsylvania Infrastructure Technology Alliance (PITA), (c) the U.S. Federal Highway Administration Cooperative Agreement Award DTFH61-07-H-00040, and (d) the U.S. Office of Naval Research Contract Number N-00014-08-0188 is gratefully acknowledged. The opinions and conclusions presented in this paper are those of the writers and do not necessarily reflect the views of the sponsoring organizations.

REFERENCES

Bocchini, P., and Frangopol, D. M. (2011a). “Optimal resilience- and cost-based post-disaster intervention prioritization for bridges along a highway segment.” *Journal of Bridge Engineering*, ASCE, doi: 10.1061/(ASCE)BE.1943-5592.0000201 (in press and already available on line).

Bocchini, P., and Frangopol, D. M. (2011b). “A stochastic computational framework for the joint transportation network fragility analysis and traffic flow distribution under extreme events.” *Probabilistic Engineering Mechanics*, Elsevier, doi: 10.1016/j.probengmech.2010.11.007 (in press and already available on line).

Bruneau, M., Chang, S. E., Eguchi, R. T., Lee, G. C., O'Rourke, T. D., Reinhorn, A. M., Shinozuka, M., Tierney, K., Wallace, W., and Winterfelt, D. V. (2003).

"A framework to quantitatively assess and enhance the seismic resilience of communities". *Earthquake Spectra*, EERI, 19(4), 733-752.

Cimellaro, G. P., Reinhorn, A. M., and Bruneau, M. (2010). Seismic resilience of a hospital system. *Structure and Infrastructure Engineering*, Taylor and Francis, 6(1), 127-144.

Deb, K. (2001). *Multi-Objective Optimization Using Evolutionary Algorithms*. John Wiley and Sons.

DHS (2009). *HAZUS-MH MR4 Earthquake Model User Manual*. Department of Homeland Security; Federal Emergency Management Agency; Mitigation Division. Whashington, DC.

FHWA (2009). *National Bridge Inventory*. Federal HighWay Administration. Available on line at http://www.fhwa.dot.gov/bridge/nbi.htm (visited on December 14, 2010).

Goldberg, D. E. (1989). *Genetic Algorithms in Search, Optimization, and Machine Learning*. Addison-Wesley Professional.

Seismic Repair of RC Bridge Piers using Shape Memory Alloys

Moochul Shin[1] and Bassem Andrawes[2]

[1]Graduate Research Assistant, Department of Civil and Environmental Engineering, University of Illinois at Urbana-Champaign
Address: 3109 Newmark Civil Engineering Lab, 205 North Matthews Ave, Urbana, IL 61801, USA
Email: mshin7@illinois.edu (Presenter)

[2]Assistant Professor, Department of Civil and Environmental Engineering, University of Illinois at Urbana-Champaign
Address: 3122 Newmark Civil Engineering Lab, 205 North Matthews Ave, Urbana, IL 61801, USA.
Email: andrawes@illinois.edu (Corresponding Author), Phone: (217) 244-4178

ABSTRACT

This experimental study focuses on investigating the feasibility of using shape memory alloy (SMA) spiral to conduct emergency repairs on severely damaged reinforced concrete (RC) bridge piers. The studied repair technique can be implemented in less than 24 hours and hence can be used to rapidly restore the functionality of lifeline bridges that are severely damaged by an earthquake. The proposed repair technique can also ensure the safety and structural integrity of important bridges against strong aftershocks. Unlike other repair techniques such as composite jackets, which utilize the concept of passive confinement, this proposed technique relies on the concept of concrete *active confinement* to enhance the strength and ductility of severely damaged concrete. Research has shown that active confinement is a more superior confinement technique to passive confinement; however, with conventional materials, its fast application on-site in case of an emergency could be a challenge. This study presents an easy and fast method to apply active confinement using SMAs. The thermally activated shape recovery feature of SMAs is used to apply the active confining pressure at the damaged locations. To examine the proposed technique, two 1/3-scale RC columns which were severely damaged are repaired using SMA spirals and retested. The damage sustained by the two columns is localized primarily at the column base (i.e. at the plastic hinge zone), which is typical in seismically damaged slender columns. The damages in both columns are in the form of concrete cover spalling, concrete core crushing, and buckling and rupture of at least one of the longitudinal rebars. The repaired columns are tested under quasi-static cyclic loading. The results are compared with those of the as-built columns. The experimental results show that the repaired columns have fully restored their lateral stiffness, strength and hysteretic energy dissipation capability. The results of this study clearly illustrate the effectiveness of the proposed technique for emergency repair applications.

INTRODUCTION

There is a continuous need for developing rapid and robust emergency structural repair methodologies for ensuring the safety of our societies from natural hazards such as earthquakes. In order to mitigate the impacts of such hazards on our societies,

one approach is to secure critical life-line structures against possible damages and malfunction. When life-line bridges are severely damaged, the functionality of the entire transportation network is impacted, thus delaying emergency response teams from taking a swift action. In many cases, severely damaged reinforced concrete (RC) columns supporting life–line bridges have jeopardized safety and functionality of the bridges. Therefore, this paper focuses on addressing the emergency repair of severely damaged RC bridge columns.

The majority of the repair techniques currently at hand suggest the use of either fiber reinforced polymer (FRP) sheets or concrete jackets. One of the recent studies that explored the use of carbon-FRP (CFRP) sheets to repair already damaged columns was conducted by Vosooghi et al. (2008). Prior to this study there was another study that focused on using prefabricated FRP composite straps for seismic damage repair of circular and rectangular columns (Saadatmanesh et al. 1997). These studies reported improvements in the strength and ductility of the repaired columns. However, a major challenge when using FRP sheets for rapid repair is the time required for the resin to cure under ambient climate conditions which could extend up to a week or more. On the other hand, some studies attempted the use of concrete jackets for repair (Bett et al. 1988; Fukuyama et al. 2000; Lehman et al. 2001). The results of the research were satisfactory; however, this technique also requires considerable labor and time, which will impose significant delays in the opening of damaged bridges. Therefore, this paper focuses on presenting and investigating experimentally a new rapid repair technique for severely damaged RC columns using shape memory alloy (SMA) spirals. The new technique is designed specifically for emergency situations, and thus will help in restoring the functionality of severely damaged structures in less than 24 hours. Two damaged RC columns were repaired and tested under quasi-static cyclic loads.

REPAIR TECHNIQUE USING SMA SPIRALS

Utilizing the recovery stress of prestrained SMA spirals associated with the shape memory phenomenon of SMA is the key point of the new repair technique. As wrapping the damaged region of the RC column with the prestrained SMA spirals and providing the spirals with high enough temperature, an active confining pressure is applied in the form of hoop stress on the damaged region of the column, and the active confining pressure contributes to restore the strength and flexural ductility of the damaged column.

For this particular application, approximately 6%-prestrained SMA wires in a martensite phase by manufacturer were used. It is important to maintain the active confining pressure even at a wide range of ambient temperature for its service life. Therefore, an alloy whose thermal hysteresis is wide enough has to be used, and the ternary NiTiNb alloy was selected in this study for that reason. The thermal hysteresis width of NiTiNb is typically around 130 ^{o}C, with its martensite start temperature (M_s) being approximately -50 ^{o}C (Duerig et al. 1990). Figure 1 depicts schematic of a wide hysteresis SMA with the expected range of ambient temperature. Since the expected range of ambient temperatures is greater than M_s, the alloy should remain in the austenite phase when the ambient temperature drops down after heating.

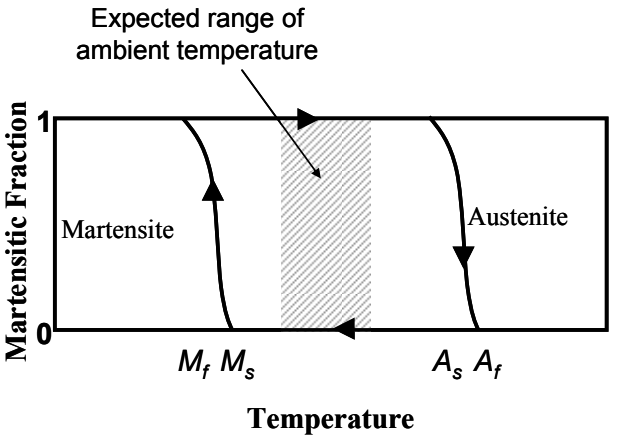


Figure 1. Martensitic fraction vs. temperature of a SMA with wide thermal hysteresis.

In an earlier study by the authors, thermo-mechanical tests on the NiTiNb wires were conducted (Shin and Andrawes, 2010a). From the experimental tests, the stabilized recovery stress of SMA was recorded as 459.9 MPa even at room temperature (16 ^{o}C) after the temperature of SMA wire was heated approximately up to 200 ^{o}C. This stable recovery stress was continually exploited in this study to apply the active confining pressure as a rapid repair technique to restore damaged columns' strength and flexural ductility.

The proposed repair technique consists of the following steps: (1) removing loose concrete, (2) straightening and/or coupling any buckled or ruptured longitudinal reinforcing bars, (3) injecting epoxy into concrete cracks, (4) applying quick-setting cement-based mortar to replace the removed concrete, (5) wrapping the damaged portion with the prestrained SMA wire in the form of a spiral, and heating the SMA spiral by using a fire torch or by passing an electric current.

SPECIMENS DESCRIPTION AND DAMAGE HISTORY

As-built Specimens

Two reduced scale (1/3-scale) single-cantilever RC columns were repaired with the proposed technique using SMA spirals, and tested under quasi-static lateral cyclic loading. The damaged columns in a previous study conducted by the authors (Shin and Andrawes, 2010b) were used. One of the columns (C1) was damaged under an incrementally increasing displacement-controlled lateral cyclic load, while the other column (C2) was damaged accidentally due to an error in the control system which caused the column to fail under excessive monotonic load. Figure 2 shows details of the as-built columns and the steel reinforcing rebars. The effective height of the column was 1270 mm, and the diameter of the cross section of the column was 254 mm with 25.4 mm clear cover. The dimensions of the footing were 1168 mm x 1168 mm x 406 mm. Eight No.4 (13 mm diameter) reinforcing bars were used for the longitudinal reinforcements, while No. 2 (6 mm diameter) transverse ties were placed every 102 mm for the transverse reinforcement. The average compressive strength of

the concrete was 40 MPa at the day of testing. Figure 3 shows the load protocol adopted in the tests.

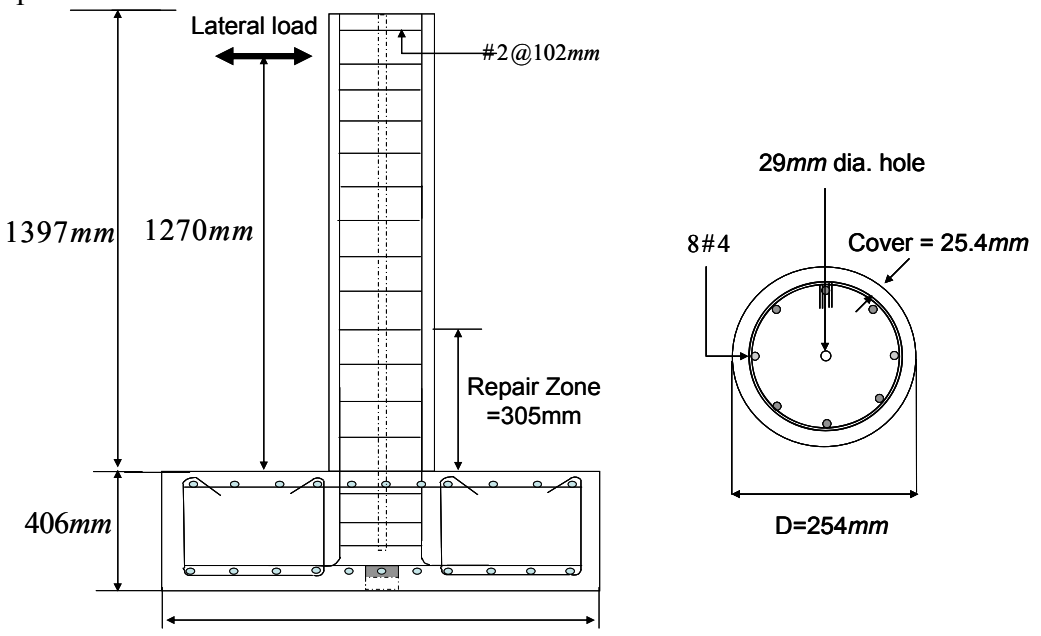


Figure 2. Elevation and cross section of as-built columns.

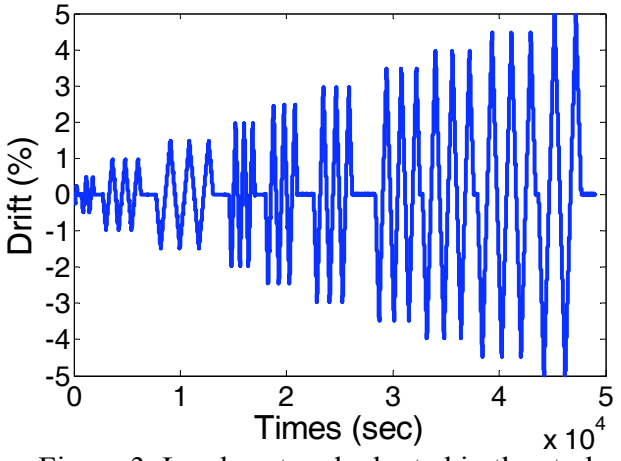
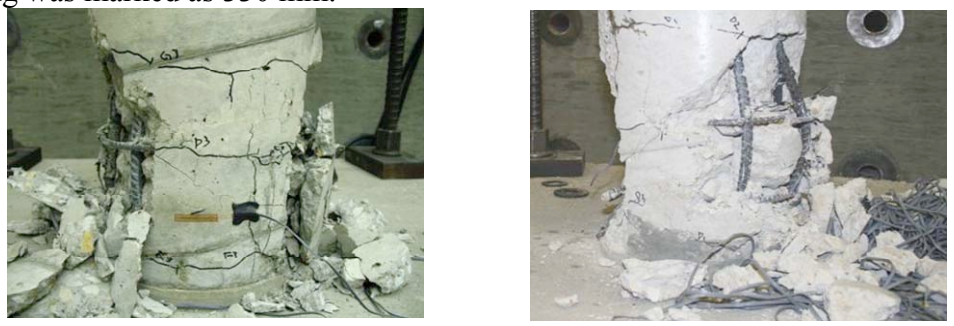


Figure 3. Load protocol adopted in the study.

Behavior and Damage of As-built Column C1

When column C1 reached the 1.5% drift ratio, the longitudinal reinforcing bars started yielding, and the average maximum strength was recorded as 34.0 KN. Also, at the drift ratio of 3.5%, cover concrete had spalled significantly, after which, the core concrete and the two longitudinal bars located near the extreme fibers started crushing and buckling, respectively. When the column reached 4.2%-drift, one of its longitudinal rebars ruptured, which resulted in the degradation of the strength abruptly by 23%. The maximum drift the column experienced was 5%-drift ratio. Figure 3.a shows a picture of the damaged C1 column. The damage of the column consisted of: 1) crushed cover and core concrete on both sides of the column, 2) one ruptured and five buckled longitudinal reinforcing bars, and 3) excessive opening of

transverse reinforcement. The height of the formed plastic region from the top of the footing was marked as 330 mm.



(a) C1 (b) C2

Figure 3. Damage sustained by columns C1 (a) and C2 (b).

Behavior and Damage of As-built Column C2

It was planned for Column C2 to be tested under the same cyclic load protocol used for the column C1. However, at a drift ratio of 1.5%, the hydraulic actuator went out of control exerting a maximum drift ratio of about 7% on the specimen in one direction. Due to the accident encountered during testing, no data was recorded after the 1.5% drift. Figure 3.b shows a picture of the damaged specimen under the excessive monotonic loading. Since the column failed primarily under the monotonic loading in one direction, the concrete at one side was completely crushed, while at the other side, the concrete was cracked due to excessive tension. Therefore the damage of the column c2 was unsymmetrical while the damage of the column C1 was symmetrical. In addition, since column C2 was not subjected to significant cyclic loading at high drift ratios as column C1, the reinforcing bars of column C2 had buckled without experiencing any ruptures. The height of the damaged plastic region was marked as 330 mm.

REPAIRED SPECIMENS

In order to repair the two damaged columns and restore the functionalities of the columns in less than 24 hours, a five-step repair process had been taken. Each step of the repair process was illustrated in figure 4. First, crushed and loose pieces of concrete were removed from the damaged region of the columns, and the steel reinforcing bars were exposed. Figure 4.a shows the concrete surface of column C1 after removing the crushed concrete. Second, slightly buckled longitudinal reinforcing bars were straightened, and the ruptured bars were connected using rebar couplers (figure 4.b). As noted earlier, only one reinforcing bar was ruptured and needed coupling in column C1. For column C2, however, no longitudinal rebars were ruptured, but three of the rebars buckled severely after being damaged by the excessive monotonic loading. To adjust these severely buckled rebars, it required to cut the bars, and reconnect them with couplers. Third, pressurized epoxy was injected to fill the cracks of the concrete in this repair process (figure 4.c.). Steps one through



(a) Concrete removal



(b) Steel adjustment



(c) Epoxy injection



(d) Mortar application



(e) Heating SMA spirals



(f) Repaired column

Figure 4. Pictures of the five-step emergency repair process.

three took approximately three hours. Forth, the damaged region was filled with quick-setting mortar (figure 4.d). The nominal compressive strength of the mortar under controlled environmental conditions at an age of 24 hours was 31.0 MPa. To examine the strength of the mortar in the laboratory environment where the columns were tested, three 76 mm x 152 mm cylinders were cast using the quick-setting mortar and tested after 24 hours. The strength of the cylinders was found to be 21 MPa, which is 53% of the compressive strength of the concrete used in casting the as-built columns. While curing the mortar, the fifth step of the repair process proceeded. The columns were wrapped with the SMA spirals at the repaired region (i.e. 330 mm

from the column base) with 25mm pitch spacing, and heated using a fire torch as shown in figure 4.e. Figure 4.f shows a picture of the repaired column after the completion of the repair process. It took approximately 24 hours from the first step of repair process until the onset of the column testing. However, it is important to note that the whole repair process from the first step to the fifth step was completed in less than 15 hours.

TEST-SETUP

Figure 5 shows schematic of the test setup used in this study. The columns were subjected to quasi-static lateral cyclic loading protocol similar to the one previously shown in figure 3. A 445 KN servo-controlled hydraulic actuator with a stroke of ± 254 mm was used to apply the lateral loading at the effective height of 1270mm. The constant axial force was applied on the column during the test, and it was maintained as 116 KN, which represented 5% of the gross section compressive strength of the as-built columns. A 445 KN hydraulic actuator was used to apply the axial force, and a load cell was mounted on the top of the column, and the load cell was anchored to a 15.2 mm-diameter seven wire steel strand located at the center of the column. Additionally, to measure the net displacements of the column, four Linear Variable Differential Transformers (LVDTs) were installed Three LVDTs were placed between the floor and the footing to capture the rotation of the footing and its displacement relative to the floor. The last LVDT was installed to measure the relative displacement between the reaction wall and the actuator's steel and concrete blocks.

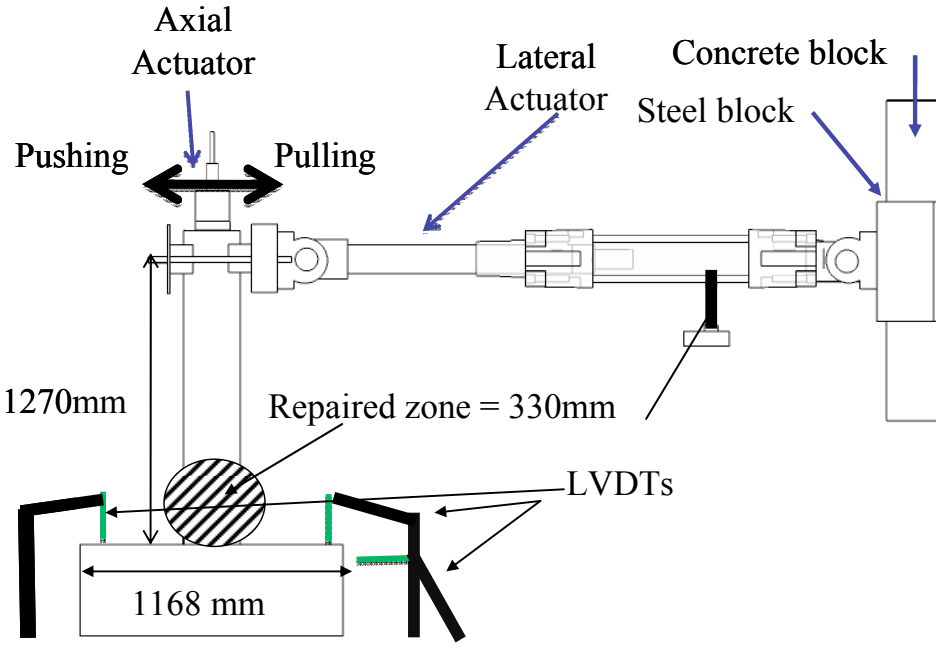


Figure 5. Schematic of the test set-up

TEST RESULTS

Column C1

Figure 6 shows a comparison between the lateral force versus displacement relationships of the as-built and the repaired C1 column. The repaired column started yielding at a drift ratio of 0.7%, and the average maximum strength recorded under pushing and pulling was 34.2 KN. At a drift ratio of 2%, the strength of the repaired column dropped abruptly by 28% due to the rupture of one of the longitudinal reinforcing bars. In the succeeding cycle, another rebar was ruptured, which resulted in reducing the strength to 52% of its maximum strength. Based on the comparison between the average strengths of the repaired and as-built columns, it was concluded that the emergency repair technique using SMA spirals performed on the severely damaged column was capable to fully restore the as-built column's lateral strength. Furthermore, the average initial stiffness of the repaired column was found to be 3.4 KN/mm, which is 54% higher than that of the as-built column and 930% higher than the residual (secant) stiffness of the damaged column.

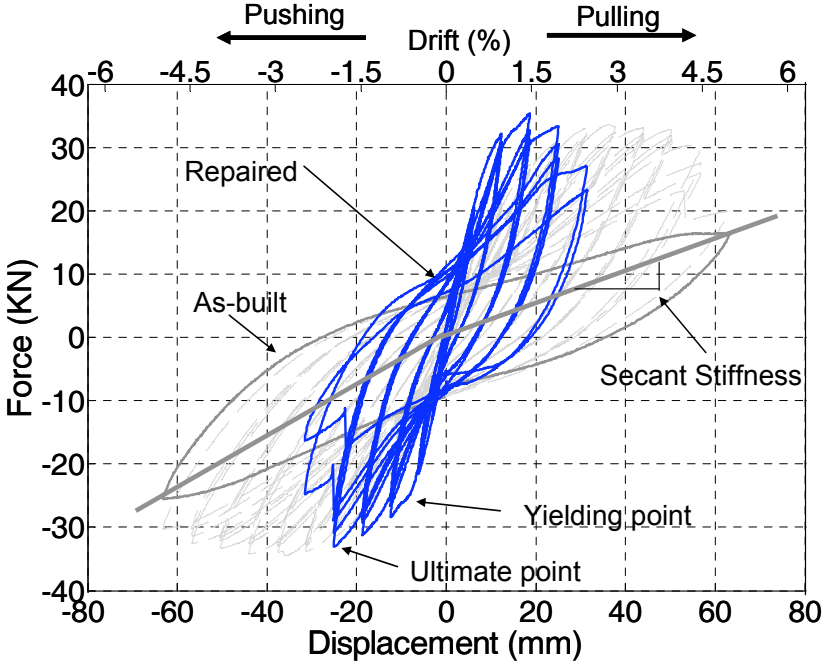


Figure 6. Comparison between the cyclic force vs. displacement relationships of the as-built (dashed line) and the repaired (solid line) C1 column.

Column C2

Figure 7 shows a comparison of the lateral force versus displacement relationship between the as-built and the repaired column C2. The repaired column started yielding at a drift ratio of 0.6%, and the maximum strength recorded was 41.3 KN at 1.5% drift ratio. The cyclic behavior of the repaired column C2 was unsymmetrical, and the lateral strength of the column degraded gradually, instead of showing an

sudden drop unlike the repaired column C1. The slippage of the coupled rebars located on one side of the repaired column during testing was identified as a main reason for the unsymmetrical behavior of the repaired column C2 after the completion of the test. The failure of the couplers to fully connect the rebars resulted in a reduced strength of the rebars, which led to significantly less strength for the column when "Pushed" (see figure 7). On the other hand, when the column was "Pulled", it showed satisfactory behavior since the rebars resisting tension were relatively in fair condition and only sustained minimal damage during the first round of testing. Assessing the behavior of the column when pulled, one can observe that the strength of the repaired column exceeded that of the as-built column by 21% (based on the predicted maximum strength of the as-built column, 34.5 KN). Also, the average initial stiffness of the repaired column in both pulling and pushing directions was 4.2 KN/mm, which exceeded the initial stiffness of the as-built column by 47%.

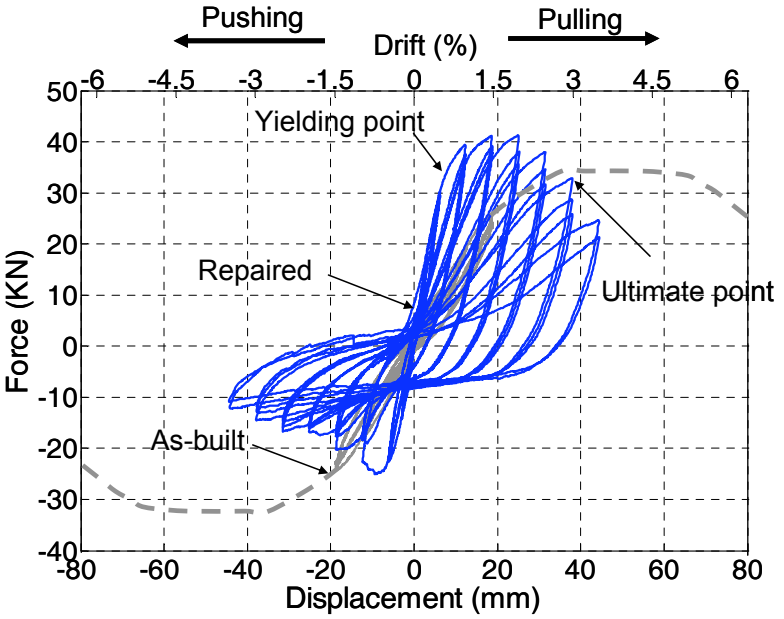


Figure 8. Comparison between the force vs. displacement relationships of the as-built (dashed line) and the repaired (solid line) C2 column.

CONCLUSIONS

This paper presented a new emergency repair technique for severely damaged RC columns using prestrained SMA spirals. The thermally-triggered recovery stress of prestrained SMAs was used to exert large external active confining pressure on the concrete at the repaired region of the damaged column in a short time. Two reduced scale (1/3-scale) RC single cantilever columns (C1 and C2) that were severely damaged in a previous study were repaired using the new repair technique, and retested under quasi-static lateral cyclic loading. The repair process of each column was conducted in less than 15 hours and the columns were tested in less than 24 hours. Test results revealed that the lateral strengths and the initial stiffness of both repaired columns were fully restored or even enhanced, It is important to note that the

recovered properties of the repaired columns are mainly attributed to the ability of the SMA spirals to apply and maintain active confining pressure on the damaged region of the columns, which increased the strength of the already damaged concrete and delayed its damage by increasing its ultimate strain. Finally, this paper showed that the proposed repair technique is effective and could be implemented successfully in a short time and thus could be used in emergency situations to maintain or restore the functionality of damaged lifeline structures.

REFERENCES

Bett, B. J., Klingner, R. E. and Jirsa, J. O. (1988) "Lateral Load Response of Strengthened and Repaired Reinforced Concrete Column." *ACI Structural J.,* 499-508.

Duerig, T. W., Melton, K. N., and Proft, J. L. (1990) "Wide Hysteresis Shape Memory Alloys." *Engineering Aspects of Shape Memory Alloys,* 130-136.

Fukuyama, K., Higashibata, Y., and Miyauchi, Y. (2000) "Studies on repair and strengthening methods of damaged reinforced concrete columns." *Cement & Concrete Composites,* 22, 81-88.

Lehman, D. E., Gookin, S. E., Nacamuli, A. M., and Moehle, J. P. (2001) "Repair of Earthquake-Damaged Bridge Columns." *ACI Structural J.* **,**98, 233-242.

Saadatmanesh, H., Ehsani, M. R., and Jin, L. (1997) "Repair of Earthquake-Damaged RC Columns with FRP Wraps." *ACI Structural J.,* 94, 206-214.

Shin, M. and Andrawes, B. (2010a) "Experimental investigation of actively confined concrete using shape memory alloys." *Engineering Structures,* 32, 656-664.

Shin, M. and Andrawes, B. (2010b) "Experimental Study of Concrete Columns confined with Shape Memory Alloys." *9th U.S. National and 10th Canadian Conference on Earthquake Engineering, Toronto, Canada, July 25-29.*

Vosooghi, A., Saiidi, M. S., and Gutierrez, J. (2008) "Rapid repair of RC bridge columns subjected to earthquakes." *Proceedings of 2nd International Conference on Concrete Repair, Rehabilitation, and Retrofitting (ICCRRR 2008), Cape Town, South Africa*

Seismic Protection of Bridge Structures using Shape Memory Alloy-based Isolation Devices

O. E. Ozbulut[1] and S. Hurlebaus[2]

[1]Zachry Department of Civil Engineering, Texas A&M University, 3136 TAMU College Station, TX 77843; PH (979) 845-9300; email: ozbulute@tamu.edu
[2]Zachry Department of Civil Engineering, Texas A&M University, 3136 TAMU College Station, TX 77843; PH (979) 845-9570; email: shurlebaus@civil.tamu.edu

ABSTRACT

This study compares the performance of two smart isolation systems that utilize superelastic shape memory alloys (SMAs) for seismic protection of isolated bridges during strong earthquakes. The first isolation system is an SMA/rubber-based (SRB) isolation system and consists of a laminated rubber bearing that decouples the superstructure from the bridge piers and an SMA device that provides additional energy dissipation and re-centering capacity. The second isolation system, named as superelastic-friction base isolator (S-FBI), combines the superelastic SMAs with a flat steel-Teflon bearing rather than a laminated rubber bearing. Seismic energy equations of a bridge structure with SMA-based isolation systems are established by absolute and relative energy balance formulations. Nonlinear time history analyses are performed in order to assess the effectiveness of the isolation systems and compare their performance. The program RspMatch2005 is employed to generate spectrum compatible ground motions that are used in dynamic time history analyses of the isolated bridge. The results indicate that SRB isolation system produces higher seismic input energy, recoverable energy and base shears as compared to the S-FBI system. Also, it is shown that combining superelastic SMAs with a sliding bearing rather than rubber bearing significantly reduce the amount of the required SMA material.

INTRODUCTION

Strong earthquakes can be considered as the most significant and possibly most frequent natural hazard that causes damage to the bridge structures. Severe damages or complete collapses have been observed in numerous bridges during the past earthquakes. Since the bridges are lifelines of the transportation network, damaged bridges within the highway system cause an increase in travel time and distance. Therefore, indirect economic loss can reach to significant levels besides the direct loss resulting from bridge damage (Enke *et al*., 2008). To reduce the damaging effects of earthquakes on bridge structures, there have been intensive research efforts in the field of structural engineering over the past decades. Several innovative design strategies have been developed and employed to improve response of bridges

subjected to seismic loads. Among them, seismic isolation has been most commonly used method to minimize the damaging effects of strong ground motions.

Seismic isolation aims to reduce earthquake energy that enters to the structure by providing flexible interfaces which decouple the support of a structure from the horizontal motions of the ground. For seismically isolated bridges, the isolation bearings are placed between the superstructure and the top of the substructure (the piers and abutments). Under service loading, they behave as a conventional bridge bearing. During an earthquake loading, the seismic isolation (i) reduces the lateral forces in the superstructure by elongating the fundamental period of the structure and dissipating energy and (ii) concentrates the lateral displacements at the isolation level, i.e. limits the structural deformations of the piers. A variety of devices including rubber isolation systems that combine laminated rubber bearings and some mechanical dampers as well as sliding-type isolation systems that filter out earthquake forces via the discontinuous sliding interfaces have been developed and used for seismic isolation.

To improve the response of isolated structures, several researchers have proposed smart isolation systems which combine smart materials with conventional bearings. Shape memory alloys (SMAs) are a unique class of metal alloys that have the ability to recover extensive deformations upon removal of the external load. Superelastic SMAs display hysteretic energy dissipation capacity and have substantial resistance to fatigue and corrosion. Due their appealing characteristics, superelastic SMAs have been considered as an isolation component by a number of researchers to develop a smart isolation system. Wilde *et al.* (2000) proposed a base isolation system that is composed of a laminated rubber bearings and an SMA device for protecting elevated highway bridges from the hazard of earthquakes. Ozbulut and Hurlebaus (2010a) studied the performance of a superelastic-friction base isolator (S-FBI) that combines a flat sliding bearing and a superelastic SMA device. They identified the optimum design parameters of the S-FBI system for seismic protection of bridges against near-field earthquakes. As an alternative to conventional rubber isolators, Ozbulut and Hurlebaus (2010b) evaluated the performance of a smart rubber bearing system with shape memory alloys. In particular, they explored the effectiveness of SMA/rubber-based (SRB) isolation systems in mitigating response of the bridge structures subjected to near-field earthquakes by performing a sensitivity analysis. Although both the S-FBI system and SRB system have been found to be an effective isolation system when their design parameters are judiciously selected, further work is needed to compare the efficiency of these two SMA-based isolation systems.

Energy-based concepts have been considerably used in the earthquake resistant design of structures since an energy-based design method was introduced by Housner (1956) in the mid 1950s. The basic idea in the energy-based design is that the *energy demand* during a seismic excitation should be less than the *energy supply* of a structural system. In view of energy-based concepts, in seismic isolation, the goal is to reduce the seismic input energy to the system and dissipate the input energy through damping mechanisms. Therefore, an optimal isolation system should minimize the energy transmitted to the structure while dissipating the most of the energy through nonlinear hysteretic deformations in the isolation device with only a

small amount of left energy that can cause damage on the main structural system (Austin and Lin, 2004).

The goal of this study is to assess and compare the effectiveness of two different SMA-based isolation systems, namely the S-FBI system and SRB isolation system by conducting nonlinear time history analyses with energy balance assessment. First, the energy balance equations are formulated for an isolated bridge structure. Both absolute and relative energy formulations are considered and the relevance of using them for the seismic evaluation of structures subjected to various earthquakes is discussed. Then, the efficacies of the S-FBI system and SRB isolation system for seismic protection of bridges are assessed by conducting nonlinear time history analyses.

MODELING OF ISOLATED BRIDGE AND SELECTED GROUND MOTIONS

A three-span continuous bridge is selected for the numerical simulations (Wang *et al*., 1998). The deck of the bridge has a mass of 771.1×10^3 kg, and the mass of each pier is 39.3×10^3 kg. The bridge has a total length of 90 m, and each pier is 8 m tall. The moment of inertia of piers and Young's modulus of elasticity are given as 0.64 m^4 and 20.67×10^9 N/m^2, respectively. The fundamental period of non-isolated bridge is 0.45 s. Since the isolation systems installed at the abutment and pier have similar characteristics and therefore, the seismic response of the bridge at the abutment and pier have the same trend, only an internal span is modeled.

Figure 1 shows a two-degree-of-freedom model of the isolated bridge with the S-FBI system and SRB system. The S-FBI system combines a superelastic SMA device with a flat steel-Teflon bearing, whereas the SRB isolation system combines the SMA device with a laminated rubber bearing rather than a sliding bearing. The SMA device simply consists of multiple loops of superelastic NiTi wires wrapped around low-friction wheels. The pier is assumed to remain linear-elastic and modeled with a linear spring and dashpot. The restoring force of the S-FBI system is given as

$$F_{SFBI} = F_f + F_{SMA}, \tag{1}$$

where F_f and F_{SMA} denote the frictional resistance force of the steel-Teflon sliding bearings and the nonlinear force of the SMA device, respectively. A hysteretic model is used to simulate the force of the sliding bearings (Constantinou *et al*., 1990). The frictional force at a sliding interface is given by

$$F_f = \mu W Z \tag{2}$$

where μ represents the coefficient of friction, W is the normal load carried by the bearing interface, and Z is a hysteretic dimensionless quantity computed from following equation

$$Y\dot{Z} + \gamma|\dot{u}_b||Z||Z|^{n-1} + \beta\dot{u}_b|Z|^n - \dot{u}_b = 0\,, \tag{3}$$

where Y is the yield displacement of the sliding bearing chosen as 0.0005 m and, γ, β, and n are dimensionless parameters that control the shape of the hysteretic curve and have the values of 0.9, 0.1 and 1, respectively.

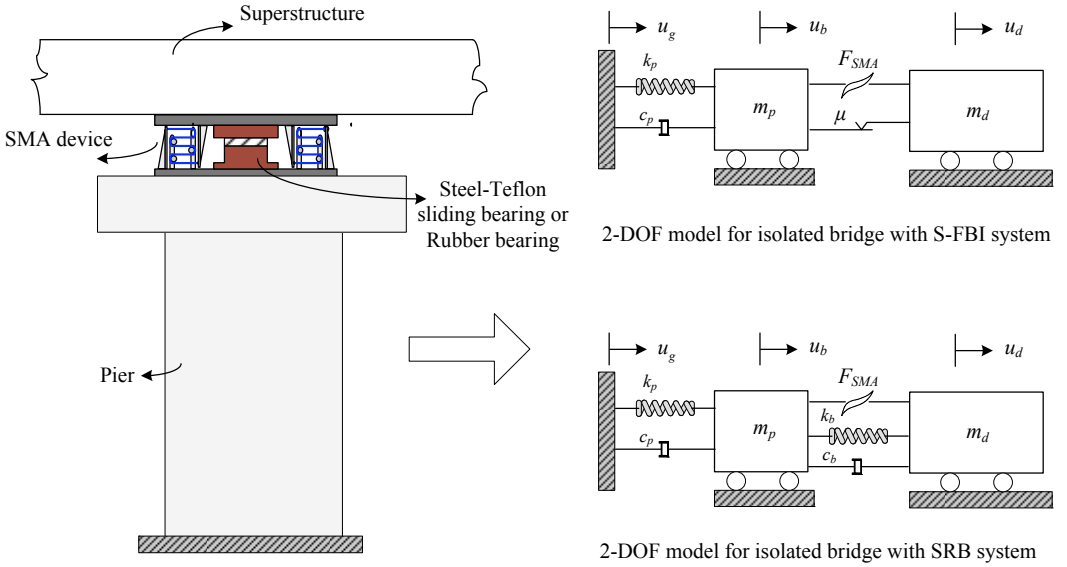


Figure 1. Model of isolated bridge structure

A neuro-fuzzy model developed by Ozbulut and Hurlebaus (2010c) is used to simulate the force-deformation behavior of the SMA device. Neuro-fuzzy modeling refers creating a fuzzy inference system (FIS) that is trained by a learning algorithm based on neural networks. The FIS maps an input space to an output space by means of fuzzy if-then rules. Adaptive neuro-fuzzy inference system (ANFIS) is a soft computing approach that employs neural network strategies to develop a fuzzy inference system whose parameters cannot be predetermined. Ozbulut and Hurlebaus (2010c) used the ANFIS to create a model of superelastic SMA wires and the details in regard to the neuro-fuzzy model of the NiTi wires can be found in their work.

The restoring force developed in the SRB isolation system is given by

$$F_{SRB} = c_b \dot{u}_b + k_b u_b + F_{SMA} \tag{4}$$

where c_b and k_b are the viscous damping and initial stiffness of the laminated rubber bearing, respectively; $\dot{u}_b$ and u_b are the velocity and deformation of the bearing, respectively; and F_{SMA} is the force of the SMA device.

Four ground motion records, namely, 1940 El Centro, 1992 Landers, 1992 Erzincan, 1999 Kocaeli are selected as seismic loading. Note that the 1940 El Centro record resembles a typical far-field ground motion; the 1992 Landers and 1992 Erzincan records are near-field ground motions characterized by forward directivity and the 1999 Kocaeli record is a near-field earthquake with fling effect. Near-field earthquakes are characterized by long period and large- velocity pulses. While the near-field records with forward directivity have double-sided velocity pulses, fling motions are characterized by a unidirectional large amplitude velocity pulse.

The program RSPMatch 2005 is used to modify selected time histories so that their response spectra are compatible with the selected target spectrum. A response spectrum constructed as per the International Building Code (2000) for a site in

southern California, assuming firm rock conditions is selected as the target spectrum (Malhotra *et al*., 2003). Figure 2 shows the target response spectrum used in the analysis and response spectra of selected ground motions for 5% damping level before and after spectral matching.

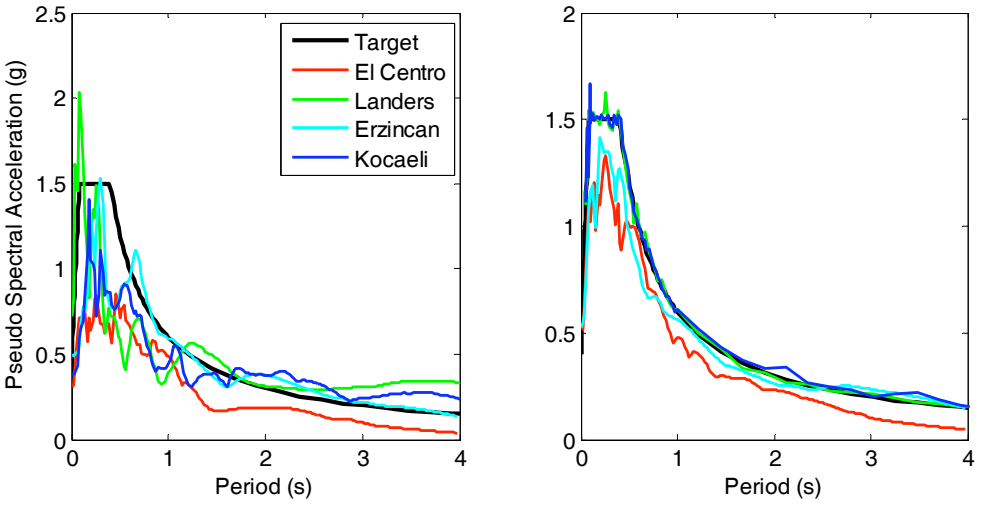


Figure 2. Model of isolated bridge structure

SEISMIC INPUT ENERGY FORMULATIONS FOR AN ISOLATED BRIDGE

In previous studies, in order to quantify the energy imparted to the structures, the absolute energy equation was used by some researchers (Park and Otsuka, 1999; Takewaki, 2004), while the relative energy formulation (Fajfar and Vidic, 1994; Ordaz *et al.* 2003) was employed by others. Kalkan and Kunnath (2008) investigated the relevance of using absolute and relative energy formulation in seismic evaluation of structures that are subjected to near-field ground motions. They found that the difference between absolute and relative energy input to structural systems during near-field earthquakes is much larger than that of in the case of far-field earthquakes. They suggested that selection of appropriate energy measure for near-field earthquakes should be based on the shape and period of the dominant pulse in the ground motion record and the vibration properties of the structural system. It was noted that arbitrarily using absolute or relative energy definitions for near-field ground motions can result in overlooking significant information.

The absolute energy balance equation of an isolated bridge modeled as two-degrees-of-freedom system can be written as

$$\frac{1}{2}\{\dot{u}_t\}^T\mathbf{M}\{\dot{u}_t\}+\int_0^t\{\dot{u}\}^T\mathbf{C}\mathrm{d}\{u\}+\int_0^t\mathbf{F}[u,\dot{u}]\mathrm{d}\{u\}=\int_0^t\{m\}^T\{\ddot{u}_t\}\mathrm{d}u_g(\tau) \qquad (5)$$

where $\{u_t\}$is the vector of absolute displacements of the system, $\{u\}$is the vector of relative displacements of the system, $\mathbf{M}$ = (2×2) diagonal mass matrix, $\mathbf{C}$ = (2×2) damping matrix, and $\mathbf{F}[u,\dot{u}]$= (2×1) vector of restoring forces, $\{m\}$= (2×1) vector of lumped masses and u_g is the ground displacement. Equation (5) can be simply expressed as

$$E_K + E_\xi + E_A = E_I \,, \tag{6}$$

where

$$E_K = \frac{1}{2}\{\dot{u}_t\}^T \mathbf{M}\{\dot{u}_t\} \tag{7}$$

$$E_\xi = \int_0^t \{\dot{u}\}^T \mathbf{C}\mathrm{d}\{u\} = \int_0^t \{\dot{u}\}^T \mathbf{C}\{\dot{u}\}\mathrm{d}\tau \tag{8}$$

$$E_A = \int_0^t \mathbf{F}[u,\dot{u}]\mathrm{d}\{u\} = \int_0^t \{\dot{u}\}^T \mathbf{F}[u,\dot{u}]\mathrm{d}\tau \tag{9}$$

$$E_I = \int_0^t \{m\}^T \{\ddot{u}_t\}\mathrm{d}u_g(\tau) = \int_0^t \{m\}^T \{\ddot{u}_t\}\dot{u}_g \mathrm{d}\tau \tag{10}$$

Here, E_K denotes the absolute kinetic energy, E_ξ is the damping energy, E_A is the absorbed energy, which is composed of the recoverable elastic strain energy E_S and the irrecoverable hysteretic energy E_H and, E_I represents the absolute input energy.

Similiarly, the relative energy equation for the isolated bridge can be written as follows

$$\frac{1}{2}\{\dot{u}\}^T \mathbf{M}\{\dot{u}\} + \int_0^t \{\dot{u}\}^T \mathbf{C}\mathrm{d}\{u\} + \int_0^t \mathbf{F}[u,\dot{u}]\mathrm{d}\{u\} = -\int_0^t \ddot{u}_g \{m\}^T \mathrm{d}\{u\} \tag{11}$$

or

$$E_K^{'} + E_\xi + E_A = E_I^{'} \,, \tag{12}$$

where

$$E_K^{'} = \frac{1}{2}\{\dot{u}\}^T \mathbf{M}\{\dot{u}\} \tag{13}$$

$$E_I^{'} = -\int_0^t \ddot{u}_g \{m\}^T \mathrm{d}\{u\} = -\int_0^t \{m\}^T \{\dot{u}\}\ddot{u}_g \mathrm{d}\tau \tag{14}$$

The difference between absolute and relative energy formulations is essentially the difference in the kinetic energy terms and can be computed as

$$E_I - E_I^{'} = E_K - E_K^{'} = \frac{1}{2}\{\dot{u}_t\}^T \mathbf{M}\{\dot{u}_t\} - \frac{1}{2}\{\dot{u}\}^T \mathbf{M}\{\dot{u}\} \tag{15}$$

Note that the definition of E_ξ and E_A is the same for both absolute and relative energy formulation.

In order to illustrate the difference in absolute and relative energy input to a structure during a typical far-field and near-field earthquake, Figure 3 energy response history of the non-isolated bridge subjected to a far-field (1940 El Centro) and a near-field (1992 Kocaeli) ground motion. It can be seen that the two different energy formulations result in similar input energy response histories for far field earthquake and input energy gradually builds up and reaches to a maximum near the end of the ground motion. In contrast, for near-field earthquakes, instantaneous energy spikes that have considerably larger values than the energy accumulated at the end are present in the response time history. The values of absolute and relative input energy differ significantly during these energy spikes. Therefore, both absolute and

relative energy balance formulations are considered to evaluate the energy response of the isolated bridge with SMA-based isolations systems subjected to different earthquakes in the next section.

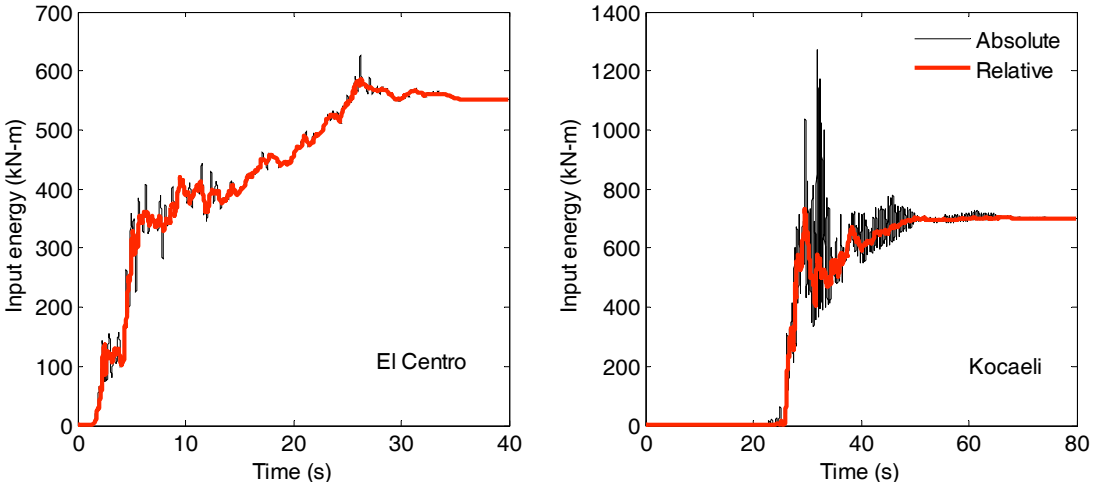


Figure 3. Input energy time histories for a typical far-field and near-field earthquake

NUMERICAL STUDY

In this section, an energy-based methodology is used to compare the performances of the S-FBI system and the SRB isolation system for protecting bridge structures against various earthquakes. Figure 4 shows idealized force-deformation curve of an SMA device. In the figure, F_y and u_y represent forward transformation force and displacement of the SMA device; k_{SMA} and αk_{SMA} denote initial and post transformation stiffness of the device, respectively. For the NiTi wire considered in this study, α, which represents the ratio of post transformation stiffness and initial stiffness of the SMA device, is observed to be 0.1 and the forward transformation strain of SMA wire ε_y is about 1%. Here, the forward transformation displacement u_y and the normalized forward transformation strength of the SMA device F_o which is defined as, $F_o = F_y / W_d$ where W_d is the weight of the bridge deck are selected to characterize the SMA device of the smart isolation systems. Note that once u_y and F_y are given, the geometric dimensions of the SMA elements can be computed from

$$u_y = \varepsilon_y \cdot L_{SMA}$$
$$k_{SMA} = \frac{F_y}{u_y} = \frac{A_{SMA} \cdot E_{SMA}}{L_{SMA}}, \tag{16}$$

where E_{SMA}, A_{SMA} and L_{SMA} are the Young's modulus, cross-sectional area and length of the SMA wires, respectively.

Based on the findings of the work of Ozbulut and Hurlebaus (2010b), an optimal SRB isolation system is designed with the parameters of u_y = 40 mm and F_o = 0.20 for the SMA device and k_b = 25 kN/cm and 2% viscous damping ratio for the laminated rubber bearing. The optimum design parameters for the S-FBI system are

adopted from Ozbulut and Hurlebaus (2010a). For the S-FBI system, the flat sliding bearings has a friction coefficient of 0.10 and the parameters of the SMA device are u_y = 30 mm and F_o = 0. 06. Note that for the above design parameters, the volume of the SMA wires used in the S-FBI system is 70% less than the volume of the SMA material employed in the SRB isolation system.

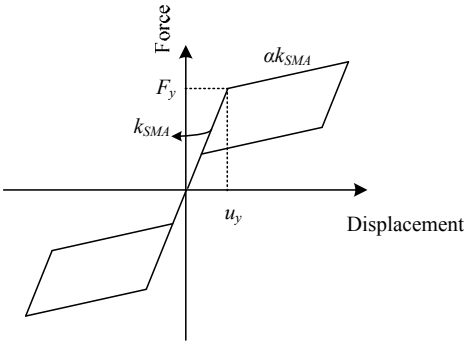


Figure 4. Idealized force-deformation curve of SMA device

Figure 5 through Figure 8 shows the time histories of the various response quantities for the isolated bridges subjected to El Centro, Landers, Erzincan and Kocaeli earthquakes, respectively. In particular, the time histories of input energy and recoverable energy (kinetic energy + strain energy) for absolute and relative energy balance formulations as well as the time histories of the deck drift and base shear normalized by the weight of the deck are plotted in each figure.

It can be seen that absolute and relative input energy are very similar and cumulatively increase and reach a maximum at the end of the motion for both the SFBI and SRB isolation systems for El Centro earthquake. However, for near-field earthquakes, energy spikes are observed especially in the absolute input energy at the early stages of the excitation. Specifically, Kocaeli earthquake produces considerably high absolute instantaneous energy spikes for both isolation systems. It should be noted that peak input energy, either computed through absolute or relative energy formulations, is smaller for the S-FBI system compared to the SRB system for all excitation cases.

When the time histories of recoverable energy transmitted to the bridge structure are compared, it can be seen that there is a substantial reduction in recoverable energy, which is the cause of damage in the structure, for the S-FBI system in comparison with that of the SRB system. This is observed for all excitation cases and irrespective of absolute or relative energy formulation except the Kocaeli earthquake, where the S-FBI system has larger recoverable energy for relative energy formulation. This is due to the fact that the force transmitted to the superstructure by the S-FBI system is considerable smaller than that by the SRB system, which will be shown later.

From the time-histories of the deck drift, it can be seen that the S-FBI system reduce the peak deck drift considerably more than the SRB system when the isolated bridges subjected to El Centro and Kocaeli earthquakes, while both systems produce similar peak deck drift in the case of Landers and Erzincan excitations. However, note that the SRB isolation system damps out the vibrations over longer time. The S-

FBI system also has consistently smaller peak base shear for the considered earthquakes.

Figure 9 illustrates the energy absorbed by the subcomponents of SMA-based isolation systems, i.e., the rubber and steel-Teflon bearings and the SMA device for the S-FBI system and the SRB isolation system subjected to different earthquakes. It can be seen that the energy is dissipated mainly by the SMA device for the SRB isolation system whereas the SMA device serves as a re-centering component in the S-FBI system and the energy is dissipated through friction in the sliding surface for the S-FBI system.

CONCLUSION

This study compares the performances of two different SMA-based isolation systems, namely S-FBI system and SRB isolation system by conducting nonlinear time history analyses with energy balance assessment. First, absolute and relative energy balance equations are derived for an isolated bridge. Then, a numerical study is performed to compare the response of a three-span isolated bridge structure with an S-FBI system and that of an SRB isolation system.

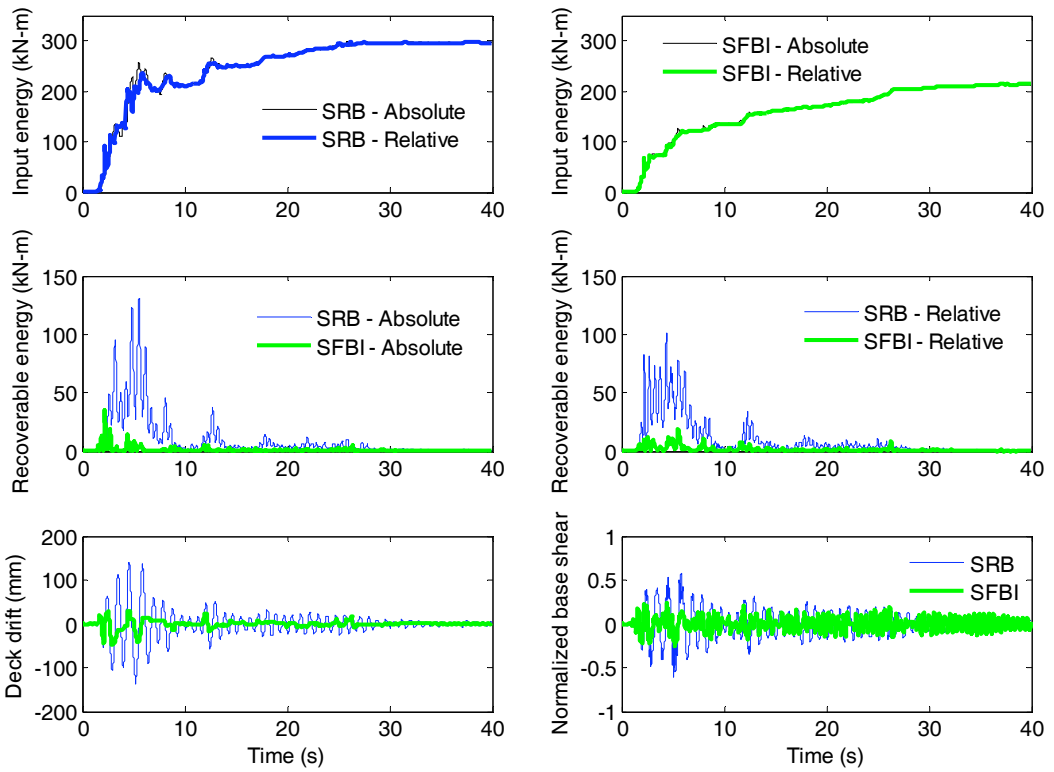


Figure 5. Time histories of various response quantities for El Centro earthquake

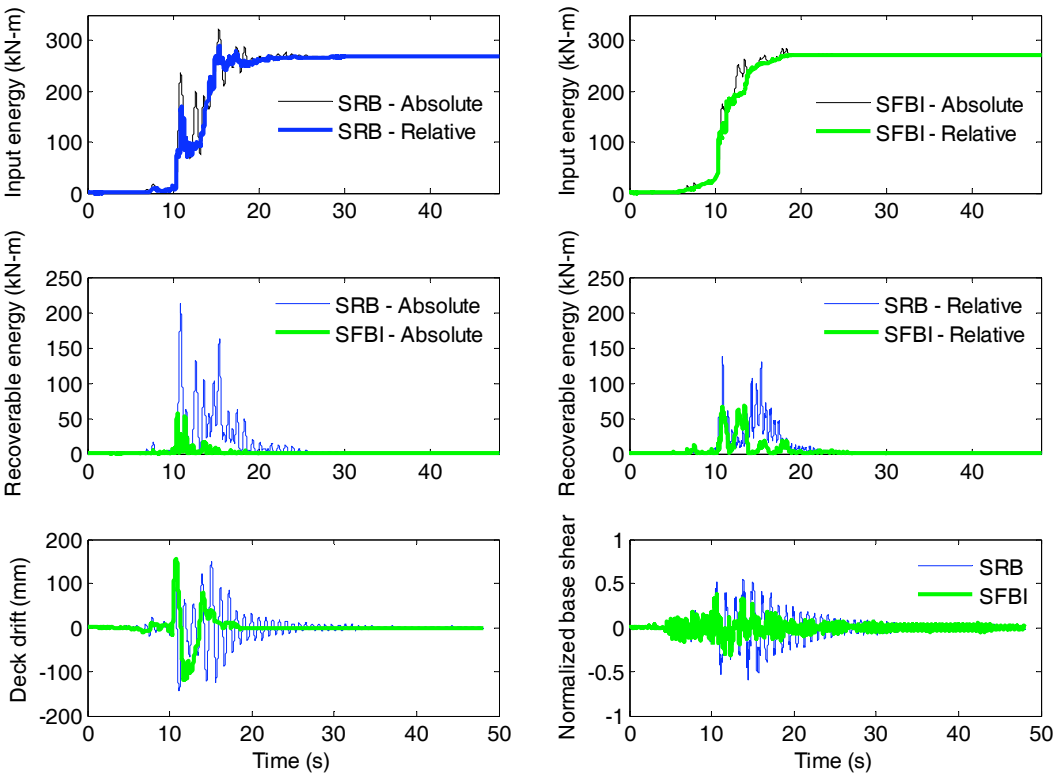


Figure 6. Time histories of various response quantities for Landers earthquake

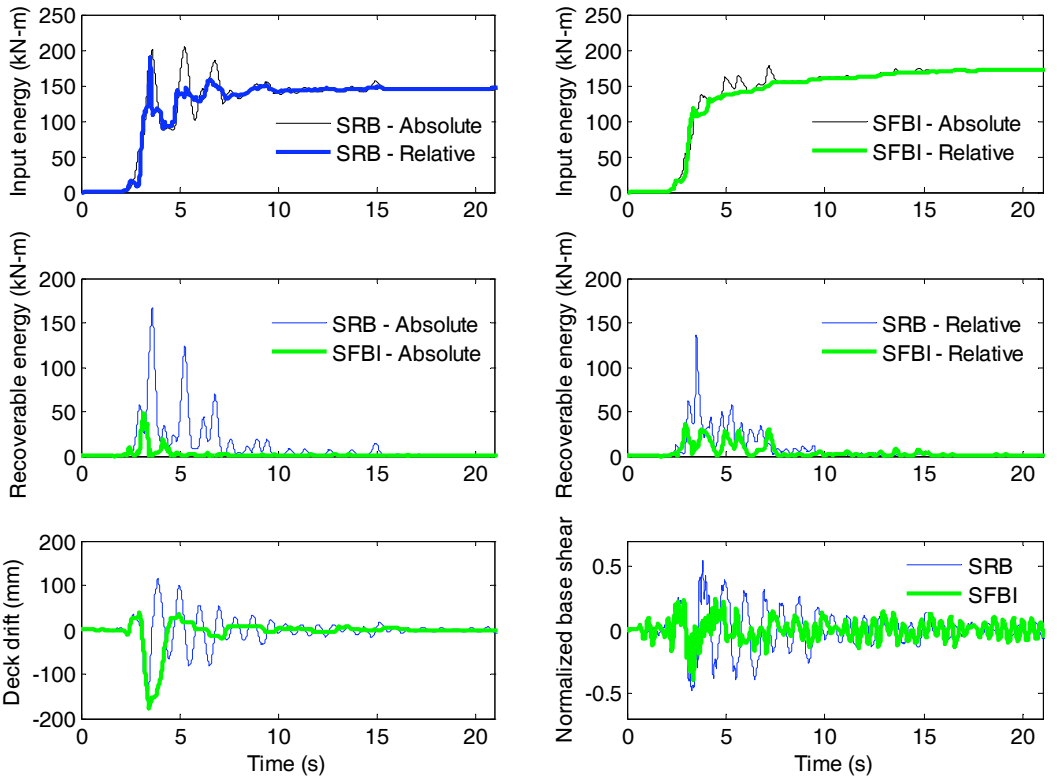


Figure 7. Time histories of various response quantities for Erzincan earthquake

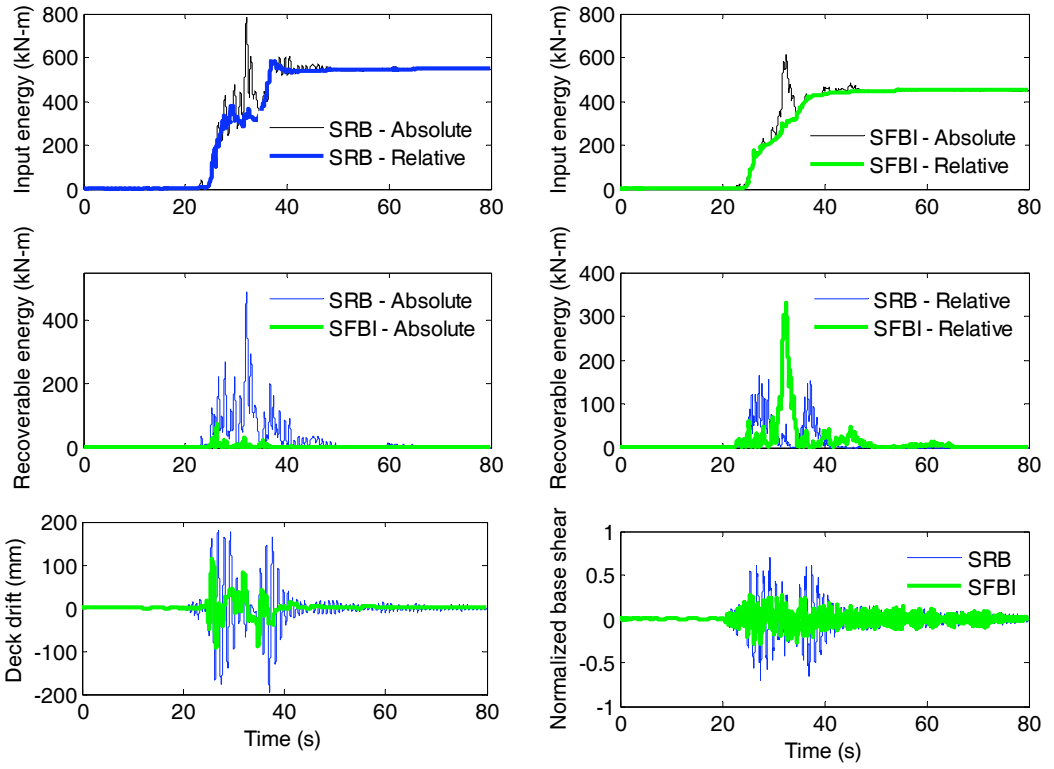


Figure 8. Time histories of various response quantities for Kocaeli earthquake

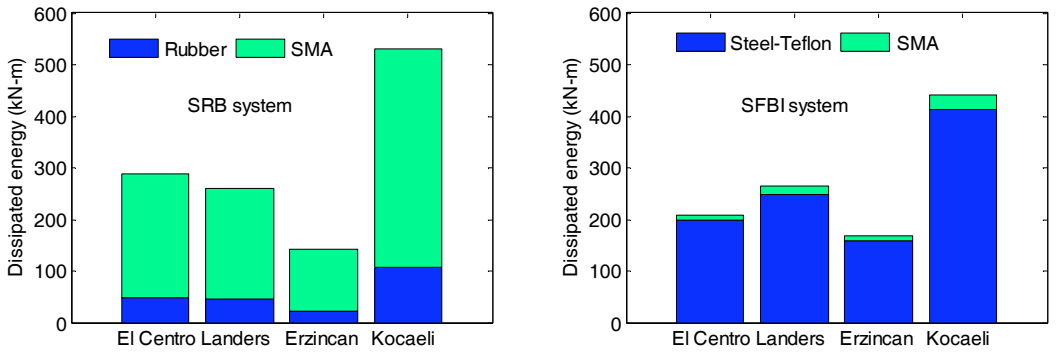


Figure 9. Energy dissipated by the subcomponents of the S-FBI and SRB isolation systems

It is found that the bridge structure isolated by either the SRB isolation system or the S-FBI system can effectively limit the peak deck drift response for considered excitations. However, it is noted that the peak base shear exhibits higher values in the case of the SRB isolation system. It is also observed that the S-FBI system attracts smaller quantities of input energy than the SRB system. It is shown that the energy is mainly dissipated by the SMA components for the SRB isolation system. On the other hand, the energy dissipation in the S-FBI system is through friction, while the SMA component of the isolation system serves as a re-centering device. Since the energy dissipation in the SRB isolation system almost solely relies on the hysteretic behavior of SMAs, and, the energy dissipation capabilities of the superelastic SMAs are limited, larger amount of SMA material is required for the SRB isolation system.

To be more specific, the S-FBI system employs superelastic SMA wires that are 70% less in volume as compared to those used in the SRB isolation system.

Noting that the high cost of the SMA is mostly cited as one of the main barriers that preclude the use of SMAs in a full-scale seismic application and considering superior structural response of the S-FBI system, it can be concluded that the S-FBI system which combines SMAs with flat sliding bearings has more favorable properties than the SRB isolation system which consists of a laminated rubber bearing and an SMA device.

REFERENCES

Austin, M. A., and Lin, W. J. (2004). "Energy balance assessment of base isolated structures." *Journal of Engineering Mechanics*, 130(3), 347-358.

Casciati, F. and Faravelli, L. (2009). "A passive control device with SMA components: from the prototype to the model," *Structural Control and Health Monitoring*, 16, 751-765.

Constantinou, M., Mokha, A., and Reinhorn, A. (1990). "Teflon bearing in base isolation II: Modeling." *Journal of Structural Engineering*, 116(2), 455-74.

Enke, D. L., Tirasirichai, C., and Luna, R. (2008). "Estimation of earthquake loss due to bridge damage in the St. Louis metropolitan area. II: Indirect losses." *Natural Hazard Review*, ASCE, 9, 12-19.

Fajfar, P., and Vidic, T. (1994). "Consistent inelastic design spectra: hysteretic and input energy." *Earthquake Engineering and Structural Dynamics*, 23, 523–537.

Housner, G. W. (1956). "Limit design of structures to resist earthquakes." *Proceedings of the 1st World Conference on Earthquake Engineering*, Berkeley, CA.

IBC 2000 *International Building Code* International Code Council: Falls Church VA

Kalkan, E., and Kunnath, S. H. (2008). "Relevance of absolute and relative energy content in seismic evaluation of structures." *Advances in Structural Engineering*, 11, 1-18.

Malhotra, P. K. (2003). "Strong-motion records for site-specific analysis." *Earthquake Spectra*, 19, 557-578.

Ordaz, M., Huerta, B., and Reinoso, E. (2003). "Exact computation of input-energy spectra from Fourier amplitude spectra." *Earthquake Engineering and Structural Dynamics*, 32(4), 597-605.

Ozbulut, O. E., and Hurlebaus, S. (2010a). "Optimal design of superelastic-friction base isolators for seismic protection of highway bridges against near-field earthquakes." *Earthquake Engineering and Structural Dynamics*, doi:10.1002/eqe.1022.

Ozbulut, O. E., and Hurlebaus, S. (2010b). "Performance evaluation of shape memory alloy-based rubber isolation systems for seismic response mitigation of bridges." *Proceedings of SPIE*, Vol. 7647, 76473X, San Diego, CA.

Ozbulut, O. E., and Hurlebaus, S. (2010c). "Neuro-fuzzy modeling of temperature- and strain-rate-dependent behavior of NiTi shape memory alloys for seismic applications." *Journal of Intelligent Materials and Structures*, 21, 837-849.

Park, J. G., and Otsuka, H. (1999). "Optimal yield level of bilinear seismic isolation devices." *Earthquake Engineering and Structural Dynamics*, 28, 941-955.

Takewaki, I. (2004). "Bound of earthquake input energy." *Journal of Structural Engineering*, 130, 1289-1297.

Wang, Y. P., Chung., L. L., and Liao W. H. (1998). "Seismic response analysis of bridges isolated with friction pendulum bearings." *Earthquake Engineering and Structural Dynamics*, 27, 1069-1093.

Wilde, K., Gardoni, P., and Fujino, Y. (2000). "Base isolation system with shape memory alloy device for elevated highway bridges." *Engineering Structures*, 22, 222-229.

A Shape Memory Polymer Based Self-Healing Syntactic Foam Sealant for Expansion Joint

Guoqiang Li[1,2,*] and Tao Xu[1]
[1]Department of Mechanical Engineering
Louisiana State University
Baton Rouge, LA 70803

[2]Department of Mechanical Engineering
Southern University,
Baton Rouge, LA 70813

[*]Corresponding author
Tel. (225) 578-5302; Fax: (225) 578-5924; E-mail: guoli@me.lsu.edu
Homepage: http://me.lsu.edu/~guoli

Abstract

Failure of expansion joints is a leading cause of damage to bridge superstructures. Cohesive and/or adhesive failure of joint sealant material facilitates decay of the structures beneath it. The objective of this study is to develop a novel smart joint sealant to self-heal cohesive damage and eliminate adhesive failure of expansion joints. This sealant will be a shape memory polymer (SMP) based syntactic foam material. A key feature of this sealant is that it utilizes the shape memory functionality for the purpose of self-healing damage. In particular, internal cracks can be narrowed or fully closed by confined shape recovery of the smart sealant. Also, the sealant can be programmed to consistently and autonomously apply a compressive stress to the edge of the concrete deck and restrict the upward expansion, so that adhesive failure or debonding can be eliminated and a smooth joint can be maintained. In this study, a shape memory polymer (SMP) based syntactic foam sealant was prepared by dispersing 40% by volume of glass microballoons into a SMP matrix. After curing, this foam sealant was first programmed under 2-D stress condition (compression in longitudinal direction and tension in transverse direction) by a specially designed 2-D test fixture and then freely recovered. The effect of the prestress levels and the number of programming-recovery cycles on the thermomechanical behavior and shape fixity and shape recovery ratios, was investigated. The potential of this sealant for eliminating adhesive failure and healing cohesive damage was discussed.

1. Introduction

Expansion joints are weak links in bridge decks or concrete pavements. Expansion joint failure is a leading cause for structural damage to bridge

superstructures. Various types of sealants have been utilized to seal expansion joints in bridge decks and pavements. These sealants are typically hot-poured, cold-poured, or preformed. A comprehensive review of the existing sealants used in concrete pavements has shown that the failure of these sealants is dominated by adhesive failure and cohesive failure besides aging (Odum and Attoh, 2008).

Damage related to poorly performing expansion joints in bridge decks in the United States amounts to hundreds of millions of dollars each year. A survey conducted by the Federal Highway Administration indicated that, in a five-year evaluation period, over 60% of the expansion joints were leaking water and the remaining 40% were experiencing problems that would shorten their service life (Fincher 1983; Wallbank 1989). Joint failure remains an unsolved problem in the transportation community.

Due to the critical role played by joints in bridge decks and pavements, joint sealant has been a topic of intensive research for many years. Various factors that cause the failure of sealed joints have been identified (Price, 1984; Lee, 1994; Chang and Lee, 2002). The most frequently used types of sealed joints in the United States include, but are not limited to, (1) Field-poured silicone and polymer modified asphalt joints; (2) Compression seal joints; (3) Strip seal joints; (4) Polymer modified asphalt plug joint system; (5) Inflatable neoprene joints; and (6) Modular joint sealing system. According to some recent surveys of practical experiences (Chang and Lee, 2002; NCHRP#319, 2003), each type of sealant has its own pros and cons. Recently, a new silicone foam based seal material was developed for field-poured sealant (Malla, 2007). One advantage of this new material is its high ductility. Since the accommodation to movement of field-poured sealant is realized through the high ductility of sealant under both tension and compression, the adhesion to the concrete edge and cohesion in sealant itself are critical. However, one problem of the normal foam sealant used for compression seal joint is the loss of compression over time. It was reported that large sustained compressive movements force air out of the seal material (gas leakage) (Malla, 2007), which may not recover when the joint expands, and thus causes compression loss in the compression seal joint under cyclic loading.

Another problem of foam sealant is the filling of the open cells (void) with water in the foam sealant after long-term service. This problem can accelerate and magnify due to micro-cracking and damage caused by thermal stress and traffic load. In the field, the bond between the sealant and concrete can be weakened by the presence of moisture at bond interface. Such moisture deteriorated bond is especially vulnerable to tension stress (Ouyang and Wan, 2008), and thus leads to adhesive failure at the bond interface. When sealants serve in dry conditions, the presence of tension stress due to deck's movement

normally causes cohesive failure within sealant materials (Odum and Attoh, 2008). Additionally, a problem with solid sealants is that they are squeezed out of the joint when the expansion joint narrows due to the thermal expansion of the structural elements.

Shape memory polymer (SMP) is a new member of the family of shape memory materials. It has been found that SMPs can be deformed and fixed into a temporary shape and recover their original permanent shape only on exposure to external stimuli such as heat, light, magnetic field, etc. (Koerner et al., 2004; Lendlein et al., 2005; Mohr et al., 2006). The driving force for shape recovery is the conformational entropy of the molecular segments in terms of micro-Brownian thermal motion. Thermodynamically, the molecular segments experience a change from a temporary and ordered configuration to its random and coiled configuration during the shape recovery process. Since this process is accompanied by an increase in entropy, it is an autonomous process.

A recent development in SMPs is the use of confined shape recovery for the purpose of self-healing structural-length scale damage. Li and John investigated the concept for SMP based syntactic foam to repeatedly heal impact damage (Li and John, 2008). Later, it has been proved that SMP based syntactic foam can be used in grid stiffened SMP based syntactic foam cored sandwich and 3-D woven fabric reinforced SMP based syntactic foam panel for repeatedly and efficiently heal impact damage (John and Li, 2010; Nji and Li, 2010a). Most recently, a two-step close-then-heal self-healing scheme has been proposed by Li and Nettles (2010) and Xu and Li (2010), and elucidated by Li and Uppu (2010). This is a scheme by mimicking self-healing of biological systems such as human skin. This concept has been experimentally validated by Nji and Li (2010b), which shows that this system can heal structural-length scale damage repeatedly, efficiently, timely, molecularly, and almost autonomously.

We believe that an ideal sealant should be able to apply a consistent compressive stress to the concrete wall so that adhesive failure can be avoided. Also, the sealant needs to maintain in the groove when the groove narrows due to thermal expansion of the concrete. Additionally, the sealant should prevent water from seeping into it and also have self-healing capabilities so that cohesive failure can be healed. To this end, we propose to use shape memory polymer based syntactic foam as a sealant for expansion joint. First, the foam sealant can be programmed or trained by a 2-D stress condition: compression in the longitudinal (horizontal or traffic direction) and tension in transverse or vertical direction; see Figure. 1 (a). When the foam sealant is installed at the lowest temperature the sealant will experience, the sealant will always apply a compressive stress to the concrete wall; see Figure. 1 (b). When the temperature rises, the compressive

stress applied to the sealant will increase, which further ensures that the sealant applies a compressive stress to the concrete wall and adhesive failure can be avoided. Also, because the stiffness of the SMP based sealant reduces as temperature rises, the compressive stress will not become excessive such that compressive failure of the concrete occurs. However, the squeezing out problem dominates due to Poisson's ratio effect. With SMP based sealant and the special 2-D training, this problem can be solved because the rising temperature will trigger the shape recovery process of the sealant, which makes the sealant contracts in vertical direction. If properly trained, the Poisson's effect (squeezing out) and shape recovery effect (contracting) can be balanced and the sealant may maintain at the same level; see Figure. 1 (c). When temperature drops, the shape recovery stops and the sealant returns to Figure. 1 (b). As discussed by Li and Uppu (2010), each compressively constrained shape recovery completes a new cycle of programming. It is thus believed that this sealant will be able to experience many such cycles without failure.

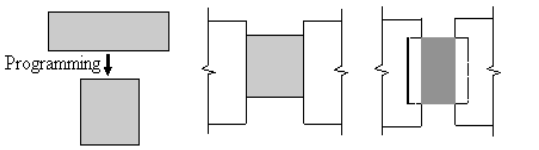


Figure 1. Work principle of SMP based syntactic foam sealant.

In order to solve the problem of water damage, we propose to use close-celled foam instead of open-celled foam. Therefore, we believe that a SMP based syntactic foam trained by 2-D programming (compression in one direction and tension in the transverse direction) would be a viable alternative as a sealant for expansion joint. The purpose of this study is to experimentally investigate the 2-D programming and shape recovery of a SMP based syntactic foam sealant.

2 Experimentation

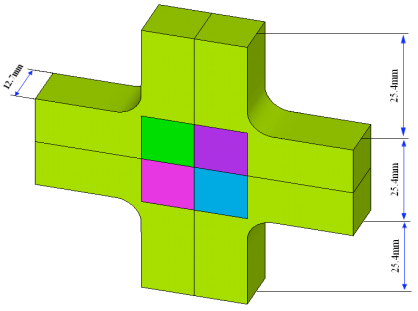
2.1 Raw materials

The syntactic foam consists of hollow glass microspheres dispersed in a shape memory polymer matrix. The polymer is a styrene based thermoset SMP resin system (T_g= 62^{o}C) sold commercially by CRG Industries under the name Veriflex®. The glass microballoons (hollow spheres) were purchased from Potters Industries (Q-CEL6014: 85μm average outer diameter, effective density of 0.14 g/cm^3, maximum working pressure of 1.73MPa, and 0.8μm wall thickness). These raw materials have been used previously for the smart syntactic foam (Li and Nettles, 2010; Nji and Li, 2010a).

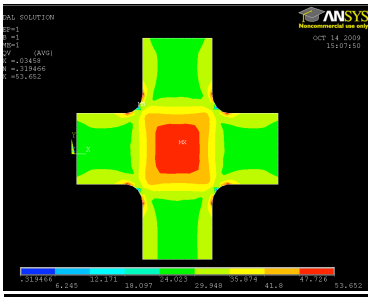
2.2 Biaxial specimen preparation

The SMP based syntactic foam sealant consists of hollow glass

microballoons and SMP matrix, which was fabricated by dispersing 40% by volume of microballoons into the SMP resin. The microspheres were added to the resin while slowly stirring the mixture to minimize air bubbles in the resin. The microspheres were added in multiple steps to avoid agglomeration. After dispersion, a hardening agent was added and the mixture was mixed for 10 min. The composite was poured into a 229×229×12.7 mm steel mold and placed in a vacuum chamber at 40kPa for 20 min in order to remove any air pockets introduced during the mixing process. Based on our previous study (Li and Nettles, 2010), the curing cycle was 79°C for 24h, 107°C for 3h, and 121°C for 9h. After curing, the sealant panel was de-molded and was machined into biaxial specimens for programming and further testing. The cruciform specimen dimensions were given in Figure. 2 (a). With such a dimension, the central square is roughly under a 2-D stress condition as validated by a finite element analysis; see Figure. 2 (b).



(a) A schematic diagram of biaxial specimen dimensions



(b) von Mises stress distribution in the specimen (there is a piece of square material (red color) at the center of the specimen (about 25.4mm by 25.4mm) that is subjected to a uniform 2-D stress condition)

Figure 2. Cruciform specimen for 2-D programming.

2.3 2-D programming of biaxial specimen

In order to make the polymer smart, it usually subjects to a typical three-step thermomechanical cycle called programming (Li and John, 2008). The energy that is restored with shape recovery is a growing function of the energy supplied during the deformation at a high temperature (Miaudet et al., 2007). The

SMP based foam sealant can be programmed to consistently and autonomously apply a compressive stress to the edges of the concrete deck/pavement regardless of the environmental conditions (expansion or contraction) of the expansion joint. This feature ensures that the debonding problem can be avoided by preventing tensile stress from occurring at the interface.

After machining the cruciform foam sealant specimen, two small steel tabs were fixed by using strong glue along the edge of the central square (uniform 2-D stress condition as shown in Figure. 2 (b)) on to one side surface of the specimen (one in the vertical and the other in the horizontal direction) to measure the displacement of the two directions (see Figure. 3(a)). Then the cruciform specimen was introduced into the truss-form fixture and the bolts were tightened to grip the four arms of the specimen, with each arm by 12.7mm (as shown in Figure. 3(b)). The truss fixture can transform 1-D compression into 2-D loading (vertical compression and horizontal tension) by directly applying compressive load to the top and bottom nodes of the truss fixture. The ratio of the vertical load and horizontal load can be adjusted by changing the length of the members of the truss fixture. Finally the temperature was monitored with the help of thermocouples connected to a Yokagawa DC100 data acquisition system.

According to the previous study (Li and Nettles, 2010), the glass transition region of the foam is 63.69–76.19^{o}C with a glass transition temperature of T_g = 70.50^{o}C. In order to perform efficient programming and shape recovery tests, we chose 79^{o}C as a testing temperature since it is just above the upper limit of the T_g region in the foam. We started with putting the device into a chamber and heating up to 79^{o}C and holding for about 25 minutes, and then retightening the bolts to clamp the sample better because the specimen became soft at 79^{o}C. After retightening, place the set-up back into the chamber and install two linear variable differential transducers (LVDT) in conjunction with the two pre-attached tabs in the vertical and horizontal direction, respectively (see Figure. 3(c)). Also install the weight-bearing rod to the top node of the truss fixture and reheat the system up to 79 ^{o}C for another 20 minutes for temperature equilibration.

Immediately following, a load was applied onto the rod by hand. This loading method caused the sample into compression condition in the vertical direction and tension condition in the horizontal direction. Approximately 20 min were allowed for the deformation to stabilize. This completed the first step (pre-strain) of the programming. In the next step (cooling), the heating was first stopped, and the chamber was kept closed and the system was allowed to naturally cool for 8-10h to room temperature while maintaining the applied load constant. The strain gauges and LVDT tracked the shape changes of the specimen during this cooling step. Because of creep and contraction during cooling, the strain was

continuously increased until the temperature reached room temperature. Then the specimen was unloaded. This completed the 2-D thermo-mechanical programming or shape fixity process of the cruciform foam sealant.

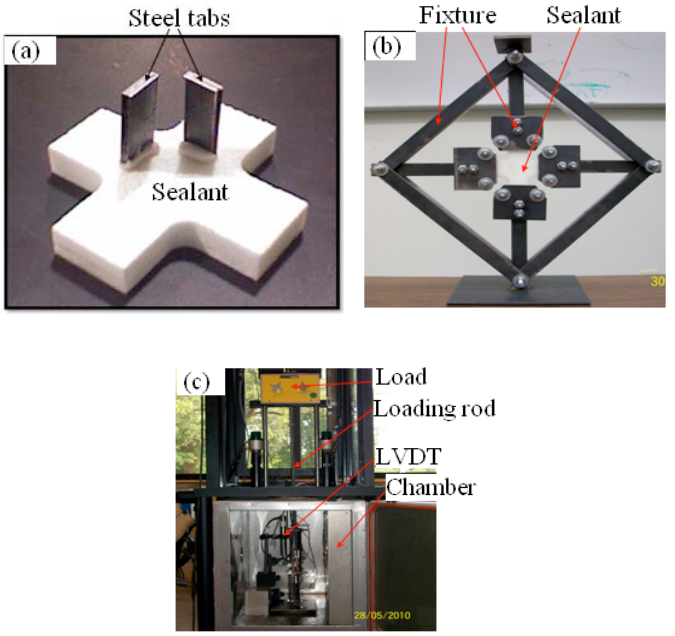


Figure 3. Programming setup and testing method of cruciform foam sealant specimen.

After completing the specimen programming, the core area of the programmed cruciform specimens was machined to four smaller cube specimens with an edge length of 12.7mm (see Figure. 4) for further shape recovery testing. In Figure 4, Orientation-1 is subject to compressive prestress; Orientation-2 is subject to tensile prestress; and Orientation-3 is free of stress.

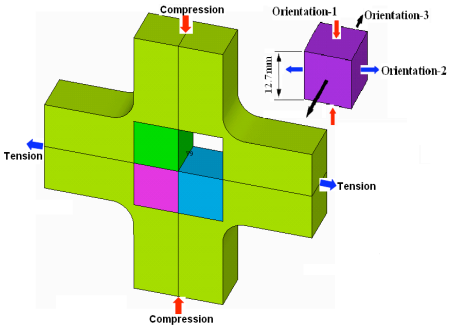


Figure 4. A schematic diagram of the preparation for programmed sealant specimen.

In order to evaluate the effect of prestress level on the thermomechanical behavior, four compressive prestress levels in the vertical direction were used. They were 168.3kPa, 207.7kPa, 247.6kPa, and 300.7kPa, respectively. Because of

the symmetry of the truss fixture and the specimen, the tensile prestress in the horizontal direction was the same as the corresponding vertical compressive prestress. In addition, some specimens with 300.7kPa prestress experienced 10 thermomechanical cycles to evaluate the functional stability of the foam sealant.

2.4 2-D shape recovery of biaxial specimens

2-D free-shape recovery started after the completion of the programming by using the same heating chamber and LVDT system. The chamber was heated up quickly from room temperature to 49^{o}C and allowed to soak for 20 min. Then the heating was continued again at an average heating rate of 0.3^{o}C/min until 77^{o}C. After 7 minutes, the heating was ramped quickly to 79 ^{o}C and holding for 30 minutes. This completed the 2-D free shape recovery.

3. Results and Discussion

3.1 Thermomechanical behavior of biaxial specimens

Figure 5 shows the typical strain evolution during the entire thermomechanical cycle subjected to various prestress levels. Similar to previous 1-D stress controlled programming and free shape recovery (Li and Nettles, 2010), each direction (compression in the vertical direction and tension in the horizontal direction) shows similar four-step thermomechanical behavior. From Figure 5, the thermomechanical cycle includes four steps: Step1 (loading), Step 2 (cooling while holding the load constant), Step 3 (unloading), and Step 4 (recovery). The small spikes are due to manual control of the testing setup.

Based on Figure 5 (a) and (b), the shape fixity ratio and shape recovery ratio are obtained. The shape fixity ratio is 95.6%, 96.7%, 98.6%, and 99.2% for the four prestress levels, respectively. The corresponding shape recovery ratio is 97.3%, 95.4%, 94.1%, and 91.6%. It is clear that as the prestress level increases, the shape recovery ratio decreases. This is understandable because higher prestress may cause some damage to the foam (such as crushing of microspheres), which is unrecoverable during shape recovery. For the shape fixity, with the increase in the prestress, the foam sealant specimen becomes denser and stiffer, resulting in a smaller springback and higher shape fixity.

From Figure 5 (c), the horizontal and vertical strain after 10 thermomechanical cycles is close to the strain development of the first thermomechanical cycle. The shape fixity ratio is 98.5 %, and the shape recovery ratio is 88.3%. It is noted that the shape fixity ratio is slightly higher, and the shape recovery ratio is slightly lower than that in the first thermomechanical cycle under the same prestress level (300.7KPa). This is because more unrecoverable damages are accumulated during each additional thermomechanical cycle, which lead to the decrease in shape recovery ratio and increase in shape fixity ratio.

However, this change is shape recovery ratio and shape fixity ratio is comparatively small. Therefore, the shape recovery functionality of this foam sealant is stable and sustainable.

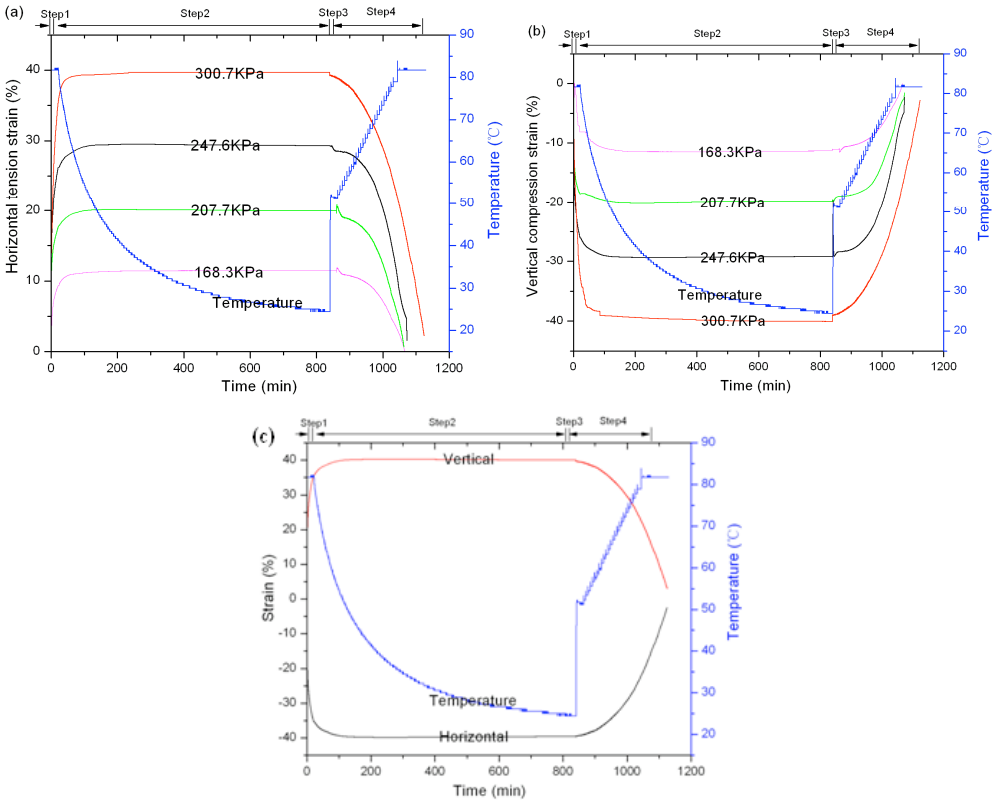


Figure 5. (a) Horizontal and (b) Vertical strain of the cruciform sealant sample under various stress levels during programming and recovery (Steps 1-3 represent programming and Step 4 represents free shape recovery) and (c) Horizontal and vertical strain of the 10th thermo-mechanical cycle under the prestress level of 300.7kPa.

To visualize the programming and recovery process, Figure 6 shows the original and programmed cruciform foam sealant specimen and its recovery process under various temperatures. During Step 1 and Step 2 of the programming, the 2-D stress condition causes the orientation of the macromolecular chains of SMP aligns along both vertical and horizontal directions. This leads to a decrease in entropy of the material system in the programming process (Hossein et al., 2007; Jalil and Hossein, 2005). Meanwhile, some microspheres may be bent or buckled, and the deformed microspheres or crushed debris are aligned in the tension orientation due to the compression in the transverse direction. Furthermore, a wrinkle-like pattern can be seen with the naked eye on the stretched specimen surface along both directions, as shown in Figure 6 (b). This reflects the 2-D stress conditions. It is believed that the central square of the

cruciform foam sealant specimen is changed from isotropy to anisotropy. From Figure 6 (c-f), the recovery rates in horizontal and vertical directions are faster when the temperature is up to T_g, which is consistent with strain development shown in Figure 5. Additionally, the recovery process occurs in both directions simultaneously, which is important for the sealant in expansion joints to expand in the horizontal direction and contract in the vertical direction without distortion. It is beneficial to achieve the design purpose of smart foam sealant proposed in this study.

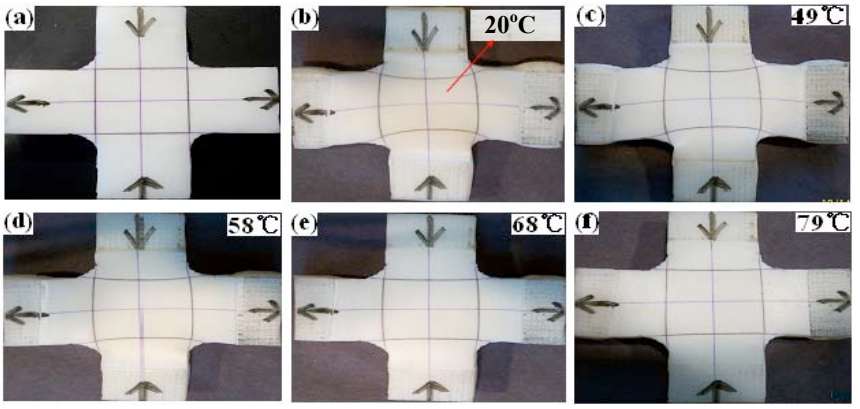


Figure 6. (a) Original and (b) programmed cruciform foam sealant specimen and (c-f) its recovery process under various temperatures.

4. Conclusion

Based on the comprehensive tests, the following conclusions are obtained:

(1) A special 2-D programming method for SMP based foam sealant is developed. The foam sealant has good shape memory functionality under the 2-D stress condition. The 2-D programming method may cause the sealant to transform into anisotropy from isotropy.

(2) The 2-D programming method has a potential to solve squeezing-out problem of the foam sealant when the expansion joint narrows. The number of thermomechanical cycles has a slight effect on thermomechanical behavior of the foam sealant, indicating good stability of the shape memory functionality of the foam sealant.

Acknowledgments

The work is funded by Transportation Research Board/NCHRP/IDEA and Louisiana Transportation Research Center (LTRC) under grant number NCHRP/IDEA-142. Dr. Inam Jawed is the TRB program manager and Mr. Walid Alaywan is the LTRC project manager. The financial support is greatly appreciated.

The contents of this paper reflect the views of the authors who are

responsible for the facts and the accuracy of the data presented herein. The contents do not necessarily reflect the views or policies of the funding agencies.

References

Boyce M.C., Parks D.M., and Argon A.S. (1988). Large inelastic deformation of glassy polymers: Rate dependent constitutive model. Mech. Mater., 7: 15–33.

Chang L.M. and Lee Y.J. (2002). Evaluation of performance of bridge deck expansion joints. J. Perform. Constr. Fac., 16: 3–9.

Choi J. B. and Lakes R. S. (1995). Analysis of elastic modulus of conventional foams and of re-entrant foam materials with a negative poisson's ratio. Int. J. Mech. Sci., 37: 51– 59.

Fincher H.E. (1983). Evaluation of rubber expansion joints for bridges. Report No. FHWA/IN/RTC-83/1, Washington, D.C., 15–16.

John M. and Li G.Q. (2010). Self-healing of sandwich structures with grid stiffened shape memory polymer syntactic foam core. Smart Mater. Struct, 19, pp. 1-12 (paper No. 075013).

Khonakdar H.A., Jafari S. H., and Rasouli S. (2007). Investigation and Modeling of Temperature Dependence Recovery Behavior of Shape-Memory Crosslinked Polyethylene. Macromol. Theory Simul., 16: 43–52.

Koerner H., Price G., Pearce N.A., Alexander M., and Vaia R.A. (2004). Remotely actuated polymer nanocomposites- stress-recovery of carbon-nanotube-filled thermoplastic elastomers. Nat. Mater., 3: 115–120.

Lee D.J. (1994). Bridge bearings and expansion joints. Alden Press, Oxford, U.K.

Lendlein A., Jiang H., Jünger O., and Langer R. (2005). Light-induced shape-memory polymers. Nature, 434: 879–882.

Li G.Q. and John M. (2008). A self-healing smart syntactic foam under multiple impacts. Compos. Sci. Technol. 68: 3337–3343.

Li G.Q. and Nettles D. (2010). Thermomechanical characterization of a shape memory polymer based self-repairing syntactic foam. Polymer 51: 755–762.

Li G.Q. and Uppu N. (2010). Shape memory polymer based self-healing syntactic foam: 3-D confined thermomechanical characterization. Compos. Sci. Technol. 70: 1419–1427.

Liu Y.P. and Hu H. (2010). A review on auxetic structures and polymeric materials. Sci. Res. Essays., 5:1052–1063.

Malla R.B., Shaw M.T., Shrestha M.R., and Brijmohan S.B. (2007). Development and laboratory analysis of silicone foam sealant for bridge expansion joints. J. Bridge Eng., 12: 438–448.

Miaudet P., Derré A., and Maugey M. (2007). Shape and temperature memory of nanocomposites with broadened glass transition. Science, 318:1294–1296.

Mohr R., Kratz K., and Weigel T. (2006). Initiation of shape-memory effect by

inductive heating of magnetic nanoparticles in thermoplastic polymers. Proceedings of the National Academy of Sciences of the United States of America, 103:3540–3545.

Morshedian J., Khonakdar H. A., and Rasouli S. (2005). Modeling of Shape Memory Induction and Recovery in Heat-Shrinkable Polymers. Macromol. Theory Simul., 14: 428–434.

NCHRP Synthesis Report #319 Project: NCHRP 20-05(2003).Washington, D.C.

Nji J. and Li G.Q. (2010a). A self-healing 3D woven fabric reinforced shape memory polymer composite for impact mitigation. Smart Mater. Struct., 19: pp.1-9 (paper No. 035007).

Nji J. and Li G.Q. (2010b). A biomimic shape memory polymer based self-healing particulate composite. Polymer, 51: 6021-6029.

Odum-Ewuakye B. and Attoh-Okine N. (2006). Sealing system selection for jointed concrete pavements – a review. Constr. Build. Mater, 20: 591–602.

Ouyang Z. and Wan B. (2008). Experimental and numerical study of moisture effects on the bond fracture energy of FRP/concrete joints. J. Reinf. Plast. Comp., 27: 205–223.

Patankar S.N.and Kranov Y.A. (2010). Hollow glass microsphere HDPE composites for low energy sustainability. Mater Sci. Engin. A, 527: 1361–1366.

Price A.R. (1984). The performance in service of bridge expansion joints. TRRL Report LR 1104, Transport and Road Research Laboratory, Crowthorne, U.K., 4–10.

Wallbank E.J. (1989). The performance of concrete in bridges: a survey of 200 highway bridges. Department of Transport, HMSO, London.

Wouterson E. M., Boey F.Y.C., Hu X., and Wong S.C. (2005). Specific properties and fracture toughness of syntactic foam: Effect of foam microstructures. Compos. Sci. Technol., 65: 1840–1850.

Xu W. and Li G.Q. (2010). Constitutive modeling of shape memory polymer based self-healing syntactic foam. Int. J. Solids Struct., 47: 1306–1316.

Report of the Terminology and Procedures Sub-Committee (SC1): *Recommendations for Design against Disproportionate Collapse of Structures*

U. Starossek[1], R. Smilowitz[2], M Waggoner[3],
K. J. Rubenacker[4], and Marco Haberland[5]

[1]Hamburg University of Technology, Denickestr. 17, 21073 Hamburg, Germany.
email: starossek@tuhh.de
[2]Weidlinger Associates, Inc., 375 Hudson Street, New York, NY 10014-3656.
email: smilowitz@wai.com
[3]Walter P. Moore and Associates, Inc., 221 West 6th Street, Suite 800, Austin, Texas 78701.
email: mwaggoner@walterpmoore.com
[4]Gilsanz Murray Steficek LLP, 129 West 27th Street, 5th Floor, New York, NY 10001.
email: karl.rubenacker@gmsllp.com
[5]Hamburg University of Technology, Denickestr. 17, 21073 Hamburg, Germany.
email: m.haberland@tuhh.de

INTRODUCTION

The ASCE SEI Committee on Disproportionate Collapse Standards and Guidance is developing a guidance document for design against disproportionate collapse of structures. A Terminology and Procedures Sub-Committee was created to focus on definitions of terms and to develop a conceptual framework. The Sub-Committee prepared a draft that was discussed and accepted in principle by the Committee at its meeting on 13 May 2010. The draft is published here in its latest but shortened version for rapid dissemination and discussion. The complete draft is available on request.

The draft starts with a comprehensive and consistent set of definitions of relevant terms such as collapse resistance, robustness, vulnerability, exposure, direct design, indirect design, threat-specific design, non-threat-specific design, and many more, which up to now have not been consistently defined and used. These definitions are strongly cross-referenced and a hierarchical system of interrelated definitions thus emerges. On this basis, a conceptual framework of design criteria comprising design requirements, design objectives, design methods, and verification procedures is developed. This framework will serve as the outline for the Committee's design guidance document. Specific content for a number of sections and an appendix still need to be developed by dedicated Sub-Committees (SC). These tasks are clearly defined by the framework.

The draft consists of recommendations and commentary. In the following, recommendations are set in normal font and commentary in italics. The section numbering of the draft is substantial to cross-referencing and thus retained. Specific content still to be developed by dedicated Sub-Committees is indicated in brackets. Numbers given in tables are intended to illustrate the possible final content of these tables and to stimulate discussion. They should be understood as placeholders for the final content to be specified by the respective Sub-Committee.

TERMINOLOGY AND PROCEDURES SUB-COMMITTEE DRAFT

1 Scope

These recommendations concern the design for the prevention of disproportionate collapse of structures. A performance-based framework of design criteria comprising design requirements, design objectives, design methods, and verification procedures is given. It applies to the design of new structures and the retrofit design of existing structures. *In general, the design criteria are specified on a project-by-project basis by the parties involved in and affected by a given project. This specification can be based on the provisions presented here as long as they are applicable. If not, other applicable provisions can be used. (...)*

2 Definitions

2.1 Abnormal event. An event that is unforeseeable or occurs with very low probability and is not considered in the ordinary design of a structure. *This term refers to the abnormal conditions that might actually occur. In contrast, the abnormal conditions assumed in the design against disproportionate collapse are called hazard scenarios (see Sect. 5.2).*

2.2 Action. A condition that affects a structure and can be characterized by physical quantities. *In most cases, actions are applied loads or imposed deformations or displacements. However, the definition also includes heat action (fire) and corrosive action. Abnormal events and hazard scenarios may or may not result in actions.*

2.3 Alternative load paths. Alternative paths for a load to be transferred from a point of application to a point of resistance. Enable a redistribution of forces originally carried by failed components thus preventing a failure from spreading. *Providing alternative load paths is one of the design methods (see Sect. 2.10, 6.1, and 6.5).*

2.4 Authorities. The Authorities are the construction authorities that hold jurisdiction over the structure in question.

2.5 Client. The Client is understood here to be the collective of the owner of the structure and all the parties affected by its possible collapse. *The need to include affected parties derives from the indirect consequences of a collapse. For a storage structure filled with hazardous material, important bridges and tunnels, and other lifeline structures, for instance, possible indirect consequences are an impairment of public infrastructure and of civil and national defense. Examples of affected parties are military authorities, external local authorities, utility companies, concessionaires, financial institutions, and insurance companies. Defining the collective will of the Client can require an administrative or political decision on a national or international level.*

2.6 Collapse resistance. Insensitivity to abnormal events. A structure is collapse resistant if abnormal events do not lead to disproportionate collapse. A precise definition requires reference to specified design objectives: a structure is collapse resistant if the hazard scenarios affecting the structure do not lead to an extent of damage that violates the performance objectives. The hazard scenarios affecting the structure, referred to in this definition, do not include hazard scenarios averted by event control. *Collapse resistance is a property that depends on the structure and the abnormal events. A robust structure is collapse resistant because an initial damage does not spread disproportionately (see Sect. 2.34). A non-robust structure can be made*

collapse resistant by reducing its vulnerability to prevent or lessen initial damage (see Sect. 2.42). See also Figure 2. A disproportionate collapse can be prevented by providing collapse resistance or by reducing the exposure (event control).

2.7 Consequences. The consequences of the collapse of a structure. *Being all-embracing, this term refers to the sum of all direct and indirect losses resulting from a collapse (see Sect. 4.3). (...)*

2.8 Continuity. Continuous connectivity between structural components. *Extraordinary load-transfer mechanisms, such as catenary action, can be enabled by continuity. In this way, the redundancy and robustness of a structure can be increased. However, an increase of robustness can also be achieved by a break of continuity at segment borders.*

2.9 Design criteria. The design criteria form the framework of performance-based design. They consist of design requirements, design objectives, design methods, and verification procedures. *(...)*

2.10 Design methods. Methods that aim at preventing disproportionate collapse of a structure. *(...)*

2.11 Design objectives. Design objectives are the basis of direct design. They comprise hazard scenarios, performance objectives, and applicable combinations of actions and safety factors. *(...)*

2.12 Design requirements. Specification of whether design against disproportionate collapse is required for a structure and, if yes, specification of the level of requirements on design objectives, design methods, and verification procedures. *(...)*

2.13 Direct design. The terms direct and indirect design categorize approaches for designing collapse-resistant structures: (a) direct design aims at explicitly ensuring collapse resistance by demonstrating that the structure meets specified performance objectives when specified hazard scenarios occur and affect the structure; (b) indirect design aims at increasing the collapse resistance of a structure implicitly by incorporating consensus-approved design features; this is done by applying prescriptive design rules and thus without explicit consideration of hazard scenarios and without demonstrating that performance objectives are met. *(...) Protection, increased local resistance, alternative load paths, and segmentation (i.e. the structural methods, see Sect. 2.39) can be implemented within a direct or indirect design approach.*

2.14 Disproportionate collapse. A collapse that is characterized by a pronounced disproportion between a relatively minor event and the ensuing collapse of a major part or the whole of a structure. A precise definition requires reference to specified design objectives: a collapse is disproportionate if the hazard scenarios lead to an extent of damage that violates the performance objectives. *The terms disproportionate collapse and progressive collapse are often used interchangeably because disproportionate collapse often occurs in a progressive manner and progressive collapse can be disproportionate. Disproportionate collapse is the more appropriate term in the context of design and performance because a precise definition of disproportionate requires specified design objectives. The term progressive collapse is more suitable when referring to the physical phenomenon and mechanism of collapse (see Sect. 2.30).*

2.15 Ductility. The ability of a structural component or structure to sustain large plastic deformations without rupture. *Ductility can increase the redundancy and robustness of a structure. However, an increase of robustness can also be achieved by non-ductile behavior at segment borders.*

2.16 Engineer. The Engineer is the person or entity responsible for the design of the structure and of any external structural measures of protection.

2.17 Event control. Reducing the probability of occurrence and the intensity of abnormal events through non-structural measures. *Event control is one of the design methods (see Sect. 2.10, 6.1, and 6.2).*

2.18 Exposure. The exposure results from the abnormal events that possibly affect a structure during construction and lifetime and are not considered in ordinary structural design. *The exposure of a structure is one of the conditions from which the design requirements are derived (see Sect. 4). The disproportionate collapse of a structure can be prevented by reducing its exposure which in turn can be achieved by event control (see Sect. 2.17). See also Figure 2.*

2.19 Hazard scenarios. The abnormal conditions to be assumed in design to occur during construction and lifetime of a structure. *The hazard scenarios are specified as part of the design objectives (see Sect. 5).*

2.20 Increased local resistance. An increase (or confirmation of adequacy) of local structural resistance. Aims at preventing or reducing initial damage that could otherwise lead to disproportionate collapse. *Providing increased local resistance is one of the design methods (see Sect. 2.10, 6.1 and 6.4). Within direct design, this is called specific local resistance (see Sect. 2.38). Within indirect design, this is called prescribed local resistance (see Sect. 2.28).*

2.21 Indirect design. See Sect. 2.13.

2.22 Initial damage. The damage to a structure that can be ascribed directly to an abnormal event (without resorting to the response of the structure as a whole) or a notional damage as determined from the hazard scenarios. *An initial damage results in a reduction (sectional weakening) or a complete loss (component failure) of the load-carrying capacity of a part of the structure. It is usually locally limited.*

2.23 Integrity. (…) *The term general structural integrity has been defined as the property of being able "to sustain local damage with the structural system as a whole remaining stable and not being damaged to an extent disproportionate to the original local damage" [1]. This corresponds to the term robustness as defined in Sect. 2.34. However, the term integrity is used only occasionally to denote this particular meaning. Furthermore, it could also be defined in a different manner more in line with general usage, namely as the wholeness and intactness of a structure. Integrity would thus refer to the state of a structure and not to its behavior. It is therefore recommended to discontinue the usage of the term integrity in the firstly mentioned sense and to use the term robustness instead.*

2.24 Key element. A structural component (or a part of the structure) that meets two conditions: (a) it is not larger than the structural part assumed to initially fail as determined from the hazard scenarios; (b) its failure entails further damage that violates the performance objectives. *Examples of possible key elements are a building column, a pier of a continuous bridge, a cable in a cable-supported structure, an individual anchor of an anchored retaining wall, certain areas of the subsoil, and components of temporary bracing or shoring during construction.*

2.25 Non-structural methods. See Sect. 2.39.

2.26 Non-threat-specific design. See Sect. 2.40.

2.27 Performance objectives. The acceptable response of a structure to hazard scenarios. *The performance objectives are specified as part of the design objectives (see Sect. 5).*

2.28 Prescribed local resistance. A local increase of structural resistance implemented as an indirect design measure. *Prescribed local resistance is the indirect-design version of the design method increased local resistance described in Sect. 2.20. Instead of prescribed local resistance, the term enhanced local resistance has occasionally been used in the past.*

2.29 Prescriptive design rules. Consensus-approved features of indirect design (…) codified in standards and guidelines or specified for a particular project. *See Sect. 6.8.*

2.30 Progressive collapse. A collapse that commences with the failure of one or a few structural components and then progresses over successively affected other components. *See Sect. 2.14. There are various types of progressive collapse that differ with respect to the mechanism of collapse and the propagating action such as pancake-type collapse, zipper-type collapse, domino-type collapse, (...) and mixed-type collapse. Different kinds of structures can be susceptible to different types of progressive collapse. (...)*

2.32 Protection. Mitigating the effect of abnormal events through external structural measures. Aims at preventing or reducing initial damage that could otherwise lead to disproportionate collapse. *Providing protection is one of the design methods (see Sect. 2.10, 6.1, and 6.3).*

2.33 Redundancy. Availability of alternative load paths. *See Sect. 2.3. Redundancy is one possibility to enhance robustness. Both terms denote different properties of the structure though and should be clearly distinguished.*

2.34 Robustness. Insensitivity to initial damage. A structure is robust if an initial damage does not lead to disproportionate collapse. A precise definition requires reference to specified design objectives: a structure is robust if an initial damage as determined from the hazard scenarios does not lead to an extent of damage that violates the performance objectives. *Robustness is a property that depends on the structure and the location and amount of initial damage. If the initial damage is specified as a notional damage, its cause is immaterial and robustness becomes a purely structural property. This is in contrast to a broader definition of robustness – as it is given, for instance, in Eurocode 1 [2] – that refers to abnormal events. Such a broader conception is close to the term collapse resistance defined in 2.6. A robust structure is collapse resistant but not vice-versa (see Sect. 2.6). Robustness can be achieved by alternative load paths (see Sect. 2.3) or segmentation (see Sect. 2.36). See also Figure 2.*

2.35 Segment border. A border of a segment of a structure at which a failure within the segment is isolated from the remaining structure and thus brought to a halt. *See Sect. 2.36 and Sect. 6.6.*

2.36 Segmentation. Segmenting a structure by dedicated segment borders to isolate a failure that occurs in a segment within that segment thus preventing a failure from spreading. *Segmentation is one of the design methods (see Sect. 2.10, 6.1, and 6.6). Instead of segmentation, the term compartmentation (or compartmentalization) has occasionally been used in the past. (...)*

2.37 Significance. The significance of a structure is determined by the consequences of its collapse. *The significance of a structure is one of the conditions from which the design requirements are derived (see Sect. 4).*

2.38 Specific local resistance. A local increase of structural resistance implemented as a direct design measure. *Specific local resistance is the direct-design version of the design method increased local resistance described in Sect. 2.20.*

2.39 Structural methods. Structural methods aim at preventing a disproportionate collapse through the structural design of the structure itself (internal methods) or of external structural measures of protection, thus enhancing collapse resistance. In contrast, non-structural methods aim at preventing abnormal events from affecting a structure, thus reducing the exposure, without requiring a structural design for this purpose. *Protection, increased local resistance, alternative load paths, and segmentation are structural methods. Event control is a non-structural method. Structural methods can be implemented within a direct or indirect design approach (see Sect. 6.7 and 6.8).*

2.40 Threat-specific design. The terms threat-specific and non-threat-specific design categorize the manner hazard scenarios are specified: (a) threat-specific design is based on specific threats that possibly occur (specific abnormal events); (b) non-threat-specific design is based on the assumption of notional actions or notional damage. *Direct design can be based on threat-specific or non-threat-specific hazard scenarios. Indirect design is not based on hazard scenarios and therefore is neither threat-specific nor non-threat-specific (see Sect. 6.8). (...)*

2.41 Verification procedures. Procedures for demonstrating that specified performance objectives are met when specified hazard scenarios occur. Used in the context of direct design and event control. *The verification procedures are specified as part of the design criteria (see Sect. 3 and 7).*

2.42 Vulnerability. Susceptibility of a structure to suffer initial damage when affected by abnormal events. *This definition is based on Ref. [3] according to which vulnerability accounts for the direct consequences of an abnormal event, which are related to the component behavior. A structure can be made collapse resistant (see Sect. 2.6) by reducing its vulnerability which in turn can be achieved by protection (see Sect. 2.32) or increased local resistance (see Sect. 2.20). See also Figure 2.*

3 Design criteria

3.1 General. The design criteria form the framework of performance-based design against disproportionate collapse. They consist of design requirements, design objectives, design methods, and verification procedures. *(...) The framework suggested here is illustrated in Figure 1.*

3.2 Specification of design criteria. In general, the design criteria are specified on a project-by-project basis by the Client and the Engineer and approved by the Authorities as further detailed below. This specification can be based on the provisions of Sect. 4 to 7 if applicable. If not, other applicable provisions can be used. (…) *Due to the complexity and diversity inherent in major structures, a project-related specification of design criteria is required for such structures. Such a specification entails a decision-making process possibly supported by specialist consultants. In some cases, the design criteria can be established on the basis of a classification of structures. Such a classification is outlined below. It is anticipated, however, that a generally binding specification of design criteria on the basis of a classification of structures will at best be possible for small to medium-sized structures. Some of the design criteria listed here have been codified for specific types of structures: Eurocode 1 [2], General Services Administration guidelines for federal office buildings [4], Unified Facilities Criteria for Department of Defense projects [5], Approved Document A of the UK Building Regulations [6], Post-Tensioning Institute recommendations for stay cable design, testing and installation [7].*

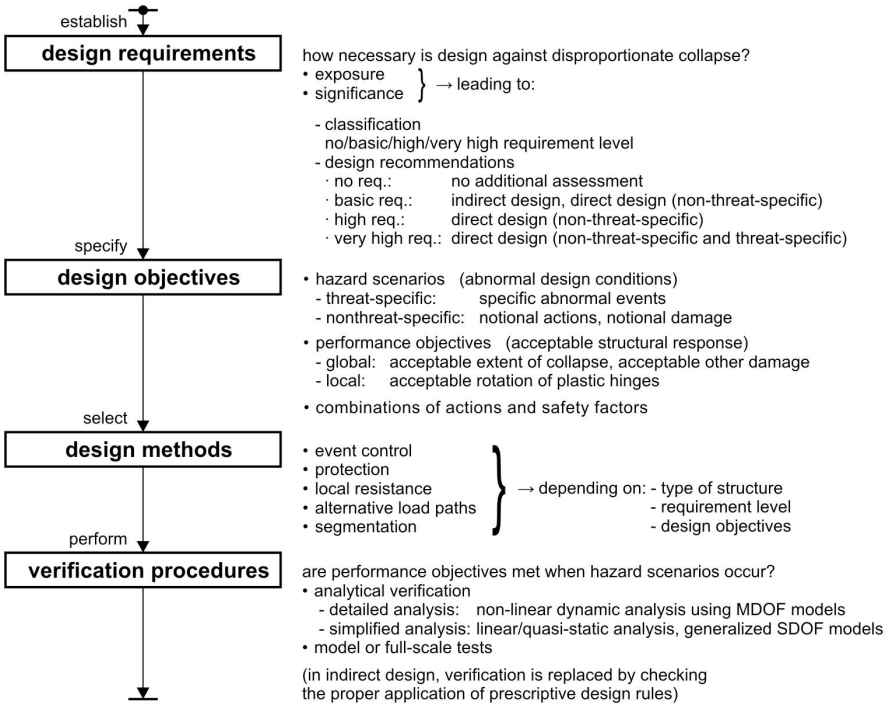


Figure 1: Framework for design against disproportionate collapse

4 Design requirements

4.1 General. The design requirements specify whether design against disproportionate collapse is required for a structure. If such a design is required, they can specify the level of requirements on design objectives, design methods, and verification methods. The design requirements are usually based on the exposure and the significance of a structure. *In view of cost effectiveness, design against disproportionate collapse will not be required for every structure. It is suggested that the following four levels of requirements be distinguished: no requirements, basic requirements, high requirements, and very high requirements.*

4.2 Exposure. The exposure results from the threats that possibly affect a structure during its construction and lifetime. In the context of disproportionate collapse, only the threats not considered in the ordinary design of a structure are of interest. When they occur they are called abnormal events. *(...) A list and classification of possible abnormal events is given in Table 1 (...).*

4.3 Significance. The significance of a structure is determined by the consequences of its collapse. *The consequences of a collapse are the sum of all direct and indirect losses. They go beyond the immediate human and material losses and include indirect consequences such as impairment of public infrastructure and of civil and national defense. (...)*

4.4 Specification of design requirements. The design requirements are specified by the Client and approved by the Authorities. This specification can be based on the classification suggested in Table 3 if applicable or on other applicable provisions. *Structures can be classified according to their exposure and significance. The resulting classes of structures can be linked to levels of requirements. Such a classification*

Table 1: List and classification of abnormal events

Faults			Errors
External		Immanent	
Man-made (accidental/intentional)	Environmental		
Impact (car, train, ship, aircraft)	Earthquake	Lack of strength	Design errors
Explosion (gas, explosives)	Extreme wind forces	Cracks	Construction errors
Fire	Heavy snow fall		Usage errors
Excessive loading (live load)	Floods (scour)		

[To be revised and completed by the Requirements and Objectives Sub-Committee]

Table 2: List and classification of consequences
[To be drafted by the Requirements and Objectives Sub-Committee]

Table 3: Classification of structures and design requirements

Basis of classification	Classification of structures	Examples of structures	Requirement level
Significance low	Structures whose failure does not result in major human or material losses	Buildings rarely occupied by humans; Short bridges on secondary roads	1 – No requirements
Significance medium	Structures whose failure results in limited human or material losses	Buildings with up to 50 occupants; Bridges and tunnels of up to 100 m length and up to four lanes	2 – Basic requirements
Exposure or significance high	Structures which are highly exposed or whose failure results in major human or material losses	Embassy and military buildings. Structures and clusters of structures with up to 1000 occupants; Bridges and tunnels of up to 1000 m length and up to six lanes	3 – High requirements
Exposure and significance high	Structures which are highly exposed and whose failure results in major human or material losses	Lifeline structures; Buildings in which hazardous products are stored or processed; Structures and clusters of structures with more than 1000 occupants; Bridges and tunnels of more than 1000 m length or more than six lanes	4 – Very high requirements

[To be revised and completed by the Requirements and Objectives Sub-Committee]

is suggested in Table 3. (...) Specifying design requirements is not intrinsically an engineering problem. It can be supported by professionals but must reflect the will of (...) Client and Authorities. Therefore, the classification suggested in Table 3 is a non-binding orientation guidance. (...)

5 Design objectives

5.1 General. Design objectives are the basis of direct design. They comprise hazard scenarios, performance objectives, and applicable combinations of actions and safety factors.

5.2 Hazard scenarios. The hazard scenarios are the abnormal conditions to be assumed in the design to occur during the construction and lifetime of a structure. They can be specified as specific abnormal events, as notional actions or as notional damage. Notional damage is typically specified as cases of initial local failure. *In threat-specific design, the hazard scenarios are specific abnormal events. In non-threat-specific design, they are notional actions or notional damage.*

The abnormal conditions possibly affecting a structure can differ substantially from project to project. Therefore, it is difficult to specify the hazard scenarios in a standardized manner. (…) Threat-specific design requires the identification and quantification of all threats possibly affecting the structure and the ensuing effects on it. These input data are likely to be incomplete and imprecise because some threats remain unpredictable. Threat-specific design, if used, should therefore be complemented by elements of non-threat-specific design, in particular by the assumption of notional damage. For the same reason, preference should normally be given to non-threat-specific design, possibly complemented by elements of threat-specific design. With respect to notional damage, the applicable design methods are limited to alternative load paths and segmentation (see Sect. 6). (…)

5.3 Performance objectives. The performance objectives are the acceptable response of a structure to the hazard scenarios. (…) *The performance objectives can be defined on a global level, that is, as acceptable extent of collapse and acceptable other damage, or on a local level, for instance, as acceptable rotation of plastic hinges. Other damage includes damage to the non-collapsed remaining structure, damage to the surroundings, and indirect losses resulting from an impairment of public infrastructure and of civil and national defense. (…) Global performance objectives are generally more meaningful. Local performance objectives can serve as simplified and substitute criteria for achieving global objectives. (…)*

5.4 Combinations of actions and safety factors. The combinations of actions and safety factors to be applied in analytical verifications pertaining to direct design must be specified. *In ordinary design, this specification is mathematically derived from the requirement to achieve a uniform level of safety. This is not currently possible in the context of disproportionate collapse. A reasonable level of safety can nevertheless be achieved by using reasonable combinations of actions and safety factors. It is suggested that the actions determined from the hazard scenarios and actions resulting from an initial damage be combined with dead load, live load, and environmental loads. (…) It is suggested that stricter safety factors be required when disproportionate collapse is intended to be prevented by specific local resistance (see Sect. 6.4).*

5.5 Sets of design objectives. The design objectives can be specified as sets or functions of interrelated data. *When the design objectives are specified as more than one set of data, the performance objectives can be specified differently for hazard scenarios of different kind or extent. Such dependency can be expressed by a number of sets of design objectives or by functional relationships. (…)*

5.6 Specification of design objectives. The design objectives are specified by the Client and approved by the Authorities. This specification can be based on the provisions suggested in Tables 4, 5, and 6 if applicable or on other applicable provisions. The hazard scenarios shall not be specified against the advice of the Engineer. *The design objectives can be established depending on the level of requirements. Corresponding design objectives are suggested in Tables 4, 5, and 6. (…) The level of requirement in these tables can be determined from the classification of structures suggested in Table 3 if applicable. (…)*

Table 4: Hazard scenarios depending on the level of requirements
[To be revised and completed by the Requirements and Objectives Sub-Committee]

Table 5: Performance objectives depending on the level of requirements

Requirement level	Acceptable extent of collapse	Acceptable other damage
2 – Basic requirements	10 % of the structure in terms of masses, volumes, or floor area (in buildings).	A cost equivalent of 10 % of the construction costs of the structure.
3 – High requirements	10 % of the structure in terms of masses, volumes, or floor area (in buildings).	A cost equivalent of 10 % of the construction costs of the structure but not more than USD 20 M.
4 – Very high requirements	5 % of the structure in terms of masses, volumes, or floor area (in buildings).	A cost equivalent of 5 % of the construction costs of the structure but not more than USD 20 M.

[To be revised and completed by the Requirements and Objectives Sub-Committee.]

Table 6: Combinations of actions and safety factors depending on the level of requirements

Requirement level	Design method	Combinations of actions and load safety factors	Resistance safety factors
2 – Basic requirements	Specific local resistance	1.3 HSA + 1.1 IDA + (0.95 or 1.1) DL + 0.7 LL + 0.2 EL	Concrete: 0,65 Steel: 0,9
	Alternative load paths, Segmentation	1.1 HSA + 1.1 IDA + (0.95 or 1.1) DL + 0.7 LL + 0.2 EL	Concrete: 0,7 Steel: 0,95
3 – High requirements	Specific local resistance	1.5 HSA + 1.1 IDA + (0.95 or 1.1) DL + 0.7 LL + 0.2 EL	Concrete: 0,65 Steel: 0,9
	Alternative load paths, Segmentation	1.2 HSA + 1.1 IDA + (0.95 or 1.1) DL + 0.7 LL + 0.2 EL	Concrete: 0,7 Steel: 0,95
4 – Very high requirements	Specific local resistance	1.7 HSA +1.3 IDA + (0.9 or 1.3) DL + 1,0 LL + 0.3 EL	Concrete: 0,6 Steel: 0,85
	Alternative load paths, Segmentation	1.3 HSA + 1.3 IDA + (0.9 or 1.3) DL + 1,0 LL + 0.3 EL	Concrete: 0,65 Steel: 0,9

HSA = actions determined from hazard scenarios; IDA = actions resulting from initial damage; DL = dead load; LL = live load; EL = environmental load; (see Sect. 5.4 for further explanations)

[To be revised and completed by the Requirements and Objectives Sub-Committee.]

6 Design methods

6.1 General. Design methods are methods that aim at preventing disproportionate collapse of a structure. The available design methods are event control and protection, which are external methods, and increased local resistance, alternative load paths, and segmentation, which are internal methods. Event control is a non-structural method, whereas protection and the internal methods are structural methods. Structural methods can be implemented within a direct or indirect design approach. *Internal methods apply to the design of the structure itself. External methods do not directly apply to the design of the structure itself. (…) The classification of design methods suggested here is illustrated in Figure 2.*

6.2 Event control. Event control reduces the probability of occurrence and the intensity of abnormal events through non-structural measures. *Event control reduces the exposure of a structure. The kind of abnormal event to be controlled must be anticipated for implementing event control. It is thus a threat-specific method. Examples of event control are the control of public access to the structure, the enforcement of standoff distances, aerial surveillance, and anti-aircraft defense. (…)*

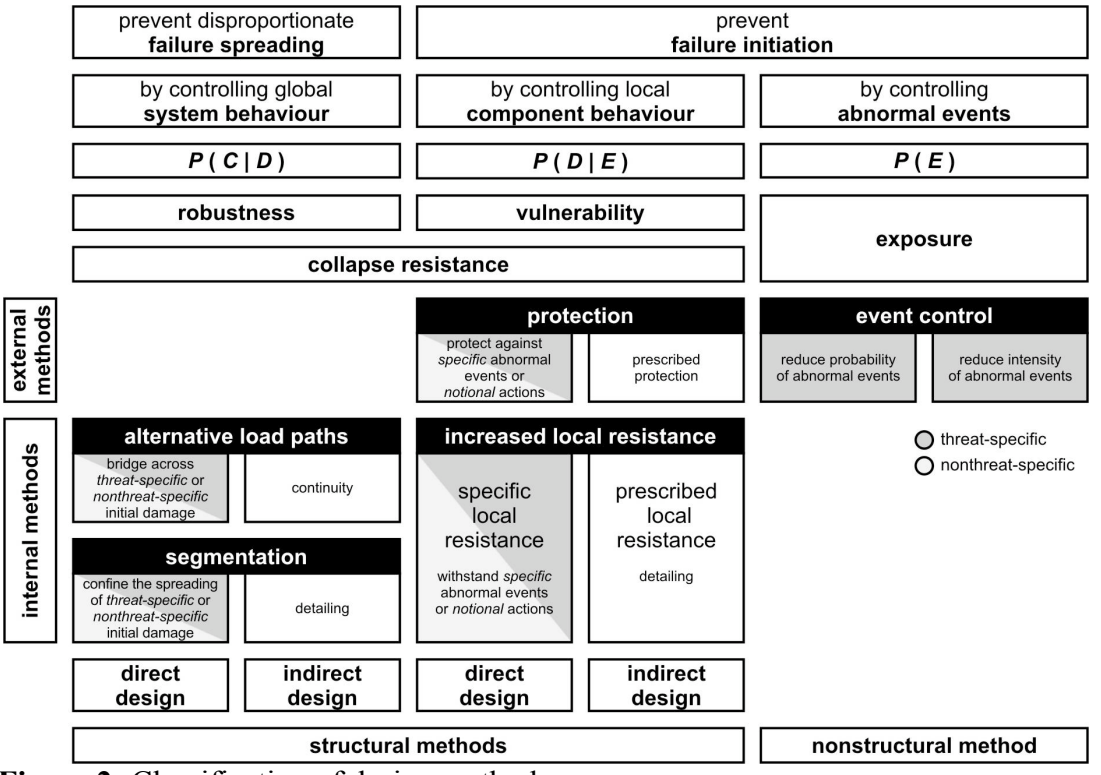


Figure 2: Classification of design methods

6.3 Protection. Protection mitigates the effect of abnormal events through external structural measures. It aims at preventing or reducing initial damage that could otherwise lead to disproportionate collapse. *Protection reduces the vulnerability of a structure. It usually focuses on the key elements of a structure. External structural measures of protection are additional auxiliary components or structures as long as they are not components of the load-transfer system of the structure being protected. Examples of protection are barriers, walls, and dams that resist and shield from impact and blast.*

6.4 Increased local resistance. The local structural resistance is increased or confirmed to be adequate by this design method. It aims at preventing or reducing initial damage that could otherwise lead to disproportionate collapse. Within direct design, this method is called specific local resistance. Within indirect design, this method is called prescribed local resistance. *Increased local resistance reduces the vulnerability of a structure. This method usually focuses on its key elements. (...) Providing specific local resistance is based on specified hazard scenarios. These can be specific abnormal events not averted by event control (threat-specific) or notional actions (nonthreat-specific). In either case, these input data are possibly imprecise. Furthermore, the failure of any one key element is likely to lead to immediate disproportionate collapse (contrary to the failure of an alternative load path or a segment border). It is therefore suggested that an increased margin of safety be required when disproportionate collapse is intended to be prevented by specific local resistance. (...)*

6.5 Alternative load paths. Alternative load paths provide alternatives for a load to be transferred from a point of application to a point of resistance. They enable a redistribution of forces originally carried by failed components and thus prevent a failure

from spreading. *Alternative load paths enhance the robustness of a structure. Alternative load paths can form through ordinary or extraordinary load-transfer mechanisms. (…) Alternative load paths can be added by increasing continuity, strength, and ductility.*

6.6 Segmentation. A structure is divided into segments by dedicated segment borders. This allows a failure that occurs in a segment to be isolated within that segment and thus to prevent a failure from spreading. *Segmentation enhances the robustness of a structure. Segment borders can produce their isolating effect by three different modes of effectiveness: (a) by accommodating large forces, that is, by high local resistance; (b) by accommodating large deformations and displacements, that is, by eliminating continuity or reducing stiffness; (c) by accommodating large forces and large displacements at the same time, which can be achieved by high ductility and results in large energy dissipation capacity. (…)*

6.7 Direct design. Direct design aims at explicitly ensuring collapse resistance by demonstrating that specified performance objectives are met when specified hazard scenarios occur and affect the structure. *For structures of high exposure or significance, direct design is preferable to indirect design. It takes into account the diversity and complexity emerging in structures and ensures collapse resistance in a reasonably reliable, verifiable, and economical manner.*

6.8 Indirect design. Indirect design aims at implicitly increasing the collapse resistance of a structure by incorporating consensus-approved structural design features. This is done without explicit consideration of hazard scenarios and without demonstrating that performance objectives are met. Such features can be codified in standards and guidelines or specified for a particular project, both as prescriptive design rules. *The verification effort required in direct design may become disproportionate for structures of low or medium significance. If therefore direct design is not used, a certain degree of collapse resistance by using indirect design may still be desired. The prescriptive design rules codified so far are detailing rules that intend to provide tension ties, to enable catenary action, or to provide ductility in building structures. These measures aim at providing increased local resistance or alternative load paths. If potential alternative load paths are not provided with the strength required for a redistribution of forces, a failure spreading is possibly not prevented but promoted. Therefore, prescriptive design rules aiming at providing alternative load paths should be applied only to structures strictly within the scope of the applicable provisions or when their safety has been approved otherwise. Prescriptive design rules for specific and specified types of structures are suggested in an Appendix [to be drafted by the Indirect Design Sub-Committee].*

6.9 Combination of design methods. (…) *The design methods can be combined in different ways and for different purposes. (…)*

6.10 Specification of design methods. The structural design methods are selected by the Engineer and approved by the Authorities. This selection can be based on the provisions suggested in Table 7 if applicable or on other applicable provisions. The complementary or alternative use of event control requires adequate professional and organizational support for reliably implementing such non-structural measures and the explicit consent of the Client, the Engineer, and the Authorities. *The applicable structural design methods, including the respective design approaches, can be specified depending on the level of requirements. Such a specification is suggested in Table 7. (…)*

Table 7: Specification of structural design methods

Requirement level	**Design approaches**	(…)
2 – Basic requirements	Indirect design (prescriptive design rules);	
	Direct design (based on non-threat-specific hazard scenarios	(…)
3 – High requirements	Direct design (based on non-threat-specific hazard scenarios possibly complemented by threat-specific hazard scenarios)	(…)
4 – Very high requirements	Direct design (based on non-threat-specific hazard scenarios complemented by threat-specific hazard scenarios)	(…)

[To be revised by the Requirements and Objectives SC and the Direct Design SC]

7 Verification procedures

7.1 General. Verification procedures are used to demonstrate that specified performance objectives are met when specified hazard scenarios occur. They are used in the context of direct design and event control. In an analytical verification, the analysis including the modeling of hazard scenarios, structure, measures of protection, and event control should be sufficiently detailed. (…) *Verification is usually performed by analysis. In particular cases, it can be performed by model or full-scale tests. In indirect design, verification is replaced by checking the proper application of prescriptive design rules.*

7.2 Detailed analysis. The required level of detail is generally high. *An analytical verification generally requires non-linear dynamic analysis allowing for large displacements and non-linear material behavior, and using multi-degree-of-freedom models.*

7.3 Simplified analysis. In some cases, simplified analysis can be used. *Simplification, where admissible, resorts to linear analysis, quasi-static analysis, and generalized single-degree-of-freedom models. Simplified analysis can be sufficient if the failure spreading does not involve impact loading. This is not usually the case for structures susceptible to pancake-type collapse (...). [To be revised and completed by the Direct Design Sub-Committee.]*

7.4 Specification of verification procedures. The verification procedures are selected by the Engineer and approved by the Authorities. *It is suggested that generally detailed analysis be required. Simplified analysis can be allowed on the basis of further research into the relationship between type of structure, type of progressive collapse (...), and type of structural response. [To be revised and completed by the Direct Design Sub-Committee.]*

8 Documentation

8.1 General. The design criteria and the structural analysis and design with respect to disproportionate collapse shall be documented as necessary for design checking, construction, structure management, and emergency response. *(...)*

8.2 Construction documents. Key elements, identified during and remaining after design, that exist in the various construction stages and in the completed structure shall be stated in the construction documents. *The initial failure of any remaining key element is likely to lead to disproportionate collapse. To make such initial failure less probable, structural design and construction (including soil investigation) should meet enhanced requirements when key elements are concerned. In design, this is reflected by the design methods event control, protection, and increased local re-*

sistance. In construction, this is ensured by enhanced quality and safety requirements. The key elements should be stated in the construction documents to enable the Client and the Authorities to specify and to enforce such enhanced construction requirements. The components of temporary works can be key elements. The design of such components is within the scope of these Recommendations.

8.3 Building safety provisions. The design criteria shall also be documented as part of the building safety provisions (…). This documentation shall include a commentary that provides efficient guidance to structure management, users, and emergency response personnel in the case of an abnormal event. *The commentary should include, for instance, the size and location of initial damage that can safely be tolerated by the structure without leading to disproportionate collapse. (...)*

9 References

[1] American Society of Civil Engineers. Minimum Design Loads for Buildings and other Structures (ASCE 7-05). ASCE, Reston, Va., 2005.

[2] Eurocode 1: Actions on structures—Part 1-7: General actions—Accidental actions; BS EN 1991-1-7:2006. Sept. 2006

[3] Joint Committee on Structural Safety. Risk Assessment in Engineering. Principles, System Representation & Risk Criteria. JCSS, Zürich, Switzerland, 2008.

[4] U.S. General Services Administration. Progressive collapse analysis and design guidelines for new federal office buildings and major modernization projects. GSA, June 2003.

[5] U.S. Department of Defense. Unified Facilities Criteria—Design of buildings to resist progressive collapse. UFC 4-023-03, Jan. 2005.

[6] The Building Regulations 2000—Structure: Approved document A. Office of the Deputy Prime Minister, UK, Apr. 2006.

[7] Post-Tensioning Institute. Recommendations for stay cable design, testing and installation. PTI Cable-Stayed Bridge Committee, Phoenix, Ariz., 5th Edition, 2007.

CONCLUSIONS

A draft has been presented that will serve as the outline for the design guidance document to be developed by the ASCE SEI Committee on Disproportionate Collapse Standards and Guidance. It contains a comprehensive set of definitions of terms relevant to disproportionate collapse of structures and, on this basis, a conceptual framework of design criteria encompassing the entire design process. Specific content for a number of sections and tables and an appendix still needs to be developed. This will be done by the Requirements and Objectives Sub-Committee, the Direct Design Sub-Committee, and the Indirect Design Sub-Committee. The scope of these Sub-Committees is defined by the conceptual framework presented here.

A Framework for Optimizing Civil Infrastructure Resiliency

D.A. Reed, M. ASCE [1], Z.B. Zabinsky[2] and L.N. Boyle[3]

[1] Civil and Environmental Engineering, University of Washington, Seattle WA 98195-2700, reed@uw.edu
[2] Industrial and Systems Engineering, University of Washington, Seattle WA 98195-2650, zelda@uw.edu
[3] Industrial and Systems Engineering and Civil and Environmental Engineering, University of Washington, Seattle WA 98195-2650, linda@uw.edu

ABSTRACT

Civil infrastructure systems are complex networks of tightly coupled, interdependent subsystems that involve many factors and system constraints. Their resiliency is critical for the proper functioning of society during and following extreme events such as hurricanes and earthquakes. The goal of this paper is to outline the formulation of a framework that provides strategies for increased resiliency. These strategies will be expressed in a common rule-based form of "If-Then" statements. A rule-based model is flexible and can incorporate social performance measures in addition to traditional metrics. The rule-based model also has the capability to reflect the performance of interdependent networks of multiple systems. These rules may be formulated in a manner so as to be incorporated in a multi-objective optimization algorithm that can improve system performance. A brief example of the proposed framework is provided.

INTRODUCTION

Civil infrastructure systems are considered the foundation of a properly functioning society. The constituent subsystems include power delivery, transportation systems such as roadways, and utilities such as water supply. The resiliency of such systems depends not only upon the physical aspects of the systems but the community in which they are located. As defined by MCEER[1] [Bruneau et al. (2003)], *resiliency* for infrastructure systems has the dimensions of *robustness*, *resourcefulness*, *redundancy* and *rapidity*. Although many of these dimensions may be evaluated as technically-based functions of the physical systems such as fragilities, some implicitly include the social and organizational aspects of the community in which the infrastructure exists. For example, *resourcefulness* is a function of both physical resources and the abilities of the community members to respond to and recover from disaster events. Relating the social and organizational "abilities" and traits to the technical functions involving physical systems is extremely challenging.

[1] Multidisciplinary Center for Extreme Event Research, University of New York at Buffalo, NY.

Cimellaro et al. (2009) developed a metamodel for hospital organizational recovery post-earthquake that incorporated uncertainties and interdependencies of transportation roadways, structural performance, and the quality of care at health care facilities. In our approach, we implement a rule-based method to capture the organizational aspects of recovery. These aspects are based upon a system of rules derived both pre and post event for post-disaster recovery from technical sources as well as social strategies consciously or unconsciously developed by community members. Indeed, the rule-based format allows for the introduction of complex community social dynamics determined through surveys and other tools.

In the US, post-disaster emergency response efforts are traditionally designed with a top-down approach designated as "command and control" [e.g., DHS (2009)] while many participants within affected systems approach their response from a less structured bottom-up approach. Figure 1 illustrates this response situation. Communication in both directions is crucial to an effective response. Bridging the gap between these two approaches can provide a framework for a decision support system that best synergizes the command and control with the community-based social systems.

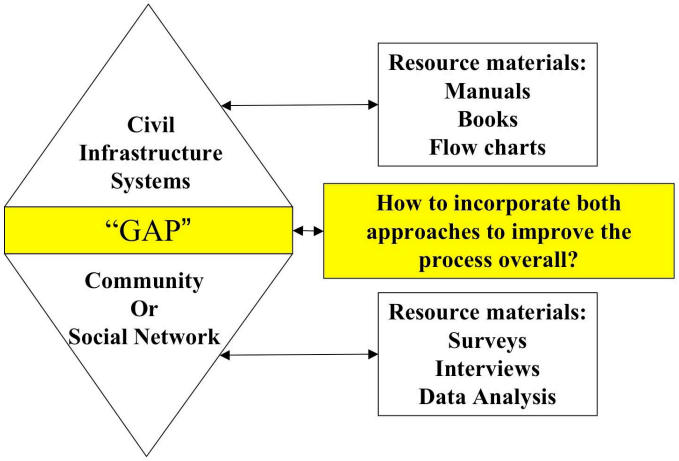


Figure 1. Perspectives of emergency response approaches to management post-event.

In order to build our framework, we must incorporate aspects of systems engineering, social science, optimization and civil engineering. The relevant aspects of these are outlined in the next section.

BACKGROUND.

An interdependent model of civil infrastructure resiliency is comprised of multiple dimensions that include post-event community-based social performance measures and multi-criteria optimization of complex systems based upon rules. Each of these will be defined and outlined in this section before our proposed framework is presented.

Civil Infrastructure Systems.

"Civil infrastructure" is defined in this context as "interconnected lifelines". "Lifelines" are networks that provide for the proper functioning of modern society, such as electric power delivery, transportation systems and water supply. The present networked infrastructure developed in an ad-hoc manner through varying stages of technological innovation without consideration for the interconnected behavior. Individual aging lifelines such roadways continue to decline [ASCE (2009)]. Figure 2 illustrates the system of systems discussed in this paper.

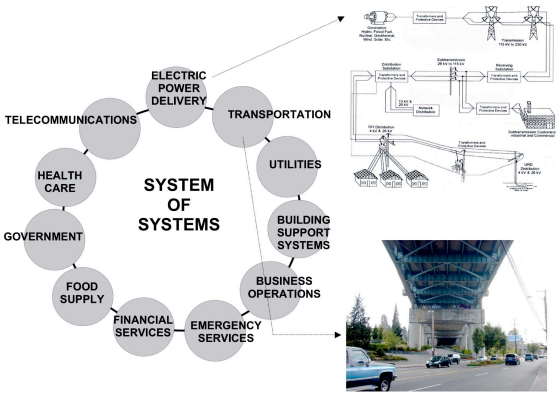


Figure 2. The system of systems that describe the civil infrastructure.

Our network model is derived from the eleven-system interdependent infrastructure as postulated by Chang et al. (2005). The eleven systems $S_1,...S_{11}$ are denoted by index values as follows:

$$\begin{Bmatrix} S_1 \\ S_2 \\ S_3 \\ S_4 \\ S_5 \\ S_6 \\ S_7 \\ S_8 \\ S_9 \\ S_{10} \\ S_{11} \end{Bmatrix} = \begin{Bmatrix} \text{Electric power delivery, with subsystems distribution, transmission and generation.} \\ \text{Transportation, with subsystems air travel, roadways, fueling, transit, rail, water and port facilities.} \\ \text{Utilities, with subsystems water supply, sewage treatment, sanitation.} \\ \text{Building Support Systems, with subsystems HVAC, elevators, security and plumbing.} \\ \text{Business Operations, with subsystems computer systems, hotels, insurance and gaming.} \\ \text{Emergency Services, with subsystems 911, ambulance, fire, police and shelters.} \\ \text{Financial Systems, with subsystems of ATM, banks, credit cards and stock exchange.} \\ \text{Food Supply, with subsystems of distribution, storage, preparation and production.} \\ \text{Government, with subsystems of offices and services;} \\ \text{Health Care, with subsystems of hospitals and public health.} \\ \text{Telecommunications, with subsystems of cable, cellular, Internet, landlines and media.} \end{Bmatrix} \quad (1)$$

Rule-based Optimization.

Complex systems have complicated rules that describe their operation and performance. Instead of using a traditional optimization model with closed form mathematical equations, we apply a recently developed multi-objective interacting particle algorithm that operates directly on If-Then logic rules [Mete and Zabinsky (2010) and Mete (2010)].

In traditional approaches, mathematical modeling must be implemented to create linear or non-linear functions to characterize the real system. The If-Then approach allows users to create and modify the rules that represent the operational or

performance metrics of the system. Mete and Zabinsky (2010) developed an algorithm that operates directly on the rules and produces estimates of the Pareto optimal solutions. The methodology has been applied successfully to scheduling and resource allocation problems defined by business rules [Mete, 2010].

The primary advantage of a rule-based approach is that it employs the natural language of users and is similar to the human cognitive process [Giarratano and Riley (2005); Newell and Simon (1972)]. A popular type of expert systems, rule-based systems, have been successfully implemented for true/false evaluations, such as credit eligibility [Hu and Ansell (2007)]. The current methodology also requires optimization in order to constrain the solution with imposed rules.

In the definition of the problem, the rules are classified as "hard" or "soft". Hard rules provide boundaries so that all solutions must satisfy them. Soft rules represent preferences for the solution. Hard rules are analogous to constraints and soft rules are analogous to *goal programming* in traditional modeling approaches, which result in multiple objectives. Hard rules have true or false (binary) outputs that indicate feasibility of a solution, whereas soft rules have measurable outputs and quantify the degree to which the rule is satisfied. If a soft rule is not completely satisfied, a penalty function *"f"* is assessed.

Mathematically, the defined variables are mapped into Euclidean space where the variables may be real or integer-valued. Variables are associated with solutions that are evaluated for feasibility with hard rules and degree of satisfaction by soft rules. This formulation provides a framework for stochastic optimization. If x is a solution and $f_1,\ldots,f_m$ denote the degree of satisfying soft rules $1,\ldots,m$, respectively, the mathematical problem is

$$\begin{aligned} &\text{minimize: } f_1(x), f_2(x), \ldots, f_m(x) \\ &\text{subject to: } \textit{hard rules} \end{aligned} \tag{2}$$

The functions $f_1,\ldots, f_m$ are smallest when the soft rules are satisfied and larger when they are not. They act as penalty functions. The main flow of the Multi-objective Rule-based Interactive System is presented in figure 3 [Mete (2010)]. The concept is that a group of users may interact through the decision support system to develop hard and soft rules that accurately account for operation and performance of the network of infrastructures. This would facilitate incorporating rules from the top-down command and control structure as well as rules from community-based systems that relate individual responses in various solutions. The rules may also provide interdependency relationships between infrastructures.

When solutions are added to the estimated Pareto optimal list, the decision-makers can discuss the alternatives to come to solutions to implement. If needed, the rules can be modified as the decision-makers explore the impact of non-dominated solutions on the various performance metrics and understand the consequential tradeoffs.

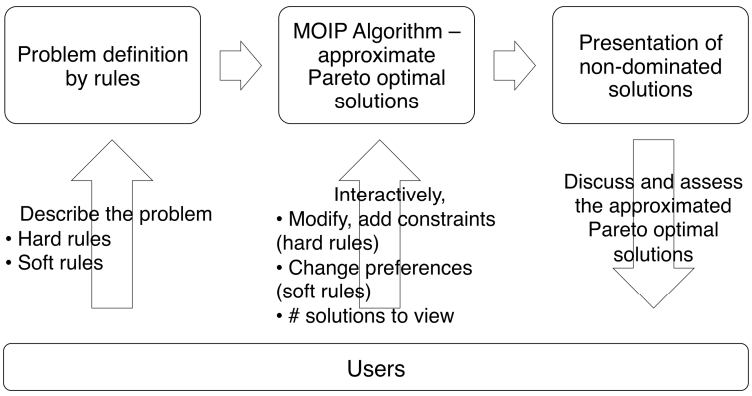


Figure 3. Flow of Multi-objective Rule-based Interactive System. Based on [Mete (2010)].

The multi-objective interacting particle (MOIP) algorithm is used for optimization directly on rules. This algorithm is a combination of a simulated annealing type algorithm and a population-based algorithm (such as genetic algorithms). The MOIP algorithm is inspired by theoretical results from physics that allow us to provide some convergence results. Details on the MOIP algorithm are provided in Mete (2010) and Mete and Zabinsky (2010). Candidate solutions are generated and checked by the hard and soft rules that lead to an estimated Pareto optimal list.

Social Performance Metrics.

The resourcefulness of communities in recovery and response efforts varies as can be evidenced from recent events such as the aftermath of communities in Haiti and New Zealand following major earthquakes. Predictions of community behavior are challenging. The information we seek is ill-defined and highly dependent on the characteristics of the groups seeking assistance. In order to provide models of social behavior post-event, survey instruments traditionally employed in other scenarios such as driver attitudes and behavior in roadway activities may be used [e.g., Donmez et al. (2006)]. To examine various subgroups, stated preferences for resources need to be captured using techniques such as those employed by Ng, Barfield, and Mannering (1998). The surveys will need to address individual's capabilities and limitations within the network [Dickie and Boyle (2009)]. In investigating the attitudes of individuals, we will attempt to answer the following questions:

- How are social groups defined for the community under investigation?
- What resources are required by various social groups post-event and for how long?
- Do individuals act as directed by local, state or federal government?
- Are individuals more closely organized by extended family and neighborhood groups or by governmental institutions?
- What roles do religious organizations and community centers play?
- What preferences are stated for seeking shelter and assistance?

Knowledge gleaned from the surveys will be embedded into the rules of the MOIP system.

FRAMEWORK APPLICATION.

As an example, we outline the approach for an earthquake scenario in the Puget Sound region of the Pacific Northwest. We assume that a magnitude 6.8 deep focus event has occurred. Decisions for roadway restoration by Seattle Department of Transportation [SDOT] and Washington State Department of Transportation [WSDOT] include the following:

- Assess the spatial extent of damage
- Identify if additional resources beyond the local capability will be necessary
- Set priorities for bridge inspection
- Allocate crews and equipment
- Decide road closures and openings

Example rules related to these decisions are listed as follows:

Hard Rules:

- All roads closed in affected areas until crew approves.
- Personnel must be available for rerouting traffic.
- Allocated crews require specific equipment.

Soft Rules:

- Route crews on shortest path if possible.
- Allocate full crews if possible.
- Prioritize bridge inspection on driver behavior.
- Incorporate driver behavior in traffic rerouting.

In the civil infrastructure recovery problem, many rules are derived from preparedness plans. As an example, a solution, x, could be the scheduling and assignment of teams and equipment to locations where the roadway (lifeline) needs to be restored. Hard rules can include the necessity to use equipment, whose operation depends on operator availability. Further, it is necessary to ensure that no equipment is allocated to two places at any given time.

The soft rules relate to rules for ideal situations as well as alternative solutions. For example, it may be ideal to have a three-person team at the site to inspect and open roadways. However, a two-person team can be feasible, but it would take additional time; that is, there is a penalty, f_1, incurred. Another soft rule could encompass the ideal origin-to-destination route. The ideal route would transport equipment and operators to the site the quickest, but an alternate route is feasibility with additional time (penalty, f_2).

The social performance metrics will form the basis for other soft rules. For example, there may be a need to restore traffic to locations not easily identified in the command-control approach. Some individuals find comfort in places that are more familiar such a church, temple, or neighborhood community centers. The information gathered from the survey will provide insights on the likelihood that they will seek shelter at a location not already identified in the top-down approach. The ideal place to restore traffic will be identified as the highest priority by the majority of survey

respondents. It is also recognized that there may not be easy access to some of these locations and hence, an alternative location based on the next highest priority location will be targeted for restoration. However, the penalty of the alternative location is the number of people that can actually be reached (f_3).

It is also likely that subgroups of the population will use only certain facilities. For example, the elderly may be more likely to seek shelter in a faith-based organization while those younger to middle-aged may be more likely to travel to the community center. These differences in subgroups will also need to be accounted for in the algorithm.

Sample Solutions.

The recovery of lifelines is usually characterized by a resilience metric, *Q(t),* or quality. When *Q(t)* equals 100 percent, the lifeline is operating at full capacity. At *Q(t)* equal to zero, the lifeline is not operating at all. Intermediate values of system performance are in-between these two values. We compare a base case scenario (our roadway recovery without MOIP) with two different MOIP solutions in Figure 4.

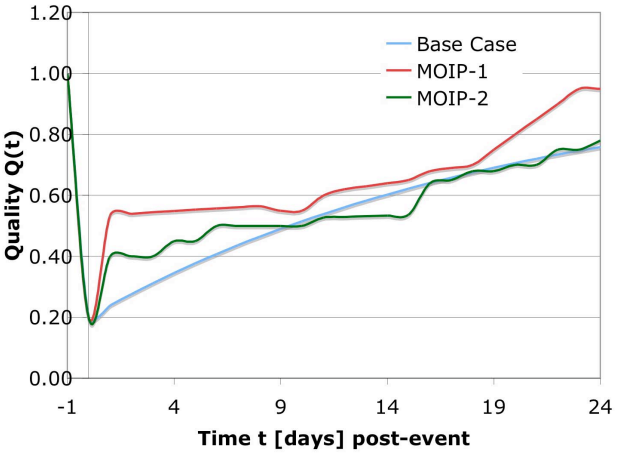


Figure 4. Comparison of *Q(t)* functions.

It is anticipated that the MOIP solutions will provide more rapid recovery. Differences among the recovery functions may be evaluated by decision-makers to improve resource allocation and possibly infrastructure design. Finally, because there are *Q(t)* functions for each system S_i as given in Eqn. (1), and these systems are interdependent [e.g. Reed et al. (2009)], we propose the use of a radar resiliency plot for all eleven systems, at regular time intervals, to assess the recovery of the entire infrastructure system. An example is given in Figure 5 for one time interval.

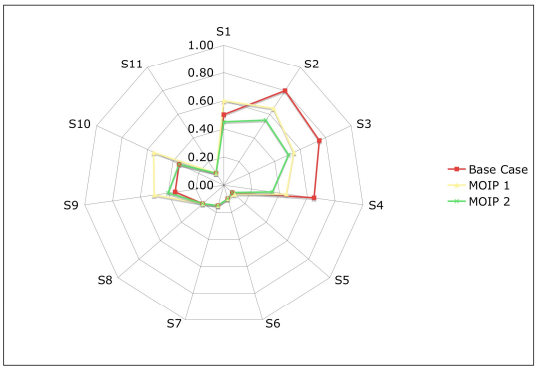


Figure 5. Radar resiliency plot for one time interval.

SUMMARY AND CONCLUSIONS.

We have outlined an alternative approach denoted as "rule-based MOIP" to modeling post-disaster decision-making regarding emergency response and recovery of civil infrastructure systems. Hard and soft rules incorporate constraints and preferences. MOIP provides quantitative information for discussion of mutual interests at the top level of emergency management. It has the potential to transform the process. Improved design of CIS and resource allocation post-event are possible through the application of the proposed methodology.

REFERENCES.

ASCE (2009). *Report Card on America's Infrastructure.* http://www.infrastructurereportcard.org/, last accessed on Dec. 15, 2010.

Bruneau, M., et al. (2003). "A framework to quantitatively assess and enhance the seismic resilience of communities." *Earthquake Spectra*. 19, 733-752.

Chang, S.E. et al. (2005). "Mitigation of Extreme Events: Electric Power Outage and Infrastructure Failure Interactions," *The Economic Impacts of Terrorist Attacks*. Ed. By Harry W. Richardson, Peter Gordon and James E. Moore II, Cheltenham, UK: Edward Elgar Publishing, pp. 70-90.

Cimerallo, G.P. et al. (2009). *Quantification of Disaster Resilience of Health Care Facilities.* Technical Report MCEER-09-0009, Sept. 14.

Department of Homeland Security. (2009). *National Infrastructure Protection Plan*. http://www.dhs.gov/files/programs/editorial_0827.shtm, last accessed December 15, 2010.

Dickie, D. and Boyle, L. (2009). "Drivers' understanding of adaptive cruise control limitations". *Proceedings of the Human Factors Society 53rd Annual Meeting*, San Antonio, TX., pp. 1806-1810.

Donmez, B., Boyle, L., Lee, J. and McGehee, D. (2006). "Driver acceptance and trust of distraction mitigation strategies: effects of age, accuracy, and presentation mode." *Transportation Research Part F*, 9, 6, 387-398.

Giarratano, Joseph C. and Gary Riley. (2005). *Expert Systems: Principles and Programming. Thomson Course Technology*. Australia; Boston, Mass.

Hu, Y.C. and J. Ansell. (2007). Measuring retail company performance using credit scoring techniques. *European Journal of Operational Research*, 183(3):1595–1606.

Liu, H., Zabinsky, Z. B., and Kohn, W. (2010). "Rule-based Forecasting and Production Control System Design Utilizing a Feedback Control Architecture." *IIE Transactions*. To appear.

Mete, Huseyin O. and Z. Zabinsky. (2010). "Multi-Objective Interacting Particle Algorithm for Global Optimization." manuscript under review by *INFORMS Journal on Computing*.

Mete, Huseyin O. (2010). "Multi-Objective Optimization of Complex Systems Defined by Rules." University of Washington Dissertation. (2010).

Ng, L., Barfield, W., and Mannering, F. (1998). Multivariate analysis of private drivers' commuting and commercial drivers' work related driving behavior. *Transportation Research Record,* 1621*,* 27-33.

Newell, Allen and Herbert A. Simon. (1972). *Human Problem Solving*. Prentice-Hall, Englewood Cliffs, N.J.

Reed, D.A. and J. Wang. (1993). *An Emergency Response Plan for Bridge Management, Report No. WA-RD 289.1.* Washington State Transportation Center [TRAC], Seattle WA 98105-4631, Dec.

Reed, D.A., K.C. Kapur and R.D. Christie. (2009). "Methodology for Assessing the Resilience of Networked Infrastructure." *IEEE System Journal*. Vol. 3. No. 2, June, pp. 174-180.

A special solution for lateral-resisting systems capable of multiple seismic performances

Tomaso Trombetti, Stefano Silvestri, Giada Gasparini, Ilaria Ricci[1]

[1]Department of Structural Engineering , University of Bologna, Viale Risorgimento 2 , 40136 Bologna, Italy; Tel: ++39 051 2093258: Fax: ++39 051 2093236; E-mail: stefano.silvestri@unibo.it email, ilaria.ricci6@unibo.it

ABSTRACT

This paper aims at presenting an innovative approach for an optimised/full-controlled seismic design of structures which combines recent contributions in the field of earthquake engineering and overcomes the traditional design approach leading to the identification of the characteristics of the lateral-resisting system capable of satisfying multiple seismic performance objectives. In this respect, it is fundamental the total conceptual separation between the structural systems resisting to vertical and horizontal loads. With reference to both (1) a braced pendular frame structure and (2) a shear-type frame system coupled with a lateral-resisting element (such as a reinforced concrete core or a bracing system), the approach here presented identifies the characteristics (strength, stiffness, ductility, energy-absorption) of the system resisting to horizontal loads which enables to satisfy prescribed seismic performance objectives. This is achieved through the identification of an objectives curve, in the Force-Displacement diagram, of the mechanical characteristics of the structure. The lateral-resisting system is obtained by means of (1) special braces in the case of the braced pendular frame structure and (2) special connection elements in the case of the shear-type system coupled with a lateral-resisting element.

1. INTRODUCTION

The design of building structures capable of providing given seismic performances represents a difficult task due to the complex characterization of the seismic action (not a single action but a set of possible actions of different strength and probability of occurrence) and of the structural response. Many recent contributions in the field of seismic engineering have opened up new possibilities for the structural engineer in terms of conceiving and dimensioning a structural system which offers predetermined seismic performances. Skipping all details, these recent contributions may be summarized as follows: (i) the PBSD approach (SEAOC Vision 2000 1995, Bertero and Bertero 2002) formalized the need of satisfying a multiplicity of performance objectives, (ii) the Direct Displacement-Based Design (DDBD) (Priestley et al. 2007) introduced the displacement analysis as a tool for seismic design of structures and (iii) the wide use of protection devices and techniques (e.g. unbounded braces, dampers (Soong and Dargush 1997, Christopoulos and Filiatrault 2006), seismic isolators (Kelly 1997)) allowed the mitigation of the seismic effects on the structures and strongly suggested the conceptual separation between the structural systems resisting to vertical and horizontal loads.

This paper (i) presents a design approach for a full-controlled seismic design of structures which combines these recent contributions and overcomes the traditional

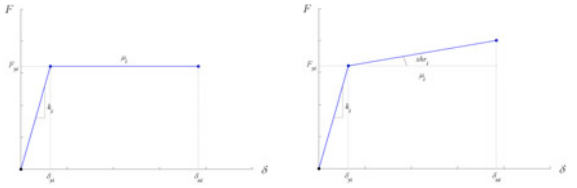
one, and (ii) proposes a special solution for lateral-resisting systems capable of multiple seismic performances constituted by specifically developed "calibrated-shape devices".

2. IDEA AND NEW ASPECTS OF THE PROPOSED DESIGN APPROACH

The basic idea behind the design approach here proposed lies in the identification of the characteristics (strength, stiffness, ductility, energy-absorption) of the structural system resisting to horizontal loads which enables to satisfy a multiplicity of seismic performance objectives, as required by the PBSD and as already faced in other research works (Liu et al. 2004), by adapting and exploiting the complete DDBD approach (Xue and Chen 2003).

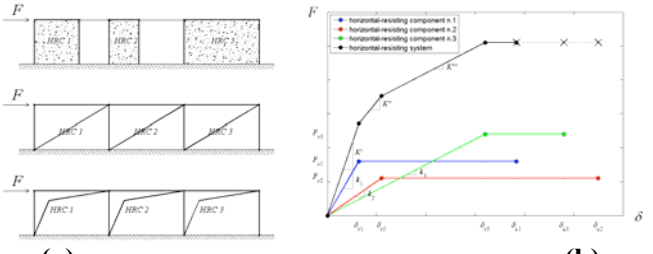
In general, the horizontal-resisting system (hereafter referred to as HRS) of a given building structure can be seen as composed of a series of single horizontal-resisting elements (hereafter referred to as "horizontal-resisting components", HRC), working together. The mechanical characterization of each component (being either a shear wall, a bracing system or other) of the horizontal-resisting system necessarily requires to capture both its elastic and inelastic behaviour. Without loss of generality, the mechanical characterization of each elementary component can be assumed to be an elastic-perfectly plastic one or a bilinear one with hardening, as represented in Figure 1 (a) and (b), respectively. The independent parameters, which are necessary to fully characterize the HRC behavior, are only four and they are stiffness, strength, ductility and strain hardening ratio. For sake of simplicity, in order to present the basic ideas of the design approach here proposed, in the following parts of this paper, the elastic-perfectly plastic model (strain hardening ratio = 0) has been assumed.

The mechanical characterization of the whole horizontal-resisting system (Figure 2b), as composed of the n horizontal-resisting components working in parallel (Figure 2a), can be directly obtained by adding the mechanical characterization of each single component.



(a) **(b)**

Figure 1: F - δ constitutive law of the *i*-th HRC. (a) Elastic-perfectly plastic model; (b) Bilinear model with hardening.



(a) **(b)**

Figure 2. (a) Different SDOF structural systems, each one composed of three homogenous horizontal-resisting components. (b) F - δ constitutive law of a

HRS composed of three HRCs, as obtained combining the constitutive laws of the single HRCs.

The new aspects of this design approach lie:
- in a sound and active combination of the most recent contributions in the field of the earthquake engineering (PBSD, DDBD and protection systems),
- in the total "*separation*" between the structural system resisting to vertical loads ("vertical-resisting system") and the structural system resisting to horizontal loads ("horizontal-resisting system"),
- in the development of a special solution for the horizontal-resisting system based upon the smart use of peculiar devices which are specifically calibrated in their shape to satisfy multiple performance objectives.

3. THE PROPOSED DESIGN APPROACH

The previous considerations, which show how a backbone F-δ curve can be developed and controlled acting on each single HRC, can be collected and formalized in a 3-Phases seismic design approach which is aimed at identifying the characteristics of the structural system resisting to horizontal loads which enables to directly satisfy given seismic performance objectives (without recurring to any trial-error processes). The approach is composed of the following 3-phases:
- Phase 1: starting from selected seismic performance objectives, identification of the F-δ objectives curve of the structural system to be designed;
- Phase 2: development of "calibrated-shape devices" which are capable of satisfying the selected performance objectives when used either (i) as special braces in the case of a pendular frame structure or (ii) as special connections in the case of a frame coupled with a lateral-resisting element;
- Phase 3: verification, by means of appropriate time-history analyses, of the seismic performances achieved.

The approach is illustrated in the following part of the paper with reference to two applicative examples, as developed with reference to:
1) a braced pendular frame structure, and
2) a shear-type frame system coupled with a lateral-resisting element (such as a reinforced concrete core or a steel bracing system).

4. FIRST APPLICATIVE EXAMPLE

The first applicative example is carried out with reference to a building structure composed of seven-storey pendular steel frames (for sake of simplicity it is here assumed that there is no transmission of bending moments at the column-beam connections). The building plan is 36 x 18 m, inter-storey height is 3.5 m and the total building mass is $4.54 \cdot 10^6$ kg. The building is assumed to be located in Bologna (Italy) on D.M. 14/01/2008 soil type C and on topographic surface S1. It is designed to meet the D.M. 14/01/2008 provisions.

The structure is characterized by the separation between the vertical-resisting system (beams and columns) and the horizontal-resisting system (special bracing system). The vertical-resisting system is sized to support just the vertical loads. The horizontal-resisting system is designed to display a controlled inelastic behaviour at the ground level and to behave elastically from the second storey up. It is composed

of: (1) special bracing elements, named “calibrated-shape devices” placed between the ground storey and the first storey, (2) traditional diagonal bracing elements from the second storey up. The horizontal-resisting system, placed between the ground and the first storey, is calibrated, within a Performance-Based Seismic Design approach, to satisfy a multiplicity of performance objectives through the identification of a "objectives curve", in the Force-Displacement diagram, of the mechanical characteristics of the structure. The horizontal-resisting elements from the second storey up can be designed through a capacity design approach and will not be considered in the following analyses. Figure 3 shows the geometry of one of the two perimeter pendular steel frames in both the North-South (NS) and the East-West (EW) directions.

The seismic behaviour of the building along each direction may be schematised as the one of a SDOF system characterized by a mass corresponding to that of the whole superstructure (second storey up) and by the lateral force-displacement relationship controlled by the HRSs composed of 8 HRCs along both the NS and the EW directions, respectively, together with the little contribution to the lateral resistance provided by the vertical-resisting systems. In the following part of the paper, for sake of conciseness, only the seismic behaviour of the building along the NS direction will be considered.

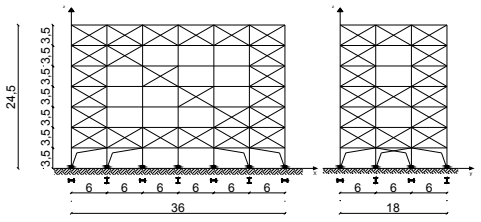


Figure 3. Schematic representation of the building structure considered.

4.1 Identification of the F-δ Objectives curve (Phase 1)

The selected performance objectives

With the aim of obtaining a desired behaviour for the structure at hand and designing the horizontal-resisting system, we imposed the following Basic Objectives as defined in the Vision 2000 document:

1) First Performance Objective (PO1): defined as a coupling of the Fully Operational performance level with the Frequent Earthquake Design Level;
2) Second Performance Objective (PO2): defined as a coupling of the Operational performance level with the Occasional Earthquake Design Level;
3) Third Performance Objective (PO3): defined as a coupling of the Life Safe performance level with the Rare Earthquake Design Level.

Objectives Curve in the force-displacements diagram

Imposing on the considered structure the previous performance objectives (making use of the tools of the typical Priestley’s DDBD approach, such as the identification of the seismic demands by equating equivalent viscous damping and reading off an effective period from highly-damper displacement spectra), we have obtained the *objectives curve* in the Force-Displacements diagram, for the city of Bologna, for D.M. 14/01/2008 soil type C and for topographic surface S1. For sake of conciseness, it is here only represented in graphical form in Figure 4, which

illustrates the target points for an optimised/controlled seismic behaviour of the structure (performance objectives PO1, PO2, PO3). As illustrative example, as far as PO1 is concerned, F_{PO1} = 4.41 MN, δ_{PO1} = 1.75 cm and $K_{PO1} = K_{target}$ = 253790kN/m.

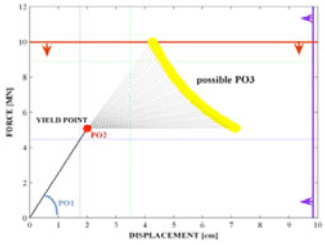


Figure 4. *Objectives curve* in the Force-Displacements diagram.

4.2 Identification of the characteristics of each single horizontal-resisting component (Phase 2)

In this section, the physical characteristics of the horizontal-resisting system are obtained taking into account also the mechanical properties along the horizontal direction of the vertical-resisting system.

Lateral stiffness of the vertical-resisting system

For the case-study at hand, the lateral stiffness (initial inclination of the force-displacement relationship) of the vertical-resisting system, as composed by 28 equal HEA300 columns (14 of which placed to act in weak direction and 14 of which in strong direction), is computed as:

$$K_{VRS} = \sum_{i=1}^{28} k_i = \sum_{i=1}^{14} 1.6\frac{EJ_y}{h^3} + \sum_{i=1}^{14} 1.6\frac{EJ_x}{h^3} = 80060\frac{\text{kN}}{\text{m}} \quad (1)$$

where E = 210000 MPa (Young modulus), J is the moment of inertia along the considered direction (J_y =19380cm^4 and J_x =58220cm^4), and h = 3.5 m (inter-storey height). The stiffness coefficient 1.6 derives from the specific static scheme corresponding to pendular columns which are constrained to move together, along the X-direction, in the upper stories due to the presence of traditional diagonal bracing elements. Figure 5 shows the contribution to the lateral resistance provided by the vertical-resisting system, together with the *objectives curve*, in the Force-Displacement diagram. It is possible to note that the vertical-resisting system alone is not able to satisfy the performance objects imposed.

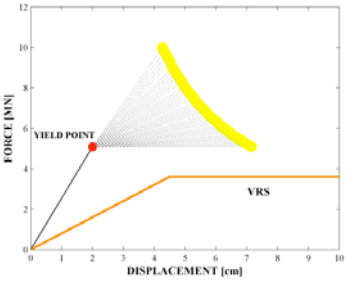


Figure 5 Vertical-resisting system F-δ diagram on the *objectives curve*

Lateral stiffness of the horizontal-resisting system

Without modifying the lateral stiffness of the vertical-resisting system, we assign the part of the lateral stiffness, required for satisfying the performance objectives, to

the horizontal-resisting system placed between the ground and the first storey. Figure 6 shows the "objectives curve" of each HRC. It is obtained subtracting from the structure "objectives curve" the lateral contribution of the vertical-resisting system and dividing by the total numbers of horizontal-resisting components which compose the horizontal-resisting system along the considered direction. Let us indicate the lateral stiffness of the horizontal-resisting system with ΔK or K_{HRS}:

$$\Delta K = K_{\text{HRS}} = K_{\text{Target}} - K_{\text{VRS}} = 173730 \ \frac{\text{kN}}{\text{m}} \tag{2}$$

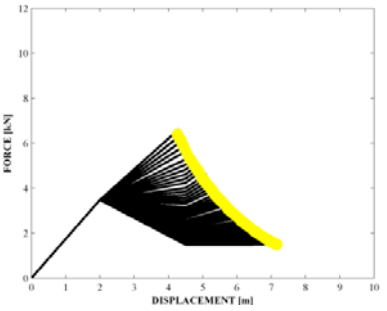


Figure 6 "Objectives curve" of each couple of HRCs.

Design of the linear mechanical/geometrical characteristics of the calibrated-shape device

The lateral stiffness of each couple of horizontal-resisting components (one brace in compression + one brace in tension) is 1/4 of the lateral stiffness of the horizontal-resisting system (there are four Calibrated-shape devices on each face of the building in North-South direction):

$$K_{\text{2HRC}} = \frac{K_{\text{HRS}}}{4} = 43440 \ \frac{\text{kN}}{\text{m}} \tag{3}$$

Figure 7 shows the generic couple of calibrated-shape devices.

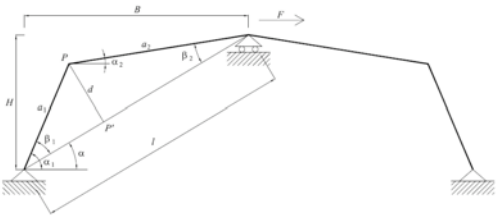


Figure 7 Generic couple of two calibrated-shape devices.

The Virtual Works Principle gives the lateral stiffness of the single crescent shaped brace as follows:

$$\frac{K_{\text{2HRC}}}{2} = \frac{3EJ\cos^2\alpha}{d^2 \cdot (a_1 + a_2)} \tag{4}$$

Where E is the steel Young Modulus; J is the inertia moment of the HRC's cross section; α is the inclination of the portal's diagonal; d is the distance of the knee point, P, from the portal diagonal; $a_1 + a_2$ is the length of the calibrated-shape device.

The first equation for sizing the single crescent shaped brace can be found imposing the equality between Eq. (3) and Eq. (4):

$$\frac{J}{d^2} = \frac{(K_{2HRC}/2)\cdot(a_1 + a_2)}{3E\cos^2\alpha} \quad \textit{(5)}$$

The structure first yield displacement, $_{y1}$, is also the single horizontal-resisting component first yield displacement. So, when each crescent shaped brace has reached its first yield displacement, the bending moment in the most stressed section reaches the first yielding moment, M_y.

The maximum bending moment at point P is given by:

$$M_P = \frac{F}{\cos\alpha}\cdot d \quad \textit{(6)}$$

The first yielding moment is given by:

$$M_y = f_y \cdot W_{el} \quad \textit{(7)}$$

where f_y is the steel yielding tension ($f_y = 275$ MPa) and W_{el} the section modulus of the HRC's cross section.

The second equation for sizing the single crescent shaped brace can be found imposing the equality between Eq. (6) and Eq. (7):

$$\frac{W_{el}}{d} = \frac{(F_{y1,\,2HRC}/2)}{\cos\alpha}\cdot\frac{1}{f_y} \quad \textit{(8)}$$

where h is the height of the cross section and $F_{y1,\,2HRC}/2$ is the first yielding force of each couple of HRCs.

The number of the unknown quantities (J, W_{el}, d) is greater than the number of the equation, hence it is necessary to fix one of the three unknown quantity.

Fixing d = 1 m, we obtain $J = 33414$ cm^4 and $W_{el} = 1789$ cm^3. At this point, several cross-sections may be found with these prescribed values of J and W_{el}. As illustrative examples, the following two cross-sections can be taken into account:

- ***rectangular cross-section characterised by h = 35 cm and b = 9.5 cm ($J = 33943$ cm^4 and $W_{el} = 1940$ cm^3);***
- ***HEB 340 profile modified (t_w=1.3cm, t_f =2.5cm) ($J = 36656$ cm^4 and $W_{el} = 2160$ cm^3).***

In the following section, for sake of brevity, only the "effective" constitutive law of the rectangular cross-section has been reported as obtained by an accurate push-over analysis.

Design of the non-linear mechanical characteristics of the calibrated-shape device

Provided that there are different possibilities regarding the second non-linear branch of the objectives curve (the satisfaction of the PO3 does not lead to a unique objectives curve, but many different solutions may be feasible), the constitutive law of each couple of HRCs has been numerically obtained (Figure 8a) with a non-linear static push-over analysis (displacement control) and then checked with respect to the possibilities of the objectives curve. The couple of braces has been modelled in the STRAUS7 version 2.2.3 package using 2D plane-stress plate elements with the typical stress-strain curve for mild steel material (S275), considering both mechanical and geometrical non-linearities.

Figure 8b shows the constitutive law of each couple of HRCs as reported above the *objectives curve*, together with the contribution of the single column of the vertical-resisting system, which may be considered negligible. Inspection of Figure

8a also indicates that the system is far from the ultimate displacement capacities of both the columns (128 cm) and the calibrated-shape devices (larger than 40 cm). It is clear that the single couple is able to satisfy the performance objective, consequently, also the structure should be able to satisfy the imposed performance objectives. This will be verified in next Phase 3. From Figure 8b, it can be noted that the imposed (designed) displacement under the Rare Earthquake is equal to 4.6 cm.

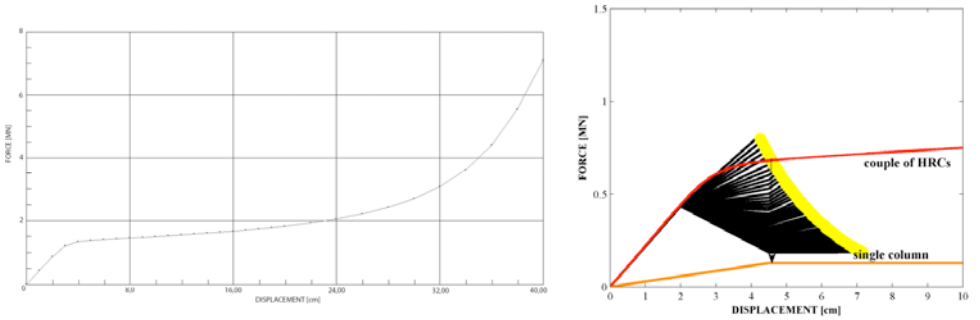


Figure 8. (a) Constitutive law of each couple of HRCs. (b) The constitutive law and the *objectives curve* of each couple of HRCs.

4.3 Analysis and verification (Phase 3)

In this phase, the analysis of the structure so obtained is carried out to verify if the actual structural behaviour is congruent with the expected/imposed performances. A plane model of the structure has been realized using the SAP2000 v14 package, and each crescent shaped brace has been modelled with a synthetic non-linear link element, characterised by a reasonable schematization of the sophisticated constitutive law obtained in the previous Phase 2.

Non-linear time-history dynamic analysis have then been developed on the structural model, using as earthquake ground motions, two groups of seven accelerograms. The first group is composed of seven accelerograms which are overall compatible with the design spectrum of the Italian code corresponding to the Frequent Earthquake. The second group is composed of seven accelerograms which are overall compatible with the design spectrum of the Italian code corresponding to the Rare Earthquake. The accelerograms have been obtained using the program REXEL v 2.2 (beta) (Iervolino 2008). Tables 1 (a) and (b) show the maximum displacements of the first storey caused by the seven accelerograms corresponding to the Frequent Earthquake and by the seven accelerograms corresponding to the Rare Earthquake, respectively. In these tables the average values of the these displacements are also reported. The average values of the displacements of the first storey represent the average displacement demand required by the earthquakes. Comparing the average value of the displacement demand with the value of the displacement demand imposed in Phase 1 for each performance objective, it is possible to note that the value are almost the same (1.76 cm vs. 1.75 cm, and 5.34 cm vs. 5 cm).

Table 1. Maximum displacements and average value of the first storey caused by the seven accelerograms corresponding to the (a) Frequent Earthquake, (b) Rare Earthquake.

(a)

TABLE: Joint Displacements					
Joint	OutputCase	CaseType	StepType	U1	U1
Text	Text	Text	Text	cm	cm
68	DIN_NL_S1_FO	NonDirHist	Max	1.1761	
68	DIN_NL_S1_FO	NonDirHist	Min	-1.1844	1.1844
68	DIN_NL_S2_FO	NonDirHist	Max	3.7342	
68	DIN_NL_S2_FO	NonDirHist	Min	-2.9317	3.7342
68	DIN_NL_S3_FO	NonDirHist	Max	1.3759	
68	DIN_NL_S3_FO	NonDirHist	Min	-1.5391	1.5391
68	DIN_NL_S4_FO	NonDirHist	Max	1.676	
68	DIN_NL_S4_FO	NonDirHist	Min	-1.5505	1.676
68	DIN_NL_S5_FO	NonDirHist	Max	1.9666	
68	DIN_NL_S5_FO	NonDirHist	Min	-2.0353	2.0353
68	DIN_NL_S6_FO	NonDirHist	Max	1.162	
68	DIN_NL_S6_FO	NonDirHist	Min	-1.383	1.383
68	DIN_NL_S7_FO	NonDirHist	Max	0.7457	
68	DIN_NL_S7_FO	NonDirHist	Min	-0.6863	0.7457
			AVERAGE VALUE		1.76

(b)

TABLE: Joint Displacements					
Joint	OutputCase	CaseType	StepType	U1	U1
Text	Text	Text	Text	cm	cm
68	DIN_NL_S1_LS	NonDirHist	Max	6.5233	
68	DIN_NL_S1_LS	NonDirHist	Min	-2.0428	6.5233
68	DIN_NL_S2_LS	NonDirHist	Max	4.2111	
68	DIN_NL_S2_LS	NonDirHist	Min	-2.6618	4.2111
68	DIN_NL_S3_LS	NonDirHist	Max	5.8419	
68	DIN_NL_S3_LS	NonDirHist	Min	-2.1442	5.8419
68	DIN_NL_S4_LS	NonDirHist	Max	3.8728	
68	DIN_NL_S4_LS	NonDirHist	Min	-4.3206	4.3206
68	DIN_NL_S5_LS	NonDirHist	Max	5.589	
68	DIN_NL_S5_LS	NonDirHist	Min	-4.6937	5.589
68	DIN_NL_S6_LS	NonDirHist	Max	3.5379	
68	DIN_NL_S6_LS	NonDirHist	Min	-4.4976	4.4976
68	DIN_NL_S7_LS	NonDirHist	Max	6.383	
68	DIN_NL_S7_LS	NonDirHist	Min	-2.9985	6.383
			AVERAGE VALUE		5.34

5. SECOND APPLICATIVE EXAMPLE

The second applicative example is carried out with reference to a building structure composed of five-storey steel shear-type frames coupled with a lateral-resisting element (i.e. a r.c. wall). The connection between the frame and the lateral-resisting element is realized through the spread placement of hysteretic dissipative devices (therefore referred as HDDs) at each floor of the structure (Figure 9). The building plan is 36 x 18 m, inter-storey height is 3.5 m and the total building mass is $5.40 \cdot 10^6$ kg. The building is assumed to be located in Bologna (Italy) on D.M. 14/01/2008 soil type C and on topographic surface S1. It is designed to meet the D.M. 14/01/2008 provisions.

The structure is characterized by the separation between the vertical-resisting system (beams and columns) and the horizontal-resisting system (r.c. walls of the core). The vertical-resisting system is sized to support just the vertical loads whilst the lateral-resisting element is sized to support just the horizontal loads. The HDDs are calibrated, within a Performance-Based Seismic Design approach, to satisfy a multiplicity of performance objectives through the identification of a "objectives curve", in the Force-Displacement diagram, of the mechanical characteristics of the structure.

In this second case, the seismic behaviour of the building along each direction may be schematised as the one of a MDOF system.

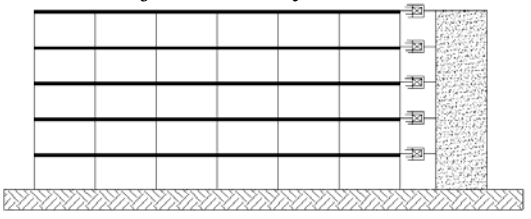


Figure 9. Schematic representation of the building structure considered.

5.1 Identification of the F-δ Objectives curve (Phase 1)

As far as the identification of the F-δ objectives curve (Phase 1) is concerned, the same Basic Objectives have been imposed on the considered structure to obtain the *objectives curve* in the Force-Displacements diagram.

5.2 Identification of the characteristics of each single horizontal-resisting component (Phase 2)

Since the structure at hand is a MDOF system, the HDDs should be calibrated along the height of the building. A tri-linear constitutive law is imposed for each HDD according to the following procedure:

1. Step 1: identification of the total stiffness which the lateral-resisting system should provide to the structure for satisfying the imposed performance objectives;
2. Step 2: distribution of the stiffness of each HDD along the height of the structure;
3. Step 3: identification of the yielding force of each HDD;
4. Step 4: selection of the slope of the second post-yielding branch, of the slope of the third hardening branch, and of the ultimate displacement.

Step 1: identification of the total stiffness for the HDD

The following criterion has been envisaged to obtain a reasonable total stiffness. The total stiffness is evaluated through the equation (9) accounting for the stiffness of the device placed on the first floor, $k_{d,floor1,new}$. This latter is evaluated multiplying the floor stiffness of the shear-type frame, $k_{p,floor,old}$, by a coefficient corresponding to the maximum ratio between the maximum inter-storey drift calculated from the linear analysis ($\max(id)_{floor}$) and the displacement corresponding to PO1, δ_{PO1}, or the elastic displacement of the structure, δ_{el}:

$$k_{d,floor1,new} = k_{p,floor,old} \cdot \max\left(\frac{\max(id)_{floor}}{\delta_{PO1}}, \frac{\max(id)_{floor}}{\delta_{el}} \right) \quad \textbf{(9)}$$

Step 2: distribution of the stiffness of each HDD along the height of the structure

For the distribution of the stiffness of each HDD along the height of the structure different criteria have been envisaged and analysed:

- Criterion 1: transformation of a *n*-DOF system (where *n* is the number of floors) in one made up of *n* unrelated SDOF systems characterized by the same stiffness:

$$k_d = \frac{4\pi^2 m_{floor}}{T_{Frequent}^2} \quad \textbf{(10)}$$

  where $k_{d,i}$ is the stiffness of the *i*-th device (where $k_{d,1} = k_{d,2} = ... = k_{d,i} = ... = k_{d,N}$), m_{floor} is the mass of the floor (which is assumed to be the same for each floor), $T_{Frequent}$ is the period of the whole structure corresponding to the initial imposed stiffness.
- Criterion 2: calibration of the stiffness of the *i*-th device based of the *i*-th shear floor (evaluated through a linear modal analysis) of the shear-type frame; in this case the stiffness of the devices varies from floor to floor:

$$k_{d,i} = \frac{T_i}{\delta_{PO1}} \quad \textbf{(11)}$$

  where $k_{d,i}$ is the stiffness of the *i*-th device, δ_{PO1} is the imposed displacement at PO1.
- Criterion 3: iteration carried out upon Criterion 2 which stops when the variation of the group of stiffness between two consecutive is negligible;

- Criterion 4: transformation of *n*-DOF system in one made up of *n*-linked SDOF systems. This conception is able to consider the shear contribute of overhanging floors.
- Criterion 5: optimization of the initial stiffness through Genetic Algorithms.

On the basis of the results obtained, the best methodology has been identified in Criterion 3, and, for design purpose, it has been deduced the following simplified formula: the relative values of the storey stiffnesses are roughly positioned on a line described by:

$$i_r,2 = \frac{i}{S(n)}; \quad S(n) = \sum_{i=1}^{n} i = \frac{n \cdot (n+1)}{2} \qquad \textit{(12)}$$

where n is the number of floors and i is the floor index (floors are numbered in a crescent order from the top to the bottom).

Step 3: identification of the yielding force of each HDD

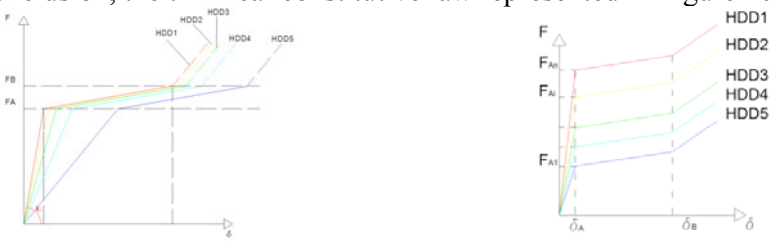
Two criteria have been envisaged to identify the yielding force of each device:

1. the first one considers the same yielding force for all the devices (the yielding force of the device placed on the first floor has been chosen);
2. the second one considers the same yielding displacement for all the devices (the yielding displacement corresponding to the PO1 has been chosen).

Step 4: selection of the slope of the second post-yielding branch, of the slope of the third hardening branch, and of the ultimate displacement

The slope of the second post-yielding branch is defined as the 3% of the initial stiffness of each device, in order to limit the forces on the structural elements. The slope of the third hardening branch is defined as the 50% of the initial stiffness of each device. The ultimate displacement is defined on the basis of the PO3.

In conclusion, the tri-linear constitutive law represented in Figure 10 is obtained.



(a) **(b)**

Figure 10. Constitutive law of HDDs (a) same yielding force and (b) same yielding displacement.

5.3 Analysis and verification (Phase 3)

A plane model of the structure has been realized using the SAP2000 v14 package, and each connection element has been modelled with a synthetic non-linear link element, characterised by a constitutive law obtained in the previous Phase 2. Non-linear time-history dynamic analysis have then been developed on the structural model with the same earthquake ground motions used in the previous example.

Figure 11 displays the on the *objectives curve* of the first floor the results obtained through the non linear analysis.

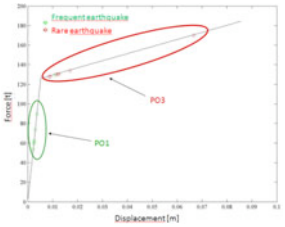


Figure 11. Verification of the seismic performances of the HDDs. *Objectives curve* for the first floor and results of the non-linear time-history analysis.

6. CONCLUSIONS

This paper presents an innovative seismic design approach which allows to exploit at their best all the potentialities offered by both the PBSD framework and the DDBD methodologies.

This approach, which has been applied to the case studies of a (1) moment-resisting frame structure and (2) shear-type frame system coupled with a lateral-resisting element, leads to the identification of the characteristics of the (1) structural system resisting to horizontal loads (special calibrated-shape braces) in the first case-study and (2) special connection elements in the second case-study, which enable to satisfy given seismic performance objectives. This is achieved by considering a total conceptual separation between the structural systems resisting to vertical and horizontal loads and by the use of peculiar calibrated-shape devices as horizontal-resisting system.

ACKNOWLEGEMENTS

Financial supports of Department of Civil Protection (Reluis 2010-2013 Grant – Thematic Area 2, Research line 3, Task 2: “Development and analysis of new technologies for the seismic retrofit”) is gratefully acknowledged.

The authors gratefully acknowledge Maria Cristina Todisco for her contribution in the development of the second case-study.

REFERENCES

SEAOC Vision 2000 Committee. Performance-Based Seismic Engineering. Report prepared by Structural Engineers Association of California: Sacramento, CA, 1995.

Bertero R. D., and Bertero V. V., “Performance-based seismic engineering: the need for a reliable conceptual comprehensive approach, Earthquake Engineering and Structural Dynamics, vol. 31, no. 3, pp. 627-52, 2002.

Kelly J. M., “Base isolation: linear theory and design”, Earthquake Spectra, vol. 6, no. 2, pp. 223-244, 1997.

Soong T. T., and Dargush G. F., Eds., Passive Energy Dissipation Systems in Structural Engineering, John Wiley & Sons, Baffins Lane, Chichester, West Sussex PO19 1UD, England, 1997.

Christopoulos C., and Filiatrault A., Principles of Passive Supplemental Damping and Seismic Isolation, IUSS Press: Pavia, Italy, 2006, p. 480.

Priestley M. J. N., Calvi G. M., and Kowalsky M. J., Direct Displacement-Based Seismic Design of Structures, IUSS Press: Pavia, 2007.

Liu M., Burns S. A., and Wen Y.K., "Multiobjective optimization for performance-based seismic design of steel moment frame structures", Earthquake Engineering & Structural Dynamics, vol. 34, no. 3, pp. 289-306, 2004.

Villaverde R., Fundamental concepts of Earthquake Engineering", CRC Press, 2009

"Norme Tecniche per le Costruzioni" accepted with D.M. 14/01/2008 and published in S.O. No. 30 to G.U. (Official Gazette) No. 29 on date 04/02/2008.

Iervolino, Galasso C., and Cosenza E., Selezione assistita di input sismico e nuove Norme Tecniche per le Costruzioni, Atti del Convegno Valutazione e riduzione della vulnerabilità sismica di edifici esistenti in c.a., Roma, 29-30 maggio 2008.

Blast Vulnerability Evaluation of Concrete Masonry Unit Infill Walls Retrofitted With Nano Particle Reinforced Polyurea: Modelling and Parametric Evaluation

M. IRSHIDAT, A. AL-OSTAZ, A.H.-D. CHENG, AND C. MULLEN

Nano Infrastructure Research Group-Department of Civil Engineering
University of Mississippi
Oxford, Mississippi, 38677-1848, USA

ABSTRACT

This paper focuses on blast vulnerability assessment of concrete masonry infill walls retrofitted with nano particle reinforced polyurea. Quarter scale model concrete masonry infill walls made of scaled down brick units were retrofitted with Polyhedral Oligomeric Silsesquioxane (POSS) reinforced polyurea and subjected to a pre-adjusted airblast pressure and impulse in the ERDC Blast Load Simulator facility. A computationally-efficient model was built using an explicit hydrocode called ANSYS AUTODYN to replicate with reasonable accuracy the behavior of retrofitted infill walls subjected to blast loads. A series of finite element analysis was conducted. The focus was to study the effect of some factors such as boundary conditions, thickness and arrangement of retrofitted layers, and ductility of retrofitted materials on the behavior of the system during and after blast. Results from blast experiments showed that POSS reinforced polyurea significantly enhanced the performance of masonry walls sustaining blast load. The finite element parametric evaluation results show that for the case of retrofitting with elastomeric materials it is better to apply the retrofit at the back side since this will be associated with no failure, when compared to front side retrofit, and a larger deflection (e.g. more energy dissipation) when compared with two side retrofit with a smaller amount of material.

1. INTRODUCTION

Conventional building components are highly vulnerable to terrorist bomb attack. One of the greatest threats from blast loading is the fragmentation–pieces from walls, windows, equipment, or vehicles flying at such high speeds that they can result in extensive injury or death. Un-reinforced masonry (URM) walls have low resistance to out-of-plane blast loadings due to low flexural capacity and brittle mode failure. These problems lead to a critical need to develop effective retrofitting techniques to improve the load carrying capacity of such members to resist blast loads. Good amount of work had been done on using elastomeric materials as a retrofit technique. Johnson, et al (2005) conducted a series of static and dynamic experiments to investigate the potential benefits of using both reinforced and unreinforced elastomeric materials to retrofit hollow, unreinforced, concrete masonry walls. The static experimental results demonstrated an increase in the ultimate flexural resistance of the retrofitted CMU walls. And it supported the idea that the polyurea spray-on materials did significantly increase the stiffness of the reinforced polyureas as compared to the unreinforced ones. Dynamic results showed that the unreinforced polyureas did add minor additional flexural resistance to the hollow unreinforced CMU wall, whereas the addition of reinforcement to the polyurea retrofit system significantly increased the flexural resistance of the CMU walls. Davidson, et al (2004) used full-scale

explosive tests to determine the effectiveness of using sprayed-on polymers to improve blast resistance of unreinforced masonry walls. They concluded that a sprayed-on polymer retrofit approach to strengthening masonry walls against blast loads was an effective technique. Davidson, et al (2005) experimentally and numerically studied damage and failure mechanisms of polymer reinforced concrete masonry walls subjected to blast loadings. They observed that a thin elastomeric coating on the interior face of the wall can be effective in minimizing the fragmentation and potential for collapse of unreinforced concrete masonry walls resulting from a blast. They also found that the elongation capacity was more important for damage reduction than having a high stiffness, so an effective balance between stiffness and elongation potential was required. Finite element results indicated that a spray-on polymer reinforcement approach can be effective in reducing the vulnerability of unreinforced CMU walls subjected to blast loading. Eamon, et al. (2004) analyzed CMUs subjected to blast pressure using the Finite Element Method. Their model had the ability to replicate experimental results with good agreement, generally matching the failure shape, the location of break lines, and the size and the number of primary pieces of debris. In order to protect the nation's infra structure one need to employ the best available materials. When existing materials cannot deliver the performance, it is important to design new material. Recent interest in the use of polymer based composite materials in infrastructure applications requires further improvements in blast resistance of these materials. The main objectives of this study are to investigate the ability of nano particle reinforced polymers to protect masonry infill wall against blast loading, and to study the effect of some factors like boundary conditions, thickness and arrangement of retrofitted layers, and ductility of retrofitted materials on the behavior of the system during and after blast.

2. DESCRIPTION OF MATERIALS USED

Polyhedral Oligomeric Silsesquioxane (POSS) reinforced polymers were used in the current research to protect masonry walls against blast loads. The polymer used in was polyurea Line-XS 350 produced by Protective Coatings Inc.

2.1. Material Properties

The static stress-strain behavior of POSS reinforced polyurea was determined by performing standard direct tension tests using a Servo-hydraulic Material Test Systems (MTS) machine on coupons cut from large panels. Important mechanical properties such as modulus of elasticity, tensile strength, and strain at failure were obtained directly from the generated curve. Table 1 lists the average modulus of elasticity, ultimate tensile strength, and strain at failure. Figure 1 shows typical stress-strain curves for one tested specimen.

Table 1: POSS reinforced polyurea mechanical properties

Modulus of Elasticity (MPa)	210.56
Ultimate Strength (MPa)	13.81
Strain at Rupture (%)	116

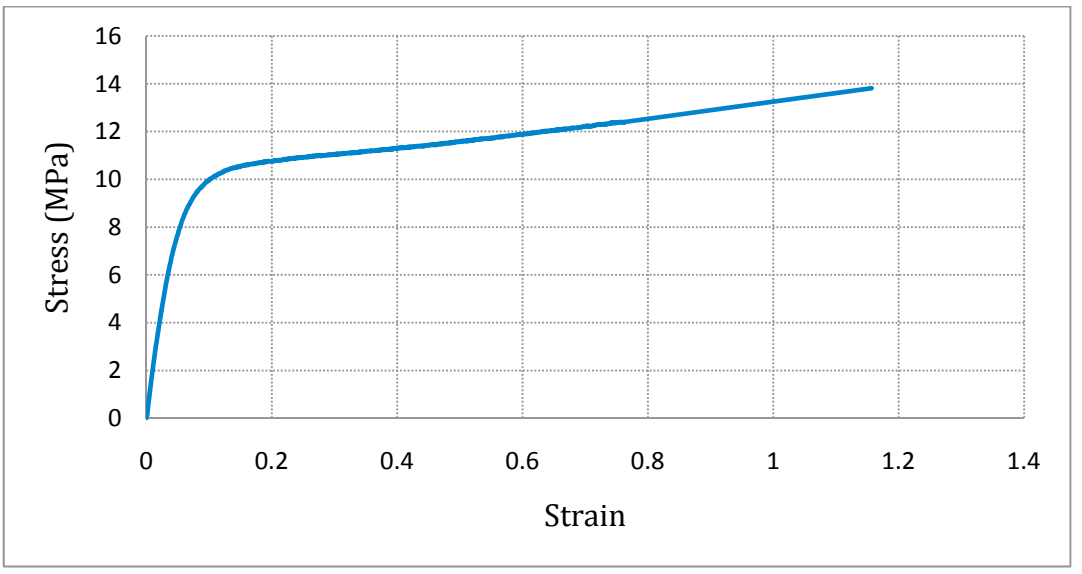


Figure 1: Typical stress-strain behavior for POSS reinforced polyurea under quasi-static tensile loading

Limited number of tensile dynamic testing was performed for POSS reinforced polyurea being used in this research using SHPB in order to compare the high strain rate response to quasi-static response. The results are shown in Figure2.

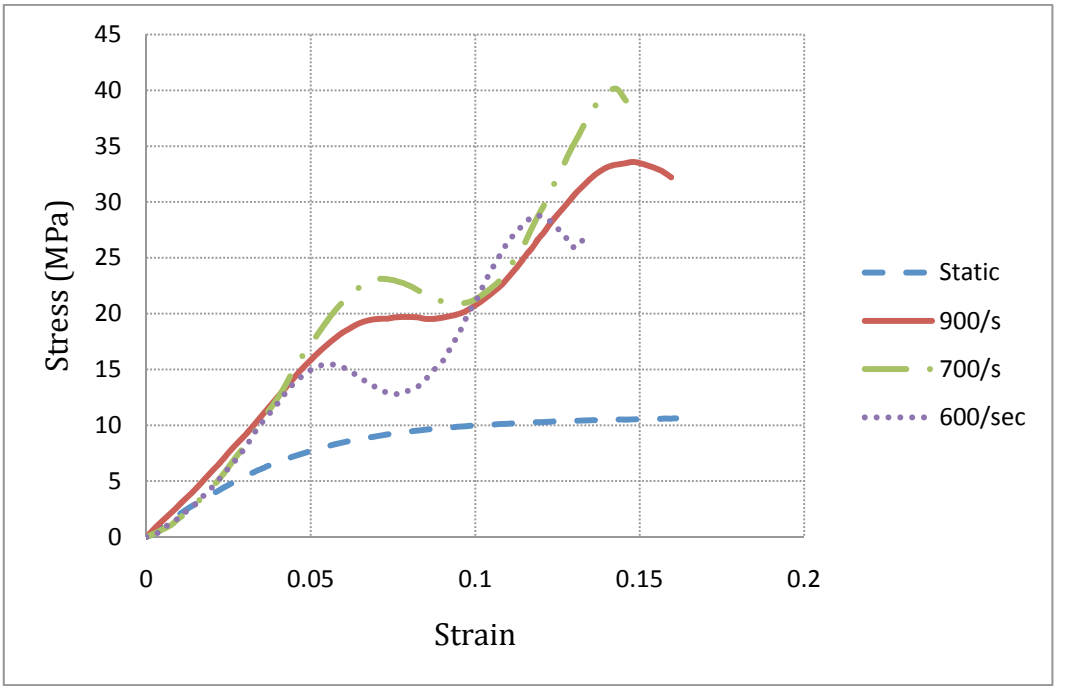


Figure 2: Stress-strain relation for POSS reinforced polyurea under dynamic tensile loading (SHPB)

3. EXPERIMENTAL WORK

Quarter scale model walls made of scaled down brick units (Figure3) were used to investigate the response of POSS reinforced polyurea retrofitted CMU panels subjected to air blast loading produced by Blast Load Simulator (BLS). The average mass of brick units was 252 gm. The walls were fully grouted with approximately 16 blocks tall and 12 blocks wide as shown in Figure3 below. The wall was casted in a steel frame with dowels at top and bottom to simulate simply supported conditions and free boundary conditions at left and right. The average unconfined compressive strength and density of the mortar were 15.9 MPa and 1.700 kg/m^3, respectively, and the average unconfined compressive strength and density of the grout were 15.9 MPa and 1.800 kg/m^3 respectively. The walls were tested at the US Army Engineer Research and Development Center (ERDC) using the blast simulator (Figure4).

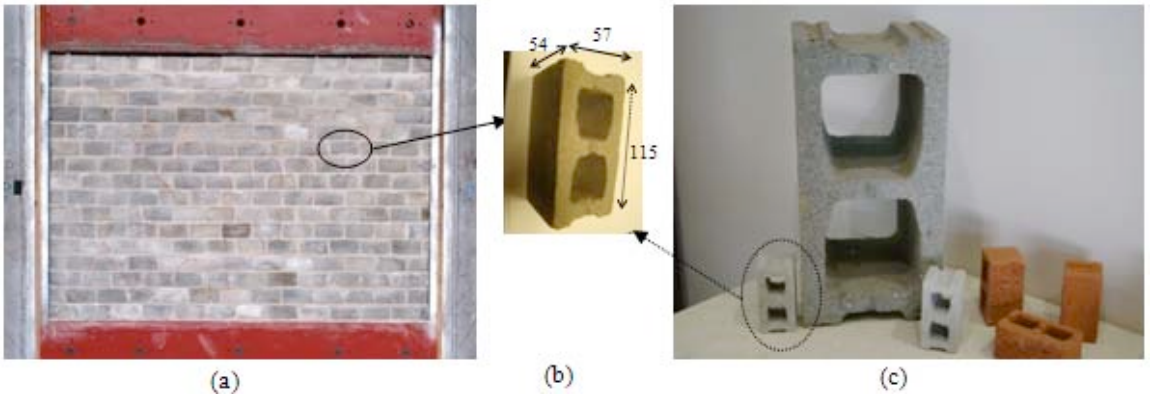


Figure 3: Masonry wall panel (b) Concrete masonry unit brick (all dimensions in mm) (c) Comparison between full scales and scaled down dimensions of masonry unit



Figure 4: Blast simulator at ERDC, Vicksburg, MS

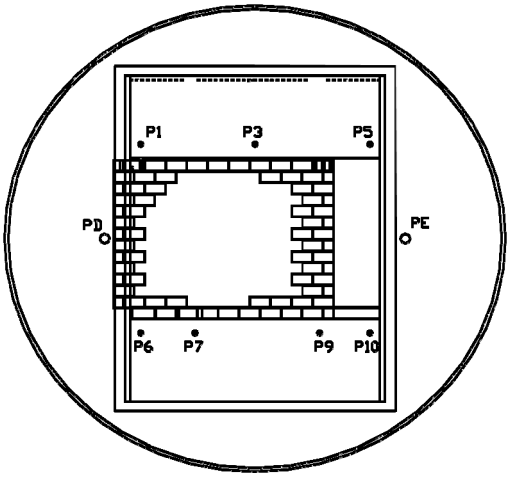
3.1. Experimental Setup

Spraying technique was used to apply POSS reinforced polyurea to the back (interior face) of the CMU infill walls (Figure5). This technique was used because of the fast reaction between the polyurea resin and the *cyanates* hardener. The walls were sprayed back and forth three times. Retrofitted layer thickness was observed to be 1.8mm.



Figure 5: Spray-on retrofitted material

A pre-adjusted air blast pressure and impulse were applied to each wall. Nine pressure sensors mounted on the steel loading frame were used to collect pressure time history (Figure6). Typical pressure time history and calculated impulse time history are shown in Figure 7.



Gage	P (psi)	I (psi-msec)
P1	33.66	71.7
P3	33.13	71.5
P5	29.5	72.1
P6	32.21	70.1
P7	31.63	71.5
P9	27.96	71.1
P10	30.87	71.6
PD	35.22	72.3
PE	31.6	73.2
Sum	285.76	645.1
Avg	**31.75**	**71.7**
IP1	0.37	

Figure 6: Locations of pressure sensors and typical peak pressure values

It was noted that, for all cases, there was an initial rise to a peak reflected pressure (compression pressure wave) followed by a decay to zero pressure and then a negative phase (suction pressure wave). Therefore, if a wall system can be retrofitted adequately to resist the initial compression pressure wave, then it can be allowed to fail on the opposite side (non occupant side) when subjected to the negative pressure wave. Average values of reflected pressure and impulse subjected to the wall were observed to be 218.91 kPa and 494.35 kPa.ms respectively.

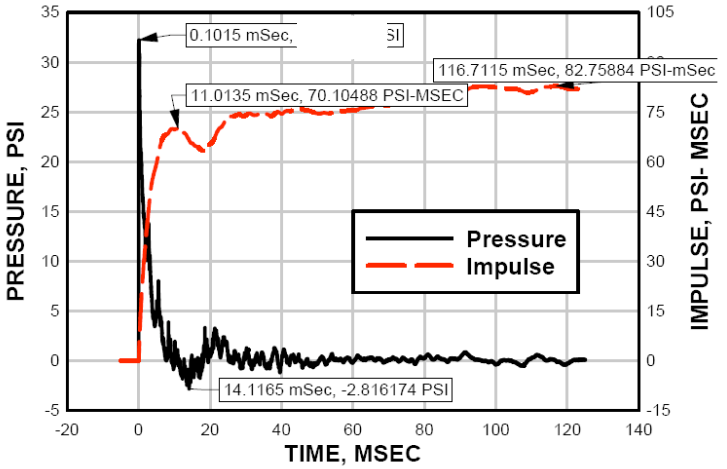


Figure 7: Typical pressure-time history and associated impulse time history obtained using pressure Sensor.

3.2.Experimental Investigation

Wall retrofitted with POSS reinforced polyurea had hairline shear and horizontal crack at blast peak pressure of 218.91 kPa. Shear damage was observed at the top left corner of the wall at the same peak pressure. The results showed that the addition of POSS reinforcement to the polyurea retrofit system increased the flexural resistance of the CMU INFILL wall significantly. However, the retrofit helped the whole panel to have no damage (Figure8).



Figure 8: Wall #3 (a) Back view after the blast event (b) Front view after the blast event

4. COMPUTATIONAL MODELING

To study the effect of blast loads on CMU infill walls and to understand the behavior of these structures under previously noted loading conditions, a number of experiments is required to get enough data that allow the researchers to analyze clearly and process the results. Unfortunately, the expense involved in blast experiments limits the number of tests that are predictable at a given time. Alternative methods as substitutes for actual experimentation had to be sought. The focus of this part of the study is to develop a computationally-efficient model that can replicate with reasonable accuracy the behavior of retrofitted CMU infill wall subjected to blast loads.

Finite Element (FE) models provide cost and time effective solutions compared to the experimental alternative. A finite Element model was built into this research to predict the experiments as mentioned previously. Due to time and cost constraints of the research program, development of a specific finite element analysis code for this project was not feasible. Therefore, ANSYS AUTODYN, an explicit hydrocode that used finite difference, finite volume, and finite element techniques to solve a wide variety of non-linear dynamic problems in solids, fluids, gases, and their interactions, was used to model and analyze the Nano Reinforced Elastomeric Materials retrofitted masonry walls subjected to blast loading.

4.1. Finite Element Configuration and Mesh

The importance of the computational modeling was measured by the ability of the finite element model to replicate with reasonable accuracy the experimental behavior of the system. Therefore, the same 16 blocks tall and 12 blocks wide CMU infill walls used in the experimental work were modeled using finite element software called AUTODYN. Each retrofitted wall was represented by 8670 Lagrangian cells, 3840 of which were filled with masonry material to represent the bricks; 2440 were filled with the mortar material bonding the bricks together; with remainder represented the retrofitted material. Figure9 shows the geometry and the mesh of the walls.

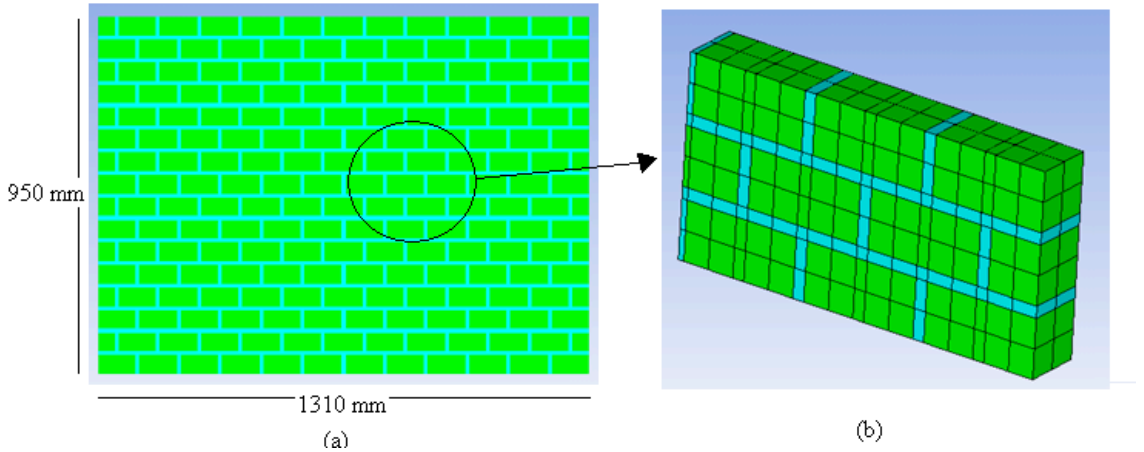


Figure 9: (a) Wall geometry (b) F.E. mesh

4.2. Material Modeling

To model a new material in AUTODYN, the parameters of equation of state (EOS), strength model, and failure model should already be defined.

Unreinforced masonry

The response of masonry under shock loading is a complex phenomenon. A variety of constitutive models for the dynamic and static response of masonry have been proposed over the years. In this research, Porous equation of state (EOS), Drucker-Prager strength model, and Hydrodynamic tensile failure (P_{min}) model were used to represent the unreinforced masonry. These models are discussed in detail in AUTODYN theory manual.

Mortar

Compaction equation of state (EOS), Mo Granular strength model, and Hydrodynamic tensile failure (P_{min}) model were used to represent the mortar.

POSS

A real EOS should be defined for these new elastomeric materials; however, due to the low pressure level introduced by blast waves, a linear equation of state works as a start for this study. Equation 10 shows the linear EOS used to model all three retrofitted materials,

$$P = K\mu \tag{10}$$

Whereas, K is the material bulk modulus; μ is volumetric strain as given by Equation 11; ρ is the material density; and ρ_o is the reference density.

$$\mu = \frac{\rho}{\rho_o} - 1 \tag{11}$$

Johnson-Cook Strength Model and Principal Strain Failure Criterion were used to model these materials. All material models used in this research are summarized in Table 2. More details are available in AUTODYN Theory Manual.

Table 2: Material models

Material	EOS	Strength Model	Failure Model
Masonry	Porous	Drucker-Prager	Hydrodynamic tensile failure (P_{min})
Mortar	Compaction	Mo Granular	Hydrodynamic tensile failure (P_{min})
Polyurea with POSS	Linear	Johnson-Cook	Plastic strain
E-glass/ Epoxy	Puff	Von Mises	Hydrodynamic tensile failure (P_{min})

4.3. Finite Element Results and Discussion

Un-retrofitted wall (Base Line)

Results of FEA showed a maximum midpoint deflection of 95 mm and maximum debris velocity of 6.834 m/s as compared to a maximum midpoint deflection of 86 mm and a maximum debris velocity of 5.91 m/s obtained experimentally (Table 5). FEA experiments likewise showed that the wall failed in four main segments, and that all debris was captured by the retrofit material. Table 3 shows good agreement between experimental and numerical deformation shapes at the time of maximum deflection and at the end of the test.

POSS reinforced polyurea retrofitted wall

Results of FEA showed a maximum midpoint deflection of 112 mm as compared to a maximum midpoint deflection of 95.65 mm obtained experimentally (Table 5). The wall did not fail in either experiment or FEA. Table 4 shows good agreement between experimental and numerical deformation shapes at time of maximum deflection and at the end of the test.

Table 3: Numerical and experimental results comparison for the case of un-retrofitted CMU infill wall

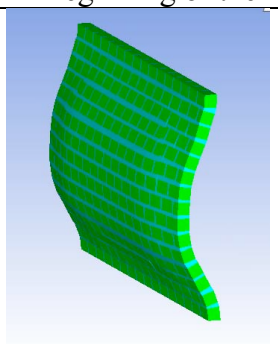
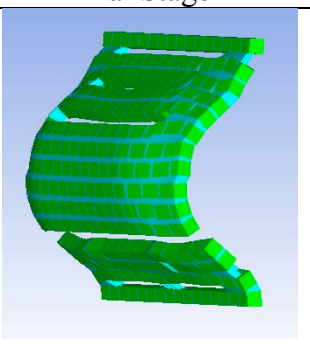
Beginning of the Failure	Final Stage	
		Numerical results obtained using AUTODYN hydrodynamic code
		Experimental results obtained using BLS

Table 4: Numerical and experimental results comparison for the case of CMU infill wall retrofitted with POSS reinforced polyurea

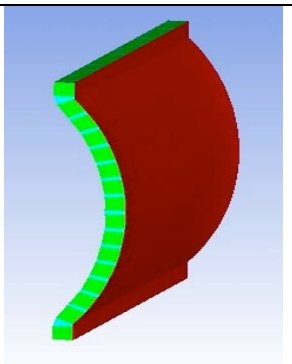
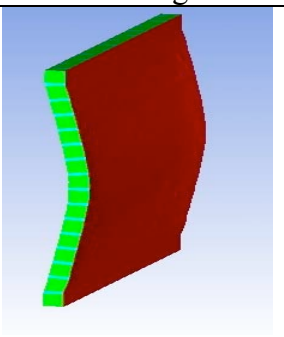
Maximum deflection	final stage	
		Numerical results obtained using AUTODYN hydrodynamic code
		Experimental results obtained using BLS

Table 5: Midpoint deflection and debris velocity

Wall	Maximum Midpoint deflection (mm)		Maximum debris velocity m/s	
	Experiments	Finite element	Experiments	Finite element
Un-retrofitted wall	86.0	95.0	5.9	6.8
Retrofitted wall	95.7	112.0	N.A	N.A.

5. PARAMETRIC EVALUATIONS

To get complete and better understanding of the behavior of retrofitted CMU infill wall under blast loading, a series of finite element analysis was conducted. The focus was to study the effect of some factors such as boundary conditions, thickness and arrangement of retrofitted layers, and ductility of retrofitted materials on the behavior of the system during and after blast.

5.1. Effect of Boundary Conditions

Two types of boundary conditions were applied to the top and bottom of the wall: simply supported (S.S.) and fixed. All retrofitting was applied at the back side of the wall. To neglect the thickness effect, thickness of retrofit layer was kept constant at 1.8mm for all simulations. Same finite element model in the previous section was used here. The effect of the boundary conditions was clear in the results. Using simply supported boundaries allowed the wall to deflect much more than fixed boundaries (Figure10). Both walls did not fail.

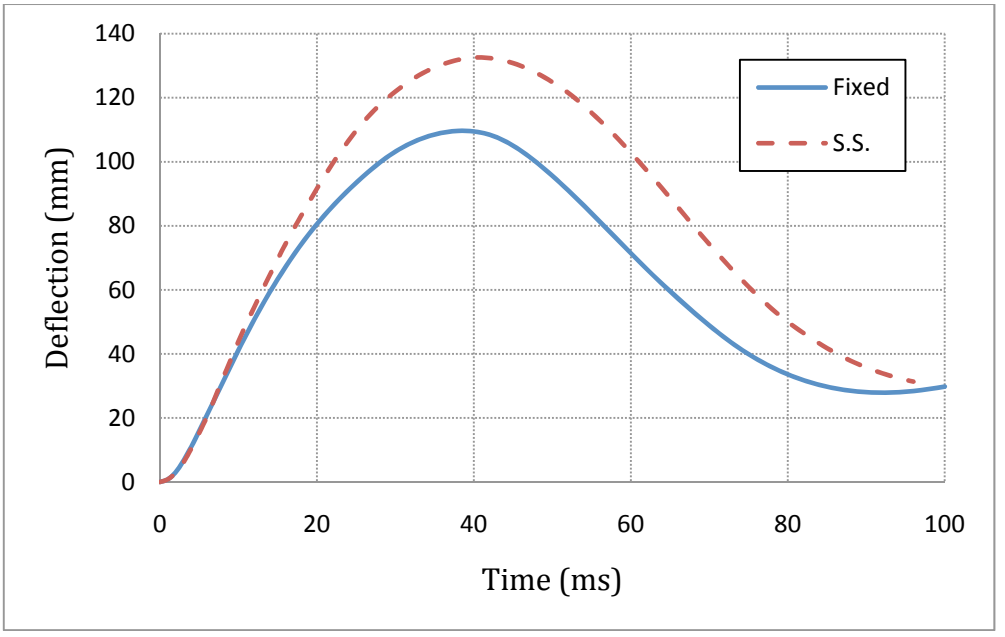


Figure 10: Midpoint deflection of retrofitted CMU infill wall with different B.C. under blast loading

The maximum deflection was observed to be 133mm and 110mm for the case of simply supported and fixed boundaries, respectively. By allowing the retrofitted wall to deform, more energy will be absorbed by the system as shown in Figure 11. The more energy absorbed the less

reaction forces transmitted to the beams and columns (Figure 12) where the energy will be dissipate to deform the panel, to destroy the wall itself, or to separate the retrofitted layer from the wall.

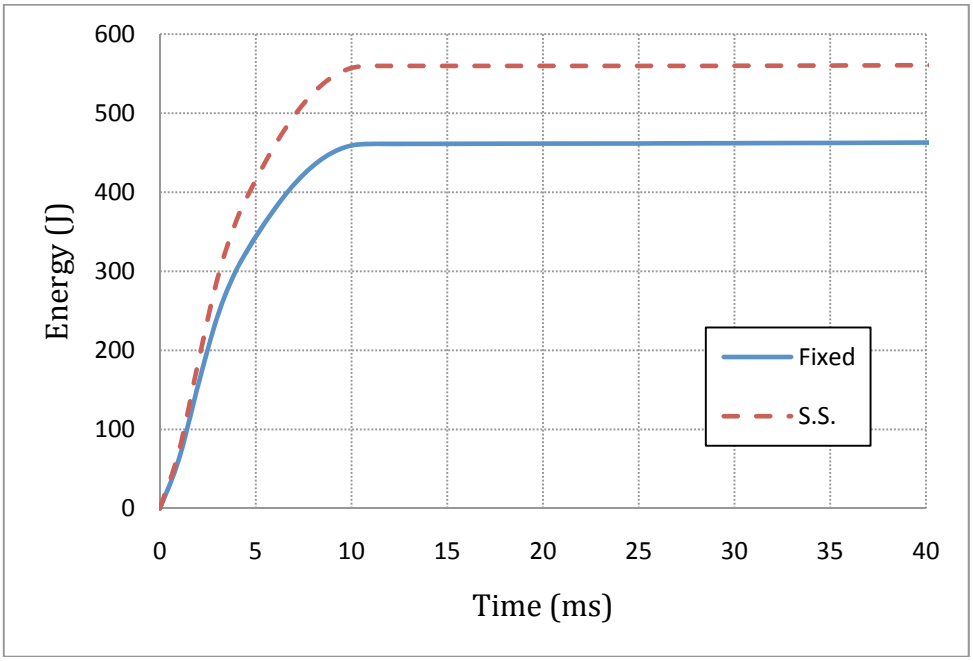


Figure 11: Energy absorbed by retrofitted CMU infill wall with different B.C. under blast loading

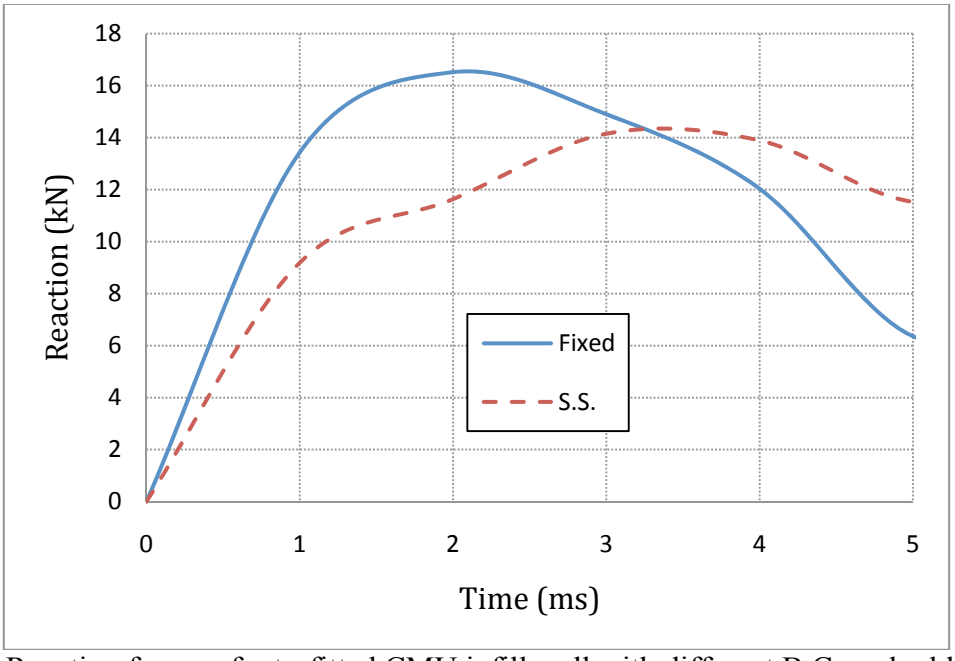


Figure 12: Reaction forces of retrofitted CMU infill wall with different B.C. under blast loading

5.2. *Effect of Retrofitted Layer Thickness*

In order to study the effect of retrofitted layer thickness, the wall was coated with POSS reinforced polyurea with various thicknesses; 1.25mm, 1.5mm, 1.8m, and 3.0mm. All retrofitting was applied at the back side of the wall. The top and the bottom of the wall were fixed, while the two sides were left free for all simulations. The results show that the less thickness the more deformation due to blast until the wall failed when it was coated with 1.25 mm POSS reinforced polyurea at the opposite side of the blast (Figure 13).

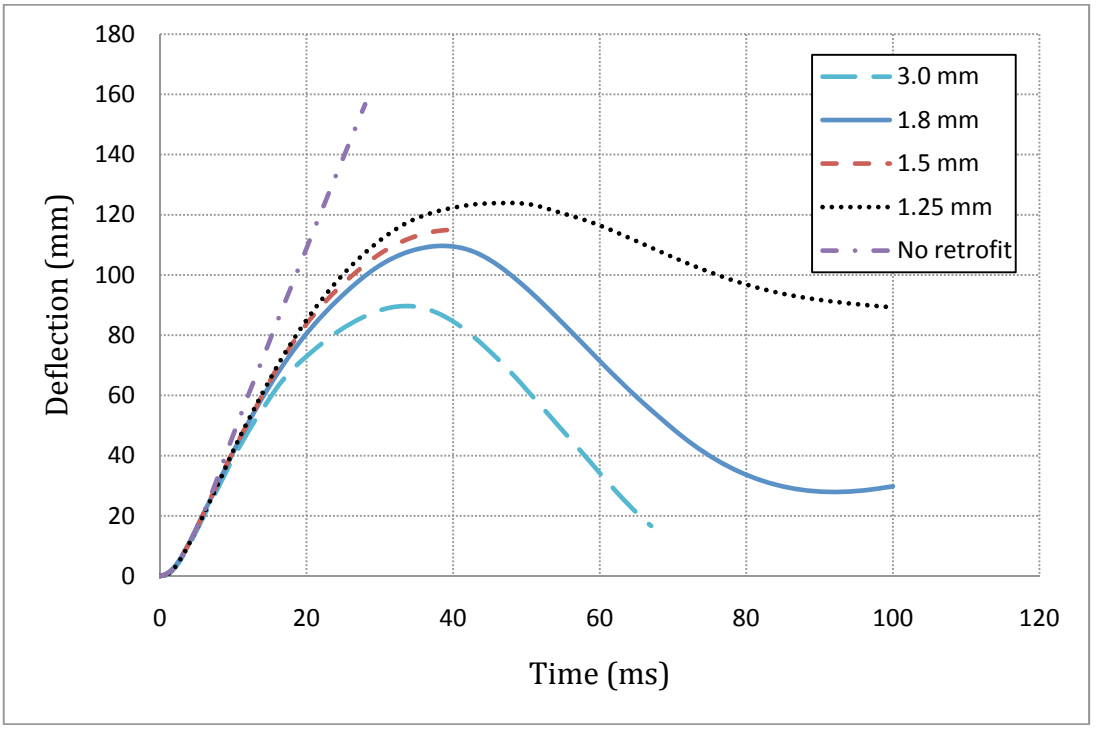
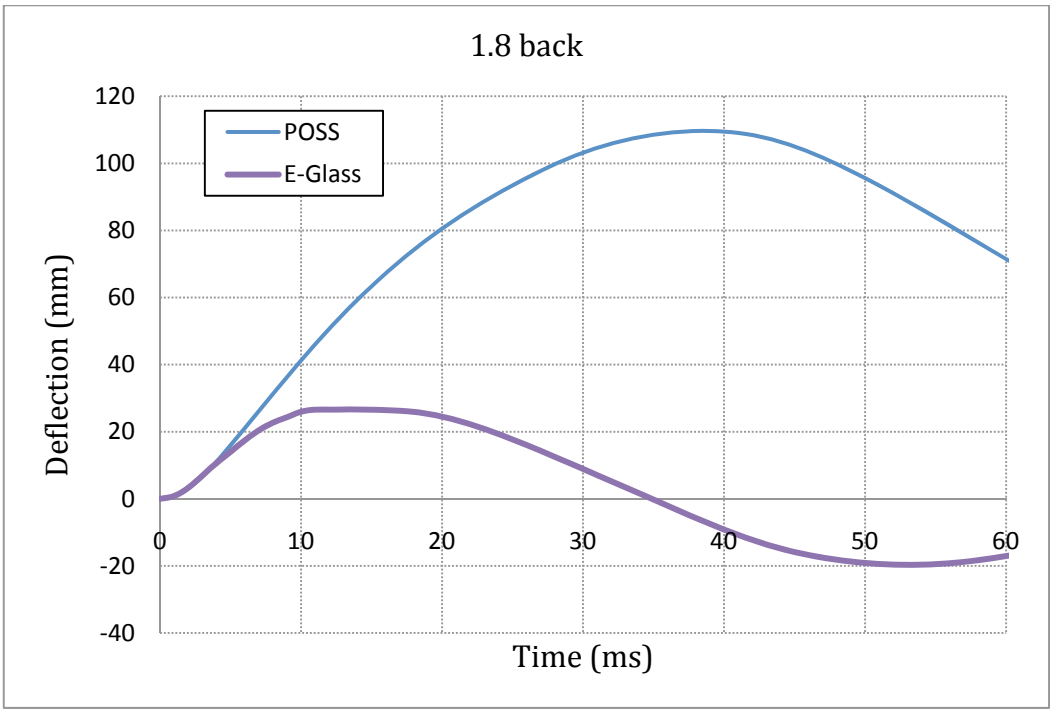


Figure 13: Midpoint deflection of retrofitted CMU infill wall with various coating thicknesses under blast loading

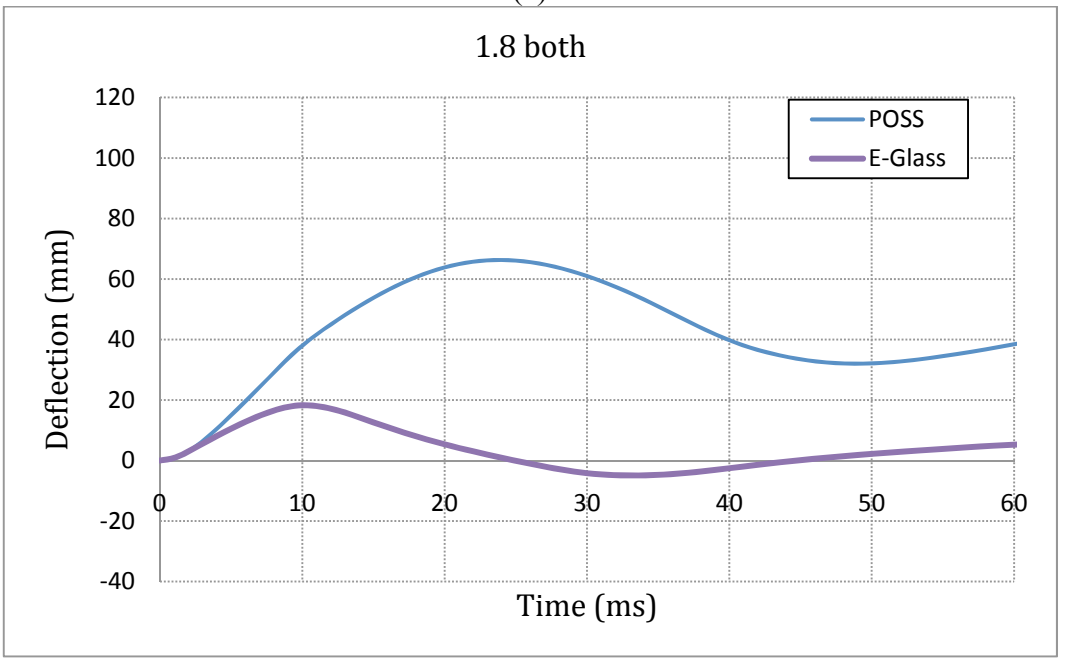
5.3. *Hybrid Retrofitting System*

In order to investigate the ability of using hybrid retrofitting system, one can play with the arrangement of retrofit layers and the ductility of retrofitted materials. A series of finite element analysis was conducted on different retrofit scenarios (back retrofit, front retrofit, and both sides retrofit) for two extreme cases of retrofit materials: rigid (E glass- epoxy) and relatively softer materials (POSS reinforced polyurea). To neglect the thickness effect, thickness of retrofit layer was kept constant at 1.8mm for all cases. The results (Figure 14 and Table 6) show that for the case of retrofitting with elastomeric materials it is better to apply the retrofit at the back side since this will be associated with no failure, when compared to front side retrofit, and a larger deflection (e.g. more energy dissipation) when compared with two side retrofit with a smaller amount of material. In the case of retrofitting with rigid materials, it was also observed that applying the retrofit at the back side was the best scenario.

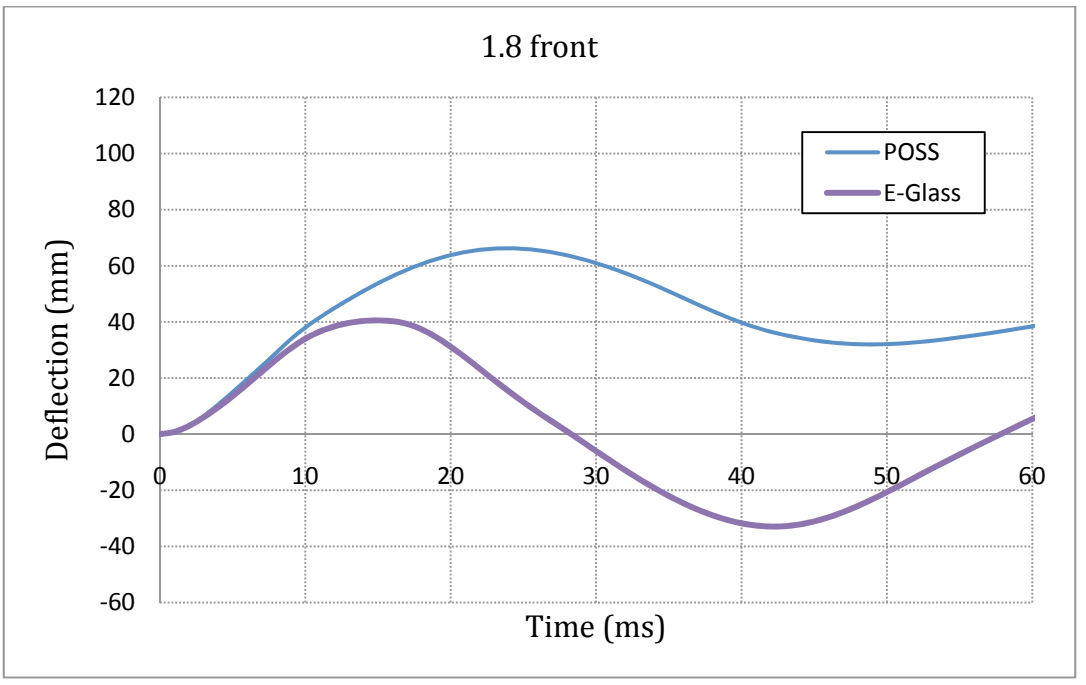
In order to evaluate effect of wall retrofitting on structural elements (e.g. columns and beams), reaction forces were compared for two extreme retrofit cases. The results of FEA parametric evaluation (Figure 15) showed that retrofitting with rigid material will result in a higher reaction force. This means a higher possibility of failure beams and columns, which leads to failure of the whole structure.



(a)



(b)



(c)

Figure 14: Midpoint deflection of CMU infill walls retrofitted with two different materials under blast loading (a) Back side retrofit (b) Front side retrofit (c) Both sides retrofit

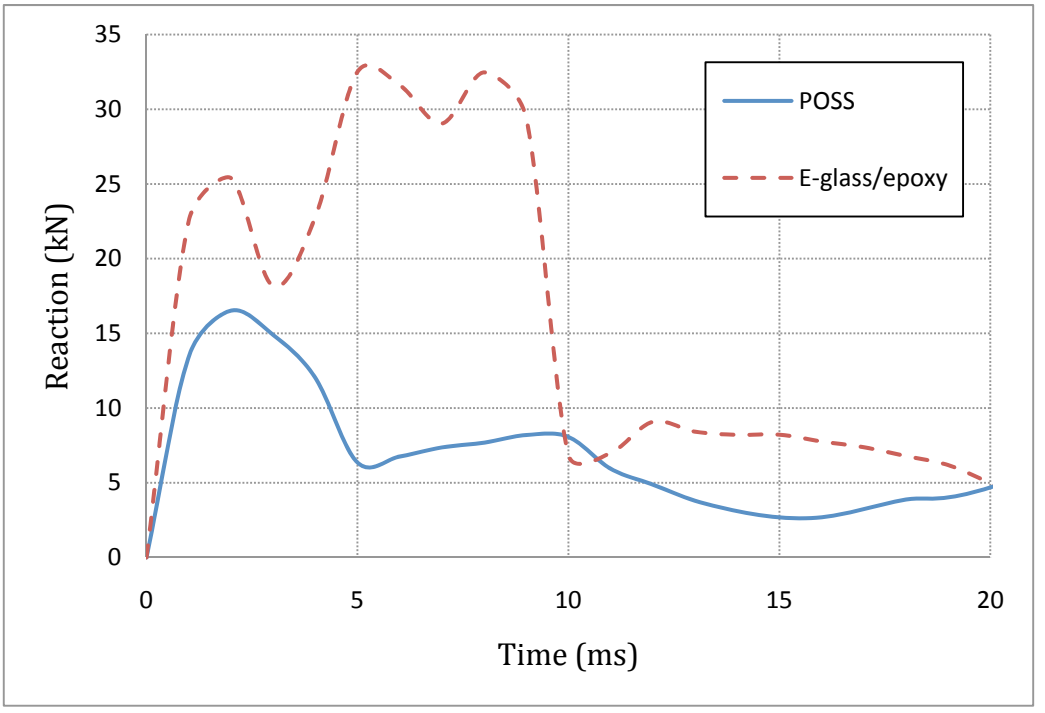
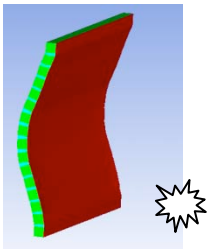
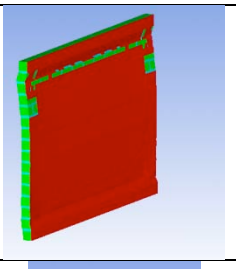
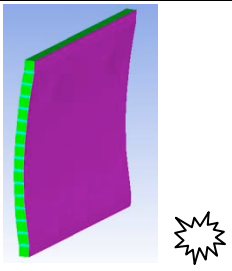
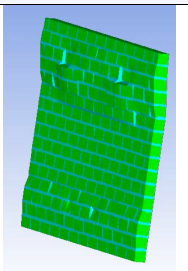
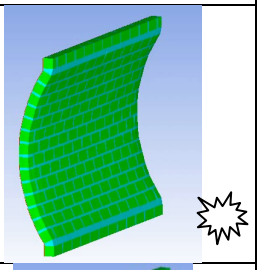
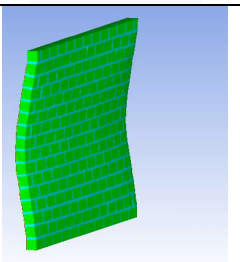
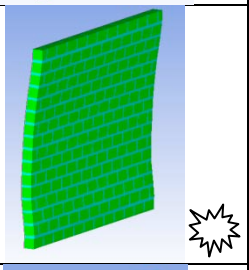
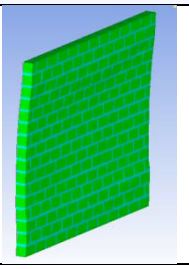
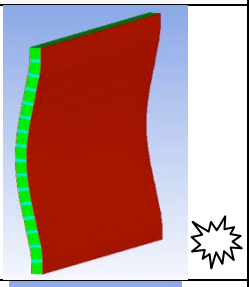
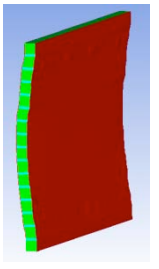
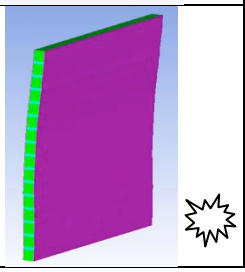
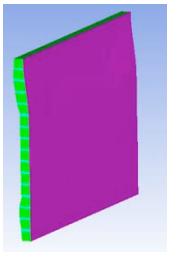


Figure 15: Reaction forces of CMU infill walls retrofitted with two different materials under blast loading

Table 6: Effect of retrofit scenarios

Type of Retrofit	At max. deflection	Final stage	Max. deflection (mm)
Blast Side (POSS)			Failed
Blast Side (Glass-Epoxy)			Failed
Back Side (POSS)			110
Back Side (Glass-Epoxy)			27
Both Sides (POSS)			66
Both Side (Glass-Epoxy)			18

6. CONCLUSION

This study focused on blast vulnerability assessment of concrete masonry infill walls retrofitted with nano particle reinforced polyurea. Quarter scale model concrete masonry infill walls made of scaled down brick units were retrofitted with Polyhedral Oligomeric Silsesquioxane (POSS) reinforced polyurea and subjected to a pre-adjusted airblast pressure and impulse in the ERDC Blast Load Simulator facility. A computationally-efficient model was built using an explicit hydrocode called ANSYS AUTODYN to replicate with reasonable accuracy the behavior of retrofitted infill walls subjected to blast loads. Finite element parametric evaluation was conducted to study the effect of boundary conditions, thickness and arrangement of retrofitted layers, and ductility of retrofitted materials on the behavior of the system during and after blast. Results from blast experiments showed that POSS reinforced polyurea significantly enhanced the performance of masonry walls sustaining blast load. The parametric evaluation results show that for the case of retrofitting with elastomeric materials it is better to apply the retrofit at the back side since this will be associated with no failure, when compared to front side retrofit, and a larger deflection (e.g. more energy dissipation) when compared with two side retrofit with a smaller amount of material.

7. ACKNOWLEDGEMENT

This work was partially supported by the funding received under a subcontract from the Department of Homeland Security-Sponsored Southeast Region Research Initiative (SERRI) at the Department of Energy's Oak Ridge National Laboratory, USA. The preparation of the XGnP reinforced polyurea and the consultation on material properties provided by Dr. Larry Drzal of Michigan State University and XG Sciences is deeply appreciated. The preparation of POSS reinforced polyurea and consultation provided by Drs. Joe Lichtenhan and Bruce Fu of Hybrid Plastics is also gratefully acknowledged.

REFERENCES

[1] Davidson, J. S., Porter, J. R., Dinan, R. J., Hammons, M. I., and Connell, J. D. (2004). "Explosive testing of polymer retrofit masonry walls", *ASCE Journal of Performance of Constructed Facilities*, 100-106

[2] Davidson, J. S., Fisher, J. W., Hammons, M. I., Porter, J. R., and Dinan, R. J. (2005). "Failure mechanisms of polymer-reinforced concrete masonry walls subjected to blast", *ASCE Journal of Structural Engineering*, 1194-1206.

[3] Eamon, C. D., Baylot, J. T., and O'Daniel, J. L. (2004) "Modeling concrete masonry walls subjected to explosive loads", *ASCE Journal of Engineering Mechanics*, 1098-1106.

[4] Johnson, C. F., Slawson, T. R., Cummins, T. R., and Davis, J. L. (2005). "Concrete masonry unit walls retrofitted with elastomeric systems for blast loads", *Proceedings for the Army Science Conference (24th)*, Orlando, Florida.

Overview of ASCE 4 Rev 2

O.Gurbuz[1], S.A Short[2], and M.W. Salmon[3]

[1]Gurbuz Consulting, 16162 Tortola Circle, Huntington Beach, CA, 92649; PH (714) 625-0656; email: ogurbuz@verizon.net
[2]Simpson Gumpertz & Heger, 4000 MacArthur Blvd, Suite 710, Newport Beach, CA, 92660; PH (949) 930-2159; email: sashort@sgh.com
[3]Los Alamos National Laboratory, P. O. Box 1663, MS K575, Los Alamos, NM, 87545; PH (505) 665-7244; email: salmon@lanl.gov,

ABSTRACT

ASCE 4, "*Seismic Analysis of Safety-Related Nuclear Structures and Commentary*," was first issued in 1986. It was expanded, revised and re-issued in 1998. The second revision of the standard will soon be completed by the Working Group on Revision of ASCE 4, which is part of the ASCE Committee for Dynamic Analysis of Nuclear Structures.

This standard provides prescriptive criteria for the analysis of safety-related (Seismic Category I) structures, systems and components (SSCs). It is designed to be used in conjunction with ASCE-43/SEI 43-05, "Seismic Design Criteria for Structures, Systems and Components in Nuclear Facilities." It addresses all aspects of seismic analysis: site response, modeling, and analysis for all types of SSCs. The standard also provides guidance on Quality Assurance requirements and Peer Review needs. Taken together, ASCE4 and ASCE/SEI43-05 may be adapted by federal agencies such as the U.S. Nuclear Regulatory Commission and the U.S. Department of Energy as the minimum expected seismic analysis and design requirements for nuclear facilities.

This overview paper highlights the proposed changes to the ASCE 4-98 Standard proposed by the Working Group. These changes, if adapted, will become effective following consensus balloting and public comment of the proposed changes.

CHANGES TO THE CONTENTS AND FORMAT

There were many changes suggested to the content and also to the format of the document as summarized below:

- A multistep method of analysis which is commonly used in current practice was added. In this approach an initial analysis is conducted to determine the global structural response. Then, using the global response parameters, a detailed analysis is performed for structural and subsystem design.

- Nonlinear response analysis methods using time history and response spectrum methods as well as the nonlinear static analysis are now included in the standard.

- The 4-98 Standard does not prescribe the minimum number of time-histories to be used for dynamic analysis when time-history methods are used. The revised standard provides new criteria

- Criteria for the analysis of sliding and rocking analysis of unanchored components are not presented in ASCE 4-98. A new section is suggested for components and structures using approximate methods. These subjects are presented in ASCE//SEI 43-05 and are now included in ASCE 4.

- The section on Seismic-Isolated Structures was completely revised to bring in the current methods used by practitioners.

- The 4-98 Standard is reorganized to provide sections and subsections using 2 or 3 or 4-digit numbering system. This reorganization is expected to facilitate the use of the document.

- The ASCE 4-98 S first presented the "requirements" and then the "commentary." The proposed revision brings the commentary after each section or subsection. Depending on the need, commentary is provided immediately after the requirements section for each 2-, 3-, or 4-digit section.

- References are updated extensively and those that cannot be obtained through university libraries are deleted. The references are given as part of the commentary after each chapter; again to facilitate use the standard.

GOAL OF THE STANDARD

The overall goal of this standard is to produce a targeted level of seismic demand, conditional on the design basis ground motion occurring, that, when used with code capacities from the design standard, ASCE/SEI 43-05, the resulting design will achieve both of the following:

1. Less than about a 1% probability of unacceptable performance for the Design Basis Earthquake (DBE) ground motion, and:

2. Less than about a 10% probability of unacceptable performance for a ground motion equal to 150% of the DBE.

The 150% is a design check to assure acceptable behavior of the SSC at this level of earthquake. It should not be confused with the term "beyond design basis earthquake."

Commentary to ASCE/SEI 43-05 (Ref. 1) shows that the above performance goals will be met if the demand and capacity calculations are carried out to achieve the following:

1. Demand is determined at about 80% chance of not being exceeded for the specified input response spectrum. Consequently, the requirements of this

standard are set to produce demand estimates at 80% non-exceedance level; whether deterministic or probabilistic analysis methods are used. It should be noted that, for certain special structures (in Chapter 7) where greater uncertainty may exist due to highly variable properties, additional conservatism is incorporated into the analysis process to preclude underestimation of responses.

2. Design capacity is calculated at about 98% exceedance probability. Use of code capacity equations (with minimum specified strengths and code strength reduction factors) will result at about 98% exceedance probability (Ref. 1).

There have been a limited number of comparative studies between deterministic and probabilistic seismic analyses (Refs. 2 to 4). References 2 and 3 concluded that following the provisions of this standard will indeed provide demands that are reasonably close to the 80% non-exceedance level. Ref. 4 reached a similar conclusion except that under certain conditions the deterministic responses were below the probabilistically determined 80% non-exceedance level. It is expected that more studies will be carried out to further define the requirements with which 80% non-exceedance level can be assured.

Based on the current standard of knowledge, it is recommended that the updated ASCE 4 be used together with ASCE/SEI 43-05 (and the design codes specified in that standard) to achieve an acceptable level of conservatism in design.

SITE RESPONSE ANALYSIS

Modern probabilistic seismic hazard assessments are required for use in the design of most nuclear facilities. The probabilistic seismic hazard assessment will provide a mean horizontal and vertical Uniform Hazard Response Spectra (UHRS) at known annual frequencies of exceedance. Using the UHRS, performance-based, smoothed Design Response Spectra (DRS) are developed as input for the design of the facility (Ref. 1). DRS may be at the surface (DRS_S) or at the building foundation level as in-layer spectra (DRS_{FI}).

When time history analyses are to be used, sets of input motions to be used for subsequent conditioning shall be based on actual earthquake recordings (two horizontal and one vertical). Three options are proposed for time history analyses of structures:

1. A single time-history set (2H+1V) may be used provided that the 5% damped spectra produced by the conditioned records match or envelop the target spectra. In addition, the calculated spectra at 2% and 20% damping must exceed 90% of the respective target spectra.

2. Alternatively, three time-history sets that match the target spectrum at 5% damping may be used in which case the design is based on maximum responses.

3. The third alternative is to use five or more time-history sets in which case the design is based on the average response from the suite.

The above requirements are for linear time history analyses. For nonlinear time history analyses, a minimum of three time-history sets are required. If less than 7 time-history sets are used, the peak maximum component response is used for design. If 7 or more time-history sets are used, the median component response may be used for design.

SOIL-STRUCTURE INTERACTION (SSI) ANALYSIS

Soil-structure interaction (SSI) is expanded from ASCE 4-98 significantly. The proposed standard requires that SSI analyses be performed for all nuclear structures not supported by rock or rock-like foundation material. At sites with a shear wave velocity of 8000 ft/sec or greater at low shear strains, a fixed-base analysis is acceptable. Effects of mat foundation flexibility need not be included in the global response analysis for typical shear wall structures.

In general, the SSI analyses should account for the nonlinear behavior of the soil, uncertainties in soil properties and structure-to-structure interaction. Variation in the soil properties can be addressed by repeating the analyses for upper bound, median and lower bound soil stiffness cases and then enveloping the resulting responses. Alternately, probabilistic SSI analyses may be performed from which the 80^{th} percentile response may be extracted. The structure model to be used in the SSI analysis may be the detailed model used for determining the design forces and displacements or a simplified model. In the latter case, sufficient studies should be carried out to ensure the simplified model is truly representative of the detailed model. Embedment effects shall also be taken into consideration as they may affect the response characteristics of the system.

In recent years, wave incoherency has been shown to be an important factor in SSI analyses, particularly in the high frequency range and at stiff soil sites. Seismic wave incoherency arises from the horizontal spatial variation of both horizontal and vertical ground motions. Incoherency effects reduce the translational motions of the foundation but may produce foundation rotational motions.

Subsurface material properties significantly affect the seismic response of the structure. Therefore, accurate determination of the material properties by field and laboratory testing is important. The most important material properties to be determined are shear modulus and damping, as a function soil strain. Other properties that are needed in analyses include material unit weight and Poisson's ratio.

SSI analysis can be performed using the direct method or the sub-structuring method. In the direct method, the boundaries of the soil-structure model and the input motions at these boundaries are defined. With boundary input motions, soil-structure system is analyzed directly to determine the responses at any point in the system.

In recent years, sub-structuring methods have been more commonly used for the SSI analysis. A brief description of the two widely used sub-structuring methods follows:

1. A continuum mechanics approach in which the soil profile is modeled as semi-infinite layers overlying the half space. Free-field motions are defined at the "control" points. Interaction problem is solved using Green's functions. The primary example in this category is the CLASSI computer code.

2. Frequency-domain solution using a 2 or 3D finite element model. In this group the most frequently used computer code is System for Analysis of Soil-Structure Interaction (SASSI).

The standard also permits a probabilistic approach to develop seismic responses of the soil-structure system. In this method the range of parameters that define the soil and structural properties are defined. A series of SSI analyses are performed and responses at the 80% percentile level are calculated.

The proposed changes to ASCE 4-98 are intended to capture all the recent developments in SSI methods. The adaption of the proposed changes will help to provide a consistent application of SSI techniques in the design of nuclear facilities.

MODELING OF STRUCTURES AND SYSTEMS

Modeling used for the dynamic response of civil structures continues to evolve and become more complex. Today, structural models of one hundred thousand degrees of freedom or more are commonly used in nuclear projects. The emphasis is on the finite element analyses using a variety of computer codes which may have widely varying capabilities. Both linear and nonlinear analyses are routinely performed.

The standard focuses on aspects of modeling that will lead to accurate analytical solutions. Since different structural models are often used, their purposes should be clearly defined and the underlying assumptions should be explicitly stated. In developing the seismic analysis model, the frequency range of interest (the earthquake input amplified region and the building and soil response frequencies) should be carefully considered. The model for seismic analysis should be sufficiently refined to capture the high frequency content of the input motion; the model should be able to transmit motions up to 50 Hz. Lumped mass stick models that have been used in the past are no longer considered adequate for seismic analysis in the high frequency range.

There are many parameters that need consideration to produce a good model to obtain reasonably accurate solutions. These include: element types to be used, mesh sizes, types of analyses, material properties, significance of nonlinear behavior, modeling of mass, damping in seismic analysis and so on. The standard provides guidance on defining these parameters in practical applications.

The standard will also require explicit consideration of "response parameters of interest." If the purpose is to develop In-Structure Response Spectra (ISRS), the results should be accurate up to 100 Hz. The points at which ISRS are needed should be modeled accurately. On the other hand, if the purpose is to determine the seismic design forces, the model should permit capturing of important responses, such as forces or moments at the base of a wall. Since out-of-plane bending of slabs is important, the standard will require adequate number of elements in each direction to capture the bending moments. Unless a specific study is carried out, slabs should have eight elements along the long side and six elements along the short side.

In multi-step analysis, compatibility of the seismic analysis model with the detailed model that may be used in subsequent analyses must be demonstrated. This demonstration should include not only comparison of the design forces but also the ISRS at critical locations.

The decoupling criterion has been clarified; coupling of a subsystem with the primary structure is required when the values of key design parameters from the coupled model are more than 10% higher than those from the uncoupled model.

The standard provides additional guidance for the analyst in modeling reinforced concrete elements. When modeling reinforced concrete sections the analyst must choose whether to model the sections as gross, cracked, or somewhere in-between depending on the expected stress level in the structural element during earthquake response. The general consensus of the Working Group was that the assumption of uncracked (gross) properties is acceptable for in-plane responses for both walls and diaphragms. For out-of-plane responses, cracked section properties should be used for slabs if cracking is expected under the gravity loads. Out of plane response of walls must be evaluated from preliminary seismic evaluations to assess cracking potential. There are different assumptions for the cracked section properties, ranging from $0.7I_g$ to $0.5I_g$ in different standards. Analysts will need to carefully evaluate the demand-capacity ratios prior to making an assumption regarding the modeling of stiffness. Additional commentary is added to the standard to guide the analyst with making this decision.

ANALYSIS METHODS

The major change in the analysis chapter of the revised standard is the elimination of most of the equations. It was reasoned that these equations are found in many readily available references (books and papers) and repeating them in the standard would not serve a useful purpose. Therefore, the focus was on the methodology and criteria to be used in the analyses. The references for this chapter were carefully reviewed and many of them were removed due to difficulty in obtaining them. New references were added to provide background information in the recent developments in analyses approaches.

There were few changes in the sections on time history and response spectrum analyses (RSA). Both methods can be used to determine the seismic responses for design and ISRS for subsystem design.

The section on multistep analysis has been extensively revised. The requirements for the initial analysis in which the gross response of the structure is determined are defined. The standard permits the subsequent analyses to be static or dynamic (both RS and TH analyses).

For determining the total response due to the three components of an earthquake, the standard allows the use of the square-root-of-the-sum-of-squares (SRSS) method or the 100-40-40 rule (also termed the factor method), consistent with U.S. NRC Regulatory Guide 1.92 (Ref. 5). In the factor method, permutation of responses from each direction (considering signs) generally results in 24 spatial response combinations. The design is then carried out for all these combinations. When a single parameter is dominant in design, the results from SRSS and the factor method are essentially the same. However, when multiple design parameters are involved, the differences can be quite significant. The factor method generally results in more realistic designs. The SRSS method can be overly conservative.

As an example, consider a shear wall oriented in the north-south direction with seismic responses for four design parameters, P=axial load, V=shear, M_{ip}=in-plane moment, M_{op}=out-of-plane moment. Assume that responses for these parameters have been obtained from dynamic analysis as shown in Table 1. (Note: for simplicity the signs are ignored in this example.)

The first three rows in the table show the calculated responses due to seismic input in each direction. The fourth row is the SRSS combination results and these values would be used in design. The next three rows give the design values using the factor method. All three rows obtained from the factor method would be used in design.

As can be seen from the table, the most severe design condition is produced by the SRSS method. This is the case when each response parameter is dominated by a particular earthquake direction. On the other hand, the design resulting from each of the three factor method combinations will be less demanding, and the final design will be more realistic as each of these spatial response combinations are likely to occur.

A recent development has further complicated the issue. On some projects, reviewers have contended that, after obtaining the spatial combination results, the design should be based on the maximums of each parameter, regardless of the combinations that produced each maximum. The last row (factored-enveloped) in the table shows the resulting design condition. This is inconsistent with the goal of seismic design which is to use the parameters that are most likely to occur simultaneously.

Review of the table indicates that the SRSS design values are close to the factored-enveloped numbers. This suggests that the design parameters as calculated by the SRSS method are also unlikely to occur simultaneously.

Table 1. Example of Design Parameters using the SRSS and Factor Methods

Seismic Load	P, kips	V, kips	M_{ip}, ft-k	M_{op}, ft-k	Comment
N-S Earthquake	0	500	10000	100	
E-W Earthquake	0	30	500	500	
Ver Earthquake	400	0	0	0	
SRSS	400	501	10012	510	SRSS design
Factored 1: 100+40+40	160	512	10200	300	Consistent factor method design cases
Factored 2: 40+100+40	160	230	4500	540	
Factored 3: 40+40+100	400	212	4200	240	
Factored-enveloped	400	512	10200	540	Inconsistent factor method

SPECIAL STRUCTURES

SSCs with unique features that require special analytical approaches for seismic response determination have been collected in Chapter 7. Sections of Chapter 7 include:

- Buried pipes and conduits,
- Earth-retaining walls,
- Above ground vertical cylindrical tanks,
- Distribution system,
- Sliding and rocking of unanchored rigid bodies, and
- Seismically isolated structures.

There have not been many changes in the section on buried pipes and conduits, as there have not been significant new developments in the state of practice. One significant improvement is that a recommended value for the apparent shear wave velocity is provided for use in assessing pipe strains.

For earth-retaining walls, including the buried walls of safety-related concrete structures, new methods of analyses have been developed since the last edition. SSI analyses can now be used directly to obtain the soil pressures on the walls. On the

other hand, classical methods for flexible and rigid walls are still being used in the industry. A new method that combines the response from SSI analysis with an analytical approach for determining seismic-induced wall pressures has been introduced. This section now includes all these methods and provides specific guidance to the user.

Above-ground vertical cylindrical tanks have also been the subject of many studies. The section on these tanks was updated to include the state-of-the-art methods of both horizontal and vertical responses.

In ASCE 4-98 the only distribution system that was addressed extensively was the raceway systems. The proposed edition will include treatment of piping and pipe supports, tubing, ductwork as well as raceways. The expanded treatment of the distribution systems was reviewed by specialists in the industry to capture the industry experience.

Criteria for the analysis of unanchored components and structures are not included in ASCE 4-98. This revision proposes criteria consistent with ASCE/SEI 43-05. The committee proposes that the criteria be removed from ASCE/SEI 43-05 in subsequent revisions, and be retained in ASCE/SEI 4

The section on seismically isolated nuclear structures has been completely revised. The main advantage of seismic isolation is the reduced seismic response in the horizontal direction. Nuclear safety-related structures are stiff, with fundamental horizontal frequencies in the range of 2-10 Hz. The design response spectra may have their peak spectral accelerations also in the same range, thus maximizing the horizontal responses. Base isolation can bring the fundamental frequency below 1 Hz (typically around 0.3 Hz), thus significantly reducing the seismic response and hence the demand on systems and components. Unfortunately, these benefits are not readily available in the vertical direction; but the magnitude of the issue can be reduced by creative layout of the systems and components.

The standard covers three types of seismic isolators that are considered as viable alternatives for nuclear safety-related structures:

1. Low-damping elastomeric bearings,
2. Lead-rubber elastomeric bearings, and
3. Sliding bearings with restoring forces provided by gravity.

The standard addresses environmental and operating conditions, isolator performance, and modeling and analyses requirements. Multiple nonlinear analyses are required to determine the demands at the 80% exceedance level, consistent with the basic philosophy of the standard.

CONCLUSIONS

The American Society of Civil Engineers, Codes and Standards Committee has required that the ASCE Standards be updated on a tri-annual basis, unless special exceptions are granted. A proposed revision to ASCE 4-98 is working its way through the standards process by the Dynamic Analysis of Nuclear Structures working group. The proposed revision to ASCE 4-98, if adapted, will bring the state-of-the-art engineering practices to the design community for use in the design of the next generation of nuclear facilities. This overview has led to the following conclusions:

- The proposed revision standard is vastly improved in terms of extent and depth of the topics covered. It also reflects closely the current state of practice.
- As a result, the volume of the document is increased by more than two-fold.
- The proposed revision is expected to be a key document for the nuclear industry, hopefully eliminating (at least reducing) the contentious positions between the practitioners and the regulators.
- To that end, it is hoped that the new document will be endorsed by the regulators in its entirety
- Notwithstanding the above optimistic viewpoint, the proposed standard still lacks guidance on some analysis needs of designers of nuclear structures subjected to earthquakes Authoritative guidance on additional topics will go a long way toward designing better nuclear facilities while increasing the public confidence in the engineering of these facilities. Some of the topics that are being considered for inclusion in the next revision include:
    - Analyses of cranes,
    - Fragility calculations,
    - Seismic 2/1 evaluations.

    Others could conceivably be added to the above list to extend the reach and appeal of this standard worldwide.

ACKNOWLEDGEMENTS

The authors are grateful all members of the ASCE Working Group who have contributed to this document as volunteers for many years. The authors would also like to thank Bechtel Corporation which has generously supported earlier drafts of the revised standard for many years.

REFERENCES

1. "Seismic Design Criteria for Structures, Systems, and Components in Nuclear Facilities" ASCE/SEI 43-05, American Society of Civil Engineers, 2005.

2. Hashemi, A., Elkhoraibi, T., and Ostadan, F. "Probabilistic and Deterministic Soil Structure Interaction Analysis", 11th International Conference on Application of Statistics and Probability in Civil Engineering (ICASP), Zurich, Switzerland, August 2011 (Paper in preparation).

3. Eggers, Daniel and S, Bolourchi, and F. Ostadan "Probabilistic and Deterministic Seismic Soil-Structure Interaction Analysis of the Lotung Quarter-Scale Containment Model," Paper in preparation.

4. Houston, T., M. Costantino, and C. Costantino, "Hazard Consistent Structural Demands and In-Structure Design Response Spectra," 20th SMIRT Conference, Finland, August 2009.

5. Regulatory Guide 1.92, "Combining Modal Responses and Spatial Components in Seismic Response Analysis," Rev. 2, USNRC, July 2006.

Benchmark Analysis of Seismically Induced Fluid-Structure Interaction in Liquid-Containing Tanks with Insufficient Freeboard

F.G. Abatt[1]

[1]M&D Professional Services, Inc., 114 Columbia Point Drive, Suite A, Richland, WA, 99352; PH (509) 943-1625; email: george@mdpsi.com

Abstract

Parameters of interest in the seismic analysis of liquid-containing tanks include reaction forces, slosh heights, and peak wall pressures. Numerous references including Section 7.4 of ASCE 4 have simplified expressions for wall pressures, overturning moments, and slosh heights for tanks with excess freeboard. For tanks with insufficient freeboard, less guidance is available. As an example, ASCE 4 requires that if tanks have insufficient freeboard, the liquid level must be lowered or the tank roof and wall must be designed to withstand the impact of the sloshing fluid. However, ASCE 4 does not provide specific guidance on evaluating the impact of liquid with the tank roof.

The present study evaluates seismically induced fluid-structure interaction in flat-top and domed tanks with insufficient freeboard using the explicit finite element program MSC.Dytran®[2] and the results of the study are compared to approximate solutions. For the systems considered, the study shows that the peak wall pressures in the domed tank are nearly the same as for a vertical-walled tank with excess freeboard. However, for the flat-top tank, the peak roof pressures are significantly higher than predicted using the approximate methods. In all cases, peak wall pressures lower in the tanks are unaffected by local roof or dome interactions.

INTRODUCTON

This study was motivated by the need to update the seismic analysis of record for the Double Shell Underground Waste Tanks (DSTs) at the US Department of Energy Hanford Site north of Richland, Washington. The DSTs have a nominal capacity of one million gallons and consist of a primary steel tank surrounded by an annular space and supported by a circular cylindrical concrete vault with a domed roof. The inner primary tanks have a radius of 37.5 feet. The vertical walls of the primary tank are approximately 35.5 feet high and the dome height of the primary tank is approximately 11.5 feet, giving a total height from the primary tank base to the dome apex of approximately 47 feet. Some tanks contain liquid with an initial free surface

[2] Dytran is a registered trademark of MSC Software Corporation, Santa Ana, California.

high enough to result in significant fluid-structure interaction with the tank dome for the level of seismic excitation considered.

The purpose of the studies described herein was to better understand the effects of this interaction on the tank demands. It was of particular interest to determine if the methodology described in Appendix D of BNL (1995) for predicting maximum wall and roof pressures for curved roofs would provide conservative estimates. Thus, results from time-history computer simulations using the finite element code MSC.Dytran® were compared to results using the methodology from BNL (1995) both for tanks with excess and insufficient freeboard. Similar comparisons were made also to predictions using the simplified estimates described in Malhotra (2005).

The response parameters that were monitored during the computer simulations were the impulsive, convective, and breathing mode frequencies, the horizontal and vertical reaction forces, the maximum unconstrained slosh heights, and the wall and roof pressures.

SYSTEMS CONSIDERED

Before evaluating the flexible-wall tank with a curved roof, two simpler systems were considered. The first of these was a rigid circular cylindrical flat-top tank that was evaluated at four liquid levels. The lowest liquid level represents the situation of a tank with excess freeboard, and was run as a benchmark case. Two intermediate liquid levels included liquid interaction with the roof. The last case was a completely full tank (no head space) that was also run as a benchmark case. The last case is not discussed herein except to note that the results of the computer simulation matched the known solution.

The second simplified system was a rigid tank with a curved roof having the same configuration of the flexible-wall tank of ultimate interest. Finally, the flexible-wall tank with the curved roof was evaluated. All models were three dimensional and incorporated a Lagrangian formulation for shell elements and an Eulerian formulation for fluid elements.

RIGID FLAT-TOP TANK

The flat-top tank considered has a radius of 450 inches and a height of 500 inches. The initial liquid heights considered were 460, 480, 490, and 500 inches. The two intermediate liquid heights resulted in intermittent interaction between the liquid free surface and the tank roof, and are of the most interest. For the seismic input to the system, the 480 inch initial liquid height represents a freeboard height (h_0) to maximum unconstrained slosh height (h_s) of 0.8. The 490 inch initial liquid level represented a freeboard height to maximum unconstrained slosh height of 0.4. Only horizontal seismic excitation was applied to the rigid flat top tank model. The apparent damping in the rigid flat-top system as determined by the logarithmic decrement of the convective response was a few tenths of a percent of critical damping. The system damping consisted exclusively of the artificial bulk viscosities

inherent in Dytran®. A plan view and elevation view of the flat-top tank model showing liquid element sets at which pressures were monitored are shown in Figure 1 and Figure 2.

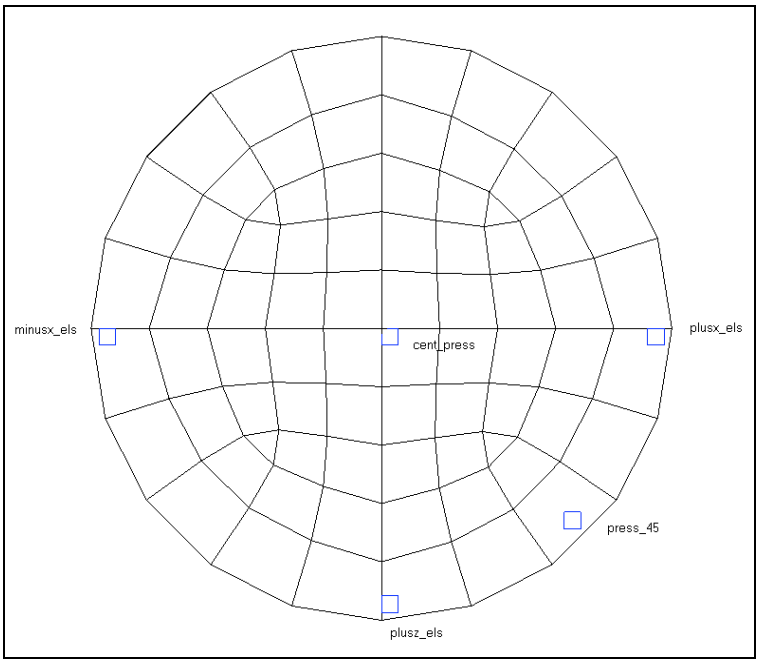


Figure 1. Plan View of Model Showing the Angular Locations of Fluid Elements at Which Pressures Were Monitored.

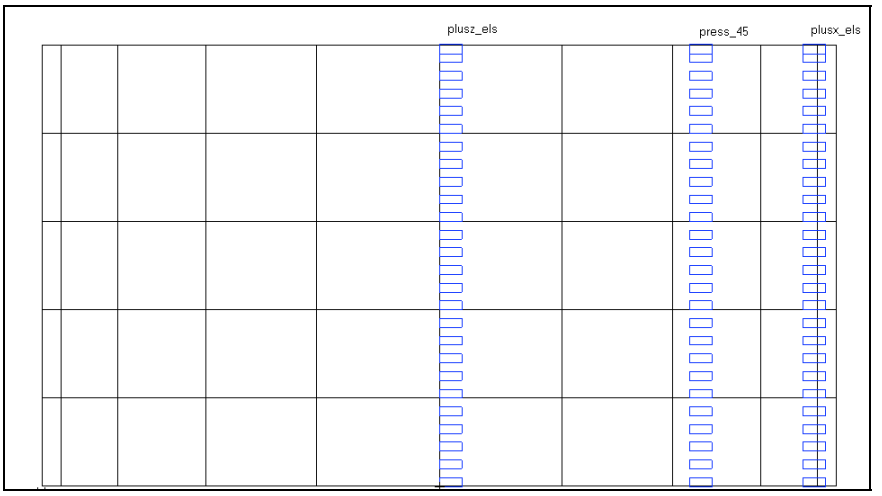


Figure 2. Elevation View of Model Showing the Locations of Selected Fluid Elements Sets at Which Pressures Were Monitored.

At the 460 inch initial liquid level, the peak horizontal reaction force predicted by the Dytran® model was 106% of the value given by the BNL methodology for a tank with excess freeboard if the impulsive and convective contributions are summed using an SRSS combination, and 90% of the value given by the BNL methodology if the two components are summed absolutely. The Dytran® prediction is equal to the

value given by the Malhotra estimate when the two contributions are summed using the SRSS method and is 91% of the Malhotra estimate when the two terms are summed absolutely. Because the tank is rigid, the spectral acceleration for the impulsive mode that is used to calculate the peak reaction force is taken as the peak ground acceleration.

The maximum wall pressures predicted by the Dytran® model for the tank with excess freeboard were almost identical to those predicted using the BNL methodology for a tank with excess freeboard at all heights. The convective frequency given by the Dytran® simulation was the same as predicted by BNL (1995) and Malhotra (2005). The maximum slosh height of 26.9 inches predicted by the Dytran® simulation was 7% greater than predicted by the BNL methodology and 9.5% less than given by ASCE (1998) and Malhotra (2005). The peak horizontal reaction force due to convective effects only was 25% less than predicted using the BNL methodology. In this case the BNL prediction of the convective reaction force was either 15% or 18% of the total reaction force per the BNL estimate depending on whether the impulsive and convective components are summed absolutely or via SRSS, respectively.

At the 480 inch initial liquid level (h_0/h_s=0.8), the peak horizontal reaction force predicted by the Dytran® model was 82% of the value predicted by the BNL methodology for a flat-top tank with insufficient freeboard if the impulsive and convective contributions are summed using an SRSS combination, and 76% of the BNL value of the impulsive and convective components are summed absolutely. The Dytran® prediction is 88% of that given by the Malhotra prediction for a tank with insufficient freeboard using an SRSS combination and 80% using an absolute sum.

The maximum wall pressures predicted by the Dytran® model are essentially the same as for a tank with excess freeboard on the lower 70% of the tank wall, but diverge from this solution in the upper 30% of the tank where the effects of roof interaction become apparent. The total absolute pressures shown in Figure 3 indicate that the BNL estimate is conservative for predicting peak wall pressures in the majority of the wall height, but that it underestimates peak wall forces near the top of the tank. The peak dynamic roof pressure predicted from the Dytran® solution is approximately twice that given by the BNL estimate and more than 20 times greater than given by the Malhotra estimate.

The convective frequency from the Dytan solution is the same as determined for the 460 inch initial liquid level with no roof interaction, and the convective response does not show any additional apparent damping due to interaction with the roof. However, the maximum magnitude of the convective response is approximately half of that determined for the case of no roof interaction. This inhibited convective response evidently is due to the interaction with the roof preventing the development of the unconstrained convective mode shape.

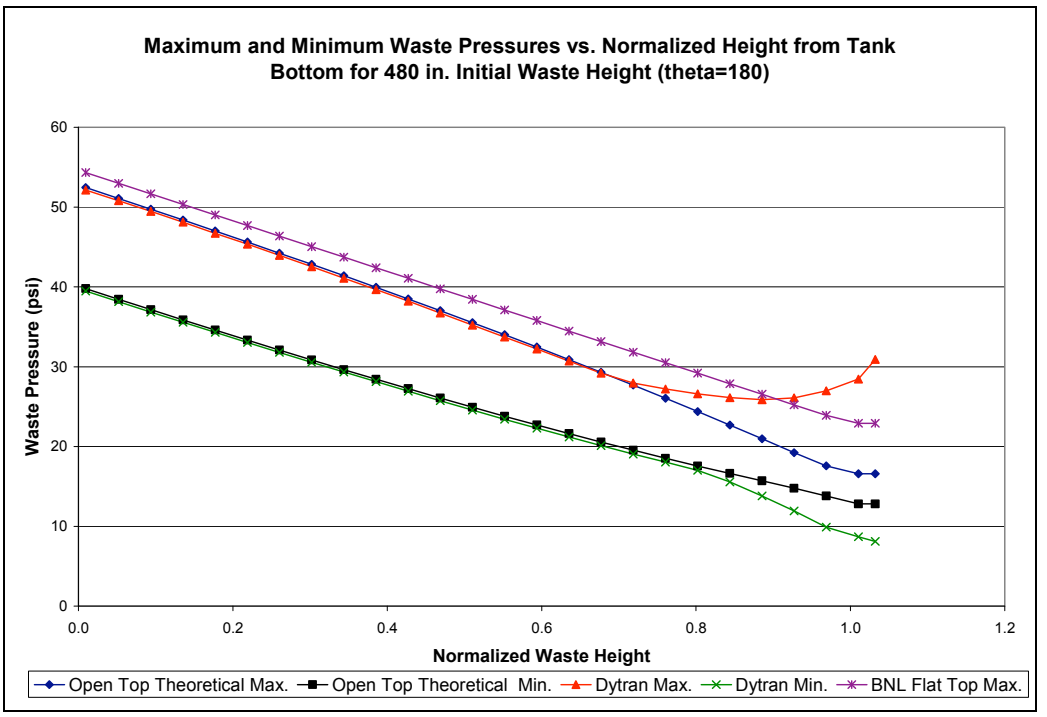


Figure 3. Maximum and Minimum Total Absolute Wall Pressure Comparison for the Roofless Tank, BNL Flat Top Estimate, and Dytran® Solution at the 480 inch. Liquid Level Along the Plane of Excitation.

At the 490 inch initial liquid level (h_0/h_s=0.4), the peak horizontal reaction force predicted by the Dytran® model was 83% of the value predicted by the BNL methodology for a flat-top tank with insufficient freeboard if the impulsive and convective contributions are summed using an SRSS combination, and 78% of the BNL value of the impulsive and convective components are summed absolutely. The Dytran® prediction is 78% of that given by the Malhotra prediction using an SRSS combination and 75% using an absolute sum.

The maximum wall pressures predicted by the Dytran® model are essentially the same as for a tank with excess freeboard on the lower 60% of the tank wall, but diverge from this solution in the upper 40% of the tank where the effects of roof interaction become apparent. The total absolute pressures shown in Figure 4 indicate that the BNL estimate is conservative for predicting peak wall pressures in the majority of the wall height, but that it underestimates peak wall forces near the top of the tank. The peak dynamic roof pressure predicted from the Dytran® solution is approximately 50% greater than given by the BNL estimate and more than eight times greater than given by the Malhotra estimate. The Dytran® solution also predicts that the peak roof pressure at the 480 inch liquid level is 30% higher than for the 490 inch liquid level, which is consistent with a higher impact pressure occurring when the liquid has more headspace available to develop impact energy at the roof.

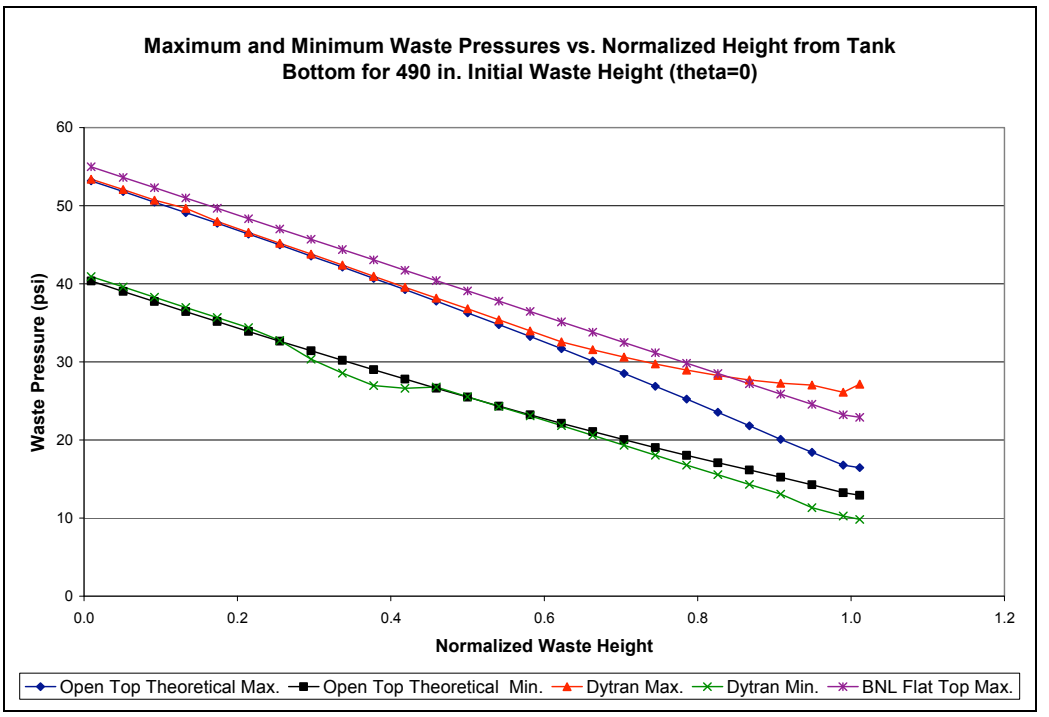


Figure 4. Maximum and Minimum Total Absolute Wall Pressure Comparison for the Roofless Tank, BNL Flat Top Estimate, and Dytran® Solution at the 490 inch. Liquid Level Along the Plane of Excitation.

When the available freeboard is only 40% of the maximum unconstrained slosh height, the convective response following the termination of the seismic excitation shows two interesting characteristics that are illustrated in Figure 5. First, the interaction with the roof has the effect of adding apparent damping to the convective response. Based on the logarithmic decrement of the free convective response, the decay of the convective reaction force is consistent with an effective critical damping ratio of approximately 6%. Second, the interaction with the roof has the effect of significantly increasing the apparent convective frequency relative to the roofless tank response. Rather than the 0.2 Hz convective frequency for the roofless tank, the frequency is increased to an average frequency of approximately 1.67 Hz due to the interaction with the roof. The increased convective frequency is reasonable since the presence of the roof inhibits the longer-period free convective oscillation of the liquid.

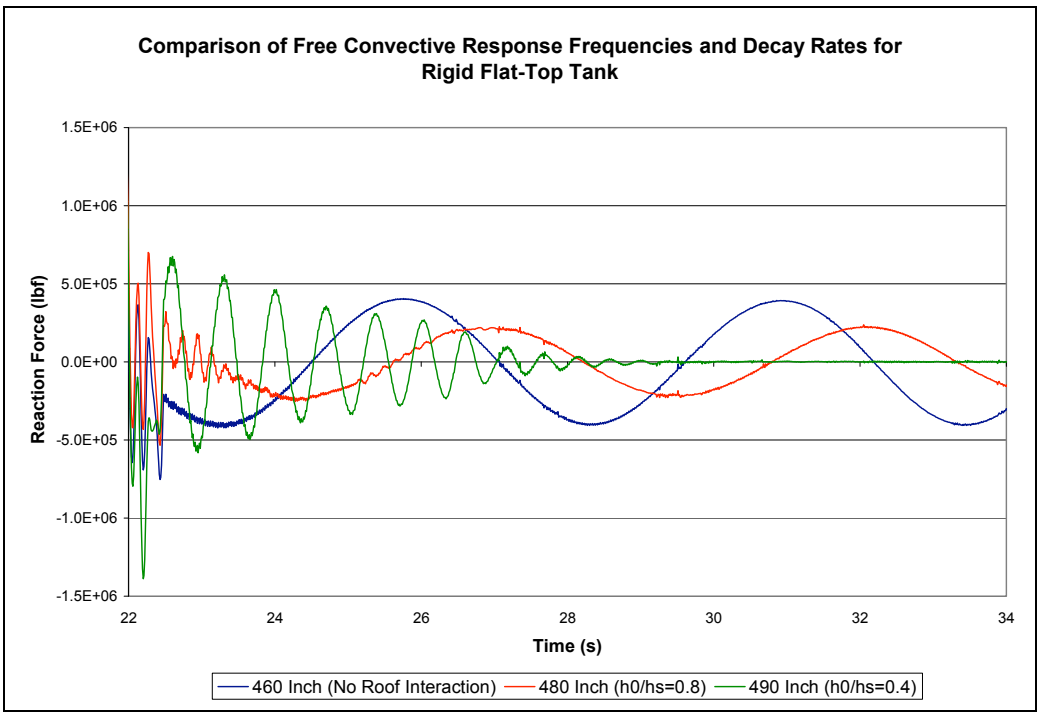


Figure 5. Frequencies and Decay Rates of the Free Convective Response of the Liquid in Rigid Flat-Top Tank at Three Headspace Levels.

RIGID DOMED TANK

Both the rigid and flexible-wall tanks have an initial liquid level of 460 inches and were evaluated using an equivalent flat-top roof height of 484 inches per Kennedy (2003). A plan view of the tank geometry along with selected fluid element sets at which pressures were monitored is shown in Figure 6. As with the rigid flat-top tank, the damping in the rigid dome tank system as determined by the logarithmic decrement of the convective response was a few tenths of a percent of critical damping. The horizontal seismic input for both dome tanks was the same as used for the previously discussed flat-top models.

The peak horizontal reaction force predicted by the Dytran® model was 111% of the value predicted for a tank with excess freeboard when the impulsive and convective contributions are summed using an SRSS combination and is 94% of the value for a tank with excess freeboard when the impulsive and convective contributions are summed absolutely. The percentages are nearly the same using the Malhotra methodology for a tank with excess freeboard.

The peak horizontal reaction force predicted by the Dytran® model was 93% of the value using the BNL equivalent flat top procedure using an SRSS sum and 83% of the BNL estimate based on an absolute sum. Similarly, the Dytran® prediction was 96% of the Malhotra estimate using SRSS, and 86% of the Malhotra estimate using

an absolute sum. That is, the equivalent flat-top predictions for peak horizontal reaction force are conservative relative to the Dytran® prediction.

The maximum liquid pressures were nearly identical to those for a vertical-wall tank with no liquid interaction with the dome over the lower 90% of the tank wall. That is, the pressure deviations from the solution for a vertical-wall tank with excess freeboard were limited to the upper 10% of the liquid, and were minor except at the free surface. The peak dynamic wall pressure predicted by Dytran® at the free surface was 2.7 times higher than for the vertical wall tank with excess freeboard and approximately 62% of the value predicted for the equivalent flat-top tank using the estimate from Appendix D of BNL (1995). Thus, the BNL methodology provided conservative estimates for the maximum liquid pressures in the tank.

The convective frequency of 0.207 Hz predicted by Dytran® represents a slight increase relative to the convective frequency of 0.196 Hz for a vertical-wall tank with ample freeboard as determined using the BNL, Malhotra, or ASCE 4 equations. The slight increase in the apparent convective frequency is consistent with behavior noted for the flat-top tank as shown in Figure 5, though to a lesser degree. The maximum magnitude of the horizontal reaction force caused by the convective response only is 56% of that determined for the case of a vertical wall tank with excess freeboard. For this case, the convective component of the peak reaction force as determined by the BNL estimate is approximately 10% of the total peak reaction force. This reduction in convective response for a tank with insufficient freeboard is consistent with the observation that for a completely full tank, there is no convective response.

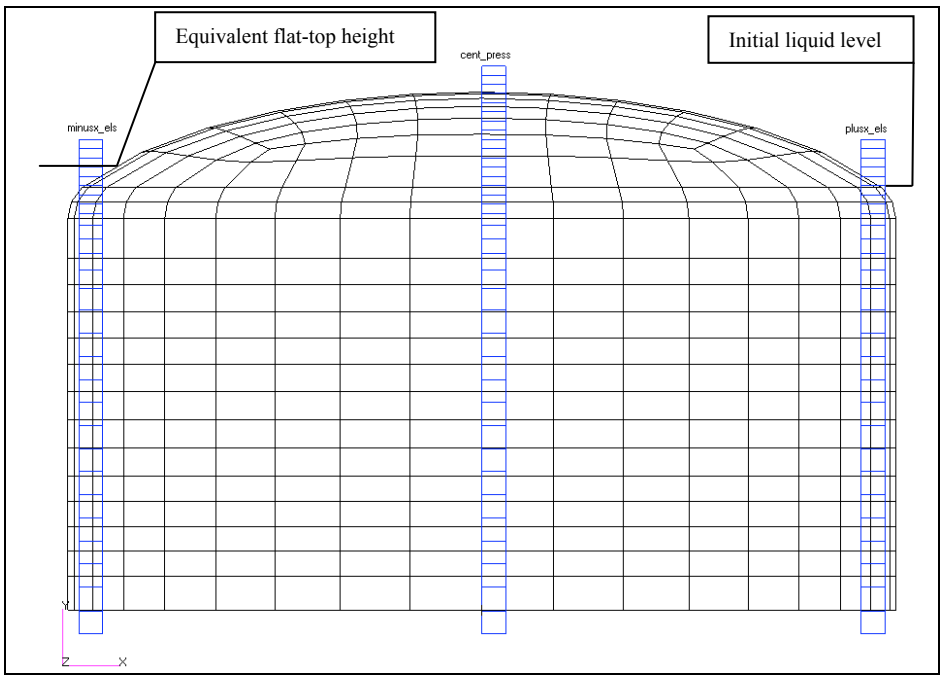


Figure 6. Elevation View of Rigid Domed Tank Model Showing the Locations of Selected Fluid Elements Sets at Which Pressures Were Monitored.

FLEXIBLE-WALL DOMED TANK

In contrast to the rigid tank systems, damping in addition to the inherent bulk viscosities was implemented in the flexible-wall tank. This was via a damping parameter introduced in the central difference integration scheme. The damping was calibrated to provide approximately 3-5.5% critical damping in the impulsive and breathing mode responses in the tank. The range of damping is a result of slightly lower apparent damping based on the decay of the breathing mode response of the system and slightly higher apparent damping based on the decay of the impulsive response of the system. Also, although not shown in Figure 6, the mesh resolution for the fluid elements in the flexible-wall tank system is significantly higher in the vertical direction than it was for the rigid domed tank.

The theoretical calculation of the maximum horizontal reaction force for the flexible-wall domed tank depends on the impulsive frequency of the tank-liquid system as well as the associated spectral acceleration at that frequency. It also depends on the spectral damping corresponding to the impulsive response. The impulsive frequency calculated via the BNL methodology for a tank with excess freeboard is 6.5 Hz. The impulsive frequency calculated for a tank with excess freeboard using the Malhotra estimate is 5.4 Hz. The impulsive frequency for the flexible-wall domed resulting from the Dytran® simulation was 6.25 Hz.

The results of the Dytran® simulation show that the maximum horizontal reaction force is slightly less than predicted for a vertical-wall tank with excess freeboard, and

approximately 30% less than predicted for an equivalent flat-top tank using the BNL or Malhotra estimates with an SRSS combination of impulsive and convective components. The convective frequency and maximum horizontal reaction force due to convective effects only is the same as for the rigid domed tank as expected, but for the flexible-wall tank, the maximum convective reaction force per the BNL estimate is only 5% of the total reaction force owing to amplification of the impulsive response. Further details on the combinations of impulsive frequencies, effective damping, and solution methods used to arrive at the above estimates are provided in Appendix C of Abatt and Rinker (2008b).

One might expect that the reaction force for the domed tank would be greater than that for the corresponding vertical-wall tank with excess freeboard. However, the comparison here is not a direct one because some of the interaction between the tank and contained liquid in this problem occurs in the rigid dome area. The interaction between the liquid and rigid portion of the tank is not amplified by the impulsive frequency, and this may lead to a slightly lower overall reaction force.

A comparison of peak wall pressures showed that in the lower 95% of the tank wall the maximum pressures from the Dytran® solution were essentially the same as those predicted for a vertical-wall tank with excess freeboard. The pressures predicted by Dytran® increased relative to vertical-wall tank solution in the upper 5% of the liquid with the peak dynamic wall pressure nearly three times greater than for the vertical-wall tank, but less than a third of the value predicted for the equivalent flat-top tank using the BNL estimate. In this case, the BNL methodology provided estimates of maximum liquid pressures that are even more conservative than for the rigid domed tank.

DISCUSSION

Dytran® agrees well with the BNL and Malhotra solutions for the vertical-wall tank with excess freeboard. There were two notable observations for this case. First, the BNL solution for the peak horizontal reaction force was slightly unconservative relative to the Dytran solution and the Malhotra estimate when combining impulsive and convective contributions via the SRSS procedure. Second, the peak horizontal reaction force due to convective effects only that was determined using Dytran® was significantly lower than predicted using the BNL or Malhotra estimates.

When the available freeboard was 80% of the maximum unconstrained slosh height (initial liquid level of 480 inches), the peak pressures predicted by Dytran® matched the BNL predictions for a tank with excess freeboard over the lower 70% or more of the tank. Moreover, the BNL solution for a tank with insufficient freeboard is conservative over the lower 90% of the tank. It is only in the upper 10% of the tank that the pressures exceed those predicted by the BNL solution, but near the top, the peak dynamic pressures are approximately twice that given by the BNL estimate and more than 20 times greater than given by the Malhotra estimate. In this case, the interaction with the tank roof is evidently localized enough that it does not affect the

convective frequency, or the apparent convective damping. However, the peak horizontal reaction force due to convective effects only is reduced.

When the available freeboard was 40% of the maximum unconstrained slosh height (initial liquid level of 490 inches), the peak pressures matched the BNL predictions for a tank with excess freeboard over the lower 60% or more of the tank. The BNL solution for a tank with insufficient freeboard is conservative over the lower 85% of the tank. It is only in the upper 15% of the tank that the pressures exceed those predicted by the BNL solution, but the peak dynamic pressures are approximately 50% greater than given by the BNL estimate and more than eight times greater than given by the Malhotra estimate. In comparison to the previous case, although the peak roof pressures are higher in that case, the effects on liquid pressures are also more localized near the top of the liquid column when more freeboard is available.

The additional interaction with the tank roof that occurs when the available freeboard was 40% of the maximum unconstrained slosh height also dramatically increases the apparent convective frequency and apparent convective damping. The results also showed that the BNL and Malhotra estimates for the peak horizontal reaction force are more conservative relative to the Dytran® results for flat-top tanks with insufficient freeboard than for tanks with excess freeboard.

The disparity in the peak roof pressures predicted by the different methods should not be surprising. The Malhotra estimate of roof pressures is based on the contained liquid in the tank subjected to a lateral acceleration equal to the spectral acceleration at the convective frequency of the system. Accordingly, impulsive effects are not reflected in this estimate. In contrast, the BNL estimate of peak roof pressures for a tank with insufficient freeboard is based on the contained liquid in the tank subjected to a lateral acceleration equal to the spectral acceleration at the impulsive frequency of the system (which is the same peak roof pressure predicted for a completely full tank subjected to the impulsive acceleration). The Dytran® simulation naturally captures the convective and impulsive effects plus the dynamic impact effect that is not reflected in either of the other estimates.

The Dytran® simulation at the 480 inch and 490 inch initial liquid levels for the flat-top tank shows non-zero dynamic roof pressures at outside of the central half-angles predicted by BNL or Malhotra. The higher peak roof pressures predicted by Dytran® for the flat-top tank coupled with non-zero dynamic pressures outside the predicted central half-angle *suggests* that the total peak roof force may be higher for flat-top tanks than predicted by the BNL or Malhotra estimates. However, the total peak roof force and variation of the contact area of the liquid with the roof were not parameters that were of primary interest for this study and thus the total roof force was not monitored. Consequently, this investigation does not provide enough information to support a conclusion regarding the peak roof forces predicted by the BNL or Malhotra estimates. This is perhaps the most important practical result that was not provided by this study.

In the two cases of the domed tanks, the estimates of the peak horizontal reaction forces provided by the BNL and Malhotra procedures for are conservative relative to the Dytran® solutions, especially for the flexible-wall tank. The peak liquid pressures for the rigid domed tank are very similar to the solutions for vertical-walled tanks with excess freeboard up to at least 90% of the normalized initial liquid level. This behavior is consistent with results for flat-top tanks, but the agreement between the solutions for the domed tanks and for vertical-wall tanks with excess freeboard extends further up the tank wall than for flat-top tanks. In the flexible-wall domed tank, the peak liquid pressures are indistinguishable from those predicted for a vertical-wall tank with excess freeboard in the lower 95% of the liquid. In both cases, this is consistent with a milder effect of roof interactions for a curved roof relative to a flat roof.

The liquid interaction with the tank dome was captured by the Dytran® simulations as evidenced by the significant increase in peak wall pressures relative to those predicted for vertical-wall tanks with excess freeboard. On the other hand, the peak roof pressures determined using the BNL estimates for equivalent flat-top tanks were conservative, especially for the flexible-wall domed tank. In fact, the peak liquid pressures at all elevations were conservatively estimated by the BNL procedure, and very conservatively estimated for the flexible-wall tank. The peak roof pressures given by the Malhotra estimate are the same as for the rigid domed tank because the estimate depends in the convective acceleration, but not on the impulsive acceleration, which is higher for the flexible-wall tank. In both cases, the maximum roof pressures were dramatically underestimated using the Malhotra procedure.

Part of the conservatism inherent in the BNL solution for predicting peak liquid pressures for equivalent flat-top tanks is due to the assumption that within the central half-angle, the fluid column is trapped between the floor, wall, and roof, and that the dynamic pressure is independent of height on the column. This is in contrast with the prediction from the Dytran® simulations that the peak pressures over the majority of the tank height are not increased by the presence of the roof.

CONCLUSIONS

The following conclusions are supported by the results of this study:

1. The peak horizontal reaction force estimate per BNL for a vertical-wall tank with excess freeboard was conservative relative to the Dytran® solution when the impulsive and convective components were summed absolutely, but slightly unconservative when the two components were summed via the SRSS method.
2. The peak reaction force estimates provided by BNL and Malhotra were conservative for flat-top tanks with insufficient freeboard and for domed tanks regardless of whether the impulsive and convective components were summed via the SRSS method or using an absolute sum.
3. Peak liquid pressures in flat-top tanks with insufficient freeboard or in domed tanks agree with the peak pressures for vertical-wall tanks with excess

freeboard in the lower 60% to 95% of the liquid column, depending on the tank configuration.

4. The effects of the roof or dome interaction on the peak liquid pressures are limited to the upper portions of the tank and the effects are quite localized for the domed geometry considered.
5. In the case of flat-top tanks with insufficient freeboard, the peak roof pressures predicted by the Dytran® simulations were higher than given by the BNL equivalent flat-top tank estimates because the BNL estimate does not include dynamic impact effects.
6. In the case of domed tanks, the BNL equivalent flat-top tank estimates of the peak roof pressures were conservative, especially for the flexible-wall tank.
7. The peak roof pressures predicted using the Malhotra estimate were dramatically lower than either of the other two methods because the estimate does not account for impulsive effects or dynamic impact effects.

REFERENCES

Abatt FG, and MW Rinker (2008a), "Hanford Double-Shell Tank Thermal and Seismic Project - Dytran® Benchmark Analysis of Seismically Induced Fluid-Structure Interaction in Flat-Top Tanks", RPP-RPT-30807, Rev. 1, Prepared by M&D Professional Services, Inc. for Pacific Northwest National Laboratory, Richland, Washington. Available at www.osti.gov/bridge.

Abatt FG, and MW Rinker (2008b), "Dytran® Benchmark Analysis of Seismically Induced Fluid-Structure Interaction in a Hanford Double Shell Primary Tank", RPP-RPT-28963, Rev. 1, Prepared by M&D Professional Services, Inc. for Pacific Northwest National Laboratory, Richland, Washington. Available at www.osti.gov/bridge.

ASCE (1998), "Seismic Analysis of Safety-Related Nuclear Structures and Commentary", ASCE 4-98, American Society of Civil Engineers, Reston, Virginia.

BNL (1995), "Seismic Design and Evaluation Guidelines for the Department of Energy High-Level Liquid Storage Tanks and Appurtenances", Report No. 52361, October 1995, Engineering Research and Applications Division, Department of Advanced Technology, Brookhaven National Laboratory, Associated Universities, Inc., Upton, New York.

Kennedy, R.P., (2003), "Review Comments Concerning Evaluation of Proposed Increase to Double-Shell Tank Liquid Level", May, 2003, RPK Structural Mechanics Consulting, Escondido, California.

Malhotra, Praveen K. (2005), "Sloshing Loads in Liquid-Storage Tanks with Insufficient Freeboard", Earthquake Spectra, Volume 21, No. 4, pp. 1185-1192, November 2005.

Modeling and Analysis for Seismic Evaluation of Nuclear Structures

S.A. Short,[1] O. Gurbuz[2], A.S. Whittaker[3], and M. Shams[4]

[1]Simpson Gumpertz & Heger, 4000 MacArthur Blvd, Suite 710, Newport Beach, CA, 92660; PH (949) 930-2159; email: sashort@sgh.com
[2] Gurbuz Consulting, 16162 Tortola Circle, Huntington Beach, CA, 92649; PH (714) 625-0656; email: ogurbuz@verizon.net
[3]University of Buffalo, State University of New York, Red Jacket Quadrangle, Buffalo, NY, 14261; PH (716) 645-4364; email: awhittak@buffalo.edu
[4]United States Nuclear Regulatory Commission, 11555 Rockville Pike, Rockville, MD 20852; PH (301) 415-0501; email: mohamed.shams@nrc.gov

ABSTRACT

Nuclear structures are typically reinforced concrete shear wall buildings constructed either embedded in or on the ground surface. Nuclear structures contain equipment, systems, and components that are safety-related and generally require seismic qualification by either full-scale testing or analysis. Evaluation of a safety-related nuclear structure is typically performed by dynamic analysis of a finite element model of the structure considering three orthogonal components of input motion. The paper addresses updates to ASCE 4 in the areas of finite element modeling, damping for multiple levels of response, modal response combination, frequency domain response methods, multi-step analyses, and nonlinear seismic analysis.

MODELING OF STRUCTURES

General Requirements. The arrangements of nuclear plant buildings and major components are structurally complex, and the development of mathematical models for seismic effects requires careful consideration. The amount of detail used to represent a structure in a mathematical model depends on the structural configuration and the use of the model. Specific considerations and requirements pertinent to idealizing complex plant structures are provided in the standard.

The seismic response of a structure shall be determined by preparing a mathematical model of the structure and calculating the response of the model to the prescribed seismic input. Mass and stiffness distribution in the structure shall be appropriately included. The mathematical model shall represent, at a minimum, the structural elements that form the primary load resisting system of the structure. The hydrodynamic effects of any significant water mass interacting with the structure shall be considered in modeling the inertial characteristics. The response parameter(s) of interest shall be identified. Response parameter(s) of interest are defined as the desired results of a specific analysis that will be used in design and/or evaluations. Different structural models are often developed for different purposes and the purpose of each model should be clearly identified.

The frequency range of interest shall be identified and the mathematical model shall adequately represent the frequency range of interest. The frequency range of interest is the intersection of (1) the frequency range of the earthquake input; (2) the frequency range of building response; and (3) the frequency range of the response parameter of interest. Refined finite element meshes and increased analytical rigor are generally required to transmit higher frequencies through the analytical models.

Structural design forces, such as base shear, are functions of relative displacement and are typically not sensitive to high frequency response. Equipment response may, depending on the component, be sensitive to high frequency response. Thus, an analytical model developed solely to determine structural design forces may have a lower frequency range of interest than an analytical model developed to generate in-structure response spectra for high frequency sensitive equipment evaluations. Typical nuclear construction, such as heavy reinforced concrete shear wall confinement/containment structures are generally capable of transmitting high frequency response throughout the structure. The seismic input for a western US site or an eastern deep soil site has much lower frequency content than an eastern US rock site. Where the frequency range of interest extends to high frequencies, it is required that (1) the soil-structure interaction (SSI) and structural models are adequately refined to sufficiently capture the high frequency content of the seismic input in the structural response; (2) the range of high frequency to be transmitted should cover a model refinement frequency of at least equal to 50 Hz; and (3) in-structure response spectra (ISRS) computed using a refined model should contain spectral responses up to 100 Hz.

Models for Horizontal and Vertical Motions. When significant coupling exists between horizontal and vertical structural responses, one combined analytical model (a three-dimensional model) shall be used for the seismic response analysis. Otherwise, separate analytical models for horizontal and vertical excitations may be used. Because of the complexity of structures, equipment locations, and non-uniform mass distribution, eccentricity between the center of mass and the center of rigidity often exists in nuclear plant structures. This creates coupling between the three orthogonal structural responses.

Selection of Finite Element Type. There are two factors to be considered in the selection of finite element types for analysis: (a) type of the structural members to be modeled and, (b) type of the response parameters of interest that are critical to the design of the SSC. The selection of the element type shall also consider the analytical theory on which the element is based, in order to represent major characteristics of the structural system and to capture the response parameter(s) of interest. The selection of the discretization parameters shall consider the size, shape, and aspect ratio of the elements; the internal node points; type of deformation to be modeled (e.g. out-of-plane shear deformation); and the number of nodes required to define the element.

For frame structures, the beam and truss elements should be used; the latter being necessary for members with axial load capability only. When modeling with beam elements, a single element between the support points is sufficient unless determination of dynamic response between the nodes is necessary. Also, it must be recognized that multiple elements with distributed masses between the support points will result in local modes in dynamic analysis that may not be important to behavior of the overall structure but increases the number of modes below the specified cut-off frequency. For shear wall structures, it is preferred to use shell elements that will calculate the variation of stresses within the element as well as out-of-plane shears. Shell elements with transverse shear deformation are required in many nuclear structures with thick slabs and walls and relatively short spans. 3D solid elements may be used to represent massive solid components and are often used to represent soil. Different types of elements can be combined in one model provided that compatibility of forces and displacements at the boundaries are assured.

Selection of Mesh Size. The finite-element model shall produce response parameters of interest critical to design that are not significantly affected by further refinement in the element mesh size and shape. The mesh size must be capable of transmitting the entire frequency range of interest. The selection of element sizes is essentially an exercise of engineering judgment, since the "true solution" to which the results can be compared is often not known. Mesh refinement guidelines include:

- For in-plane shear, piers should have at least three elements vertically.
- For transverse bending in slabs, element size should be smaller of the short side/6 or the long side/8.
- For transverse bending in walls, four elements across vertical spans should be used.
- If transverse bending is important in walls, such as exterior walls resisting soil pressure, mesh the walls as a slab.
- If concentrated loads are important, arrange elements to provide punching shear on critical sections.
- Provide additional refinement around discontinuities, unusual openings and high stress areas.

Damping. Values of damping to be used in dynamic analyses are given in Table 1 as a function of stress level. The stress level is calculated on a member basis and is given as:

- Stress Level 1 structures have low stresses. The member forces calculated for the loading combination are generally less than about 50% the code ultimate strength or stresses are generally less than about 50% yield capacity in the major resisting building elements.

- Stress Level 2 structures correspond to structures with demands less than the nominal ACI, AISC member capacities. The member forces calculated for the loading combination, are generally between about 50% and 100% of the code

ultimate strength or stresses are generally between about 50% and 100% of yield capacity in the major resisting building elements.

- Stress Level 3 structures have responses ranging from "Limited Permanent Distortion" to "Large Permanent Distortion" which corresponds to ASCE 43 Limit States C, B or A. The member forces calculated with F_μ=1, for the loading combination, must exceed the nominal code capacity or stresses must exceed the yield strength in major load resisting building elements.

Table 1 Viscous Damping Expressed as a Fraction of Critical Damping

Structure Type	Stress Level 1	Stress Level 2	Stress Level 3
Welded aluminum structures	0.02	0.04	0.04
Welded and friction-bolted steel structures	0.02	0.04	0.07
Bearing-bolted steel structures	0.04	0.07	0.10
Prestressed concrete structures (without complete loss of prestress)	0.02	0.05	0.07
Reinforced concrete structures	0.04	0.07	0.10
Reinforced masonry shear walls	0.04	0.07	0.10

These values are applicable to all modes of a structure constructed of the same material. Damping values for systems that include two or more substructures, such as a combined concrete and steel structure, or soil-structure systems require special treatment. For generating input motions to subsystems (i.e., equipment or piping attached to a building) or for evaluating structural displacements, the level of damping will depend upon the calculated stress levels. In lieu of iterative analyses to determine the actual Stress Level and associated damping value, Stress Level 1 damping values may be used for generation of in-structure spectra and displacements. Stress Level 1 damping shall be used if the design is governed by an elastic buckling mode.

For the design or analysis of safety-related structures limited to elastic response, Level 2 damping values may be used independent of the state of stress in the structures. Damping values higher than Stress Level 2 values are generally appropriate for structures responding well into their nonlinear range. The analysis may account for such damping, if properly justified, either through the use of a Stress Level 3 viscous damping value, or a combined Stress Level 1 viscous damping value and hysteretic energy dissipation mechanism. For structural design or analysis, the use of the higher damping values (Stress Level 3) is justified because, before the structural elements would reach a displacement limit, they would experience Stress Level 3. The exception is made for elastic buckling where the limiting value may be reached before Stress Level 3 or 2 is reached.

The use of damping values higher than those in Table 1 is permitted if the damping values are properly justified.

Modeling of Stiffness. The mathematical model shall represent, at a minimum, the structural elements that form the primary load resisting system of the structure. The stiffness of secondary elements, which are not part of the primary load path, may be omitted from the mathematical model provided that secondary elements do not unconservatively affect the response parameters of interest by more than 10%. Elements which are rigid compared to the stiffness of other elements in the load path may be considered as rigid bodies in the analysis, provided that the inclusion of rigid elements does not affect the response parameters of interest by more than 10%.

Reinforced concrete elements may be modeled as cracked or uncracked sections, depending on their stress levels due to the most critical seismic load combination. For the generation of input motion to subsystems, consideration shall be given to the uncertainties in the stiffness properties of the concrete elements. The ±15% peak broadening of in-structure response spectra, as required in the standard, is intended to account for the variability in structural properties.

Modeling of Mass. The inertial mass properties of a structure may be modeled by assuming that the structural mass and associated rotational inertia are discretized and lumped at node points of the model. Alternatively, the consistent mass formulation may be used. When appropriate, three translational and three rotational degrees of freedom shall be used at each node point. Mass for some degrees of freedom, such as rotational, may be neglected, provided that their exclusion does not affect the response significantly. The following conditions shall be met:

- Structural mass shall be lumped so that the total mass, as well as the center of gravity, is preserved, both for the total structure and for any of its major components that respond in the direction of motion.

- The number of dynamic degrees of freedom, and hence the number of lumped masses, shall be selected so that all significant vibration modes of the structure can be evaluated.

Mass included in the model used for dynamic analysis shall include all mass expected to be present at the time of the earthquake and shall not include added conservatism. This mass will include the effects of dead load, stationary equipment, piping, and the appropriate part of the live load. The mass shall account for the expected live load, but not less than 25% of the specified design live load for design loads 200 psf and smaller, and not less than 50 psf for design live loads greater than 200 psf.

Modeling of Damping. Damping coefficients listed in Table 1, shall be used for structures composed of the same material or with similar damping characteristics. For structural systems that consist of substructures with different damping properties, composite damping methods, damping matrix sub-structuring, or composite modal damping may be used. The entire frequency range of interest shall be considered when selecting the damping model.

ANALYSIS OF STRUCTURES

General Requirements. The seismic analysis of safety-related structures is typically performed by analysis of linearly elastic mathematical models. Nonlinear analysis may be performed in some cases, especially for beyond design basis calculations. The following methods of seismic analysis are acceptable:

Linear analysis	Nonlinear analysis
Time-history method	Time-history method
Response-spectrum	Response-spectrum
Frequency-domain	Nonlinear static
Equivalent static	
Multistep	

Analyses shall be performed for three orthogonal (two horizontal, one vertical) components of earthquake motion. The axes shall, in general, be aligned with the principal axes of the structure. Nuclear structures are generally stiff, massive and embedded structures for which soil-structure interaction (SSI) effects are likely to be important. Accordingly, regardless of the method chosen for analysis, the mathematical model of the structure shall account for SSI effects as appropriate.

Linear Time-History Analysis. Dynamic analysis of linear (and nonlinear) systems is based on the solution of a set of simultaneous differential equations involving mass, damping and stiffness matrix representations of the structure. Alternate methods, including direct integration and modal superposition, are available to solve the equations. Earthquake effects are imposed in the form of three-component acceleration time histories. A single set of time histories may be used provided that the 5% damped spectra match or envelop the target spectra and the calculated spectra at 2% and 20% damping must exceed 90% of the respective target spectra. Alternately, 3 independent sets of three component time-series can be used from which the peak maximum component response is determined. If 5 or more sets of time-series are used for linear analysis, median maximum component response shall be used.

Linear Response Spectrum Analysis. Methods of response-spectrum analysis are well established in codes, standards and guidelines for seismic analysis and design. A sufficient number of modes shall be included in the analysis to ensure that the inclusion of the remaining modes does not result in more than a 10% increase in the responses of interest. A residual mode may be used to include higher modes in the response calculations, where the residual mode frequency is equal to that of the ZPA.

Combination of Modal Responses. Modal responses shall be combined in a manner that accounts for the relative phasing between modes. Low-frequency modes are out of phase with each other, high-frequency modes are in phase with each other, and modes in between are in transition phasing as shown in Figure 1.

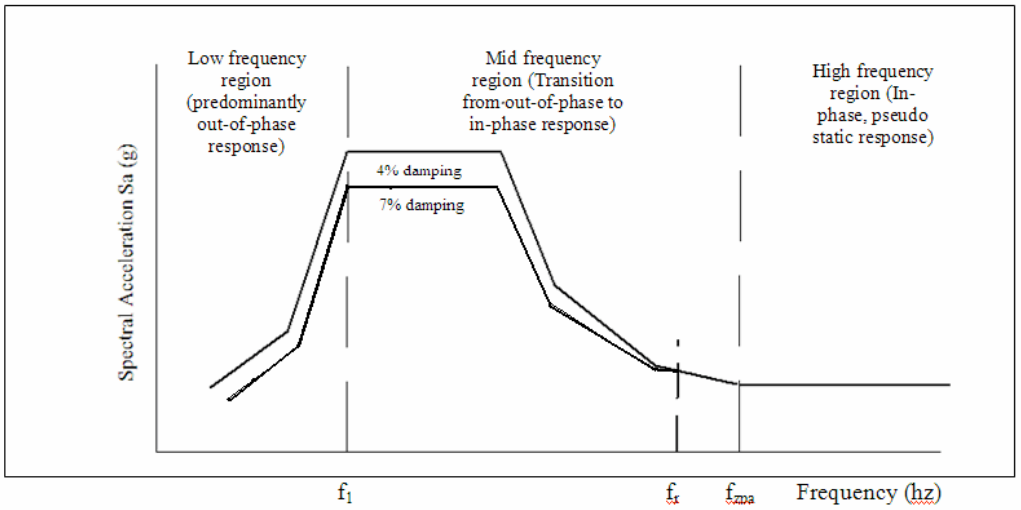


Figure 1. Modal Phasing and the Ground Response Spectrum

Combination of Out-of-Phase (Periodic or Low Frequency) Modal Responses. Combination of the modal responses for the Ith component of motion is calculated using the following double sum equation:

$$R_I = \pm\sqrt{\sum_i \sum_j \varepsilon_{ij} R_{Ii} R_{Ij}} \qquad \text{(Eq. 1)}$$

where: R_I = the response for the I^{th} component of motion

R_{Ii}, R_{Ij} = the signed modal response of interest in the i^{th} (j^{th}) mode, including the residual mode

ε_{ij} = modal correlation coefficients

Eq. 1 is the standard double-sum equation in which the coupling terms, ε_{ij}, account for the correlation between modal responses. If the frequencies of all modes are sufficiently separated, it is acceptable to combine out-of-phase modal responses using the SRSS method. In this approach, ε_{ij} is equal to 1.0 when i is equal to j and equal to 0.0 when i is not equal to j. If there are closely spaced modes, it is permissible to use either of the following two approaches for modal combination. Each of these methods have specific correlation coefficients, ε_{ij}.:

- Modified Rosenblueth's Correlation Coefficient
- Der Kiureghian's Correlation Coefficient (Complete Quadratic Combination or CQC)

Combination of Rigid (In-Phase or High-Frequency) Modal Responses. In the high-frequency region (greater than rigid frequency, f_r, as shown in Figure 1), rigid response is predominant and modal responses are to be combined by algebraic sum:

$$R_{Ir} = \sum_{i=1}^{n} R_{Iri} \qquad \text{(Eq. 2)}$$

where: R_{Ir} = the combined response of the I^{th} component of motion for all modes at frequency greater than rigid frequency f_r.

R_{Iri} = the response of the I^{th} component of motion for mode i for all modes at frequency greater than rigid frequency f_r.

f_r = the rigid frequency that can be identified as the frequency at which response spectra curves for different damping ratios converge.

Combination of Modes with Both Periodic and Rigid Responses. For the general case in which there are both periodic and rigid modal responses, it is permissible to use either of the following two approaches for modal combination:

- Gupta Method (also General Modal Combination or GMC)
- Lindley-Yow Method

These methods address both periodic and rigid modes as well as those modes in the transition region between frequencies f_1 and f_r in Figure 1.

The previous edition of the standard permitted an assumption of abrupt change between periodic and rigid response at a frequency of $1/2\, f_r$. This approximation is no longer permitted in the current standard. Recent work has indicated that periodic response is very strong close to the rigid frequency.

Frequency Domain Analysis. Frequency-domain analysis is generally employed for soil-structure interaction analysis. The frequency-domain analysis method permits the direct use of frequency-dependent parameters such as foundation radiation damping in the equations of motion. In frequency-domain analysis, the input motions shall be generally specified as an acceleration time-series. Each time series is transferred into frequency domain using Fourier transform techniques and once the solution is obtained the response is transformed back into the time domain using the inverse Fourier transform. For frequency-domain analysis, the following requirements shall be met:

- If acceleration time-series are used as input, the time step for the input acceleration time-series shall be chosen so that the maximum frequency of interest is retained. If random vibration theory is used, frequencies should be selected to accurately characterize the response or power spectrum of the input motion for the entire frequency range of interests.

- The frequency interval used to generate transfer functions shall be selected to enable calculation of transfer functions at key structural frequencies and any other frequencies of interest. If interpolation schemes are used to interpolate between these frequencies, the resulting transfer functions shall be checked.

Multistep Analysis. In a multistep analysis, dynamic response analysis is performed as a first step to establish system-level responses, including floor acceleration time series and floor displacement histories. Calculations of demands on components of the structural system are performed in subsequent steps. The mathematical model used for the subsequent analysis is generally more detailed than the model used for the initial dynamic analysis as the latter model is used for the calculation of forces for design and detailing of structural components and systems.

Initial Analysis. The seismic analysis of the structure is performed in the three orthogonal directions. Soil-structure interaction shall be considered. System-level acceleration, velocity and displacement results shall be recorded for subsequent steps in the analysis. In-Structure Response Spectra (ISRS) shall be developed for analysis of the systems, structures and components (SSCs) in or attached to the structure..

Subsequent Static Analysis. For subsequent analysis, the structure is typically modeled with a fixed base. Equivalent static forces shall be calculated as the product of maximum accelerations from the initial analysis and nodal masses and applied to a detailed model of the structure. The analyst should verify that the signs of the values used for the static analysis do not lead to an underestimation of demand on structural components and systems. The use of the static method of analysis to calculate demands on structural components may be very conservative because the maximum values of total acceleration are assumed to occur simultaneously.

Subsequent Dynamic Analysis. Response-spectrum or time (response)-history analysis can be used to determine forces for design of structural components. The use of an envelope response spectrum at the level of the foundation of the structure assumes that the effects of rocking and torsion are small and this assumption shall be verified. If the initial analysis indicates that rocking or torsion effects are significant, the time-history method of analysis is preferred because histories of rocking and torsion can be input at the base of the structure.

Nonlinear Time-History Analysis. Nonlinear time-history analysis shall be used for analysis of seismically isolated nuclear structures for design basis and beyond design basis shaking and may be used for analysis and design of all nuclear structures. Direct integration of the equations of motion and fast nonlinear analysis (FNA), which is best suited to structures with a limited number of nonlinear elements, can be used. A nonlinear representation of force-deformation behavior is typically used for all structural components. A linear elastic component model can be substituted for a nonlinear component model only if elastic response is anticipated and confirmed for the selected intensity of shaking. Nonstructural components that contribute significant lateral strength and/or stiffness to the structure, such as infill masonry walls, shall be modeled using equivalent beam-column or strut elements, or appropriate finite elements. Nonlinear models of components shall be based on test data where available. Nonlinear models of structural components (other than seismic isolators) will generally be enveloped by the basic form of the force-displacement relationships shown in Figure 2.

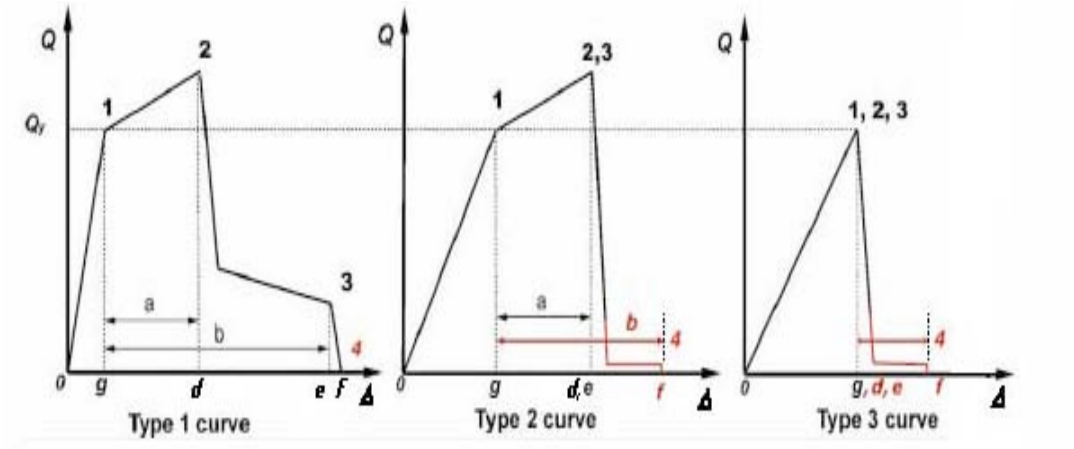


Figure 2 Generalized Force-Displacement Behavior of Structural Components

- The Type 1 curve is representative of ductile behavior characterized by an elastic range (points 0 to 1) and a plastic range (points 1 to 3). The plastic range includes a strain hardening or softening range (points 1 to 2) and a strength-degraded range with residual strength to resist lateral and gravity loads (points 2 to 3). Loss of lateral-force-resisting capacity occurs at point 3, which is followed by loss of vertical-force-resisting capacity at point 4.

- The Type 2 curve is representative of limited ductile behavior where there is an elastic range (points 0 to 1) and a plastic range (points 1 to 3), followed by loss of lateral-force-resisting capacity at point 3 and loss of vertical-force-resisting capacity at point 4.

- The Type 3 curve is representative of brittle or non-ductile behavior where there is an elastic range (points 0 to 1) followed by loss of lateral-force-resisting capacity at point 3 and loss of vertical-force-resisting capacity at point 4.

Three-component sets of earthquake ground motions shall be applied simultaneously to the mathematical model of the structure. A minimum of 3 independent sets of three component time-series shall be used for analysis. If 3 sets of time-series are used for analysis, the peak maximum component response shall be used for design. If more than 6 sets of time-series are used for analysis, the median maximum component response shall be used for design.

Nonlinear Response- Spectrum Method. If the nonlinear response spectrum method is used to estimate demands on components and systems, an acceptable method of nonlinear analysis for nuclear structures is to determine initially the response of the components of a structure using linear methods of analysis with an input excitation consistent with an elastic design response spectrum. The component elastic forces are then reduced by component-specific inelastic energy absorption factors, F_{μ}, to obtain inelastic member forces. Larger values of F_{μ} may be used for

ductile actions but smaller values of F_μ (but 1 or greater) must be used for brittle or less ductile members. For more hazardous facilities, lower values F_μ values are used to add conservatism to the design or evaluation, to reduce the likelihood of unacceptable performance. Recommended values for F_μ consistent with performance levels appropriate for nuclear facilities are presented in ASCE/SEI 43-05.

Nonlinear Static Analysis. The use of nonlinear static analysis shall be limited to low-rise, regular nuclear structures in which second and higher mode effects are not significant. Nonlinear static analysis involves the incremented lateral displacement of a nonlinear model of building frame using user-specified lateral force patterns. The analysis is terminated after the displacement of a control node exceeds the target displacement. The selection of a control node, the lateral load patterns, calculation of the fundamental frequency, analysis procedures, and treatment of soil-structure-interaction shall comply with the requirements of Chapter 3 of ASCE 41.

The target displacement of the building frame shall be calculated by either the coefficient method or the capacity spectrum method. The effect of the earthquake shaking is characterized using a spectral displacement that is transformed into a target displacement for the purpose of component checking. In the coefficient method, the target displacement is calculated as the product of the elastic spectral displacement at the first mode frequency of the structure in the direction under consideration and a series of calibrated factors that transform spectral displacement to roof displacement, elastic displacement to inelastic displacement, and account for the effects of hysteresis loop shape and dynamic second-order effects. In the capacity spectrum method, the target displacement is calculated by plotting the elastic response spectrum in terms of spectral acceleration versus spectral displacement, reducing the ordinates of the elastic spectrum to account for the effects of hysteretic energy dissipation (generating the demand curve), overlaying the results of nonlinear static analysis of the structure in the same coordinate system used for the spectra (generating the capacity curve), and determining the displacement at which the demand and capacity curves intersect.

CONCLUSIONS

Conclusions of this paper are where ASCE 4-98 has been significantly updated in the areas of modeling and analysis.

1. The basic requirement is that nuclear structures are represented by a detailed finite element model for which a three dimensional dynamic analysis is performed. More simplified modeling or analysis may be used, if justified.
2. Eastern United States seismic hazard estimates now indicate significant high frequency amplified seismic input at high frequencies on the order of 25 Hz. As a result, the standard provides modeling guidelines such that high frequency seismic response can be accurately captured. The range of high frequency to be transmitted should cover a model refinement frequency of at least equal to 50 Hz; and in-

structure response spectra (ISRS) computed using a refined model should contain spectral responses up to 100 Hz.

3. Mesh refinement guidelines are provided in the updated standard to capture accurate seismic response.

4. Structural damping levels have been added in this standard update for Stress Level 3. This is for the level of response where limited inelastic behavior is permitted in accordance with Limit States A, B, or C of ASCE/SEI 43-05.

5. Combination of modal responses for response spectrum analyses has been expanded in this standard update. Mode phasing in the low frequency amplified range, the high frequency rigid range, and the transition range in between have been identified and mode combination methods appropriate for each range are discussed.

6. Frequency domain analysis discussion has been updated for this version of the standard. Frequency domain analyses are the standard for consideration of SSI in computed programs such as SASSI and CLASSI to accurately treat frequency-dependent impedance and scattering behavior.

7. Multi-step analyses requirements have been added to this update of the standard in which a less refined SSI model is used to obtain global responses. The global response is then used as input to very refined models to obtain seismic response for purposes of design.

8. Updates include an expansion of the discussion of nonlinear analysis including time history approaches, the response spectrum method that is the basic method in ASCE/SEI 43-05, and static or pushover approaches.

REFERENCES

Clough, R. and Penzien, J., (2003), *Dynamics of Structures*, Second Edition, Computers and Structures, Berkeley, CA.

Chopra, A. K., (2001), *Dynamics of Structures: Theory and Applications to Earthquake Engineering*, Prentice Hall

Wilson, E. L., (2004), *Static and Dynamic Analysis of Structures*, Fourth Edition, Computers and Structures, Berkeley, CA.

United States Nuclear Regulatory Commission (USNRC), (2006), *Combining Modal Responses and Spatial Components in Seismic Response Analysis, Regulatory Guide 1.92*, Revision 2, Washington, DC.

American Society of Civil Engineers (ASCE), (2006), *Seismic Rehabilitation of Existing Buildings*, ASCE/SEI Standard 41-06, Reston, VA.

American Society of Civil Engineers (ASCE), (2005), *Seismic Design Criteria for Structures, Systems and Components in Nuclear Facilities and Commentary*, ASCE/SEI Standard 43-05, Reston, VA.

Sliding and Rocking of Unanchored Components and Structures: Chapter 7.6 ASCE 4 Revision 2

S. R. Jensen[1] and O. Gurbuz[2]

[1]Idaho National Laboratory, Idaho Falls, ID, P. O. Box 1625, Idaho Falls, ID 83413-7101, Ph (208) 526-9137 stuart.jensen@inl.gov
[2]Gurbuz Consulting, 16162 Tortola Circle, Huntington Beach, CA 92649, Ph (714) 625-0656, ogurbuz@aol.com

ABSTRACT

Section 7.6 of ASCE 4-Rev 2, *Seismic Analysis of Safety-Related Nuclear Structures: Standard and Commentary*, provides updated guidance for analysis of rocking and sliding of unanchored structures and components subjected to seismic load. This guidance includes provisions both for simplified approximate energy-based approaches, and for detailed probabilistic time history analysis using nonlinear methods. Factors to be applied to the analytical results are also provided to achieve demand estimates at the 80% non-exceedance probability level. The present paper surveys the published literature supporting these provisions. The results of available testing and analyses are compared to results produced by both simplified and probabilistic approaches. In addition, adequacy of the standard's provisions for analysis methods and factors is assessed. A comparison is made between the achieved level of conservatism and the standard's non-exceedance probability target.

BACKGROUND/INTRODUCTION

Section 7.6 of ASCE 4-Rev 2, *Seismic Analysis of Safety-Related Nuclear Structures: Standard and Commentary* (ASCE, 2011), provides guidance for analysis of rocking and sliding of unanchored structures and components subjected to seismic load. Hereafter in this paper, "ASCE 4" shall refer to the draft standard, not to be confused with the existing ASCE 4-98. The guidance in ASCE 4 Section 7.6 is consistent with the current revision of ASCE/SEI 43-05, *Seismi Design Criteria for Structures, Systems and Components in Nuclear Facilities* (ASCE/SEI 43-05), but does provide some evolutionary updates as will be explained throughout this paper.

Seismic design and evaluation of nuclear structures can be divided into to two main tasks, which are each addressed by separate ASCE standards. Analysis of structures to determine seismic demands is governed by ASCE 4, while criteria to be used in the design of these structures are given by ASCE/SEI 43-05. The acceptability of the design is determined by the comparison of demands to capacities, as outlined in ASCE/SEI 43-

05. These standards in combination are intended to satisfy a performance goal, described in ASCE/SEI 43-05 as to reasonably achieve both of the following criteria:

> 1. Less than about a 1% probability of unacceptable performance for the DBE ground motion
>
> 2. Less than about a 10% probability of unacceptable performance for a ground motion equal to 150% of the DBE ground motion.
>
> (ASCE/SEI 43-05 Section 1.3)

Each standard provides a controlled degree of conservatism. ASCE 4-98 stated an intent to produce demands with a non exceedance probability (NEP) of approximately 90%. The new draft of ASCE 4 will change that target to an NEP of approximately 80%. ASCE/SEI 43-05 states an intent to produce capacities with an exceedance probability of approximately 98%. These two margins, one on analysis and one on design, when combined are shown in the ASCE/SEI 43-05 commentary to satisfy the performance goal.

However, ASCE 4-98 did not contain provisions for rocking and sliding of unanchored components. Because the working group felt it would be useful to provide some guidance, ASCE/SEI 43-05 was issued including Section 7.1 containing provisions for evaluation of sliding and rocking of unanchored components. It was necessary under those circumstances to combine the conservatism for analysis and design into the design criteria standard. This conservatism is presented in ASCE/SEI 43-05 as factors of safety to be applied to the best-estimate (median centered) sliding distance or rocking angle to develop design values. These factors of safety were based upon judgment formed by preparation and review of a number of non-published nonlinear time history analysis studies. The ASCE/SEI 43-05 factors are as follows:

Sliding: $\boldsymbol{FS_S} = 3.0$
Rocking: $\boldsymbol{FS_R} = 2.0$

ASCE 4, SECTION 7.6 METHODOLOGIES

As in ASCE/SEI 43-05, the new draft of ASCE 4 provides three general approaches to analyze rocking and sliding of unanchored components:

- Static Evaluation
- Conservatively Biased Reserve Energy
- Time History Analysis

Static Evaluation. The static evaluation is generally consistent with longstanding procedures established in building codes and in the NRC Standard Review Plan. Static evaluation entails an analysis (which generally considers dynamic effects and soil-structure interaction) to develop base shear and overturning moments, which are then multiplied by a safety factor of 1.1. These analyses usually assume the foundation is essentially rigid. Pressures applied to the foundation medium should be verified to be acceptable. If the resulting demand is less than the static resisting capacities, the

component (or structure) will not slide or rock and no further evaluation is necessary. If the factored demands are greater than the static resistance capacities, then nonlinear analysis is required. Two general nonlinear approaches are described.

Reserve Energy Method. The simplified nonlinear approach provided in ASCE 4 is a reserve energy method, with formulations for both rocking and sliding. This method is well described in the appendices of ASCE/SEI 43-05 and elsewhere (Blume 1960, Yim et al. 1980, Aslam et al., 1980), and benchmarked against alternative approaches (Esfendari et al. 2009). It has been shown to be conservative with respect to more rigorous time-series analysis (ASCE 2005). In ASCE/SEI 43-05, the generous conservatism of particularly the sliding analysis is credited by reducing the required general factor of safety from 3, if a true best-estimate is developed, to 2, if the conservatively biased reserve-energy method is used. In ASCE 4 the treatment of safety factors has been changed in general, as will be discussed later, and in particular for the reserve energy sliding analysis, there is no longer any distinction made between this conservative approach and a true best estimate. The reserve energy solutions for both sliding and rocking analyses are treated as best-estimates or mean solutions. These solutions assume rigid rocking or sliding bodies interacting with an undeformable foundation through a coefficient of restitution, and are only appropriate when such conditions approximately apply.

Time History Analysis. Two approaches to nonlinear time history analysis are provided; for each approach a number of sets of time histories matching the design basis earthquake (DBE) spectra and conforming to the requirements of Chapter 2 are required. In the first approach, 5 different time histories (sets) are applied to the same deterministic model. The mean of the 5 solutions is taken as the best estimate. In the second approach, a fully probabilistic solution modeling all significant sources of variability and uncertainty in the particular problem, including time histories, friction coefficients, dynamic stiffness of the support, stiffness of the object, damping, and geometric tolerances is generated. At least 16 independent realizations are required. The 80^{th} percentile non-exceedance probability (NEP) response is taken as the analytical demand. The time history problem may be solved in two or three dimensions, depending upon the relevant geometries.

Adjustment for Analytical Demand Conservatism. The intent of the standard is to produce analytical demands at about the 80% NEP level. The probabilistic time history analysis approach can directly generate this 80% NEP result. The deterministic approaches, reserve energy and the time history mean-of-5, generate results that are taken as mean or best estimates, and which require adjustment up to the 80% NEP level. This is achieved by multiplying the deterministic best estimate by a factor of 1.5. This factor will be shown later in this paper to produce a reasonable estimate of the 80% NEP analytical demand.

Consideration of Uncertainties. Sliding and rocking problems are known to be sensitive to parameters which are usually not well-characterized. These may involve such phenomena as friction, surface irregularity, and phasing of input motions. To control and account for these effects, provisions are made for the consideration of uncertainties. For

deterministic analysis, friction is to be taken at the 95% NEP level for rocking, and at the 5% NEP level for sliding. Alternatively, pure rocking or pure sliding may be assumed. However, displacements due to rocking and displacements due to sliding need not be combined. For probabilistic analysis, friction is to be varied over an appropriate interval. Any combination of rocking and sliding may result and will factor into the reported displacement parameter.

Adjustment for Capacity Conservatism. To ensure the performance goals of ASCE/SEI 43-05 are satisfied, capacity factors precluding potential adverse interactions due to rocking or sliding are provided. Ideally these factors would be provided in ASCE/SEI 43-05 rather than in ASCE 4, because they have to do with capacity margin rather than demand margin. However, as an interim step that will allow future migration of the capacity factors to ASCE/SEI 43-05, ASCE 4 separates the demand factors from the capacity factors. A minimum capacity factor of 2.0 is required for both rocking angle and sliding displacement. The basis for this factor is judgment formed by familiarity with unpublished time history analyses results. Further development of a basis for these factors, particularly computed for the highly nonlinear rocking and sliding responses, may be an appropriate activity in support of the next revision of ASCE/SEI 43-05. However, based upon typical variability in seismic capacities as discussed in ASCE/SEI 43-05 Commentary, a factor of two will result in a capacity with approximately 98% probability of exceedance. In combination with the 80% NEP demand, this is expected to satisfy the ASCE 43-05 performance goal.

The combined demand and capacity factors result in a factor of safety of 3.0 relative to the best estimate. This is consistent with the factor of safety required for sliding in ASCE/SEI 43-05, and slightly higher than that previously required for rocking.

Response Limits. Solutions to rocking problems tend to become unpredictable at rocking angles approaching the stability limit. For example, it has been shown (DeJong 2009) that for ground motions which challenge gross stability, responses to multiple time histories with different phasing matching the same response spectrum can vary from less than 10% of the overturning angle all the way to overturning. Furthermore, this response is also shown to be sensitive to the duration of the shaking, which is not specified by a response spectrum.

To ensure a predictable response, the factored (80% NEP) rotation angle demand is limited to no more than 75% of the stability limit. For time history analysis, configurations which lead to any realization (either deterministic or probabilistic) overturning are prohibited. This prohibition is necessary for deterministic analysis based upon the mean response to 5 time histories because it would not be meaningful to average an overturned response with stable responses. A probabilistic analysis where some of the solutions result in overturning (when overturning is unacceptable) would be considered an “alternative methodology” as permitted in ASCE 4 Section 1.1.3.3. However, where, in general, alternatives to standard methodologies would need to demonstrate at least an 80% NEP, in the case of rocking and sliding ASCE 4 also provides the capacity factors required to achieve the ASCE/SEI 43-05 performance goals.

Therefore, alternative rocking and sliding analyses in which some realizations overturn would need to demonstrate both a 1% or less probability of exceedance given the DBE, and a 10% or less probability of exceedance given 1.5 times the DBE. This would require a large number of solutions, depending in part upon the number of realizations which overturn.

An additional consideration applies to rocking of cylindrical components or of components whose bases have rounded cross sections. The reserve energy method accounts for dissipation of energy as the base impacts the foundation at each transition through the 0° rotation angle. This coefficient of restitution-based energy dissipation is converted into an equivalent viscous damping, which is used to select the appropriately damped input response spectrum. However, it is possible that objects whose bases have circular cross sections may roll around the edge of their base when rocking. This type of response will exhibit much less energy dissipation than a pure rocking response, and the assumptions used to derive equivalent viscous damping are not accurate. To ensure a conservative analytical approach for components with circular bases, the rotation angle demand (80% NEP level) calculated by the simplified method (reserve energy) is limited to less than 10% of the angle at the stability limit. Detailed three dimensional nonlinear analysis can accurately model the rolling behavior of a round-based object, because energy dissipation is not dependent upon a linearization of the impact phenomenon (Sandia 2005). Therefore, when three dimensional time history analysis adequately models the potential rolling behavior of a component, the rocking angle limit remains 75% of the stability limit.

Summary of Methodologies. The nonlinear analysis methodologies and provisions are summarized in flowchart form in Figure 1.

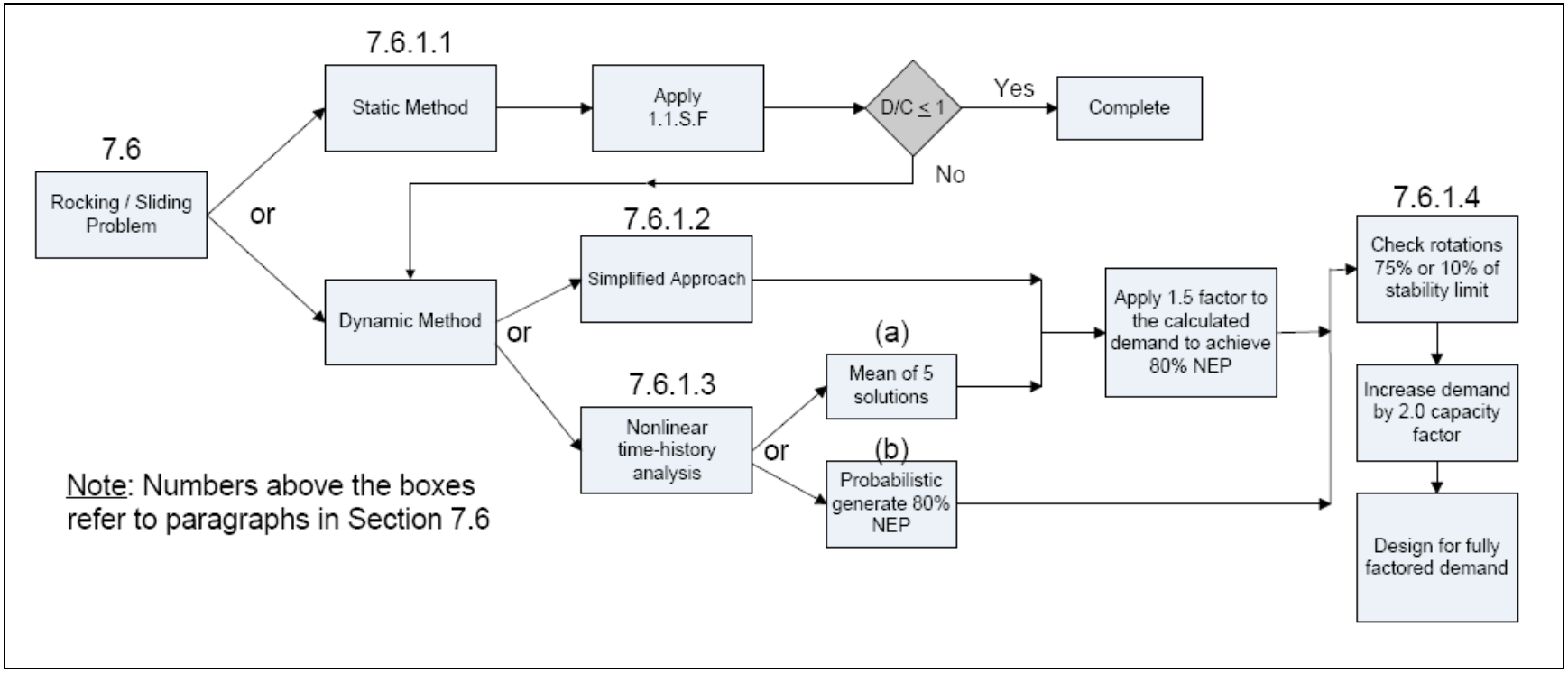


Figure 1: Summary of Rocking and Sliding Analysis Provisions

ADEQUACY OF ANALYTICAL DEMAND CONSERVATISM

Standard Intent. The intent of the standard is to produce analytical demands at approximately the 80% NEP level, given the design basis earthquake (DBE). A key element in this approach is that the mean response, multiplied by the demand factor of 1.5, will produce an approximately 80% NEP response.

Studies (Hutchinson and Chaudhuri 2006, Sandia 2005) have shown that rocking and sliding responses to various time histories matching a given demand response spectrum approximately follow a lognormal probability distribution. To the extent this formulation applies, a demand factor can be calculated from the assumed lognormal standard deviation, β_D,(=($\beta_R^2 + \beta_U^2$)$^{0.5}$ where β_R and β_U are the logarithmic standard deviation for the inherent randomness and uncertainty, respectively, of the seismic response. The 80% NEP demand is given by the following equation,

$$\frac{F_D}{F_C} = e^{0.84\beta_D} \qquad \text{(Eq 1 of 1)}$$

where 0.84 is the standardized normal variable for the 20% (one-sided) exceedance probability level (that is, the 80$^{\%}$ NEP level), F_D is the factored demand and F_C is the calculated median demand, and β_D is the composite lognormal standard deviation of demand. Note that the factor thus calculated applies to the median value, which will be lower for a lognormal distribution than the mean value. Because ASCE 4 applies the demand factor to the calculated mean (or best estimate), Equation 1 is conservative. Values of F_D corresponding to a range of values of β_D are tabulated in Table 1 below.

Table 1. Example Values of F_D/F_C

β_D	F_D/F_C
0.3	1.29
0.35	1.34
0.4	1.40
0.45	1.46
0.5	1.52
0.55	1.59
0.6	1.66

As can be seen from Table 1, a demand factor of 1.5 will produce a reasonable estimate of the 80th percentile demand for problems having lognormal standard deviations of about 0.5 or less, since the required multiplier in Table 1 is less than 1.5.

Seismic response of components typically will have lognormal standard deviations in the range of about 0.2 to 0.4 (ASCE 2005); therefore, the factor of 1.5 provides a reasonable estimate of the demand at the 80% NEP level.

Rocking and Sliding Problems. However, rocking and sliding problems exhibit highly nonlinear and unique behavior. In this section new statistical processing of previously published results of a detailed three-dimensional study of the rocking response of cylindrical casks and rectangular storage modules using nonlinear time history analysis (NUREG/CR-6865, Sandia 2005) is reported. This will serve as an example to illustrate the variability of the responses in this class of problems and to test the adequacy of the ASCE 4 demand factor. NUREG/CR-6865 presents rocking results for casks and modules analyzed to three different standard spectral shapes, with five unique and spectrum-appropriate (magnitude, distance, tectonic environment) time history record sets fitted to each of the three spectra. The spectra are normalized to peak ground accelerations of 1.0g, and the time histories are scaled to various enveloping acceleration levels. For the cylindrical casks there are five acceleration levels, and for the rectangular casks there are four. Other parameters varied include foundation stiffness and coefficient of friction. Various output parameters are reported with analysis; only peak rotations are considered here.

Because of the relatively coarse binning of the model parameters, results from different friction sets and foundation stiffness sets are assumed here to represent distinct statistical populations. Therefore, the statistical analysis is performed on a series of results sets with only five results in each set. While this probably is an adequate sample size to define a mean, it is not considered adequate to define an 80% confidence interval. However, the large number of sample sets, each representing different permutations of friction and foundation stiffness, taken together are considered to provide a meaningful test of the adequacy of the ASCE 4 demand factor as applied to the rocking problem. Significantly, the results reported in NUREG/CR-6865 show demonstrable rolling on the base by the cylindrical casks. In total, there are nine results sets (permutations of three friction coefficients and three foundation stiffnesses) for each spectral shape, each scaled acceleration level, and each component type. In total 243 sets of five results each were processed and are reported here.

Figure 2(a)-(f) below presents the ratios of the estimated 80^{th} percentile peak response to the mean peak response, calculated assuming lognormal distribution of the five results in each result set. There are two reasons why many of the sets are not shown in the figures. First, for low acceleration levels and particularly for the rectangular components, there was numerically zero variability (sometimes due to zero response), which precludes calculation of an 80^{th} percentile response level. Secondly, in cases of higher responses, some of the cylindrical components overturned, which precludes even calculation of the mean.

As can be seen in Figure 2, it is reasonably conservative to estimate the 80^{th} percentile rocking response by multiplying the mean of five time history responses by

a demand factor of 1.5 in accordance with ASCE 4. These figures the result of additional statistical processing of the results published in NUREG/CR-6865).

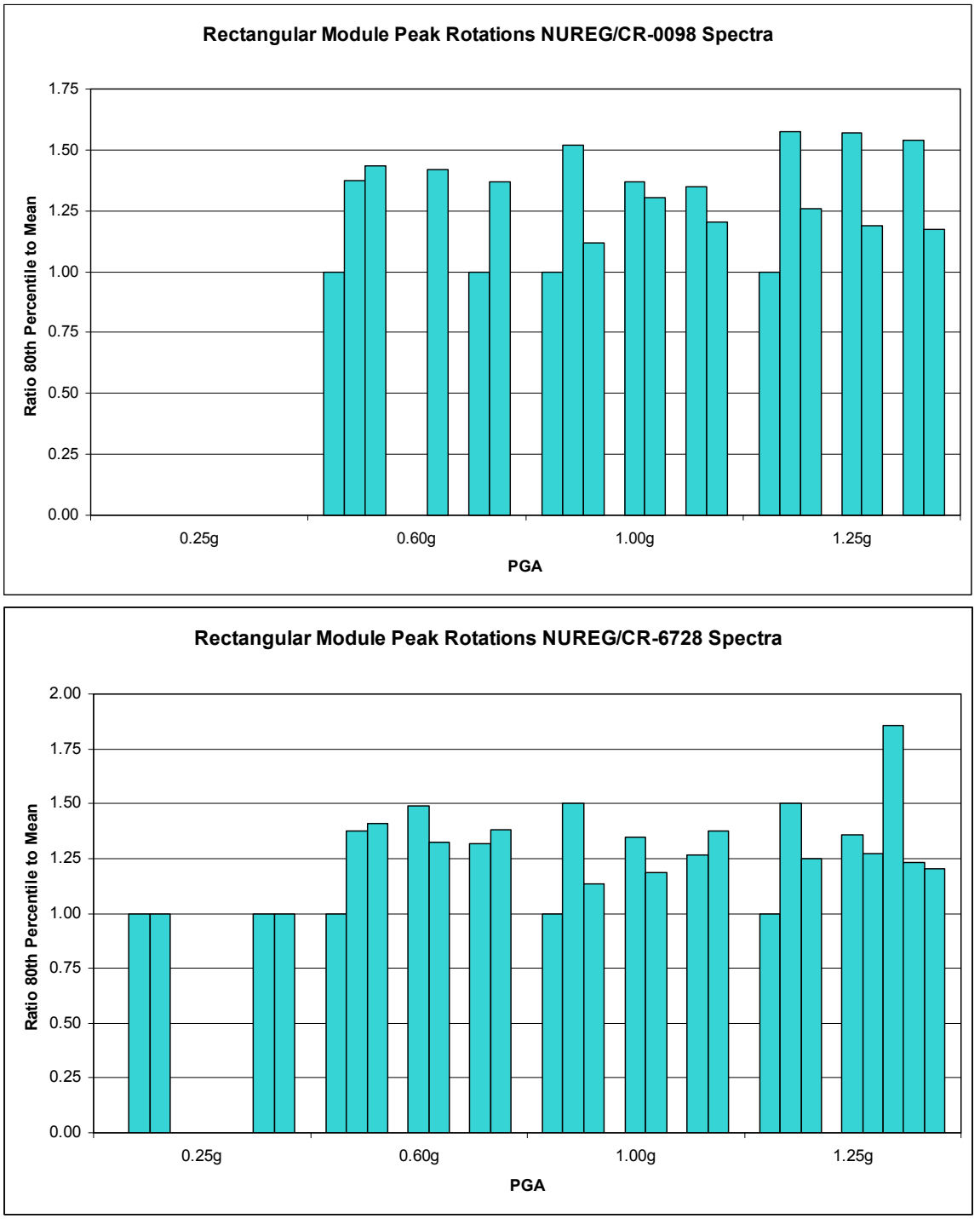
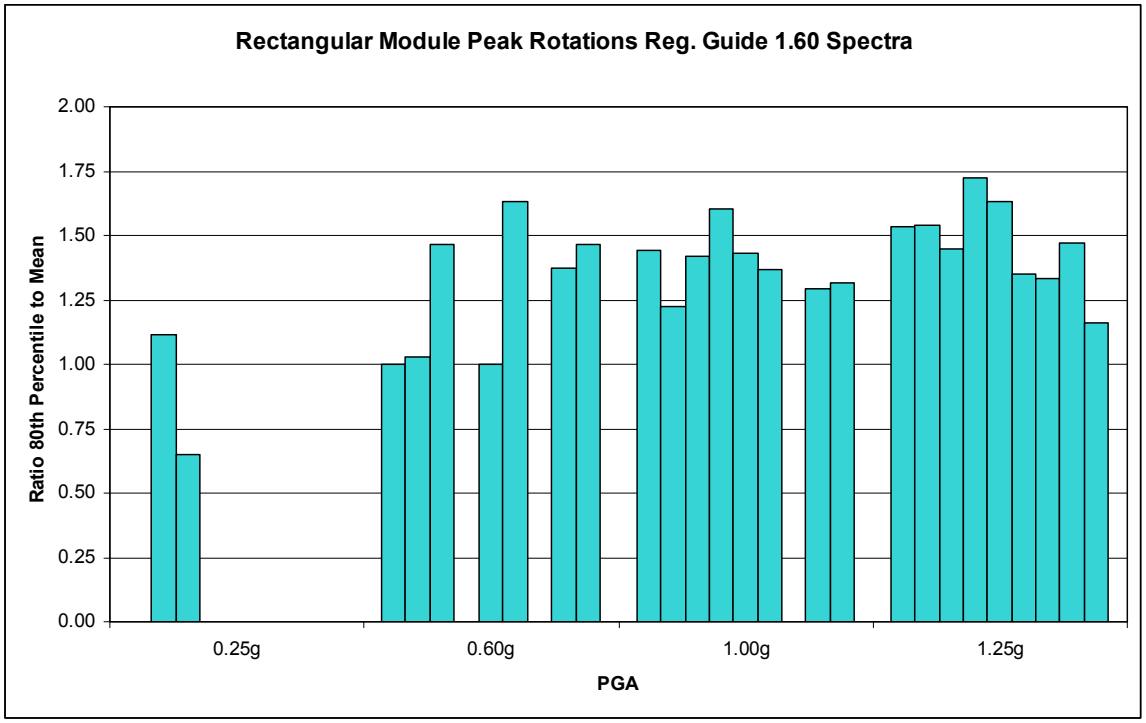


Figure 2(a) and (b): Rocking Response Ratio, $80^{\%}$ NEP to Mean



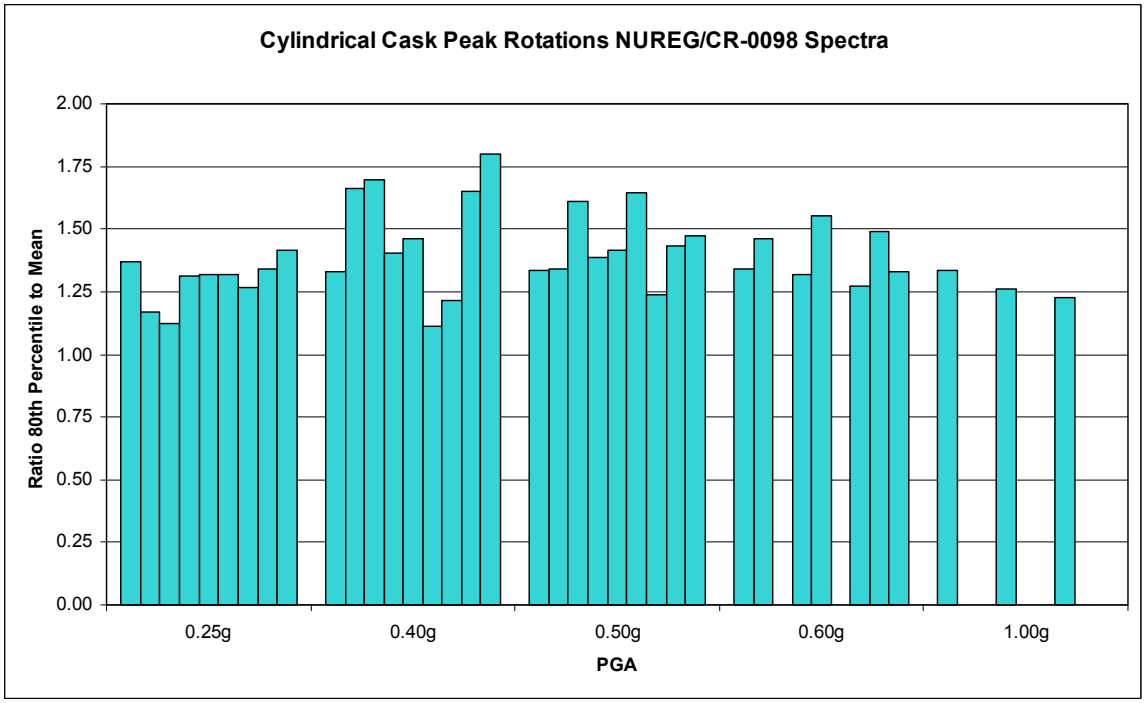
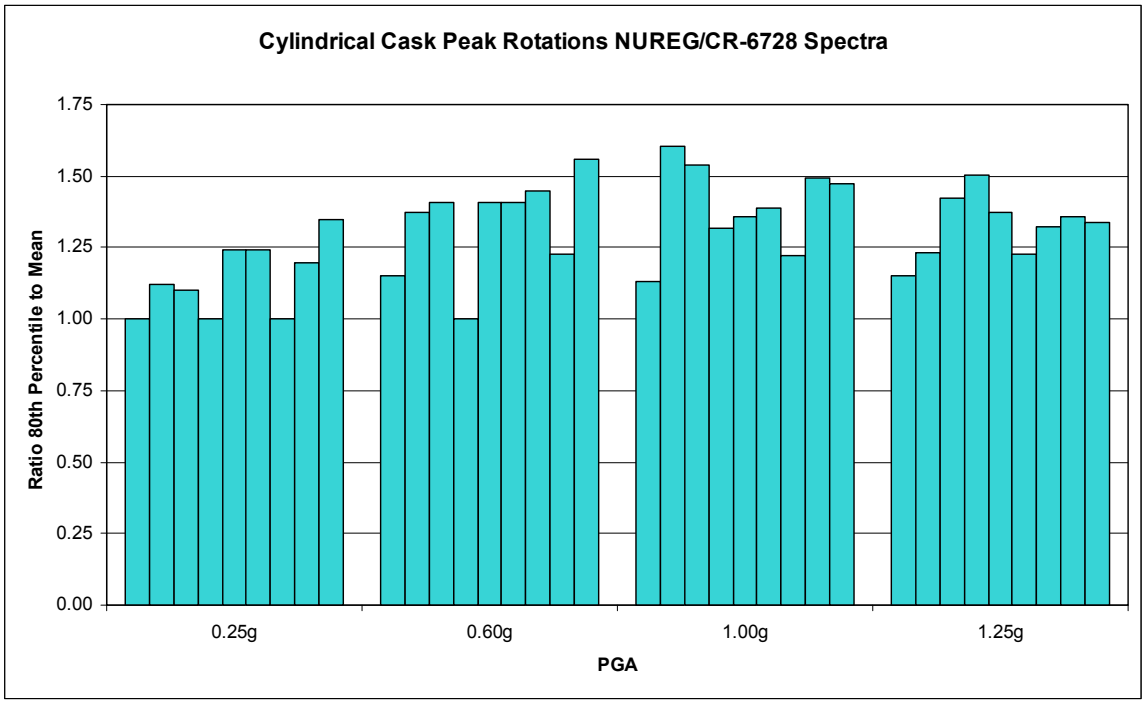


Figure 2(c) and (d): Rocking Response Ratio, 80% NEP to Mean



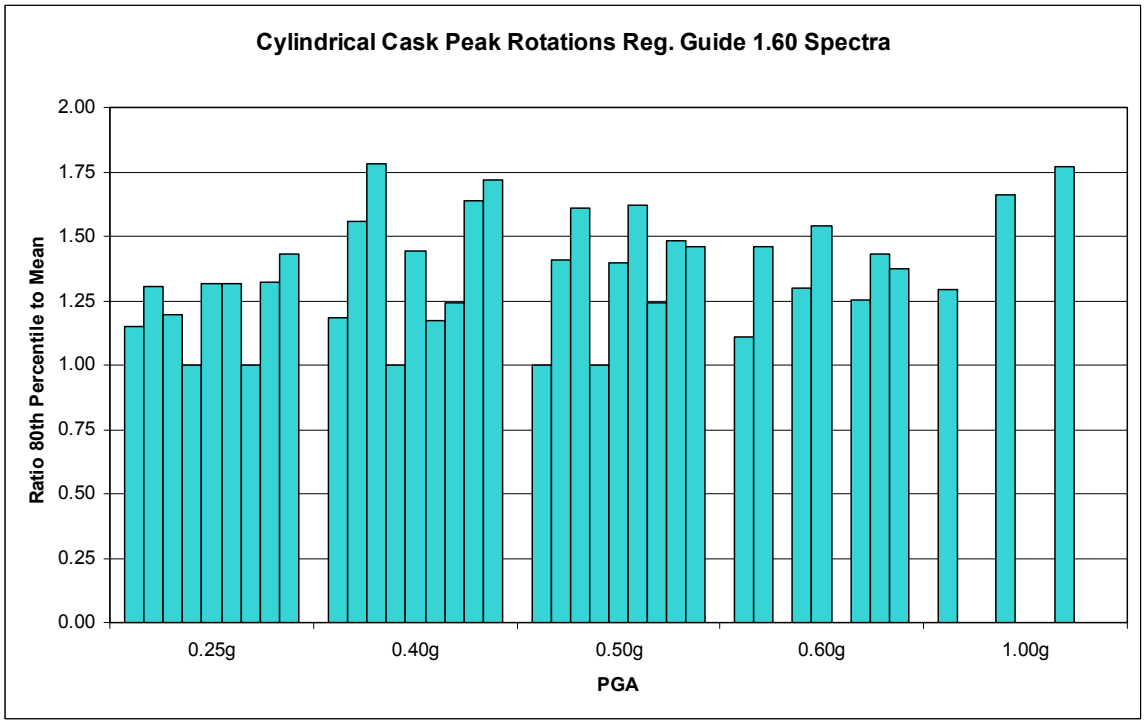


Figure 2(e) and (f): Rocking Response Ratio, $80^{\%}$ NEP to Mean

CONCLUSION

The new addition to ASCE-4 as Section 7.6 provides evolutionary guidance for seismic evaluation of rocking and sliding of unanchored bodies. Following the

provisions of Section 7.6 will produce reasonably conservative estimates of the 80th percentile rocking or sliding demands.

ACKNOWLEDGEMENTS

This manuscript has been authored by Battelle Energy Alliance, LLC under Contract No. DE-AC07-05ID14517 with the U.S. Department of Energy. The United States Government retains and the publisher, by accepting the article for publication, acknowledges that the United States Government retains a nonexclusive, paid-up, irrevocable, world-wide license to publish or reproduce the published form of this manuscript, or allow others to do so, for United States Government purposes.

REFERENCES

American Society of Civil Engineers, ASCE 4-98, *Seismic Analysis of Safety-Related Nuclear Structures: Standard and Commentary*, 1998.

American Society of Civil Engineers, ASCE 4-Rev 2, *Seismic Analysis of Safety-Related Nuclear Structures: Standard and Commentary*, Pending 2011.

American Society of Civil Engineers, ASCE/SEI 43-05, *Seismic Design Criteria for Structures, Systems and Components in Nuclear Facilities,* 2005.

Aslam, M, Godden, W.G., and Scallse, D.T. "Earthquake Rocking Response of Rigid Bodies," *Journal of Structural Engineering,* 1980.

Blume, J.A., "A reserve energy technique for the earthquake design and rating of structures in the inelastic range." *Proceedings of the Second World Conference on Earthquake Engineering,* Tokyo and Kyoto, Japan, 1061–1083, 1960.

Dejong, M. J., *"Redefining the Vulnerability of Rocking Structures to Horizontal Ground Motion*" c.2009.

Esfandiari S., Wandell, Christopher, "*Comparison of Approximate Methods for Sliding and Rocking Evaluation of Unanchored Platforms*", SMiRT 2009.

Hutchinson, T .R. and S. R. Chaudhuri, *"Simplified Expression for Seismic Fragility Estimation of Sliding-Dominated Equipment and Contents,"* Earthquake Spectra, Volume 22 No. 3, pages 700-732, August 2006.

Sandia National Laboratories, NUREG/CR-6865, *Parametric Evaluation of Seismic Behavior of Freestanding Spent Fuel Dry Cask Storage Systems,* 2005.

Yim, S.C.-S., Chopra, A.K., and Penzien, J. "Rocking response of rigid blocks to earthquakes." *Earthquake Engineering and Structural Dynamics*, Vol. 8, 565–580, 1980.

Applicability of Nonlinear MDOF Modeling for Design

Michael Valley[1]

[1]Consulting Structural Engineer; email: michael@mmvalley.net

ABSTRACT

Codes, standards, and guidelines commonly used in the evaluation and rehabilitation of existing buildings recognize and allow various performance-based engineering analysis methods, but much of their focus is on nonlinear static procedures (NSPs). The NSPs codified in those documents are based on single-degree-of-freedom (SDOF) models, which are easy to understand but may not capture adequately the complex behavior of structures with multiple-degree-of-freedom (MDOF) effects. The NEHRP Consultants Joint Venture has completed a project (ATC-76-6, with results published in NIST GCR 10-917-9) to improve the practical application of NSPs and nonlinear response history analysis (NRHA) to structures with MDOF effects.

The NIST GCR 10-917-9 project report summarizes both recent MDOF modeling research and current structural analysis practice as specified in codes, standards, and guidelines and as implemented by leading practitioners. The work of the project includes synthesis of available research and performance of new problem-focused studies. The primary studies compare results from NSP and NRHA for both detailed structural archetypes and simplified models. Issues addressed in ancillary studies include examination of demand parameter sensitivity to ground motion selection and scaling methods, direct determination of NSP target displacement, and practical implementation of the nonlinear analysis methods. Based on available past research and on the new studies, the project report provides guidance on selection of simple nonlinear analysis methods appropriate for design, on implementation of nonlinear analysis methods, and on incorporating uncertainty in nonlinear dynamic and nonlinear static analysis.

Related to the ATC-76-6 project, this paper provides background, a summary of the work performed, and a summary of key findings and recommendations. Related papers provide more detail of the technical work performed.

BACKGROUND

Prevailing practice for Performance-Based Seismic Design (PBSD) is based largely on products that have been developed under the direction of National Earthquake Hazards Reduction Program (NEHRP) agencies and other key contributors. Many of these documents recognize and allow several different performance-based analytical methods, but much of their focus is on nonlinear static analysis procedures.

Using FEMA 440 as a starting point, the purpose of this project was to improve nonlinear MDOF modeling for structural design practice by providing guidance on: (1) the minimum level of MDOF model sophistication necessary to make performance-based engineering decisions; (2) selection of appropriate nonlinear analysis methods; and (3) possible alternative approaches to analytical modeling.

The scope of the investigative effort included two primary activities. The first was to review current research and practice on nonlinear modeling of multiple-degree-of-freedom effects. The second was to conduct focused analytical studies to fill gaps in available research and synthesize available information. A workshop of invited experts was convened to obtain feedback on preliminary findings and to refine the resulting recommendations.

WORK PERFORMED

Review of Current Structural Analysis Practice

Current structural analysis practice often is based on available codes, standards, and guidelines for performance-based seismic design. The project report includes detailed summaries for the following documents relevant to multiple-degree-of-freedom modeling in current engineering practice: ATC 40, FEMA 351, FEMA 352, ASCE/SEI 31-03, FEMA 440, ASCE/SEI 41-06, FEMA P-440A, FEMA 750, ASCE/SEI 7-10, and PEER/ATC-72-1. Those summaries identify the scope, applicability, direction on modeling, analytical requirements, ground motion characterization, and response quantities or demand parameters addressed in each document.

The approaches employed by individual practitioners can differ from prescribed methods for a variety of reasons, including differences in the focus of their practice, the need to resolve engineering issues not fully addressed in available resources, past experience, familiarity with more recent research, or judgment that the documents are deficient in some way. While most practitioners employ linear static and linear dynamic analysis procedures for nearly all design, evaluation, and rehabilitation projects, some advanced practitioners routinely use nonlinear analysis procedures in their work. To establish the context of the ATC-76-6 project, information was obtained from practicing engineers who routinely perform nonlinear structural analysis using various methods. Their observations are summarized in the project report.

Review of Recent MDOF Modeling Research

The scope of the investigative effort included an extensive review of existing research on MDOF modeling. The purpose of this review was to identify and assemble recent available research that could be used to address the challenges associated with nonlinear MDOF modeling in current engineering practice. Review of available research was focused on identifying possible improvements to nonlinear static analysis procedures and possible methods of performing simplified nonlinear response history analyses and was limited to sources published in 2002 and later.

While there was an extensive volume of research investigating nonlinear MDOF effects, much of it proposing variations, complications, and enhancements to nonlinear static analysis procedures, there had not been a single comprehensive study evaluating different analytical methods and their limitations, considering a broad variety of response quantities, across a broad range of structural systems and configurations, using a consistent suite of ground motion records (or response spectra). Review of available research on nonlinear MDOF effects, led to the following

conclusions that affected the problem-focused and ancillary studies conducted as part of the project:

- No single method has been identified in the literature as being uniformly applicable, consistently accurate, and relatively simple in capturing all nonlinear MDOF response quantities of interest.
- Nonlinear static analysis methods generally are incapable of representing the development of multiple inelastic mechanisms, the variety of modal interactions, and timing that produce maxima in nonlinear response history analyses.
- Of primary importance is whether or not simplified nonlinear static analysis methods can produce good estimates of the central tendency (mean or median) of a variety of response quantities needed for design.
- Investigation of various invariant load patterns, adaptive load patterns, single-mode pushover procedures, and multi-mode pushover procedures may help to define the domain over which pushover procedures can be relied upon in design.
- It is possible that a relatively small set of ground motions could be used to establish relevant response statistics in a design context.
- Inelastic spectral displacement, S_{di}, may be useful as an intensity measure for simplified record selection.

Problem-Focused Analytical Studies

The ATC-76-6 project team conducted new analytical studies to fill gaps in available research and synthesize available information into recommendations for improving nonlinear multiple-degree-of-freedom (MDOF) modeling. This section summarizes the different analysis methods, component modeling techniques, software packages, response quantities of interest, ground motion records, and structural system characteristics that were investigated.

The approach taken in conducting problem-focused analytical studies emphasized practical application. Nonlinear response history analysis, which is the most rigorous analysis method available for prediction of structural response to earthquake ground motion, is used as a benchmark against which the accuracy and complexity of less rigorous methods are measured. Rather than seeking to calibrate and further refine the approximate methods that are available at present, studies were used to assess the accuracy and complexity of those methods as they would be employed in practice.

Nonlinear static analysis methods. Three nonlinear static analysis methods were specifically investigated in the focused analytical studies. The Nonlinear Static Procedure (NSP), defined in ASCE/SEI 41-06, is the basic pushover procedure used in practice. It utilizes the application of a single invariant load pattern to determine structural response. As defined in ASCE/SEI 41-06, the load pattern is based on the first mode shape, and the target displacement is determined using the coefficient method. The Modal Pushover Analysis (MPA) procedure, initially proposed by Chopra and Goel (2001), combines results from multiple pushover analyses generated by

assuming load patterns based on the first mode and one or more higher modes. Although various authors have suggested further adaptations of the MPA method, this project used the approach favored by practitioners of determining all response quantities in a single analysis phase. The Consecutive Modal Pushover (CMP), developed by Poursha et al. (2009), considers up to three modes, applied consecutively in stages in a single pushover analysis after the application of gravity loads. Modal forces applied in each stage have an invariant load pattern. First mode forces are applied until a certain displacement is reached. The analysis then continues with incremental forces applied using a second mode distribution, and then a third mode distribution. The maximum values of response quantities in each pushover analysis are retained. Additional ancillary studies were also conducted using an extension of the CMP procedure, by changing the order in which the modal force patterns were applied, varying the signs used in load application, and computing both enveloped and averaged responses.

Software platforms. Analytical models of MDOF systems were developed using the following software platforms commonly used in research and practice: Drain-2DX, *Static and Dynamic Analysis of Inelastic Plane Structures* (Prakash et al., 1993), OpenSees, *Open System for Earthquake Engineering Simulation* (McKenna, 1997), Perform 3D, *Nonlinear Analysis and Performance Assessment for 3D Structures* (Computers and Structures, Incorporated), and SAP2000, *Integrated Software for Structural Analysis and Design* (Computers and Structures, Incorporated).

Response quantities of interest. The response quantities of interest for engineering design (i.e., demand parameters) investigated in the project are listed below. Story-level demand parameters were emphasized, but since design codes and standards generally focus attention on component-level force and deformation demands, focused studies examined the correlation between component-level demand parameters and story-level demand parameters. In each case comparisons are made between peak values, rather than time-varying values, of the parameters. Primary demand parameters addressed in all of the studies include story drift ratios, story shear forces, and floor overturning moments.

Ground motions. Nonlinear response history analyses were performed using the suite of 44 ground motion records of the far-field record set utilized in FEMA P-695 (FEMA, 2009b). Ground motion records are normalized on the basis of peak ground velocity, as discussed in FEMA P-695, and scaled by scale factors equal to 0.5, 1 and 2. These scale factors correspond to ground motions at a Los Angeles, California site with mean recurrence intervals of approximately 100, 400, and 2475 years, respectively.

Codes, standards, and guidelines governing the application of nonlinear response history analysis prescribe, for example, the use of maximum of three or average of seven ground motions, as single components or in pairs. FEMA P-750 (FEMA, 2009d) states that while such ground motion suites might "provide reasonable estimates of mean response for the individual response parameters", they certainly are not "adequate to give an accurate estimate of the variability." Because focused studies aimed to examine the relative accuracy of different analysis methods in

the context of realistic variations in response, the blind application of such codified rules was considered inadequate, and alternatives were studied. Those alternatives include other intensity measures, scaling methods, and subset selection techniques.

System prototypes. Structural system prototypes were used to test the analytical procedures, model types, demand parameters, and ground motions outlined above. Prototypes for regular structural systems and systems with special characteristics were developed. The regular structural system prototypes investigated are steel moment frames, reinforced concrete moment frames, and reinforced concrete shear walls. Individual prototypes were selected based on several criteria: (1) structure types that are commonly encountered in practice; (2) structures for which nonlinear static procedures are expected to produce accurate results and some for which they are not; and (3) structures from previous studies funded by FEMA and NIST to reduce modeling effort. Additional prototypes with special structural characteristics, including systems with explicitly modeled gravity framing, load-pattern-sensitive story mechanisms, weak-story irregularities, concentrically braced frames, and flexible roof diaphragms, were also investigated. Specific design and modeling information for individual structural system prototypes are provided in the project report.

Tables 1 and 2 summarize the problem-focused studies performed.

Table 1 Structural System Prototypes, Nonlinear Static Analysis Methods, and Software Platforms Used in Focused Analytical Studies

System prototype	Nonlinear Static Analysis Methods				Software Platforms			
	NSP	MPA	CMP	Extended CMP	OpenSees	Drain-2DX	SAP 2000	Perform 3D
2-story SMRF	x				1-bay	3-bay		
4-story SMRF	x	x			1-bay	3-bay		
8-story SMRF	x	x			1-bay	3-bay		
2-story RCMF	x	x	x		x			
4-story RCMF	x	x	x		x			
8-story RCMF	x	x	x		x			
2-story RCSW	x				x			
4-story RCSW	x	x			x			
8-story RCSW	x	x			x			
6-story SMRF	x	x	x	x			x	
3-story SCBF	x	x	x	x				x

Table 2 Structural System Prototypes, Component Models, and Damping Models Used in Focused Analytical Studies

System prototype	Component models		Damping models
2-story SMRF 4-story SMRF 8-story SMRF	Beam: Column: Panel zone:	lumped plasticity flexure lumped plasticity flexure (no axial load dependence) trilinear shear (nondeteriorating)	Rayleigh (proportional to mass and initial stiffness) 2.5% at T_1 and $0.2T_1$
2-story RCMF 4-story RCMF 8-story RCMF	Beam: Column: Joints:	lumped plasticity flexure lumped plasticity flexure shear distortion and bond slip	Rayleigh (proportional to mass and initial stiffness) 5% at T_1 and T_3
2-story RCSW 4-story RCSW 8-story RCSW	Flexure: Shear: 4-story:	fibers translational spring separate models were used with simplified rotational flexure springs and translational shear springs capped at $1.5V_n$ with pinched hysteresis)	Rayleigh (proportional to mass and initial stiffness) 2.5% at T_1 and $0.2T_1$
6-story SMRF	Beam: Column:	lumped plasticity flexure lumped plasticity flexure (no axial load dependence)	Rayleigh (proportional to mass and initial stiffness) 5% at T_1 and T_2
3-story SCBF	Brace: Beam: Grade beam: Column: Foundation: Roof deck:	asymmetric axial (with compression buckling, tension yielding, and cyclic pinching) lumped plasticity flexure with cyclic degradation lumped plasticity flexure with cyclic degradation lumped plasticity flexure with cyclic degradation (and axial load dependence) (undamped) uplift elements to allow rocking shear with strain hardening and cyclic degradation	5% thus: 2% Rayleigh (proportional to mass and initial stiffness) and 3% modal

Ancillary Studies

Ancillary studies were undertaken to expand the coverage provided by the basic systems and to investigate specific issues. The first ancillary study investigated relationships between demand parameter dispersion, ground motion scaling method, and size of ground motion data set, with the goal of finding more economical approaches for nonlinear response history analysis. The second ancillary study tested the practicality of directly determining target displacement for nonlinear static analysis. The third ancillary study (which is included in summary Tables 1 and 2 above), conducted by practicing structural engineers, applied the methods tested in primary studies (with some extensions) to models of special-case buildings encountered in practice using production software in common use among practitioners. The objective of this third study was to test the accuracy of the methods and to identify practical challenges to their implementation.

KEY FINDINGS AND RECOMMENDATIONS

Problem-Focused Analytical Studies

Table 3 summarizes ratios of response quantity estimates to median results from nonlinear response history analysis (NHRA), for each simplified analysis procedure, each demand parameter, and each regular structural system prototype. It permits head-to-head comparison of the methods employed and systems investigated, but obscures potentially meaningful differences in response over height and at various levels of intensity, which can be observed more readily in figures. Ratios less than 1.0 indicate that the nonlinear static analysis underestimates the median nonlinear response history analysis results; ratios greater than 1.0 indicate overestimation. As shown in Figure 1, the response quantity ratios tell only part of the story. Not only are the ratios for peak story drift of the 8-story steel moment frame worse than those for the 4-story structure (as seen in Table 3); for the 8-story structure, the overall deformation pattern is markedly different and the estimated response can fall outside the range of response predicted for all 44 ground motion records considered.

Table 3 Summary Ratios of Response Quantity Estimates to Median NHRA Results

System Prototype	Response Quantity Ratios[1]			
	Displacement	Story Drift	Story Shear	Floor Overturning Moment
Single-Mode Nonlinear Static Analysis				
2-story SMRF		0.9 to 1.1	0.8 to 1.0	0.8 to 1.0
4-story SMRF		0.6 to 1.3	0.3 to 0.9	0.3 to 1.0
8-story SMRF		0.4 to 1.6	0.3 to 1.0	0.3 to 1.1
2-story RCMF	0.9 to 1.1	0.9 to 1.1	0.8 to 1.0	0.8 to 1.0
4-story RCMF	1.0 to 1.2	0.8 to 1.2	0.6 to 1.0	0.6 to 1.0
8-story RCMF	0.9 to 1.5	0.4 to 1.4	0.4 to 1.0	0.4 to 0.9
2-story RCSW		1.2 to 1.6	0.9 to 1.2	0.9 to 1.3
4-story RCSW		1.1 to 1.8	0.8 to 1.3	0.8 to 1.4
4-story RCSW (δ_t – ESDOF)		0.9 to 1.1	0.8 to 1.0	0.8 to 1.1
8-story RCSW		1.3 to 2.5	0.7 to 1.3	0.7 to 1.4
Multi-Mode Nonlinear Static Analysis (Modal Pushover Analysis)				
4-story SMRF		0.7 to 1.1	0.8 to 1.0	0.8 to 1.0
8-story SMRF		0.7 to 1.9	0.7 to 1.2	0.8 to 1.2
2-story RCMF	0.9 to 1.1	0.9 to 1.1	0.8 to 1.0	0.8 to 1.0
4-story RCMF	1.0 to 1.2	0.8 to 1.2	0.8 to 1.0	0.8 to 1.0
8-story RCMF	1.0 to 1.5	0.7 to 1.5	0.8 to 1.1	0.8 to 1.2
4-story RCSW		1.0 to 1.6	1.0 to 1.3	1.0 to 1.8
8-story RCWS		1.0 to 1.4	0.8 to 1.2	0.9 to 1.2

System Prototype	Response Quantity Ratios[1]			
	Displacement	Story Drift	Story Shear	Floor Overturning Moment
Multi-Mode Nonlinear Static Analysis (Consecutive Modal Pushover)				
2-story RCMF	0.9 to 1.1	0.9 to 1.1	0.8 to 1.2	0.8 to 1.2
4-story RCMF	1.0 to 1.2	1.0 to 1.4	0.7 to 1.4	0.7 to 1.4
8-story RCMF	0.9 to 1.5	0.4 to 1.4	0.4 to 1.0	0.4 to 0.9

[1] Values are the minimum and maximum ratios of estimated response quantity to median value from nonlinear response history analysis.

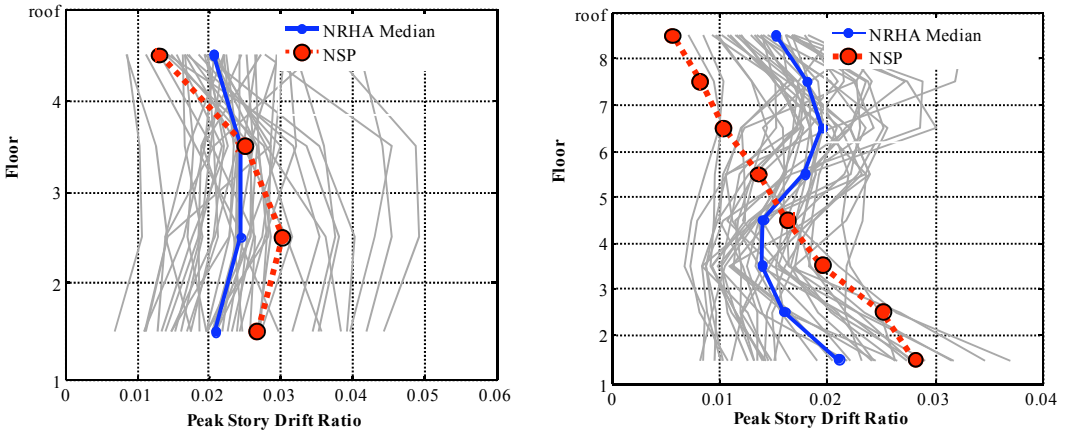


Figure 1 Comparison of nonlinear response history analysis results (median and dispersion) to results from single-mode nonlinear static analysis for 4-story and 8-story steel moment frames (at a scale factor of 2.0)

For the regular structural system prototypes investigated, the following general observations were made:

- For the 2-story systems considered, response quantities from single-mode nonlinear static analysis generally agree well with median results from nonlinear response history analysis. Results for systems with special characteristics, however, show that this observation may not always hold true.
- The accuracy of response quantities from single-mode nonlinear static analysis decreases with increasing height. Response may be underestimated substantially for 4-story steel moment frames and 8-story reinforced concrete moment frames. Underestimation of response occurs mostly in the upper stories and varies significantly between story drift, story shear, and floor overturning moment response parameters.
- In general, estimates of demand parameters for reinforced concrete shear wall structures were better than those for moment frame structures of the same height, provided the target displacement estimate is reasonably accurate.

- Use of multi-mode nonlinear static analysis generally improves the prediction of demand parameters for regular steel and reinforced concrete moment frame systems. In the case of 8-story structures, however, response prediction was still substantially underestimated.
- Use of multi-mode nonlinear static analysis may improve or worsen the prediction of demand parameters for reinforced concrete shear walls, but in most such cases, the response is overestimated.

When judging the adequacy of analytical methods for design decisions, the relevance of the response quantity to design should be considered. For instance, column axial forces due to earthquake loading, which are related to floor overturning moments, may be a more critical design consideration in lower stories than in upper stories. Also, differences in analytically predicted response quantities can indicate changes in performance, but the significance of such differences must be considered in light of the acceptance criteria that define performance. In some cases (e.g., non-ductile components) small changes in a response quantity can lead to large differences in expected performance, but in other cases (e.g., ductile components) performance can be relatively insensitive to changes in a response quantity.

Ancillary Studies

Ground motion subset selection. The approaches studied were successful at producing estimates of median and dispersion values with relatively small subset sizes. Error in the estimates generally decreased as the subset size increased, with relatively good estimates being obtained with 5 records. For estimates of the median using 5 records, mean absolute errors (for story drift, floor acceleration, story shear, and overturning moment) ranged between approximately 3 and 10%, while maximum absolute errors ranged between 20 and 30%. Mean and maximum errors for component-level response quantities (e.g., beam and column plastic rotations) were much larger.

Direct determination of target displacement. In nonlinear static analysis, target displacements have conventionally been determined by equivalent linearization or displacement coefficient approaches, using relationships between the peak displacement response of a yielding SDOF oscillator and that of an elastic counterpart, established on the basis of past computations. An ancillary study investigated the determination of target displacement by two alternative approaches: direct computation by means of nonlinear response history analysis of an equivalent SDOF system, and application of the open source software tool, Static Pushover 2 Incremental Dynamic Analysis, SPO2IDA (Vamvatsikos and Cornell, 2005).

Both approaches were found to produce useful estimates of peak displacement and are recommended as replacements for the displacement coefficient and equivalent linearization approaches. In particular, they are highly recommended in cases where: (1) the target displacement is in the negative tangent stiffness region of the global pushover curve, and (2) the pushover curve is not close to linear before global yielding occurs (e.g., stiffness changes that occur between the pre- and post-cracking regimes of reinforced concrete or masonry structures).

Practical implementation of analysis methods. This ancillary study identified the following challenges to practical implementation of nonlinear response history analysis:

- More information is needed to perform nonlinear response history analysis than is needed for pushover analysis. Appropriate models must be selected and implemented for structural damping and cyclic hysteretic behavior, and proper calibration requires interpretation of experimental test data.
- Ground motion records must be appropriately selected and scaled and applied to the model. At present there is no standard set of procedures for selecting and scaling ground motions.
- A wide variety of structural analysis software is currently in use by practicing engineers, yet only a limited subset of these is capable of nonlinear response history analysis. Software that is capable of advanced analysis is often less capable of more basic structural analysis and/or design tasks, necessitating the development of multiple structural models.
- Since nonlinear response history analysis requires more solution steps than pushover analysis, a nonlinear response history analysis model might need to be smaller and less complex than a pushover analysis model.

Preliminary work to extend the Consecutive Modal Pushover method found that varying the sequence and sign of the modal responses could encompass the various deformation mechanisms found to occur in the corresponding suite of response history analyses. If each CMP analysis is treated as a separate "earthquake," it may be useful to average results for deformations and envelope results for forces, but further investigation is needed to better understand potential limitations in the application of the Extended CMP concept.

Assessment of Nonlinear Analysis Methods

Engineering design decisions are concerned with component forces and deformation demands. Methods for prediction of response, whether local (e.g., component forces and deformations), intermediate (e.g., story drifts and shears), or global (e.g., roof displacement or collapse), depend on the design objective. Good seismic design goes beyond code-based quantitative demand assessment to include good judgment and qualitative evaluation, in which exact numbers are less relevant than understanding of behavior. Simple nonlinear static analysis methods can provide valuable qualitative insight in the evaluation and design process, but care is necessary when they are used alone to establish design quantities.

Nonlinear static procedures. By definition, nonlinear static procedures cannot, except in very simple cases, provide accurate demand predictions for dynamic loading. Many attempts have been reported in the literature to account for these effects, but in most cases the effort needed for implementation defeats the purpose of simplified analysis. Justification for the use of a nonlinear static procedure depends on the procedure employed, the type and configuration of the structural system, the degree of inelastic response expected, and the objectives of the analysis effort.

In general, nonlinear static analysis is always useful and should be part of every evaluation process concerned with inelastic behavior, whether or not the objective is rigorous quantification of demand parameters. Nonlinear static analysis is helpful in many situations, including the following:

- Checking and debugging a nonlinear analysis model, and evaluating the fairness of modeling assumptions
- Augmenting understanding of the yielding mechanisms and deformation demands
- Understanding of behavior and of existence of an adequate load path
- Investigating alternative design parameters and how variations in the component properties can affect inelastic response
- Providing an estimate of the lateral strength of the structure, and estimating structure overstrength in relation to seismic design loads
- Providing information to help establish a force-displacement capacity boundary of a structure in order to estimate global response characteristics such as roof displacement using an equivalent SDOF system
- Providing a global understanding of base shear versus roof displacement response, including estimates of post-yield stiffness and displacement at which the tangent stiffness becomes clearly negative or behavior is close to collapse
- Discovering locations of excessive deformation demands that should become the focus of more detailed study
- Discovering potential problems caused by overloading components with inadequate ductility
- Discovering potential problems caused by story-based strength and stiffness discontinuities, P-Delta effects, and strength deterioration

Nonlinear response history analysis. In practice, appealing features of nonlinear response history analysis include the following:

- More realistic and explicit modeling of response is possible, producing more reliable assessment of seismic performance.
- Possible responses, and their corresponding probabilities, can be determined.
- Generation and application of artificial static load patterns is not required.
- The significance of cyclic loading and associated deterioration can be assessed directly.
- Lateral dynamic instability can be addressed directly.

However, these improvements come at a cost of additional effort and complexity of the procedure. In concept, the major differences associated with modeling for nonlinear response history analysis include the need for a representative set of ground motions, and the need to model more completely the hysteretic behavior of structural components.

It is suggested that demand prediction from nonlinear response history analysis based on the simplest hysteresis diagram is more realistic than demand prediction from a nonlinear static analysis. Modeling of the "backbone curve" (or force-displacement capacity boundary) of individual components is needed one way or another, and the use of a simple component model becomes the core of facilitating the use of nonlinear response history analysis.

Treatment of Variability in Design

Treatment of uncertainty and variability in current code provisions is completely obscured in nonlinear static procedures, and extremely simplistic in nonlinear response history analyses. This neglect of uncertainty may compromise the ability to design for reliable performance.

Even where design decisions are based on central tendencies without explicitly including variability, awareness of the sources of variability (and their corresponding magnitudes) can inform qualitative judgments made in selecting and applying design and analysis methods. For instance, recognizing the likely range of displacement response or the degree to which a small subset of ground motion records reflects the inherent variability of a larger population of representative records may prevent unrealistic confidence in marginal analysis results or may mitigate concern about inaccuracies in simple analysis methods.

Codes, standards, and guidelines that address nonlinear analysis often target median or mean response quantities but require consideration of variability in some manner. Application of probabilistic methods allows direct consideration of such variability. While the characterization of uncertainty is somewhat crude at present, explicit incorporation of rough measures of uncertainty is preferable to ignorance and neglect. The project report recommends an approach to include explicit consideration of variability in nonlinear response history analysis, with possible extensions for nonlinear static analysis.

ACKNOWLEDGEMENT

This paper relies on results obtained under Task Order 6 of the NEHRP Consultants Joint Venture (a partnership of the Applied Technology Council and the Consortium of Universities for Research in Earthquake Engineering), under Contract SB134107CQ0019, Earthquake Structural and Engineering Research, issued by the National Institute of Standards and Technology. The views expressed do not necessarily represent those of the organizations identified above.

REFERENCES

ASCE, 2003, *Seismic Evaluation of Existing Buildings*, ASCE Standard ASCE/SEI 31-03, American Society of Civil Engineers/Structural Engineering Institute, Reston, VA.

ASCE, 2007, *Seismic Rehabilitation of Existing Buildings*, ASCE Standard ASCE/SEI 41-06, American Society of Civil Engineers/Structural Engineering Institute, Reston, VA.

ASCE, 2010, *Minimum Design Loads for Buildings and Other Structures,* ASCE Standard ASCE/SEI 7-10, American Society of Civil Engineers/Structural Engineering Institute, Reston, VA.

ATC, 1996, *Seismic Evaluation and Retrofit of Concrete Buildings*, ATC 40 Report, Volumes 1 and 2, Applied Technology Council, Redwood City, CA.

Chopra, A.K. and Goel, R.K., 2001, *A Modal Pushover Analysis Procedure to Estimate Seismic Demands for Buildings: Theory and Preliminary Evaluation*, PEER Report 2001/03, Pacific Earthquake Engineering Research Center, University of California, Berkeley.

FEMA, 2000a, *Recommended Seismic Evaluation and Upgrade Criteria for Existing Welded Steel Moment-Frame Buildings,* FEMA 351 Report, prepared by the SAC Joint Venture, for the Federal Emergency Management Agency, Washington, D.C.

FEMA, 2000b, *Recommended Postearthquake Evaluation and Repair Criteria for Welded Steel Moment-Frame Buildings,* FEMA 352 Report, prepared by the SAC Joint Venture, for the Federal Emergency Management Agency, Washington, D.C.

FEMA, 2005, *Improvement of Nonlinear Static Seismic Analysis Procedures*, FEMA 440 Report, prepared by the Applied Technology Council for the Federal Emergency Management Agency, Washington, D.C.

FEMA, 2009a, *Effects of Strength and Stiffness Degradation on Seismic Response,* FEMA P-440A Report, prepared by the Applied Technology Council for the Federal Emergency Management Agency, Washington, D.C.

FEMA, 2009b, *Quantification of Building Seismic Performance Factors,* FEMA P-695 Report, prepared by the Applied Technology Council for the Federal Emergency Management Agency, Washington, D.C.

FEMA, 2009c, *NEHRP Recommended Provisions for Seismic Regulations for New Buildings and Other Structures*, FEMA P-750-1/2009 Edition, Part 1: Provisions, Federal Emergency Management Agency, Washington, D.C.

FEMA, 2009d, *NEHRP Recommended Provisions for Seismic Regulations for New Buildings and Other Structures*, FEMA P-750-1/2009 Edition, Part 2: Commentary, Federal Emergency Management Agency, Washington, D.C.

McKenna, F., 1997, *Object Oriented Finite Element Programming Frameworks for Analysis, Algorithms and Parallel Computing,* Ph.D. Dissertation, University of California, Berkeley.

NIST, 2010a, *Applicability of Nonlinear Multiple-Degree-of-Freedom Modeling for Design*, NIST GCR 10-917-9, prepared by the NEHRP Consultants Joint Venture for the National Institute of Standards and Technology, Gaithersburg, MD.

NIST, 2010b, *Evaluation of the FEMA P-695 Methodology for Quantification of Building Seismic Performance Factors*, GCR 10-917-8, prepared by the NEHRP Consultants Joint Venture for the National Institute of Standards and Technology, Gaithersburg, MD.

NIST, 2010c, *Nonlinear Structural Analysis for Seismic Design: A Guide for Practicing Engineers*, GCR 10-917-5, prepared by the NEHRP Consultants Joint Venture for the National Institute of Standards and Technology, Gaithersburg, MD.

PEER/ATC, 2010, *Modeling and Acceptance Criteria for Seismic Design and Analysis of Tall Buildings*, PEER/ATC-72-1, prepared by the Applied Technology Council in cooperation with the Pacific Earthquake Engineering Research Center, Redwood City, CA.

Poursha, M., Khoshnoudian, F., and Moghadam, A.S., 2009, "A consecutive modal pushover procedure for estimating the seismic demands of tall buildings," *Engineering Structures*, Vol. 31, No.2, pp. 591-599.

Prakash, V., Powell, G.H., and Campbell, S., 1993, "DRAIN-2DX: Basic program description and user guide," Report No. UCB/SEMM-1993/17, University of California, Berkeley.

Vamvatsikos, D. and Cornell C.A., 2005, "Direct estimation of the seismic demand and capacity of MDOF systems through Incremental Dynamic Analysis of an SDOF Approximation," *Journal of Structural Engineering,* Vol. 131, No.4, pp. 589–599.

Seismic Evaluation of Steel Moment Frames and Shear Walls Using Nonlinear Static Analysis Procedures

D. G. Lignos[1], C. Putman[2], F. Zareian[3], and H. Krawinkler[4]

[1]McGill University, Department of Civil Engineering and Applied Mechanics, Room 278C, Montreal, QC H3A 2K6; PH (514) 398-2198; FAX (514) 398-7361; email: dimitrios.lignos@mcgill.ca
[2]Degengolb Engineers; 300 Frank H. Ogawa Plaza, Suite 450, Oakland, CA 94612; PH (510) 250-1242; email: cputman@degenkolb.com
[3]University of California at Irvine, Department of Civil and Environment Engineering EG E4141; CA 92697-2175; PH (949) 824-9866; FAX (949) 824-2117; email: zareian@uci.edu
[4]Stanford University, Department of Civil and Environmental Engineering, Room 231; 473 Via Ortega Stanford, CA, 94305; PH (650) 723-4129; FAX (650) 723-7514; email: krawinkler@stanford.edu

ABSTRACT

This paper discusses the effectiveness of simplified nonlinear static methods for predicting the seismic response of various steel moment resisting frames (MRFs) and shear wall structures. Different nonlinear static analysis procedures are discussed. Results from focused studies of different archetype structural systems are compared with nonlinear response history analysis (NRHA). The main engineering demand parameters considered are story drift ratios, story shear forces and overturning moments. Suggestions are made for improving accuracy and required effort of alternative nonlinear static procedures used to predict the seismic response of steel MRF and shear wall structural systems.

INTRODUCTION

In civil engineering practice it is common to employ nonlinear static analysis procedures (known as pushover analysis) for design, evaluation and rehabilitation of structural systems. The pushover analysis (PA) is a useful analytical tool in order to assess in an approximate manner the inelastic seismic demands of a structural system, such as story drift ratios, story shear force distributions, overstrength and inelastic element deformations. Further, PA can identify regions in which the deformation demands of a structural system are high, and story mechanisms due to strength discontinuities that may not appear in an elastic analysis(Krawinkler and Seneviratna, 1998). Guidance on utilization of nonlinear static analysis procedures has been provided in various engineering documents, such as ATC-40 (ATC, 1996), ASCE/SEI 31-03 (ASCE, 2003), FEMA 440 (FEMA, 2005) and ASCE/SEI 41-06 (ASCE, 2007) and more recently in FEMA P-440A (FEMA, 2009a).

FEMA 440 concluded that current nonlinear static analysis procedures, which are based on single-degree-of-freedom (SDOF) models, are limited in their ability to capture the complex behavior of structures that experience multiple-degree-of-

freedom (MDOF) response, and that improved nonlinear analysis techniques to more reliably address MDOF effects were needed. This paper summarizes part of a study that was initiated by the National Institute of Standards and Technology (NIST) to address this need. Using FEMA 440 as a starting point, the goal is to improve nonlinear MDOF modeling for structural design practice by providing guidance on: (1) the minimum level of MDOF model sophistication necessary to make performance-based engineering decisions and (2) selection of appropriate nonlinear analysis methods.

ARCHETYPE STRUCTURAL SYSTEMS

In order to evaluate important engineering demand parameters (EDPs) from results obtained from "best estimate" nonlinear response history analysis (NRHA), we use 2-dimensional numerical models of 2-, 4- and 8-story special steel moment frames (SSMF) and reinforced concrete shear wall (RCSW) structures. These structural systems are archetypes that were designed and analyzed as part of the ATC-76-1 project concerned with evaluation of the FEMA P-695 (FEMA, 2009b) Methodology for Quantification of Building Seismic Performance Factors. Both the SSMF and RCSW structures were designed for seismic design category D_{max} (S_{DS} = 1.0g and S_{D1} = 0.60g). The EDP values obtained from such NRHA serve as benchmark values for assessing predictions by means of simplified methods. Details regarding the design of these structural systems are summarized in NIST (2010).

Steel Moment Resisting Frames: The structures comprise 3-bay moment resisting frames that serve as the lateral load resisting system of steel buildings. The final report of this project (NIST, 2010) describes the SSMFs in detail. The subset consists of three structures that have been designed based on response spectrum analysis (RSA). In summary, these buildings are,

- 2-story SSMF (Archetype ID 2-D_{max}-RSA)
- 4-story SSMF (Archetype ID 4-D_{max}-RSA)
- 8-story SSMF (Archetype ID 8-D_{max}-RSA)

Reinforced Concrete Shear Walls: The salient features of the subset of RCSWs utilized in this study are summarized below. The subset consists of three structures, designated here as,

- 2-story ATC-76-1 RCSW (Archetype ID 12)
- 4-story ATC-76-1 RCSW (Archetype ID 13)
- 8-story ATC-76-1 RCSW (Archetype ID 14)

Note that the structures have been designed with a low $0.075A_g f_c'$ axial stress level.

NUMERICAL MODELING OF STRUCTURAL SYSTEMS

Steel Moment Resisting Frames: The bare frame structure is analyzed with the latest version of either the Drain-2DX program (Prakash et al., 1993) or the Open System for Earthquake Engineering Simulation (OpenSees) platform

(http://opensees.berkeley.edu, McKenna, 1997, Version 2.1.1), utilizing recently developed component moment-rotation models (Lignos and Krawinkler, 2009, 2011). The models for flexural behavior of steel components, which are identical in the Drain-2DX and OpenSees versions used in this study, are based on the point hinge concept and utilize a backbone, a bilinear hysteretic model, and cyclic deterioration parameters discussed in detail in Lignos and Krawinkler (2009, 2011). The deterioration parameters are based on regression equations derived from experimental results and provide different values for different steel W-sections as a function of geometric section properties and material properties that control deterioration in strength and stiffness due to local and lateral torsional buckling (Lignos and Krawinkler, 2011). This component model is referred to as the "modified IK model," and analysis performed based on this component model is referred to as Analyt.M1. Results obtained with Analyt.M1 account for cyclic deterioration in NRHA but they do not account for cyclic deterioration in a pushover analysis, which is based on the initial backbone curve. An example of global pushover curves for the 4- and 8-story SSMFs is shown in Figure 1 after utilizing the Analyt.M1 component model.

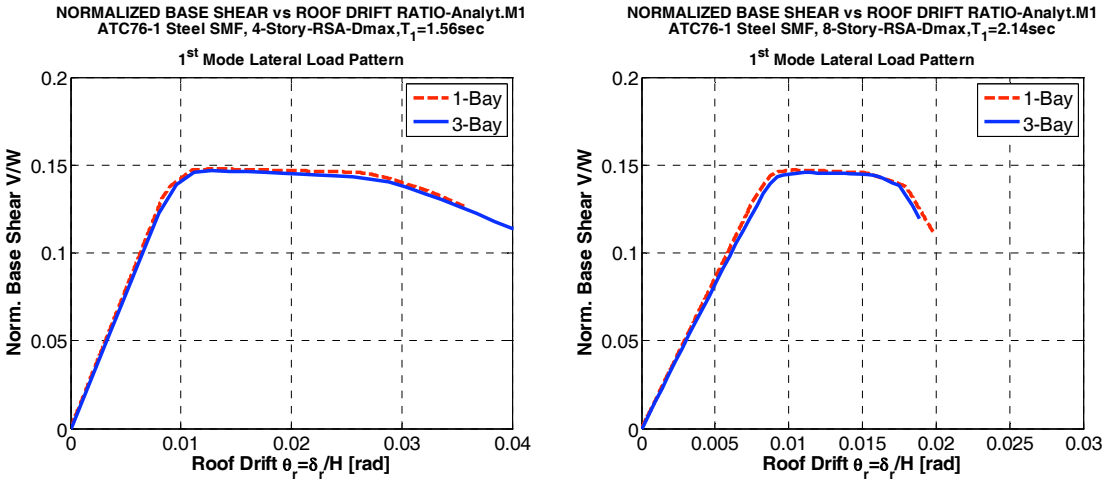


Figure 1. Comparison of global pushover curves ($V_l/W - \theta_r$) of 1- and 3-bay steel SMF analytical models, 4-, and 8-story steel SMFs.

It is often acceptable to represent all moment resisting frames by a single bay frame, resulting in a simplified model. Such a model reduces the computational effort and often facilitates interpretation of global results. But the simplified model may not be adequate to extract local demands such as plastic hinge rotations in individual components and axial and shear forces in columns. Thus, its primary purpose is to assess global and story level EDPs and to detect weaknesses that may become the subject of a more detailed evaluation. The resulting single bay frame is similar to the 'fishbone' model used extensively in Japan (Luco et al., 2003), with the added advantage that overturning moments and column axial deformation effects are represented in the model. Figure 1 shows a comparison of global pushover curves of 1- and 3-bay steel SMF analytical models of the 4-story and 8-story steel SMFs. Details regarding the improved 'fishbone' model are summarized in NIST (2010).

Reinforced Concrete Shear Walls: Displacement-based beam-column elements together with translational shear springs were used to model wall elements for all the shear wall archetypes. The OpenSees C02 model was used for modeling both confined and unconfined concrete. Concrete crushing was taken as the point where the post-peak linear descending branch reaches the residual concrete stress (defined as 20% of the peak confined concrete stress). Confined concrete model parameters were varied over the wall height at locations where transverse reinforcement changed. Concrete tensile strength (f_t), concrete tensile modulus (E_t), and unloading parameter (λ), which defines the unloading slope in terms of the initial concrete modulus (unloading slope = λ_{E_0}), were selected based on the information provided by Orakcal et al. (2006). Reinforcement was modeled as a "hysteretic material" in OpenSees. Expected values of yield and ultimate strength of reinforcement were taken as 68 ksi and 100 ksi, respectively. A tensile strain value of 0.05 was selected to correspond to failure associated with rebar buckling and subsequently rebar fracture. After reaching a strain of 0.05, the stress capacity of the reinforcing bar drops to near zero. Flexural behavior was modeled by 6"x6" fiber elements. Shear behavior was modeled by a translational shear spring. Such a spring was inserted in every story. The properties of the shear spring were based on the NIST (2010) study.

NONLINEAR STATIC PROCEDURES

Given a prescribed lateral load pattern, there are different options for modeling a structure for pushover analysis and for selecting the method for target displacement prediction. In general, the latter is based on predicting the displacement demand for an equivalent single-degree-of-freedom (SDOF) system that represents the first mode characteristics of the multi-degree-of-freedom (MDOF) structure and mapping this demand back to the global pushover curve to find the point at which the structure should be evaluated (sometimes referred to as performance point). In the ASCE/SEI 41-06 coefficient method (ASCE, 2007) this process is greatly simplified and the equivalent SDOF system does not become an explicit part of the target displacement estimation. Figures 2 and 3 show an example of the global pushover analysis of a 2-story SSMF and 4-story RCSW structure, respectively, together with an equivalent single degree of freedom system.

Pushover Analysis Options for SSMFs: The following two options are explored for models of structural components, which then are assembled in the OpenSees analysis platform:

- **ASCE41:** ASCE/SEI 41-06 component models are used, but assuming a post-capping stiffness obtained by linearly connecting peak point C and point E of the generic ASCE/SEI 41-06 model. This modification is made in order to avoid

numerical analysis stability problems and to conform better to data and analysis models developed over the last decade.

- **Analyt.M1:** Modified IK component model with monotonic backbone curve is used, i.e., ATC-72-1 analysis option 1 (PEER/ATC, 2010); cyclic deterioration is not reflected in pushover analysis.

Pushover Analysis Options for Reinforced Concrete Shear Walls: In this study the following options are explored for models of structural components, which then are assembled in the OpenSees analysis platform:

- **ASCE41:** ASCE/SEI 41-06 component models are used, but assuming a post-capping stiffness obtained by linearly connecting peak point C and point E of the generic ASCE/SEI 41-06 model.
- **FM:** Fiber model described in NIST (2010) is utilized to represent flexural behavior, and a story shear spring is used to represent shear behavior.

The FM analysis option was executed for all three RCSWs, whereas the ASCE41 option was explored only for the 4-story RCSW.

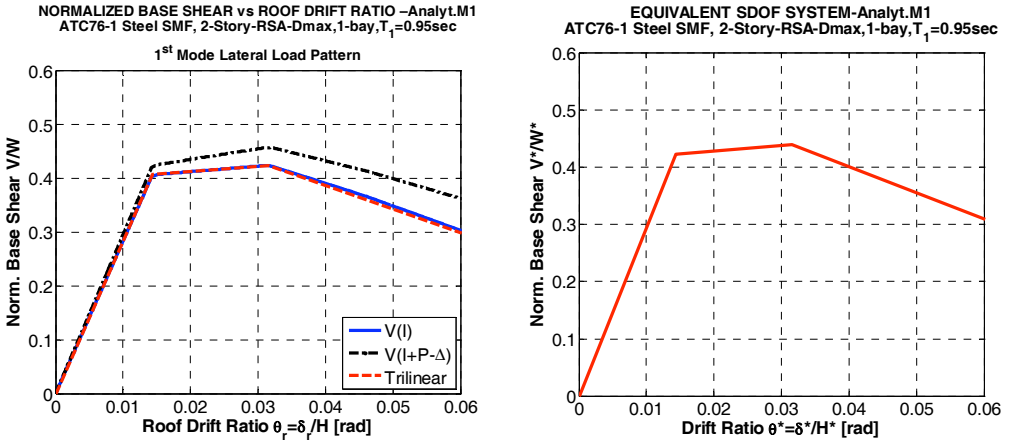


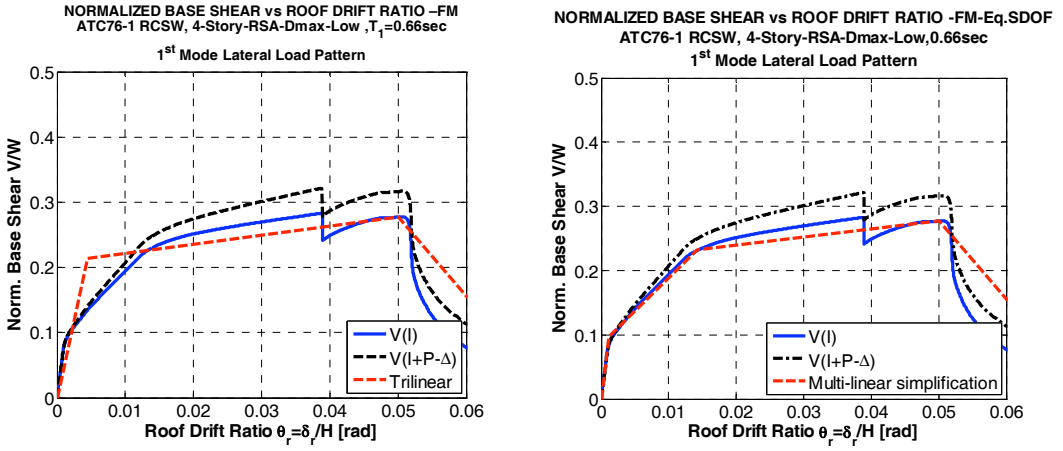
Figure 2. Utilization of global pushover of 2-story SSMF to develop and equivalent SDOF system

Target Displacement Options for Steel Moment Resisting Frames and Reinforced Concrete Shear Walls

- **ASCE41**: Target displacement obtained from ASCE/SEI 41-06 coefficient method. For a shear wall system the target displacement is obtained with an idealized trilinear force-displacement curve recommended in ASCE 41-06 as shown in Figure 3a. This curve utilizes an effective elastic stiffness obtained by placing a line through the displacement at $0.6V_y$.
- **EqSDOF:** Target displacement based on median displacement obtained from a first mode equivalent SDOF system and NRHA using the 44 ground motions of the FEMA P-695 set and the analysis tool IIIDAP (Lignos, 2009). Equivalent SDOF properties are obtained from the base shear V_I – roof displacement pushover curve (not the $V_{I+P-\square}$ – roof displacement pushover curve), which implies that P-delta effects are accounted for approximately in the development of

the equivalent SDOF system (see Figure 2). In the case of shear wall structures in which the global pushover curve shows a clear kink around cracking, the idealized force-displacement curve is better represented by a multi-linear curve that has at least 4 stiffnesses (pre-cracking, post-cracking, post-yielding, and post-capping) as shown in Figure 3.

It should be noted that the primary focus is on target displacements that correspond to three scale factors (SF) of median ground motion intensity (SF=0.5, 1.0 and 2.0)



(a) (b)

Figure 3. Utilization of global pushover of 4-story RCSW to develop an equivalent SDOF system; (a) ASCE 41 procedure; (b) Eq.SDOF system

Findings for Special Steel Moment Frames: Only a summary of results from all the studies is presented herein due to brevity. For illustration, peak story drift ratios, peak story shear forces and peak floor overturning moments for a scale factor of 2 are compared between NSP and NRHA for the 4- and 8-story SSMFs. A summary of findings for the 2-story frame structure is also included. It should be noted that story shear forces are obtained as the summation of the inertia and P-Delta forces noted as $V_{I+P-\Delta}$. Story shear forces are normalized with respect to the seismic weight W of the frame structure. Similarly, floor overturning moments are based on $V_{I+P-\Delta}$ multiplied by the individual story heights and are normalized with respect to the seismic weight W multiplied by the total height H of the frame structure.

2-story Steel Moment Resisting Frame: In the Analyt.M1 component model the post-yield stiffness is caused by a 10% increase in M_y regardless of the amount of pre-capping plastic hinge rotation capacity.

The ASCE/SEI 41-06 criteria for post-capping behavior result in a steep post-capping tangent stiffness leading to rapid deterioration. This does not correspond to statistical data from component tests on which the Analyt.M1 model is based (Lignos and Krawinkler, 2009, 2011). The ASCE/SEI 41-06 coefficient method pays no attention to the aforementioned differences, i.e., it results in the same target displacement prediction for both the ASCE41 and Analyt.M1 pushovers.

All target displacement predictions are within 10% of the median roof drift obtained from NRHA. NSP results compare well with NRHA results, except for the story drift predictions for SF = 2.0 based on the ASCE/SEI 41-06 pushover. The reason is the negative tangent stiffness in the post-yield range of the ASCE41 pushover.

4- and 8-story Steel Moment Resisting Frames: In theses structures the ASCE/SEI 41-06 pushover underestimates post-yield strength and deformation capacities of structures compared to the Analyt.M1 model. The latter model is based on expected values of component properties, whereas more conservative (low) values have been selected intentionally in the ASCE/SEI 41-06 modeling criteria.

The use of the low estimate ASCE/SEI 41-06 pushover model together with an equivalent SDOF model for target displacement prediction (ASCE41-EqSDOF) may provide estimates of performance that are lower than NRHA but might be justifiable. For SF = 2.0 the EqSDOF leads to 33 collapses, which are direct consequences of the relatively short yield plateau obtained in the ASCE/SEI 41-06 pushover. For all options, NSP story drift predictions show a significant deviation from median NRHA values (see Figure 4). In the inelastic range (SF = 2.0) drifts in the lower stories are overestimated and drifts in the upper stories are underestimated. This can be seen in Figure 4 that shows a comparison between peak story drift ratios along the height of the 4- and 8-story SSMFS as obtained from NRHA and alternative NSP methods.

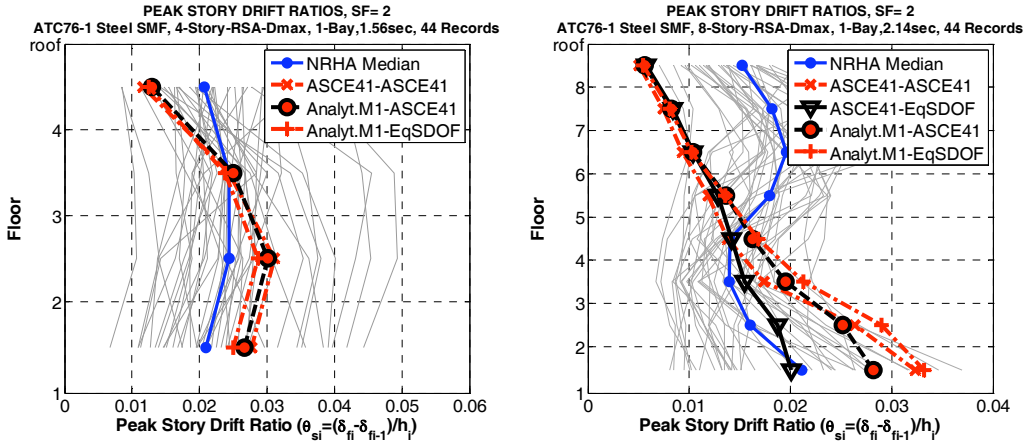


Figure 4. Peak story drift ratios for SF=2 for 4- and 8-story SSMFs

NSP story shear predictions are not good representations of NRHA results in the inelastic range (SF = 2.0). Story shears are consistently underestimated, particularly in the upper stories. But also the maximum NSP base shear, which corresponds to the peak of the $V_{I+P\text{-}delta}$ pushover curves is about 25% below the NRHA median base shear. The reason is dynamic redistribution, which amplifies story shear forces compared to those obtained from a predetermined lateral load pattern. If story shears are an important performance consideration, then the validity of quantitative values obtained from a pushover analysis diminished for the 4- and 8-story steel SMFs (see Figures 5a and 5b). Similar observations apply to floor

overturning moments, which control axial forces in columns of frame structures. In the upper stories the NSP predictions are less than half of those obtained from NRHA. This can be seen from Figures 5c and 5d that show a comparison between the peak floor overturning moments along the height of the 4- and 8-story SSMFs, respectively, as obtained by NRHA and various NSP methods. The situation is better at the base, because maximum shear forces in individual stories occur at different times. The outcome is that even for this relatively low-rise steel SMF structure NSP predictions may provide misleading quantitative information, particularly for force quantities.

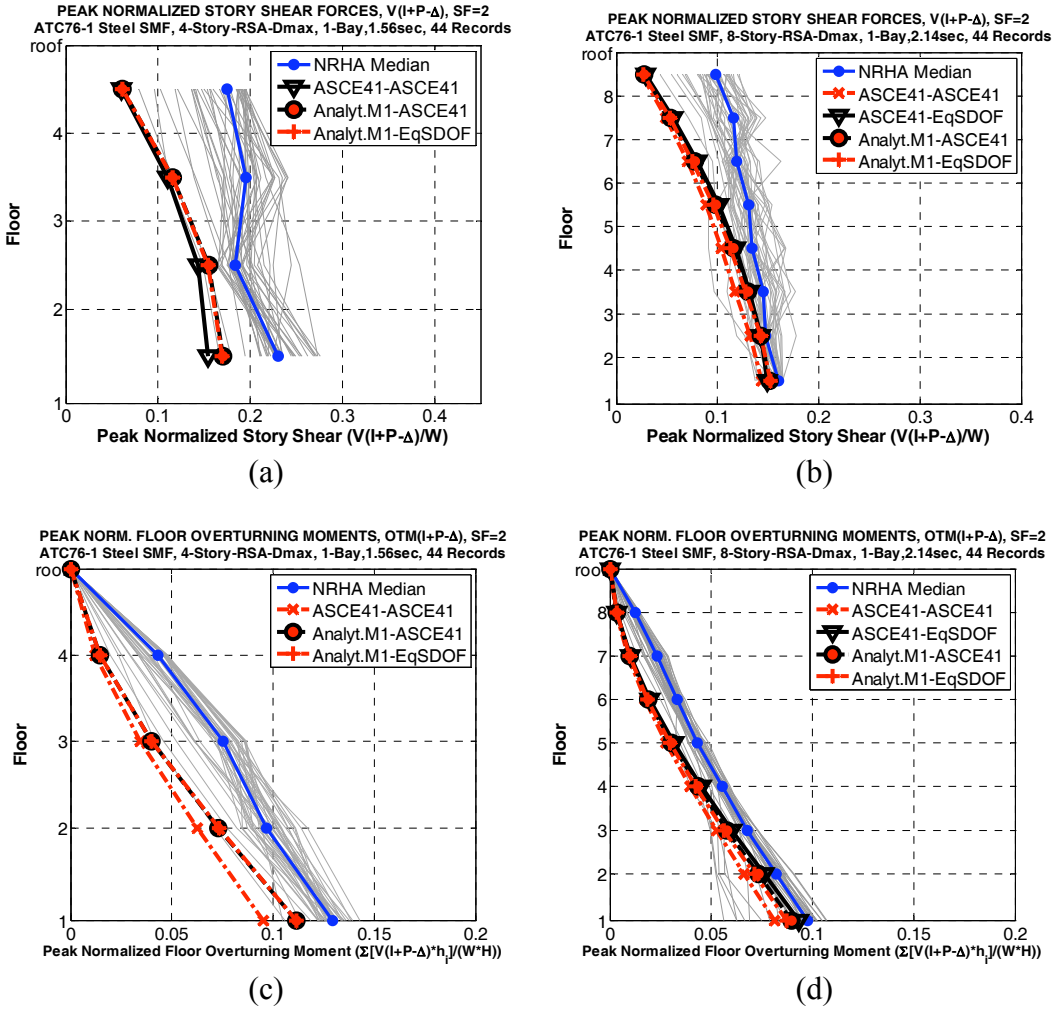


Figure 5. Peak normalized story shear forces and floor overturning moments for the 4- and 8-story SSMFs for SF=2

Findings for Reinforced Concrete Shear Walls: For all RCSW structures (2, 4, and 8 stories) the FM-ASCE41 NSP option (as recommended presently in ASCE/SEI 41-06) leads to rather poor predictions of story drift ratios. An example can be seen from Figure 6 for the 4-story RCSW. Therefore, emphasis was placed on a better representation of the global pushover curve in the equivalent SDOF system in order to obtain a better estimate of the target displacement. For this purpose the global

pushover curve was represented in a multi-linear manner rather than the trilinear manner recommended in ASCE/SEI 41-06. An example of this improved SDOF system can be seen in Figure 3b. The target displacement of the corresponding equivalent SDOF system was predicted with the program IIIDAP (Lignos, 2009), by subjecting the equivalent SDOF system to the set of 44 FEMA P-695 ground motions and computing the median displacement, which was then mapped back to the MDOF domain. This mapped value was used as target displacement to predict the EDPs from the global pushover. The EDP predictions obtained in this manner (denoted as FM-Eq.SDOF) show a large improvement over the predictions obtained from use of the trilinear ASCE/SEI 41-06 equivalent SDOF system for SF=0.5 and 1.0. Figures 6 and 7 summarize the peak story drift ratios, normalized peak story shear forces and peak normalized overturning moments along the height of the 4-story RCSW structure for the two scale factors of interest.

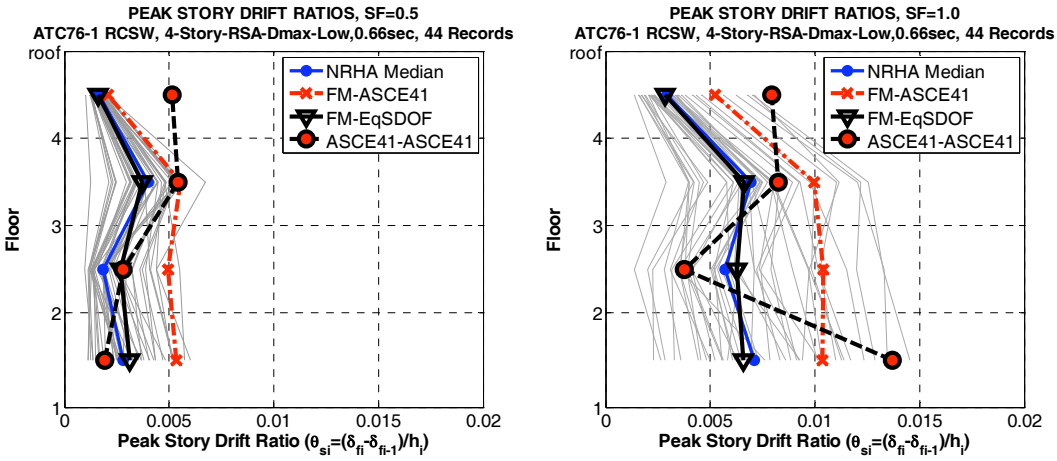


Figure 6. Peak story drift ratios for the 4- story RCSW for SF=0.5 and 1.0

As an alternative, EDP predictions for the 4-story RCSW were also obtained from using ASCE/SEI 41-06 component models to perform the pushover analysis together with the ASCE/SEI 41-06 target displacement procedure (ASCE41-ASCE41 option). The challenge here was to determine moment and shear force strength properties based on ASCE/SEI 41-06 recommendations. The values for bending strength obtained from the FM model and computed from ACI criteria together with ASCE/SEI 41-06 criteria for expected material properties differ by a significant amount. Due to brevity, details about this model can be found in NIST (2010) report.

The estimated strength values (M_c) are significantly larger than would be calculated from basic engineering models and using the reinforcement layout provided in the NIST (2010) report. The FM peak moment value M_c can be obtained only with a much larger axial force that was used in design of this structure. The bending capacity of the wall is very sensitive to the axial force in the wall. A small difference in axial force changes the bending capacity by a large amount, and consequently the failure mode in the wall may change from bending to shear or vice versa. Nonlinear dynamic response in a wall that deforms primarily in shear may be very different from that deforming primarily in bending. This is the reason for the large differences between NSP predictions (ASCE41-ASCE41) compared to those

obtained from FM-ASCE41 and FM-Eq.SDOF in story drift ratios (see Figure 6) and peak story shear forces and overturning moments (see Figure 7). ASCE41-ASCE41 predictions were possible only for SF = 0.5 and 1.0, because for larger ground motion scale factors the predicted roof drift exceeded the deformation capacity indicated by the ASCE/SEI 41-06 pushover.

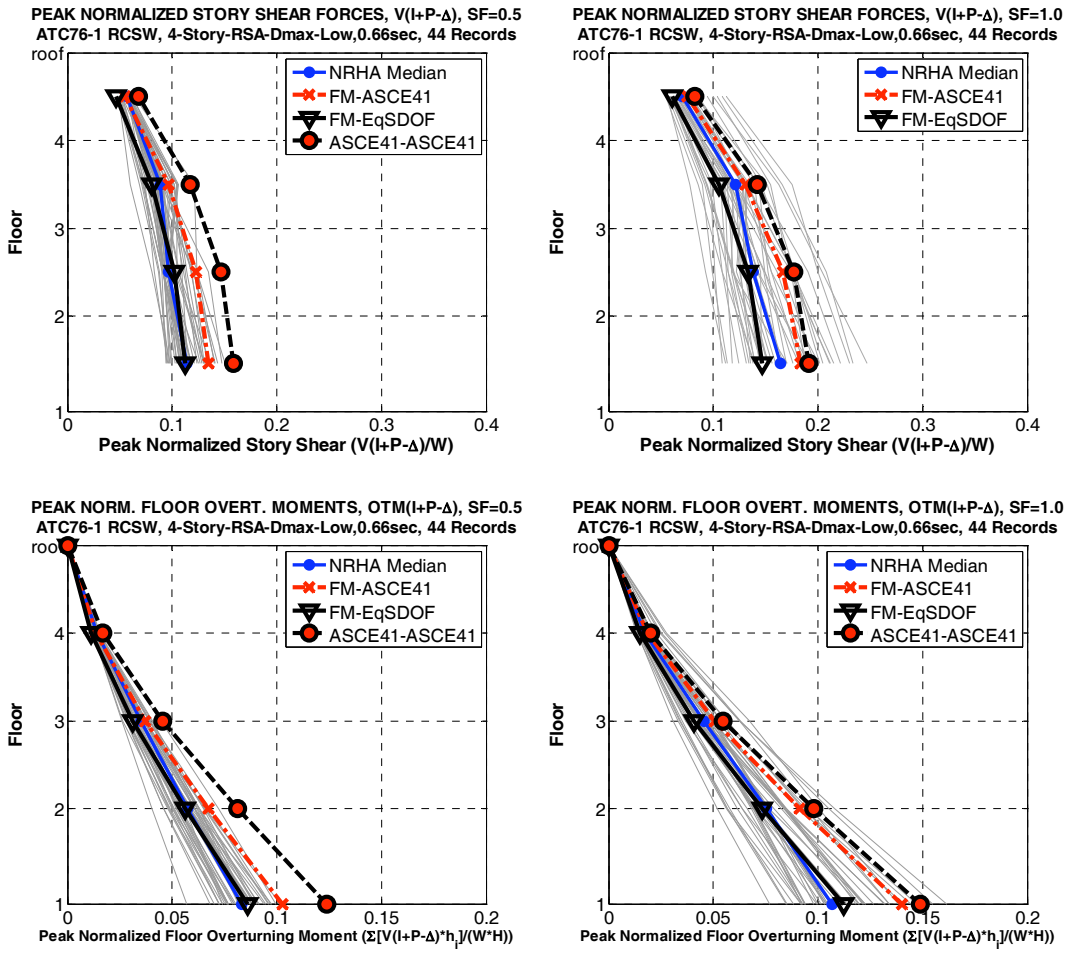


Figure 7. NSP to NRHA comparison, 4-story ATC-76-1 RCSW, three different NSP options, SF = 0.5 and 1.0.

The upshot is that there is a large discrepancy between EDP predictions obtained from a fiber model pushover analysis and an ASCE/SEI 41-06 pushover analysis. This study can only point out this discrepancy but cannot attempt to solve it. The discrepancy is evident in the NSP predictions. The ASCE41 pushover predicts unacceptable performance (represented by intolerable roof drift in the ASCE/SEI 41-06 pushover and by collapses in NRHA with the FM model) at ground motion intensities (represented by the scale factor SF) less than one third of that predicted by the FM model. These observations do not imply that the ASCE/SEI 41-06 component models are incorrect; it merely implies that there are huge differences between a pushover curve obtained from ASCE/SEI 41-06 and a pushover curve obtained from the FM model used in the ATC-76-1 study.

Given that the FM model is an appropriate model to predict EDPs by means of NRHA, it is important to note that the FM-Eq.SDOF NSP approach provides a very good match with NRHA median results for all three story EDPs (drift, shear force, and OTM) – up to a ground motion scale factor of 2.0. The improvement is the multi-linear representation of the pushover curve for formation of the equivalent SDOF system, as compared to the FM-ASCE41 approach in which the pushover curve is represented by a trilinear diagram. The latter does not lead to good EDP predictions in most cases.

SUMMARY

This paper summarizes part of a study that was conducted in order to provide guidance on the selection of nonlinear static procedures (NSPs) for steel special moment frame and reinforced concrete shear wall structures. It also summarizes limitations of use for NSPs to predict engineering demand parameters. Rather than developing new, complex NSP methods, improvements on current NSP methods that are utilized in various guideline documents are suggested.

ACKNOWLEDGEMENTS

This paper relies on results obtained under Task Order 6 of the NEHRP Consultants Joint Venture (a partnership of the Applied Technology Council and Consortium of Universities for Research in Earthquake Engineering), under Contract SB134107CQ0019, Earthquake Structural and Engineering Research, issued by the National Institute of Standards and Technology. The views expressed do not necessarily represent those of the organizations identified above.

REFERENCES

ATC (1996). *"Seismic evaluation and retrofit of concrete buildings,"* ATC 40 Report, Volumes 1 and 2, Applied Technology Council, Redwood City, CA.

ASCE (2003). *"Seismic evaluation of existing buildings,"* ASCE Standard ASCE/SEI 31-03, American Society of Civil Engineers/Structural Engineering Institute, Reston, VA.

ASCE (2007). *"Seismic rehabilitation of existing buildings,"* ASCE Standard ASCE/SEI 41-06, American Society of Civil Engineers/Structural Engineering Institute, Reston, VA.

FEMA (2005). *"Improvement of nonlinear static seismic analysis procedures,"* FEMA 440 Report, prepared by the Applied Technology Council for the Federal Emergency Management Agency, Washington, D.C.

FEMA (2009a). *"Effects of strength and stiffness degradation on seismic response,"* FEMA P-440A Report, prepared by the Applied Technology Council for the Federal Emergency Management Agency, Washington, D.C.

FEMA (2009b). *"Quantification of building seismic performance factors,"* FEMA P-695 Report, prepared by the Applied Technology Council for the Federal Emergency Management Agency, Washington, D.C.

Krawinkler, H., Seneviratna, G. D. P. K. (1998). "Prons and cons of a pushover analysis of seismic performance evaluations," *Journal of Engineering Structures*, Vol. 20 (4-6), pp. 452-464.

Lignos, D.G., (2009) "Interactive Interface for Incremental Dynamic Analysis, IIIDAP: Theory and example applications manual, Version 1.1.5," Department of Civil and Environmental Engineering, Stanford University, CA.

Lignos, D.G., and Krawinkler H. (2009). "Sidesway collapse of deteriorating structural systems under seismic excitations," *Report No. TR 172*, John A. Blume Earthquake Engineering Center, Department of Civil Engineering, Stanford University, CA.

Lignos, D.G., and Krawinkler, H. (2011). "Deterioration modeling of steel components in support of collapse prediction of steel moment frames under earthquake loading," *ASCE, Journal of Structural Engineering* (accepted for publication).

Luco, N., Mori, Y., Funahashi, Y., Cornell, A., Nakashima, M. (2003). "Evaluation of predictors of non-linear seismic demands using 'fishbone' models of SMRF buildings," *Earthquake Engineering and Structural Dynamics*, Vol. 32(14) pp. 2267-2288.

McKenna, F. (1997). "Object oriented finite element programming frameworks for analysis, algorithms and parallel computing," *Ph.D. Dissertation*, University of California, Berkeley.

NIST (2010). *"Evaluation of the FEMA P-695 methodology for quantification of building seismic performance factors, GCR 10-917-8,"* prepared by the NEHRP Consultants Joint Venture for the National Institute of Standards and Technology, Gaithersburg, MD.

Orakcal, K., Massone, L. M., Wallace, J. W. (2006). "Analytical modeling of reinforced concrete walls for predicting flexural and coupled-shear-flexural responses," *Report 2006/07*, Pacific Earthquake Engineering Research Center, University of California, Berkeley, 2006.

PEER/ATC (2010). *"Modeling and acceptance criteria for seismic design and analysis of tall buildings,"* PEER/ATC-72-1, prepared by the Applied Technology Council in cooperation with the Pacific Earthquake Engineering Research Center, Redwood City, CA.

Prakash, V., Powell, G.H., and Campbell, S. (1993). "DRAIN-2DX: Basic program description and user guide," *Report No. UCB/SEMM-1993/17*, University of California, Berkeley.

Applicability of Nonlinear Static Procedures to RC Moment-Resisting Frames

Michalis Fragiadakis[1], Dimitrios Vamvatsikos[2], and Mark Aschheim[3]

[1] Post-doctoral Scholar, University of Cyprus, Nicosia, Cyprus, mfrag@mail.ntua.gr;
[2] Lecturer, National Technical University of Athens, Greece, divamva@gmail.com;
[3] Professor, Santa Clara University, Santa Clara, CA, USA, maschheim@scu.edu.

ABSTRACT

The applicability of nonlinear static procedures for estimating seismic demands in a variety of building types was evaluated within the recently concluded ATC-76-6 project. Results are reported herein for several pushover methods applied to three RC moment frame buildings, relative to baseline data provided by nonlinear response history analysis. Response quantities include peak interstory drifts, floor accelerations, story shears, and floor overturning moments. The single-mode pushover methods that were evaluated include the N2 and ASCE 41 coefficient methods. Multi-modal pushover methods include the modal pushover with elastic higher modes, and the consecutive modal pushover. Target displacements were estimated using typical R-C_1-T relationships.

Results indicate that the good performance of the single-mode methods for low-rise buildings rapidly deteriorates as the number of stories increases. Multi-mode techniques generally can extend the range of applicability of static pushover methods, but at the cost of significant additional computation and with uncertainty about the reliability of the results.

INTRODUCTION

Nonlinear Response History Analysis (NRHA) is recognized as the most rigorous method available for the analysis of structures undergoing inelastic response to earthquake excitation, but its use in practice is limited because of doubts regarding the selection and scaling of ground motions, the interpretation of dispersion in the results, the effort required to develop valid models where cyclic degradation is modeled, and the time required for analysis of complex models. In contrast, Nonlinear Static Procedures (NSPs) have been attractive because of their relative simplicity; their use of smoothed design spectra as input (which dispenses with questions about ground motion selection) and their output of point estimates of response quantities. Nevertheless, questions have been raised about their validity, given their inability or limited ability to consider dynamic interaction of the "modes" of response. Recognition of potential limitations was made in ATC-40 (1996) and demonstrated clearly in FEMA 440 (2005). This resulted in the use of single-mode pushovers being removed from the main body of the *NEHRP Provisions and Commentary* and being restricted for the structural design of new buildings to

buildings less than 40 ft. in height in a non-binding Resource Paper in Part 3 of the *Provisions and Commentary* (BSSC 2009). A more precise quantification of the potential and limitations of pushover methods was sought in the ATC 76-6 project.

This project utilized building designs and models developed in the previous ATC projects. Only relatively simple single-mode and multimode pushover methods were considered, because NRHA generally will be preferred over pushover methods that impose complex analysis requirements on the user and those for which analysis results may have poor or uncertain reliability. Since the applicability of the simple pushover methods to one-story buildings that can be modeled using lumped mass as single-degree-of-freedom (SDOF) systems is not in question, one may view the study as evaluating the point at which additional stories cause the pushover methods to introduce unacceptable error. Evaluation of error in any response parameter may be considered relative to the mean and dispersion obtained in the response parameter obtained in NRHAs of the model for a large number of ground motions considered representative of the hazard level of interest.

BUILDINGS AND MODELS

Although a variety of building types were considered within the ATC 76-6 project, only results obtained for three reinforced concrete (RC) moment-resistant frame (MRF) buildings are reported in this paper. The 2-, 4-, and 8-story RCMRF buildings each have three bays and are regular and symmetric. Each was designed according to the 2003 IBC as described in the FEMA P695 (2009) report. Column sizes were determined to satisfy flexural strength requirements at beam-column joints as well as joint shear requirements.

Models of the building frames reported in FEMA P695 were used in the analyses reported herein. Seismic framing was modeled along with a leaning column to represent P-Δ effects, using planar (2D) models containing one-dimensional line-type elements. Gravity loads were considered using a load combination of 1.05(Dead Load) + 0.25(Live Load) for P-Δ effects as well as for determining the flexural strengths of columns; the effect of potential variation of axial load on column strength was not represented. Nonlinear in-cycle degrading response of beams, columns and joints was simulated, e.g., for beam-column plastic hinges as shown in Figure 1. Typical models have an initial elastic branch, a strain hardening branch, and a descending branch that terminates at an ultimate chord rotation equal to 0.1 rad. An initial uncracked stiffness as well as the potential for shear failures were not modeled. Rayleigh damping amounting to 5% of critical damping was assigned to the 1st and the 3rd mode of vibration, at all beams and all columns, but not at the joints. To compensate for the absence of damping in the joints, the stiffness proportional damping coefficients were increased by 10%. First mode periods based on cracked section stiffness were 0.625, 0.855, and 1.80 sec for the 2-, 4-, and 8-story frames, respectively.

GROUND MOTIONS

NRHAs were performed using the suite of 44 far-field ground motion records identified in FEMA P-695 (2009). The records were normalized as discussed in FEMA P-695. In the present study, the amplitudes of these ground motions were

further scaled by scale factors (SF) equal to 0.5, 1 and 2. These scale factors correspond to ground motion at a Los Angeles, California site with mean recurrence intervals of approximately 100, 400, and 2475 years. Figure 2 shows the mean and the median design spectra for a 400-year mean recurrence interval (SF = 1.0).

NONLINEAR STATIC PROCEDURES (NSPs)

Estimates of response parameter values were determined according to the following five analysis procedures:

- *ASCE/SEI 41-06*: Buildings are "pushed" with a first-mode lateral load pattern according to ASCE 41 until the roof reaches a target displacement defined as:

$$d_t = C_0 C_1 C_2 C_3 S_a(T_e) \frac{T_e^2}{4\pi^2} g \quad (1)$$

where S_a is the elastic spectral acceleration value at effective period T_e, C_0 is the modal participation factor, C_1 is obtained with the improved R-C_1-T relationship developed in FEMA 440 (2005):

$$C_1 = 1 + \frac{R-1}{aT_e^2} \quad (2)$$

C_2 is calculated with the formula suggested in ASCE/SEI 41-06:

$$C_2 = 1 + \frac{1}{800}\left(\frac{R-1}{T_e^2}\right)^2 \quad (3)$$

and C_3 is assumed to be equal to 1. In the preceding, R is the strength reduction factor ($R = S_a C_m W / (V_y g) \geq 1$), and C_m is the modal mass participation ratio (M_n^* / W). Site Class B soils were assumed, and therefore $a = 130$ in Equation (2).

- *Eurocode/N2 method:* The N2 method proposed by Fajfar and Fischinger (1988) has been codified in Eurocode 8 (2004). A pushover analysis is done and the resulting capacity curve is idealized using an elasto-perfectly plastic relationship to determine the period T_e of the equivalent SDOF (ESDOF) system. Different expressions are suggested for short and for medium-to-long period ranges; for the latter case d_t^* is equal to the displacement of the corresponding elastic SDOF system, calculated as:

$$d_{et}^* = S_a(T_e)\left[\frac{T_e}{2\pi}\right]^2 \quad (4)$$

where $S_a(T_e)$ is the elastic acceleration response spectrum at the period T_e.

- *Modal Pushover Analysis (MPA)*: This procedure, initially proposed by Chopra and Goel (2002), determines response parameter values for independent modal pushover analyses in the 1st, 2nd, and possibly 3rd elastic modes of vibration. Although subsequently Goel and Chopra (2005) recommended deformations determined by MPA be imposed on the structure in a second pushover analysis phase to determine member forces, the more common practice of determining all

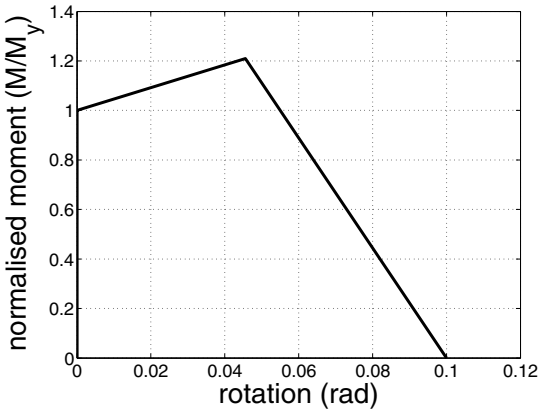


Figure 1. Typical moment-rotation relationship used for the plastic hinge part of component models.

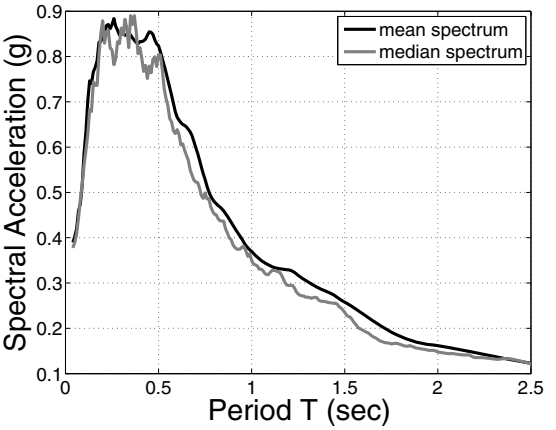


Figure 2. 5%-damped unscaled mean and median response spectra of the 44 ground motion records used in this study.

response quantities by SRSS combination of independent modal analyses (Chopra and Goel (2002)) was followed in this work. Target displacements δ_t for each mode were determined using the ASCE/SEI 41-06 R-C_1-T relationship. Each pushover analysis was done with gravity loads present; the effects of gravity loads, as determined in a separate gravity load analysis without imposed lateral displacements were then subtracted from the modal response quantities, SRSS combinations were taken, and the gravity load effects were then added to the result. Two modes were used for the 2-story RCMRF and three for the 4- and 8-story RCMRFs.

- *Consecutive Modal Pushover (CMP):* This procedure applies lateral loads approximately corresponding to the first, second, and possibly third elastic modes in sequence, all as part of a single pushover analysis. Thus, interaction of multiple modes is considered in a way that may cause different inelastic mechanisms to form. Also, the consecutive application of modal responses may come closer to representing the higher mode responses that take place when the peak displacement response is realized dynamically. Finally, member forces resulting from the analysis are consistent with member capacity limits (e.g. beam shears do not exceed the shears associated with development of a plastic mechanism). As presented by Poursha et al. (2009), the first pushover analysis uses an inverted triangular load pattern for medium-rise buildings and a uniform force distribution for high-rise buildings. A second pushover analysis is done, consisting of a sequence of first and second mode forces. The first mode forces are applied until the roof displacement equals $a_1\delta_t$, where a_1 is the first mode modal mass ratio and δ_t is the target displacement determined for the first mode. Upon reaching $a_1\delta_t$, incremental forces are applied that follow a second mode pattern. Thus, the incremental displacement used for this analysis stage is $(1\text{-}a_1)\delta_t$. A third pushover analysis is required for buildings with periods of 2.2 seconds or higher. The peak value of any demand parameter in each separate pushover analyses is compared to identify the largest (or envelope) value.
- *Modal Response Spectrum Analysis (MRSA):* For buildings responding inelastically whose deformed shapes resemble their elastic mode shapes, perhaps the simplest multimodal approach to estimate deformations is to extrapolate linear

modal response spectrum analysis results into the inelastic regime. In this case, lateral load patterns, matching those used in the MPA procedure, are used in a linear elastic analysis. Target displacements are calculated using the C_1 and C_2 relationships of ASCE/SEI 41-06; the coefficient C_3 was taken equal to 1.0. SRSS combinations of modal demand parameter values are taken to obtain the final response estimate.

RESULTS

Nonlinear Response History Analysis. Figure 3 presents selected results from nonlinear response history analysis. Median results are plotted for different scale factors. Dispersion in response values (e.g. Figure 8) to some degree reflects the method used to scale ground motion records in FEMA P695, which is based on the geomean of peak ground velocities of orthogonal ground motion components. Results for these structures indicate:

- Maximum story drift demand is higher in the lower stories while the minimum values are always at the top story. Story drift tends to concentrate in the lower stories with increasing scale factor. Higher modes appear to have an appreciable effect on story drift and story shears.
- Overturning moments tend to follow the concave pattern associated with first mode or code equivalent lateral force patterns. Dispersion in overturning moments is relatively small, attributable to the contributions of higher mode lateral forces to the overturning moment at any level tending to cancel out. Overturning moments tend to "saturate" as the scale factor increases.
- Story shears in the upper stories are significantly larger than would be expected from first mode or code equivalent lateral force patterns. Base shears developed in the dynamic analyses are larger than the capacities indicated by a first-mode pushover analysis. Story shears tend to "saturate" as the scale factor increases.

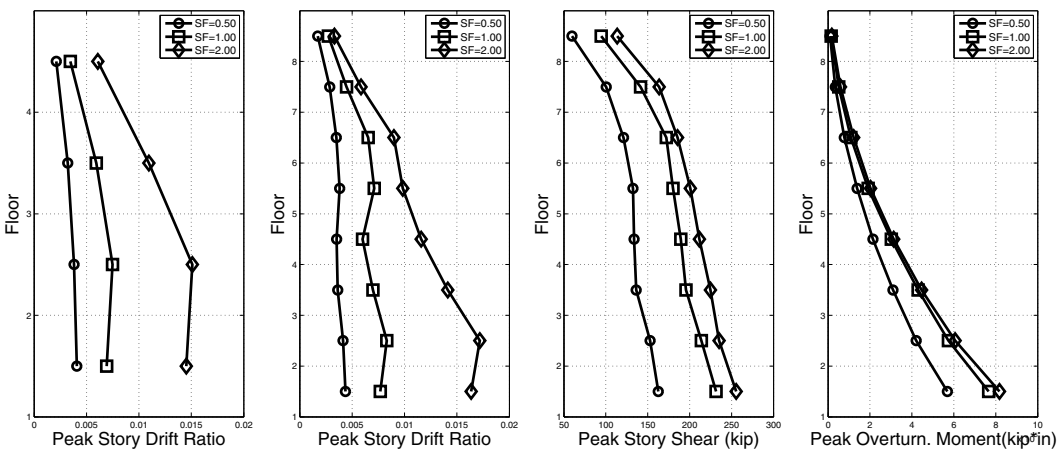


Figure 3. Profiles of median peak response quantities for SF=0.5, 1.0, and 2.0: (a) story drifts for the 4-story RCMRF, and (b) story drifts, (c) story shears, and (d) overturning moments for the 8-story RCMRF.

First Mode Nonlinear Static Analysis. Figure 4 shows the capacity curves obtained in first-mode pushover analyses of the three moment frames and the target displacements determined using the formulas of ASCE-41 and Eurocode 8 for the mean spectra scaled by SF=0.5, 1.0, and 2.0. Both methods produce nearly identical target displacement estimates for the three moment frames; for this reason only ASCE-41 target displacements were used for estimating response quantities in first-mode pushover analyses. Roof displacements at yield are about 0.5 - 0.6% of the height. Target displacements for a scale factor of 0.5 are in the elastic regime, those for the records scaled by 1.0 are nearly elastic, and those for a scale factor of 2.0 cause moderate inelastic response, developing system ductilities of 2-3.

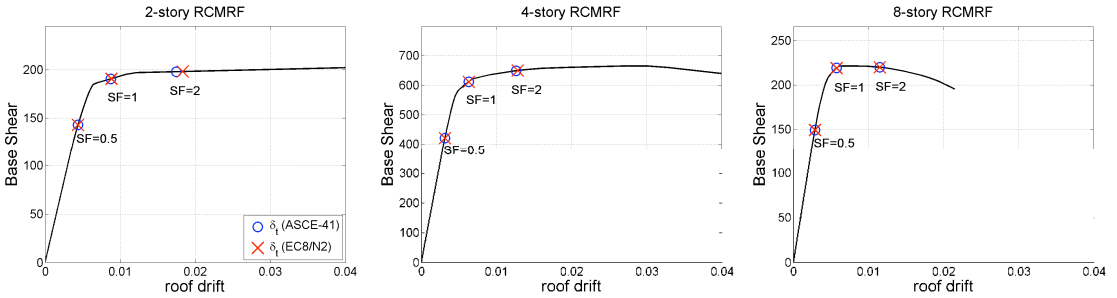
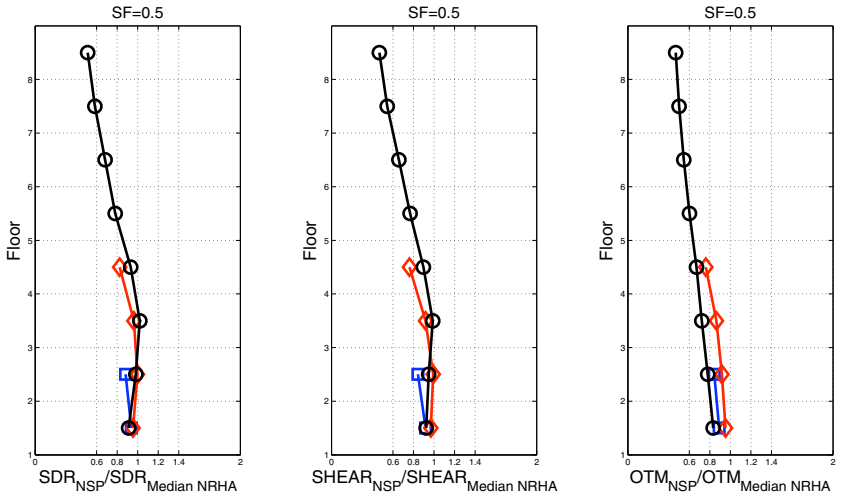


Figure 4. First mode static pushover curves and target displacement estimates for the 2-, 4-, and 8-story reinforced concrete moment frames, for ground motion scale factors of 0.5, 1.0, and 2.0.

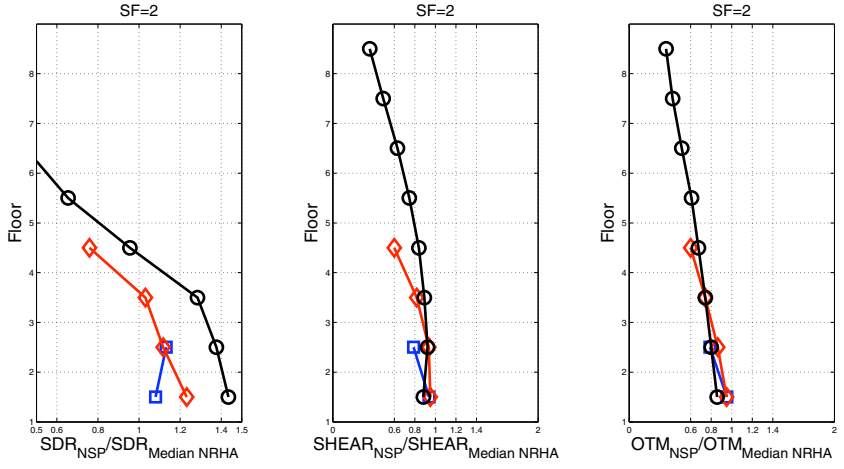
Ratios of demand parameter values determined by first mode pushover analysis and medians of the peak values obtained in NRHA are plotted over the height of each frame in Figure 5 (SF=0.5) and Figure 6 (SF=2.0). Accuracy clearly varies with scale factor (e.g. Figures 5a and 6a), response quantity (Figures 6a and 6b), and number of stories. Accuracy in the estimation of one response quantity does not signify accuracy in the estimation of other response quantities even for the same scale factor and structural model. Reasonable accuracy was obtained for the three demand parameters considered for the 2-story RCMRF, although the error in shear at the upper story slightly exceeded 20%. For the 4-story frame, the accuracy of story drifts, story shears and overturning moments degraded as the scale factor increased from 0.5 to 2.0. Errors in story drift, story shear, and floor overturning moments exceeded 20% at some locations and some scale factors at some locations in the 4-story frame. The degradation in accuracy with increase in scale factor was more pronounced for story drifts. The accuracy of NSP estimates also degraded with increase in scale factor for the 8-story frame, where the error in the top stories of story shears and overturning moments was of the order of 60%. In general, larger errors were encountered in the buildings with more stories.

Modal Pushover Analysis. Figure 7 shows the modal pushover curves for the 2-, 4-, and 8-story reinforced concrete moment frames. Target displacements determined using mean elastic response spectra for scale factors of 0.5, 1.0, and 2.0 are shown. The higher mode pushover curves did not display reversals (e.g. Hernández-Montes et al. 2004). Target displacements were such that elastic response was predicted in the independent 2nd and 3rd mode pushover analyses.



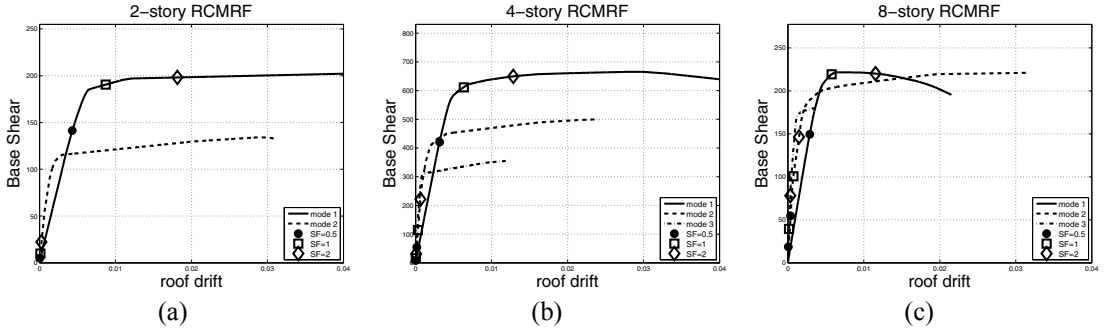
(a) (b) (c)

Figure 5. Ratios of first mode NSP and NRHA response estimates for SF=0.5: (a) peak story drifts, (b) peak story shears, and (c) peak overturning moments.



(a) (b) (c)

Figure 6. Ratios of first mode NSP and NRHA response estimates for SF=2.0: (a) peak story drifts, (b) peak story shears, and (c) peak overturning moments.



(a) (b) (c)

Figure 7. Static pushover curves and target displacement estimates for the 2-, 4-, and 8-story reinforced concrete moment frames, for ground motion scale factors of 0.5, 1.0, and 2.0.

For the 2-story frame, second mode contributions to floor displacements (not shown), story drifts (Figure 8a), and overturning moments (not shown) were negligible; reasonably accurate estimates of these quantities were obtained with the first mode estimates. While story shears were estimated with reasonable accuracy for a scale factor of 0.5 even with single mode pushover analysis (Figure 5b), the inclusion of second mode contributions in the modal pushover analysis procedure, while beneficial, did not sufficiently increase the story shear estimates to result in an accurate estimate of story shear at a scale factor of 2.0 (Figure 8b). This suggests a relatively severe constraint on the reliable application of both single mode and simple multimodal pushover methods.

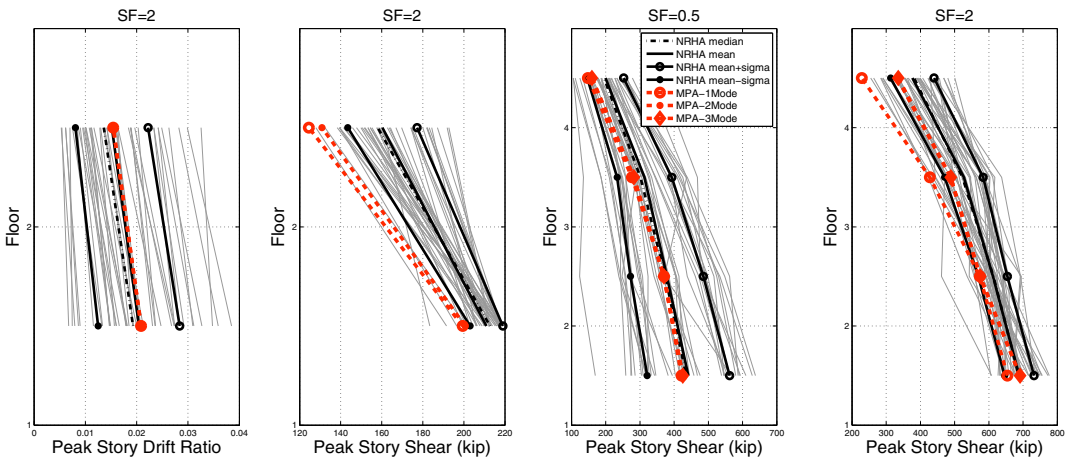


Figure 8. Estimates made with modal pushover analysis and profiles of (a) story drifts and (b) story shears for the 2-story RCMRF at SF=2, and profiles of story shears for the 4-story RCMRF at (c) SF=0.5 and (d) SF=2.

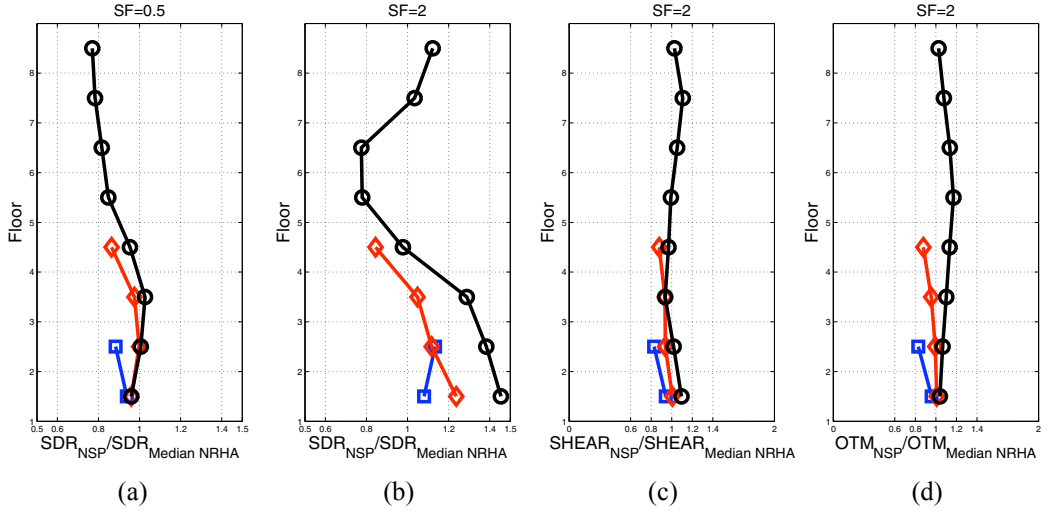


Figure 9. Ratio of modal pushover analysis results and nonlinear response history analysis results for the reinforced concrete moment resisting frames: (a) peak story drift (SF=0.5), (b) peak story drift (SF=2.0), (c) peak story shears (SF=2.0), and (c) peak overturning moments (SF=2.0).

For the 4-story frame, second and third mode contributions to floor displacements (not shown) and story drifts (Figure 9b) were negligible; reasonably accurate estimates of these quantities were obtained with first mode estimates at a scale factor of 0.5 (Figure 5a and Figure 6a). In contrast to the 2-story frame, the accuracy of modal pushover analysis estimates of story shears improved as the scale factor increased from 0.5 to 2.0 (Figure 8c and Figure 8d). While second mode shears had a significant and beneficial effect, third mode story shears, while beneficial, had a relatively small contribution. Relatively accurate estimates of overturning moments were made, and these benefited from inclusion of the second mode contribution (Figure 9d compared with Figure 6c).

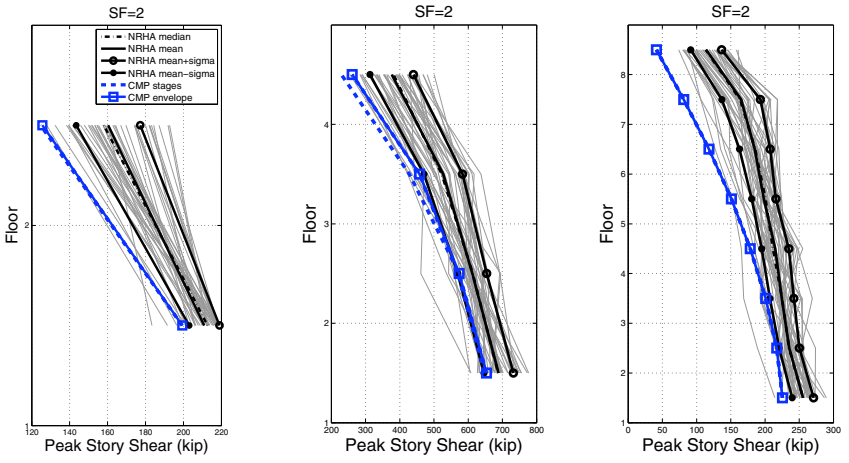
For the 8-story frame, second mode contributions to story drift were not negligible and improved the story drift estimates (Figure 9 compared with Figure 5a and Figure 6a), but accuracy varied with location and scale factor. In particular, the accuracy of story drift estimates improved at the upper stories at a scale factor of 2.0. The accuracy of story shear estimates also varied with location and scale factor. Both second and third mode contributions to story shears were appreciable (Figure 9c compared with Figure 6b); inclusion of higher mode story shears improved story shear estimates at the upper stories. Second mode contributions to overturning moments were not negligible and improved the estimates; overturning moments tended to be underestimated at a scale factor of 0.5 (not shown), and were slightly overestimated at a scale factor of 2.0 (Figure 9d).

Consecutive Modal Pushover. Selected results obtained by application of Consecutive Modal Pushover (CMP) analysis to the three RCMRFs are shown in Figure 10 and Figure 11. Figure 10 shows story shear results with dashed lines for the two CMP stages and with solid lines for their envelope, in addition to the single-record and NRHA curves.

For the 2-story frame, story drifts were estimated with reasonable accuracy (not shown). However, story shears were accurately estimated at a scale factor of 1.0, were significantly overestimated at a scale factor of 0.5, and were significantly underestimated at a scale factor of 2.0. Thus, relatively severe limitations on the reliable applicability of the CMP are apparent.

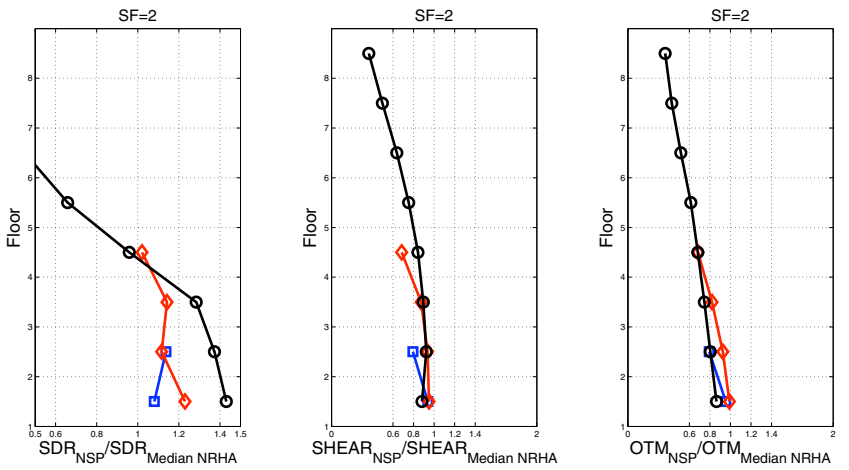
For the 4-story frame, the accuracy of estimates of story drift, story shear, and floor overturning moments varied with location and scale factor. For example, story shears in the upper stories were significantly overestimated at a scale factor of 0.5, and story shears over the height of the building were significantly underestimated at a scale factor of 2.0 (Figure 10b).

For the 8-story frame, peak displacements were overestimated at a scale factor of 2.0, just as occurred with the first mode and multiple mode pushover analyses. As for the 4-story frame, the accuracy of estimates of story drift, story shear, and floor overturning moments varied with location and scale factor.



(a) (b) (c)

Figure 10. Story shear estimates using consecutive modal pushover analysis for the 2-, 4-, and 8-story reinforced concrete moment resisting frame



(a) (b) (c)

Figure 11. Ratio of Consecutive Modal Pushover Analysis results to NRHA results for the reinforced concrete moment resisting frames, for SF=2: (a) peak story drifts, (b) peak story shears, and (c) peak overturning moments.

Elastic Modal Response Spectrum Analysis. Selected results from elastic modal response spectrum analysis are shown in Figure 12 for selected response quantities at scale factors of 0.5 and 2.0. In Figure 12 it is apparent that the accuracy of story drift estimates, while a function of scale factor, is on par with that of the multimodal pushover analysis method (Figure 9a and Figure 9b), while relatively good shear (Figure 12c) and overturning moment (Figure 12d) estimates were obtained under elastic response (SF=0.5) for the 2-, 4-, and 8-story frames. However, even for elastic response (SF=0.5), story shears at the upper stories and overturning moments generally were underestimated for the 4- and 8-story RCMRFs.

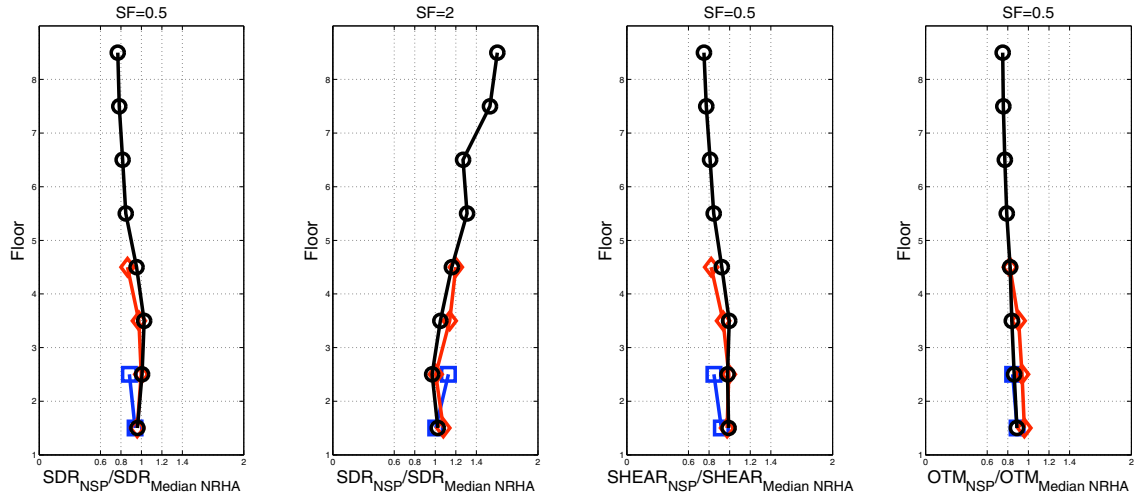


Figure 12. Ratio of elastic Modal Response Spectrum Analysis results to NRHA results for the reinforced concrete moment resisting frames, for SF=0.5: (a) peak story drifts, (b) peak story shears, and (c) peak overturning moments.

CONCLUDING REMARKS

Single-mode pushover analysis is valuable for its ability to characterize inelastic response of a building in the first mode and for illustrating the nature of the inelastic mechanism that develops in first mode response. Pushover methods often will identify, or even exaggerate, the potential for weak story response. However, neglect of higher mode contributions and interaction of "modes" in potentially causing different inelastic mechanisms to develop is a weakness in using NSP methods as a quantitative tool for evaluation of demands in multistory construction.

Accuracy of NSP estimates depends on the response quantity of interest, the intensity of inelastic response (or excitation), as well as the mechanism that develops. Acceptable error relative to median NRHA results depends on the consequences. In non-critical locations a large percentage error may be acceptable while small absolute errors may be critical in other cases. Alternatively, acceptable error might be judged relative to dispersion in NRHA results. In the authors' judgment, without proper consideration of the response dispersion inherent in multi-record NRHA, the limit of reliable applicability of single-mode pushover analysis for local response assessment appears to be about 2 stories for moment-resistant frames, while multimode-pushover analysis appears to be limited to about 4 stories. Although these limits are suggested based on limiting errors relative to median NRHA results, they are not absolute. The development of different mechanisms and issues related to degradation of components and duration of ground motion, not considered in this work, may be important. For the regular frames explored in this study, linear elastic modal response spectrum analysis provided estimates of interstory drift on par with the best multimodal pushover methods. Potential improvements to the consecutive modal pushover analysis method should be explored before fully assessing this method.

With these limitations in mind, appropriate care is advised in all applications of nonlinear static methodologies when used for quantitative, rather than qualitative, estimation of seismic performance.

ACKNOWLEDGMENTS

This paper relies on results obtained under Task Order 6 of the NEHRP Consultants Joint Venture (a partnership of the Applied Technology Council and Consortium of Universities for Research in Earthquake Engineering), under Contract SB134107CQ0019, Earthquake Structural and Engineering Research, issued by the National Institute of Standards and Technology. The views expressed do not necessarily represent those of the organizations identified above.

REFERENCES

Applied Technology Council (ATC), 1996, *Seismic Evaluation and Retrofit of Concrete Buildings*, *Volumes 1 and 2, Report No. ATC-40,* Redwood City, CA.

Applied Technology Council (2005). *Improvement of nonlinear static seismic Analysis procedures,* Rep. No. FEMA-440, Washington, D.C.

American Society of Civil Engineers (2006). *Seismic rehabilitation of existing buildings*, ASCE Standard No. ASCE/SEI 41-06, Reston, 2006.

Building Seismic Safety Council (BSSC), 2009. *NEHRP Recommended Provisions for Seismic Regulations for New Buildings and Other Structures*, Federal Emergency Management Agency, Washington D.C.

CEN (2004) Eurocode 8, Design of structures for earthquake Resistance—Part 1: general rules, seismic actions, and rules for buildings. EN 1998-1:2004. Comité Européen de Normalisation, Brussels.

Chopra, A. K. and Goel, R. K. (2002). A modal pushover analysis procedure for estimating seismic demands for buildings, *Earthquake Engineering & Structural Dynamics*, Vol. 31, no. 3, pp. 561-582.

Fajfar, P. and Fischinger, M. (1988). N2—A Method for Non-Linear Seismic Analysis of Regular Buildings, *Proceedings of 9th World Conference on Earthquake Engineering*, Tokyo-Kyoto, Japan, August 2-9

Federal Emergency Management Agency (FEMA) (2009). FEMA P695 Recommended Methodology for Quantification of Building System Performance and Response Parameters, Project ATC-63, prepared by the Applied Technology Council, Redwood City, CA.

Goel, R. K, and Chopra, A. K. (2005). Extension of Modal Pushover Analysis to Compute Member Forces, *Earthquake Spectra,* Vol. 21, no. 1, pp. 125-139.

Hernández-Montes, E., Kwon, O-S, and Aschheim, M. (2004), "An Energy-Based Formulation for First- and Multiple-Mode Nonlinear Static (Pushover) Analyses, *Journal of Earthquake Engineering*, 8(1):69-88.

International Code Council, 2003, International Building Code, Falls Church, VA.

Poursha, M., Khoshnoudian, F., Moghadam, A.S. (2009). A consecutive modal pushover procedure for estimating the seismic demands of tall buildings, *Engineering Structures*, Vol. 31, no. 2, pp. 591-599.

Prediction of Nonlinear Response - Pushover Analysis versus Simplified Nonlinear Response History Analysis

Helmut Krawinkler[1], Dimitrios G. Lignos[2], and Chris Putman[3]

[1]Dept. of Civil & Environmental Engineering, Stanford University, Stanford, CA 94305; PH (650) 723-4129; FAX (650) 723-7514; e-mail: krawinkler@stanford.edu
[2]McGill University, Department of Civil Engineering and Applied Mechanics, Montreal, QC H3A 2K6; PH (514) 398-2198; FAX (514) 398-7361; email: dimitrios.lignos@mcgill.ca
[3]Degenkolb Engineers, 300 Frank H. Ogawa Plaza, Suite 450, Oakland, CA 94612; e-mail: cputman@degenkolb.com

ABSTRACT

This paper discusses the pros and cons of predicting structural behavior and important engineering demand parameters (EDPs) by means of either nonlinear static pushover (NSP) analysis or nonlinear response history analysis (NRHA) with simple hysteretic models. It will be demonstrated that NRHA comes out as a clear winner if the issue is quantification of EDPs, except for low-rise first mode controlled structures in which torsion is not an important consideration. It also will be demonstrated that NSP analysis has much value in understanding important behavior characteristics that are not being explored in a NRHA in which engineers usually focus on a demand/capacity assessment rather than visualization of response. The conclusion is that both NSP and NRHA have intrinsic value and that it is advisable to employ a combination of both to understand seismic performance and quantify important engineering demand parameters.

INTRODUCTION

Engineering design decisions conventionally are concerned with component forces and story drift. From basic mechanics principles it is clear that component forces depend on component deformations once a structure enters the range of nonlinear behavior. Since component strength decreases when deformations become excessive, recent design provisions for design of new structures and for retrofit of existing structures place limits, either directly or indirectly, on acceptable component deformations. Emerging performance-based design criteria place emphasis also on damage control, which necessitates control of floor accelerations and residual drift, and on explicit consideration of collapse safety, which necessitates the estimation of collapse probability for a given hazard level or for a given life span of a structure.

The upshot is that suitable methods for prediction of demands, whether local (such as component forces and deformations), or intermediate (such as story drifts and shears), or global (such as roof displacement), depend on the design objective. To put the following discussion into perspective, it is emphasized that good seismic design includes more than code based quantitative demand assessment, usually represented by demand/capacity ratios. It includes good judgment and qualitative

evaluation, in which exact numbers are less relevant than understanding of behavior. And here the value of simplified analysis, even if less accurate, increases. This point needs to be considered when judging suitability of various analysis techniques.

The following discussion presents arguments pro and con various analysis techniques, based on the experience acquired in the NIST sponsored ATC 76-6 project (NIST 2010) in which static and dynamic methods for predicting demand parameters are evaluated on 2 to 8 story archetypes of steel and reinforced concrete frame structures and reinforced concrete shear wall structures. The archetypes are described elsewhere in these proceedings (Lignos et al. 2011, Fragiadakis et al. 2011). Most of the archetypes are those designed for evaluation of the FEMA P695 methodology (FEMA 2009) summarized in NIST 2010a.

COMPONENT MODELS AND ANALYSIS PLATFORM

The following component models were utilized in predicting the static and dynamic response of the archetype structures.

ASCE41. This component model is a point hinge model based on the generic ASCE/SEI 41-06 backbone curve (ASCE 2006) but assuming a post-capping stiffness obtained by linearly connecting peak point C and point E. This modification, illustrated in Figure 1, is made in order to avoid numerical instability problems in the analysis, and to better conform to component test data developed over the last decade. This model is used only for pushover analyses.

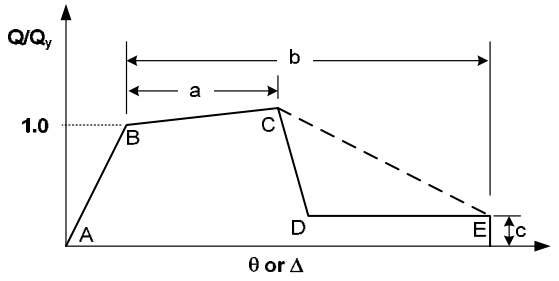


Figure 1. Modified ASCE 41 component model (PEER/ATC 2010).

Monotonic/cyclic deterioration model, Analyt.M1. This component model is a point hinge model that utilizes a modified Ibarra-Krawinkler backbone curve of the type shown in Figure 2 (Ibarra et al. 2005, Lignos and Krawinkler 2009, 2011), a bilinear hysteretic model (for steel frame structures), and cyclic deterioration parameters per analysis option 1 in PEER/ATC-72-1 (PEER/ATC 2010). The deterioration parameters for steel frame structural components are based on regression equations derived from experimental results and provide different values for different steel W-sections as a function of geometric section properties and material properties that control deterioration in strength and stiffness due to local and lateral torsional buckling (Lignos and Krawinkler 2009, 2011). Nonlinear response history analyses (NRHA) utilizing this component model accounts for cyclic deterioration effects explicitly. Nonlinear static analysis utilizing this component model does not account for cyclic deterioration because it is based on the initial

(monotonic) backbone curve. For pushover analysis a modified version of this model (Analyt.M3) was also employed in which the post-yield properties were reduced to account for cyclic deterioration effects in an approximate manner per analysis Option 3 in PEER/ATC-72-1. The pushover results obtained from all three models (ASCE41, Analyt.M1, and Analyt.M3 were very similar until the capping point (point C in Figure 1) was exceeded in several components. Thereafter, the results deviated considerably from each other.

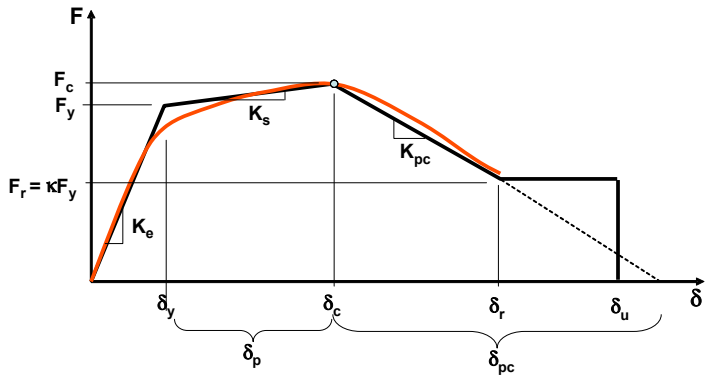


Figure 2. Backbone curve for component model Analyt.M1 (PEER/ATC 2010).

Fiber Model. For shear walls a fiber element model is employed utilized displacement-based formulation together with translational shear springs. Nonlinear degrading properties of concrete and steel materials are explicitly considered. Concrete crushing was taken as the point where the post-peak linear descending branch reaches a residual stress of 20% of the peak confined concrete stress. Confined concrete model parameters were varied over the wall height at locations where transverse reinforcement changed. Reinforcement was modeled as a "hysteretic material" in OpenSees. A tensile strain value of 0.05 was selected to correspond to failure associated with rebar buckling and subsequently rebar fracture. Details of the fiber element are presented in NIST 2010a.

Simplified Spring Model. As alternative to modeling shear wall flexural/axial behavior by means of a fiber model, simplified plastic hinge spring models were used to assist in evaluating results obtained from fiber models. Use of simplified spring models permits explicit modeling of post-yield and post-capping behavior, using modeling parameters similar to those used for the deterioration model shown in Figure 2.

Analysis Platform. Analysis was performed with the latest version of the OpenSees platform (http://opensees.berkeley.edu). The study was concerned only with 2-dimensional modeling of structures. In all analyses Rayleigh damping of 2.5% is assigned at the first mode period T_1 and at $T = 0.2T_1$.

ANALYSIS MODEL SIMPLIFICATIONS

In modeling the steel frame structures, the following simplifications have been explored. A 2-dimensional model of a moment resisting frame structure should represent, at least, the moment-frame(s) as well as all P-Delta effects tributary to the

moment frame(s). If several moment-resisting frames exist, they may be placed in parallel, presuming that the assumption of a rigid diaphragm is reasonable. Thus, a 2-D model consists of moment resisting frames, a P-Delta column, and, if presumed to be important, may incorporate a representation of the gravity system. If the focus is on global and story level engineering demand parameters (EDPs), such as story drifts and shears, it is often acceptable to represent all moment resisting frames by a single bay frame, resulting in the simplified model illustrated in Figure 3. Such a model greatly reduces the computational effort and often facilitates interpretation of global results. But the simplified model may not be adequate to extract local demands such as plastic hinge rotations in individual components and axial and shear forces in columns. Thus, its primary purpose is to assess global and story level EDPs and to detect weaknesses that may become the subject of a more detailed evaluation.

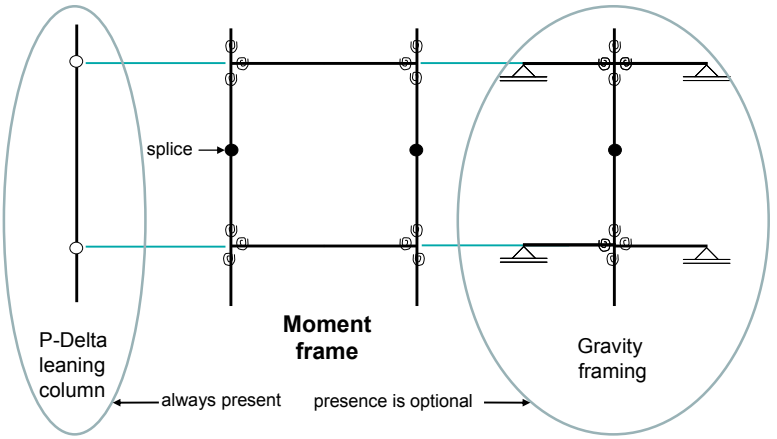


Figure 3. Simplified model of moment-resisting frame structure.

Lumping together multi-bay frames into a single bay frame can be accomplished by setting $\Sigma EI_i/L_i$ and ΣM_p of all beams equal to EI/L and M_p of the single bay beam, respectively, and setting ΣEI_i and ΣM_{pc} of all columns equal to $2EI$ and $2M_{pc}$ of the single bay columns, respectively. For taller frames in which overturning moment and axial deformations in columns are important, these effects can be approximated by setting L of the single bay frame equal to the distance between end columns of the multi-bay frame, and setting the area of the single bay column equal to the area of the end column of the multi-bay frame. This simplification is based on the assumption that overturning effects are resisted mostly by the two end columns. The approximations summarized in this paragraph are reasonable if all bays of the SMF are of about equal width, and become more approximate when spans of the SMF vary considerably.

A fishbone type model can be used to represent the strength and stiffness properties of the gravity framing that is not part of the moment resisting frame, as is shown in the right portion of Figure 3. If the gravity framing is included in the analytical model, then the column of the fishbone can be used also to represent P-Delta effects not directly attributed to the moment resisting frame. Otherwise, the need exists to provide a P-Delta (leaning) column as shown on the left of Figure 3.

The single bay simplification has been tested for the steel SMF structures. Comparisons of results obtained from a 3-bay model and the corresponding single-

bay model (both incorporate a P-Delta column) can be made from Figure 4, which shows peak story drifts obtained from NRHA in which the models are subjected to the FEMA P695 ground motion set scaled by a factor of 2.0 (FEMA 2009).

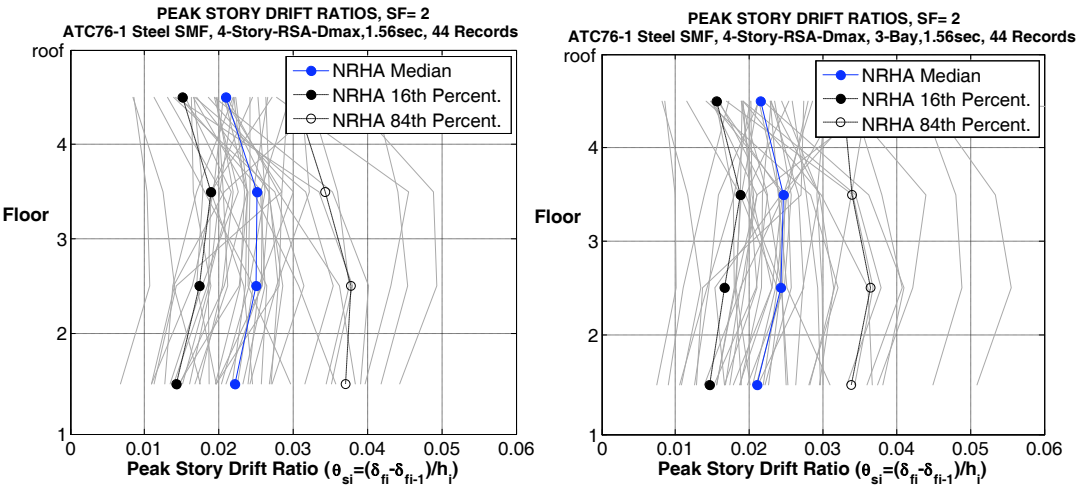


Figure 4. Comparison of peak story drift ratios from NRHA with 44 ground motions, 1- and 3-bay models of 4-story steel SMF

ASSESSMENT OF NONLINEAR STATIC PROCEDURES

By definition, nonlinear static procedures cannot, except in very simple cases, provide accurate demand predictions for dynamic loading. The reasons are higher mode effects and inelastic redistribution that affect modal contributions in every increment of inelastic response. Many attempts have been reported in the literature to account for these effects, but in most cases the effort needed for implementation defeats the purpose of simplified analysis. Justification for the use of a nonlinear static procedure depends on the procedure employed, the type and configuration of the structural system, the degree of inelastic response expected, and the objectives of the analysis effort.

As a preamble, nonlinear static analysis is always useful and should be part of every evaluation process concerned with inelastic behavior, whether or not the objective is rigorous quantification of demand parameters. An incomplete list of arguments for performing nonlinear static analysis is as follows:

- Check and debug a nonlinear analysis model
- Evaluate the fairness of modeling assumptions
- Augment understanding of the yielding mechanisms and deformation demands
- Augment understanding of behavior and of existence of an adequate load path
- Investigate alternative design parameters and how variations in the component properties may affect response
- Augment understanding of behavior close to collapse
- Provide a relatively good estimate of the lateral strength of the structure
- Estimate structure overstrength in relation to seismic design loads

- Provide information that helps to establish a force-capacity boundary of the structure that can be used to estimate global response characteristics (e.g., roof displacement) from an equivalent SDOF system.
- Provide a global picture of the structure's base shear – roof displacement response, including estimates of post-yield stiffness and displacement at which the tangent stiffness becomes clearly negative
- Discover locations of excessive deformation demands that should become the focus of more detailed study
- Discover potential problems caused by overloading components with inadequate ductility
- Discover potential problems caused by story based strength and stiffness discontinuities
- Discover potential problems caused by P-Delta effects and strength deterioration

In practice, the use of nonlinear static analysis methods for quantification of demand parameters (and demand/capacity ratios) is appealing because this type of analysis produces a single, clear result without the need for selection and scaling of ground motion records. However, with those positive features come the following drawbacks:

- The single, clear, static result will deviate from the median result obtained from NRHA with a set of representative ground motions. The amount of deviation depends on the importance of higher mode contributions and inelastic redistribution. Demand parameter values can be significantly under- or over-estimated.
- A single, deterministic answer will not provide information on all mechanisms that potentially may develop when the structure is subjected to a set of ground motions with different frequency characteristics.
- No information is obtained on response uncertainties
- Lateral dynamic instability cannot be addressed directly.

The amount of deviation from median values obtained from nonlinear response history analysis has been the subject of the exploratory studies carried out in the ATC 76-6 project. These studies are not, and cannot be, comprehensive because of the large variability in system configurations and design decisions, which will affect the deviation to various degrees. The following is a compendium of summary observations drawn from these studies. These summary observations are case specific and are intended to aid in the decision process when and to what degree an engineer can rely on quantitative demand parameter predictions obtained from a nonlinear static analysis. The observations are drawn from results of the type shown in Figure 5, which shows comparisons of peak EDPs (engineering demand parameters) obtained from pushover analysis and NRHA. Only one representative example each is shown for steel special moment frames (SMFs) and reinforced concrete shear walls (RCSWs).

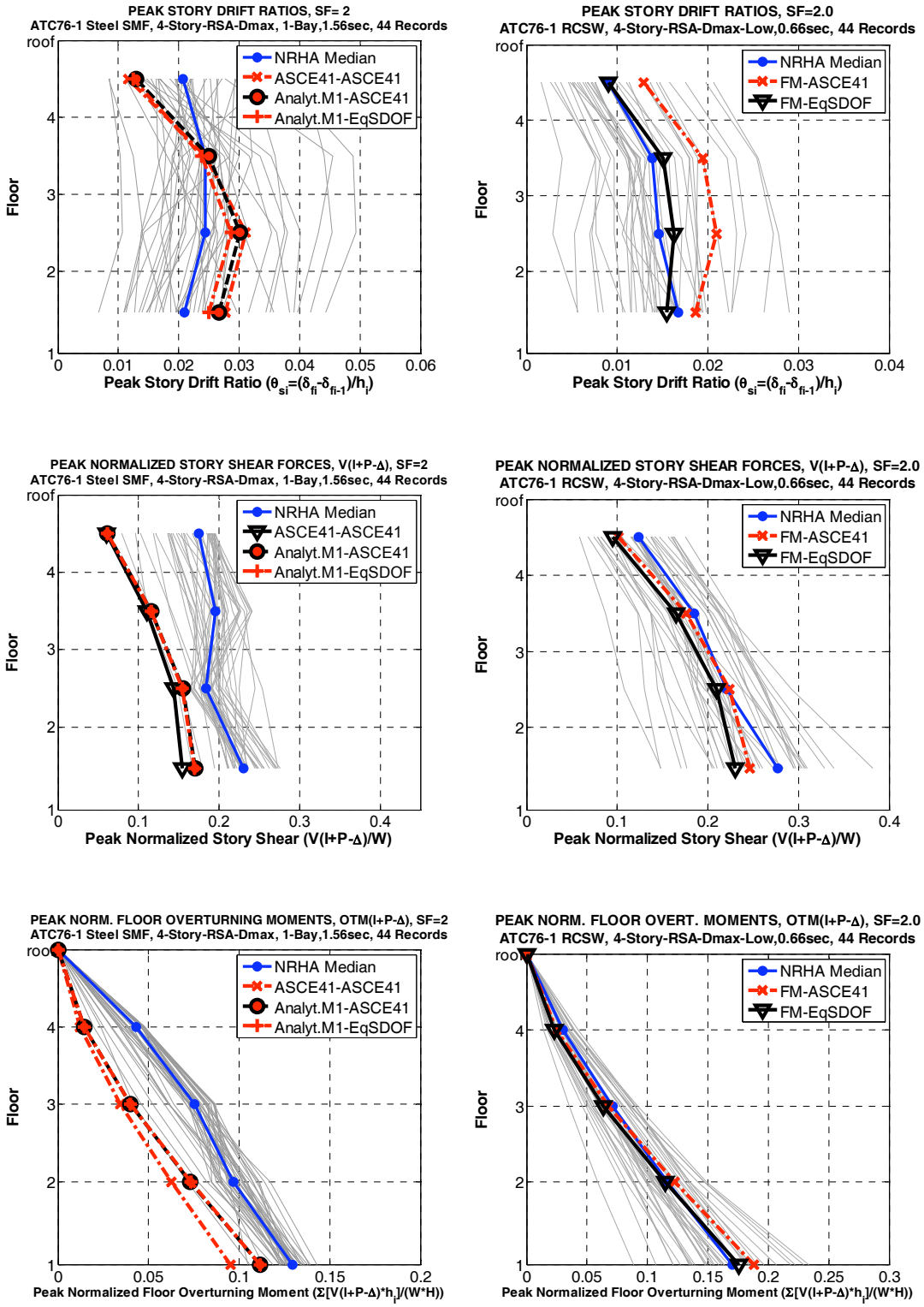


Figure 5. NSP to NRHA comparison of peak story drifts, peak story shears, and peak floor overturning moments; 4-story steel SMF (left) and 4-story RCSW (right); FEMA P695 ground motion set with scale factor of 2.0

First Mode Nonlinear Static Analysis with Invariant Load Pattern

In this procedure a lateral load pattern corresponding to the elastic first mode deflected shape is applied and is incremented to provide a global pushover curve. The target displacement is obtained from the elastic response spectrum under which the response is to be evaluated, using either the ASCE-41 coefficient method or the median displacement obtained from an equivalent SDOF system subjected to a set of ground motions whose spectra represent, in average, the elastic response spectrum. The method should be used with smooth spectra and not with spectra of individual ground motions. The following general observations are made:

- Adequacy of demand predictions from first mode nonlinear static analysis depends on system type and configuration, on the first mode mass participation (related to system type and number of stories), on the extent of inelastic deformations, on the relative spectral accelerations at the modal periods, on the sensitivity of story yield strength to the applied load pattern, on the variation of story strength and stiffness over the height, and on the mechanism controlling inelastic response.
- For the regular 2-story systems considered in this project, response quantities from first mode nonlinear static analysis generally agree well with median results from nonlinear response history analysis.
- The deviation from the median of nonlinear response history analyses increases with increasing height. Response may be underestimated substantially for 4-story steel moment frames and 8-story reinforced concrete moment frames. Underestimation of response occurs mostly in the upper stories and varies significantly between response parameters story drift, story shear, and floor overturning moment. When judging adequacy of first mode nonlinear static analysis, the user needs to consider the relevance of the response parameters for design. For instance, column axial forces due to earthquake loading, which are related to floor overturning moments, may not be a critical design consideration in the upper stories of a moment frame.
- Estimates of demand parameters for the reinforced concrete shear wall structures studied here generally are better than those for moment frame structures of the same height – provided that the estimate of the target displacement is displacement is reasonable. The ASCE-41 coefficient method, which is based on an effective elastic stiffness, often will not result in a good estimate of the target displacement if the pre- and post-cracking stiffnesses of the global pushover curve are clearly different. In such cases it is recommended to compute the target displacement from nonlinear response history analysis of equivalent SDOF systems.
- If the target displacement is in the negative tangent stiffness region of the pushover curve, it is recommended to compute it from nonlinear response history analysis of an equivalent SDOF system. Prediction of target displacements from the ASCE-41 coefficient method is likely to be inadequate in such cases.
- The invariant load pattern might create a perceived weak story if the relative strength of stories is sensitive to the load pattern. If the pushover indicates an irregularity that concentrates drift in a single story, mechanics principles should

be employed to estimate story strength in order to assess whether a weak story indeed exists or whether the perception of a weak story is created by the application of an invariant load pattern.

- If a strength irregularity exists and it is concentrated in a single story, then the first mode nonlinear static procedure is expected to provide good estimates of drift and force demand parameters. If strength irregularities exist in more than one story, then an invariant static load pattern rarely will detect more than the first irregularity, likely producing misleading results. Therefore, if irregularities exist in more than one story, it is recommended to either rectify the irregularities or perform nonlinear response history analysis.
- Pushovers with an invariant load pattern might lead to a misleading perception of the dominant yielding mode. A classical example is the issue of shear versus bending yielding in a shear wall. It has been shown in many nonlinear response history analyses (e.g., Krawinkler and Seneviratna 1998) that for taller structures the maximum shear force in walls, in which a pushover indicates bending yielding at the base, gets amplified by a factor that might be larger than 2.0. Thus, the wall might actually yield in shear rather than bending. For low-rise wall structures this factor will be smaller, but still clearly larger than 1.0. This is an important issue because shear yielding is viewed as much less ductile than bending yielding. Applying an amplification factor to wall shear is one way to mitigate this problem. Another one is to perform nonlinear response history analysis.
- Collapse is an important issue if the target displacement is in the negative tangent stiffness region of the pushover curve (Zareian and Krawinkler 2009). FEMA P-440A (FEMA 2009a) recommends the use of a parameter R_{di} to safeguard against collapse if the target displacement becomes very large. This parameter is useful for the intended purpose, except that the third term in the equation can rarely be quantified with confidence for a structure pushover curve. It is recommended to omit the third term unless all parameters are well defined in the pushover curve.

Multi-Mode Nonlinear Static Analysis Options

The following three multi-mode analysis options were tested in various parts of the ATC 76-6 project: elastic modal response spectrum analysis, multi-mode nonlinear static analysis (commonly referred to as modal pushover analysis, MPA), and consecutive modal pushover (CMP) analysis. General observations on the first two methods are as follows:

- Elastic modal response spectrum analysis is a very useful tool for predicting deformation and force demand parameters, as long as the structure is in the elastic range or close to it. For inelastic systems this method provided estimates of floor displacement and story drift that were as good as or better than those from nonlinear static analysis methods - but only for structures without strength irregularities. The method consistently overestimated story shears and overturning moments for yielding systems, and did so by a large amount for structures responding highly inelastic.

- This analysis method is valuable as a backup method for predicting story drifts for regular structures, but it cannot be considered a generally applicable method for inelastic response prediction because of its inability to account for limited component strength that might control inelastic response.
- Use of multi-mode nonlinear static analysis (MPA) improved the prediction of demand parameters for regular structures, and in many cases by a considerable amount. The results appear to be acceptable for the 8-story structures, which are the tallest structures investigated in this project.
- In many cases this method over-estimated demands in the lower stories of the structure, but did a much better job than the first mode nonlinear static analysis in estimating demands in the upper stories.
- The MPA, which uses invariant modal load patterns, does not protect against misleading drift information that may be caused by load pattern sensitive story mechanisms in more than a single story.
- In most of the regular structures investigated here the second mode contribution was elastic, which simplifies the modal combination and avoids ambiguities that might be caused by displacement reversals sometimes observed in inelastic higher mode pushover analyses.
- When the MPA method is employed, the reader should be aware that the option exists to compute component forces from component deformations, as discussed in Goel and Chopra 2005. This will lead to an improved estimate of component forces but necessitates the execution of a second analysis phase.
- There are many additional options for executing a nonlinear static analysis. Many of these methods have clear advantages in specific applications, but none have been found to be applicable for all conditions. And all these methods involve additional computational efforts. No general recommendations can be made for preference of any of these methods.

ASSESSMENT OF NONLINEAR RESPONSE HISTORY ANALYSIS

The use of nonlinear response history analysis (NRHA) has many hurdles to overcome. Some of them are real (such as increased complexity and the "can't see the forest because of the many leaves on the trees" syndrome) and some are fictional (such as fear of complex modeling). The challenge is to reduce complexity, so that time investment is minimized, and increase the ability to inspect and visualize response so that final design decisions can be based on good engineering judgment rather than numerical results alone. The former requires simplicity in modeling, and the latter requires thoughtful post-processing of analysis data. Thoughtful post-processing of data is under control of the practitioner and the professional program developer who wants to accommodate the practitioner's desire for efficient communication of results. This is only a time-limited stumbling block.

Simplicity in modeling is at the core of facilitating the use of nonlinear response history analysis. In concept, the major difference between modeling for nonlinear static analysis and nonlinear response history analysis lies in the need to model hysteretic behavior of structural components. Modeling of the "backbone curve" of individual components is needed one way or another. It is postulated here

that demand prediction from response history analysis based on the simplest hysteresis diagram is more realistic than demand prediction from a nonlinear static analysis. The latter is based on a simplified global pushover curve and on target displacement prediction that is derived from simplified SDOF models and assumed (usually bilinear) hysteresis diagrams. So, why not use a simple hysteresis diagram for structural components and perform nonlinear response history analysis rather than take a detour of static analysis and a postulated target displacement.

The PEER/ATC-72-1 report (PEER/ATC 2010) provides recommendations for simple component modeling. This could mean a bilinear hysteresis model for steel structural components or a peak-oriented hysteresis model for reinforced concrete components. The associated backbone curve could include a post-capping range of negative tangent stiffness if this range is deemed to be important in response predictions. One could use the modified ASCE-41 force-displacement model (Figure 1) as the backbone curve. Since the tabulated ASCE-41 properties of this model account for cyclic deterioration, there would be no need to incorporate cyclic deterioration in the analysis (PEER/ATC-72-1 analysis option 3). Thus, the modeling effort for NRHA should not be much more complex than the one for nonlinear static analysis. The better alternative is to employ component models that account explicitly for cyclic deterioration (for instance, Analyt.M1).

Appealing features of NRHA include (a) more realistic modeling of response, producing more reliable assessment of seismic performance, (b) exploration of the various possible types of response and their corresponding probabilities, (c) assessment of the significance of cyclic loading and associated deterioration, and (d) lateral dynamic instability can be addressed directly.

These improvements come at a cost, including somewhat more complex modeling and much more complex data interpretation. But most important, execution of nonlinear response history analysis necessitates the availability of a representative set of ground motions associated with the hazard at which demand parameters are to be evaluated. This is the most challenging issue that deserves much attention in order to advance the state of the practice for seismic demand prediction.

CONCLUSIONS

Both NSP and NRHA have intrinsic value, and it is advisable to employ a combination of both to understand seismic performance and quantify important engineering demand parameters.

ACKNOWLEDGMENT

This paper relies on results obtained under Task Order 6 of the NEHRP Consultants Joint Venture (a partnership of the Applied Technology Council and Consortium of Universities for Research in Earthquake Engineering), under Contract SB134107CQ0019, Earthquake Structural and Engineering Research, issued by the National Institute of Standards and Technology. The views expressed in this publication do not necessarily represent those of the organizations identified above.

REFERENCES

ASCE (2006). "*Seismic Rehabilitation of Existing Buildings*," ASCE Standard ASCE/SEI 41-06, American Society of Civil Engineers/Structural Engineering Institute, Reston, VA.

FEMA (2009). "*Quantification of Building Seismic Performance Factors,*" FEMA P-695 Report, prepared by the Applied Technology Council for the Federal Emergency Management Agency, Washington, D.C.

FEMA (2009a). "*Effects of Strength and Stiffness Degradation on Seismic Response,"* FEMA P-440A Report, prepared by the Applied Technology Council for the Federal Emergency Management Agency, Washington, D.C.

Fragiadakis, M., Vamvatsikos, D., and Aschheim, M. (2011). "Applicability of Nonlinear Static Procedures on RC Moment-Resisting Frames," *Proceedings, ASCE Structures Congress 2011*.

Goel, R.K. and Chopra, A.K. (2005). "Extension of Modal Pushover Analysis to compute member forces," *Earthquake Spectra,* Vol. 21, No. 1, pp. 125-139.

Ibarra L. F., Medina R. A., and Krawinkler H. (2005). "Hysteretic models that incorporate strength and stiffness deterioration", *Earthquake Engineering and Structural Dynamics*, 34(12), 1489-1511.

Krawinkler, H. and Seneviratna, P. (1998). "Pros and cons of a pushover analysis for seismic performance evaluation," *Journal of Engineering Structures*, Vol. 20, No. 4-6.

Lignos, D.G, and Krawinkler, H. (2009). "Sidesway collapse of deteriorating structural systems under seismic excitations", *Rep. No. TB 172*. The John A. Blume Earthquake Engineering Center, Stanford University, Stanford, CA.

Lignos, D.G. and Krawinkler H. (2011). "Deterioration modeling of steel components in support of collapse prediction of steel moment frames under earthquake loading," *J. Struct. Eng*., ASCE, accepted for publication.

Lignos, D.G., Putman, C., Zareian, F., and Krawinkler, H. (2011). "Seismic Evaluation of Steel Moment Frames and Shear Walls Using Nonlinear Static Analysis Procedures," *Proceedings, ASCE Structures Congress 2011*.

NIST (2010). "*Applicability of Nonlinear Multiple-Degree-of-Freedom Modeling for Design*," GCR 10-917-9, prepared by the NEHRP Consultants Joint Venture for the National Institute of Standards and Technology, Gaithersburg, MD.

NIST (2010a). "*Evaluation of the FEMA P-695 Methodology for Quantification of Building Seismic Performance Factors*," GCR 10-917-8, prepared by the NEHRP Consultants Joint Venture for the National Institute of Standards and Technology, Gaithersburg, MD.

PEER/ATC (2010). "*Modeling and Acceptance Criteria for Seismic Design and Analysis of Tall Buildings*," PEER/ATC-72-1, prepared by the Applied Technology Council in cooperation with the Pacific Earthquake Engineering Research Center, Redwood City, CA.

Zareian, F., and Krawinkler, H. (2009). "Simplified Performance-Based Earthquake Engineering," *John A. Blume Earthquake Engineering Center Report No. TR 169,* Department of Civil Engineering, Stanford University.

Kalman Filter-Based Identification of Bridge Fragility Parameters

Swagata Banerjee[1], Chao Chi[2] and Masanobu Shinozuka[3]

[1]Assistant Professor, Department of Civil and Environmental Engineering, Pennsylvania State University, University Park, PA 16802; PH (814) 863-2936; email: swagata@engr.psu.edu
[2]Graduate Student, Department of Civil and Environmental Engineering, Pennsylvania State University, University Park, PA 16802; email: cuc228@psu.edu
[3]Distinguished Professor, Department of Civil and Environmental Engineering, University of California, Irvine, CA 92697; email: shino@uci.edu

ABSTRACT

The study describes a procedure to identify bridge fragility parameters utilizing its vibration response recorded during experimental study. For this purpose, bridge damage data observed in a near full-scale shake table experiment is utilized. The bridge was tested under a sequence of earthquake ground motions with increasing intensities. Low and high amplitude tests were performed in series to observe the seismic performance of the bridge starting from yielding to complete failure. In the present study, recorded bridge acceleration during high amplitude tests is utilized and further analyzed to evaluate the degraded performance of the bridge after each high amplitude test. This is done by using extended Kalman filtering (EKF) technique as a tool. The degraded performance of the bridge after each run is measured in terms of degraded stiffness of the bridge at pier ends. In parallel, finite element (FE) model of the same bridge is developed in order to perform time history analysis under a set of earthquake ground motions with various hazard levels. Before applying the ground motions, the FE model is updated with the degraded stiffness of the bridge obtained from EKF after each high amplitude test. This is important to numerically simulate the gradual progression of bridge damage when subjected to earthquake ground motions in sequence. After each time history analysis, bridge response is obtained in terms of the rotation at bridge pier ends. Thus obtained response from time history analyses is used for fragility curve development. The change in fragility parameters represents the progressive damage of the bridge when subjected to ground motions with incremental intensity.

INTRODUCTION

Bridge safety and serviceability are the major concerns to civil engineers. Experience showed that bridges are the most vulnerable components of highway transportation systems. Performance of a highway transportation network under extreme natural disasters greatly depends on the performance of its constituent bridges. During the most recent major earthquake in past, 1994 Northridge

earthquake in California, seven major freeway bridges in the neighborhood of Los Angeles collapsed and a number of bridges suffered from major damage. This resulted in a significant functional degradation of the Los Angeles area highway transportation network. Similar scenario is observed during the Hurricane Katrina in 2005; several bridges were destroyed making the highway transportation system in Louisiana, Mississippi and New Orleans totally disrupted. Hence to minimize such negative consequences of extreme disasters, it is important to evaluate bridge performance under future scenario events and assess the expected risk of highway transportation systems under regional hazards.

Development of bridge fragility curves in one of the most convenient ways to express bridge performance under external loading. Fragility curves represent the failure probabilities of bridges at a damage level under certain loading intensity. These curves can be developed by utilizing bridge damage data obtained from various sources such as numerical and experimental research and real-time seismic events. Numerous studies have been performed over last few decades to numerically simulate bridge performance under seismic excitation and to develop seismic fragility curves. In contrast, availability of bridge fragility curves generated using experimental result is rather scarce. This is because large-scale experiments involving entire bridge models are expensive; component level testing is more common for this purpose. Even if bridge response from large-scale experiments is available, bridge fragility analysis utilizing the recorded response has not been done yet. For example, a near full-scale shake table test is performed on a two span reinforced concrete bridge model and the recorded bridge response is processed to gain desired knowledge on the progressive damage of the bridge under seismic excitations (Johnson *et al*. 2006). However, recorded data has not been analyzed to identify bridge fragility characteristics. Such fragility curves are important indeed not only to characterize the seismic vulnerability of bridges having similar attributes and configurations as of the experimental model, but also to investigate how bridge fragility behavior changes after earthquake events.

The objective of the present study is to identify bridge fragility characteristics by analyzing its experimentally recorded vibration response data. Bridge damage data observed in a near-full scale shake table experiment (Johnson *et al*. 2006) is utilized for this purpose. In this experiment, the bridge was tested under a sequence of seismic ground motions with increasing intensities. In this present research, recorded bridge response is analyzed using Extended Kalman Filter (EKF) in order to quantify the degraded performance of the bridge after each run. The degraded performance of the bridge is measured in terms of degraded stiffness at bridge pier ends.

For fragility analysis, numerical study is performed to simulate the seismic response of the same bridge. Finite element (FE) model of the experimental bridge is developed in SAP2000 Nonlinear (Computer and Structures, Inc. 1995). Time history analyses are performed under a set of ground motions with various hazard levels. Before analyzing the bridge under these ground motions, FE model is updated with the degraded stiffness obtained through EKF. By doing this, FE model of the bridge is calibrated with the experimental model for sequential ground motion run. Obtained bridge response is presented in the form of fragility curves. Change in fragility parameters indicates the degradation of bridge performance due to seismic events.

REVIEW OF EXPERIMENTAL STUDY AND OBSERVED RESULTS

The present study uses the vibration measurement data of a two span reinforced concrete bridge under earthquake ground motions. The data is obtained from large-scale shaking table tests conducted at the University of Nevada, Reno (Johnson *et al*. 2006). Experimental results include bridge response (acceleration time histories and rotational and translational deformations) and the nature of bridge failure from yielding to complete collapse under ground motions with increasing intensity levels. Figure 1 shows the bridge model and experimental plan. Bridge instrumentation plan (i.e., locations of accelerometers) can be found in Soyoz and Feng (2007). Total height of this specimen was 3.28 m from the bottom of the footing block to the top of the superstructure. Bridge spans, each 9.14 m long, were supported on three pier bents with the tallest one at middle. Clear heights of these bents were 1.83 m, 2.44 m and 1.52 m. Each bent consisted of two piers of the same cross-sectional and material properties. The bridge deck was a solid slab post-tensioned in both the longitudinal and transverse directions of the bridge. The axial force was estimated to be 209.2 kN in bent 1 and 3, and 182.2 kN in bent 2. Additional details of the bridge and the experiment are given in Johnson *et al*. (2006).

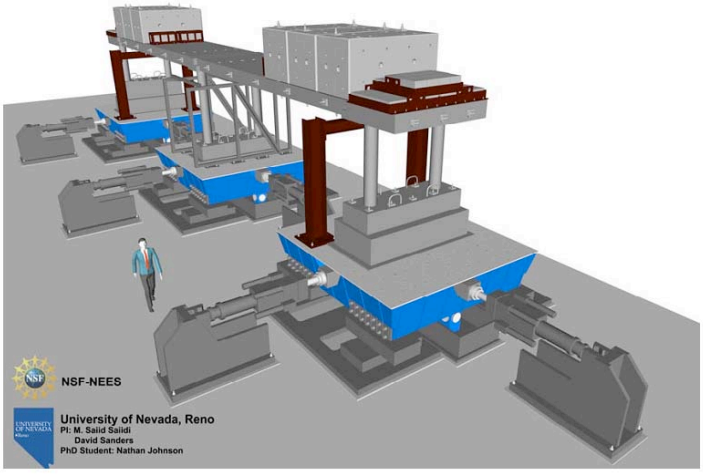


Figure 1. Experimental model of a 2-span reinforced concrete bridge (adopted from Johnson *et al.* 2006)

The experiment was performed by applying the input ground motion acceleration time histories in the transverse direction of the bridge. Low and high amplitude tests were performed in series. No damage was observed during low amplitude tests. Therefore it was assumed that the bridge remained in elastic range during the low amplitude tests. Following these, nine high amplitude tests (Ti, i = 12 ~ 20) were performed. Ground motion intensities during these high amplitude tests were increased gradually to observe the seismic performance of the bridge starting from yielding to complete failure.

Bridge response during high amplitude tests T12, T13, T14, T15, T17 and T18 are used in the current study. Table 1 represents the peak ground accelerations (PGAs) used during these tests and observed damage (in general) in bridge piers.

During Test 19, more than one rebar buckled in Best 3 which was regarded as the failure of the bridge. Following this, an additional test T20 was performed to generate more damage in Bents 1 and 2.

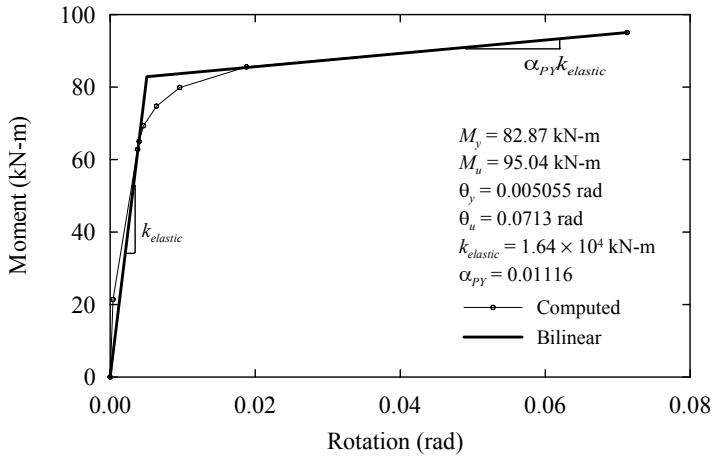
Table 1. Input PGAs and corresponding damage during high amplitude tests

High amplitude test	PGAs (g)	Damage in bridge piers
T12	0.075	No damage
T13	0.15	No damage
T14	0.25	Hairline cracks
T15	0.50	Minor cracking or spalling in cover concrete
T17	1.00	Minor cracking and significant spalling
T18	1.33	Significant spalling

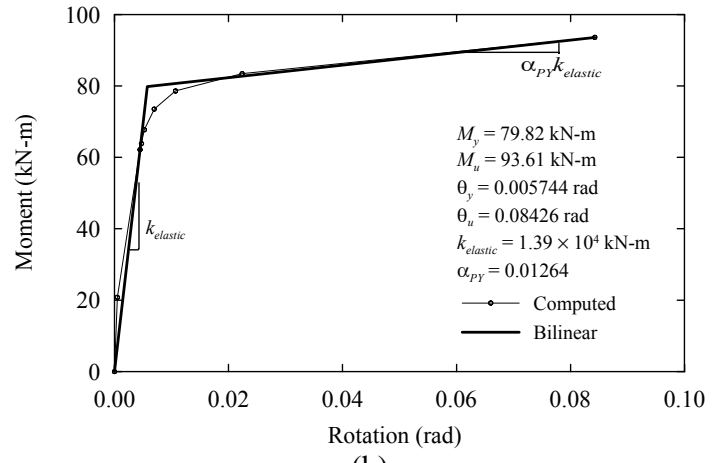
According to the nature of damage observed in bridge piers during high amplitude tests, bridge damage is categorized into four damage levels starting from no damage to major damage (Banerjee and Shinozuka 2008). This categorization is done in accordance with the qualitative damage state descriptions presented in HAZUS (1999). Table 2 lists these damage states and corresponding damage in bridge piers. Moment-rotation relationships of bridge piers in the three bents are also developed in Banerjee and Shinozuka (2008) and shown in Figure 2.

Table 2. Bridge damage states

Damage states	Descriptions of physical damage
No Damage	No damage in bridge piers
Minor Damage	Height of pier flaking/spalling ≤ 80 mm
Moderate Damage	Height of pier spalling > 80 mm or exposure of pier reinforcement
Major Damage and beyond	Significant spalling to buckling of reinforcing bar(s)



(a)



(b)

Figure 2. Moment-rotation relationships of bridge piers in (a) Bent 1 and Bent 3 (b) Bent 2 (adopted from Banerjee and Shinozuka 2008)

QUANTIFICATION OF DEGRADED STIFFNESS OF BRIDGE PIERS THROUGH EXTENDED KALMAN FILTER (EKF)

Quantification of structural damage and the evaluation of post-event structural capacity can be done by calculating the degraded stiffness values of structural elements. This also facilitates the identification of damage locations in the structure. Extended Kalman filtering (EKF) method is an effective tool for this purpose (Mohinder and Angus 2008). This technique has been extensively used over last three decades for structural damage identification (Yun and Shinozuka 1980, Hoshiya and Saito 1984, Loh and Chung 1993, Loh and Tou 1995, Ghanem and Ferro 2006, Soyoz and Feng 2007, Yang *et al*. 2007). Through EKF, the state of a dynamic system can be estimated from its vibration measurement data. The technique is essentially a set of mathematical equations that filters observed measurements (may be associated with noise and inaccuracies) to obtain true state of the structure. In the present study, a

program on EKF is developed using Matlab (Mathworks Inc. 2008). Time histories of bridge acceleration recorded in accelerometers during the high amplitude tests are used as input to the program. Additionally, ground motion time histories at the table level are used as the input ground motions. The program yields the degradation of bridge stiffness at top and bottom of each bridge pier in a dimensionless format (i.e., degraded stiffness/initial elastic stiffness). Table 3 shows these dimensionless stiffness quantities obtained after each high amplitude test. In Test 12, the starting stiffness is taken as the elastic stiffness of the bridge. After this test, obtained degraded stiffness from EKF is presented in Table 3 under T12. This degraded stiffness is considered to be the initial stiffness for T13. After T13, obtained degraded stiffness from EKF is presented in Table 3 under T13 which is again considered as initial value in EKF for T14. The process is continues for all the high amplitude tests. This way the bridge model is updated in EKF program after each high aptitude test before the following test is done to calculate stiffness degradation.

Table 3. Dimensionless stiffness (degraded stiffness/initial elastic stiffness) at bridge pier ends after high amplitude tests

Location of bridge piers		T12	T13	T14	T15	T17	T18
Bent 1	Top	1.00	1.00	0.99	0.91	0.66	0.41
	Bottom	1.00	1.00	0.99	0.94	0.78	0.61
Bent 2	Top	1.00	0.99	0.96	0.84	0.63	0.36
	Bottom	1.00	1.00	0.99	0.97	0.93	0.86
Bent 3	Top	1.00	0.99	0.94	0.78	0.51	0.45
	Bottom	1.00	0.99	0.97	0.86	0.67	0.63

NUMERICAL ANALYSIS FOR FRAGILITY CURVE DEVELOPMENT

Experimental study provides limited data. For fragility analysis, however, a set of bridge damage data is required that represents bridge performance under a variety of earthquake ground motions. For this purpose, a finite element (FE) model of the same experimental bridge is developed and analyzed under 60 earthquake ground motions. Obtained bridge response is used for fragility curve development. The following paragraphs provide the detail of this numerical study.

Bridge Model and Input Ground Motions

The finite element model of the bridge is developed in SAP2000 Nonlinear. Figure 3 shows a 3D view of the bridge model. The bridge is analyzed under 60 ground motion time histories. These motions were originally developed for the area of Los Angeles, CA for the purpose of Federal Emergency Management Agency

(FEMA) SAC steel project[1]. The motions are categorized in 3 sets, each having 20 records of horizontal ground accelerations derived either from historical recordings or from simulations. Each set of 20 records is scaled linearly in order to have return periods of 2500 years, 475 years and 72 years (exceedance probabilities respectively of 2, 10 and 50% in 50 years). These ground motions are applied in the transverse direction of the bridge to be consistent with the experimental research.

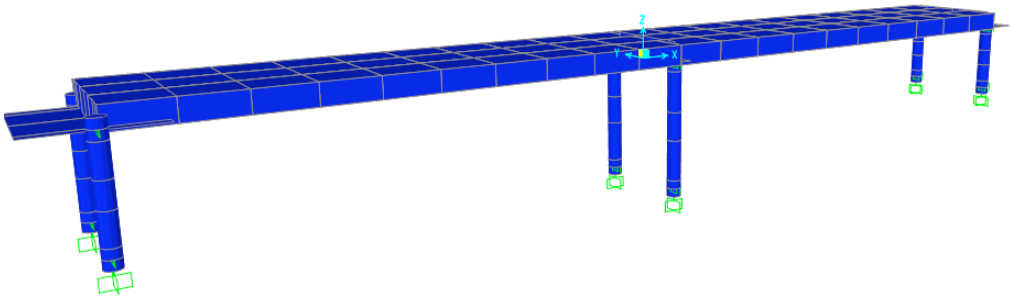


Figure 3. 3D view of FE bridge model

During seismic excitations plastic hinges are likely to generate at top and bottom of bridge piers. This is modeled in SAP2000 by introducing nonlinear links at both ends of each pier. The middle portion of each pier is assumed to be linear. At the beginning, bridge stiffness is taken as the initial (i.e., pre-damaged) stiffness. Thus the moment-rotation values shown in Figure 2 are assigned to the FE model.

Dynamic response of this bridge under 60 LA motions is recorded in terms of rotation at pier ends. This response is assumed to be the representative of bridge seismic performance. In the following step, bridge stiffness is updated with that obtained from EKF after T12 (Table 3) and thereafter analyzed under 60 LA motions. Rotations are recorded at bridge pier ends, which represent bridge seismic performance when the bridge has already experienced an earthquake similar to that used in T12. Following this, the stiffness of FE model is updated again with that obtained from EFK after T13 and a new set of time history analysis under 60 LA motions are preformed. The new recorded response represents bridge seismic performance when the structure was partially degraded due to an earthquake event similar to that used in T13. The process is continued until T18. Each time, bridge stiffness is updated to the appropriate degraded stiffness values so that the numerical model can actually represent the degraded state of the bridge after it experiences a seismic event. A flowchart in Figure 4 shows the process.

[1] http://nisee.berkeley.edu/data/strong_motion/sacsteel/ground_motions.html

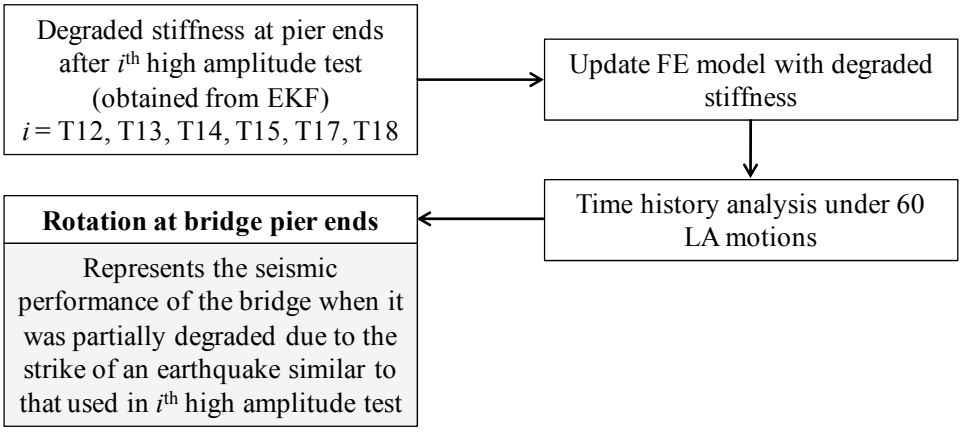


Figure 4. Flowchart showing the steps in numerical study

Seismic Fragility Curves of the Bridge

Prior to the development of fragility curves, bridge response obtained from time history analysis is categorized into different damage states (as discussed in Table 2). This is done by using threshold limits (numeric values) of bridge damage states that correspond to the physical descriptions presented in Table 2. Banerjee and Shinozuka (2008) quantified these limits in terms of rotational ductility by analyzing bridge damage data obtained from the same experimental study. By definition, rotational ductility represents the ratio of observed rotation to the yield rotation. The threshold rotational ductility values are calculated as 3.14 for minor damage, 5.90 for moderate damage and 9.42 for major damage and beyond. That means if obtained rotational ductility from numerical analysis exceeds 3.14, the bridge is no longer in minor damage state; it goes to the moderate damage.

Using rotations at each pier ends from time history analyses, values of rotational ductility are calculated. It should be noted here that piers in Bent 1 and 3 have yield rotation different from that in Bent 2 (Figure 2). Therefore for calculating rotational ductility at pier ends, appropriate values of yield rotation are taken. Damage states are decided by comparing the rotational ductility values with the threshold limits, and used further for the development of fragility curves.

Fragility curves represent probability of bridge failure in a damage state under certain ground motion intensity such as peak ground acceleration or PGA. The current study follows the procedure described in Shinozuka *et al*. (2000) to develop fragility curves at minor, moderate and major damage states of the bridge. A two-parameter lognormal distribution is used to represent the fragility curve. The parameters, median and log-standard deviation, define the shape of the fragility curve. Lower median value indicates weaker curve, as it has high probability of exceeding the damage state at lower intensity level. Thus, it also indicates higher vulnerability (or damageability) of the bridge under seismic excitations.

Table 4 shows the fragility parameter (median value) of the bridge after each high amplitude test. The fragility curves are shown in Figure 5, 6, and 7 respectively for minor, moderate and major damage states of the bridge. For all of these curves,

log-standard deviation is taken as 0.5 so that any two curves cannot cross each other and the curves can be compared in terms of their median values.

Table 4. Fragility parameter (median value in g) of the bridge after high amplitude tests

Damage State	Median value in g					
	T12	T13	T14	T15	T17	T18
≥ minor	0.49	0.48	0.48	0.45	0.36	0.20
≥ moderate	1.10	1.10	1.10	0.91	0.63	0.48
≥ Major	2.43	2.05	2.05	2.05	1.10	0.72

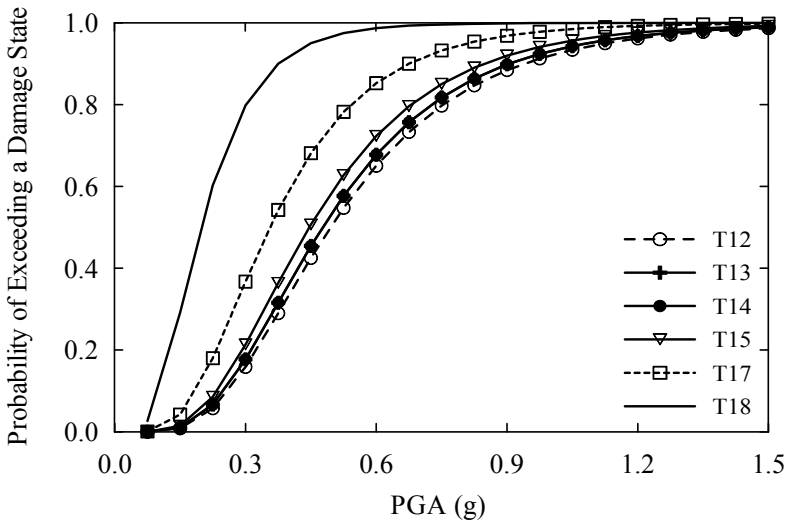


Figure 5. Bridge fragility curves at minor damage state after high amplitude tests

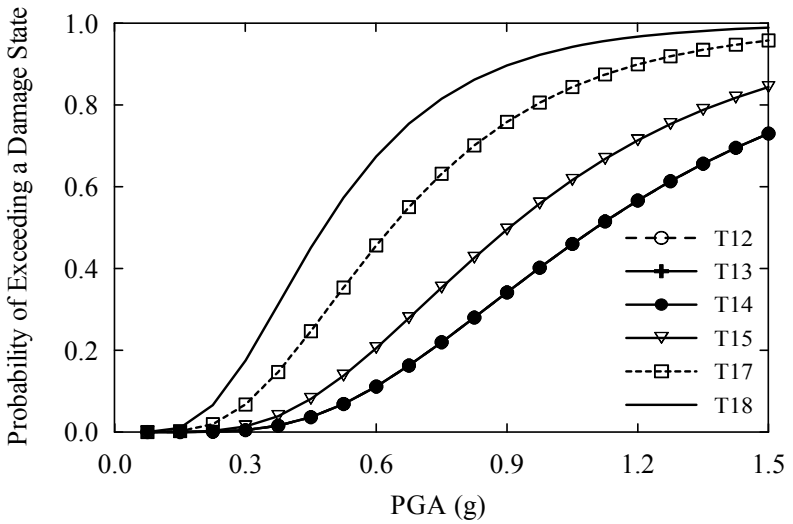


Figure 6. Bridge fragility curves at moderate damage state after high amplitude tests

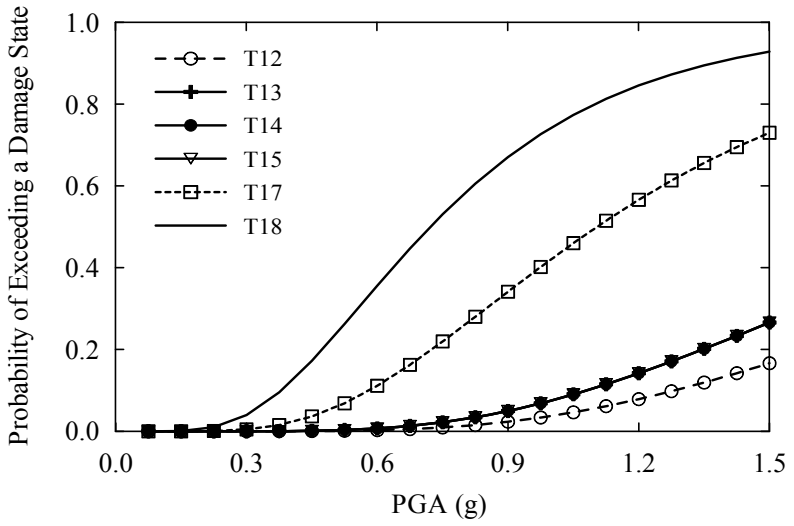


Figure 7. Bridge fragility curves at major damage state after high amplitude tests

PROGRESSIVE DEGRADATION OF BRIDGE FRAGILITY CHARACTERISTICS

The fragility curves in Figures 5, 6, and 7 represent bridge vulnerability under seismic ground motions. As these curves move towards left (i.e., median value decreases), bridge seismic vulnerability increases. It is evident from these figures that bridge vulnerability increases after each high amplitude test. This is quite obvious because bridge stiffness degrades in a progressive manner with the high aptitude tests. Not much degradation was observed in test T12 to T14 during the experiment (Table 1). This reflects properly in bridge fragility characteristics. For all three damage states, median fragility parameters do not have significant change from T12 to T14. Following T15, bridge stiffness degrades to a large extent so as the fragility curves. After T17 and T18, bridge seismic performance in major damage changes rapidly indicating a very high probability of having bridge failure in the higher damage state. The similar phenomenon is observed during the experiment. After T18, more than one rebar buckled in bridge piers, which was regarded as the failure of the bridge.

CONCLUSION

The study establishes a procedure of utilizing structural vibration response recorded from dynamic testing and/or from embedded sensors to determine its fragility characteristics under ambient vibration and natural events. The result shows how bridge seismically vulnerable increases after seismic events. Even if there is not much visible damage in a bridge due to a seismic event, the stiffness may get reduced to some extent which may has significant impact on the bridge seismic behavior. Therefore, consideration of initial (i.e., pre-damaged) condition for the seismic performance evaluation of an existing bridge is misleading; this may overestimate the actual capacity of the bridge. Use of such result in the seismic performance evaluation of highway transportation networks is not desirable.

REFERENCES

Banerjee, S. and Shinozuka, M. (2008). "Experimental verification of bridge seismic damage states quantified by calibrating analytical models with empirical field data." *Earthquake Engineering and Engineering Vibration*, 7(4), 383-393.

Computer and Structures, Inc. (1995). SAP2000 Nonlinear, Berkley, CA, Version 14.1.0.

Ghanem, R. and Ferro, G. (2006). "Health monitoring for strongly non-linear systems using the Ensemble Kalman Filter." *Structural Control and Health Monitoring*, 13(1), 245-259.

HAZUS (1999). *Earthquake Loss Estimation Methodology*, Technical Manual SR2, Federal Emergency Management Agency through agreements with National Institute of Building Science, Washington, D.C., USA.

Hoshiya, M. and Saito, E. (1984). "Structural identification by extended Kalman Filter." *Journal of Engineering Mechanics*, 110(12), 1757-1772.

Johnson, N., Saiidi. M., and Sanders, D. (2006). *Large-scale experimental and analytical seismic studies of a two-span reinforced concrete bridge system*, CCEER-06-02, Reno, NV.

Loh, C.H. and Chung, S.T. (1993). "Three-stage identification approach for hysteretic systems." *Earthquake Engineering and Structural Dynamics*, 22(2), 129-150.

Loh, C.H. and Tou, I.C. (1995). "System identification approach to the detection of changes in both linear and non-linear structural parameters." *Earthquake Engineering and Structural Dynamics*, 24(1), 85-97.

Mathworks, Inc. (2008). Matlab. Natick, MA. Version 7.7.

Mohinder, G. and Angus, A. (2008). *Kalman Filtering Theory and Practice Using MATLAB*, John Wiley & Sons, Inc., New York.

Shinozuka, M., Feng, M.Q., Lee, J., and Naganuma, T. (2000). "Statistical analysis of fragility curves." *Journal of Engineering Mechanics*, 126(12), 1224-1231.

Soyoz, S. and Feng, M.Q. (2007). "Instantaneous damage detection of bridge structures and experimental verification." *Structural Control and Health Monitoring*, 15(7), 958-973.

Yang, J.N., Pan, S. and Huang, H. (2007). "An adaptive extended Kalman filter for structural damage identifications II: Unknown inputs." *Structural Control and Health Monitoring*, 14(3), 497-521.

Yun, C.B. and Shinozuka, M. (1980). "Identification of nonlinear structural dynamic systems." *Journal of structural mechanics*, 8(2), 187-203.

Sensitivity of Reliability Index of Bridge Girders to Random Variables and Average Daily Truck Traffic

O. Kwon[1], E. Kim[2], and S. Orton[3]

[1] Assistant Professor (os.kwon@utoronto.ca), Department of Civil Engineering, University of Toronto. Toronto, Ontario, M5S 1A4. Canada.
[2] Graduate Research Assistant (ekwb8@mst.edu), Missouri University of Science and Technology. Rolla, MO., 65409.
[3] Assistant Professor (ortons@missouri.edu), Department of Civil and Environmental Engineering, University of Missouri, Columbia. Columbia, MO, 65211.

ABSTRACT

The objective of the presented study is to evaluate the sensitivities of the random variables and Average Daily Truck Traffic (ADTT) on the evaluated reliability of bridges. The reliability analysis is carried out for the Strength I Limit State in the AASHTO LRFD Bridge Design Specification. The Weigh-In-Motion (WIM) data recorded at 24 WIM stations in Missouri are processed and used as an input to simulate realistic live loads due to truck traffic. Gumbel Type I extreme value distribution is used to represent daily maximum positive moments and extreme value theory is used to project the daily maximum values to the maximum values in 75 years of bridge lifespan. Sensitivity analysis is conducted to understand the relative effects of random variables and ADTT on the calculated reliability index. The result shows that the ADTT affects the reliability index as sensitively as other random variables, such as dead load, girder distribution factor, and dynamic impact factor. Hence, explicit consideration of uncertainties in ADTT is suggested for future calibration studies. Alternatively, the reliability index needs to be assessed conditioned on deterministic ADTT.

INTRODUCTION

Bridge design philosophies and specifications have been developed over the years to design bridges with a desired level of reliability. When AASHTO began publishing the standard specification for highway bridges in the 1930s, a factor of safety was used to ensure that the resistance of a bridge is greater than the combination of service loads. The design method is referred to as Allowable Stress Design (ASD). In the 1970s, uncertainties in load prediction were considered by using different load factors depending on the engineer's ability to predict the loads. This design approach is referred to as Load Factor Design (LFD). Recently, the bridge engineering profession has been moving toward the Load and Resistance Factor Design (LRFD). Load factors and resistance factors in the LRFD specification were developed based on the reliability analysis of bridges. FHWA mandated that the AASHTO LRFD Bridge Design Specification should be used for new bridges on which states initiate preliminary engineering from October 2007.

The load factors in the AASHTO LRFD Specification have been calibrated through several NCHRP research projects. The NCHRP Project 12-33 produced

NCHRP Report 368 (Nowak 1999), which is the basis of the current LRFD Specification. For the project, the truck survey results from the Ontario Ministry of Transportation were used to calibrate the live load factor. It was assumed that the surveyed truck data from Ontario in mid 1970s represented two-weeks of heavy traffic on a two lane bridge with Average Daily Truck Traffic (ADTT) of 1,000 in one direction. The development of live load factor was based on reliability analyses of around 200 representative bridges from various geographical regions in the United States. From the evaluated reliability indices, the live load factor of 1.7 was proposed. In NCHRP Report 20-7/186 (Kulicki et al. 2007), the live load factor was increased from 1.7 to 1.75 due to the increase in the design ADTT from 1,000 to 5,000.

Recently, several states in the U.S. calibrated the load factors to consider state-specific traffic environment (traffic volume and truck weights) and bridge configurations. So far, the Michigan DOT has proposed an adjustment factor to increase the live load to account for heavy truck traffic in metropolitan areas (Van de Lindt et al. 2006; Fu et al. 2006). In addition, Oregon, Florida, and New York DOTs calibrated live load factors for Load and Resistance Factor Rating (LRFR) using Weigh-in-Motion (WIM) data collected in each state. Missouri DOT recently completed a research project in which the live load factor is calibrated based on state-specific traffic environment and bridge configurations (Kwon et al. 2010a, 2010b).

In the reliability analysis procedure in the above studies, several random variables are involved in resistance, live loads, and dead loads. While the procedures are thorough and rationale, no attempts has been made yet to understand which random variable contribute the most to the evaluated bridge reliability. In addition, how the local traffic environment (such as ADTT in this study) affects the reliability of bridges has not been quantitatively evaluated yet. Hence, the objective of the presented study is to evaluate the sensitivities of the random variables and ADTT on the evaluated reliability of bridges. The reliability analysis procedure in this study is based on the study by the authors (Kwon et al. 2010a, 2010b).

In the following, overview of the reliability analysis procedures is introduced, which is followed by the introduction on localities of traffic environment in Missouri. The reliability analysis procedure is demonstrated with a typical pre-stressed concrete bridge. Then, the sensitivity analyses of random variables on evaluated reliability are carried out.

OVERVIEW OF RELIABILITY ASSESSMENT PROCEDURE

The reliability assessment of bridge girders requires identification of uncertain parameters in the expected loads and resistance of bridge girders as depicted in Figure 1. The expected loads need to be assessed considering the uncertainties in dead loads and live loads. Since the assessed reliability will be ultimately used to calibrate the load factor in the design specification, the uncertainties in the live loads should take into account the maximum live load effects throughout the life span of bridges and the expected traffic volume which is generally represented with Averaged Daily Truck Traffic (ADTT). The expected live load needs to be based on a realistic vehicle load model customized for a specific state or recorded vehicle weights from Weigh-In-Motion (WIM) stations. Hence, the evaluation of loads consists of the assessment of short-term live load effects (daily maximum load effects in this study) and the

projection of those to 75 year effects. The procedure for live load assessment is illustrated in the left most column in Figure 1. In addition to the live loads, the uncertainties in dead loads need to be included as shown in the middle column in Figure 1. In terms of bridge resistance, comparison of girder strengths in as-built condition with minimum strengths required by the code shows that the as-built strengths are mostly higher than the minimum required strengths for the Strength I condition (Orton et al. 2010). Since this study is carried out to calibrate the load factors in the bridge design specification, the minimum strength required by the code is used as girder strengths rather than strength in as-built condition.

Even when a bridge girder is optimally designed to have a minimum required strength, previous research showed that structural members tend to have over-strength due to the bias in actual material strength and nominal material strengths. In addition, since the properties of structural materials are not deterministic, the strengths of structural members are inherently random in nature. Hence, the uncertainties in minimum required strengths are evaluated considering the uncertainties in material strengths, fabrication, and professional parameters (Orton et al. 2010).

The reliability assessment of bridge girders requires assessment of the random variables discussed in the above. In addition, the expected ADTTs of the studied bridges need to be carefully determined. In the next section, the localities of traffic environments within a state are discussed which shows the range of ADTTs that bridges are subjected to.

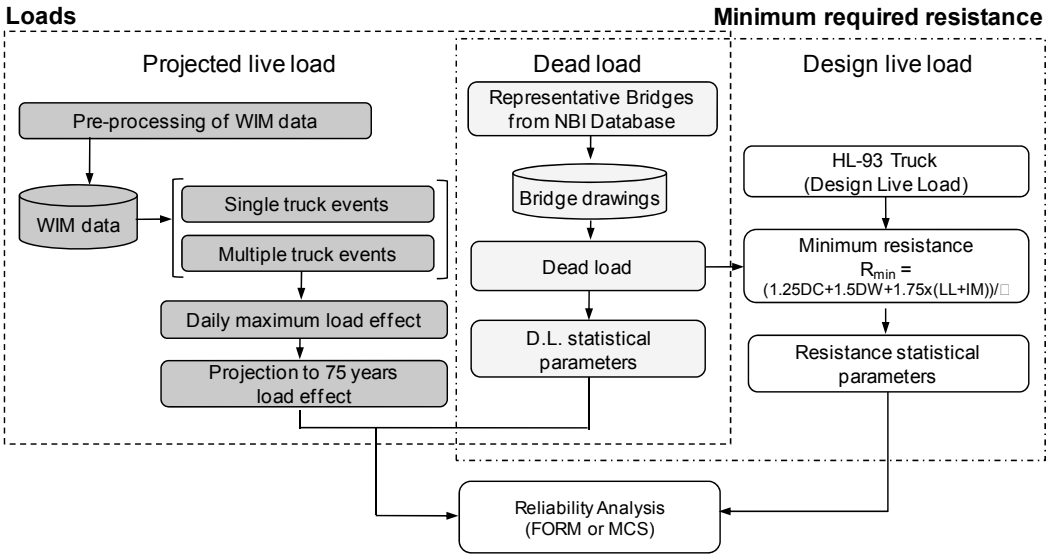


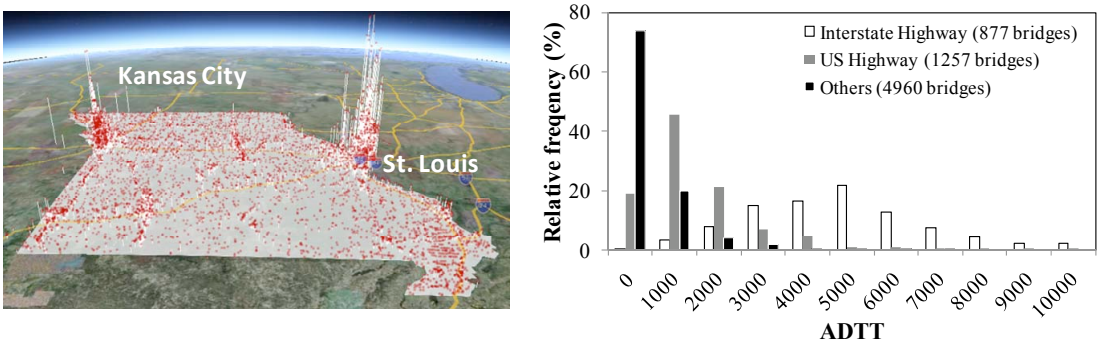
Figure 1. Overview of reliability analysis procedure for bridge girders

LOCALITIES OF TRAFFIC VOLUME AND TRUCK WEIGHT

The traffic volume and truck weights are parameters that significantly affect the assessed reliability of bridge girders. With higher truck weights and volumes, the reliability of bridge girders decreases. While the localities of the traffic environments were discussed in literature (Van de Lindt et al. 2006; Kwon et al. 2010a, 2010b), the load factors in the current design specification, which were developed based on

assumption that ADTT is 5000, are universally applied in most states except a few states which carried out calibration studies based on local traffic data.

To illustrate the level of distributions in traffic volumes, the geographical distribution of ADTTs in Missouri is depicted in Figure 2(a). Each mark in the figure indicates the location of a bridge. The height of the mark shows the relative ADTT. As it can be observed from the figure, a high volume of truck traffic is concentrated in the metropolitan areas of Kansas City and St. Louis. For many bridges in rural areas, the ADTTs are very small. Figure 2(b) compares the distribution of ADTT for bridges in the Interstate Highway system, in the US Highway system, and other rural roads. The average ADTT of Interstate Highway bridges is close to 5,000, which was used for the calibration of the live load factor in current AASHTO LRFD. The distribution of ADTT is close to the normal distribution with fairly large standard deviation. The average ADTT of the US highway bridges is only around 1,100 and bridges on other roads have an average ADTT of only 415. Considering that the majority of bridges in Missouri carry US highway (1257 bridges or 18% of total bridge inventory) or local roads (4960 bridges or 70%), a different live load factor may need to be applied for these bridges in order to have a uniform safety margin. The discussion on the effect of ADTT on the reliability of bridges is provided in more detail later in this paper.



(a) Geographic distribution (b) Histogram of ADTT in different roadways

Figure 2. Regional and roadway dependency of ADTTs in Missouri

Figure 3 compares the distribution of gross vehicle weights (GVW) of three different WIM stations in Missouri. The figures clearly show that even within a state, the distribution of GVWs varies. Even though not investigated in this study, it is speculated that the distribution of GVWs may vary in different states with following reasons; 1) some states in the U.S. have different legal loads and/or different practices in issuing overweight permits, 2) states have different industry which requires transportation of heavy raw materials or final products, and 3) distribution of population and associated traffic demands are not uniform in the U.S. Hence, to achieve the objective of having uniform reliability of bridges through the transition from LFD to LRFD, it is imperative to evaluate traffic environments of each state and calibrate load factors based on the evaluation. In terms of traffic environments, the scope of the study presented in this paper is limited to the effects of ADTT on the assessed reliability index, which will emphasize the importance of defining appropriate ADTT in reliability assessment procedure.

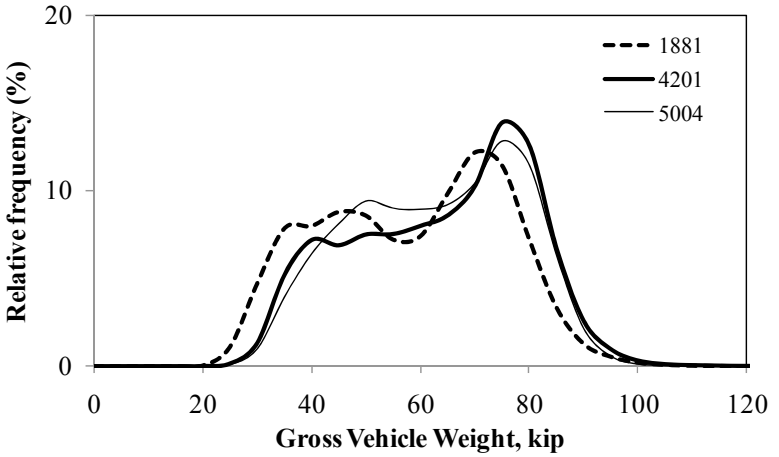


Figure 3. Distribution of GVW of vehicle class 9 (Stations 1881, 4201, 5004)

RELIABILITY ASSESSMENT OF AN EXAMPLE BRIDGE GIRDER

Reliability assessment procedure is discussed in detail with a typical prestressed concrete bridge in Missouri. The bridge consists of a simple span with span length of 90ft and span width of 26ft. Four pre-stressed concrete girders are used to transfer loads to abutments. While the actual bridge carries rural roadway, for traffic simulation it is assumed that the bridge carries Interstate Highway and vehicles run at highway speed.

Minimum Required Resistance

The minimum required resistance consists of live load (HL93 design truck) and dead load. Based on the moving load analysis with the design truck, the maximum positive moment of the bridge span from the live load is found to be 2,313 kip-ft, which includes dynamic impact factor of the design truck load. Maximum moment to an interior girder (1742 kip-ft) is calculated by applying girder distribution factor of 0.753, which is calculated from the geometry of the bridge section and considering the multiple presence factor for the two-lane bridge. The multiple presence factor takes into account the effects of two HL93 design trucks running in parallel on bridge girders. The dead load consists of component dead load (DC, total 1480 kip-ft) and wearing surface dead load (DW, 248 kip-ft). The required minimum resistance is calculated from the load combination of Strength I limit state:

$$M_{req} = (1.25(DC) + 1.5(DW) + 1.75(LL + IM))/\square.$$

From the load combination, the nominal positive moment for an interior girder is found to be 5270 kip-ft. This value is assumed as ‘nominal resistance’ of the bridge girder as a properly designed bridge girder will have a moment strength equal to or greater than 5270 kip-ft.

The deterministic minimum required resistance is converted to a random variable by applying a bias factor and a coefficient of variation (COV). The bias factor and the COV of a prestressed concrete girder section are estimated from the statistical analysis of existing girder sections in which the probabilistic distribution of

materials, fabrication, and professional parameters are considered. The adopted bias factor and the COV are 1.055 and 0.069 (Orton et al. 2010), which are evaluated using the latest material parameters available in literature.

Load Demands throughout the Lifespan of a Bridge

The load demands consist of dead loads and live loads. The dead loads are assumed to be identical with those used for minimum resistance calculation except that the dead loads follow lognormal distribution. Different bias factors and COVs are applied to factory-made members, cast-in-place members, and wearing surface based on the study by Nowak (1999). The live load demands are calculated from Monte-Carlo simulation of moving trucks considering traffic volume (ADTT) and WIM data recorded in Missouri. The WIM data are processed to remove unreliable data points as briefly introduced in the following section.

Filtering of WIM data

The WIM data used in this study were collected for five years between 2004 and 2008 at 22 permanent and 2 temporary WIM stations in Missouri. Approximately 41 million WIM data were collected at the 24 WIM stations and 84% of the data were recorded on Interstate Highways. Since WIM data are recorded while trucks ran at highway speeds, the recorded data are prone to error. Inspection of the recorded data showed that a non-negligible portion of the data has unrealistically large axle weights, gross vehicle weights, or axle spacing. Hence, after reviewing the time series of daily average GVW from all WIM stations, the erroneous data segments, which show unrealistic values are removed from the database. After screening WIM data based on the daily average GVW, the screening criteria in NCHRP Web-Only Document 135 (Sivakumar et al. 2008) is applied to remove outlier data points.

Effects of single heavy truck

The daily maximum moment in a bridge girder may result from a single heavy truck or multiple trucks running in parallel or in series. In the minimum resistance calculation, the multiple presence factor in LRFD Specification takes into account the multiple truck events. For live load demand calculation, the multiple presence effects should be realistically simulated in which the chances of having multiple truck events and distribution of moments to each girder can be appropriately considered.

For single truck events, it is not necessary to run analysis with all ADTT number of trucks to find daily maximum moment as only heavy trucks affect the maximum moment. To understand how the maximum moments are correlated with the GVWs of trucks, the correlation coefficient between GVWs and the maximum moments is calculated. While not presented in this paper for the sake of brevity, the correlation between GVWs and maximum moments is approximately 0.95. A reference is made to Kwon et al. (2010b) for more information. Based on the close correlation, trucks only within top 5% of GVWs are used to find maximum moment due to single truck events.

Simulation of multiple truck events

The chance that multiple trucks exist on a bridge highly depends on the bridge length, number of lanes, average daily traffic, average daily truck traffic, and the traffic flow. In the previous calibration studies (NCHRP 368 and NCHRP 20-7), the following assumptions were used based on limited observation of truck traffic; every 50^{th} truck is followed by another truck with the headway distance less than 100 ft, every 150^{th} truck is followed behind by a partially correlated truck, every 500^{th} truck is followed behind by a fully correlated truck. Similar assumptions were also used for trucks running on bridges with two or more lanes.

In this study, the traffic flow is modeled as a Poisson process. When an event follows a Poisson process, the time between vehicle's arrival to a bridge, is described by an exponential distribution (Cowan 1975). Since vehicles keep certain level of headway distance, the shifted exponential distribution can be used to take into account the headway distance. The vehicle's arrival time to a bridge can be numerically simulated using the distribution, and the distance between vehicles can be compared with the length of a bridge to determine how many multiple presence effects should be considered for moving load analysis. Figure 4 illustrates how the multiple trucks running in series or running in parallel are selected for moving load analysis. For the example bridge, it is found that when ADTT is 5,000, on average 180 multiple truck events per one-day of traffic simulation need to be included in the moving load analysis.

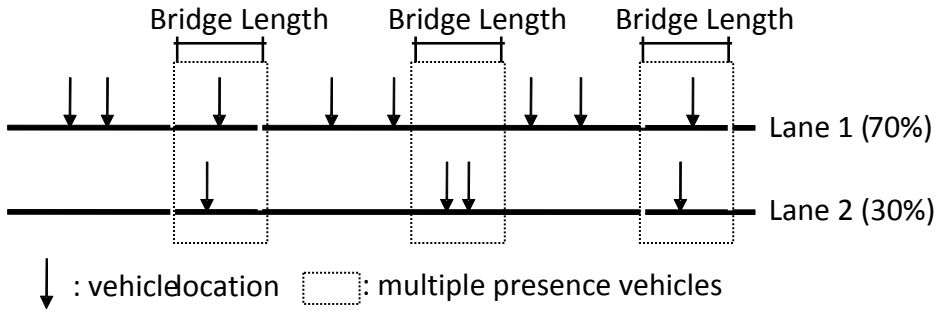


Figure 4. Simulation of multiple truck cases

Based on the 2007 NBI database and field monitoring of traffics at three different locations on IS-44 (near Rolla, Missouri), around 25% of daily traffic (ADT) was found to be truck traffic. In addition, traffic monitoring conducted for this research showed that approximately 70% of vehicles use the travel lane and the remaining use the bypass lane in the IS highway without having traffic congestion. Even though the observation was limited to the specific highway and observed time, this data was used to simulate multiple truck events due to lack of data available in literature.

Distribution of load effects to girders and consideration of dynamic impact

The moving load analysis in the above can result in maximum moment for the entire section of the bridge span. As the reliability analyses are carried out in bridge

girder level not bridge section level, it is necessary to distribute the moment to each girder. For this purpose, the girder distribution factors in AASHTO LRFD specification are adopted. Note that in a real bridge, multiple trucks may not run perfectly in parallel as it was assumed in the multiple presence factor in LRFD Specification. Hence, it is not appropriate to directly apply the multiple presence factor in the LRFD Specification to the moments calculated from truck traffic simulation. Thus, the load distribution factor in the specification is modified to take into account the multiple lane effects from traffic simulation. For more details on girder distribution factors adopted in this study, reference is made to Kwon et al. (2010a).

Due to the roughness of bridge surface and dynamic interaction between bridge superstructure and vehicles, a dynamic amplification factor is applied to the load effects from vehicular live loads. In this study, to be consistent with the procedure adopted for the development of the current AASHTO LRFD Specification, the mean values and the coefficient of variation used by Hwang and Nowak (1991) are adopted to reflect the uncertainties in the dynamic impact. The mean dynamic impact factors of 0.10 and 0.15 are taken for multiple truck events and single truck events, respectively. The coefficient of variation for the dynamic impact factor is taken as 0.8.

Daily maximum values and projection for 75-year load effects

Simulation is carried out for one hundred days of traffic. On each day the simulation considers a number of trucks equal to the ADTT. Both single truck events and multiple truck events are simulated following the procedure discussed in the previous sections. As each daily maximum value is an extreme value of the day, the distribution of the daily maximum values is assumed to follow extreme value distribution. It is assumed in this study that the daily maximum value follows Gumbel Type I distribution:

$$F_{X-1day}(x) = \exp\left(-\exp\left(-\frac{x-u}{\alpha}\right)\right)$$

in which α and u are scale parameters and location parameters, respectively. The distribution of maximum load effect for 75 years, $F_{X-75\,years}$ can be projected using the distribution of daily maximum load effect as follows:

$$F_{X-75\,years}(x) = \left[F_{X-1day}(x)\right]^N = \left[\exp\left(-\exp\left(-\frac{x-u}{\alpha}\right)\right)\right]^N = \exp\left\{-\exp\left(-\frac{x-u_n}{\alpha_n}\right)\right\}$$

where N is the number of days in 75 years. Note that in a previous study (Nowak 1999) the normal probability paper was used to project short-term simulations to estimate long-term (75 years) effects. A comparison of the different projection methods showed that the method adopted in this study is more consistent and conservative than the other method. Detailed comparison of the two projection methods can be found in Kwon et al. (2010b).

Figure 5(a) shows the Cumulative Distribution Function (CDF) of daily maximum positive moments. Note that some of the maximum values result from multiple truck events and others are from single heavy trucks. It can be observed from

the figure that the Gumbel Type I distribution can describe the simulated data points with acceptable accuracy. In Figure 5(a), the mean daily maximum moment for the example bridge is around 875 kip-ft, which is far less than the maximum live load from HL93 design truck (1742 kip-ft including lane load and 1286 kip-ft excluding lane load) despite the fact that the GVW of the heavy trucks in WIM data is generally greater than GVW of HL93 design truck. This difference mainly results from the use of different multiple presence factors in resistance calculation and in load demand calculation. In resistance calculation, the multiple presence factors were developed based on assumption that two design trucks run in parallel, hence, the multiple presence factor is relatively large. In the load demand calculation, on the other hand, multiple presence effects are considered through traffic simulation in which the chance of having two heavy trucks running in parallel is low.

Figure 5(b) presents distribution of the maximum moment in 75 year of lifespan of the bridge. It is important to note that the projected curve mainly relies on the shape of tail portion of the CDF of the short-term simulation (daily maximum value distribution, Figure 5(a)). The maximum moment in 75 year has mean value of 1,637 kip-ft and COV of 0.18.

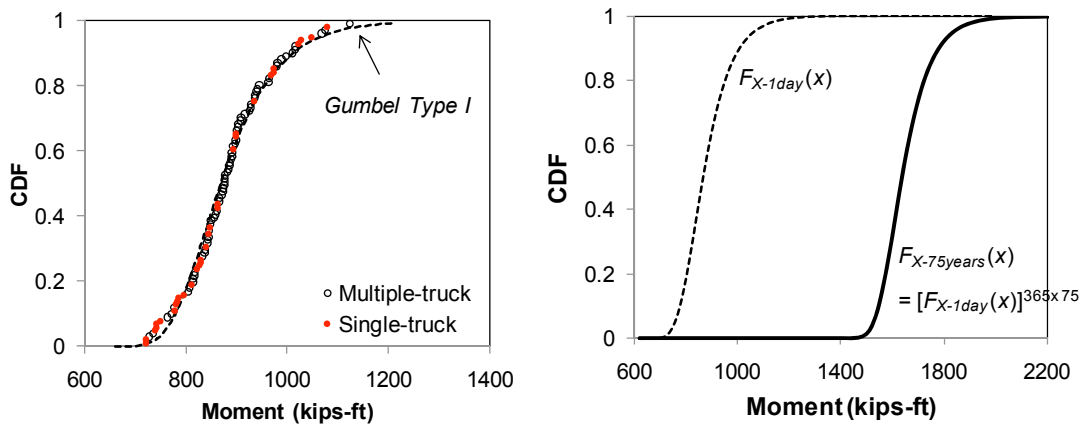


Figure 5. Distribution of 75-year maximum moment

Reliability Assessment

The probabilistic distribution of load demand throughout the lifespan of the bridge and minimum required resistances are estimated following the procedure discussed in the above. The Table 1 summarizes distribution of random variables used in the reliability assessment. Note that some of the uncertainties are propagated into other derived random variables. For instance, the uncertainties in material properties, which are not presented in this paper, are reflected in the uncertainties in resistance. In addition, the uncertainties in impact factor and girder distribution factors are reflected in the load demand. Based on the statistical distribution of resistance and load demand, the reliability index of the example bridge girder is found to be 5.91 using the First Order Reliability Method (FORM). The reliability index of 5.91 is far greater than the target reliability index of 3.5 used for the calibration of load factors in current AASHTO LRFD Specification. The main sources of the difference could be 1) the simulation method for truck traffics, 2) girder distribution

factors to consider multiple presence effects, and 3) projection methods. Each of these is in fact requires further in-depth research as it involves large assumptions which can directly affect the derived reliability index.

Table 1. Statistical parameters for dead load

Random variables	Distribution	Parameters	
		Bias factor	COV
Factory-made members (DC1)	Log-normal (Nowak 1999)	1.03	0.08
Cast-in-place members (DC2)		1.05	0.10
Cast-in-place members (DC3)		1.05	0.10
Wearing surface (DW)		1.00	0.25

Table 2. Statistical parameters for distribution factor (mg) and impact factor (IM)

Random variables	Distribution	Parameters	
		Mean	COV
mg for single lane load	Normal (Hwang and Nowak 1991)	0.536	0.12
mg for multiple lane loads		0.752	0.12
IM for single lane load		0.15	0.80
IM for multiple lane loads		0.10	0.80

Table 3. Statistical parameters for resistance (positive moment, PS girder)

Random variables	Distribution	Parameters	
		Bias factor	COV
PS concrete girder	Normal (Orton et al. 2010)	1.055	0.069

Sensitivity Analysis

Several random variables contribute to the uncertainties in the estimated reliability index. To understand how the reliability index is sensitive to each random variable, sensitivity analysis is carried out with dead load, girder distribution factor, dynamic impact factor, resistance, and ADTT. The mean of the selected random variables is changed between mean minus standard deviation and mean plus standard deviation and reliability index of the bridge girder is revaluated. Note that only mean values are changed for the sensitivity analysis not dispersion parameters. In addition, as ADTT is assumed to be deterministic value in this study, the ADTT is arbitrarily varied from 500 to 50,000, which covers the range of actual ADTTs in Missouri, Figure 2(b). The effect of ADTT is considered only in the projection of daily maximum load effects, not in the traffic simulation.

Figure 6 compares the reliability indices when the mean values of selected random variables are changed. For dead load, the mean value on dead load demand is varied and the dead load for resistance calculation is kept constant. Hence, by increasing mean value from mean-σ to mean+σ, the reliability index decreases. In the same way, as the girder distribution factor and dynamic impact factor in demand calculation increases from mean-σ to mean+σ, the reliability index decreases. As resistance increases, the reliability index increases as expected. It is worth to note that when ADTT varies from 500 to 50,000, the reliability index varies from 6.5 to 5.3. The sensitivity of reliability index to ADTT between ADTT of 500 to 50,000 is close

to that of other random variables such as dead load, distribution factor, or dynamic impact factor. As the multiple presence effect is not fully considered in the sensitivity analysis, the actual effect of ADTT on reliability index could be much higher.

In all previous studies, including the one by the authors (Kwon et al. 2010), the ADTT is assumed deterministic value. As ADTT has as significant effect as other random variables as observed in Figure 6 and as ADTT significantly varies depending on bridges as shown in Figure 2, it is proposed that ADTT needs to be considered as a random variable in the reliability assessment, or the derived reliability index should be conditioned on ADTT as in Kwon et al. 2010.

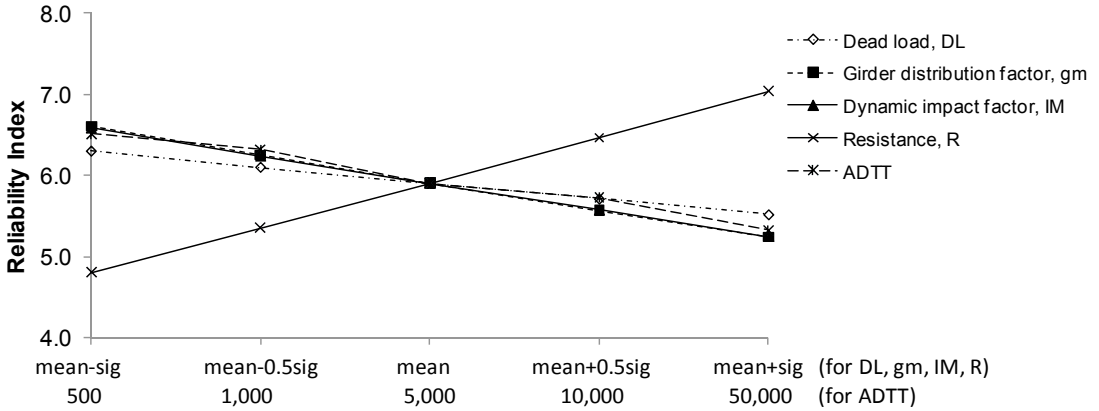


Figure 6. Sensitivity analysis of random variables adopted in the reliability analysis

CONCLUSIONS

The paper presents a procedure for the reliability assessment of a bridge girder using a simply supported prestressed concrete bridge as an example. The main focus of discussion is on localities of traffic environment and sensitivities of reliability index to random variables adopted in the process. Here are summary of findings from this study.

- The NBI Database shows that the traffic volume in terms of ADTT greatly varies depending on the area within a state and roadway system. Thus, it is expected that when calibration study is carried out for the refinement of LRFD specification, either ADTT needs to be considered as a random variable or the reliability index needs to be conditioned on ADTT.
- The collected WIM data shows that statistical distribution of GVW varies depending on WIM stations. It is expected that the distribution of GVW could be different for each state as main industry and legal limits varies depending on states.
- The reliability index has similar sensitivity to dead load, girder distribution factor, and dynamic impact factor.
- When ADTT varies from 500 to 50,000, the reliability index varies approximately from 6.5 to 5.5, which is similar to the range of reliability index when mean values of other random variables (dead load, girder distribution factor, and impact factor) vary from mean minus standard deviation to mean plus standard deviation.

The derived reliability index from this study is higher than the target reliability index used in the previous study as different procedures for traffic simulation, consideration of multiple presence effects, and projection methods are adopted in this study. For more accurate reliability assessment, these procedures require further investigation.

ACKNOWLEDGEMENT

This study was funded by the Missouri Department of Transportation (MoDOT) and Missouri S&T National University Transportation Center (NUTC). All findings and conclusions are those of the authors and do not represent MoDOT or NUTC.

REFERENCES

Fu, G. and Van de Lindt, J.W. (2006), *LRFD Load Calibration for State of Michigan Trunkline Bridges*, Report RC-1466, Michigan Department of Transportation, MI.

Hwang, E.S. and Nowak, A.S. (1991), "Simulation of dynamic load for bridges." *Journal of Structural Engineering*, ASCE, Vol.117, No.5, pp.1413–1434.

Kulicki, J. M., Prucz, A., Clancy, C. M., Mertz, D. R., and Nowak, A. S. (2007). *Updating the Calibration Report for AASHTO LRFD code*, Final Report, Project No. NCHRP 20-7/186, Transportation Research Board of the National Academies, Washington, D.C.

Kwon,O., E. Kim, and S. Orton (2010a), "Calibration of the Live Load Factor in LRFD Bridge Design Specifications Based on State-Specific Traffic Environments," *Journal of Bridge Engineering*, posted ahead of print on 13 December 2010.

Kwon,O., E. Kim, S. Orton, H. Salim, and T. Hazlett (2010b), *Calibration of the Live Load Factor in LRFD Design Guidelines*, Project 2a Report, Missouri Department of Transportation, MO.

Nowak, A.S. (1999), *NCHRP Report 368: Calibration of LRFD Bridge Design Code*, Transportation Research Board, National Research Council, Washington, DC.

Orton, S., Kwon, O., and Hazlett, T. "Statistical Distribution of Resistance of Bridges Using Updated Material Parameters," *Journal of Bridge Engineering* (in review).

Sivakumar, B., Ghosn, M., and Moses, F. (2008), *Protocols for Collecting and Using Traffic Data in Bridge Design*. NCHRP web-only document 135, Transportation Research Board, National Research Council, Washington, D.C.

Van de Lindt, J.W., Fu, G., Zhou, Y., and Pablo Jr., R. (2006), "Locality of Truck Loads and Adequacy of Bridge Design Load," *Journal of Bridge Engineering*, ASCE, Vol.10, No.5, pp.622-629

Coastal Bridge Reliability during Hurricane Events: Comparison of Fragility Curves by Static and Dynamic Simulation

Navid Ataei[1], Jamie E. Padgett[2]

[1]Graduate Research Assistant, Department of Civil and Environmental Engineering, Rice University, 6100 Main Street, MS-318, Houston, TX 77005;
E-mail: navid.ataei@rice.edu

[2]Assistant Professor, Department of Civil and Environmental Engineering, Rice University, 6100 Main Street, MS-318, Houston, TX 77005; PH: 713-348-2325;
E-mail: jamie.padgett@rice.edu

ABSTRACT

Post-hurricane functionality of the transportation system is vital for emergency response and recovery activities. Coastal bridges are among the most critical components of the transportation system susceptible to hurricane induced wave and surge loads that may hamper this functionality. This study explores alternative approaches to develop probabilistic statements of coastal bridge damage potential conditioned upon hazard intensity, known as fragility. Fragility surfaces for a representative bridge structure of the Houston/Galveston area are developed using two different approaches: static analysis and nonlinear dynamic simulation. The static approach is efficient and can provide sufficient fragility models for simply supported bridges with limited connectivity between the super structure and substructure, since their predominant mode of failure is deck unseating or shifting due to connection failure. Nevertheless, for bridges with strong connection between sub and superstructure, the force transfer can cause other components to exceed their limit state. Hence the full dynamic behavior of structure becomes more critical in the fragility modeling of bridges with high strength connections.

INTRODUCTION

High exposure of the transportation system in coastal regions to hurricane events (Chen et al. 2007) along with the continuous development in these areas (Crossett et al. 2004) underscore the importance of studying the vulnerability of the transportation network due to coastal storms. Any damage to the transportation network affects the post event recovery and restoration of a region and also leads to significant economic losses. Since bridges are the key components in the transportation infrastructure which their susceptibility to hurricane induced surge and wave loads was illustrated in past events along the Gulf Coast, this study focuses on the reliability assessment of coastal bridges.

Damages to bridges in recent hurricane events, such as Ivan (2004), Katrina (2005) Ike (2008), drew the attention of the research communities to the performance of bridge structures vulnerable to coastal storms. The study of the bridge performance has started by the reconnaissance lessons (Mosqueda et al. 2007; NIST 2006; Okeil and Cai 2008; Padgett et al. 2008; Robertson et al. 2007). Along with these field observations, coastal researchers have reported on the hydrological aspects of the hurricane induced wave and surge by hind-casting of wave and surge parameters (Chen et al. 2009; Chen et al. 2007; Cheung et al. 2003; Levinson et al. 2010; Panigrahi and Misra 2010; Zhixia et al. 2009). Another critical advance in the field has been developed by the beginning of studies on the evaluation of wave forces on bridge decks (Chen et al. 2009; Douglass et al. 2006; Huang and Xiao 2009; Marin and Sheppard 2009; Meng and Jin 2007; Schumacher et al. 2008); which finally have led to the first specifications for bridges vulnerable to coastal storms (AASHTO 2008). These studies have eased the path toward the probabilistic assessment of the susceptibility of coastal bridges, which is currently lacking in the literature. These models are essential for regional risk and loss estimates, determining the potential damage to major transportation routes and support risk mitigation plans and decision-making about retrofitting.

This paper proposes and evaluates different methodologies for developing of fragility curves for bridges susceptible to hurricane induced loads. Fragility curves provide conditional probability estimates of failure, or of exceeding a particular damage state, given hazard intensity. Analytical fragility curves may be developed by employing dynamic time history analysis of nonlinear finite element models that are capable of capturing evolving structural demand on different bridge components across various modes of failure. However, a static analysis approach has the advantage of computational efficiency that may be sufficient to capture one important failure mode of the bridge structure, deck shifting or unseating. In the static analysis approach, the vertical resistance of superstructure is compared with the maximum demand of the wave forces. Hence this method is appropriate for simply supported bridges, where according to the field observations deck unseating is the most common mode of failure (Chen et al. 2009; Meng and Jin 2007; Padgett et al. 2008).

This paper describes both static and dynamic analysis approaches to develop the fragility curves for coastal bridges and demonstrates the application of these methodologies through a case study representative bridge of Houston/Galveston bridge inventory. Key features include the identification and propagation of uncertainty in the performance assessment for both demand and capacity estimation.

STATIC FRAGILITY MODELING OF DECK UNSEATING UNDER STORM SURGE AND WAVE LOADS

For any given damage state, fragility surfaces provide us with conditional probability of failure (exceeding the given damage state) for given hazard parameter(s), known as intensity measure(s) (IMs). In other words, fragility surfaces introduce the probability of structural demand exceeding structural capacity for the entire reasonable range of intensity measure(s).

For the static analysis of deck unseating, failure is considered when the vertical uplift force is greater than the vertical uplift capacity. Consequently, the bridge span moves freely due to wave transverse and vertical forces. The following subsections describe the probabilistic modeling for estimation of vertical uplift capacity and demand. After attaining the probability distributions of capacity and demand as explained in these sections, the probability of failure of each span can be assessed. Fragility surfaces are obtained by performing 1000 Monte Carlo simulations per unique span of each bridge for each combination of IMs. The spans are considered as series system, thus failure in any of them results in the failure of the entire system. The probability of failure of each span is considered to be independent from others. Hence, the probability of the deck shifting or unseating for the entire bridge, P_F, is the union of probability of failure of each individual span.

Surge and Wave Forces: Demand Modeling

An appropriate wave and surge load model is essential to evaluate the forces on bridge deck. There was a gap in the literature for calculation of wave forces, since these forces were traditionally not considered in bridges design. However, empirical evidence reveals their potential to yield bearings, damage guardrails, shift and unseat spans, among other component damage. Subsequently, a recent body of research has focused on hazard modeling and estimation of surge and wave forces on bridge superstructures (Cuomo et al. 2009; Huang and Xiao 2009; Marin and Sheppard 2009; Meng and Jin 2007; Okada et al. 2006). Douglass et al. (2006) and Aguíñiga et al. (2008) provide reviews of available methods to calculate wave forces on bridge superstructure. The basis of many of the equations for wave loads on bridge decks are from previous works in offshore engineering. Nevertheless, modification is needed to the offshore equations since coastal bridges are located in shallow bodies of water and different geometry. In this paper, the load estimates used to illustrate the bridge response to deck wave forces is derived from the recent AASHTO specifications for bridges vulnerable to coastal storms (AASHTO 2008). The load models were derived from the extensive studies of Sheppard and Marin (2009) and have been selected due to their accuracy with experimental and field data.

The wave imparts two different loads on bridge deck: a slowly time varying force; refer to as quasi-static and a sudden impulse-like force attributed to trapped air. The quasi-static force is composed of a drag, inertial and buoyant force. The calculation of these forces have a theoretical background based on Kaplan's work for offshore platforms and Morrison's equation improved by the added mass computation and discritizing the domain (Marin and Sheppard 2009). Drag and inertial coefficients are found based on experimental tests. The complete equations of the wave peak forces and corresponding coefficients are presented in AASHTO 2008.

Four hazard parameters are used for demand estimation: maximum wave height (H_{MAX}), wave period (T_p), wave length (λ) and relative surge elevation (Z_c). Due to the complexity of wave forces under storm surge and wave passage, it is not possible to condition the probabilistic demands or probability of failure on any one of the wave and surge parameters alone and randomly propagate uncertainties in other parameters while still maintaining accuracy and efficiency in the predictive model. The failure probability is therefore conditioned on at least two hazard parameters as

concluded in recent work (Ataei and Padgett 2010). Implementing the relative surge elevation as one of the hazard intensity measures (IMs) is critical, since as its name suggests, it delineates the elevation of the bridge deck relative to the water surface, and the responses change clearly with its alteration. In addition, the three wave parameters are related to each other, as it is shown for example in proposed equations of (AASHTO 2008), and other ocean engineering literature (Le Roux 2007); hence, it is not rational to employ all of them independently. Thus, a two parameter vector based IM has been implemented, given relative surge elevation along with any of the wave parameters, adopted as wave height herein due to the criteria of "hazard computability".

For probabilistic assessment of structural performance, uncertainties associated with each parameter realization should be taken in to account. Table 1 defines the structural, wave and surge parameters that are considered in the reliability analysis and their corresponding probability distributions. Probability distribution of wave period is briefly introduced here. Wave period corresponds to maximum wave height is calculated using the Longuet-Higgins joint probability of wave height and wave period (Longuet-Higgins 1983). The value of wave spectral density, v, is required for the use of this distribution. In general, the value of v is small during the storm surge. 0.3 is chosen for v according to the Massel's suggestion (Massel 1997).

Table 1. Parameters required for demand and capacity estimation.

Wave and surge parameters					
			Distribution Parameters		
Variable	**Symbol**	**Distribution**	**1**	**2**	**Unit**
Maximum wave height	H_{MAX}	Function of H_s	-	-	m
Wave Period	T_p	Longuett-Higgins	$\nu^1 = 0.3$	-	s
Wave length	λ	Function of T_p	-	-	m
Relative surge elevation	Z_c	Uniform	$l^2 = 90\%$	$u^3 = 110\%$	m
Structural parameters					
Width	W	Deterministic	-	-	m
Girder height	d_g	Deterministic	-	-	m
deck thickness	d_b	Uniform	$l^2 = 95\%$	$u^3 = 105\%$	m
Concrete strength	f'_c	Normal	$\mu^4 = 21$	$\sigma^5 = 4.3$	MPa
Steel strength	f_y	Lognormal	$\lambda^6 = 6.02$	$\zeta^7 = 0.08$	MPa
Concrete density	γ_c	Normal	$\mu^4 = 2400$	$\sigma^5 = 96$	kg/m^3
Steel density	γ_s	Normal	$\mu^4 = 7850$	$\sigma^5 = 78.5$	kg/m^3

[1] Wave spectral density.
[2] Lower bound for uniform distribution, in percentage.
[3] Upper bound for uniform distribution, in percentage.
[4] Mean value of normal distribution.
[5] Standard deviation of normal distribution.
[6] Mean value of lognormal distribution.
[7] Standard deviation of lognormal distribution.

In order to take into account uncertainties associated with the surge elevation, a uniform distribution for surge elevation with lower and upper limit of 90% and 110% is considered. Relative surge elevation, which is the difference between deck clearance and surge elevation, is used in the calculation of wave forces. To be consistent with capacity modeling, a uniform distribution for the deck thickness is also considered in demand modeling, where the thickness can be varied from 95% to

105% of the nominal value presented in as built drawings. Other structural geometric parameters that are required for forces estimation are considered deterministic, as the small variation in them cause a negligible effect on the magnitude of wave forces.

Capacity Modeling

The vertical resistance of the span to uplift consists of the dead weight of the deck as well as the connection strength between superstructure and substructure, if any exists. The dead weight of each bridge span is assessed considering uncertainty in the unit weight of construction materials as well as some workmanship or construction errors to reflect uncertainty in as-built plans relative to field condition. A normal distribution for concrete and steel density is selected based upon (JCSS 2001), and the corresponding values are presented in Table 1. To account for workmanship and construction errors, a uniform distribution for deck thickness is considered with lower and upper limit of 95% and 105% of the as-built plan thickness, thereby affecting the span volume and dead weight estimate. Other geometric parameters, such as the girder type and height, are taken as deterministic.

If vertical connectivity is present, its contribution to the capacity model can be characterized by the pullout or yield strength of the dowel bars, depending upon its embedment length. Concrete and steel strengths are also required to estimate the required development length of the dowels and connection strength. The steel and concrete mean strength are based on the properties of the bridge inventory of larger Houston area, and the coefficients of variations are based on (Ellingwood and Hwang 1985) as shown in Table 1. The summation of the deck weight and connection strength per unit length is the total uplift capacity of the deck.

DYNAMIC FRAGILTY MODELING

The use of nonlinear time history analysis is typically preferred over linear static approaches for reliability assessment of the structures since it can capture displacement based demands and account for accumulation of damage over time. For the dynamic simulations, the same structural and wave probability distributions are adopted as those presented in the previous section (Table 1). Since the dynamic analysis requires time history of the loads, the following subsection briefly describes a simplified model to estimate the wave loads time series. The structural demand is measured in the terms of deck displacement for the deck unseating mode of failure. Additionally, column curvature ductility demand and dowels deformation are also recorded during the analysis to allow the fragility modeling of these components presented in a later section.

Surge and Wave Forces: Demand Modeling

The AASHTO equations (AASHTO 2008) adopted for the evaluation of the peak value of wave and surge loads are extrapolated in a simplified deck load time history model. The model is based on previous reports of wave loads with assumptions briefly described herein. Forces are in phase with the wave, hence, the wave forces in this research have been taken as a sinusoid with a period equal to that of the wave and maximum amplitude equal to that of the maximum quasi-static load. The impact

loads are then superimposed on the quasi-static forces. The impact loads were observed to have an effect on the bridge for approximately 5/8 the period of the wave, based on visual observation of results given by (Sheppard and Marin 2009). It is assumed that the wave is moving at a constant velocity. In addition to the vertical and horizontal forces, moment induced by wave should also be considered. When a wave passes over a bridge deck, the forces imparted change dramatically with time, and those forces cause moments on the bridge deck. The moment is calculated about the center of the bridge deck at each time step using the moment arm method. More discussion on the wave load model is provided in (Ataei et al. 2010). Since the bridge deck is allowed to uplift during the simulation if the vertical loads overcome the vertical resistance, the relative surge elevation changes during the analysis. Hence, a procedure is written to update the wave forces during the analysis based on the position of the deck.

Description of Bridge Finite Element Model

The representative bridge of the area of interest that will serve as a case study is a three-span simply supported concrete box beam bridge. The selected bridge is the most common bridge type in the Houston/Galveston bridge inventory. The spans' length is 15.2 m, and the width is 10.9 m. The outmost spans of the bridge are supported on seat type abutments. The substructure consists of two bent caps, each supported with three 0.9m diameter circular concrete columns; all of them with eight #9 longitudinal reinforcement. The bent caps have a rectangular 0.87m width and 0.91m depth cross section. Two different models with different pier-deck connection capacity are analyzed. The first one has a weak connection, where limited resistance to uplift is provided only by the deck weight and resistance of four dowels with the embedment length of 0.2m at each side of the spans. The strong connection model has twelve dowels at each side with 0.7m embedment length. For the dynamic simulation, the bridge deck is considered as unseated if the vertical displacement is more than the embedment length or transverse displacement is larger than 1m, although these limits are easily adaptable.

The numerical model for the bridge is developed in OpenSees, based largely upon past recommendations for typical CSUS concrete bridges (Nielson 2005). Unique consideration, however, is made in the connection modeling to capture the response of the bridge under the coupled vertical and horizontal forces of waves appropriately. Specifically, a contact element has been incorporated to allow the deck to be uplifted from the supports, and settle back on the bent beam when the vertical force reduces during wave passage. This vertical contact element is used in conjunction with a pounding element to reflect the impact loads and energy dissipation upon slamming of the deck back on the supports after uplift. The pounding element is a bilinear spring with properties are calculated based on (DesRoches and Muthukumar 2002) recommendations for impact elements. Contact elements are used in parallel with springs representing the dowel bars. Since the embedment length of the dowels is less than the required development length in tension, their behavior is governed by a pullout model. The properties and probability densities that are used for material strengths and weights are described in Table 1.

Deterministic Response Analysis

A sample deterministic response analysis is conducted to illustrate the dynamic response of the representative bridge with limited connection capacity under hurricane induced surge and wave loading. The mean values for material properties are employed for this deterministic study. The wave and surge parameters are H_{MAX} = 1.9m, Z_c = -0.63m, T_p = 5.8s and λ = 34m. Figure 1 illustrates the deck displacement as well as dowel bars force-deformation behavior. The embedment length of dowel is approximately 200 mm, and as shown in Figure 1, the dowel is completely pulled out after this displacement and does not carry any more force. The deck is fully uplifted and slammed back to its support and large displacements are observed in both the transverse and vertical direction.

Figure 2 depicts the transverse moment-curvature response of the column in the waveward direction of the pier supporting decks 1 and 2, as well as axial force time history. Large axial forces transfer to the column after impact. Also, before failure of the dowels, the column axial load changes from compression to tension due to vertical load. This reveals the important interaction between deck and pier under surge and wave loading, and the potential of strong connections to transfer damage from the super- to substructure—an important consideration in later system fragility analysis considering multiple failure modes.

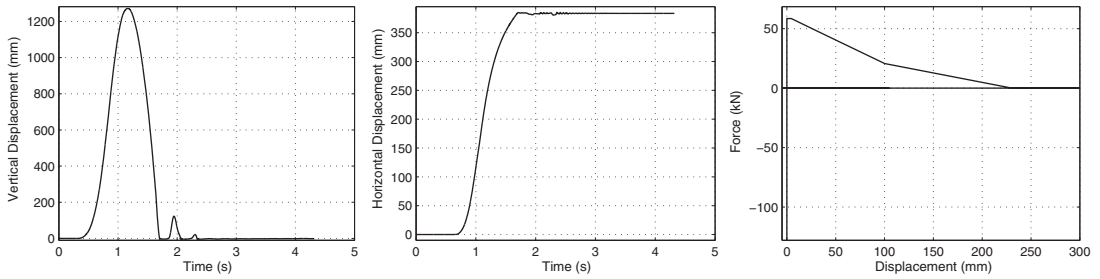


Figure 1. Deck vertical and transverse displacement, and dowel force – pullout model.

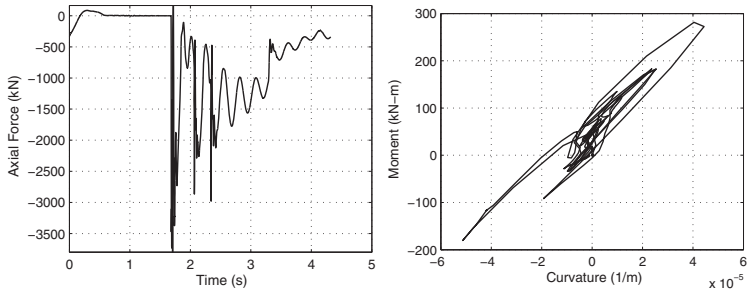


Figure 2. Time history of axial force and moment curvature for one of the columns - pullout model.

COMPARISON OF DECK UNSEATING FRAGILITIES FROM DYNAMIC AND STATIC APPROACHES FOR THE BRIDGE WITH LIMITED CAPACITY CONNECTION

Fragility surfaces for deck unseating have been developed for the representative bridge with pullout connection adopting both dynamic simulation and static analysis strategies. For the bridge with weak connection, all of the components except

connection dowels remain in their elastic range. From the results of the analysis it has been concluded that for the multi span simply supported bridges with limited connectivity, most ranges of realistic hurricane induced hazard parameters lead to extreme cases of deck response (e.g., either well below damage level or resulting in severe deck displacement); hence adopting a higher value for vertical displacement limit leads to almost identical fragility surface. Furthermore, employing the vertical displacement limit state without considering transverse displacement limit state for dynamic analysis leads to the similar reliability estimates. The extreme response of the deck due to wave and surge loads leads to similar probabilistic estimates for static and dynamic analysis, where Figure 3 compares the result of static and dynamic simulation. The findings demonstrate the potential viability of the static approach for assessment of the deck unseating failure mode for bridges with limited capacity connections prevalent in the Gulf coast inventory, and particularly in the Houston/Galveston region.

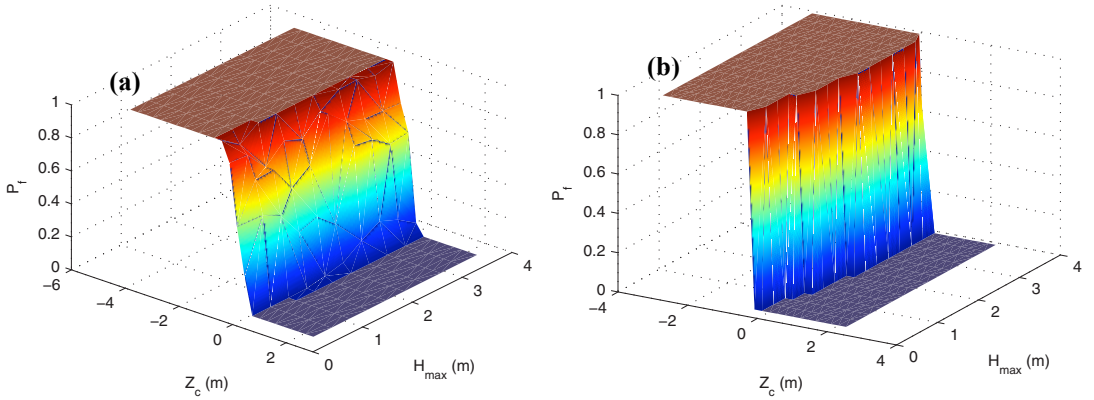


Figure 3. Fragility surfaces for deck unseating: (a) static; and (b) dynamic analysis.

FRAGILITY SURFACES CONSIDERING MULTIPLE COMPONENT FAILURES FOR THE BRIDGE WITH HIGH STRENGTH CONNECTIONS

The fragility under surge and wave load is assessed in this section for the multiple span simply supported concrete box beam bridge with high strength connections. In this model, the connection dowels reach their yield strength prior to pullout. Strengthening the deck-pier connection is also one new design or retrofit detail that has been considered to help avoid unseating of coastal bridges. This strong connection causes significant force transfer to the substructure, thus introduces large demands on columns. Since the column axial force is not constant during wave passage, its yield and ultimate curvature changes during the simulation, which is taken into account by calculating the yield and ultimate curvature at each time step. In this study, two different limit states are considered: yield (major) and complete. For the columns, considering flexural failure by measuring curvature ductility demand as the only demand parameter is not sufficient since another important mode of failure is possible with this strong connection, which is the tensile failure of the columns. For this particular demand (EDP), a column assumed at the major damage state if the axial force is larger than the cracking load of the section, and at the complete state if the tension force exceeds the required force to yield the longitudinal reinforcement.

This discussion reveals that considering both tensile force and curvature ductility demand is required for the columns. Hence, a column reaches the major damage state if the demand curvature passes yield curvature or tensile force exceeds the cracking load. Table 2 illustrates the limit states for the structural components as well as for the entire system. The deck unseating is also considered as one of the complete failure modes by considering the fracture displacement of dowels, as noted in Table 2. However, for the assumed connection type columns exceed the complete limit state before the deck unseating. Nevertheless, the results of this section can be generalized to the cases where the deck unseating occurs before any collapse in substructure by dividing the failure probability into two parts and applying the total probability theorem, as, for example, illustrated in (Baker and Cornell 2005).

Table 2. Limit states.

Limit State	Columns	Connections	System
Yield	$c/c_y>1$ *or* $P_t>F_{crack}$	d_d> yield disp.	Columns or connections in major damage state
Collapse	$c/c_c>1$ *or* $P_t>F_{tmax}$	d_d> fracture disp.	Columns or dowels in complete damage state

Contrasting the deck unseating analysis for the weak connection bridge, it is possible to observe a functional relationship between the EDPs (displacement, curvature ductility demand, or axial force) and the wave and surge parameters. Table 3 shows the relationship and the test of goodness of fit in terms of R^2. It should be noted that the initial clearance of the bridge (Z_{c0} of zero surge) is added to the values of negative of Z_c, since it can take negative values (submergence).

Table 3. Coefficients for functional relationship $\ln EDP = a \ln(-Z_c + Z_{c0}) + b \ln H_{MAX} + c$.

Analysis	*EDP*	Symbol	*a*	*b*	*c*	R^2
Dynamic	Maximum tensile force ratio	P_t/F_{tmax}	3.9121	-0.0679	-7.155	0.781
	Curvature ductility demand	c/c_y	1.9741	-0.0123	-9.568	0.746
	Ultimate curvature ratio	c/c_u	2.8885	0.0948	-14.6789	0.796
	Dowel deformation	d_d	12.162	0.3254	-24.072	0.751
Static	Maximum tensile force ratio	P_t/F_{tmax}	3.7373	-0.0381	-6.237	0.832

For comparison, the maximum forces in columns are also calculated by adopting maximum wave forces in static approach and performing a linear structural analysis. The column curvature and dowel bar deformation are not calculated, since the analysis is linear. The resulting equation for the maximum tensile demand is similar to the dynamic analysis, and the corresponding coefficients are presented in the last row of Table 3.

Fragility surface for each component can be assessed, assuming that distribution of EDPs in logarithmic space is normal, according to the following equation:

$$P(EDP \geq LS \mid \mathbf{im} = [Z_c \;\; H_{MAX}]) = 1 - \Phi\left(\frac{\ln LS - (a \ln(-Z_c + Z_{c0}) + b \ln H_{MAX} + c)}{\sigma}\right)$$

Where Φ is the normal cumulative distribution function and σ is the standard deviation of the regressed functional relationship in the logarithmic space. Figure 4 plots the fragility surfaces for the columns tensile demand and dowel bar deformation

for major damage state. It should be noted that applying either static or dynamic approach yields similar fragility surface for the columns tensile demand. However, this limit state is force-based, and other limit states based on deformation may not be feasible to assess under such simplified analyses methods.

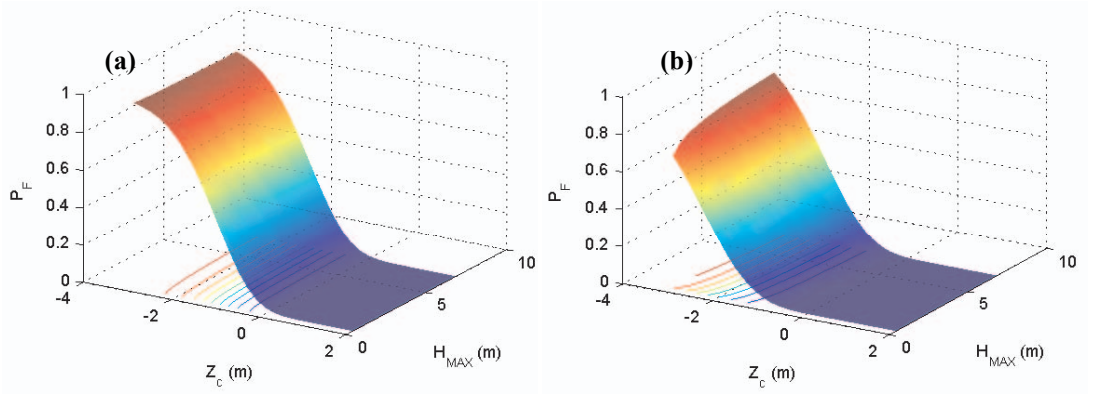


Figure 4. Fragility surface for yield damage state: (a) column tensile demand; and (b) dowel deformation.

The fragility for the entire structure is constructed by the assumption of series system, i.e. the system is in a particular damage state if any of its components is in that damage state. The probability distributions of components are combined into a joint normal probability distribution in the transformed logarithmic space. By this methodology, the system level fragility is shown in Figure 5. For the case study bridge structure, the system fragility is mostly influenced by the columns tensile limit state, in both damage states. Hence, the static fragility for the columns may serve as an efficient and viable lower bound of the system fragility. Future work will investigate alternative system definitions appropriate for capturing the failure modes and consequences of damage for bridges under surge and wave loading.

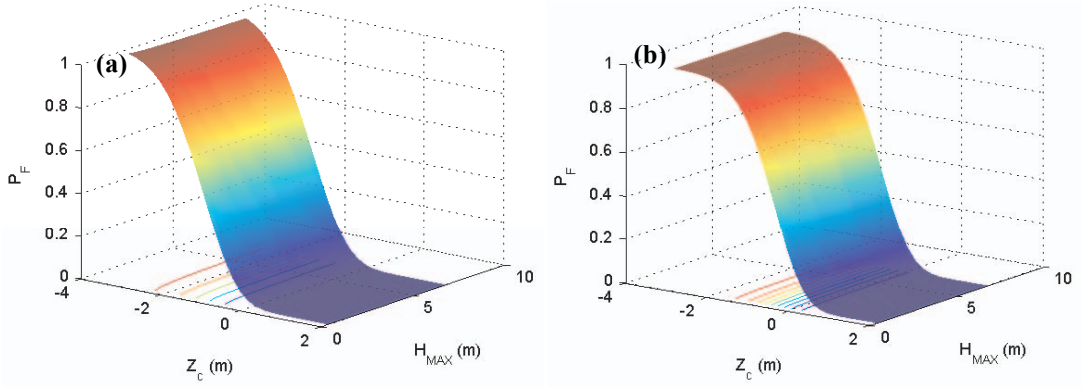


Figure 5. System fragility surface: (a) major; and (b) complete.

CONCLUSIONS

This paper proposes two different analytical methodologies to probabilistically assess the reliability of coastal bridges susceptible to hurricane induced storm surge and wave. A simply supported concrete bridge, as a representative bridge of Houston/Galveston area, is selected for the case study to demonstrate the application of the static and dynamic methodologies for the development of conditional probability estimates given hazard parameters (fragility surfaces). The results of this study reveal that for simply supported bridges, deck unseating is the predominant mode of failure and that a static approach with rigorous uncertainty treatment may approximate the fragility with acceptable accuracy. Conversely, when a strong deck-pier connection exists, the structural demand on substructure should also be taken into account, since large forces are transmitted through the connection from the bridge deck to the substructure. In particular, results show large tensile forces in columns, which is not typical in design of columns and foundations. Currently, the linear static approach is able to account for the columns tensile demand. However, it is not able to correctly account for displacement based demands such as the column curvature. Hence, for a complete system reliability assessment of bridges with strong connections between sub and superstructure, nonlinear dynamic analysis is preferred. Nonlinear static analysis is part of the ongoing research to evaluate its possible applicability for this type of bridge with strong connection, as well as the investigation of system logic for system fragility modeling of bridges under surge and wave loading.

ACKNOWLEDGEMENTS

The authors would like to acknowledge the support of the Houston Endowment.

REFERENCES

AASHTO. (2008). *Guide Specifications for Bridges Vulnerable to Coastal Storms*, American Association of State Highway and Transportation Officials (AASHTO).

Ataei, N., and Padgett, J. "IM Study for Probabilistic Modeling of Coastal Bridges Susceptible to Hurricane Events." *International Symposium on Reliability Engineering and Risk Management (ISRERM2010)*, Shanghai, China.

Ataei, N., Stearns, M., and Padgett, J. E. (2010). "Response Sensitivity for Probabilistic Damage Assessment of Coastal Bridges under Surge and Wave Loading." *Transportation Research Record*, 2202 (3), 93-101.

Baker, J. W., and Cornell, C. A. (2005). "A vector-valued ground motion intensity measure consisting of spectral acceleration and epsilon." *EARTHQUAKE ENGINEERING AND STRUCTURAL DYNAMICS*, 34, 1193-1217.

Chen, Q., Wang, L., and Xhao, H. (2009). "Hydrodynamic investigation of coastal bridge collapse during Hurricane Katrina." *Journal of Hydraulic Engineering*, 135(3), 175-186.

Chen, Q., Wang, L., Zhao, H., and Douglass, S. L. (2007). "Prediction of storm surges and wind waves on coastal highways in hurricane-prone areas." *Journal of Coastal Research*, 23(5), 1304-1317.

Cheung, K. F., Phadke, A. C., Wei, Y., Rojas, R., Douyere, Y. J. M., Martino, C. D., Houston, S. H., Liu, P. L. F., Lynett, P. J., Dodd, N., Liao, S., and Nakazaki, E. (2003). "Modeling of storm-induced coastal flooding for emergency management." *Ocean Engineering*, 30(11), 1353-1386.

Crossett, K. M., Culliton, T. J., Wiley, P. C., and Goodspeed, T. R. (2004). "Population Trends Along the Coastal United States:1980-2008." National Oceanic and Atmospheric Administration (NOAA).

Cuomo, G., Shimosako, K.-i., and Takahashi, S. (2009). "Wave-in-deck loads on coastal bridges and the role of air." *Coastal Engineering*, 56(8), 793-809.

DesRoches, R., and Muthukumar, S. (2002). "Effect of pounding and restrainers on seismic response of multiple-frame bridges." *Journal of Structural Engineering*, 128(7), 860-869.

Douglass, S. L., Chen, Q., Olsen, J. M., Edge, B. L., and Brown, D. (2006). "Wave Forces on Bridge Decks." Office of Bridge Technology, Washington, D.C.

Ellingwood, B., and Hwang, H. (1985). "Probabilistic descriptions of resistance of safety-related structures in nuclear plants." *Nuclear Engineering and Design*, 88(2), 169-178.

Huang, W., and Xiao, H. (2009). "Numerical modeling of dynamic wave force acting on Escambia bay bridge deck during Hurricane Ivan." *Journal of Waterway, Port, Coastal and Ocean Engineering*, 135(4), 164-175.

JCSS. (2001). "JCSS PROBABILISTIC MODEL CODE - PART 3: RESISTANCE MODELS." Joint Committee on Structural Safety.

Le Roux, J. P. (2007). "A simple method to determine breaker height and depth for different deepwater wave height/length ratios and sea floor slopes." *Coastal Engineering*, 54(3), 271-277.

Levinson, D. H., Vickery, P. J., and Resio, D. T. (2010). "A review of the climatological characteristics of landfalling Gulf hurricanes for wind, wave, and surge hazard estimation." *Ocean Engineering*, 37(1), 13-25.

Longuet-Higgins, M. S. (1983). "On the Joint Distribution of Wave Periods and Amplitudes in a Random Wave Field." *Proceedings of the Royal Society of London. Series A, Mathematical and Physical Sciences*, 389(1797), 241-258.

Marin, J., and Sheppard, D. M. "Storm Surge and Wave Loading on Bridge Superstructures." *Structures Congress 2009*, Austin, Texas, 62-72.

Meng, B., and Jin, J. (2007). "Uplift Wave Load on the Superstructure of Coastal Bridges." Structures Congress: New Horizons and Better Practices.

Mosqueda, G., Porter, K. A., O'Connor, J., and McAnany, P. "Damage to Engineered Buildings and Bridges in the Wake of Hurricane Katrina." *Forensic Engineering Symposium*, Long Beach, California, USA, 4-14.

Nielson, B. (2005). "Analytical Fragility Curves for Highway Bridges in Moderate Seismic Zones," Georgia Institute of Technology, Atlanta.

NIST. (2006). "Performance of Physical Structures in Hurricane Katrina and Hurricane Rita: A Reconnaissance Report."

Okada, S., Mitamura, H., and Ishikawa, H. (2006). "The collapse mechanism and the temporary restoration of Omori Bridge damaged by the storm surge of Typhoon No. 18 in 2004." Technical Memorandum of Public Works Research Institute, 185-192.

Okeil, A. M., and Cai, C. S. (2008). "Survey of short- and medium-span bridge damage induced by Hurricane Katrina." *Journal of Bridge Engineering*, 13(4), 377-387.

Padgett, J., Desroches, R., Nielson, B., Yashinsky, M., Kwon, O.-S., Burdette, N., and Tavera, E. (2008). "Bridge damage and repair costs from Hurricane Katrina." *Journal of Bridge Engineering*, 13(1), 6-14.

Panigrahi, J. K., and Misra, S. K. (2010). "Numerical hindcast of extreme waves." *Natural Hazards*, 53(2), 361-374.

Robertson, I. N., Riggs, H. R., Yim, S. C. S., and Young, Y. L. (2007). "Lessons from Hurricane Katrina Storm Surge on Bridges and Buildings." *Journal of Waterway, Port, Coastal, and Ocean Engineering*, 133(6), 463-483.

Schumacher, T., Higgins, C., Bradner, C., Cox, D., and Yim, S. C. (2008). "Large-Scale Wave Flume Experiments on Highway Bridge Superstructures Exposed to Hurricane Wave Forces." The Sixth National Seismic Conference on Bridges & Highways, Charleston, South Carolina.

Sheppard, D. M., and Marin, J. (2009). "Wave loading on Bridge Decks." Florida Department of Transportation, Tallahassee, Florida.

Zhixia, Z., Yang, Y., and Ke, Z. "A numerical simulation method of typhoon waves." *Proceedings of the International Offshore and Polar Engineering Conference*, 800-805.

EFFECTS OF THE JANUARY 2010 HAITIAN EARTHQUAKE ON SELECTED EQUIPMENT AND THE IMPLICATIONS FOR THE SEISMIC DESIGN OF CRITICAL NON-STRUCTURAL COMPONENTS REQUIRED FOR POST-EARTHQUAKE RECOVERY OPERATIONS IN DEVELOPING COUNTRIES

Nathan C. Gould, D.Sc., P.E., S.E.[1], Barry J. Goodno, Ph.D., P.E., F.ASCE[2], Phillip L. Gould, Ph.D, P.E., S.E., F. ASCE[3], Philip Caldwell[4]

[1]Director and Chief of Technology, ABS Consulting, 77 Westport Plaza, Suite 210, St. Louis, MO 63146; Ph (314) 819-1550; email: ngould@absconsulting.com
[2]Professor, School of Civil & Environmental Engineering, Georgia Institute of Technology, Atlanta, GA, 30332-0355, Ph (404) 894-2227, email:bg6@ce.gatech.edu
[3]Harold D. Jolley Professor, MEMS Department, Washington University, St. Louis, MO; Ph (314) 935 6383; email: pgoul@seas.wustl.edu
[4]Schneider Electric Codes & Standards, 1990 Sandifer Blvd., Seneca, South Carolina 29678, Ph (864) 886-1471; email: philip.caldwell@us.schneider-electric.com

INTRODUCTION

A team of engineers, funded by an NSF RAPID Grant, investigated selected critical electrical equipment, such as switchgear, motor control centers and inverters, at ten sites located in the Port-Au-Prince region that were subjected to strong ground motion during the 12 January 2010 Haiti earthquake. The investigations included a site survey of both damaged and undamaged electrical equipment, and included not only documentation of the physical damage to the equipment, but also consideration of the resulting consequences of the loss of use of the specific equipment and related systems.

While the observed damage modes for the selected equipment when subjected to strong ground motion were not unexpected, it was the consequences of the loss (actual or potential) of the use of the damaged equipment that presented important lessons for the investigating team.

This paper will detail the observed damage for selected non-structural elements subjected to strong ground motion during the 2010 Haiti earthquake. In addition, the paper will discuss the consequences of the loss of critical equipment at selected facilities in the Port-Au-Prince region and possible implications for the seismic design of critical non-structural components required for post-earthquake recovery operations in developing countries.

SURVEY OF SITES SURVEYED IN PORT-AU-PRINCE

Extensive planning prior to the visit to the Port-Au-Prince region allowed the Haiti mechanical and electrical equipment (MEP) survey team to maximize data acquisition activities during their time on site (April 11-15, 2010). The investigation team visited ten sites in and around Port-au-Prince in search of damage to mechanical and electrical equipment. The ten sites are listed in Table 1 and are identified on a map (Figure 1) which shows their general location in relation to the epicenter of the January 12, 2010 earthquake. While the focus was on damage to MEP components, the team observed and made note of damage to nonstructural elements and systems in general, if visible, during the guided tour of each site. Each site was given a unique two character ID (see Table 1) for use in cataloging and cross referencing the hundreds of digital photos and other information obtained by each member of the team.

The specific types of equipment found at selected sites as well as the types and severity of damage to each are discussed in follow on sections of this report. At each location, the team looked for and recorded the following information:

- Facility name, function, and local personnel contact information
- For selected equipment, the equipment name, and model, as well as the specific location and the function of the equipment within the facility
- The latitude and longitude of the equipment location (using hand-held GPS equipment)
- Damage to the equipment as a result of the strong ground motion; if damage occurred, evaluation of possible damage mode(s) (internal vs. external, anchorage, overturning, translation, etc.)
- Impact of the loss of the selected equipment from both a disaster response and disaster recovery perspective
- Contribution of the loss of the selected equipment to significant business interruptions at the facility, and associated level of financial impact of the loss of the equipment
- Detailed digital photographs, engineering sketches and measurements of the equipment layout, the supporting equipment pad, and any existing lateral restraint or anchorage
- Assessment of how long it will take the facility to replace or repair the damaged equipment.

Site	ID	Latitude	Longitude	Distance to epicenter (miles)
Center Petion Power Plant	PP	18.53574	72.38551	13.1
Adventiste Hospital	AH	18.53132	72.38644	13.1
ADRA Warehouse	AW	18.52672	72.38717	13.1
University Adventiste	UA	18.52671	72.38383	13.1
Port-au-Prince General Hospital	GH	18.53973	72.33938	13.1
Union School	US	18.51800	72.29913	18.4
Prestige Beer Plant	PB	18.57395	72.30482	19.2
U.S. Embassy	UE	18.56411	72.24883	22.4
CDTI Hospital	CH	18.53702	72.33125	16.7
Digicel	DB	18.53273	72.32324	16.7

TABLE 1 – SITES VISITED BY PROJECT TEAM TO RECORD MEP DAMAGE

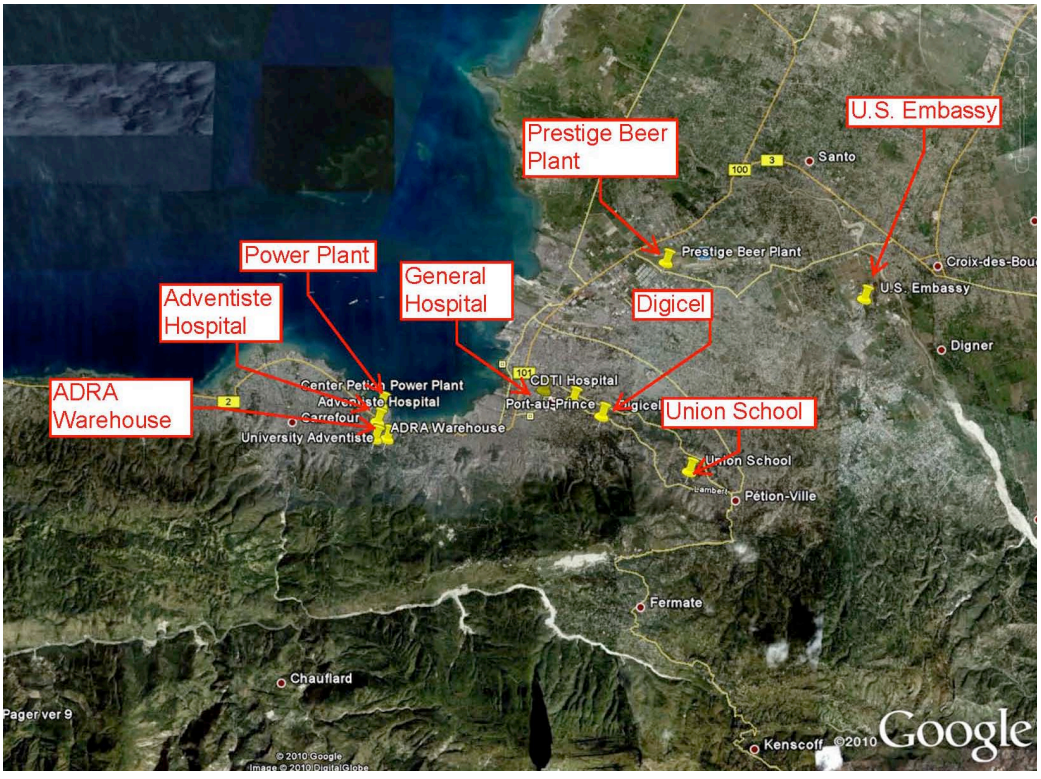


FIGURE 1 – MAPPED LOCATION OF THE TEN SITES VISITED BY THE PROJECT TEAM

TYPES OF ELECTRICAL EQUIPMENT SURVEYED

Facility electrical power distribution and control equipment, as well as system design and installation methods, surveyed at all sites were typical of what would be found in similar facilities in North America. Origin of manufacture was North America for a majority of the power system components (switchgear, transformers, conduit, etc.) at all locations.

Of note was that electrical system design and installation methods in two of the hospitals, Adventiste and Port-au-Prince General, were not as robust as and of less capacity than for similar size facilities in North America. Portions of the installations would not meet basic North American standards, much less the required seismic lateral restraint requirements, due to the absence of conduit or missing cover plates on junction boxes resulting in exposed power conductors and other poor installation practices.

Uniquely different from North American facility electrical systems was the common use of on-site diesel generators as the primary source of power. While all facilities had provisions for service entrance connection to the public utility power grid, very few used the grid as a sole source of power, even before the earthquake, due to reliability and cost. As a result, the North American paradigm of "emergency generator" does not exist in Haiti since on-site generation is frequently the normal source of power. This heavy reliance on user-owned diesel generators has significant implications for post disaster return-to-operational status for critical facilities due to interruptions in fuel availability and delivery. Assessment of the public electrical power utility system was not a focus of this survey but anecdotal evidence suggests that the local overhead electrical power distribution system was heavily damaged by building collapses, thus power was still not available in most of the Port-au-Prince area at the time of this survey. (The team was unable to obtain permission to enter and inspect EDH (Electricity de Haiti), the government owned and operated power plant located adjacent to Center Petion Power Plant.)

It was also common to see inverters used to supply power from deep cycle storage batteries to emergency lighting and similar essential loads during off hours when the generators were shut down. Inverters were also used during power interruptions associated with the transition from normal to alternate sources for facilities without paralleling transfer systems.

OBSERVED DAMAGE AT SELECTED SITES

Damage to electrical components and equipment was observed at all sites to some extent, although a disproportionate amount of damage to electrical equipment and components was observed at several key sites. Displacement of electrical equipment due to the absence of or inadequate anchorage was the most commonly observed damage state. Falling building debris and building displacement induced damage was also an issue. Observed displacement damage states typically had little or no impact

on electrical equipment functionality and any needed repairs had been or could be carried out with local resources. Had the ground motions been larger or lasted longer, the outcome may have been very different. Due to the space limitations of the paper, only damage at selected sites will be discussed below. Readers can find a more in-depth discussion of the damage observed at sites in other publications.

Digicel Building (DB):

Digicel is the main provider of wireless communications in the region. The primary Digicel facility in Port-Au-Prince consists of two major building, one of which sustained considerable structural damage. In addition to the buildings, the site also includes numerous auxiliary non-structural elements that are critical to the functionality of the communications facility.

An unanchored UPS system at Digicel, shown in Figure 2 below, consisted of multiple free standing cabinets located at grade level with top entry and exit electrical conduits. Cabinets were not fastened together, so they could slide independently. The UPS systems provide power to servers that control the cellular network node covering the Port-au-Prince area. As such, the UPS systems were a critical element for the cellular network. Attachment points for the conduit were the ceiling bracket just after the first 90 degree elbow and the top of the UPS enclosure. Stresses on the conduit and the attachment points were at a maximum between these points. UPS cabinets displaced to the right of their initial installation position as can be seen by the offset of their cabinets (left photo, Figure 2). The cabinets may have displaced laterally as much as five inches or more during the earthquake (right photo, Figure 2) in addition to an undetermined floor-to-ceiling interstory drift. Despite displacement demands on the conduit, the connections to the enclosures remained intact.



FIGURE 2 – DISPLACEMENT OF THE UPS CABINETS AT THE DIGICEL FACILITY

There were also multiple microwave antennas located on top of a trussed tower adjacent to the buildings, as shown in the photograph on the left in Figure 3 below. Each antenna either links with major nodes of the carrier's network or serves as an end point link to local cell sites in the Port-au-Prince area. Microwave links at these frequencies are highly directional, requiring highly specialized instruments and technicians to achieve the precision alignment required for reliable data links. The carrier operations manager reported that none of their tower-mounted microwave links required realignment after the earthquake. The only cellular antenna arrays reportedly damaged beyond repair were those at local sites on buildings that collapsed.

While the tower and microwave antennas were undamaged, the cable tray running from the cell tower to the Digicel low-rise building, which contains RF coaxial cables for antennas and microwave links, experienced considerable damage, as seen in the photograph on the right in Figure 3. The cable tray separated from its attachment to the building, probably due to significant differential interstory displacements of the heavily damaged low-rise building. The damage was limited to the cable tray attachment while the cell system itself remained functional. Had the RF coaxial cables been damaged, the ability of the Digicel to quickly restore system wide operation throughout Haiti would have been seriously impaired.

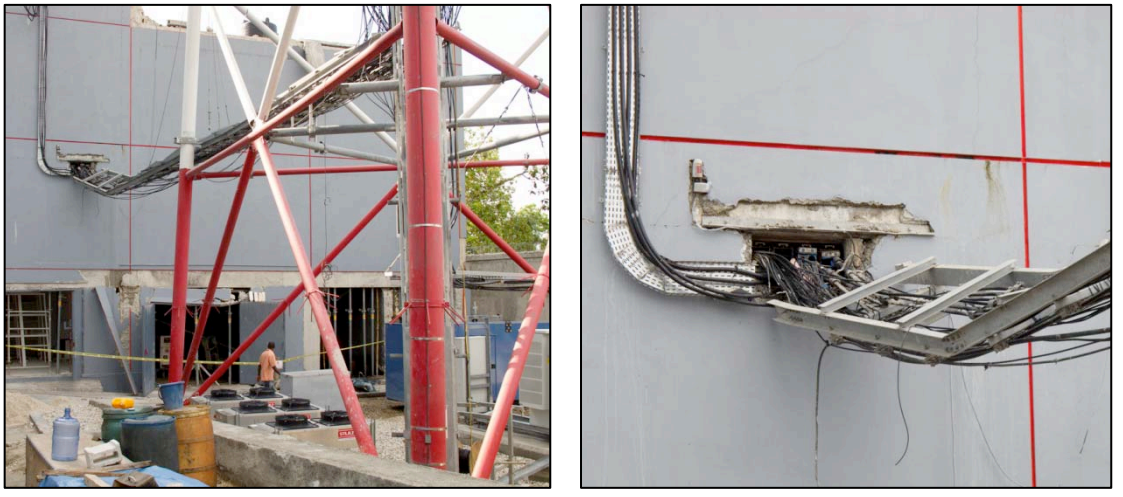


FIGURE 3 – MICROWAVE TOWER AND DAMAGED CABLE TRAY

General Hospital (GH):

Damage to the EDH public utility electrical service entrance area was visible at the Port-au-Prince General Hospital. Major components on site were a station circuit breaker, a diesel generator, an automatic transfer controls cabinet, a liquid filled pad-mounted transformer, and two voltage instrumentation transformers.

The general purpose cabinet with controls installed for automatic transfer of facility power source between the public utility and an on-site generator is shown in the photo on the left in Figure 4 below. The control wiring conduit at grade level pulled out of the cabinet when the cabinet moved off of its concrete pad due to a lack of anchorage, as shown in the photo on the right. Repairs to the cabinet and wiring appeared to be within capabilities of local resources.

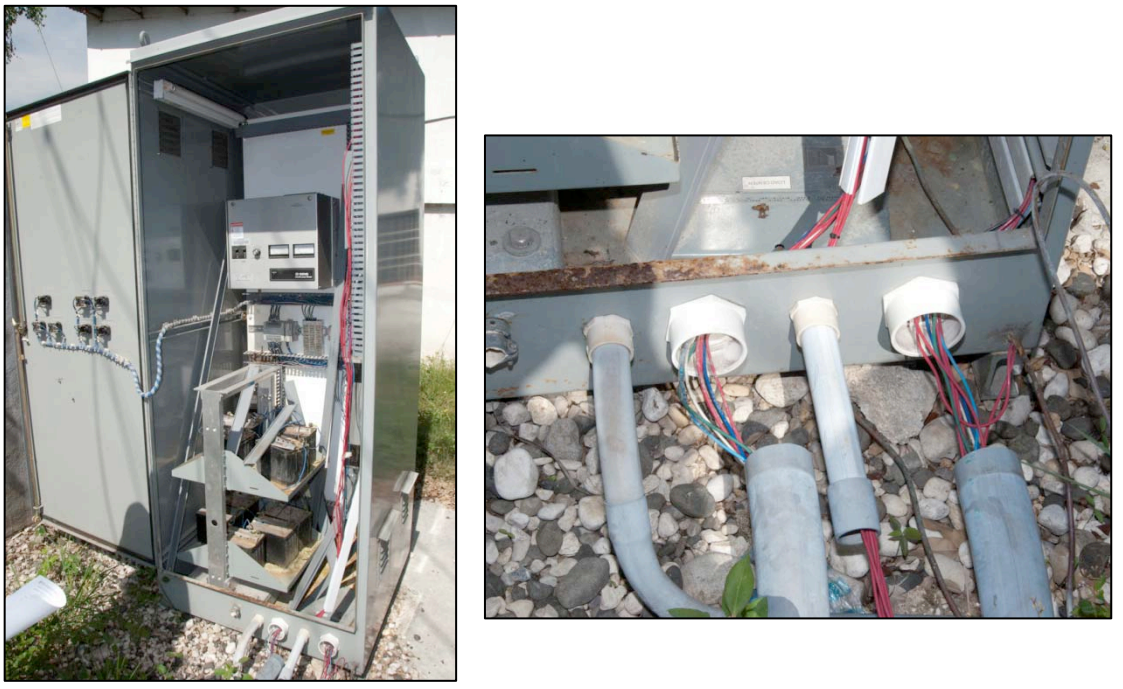


FIGURE 4 – DAMAGE TO AUTOMATIC CONTROL CABINETS

US Embassy (UE):

Overall, the U.S. Embassy buildings performed very well in the earthquake (Sawyer, 2010). There was no visible damage to the building itself, and only very minor damage was noted to selected non-structural elements. This represents validation of U.S. codes and practice for seismic design and construction, especially for structures and non-structural elements that are designed for a higher level of seismic performance.

The only damage visible in the facility's electrical switchgear room was to a general purpose free standing cabinet housing a power quality monitoring system. This cabinet is located on the equipment pad to the right of the draw-out switchgear for the incoming utility power system and was not attached to the draw-out switchgear. The cabinet was poorly anchored; the anchor bolt at the front left corner was observed to have backed out with damage to the flat washer, as shown in the photograph on the left in Figure 5 below. This damage appears to have been caused by impact due to left front corner uplift of the cabinet during rocking motion induced by the

earthquake. The photograph on the right shows damage to the right front corner of the cabinet pad. This corner failure appears to have been caused by a prying moment on the embedded anchor due to cabinet rocking during the earthquake.



FIGURE 5 – DAMAGE TO POWER QUALITY MONITORING CABINET

IMPACT OF LOSS ON DISASTER RESPONSE AND RECOVERY

The impact of the loss of power on the sites that were involved in the response and recovery effort appeared to be substantial. The Adventist and General Hospitals, both of which received a tremendous influx of patients following the earthquake, were limited in their operations due to the lack of city power and the finite capacity of their emergency generators. Staff at both hospital facilities mentioned that the lack of dependable power had an adverse impact on their ability to perform essential medical procedures and to deliver quality medical care.

At the General Hospital, a 440 kw generator that appeared to be in good condition was not being used because it was dedicated for use in the radiology department, which was not in service due to damaged equipment. In discussions with staff, it was unclear why the generator could not be re-tasked for use in another part of the hospital, although there were indications that the skilled labor required to remove and re-install the generator may not have been available following the earthquake.

The ADRA facility, which secures, stores and distributes food and other supplies to those in need, was a key component in the local earthquake response and recovery effort. The ADRA facility was well prepared to sustain post-earthquake operations even with a loss of city power, with relatively large generators in place given the size of the facility. However, it was noted that the anchorage and lateral restraint of the generators and their associated starter batteries appeared marginal at best. If the ground motion at this location had been stronger and/or of longer duration, the chance that the generators and starter batteries would have sustained significant damage would have increased substantially. A loss of emergency power generation capacity

at a facility such as ADRA would have a major negative impact on the response and recovery effort in that region of Port-Au-Prince.

SUMMARY AND CONCLUSIONS

The enormous scale of deadly destruction in Haiti can easily mask important lessons to be learned from the Haiti earthquake that should not be overlooked. Given that the sites surveyed were located approximately 13 to 23 miles from the epicenter of a M 7.0 earthquake with an estimated depth of 8 miles, the Haiti event is typical of an earthquake that could occur during the life of a critical facility located in any moderate to high seismic region of the world. The investigations of the project team at selected facilities in Haiti confirmed that non-structural elements that are well anchored and/or laterally restrained, such as those elements observed at the U.S. Embassy, will perform well during a moderate seismic event. However, the investigation also revealed that many critical institutions in an underdeveloped country such as Haiti do not utilize the state-of-the-art engineering design or construction practices when installing non-structural elements that are key to their post-earthquake operations.

While there is and always will be uncertainty about the exact nature of ground motions from the Haiti event, the damage survey observations were generally consistent with the performance goals of modern building seismic design standards such as ASCE 7-05. Completed in 2008, the new U.S. Embassy in Haiti was a text book example of how effective properly implemented seismic mitigation measures for building equipment and related systems can be in meeting the performance goal of operational after the event.

The focus of this survey team was to evaluate the performance of mechanical and electrical systems in selected critical facilities. The most significant finding was that absent or poorly implemented equipment seismic anchorage hampered the ability to restore essential systems to operation after the event. The survey team also noted that even when there is an awareness of the need to anchor and/or restrain non-structural elements, implementation of the lateral anchorage/restraint in accordance with the procedures detailed in ASCE 7-05 or other similar standards may not be practical due to financial and logistical issues in developing countries like Haiti.

Observations from selected Haiti critical facilities also demonstrate that even for very well designed and constructed critical facilities, a fundamental understanding of how to design, install and inspect electrical equipment seismic restraint is lacking and, as such, poses a significant risk to the post event operability of critical facilities. This long established fundamental knowledge gap suggests that effective methods to advance the state-of-the-art in seismic mitigation for critical facilities must be developed.

Designers of facilities that are being constructed in regions of the world where modern design standards are not typically utilized should be sensitive to the need to provide details for the lateral anchorage and/or restraint of critical non-structural elements that can be installed by the local construction trades. In addition, design professionals should advocate for construction observation to be provided at these critical facilities to ensure proper installation of anchors and lateral restraining elements. Observations of the project team following the Haiti earthquake suggest that there is a need to improve local installation practices for critical non-structural equipment, especially in under-developed regions of the world. Specifically, follow on studies should be targeted at designing and distributing installation details for non-structural elements in facilities that are critical to the post-earthquake response in under-developed countries (e.g., similar to that presented in FEMA 413, 2004 and 74, 2005.)

ACKNOWLEDGEMENTS

This research was sponsored by a National Science Foundation RAPID Grant (1034794). All results, conclusion and findings are solely those of the authors and do not necessarily represent those of the sponsors.

REFERENCES

Sawyer, Tom, "U.S. Embassy Tour Shows Small Measures Pay Off Bigtime", Engineering News-Record (ENR.com), April 21, 2010

ASCE 7-05, Minimum Design Loads for Buildings and Other Structures, American Society of Civil Engineers, 2005

FEMA 413. 2004, Installing Seismic Restraints for Electrical Equipment, Federal Emergency Management Agency

FEMA 74. 2005, Reducing the Risks of Nonstructural Earthquake Damage: A Practical Guide, Federal Emergency Management Agency

Structural Analyses to Replicate the Observed Damage to Engineered Buildings from the January 2010 Haiti Earthquake

D. Zhang [1], G. Federico[1], K. Telleen[2], A. Schellenberg[2], R. Fleischman[1], J. Maffei[2]

[1]Dept. of Civil Engineering & Eng. Mechanics, University of Arizona, 1209 E. Second St, Tucson, AZ 85721; PH (520) 621-2266; email: zdc@email.arizona.edu
[2]Rutherford & Chekene, 55 Second Street, Suite 600, San Francisco, CA 94105, PH: (415) 568-4400; FAX: (415) 618-0684; email: jmaffei@ruthchek.com

ABSTRACT

Although the majority of devastation in the January 12 2010 Haiti earthquake was from non-engineered structures, the earthquake also damaged several modern engineered buildings in the capital city of Port-au-Prince. Data gathered on the observed performance of a selection of these structures is being used for the purposes of comparison with, and calibration of, analysis-based predictions used in seismic assessment procedures. Structures were selected for investigation based on their damage state, available design information, and accessibility. These buildings are a small set of important engineered reinforced concrete structures within Port-au-Prince. The available information is being used to construct analytical models using state-of-the-art techniques for nonlinear dynamic analysis. Seismic hazard levels are being estimated by indexing to the level of demand required to bring about the observed damage. Conclusions on the efficacy of these methods are being drawn through comparisons of the predicted response to actual outcomes. The final deliverable is a report documenting the structure and design information; the post-earthquake state; the modeling techniques; analytical results/comparison and evaluation of the methods. As an interim report, this paper presents: (1) general Haiti earthquake information; (2) damage mapping of candidate structures; (3) preliminary analytical modeling.

1. INTRODUCTION

Although the majority of devastation in the January 12 2010 Haiti earthquake was from non-engineered structures, the earthquake also damaged several modern engineered buildings in the capital city of Port-au-Prince. Data gathered on the observed performance of a selection of these structures is being used for the purposes of comparison with, and calibration of, analysis-based predictions used in seismic assessment procedures. The work is being performed as a partnership between academia and industry with university researchers working alongside professionals from the earthquake engineering consultant firm Rutherford & Chekene.

Structures were selected for investigation based on their damage state, available design information, and accessibility. These buildings are a small set of important engineered reinforced concrete (RC) structures within Port-au-Prince: the Teleco high-rise office building, and the cafeteria and classroom buildings at the St. Louis de Gonzague School. The design, site conditions, and observed damage of these structures have been documented by the team, with on-site visual inspection providing failure modes, damage intensity/patterns, and residual state.

The available information is being used to construct analytical models using state-of-the-art techniques for nonlinear dynamic analysis. Seismic hazard levels are being estimated by indexing to the level of demand required to bring about the observed damage. Then, the analytical models are used to predict building response according to accepted seismic assessment techniques in the U.S., and the predicted response is compared to the observed actual performance. In particular, the effectiveness of the structural models to produce similar behavior modes, overall patterns of damage, and appropriate assessment decisions is being evaluated. This paper written during ongoing work presents: (1) general Haiti earthquake information; (2) damage mapping of candidate structures; (3) preliminary analytical modeling.

2. BACKGROUND

The Mw 7.0 earthquake that struck the Republic of Haiti on January 12, 2010, is among the most destructive earthquakes in recorded history. The earthquake occurred at 4:53 PM local time on January 12, 2010 with duration of about 30sec. The USGS reports that the earthquake epicenter was located at 18.457N, 72.533W. Port-au-Prince, with an estimated population of between 2.5 and 3 million people, is located 25 km ENE of the epicenter. Fig.1. shows main shock and aftershock locations (M7 indicated as star; M5-M6 indicated as dark circles and M4-M5 indicated as light circles). Despite recent seismic quiescence, Haiti has suffered similar devastating earthquakes in the historic past (1701, 1751, 1770, and 1860).

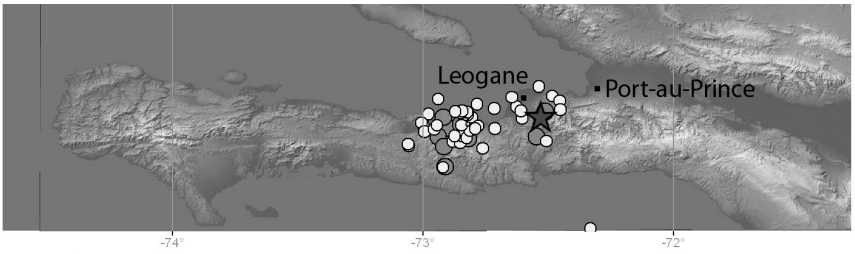


Fig.1. Topographic map of Haiti with the January 12, 2010 (USGS, 2010).

The loss in the earthquake includes: 222,000 deaths, 300k injured and 1,300,000 displaced; 97,000 houses destroyed, 188,000 houses damaged and 20% of structures in Port-au-Prince collapsed. Haiti had no seismograph stations during the main earthquake, so it is difficult to estimate accurately the intensity of ground motions. Nonetheless, the wide range of buildings damaged suggests that the ground motions contained seismic energy over a wide range of frequencies.

Partly because of the recent seismic quiescence since the last devastating earthquake in 1860, most buildings are designed for gravity only and generally no specific provisions for lateral design were considered in the past. This is apparent from the following post-earthquake observations:

(1) Unreinforced masonry is used extensively for partition walls. This is effective for insulation against temperature and noise, but it tends to exhibit little ductility in seismic shaking.

(2) Concrete beams and girders are not always connected with each other in the same plane but instead beams often run across the top of girders.

(3) Reinforcing bar ties in concrete columns tend to have large spacing and small diameter (e.g. #2 ties @15-30cm o.c.) which provides limited shear strength and confinement.

(4) Heavy floor systems with small columns are common. Beams tend to be stronger than columns, which resulted in soft story earthquake response in many buildings.

3. DAMAGE MAPPING FOR SELECTED STRUCTURES

In order to gather the required information a field trip was conducted by the team in May 2010. During this trip, many sites were visited and a few structures were selected for investigation based on damage state, availability of the design information, and accessibility. Ideal structures for this study are those that are engineered construction with the potential for design documentation, suffered documentable damage during the January 2010 earthquake, and were safe and accessible for the team to enter to perform reconnaissance work. The selected structures represent a variety of structural configurations, ranging from single story to multistory frame and from regular plan to irregular plan:

(1) Saint Louis De Gonzague School (SLG) Complex
   a. Cafeteria: C-shaped building consisting of 3 single-story RC frame units, one of which has an underground storage floor;
   b. Canopy: single story cantilever column structure;
   c. Classroom building: 2-story 8-bay RC frame structure

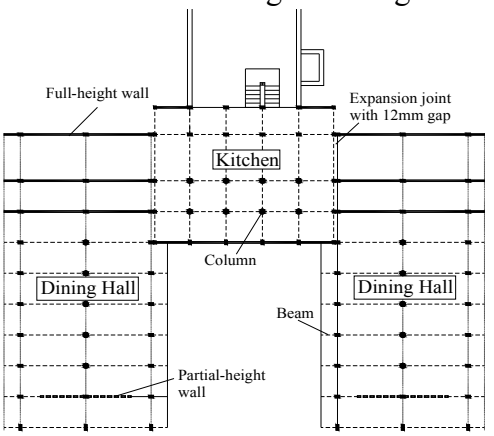
(2) Teleco Building: 9-story V shaped RC structure

(3) St. Joseph School (SJC): 4-story RC frame structure

Saint Louis de Gonzague School: Cafeteria Building

The cafeteria is a C-shaped one-story building that consists of three structures separated by expansion joints with a gap of ~12 mm (Fig.2). The kitchen in building rear is disconnected from the two dining hall wings which are located on either side of the kitchen. The vaulted concrete shell roof is supported by gravity beams and columns. None of the full-height masonry infill walls in the building rear (kitchen and dining hall areas) act as bearing walls. Nonstructural, partial-height, unreinforced masonry walls abut the center columns in the front of both dining hall wings.





(a) Photo (b) Plan view

Fig.2. One story cafeteria buildings.

Two main areas of structural damages were observed in the building:

(1) Spalling and shear damage of concrete and buckling of longitudinal bars of the columns in the front of the two dining hall wings, just above the top of the partial-height masonry walls (Fig.3). The shear damage at the top of these concrete columns was most likely caused by a combination of the partial-height masonry walls that reduced the clear-height of the columns and also by the large displacement demands caused by the geometry (torsional response) of the building. The combined center of stiffness of the three structures is in the back of the cafeteria whereas the center of mass of the whole structure is further to the front of the building. Hence the cafeteria building tended to rotate around its center of stiffness imposing large displacement demands on the columns in the front of the two dining hall wings.



Fig.3. Column shear damage in cafeteria building.

(2) Extensive damage to the columns and full-height masonry walls in the area of the two expansion joints between the kitchen and the two dining hall wings (Fig.4). The damage was caused by pounding of the three structures across the 12 mm expansion joints. Observations indicate that pounding occurred in both directions. Longitudinal cracks observed in the vaulted ceiling were most likely preexisting (long-term discoloration of paint due to moisture/water intrusion through cracks). However, they might have been enlarged during the shaking.

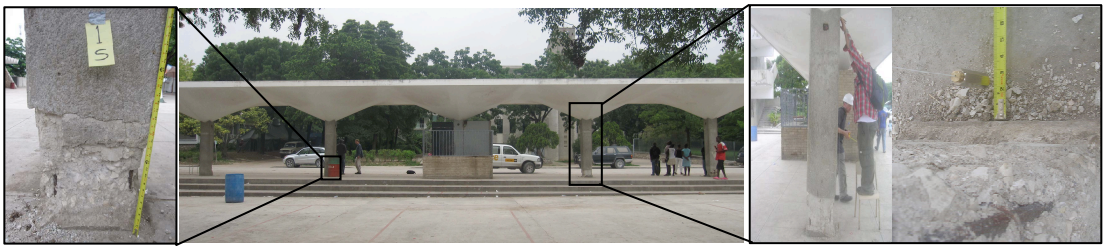


Fig.4. Pounding failure in cafeteria building.

Other columns in the building appear to have performed well, indicating that the typical column shear reinforcement may be sufficient if the column is free over the full story height (no constraining walls). Columns with full-height masonry walls on both sides appear to have performed adequately as well.

Saint Louis de Gonzague School: Canopy Structure

This structure consists of a concrete shell roof supported by six square concrete columns placed in a line (Fig.5b). In the transverse direction the canopy behaves like a cantilever and in the longitudinal direction it behaves like a one-story-five-bay frame. Columns appear to be flexure-governed at the base where they form plastic hinges with noticeable concrete spalling (Fig.5a) and up to 2.9% residual drift in the transverse direction (Fig.5c).

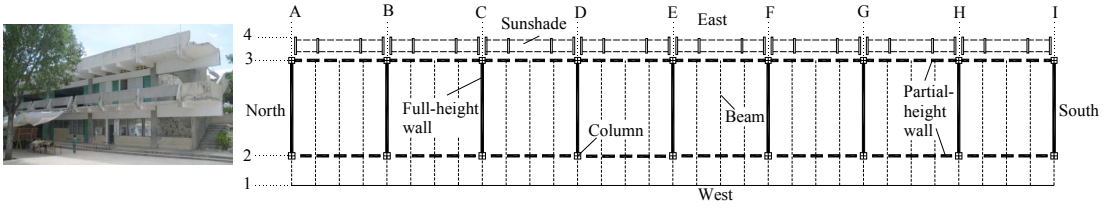


(a) Column damage (b) Canopy structure (c) Residual drift

Fig.5. Photo of canopy structure.

Given the well-defined canopy structure with its localized damage and residual drift it is possible to perform nonlinear incremental time history analyses to find a suitable ground motion and its intensity to replicate the damage. Hence, the canopy structure is serving as a tool to calibrate ground motions, which can then be used to analyze the other structures (classroom and cafeteria) at the Saint-Louis de Gonzague school. Local variations in soil properties throughout the school campus may affect the ground motions experienced by each separate building, which complicates the calibration.

Saint Louis de Gonzague School: Classroom Building



(a) Photo (b) Plan view

Fig.6. 2-story classroom building.

This classroom building is a two-story, eight-bay frame structure with story heights of 3.7 m and bay widths of 8.2 x 8.2 m (Fig.6). The member (beam, column) dimensions in both stories and all eight bays are the same. Most of the participating mass of the classroom building comes from the two suspended levels (2nd and Roof). In addition, a concrete sunshade structure (2 m deep) occurs in the back of the building and contributes some mass but little stiffness to the overall structure. Full-height infill masonry walls exist in all the EW-frames and partial height (mostly 1/3 of column height) infill walls exist in the east NS-frames in the back of the building.

Several major damages were observed in this building:

(1) The front (west side) of the building had partial height infill masonry walls that had mostly been demolished and removed when the team arrived. These infill walls did not directly bear against the columns because of door frames on both sides. Therefore they did not significantly influence the rest of the structure during the earthquake but behaved independently and most likely collapsed due to out-of-plane inertia loads (Fig.7). Due to the larger shear forces in the first story but same member sizes in both stories and the weak-column strong-beam design, the classroom building tended to form a soft story mechanism at the 1st story. This was visible from flexural hinges that formed at the top and bottom of the 1st-story columns along the west NS-frames of the building (Fig7).



Fig.7. Flexural hinge damage in the west NS-frame.

(2) On the NS-frame on the east side of the building, partial-height infill masonry walls abut most columns, shortening the column clear height and leading to shear-governed or flexure-shear behavior. The worst cases are shear failures at the 1st story columns H3 and I3, which are the two locations where masonry partial-height walls are higher than usual because of a restroom (Fig.8). This is aggravated by the fact that column bar splices that occur at the top and bottom of each story, in the regions of the column subject to the greatest moments and shear forces.



Fig.8. Shear-flexural damage in column H3 of the east NS-frame.

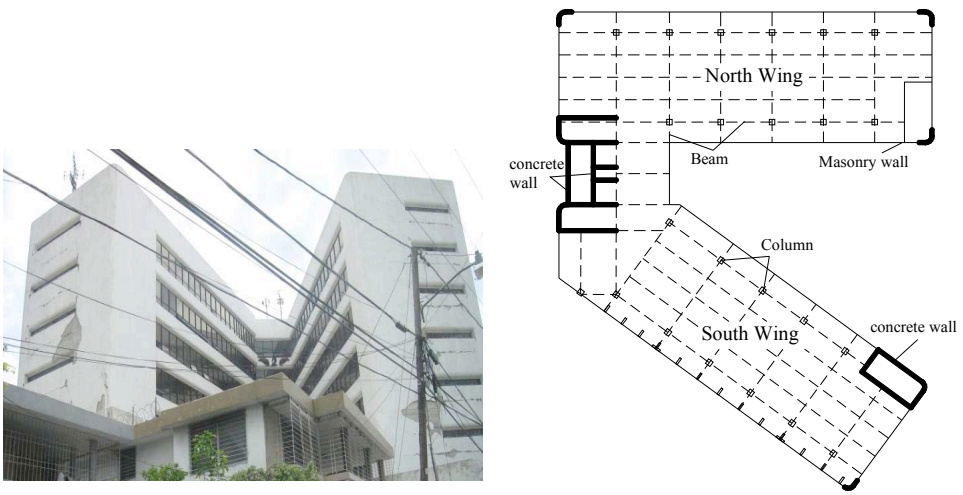
(3) In the EW direction, performance is generally acceptable. Full-height masonry infill partitions on every line at both levels provide strength, stiffness, damping, and regularity in this direction. There is spalling around the edges of most of these partitions and crushing at some corners (Fig.9), but little evidence of out-of-plane falling hazards.



Fig.9. Damage in the corners of full-height masonry partitions infilling the EW-frame.

Teleco Building

The Teleco building is a reinforced concrete structure, V-shaped in plan, that has one basement level and eight stories above ground (Fig.10). The North wing of the building is perpendicularly connected to the concrete core of the structure, which contains a stairwell, two elevator shafts and mechanical utility rooms. The South wing of the building is connected to the core at an angle of 55° meaning that the inside angle of the V is equal to 35°. Two additional stairwells exist at the ends of the two wings. The stairwell walls at the end of the North wing are mostly CMU walls except for the outside corner column which is concrete. On the other hand, all four stairwell walls of the stairwell in the South wing are reinforced concrete. Columns change their dimensions and presumably their reinforcement as they go up the building. Most of the girders that span between columns have haunches at their ends (possibly needed for added shear strength) but beams spanning between girders and cantilevering off columns have no haunches. Partial-height unreinforced masonry walls exist in many locations on the building facade where the windows are smaller than the story height (e.g. executive offices and bathrooms adjacent to the core. Interior full height unreinforced masonry walls also exist in the same two areas on both sides of the core.



(a) Photo (b) Plan view

Fig.10. Teleco building.

The Teleco building suffered its greatest damage on the second (ground) level and third level. Many of the columns on these levels showed 2mm to 5mm wide shear cracks (Fig.11a) and some flexural hinging was observed as well. Due to the additional stiffness and strength that was provided by the concrete stairwell at the end of the South wing, displacement demands were smaller on the columns in this wing compared to the ones in the North wing, where the stairwell was unreinforced masonry and suffered significant damage (large shear cracks and destroyed masonry units). Most of the unreinforced masonry walls throughout the building suffered significant damage (shear cracks) from in-plane loading, or they collapsed from out-of-plane inertia loading (Fig. 11b). Because of the end-haunches in most of the girders, columns were generally weaker than the girders, which showed no damage.



(a) Column shear crack (b) Masonry wall crack

Fig.11. Observed damage in the Teleco building.

Openings in the concrete core wall (4 square openings in a row at each story, for ventilation fans near the elevator core, visible from outside at the point of the "V") create a weak plane in the core wall and also tend to be constructed with poorly consolidated concrete. This led to shear failure of the piers in between these openings at Level 3, concentrating seismic drifts in this story (Fig.12). There is also a diagonal crack across the solid portion of the core at this level (visible from the outside), but from limited visual observation from the inside, this crack appears to be only in the mortar façade, not through the concrete structural wall.

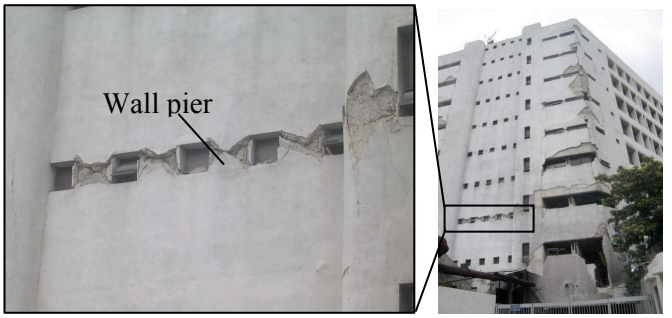


Fig.12. Observed damage in the RC core wall of Teleco building.

4. ANALYTICAL STUDY

Using the information and damage mapping obtained from field work, analytical models are being developed for the investigated structures. The seismic demand and damage predictions are being estimated using nonlinear dynamic

analyses. Several preliminary analytical modeling works are presented in this paper including: (1) selection of ground motions; (2) estimation of material properties; (3) modeling technique; (4) preliminary results and (5) future work.

(1) Selection of Ground Motions

A suite of three earthquake ground motions (group I in table 1) was selected for the dynamic analyses from the PEER Strong Motion Database (PEER 2000) with the following selection parameter matching the 2010 Haiti earthquake: (a) fault mechanism, strike slip; (b) magnitude, 6.9~7.1; (c) distance, 20-30km; (d) PGA, 0.3~0.5g; (e) PGV, 20-80cm/sec. Additional earthquake ground motions were selected by releasing the selection criterion of distance (10-80km, group II). The response spectra of the selected earthquake motions is shown in Fig. 13 with the USGS estimation (USGS 2010) indicated (dash line).

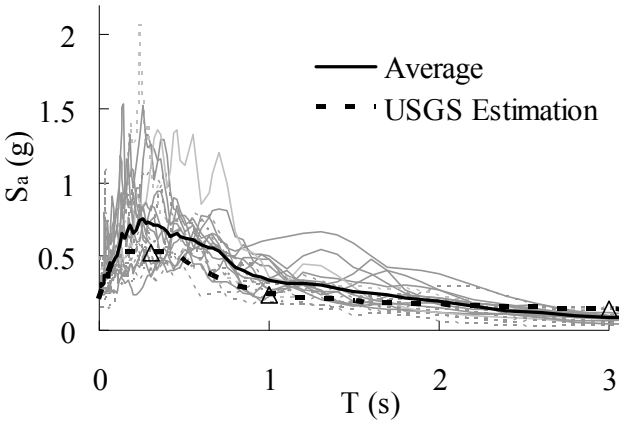


Fig.13. Response spectra of selected earthquake ground motions.

Table.1 Parameters for selected earthquake ground motions

Group	EQ	PGA (g)	PGV (cm/s)	Dist. (km)	Soil class	Direction
I	Imperial Valley	0.309	36.3	23.6	C	85
	Kobe	0.345 0.251	27.6 18.7	26.4	D	90 0
	Landers	0.417 0.283	42.3 25.6	21.2	B	Trans Long
II	Imperial Valley	0.315	31.5	10.4	C	140
	Imperial Valley	0.351 0.238	33 26	43.6	C	352 262
	Imperial Valley	0.313 0.215	29.8 30.2	8.3	C	180 270
	Imperial Valley	0.37 0.221	35.6 42.4	12.9	B	3 273
	Imperial Valley	0.364 0.38	34.5 42.1	12.6	C	140 230
	Kocaeli, Turkey	0.312 0.358	58.8 46.4	12.7	C	180 270

(2) Estimation of Material Properties

The material properties used for creating the analytical model are being estimated from ASCE-41 (2006) and sample material tests conducted by other researchers (Chambers et al. 2010) (KAKO 2010).

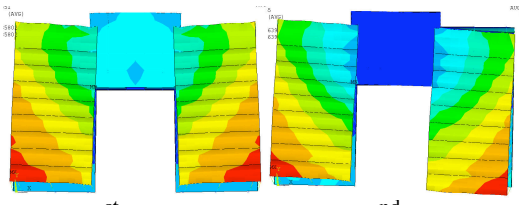
(3) Modeling Technique

The analytical models are being constructed using state-of-the-art techniques for nonlinear dynamic analysis. The nonlinear dynamic analyses are being performed using both research software (e.g. ANSYS and OPENSEES) and design office software (SAP2000 and PERFORM 3D). In order to capture the damage observed in the candidate structures during the Haiti earthquake, several structural members must be modeled as nonlinear elements including: columns, beams, shear walls, masonry walls and pounding effects.

The RC beams, columns and shear walls are modeled as elastic elements with plastic hinges at the critical sections determined based on the damage mapping. The plastic hinge is modeled nonlinearly to capture axial/flexural inelastic response using groups of nonlinear coupled springs and to capture shear limit states using nonlinear shear springs (Yavari et al. 2008). For certain cases where the column is under significant combined axial, shear and flexure loading, the fiber model with axial-shear-flexure coupling capability will be used (Ceresa et al. 2009).

Masonry walls, which have a significant impact on the response of the columns as discussed in damage mapping, are being modeled with nonlinear strut-tie models based on in-plane and out-of-plane behavior (Mosalam 2007).

The observed pounding effect is being modeled with high stiffness contact element serials connected with a nonlinear crush spring.



(a) 1st mode (b) 2nd model

Fig.14. Modal analysis of cafeteria building.

(4) Preliminary Analytical Results

The preliminary analytical results include: modal analysis of the cafeteria building and nonlinear dynamic analysis of the canopy structure. Both analyses are performed using the general-purpose finite element software ANSYS.

An elastic model with cracked section properties is used for the modal analysis of the cafeteria building. Fig.14 shows the first two modes from the analysis.

As seen in Fig. 15, the canopy structure is modeled with elastic elements (shell elements for the canopy and beam elements for the columns). Nonlinear coupled springs are used at ends of each column for modeling the plastic hinge. Fig. 16 shows the dynamic analysis results: (a) roof drift time history in the transverse direction with the measured residual drift indicated by the dashed line; (b) moment-rotation response at the column base in the transverse direction. As shown in Fig. 16(a), after

calibrating the ground motions, the model predicts a damage pattern and residual drift similar to that observed in the field.

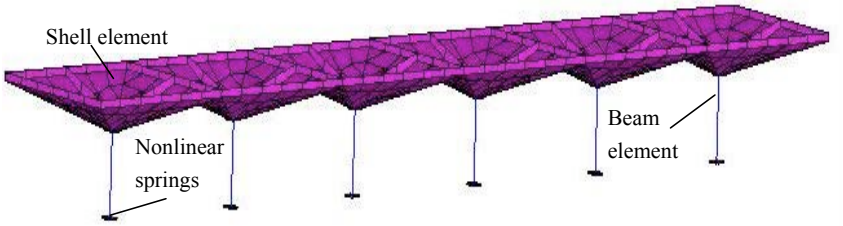
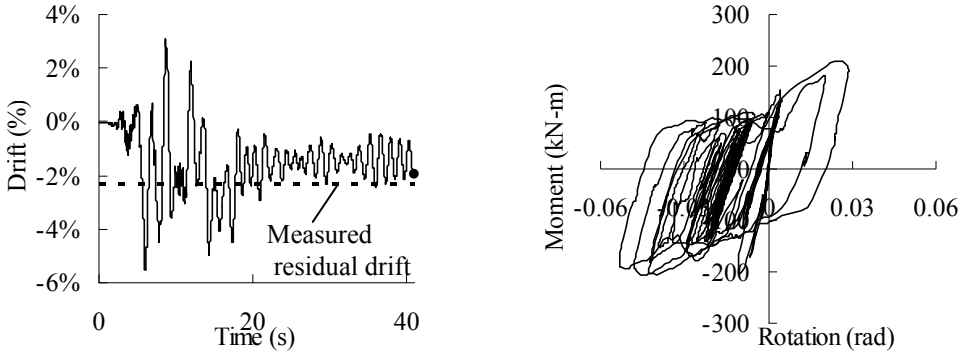


Fig.15. Canopy structure model.

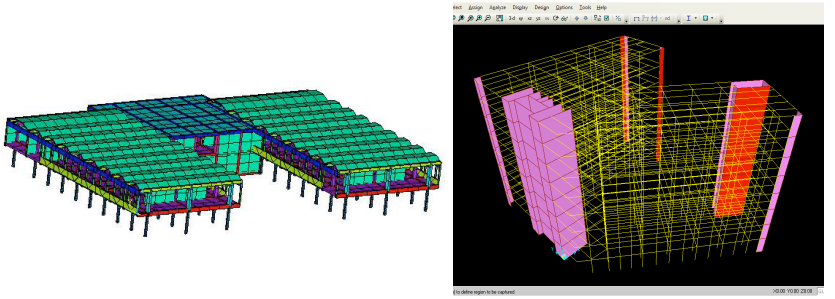


(a) Roof drift time history (b) Moment-rotation response at base

Fig.16. Dynamic analysis results of canopy structure in the transverse direction.

(5) Future work

Nonlinear dynamic analyses on the candidate structures will be performed. 3D nonlinear models of the candidate structures are being developed using the techniques described above, i.e., 3D SLG cafeteria model in ANSYS (Fig.17a) and 3D Teleco building model in SAP2000 (Fig.17b). The efficacy of these analytical models will be evaluated through comparisons of the predicted response to actual observed damage.



(a) SLG cafeteria building model (b) Teleco building model

Fig.17. 3D nonlinear models for the candidate structures.

5. CONCLUSION

Perishable data on the design of several engineered structures and details of their earthquake damage has been documented from field work in Port-au-Prince. That information is being used to construct analytical models using state-of-the-art

techniques for nonlinear dynamic analysis. Seismic hazard levels are being estimated by indexing to the level of demand required to bring about the observed damage. Nonlinear analysis results to date are able to replicate the behavior mode and residual deformation of the canopy structure. This analysis helps to index the amplitude of graound motions in Port-au-Prince. Further conclusions on the efficacy of these methods are being drawn through comparisons of the predicted response to field observations. The final deliverable is a report documenting the structures and design information; the post-earthquake state; modeling techniques; a comparison of analytical results and field observations; and evaluation of the methods with possible recommendations for refinement of current assessment procedures.

6. ACKNOWLEDGEMENTS

This research was supported by the National Science Foundation (NSF) under Grant 1034874. The authors are grateful for this support. Any opinions, findings, and conclusions or recommendations expressed in this material are those of the author(s) and do not necessarily reflect the views of the National Science Foundation. The authors wish to acknowledge the key assistance of Dr. Patrick Paultre of Univ. of Sherbrooke who coordinated the Haiti trip, and to those in Haiti who generously assisted the authors with the field work: Mr. Roger Laplanche, Mr. Gregory Lewis, Brother Farell Duvert of SLG and Mr. Giovanni Levy of SJC.

7. REFERENCE

USGS (2010). “Earthquake Hazard Program”. < http://pubs.usgs.gov/>

PEER (2000). “Strong Motion Database”. < http://peer.berkeley.edu/smcat/>

ASCE-41 (2006). “Seismic Rehabilitation of Existing Buildings”. American Society of Civil Engineers, 1st Edition.

Chambers, M., Zeleschuk, K. and Brzev, S. (2010) “Haiti Blocks Testing – Density and Compressive Strength”. BCIT Material Lab Report. May.

KACO. (2010) “Report of Compressive Strength Test”. Kaderabek Company. Mar.

Yavari, S., Elwood, K.J. and Wu C. (2009). “Collapse of a Nonductile Concrete Frame: Evaluation of Analytical Models”. Earthquake Engineering and Structural Dynamics. V38:225-241.

Ceresa, P., Petrini, L., Pinho, R. and Sousa, R. (2009). “A fiber flexure-shear model for seismic analysis of RC-framed structures”. Earthquake Engineering and Structural Dynamics. V38:565-586.

Mosalam, K.M. (2009) “Modeling of Unreinforced Masonry Infill Walls Considering In-Plane and Out-of-Plane Interaction”. Pacific Earthquake Engineering Research Center Report 2008-102.

Conceptual Transparency: Examples from the Work of Robert Maillart and Jörg Schlaich

E. M. Hines[1]

[1]Professor of Practice, Tufts University; Principal, LeMessurier Consultants, Cambridge, MA 02139; PH (617) 868-1200; email: emhines@lemessurier.com

ABSTRACT

Design processes and design calculations are reviewed for the 1925 Valtschielbach Bridge by Robert Maillart and the 1998 Ingolstadt Bridge by Jörg and Michael Schlaich. This review emphasizes the importance of conceptual transparency in structural design and demonstrates the interconnected nature of theory and practice in actual design processes. It helps to establish engineering thinking as distinct from scientific or mathematical thinking, and allows detailed consideration of how structural design processes may be taught in the university. Examples from the author's own practice and teaching demonstrate the potential for learning environments where university students are introduced to the tools and disciplines essential to creating original work based on fundamental understanding of engineering concepts.

SESSION DEDICATION AND INTRODUCTION: WHAT CAN WE LEARN FROM THE GREAT STRUCTURAL DESIGNERS?

We have assembled this session in order to honor the career of Professor David P. Billington of Princeton University, whose scholarship and voice have influenced countless members of our profession, encouraging us to seek the human stories behind the great works of structural engineering. It is through these stories that Professor Billington has conveyed to us not only the character of the great designers themselves, but also the very ideas and contexts that have made great designs possible. Our collection of perspectives on these ideas amounts to a modest *Festschrift*, recollecting the documents produced by students and colleagues to honor their mentors, documents we have stumbled across over the years working alongside Professor Billington in his Maillart Archive at Princeton.

Session Papers:

- Maria E. Moreyra Garlock: "Felix Candela and the Origins of Inspiration"
- Eric M. Hines: "Conceptual Transparency: Examples from the Work of Robert Maillart and Jörg Schlaich"
- Abbie Liel: "The Influence of Engineering Organization on Design and Construction Processes at Tennessee Valley Authority Dams of the 1930s"

The distinction between theory and practice leads many to assume that engineering design consists of following procedures generated as the results of scientific research. A closer look at the design processes for significant historical structures, however,

reveals intensive engagement between engineering imagination, fundamental principles, technical know-how and human will. Based on this insight, the session showcases some examples of compelling design processes and considers the implications for university engineering education. Attention is given to the distinction between a design process—which implies a personal way of directing creative thinking toward the solution of an actual problem; and a design procedure—which implies rote application of equations and methods. Understanding this distinction opens up possibilities for several important projects including: establishing engineering design as a creative and intellectual discipline equivalent in stature to research, working to reduce code complexity by placing emphasis on principles as opposed to rules, establishing the limits of computer analyses and their relationship to the imaginations of competent designers, and ensuring that engineering students master fundamental concepts in a way that allows them to think creatively.

INTRODUCTION

The calculations and the sketches behind the two structures featured in this paper constituted my introduction to the structural engineering design process under the guidance of Professor Billington. The stories behind both structures have proven to be durable and reliable landmarks on my professional path as a structural engineer. While these calculations and sketches were instrumental in the creation of sophisticated, original structures, they are themselves quite clear and simple. In a world enamored of complexity and computational power, where high-tech is often equated with intellectual merit, they demonstrate a higher level of thinking—one that radically distinguishes the essential characteristics of a system from the trivial—*conceptual transparency*. This power of abstraction serves a vital role in the design of large-scale structures, where failures are catastrophic and experimental prototypes are prohibitively expensive. Overlay these warnings with the imperative of economy and the desire for beauty, and it becomes clear that conceptual transparency addresses equally the need to assume responsibility and the opportunity to work creatively.

ROBERT MAILLART'S VALTSCHIELBACH BRIDGE

The chief concern of engineers is the quality of their assumptions. One of the clearest examples of this point in engineering history, as told by Professor Billington in *The Tower and the Bridge*, relates to Robert Maillart's development of reinforced concrete deck-stiffened arch bridges in the mid 1920's.

> Robert Maillart, the Swiss bridge designer, developed in 1923 a limited theory for one of his arched bridge types which violated in principle the general mathematical theory of structures and thereby infuriated many Swiss academics between the wars. But Maillart's limited theory worked well for that special type of form. Within that category type, Maillart's theory was useful and had the virtue of great simplicity; he developed the theory to suit the form, not the form to suit the theory. In the United States, by contrast, some of our best

> engineers understood the general theory well, but not understanding Maillart's specific ideas, they failed to see how new designs could arise. They were trapped in a view of an engineering analysis which was so complex that it obscured new design possibilities.(Billington 1983, 9-10)

Adherence to a general theory in this case is tantamount to the blind application of equations so often observed in the work of engineering students in fundamental classes. Maillart's much simpler approach, however, with its emphasis on new possibilities for arched bridge forms, represents the heart of creative engineering thinking—creativity not only with respect to the appearance of form, but also with respect to its engineering substance. Even Maillart's calculations were creative. In other words, Maillart recognized that there was more than one way to approximate the structural behavior of his deck-stiffened arch systems and he chose an approximation that exhibited a high degree of conceptual transparency. In the appropriate context, Maillart's calculations were entirely correct. That was precisely what angered Maillart's academic peers, and distinguished Maillart's engineering thinking. Maillart's calculations for the deck-stiffened Valtschielbach bridge, pictured in Figure 1, total 3 ½ pages. The calculations that represented Maillart's conceptual leap filled the last half page, and are shown in Figure 2.

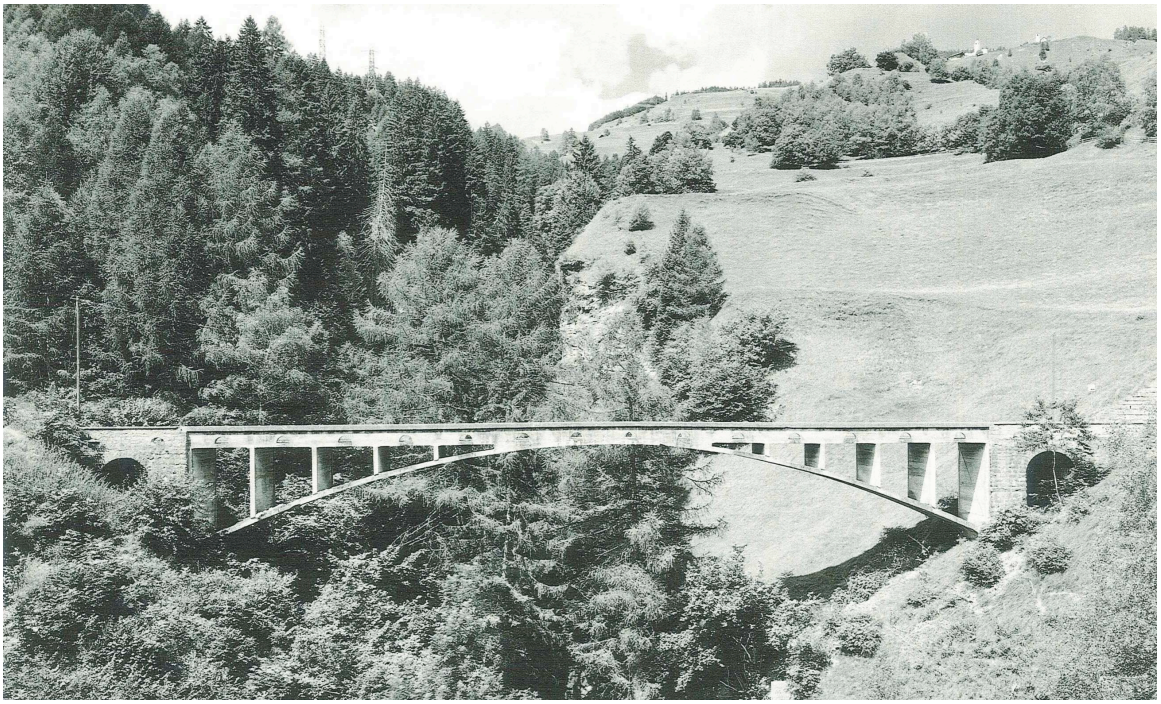


Figure 1. Robert Maillart's 1925 Valtschielbach Bridge in Switzerland (image credit: Billington 2005).

Seldom has the point been made more clearly that the engineering genius of the work rests on the *assumption* supporting this half page, and not on the calculations themselves. Based on the full scale behavior of his previous bridges, Maillart made

the assumption that the deck and the arch deform together, and would thus carry bending moments in proportion to their flexural stiffness. Since the deck was significantly stiffer than the arch, Maillart designed the deck to carry all the bending of the system. Such a conceptual leap reflects at least the same level of intellectual quality as the creation of any general theory, and far surpasses the technical exercise of applying such a theory. From a human point of view, Maillart's conceptual leap exceeded the generalized theory in value, because it led to more economical bridges that have become artistic icons as they have remained both serviceable and durable.

The essence of Maillart's engineering calculation for the Valtschielbach bridge in Figure 2 is represented by the equation

$$M = \frac{pL^2}{2 \cdot 8 \cdot 4} = \frac{0.9 \cdot 40^2}{64} = 22.5tm$$

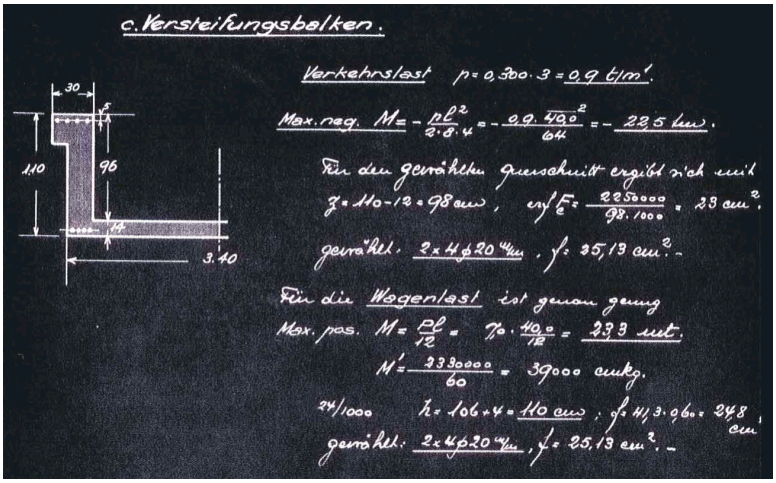


Figure 2. Robert Maillart's deck stiffening calculations for the Valtschielbach Bridge (image credit: Billington 2005).

Using the arch allowed Maillart to reduce his dead load bending moments to zero, while reducing his live load bending moments to approximately 22% of the same moments on a simply-supported beam. Figure 3 shows conceptually the Valtschielbach arch on the left and a simple beam on the right, each with a span of 40 m (131 ft). Assuming the distributed live load of 0.9 t/m (0.603 k/ft) for this example, the live load bending moments shown for the arch and the beam at the bottom of Figure 3 are 162 kft [22.4 tm] and 730 kft. This difference is impressive, but does not emphasize the relative efficiency of Maillart's bridge, which is more efficient than a simple beam by more than a factor of 8.

The top of Figure 3 shows the same spans under uniform load. For this example the same live load has been used for consistency, although it would be more appropriate to use the actual dead load, which is larger than the uniform load shown at the top of Figure 3. The moments under uniform load in the arch are zero, while in the beam they are 8 times higher than in the arch under live load.

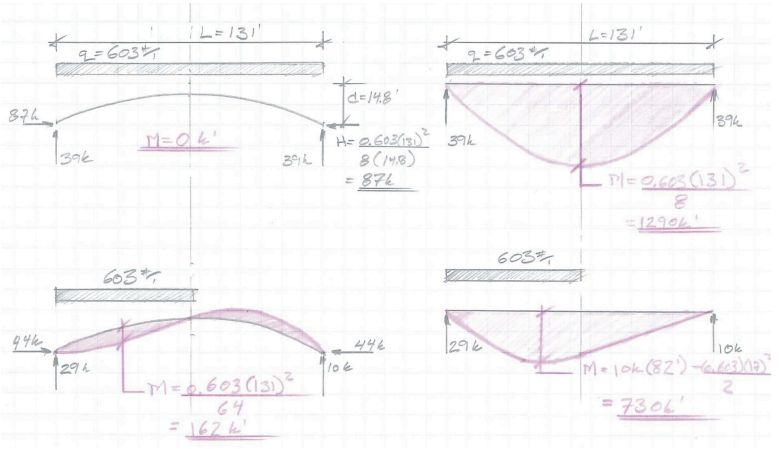


Figure 3. Valtschielbach bending moments explained conceptually.

For this example, it is most appropriate to compare maximum bending overall moments, not just maximum bending moments from a given load case. If the dead loads of the structure are just 25% higher than the live loads, then it can be demonstrated that the deck-stiffened arch reduces bending moments by an order of magnitude compared to the simple beam. See Chapter 9 of *Robert Maillart's Bridges* (Billington 1979) for a complete historical discussion of Maillart's deck stiffened arches and their relevance to the difference between science and engineering.

JÖRG AND MICHAEL SCHLAICH'S INGOLSTADT BRIDGE

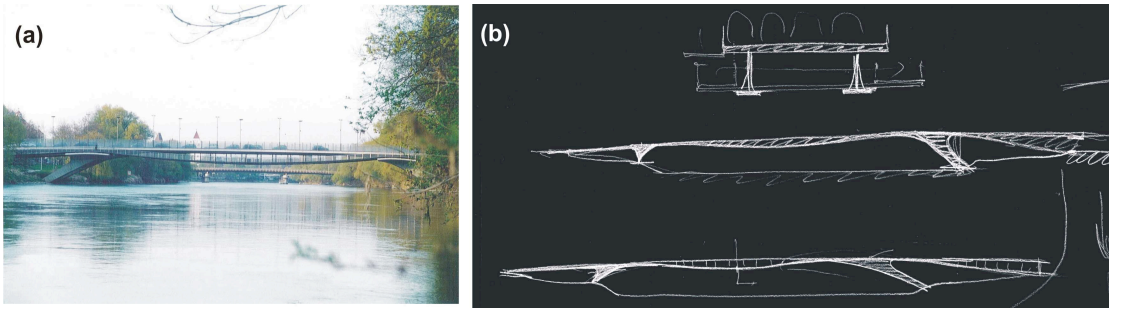


Figure 4. Danube River bridge in Ingolstadt. (a) Elevation. (b) System concept sketches.

Figure 4(a) shows the third bridge over the Danube River in Ingolstadt, Germany, which won a design competition in 1993 and was completed in 1998. Jörg and Michael Schlaich generously allowed us to photocopy many sketches from their collaborative design process for this bridge with Architects Kurt and Peter Ackermann. These sketches and several interviews formed the basis for our story of this design process and the design competition (Hines and Billington 1998). In the discussion of conceptual transparency, these sketches complement the simplicity of Maillart's Valtschielbach calculations by demonstrating the power of drawing as a language of creative expression.

One of the important early system sketches is pictured in Figure 4(b). While simple, this sketch captures the essential ideas of the proposed system: a slender deck, supported as an inverted suspension span, and longitudinally prestressed by the arching action beween two raked piers. The separation between the road and the pedestrian can be seen in the section at midspan. The second elevation below shows a representation of massing with vertical supports between the cables and deck. The sketches are executed quickly in the company of collaborators. They are the standard means of communicating between designers. Yet, it is rare that we consider closely and discuss the sketches that represent the creative process. They are often considered either to stand alone as a flash of genius or to be mundane in their multitude. As representatives of hundreds of sketches developed during a design process, the sketches in Figure 4(b) and in Figure 5 show the kind of communication that is essential to the creative development of an idea in structural engineering.

Often these sketches are accompanied by simple calculations and text. Their value lies in their ability to represent clearly and accurately a dynamic process that is invisible to most students in its human character—composed of sketching, simple calculations, discussion, debate and an iterative approach to the development of an idea. I tell my students that if our imaginations were perfect, we would not need to worry about the discipline of creativity. Our ideas would come fully formed out of our imaginations. Instead, most of us harness the power of our ideas by communicating about them. We communicate with ourselves, with our colleagues, and with our critics. In this communication, we learn more about our ideas and develop them further. While it may not be possible to teach creativity per se, it is certainly possible to teach the discipline required for creative work. And the first step in teaching such a discipline is to demonstrate it by example.

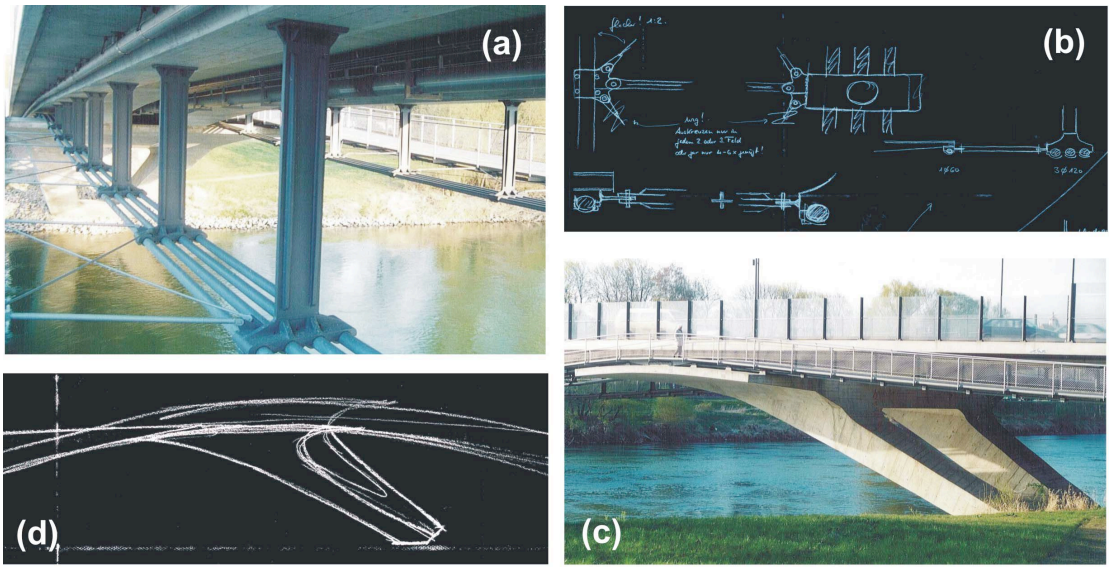


Figure 5. Ingolstadt details and concept sketches. (a) deck support on cables with bracing to pedestrian walkway; (b) concept sketches for connections between deck support cables and pedestrian walkway; (c) skewed pier with deck and pedestrian walkway; (d) pier sketch.

Figure 5 shows this discipline in further details. It is not enough simply to sketch a system. The system relies on its details, and conceptual transparency is largely concerned with the interaction between a system and its details. Figure 5(a) shows the supports between the cables and the deck, along with the horizontal ties between these cables and the pedestrian walkway. Figure 5(b) shows sketches of these details that were developed in close proximity to the sketches in Figure 4(b). Figure 5(c) shows the skewed support, which evolved to retain a high degree of plasticity from a very simple decision to skew the supports by 20 degrees. Figure 5(d) shows the early conceptualization of this support as a plastic element.

The example set in Figures 4(b) and 5 is that the creative work of engineers involves intense communication between the idea of a system and ideas for its details. This communication poses a challenge, because it is easier to fall into a habit of focusing only on the big picture or only on the details. The sketches in a design process need to be effortless because they need to be disposable. The value of any given sketch resides in its relation to all the other sketches and the design process—not in its quality as an independent work of art. The disposable nature of these sketches gives them their value—they record fleeting thoughts and ideas, set down quickly for the purpose of critical evaluation and discussion. To produce them fluently is to speak the language of the engineer. Leonardo Da Vinci's sketch books are compelling precisely because they exhibit his artistic talent not for its own sake but as eloquence in the language of drawing.

DRAWING, THE LANGUAGE OF THE ENGINEER

The concept of drawing as a language was coined by Carl Culmann in the mid 19th century as he developed graphic statics (Billington 2003, Lehmann and Maurer 2006), however for this discussion I would like to consider drawing even more broadly—as a language requiring multiple levels of abstraction, and possessing tremendous intellectual richness.

Expression of thought through language is creative. Creativity involves choice. Intellectual disciplines contribute to creative work when they facilitate judgments required to make choices. Engineering requires the command of three primary languages:

1. The written word and spoken word communicate action—a narrative of what has happened, is happening or will happen.
2. Mathematics communicates quantity.
3. Drawing communicates substance—a real object that is best understood by its appearance is communicated as an ideal through drawing.

University culture clearly recognizes the value of the written/spoken word and mathematics as forms of communication, and the act of acquiring a liberal education involves the extensive use of these languages. Drawing, on the other hand, has often been misunderstood outside of the fine arts, and in engineering has been branded as a

technical discipline. As a form of communication however, drawing is similar to writing, speaking and mathematics: it requires skill, but it also requires intellectual depth. In fact, the two are inextricably linked.

Similar to written and oral communication, the audience matters tremendously. For presentation to an owner, realistic appearance is often helpful. For communication with architects, realistic appearance is also valuable, but can be tempered with abstraction and style in a manner that facilitates a collaborative, creative process. For contractors developing an estimate, depicting quantities and the general level of complexity are helpful. For contract documents more detail is generally more helpful. It requires experience and thoughtfulness, however, even with the most powerful computer modeling systems, to develop contract drawings that are well coordinated. Providing information that is incorrect can be more harmful in the context of a contract than not providing any information.



Figure 6. Lobby Renovation, 100 High Street, Boston, Massachusetts. (a) Before: two levels of retail space at base of 28 story building (photo credit: CBT Architects). (b) After: two-story lobby with structural glass wall hung from cantilevered third floor.

In order to provide contract information in a manner that is consistent and easily understood by an expert, engineers have developed several abstractions such as weld symbols, elevation marks, tolerance numbers and typical details. These abstractions, while often communicated in the form of drawings, are generally not comprehensible to a person who does not speak this language.

In order to provide context for the characteristics of drawing discussed above, I will discuss two recent lobby renovations in Boston and their role in my teaching the 3rd-

Year structural systems design course at Tufts University. Figure 6 shows before and after photos of a lobby renovation completed with CBT Architects at 100 High Street in Boston in the spring of 2009. The former entrance to the building in Figure 6 was located at 150 Federal Street. The lobby renovation consisted of removing three bays of slab framing from the second story in order to create a new 2-story high lobby with a structural glass façade by W&W Glass/Pilkington Planar.

Figure 7 shows the framed area before and after the slab was removed. Since the new glass wall was to be hung from the cantilevered third floor framing, reinforcement of the columns prior to demolition of the slabs required not only considerations of column stability under 28 stories of building dead and live loads, but also of column flexural deflections and their effect on cantilevered slab deflections.



Figure 7. Lobby Renovation, 100 High Street, Boston, Massachusetts. (a) Before: columns and cantilevered girders reinforced prior to removal of three 30 ft x 30 ft bays. (b) After: three bays of slab framing removed, and column reinforcement completed.

Figure 8(a) shows original sketches and calculations developed during concept design of this slab removal. While it may seem natural that sketches, calculations and word occupy the same page of work (as do also graphs and tables often times), it is important to note that many students are not educated to communicate in this kind of language. At the top of Figure 8(a) is a sketch of the plan, which gives context and which will become the primary form of communication in later contract documents. Also listed are the assumed loads. These loads are deliberately simple, and their importance lies in the fact that they allow this communication to stand alone, without reference to other documents. This makes the work easier to check and to discuss with colleagues. For columns supporting a fully-occupied 28-story building, it

became important to be able to check both the relevant assumptions and calculations many times, with many different colleagues. The intellectual merit of the problem lay in distilling the problem down to its essence—to make it so simple that the unconscious could continue to consider the problem at all hours—so simple that one could wake up in the middle of the night and check the work at bedside. The analysis on the lower portion of Figure 8(a) is a simple, single degree of freedom moment distribution, which could be carried out on half a page. A sketch of the physical system, with moment diagrams drawn directly on top of the sketch helped to facilitate this level of conceptual transparency.

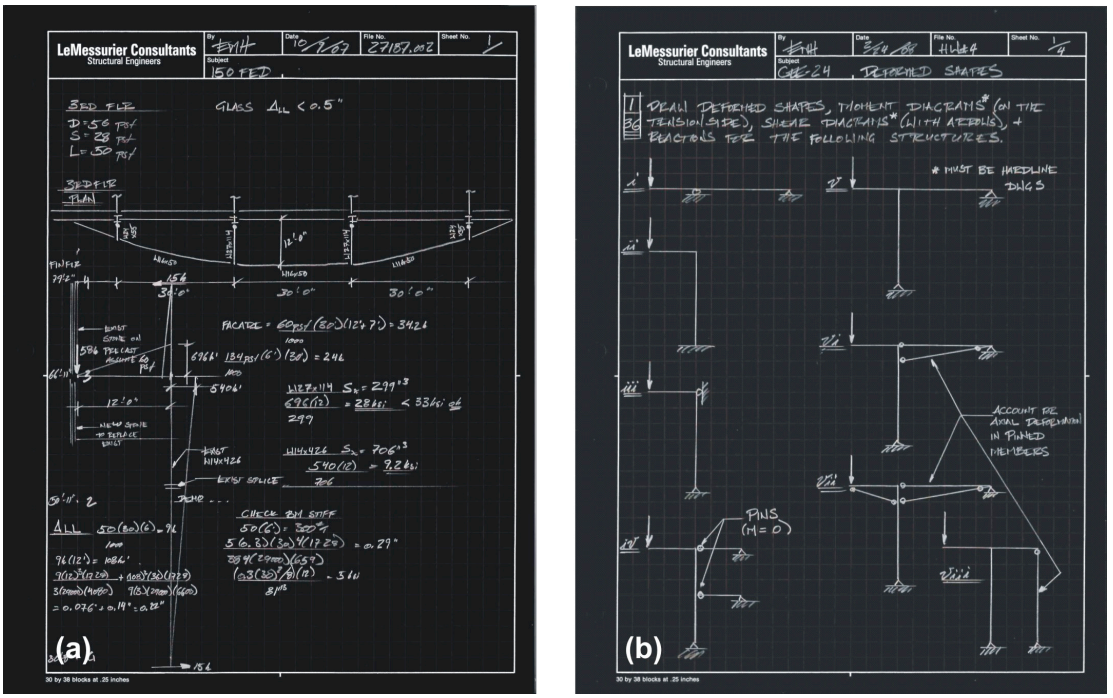


Figure 8. Lobby Renovation, 100 High Street, Boston, Massachusetts. (a) Initial analysis of third floor framing to support hung glass wall. (b) 3rd-Year structural systems homework assignment reflecting the parametric investigation of system behavior completed prior to final design.

Figure 8(b) shows a series of exercises assigned to 3rd-Year structural engineering undergraduate students at Tufts University based on a parametric investigation that followed the calculations in Figure 8(a). The object of the investigation was to determine the stiffening effects due to a range of possible reinforcement schemes for the cantilever and its beam and column back-spans. I learned from assigning this series of problems that there was a significant difference between how I saw these simple sketches versus how my students and teaching assistants saw them. I saw several variations on one theme—a cantilever with a backspan. The variations entailed different types of backspans resulting in different levels of rotational stiffness at the root of the cantilever. My students, however, saw eight different problems, with little or no conceptual thread running through them.

When I solved these problems in Figure 8(b), the moment diagrams and axial force diagrams yielded significant insight into system behavior—even before I calculated any numbers. From the principle of virtual work, more area under these diagrams implied more system flexibility. In other words, the diagrams appear more simple than they actually are—this speaks to the subtlety and effectiveness of their abstraction. Only an expert can see all they have to offer. And to an expert—they facilitate a powerful understanding. A similar observation was treated extensively by the National Research Council in Chapter 2 of their summary of education research entitled *How People Learn*.

> Experts' abilities to reason and solve problems depend on well-organized knowledge that affects what they notice and how they represent problems… The fact that experts are more likely than novices to recognize meaningful patterns of information applies in all domains, whether chess, electronics, mathematics, or classroom teaching… Because of their ability to see patterns of meaningful information, experts begin problem solving at "a higher place." (NRC 2000, 48)

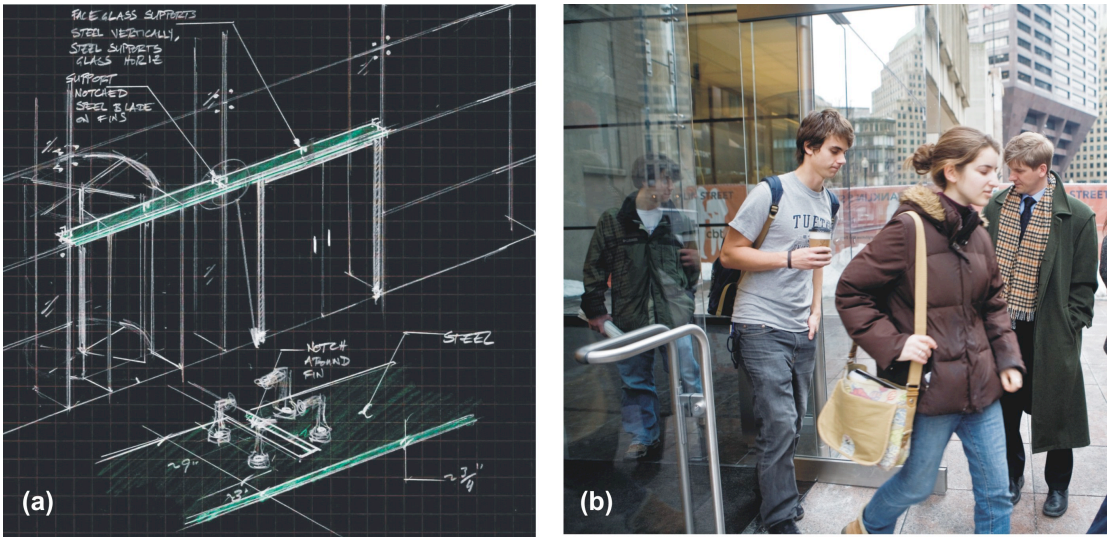


Figure 9. Lobby Renovation, 225 Franklin Street, Boston, Massachusetts. (a) Engineer's sketch of steel reinforcement for glass door header. (b) 3rd-Year Tufts University students walking through the doors depicted in (a) (photo credit: Tufts University).

Figure 9(a) shows a sketch for another structural lobby renovation at 225 Franklin Street in Boston. I developed this sketch during a coordination meeting with the architect, the glass installer and the general contractor. During the meeting, the sketch helped our team to align our interests with regard to developing an extremely light steel header that could be attached to the glass system. Both the system and the details were important to all parties involved, and the actual engineered header system ended up resembling this concept sketch very closely. Figure 9(b) shows my 3rd-Year students walking out of this doorway after having toured the new 225 Franklin Street Lobby.

CONCLUSION: THE ROLE OF DESIGN IN UNIVERSITY ENGINEERING EDUCATION

The role of design in university engineering education is to *motivate and challenge students' fundamental understanding* of the physical world. Design is relevant in the university, not because it prepares students for the working world, but because it is what *motivates and challenges* students' understanding of the fundamentals in the best possible way. Design requires a personal way of directing creative thinking toward the solution of an actual problem, and has little use for rote application of equations that a student may or may not understand. Design requires a philosophical approach rooted strongly in the fundamentals of the discipline, which is the necessary foundation for conceptual transparency. Fundamentals are not just theory, but how theory is applied in a context. To separate theory from practice is to ignore context—and hence to forsake what is most human and most wonderful in engineering.

REFERENCES

Billington, D.P. (1979) *Robert Maillart's Bridges*, Princeton University Press, Princeton, New Jersey, 146 pp.

Billington, D.P. (1983) *The Tower and the Bridge*, Princeton University Press, Princeton, New Jersey, 306 pp.

Billington, D.P. (2003) *The Art of Structural Design: a Swiss Legacy*, Princeton University Art Museum, Yale University Press, New Haven, CT, 211 pp.

Billington, D.P. (2005) *Civ 262: Structures and the Urban Environment*, Powerpoint Lectures, Department of Civil and Environmental Engineering, Princeton University, Princeton, New Jersey.

Hines, E.M. and Billington, D.P. (1998) "Case Study of Bridge Design Competition," ASCE Journal of Bridge Engineering, 3(3), Aug., pp. 93-102.

Lehmann, C. and Maurer, B. (2006) *Karl Culmann und die graphische Statik: Zeichnen, die Sprache des Ingenieurs*, Ernst & Sohn, Berlin, Germany, 207 pp.

National Research Council (2000) *How People Learn: Brain, Mind, Experience and School—Expanded Edition*; J.D. Bransford, A.L. Brown and R.R. Cocking, editors; National Academy Press, Washington, D.C., 374 pp.

Félix Candela and the Origins of Inspiration

Maria E. Moreyra Garlock[1] and David P. Billington[2]

[1]Assistant Professor, Department of Civil and Environmental Engineering, Princeton University, Princeton, NJ, 08540; PH 609-258-2728; email: mgarlock@princeton.edu
[2]Professor Emeritus, Department of Civil and Environmental Engineering, Princeton University, Princeton, NJ, 08540; email: billington@princeton.edu

ABSTRACT

Félix Candela is widely acknowledged to be one of the great structural artists of the twentieth century. Candela was born in Spain, and was exiled in 1939 to Mexico where he created all of his major thin shell concrete constructions. This paper examines Candela's process of design and illustrates through his major works that he acted first as a builder who not only constructs, but also makes the engineering design. He also takes a general form and plays with it to make *structural art*. Structural art implies efficiency, economy, and elegance; but we also illustrate how structural art also implies a sustainable design. Finally, we show that the *inspiration* for the designs of structural artists come from a process that begins with imitation, followed by innovation. Education is crucial for the future of structural art, and in studying it, educators, practitioners, and the general public can recognize the potential for this new art form in the 21st century.

INTRODUCTION

Modern master builders exhibit two characteristics that are fundamental to the best-engineered structures: the ethos of *efficiency* and the ethic of *economy*. Efficiency in this sense means the search for forms that use a minimum of materials consistent with sound performance and assured safety; economy signifies a minimum of construction costs consistent with low expense for maintenance. These two fundamentals imply a plan that pays attention to both design and construction. An engineer who designs efficiently and with a builder's mentality is considered a master builder. But a *structural artist* is an engineer who has all the qualities of a master builder and possesses *aesthetic* motivation in addition. An engineer can be a master builder without being a structural artist, but one cannot be a structural artist without being a master builder.

Many master builders are engineers who work for architects and consider the aesthetic to be the province of the architect; hence, they think of their structures as part of architectural art. While this approach is common practice, it has contributed to one of the greatest myths in our structural engineering profession: that elegance in structural engineering is the province of architects and that while engineers ensure

that it will stand, only architects can make it a work of art. This argument is contradicted by the most talented structural engineers over the last 200 years whose motivation included appearance along with efficiency and economy. One such engineer was Félix Candela.


Figure 1: Félix Candela

Félix Candela (1910-1997) (Fig. 1) was a world-renowned structural artist of thin-shell concrete-roof structures in the mid 20th century. Shortly after completing his degree in architecture in Madrid, the Spanish Civil War broke out and in 1939 Candela was exiled to Mexico. After a few years, he returned to reading the publications on thin shell analysis and design (which he had begun to read on his own incentive in Madrid) and then began to experiment with building thin shell structures. His work was directed toward understanding the performance of thin-shell concrete structures under load, but, in addition, he was gaining insight into the building process for such forms. He was beginning to think like a builder, making forms—not on paper out of drawings but in the field out of concrete. Thus, when he formed his company, it was decidedly neither an architectural nor a consulting-engineering firm but rather a business devoted to building—he became a construction contractor.

Since Candela's formal education was in architecture, and since his shell designs are elegant, most people identify Candela as an "architect". However, based on his career as a builder and designer, and his own words, we can demonstrate that Candela practiced as one of the greatest structural engineers of the twentieth century, and hardly at all as an architect. He remarked at the time that "every day I feel less and less an 'architect'; I am losing interest in making plans and window details and things like that." (Faber 1963) He identified himself more as an engineer and builder: "I must say . . . that although an architect by training, in practice I am a constructor and building contractor," (Candela 1955) and one who makes his own engineering designs. This disassociation from thinking of himself as an architect was reflected even more pointedly in an essay he wrote for a symposium honoring Robert Maillart at Princeton University in 1972. The organizers who invited him to speak suggested "New Architecture" as a title for his paper. Candela began his paper and lecture saying, "The title of my lecture is 'New Architecture'; but I cannot avoid the feeling that I have not too much to do with this subject. I don't think I can speak of my work as of any new architecture or even as architecture at all." (Candela 1973) Later, when Candela republished this paper in Spanish, he renamed it "La Herencia de Mailllart" (Maillart's legacy).

This paper examines Candela's process of design and illustrates, through his major works, that he acted first as a builder who not only constructs, but also makes the design, which then can be expressed through a simplified analysis (Faber 1963, p. 199). He also takes a general form, which sometimes comes from somewhere else,

and plays with it to make structural art. Structural art implies efficiency, economy, and elegance; but we also illustrate how structural art also implies a sustainable design. Finally, we show that the *inspiration* for the designs of structural artists come from a process that begins with imitation, followed by innovation. Education is crucial for the future of structural art, and in studying it, educators, practitioners, and the general public can recognize the potential for this new art form in the 21st century.

CANDELA'S PROCESS OF DESIGN

His Major Works

All of Candela's significant structures were of one geometric form, the hyperbolic paraboloid (hypar), and with that discipline he could build them only 1.5 inches (4 cm) thick. The doubly curved surface of the hypar form (Fig. 2) is developed with two straight line generators; thus, Candela achieved economy of construction by avoiding curved boards for his falsework in construction. While the climate in Mexico is more moderate than that in the United States, other designers successfully have built similar thin shell structures in harsh environmental conditions. For example, Heinz Isler designed many thin shell concrete structures in Switzerland; typically these were 3 inches thick and, like Candela's designs, they serve as models of efficiency, economy, and elegance (Billington 2003)

.

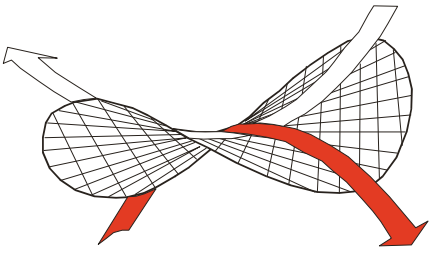


Figure 2: The hyperbolic paraboloid (hypar)



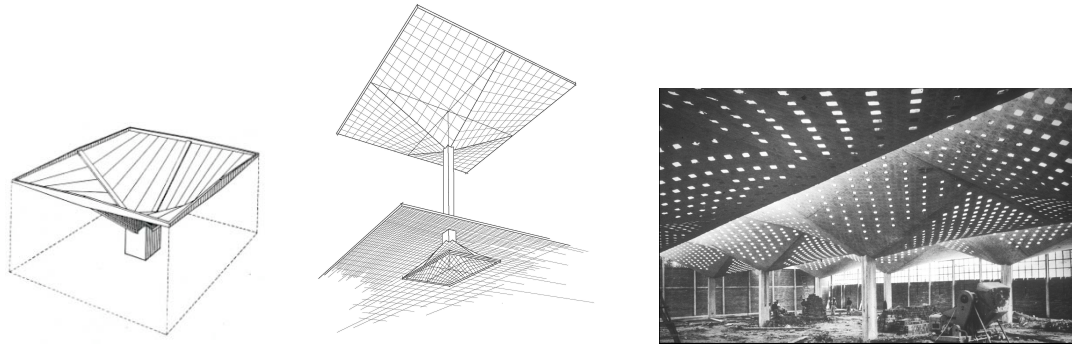
Figure 3: The Cosmic Rays Laboratory (1951) (photo by Bruce White)

When asked to name his favorite structures, Candela replied: Church of Our Lady of the Miraculous Medal (Milagrosa), the Chapel at Cuernavaca, Restaurant Los Manantiales at Xochimilco, and the Bacardi Rum factory (Basterra and Valero 1998). We will examine these self-proclaimed favorite structures plus his first hyperbolic paraboloid shell (Cosmic Rays Laboratory) and his umbrella shells that comprised the bulk of his work. From all these works, the same pattern emerges. Candela the builder makes the engineering design, and then takes a general form and plays with it to make structural art.

In the Cosmic Rays Laboratory of 1951 (Fig. 3), the architect already had a form—barrel shells—and when Candela took on the construction, he decided to change the

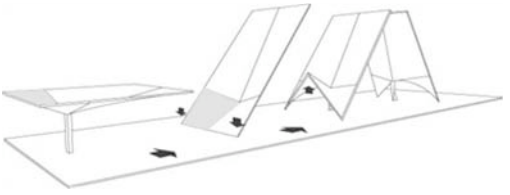
barrels to hyperbolic paraboloids, his first such structure. Although no calculations seem to have survived, Candela certainly became the structural engineer, calling on his earlier study of French and German publications from the 1930s (Garlock and Billington 2008, Kelly et al. 2010).

With the umbrella shells, he recalled his earlier study of a 1936 paper by Aimond (Aimond 1936), who showed a single umbrella with the same basic form that Candela would follow. Since he considered Aimond's umbrella shape (Fig. 4a) visually dull, he refined it by 1952 to achieve a more elegant appearance (Fig. 4b,c). The umbrella he transformed into a church in 1953, Church of Our Lady of the Miraculous Medal (Fig. 5), which resulted from an unusual opportunity that afforded Candela to be the builder, designer, and artist for a structure that is traditionally a work of architecture. Again, however, the project was first a construction and a design second.



(a) Aimonds sketch (b) Candela's umbrella (c) High Life Textile Factory (1954)

Figure 4: Umbrellas



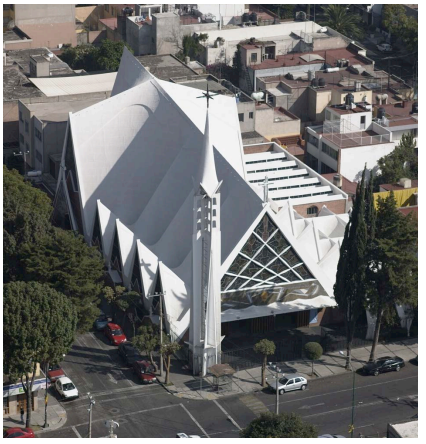


Figure 5: Our Lady of the Miraculous Medal Church (Milagrosa) (1955) (photo by Bruce White): above, evolution of form from the umbrella

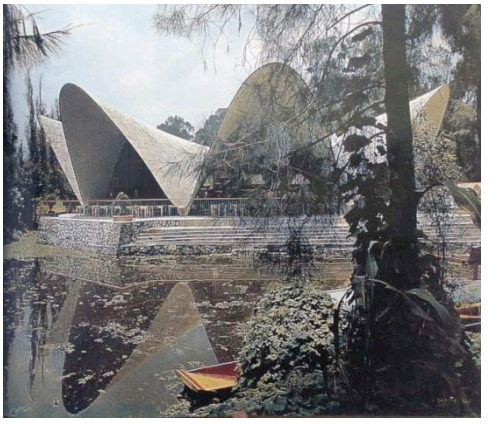


Figure 6. Félix Candela's Restaurant Los Manantiales in Mexico City, Xochimilco, 1958.



Figure 7: Chapel Lomas de Cuernavaca (1958)

For the restaurant Los Manantiales at Xochimilco (Fig. 6), Candela was asked by colleagues to take the project as both designer and builder, but once again the basic shape was not his idea. Colin Faber, working then at Candela's construction company Cubiertas Ala, made a sketch similar to what eventually became the shape of the restaurant. Candela considered the sketch a good beginning and proceeded to refine it carefully (Garay 1994). The restaurant is pure structure and reflects the hand of a structural artist. The same pattern emerged for the Cuernavaca chapel (Fig. 7); the architect approached Candela to be the builder and brought him a sketch of a triangular raised roof. Candela reshaped the form into the thin curved structure that made the chapel unique and dramatic (Draper 2008).

Finally, for a new project he was stimulated by the cylindrical the groin vaults of the St. Louis Airport terminal building designed by the architect Minoru Yamasaki and modified strongly by the engineer Anton Tedesko. For the next project Candela gained, he decided that whatever its function he was determined to create three groined vaults as in St. Louis; it so happened to be a Bacardí Rum bottling plant (Fig. 8). Once again, the client employed Candela as builder first, but that assignment also included, as did most of his other projects, functioning as structural designer. The building is pure structure in a series of hyperbolic parabolid groined vaults. (Segal at al. 2008).

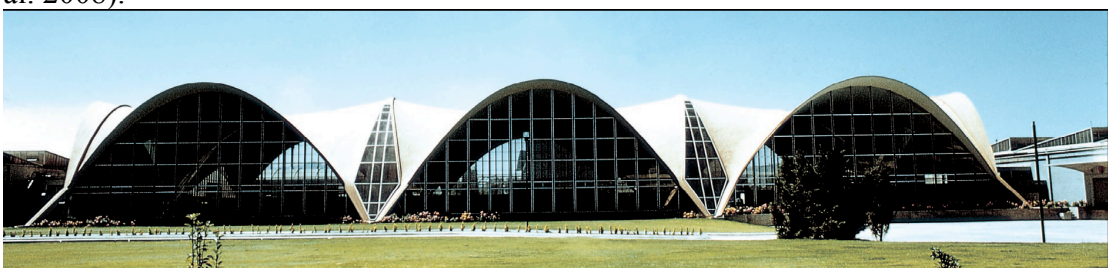


Figure 8: Bacardi Rum Factory, 1960

Sustainability

Fashionable new terms like "sustainability" really mean something that has been part of the tradition of structural engineers – especially those who stand out as the greatest ones over the past 200 years – essentially structural artists. Great structural designers understood the need to conserve resources and protect the environment, even before we had the terminology (e.g., "sustainability", "green design") or a metric (e.g. LEED) to define it. Since structural art is defined by efficiency and economy, it implies a sustainable design.

Efficiency, in the context of sustainability and structural design, means not wasting materials and using locally available resources. Candela used local materials which

eliminates the need to transport materials from afar (an environmental and energy advantage). He also designed the structures to be the minimum practical thickness. Since the form of the shell was correct, not a lot of material was needed for strength and stiffness. Furthermore, Candela conserved material during the construction process by reusing the form work.

Economy, in the context of sustainability and structural design, means durability and energy efficiency. Candela's reinforced concrete shells have proven to be durable and easy to maintain. The first author visited several of Candela's structures in Mexico and found all of his shells in good condition (even with more than 50 years of service) despite the thinness of the shell and the frequent earthquakes. Also, many of Candela's structures allow natural light to enter and illuminate the interior, reducing and often eliminating the need for electric lights during the day. For Candela, there was a practical limit in the size of the shells that he was designing based on structural engineering concerns (e.g., problems of deformation), but on energy efficiency as well. Candela has commented that "if one increases the scale, the size increases and the volume gets larger, for example, in the site where one has to place air conditioning. This constitutes a serious limitation." (Garay 1994)

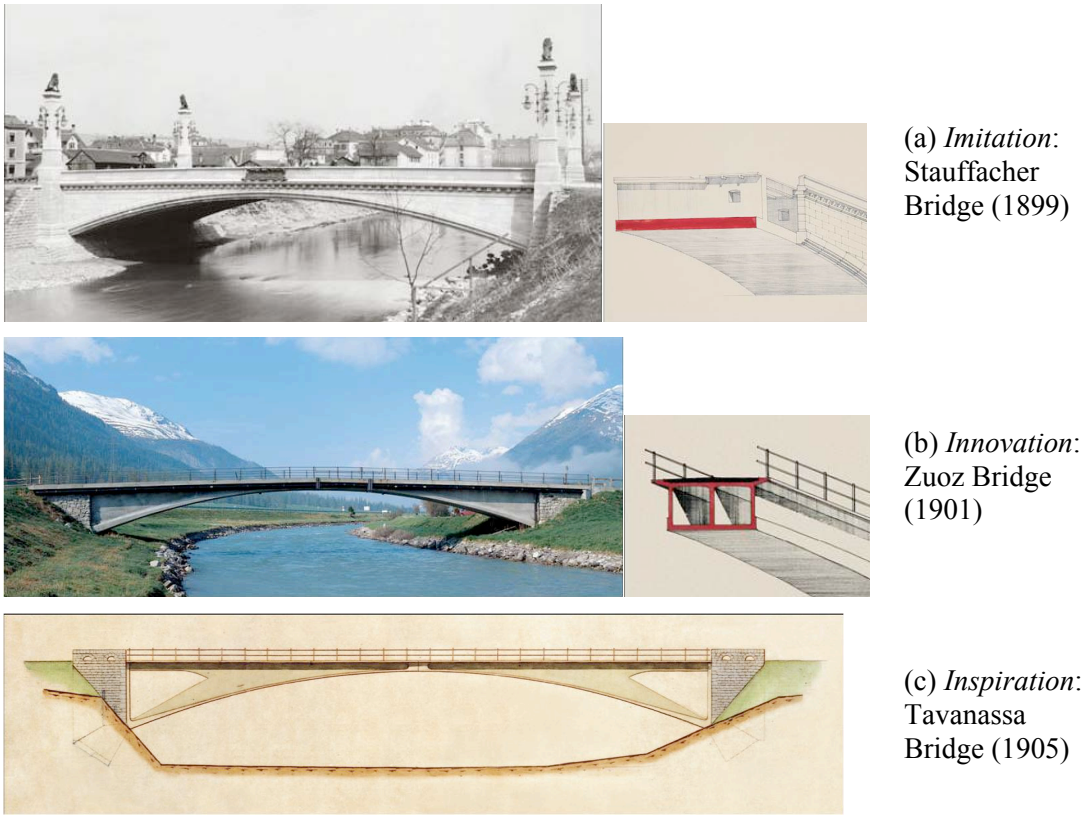
This connection between sustainability and structural artists can be found in designers other than Candela. For example, Heinz Isler has written that the life of a building "should not be just a few years but three generations, about three times twenty, or sixty years without any damage or need for repairs" (Isler 2008, p. 87). Further, when Isler was young, he was against building because he saw how building can destroy nature. Isler was careful not to waste materials, which is good ecologically.

THE ORIGINS OF INSPIRATION

Imitation, Innovation, and Inspiration

Robert Maillart (1872-1940), a Swiss engineer, was one of the greatest structural artists of the twentieth century. Maillart critically studied his built structures and was always striving to improve them. With his Stauffacher Bridge (Fig. 9a) he imitated a bridge built in Geneva that had fake stone walls. This style of design was an inefficient use of concrete since the walls were not structural. With the Zuoz Bridge (Fig. 9b), the walls were part of the structure and the cross section was an efficient hollow box – an innovation of Maillart's. Finally, in the Tavanassa Bridge (Fig. 9b), he eliminated the walls near the abutment that would otherwise crack but not necessary for carrying any loads. This evolution of design (illustrated in Fig. 9) is an example of how structural artists go from imitation to innovation to inspiration.

Candela also began by imitating forms. For example, his umbrella forms were an imitation of something he had seen in an article (Fig. 4a). But the form was re-proportioned to make it more elegant (Fig. 4b,c), and through experimentation, he optimized the rise of the umbrella (Draper et al. 2010). His umbrella-derived inspiration of Milagrosa (Fig. 5) is based on creativity that is rooted in engineering principles of design.



(a) *Imitation*: Stauffacher Bridge (1899)

(b) *Innovation*: Zuoz Bridge (1901)

(c) *Inspiration*: Tavanassa Bridge (1905)

Figure 9: Evolution of Robert Maillart bridges

In addition, Candela's first vaulted shells were of the traditional forms (such as barrels and funicular) – an imitation. His Cosmic Rays Laboratory was an innovation of a hypar shell form – but not an inspiration. Another innovation was the hidden "V-beams" in the groins of "intersecting hypars", i.e. groined vaults. These V-beams were not visible and they stiffened the shell and attracted the forces to the groins, which would carry the load to the foundation. These innovations and his "disciplined play", led him to many creative yet technically correct forms such as Restaurant Los Manantiales (Fig. 6) and Bacardi Rum Factory (Fig. 8) – examples of inspirations.

Influence of Structural Artists

Structural artists are sometimes stimulated by other structural artists. For example, through studying the writings and works of many engineers, Candela was able to educate himself. In particular, structural artist Robert Maillart stands out as his greatest influence: "[Robert Maillart] may have been one of the strongest influences at the critical moment in my career in which I was trying to become a builder of shells." He discovered Maillart's works in two books, Sigfried Giedion's Space, Time, and Architecture and Max Bill's Robert Maillart. Maillart had constructed many slender, elegant arched bridges and pioneered new building forms out of reinforced concrete, striving for new forms that were efficient. Candela devoured his writings, and Maillart's papers opened his eyes to a new way of approaching structures. The Swiss structural artist used simplified calculations rather than rigorous analysis (which he had studied at the ETH in Zurich), a strategy that Candela found

"delightfully sympathetic and encouraging." (Félix Candela, unpublished autobiography)

Robert Maillart influenced Candela, but in turn, Candela influenced other developing structural artists. For example, in the early 1960s, Swiss shell designer Heinz Isler came across a book cover with a photograph of the Restaurant Los Manantiales designed and built by Candela (Fig. 6); its forms were completely new to Isler and appeared almost paper thin, and stimulated Isler to think about how he might express the same kind of thinness (Billington 1985). He was not able to achieve it with his traditional pneumatic forms, but did succeed with his hanging forms, as demonstrated for example by the BP service station built in 1968 (Fig. 10).



Figure 10. Heinz Isler's hanging form of the BP Service Station (1968)



Figure 11. Jack Christiansen's umbrellas.

Jack Christiansen designed many fine thin shell concrete structures in the US. Like Candela, he admired and was also influenced by the works of Maillart and others; but also, he was influenced by Candela. When he learned of Candela's work, he called it "Love at first sight" (Segal 2008). Like Candela, Christiansen designed many shells out of the hypar form such as the umbrellas used at Seattle's World fair (Fig. 11). Other current designers such as Jorg Schlaich (Schlaich 2008, p. 171) and Bill Baker (Baker, 2008) also give credit to Candela for inspiring them with forms

Education and Teachers

Structural art has flourished most impressively in Switzerland, in no small part because of the engineering educational tradition at the Federal Institute of Technology (ETH) in Zurich, and two exemplary teachers in particular: Wilhelm Ritter (1847–1906) and Pierre Lardy (1903–1958). Ritter made a deep personal impression on his students, conveying to them his emphasis on the importance of aesthetics in the education of civil engineers. The strong visual component of his teaching related applied mechanics to structural form and he encouraged his students to visualize the flow of forces within a structure, as well as the ways in which different forms could change that flow. It is not surprising that his teaching produced two of the most outstanding bridge engineers of the 20th century: Robert Maillart (1872–1940) and Othmar Ammann (1879–1965).

The most significant aspect of Lardy's teaching was his continued reference to the aesthetics of structure (especially those of Maillart), not as an isolated topic but as one integral to the engineer's design. Once again, we see the product of his technical teaching combined with an aesthetic emphasis in the works of his students, including Heinz Isler (1926-2009) and Christian Menn (born 1927). Heinz Isler has written that (Isler, 2002)

> "I think that the most important contribution we students got from our teacher Lardy is this:
> He reminded us, the engineering students,
> a) that we have in us a sense for esthetics
> b) that we have the right to use it
> c) that we are allowed to mention our opinion
> d) and that we can find and express it in our projects
> This to my opinion was the invaluable, great, and unique contribution he gave to us. Not the statics, not the theories, not the investigations were his greatest and lasting influence, but encouraging us to find and apply esthetics from within us.
> And for this I am very grateful to him."

Structural engineering education, done properly, can thus inspire students to reach the pinnacle of design: structural art. Teaching structural art is also important because structural engineering since the Industrial Revolution has become a *new art form* parallel to but independent from architecture. It must therefore form an important part of the education of civil engineers. Just like other forms of art – painting, sculpture, music and literature – structural engineering should focus on the exemplary works of structural artists in the education of engineers and in the broader education of *all* students.

This form of teaching is done at Princeton University through the course "Structures and the Urban Environment", which was developed by David Billington and has been taught continually by him since 1974 (with its largest enrollment ever this year of about 240 students). This is a required course for structural engineering majors, who typically constitute less than 10% of the class. About 80% of those enrolled are *non* science or engineering majors. The course centers on fourteen of the greatest structural engineers and discusses what leads us to designate them as artists – structural artists. This argument appears in the basic text for the course *The Tower and the Bridge: The New Art of Structural Engineering* (Billington 1985) but it is more visually expressed and better generalized in the most recent course texts: *Félix Candela: Engineer, Builder, Structural Artist* (Garlock and Billington 2008) and *The Art of Structural Design: A Swiss Legacy* (Billington 2003), the latter of which consists of Swiss structural artists Robert Maillart, Christian Menn, Heinz Isler, and Othmar Ammann along with chapters on their teachers Ritter and Lardy.

CONCLUSIONS

Structural artists are engineers who consider it their mission to create the form—the aesthetic of a structure—as well as to conceive the technical design and the

construction plan. Structural art can only arise when that play is disciplined by efficiency and economy. As Candela explained: "But an efficient and economical structure has not necessarily to be ugly. Beauty has no price tag and there is never one single solution to an engineering problem. Therefore, it is always possible to modify the whole or the parts until the ugliness disappears. This aversion to ugliness is quite the opposite of the task of the professional artist who has to produce beauty as an obligation or of today's star-architect who has to be original at any cost in each new project." (Candela 1973)

A work of structural art satisfies all the above criteria and it is always the product of one person's imagination: an individual who develops the form based on the engineering imagination, makes appropriate calculations, and develops a means of building it. Candela seems never to have created a new form in the sense that some architects do, often without any relationship to efficiency and cost. While Candela worked with architects on some of his projects, the designs were based on his innovative ideas, which in turn were based on the *engineering imagination*.

The *inspiration* for the designs of structural artists come from a process that begins with imitation, followed by innovation. This concept was illustrated through the examples of the designs of Robert Maillart and Félix Candela. Sometimes, the inspiration comes from another structural artist. For example, Candela was stimulated by Maillart, and Isler was stimulated by Candela to express the thinness.

In a design profession it is of the utmost importance to teach the greatest works along with the discipline of calculations. Student engineers need to be exposed to the best that has been done and *all* students need to be educated in structural art so that as citizens they can call for such works in the future and to be able to choose them over the sometimes flashy but excessively costly structures that are wasteful of material and moneys and are difficult to sustain. Education is therefore crucial for the future of structural art and in studying it educators, practitioners, and the general public can recognize the potential for this new art form in the 21st century.

ACKNOWLEDGEMENTS

All photographs are courtesy of Princeton University Structural Engineering Archive, which is largely comprised of materials on Maillart, Candela, and Tedesko.

REFERENCES

Aimond F. (1936). "Étude statique des voiles minces en paraboloide hyperbolique travaillant sans flexion," Publications, International Association for Bridge and Structural Engineering (IABSE) 4

Baker, William (2008). "Learning from Candela: Structural Forms in Architecture", presentation in *Symposium on Felix Candela: His influence for today and the future*, Princeton University, Princeton, N.J., October.

Basterra, A. and Valero, E. (1998). "La Aventura Mexicana: Entrevista con Félix Candela," Arquitectura Viva 58, January–February.

Billington, David P. (1985). *The Tower and the Bridge: The New Art of Structural Engineering*. Princeton: Princeton University Press,

Billington, David P. (2003). *The Art of Structural Design: A Swiss Legacy*, New Haven, 13.

Candela, F. (1955). "Encuestra espacios" (an interview with Félix Candela), Espacios: Revista integral de arquitectura, planification, artes plasticos 28, November – December.

Candela, F. (1973). "New Architecture," The Maillart Papers, ed. David P. Billington et al. , Princeton, 119–26.

Candela, F. (1990). Felíx Candela's autobiography; written in the 1990s, it remained unfinished and was never published. A copy of the manuscript was obtained courtesy of Mrs. Dorothy Candela and is housed in the Princeton University Candela Archives, Department of Civil and Environmental Engineering, Princeton University; trans. Maria Garlock.

Draper, P., Garlock, M.E.M., Billington, D.P.(2010). "Structural Optimization of Félix Candela's Hyperbolic Paraboloid Shells", Journal of the International Association for Shell and Spatial Structures, v 51, n 163, p 59-66.

Draper, P., Garlock, M., Billington, D. (2008). "Finite Element Analysis of Félix Candela's Chapel of Lomas De Cuernavaca", Journal of Architectural Engineering, ASCE, v 14, n 2, p 47-52.

Faber, C. (1963). *Candela: The Shell Builder.* New York: Reinhold Publishing, 1963.

Garay, G. (1994). "Proyecto de Historia Oral de la Ciudad de Mexico: Testimonios de sus Arquitectos (1940–1990), Entrevistas Arquitecto Félix Candela", Mexico, August: third interview, 15; trans. Maria Garlock.

Garlock, Maria E. M. and Billington, David P. (2008). *Félix Candela: Engineer, Builder, Structural Artist*. New Haven: Yale University Press.

Isler, Heinz (2002). Letter from Heinz and Maria Isler to Phyllis and David Billington, April 2, 2002.

Isler, Heinz (2008). "Shell Structure: Candela in America and What We Did in Europe", in *Seven Structural Engineers: The Felix Candela Lecture Series*, The Museum of Modern Art, New York, edited by Guy Nordenson.

Kelly. K., Garlock, M.E.M., Billington, D.P. (2010). "Structural Analysis of the Cosmic Rays Laboratory", Journal of the International Association for Shell and Spatial Structures, Vol 51, No. 1., p 17-24

Schlaich, Jorg (2008). "On the Cultural and Social Responsibility of the Structural Engineer", in *Seven Structural Engineers: The Felix Candela Lecture Series*, The Museum of Modern Art, New York, edited by Guy Nordenson.

Segal, E., Garlock, M., Billington, D. (2008). "A Comparative Analysis of the Bacardí Rum Factory and the Lambert-St. Louis Airport Terminal", Proceedings of the International Symposium IASS-SLTE 2008, Acapulco, Mexico, Oct. 27-31.

Segal, E. M. (2008). "The Thin Concrete Shells of Jack Christiansen", A Master of Science in Engineering Thesis, submitted to the Department of Civil and Environmental Engineering, Princeton University, May.

Thrall, A., Garlock, M.E.M. (2010). "Analysis of the Design Concept for Iglesia de la Medalla Milagrosa" Journal of the International Association for Shell and Spatial Structures, v 51, n 163, p 27-34.

The Influence of Engineering Organization on Design and Construction Processes at Tennessee Valley Authority Dams of the 1930s

A.B. Liel[1]

[1]Assitant Professor, University of Colorado, Boulder, CO 80309; PH (303) 492-1050; email: abbie.liel@colorado.edu

ABSTRACT

This study examines engineering design processes and organization at the Tennessee Valley Authority in its early years from 1933 to 1936. During this time, Norris and Wheeler dams were constructed and plans and designs were begun for several additional dams. The TVA experience provides insights into how design processes evolved and were managed in a large engineering organization. A particularly innovative decision was the choice to build TVA dams by force account, i.e. by hiring their own employees, rather than by selecting contractors through a traditional bidding process. TVA engineers believed this approach would reduce overall design and construction costs, as well as reduce time to completion. Case studies of civil engineering history, like this one, provide an important tool for introducing students to design processes and engineering decision making.

DAM DESIGNERS

Unlike many of the landmark civil engineering works of the 20th century, which can largely be attributed to the engineering know-how and imagination of one individual, such Othmar Amman's George Washington Bridge, the construction of each of the massive federal dams during the 1930s and 1940s largely represents a collaboration of engineering design expertise among many individuals. This collaboration likely resulted from the unique challenges of dam design, which require integration of design of structures, water passage systems, turbines, transmission, and mechanical systems and involve each of the major branches of engineering. As a result, both the expertise and creativity of individual engineers and their interactions to integrate different aspects of the design are critical to the design process.

This study examines one major dam-building agency, the Tennessee Valley Authority (TVA), and their engineering design processes and organization. Much has been written about the TVA: the politics of its early proponents in the 1920s, its origins during the Great Depression, the controversy of creating a multi-state organization to manage a river basin, the conflict between its early board members, and the technical features of its concrete dams. However, little has been written about the development of the engineering organization within this unique and complex political instrument. The story of TVA engineering management during these early years provides an important case study of how an organization grew from nothing in 1933 to build major engineering works, including the planning, design and construction of six major dams by 1940.

THE TENNESSEE VALLEY AUTHORITY CONTEXT

President Franklin Roosevelt signed the act authorizing the Tennessee Valley Authority (TVA) on May 18, 1933, and chose Arthur Morgan as the organization's chairman. Morgan had gained renown as chief engineer of the Miami Conservancy District, for which he devised a flood control plan for the Miami Valley of the Ohio River (1915-1921), and administrative experience from his time as president of Antioch College (1921-1933). He also had experience designing earthen dams, but none with concrete dams or managing a large regional development project. Two others completed the Board of Directors: Harcourt Morgan, president of the University of Tennessee and David Lilienthal, lawyer for the Wisconsin Public Services Commission. In the summer of 1933, the government launched the new Authority with neither employees, technical expertise in the building of concrete dams, nor an organizational structure, but with three board members coming from diverse backgrounds and a desire to quickly begin construction of Norris Dam.

Decisions had to be made on how construction would be carried out, and how the TVA would be organized. Under Morgan's leadership, TVA began by removing the U.S. Army Corps of Engineers from the Tennessee River. The Corps had already begun plans for restructuring the valley, but both Roosevelt and Morgan felt that the duality of their engineering and social goals for the region could be better accomplished by a completely autonomous agency. The Corps of Engineers' legacy was a report that prioritized Norris Dam, on the Clinch River, and Wheeler Dam, on the Tennessee River, ahead of other proposed projects in the region.[1] In other areas, Arthur Morgan's previous experience at the Miami Conservancy clearly influenced early board decisions. Most importantly, the directors chose to build their dams by force account, hiring their own employees, as had been done at the Miami Conservancy. Morgan and other TVA engineers were strong proponents of this system, although little evidence existed as to its superiority and much of the engineering profession remained unconvinced as to its merits. Both the Bureau of Reclamation and the Army Corps of Engineers, for example, usually used the traditional contractor-bid method. Drawing on his connections with the engineering profession and previous employees, Morgan rapidly established a talented engineering staff, but he felt it was essential, too, to enlist the Bureau of Reclamation's assistance in the design of the first two dams.

TVA'S EARLY ENGINEERING ORGANIZATION

Since Morgan was chosen as TVA chairman prior[2,3] to the official authorization of the TVA by Congress, he influenced the writing of the legislation and the initial

---

[1] United States Army Corps of Engineers. The Tennessee River and Tributaries: North Carolina, Tennessee, Alabama and Kentucky. Washington: Government Printing Office, 1930.

[2] Roosevelt announced that Morgan would lead TVA the day he signed the Act in May, 1933. By mid-April, 1933, Morgan and Roosevelt had begun communicating regarding plans for the TVA and Morgan had approval to confidentially begin inquiries about potential personnel.

[3] Talbert, Roy Jr., FDR's Utopian: Arthur Morgan of the TVA, Jackson: University Press of Mississippi, 1987. See also, Letter from Franklin Roosevelt to Arthur Morgan. April 18, 1933. *[Early TVA Correspondence. TVA Library. Knoxville, TN.]*

organization of the Authority. When the congressional committee asked Morgan how many members the Board of Directors should have, Morgan suggested three, a number he and Roosevelt had discussed. In addition, Morgan insisted that the three board members serve as equals and receive equal salaries.[4]

In an interview, Gordon Clapp, who began his time at TVA in July 1933 as assistant director of personnel and later became chairman of the TVA board in 1947, discussed the contradictory understandings of organization each of the original board members brought to the young corporation. Arthur Morgan, Clapp says, focused his efforts on hiring good people; armed with a superb staff, Morgan believed a suitable organization would develop without explicit planning. In the preface to a TVA organizational manual issued in March, 1935, Morgan wrote, "I personally detest regimentation, red tape, and bureaucracy, and am willing to endure a limited amount of confusion in order to give freer play to loyalty, initiative and enthusiasm."[5] Conversely, Harcourt Morgan, the lone member of the board with any experience in public administration, felt that a well-structured organization was essential.

Under the original organizational plan, Arthur Morgan became the general manager of the organization, responsible for coordinating and administrating the various activities of the organization, while the entire board would be responsible for general policies. However, this plan was abandoned only two months later, in August 1933, as Harcourt Morgan and David Lilienthal grew "dissatisfied with what they felt to be a lack of an adequate plan of administration or an effective overall method of control and review of the TVA program."[6] The new organization consisted of a tri-section of the board that continued until the 1936. Under this reorganization, the entire bard maintained responsibility for general policy formulation. Arthur Morgan took responsibility for the engineering and construction programs, with Carl Bock as his assistant engineer. Within the engineering department, separate divisions were created for both of the major projects, Norris and Wheeler, as well as engineering services, maintenance and construction, and reservoir clearance.[7] Harcourt Morgan took charge of agriculture and fertilizer considerations, and David Lilienthal assumed jurisdiction over electric power issues.

DESIGN OF NORRIS DAM

Having obtained the Army Corps of Engineers' designs, the Board of Directors asked the Bureau of Reclamation, the federal dam-building agency with the greatest experience in large concrete dams, to do the design work for both Norris and Wheeler dams, their first projects.[8] The Bureau of Reclamation engineers, led by J.L. Savage, redesigned the dams and furnished TVA with complete designs and specifications. The decision to discard the Corps' designs seems to have been largely based in politics rather than engineering and, particularly, Morgan's well-documented dislike

[4] Arthur Morgan, Making of the TVA, Buffalo: Prometheus Books, 1974.
[5] C. Herman Pritchett. The Tennessee Valley Authority: A Study in Public Administration, Chapel Hill: The University of North Carolina Press, 1943, pg. 155.
[6] *Ibid*, pg. 154.
[7] *Ibid*, pg. 171.
[8] None of the archival materials available make it clear whether the decision to involve the Bureau of Reclamation was predominantly made by Morgan, or a decision involving the entire board.

of the Corps of Engineers. Sherman Woodward, the TVA water resources engineer charged with reviewing the Corps of Engineers' designs, deemed them "naïve and in need of improvement."[9] However, careful evaluation of the two designs shows this negative assessment to be unjustified; the final Norris dam design had a lower reservoir elevation and removed the Corps' planned navigational lock, but the general shape of the dam remained similar to the Corps' original design and, certainly, the Bureau of Reclamation engineers had the Army Corps' design at their disposal. As well, there is some indication that the Bureau engineers utilized designs from recently completed Madden Dam on the upper Chagres River, in Panama, for the Norris design.[10] The Army Corps' preparation work, as well as the engineering expertise provided by the Bureau of Reclamation and mapping assistance from the United States Geological Survey, allowed TVA to begin construction of Norris and Wheeler Dams almost immediately. This quick start was imperative, in light of the politics of the Great Depression. TVA hired construction forces at the same time as the Bureau prepared the plans.

FORCE ACCOUNT CONSTRUCTION

TVA design plans and specifications were not put out to bid for contractors, but rather, were built by the organization's own construction employees, the so-called "force account" construction method. Arthur Morgan's experience at the Miami Conservancy District greatly influenced the decision to use the force account method for engineering and construction. Morgan originally had planned to use the traditional contract method for the Miami Conservancy dams. However, World War I led to fluctuations in materials and wages, and contracts included contingencies. Unwilling to accept these uncertainties, Morgan chose to hire his own workforce at the Miami Conservancy District. [11] Comparisons between his earlier years in private engineering practice and his years at the Miami Conservancy led Morgan to criticize the customary contract forms and specifications for their "ambiguity, repetition, [and] stereotyped phraseology."[12] Morgan viewed his plan for the Tennessee Valley as a scaling-up of the work he had done at the Miami Conservancy, and wanted to incorporate the same non-traditional construction methods. In his later writings, Morgan claimed that "the idea to take this course [the force account method] was mine."[13] Though the Bureau of Reclamation's construction work has always been done through the traditional bid-contracting system, Savage, the Bureau's chief design engineer, supported the choice of the force account method. The minutes of the July 29, 1933 board meeting read, "Mr. Savage believes the best and most economical results will come from the direct responsibility of the construction superintendent to the Authority, without the intervention of a contractor."[14]

---

[9] Morgan, Making of the TVA.
[10] H.A. Sargent. "Memorandum to Barton M. Jones: Study of Design Costs" May 12, 1937. *[Carl Bock Papers. National Archives. East Point, GA.]*
[11] Morgan, Making the TVA, pg. 95.
[12] Arthur Morgan. The Miami Conservancy. New York: McGraw-Hill, 1951.
[13] Morgan, Making the TVA, pg. 95.
[14] "Minutes July 29, 1933 Meeting, Board of Directors" *[TVA Library. Knoxville, TN.]*

TVA leaders were convinced that the force account method shortened time to completion of the projects. At a July 29, 1933 board meeting, the directors acknowledged that plans for Norris Dam could not be finished for six months and that "it would be difficult to take bids until the plans are finished, but it is possible to begin work very soon by force account."[15] The extra time required to use the traditional contracting method was certainly unpopular in the midst of the Great Depression. Praising the original board's decision in retrospect, Gordon Clapp described the shortened construction time-line as the major advantage of TVA's force-account method: "Building a dam by contract, in fact, is to build a dam at least twice, once on the drawing boards before you move a cubic yard of dirt and building it again on the site."[16] There is, however, little empirical evidence that TVA's use of the force account method significantly reduced project completion time.

In addition, the TVA board believed that the interaction between construction and design teams facilitated the realization of improvements that could be made and added to the as yet unfinished plans, a concept Morgan referred to as "dynamic design". In describing the advantages of the force account method, Morgan wrote, "I had found [at Miami Conservancy] that in large outdoor constructions there would almost certainly be actual conditions that could not be anticipated at the start."[17] Ross White, construction superintendent at Norris Dam, advocated the force account construction method saying, "It may be necessary to change substantially the foundation plans when the excavation for the foundation has exposed the nature of the underlying rock."[18] Morgan later claimed that several changes at Norris Dam made late in the design process, including the decision to increase concrete density, thereby increasing the safe reservoir level by 10%, would have been impossible to make in a traditional contractor-bid system.[19]

The Board of Directors further justified doing their own construction because it would allow the Authority to provide good working conditions, a characteristic Morgan wanted to be a hallmark of the TVA organization. In particular, TVA employees worked a total of six 5.5 hour days per week, with three days spent on the construction site, the others in training programs. The board felt that the feasibility of this type of work schedule under the typical contractor-bid systems would have been very difficult, if not impossible: "the whole training program depends on the direct handling of the work by the authority."[20]

The implementation of the force account method meant that the final design of Norris dam was only a few weeks ahead of construction. However, the board members' criticism of the traditional contracting methods and promotion for the force account were unusual. Excepting those in the Tennessee Valley, all major federal American dams were built in the traditional method. TVA eventually utilized this force account method of construction for each of its major dams.

---

[15] *Ibid.*
[16] Gordon Clapp. "Men and Management Rebuild a River." Six Lectures at the University of Chicago. (Chicago: University of Chicago Press), pg. 9.
[17] Morgan, Making of the TVA, pg. 95.
[18] "Minutes of July 29, 1933 Meeting, Board of Directors." *[TVA Library. Knoxville, TN.]*
[19] Morgan, pg. 95.
[20] "Minutes of July 29, 1933 Meeting, Board of Directors." *[TVA Library. Knoxville, TN.]*

TVA ENGINEERS

TVA engineers were chosen based on their previous engineering work and a particular ideology, including previous "progressive" work and a belief in "the feasibility of this [TVA] approach [for multi-purpose dams]."[21] During the summer of 1933, Arthur Morgan, and Bock, his assistant hired a team of respected engineers, drawing on Morgan's personal connections to quickly recruit technical staff.[22] Barton Jones, who eventually became TVA's chief design engineer, had worked with Morgan at Morgan's own firm, Morgan Engineering Company, the Miami Conservancy, and Antioch College. Morgan had also previously employed other high-level TVA engineers, including Bock, Woodward, Ross Riegel and Ned Sayford, James Bowman, and Emerson Chandler. In addition, Morgan recruited Dudley Dawson, head of training, from among the faculty at Antioch College. Morgan himself acknowledged the important legacy of Miami and his employees there, writing, "The general plan of the river control of the TVA and the dam building and administrative organization there was largely the work of men trained on the Miami Conservancy Project."[23]

The TVA also recruited a number of employees with previous dam-building experience with the U.S. Army Corps of Engineers or the Bureau of Reclamation. Theodore Parker, chief construction engineer, and Nicholls Bowden, hydraulic engineer, had both worked on large hydraulic projects with the Army Corps of Engineers. Byrum Steele and Robert Moore were former Bureau of Reclamation employees, Steele having worked on Hoover Dam.[24] Moore, who joined TVA in 1937 as assistant director of water control planning, had previously worked as the Senior Engineer in Charge of Structural and Hydraulic Design for the Bureau of Reclamation and played a major role in that organization's designs for Norris and Wheeler Dams.

ORGANIZATIONAL CHALLENGES

TVA Organization. The tri-section of the Board of Directors created the most fundamental organizational problem during TVA's first three years as it required the directors to split their time between leadership and general administration and oversight of the daily operation of the Authority. The TVA's organization at this time was unlike most private corporations, which tend to have a larger board of directors and a separate group of managers who direct the day-to-day operations of the organization.

Facing dual responsibilities, each director did not have adequate amount of time to address both the administrative and the operational issues. Although splitting their responsibilities was beneficial when initially conceived because it allowed each member of the board to focus especially on a particular aspect of the organization, the personal projects and personality clashes soon damaged the overall organization. John

[21] Clapp, "Men and Management Rebuild a River", pg. 9
[22] Personnel decisions had to also be approved by President Roosevelt. *[Early TVA Correspondence.]*
[23] Morgan, The Miami Conservancy.
[24] Personal communication with Donald Jackson, Professor of History, Lafayette College.

Blandford, secretary to Arthur Morgan, and, later, TVA general manager, described the characteristics of the board between 1933 and 1936: "In reality, there was no board then in existence. Officials had to catch each director severally by his coat tails and get the necessary documents signed."[25] Separation between the three directors allowed each to hire based on personal relationships or convenient political appointments. This intense interest in specific projects and people, as well as personality clashes amongst the board members significantly decreased the effectiveness of the tri-section of the organization. F.X. Reynolds, an employee in the personnel department, reflected in an interview, "disagreement was not taken kindly, and irritations caused reprisals and hindrances, and, they tended to deny to each other the things to which each was entitled. It was this spirit rather than the mere organization that caused the trisection to operate worse than could be deduced merely from structure."[26] On an undated organizational chart, Carl Bock wrote, "Mature consideration indicates the desirability of having the Directors retire from the administration of those phases of the TVA program which they collectively delegated themselves as individual directors back in the fall of 1933."[27] However, no provision was made, and organizational remedies were not made until 1936.

Although much of the personal squabbling was limited to the Board of Directors, bureaucracy and "red tape" led to a loss of morale that permeated all levels of the organization. Those employees who reported directly to the Board of Directors complained of inadequacies in the service departments and of time wasted on bureaucratic and administrative decisions. The accounting department was described as both "unsatisfactory" and "inefficient" and the personnel department found to be unresponsive to engineering needs.[28] Carl Bock wrote, "These problems require more than half my own time and energy to combat... They are likewise sapping the energy of heads of our engineering departments, and this situation, coupled with failure to authorize some much needed assistance, creates a serious situation." The bureaucratic problems, Bock believed, were not a result of the people hired, but rather the organizational system that had developed.[29]

The morale problem extended beyond the existing organization as managers reported a difficulty in hiring as the public gained knowledge of the conflicts among the Board of Directors: "Recent contacts with high grade prospects for key position invariably elicit questions as to the probable effect of this split on the candidate's situation."[30] Concerns about morale at all levels also inhibited the adoption of suggestions for reorganization, as the administration believed they would further worsen the situation.[31]

---

[25] "Interview with Clapp." *[Herman Finer Papers. National Archives. East Point, GA.]*
[26] " Interview with Reynolds." *[Herman Finer Papers.]*
[27] "Undated Organizational Chart." *[Carl Bock Papers.]*.
[28] "Suggestions for the Improvement of Administrative and Routine Procedures in the Engineering and Construction Departments by the Supervisory Staff of these Departments." *[Herman Finer Papers]*
[29] Mr. Woodward's Comments of October 15 on Red Tape. *[Carl Bock Papers.]*
[30] Carl Bock. "Engineering Organization and Administrative Problems of the Tennessee Valley Authority." April 26, 1937. *[Herman Finer Papers.]*
[31] " Correspondence regarding Architectural Design." 1937. *[Carl Bock Papers.*]

Engineering and Construction Organization. On an undated organizational chart from the mid-1930s, Carl Bock noted that "the authority is slowly changing from a planning and construction agency to a construction and operating agency."[32] He also acknowledged, "It was fundamentally impossible to design a suitable organization at the beginning because there had been no precedent for an enterprise such as the TVA. With the benefit of actual experience it should now be possible to introduce desirable forms of reorganization and this ought to be accomplished to the fullest extent possible."[33] In particular, the organization could learn from the design and construction experience at Norris and Wheeler dams. These changes in function of the authority required an alteration in the organization of the design and construction departments between 1933 and 1936.

Archival letters, interviews and other papers indicate a number of specific complaints regarding the engineering and construction organization. In particular, engineers frequently lamented the separation between electrical engineers, who were in the commercial electricity department, from the rest of the engineering division. This separation hampered communication between engineers and transmission power planners; while the engineers determined power capacity at dams, the electrical engineers designed the transmission lines, often without consulting each other, leading to repeated work once conflicts were discovered.[34] According to Reynolds, organizational difficulties increased costs: "in engineering, program money was lost because decisions were not agreed upon between the electrical engineers and the dam-building engineers."[35] The separation between the design department and the operating division also led to inefficiencies in TVA operation. Parker, Jones and Woodward, the three highest-ranking engineers, reported in October, 1936, that while they designed Norris to be operated by twelve people, twenty-eight men were on site, and, as a result, more facilities were needed.[36]

TVA engineers also found basic workplace amenities to be lacking.[37] The engineering design team reported that they had been moved from office to office often, and were not given enough space to work. The rapid increase in workforce from TVA's inception in May, 1933 to nearly 10,000 employees by July, 1934 exacerbated problems with workplace facilities. As TVA people and projects increased, difficulties emerged in employee training programs as well. The large number of isolated construction camps made it a necessity to provide a branch of training at each construction and operating center, requiring duplication of some training programs.[38]

Archival papers show that the organizational structure created animosity between the engineering department and other divisions, particularly the staff in the

---

[32] "Suggested organizational charts." *[Carl Bock Papers.]*
[33] "Suggestions for reorganization of the TVA." *[Carl Bock Papers.]*
[34] "Memo". April 21, 1937. *[Carl Bock Papers.]*
[35] "Interview with Reynolds". *[Herman Finer papers.]*
[36] Theodore Parker, Barton Jones and Sherman Woodward. "Report on Operation and Maintenance of Navigation, Flood Control and Power Facilities. October 1936." *[Herman Finer Papers]*.
[37] "Suggestions for the Improvement of Administrative and Routine Procedures in the Engineering and Construction Departments by the Supervisory Staff of these Departments." Oct.1936. *[Herman Finer papers.]*
[38] "Interview with George F. Gant." April 22, 1936. *[Herman Finer papers.]*

personnel office. Steele discussed the barriers he found in hiring talented engineers: "past experience has shown that there were many difficulties in building up the design force to adequate strength to handle the work under consideration. These difficulties, however, have increased rather than decreased, due to the bureaucratic procedure established by the Personnel Department."[39] An unsolicited memo on suggestions for improvement written by members of the engineering staff described the personnel department as one of their most significant problems. Signatures on this memo included the head construction plant engineer (Ackerman), the chief engineer (Parker), the chief design engineer (Steele), the acting chief design engineer (Jones), the general construction superintendent (White), and several project and construction engineers.[40] Salary policy, developed by the personnel department, was another point of contention. Exit interviews conducted when engineers left the organization indicated that engineers felt that the aim of the new salary policy was to "throttle their opportunities with TVA."[41] The combination of the bureaucratic hiring process and unpopular salary policy made it difficult for the engineering organization to maintain and hire the staff necessary for their operations. A 1937 report in *Engineering News Record* that private engineering hires had increased further increased concern among TVA engineers about their ability to hire the best engineers.[42]

These organizational difficulties challenged the original fluid organizational strategy, proposed by Arthur Morgan. Personal animosities and the tri-section of the board hampered the productivity of the leadership of the organization; excess red tape and loss of morale decreased the effectiveness of the engineers and laborers. Though TVA successfully hired what Morgan considered to be "good people", organizational difficulties did not solve themselves, and, by 1936, a major restructuring of the organization, of the type originally advocated by Harcourt Morgan, was necessary. One of the critical changes was the institution of the office of general manager. The position was given to Blandford, who had joined the organization as Morgan's personal assistant in September, 1933.

ENGINEERING ECONOMY: TVA DESIGN COSTS

Despite the expectation that the force-account construction method would reduce the overall cost of TVA projects, A.J. Ackerman, the head construction plant engineer, acknowledged in 1937 that "design costs are way out of line," and that there were "possibilities here for introducing economies."[43] Though Ackerman's memo emphasized that he does not have enough data to make comparisons to other engineering organizations, the high design costs of the first TVA dams beg

---

[39] Byrum Steele. "Report on Engineering Design in the Engineering and Construction Departments". October 1936. *[Carl Bock Papers]*.

[40] "Suggestions for the Improvement of Administrative and Routine Procedures in the Engineering and Construction Departments by the Supervisory Staff of these Departments." Oct.1936. *[Herman Finer Papers.]*

[41] "Salary Policy." From a preliminary report by Chairman Morgan on Organizational Problems of the TVA. 1936 – 1938. *[Arthur Morgan Papers. National Archives, East Point, GA.]*

[42] *Ibid.*

[43] Ackerman, A.J. "Memo to Carl Bock." Feb. 15, 1937. *[Carl Bock Papers.]*

comparison with dams built either by private sector or the other federal dam building organizations.

Total design costs at TVA dams, as a percentage of total structural cost, range from 2.2% at Wheeler to 6.8% at Hiwassee, as shown in Table 1. The two dams designed entirely by TVA forces (Pickwick Landing and Guntersville) had higher design costs than Norris and Wheeler, designed by the Bureau of Reclamation. Although Wheeler Dam probably had low design costs because the strong foundation material allowed the Bureau of Reclamation to use a particularly repetitive design, the total design cost for Pickwick Landing was twice that of Wheeler. Moreover, Hiwassee, the first tributary dam constructed after Norris, also had markedly higher design costs than either Norris Dam or Tygart Dam, constructed by the Army Corps of Engineers on the Monongahela River. However, overall structural costs among all the structures are similar.

Table 1. TVA dam design costs, in relation to total structural cost.

Dam	Year completed	Design cost	Total cost	Design costs as % of total structural cost
Norris[44]	1936	$561,248	$15,733,562	3.7%
Wheeler	1936	$507,927	$20,806,321	2.5%
Pickwick Landing	1938	$1,076,229	$21,902,776	5.1%
Guntersville	1939	$746,670	$17,837,168	4.5%
Hiwassee[45]	1940	$734,549	$10,764,624	6.8%
Tygart[46]	1938	$675,000	$18,400,000	3.8%

TVA engineers and administration attributed the large design costs in part to the TVA's young organization and lack of engineering experience. While other dam building organizations were able to reuse previous designs, TVA had no design experience to build on. By the 1930s, the Bureau had a standardized routine that lowered their design costs. Perhaps even more importantly, the force account method uniquely employed by TVA may have increased the design costs, while reducing the overall cost of construction, reflecting the mantra that, "With force account work, it is generally possible to apply the principle of spending another dollar to save two dollars."[47] While other dam building agencies were unable to make significant modifications in design after contractor bidding, the TVA design team worked with the field engineers and construction team to make modifications as the project progressed. Justifying the large design costs to the Board of Directors, Bock said, "it is our considered policy to scrap designs and make them over when by so doing a better construction will result or when substantial sums can be saved on construction

[44] Design costs for Norris, Wheeler, Pickwick Landing and Guntersville dams are given in the TVA memos: "Comparison of Design Costs of TVA Projects," dated May 12, 1937. *[Carl Bock Papers]*.

[45] The best estimate available for the design costs at Hiwassee is in TVA's technical report, The Hiwassee Project (Washington: Government Printing Office, 1946).

[46] The estimate of Tygart design costs is based on a letter from the Secretary of War, Harry Woodring, to West Virginia Senator Rush Holt on July 19, 1937. *[RG 77/111 Box 1682, Folder 5221. National Archives. College Park, MD.]*

[47] "Letter to Board of Directors." Feb. 15, 1937. *[Carl Bock Papers.]*

operation."[48] Cost engineer H.A. Sargent also acknowledged that some of the redesign was the result of having started the design before structural characteristics or equipment to be used were determined.[49]

To demonstrate these overall savings, the engineering department completed a detailed study of design changes and resulting economies for Norris Dam. As construction work progressed and more knowledge about the Norris site became available, TVA, together with the original Bureau design team, altered the diversion scheme to use spillway blocks rather than diversion tubes, eliminated the need for needle valve outlet conduits to regulate outflow, redesigned and moved the powerhouse, and removed a cutoff trench at the heel of the dam. Each of these changes increased the design costs, but resulted in estimated total savings of $980,335, a remarkable result considering the $561,248 total design price tag.[50] Similar TVA studies showed significant savings from redesign and the force account method at Pickwick Landing, Guntersville and Chickamauga Dams as well.[51]

CONCLUSIONS: THE IMPORTANCE OF STORIES IN ENGINEERING EDUCATION

In the words of the *American Society of Civil Engineers,* in civil engineering education we aim to prepare and inspire our students to,

> *serve competently, collaboratively, and ethically as master: planners, designers, constructors, and operators of society's economic and social engine, the built environment; stewards of the natural environment and its resources; innovators and integrators of ideas and technology across the public, private, and academic sectors; managers of risk and uncertainty caused by natural events, accidents, and other threats; and leaders in discussions and decisions shaping public environmental and infrastructure policy.*[52]

While ensuring that students gain the necessary technical expertise is essential to meeting these goals, it is insufficient. Case studies and stories of past civil engineering successes and failures provide a powerful tool for teaching students about the economic, societal and political impacts and considerations that affect any major engineering effort. In the early Tennessee Valley Authority described here, a group of political and engineering leaders set out to restructure the Tennessee River and the region's economy. Their story illustrates how one organization designed major civil engineering structures. Of particular importance are the insights into how the TVA went about building the human capital and technical expertise to design and construct the early dams. The early TVA engineering efforts also demonstrate the important role of engineering management and organization in facilitating or hindering design processes. In the mid-1930s, the engineering organizational structure seems to have

---

[48] *Ibid.*
[49] H.A. Sargent. "Memorandum to Barton M. Jones: Study of Design Costs" May 12, 1937. *[Carl Bock Papers.]*
[50] "Major Design Changes and Resulting Economies, Norris Dam" May 12, 1937. *[Carl Bock Papers.]*
[51] "Pickwick Landing Project: Major Design Changes", "Guntersville Project: Major Design Changes", "Chickamauga Project: Major Design Changes". All dated May 12, 1937. *[Carl Bock Papers]*
[52] American Society of Civil Engineers (ASCE). Civil Engineering Body of Knowledge for the 21st Century Preparing the Civil Engineer for the Future (2nd Edition). Reston, VA, 2008.

complicated efforts to collaborate across different branches of the organization and to integrate the different components of dam design (civil, mechanical, electrical and chemical). Even so, the TVA introduced a major innovation in design and construction, choosing to design and build the dams in-house. This design-build approach, which has recently gained increased popularity, probably facilitated the introduction of certain design changes and unique engineering features late in the dam design process and, in the process, provided design engineers with the flexibility to cope with some of the organizational and communication challenges they were faced with. These lessons – and others like them – can help our students better understand and navigate engineering design processes, including technical considerations of economy and efficiency and human considerations.

ACKNOWLEDGEMENTS

I first undertook the study that provides the basis for this paper as an undergraduate research project at Princeton University. It would not have been possible without the guidance, wisdom, and mentorship of Professor David P. Billington of Princeton University who introduced me to a love of scholarship and engineering stories. Sinead MacNamara and Angela Ovecka gathered some of the archival research materials.

A Comprehensive Assessment of Building Damage after the January 12, 2010 Haiti Earthquake

Ronald T. Eguchi[1], Stuart Gill[2], Shubharoop Ghosh[1], Walter Svekla[1], Galen Evans[2], Joaquin Toro[2]

[1] ImageCat, Inc., 400 Oceangate, Suite 1050, Long Beach, CA, USA; PH (562) 628-1675; FAX: (562) 628-1676; rte@imagecatinc.com
[2] The World Bank, Disaster Risk Management LABS, Global Facility for Disaster Reduction and Recovery (GFDRR), 1818 H Street, NW, Washington DC 20433, USA.

ABSTRACT

This damage assessment relied heavily on the use of remote sensing technology. Never before has the availability of high-resolution satellite and aerial imagery been so open and accessible. Data from different missions (World Bank-ImageCat-RIT Remote Sensing Mission (15cm optical and 2 pt/m2 LiDAR), Google (15cm optical), NOAA (25cm optical), Pictometry, as well as satellite imagery from GeoEye and Digitalglobe) has allowed damage from the Haiti earthquake to be viewed through multiple sensors and at different times. These multi-dimensional perspectives have been invaluable in understanding the magnitude and scope of damage caused by this earthquake.

BACKGROUND

This paper provides a brief account of how technology, inspiration and collaboration were used to quickly assess the amount of damage caused by the January 12, 2010 Haiti earthquake. In less than a minute, this event leveled approximately 20 percent of the buildings in greater Port-au-Prince; killed close to a quarter of a million people; injured as many; and left over a million individuals homeless. While not considered a *great* earthquake (from seismological standards), this event will rank as one of the deadliest earthquakes of the 21st century.

This event will also be known as one of the first events where technology (especially high-resolution imagery) was embraced at such a large scale in a real operational sense. Almost from the very onset of the disaster, high-resolution satellite imagery was available to provide the first glimpse of the devastation caused by this earthquake. Days later, very-high resolution aerial imagery was available to provide even more detail on the damage caused in this event. Together, these valuable datasets allowed a small army of remote sensing experts to provide one of the most accurate assessments of building damage in the last decade. Furthermore, this information was shared with Haitian government officials in relatively short time – within two months of the earthquake – in the

form of a *Building Damage Assessment Report* in support of the Post-Disaster Needs Assessment (PDNA) and Recovery Framework.

This paper discusses how three key international organizations – the World Bank (WB), the United Nation Institute for Training and Research (UNITAR) Operational Satellite Applications Programme (UNOSAT) and the European Commission's Joint Research Centre (JRC) – worked together, in the framework of the joint declaration signed in 2008 between the World Bank, European Commission and the United Nations Development Group on post-crisis Assessments and Recovery Planning, to produce this rapid assessment of building damage and how these organizations are continuing this collaboration to improve response protocols for future disasters. It is clear from the Haiti experience that the future of post-disaster damage assessments has changed dramatically and that the "bar has been raised" for the next event. The main purpose of this chapter is to document key lessons from the Haiti experience and to recommend improvements that can be implemented by future responders.

DAMAGE ASSESSMENT

The main outcome from the joint collaboration was the *damage assessment*. Damage was measured by the number of buildings in different damage states. For ease of use, the joint team agreed to use a damage scale that was developed several years ago in Europe – the European Macroseismic Scale – 1998 version. Fundamentally, this was one of the most important decisions made by the WB-UNOSAT-JRC team because it ensured a common basis for measuring the effects of the earthquake. By agreeing to use this scale, the damage assessment results from each organization could be combined without significant re-adjustment.

Table 1 shows the damage totals for the ten communes that were significantly affected by the earthquake. In total, over 90,000 buildings were either destroyed or experienced heavy damage. This represents slightly less than one third of the building inventory in the affected areas. Most of the damage occurred in Port-au-Prince; however, significant numbers of buildings were also destroyed in Carrefour, Delmas, Leogane and Petion-Ville. Based on median floor area estimates for different occupancy uses, this damage translates roughly to over 26 million square meters in building area affected with about one third of this total associated with buildings that will have to be either replaced or significantly repaired. The total repair cost to buildings is estimated to be over $6 billion (US).

SIGNIFICANT BREAKTHROUGHS

Years from now, many of the details of the joint WB-UNOSAT-JRC Haiti response will be forgotten; however, there are a number of outcomes that will remain a legacy of this monumental effort. What was accomplished during the Haiti campaign changed the landscape of global disaster response forever. The sheer magnitude of the event and its impact on the country of Haiti and its people required a new paradigm of data collection and damage assessment. Some of the notable accomplishments include:

- PDNA damage assessment based primarily on the use of remote sensing technologies,
- Crowd-sourcing technology as a means of mobilizing the expertise and passion of hundreds of volunteers around the world to rapidly assess the level of building destruction in greater Port-au-Prince, and
- A myriad of geo-spatial products that helped to chronicle the relief efforts of tens of volunteer organizations over time.

Table 1 - Number of Buildings Grouped by EMS-98[1] Damage Grade and Commune

	EMS-98[1] Damage Grades				
COMMUNE	**5**	**4**	**3**	**2**	**1**
Carrefour	2763	5905	5920	3220	35219
Cite Soleil	1012	549	1073	576	6403
Delmas	5012	2814	5064	2881	29478
Grand-Goave	148	541	421	276	2175
Gressier	565	289	567	319	3436
Jacmel	214	1785	1489	857	8799
Leogane	2220	5985	4139	2360	24736
Petion-Ville	2027	906	1693	708	10614
Petit-Goave	173	104	167	116	770
Port-Au-Prince	9902	15257	12351	6699	62693
Tabarre	532	365	663	383	3914
Total	**24062**	**34500**	**33546**	**18395**	**188236**

Note: 1-EMS-98: European Macro-seismic Scale (1998)

PDNA Damage Assessment – Past post-disaster damage assessments in support of a PDNA have been based on a variety of methods and data sources. Most common were field reports that attempted to capture the magnitude and scope of the disaster by focusing on heavily-affected areas and "extrapolating" these observations to the rest of region. In the past decade, remote sensing technology has had a role in these damage assessments but primarily as a verification source or as a means to visually portray to decision-makers and the public the amount of damage that had been sustained in the disaster. The notion of using remote-sensing technology as the primary basis of establishing the "damage estimate" is new and the fact that the Post-Disaster Needs Assessment framework adopted by the Haitian government is based on a direct result of this assessment is noteworthy. What was fundamentally a slow and tedious process was greatly enhanced by free and widely-available high-resolution satellite and airborne imagery. Rather than taking months to complete a preliminary count of damaged buildings, the application of remotely-sensed data allowed this damage assessment process to be shortened by a factor of two or three.

[1] EMS-98 scale includes five damage grades: 1 – no visible damage; 2 – minor damage; 3 – moderate damage; 4 – very heavy damage; and 5 – Destroyed.

Currently, there is a Ministry of Public Works effort designed with support from the World Bank and co-financed by the World Bank, GFDRR[2] and USAID[3] OFDA[4] that is focused on conducting a "house-to-house" assessment of building damage levels in order to ensure the safety of each building and to estimate the rebuilding or repair costs of all affected structures. This level of investigation is considered the most reliable and most accurate indicator of damage and thus represents the benchmark to which the remote-sensing assessment must be based. Since this process is still ongoing, a final comparison is not possible at this stage; however, early indications are that the remote-sensing based results are highly reliable with respect to counts of heavily-damaged or destroyed buildings. The World Bank/GFDRR financed portion of the structural building assessment is being implemented by UNOPS and the USAID OFDA portion is implemented by PADF[5].

Despite the obvious power of remote sensing technology, it is not without limitations. As we observed from ground surveys, much of the damage that resulted in the Haiti earthquake could not be detected from traditional aerial imagery (i.e., nadir views). With damage phenomena known as "soft-story" failures"[6] so prevalent in this earthquake, ground surveys played an important role in "filling in" the complete picture of damage. One of the key recommendations of this effort is the need for detailed protocols that systematically identify where these ground surveys are to be completed and to what extent. Some research is already being performed to help answer these questions (Saito et al, 2010).

Future post-disaster damage assessments – whether for earthquakes or for other hazards – will surely include a major remote-sensing component. As the technology improves in both resolution and delivery, the use of remote sensing will be commonplace not only for the most spectacular events but for smaller and moderate-sized events. And the Haiti earthquake will serve as the benchmark for what can and should be accomplished in these disastrous events.

Crowd-sourcing – Crowd-sourcing or human computation is a relatively new development and certainly a new concept in the area of disaster response. The notion of using a large community of experts to help perform damage assessments in disasters has been introduced by a number of individuals and organizations. With the Internet becoming the foundation of "social networking," it is not unexpected that virtual damage surveys using high-resolution imagery displayed on "Google Earth" type platforms emerged as a major source of damage information for the Haiti PDNA. After the Haiti earthquake, hundreds of individuals from around the globe passionately sought ways of contributing their expertise, time and knowledge to help support the people of Haiti.

---

[2] Global Facility for Disaster Reduction and Recovery

[3] United States Agency for International Development

[4] Office of Foreign Disaster Assistance

[5] Pan American Development Foundation

[6] These types of structural failures occur when the stiffness of the lower stories of a building are much "softer" that than upper portions of a building. Soft floors usually result when large open spaces at the first level. The effect when significant ground shaking occurs is for the upper floors to collapse onto the lower story. Many of these failures were observed in Haiti.

ImageCat working with a network of partners including the Earthquake Engineering Research Institute[7] reached out to the engineering and scientific community to help in quantifying the extent of damage caused by the Haiti earthquake. In direct response to this event, ImageCat and EERI formed the GEO-CAN (Global Earth Observation – Catastrophe Assessment Network) community to help the World Bank in its effort to quantify building damage. Using very high-resolution aerial imagery, this community was able to identify the number of heavily-damaged and destroyed buildings in greater Port-au-Prince. A major product from this effort was the delineation of the pre-earthquake footprints of these buildings that would later be used by the joint WB-UNOSAT-JRC effort to quantify the amount of building area that needed to be replaced or repaired. In addition, the footprints offered an efficient way of combining the damage assessment results from the World Bank effort (GEO-CAN), and the UNOSAT and JRC teams. Using crowd-sourcing as the main information technology tool for post-disaster damage assessment, the GEO-CAN community was able to deliver its first count of damaged buildings in less than a week.

The GEO-CAN community consisted of over 600 experts from 23 different countries with over 60 major universities represented, about 20 government agencies and non-profit organizations, and over 50 private companies[8]. Current efforts by the World Bank, EERI and ImageCat are ongoing to institutionalize the GEO-CAN community as a permanent tool in the World Bank damage assessment toolbox.

Geo-Spatial Products – Led primarily by the UNITAR/UNOSAT group, a myriad of geo-spatial products emerged throughout the post-Haiti earthquake campaign. Early products were used for tracking emergency response activities, such as the locations Internally Displaced Persons (IDP). Later products included atlases that showed the locations of severely-damaged and collapsed buildings – see Figure 1. These damage atlas sheets were critical in deploying emergency teams to assess the safety and integrity of all buildings in the greater Port-au-Prince area.

Some other novel applications include 3-D models of Port-au-Prince that were constructed using LiDAR data collected during the World Bank-ImageCat-Rochester Institute of Technology Remote Sensing Mission (see Figure 2). A final report prepared by the World Bank and ImageCat contains a more comprehensive discussion of the various data products that were prepared by numerous organizations using high-resolution satellite, aerial (both nadir and oblique) optical imagery and LiDAR data (World Bank and ImageCat).

One of the important lessons learned from the Haiti earthquake was that free access to high-quality imagery was an important factor in motivating researchers and response organizations from around the world in producing rapid and transparent damage assessments. Corroboration of damage results was possible because of the number of

[7] The Earthquake Engineering Research Institute is a professional organization of engineers and scientists that are dedicated to reducing the effects of earthquake on people and structures. Founded in the late 1960's, its membership exceeds several thousand individuals. For more information on the organizations and its accomplishments over the last several decades, please see http://www.eeri.org.

[8] See http://www.virtualdisasterviewer.com for a complete list of organizations that participated in the GEO-CAN Haiti Initiative.

independent studies that were performed in this event. Although manual interpretations of damage were most common, many studies focused on automated or semi-automated approaches. Over the next year, we will be able to evaluate what methods were most effective at quantifying the scope of damage in this disaster. Already several major journals have committed to publishing special issues on the Haiti earthquake with special attention to remote sensing technologies. Through these reviews and exchanges in information knowledge, the response community will be able to build on the lessons learned in the Haiti earthquake so that the process of damage assessment will be even more robust and efficient in the future.

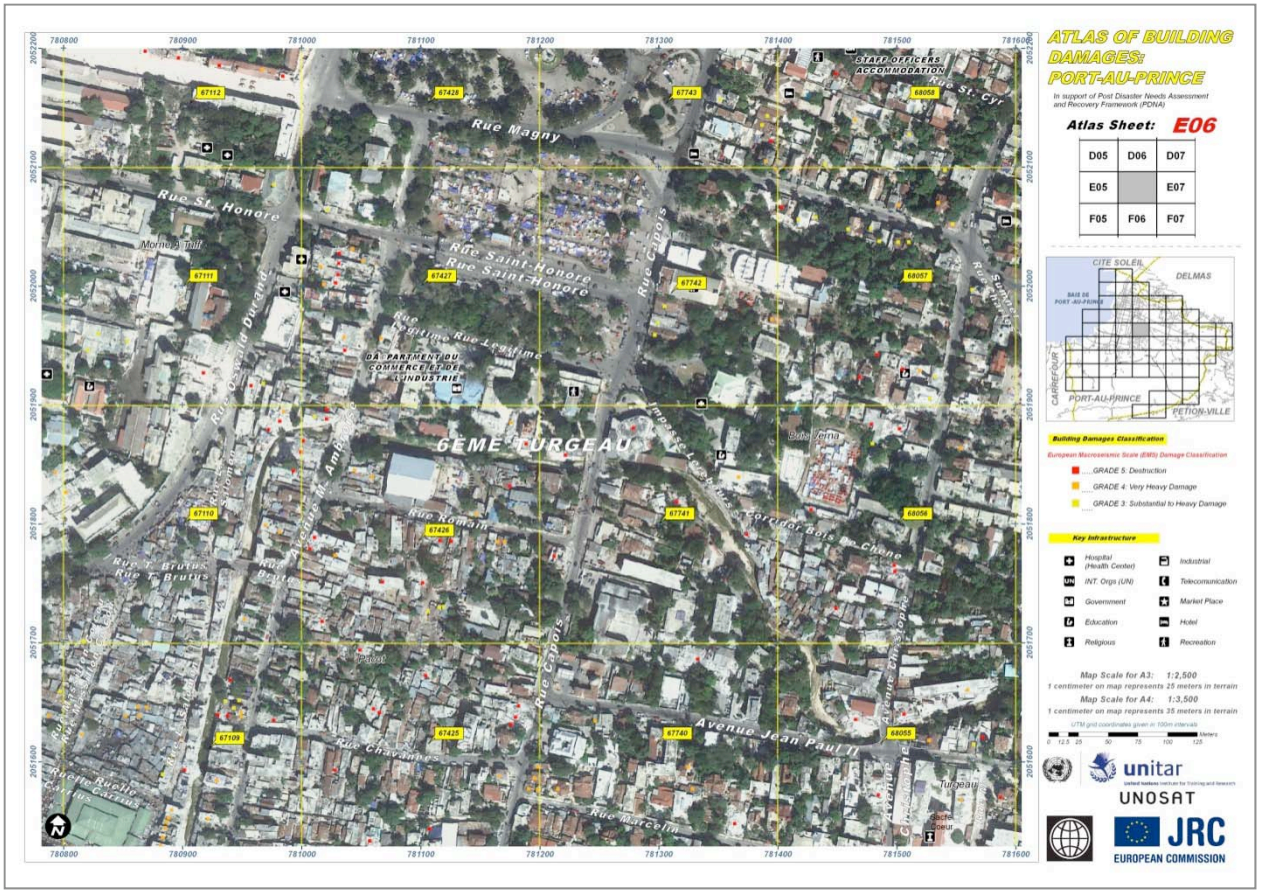


Figure 1 - Damage Atlas Sheet – Haiti Earthquake



Figure 2 - Purdue University's 3-D building Models as viewed in Google Earth

CONCLUSIONS

While the area of remotely-sensed damage assessment took a quantum step forward in the Haiti campaign, there is still significant room for improvement. Some of the areas that deserve further investigation or review are:

1. The establishment of standard operating procedures to ensure that damage assessments performed by multiple groups are consistent, transparent and combinable. An important element of any protocol will be standard definitions of damage and a damage scale based primarily on remotely-sensed imagery. Current efforts by the joint WB-UNOSAT-JRC team are focusing on a preliminary set of guidelines in this area (JRC et al., 2010).
2. The availability of high-quality imagery in near real-time. A key factor in the success of the Haiti response was having access to very high-resolution imagery within a matter of days. Rapid access to these data allowed a number of operations to proceed with greater confidence, i.e., deployment of emergency personnel to assess the safety of damaged structures. The fear of "overcommitting" resources before the priorities were known was somewhat mitigated by having these early "snapshots" of the devastation caused by the earthquake.

3. More work in training field personnel in how to use the "derived" products of satellite and aerial imagery. What was evident from post-earthquake interviews with field personnel was that existing workflow processes did not include the use of high-resolution imagery or derived damage products in the early emergency phase. For that reason, the use of the damage atlas sheets and general damage statistics was limited at that stage. Perhaps, an important purpose of the standard operation procedures discussed above could include clear guidance on how these damage products could be used for building safety assessments, siting of evacuation camps, siting of relief centers, etc. Additionally, there is an opportunity to integrate remotely-sensed products into the recovery process. For example, tracking and monitoring the progress of rebuilding or reconstruction can be a product of remote sensing technologies.
4. Refining the application of crowd-sourcing techniques in both damage assessment and in exposure mapping. In Haiti, one of the most severe impediments to the rapid mapping process was not having quantitative information on what was there before the earthquake. In most developed countries, property information (parcel locations, building sizes, some structural data) is typically available through cadastral and tax records or other government databases. This information is important in identifying what the reconstruction needs are because it provides data on what existed before the disaster. Because this information was largely absent in Haiti, a significant amount of time was spent trying to construct this information post-event by "digitizing" remote sensing images. Because there are a number of countries that would be in the same situation as Haiti, refining crowd-sourcing techniques to quickly develop key datasets, including locations of damaged structures and as spectacularly demonstrated by the Open Street Map initiative[9], is highly recommended.
5. Exploiting the lessons learned from the Haiti Earthquake. The response to the Haiti earthquake with respect to technology exploitation was phenomenal. In many respects, the event served as a testbed for assessing the efficacy of a wide range of technologies, including remote sensing. The lessons learned from this event must be leveraged so that when the next mega disaster occurs, we are not "re-learning" how to respond or how to implement these new and emerging technologies. What is needed is a "tsunami" of publications, reports, briefs, book chapters that document our successes and failures, in a way that also guides the way forward for future applications. It is the hope of the current authors that this book chapter contributes to this mission and that in a small way, we have defined part of that direction.

[9] http://wiki.openstreetmap.org/wiki/WikiProject_Haiti for a description of the OSM crisis mapping activities and http://haiti.openstreetmap.nl/ for access to the map data.

ACKNOWLEDGMENTS

There are many organizations and individuals that contributed to this joint damage assessment mission. We would like to acknowledge the following groups/individuals:

- BFP Engineers, Inc., USA
- DigitalGlobe, USA
- Earthquake Engineering Field Investigation Team (EEFIT), UK
- Earthquake Engineering Research Institute (EERI), USA
- EC/Joint Research Centre, Italy
- GeoEye, USA
- Google, USA
- Open Street Map, USA
- Pictometry, USA
- Rochester Institute of Technology, USA
- Stanford University-Pacific Earthquake Engineering Research Center, USA
- Swisstopo, SUI
- University at Buffalo, USA
- University of Zurich, SUI
- UN/UNITAR/UNOSAT, SUI

REFERENCES

Coyle, Diane and Patrick Meier, *New Technologies in Emergencies and Conflicts: The Role of Information and Social Networks*. Washington, D.C. and London, UK: UN Foundation-Vodafone Foundation Partnership, 2009.

Joint Research Centre, UNITAR/UNOSAT, World Bank (GFDDR), ImageCat and Cambridge Architectural Research, Standard Operating Procedures - Collaborative Post-disaster Damage Assessment Using Remote Sensing, 2010.

Saito, K., Spence, R., Booth, E., Madabhushi, M, Eguchi, R. and Gill, S., "Damage Assessment of Port-au-Prince using Pictometry," *Proceedings of the 8th International Workshop on Remote Sensing and Disaster Management*, Tokyo, Japan, September 30 – October 1, 2010.

World Bank – ImageCat, *Post-Disaster Building Damage Assessment using Satellite and Aerial Imagery Interpretation, Field Verification and Modeling Techniques*, 2010.

Procedures for Fatigue Crack Growth Monitoring and Fatigue Life Prediction Using Acoustic Emission Data and Neural Networks

F.F. Barsoum, M.ASCE[1], E.v.K. Hill[2], Y. Zhang[3], A. Korcak[3], and J. Suleman[3]

[1]Associate Professor, Mechanical and Civil Engineering Department, Embry-Riddle Aeronautical University (ERAU), Daytona Beach, FL 32114, USA; (386) 226-6618; email: Fady.Barsoum@erau.edu
[2] Professor, Aerospace Engineering Department, ERAU
[3] Student, ERAU

ABSTRACT

This research applied the nondestructive testing (NDT) technique of acoustic emission (AE) to monitor fatigue cracking in steel structures and utilized artificial neural networks (ANNs) for fatigue life prediction. The neural network classification network known as a Kohonen self organizing map (SOM) was first used to classify the AE data into the different source mechanisms occurring during fatigue cracking. This research developed methodologies for placing sensors, collecting acoustic emission data and eliminating noise from the raw data. The ultimate goal of this research was to monitor for steel fatigue cracking and accurately predict remaining fatigue lives using AE flaw growth data and back propagation neural networks (BPNNs). The procedures for doing so are presented herein.

INTRODUCTION

Acoustic emission is a powerful NDT technique when evaluating the health of structures. Artificial neural networks can be used to classify the AE data into different source mechanisms using a Kohonen SOM neural network and to predict the fatigue or residual life of the structure using the AE flaw growth data as input to a BPNN. Laboratory testing has been performed on notched A572-G57 steel bars for prediction using BPNNs (Barsoum et al. 2009). The AE sources were classified into plastic deformation plus plane strain and plane stress fracture mechanisms. Fatigue lives were predicted with a maximum error of under ± 20%. Notched steel I-beams were also tested in the laboratory, and the maximum prediction error was 5.3 % based on the third quarter of data (50-75%) of the average fatigue life (Korcak 2010 [1]). Field testing has been conducted on a Florida girder bridge which was examined to be structurally deficient (Korcak et al. 2010 [2]). The acoustic emission data were classified using a SOM into three different mechanisms, which included possible concrete cracking. A similar test was conducted on two Florida mast arm poles susceptible to fatigue cracking in order to identify and locate the fatigue crack (Korcak et al. 2010 [3]). This paper proposes a procedure for structural health monitoring of steel structures using acoustic emission and neural networks. Sensor placing methodology and effective

noise filtering techniques are addressed. Valid neural network setup for source classification using a SOM and fatigue and residual life predictions using BPNNs are demonstrated.

LABORATORY TESTING

A572-G50 Steel Bar Testing

Twenty A572-G50 steel bars with a 3.81mm (0.15 in) deep V-notch were fatigued at six discrete stress levels for prediction purposes using AE and BPNNs (Barsoum et al. 2009). To ascertain the noise behavior coming from the testing machine and environment, before the actual testing, several noise tests were performed as the MTS machine was switched on, but both the mean cyclic load and the span setting were set at zero. Readings from the two-channel PocketAE[1] system (with AEwin[2] software imbedded) were recorded for half an hour, and three graphs were plotted to illustrate the noise behavior. The sources of noise present were (1) the hydraulic pump, hydraulic valves, and actuator piston; (2) the hydraulic grips that contributed rubbing noises; and (3) electromagnetic interference from the PocketAE charger interface, which is a long duration signal. The average frequency (counts/duration) histogram of the noise spectrum is shown in Figure 1, with the bulk of it falling between the ranges of 1 kHz to 30 kHz.

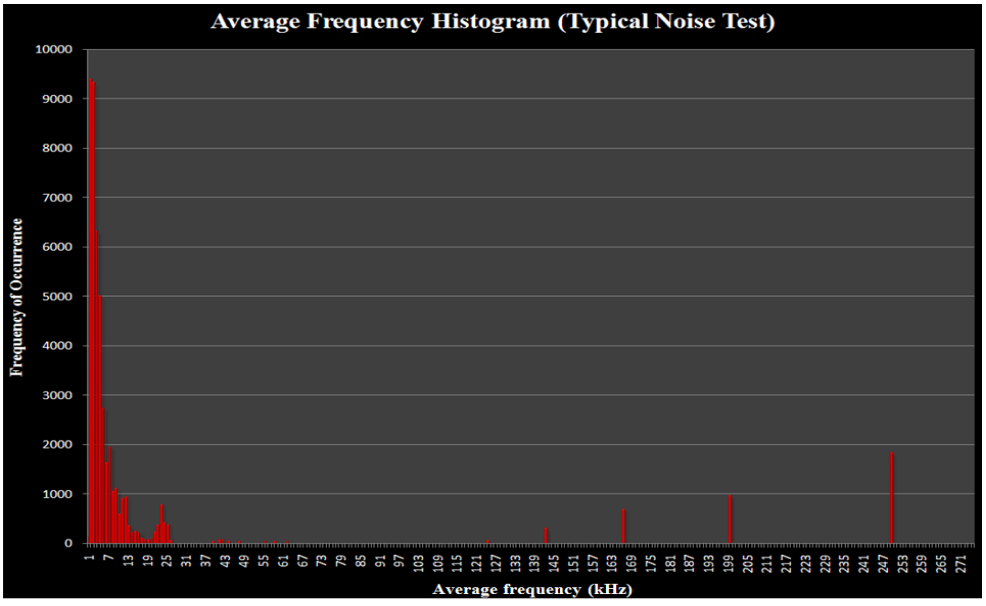


Figure 1: Average frequency histogram for a noise test (Barsoum et al. 2009)

The duration vs. counts plot is shown in Figure 2, and the average frequency (counts/duration) limits can be established as labeled in the plot, which agrees with the findings in Figure 1.

[1,2] Physical Acoustics Corporation

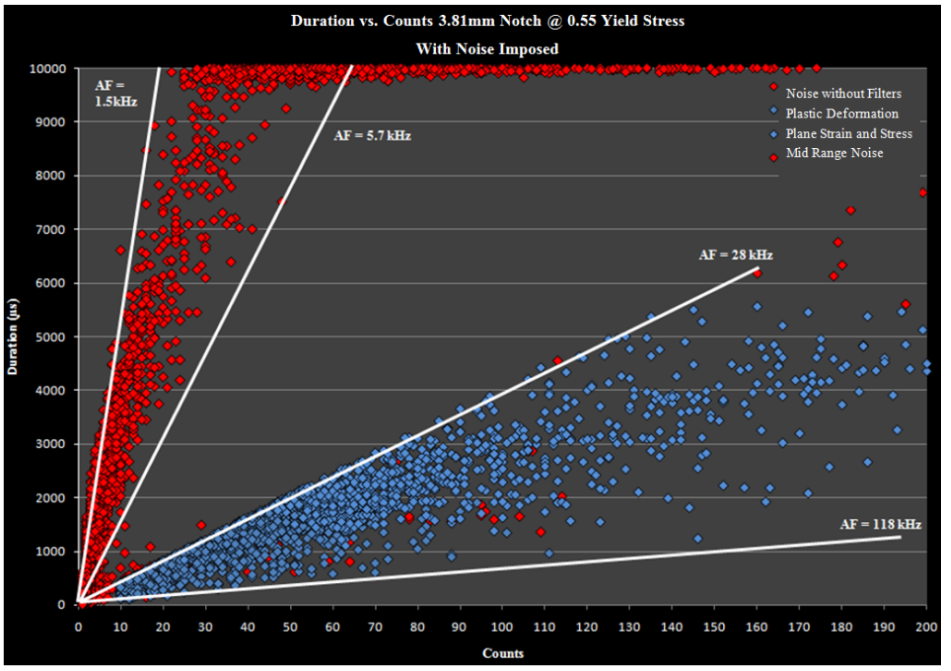


Figure 2: Duration vs. counts point plot with noise overlap (Barsoum et al. 2009)

A plot of the amplitude histogram of the noise signal indicates an amplitude range between 30 to 34 dB. As two filters can be applied to each of the transducers based on the findings, one filter was set to remove the AE hits of average frequency less than 25 KHz, and the other removed hits of counts less than 10. The constant noise signals of particularly long duration were later removed manually from individual files.

The actual AE data from the fatigue testing was later classified by SOM[3] into three mechanisms: plastic deformation plus plane strain and plane stress cracking. A BPNN[4] was then trained on eight bar specimens, and fatigue life was predicted using the data from the first quarter (0-25%) and the third quarter (50-75%) of the experimental fatigue life. The prediction results were within ±20% for first quarter data and ±12% for third quarter. These results indicated that, as might be expected, constant crack growth rate AE data yielded better predictions than crack initiation AE data (Korcak 2010 [1]).

Steel I-Beam Testing

In attempt to predict the fatigue life of bridge girders, ten simply supported S4x7.7 steel I-beams with span of 2.84 m (112 in) were tested (Korcak 2010 [1]). A 10 kip MTS actuator was used to apply a cyclic loading of 300 to 3,800 lb_f sinusoidal at 1 Hz. Each I-beam had a 0.254 cm (0.10 in) deep notch cut into the bottom

[3,4] NeuralWorks Professional II/Plus software

flange. Two transducers were mounted with hot melt glue on both sides of the notch. The noise tests indicated a noise amplitude threshold at 40 dB. One filter of the PocketAE system removed hits of average frequency less than 14 KHz, while the other removed hits with counts of less than 5. The ten beams tested had fatigue lives ranging from 11,811 to 19,653 cycles. The BPNN was trained on five specimens and used to predict fatigue lives on the other five with a maximum prediction error of ±18.4% for the 1st quarter data, -16.8% for the 2nd quarter data, and 5.3% for the 3rd quarter data. The prediction yielded less error when the data from the third quarter of the fatigue life was used, which is preferable in the actual bridge testing as fatigue monitoring becomes more crucial.

FIELD TESTING

Florida Girder Bridge

AE testing was done on a Florida steel girder bridge (Korcak et al. 2010 [2]) in order to monitor for any fatigue cracking and then predict remaining fatigue life using the recorded AE data and a BPNN. The 55.5 m (182 ft) long bridge had four spans and steel girders supporting a reinforced concrete deck. It was built in 1951 and had recently been classified as structurally deficient. The Florida Department of Transportation (FDoT) loaded the bridge on its two lanes with two trucks carrying concrete blocks, simulating a loading of 80,000 lb_f. A four-channel acoustic emission system was used to obtain the acoustic information from the different bridge members during the load testing as well as from live traffic. A robust four-channel AE PCI/DSP-4[5] system was used, connected to a laptop with AEWin software, which collected and recorded the data as shown in Figure 3. Four integrally pre-amplified 150 kHz piezoelectric transducers were hot melt glued onto the top side of the bottom flange of the beam, since the coating of the bridge made it difficult to bond anything to it. The bottom I-beam flange had a flat plate welded to it, where the rubbing of the surfaces or even cracking of the welds could generate acoustic activity. Figure 3 shows the welded plate and one of the AE transducers.

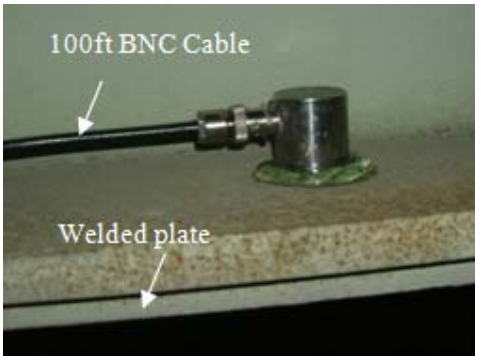


Figure 3: Transducer placement (Korcak et al. 2010 [2])

[5] Physical Acoustics Corporation

AE hits of zero duration or rise time were removed from the raw data as they were clearly noise. The data were then classified into three different mechanisms using a SOM, as shown in Figure 4 in an amplitude histogram. It should be noted that both the amplitude distributions for AE sources above the threshold amplitude resembled normal distributions. From Figure 4, Mechanism 1 had a wide range of amplitudes consistent with concrete cracking at the top of the I-beam; Mechanism 2 was thought to be rubbing of the welder reinforcing plate; and Mechanism 3 appeared to be rubbing from the side supports (Korcak et al. 2010 [2]). However, with these sources of AE data, no fatigue life prediction could be made.

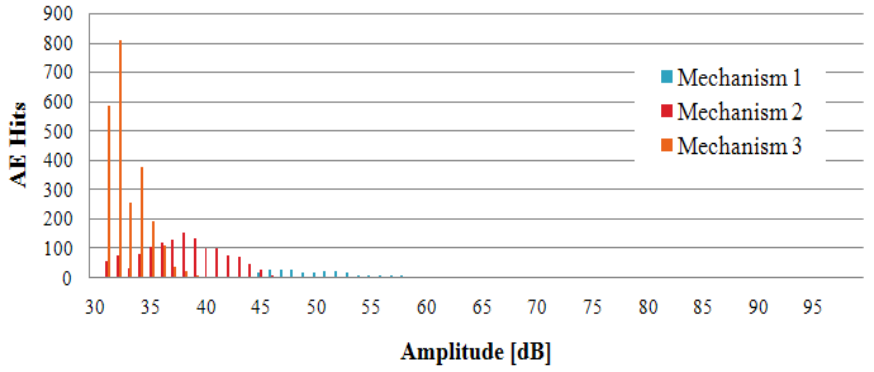


Figure 4. Source classification (Korcak et al. 2010 [2])

Florida Mast Arm Poles

Two Florida mast arms identified by FDoT to be highly susceptible to fatigue and large vibrations were tested to demonstrate the capability of real time monitoring for fatigue cracking as well as residual life prediction (Korcak et al. 2010 [3]). Monitoring was done on one pole without a known crack and another with a known crack. The PocketAE system was used in both tests. For the pole without a known crack, the two 150 kHz transducers were placed on opposite sides of the pole, close to the bottom where the maximum stress was expected, as shown in Figure 5 (a). Figure 5 (b) shows welds around the pole bottom. A defect in the weld can initiate a crack; moreover, the area of interest included bolt attachments which introduced rubbing noises.



(a) PocketAE and transducer placement (b) Welds

Figure 5. Two-channel PocketAE setup (Korcak et al. 2010 [3])

A preliminary classification of the AE data is shown in Figure 6. Two AE parameters (amplitude and average frequency) were fed into the SOM neural network which subsequently classified the AE data into two mechanisms.

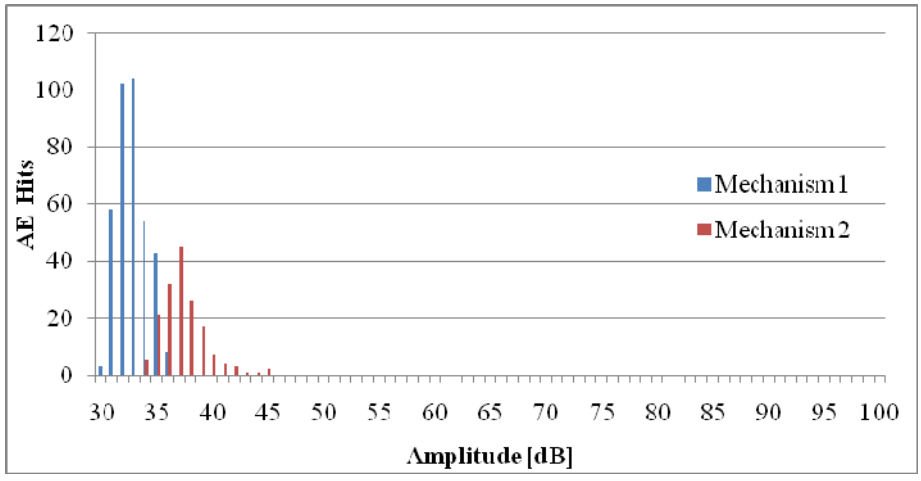
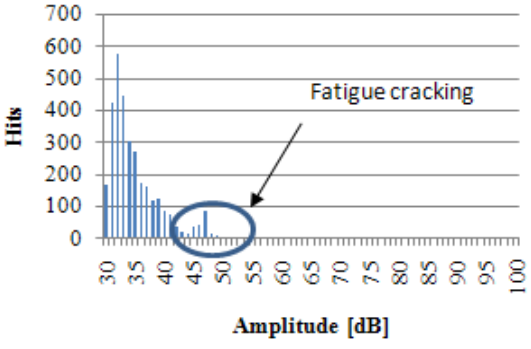


Figure 6: Source classification (Korcak et al. 2010 [3])

Two transducers were placed on either side of the crack on the second pole to verify the source in order to identify whether the emissions are coming from the crack or the rubbing of the bolt nearby. The test setup and AE data are shown in Figure 7. From Figure 7 (b), the separate high amplitude hump without overlap is most likely fatigue cracking. With the small data set for fatigue cracking no attempt was made here to predict fatigue life.





(a) AE test setup (b) AE data amplitude histogr

Figure 1: Cracked pole testing and AE data result (Korcak et al. 2010 [3])

Procedure for Fatigue Monitoring

The actual field and experimental testing shown above are examples of steel structure fatigue monitoring, failure mechanism classification and fatigue life prediction. The general procedure for real time structural steel fatigue crack monitoring is summarized below.

1. Transducer placement
   a. Transducers are mounted on the surface of the steel structure using hot melt glue. The surface where the transducers are attached should be free of rust or dirt.
   b. If the fatigue crack location is known, two transducers can be placed on either side of the crack (Figure 7) to verify the location of the source (can be observed from the events vs. x-position plot from AEWin software). This should be used to ensure that the data utilized are from the known crack location.
   c. If the crack location is unknown, the transducers should be placed near the component that has the highest tensile stress.
   d. The nearby bolts or welded reinforcing plates can contribute rubbing noises which will also be recorded by the transducers. This requires special attention during post test analysis.
2. AEWin Software Setup

   AEWin software was utilized in this research when both the four-channel system and the two-channel PocketAE system were used. The amplitude threshold setup of 30 dB is recommended for isotropic materials. The maximum duration should be set high enough to allow all data of interest to be captured. The AE waveform parameters -- peak definition time (PDT), hit definition time (HDT), and hit lock-out time (HLT) -- as illustrated in Figure 8, are set to separate noise from fatigue cracking data. Typical values for PDT, HDT, and HLT for common materials are listed in Table 1.

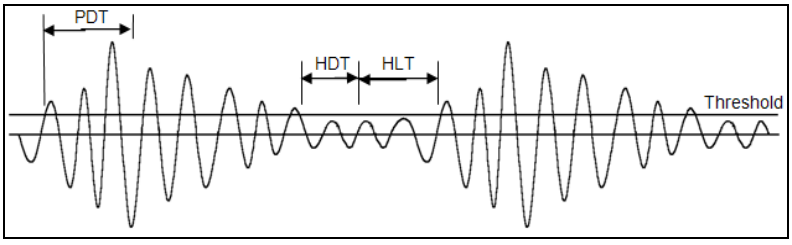


Figure 8: AEWin Waveform Parameters (Dorfman 2004)

Table 1. Waveform parameter values for common materials (Dorfman 2004)

Material PDT (µs) HDT (µs) HLT (µs)			
Composites, Non-Metals 20 - 50 100 - 200 300			
Small Metal Specimens 300 600 1000			
Metal Structures (High Damping) 300 600 1000			
Metal Structures (Low Damping) 1000 2000 20000			

3. Noise filtering
    a. In laboratory testing, noise can be monitored before the actual testing by simply turning on the testing machine with the specimen in the grips, but with the load set to zero. The AE data from the noise test can be plotted in three graphs: average frequency histogram (Figure 1), duration vs. counts (Figure 2), and an amplitude histogram. These graphs indicate the average frequency and count characteristics of the noise signal, which will be applied to the filters. However, AE hits with zero duration or rise time, or extra long duration are also noise and should be removed manually from the individual data files. Efforts should also be made to reduce any friction between the contacts (in steel-steel connection, noise emissions will be transferred), for example, a plastic block can be placed between the actuator and testing specimen.
    b. In field testing for infrastructure, it is preferable that the same noise monitoring procedure discussed above should be performed before the actual test whenever feasible. In addition, rubbing of surfaces in contact or bolt connections (Figure 3 and 5) will always contribute to noise that will be captured by the transducers, and will be later identified during source classification as displayed in Figure 4. As the AE data is acquired, AE hits of small counts and zero duration or rise time should be deleted manually in every data file.
    c. For prediction purposes, after the failure mechanisms are classified, the indicated noise data can be further removed to make better prediction training files.
4. AE Data Acquisition and Processing
    a. AE data acquired by the AEWin software are saved as an ASCII file for further processing. The data file should include time, channel, rise time, duration, amplitude, average frequency, etc. One can perform multiple tests and append all the data files into one file.
    b. Using a spread sheet such as Microsoft Excel, the data file is edited further to remove noise as explained above in step 3.
5. Source Classification using a SOM
    a. To prepare the input file, all AE hits of different parameters are compiled into an ASCII file without time information, labels and titles (only numbers).
    b. Open NeuralWorks Professional II/Plus software and choose **Self Organizing Map** in the **InstaNet** menu; the window display is as shown in Figure 9. The **Input** value should be the number of AE parameters provided in the input file. The product of **Rows** and **Columns** yields the

number of failure mechanisms. Note that a valid classified mechanism plot should resemble a normal distribution. In **I/O Files**, the **Learn** and **Recall** file should be the same input file. The rest of the setup follows the default values shown in Figure 9.

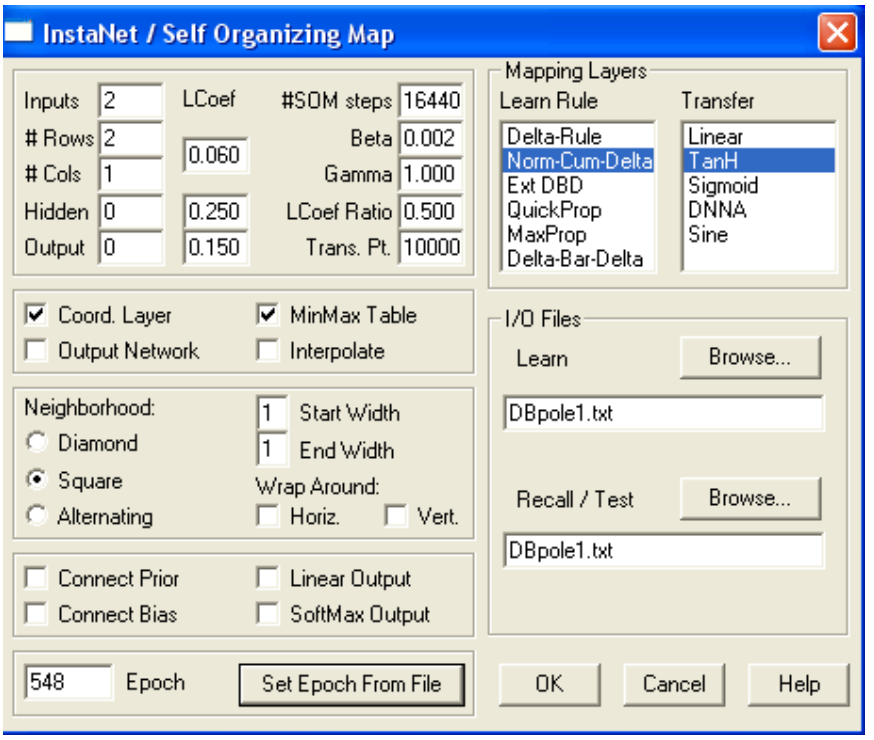


Figure 9. SOM setup window

c. The rest of the steps follow that of the SOM tutorial (Hearn et al. 2004). The output file includes two mechanisms (0 and 1), as the product of **Rows** and **Columns** in the above step is set to 2. Append the output file to the AE hits data, and sort one column of the mechanism from smallest to largest (zeros to ones) to get data sorted into two mechanisms. Graphs of interest such as amplitude histogram, average frequency versus amplitude and energy versus amplitude are then plotted.

6. Fatigue Life Prediction using a BPNN

a. To predict the fatigue life (or residual life) of the steel structure, for this research, the amplitude distributions were used as input data. Take the 1st quarter data (0-25% of fatigue life) of the steel bar testing as the training file input to the BPNN (Barsoum et al. 2009); the software is then trained on eight specimens, and predicts on the remaining three. The training and testing files are given in Tables 2 and 3, where the number in bold is the actual experimentally determined fatigue life which is used to train the

network. For small data sets, the training file should include a good sample of the data (low fatigue life, high fatigue life, and some in between), and a rule of thumb is that that 60% of the AE data should be used to generate the training file, and the remaining 40% for the testing file (Barsoum et al. 2009).

Table 2: 25% steel bar BPNN training file (Barsoum et al. 2009)

Sample	Amplitude Histogram 30-100 dB @1dB incriments
0.15 inch	0 0 0 0 10 21 39 37 37 49 43 68 51 25 21 17 18 9 9 7 12
0.55 yield	7 9 5 5 5 3 4 2 4 2 0 1 1 2 0 1 1 1 1 0 0 0 0 0
Test 1	0 1 1 0 0 0 0 0 0 0 0 0 0 0 0 0 0 0 0 0 0 0 0 0 0 0 0 **22206**
0.15 inch	0 0 0 23 167 407 320 354 522 854 1296 1222 864 473 212 76 19 15 16 10 4
0.55 yield	4 1 1 1 4 1 2 1 1 0 0 0 1 0 0 0 0 0 0 0 0 0 0 0
Test 3	0 0 0 0 0 0 0 0 0 0 0 0 0 0 0 0 0 0 0 0 0 0 0 0 0 0 0 **24246**
0.15 inch	0 0 0 3 9 58 72 69 43 31 19 29 31 36 29 34 45 40 36 26 18
0.6 yield	10 10 11 10 5 9 3 2 5 6 1 2 0 2 0 0 0 1 0 0 0 0 0 0 0
Test 2	0 0 0 0 0 0 0 0 0 0 0 0 0 0 0 0 0 0 0 0 0 0 0 0 0 0 0 **13861**
0.15 inch	0 0 0 0 18 163 535 1127 1204 966 588 417 600 855 906 531 164 41 19 9 12
0.6 yield	12 12 5 7 1 2 7 1 3 4 5 2 0 2 1 0 0 0 1 0 0 0 0 0 0
Test 3	0 0 0 0 0 0 0 0 0 0 0 0 0 0 0 0 0 0 0 0 0 0 0 0 0 0 0 **15808**
0.15 inch	0 0 1 72 129 137 57 55 46 20 35 37 34 31 22 27 27 17 22 13 13
0.6 yield	16 6 9 11 5 5 4 2 1 3 1 2 3 4 0 0 0 0 0 1 1 0 0 0 0
Test 4	0 0 0 0 0 0 0 0 0 0 0 0 0 0 0 0 0 0 0 0 0 0 0 0 0 0 0 **14160**
0.15 inch	0 0 0 10 28 81 73 101 150 315 532 325 76 21 23 22 21 11 13 9 7
0.66 yield	8 9 0 7 5 1 4 0 3 4 3 0 0 0 1 1 0 2 0 2 1 2 0 0 0
Test 3	0 0 0 0 0 0 0 0 0 0 0 0 0 0 0 0 0 0 0 0 0 0 0 0 0 0 0 **10969**
0.15 inch	0 0 0 0 7 19 28 34 53 43 37 59 45 45 37 26 26 22 18 16 14
0.66 yield	6 12 5 8 1 2 7 2 0 3 3 1 0 1 1 0 0 0 0 0 0 0 1 1
Test 4	0 0 0 0 0 0 0 0 0 0 0 0 0 0 0 0 0 0 0 0 0 0 0 0 0 0 0 **10462**
0.15 inch	0 0 0 2 32 36 24 18 15 14 10 12 10 11 6 5 5 2 5 6 1
0.66 yield	4 4 3 2 1 0 0 1 1 0 0 0 0 1 0 0 0 0 0 0 0 0 0 0 0
Test 5	0 0 0 0 0 0 0 0 0 0 0 0 0 0 0 0 0 0 0 0 0 0 0 0 0 0 0 **9771**

Table 3: 25% steel bar BPNN testing file (Barsoum et al. 2009)

Sample	Amplitude Histogram 30-100 dB @1dB incriments
0.15 inch	0 0 0 1 0 11 13 24 31 31 23 31 13 16 11 10 7 8 8 5 9
0.55 yield	8 1 3 6 1 2 1 1 0 2 1 0 0 0 0 1 0 0 0 0 0 0 0 0 0
Test 2	0 0 0 0 0 0 0 0 0 0 0 0 0 0 0 0 0 0 0 0 0 0 0 0 0 0 0
0.15 inch	0 0 0 0 1 7 7 26 21 19 20 18 27 22 18 17 14 7 10 11 11
0.6 yield	8 7 5 8 6 1 4 3 2 3 1 2 2 1 0 1 1 0 0 0 1 0 0 0 0
Test 1	1 0 0 0 0 0 0 0 0 0 0 0 0 0 0 0 0 0 0 0 0 0 0 0 0 0 0
0.15 inch	0 0 0 0 5 10 18 24 23 29 27 21 23 18 17 18 18 16 15 5 11
0.66 yield	5 7 8 5 2 5 3 3 0 0 0 0 1 0 0 0 0 0 0 0 1 0 0 1 0
Test 1	0 0 0 0 0 0 0 0 0 0 0 0 0 0 0 0 0 0 0 0 0 0 0 0 0 0 0

b. Open the NeuralWorks Professional II/Plus software and choose **Back Propagation** in the **InstaNet** menu; the window display is as shown in Figure 10. The **Input** indicates the number of the input values in the training file (not including the fatigue life), which in this case is the 71 amplitude frequencies of occurrence (30-100 dB), as shown in Table 2. The hidden layer 1 (**Hid 1**) value follows the 2n + 1 rule, where n is the number of failure mechanisms classified by SOM. The other training

parameters have to be determined through trial and error iterations to obtain the optimized setup, by comparing the output error after each parameter change in the initial settings.

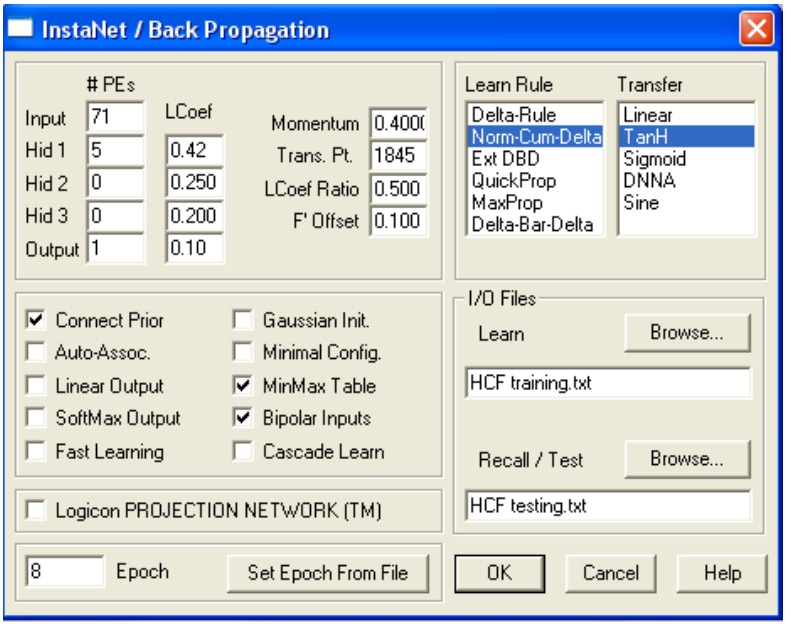


Figure 10. BPNN setup window

c. The rest of the steps follow that of the BPNN tutorial (Horvath et al. 2007). The **Convergence Criterion** should be adjusted to specify a stopping criterion based on the **RMS** error for the eight files in the training set.
d. The output file includes the predicted fatigue life, and the errors between the predicted value and actual value can be compared as shown in Table 4.

Table 4: 25% steel bar fatigue prediction results (Barsoum et al. 2009)

TestedExperimental		**Trained HCF BPNN**	
SampleFatigue life	**Predicted**	**% error**	
0.15-0.55Y-T22	7401720417.0		
0.15-0.60Y-T11	49011202619.3		
0.15-0.66Y-T11	02188240		**19.4**

Conclusions

This paper provided a procedure for structural steel fatigue crack monitoring using the acoustic emission technique. This included failure mechanism classification using a self organizing map (SOM) neural network and fatigue life prediction using a back propagation neural network (BPNN). Methodologies for transducer

placement, noise filtering and neural network software setup were presented with details. The fatigue life prediction of steel specimen based on the AE data from the first 25% of experimental life (crack initiation data) herein yielded errors of less than ±20%; however, worst case errors in the ±5% range have been obtained from the third quarter (50-75% constant crack growth rate) AE fatigue data (Korcak 2010 [1]). From this it can be concluded that acoustic emission and neural networks are effective techniques for fatigue crack growth monitoring and predicting the fatigue and residual life of steel structures.

References

Barsoum, F.F., Suleman, J., Korcak, A., and Hill, E.v.K. (2009)*Acoustic Emission Fatigue Life Prediction in Axially Loaded Notched Steel Specimens,* Embry-Riddle Aeronautical University, FL.

Dorfman, M.D. (2004) *Ultimate Strength Prediction in Fiberglass/Epoxy Beams Subjected to Three-Point Bending Using Acoustic Emission and Neural Networks*, MSAE Thesis, Embry-Riddle Aeronautical University, FL.

Hearn, D., Nguyen, T.K., Dorfman, M., and Nimis, R. (2004) *Tutorial for Self Organizing Maps Using NeuralWorks Professional II/Plus Software,* Embry-Riddle Aeronautical University, FL.

Horvath, M., and Mueller, A. (2007) *NeuralWorks Professional II/Plus Tutorial: Backpropagation Neural Network,* Embry-Riddle Aeronautical University, FL.

Korcak, A. (2010) *Fatigue Life Prediction in Steel Using Acoustic Emission Amplitude Histograms and Back Propagation Neural Networks,* MSAE Thesis, Embry-Riddle Aeronautical University, FL.

Korcak, A., Barsoum, F., and Hill, E.v.K. (2010) *Acoustic Emission Monitoring of a Florida Steel Girder Bridge During a Load Test*, NDE/NDT For Highways and Bridges: Structural Materials Technology (SMT), American Society for Nondestructive Testing, NY, pp. 296-302.

Korcak, A., Barsoum, F., Hill, E.v.K., Zhang Y. (2010) *Acoustic Emission Monitoring of Florida Mast Arms Susceptible to Fatigue*, NDE/NDT for Highways and Bridges: Structural Materials Technology (SMT), American Society for Nondestructive Testing, NY, pp. 671-677.

Large-Scale Experimental Evaluation of Building System Response to Sudden Column Removal

Wei-Jian Yi[1], Sashi K. Kunnath[2], F.ASCE, Fan-Zhen Zhang[1] and Yan Xiao[3], M.ASCE

[1]College of Civil Engineering, Hunan University, Changsha, China 410082, China; email: hunuyi2006@gmail.com
[2]Department of Civil Engineering, University of California, Davis, CA 95616; email: skkunnath@ucdavis.edu
[3]Department of Civil Engineering, University of Southern California, Los Angeles, CA 90089; Director, MOE Key Laboratory of Building Safety and Energy Efficiency, Hunan University, Changsha, China; email: yan.xiao@usc.edu

ABSTRACT

Two large-scale experiments are currently in progress in the structural laboratory at Hunan University, China to assess the progressive collapse behavior of reinforced concrete (RC) building systems: the first system comprises a flat-plate structure while the second is a beam-column moment frame. Results from the first test are reported in this paper while construction of the second system is in progress with collapse testing scheduled during the summer of 2011. The collapse experiment of the flat-plate structure consisted of a push-down test to simulate the loss of an interior column. The next proposed test will assess the system response of a half-scale three story RC frame building to sudden column removal. The tests will enable a clearer understanding of force redistribution, slab contribution and catenary effects during progressive structural collapse.

INTRODUCTION

A comprehensive computational and experimental investigation of the progressive collapse resistance of reinforced concrete (RC) structures is presently underway as part of a collaborative effort between the National Institute of Standards and Technology (NIST), the University of California, Davis and Hunan University, China. Full-scale component tests have been conducted by NIST, large-scale frame tests are ongoing at Hunan University and computational studies in support of these experiments are in progress at UC Davis.

This paper summarizes preliminary findings from the recently concluded collapse testing of a flat plate frame model. Also outlined is the proposed progressive collapse test on a half-scale 3-story moment frame building due to sudden column removal scenarios.

FLAT PLATE FRAME MODEL TEST

The flat plate frame structure was designed to resist a total dead load of 5.25 kN/m^2 and a live load of 5.0 kN/m^2 in accordance with the building code requirements in China. The 1:2.34 model frame constructed for progressive collapse testing was composed of a 2x2 bay single story structure as shown in Figure 1. The column height was 1.4m with cross-section dimensions of 216x216 mm and the thickness of the flat plate was 90 mm. Reinforcement in the middle strip comprised 6.5mm bars at 150 mm in 2 layers at the top and bottom whereas the column strip was composed of 2 layers of 6.5mm bars spaced at 90mm at the top and 150 mm at the bottom. The concrete used in the construction had a cube (150mm) strength of 39.5 MPa and the yield strength of the reinforcement was 425 MPa.



Figure 1. Model structure (left) and imposed distributed load on slab (right).

Collapse Loading. The model frame was fixed on the strong floor of the lab with the help of a foundation beam. In order to approximately simulate the impact effect of the original loads on the flat plate due to sudden column loss, the total applied uniform load was 2 times the design load. The load was applied in 9 stages: sand bags were used in the first six stages and steel blocks were used in the final three stages of loading. The model structure with all of the imposed loading is shown in Figure 1.

The removed column was replaced by a hydraulic jack attached to a load cell as shown in Figure 2. After the 4th stage of loading the imposed load was 10.25 kN/m^2 (corresponding to the design dead and live load), and the force in the jack was released to attain a zero force state. Loading of the cantilever portion of the floor was ceased at this stage. The next 3 loading phases consisted of applied uniform loads of 2.4 kN/m^2 each and the hydraulic jack was released at the end of each stage to measure the corresponding slab deformations and bar strains. The final 2 stages composed of applied uniform loads of 1.98 kN/m^2 and 1.15 kN/m^2, respectively. Test measurements include: the horizontal and vertical displacement of the flat plate, the inclination of the plate surface, the concrete strain at the top and bottom surface of the plate, the strains in the longitudinal reinforcement at the top and bottom, and the vertical displacement and residual axial force in the interior “removed” column.

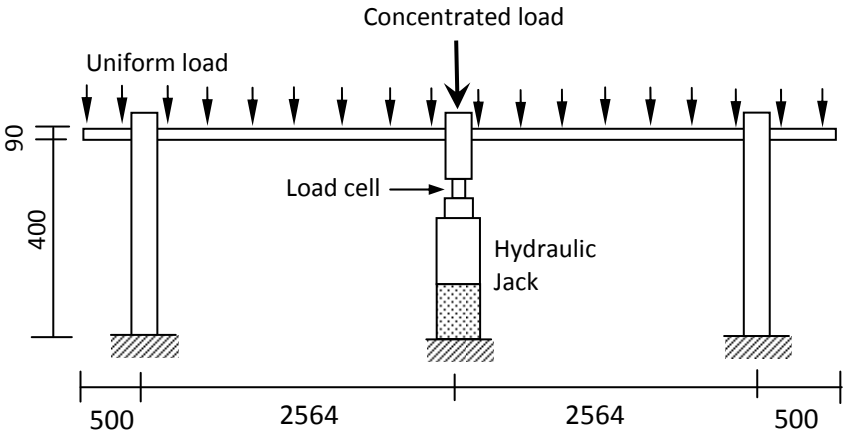


Figure 2. Schematic view of imposed slab loading

Preliminary Results. Following the applied load of 10.25 kN/m^2, the measured vertical displacement beneath the removed column was 90 mm. At this stage, a concentrated push-down load was applied through an actuator attached to the top of the interior column (see loading frame above the floor in Figure 1 and also the schematic view of the applied loads in Figure 2). Push-down vertical loading continued till the displacement reached approximately 285 mm at which stage a punching shear failure of the slab occurred. The final damaged state of a typical exterior column is shown in Figure 3. Also shown is the complete overview of the cracking pattern in the top surface of the slab where the yield lines are clearly visible. It is of importance to note that the longitudinal reinforcement in the slab was continuous through the column section.

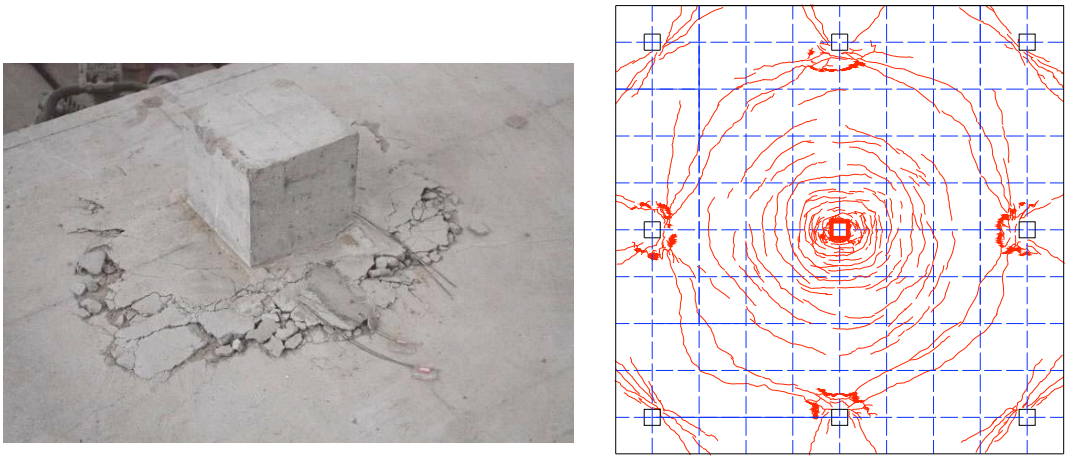


Figure 3. Punching shear failure of exterior slab-column section (left) and overview of observed cracking and yield lines on slab at failure (right).

PROPOSED HALF-SCALE MOMENT FRAME TEST

The second phase of the large-scale experimental collapse test will feature a half-scale model of a moment frame building. The three-story model represents the lower floors of a ten-story moment frame structure designed to meet the requirements of Seismic Design Category "C" as per ASCE 7-2005 and detailed to ACI 318-08 specifications. The imposed gravity loads include 30 psf superimposed dead load (SDL) and 100 psf live load (LL). The half-scale test structure was designed for 200 psf (1.2SDL + 1.6LL) of uniformly distributed superimposed load. The plan and elevation of the model building are displayed in Figure 4.

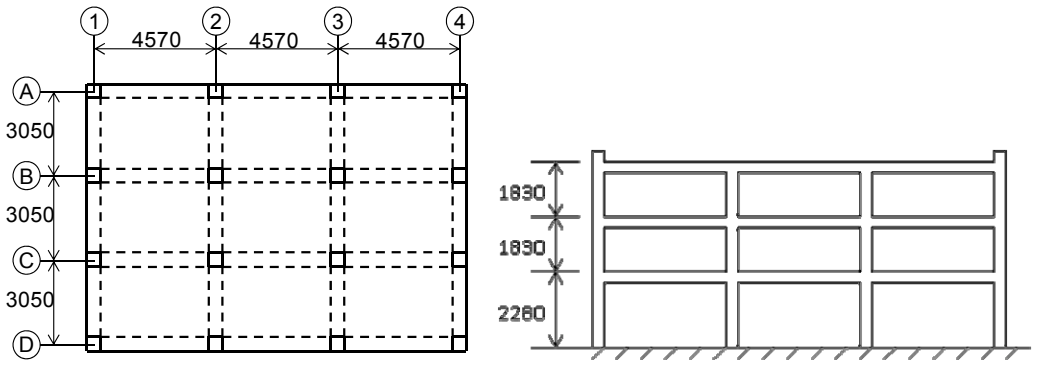


Figure 4. Model frame configuration

The proposed test plan includes sudden column removal by controlled explosion or other means followed by push-down loading of the removed column. The initial sequence of column removals was as follows: Removal of corner column D1 followed by removal of columns C4 and B2. To gain an understanding of the system response to these loading scenarios, numerical simulations were carried out using a macromodeling approach (Bao et al., 2008). The macromodeling simulations were also complemented by more refined analyses using LS-DYNA (Hallquist 2005) to incorporate slab effects. Results of the simulation are presented in Figure 5.

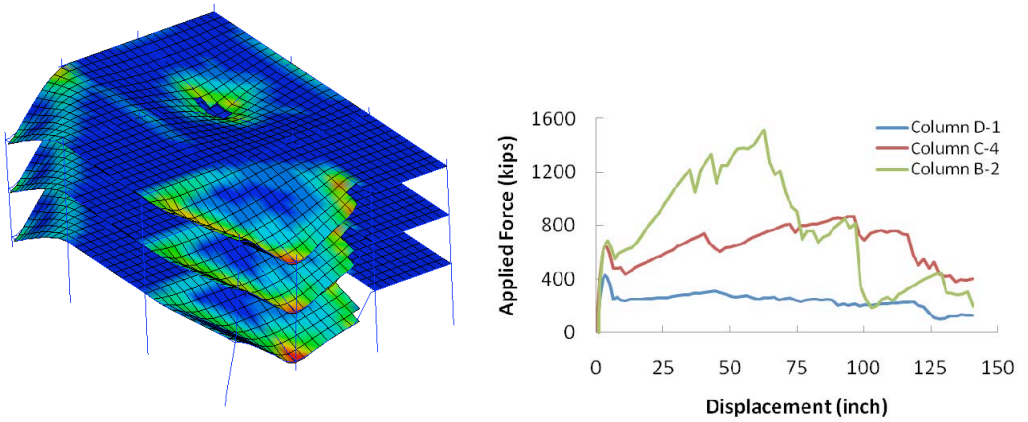


Figure 5. Numerically simulated push-down simulations for different column removal scenarios

Additional studies are underway to consider alternative column removal scenarios including the removal of multiple columns. Final testing details will be established following a comprehensive computational study which is expected to conclude by the end of January 2011.

CONCLUDING REMARKS

The proposed tests will enable a clearer understanding of force redistribution, slab contribution and catenary effects during progressive structural collapse. As indicated earlier, the test program is part of a larger effort to develop modeling guidelines for progressive collapse analysis of RC structures as well as establish measures of structural robustness to progressive collapse following the loss of one or more primary load-carrying elements in a building.

REFERENCES

Bao, Y., Kunnath. S. K., El-Tawil, S. and Lew, H.S. (2008), "Macromodel-Based Simulation of Progressive Collapse: RC Frame Structures," *Journal of Structural Engineering*, ASCE, 134(7), 1079-1091.

Hallquist, J. (2005). LS-DYNA, Livermore Software Technology Corp, Livermore, California.

Zhang, F-Z. (2011). "Collapse Testing of a Flat-Plate Frame Structure." Ph.D. Dissertation, Hunan University, China (to be completed; in Chinese).

New Methods for Progressive Collapse Testing and Simulation

David Vaughan[1], David Milner[2], James Gran[3]

[1]Weidlinger Associates, Inc., 399 W. El Camino Real, Suite 200, Mountain View, CA, 94040; PH (650) 230-0210; email: vaughan@wai.com
[2]Weidlinger Associates, Inc., 399 W. El Camino Real, Suite 200, Mountain View, CA, 94040; PH (650) 230-0210; email: milner@wai.com
[3]SRI International, 333 Ravenswood Avenue, Menlo Park, CA 94025-3493; PH 650-859-4472; email: james.gran@sri.com

ABSTRACT

A number of analytic tools have been applied to or developed for progressive collapse modeling. However, the lack of relevant experimental test data makes it difficult to validate these tools or identify which aspects of the modeling approaches or software formulations may need additional refinement. The cost of full scale testing to validate these analytical tools is extraordinarily expensive due to the physical size of the structures that need to be tested and the range of phenomenology that needs to be investigated. This paper investigates the use of small scale building models, which can be tested in a centrifuge to provide properly scaled gravitational loads, for studying progressive collapse of damaged buildings. For this effort, a reinforced concrete building (3-bay x 4-bay, 4-story) was designed, constructed at 1/18th scale and tested in a centrifuge while several ground floor support columns were dynamically removed. The test data, including overall collapse response, were compared with the results of pretest analyses performed using a high fidelity, explicit finite element code. This testing effort was designed to contribute to improved validation of simulation tools for progressive collapse modeling.

INTRODUCTION

'Progressive' collapse of a building damaged by an explosion means that damage to the structure is not limited to the area directly affected by the weapon(s) blast loading, i.e. the region of collapse may continue to expand beyond the region of direct blast damage. Potentially, this progressive failure of the building can result in the complete collapse of the entire structure. A well known example of partial progressive collapse occurred in the Oklahoma City bombing which occurred in 1995. An explosion destroyed several support columns on one side of the building but the damage zone progressed to include approximately ½ of the structure before finally being arrested by the stability of the remaining structure. The threat of terrorist attacks against civil structures has increased the need to design buildings resistant to progressive collapse. This requires improved simulation tools for assessing the likelihood of progressive failure for a structure should the load carrying capacity of one or more structural members be seriously compromised.

Although various analytic tools for progressive collapse assessment have been developed to date, the lack of experimental test data makes it difficult to validate them or identify which aspects of these tools may need additional refinement.

This paper considers 'small scale' testing technology that is applicable to testing progressive collapse of structures in the laboratory. The successful use of small scale testing in combination with good correspondence between test response and high fidelity modeling of collapse response provides a clear demonstration of how this testing approach can be applied to advance the state-of-the-art in understanding progressive collapse behavior of buildings. The results of this work contribute to validating models for progressive collapse simulations. Increased accuracy of and confidence in progressive collapse assessment tools will result in advances in effective progressive collapse resistant design methods and criteria.

PROGRESSIVE COLLAPSE TESTING

In order to assess the validity of progressive collapse simulation methods, applicable and accurate testing methods and procedures are needed. For any testing procedure to produce accurate and reliable results, it must reproduce basic features of progressive collapse events. Weidlinger (2003) and Ettouney (2006) have shown that progressive collapse is both a local and global event. The collapse will progress from one structural component to the next: which will require accurate modeling of those components (columns, beams, joints, etc.). In addition, it was shown that the process of complete structural collapse can be considered as a global loss of structural stability: which requires accurate modeling of the global structure. This local/global behavior is a major challenge for developing valid full scale tests for progressive collapse. As a result, very little test data is available to validate either simplified or complex three dimensional models used for blast initiated progressive collapse predictions.

The cost of full scale testing for a sufficiently complex structure can be extraordinarily expensive due to the physical size of the structures required to be tested and the range of phenomenology that needs to be investigated. Real world events that have resulted in progressive collapse of full scale structures are generally not instrumented. To date, laboratory or field testing of full scale test articles generally involve small assemblies of structural components. These tests are useful and produce data that aid in validating some aspects of progressive collapse behavior. However, they do not provide a rich enough testing set to fully assess analytic models that might be applied to collapse simulations.

Performing progressive collapse tests on sub scale structures, such as 1/2 or 1/3 scale, are less expensive than full scale tests due to the reduced cost of construction but face the fundamental challenge that the gravitational loads that drive progressive collapse are not properly scaled. That is, full scale gravitational loads are applied to sub scale test articles. To achieve a 'properly scaled' test for a sub scale structural model, the gravitational loads must be increased. For example, consistent gravitational loads for

a 1/2 scale structure would be 2 Gs, for a 1/3 scale structure, 3 Gs, etc. Clearly, it is impractical to properly scale gravity for structural test articles of substantial size.

Small scale testing is another approach that can be considered for progressive collapse investigations. Using 'replica scaling', the small-scale model is built by reducing all the lengths in the full-scale design by the scale factor. For example, a 1/18-scale reinforced concrete beam is 1/18 the length, width, and height of the full-scale beam. The experimental effort described herein applies replica scaling methods to the problem of progressive collapse testing of a reinforced concrete moment frame building. The use of replica scaling at small-scale to solve reinforced concrete design problems is well established with many universities and laboratories around the world having contributed to the development of fabrication techniques, see (Harris 1966, White 1970, Carpenter 1972, Mirza 1972, Harris 1980, Gran 1982 and Harris 1999).

As mentioned above, Earth gravity does not 'scale' appropriately when using replica scaling. For example, gravity in a 1/18-scale experiment should be increased to 18 g. This is of particular interest for progressive collapse testing because all of the loads in the problem are gravitationally induced loads. Small scale models that can physically be placed in a centrifuge can benefit from having properly scaled gravitational forces. This is the basic idea behind performing small-scale progressive collapse experiments in the centrifuge.

There are other parameters that do not scale naturally to the required value when using replica scaling. Specifically, viscosity and fracture toughness, both of which are material properties. In some cases, the small scale material can be adjusted to match the required properties. For example, in the case of steel, a different alloy or heat treatment can be selected to attain the desired properties. With concrete, it is not practical to independently control the strain-rate dependence and fracture toughness while maintaining a match to the compressive strength. For progressive collapse problems, the effects of strain rate are expected to be minor, even for small-scale models. The fracture toughness of the model concrete, which mostly affects cracking but not ultimate failure, is generally secondary to compressive strength.

DESIGN OF TEST STRUCTURE

This testing effort involved designing a code compliant full scale structure, then fabricating it at $1/18^{th}$ scale and finally testing it in the centrifuge under 18 g gravity. The structural configuration was chosen to be 4 bays x 3 bays x 4 stories tall as shown in Figure 1. The full scale bay size was chosen to be 20 feet in both directions. Each story height was 12 ft. The overall size of the structure was chosen so that a $1/18^{th}$ scale test article would fit within the size constraints of the centrifuge test platform.

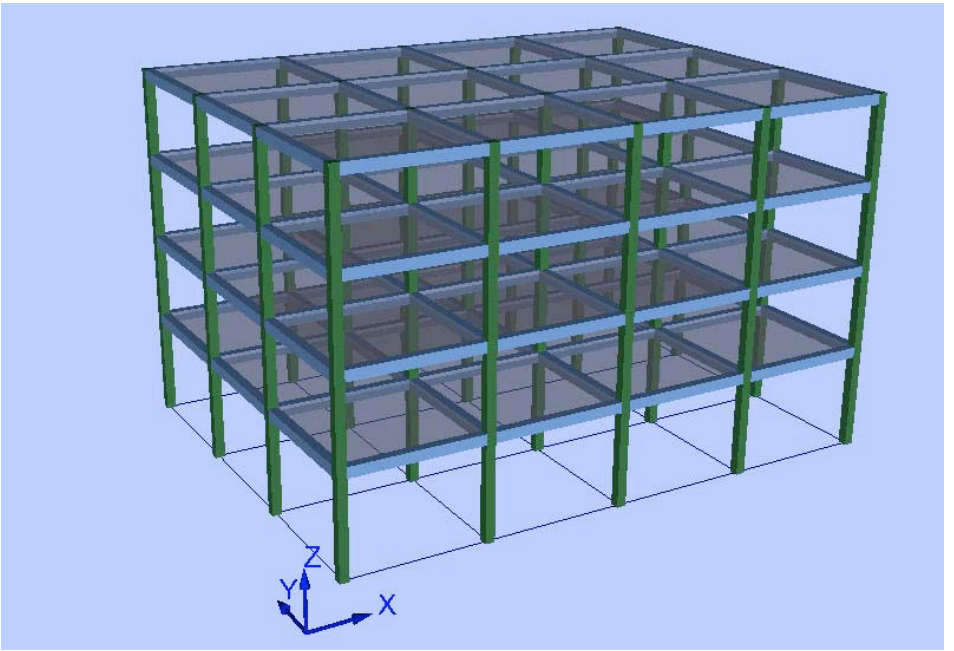


Figure 1 Multi-Story Test Structure

The building was designed according to the 2003 IBC design code for low seismic regions and typical wind conditions of 90 MPH. The availability of 1/18th scale equivalents for #9 and #11 reinforcing bars guided the designer to utilize these size bars as the primary reinforcing in the design. All full scale dimensions were scaled down by 1/18th to define the appropriate dimensions for the small scale test article.

FABRICATION OF TEST STRUCTURE

Maintaining reasonable consistency between small scale and full scale material behavior is one of the primary challenges of performing small scale testing. In this effort, a 1/18 scale reinforced concrete structure was constructed. To represent the concrete material, a close approximation to the Fine Aggregate Cementitious Material (FACM) developed by the U. S. Army Corps of Engineers ERDC (Gran 1996) was used. This material was selected because it has an aggregate size distribution appropriate for the 1/18-scale structure and it has mechanical properties that are a good match to full-scale concrete.

To represent 1/18 scale steel reinforcing, all physical dimensions of the reinforcing needed to be scaled accordingly. The main steel reinforcing bars in the beams and columns of the test structure were modeled with steel threaded rods. Previous investigations have shown that the threads provide a reasonably good match to the bond between full-scale rebar and concrete. The nearest matches of standard thread sizes to the desired rod diameters are 1-64 threads for 1/18-scale #9 bars and 2-56 threads for 1/18-scale #11 bars. The pitch diameter of the 1-64 thread is about 0.058 in. and the pitch diameter of the 2-56 thread is about 0.067 in. For comparison, 1/18-scaled diameters of #9 and #11 bars are 0.062 in. and 0.076 in., respectively.

Because the threading process induces strain hardening in the steel, the annealing schedule during the cold-drawing of the bare wire was adjusted in order to approximately match the desired strength of the finished threaded rods. No heat-treatment of the rods was done after threading.

Testing was performed to characterize the small scale concrete and steel material behavior. This allowed appropriate constitutive model fits that account for differences between full scale and small scale materials to be developed and used in a high-fidelity computational model of the small scale structure's response.

The 1/18th scale test article was fabricated by SRI International (Gran 2010) using precision construction procedures. Metal forms were created to facilitate placement of the small scale reinforcing steel and pouring the fine aggregate concrete. All longitudinal and stirrup reinforcing steel in columns, beams and slabs was fabricated with fine tolerance and placed for one complete floor level of the structure at a time as shown in Figure 2. Then the concrete was prepared and poured for that floor level. Model concrete was mixed and placed in three batches for each story, one for the columns, one for the beams, and one for the floor slabs. By far, the most difficult placement was in the columns because of the need to push the concrete through the closely spaced beam reinforcing steel. To assist with placement, electric engraving pencils were fitted with extended probes to use as internal vibrators to remove air voids in the columns. The concrete was left to harden for about a week before the forms were removed, cleaned, and reassembled for the next story, Figure 3. Two vertical laser beams mounted above the assembly area were used to accurately locate each floor in the horizontal plane. By aligning each story with the lasers, leaning and twist of the structure was prohibited. The completed test article is shown in Figure 4.

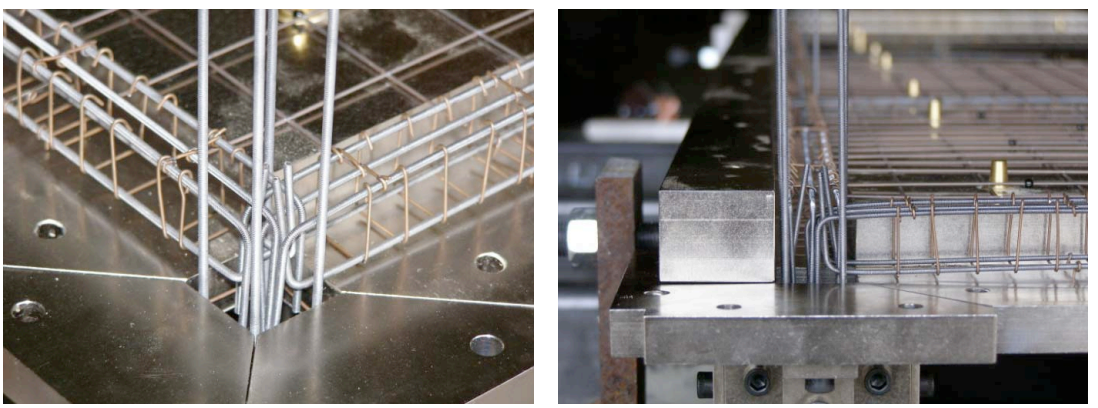


Figure 2 Two Close-up Photos of Steel Reinforcment Placement for 1/18th Scale Building



(a) From above with forms in place (b) From below with forms removed

Figure 3 Photo of Completed 1st Floor of 1/18th Scale Building



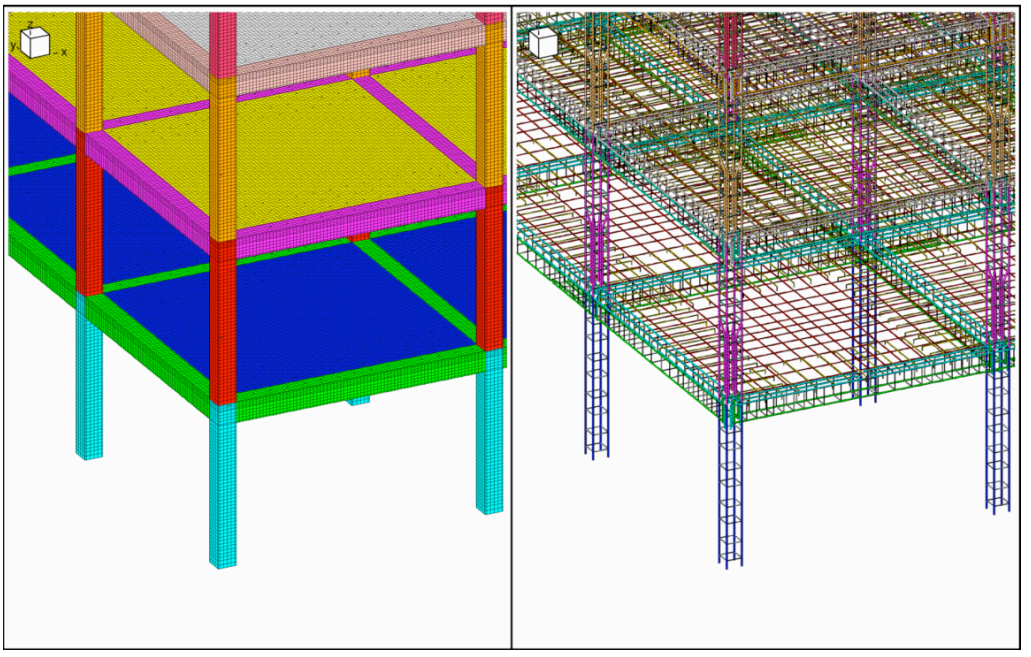
Figure 4 Completed Four-story Reinforced Concrete 1/18th Scale Building

HIGH FIDELITY SIMULATION MODEL

The NLFlex finite element code, (Vaughan 1983), was used to perform high fidelity simulations of the 1/18th scale structure to plan the specific details of the centrifuge testing series. NLFlex has been extensively validated for blast effects modeling of reinforced concrete and steel structures under a wide range of Department of Defense field test programs. It uses advanced constitutive models (Mould 1993, Mould 1994) for representing the full range of nonlinear material behavior that occurs for steel and concrete materials during a collapse event. The NLFlex constitutive models for steel and concrete were fit to available lab data for the small scale steel reinforcing and small scale concrete actually used to construct the test article.

Pretest simulations were performed to investigate the response of the small test article under various floor load levels and a variety of potential damage states. Structural damage scenarios considered involved the dynamic removal of one or more ground floor support columns.

The high fidelity models of the test structure used continuum elements to represent the concrete material in the building and beam and bar structural elements to explicitly represent all of the reinforcing steel in the structure. Figure 5 presents a close up view of the model illustrating the refined finite element discretization used in the model. Note that the display tones were chosen to aid visual identification of the individual structural components associated with different floor levels in the building.



(a) Discretization of Concrete (b) Explicit Steel Reinforcing

Figure 5 High Fidelity Finite Element Model Details

CENTRIFUGE TESTS

The testing approach used for this investigation was to subject the 1/18th scale test structure to the properly scaled gravitational loading (i.e. 18 g) and then dynamically remove one or more ground level support columns. The gravitational loading on the structure would either be successfully redistributed to neighboring components or the structure would experience either a local or more global collapse.

A key factor contributing to the collapse of structures is the amount of mass loading the structure is supporting at the time one or more of its support columns are damaged. In addition to the 'self weight' of the reinforced concrete structural members (i.e. columns, beams and slabs), an actual building will also contain a large amount of non structural 'dead load' such as electrical and air conditioning systems, plumbing, non structural building façade, etc. Also, there is a significant amount of non structural 'live load' including office furniture, interior movable partitions, etc.

The self weight of the multi-story test article is fairly minimal and distributed mass loading representing additional dead and live load contributions were added to the structure for the tests. Bags of steel shot were adhered to each concrete slab in the test article to provide additional dead and live loading of approximately 250 lb/ft^2.

The 1/18th scale test article was installed in the centrifuge at the U.S Army Corp of Engineers centrifuge located at Vicksburg, MS, see Figure 6. It was subjected to two different tests in which ground floor column supports were dynamically removed while the structure was subjected to 18 g gravity. The first test removed one column adjacent to the corner column of the building. Pretest simulations had predicted no collapse for this damage scenario and the test results corresponded to the simulation results. The second test, performed at a later date, removed two additional columns (see Figure 7).



Figure 6 Multi-story Building Test Article Installed on Centrifuge Platform

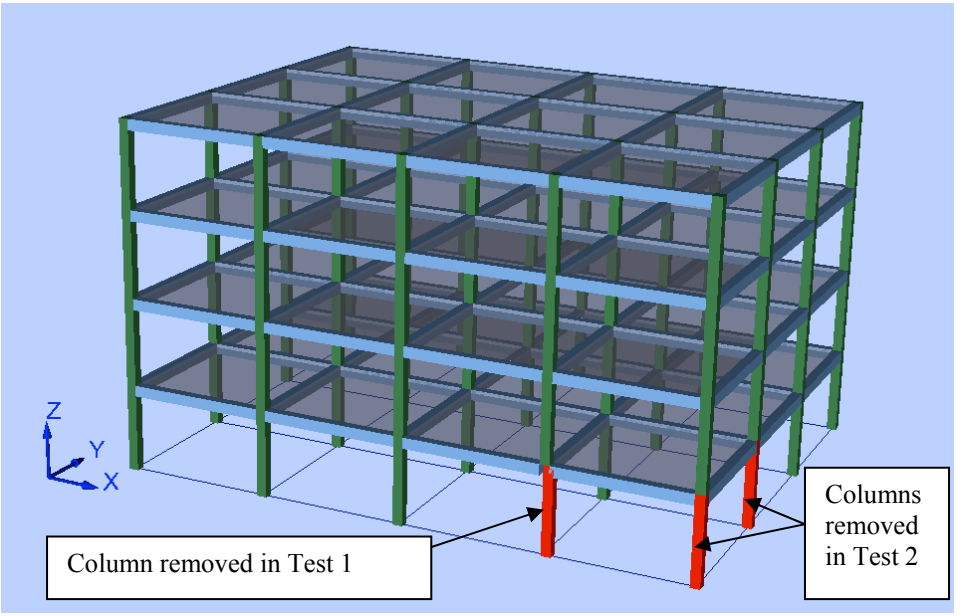


Figure 7 Multi-story Building Showing Columns Removed During Centrifuge Tests

Pretest simulations had predicted a partial collapse of the structure. The predicted collapse zone was consistent with the results of the actual test as shown in Figure 8. Figure 9 presents snapshots from the NLFlex pretest simulation using a roughly similar view position as was used for the high speed camera recording the building's response during the test. The images show the complex deformations and interactions that are occurring in both the test and the simulation. It's interesting to note the overall level of qualitative agreement between the simulation and the test article's response although specific details vary.

Direct comparison of laser displacement gage measurements and pretest simulation results are presented in Figure 10. These records represent the displacements for vertical measurements made on the collapsing portion of the structure. Note that several of the collapsing gauges quit providing data once deflections reached the point that the laser gauge was compromised. It is clear that the first order response characteristics are well represented between the pretest simulation and measurement.

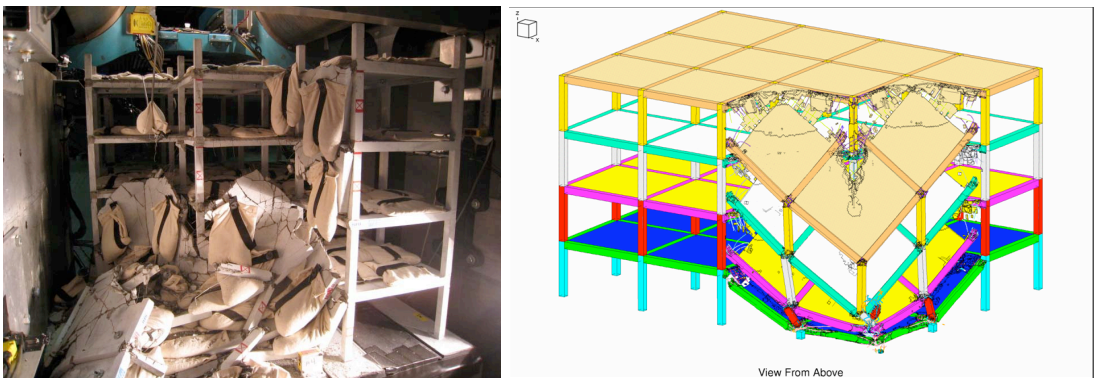


Figure 8 Post-test photo of Test Article Showing Collapsed Region Compared with Snapshot from Pretest Simulation Showing Collapsing Section of Model

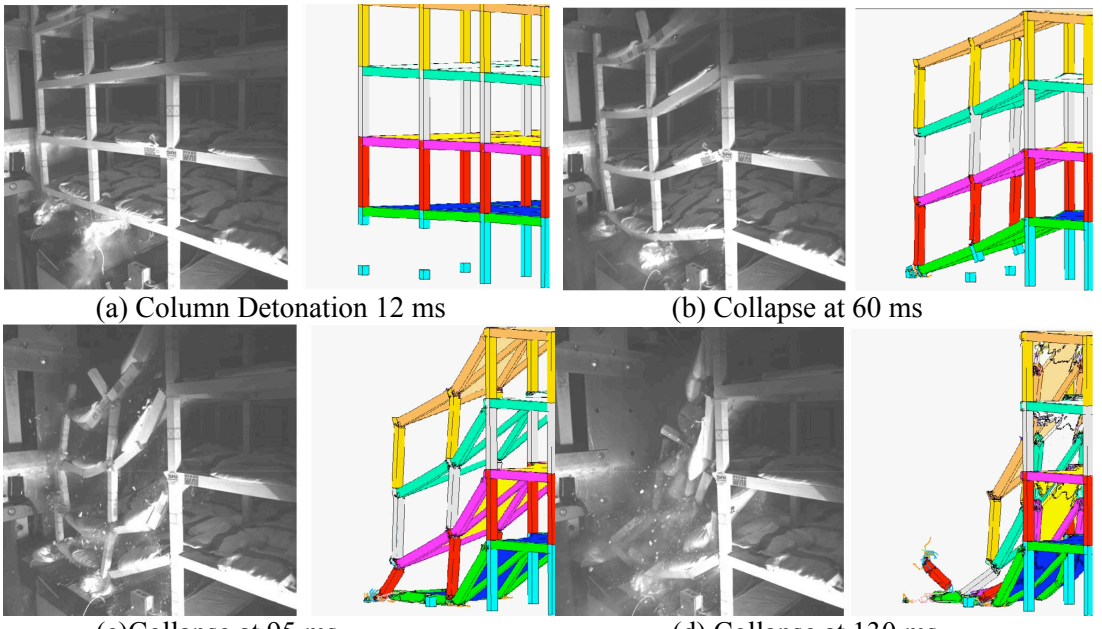


Figure 9 Comparison of High Speed Camera Images with Equivalent Snapshots from Pretest Simulation

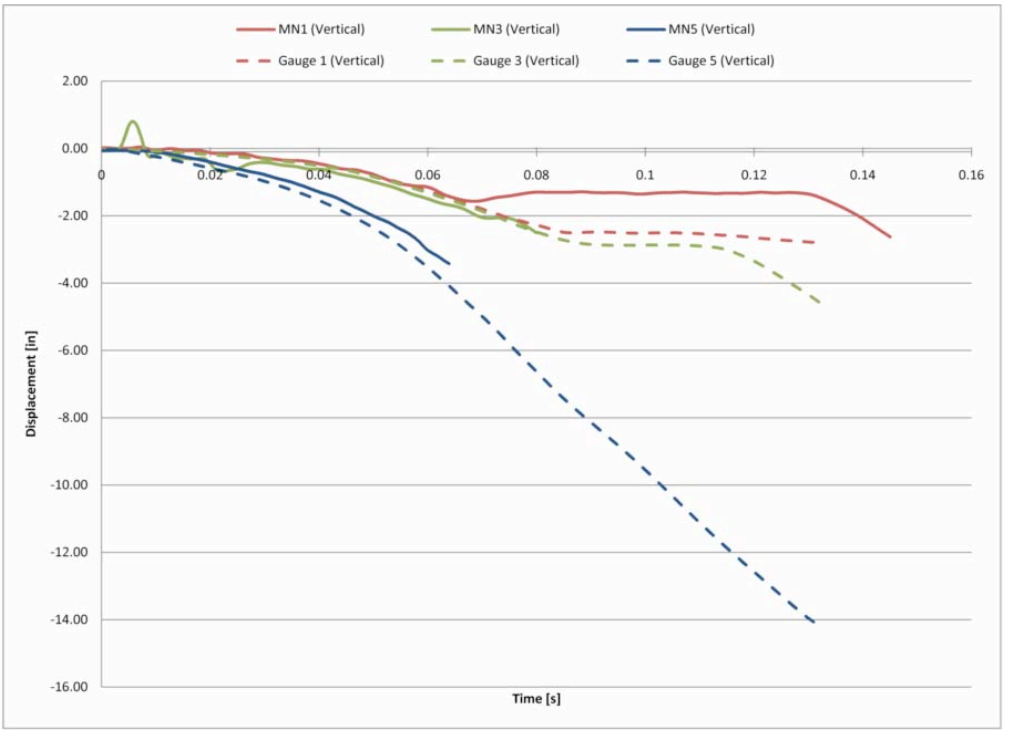


Figure 10 Test 3 Comparison of Pretest Calculated and Measured Vertical Displacements for Collapsing Section of Structure

Conclusions

A full scale multi-story building structure was designed according to standard building codes and fabricated with high precision at 1/18th scale using replica scaling. Pretest planning simulations using the NLFlex finite element software were used to map out a sequence of tests which provided a representative range of structural response to several different levels of damage. Pretest predictions were in good agreement with all major aspects of collapse behavior for the structure. The test results provided a significant validation demonstration of the NLFlex software for progressive collapse applications.

This effort pioneered the use of small scale testing under properly scaled gravity loads for progressive collapse applications. Small scale testing was found to be practical and useful for studying progressive collapse phenomena.

Although there are differences between full scale and small scale structures due to scale effects and the practical challenges of manufacturing a small scale structure, simulation tools can effectively account for these scaling effects within the computational model.

References

Carpenter, J. E. (Ed.), "Models of Concrete Structures," ACI Committee 444, American Concrete Institute Annual Convention, Dallas, TX (1972).

Ettouney, M., Smilowitz, R., Tang, M. and Hapij, A., "Global System Considerations for Progressive Collapse, with Extensions to Other Natural and Manmade Hazards," ASCE J. of Constructed Facilities, November, 2006.

Gran, J. K., J. R. Bruce, and J. D. Colton, "Scale Modeling of Buried Reinforced Concrete Structures under Air-Blast Loading," in Dynamic Modeling of Concrete Structures, H. G. Harris, ed., ACI Publication SP-73, pp. 125-142 (1982).

Gran, J. K., and P. E. Senseny, "Compression Bending of Scale-Model Reinforced Concrete Walls," *ASCE Journal of Engineering Mechanics*, Vol. 122, No 7., pp. 660-668 (July 1996).

Gran, J., Vaughan, D and Vanadit-Ellis, W., "Progressive Collapse Testing of a Four Story Reinforced Concrete Structure at 1/18th Scale", 81st Shock and Vibration Symposium, Orlando, FL, Oct. 25-29, 2010.

Harris, H. G, G. M. Sabnis, and R. N. White (1966), "Small-Scale Direct Models of Reinforced and Prestressed Concrete Structures," Department of Structural Engineering, Cornell U., Report No. 326.

Harris, H. G. (Ed.) (1980), Dynamic Modeling of Concrete Structures, ACI Publication No. 73.

Harris, H. G. and G. M. Sabnis, Structural Modeling and Experimental Techniques, CRC Press, Washington, D.C. (1999).

Mirza, S (Ed.), "Structural Concrete Models, A State of the Art Report," McGill University, Montreal, Quebec (1972).

Mould, J. C., Jr. and H. S. Levine (1993), "A Rate-Dependent Three Invariant Softening Model for Concrete," published in Studies in Applied Mech., Mech. and Materials and Structures, Ed. by G. Voyiadjis, L. Bank and L. Jacobs, Elsevier, 1994.

Mould, J., H. Levine and D. Tennant (1994), "Evaluation of a Rate-Dependent Three Invariant Softening Model for Concrete," Fracture and Damage in Quasi-brittle Structures, edited by Z.P. Bazant et al., Chapman and Hall, London, UK, 1994, pp. 231.

Vaughan, D.K., "FLEX User's Guide," Report UG8298, Weidlinger Associates, Mountain View, CA, May 1983 plus updates through 2010.

Weidlinger Associates, Inc. (2004). "TSWG Method for Progressive Collapse Analysis and the ProCAT Computer Program." Prepared by Weidlinger Associates, Inc. for the Technical Support Working Group. Contract #N41756-02-C-4704, Washington, D.C, June 2004.

White, R. N. (Ed.), "Models for Concrete Structures," ACI Publication No. 24, American Concrete Institute, Detroit, MI (1970).

VISUALISATION-A CONCEPTUAL DESIGN AID

Yaqub Rafiq,

Faculty of Science and Technology, University of Plymouth, UK

Yaqub.rafiq@plymouth.ac.uk

Tel: (++44) 1752 586144

ABSTRACT

Due to highly fragmented nature of the of Architecture Engineering Construction (AEC) industry and time constraints, little attention has been devoted to the conceptual design process. Multidisciplinary teams start with a limited set of requirements, mostly imposed by the Architect, to work on only a restricted number of design alternatives. Therefore, final designs often lack satisfactory performance throughout its life. This paper uses a decision support tool, the IVCG, which combines the searching power of evolutionary computation with the exploration power of an interactive visualisation tools to assist designers at the conceptual design stage. This approach facilitates members of the different disciplines involved to interact with the system independently to identify those regions of the search space which best satisfy the requirements of their individual disciplines. It then allows them to agree on a 'mutually inclusive' region that partially satisfies the needs of all parties involved in the design. The system also uses the Pareto optimisation algorithm to focus on a limited number of solutions, inside the Pareto front, for the multi-disciplinary team to interactively explore solutions within this region. This enables selection of a workable number of 'compromised solutions' that are acceptable to all parties involved.

Keywords: Evolutionary computation, Visualisation, Exploration, Conceptual design, Decision support, Compromised solution.

INTRODUCTION

The impacts of global warming have significantly alarmed nations towards acting more responsibly. Additionally, there is an increasing awareness about the negative impact of buildings on the environment. According to USGBC 2007, in the U.S. over 70% of electricity, 40% of raw materials and 12% of water consumption is attributed to buildings alone. This is an alarming situation. Furthermore, Turner and Frankel (2008) argue that the lifecycle performance of many new buildings is below that of older buildings and often below code requirements. According to Miller (1993), the overall design cost is less that 10% of the building cost while the construction costs are around 80%. Research has shown that decisions made that the conceptual stage are responsible for committing about 70 to 80% of the building costs. In current conditions, time is a major limiting factor in the conceptual stage of the design. Therefore, decisions made at this stage are usually rushed, mostly fragmented and are predominantly based on heuristics and from the experiences of previous projects. Fig. 1 shows the impact of decision-making and the cost of redesign at various stages of the design.

From Fig. 1 it is clear that decisions made at the conceptual stages of the design process have much greater impact on the final design; and the cost of redesign at this stage

is negligible when compared with other design stages. These issues necessitate an urgent need for closer collaboration at the conceptual stage of the design.

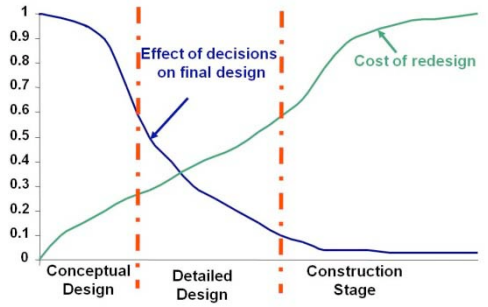


Fig. 1: Effects of decision making and the cost of redesign at different stages

Successful application of evolutionary computation (EC), particularly genetic algorithms (GAs), to solve multi-dimensional problems has shown to be promising. Applications of EC in building design goes back to the early 1990s: Grierson & Pack (1993) addressed topological and geometrical optimisation problems. Rajan (1995) also conducted a similar investigation using trusses instead of frames. Parmee and Bullock (1993) described how the GA has been successfully applied to the design of a hydropower scheme.

From 1997 to the present day, there has been a noticeable growth in interest in the application of GAs specifically to conceptual building design. One reason for this is that building design problems are highly multi-dimensional, multi-criteria and multi disciplinary problems with lots of inherently conflicting criteria. Grierson and his co-researchers in Waterloo (Grierson and Khajehpour, 1999; Grierson and Park, 1997), Rafiq et al. in Plymouth (Mathews et al., 1996; Rafiq et al., 2003) and Miles et al. in Cardiff (Miles et al., 1995; Miles et al., 2001; Sisk et al., 2003) are perhaps among the first researchers who have made particularly significant contributions to this area.

Recently, there has been recognition of the value of human-computer interaction at various stages of the design process. As the main focus of this paper is on the conceptual design process, only relevant literature in this area will be reviewed.

A comprehensive review by Takagi (2001) lists a number of approaches towards application of interactive evolutionary computation. One of the first preliminary design systems devised by Pham & Yang (1993), allowed the GA to produce configurations for the user to view and evaluate in order to formulate decisions about further redesigns. Jo (1998) discovered that adding human interaction to his evolutionary design system meant domain knowledge could be incorporated online and solutions could be independently visualized in a space layout problem which allowed the user to modify individual elements of the design. User interaction has also been further considered in a multi-objective environment: Fonesca and Fleming (1993) proposed a decision-maker (DM) that controls which objectives have more importance within a non-dominated set of solutions. Horn (1997) points out that there are three different approaches to decision making in multi-criteria problems: make a multi-criteria decision before search, make a decision after search or integrate the search and decision making. The latter approach would appear to be the most powerful, incorporating iterative search and decision making.

Mathews & Rafiq (2000 & 2003) developed a Conceptual Building Design (CBD) system using the Structured GA. This system used the objective oriented functionalities of visual C++ that allows the user to manipulate the system more interactively. A powerful

GUI was used which included a number of interactive dialogue boxes for effective user interaction. To enable better interaction at run time, the design hierarchy was made available to the designer. A tree control provides basic functionality for manipulating the nodes (different frame systems) and branches (different design options) within a hierarchy. Using this facility allows the designer to include or exclude particular design options from the GA search at the runtime. The system also enables the designer to trace the design evolution process throughout a whole run of a GA operation. This was an important facility which added transparency to the otherwise 'black box' GA operation.

Grierson and Khajehpour (2002) used Pareto optimisation techniques for the multi-criteria conceptual design with the use of colour-filtered graphics. In this investigation, a large set of Pareto non-dominated solutions were captured. Subsequently, they used colour filtering of the Pareto-optimal design set and created a large body of informative graphics that identify trade-off relationships between competing objective criteria, as well as design subsets having particular designer-specified attributes. This research demonstrated that effective use of visualisation tools enables discovery of interrelationships between design parameters.

Research in Plymouth Engineering Design Centre by Parmee and Bonham (1998) resulted in development of an Interactive Evolutionary Design System (IEDS) based on a system of iterative redefinition of variables and objective space by a designer. These ideas evolved from many years of research in using evolutionary computing to aid engineering design, starting from general ideas to locate and analyse robust regions of the search space. Development of cluster-oriented genetic algorithms (COGAs) allowed inclusion of user preferences between objectives. COGA extracts regions of good solutions from a GA run by selective filtering of high performance solutions through the search process.

INTERACTIVE VISUALISATION CLUSTRING GENETIC ALGORITHM

The Interactive Visualisation and Clustering Genetic Algorithm System (IVCGA) developed by Packham et al. (Packham 2003, Packhan & Denham 2003) was designed to focus on user interaction from the outset. This work is centred on a user interface that allows exploration of specific regions of the solution space by 'zooming in' to interactively selected regions, in order to evaluate the merit of solutions within these regions against the project requirements. It allows the designer to increase the number of solutions inside or outside these regions by creating new design alternatives using further GA runs.

The IVCGA was designed to offer the following features:

- The fast generation of diverse data by running a simple GA for a low number of generations whilst maintaining the diversity of solutions generated.
- An easy to use interface that allows direct manipulation of both the data and views. Various high dimensional visualization techniques are added that enhances human-led exploration of the solution spaces.
- An automatic clustering procedure is incorporated into the system which identifies clusters of design solutions relevant to the problem in hand. Colour is used to highlight important clusters (better design alternatives), enhancing perceptual understanding of the data.
- Extensive interaction is supported thus enabling further data generation with the GA, both inside or outside regions identified by the user.

- Permits investigation of inter-relationships between design parameters and objectives.

METHOD

Building design is a multi-disciplinary activity, involving a number of individuals from a variety of disciplines, each with a differing emphasis on the design requirements. Thus, the objective of this study is to illustrate how the IVCGA can face the challenges of multi-disciplinary design and how it is efficiently used in a multi-disciplinary design environment. This research has been conducted in close collaboration with an Architect, a Structural Engineer and a Building physicist. Differential requirements of each can be summarised as follows:

- The Architect: Space; functionality; appearance; user comfort.
- The Structural Engineer: Building stability; structural performance; strength; safety.
- The Building Physicist: Mechanical; electrical; heating cooling and ventilation systems (HVAC) and user comfort.

Some details of how the IVCGA deals with the above issues are discussed below.

Architectural requirements

A major architectural objective is to have column free spaces to maximise the utility of the building in terms of its flexibility and future use.

From literature and discussions with the architect, it was discovered that architects plan building footprints based on specific architectural grids, which are functionality dependent. The following architectural grids are commonly used by the architects: 1.0m, 1.2m, 1.5m & 1.8m. The following structural grid (bay sizes) combinations can be generated from these architectural grid sizes:

4m, 4.5m, 4.8m, 5m, 5.4m, 6m, 7m, 7.2m, 7.5m, 8m, 8.4m, 9m. These grid dimensions were used to determine the size of the building footprint.

Types of cladding, window types and window sizes determine external building appearance. Some of these aspects also overlap with the structural engineers and building physicist requirements.

For the case study presented in this paper, 4 cladding types and 4 window types are used and window ratios are varied from 25% to 100% of the bay area.

Structural Engineering requirements:

A pivotal requirement of the structural engineer is the use of optimum structural element sizes that are capable of carrying loads safely to the ground. Generally, an optimum bay size reduces the load carried by each element and hence the overall cost of the building. In this study, bay sizes have been considered to be an important structural requirement and structural steel was used as the main construction material. Column, beam and floor types were based on the UK Steel Construction Institute standard member sizes and types.

In order to minimise the calculation time, prior to the optimisation process a comprehensive parametric study was conducted and look up tables were created to enable the optimisation program to select optimum member types and sizes for each bay size. The size of the bays used are those as shown in the ‘Architectural requirements’ section. The number of storeys used in this was from 1 to 8, with inclusion of 7 different floor systems.

Building Physicist requirements:

Calculation of a building energy usage is a complex issue, which is outside the scope of this paper. However for optimisation purposes, it is necessary to include building energy usage to enable a long term cost comparison for different design concepts even if it is a relative cost of energy consumption.

Most building physicists use complex simulation programs and Energy Plus programs (http://apps1.eere.energy.gov/buildings/energyplus/) to assess building energy consumption and thermal comfort for buildings. Using these tools may be feasible for a single building, while optimisation algorithms deal with a population of designs that consist of thousands of alternatives. For this reason, in this study 'LT Method 2.0' of Baker and Steemers (1994), is used for rapid calculation of energy consumption. Of course, at the later design stages, when a few selected design alternatives are singled out by the design team, more complex simulation tools would be feasible to use for more reliable calculation of energy consumption and thermal comfort.

For the purpose of this study, 'LT Method 2.0' divides the building into active and passive regions. Active regions are those parts of the building that are not lit, heated or ventilated naturally. A 6m perimeter zone (along the outer perimeter of the building, adjacent to windows) is restricted for the passive zones; any area outside this zone is an active zone which requires mechanical lighting, heating and ventilation.

For this study the climate data for 12 months of the year for Cambridge, UK has been used. South facing buildings with large window ratios and a maximum building width of around 12m would be the optimum design solution for energy consumption.

THE PROPOSED APPROACH

Conceptual building design is a highly multi-dimensional and multi-disciplinary process. This paper introduces a novel method of resolving these multi-disciplinary issues. To tackle this problem, at first, each member of the design team interacts with the IVCGA independently to address their discipline specific needs. In this case, a multi-objective problem is simplified into three separate, single objective problems for which the main (dominant) objective is determined by each discipline running the IVCGA. During this independent interaction with the IVCGA, the system also computes values of the objectives related to the other two disciplines. This alerts the members of the individual disciplines about the consequences of choices made by one discipline on the other two members and on the overall design. Hence, the following stages are considered:

1. **Search and optimisation stage**: in this stage the solution space is widely searched to discover a population of optimum solutions that satisfy the requirements of a given discipline. Each member of the design team defines their own objectives. Some details of objectives related to each member of the team will be discussed later. The dominant objective of the search process is that determined by the discipline running the IVCGA. This objective is interactively selected using drop down menus provided by the system. It is worthwhile noting that unlike other previous optimisation processors that were trying to find a single solution "the so-called global optimum solution", the IVCGA searches the design space to locate a set of feasible solutions that best fit the problem requirements. In this optimisation process no constraints, except the upper and lower bounds of the design independent variables, are imposed. Other constraints are defined interactively by the user at run time. At the end of this stage the IVCGA identifies clusters of feasible solutions based on the single dominant

objective. Different colours are used to present clusters of solutions having similar characteristics.

2. **The exploration stage:** at this stage, members of the design team independently interact with the IVCGA to explore the suitability of the solutions generated during the search stage. They explore regions by highlighting part of the solution, using the cursor to draw boxes around regions of interest. Using their domain expertise they explore the suitability of each region and finally select a region which the domain expert thinks is a best fit for the purposes of their discipline requirements.

To simplify the output, only the building footprint is presented as the graphic outcome of the design, with a brief description of the major design components.

Once individual members of the design team have conducted independent exploration of the solution space and selected their discipline specific regions, the system superimposes these regions to find an area that overlaps the requirements for all parties. This region is called "the mutually inclusive region"; a region that contains design alternatives that partially satisfies the requirements of all parties involved in the design.

Essential discipline-related design requirements are defined as objectives specific to these disciplines, and are summarised in the following sections.

Architectural requirement

The principle objective function of the architectural requirements used in this paper is to minimise the number of fire escapes and columns used in the building (maximise column free space). To achieve this, the term "areaLoss" was introduced. AreaLoss is calculated as the sum of the area occupied by the columns and the fire escapes. Non-useable area around a column is considered to be $1m^2$ and an area of $18m^2$ per floor was used for each fire escape. In order to satisfy the architectural requirement, the areaLoss was minimised. Number and location of fire escapes are determined by fire regulations.

Structural engineering requirements:

The structural engineer requires the use of optimum structural element sizes that are capable of carrying loads safely to the ground. For this case study structural steel is used as the sole construction material. A spreadsheet was created listing optimum member sizes and recommended floor types for each bay size. This spreadsheet is used to obtain optimum floor system and optimum structural sizes. The cost of the structure is calculated as the cost of: total superstructure, substructure, foundation, ground slab, prelims & external works, finishes & walls and cladding and windows. In order to make this data more useful and comparable, all costs are converted to cost/m^2 of the floor area and stored in looking up tables to be used by the optimisation algorithm.

Building physicist requirements

Calculation of energy usage for a building is a complex issue, which is out of the scope of this paper. However it is necessary to include building energy usage in the optimisation process to give a long term cost comparison for different design concepts, even if it is a relative cost of energy consumption (termed as 'eCost' in this study). As stated previously, the 'LT Method 2.0' was used to calculate 'eCost'.

Design Variables and Objectives

From the above three disciplines, a total of seven independent variables are selected, these being:

1. Number of storeys: single to 8 storeys
2. Bay size (i.e. sizes 4m to 9m): 12 options (8 options selected for this study)
3. Number of bays along the length of building (single bay to 16 bays): 16 options
4. Concrete floor type: 8 options
5. Wall cladding type: 4 options
6. Window type: 4 options
7. Window ratio, ranging from 0.25 to 1.00: 16 options

Clearly, within a more realistic problem, many more design variables would be used. However, even with this small number of design variables and the simplicity of the assumptions made, there are approximately 3 million possible solutions. Traditionally it would be exceptionally difficult to transverse a search space of this size to find compromise solutions. Normally, designers may only consider a small fraction (i.e. numbers in the range of 4 to 5) of this search space, thus possibly missing superior alternative solutions.

The IVCGA optimisation tools use 3 core objectives (Arealoss for the architectural requirements that maximises the lettable floor space; StructCost for structural requirements that minimises the structural costs; and eCost that minimises building energy consumption.)

The IVCGA is a novel and powerful tool, with the core component of user-led exploration. A key outcome of this exploration is to enable users to explore and discover boundaries of the solutions that contain alternative designs which may best satisfy the requirement of a particular discipline. For details of the IVCGA exploration process refer to Packham and Denham (2003).

PRACTICAL EXAMPLE

Problem definition

In this paper, multidisciplinary issues regarding the design of a commercial building with a total lettable area of 8000 m^2 is investigated. Structural steel has been selected as the main construction material. As mentioned, the design team consists of three disciplines: the architect, the structural engineer, and the building physicist.

The architect view

Running the IVCGA, the architect selects the “areaLoss” as the objective of the optimisation process. Initially, a 100 population size and 21 generations are used to generate 2100 solutions. No restrictions or filtering of information, to discourage the generation of impracticable solutions, have been implemented at this stage.

Fig. 2 left hand (LH) frame shows the entire solution space satisfying the architectural objective of minimising areaLoss. Each dot on Fig. 2 represents one solution; and the darker the colour, the fitter (i.e. better) the solution is. The exploration process is interactive and the user has full control. For example to explore a preferred region for the architectural solution space, the architect draws a box around the specific region of the solution space which they signify to be useful for further exploration (e.g. total building footprint area between 7500m^2 to 8500m^2 and up to a maximum of 350m^2 areaLoss has been selected inside the box in Fig. 2 LH frame). The IVCGA automatically discards all

solutions that are outside the comfort zone of the architect and zooms into the selected area. The new solution space is shown in Fig. 2 RH frame.

The additional use of colour enables the user to emphasise the clusters that are important to the user whilst keeping other interesting data also available. For example, in Fig. 2, concepts presented by yellow and pink represent two distinct clusters of high fitness solutions.

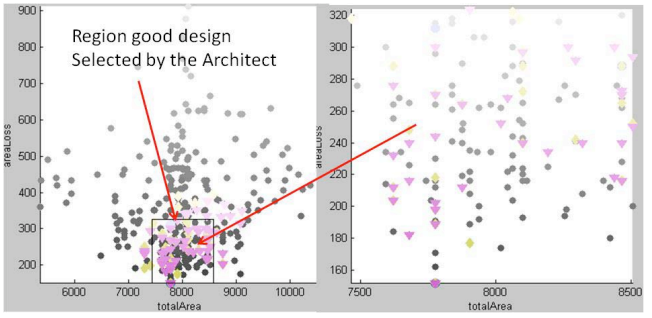


Fig. 2: LH-whole design space; RH-Zoomed in on the selected region

The system has a graphic user interface where a right mouse click on a particular solution (e.g. those shown by pink triangle or yellow diamond) presents to the user a 2D floor plan of the selected solution. It also gives some other important textural details about the selected design option, such as footprint dimensions, floor type, bay size etc. A cut-down screenshot of this process is given in Fig. 3. While this information is useful, it is a simplified graphic user interface which could easily be replaced with an interface with 3D Studio Max or even with virtual reality or building information modelling (BIM) programs such as Revit & TEKLA, which give more practical information about the building. Work in this area in progress.

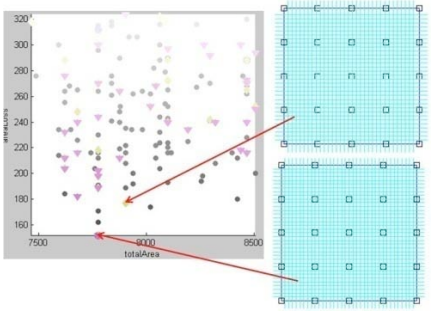


Fig. 3 samples of designs selected by the architect

It is worthwhile to note that the cyan lines in Fig. 3 represent architectural grids.

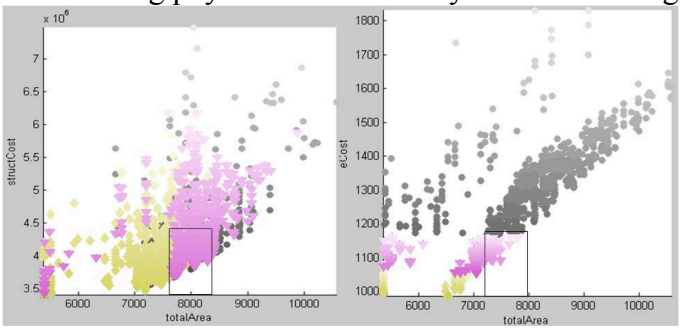
The IVCGA also allows the designer to generate more designs solutions inside the boundaries of the selected region by performing another set number of generations inside the selected area (i.e. the area within the rectangle selected interactively by the Architect.)

Using other graphic facilities of the IVCGA, the designer can conduct further explorations to enhance their understanding of the interrelationships between design parameters. This is achieved by defining which variables are plotted against each other. As an example, plot of the areaLoss against the number of storeys could provide the architect with significant information.

The structural engineer and the building physicist views

The structural engineer selects the 'structCost' and the building physicist selects the eCost as the objective of the optimisation. They minimise the overall cost of the structure and energy requirements of the building, respectively.

Like the architect, the structural engineer and the building physicist can conduct similar explorations to identify the boundaries of the solution spaces that best suit their individual disciplinary requirements. In this example, the preferred areas selected by the structural engineer and building physicist are shown by the boxes in Fig. 4.



(Structural Engineering) (Building Physicist)

Fig. 4: Solution spaces generated using structCos and eCost as objectives

Mutually inclusive region of the multi-disciplinary solution space

Once independent exploration of the solution space is completed by all members of the design team, and each has identified their regions of best solutions, these areas previously identified independently as their discipline 'comfort zones' can be superimposed on each other. This enables identification of a mutually inclusive region that partially satisfies the requirements of all disciplines involved in the design.

Fig. 5 exemplifies a superimposed solution space that contains the preferred solutions selected by all three disciplines interactively (in this case study the combined-solution spaces contains 3x2100 = 6300 alternative designs). In Fig. 5, solutions coloured purple and pink represent a mutually inclusive region of the solution space that partially satisfies the requirements of all three parties. This mutually inclusive region is identified by overlapping three clusters: cyan - the architectural preferred area; green - the structural engineer preferred area; and red - the building physicist preferred region.

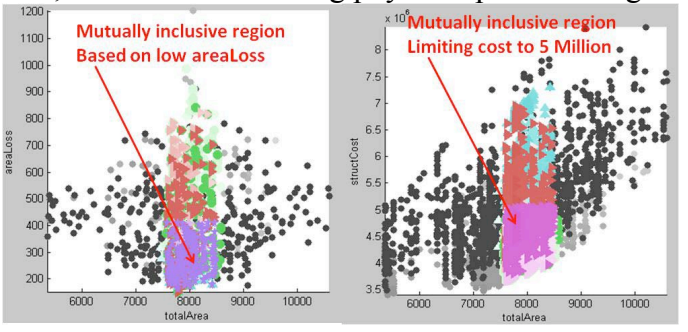


Fig. 4: Mutually inclusive regions

Pareto optimal front

Mutually inclusive region defines a framework for the future of multi-disciplinary exploration in which members of the design team can focus only on the solutions within

the boundaries of this region. For this case study, the region contains 1448 individual solutions which is by itself a large solution space to contend with. In order to narrow down the exploration space, a Pareto algorithm was implemented in a novel way to rank solutions within this region and identify a Pareto set based on the non-dominated rule defined by Pareto. Using this method, 147 designs alternatives were found to be non-dominated solutions. Fig. 5 give details of this Pareto set.

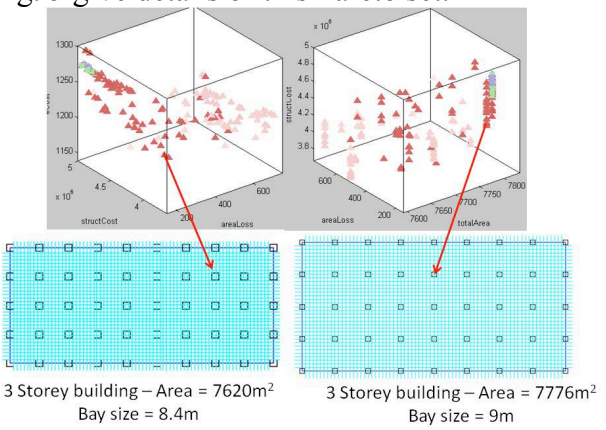


Fig. 5 Pareto non-dominated set – LH-frame: three objectives and RH- frame total area against areaLoss and structCost

In Fig. 5 - LH frame, solutions adjacent to the vertical axis are those designs which have lower values for all three objectives. Unfortunately, the total area for most of these buildings is approximately 7600m^2, considerably less than the required 8000m^2. Conversely, by plotting the 2 objectives against the totalArea it is discovered that the cluster of solutions at the RH end of the design space contain superior solutions with a floor plan area close to 8000m^2 and lower structCost. This phenomenon also demonstrates the knowledge discovery aspect of the IVCGA as a useful decision support tool.

CONCLUSIONS

- Previous research discovered that changes identified and implemented at the conceptual stage of the design process have maximal impact of final design and building costs.
- This paper demonstrates that the IVCGA, a powerful decision support tool, facilitates user interaction, enabling members of the multi-disciplinary design team to conduct fast and efficient exploration of the solution space at the conceptual design stage. This enables selection of the most suitable solution to satisfy the requirements of all 3 core disciplines involved in the multi-disciplinary team.
- User interaction through the IVCGA enhanced the multi-disciplinary design team members' understanding of the overall design issues, allowing them to appreciate the effects that their decisions have on other parties and on the overall design.
- A novel use of the Pareto optimal front was an ideal way of solely focusing on non-dominated solutions which is in the region of 10% of the overall design. This assists design team members in their decision making.
- In conclusion, the use of the IVCGA at the conceptual stage of the design process, not only enables independent user interaction, so designers can focus specifically on their discipline-specific objectives, but also upon completion of the run

combines this data to provide solutions that are acceptable to all members of the design team. This enables production of a structure that is not only structurally sound, but also cost effective with limited adverse environmental effects in a building with maximal utility of the space available.

- Further research could cover the addition of more design parameters such as: other construction materials; construction cost and time and life cycle costs. In terms of visualisation, interface with virtual reality and building information modelling tools such as Revit and TEKLA will provide a more realistic view of the building design process and life costing.

REFERENCES

Baker, N. & Steemers, K. (1994), LT Method 2.0 An Energy Design Tool for Non-domestic Buildings. Cambridge Architectural Research Limited.

Fonesca, C. M,, Flemingm, P. J. (1993). "Genetic algorithm for multi-objective optimization: Formulation, discussion and generalization". In: Fifth Int. Conf. on Genetic Algorithms; p. 416-423.

Gane, V. & Haymaker, J. (2010). "Design Scenarios – enabling requirements-deriven parametric desing space", in press.

Grierson, D. E. & Park, W. H. (1993) Optimal Sizing, Geometrical and Topological Design Using a Genetic Algorithm. *Structural Optimization,* 6**,** 151-159.

Grierson, D. E. & Park, W. H. (1997) Optimal Conceptual Topological Design. *in Advances in Structural Optimization*.

Grierson, D. E. & Khajehpour, S. (2002) Method for conceptual design applied to office buildings. *Journal of Computing in Civil Engineering,* 16**,** 83-103.

Horn, J. (1997) *Multicriteria Decision Making and Evolutionary Computation, Handbook of Evolutionary Computation*. Bristol, UK.: Bäck T., Fogel D.B. & Michalewicz Z. (eds.), Institute of Physics Publishing.

Inselberg, A., & Dimsdale, B., (1994) Multi-dimensional Lines I: Representation & Multi-dimensional Lines II: Proximity and Applications. SIAM J. Appl. Math. 1994;54(2):559-596.

Jo, J. (1998). "Interactive Evolutionary Design System: Process and Knowledge Representation". In: Gero JS, Maher ML, editors. Fourth International Round-table Conference on Computational Models of Creative Design; 1998; Heron Island, Australia: University of Sydney; p. 215-224.

Mathews, J. D., Rafiq, M. Y. & Bullock, G. N. B. (1996). "A Prototype for a Conceptual Structural Building Design System Using Genetic Algorithms". *Adaptive Computing in Engineering Design and Control, 96, 2nd Int. Conf.* Plymouth, UK, ED Parmee.

Mathews, J. D. (2000). *Optimisation and Decision Support during the Conceptual Stage of Building Design: New techniques based on the genetic algorithm* [PhD Thesis]. Plymouth, UK: University of Plymouth.

Miles, J. C., Moor, C. J. & Price, G. (1995) Design costing models: An application of heuristic substitution. *Computing Systems in Engineering,* 6**,** 521-531.

Miles, J. C., Sisk, G. M. & Moore, C. J. (2001) The conceptual design of commercial buildings using a genetic algorithm. *Computers & Structures,* 79**,** 1583-1592.

Miller, L., (1993). Concurrent Engineering "Design: integrating the best practices for process improvement". Society of Manufacturing Engineers.

Packham I. S. J. (2003), *An Interactive Visualisation System for Engineering Design using Evolutionary Computing*. PhD thesis, University of Plymouth, UK.

Packham I. S. J. and Denham S. L. (2003), "Visualisation Methods for Supporting the Exploration of High Dimensional Problem Spaces in Engineering Design". In: Roberts JC, editor.

International Conference on Coordinated & Multiple Views in Exploratory Visualization (CMV2003); 15 July, Computer Society, London, UK: IEEE; p. 2-13.

Parmee, I. C., & Bullock, G. N., (1993) "Evolutionary Techniques and their Application to Engineering Design". In: Behesti MR, Zreik K, editors. Advanced Technologies; Elsevier Science; p. 32-42.

Parmee, I. C., & Bonham, C. R., (1998) "Supporting Innovative and Creative Design using Interactive Designer / Evolutionary Computing Strategies". In: Gero JS, Maher ML, editors. Fourth International Round-table Conference on Computational Models of Creative Designeds; December 1998; Heron Island, Australia: University of Sydney; p. 187-214.

Pham, D.T., Yang, Y. A. (1993). "Genetic Algorithm Based Preliminary Design System". Institution of Mechanical Engineers, Part D: Journal of Automobile Engineering;207(2):127-133.

Rajan, S. D. (1995) Sizing, Shape and Topology Design Optimization of Trusses Using Genetic Algorithm. *The Structural Engineer***,** 1480-1487.

Rafiq, M. Y., Mathews, J.D., & Bullock, G. N., (2003) "Conceptual Building Design - an Evolutionary Approach". Journal of Computing in Civil Engineering 17(3):150-158.

Sisk, G. M., Miles, J. C. & Moore, C. J. (2003) Designer centered development of GA-based DSS for conceptual design of buildings. *Journal of Computing in Civil Engineering,* 17**,** 159-166.

Takagi, H. (2001). "Interactive Evolutionary Computation: Fusion of the Capabilities of EC Optimization and Human Evaluation". Proceedings of the IEEE 1;89(9):1275-1296.

Turner, C., Frankel, M., (2008). "Energy Performance of LEED for New Construction Buildings", White Salmon, WA: New Buildings Institute.

United States Green Building Council (USGBC 2700 modified 2008), A National Green Building Research Agenda, http://www.usgbc.org/ShowFile.aspx?DocumentID=3402 (cited 10 September 2010).

Open Sourcing the Design of Civil Infrastructure (OSD-CI): A Paradigm Shift

T. Kijewski-Correa, M. ASCE[1]

[1]DYNAMO Laboratory, Department of Civil Engineering and Geological Sciences, University of Notre Dame, 156 Fitzpatrick Hall, Notre Dame, IN 46556; PH (574) 631-2980; email: tkijewsk@nd.edu

ABSTRACT

Few will argue the importance of civil infrastructure to society, yet its condition has been allowed to deteriorate to a staggering level. Meanwhile the research and design practice dedicated to it has relied only upon limited, fractured resources scattered physically across the community with little formal collaboration. As the information used in the design, analysis and even management of civil infrastructure is trapped inside proprietary systems, these essential public works projects often do not benefit from the full expertise and latest advances available in the wider engineering community. To address this problem, a new virtual organization has been launched: **Open Sourcing the Design of Civil Infrastructure (OSD-CI),** welcoming *Citizen Engineers to* engage in four dimensions of collaboration (sharing hardware, software, knowledge and manpower). This paper presents the ongoing development of this concept, specifically focusing on two recent prototypes allowing this crowd to contribute and assess engineering data.

INTRODUCTION

A few years ago, no one would have believed that a global team of volunteers could write a major operating system kernel or a comprehensive encyclopedia. But today, Linux and Wikipedia and many similar open source projects serve as evidence that loosely organized teams can create and maintain the complex technical and intellectual infrastructure upon which society increasingly depends (Raymond 2001). These projects have succeeded not by accepting participants indiscriminately, but by creating a meritocracy that rewards expertise regardless of its source. Yet interestingly, what is viewed as the best cognitive model (the crowd) has been applied to relatively non-technical societal problems (Surowiecki 2005). Why not then tap it to address once of society's grand challenges: its aging civil infrastructure?

Interestingly, civil engineering is naturally suited towards open source concepts: complex systems like buildings, bridges and other lifelines have many different stakeholders, require many kinds of technical expertise, and have a lifetime far beyond any one contributor. As the information used in the design, analysis and even management of civil infrastructure is trapped inside proprietary systems, these essential projects often do not benefit from the full expertise and latest advances available in the wider engineering community. To address this problem, a team of civil engineers, computer scientists and social scientists at the University of Notre

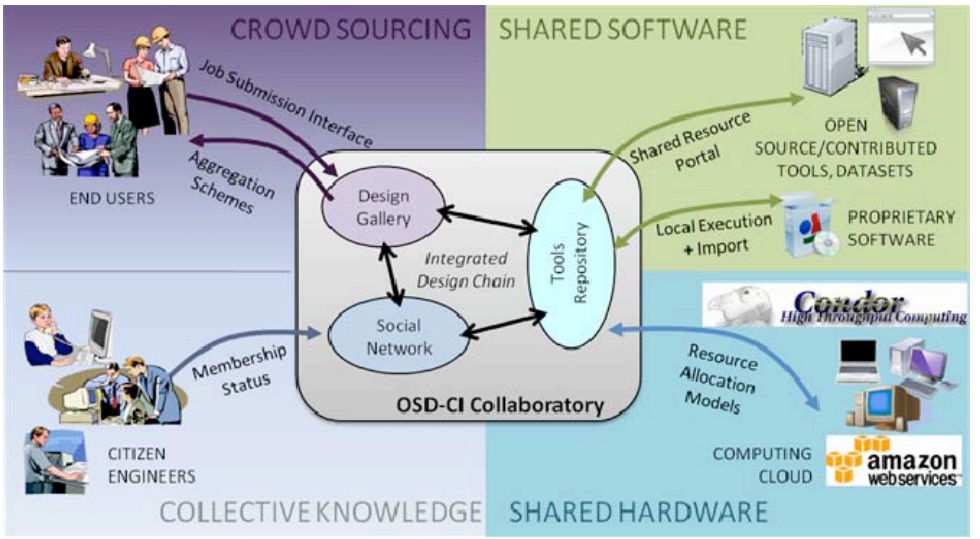


Figure 1. Four dimensions of sharing and mechanisms interfacing them in OSD-CI.

Dame are engaged in the formation of a new type of virtual organization for **Open Sourcing the Design of Civil Infrastructure (OSD-CI)**. OSD-CI will allow stakeholders – engineers, public officials, researchers, students, and even the public at-large – to review, propose, modify, evaluate, and contribute to designs, analyses, databases and other fundamental research that supports civil infrastructure and will provide these *Citizen Engineers* with unparalleled access to tools that will empower their individual inquiry.

The OSD-CI Concept

While it may seem bold to suggest that engineers would agree to crowdsource their problems, it is important to note that the profession presently operates within a limited crowd construct. Both scholarly research and state-of-the-art design depend on the efforts of predecessors and contemporaries, and the crowd, via peer review, citations, and standardization, decides whose work is best (Surowiecki 2005). This project now boldly extends that crowd to the public at large, with appropriate policies, governance structure, incentives, and control mechanisms to assure trustworthiness in technical tasks (Johnson 2006, O'Mahony and Ferraro 2007). As shown in Figure 1, this collaboratory would accept job submissions from end users (firms, researchers, fellow *Citizen Engineers*), who would specify relevant details (scope, constraints, models, etc.), deadlines, submission formats, and requisite credentials. *Citizen Engineers* with the proper credentials and membership status (a concept discussed in a later section) can volunteer to contribute to these job submissions, either individually or as part of teams, using the various computational resources and tools housed in the portal. The products produced by *Citizen Engineers* are archived in the collaboratory's design gallery and can be retrieved and commented on by any member of the public to form a truly transparent archival system for Civil Infrastructure projects. These products are ultimately delivered back to the end user through various aggregation schemes.

One may ask: what are the incentives for end users to bring their jobs to the OSD-CI portal? Eventually, every firm is faced with projects requiring expertise outside the restricted range of their staff's abilities and experiences. The crowd provides a flexible and informal mechanism to obtain needed expertise for specific projects at little to no cost. The OSD-CI therefore provides a mechanism through which firms of varying sizes can "crowdsource" specific projects, allowing the firms to both focus on their core competencies and obtain the expertise to solve problems requiring a more diverse group. Conversely, *Citizen Engineers*, whose demographics may be broad, have similarly diverse reasons to join the crowd. For members of the general public, status and ratings within a community of users and the chance to be part of a larger initiative that serves the public good has been shown to sustain involvement. However, to attract *Citizen Engineers* with higher level qualifications, other incentives are required. Networking, potentials for career advancement, and exposure to potential employers may be sufficiently attractive, especially for the legions of unemployed engineers. For licensed engineers, OSD-CI activities can be used to earn professional development hours (PDHs). Of course, direct monetary compensation will be warranted for those working on the most complex and challenging problems. Thus, one of the major research endeavors of this project is to determine which types of incentives work best for wide ranging tasks within OSD-CI.

Cyberinfrastructure Requirements

There are many successful examples of open sharing of computational resources (SETI@Home), source code (Linux), knowledge (Wikipedia), and even manpower (Amazon's Mechanical Turk); however, the unique feature of OSD-CI is that it will enable collaboration in all four of these dimensions as part of an integrated design chain shown in Figure 1. While this in and of itself is challenging, it is further compounded by the fact that these social computing principles have never been applied in high risk application domains where failure has serious implications. However before the issue of how to assure trustworthy work can be tackled, a robust cyber-platform must be developed to support these four dimensions of collaboration and their three distinct repositories of interacting data: (1) a design gallery consisting of all the active job submissions, (2) the social network representing the properties, qualifications, and actions of all the *Citizen Engineers* participating in the system, and (3) the tool repository -- a collection of open source and contributed tools from members of the collaboratory. Figure 2 provides examples of these tools such as data archives, real-time data, tele-experiments, simulation/analysis tools, and e-design aids (Kareem et al. 2008, Kwon et al. 2008). A key feature of the tool repository is the provision for both open source tools to be embedded in the system *and* the capacity to upload/download information and results to/from proprietary software whose analyses have been executed locally by a *Citizen Engineer* outside the portal. As such, *Citizen Engineers* will retain ongoing access to the analyses they trust and have access to new collective resources that all can be seamlessly integrated in the design chain. Further, since computational demands of various actions in the portal will vary widely, at times surpassing the local computational resources of the *Citizen Engineer*, there is the capability to farm computations out, e.g., to Condor or Amazon's Elastic Computing Cloud.

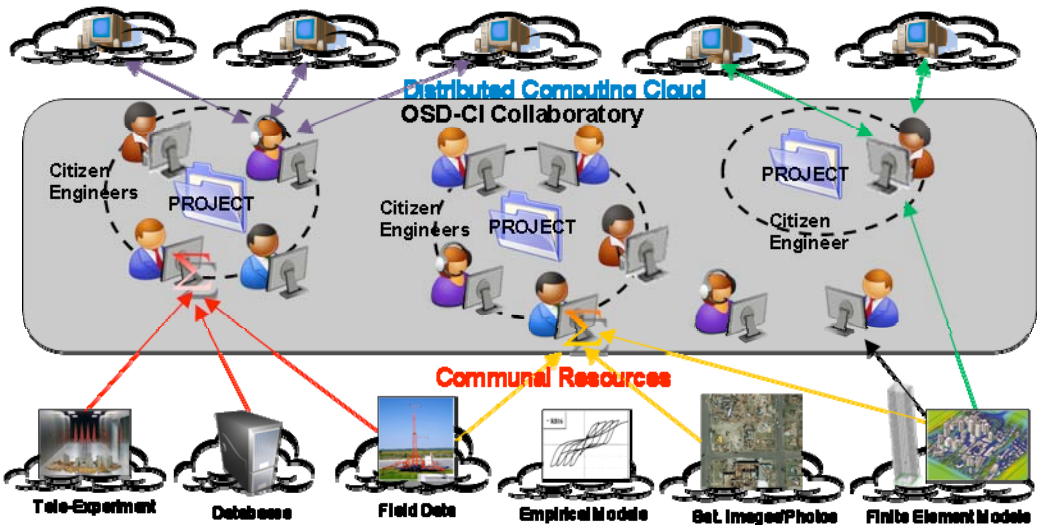


Figure 2. Schematic of *Citizen Engineer* interactions and use of distributed resources.

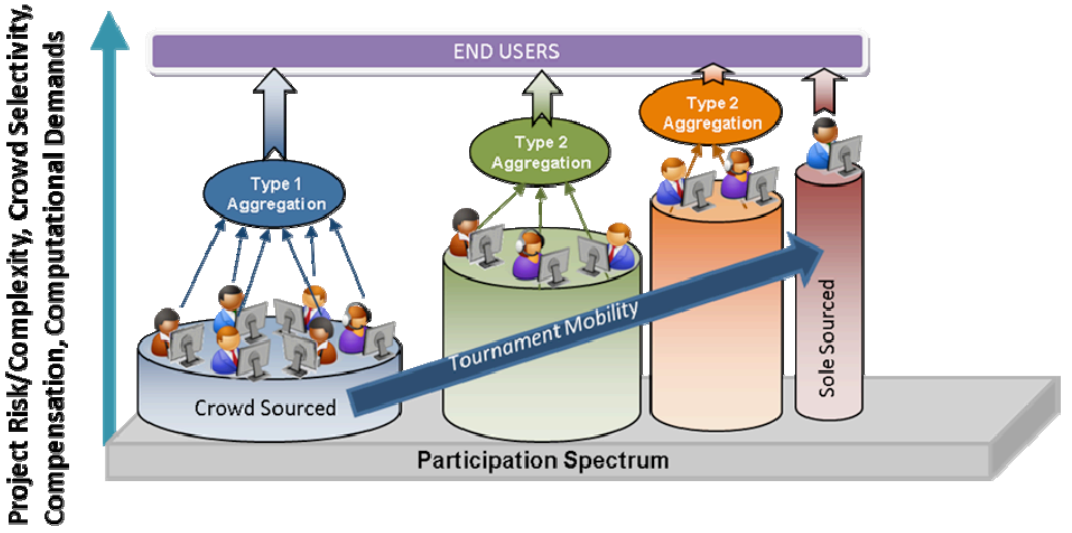


Figure 3. Tiered organizational structure of OSD-CI.

Balancing Trustworthiness and Openness

Many open source systems began with no controls in order to foster maximum openness, e.g., Wikipedia. Interestingly, its founders later regretted that structure and the lack of *a priori* roles for experts (Lih 2009). Considering the high levels of risk involved in the proposed effort, the competing requirements of trustworthiness and openness are be best optimized through a tiered collaboratory. This concept, shown in Figure 3, acknowledges that there is a wide spectrum of tasks with diverse requirements that not all members of the crowd would be qualified to address. At the highest tiers, projects would be increasingly complex, may require sophisticated analysis tools and substantial computational resources, and in turn offer higher levels

of compensation, but as a result, greater selectivity within the crowd. This produces a spectrum of participation from crowdsourced to sole sourced.

One of the major advantages of the tiered system is that it provides a mechanism for building trust through transparent credentials and rating systems for all its *Citizen Engineers*, based on the accumulated reviews received from past contributions (similar to ratings on e-Bay and Amazon). These ratings will not only create incentives, but they will also provide end users with information that they can use to pre-qualify *Citizen Engineers* for their projects and a mechanism to evaluate and even aggregate their submissions. The result would be a form of tournament mobility as shown in Figure 3, where *Citizen Engineers* would start off "competing" at lower tiers and as their efforts are positively evaluated they would become qualified to "compete" at higher levels.

EXAMPLE CROWDSOURCED PORTALS FOR CIVIL INFRASTRUCTURE

Having summarized the basic concept behind **Open-Sourcing the Design of Civil Infrastructure**, two case studies will be presented to demonstrate the cyberinfrastructure that can support various activities executed by *Citizen Engineers*.

Case Study 1: Applying a Participatory Sensing Paradigm to National Infrastructure Monitoring

There has been considerable attention paid to the concept of ubiquitous sensing for evaluation of aging infrastructure. As visual inspections are generally executed every 1-2 years, potentially significant damage can be present for sometime before the next inspection cycle. Therefore the first prototype developed in OSD-CI portal seeks to leverage the multi-sensor array with the highest on board computational and decision making power: humans. The prototype, launched late in the summer of 2010, asked *Citizen Engineers*, in this case Notre Dame engineering students and any family and friends they referred to the portal, to collect visual evidence of degrading infrastructure. By mobilizing citizens to collect images of troubled infrastructure in their communities, the capability for identifying potential troubled structures in the period between their regular inspections is greatly enhanced. Further, by these simple engagements of the general public, overall attitudes and awareness surrounding civil infrastructure can be heightened, creating more stewards of our national infrastructure and allies in reversing our infrastructure crisis.

To facilitate this crowdsourced project, the development of a robust and reliable portal was first necessary. The portal includes a welcome page (Fig. 4) with relatively standard features that permit users to create a secure account and manage their profile. The more significant objective was to create a seamless approach to receive geotagged photos acquired in the field. It was important to remove technological barriers from this process to maximize participation by citizens as they are going about their daily routines. As a result, users, after establishing an account tied to a specific email address, were provided with a detailed tutorial that demonstrated how to enable geotagging on their smart phones and a means to directly submit the images from their phones or upload them directly through the web portal (Fig. 5). In the event the participant did not have geotagging capabilities, i.e., phone does not permit geotagging or participant was using a standalone digital camera, users

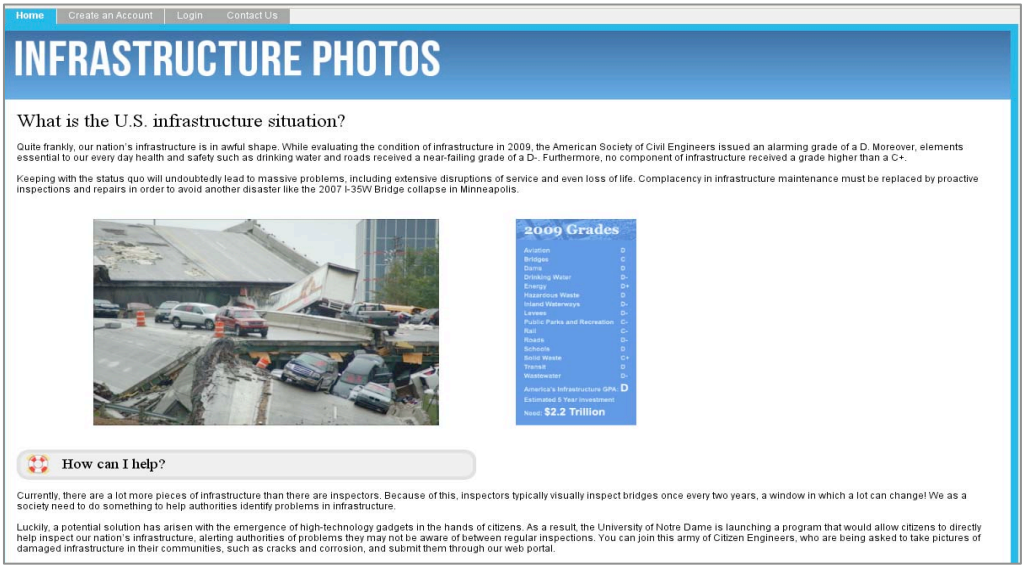


Figure 4. Front page of infrastructure photo portal.

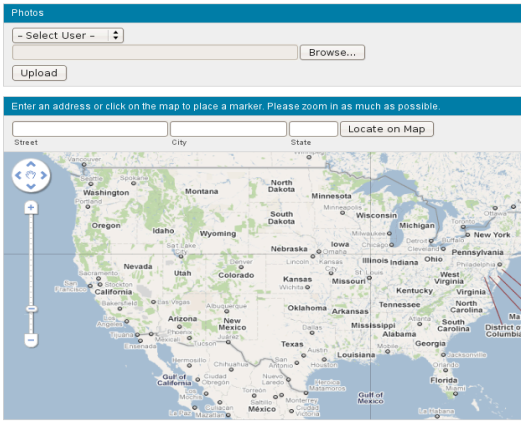


Figure 5. Manual uploading options in infrastructure photo portal.

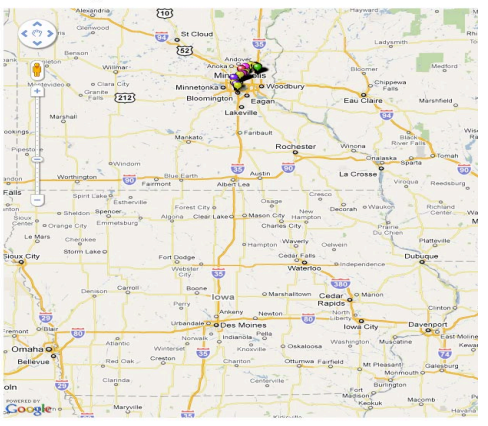


Figure 6. Google maps interface for representation and visualization of submissions.

can either input the street address or use a movable marker to pinpoint the site locations in Google Maps during the image upload process (see Fig. 5). However, the experiment found that the overwhelming majority (99%) of photos submitted were geotagged, proving that this is a seamless way to collect data on distributed infrastructure systems.

At the server side, submissions are tied to a database for indexing. This database allows all submissions to be visually represented using colored balloons/pins as shown in Figure 6, so that the details of any submission of the crowd can be easily viewed by administrators by clicking on any of these balloons/pins. Further, the use of Google Maps creates an easy to navigate interface familiar to most users.

It should be noted that the portal was opened one week before the start of classes in the Fall 2010, leaving a limited time for participation by most students.

Even so, the portal received documentation of a wide range of infrastructure degradation from cracks and holes in pavements to significantly deteriorated bridges and piers. However, only about a third (32%) of *Citizen Engineers* creating accounts actually uploaded one or more images – a common issue in virtual organizations – however the active users submitted on average 21 photos each.

Case Study 2: Applying a Crowdsourcing to Infrastructure Assessment

While the previous case study provides a demonstration of how *Citizen Engineers* can be harnessed to collect data, this data needs to be effectively analyzed to make meaningful decisions. This begs the question of what would be the most effective motivator for *Citizen Engineers* to conduct such analyses, providing their time, knowledge and effort with little or no promise of pay or recognition? The issue of motivation is central to the entire spectrum of crowdsourced activities, but specific to engineering, where the tasks are highly technical and thought intensive, the question is even more relevant. To answer this question, an experiment was developed in the Fall 2010 to evaluate the types of extrinsic motivators that are most effective in enhancing not only the quantity but also the quality of *Citizen Engineer's* contributions. In order to simulate a meaningful and authentic crowdsourced civil engineering task likely to resonate with citizens' volunteer spirit, the case study utilized a database of 400 photos of damaged reinforced concrete and masonry buildings collected by the author during field reconnaissance in Léogâne, Haiti in March 2010, two months after the catastrophic earthquake. The objective of the crowdsourced task was to ask *Citizen Engineers* to identify the type and severity of damage in each photo. Considering the large repositories of photos from reconnaissance following disasters, often not completely categorized or databased by their curators, if the crowd could be leveraged to accurately execute such a task, then an automated repository could be created and easily mobilized for future disasters.

The primary challenge was first to develop a schema that can break the classification of a damaged structure into a series of simple, progressive steps that could easily be replicated by citizens without an engineering background and could be implemented readily in the portal. The final classification schema used in the experiment is shown in Figure 7, customized for the construction style in Haiti. The schema asks which elements are visible, if they are damaged, and if so the type of damage and its severity The first three classifications are largely objective, while the fourth is quite subjective. A detailed web tutorial was created to familiarize the *Citizen Engineers* with the schema. Figure 8a shows a screen shot of part of this tutorial focused on element identification. Later stages of the tutorial introduce various damage patterns and, as shown in Figures 8b-c, allow *Citizen Engineers* to take self-quizzes to gauge their understanding of each step of the schema.

After *Citizen Engineers* create an account, complete a brief entrance questionnaire collecting various demographic and attitudinal data, and conclude the tutorial, they are unknowingly and randomly assigned to one of four groupings depicted in Table 1. An equal distribution of participants (~50) is assigned to each of these groupings, assuming a total of 200 participants. The groupings explore the effect of monetary vs. moral incentives, as well as the impact of information fed back to the participants. Specific to the latter point, all participants receive information on the number of photos they have classified or "tagged" in the database, however, 50%

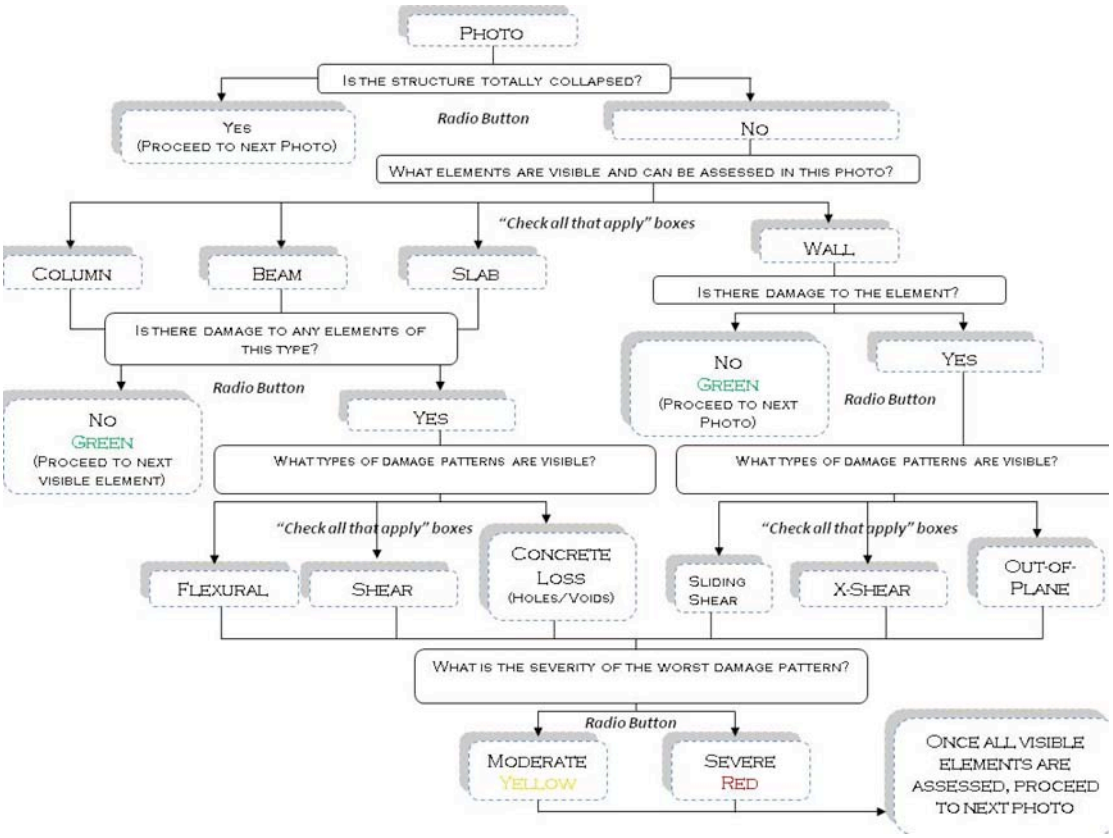


Figure 7. Schema for classifying earthquake damage to reinforced concrete and masonry structures in Haiti.

of the participants will also receive feedback on their ranking (in terms of number of photos classified) relative to others in the portal. This is expressed as a second status bar, shown at the top of each screen shot in Figure 9.

Table 1. Four possible groupings for participants in the Haiti photo classification experiment.

		Incentives	
		Utilitarian	**Moral**
Information	**Individual**	Incentive: cash prize based on performance Information: sees only personal progress	Incentive: watches short movie about earthquake in Haiti and need for help in assessing damage. Information: sees only personal progress
	Collective	Incentive: cash prize based on performance Information: sees progress relative to all other participants.	Incentive: watches short movie about earthquake in Haiti and need for help in assessing damage. Information: sees progress relative to all other participants

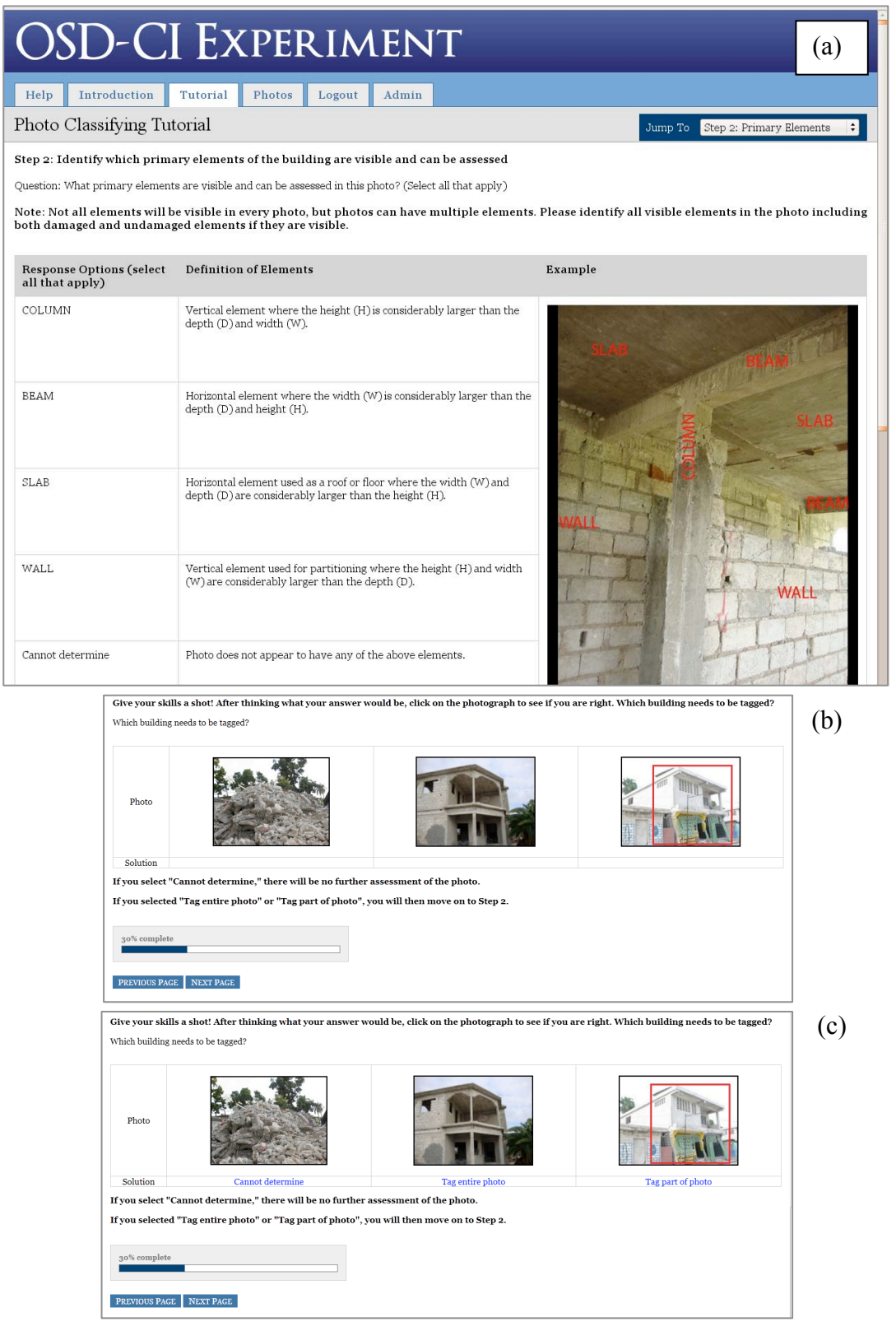


Figure 8. Screenshots of Haiti photo classification tutorial: (a) definition of structural elements, (b) self quiz, (c) self quiz with solution.



Figure 9. Screenshots of Haiti photo classification process: (a) identification of structural elements, (b) determination of damage, (c) classification of damage type. Status bars shown at top of each screen shot indicative of what a *Citizen Engineer* in the collective information grouping would see. Individual information assignees would see the same interface but with only the first status bar.

The classification process uses a set of web pages that adapt to the previous responses at each step of the schema. An example of this sequence of pages is shown in Figure 9. Each participant is asked to classify a minimum of 25 randomly assigned photos of buildings in Haiti; however it is hoped, by virtue of the incentives and information they receive, that they will classify more and possibly all 400 photos within seven days of joining the study. At the close of the seven day period, all participants complete an exit questionnaire to gauge their attitudes and identify any functional issues with the portal or classification schema.

As both quantity and quality of classification is of interest in this application, three expert taggers (structural engineers) have independently classified all 400 photos in the database to create a "key" against which each *Citizen Engineer* can be graded. The analysis of the data collected from the study that evaluates performance of the crowd as a function of their assigned groupings, wide ranging variables associated with their survey responses, as well as their monitored actions within the portal (time spent on each photo, etc.) is beyond the scope of this paper; however, space does permit a brief discussion on the participation within the portal.

The portal was opened in November 2010 to Notre Dame students. In total 242 students created accounts, hailing from the Colleges of Science, Engineering, Business, Architecture, and Arts & Letters. These users executed 9445 photo classifications over a two week period or approximately 30 classifications per user. In fact, a handful of users classified all 400 photos in the database. More importantly, this resulted in an average of 23.6 classifications for each photo in the database. This would allow the "wisdom of the crowd" to be effectively gauged for each photo with sufficient statistical significance. Again not only will this allow various incentives and motivational constructs to be evaluated, but also will determine if the crowd is capable of achieving consensus or if refinements to crowdsourced engineering tasks are required. This could, for example, include grouping *Citizen Engineer*s based on their expertise or past performance within the portal and assigning their work units accordingly.

CONCLUSIONS

This paper introduces the formation of a new virtual organization to enable **Open Sourcing the Design of Civil Infrastructure (OSD-CI)**, allowing all stakeholders – engineers, public officials, researchers, students, and even the public at-large – to engage as *Citizen Engineers* in four dimensions of collaboration: harnessing human effort, tapping collective knowledge, pooling communal software and leveraging distributed computational hardware, to rehabilitate our nation's deteriorating civil infrastructure. It should be noted that this project is particularly challenging as most social computing applications have only been attempted on projects with relatively modest technical demands, while structural design faces significant policy and technical challenges. However, this project demonstrates how the collaboration between civil engineers, computer scientists and social scientists can develop cyberinfrastructure and the appropriate policies and governance to extend one of the most powerful cognitive models – the crowd – to one of the most pressing societal problems – the design and maintenance of civil infrastructure – by leveraging an army of *Citizen Engineers*.

The two case studies presented in this paper demonstrate how cyberinfrastructure can be developed to facilitate a participatory sensing paradigm to monitor civil infrastructure using geotagged photo submissions and how extensions of these portals can be used to harness the wisdom of the crowd to assess and ultimately curate archives of reconnaissance photos of damaged infrastructure. This latter portal, using actual field data from the 2010 Haiti earthquake, has provided the opportunity to further study the incentives (moral vs. monetary) and motivators (feedback regarding *Citizen Engineer*'s status relative to others in the portal) required to maximize both the quantity and quality of voluntary work units within crowdsourced civil engineering projects. The outcomes of this research and the data collected through this latter case study will be critical to determine how best to incorporate distributed *Citizen Engineers* into a faithful design process that ensures extreme trustworthiness in technical tasks, while promoting participation as a first step in realizing the grander vision that is OSD-CI.

ACKNOWLEDGEMENTS

The author wishes to acknowledge the support of the National Science Foundation through Grant CBET-09-41565 as part of the initiative on Cyber-enabled Discovery and Innovation (CDI) and her collaborators on this effort: Professors David Hachen, Ahsan Kareem, Gregory Madey and Douglas Thain, Lead Post-Doctoral Researcher Dr. Zack Kertcher, Graduate Students Zhi Zhai and Jenny Vaydich, and Undergraduate Student Andrew Webber, all of the University of Notre Dame.

REFERENCES

Kareem, A., Kijewski-Correa, T., Tamura., and Madey, G. (2008). "Next frontiers of innovation, discovery and learning in wind engineering: A cyberinfrastructure perspective." *Proceedings of the First AAWE Workshop*, August, CD-ROM.

Johnson, J.P. (2006). "Collaboration, peer review and open source software." *Information Economics and Policy,* 18(4), 477-97.

Lih, A. (2009) *The Wikipedia revolution: How a bunch of nobodies created the world's greatest encyclopedia*, Hyperion, New York.

O'Mahony, S. and Ferraro, F. (2007). "The emergence of governance in an open source community." *Academy of Management Journal*, 50, 1079-106.

Raymond, E.S. (2001). *The cathedral and the bazaar : Musings on Linux and open source by an accidental revolutionary*; O'Reilly; Cambridge, MA.

Surowiecki, J. (2005). *The wisdom of crowds: Why the many are smarter than the few and how collective wisdom shapes business, economies, societies and nations*, Anchor Books, New York.

Kwon, D.K., Kijewski-Correa, T., and Kareem, A. (2008). "E-analysis of high-rise buildings subjected to wind loads." *Journal of Structural Engineering*, ASCE, 134(7),1139-53.

Assessment & Reduction of Transportation Structure Vulnerability Past, Present & Future

Sena Kumarasena[1], PhD, PE and Raymond Daddazio[2], PhD, PE

Abstract: Following the events of 9/11/2001, FHWA together with AASHTO commissioned a Blue Ribbon Panel (BRP) on Bridge & Tunnel Security. It was charged with the task of examining the issues and developing the initial road map for improving the bridge and tunnel security in the United States in the face of this new reality; organized terrorism on American soil. The recommendations of the panel was published in September of 2003, and has been a key reference and a source document for assessing vulnerability and planning of structural hardening of many key bridge and tunnel facilities in the US. Even though a considerable knowledge existed in related areas, especially within the military type organizations, at the time the BRP, bridge and tunnel security was in its infancy. Over the decade since 9/11, much progress has been made in both infusing the considerable knowledge that existed in other areas. These include counter terrorism intelligence, monitoring and enforcement as well as structural hardening and blast resistant design applied to military buildings and other facilities of sensitive nature. In addition to this cross-over of operational and design methodologies, considerable new knowledge and experience in vulnerability assessment and mitigation has been generated specific to bridges and tunnels. One key aspect of this evolution is the crystallization of the idea that any holistic vulnerability assessment and risk mitigation of the transportation infrastructure must consider multi-hazards and just not terrorism.

However, many challenges and considerable difficulties still remain in improving safety and security of many existing bridges and tunnels to a meaningful level. The paper examines the evolution of bridge and tunnel security, the progress to date and also the challenges and opportunities as we as look to the future in developing promising new approaches and initiatives. It can be shown that viable approaches are available to bring bridge and tunnel security to the next level in a cost effective manner in a relatively short time; same way how the earthquake security initiative of the 70's improved the seismic worthiness of bridges and tunnels in America and beyond.

[1] Vice President & Technical Director of Complex Bridges, HDR Engineering, Email: Sena.k@hdrinc.com
[2] President & Chief Executive Officer, Weidlinger Associates Inc, Email: daddazio@wai.com

1. Introduction

The transportation system and its assets are a vital component of the economic and social infrastructure of a nation and probably represent the largest component of its public investment. A catastrophic disruption to it would have immense consequences in terms of direct and indirect economic loss, breach of public safety and mobility of people, goods and services within the affected region. Due to regional and global interdependencies, the effects can reach well as beyond the area of direct impact. Also, they often generate lasting impacts on socio-psychological wellbeing of the public due to feelings of insecurity and vulnerability in the aftermath.

Historically, large scale loss of life from disruptions to the built-environment has been due to natural disasters[3] such as large magnitude seismic events, massive floods, wide-spread fires and severe wind events. Considerable gains have been made in improving the performance of structures against such conventional threats or hazards. A structure properly designed using current design codes and properly constructed do in fact perform satisfactorily against the events that they have been designed against. Nowhere have these gains been more rapid, visible, and fruitful than in the area of seismic risk mitigation as clearly evident by the satisfactory seismic performance of newer facilities properly designed and constructed in the recent past and the damage and loss of life suffered in regions where such enforcement is lacking.

The drive towards prevention of seismic damage as a critical regional issue in California was propelled forward by the San Fernando Valley Earthquake in 1971. Prior to this massive undertaking by CalTrans, seismic risk was deemed more or less something that one has to live with, its mitigation considered too expensive or impractical for wide-spread implementation, and was left largely to the intuition of the individuals designing a particular facility. Within the relatively short span of about four decades, it has matured considerably beyond its initial scope of preventing structural collapse and resulting loss of life and also beyond the initial region of focus in California to become an issue of global awareness. The bar in state-of-the-art seismic risk mitigation is no longer set at just preventing loss of life due to structural collapse of an individual facility; but at life-line engineering on one hand where the goal is to ensure availability of critical routes for emergency operations and ensuring public access to critical facilities, services, and an uninterrupted supply of food & fuel; and at performance based design on the other hand where the goal is to ensure continued “normal” operation of a given facility

[3] Except acts of war

following a major seismic event by ensuring any damage following a seismic event is minimal.

As the state of the art continues to advance in seismic hazard mitigation, the global community is facing yet another threat; equally unnerving if not more in terms of its lack of warning and potential devastation; that of organized terrorism. Terrorism brings considerable engineering challenges in hazard mitigation due to the shear magnitude of the potential blast loads that structures could become subjected to, and the evolving nature of the hazard.

Similar to the case with seismic risk mitigation, the public agencies at the federal, state and local levels and the engineering community is looking to mitigating the thereat of this latest challenge on two fronts – operational improvements designed to deny the opportunity to inflict damage and engineering improvements designed to harden the existing transportation infrastructure initially designed and built with no such considerations. Another key outcome of this recent evolution of ideas is the notion that any holistic risk mitigation of transportation infrastructure must consider multi-hazards, and not just terrorism.

2. Evolution of Blast Resistant Design

The initiating event in the design of non-military structures to explosive loading was the destruction of the United States Embassy in Lebanon in 1983, Figure 1. Prior to this, the design approaches, the data that supported these approaches and the structures were all military in nature. These approaches were codified in publications such as: TM 5-855-1[4] "Design and Analysis of Hardened Structures to Conventional Weapon Effects" and TM 5-1300[5] "Structures to Resist the Effects of Accidental Explosions." Following the 1983 terrorist attack in Lebanon, the US government developed new rules for the blast resistant design of embassies known as the Inman standards[6] calling for changes in design and siting. For new construction, these standards mandated a security setback

[4] Department of Defense, "Design and Analysis of Hardened Structures to Conventional Weapons Effects," Army TM 5-855-1, Air Force AFPAM 32-1147(I), Navy NAVFAC P-1080, DSWA DAHSCWEMAN-97, US Department of Defense, August 1998 now superseded by UFC 3-340-01, 2002.

[5] Department of Defense, "Structures to Resist the Effects of Accidental Explosions," Army TM 5-1300, Navy NAVFAC P-397, Air Force AFR 88-22, US Department of Defense, November 1990 now superseded by UFC 3-340-02, December 2008.

[6] United States Department of State, "Report of the Secretary of State's Advisory Panel on Overseas Security," 1985

of 100 feet from streets, sites of 15 acres or more, locations far from downtown and reduced use of glass. The implementation of these design standards resulted in the construction of imposing walled compounds such as the embassy in Santiago shown in Figure 2.



Figure 1: U.S. Embassy in Lebanon, 1983.



Figure 2: U.S. Embassy in Santiago

Acknowledgements: Figure 1 is from the monograph US Marines in Lebanon 1982-1984, History and Museums Division, U.S.M.C, Washington, D.C 1987. Figure 2 is from U.S. Government Website http://chile.usembassy.gov/history.html. These are public domain information and no specific permission is required for their inclusion in this paper.

Another defining event was the destruction of the Alfred P. Murrah Federal Building in Oklahoma City, Oklahoma in 1995, Figure 3. About 5000 pounds of ammonium nitrate fertilizer, nitro-methane and diesel fuel was detonated in front of the building killing 168 people. This incident remains the deadliest act of domestic terrorism in American history. At this point, the U.S. General Services Administration embarked on a building security technology program to develop the policy and requirements for building security used in the design and construction of GSA buildings. This still evolving effort has conducted explosive tests and developed design tools to assist design professionals.



Figure 3: Alfred P. Murrah Building, April 1995

Acknowledgements: Figure 3 is a public domain photograph available at http://www.photolibrary/photo_details.do?id=1562

Much of this information can be found in the Whole Building Design Guide[7] which is a program of the National Institute of Building Sciences that has been supported by federal agencies, private sector companies, non-profit organizations and educational institutions.

The attack on the World Trade Center in September 2001, Figure 4, refocused our society on the Importance of making buildings safe for the public that inhabits them. It also drew attention to our critical transportation infrastructure and with this attention a whole new set of challenges arose. The primary differences between the protection of buildings and protection of transportation infrastructure such as bridges and tunnels are related to the age of bridges and tunnels coupled with their essential function of moving people and goods. The engineer must work with century old structures where the threat, for example, a vehicle borne bomb, cannot easily be kept away from the structure as its essential function is to transport vehicles. The potential threat of large explosives coupled with small standoff distances, renders much of the military based design guidance inapplicable.



Figure 4: World Trade Center Site

Acknowledgements: Figure 4 is a public domain photograph from http://rst.gsfc.nana.gov/Sect4/Sect4_2.html

A key component to the work that has been done is full scale field testing. These tests go beyond the regimes that are encompassed in the military design manuals as the threats, structures and the fundamental behavior of these structures and components are not the same. Extensive testing has been done on steel and reinforced concrete columns, beams and connections as well as on windows and curtain wall systems. Testing has been done to develop structural designs and detailing that prevent disproportionate collapse as well as retrofit concepts for existing structures. Testing has been done to better understand air blast propagation in an urban environment and when the scaled range of the explosive is small. One lesson is clear, rational design cannot be accomplished through naïve application of the military design standards.

[7] The Whole Building Design Guide, http://www.wbdg.org/

The evolution of the work over the last quarter of a century has resulted in a better understanding of the response of structures and material to extreme loadings. This understanding is based on full scale testing and the enhancement and calibration of computational structural dynamics and computational fluid dynamics software. An experienced structural engineer can use the results of this software to accurately simulate the response of structures and together with the design team and owner communicate choices that effect rational and cost effective design that incorporate resiliency while advancing design excellence, Figure 5, where safety and security can be achieved without compromising the aesthetics and the airily appearance.



Figure 5: New U.S. Embassy in London, © Kieran Timberlake

3. Bridge & Tunnel Security Against Terrorism Following 9/11

The events of 9/11 brought the threat of organized terrorism to the infrastructure as an issue of utmost importance to national security. While terrorism has been a growing issue around the world for several decades, 9/11 dispelled the general perception that it

was largely an issue contained to known troubled spots distributed around the world. It was the watershed moment, much like the San Fernando Valley Earthquake in 1971 that crystallized the nation's determination to do everything possible to protect the public safety, economic wellbeing and the critical infrastructure against the threat of terrorism.

While a considerable prior knowledge existed with respect to blast resistant design applications involving military buildings and other critical facilities as embassies, there are some challenges in applying these directly to the transportation infrastructure, especially to large bridges and tunnels that would constitute the primary targets of terrorist organizations. These differences include:

1. Access: Buildings can be provided with barricades, large stand-off distances and other access restrictions. However, general traffic has to be provided with free access to bridge and tunnel facilities. Further they contain chambers, doorways, platforms designed specifically to make access to the critical structural elements relatively easy.
2. Vintage: Existing transportation infrastructure consists of many large scale facilities designed and built at a time when man-made sabotage was not a major considerations. These facilities contain elements critical to their overall structural integrity within close proximity of the travelled roadway.
3. Criticality: Many of these facilities represent major links in and out of large cities and are critical elements of the transportation system and the economy. Many of the urban transportation networks do not contain either the capacity or the redundancy to handle an event that would put these links out of service.
4. Practicality: Strengthening existing structures against potential threats contain serious practical limitations. The practically implementable hardening on an existing facility is often effective only against the lower end of the spectrum of the possible threats, and many structures contain areas that are very difficult to be hardened.
5. Lead Time: There is a considerable time lag from when a critical facility is considered for risk mitigation to the actual implementation of the hardening measures. There is significant time associated with assessments, prioritization, identification and development of the hardening methodology, and the needed testing and verifications before their implementation.
6. Regeneration Cycle: Building facilities are renewed and/or replaced at a considerably faster rate than bridges and tunnels. Thus the integration of newer design standards within the building industry is easier and has a much shorter implementation cycle than possible with bridges or tunnels.

7. Resource Limitations: The large number of existing bridge and tunnel facilities of critical importance and the limitations of available funding require some prioritization based on a number of parameters, and only some of the facilities identifies as needing the hardening will receive the necessary resources within a given cycle funding.
8. Evolving Nature: Terrorism is an evolving hazard where the future conditions are uncertain and cannot be predict or quantified even on a probabilistic basis. The deterministic design of hardening measures assumes parameters that may not be representative of future threats conditions.

On the other hand, the operational approaches to terrorism risk mitigation are readily transferable to the context of transportation structures. These countermeasures consist of the so called 4D's championed by USACE; Deter-Deny-Detect-Defend by removing the means of inflicting damage by focusing on the human element essential to terrorism. This will be a central strategy to safeguarding the transportation infrastructure as long as terrorism remains a threat; and will be an inseparable part no matter how advanced the state-of-the-art in structural aspects of bridge and tunnel safety and security would become. These two compliments one another where advances in engineering in making facilities more robust would lead to more effective operational approaches by allowing a sharper focus on a narrower band of potential threats.

Responding to the new challenge, FHWA together with AASHTO appointed a Blue Ribbon Panel (BRP) on Bridge and Tunnel Security. It was commissioned to identify issues in Bridge & Tunnel Security and to formulate a roadmap for moving forward, The final BRP report was published in 2003 and this is one of the most significant formal documentation of the issues with recommendations on both short term and long term courses of action. The report includes a standardized methodology for prioritization and risk assessment of the existing facilities, provides some commonsense design measures based on available knowledge. The report also provides a listing of common vulnerabilities within the existing assets, some quantification of threat levels and recommendations for future research and development.

The risk assessment procedure outlined in the BRP (2003) is applicable to a transportation network as a whole (to identify and prioritize at the facility level) or to a given facility (to identify and prioritize at the element level). Since its original publication, this basic procedure has been adopted and refined by various owner organizations to suit the particular conditions. BRP condenses down some of the essential elements to a few tables and criteria (Tables 1, 2 and 3 reproduced below):

Table 1. Bridge and Tunnel Security Issues

Key Topics in Infrastructure Security	Specific Issues
1. Foundations for Policy	• Criteria Establishing Investment Priorities • Institutional Continuity
2. Planning, Design, and Engineering	• Design Review for Secure Structures • Research and Development (R&D) Needed to Support "Design for Security" • Design Criteria • Design Specifications
3. Management and Operational Practices	• Best Practices • Practice Review • Institutional Relationships • Preparedness • Personnel and Vehicle Security • Communication/Outreach
4. Information Security	• Procurement Practices • Information Security
5. Mobilization ("Notice") and Response ("Trans-event")	• Threat Warning • Early Response • Initial Response
6. Recovery (Post-event)	• Damage Assessment • Functional Continuity

Table 2. Critical Bridge Components

Suspension and Cable-Stayed Bridges	Truss Bridges	Arch Bridges
• Suspender ropes, stay cables • Tower leg • Main cable • Orthotropic steel deck • Reinforced and prestressed bridge decks • Cable saddle • Approach structures • Connections • Anchorage • Piers	• Suspended span hangers • Continuous and cantilever hold-down anchorages • Compression chords or diagonals • Connections • Decks • Piers	• Tension-tie • Connections • Decks • Piers **Multi-girder/Freeway Overpass Bridges** • Decks • Connections • Piers

The vulnerability mitigation is divided in to two basic parts:

A. Mitigating Threats:

- Establishing a secure perimeter using physical barriers – Deny (Access)
- Surveillance, CCTV, monitoring and enforcement – Detect (Presence)
- Visible presence of security and surveillance – Deter (Perpetrators)
- Minimize time on target – Defend (Removal of threat)

B. Mitigating Consequences:

- Provide stand-off distances from critical elements –
- Increase design redundancy –
- Structural hardening / strengthening of vulnerable key elements –
- Develop a rapid response and recovery plan –

Table 3. Magnitude of Threats

Threat Type	Largest Possible	Highest Probability
Conventional explosives	Truck*: 20,000 lbs Barge: 40,000 lbs	Car bomb*: 500 lbs
Collision to structure (i.e., the size of a vehicle that could collide with a structure)	Truck: 100,000 lbs GVW Water Vessel: depends on waterway	Truck: H-15 Water Vessel: (see AASHTO spec. LRFD on vessel impact)
Fire	Largest existing fuel or propane tank Largest fuel vessel or tanker	Gasoline truck (3S-2) Fuel barge
Chemical/biological HAZMAT	These threats exist; however, the panel is not qualified to quantify them. Therefore, other experts should assess these threats in this way.	

* Largest possible conventional explosive – for a truck, based on largest truck bomb ever detonated internationally by a terrorist act. For a barge, based on the assumption that it is the largest explosive that could pass by unnoticed by current security at place at major waterways.

** The size of an explosive charge that can be concealed within the trunk of an automobile without being visually detected when inspecting the automobile.

As noted before these two complement one another and form essential components of implementing an effective security plan against terrorism. Under the leadership at the federal, state and other local agencies, considerable gains have been and are being made in implementing the identified strategies; using the protocols and the general approach outlined in BRP. Many structures have been hardened by implementation of a range of measures that protect the most vulnerable elements.

Further, some early steps have been taken in making improvements to new structures starting from the planning process. This is very critical due to following reasons; The logistical complexity, practicality and the cost involved in Mitigating Threats (Part A above) would be somewhat similar whether the facility is existing or new. So addition of these as an afterthought, while not preferable, is possible. However, there are considerable differences in the logistical complexity, practicality and the cost of Mitigating Consequences (Part B above) depending on whether the facility is an existing one or one being planned. This is due to the following:

- Many existing facilities designed and built without security as a consideration contain critical structural elements placed immediately adjacent to the roadway. Providing stand-off distances after the fact would mean restricting the travelled roadway, which often is not often possible.
- Increasing design redundancy with respect to many of the key vulnerabilities listed in BRP Table 2 on an existing bridge is typically neither practical nor economically viable[8].
- The structural hardening, especially in the light of the above, is very expensive and even then can typically be accomplished for relatively low magnitude threats noted as Highest Probability Threats in Table 3 of BRP.

Thus, examining options for enhancing safety and security must be started right from the planning and the conceptual stages as changes aimed at mitigating consequences are difficult to be implemented as a later addition.

4. Capturing The Full Potential in Bridge & Tunnel Security

Many of the recommendations of the BRP are being implemented to mitigate the risk of terrorism to select facilities from the nations' most vulnerable transportation structures. However, more work remains to be done if the maximum long-term benefits were to be gained in the most cost effective manner. As noted before, in combination with other measures, structural hardening of existing facilities (within the constraints of practical viability) remains the best option available in safeguarding public safety and public investment. However, some difficulties remain:

- Structural hardening to mitigate system vulnerabilities (Table 2) in existing structures against even the probable threat levels sometimes prove difficult
- Structural hardening for largest possible threat levels (Table 3) for many existing facilities remains elusive and a practical impossibility.
- Structural improvements may be more practical during major rehabilitations of existing structures but this require planning on a case-by-case basis, there is potential for developing a formal approach to make this happen.

[8] While there are some parallels in seismic hazard mitigation (of the past) and the process of improving bridge and tunnel safety and security, there are also some key differences. The modifications to existing bridges and tunnels needed for seismic upgrading are typically localized to bearings, and key members in the vicinity of supports. The scope of structural changes are much broader in improving safety & security

- As seen by such recent examples as I-35 collapse and the I-90 tunnel ceiling collapse, effective bridge and tunnel safety and security must go beyond terrorism and consider resiliency to a multitude of hazards in the formation of structural solutions (multi-hazard resiliency)

As we move forward, innovation towards creating economical, elegant transportation structures with considerably higher safety and security standards must remain our goal. This however requires and making some fundamental improvements to the design process to enable the newly constructed structures meet not only the challenges of today, but also some allowance for the unknowns tomorrow could bring.

While many aspects of the BRP report has come to fruition with the leadership of public agencies at all levels, one area with significant potential not yet fully explored remain the development of more resilient structures through innovations in design approaches, analysis capabilities and materials application. This area remains one of considerable potential. In general, the current state-of-the-art in bridge and tunnel security is perhaps comparable to early to mid stages of the seismic risk mitigation initiative. It has been demonstrated that there is considerable room for further innovation quite within reach to provide considerably safer, yet economical and elegant structures designed with multi-hazard resiliency as a central functional requirement (Kumarasena, 2008).

References

FHWA/AASHTO Blue Ribbon Panel on Bridge and Tunnel Security (BRP), 2003, Recommendations for Bridge and Tunnel Safety

Kumarasena, 2008, Design of Resilient Bridges, White Paper Provided to FHWA and DHS, for internal circulation, with ownership of the document retained by the primary author of this paper.

Acknowledgements

The authors wish to acknowledge following sources for some of the information contained in this paper. Figures 1 to 4 are in the public domain and the exact references are given following the photograph. Figure 5 attribution is stated in the caption. The document referenced in footnote 4 is not a classified document and the existence and the title can be confirmed at http://www.wbdg.org/ccb/DOD/UFC/ufc_3_340_01.pdf

Unresolved US Code Compliance Issues for Wind Energy Structures: The Need for Research

Nestor A. Agbayani[1], Rolando E. Vega[2], and James Newell[3]

[1] P.E., S.E., SECB, M.ASCE, Partner; MSKA Structural and Civil Engineers, 1716 Oak Street, Suite 21, Bakersfield, CA 93301-3040; email: nagbayani@sbcglobal.net

[2] Ph.D., P.E., M.ASCE, Technical Manager; ABS Consulting, Global Renewable Energy Division, 16855 Northchase Drive, Houston, TX 77060; email: RoVega@absconsulting.com

[3] Ph.D., P.E., Design Engineer; Degenkolb Engineers, 707 SW Washington Street, #600, Portland, OR 97205; email: jnewell@degenkolb.com

ABSTRACT

It has been roughly three decades of utility-scale wind farm development in the US without much clear guidance for the design and permitting of these structures. However, since late 2009 an effort has been underway to develop a US Recommended Practice for the design and permitting of wind energy structures. This task has been undertaken by a joint committee of the American Wind Energy Association (AWEA) and the American Society of Civil Engineers (ASCE).

While the stated goal of a practical design guideline for Code compliance is straightforward, technical challenges and unresolved issues have been encountered during the Recommended Practice's development process. This paper describes several of those technical issues including the following:

- Reconciling the regulatory requirements of American Code versus those of International and European wind industry commercial certification.
- Reconciling the fatigue provisions of Eurocode and AISC.
- Reconciling extreme wind speed profiles of ASCE and International Wind Turbine Standards
- Establishing Code-compliant seismic design parameters and procedures for the combination of earthquake plus turbine operational loads.
- Handling specialized design procedures used in the wind industry that are based on foreign reference documents that have not been translated into the English language.

This paper discusses possible solutions and the ongoing efforts to resolve these technical issues. The paper also makes suggestions for needed research and calls for dedicated U.S. national leadership focused in shaping an industry that is known for producing safe and reliable structures that produce alternative and cost-effective energy.

INTRODUCTION

Codes and standards. In the US, there are currently no dedicated design standards or guidelines for wind farm towers, even after more than thirty years of utility-scale development of domestic wind farms. Development of recommended practices for wind turbine support structures is currently under way by committees supported by industry groups such as the American Wind Energy Association (AWEA) and the American Society of Civil Engineers (ASCE). The draft document is titled *Recommended Practices for Compliance of Large Wind Turbine Support Structures* (AWEA/ASCE, 2010). The document is being developed by the Structures Project Team under AWEA's Large Wind Turbine Compliance Guideline Committee in conjunction with the Wind Energy Structures (WES) subcommittee under ASCE's Structural Wind Engineering Committee (SWEC). This paper discusses some of the technical challenges specifically related to tower design and permitting faced by the Tower Subgroup (hereunder "the committee") within the Structures Project Team.

A recognized document of design recommendations would result in some obvious benefits to the structural engineering design and permitting process by establishing the following (Agbayani, 2010):

- A minimum baseline for tower designs and a more uniform level of design safety and quality.
- A consistent and "level playing field" for engineers engaged in tower design by helping to define the extent of required work.
- A consistent criteria for tower design plan review among US building department jurisdictions, resulting in more uniform and streamlined structural permitting.
- A common frame for engineers to communicate terminology and conventions.

Wind Tower Structural Systems. A typical wind turbine generator system (WTGS) configuration consists of a three-blade horizontal-axis wind turbine mounted on top of a steel tower. Figure 1 shows typical lattice and tubular tower structures. The lattice towers were used predominantly in the early days (early 1980's) of the US wind industry. However, in the last decade, the utility-scale wind industry has transitioned to almost exclusive use of tubular towers that routinely reach heights of 80 m (Agbayani, 2009). The tubular tower is a thin-shell steel structure. It is a fabricated tube consisting of slightly tapered truncated cone segments called "cans." Can segments are welded together to form the longer tubular sections of the tower mast. Cans are formed from sheets of flat steel plate. Since the fabricated tube tower is the current staple of the utility-scale wind industry, the initial draft of the tower design recommendations addresses only tubular towers and no other structure type.

European Certification. The commercial wind turbine industry evolved in Europe, and European wind turbine manufacturers continue to dominate the global market. Even the newer generation of Asian turbine manufacturers complies with existing European standards. For this reason, European wind industry standards, such as the

IEC and Eurocode (or EN) standards, are the basis for most wind tower designs. Wind turbines and towers are certified (i.e., validated and plan checked) by a handful of certification agencies, such as Germanischer Lloyd (GL), Det Norsk Veritas (DNV) and the American Bureau of Shipping (ABS). Certification is achieved by demonstrating design compliance with International Electrotechnical Commission (IEC) standards such as IEC 61400-1 (IEC, 2003), agency-specific standards, e.g., *GL Rules* (GL, 2003), or a combination of both. Certification agency rules in turn reference Eurocode design standards such as EN 1993-1-6 (EC3-6, 2007) for thin shell steel strength design and EN 1993-1-9 for fatigue design. Achieving certification is the industry standard for establishing the commercial legitimacy of a turbine-tower system in a way that is analogous to a UL listing for an electronic device or to an ICC Evaluation Service test report for a structural product. The absence of such documentation would make a product appear suspect and less marketable compared to its certified competitors. Moreover, certification is often a condition of financing for utility-scale wind farm projects (Agbayani, 2008).



Figure 1. Typical lattice towers (left) and tubular towers (right). (Photographs courtesy of MSKA.) (Agbayani, 2009)

TECHNICAL CHALLENGES AND UNRESOLVED ISSUES

Several technical issues have been encountered during the development of the tower structural design best practices recommendations. While some issues have been resolved, others remain unresolved, and further research may be necessary in some cases. These issues are discussed in the following sections.

Reconciling Regulatory Code Requirements and Commercial Certification. The design basis for most utility-scale wind farm towers are the design criteria (typically based on the Eurocodes and IEC standards) provided in certification agency rules. However, regulatory requirements for structural permitting center around building code compliance, specifically with the International Building Code (IBC, 2006) and ASCE 7 (ASCE, 2005) in most of the US.

Key to reconciling the commercial and regulatory requirements is the recognition that the certification agency rules and IEC standards are very specialized for the design of wind farm towers. The building code, on the other hand, is not specialized for wind farm towers. That said, the committee at this point in time is recommending the following best practices:

1. **Design basis.** For the purpose of complete structural design, certification agency rules may serve as the most thorough design basis for the design of wind farm towers at the present time. The building code by itself is a "blunt instrument" that, although well-developed for conventional building structure design, lacks the precision and detail to be a wind turbine tower design basis.
2. **Design capacity (resistance).** For the purpose of plan review for code compliance, the most straightforward strategy may be to use the capacity equations found in US steel stack standards such as ASME STS-1 *Steel Stacks* (ASME, 2006) and the Troitsky textbook on steel stack design (Troitsky, 1990), recognizing that the thin-shell steel stack is the closest structural "cousin" to the fabricated-tube tower. This standard and reference have been used successfully for wind tower design for many years. Also, direct comparison to European tower design calculations indicates reasonable agreement in calculated design capacity. For these reasons, the current draft of the committee's design recommendations contains design strength equations derived from these sources. An excerpt of the local buckling strength equations is shown in Figure 2. Use of the American Institute of Steel Construction (AISC) specifications (AISC, 2005) would have provided a familiar design reference for the comfort of most plan reviewers, but unfortunately, the AISC provisions limit the applicability of its equations only to manufactured tubing (e.g., HSS and pipe sections), and no guidance is given in the high slenderness range encountered in thin shells.

$F_n = F_{cr}$
$\phi_c = 0.90$
Slenderness parameters:

$\lambda = D/t$ where D is the outside diameter of the tower shell and t is the shell thickness.
$\lambda_1 = 0.11E/F_y$
$\lambda_2 = 0.357E/F_y$
λ_{MAX} = No maximum value is specified, but it is rare in most practical tube towers to find slenderness values in excess of 330.
For $\lambda \leq \lambda_1$
F_{cr} should be the smaller of the following:
$F_{cr} = F_y$
F_{cr} due to flexural buckling calculated in accordance with "stepped column" procedures.
For $\lambda_1 < \lambda_p \leq \lambda_2$
$F_{cr} = QF_y$
where $Q = 0.038E/[F_y (D/t)] + 2/3$
For $\lambda_2 > \lambda <= \lambda_{MAX}$
$F_{cr} = 8000/(D/t)$

Figure 2. Excerpt from (AWEA/ASCE, 2010) showing local buckling strength equations.

3. **Design loading.** For the purpose of plan review for code compliance, the most straightforward strategies may be the following:
    a. Fatigue. See the section below titled "Reconciling the Fatigue Provisions of Eurocode and AISC."
    b. Extreme wind. See the section below titled "Reconciling the Wind Provisions of Code versus Wind Industry Standards."
    c. Earthquake. See the discussion below titled "Seismic Design Criteria."

Reconciling the Fatigue Provisions of Eurocode and AISC. Fatigue calculations may govern structural design, so they should be part of the plan review submittal. Typical wind industry design practice for fatigue is to use EN 1993-1-9 modified with safety factors from IEC 61400-1. The most direct reference standard for fatigue design would be the AISC (or AWS) fatigue provisions. Direct comparison of the most commonly used fatigue detail categories and fatigue S-N curves indicates that the European approach to fatigue design is more conservative than that of the AISC fatigue provisions. A comparison of S-N curves from Eurocode and AISC is shown in Figure 3 for normal stress in a typical girth weld of a tubular tower. Effort is ongoing to determine the reason for the differences.

In the meantime, the committee's current recommendation is simply that the tower fatigue design should be compatible with the turbine's commercial certification. Since the AISC provisions have the authority of a code reference standard, baseline Code compliance of the more conservative EN provisions would be easy to show. However, for use as a design basis, the committee cautions against using less conservative fatigue design provisions to effectively undercut the design safety of the commercial certification.

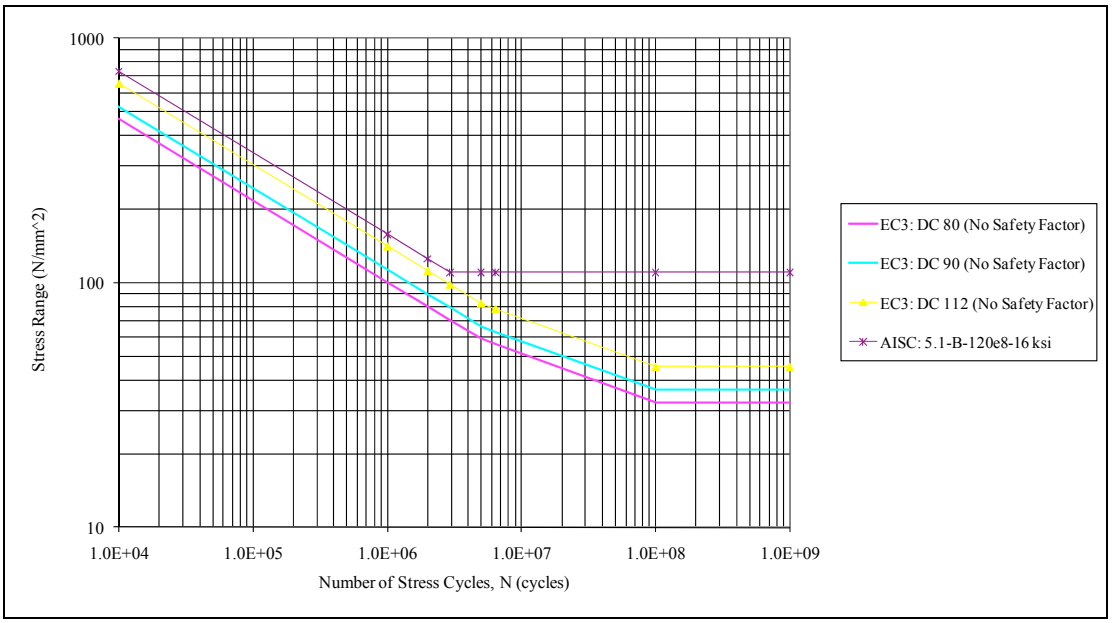


Figure 3. Comparison of Eurocode and AISC S-N curves for CJP girth welds.

Reconciling the Wind Provisions of Code versus Wind Industry Standards. In order to show code compliance for plan review purposes, the task would be to show that the IEC Site Class rating meets the Code wind requirements. However, some key differences should be observed. The tower wind design loads are based on IEC 61400-1 (IEC, 2003), and the IEC loads are obtained from a complex time series software simulation with a turbulent wind model by the turbine manufacturer's load department. It is reasonable to assume that most building departments do not have this software/analytical capability. Also, much of the turbine modeling information is proprietary and therefore not amenable to plan review scrutiny. The more straightforward and feasible strategy is to show that the IEC wind loads envelope the Code wind loading requirements.

The ASCE 7-05 design wind closely matches the definition of IEC design load case (DLC) 6.1:

- The IEC wind load factor of 1.35 is approximately similar to the ASCE wind load factor of 1.6 multiplied by a K_d (directionality factor) value of 0.95.
- Standard air density values of 1.225 kg/m^3 are equal.
- Both specify a reference wind speed defined as a 3-second, 50-year wind. Reference heights are different (10 m and hub height for ASCE 7 and IEC, respectively) but can be reconciled. The IEC velocity profile power law exponent is 0.11. At Exposure C, the exponent based on the square root of K_z is 0.105, which is approximately equal to 0.11.
- IEC application of load is within 15 degrees of the front of rotor, which is consistent with ASCE 7's projected area (0 degrees) application.

For these reasons, the committee has recommended that the IEC DLC 6.1 can be offered to the plan reviewer as the "Code compliance" wind load case on the basis of the matching wind definition. Moreover, it should be observed that other DLCs can sometimes provide larger magnitude design loads than DLC 6.1. Such cases illustrate the shortcoming of the Code wind provisions to completely assess the governing load case for wind tower design.

Seismic Design Criteria. Numerous utility-scale wind farms in the US are sited in seismically active regions. Wind farm sites by their very nature are located in regions of sustained moderate to high wind speeds and therefore the likelihood of an earthquake occurring simultaneously with typically expected wind conditions needs to be considered in design. However, ASCE 7 (ASCE, 2005) design load combinations do not consider a case with simultaneous wind and earthquake loading. For buildings the probability of a design level wind and seismic event occurring simultaneously is sufficiently low that the committee responsible for ASCE 7 felt a combined wind and earthquake load case is not required. The same cannot be said for wind energy structures and the committee has proposed best practices combined wind and seismic load combinations.

Seismic Ground Motion Values. Seismic ground motion values for tower and foundation design should be determined using the ASCE 7 procedure, except that spectral response acceleration parameters should be adjusted to 1% damped values per IEC 61400-1 Annex C instead of 5% damping as typically assumed in building design. A multiplicative adjustment factor equal to 1.4 should be used to adjust spectral response acceleration, S_a, from 5% to 1% damped values. Future research and instrumentation of WES may justify use of larger damping values.

Performance Objective. Wind farms are not capable of providing continuous electrical power due to the varying nature of wind and therefore the committee felt that they do not qualify as an Occupancy Category III structure per ASCE 7. An importance factor equal to 1.0 (Occupancy Category II) is typically used for tower and foundation design unless a higher importance factor is required due to the occupancy category of an adjacent structure.

Building code seismic design requirements do not ensure that structures will remain operational after a design level earthquake. Similarly, a wind turbine support structure designed using *Recommended Practices for Compliance of Large Wind Turbine Support Structures* may be damaged during an earthquake beyond a level that is economically repairable or the turbine components may be damaged by the earthquake induced shaking. However, wind energy is becoming an increasingly important contributor to total electricity production. Therefore, the operability of a wind farm after a seismic event may be important to recovery of the affected region.

Enhanced performance objectives, such as operational performance after a design level earthquake, may be established to meet specific owner requirements. However, a clear distinction should be made between the required minimum performance objective of the *local building code* (life-safety) versus that of any supplementary, project-specific contractual agreements. A performance factor (similar to an importance factor of 1.5 for essential facilities) may be established to improve expected earthquake response. A major consideration in establishing this performance factor is coordinating with the wind turbine manufacture to establish acceleration thresholds for turbine components that will ensure operational performance (e.g. operational performance if nacelle acceleration during an earthquake is limited to 2.0g). Using advanced analysis techniques and the established nacelle acceleration limits the Engineers can evaluate support structure options that will achieve these improved performance goals.

Seismic Load Combinations. By the very nature of their function wind turbines have a reasonable likelihood of being in an operational state during an earthquake and may also be subjected to simultaneous earthquake and emergency stop loads if a shutdown is triggered by the earthquake. ASCE 7 seismic load combinations do not include consideration of concurrent earthquake and turbine operational loads. It is of critical importance to recognize that seismic plus operational loads may in some cases govern tower and foundation design. Therefore, the committee recommends the evaluation of seismic plus operational load combinations, regardless of the absence of a codified

requirement. Figure 4 shows recommended best practices load combinations including seismic plus operational loads that should be considered in addition to ASCE 7 prescribed load combinations. Note that for these recommended load combinations the minimum specified value of the seismic response coefficient, C_s, per ASCE 7 Equations. 15.4-1 and 15.4-2 should not apply. These load combinations are based on recommendations of IEC 61400-1 Annex C and Eurocode 8 standards that do not contain a similar minimum value for the seismic response coefficient. Operational and earthquake loads should be combined as an absolute sum. Alternatively, other methods may be used to combine operational and earthquake loads provided that they are justified by rational engineering analysis.

Seismic Load Combination:

$$U = (1.2 + 0.2S_{DS})D + \rho Q_E + 1.0M$$

$$U = (0.9 - 0.2S_{DS})D + \rho Q_E + 1.0M$$

where,

M = operational loading equal to the greater of: 1) loads during normal power production at the rated wind speed; or 2) characteristic loads calculated for an emergency stop at rated wind speed.

ρ = 1.0, redundancy factor (for nonbuilding structures not similar to buildings ρ = 1.0 per ASCE 7 Chapter 12.3.4.1).

All other variables are as defined in ASCE 7 Sections 2, 11, 12, and 15.

Figure 4. Excerpt from (AWEA/ASCE, 2010) showing seismic load combination equations.

Analysis Procedures. Any analysis procedure (equivalent lateral force, modal response spectrum analysis, or response history analysis) permitted by the local building code is acceptable for use with the *Recommended Practice*.

If the equivalent lateral force procedure is used, the vertical distribution of seismic forces should be calculated based on the procedure given in ASCE 7 Chapter 12.8.3 with the following recommended modification. The effective seismic weight of the nacelle and rotor should be assumed to be located at the turbine's center of gravity, and the effective seismic weight of the tower structure (including ladders, platforms, railings, etc.) should be distributed to nodes located at tower can joints. Seismic forces should also be assumed to act at these locations.

ASCE 7 Table 15.4-2 presents response modification factors, R, for various nonbuilding structures not similar to buildings, but does not explicitly include wind turbine support structures. For evaluation of structures sensitive to buckling failure (typically one of the primary failure modes for tube towers) ASCE 7 Chapter

15.7.10.5 implies a value of R equal to 1.0. The committee recommended use of R equal to 1.0 unless a larger value is justified by rational engineering analysis that is reviewed and accepted by the Engineer of Record.

In practice, often only the peak seismic loads and peak operational loads are available. As a result, the combination of operational and seismic loads with an absolute sum procedure may be an overly conservative approach, especially considering that the respective peak loads do not occur at the same instant of time and in the same loading direction. Seismic response history analysis considering time varying earthquake ground acceleration and operational or emergency stop loads can be used to more accurately predict response and reduce potential design conservatism. Seismic response history analysis procedures should conform with the requirements of ASCE 7 Chapter 16. The committee recommends that any such analysis be conducted with analysis software capable of simulating both structural response and global turbine dynamics, including aerodynamic interaction. Future research is recommended to establish probability-based load factors for the wind plus seismic load combination, using techniques similar to those used in development of the ASCE 7 load combinations.

Specialized Design Procedures. There are several design procedures for the tower and tower components that are routinely implemented in design according to certification agency rules. Unfortunately, these design procedures have no available parallel in US reference standards. Examples of specialized design procedures include the following:

1. Special finite element analysis (FEA)
    a. Top flange eccentricity analysis. The top flange of the tower may be eccentrically loaded by the yaw bearing of the wind turbine. Involvement of the yaw bearing requires a complex nonlinear FEA of a mechanical engineering nature, not often encountered in civil engineering analysis: non-standard or exotic materials; ball bearing; nonlinear gap and contact elements; and pretensioned bolted connection. The committee approached this issue by describing this analysis and providing references to several European papers on the topic. Owing to complexity, there was no attempt to provide a design basis at this time.
    b. Hotspot analysis at shell penetrations. No US reference standards found in the Code give any guidance on this topic. For this reason, the committee felt it most effective at this time to provide reference to the International Institute of Welding (IIW) standards (IIW, 2003) that provide a thorough description of the hotspot analysis method using FEA techniques.
    c. Nonlinear buckling and pushover analysis. No US reference standards found in the Code give any guidance on this topic specifically applied to wind farm towers. For this reason and the complexity of the FEA, the committee felt it most effective at this time to provide a reference to the GMNIA analysis method (i.e., geometric and material nonlinear analysis with imperfections) as found in EN 1993-1-6 (EC3-6, 2007).

2. Bolted splice flange design. No US reference standards found in the Code give any guidance on this topic. FEA is an acceptable method for flange analysis, but unnecessarily difficult in light of simpler manual design methods available in European references. For this reason, the committee felt it most effective at this time to provide references to European papers on this topic. Since some of the reference papers are not in English language, future efforts by the committee may be a comprehensive English-language technical review of the various flange design methods.

CONCLUSION

There are no dedicated design standards or guidelines for wind farm towers in the US. This paper presented technical challenges encountered by the committee in developing best practices recommendations for wind tower structural design. Solutions to code compliance issues and also recommendations for further research and study have been discussed.

REFERENCES

Agbayani, N., and Kyatham, V., (2008), "Megacycle Fatigue Analysis Demystified: Examples from Wind Farm Tower Design," *Proceedings of the 2008 Structural Engineers Association of California (SEAOC) Convention*, SEAOC, Sacramento, California, 303-320.

Agbayani, N., (2009), "Defects, Damage, and Repairs Subject to High-cycle Fatigue: Examples from Wind Farm Tower Design," *Proceedings of the Fifth Congress on Forensic Engineering*, 2009, American Society of Civil Engineers (ASCE), Reston, Virginia, 546-555.

Agbayani, N., (2010), "The Lack of US Structural Design Guidelines for Wind Farm Towers: Basic Code Compliance Issues at the High-Tech Frontier," *Proceedings of the 2010 Structures Congress*, 2010, American Society of Civil Engineers (ASCE), Reston, Virginia.

AISC (2005), *Steel Construction Manual*, *13th Edition*, American Institute of Steel Construction (AISC), 2005, Chicago, Illinois.

ASCE (2005), ASCE/SEI 7-05 *Minimum Design Loads for Buildings and Other Structures*, 2005, American Society of Civil Engineers (ASCE), 1801 Alexander Bell Drive, Reston, Virginia.

ASME (2006), ASME STS-1-2006 *Steel Stacks*, 2006, American Society of Mechanical Engineers (ASME), Three Park Avenue, New York, New York.

AWEA/ASCE (2010), Unpublished Committee Draft (CD) (85% Draft) of *Recommended Practices for Compliance of Large Wind Turbine Support Structures*,

2010, American Wind Energy Association (AWEA), 1501 M Street NW, Suite 1000, Washington DC 20005.

EC3-6 (2007), European Standard EN 1993-1-6:2007, *Eurocode 3: Design of Steel Structures – Part 1-6: Strength and Stability of Shell Structures*, 2007, European Committee for Standardization (CEN), Brussels, Belgium.

EC3-9 (2002), Prestandard prEN 1993-1-9:2002, *Eurocode 3: Design of Steel Structures – Part 1.9: Fatigue Strength of Steel Structures*, 2002, European Committee for Standardization (CEN), Brussels, Belgium.

IBC (2006), *2006 International Building Code*, 2006, International Code Council (ICC), Country Club Hills, Illinois.

IEC (2003), International Standard IEC 61400-1, *Wind Turbine Generator Systems– Part 1: Safety Requirements*, Third Edition, 2003, International Electrotechnical Commission (IEC), Geneva, Switzerland.

IIW (2003), Document XIII-1965-03/XV-1127-03, *Recommendations for Fatigue Design of Welded Joints and Components*, 2003 (Updated 2004), International Institute of Welding (German Delegation), Paris, France.

GL (2003), *Germanischer Lloyd Rules and Guidelines, IV–Industrial Services, Part 1–Wind Energy, Guidelines for the Certification of Wind Turbines*, 2003, Germanischer Lloyd WindEnergie GmbH, Hamburg, Germany.

Troitsky, M. S. (1990), *Tubular Steel Structures—Theory and Design*, Second Edition, 1990, James F. Lincoln Arc Welding Foundation, Cleveland, Ohio, 2-3.

Analysis of Nonbuilding Structures Connected by Large Diameter Pipe while Subjected to Seismic Loads

Eric Wey[1], Dawar Naqvi[2], David Glasscock[3], and Ankur Sepaha[4]

[1]Fluor Corp, One Fluor Daniel Drive, Sugar Land, TX 77478; PH (281) 263-4060; email: Eric.Wey@Fluor.com
[2]Fluor Corp, One Fluor Daniel Drive, Sugar Land, TX 77478; PH (281) 263-1913; email: Dawar.Naqvi@Fluor.com
[3]Fluor Corp, One Fluor Daniel Drive, Sugar Land, TX 77478; PH (281) 263-2261; email: David.Glasscock@Fluor.com
[4]Fluor Corp, One Fluor Daniel Drive, Sugar Land, TX 77478; PH (281) 263-6406; email: Ankur.Sepaha@Fluor.com

ABSTRACT

It is not unusual in petrochemical plants for two adjacent nonbuilding structures to be connected together by large diameter pipe. Common examples of these nonbuilding structures include pipe racks, equipment modules, and heat exchanger structures. Typically, these structures are modeled separately from each other without considering the effects due to large diameter pipe connected to adjacent structures. The pipe is typically modeled and analyzed independent of the nonbuilding structures by considering the equipment as anchor points and the supporting structures as supports, guides or anchor points. This method of modeling nonbuilding structures connected by large diameter pipe is acceptable for static loads; however, the results can become very misleading when applied to earthquake loads. It is even more difficult to rationally apply the effects seismic displacements to these independent models. In this paper three methods of seismic analysis and corresponding results are presented using a simplified 2-D example of two nonbuilding structures connected by a large diameter pipe. The first method uses the traditional method of analyzing the two structures independently and accounting for loads due to seismic displacements from an independent pipe model. The second method utilizes a combined model which includes two nonbuilding structures connected by a large diameter pipe. The seismic load is applied statically to the structures. The third method utilizes the same combined model as the second method with analysis done using Response Spectra Analysis. The results of each method are graphically compared. The paper also includes the results and conclusions drawn from the methods which were investigated.

INTRODUCTION

Petrochemical nonbuilding structures, such as pipe racks, equipment structures, and equipment modules, are typically analyzed and designed using an independent model for each nonbuilding structure and piping system. These models do not consider the size and quantity of pipe interconnecting the adjacent nonbuilding structures. There are many advantages to using these independent models to analyze a nonbuilding structure. The independent model allows the engineer to focus on the

loads that are tributary to that structure alone. The analysis and design is broken down into simple discrete models that can be worked on independently. This work process is sufficient for configurations where there is no potential for lateral load transfer. An example of this would be two adjacent nonbuilding structures connected with small diameter pipe with flexible configurations. Lateral load transfer is likely to occur in cases where two or more nonbuilding structures are connected by large diameter pipe (typically larger than 12 inch diameter) in relatively inflexible configurations. An example of a case where lateral load transfer can occur is shown in Figure 1. This paper provides proposed guidelines for analyzing nonbuilding connected by large diameter pipe.

The design of nonbuilding structures with potential to transfer lateral loads should be approached differently than nonbuilding structures with no mechanism to transfer lateral loads between the structures. In order to transfer lateral loads a mechanism is required that acts like a collector element or drag strut such as a pipe rack strut or a connected large diameter pipe.

The following sections examine methods for analyzing seismic loads on nonbuilding structures connected by large diameter pipe. Example problems of each method are presented and the results are graphed and compared.

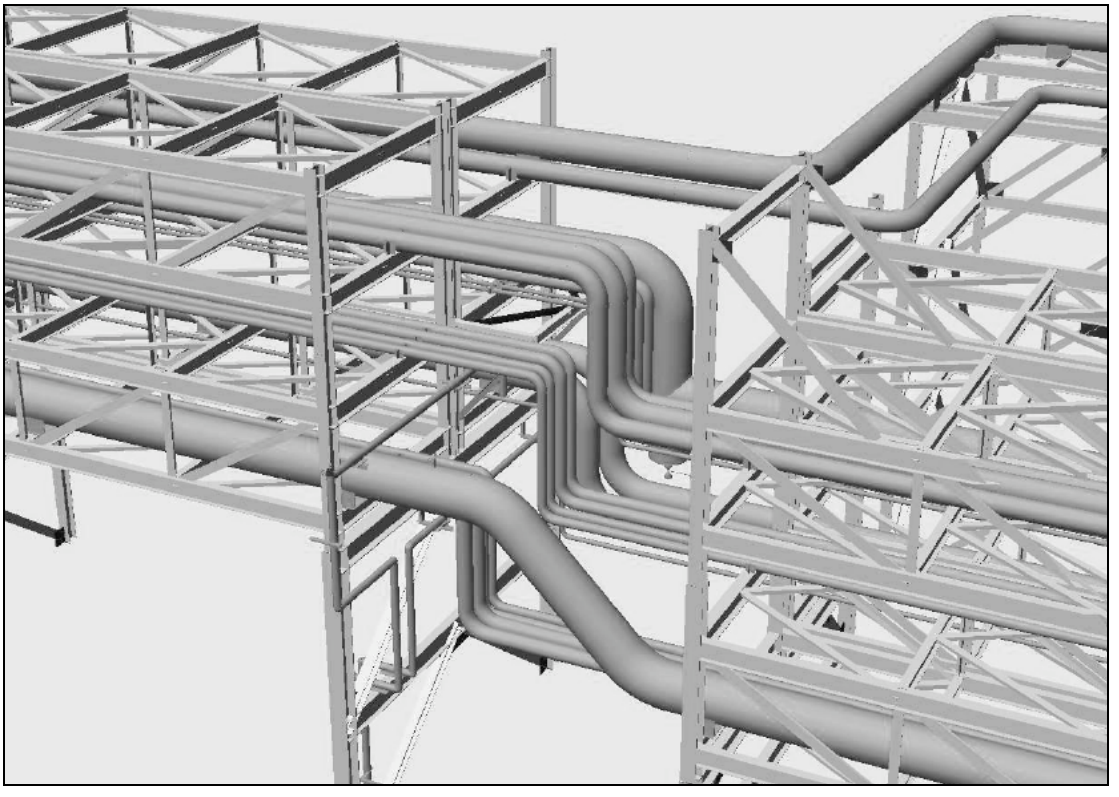


FIGURE 1: Nonbuilding Structures Connected by Large Diameter Pipe

Challenges of Seismic Analysis Nonbuilding Structures connected by Large Diameter Pipe

It is clear that there is advantage to modeling nonbuilding structures independently for cases where there is no significant lateral load transfer to adjacent structures. When substantial lateral load transfer is involved the amount of lateral load retained by an independent model is difficult to predict without also considering the stiffness and natural periods of adjacent connected structures. Considerations of seismic displacements also become problematic for an independent model of a structure that is connected by large diameter/stiff pipe to adjacent structures.

Earthquake load distribution is significantly impacted by the stiffness of the connected elements and the natural frequency of the adjacent connected structures. Industry practice is to model individual structures independently. The method of analysis is typically either Equivalent Lateral Force Procedure (ELFP) or Response Spectra Analysis (RSA). ELFP is more commonly used for simple, regular structures. Direct application of the ASCE 7 [ASCE 2005], ELFP to predict seismic shear transfer between nonbuilding structures presents several challenges, such as shear transfer and seismic displacements.

The concept of amplified seismic displacements cannot directly be applied to a independently modeled structures due to the amount of interconnecting pipe that adds stiffness to the overall system and transfers shear from one structure to another. When planning the model of connected nonbuilding structures consideration should be given to the mechanism connecting the structures. For example, if there are struts connecting the structures then they should be designed as collector elements and modeled to capture the seismic shear transfer. If there is pipe between the two structures then the flexibility of the pipe and its connection to the structures should be considered. If the pipe is not anchored or guided and allowed to slide on one structure then the friction force should be the largest force considered for effects of the seismic displacements between the structures.

Directionality of load presents another challenge. When nonbuilding structures are resisting lateral loads due to earthquake there are many possibilities for the direction of loading relative to on another due to the differences in natural periods. At one moment the structures can be moving towards each other and the next moment they will be moving away from each other. When the structures are connected by a rigid/stiff element such as a large diameter pipe their responses to seismic loads are interconnected and complicated. Sometimes the worst case response is when the structures are moving in synchronicity.

Prior to the evolution of sophisticated structural analysis programs, structural analysis models were necessarily simplified to save computing effort. Thought was put into creating these models in order to take advantage of symmetry and model only members that were necessary for the distribution of loads. This has become a lost art since computing power and memory is no longer an issue. It is now relatively easy to create and run a large structural analysis model. Unfortunately, the methods of managing and summarizing the behavior of large complicated structural analysis models have not kept up with the computer advancements.

Methods are required that account for the complexity of interconnected structures and yet capture the overall behavior when subjected to seismic loads in a way that is

clear and concise. An independent model reflects the characteristics of one structure but does not capture the distribution of forces between adjacent structures. A combined model is capable of capturing the distribution of forces but may be too complicated to provide practical information about the behavior of the connected structures. In some cases the independent model may be more appropriate. Under other circumstances the combined model may be better suited. In order to apply these methods successfully guidelines should be developed to help the engineer choose the appropriate method of analysis. Oversimplified methods may lead to overly conservative results or incorrect results. Combining all interconnected structures into one large model can become an onerous and tedious method that would bog down the practicing engineer and introduce more chances of errors.

METHODS OF ANALYSIS AND EXAMPLE PROBLEM

Three methods were examined for modeling nonbuilding structures connected by large diameter pipes. In order to effectively and concisely compare these methods example problems consisting of simplified, two-dimensional plane frame models were used. Appendix 1 presents the basic example problem common to all methods and some of the parameters used in the analysis study. The example problem includes a large diameter pipe with an expansion loop. The pipe is assumed to be anchored to each structure. The seismic weight and stiffness remains constant for the strong frame for each method in all the load cases. The stiffness of the weak frame was varied in each of the load cases; however, the seismic weight remained the same as that of the strong frame. Thus the natural period ratio was varied by only varying the stiffness of the Weak Frame. Graphed comparisons of the three methods are shown in Appendix 2. There are graphs of seismic shear distribution between the frames for different natural period ratios of the strong frame to weak frame. Results of Methods A, B and C are presented in Appendix 3. The following sections outline each method that was evaluated.

METHOD A: INDEPENDENT MODELS THAT ACCOUNT FOR AMPLIFIED SEISMIC DISPLACEMENTS

This Method considers each nonbuilding structure as an independent model. The seismic displacements are calculated for each nonbuilding structures. The seismic displacements are amplified by the seismic displacement amplification factor, C_d, and applied to the corresponding piping systems in the independent piping models. The reaction forces in the piping models at anchors and guides are applied to the corresponding locations in the independent nonbuilding structure models.

Unlike a combined model, the independent models require analysis in steps. The following steps (shown graphically in Figure 3) are typically used for seismic evaluation of independently modeled nonbuilding structures connected by large diameter pipes:

STEP 1: Independent nonbuilding structure models are analyzed for seismic loads caused by tributary seismic weight (V_{SS} and V_{SW}). Deflections due to seismic loads are calculated.

STEP 2: Independent models of the interconnecting pipe are analyzed for the amplified seismic displacements. Reaction forces (V_{DS} and V_{DW}) due to the induced amplified seismic displacements are calculated.

STEP 3: Independent nonbuilding structure models are analyzed for the combined seismic shear, V_T, due to tributary seismic weight and due to reactions of the interconnecting pipe caused by seismic displacements.
($V_{TS} = V_{DS} + V_{SS}$ and $V_{TW} = V_{DW} + V_{SW}$)

The resulting sum total base shear for the nonbuilding structures is higher than the base shear calculated for the total seismic weight. In this method the force due to the deflection of the large diameter pipe adds seismic shear to both nonbuilding structures. In reality seismic shear should be transferred from one structure to another and no additional seismic shear should be created.

METHOD B: COMBINED MODEL WITH ELFP APPLIED SEISMIC FORCES

Method B uses a combined nonbuilding structure model and the ASCE 7, ELFP for evaluating seismic loads. Several load cases are used in this method to capture the behavior of the structures. Seismic loads are applied in different directions in order to determine the worst combination of seismic shear for each of the connected nonbuilding structures.

The Strong Frame and the Weak Frame are modeled together with loading and boundary conditions such that only two dimensional behavior is observed. The models of the two frames are connected by a pipe loop which is pinned to each structure to model a combined pipe anchor and pipe guide.

Figure 4 graphically shows the load cases evaluated for the example problem using this method. The example problem has been simplified to include only two connected nonbuilding structures and two possible directions of seismic loading for each structure. The number load cases become significantly larger for cases where there are more than two connected structures and cases of orthogonal seismic loading. The limitations of this method are the same as those of the ELFP as described in FEMA 450, Section 5.2.3. In the ELF procedure, the distribution is based on simplified formulas that are appropriate for regular structures as specified in FEMA 450 [FEMA 2003] and ASCE 7 [ASCE 2005]. The ELFP is adequate for most regular structures; however, the ELFP may be inadequate in the following cases:

1. Structures with irregular vertical distribution of strength in the different levels of the structure. This may lead to possible concentration of ductility demand in a few levels of the structure.

2. Structures with irregular stiffness and mass and properties in which case the simple equations for vertical distribution of lateral forces may lead to incorrect results.

3. Structures in which the torsional motion and the lateral motions in two orthogonal directions are strongly coupled.

When these conditions occur a more thorough procedure that considers the dynamic behavior of the structure should be used.

METHOD C: COMBINED MODEL WITH SEISMIC LOADS EVALUATED USING RESPONSE SPECTRA ANALYSIS

Response Spectra Analysis is a common method of modal analysis used to analyze seismic loads on a structure. In this method the natural periods and associated mode shapes are evaluated for a specified seismic dead weight and structural stiffness. Mass participations factors are evaluated for each mode shape based upon the mass and stiffness distribution of the structure. The weighted response of each mode is calculated using the mass participation factors. These responses are added together using a process called modal superposition to determine the overall response of the structure. More background information regarding RSA can be found in dynamic analysis textbooks [Paz 1991] and [Craig 1981].

In the Response Spectra Analysis procedure, the distribution of seismic forces over the height of the structure is based on properties of the natural vibration modes, which are determined from the mass and stiffness distribution.

The results for Response Spectra Analysis were obtained using a commercially available structural analysis software called RISA-3D [RISA (2010)]. Figure 5 shows the dominant mode shapes for the example problem.

The Strong Frame and the Weak Frame are modeled together with loading and boundary conditions such that only two dimensional behavior is observed. The models of the two frames are connected by a pipe loop which is pinned to each structure to model a combined pipe anchor and pipe guide.

COMPARISON OF METHODS

Appendix 3 provides graphs of shear distribution using the three methods presented herein. Figures 6, 7, and 8, show the base shear distribution verse natural period ratio of the weak frame to the strong frame (T_{weak} / T_{strong}) for Methods A, B and C, respectively. Figure 9 shows a comparison of total seismic base shear for each method as it varies with natural period ratio.

In industry practice, a version of Method A “Independent Model Method” is most commonly used for analysis of nonbuilding structures with large diameter pipes. Method A; however, does not accurately model the distribution of seismic shear throughout the system as the natural period ratio increases. Although Method A is simpler than the combined models, the results become increasingly conservative as the seismic displacements and the natural period ratios increase. The reason why Method A yields higher base shear at larger natural period ratios is because the seismic displacements are larger at the Weak Frame. The larger seismic displacement causes a larger reaction for the pipe because the pipe is reacting against a forced displacement. The weaker the frame the more unrealistic this displacement becomes. Figure 10 shows a graph of seismic displacement ratio verses base shear. The trend in this graph is that as the seismic displacements increase the base shear increases.

The Method B: "ELFP Combined Model" is more complicated than the Method A: "Independent Model Method" and yields results that are very close or slightly more conservative than the Method C: "RSA Method" in ranges of the parameters examined in this paper.

Figure 9 shows a graph of the total base shear for all three methods with increasing natural period ratio. The downward trend in base shear in this graph is due to the natural period of the Weak Frame being in the constant spectral velocity range. This range yields a smaller base shear for the same amount of seismic weight.

In Figure 9, the graph results of Methods B and C are very similar; however, the results of Method A are more conservative for high natural period ratios and large seismic displacements. Figure 9 shows when the natural period ratio is close to unity ($T_{weak} / T_{strong} \approx 1$) and the seismic displacements are low then the independent model base shear distributions are similar to those of the combined models using ELFP and Response Spectra Analysis.

SUMMARY OF FINDINGS

The following is a summary of the findings based on the analysis and parameters studied in this paper:

1.) When using an independent model for each structure, it is difficult to accurately account for the interconnecting effects of nonbuilding structures connected by large diameter pipes. Independent models become less accurate as seismic displacements increase and natural period ratios between the connected structures become larger.

2.) Combined models of multiple nonbuilding structures can be very complicated and their use for defining the behavior of the structures can become limited. It is recommended that combined models be as simplified as possible in order to capture the load distribution and capture the essence of the structural behavior.

3.) When considering the necessity of a combined model, compare the relative stiffness of the connected structures and their relative natural periods. Structures that are very flexible and have long natural periods may transfer their seismic shear to stiffer structures with short natural periods.

4.) When designing for the shear transfer from one structure to another, account for the additional shear transfer to the structure attracting additional seismic shear load, however, design the nonbuilding structure that is shedding seismic shear for its full tributary shear. This should be done in case something is modified to the structure attracting additional seismic shear loads or the connecting mechanisms.

5.) Consider structural strut beams between structures that are connected by larger diameter pipes. This will force the structural behavior in a more controlled manner because the struts and their connections can be analyzed and designed for the load they transfer.

6.) The geometry of the interconnecting pipes may cause torsional loads on the structure or equipment nozzles which may not be captured in the independent models.

7.) Foundation mounted equipment or equipment supported on other nonbuilding structures may receive the interconnecting piping loads. It is important that the allowable nozzle loads on the equipment are not exceeded by loads from interconnecting pipes and the effects of seismic displacements. If this is the case then other mechanisms for seismic shear distribution should be investigated.

ACKNOWLEGEMENT
The authors would like to acknowledge the valued input from Josh Plummer, SE with RISA Technologies and his review.

REFERENCES

ASCE (2005). Minimum Design Loads for Buildings and Other Structures, ASCE/SEI7-05. American Society of Civil Engineers, Reston, Virginia.

Craig (1981). Structural Dynamics, An Introduction to Computer Methods, Roy Craig, John Wiley & Sons, 1981, pgs 341-379

FEMA (2003). NEHRP Recommended Provisions for Seismic Regulations for New Buildings and Other Structures, FEMA 450-03, Federal Emergency Management Agency, Washington DC.

Paz (1991). Structural Dynamics Theory & Computation, Third Edition, Mario Paz, Van Nostrand Reinhold, 1991

RISA (2010). RISA-3D, Structural Analysis and Design Software, RISA Technologies, Foothill Ranch, CA.

APPENDIX 1 : NOTATION AND EXAMPLE PROBLEM

NOTATION

C_d = Seismic Displacement Amplification factor [ASCE (2005)]
V_{DS} = Shear due to pipe reaction due to seismic displacements from Strong Frame
V_{DW} = Shear due to pipe reaction due to seismic displacements from Weak Frame
V_{SS} = Seismic shear on Strong Frame due to tributary seismic weight
V_{SW} = Seismic shear on Weak Frame due to tributary seismic weight
$V_{TS} = V_{DS} + V_{SS}$ =Total seismic shear on Strong Frame for Method A
$V_{TW} = V_{DW} + V_{SW}$ =Total seismic shear on Weak Frame for Method A
Δ_{SS} = Unamplified seismic displacement of the Strong Frame
Δ_{SW} = Unamplified seismic displacement of the Weak Frame
V_{T1} = Total seismic shear for the Load Case 1

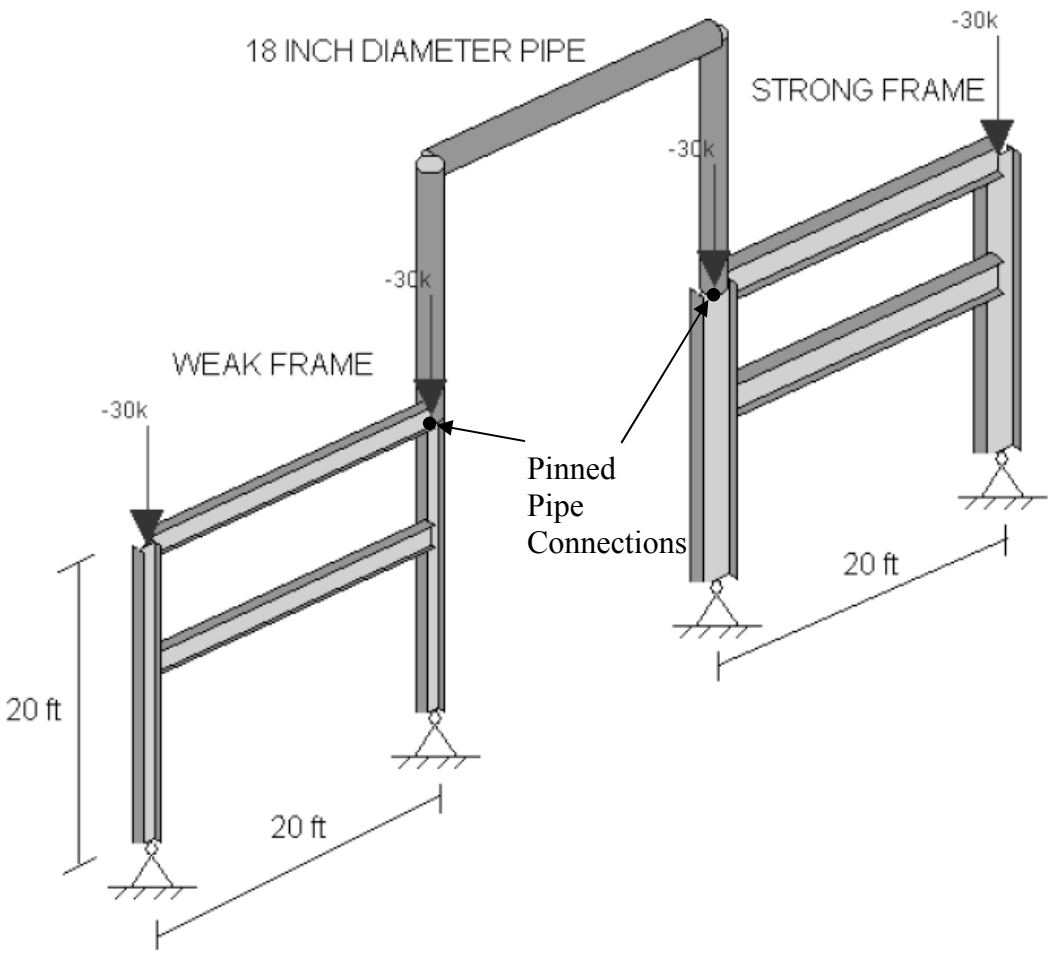
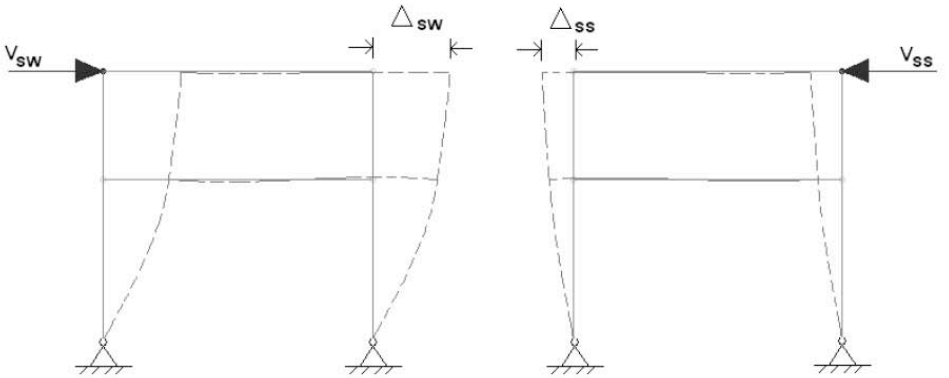
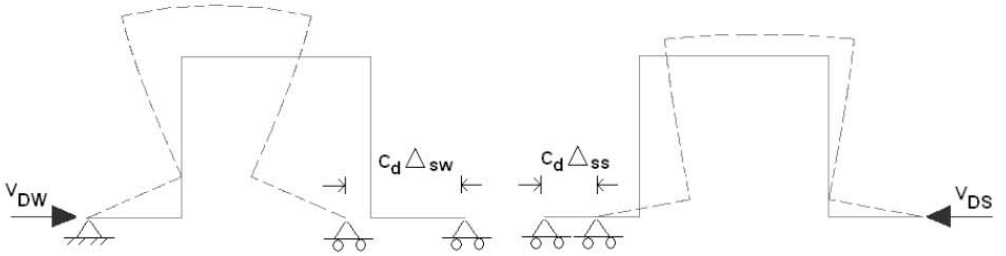


FIGURE 2 – Example Problem

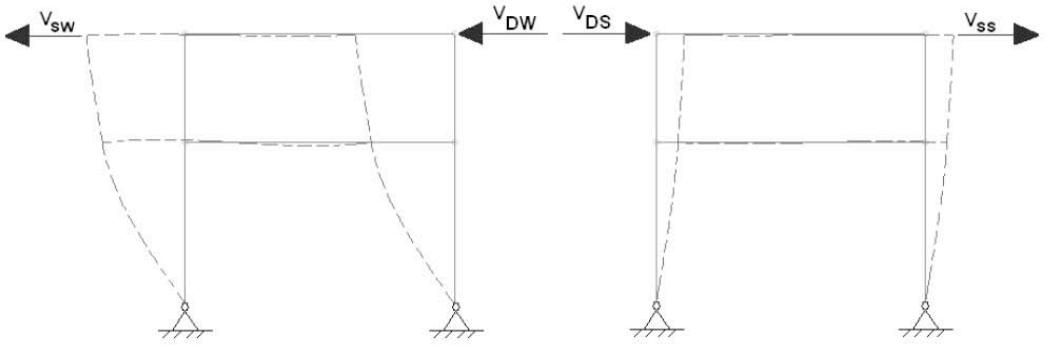
APPENDIX 2: COMPARISON OF METHODS



STEP 1: ANALYZE INDEPENDENT MODELS WITH STATIC SEISMIC LOADS

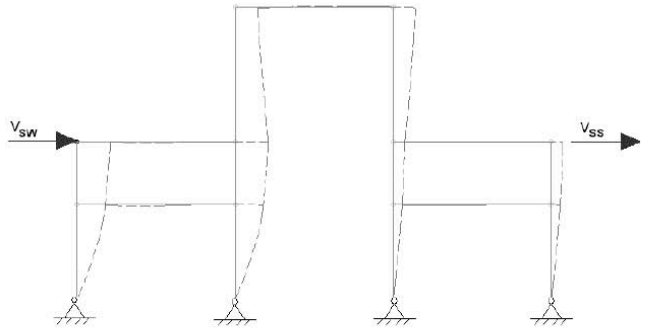


STEP 2: APPLY AMPLIFIED DEFLECTION TO INTERCONNECTING PIPE

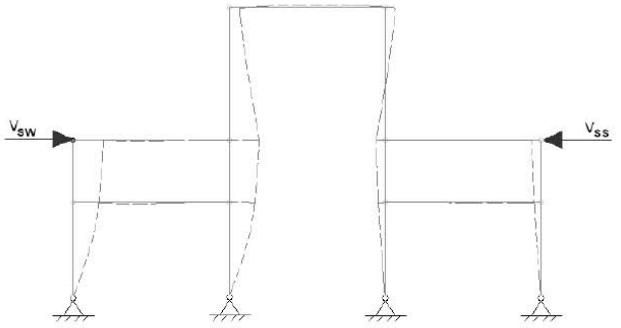


STEP 3: APPLY COMBINED SEISMIC FORCES TO THE INDEPENDENT STRUCTURES

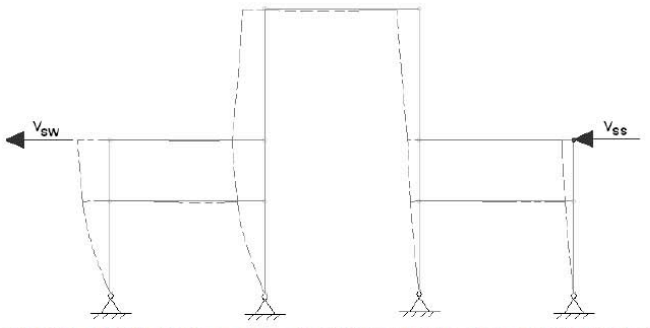
FIGURE 3 – Method A: Analysis Steps



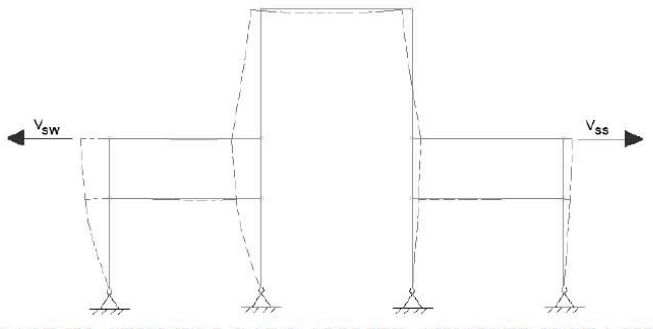
LOAD CASE I: SEISMIC LOADS APPLIED TOWARDS THE STRONG FRAME



LOAD CASE II: SEISMIC LOADS APPLIED TOWARDS EACH OTHER

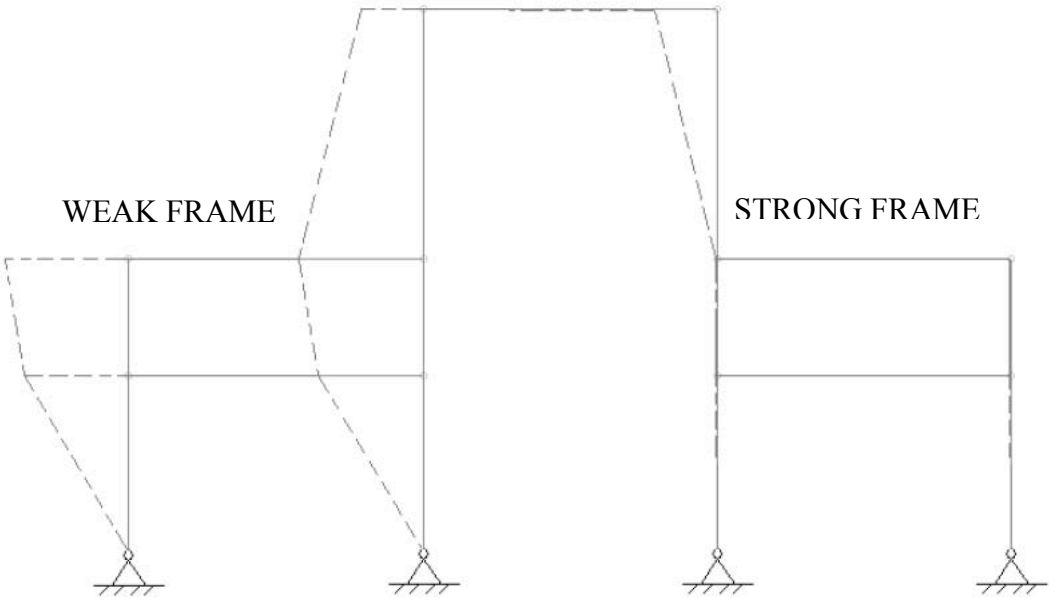


LOAD CASE III: SEISMIC LOADS APPLIED TOWARDS THE WEAK FRAME

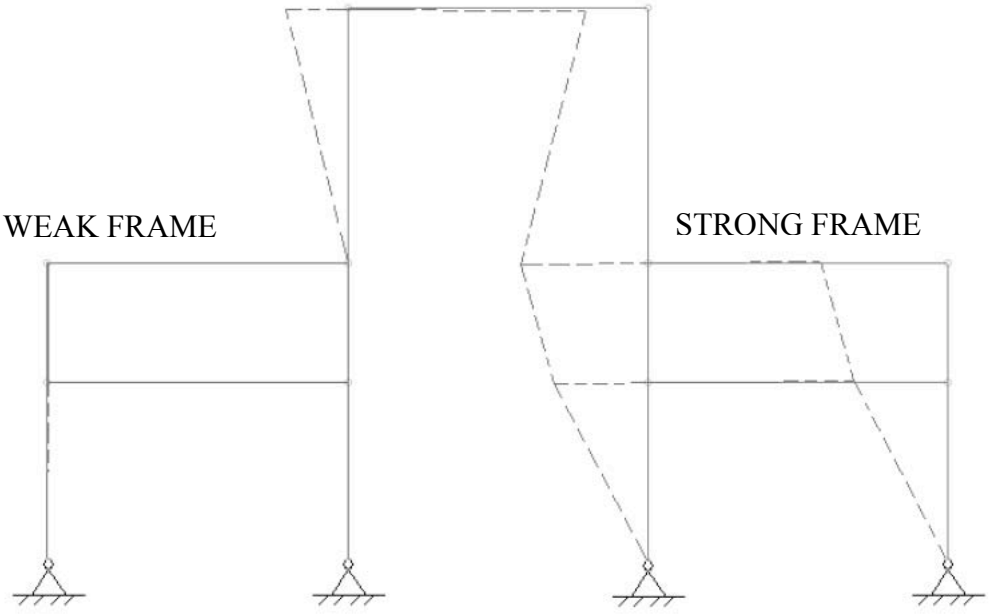


LOAD CASE IV: SEISMIC LOADS APPLIED AWAY FROM EACH OTHER

FIGURE 4 – Method B: (Static Combined Model) Analysis Load Cases



Mode Shape 1 – Weak Frame Dominate Mass Participation



Mode Shape 2 – Strong Frame Dominate Mass Participation

FIGURE 5 – Method C: (RSA Combined Model) Mode Shapes

APPENDIX 3: COMPARISON OF METHODS

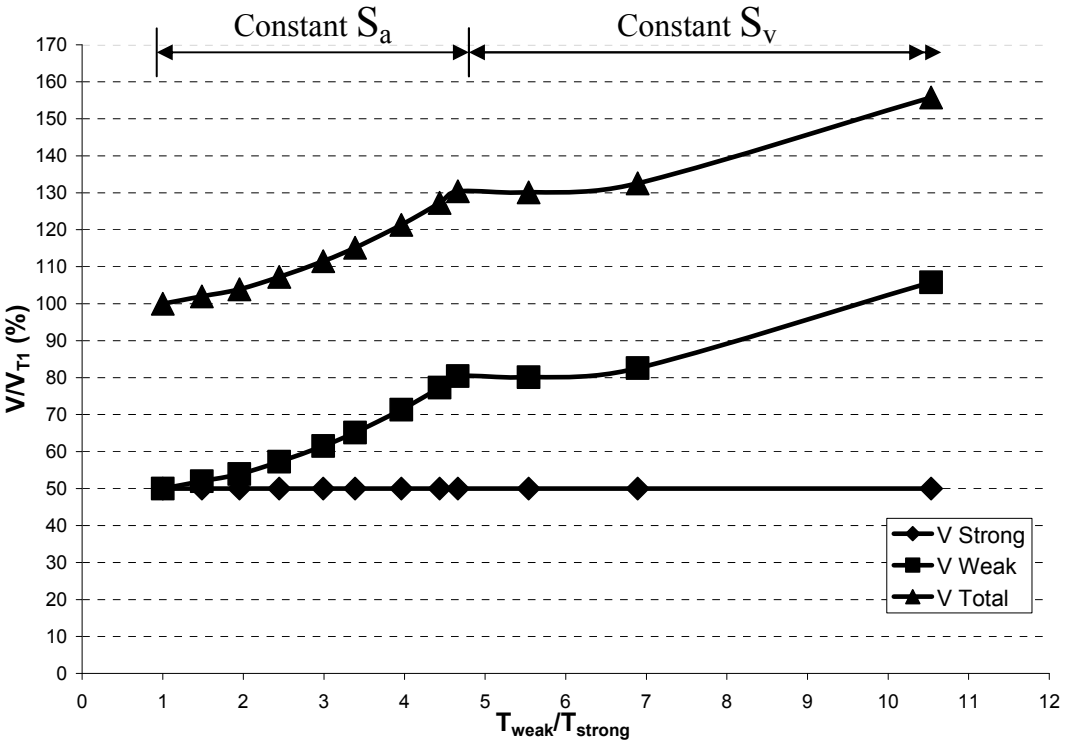


FIGURE 6 – Method A (ELFP Independent Models)Base Shear vs. Natural Period Ratio

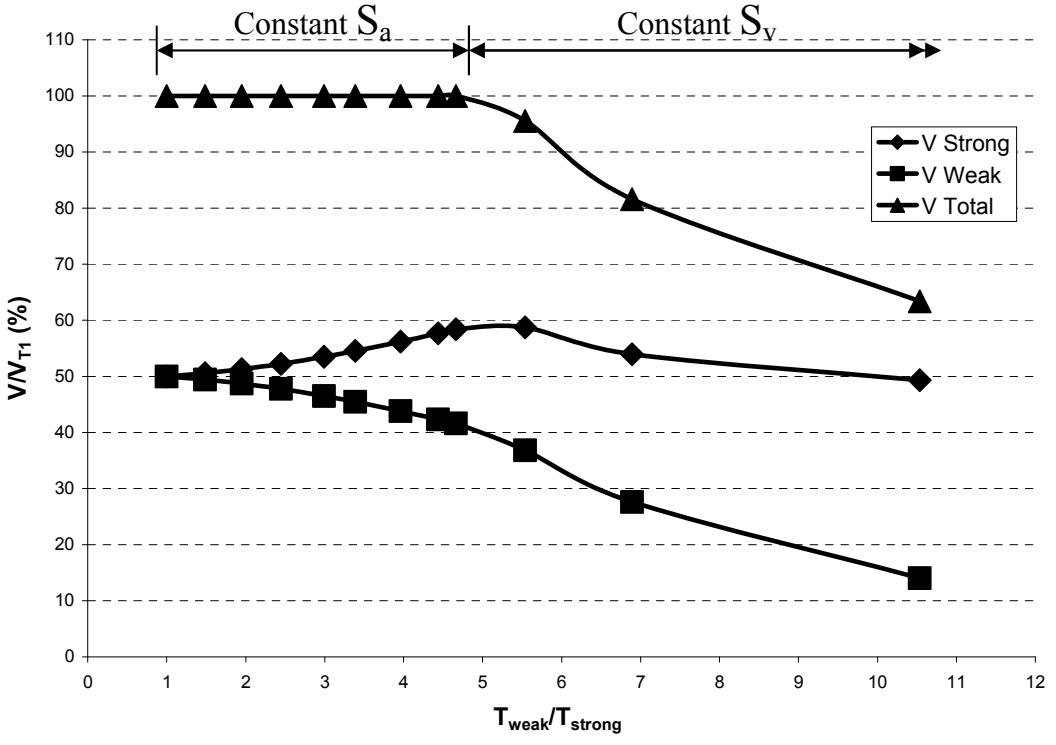


FIGURE 7 – Method B (ELFP Combined Model)Base Shear vs. Natural Period Ratio

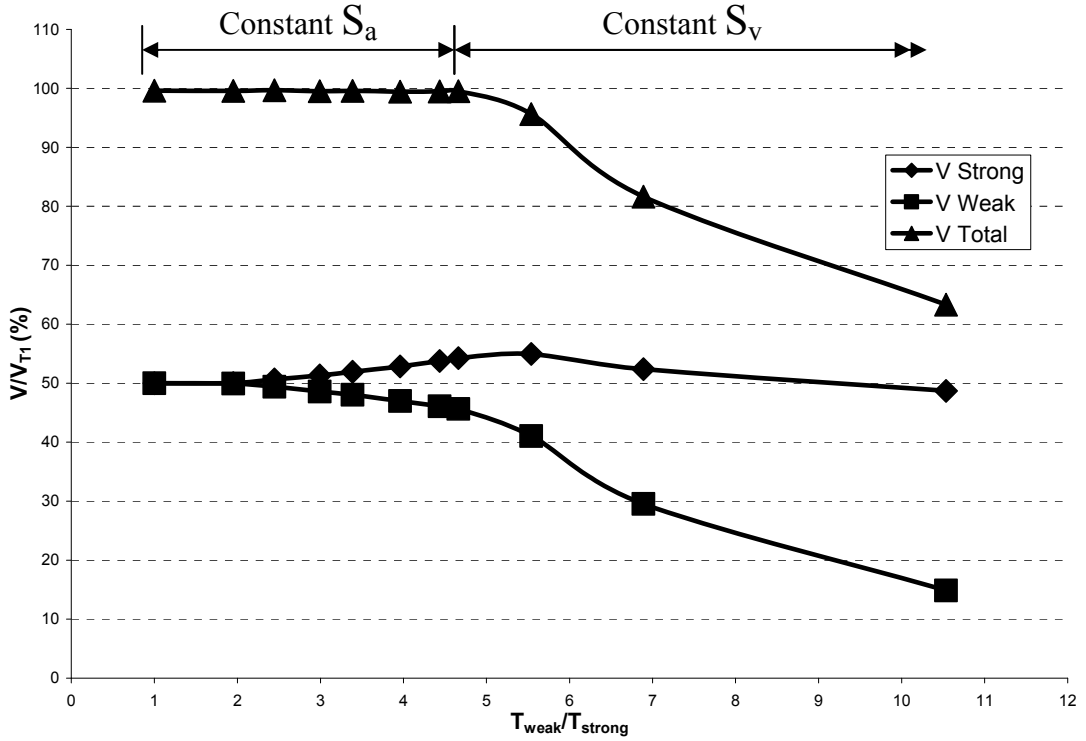


FIGURE 8 – Method C (RSA Combined Model) Base Shear vs Natural Period Ratio

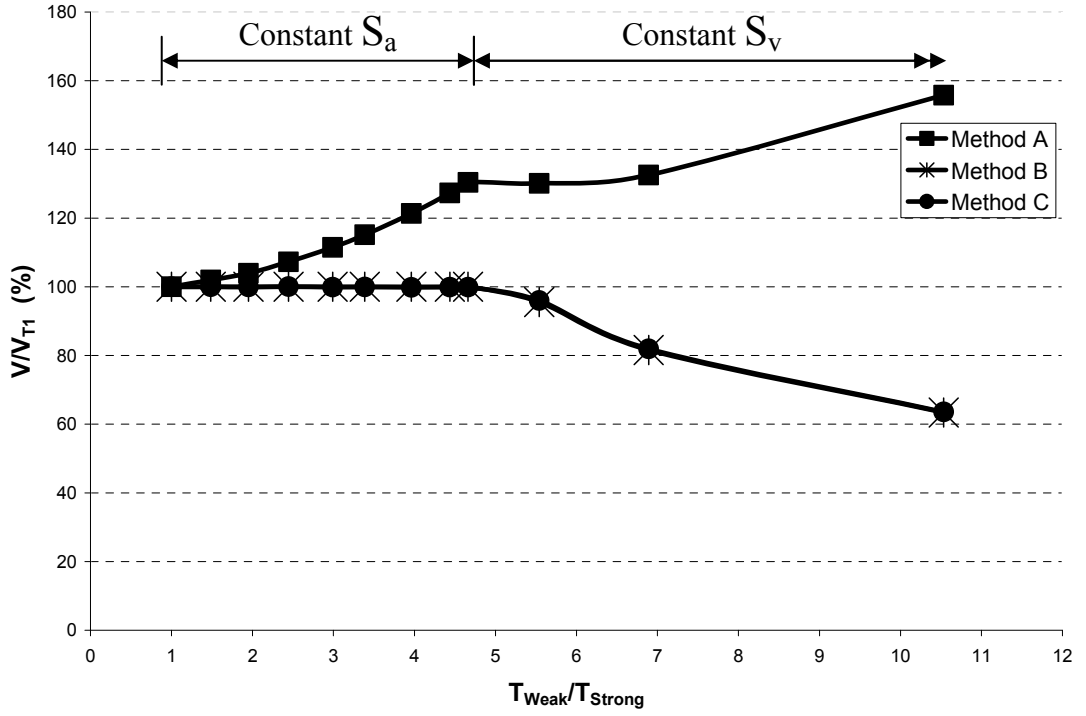


FIGURE 9: Total Base Shear vs Natural Period Ratio for all Three Method

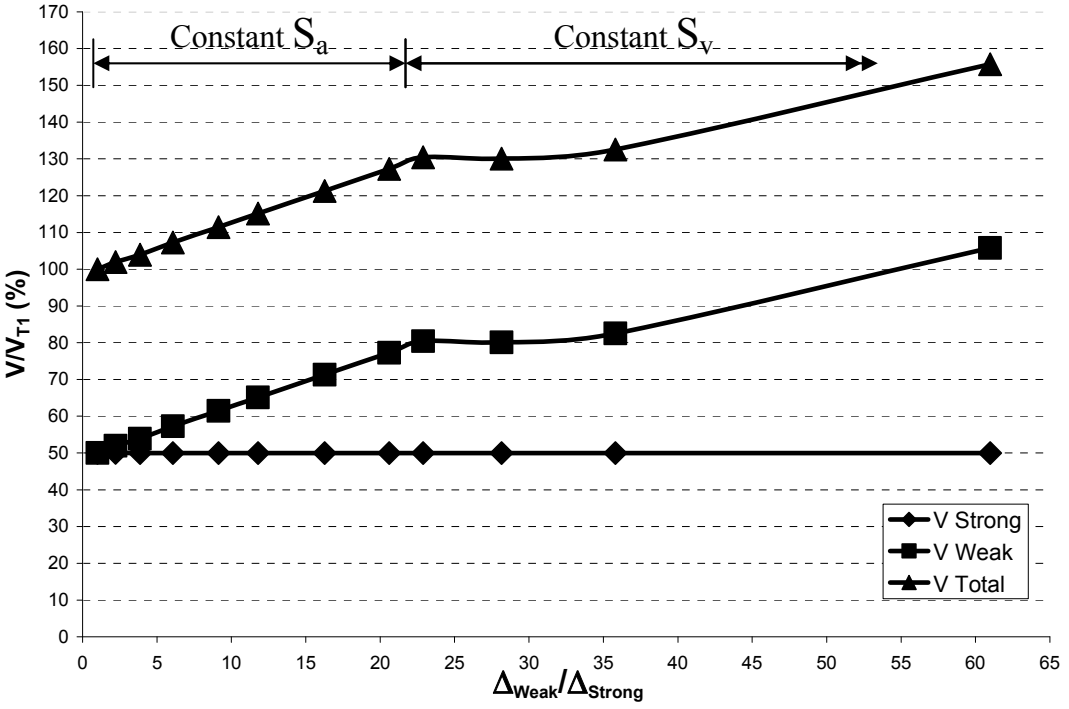


FIGURE 10: Method A – Base Shear vs. Seismic Displacement Ratio

Blast Resistant Design: Engineering Level Frame Analysis

W. L. Bounds[1], Amol Ganpatye[2], George Miller[3]

[1]Senior Fellow, Fluor Corporation, P.O. Box 5014, Sugar Land, TX 77487; email: William.Bounds@Fluor.com

[2]Design Engineer I, Fluor Corporation, P.O. Box 5014, Sugar Land, TX 77487; email: Amol.Ganpatye@Fluor.com

[3]Fellow, Fluor Corporation, P.O. Box 5014, Sugar Land, TX 77487; email: George.Miller@Fluor.com

Abstract

This paper discusses the nonlinear analysis of a structural steel frame subjected to low level far field blast loads. Such blast loads are considered typical for buildings designed for petrochemical plants. The analysis involves the use of a beam and hinge model similar to what can be used for a nonlinear seismic design. An example frame, based on Chapter 12 of ASCE 2010, "Design of Blast-Resistant Buildings in Petrochemical Facilities", is analyzed. The resulting dynamic response is compared to a simpler SDOF equivalent analysis and a to more comprehensive nonlinear finite element analysis. For simple steel frames in typical petrochemical plant applications, the use of a nonlinear hinge model provides a reasonable level of accuracy.

Introduction

The need for, and use of, blast analysis in the petrochemical industry is common. To support this activity, owner and engineering companies have produced a number of internal specifications and practices for the design of blast resistant structures. The industry standards group Process Industry Practices has published two publicly available standards (PIP STC01018 and PIP ARS08390). The American Society of Civil Engineers has published guidelines suitable for petrochemical industry buildings (ASCE 2010). In these publications, and in common practice, the predominant blast design method is a member-by-member analysis using a single degree of freedom (SDOF) equivalent approach.

SDOF equivalent methods and member-by-member approaches are adequate for many structural elements; however the need arises for a "fit for purpose" method applicable to structural members and assemblies for which the response cannot be mathematically described in terms of a SDOF system, or where coupling effects between members will have a significant effect on the response. Moment resisting frames represent such an example because of the coupling of lateral and vertical modes and because a blast wave traveling along a roof beam will excite a number of higher beam modes. ASCE 2010 and UFC 3-340-02 describe SDOF equivalent methods as acceptable for preliminary frame analysis, but prescribe the use of multi degree of freedom (MDOF) methods for a final analysis. Additionally, ASCE 2010

recommends the use of a coupled analysis if the natural periods of connected members differ by less than a ratio (greater/lesser) of 2.

The term “fit for purpose”, perhaps itself a debatable subject, refers to an appropriate level of analysis for the overall parameters and requirements of the calculation. For petrochemical type buildings subjected to blast loading, the basis for using a simple, approximate approach is based on:

- The objective is to design a safe structure with reasonable conservative accuracy given time, budget, resource, and schedule constraints.

- The most common source of an explosion is from a vapor cloud, which involves an accidental release of fuel, mixture with air, and ignition. Estimates must be made of the volume of fuel released, the volume of fuel within the explosive fuel-air mix range, the ignition location, and the degree of congestion, and the direction to an occupied building. Vapor cloud explosions are typically evaluated using release scenarios, a dispersion analysis, and risk criteria (API RP 752, API RP 753).

- Empirical formulas are used to calculate the magnitude of blast loads on the surfaces of a building. The negative blast phase is almost always considered to be insignificant and conservative to neglect. The use of more comprehensive computational fluid dynamics methods are not considered warranted unless blast wave reflections from nearby obstructions is considered to be significant.

- Computed blast loads are almost always low level and far range. The blast wave is considered to envelope the entire building and the free field overpressure is considered to be constant over the dimensions of the building.

- The response limit criteria used, consisting of ductility ratios and support rotations, is simple to implement, however the limiting values are considered conservative.

An Engineering Level Frame Analysis (ELFA) is a descriptive label for this "fit for purpose" category. There are multiple ways to implement such an analysis. The use of computer programs with a nonlinear dynamic analysis capability will be needed. ASCE 2010 mentions the use of either a frame analysis (nonlinear hinges) or a finite element analysis (nonlinear material). ASCE 2010 also recommends use of the same limiting values of ductility ratio, support rotation, and drift as used for SDOF methods.

This paper focuses on the steel frame analysis example provided in Chapter 12 of ASCE 2010 (refer to Figure 1). To avoid showcasing one particular method or computer program over another, details of the computer program implementation are not provided in ASCE 2010, so this paper also serves to provide additional detail. The Chapter 12 example analysis was performed for the original 1997 edition of the ASCE report using STABLE, an implicit nonlinear frame analysis program written by the

US Army Corps of Engineers. This computer program is no longer in use. An ASCE Structures Congress presentation in 2001 (Barker 2001) re-created the Chapter 12 analysis using ADINA, an explicit nonlinear finite element program.

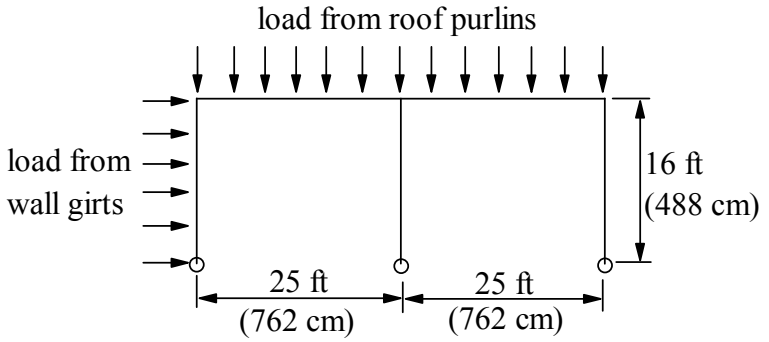


Figure 1: Steel Frame Example (ASCE 2010, Chapter 12)

This paper will examine a method of carrying out an ELFA paralleling the ASCE 2010 Chapter 12 example using a frame (nonlinear hinge) analysis. Comparisons will be made with a SDOF equivalent solution, and a more comprehensive finite element (nonlinear material) analysis.

MDOF (Nonlinear Hinge) Analysis

A MDOF analysis using beam elements is normally not thought of as a finite element analysis even though the computer program used is often the same. Programs for a beam and nonlinear hinge analysis must have the appropriate beam analysis capability using standard steel shapes, and nonlinear hinges. Programs commonly used for structural design may have included this capability for the purpose of a seismic analysis (ASCE 7, Chapter 16, or ASCE 41). The program used for this example is SAP2000 Advanced, version 14.2.0.

SAP2000 Advanced has a nonlinear direct integration capability. Nonlinear behavior is introduced by manually locating hinges on beam elements. There is no limit on the number of hinges or locations. The hinges can include the effects of interaction with axial forces and user-specified post-yield behavior. Significant advantages to this type of analysis are that the same 3D model can be used for static analysis and code checks; changes can quickly be made to member sizes, frame dimensions, and mesh criteria; and frame videos can be made with color coded hinge behavior.

MDOF (Nonlinear Hinge) Implementation

Blast loading for the ASCE 2010 Chapter 12 example was based on a provided free field blast wave (peak overpressure = 1.2 psi, positive phase duration = 50 ms). Using formulas provided in ASCE 2010 Chapter 3, frame loads were recalculated as shown in Figure 2. Rear wall rise time is calculated from ASCE 2010, Figure 3.10b.

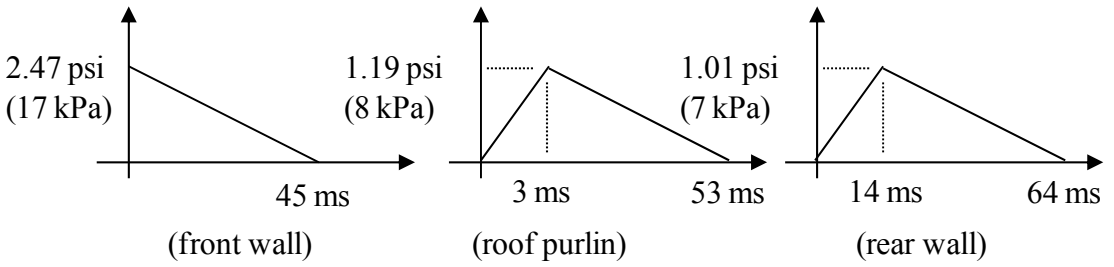


Figure 2, Frame Loading

The building has a width, perpendicular to the traveling blast wave, of 100 ft (30.5 m), length, parallel to blast wave travel, of 50 ft (15.2 m), and height of 16 ft (4.9 m). The moment resisting steel frames are oriented in the short, 50 ft (15.2 m) direction.

The externally applied blast pressures are applied to the frame at the location of each girt and purlin based on a tributary area approach. Each roof purlin supports a tributary width of 20 ft (6.1 m) and tributary length of 4 ft (1.2 m). Each wall girt supports a tributary width of 20 ft (6.1 m) and tributary height of 3 ft (0.9 m). Peak blast loads based on tributary area are 21.341 k (94.9 kN) for each front wall girt, 13.709 k (61.0 kN) for each roof purlin, and 8.726 k (38.8 kN) for each rear wall girt. Peak blast loads for more closely spaced end span girts and purlins were reduced accordingly.

The blast wave arrival time at each roof purlin was calculated using the blast wave speed of 1,169 ft/s (356 m/s) and applicable distance from the front building wall. The rear wall blast arrival time of 43 ms was calculated from the blast wave speed and 50 ft (15.2 m) building length.

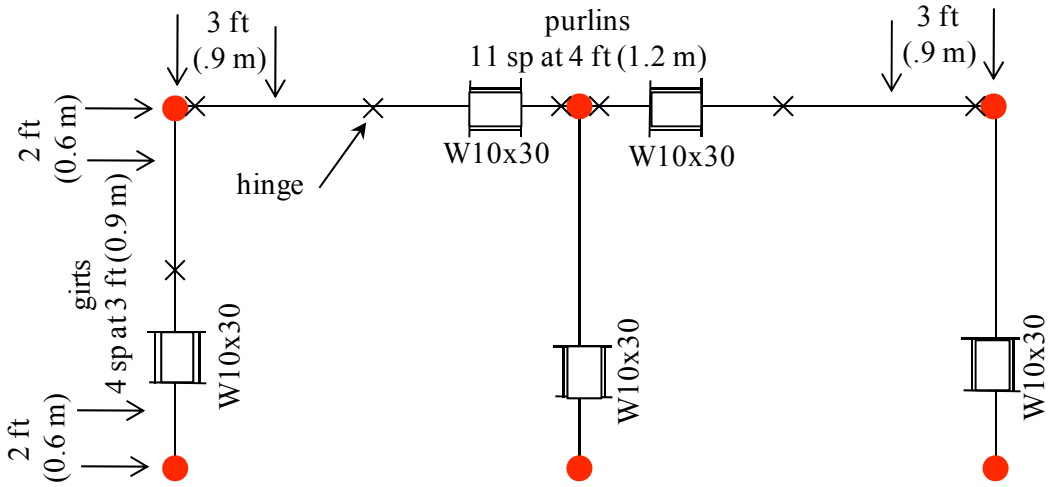


Figure 3: SAP2000 Analysis Frame

The nonlinear hinges were determined by inspection of the frame and located at the midpoint and ends of the two roof beams, and midpoint and top end of the front

face column (refer to Figure 3). SAP2000 does not limit the number of hinges, thus additional hinges could be included if desired. The analysis results can be used to confirm that yield moments are not exceeded elsewhere. The value of the hinge yield moment was manually set to $(F_{DY})(Z_X)$ or 1,866 k-ft (2,109 kN-m) as indicated in the ASCE 2010 Chapter 12 calculation. This hinge value implements the strain rate increased yield stress, F_{DY}, and plastic section modulus, Z_X. Alternatively the hinge yield moment can be calculated by SAP2000 based on the input member size, yield stress, and hinge modification factor.

Mass, manually calculated from the tributary weight of roof panels, wall panels, purlins, girts, and frame members was input as linear values for each beam and column. The program allocates mass to the nearest node, thus a suitable level of meshing must be specified. The initial static dead load was not considered in this example, but must be considered in a real design. The SAP2000 program provides for this capability.

Finally, user-specified nodes must be defined where each time-history response measurement is to be obtained.

Entering the data for this analysis proceeded quickly, and a solution was thus obtained. Though this example represents one of the simplest forms of a MDOF analysis, additional time was necessary to verify the results. Verification steps included:

- Beginning with a static linear analysis (with separate vertical and horizontal load cases) and checking that the deflected shape was as expected.
- Performing a linear dynamic analysis (without the hinges) and checking that the deflection response was as expected.
- Performing the nonlinear dynamic analysis (with the hinges) and checking that each hinge time-moment behavior was as expected.
- Varying the direct integration time step and checking for the level of variance in the results.
- Varying the mesh size and checking for the level of variance in the results.
- Reviewing a video of the overall response for anticipated global response.
- Reviewing time plots of sidesway deflection, beam deflection, column deflection, and base reactions for anticipated results.

The results of the analysis indicate a peak sidesway response at the top of the left column of 3.292 in (84 mm) at time 0.139 s. The peak vertical response at midspan of the left beam is -2.603 in (-66 mm) at time 0.155 s. The peak horizontal response at

midheight of the left column is 4.084 in (104 mm) at time 0.114 s. Displacement-time plots are provided in Figures 5, 6, and 7.

SDOF Equivalent Analysis

For comparison purposes, a SDOF equivalent analysis was performed. The method uses empirical factors to approximate the effects of distributed load and mass. The advantages of the method are that it is fast and relatively easy to understand given a basic knowledge of dynamics. Simple extensions such as for a two DOF overturning/sliding analysis can be derived if required. Limitations are that the method applies accurately only to predefined circumstances (i.e. bending, first mode), bending is the predefined mode of response unless specifically derived otherwise. More complex extensions (i.e. MDOF frames) would involve far too much effort for the benefit provided. Solutions are available in the form of closed-form equations, charts, and spreadsheets. The most versatile solution is a spreadsheet solution, thus the spreadsheet described in ASCE 2010 Chapter 6 was used for this example.

Applicability of a SDOF analysis for frame components is typically limited to trial calculations; usage for this example provides a simple approximate verification.

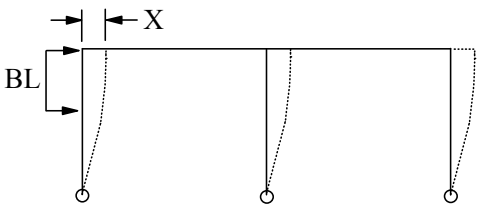


Figure 4, SDOF Equivalent Sidesway Analysis

The SDOF sidesway analysis uses load and mass calculated from a tributary area equal to the roof plus the top half of the walls (refer to Figure 4). Unlike the ASCE 2010 Chapter 12 example, the stiffness is determined by applying a lateral load to the static model used for code checks (a static model needs to be created anyway for an actual analysis). The sidesway analysis results in a peak response at the top of the left column of 3.379 in (86 mm) at time 0.0921 s.

The SDOF beam equivalent analysis uses fixed end conditions. The peak response at the midpoint of the left beam is 1.86 in (47 mm) at time 0.038 s.

The SDOF column equivalent analysis uses a fixed top and pinned base boundary condition. The peak response at the midpoint of the left column is 2.635 in (67 mm) at time 0.024 s.

Displacement-time plots are provided in Figures 5, 6, and 7.

MDOF (Nonlinear Material) Analysis

For comparison purposes, a more comprehensive analysis is desired. Because detailed input data from the previously presented results using STABLE and ADINA are not available, the analysis for this comparison was re-performed using the ANSYS finite element analysis program. The program includes the ability to use nonlinear material properties, thus the formation and location of plastic hinges are determined by the analysis.

Advantages for this form of analysis are that, given proper modeling, the analysis can consider a global response or local effects from close-in explosions, incorporate a higher level of detail (fidelity), and include modeling of connections so that the behavior can be examined.

Issues related to this form of analysis are the additional time required to program and validate the model, the additional time and computer resources required to execute the analysis, an increased complexity in making changes to the model, and the need to prepare a separate model for conventional-load static code checks.

The ANSYS model used similar configuration and loading parameters as for the SAP2000 analysis, with only a few differences. A nonlinear steel material was implemented instead of defined hinges. As for the two other analysis methods, the material was assumed to be elastic-perfectly plastic and incorporated a strain-rate adjusted yield strength.

The results of the analysis indicate a peak sidesway response at the top of the left column of 3.257 in (82 mm) at time 0.160 s. The peak vertical response at midspan of the left beam is -2.777 in (-71 mm) at time 0.159 s. The peak horizontal response at midheight of the left column is 4.119 in (105 mm) at time 0.118 s. Displacement-time plots are provided in Figures 5, 6, and 7.

Comparison of Results

A comparison of sidesway response methods is presented in Figure 5. The result indicates a very similar peak response value from the three analysis methods. The accuracy of the SDOF equivalent method in this comparison is due to the use of a lateral stiffness calculated from a static frame analysis. The MDOF methods compare favorably with each other and have a higher continuing response due to additional plastic hinges in the frame.

A comparison of roof beam response methods is presented in Figure 6. The SDOF equivalent method underestimates the peak response, mainly due to plastic hinges at the beam ends which reduce the stiffness. The beam end hinges also shift the phasing of the response. Again, the two MDOF methods compare favorably with each other.

A comparison of column response methods is presented in Figure 7. The SDOF equivalent method provides a similar first peak value, but underestimates the remainder of the response. This is mainly due to sidesway deflections at the top of the

column. Note that the peak deflection used to calculate ductility and support rotations should consider the effect of sidesway deflection at the top of the column. Thus Figure 8 is provided to illustrate adjusted response values for the two MDOF methods, where half the sidesway response is subtracted from the column midpoint deflections. Figure 8 indicates a somewhat better comparison, however the SDOF equivalent method slightly overestimates the positive peak response and underestimates the rebound response.

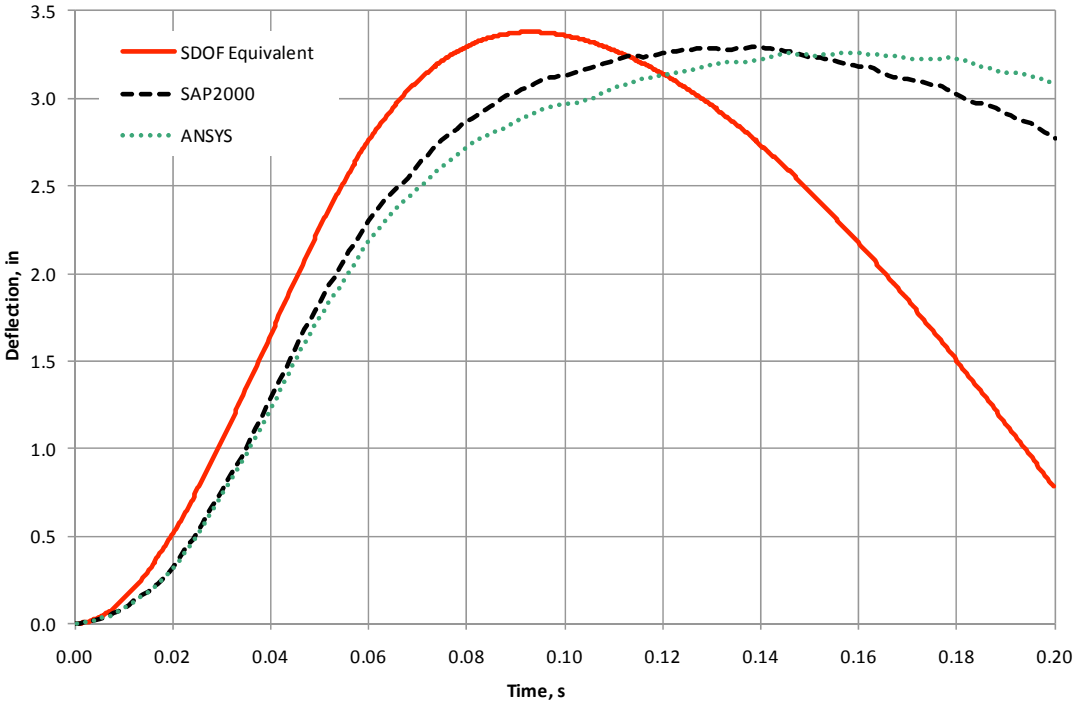


Figure 5, Sidesway Response at Top of Left Column

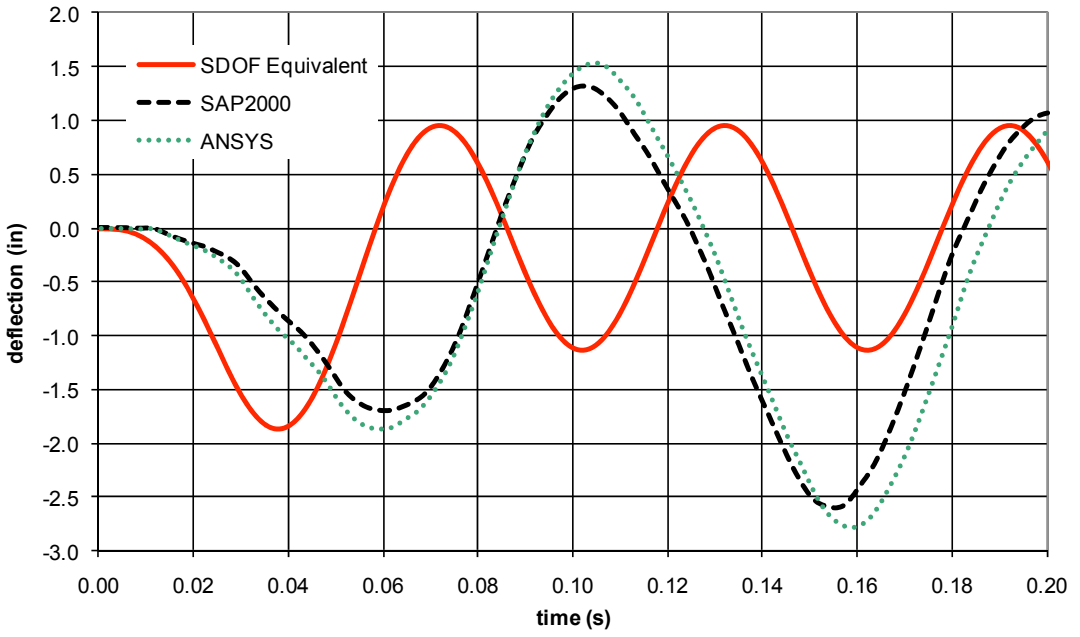


Figure 6, Beam Midspan Vertical Response

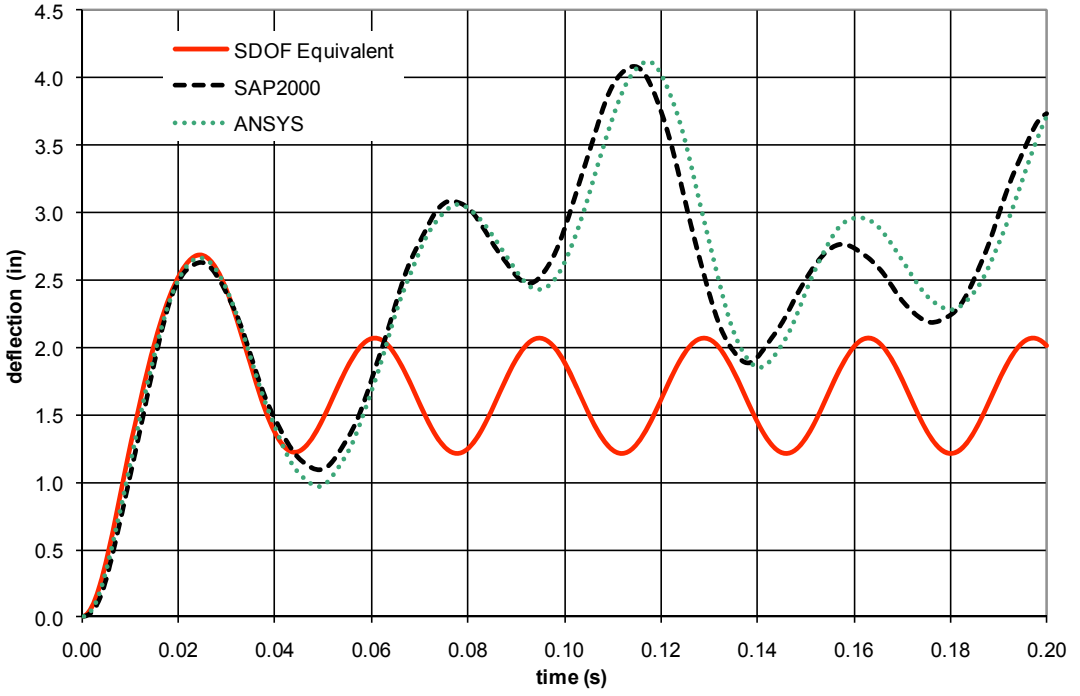


Figure 7, Column Midheight Horizontal Response

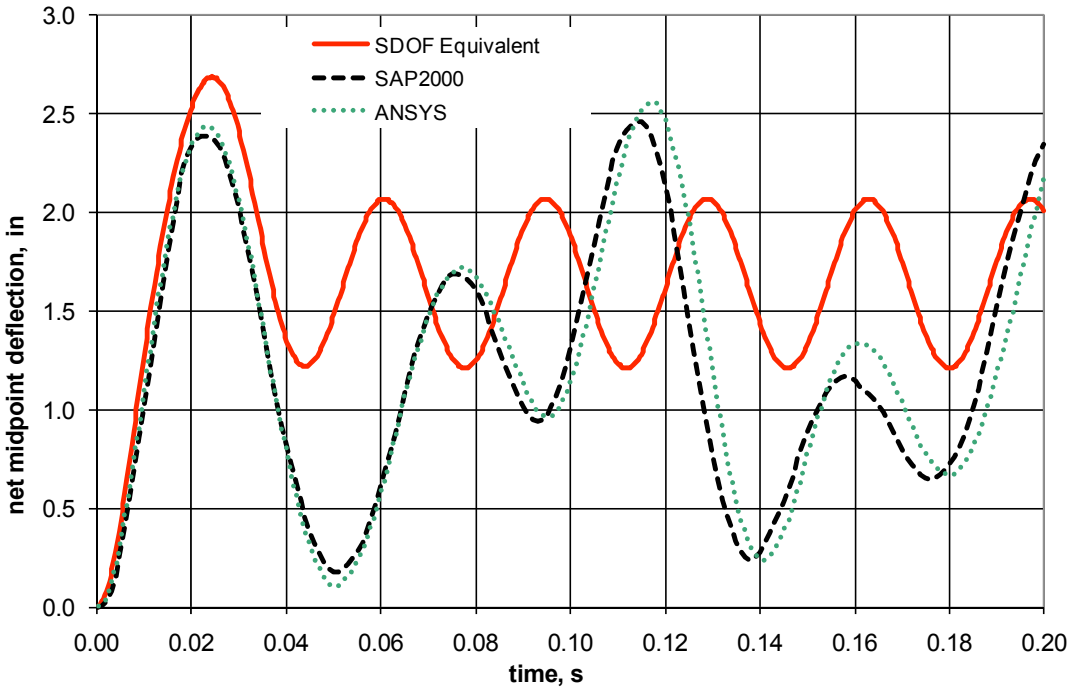


Figure 8, Sidesway-Adjusted Column Midheight Horizontal Response

Conclusions

The accuracy of results using the SAP2000 nonlinear hinge analysis compares favorably with the more comprehensive ANSYS nonlinear material analysis. Aspects of the SDOF equivalent analysis results are similar; however different frame configurations and loading could lead to greater differences. The use of SDOF equivalent method for trial calculations appears to be justified.

The SAP2000 data input for this analysis can be entered quickly and changes are simple to make. Conventional load code checks can be performed using the same model. The model verification that is vital to any computer nonlinear analysis can be more time consuming than that for data input.

The frame model in this example is intended for relatively simple steel frames subjected to low level, far field, blast loads.

The ability of framing members to reach and sustain plastic deformations must be manually verified using applicable code or specification criteria. P-delta effects can and should be included within the MDOF analysis.

References

ADINA, Adina R & D, Inc., Watertown, MA

ANSYS, Ansys Inc., Canonsburg, PA

API RP 752 (2009). *Management of Hazards Associated with Process Plant Buildings*, American Petroleum Institute, Washington DC

API RP 753 (2007). *Management of Hazards Associated with Process Plant Portable Buildings*, American Petroleum Institute, Washington DC

ASCE (2010). *Design of Blast-Resistant Buildings in Petrochemical Facilities*, American Society of Civil Engineers, Reston VA

ASCE 7 (2005), *Minimum Design Loads for Buildings and Other Structures*, American Society of Civil Engineers, Reston VA

ASCE 41 (2006), *Seismic Rehabilitation of Existing Buildings*, American Society of Civil Engineers, Reston VA

Barker, D. and Bounds, W. (2001). *Design Application - External Blast*, Presentation at the ASCE Structures Congress, Washington, DC

PIP STC01018 (2008). *Blast Resistant Building Criteria*, Process Industry Practices, Austin TX

PIP ARS08390 (2006). *Blast Resistant Doors and Frames*, Process Industry Practices, Austin TX

SAP2000, Computers & Structures, Inc., Berkeley, CA

UFC 3-340-02 (2008). *Structures to Resist the Effects of Accidental Explosions*, United States Department of Defense, Washington DC

Designing Foundations for Vibrating Machinery: Dealing With Soil & Software Issues

Amy Petrash[1], William Bounds[2], Silky Wong[3]

[1]Design Engineer I, Fluor Corporation, One Fluor Daniel Drive, Sugar Land, TX 77478; email: Amy.Petrash@Fluor.com

[2]Senior Fellow, Fluor Corporation, One Fluor Daniel Drive, Sugar Land, TX 77478; email: William.Bounds@Fluor.com

[3]Design Engineer II, Fluor Corporation, One Fluor Daniel Drive, Sugar Land, TX 77478; email: Silky.Wong@Fluor.com

ABSTRACT

The design of foundations for vibrating machinery involves solving the equations of motion. To do this, the basic values of load, mass, and impedance need to be determined. Soil / pile impedance is easily the most complex of these values. Current means of evaluating soil impedance is through the use of computer software. Because of the complexity of the calculations, such software is often seen as a "black box" that takes user input data and reports a result. Familiarity with the assumptions and formulas behind computer calculations is important, as is a visual grasp of how results will be affected by changes to input data. Also of significance is having the ability to confirm the reasonableness of computer results. This paper addresses these subjects.

BACKGROUND

Understanding and interpreting computer based results is not always easily accomplished. The calculation of stiffness and damping is relatively straightforward when dealing with soil supported mats on homogeneous soil. Values can be easily determined manually, or by using a spreadsheet. Stiffness and damping calculations for layered soil or for pile groups may appear reasonably simple in theory, but become complicated and tedious in implementation.

For soil supported foundations, several situation-specific methods are available for design which include a homogeneous halfspace, layer over a halfspace, layer over a rigid stratum, shear modulus increasing with depth, and shear modulus increasing hyperbolically to a specific depth. General purpose methods include an equivalent pile (soil column), and a cone (Wolf 2004).

Pile supported foundations involve single piles as well as the arrangement of piles in a group. Situation-specific charts and figures are available. The most commonly used general method for individual piles is the Novak plain strain approach which allows for floating piles, end bearing piles, and layering within the length of the pile. Methods for determining the impedance of pile groups are either direct (all at once), or use superpositioning (combinations of two piles).

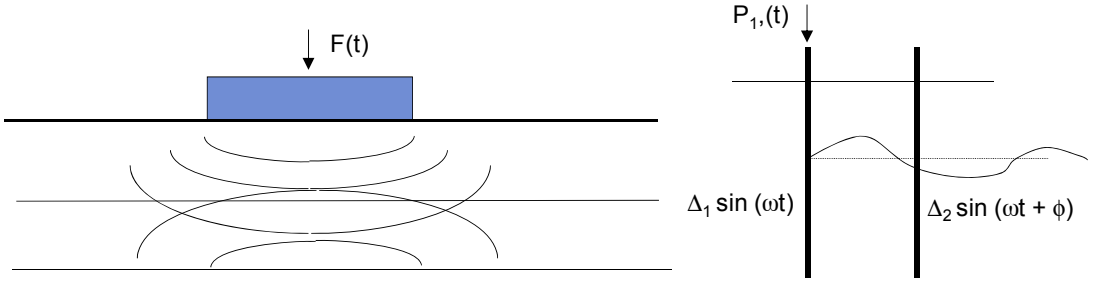
The most comprehensive method for soil / pile supported foundations is a detailed finite element analysis which usually involves a prohibitive amount of effort to implement. Even some of the "simplified" methods are considered to be time-demanding. Simplified calculations are further complicated by the use of complex numbers, which of course are not a part of normal structural calculations. For the solution of the equation of motion, complex numbers are easier to deal with symbolically and computationally. Complex numbers enter into the calculation through the implementation of material and geometric damping.

Software available on the market typically provides input and output values, but the inner workings are not accessible to the user. Thus only a "black box" calculation is available which can create design challenges for the verification of computer results. This paper provides some guidance for understanding impedance and discusses the validation of computer results.

Software authors assume that users are fully versed in the documentation and theory before attempting a design. In reality, software users may actually have only a general knowledge of the method basis. This provides a problem for verification because careful input checking alone may not be sufficient. Some potential issues when using one of the more common programs, Dyna 5, are discussed.

VISUALIZATION

The transmission of stress waves through the soil is how foundation impedance occurs. It is also a convenient way to visualize how impedance is affected by calculation parameters. Basically, stress waves that travel away from the foundation, never to return, result in a large amount of energy loss through geometric damping. Stress waves that impact a different soil layer, reflect back to the foundation and will change the impedance depending on the amount of reflection, attenuation, and phasing of the reflected wave (Figure 1a). Stress waves that impact an adjoining pile, change the total pile group impedance depending on the attenuation and phasing of the stress wave where the impact occurs (Figure 1b, Figure 2).



(a) Through Soil Layers **(b) Between Piles**

Figure 1, Transmission of Stress Waves

For soil layers, the cone analysis method (Wolf 2004) calculates the reflection and refraction of waves at each soil layer boundary with attenuation calculated from soil

layer reflection coefficients and from a spread in the shape of a cone. For pile groups, methods such as described by Gazetas (Gazetas 1991) calculate the attenuation and phasing of stress waves as they spread laterally from a source pile to a receiver pile. A close understanding of these methods provides a good understanding of the principles involved in determining impedance.

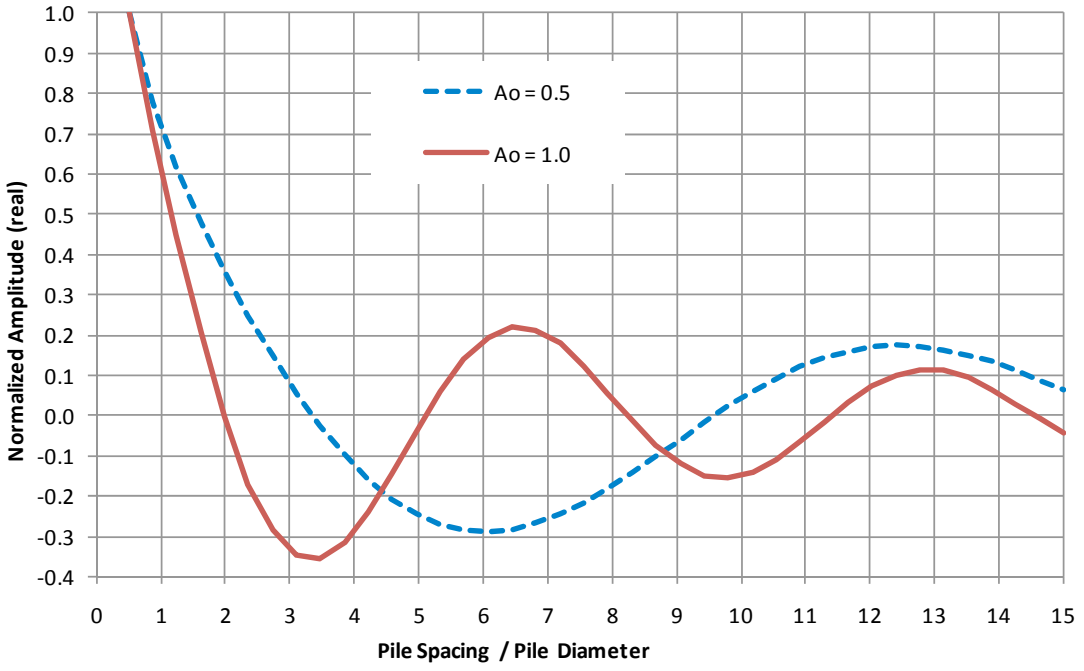
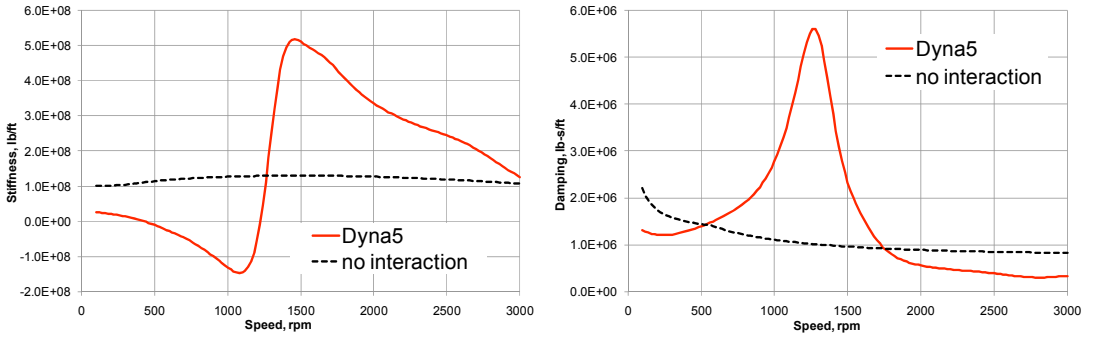


Figure 2, Attenuation & Phasing of a Shear Wave Ao = Diameter-Based Frequency Factor

The following paragraphs describe several instances of seemingly counter-intuitive results. The appropriate evaluation of results is aided by considering how the transmittal of stress waves occurs and through the use of visual aids to help put specific results in context.

EFFECT OF PILE GROUP INTERACTION

Often a software user may desire to verify the program generated group pile stiffness values by simply using the single dynamic pile stiffness multiplied by the number of piles. This rough approximation is inaccurate as the group pile interaction effects are much greater than the single pile dynamic response. Figure 3 illustrates the comparison of a range of dynamic stiffness and damping values as function of frequency. Thus single pile results will not provide insight to validate group pile program results. By observation of Figure 3, stiffness and damping values near zero rpm indicates that the use of static interaction factors would be equally unsatisfactory (i.e. a constant stiffness value over the frequency range).



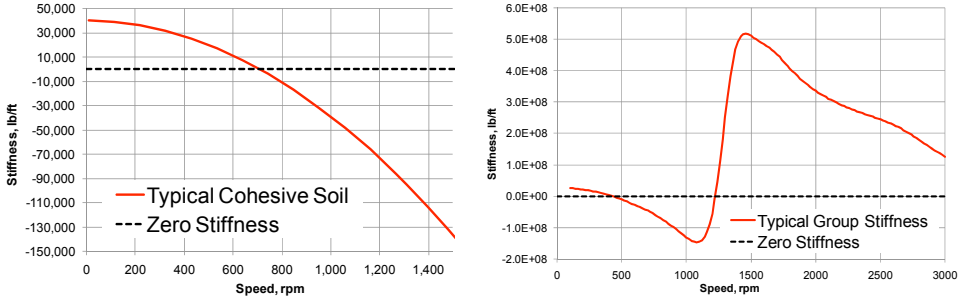
a) stiffness comparison b) damping comparison

Figure 3, Effect of Pile Group Interaction

An appendix is provided in this paper to illustrate the vertical impedance calculation for a single pile as well as for a four pile group. The calculation is based on Novak's plain strain method. The procedure is similar to that used by the Dyna5 program and the results may be used for an approximate verification of the results. The response for horizontal and rocking is more complicated due to coupling between horizontal and rocking modes, and due to soil stiffness based on a combination of shear and compression waves.

NEGATIVE STIFFNESS

One phenomenon that appears to be counter intuitive is the occurrence of negative stiffness values in the solution. The user may initially presume that there was a program malfunction. However, this can be a valid result and there are several causes. First, foundations supported on a highly cohesive soil with a high Poisson's ratio value (i.e. clay) can produce a negative stiffness at higher frequencies (Figure 4a). The effect is the result of part of the soil vibrating in phase with the foundation. Because in-phase soil mass is not included in the mass of machine-foundation models, the resulting stiffness can become negative. Secondly, a negative stiffness can result from a pile group vibrating within a specific frequency range (Figure 4b). This is a geometric effect from the shear wave velocity and the spacing between piles.



a) cohesive soil b) pile group

Figure 4, Negative Stiffness Situations

Though a negative stiffness would make a fundamental difference in a static situation, there is no practical or numeric defect when solving the equations of motion.

For most software programs dealing with block-type foundations, it is not necessary to provide any further action other than to note that the stiffness is negative and continue with the design. If a flexible structure is to be analyzed and the stiffness is to be transferred to a finite element program, a negative stiffness may not be a valid input value. Therefore, it will be necessary to convert the negative stiffness, K_N, to an equivalent positive value stiffness (usually the static stiffness, K_S, is chosen) and additional mass, M_A. The equation below, with ω as the circular frequency, can be used to accomplish this conversion.

$$M_A = (K_S - K_N) / \omega^2$$

STRONGER SOIL, LOWER STIFFNESS

Another counter intuitive phenomenon is where an increase in shear wave velocity (i.e. stronger soil) results in a decrease in pile group stiffness. When the shear wave velocity is varied, the shear waves impacting adjacent piles are shifted in phase (refer to Figure 2). The result is a decrease in stiffness, plus a shift in frequency. Figure 5 provides an illustrative sample comparison where the stiffness decreases at frequencies near 1,500 rpm.

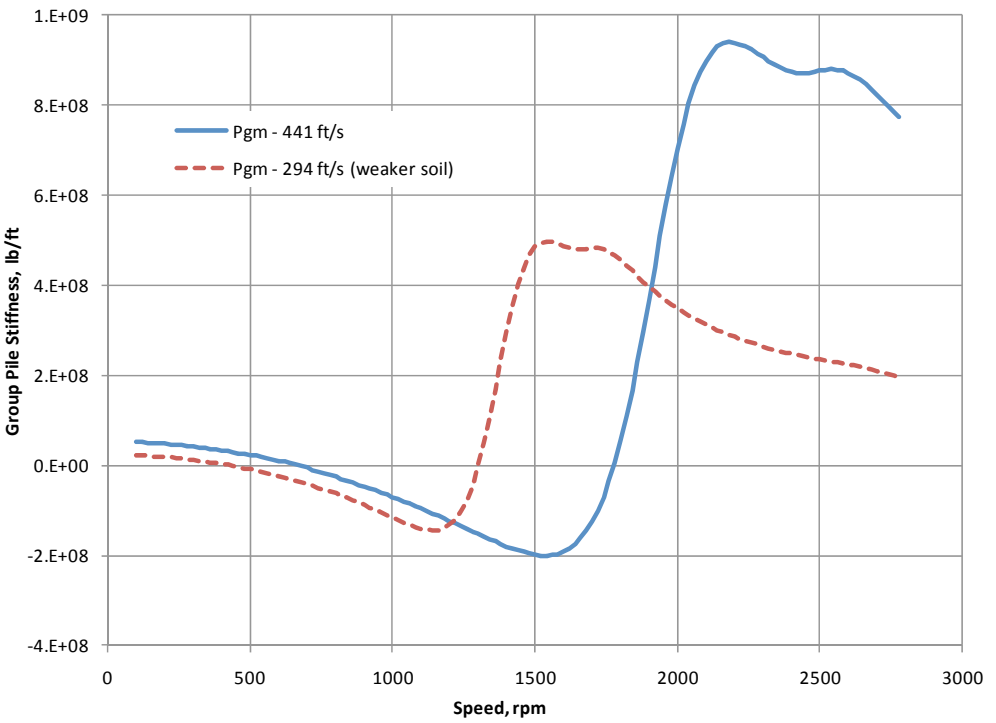


Figure 5, Effect of Group Piles Stiffness from Variation of Shear Wave Velocity

DAMPING LIMITS BASED ON CRITICAL DAMPING

The implementation of project specification criteria that specifies damping limits based on a percentage of critical damping can be problematic. Limitations on damping are used to account for variability in measured soil values. The use of critical damping based limits appears to have originated from frequency independent impedance methods for uniform soil conditions. Because geometric damping is computed as a coefficient, the damping ratio is calculated as follows:

Damping Ratio = (damping coefficient) / (critical damping coefficient)

Critical Damping Coefficient = $\sqrt{\text{stiffness} \times \text{mass}}$

The calculation of critical damping and usage of a percentage of this value can be an issue due to the following factors,

- Negative Stiffness: As discussed previously, this can occur for specific circumstances such as cohesive soils and or for pile groups (Figure 4). One logical resolution is to use a critical damping value based on the static stiffness, however the resulting static-based damping value can be unrealistic at certain frequencies.

- Change of Mass: Mass can affect the damping limit. A change in foundation mass, without any change in the soil interface, would result in a different damping limit.

- Large range of damping values in pile groups: Pile group geometric damping at certain machine speeds can be very large and the application of critical damping based limits would result in a dramatic drop in damping. At other machine speeds, damping could be below the limit and the application of critical damping based limits would result in no reduction whatsoever (Figure 6).

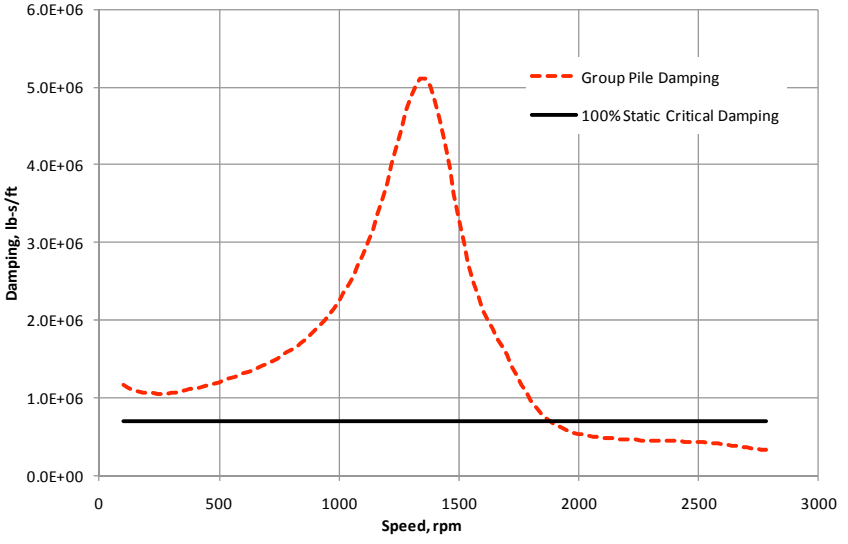


Figure 6, Group Pile Damping Versus Static Critical Damping

- Software Limitations: Some commonly used programs do not include the capability to specify a damping ratio limit, or to specify different limits for each mode of vibration.

A consistently conservative alternative is to implement a uniform reduction from the calculated theoretical damping value. Dyna 5 for example, implements a uniform reduction as a damping safety factor (For Example, DSF = 2 represents a 50% reduction).

RESONANT RANGE ISSUES

Another project specification issue is the avoidance of the resonant range. Resonance occurs when the exciting frequency is very close to the natural foundation frequency; the associated high vibration response will be detrimental to the machine. A natural frequency for an uncoupled mode occurs where the foundation stiffness, $K = M \omega^2$ (refer to Figure 7). Typically a specification will state that the frequency ratio (machine exciting frequency divided by natural foundation frequency) shall be outside a resonant range (usually given as 0.7 to 14, or 0.8 to 1.2). Alternative criteria are rarely included. Meeting resonant range criteria in project specifications can become difficult due to the following factors:

- The dynamic analysis is normally performed using the measured shear wave velocity, plus values that represent higher and lower variations resulting in additional resonant ranges.
- A flexible tabletop-type support may have hundreds of natural frequencies.
- A reciprocating machine will have primary and secondary exciting frequencies.
- A pile group may have several natural frequencies. Refer to Figure 7 which shows the resonant ranges (based on 0.8 to 1.2) to be avoided. As shown, the shaded regions indicating the resonant ranges can greatly limit the design.

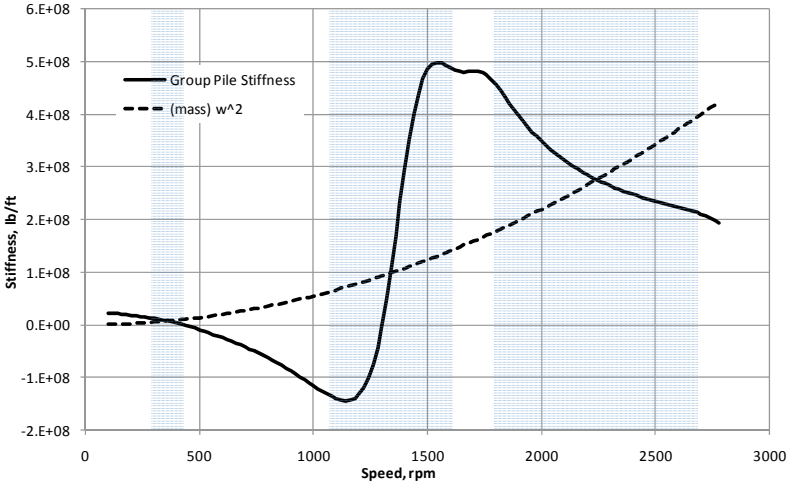


Figure 7, Indication of Three Vertical Natural Frequencies and Resonant Ranges for a Pile Group

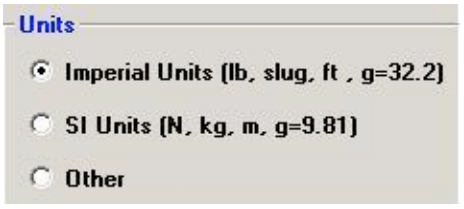
The resonant range, being a function of frequency, covers a wider range of values with higher natural frequencies. In situations where avoidance of the resonant range is not practical, an alternative would be to increase the damping reduction from theoretical values. Where 50% of the theoretical value would normally be used, 25% of the theoretical value would be used (for the Dyna5 program, this equates to a DSF = 4).

SOFTWARE ISSUES

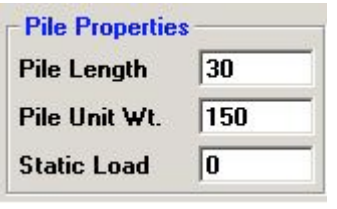
Because of the complexity of calculations, engineers must typically rely on computer software for designing vibrating equipment foundations. Design using software may not simplify the engineering process due to a lack of software usage guidance resources. Pitfalls related to the user interface can greatly affect the results. It is important to thoroughly understand the program input values as well as to verify the results in the output data. A common perception is that program input data verification will detect modeling mistakes. However, if the user is unfamiliar with the program assumptions and defaults, the user may not realize that input values are incorrect.

This paper discusses some input quirks found in Dyna 5. Dyna 5 is a commonly used program that, when used properly, produces reliable results. If other programs are used, it is recommended to look for similar issues presented in the following bullet list.

- Units: Units are defined in Dyna 5 under the setting summary (Figure 8a). The units chosen are not repeated on the data input screens (Figure 8b). In the Dyna 5 settings, it is strongly recommended to select "Echo Input Data" under the Output Flags section (Figure 8c). This option directs the program to include input values, with units of measure, in the output text file (Figure 8d).



a) units designation



b) data input



c) echo designation

```
GRAVITATIONAL CONSTANT SET TO  32.20 ft/s**2
*****************************

FREQUENCY UNITS :  RPM
***************

LENGTH UNITS : ft
*************
```

d) results with units

Figure 8, Dyna 5 Screen: Units of Measure

- Density: Density is not described as weight or mass density on the data input screen. Note that the program's imperial unit for mass is slugs. Where "Density" is shown (Figure 9), a mass density is expected by the program.

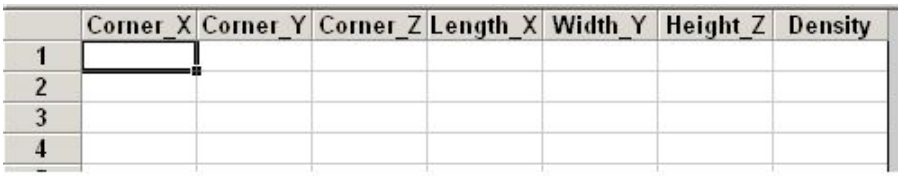


Figure 9, Dyna 5 Screen: Density Input

- Damping Values: The material damping entered in Dyna 5 (Figure 10) is defined as the tangent of the loss angle, which is equal to twice the damping ratio.

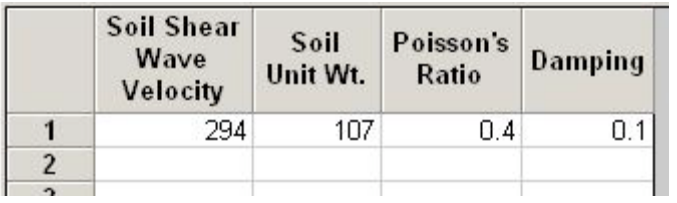


Figure 10, Dyna 5 Screen: Damping Input

- Pile Tip Condition: Dyna 5 includes an option for the pile tip condition to be "Floating" or "End-Bearing" (Figure 11). This is actually a low frequency damping modification. Geometrical damping vanishes at low frequencies, leaving only material damping. The pile tip condition determines how this is to be implemented. "Floating" is the default condition which specifies a straight line transition. "End-Bearing" is the alternate condition where Dyna 5 will calculate the deposit's first natural frequency, below which the radiation damping will be abruptly eliminated.

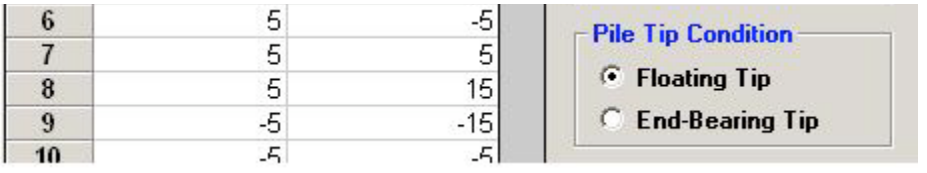


Figure 11, Dyna 5 Screen: Pile Tip Condition Input

Once input parameters have been verified, manual and visual verification of the software results must be achieved. Manual verification is performed by examination of the printed results. Visual verification is performed by using the Dyna 5 plotting capability (Figure 12). If desired, plot data can be extracted for use in other software. Note that data files must reside in the Dyna 5 program directory in order for the plotting routine to function.

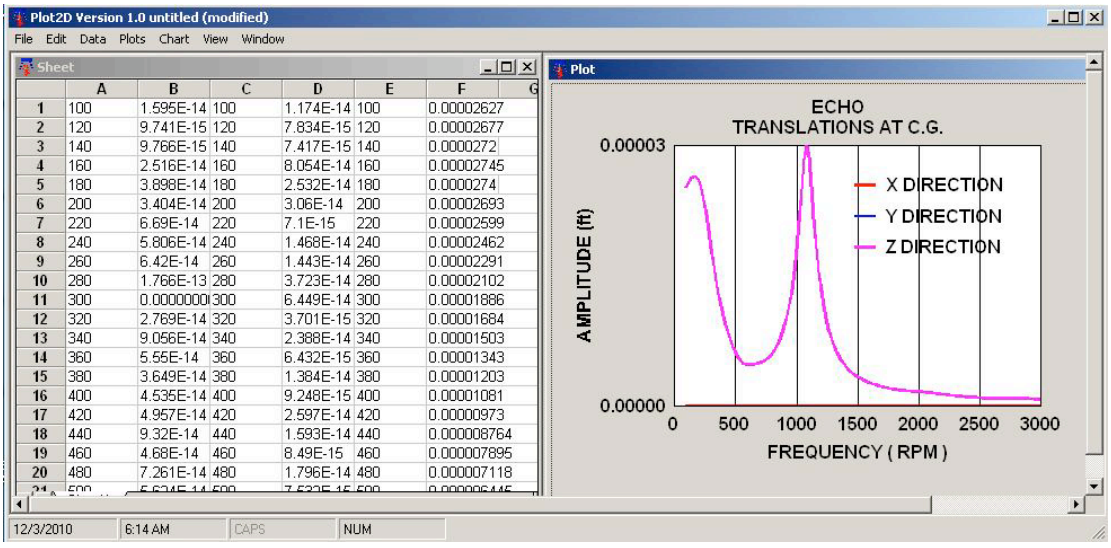


Figure 12, Dyna 5 Screen: Graphing Options

An independent manual verification of results may be necessary to validate program results. For pile impedance, the sample calculation provided in the Appendix provides a vertical impedance calculation for a four pile group. The results should be close enough to help identify if the program solution is reasonable. Manual verifications can also be based on any of a number of graphs and tables available for a variety of soil and pile situations. Note that chart data from various resources may define the frequency factor, A_O, based on either the radius, R, or the diameter, D.

$$A_O = R\,\omega / V_S \quad \text{or} \quad A_O = D\,\omega / V_S$$

In addition, pile interaction factors may be based on either a dynamic-based definition (i.e. Mylonakis & Gazetas 1998) or a static-based definition (i.e. Kaynia & Kausel 1982). If implemented properly, the result will be the same.

$$\alpha = \frac{(\text{pile 2 dynamic deflection})}{(\text{pile 1 dynamic deflection})} \quad \text{or} \quad \alpha = \frac{(\text{pile 2 dynamic deflection})}{(\text{pile 1 static deflection})}$$

SUMMARY

Designing foundations for vibrating machinery requires knowledge of both the theory and the software used. Soil / pile impedance is clearly the most complicated issue requiring software interface. It is recommended that the design engineer utilize the applicable design software with caution. While software results are highly dependant on accurate input data, the program input assumptions may not always be readily apparent to the user. In order to validate the program results, a grasp of the basic theory is required to facilitate visual and manual results verification. This paper provides a fundamental description of vibratory equipment foundation analysis methods, discussions on counterintuitive design results, and recommendations on software verification.

REFERENCES

Dyna5, Geotechnical Research Centre, University of Western Ontario, London, Ontario

Gazetas, G. and Makris, N. (1991). "Dynamic Pile-Soil-Pile Interaction. Part I: Analysis of Axial Vibration", *Earthquake Engineering and Structural Dynamics*, John Wiley & Sons, New York, NY, Vol. 20, pp 115-132

Kaynia, A. and Kausel E. (1982), "Dynamic Behavior of Pile Groups", *Proceedings of the 2nd International Conference on Numerical Methods in Offshore Piling*, Austin, TX

Mylonakis, G. and Gazetas, G. (1998). "Vertical Vibration and Additional Distress of Grouped Piles in Layered Soil, *Soils and Foundations*, Japanese Geotechnical Society, Vol. 38, No. 1, pp 1-14 1998

Novak, M., Nogami, T., and Aboul-Ella, F. (1978) "Dynamic Soil Reactions for Plane Strain Case", *Journal of the Engineering Mechanics Division*, American Society of Civil Engineers, Reston, VA, Vol 104, No. EM4, pp 953-959

Veletsos, A. and Verbic, B. (1974). "Basic Response Functions for Elastic Foundations", *Journal of the Engineering Mechanics Division*, American Society of Civil Engineers, Reston, VA, Vol. 100, No. EM2, pp 189-202

Wolf, J. and Deeks, A. (2004). *Foundation Vibration Analysis: A Strength-of-Materials Approach*, Elsevier, Burlington, MA

Appendix

Part 1: Single Pile Vertical Impedance:

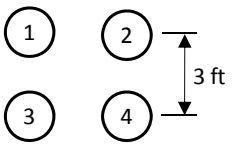
Given:

uniform soil
machine speed, MS = 750 rpm
soil shear wave velocity, V_S = 300 ft/s
soil unit weight, Y_S = 110 lb/ft^3
pile unit weight, Y_P = 150 lb/ft^3
pile radius, R_P = 0.5 ft
pile pattern = 2 piles by 2 piles

floating pile tip
soil poisson's ratio, v_S = 0.35
pile modulus, E_P = 804,230,000 lb/ft^2
soil damping ratio, β_S = 5%
pile damping ratio, β_P = 10%
pile embedment, L_P = 30 ft
pile spacing, Sp = 3 ft

1. Calculate circular frequency, ω:

$\omega = (MS)\,(\pi) / 30 = (750 \text{ rpm})(\pi) / 30 = 78.54$ rad/s



2. Calculate non-dimensional frequency, A_O:

$A_O = (\omega)(R_P) / (V_S) = (78.54 \text{ rad/s})(0.5 \text{ ft}) / (300 \text{ ft/s}) = 0.13$

3. Determine soil reaction against side of pile, S_V: (Novak 1978)

refer to Figure A1 using $A_O = 0.13$: S_V (real) = 1.9, S_V (imaginary) = 0.16

$S_V = 1.9 + i\ 0.16$

4. Calculate pile area, A_P:

$A_P = \pi (R_P)^2 = (\pi)(0.5 \text{ ft})^2 = 0.785 \text{ ft}^2$

5. Calculate pile mass per unit length, μ:

$\mu = (Y_P)(A_P) / (\text{gravity}) = (150 \text{ lb/ft}^3)(0.785 \text{ ft}) / (32.2 \text{ ft/s}^2) = 3.66 \text{ lb-s}^2/\text{ft}^2$

6. Calculate soil shear modulus, G_S and G_S':

$G_S = (Y_S)(V_S)^2 / (\text{gravity}) = (110 \text{ lb/ft}^3)(300 \text{ ft/s})^2 / (32.2 \text{ ft/s}^2) = 307{,}453 \text{ lb/ft}^2$

$G_S' = G_S [1 + i\ 2\beta_S] = (307{,}452 \text{ lb/ft}^2) [1 + i(2)(0.05)] = 307{,}452 + i\ 30{,}745 \text{ lb/ft}^2$

7. Calculate complex pile elastic modulus, E_P':

$E_P' = E_P [1 + i\ 2\beta_P] = 804{,}230{,}000 \text{ lb/ft}^2 [1 + i(2)(0.1)]$
$= 804{,}230{,}000 + i\ 160{,}846{,}000 \text{ lb/ft}^2$

8. Calculate frequency coefficient, Λ:

$$\Lambda = L_P \{[\mu \omega^2 - G_S (S_V)] / (E_P')(A_P)\}^{0.5}$$
$$= (30 \text{ ft}) \{[(3.66 \text{ lb-s2/ft}^2)(78.54 \text{ rad/s})^2 - (307{,}453 \text{ lb/ft}^2)(1.9 + i\ 0.16)] / (804{,}230{,}000 + i\ 160{,}846{,}000 \text{ lb/ft}^2)(0.785 \text{ ft}^2)\}^{0.5}$$
$$= 0.26 + i\ 0.99$$

9. Calculate pile tip resistance, R_V: (Veletsos 1974)

if $v_S < 0.4$
then $b_1 = 0.35$, $b_2 = 0.8$, $b_3 = 0$, $b_4 = 0.75$
otherwise $b_1 = 0$, $b_2 = 0$, $b_3 = 0.17$, $b_4 = 0.85$

$$R_R = 1 - (b_3)(A_O)^2 - (b_1)(b_2 * Ao)^2 / [1 + (b_2 * A_O)^2]$$
$$= 1 - (0.0)(0.13)^2 - (0.35)(0.8 * 0.13)^2 / [1 + (0.8 * 0.13)^2] = 1.0$$

$$R_I = b_4 + (b_1)(b_2)(b_2 * A_O)^2 / [1 + (b_2 * A_O)^2]$$
$$= 0.75 + (0.35)(0.8)(0.8 * 0.13)^2 / [1 + (0.8 * 0.13)^2] = 0.75$$

K_{ST} = 4 (G_S')(R_P) / (1 - v_S) = 4(307,452 + i 30,745 lb/ft^2)(0.5 ft) / (1 - 0.35)
= 946,010 + i 94,601 lb/ft

$R_V = K_{ST} (R_R + i R_I)$ = (946,010 + i 94,601 lb/ft)(1.0 + i 0.75)
= 933,094 + i 187,492 lb/ft

10. Calculate impedance coefficients, A, B, C:

sin (Λ) = 0.40 - i 1.11
cos (Λ) = 1.47 + i 0.30

A = (E_P')(A_P)(Λ)(cos Λ) / (sin Λ)(L_P)
= (804,230,000 + 160,846,000 lb/ft^2)(0.785 ft^2)(0.26 + i 0.99)(1.47 + i 0.30)) / (0.40 - i 1.11)(30 ft) = 26,495,827 + i 8,685,694 lb/ft

B = (E_P')(A_P)(Λ) / -(sin Λ) / L_P
= (804,230,000 + 160,846,000 lb/ft^2)(0.785 ft^2)(0.26 - i 0.99) / -(0.40 - i 1.11)(30 ft) = -18,400,243 - i 2,135,954 lb/ft

C = A + R_V = (26,495,827 + i 8,685,694 lb/ft) + (933,094 + i 187,492 lb/ft)
= 27,428,921 + i 8,873,187 lb/ft

11. Calculate single pile impedance:

K_V = [(A)(C) - (B)^2] / C
= [(26,495,827 + i 8,685,694 lb/ft)(27,428,921 + i 8,873,187 lb/ft) - (-18,400,243 - i 2,135,954 lb/ft)^2)] / (27,428,921 + i 8,873,187 lb/ft)
= 14,633,044 + i 9,657,535 lb/ft

12. Calculate stiffness and damping:

stiffness = K_V (real) = <u>14,633,044 lb/ft</u> (Dyna5 = 14,550,000)

damping = K_V (imaginary) / ω = (9,657,187 lb/ft) / (78.54 rad/s) = <u>122,964 lb-s/ft</u>
(Dyna5 = 122,300)

Part 2: Group Vertical Pile Impedance

1. Determine interaction factors, α:

(option 1, approximate equation) (Gazetas & Makris 1991)

$$\alpha = \text{sqrt}\,[R_P / S_P] * \exp\,[-(\beta_S + i)(S_P / R_P - 1)(A_O)]$$

(option 2, interpolate from available chart, such as attached Figure A2)
(Mylonakis & Gazetas 1998)

Note: For the following equations, the chart needs to be based on,
α = (pile 2 dynamic deflection) / (pile 1 dynamic deflection)

using option 1,

between the same pile (1-1, 2-2, 3-3, 4-4), $S_P/2R_P = 0.5 \rightarrow \alpha = 1 + 0i$
between adjacent piles (1-2, 1-3, 2-4, 3-4), $S_P/2R_P = 3 \rightarrow \alpha = 0.31 - i\ 0.24$
between diagonal piles (1-4, 2-3), $S_P/2R_P = 4.2 \rightarrow \alpha = 0.18 - i\ 0.27$

2. Assemble interaction matrix for the pile group, [α]:

$$[\alpha] = \begin{bmatrix} \alpha_{1,1} & \alpha_{1,2} & \alpha_{1,3} & \alpha_{1,4} \\ \alpha_{2,1} & \alpha_{2,2} & \alpha_{2,3} & \alpha_{2,4} \\ \alpha_{3,1} & \alpha_{3,2} & \alpha_{3,3} & \alpha_{3,4} \\ \alpha_{4,1} & \alpha_{4,2} & \alpha_{4,3} & \alpha_{4,4} \end{bmatrix} = \begin{bmatrix} (1.0 + i\,0.0) & (0.31 - i0.24) & (0.31 - i0.24) & (0.18 - i0.27) \\ (0.31 - i0.24) & (1.0 + i\,0.0) & (0.18 - i0.27) & (0.31 - i0.24) \\ (0.31 - i0.24) & (0.18 - i0.27) & (1.0 + i\,0.0) & (0.31 - i0.24) \\ (0.18 - i0.27) & (0.31 - i0.24) & (0.31 - i0.24) & (1.0 + i\,0.0) \end{bmatrix}$$

3. Calculate the inverse of the interaction matrix, [ε]. Inversion can be performed using built-in routines available in Excel or MathCad. In Excel, the Minverse routine can be used by first converting the matrix of complex numbers into an equivalent matrix of real numbers as follows:

$$\begin{bmatrix} (a_1 + ib_1) & (a_2 + ib_2) \\ (a_2 + ib_2) & (a_3 + ib_3) \end{bmatrix}^{-1} = \begin{bmatrix} a_1 & a_2 & -b_1 & -b_2 \\ a_2 & a_3 & -b_2 & -b_3 \\ b_1 & b_2 & a_1 & a_2 \\ b_2 & b_3 & a_2 & a_3 \end{bmatrix}^{-1} = \begin{bmatrix} \varepsilon_1 & \varepsilon_2 & -\varepsilon_4 & -\varepsilon_5 \\ \varepsilon_2 & \varepsilon_3 & -\varepsilon_5 & -\varepsilon_6 \\ \varepsilon_4 & \varepsilon_5 & \varepsilon_1 & \varepsilon_2 \\ \varepsilon_5 & \varepsilon_6 & \varepsilon_2 & \varepsilon_3 \end{bmatrix} = \begin{bmatrix} (\varepsilon_1 + i\varepsilon_4) & (\varepsilon_2 + i\varepsilon_5) \\ (\varepsilon_2 + i\varepsilon_5) & (\varepsilon_3 + i\varepsilon_6) \end{bmatrix}$$

Applying either inverse procedure results in,

$$[\varepsilon] = [\alpha]^{-1} = \begin{bmatrix} (1.06 - i0.28) & (-0.28 + i0.2) & (-0.28 + i0.2) & (-0.04 + i0.08) \\ (-0.28 + i0.2) & (1.06 - i0.28) & (-0.04 + i0.08) & (-0.28 + i0.2) \\ (-0.28 + i0.2) & (-0.04 + i0.08) & (1.06 - i0.28) & (-0.28 + i0.2) \\ (-0.04 + i0.08) & (-0.28 + i0.2) & (-0.28 + i0.2) & (1.06 - i0.28) \end{bmatrix}$$

4. Sum the 16 individual real and imaginary values from the inverted matrix:

$\Sigma\varepsilon = 1.88 + i\ 0.78$

5. Calculate the group impedance:

$K_{GV} = (K_V)(\Sigma\varepsilon) = (14{,}633{,}044 + i\ 9{,}657{,}535\ lb/ft)(1.88 + i\ 0.78i)$
$= 20{,}010{,}634 + i\ 29{,}677{,}526\ lb/ft$

6. Calculate stiffness and damping:

stiffness = K_{GV} (real) = <u>20,010,634 lb/ft</u> (Dyna5 = 15,480,000)

damping = K_{GV} (imaginary) / ω = (29,677,526 lb/ft) / (78.54 rad/s)
= <u>377,866 lb-s/ft</u> (Dyna5 = 397,500)

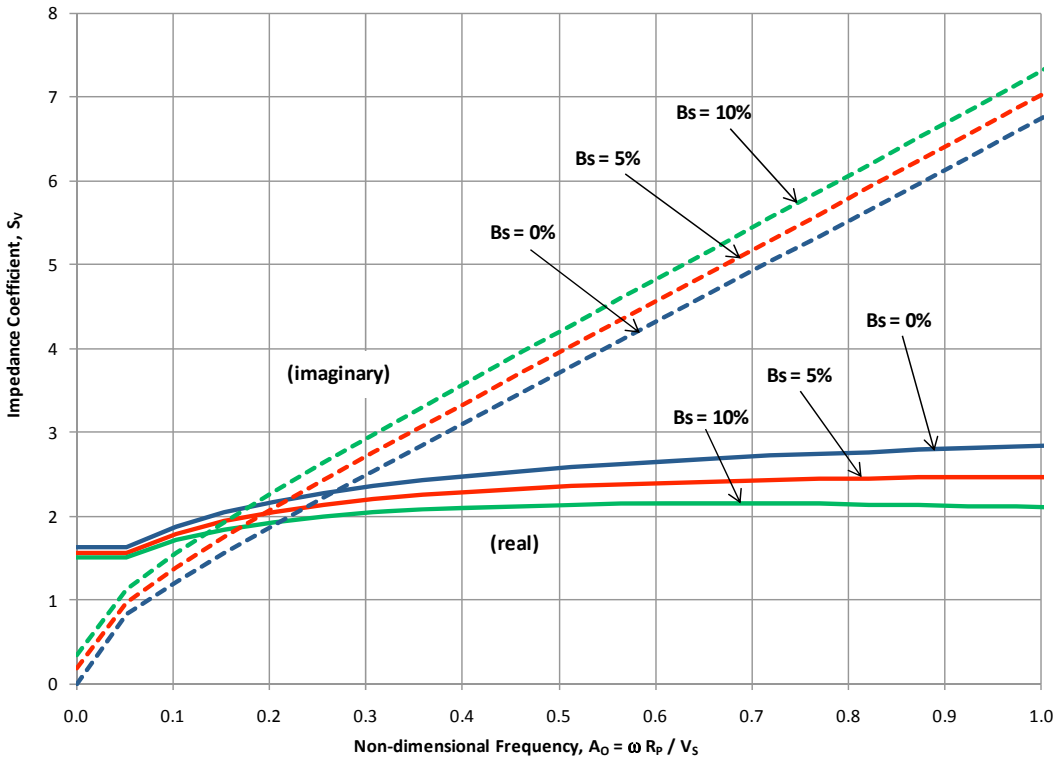


Figure A1 (S_V for low-frequency pile tip = floating)

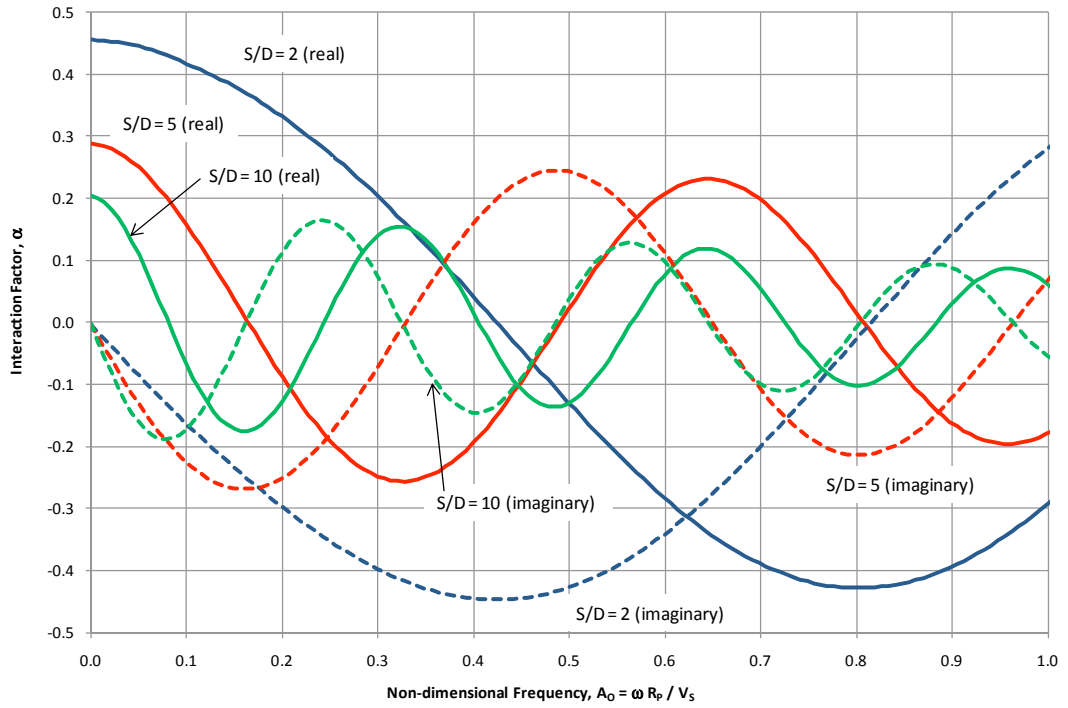


Figure A2 (values of α_V)

$L/d = 20$, $E_P/E_S = 1000$, $\upsilon_S = 0.40$, $\rho_P/\rho_S = 1.25$, $\beta_S = 5\%$

Weight Management Considerations for Onshore Modularized Petrochemical Facilities

Silky S.K. Wong[1], Alan Shive [2], and Harry Warren[3]

[1]Design Engineer II, Fluor Corp, One Fluor Daniel Drive, Sugar Land, TX 77478; PH (281) 295-6303; email: Silky.Wong@Fluor.com
[2]Director I, Design Engineering, Fluor Corp, One Fluor Daniel Drive, Sugar Land, TX 77478; PH (281) 263-4206; email: Alan.Shive@Fluor.com
[3]Senior Design Engineer, Fluor Corp, One Fluor Daniel Drive, Sugar Land, TX 77478; PH (281) 263-2678; email: Harry.Warren@Fluor.com

ABSTRACT

Modular construction is a well-proven technique for the North Slope of Alaska and the offshore petrochemical industry and is often preferred because of site conditions. Modularization is not a technique generally associated with conventional land-based petrochemical facilities, but certain project conditions, such as limited manpower availability and severe weather conditions, can make it the best construction execution method to achieve cost savings. Structural engineering for modular structures is more complex than for conventional structures due to requirements associated with transport, handling, and final placement of complete modules or major sub-assemblies. A primary source of the additional complexity is the need for structural engineers to participate in the Weight Management process.

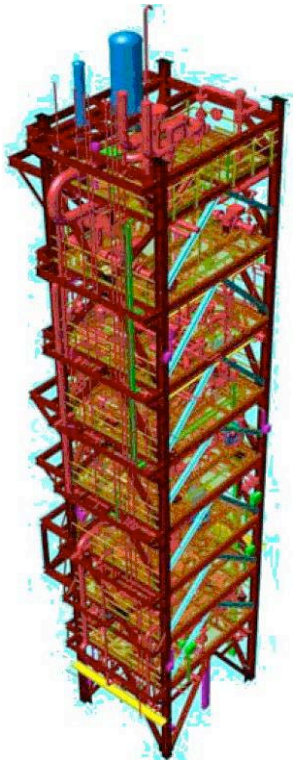
Determination of module weight and Center-of-Gravity (COG) location is a key component of the Weight Management process. This paper provides an overview of the Weight Management process and presents a structural engineer's roles in this process. An implementation example is provided to show how the weight control data is generated by the weight reporting scheme to be used to assist project planning and management, specifically in material procurement and transportation logistics planning.

INTRODUCTION

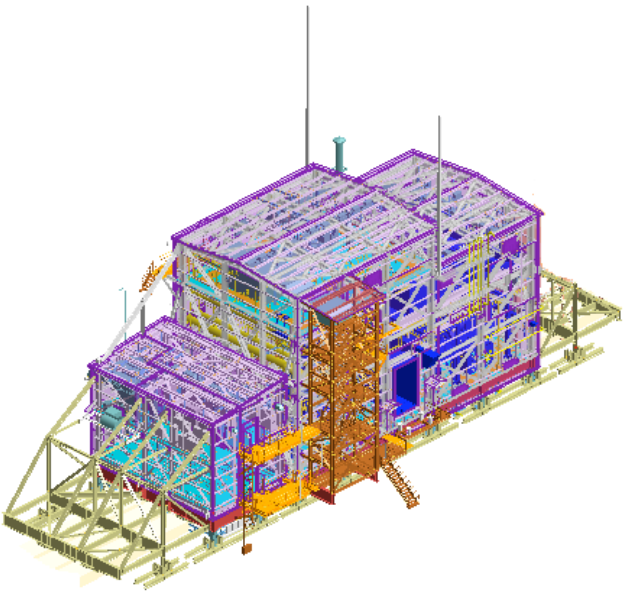
Modular construction[1], or modularization, refers to the assembly of components into packaging facilities that can be transported from the established offsite fabrication shops and yards to the project construction site for installation and pre-commissioning activities. Figure 1 illustrates 3-D isometric views of modules for onshore petrochemical facilities. Modular units generally cost 10%-15% higher than field erected units. However, the higher cost of modularization is often offset by performing the work at the fabrication site instead of in the field. Modularization

[1] Module - A transportable pre-assembly of process plant components designed to minimize site installation and commissioning labor costs.
Stick Built - The concept of erecting items at the job site from basic fabricated pieces without the use of pre-assembly or modularization.

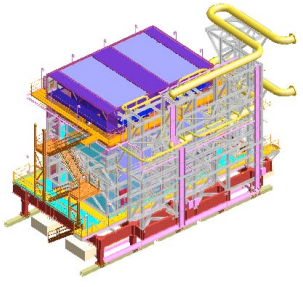
reduces the overall project cost due to lower field construction costs and a shorter field construction schedule. Onshore modular construction is found to be attractive due to the following potential benefits: better productivity, increased quality, reduced construction support requirements, minimized site congestion and interferences, lower direct labor rates, reduced safety risks associated with elevated work activities, and better supplier access.



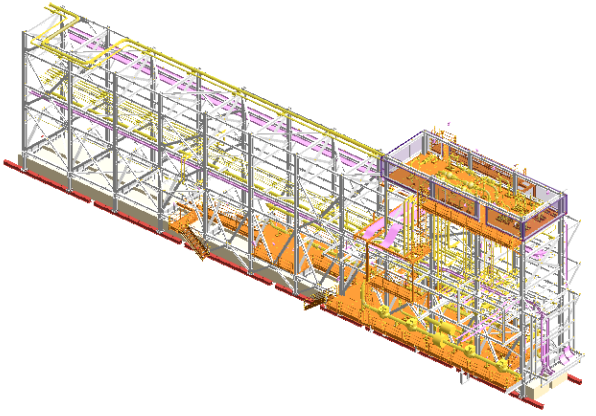
(a) Tower Module



(b) Gas Compression Module



(c) Air Cooler Module



(d) Piperack Module

Figure 1. Isometric Views of Modules for Onshore Petrochemical Facilities.

Currently developed onshore modularization techniques require careful attention with regard to internal access, methods of module transport, methods of placement, and problems associated with the greater compactness of a modular plant, including the limitations on the design of foundations, underground services, and cable routing.

These considerations must be incorporated into the onshore modularization Weight Management process throughout the project life cycle.

Among all engineering disciplines, Structural is the most involved discipline because modular structural steel must be designed to support all module components, withstand dynamic forces during transportation, and allow for installation by crane or transporter at the construction site. During a project feasibility study, structural engineers are often requested to provide technical evaluations and recommendations with respect to module identification, size limit, weight restriction, etc. It is not uncommon for a structural engineer selected to be the weight control engineer. Thus, a thorough understanding of the structural engineer's roles throughout the Weight Management process facilitates successful modularization project execution.

The following sections provide an overview of a recommended onshore module Weight Management process illustrated with flowcharts and the structural engineer's roles throughout the process. An implementation example is presented in the Appendix to demonstrate a typical periodic weight and COG data reporting process.

OVERVIEW OF THE ONSHORE MODULE WEIGHT MANAGEMENT PROCESS

Figures 2 (a) and (b) illustrate a typical Weight Management process associated with various project execution stages and facilitate the following:

- Evaluation of the current project condition with respect to the design development status.
- Evaluation of the defined constraints of Weight Management.
- Determination of whether the design should proceed.
- Determination of whether a design cycle should be repeated.

The extent, level, and frequency of weight reporting as part of a Weight Management process vary depending on the sensitivity of the specific module designs, the associated technical requirements, and whether weight considerations and COG are of a high priority in the project.

Decisions to be made during the process are heavily dependent on historical information by keeping good records of previous experience and continuous evaluations of weight and COG predictions across various project stages. A weight control reporting system is required to support the Weight Management process whereby at any time, accumulated weights can be checked against previously predicted weights. If discrepancies are found, the weight control reporting database can be managed and analyzed, so that the final weight can be achieved within the specified target weight.

If early weight estimates are based on relevant experience and reliable records, the process often demands no more than monitoring the weight of the structure as the project proceeds. Conversely, if early weight estimates are poor and low, the weight

control effort for the remainder of the project will become exceptionally arduous and require substantial management involvement in addition to monitoring weights and COGs. This will lead to additional design work by all disciplines during and after detailed design, causing schedule delays and increased cost.

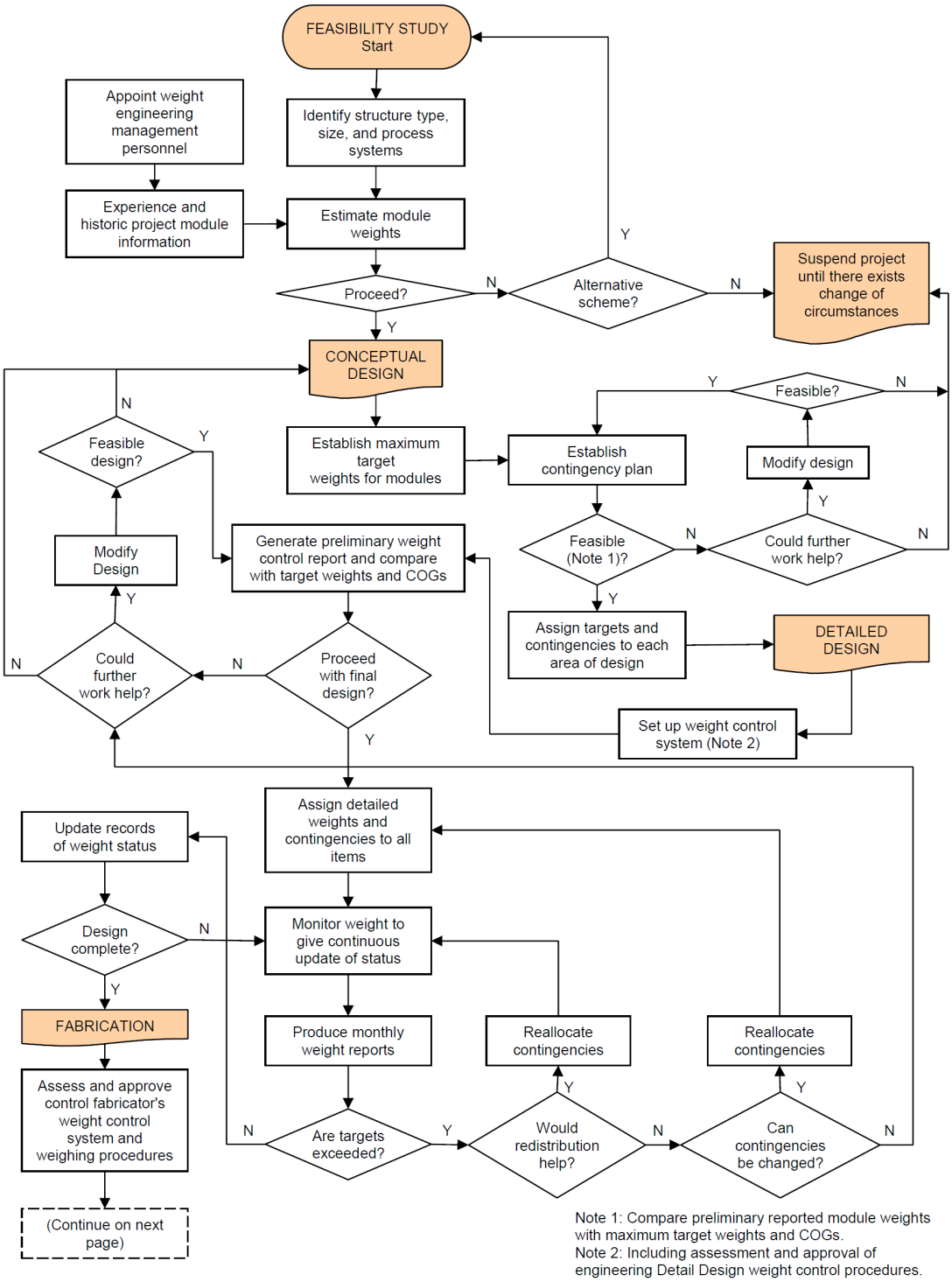


Figure 2(a). Recommended Onshore Modularization Weight Management Process.

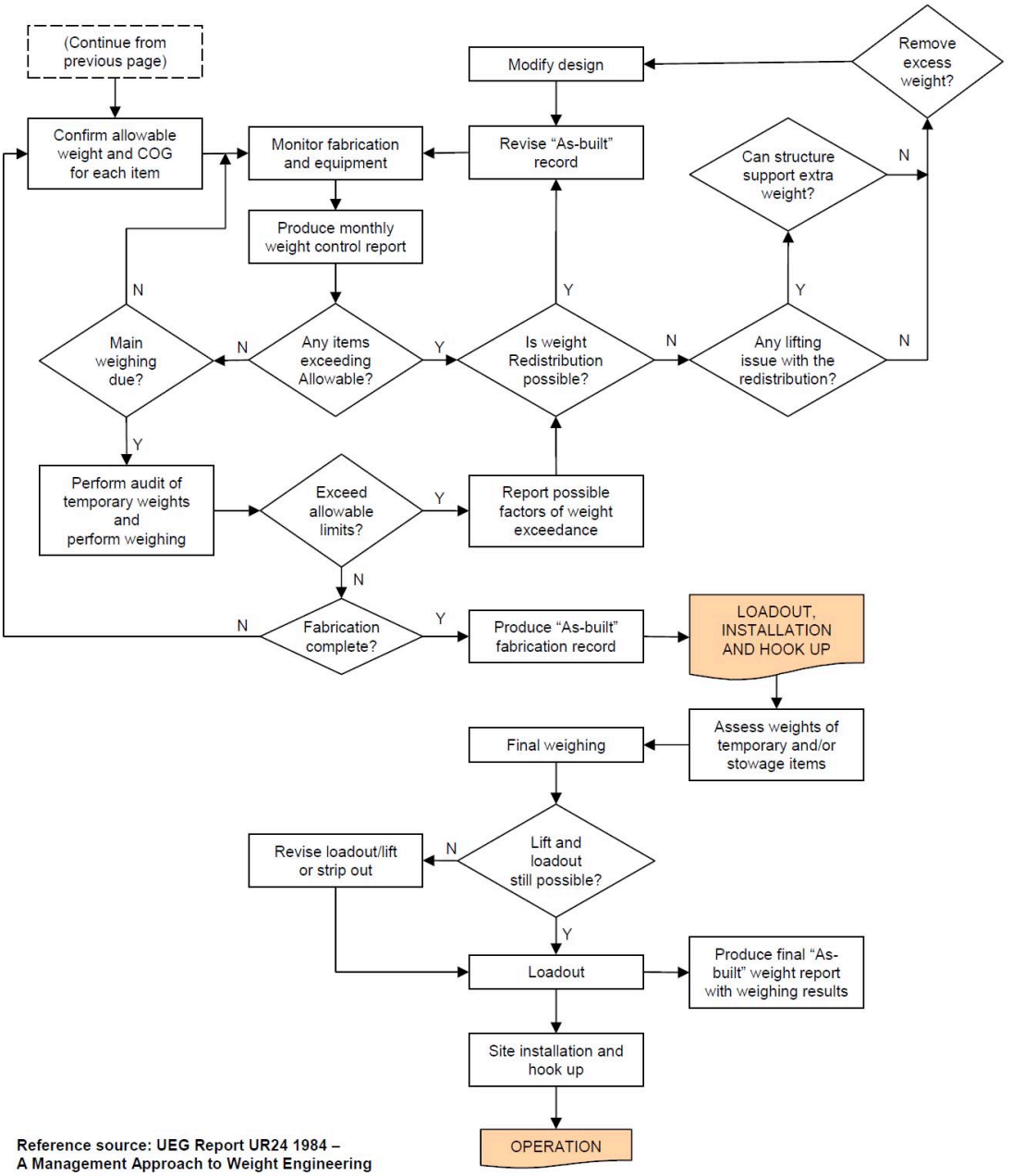


Figure 2(b). Recommended Onshore Modularization Weight Management Process (Continued).

STRUCTURAL ENGINEER'S ROLES THROUGHOUT THE WEIGHT MANAGEMENT PROCESS

The following discussion assumes that modules are fabricated and then transported by barge and over land, to a site where they are lifted and set on foundations.

For onshore modularization projects, the structural steel weight may reach as high as 70% of the total module weight, therefore, the Structural discipline is viewed to be primarily responsible for module design, its evaluation and acceptance, and

construction support. Structural engineers should engage in well-facilitated discussions about the project Weight Management plan starting from the feasibility study stage.

Stage 1 – Feasibility Study
Since data often is not readily available from previous projects, most of the weight estimates are expected to be based on the personal experience and expertise of the study leader. Structural engineers, who should have the best sense of weight accuracy and understanding among all the engineering disciplines, should participate in preliminary feasibility studies with project management and client representatives to assist in the development of schedule, risk analysis, and modularization strategy from a Weight Management perspective.

Stage 2 – Conceptual Design
The naval architect and the lifting contractor should be brought in at this stage to ensure that all the requirements of construction, transport and final installation can be met. However, this is not always possible due to client's project funding and resource allocations. The structural engineer should perform preliminary analysis to set up barge and lifting requirements, such as maximum weight and required barge deck stiffness. For land transportation, heavy haul routes should be identified considering transporter requirements, preliminary module configuration and weight limitations, as well as fabrication yard and project site constraints.

Stage 3 – Detailed Design
The use of a computerized weight control scheme becomes essential at this stage. In a large scale project, the number of module items may reach as many as 15,000 or more. Each of these items requires regular revision when information becomes more accurate. The weight status levels would typically be:

1. Current Estimated Weight
2. Weight with Well-Supported Information (such as developed drawings, supplier certified data, etc)
3. Weight without Well-supported Information
4. Final Weight

Current Estimated Weight (item 1) is equal to Weight with Well-Supported Information (item 2) plus Weight without Well-supported Information (item 3), which includes a suitable contingency. As the detail design progresses, item (2) improves, item (3) decreases, and items (1) and (4) should ideally converge.

Data of total weights and COGs for each installation phase (such as upon fabrication completion, during barge loadout, at project site installation and hook-up, etc) should be stored in the weight control database, in which the user is allowed to edit each data item separately, so that up-dates can be carried out quickly and effectively. A highly refined editing system should be developed to provide a concise summary with focuses on the major trends in weight build up and a breakdown of total weights by

each discipline. The structural engineer should participate in the development of this database and ensure correct generation of COG data.

Considerations in Determination of Module Weight and COG Location

An acceptable COG envelope should be developed based on combined weight and COG acting under various load conditions, including lift, transport, in-place, etc. The module structural engineer can conduct a sensitivity assessment to ascertain the effect of load distribution on the COG.

The following are various parameters that may require to be considered:

- Lift capacity
- Jacking capacity during weighing (Figure 3)
- Pile capacity
- Sea and land transport stability (Figure 4)
- In-place stability



Figure 3. Module Weighing by Hydraulic Jacking Load Cells.

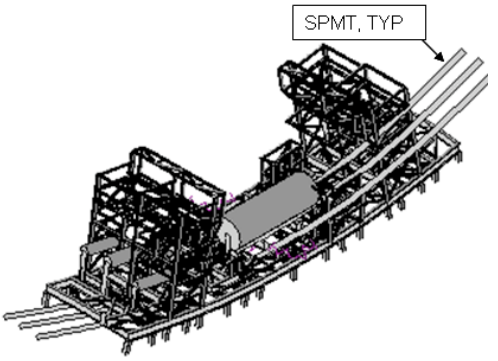


Figure 4. Module Deflected Shape Without Outrigger During Transportation.

The structural engineer should discuss with the client any design risk associated with the weight and COG characteristics, including special weight control problems and the areas to receive the weight control emphasis. During design development, it is not unusual that the projected COG approaches or exceeds the acceptable COG envelopes; the module structural engineer should re-evaluate these situations and determine if immediate actions are needed.

If the weight reports indicate that target weights are being exceeded, or module COGs are becoming unacceptably offset from the envelopes, a corrective action is required either by modifying the structure to accommodate the change or by distributing or repositioning the excessive weight.

Structural Design and Analysis Considerations

The following presents the considerations of structural design and analysis during detailed design phase:

- Detailed module structural analysis should validate a land transportation scheme, such as Self Propelled Modular Transporter (SPMT). Analysis should incorporate

a hydraulic load balancing system between each module and the SPMT. In order to minimize strengthening steelwork, the module's self weight should be evenly distributed over the SPMT support points.

- Module structural analysis models should be created for different transport scenarios, such as loadout, transport, installation, etc. To ensure that overall module stability considerations are properly addressed, the target weight and COG envelopes should be applied to these models, with added safety factors applied in accordance with project specifications. The benefit of using this approach is: When final weights and COGs are obtained during fabrication stage, the previously conducted analyses will still be valid and re-work will be avoided.
- Module lifting and feasibility studies are recommended to be performed by module design structural engineers.
- When structural engineers review vendor drawings for structural load calculations, they should ensure that weights shown on these drawings are accurately reflected on the weight reports from other disciplines.
- Weight factors to account for mill tolerances, welding, and paint should be added to the analysis process.
- Structural engineers should be involved in establishing the method and degree of weight control that will be required for subcontractors and vendors.
- Structural item contingencies should be updated on a regular basis with an understanding of how other disciplines provide their current item contingencies.
- Generating module transportation logistic data drawings for land transportation contractor would reduce the risks associated with problematic weight, stability, and clearance issues.

Weight Reporting Quality Assurance Considerations

Quality assurance can be delivered for reported weight data by developing a verification scheme and the following list:

- Establish common terminology for weight items.
- Develop procedures to maintain consistency in reporting methodology.
- Develop database specific to each module.
- Ensure consistent breakdown of discipline data.
- Employ discipline checklists to ensure that there are no missed items or double dipping.
- Verify equipment weight and COG data against the latest Master Equipment List.

Module Design Documentation Considerations for Weighing

The following module design records and any criteria specific to weighing should be clearly identified and provided to the fabricator:

- Completed sets of weight data collection sheets and related information, such as assumptions, sources of weight and COG data, references, etc.
- Records of the information used to develop estimates and reports.
- Design history and changes.
- Preliminary weight control plan.
- The constraints associated with the weight and COG limits.

Stage 4 – Procurement, Fabrication and Construction
This stage includes module fabrication, all installation, and hook-up work before operations.

During the fabrication stage, fabricators should report and monitor weight growth, but not manage weight growth. The engineering team should be aware that module weighing can be done using different methods, some of which are more accurate than others while some are less expensive. The selected weighing process and operations, including weighing method and in-situ weight monitoring, must be included in the weighing procedure. Prior to the management approval of the fabricator's weighing procedure, the structural engineer should provide technical recommendations and comments considering the module structures and project conditions.

Weight Management strategies at this stage should include supervision during fabrication to ensure that detailed weight reporting is occurring. Additionally, the weighing plan needs to be developed, because the selected weighing technique may affect the erection and/or transportation process. For example, load cell locations established by the fabricator should be submitted for structural engineer's approval, so that the structural members can be confirmed to resist jacking reactions properly. Also, the proposed load cell locations can be verified not to hinder any transporter arrangements.

The weight control manager may assign the module structural engineer to review predicted module weighing reports and final module weighing result reports before module loadout from fabrication yard. Module fabricator may add temporary items before loadout. Structural engineer's review on these weighing reports would prevent overstress of structural members, as the added temporary items may exceed the stowage weight considered in structural design.

THE WEIGHT CONTROL REPORTING SCHEME

Weight control reporting is the most significant activity throughout the Weight Management process. An example is presented in the Appendix as a guideline for the determination of module weight and COG data, as well as proposals on corrective actions when the target weight is exceeded and/or an unacceptable module COG offset is indicated. The main results of module weights and COGs, considering various transport load case conditions, are illustrated and discussed.

Challenges of Implementing an Effective Weight Control Reporting System
The significance of weight control reporting system is often overlooked due to a lack of disciplined "weight thinking" within the industry. Weight control is often regarded as an unnecessary and unfulfilling task, thus insufficient effort has been taken to make the systems work effectively. Weight control personnel often have insufficient authority within the design team to carry out their true function, as a result, the methods are ineffectively applied. Workflows among disciplines are often not created with the explicit goal of engaging fabricators and contractors early in design to ensure

that constructability considerations in the weight control reporting system are properly addressed. An undisciplined weight control approach is particularly apparent in projects which involve innovative concepts (i.e., lack of previous experience).

Another common misconception in weight control reporting is that the weight control manager may provide recommendations on the periodic weight reports without acquiring further verification and evaluation from structural engineers. However, some of the recommendations, such as weight shedding opportunities and addition of temporary items, may alter the structural design criteria and assumptions. The outcome may be detrimental if a module's structure is indeed required to be modified to accommodate the proposed changes.

CONCLUSION

Successful Weight Management for onshore modularized petrochemical facilities depends on a disciplined approach to record and update weight data related to each module component. Such a system is best developed at the outset of the Weight Management process, so that all engineering discipline weight control personnel acknowledge and appreciate the importance of their roles and responsibilities in the overall Weight Management effort.



Figure 5. A Piperack Module Sail Out with a Successful Weight Management Approach.

The challenge for the weight control team is to incorporate "weight thinking" into current discipline responsibilities and create an integrated weight reporting system across all disciplines.

This paper strives to introduce the onshore modularization Weight Management considerations to the structural engineering community. The general aspects of the Weight Management process, as well as structural engineer's roles throughout the process, are presented and discussed. Specifically, the importance of weight control reporting, as part of the Weight Management process, is emphasized and demonstrated with an example.

ACKNOWLEDGEMENT

The authors would like to sincerely acknowledge Exxon Neftegas Limited (ENL) [Photos] and Mammoet USA Inc. for their input. The authors also gratefully acknowledge the support from the P4 (Professional Publications and Presentations Program) committee of Fluor Corporation.

REFERENCES

Ainslie, S.H., Burns, P.D. and Clark R.J. (2005). *Modularization Techniques and Structural Steel Procurement on OPTI-NEXEN'S Long Lake Upgrader Project*, Proceedings of the 33rd Annual General Conference of the Canadian Society for Civil Engineering, Ontario, Canada.

Bounds, W. (2005). *Structural Engineering Challenges Designing Modules for the Sakhalin I Project*, Presentation at the Structural Engineers Association of Texas, Houston, Texas.

CAN/CSA-ISO 19901-5. (2005). *Specific Requirements for Offshore Structures - Part 5: Weight Control during Engineering and Construction*, Canadian Standards Association, Ontario, Canada.

Jani, R.P. and Thakar, M.A. (2006). *Conceptualization, Simulation and Structural Analysis of Modules during Land Transportation by Self Propelled Modular Transportation (SPMT),* Proceedings of the 10th East Asia-Pacific Conference on Structural Engineering & Construction, Bangkok, Thailand.

Jani, R.P. and Thakar, M.A. (2006). *Barge Transportation Analysis and Load-out Activities in Modular Construction,* Proceedings of the 10th East Asia-Pacific Conference on Structural Engineering & Construction, Bangkok, Thailand.

UEG Publication UR24. (1984). *A Management Approach to Engineering*, UEG Offshore Research, Westminster, London.

APPENDIX: WEIGHT CONTROL REPORTING EXAMPLE

The periodic weight and COG reporting of bargeable piperack Module PR-01 is covered in this example, given that:



Figure A1. Bargeable Piperack Module PR-01.

- Units: weight units are in Metric Tonnes (MT). All dimensions or coordinates are in meters (m).
- Client Established Target Weight: 730 MT
- Contingency: The project is at the end of conceptual design phase, the weight Contingency is set at 15% except Piping and Structural, since their calculated weights were based on data extraction from the 3D schematic modeling.
- Non-module weights (including piling, fencing, etc.) are excluded.
- Wet or operating module weights are not considered.

1. Provide discipline classification.
The weight is classified into the following engineering disciplines when applicable:

- Architectural
- Electrical
- HVAC
- Instrumentation, Automation and Telecommunication
- Loss Control (Fire & Safety)
- Mechanical
- Piping
- Structural

2. Define load cases.
During this reporting period, four (4) load cases are monitored for each module as shown in Table A1:

Table A1. Module Reported Weight Descriptions at Each Load Condition.

Condition Description	Reported Weight Description	Remarks
Loadout	= Subtotal + Temporary + Ship-Loose	Inclusive of any ship-loose items on the module, internal sea fastening, and temporary equipment items or installation components that may be on board at the time of loadout.
Transport	= Subtotal + Temporary + Tiedowns (+ Ship-Loose)	Inclusive of any ship-loose items transported on the module, internal and external sea fastening and tiedowns, and temporary equipment items or installation components that may be on board. Note: Ship-loose items are currently not

		planned to be transported directly on the module, .i.e., they are not considered as part of the barge transport weight.
Installation	= Subtotal + Temporary + Ship-Loose	Inclusive of any ship-loose items transported on the module, internal sea fastening, and temporary equipment items or installation components that may be transported on road.
In-Place (Dry)	= Subtotal + Ship-Loose + Site-Installed	Inclusive of module structure, equipment, piping bulks, electrical bulks and, if any, accommodation (but without items of consumable or variable loads, stores, crews and their effects). In-place dry weight also excludes external loads.

3. Check module dimensions are within maximum allowable values.

In this reporting period, module dimensions are within client approved module maximum allowable and dimensions as established in Table A2 based on historic data:

Table A2. Module Dimensions Summary.

	Module PR-01	Allowable	Exceed Allowable?
Length (m)	60	70	No
Width (m)	8	9	No
Height (m)	15	20	No

4. Define COG coordinates and constraints.

In this reporting period, module COG constraints are established in Table A3 based on historic data and preliminary input from the transportation contractor.

Table A3. Module COG Constraints.

Module Type	Longitudinal COG (X)	Transverse COG (Y)	Vertical COG (Z)
Piperack	Within L/3	Within W/3	Within H/2 + Height of trailers (1.5 m)

Note: Effect of trailer/SPMT arrangement is not included in the COG constraints.

A local coordinate system as shown in Figure A2 is used for the calculation of module COGs. The Z origin is based on the bottom of column base plate elevation. The X and Y origins are at southwest outer corner of the module outline (Note that module local coordinate system should not be changed once it is established for the project, but this information should be provided in each weight report).

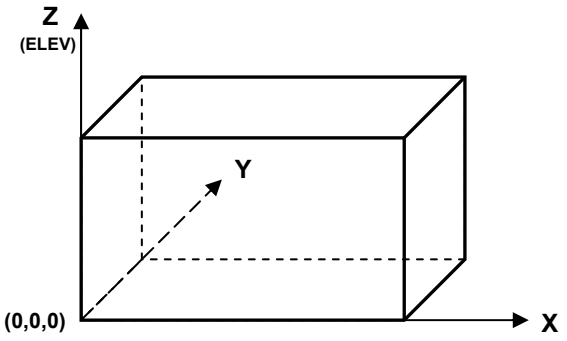


Figure A2. Module Local Coordinate System.

5. Generate up-to-date predicted module weight and COG information from discipline input.

Table A4. Discipline Reported Weights and COGs.

Discipline Description	Source	Status	Total Dry Weights (MT)			C.O.G. Coordinates (m)		
			Calculated Weight	% Contingency	Reported Weight	X	Y	Z
Architectural	S	E	1.37	15.00%	1.58	46.05	3.00	20.34
Electrical	S	E	5.83	15.00%	6.70	41.55	1.21	6.00
HVAC	S	E	0.00	15.00%	0.00	0.00	0.00	0.00
Instrumentation, Automation and Telecommunication	S	E	0.30	15.00%	0.35	43.68	3.51	5.82
Loss Control (Fire & Safety)	S	E	0.10	15.00%	0.12	43.68	3.51	5.82
Mechanical	-	-	0.00	0.00%	0.00	0.00	0.00	0.00
Piping	F	P	255.36	10.00%	280.90	44.95	3.51	7.99
Structural	F	P	367.71	10.00%	404.48	40.57	3.09	8.59
				Subtotal (MT)	694.12			
Temporary	F	E	7.80	15.00%	8.97	41.55	1.21	6.00
Temporary (Tiedowns)	F	E	30.56	15.00%	35.14	30.00	1.21	6.00
Ship-loose (All Disciplines)	S/F	E	6.47	15.00%	7.44	30.00	3.00	4.00
Site-Installed	S/F/C	E	4.90	15.00%	5.64	30.00	3.00	4.00

Notes:
(1) Source Codes: S - Supplier Information; F - Fabricator; C - Client Supplied Information
(2) Status Codes: E – Estimated; P – Preliminary; F – Final; W – Weighed

6. Process information to present facility weight status for the modules at the load cases stated in Step 2 and provide a summary of results, including areas of concern and recommended actions.

Table A5. Summary of Module Reported Weights and COGs.

Condition Description	Reported Weight (MT)	COG Coordinates (m)			COG Constraints [Min - Max] (m)		
		X	Y	Z	X	Y	Z
Loadout	710.5	**42.23***	3.21	8.28	20 – 40	2.7 – 5.3	0 – 9
Transport	**738.2 (NG)**	**41.77***	3.12	8.21	20 – 40	2.7 – 5.3	0 – 9
Installation	710.5	**42.23***	3.21	8.28	20 – 40	2.7 – 5.3	0 – 9
In-Place (Dry)	707.2	**42.14***	3.24	8.27	20 – 40	2.7 – 5.3	0 – 9

Note: *Exceeds the allowable COG offset envelope.

Module PR-01 currently falls outside the transportation constraints in the longitudinal (X) direction as indicated in Table A5. The following are the factors of the above preliminary COG results:

- The COGs were calculated using data in the computer model which is in development and only 20% complete. COGs for piping and equipment (including data for inline instruments and electrical weights) were calculated manually.
- The Pressure Safety Valve (PSV) platform design by vendor has been changed and the revised equipment and platform layout drawings will be developed.

- Any material or equipment that is currently defined as a ship-loose item is subjected to change.

It is recommended to consider the first floor East-West access walkway as a ship-loose item. The predicted weight after weight shed during transport condition will become 714 MT (refer to Tables A6 and A7 below). The proposal will ensure that the module weight is within transportation envelopes (i.e., 730 MT) and thus to minimize future rework in the detail design phase. This action requires further structural analysis and client agreement.

Table A6. Discipline Reported Weights and COGs with Weight Shed.

Discipline Description	Source	Status	Total Dry Weights (MT)			C.O.G. Coordinates (m)		
			Calculated Weight	% Contingency	Reported Weight	X	Y	Z
Architectural	S	E	1.37	15.00%	1.58	46.05	3.00	20.34
Electrical	S	E	5.83	15.00%	6.70	41.55	1.21	6.00
HVAC	S	E	0.00	15.00%	0.00	0.00	0.00	0.00
Instrumentation, Automation and Telecommunication	S	E	0.30	15.00%	0.35	43.68	3.51	5.82
Loss Control (Fire & Safety)	S	E	0.10	15.00%	0.12	43.68	3.51	5.82
Mechanical	-	-	0.00	0.00%	0.00	0.00	0.00	0.00
Piping	F	P	255.36	10.00%	280.90	44.95	3.51	7.99
→ **Structural**	F	P	**345.74**	10.00%	**380.31**	36.84	3.20	8.88
				Subtotal (MT)	669.95			
Temporary	F	E	7.80	15.00%	8.97	41.55	1.21	6.00
Temporary (Tiedowns)	F	E	30.56	15.00%	35.14	30.00	1.21	6.00
→ **Ship-loose (All Disciplines)**	S/F	E	**28.44**	15.00%	**32.71**	30.00	3.00	4.00
Site-Installed	S/F/C	E	4.90	15.00%	5.64	30.00	3.00	4.00

Notes:
(1) Source Codes: S - Supplier Information; F - Fabricator; C - Client Supplied Information
(2) Status Codes: E – Estimated; P – Preliminary; F – Final; W – Weighed

Table A7. Summary of Module Reported Weights and COGs with Weight Shed.

Condition Description	Reported Weight (MT)	COG Coordinates (m)			COG Constraints [Min - Max] (m)		
		X	Y	Z	X	Y	Z
Loadout	711.6	39.86	3.27	8.27	20-40	2.7-5.3	0-9
Transport	**714.1 (OK)**	39.82	3.18	8.35	20-40	2.7-5.3	0-9
Installation	711.6	39.92	3.27	8.28	20-40	2.7-5.3	0-9
In-Place (Dry)	708.3	39.82	3.30	8.27	20-40	2.7-5.3	0-9

Note: All COGs are within the allowable COG offset envelopes.

Repair and Retrofit of a Failed Deep Underground Sewage Pump Station

Prasad Samarajiva[1], Ph.D., P.E., M. ASCE and Narendra Gosain[2], Ph.D., P.E., M. ASCE

[1]Walter P Moore, 1301 McKinney Street, Suite 1100, Houston, Texas 77010, PH (713) 630-7300; Fax (713) 630-7396; PSamarajiva@WalterPMoore.com

[2]Walter P Moore, 1301 McKinney Street, Suite 1100, Houston, Texas 77010, PH (713) 630-7300; Fax (713) 630-7396; NGosain@WalterPMoore.com

ABSTRACT

Built 100' deep into dolomite bedrock, the influent pump station at Valley Creek Wastewater Treatment Plant in Alabama is approximately 360' long and 230' wide. Several elements of this underground structure failed in April 2005 only a few weeks after its commissioning, partially flooding the pump station and rendering it inoperable. After the causes of the failure were determined, the engineer presented several repair options. The accepted repairs included wall and floor thickening using 25,000 epoxy grouted steel dowels, uplift stabilization of the entire underground structure using 700 high-capacity rock anchors, installation of concrete and steel transverse bracing for previously laterally unsupported basement walls, modifications to various structural elements for reconfigured load paths by new transverse bracing, hydrophilic urethane crack injection in the mat slab to reduce groundwater infiltration, and epoxy injection of numerous cracked structural concrete elements. Despite the magnitude and the challenges of the repairs, the pump station was restored within three years of the failure and is fully operational.

INTRODUCTION

Valley Creek Wastewater Treatment Plant is an 85 Million Gallons per Day (MGD) sewage treatment facility (Photo 1). With the pump station in operation, it has 600 MGD of peak flow treatment capacity.

The pump station is built in a 100' deep excavation into dolomite bedrock. The footprint of this underground concrete structure is approximately 360' long and 230' wide and extends out 35' from each side of the substructure's long span. The underground concrete structure has three major functional areas: the wet well, the dry well, and the flume (Figure 1 and Figure 2). The wet well, which is continuous through the total depth of the pump station, is the receiving point of influent. The dry area located in the middle part of the pump station along the long span houses about 20 large pumps and discharge lines. The 35' wide and 35' high flume, which runs along the long span of the pump station on the opposite side of the wet well is supported by 53'tall concrete space frame of columns and beams. In addition, two stair wells, an elevator shaft, and an air shaft are located in the flume area.

The superstructure, which houses the control room, restrooms, loading dock, and storage rooms, is a 55'-tall steel and concrete frame structure with concrete masonry units (CMU) infill walls. Movement of heavy equipment in and out of the pump station is performed by an overhead gantry crane system running along the long axis of the pump station.

Several elements of the underground structure, including the mat slab, failed on April 2, 2005. Damage was visible in numerous concrete structural elements in the form of cracks and spalls. After the failure of the mat slab, groundwater flowed into and partially flooded the pump station, with the water level in the dry well of the station reaching 14' above the base mat. Heavy rains fell in the area days prior to the failure. The groundwater level outside of the pump station two days after the failure was approximately 68.5' above the base of the mat slab.

This paper presents the details of repair and retrofit procedures that were followed after determination of the cause of failure.

INVESTIGATION

The forensics engineering team conducted field observations performed a detailed structural analysis and design review, and conducted geotechnical testing and analysis. Details of this investigation was published in the proceedings of ASCE Structures Congress -2010 (Samarajiva and Gosain, 2010).

Distress observed in the field investigation can be summarized as follows:

1. A crack in the mat slab 2" wide and 100' long in the dry well adjacent to the wall that separates wet and dry wells;
2. Numerous cracks in the mat slab, flume structure, columns, beams, and walls;
3. Heaving of the mat slab.

In order to conduct a failure analysis, a finite element analytical model of the entire underground structure was implemented. The detailed failure analysis concluded the following:

1. The structural failure of the mat slab was caused by groundwater uplift pressure on the mat slab;
2. The underground perimeter walls of the structure were not designed to withstand the groundwater pressure present at the time of failure;
3. The structure as a whole did not have sufficient capacity to resist uplift forces under hydrostatic pressure if the groundwater elevation was close to the surface;
4. The strength of the structure was inadequate to resist the lateral earth pressures even without the presence of groundwater.

REPAIR OPTIONS AND CRITERIA

All repair options had to address four structural issues:

1. Repairing the damaged beams and columns under the flume;
2. Grouting or injecting the cracks in the mat slab to reduce infiltration of ground water if no dewatering system is installed;

3. Strengthening the perimeter walls to resist lateral loads due to earth pressure and groundwater;
4. Anchoring the mat slab to reduce buoyancy of the structure or installing a permanent dewatering system.

Based on the owner's input, five conceptual repair schemes depicted in Figure 3 were developed with approximate construction costs. After evaluating the associated risk, construction issues, cost and life expectancy of the pump station, the owner chose a combination of Options C and D. This included strengthening the structure to resist the hydrostatic lateral pressure due to groundwater and yet put in place a dewatering system to maintain the groundwater levels below a chosen threshold.

ENGINEERING CHALLENGES

Given the challenging nature of the project, the engineer consulted the facility's original general contractor and a subcontractor to develop a better understanding of challenges associated with the proposed repair options. The presence of the structural frames inside and large shot rock fill in the basin outside led the subcontractor to recognize that installation of rock anchors of the perimeter walls would be highly cost prohibitive. Therefore, Options A and B were abandoned. The geotechnical engineer found that complete grouting of the shot rock fill would be virtually impossible, and therefore Option C was also dismissed. The partially excavated backfill Option E would limit accessibility to the pump station. In addition, the buried lines in the proposed excavation area would hamper sewage transfer operations. Also, the owner wanted to limit the repair work only within the pump station.

As a result, repairs were limited to Option D or a variation of this option. Even though the impact of wall strengthening on the sewage retention capacity in Option D appeared to be insignificant, the introduction of an internal bracing system would severely hamper the pump station maintenance operations. For example, it would be virtually impossible to remove and replace the pumps if transverse braces were installed at every current frame location. Furthermore, installing transverse braces at the lowest level of beams would limit maneuvering space for internal operations of the pump station.

Based on those restrictions and the owner's operational requirements, the transverse bracing locations were limited to every other frame and these were installed only above the first beam level. As a result, the walls needed to be strengthened together with the installation of the transverse braces.

After considering all the associated issues and the owner's desire to have the pump station operational even during a failure of the ground water pumping system, the repairs items 1 to 11 pictured in Figure 4 were designed. These are described below.

During construction, some additional structural deficiencies were discovered. The majority of these deficiencies can be attributed to the discovery of the substitution of precast hollow core slab panels for a cast-in-place reinforced concrete slab at the

ground level to function as a diaphragm. It was determined that these hollow core slab panels were not designed to act like a diaphragm. As a result, creating new access hatches for the wet well repairs became impossible without strengthening the diaphragm slab. In addition, the concrete corbels for the bridge crane and the transfer beams under the crane columns were found to be structurally deficient. In order to address the later identified deficiencies, the repairs items 12 to 16 pictured in Figure 4 were also designed which are described below.

REPAIR DESCRIPTIONS

1. Anchoring the Mat Slab Using Rock Anchors

Nearly 680 rock anchors were installed on 9'x9' grid in the dry well and 9'x12' grid in the wet well (Photo 2). Finite element analysis was used to ensure effectiveness of the anchors when they were repositioned beyond the allowable 2' tolerance. Each anchor was design to sustain a tensile force of 580 kips. About 55 of these anchors were randomly subjected to Proof Tests and about 5 of these anchors were subjected to Extended Creep Tests.

2. Mat Slab Major Crack Injection

The major crack in the mat slab was injected to its full depth using hydrophilic polyurethane grout (Photo 3). Injection could be stabilized only after several attempts to bridge the gap.

3. Housekeeping Topping Slab Overlay for the Base Mat

Presence of many fractures in the area made it difficult to seal all the cracks. An 18" housekeeping topping slab was placed over the existing mat slab by sandwiching a drainage mat in between (Photo 4). The purpose of the drainage mat was to ensure free dissipation of ground water seeping through numerous cracks in the base mat.

4. Transverse Bracing

New 36"x36" transverse bracing struts were designed to match the existing beams. Concrete was chosen for the wet well section to and galvanized hollow structural steel square sections were chosen in the dry areas (Photo 5). Galvanized steel braces were chosen mainly to expedite the repair process. Use of galvanized steel was not a suitable option in the wet well due to the possibility of corrosion, The complexity of precise positioning of the bracing struts was met by the contractor.

5. Waler Beam in Wet Well

A new 96"x60" high strength concrete waler beam was attached to the concrete wall with epoxy grouted galvanized dowels (Photo 6). The purpose of this beam was to transfer lateral earth forces more uniformly than the existing wall. For accessibility reasons, the locations of construction joints, stirrups assembly, and lap splicing were

customized so the contractor could conduct other repair tasks simultaneously in the level below.

6. Wall Strengthening

Existing perimeter walls were thickened to increase the shear capacity (Photo 7). These 72"thick perimeter walls were thickened over a 35' height above the mat slab with thickness varying from 72" at the bottom to 24" at the top of the thickened section using high strength concrete. Epoxy grouted galvanized steel dowels were used to ensure composite action between the existing wall and the new wall.

7. Epoxy Inject Cracked Beams, Columns, and Walls

All minimally cracked structural concrete elements were epoxy injected. The purpose of epoxy injection was to reestablish aggregate interlock lost during the failure.

8. Recasting Heavily Damaged Concrete Beams

Some concrete beams were distressed beyond repair due to yielding of steel. Such heavily damaged concrete beams were demolished and recast to their original sizes. However, reinforcement was redesigned in the beams to function as struts.

9. Externally Bonded Ties for Columns and Struts

Structural columns were originally designed without column ties and introduction of the cross bracing frame caused some beams to function as struts. As a result, new externally bonded steel plates were designed for the columns and beams to function as ties. Epoxy anchors were used to attach steel plates to the columns and beams (Photo 8).

10. Repair Concrete Spall

Concrete spalls throughout the structure were repaired using standard repair methods using polymer cementitious mortar. The purpose of spall repairs was to ensure adequate concrete cover over the reinforcement.

11. Permanent Dewatering System

Based on a ground water study, a new programmable 4-pump dewatering system was installed. This system is capable of autonomously maintaining groundwater levels between user set limits.

12. Wet Well Diaphragm Strengthening

A new high strength concrete overlay slab was installed over the wet well topping slab to improve the diaphragm capacity (Photo 9). Epoxy anchors were used to ensure adequate shear transfer between the topping slab and the overlay.

13. Concrete Beams Inside the Flume

Certain parts of the superstructure were directly supported on hollow core concrete planks. These hollow core concrete planks were found to be inadequate to take the superstructure design loads. Therefore, 36”x36” concrete beams were installed inside the flume under the superstructure. In order to establish contact between the hollow core plans and the new beams, self-consolidating concrete was poured into the formwork through ports in the existing hollow core planks.

14. Steel Trusses to Support Crane Beams

The crane support beams were found to be under designed for the rated capacity of the pump station crane. This beam was at a location where it is difficult to install a fully assembled truss (Photo 10). Therefore, a series of galvanized steel trusses were designed to facilitate field assembly so workers could install them in pieces without the use of a heavy crane.

15. Corbel Strengthening

The crane supporting concrete corbels did not meet the minimum reinforcement requirement in design codes (ACI-318). As a result, additional reinforcing bars were epoxy grouted into the crane support corbels to meet the necessary strength requirements.

16. Closure of the Stair Well Openings

Existing stairwell openings were found to have reduced the diaphragm capacity below acceptable limits. As a result, the stair well openings in the middle of the top diaphragm were closed to ensure continuity in diaphragm action. New stair well segments were designed to provide access to the stair wells from the exterior (Photo 11).

CONCLUSIONS

After six months of investigation and analysis and five months of repair design, a plan was accepted by the owner to repair the pump station. These repairs included 700 rock anchors, nearly 25,000 epoxy-grouted dowels, 650 tons of steel and 8,000 cubic yards of concrete. The total cost of repairs amounted to $ 33 million and the original construction cost was about $52 million. Photo 12 shows the interior view of the structure after the repairs were completed.

Despite the magnitude and challenges of the repairs, the pump station was restored and fully operational to the owners’ satisfaction in less than three years from the time of failure. The success of these unusual repairs should be credited to the exceptional team work and creative structural solutions by all parties engaged and the owner’s unwavering commitment to restore the pump station to serve the community.

REFERENCES

ACI-318, "Building Code Requirements for Structural Concrete (ACI 318-99) and Commentary (ACI 318R-99)," June 1999, American Concrete Institute.

Samarajiva, P. and Gosain, N. (2010), "Investigation and Failure Analysis of Deep Underground Sewage Pump Station," Proceedings of Structures Congress, ASCE, May 2010.



Photo 1. Partial Interior View of the Pump Station Before Repairs

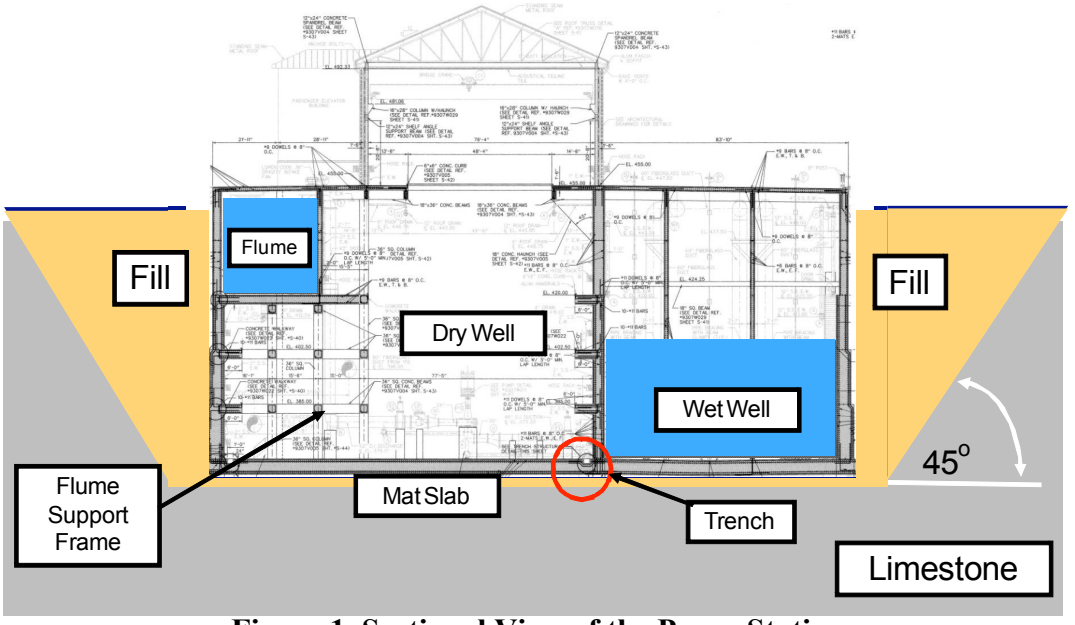
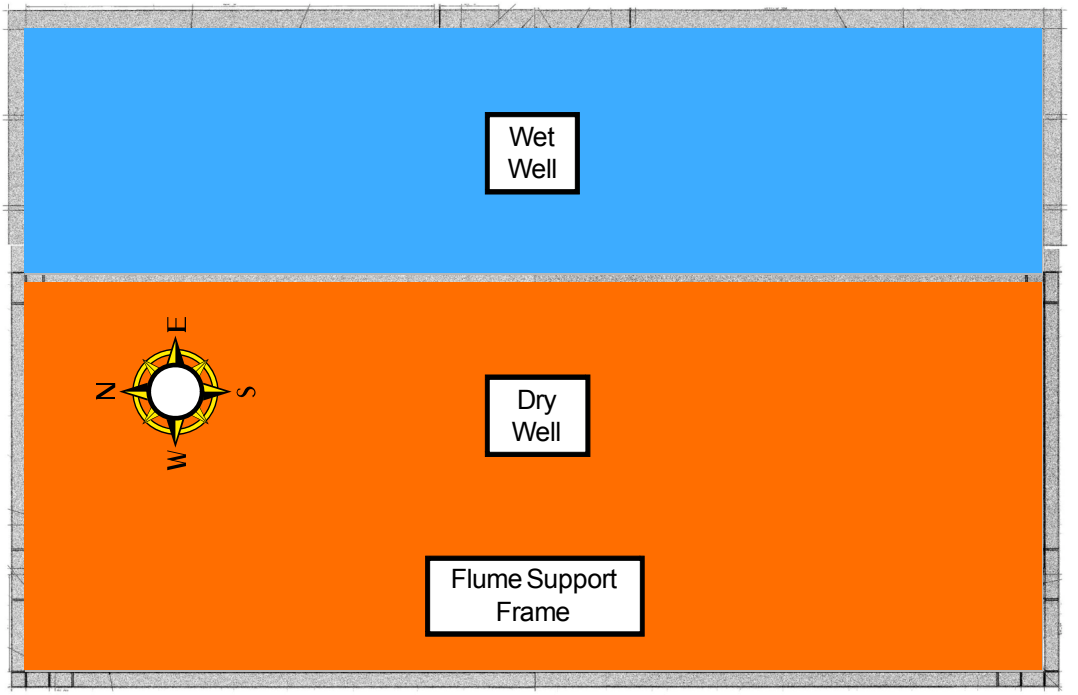
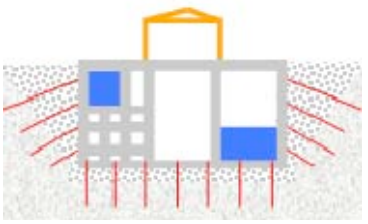


Figure 1. Sectional View of the Pump Station

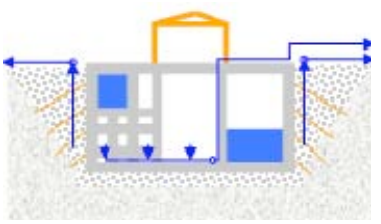


Plan View

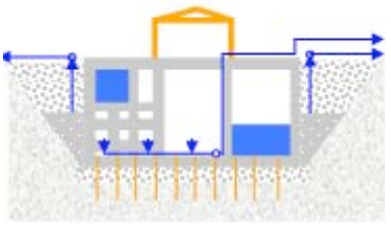
Figure 2. Schematic Layout of the Pump Station



(A) Fully Anchored System Without Dewatering



(B) Partially Anchored System With Dewatering



(C) Grouted Shotrock Fill



(D) Internal Cross Bracing Frame Without Dewatering



(E) Partially Excavated Backfill

Figure 3. Proposed Repair Options

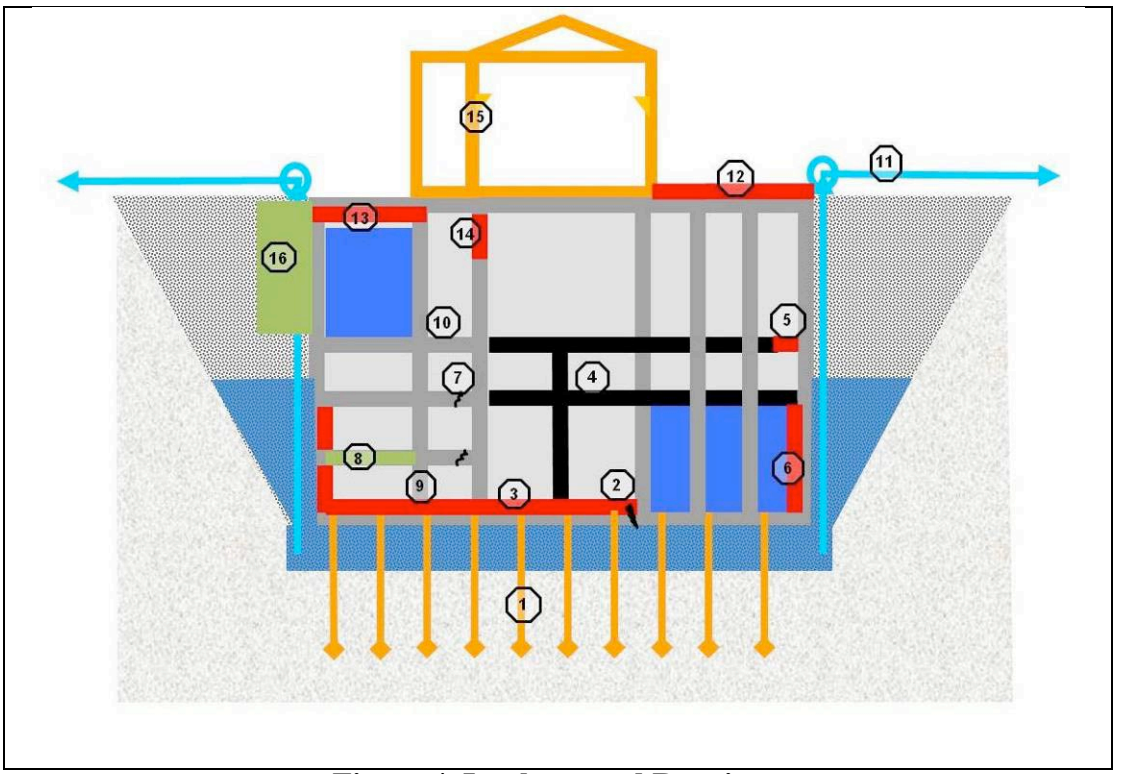


Figure 4. Implemented Repairs

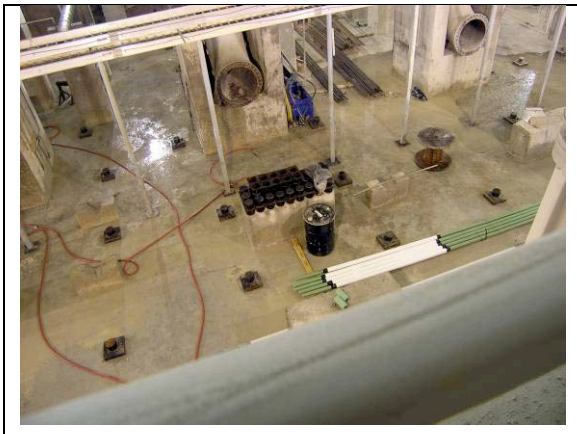


Photo 2. Installation of Rock Anchors



Photo 3. Urethane Crack Injection in Progress



Photo 4. House Keeping Slab Installation



Photo 5. Steel Strut Installation in Progress



Photo 6. Waler Beam Epoxy Doweling in Progress



Photo 7. Wall Strengthening in Progress



Photo 8. External Compression Ties



Photo 9. Installation of Dowels for Wet Well Diaphragm Overlay

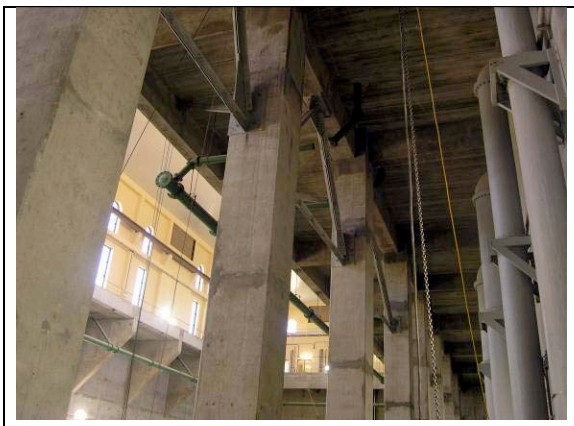


Photo 10. Crane Beam Support Truss



Photo 11. Exterior Stair Well Installation in Progress



Photo 12. Partial Interior View of the Pump Station After Repairs

SCR Pile Cap Foundation Design Using STAAD v8i & Excel

Jonathan Meyer, P.E.
Principal Engineer, WorleyParson Group Inc., 2675 Morgantown Road, Reading, PA 19607-9676

ABSTRACT: To expedite the design of foundations for the SCR support structure (40 m wide x 170 m long x 85 m high) at a Southeastern U.S. coal fired power plant, a number of STAAD Pro v8i (Bentley Systems, Inc., 2008) models were developed and Excel (Microsoft 2003) spreadsheets utilized. The forces were summarized in Excel to assist in the reinforcing design. There were a large number of primary load cases which resulted in thousands of service and strength load cases that needed to be analyzed. The large amount of data generated required post processing using Excel to consolidate and summarize the information. Typically, information is copied from STAAD Pro v8i and pasted into the appropriate location in the spreadsheet, however, one spreadsheet was utilized which uses Open STAAD (A library of exposed functions) to extract the pertinent information and combine the plate forces (Mx, My & Mxy). This spreadsheet was enhanced by graphics of the foundation plates that were then color coded to represent the extent of the required reinforcing. This provided a convenient visual representation of the extents of the required reinforcing.

Due to poor soil capacity and large loads, micro piles to rock were required to support the pile caps. The micro piles were modeled in STAAD Pro v8i and the forces extracted to an Excel spreadsheet which compared the values to allowable capacities. Foundation thickness was confined due to existing obstructions (feed water pipes, electrical duct banks, etc) which limited the foundation shear capacity. In a number of locations micro piles were located within *d* of the columns requiring a deep beam shear check of the foundation. Another spreadsheet was developed to provide this check by extracting the plate moments and shear for each load case and applying it with the appropriate deep beam shear formula. A comparison between the allowable deep beam shear and the actual was then made.

INTRODUCTION

Plant Robert W. Scherer, located near Macon, Georgia, is an electric generating facility consisting of four coal-fired units having a total capacity of approximately 3,500 megawatts. A large environmental controls initiative at the facility includes the construction of bag houses, selective catalytic reduction (SCR) facilities, and flue gas desulfurization (FGD) facilities. The Selective Catalytic Reduction (SCR) structures support numerous pieces of equipment used in the reduction of nitrogen oxides from the flue gas. The SCR reactors and dampers, as well as inlet and outlet ducts, are supported at various locations throughout the structure. Each SCR structure is approximately 40m wide by 170m long. The Units 1 and 2 structure is approximately 105 m high, while the Units 3 and 4 structure is 85m high. Each structure spans over two existing precipitators and is located between the boiler house and stack (See Figure 1). (Adeyefa, A. 2011, et al)

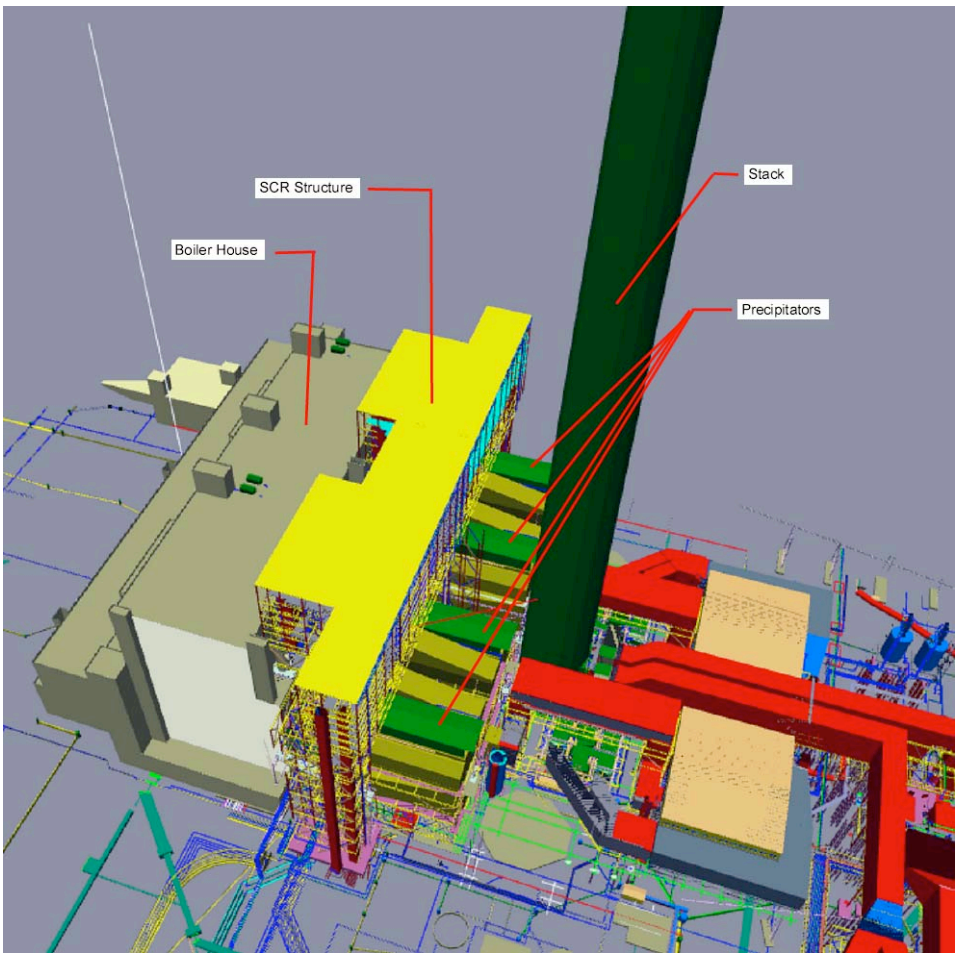


Figure 1 – SCR Structure – Units 1 & 2

The SCR structure has 70 columns to grade which are supported on numerous concrete foundations embedded on micro piles which extend to rock. This was necessary due to the limited soil capacity and the magnitude of the loading from the SCR structure. In addition the thickness of the pile caps was restricted due to existing underground obstructions such as piping and electrical duct banks.

Due to the number of loads and load combinations, as well as the number of foundations required to support the SCR structure, STAADPRO v8i was used to analyze both the structure and the foundations. Excel was used to extract data from STAAD v8i and to assist in the design of the foundation reinforcing. This paper describes the techniques used to determine the pile cap forces, pile forces and the design of the reinforcing for the pile caps for the units 1 & 2 SCR structure.

MASTER FOUNDATION MODEL

The SCR Structure was modeled in STAAD Pro v8i and consists of 10,292 beams, 4249 nodes, 74 primary load cases and 480 service load cases. It supports numerous pieces of equipment as well as dampers and large duct runs. The SCR structure is supported on 70 columns which in turn are supported on 21 pile caps with a total of 845 micro piles

drilled to rock. A master foundation model was created which contained all of the pile caps, piles and the primary loads from the steel model of the SCR structure. From this master model the individual pile caps were extracted and designed. The pile caps were modeled as four node or three node plate elements and the micro piles were modeled as prismatic members. Rigid links were utilized to simulate the foundation thickness to the support node of the SCR columns. An average pile length of 3 m was used with the properties of the section adjusted to address the average expected length of the micro piles. The plates were given the properties of concrete with f'c =34.47 MPa, E= 26 GPa and a density of 23.5 kN/m^3.

The ASCE/ACI service and strength load combinations as per the ASCE 7-05 and ACI 318-05 were then developed and input into the master foundation file. This resulted in 115 (LC #1 to 116) primary load cases, 615 service load cases (LC#120 to 734) and 774 strength load cases (LC#1000 to 1774). The individual foundation models were run and the results were extracted from STAAD v8i to spreadsheets to design the reinforcing and check the micro pile capacity.

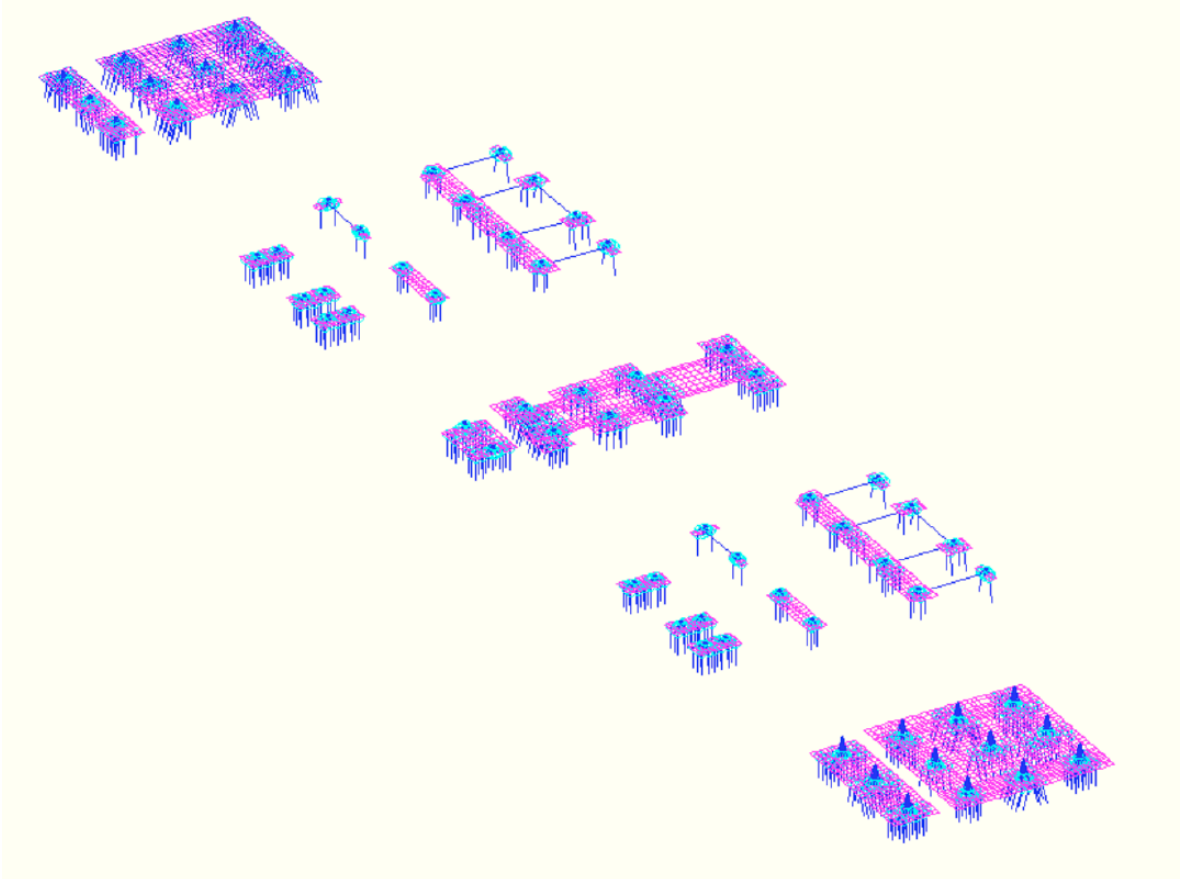


Figure 2 - Master Foundation STAAD Model

PILE CAPACITY CHECK AND PILE CAP REINFORCING DESIGN

To check the pile capacity, the service load reactions for the micro-piles were enveloped in STAAD Pro V8i and copied to the pile support reaction spreadsheet which summarized them in a handy table (See Figure 5). This table was then conditionally formatted using the allowable loads for the micro-piles, which were provided by the project geotechnical engineers. The conditional formatting colored the cells yellow if they were within the allowable loads and red if they exceeded the allowable loads. In this manner the micro-pile layout and number were checked to determine if the micro-pile configuration and number were acceptable.

To assist in the design of the pile cap another spreadsheet utilizing OpenSTAAD (Bentley Systems, 2008) was developed by WorleyParsons to extract the plate information, combine the moments and summarize them in a table. Worksheets were added to this spreadsheet to extract the top and bottom moments, Mx & My, and display them for each plate. Reinforcing capacities were input into the spreadsheets and the cells colored to represent the extent of the required reinforcing. Similar worksheets were made for the shear values, Vx & Vy.

To complete the process a calculation package was developed for the foundations with an appendix containing the design for each individual foundation. The main body of the calculation summarized the results for each foundation. In this manner all 18 foundations that support the SCR structure were designed and documented.

EXAMPLE FOUNDATION

The first foundation that was designed using this methodology was the south tower west foundation (STWF), which will be used as an example. The foundation is 6 m x 19.5 m x 2 m thick and is supported on 64 – 0.244 m diameter micro piles. The foundation supports three columns of the SCR structure. The micro piles surrounding the center column are battered at 14 degrees to the north and south respectively (12 north & 12 south). The 20 micro piles under the south end were symmetrically placed about the column. The 20 micro piles under the north end could not be placed symmetrically due to underground obstructions. The STAAD v8i model is shown in Figure 3.

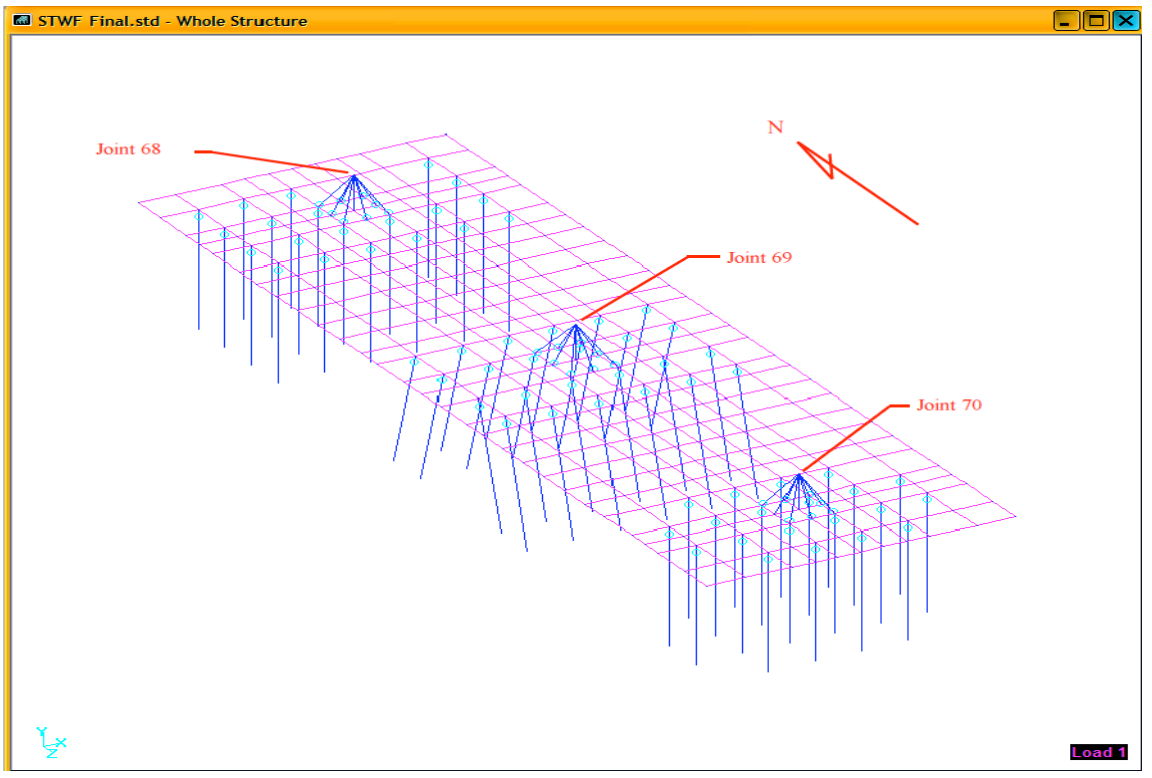


Figure 3 - STAAD Model

Design Loads

To gain a perspective on the loading of the foundation Figure 4 lists a number of the load cases and their respective values. Joint 68, 69 and 70 refer to the north, center and south columns on the foundation.

```
LOAD 1 SELF WEIGHT
SELFWEIGHT Y -1
JOINT LOAD
68  FX -5.55 FY -2286.91 FZ -115.52
69  FX -0.97 FY -1177.3 FZ 293.15
70  FX -2.79 FY -2759.48 FZ 326.08
*
LOAD 2 DEAD LOAD - ROOF, SIDING, GIRTS
JOINT LOAD
68  FX -0.25 FY -59.04 FZ 2.53
69  FX -0.05 FY -39.12 FZ 24.59
70  FX -0.14 FY -125.23 FZ 17.53
*
LOAD 3 DEAD LOAD - PLATFORMS
JOINT LOAD
68  FX -0.85 FY -134.68 FZ 13.37
69  FX -0.14 FY -106.38 FZ 81.04
70  FX -0.51 FY -366.48 FZ 53.9
*
LOAD 4 DEAD LOAD - DUCT AND REACTOR
JOINT LOAD
68  FX -2.69 FY -701.67 FZ 85.55
69  FX -0.53 FY -597.06 FZ 476.9
70  FX -1.99 FY -2173.37 FZ 311.16
*
*(LOAD 5 DEAD LOAD - PIPES/TRAY/CONDUIT)
*(LOAD 6 LIVE LOAD - STRUCTURE NOT IN STAAD)
*
LOAD 7 LIVE LOAD - PLATFORMS
JOINT LOAD
68  FX -6.87 FY -1182.48 FZ 51.96
69  FX -1.14 FY -813.42 FZ 509.51
70  FX -3.94 FY -2566.35 FZ 366.71
*
LOAD 8 LIVE LOAD - DUCT AND REACTOR
JOINT LOAD
68  FX -0.16 FY -57.78 FZ 4.48
69  FX -0.03 FY -43.26 FZ 30.9
70  FX -0.07 FY -149.92 FZ 20.93
ELEMENT LOAD
1 TO 280 PR GY -14.36
*
LOAD 10 LIVE LOAD - ROOF
JOINT LOAD
68  FX -0.25 FY -59.04 FZ 2.53
69  FX -0.05 FY -39.12 FZ 24.59
70  FX -0.14 FY -125.23 FZ 17.53
*
LOAD 11 LIVE LOAD - ASH
JOINT LOAD
68  FX -0.14 FY -64.75 FZ 2.58
69  FX -0.03 FY -43.03 FZ 26.76
70  FX -0.04 FY -140.55 FZ 19.07
```

```
LOAD 31 WIND LOAD (N->S) - OPEN LOWER STEEL
JOINT LOAD
68  FX 12.75 FY 8846.1 FZ 1047.56
69  FX 0.29 FY -230.4 FZ 1440.8
70  FX -5.23 FY -10341.05 FZ 1138.48
*
LOAD 32 WIND LOAD (S->N) - OPEN LOWER STEEL
JOINT LOAD
68  FX -12.75 FY -8845.7 FZ -1047.56
69  FX -0.29 FY 230.4 FZ 1440.8
70  FX 5.23 FY 10341.05 FZ -1138.48
*
LOAD 33 WIND LOAD (E->W) - OPEN LOWER STEEL
JOINT LOAD
68  FX -26.3 FY -7377.34 FZ 649.55
69  FX -12.17 FY -3165.26 FZ 150.37
70  FX -23.8 FY -6273.3 FZ 624.31
*
LOAD 34 WIND LOAD (W->E) - OPEN LOWER STEEL
JOINT LOAD
68  FX 26.3 FY 7377.7 FZ 649.55
69  FX 12.17 FY 3165.29 FZ -150.37
70  FX 23.83 FY 6273.52 FZ -624.31
*
LOAD 35 WIND LOAD (N->S) - OPEN UPPER STEEL
JOINT LOAD
68  FX 1.7 FY 1171.79 FZ 139.78
69  FX 0.13 FY 24.7 FZ 181.42
70  FX 0.11 FY -1135.5 FZ 129.11
*
LOAD 36 WIND LOAD (S->N) - OPEN UPPER STEEL
JOINT LOAD
68  FX -2.01 FY -1306.84 FZ -150.81
69  FX -0.18 FY -83.01 FZ -176.61
70  FX -0.36 FY 1015.34 FZ -116.78
*
LOAD 37 WIND LOAD (E->W) - OPEN UPPER STEEL
JOINT LOAD
68  FX -4.86 FY -1744.99 FZ -159.86
69  FX -1.03 FY -730.58 FZ 16
70  FX -4.63 FY -1424.45 FZ 132.97
*
LOAD 38 WIND LOAD (W->E) - OPEN UPPER STEEL
JOINT LOAD
68  FX 5.12 FY 1855.67 FZ 168.92
69  FX 1.07 FY 768.91 FZ -17.83
70  FX 4.76 FY 1481.87 FZ -139.18
*
```

Figure 4 -- Column Loads on the Foundation (Units kN & kPa)

Pile Forces

After the model was analyzed the pile forces for the service load cases were enveloped and copied into the pile support reactions spreadsheet. The spreadsheet summarized the information and provided the summary, a portion of which is reproduced Figure 5.

Pile Reaction Stat.			
Vertical	Compression(+)	1222.591	kN
	Tension(-)	-793.078	kN
Horizonal	Fy (Local)	20.768	kN
	Fz (Local)	23.156	kN

Note: Blue fonts are compression piles,black fonts are tension and compression piles.

	Node #	Max FX	Min Fx	Max Fy	Min Fy	Max Fz	Min Fz
5	4186	984.456	-480.5	1.072	-1.489	13.394	-23.098
13	4172	978.398	-489.311	1.071	-1.485	13.201	-22.91
21	4191	1086.727	-549.931	1.067	-1.48	13.396	-23.102
29	4175	1081.424	-558.823	1.067	-1.482	13.203	-22.914
37	4183	1020.79	-506.467	1.072	-1.487	13.338	-23.053
45	4185	1129.493	-579.076	1.067	-1.481	13.338	-23.053
53	4177	1015.901	-507.621	1.072	-1.487	13.274	-22.991
61	4182	1124.604	-580.23	1.067	-1.481	13.274	-22.991
69	4116	791.381	-427.83	1.193	-1.638	13.205	-22.887
77	4147	895.117	-494.079	1.199	-1.645	13.399	-23.077
85	4137	877.172	-484.161	1.199	-1.646	13.339	-23.018
93	4127	842.436	-461.979	1.193	-1.638	13.274	-22.955
101	4244	548.669	-576.542	20.599	-11.526	1.014	-1.404
109	4264	597.93	-604.492	20.731	-11.629	1.015	-1.406
117	4258	585.281	-595.814	20.7	-11.596	1.015	-1.405

Figure 5 - STWF Pile forces Summary

The value for compression, tension and shear were then compared to the allowable loads that were provided by the geotechnical engineers of 2002 kN compression, 1001 kN kips tension and 89 kN of shear. Since the pile forces were all less than the allowable pile forces, no modifications were required to be made to the pile layout. If any of the values would have exceeded the allowable values, the pile layout would have been revised to add vertical or battered piles or move piles. The model would be re-analyzed and the results copied to the pile forces spreadsheet for review. This process would be repeated until the all the pile forces were below the allowable pile forces.

Pile Cap Design

The design of the pile cap utilized a spreadsheet that was developed at WorleyParsons. This spreadsheet contains VBA macros which opens the STAAD file selected by the user, extracts the Mux, Muy, Muxy, Vx & Vy values, combines the Mux, Muy & Muxy values as per Wood (Wood, R.H., 1968) and Armer (Armer, R.G.T., 1968), separates the top and bottom Mux & Muy values and the maximum and minimum Vx & Vy values and writes them to a data file. It then summarizes the information in a convenient table and gives the user the option of writing the data to a pivot table adjacent to the analysis summary. All this is accomplished via the “Calculate” command button; see Figure 6 and Figure 7.

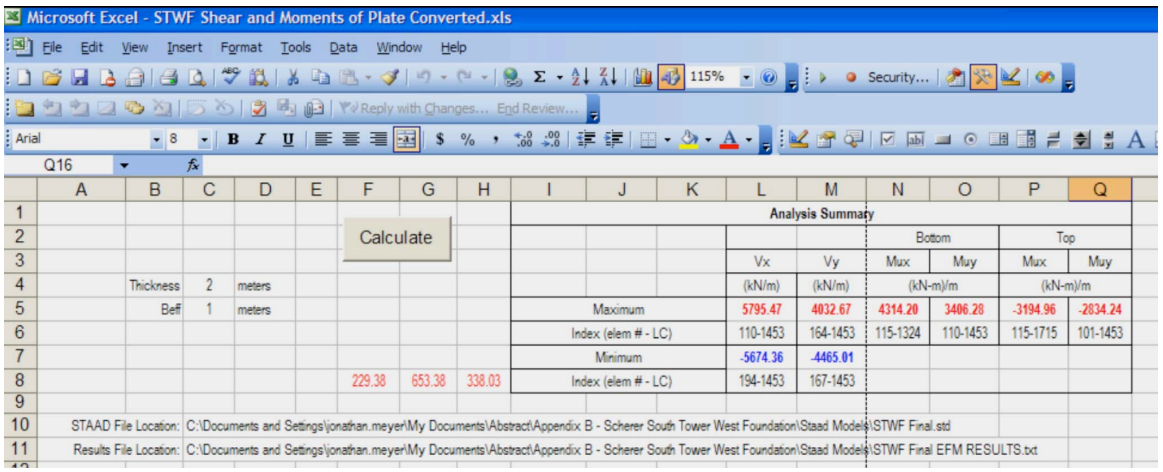


Figure 6 - Shear and Moments of Plate Summary

S	T	U	V	W	X	Y	Z	AA
Elem #	MAX of Mux	MAX of Muy	MIN of Mux	MIN of Muy	MAX of Vx	MIN of Vx	MAX of Vy	MIN of Vy
1	9.190	35.400	-36.490	-69.921	6.240	-34.960	142.880	-223.703
2	121.500	148.530	-206.760	-258.290	112.950	-237.890	172.080	-113.358
3	221.150	264.030	-346.640	-399.513	0.000	-56.580	521.260	-304.122
4	263.990	419.110	-401.700	-577.232	0.000	-50.720	248.540	-110.713
5	335.250	772.530	-509.990	-981.543	71.500	-208.600	578.780	-265.572
6	302.000	1060.370	-451.390	-1187.473	0.000	-60.750	936.230	-429.221
7	251.160	1206.980	-342.630	-1197.545	111.600	-81.570	746.090	-329.778
8	194.180	1384.640	-276.180	-1276.225	96.670	-62.940	535.250	-240.550
9	156.860	1547.270	-208.680	-1373.024	77.430	-42.970	348.730	-184.277
10	144.060	1674.220	-166.700	-1484.067	64.560	-30.690	197.010	-161.060
11	177.350	1770.610	-170.060	-1614.641	67.680	-31.490	144.310	-238.527

Figure 7 - Shear and Moment of Plate Pivot Table

To facilitate the pile cap design, additional worksheets were added to show the moments in each plate and color code them to selected reinforcing. The following lists the worksheets that were added and a short description of what it does:

"Mat" – Contains a map of the foundation plates with the plate numbers that correspond to the model.

"Mux Bottom" – Reads the plate number from the "Mat" worksheet and extracts the plate's maximum value of Mux from the pivot table which is the bottom moment in the plate in the x direction. See Figure 8.

"Muy Bottom" - Reads the plate number from the "Mat" worksheet and extracts the plate's maximum value of Muy from the pivot table which is the bottom moment in the plate in the y direction.

"Mux Top" – Reads the plate number from the "Mat" worksheet and extracts the plate's minimum value of Muy from the pivot table which is the top moment in the plate in the x direction.

"Muy Top" - Reads the plate number map from the "Mat" worksheet and extracts the minimum value Muy from the pivot table which is the top moments in the plate in the y direction.

"Vx" – Reads the plate number map from the "Mat" worksheet and extracts the largest absolute value Vx from the pivot table which is the maximum shear in the x direction.

"Vy" - Reads the plate number map from the "Mat" worksheet and extracts the largest absolute value Vy from the pivot table which is the maximum shear in the y direction.

Figure 8 shows the Mux Bottom worksheet for the STWF. The dots represent the pile locations, and the numbers in the cells are the values of the moments along the x direction for that plate. The outlined borders approximately represent either a distance d from the pier or the outline of the edge of the pier (column base plate). The cells have patterns which correspond to the reinforcing required in that area.

To determine the reinforcing required, the moment & shear capacities of various configurations of bars was calculated. Since the maximum value for each worksheet is shown, the user can select reinforcing that meets the demand of the foundation, input the FMn value in the appropriate cells and see where the reinforcing is required by the patterns in the cells. Along the top and left side is a distance from the start of the foundation to enable easy recognition of the extent to which reinforcing is required. This methodology was followed for each of the moment and shear worksheets (deep beam shear was also checked when applicable utilizing another spreadsheet).

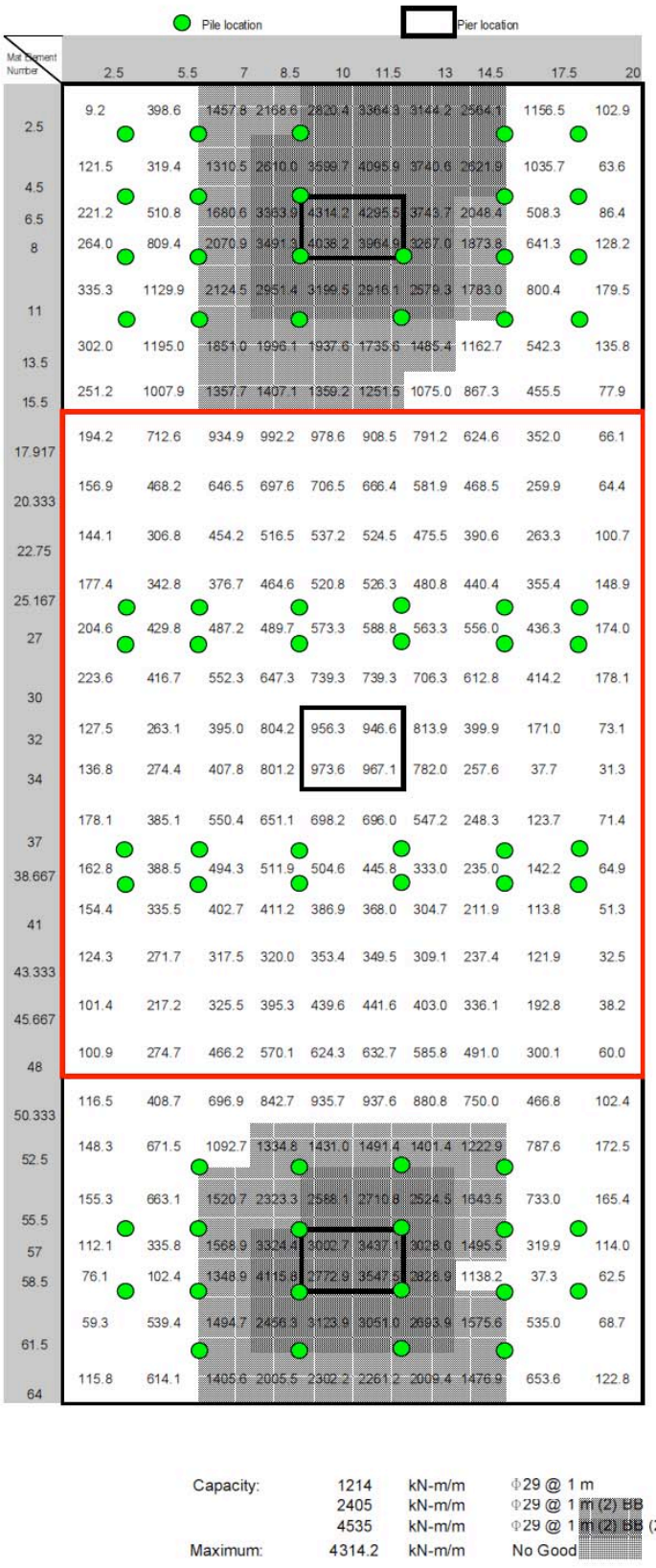


Figure 8 - Mux Bottom Worksheet

CONCLUSIONS

The design of the unit 1 & 2 SCR structure's foundations was able to be systematically approached via outlined procedure using STAAD v8i to analyze the foundation and Excel spreadsheets to post process the data. Once familiar with the spreadsheets the design of the foundations proceeded quickly. If additional manpower was available, it would have also been possible to have more than one engineer participate in the design. In addition, when presented with field changes, (i.e. existing adjacent caissons being larger than shown on the design drawings, or rock being deeper than expected) the models were quickly modified, the results exported to the spreadsheets and the effect on the foundations evaluated. In some cases this resulted in additional reinforcing being added, existing caissons being trimmed back to allow for clearances or piles being skewed to avoid interferences. Using these design procedures proved to be very effective and efficient in both the original design process and when confronted design modifications due to field changes.

ACKNOWLEGMENTS

I would like to thank the management and staff of The Southern Company and WorleyParsons for the opportunity to participate in the design of the unit 1 & 2 SCR foundations.

REFERENCES

Adeyefa, A., .Bolton, K., Pegues, J.C., (Accepted for publication, 2011), High Capacity Micropiles in Intermediate Geomaterials: Partial vs. Full Length Casing

Wood, R. H., (1968), "The Reinforcement of Slabs in Accordance with a Pre-Determined Field of Moments", *Concrete*, vol. 2, pp69-76, February 1968.

Armer, G. S. T., (1968), "Discussion of The Reinforcement of Slabs in Accordance with a Pre-Determined Field of Moments", *Concrete*, vol. 2, pp 319-320, August 1968.

Bentley Systems, Inc. (2008)

Microsoft Corporation (2003)

Concrete Shear Strength of Elevated Water Storage Tank Pedestals

Atis A. Liepins[1] and Gunjeet Juneja[2]

[1]Simpson Gumpertz & Heger Inc., 41 Seyon Street, Building 1, Suite 500, Waltham, MA 02453; PH (781) 907-9212; email: aaliepins@sgh.com
[2]Simpson Gumpertz & Heger Inc., 41 Seyon Street, Building 1, Suite 500, Waltham, MA 02453; PH (781) 907-9263; email: gjuneja@sgh.com

INTRODUCTION

Concrete pedestals of elevated water storage tanks support a steel vessel, schematically shown in Figure 1, or a concrete vessel, schematically shown in Figure 2.

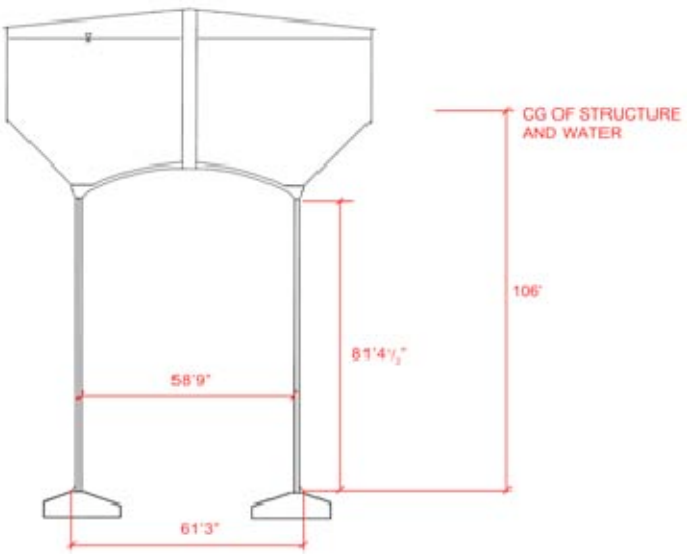


Figure 1. 2.0 MG composite elevated water storage tank.

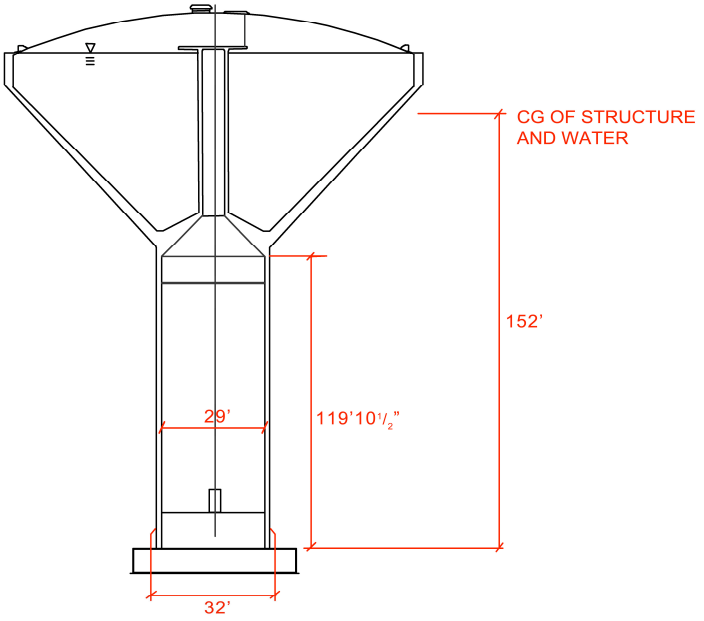


Figure 2. 2.0 MG concrete elevated water storage tank.

ACI Report 371R-08 [1] recommends that elevated tank pedestals be designed in accordance with ACI 318 (Code) [2]. The Code permits the shear strength of members to be calculated as the sum of the strength provided by concrete alone and the strength provided by shear reinforcement. For the concrete contribution to shear strength, Chapter 11 of the Code allows the designer of tank pedestals the choice of considering the pedestal as a compression member or as a shear wall. The Code provisions for compression members are based on tests of beams and beam columns of rectangular and solid circular cross sections. The Code provisions for shear walls are based on tests of walls of rectangular sections. The pedestals of tanks exemplified by the pedestals shown in Figures 1 and 2 are of thin-walled circular hollow sections. In addition, Chapter 21 of the Code provides requirements for structural walls subjected to seismic forces.

This paper discusses the concrete shear strengths of elevated tank pedestals obtained from ACI 318, proposes alternate concrete shear strengths based on theory and test results on plain concrete, and presents concrete shear strength and limit state obtained from a pushover analysis of the pedestal shown in Figure 2.

SHEAR STRENGTH OF PEDESTALS FROM ACI 318

ACI 318 allows the shear strength of the pedestal to be the sum of the shear strength contributed by concrete and shear strength contributed by shear reinforcement. Considered in this paper is the contribution of concrete without shear reinforcement to the total shear strength of the pedestal.

To apply ACI 318, the concrete pedestal can be considered to act as a member subjected to shear, flexure, and compression or, alternatively, to act as a wall.

For compression members with circular sections, the Code states that the area of the section to be used in computing the shear load can be taken as the product of

the diameter, D, and d = 0.8D, where d is the location of flexure steel relative to extreme compression fiber. This approximates closely the gross area of the concrete section A_g. We consider that A_g and d so defined also apply to hollow circular sections such as those found in pedestals.

With the section of the member so defined, for normal-weight concrete subjected to shear and flexure without compression, the Code allows the shear strength

$$V_c = 2\sqrt{f_c'}A_g \quad (1)$$

This corresponds to a shear stress $v_c = 2\sqrt{f_c'}$ uniformly distributed over the area of the section.

For members with compression, the Code shear strength is

$$v_c = 2\sqrt{f_c'}[1 + f_{cu}/2000] \quad (2)$$

where
$f_{cu} = N_u/A_g$ and
N_u = factored vertical compression load comprising a full vessel of water and the dead weight of the structure above the section investigated.

At the base of the pedestal of the composite tank, shown in Figure 1, f_{cu} = 960 psi and (2) leads to $v_c = 3.0\sqrt{f_c'}$. At the base of the pedestal of the all-concrete tank, shown in Figure 2, f_{cu} = 1,690 psi and (2) leads to $v_c = 3.7\sqrt{f_c'}$.

The Code also permits an alternate computation of shear strength of a compression member that includes the effect of flexure steel as well as bending, shear and compression. This alternate is not considered here because recent tests [3] show that it may lead to low factors of safety.

The Code provisions for shear strength of walls include a pair of expressions of which the lesser strength of the two governs.

$$v_c = 3.3\sqrt{f_c'} + 0.25\, f_{cu} \quad (3)$$

where
$f_{cu} = N_u/A$ and
$A = hd$

The second of the pair, taking $l_w = D$, $N_u/l_w h = f_{cu}$, and $M_u/V_u l_w$ approximately equal to H/l_w where H is the approximate location of the center of gravity of the structure plus a full vessel of water, is

$$v_c = 0.6\sqrt{f_c'} + (1.25\sqrt{f_c'} + 0.2\, f_{cu})/(H/l_w - 0.5) \quad (4)$$

Pedestals of elevated tanks are commonly constructed of 4,500 psi concrete. For the composite tank, $H/l_w = 1.7$, (4) governs, and $v_c = 3.9\sqrt{f_c'}$. For the all-concrete tank, $H/l_w = 4.7$, (4) also governs, and $v_c = 2.1\sqrt{f_c'}$.

The seismic provisions of the Code for structural walls limits the strength contributed by concrete to

$$v_c = V_c/A_{cv} = \alpha\sqrt{f_c'} \quad (5)$$

where $\alpha = 3.0$ for $h_w/l_w \leq 1.5$, $\alpha = 2.0$ for $h_w/l_w \geq 2.0$ and varies linearly between 3.0 and 2.0 for h_w/l_w between 1.5 and 2.0. With h_w equal to the height of the pedestal, (5) leads to $v_c = 3.0\sqrt{f_c'}$ for the composite elevated tank and $v_c = 2.0\sqrt{f_c'}$ for the all-concrete tank.

In summary, ACI 318, as applied here, limits concrete shear strength in pedestals of elevated tanks shown in Figures 1 and 2 as follows:

Loading Condition	Concrete Strength, $v_c/\sqrt{f_c'}$	
	Composite Tank	All-Concrete Tank
Seismic	3.0	2.0
Nonseismic	3.6	2.1

PROPOSED ALTERNATE SHEAR STRENGTH OF CONCRETE FOR PEDESTALS

We base our proposal for concrete shear strength of elevated water storage tank pedestals on the three invariant cap model of Schwer and Murray [4]. The model uses the first invariant of the stresses,

$$I_1 = \sigma_1 + \sigma_2 + \sigma_3 = 3P, \quad (6)$$

the second invariant of the deviatoric stresses,

$$J_2 = [(\sigma_1 - \sigma_2)^2 + (\sigma_2 - \sigma_3)^2 + (\sigma_3 - \sigma_1)]/6, \quad (7)$$

and the third invariant of the deviatoric stresses,

$$J_3 = s_1 s_2 s_3 \quad (8)$$

where
σ_1, σ_2, σ_3 = principal stresses,
s_1, s_2, s_3 = principal deviatoric stresses,
P = hydrostatic pressure,
and positive stresses are considered compressive.

The failure function is based on these three invariants and the cap hardening parameter, κ, as follows:

$$F(I_1, J_2, J_3, \kappa) = J_2 - R^2 F_f^2 F_c = 0 \quad (9)$$

where
F_c = hardening cap function [4],
R = Rubin function [4],
$F_f = \alpha - \lambda \exp(-\beta I_1) + \theta I_1$, (10)

and α, λ, β, and θ are parameters determined from calibrations of triaxial compression tests on plain concrete test specimens.

The failure surface, F, can be visualized as a surface in Haigh-Westergaard principal stress space with the hydrostatic axis at equal angles from the principal stress axes, the deviatoric plane perpendicular to the axis at a distance from the origin that is proportional to the hydrostatic pressure, a radius in the deviatoric plane that is a function of $\sqrt{J_2}$, and its polar location at an angle that is a function of J_2 and J_3. The intersection of the failure surface by a plane that contains the hydrostatic axis and deviatoric radius at polar angle of zero is F_f, and is known as the compression meridian. Points on the compression meridian are obtained from triaxial tests, frequently on cylindrical test specimens, but cubes as well, in which the confining pressure on the cylindrical surface is held constant and the axial stress is increased to failure. Figure 3, based on calibrations found in Reference [5], shows the compression meridian corresponding to $f_c' = 4{,}500$ psi a commonly used concrete strength in the construction of elevated tank concrete pedestals. In Figure 3, σ_1 is the axial stress and σ_3 is the confining stress in a test of a cylindrical specimen and $\sigma_1 - \sigma_3 = \sqrt{(3J_2)} = \sqrt{3}F_f$.

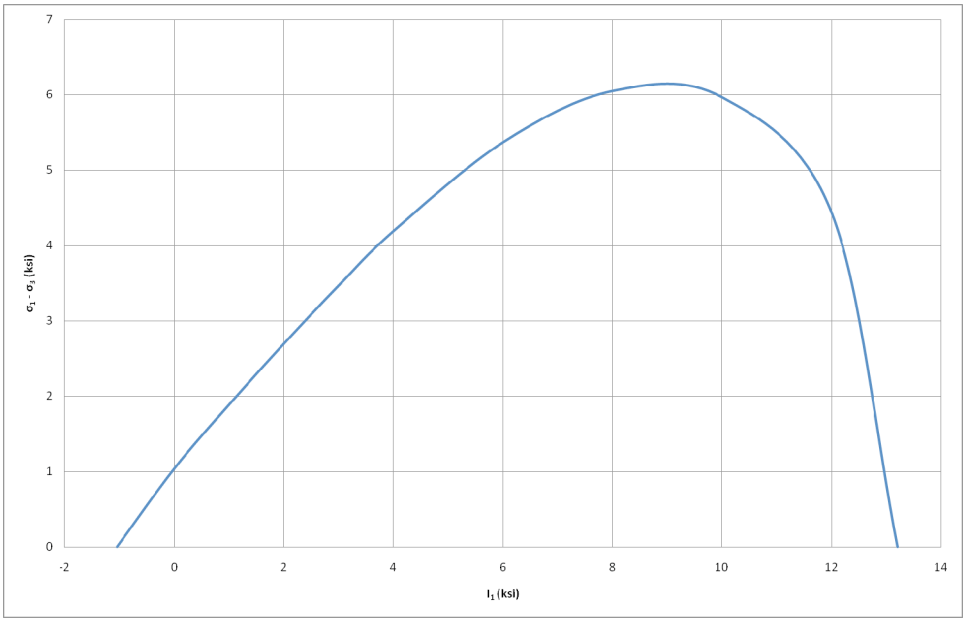


Figure 3. Compression meridian.

Two other meridians of the failure surface include the extension meridian and the shear, or torsion meridian. Points on the extension meridian are obtained from triaxial tests where the axial stress is held constant and the confining stress is increased to failure. Points on the shear meridian are obtained from triaxial tests where the axial stress is increased and the confining stress decreased, or the axial stress is decreased and the confining stress increased, so that I_1 remains constant.

The Rubin function, R, scales the extension, shear, and other meridians to the compression meridian, therefore, R = 1 for the compression meridian [4]. The shear meridian value at $I_1 = 0$ is pure shear and is equal to $(\sigma_1 - \sigma_3)/3$.

Figure 3 shows that at $I_1 = 0$ the variation of $(\sigma_1 - \sigma_3)$ is nearly linear. A similar observation holds for the shear meridian. This suggests that the shear strength of confined concrete may be taken as

$$v_c = C_1 + C_2 I_1 \tag{11}$$

where C_1 and C_2 are functions of f_c'.

Since the shear strength of concrete is commonly taken proportional to the square root of f_c', we take $C_1 = k_1\sqrt{f_c'}$, and inspection of available test results suggests that C_2 could be taken proportional to the cube root of f_c': $C_2 = k_2(f_c')^{1/3}$, where k_1 and k_2 are constants to be determined from available test results. Then,

$$v_c = k_1\sqrt{f_c'} + k_2(f_c')^{1/3}I_1 \tag{12}$$

and

$$I_1 = \sigma_1 + \sigma_2 + \sigma_3 = \sigma_v + \sigma_h + \sigma_r \tag{13}$$

where
σ_v = vertical stress in the pedestal,
σ_h = hoop stress in the pedestal,
σ_r = radial stress in the pedestal.

The radial stress σ_r, is zero, considering the pedestal as a cylindrical shell. The hoop stress σ_h, is a secondary stress resulting from discontinuity of deformation at the base of the pedestal which can be neglected. Then,

$$v_c = k_1\sqrt{f_c'} + k_2(f_c')^{1/3}\,\sigma_v. \tag{14}$$

To determine k_1 and k_2, we use the laboratory tests conducted by Kupfer, Hilsdorf, and Rusch [6]; Mills and Zimmerman [7]; Launay and Gachon [8]; Khaloo and Ahmad [9]; Cardenas, Hanson, Corley, and Hognestad [10]; and strength results included in Reference [5]. The data in the above references were plotted to obtain part of a compression meridian near $I_1 = 0$, similar to that shown in Figure 3 and the Rubin function, that has been calibrated in Reference [5] for the concrete strengths in Reference [5], was applied to obtain the shear meridian. Table 1 summarizes the k_1

and k_2 values so obtained. Reference [11] includes an extensive list of test results conducted by others. These are not used here because the required extrapolations lead to k_1 values that are twice and three times as large as those in Table 1 and the extrapolated values were considered inaccurate.

Table 1. Values of k_1 and k_2 Based on Published Data.

Reference	f_c', psi	k_1	k_2	Test Specimen
4	2,700	3.5	0.022	7.9 in. X 7.9 in. X 2
	4,450	3.8	0.020	in.
	8,350	4.4	0.014	
5	3,340	6.9	0.019	2.25 in. X 2.25 in.
	3,910	7.1	0.018	cubes
	5,235	6.6	0.018	
6	5,290	4.2	0.011	5.5 in. X 5.5 in. cubes
7	5,850	4.3	–	75 in. X 75 in. 3 in. wall
8	5,500	5.6	–	3 in. X 9 in. cylinders
	8,000	5.7	–	
2	2,900	3.6	0.021	Published data
	4,060	4.9	0.021	
	5,510	5.5	0.020	
	6,670	5.5	0.020	
	8,410	4.9	0.018	
Average	**5,345**	**5.1**	**0.018**	

For $f_c' = 4{,}500$ psi, a frequently used concrete strength in the construction of elevated water storage tank pedestals, the average values of k_1 and k_2 in Table 1 lead (14) to

$$v_c = 340 + 0.30\,\sigma_v \tag{15}$$

where σ_v is positive when compressive.

The pedestal of the composite steel-concrete water storage tank, shown in Figure 1, works at a compression stress of approximately 650 psi due to self-weight and the weight of a full vessel of stored water. For this condition and for this tank, (15) leads to $v_c = 535$ psi $= 8\sqrt{f_c'}$. The pedestal of the all concrete water storage tank, shown in Figure 2, works at a compression stress of approximately 1,200 psi. For this tank, (15) leads to $v_c = 700$ psi $= 10\sqrt{f_c'}$. These shear strengths of $8\sqrt{f_c'}$ and $10\sqrt{f_c'}$ would result if the cross section of the pedestals were uniformly compressed. However, under lateral loading of the pedestals, maximum compression will result only at one point on the section and diametrically opposite to it tension and cracking may result. To compare the shear strength of (15) to the shear demand of the uncracked and cracked sections, we performed a pushover analysis of the pedestal of the tank shown in Figure 2.

PUSHOVER ANALYSIS OF THE PEDESTAL OF THE ALL-CONCRETE TANK

The pushover analysis was performed with a finite element model of the all-concrete tank shown in Figure 2. The model included one-half of the tank defined by a vertical plane that included the vertical center line of the axisymmetric structure of the tank. Symmetry conditions on the vertical edges of the model included the structural action of the excluded half of the tank. Solid elements, 1 element through the thickness, 50 elements around the circumference, and 120 elements over the height of the pedestal wall modeled the concrete of the pedestal. Rod elements connected to the nodes at the corners of the solid elements modeled the vertical reinforcing. The circumferential reinforcing was excluded from the model, as it was considered to be shear reinforcing. A lumped mass, approximately at the center of gravity, represented the mass of the vessel and the contained water. The lumped mass was rigidly connected to the top edge of the pedestal. The three components of displacement were restrained at all nodes at the base to model a fixed base.

The response of the model was computed with LS-DYNA using Material 159. Material 159 is based on the three invariant concrete model defined in [4]. Material 159 has been calibrated with published results of triaxial tests, laboratory impact tests on beams, and test results of selected structures. The push was effected by applying a low lateral velocity to the lumped mass.

RESULTS OF THE PUSHOVER ANALYSIS

The results of the pushover analysis are presented in Figures 4 through 10. Figure 4 shows the pushover lateral force as a function of the lateral displacement at the lumped mass.

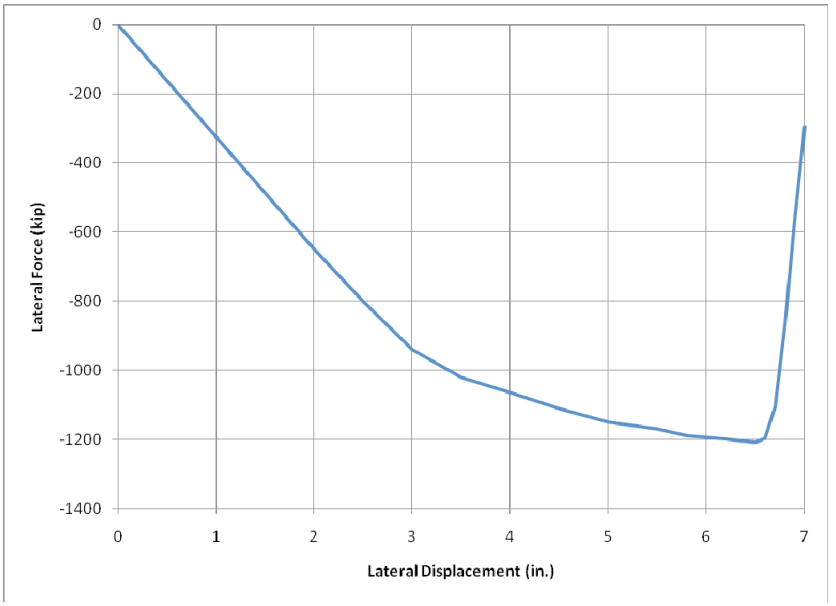


Figure 4. Variation of pushover lateral force (kip) with lateral displacement (in.).

The first flexural crack starts at the base at a lateral displacement of 2.5 in. Immediately before the development of the crack, Figure 5 shows that the shear strength given by (15) exceeds the shear stress demand at all points on the circumference of the base. For the stress conditions at the crack, a lengthy calculation, not shown here, results in the Rubin function value of 0.47 consistent with the polar angle value of 52° close to the extension meridian of the failure surface. This stress condition relative to the compression meridian is shown in Figure 6. Following the initial flexural crack, flexural cracking proceeds circumferentially and inclined cracks are indicated by the accumulated damage above the base shown in Figure 7.

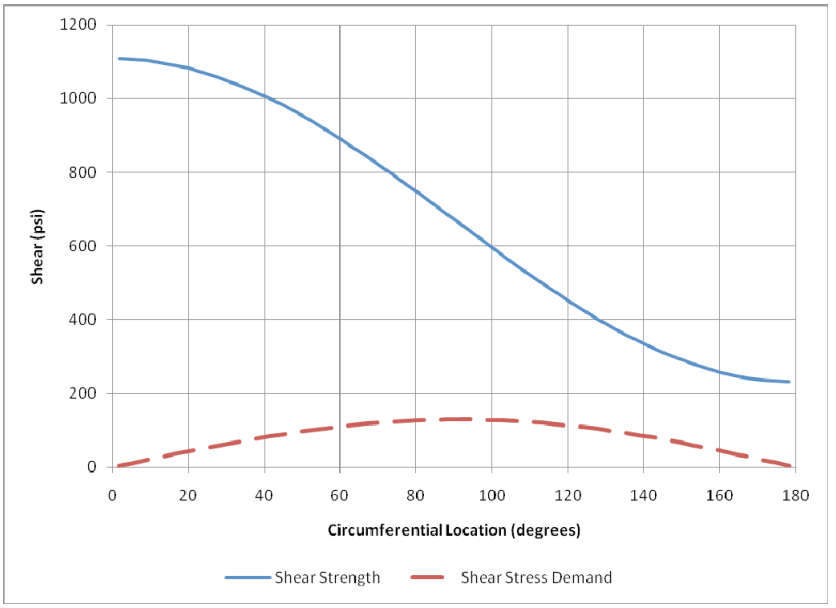


Figure 5. Circumferential variation of shear strength (psi) and shear stress demand (psi) at the base for a lateral displacement of 2.5 in.

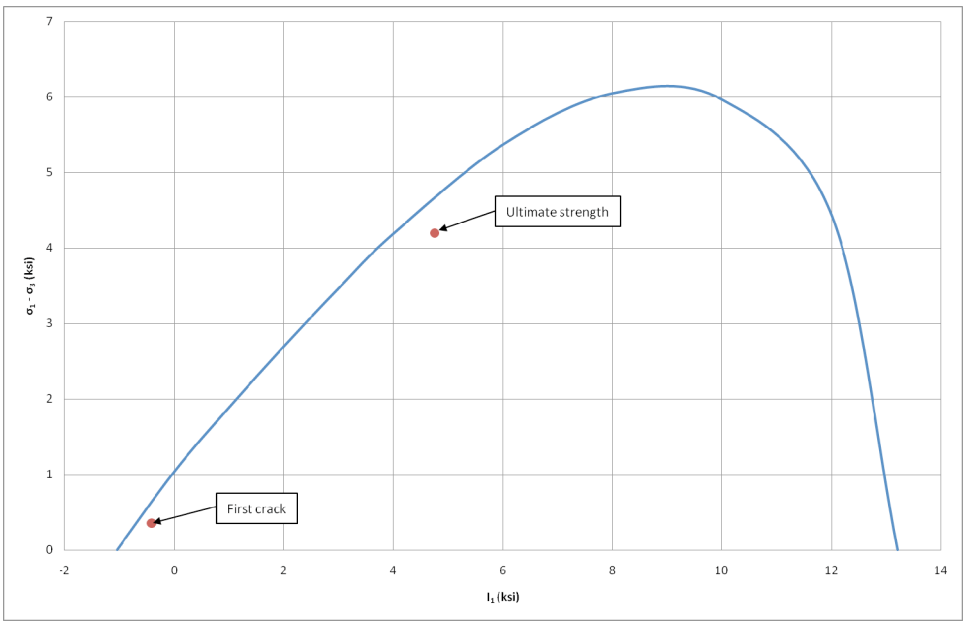


Figure 6. Points on failure surface at first crack and at ultimate strength.

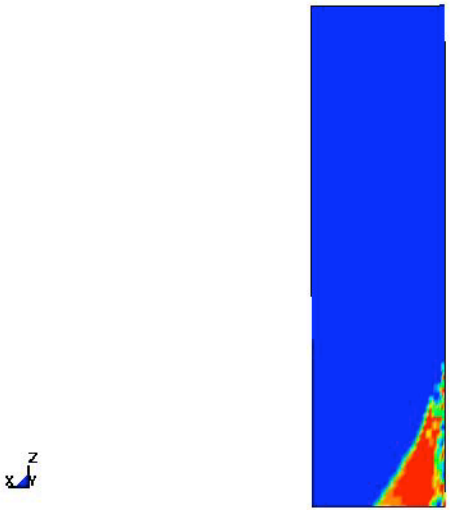


Figure 7. Accumulated damage indicating cracking above the base for a lateral displacement of 5 in.

At a lateral displacement of approximately 6.6 in, the lateral force reaches its maximum of approximately 1,200 kips on one half of the pedestal or 2,400 kips on the complete pedestal. At this force level, Figure 8 shows that the shear strength given by (15) exceeds the shear stress demand at all points on the circumference of the base. Also at the maximum lateral force, the average shear stress over an uncracked section is 116 psi = $1.7\sqrt{f_c'}$. Figure 9 shows the circumferential variation of the first stress invariant and the principal stress difference. At the most highly compressed point on the circumference, the Rubin function is equal to 0.92 consistent with the polar angle of 8° close to the compression meridian of the failure surface.

This stress condition, shown in Figure 6, indicates compression failure of the concrete. The circumferential distribution of stress in the vertical reinforcement, shown in Figure 10, indicates that steel stress is low relative to yield stress. A statics calculation indicates that the eccentricity produced by the lateral load is 96% of the mean radius of the pedestal wall and, therefore, close to the tipping point.

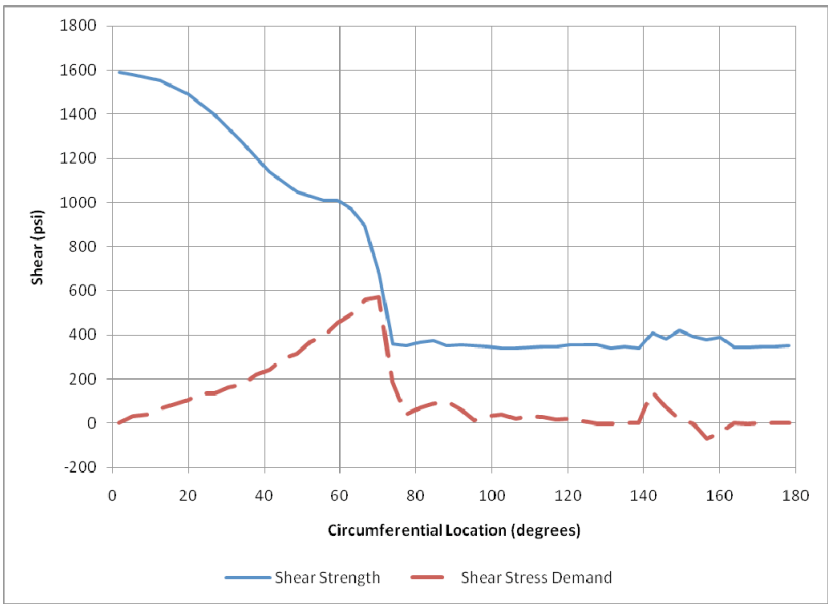


Figure 8. Circumferential variation of shear strength (psi) and shear stress demand (psi) at the base for a lateral displacement of 6.6 in.

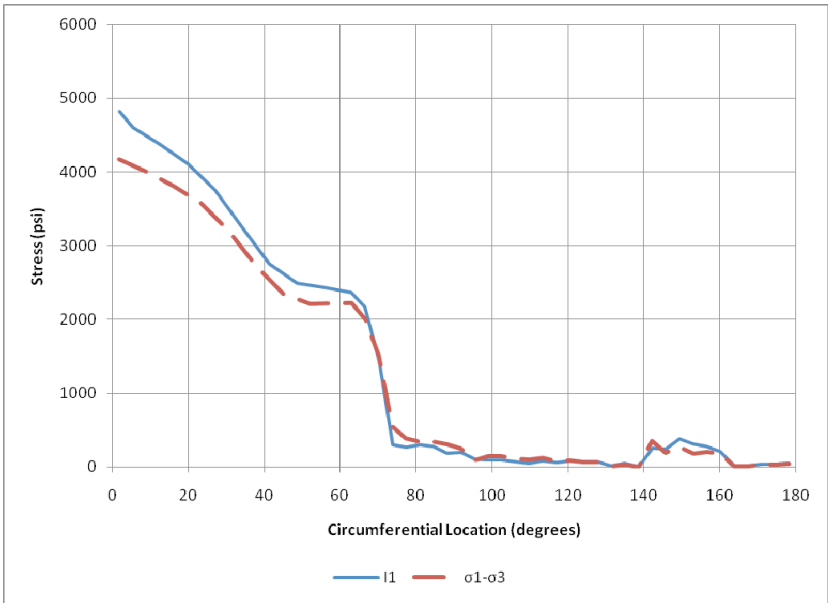


Figure 9. Circumferential variation of first stress invariant (psi) and principal stress difference (psi) at the base.

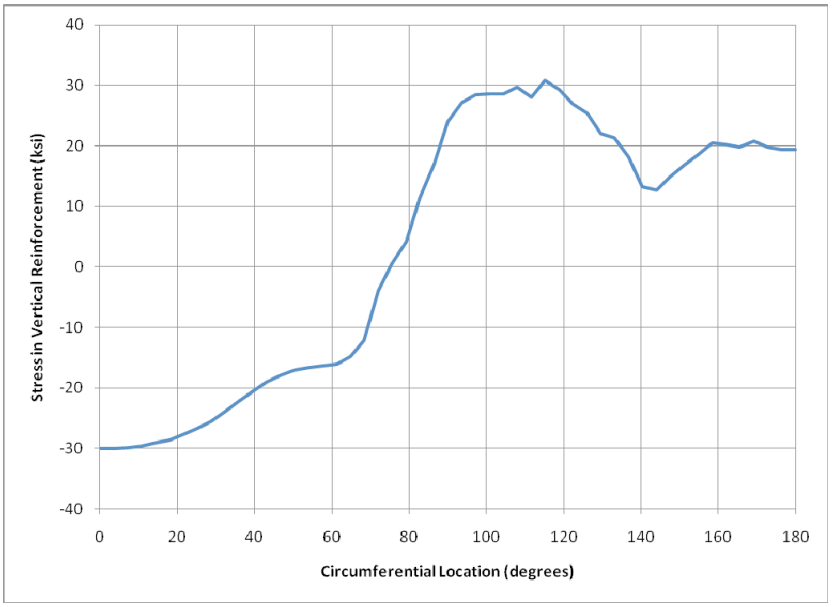


Figure 10. Circumferential distribution of stress (ksi) in the vertical reinforcement

DISCUSSION

The proposed concrete shear strength that includes the beneficial effect of compression is based on limited test data. The reason for this is that the bulk of triaxial test data available in the literature do not include loadings that result in tensile first invariant of stresses, I_1, or loadings that result in near zero value of I_1. More triaxial tests on plain concrete are required for better definition of concrete shear strength in presence of compression.

The pushover analysis of the all-concrete elevated tank pedestal shown in Figure 2 indicates that concrete compression rather than concrete shear strength and flexural steel strength are limiting the ultimate lateral strength of the pedestal. The ductility requires a study that should include the contribution of the vessel and the base slab.

The pedestal of the composite elevated tank shown in Figure 1 has a lower height-todiameter ratio. Its geometry will resist a larger overturning moment and, therefore, concrete compression may not be the limiting strength. A pushover analysis needs to be conducted to determine if concrete shear strength or steel stress limits its ultimate lateral strength.

During the calculation of the pushover several questions arose that require further investigation. The lateral load was generated by applying a low velocity at the center of gravity of the mass representing the structure and the stored water. The intent was to achieve quasi-static loading. This follows the suggestion of the developer of the Material 159 in the LS-DYNA software. The calculated response indicates that a small amount of dynamic variation of the force resulted. This suggests that variation of the applied velocity should be explored to arrive at an optimal velocity that reduces the dynamic effect to an acceptable level while

controlling the amount of output that is generated. Also, the effect on the calculated response of initialization of the applied velocity and the time step used should be explored.

REFERENCES

[1] American Concrete Institute (2008). *ACI 371R-08 – Guide for the analysis, design, and construction of elevated concrete and composite steel-concrete water storage tanks.* American Concrete Institute, Farmington Hills, MI.

[2] American Concrete Institute (2008). *ACI 318-08 – Building code requirements for structural concrete*. American Concrete Institute, Farmington Hills, MI.

[3] Gupta, P.R., and Collins M.P. (2001). "Evaluation of shear design procedures for reinforced concrete members under axial compression," *ACI Structural Journal*, 98(4), 537-547.

[4] Schwer, L.E., and Murray, Y.D. (1994). "A three-invariant smooth cap model with mixed hardening." *International Journal for Numerical and Analytical Methods in Geomechanics*, 18, 657-688.

[5] Murray, Y.D. (2007). "Users manual for LS-DYNA concrete material Model 159," FHWA-HRT-05-062, Federal Highway Administration, U.S. Department of Transportation, McLean, VA.

[6] Kupfer, H., Hilsdorf, H.K., and Rusch, H.(1969). "Behavior of concrete under biaxial stresses." *ACI Journal*, 656-666.

[7] Mills, L.L., and Zimmerman, R.M. (1970). "Compressive strength of plain concrete under multiaxial loading conditions." *ACI Journal*, 802-807.

[8] Launay, P., and Gachon, H. (1972). "Strain and ultimate strength of concrete under triaxial stress." *Concrete for Nuclear Reactors – Vol. 1*. ACI SP 34, 1972.

[9] Khaloo, A.R., and Ahmad, S.H. (1988). "Behavior of normal and high-strength concrete under combined compression-shear loading." *ACI Materials Journal*, 551-559.

[10] Cardenas, E.E., Hanson, J.M., Corley, W.G., and Hognestad, E. (1973). "Design provisions for shear walls." *ACI Journal*, 221-230.

[11] Gunawan, L. (2003). "Ultimate strength of plain concrete subjected to triaxial stress." PhD thesis, Illinois Institute of Technology, Chicago, IL..

Metal Liquid Storage Tanks on Sloped Foundations… What Could Possibly Go Wrong?

Richard A. Dethlefs[1], Zeno Martin[2], and Aaron J. Sterns[3]

[1]Wiss, Janney, Elstner Associates, Inc., 960 South Harney Street, Seattle, WA 98108; PH (206) 622-1441; FAX (206) 622-0701; email: rdethlefs@wje.com
[2]Wiss, Janney, Elstner Associates, Inc., 960 South Harney Street, Seattle, WA 98108; PH (206) 622-1441; FAX (206) 622-0701; email: zmartin@wje.com
[3]Wiss, Janney, Elstner Associates, Inc., 960 South Harney Street, Seattle, WA 98108; PH (206) 622-1441; FAX (206) 622-0701; email: asterns@wje.com

ABSTRACT

Wiss, Janney, Elstner Associates, Inc. (WJE) was asked to investigate cracking and spalling of the concrete foundations of a number of liquid storage tanks at an ethanol manufacturing plant located in western Oregon. The plant was new at the time and the cracking and spalling of the foundations occurred immediately after the tanks were put into service. An initial attempt by the plant to repair the foundations failed immediately. WJE was asked to investigate the cause of the cracking and make recommendations for repairs.

There were twenty metal liquid storage tanks at the plant ranging in size from 62 feet in diameter and 52 feet in height to 14 feet in diameter and 5-1/2 feet in height. All twenty tanks were constructed on foundations with a 1 in 12 slope. The only attachments of the tanks to the foundations were hold down bolts spaced evenly around the perimeter of the tanks, which were intended to prevent overturning.

Although analysis indicated that friction between the base plates and the compacted fill was sufficient to resist sliding of the tanks due to gravity, wind and earthquake forces, it was evident that the tanks were sliding down slope. A study of the thermal expansion and contraction characteristics of the tanks by WJE found that thermal cycling would cause the tanks to migrate down slope.

Ultimately, WJE was tasked with determining which of the twenty tanks were at risk of additional damage and determining if (and how) the process could be arrested. This paper discusses the problems with constructing metal storage tanks on sloped base foundations and proposes an innovative method to prevent downward sliding of these types of tanks.

INTRODUCTION

In mid-2008, WJE was asked to investigate cracking and spalling of the concrete foundations of a number of liquid storage tanks at an ethanol manufacturing plant located in western Oregon. The plant was new at the time and the cracking and spalling of the foundations occurred immediately after the tanks were put into service.

An initial attempt by the plant to repair the foundations failed immediately. The cracking, which although initially was only observed in the foundations of a limited number of tanks, caused concerns regarding the integrity of the remaining sloped base tanks. Consequently, WJE was asked to: 1) determine if the other sloped base tanks were also experiencing damage; 2) determine the risk of future damage for the other sloped base tanks; and 3) develop schematic repairs to prevent future damage to the sloped base tanks that were determined to be at risk. This paper describes our work.

BACKGROUND

Twenty of the liquid storage tanks at the plant were constructed on sloped base foundations. Typically, liquid storage tanks of this type have bases that slope to center. In tanks with bases that slope to center, the outflow pipes attach to the center of the tank beneath the tank. Presumably, the designer of the tanks at this ethanol plant hoped to avoid the construction and maintenance difficulties of having underground outflow pipes by constructing the tanks on sloped foundations located above grade (Figure 1). By constructing the tanks in this manner, the outflow pipes could attach at the side of the tanks at the low end.

The tanks were of varying diameters and heights but otherwise of similar construction. The tanks ranged in size from 62 feet in diameter and 52 feet in height, to 14 feet in diameter and 5-1/2 feet in height. The tanks were generally constructed with 1/4 inch and 3/16 inch thick stainless steel plate walls. All of the tanks had 3/16 inch thick base plates. The tanks were supported by perimeter reinforced concrete foundation walls with continuous spread footings. The foundations were backfilled with compacted fill. The tanks and foundations were all constructed on a 1 in 12 slope.

The foundation wall thickness varied but was generally 14 or 16 inches thick. The walls were generally reinforced with two mats of reinforcing steel with both vertical and horizontal reinforcing. The tanks were anchored to the foundation walls with hold down anchor bolts, generally 1-1/4 to 2 inch diameter bolts, spaced evenly around the perimeters of the tanks. The anchor bolts were attached to the tanks with welded steel anchor chairs generally located 1-1/2 to 2 feet above the base of the tanks. The design drawings indicated a gap between the edge of the tank base plates and the anchor bolts of approximately 1/8 inch to 1/4 inch.

At the low end of the tanks, there was a notch in the foundation walls for the attachment of the outflow pipes. The outflow pipes were generally welded to the base of the tanks at the low end and the notches were in-filled with unreinforced concrete.

Nine of the tanks were fully clad with light gauge metal siding panels. Eleven of the tanks did not have cladding. The anchor bolts were hidden at the tanks that had cladding and were exposed at the tanks that did not have cladding. Most of the tanks operated at high temperatures (170 to 180 degrees Fahrenheit) and some tanks also had internal agitators that caused the tanks to vibrate.

FOUNDATIONS IN DISTRESS

We were first contacted because concrete was spalling off the foundation walls around the low end anchor bolts and around the outflow pipe of the Process Condensate Tank. The Process Condensate Tank is a 44-1/2 foot diameter by 40 foot tall tank with 24 anchor bolts located around its perimeter. At eight of the low end anchor bolts and at the outflow pipe, the concrete at the outer edge of the foundation had broken out (Figures 2 and 3). It was reported that the concrete at these locations spalled and cracked shortly after the tank was put into service. Initial repair attempts by the plant included cutting and chipping the affected concrete and patching with a cementitious repair mortar. The patches subsequently failed and were chipped away again prior to our inspection.

Eleven of the tanks did not have exterior cladding and we were able to measure the positioning of the tanks relative to the anchor bolts. At ten of the eleven tanks, it was observed that the tank base plate was in contact with and engaging the low end anchor bolts. Observations at the mid-slope anchor bolts at many of the tanks also demonstrated down slope movement of the tanks (Figure 4).

At the ten tanks where the base plate was in contact with the low end anchor bolts, distress in the concrete foundations included cracked and delaminated infill concrete around the outflow pipes, cracked and de-bonded grout between the tank base plate and foundation wall, and vertical cracking of the foundation walls at the low end anchor bolts.

Measurements of tank movement were difficult to obtain at the tanks with exterior cladding because the cladding concealed the anchor bolts. At these tanks, observations were limited to the condition of the concrete foundation walls.

At six of the tanks with cladding the distress in the concrete foundations was limited to cracking and delamination of the concrete infill around the outflow pipes. At two tanks, the loose, cracked concrete around the outflow pipes was removed and replaced prior to our visit. By the time of our inspection, new cracking and delaminations were already observed in the repair patches indicating that the tanks were continuing to move (Figures 5 and 6).

WHY ARE THE TANKS SLIDING?

A review of the original design calculations indicated that friction between the underside of the tanks and the compacted fill was relied on to resist wind and earthquake sliding shear forces. WJE's analysis, and observations, demonstrated that friction was adequate to resist the effects of the down slope component of gravity and dead load acting on the tanks. However, our observations indicated that the tanks were clearly moving down slope. The question was why?

The tanks, which were primarily constructed of stainless steel plates, expand when heated and contract when cooled. The frictional forces acting on the bottom

plate always act opposite of the direction of movement. A tank that heats and cools on a level foundation will expand and contract about the center of the tank since that is the only point about which the sum of the frictional forces resisting the tank movement will be in equilibrium in all directions. For a tank on a sloped base, there is a force due to gravity and the dead load of the tank that always acts in the direction down slope. As a result, when the tank expands or contracts, for the sum of the forces acting up and down slope to be in equilibrium, the frictional forces acting on the underside of tank cannot be equal in both directions. The result is that the center of gravity of the tank moves slightly down slope with each heating and cooling cycle.

To simplify the description of the analysis, the circular tank base can be idealized as a flat steel bar resting on a sloped base. In Figure 7, the forces due to thermal expansion are shown on the idealized steel bar with a component of the tank weight acting down slope due to gravity. As the bar expands due to heating, more of the bar must expand down slope in order for the up slope and down slope frictional force components and the down slope component of dead weight to be in equilibrium. Conversely, as shown in Figure 8, when the bar contracts due to cooling, a longer portion of the bar must contract on the high side of the bar in order for the frictional forces and the down slope component of dead weight acting on the bar to remain in equilibrium.

As a result, the low end of the bar does not contract upward as far during the cooling cycle as it expanded downward during the heating cycle resulting in a net movement downward. Similarly, the high end of the bar expands upward a small amount during expansion and contracts downward a larger amount during cooling resulting in a net movement downward.

We decided for a number of reasons that determining the actual magnitude and number of thermal cycles would be a nearly impossible task. One problem was the tanks were enclosed and were subjected to both daily and seasonal temperature cycles both before and after being placed into service. Although any temperature change can theoretically cause a tank to expand or contract, a study to develop a correlation between daily temperature fluctuations and changes in the average temperature of the steel base plates for twenty different tanks was beyond the scope of the project. A study to determine the level at which small temperature cycles could offset the elastic response of the soil and develop frictional forces was also beyond the scope of the project. Luckily, this level of analysis was unnecessary. Our analysis had identified that a mechanism for movement of the tanks existed and the observed movement of the tanks was consistent with the mechanism.

CAUSE OF DAMAGE

What happens when the tanks try to expand after they have already come into contact with the low end anchor bolts? After the tanks come into contact with the low end anchor bolts all future tank expansion is forced to occur up slope. When this occurs the anchor bolts must resist the forces developed due to friction acting across the entire tank bottom as well as the down slope component of the dead load. Our

analysis found that when the tanks were full of liquid, these forces could be huge. Figure 9 demonstrates this load condition.

Frictional resistance is applied in the direction opposite of movement. The magnitude of the frictional force is equal to the product of the normal force acting on the friction plane and the coefficient of friction between the two materials (in this case the stainless steel base plate and the compacted fill). The tank weight is calculated from the weight of the tank components. The fluid weight is calculated from the volume and density of the fluids used in the tank. In our analysis, we assumed a coefficient of friction of 0.3 between the base plate and the compacted fill.

Our analysis indicated that if the Process Condensate Tank, which was 44-1/2 feet in diameter and 40 feet in height, was in contact with the anchor bolts and full of liquid during a heating expansion cycle, it could generate 1,432,000 pounds of horizontal force on the down slope anchor bolts. The capacity of the anchor bolts was found to be controlled by concrete breakout strength and was approximately 7,700 pounds per bolt. Since only ten anchors were determined to be effective in resisting downward movement of the tank, the demand-to-capacity ratio (DCR) was approximately 18.7.

The Process Condensate Tank has an operating temperature of approximately 175 degrees Fahrenheit when filled with liquid and in operation. Based on the fact that the concrete broke away from the low end anchor bolts as soon as this tank was placed into service, it was apparent that the tank had migrated down slope due to ambient temperature variations while it was still empty. As soon as the tank was filled and heated, the tank simply expanded and pushed the low end anchor bolts outward failing the concrete around the bolts. It was also not a surprise to find that the first attempt to patch these locations also failed.

FUTURE RISK ASSESSMENT

Once the mechanism for movement and damage was identified, the question became one of future risk of the remaining tanks at the plant. During our inspections, we found that most of the tanks were already bearing on the low end anchor bolts. At many of the tanks, there was already cracking and incipient spalling of the foundation walls at the low end anchor bolts.

A demand-to-capacity based risk analysis was performed for all of the twenty sloped base tanks. In the analysis, the sliding resistance of the existing hold down anchors was calculated and compared to the maximum possible down-slope force demands that could be generated by the tanks accounting for frictional and gravity forces.

The anchor bolts were originally designed only to provide uplift resistance to prevent tank overturning and were not intended to resist horizontal sliding of the tanks. However, for the risk assessment, horizontal force capacities were assigned to

each of the anchor bolts. The capacity of the individual bolts was determined to be the lesser of the following:

1. Bearing capacity of the tank bottom plate against the anchor bolt
2. Shear strength of the anchor bolt
3. Concrete breakout strength of the side of the foundation walls

Bearing capacity of the tank bottom plate against the anchor bolts was determined in accordance with AISC 360-05 *Specifications for Structural Steel Buildings* design provisions using properties for stainless steel from the Specialty Steel Industry of North America (SSINA).

The anchor bolts are ASTM F-1554 Grade 55 galvanized steel bolts. The shear capacity of the bolts was determined in accordance with AISC 360-05 design provisions.

Concrete breakout strength was determined in accordance with ACI 318-05 *Building Code Requirements for Structural Concrete*, Appendix D. In all cases, concrete breakout strength was determined to be the controlling failure mode for the horizontal force capacities of the anchor bolts. Observations at the Process Condensate tank and at one other tank confirmed that concrete breakout was the controlling failure mode.

The total capacity that the foundations have to resist the horizontal forces generated by tank expansion and gravity effects is equal to the number of anchor bolts providing resistance multiplied by the horizontal force capacities of the individual bolts. In the risk analysis, we typically utilized half the total number of anchor bolts (those on the down slope side of the foundation). In some instances, the number of anchors effective was half the anchors minus one, depending on the bolt layout for each tank. Bolts that aligned at the exact mid-point of the tank were determined not to be effective in resisting sliding.

Our assumption that all of the bolts in the lower half of the circumference provide equally effective resistance to sliding is generous. More likely, the anchors located in just the bottom third of the circumference would provide the majority of resistance to tank sliding.

Our analysis indicated that nineteen of the twenty sloped base tanks were at risk of sliding and causing damage to the foundations at the down slope end. The DCRs for the nineteen tanks at risk varied from a low of 2.6 to a high of 18.7. Only the smallest tank, which had a diameter of 14 feet and a height of 5-1/2 feet, was not at risk. Confirming our analysis was the fact that that the tank with the highest calculated DCR, the Process Condensate Tank, was the first to experience advanced stages of distress. Generally, our observations of tank performance and level of foundation distress coincided with the calculated DCRs. A number of tanks with calculated DCRs in the 11 to 12 range appeared to be at the beginning stages of concrete breakout.

It was interesting to note that larger diameter tanks were generally found to be at higher risk of foundation breakout failure. This was because there were relatively more anchor bolts for the smaller diameter tanks since these tanks are generally more susceptible to overturning than the larger diameter tanks.

THE REPAIR

If allowed to progress unabated, further sliding would likely lead to damaged piping and mechanical equipment as well as possible heavy damage to the tanks and foundations. A number of different repair concepts were considered; however, the challenges were numerous.

One repair concept was to simply add anchor bolts around the perimeter of the tanks. Although this approach would arrest the sliding of the tanks, it would generate large forces at the new anchor bolts when the tanks attempt to expand and contract with future temperature changes. We determined that bolting the tanks to the foundation walls would likely cause damage to occur.

Another approach considered was to buttress the tanks at the low end of the foundations. This repair approach was problematic for a number of reasons. First, the magnitude of forces that could be generated by the tanks at the low end was enormous. So any attempt to buttress the tanks would have involved large soil excavations and addition of considerable volumes of additional concrete at each tank. Second, the tanks were simply not constructed to be loaded in this manner. There was a likelihood of tank wall buckling if the tanks were buttressed at the low end. As a result, any attempt to buttress the tanks from the low end of the foundation would also have had to include significant strengthening and bracing of the tank walls or base plates, or both.

Ultimately, WJE developed a conceptual retrofit design that included adding a series of springs (tie rods) on the high end of the foundations. The concept was to pre-tension the springs to exactly offset the down slope component of dead load acting on the tanks. The springs would all be oriented so that they only generated forces parallel to the slope of the foundation. By installing retrofit anchors of this type, the tanks would still be allowed to expand and contract due to thermal cycling in all directions; however, there would no longer be a driving force acting down slope to cause the tanks to migrate in that direction with each heating and cooling cycle. The conceptual retrofit anchor design is schematically shown in Figures 10 and 11.

There are a number of additional benefits to the proposed solution. One is that the horizontal forces imparted on the springs are directed back to the existing foundation on the high end. There is no need to add significant additional size or weight to the existing foundations in order to offset the forces in the new anchors. Another benefit is that the forces are transmitted to the tanks in tension directly to the base plate at the high end of the foundations. As a result, there were no concerns with

buckling of the tank walls or plates and there was no need to modify or strengthen the existing tank construction.

The pre-loaded springs solution would also accommodate a number of different load conditions. In the event that the tanks were emptied, the springs would pull the tanks slightly up slope, but in so doing, would relieve the forces in the springs. In the event that the tanks were re-filled and again began experiencing thermal cycles, the tanks would migrate down slope until the forces in the springs became equal to the down slope component of dead load. At that point, the tanks would be back in equilibrium and additional thermal cycles would not cause the tanks to move upward or downward.

After the proposed new tie-rod attachments were to be installed, the damaged concrete around the low end anchor bolts and outflow pipes could be repaired with normal concrete patching procedures.

Although schematic repairs were developed to address the sliding of the tanks, a final design was not developed and the repairs were never instituted because the plant was shut down for economic reasons not related to the condition of the tanks.



Figure 1 - Typical tank on sloped foundation



Figure 2 - Concrete broken out at Process Condensate Tank anchors



Figure 3 - Concrete broken out and removed at outflow pipe



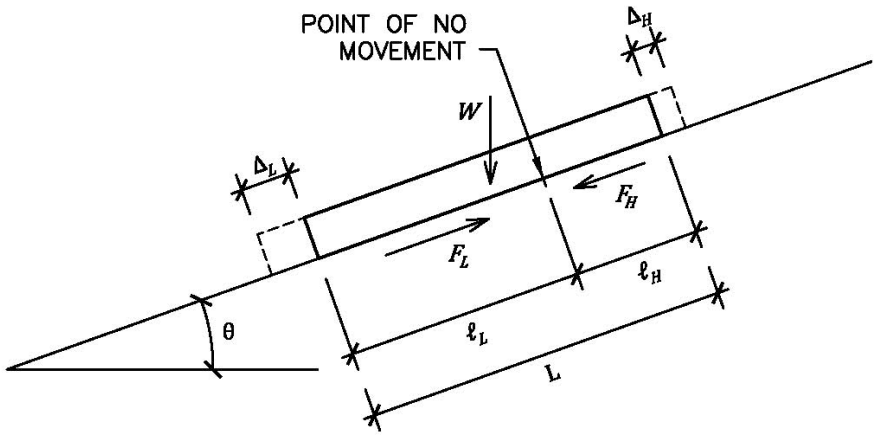
Figure 4 - Mid-slope anchor bolts indicate tank movement



Figure 5 - Cracking of infill concrete repair patch at outflow pipe

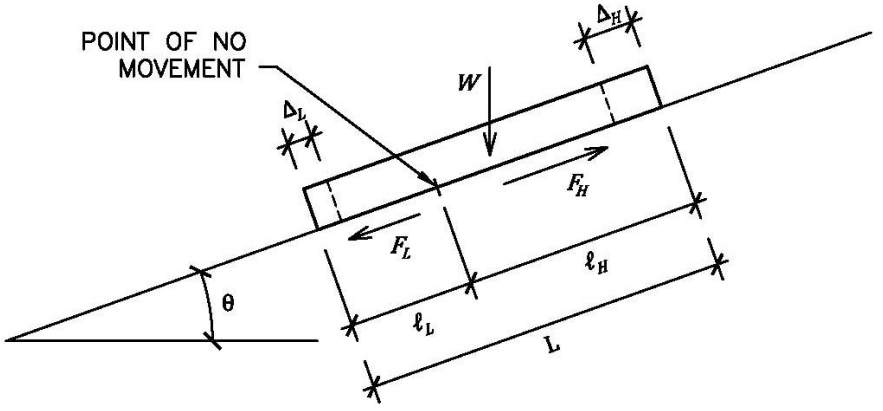


Figure 6 - Cracking of infill concrete repair patch at outflow pipe



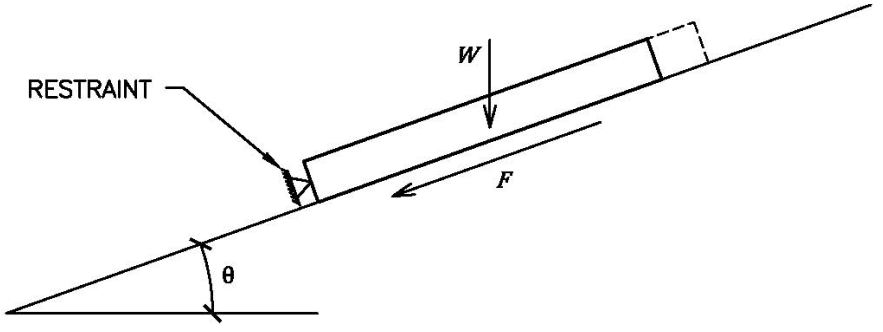
For equilibrium: $F_H + W \sin\theta = F_L$; therefore $F_L > F_H$; which means $\ell_L > \ell_H$; which means the center of gravity of the bar moves down hill.

Figure 7 - Heating Cycle



For equilibrium: $F_H = F_L + W \sin\theta$; therefore $F_L < F_H$; which means $\ell_L < \ell_H$; which means the center of gravity of the bar moves down hill.

Figure 8 - Cooling Cycle



For equilibrium: $R = F + W \sin\theta = W \cos\theta\, \mu + W \sin\theta$

Figure 9 - Heating after contact with rigid restraint

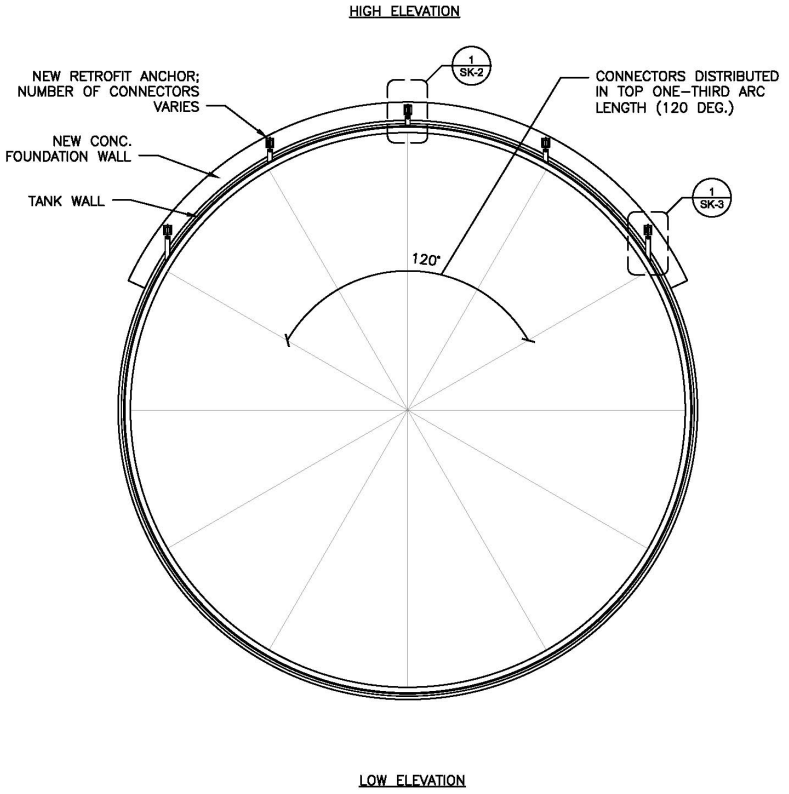


Figure 10 - Retrofit Plan

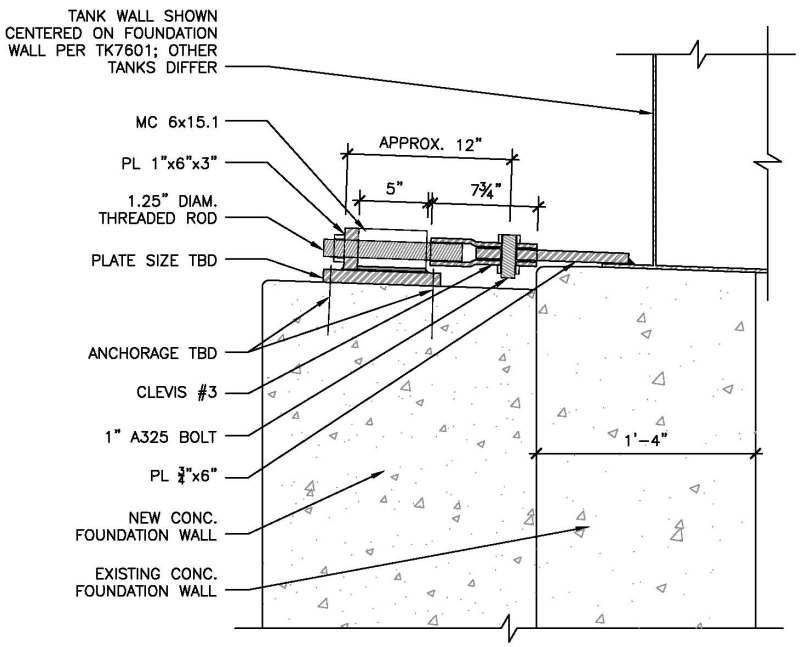


Figure 11 - Retrofit Section

Considerations for Retrofitting Existing Pipe Bridges

Xiapin Hua, Fluor Corporation, Sugar Land, TX, xiapin.hua@fluor.com

ABSTRACT

Pipe bridges are widely used to cross over roads, highways, railroads and obstructions. Retrofitting of existing pipe bridges are required for many reasons such as additional levels, outriggers, and past modifications which were not considered in the original design. There are many items to consider when evaluating, analyzing and reinforcing existing pipe bridges such as operating loads, test loads, seismic loads, wind loads, analysis methods, and reinforcement plans.

Pipe bridges are classified as pipe rack structures, which belong to non-building structures. The nature of pipe bridge structures are not similar to regular building structures, which have less redundancy to resist seismic or wind loads. Wind load determination can be a challenging topic due to the lack of research and design guidelines. In this paper, there is a comparative study of wind load determination, which is based on ASCE 7, ASCE Wind Loads on Petrochemical Facilities, a reference calculation performed in the 60s, current design practices and AASHTO wind pressures. The consideration of operating loads, test loads, seismic loads and load combinations for pipe bridges are also discussed in this paper.

Usually, existing pipe bridge evaluations and retrofit plans will rely on a structural analysis of the existing bridge. In order to eliminate or minimize the extent of upgrades and satisfy client expectations, several design approaches and options need to be tried and compared. These efforts are also important to meet the project schedule and budget requirements. In some cases, obstructions will add to the difficulties of the retrofit project that requires additional efforts for passing code check, connection verifications and foundation reinforcement. Spring boundary conditions and analysis modeling options are discussed in this paper. It is found that the force redistribution among the structural members and foundations is important for retrofit projects, especially for pipe bridges located in congested areas. The enhancement for pipe bridge members, connections and foundations are also discussed and presented in this paper.

WIND LOAD CONSIDERATIONS

Unlike regular open structures with beams and columns, trussed pipe bridges consist of many lattice members that may produce a larger area projected on a plane normal to the wind. The maximum force depends on the wind angle of attack.

ASCE-7-05 [1] equation 6-28 specifies the general procedure for wind load on open structures. The shape factor of 1.6 to 2.0 is recommended for flat sided members per Fig. 6-22, and 0.7 to 1.2 for pipes $(D_1(q_z)^{1/2} \leq 2.5)$ per Fig. 6-21. The shape factor depends on the ratio of solid area to gross area, round member size and velocity pressure calculated at height z above ground.

Per ASCE Wind load for petrochemical facilities [2], a minimum of shape factor 0.7 for pipes is suggested. The total loads on pipes are determined per the diameter of the largest pipe plus 10% of the width of the pipe rack (A_s=(D+0.1W)L). In chapter 4.2, the force coefficient C_f is calculated as the functionality of frame solidarity ratio and number of frames. The optional calculation method for the force coefficient C_f is also provided in Appendix 4A. This method provides a greater range of solid ratios and frame spacing variations.

It is found that some of the existing pipe bridges built in the 1960's that still stand today were designed for a wind load of 30 psf on one truss, in which the wind load is assumed acting at 45°. In the original calculations, the shape factor of 0.6 for pipes, 1.3 for columns and 1.0 for the truss members are utilized and the wind load is assumed to apply on one truss only plus wind on the front surface of pipes.

Rutz [3] listed the wind pressure recommendations from late 19th century and early 20th century, in which a table contains 5 references to address the recommendation of 30 to 40 psf wind load to be used**.** Smith [3] addresses wind pressure on both trusses and the surface of a railroad train on the bridge. In table three, it states that some trussed bridges designed for 30 to 50 psf on one truss with or without the wind on train in the design of the 1880's bridges.

The equation 3-1 of AASHTO signs [4] provides similar design methods as ASCE -7. Table 3-6 provides a wind drag coefficient (Cd) for trusses and states "the drag coefficient for a truss with a very small solidity ratio is merely the sum of the drags on the individual members". According to note 3 of table 3-6, the magnitude of drag coefficient depends on member solidity ratio and the spacing of the elements in line with the wind. The drag coefficient of 2.0 is selected for the truss bridges in AASHTO Pedestrian Bridge specifications [5].

Table 3.8.1.2.1-1 of AASHTO LRFD bridge design specification specifies that windward of 50 psf and leeward of 25 psf for the trusses and columns are to be used, which is based on 100 mph wind speed. Table 3.8.1.2.2-1 further provides the base wind pressure for various angles of attack, in which the wind pressure varies from 75 to 17 psf laterally versus 50 to 0 psf longitudinally, based on 0-60 degree skew wind angle variations.

Table 1 provides the comparative study of wind loads on the boxed trusses using five different methods, in which the projected vertical area of truss members (see Fig. 1) is calculated as follows: Chords: 150*2*0.50=150 ft^2, Verticals: 8*8*0.25=16 ft^2, Diagonals: 11*20*0.25= 55 ft^2, and Columns 3x1.22*8=29.3 ft^2, Total area per truss A_s= 250 ft^2. For simplicity, the dimension of center to center instead of out to out is used in this study.

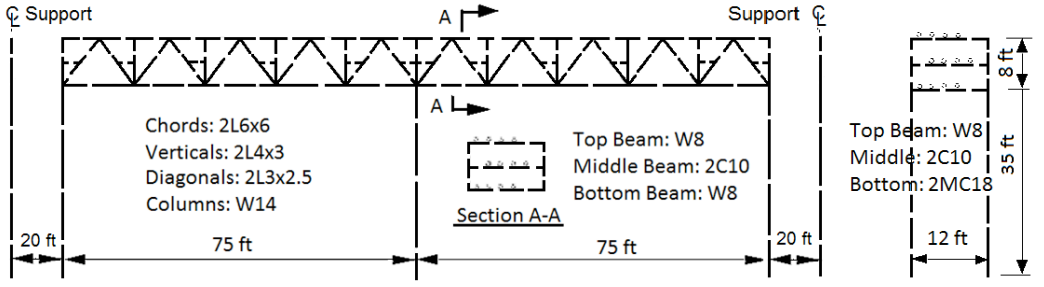


Figure 1. Pipe Bridge Elevation View and Section View

Table 1 Wind Load Calculations [3]

Method 1is based on ASCE 7 [1] and Wind Load on Petrochemical facilities [2]:
Assuming wind speed 90 mph and exposure category B, the velocity pressure at height z is q_z = 0.00256(Kd)(Kz)(Kzt)(V^2) I = 13.75 psf (Equation 6-28 of ASCE 7-05), where Kz is the exposure factor = 0.78 (Table 6-3 for a height of 43 ft), I = 1.0 (Table 6-1), K_d = 0.85 (Table 6-4), K_{zt} = 1.0, C_f = 1.8 (Fig. 6-22) and G = 1.14 for comparison purpose. Wind loads [1] on the truss members can be calculated as $F_{member}=q_z$ G C_f A=(15.7) 1.8 (2 trusses*250) = ***14.2 kips***. The wind load on the pipes [2] is $F_{pipe} = A_s$ (0.7) (13.75 psf) = A_s (0.7) (13) = 8.3kips, where A_s= (D+0.1W)L = 3x (6/12 + 0.1x12) 170=870 ft^2**.** Total wind load in the transverse direction is F_{tl}= 22.5 kips.
Method 2 is based on the reference calculations in the 60's:
The wind loads on the truss members is calculated as F_{member}= 30 psf (150+16+55+1.3x29.3) = 7.8 kips. F_{member}= 0.707 (7.8) =***5.5 kips*** based on 45^o wind skewed angle. The wind load on the pipes is $F_{pipe} = A_s$ (0.6) (30psf) = 4.6 kips, where A_s=6/12*3*(75x2+20)= 255 ft^2**.** Assuming 12.4 kips (7.8+4.6=12.4 kips) acting at 45^o to the truss, total wind load in the transverse direction is F_{tl}= 0.707(12.4) = 8.77 kips. Same wind force is assumed in the longitudinal direction.
Method 3 is based on Ch. 4 and appendix 4A of ASCE Petrochemical wind [2]:
In the transverse direction: A_{gross}= 150*8 =1200 ft^2, Solid Ratio ε = 250/1200 = 0.21, N=2, S_f = 12', B = 151' (per Fig. 4.1, assuming verticals as the columns), S_f / B = 0.08, α_{max}=(10+52 ε)^o =21^o. Per Fig. 4A.3, the force coefficient is C_f =2.7. Wind loads on the truss memers can be calculated as F_{member}=(15.7) 2.7 (250) = ***10.7 kips*** (for two trusses). In the longitudinal direction: A_{gross} = 8'*12'=96 ft^2, A_{net}= 8x0.33x2+ (8+10+18) 12/12 =41.3 ft^2, Solid Ratio ε = 41.3/96 = 0.43, N=11, S_f = 15', B = 13.22', S_f / B = 1.03, α_{max}=(16+52 ε) ^{o} =38 ^{o}. Per Fig. 4A.3, the force coefficient is C_f =10.8 (approximate). Wind loads on the truss members can be calculated as $F_{member2}$=(15.7) 10.8 (41.3) = ***7.2 kips***.
Method 4 is based on AASHTO signs [4]
Assuming wind speed 90 mph and wind exposure B, the velocity pressure at height z is p_z=0.00256 (Kz) G (V^2) I_r (C_d)= 37.5 psf per Eq. C3-1, where K_z is the height and exposure factor = 0.78 (per ASCE-7 for a height of 43 ft, AASHTO only provides K_z=1.05 for wind exposure C), G = gust effect factor= 1.14 (minimum), Ir = 1.0 (per Table 3-2), C_d = wind drag coefficient = 2.0 per table 3-6. The wind load in the transverse direction is F_{member}= (250*2 trusses* 0.0375) = ***18.75 kips***.
Method 5 is based on AASHTO LRFD Bridge Design Specifications [5]
Assuming wind load acting at 21 ^{o} normal to the truss. As the values used in AASHTO Table 3.8.1.2.2-1 are based on 100 mph wind speed and exposure C, the reduction factors of 0.81 and 0.75 are used here for the wind speed of 90 mph and exposure B. In transverse direction, F_{member}= (250*2 trusses) *0.068 (0.81*0.75) =***20.4 kips***, in the longitudinal direction, F_{member} =(42x11) 0.020 (0.81*0.75) = ***5.61 kips***.
(1) ASCE 7 section 6.5.12.3 requires that MWFRS (Main Wind Force Resisting Systems) shall be designed for the wind load cases in any directions. For method one, wind load analysis in the longitudinal direction is not included.
(2) Wind load on pipes is based on reference [2].
(3) Wind load on the columns below boxed truss is not considered.

This comparison study shows that 1) Methods 4 and 5 yield the highest wind loads compared to the other three methods, in which no shielding is considered; 2) Method 2 yields the least wind design force in the transverse direction, in which 45^o skew wind angle is considered; 3) Method 3 reduces the wind loads in the transverse direction by 25% compared to method 1 (see Fig. 2 for details).

Conclusions and Suggestions: 1) Both method 1 and 3 are reasonable for estimating wind loads on the truss members and method 3 may be utilized to estimate the wind load in the longitudinal direction. 2) Further research and study will be needed, which should include the wind tunnel testing of truss members and pipes.

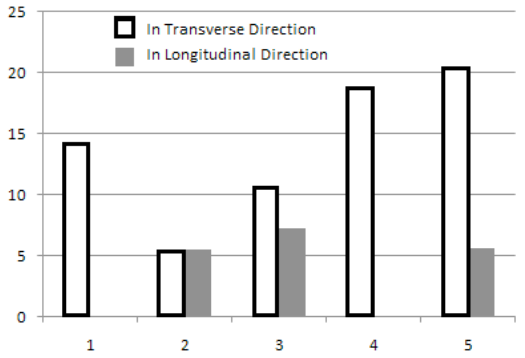


Figure 2. Wind Loads on the trusses (kips)

SEISMIC LOAD CONSIDERATIONS

Pipe bridges have less redundancy than buildings and lack the non structural components which increase damping and energy absorption during a seismic event. The dead load participation of piping systems in the existing structure may not be easily estimated. The intent of a seismic retrofit depends on the regulatory requirements and the wishes of the owners. Due to constraints of project schedule and budget, assumptions need to be made because of limitations and uncertainty in the absence of significant investigations and detailed analysis.

Old pipe bridges were usually not designed for seismic loads nor seismic detailing, so upgrading the existing pipe bridge for today's code is difficult and may be impossible. ASCE 7 Table 15.4-1 [1] provides seismic coefficients for non-building structures similar to buildings, in which the detailing of AISC 341 [7] is not required if the response modification R = 1.0, Ω_0=1 and C_d=1 for steel ordinary moment frames is utilized. This option usually yields a huge seismic design force that requires significant upgrades to the existing structures. This may not be suitable for a retrofitting project. To eliminate the AISC 341 detailing requirement, the seismic design category may need to be changed to category C or lower. If R =3, Ω_0=3 and C_d=3 are selected for non-building type structures, AISC seismic detailing will not be required. Besides, this option provides lower seismic design forces in that the redundancy factor ρ is reduced from 1.3 to 1.0. To reduce the seismic design category, verifications of existing soil conditions may be needed. In some cases, soil improvement may be required to achieve required the site class. Site specific ground analysis will be helpful for the possible reduction of peak ground accelerations.

The seismic force determination is affected by many factors. The goal is to reduce the seismic design forces as much as possible and avoid a significant upgrade to the existing structures. In this study, the period determination for static analysis (Table 2) is per model response spectrum results (Table 3). Factors considered include two design cases (Fig. 3) along with two different boundary conditions, the directions of the

forces applied, the design parameters of structure period (T_2), model base shear (V_t), and force scaling factors which are summarized in Table 3.

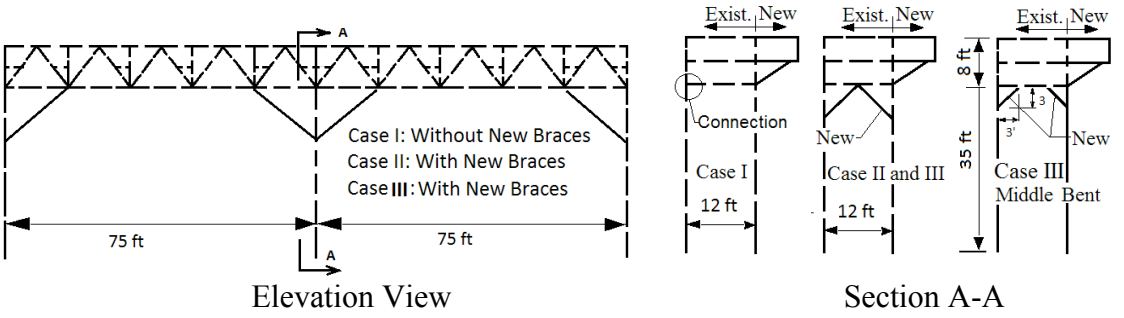
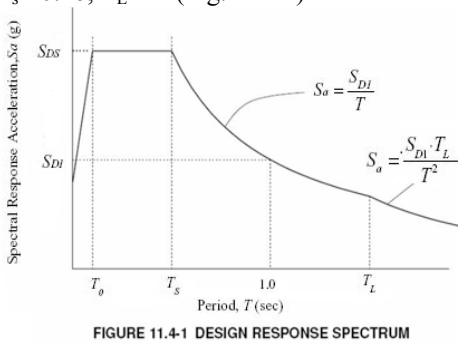
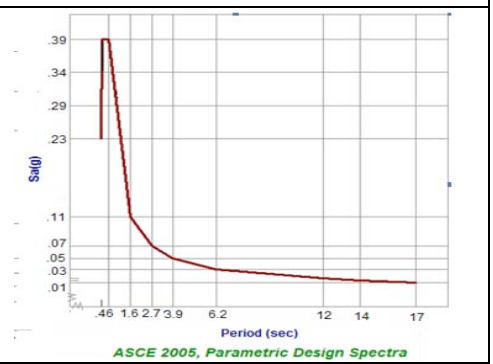


Figure 3. Exisitng Pipe Bridge With Modifications

Table 2 Seismic Load Calculations

Method 1 ASCE-7 Equivalent lateral force procedure [1]	
seismic design category C, group II, I_e =1.0 (Table 11.5-1) R = Ω_0 = C_d = 3 Per Item H in Table 12.2-1. $W_{DL+Operating}$ =330 kips	T_0= 0.2, S_{ds} =0.39, S_{dl} =0.18. S_{dl} /S_{ds}=0.09, T_s =0.46, T_L=12 (Fig. 22-12)  FIGURE 11.4-1 DESIGN RESPONSE SPECTRUM
C_s = S_{ds}/(R/I_e) = 0.13 (12.8-2) $C_{s(min)}$ = 0.044 $S_{ds}I_e$=0.017 (15.4-1) $C_{s(min)}$ = 0.03 (Control) (15.4-1) T_2 = 0.9 ~ 3.5 from Table 3 (Note: section 12.8.2 is not used for determining the period of the bridge) $C_{s(max)}$ = S_{d1}/T/(R/I) =0.03~0.07 (12.8-3) V_1 = C_s W= 9.99~22 kips (see table 3) (12.8-1)	
Method 2 ASCE-7 Response Spectrum analysis	
Model Response Parameter I/R=0.33 (ASCE Sec. 12.9.2) For case II pinned condition, the spectrum load in the transverse direction =32.4 kips Model base shear V_t =0.33 (32.4) = 10.6 kips Scaling of Forces: Scale factor $SF_{(force)}$ = 0.85 V_1/V_t = 0.88<1, use 1 (Per ASCE 12.9.4.1, the Dynamic Analysis base shear cannot be less than 85 percent of the Static Analysis)	

For the model response spectrum analysis (method two), there are 20 modes participation with seismic category S_{ds} =0.39 and S_{dl} =0.18. The design response spectrum is plotted by using Risa 3D version 8, which matches ASCE 7 Fig. 11.4.1 shown in Table 2. The analysis results indicate 97% of the mass participation in both horizontal directions. The period of the structure varies from 0.9 to 3.5 which depend on structure types and the boundary conditions listed in Table 3.

This study shows that 1) The spectrum loads for the pinned base analyses decreased by 50% from the fixed base values due to a longer period; 2) The super structure rigidity affects the seismic design forces, in which the spectrum loads of the braced frame in the transverse direction is 20% to 40% higher than these of the un-braced frames. 3) The base shear of case II fixed condition is the highest due to a shorter period.

Table 3 Comparison of Static and Dynamic Analysis Results

Type Cases of analysis	Boundary Conditions	T_2 (sec)	Spectrum load (kips)	V_t (kips)	$C_{s(max)}$	V_1(kips)	$SF_{(force)}$
$A^{(1)}$ case I	fixed	1.7	33.3	11	0.035	11.6	1.0
	Pinned	3.5	16.4	5.4	0.030	9.9	1.6
$A^{(1)}$ case II	fixed	1.3	47.2	15.5	0.046	15.2	1.0
	Pinned	2.4	23.6	7.8	0.030	9.9	1.1
$B^{(2)}$ case I	fixed	1.1	50.3	16.6	0.055	18.0	1.0
	Pinned	2.2	25.8	8.5	0.030	9.9	1.0
$B^{(2)}$ case II	fixed	0.9	61.7	20.4	0.067	22.0	1.0
	Pinned	1.8	32.4	10.6	0.033	11.0	1.0
(1) A- in longitudinal direction, (2) B-in transverse direction, T_2 – Period per spectrum analysis							

OPERATING LOAD CONSIDERATIONS

A retrofit project usually starts with a walkthrough for evaluating the existing conditions to determine the weakness and obstructions which may not appear in the existing drawings or calculations.

For the case of demolishing existing pipe to make room for new pipe and cable trays or adding pipe using empty space, the structural retrofit will usually not be required if the new loads are equal to or less than the original design operating loads. If additional steel levels or significant outriggers are added to the existing pipe bridges, the structure system may have to be reinforced to pass the code check. In some cases, even if the new loads are not significant, the evaluation for the existing structure may still be important in that the existing structure may have been previously upgraded several times and may not have been verified in the past design.

The operating loads for old pipe bridges could be very light and may only be 50% of the pipe operating loads used today. A review of the existing structure drawings can help with understanding the original design and past modifications. Original piping drawings are also a good source for evaluating the products in the existing pipe. Coordination with the owner and field trips will be an important step for verifying the actual operating loads.

TEST AND THERMAL LOAD CONSIDERATIONS

Test loads (such as hydro test) for the newly added pipes could cause the failure of the existing structures, especially the existing structure loaded with pipes in larger sizes. In order to secure the existing structures during the test, temporary supports or crane lifting may be necessary. An air test is also an option.

The verification of existing friction and thermal loads could be a complicated task that requires coordinating with piping and the owner. If friction load controls the

design, wind load shall not be considered simultaneously. For a bridge supporting large and rigid pipes, modeling the pipes using a link (such as a compression only link) between pipes and the structure members can be helpful to pass the structural code check. Reduction of the lateral pipe stresses can also be achieved by coordination with the piping group. For example, providing the lateral stiffness of the structure at the guide locations may be an option.

LOAD COMBINATIONS

ASCE 7 chapter 2.3 and 2.4 provide the general requirements of load combinations based on factored loads for strength design and nominal loads for allowable design. Other considerations may be needed when applying the load combinations. For example, the consideration of certain percentage of contents left in the equipment [8] for the combination of dead load and wind load could be important for verifying the existing structures**.** This can help on reducing the calculated overturning moment in an extreme wind load condition.

EVALUATION AND ANALYSIS

In a conventional design, the design sequence is to calculate the loads first, design the super structures, and then design the foundations. For a retrofit project, evaluating the existing structure becomes the first priority of making the retrofit plan. The design sequences may have to be set backwards to check the column base connections or the foundation capacities first and then verify the super structures. This is due to the limited anchor connection capacities. The retrofit constraint for modifying existing foundations could also be a major concern. The redistribution of design forces may have to be considered when underground obstructions are present and/or modification to the existing structure is impossible. An example of this consideration is to add knee braces to the bent framing in the transverse direction. This will help to reduce the column base moment reactions and eliminate the modifications to the foundations.

To study and compare the different design options, corresponding member stresses, deflections and design forces are calculated as shown in Fig. 3 and table 4. Design case I and II consist of three different boundary conditions. Design case III only includes a spring boundary condition. The load combination of 0.9D+1.6W and 1.2D+1.6W in transverse direction is used for studying these three cases.

The fixed boundary condition assumes that existing foundations are strong enough to take the additional loads. The advantage of this option is to keep the flexible structure unmodified. The pinned boundary condition assume**s** a weak base connection or weak foundation capacities. In this case, the super structure framing may need to be strengthened for the load redistribution. The spring boundary condition is to utilize the foundation flexibility to reduce member stresses, connection design forces and lateral deflections of the super structures. This option may yield none or fewer modifications to the existing structures. Case III is to consider obstructions in the middle bent, in which the knee brace geometry is modified to fit the existing condition (Fig. 3).

In reality, there are no absolute fixed or pinned base conditions. The behavior of the connection rigidities depends on the overall soil-structure interactions. When modeling the spring boundary conditions, factors of existing anchorage capacity and foundation flexibility may need to be considered. In this study, 4000 k-ft/rad is used for spring boundary conditions. To calculate the rotation constant, both steel and spread footings are modeled in one analysis file and the subgrade spring constant of 50 kips per cubic inch is utilized. The rotation constant is determined by dividing the column base moment by the rotations read at the column base joint. It is also found that the magnitude of rotation constants is affected by the footing sizes and the super structure rigidity. In table 4, numbers in the shaded area represent the failure of structure members, column base anchorage, steel connections or framing drift criteria.

This study shows that original structure is overstressed either in the base connection, moment connections or steel members (see Table 4 and Fig. 3). The added knee braces will help redu**ce** the design moments at the connections and column bases.

Table 4 Check for Member Stress Ratio (SR), Connection, Drift and Base Reactions

A	B	SR for Bottom Beam		Column SR		Drift (In)	Max Base Reactions (kips)				Bot. Beam to Column Connection in kips-ft,			
		C	D	N	S		P	T	V	M	M_1	M_2	N_1	N_2
I	Fixed	0.75	0.86	0.66	0.57	2.22	***172***	***14***	***12***	***239***	180	234	8	12
I	Pinned	***1.46***	***1.84***	1.07	0.98	***9.90***	217	46	14	0	***351***	***445***	8	13
I	Spring	***1.18***	***1.32***	0.85	0.78	***6.90***	198	34	12	80	285	***355***	8	13
II	Fixed	0.25	0.29	0.54	0.44	1.56	***183***	***17***	***12***	***212***	52	74	32	45
II	Pinned	0.32	0.39	0.80	0.75	**6.33**	222	44	14	0	59	88	61	82
II	Spring	0.29	0.35	0.65	0.59	4.63	206	36	13	62	57	81	51	69
III	Spring	0.32	0.67	0.69	0.68	5.12	195	42	12	64	64	170	45	69

A- Design Cases, B-Boundary Conditions, N-North, S-South, C-bent 1, D-bent 2,
P-compression force , T-tension, V-shear, M-moment
M_1-moment (kip-ft) for bent 1, M_2-moment (kip-ft) for bent 2, N_1-axial force (kips) for bent 1, N_2-axial force (kips) for bent 2

In summary, the column base moment is the highest for fixed boundary conditions, which significantly exceed the existing column base connection capacities; the pinned boundary condition causes high drift along with big moments at the bottom beam to columns of the transverse bents that need review; it is found that spring boundary conditions offer the best solution that meet all design criteria. (See Table 4 and Fig. 3).

FOUNDATIONS

A walk down of the area is an important step for checking out obstructions and constructability limitations that may prohibit foundation modifications. Other considerations are to verify the capacity of column anchorage to the concrete pedestal at the early planning stage. These connections may have very limited capacities. Many old anchor bolts are hooked L bolts that have less capacity than headed bolts.

ACI 318 appendix D Section D3.3.4 requires that anchors shall be governed by the steel strength of a ductile steel element. For anchors loaded with a combination of tension and shear, the strength in all loading directions must be controlled by the steel strength of the ductile steel anchorage element. The pull out strength in the tension of single hooked bolts is described in Table 5.

Table 5 Pull Out Strength of Hooked Bolts

for ductile steel failure mode governs: $0.75\ \phi N_{pn}\Psi \geq N_{ua}$ and $\phi N_{pn} > \phi N_{sa}$, (Section D3.3.3) N_{sa} is nominal strength governed by the steel, $N_{sa} = nA_{se,N}f_{uta}$ (D-3) Where $\phi = 0.70$ (Section D 4.4(c) (ii))	$N_{pn}=\Psi_{c,p}N_p$, (ACI 318 D-14) $\Psi_{c,p}= 1.0$ (Section D 5.3.6) $N_p = 0.9f_c' e_h d_a$, (ACI 318 D-16) where $3\ d_a <= e_h <= 4.5\ d_a$ (Section D 5.3.5)
If e_h= 5.5", d_a= 1.25" and f_c' =3 ksi are assumed, N_p= 18.6 kips, ϕN_{pn} = 0.7(18.6) = 13 kips, for moderate or high seismic region, pull out strength = 0.75(13) = 9.7 kips per bolt.	

For the pier design, ACI [10] requires a minimum of 2 #4 ties or 3 #3 ties distributed within 5" of the top pedestal. A similar requirement can be found in the other references [2] [11]. For old existing piers, this requirement is rarely met because existing piers usually consist of very few ties compared to the current standards (see Fig. 4). It is also very expensive to upgrade existing piers to meet today's code. Figure 5 shows a pier strengthening detail, in which additional reinforcement including dowels with 90 degree hooks and new ties around the existing pier can provide additional strength.

Post installed reinforcement either is determined on the basis of bond/plain concrete cone failure or designed as a lap splice per provider's technical data. For a project located in a seismic zone, a conservative design approach may be required in that the cyclic loading may result in reductions in bond strength.

In order to balance the foundation stability, thickening the existing footings or combining individual footings together may be required. This will increase the moment capacities of the spread footings. In some cases, the footings sizes may need to be enlarged to not overload the soil strength. Typical details for thickening and enlarging existing footings are shown in Figure 5. Special constructability should be considered to make sure that the reinforcement can be placed in the field. Through dowels are much stronger than regular dowels in that they do not rely on bonding to deliver the forces. This option is usually limited by the available working space. Verifying the overall structural stability during foundation construction is also important. Reduced wind loads [9] can be used for the verification.

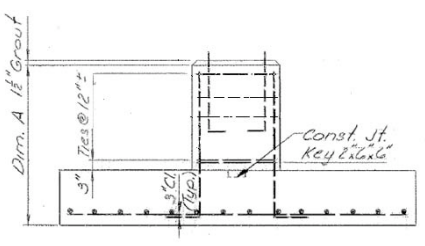


Figure 4. Existing Spread Footing

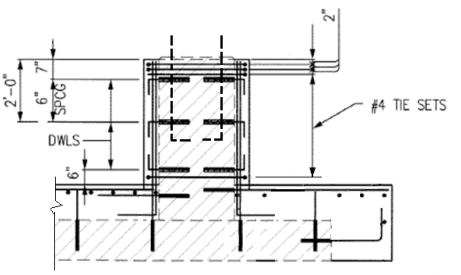


Figure 5. Foundation Reinforcement

SUPER STRUCTURE ENHANCEMENT CONSIDERATIONS

Steel member and connection reinforcement could be difficult due to limited material strength. Verifications could be more difficult if the existing drawings are not available. AISC design guide 15 includes the historic summary of ASTM structural steel and bolt information, which can provide the design information for the existing structural elements [12].

When retrofitting, constructability is a key consideration. A field survey for the existing structures may be required because the existing column orientation, size of anchor bolts and structure members may be different from these shown on the existing drawings. Field drilling and bolting is always preferred over field welding to avoid hot permitting process and lead released during construction. Old bolts may not be marked as today's bolts. To avoid overestimating the existing bolt capacity, replacing the bolts can be a quick and conservative way for a retrofit project. When replacing bolts, structural accessibility and potential interferences are key elements to be considered. Chapter 14 of AISC guide 15 provides guidance and details for the enhancement options of existing connections.

Many existing trussed bridges were designed as warren trusses with a moment framing system in both directions. Adding new structure members to release the design forces in the existing connections can be an easy way in the retrofit plan.

Fig. 6 and 7 show the connection detail 1 and detail 2 used for the newly added braces. In detail 2, a connector that consists of an end plate and cover plates is designed so that the axial force will be transferred to the channel webs. Fig. 8 shows the brace connection detail if knee braces are required in the longitudinal direction. In this detail, the knee brace is connected to the existing column web using an end plate connection. To transfer the horizontal force component to the column flange, a T plate and a set of angles are bolted on the other side the column. Bolted connections are selected due to hot permit limitations.

In some cases, the horizontal braces of a boxed truss bridge may not be strong enough to resist the new loads. If strengthening a horizontal diaphragm is required for distributing the lateral forces, the horizontal framing connections for the bridge will need to be verified and reinforced. If the replacement of the structure braces and connections are required, construction sequences will have to be considered to avoid the failure of the structural system during the construction period.

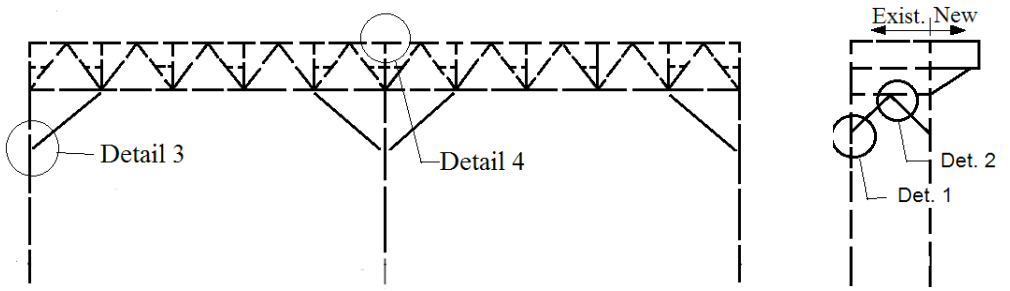


Figure 6. Connection Locations

To maintain the structure integrity during construction, minimum lateral resistance has to be maintained to resist the lateral, operating and construction loads. In this case, the replacement of the braces may need to be specified such as replacing one connection at a time. The design loads during construction can be found in ASCE 37 Design Loads on Structures during Construction [9].

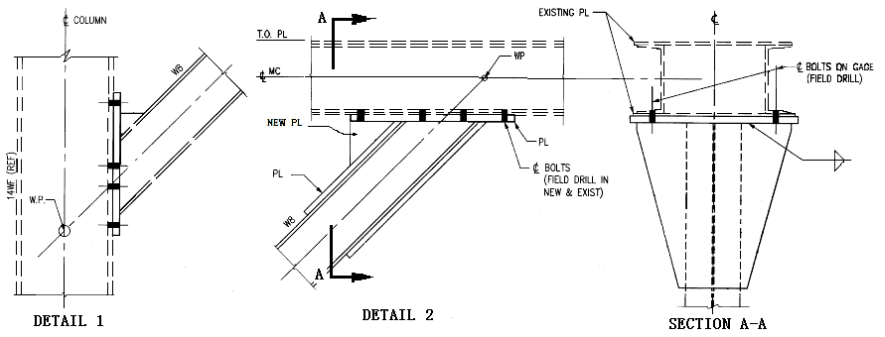


Figure 7. Detail 1 and 2 - Brace connections in Transverse Direction

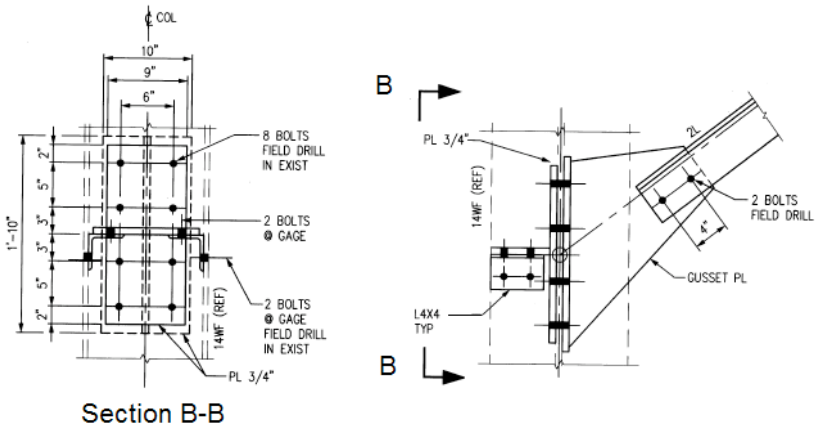


Figure 8. Detail 3 - Brace Connection in Longitudinal Direction

For continuous span trusses, top chord connections to the bent structures usually present high tension forces. Connection reinforcement may be required. Detail 4 in Fig. 9 uses a cover plate to transfer the unbalanced axial forces.

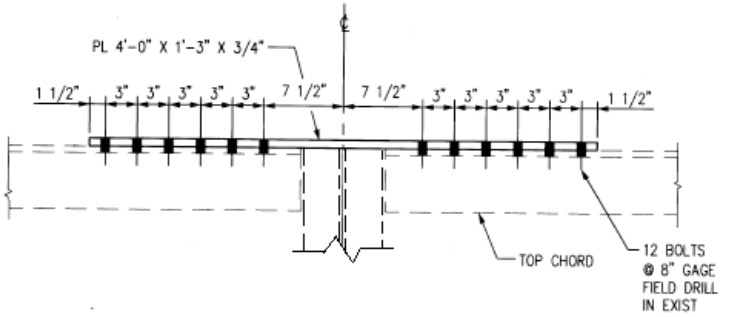


Figure 9. Detail 4 – Top Chord Connection in Longitudinal Direction

SUMMARY

Loading determinations for a retrofit project is a complex task that requires code interpretation, literature research, site verification and the considerations of construction, permitting and the owner's requirement. The structural analysis for an existing pipe bridge with new additions is different from the method used for designing a new structure, which requires efforts of trial and error and by comparing several different options to achieve the best solution. Constructability is the key element for determining the final details of the structure reinforcement.

ACKNOWLEDGMENT

Author likes to thank David E. Goolsby and Yun-Tien Lin for reviewing and the valuable comments for this paper.

REFERENCES

[1] ASCE Standard ASCE/SEI 7 (2006), "Minimum Design Loads for Buildings and Other Structures'. *America Society of Civil Engineers.*

[2] ASCE (1997) "Wind Loads and Anchor Bolt Design for Petrochemical facilities", *America Society of Civil Engineers.*

[3] Rutz, F. R. and Rens, K. L. (2007), "Wind Load for 19th Century Bridges: Design evaluation, historic failures, and modern preservation*", Journal of performance of constructed facilities*, ASCE, March/April.

[4] AASHTO (2001), "Standard Specifications for Structural Supports for Highway Signs, Luminaries and traffic Signals", Washington, D.C.

[5] AASHTO (2009), "*LRFD Guide Specifications for the Design of Pedestrian bridges*", Washington, D. C.

[6] AASHTO (2007), "*LRFD Bridge Design Specifications*", Washington, D. C.

[7] AISC 341 (2005), "Seismic Provisions for Structural Steel Buildings", *American Institute of Steel Construction.*

[8] Gilbert, R. T., Bailey, J. R., Rennalls, N. and Young, G. B. (2009), "*Wind load considerations for existing petrochemical structures*", *Structural Congress Proceedings*, ASCE.

[9] ASCE Standard ASCE/SEI 37 (2002), "Design Loads on Structures during Construction", America *Society of Civil Engineers* construction.

[10] ACI 318 (2008) "Building Code Requirements for Structural Concrete and Commentary", American *Concrete Institute.*

[11] PIP STE05121 (2006) "Anchor Bolt Design Guide", *PIP Process Practices.*

[12] AISC Design Guide 15 (2002) "AISC Rehabilitation and Retrofit Guide" *American Institute of Steel Construction.*

Structural Strengthening of Aloha Stadium

C.M. Moe[1], C. Paulson[2], G.R. Searer[3], A.A. Erickson[4] and B. Wonneberger[5]

[1] Senior Associate, Wiss, Janney, Elstner Associates, Inc., 10 South LaSalle Street, Suite 2600, Chicago, IL 60603; Phone: (312) 372-0555; cmoe@wje.com
[2] Principal, Wiss, Janney, Elstner Associates, Inc., 10 South LaSalle Street, Suite 2600, Chicago, IL 60603; Phone: (312) 372-0555; cpaulson@wje.com
[3] Associate Principal, Wiss, Janney, Elstner Associates, Inc., 2550 N. Hollywood Way, Suite 502, Burbank, CA 91505; Phone: (818) 303-1300; gsearer@wje.com
[4] Associate III, Wiss, Janney, Elstner Associates, Inc., 1441 Kapiolani Blvd., Suite 1700, Honolulu, HI 96814; Phone: (808) 591-2728; aerickson@wje.com
[5] Principal, Wiss, Janney, Elstner Associates, Inc., 1441 Kapiolani Blvd., Suite 1700, Honolulu, HI 96814; Phone: (808) 591-2728; bwonneberger@wje.com

ABSTRACT

Built in the early 1970s, Aloha Stadium is a welded plate girder and steel frame structure located in Honolulu, Hawaii that was not designed for contemporary hurricane wind loads, much less the large earthquake design forces that current code now prescribes. The owner of the stadium elected to voluntarily upgrade the structure to resist current-code-level wind and seismic events. This paper presents the results of a multi-year detailed structural analysis and a multi-year structural strengthening project for Aloha Stadium.

INTRODUCTION

Built in the early 1970s, Aloha Stadium is a welded plate girder and steel frame structure located in Honolulu, Hawaii that was not designed for contemporary hurricane wind loads, much less the large earthquake design forces that current code now prescribes. The owner of the stadium elected to voluntarily upgrade the structure to resist current-code-level wind and seismic events.

Structural System

The stadium is comprised of six primary structural "modules" that can be thought of as distinct or separate structures: two end-zone seating stands and four sideline seating stands. Large welded plate girder raker frames form the primary structure supporting the main roof and seating areas. In the end-zone stands, the raker frames are supported by a concrete substructure that also includes the lower areas of seating at the field level. In the sideline stands, the steel raker frames are supported by steel space frames that also support the field level seating areas at the sidelines. The slideline stands typically cantilever beyond their foundation supports. Figures 1 through 4 show overall views of the stadium structure.

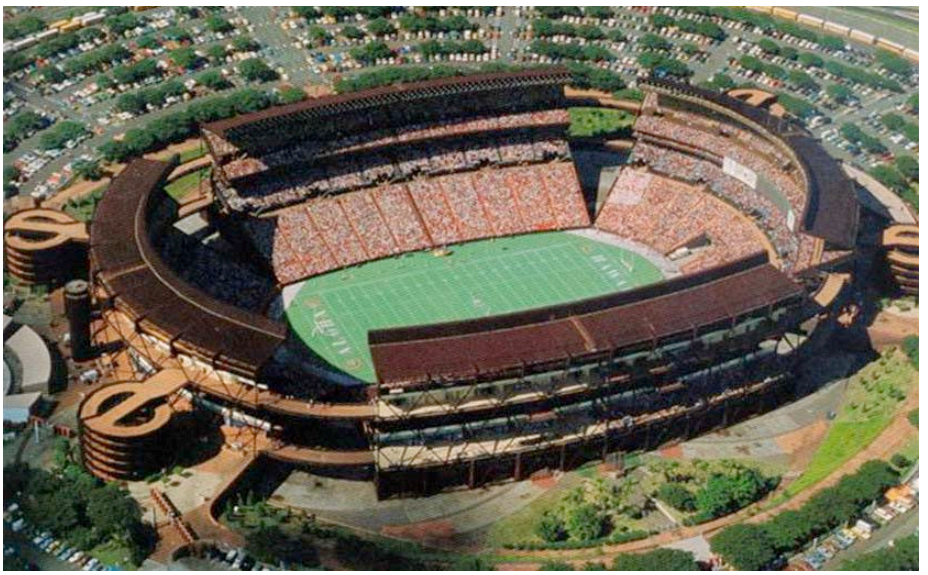


Figure 1: Overall view of Aloha Stadium in football configuration.



Figure 2: View of the typical raker frame at the end of the sideline stands.



Figure 3: View of the sideline stands from the exterior of the stadium.

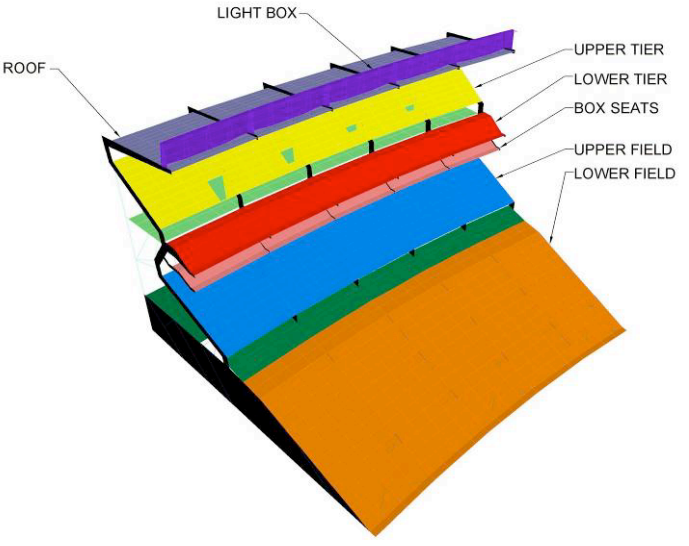


Figure 4: Bird's eye schematic view of sideline seating stands, defining stadium features.

The facility contains approximately 50,000 seats primarily for the viewing of athletic events. The stadium previously had the ability to move four of the six sections of seating stands to allow the stadium to be changed between either football or baseball configurations. During 2006, a policy decision was made by the owner to permanently maintain the stadium in the football configuration.

LIVE AND DEAD LOADS

Design dead loads are not significantly changed from the original design criteria and although design live loads for fixed stadium seating have actually decreased compared to the original design criteria, our analysis predicted significant overstresses in the as-designed connections of one of the large space frame trusses that support the sideline stands, and overstress conditions and vibration-related complaints were also identified in the pedestrian bridges due to live loads.

Space Truss Connections

Large trusses span parallel to the field and cantilever beyond the last foundation support, resulting in very large tension forces in the top chord of the truss. The connections of concern consist of two bolted, bent steel plates that behave as combined tension and shear connections (Figure 5), typical at 16 locations. Close observation of these connections revealed that the connections were indeed experiencing distress: paint had locally flaked away from some of the connections, indicating that yielding had occurred in the connecting angles, and a number of connections had clearly moved or slipped since the structure had last been painted about 20 years ago (Figure 5), suggesting possible deformation at the bolt holes in the web of the chord member.



Figure 5: View of the problematic connection (left), and close-up (right) showing localized flaking of paint, which is evidence of yielding, and a gap in the paint along the toe of the connecting bent plate, which is evidence of movement (arrow).

The combination of the sufficiently large calculated overstresses due to dead and live load only and the evidence of yielding and movement resulted in the recommendation

that strengthening of these connections be expedited and completed prior to the next use of the stadium. In the interim, movement gages were installed to assess whether additional movement under dead loads and nominal live loads was occurring.

Strengthening measures were completed a few months after identification of the problem and prior to any scheduled events at the stadium; strengthening included addition of top and bottom connection plates to deliver the tension load in the truss top chord to the other members that frame into the connection (Figure 6).



Figure 6: Connection plates were added to the truss chord top flange (flange cover plate, arrow in figure on the left) and bottom flange (triangular gusset-style plate, arrow in figure on the right).

Pedestrian Bridges

Eight previously removable curved pedestrian bridges exist connecting concourses between the seating stands. An overstress condition was identified in the curved steel girders, along with longstanding pedestrian-induced vibration and deflection issues. A system of tension rod stays was installed, which shifted the natural period away from the dynamic pedestrian loading and improved the structural performance of the bridges.

WIND LOADS

The original structural drawings for the stadium, which were prepared in the early 1970s, specify a uniform projected wind design pressure of only 20 pounds per square foot (psf). Given that hurricanes can strike the Hawaiian Islands, the original design pressure is significantly underconservative compared to the plausible if not likely wind pressures that might result from a hurricane strike. Therefore, due to the unique building facade conditions and shape of the Aloha Stadium structure, wind tunnel modeling of the

Aloha Stadium was performed during 2007 and 2008. Cermak Peterka Petersen (CPP), of Fort Collins, Colorado, performed the wind tunnel studies. The wind tunnel testing, data extraction, and final data interpretation were all performed in general conformance with *Minimum Design Loads for Buildings and Other Structures* (*ASCE 7-05)*.

Through a series of iterations between CPP, who analyzed the pressure tap data, and WJE, who reviewed the structural effect of the pressure data utilizing the structural analytical models, design wind pressures were developed for 12 main wind force resisting system (MWFRS) global load cases.

Due to hurricane wind directionality effects, global and local MWFRS wind load cases were developed separately for each of the north and south end-zone seating stands. In addition, using the wind tunnel results from all four sideline structures, envelope-type load cases were developed for a single sideline stand that were representative of wind loading on all four sideline seating stands.

Structural analyses were undertaken, using the design wind pressure results of the wind tunnel modeling, to better understand the weaknesses of the existing structural design, and to develop structural strengthening for this complicated, multi-structure stadium.

SEISMIC EFFECTS

The stadium was designed at a time when Honolulu was only seismic Zone 1 (described as "only minor damage anticipated") in the 1970 *Uniform Building Code* (UBC), and when modern seismic design philosophies, including ductile design detailing, were still being developed. In the *International Building Code* (IBC), the stadium is assigned to Seismic Design Category D, which is indicative of significant seismic hazard. Although voluntary seismic improvements are not required to conform to any standard, the owner desired that any seismic-related strengthening work conform to the seismic requirements of the 2003 IBC, with the added goal of conforming to the 2006 IBC where possible. Comparison of the seismic design provisions between the 2003 and 2006 editions of the IBC finds that the specified seismic design forces for "cantilever columns", such as those that support the main roof at Aloha Stadium, double when going from the 2003 IBC to the 2006 IBC due to corresponding changes between ASCE 7-02 and ASCE 7-05. It should be noted that since both of these versions of ASCE 7 require that connections be designed for the basic seismic design forces multiplied by an overstrength factor, which means that connections are required to stay essentially elastic. Thus, the net effect of this change on connection design forces is not as drastic as it might initially appear; however, the relative change from the requirements of the 1970 UBC to current code is quite large, as shown in Figure 7, and significant strengthening was required to meet the requirements of current code. Further, since the connections were designed to remain essentially elastic, the ductility demands on the connections, which consist of circa 1970s welded connections with potentially non-ductile details and bolted connections, are extremely low.

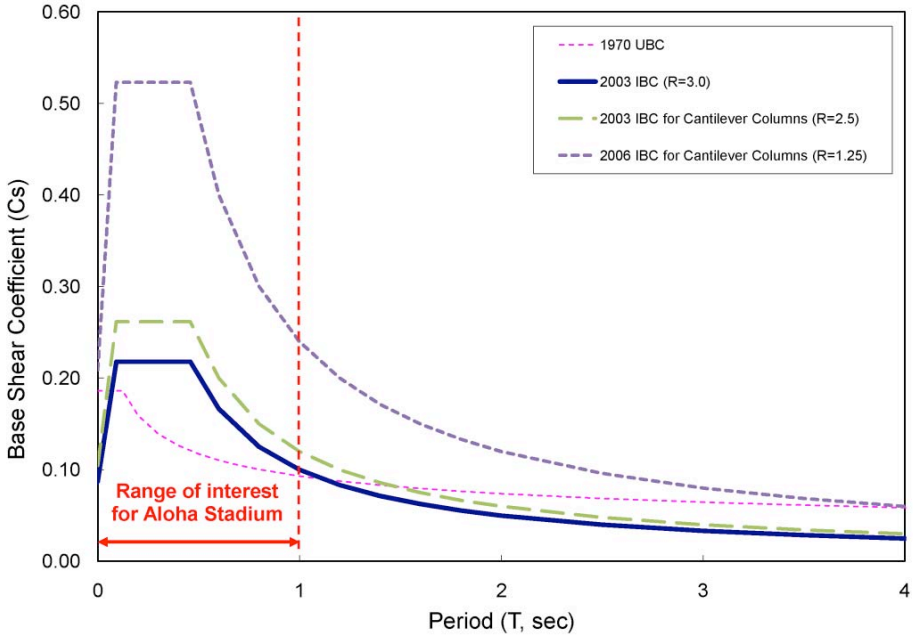


Figure 7: Spectra of seismic base shear design coefficients for Aloha Stadium.

In our analyses, the horizontal response spectra were based on the requirements of the 2006 IBC, using a response modification factor, R, of 1.25 and an Importance Factor, I, of 1.25, to address the conceivable, though not particularly likely, possibility that the stadium could be occupied during a design-level earthquake. The vertical response spectrum was defined as two-thirds of the spectrum used for lateral response, which is commonly accepted practice for seismic structural design.

When combining two orthogonal directions, ASCE 7-05 requires 100 percent of the force in a single direction to be combined with 30 percent of the force in the perpendicular direction. This requirement is based on the assumption that the building being analyzed is generally simple and regular, with a single, clearly apparent reference coordinate system; however, the Aloha Stadium seating stand structures are complex, irregular, curving structures that do not necessarily have a single easily defined reference coordinate system. Due to this complexity, the square root of the sum of the squares (SRSS) approach was taken to combine the three different directions of seismic response. The appropriateness of using the SRSS method for combining directional seismic load effects with complex structures is described by Wilson *et al*. (1995).

Because seismic design forces were based on modal response spectrum analyses, scale factors were applied to the two horizontal base shear components as specified by ASCE 7-05. For the sideline stand model, the adjustment factor was 1.60 for the longitudinal direction and 1.05 for the transverse direction. For both endzone stand models, the adjustment factor was approximately 1.55 in both directions. The general use of the response spectrum scaling factors from ASCE 7-05 for analyzing Aloha Stadium is conservative in our opinion. This is because the scaling factors were

developed for normal, structurally regular, generally rectangular buildings with distinct horizontal diaphragms and concentrated masses at discrete floor levels, and are thus conservative when applied to an irregular structure with inclined diaphragms and well distributed mass, and for which separate orthogonal design base shear forces may not have much meaning. When these scaling factors are combined with the response modification factor R of 1.25 and importance factor I of 1.25, the resulting seismic design forces are well within the elastic seismic response range; that is, the final effective R factor is likely less than 1.0. Note that according to strict interpretation of ASCE 7-05, a new stadium relying on an ordinary steel moment frame would not be permitted in Seismic Design Category D due to the arbitrary height limits found in ASCE 7-05; however, since this is an existing structure that is in essence being checked for fully elastic or even "greater-than-elastic" forces, we believe that the existing structure will meet or even exceed the intent of the 2006 IBC after implementation of structural improvements.

STRENGTHENING FOR WIND AND SEISMIC LOADS

With respect to wind and seismic loads, the major nonconformities identified by the structural analyses involved the vertically cantilevered raker frame columns that support the main roof and some members of the braced frame system. Raker columns were strengthened; beams and bracing members were strengthened and stiffened; and critical connections were strengthened or replaced, as described below.

Raker Frames

The welded plate girder raker frames were overstressed in both strong- and weak-axis bending as well as web shear in the elbow joints. To address these overstresses, cover plates were added to the top flanges of selected raker roof beams and rear flanges of selected raker columns, and haunch plates were added to the undersides of the roof raker beams and to the interior faces of the raker columns just below the roof level. Steel plate shear walls parallel to the exterior of the stands were also added to resist lateral forces that would otherwise cause weak axis response in the raker columns. Finally, diagonal web stiffener plates were added to the raker elbow joints to increase both the shear strength of the web and create tension/compression struts to transfer bending stresses around the corners of the elbow. Figure 8 shows installation of new column haunch plates and steel plate shear walls; Figure 9 shows installation of a new raker beam cover plate; and Figure 10 shows new diagonal web stiffener plates at raker elbows.



Figure 8: View from the upper seating level, looking outward. The arrows indicate the new steel shear walls and the new haunch plates.



Figure 9: Typical new steel plate added to the top of a raker roof beam.

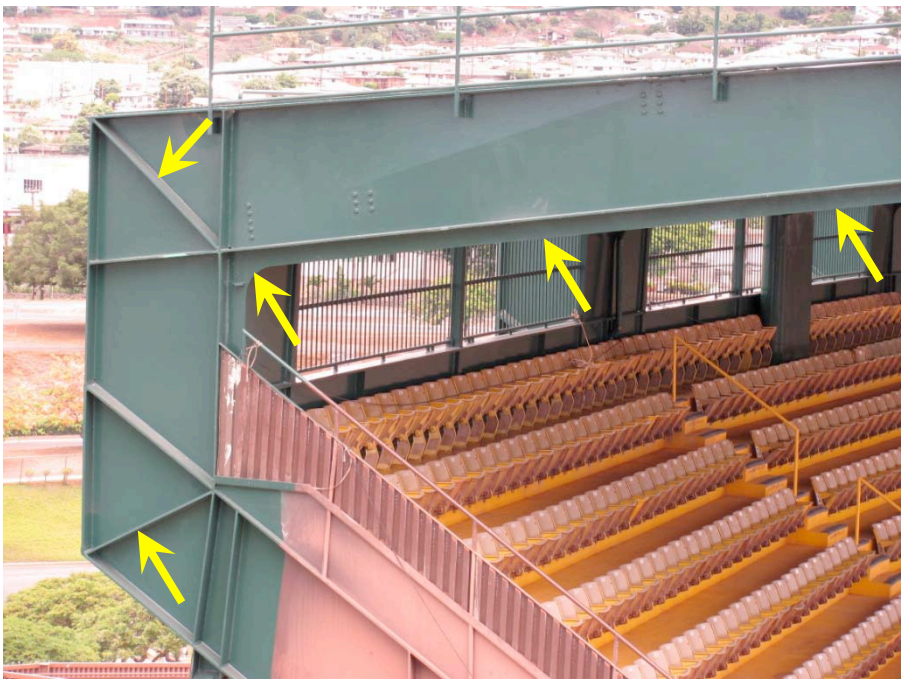


Figure 10: New diagonal web stiffener plates at raker elbows and new haunch plate, as indicated by arrows.

Connections of Raker Frames to Diagonal Bracing

Web compression stiffeners in raker beams were also substantially overstressed due to lateral bending just above the termination of the perimeter diagonal braces, so diagonal HSS braces were added to strengthen and laterally stabilize this region of the raker frame. The new braces also serve to transfer loads from the new steel plate shear walls to the work point at the top of the existing diagonal bracing system (Figure 11).

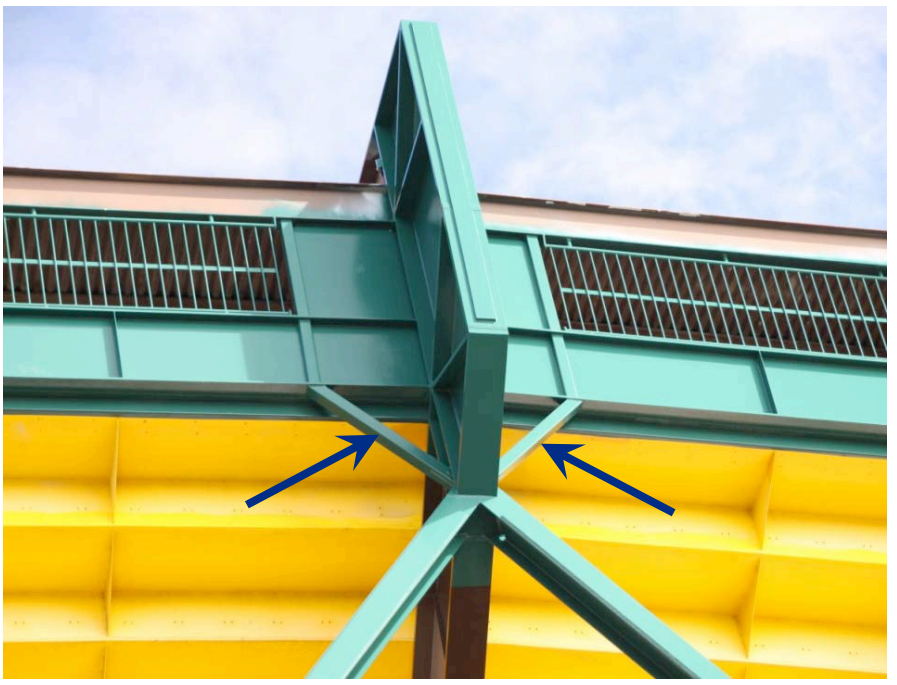


Figure 11: New HSS braces were added to connect the tops of the perimeter diagonal bracing to the new steel plate shear walls.

Strengthening of Exterior Diagonal Bracing

The last major strengthening to be implemented was improvement of the compression buckling strength of the exterior diagonal bracing on the sideline stands. A large number of braces were calculated to be exceedingly slender, so much so that interaction of compressive axial load from seismic loads and the relatively minor bending caused by member self-weight or seismic vibration perpendicular to the longitudinal axis of the brace member tended to cause unusually large calculated design interaction ratios. Addition of flange cover plates that terminated short of each brace end connection (Figure 12) improved the compression buckling strength of the braces without increasing the tension capacity, thereby averting a need for strengthening of the tension capacity of the brace end connections.



Figure 12: Steel plates were added to diagonal bracing on the sideline stands.

Identification of Other Elements for Future Strengthening

Due to the phased construction approach that was necessary to keep this structure in service during construction work, all wind and seismic strengthening was not performed in a single construction project. As part of our assignment, we identified elements to be included in future strengthening phases, including:

- Strengthening of selected lower portions of the raker frames, similar to the strengthening described herein for the upper portions;
- Strengthening of selected connections elsewhere in the structure that are overstressed due to seismic loads;
- Modification of connections of pedestrian ramps and bridges to the stadium stands to allow greater differential movement between the various structures; and
- Anchoring the now-disused transporter frame assemblies that support the sideline seating stands to the foundations to resist sliding of the sideline stands.

CONCLUSIONS

Aloha Stadium was designed and constructed during the 1970s, before the advent of modern seismic building codes and long before the potential for a direct hurricane strike on the island of Oahu was recognized by the building code. The authors were retained to design strengthening measures for the stadium that would bring the structure into general conformance with the modern building code. A number of existing structural members were strengthened and stiffened. Further seismic strengthening measures will be implemented in future phases of the project. In

addition to the need for seismic- and wind-related strengthening, which is not unusual for a building of this age, a significant and unexpected deficiency relating to dead and live load was discovered in a series of connections; the overstresses in these connections were so large that the connections in question had yielded under service loads. These deficient connections were strengthened as well.

REFERENCES

American Society of Civil Engineers (2002), *ASCE SEI 7-02, Minimum Design Loads for Buildings and Other Structures*, American Society of Civil Engineers, Reston, VA.

American Society of Civil Engineers (2005), *ASCE SEI 7-05, Minimum Design Loads for Buildings and Other Structures*, American Society of Civil Engineers, Reston, VA.

International Code Council, Inc. (2003), 2003 *International Building Code*, International Code Council, Inc., Washington, D.C.

International Code Council, Inc. (2006), 2006 *International Building Code*, International Code Council, Inc., Washington, D.C.

International Conference of Building Officials (1970), *Uniform Building Code, 1970 Edition*, International Conference of Building Officials, Whittier, CA.

Wilson, E.L., Suharwardy, I., and Habibullah, A. (1995), "A Clarification of the Orthogonal Effects in a Three-Dimensional Analysis", *Earthquake Spectra*, Earthquake Engineering Research Institute, Vol. 11, No. 4.

Seismic Design Retrofit & Detailing for Special Structures

Crystal Roe Starr, P.E., LEED AP, Engineer, MWH Americas Inc., Walnut Creek, CA 94596; email: crystal.starr@us.mwhglobal.com

ABSTRACT

With increasing knowledge of structural performance during seismic events, new building design has evolved to include redundancy, building regularity, ductile detailing, and continuity among many changes that set precedence for the retrofit of existing buildings. Many existing buildings require a seismic retrofit not only to perform to the level of similar new buildings during an earthquake but to even perform at all. However, it is impractical to seismically retrofit all existing buildings. This is why priority is given to retrofitting various essential facilities and in many instances, enforced through regulations. Many municipalities are required to seismically retrofit many of their essential facilities because of the economical and life safety impacts of not doing so. This paper will outline the seismic retrofit of an essential water storage facility for the City of San Francisco in accordance with ASCE 41-06. In addition, this paper will discuss in brief the temperature analysis performed on the reservoir.

INTRODUCTION

The University Mound Reservoir North Basin (UMRNB) was originally constructed in 1885 as an open-cut, in ground 55-MG reservoir with an earthen embankment dam and concrete floor slab (Figure 1). In 1962, UMRNB was upgraded with a thin pan-joist concrete roof system with girders in one direction, supported primarily on cast-in-place columns and footings which are integral with the concrete lining. The thin roof slab with overall dimensions of approximately 750’ x 650’ is divided into 15 segments separated by seismic joints. There were 12 segments along its perimeter and 3 at the interior (Figure 2).

The goal of the UMRNB seismic retrofit performed in 2007 by MWH Americas Inc. was to provide assurance that the reservoir would be capable of supplying fire fighting and drinking water after the maximum credible earthquake. The maximum credible earthquake is based on the 8.2 km proximity of the site to the nearest fault, the San Andreas Fault. The earthquake magnitude considered was the repeat of the 1906 type earthquake with a moment magnitude (Mw) of 7.9. The deterministic site-specific response spectra at the median plus one standard deviation (or the 84th percentile) level was used. This is also the required maximum credible earthquake

required for design by the Division of Safety of Dams (DSOD), a regulatory agency who oversees the protection of the lives and property due to dam failure. The potential loss of surrounding property due to failure of the embankments on the north and east sides of the UMRNB dictates the jurisdiction of DSOD.

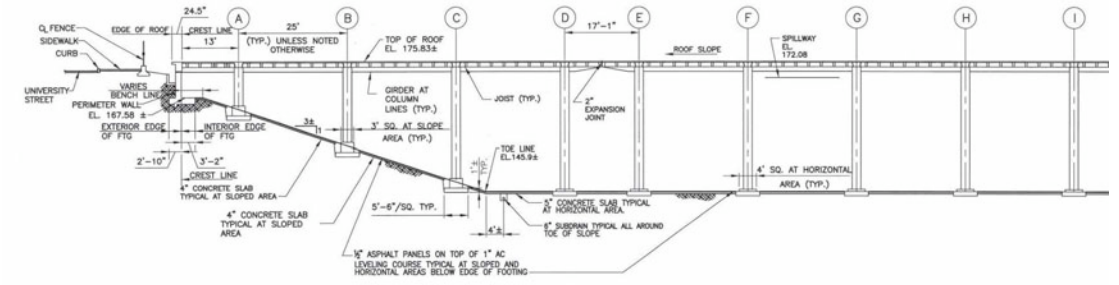


Figure 1. Existing Typical Section

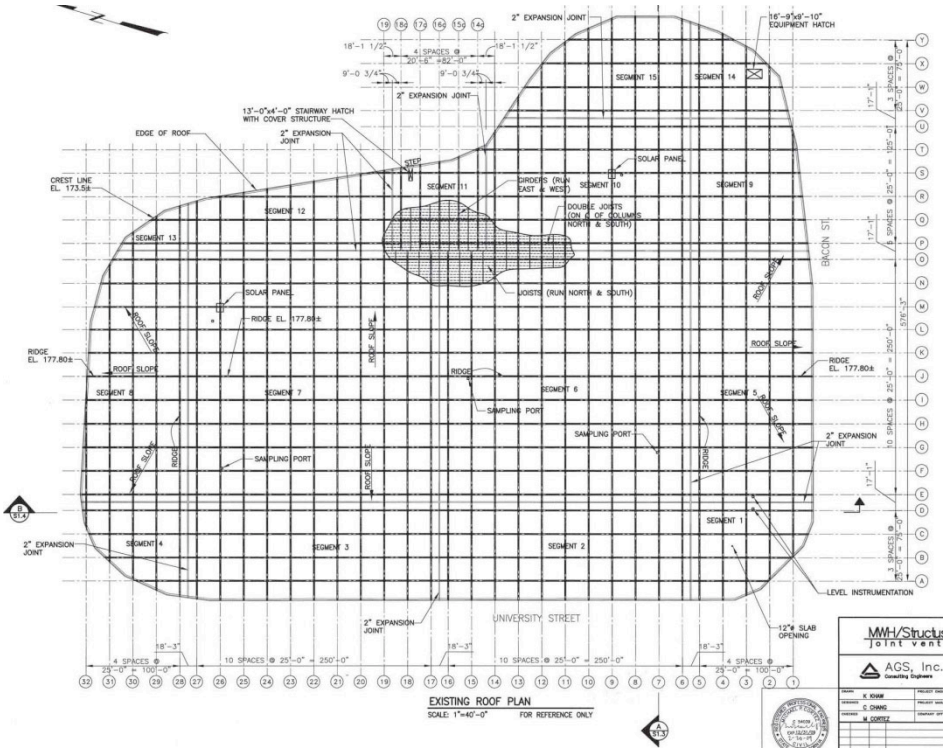


Figure 2. Existing Roof Plan

SEISMIC CRITERIA

Seismic design and evaluation for retrofit of the reservoir was based on the standard for *Seismic Rehabilitation of Existing Buildings*, ASCE 41-06 requirements in conjunction with the City building standards. The provisions of ASCE 41 are based on FEMA 356 Prestandard and FEMA 274. ASCE 41 supersedes FEMA 356, however FEMA 274 is still an active standard.

Seismic rehabilitation in accordance with ASCE 41 is a performance-based design, which differs from procedural new building design. Performance-based design is ideal for seismic retrofit design because with increasing knowledge of building behavior and advanced structural modeling tools, building performance can be predicted. For this reason, new building design procedures include redundancy, emphasis on building regularity, ductile detailing, and element continuity. With most existing buildings designed using dated building codes that do not achieve this level of performance (hence the premise of ASCE 41), it is difficult to predict the performance of the buildings. Therefore, a procedural based design for retrofit of existing building is unrealistic and a performance based analysis must be utilized.

The performance-based design of ASCE 41, prescribes performance levels based on findings from a seismic evaluation that must be conducted. The performance level is defined as the extent of damage that a building and its occupants can afford during and after a seismic event. The performance level can be categorized as one of the following, in order of severity from least to most severe; Operational, Immediate Occupancy, Life Safety, or Collapse Prevention. Table 1 shows the performance level classifications used on the project.

Table 1. Structural Performance Objectives

Component	Earthquake Level	Structural Performance Level	Non-Structural Performance Level
Reservoir Roof	BSE – 1	Immediate Occupancy	Operational (1-A)
	BSE – 2	Immediate Occupancy	Immediate Occupancy (1-B)

During the seismic evaluation, certain considerations must be analyzed which include the structural characteristics, site seismic hazards, occupancy, societal impacts, and economic considerations. Once the performance level is determined the Rehabilitation Objective can be selected. There are three Rehabilitation Objectives, Basic Safety Objective (BSO), Enhanced Objective and Limited Objective. The UMRNB rehabilitation program fell into the Enhanced Rehabilitation Objectives

category in accordance to Table C1-1. *Rehabilitation Objectives* of ASCE 41. Following the guidelines of the Enhanced Rehabilitation Objectives, UMRNB retrofit design was to be analyzed at a Basic Safety Earthquake-1 (BSE-1) and Basic Safety Earthquake-2 (BSE-2) hazard level.

The BSE-1 is a "Design Earthquake" defined as an earthquake with a 10% probability of exceedance in 50 years, and a mean return period of approximately 475 years. However, since the BSE-2 is required for design and more critical, the BSE-1 analysis is moot for seismic retrofit design.

The BSE-2 is a "Maximum Earthquake" defined as an earthquake with a 2% probability of exceedence in 50 years, and a return period of approximately 2475 years. However this earthquake shall not exceed the maximum earthquake ground shaking based on a deterministic approach (84% MCE- 84 percentile of the Maximum Credible Earthquake).

SEISMIC ANALYSIS

In accordance with ASCE 41, linear or nonlinear analysis procedures may be selected for an existing building evaluation. The building must meet the requirements of the standard. It is evident that all existing buildings have some nonlinear response or ductility, but not all buildings need to be designed with nonlinear procedures. A linear analysis can be selected for a building with spatial regularity where nonlinear response can be distributed uniformly throughout the structure at the response level to which the building is to be evaluated based on the performance objectives. The nonlinear analysis procedures provide results that are close approximations of the expected response of the structure for the given performance level.

A Linear Analysis was selected for the UMRNB Project as the structure met the requirements for linear design. Linear Analysis in accordance with ASCE 41 is similar to traditional new building design but includes adjustments for some nonlinear behavior of the structure.

All component actions must be identified as either deformation-controlled or force-controlled. Deformation-controlled action is the yielding behavior of a component. Type 1 and Type 2 curves in the stress-strain diagrams of Figure 3 represent the ductile yielding of a component with an initial elastic range followed by a plastic range. In the plastic range the component has a residual strength gain followed by a loss of strength with increasing plastic deformation during the strain-hardening phase. Alternatively, force-controlled action is the nonductile and brittle behavior of a

component. Type 3 curve of Figure 3 represents a force-controlled stress-strain diagram where an element experiences elastic behavior followed by a loss of strength. Table 2 shows possible deformation-controlled and force-controlled actions identifications for various components as were used for the UMRNB design elements.

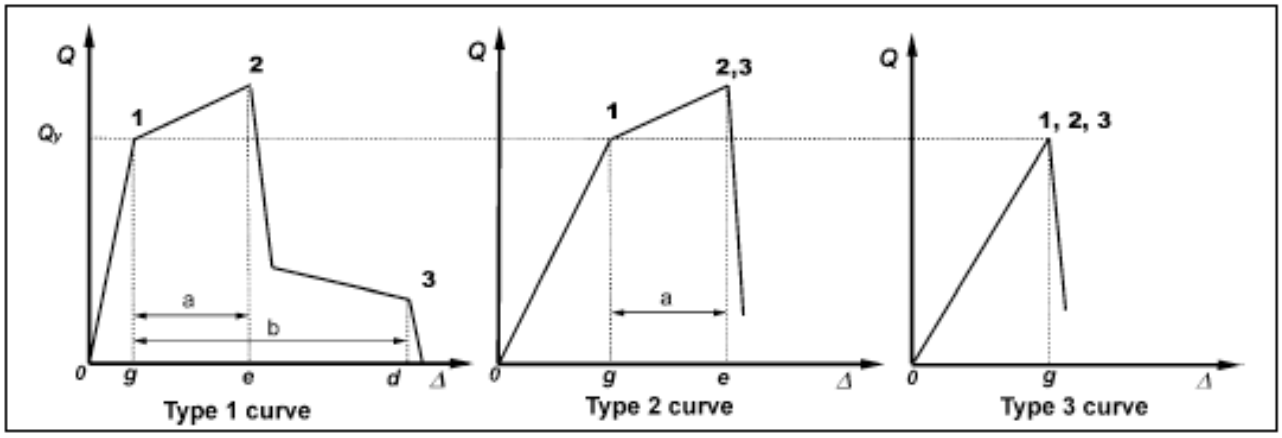


Figure 3. Component Force vs. Deformation Curves

Table C2-1 Examples of Possible Deformation-Controlled and Force-Controlled Actions

Component	Deformation-Controlled Action	Force-Controlled Action
Moment Frames		
• Beams	Moment (M)	Shear (V)
• Columns	M	Axial load (P), V
• Joints	--	V[1]
Shear Walls	M, V	P
Braced Frames		
• Braces	P	--
• Beams	--	P
• Columns	--	P
• Shear Link	V	P, M
Connections	P, V, M[3]	P, V, M
Diaphragms	M, V[2]	P, V, M

1. Shear may be a deformation controlled action in steel moment frame construction.
2. If the diaphragm carries lateral loads from vertical seismic resisting elements above the diaphragm level, then M and V shall be considered force-controlled actions.
3. Axial, shear, and moment may be deformation-controlled actions for certain steel and wood connections.

Table 2. Component Identification

MODELING

Three-dimensional finite element models of UMRNB were developed using SAP 2000, Version 11, a finite element software (Figure 3). Both the existing structure and the proposed seismic upgrade elements were included in the models. The models were used for static, non-linear pushover and thermal analysis.

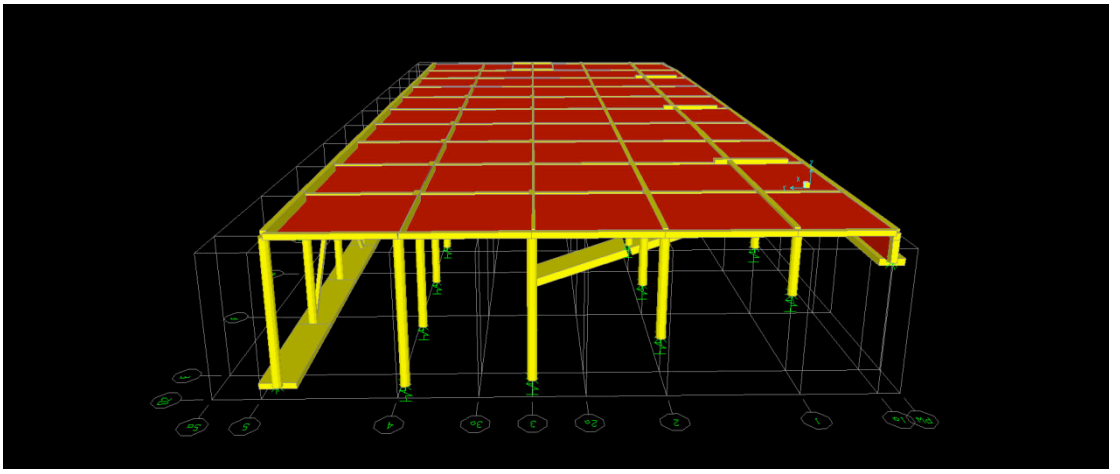


Figure 3. SAP model of a single roof segment

The foundation elements of the structure were modeled with springs based on geotechnical recommendations and calculated values to represent the soil structure interaction. The elastic spring constants were a function of the stiffness, length and embedment of the foundation with respect to the stiffness of the soil in accordance with FEMA 356 Chapter 4. All the supports were restrained in the lateral direction and moment resistance was released in all directions. The existing column footings were modeled as pinned supports with elastic springs. The perimeter wall footings were modeled with linear springs below the footing. New foundation elements, grade beams and shear walls were modeled with similar linear springs. However, rotational springs were added to the base of the shear walls to allow out-of-plane bending.

Cracked section properties were used for dynamic analysis. Effective moment of inertia was assumed to be 50% of gross moment of inertia for the beams, columns and cracked walls.

RETROFIT ELEMENTS

The UMRNB retrofit elements were selected based on stiffness requirements and space constraints. Shear walls, brace frames, moment frames and collectors served as the new lateral force resisting elements (Figure 4).

The perimeter walls provided vertical support of the perimeter roof segments without lateral resistance. The new lateral resisting elements in the long span were new shear walls directly in front of the perimeter wall and braced frames at the opposite side of the segment. Adjoining the roof and perimeter wall was considered by this forced too much load into the perimeter wall and put torsion of the roof segment. Braced frames were chosen for the bays toward the center of the structure because they would allow more water circulation than would shear walls. In the short span of the segments, shear walls were provided along the embankment slope. Forces were transferred through the diaphragm through collectors in the roof that were attached to existing girders and double joists. At the floor, grade beams transferred forces through the floor slab.

Shear walls were designed integral with the existing columns. The instability of the shear walls due to overturning, was restisted by a micropile foundation. Micropiles were selected in lieu of large diameter piles because we wanted to minimize any disturbance to the embankment.

The new lateral system at the interior segments were new concrete moment frames. The concrete moment frames would allow the roof segments to move.

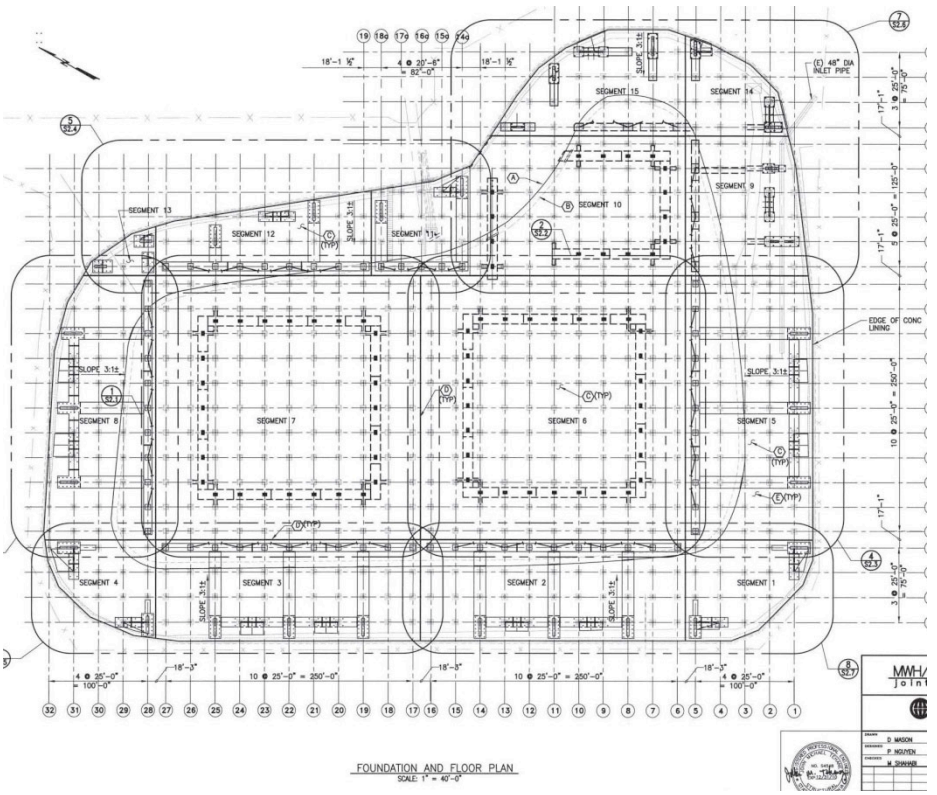


Figure 4. New foundation and floor plan

THERMAL ANALYSIS

A thermal analysis was a design consideration that became a governing load condition for the UMRNB design. The original scope of work for the project included a basic thermal analysis check. However, thermal movement was observed at a similar reservoir retrofit which warranted a detailed thermal investigation of the University Mound Reservoir based on measured expected temperatures.

The reservoir was undergoing a retrofit of a similar nature, with major moment frames, braced frames and shear wall components. This reservoir retrofit was the basis of our design for UMRNB. We were fortunate that this reservoir was in construction during the design phase of UMRNB. Of many lessons learned and taken from this reservoir, temperature considerations was the most prevailing. During visits to the site, some cracking of the roof and noises within the reservoir were observed after the braced frames and shear walls were locked to the roof slab.

We performed a detailed SAP thermal analysis of the roof slab for the UMRNB (Figure 5). To no prevailing surprise, thermal expansion and contraction is prevented in the roof slab once the braced frames and shear walls are locked to the roof. This type of restraint imparts significant tension and compression stresses in the roof. Compression on hot days as the roof slab wants to expand and tension on cold days

when the roof wants to contract. To mitigate overstressing our 3-inch thick roof slab reinforced with welded wire fabric, we identified the areas of high stress concentration using our SAP analysis models. The areas of large stress as predicted were located where the roof is restrained, at the braced frames and shear walls.

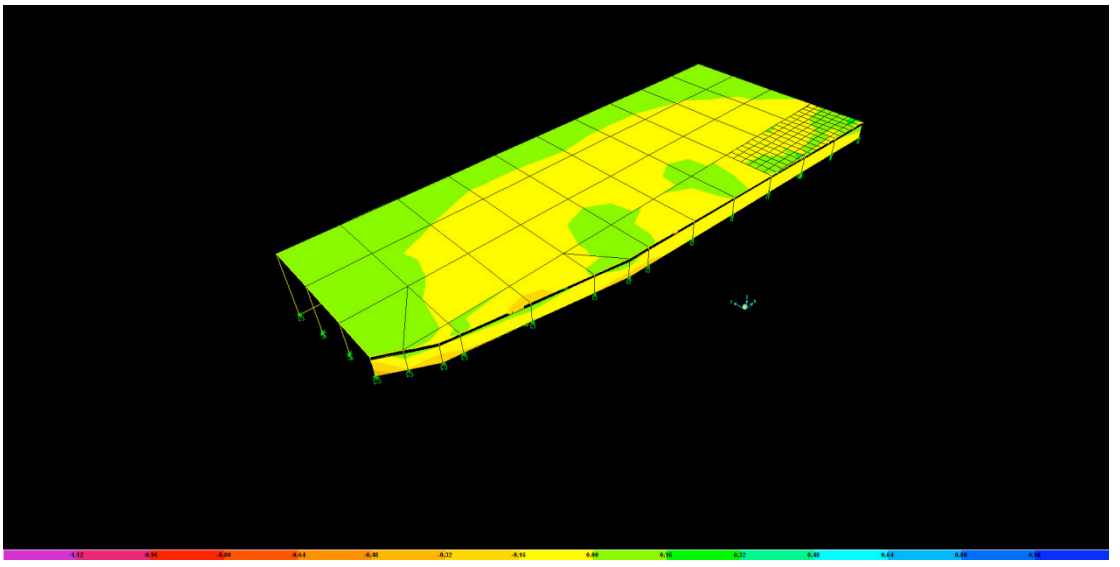


Figure 5. Thermal SAP analysis model of a single roof segment

For our thermal analysis, we used measured field and historical temperatures. The exterior roof surface temperature was observed to be within the range of 20°F higher than ambient temperature. Our estimated modeling temperatures at the exterior roof surface were 130°F on a hot day and 22°F on a cold day. These temperatures were the maximum and minimum expected roof surface temperatures. However, we discovered a reflective white coating that can be applied to the roof surface that would radiate direct sunlight that could be used to restrict the heat absorbed by the roof slab at its surface. The manufacturer of the reflective coating guaranteed the roof temperature would remain at ambient temperature with the use of this product. Our new modeling roof surface temperatures became 108°F at maximum and 22°F at minimum. The estimated temperatures within the reservoir were 60°F in the summer and 50°F in the winter. When the roof was analyzed under the thermal gradient 108°F to 60°F and 22°F to 50°F, the roof was significantly overstressed. We knew we could increase the tensile strength of the roof by adding FRP, however the compression capacity of the roof is limited to the existing capacity of the roof slab.

We devised a plan to specify an installation temperature for the roof to brace frames and roof to shear wall (or locking temperature) that is based on the temperature range in which we know the roof can be stressed under without exceeding its capacity. This locking temperature was determined to between 80°F and 60°F. This would set summer installation temperatures between 108°F and 60°F. Likewise, the winter

installation temperatures were set between 22°F and 80°F. Notice the lower bound temperature is used for summer installation temperatures and higher bound temperature is used for the winter installation temperature which produces the largest thermal gradient.

Not only was the roof capacity checked, but the member capacities were checked for thermal loading. For seismic design in accordance with ASCE 41, a phi factor of 1.0 is allowed. However, for thermal analysis which isn't included in ASCE 41, typical code level reductions are used for member designs. Therefore, it could not be assumed that seismic conditions governed member design.

CONCLUSIONS

Construction sequencing must be clearly defined in the Specifications and scope of work. Poor construction sequencing was evidenced by the difficulty of achieving the locking temperature in the field. The Contractor was able to lock in most of the braced frames and shear walls to the roof slab in the summer months when the locking temperatures were achievable. However, remaining braced frames were difficult to lock into place when it became cold in the winter months because the reflective coating was placed above the roof. The reflective coating would prevent the roof from absorbing any natural sunlight, which poses difficulty in the winter months. In hindsight, proper sequencing and scheduling would have negated this problem. The reflective coating should have been placed after the braced frames and shearwalls were locked to the roof at the locking temperature.

DISCLAIMER: "This document has been prepared specifically for the 2011 Structural Congress in relation to the University Mound North Basin Reservoir Project and should not be relied upon by other parties nor used for any other purpose other than for the Structural Congress without initial consent from MWH."

REFERENCES

Prestandard and Commentary for the Seismic Rehabilitation of Buildings (FEMA 356). (November 2000). *American Society of Civil Engineers*, Reston, Virginia.

ASCE/SEI 41-06, Seismic Rehabilitation of Existing Buildings. (2007). *American Society of Civil Engineers*, Reston, Virginia.

Improvement of Nonlinear Static Seismic Analysis Procedures (FMA 440). (June 2005). *Applied Technology Council (ATC-55 Project).* Redwood City, California.

Floating Stair using High Performance Structural Materials

Mark C. Waggoner

Principal, Walter P. Moore and Associates, Inc., 221 West 6th Street, Suite 800, Austin, Texas 78701; PH 512.330.1270; email: mwaggoner@walterpmoore.com

Abstract

In 2007 Walter P Moore relocated its corporate headquarters in Houston, TX, in 2007 to three floors in a tall building in downtown Houston designed by the firm. Working with the architecture firm Gensler, initial planning efforts identified the need to connect the workflow of the office via a new, common central stair atrium cut into the existing floor plates. The final design for the stair was chosen from an internal design competition that sought to identify a lightweight, progressive structural solution that highlighted the creative abilities of the firm.

The design implemented for the stair consists of a cantilevered, stringerless arrangement that takes advantage of the intrinsic elements that exist functionally in a stair by rewriting the structural behavior of the stair through manipulation of the boundary support conditions. Using this design framework, individual elements of the stair were minimized through the use of high performance materials, including ultra-high performance fiber reinforced concrete (UHPFRC) and high strength steel cables.

In addition to the optimization process that enabled the ultra-thin sections, a unique approach to vibration design was taken. The stair was intentionally designed to be somewhat flexible, allowing a platform for discussion of vibration perception topics with the clients who visit the office. The stairs are outfitted with a small tuned mass damper (TMD) and instrumented with accelerometers whose output is displayed on a large screen at the bottom of the stair.

Stair Concept

What are the essential elements of a stair? Functionally, a stair must have treads, guard rails, handrails, and stringers for structural support. Or does it? The design concept of the stair emerged from a fundamental examination of the basic components of a stair and how they might be exploited as structure. The inspiration was to eliminate any elements that acted only as structure, and simply use the basic essential functional elements of a stair to provide support.

Looking at the fundamental elements of the stair, the walking surface typically consists of thin but wide slabs of concrete – quite suitable to take compressive loads. Likewise, the handrails and guardrails are thin, linear elements which are well proportioned for tensile loads but unsuitable for compression. However, the manner by which stairs are typically supported at either end produces bending forces that place compression in the upper elements and tension in

the lower elements – exactly the opposite of the available structural opportunities in the stair elements.

By flipping the stair on its end and cantilevering it from the top, the forces induced in the stair elements – tension on top, compression on bottom – match the suitable structural functions of the respective stair tread and railing elements. Thus the stair is not supported at its lower end, allowing the dramatic floating appearance but in fact only as a by-product of the manipulation of structural forces. Resolution of the horizontal forces at the top end of the stair is provided by a vertical W16 beam, which easily spans to the existing building floor levels to distribute forces to the floor diaphragms.

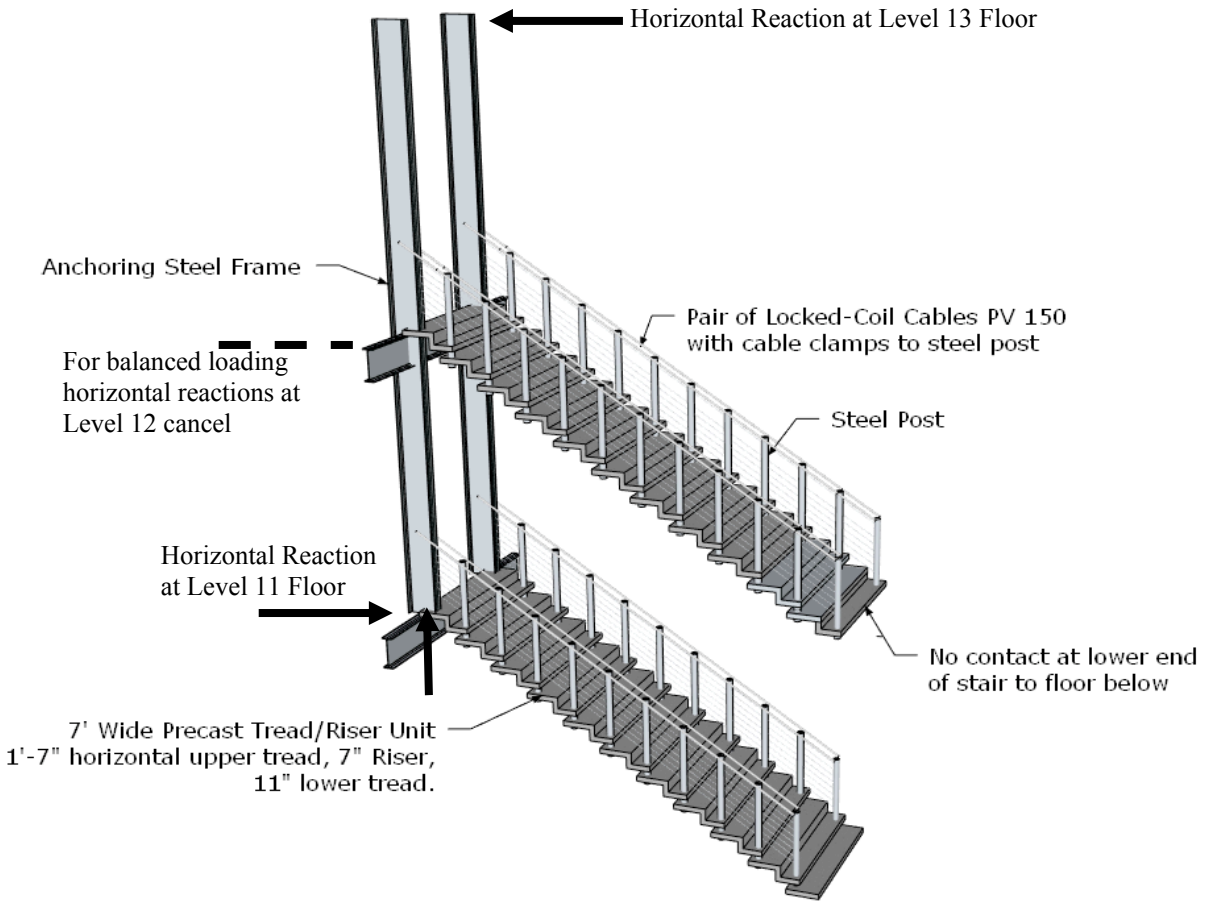


Figure 1: Stair Design Concept

Stair Elements

The "cantilevered beam" consists of a trussing of the upper tension elements with the lower compressive elements. Using the 42" height required of the guardrail provided a robust depth for the span – the equivalent of span/15 in structural terms. Rather than introduce diagonals to

create the truss, a clean appearance was maintained by utilizing flexural stiff vertical posts rigidly connected to the treads and risers to create a vierendeel system.

Using this basic form, the various stair elements were realized in state-of-the-art high strength structural materials to allow the lightest elements possible, and also to create a demonstration of use of advanced materials. Ultra-high performance fiber reinforced concrete (specifically, Ductal by LaFarge) was used for the precast tread and riser units. Using UHPFRC enabled the units to be only 1" thick typically, with a stiffening rib at the connection to the steel post. Combined with a compressive strength around 18,000 psi, the UHPFRC utilized high performance organic fibers that enabled elimination of most rebar in the tread/riser units. Design of the UHPFRC was accomplished using a code framework developed by the Japanese Society of Civil Engineers (JSCE, 2006). In this stair application the UHPFRC is enhanced by the inherent compressive forces flowing through the bottom chord of the truss, effectively prestressing the concrete material.



Figure 2: UHPFRC Precast Tread/Riser Units

The guardrail of the stair, working as the top tension chord of the truss, is made of two 1½" diameter locked coil cables. Not needed for strength, sizing of the cable is based on a combination of stiffness requirements and prescriptive code requirements for guardrail dimensions. Each pair of cables is clamped to the tops of the solid 3½" stair posts through a machined cable clamp, which is bolted to the top of the steel post through a tapped, threaded hole. The top ends of the cables are anchored with an open spelter socket.

The steel posts are solid 3½" A36 steel rods, selected from common bar stock. At the lower connection to the precast units, the post is threaded externally and passes through a blocked out hole in the unit above. Nuts clamp the concrete rib and transfer the moment from vierendeel

truss action through bearing and bending in the steel post. A high strength A490 bolt is threaded up through a hole in the lower precast into a hole in the end of the pipe to secure the lower precast element.



Figure 3: Cable Clamps



Figure 4: Post Connection to Precast Units

Vibration Design

A unique approach was taken to design of the stair for vibration. Rather than seek to eliminate vibration, a common request of our clients, we chose to feature the movement of the stair. At a base frequency of 3.5 Hz without taking any enhancement to the design for vibration, the stair was in a range where perceptible accelerations could be expected.

Our design practice frequently tackles complex problems of vibration design and the associated human perception issues. We frequently attempt to explain to clients what different levels of vibration might feel like so that they may make important and often very costly decisions on tradeoffs of cost in implementing various levels of acceleration control. Such explanation is often futile without physical demonstration to the layman. In order to help better educate our clients on vibration issues and what it means to "feel" a structure move, we chose to target our stair design flexibility in a range to facilitate these discussions.

To better understand what actual performance might be expected, extensive time history analysis was conducted of an analytical model of the stair. Simulations of one, two, four, and six people traveling on the stair simultaneously was conducted using various pacing rates. Predicted accelerations were in the 2 to 3 percent gravity range, a level that is readily perceptible.

As a measure to allow the flexibility to tune and limit the acceleration levels, the cantilever stair concept offered an excellent opportunity to incorporate a tuned mass damper (TMD) at the tip of the cantilever. A pivoting TMD was bolted to the underside of the stair at the lower two post locations. The pivot arm contains an offset mass aligned with an air damper, and reacts on a steel spring bearing on the underside of the lower tread unit. The mass is provided by steel plates which can be adjusted in both number and position to tune the properties of the TMD. The damper is an off the shelf air damper.

To provide real time feedback on the stair response, the lower end of the stair near the TMD was equipped with an accelerometer which is linked to a display read out at the bottom of the stair. The TMD is also equipped with a lock-down mechanism such that it can be turned "off", so that the user can experience the effectiveness of the TMD in reducing the response of the stair. Measurements indicate that the stair damping was enhanced from 0.5% critical for the bare stair to around 6% critical with the TMD engaged.

Erection

The stair was erected from the top down by progressively hanging each post and precast unit onto the top lock coil cables. Due to the sequential nature of the deflections, Walter P Moore provided the erector with setting dimensions based on simulation of the stair erection using a staged construction analysis. Interestingly, one flight of stairs was erected properly to specified setting dimensions and came to the correct elevation at the lowest tread, an important consideration to meet the code tolerances on variation in tread height. The second flight was set without consideration for the preset dimensions, and came out of tolerance but was easily adjusted through jacking and shimming at the top of the cantilever.

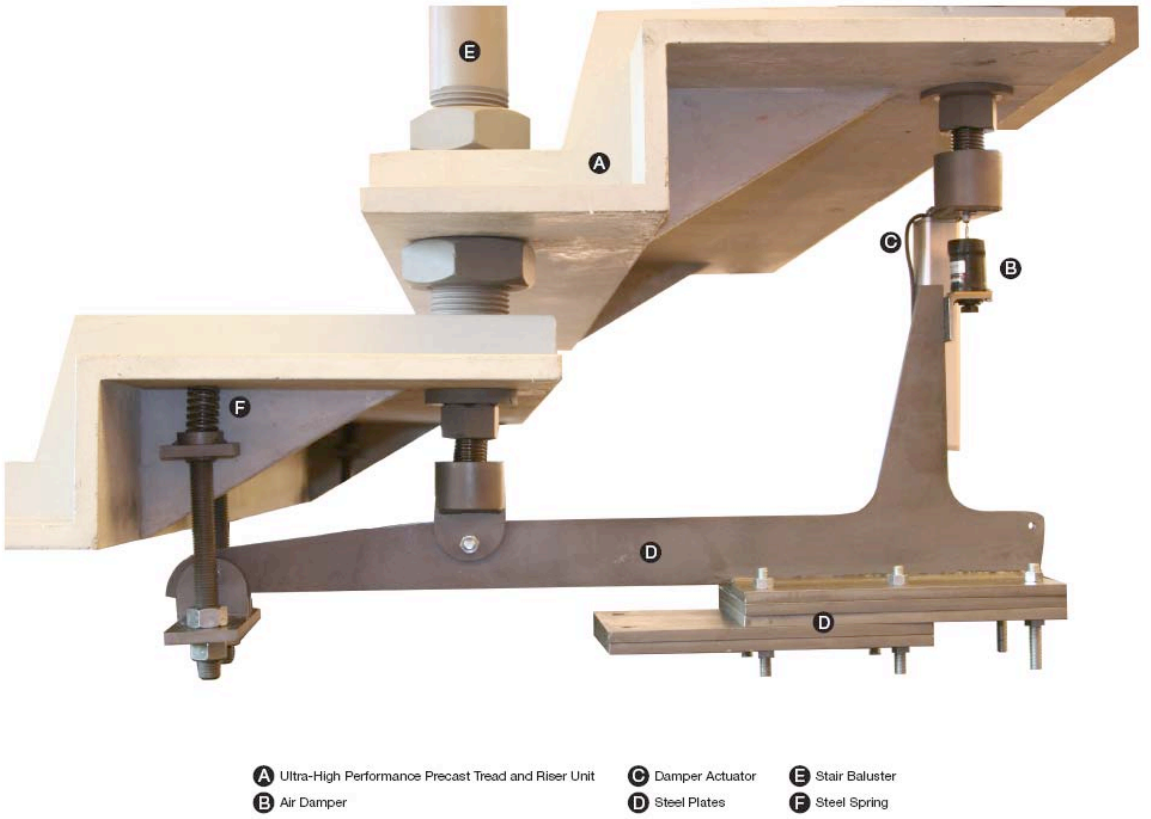


Figure 5: Tuned Mass Damper

Conclusions

The Walter P Moore Houston office stair has been conceived to defy all conventional notions of how a stair behaves. The inverted structural form replaces a conventional spanning notion, and budget normally spent on expensive architectural finishes is vastly reduced by the use of high performance structural materials. Conventional notions of a rigid feeling stair experience are replaced by celebrating the experience of traversing the stair through a real time read out of the participant's effect on the structure. After completion, the stair has proved to be a highly entertaining feature for both staff and clients, and has provoked extensive discussion on its inner workings.



Figure 6: Completed Stair

References

Niwa, J. Ed. (2006) *Recommendations for Design and Construction of Ultra High Strength Fiber Reinforced Concrete Structures (DRAFT)*, Japanese Society of Civil Engineers, Tokyo.

Staircase Vibrations Due to Human Activity

Rami Eid[1], Michael Seica[2], David Stevenson[2], and Brian Howe[3]

[1]SCE – Sami Shamoon College of Engineering, P.O. Box 950, Beer Sheva 84100, Israel, ramiei@sce.ac.il (formerly of Halcrow Yolles, 207 Queen's Quay West, Toronto, Ontario, Canada M5J 1A7)
[2]Halcrow Yolles, 207 Queen's Quay West, Toronto, Ontario, Canada M5J 1A7
[3]HGC Engineering, 2000 Argentia Road, Mississauga, Ontario, Canada L5N 1P7

ABSTRACT

Feature staircases are very popular in the architectural design of institutional and commercial buildings in North America and elsewhere. Generally, the iconic staircase is constructed from steel, has long unsupported spans and often consists of unique geometries. The gravity design of such staircases is trivial; however, designing the staircase to be insensitive to vibrations due to human activity is often challenging. The long spans, low mass, in conjunction with a low damping ratio, can result in a low-frequency system that responds with high human-induced accelerations. The damping ratio and the pace frequency have a significant influence on the vibration behavior of the structure. The AISC 11 design guide, which is the document used predominantly in North America for vibration design, does not contain any specific requirements for staircases. The UK design guide SCI P354, however, provides some specific information pertaining to their design. This paper examines the approaches of different vibration design guidelines and, along with the assumptions used in the analytical model, presents their application to the design of a feature staircase at a prominent academic institution in Toronto, Ontario, Canada. The four-story steel staircase, analyzed for vibrations using the finite element program SAP2000, has a nine meter cantilever span, with stone finishes and composite steel landings. To determine the best estimate for the actual damping ratio needed to be used in the analysis, acceleration measurements were performed on an existing staircase with similar characteristics. The study demonstrates that a large and inconsistent scatter of accelerations is obtained using the approaches specified in the different guidelines. It also emphasizes that the damping ratios recommended in the guidelines may not be indicative of the actual values and should be used with caution. Recommendations for damping ratios and pace frequencies for staircases are also provided.

INTRODUCTION

Over the past decades, resonance due to human activity has been typically ignored in the design of floors, staircases, and footbridges. Recently however, several analytical procedures have been proposed to evaluate the behavior of structural elements for human comfort arising from a specific activity and for suitability for sensitive equipment (AISC 1997, SCI 2007, FIB 2005). Such analytical tools require, in general, the calculation of the first natural frequency of the element under consideration and the maximum amplitude of acceleration for a specific human-induced excitation. The damping in the structural system is an important parameter that has to be estimated in order to obtain meaningful results. An acceptance criterion for human comfort or sensitive equipment is then used to determine whether the structural system meets serviceability requirements.

Feature staircases are very popular in the architectural design of institutional and commercial buildings in North America and throughout the world. Generally, the iconic staircase is constructed from steel, has a long unsupported span and often includes unique geometries. The structural design for gravity loads of such staircases is trivial; however, designing the staircase to be insensitive to vibrations due to human activity is often a challenging task. The long spans, low mass, in conjunction with a low damping ratio, can result in a low-frequency system that responds with high human-induced accelerations. While the mass influences both the frequency of the system and the response, the damping ratio and the pace frequency also have a significant influence on the vibration behavior of the structure (Kerr 1998, Kerr and Bishop 2001).

Three main parameters are required to properly evaluate the vibration sensitivity of staircases for human-induced vibrations: the damping ratio, the forcing or pace functions, and the acceptance criteria for human comfort. At present, there is no clear consensus in the research community on the determination of these values. The vibration behavior of a staircase based on two widely used design guides, AISC (1997) and SCI (2007), is examined herein.

DESIGN GUIDES REQUIREMENTS

Generally, vibration problems involve repeated forces caused by machinery or human activities such as walking, dancing, or fitness activity. In general, a repeating force can be represented by a combination of sinusoidal forces whose frequencies, f, are multiples, or harmonics, of the base frequency of the force repetition, e.g., the step frequency, f_{step}, in the case of human activities. The time-dependent repeating force can be represented by Fourier series as follows (e.g., AISC 1997):

$$F = P\left[1 + \sum_{i=1}^{n} \alpha_i \sin(2\pi i f_{step} t + \phi_i)\right]$$

where,

P is the person's weight
α_i is the dynamic or Fourier coefficient for the i^{th} harmonic force component
i is the harmonic multiple of the step frequency
f_{step} is the step frequency
t is time
ϕ_i is the phase angle for the i^{th} harmonic
n is the total number of contributing harmonics

The step or forcing frequencies, Fourier coefficients and other requirements of the two most widely used vibration design guides, AISC (1997) and SCI (2007), are presented below for footbridges and staircases, respectively.

1. AISC Guidelines

The American Institute for Steel Construction (AISC) design guide 11 "Floor Vibrations Due to Human Activity" (AISC 1997), which is the document used predominantly in North America for the design against vibration, contains no specific requirements for staircases. However, it provides requirements for footbridges which, for the purpose of this study, could be assimilated for the design of staircases. In this guide, the walking person is assumed to have a weight of 0.7 kN and the recommended damping ratio for footbridges is 1% of critical. The footbridge system is satisfactory if the peak acceleration due to walking excitation, as a fraction of the acceleration of gravity, g, does not exceed the acceleration limit of 1.5% for indoor footbridges and 5.0% for outdoor footbridges. The excitation (or forcing) frequency ranges and the dynamic (or Fourier) coefficients are given in Table 1.

Table 1. Forcing frequencies, f, and Fourier coefficients, α_i, for walking excitation (AISC 1997).

Harmonic, i	f (Hz)	α_i
1	1.6-2.2	0.5
2	3.2-4.4	0.2
3	4.8-6.6	0.1
4	6.4-8.8	0.05

2. SCI Guidelines

In contrast, the design guide prepared by the UK Steel Construction Institute (SCI 2007) provides specific requirements for the design of staircases. According to this guide, the walking person weight is assumed to be 0.746 kN and the recommended damping ratio is 0.5% of critical for fully welded steel structures, such

as staircases. For vibration frequencies between 4 and 8 Hz, the recommended peak acceleration for human comfort for vibrations due to human activities is equivalent to 2.31% of *g*, for stairs with light use. In this guide, and based on the ISO 10137 standard (ISO 2007), the human footfall loading on stairs during ascending and descending is different in frequency and magnitude compared to that induced by walking on flat surfaces. The excitation forcing frequencies and the Fourier coefficients are given in Table 2.

Table 2. Forcing frequencies, f, and Fourier coefficients, α_i, for walking excitation on staircases (SCI 2007).

Harmonic, i	f (Hz)	α_i
1	1.2-4.5	1.1
2	2.4-9.0	0.22

Walking-Induced Lateral Loading

In addition to the vertical excitation, the lateral component of the human-induced walking loading may have a significant contribution but it is not specified in the above two design guides. Based on other resources (FIB 2005, Bachmann 1987, Bachmann and Ammann 1995), the frequency of the lateral loading is taken as half the walking frequency and the Fourier coefficients are $\alpha_1 = 0.1$, $\alpha_2 = 0.01$, and $\alpha_3 = 0.1$.

STAIRCASE MODELING

The four-story steel atrium staircase, shown in Figure 1, was modeled and analyzed using the commercially-available finite element (FE) program SAP2000 (CSI 2009). The staircase has a nine meter cantilever span, with stone finishes and composite steel construction landings (100 mm concrete placed on 8 mm steel plate). The balustrade is constructed using a 20 mm thick inner plate and an 8 mm thick outer steel plate. The stair stringers are HSS356x102x13 and HSS203x102x13, whereas the posts supporting the balustrade (located between the two plates) are HSS102x102x9.5 (Figure 2). The latter, together with the steel plates, effectively create a structural element which, jointly with the stringers and the rest of the structure, contributes to the overall stiffness against vibrations. The yield strength of all steel elements is $f_y = 345$ MPa. The main floors of the building consist of a 250 mm thick reinforced-concrete flat slab with 500 mm drop panels at the columns and at the edge, where the stair is connected to the slab. The drop panels at the edge provide an element with increased stiffness for the support of the stair. The concrete strength is typically $f_c' = 30$ MPa; however, at the connection between the stair and the slab a 60 MPa strong concrete is utilized. The dynamic modulus of elasticity for

concrete was taken as 35,000 MPa and 41,200 MPa, corresponding to the 30 MPa and 60 MPa concrete strengths, respectively.

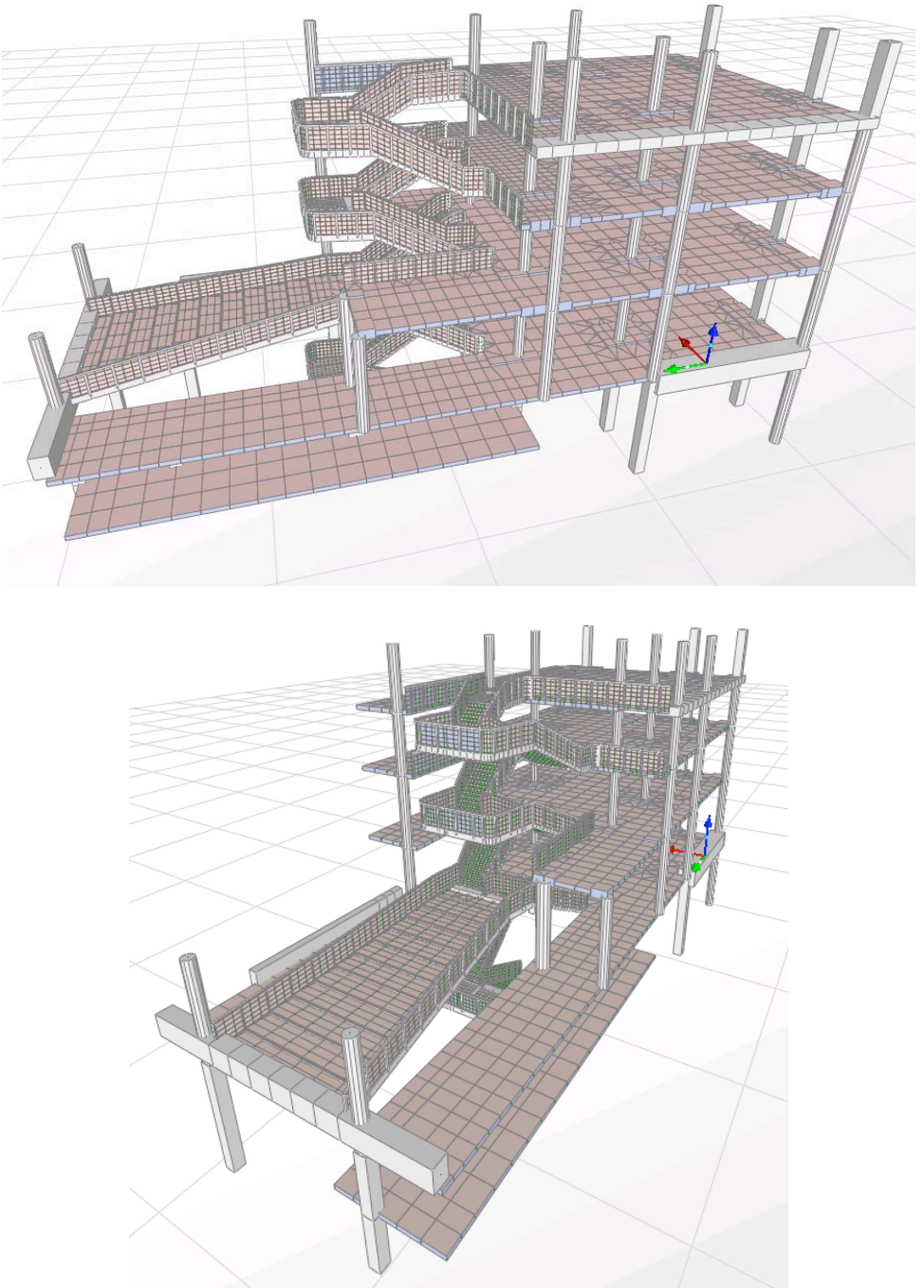


Figure 1. Feature staircase at a prominent academic institution in Toronto, Ontario, Canada.

The gravity loads applied to the staircase consist of the self weight of the structure, superimposed dead load of 1.9 kPa, and live load of 4.8 kPa. The gravity loads applied to each floor of the building consist of the concrete self weight, superimposed dead load of 1.5 kPa (at the floors above the ground) or 4.8 kPa (at ground floor), and live load of 4.8 kPa. For the dynamic analysis, the mass of the structure is based on the entire self weight and superimposed dead load, and 10 % of the live load. Four-noded shell elements were used for the modeling of area elements (floors, landings, stair treads, balustrade, etc.) and the consistent meshing was done manually to ensure proper connectivity between the nodes of the elements.

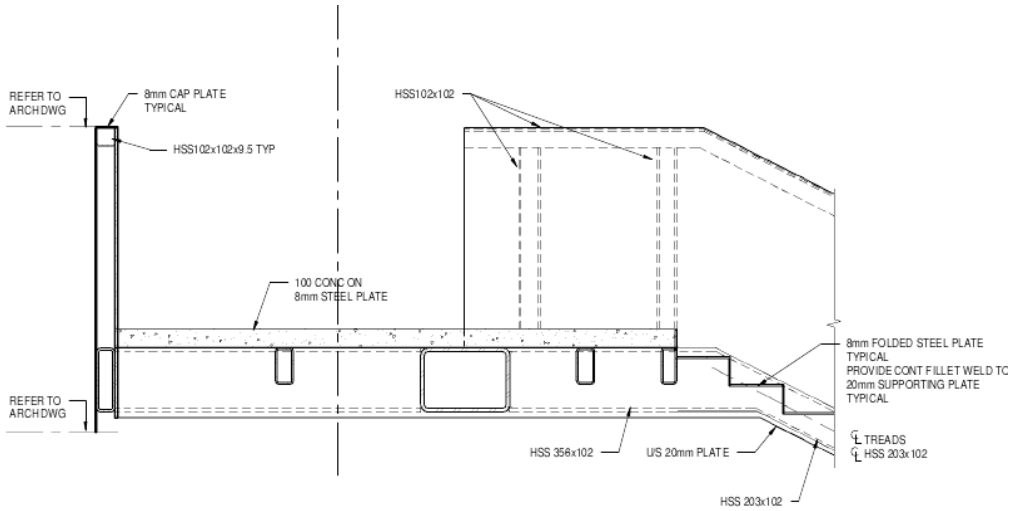


Figure 2. Detail of the staircase indicating steel sections used.

WALKING EXCITATION – LOAD CASES

Walking up and down the stair introduces an additional dynamic effect to the magnitude of excitation force imparted to the stair structure due to the body lifting or dropping onto the next tread. Hence, in applying the pace frequencies and the dynamic coefficients a differentiation was made between walking up and down the stair and walking on the landings. For the former case, the SCI (2007) parameters were incorporated in load case 1, where the loading function was applied at a small distance from the last tread (refer to load 1 in Figure 3). In load case 2 the SCI (2007) loading function was applied at the same location as for case 1; however, the measurement of the acceleration was made at a distance equal to one quarter of the mid-landing width, measured from the staircase edge (refer to loads 2 and 3 in Figure 3). Finally, in load case 3, the AISC (1997) loading function was applied at a distance equal to one quarter of the mid-landing width, measured from the edge of the staircase (refer to load 3 in Figure 3). This point is close to the maximum modal displacement for the first and second vertical vibration mode shapes.

The AISC vibration guidelines also specify a reduction factor, *R*, that accounts for the fact that full steady-state resonant motion is unlikely to be achieved for walking and that the person walking and the person feeling the resulting acceleration are not simultaneously at the location of maximum modal displacement (AISC 1997). The reduction factor should be taken as 0.5 for floors and 0.7 for pedestrian bridges (stairs qualify as indoor footbridges). For consistency, this factor was used also for the SCI loading function. However, it is to be noted that, for load case 2, the reduction factor *R* was taken as 1.0 (and not 0.7 as for the other load cases) because the measurement was not taken at the same point as that of the load application.

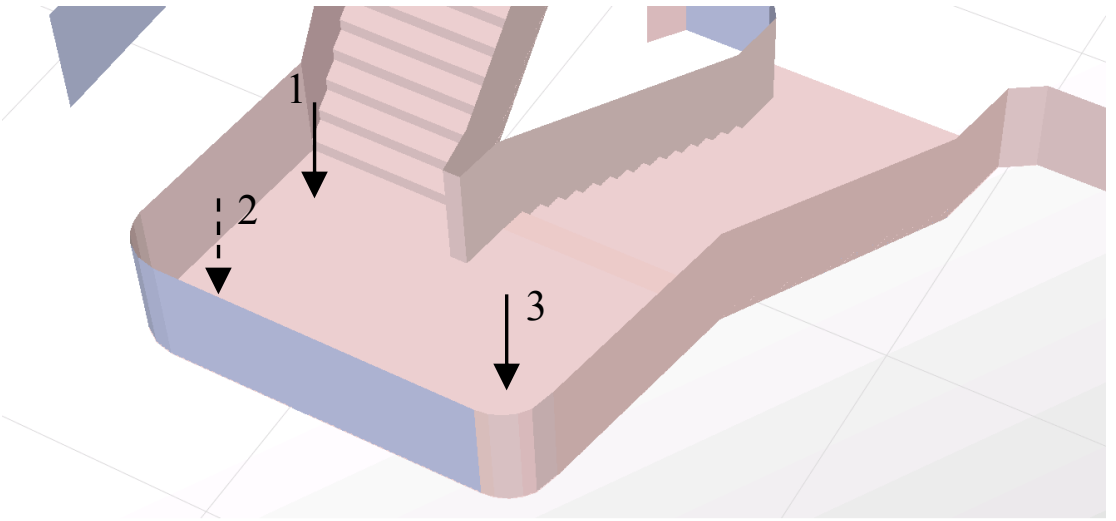
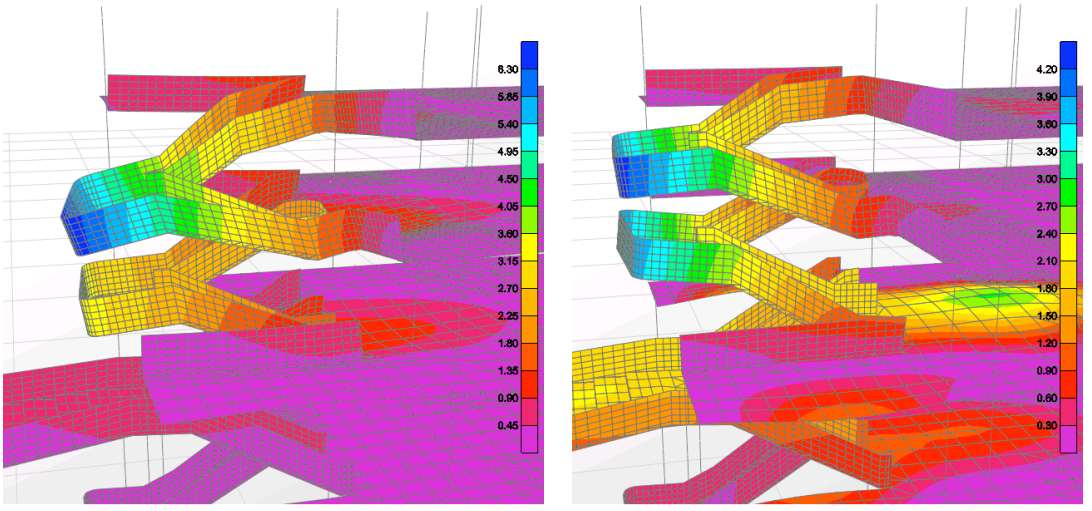


Figure 3. Walking excitation load cases for the staircase.

ANALYSIS RESULTS

The linear time-history dynamic analysis was performed using the FE program SAP2000 (CSI 2009). The first and second modes of the stair are shown in Figure 4 and their periods are 0.202 and 0.157 seconds, respectively. Figure 5 shows the acceleration as a function of time for the three load cases mentioned previously.

Damping has a significant effect on accelerations. It is well known that there is a linear relationship between the two parameters such that increasing the damping ratio by a certain percentage results in a decrease of the acceleration by a similar percentage. For example, accelerations are expected to double by using a damping ratio of 0.5% of critical (as per the SCI P354 guidelines) instead of 1.0% (as per the AISC guide 11). To determine the best estimate for the actual damping ratio to be used in the numerical analysis, dynamic measurements were conducted on a relatively similar existing atrium stair. The data was collected through acceleration measurements using a heel drop technique on the stair ramps and two landings. As a result, the percentage of critical damping thus obtained was consistent for both the lower and upper landings at slightly over 4%.



(a) (b)

Figure 4. Mode shapes of the staircase
(a) First mode (T=0.202 s) and (b) Second mode (T=0.157 s).

The modal damping ratios at the lower and higher frequencies of the stair vibration spectrum were similar and in the range of 4 to 5% of critical damping. However, it is to be noted that the heel drop measurement technique tends to overestimate the damping because it measures not only the energy dissipation but also the transmission of vibrational energy to other structural components, the latter being known as geometric dispersion (AISC 1997). For typical office buildings this technique gives 190 % higher values than the method based on the Fourier spectrum of the response to impact (AISC 1997). Therefore, from the performed measurements on the existing staircase it was concluded that a damping ratio around 1.0 % would be an appropriate estimation for such type of steel structure.

Figure 5 shows that the peak acceleration values obtained for load cases 1, 2 and 3 are 1.65, 3.21 and 1.98% of *g*, respectively, when a damping ratio of 0.5% of critical is considered. For a damping ratio of 1.0% of critical, the maximum acceleration values obtained for load cases 1, 2 and 3 are 0.84, 1.64 and 1.05% of *g*, respectively. These values were compared to vibration design criteria given in the SCI (2007) and AISC (1997) guidelines and the stair satisfied the criteria for a damping ratio of 1% of critical. The former guidelines indicate an RMS acceleration limit of 2.31% of *g*, and this corresponds to load cases 1 and 2, whereas the latter recommend a peak acceleration limit of 1.5% of *g*, which is applicable to load case 3. It is interesting to also note that, for a load case that is similar to load case 3 but in which the forcing frequencies and Fourier coefficients prescribed by the SCI guidelines were used, the resulting peak acceleration amplitudes were 4.59 and 2.34% of *g*, for damping ratios of 0.5 and 1.0% of critical, respectively. This is represented by load case 3-SCI-P354 illustrated in Figure 5(d). The latter values are more than double the values obtained from load case 3, which is based on AISC 11 design guide.

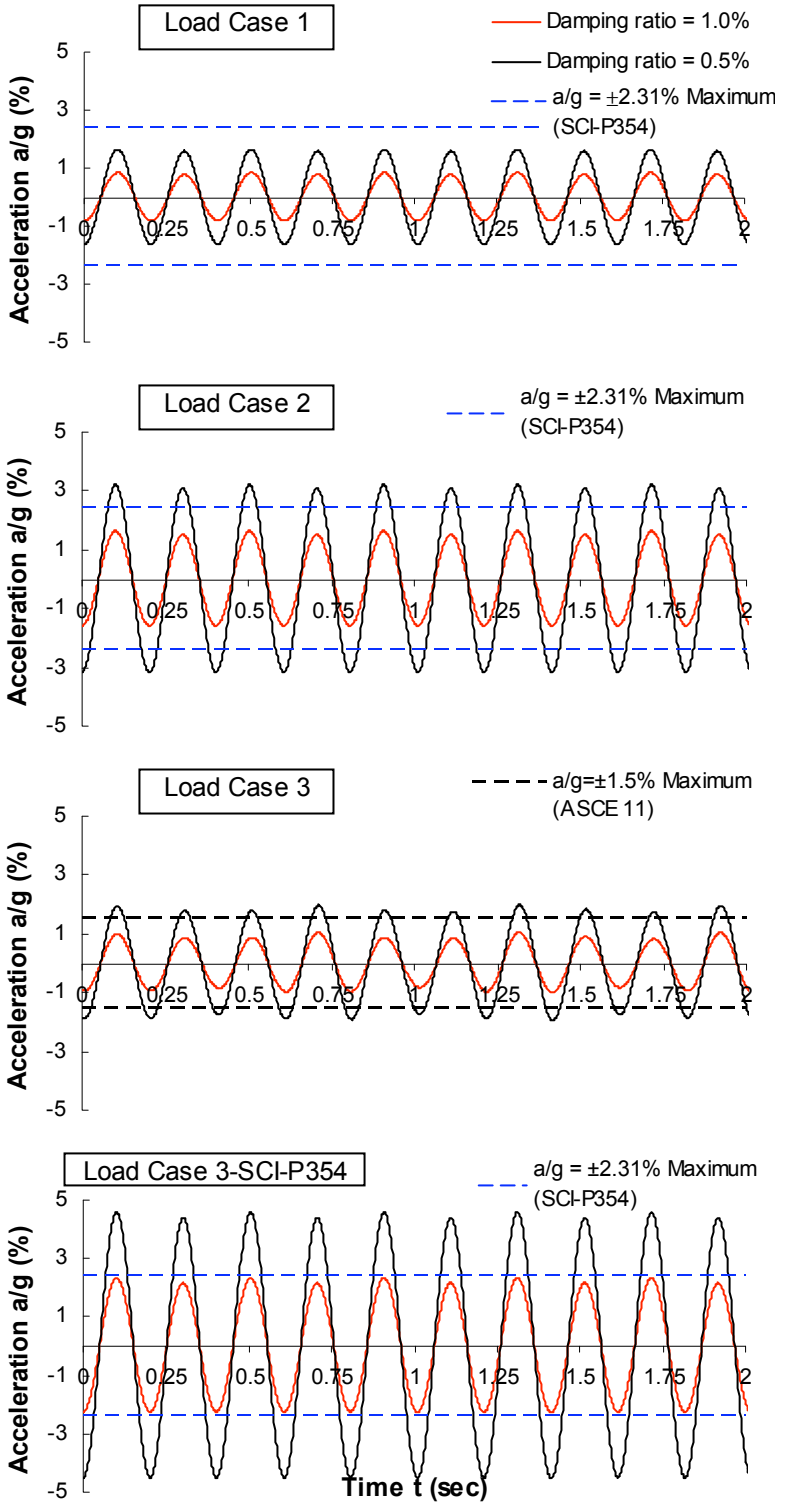


Figure 5. Acceleration-time curves for the four load cases with damping ratios of 0.5 and 1.0% of critical.

CONCLUSION

Designing a staircase to be insensitive to vibrations due to human activity is often challenging. The long spans, low mass, in conjunction with a low damping ratio, can result in a low-frequency system that responds with high human-induced accelerations. The damping ratio and the pace frequency have a significant influence on the vibration behavior of the structure. The AISC 11 design guide, which is the document used in North America predominantly for vibration design, contains no specific requirements for staircases. The UK SCI-P354 design guide, however, provides some specific information pertaining to the design of staircases. The study demonstrates that a large and inconsistent scatter of accelerations is obtained from the FE analysis by using the approaches specified in different guidelines. It also emphasizes that the damping ratios recommended in the guidelines may not be indicative of the actual values and should be used with caution when designing staircases for vibrations. It is recommended that more research should be performed to reach a consensus in order to provide better estimates of the damping ratio and forcing functions for vibration-sensitive structures. Based on the presented study, a damping ratio of 1% of critical is recommended for welded steel staircases with stone finishes and composite landings, or similar construction. In addition, pace frequencies of 1.6-2.2 Hz using the Fourier coefficients indicated in the AISC 11 guide should be used at the landings, whereas pace frequencies of 1.2-4.5 Hz and Fourier coefficients specified in the SCI P354 guide are recommended along the stair treads.

REFERENCES

American Institute for Steel Construction (AISC). (1997). *Floor vibrations due to human activity*, steel design guide series 11, Chicago, IL.

Bachmann, H., and Ammann, W. (1987). *Vibration in structures induced by man and machines,* International Association for Bridge and Structural Engineering, IABSE, Zurich, Switzerland.

Bachmann, H. (1995). *Vibration problems in structures: practical guidelines,* Birkhauser Verlag Basel, Switzerland.

Computers and Structures Inc. (CSI). (2009). Structural Analysis Program, SAP2000, version 12.0.2, Berkeley, CA.

Federation internasional du Beton (FIB). (2005). *Guidelines for the design of footbridges*, Bulletin 32, Lausanne, Swizerland.

International Organization for Standardization (ISO). (2007). *Bases for design of structures – Serviceability of buildings against vibration*, ISO 10137, Geneva, Switzerland.

Kerr, S. C., and Bishop, N. W. M. (2001). "Human induced loading on flexible staircases." Engineering Structures, 23(1), 37-45.

Kerr, S. C. (1998). *Human induced loading on staircases*, PhD Thesis, Mechanical. Engineering Department, University College London, UK.

Steel Construction Institution – SCI, (2007). Design of floors for vibration – A new approach, Ascot, Berkshire, UK.

How to Keep Monumental Stairs from Vibrating

Daniel J. Huntington, SE, PE, CE, LEED® AP[1] and Jon W. Mooney[2]

[1]Associate Principal, KJWW Engineering PC, 623 26th Avenue, Rock Island, IL 61201; PH (309) 788-0673; FAX (309) 786-5967; e-mail: huntingtondj@kjww.com
[2]Senior Acoustics Engineer, KJWW Engineering PC, 623 26th Avenue, Rock Island, IL 61201; PH (309) 788-0673; FAX (309) 786-5967; e-mail: mooneyjw@kjww.com

ABSTRACT

This paper presents a case study of a 39-foot long, curved, conventionally framed monumental stair. The stair experienced considerable vibration issues under normal loading. A retrofit solution was designed and implemented to mitigate the vibrations. Before and after vibration results are included, as well as the design calculations for determining the repair.

The paper includes an additional case study of a concrete slab on steel beam framed office building that started to experience vibration problems when the Owner removed steel and glass partitions during a remodel. The design solution, equations, and before and after results are presented.

CASE STUDY 1: 39-FOOT CURVING MONUMENTAL STAIR

The monumental stair in the main lobby of Sherman Hospital in Elgin, Illinois (Figure 1) was envisioned to take pedestrians up and around the massive, four-story Tree of Life centerpiece sculpture without calling attention to the stair itself. To this end, the stair was designed with transparent glass guard panels and with a structural spine only 12 inches deep. To complete the visual effect, the stair was designed such that no supports were needed at the mid-span landing. The structure of the stair comprises three 2x12-inch sloping, curved plate stringers with a 1/2 inch thick, folded steel tread plate. Stair treads are topped with 1-1/2 inch thick terrazzo tile. The 12-ton stair was manufactured in three sections in the shop of Chicago's David Architectural Metals, Inc., and was then transported and assembled at the job site. During final assembly, deflection at the mid-span landing was measured to be in excess of the expected 0.9 inch (refer to Table 2). The additional deflection was traced to movement of the end attachment points, which were subsequently reinforced.

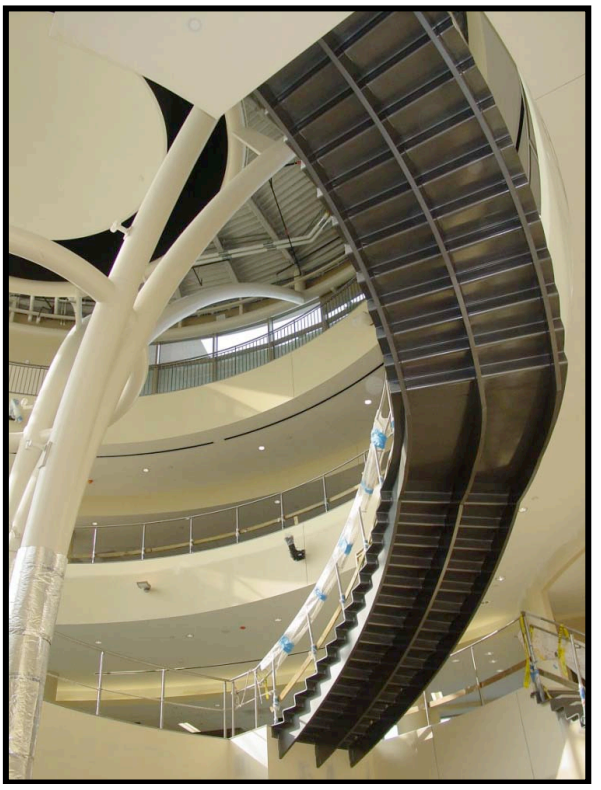


Figure 1. Bottom view of 39-foot curving monumental stair

Five months before the scheduled opening, the Owner started to complain of excessive vibration of the stair. Several options to remediate the vibration were discussed, including tensioning the stair with cables, adding a mid-span support, adding flanges to the bottoms of the stringers, and adding a tuned mass damper. The Construction Manager, Owner and Engineer decided the tuned mass damper offered the most cost-effective, aesthetically pleasing solution. Costs would be half, and the fabrication and installation labor would only be a fifth, of that needed for the other options. Before making a final decision to design a tuned mass damper solution, KJWW tested the stair to determine the nature of its vibration response.

Vibration testing was performed using Gulf Coast Data Concepts Model X6-2 USB accelerometer (Figure 2). This is an inexpensive, self-contained, three-axis recording accelerometer with a USB interface for setup and data download to a computer. At the time of the pre-installation test, the X6-2 software gave it a resolution of 0.001 G and a frequency limit of 160 Hz.

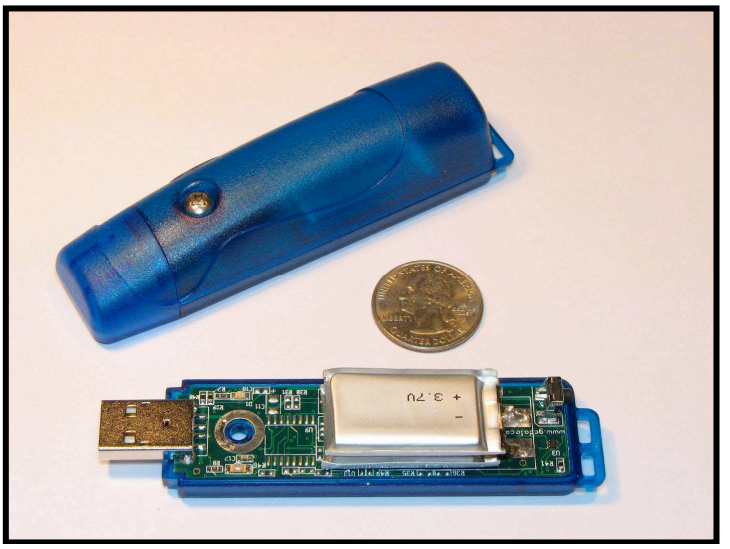


Figure 2. Gold Coast Data Concepts Model X6-2 Accelerometer

Pre-installation testing consisted of one or two people walking up or down the stair, with one or no people standing on the mid-span landing. The accelerometer was placed near the outer edge of the mid-span landing. No effort was made to normalize the test to match the test loading, frequency, position, and duration to those assumed for the Design Guide 11 criterion (Murray, Allen & Ungar, 1997). Table 1 lists the results. Figures 3 and 4 show the acceleration time trace and velocity spectra for Test #4. Note the spectra displays 1/3 Hz increments and, therefore, the response levels indicated in Figure 4 are somewhat less than the true 1 Hz spectrum levels of the stair. From the results, KJWW concluded: 1) the stair has a fundamental frequency of 4.23 to 4.56 Hz, 2) the vibration movement at the mid-span landing is 21.04 to 21.39 degrees from vertical, and 3) the vibration response of the stair to typical loading conditions is within the Reiher-Meister "strong" range.

Table 1—Results of Pre-Remediation Stair Vibration Testing

Test #	# people on landing	# people walking	Up or down	Frequency (Hz)	Vz (in/sec)	Vx (in/sec)	Angle (deg)	Peak G
1	0	1	Up	4.56				
3	0	1	Down	4.23	0.104	0.040	21.04	0.008
4	1	1	Up	4.23	0.263	0.103	21.39	0.019
5	1	1	Down	4.56				
6	0	2	Down	4.23	0.139	0.054	21.23	0.010

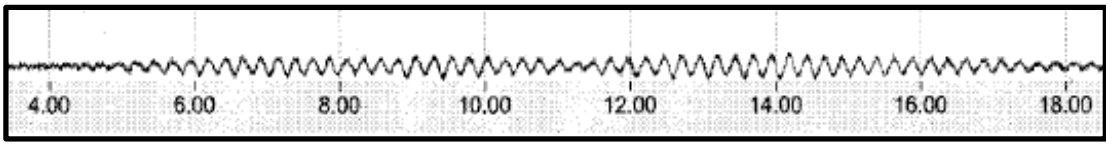


Figure 3. Pre-Installation Test #4 - Acceleration Time Trace

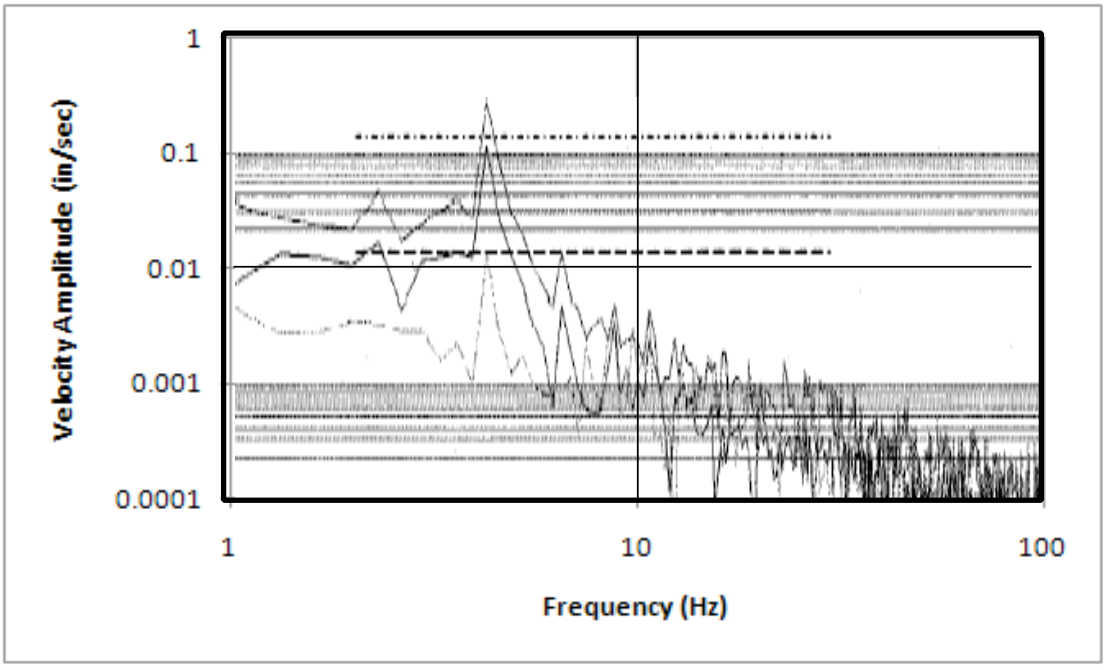


Figure 4. Pre-Installation Test #4 - Velocity Spectra of Acceleration Trace Shown in Figure 3

While testing proceeded, KJWW reviewed the design of the stair according to the recommendations of Steel Design Guide Series 11 "Floor Vibrations Due to Human Activity." (Murray, Allen & Ungar, 1997) Following the procedure outlined in Chapter 4 of Design Guide 11 for determining the acceptability of an indoor footbridge, the stair was evaluated using two different simplifying assumptions. The stair was viewed as: 1) a pinned-pinned beam loaded by a constant value running load and 2) a pinned-pinned curved beam loaded by a constant value running load. In both simplifications, mid-span deflections were calculated as if the stair were rotated to horizontal, however, neither simplification is fully accurate. Analyzing the stair as a beam neglects the torsional loading of the stair. Analyzing the stair as a curved beam neglects the helical shape of the stair. In addition, the effect of adding a 1/2-inch thick bottom plate to the entire length of stair was calculated using the curved beam assumption. Table 2 lists the results of each calculation step.

Table 2: Results of Design Guide #11 Calculation Steps

Calculation	Analyzed as beam	Analyzed as curved beam	Added bottom plate
Span (ft)	39.4	39.4	39.4
Running mass (lbm/ft)	590.7	590.7	704
Bending Moment of Inertia (in^4)	2181	2181	3913
Polar Moment of Inertia (in^4)	n/a	72679	74411
Radius of Curvature (ft)	n/a	23.4	23.4
Self weight deflection (in) **1**	0.51	0.95	0.64
Natural frequency (Hz) **2**	4.97	3.64	4.43
Weight (lbm):	23283	23283	27767
Peak acceleration (G) **3**	0.069	0.111	0.070
Maximum acceptable peak acceleration [150% DG#11] (G)	0.023	0.024	0.023

Note 1. Field testing measured an actual self weight deflection of 1.0 inch.
Note 2. Field testing measured a natural frequency of 4.23 to 4.56 Hz.
Note 3. Field testing measured a peak acceleration of 0.019 G.

Comparing the calculation results in Table 2 with the test results in Table 1, the measured natural frequency of the stair falls between the two calculated values. The maximum measured peak acceleration of 0.019 G was only 17% to 28% of the predicted values of 0.069 to 0.111 G. This difference is mainly due to the tests being conducted with a forcing frequency of approximately 3.9 Hz instead of the 4.23 Hz natural frequency of the stair. Figure 5 illustrates the theoretical response curve of a harmonically forced, single degree of freedom system having 1% to 10% damping. Since the tests were conducted at approximately 0.9 times natural frequency, and the stair damping is assumed to be 1%, Figure 5 shows that, all other variables being equal, the stair acceleration produced in the tests would have been expected to be only 9% of those predicted. The steepness of the response curve for forcing frequency ratios between 0.8 and 1.2, combined with the fact that it took 14 seconds to traverse the 27 steps, suggest that, had the walker's step been just 0.02 seconds quicker, the measured stair acceleration would have reached peak response levels. Also, it should be expected that the forcing function created by descending a stair has a higher amplitude than that created by walking a level footbridge due to the added vertical kinetic energy of the walker. These test results suggest that, for stairs, the value of the constant force used in Equation 2.3 of Design Guide 11 may be one to two times the weight of the person. This is analogous to increasing the value of dynamic coefficient in Equation 2.4 of the Design Guide when considering the response of floors to rhythmic activity.

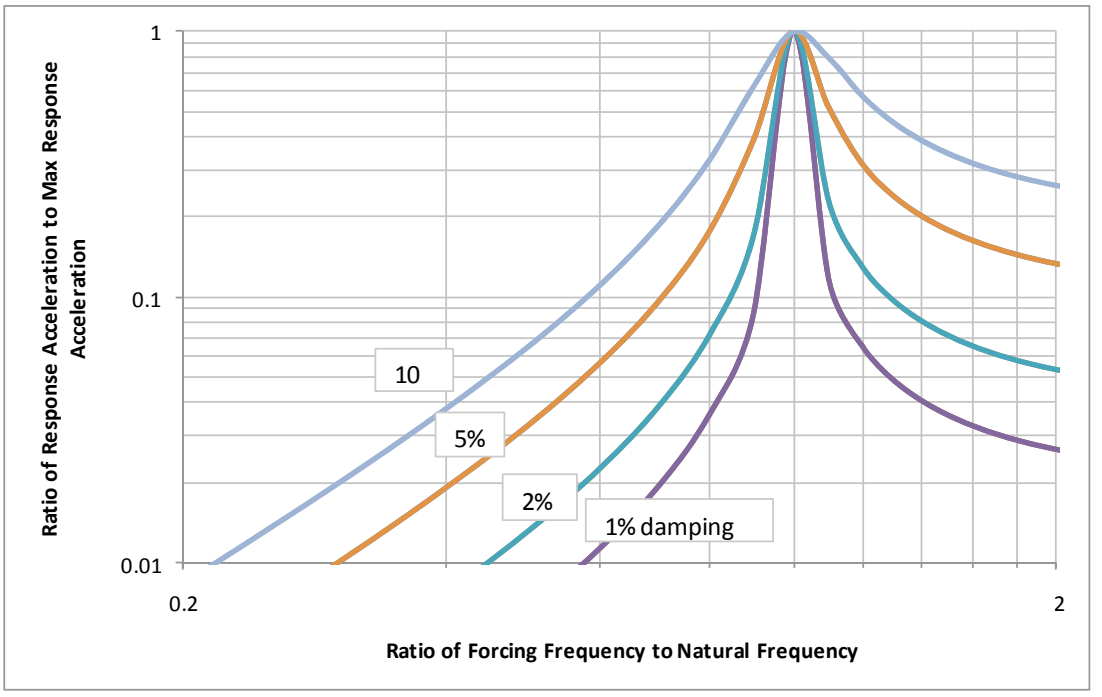


Figure 5. Theoretical response curve of a harmonically forced, single degree of freedom system having 1% to 10% damping

With test data and vibration calculations in general agreement, the option of adding a bottom plate was ruled out, and a tuned mass damper appeared to be the best choice for mitigating stair vibration while maintaining the intended look of the structure. The tuned mass damper would need to fit under the mid-span landing. Once installed, a thin sheet of metal would be welded across the bottoms of the stringers under the landing to hide the assembly from view. The allotted space limited the design. To avoid the complications of multiple dampers, it was decided to design one damper to fit between the middle and outer stringers. To minimize the magnitude of secondary rotational damper oscillations, the damper was limited to a footprint of 2x3 feet.

The tuned mass damper design started with estimates of its size and performance. With an available headroom under the mid-stair landing of only 12 inches, the damper mass was estimated as equivalent to four, 2x3 feet by 1/2-inch thick steel plates, with a total weight of 484 pounds. A 484-pound damper on a 23,283-pound stair should yield a damping ratio of approximately 0.07 and replace the 4.23 Hz natural frequency peak of the stair with two smaller peaks at 3.93 Hz and 4.55 Hz. Matching the measured 4.23 Hz frequency of the stair, the 484-pound tuned mass damper would require a total spring constant of 886 pounds per inch. To allow for tuning of the mass damper, an additional 143 pounds would be required to cover the 3.93 to 4.55 Hz damped frequency range. For the 92-pound step function called out in Design Guide 11, the expected damper spring deflection would be approximately 0.1 inch.

Using the above estimates as a guide, four off-the-shelf equipment mounting springs were selected for the design. The Mason SLFH-104 springs are rated for 200

pounds per inch and a 500-pound load, which gives the tuned mass damper an 800 pound per inch spring constant.

A complication in the design was the fact that the landing does not vibrate vertically, but rather 21° from vertical. To achieve a parallel motion in the tuned mass damper, the damper weights were designed to follow a 21° cam while the weights themselves remain horizontal throughout the cycle. To allow fine tuning, the weight assembly consists of three 101-pound plates, one 61-pound plate, two 30-pound plates, and ten 10-pound plates.

Before installation, the effectiveness of the tuned mass damper on the stair was determined by allowing it to operate on top of the landing. Table 3, and Figures 6 and 7 show results from a typical test in this series.

Table 3—Results of TMD Stair Vibration Testing

Test #	# people on landing	# people walking	Up or down	Frequency (Hz)	Frequency (Hz)	Vz (in/sec)	Vx (in/sec)	Angle (deg)	Peak G
1	1	1	Down	3.91	4.90	0.107	0.048	24.2	0.007

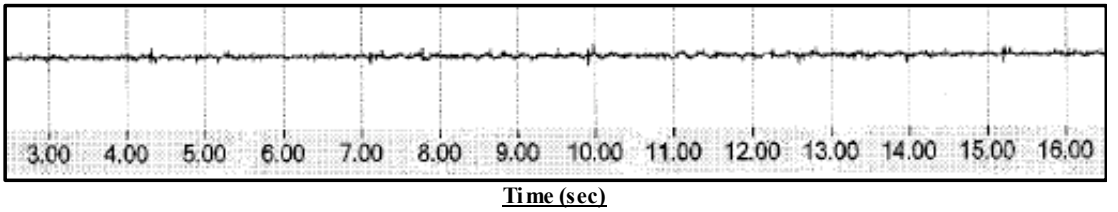


Figure 6. TMD Test #1 - Acceleration Time Trace

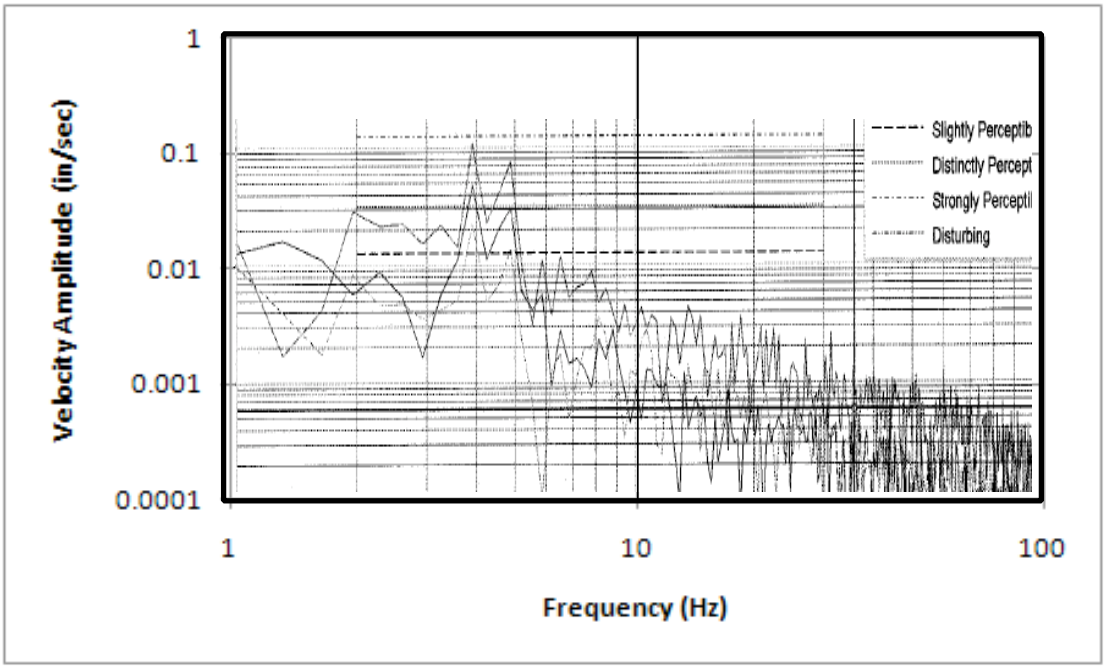


Figure 7. TMD Test #1 - Velocity Spectra of Acceleration Trace Shown in Figure 6

Figure 8 shows the tuned mass damper assembled for testing. Also visible in this figure is one of the two 21° cam followers. Figures 9a and 9b show two views of the installed damper.

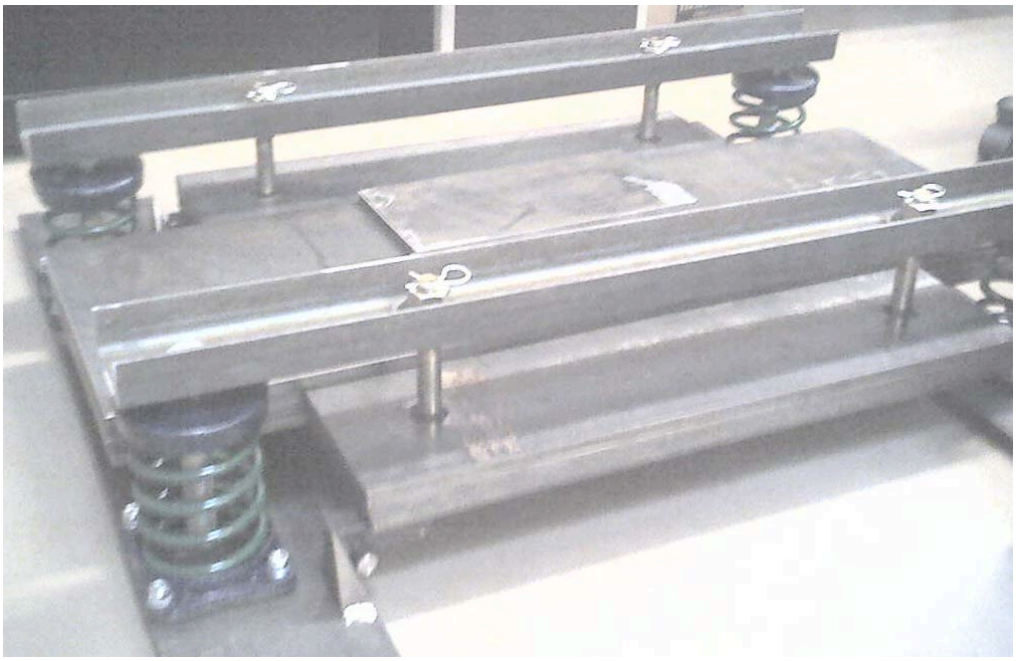


Figure 8. Tuned Mass Damper Assembled for Testing 21° Cam and Follower in Foreground



Figure 9a. Tuned Mass Damper Installed Under Mid-Span Landing

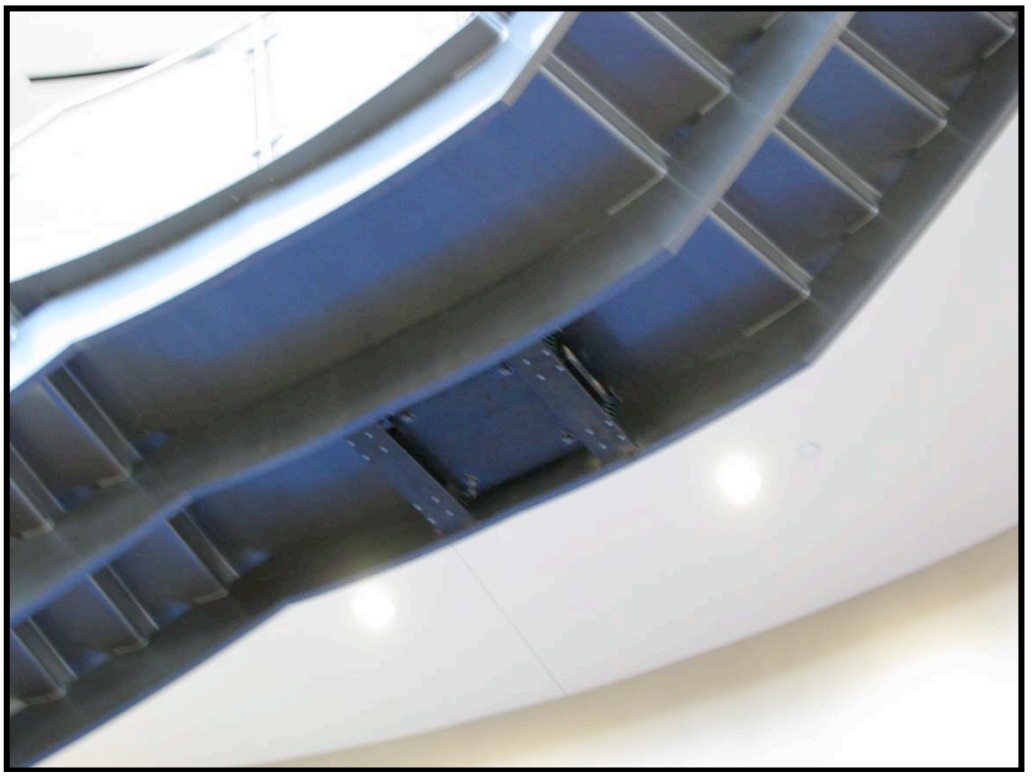


Figure 9b. Tuned Mass Damper Installed Under Mid-Span Landing

Comparing the pre- and post-damper measured responses, the stair vibration fell from levels just above those recommended in Design Guide 11 for indoor footbridges to levels just above those recommended for offices. Comparing the before and after acceleration traces of Figures 3 and 5 illustrates the relatively huge increase in damping. Responses to single jumps, which initially rang for 20 seconds and longer, were reduced to less than a second.

CASE STUDY 2: RETROFIT OF AN EXISTING OFFICE BUILDING

KJWW was retained when non-structural renovations to an existing office building resulted in floor vibrations noticeable to the occupants. The floor design of the existing office building is divisible into a row of 30x45 foot bays on each side (north and south) of a center hallway. The floor is a 3-inch deep steel form deck with concrete poured to 2.5 inches above the steel. The floor is supported by 10W29 joists spaced nine feet apart. The joists are supported by 21W82 girders connected to either side of columns spaced 30 feet apart. As part of the renovation of the building, the original three-quarter height glass and metal frame office partitions were removed. The dotted lines in Figure 10 illustrate the typical placement of the original partitions. The heavy plaster panel hallway wall (represented in Figure 10 by the wide black line) was left intact. Of special concern is the fact that the curtain wall rests on its own joist, and, therefore, the floor is not connected to the sides of the building. As renovations continued, office workers began complaining of excessive floor vibration.

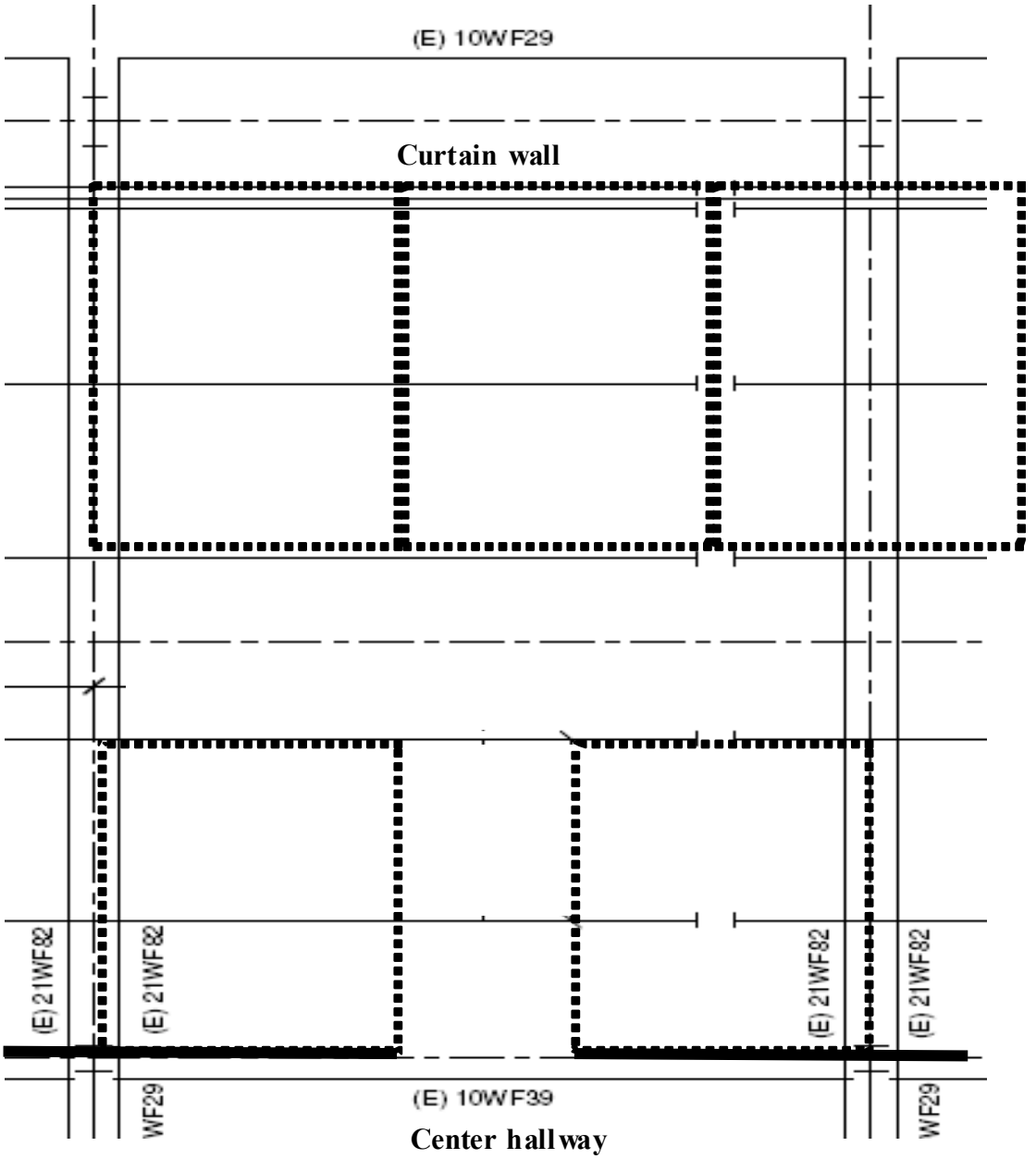


Figure 10. Diagram of Office Bay Showing Placement of Original Partitions (Dotted Lines)

Table 4 lists the results of each Design Guide 11 calculation step for the floor before and after removing the partitions. Since the floor edge is not supported by the exterior wall, the effective width for the joist panel vibration mode was reduced 50%. The removal of the original partitions had two effects: reducing the floor loading by 19 psf and decreasing the floor damping ratio from 0.05 to 0.02. Possible reduction in joist mode moment of inertia was suspected but not pursued.

Table 4: Results of Design Guide #11 Calculation Steps for Floor		
Calculation	**Before renovation**	**After renovation**
Joist mode bending moment of inertia (in^4)	660	660
Joist mode running load (lbf/ft)	783	614
Joist mode deflection (in)	0.746	0.585
Joist mode frequency (Hz)	4.10	4.62
Joist mode effective panel weight (lbm)	69,296	54,339
Girder mode bending moment of inertia (in^4)	5833	5833
Girder mode running load (lbf/ft)	2692	2129
Girder mode deflection (in)	1.468	1.161
Girder mode frequency (Hz)	2.92	3.28
Girder mode effective panel weight (lbm)	227,743	180,113
Combined natural frequency (Hz)	2.38	2.68
Combined effective weight (lbm)	174,355	137,972
Damping Ratio	0.05	0.02
Peak acceleration (G)	0.0032	0.0092
Maximum acceptable peak acceleration [150% DG#11 offices] (G)	0.0097	`0.0092

Vibration testing of the floors showed primary level peaks at 4.4 Hz corresponding to the joist mode vibration, and a secondary level peak at 2.5 Hz corresponding to the combined mode vibration. Measured vibration levels varied with floor, bay, and time of day, ranging from "slightly perceptible" to "distinctly perceptible" on the Reiher-Meister scale.

Since complaints centered on vibrations traveling from bay to bay, the investigation focused on joist mode vibration. Finite element modeling of the bay was used to determine the effect of various options to stiffen the bay. The addition of column supports was not considered feasible since this required a minimum of three columns per bay and would require considerable adjustment to the open plan office design. The model suggested that adding bracing at each joist/girder intersection would add enough stiffness to the joist mode vibration to put the floor well within the recommended vibration limits for office spaces. This was done in two bays by adding two 6-foot long L6x6x3/8 kickers to each joist/girder intersection. Ambient vibration measurements made after this installation showed peak levels of 0.0014 G @ 4.4 Hz, and complaints from this section of the building were significantly reduced.

The high installation costs of adding kickers to the joists prompted a search for a less expensive solution to handle complaints of excessive vibration in other

parts of the building. Since the seating locations of the complainants did not necessarily coincide with the locations of measured maximum vibration, a tuned mass damper was considered a good option to reduce vibrations local to the complaint. Figure 11 shows the tuned mass damper, designed to hang between joists, mounted on a test dolly that was used to tune and test the damper on various locations of the bay. Tests of a bay after installation of the tuned mass damper in the second joist interstice from the center hall measured vibration levels of 0.0006 G @ 4 Hz, with no identifiable peak at the position directly above the damper. Vibration levels at the fourth joist interstice measured 0.0013 G @ 4 Hz, with no identifiable peak with periodic (one per hour) brief (40 second) duration events of 0.0195 G @ 4 Hz. These results suggest the tuned mass damper is only locally effective for this application. At the time of writing, an additional damper was scheduled to be installed at the fourth joist interstice.



Figure 11. Tuned Mass Damper Mounted on Test Dolly

CONCLUSIONS

Test results suggest that, when using Design Guide 11, Equation 2.3 to evaluate the vibration acceptability of a stair, the designer may consider increasing P0 to a value of 157 pounds to 314 pounds to account for the added vertical kinetic energy of a person descending the stair. This is analogous to increasing the value of dynamic coefficient in Equation 2.4 of the Design Guide when considering the

response of floors to rhythmic activity. Since the tests were not designed to study this hypothesis, this is a suggestion for further study rather than a recommendation.

When the vibration acceptability of a floor is marginally acceptable, the seating locations of the complainants may not necessarily coincide with the locations of measured maximum vibration. Placing a tuned mass damper at the location of the complainant demonstrated a significant local reduction in vibration. Vibration levels at other locations in the same bay remained relatively unchanged.

REFERENCE

Murray, Allen & Ungar. (1997). *Steel Design Guide Series 11, Floor Vibrations Due to Human Activity.* Chicago: American Institute of Steel Construction.

Title: The Feature Stair at Louis Vuitton in Crystals at CityCenter

Authors: Crispin Howes, PEng, Associate, Halcrow Yolles Toronto
Michal Krynski, PEng, Design Engineer, Halcrow Yolles Toronto
Stephan Kordt, SE, PE, Principal, Halcrow Yolles Las Vegas

Abstract: *In December 2009, Louis Vuitton opened their largest North American store in the retail component of the CityCenter development in Las Vegas. The three retail floors of the flagship store are interconnected with an elegant feature staircase clad in polished stainless steel, glass, and exotic hardwood.*

The steel structure is comprised of stepped stringers with folded plate to form the treads and risers. The staircases finishes are closely fitted to three sides of each stringer\. The slender profile of the staircase was achieved by minimizing the depth of the stringer to 8 in even though the mi-landing is cantilevered 20' from the supporting landings. Extensive structural and vibration analyses and precise detailing of the integral glass guard ensure the performance of this monumental staircase.

This paper presents a review of the analysis, design, and detailing of this feature stair steel structure and integral glass guard.

1.0 Introduction

Louis Vuitton opened their largest North American store in the retail component of the CityCenter development in Las Vegas in 2009. The program for the store included 14,000 sq. ft of luxury retail space over 3 floors with additional area for administration services. The architects for the project were the New York based firm of Gertler & Wente Architects. As one of the key tenants on Las Vegas Boulevard, the design and construction of the store was realized with a fast track schedule to meet the opening date of the overall CityCenter development.

As the flagship store for North America, the design of the store has several features befitting the luxury brand. On the exterior of the store is clad with embossed stainless steel panels embedded with 4000 programmable LEDs. Interior features include a 31ft diameter chandelier, a two story high luggage display unit, and a 103in. plasma screen display.

One of the most prominent interior design elements is the elegant feature stair which is clad with polished stainless steel, hardwood and glass. The stair interconnects the 3 retail floors of store. The first leg of stair spans from street level to mezzanine level with a height of 12ft between floors. The next two legs connect the mezzanine level to Level 1, also with a floor to floor height of 12 ft. A mid-height landing is provided between these two legs. At the outside edge of the mid-landing, the stair is cantilevered 20ft from the supporting floor structure.

2.0 Design Concepts

The architectural design intent for this stair was to maintain an overall expression of a slender stepped plate with the soffit of the stair as a direct offset from the treads and risers. As is sometimes the case, the architectural concept was developed prior to the opportunity to prove the structural concept. The overall depth of stair assembly was to limited to 8in to maintain the appropriate slender envisioned in the architectural concept. Allowances for the cladding finishes, hardwood flooring on top and polished stainless steel panels on the soffit, were included within total depth. After the allowances for the finishes were subtracted from 8in depth only 6in was available for the structural framing.

The plate-like expression for the stair might suggest a similar type of structural solution, a cast-in-place structural slab, for example. However, such as solution would not have been feasible for several reasons. The cost of custom formwork and shoring would have been substantial. The 6in available for slab depth would have required considerable cambering to control self-weight deflection. The stepped slab profile does not allow for continuous rebar in the direction of the slab span so rebar would need to be cranked with tension splices at each step to maintain continuity moment resistance in the slab. Therefore, the appropriate choice of material was structural steel.

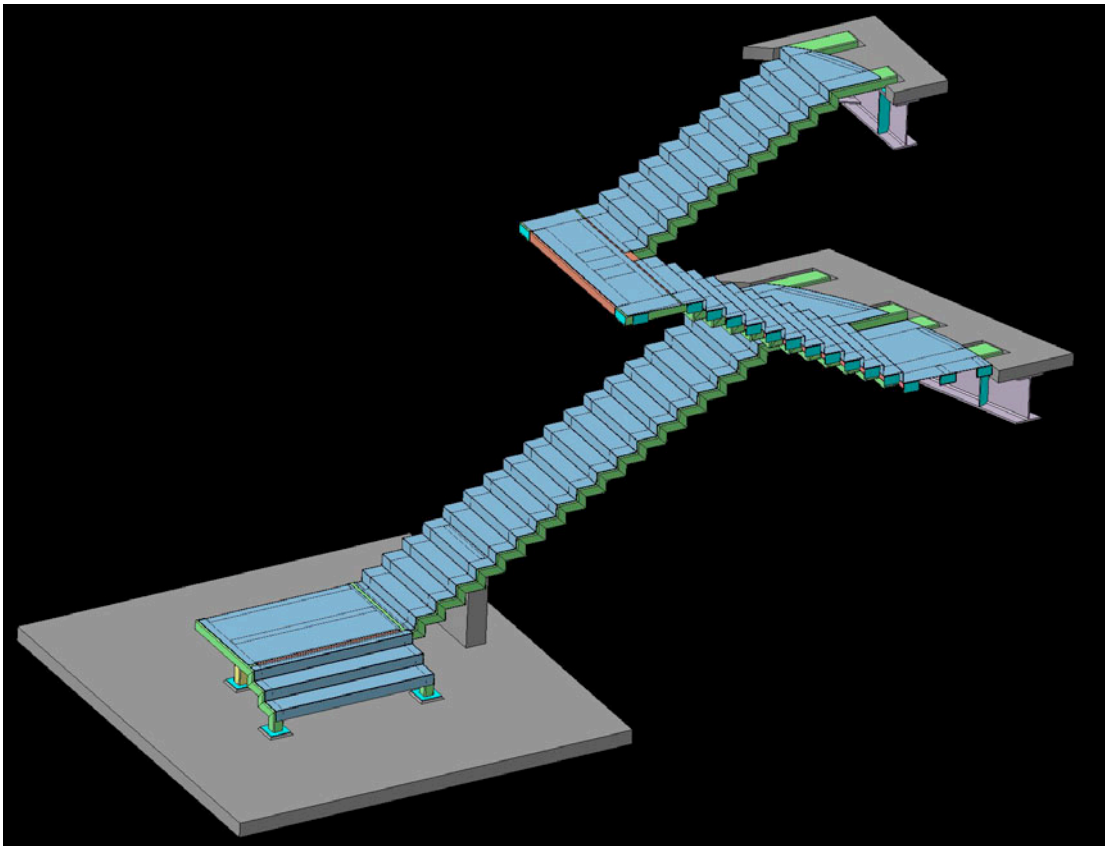


Figure 1: Structural Coordination Model of Stair Framing in CATIA

3.0 Structural Solution

The initial underlying structural solution was similar to many stairs beginning with two exterior stringers. Hollow Structural Section (HSS) were utilized for framing to maximize the capacity in the available structural depth. However, the stepped profile of the stair assembly required the stringer to be stepped as well. At each step, the HSS had to be cut and mitred with corresponding horizontal and vertical pieces. To help mitigate the extent of the required welding all the wall thickness of the HSS were increased by at least 1/8" above required so partial penetration welds could be used to achieve the needed capacity rather than specifying full penetration welds at all the mitres.

The sizes used for stringers were HSS 6x12 and HSS 6x10. The HSS were oriented with the long leg horizontally. This horizontal orientation was not the most structurally efficient but was necessary to fit within the space requirements of the stair assembly while meeting the structural requirements for strength and serviceability. The cantilever mid-landing between the two upper legs was framed by providing two HSS 6x10 members that span between the exterior stingers. The interior stringers are moment connected to the interior landing member providing moment continuity between the two stringers via torsion in the landing member. Refer to Figure 2 for a plan of mid-landing framing.

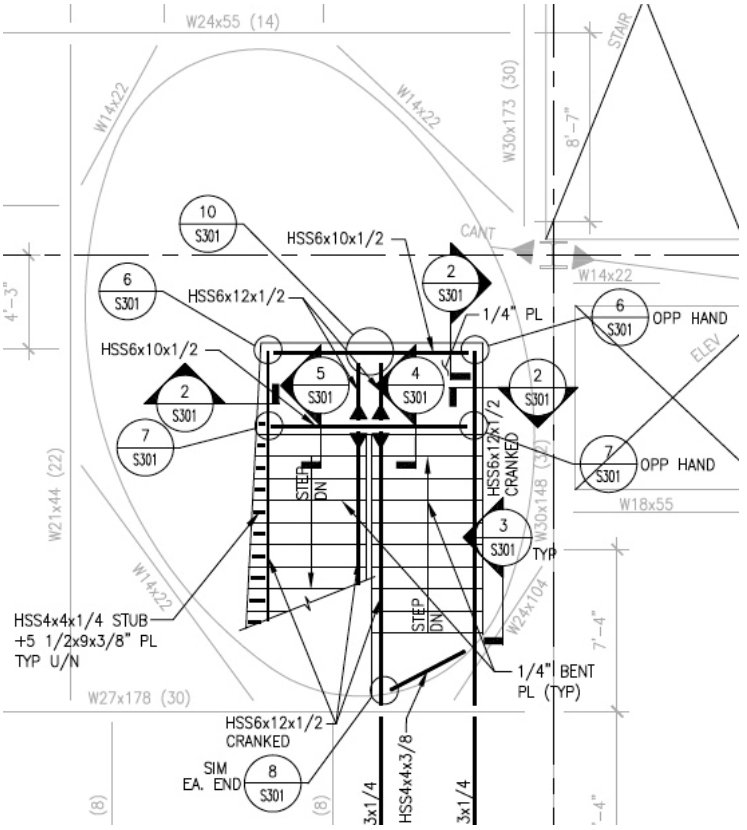


Figure 2: Cantilever Mid-Landing Framing Plan

Spanning between the two stringers, ¼" bent steel plate provides supports for the treads and risers. Concrete slab on steel deck was another option initially considered. However, the slab on deck assembly could not have been placed on top of the stringers and would have been required to fit between the stringers. Bent steel plate was a more appropriate choice, as it could be placed on top of the stringer within a minimal increase to structural depth. In addition to supporting the direct gravity loads of stair users, the bent plate provides a continuous diaphragm to maintain the horizontal stability of the overall stair structure. The connection of the bent plate to the stringer with welds near the interior and exterior faces of the HSS, provides additional stability to the stringer allowing torsion generated by loads on the glass guard to be resisted as mend moments in the bent plate profile.

4.0 Analysis

The analysis and design of the overall stair structure utilized SAP2000 Non-Linear. Per figure 3, the analysis model consisted of the entire stair structure including the glass guards and the local supporting floor framing of the base building. Plates, slabs, and glass guards were modeled as area elements while steel beams were modelled as frame elements. The glass guards were included in the model to assess the resulting internal stress distribution under the stairs loads. The supporting base building framing was included in the model to account for its stiffness under stair and floor loads and to capture the internal force re-distribution resulting from varying stiffness between supporting members.

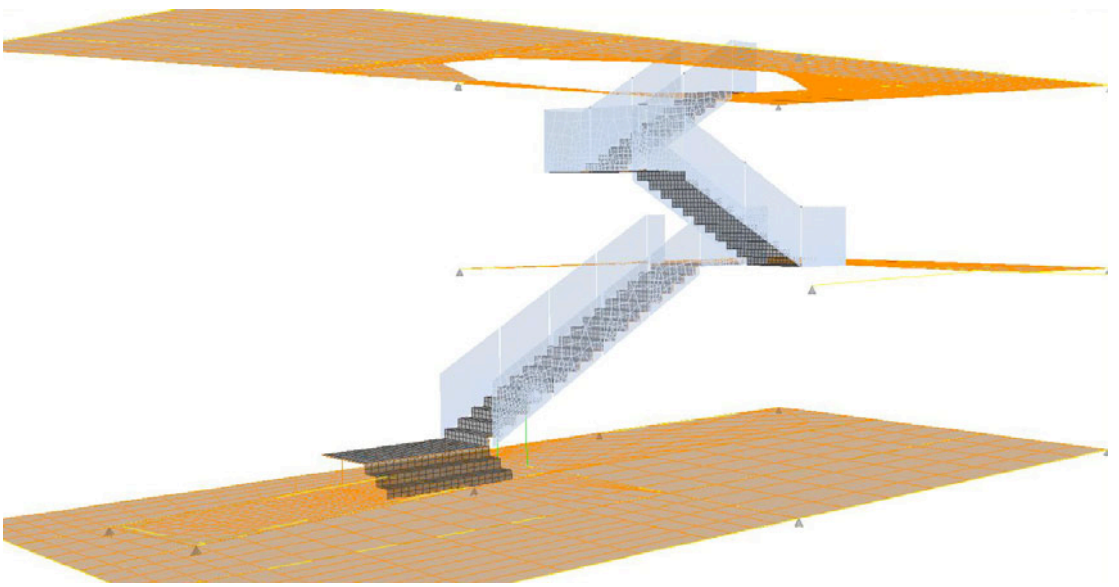


Figure 3: SAP2000 Non-Linear analysis model of stair framing

5.0 Detailing

Although the structural steel is not exposed to view, the detailing of steel connection needed to be mindful of the architectural expression. With cladding finishes fitting tight to the structural framing, welded connections were necessary as there was no opportunity to allow for connection plates that would project beyond the member profile.

6.0 Connections to Base Building

Connections to the base building floor framing were provided by sawcutting into the existing slab edge to create a trench in which to install the stair stringers. A series of field-welded stepped shims filled the gap between the as-built top of floor beam and the underside of the stringer and provided a connection capable of transferring shear and axial forces from the stinger to base building floor framing. At the each connection point, the base building beams were local stiffened and an HSS 3x3 was connected from the supporting floor beam to the next adjacent floor beam to act as a dragline to distribute the axial force deeper into the floor slab diaphragm. Figure 4 illustrates a typical connection to base building.

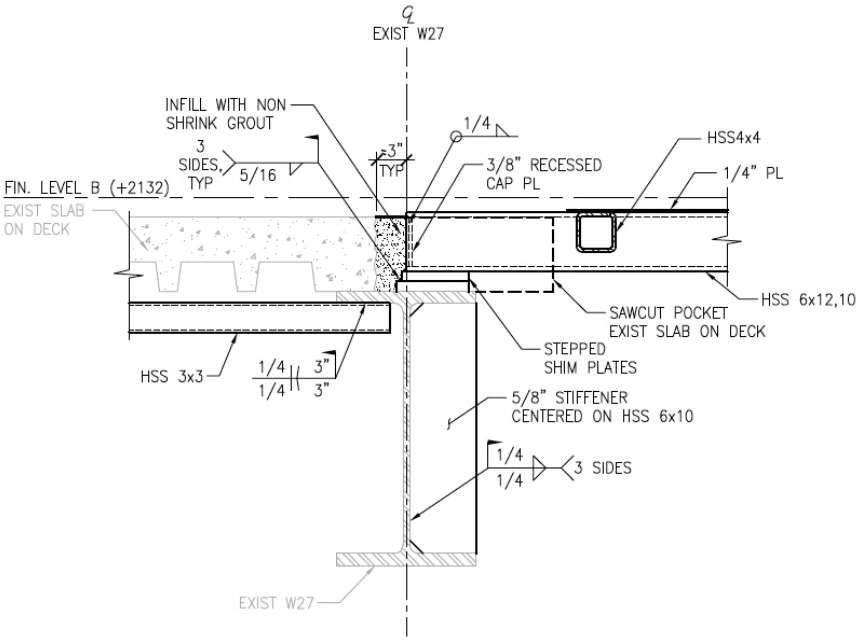


Figure 4: Typical connection of stair stringer to base building floor framing

7.0 Vibration Analysis

As with almost all slender stair structures, an evaluation of the dynamic response of structure under walking excitation is a necessary step in the design process. Our analysis indicated that, horizontally, the combination of the wide HSS stringer with the continuous steel bent plate diaphragm comfortably met our limits for acceleration limit of 0.5%g with 1.0% damping

Vertically, the reference criteria was an acceleration of 1.5%g with 1% damping as recommended for indoor footbridges in the AISC Steel Design Guide for Floor Vibrations due to Human Activity. Due to the limited structural depth in the vertical direction, the structural steel framing was unable to meet the limit. However, by engaging the glass guard in combination with the steel framing, the limit was met. The detailing of this connection between the steel and glass needed to be carefully considered to be able to transfer the required in-plane shear forces and out of plane moment from the glass guard to the steel stringer while avoiding excessive confinement that could lead to internal stress concentrations.

7.0 Glass Guard Connections

Connections between the glass guard and the stair stringer, as shown in Figure 5, were provided at every second tread. The arrangement of two connectors per connection location resisted out of plane moment due to lateral loads on the glass guard by providing a push-pull couple. The in-plane shear is transferred through friction at the two connectors. A ¾” bolt centered in an oversized hole within the glass is used to pre-compress the connection assembly clamping the glass against the stringer providing sufficient friction to transfer the shear while avoiding stress concentrations by transferring shear over a relatively large area. Refer to Figure 6 for a typical section through the glass connection.

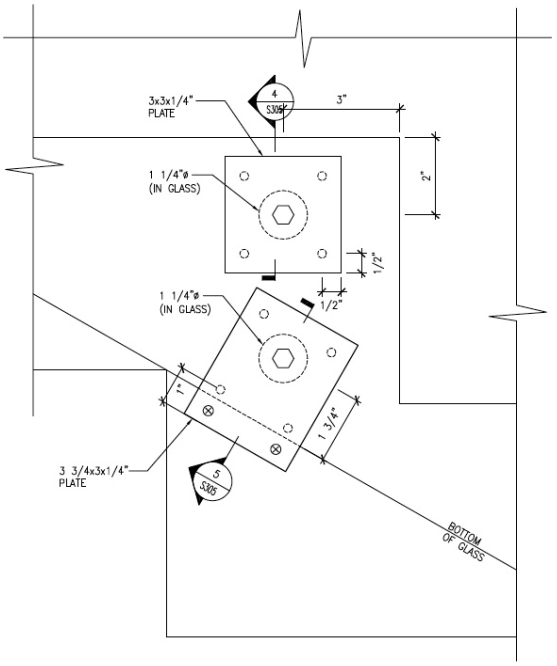


Figure 5: Elevation of glass guard connection to stair stringer

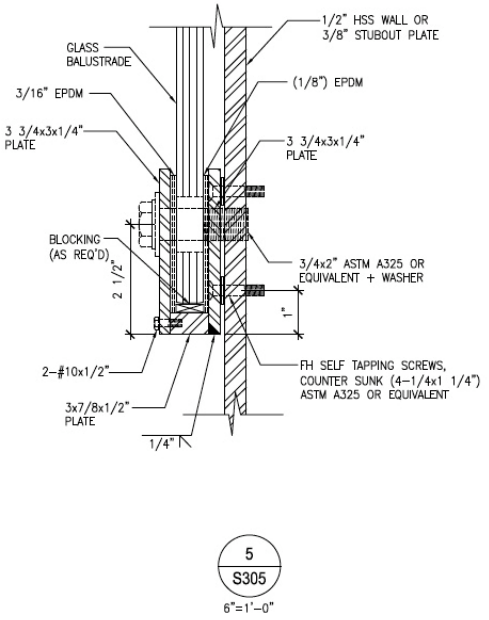


Figure 6: Section through glass guard connection to stair stringer



Figure 7: Erection of cantilever mid-landing,



Figure 8: Erection of Stair Framing, photo courtesy of Gertler & Wente Architects



Figure 9: Finished Feature Stair, photo courtesy of Gertler & Wente Architects

8.0 Conclusions

Although the structural steel framing is not exposed to view, it has been carefully sized and detailed with consideration for the architectural expression. In addition, a subtle and economical connection between the glass and steel helps minimize the depth of structure. With the structure in a supporting role, the architectural vision is maintained contributing to the overall shopping of experience of the clientele of Louis Vuitton.

Title: The Spiral Stairs at the Art Gallery of Ontario

Authors: Crispin Howes, PEng, Associate, Halcrow Yolles Toronto
Eric Gordon, PEng, Senior Principal, Halcrow Yolles Toronto

Transformation AGO is the recently completed renovation of the Art Gallery of Ontario by Frank Gehry.

Within the building, visitors are intuitively drawn to Walker Court, the heart of the AGO bathed in natural light. The focal point of Walker Court is the Feature Spiral Staircase. From the ground floor the stair is experienced as a sculptural form clad in douglas fir panels. Upon entering the staircase at the 2nd floor level, visitors travel through the roof of Walker Court and upward 90 ft on the north elevation of the new Contemporary Tower with landings on the 3rd, 4th, and 5th floors.

On the south elevation, an enclosed staircase, clad in stainless steel and glass, cantilevers 30 ft from the face of the building directly above the 4th oldest surviving building in Toronto. The staircase has been dubbed the "Barnacle Stair" for the manner in which it appears to cling to the face of the Contemporary Tower.

This paper will provide an overview of the design and construction processes related to the two monumental stairs.

1.0 Project Introduction

The Art Gallery of Ontario (AGO), located in Toronto, Ontario, Canada has existed for over 100 years. Over that time the building has been renovated and expanded numerous times. Transformation AGO was the latest completed and most dramatic renovation\expansion. Completed in 2008, the total cost was $276 million CDN. The design by Frank Gehry involved extensive renovations to the existing galleries, the addition of a new tower for contemporary art, and the addition of several feature elements. In addition to the two monumental stairs, other feature elements of Transformation AGO included a 300ft long glulam and glass façade, a serpentine ramp, and skylights angled to control direct sunlight but still providing the opportunity to view light under natural light.

2.0 The Feature Stair

2.1 Introduction

One of the highlights of touring Transformation AGO is the experience of entering the Walker Court from the north, looking to the south and taking pause to reflect upon the sensuous curves of the feature staircase. Clad in douglas fir panels, the stair traces a path that starts above the south entrance of Walker Court, curves towards west wall,

back to the east wall and reaches to the new glazed roof above. Moving further to the south and looking upward reveals the staircase actually penetrates through roof and climbs up the north face of the new Contemporary Tower.

From the ground floor, the stair can only be experienced as a sculptural form. Visitors access the stair from the new second floor walkway that encompasses the exterior of Walker Court. Above the second floor, the stair links the 3rd, 4th and 5th floors of the Contemporary Tower. Below the new roof of Walker Court the stair is interior with a U-shaped cross-section, while above the roof the stair is exterior and enclosed with a roof and stainless steel and glass cladding.

2.2 Structural Solution

Two steel plate girders, concealed within the balustrade finishes, run parallel to each other for the entire length of the stair. The exterior plate girder is interrupted by the floor landings which provide support to the stair with two wide flange beams cantilevered from the tower floor framing. The interior plate girder is continuous from 2nd floor to 5th floor, a total distance of 180ft. The balustrade plate girders are comprised of 6 5/8in XXS pipe for the top and bottom flanges and a 5/8in curved steel plate for the web. Along the length of the stair the height of the balustrade varies in a non-linear fashion. With top and bottom of the balustrade curving in both plan and elevation, the flange pipes were required to be bent into 3D splines. The two plate girders are interconnected at regular intervals with integral U-shaped frames of 5 9/16in XXS pipes. The rigid welded connections of the U frames ensure that the two plate girders work in unison. Pipe bracing which zigzags between the bottom pipes of the plate girders provides horizontal stiffness. ¼" bent plates were used to form the tread and riser assembly which were then topped with a 2" concrete infill.

Above the roof of Walker Court, vertical 5 9/16in XXS pipes were positioned to align with joints in the curved glazing. These pipes support the roof above which encloses the stair. Framing of the roof maintained the solution developed for the Barnacle Stair where 3/8" x 2 1.2" straight bars were located on ruling lines in the curved roof surfaces. A 1/4in plate was installed to conform to the surface dictated by the ruling lines.

Being a conditioned environment, there were multiple requirements for the structural framing to accommodate the mechanical distribution systems. At floors 3, 4 and 5, the mechanical ducts enter stair below the landing framing. This is also the zone required for the structural support of the stair. To minimize the overall depth of the landing, large plated web openings were introduced to feed the ducts through the structure. These ducts supply a plenum which runs in the zone between the stair soffit and the under side of the tread and riser assembly. At regular intervals, this under stair plenum connects to vertical plenums with the balustrade on each inside of the stair. To facilitate this connection, 6"x4" openings were cut into the curved web of the plate girder.

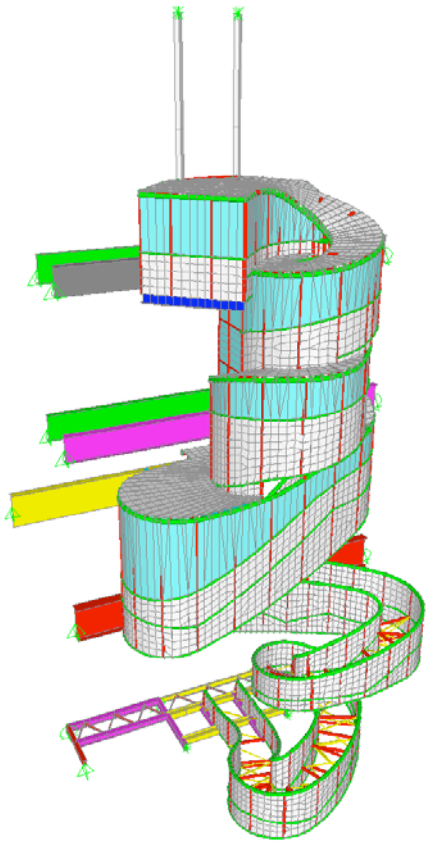


Figure 1: SAP2000 analysis model of the Feature Stair



Figure 2: Structural CATIA Model of the Barnacle Stair

3.0 The Barnacle Stair

3.1 Introduction

Visitors viewing the new Contemporary Tower of the Art Gallery of Ontario from the south in historic Grange park, will identify the Barnacle Stair as a prominent feature. The stainless steel and glass clad sculptural form softens the appearance of the rectilinear tower. The stair, nicknamed the barnacle for the manner in which it appears to "clings" to the tower, interconnects the 4th and 5th floors. Visitors in Grange Park will also notice that the stair is located directly above the Grange House. A Georgian-style manor, the Grange House was constructed in 1817 and is the fourth oldest surviving building in Toronto. Within the stair, visitors are treated to number of spectacular views to the south as they walk up and down the stair. The most prominent view comes at the tip of the stair, 30 feet from south tower and aligned with the centre of Grange park, where observers can look south along John Street down to Lake Ontario.

Achieving such a daring sculptural form that also must function as fully condition enclosed space requires a unique structural solution. From a large scale viewpoint, the framing of the stair can be viewed as a steel tube, with material distributed around the perimeter of the stair cross-section to resist bending and twist as the stair cantilevers out and curves back on itself. The interior of the tube is hollow achieving the function of the stair, to allow visitors to move between the galleries of the 4th and 5th floors.

3.2 Structural Solution

From a component level viewpoint, there are a number of requirements that shape the exact layout of the framing. A key requirement is a band of curved that runs on both sides of the stair for its entire length. This zone of transparency severs the top of the tube from the bottom. However, structurally, framing between the top and the bottom is essential for the overall structural action, so 5 9/16" XXS vertical pipes were provided which align directly with the joints in the glazing. By adding corresponding 5 9/16" XXS pipes transversely at the top and bottom of the stair cross section and aligned with the vertical pipes, a series of strong hoops was created along the entire length of the stair. These hoops are interconnected with 6 5/8" XXS pipe located at the four corners of the stair cross-section and at the top of the balustrade. As the interconnecting pipes had to be concealed within the interior and exterior finishes of the balustrade, the pipes were curved to fit within the structural "zone".

Welded rigid connections between pipes were provided to resist racking of the stair cross-section as well as to act as a vertical Veerindeel truss. The truss was further stiffened with curved ½" steel plates located within balustrade zone.

On the roof of the stair, a requirement was to provide a continuous surface to support and set out the geometry for the roof cladding. Analyzing the curvature of the surface within CATIA, ruling lines, which are straight lines which lie on curved surfaces,

were identified. 3/8" x 2 1/2" steel bars were placed on these ruling lines spaced at approximately 12" c/c. On top of these bars, a ¼" steel plate could be warped to conform to the geometry set out by the ruling lines. This ¼" plate provided the required continuous surfaces but also acted as a diaphragm to stiffen the roof of the stair horizontally. On the soffit of stair, there was no requirement to support cladding, so bracing pipes sawtooth between hoops for the entire length of the stair providing horizontal stiffening.

At the 4th and 5th floors, the stair framing is anchored to portal frame comprised of built-up the face of the building.

Beneath the oak flooring, ¼" steel bent plate topped with concrete provides support for the treads and riser of the stair. While at landings, 1 ½" composite steel deck spans across the stair as formwork for a 2 ½" concrete slab. A plenum is contained within the zone between the stair soffit and tread and riser assembly. This plenum is interconnected at regularly intervals to a vertical plenum located within the balustrade assembly. To facilitate this interconnection, corresponding 6"x4" openings in steel box sections. Two vertical box sections extend from the 4th floor to 5th floor and from the 5th floor to the Roof to resist pushing into the building or pulling away from the building. A horizontal box section, located at the stair roof level, rigidly connects to the vertical to resist loading parallel to the ½" curved plates were required. Additional requirements to accommodate mechanical systems were encountered at the connection to 4th and 5th floors. Connections in these areas are the most critical for the stair framing. Large openings for ductwork had to be carefully integrated to maintain structural integrity while allowing proper conditioning of the stair.

4.0 Tuned Mass Damper

Early in design process of the stairs, the dynamic response of the structure to walking excitation was evaluated in both vertical and horizontal modes. The evaluation limit for vertical acceleration was 1.5% g with 2% damping based in the AISC Design Guide for Floor Vibrations due to Human Activity. The limit for horizontal acceleration was 0.5% with 2% damping. The robust structure of the Feature Stair was well within the acceptable limits. The Barnacle Stair on the other hand could not meet the specified limits. Stiffening the structure by adding additional steel was not an option has it would increase the overturning moment needed to be resisted by the supporting framing. Instead, a Tuned Mass Damper (TMD) was specified to control the dynamic response of the structure.

Below the mid-landing furthest away from the tower, a pie shaped volume was allocated for the TMD. Refer to Figures 3 and 4 The specified properties of the TMD were a mass of 4850 lbs, damping of 6%, and a tuned frequency of 2.40Hz. The TMD was designed, manufactured, and installed by GERB GmbH. Third party testing following the installation verified the TMD was performing to the specified requirements.



Figure 3: TMD prior to stair erection



Figure 4: TMD after stair erection

5.0 Erection of the Stairs

A modular approach was utilized in the erection of the stair which provided a balance of efficient shop welding with field adjustability. The overall framing was subdivided into modules that would fit within shipping requirements. Each of the modules was fabricated on a jig in the shop and subsequently test-fitted to the modules directly above and below. Once in the field the modules were connected with field welds.

The Barnacle was erected in eight modules starting at both the 4th and 5th floors with modules added in succession until meeting in the middle. The presence of the Grange House, the fourth oldest surviving building in Toronto, precluded to possibility of providing temporary shoring. The Feature Stair, on the other hand, was erected temporary shoring cantilevered of the Contemporary Tower structure. Once the erection was complete from 2nd to 3rd floor the shoring was released and the as-built structure support the erection of the remainder of the framing up to the 5th.

6.0 3D Model Documentation

All of the feature elements on the Transformation AGO project were structurally and architecturally coordinated with CATIA\Digital Project. The models were subsequently issued as construction documents in combination with traditional 2D documentation. 2D documents provided members sizes, connection forces and other

connection requirements. Geometry was specified by the CATIA master models and dimension information was removed from 2D documents.

Two models were issued for each element. The master models contained only wireframe and surfaces that represented framing members, plates, and slabs. The contractor was directed to use the master models as the basis for structural detailing by extruding the member sizes specified on the 2D documents about the specified wireframes. The second type of model was the reference model which contained many of the elements modeled for coordination during the design phase. Modeled elements included member extrusions or sample connection details. The contactor was directed not to use the reference models as the basis for structural detailing as there was a possibility that modeled elements may not corresponded to information specified on the 2D documentation. These models were provided to aid the contractor in early visualization prior to developing their detailing model.

The list of submittals required by specifications was updated to include models in CATIA\Digital Project format. Prior to the production of shop drawings models were submitted to by the consultants for geometry review and to the General Contractor for interference review with the adjacent trades. The subsequent advantage of this approach was that once the 2D shop drawings were submitted for review they could reviewed and returned to the contractor substantially quicker than with a traditional approach.

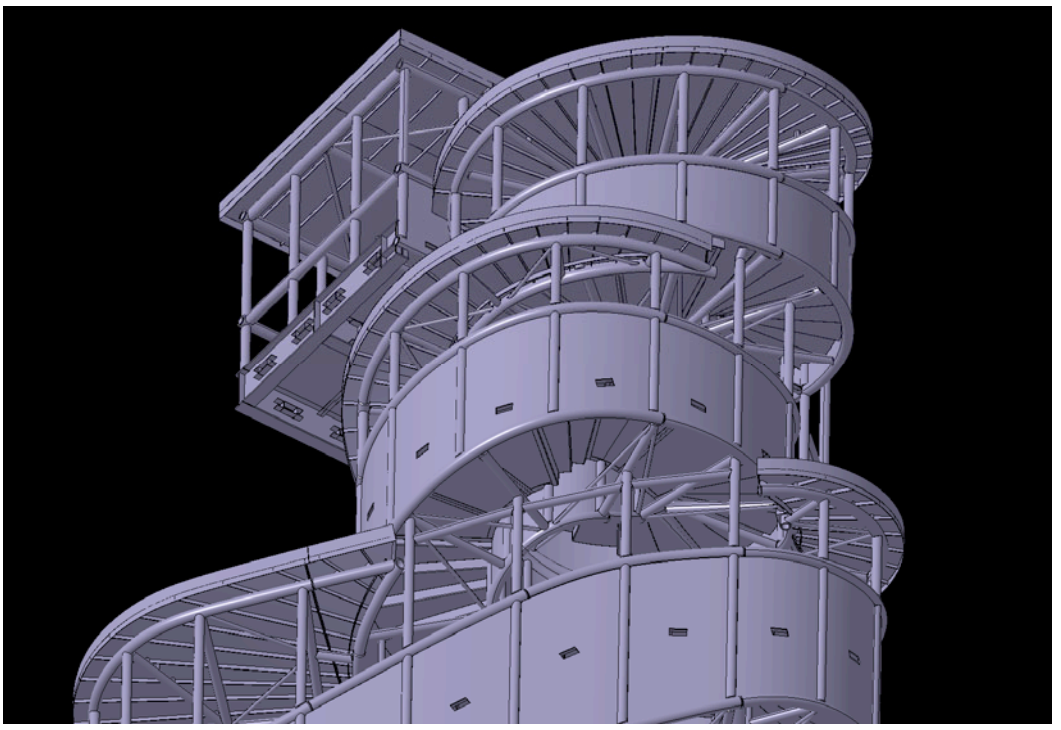


Figure 5: CATIA detailing model for the Feature Stair prepared by Mariani Metal Fabricators

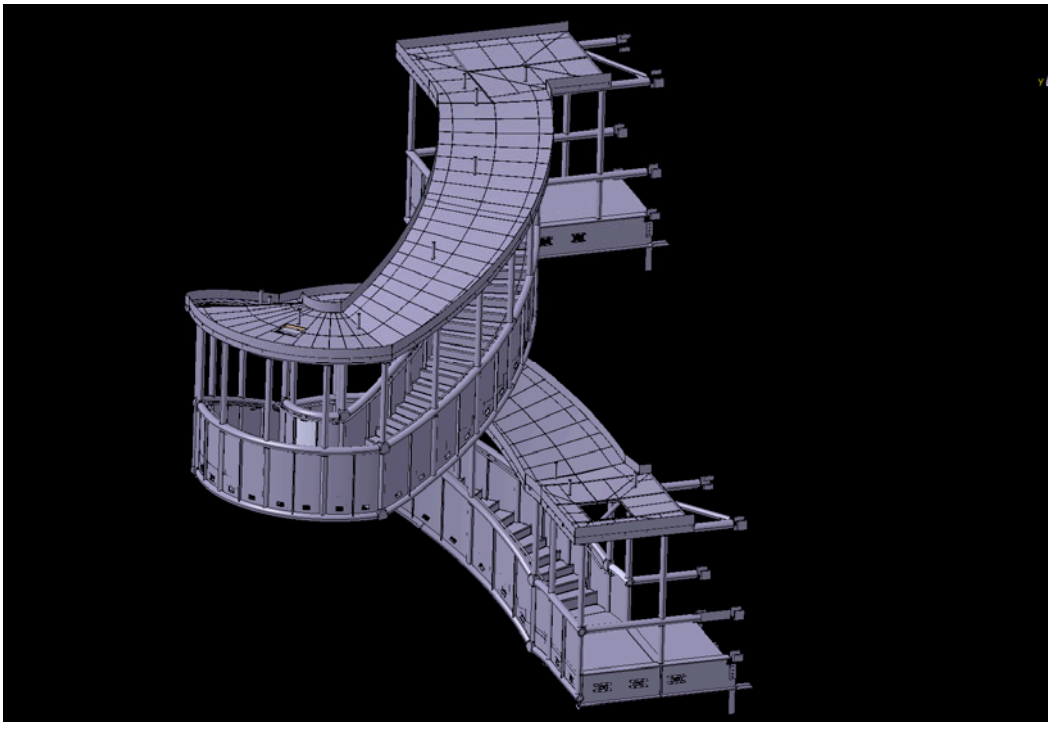


Figure 6: CATIA detailing model for the Barnacle Stair prepared by Mariani Metal Fabricators



Figure 7: Erection of structural steel framing for the Feature Stair



Figure 8: Erection of structural steel complete and installation of finishes underway on the Barnacle Stair



Figure 9: The Feature Stair viewed from within Walker Court,
photo courtesy of the Art Gallery of Ontario



Figure 10: The Barnacle Stair on the south Elevation of the Contemporary Tower, photo courtesy of the Art Gallery of Ontario

7.0 Conclusions

The Feature and Barnacle Stairs, as well as other feature elements, at the Art Gallery of Ontario were a challenge to design, coordinate, fabricate, and erect. However, the overall project was realized on budget and within a month of the original opening date. Much of the success was attributable to the use of 3D modeling through out the design and construction process. While pre-dating the current Building Information Modeling (BIM), the process used on the Transformation AGO provided proof of the claimed benefits including clash detection and a reduction in the number of Requests for Information.

Large Temporary Structure for Special Event

M. G. Paschetto[1], T. D. Heidersdorf[2], and D. M. Campbell[1]

[1]Geiger Engineers, 2 Executive Boulevard, Suite 410, Suffern, NY 10901; PH (845) 368-3330; FAX (845) 368-3366; email: mgp@geigerengineers.com
[2]Heath Tecna Inc., 3225 Woburn Street, Bellingham, WA 98226; PH (360) 738-2005; FAX (360) 715-3999; email: ted.heidersdorf@heath.com

ABSTRACT

As the entertainment industry continues its efforts to attract audiences and audiences search for ever more dramatic events, engineers are being asked to design and analyze a widening variety of temporary entertainment structures. Whereas concert tours and music festivals typically employ a standard range of modular stages, some events have started using stage structures that are unique and used for one event only. Wrestlemania XXVI in the spring of 2010 at University of Phoenix Stadium is an especially interesting example of this. Standard Stageco rental equipment was combined with several custom-built pieces to create a four-legged pyramid over the main event wrestling ring. In all, 40,000 lbs' worth of truss supported rigging loads equaling 63,000 lb.

Unique, one-off entertainment structures present specific challenges for the engineer, not least because of the normally tight schedules. The loads and structure dimensions can be significant despite the temporary nature of the installations. And it is most often not feasible when problems arise to take the time to determine the cause(s). Usually, issues must simply be worked around if the event is to take place safely and on time. In working on entertainment projects, engineers need to be flexible and creative.

BACKGROUND

The Stageco Group, headquartered in Tildonk, Belgium, has been in operation since 1985. The traditional part of Stageco's business is providing modular truss systems for temporary structures to be installed at a wide variety of entertainment, sporting, and promotional events. However, Stageco also works with production designers to create unique "one-off" structures that will be used only as part of a specific tour or even just a single event.

Beginning in 2003 with Wrestlemania XIX, Stageco has been involved in the staging of World Wrestling Entertainment's (WWE) signature annual event. The WWE wanted a large pyramid structure to support the lighting and audio equipment and video screens above the ring for Wrestlemania XXVI held in the spring of 2010.

THE PYRAMID

The structure envisioned for Wrestlemania XXVI was a straightforward assembly of four trussed legs angled to meet at a point and thereby forming the outline of a

pyramid. The pyramid would be 185 feet per side at ground level and 105 feet high. The base perimeter would be formed by cables tying the legs together. Figure 1 shows the pyramid during erection.

A 70'-6" square rigging grid was incorporated into the structure at a height of 58 feet. The rigging grid was constructed of one of Stageco's larger stage roof trusses from their standard equipment inventory. All told the equipment rigged from the pyramid amounted to 63,000 pounds.

The overall structure's size and large payload required that Stageco ship their heaviest-duty truss from Belgium so it could be used for the pyramid's four legs. This steel triangular truss has a depth of 5'-11" with 3.5" diameter chords. The overall strong axis moment capacity is 235,000 ft-lb.

Stage roof truss towers and buttresses in the Stageco system are founded on 6.5' square, steel encased concrete block bases. Each base weighs 4,840 lbs. One of these bases was employed at the bottom of each pyramid leg.

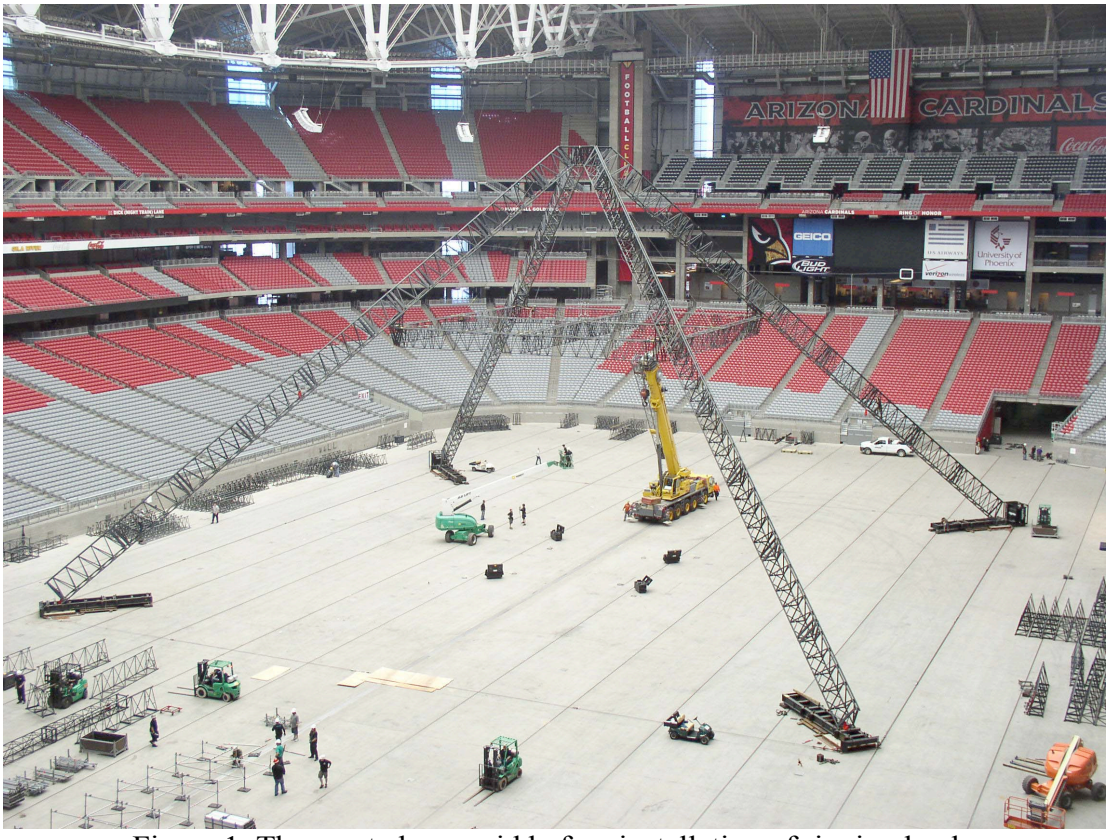


Figure 1. The erected pyramid before installation of rigging loads.

THE VENUE

A state of the art structure with both the roof and natural grass field being retractable, the University of Phoenix Stadium opened in August 2006. The dimensions of the retractable roof opening are 360' x 120'. During Wrestlemania XXVI, the roof was to be open and the grass field was to be in its outdoor location.

Planning to have the stadium roof open during the event engendered much discussion because there was no data available on the wind effects inside the stadium when the roof was retracted. No provisions had been made for wind ballast because the pyramid was being installed indoors. However, the WWE was firm in its decision to keep the roof open. Therefore it was not an option to specify that the roof be closed in the event of the outside wind reaching a certain speed.

For analysis purposes, it was finally agreed that a basic wind speed of 40 mph would be used. Any air turbulence around the roof opening would not have a significant impact on the pyramid because its height was well below the stadium's roof. So in this instance, the Engineer of Record was confident that 40 mph was conservative for a design wind speed. The maximum lateral design force from 40 mph wind on the pyramid was calculated to be 15,200 lb.

THE PYRAMID'S BASE REACTIONS

As with any structure of this type, there was significant outward thrust at the leg bases. When the pyramid was fully loaded, the thrust was 33,000 lbs per leg. Handling forces this large especially from a temporary structure presented quite a challenge. Entertainment projects almost always have a very short lead time and the schedule must be maintained if the event is to occur.

Computer analysis of the pyramid showed that creating a pinned condition at the leg bases would cause some truss members to become overstressed when all loads were applied. At the other extreme, allowing the leg bases to slide freely under load caused the trusses to become even more overstressed than in the pinned configuration. Further computer analysis of the pyramid with intermediate amounts of restraint at the bases found that allowing some spreading reduced all trusses' internal forces to allowable levels.

There was no ability to follow any design path except this last one, allowing the bases to spread a specified distance. Stageco's most heavy duty truss was already being used so the legs could not be made stronger. The rigging loads could not be significantly reduced because the client would be left with a lackluster show. The issues associated with partially restraining the bases would have to be dealt with, namely how to stabilize the bases once the desired displacements have occurred and how to ensure the bases' sliding will take place in a controlled manner.

Leg Base Restraint Methods. Two ways the bases could have been secured once they had moved the correct distance were quickly dismissed - anchoring the bases to the stadium floor or adding more ballast to them to maintain their positions. There was no doubt that neither the University of Phoenix nor Stageco would be interested in drilling into the stadium's concrete floor for anchorage. Similarly, from an engineering perspective it was considered inadvisable to rely on ballast alone to keep the bases in their proper locations because if the they spread too much the entire structure would fail.

Clearly, the base cables that were part of the original designer's concept would be a suitable alternative. These base perimeter cables that tied the legs together would be sized not just for strength but also for the right amount of stretch.

The elongation of the cables would partially release the legs and allow them to spread the desired distances. Beyond that, the cables would restrain the bases from any further spread. The final cable force was 22,000 lbs with the bases each displaced a total of 7 inches outwards.

Once the pyramid reached the desired deflected shape, gravity loads would provide enough friction at the bases to resist sliding forces that might arise from wind forces. The maximum lateral force for 40 mph wind was calculated to be 15,200 lbs. A 3,000 lb water tank was attached to each base to bring the total normal force up to a safe level for sliding resistance assuming a friction coefficient of 0.3 and including a factor of safety of 1.5.

Base Sliding. It was crucial that the bases spread a specified amount in order to keep the structure from being overstressed when fully loaded. Implied in this is that the bases needed to displace equally and in a straight outward line. See Figure 2 for the idealized displaced pyramid shape.

One fear was that a base which had not moved far enough under dead load might suddenly and violently release when rigging loads were being applied. Also, unequal movement of the bases would put additional, undesirable stress on the structure. The truss legs were strong in major axis bending and axial loading but they were not intended to resist any significant amount of weak axis bending. Although in theory the normal loads on the bases would not be high enough to create adequate frictional force to resist the thrust, in practice each base would see different floor conditions and one could easily get stuck. See Figure 3 for the expected displaced shape for this particular problem.

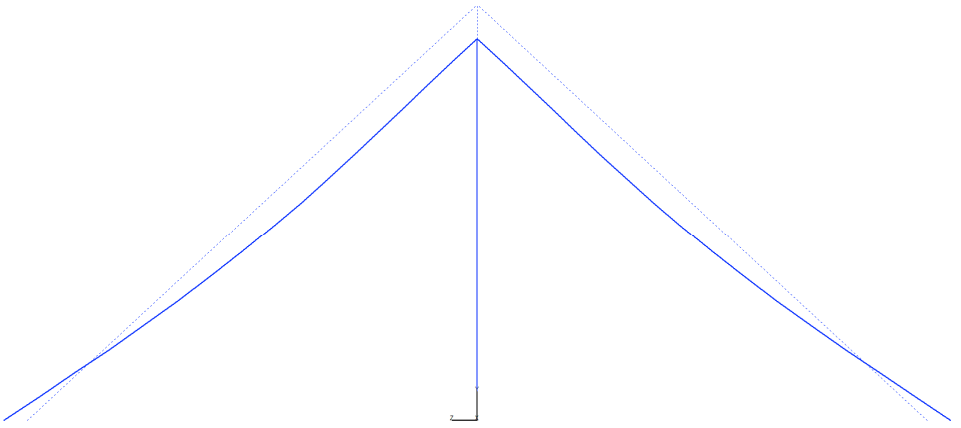


Figure 2. The desired deflected shape for the pyramid.

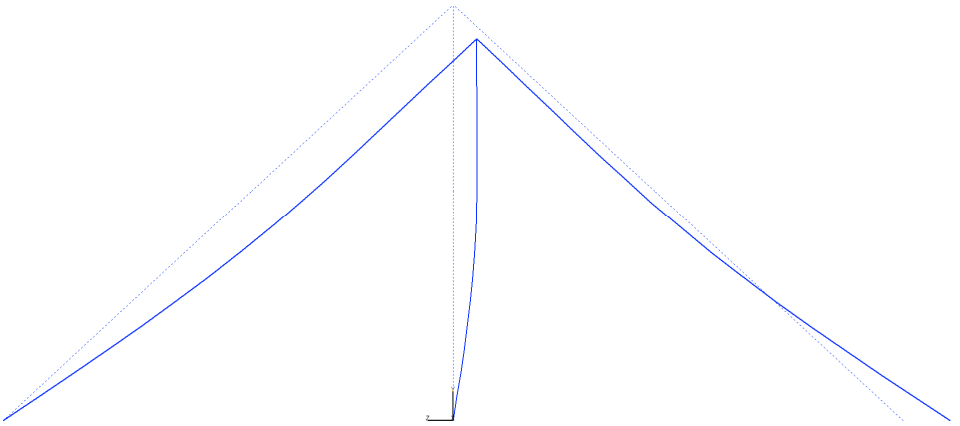


Figure 3. The deflected pyramid if the left hand base does not slide and the other three bases slide as needed.

Overall Sliding Resistance. The pyramid legs must slide during loading. However, they must also not be allowed to slide under wind forces once the structure has been completed and fully rigged. Whatever was designed to guide the legs during sliding, it would have to include a method for removing, at the appropriate point during installation, the ability to slide.

SLIDE BEARINGS

It was clear that some form of slide bearing would have to be designed for the pyramid bases. This was the only viable choice despite the attendant challenges. The remaining questions then were how to design something that could be quickly fabricated, easily installed on site, and safely used by the rigging crew.

When these decisions were being made, time and budget had become very short. The slide bearing design was therefore focused on using wood products. They were available at local DIY stores, easy to work with, lightweight, and inexpensive. Essentially, large wooden sleds were envisioned to receive and guide the pyramid's concrete bases. A plywood pad would be laid on the concrete floor of the stadium with another plywood pad on top of it and the concrete base on top of that. The plywood to plywood interface material would be selected to have a very low coefficient of friction. Blocks of wood would be nailed to the bottom pad to ensure that the legs did not slide sideways. And when the time came, the two plywood pads would simply be nailed together to secure the bearing pad assembly.

Below is provided for reference the equipment list and set of instructions given to the Stageco crew for the slide bearings. See Figure 4 for a photo of an assembled slide bearing.

Equipment:
8x4' sheet of ¾" plywood, 16 required
8x4' masonite sheet, approx. 3/16-1/4" thick, 16 required
250 ct. ¼" x 1-3/4" lag bolts

250 ct. ¼" x ¾" long flathead wood screws
lithium grease

Steps:

1. Assemble the slide bearing pads. One pad is to be made up of 4 panels in two layers – two plywood sheets in one layer and the masonite sheets in the other layer. It is important that the rougher side of the masonite, if there is one, is placed against the plywood. The smoothest face of the masonite should be the sliding surface. The bottom two sheets run in the perpendicular direction of the top sheets. The top and bottom layers are to be glued and screwed together.
2. Half of the slide bearing pads are to be cut down to 7' square overall dim's. These will be the top layers of the slide bearings.
3. Screw a guide block onto each offstage side of the exposed masonite surface of each of the 8' x 8' bottom slide bearing pads.
4. Place the 8' x 8' bottom slide bearing pads in the stadium with the masonite surface up and the masonite seam running parallel to the direction of slide. Proper alignment of the bottom pad along the direction that the base will move is critical.
5. Liberally grease the entire top masonite surface of each bottom slider bearing pad as well as the inner faces of the guide blocks.
6. Place the 7' x 7' top slide bearing pads on top of the bottom pads with the masonite surface down.
7. Place the concrete base on the slide bearing.
8. Put together the base cube assembly with the ground perimeter cables. Do not yet attach the base frames to the base cubes.
9. Tighten the perimeter cables to remove any slack.
10. Mark the current, unloaded location of the slide bearings' top pads relative to the bottom pads. Continue with assembly of the pyramid structure.
11. Once the pyramid is pinned to the base cubes, have the crane operator slowly release the load. The slide bearings should all move outwards approximately the same distance at each base – the concrete base and top pad moving together over the bottom pad – as the pyramid "settles". The guide blocks will prevent unintentional side to side movement. Note should be made of how far each base moves under self weight and also under self weight plus full rigging loads.
12. Check that each slide bearing seems to be moving properly. If there is any binding up, stop and resolve the issue. A strong hammer hit may be sufficient.
13. Once the entire self weight of the pyramid has been released from the crane, check the amount of overall movement in the slide bearing at each base. The distances should be approximately 4" and all about the same.
14. Rig the structure. The slide bearings will continue to move outwards as load is added to the pyramid.
15. Once all of the live load is in place, make one final check that each slide bearing moved a total of approximately 7" outwards.

16. Screw each slide bearing top pad to the bottom pad with 60 screws evenly spaced around the perimeter of the concrete base.
17. Attach the base frames.
18. For strike, reverse the above steps.



Figure 4. Assembled slide bearing shown with concrete base and steel base frame on top awaiting pyramid leg attachment.

IMPLEMENTATION

Challenges continued to crop up when the pyramid with its slide bearings was erected. The pyramid was assembled, still suspended from the crane, and pinned into the bases. As the crane released its load, the turnbuckle in one of the perimeter ground cables unwound, one of the bases did not slide, and the opposing base moved twice the distance it should have.

Work was halted and the structure was inspected. There was clear warping of the pyramid truss legs, as illustrated in Figure 3. It was decided that the crane operator should re-engage the pyramid in the hopes that the bases would return to their original positions. As the crane picked up load, there was some amount of rebound but not enough. Forklifts were used to "encourage" each slide bearing to return to its starting location. After several impacts from the forklifts, the slide bearings were acceptably close to where they should have been.

The turnbuckles were checked and tightened as necessary so that each perimeter cable was, as nearly as possible, under the same amount of tension. The

crane operator was again directed to start releasing the pyramid structure. This time a forklift was stationed at the previously stuck base so that it could be pushed if it still did not move.

The bases moved the correct distances after some prodding. However, there was a great deal of concern over whether the bases would slide evenly when the rigging loads were applied to the structure. It was thought that the best way forward was to add pre-stress to the perimeter ground cables. This would put inwards force on the bases which would be counteracted as the live load outward thrust started to act. Accordingly, the turnbuckles were tightened an amount that corresponded to the desired cable length decrease necessary to match the tension that would arise from the live load thrust. The pyramid was rigged without further problems and Wrestlemania went off without a hitch. The above steps were reversed for strike and went smoothly.

In hindsight, it was thought that two things were the most to blame for the stuck bearings. One was that the lithium grease seeped into the masonite and either caused it to swell or somehow become sticky. By the time the event was over and the structure was being taken down, the bearings had completely dried out and loosened up. And indeed the bearings behaved as they should have during strike. The other factor was a pair of guide blocks that had been attached too closely to the sides of the upper bearing pad of the slide bearing assembly that had caused the most problems during installation.

CONCLUSION

Unique, one-off entertainment structures present specific challenges for the engineer, not least because of the tight schedule constraints. The loads and structure dimensions can be significant in light of the temporary nature of the installations. And as with anything that is only designed and built once, there are always unforeseen issues that arise and must be addressed.

The slide bearings for the Wrestlemania pyramid are a case in point. In particular, one of the four slide bearings did not behave as expected and there was no time to disassemble the pieces to find the cause. The problem simply had to be worked around if the WWE event was going to take place safely and on time. In working on entertainment projects, engineers must be willing to deal with this type of situation on a regular basis if their clients are to be well served.

Assessing Existing Theater Structures and Rigging Infrastructure for Large Production Demands

T. D. Mills, M. G. Paschetto, P.E.[2], and D. M. Campbell, P.E.[1]

[1]Principals at Geiger Engineers, 2 Executive Boulevard, Suite 410, Suffern, NY 10901; PH (845) 368-3330; FAX (845) 368-3366; email: tdm@geigerengineers.com; dmc@geigerengineers.com
[2]Geiger Engineers, 2 Executive Boulevard, Suite 410, Suffern, NY 10901; PH (845) 368-3330; FAX (845) 368-3366; email: mgp@geigerengineers.com

ABSTRACT

The ever increasing load demands placed on existing theaters by modern live entertainment pose unique challenges for the structural engineer. One of the more difficult aspects for the engineer is the fact that many of the older theaters have limited, or no, design/construction documentation in existence. In the absence of drawings, investigations must be based solely on surveys of the existing conditions of the stage supporting structures and the grid-iron and fly systems. Typically, one finds that structural modifications have been made over the years for various shows without the benefit of engineering reviews. The Hammerstein Ballroom Theater (circa 1906) and the Howard Gilman Opera House at the Brooklyn Academy of Music (circa 1908) are two particularly interesting examples of old theaters requiring structural reviews for recent productions of new shows whose loads would impose a high demand on the existing structures.

BACKGROUND

Theater stagehouses provide an area over the stage for the rigging of hanging show elements. A stagehouse of a typical theater with a seating capacity of 1300 would usually have clear dimensions (with no obstructions from beams, columns, floors, etc.) of 50 ft x 90ft wide x 90ft high. Within the stagehouse is a counterweighted hanging system called a *Fly System* that allows technicians to move scenic elements such as lighting, video, audio, scenic flats and special effects vertically between the show's visible performance area behind the stage proscenium opening to the large stagehouse directly above. A schematic of a single manually operated lineset in a typical theater Fly System is depicted in Figure 1.

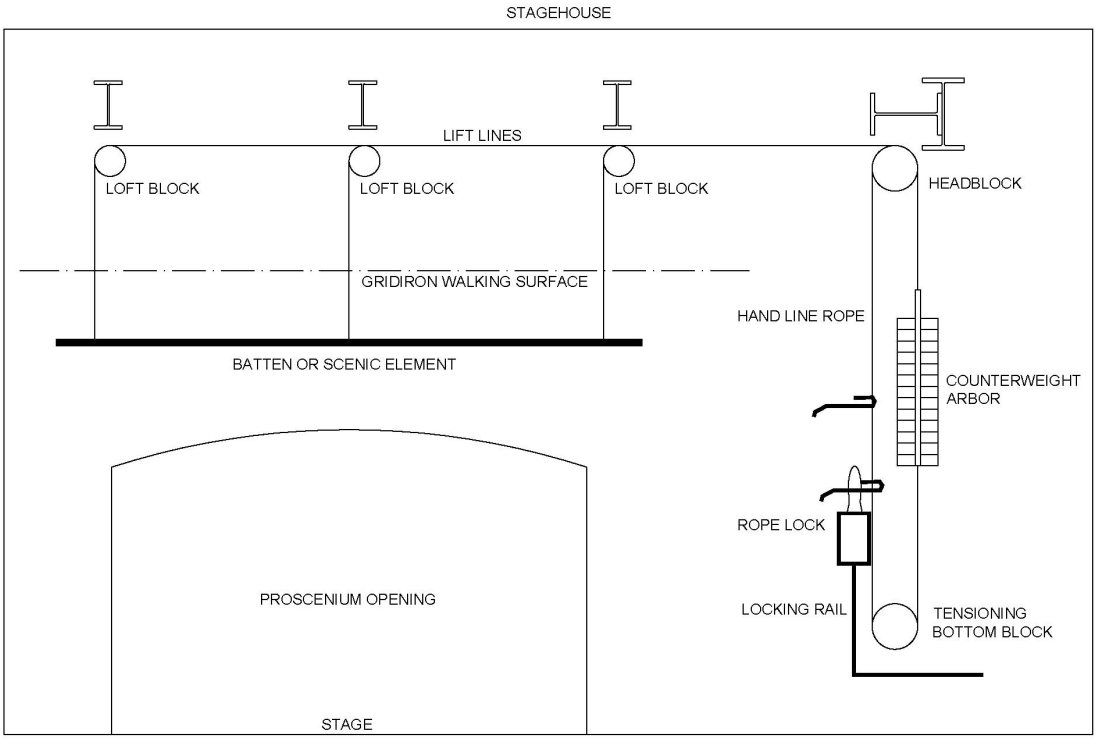


Figure 1 – Schematic of a Typical Manual Lineset in a Fly System

The counterweight arbor is brought into balance with the scenic load by adding and removing arbor weight plates. The average small theater, such as found in a high school, has 10 to 40 of these linesets. Theater facilities such as performing arts centers, and commercial Broadway and local theaters can have hundreds of linesets with multiple catwalk 'bridges' located along the side of the stagehouse wall to facilitate the loading and unloading of counterweight plates. A single lineset can have a lifting capacity of as much as 1600 lbs. The linesets range across the ceiling of the stagehouse spaced at 4 to 12 inches on center. Larger theaters typically employ a lattice grid of structural steel (called the *flygrid* or *Gridiron*) which is used as a walking surface to service the loft blocks and to support other rigging. The narrow spaces between the grid steel members allow the lift lines to pass through. The loft blocks may be attached to the gridiron itself or the stagehouse ceiling above. Figure 2 shows these two most common configurations.



(a) Gridiron Mounted Loft Blocks (b) Ceiling Mounted Loft Block

Figure 2 – Typical Stagehouses with a Gridiron (a) or without a Gridiron (b)

Occasionally, temporary rigging may be employed where chain hoists are attached to the gridiron or ceiling of the stagehouse. Typical chain hoists used in the entertainment industry have lifting capacities of 1 and 2 tons. It is not uncommon for productions to use more than 100 of these units to rig the scenic elements of a show.

Recent advances over the last 20 years have added automated, computerized rigging systems to theaters which provide accuracy of timing and positioning of scenery and special effects. As a consequence of going to motorized systems, operating speeds have increased along with the attendant dynamic loads. Automated rigging systems typically use a grooved drum wire rope hoist, which eliminates the need for counterweights and consequently lowers the gravity loads on the stagehouse structure.

Modern theaters are designed using recent code criteria where previously there were no or only limited provisions for stagehouse rigging loads. The NYC Building Code requires stage structures that support rigging to carry 100% of the rigging loads plus a 25% impact factor as well as a 50 psf live load on the gridiron. The International Building Code and the State of California also now have minimum design criteria for theater stagehouse rigging loads. For automated systems, there are also provisions in the International Building Code and ASCE for machinery impact loads.

Typically, gridirons are supported by the stagehouse roof structure. Therefore, design criteria for rigging loads are usually considered as an additional live load and used within load combinations that include environmental loads. Since there is a remote possibility that 100% of the rigging loads would be acting simultaneously over the entire gridiron, a reduction factor is typically employed. In practice, many engineers will reduce the load over the entire area, often by up to 25%.

Older theater fly systems were designed to hang simple wood-frame and painted scenery flats and other light weight loads. Although one finds that the early gridirons were built conservatively for the loads of yesteryear, modern productions push the limits of the gridiron and stagehouse structure's capacity. Making matters worse, one finds that structural modifications

have been made over the years for various shows without the benefit of engineering reviews or guidance.

Two interesting examples of old turn-of-the-century theaters requiring structural reviews for new shows whose loads would impose a high demand on the existing structures are presented herein.

HOWARD GILMAN OPERA HOUSE AT THE BROOKLYN ACADEMY OF MUSIC

Built around 1908, the Howard Gilman Opera House at the Brooklyn Academy of Music (BAM) is one of the oldest theaters in New York City and is a typical example of a large playhouse with a full stagehouse gridiron and loft blocks attached to the ceiling structure – see Figure 3.

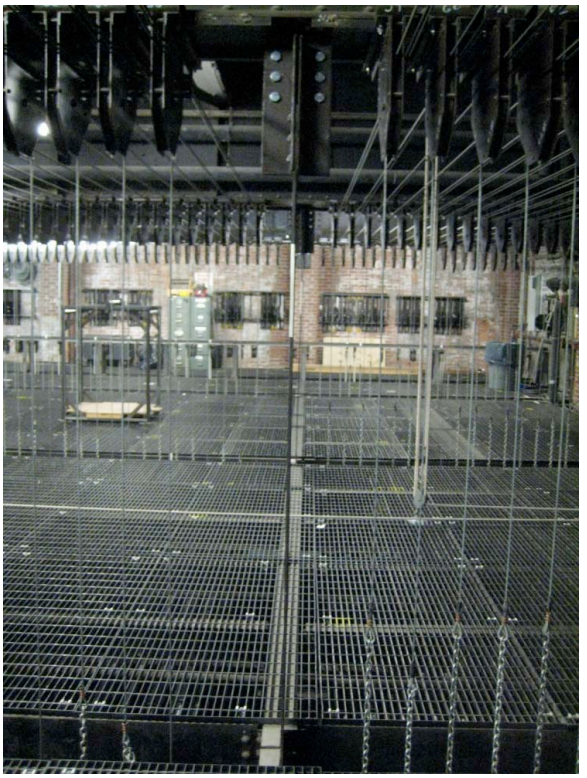


Figure 3 –Brooklyn Academy of Music Stagehouse Gridiron

In the summer of 2009, VH1's Diva/HHH show was engaged by BAM for a one-time event. The show wanted to rig fifty one (51) 1-ton chain motors to the gridiron of BAM's stagehouse. See Figure 4.

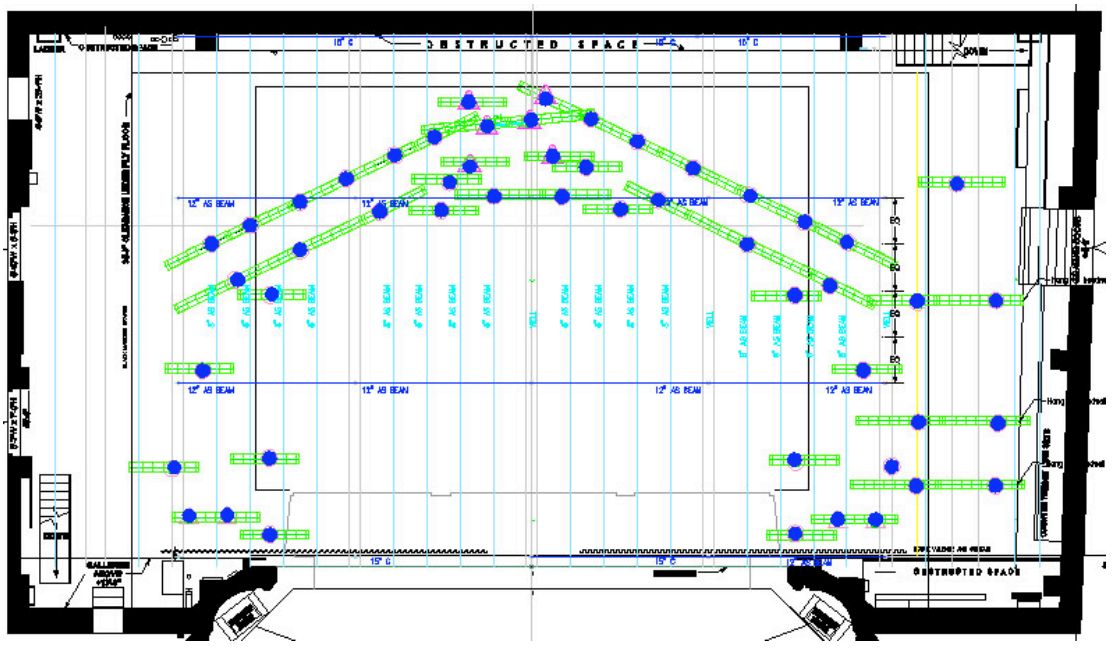


Figure 4 – VH1 Divas/HHH Show Rigging Points on Brooklyn Academy of Music Gridiron

As is common with most gridiron structures, BAM's gridiron is hung from the roof structure and is approximately 76' feet above the stage deck in the stagehouse. All loft blocks are hung from the roof structure, so the gridiron does not support loads from the permanent fly system. As a consequence, the gridiron steel structure is only used to support small hung loads and loads from the bar grating walking surface.

The Divas/HHH show required rigging from the gridiron's steel structure, so the engineering review concentrated on the capacity of the gridiron support structure. Since the Divas/HHH show did not take place in winter, the fly house roof structure was not reviewed because the roof's snow load capacity was assumed to be greater than the Divas/HHH show loads.

Based upon on-site inspections, it was found that the gridiron's original walking surface of 2" x ¼" steel slats had been replaced by modern bar grating sometime in the 1980s. It is easy to understand why the facility replaced the slats; they were bouncy and had 'dished' over the years as riggers walked on it. This left the slatted surface across the gridiron wavy with hills over the beams and valleys in between. Evidence was found of the original slats' attachments along all of the tops of the gridiron support beams. The original attachments consisted of clamping bars that grabbed both edges of the top flanges of the beams of the gridiron support structure. A small area containing some of the original slats as can be seen in figure 5.

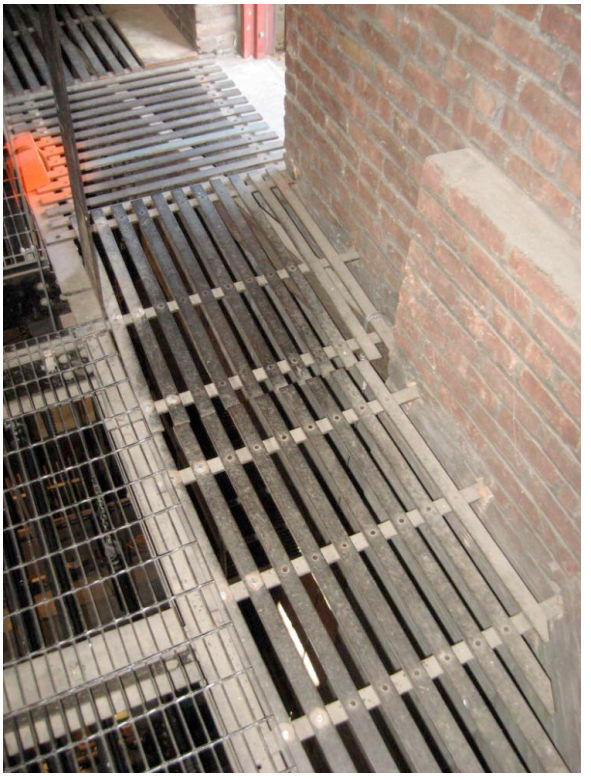


Figure 5 – Section of Original Slat Walking Surface of Gridiron (note modern bar grating to left)

The original slats provided continuous lateral beam bracing to most of the gridiron support structure. However the new bar grating with four hold-down clips at each corner of each grating panel did not provide the same level of lateral bracing for the beams. See Figure 6.

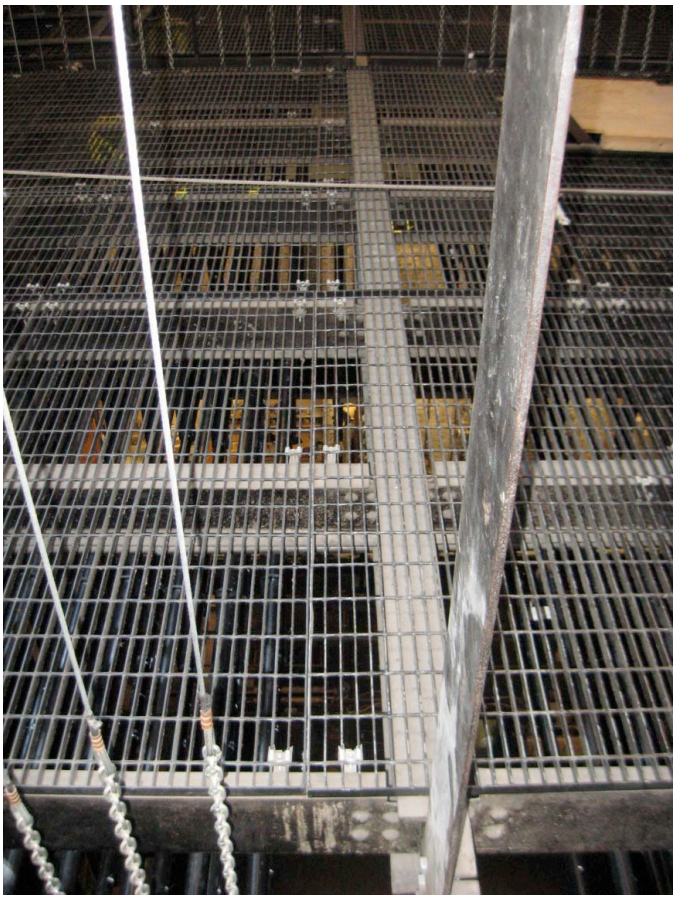


Figure 6 – Bar Grating Panels with Each Panel Secured With a Clip at Each Corner

The reduction in the amount of lateral bracing meant that the gridiron structure had very low rigging load capacity above the minimum required loads for the grating surface. To rig the Divas/HHH show, the production was required to remove the bar grating panels in the affected areas and add temporary blocking/bracing between the beams. The bracing had to be installed between the webs of the beams so as not to protrude above the tops of the flanges which would prevent the bar grating panels from being replaced. See Figure 7

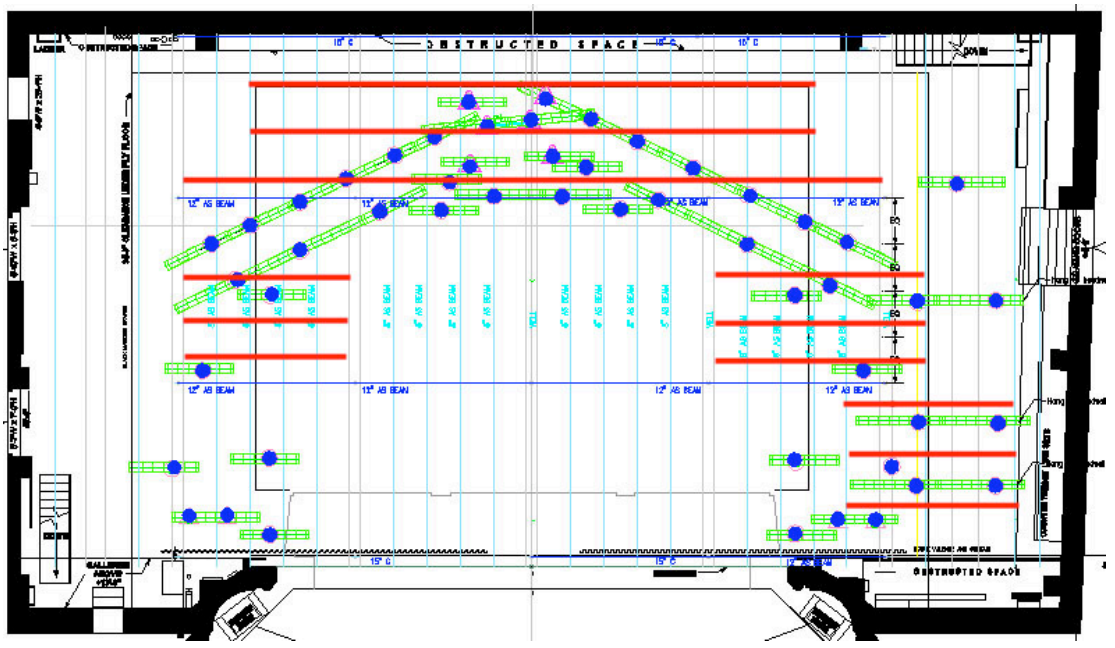
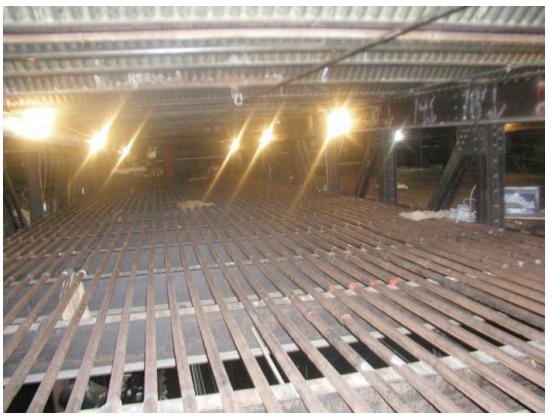


Figure 7 – Divas/HHH Show Gridiron Beam Bracing Plan

By replacing the original gridiron slats, the theater unwittingly had drastically reduced the load capacity of their gridiron. Unless and until they install permanent beam bracing, any show that desires to rig from the gridiron must now have temporary bracing added to the structure. This situation is typical of structural modifications made in theaters without the benefit of engineering guidance. This type of occurrence is possible because theaters are able to install shows and make modifications without building permits. Over the years a mindset develops where it is thought that theater rigging alterations do not warrant engineering review.

THE HAMMERSTEIN BALLROOM

Built around 1906, the Hammerstein Ballroom may be the oldest theater in New York City. Sometime in the 1970s, major renovations of the Ballroom were undertaken. The renovation included the construction of an addition to the original Hammerstein Ballroom structure. This newer structure is called the Grand Ballroom. The Grand Ballroom's stage was built on top of the Hammerstein Ballroom's original stagehouse roof. See Figure 8.



(a) Hammerstein Gridiron and Original Stagehouse Roof



(b) Grand Ballroom Stage Added to Hammerstein Stagehouse Roof

Figure 8 – Renovated Hammerstein Stagehouse with Added Stage Structure

Three Hammerstein stagehouse trusses help support the Grand Ballroom's stage. The fly house trusses are supported by deep plate girders at the stagehouse's left and right walls. See Figure 9.



(a) A Hammerstein Stagehouse Truss



(b) Hammerstein Plate Girders

Figure 9 –Hammerstein Stagehouse Gridiron and Grand Ballroom Support Structure

The original fly system had loft blocks attached to the stagehouse roof but this fly system was removed so there was a reduction of rigging loads on the stagehouse roof. While the Hammerstein stagehouse trusses were originally designed to carry gridiron and roof loads that include snow and wind, the addition of the Grand Ballroom stage has caused a net increase in the loads the trusses must support despite the removal of the snow, wind, and fly system loads. The engineering evaluation was to determine by how much the added loads from the Grand Ballroom stage reduced the capacity of the fly house trusses and how that impacted the rigging capacity of these trusses for shows in the Hammerstein Ballroom.

Computer analysis models were created for the three typical fly house trusses and the plate girder based on the site visit sketches and notes. Site visit sketches were compared to existing drawings and calculations from previous renovations to the structure. Note that while the existing documentation found was incomplete regarding the stagehouse, enough information was obtained to properly evaluate the stagehouse trusses and plate girder (but not the plate girder connections hidden within the masonry of the proscenium and stagehouse walls).

Loads applied to the computer analysis models were determined from the site visit notes, knowledge of typical construction material weights, and AISC reference materials pertaining to turn of the 20th century steel construction. Many steel mills at that time had their own steel shapes and identification of sections and materials were made from the manufacturer's markings on beams. See Figure 10.



Figure 10 – Turn of the 20th Century Steel Beam Manufactured by Steel Mill 'PHOENIX'

Codes require a 150 psf live load for stage structures. However, in determining a realistic tributary load for the three main structural elements, 100 psf was chosen since it is highly unlikely that the full 150 psf would be reached over the entire stage area all at once.

Initial findings indicated that the stagehouse trusses' top chords were at 110% of capacity per allowable AISC code stresses when a 100 psf load was applied to the Grand Ballroom stage which directly loads these trusses. This overstress condition precluded additional capacity for handling any rigging over the Hammerstein stage which would be tributary to these same trusses. Essentially, no rigging should occur in the Hammerstein stagehouse if there is any event occurring at the same time in the Grand Ballroom. Indeed, any Hammerstein Ballroom rigging should be evaluated with the stagehouse trusses' limited capacities in mind, whether there was a concurrent event in the Grand Ballroom or not.

Further investigation also found that the plate girders supporting the stagehouse trusses would be over capacity if a 100 psf live load is applied to the Grand Ballroom stage at the same time as rigging loads for the Hammerstein Ballroom. There was no exploration of possible solutions for reinforcing the stagehouse trusses and plate girders.

CONCLUSION

It is common to find that significant renovations have been made to theaters' structural components that are involved in supporting show loads. Because theatrical productions have historically been outside the purview of building departments, these renovations were often implemented without engineering oversight. For this reason, extra care should be taken to capture the structural ramifications of previous, perhaps undocumented changes when one is inspecting and evaluating existing theater structures.

Touring Stages for Outdoor Concert Productions

Karen A. Lynch P.E., M.ASCE[1], Paul A. Gossen P.E. F.ASCE [2]:

[1] Associate of Geiger Gossen Hamilton Campbell Engineers P.C.
2 Executive Blvd Suite 410, Suffern, NY 10901
Ph (845) 368-3330 Fax (845) 368-3366; e-mail kal@geigerengineers.com
[2] Principal of Geiger Gossen Hamilton Campbell Engineers P.C.
2 Executive Blvd Suite 410, Suffern, NY 10901
Ph (845) 368-3330 Fax (845) 368-3366; e-mail pag@geigerengineers.com

ABSTRACT

This paper presents the experience of the authors engineering stages for touring productions for outdoor concerts in stadia and other large outdoor venues. Stage structures spanning as much as 30m (100 ft) capable of supporting as much as 50 tons of entertainment equipment are regularly erected, dismantled, trucked and re-erected dozens of times in a major tour. Structures assembled in three days from modular steel components and platforms supported on scaffold systems are employed to create large stages often for a single performance at a venue. Most structures are designed to be supported at grade, often on sports turf fields, creating unique engineering challenges.

INTRODUCTION

Each year dozens of rock bands, country music artists, and other performers spend the summer travelling across North America and around the world playing night after night to stadiums packed with adoring fans. In addition to the musical talent a key component of every successful show is the stage structure which supports the sound, lighting, and video as well as the performers. The stage structure is comprised of many modular elements that can readily be erected, dismantled, trucked, and re-erected dozens of times in a major tour.

STAGE CONFIGURATION

A typical concert stage is 25600mm (84ft) wide by 19500mm (64ft) deep. With sound wings and additional video display on either side of the main stage, the overall width may be as much as 63700mm (209ft). The stage itself is comprised of a deck

on 1900mm (6'-3") high scaffolding. The roof over the main stage is 15600mm (51'-6") high supported on eight or ten trussed tower legs. (Figure 1) Additional trussed tower legs support the wings. Though various components of the stage and roof are pre-engineered, the entire system still must be evaluated for the specific loads for the show and for the code required environmental loads for every venue.

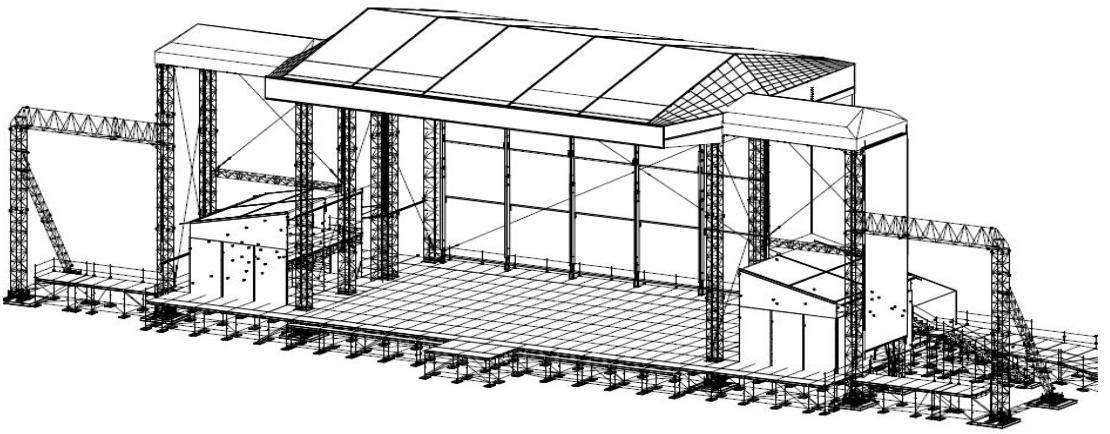


Figure 1. Touring Stage- Isometric View

LOADING

These touring stage structures are subject to the same load requirements as all other structures. However, these structures are used in multiple locations, so they must meet the load requirements of many different jurisdictions. Design loads should be determined from the building code in the structure's jurisdiction and per the reference standard ASCE 7.

The dead load of the structure is extremely light because the components must be quickly assembled and disassembled by a road crew without the benefit of heavy lifting equipment. The weight of the system is also minimized in order to reduce the transportation cost. The primary gravity load comes from the sound, lighting, and video equipment. These components are highly concentrated in a small space and so pose unique loading problems.

ROOF RIGGING LOAD

The main roof supports lighting, video, and other suspended show effects. The hung effects are usually well distributed over the roof. However, a major effect that has been incorporated in many events in recent years is the video wall. The video wall is located towards the upstage edge of the roof (the back wall of the stage) and generally spans the entire 24380mm (80ft) width of the stage. The weight of the wall, varying between 44 and 71kN (10 and 16k), must be shared between two cross-stage roof trusses since the video wall alone nearly loads a truss to its limit.

Many of the lights are located at the downstage edge of the roof (front of stage) in order to illuminate at the act on stage. This edge of the roof is a cantilever so the load at the outer edge is limited.

WIND LOAD

Wind load is the primary concern in evaluating touring stages. The main stage is covered by a roof and enclosed by semi-permeable walls (known as skin or scrim) on three sides. Large stacks of hung speakers fill the sound wings, and video walls fill the outer wings. This complete system does not conform to any of the structural systems defined in ASCE 7. Consequently, the structure has to be evaluated as several individual systems and then the resulting forces combined.

The main stage system can be evaluated as a Building Structure because it has a roof with three closed sides. However, in high wind conditions, the walls need to be lowered, creating a "Roof Only" Structure. The sound and video wings need to be evaluated as Non-Building Solid Freestanding Walls. Often there are other sub-structures located within the main stage system. Additionally, the wind load on the truss tower legs must be computed. The loads from these various components are transmitted to the 750mm x 750mm (30.5in x 30.5in) truss tower legs and then to grade.

In the upstage/downstage direction, the wind exposure of the fully rigged touring stage is approximately 1078m^2 (11,610ft^2) with a distance between the upstage and downstage tower legs of only 14400mm (47'-3"). Figure 2 and Figure 3 illustrate the front elevation and side elevation respectively. As shown in Figure 3, the lateral load on the structure is transferred to the stage level through diagonal bracing cables. The narrow footprint in the upstage/downstage direction and the limited number of truss towers lead to high vertical reactions from lateral loads.

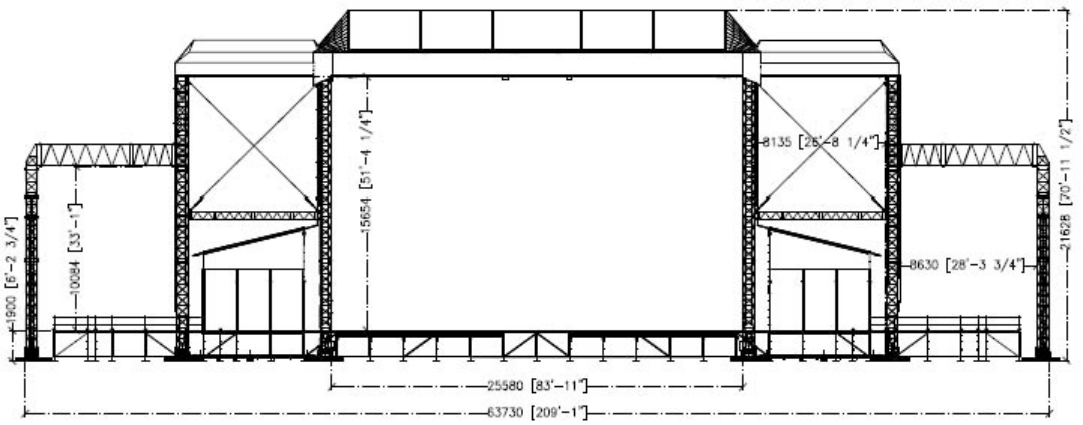


Figure 2. Touring Stage- Front Elevation

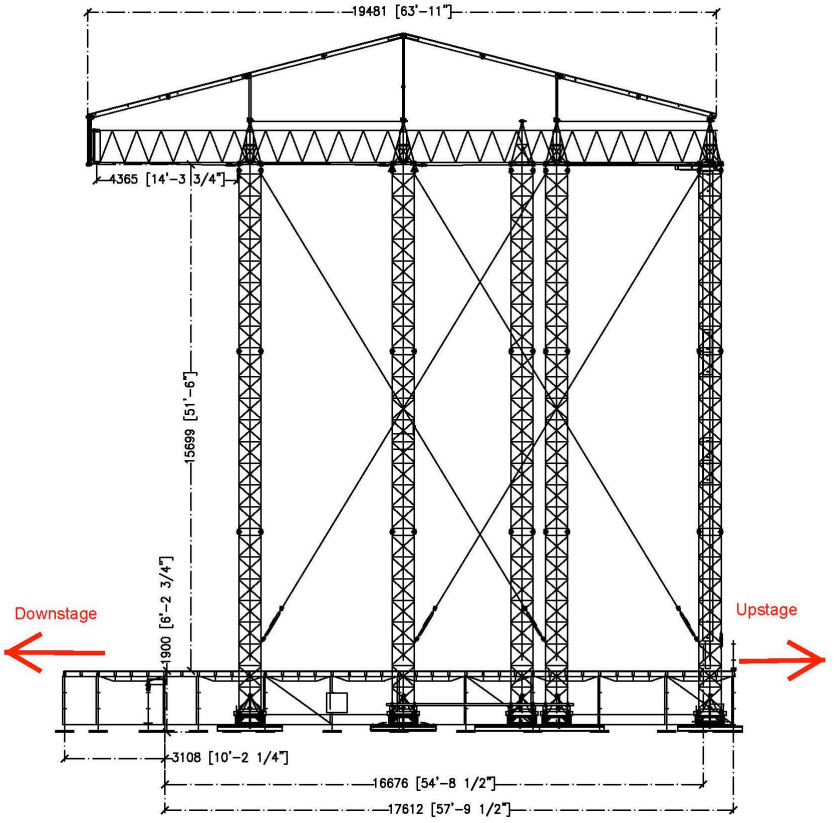


Figure 3. Touring Stage- Side Elevation

The stage is a temporary structure that is not in one venue for more than a week. SEI/ASCE 37-02, "Design Loads on Structures during Construction" provides reduction factors for "construction periods". For a "construction period" of less than 6 weeks the basic wind speed from ASCE/SEI 7 is multiplied by 0.75. Occasionally, stage structures are erected as a seasonal venue to be used for performances by different acts over the period of several months. The factor for these structures is 0.8. The reduced construction load is considered to have the same probability for a temporary structure as the non-hurricane 1 in 50 year return storm. However, the structure must be evaluated for the rigging load for each show.

BRACING

The trussed tower legs are slender elements and provide negligible lateral resistance. A pair of 16mm (5/8in) or 20mm (3/4in) diameter X-bracing cables is provided in the upstage face of the structure and multiple sets are provided in the upstage/downstage walls. These deliver the lateral load to the stage deck level. Similarly, the scaffolding legs are too slender to provide lateral resistance so an array of diagonals in the stage scaffolding delivers the load to grade.

SLIDING & OVERTURNING

The rigging loads are not distributed uniformly over the structure. The majority of the loads are hung from the downstage third of the structure with the speakers and often video walls on the downstage face. Additionally, the roof cantilevers over the downstage legs, so lighting trusses and effects hung on the front edge add substantial load to the downstage legs. With wind from upstage, the compression load on the downstage legs can reach 170kN (38k), with uplift forces on the upstage legs. To resist these vertical reactions, coupled with the lateral loads that are delivered primarily to the upstage and downstage legs poses an interesting challenge.

Often ballast is required to resist both sliding and uplift. A factor of safety of 1.5 is used in calculating the required ballast, however the coefficient of friction, μ, used for calculating sliding resistance varies depending on the surface conditions. Additionally, since the structures are supported on grade on either natural or artificial turf, the load has to be distributed so that the soil capacity is not exceeded. Therefore the tower loads and the ballast loads need to be distributed among the tower legs. Ballast is generally provided by concrete road barriers, concrete blocks, or tanks of water. Steel frames or beams are often required at grade to connect the tower bases and distribute load. In lieu of ballast, soil anchors are also employed.

Several stage systems have water tanks integrated into the base frame design. Other systems have heavy steel base frames. The lightweight tanks are shipped with the structure and filled with water during assembly. Concrete ballast is usually procured locally at each venue to eliminate shipping costs. Ballast required for an event varies between 40 and 196kN (9 and 44k).

Touring stages are used inside of stadia as well as in open outdoor venues. Although a stadium provides a measure of protection against wind, each condition is unique and requires analysis of wind from all directions.

WIND MANAGEMENT PLAN

Touring stages are primarily used during the summer months. On the east coast, however, the summer months coincide with hurricane season. Per ASCE/SEI 7, the design wind speed along most of the coast is as high as 150mph. Numerous major east coast cities including Miami, Washington DC, New York, and Boston are along this hurricane coastline and are popular destinations for concert tours.

A fully clad structure (See Photo 1 and Photo 2) is not capable of resisting hurricane force winds. Fortunately, current technology and weather forecasting are able to provide early warning of impending hurricanes. Various measures can be taken in anticipation of an extreme wind event in order to mitigate the effects on the structure. We provide the production team with a “Wind Management Plan” which defines

measures to be taken at various increasing wind speeds to protect the structure, the equipment, the personnel, and the audience.



Photo 1. Touring Stage- Fully Clad Stage with Sound and Video Wings

In addition to hurricanes, major thunder storms with strong winds are very common in the summer months. These storms often come with very little warning. The use of an anemometer, strategically placed at the top of the structure, provides accurate wind speed readings which are necessary for properly implementing the plan.

The structure is analyzed for the service condition, with all enclosure "skins", scenic panels, and suspended equipment in place, for wind gusts of up to 40mph. For the maximum design wind speed of 67.5mph (0.75x90mph) the structure is analyzed with only its self weight and significantly reduced rigging load.

The Wind Management Plan is outlined specifically for each show and each site and accounts for the rigging load distribution and the ballast. An example from one show is as follows:

Elements and components must be removed, stowed or secured as wind speed increases. The following must occur to maintain a safe condition. Items are listed in order of importance.

<u>Wind gusts approach 35 mph:</u>

Back wall skins or scrim in the PA wings are to be lowered and removed.
Main stage back wall skins are to be lowered and removed.
All side wall skins or scrim are to be lowered and removed.

Wind gusts approach 40 mph:

All video walls are to be lowered to the stage deck and secured.
All scenic trusses are to be lowered to the stage deck and secured.
PA stacks should be lowered to the deck and secured.
LED walls should be lowered to the deck, dismantled, and secured.

Storms with wind gusts expected in excess of 67.5 mph:

The stage structure without sidewalls and suspended equipment can resist design wind events with gusts to 67.5 mph. In the event of a severe storm forecast with potential winds in excess of 67.5 mph, the stage structure should be dismantled. In the event that it is impractical to dismantle the structure, efforts should be undertaken to secure whatever structure cannot be removed against severe wind. In no instance should the structure be occupied during a severe wind event. To the greatest extent feasible all cladding, skins, roof, and decking should be removed and stowed inside a building. The structures should be temporarily guyed or secured as is feasible.



Photo 2. Touring Stage- Fully Clad Stage with Sound Wings

Fortunately, in the event of an impending hurricane concerts are customarily cancelled. Above a wind speed of about 67.5mph (0.75 x 90mph) the concern is for protecting and securing the stage and equipment. The structure should not be occupied during a severe wind event. The structure is analyzed at each of these wind speeds to account for the different clad area and load for each condition.

CONCLUSION

Stages and show configurations vary widely and must be analyzed individually for the jurisdiction in which they are employed. Resulting forces from overturning from wind is a critical load case for these structures and often requires the addition of ballast. The monitoring of environmental loads, especially wind, is a design requirement necessary to define measures to be implemented to prevent overstress of the structure.

REFERENCES

ASCE/SEI 7-05, "Minimum Design Loads for Buildings and Other Structures", Published by American Society of Civil Engineers

ASCE/SEI 37-02, "Design Loads on Structures during Construction", Published by American Society of Civil Engineers

"Portfolios." *Stageco.* Web. 01 Jan. 2011. <http://www.stageco.com/us-en/references/category/36>.

UNDERSTANDING WALL/SLAB BENDING MOMENT AND SHEAR TRANSFER IN LIQUID CONTAINING STRUCTURES

Almanzar-Micheli, Leonel I. PhD, PE[1]
Morris, Jordan MSCE, EIT[2]

[1]CDM, 4835 East Cactus Road, Suite 360, Phoenix, AZ 85254. PH (602)281-7856, email: almanzarli@cdm.com

[2]CDM, 4835 East Cactus Road, Suite 360, Phoenix, AZ 85254. PH (602)281-7924, email: morrisjl@cdm.com

ABSTRACT

During structural design of reinforced concrete liquid containing structures, it is very important to visualize how shear and moments are transferred from the wall to the foundation slab. This article presents simple explanations to understand the behavior of the shear/moment connection in reinforced concrete tanks. This includes figures and sketches to aid engineers in properly locating reinforcement, splices, and hook requirements. The proper reinforcement location, taking into account the development of the stresses transferred, is one of the most important detailing challenges in liquid containing structures in order to avoid crack formation and potential leaking. Using the tips and explanations presented, the engineers will be able to minimize cracking in the connection, as well as to understand the structural behavior of the wall/slab joint of liquid containing structures.

INTRODUCTION

Liquid containing structures' joints shall be designed to transfer loads through joint while remaining water tight. Specifically, the joint between the wall and the slab shall be properly detailed in order to obtain these objectives. Detailing mistakes at this location are commonly made and can easily be avoided. For the entirety of this paper the boundary condition between the wall and slab will transfer both shear and bending (fix connection) stresses.

Two scenarios are often encountered, interior water loading (opening moment) and exterior soil loading (closing moment). Each of these scenarios poses similar detailing challenges. In order to meet these challenges understanding stress transfer is critical. To gain insight to the behavior of these stresses a simple three dimensional solids elastic finite element model was developed in ANSYS 11.0. The wall and slab were modeling using SOLID65 solid elements. Both, opening and closing moment were applied to the joint and the stresses contours are shown in Figures 1, 2 & 3. This model represents un-cracked concrete condition at low stresses. When the concrete cracks, the strain field is disrupted, causing redistribution of the internal forces. Using finite element model to understand where the elastic internal

forces are developed, a simple truss analogy system has been developed for the cracked concrete (Figure 4). By using this truss analogy, it is assumed that the stress does not vary linearly through the joint.

The Y & Z normal stresses in Figure 1 & 2 illustrate the tension and compression regions within the concrete. Y normal stress illustrates the location for the wall reinforcement. Z normal stress illustrates the location for the base slab reinforcement. The YZ shear stress illustrates the transition of normal and shear stresses within the joint. As the normal stress propagate toward the center of the joint, they are transformed into shear stress, as the shear stress propagates away from the center of the joint, the stress are transformed into orthogonal normal stress.

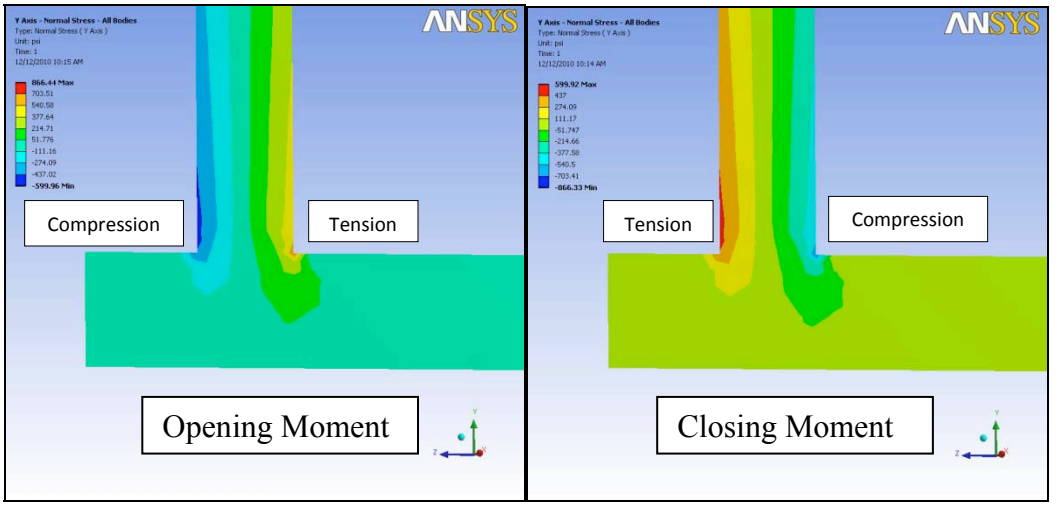


Figure 1. Y Normal Stresses

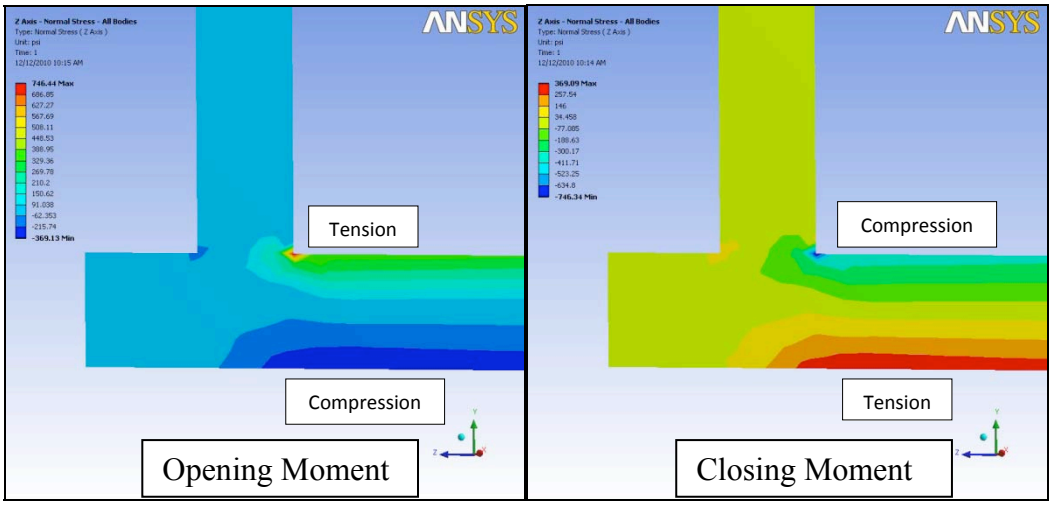


Figure 2. Z Normal Stresses

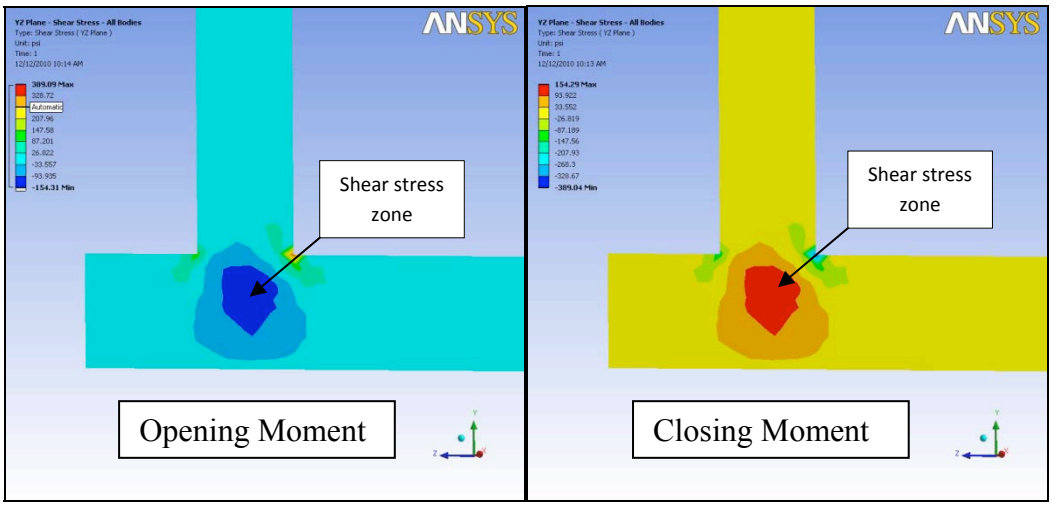


Figure 3. Shear Stress

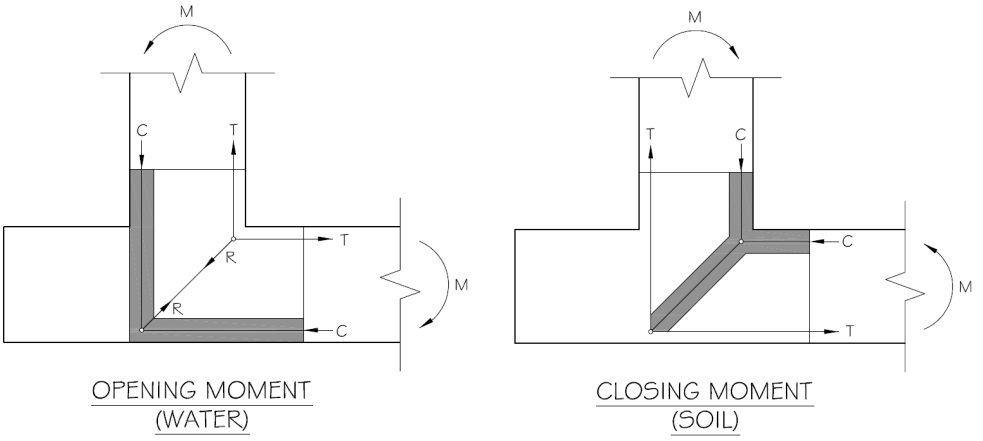


Figure 4. Truss Models

MOMENT AND SHEAR TRANSFER

Strength requirements for transfer of forces to the base slab through the joint shall be satisfied, rotation and deflection shall be minimized in order to prevent non desirable cracks, and bearing pressure shall be minimized to prevent excessive settlement. To investigate how some of these parameters affect the design, several finite element plate models were developed (Figure 5). The height of the wall and applied lateral load were held constant. In each of the models the toe length was then

varied. The results for the opening and closing moments in the slab are shown in (Figures 6 & 7). These plots clearly show that the moment that is transferred to the slab when there is no toe is approximately equal in magnitude to the base moment of the wall. For both scenarios the moment decreases as the toe is increased. This distribution is a function of both the wall/slab stiffness and the soil stiffness. Once the toe length reaches some distance the moment in the base slab should be approximately one half of the wall moment. A second advantage of toe length increase is a decrease in wall rotation and deflection (Figure 8). This decrease in rotation and deflection is also accompanied by a decrease in bearing pressure.

Often the wall and slab are casted in two separate pours that create a construction joint. Conventional shears capacities per ACI 350-06§11.3 are analyzed at a distance "d" from the joint in order to verify whether the wall has adequate shear capacity. The base shear is checked using the shear friction equation in accordance with ACI 350-06§11.7.4. There is often confusion on how the bending affects the shear friction, detailed explanation is included in ACI 350-06§R11.7.7. Usually, it is not necessary to provide additional reinforcement to resist the shear by friction. The flexural tension reinforcement is located in one face of the wall and the compression reinforcement located in the other face can be used for the shear friction transfer. Once the base shear is transferred through the joint it is transferred to the base slab as either a tension or compression. Globally this shear is satisfied by an equal and opposite lateral force from the opposite wall. Internally, in order for the global equilibrium to be satisfied the tension is resisted by the slab reinforcement. Often two mats of reinforcement are placed in the base slab and only one face of the mats is being utilized for bending. Therefore the other mat can resist the tension values, so that these tension and compression values are often ignored.

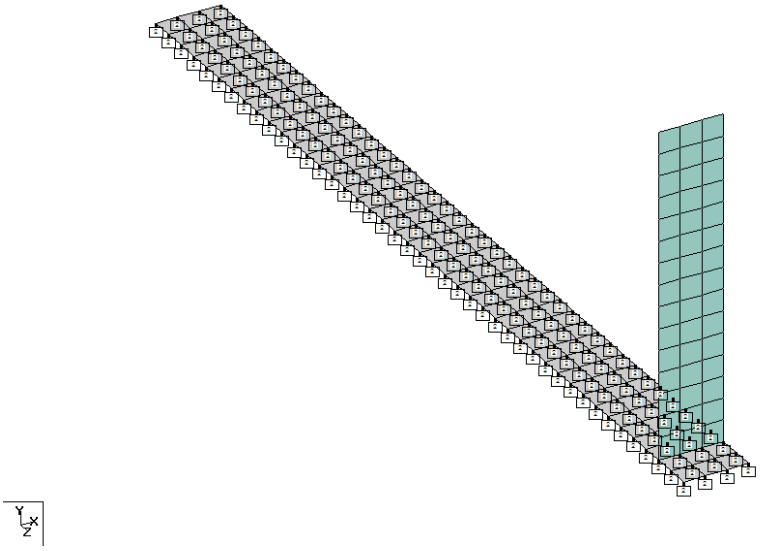


Figure 5 – Plate Model (STAAD)

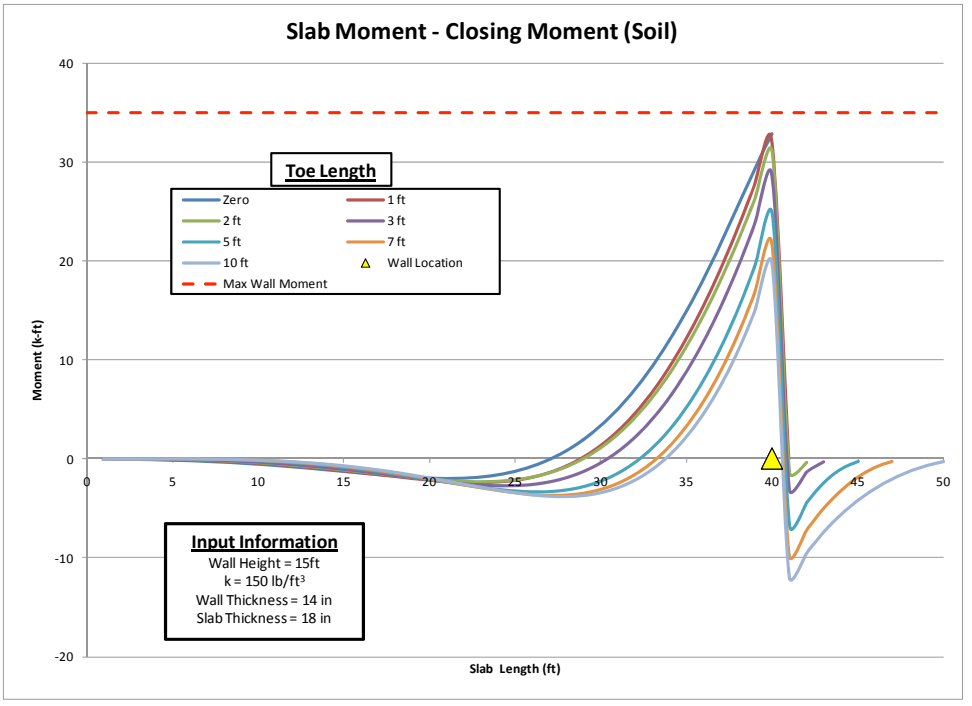


Figure 6 Slab Moment (Soil)

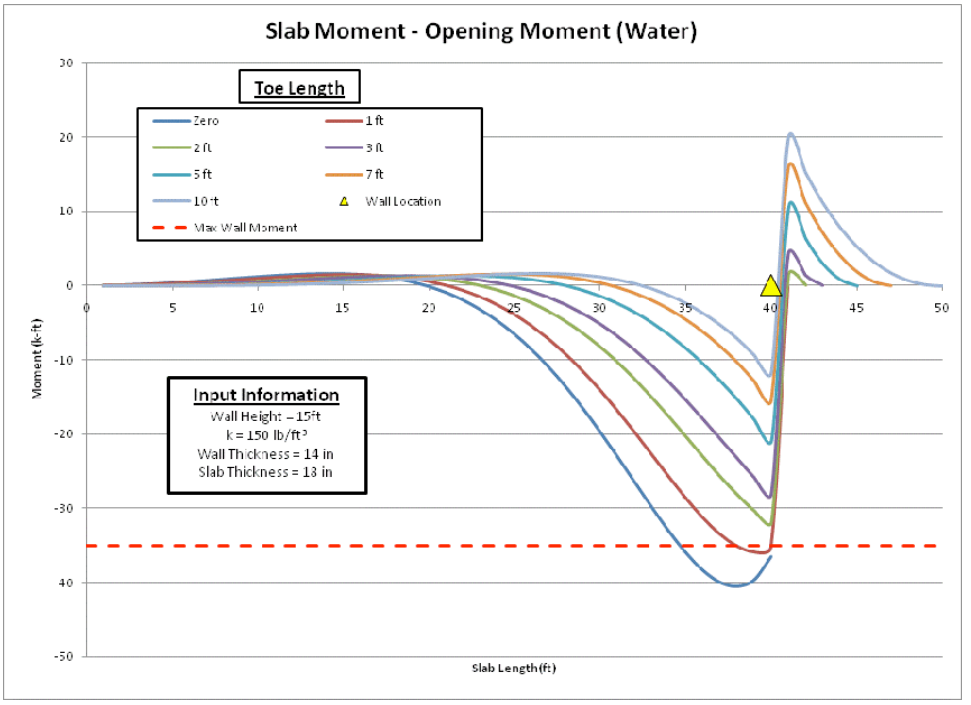


Figure 7. Slab Moment (Water)

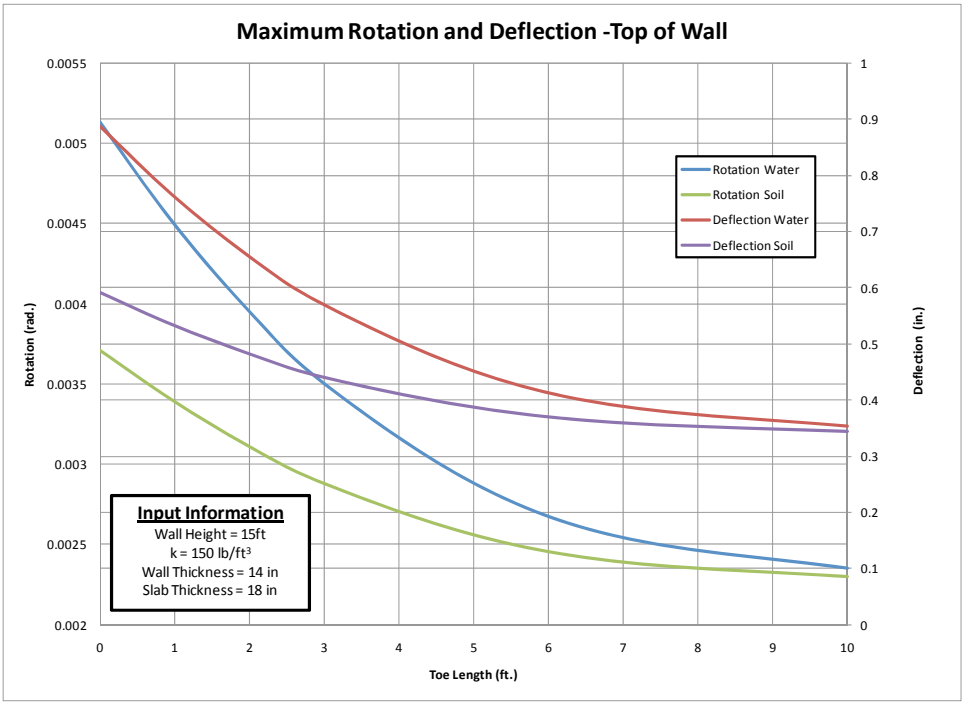


Figure 8. Maximum Rotation and Deflection

JOINT DETAILING

When detailing the reinforcement of the joint the designer's primary objective is to provide reinforcement for strength and cracking control. The design includes determining wall and slab thicknesses and reinforcement. Having done the design, the next objective is to insure proper reinforcement and anchorage detailing. Proper detailing includes reinforcement development and hook requirements for anchorage of reinforcement. All development and hook lengths shall be determined in accordance with ACI 350-06 Chapter 12. See Figure 9 for typical reinforcement details for opening and closing moments.

Using Figure 4, reinforcement is laid out in the tension zones of the wall and slab. This reinforcement is sized and spaced based on the bending moments at the base of the wall. When determining the reinforcement required in the base slab, it was shown in Figures 6 & 7 that the bending moment transferred to the base is approximately equal to the bending moment in the wall (this applies for most scenarios). The bending moment capacity of the base slab shall not be less than moment capacity of the wall. Reinforcement spacing shall be minimized to minimize cracking formation; ACI 350-06 has stringent stress limits and uses a durability factor (ACI 350-06§9.2.6) to account for the serviceability requirements in water containing structures. It is common practice to space smaller bars at a tighter spacing.

The tension reinforcement must have adequate anchorage /development. It is critical when determining the development length to understand where the

development starts. Development typical begins at the cracked section or the joint face. In Figure 9, it is assumed that the development for the reinforcement begins where the orthogonal reinforcement will first intersect the crack. The cracked section is assumed to be 45 degrees across the joint. The base slab thickness needs to at least be thick enough to develop the wall reinforcement and the toe shall be long enough to develop the base slab reinforcement.

The use of starter wall in figure 9 is to serve as a means to avoid conflict between the base slab reinforcement and the waterstop. Typical the starter wall height is between 1.5-3.0 inches, waterstop height is 4-9 inches and clear cover 2-3 inch. In lieu of a starter wall there are several other options, e.g., shear key, mounded base (used for thicker walls), or increased clear cover on base slab reinforcement.

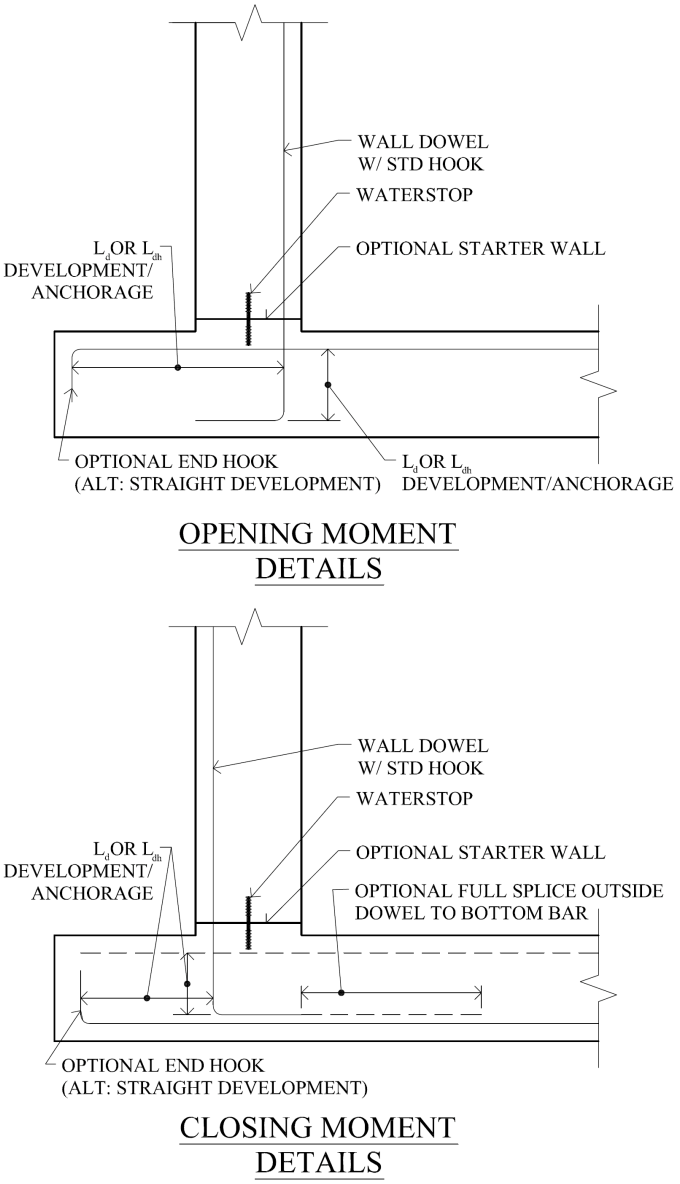


Figure 9. Typical Reinforcement Details

SUMMARY

One of the most critical tasks in water containment structures is preventing cracking. It is concretes nature to crack. By understanding how the bending moment and shear are transferred through the base slab and wall connection allows for proper detailing and analyses which lead to fewer failures. The presented details provided are example only; each structure shall be carefully analyzed for its associated loading conditions. It is also important to consider that there are several slab/wall connections used throughout the industry with success.

Typical guidelines for joint detailing:

1. Assume the opening or closing moment transferred from the wall to the base slab is at least the same in magnitude as the wall base moment.
2. Thickness of base slab and toe lengths must accommodate development lengths, hooks and clear covers.
3. The thickness of the base slab shall be no thinner than the wall thickness.
4. The toe width shall be at least the wall thickness or longer.
5. Check clearances for waterstops.
6. Space smaller bars at closer spacing.

The designer shall account for the stiffness interaction between the wall, base slab and soil, in order to properly predict the stresses transferred from the wall to the slab. The designer shall also carefully select the proper loading conditions in the structure, leading to an opening moment design, closing moment design, or both.

REFERENCES

American Concrete Institue. (2006). *Code Requirements for Environmental Engineering Concrete Structures and Commentary, ACI 350-06.* Farmington Hills, MI.

ANSYS Academic Research, v.11.0. (2008).

Boresi, A. P., & Schmidt, R. J. (2003). *Advanced Mechanics of Materials.* Hoboken: John Wiley & Sons, Inc.

Johansson, M. (2001). Reinforcement Detailing in Concrete Frame Corners. *ACI Structural Journal* , 105-114.

Nilson, A. H., Darwin, D., & Dolan, C. W. (2004). *Design of Concrete Structures.* New York: McGraw-Hill .

Nilsson, I. H., & Losberg, A. (1976). Reinforced Concrete Corners and Joints Subjected to Bending Moments. *Journal of the Structural Divison* , 1229-1253.

STAAD Pro. (2007). *Research Engineers.* Bentley.

On the Application of the Meck Plot in Elastic Buckling

Tadeh Zirakian

Ph.D. Student, Department of Civil and Environmental Engineering, University of California, Los Angeles, CA 90095-1593; PH (818) 522-5997; email: tzirakian@ucla.edu

ABSTRACT

The Meck Plot is an adapted version of the well-known Southwell method for determining experimentally the critical load of a structure undergoing lateral-torsional buckling. It has been demonstrated that lateral displacement and rotation are directly coupled when lateral-torsional buckling occurs. Recently, it has also been interestingly shown that lateral displacement of an I-beam undergoing lateral-distortional mode of buckling is directly coupled with the web transverse strain, and satisfactory results have been obtained as a result of application of the Meck's method on these deformation variables. In this paper, one further step is taken in this regard and it is shown that web transverse strain may even be used with either web longitudinal strain, vertical deflection, or angles of twist of top and bottom flanges of an I-beam undergoing lateral-distortional buckling and still good results be obtained as a result of application of the Meck Plot on each pair of these deformation variables.

INTRODUCTION

In 1977, Meck (Meck 1977) proposed an extrapolation technique for experimental determination of the buckling load in problems of lateral-torsional buckling. He believed that it is necessary to consider both lateral displacement (δ_L) and rotation (ϕ) of the section in lateral-torsional buckling mode. Of course, later on, Mandal and Calladine (Mandal and Calladine 2002) showed that lateral displacement tends to be proportional to rotation as deformations increase in case of lateral-torsional buckling. Meck suggested to make a plot of (ϕ/M) against δ_L, and another of (δ_L/M) against ϕ; and that the respective slopes of the straight-line portions of these two plots will be $1/\alpha$ and $1/\beta$, and consequently M_{cr} will be the geometric mean of the slopes of the two plots (Eq. (1)).

$$M_{cr} = (\alpha\beta)^{0.5} \tag{1}$$

Recently, in an experimental study on the lateral-distortional buckling of I-beams (Zirakian 2008), it was revealed that in this mode of buckling, lateral displacement tends to be proportional to web transverse strain as deformations increase, and on the basis of this finding, reliable predictions were obtained for the critical buckling load as a result of application of Meck's method on δ_L and ε_T.

In this paper, a further step is taken in this regard and the possibility of application of the web transverse strain in I-beams undergoing lateral-distortional buckling with other deformation variables such as web longitudinal strain (ε_L), vertical deflection (δ_V), and angles of twist of top and bottom flanges (θ_{TF} and θ_{BF}) is explored. Accordingly, the relationship between web transverse strain (ε_T) and the aforementioned deformation variables is initially investigated, and subsequently the Meck Plot method is applied on each pair of these deformation variables which are also shown in Table 1.

Table 1. Case studies and the deformation variables.

Case	$d.v.1$ *(first deformation variable)*	$d.v.2$ *(second deformation variable)*
1	web transverse strain (ε_T)	web longitudinal strain (ε_L)
2	web transverse strain (ε_T)	vertical deflection (δ_V)
3	web transverse strain (ε_T)	angle of twist of top flange (θ_{TF})
4	web transverse strain (ε_T)	angle of twist of bottom flange (θ_{BF})

DETAILS OF ANALYSIS

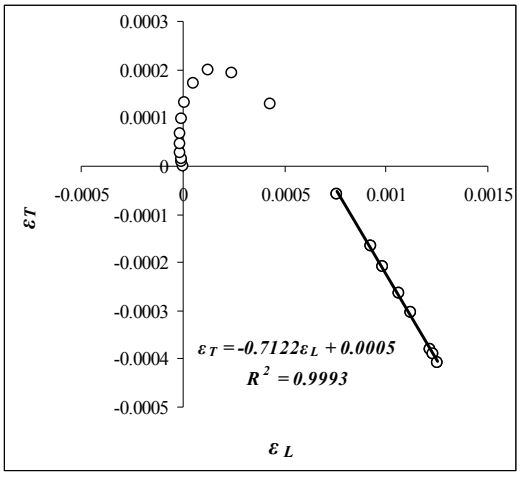
ABAQUS software (ABAQUS 2005) is used to develop lateral-distortional buckling solution and the cross-section components of the I-beam are modeled using the S4R5 shell element. The various deformation variables are captured at the midspan of a simply-supported I-beam loaded in uniform bending with dimensions $h_w = 900$ mm, $b_f = 240$ mm, $t_w = 5$ mm, $t_f = 20$ mm, and $L = 7000$ mm.

In addition, geometric nonlinear and linear elastic material analysis solutions are conducted on the beam with half sinusoidal curvature and twist as initial geometrical imperfections. The initial lateral crookedness and twist at the center of the beam are chosen as follows: (1) $\delta_{Loc} = 20$ mm and $\delta_{Voc} = 20$ mm; and (2) $\phi_{oc} =$ 0.04363 rad.

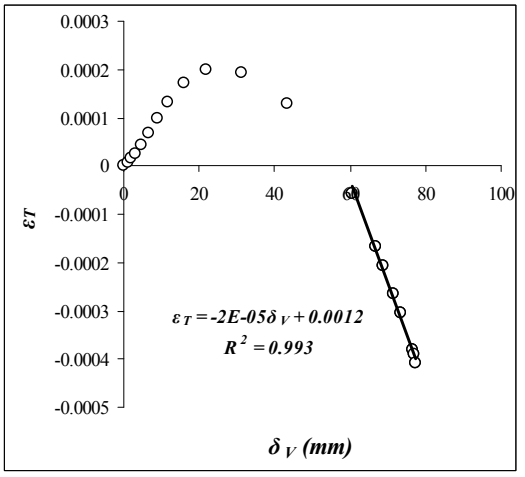
RELATIONSHIP BETWEEN DEFORMATION VARIABLES

In this part of the study, web transverse strain ($d.v.1$) is straightforwardly plotted against other deformation variables ($d.v.2$) and the respective plots of the four considered cases are provided in Figure 1. The linear equations obtained using

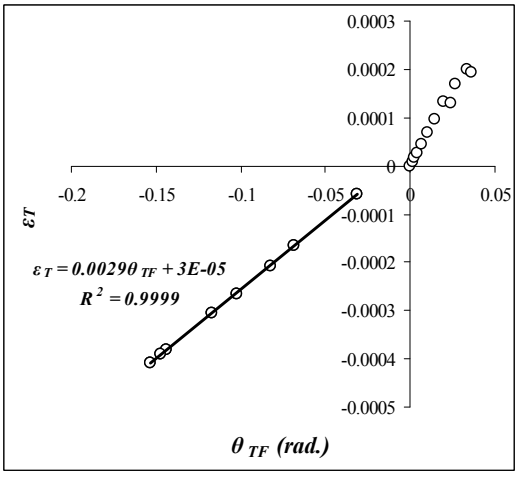
the least squares method as well as the respective R-squared values are also displayed in the figures.



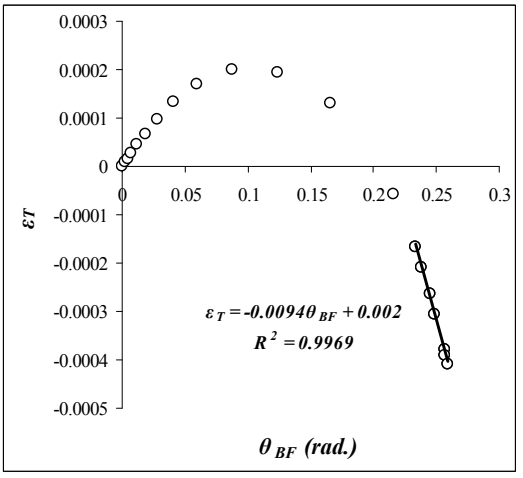
(a) ε_T vs. ε_L



(b) ε_T vs. δ_V



(c) ε_T vs. θ_{TF}



(d) ε_T vs. θ_{BF}

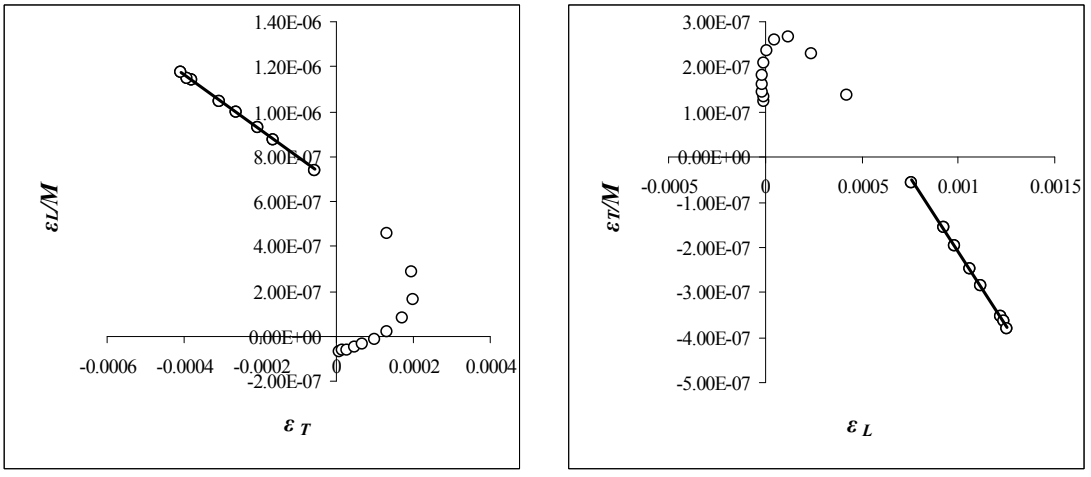
Figure 1. Relationship between deformation variables.

As it is seen in the figures, the data points in all cases, apart from the initial few, eventually lie on straight lines, which is indicative of proportionality between web transverse strain and the other considered deformation variables.

Based on these proportionality findings, it is now logical to apply the Meck Plot method and confidently expect to obtain reliable predictions for the critical buckling moment.

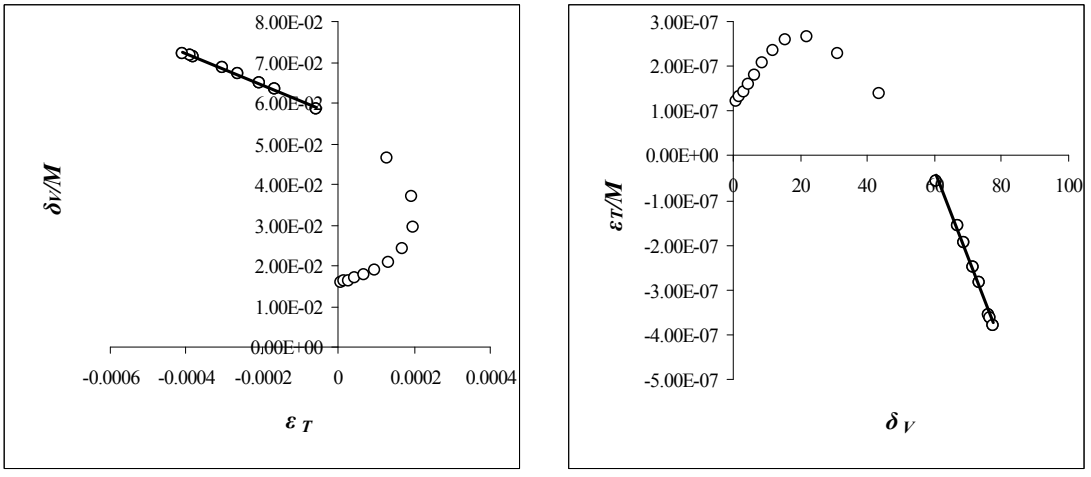
APPLICATION

In accordance with Meck's prescription, plots are made of $d.v.2/M$ versus $d.v.1$ and of $d.v.1/M$ versus $d.v.2$ for the four considered cases, which are shown in Figures 2 to 5.



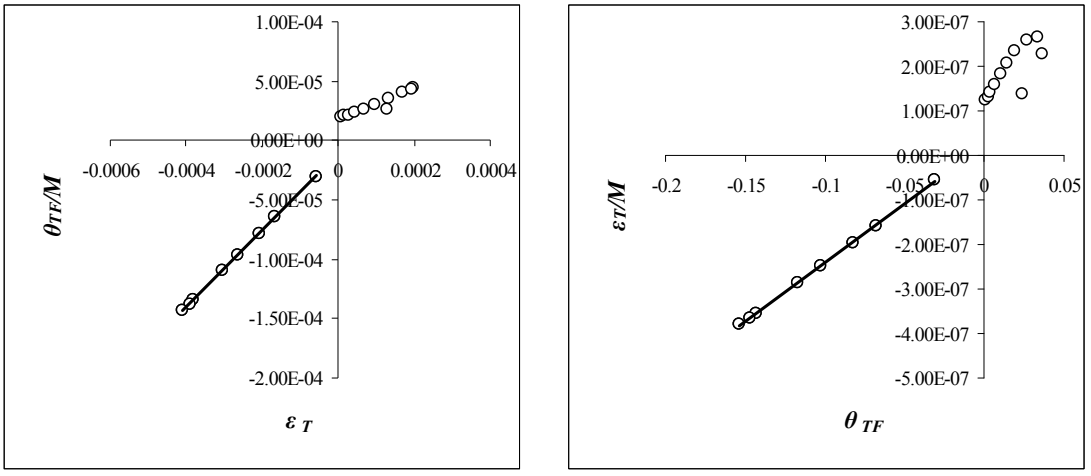
(a) *(b)*

Figure 2. Plots of ε_L/M against ε_T and ε_T/M against ε_L.



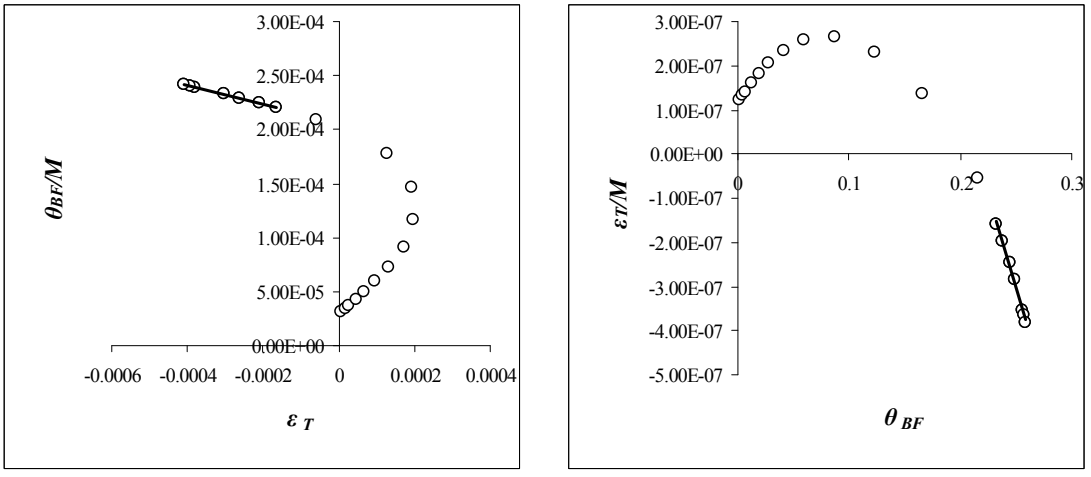
(a) *(b)*

Figure 3. Plots of δ_V/M against ε_T and ε_T/M against δ_V.



(a) *(b)*

Figure 4. Plots of θ_{TF}/M against ε_T and ε_T/M against θ_{TF}.



(a) *(b)*

Figure 5. Plots of θ_{BF}/M against ε_T and ε_T/M against θ_{BF}.

As it is seen in the figures, the points in all cases tend to eventually lie on a straight line, and according to Eq. (1), the product of the inverse slopes of the straight-line portions in the two aforementioned plots is equal to the square of the critical moment. The values of α and β, Meck Plot predictions as well as the ultimate failure moment are summarized in Table 2.

Table 2. Values of α and β, Meck Plot predictions, and the ultimate failure moment.

Case	α	β	M_{Meck} (kN.m)	M_u (kN.m)
1	-833.3	-1,428.571	1091.09	1072.63
2	-0.026	-50,000,000	1146.05	1072.63
3	3.105	333,333.3	1017.29	1072.63
4	-11.834	-111,111.1	1146.70	1072.63

In spite of some scatter in the results due to application of various deformation variables, it can be seen from the table that the extrapolated moments are in good agreement with the ultimate failure moment. These findings indicate that the applicability of the Meck Plot method for experimental determination of the critical buckling loads of structures does not really need to be limited to the use of certain deformation variables, since other *directly-coupled* deformation variables may yield similar and acceptable predictions as well.

CONCLUSION

It was demonstrated that web transverse strain in I-beams undergoing lateral-distortional mode of buckling is linearly related with other deformation variables including the web longitudinal strain, vertical deflection, and angles of twist of top and bottom flanges. On this basis, Meck's plotting method proposed for lateral-torsional buckling mode was extended to the lateral-distortional mode, and consequently good predictions were obtained in all considered cases as a result of application of Meck Plot on the two deformation variables of each individual case.

REFERENCES

ABAQUS (2005). *ABAQUS Analysis User's Manual*, Ver. 6.5.

Mandal, P., and Calladine, C. R. (2002). "Lateral-torsional buckling of beams and the Southwell Plot." *Int. J. Mech. Sci.*, 44, 2557-2571.

Meck, H. R. (1977). "Experimental evaluation of lateral buckling loads." *Proc., J. Eng. Mech. Div.*, ASCE, 103, 331-337.

Zirakian, T. (2008). "Lateral-distortional buckling of I-beams and the extrapolation techniques." *J. Constr. Steel Res.*, 64(1), 1-11.

NOTATION

b_f flange width

h_w distance between flange centroids
L length of beam
M applied major axis end moment
M_{cr} critical value of M
M_{Meck} extrapolated critical moment obtained from Meck Plot
M_u ultimate failure moment
R Pearson product moment correlation coefficient
t_f flange thickness
t_w web thickness
α reciprocal slope of the straight-line portions of plots of $d.v.2/M$ versus $d.v.1$
β reciprocal slope of the straight-line portions of plots of $d.v.1/M$ versus $d.v.2$
δ_L lateral displacement of the beam, measured at midspan
δ_{Loc} initial lateral displacement (*i.e.* imperfection) at the center of the beam
δ_V vertical (in-plane) deflection of the beam, measured at midspan
δ_{Voc} initial vertical displacement (*i.e.* imperfection) at the center of the beam
ε_L web longitudinal strain, measured at mid-height and midspan
ε_T web transverse strain, measured at mid-height and midspan
ϕ rotation of the section in lateral-torsional buckling mode
ϕ_{oc} initial rotation (*i.e.* imperfection) at the center of the beam
θ_{BF} angle of twist of bottom flange, measured at midspan
θ_{TF} angle of twist of top flange, measured at midspan

A New Approach to Office Construction: Deacero Headquarters, Monterrey, Mexico

Anton Nelson PE[1], Brendan McPhail[1], Elliot Weinstock EIT LEED®AP[1], Juan Porral RIBA[2]

[1]Dewhurst Macfarlane and Partners PC, 45 E20th St, New York, NY 10003; PH (212) 375-1600; email: anton.nelson@dewmac.com
[2]Grimshaw Architects PC, 637 W27th St, New York, NY 10013; PH (212) 967-8790; email: juan.porral@grimshaw-architects.com

ABSTRACT:

The new Deacero Headquarters in Monterrey, Mexico is a building focused on the changing world. The building was designed and engineered in a holistic fashion around two central tenents- flexibility and sustainability- while presenting it in a cutting edge architectural form.

The structure was developed to maximize flexibility of the space. The structure was designed on a 17m x 17m (56 ft. x 56 ft.) column grid without the use of internal columns or bracing. All bracing is accomplished through a unique Vierendeel Truss framing system.

The dry, hot environment of Monterrey presented a number of challenges to the façade system. To minimize heat gain on the structure, a sophisticated façade and louver system was developed.

Some of the interior architectural features, namely a very slender elevator support frame, presented a challenging structural problem. These features required careful consideration of the analysis and the design to fully capture its architectural intent.

The building has an extensive and sophisticated water management system that allows the building to be highly sustainable in a hot, dry environment. The system employs on-site water reclamation, bio-treatment and water recycling strategies. All of this results in a surplus of water which can be returned to the city.

INTRODUCTION:

After the successful completion of the Museo de Acerco in Monterrey, Mexico, Deacero S.A. de C.V. retained Grimshaw Architects of New York to design a new headquarters building for them. Grimshaw in turn retained Dewhurst Macfarlane and Partners, also of New York, to provide structural and façade engineering services.

Dewhurst Macfarlane worked closely with Grimshaw to develop a concept scheme and design criteria for the main structure as well as design development level drawings for some of the architecturally demanding elements. Dewhurst Macfarlane stayed involved in a design assist capacity through the completion of construction documents to ensure that that the engineer of record, GPI y Asociados of Mexico City, maintained the design intent laid out by the Grimshaw-Dewhurst Macfarlane team. Additionally, the construction documents of the façade were prepared by Dewhurst Macfarlane.



Figure1 – ExteriorView

Deacero is one the leading producers of steel wire and wire products in the world. The company, which is increasing their environmental stewardship, wanted their new building to reflect this growing commitment and be a showcase of sustainable building design in Mexico. The new building would form a new addition to their expanding corporate campus on the outskirts of Monterrey.

The new buildings would occupy a 68m x 68m (225-ft x 225-ft) footprint with 4 levels of subgrade parking and a 4-story, 10,500m^2 (120,000 SF). U-shaped building above grade. The program also included a 1,150m^2 (12,500 SF), enclosed atrium.

THE STRUCTURE:

To facilitate a modern office environment and allow for the possibility of leasing the building in the future, the offices needed to be as flexible as possible. Dewhurst Macfarlane was involved with Grimshaw at the earliest stages of concept design to

provide engineering and design input to vet and refine the architectural concepts as they were developed by the architects.

The design team quickly migrated towards a design which displayed many of the aspects of a classic modernist style in the tradition of Ludwig Mies van der Rohe. Interestingly, Dewhurst Macfarlane had completed the design for a much smaller structure with similar proportions for the Boston Logan 9-11 Memorial several months earlier.

The Logan 9-11 Memorial was a 6m (20 ft) cube. The architect for that project, Moskow Linn Architects of Boston, Massachusetts, wanted a structure that had very slender columns with no cross bracing. The small scale of that project allowed Dewhurst Macfarlane to investigate a large number of possible design solutions that would fit within the architectural desire. In the end, a Vierendeel frame was recommended for the memorial structure. For a variety of reasons, the memorial structure was completed using a different structural system, but it did give Dewhurst Macfarlane valuable insight into alternative framing systems, one of which would be used on the Deacero Headquarters.

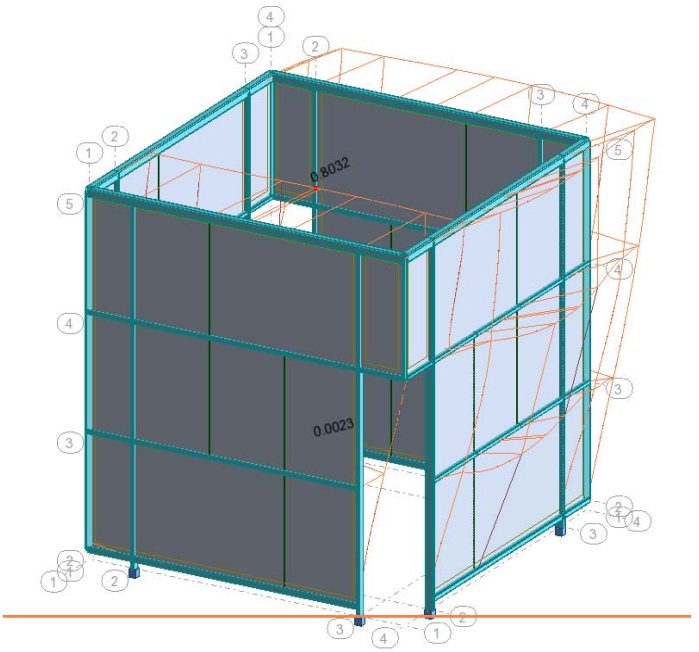


Figure 2 - Model of Logan 9-11 Memorial Model

Like the Logan 9-11 Memorial design (Figure 1), Dewhurst Macfarlane was privileged to work with an architect who was looking for an innovative design solution. Looking back on our recent experience, Dewhurst Macfarlane recommended an external Vierendeel frame for the bracing of the upper three floors and a traditional shear wall for the ground level. Besides providing lateral bracing, the Vierendeel frame also helped reduce the weight of the edge girders which carried the floor beams.

The Vierendeel frame allowed for a structure which was laid out on a 17m by 17m (55-ft x 55-ft) grid with no internal columns. This is one of the inherent and least pronounced sustainable aspects of the building. The large open floor plate allows for maximum flexibility in future use and planning. Floor beams where spaced at 3.4m which allows for future stairs and elevators to be cut in with a minimum amount of

structural modification in the future. The lack of internal bracing and a pronounced core allows for rooms with required fixed walls such as bathrooms and conferences rooms to be rearranged in the future without impacting occupiable space and architectural layout. In the end, the office floors exhibited a near 100% floor utilization factor and a 100% floor utilization factor if the full flexibility in installation of fixed rooms is taken into account.

To verify that the building performed adequately compared to a traditional structure, a number of parametric studies were done to compare the Vierendeel frame to a traditional structure with braced and moment frames. This comparison was not based purely on building performance but also on structural weight savings. As can be seen in Table 1, the Vierendeel system is comparable or superior in performance to other structural systems. Additionally, based on preliminary estimates, there was about a 50% steel reduction in using the Vierendeel scheme over a traditional moment frame.

Table 1. Comparison of different framing options examined. Framing options are shown in Figure 3.

	Deflection mm (in)	H/XXX
DHQ-Baseline	29.7 (1.169)	354
DHQ-X Brace	20.7 (0.815)	508
DHQ-1	28.4 (1.118)	370
DHQ-2	18.5 (0.731)	566
DHQ-3 (preferred scheme)	14.3 (0.562)	737

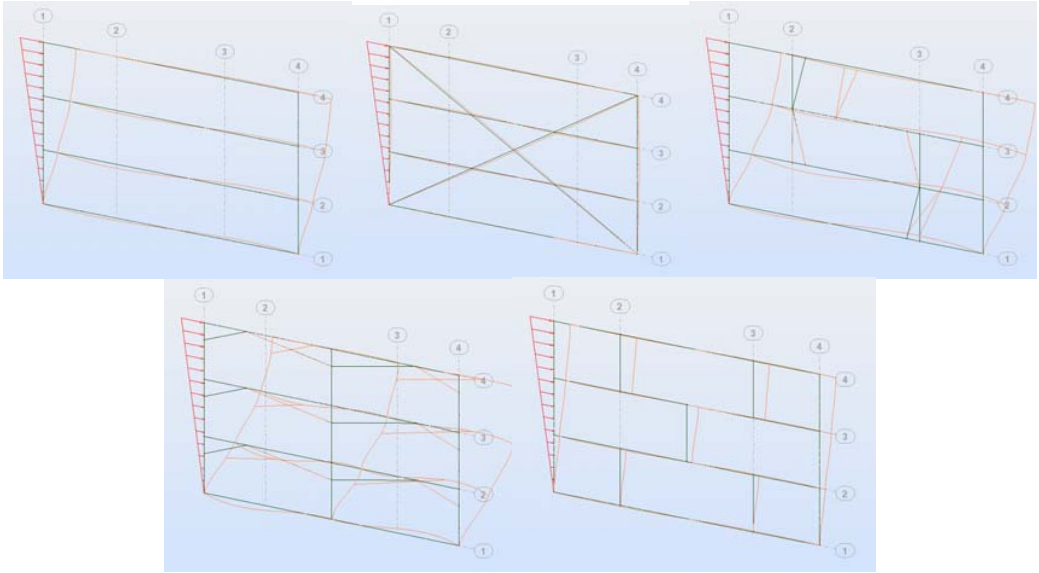


Figure 3. Five framing options compared in Table 1. Clockwise from top left: DHQ-Baseline, DHQ-X Brace, DHQ-1, DHQ-2, DHQ-3

The hardest aspect of designing the Vierendeel frame is a problem inherent in all frame structures- in order not to overstress the structural elements, they need to get larger, and as they get larger, they become stiffer and hence attract more load, which in turn causes them to get even larger, and the cycles continues until you have a

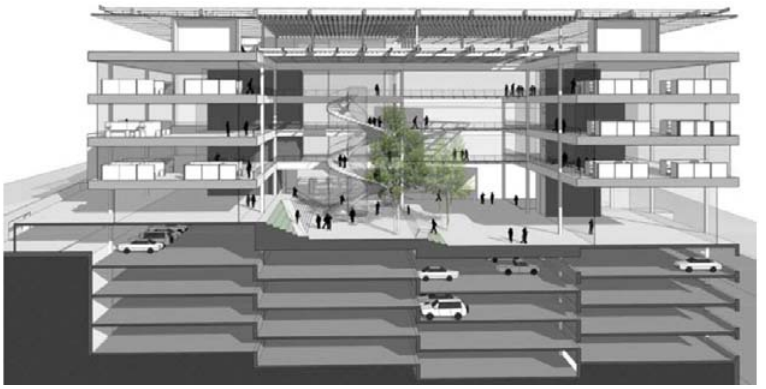


Figure 4 – Building Section

structure which is very stiff but also has a large aesthetic impact. This runs contrary to the architectural intent of the building which was to have as minimal a structure as possible, maximizing the amount of natural daylight. This required Dewhurst Macfarlane to look for elements which were strong but not stiff. While this is somewhat counterintuitive, small heavy sections, in this case a W10x60, (later changed to built-up 300mm by 300mm sections) were used. The highly compact shape with large cross-sectional area allowed Dewhurst Macfarlane to "cut the feedback loop" of strength and stiffness. The resulting stiffness was 16mm (5/8 in), H/1500, more than adequate for the structure.

What made this structural scheme even more attractive to Dewhurst Macfarlane was that the Vierendeel elements became a key part of the building's aesthetic with the architects from Grimshaw arguing just as vigorously for them as the engineers from Dewhurst Macfarlane and Partners when the scheme was first presented to the engineers of record- GPI. In the end, GPI came to understand and appreciate the scheme which was developed by Dewhurst Macfarlane and Grimshaw, but without the support of the architect, it may have been a harder sell.

One last note on the Vierendeel frame which was not fully realized when it was first proposed, but came up as the design was progressing, was the degree of structural redundancy this scheme provided. The Vierendeel frame allows for the loss of an



Figure 5– Typical office floor with conference room

edge beam connection on one floor or the loss of a column without a structural collapse via load sharing through the frame. A traditional moment frame would not have this kind of redundancy. The particular aspect of the frame's beneficial nature was realized in the extensive discussion the design team had on fire protection of the exposed steel frame.

Early in the design process it was realized that traditional notions of structural efficiency were different in Mexico than in the United States. In the U.S, it is standard practice to develop structures and details which favor labor efficiency over material efficiency, while in Mexico the opposite is true. In many ways this makes the design process more interesting to the engineer.

This logic was explored along a number of avenues in the development of the structural concept. Rather than using rolled section for the long span floor beams, a specialized steel truss was designed. This truss was design so that the top and bottom flanges would be steel plated rather than employing a steel shape and the diagonal

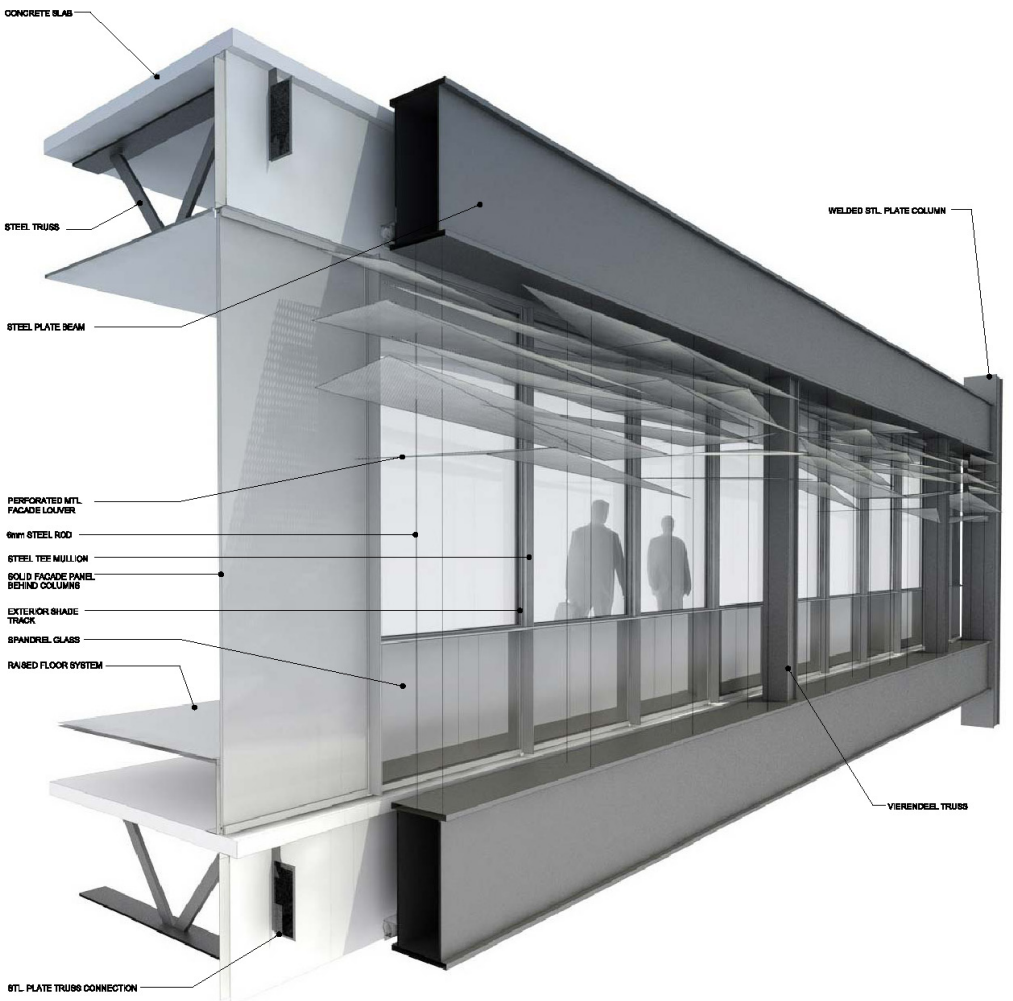


Figure 6 – Wall Section

members were made sufficiently large so that air ducts and plumbing could be run under the floor without having to drop the ceiling or create a web penetration in the floor beams, again adding to the structures' future flexibility. Additionally the floor beams were made composite with the floor slabs. These floor beams framed into box edge beams. The box shape was purely for architectural reasons since the frame of the structure was to be exposed.

The columns, and later the Vierendeel members, were designed as welded box sections 600mm (24 in) square. Along two sides the plates were recessed 50mm (2 in), to ease fabrication. This, like the Vierendeel frames, was embraced by the architect as an architectural element.

THE FAÇADE:

The environmental features of the building extended to the façade. We worked with the architect to provide completely custom designed thermally broken and insulated facades. The window wall system is a fabricated steel tee mullion system with insulated glazing, with low-e coating, and insulated panel infill.



Figure 7 – Interior Courtyard Looking towards Entrance Facade

To provide additional shading to the façade, a series of bent metal louvers made from expanded metal were employed. The louvers were cut and folded to a variety of shapes, each one analyzed using finite element software. We experimented with possible details to fix the louvers to the building. Several variations of the louver system were mocked up by local fabricators to assist in visualizing the finished product. There are 2730m^2 (29400 SF) of the standard window wall system on the building, presenting the bulk of the façade.

Another façade element it the skylight which is an integral part of the open atrium design by the architect. The skylight is supported from structural steel trusses and hung from above. The skylight structure itself is comprised of standard aluminum skylight framing members and fixed by hung rods to the structure above. The skylight itself is made from insulated glazing and uses structural silicone to connect to the

framing members. The node where the hanger rod connects to the skylight framing is thermally broken to ensure minimum heat transfer.

The main entrance to the building is through an impressive 4 story high glass wall. The wall is approximately 22m high x 34m wide (72 ft x 112 ft). The curtainwall is a custom designed system that provides support to bridges at each level that allows building users to cross the atrium space. The mullions are steel fabricated box sections at 1.85m (6-ft) centers and span vertically between the bridges and provide the lateral stiffness to the curtain wall system.

We selected materials to suit the local construction industry, but pushed for stricter usage of insulation and thermal performance than the standard requirements of Mexico in detailed drawings and specification. Together, the façade systems provide a uniquely green approach to building construction in Mexico and would be respected as an eco-friendly solution anywhere in the world.

BRISE SOLEIL:

Included in Grimshaw's design was a rooftop brise soleil. The brise soleil would help shade and lower the energy costs of the building by using mesh manufactured by the client attached to the framing. The brise soleil was supported by the interior columns of the building only, so that no support structure for the brise soleil was visible from the ground. This meant that the structural steel for the brise soleil cantilevered 17m (55 ft). The primary members for the framing were steel trusses with a depth of 2m (6 ft-6 in), but tapering to 600mm (2 ft) at the edges, giving this rooftop structure a lighter feeling.

ELEVATOR FRAMING SYSTEM:



Figure 8 – Elevator Enclosure

The architect desired an elevator core rising from open atrium below, nearly detached from the rest of the structure. Following the eco-friendly nature of the building, the decision was made to use the new Otis Gen2 elevator, a highly efficient machine roomless elevator. Grimshaw was interested in keeping the elevator structure open, with the only main framing being the elevator columns, and the elevator shaft clad in architectural mesh.

There were two challenges associated with the structural framing for the elevator. First was that the base floor for the elevator serving the office floors would be at the plaza, meaning that the base of the core rested above several levels of the subgrade parking structure. Additionally, the installation tolerance and allowable stiffness for the elevator framing are significantly higher than for a normal structure.

The first problem was dealt with by running a 1.2m (4 ft) deep truss beneath the elevator shafts. This truss needed to be strong enough to withstand the loads imparted by the elevators, but also stiff enough to be able to control the overall deflection for the elevator framing columns.

The second challenge was ensuring the proper deflection criteria to meet Otis' requirements- a maximum deflection of 6mm (¼ in). These columns were braced at every floor, but in their strong direction. In order to ensure the deflection of the elevator columns was kept within the allowable tolerances, we designed columns to be 800mm x 200mm (32 in x 8 in) steel columns with 25mm (1 in) thick plates.

The bracing of the columns at each floor level did not lead to an obvious choice of a "k" value for column design. Instead the *Direct Analysis Method* from the AISC Steel Construction Manual was used to capture the architectural intent of the columns. The columns were analyzed assuming that the columns were out of plumb by H/500 in each direction. In this case, this would be a very conservative assumption, since the elevator columns must be installed to a higher tolerance to ensure proper functioning of the elevator. The result of this analysis was a column which had minimal bracing back to the existing structure and had a very slender profile exposed to the atrium, which met the intent of the architect.

ENVIRONMENTAL FEATURES:

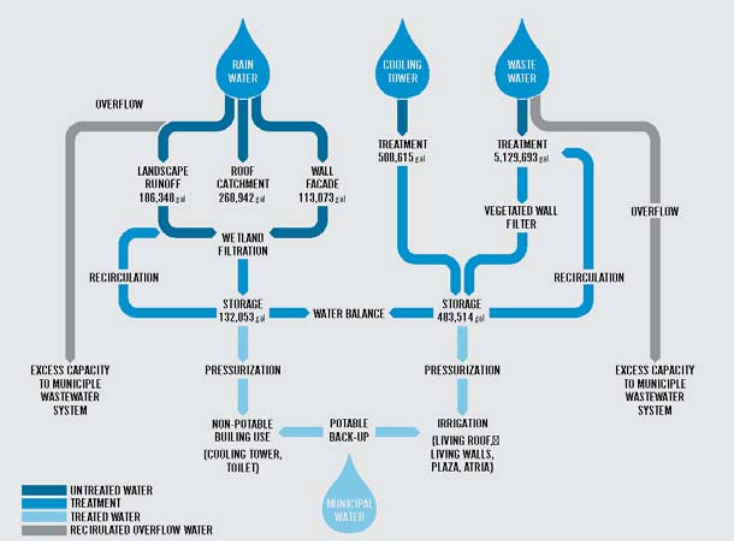


Figure 9 – Process Flow Diagram

Another very important and resonating project goal emerged more gradually in the design process and encompassed a holistic approach to the valuable and scarce resource of water. Monterrey has very limited freshwater resources and with a combined sewer system flash flooding is a dangerous and common problem. On-site water reuse addresses these

issues by providing resource efficiency, reducing sewage loads, minimizing infrastructure improvements and realizing financial return on investment. Project goals related to water include minimising potable water use for non-potable uses and a significantly reducing the volume of wastewater discharged into the municipal system. Deacero could not ignore the many benefits that these goals added to the project and so a water treatment and reuse system became an integral component of the building design.

Local code dictates that municipal water is used to supply potable demand including sinks, lavatories, janitorial uses and pantries. This is roughly 29% of the building's total consumption. The remaining 71% of consumption is non-potable demand for mechanical equipment, irrigation and toilets and can be supplied from on-site treated sources. In-depth analysis of building needs and water supply show that treatment and reuse of all building wastewater including both gray and blackwater was the most economic and efficient strategy. Initially, a system treating only graywater was considered, but this system was discarded because it required double plumbing throughout the building. This was a significant cost and resulted in the treatment and reuse of a small quantity of water compared to the current design. An integrated gray and blackwater treatment and reuse system uses a combination of biological and mechanical processes to treat 100% of building wastewater. The system manifests itself externally via significant water purification wetland terraces. This engineered wetland lines the entrance of the building from underground parking levels. Throughout the building, water features and green walls complete the circuit and highlight the story of water.

Wastewater treatment is the biological, physical, and mechanical removal of water contaminants. Each of these treatment processes occurs at different stages within the system at Deacero Headquarters. By using these processes in succession, wastewater can be treated to a level considered safe by regulatory agencies for reuse. The essential functions of the wastewater treatment system are to reduce Biological Oxygen Demand (BOD), destroy pathogens, filter particulates, reduce

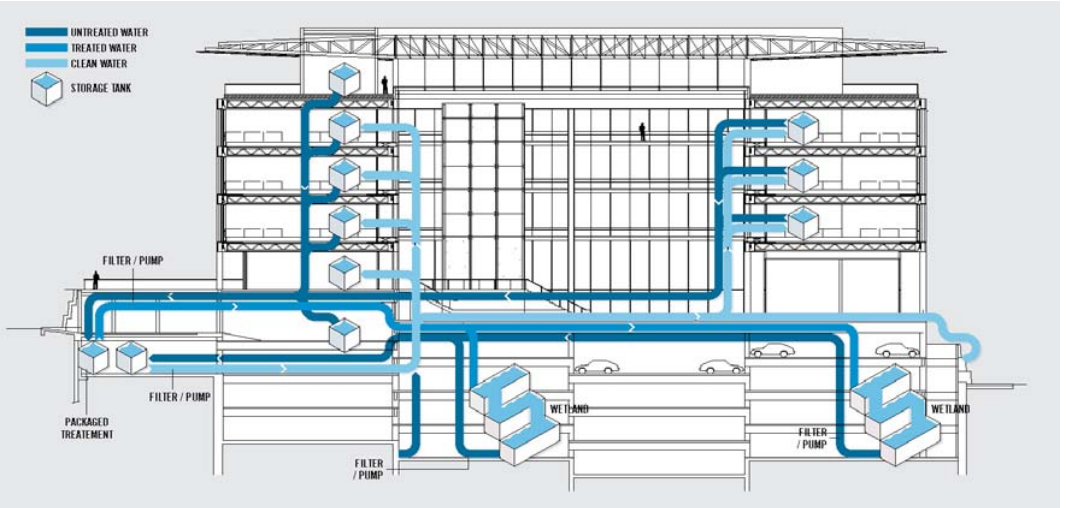


Figure 10 – Diagram of Complete Wetland System

nitrogen, phosphorous and Volatile Organic Compounds (VOCs) and stabilise or dispose of toxins. These treatment functions occur faster in constructed wetlands and biological systems than in conventional treatment systems.

Constructed wetlands are biologically complex systems, which adapt and respond to varying wastewater concentrations and changes in climate. The system is designed to emulate the systems that have naturally treated water in nature for millions of years. Naturally occurring wetlands encompass large areas and may treat water for an entire drainage basin. Studying how these systems function enables their re-creation for use in built environments. These urban wetlands are highly engineered, more efficient and able to function with less space than their natural counterparts.

The system at the new Deacero building, combines packaged biological treatment (a membrane bioreactor) with a constructed wetland to purify the water. All wastewater produced in the building is collected and directed to the membrane bioreactor (MBR) where pathogens, VOCs, most toxins and large particles are removed. The MBR is sourced locally from one of the various companies that compete in this emerging market. Water is then disinfected with ultraviolet light. From there, water is collected in a storage tank and pumped to the terraced wetlands in the parking garage. Since pathogens are removed by the MBR, water can be free flowing across the surface of the wetland without any unpleasant sights or smells. The wetland provides 'polishing treatment.' After water emerges from the bioreactor it is 'lifeless' and still contains high nutrient levels. Plants and microbes in the wetland remove excess nutrients and breathe life back into the water improving the quality for irrigation use. The recirculation of the water from storage to wetlands and through the atrium water feature prevents bacteria from developing in the tank and the water from getting stagnant. After treatment in the wetlands, water is pumped back to storage and then re-circulated throughout the building for reuse in toilets, mechanical equipment and irrigation of all indoor and outdoor vegetated features. The volume of clean water saved from non-potable uses is up to 3.6 million gallons per year- 750,000 gallons more than the building’s demand.

Two terraced planting areas which provide circulation up from the parking levels quickly evolved into the treatment wetlands, integral to the gray and blackwater treatment system. The sound of water streaming down multiple waterfalls over four stories, together with smells from the fragrant planting and the colors of seasonal foliage and flowers, feed the senses as one enters the building at the beginning of the day, or exits on the way home. Different textures in materials used to create the terracing can also be touched or viewed, completing the response to all of the senses. These wetlands are the only part of the water treatment system that is visible to staff and visitors alike. The wetlands manifest Deacero’s stewardship of natural resources in a prominent way, enrich the experience of approaching and leaving the building and perform the more mundane task of masking the sounds from the parking garage and the busy adjacent highway.

A return on investment analysis showed net savings on up-front water costs and discharge fees of some $35,000 per annum, which is about the capital cost of the blackwater treatment system. Therefore the system effectively pays for itself after one year. Continued annual savings will also cover wetland installation and system maintenance costs.

CONCLUSION:

The focus of the architect's design philosophy for this project was providing a new headquarters with a limited impact on the physical world around it. This was evident in the environmental features of the building, but Dewhurst Macfarlane and Partners, as the structural engineer, was able to expand on this vision and carry some of the same concepts to the engineering of the structure.

We were able to use a design that uses the efficiency and strength in the Vierendeel Truss framing system. The use of the Vierendeel trusses increased the stiffness of the structure, lowered the amount of steel required, and lent itself to Grimshaw's aesthetic vision for the structure. The remainder of the building's framing elements are very efficient since they make use of the approach in Mexico, where the focus is on the efficiency in materials instead of an efficiency of labor.

Additionally, the louvers, skylight, and brise soleil all have a limited visual impact, but with the shading mechanisms attached, they provide great insulating values and lower the cooling requirements for the structure. The spacing of the framing members is also an environmentally-friendly design, requiring less construction and waste when internal fit-out features are added, removed, or moved.

Working as a cohesive team, Dewhurst Macfarlane and Partners, Grimshaw Architects and GPI y Asociados were able to deliver an efficient structure to the client that was designed with each part of the design team working in unison.

ACKNOWLEDGEMENTS:

Dewhurst Macfarlane and Partners would like to acknowledge Richard Yoo, the project architect, from Grimshaw Architects in New York for the help in preparing this paper. We would also like to thank Vincent Chang, the partner in charge, and the whole design team from Grimshaw for their work on this project.

Dewhurst Macfarlane and Partners would also like to acknowledge that the section of this paper on *Environmental Features* was adapted from the article "Living Systems at the Deacero Headquarters" by Juan Porral, in collaboration with Gabrielle Fladd, published in Grimshaw's in-house journal "Blue".

CityCenter's Long Span Porte Cochères

Dennis Poon[1], I. Paul Lew[2], John Barry[3]

[1]MSCE, PE, Managing Principal, Thornton Tomasetti, Inc., 51 Madison Avenue, 17th Floor, New York, NY 10010; PH (917) 661-7800; email: dpoon@thorntontomasetti.com

[2]MSCE, MArch, PE, RA, Senior Vice President, Thornton Tomasetti, Inc., 51 Madison Avenue, 17th Floor, New York, NY 10010; PH (917) 661-7800; email: plew@thorntontomasetti.com

[3]MSCE, PE, Project Engineer, Thornton Tomasetti, Inc., 51 Madison Avenue, 17th Floor, New York, NY 10010; PH (917) 661-7800; email: jbarry@thorntontomasetti.com

ABSTRACT

Welcoming guests to Aria, CityCenter's 4,004 room hotel and casino, are two feature porte cochères: the Harmon Canopy to the north at the Aria Hotel lobby, and the Casino Circle Canopy to the east at the City Center Casino entrance.

The canopies, with heights of 102' and lengths of 157', are large, three dimensional structures that use their geometry to resist loads and integrate into the surrounding program. The primary system to create the canopies' cantilevers are a series of cable stayed box girders on a radial grid attached to box columns. A single cable between the box beam and column is tensioned against pairs of compression struts to resist uplift forces in the canopy.

Perpendicular to the frame of the box beam and column is a lattice work of stayed girts that support the inverted glass roof hung below. A series of in plane rods, bracing and radial struts create a diaphragm between the box girders to resist both seismic and wind lateral loading. In addition, the diaphragm stiffens the frames to reduce both periods and deflections.

The extreme fast-track nature of the CityCenter construction schedule led to unique problems and solutions in executing the design and construction of the two canopies.

INTRODUCTION

City Center is the largest privately financed construction project ever completed in the United States at a cost of $8.5 billion (Karlinsky 2009). Construction of the 76 acre development began in June of 2006 with the pour of Aria Hotel's mat foundation. The grand opening was just 42 months later in December of 2009.

As one of the largest and grandest resorts and casinos on the Las Vegas Strip an entry befitting of the project was required. Pelli Clarke Pelli Architects (PCP), the design architect of Block A, which included the 61 story Aria Hotel, the West Podium, housing the spa, pool deck, restaurants, back of house storage and parking; the East Podium, housing the casino, restaurants, valet parking and taxi cues; the Convention Center at Aria and the Cirque du Soleil theater, designed two large porte cochères for the major entrances to the Aria Complex.

Harmon Avenue provides direct access by car from Las Vegas Boulevard, also known as "the Strip," to the lobby of the Aria Hotel. Guests enter the multi-level lobby with a hybrid cable supported glass wall that is suspended from the porte cochère which provides a canopy 29' above the roadway, 84' wide and 280' in length. The Harmon Canopy is grand in both size and design.

At the opposite side of the Aria Hotel is the larger of the two porte cochères, Casino Circle Canopy, providing cover to guests as they enter the casino by both car and foot. The porte cochère at Casino Circle shares similar design elements with the Harmon Drive Canopy but with a very different layout. The canopy varies from 31' to 37' above the roadway, up to 137' wide and 604' in length.

Each of the porte cochères provided different structural design challenges based on their size, location and sequence of construction. Because of the fast-track nature of the job and compressed construction schedule, structural components were being fabricated and built in sequences that often preceded the final architectural design.

The structural design of both canopies began at the same time, shortly after ground breaking in July of 2006. Construction of the Aria Hotel was already underway, introducing complexities of integrating the Harmon Canopy with existing conditions. The design of the East Podium where the Casino Circle Canopy is located would not be released for another two months, allowing for the integration of that canopy into the surrounding structure.

HARMON CANOPY – The Aria Hotel Porte Cochère

The Harmon Canopy has a fan shape in plan with nine radial frames (Figure 1). Each frame consists of one built-up, inclined, steel plate box column and one cantilevered built-up steel plate box beam (Figure 2). The canopy spans the 75' of the three level lobby from its foundations on grade at Level S to the roof on Level 3 and then cantilevers an additional 27' past the top of the roof for a total height of 102'-5".

The canopy structure's nine radial frames form eight equal bays 36' apart at the widest point and integrates into the lobby of the Aria Hotel. Of the eight bays, six have an inclined glass wall supported by cables suspended from the canopy which run the entire height of the lobby. Two of these bays also support the vestibule into the lobby at Level 1, 25' above the base of the canopy. At the remaining two bays the lobby wall pulls away from the canopy, providing clear column spans from the foundation to the roof.

Because of the lead time required to build the Aria Hotel, construction of the tower was already at Level 1 before the Harmon Canopy design was finalized. This required any lateral loading from the canopy due to seismic wind or gravity induced lateral loads from sloping columns, which would ultimately be resolved in the tower core, to be transferred through the tower's concrete slab. It was therefore not possible to transmit the required lateral load into the existing slab at Level 1. The slab at Level 2 was a mezzanine that did not attach to the canopy, therefore all lateral loads would have to be transferred to the tower's core through a roof diaphragm at Level 3.

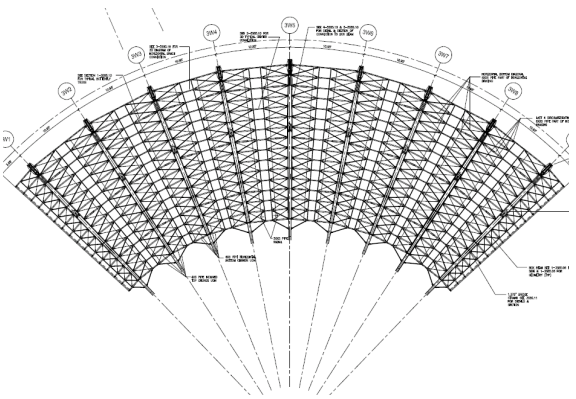


Figure 1. Harmon Canopy Plan

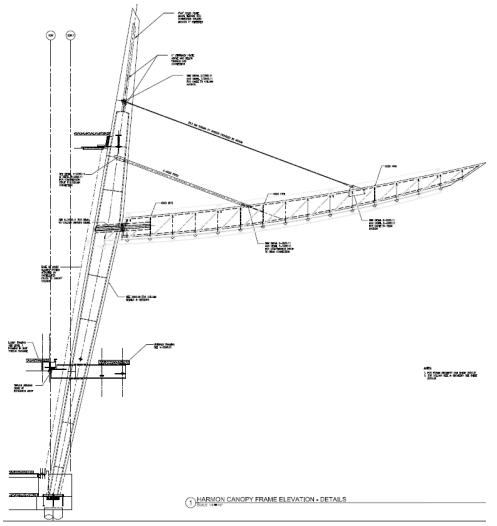


Figure 2. Harmon Canopy Section

Harmon Canopy Loading

The CityCenter site is in an area of high seismicity. Based on the site specific geotechnical report the site class was C, more favorable than the code required site class of D. The report provided a site specific spectral response which was used in the design of all components of the project. An importance factor of 1.25 was used because of the high occupancy of the structure.

Due to the complex nature of the connections of the Harmon Canopy, which are often architecturally driven, it would have been difficult to detail as required for seismic design. It was therefore decided to use a Response Modification Factor (R) of 3, "Structural Steel Systems Not Specifically Detailed for Seismic Resistance" (IBC 2000). The choice would increase lateral forces in the design from 7.4% of W, 126 kips to 12.4%, 210 kips, but would allow the most versatility in detailing of the structure. The lateral forces, however, were very small compared to sizes required by the large spans of the structure. The increased lateral forces therefore came at a negligible premium to the steel sizes and tonnage.

The wind analysis for the entire block A was conducted by Rowan Williams Davies and Irwin Inc. (RWDI). Both canopies were tested in a wind tunnel with the surrounding structures modeled. Particular attention was given to the harmonic excitation of the cantilevered canopy to prevent fluttering in the wind between adjacent frames. Infill butterfly trusses linked adjacent box columns to minimize differential movements. The first period that induced fluttering in the canopy in the form of a 1/2 sine wave occurred at .74 seconds. It was advised by RWDI that periods less than 1 second would not be excitable by wind induced excitations.

The RWDI report provided a uniform wind pressure of +/- 25 psf with peak pressures up to +30 psf. In addition, unbalanced loading was provided on the canopy both globally across all nine frames and locally for each frame. The unbalanced load induced torsion within the box beams and additional bending stresses in the infill butterfly trusses. The differential unbalance loading was a maximum of 15 psf.

At the lobby on Level 1 a cantilevered elevated exterior sidewalk from the box columns was provided that linked all nine frames. The sidewalk, part of the canopy Block A structure, adjoined the elevated roadway of Block B for guest drop-off, which had a separate design team. A 6" expansion joint was provided between the sidewalk and roadway to allow for differential seismic movement. Because of the sidewalk's location adjacent the roadway it was required to design the sidewalk for vehicular loads, in particular for emergency vehicles and equipment that may jump the curb onto the sidewalk. A 600 psf live load was used to design for the loading of emergency vehicles in addition to the weight of the sidewalk slab and finish.

Harmon Canopy Components

The main support for the canopy and the adjoining lobby are nine 106'-11" box columns on a radial grid spaced 36'-6" apart at the footing. The columns slope away from the hotel lobby at 10 degrees with a glass wall following the slope of the column attached on the back side. The columns provide gravity support for the lobby steel framing at Level 1 and the roof at Level 3. In addition the column supports a cantilevered sidewalk at Level 1 and a stayed box beams of the canopy at level 2.

The columns are unbraced for 75' between Level S and Level 3 and therefore are best suited as a box to increase the buckling capacity. The major axis of the column is radial from the hotel lobby and varies from 3'-3" in depth at the base to 6'-0" at the highest moment at the beam intersection. The column has a constant width of 1'-4" and is fabricated from 1" thick webs and 2" thick flanges, all grade 50 steel plate. Flanges are recessed 6" from the webs allowing for continuous 3/8" fillet welds at the intersection. Internal stiffeners are used at 10' centers to keep the column square during fabrication and erection.

The columns are keyed at their base into 5' square caisson caps on single 4' diameter drilled caisson. Caissons are tied together with grade beams in both directions to form fixed caps. At Level 3 the columns are tied into the roof structure of the lobby. The canopy column provides the gravity support for the roof steel but the roof steel provides lateral support for the canopy column through a network of in plane double angle braces. The braces tie back to the tower's concrete edge beam which transfers the load to the tower core walls.

At Level 1 the box columns support W36 beams which pass in between the webs of the column supporting a 6'-9" cantilevered sidewalk outside the lobby as well as the steel floor framing inside the lobby. Below the sidewalk, which connects all nine box columns together, double angle bracing was installed to provide overall lateral stability by coupling the columns at their mid-point. Because of the design and construction sequence lateral loads could not be transmitted to the tower core at Level 1. It was therefore necessary to introduce slide bearings fabricated by Fabreeka between the W36 and lobby steel to allow translational movement of the canopy columns both in and out of plane while still supporting the gravity load of the lobby floor (Figure 3).

At 29' above the sidewalk and 54' above the ground is the attachment of the canopy box beam to the box column. The box beam extends 81' beyond the column and is stayed two thirds down the length of the beam by a post tensioned 36mm cable fabricated by Pfeifer that ties back to the cantilevered portion of the box column above the lobby roof. The cable is tensioned against a pair of 6" double extra strong pipes acting as compression struts that connect the box beam at its third point back to the box column slightly below the lobby roof.

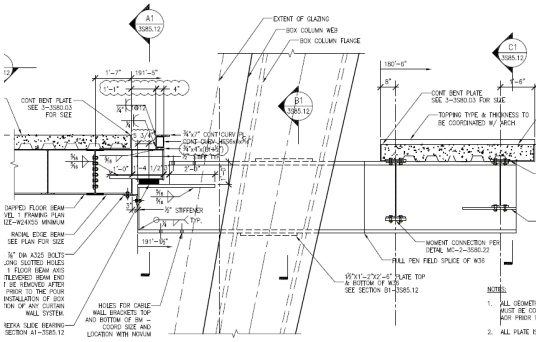


Figure 3. Slide Bearing Connection

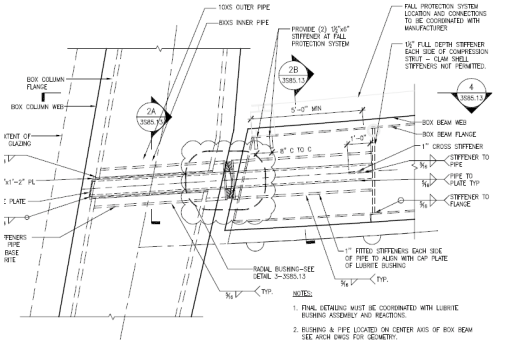


Figure 4. Harmon Canopy Radial Bearing

The box beam's geometry tapers in section from 4'-6" at the column interface to a point at its end. The beam also flares and tapers in plan, from 1'-4" wide at the column to 2'-0" wide at the compressions strut connection and down to 1'-0" in width at the tip. Both the webs and flanges of the beam are constructed of ¾" grade 50 steel plate. The flanges of the beam are recessed 4" from the web allowing for a continuous 5/16" fillet weld.

The architectural design required a reveal at the connection between the box beam and box column. To create the reveal all plates of the box beam had to stop 7" from the column, the point of highest moment in a cantilever. To make the connection work it was necessary to ensure that no moment was transferred across the joint by forming a true pin at the interface. A radial bearing, manufactured by Lubrite Technologies, was introduced between the column and beam. To ensure that the beam and column maintained in contact in the event of uplift on the canopy, therefore maintaining shear transfer from the beam to the column, an 8" double extra strong pipe was threaded through the center of the bushing tying together the column and beam (Figure 4). The connection allowed vertical rotation without vertical translation.

The cable and compression strut along with shear transfer at the radial bearing provide for the required resistance against the vertical forces of wind and gravity. To stabilize the canopy structure against the lateral forces of wind and seismic a dual purposed infill truss was used connecting each of the box beams. The infill trusses, referred to as butterfly trusses because of their shape, provided a three dimensional diaphragm in the plane of the roof allowing lateral loads to be taken as a couple between the outer box columns as well as providing attachment locations for under hung glass which formed the cover of the canopy.

The butterfly trusses spaced 5'-0" on center, matching the segmentation of the hung glass panels, were comprised of four elements. The first element, which the glass panels were directly hung from, were 6" diameter pipes hung below the box

beams from 1" fin plates. The 6" pipes were horizontal and segmented radially in plan between the box beams. At the midpoint between box beams the architect desired the pipes to reduce in section, forming a 5' long reveal. It was necessary to maintain full moment capacity across the reveal, therefore a thicker walled but reduced diameter pipe was sleeved inside the 6" pipe maintaining the section modulus.

The 6" horizontal pipe alone was not capable of spanning the required 34' without buckling under compressive loads or excessive deflection from the hung glass weight. A second element, a diagonal strut in both elevation and plan, was added forming a cantilevered truss from the box beam to brace the 6" pipe and remove shear force through tension and compression. Three and a half inch diameter pipes were used on either side of the reveal connecting back to the top of the box beams. The architect requested tapered fittings at each end of the strut to stop the connections from looking bulky. Thirteen hundred custom tapered cone cast fittings were fabricated to attach to the ends of the struts that would provide a single pin connection to gusset plates welded to the box beam.

All of the diagonal struts were inclined in the same planar direction away from the lobby. This created a force component in plan from the gravity load that needed to be resolved. A third element, in plane rod bracing in a zig-zag pattern, was added to resolve this force. The rods were stainless steel, 16 mm in diameter with pinned stainless steel fittings on each end. The rods connected alternate nodes at the reveal to the 6" horizontal pipe intersection with the box beam.

The final element was a pair of 2 3/8" struts that spanned 5' between trusses on either side of the reveal. The struts had a dual purpose. Every other connection of the strut to the horizontal pipe had no resolution to the in plane force because of the alternating connection of the zig-zag rods. The force could be accumulated in the pair of struts and then transferred where the zig-zag rods connected. The second use was to tie all of butterfly trusses together at their midpoint alleviating differential deformations in plane that could induce excessive compression forces in the attached glass below.

The butterfly trusses resolved the lateral force in the canopy back to the outer box columns which could then transfer the load to the Level 3 lobby roof and ultimately to Aria's tower core. This system prevented the need for any bracing in elevation between the box columns, a major criterion of the architects. A similar structural system was employed at the Casino Circle, except that there was no tie back at the top of the columns to resolve the lateral force.

CASINO CIRCLE CANOPY – City Center's Casino Porte Cochère

Unlike the Harmon Canopy the Casino Circle Canopy had no connection at the top of its box columns to resolve lateral load. Instead the Casino Circle Canopy cantilevers from a partially fixed base at Level 1, the drop off to the casino, 42'-6" above its foundations. A system of moment frames and braced frames, continuing three levels below Level 1, allows the box columns to act as propped cantilevers between Level S and Level 1. Because the construction of the East Podium where the Casino Circle Canopy is located lagged that of the Aria Hotel it was possible to fully integrate the canopy's required support structure into the East Podium framing.

The Casino Circle Canopy, which covers over half the circumference of the drop-off circle, is comprised of thirteen radial frames (Figure 5). Eight of the frames are made up of one inclined steel box column, 69' in height, and one cantilevered steel box beam 79' in length (Figure 6). These frames comprise the Small Canopy. Four of the frames are made up of two inclined steel box columns, 89' and 99' in height, and one cantilevered steel box beam, 157' in length, that intersects both columns (Figure 7). These frames comprise the Large Canopy. At the intersection of the Small and Large Canopies is one hybrid frame that combines the beams of both the Small and Large Canopies into the two box columns of the Large Canopy (Figure 8).

The columns of the Small Canopy and the back columns of the Large Canopy slope 12 degrees towards the entrance of the casino following a feature water wall that slopes the same angle. The beams of both Small and Large Canopies extend over the casino with the Small Canopy beams being tied vertically to building columns to reduce lateral deflections. The Large Canopy, with a second set of columns at the front slopping 8.5 degrees towards the center of the circle, has no ties between its box beam and the building below.

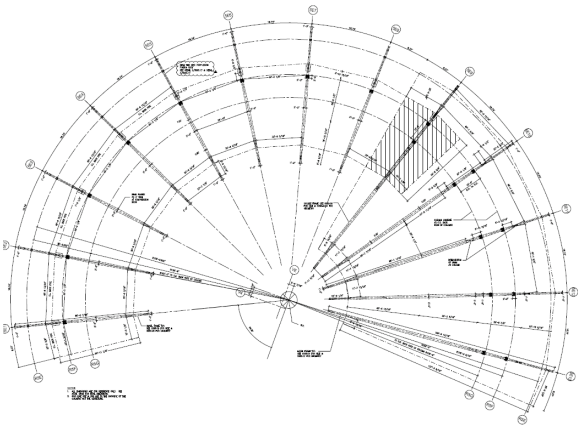


Figure 5. Casino Circle Canopy Plan

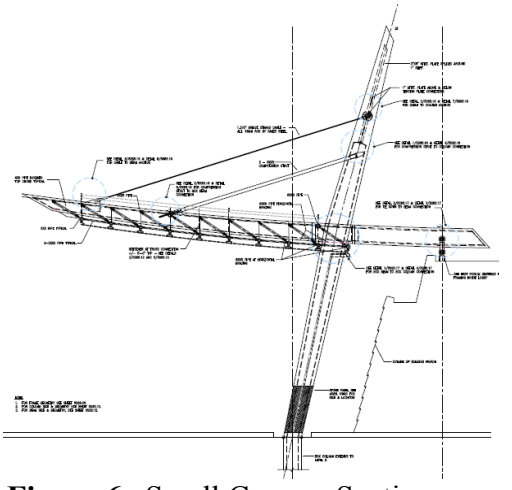


Figure 6. Small Canopy Section

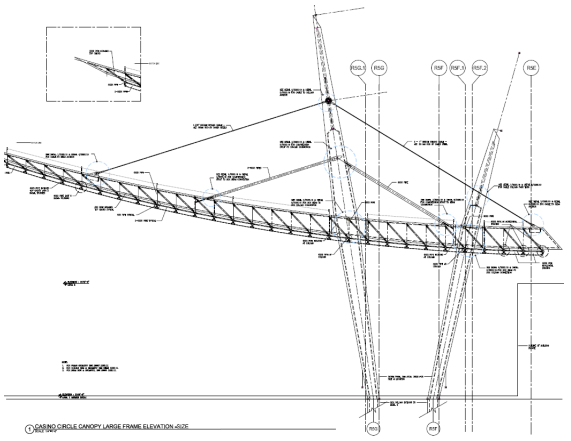


Figure 7. Large Canopy Section

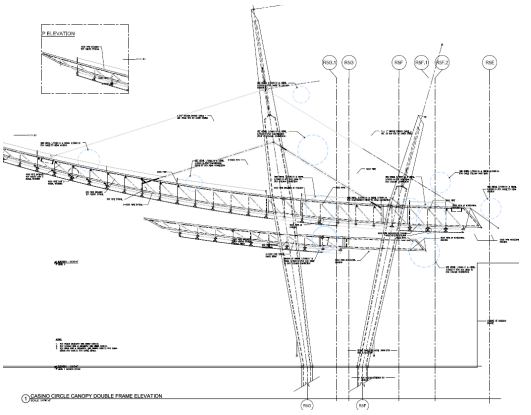


Figure 8. Hybrid Canopy Section

Casino Circle Canopy Loading

The Casino Circle Canopy shared the same seismic design criteria as the Harmon Canopy. Using a Response Modification Factor (R) of 3 the total lateral forces for seismic design was 349 kips, 14.9% of W. Lateral loads from the canopy level are transferred to the base building at Level 1 through strong and weak axis bending of the box column taking shear force and strong axis bending of the box column taking torsion in a couple through the outer columns.

Harmonic excitation of the canopy structure from wind induced fluttering was also a concern at Casino Circle. It was found in the Large Canopy that the first mode that induced oscillations in the form of a 1/2 sine wave occurred at 1.09 seconds. This exceeded the RWDI recommended maximum of 1 second, but was determined to be acceptable. For the Small Canopy the same behavior occurred at .73 seconds, under the recommended value.

The RWDI report provided a uniform wind pressure of +/- 25 psf with peak uplift pressures up to -35 psf. In addition, unbalanced loading was provided on the canopy, both globally and locally for each frame, of the Small and Large Canopies. The differential unbalanced load, inducing torsion within the box beams and additional bending stresses in the infill butterfly trusses, was a maximum of 14 psf at the Small Canopy and 18 psf at the Large.

Casino Circle Canopy Components

The main support of the Large and Small Canopies are their eighteen box columns on a radial grid spaced 44’ apart at their base. The columns are un-braced for their entire length ranging from 69’ to 99’and are best suited as boxes to resist

buckling. The major axis of the column is radial from the casino and varies from 3'-0" in depth at the base to 4'-3" at the intersection of the box beam for the Small Canopy and 6'-0" at the intersection of the box beam for the Large Canopy. Both canopies' box columns taper to a point at their tips. The width of all columns is a constant 1'-4". The webs and flanges of the column are constructed of 2" thick grade 50 steel plate. The flanges of the column are recessed 6" from the webs allowing for a continuous 3/8" fillet weld.

The canopy box columns transition at Level 1 to a three level steel structure below (Figure 9). To allow for erection tolerance in the field a 4" thick transition plate caps the building columns directly below the location of the canopy columns. The transition plate provided a surface to full penetration weld the canopy box column to. To provide the greatest fixity at the column connection a box column identical to that of the canopy was extended 26' below Level 1 transitioning 3'-0" above Level S to heavy W14 columns which continue down to caisson caps sitting on 4' diameter drilled caissons at Level S2.

The columns under the Small Canopy sit centered on a caisson cap over a pair of caissons. Each set of columns at the Large Canopy sit on a caisson cap over three caissons in line. The front and heavier loaded Large Canopy column straddles two caissons and the back column sits over one caisson, all sharing the same cap. All caissons are tied together with grade beams in both directions to form fixed caps.

At Level 1, 2' below the transition plate, beams that frame into the box columns are upsized and moment connected in both directions to provide increased stiffness for the canopy column connections above. Braced frames are also provided between the pairs of columns at the Large Canopy between Level S2 and Level 1. The propped cantilever, moment connected beams and braced frames were all required to provide sufficient stiffness at the canopy column connections to minimize the canopy's period and deflection.

The box beams are similar in construction at the Casino Circle Canopy as the Harmon Circle Canopy. Both webs and flanges are constructed of ¾" grade 50 steel plate. Unlike the Harmon Canopy the beams are moment connected to the box columns. At approximately 18" from the moment connection to the box column flange plates of the box beam are increased to 2" thick. At the Large Canopy columns the flanges are increased to 2" thick as well.

The Small Canopy shares a similar design to the Harmon Canopy with 36 mm post-tensioned cables and a pair of 6" double extra strong compression struts connecting the box beam at its two thirds and one third points respectively back to the box column. To reduce vertical translation of the Small Canopy an additional connection was required at the back of the box beam to the casino roof columns. The requirement for an open floor plan at the casino prevented the introduction of braces

in the casino. It was therefore desired to only load the building columns in tension and compression while inducing minimal lateral forces.

A pair of 2 13/16" thick dog bone shackles 30" in length were introduced, one on each side of the box beam, to allow lateral translation of the canopy while still transferring vertical loads (Figure 10). Each dog bone was fitted with two spherical bearings, one on each end, with a 3 ¾" 62 ksi solid steel pin connecting the box beam and building columns to the spherical bearings. The spherical bearings allowed the dog bone to rotate in both directions with lateral translation of the canopy box beam.

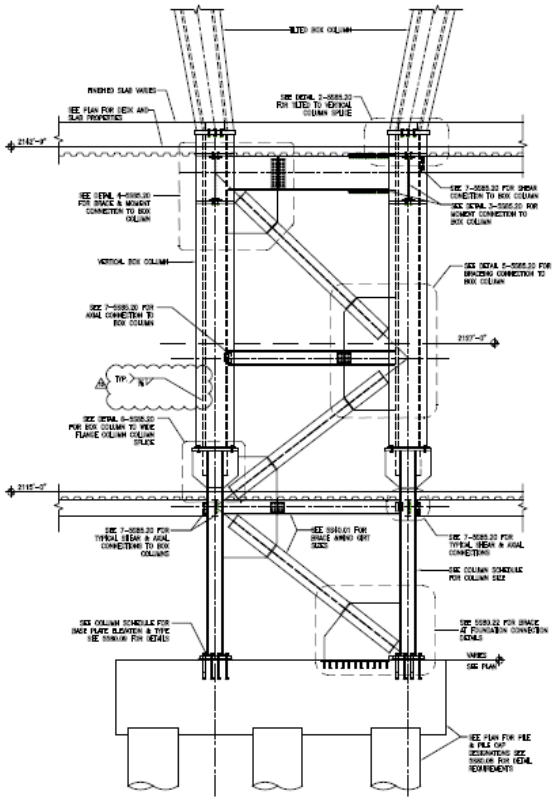


Figure 9. Large Canopy Transition

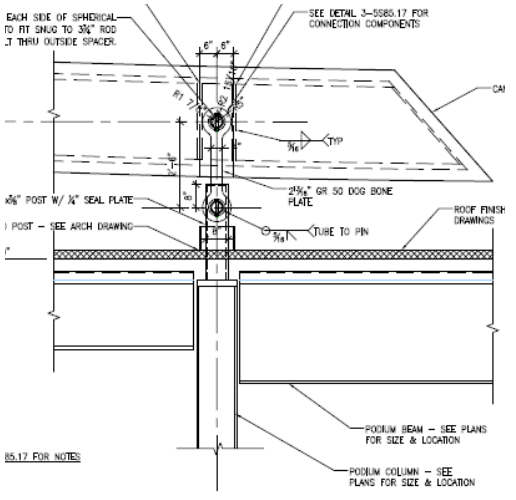


Figure 10. Dog Bone Connection

The Large Canopy, similar to the Small Canopy, has a 36 mm post-tensioned cable and pair of 6" double extra strong compression struts between the cantilevered beam and front box column. In addition aligning in elevation with the cable and struts from the front of the box column are a pair of 28 mm post-tensioned cables and a single 8" double extra strong compression strut between the front column and the back span of the cantilevered beam, with the back cables passing though the rear box column. The symmetric loading of the front column helps to reduce unbalanced loading, induced bending and deflection into the column.

A series of butterfly trusses spaced 5'-0" on center, similar to the Harmon Canopy, span between the box beams of both the Small and Large Canopies. The trusses provide a three dimensional diaphragm allowing lateral loads to be taken as a couple between the outer box columns at both the Large and Small Canopy as well as providing attachment locations for the glass hung below. The trusses comprised the same four elements as the Harmon Canopy; segmented horizontal radial chords to the bottom of the box beam, inclined struts to the top of the box beam, zig-zag steel rods, and a pair of struts linking the midpoint of the radial chords.

CONCLUSION

The porte cochères at CityCenter provided unique engineering problems in their size and complexity. A similar architectural and structural design ties all the canopies together while three different layouts required three individual solutions.

By using the geometry of the structure effectively a clean and rational approach to the design could provide simple yet elegant entries to the hotel. By integrating the canopies into the surrounding structure, structural elements could be minimized or eliminated.

A collaborative effort between the architect, structural engineer, fabricators, erectors, project manager and contractors led to successfully executing the design and installation of the large and complex canopies.

REFERENCES

Karlinsky, Neal and Harper, Eloise. "Las Vegas Gambles on $8.5 Billion CityCenter." ABC - News / Nightline. Web. 16 December 2009.

International Code Council (ICC). (2000). *International Building Code (IBC 2000)*, Washington, DC.

American Society of Civil Engineers (ASCE). (1999). *Minimum Design Loads for Buildings and Other Structures (ASCE 7-98)*, Reston, Virginia.

Accuracy of Applying "Stiff-Girder" Approach in Reinforced Concrete Bridges

M. AbdElLatef

Graduate Student, Department of Civil and Environmental Engineering, Washington State University, Phone (509) 432-4032; email: mohammed.abdellatef@email.wsu.edu

Abstract:

It is very common to consider the cross girder of a slab-girder bridge as a stiff-*Rigid*-girder rested on springs while distributing loads to main girders for simplification. This approach gives suitable results for primary manual analysis for bridges that have cross girder depth almost equal to main girder depth, small spacing between main girders, large spans of the bridge vent, and monolithically casted elements.

Two simplified models were studied in this paper: an infinitely rigid beam rested on springs having an applied concentrated load, and an *imaginary* very flexible beam rested on springs having the same loading condition. These two models were studied to indicate the extreme conditions of the cross girder. An approximate governing equation is proposed to correlate the bridge geometry to the accuracy of applying the stiff girder approach. Concrete sections of main and stiff girders were considered to be cracked sections in either working or ultimate stages.

It was obvious from the results that the bridge deformation) which is calculated by the stiff girder approach) is changing dramatically while changing bridge geometry. But the straining action of the bridge may not exceed the resistance values, before or after plastic hinges deformation.

Slab-Girder Reinforced concrete bridge:

One of the most common reinforced concrete bridges is the slab-girder bridge. This type of bridge consists of: slab, cross girders and main girders (figure 1). Usually this type of bridge is used to cover medium spans.

For primary analysis of this kind of bridge, the cross section could be considered as a rigid or semi rigid beam supported by the main girders as elastic supports. This approach is commonly used to estimate the straining actions in the cross girder, as well as determining the design traffic loads distribution for each main girder.

Assuming that cross girder is a rigid beam simplifies the calculations for load distribution as will be mentioned later. The main reason to simplify the cross girder as a rigid beam is that it has almost the same depth of the main girders. Also it has a very short span compared to that of the main girder.

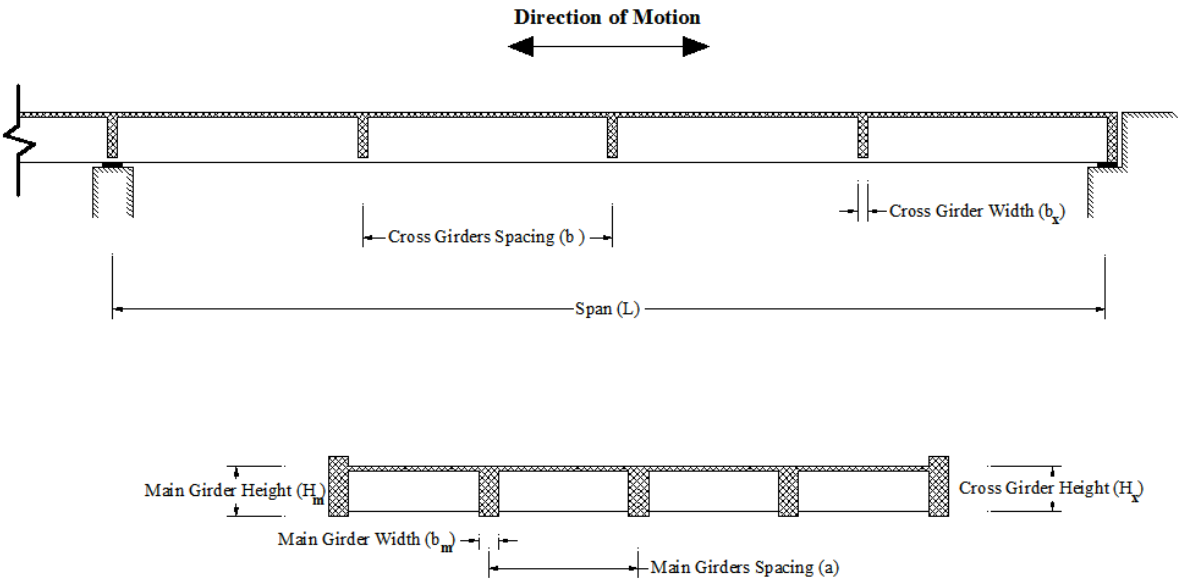


Figure 1. Typical components of concrete slab-girder bridge.

Objectives:

The main objective for this paper is to present the effect of reducing the cross girder depth or increasing its span (by increasing the spacing of main girders) on the accuracy of calculating the distributed loads on each main girder.

Two extreme approaches will be considered: the rigid approach for the cross girder and an imaginary approach for much more flexible cross girder. From the limits obtained from these two cases, a general trend will be concluded for any other case.

Also, the effect of using the effective moment of inertia of the reinforced concrete sections instead of the gross moment of inertia on the calculations will be considered.

Rigid Approach

In this approach, the stiffness of the cross girder was considered infinite compared to the stiffness of main the girders, so that it deforms as a rigid body (Figure 2). Assuming that the main girders are spaced at distance a and the springs represent n main girders with stiffness k, the force acting on each main girder R_i and the deflection δ_i will be:

$$R_i = \frac{p}{n} \pm \frac{Pe}{\sum_{i-1}^{n} r_i^2} r_i \quad [1] \quad , \quad \delta_i = \frac{R_i}{k} \quad [2]$$

where p is a concentrated load applied on the cross girder, e is the eccentricity of the load p from the center of supports and r_i is the absolute distance between support i and center of supports. "*Center of supports* is defined as the position of loading which causes the same displacement at all supports"

This case will be considered the datum for other cases, so the sum of the absolute value of errors in calculation of support reactions (displacements) and the standard deviation of these values in this case are equal to zero.

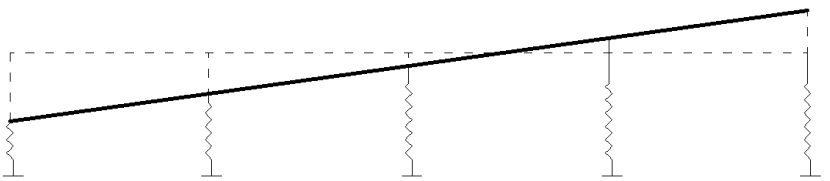


Figure 2. Structure system and deformations for stiff cross girder.

Imaginary flexible Approach

In this approach, the cross girder was assumed to be a member with no stiffness such that the entire load is transferred to adjacent supports. The goal of this approach was to calculate the maximum *sum of absolute value of errors in calculation of support reactions* (displacements) and the maximum standard deviation of these values for a unit load (displacement).

Consider the case of an odd number of supports with the load at the center of supports (figure 3). The general formula for calculating the sum of absolute value of errors and the standard deviation are:

$$e_o = \frac{1}{n}(n-1) + (1-\frac{1}{n}) \qquad [3] \quad , \quad s_o = \sqrt{\frac{\frac{1}{n^2}(n-1) + (1-\frac{1}{n})^2}{n}} \qquad [4]$$

These two equations can be simplified to:

$$e_o = \frac{2n-2}{n} \qquad [5]$$

$$s_o = \frac{1}{n}\sqrt{n-1} \qquad [6]$$

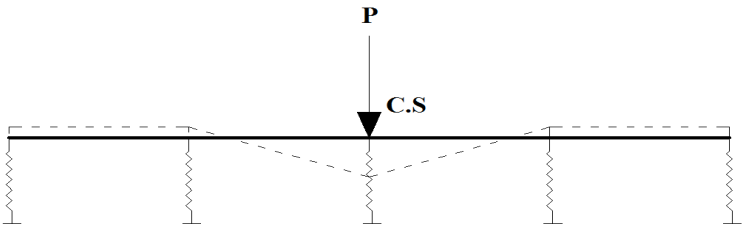


Figure 3. Cross girder with odd number of supports and loaded at the center of supports.

Consider the case of an odd number of supports with the load at the edge of the cross girder (figure 4). First, it is important to find the position where the stiff approach will have no displacement η in order to calculate the absolute value of errors. η can be calculated by solving the following equation

$$\frac{1}{n} - \frac{a(n-1)/2}{2\sum_{i=1}^{(n-1)/2}(ia)^2}\eta a = 0 \qquad [7]$$

For summation, it is required to find the last support that will have the same direction of displacement as the load. This support will be numbered as I from the center of supports.

The general formula for calculating the sum of absolute value of errors and the standard deviation of the errors are:

$$e_o = (\frac{p}{n}) - \sum_{i=1}^{I}(\frac{1}{n} - \frac{(n-1)/2}{\sum_{j=1}^{(n-1)/2} j^2} i) - \sum_{i=I}^{(n-1)/2}(\frac{1}{n} - \frac{(n-1)/2}{\sum_{j=1}^{(n-1)/2} j^2} i) + \sum_{i=1}^{[(n-1)/2]-1}(\frac{1}{n} + \frac{(n-1)/2}{\sum_{j=1}^{(n-1)/2} j^2} i) + (1 - (\frac{1}{n} + \frac{(n-1)/2}{\sum_{j=1}^{(n-1)/2} j^2} \times \frac{n-1}{2})) \qquad [8]$$

$$s_o = \sqrt{\frac{(\frac{p}{n})^2 + \sum_{i=1}^{(n-1)/2}(\frac{1}{n} - \frac{(n-1)/2}{2\sum_{j=1}^{(n-1)/2} j^2} i)^2 + \sum_{i=1}^{(n-1)/2-1}(\frac{1}{n} + \frac{(n-1)/2}{2\sum_{j=1}^{(n-1)/2} j^2} i)^2 + (1 - (\frac{1}{n} + \frac{(n-1)/2}{2\sum_{j=1}^{(n-1)/2} j^2} \times \frac{n-1}{2}))^2}{n}} \qquad [9]$$

These equations can be simplified to:

$$\eta = \frac{n+1}{6} \qquad [10] \qquad , \quad I = \text{int}\,ger(\eta) \qquad [11]$$

$$e_o = \frac{(n-1)(5n-7) + 4I(n-3I-2)}{2n(n+1)} \qquad [12]$$

$$s_o = \frac{1}{n}\sqrt{\frac{(n-1)(n-2)}{(n+1)}} \qquad [13]$$

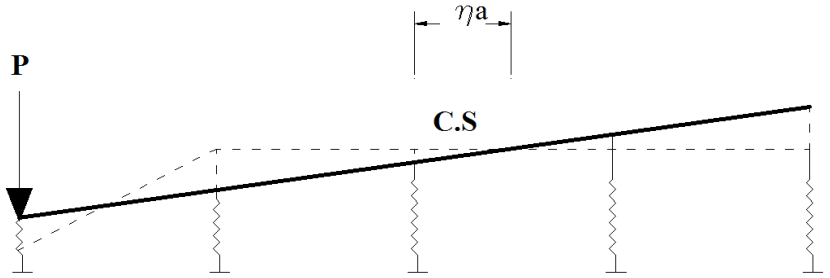


Figure 4. Cross girder with odd number of supports and loaded at the edge.

Consider the case of odd number of supports loaded at a support with eccentricity of βa (figure 5). First, it is important to find the position where the stiff approach will have no displacement η in order to calculate the absolute value of errors. η can be calculated by solving the following equation:

$$\frac{1}{n} - \frac{\beta a}{2\sum_{i=1}^{(n-1)/2}(ia)^2}\eta a = 0 \qquad [14]$$

For summation, it is required to find the last support that will have the same direction of displacement as the load. This support will be numbered as I from the center of supports.

The general formula for calculating the sum of absolute value of errors and the standard deviation of the errors are:

$$e_o = (\frac{p}{n}) - \sum_{i=1}^{I}(\frac{1}{n} - \frac{\beta}{\sum_{j=1}^{(n-1)/2} j^2} i) - \sum_{i=I}^{(n-1)/2}(\frac{1}{n} - \frac{\beta}{\sum_{j=1}^{(n-1)/2} j^2} i) + \sum_{i=1}^{\beta-1}(\frac{1}{n} + \frac{\beta}{\sum_{j=1}^{(n-1)/2} j^2} i) + \sum_{i=\beta+1}^{(n-1)/2}(\frac{1}{n} + \frac{\beta}{\sum_{j=1}^{(n-1)/2} j^2} i) + (1 - (\frac{1}{n} + \frac{\beta}{\sum_{j=1}^{(n-1)/2} j^2} \times \beta)) \qquad [15]$$

$$s_o = \sqrt{\frac{(\frac{p}{n})^2 + \sum_{i=1}^{(n-1)/2}(\frac{1}{n} - \frac{\beta}{2\sum_{j=1}^{(n-1)/2} j^2} i)^2 + \sum_{i=1}^{\beta-1}(\frac{1}{n} + \frac{\beta}{2\sum_{j=1}^{(n-1)/2} j^2} i)^2 + \sum_{i=\beta+1}^{(n-1)/2}(\frac{1}{n} + \frac{\beta}{2\sum_{j=1}^{(n-1)/2} j^2} i)^2 + (1 - (\frac{1}{n} + \frac{\beta}{2\sum_{j=1}^{(n-1)/2} j^2} \times \beta))^2}{n}} \qquad [16]$$

These equations can be simplified to:

$$\eta = \frac{n^2 - 1}{12\beta} \qquad [17] \quad , \; I = \text{int}\, ger(\eta) \le \frac{n-1}{2} \qquad [18]$$

$$e_o = \frac{2I[(n^2-1)-6\beta(I+1)]+(n^2-1)(n-1)-24\beta^2+3\beta n^2-3\beta}{2n(n^2-1)} \quad [19]$$

$$s_o = \frac{1}{n}\sqrt{\frac{n^3-n^2-n+1-12\beta^2}{(n^2-1)}} \quad [20]$$

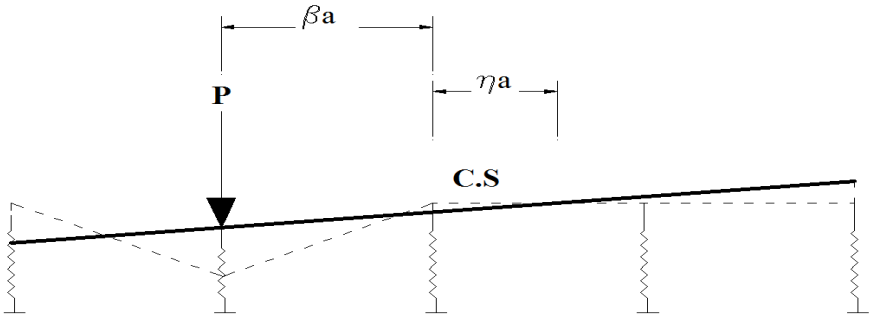


Figure 5. Cross girder with odd number of supports and loaded at any support.

Consider the case of an even number of supports with the load at the center of supports. The load will be applied to the two intermediate supports directly as an approximation because it is meaningless theoretically to but it on a member has no stiffness (figure 6). The general formula for calculating the sum of absolute value of errors and the standard deviation are:

$$e_o = \frac{1}{n}(n-2)+2(\frac{1}{2}-\frac{1}{n}) \quad [21] \quad , \quad s_o = \sqrt{\frac{\frac{1}{n^2}(n-2)+2(\frac{1}{2}-\frac{1}{n})^2}{n}} \quad [22]$$

These two equations can be simplified to:

$$e_o = \frac{2n-4}{n} \quad [23]$$

$$s_o = \frac{1}{n}\sqrt{\frac{n-2}{2}} \quad [24]$$

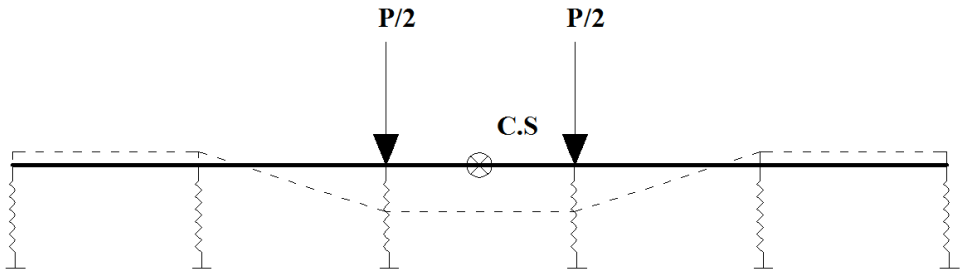


Figure 6. Cross girder with even number of supports and loaded at the middle supports.

Consider the case of even number of supports with the load at the edge of the cross girder (figure 7). First, it is important to find the position where the stiff approach will have no displacement η in order to calculate the absolute value of errors. η can be calculated by solving the following equation:

$$\frac{1}{n} - \frac{a(n-1)/2}{2\sum_{i=1}^{n/2}[(i-0.5)a]^2}\eta a = 0 \qquad [25]$$

For summation, it is required to find the last support that will have the same direction of displacement as the load. This support will be numbered as I from the center of supports.

The general formula for calculating the sum of absolute value of errors and the standard deviation of the errors are:

$$e_o = \sum_{i=1}^{I}[\frac{1}{n} - \frac{(n-1)/2}{2\sum_{j=1}^{n/2}(j-0.5)^2}(i-0.5)] - \sum_{i=I}^{n/2}[\frac{1}{n} - \frac{(n-1)/2}{2\sum_{j=1}^{n/2}(j-0.5)^2}(i-0.5)] + \sum_{i=1}^{[n/2]-1}[\frac{1}{n} + \frac{(n-1)/2}{2\sum_{j=1}^{n/2}(j-0.5)^2}(i-0.5)] + [1-(\frac{1}{n} + \frac{(n-1)/2}{2\sum_{j=1}^{n/2}(j-0.5)^2} \times \frac{n-1}{2})] \qquad [26]$$

$$s_o = \sqrt{\frac{\sum_{i=1}^{n/2}[\frac{1}{n} - \frac{(n-1)/2}{2\sum_{j=1}^{n/2}(j-0.5)^2}(i-0.5)]^2 + \sum_{i=1}^{(n-1)/2-1}[\frac{1}{n} + \frac{(n-1)/2}{2\sum_{j=1}^{n/2}(j-0.5)^2}(i-0.5)]^2 + [1-(\frac{1}{n} + \frac{(n-1)/2}{\sum_{j=1}^{n/2}(j-0.5)^2} \times \frac{n-1}{2})]^2}{n}} \qquad [27]$$

These equations can be simplified to:

$$\eta = \frac{n+1}{6} \qquad [28] \quad , \; I = \text{int}\, ger(\eta + 0.5) \qquad [29]$$

$$e_o = \frac{(n-2)(5n-4) + 4I(n-3I+1)}{2n(n+1)} \qquad [30]$$

$$s_o = \frac{1}{n}\sqrt{\frac{(n-1)(n-2)}{(n+1)}} \qquad [31]$$

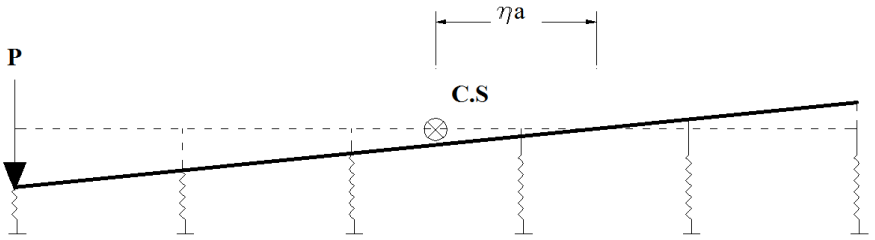


Figure 7. Cross girder with even number of supports and loaded at the edge.

Consider a case of even number of supports loaded at a support with eccentricity of $[(\gamma - 0.5)a]$ (figure 5). First, it is important to find the position where the stiff approach will have no displacement η in order to calculate the absolute values of errors. η can be calculated by solving the following equation

$$\frac{1}{n} - \frac{(\gamma - 0.5)a}{2\sum_{i=1}^{n/2}[(i-0.5)a]^2}\eta a = 0 \qquad [32]$$

For summation, it is required to find the last support that will have the same direction of displacement as the load. This support will be numbered as I from the center of supports.

The general formula for calculating the sum of absolute value of errors and the standard deviation of the errors are:

$$e_o = \sum_{i=1}^{I}[\frac{1}{n} - \frac{(\gamma-0.5)}{2\sum_{j=1}^{n/2}(j-0.5)^2}(i-0.5)] - \sum_{i=I}^{n/2}[\frac{1}{n} - \frac{(\gamma-0.5)}{2\sum_{j=1}^{n/2}(j-0.5)^2}(i-0.5)] + \sum_{i=1}^{\gamma-1}[\frac{1}{n} + \frac{(\gamma-0.5)}{2\sum_{j=1}^{n/2}(j-0.5)^2}(i-0.5)] + \sum_{i=\gamma+1}^{n/2}[\frac{1}{n} + \frac{(\gamma-0.5)}{2\sum_{j=1}^{n/2}(j-0.5)^2}(i-0.5)] + [1-(\frac{1}{n} + \frac{(\gamma-0.5)}{2\sum_{j=1}^{n/2}(j-0.5)^2} \times (\gamma-0.5))] \qquad [33]$$

$$s_o = \sqrt{\frac{\sum_{i=1}^{n/2}[\frac{1}{n} - \frac{(\gamma-0.5)}{2\sum_{j=1}^{n/2}(j-0.5)^2}(i-0.5)]^2 + \sum_{i=1}^{\gamma-1}[\frac{1}{n} + \frac{(\gamma-0.5)}{2\sum_{j=1}^{n/2}(j-0.5)^2}(i-0.5)]^2 + \sum_{i=\gamma+1}^{n/2}[\frac{1}{n} + \frac{(\gamma-0.5)}{2\sum_{j=1}^{n/2}(j-0.5)^2}(i-0.5)]^2 + [1-(\frac{1}{n} + \frac{(\gamma-0.5)}{\sum_{j=1}^{n/2}(j-0.5)^2} \times (\gamma-0.5))]^2}{n}} \qquad [34]$$

These equations can be simplified to:

$$\eta = \frac{n^2 - 1}{6(2\gamma - 1)} \qquad [35] \quad , \; I = \text{int}\,ger(\eta + 0.5) \le \frac{n}{2} \qquad [36]$$

$$e_o = \frac{2n^3 - 7n^2 - 2n - 48\gamma^2 + 48\gamma - 8 + 6\gamma^2 n + 4I[n^2 - 1 - 3I(2\gamma - 1)]}{2n(n^2 - 1)} \qquad [37]$$

$$s_o = \frac{1}{n}\sqrt{\frac{n^3 - n^2 - n - 3(2\gamma - 1)^2 + 1}{(n^2 - 1)}} \qquad [38]$$

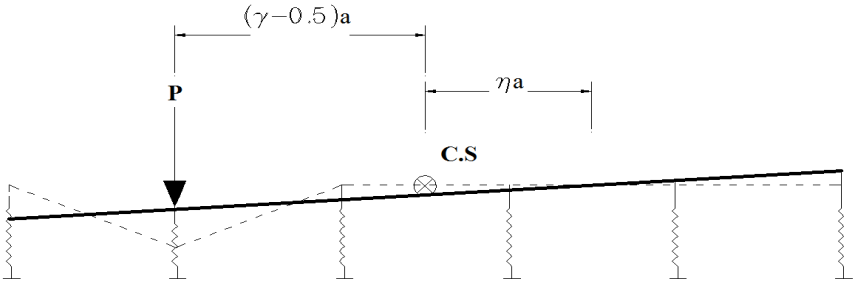


Figure 8. Cross girder with even number of supports and loaded at any support.

General Case for Main and Cross Girder Stiffness

It is extremely difficult to reproduce the previous equations for arbitrary relative stiffness of the cross girder and main girder. In that case, it is required to invert a stiffness matrix with order of $(2nX2n)$, and then do the previous operations on the values representing displacements in the column affected by load P.

The basic idea of this paper is that the extreme limits were studied, and the values of absolute error sum and standard deviation were calculated. By solving as many numerical problems as possible, a suitable approximation for the trend could be produced as follows

$$e_x[s] = \frac{e_o[s_0]}{\alpha k' + 1} \qquad [39]$$

$$k' = \frac{EI_x}{K_m a^3} \qquad [40]$$

	even	odd
e_x	$\alpha = \frac{237.25}{n^{3.43}}$ [41]	$\alpha = \frac{557.1}{n^{3.78}}$ [43]
S	$\alpha = \frac{211.35}{n^{3.38}}$ [42]	$\alpha = \frac{418.65}{n^{3.5}}$ [44]

where E is the modulus of elasticity, I_x is the moment of inertia of the cross girder, and K_m is the stiffness for the equivalent spring of the main girder.

Effective stiffness of Main and Cross Girder Concrete Moment of Inertia

It is obvious at this point that it is necessary to calculate the effective moment inertia for the considered concrete sections to get the true results. Loading codes consider the concrete section to be in the working stage of "linear stress strain relation for concrete" while it is under working loads (figure 9).

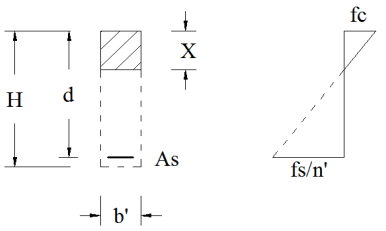


Figure 9. Effective concrete section in the working stage.

From the moment of effective areas about the neutral axis, where the tensile reinforcement ratio $\mu = \frac{A_s}{b'd}$, and $n' = \frac{E_s}{E_c}$ is the ratio between the steel and concrete modulus of elasticity : $b'\frac{x^2}{2} = n'(\mu b'd)(d-x)$ [45]

It could be concluded that: $x = (\sqrt{n'^2\mu^2 + 2n'\mu} - n'\mu)d = \alpha' d$ [46]

And by substituting in equation $I_{NA} = \frac{b'x^3}{3} + n(\mu b'd)(d-x)^2$ [47], it could be derived that:

$$I_{NA} = \frac{b'd^3}{12}[4(\alpha'^3 + 3n'\mu(1-\alpha')^2] \quad [48]$$

Note that, in some cases the moment of inertia of the attached slab increases the total inertia with significant value.

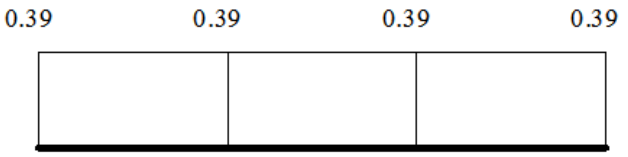
Numerical example

Consider a single span bridge with 5 cross girders, and the ratio of $\frac{b}{a}=2$. For design purposes, the following values could be assumed ($H_m=\frac{L}{10}$, $H_x=0.9H_m$, $d=0.9H$, $b_m=2b_x$, $n'=10$) . Usually, cross girder reinforcement ratio is close to the minimum reinforcement ratio and the main girder reinforcement ratio is close to the maximum reinforcement ratio , so it could be assumed that ($\mu_m=1.5\%$, $\mu_x=0.15\%$). From this data, $\frac{I_x}{I_m}=0.117$ which is much smaller than the value would be calculated using the gross moment of inertia.

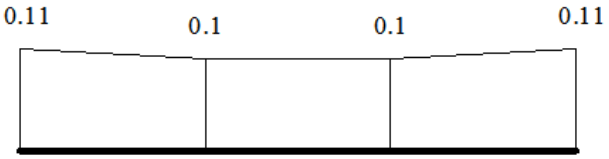
For the middle cross girder, the equivalent spring stiffness for the main girder is $K_m=\frac{p}{\delta}=\frac{384EI_m}{5L^3}$.

Consider two cases of 4 cross girders and five cross girders respectively. The influence lines for sum of absolute errors and standard deviation are drawn.

For 4 supports:

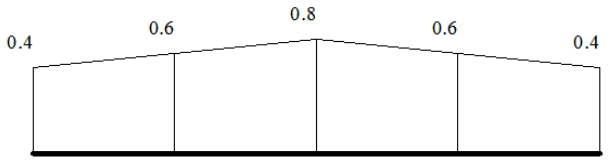


I.L. e_x

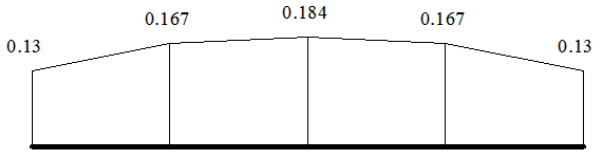


I.L. s

For 5 supports:



I.L. e_x



I.L. s

"Note that the equations were derived for loaded supports only, so it is an approximation to use straight line to describe the values between supports."

CONCLUSION

1-Applying the stiff approach to the cross girder of slab girder bridges has a significant amount of error, even in the most common geometry of the bridge. But it could be used for preliminary design under conservative conditions.

2- Considering the gross moment of inertia of the concrete thickness changes the results dramatically.

REFERENCES

American Concrete Insitiute (ACI). (2008). Building Code Requirements for Structural Concrete (ACI 318-08) and Commentary, ACI Committee 318.

Helmy, M., Shukry. M., and Sultan. A. (1992). "R.C. Design Handbook" Alexandria University. Egypt. 300 pp.

Mahmood, Z (PhD). Class lectures. Cross girder analysis. "Reinforced *Concrete Bridges design." Alexandria University. Egypt. September- October 2006.*

Research Centre for Housing and Construction (2001). Egyption code for practice (ECP203-2001). ECP Permanent committee.

Influence of the Guide Specifications for LRFD Seismic Bridge Design in Alabama

Paul J. Coulston[1] and Justin D. Marshall[2]

[1]Graduate Research Assistant (Presenter), Department of Civil Engineering, 238 Harbert Engineering Center, Auburn University, Auburn, AL 36849; email: coulspj@auburn.edu
[2]Assistant Professor, Department of Civil Engineering, 238 Harbert Engineering Center, Auburn University, Auburn, AL 36849; email: jdmarshall@auburn.edu

ABSTRACT

The Alabama Department of Transportation (ALDOT) is in the process of transitioning from the AASHTO Standard Specification for Highway Bridges to the LRFD Bridge Design Specifications. One significant difference between the two specifications is the seismic design provisions. From a practical point of view, the desire is that typical details can be developed for the worst case scenarios which can be implemented for bridges throughout the state without a significant cost premium. To determine the effects of the updated seismic provisions on current practice, an initial study of existing bridges was completed. Three typical, multi-span, prestressed concrete I-girder bridges were selected for the study. In order to bracket the demands for typical bridges, the primary bridge geometry variables were span length, pier height and pier configuration.

The bridges' Earthquake Resisting Systems were re-designed for the worst conditions for the state of Alabama. After doing the initial calculations with Site Class D as the soil condition, it was found that the Seismic Design Catergory B was the worst case for Alabama. The AASHTO Guide Specifications for LRFD Seismic Bridge Design was used for analysis and design of the three bridges. This paper discusses the changes made to two of the bridges in order to meet the requirements. The reinforcing detailing requirements in the pier for the hinge location were increased, the pier cap and drilled shaft were designed in accordance with capacity-based design, and the connection between the pier cap and girder was re-designed.

PROBLEM STATEMENT

Alabama Department of Transportation (ALDOT) has been designing bridges using the AASHTO Standard Specification for Highway Bridges (Standard Specification); however, due to Federal Highways Administration (FHWA) requirements, ALDOT will be required to begin designing bridges in accordance with AASHTO LRFD Bridge Design Specifications (LRFD Specification). Under the Standard Specifications most of the state was classified as Seismic Performance Category A which required minimal seismic detailing and no additional analysis. The new requirements will influence future bridge design. Specifically, the

substructure elements, the superstructure-to-substructure connections, and the foundations will see the most change. From a practical point of view, ALDOT Bridge Bureau's desire is that typical details can be developed for the worst case scenarios which can be implemented for bridges throughout the state without a significant cost premium.

This study was done to update the seismic bridge design in the state of Alabama. Three existing standard, multi-span, prestressed concrete I-girder bridges were selected to be redesigned according to the specifications in the AASHTO Guide Specifications for LRFD Seismic Bridge Design (Guide Specification). The results of two of those bridges are reported here. The main objectives were the following:

1. To determine the effects of LRFD seismic provisions on design and detailing and
2. To determine if typical, economically feasible details can be utilized for all the selected bridges.

INTRODUCTION

The major differences between the Guide Specification and the Standard Specification are described in the following section. The differences can be broken down into the following categories:

- New Ground Acceleration Maps

The Standard Specification currently uses ground acceleration maps created by the United States Geological Survey (USGS) in 2002. The map assumes the soil condition to be rock. The seismic loads represented by the acceleration coefficients have a 10% probability of exceedance in 50 years which corresponds to a return period of approximately 475 years. For the Guide Specifications, the ground acceleration maps depict probabilistic ground motion and spectral response for 7% probability of exceedance in 75 years which corresponds to a return period of approximately 1000 years. Also, the Guide Specification has maps for peak ground acceleration (PGA), 0.2 second spectral response acceleration (S_S), and 1.0 second spectral response acceleration (S_1) instead of just one map. The change in the ground acceleration maps generates an increase in design earthquake load for a bridge. These changes are due to larger return period for the design earthquake and the significant amount of research completed on the New Madrid and East Tennessee faults.

- New Design Spectral Shape

In the AASHTO Standard Specification, the spectral acceleration maximum is 2.5*Acceleration coefficient, A. Unless the ground acceleration is greater than or equal to 0.3, then the maximum spectral acceleration is 2.0*A. The equation for the elastic seismic response coefficient can be seen in Equation 1. The response coefficient is decaying a rate of $1/T^{2/3}$. However, the response spectrum decreases at a rate of 1/T, but because of the concerns associated with inelastic response of

longer period bridges it was decided that the ordinates of the design coefficients and spectra should not decrease as rapidly as 1/T but should be proportional to $1/T^{2/3}$ (AASHTO 2002). The response spectrum in the Guide Specification decreases at a rate of 1/T. In Figure 1, the response spectrum for the Guide Specification and Standard Specification is compared. The Guide Specification design response spectrum includes the short-period transition from the acceleration coefficient, A_S, to the peak response region, S_{DS}, unlike the Standard Specification. This transition is effective for all modes, including the fundamental vibration modes. Use of the peak response down to zero period is felt to overly conservative, particularly for a displacement-based design. (AASHTO 2008)

$$Cs = \frac{1.2 * A * S}{T^{2/3}} \qquad \textbf{Equation 1}$$

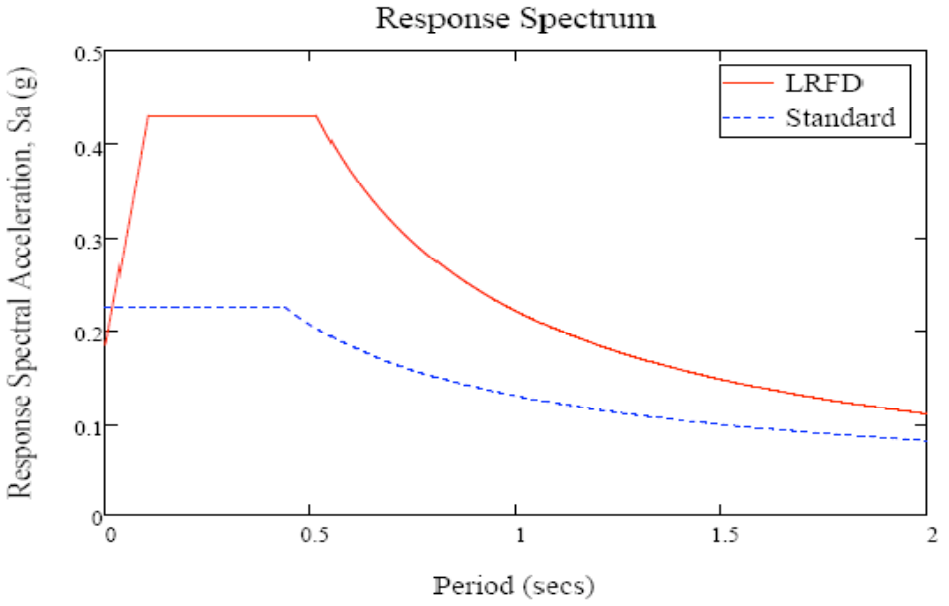


Figure 1 Comparison of the response spectrum for the Standard Specification and Guide Specification

- Site Factors

The Standard Specification has four different soil profiles which correspond to four site factors. The seismic performance category is first chosen, and then according the soil condition, the elastic seismic response coefficient is amplified. The Guide Specification has six soil profiles which correspond to six soil factors. The site class is chosen before the seismic design category is selected in contrast with the Standard Specification. These factors affect the spectral response coefficients which in turn affects the seismic design category.

GENERAL SEISMIC BRIDGE DESIGN

The initial seismic calculations and checks were the same for all of the three bridges. This is the case because the worst case for seismic design in Alabama was chosen for this project. Therefore, the location of the bridges given for redesign is irrelevant. The steps, checks and calculations described in this section are the same for the three bridges designed for this project.

A design worksheet for concrete bridges in SDC B was created using Mathcad to facilitate the design (Parametric Technology Corportation 2007). The design worksheet allows the user to input data that is required for design. The designer will have to make some changes to the worksheet as a new bridge is being designed. Mathcad is set up in a way where the input data and output can be seen easily. The checks for design are already in the worksheet; therefore, the designer must only verify that they are satisfied. This worksheet will decrease the amount of time it takes to seismically design a bridge.

The Guide Specification supplies flowcharts which can be followed to ensure all the requirements for seismic design are checked. First of all, the initial sizing of columns should be done for strength and service load combinations defined in the LRFD Specification (AASHTO 2007). The first thing to be done is to check and verify that the Guide Specification can be used for the bridge design. The Guide Specification applies to the design and construction of conventional bridges to resist the effects of earthquake motions. Critical and Essential bridges are not specifically addressed in the Guide Specification (AASHTO 2008). The bridges that were analyzed and design are classified as conventional bridges.

The next item to be investigated is under what performance criteria will be used. According to the Guide Specification, "Bridges shall be designed for life safety performance objective considering a seismic hazard corresponding to a 7% probability of exceedance in 75 years. Life Safety for the design event shall be taken to imply that the bridge has a low probability of collapse but may suffer significant damage and that significant disruption to service is possible. Partial or complete replacement may be required." (AASHTO 2008)

A foundation investigation needs to be done in the location the bridge will be built. For bridges in SDC B and where loose to very loose saturated sands are in the subsurface profile, the potential of liquefaction should be considered since the liquefaction of these soils could affect the stability of the structure. The commentary of the Guide Specification discusses when liquefaction needs to be considered for SDC B. It was assumed that the structures in this paper would not be affected by liquefaction.

For SDC B, the identification of an earthquake resisting system (ERS) should be considered. For the bridges in the study, a Type 1 earthquake resisting system was chosen. Type 1 structures have "ductile substructures with essentially elastic superstructure: This category includes conventional plastic hinging in columns and walls and abutments that limits inertial forces by full mobilization of passive soil resistance. Also included are foundations that may limit inertial forces by in-ground hinging, such as pile bents and integral abutments on piles" (AASHTO 2008).

A response spectrum should be created for the bridge being designed. The response spectrum is created by using the seismic hazard maps and the site classification. The USGS seismic parameters CD-ROM accompanying the Guide

Specification with the seismic hazard maps will calculate the accelerations based on the longitude and latitude. After determining these values, a response spectrum can be created by using a series of equations. The next step in the design process is to select the seismic design category. This is based on the 1-second period spectral acceleration which is dependent on location and site classification. For all the bridges in this project, the seismic design category is B. After this step in the process, the design will change depending on the bridge.

Introduction to the Bridges

ALDOT has chosen three existing bridges to be redesigned according to the Guide Specification. The bridges selected were standard concrete bridges. Below, two of the bridges which were redesigned are discussed. The expected changes in the transverse reinforcing and connection of the substructure and superstructure were seen in these bridges.

Bridge 1

Bridge 1 consists of three 80 ft, simple spans. The concrete bridge is 240 ft long and 32 ft 9 in. wide. The substructure has a 7 in. concrete deck supported by four AASHTO Type III girders that are equally spaced. The bridge has two bents which are made of a bent cap beam that is 4 ft x 5 ft x 30 ft, two 42 in. circular concrete columns, and two 42 in. circular drilled shafts. The abutments, which are 3 ft x 3.5 ft x 35 ft, are supported by two 42 in. circular drilled shafts. The columns have an average above ground height of 9 ft. Currently, the column and drilled shaft reinforcing are 12 number 11 bars for the longitudinal reinforcing and No. 5 hoops at 12 in. on center for the transverse reinforcing.

The first step in the seismic design process was to input all the information about the bridge into the design worksheet. An equivalent static analysis was used to analyze the bridge. Both uniform load method and single mode spectral method was completed for this bridge, but since the results were similar, the easiest method was selected. In order to do a seismic analysis, a bridge model was created in SAP 2000 Bridge Modeler (Computer & Structures 2007). A uniform load of 1 kip/ft was converted into joint loads and applied to the bridge in both the transverse and longitudinal direction. The maximum joint deflection was used to calculate the equivalent stiffness in both the transverse and longitudinal direction. The weight of the bridge was then calculated. An equivalent lateral load was created by multiplying the spectral acceleration by the weight and dividing it by the length of the bridge for both directions. Instead of re-inputting the loads into the bridge model, the designer is allowed to scale the deflection from the 1 kip/ft load by the equivalent lateral load. The bridge had maximum deflections in the longitudinal and transverse directions of 0.201 in. and 0.904 in., respectively.

Next, the displacement capacity of the columns had to be verified. For SDC B, simplified equations can be used. When the simplified equations were checked for the above ground height, the columns failed the capacity equations. Therefore after discussing this with ALDOT, it was decided to allow hinging to occur below ground. The point of fixity was assumed at the rock line. After allowing below ground

hinging, Bent 3 satisfied the simplified equations; however, Bent 2 still did not satisfy the equations because of the length-to-diameter ratio was too large. It was determined that in order to satisfy the equations with a 42 in. diameter column the clear column height would have to be 20 ft. The Bent 2 clear column height was 18 ft, and Bent 3 column height was nearly 26 ft. According to the Guide Specification, a pushover analysis can be done to verify the displacement capacity of the bridge. The bridge satisfied the pushover analysis. After completing the displacement capacity check, the seat widths were calculated to around 18 in. for the bents and abutments.

According to the Guide Specifications, the shear demand for columns in SDC B can be designed for force obtained from a linear elastic seismic analysis or the force corresponding to plastic hinging of the column including the overstrength factor (AASHTO 2008). For Bridge 1 the plastic hinging force of the column was used in design. PCA Column (PCA 2004) was used to create an interaction diagram which was used to calculate the moment capacity of the column and to ensure the column had sufficient strength to resist the applied moments from the dead load and seismic loads. The moment capacity was then amplified by an overstrength factor of 1.4. The plastic hinge zone for the columns in both Bents 2 and 3 was controlled by 1.5 times the column diameter, which is equal to 63 in. The maximum spacing of seismic hoops within the hinge zone is set at 6 in., and this is what controlled the design of these columns. Therefore within the plastic hinge zone, the columns are reinforced with No. 5 seismic hoops at 6 in. on center. The hoops within the hinge zone require 135 degree hooks or must be welded. The close spacing of the hoops provides confinement of the core which is critical during a seismic event. The shear strength of the columns was more than adequate. Also, a requirement for an extension of the hinge zone reinforcing into the bent cap beam and drilled shaft out of the LRFD Specification was used in the design. The extension zone reinforcing for these columns is 21 in. which is governed by half the diameter of the column. This is not specifically required for SDC B in the Guide Specification, but in order to avoid a plane of weakness at the joint, it has been considered important to have the extension in the design. Outside the plastic hinge zone, the columns are designed according to the LRFD Specification. Currently, outside the plastic hinge zone the No. 5 hoops were spaced a 12 in. on center, and this proved to be adequate to resist the shear force. The hoops outside the hinge zone can have tension lap splices. The drilled shafts' lateral reinforcing was designed like the column's lateral reinforcing outside the hinge zone. Hence, the drilled shaft's lateral reinforcing is No. 5 hoops at 12 in. on center. A comparison of the increase in column design can be seen in Table 1. Figures 2 and 3 compare the transverse reinforcing from the Standard Specifications and the Guide Specification for Bent 3 and Bent 2, respectively.

The change from the Standard Specification to the Guide Specification not only affects the column reinforcing but also the connection of the girder to the bent cap. The shear load the connection must be designed for has increased which in turn has affected design. Currently ALDOT is using an L6x6x1/2 by 12 in. long for the connection between the girder and bent cap beam. An anchor bolt is used to connect the angle to the bent cap beam and precast screw inserts are used to connect the vertical leg of the angle to the girder. However, a through bolt in the girder has been proposed as an option instead of the precast screw inserts. The anchor bolts and

through bolts will be designed for the same forces. Also, other types of connections are being investigated in order to avoid the construction problems with the anchor bolt locations not matching the plans. For the connection between the bents and the girders, two 1.25 in. diameter anchor bolts had to be used versus one anchor bolt, but for the connection between the abutment and girder, the same anchor bolt as before can be used. The change in the connection can be attributed to the increase in shear force demand. The increase in shear force from the previous design causes a necessary increase of the bending strength of the angle. The bending criteria for the angle could be met by lengthening the angle, adding stiffeners, or increasing the angle thickness. For this bridge, the angle thickness has been increased to 0.875 in. and 0.75 in. for the bents and abutments, respectively.

Table 1 Column design comparison

Category	Standard Specification	Guide Specification
	Bent 2 &3	**Bent 2 &3**
Stirrup Size	#5	#5
Stirrup Spacing Outside Plastic Hinging Region	12 in. o.c.	12in. o.c.
Stirrup Spacing Inside Plastic Hinging Region	12 in. o.c.	6.0 in. o.c.
Length Plastic Hinge Region	0	63 in.
Number of Stirrups per Column	34	51
% Increase in Stirrups	0	33%

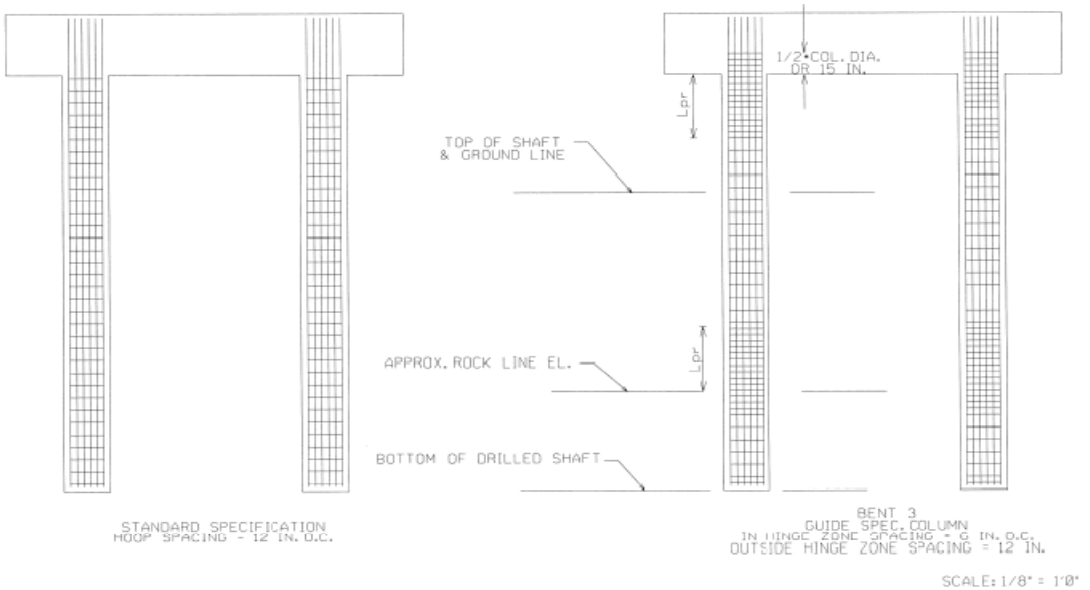


Figure 2: Column Transverse Reinforcing for Bent 3

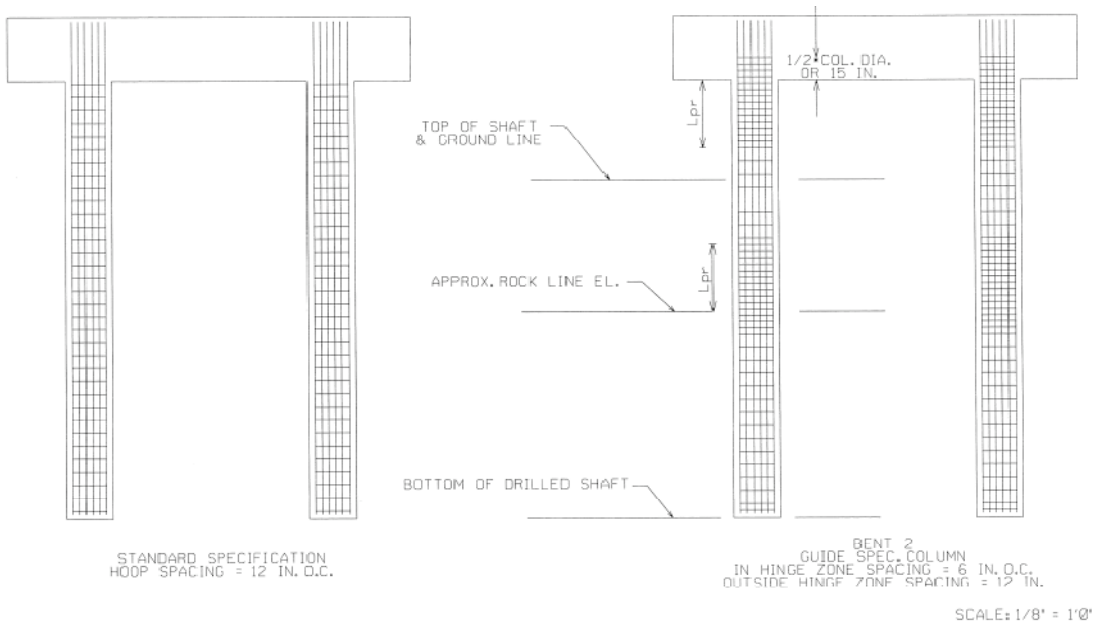


Figure 3: Column Transverse Reinforcing for Bent 2

Bridge 2

Bridge 2 is a three span concrete prestressed I-girder bridge with side spans 85 ft long and the middle span 130 ft. The total length and width of the bridge is 300 ft and 42 ft 9 in., respectively. The short span's superstructure consists of a 7 in. concrete deck supported by six AASHTO Type III girders spaced equally. The long span's superstructure consists of a 7 in. concrete deck supported by six BT-72 girders equally spaced. There are two bents which consist of a cap beam and two 54 in. circular columns which are supported by 60 in. circular drilled shafts. The columns and drilled shafts longitudinal reinforcing is 24 No. 11 bars. The bent cap beam allows for the change in size for the girders and has a total depth of 9 ft 4 in., width of 5 ft. and length of 40 ft. Bent 2 has an above ground height of 12 ft, and Bent 3 has an above ground height of 16 ft 8 in. Abutment 1, which is 3 ft x 3.5 ft x 45 ft, is supported by three 42 in. circular drilled shafts. Abutment 2 has the same dimension of Abutment 1, but it is not supported by drilled shafts.

The same procedure used to design the Bridge 1 was used to design Bridge 2. A model was built in SAP, and then the uniform loads were applied to the bridge in both transverse and longitudinal directions. When the abutment that is not supported by drilled shafts was modeled, it was only restrained in the vertical direction; therefore, the max deflection in the transverse direction is at this end of the bridge. The maximum displacements in the transverse and longitudinal direction are 1.486 in. and 0.448 in.

When designing this bridge, it was determined that it was not practical to design it for the capacity of the column, but to design it for the elastic forces from a linear elastic seismic analysis. PCA Column was used to create interaction diagrams for the columns and drilled shafts in each bent. After looking at the interaction diagrams for the column and drilled shaft for Bent 3, it was concluded that the longitudinal reinforcing needed to be increased because the combination of the uplift

case for the earthquake load and the dead load was so small. The column longitudinal reinforcing was increased to 28 No. 11 bars, and the drilled shaft reinforcing was increased to 32 No. 11 bars. This is not a problem in the design or construction process because the volumetric ratio was still small.

When the simplified displacement capacity equations were calculated, the columns failed this check; therefore, a pushover analysis was done on the bridge, and it satisfied the displacement demands. The shear forces for the design of the columns and drilled shafts were taken from the bridge model. Tables 2 and 3 display the difference in design between the Standard Specification and the Guide Specification. Figures 4 and 5 compare the transverse reinforcing from the Standard Specifications and the Guide Specification for Bent 3 and Bent 2, respectively. The plastic hinge zone is control by 1.5 times the column diameter. The spacing within the hinge zone is 6 in. on center. The spacing outside the hinge did change from 12 in. to 10.5 in. on center because the minimum transverse reinforcement specification was not met. The drilled shafts are reinforced with No. 6 hoops at 12 in. on center. The drilled shafts had a slight increase in transverse reinforcing, but this was due to the extension of the seismic hoop reinforcing. The extension into the drilled shaft and bent cap beam is 27 in. which is controlled by half the column diameter.

Table 2 Column design comparison for Bent 2

Category	Standard Specification	Guide Specification
Stirrup Size	#5	#5
Stirrup Spacing Outside Plastic Hinging Region	12 in. o.c.	10.5 in. o.c.
Stirrup Spacing Inside Plastic Hinging Region	12 in. o.c.	6.0 in. o.c.
Length Plastic Hinge Region	0	81 in.
Number of Stirrups per Column	12	29
% Increase in Stirrups	0	59%

Table 3 Column design Comparison for Bent 3

Category	Standard Specification	Guide Specification
Stirrup Size	#5	#5
Stirrup Spacing Outside Plastic Hinging Region	12 in. o.c.	10.5 in. o.c.
Stirrup Spacing Inside Plastic Hinging Region	12 in. o.c.	6.0 in. o.c.
Length Plastic Hinge Region	0	81 in.
Number of Stirrups per Column	17	36
% Increase in Stirrups	0	53%

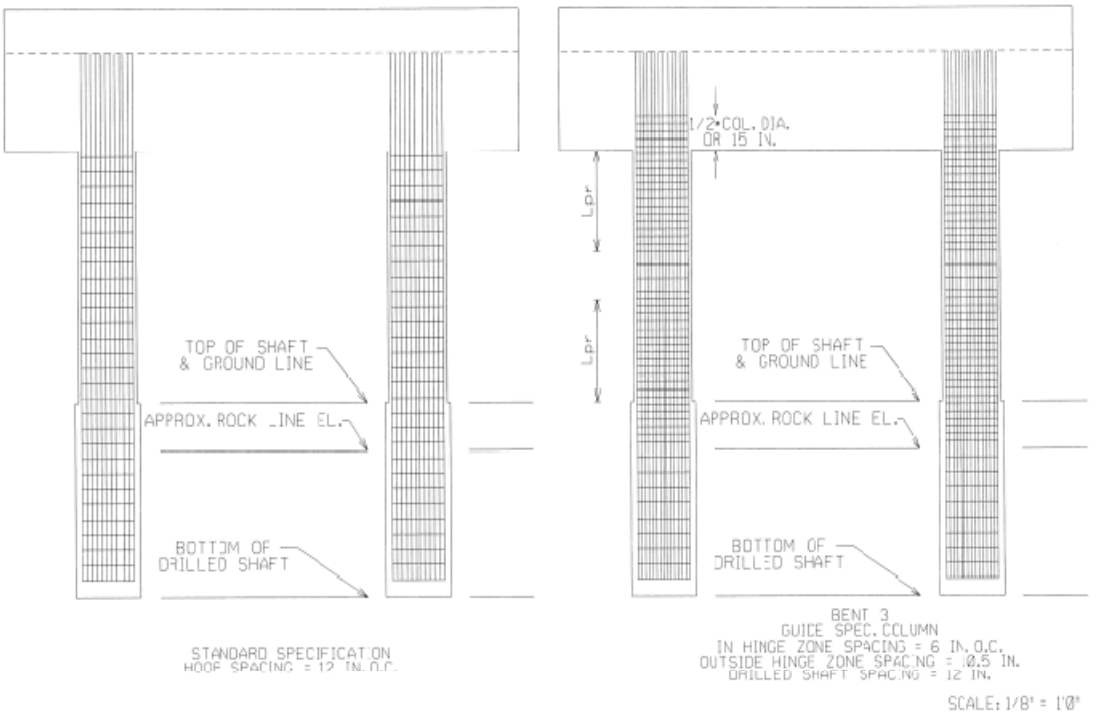


Figure 4: Column Transverse Reinforcing for Bent 3

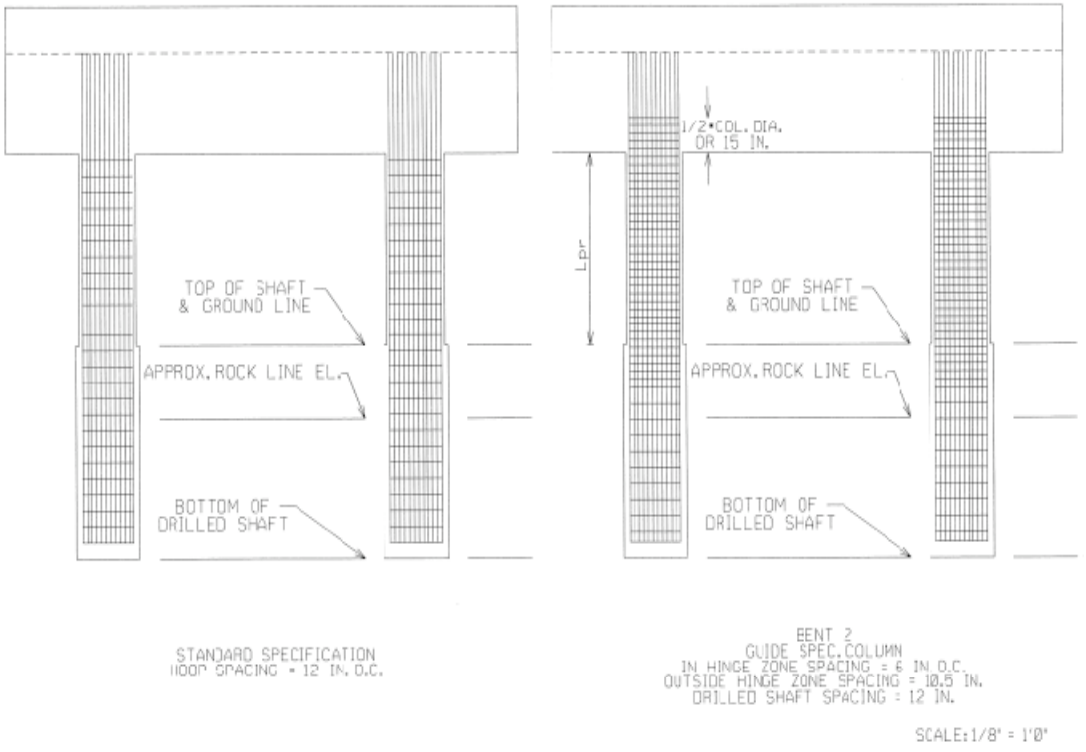


Figure 5: Column Transverse Reinforcing for Bent 2

For the Bridge 2, the connection between the superstructure and substructure had to be changed. For this bridge, the connection between the girder and bent cap beam is still an L6x6x1/2 by 12 in. long angle. For the Guide Specification, the same

connection was able to be used for both the Type III girder and the BT-72 girder. The diameter of the anchor bolt had to be increased to 1.5 in. The increase in shear force from the previous design causes a necessary increase of the bending strength of the angle. The thickness of the angle has been increased in this case.

CONCLUSIONS

Valuable information has been discovered from the two bridges whose substructures have been redesigned. From these two bridges, it is concluded that there is no problem in meeting the displacement capacity qualifications set by the Guide Specification. The shear force in the bridges has increased since the ground hazard maps have changed from the Standard Specifications. Since the bridges currently being designed do not take into account plastic hinge zones, it is concluded that there will be an increase in hoop reinforcing in most of the bridges in Alabama as seen with these two bridges. There also will be an increase in the anchor bolt diameter or number in order to carry the shear force. The angle must be strengthened in some manner in order satisfy the bending force. The redesign of the two bridges has aided in the understanding of what significant changes will need to be made in the state of Alabama.

ALDOT's goal was to develop standard details for the worst case seismic scenario in the state. From the results of these two bridges, it seems to be unlikely that will happen. In the plastic hinge zone, it can be assumed the spacing of the reinforcing will be 6 in. on center for most bridges in Alabama. Mostly likely, it can be concluded that the plastic hinge zone length will be controlled by 1.5 times the column diameter. However, the plastic hinge zone length and spacing need to be checked. If more bridges are investigated, it may be concluded that plastic hinge zone length and spacing can be assumed to be 1.5 times the column diameter and 6 in., respectively. Even though standard details may not be developed, the design worksheet that has been created for seismic design of concrete bridges in SDC B will ease the process of seismically designing bridges.

REFERENCES

AASHTO (2008). *AASHTO Guide Specifications for LRFD Seismic Bridge Design.* Washington D.C.: American Association of State Highway and Transportation Officials.

AASHTO (2007). *AASHTO LRFD Bridge Design Specifications.* Washington D.C.: American Association of State Highway and Transportation Officials.

AASHTO (2002). *Standard Specification for Highway Bridges 17th Edtion.* Washington D.C.: American Association of State Highway and Transportation Officials.

Computer & Structures, Inc. (2007). *SAP2000 User's Guide.* Berkeley, CA: Computer & Structures, Inc.

Parametric Technology Corportation (2007). *User's Guide Mathcad 14*. Needham, MA: Parametric Technology Corporation.

PCA (2004). *PCA Column*. Portland Cement Association.

HIGH QUALITY, TWO-NODES COMPONENT-BASED MODELING OF SEMI-RIGID BEAM-TO-COLUMN CONNECTIONS FOR COMPUTER-ORIENTED ANALYSIS

T. W. Aure[1] and S. Taye[2]

[1] Doctoral student, Department of Civil & Environmental Engineering, P.O. Box 21007, University of Cincinnati, Ohio, USA; Phn: (513) 476-9906, USA; Phn: (513) 476-9906; email: temesgen_wond@yahoo.com

[2] Assoc. Professor, Addis Ababa Institute of Technology, Addis Ababa University, P.O. Box 385, Addis Ababa, Ethiopia; Phn: (251 11) 123-2437, Fax: (251 11) 123-9480, email: staye@ceng.aau.edu.et

ABSTRACT

A new component-based, two-node, simplified, semi-rigid beam-to-column-connection element than can easily be used in conjunction with many available structural-engineering software products is proposed for computer-oriented structural analysis. Relevant connection element properties, such as its stiffness matrices, have been established. The proposed model circumvents the iterative procedure proposed by several code standards for determining the resistance capacity and rotational stiffness of beam-to-column connections while at the same time it also alleviates the inapplicability of four-node elements that have been proposed by several researchers for use in commonly available high-end structural engineering software products.

In the process of formulating the analytical model, panel shear deformation of the joint has been taken care of by allowing the joint region of the column to undergo shear deformation.

Numerical experience has been gained by processing several frame structural models. Application will be demonstrated using the general purpose finite element package ANSYS by way of applying to study a typical frame. Results have also been compared with those obtained by other researchers and a high-quality correlation between and among results have been obtained. In all cases, values obtained by the proposed two-node connection model have been acceptable for design purpose.

1. INTRODUCTION

The study of the behavioral response of semi-rigid joints, characterized by non-full fixity or unconstrained free rotation of the connected members, has been a research topic since the last couple of decades. Extensive studies have been carried out over the past three decades to establish the actual behavioral response of semi-rigid joints. A large number of findings have been produced on composite- and steel semi-rigid connections, covering the state of the art (Bjorhovde *et al*, 1996), numerical studies and experimental tests [such as, for example, Chen and Toma (1994), Bayo *et al* (2006), among many others] which lead to code specifications.

Most design codes also address methods and procedures for the determination of their resistance capacity and rotational stiffness. The European Code Standards

EC3 (CEN, 2004), for example, allows the use of the so called *component method* to simulate the semi-rigid behavior of such joints. In order to account for the panel shear deformation, the Code allows the use of an interaction parameter which is defined based on the internal forces at the joint thereby calling for a computationally demanding iterative process during global analysis. However, this later approach is quite inefficient and, thus, it is not generally accepted in practical design environments.

In order to avoid this iterative process Bayo *et al* (2006) proposed a new four-node element that accounts for various deformation modes in its formulation. These four-node elements, however, could not easily be practiced in commonly available structural engineering software.

Despite the fact that a large knowledge-base now exist with regard to semi-rigid connections, the design of such connection is barely practiced in several instances. This phenomenon is explained in part by the lack of effective tools for the analysis of such frames, and insufficient experimental data and the sizable cost involved in organizing such experiments. Apart from this, many available structural-engineering software products do not accommodate some of the available semi-rigid joint modeling findings.

In this paper a new component-based, two-node connection element is proposed to alleviate shortcomings of the four-node elements with particular emphasis on their computerized implementation. The local deformation of the column panel zone is accounted for by allowing shear deformation. General purpose finite element package ANSYS (2004) been used to study a series of frames under several loading and geometric conditions.

2. CONNECTION CLASSIFICATION

Realizing the potential influence of connections on frame performance, various design codes, among which Eurocode 3 is one (CEN, 2004), have introduced provisions to allow designers to consider explicitly the behavior of connections in the design of structural steel frames.

Most design codes tend to identify three types of connections for designing multistory frames: Type I (rigid framing), Type II (simple framing), and Type III (semi rigid framing). To be pertinent, the rigidity of the connection should be defined with respect to the rigidity of the connecting members. For general application to a wide range of beam-to-column connections, Bjorhorde *et al* (1996) introduced a non-dimensional system of classification that compares the connection stiffness to the beam stiffness. With particular reference to semi-rigid connections, they have used the following expression as their range of definition; viz.

$$\begin{cases} 0.2 \le \overline{m} \le 0.7 & \text{in terms of strength} \\ 0.5\overline{\theta} \le \overline{m} \le 2.5\overline{\theta} & \text{in terms of stiffness} \end{cases} \tag{1a}$$

where the non-dimensional parameters $\overline{m}$ and $\overline{\theta}$ used in the classification of connections are given by:

$$\bar{m} = \frac{M}{M_p}, \qquad \bar{\theta} = \frac{\theta_r}{\theta_p} \tag{1b}$$

where again,

θ_r is the relative deformation angle of the connection,

$\theta_p = \frac{M_p}{(EI_b/5d)}$ in which I_b denotes the moment of inertia of the beam

M_p represents the full plastic moment capacity of the beam.

3. MODELING OF SEMI-RIGID CONNECTIONS

There have been developed various approaches for modeling semi-rigid connections. The summary of the various approaches with fairly reasonable discussion on component-based methods is provided subsequently.

3.1 *Existing Models*

Several analytical models have been developed to represent connection flexibility using available experimental test data. Semi-rigid connections have been modeled on available experimental test data through curve-fitting techniques. Indeed, the most commonly used approach to describe M-θ_r curve is to simulate the experimental data with simple expressions. Such models include the Frye-Morris Polynomial model, the Modified Exponential Model developed by Kishi and Chen as a refinement of Chen-Lie exponential model, and the Three Parameter Power Model proposed by Chen *et al* [all referred to in Chen and Toma (1994)], and finally the Four Parameter Power Model of Richard and Abbott [referred to in Scott and Burns (2003)].

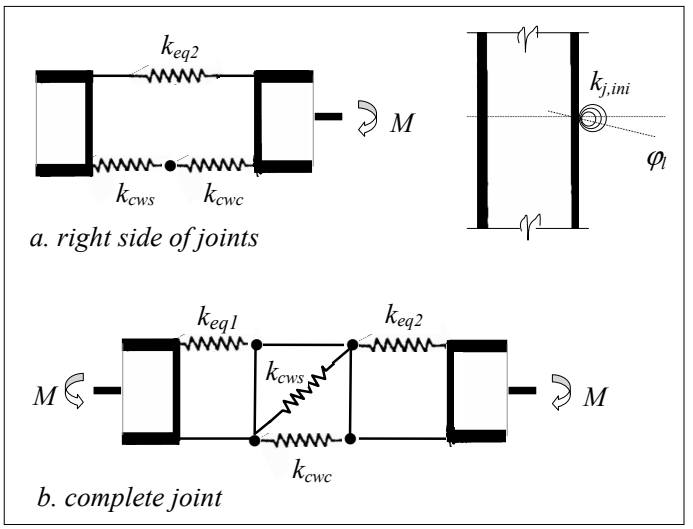


Figure 1. Spring model for the semi-rigid joint.

The finite element representation of semi-rigidly connections has also been explored. One such proposal has been by Xu [referred to in Scott and Burns (2003)]. In this modeling approach, a member is assumed to be consisting of the originally fully rigidly connected member and zero length spring elements (with spring constant equal to the appropriate secant stiffness of the semi-rigid connection it

simulates) attached to each member end. The relationship between end-moments and end-rotations of a beam can be developed. Finally, the elastic element stiffness matrix of a semi-rigidly connected member can be formulated.

The finite element modeling of semi-rigid connection takes into account geometrical non-linearity as well. The geometrical stiffness matrix has been developed by Xu [referred to in Scott and Burns (2003)] and it is specifically suited for semi rigidly connected members. The main drawback associated with this modeling approach, however, is that one needs to write an analysis program accounting for semi-rigid behavior. The other shortcoming of this model is its inability to account for the panel shear deformation.

An alternative for modeling semi-rigid connections is the so-called component-based joint modeling which is the main subject of this paper. This is a mechanical model joint in which each component is modeled by an equivalent linear spring (CEN, 2004).

Figure 1 shows a condensed model of the right side connections in which K_{eq2} is the resultant of the stiffness originating from a number of contributing parts consisting of column-web in tension, column right flange in bending, end plate in bending, angles, and bolts in tension. The springs K_{cws} and K_{cwc} represent the stiffness of the panel zone (column web) under shear and compression, respectively.

These springs are assembled to form a single bi-linear (elastic-plastic) rotational spring that models the connection and this later one is attached at the intersection of beams and columns for global analysis. The bilinear model is characterized by an initial stiffness $K_{j,ini}$ (resultant of all the components) and moment resistance $M_{j,Rd}$ which are defined, respectively, by the following expressions:

$$K_{j,ini} = \frac{h^2}{\frac{1}{K_{cws}} + \frac{1}{K_{cwc}} + \frac{1}{K_{eq}}} \tag{2a}$$

$$M_{j,Rd} = \sum F_{lt,i,Rd} h_i \tag{2b}$$

where h is the lever arm and $F_{Lt,i,Rd}$ is the resistance of each component (CEN, 2004)] (details are shown later in Figure 3).

Shear stresses in the column panel zone of the beam-column connection joint play significant role influencing the nature of the connection itself. The shear force acting on the panel zone is defined as (Bayou *et al*, 2006):

$$V_{cw} = \frac{M_1}{h}\left[\left(1 + \frac{M_2}{M_1}\right) - \frac{h}{2M_1}\left(V_{c1} + V_{c2}\right)\right] = \frac{M_1}{h}\beta_1 \tag{3a}$$

$$V_{cw} = \frac{M_2}{h}\left[\left(1 + \frac{M_1}{M_2}\right) - \frac{h}{2M_2}\left(V_{c1} + V_{c2}\right)\right] = \frac{M_2}{h}\beta_2 \quad) \tag{3b}$$

where M_1 and M_2 are the bending moments acting at the left and right side of the joint, and V_{c1} and $V_{c2,}$ are the shear forces in the upper and lower columns, respectively.

The expressions in brackets of Eqs. (3a, b) constitute the interaction factors β that are used in EC3 to define the shear forces acting on the panel zone. EC3 further simplifies Eq. (3) by omitting the beneficial effect of the shear forces V_{c1} and V_{c2} (CEN, 2004), and by limiting β to positive values less than 2.0, as in the following equation:

$$\beta_1 = \left| 1 + \frac{M_2}{M_1} \right| \leq 2 \qquad \text{and} \qquad \beta_2 = \left| 1 + \frac{M_1}{M_2} \right| \leq 2 \tag{4}$$

These β factors affect the values of the joint stiffness $K_{j,ini}$ and moment resistance $M_{j,Rd}$. However, the bending moments M_1 and M_2 and shear forces V_{c1} and V_{c2} coming from different elements (beams and columns) can only be established after a global analysis. Therefore, an initial guess of these values and a subsequent iteration procedure are needed to update the joint characteristics and to obtain the final distribution of internal forces and moments.

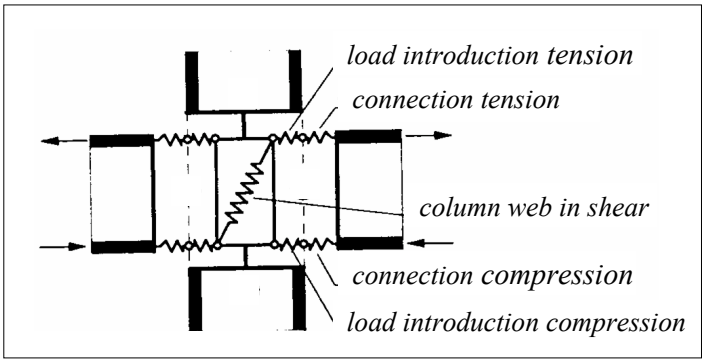


Figure 2. General model for steel joints [3]

Bayo *et al* (2006) proposed an EC3 component-based finite dimensioned elastic-plastic 4-node joint element which takes into account the actual size of the joint, its deformation characteristics (components) including those of the panel zone, local phenomenon and all the internal forces that concur at the joint. As a consequence, this new element avoids the use of the β-factor and the inherent initial guessing and iterative process that it requires. Since the element is attached to the adjacent beams and columns, the eccentricities of the internal forces coming from them are also taken into account.

For an interior joint the components are shown in Figure 1. The springs K_{eq1} and K_{eq2} represent the left and right connection stiffness, respectively. The springs K_{cws} and K_{cwc} represent the stiffness of the panel zone (column web) under shear and compression, respectively; which are usually the most critical components of the joint. All these values may be obtained by means of formulas described in EC3. Figure 3 shows the new base element with 4 nodes and 9 degrees of freedom, proposed by Bayo, *et al* in which the rigid body modes have been restrained.

The dimension *d* noted in Figure 3a is that of the width of the column, and the height *h* corresponds to the lever arm defined in EC3, Part 1.8 (CEN, 2004).

This base element will be used to obtain the basic flexibility and stiffness matrices. Afterwards, the contribution of the rigid body modes will be added to obtain the complete stiffness matrix in terms of the 12 degrees of freedom shown in Figure 3b.

In order to develop the flexibility matrix the following deformation modes are considered:

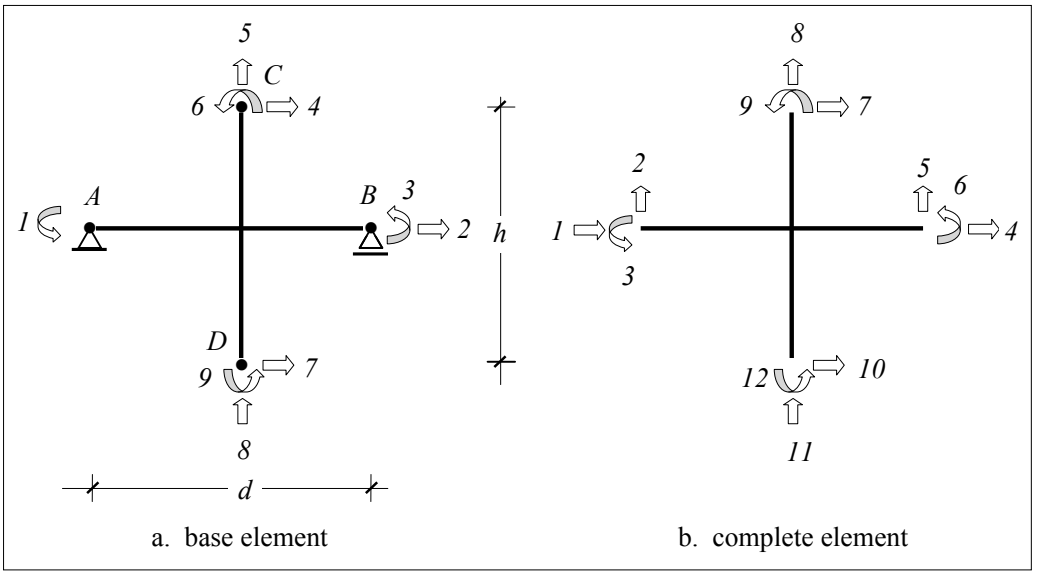


Figure 3. Degrees of freedom of the base element and complete element

- Shear deformation of the panel zone
- Tension and compression of the panel zone
- Column flange and end-plate under bending
- Elasticity and configuration of the bolts
- Bending deformation of the column
- Axial deformation of the column

Due to the stiffening effect of the column flanges the segment AB (see Figure 3) is assumed to be rigid under the shear forces coming from the beams. Thus, considering the remaining 9 degrees of freedom of element of Figure 3a and the deformation modes, the resulting non-zero elements of the upper triangular part of the flexibility matrix are derived and these are given by the various terms as in Eq. (5) in which A_c and I_c represent the area and moment of inertia of the column, respectively. All other terms F_{ij} not shown in Eq. (5) are of zero value.. The bilinear behavior of the springs is defined according to the values given by EC3.

Once the flexibility matrix has been obtained, the *basic stiffness matrix* may be calculated through matrix inversion as in $\mathbf{K}_b = \mathbf{F}^{-1}$**.** Following standard procedures in matrix structural analysis, the rigid body modes may be added by means of a transformation matrix ***T*,** which is shown in Eq. (6).

Thus, the basic stiffness $\boldsymbol{K}_b$ may be transformed to obtain the general stiffness matrix in terms of the twelve degrees of freedom (Figure 3b) as $\mathbf{K} = \mathbf{T}\mathbf{K}_\mathbf{b}\mathbf{T}^{\mathrm{T}}$.

$$
\begin{aligned}
F_{11} &= \frac{1}{h^2}\left(\frac{1}{K_{cws}} + \frac{1}{K_{cwc}} + \frac{1}{K_{eq1}}\right) & F_{13} &= \frac{1}{h^2}\left(\frac{1}{K_{cws}}\right) \\
F_{14} &= -\frac{1}{2h}\left(\frac{1}{K_{cws}}\right) & F_{17} &= \frac{1}{2h}\left(\frac{1}{K_{cws}}\right) \\
F_{22} &= \frac{1}{K_{eq1}} + \frac{1}{K_{eq2}} & F_{24} &= \frac{1}{2K_{eq1}} + \frac{1}{2K_{eq2}} \\
F_{27} &= \frac{1}{2K_{eq1}} + \frac{1}{2K_{eq2}} & F_{33} &= \frac{1}{h^2}\left(\frac{1}{K_{cws}} + \frac{1}{K_{cwc}} + \frac{1}{K_{eq2}}\right) \\
F_{34} &= -\frac{1}{2h}\left(\frac{1}{K_{cws}}\right) & F_{37} &= \frac{1}{2h}\left(\frac{1}{K_{cws}}\right) \\
F_{44} &= \frac{1}{4K_{cws}} + \frac{1}{2K_{eq1}} + \frac{1}{2K_{eq2}} + \frac{h^3}{24EI_c} & F_{46} &= -\frac{h^2}{8EI_c} \\
F_{47} &= -\frac{1}{4K_{cws}} + \frac{1}{2K_{eq1}} + \frac{1}{2K_{eq2}} + \frac{h^3}{24EI_c} & F_{55} &= \frac{h}{2EA_c} \\
F_{66} &= \frac{h}{2EI_c} & F_{77} &= \frac{1}{4K_{cws}} + \frac{1}{2K_{eq1}} + \frac{1}{2K_{eq2}} + \frac{h^3}{24EI_c} \\
F_{88} &= \frac{h}{2EA_c} & F_{99} &= \frac{h}{2EI_c}
\end{aligned}
\tag{5}
$$

$$
\mathbf{T} = \begin{bmatrix}
0 & -1 & 0 & -1 & 0 & 0 & -1 & 0 & 0 \\
\frac{1}{d} & 0 & -\frac{1}{d} & -\frac{h}{2d} & -\frac{1}{2} & \frac{1}{d} & \frac{h}{2d} & -\frac{1}{2} & \frac{1}{d} \\
1 & 0 & 0 & 0 & 0 & 0 & 0 & 0 & 0 \\
0 & 1 & 0 & 0 & 0 & 0 & 0 & 0 & 0 \\
-\frac{1}{d} & 0 & -\frac{1}{d} & \frac{h}{2d} & -\frac{1}{2} & -\frac{1}{d} & -\frac{h}{2d} & -\frac{1}{2} & -\frac{1}{d} \\
0 & 0 & 1 & 0 & 0 & 0 & 0 & 0 & 0 \\
0 & 0 & 0 & 1 & 0 & 0 & 0 & 0 & 0 \\
0 & 0 & 0 & 0 & 1 & 0 & 0 & 0 & 0 \\
0 & 0 & 0 & 0 & 0 & 1 & 0 & 0 & 0 \\
0 & 0 & 0 & 0 & 0 & 0 & 1 & 0 & 0 \\
0 & 0 & 0 & 0 & 0 & 0 & 0 & 1 & 0 \\
0 & 0 & 0 & 0 & 0 & 0 & 0 & 0 & 1
\end{bmatrix}
\tag{6}
$$

3.2 *Simplified Two-Node Component-Based Joint Model*

The four node element proposed in the previous section is not suitable to use in many commercial software systems available to practicing or research engineers. In order to use the standard element library MATRIX27 of ANSYS (2005), for example, a two node element is proposed as shown in Figure 4. The shear spring introduced represents the web panel deformation of the column web. This shear spring is assumed to be rigid in the horizontal direction but flexible in the vertical and rotational directions.

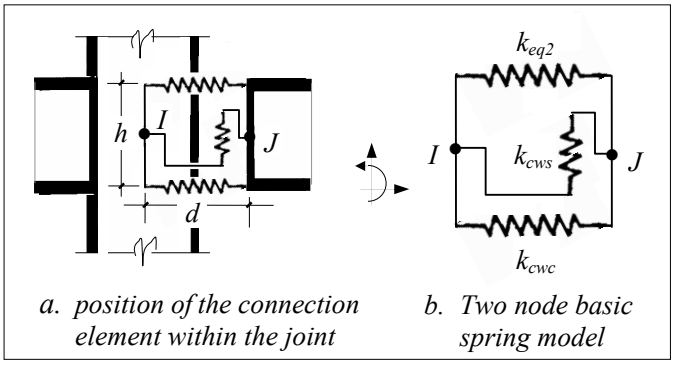


Figure 4 Position and simplified effective modeling of semi-rigid connections.

In order to derive the stiffness matrix of the connection element, the simplest case of the element with only three springs is considered, as shown in Figure 4b. As in the original component method it is assumed that a joint will primarily deform in its plane, and all other out of plane and torsional degrees of freedom (DOF) are assumed to be rigidly connected. This reduces the problem to a two node element with three DOF per node, suitable to use available routines already implemented in high-end structural-engineering products such as, for example, the stiffness matrix element MATRIX27 in the ANSYS library. If now each of these DOF is activated individually, as shown in Figure 5, and the resulting spring forces are calculated, it is possible, with the help of some geometrical considerations and the spring characteristics, to derive the stiffness matrix of the basic connection element.

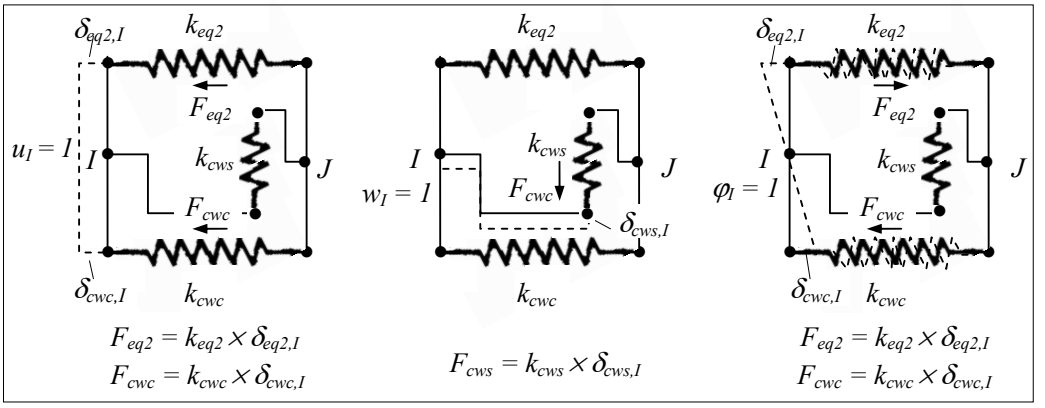


Figure 5. Derivation of stiffness terms for Node I of the basic connection element.

The stiffness matrix, generated in the manner, for the *basic* two-dimensional connection element is shown in Eq. (7).

$$\boldsymbol{K}_{el} = \begin{bmatrix} K_1 & 0 & -\frac{h}{2}K_2 & -K_1 & 0 & \frac{h}{2}K_2 \\ 0 & K_{cwc} & 0 & 0 & -K_{cwc} & 0 \\ -\frac{h}{2}K_2 & 0 & h^2K_3 & \frac{h}{2}K_2 & 0 & -h^2K_3 \\ -K_1 & 0 & \frac{h}{2}K_2 & K_1 & 0 & -\frac{h}{2}K_2 \\ 0 & -K_{cwc} & 0 & 0 & K_{cwc} & 0 \\ \frac{h}{2}K_2 & 0 & -h^2K_3 & -\frac{h}{2}K_2 & 0 & h^2K \end{bmatrix} \tag{7}$$

where, for brevity, the following substitutions have been used:

$$K_1 = K_{cwc} + K_{eq2} \qquad K_2 = K_{eq2} - K_{cwc} \qquad K_3 = \frac{1}{\frac{1}{K_{cwc}} + \frac{1}{K_{cws}} + \frac{1}{K_{eq2}}}$$

This is the desired stiffness matrix for the simplified, two-nodes semi-rigid beam-to-column connection model. The computational quality of this element matrix has been verified and validated on a series of frame models (Aure, 2007).

3.1 NUMERICAL EXPERIENCE

An extensive set of plane frames have been investigated among which the fairly simple two-story frame shown in Figure 6 is presented herewith in order to verify and validate the proposed two-node element formulation of semi-rigid joints.

The characteristics of the connections, computed based on EC3 component-based method, are provided in Table 1 and the locations of the joints are illustrated in Figure 6. ANSYS library element MATRIX 27 has been used to model the proposed two node element.

The connection region of the column has been allowed for shear deformation. The output result is given in Table 3.3. Comparison of moments (kNm) at the joints and beam mid-spans is shown. The results indicate that the moments at the semi rigid joints reduced significantly (which will reduce the cost of connection detailing).
The results are tabulated in Table 3.1. As can be seen from the table the proposed model provides comparably good result as compared to EC3 approximate analysis and the four node accurate element proposed by Bayo *et al.*

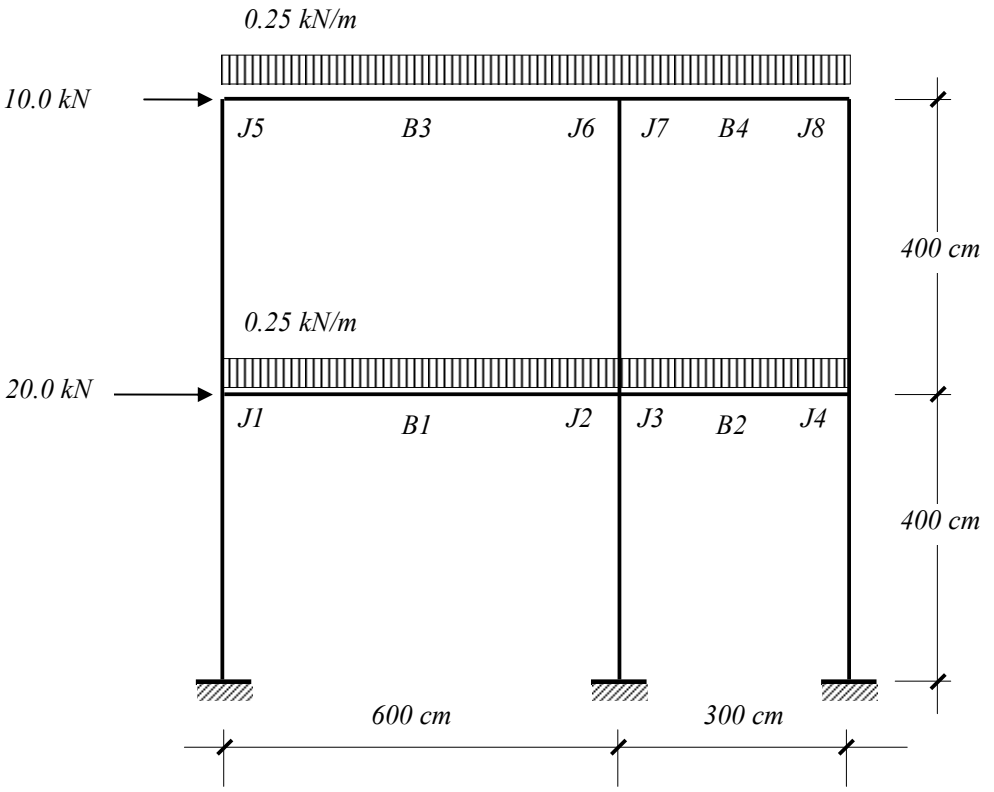


Figure 6. Reference Frame

Table 1. Characteristics of the semi rigid connection used for frame in Figure 6.

Joint	Connection Characteristics					
	K_{cws} [kN/cm]	K_{cwc} [kN/cm]	K_{eq} [kN/cm]	Resistance [kN.cm]	h [cm]	d [cm]
J1	4852	20875	10790	7342	29.35	16
J2	5583	19420	10760	8306	29.35	18
J3	8432	29290	10130	5413	19.70	18
J4	7330	20465	10160	4824	19.70	16
J5	4852	20875	10790	7342	29.35	16
J6	5583	19420	10760	8306	29.35	18
J7	8432	29290	10130	5413	19.70	18
J8	7330	20465	10160	4824	19.70	16

Table 2. Comparison of results (moment, kNm) obtained by the various methods

[1]	[2]	[3]	[4]	[5]	[6]	[7]
Location	Proposed model	Bayo *et al*	using β of EC3	Rigid	$\|\Delta\|$%[3]	$\|\Delta\|$%[4]
J1	22.24	16.37	18.81	27.54	5.87	3.43
J2	75.28	78.11	71.78	92.04	2.83	3.50
J3	8.92	16.87	9.38	18.56	7.47	0.46
J4	23.34	18.67	19.83	23.69	4.67	3.51
J5	24.80	17.79	19.71	28.41	7.01	5.09
J6	58.37	63.77	57.18	74.35	5.40	1.19
J7	18.45	28.72	21.00	32.42	10.14	2.55
J8	13.15	8.33	9.26	11.10	4.82	3.89
B1	63.79	57.88	59.83	52.71	5.91	3.96
B2	12.01	6.72	9.90	7.01	5.29	2.11
B3	71.21	64.35	66.68	61.12	6.86	4.53
B4	12.34	5.98	9.37	13.00	6.36	2.97

CONCLUDING REMARKS

In this study a two-node simplified connection element is proposed. The panel shear deformation of the joint has been taken care of by allowing the joint region of the column to undergo shear deformation.

The proposed model has given a good result as compared to the EC3 component method, using the interaction parameter $\beta-$factor. Though there are some discrepancies between the results obtained by Bayo *et al* and the proposed model at some locations, findings are generally within ranges acceptable for design purposes. The analysis response of the frames has indicated that a reduction in the joint moment is accompanied by an increase in the span moments. Reducing joint moments is advantageous as detailing, modeling and design of joints is the most cumbersome part of steel frame design.

Though there is an increase in moment at mid spans, usually steel sections, especially if laterally restrained, will be capable of resisting these moments as compared to the support region.

.REFERENCES

Bjorhovde, R, Colson, A and Zandonini, R. (1996). "Connections in Steel Structures III." BPC Wheatons Ltd

Chen, W.F. and Toma, S. (1994), "Advanced Analysis of Steel Frames" CRC Press , Inc

Bayo, E.,Cabrero, J.M. and Gil, B. (2006), " An Effective Component Based Method to Model Semi-Rigid Connections for the Global Analysis of Steel and Composite Structures", *Engineering Structures* 28, 97-108

Scott, L., and Burns, A. (2003). "Multiple Fully Stressed Designs of Steel Frame Structures with Semi Rigid Connections". *International Journal for Numerical Methods in Engineering* 58, 821-838

CEN (2004). "Eurocode 3: Design of Steel Structures.Part1.8: Design of Joints (prEN 1993-1-8)", Stage 49 Draft Edition

Aure, T. W. (2007). "Behavior Modeling of Semi-Rigid Steel Beam-to-Column Connection". A Thesis Submitted to the Graduate School of the Addis Ababa University in Partial Fulfillment of the Requirements for the Degree of Master of Science in Civil Engineering, Addis Ababa, Ethiopia

Evaluation of the ASCE 7-05 Standard for Dual Systems: Response History Analysis of a Tall Buckling-Restrained Braced Frame Dual System

L. J. Aukeman[1] and P. Laursen[2]

[1]Graduate Student, Department of Architectural Engineering, California Polytechnic University, San Luis Obispo; email: laukeman@calpoly.edu
[2]Assistant Professor, Department of Architectural Engineering, California Polytechnic University, San Luis Obispo, 1 Grand Ave. San Luis Obispo, CA 93407; PH (805) 756-1314; email: plaursen@calpoly.edu

ABSTRACT

In mid-to-high rise structures, dual systems (DS) enable a structural designer to satisfy the stringent drift limitations of current codes without compromising ductility. Currently, ASCE 7-05 permits a variety of structural systems to be used in combination as a dual system yet the design requirements are limited to the following: Moment frames must be capable of resisting 25% of the seismic forces while the moment frames and braced frames or shear walls must be capable of resisting the entire seismic forces in proportion to their relative rigidities.

This paper assesses the significance of the 25% design requirement for the secondary moment frames (SMF) in dual systems with consideration of current structural engineering practice. Three 20-story buckling-restrained braced frame (BRBF) dual system structures have been designed with varying relative strengths between the braced and special moment frame systems. The SMF system has been designed for 15%, 25%, and 40% of seismic demands and the BRBF system design has been adjusted accordingly based on its relative stiffness with respect to the moment frame. These structures have been examined with nonlinear static and nonlinear dynamic procedures with guidance from ASCE 41-06.

The drift, displacement and ductility demands, and the base shear distribution results of this study show similar responses of the three prototype structures. These results indicate a secondary moment frame designed to less than 25% of seismic demands may be adequate for consideration as a dual system regardless of the 25% rule.

INTRODUCTION

Design requirements for dual systems were first written into code in the 1959 SEAOC Blue Book and the 1961 UBC. Currently, ASCE 7-05 permits a variety of structural systems to be used in combination as a dual system yet the system specific design requirements are still limited to the following: “For a dual system, the moment frames shall be capable of resisting at least 25% of the design seismic forces. The

total seismic force resistance is to be provided by the combination of the moment frames and the shear walls or braced frames in proportion to their rigidities" (ASCE 2006).

Specifically, dual systems comprised of steel moment resisting frames (MRF) with reduced beam sections (RBS) and buckling-restrained braced frames (BRBF) provide benefits from both an architectural as well as a structural standpoint. While the MRFs maintain space flexibility and architectural openness, the BRBFs help provide stiffness and control interstory drifts in mid-to-high rise structures (SEAOC Seismology Committee 2007). This drift control by the BRBFs is particularly apparent in the lower levels. In the upper levels, the MRFs will be a more effective system for drift control. This behavior is illustrated in Figure 1 where the idealized resultant DS displaced shape is linear with respect to the buildings height (Maley et al. 2010).

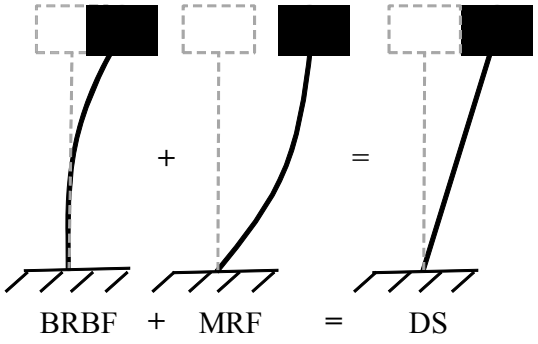


Figure 1: Simplified displaced shape of respective systems in tall buildings

Buckling-restrained braces (BRBs) provide damping to a structure in the event of the earthquake due to their low post-yield stiffness and hysteretic behavior. Typically, while dissipating energy, this behavior causes relatively large residual displacements after a large earthquake. Providing a MRF to remain elastic until after the BRBF yields allows force re-distribution from the BRBFs to the MRFs to restrict these large displacements and protect the structure. Using both MRFs and BRBFs together in a dual system allows the benefits of both systems to be utilized and the short-comings of both the BRBFs and MRFs to be mitigated by the other (EERI 1994).

The purpose of this paper is to compare the inelastic behavior of three dual system models specifically designed for this analysis. The effect of designing a secondary system for 15% (not meeting code requirements), 25%, and 40% (exceeding code requirements) of the base shear has been examined through nonlinear static pushover (NSP) and response history analysis (RHA) and conclusions are drawn from the effects of the backup system strength on the behavior and intent of a the dual system.

PROTOTYPE MODELS

A 20 story building was chosen to be examined for this study, with a rectangular plan of dimensions 144′ by 100′. The 2-dimensional analysis represented

the lateral force resisting system of the structure in one direction. One exterior braced frame line was modeled in series with an interior moment frame line connected by a rigid diaphragm. The typical bay sizes in the direction modeled are 24′-0″ with story heights of 13′-0″ and an 18′-0″ first floor lobby (Figure 2). The alternating pattern of the braces on the building elevation helps reduce column sizes by coupling the tension and compression braces.

Similar gravity loading criteria was used from the SAC project for assessment of moment frames in response to the 1994 Northridge Earthquake (FEMA 355C).

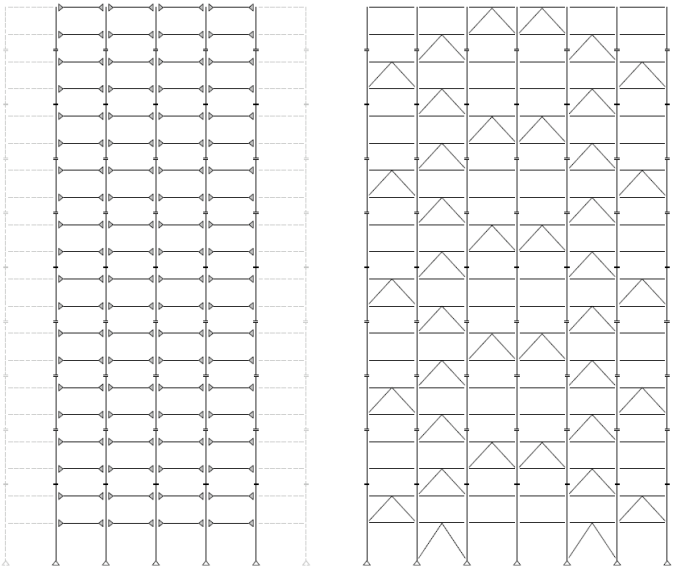


Figure 2: Elevation of dual system

The prototype structures were designed for a theoretical location of Los Angeles, California. Per the United States Geological Survey (USGS), the maximum spectral acceleration seen at the site is approximately 2*g* for short period buildings, and attains around 0.25g for long period structures. Based on ASCE 7-05 including supplement II, the upper limit fundamental period (1.8 seconds) and the minimum base shear governed the design of the structure. For an overall building weight of 29,000 kips distributed evenly among the floors, the total calculated base shear of the structure is approximately 6% of the total building weight. A Response Modification Coefficient of R= 8 was adopted per ASCE 7-05 Table 12.2-1.

Three separate buildings were designed for this analysis. The baseline model is a dual system with a backup special moment-resisting frame (SMRF) designed for 25% capacity of the seismic demands on the structure. Results reported are bound by two other models with a backup SMRF designed to 15% and 40% strength.

DESIGN PROCEDURE

The three step design procedure below was used for the prototype models in this analysis as described by Magnusson, 1997:

1. Design BRBF for full lateral resistance based on the equivalent static force procedure given in ASCE 7-05 §12.8.

2. Design SMRF for 15%, 25%, and 40% of demands per ASCE 7-05 §12.8.
3. Combine systems and reduce BRBF designs based on the relative rigidity of the BRBF to SMRF using modal response spectrum analysis as described in ASCE 7-05 §12.9.

The design utilized ASTM A992 Grade 50 steel (yield stress of 50 ksi) for all beams and columns. The BRB core yield stress was taken as 38 ksi for design. In order to develop an anticipated yielding sequence from the top of the structure down, demand-capacity-ratio (DCR) values were most conservative at the bottom levels and near unity at the top of the structure.

Typical brace core areas in Models 15, 25, and 40 are 2.0 in^2 at the roof for all structures, and 10.75 in^2, 10.5 in^2, and 10.25 in^2 at the first floor, respectively. SMRF beams used are W21x44, W21x44, and W21x50 at the roof and W21x50, W24x76, and W24x94 at the first level for Models 15, 25, and 40, respectively. Columns at the first floor are W14x455 and W14x550 for the interior braced frame and moment frames respectively in Models 15 and 25 and W14x455 and W14x605 for the interior braced frame and moment frames respectively of Model 40. W14x53 columns are used at the roof of each braced frame and the SMRF of all three models uses W14x132 columns. Additional member sizes and model information is provided in Aukeman, 2011.

Static analysis of the design forces show the stiffness ratio of the MF to BF of Model 15, 25, and 40 is 17%, 19% and 22% respectively.

MODELING FOR NONLINEAR ANALYSIS

Nonlinear elements used in Perform 3D are BRB element compounds, moment-rotation hinges for reduced beam sections and BRBF beams outside gusset connections, P-M2-M3 (PMM) Rotation Hinges for columns to consider the axial moment interaction. In addition, elastic section properties were assigned to beams and columns where nonlinear behavior was not expected and rigid elements at beam-column intersections and gusset locations in the BRBF.

The base of the SMRF elevation was assumed to be pinned with a large steel grade beam while the BRBF columns were fixed where the braces are located at the foundation and pinned elsewhere. All elements were modeled with expected yield stresses (55 ksi for beams and columns and 46 ksi for braces).

NONLINEAR ANALYSIS

The nonlinear response of the building was assessed by means of nonlinear static (pushover) and nonlinear dynamic analyses.

Nonlinear Static Analysis. A modal pushover was executed to reveal the relative behavior between the BF and MF for each model. Loading was applied based on the first mode force distribution where story forces vary with respect to story elevation as calculated in the linear static procedure.

The total base shear and the base shears in the braced frame and moment frame are shown below in Figure 3 as a function of the roof drift angle. For each model, the target displacement δ_t was calculated based on the modal pushover analyses for the design earthquake values using ASCE 41-06 §3.3.3.3.2 and is indicated in Figure 3 around 0.0068 radians or 22 inches roof displacement.

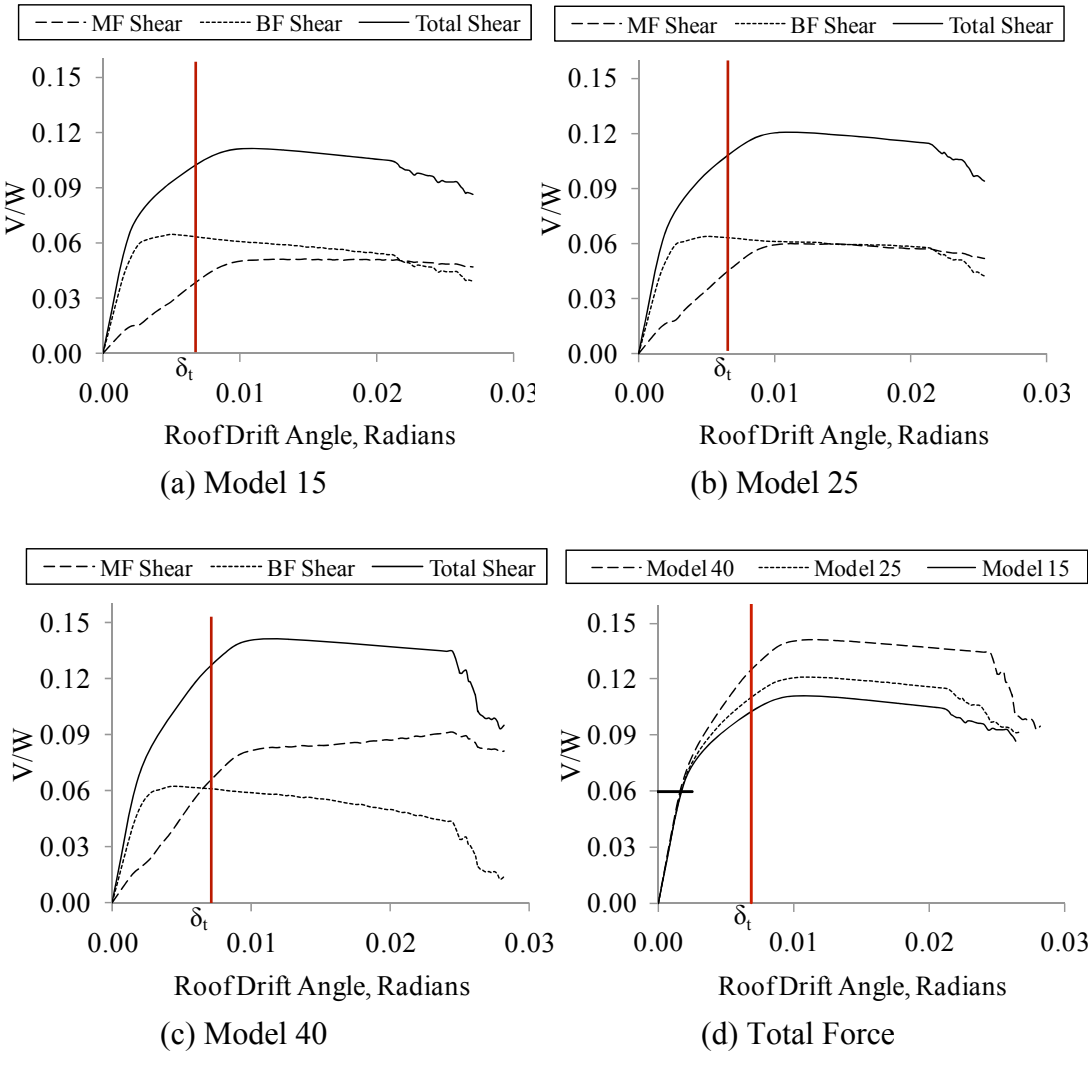


Figure 3: Modal Pushover Force Displacement Curves

The base shear value that causes first yield is approximately equal to the design base shear of 0.06W (see Figure 3 (d)). In the figures below the yielding of the braces at the upper levels cause the initial change in stiffness; however the capacity continues to increase as the conservatism of design is apparent as a result of safety factors, the gradual propagation of yielding and strain hardening. For all three models, failure is caused by a lower level column being loaded beyond its allowable axial-flexure interaction envelope and the pushover analysis is stopped. While this is not a desirable failure mechanism, the structure has been loaded well beyond its design force and has displaced to beyond 0.025 radians (6'-8") or almost four times the target displacement, δ_t, as described in ASCE 41-06.

Figure 3 (c) shows the uniqueness of Model 40 and the MF has a significantly higher capacity than the BRBF. Since ASCE 7-05 allows a reduction in strength of the braced frame (based on stiffness), the overall force displacement relationships of the different models were compared for each load pattern. Small strength reductions were made to the braced frames due to the small relative stiffness of the MF to the BF. With these reductions, the largest difference in force-displacement relationship was seen as a result of the moment frame strength rather than the reduced braced frame strength. This can be observed in Figure 3 as each BRBF has approximately the same maximum strength equal to 0.06W.

Nonlinear Dynamic Analysis. To explore the variability of seismic ground motions, a suite of 7 earthquakes were selected and the median and 84th percentile response quantities are reported below. The 7 records were scaled to the design spectrum using the amplitude scaling procedure according to ASCE 41 1.6.2.2. A list of ground motions, their unscaled peak ground accelerations and the amplitude scale factors used for this analysis is shown in Table 1. The response spectrum for the suite is shown below in Figure 4.

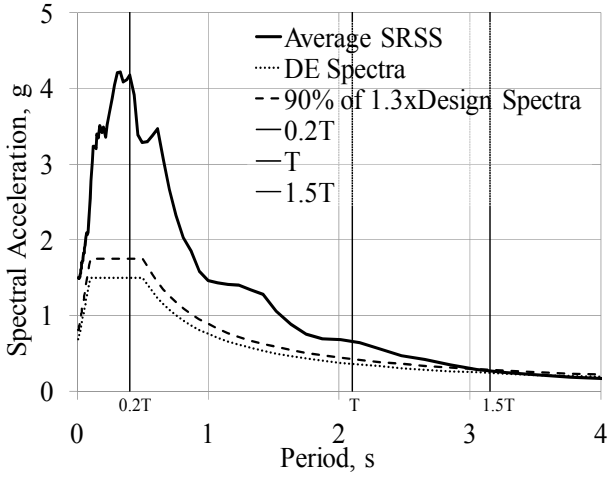


Table 1: Earthquake record data

Earthquake	Record Station	PGA (g)	Scale Factor
Northridge	Canoga Park	0.36	2.15
Loma Prieta	Capitola	0.53	2.55
Imperial Valley	Bonds Corner	0.78	2.03
Imperial Valley	El Centro	0.35	2.18
Kalamata	Kalamata	0.25	3.88
Coalinga	Pleasant Valley	0.38	3.52
Northridge	Saticoy Station	0.37	1.77

Figure 4: Earthquake spectral scaling for response spectrum

BRB hysteresis properties and modal damping of 1.9% has been assigned in Perform 3D along with a small 0.1% Raleigh damping at 0.5T and 1.5T (varying at other periods) to account for additional damping in short period modes.

For all three models, only the El Centro record induced deformations high enough to terminate the analysis. This ground motion exhibited a large pulse around 6.0 sec into the record causing large roof displacement and high ductility demands in the BRB elements that cause termination. All data from the El Centro record includes only building response data for the first 6.5 seconds (or until the maximum allowable BRB deformation of 15 times the yield displacement is reached). The remaining 6 records did not cause deformations beyond the elements maximum deformations.

For the results presented from the response history analysis, the median and 84th percentile values have been indicated. The median is reported as the value of the 4th highest result of the 7 records while the 84th percentile result is approximated as

data point 6 (since 6/7=0.86 which is nearest 0.84). The 84th percentile value can be regarded as the median response plus one standard deviation. This method was used in FEMA 355C for the SAC project when one or more earthquake records caused failure of the structure

Interstory Drift. The median and 84th percentile values for the maximum interstory drift angle for each level (not concurrent) are shown in Figure 5.

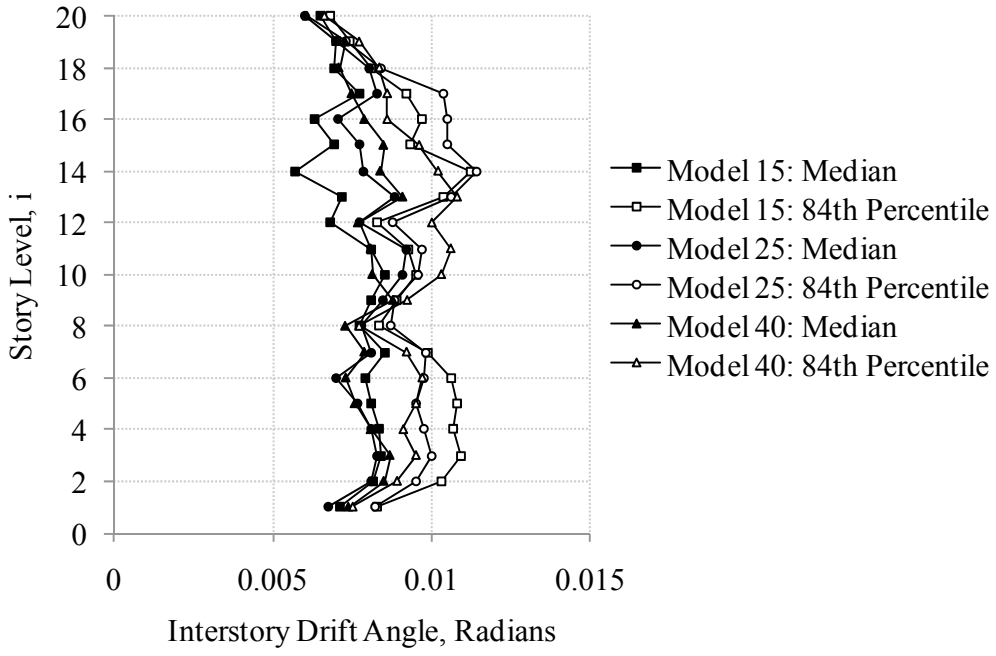


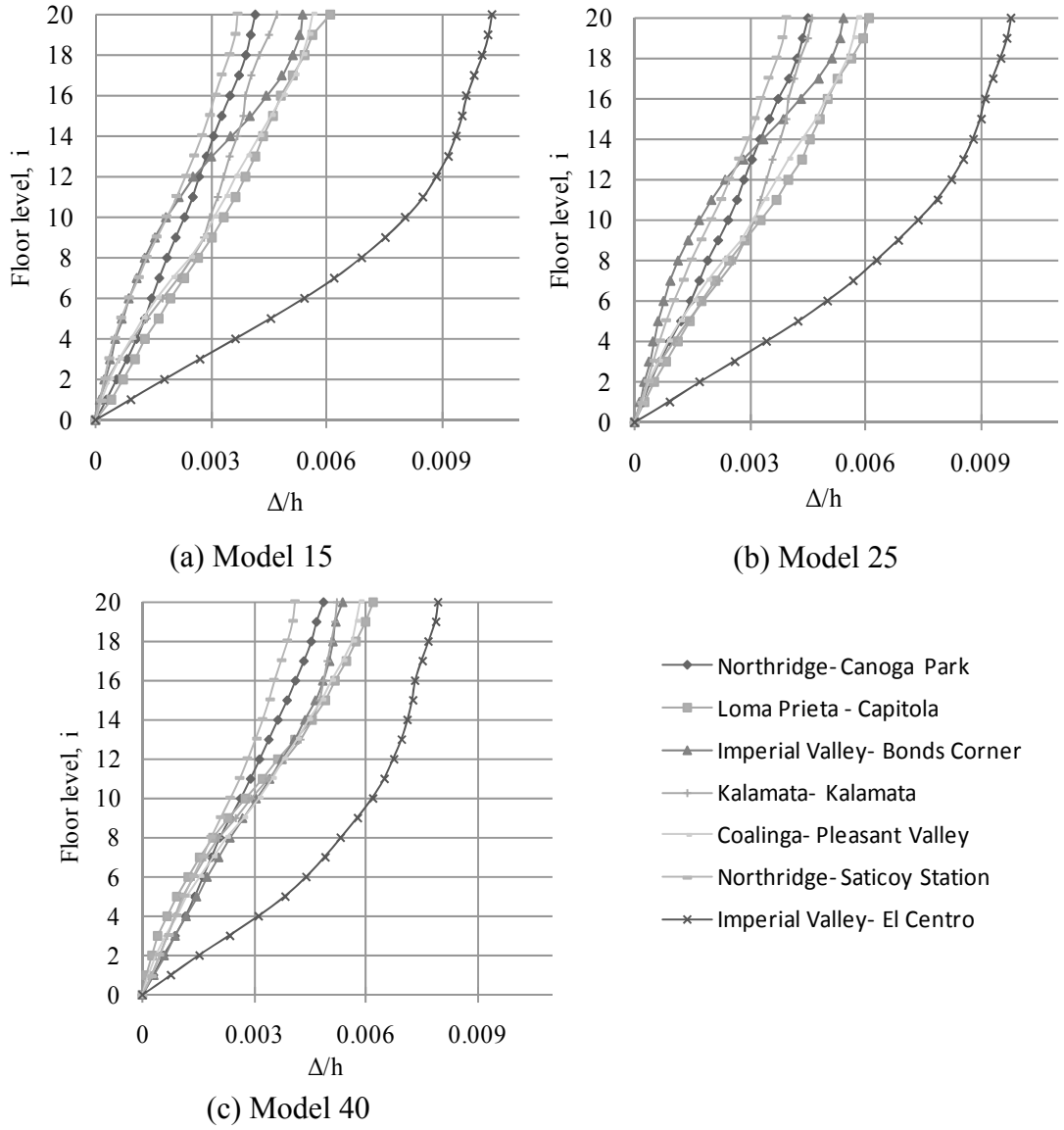
Figure 5: Nonlinear dynamic interstory drift results

The varying design criteria between models results in unique interstory drift demands. Model 25 experiences the overall highest 84th percentile interstory drift ratio equal to 0.012 radians at level 14. Model 15 experiences the largest range of drift values as the difference between the median and 84th percentile results is the highest. As the moment frame strength increases in the models, the range between the median and 84th percentile results decrease. Different trends can be observed for the upper and lower portions of the structure as an inflection point is observed near level 9. This behavior corresponds to the way the BF and MF engage each other as shown in Figure 1. These results show that no conclusive statement can be made about which design is optimal for minimizing interstory drift. ASCE 7-05 provides a limit of $0.020h_{sx}$ for drift in Table 12.12-1. Figure 5 shows that all three models performed well within the code limits for interstory drift. If a stricter drift limit of $0.010\ h_{sx}$ is used, only Model 40 would pass. Such a drift limit could be applied to high performance structures and hospitals.

Displacements. The displaced shape corresponding to the maximum roof displacement normalized by the roof height is displayed in Figure 6. Similar behavior is observed between the three models. The magnitude of the median roof drift is

approximately 0.005 for each model which is less than the target displacement roof drift of 0.0068 radians.

The displacement data of Model 40 shows the least variability between earthquake records while Model 15 demonstrates more scattered results at the lower levels. For all three structures the El Centro record induced the highest roof displacements. For the El Centro ground motion specifically, the stronger moment frame structures underwent less roof displacement at the time the lowest level braces reached their maximum allowable ductility.



(a) Model 15

(b) Model 25

(c) Model 40

Figure 6: Nonlinear Dynamic Maximum Roof Displacement

Ductility. For each structure, the ductility ratios have been calculated as the ratio of element demand to yield capacity. As shown below in Figure 7, the 84th percentile RBS ductility ratio for all three models ranges from 1.25 to 1.75 which classified by

ASCE 41-06 as the Immediate Occupancy performance category. This means that only mild plastic behavior was seen from the RHA. The 84th percentile results also show Model 40 is likely to see the least ductility demand in an earthquake.

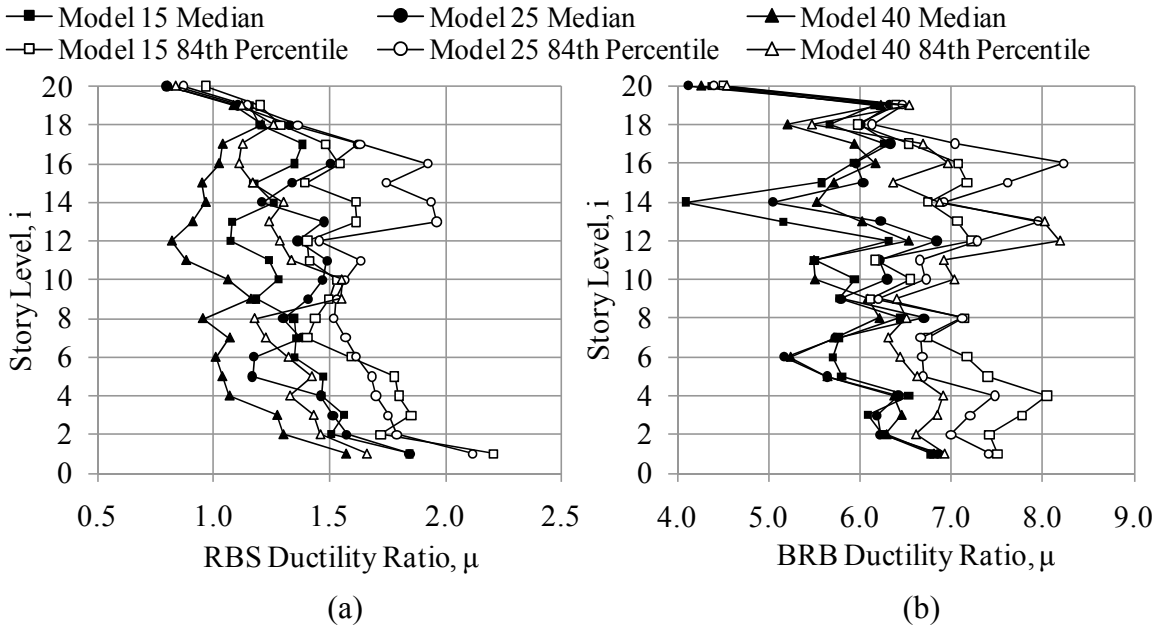


Figure 7: Nonlinear Dynamic Ductility Ratios

The results for maximum BRB ductility demands reported in Figure 7 for levels 1 through 9 show a clear trend in the 84th percentile data as Model 40 experiences the least ductility and Model 15 experiences the most. 84th percentile ductility values at levels 12 through 16 correspond to relatively higher interstory drifts in Figure 5. In the case of model 25, where BRB ductility is highest, the RBS ductility is also higher as demands shed from the BRBF into the MF as intended.

The 84th percentile results of all three models for BRB ductility in Figure 7 (b) range from 6.5 to 8.0. BRB element testing shows core yielding beyond 15 times the yield displacement is unsafe. For all BRB elements in the three models, the 84th percentile data presented above is also within the Immediate Occupancy to Life Safety range. Both RBS and BRB ductility responses show the 3 prototype structures behave similarly.

Base Shear. The median values for the base shear distribution is shown below for the instant at which the total base shear was a maximum in the Nonlinear Dynamic (ND) analysis (Figure 8 (a)) and the instant at which the MF shear was a maximum (Figure 8 (b)). These results show the total ND base shear demands far exceed the overall design base shear of 0.06W. Also, the nonlinear force distribution shows the MF appropriately take on more load as the structure yields to maintain drift control during the ND analysis. For all three models, the MF shear demands are approximately 50% or more of the overall shear. In Figure 8 (b), when the MF resists the maximum load, the shear distribution ratio is greater than 50%. The maximum total base shear imposed on Model 25 (and similarly Models 15 and 40) exceeds the ultimate capacity

shown in Figure 3. Aside from the difference in procedure, the hysteretic behavior of the BRB elements has been modeled explicitly based on test data. Due to cyclic strain hardening the capacities of the BRB elements increase as the members cycle back and forth.

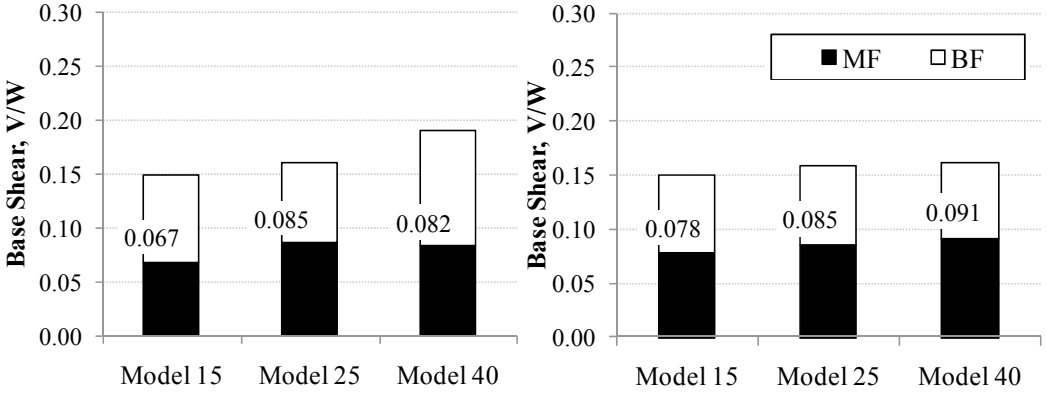


Figure 8: (a) Median ND total base shear. (b) Median ND base shear at maximum MF base shear.

CONCLUSION

Drift and displacement demands did not show one model as performing significantly better than another. The MF designed to 40% of the design base shear resulted in the least scatter of results from the 7 ground motions, however all models performed adequately based on ASCE 7-05. The general displacement profile for each structure was close to linear as expected for a BRBF and MF Dual System.
In terms of 84th percentile demands from the RHA, the interstory drift demands remained below 0.012. The ductility demands for the BRBs remained below 8.3, well within the acceptable range. The RBS ductility demands attained by the MF are approximately 2—only mildly inelastic.

As expected, the story shear results showed that the stronger moment frames resisted the highest base shear in the nonlinear pushover as well as the response history analyses in general.

Shear reversal (MF and BRBF working against each other) was observed in levels where braces occurred in adjacent interior bays. The implications of such shear reversal are unclear and should be examined further. This is related to the alternating brace patterns.

ASCE 7-05 requires a secondary system to be designed for a minimum of 25% of the seismic base shear; however the results show that the Model 15 performs similar to the Model 25. Thus there appears to be no clear argument to not categorize it as a dual system. Clearly, the design technique presented here for a dual seismic force resisting system provides a high performance structure. This paper shows that advanced analysis is required in order to fully quantify the system performance and required MF strength with respect to the performance criteria, and to quantify the added cost of the backup MF system.

This paper shows that the 25% design rule at best is arbitrary. It should be investigated if a better design rule could be based purely on strength distribution between the BRBF and MF, e.g. 75%/25%. Otherwise the BRBF design hardly changes with varying MF strength causing uneven levels of conservatism.

The allowed strength reduction of the BRBF (step 3 in design procedure) was relatively small for these systems and did not cause any deficiencies in the dual system performance.

Overall, all models were found to easily satisfy the drift and ductility limitations. However, for a more complete picture of the dual system performance, an additional study should be completed for a pure BRBF to quantify the MF contribution to the overall dual system behavior.

The results presented above may vary dramatically between dual system types as well as building layouts. It is suggested that this research may be continued with additional variations to better understand the design implications of mixing stiff and flexible systems in a dual seismic force resisting system.

REFERENCES

American Society of Civil Engineers (ASCE) (2006). *ASCE 7-05 Minimum Design Loads for Buildings and Other Structures.*

American Society of Civil Engineers (ASCE) (2007). *ASCE 41-06 Seismic Rehabilitation of Existing Buildings*. Reston, Virginia.

Aukeman, L. J. et. al. (2011) *Evaluation of the ASCE 7-05 Design Rule for Relative Strength in a Tall Buckling-Restrained Braced Frame Dual System.* San Luis Obispo, CA.

Earthquake Engineering Research Institute (EERI) (1994). *Connections: The EERI Oral History Series, Henry J. Degenkolb.* Stanley Scott interviewer/editor, Oakland, CA.

Federal Emergency Management Agency (*FEMA). 2000. FEMA 355C State of the Art Report of Systems Performance of Steel Moment Frames Subject to Earthquake Ground Shaking*. Redwood City, CA.

Magnusson, J. D. (1997). "Earthquake-Resisting Dual Systems and the 25% Rule." *Building to Last: Proceedings of Structural Congress*. vol 1. ASCE, NY 1997.

Maley T. et al. (2010). "Development of a Displacement-Based Design Method for Steel Dual Systems with Buckling-Restrained Braces and Moment-Resisting Frames", *Journal of Earthquake Engineering*, 14:1, 106-140.

Structural Engineers Association of California (SEAOC) Seismology Committee. (2007).
The SEAOC Blue Book: Seismic Design Recommendations, Jan. 2007, 17 Aug. 2009. <http://www.seaoc.org/bluebook/index.html>.

International conference of Building Officials (ICBO). (1961). *Uniform Building Code*, Whittier, CA.

Florida Tampa International Airport Interchange Steel Bridges Design

Arun P. Khatri[1], P.E., Allan Berry[2], P.E., and Dongzhou Huang[3], P.E., Ph. D.

[1]PBS&J, an Atkins company, 4030 West Boy Scout Blvd, Suite 700, Tampa, FL 33607, APKhatri@pbsj.com; [2]PBS&J, an Atkins company, 2001 N.W. 107 Ave., Miami, FL 33172, ajberry@pbsj.com, [3]PBS&J, an Atkins company, 4030 West Boy Scout Blvd, Suite 700, Tampa, FL 33607, dhuang@pbsj.com.

Abstract: Tampa international airport interchange consists of two sub-interchanges: Courtney Campbell Causeway (CCC) and Spruce Street/S.R. 60 sub-interchanges. The objective of this paper is to present the unique and economic design of the steel bridges in the CCC sub-interchange. First, a brief description of the whole project is given. Then, a detailed discussion is presented of the most important bridge design issues influencing the selection of the best bridge alternative. Finally, some unique and innovative designs are discussed. The information presented in this paper is of benefit to both the novice and experienced bridge engineers.

INTRODUCTION

Tampa international airport interchange includes 10 steel bridges, 9 concrete bridges, and 43 permanent retaining walls. All of the steel bridges are curved I-girder bridges with a total length of over 2734.1 m (8,970 ft), many of them with very sharp skew angles and difficult site and geometric constraints. The interchange was designed in 2004; the construction of this mega project was started in 2005 and finished in 2010, at a cost of approximately $230 million. The interchange consists of two sub-interchanges: Courtney Campbell Causeway (CCC) and Spruce Street/S.R. 60 sub-interchanges. The CCC interchange improvements consist of major reconstruction replacing the existing interchange at SR 60 (Memorial Highway) and the Courtney

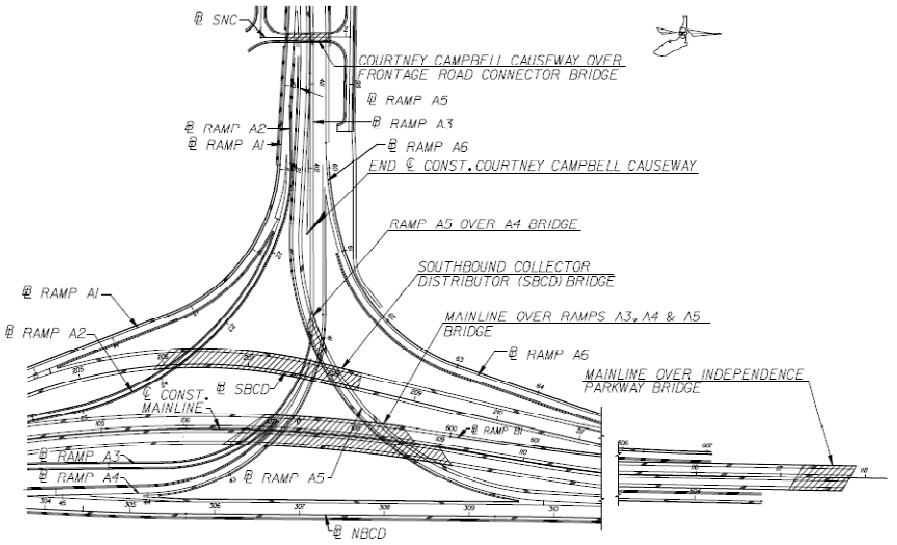


Fig.1. Bridges Layout

Campbell Causeway (CCC) with a three leg multi-level directional interchange (Fig. 1). Changes to increase traffic capacity and safety of the interchange included geometric revisions, an increase in the number of travel lanes and the elimination of two traffic signals. The project limits extend from Courtney Campbell Causeway at approximately Sta. 400+50 to the Express Lane Centerline Sta. 100+00 (South of Fish Creek). Improvements also included construction of the Mainline Express Lanes and Collector-Distributor (CD) roads from Sta. 100+00 to approximately Sta. 117+80. The Mainline Express Lanes provide a connection to the Veterans Expressway which begins at the northern terminus of this project. This project was coordinated with, and designed to match the SR60/Spruce Street Interchange at the Southern Terminus; the Veterans Expressway at the North Terminus; and the existing Courtney Campbell Causeway which consists of a 6-lane divided roadway at the Western Terminus. There are five bridges within the limits of this project. The paper focuses on the discussion of unique and innovative designs of three bridges: Southbound CD Bridge, Ramp A5 over A4 Bridge and SR 589 Mainline over Ramps A3, A4 and A5 Bridge.

SOUTHBOUND CD BRIDGE

The baselines of Southbound CD and all the ramps are on curved alignments. The minimum vertical clearance is 5.05 m and the total bridge width is 22.55 m with four travel lanes and two shoulders (see Fig. 2).

There was a partial overlap between the existing and proposed SBCD movements. Therefore, the bridge design proceeded with a staged construction scenario. Stage 1 construction (toward the outside of the curve) was 12.485 meters followed by a 8.615 meter wide Stage 2 construction (toward the inside of the curve). Stage 3 construction was a 1.45 meter closurepour.

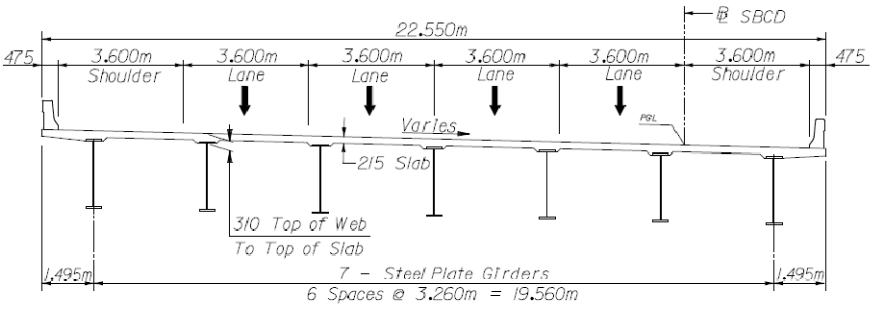


Fig.2. Southbound CD Bridge Section

Five alternatives were investigated during the project development phase and four of them will be discussed.

Alternative 1

The span arrangement for Alternative 1 consists of four spans with a steel plate girder superstructure and radial substructure (Fig. 3 (a)). End bents and piers are placed normal to the baseline of Southbound CD. The required clear zone of 4.2 meters to

the south end bent of the bridge has been provided on the south side of Ramp A2. Similarly, a clear zone of 5.7 meters has been provided on the north side of Ramp A2. A pier is located between Ramps A4 and A5 and a barrier was provided on both sides of the pier in lieu of the clear zone. A barrier is also provided on the north side of Ramp A5. This barrier, on the north side of Ramp A5 is required for the span arrangements of the bridges immediately to the east (SR 589 Mainline over Ramps A3, A4 and A5 Bridges) and the MSE wall and bridge immediately to the west (Ramp A5 over A4 Bridge), and therefore, is provided for the Southbound CD bridge for purposes of continuity. The barrier is provided just outside the sight distance line which is 4.4 meters from the edge of the lane. The resulting span arrangement is a four span structure with spans of 71.880 m + 71.870 m + 68.220 m + 45.630 m with a total bridge length of 257.600 m along the Southbound CD baseline.

Alternative 2

The span arrangement for Alternative 2 consists of four spans with a steel plate girder superstructure and skewed substructure (Fig. 3(b)). The skews are limited to a maximum of 45 degrees for this alternative. The horizontal clearances are similar to those of Alternative 1. The resulting span arrangement is a four span structure with spans of 57.610 m + 70.268 m + 70.285 m + 49.007 m for a total bridge length of 247.170 m along the Southbound CD baseline.

Alternative 3

The span arrangement for Alternative 3 consists of five spans with a steel plate girder superstructure and skewed substructure (Fig. 3 (c)). The skews are limited to a maximum of 30 degrees for this alternative. The horizontal clearances are similar to those of Alternative 1. The resulting span arrangement is a five span structure with spans of 62.040 m + 63.280 m + 49.360 m + 36.410 m + 42.260 m for a total bridge length of 255.350 m along the Southbound CD baseline. The alternative with two superstructure units (Span 1 and 2 as Unit 1 and Spans 3, 4 and 5 as Unit 2 was considered. The advantage of having two units would be the ability to optimize the structure depths for the larger spans in Unit 1 and the smaller spans in Unit 2 separately. The disadvantage would be the compromised aesthetics (with the variable structure depths within one bridge) and the introduction of an additional expansion joint. Considering that the cost advantage for the two unit arrangement is likely to be minimal, it was proposed to construct the five spans as one continuous unit.

Alternative 4

The span arrangement for Alternative 4 consists of five spans with a steel plate girder superstructure and normal substructure (Fig. 3(d)). A five-span single-unit superstructure is used as discussed for Alternative 3. The horizontal clearances are similar to those of Alternative 1. The span arrangement is a five span structure with spans of 63.380 m + 57.000 m + 47.960 m + 36.410 m + 44.350 m for a total bridge length of 249.100 m along the Southbound CD baseline.

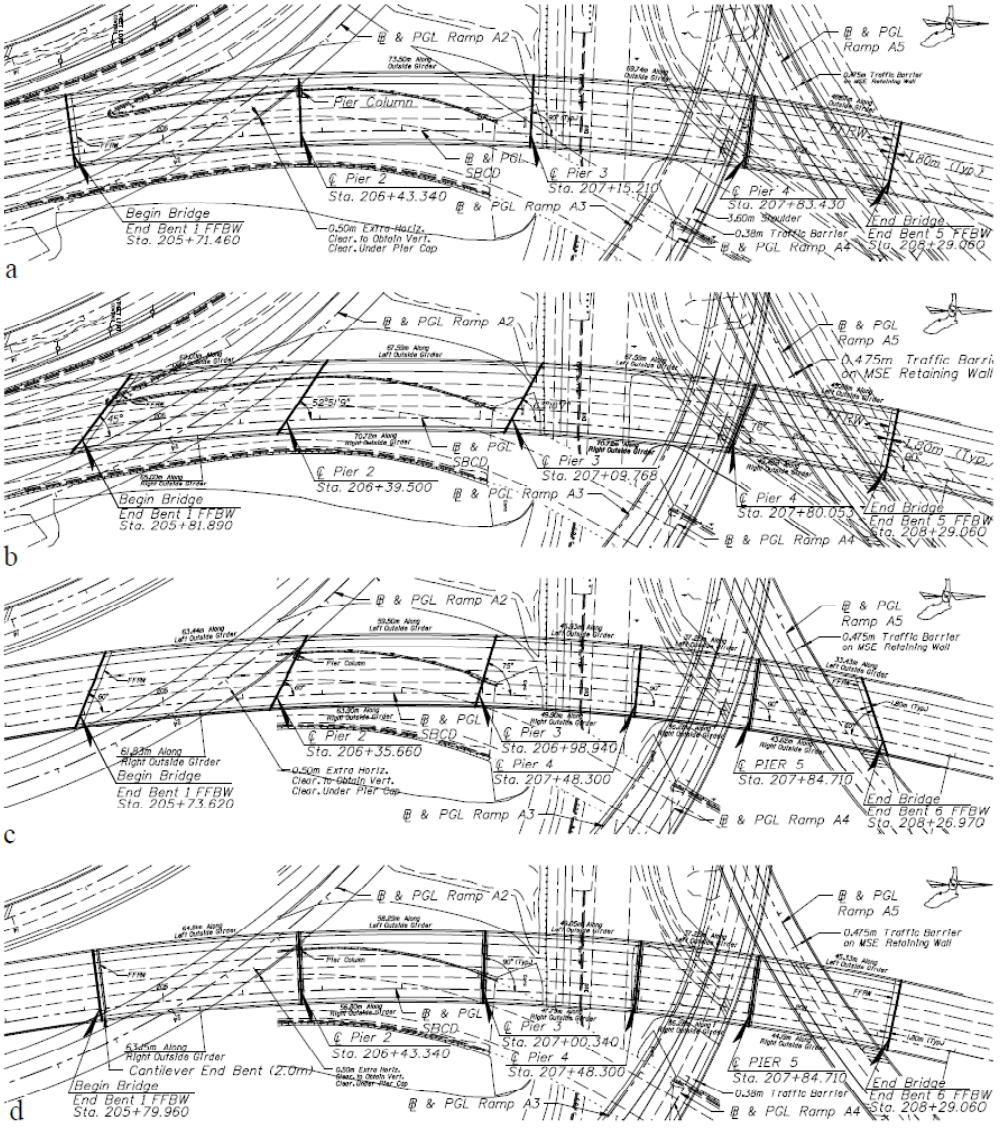


Fig.3. Southbound CD Bridge Alternatives, (a) Alternative 1, (b) Alternative 2, (c) Alternative 3, (d) Alternative 4

Unique Design Features

Of special interest in Alternative 4 is the southeast corner of the bridge. It can be seen that the crossing angle of the alignments of the Southbound CD and Ramp A2 are highly skewed. For a normal bent arrangement, this results in an unusually long end span, about 73.5 meters to cross over a relatively narrow ramp. As a means of shortening the length of Span 1, the southeast corner of the end bent was clipped such that a portion of the end bent and the approach slab would cantilever over the clear zone area. The fascia beam would not be supported on the traditional end bent pile and cap system but rather on a special foundation system integrated into the end bent.

This results in a substantial reduction in the end span length. Vertical clearance requirements would be maintained. The arrangement and details of this corner, as explained above, are shown in Figs. 4 and 5.

Substructure System

The two column hammerhead type pier was adopted for the piers on this bridge. A single column hammerhead pier may be structurally feasible with bulky sections. However, the width of the bridge makes the two column pier better suited for this

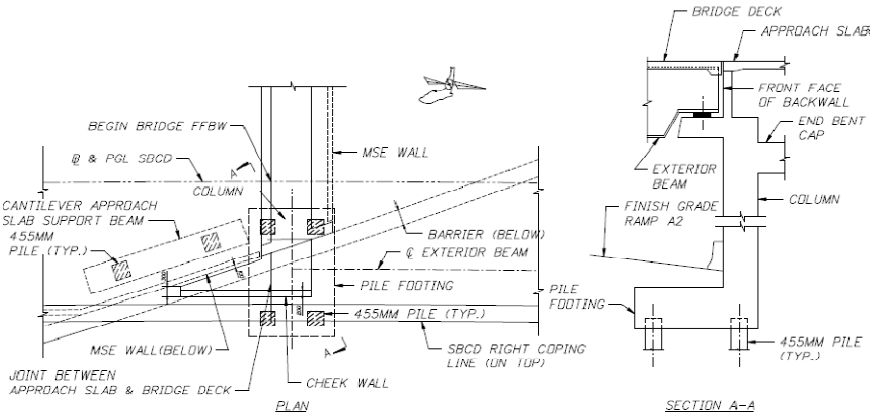


Fig.4. End Bent Details of Southbound CD Bridge

bridge. The piers have chamfered columns and caps. The wider face of the columns have vertical striations to provide a perception of a more slender appearance (see Fig. 5).



Fig.5 Southbound CD Bridge

Recommended and Constructed Alternative

In order to select the best alternative, the estimated costs for the alternatives evaluated are summarized in the Table 1. The most cost effective 4-span arrangement (Alternative 1) costs about $730K (18%) more than the most cost effective 5-span arrangement (Alternative 4). Therefore, the three 4-span arrangements were not pursued further. Alternatives 3 and 4 were the remaining alternatives requiring further consideration.

One consideration in the selection of the recommended alternative was that the bridge would require lateral staging for maintenance of traffic. The first stage of construction was 12.485 m wide, and then Stage 2 construction was 8.615 m. Stage 3

Table. 1 Estimated Costs for Southbound CD Bridge

Alternative	Est. Total Construction Cost	Cost Ratio*	Construction Cost per Square Meter
1	$4,883,312	1.18	$841
2	$4,892,690	1.18	$854
3	$4,356,454	1.05	$763
4	$4,153,411	1.00	$739

*Using the estimated cost of Alternative 4 as the base cost.

construction was a 1.45 meter closure pour. It is important to minimize any differential deflections, twisting, dead load deflections, and racking (due to skew, curvature, etc.) in order to lower the potential for erection and constructability problems during steel girder erection and concrete deck pouring. One example of a potential construction problem is after Stage 1 is constructed, the Stage 2 girders will be erected in the cambered position (before Stage 2 concrete pour). There will be a large vertical differential between stages until the Stage 2 concrete is poured. Predicting accurate deflections is critical, and large deviations for any reason could be a problem during construction. The simpler the layout, the less potential there is for construction problems. Skewed substructures cause differential deflections, twisting and racking. Therefore, the skew of the substructures should be minimized as much as possible. In addition, Alternative 3, with a skewed substructure, costs more ($203K) than Alternative 4 with the radial substructures. Therefore, Alternative 4 with all radial substructures was recommended for the Southbound CD Bridge. It should be noted that during construction the contractor eliminated the lateral construction staging and built the bridge in one stage.

RAMP A5 OVER A4 BRIDGE

The baseline of Ramp A5 crosses over the baseline of Ramp A4 at Station 54+10.176 of Ramp A5. Also, the baseline of Ramp A5 crosses over the baseline of Ramp A3 at Station 53+87.112 of Ramp A5. At this location, both Ramp A5 and A4 are on

curved alignments. The minimum vertical clearance is 5.05 m and the total bridge width is 14.7 m with two travel lanes and two shoulders (see Fig.6).

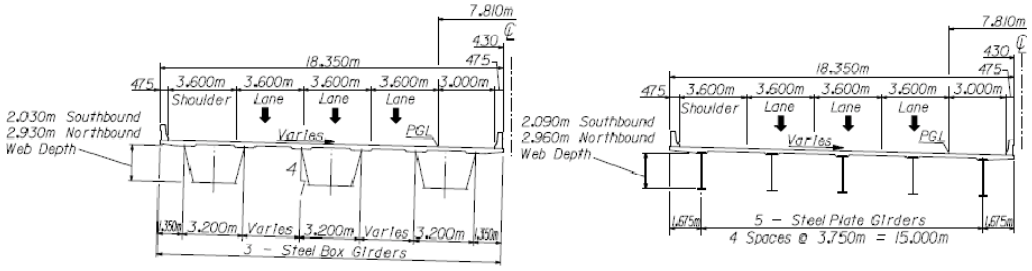


Fig.6. Ramp A5 over A4 Section, (a) Box Girder Alternative, (b) I-Girder Alternative

Four alternatives were investigated during the project development phase. Alternative 1 and 2 consist of one span and Alternative 3 and 4 consists of two spans. The two-span Alternatives, 3 and 4, were not recommended due to the higher cost and reduced aesthetics as compared to the single span alternative. Therefore, only the single-span alternative was considered and described as follows.

Alternative 1

Alternative 1 consists of a single span with a steel box girder superstructure (see Fig. 7 a). End bents are placed normal to the baseline of Ramp A5. Providing full clear zone for Ramps A3 and A4 results in a span length in excess of 85 m. This span length is not considered practical from a structure depth, cost and aesthetics point of view. Therefore, barriers are provided on Ramps A3 and A4 to result in a more practical span length. The resulting span length is 68.68 m. On the north side of Ramp A4, the barrier is placed just outside the 3.6 m wide shoulder. On the south side of Ramp A3, the barrier is placed just outside the horizontal sight distance line.

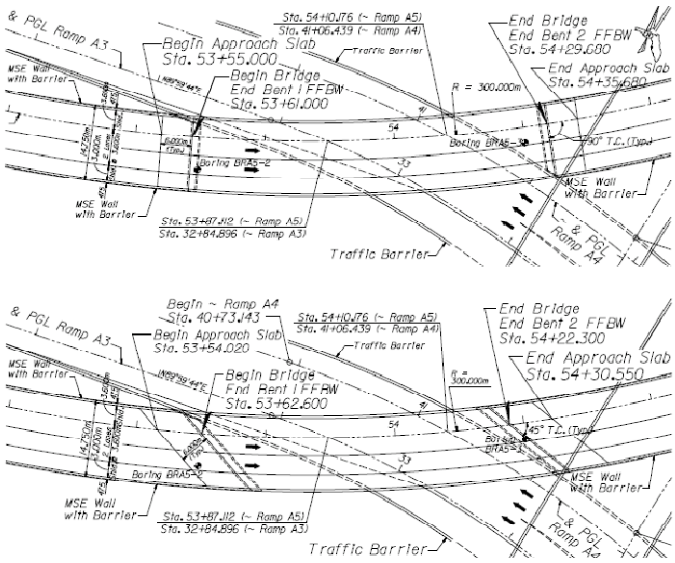


Fig.7. Ramp A5 over A4 Bridge Alternatives, (a) Alternative 1, (b) Alternative 2

Alternative 2

Alternative 2 consists of a single span with a steel plate girder superstructure (see Fig. 7(b)). End bents are skewed at 45 degrees to the baseline of Ramp A5. Providing full clear zone for Ramps A3 and A4 results in a span length in excess of 75 m. This span length is not considered practical from a structure depth, cost and aesthetics point of view. Therefore, as in Alternative 1, barriers are provided on Ramps A3 and A4 to result in a more practical span length. The resulting span length is 59.70 m. On the north side of Ramp A4 the barrier is placed just outside the 3.6 m wide shoulder. On the south side of Ramp A3, the barrier is placed just outside the horizontal sight distance line.

Unique Design Features

The crossing angle of the alignments of A5 and A4 are not close to normal. This results in an unusually long span for the A5 Bridge to cross over a relatively narrow ramp. As a means of shortening the bridge length, the corners of the end bents are clipped such that a portion of the approach slab will cantilever over the traffic shoulder (see Fig. 8). This relatively inexpensive modification results in a reduction in span lengths of 7.96 and 7.5 meters for Alternatives 1 and 2 respectively.

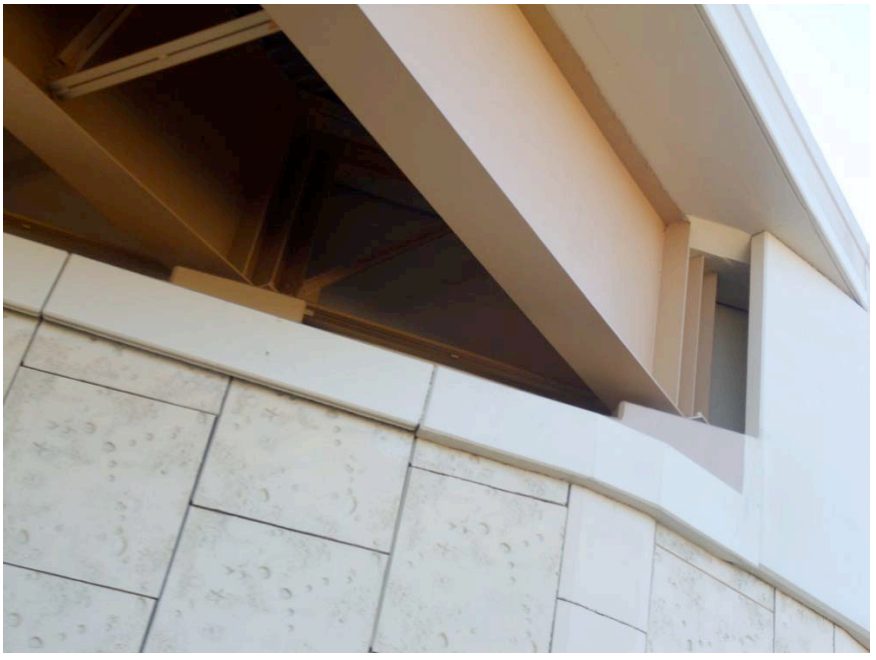


Fig.8. Clipped Corners of End Bents

Recommended and Constructed Alternative

Alternative 2 was the most cost effective alternative (refer to Table 2) and was recommended and constructed (see Fig. 9)

Table 2. Estimated Costs for Ramp A5 over A4 Bridge

Alternative	Est. Total Construction Cost	Cost Ratio *	Construction Cost per Square Meter
1	$1,083,267	1.22	$981
2	$885,819	1.00	$819

*Using the estimated cost of Alternative 2 as the base cost.



Fig.9. Ramp A5 over A4 Bridge

SR 589 MAINLINE OVER RAMPS A3, A4 AND A5 BRIDGE

At the bridge location the baselines of SR 589 and all the ramps are on curved alignments. The bridge is separated into northbound and southbound structures with an 860 mm "gap" between them (see Fig. 10). The gap is required because the superelevation of the northbound and southbound structures are in the same direction with independent PGL's, creating a step at the centerline of construction. The gap was determined using the 7.810 m distance between the PGL's, the 3.00 m shoulders, and the 475 mm traffic barriers.

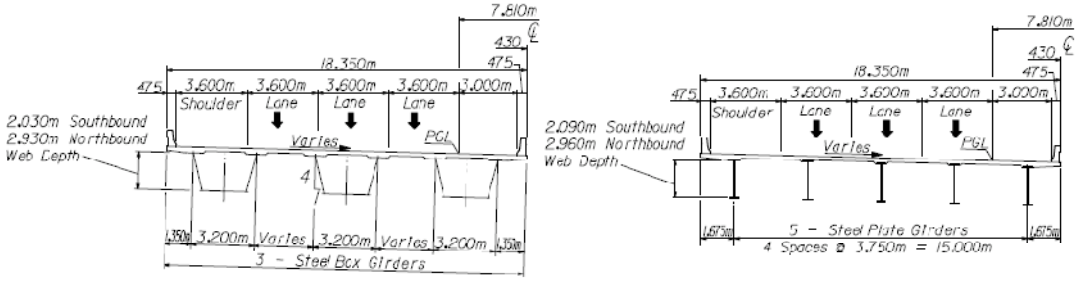


Fig. 10. SR 589 Mainline over Ramps A3, A4 and A5 Bridge, (a) Box Girder Alternative, (b) I-girder Alternative

Alternative 1

The span arrangement for Alternative 1 consists of a steel box girder superstructure (see Fig. 11 (a)). End bents are placed normal to the baseline of SR 589. A clear zone of 4.2 meters to the south end bent of the bridge is required on the south side of Ramp A3. However, at this location the horizontal sight distance requirement is 6.67 meters and is provided as a minimum. A horizontal clearance of 7.3 meters adjusted to 10.3 meters for curvature is required and provided on the north side of Ramp A4. On the south side of Ramp A5, a barrier is provided just outside the shoulder width in lieu of a clear zone of 9.5 meters adjusted for curvature from 7.3 meters. Similarly, on the north side of Ramp A5 a barrier is provided just outside the sight distance line of 4.4 meters in lieu of a clear zone of 7.3 meters. Eliminating these barriers and providing clear zones around Ramp A5 results in the north end span being greater than 82 meters which is not considered practical especially for the end span. A variance was obtained for not providing the full clear zone on the north side of Ramp A5. The end bents and piers of the northbound bridge are staggered from the end bents and piers of the southbound bridge, to provide as close to a balanced span arrangement as possible. The crossing angle of the alignments of Ramps A3 and A5 with the SR 589 mainline are not close to 90 degrees. This results in an unusually long end span, especially for the northbound bridge. The resulting span arrangement for the northbound bridge is a four span structure with spans of 71.000 m + 55.710 m + 55.710 m + 73.420 m for a total bridge length of 255.840 m long the SR 579 baseline. The resulting span arrangement for the southbound bridge is a three span structure with a span arrangement of 56.810 m + 73.140 m + 57.300 m for a total bridge length of 187.250 m along the SR 589 baseline.

Unique Design Features

As a means of shortening the bridge length for this alternative, the corners of the end bents are clipped such that a portion of the approach slab will cantilever over the traffic shoulder.

Alternative 2

The span arrangement for Alternative 2 consists of a steel plate girder superstructure (see Fig. 11 b). The span arrangement and horizontal clearances are similar to Alternative 1 except that the bents have a skew of 45 degrees. Another difference is that the piers for the northbound and southbound bridge are not staggered as in Alternative 1 but are lined up. The resulting span arrangement for the northbound bridge is a four span structure with a span arrangement of 62.610 m + 48.640 m + 48.640 m + 68.980 m for a total bridge length of 228.870 m along the SR 589 baseline. The resulting span arrangement for the southbound bridge is also a four span structure with a span arrangement of 50.810 m + 48.640 m + 48.640 m + 41.260 m for a total bridge length of 189.350 m along the SR 589 baseline.

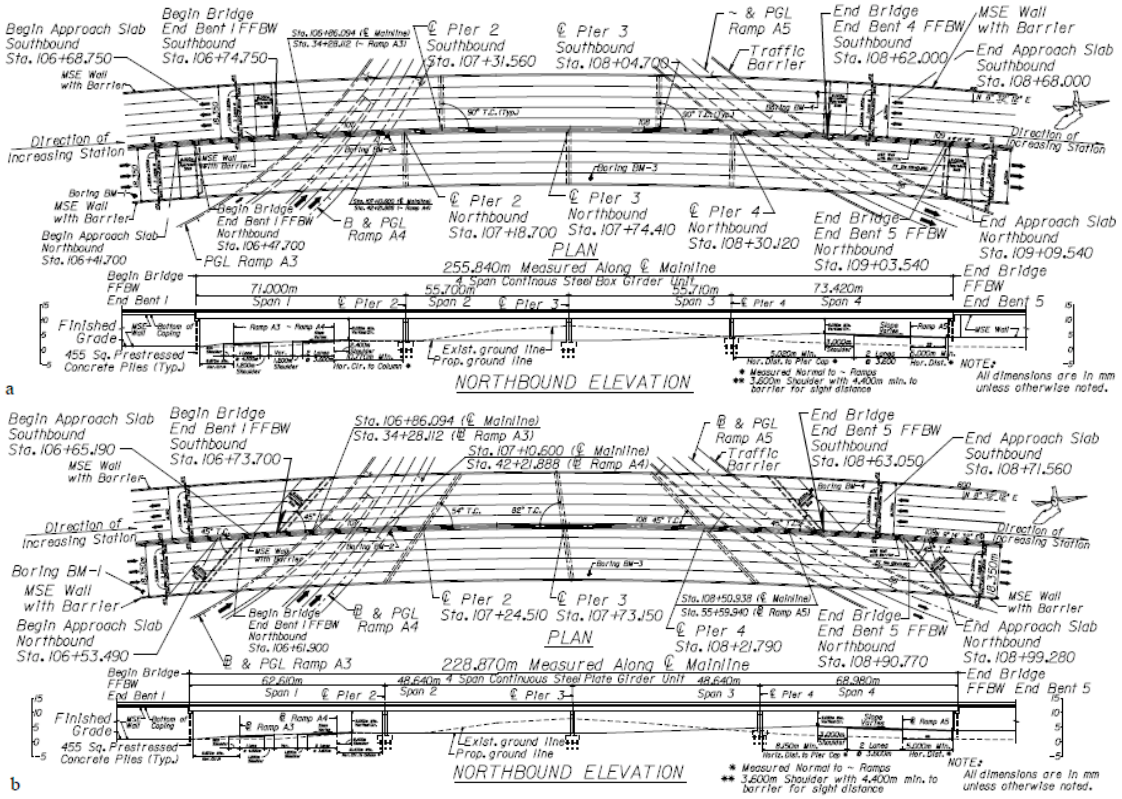


Fig.11. SR 589 Mainline over Ramps A3, A4 and A5 Bridge Alternatives, (a) Alternative 1, (b) Alternative 2

Recommended and Constructed Alternative

An estimate of probable construction costs was prepared for the two alternatives evaluated. Since the alternatives have a different amount of deck area, the cost estimates have been modified to reflect the additional embankment and wall area required for the shorter bridges. The results are summarized in the Table 3. Alternative 2 was the most cost effective alternative and was recommended. It should be noted that only the northbound roadway and bridge was constructed in this contract. The southbound roadway and bridge is planned for future construction (see Fig. 12).

Table 3. Estimated Costs for SR 589 Mainline over Ramps A3, A4 and A5 Bridge

Alternative	Est. Total Construction Cost	Cost Ratio *
1	$7,228,661	1.16
2	$6,206,427	1.00

*Using the estimated cost of Alternative 2 as the base cost.

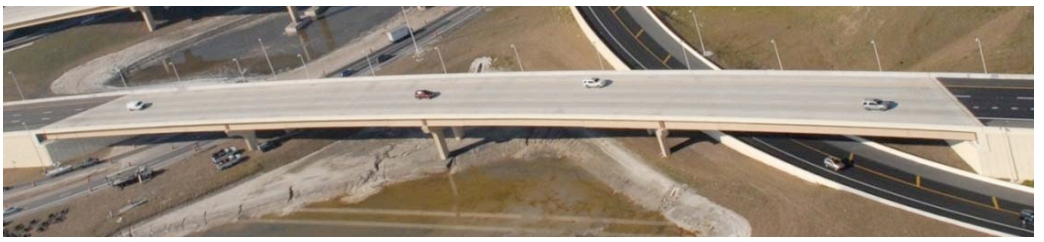


Fig.12. SR 589 Mainline over Ramps A3, A4 and A5 Bridge

CONCLUSION

Though there are many steel bridges that have successfully been built, each bridge has its unique geometric, geologic, and other site features. How to design an economic and aesthetic bridge is still a great challenge to bridge engineers. This paper presented how to select the most cost effective alternative while maintaining the required aesthetic level for three different site conditions. For phased construction, it is important to minimize the skew of the substructures as much as possible to reduce differential deflections, twisting, racking, and potential construction problems. As a means of shortening the bridge length, the corners of the end bents can be clipped such that a portion of the approach slab will cantilever over the traffic shoulder. Proper use of barriers can significantly reduce the construction costs.

ACKNOWLEDGMENTS

The writers would like to express their sincere appreciation to Mr. Brett Rakita, P.E. and Ms. Jessica Johnson for their help in preparing the figures contained in this paper.

REFERENCE

PBSJ (1998), “Memorial Highway Improvements, Courtney Campbell Causeway to South of Fish Creek”, Bridge Development Report, Florida Department of Transportation, District Seven, Tampa, Florida.

Experiment of Slender Confined Masonry Panels under Monotonic and Cyclic Loading

Y. H. Tu[1], T. H. Chuang[1], P. C. Lin[1], P. W. Weng[2], and Y. T. Weng[2]

[1] Department of Architecture, National Cheng Kung University; #1, University Road, Tainan City 701, Taiwan; PH +886(6)275-7575 ext 54140; FAX +886(6)274-7819; email: yhtu@mail.ncku.edu.tw
[2] National Center for Research on Earthquake Engineering; # 200, Sec. 3, HsinHai Road, Taipei City 10668, Taiwan; PH +886(2)6630-0888; FAX +886(2)6630-0858

ABSTRACT

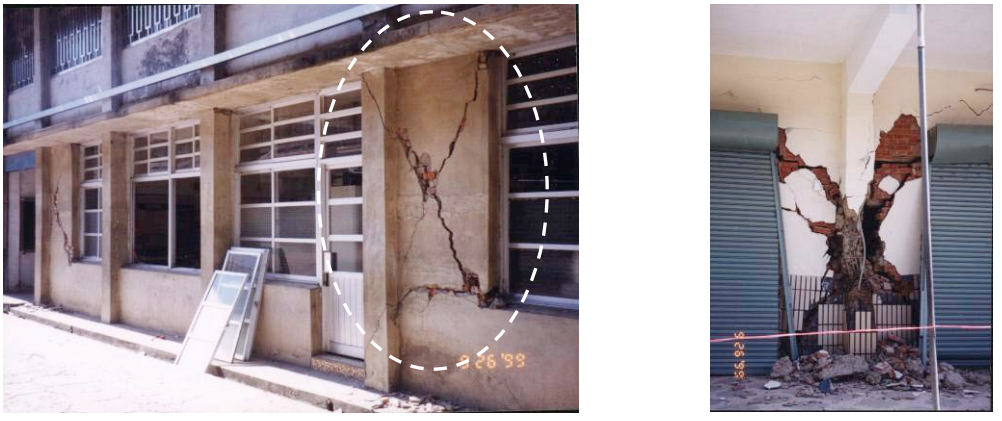
Confined masonry (CM) consists of masonry panels surrounded by cast-in-place RC boundary frames that provide confinement to the panels. When a CM panel is perforated for the needs of opening, the confining effect becomes questionable. This research is aimed at the slender CM panel segments between openings and tie columns. A series of test was carried out to study the failing behavior of this type of panels under in-plane loading. The main variables are the position of tie columns, the number of panels, and the loading pattern. Three specimens were tested under monotonic loading, including two single wing-walls with a tie column placed at the tensile and compressive side respectively and one twin wing-wall with the tie column place at the middle. Another single wing-wall and twin wing-wall specimens were tested under cyclic loading for comparison. The test result indicated that the failing behavior of the specimens was considerably affected by the position of tie column but not by the loading pattern.

INTRODUCTION

Confined masonry (CM) panels are commonly used as infill walls and partitions in low-rise RC buildings in Asian countries such as China [Hori et al. 2006], Indonesia [Sanada et al. 2009], India [Sivarama Sarma et al. 2003], and Taiwan [Tu et al. 2010]. It is also widely used in most Latin-American countries like Mexico [Tena-Colunga et al. 2009] and Chile [Gent Franch et al. 2008]. Seismic assessments for these buildings are complicated, since they combine the behaviors of RC frames and masonry panels and the interactions between frames and panels. Practical guidance for the seismic evaluation of concrete buildings with masonry infill panels can be found in FEMA 356 [FEMA 2000], where solidly infilled masonry panels are considered to be equivalent to compression struts. However, no adequate guidance is provided for partially infilled masonry panels or panels with openings. Most engineers tend to neglect the strength and stiffness of perforated masonry infill panels when designing a new building. In the commentary for section 7.5.2.1 of FEMA 356, it is suggested that a perforated infill panel can provide load-resisting system through the panel segments between openings, as proposed by Hamburger (1993). However, theoretical studies and experimental data

are insufficient for establishing reliable guidelines; the use of this approach requires judgment on a case-by-case basis.

Typical low-rise RC school buildings and street side buildings in Taiwan have a common structural system, where adjacent classrooms or street side buildings are divided by fully infilled CM partitions and the elevations normal to the partitions are opened with doors and windows. This results in an obvious weakness in seismic capacity along the corridor direction for school buildings and street direction for street side buildings. Therefore, the seismic behavior and strength of the perforated CM panels become rather important for these buildings. Figure 1 shows the two regular types of partially infilled CM panels used in typical school buildings in Taiwan, including a single wing-wall with an opening on one side and a boundary column on the other side (Figure 1(a)), and twin wing-walls with a column clamped between them (Figure 1(b)). Slenderness is a common factor in the three types, whereas the condition of the vertical boundaries is the main difference between them.



(a) Single wing-wall (b) Twin wing-wall

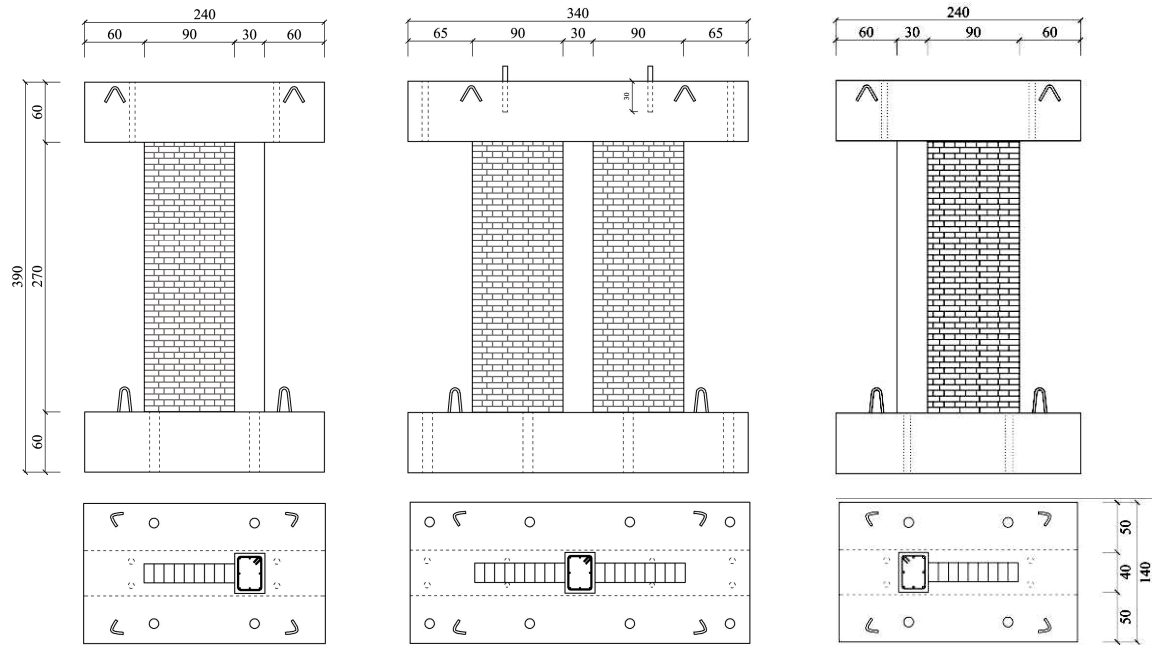
Figure 1. Regular types of partially infilled CM panels in Taiwan

Usually, a wing-wall is 900 mm wide with a clear aspect ratio exceeding 2.0, but in the examples shown in Figure 1, the failure modes are different and affected by the presence of the boundary column. In order to elucidate the capacity and the factors that affect the behavior of slender CM panels subjected to lateral load, a series of experiments were planned. The first phase of the experiment [Tu et al. 2009] included four specimens: two piers, one single wing-wall, and one twin wing-wall. Each specimen was subjected to monotonic lateral loading and constant axial force. For further study on the effect of tie column and loading pattern, the second phase of the experiment was finished in 2010. It included a single wing-wall and a twin wing-wall, both subjected to cyclic loading, and another single wing-wall subjected to monotonic loading with the tie columns positioned reversely. The test results of five wing-wall specimens are presented and discussed in this paper.

EXPERIMENTAL PROGRAM

Test specimens. A four-story existing typical school building was selected as the prototype structure. The most common section details from a damage databank for school buildings [Tu et al. 2011] were chosen to represent the existing buildings that do not meet the current design requirements.

The test specimens were full-scale, having weak columns and strong beams, as shown in Figure 2. Specimens A, AC, and C were identical single wing-walls, where specimen C was placed reversely in the test setup. Specimens B and BC were twin wing-walls with identical masonry panels used for single wing-walls. The clear height, length, and width of each panel were 2700 mm, 900 mm, and 200 mm, respectively. 200mm × 95mm × 53mm solid clay bricks were used and laid in English bond (one stretcher to one header, alternating). The panels were constructed in confined masonry; that is, the boundary beams and columns were cast after the bricks were laid. The panels have their vertical edges adjacent to the columns toothed for shear connections with the columns. The top beams were cast in place with the panels inserted in the beam base for 10~20 mm, so that the specimens could exhibit a fixed-fixed behavior, as is the case in regular CM structures. The columns had a 300 mm × 400 mm cross section, with eight #6 reinforcing bars and #3 hoops at 250 mm of spacing to represent non-ductile design details. The top beams were 400 mm × 600 mm with eight #6 reinforcing bars and #3 hoops at 100 mm of spacing.

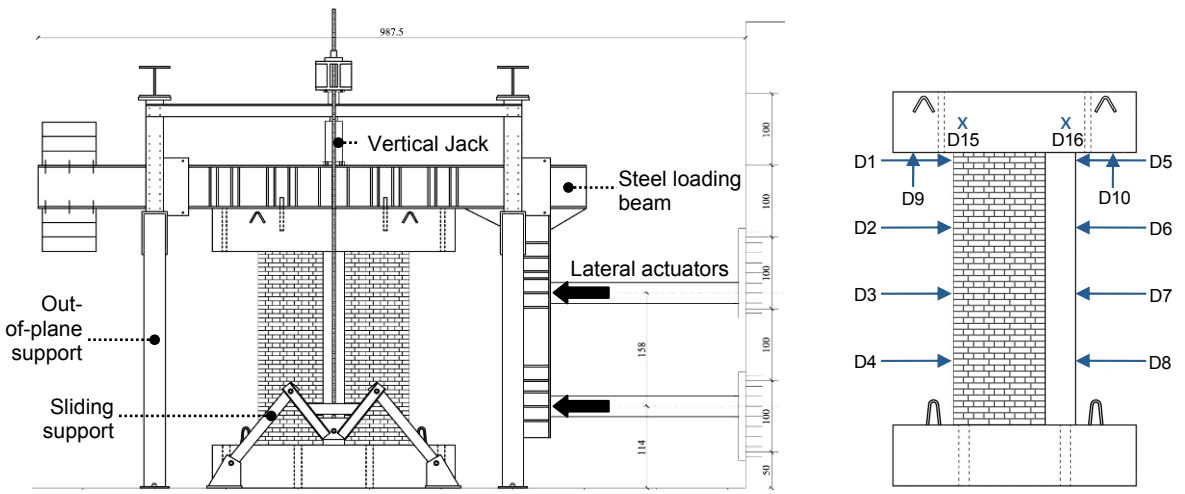


(a) Specimens A / AC (b) Specimens B / BC (c) Specimen C

Figure 2. Elevations and plans of the test specimens (unit:cm)

Test setup and instrumentation. Figure 3(a) shows the test setup. In order to ensure a fixed-fixed behavior and to maintain the top beam horizontal during the test, the lateral load was applied through an L-shaped steel loading beam by two actuators. Vertical load was applied by a jack fixed at the midline of each specimen top and connected to sliding reaction supports developed by Kuang and Wong (2005), so that no horizontal force component was produced.

Eight lateral gauges for measuring in-plane displacement were installed at different heights along the leeward (D1~D4) and windward (D5~D8) vertical edges, as shown in Figure 3(b). Four additional gauges were installed on the middle column of twin wing-wall specimens. Another two vertical gauges (D9 and D10) and two out-of-plane gauges (D15 and D16) were installed on the top beam to monitor its levelness and out-of-plane stability. Strain gauges were attached to every hoop and to both ends of the longitudinal tension and compression steel.



(a) Test setup (b) Displacement gauges

Figure 3. Test setup and arrangement of displacement gauges

Table 1. Test specimens

Specimen	Type	Lateral load	Vertical load* (kN)
A	Single wing-wall	Monotonic	313.6
B	Twin wing-wall	Monotonic	313.6
C	Single wing-wall (reversed)	Monotonic	313.6
AC	Single wing-wall	Cyclic	313.6
BC	Twin wing-wall	Cyclic	313.6

*: The weight of loading beam and jack are included.

Load patterns. As shown in Table 1, a constant vertical force of 313.6 kN (32 t) that represented the dead load was applied to each specimen during the test. Two types of in-

plane lateral loading were selected: monotonically increasing and cyclic. The cyclic load was applied with the displacement amplitudes gradually increased in each cycle. Usually, a test was terminated when severe damage was observed in the masonry panels or the residual strength was below 85% of the maximum strength.

Material properties. Material tests were conducted on the reinforcing steel, concrete, and masonry samples. These included the compression tests of standard 150 mm diameter concrete cylinders, the compression tests of brick units (Figure 4(a)), the compression tests of 50 mm mortar cubes (Figure 4(b)), and the compression tests of double wythe × double wythe × 8-course masonry prisms (Figure 4(c)). The main results are presented in Table 2.


(a) Brick units


(b) Mortar cubes


(c) Masonry prisms

Figure 4. Masonry samples for material tests

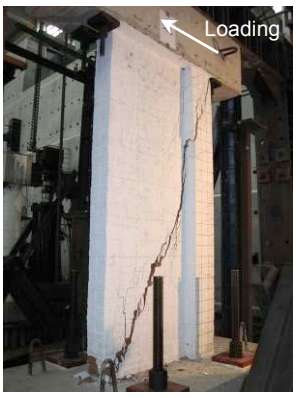
Table 2. Average strengths of materials

Specimen	Steel Yield stress (MPa)		Concrete Compressive strength (MPa)	Masonry Compressive strength (MPa)		
	#3	#6		Brick	Mortar	Masonry prism
A, B	318.9	439.2	30.4	43.6	15.5	17.4
C	400.3	490.5	30.9	44.5	13.9	19.4
AC	400.3	490.5	33.6	44.5	13.9	19.4
BC	400.3	490.5	32.4	44.5	13.9	19.4

EXPERIMENTAL RESULTS

Overall behaviors. Magenes and Calvi (1997) presented three possible failure modes for masonry walls: rocking, bed-joint sliding, and shear cracking. Rocking means that the wall rotates with flexural cracks occurring at the lower windward and upper leeward corners, ending with toe crushing at the compressed corners. Bed-joint sliding occurs along a tensile horizontal crack when the vertical load is low. Shear cracking mode is identified when the strength is governed by the formation and development of inclined diagonal cracks. In this experiment, shear cracking failure occurred in single wing-wall

specimens A, C, and AC, but the tie columns didn't fail when the panels failed. The twin wing-wall specimens B and BC had a composite behavior combining rocking and shear cracking failure, and the tie columns failed simultaneously with the panels. In all specimens, uniform tensile cracks appeared at the tie columns, suggesting that the columns acted as tension chords while the panels acted as equivalent compression struts. Figure 5 shows the photographs of the failed specimens, the value in the brackets means the drift. Figure 6 shows the lateral force-displacement curves. In some of the curves, slight load degradation happened when the actuators were paused for recording the damage condition. The damage progress of each specimen is as follows.



(a) Specimen A (1.49%)



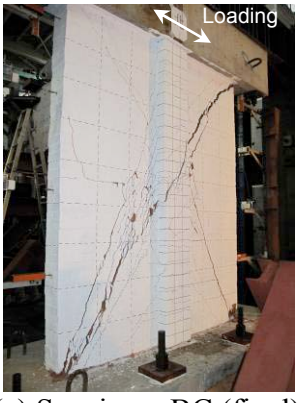
(b) Specimen B (0.51%)



(c) Specimen C (3.15%)



(d) Specimen AC (+1.48%)



(e) Specimen BC (final)

Figure 5. Photographs of failed specimens

Specimen A. This specimen exhibited asymmetric behavior due to the eccentrically placed boundary column. Uniform tensile cracks occurred in the lower portion of the column at 0.18% drift. A diagonal crack occurred in the panel and extended to the column at 0.26% drift, where the specimen also reached its peak strength, which was followed by strength degradation. The diagonal crack extended to two compression corners at 0.39% drift; it did not cause the column to fail but resulted in an

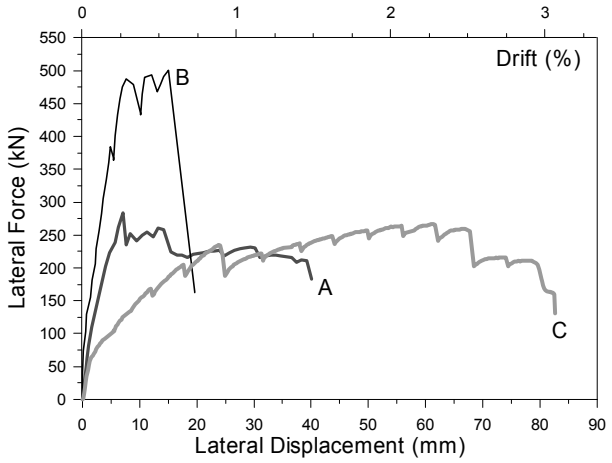
increase in the strain in the hoop passing through the crack. Toe crushing occurred at the lower leeward corner of the panel, accompanied by widening of the diagonal crack and further strength degradation at 0.53% drift. After that, brick pieces started to spall from the crack. The shear crack at the column became wider and finally caused the column to fail at 1.49% drift.

Specimen B. This specimen was slightly damaged before the experiment. When it was fixed to the floor before testing, flexural cracks appeared at its four corners due to uneven prestress in the tie-downs. These cracks closed after the prestress in the tie-downs was adjusted. Therefore, it was difficult to identify when the flexural cracks re-opened due to the lateral load. Uniform tensile cracks showed in the middle of the column soon after loading began. Flexural cracks at the upper leeward and lower windward corners started to extend at 0.08% drift, showing that the specimen was rocking as one united panel. Rocking behavior continued until 0.18% drift, when the specimen reached its first peak strength. It was followed by a diagonal crack appearing and extending to two compression corners. No obvious strength degradation occurred, but the specimen suddenly failed at 0.56% drift. The diagonal crack that extended across the both panels and the column was responsible for the sudden failure.

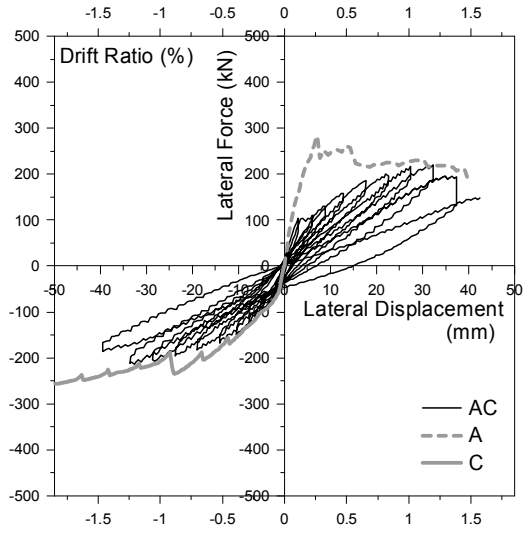
Specimen C. Usually, this type of wing-wall is considered to be invalid since the panel is located at the tensile side. However, its loading condition is actually the same with specimen A, if the top and bottom boundary conditions are completely identical. This specimen showed a cracking pattern similar to that of specimen A but upside-down. At 0.52% drift, tensile cracks occurred in the upper portion of the column and many small inclined cracks showed at the panel along its edge adjacent to the column. Longer inclined shear cracks appeared at the panel and the column bottom at 0.74% drift. The shear crack widened at 0.89% drift and a horizontal crack suddenly occurred at 1/3 height of the panel, where the first peak on the load-displacement curve also showed. The strength dropped about 20% after the peak, but returned to rising state again. After that, brick spalling kept happening along the cracks at the column-panel boundary. The specimen had the maximum strength at 2.27% drift. At 2.63% drift, a diagonal shear crack that extended across the panel suddenly appeared and divided the panel into two pieces. The failure of panel resulted in another strength degradation. Since the column was not severely damaged, the test was continued. The test was terminated at 3.15% drift, when brick crushing happened at the bottom compressive corner of the panel. At that time, only shear cracking was observed at the column.

Specimen AC. An unexpected vertical crack showed at the middle of the upper portion of the panel when the specimen was installed. It affected the initial cracking pattern of the specimen but did not change the final failure mode. At ± 0.3% drift cycle, inclined shear cracks extended from the bottom end of the vertical crack and tensile cracks started to appear at the column. A horizontal crack similar to the one of specimen C occurred at 1/3 height of the panel at –0.3%. After that, all cracks kept extended and more inclined cracks showed at the bottom 1/3 portion of the panel. The maximum strength showed at +1.19% drift. At +1.48% drift, a new diagonal crack that extended across the panel but did not extended to the column suddenly appeared and divided the

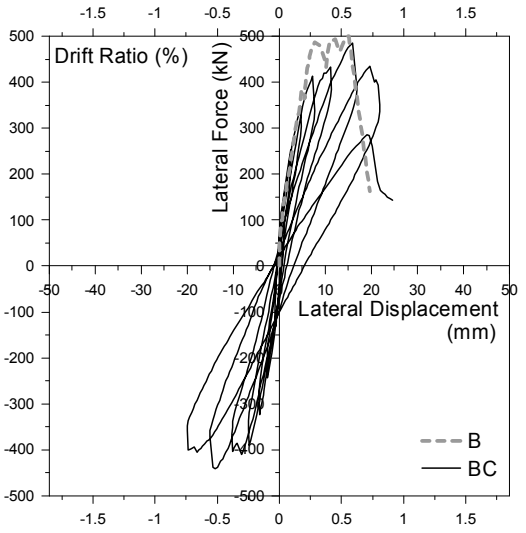
panel into two pieces. The bottom compressive corner crushed. During the next cycle, the panel broke into several segments and fell. The test was terminated when the column remained only cracked.



(a) Monotonically loaded specimens



(b) Single wing-wall specimens



(c) Twin wing-wall specimens

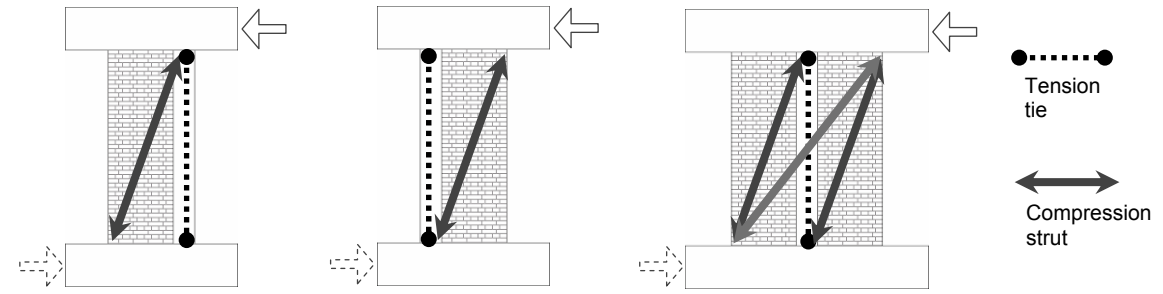
Figure 6. Lateral force-displacement curves and comparison

Specimen BC. This specimen showed quite symmetrical cracking pattern under cyclic loading. Flexural cracks appeared at the top and bottom edges of the panel at ± 0.10% drift cycle and extended to the column soon after. Inclined cracks at the panels and tensile cracks at the column showed at ± 0.25% drift cycle. At +0.56% drift, a new diagonal shear cracks showed at the panel at the compressive side. Slight toe crushing happened and the specimen showed maximum strength. At +0.75% drift, a shear crack appeared at the mid-height of the column and connected with the inclined cracks at both

panels, forming a diagonal crack extended across the entire specimen. During the next cycle, obvious sliding occurred along the diagonal crack and caused simultaneous shear failure of the panels and the column.

Effects of tie column. Figure 6(a) shows a comparison between the lateral force-displacement curves of the three specimens subjected to monotonic loading. The observation on the damage progress indicates that even though the specimens were not fully constrained in closed frames, strut-and-tie mechanism still can be developed between the panels and single tie columns. As shown in Figure 7, the lateral-load-resisting system in specimen A and specimen C should be basically the same. However, the observed behaviors of the two specimens were not identical. The difference might be due to the effect of the self-weight of panels and the asymmetry between top and bottom boundary conditions. Although the value was very small, the top beams of these specimens rotated slightly during the test. The higher yield strength of steel used for specimen C might also result in a relatively stronger column that caused the difference in failing behavior.

The failing behavior of specimen B showed that the twin panels were not independent but united with the column as a squat panel. Its cracking pattern also suggests that there might be a double layered compression stress field. As shown in Figure 7(c), one layer lies between the two extreme compressive corners of the specimen, whereas the other lies along the diagonal of each panel. In this experiment, the failure of the specimen was governed by the former layer. The comparison between specimens A, B, and C suggests that the estimation of lateral force and deformation capacities might be affected by the relationship between the individual strength of the column and the panel.



(a) Single wing-wall (b) Single wing-wall (reversed) (c) Twin wing-wall

Figure 7. Lateral-load-resisting system

Effects of loading pattern. Figure 6(b) and (c) show the comparison between the specimens subjected to monotonic and cyclic loading. In general, the monotonic load-displacement curves show good agreement with the cyclic ones. Between single wing-wall specimens, the curves of specimen A and specimen C fit well to the positive and

negative portions of the curve of specimen AC, respectively. Specimen A showed higher differences in stiffness and strength initially, but the final strength and drift at failure point agreed with specimen AC. The asymmetry between positive and negative portions of the curve of specimen AC suggests that the type of wing-wall shows different behavior when the lateral load comes from different directions and the failure is controlled by the positive case (specimen A) since the failure deformation is smaller.

The curves of specimen B and BC show good agreement in both stiffness and strength. This suggests that the loading pattern does not cause considerable influence on the test result.

CONCLUSIONS

Five confined masonry wing-wall specimens were tested with in-plane lateral load while also being subjected to a vertical compression force. In order to study the effect of the position of tie columns, the specimens included three single wing-walls with the tie columns placed eccentrically and two twin wing-walls with the tie columns placed in the middle. One twin wing-wall and two single wing-walls, where one of them was installed reversely, were tested with monotonically increasing load. The other twin wing-wall and single wing-wall were tested with cyclic loading to study the effect of loading pattern. The following conclusions can be drawn.

1. Shear cracking failure occurred in single wing-wall specimens, but the tie columns didn't fail when the panels failed. The twin wing-wall specimens had a composite behavior combining rocking and shear cracking failure, and the tie columns failed simultaneously with the panels. This suggests that the failing behavior might be affected by the position of tie column and the relationship between the individual strength of the column and the panel.
2. In all specimens, uniform tensile cracks appeared at the tie columns, suggesting that the columns acted as tension chords while the panels acted as equivalent compression struts. However, the twin wing-wall specimen acted as a united squat panel instead of two divided slender panels. This suggests that strut-and-tie models might be applied to the analysis for wing-walls, but case-by-case consideration is needed.
3. In general, the load-displacement curves of the monotonically loaded specimens showed good agreement with the curves of the cyclically loaded specimens. This suggests that the loading pattern does not cause considerable influence on the test result.

ACKNOWLEDGEMENT

The research is funded by the National Science Council, Taiwan, through grant NSC 96-2923-E-492-002-MY3. The authors gratefully acknowledge the staff of the National Center for Research on Earthquake Engineering for supporting the experiment.

REFERENCES

Federal Emergency Management Agency (FEMA). (2000). *Prestandard and Commentary for the Seismic Rehabilitation of Buildings*, FEMA 356, Washington D.C..

Gent Franch K. A., Giuliano Morbelli G., Astroza Inostroza M. A., and Gori R. E. (2008). "A seismic vulnerability index for confined masonry shear wall buildings and a relationship with the damage." *Engineering Structures*, 30, 2605-2612.

Hambergur, R.O. (1993). "Methodology for seismic capacity evaluation of steel-frame buildings with infill unreinforced masonry." *Proceedings of 1993 National Earthquake Conference*, Central U.S. Earthquake Consortium, Memphis, Tennessee, Vol. II, 173-191.

Hori N., Inoue N., Purushotam D., Nishida T., and Kobayashi J. (2006). "Experimental and analytical studies on earthquake resisting behaviour of confined concrete block masonry structures." *Earthq. Eng. Struct. Dyn.*, 35, 1699-1719.

Kuang, J. S. and Wong, H. F. (2005). "Improving ductility of non-seismically designed RC columns." *Proceedings of the Institution of Civil Engineers: Structures and Buildings*, 158, 13-20.

Magenes, G. and Calvi, G.M. (1997). "In-plane seismic response of brick masonry walls", *Earthquake Engineering and Structural Dynamics*, 26, 1091-1112.

Sanada S., Kishimoto I., Kuroki M., Sakashita M., Choi H., and Tani M. et al. (2009). "Preliminary report on damage to buildings due to the September 2 and 30, 2009 earthquakes in Indonesia." *Proceedings, 11th Taiwan- Korea-Japan Joint seminar on earthquake engineering for building structures*, Kyoto, Japan, 297-306.

Sivarama Sarma B., Sreenath H. G., Bhagavan N. G., Ramachandra Murthy A., and Vimalanandam V. (2003). "Experimental studies on in-plane ductility of confined masonry panels." *ACI Struct. J.*, 100(3), 330-36.

Tena-Colunga A., Juárez-Ángeles A., and Salinas-Vallejo V. H. (2009). "Cyclic behavior of combined and confined masonry walls." *Engineering Structures*, 31, 240-259.

Tu Y. H., Lo T. Y., Weng P. W., Chuang T. H., Chiou T. C., and Weng Y. T. (2009). "Experiment on lateral capacity of slender confined masonry walls," *Proceedings of the 11th Taiwan-Korea-Japan Joint Seminar on Earthquake Engineering for Building Structures*, Kyoto, Japan, 279-288.

Tu Y. H., Chuang T. H., Liu P. M., and Yang Y. S. (2010). "Out-of-plane shaking table tests on unreinforced masonry panels in RC frames," *Engineering Structures*, 32, 3925-3935.

Tu Y. H., Yeh P. L., and Jean W. Y. (2011). "Damage databank and its application to seismic assessment for low-rise RC school buildings." *Journal of the Chinese Institute of Engineers*, 34. (Accepted)

ASCE 31 and 41: Apocalypse Now

T.F. Paret[1], G.R. Searer[2], S.A. Freeman[3]

[1] Senior Principal, Wiss, Janney, Elstner Associates, Inc., 2000 Powell Street, Suite 1650, Emeryville, CA 94608; Phone: (510) 428-2907; tparet@wje.com
[2] Associate Principal, Wiss, Janney, Elstner Associates, Inc., 2550 N. Hollywood Way, Suite 502, Burbank, CA 91505; Phone: (818) 303-1300; gsearer@wje.com
[3] Senior Principal, Wiss, Janney, Elstner Associates, Inc., 2000 Powell Street, Suite 1650, Emeryville, CA 94608; Phone: (510) 428-2907; sfreeman@wje.com

ABSTRACT

As engineers are being guided with greater frequency to ASCE 31, *Seismic Evaluation of Existing Buildings*, and ASCE 41, *Seismic Rehabilitation of Existing Buildings*, by state and federal government requirements as well as model building codes, greater numbers of buildings are being evaluated, upgraded, and even designed in accordance with the methodologies and criteria prescribed therein. By using these flawed standards, harm is being inflicted by the structural engineering profession on society-at-large. While the contributors to the original documents have been well aware of major technical problems with these documents since long before publication, efforts to mitigate the problems have been slow, and engineering studies of buildings across the country -- including all buildings considered for lease by the Federal Government -- are being impacted by these problems. To our knowledge, no formal efforts have yet been put forth to warn anyone -- not engineers, not building owners, not government officials, and not building officials -- that reliance on the documents can easily lead to wrong results -- even though engineers most familiar with ASCE 31 and 41 acknowledge that in their own practice, use of the documents often entails modifying or ignoring major components of the published methodologies. In fact, despite the recent renewal of efforts by the associated ASCE committees to improve these standards as much as seven years after publication (and much more than a decade after the bases of these documents, FEMA 310 and 356, were published), these so-called standards remain highly flawed and continue to adversely affect the public interest.

This paper discusses a selection of mind-boggling problems with ASCE 31 and 41, focusing on some aspects about which every engineer planning to use the documents ought to be aware.

INTRODUCTION

The American Society of Civil Engineers publishes the two standards addressed herein: ASCE 31, *Seismic Evaluation of Existing Buildings* (2003), and ASCE 41, *Seismic Rehabilitation of Existing Buildings* (2006), as well as a more recently released *Supplement No. 1* (2007). Both of these standards purportedly represent the consensus knowledge of a large number of engineers and are touted as major advances in earthquake engineering. ASCE 31 and ASCE 41 were developed from

FEMA 310 (1998) and FEMA 356 (2000), respectively, with the goal of providing a set of rules, regulations, and procedures dealing with seismic assessment and strengthening of existing structures, with each set of rules, regulations, and procedures organized by basic building type, and written like a recipe. Unfortunately, however, both are evidence of the ongoing "standardization" and "cookbook-ization" of earthquake engineering (Searer *et al*., April 2008) and both dramatize the risks of disseminating performance-based earthquake engineering on a "how-to" basis. Although both documents represent a tremendous quantity of effort and contain a great deal of valuable material for reference purposes, performance-based earthquake engineering for existing buildings does not lend itself to a "how-to" formulation, and attempts to address and standardize it that way disrespect its premise, the engineering projects that are its product, and the societal stakeholders in its product.

SEAONC SURVEY

To assess how ASCE 41 is currently being used by the profession, the Structural Engineers Association of Northern California (SEAONC) conducted a non-scientific Internet survey of engineers (2010). Although the results were heavily skewed by participants from Northern California (53 percent of respondents), the results were illuminating to say the least.

Why Use ASCE 41?

When engineers were asked to select from a list of reasons why they use ASCE 41 (with multiple selections allowed) only 33 percent selected the option "provides a clear, step-by-step procedure." Other decidedly less inspiring reasons for using ASCE 41 included "industry trend" (48 percent), "required by law for California state-owned buildings" (39 percent), "company policy" (36 percent), "requested by owner" (24 percent), and "requested by building official" (16 percent). Clearly, ASCE 41 is not being used because engineers feel that it is the right tool for the job; overwhelmingly, they are required or pressured into using it.

Why NOT Use ASCE 41?

When engineers were asked why they *don't* ASCE 41 (with multiple reasons again allowed), the most frequent reason given was that most projects do not require the use of ASCE 41. Because most of the engineers who participated in the survey were California structural engineers, who presumably conduct more seismic assessments and design more seismic strengthening projects than almost any other group, the extent to which these standards appear to be manufacturing a bureaucratic need -- as opposed to filling a legitimate engineering need -- begins to be made clear. Other reasons provided for not using ASCE are equally disappointing, but of interest: "too complicated to use" (22 percent), "overly conservative results, leading to undesirable outcomes" (18 percent), "not familiar with its use" (17 percent), and "reluctant to migrate from prior practices that are satisfactory" (9 percent).

When Is a Standard Not a Standard?

In our view, and despite our predilection toward the exercise of engineering judgment when engaged in the practice of performance-based earthquake engineering, the most frightening statistic revealed by the survey was the fact that approximately 70 percent of surveyed engineers admitted to modifying or ignoring specific provisions of ASCE 41. Given this admission, ASCE 41 may be the most non-standard standard, ever. Certainly, if a greater than two-thirds majority of engineers surveyed feel that ASCE 41 gives incorrect results or requires unjustifiable amounts of analysis to the point where the same engineers admit that they have to modify or ignore portions of the standard, there must be major problems with it. Moreover, given the apparent frequency with which provisions of the standard are being modified or ignored, we seriously doubt that the structural engineering products that ostensibly rely on ASCE 41 provide anywhere near consistent standard-compliant performance -- and we challenge the profession to provide statistics demonstrating otherwise. It is therefore ethically incumbent upon the professional organizations that actively promote the use of these standards to formally notify those less knowledgeable than themselves (i.e., municipalities, government agencies and the general public who no doubt all rely on the representations of the profession that buildings "conforming" to these standards are somehow "better") that these standards leave a lot to be desired and that the hoped-for promise of these standards may be little more than false advertising or structural engineering "snake oil". To our knowledge, however, no such warnings have yet been given.

Just How Inaccurate Is It?

When the accuracy of ASCE 41 was polled, engineers were quick to point out that the results are often not accurate at all. A full 74 percent of engineers surveyed felt that ASCE 41 needs to be calibrated with the new construction provisions of the building code (e.g., some perfectly acceptable new designs are condemned by ASCE 41, and all the while, designs according to ASCE 41 are by definition less conservative than typical new construction). And when it comes to the various analysis options covered by ASCE 41 (i.e., linear static, nonlinear static, linear dynamic, and nonlinear dynamic), despite the fact that the vast majority of engineers using ASCE 41 rely on the linear static procedures therein, 64 percent of the engineers surveyed believe that the linear procedures (linear static and linear dynamic) produce results that are "too conservative", leading to excessive upgrades, and that results from the nonlinear dynamic procedure are often at odds with the results from the nonlinear static procedure. In this light, it is simply not appropriate for the engineering profession to promulgate engineering requirements that we acknowledge (but only within our little circle, with a wink and a nod) can be overly conservative and/or give conflicting or nonsensical results -- in effect selling something that consumers of our services are falsely led to believe is good engineering science and, in any case, may not really need. At the same time, of concern to us is the fact that 36 percent of engineers using the standard appear not to have recognized that the results from the linear procedures don't agree with the results from the nonlinear procedures, and that the two nonlinear procedures give results that often don't agree with each other!

ASCE 41 IS NOT EQUIVALENT TO THE BUILDING CODE

We have seen increasing evidence that ASCE 41 is being used by the engineering community to justify "equal or better" performance relative to that obtained from strict conformance to the prescriptive requirements of the building code; is being accepted by jurisdictions as equivalent to legally required code compliance; and is being pushed by the structural engineering community as a means to justify code equivalence for any work associated with existing buildings -- even the construction of additions. In fact, in states that have adopted the *International Existing Building Code*, a path now exists explicitly and legally to rely entirely on ASCE 41 to justify alterations, additions, repairs, and changes of occupancy (SEAONC, October 2010). Such uses of ASCE 41, however, are ill-advised, ill-informed, and misguided because the seismic performance obtained from ASCE 41 is in no way equivalent to that obtained from designs based on the building code. ASCE 41 itself does not even posit equivalence and expressly points out the opposite: "The level of damage and potential economic loss experienced by buildings rehabilitated to the BSO [Basic Safety Objective] may be greater than that expected in properly designed and constructed new buildings." We wonder, therefore, how exactly does that imply any equivalence between ASCE 41 and the seismic design requirements in the current building code and why exactly the structural engineering profession is pushing ASCE 41 as equivalent?

We have also long found it astonishing that the leaders of a profession that has for so long swathed itself in the mantle of public safety would suddenly reverse course and actively promote a methodology that was recognized by many of its contributors as inherently flawed -- even before it was made into a standard. But now that the profession has been told outright by the engineering community that the standard has major provisions that are regularly ignored, and that the standards lead to inconsistent and only sometimes overly-conservative results, we are floored that the *only* response of the profession has been to convene another committee to try and address the problems. When will the organizations that have brought these standards into being inform the public, local jurisdictions, and other government agencies about the problems with them? When will the organizations that developed these standards rally against allowing these standards to be used as an equivalent to the prescriptive requirements of the building code? Based on the current evidence, it appears that these organizations will never own up to what they have done; instead, and to cover their mistakes, they will create new and "improved" versions of the standards, all the while promoting continued use of the existing standards and extending their use into yet more areas for which they are inappropriate. What better way to never have to admit that buildings throughout the country are every day being evaluated and strengthened, added to, and altered, using methodologies that do not work, but can still be said to be engineered in accordance with a state-of-the art "standard"!

We hope that the following examples will illustrate the point.

Example #1

Consider the 12-story, non-ductile perimeter lightweight concrete frame / perforated shear wall structure that was designed in 1967 and is located a stone's throw away from a major California fault (Figure 1). The building had been abandoned for approximately two decades after reportedly being damaged during the Loma Prieta earthquake; because it had forfeited legal occupancy, a municipal ordinance required that the structure be brought up to current code before it could be reoccupied. In addition, the owner wanted to add another story to the top, increasing the occupant load of the structure. Based on the input of the owner's engineer to the building department, however, that ASCE 41 qualified as an alternative method under the *International Building Code*, ASCE 41 was used to justify the assessment and strengthening of the structure. The engineer-of-record evaluating the structure according to ASCE 41 determined that only relatively minor strengthening was needed beyond that required to address the soft, weak story; the engineer's design relied on the existing perimeter non-ductile concrete columns to resist a large percentage of the lateral load in the transverse direction and nearly all of the lateral load in the longitudinal direction.



Figure 1: Twelve-story non-ductile concrete frame.

The original drawings indicate that the lightweight concrete columns are shear critical -- typically with #3 hoops spaced at 10 to 12 inches on center -- or approximately "d" in the minor axis direction -- and lacking appropriate hooks. Further, an in-situ load test conducted after Loma Prieta showed that the columns are also splice/development critical -- largely the result of the #8 to #10 longitudinal reinforcement bars being spliced with compression-only mechanical couplers. The splices are staggered (but only by 30 inches), are not located at the column point of inflection, have a much shorter lap splice length than required by ACI, and are without confinement. Essentially, when the splices go into tension, the columns start to come apart. Axial loads on the perimeter columns are fairly low, and overturning of the perimeter frame can easily result in tension that overcomes the dead load pre-

compression. Bending of the columns results in further tension in the splices, and the fact that the columns are eccentric to the spandrel beams creates torsion in the column members as well. Figure 2 shows the unconventional shape and reinforcing of a typical column.

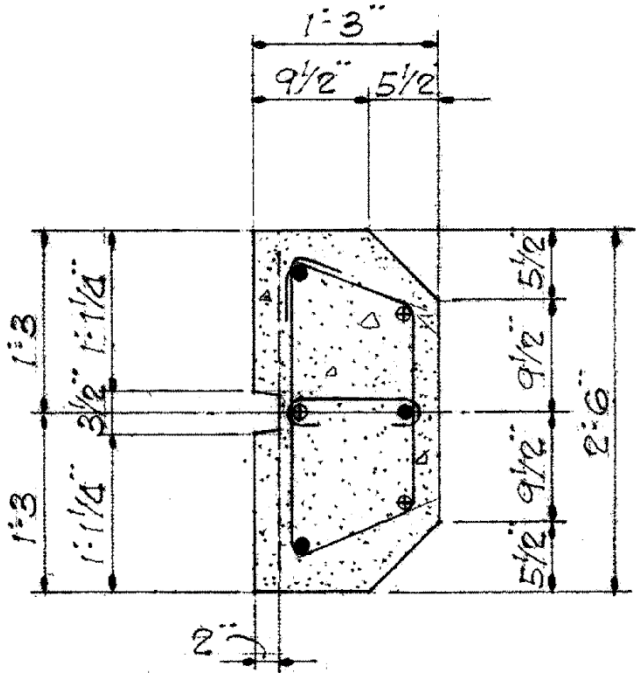


Figure 2: Typical non-ductile detailing of a column, with #3 hoops at 10- to 12-inches on center.

Even assuming that the non-ductile detailing "acceptable" to ASCE 41 would somehow preclude catastrophic failure in the event of a design-level earthquake (which the authors seriously doubt), it should be immediately obvious that these non-ductile details will not have the same *likelihood* of providing life safety or collapse prevention as a ductile design that complies with current code. Indeed, in the case of time history analysis, ASCE 41 requires only that the columns be capable of withstanding the *average* shear demand from the seven simulations required -- in effect allowing the columns to fail one-half the time under design level events. While the authors understand that in some cases, it ought to be possible to justify the use of less-than-ductile detailing, we believe that neither the owner nor the City knew what ASCE 41 was really doing, particularly that safety and resiliency were being compromised relative to what a new code-compliant design would have provided, and that the spirit and intent of the municipal ordinance in requiring code-compliance was being compromised as well. This is not a problem that can be pinned solely on the engineer; the entire profession is at fault because it has made insufficient efforts to advise the people who need to know that ASCE 41 does not provide performance equivalent to that of the code. Most unfortunately, projects like this continue to move forward and be occupied, with everyone thinking they are in seismically safe structures -- even "better than code" -- because the latest greatest "standards" were used.

Example #2

As another example, consider a proposed four-story vertical addition to an existing eight-story concrete perimeter moment-frame building (Figure 3) designed in the early 1970s located in an area of very high seismicity (Searer *et al*., October, 2008). To be permitted to add the new stories, the lateral resistance of the entire building was explicitly required by the municipal code of this major city to comply with *all* the structural design provisions applicable to new buildings in the current code. Although the concrete moment frames were apparently designed with the intent to conform to the ductile detailing requirements of the very early 1970s code, the structural drawings depict classic non-ductile detailing, including typical column hoops at greater than d/2 spacing, longitudinal reinforcing splices located outside the middle third of the column and with no confinement other than the typical widely spaced hoops, and plastic hinge confinement of heavy longitudinal steel relying on #3 cross ties. Worse still, a typical 17-inch (42-cm) thick brick-faced reinforced concrete-filled kneewall reduced the clear height of the typical columns, forcing the column hinge region up into the portion of the column with widely-spaced column hoops, creating classic "short" or captive column conditions throughout the building height, creating shear-critical columns, and increasing the flexural depth of the beams, thus creating strong-beam-weak-column conditions.



Figure 3: Photo of non-ductile concrete moment frame structure designed in the early 1970s.

Since the original building was constructed in the early 1970s with non-ductile details, bringing the building up to current code would have required substantial expense and disruption to tenants if the building could not be shown to be "conforming". The engineer initially released a report stating that the building complied with *every* detailing and strength requirement in the current code, even

considering the effect of the addition and without any strengthening whatsoever, and attempted to show "by code" that the existing building could support the four-story addition. After a peer review challenged the conformance of the existing detailing to current code requirements, the engineer selected ASCE 41 as the methodology of choice for demonstrating "equivalence", and that choice was accepted by the peer review panel and the municipality. Unnoticed and unmentioned was the brief advisement in ASCE 41 itself that it does not provide code-equivalent performance.

Using ASCE 41, and taking a few liberties with the design ground motions (which were 30% smaller than those used for code-complaint adjacent construction) and the structural analysis model (which did not include any of the kneewalls because they were so-called "architectural elements"), the engineer demonstrated via ASCE 41 that the performance of the building would provide for collapse prevention during the deterministic Maximum Considered Earthquake (MCE). As in the prior example, the ability of the columns to withstand shear was satisfied by relying on ASCE 41's provision that only the average shear from seven simulations need be considered, and based on the engineer's ASCE 41 analyses of the structure without the kneewalls modeled, the four-story vertical addition was actually approved for construction by the municipality without requiring any strengthening of the existing building!

As bizarre as this seems, but as this example clearly shows, ASCE 41 is being used to demonstrate compliance and equivalence of non-ductile detailing with the ductile detailing requirements of modern building code. Unfortunately, literally decades of learning from earthquakes about the importance of ductile detailing in concrete structures are being stripped away and dismissed by the "performance-based" analyses permitted by ASCE 41. While it may be true that a structure with limited ductility may survive a postulated design-level earthquake, it is not in the least realistic that the *confidence* that the structure will survive such an earthquake can be equated with that provided by a structure that complies with the ductile detailing requirements of the code. In no way should ASCE 41 be considered to provide the same performance or the same level of confidence that the desired performance will be achieved. Of note, ASCE 41 expressly states that ASCE 31 is understood to be even less conservative than ASCE 41 because it employs a 0.75 factor on demands when conducting a Tier 3 evaluation, which begs the question of just how many existing buildings, and projects involving additions, alterations, and changes of occupancy are being found to be "code-equivalent" on the basis of ASCE 31 Tier 3 analyses.

ASCE 31 AND ASCE 41 GIVE ANSWERS THAT ARE NONSENSICAL

The examples above notwithstanding, ASCE 31 and 41 are not always less conservative than current code; in fact, they can be far more conservative than current code, can force the performance of unnecessary calculations, and can give nonsensical results, as these next examples show.

Example #3

This structure is a one-story prefabricated steel-framed warehouse (Figure 5). Rectangular in plan, measuring 205 feet by 60 feet, and weighing just 0.4 pounds per cubic foot, this is one of the lightest structures we've ever studied.



Figure 4: Prefabricated steel-framed warehouse.

Lateral loads are resisted by steel moment frames, by diagonal cable bracing, and by the corrugated steel cladding. This building, which is in an area of moderate seismicity, was being considered for lease by the US Federal Government, which requires all buildings it leases to meet ASCE 31. With some back-of-the-envelope calculations and engineering judgment, it is possible to show not only that this structure has sufficient lengths of exterior wall that it meets the intent of current code with respect to seismic provisions, but also that hurricane-level design wind loads will govern the actual performance of the structure. Unfortunately, ASCE 31 permits neither back-of-the-envelope calculations nor engineering judgment.

Although most experienced engineers would probably consider a site with a 2475-year earthquake peak ground acceleration of 0.21g and a maximum spectral acceleration of 0.52g to be an area of moderate seismicity, the peak spectral acceleration is just 4 percent above the ASCE 31 cutoff for "moderate" seismicity.

No engineering judgment being permitted, the site is considered to have a high level of seismicity per ASCE 31. ASCE 31 then sets forth 11 pages of checklists that must be investigated to prove that the building is seismically adequate -- something that any experienced earthquake engineer should know after just a few minutes of reviewing of the structure. ASCE 31, being a cookbook, requires that torsion be checked, even though the structure is torsionally stable by inspection; several pages of calculations were required to show that torsion is adequately resisted by the structure. Further, ASCE requires that the axial stress in the cable bracing be checked but fails to require that the end connections of the cables be checked. In this case, the actual connections in this structure are so poorly engineered and constructed (Figure 5), they would be unable to develop the axial strength of the cables. ASCE 31, being a cookbook, failed to identify this potential weakness, and any inexperienced engineer relying on ASCE 31 would consequently miss this weakness as well.

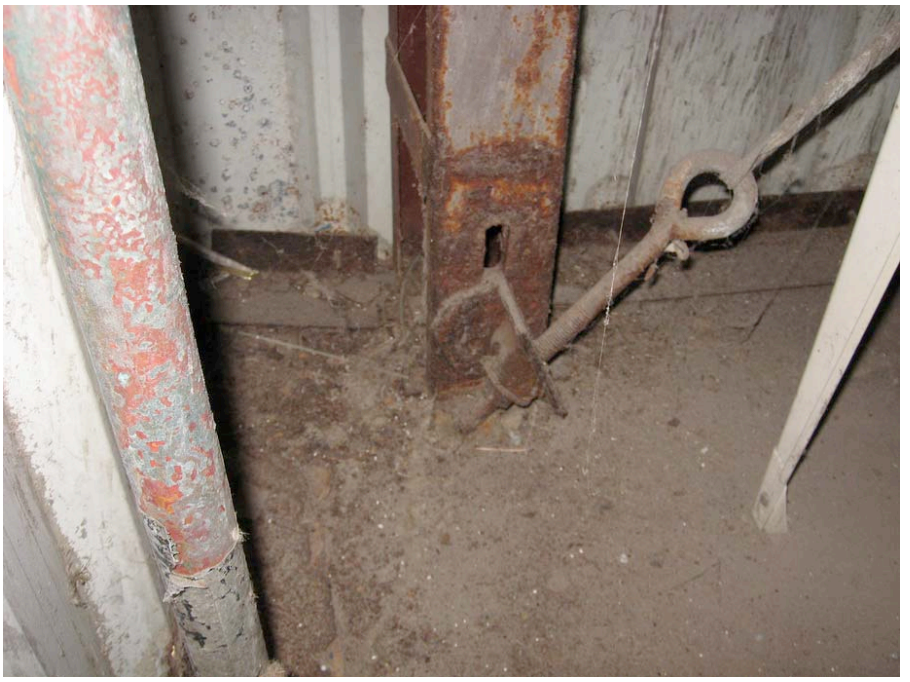


Figure 5: The connections of the cable bracing are highly eccentric and are clearly inadequate to develop the strength of the cables.

In the end, the structure "passed" ASCE 31, but for the wrong reasons. ASCE 31 required checks of elements that were clearly adequate for a structure that is likely to be unoccupied if a significant earthquake ever occurs, and failed to identify potential problems with other elements. In the end, ASCE 31 required more than 25 hours of fieldwork and analysis to prove what an hour of review by an experienced structural engineer should have been able to determine.

Example #4

ASCE 31 also fails to work properly in areas that most engineers would classify as having low seismicity. Consider the four-story unreinforced masonry structure that was originally used for manufacturing (Figure 6). The structure has since been

converted to office space and is being considered for occupancy by the U.S. Government, which requires the structure meet the requirements of ASCE 31.



Figure 6: This four story structure failed to meet the requirements of ASCE 31, despite being located in an area of relatively low seismicity.

Located on the east coast of the United States, this site has an effective peak ground acceleration of 14 percent, a peak spectral acceleration of 36 percent, and a one-second spectral acceleration of 15 percent, based on the 2475-year earthquake -- a return period that is, in the opinion of the authors, typically not appropriate for evaluation of existing buildings. A discussion of the problems with using such a long return period earthquake to evaluate existing structures is beyond the scope of this paper but can be found in Searer *et al*. (2007). In this case, the building is located in what used to be a Seismic Zone 2A in the Uniform Building Code (ICBO, 1994), and is located approximately 25 miles from an old Seismic Zone 1 -- hardly a portion of the country where earthquakes are a significant concern for well-built structures, even unreinforced masonry structures. Consequently, to occupy a portion of the structure, compliance with ASCE 31 requires that the entire building be upgraded via addition of floor- and roof-to-wall tension ties and shear transfer details -- a fairly expensive impediment to leasing space within the structure, and one that, in the authors' opinion, does not appear to be justified given the low level of seismicity to which this historic structure is exposed.

A FEW SELECTED TECHNICAL PROBLEMS WITH ASCE 31 AND 41

The ASCE standards have a myriad of technical problems, arguably enough to fill a book-length document longer than the standards themselves. A sampling of these was discussed in Searer *et al*. (April 2008); a few other head-scratchers are touched on herein.

Concrete Shear Wall Provisions

ASCE 41 provides "Numerical Acceptance Criteria for Nonlinear Procedures" for, among other things "Reinforced Concrete Shear Walls and Associated Components Controlled by Shear". The criteria are provided for, among other things, Life Safety (LS) and Collapse Prevention (CP) limit states in terms of an "Acceptable Total Drift (%)", determined using the full unreduced earthquake demands and the softening of the structure resulting from member nonlinearities. The drift criteria provided therein, which may not be exceeded without the entire structure failing the test, are 0.60 percent for LS and 0.75 percent for CP -- which makes us ask the following questions: What are the physical facts that led the authors of the document to conclude that a building -- for the sake of having an easy-to-visualize example, say a one-story concrete shear wall structure with a roof height of 10 feet -- would be a risk to the life safety of anyone when its lateral displacement at the roof during a design 475-year event was predicted to be less than ¾ inches, or would present a risk of collapse too great to accept when its lateral displacement at the roof during a 2,475-year event was predicted to be less than 1 inch? What physical facts could possibly have persuaded everyone involved that such a building was required to be seismically improved in order to make that building seismically adequate?

The provisions for reinforced concrete coupling beams have similar problems; we are not aware of any case where coupling beam damage itself resulted in the collapse of a building. What basis is there for a Collapse Prevention limit on coupling beam damage such that the safety of an entire building could be found deficient? Shouldn't the seismic adequacy of any building with coupling beams depend on whether the coupling beams are critical to the stability of the structure?

Steel Braced Frame Provisions

ASCE 41 also provides "Numerical Acceptance Criteria for Nonlinear Procedures" for, among other things "Structural Steel Components - Axial Actions" which are specifically applicable to braces. Similar to the concrete shear wall example above, the criteria provided for a primary "slender" brace in compression, say for an HSS section, which may not be exceeded without the entire structure failing the test are $5*\Delta_c$ for LS and $7*\Delta_c$ for CP, where Δ_c is the axial deformation expected at buckling load. Even a simple hand calculation, however, demonstrates that a slender brace in a bay of typical proportions could buckle at something around $^1/_{10}$ inches of axial deformation, meaning that the brace -- and thus the entire building in which the brace resided -- would fail the ASCE 41 Life Safety test if the story drift computed for the design event was short of ½ inch, and would fail the ASCE 41 Collapse Prevention test if the story drift computed for the design event was around ¾ inch. Given this,

questions similar to those raised in the preceding paragraph are certainly relevant: What are the physical facts that led the authors of this document to conclude that a building -- for the sake of having an easy to visualize example, say a one-story structure with a roof height of 15 feet -- would be a risk to the life safety of anyone when its lateral displacement at the roof during a design event was predicted to be less than ½ inch, or would present a risk of collapse too great to accept when its lateral displacement at the roof during a design event was predicted to be less than ¾ inch? What physical facts could possibly have persuaded everyone involved that such a building was required to be seismically improved in order to make that building seismically adequate? In developing these criteria, did anyone notice that these Life Safety and Collapse Prevention drift criteria are not particularly different from the drift levels used for decades to provide serviceability for wind design?

P-Delta Effects

These simple examples bring to light an underlying fundamental flaw that pervades the ASCE 41 approach; namely, that nonlinear assessment of Life Safety and Collapse Prevention limit states is typically viewed for "deformation-controlled" elements through the lens of drift-dependent element-specific criterion alone, rather than through a lens which explicitly accounts for local P-Delta effects and the structural context in which the element resides. This lapse is made clear in part by examination of the ASCE 41 acceptance criteria for structural steel columns, subject to nonlinear analysis, which are expressed in terms of "Plastic Rotation Angle, Radians". Being "plastic hinge rotations", these criteria are in some respects independent or relatively independent of the magnitude of the axial load in the column, meaning that according to ASCE 41, it does not matter whether the particular column being assessed is supporting only one story of tributary load or 100 stories -- the column being assessed is deemed to present essentially identical risk to life safety and the essentially identical collapse hazard. To our mind, however, the risk associated with any column is inextricably linked to the axial load on that column and no drift criterion alone -- such as provided by ASCE 41 -- can appropriately identify when that column will approach collapse conditions; the axial load in the column simply must be considered in tandem with the drift.

Equally, if not more, important is the subject of structural context. One criterion by which the seismic safety columns might have been judged in a pre-ASCE 41 world would have related to global buckling of the column, and the propensity of a column to buckle would have been related to whether it was located in a structure such that is either was or was not braced against sidesway. Should not the safety of a column located in a building that has shear walls be judged somewhat differently from a column located in a frame structure? Should not the safety of a column in a frame structure also be judged relative to the bracing provided by other frames in the structure? Yet this simple concept seems to not be relevant to any of the seismic safety checks in ASCE 41; in other words, the structural context of the element being evaluated does not appear to matter anymore. This is particularly ironic given that the safety of the element has, in ASCE 41, been given such weight that entire buildings

can be condemned based on the evaluation of a single element, as discussed in the following section.

Ignoring the Big Picture

As a last example, we will dwell for just a moment on the obvious -- the aspect of the ASCE methodologies that condemns entire buildings on the basis of the computed behavior of a single element. As we read the standards, assessment of the seismic adequacy of buildings is to be done on a member-by-member basis; the demands on each member in the lateral force resisting system is to be compared to the acceptance criteria applicable to that member. According to the standards, if a single primary member in a building fails the tests (including the Secondary Acceptance Criteria) the entire building fails the test, regardless of the level of redundancy and excess capacity in its remaining members and regardless of the ability or inability of the structure to redistribute loads. Unfortunately, this approach directly conflicts with what we believe are the fundamental elements and benefits of true performance-based engineering assessments, which, by employment of nonlinear analysis procedures are able to directly consider the consequences on the structure as a whole of excessive demands on individual members in a structure. The very simplistic approach required by the ASCE standards stands the intent of performance-based engineering on its head -- which it ought not to do if for no reason other than it sets itself forth as a performance-based standard. It is also simply wrong -- both in a technical sense and from an ethical one -- to automatically condemn the seismic performance of a building on the basis of the predicted response of a single element and to require that an engineer conclude on that basis that the building requires seismic strengthening.

CONCLUSIONS

While engineers familiar with ASCE 31 and 41 are well aware of the problems with these two documents, no apparent efforts have been made by either ASCE or structural engineers associations to inform other engineers, government officials, building officials, or the public with the myriad problems with these documents. Instead, these documents are being used indiscriminately by the engineering profession, resulting in inconsistent, illogical, useless, and sometimes even unsafe results. Although these documents are currently in the process of being revised, with revisions due in the fairly distant future, we are not hopeful that these documents can be improved to the point where they do more good than harm.

REFERENCES

American Society of Civil Engineers (ASCE), *Seismic Evaluation of Existing Buildings* (ASCE/SEI 31-03), 2003, Reston, Virginia.

American Society of Civil Engineers (ASCE), *Seismic Rehabilitation of Existing Buildings* (ASCE/SEI 41-06), 2006, Reston, Virginia.

American Society of Civil Engineers (ASCE), *Supplement No. 1, Seismic Rehabilitation of Existing Buildings* (ASCE/SEI 41-06), 2007, Reston, Virginia.

Federal Emergency Management Agency (FEMA), *Handbook for the Seismic Evaluation of Buildings: A Prestandard* (FEMA 310), 1998, Washington D.C.

Federal Emergency Management Agency (FEMA), *Prestandard and Commentary for the Seismic Rehabilitation of Buildings* (FEMA 356), 2000, Washington D.C.

International Conference of Building Officials (ICBO), *Uniform Building Code, 1994 Edition*, ICBO, Whittier, California, 1994.

Searer, G.R., Freeman, S.A, and Paret, T.F., "Does It Make Sense from Engineering and Economic Perspectives to Design for a 2475-Year Earthquake?", *Continental Intraplate Earthquakes: Science, Hazard, and Policy Issues*, Chapter 23, Geological Society of America, Boulder, Colorado, August 2007.

Searer, G.R., Paret, T.F., and Freeman, S.A., "ASCE-31 and ASCE-41: What Good Are They?", ASCE Structures Congress, Vancouver, Canada, April 2008.

Searer, G.R., Paret, T.F., and Freeman, S.A., "In Name Only: Peer Review of Performance-Based Engineering Projects", 14th World Conference on Earthquake Engineering, Beijing, China, October 2008.

Structural Engineers Association of Northern California (SEAONC) Existing Buildings Committee, "ASCE 41-06 Survey Results", SEAONC, San Francisco, California, September 2010.

Structural Engineers Association of Northern California (SEAONC) Existing Buildings Committee, "Perspectives on ASCE 41 for Seismic Rehabilitation of Buildings", *Structure Magazine*, National Council of Structural Engineers Associations, Chicago, Illinois, October 2010.

Seismic Evaluation of an Existing Low Ductility Braced Frame Building in California

Jeremy T. Callister[1], P.E. and Robert G. Pekelnicky[2], S.E., M. ASCE

[1]Degenkolb Engineers, 225 Broadway, Suite 1325, San Diego, California 92101; email: jcallister@degenkolb.com
[2]Degenkolb Engineers, 235 Montgomery St., Suite 500, San Francisco, California, 94104; email: rpekelnicky@degenkolb.com

ABSTRACT

Force-based seismic evaluation techniques for low ductility braced frame buildings generally will classify a braced frame structure as a potential collapse hazard if the brace connections are not capable of developing the force capacity of the associated braces. However, anecdotal evidence from major earthquakes has shown that most steel braced frame buildings have performed to a life safety or better performance level, even when brace connections have fractured. One reason for this lies with the contribution of the gravity framing participating as partially restrained moment frames. This paper discusses the seismic evaluation of a two-story 1980's braced frame building located in California. A nonlinear static analysis in accordance with *ASCE 41-06 Seismic Rehabilitation of Existing Buildings* was performed, with brace connection fracture and all the gravity frames modeled as partially restrained moment frames. The analysis showed that the building was very stiff, until the brace connections fractured. Following the connection fracture, the building became more flexible, but the gravity frames had sufficient flexibility to accommodate the earthquake induced drifts without compromising the stability of the building. The analysis showed that the building met the Life Safety performance level.

INTRODUCTION

Steel braced frame structures have been a common choice for low-rise buildings since the 1960's in many parts of California. New steel braced frame buildings in regions of high seismicity, such as coastal California, are required to either be Special Concentrically Braced Frames, Eccentrically Braced Frames, or Buckling Restrained Braced Frames (ASCE/SEI, 2006). All three of these types of braced frames have very specific design and detailing provisions that are intended to force the nonlinear response into actions that can dissipate energy such as brace yielding or buckling. Sudden failures, such as those that could occur at a connection, are prevented by requiring the connections to be designed for the capacity of the brace.

Explicit capacity based design provisions for braced frame connections were only instituted in the 1990's. Prior to the 1990's the most common type of braced frame used in low and midrise construction in California would likely be classified as a low ductility braced frame because its connections were not explicitly designed for the capacity of the braces.

The objective of this paper is to present the investigation of the seismic performance of a low ductility steel braced frame building via a nonlinear static procedure, while modeling the gravity beam to column connections as partially restrained moment frames. The purpose is to demonstrate that even though typical force based analysis procedures would show that the brace connections could not develop the capacity of the brace, and therefore would result in a classification of the building as a potential collapse hazard; the non-linear analysis indicated that the building met the Life Safety performance level.

The impetus for the assumption that the low-rise braced frame building was not a collapse hazard came first from observations of the behavior of braced frame building in major earthquakes and from some research conducted on the contribution of the steel gravity framing system behaving as a partially restrained moment frame system.

HISTORIC PERFORMANCE OF STEEL BRACED FRAMES

Past earthquakes have illustrated the susceptibility of low ductility steel braced frames to brittle failure mechanisms. These failures have typically been categorized as: i) net section fracture of the brace ii) failure of the brace to gusset connection via inadequate bolts or welds or iii) failure of the gusset plate or its connection to the beam or column. Although the documented number of brace and brace connection failures is quite extensive, the actual number of recorded building collapses due to these failures is limited, and typically only associated with older buildings with slender elements.

The 1978 Miyagi-ken Oki earthquake was one of the earliest earthquakes to illustrate potential weaknesses of modern braced-frame connections and detailing. Researchers Kato, Tanaka, and Yamanouchi (Kato, Tanaka, and Yamanouchi 1980) surveyed 454 steel buildings after the event and indicated that 107 buildings (with varying degrees of damage) had fractures of the brace elements and/or their connections. Of these 107 buildings only 6 had either collapsed or had lost their residual strength. It should be noted that a significant number of the braced frame buildings in Japan at this time consisted of slender tension-only bars or straps and light gauge steel elements, and most likely were the buildings that were categorized as collapsed. The steel building stock affected by this earthquake is not consistent with the braced frame building analyzed in this paper, and therefore, calculating probabilities of collapse from this pool and applying them to this building is unwarranted.

The 1985 Michoacan, Mexico earthquakes struck off the coast of Lazaro Cardenas on September 19th and 20th and were of magnitude 8.1 and 7.5, respectively. Investigator Martinez-Romero (Martinez-Romero 1986) surveyed 102 engineered steel buildings and reported that 10 of these had either totally collapsed or partially collapsed. Of these 10, only 3 were built after 1957 and contained diagonal braces. These 3 failures all occurred at the Pino Suarez complex, and are attributed to overstressing of slender columns, P-delta effects, and the long duration of shaking (Krawinkler and Martinez-Romero 1989). In addition, one of the 3 failures occurred

because the adjacent 21-story building collapsed onto the adjacent 14-story building. Although there was extensive damage to braced steel buildings in these earthquakes, the brace members and their connections are not representative of current detailing practices in United States, nor are they consistent with the building type investigated in this paper.

The 1994 Northridge earthquake is typically associated with having exposed the potential for brittle fractures in "ductile" moment frames and prompting investigations into various issues related to welded steel moment frame buildings; however, it also revealed the susceptibility of braced frames to non-ductile component failures. Kelly, Bonneville, and Bartoletti (Kelly, Bonneville, and Bartoletti 2000) describe damage found to a four story concentrically braced frame building that was designed to the 1980 Los Angeles building code. This building was reported to have only minor damage to its exterior; however, the interior braced bays experienced significant damage via twisting of beams at brace mid-spans, failure of brace connections to gusset plates, and fracture of bracing members at mid-spans due to local buckling. Most of the damage was concentrated at the second floor and was a result of softening that occurred to that level after initial brace failures began. It is unclear how many braced frame buildings experienced brace and component failures after the Northridge earthquake; however, there were no collapses of steel buildings.

The 1995 Hyogo-ken Nanbu earthquake caused damage very similar to the 1978 Miyagi-ken Oki earthquake, highlighting the weaknesses of slender tension-only straps and poor detailing of brace connections. Tremblay et al. (Tremblay, R. et al. 1996) summarizes a survey performed by the Architectural Institute of Japan (AIJ 1995) of 982 steel buildings. It is reported that of 452 *damaged* steel braced frame buildings, 29 had collapsed; however, 148 had only minor damage. All of these collapses were associated with slender bracing systems such as angles, flat bars and rods. Although not specifically quantified, these smaller cross sections would correlate with older building types, and therefore, as mentioned previously, are not representative of current detailing practices in United States, nor are they consistent with the building type investigated in this paper.

PARTIALLY RESTRAINED MOMENT FRAME CONTRIBUTION

After the Northridge earthquake, January 17, 1994, it was discovered that many steel welded moment frames exhibited brittle fractures in their welded moment connections; however, the performance of these buildings suggested the actual contribution of simple shear connections at the beam column joints was greater than previously thought. Liu and Astaneh-Asl (Liu and Astaneh-Asl 2000a-2000d), as part of the SAC Joint Venture Steel Project, conducted multiple full-scale cyclic tests of typical simple shear connections to very large drifts in order to establish their strength, stiffness, and ductility. These tests indicated that typical moment capacities ranged from about 20% of the plastic moment capacity of the beam (Mp) for the bare steel condition, to about 50% Mp if a concrete slab was present, and up to 80% Mp for the shear connection with a bottom seat angle and concrete slab.

ASCE 41-06 considers these types of shear connections as partially restrained (PR) moment frames and recommends modeling parameters and acceptance criteria limit states for nonlinear analysis procedures, and states that these gravity load-carrying elements could be used in the analytical model to reduce the demands on the moment frame elements. It is reasonable that specific modeling of the gravity shear connections can also be applied to non-ductile steel braced frame buildings, and therefore, act as a backup system to the non-ductile primary lateral force resisting system.

BUILDING DESCRIPTION

The existing building investigated is a two story steel braced frame building with a plan aspect ratio of approximately 3 to 1, as seen in Figure 1 and Figure 2, and a floor to floor height of 14 feet. Its design was performed in accordance with the 1976 Uniform Building Code. The gravity system is comprised of 2-inch metal deck with 3.25-inches of lightweight concrete fill spanning to steel beams, girders and columns. The beams and girders are composite members with shear studs spaced typically at 24 inches on center at gravity beams, and 12 inches on center at collector lines. The gravity beam connections are simple bolted connections with a single shear plate welded to the column as seen in Figure 3, and in some cases seat angle connections are also provided as seen in Figure 4. The foundation consists of reinforced concrete drilled piers and pier caps interconnected to each other with reinforced concrete grade beams.

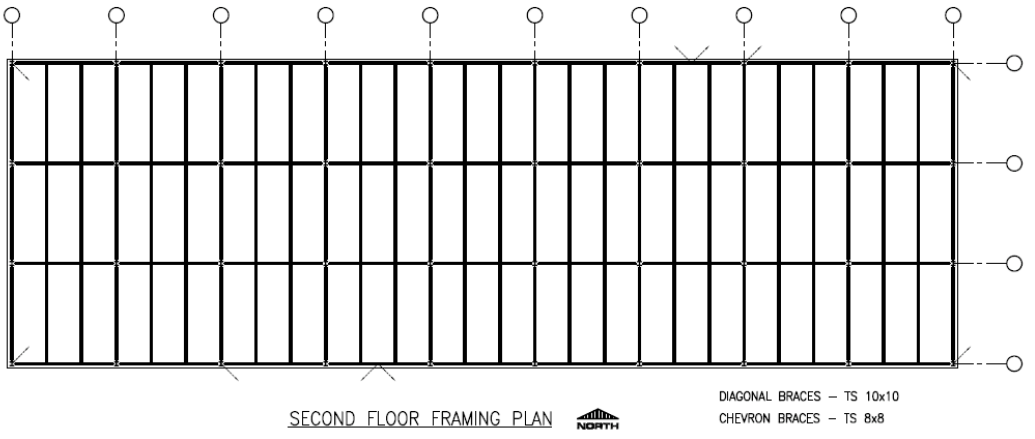


Figure 1. Second Floor Framing Plan

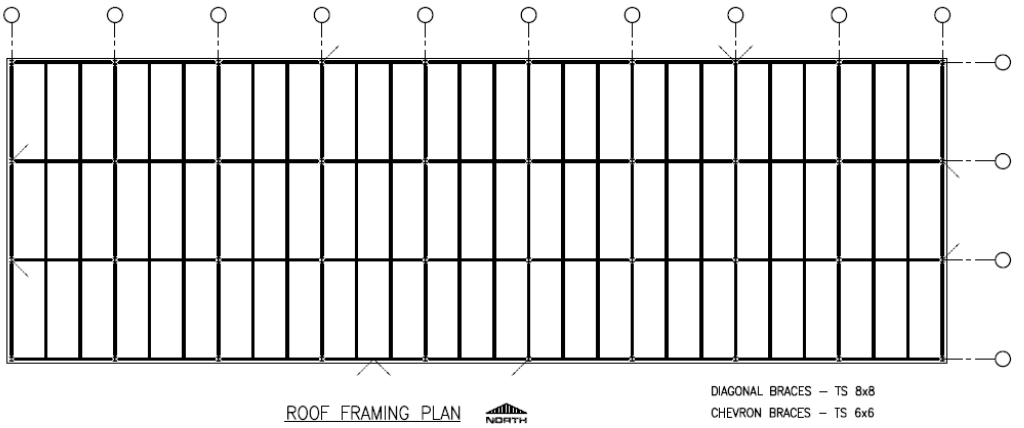


Figure 2. Roof Framing Plan

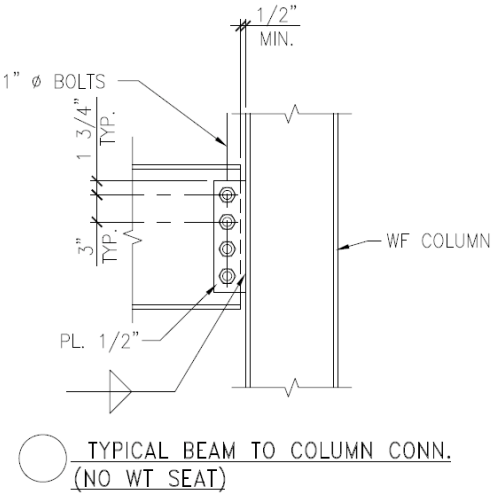


Figure 3. Typical Beam to Column Conn. (No Seat)

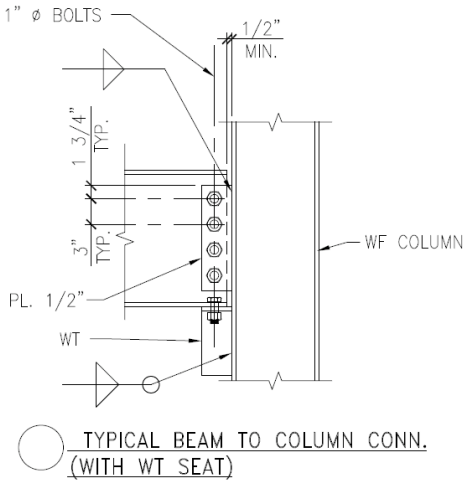


Figure 4. Typical Beam to Column Conn. (With Seat)

The lateral braces are located at each of the four exterior sides of the building, and are arranged in both diagonal and chevron bracing configurations. The diagonal braces are TS 10x10 structural sections and the chevron braces are TS 8x8 sections at the first floor. At the second floor the diagonal braces are TS 8x8 and the chevron braces are TS 6x6. The difference in brace sizes between the diagonal and chevron braces can be attributed to the longer pin-to-pin length of the diagonal brace relative to the chevron brace. The typical brace connection is depicted in Figure 5, and consists of a single gusset plate that receives the slotted tube steel brace. The absence of reinforcing plates at the net section of the brace, the short weld length of the brace to gusset connection, and the absence of detailing for ductile hinging in the gusset plate are all indicators of the potential brittleness of this connection.

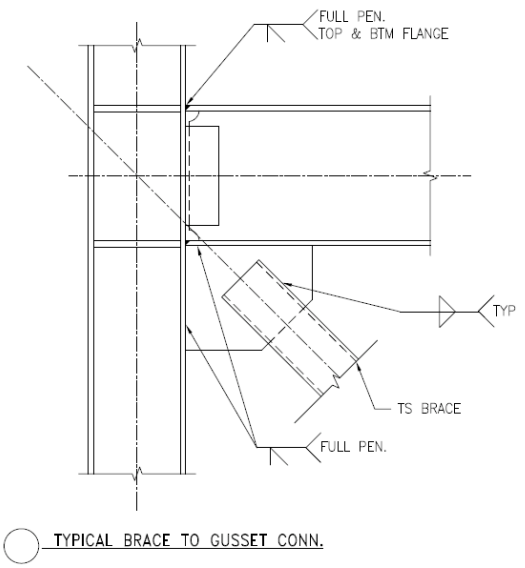


Figure 5. Typical Brace Connection

LINEAR ANALYSIS

A typical linear analysis of a braced frame building will assume the entire lateral seismic load is resisted by the brace elements, and all of the beam to column connections are assumed to have no rotational strength and stiffness (i.e. pinned connections). The compressive and tensile capacities of the braces are then checked against axial loads induced by the seismic demands. In an ASCE 7-05 procedure, the seismic demands on the braces are reduced by the system Response Modification Factor, R, and the brace capacities are based on nominal strengths (Rn) and resistance factors (phi) (AISC 360-05 and AISC 341-05). In an ASCE 41-06 procedure, the seismic demands for a particular earthquake hazard level are evaluated, and the brace capacities are based upon the expected strength of the component and the component demand modification factor (m). In both procedures, the connections of the braced frame system must be strong enough to withstand the expected yield strength of the brace in tension or the maximum load that can be delivered to the braces.

For the building considered in this paper, and true of many braced frame buildings designed and constructed prior to the code changes of the 1990's, the brace connection capacities are calculated to be insufficient to withstand the force capacity of the associated braces. Therefore, the linear analysis would classify the building as a potential collapse hazard, and costly seismic retrofitting would be required.

NON-LINEAR ANALYSIS

Simple linear analysis cannot accurately model building performance, and therefore, its inherent conservatism is more appropriate for new building design, not existing building evaluation; especially, when the existing building is a low ductility braced frame building. Therefore a nonlinear analysis of the building was performed.

As is common with ASCE 41-06 analyses, two seismic hazards were considered in this assessment. The BSE-2 seismic hazard is based on the Maximum Considered Earthquake at the building site. The BSE-1 seismic hazard is similar to a design level earthquake that would be used in new building design. Different structural performance states are assessed at each seismic hazard. In ASCE 41-06, the Basic Safety Objective (BSO) is a level which is intended to be consistent with the accepted level of seismic risk a new building would be designed to (ASCE/SEI 2007). For a building to conform to the BSO, it must meet the Life Safety performance level at the BSE-1 hazard and the Collapse Prevention performance level at the BSE-2 hazard.

The nonlinear static analysis procedure (NSP) outlined in ASCE 41-06 was used. The NSP provides a more detailed assessment of structural performance than the linear procedures contained in the building codes and ASCE 7 because it explicitly permits structural members to be stressed beyond their elastic limits and allows forces

to redistribute as they would in an actual earthquake.

In a pushover analysis, the displacement of a user-specified node is tracked against the force at the structure's base. Target displacements for the control node are calculated based on the seismic response spectrum for the site. These displacements are estimates of the maximum displacement the structure will undergo in a seismic event. Deformations in all the nonlinear hinges are then evaluated at the target displacement and checked against limits set forth in ASCE 41-06 or determined based on other rational methods. The structural elements that do not have nonlinear hinges assigned to them must then be checked to verify they have not been overstressed.

To perform the nonlinear static analysis, a three-dimensional model of the structure was created using ETABS v.9. The model included the braced frames, the concrete floor and roof diaphragms, and the main gravity framing – all the columns and all the beams along the gridlines. Because the initial assessment showed that the brace connections would not permit the braces to buckle and yield, which is the ideal way for braced frame structures to absorb seismic demands, the back-up system created by the gravity framing was included with the beam-column connections modeled as partially-restrained moment connections. Additionally, the explicit deformation characteristics of the concrete floor and roof diaphragms were modeled.

Nonlinear hinges were placed at all locations where there was a potential for the respective element to be stressed beyond its elastic limits. The hinge backbone curves were developed based on PR moment frame modeling parameters of ASCE 41-06. For the braces, ductile hinges representing the brace yielding in tension and buckling in compression were added, as were brittle hinges to represent the sudden loss of load carrying capacity in a brace when its connection is overstressed. The beams in the braced frames that had brace gusset plates attached to them were given ductile flexural hinges. The partially-restrained beam-column connections of the gravity framing had flexural hinges placed at each end to represent the behavior of their connection yielding in accordance with ASCE 41-06 and procedures developed by Liu and Astaneh-Asl (Liu and Astaneh-Asl 2004). The flexibility of the structure's foundation was explicitly modeled by placing three-dimensional springs at each drilled pier location, using upper bound stiffness values.

The model was then "pushed" in the transverse or north-south direction using a load pattern that displaces the structure elastically based on its first mode of vibration. Figure 6 shows a plot of the control node displacement, which was taken as a point on the roof near its center-of-mass, versus the base shear force (known as a pushover curve). In the analysis, the curve displays the pushover curves between zero and 150% of the BSE-2 target displacement, as ASCE 41-06 requires pushovers be carried out to. No analysis of the structure in the longitudinal, east-west direction was performed.

The structure is elastic until the point at which the connections of the second story western braces reach their limit. At that point, those connections are assumed to

fracture and render the braces ineffective, as seen in the large drop in base shear in the pushover curve. That creates a severe stiffness imbalance between the east and west sides of the second story since the eastern braces are still elastic. The roof then begins to rotate, engaging the resistance of the gravity framing and the perpendicular braced frames, which act to resist the rotation. As the roof continues to displace and rotate, the gravity framing beam-column connections yield and the perpendicular braces along the south face either buckle or fracture their connections. Those events are represented by the smaller sawtooth patterns on the pushover curves. All the while, the eastern braced frames at the second story and all the braces at the first story remain elastic.

The failure of the braced frame connections at the second story western frame creates a pronounced difference in strength and stiffness between the two stories. Because of that all the nonlinear yielding of elements occurs at the second story and the first story remains essentially elastic. At the BSE-1 target displacement, the western brace connections fracture and one of the southern braces buckle. Also, several of the gravity frame connections yield and reach their Immediate Occupancy limit. At the BSE-2 target displacement the southern brace connections fracture because of the forces imposed upon them as they resist the rotation of the roof. Most of the gravity frame connections yield. Because a significant number of the gravity connections in the roof were detailed to have a welded steel seat in addition to the standard shear-tab, those connections are capable of undergoing very large displacements without collapse and those are the connections that have the greatest rotational demand on them.

The non-linear analysis for this building indicates that when the simple shear connections are modeled as PR moment connections, these elements can have sufficient strength, stiffness, and ductility to act as a backup lateral system to the non-ductile braced frame building. The pushover curve shows that despite the fracture and/or buckling of the braces, the building can still displace well beyond the target displacement, while continuing to show increased strength in its force-displacement curve.

At the BSE-1 target displacement all the PR connections were found to have rotational demands well below the specified rotation limits for the life safety performance. Additional at the BSE-2 target displacement all the connection rotation demands were below the collapse prevention performance limits. Therefore the building met the Basic Safety Objective of ASCE 41-06.

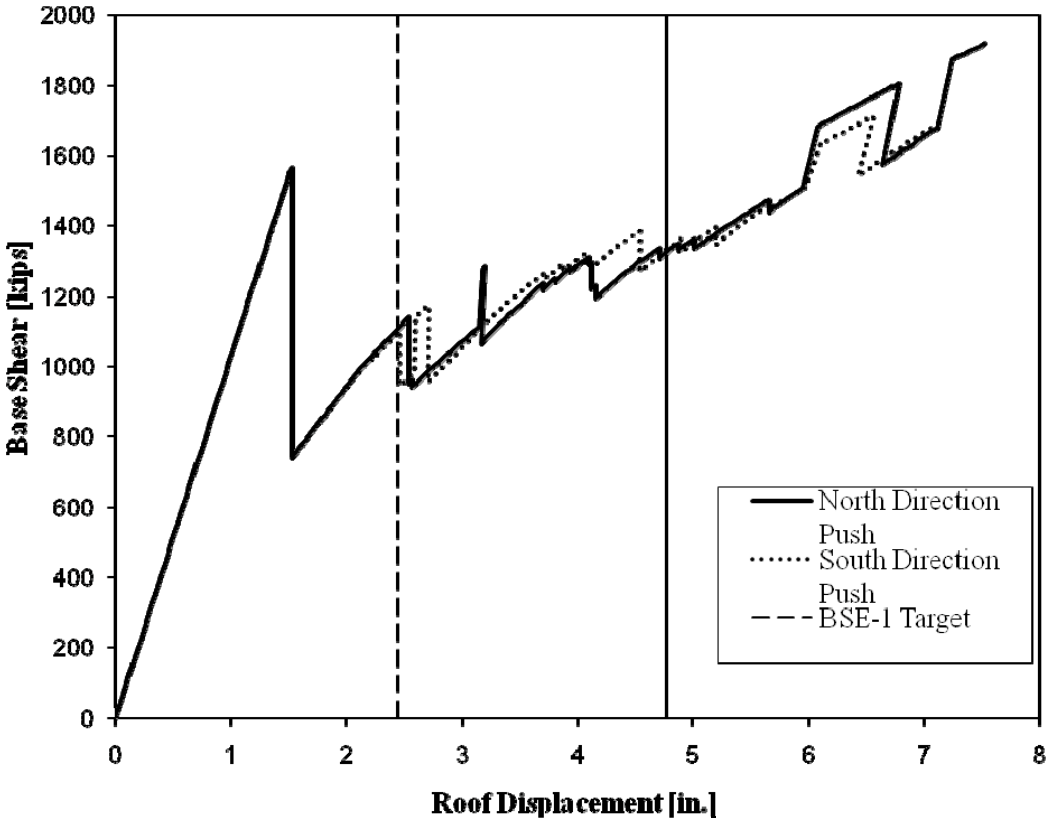


Figure 6. Nonlinear Static Pushover Curves

CONCLUSIONS

Force based or linear analysis seismic evaluations methods for low ductility braced frames will indicate that a building is a potential collapse hazard due to the inability of the brace connections to develop the capacity of the brace. As suggested by anecdotal evidence of past building performance, cyclic testing, and non-linear static modeling, the contribution of simple gravity connections in steel buildings can provide a backup system of strength, stiffness, and ductility to a building utilizing low ductility lateral braces. This contribution is significant enough that when considered in seismic evaluations, they may provide a cost-effective alternative to seismic retrofitting. This paper only considers a non-linear static procedure; however, it is expected that a non-linear dynamic procedure would yield the same conclusions, as the refinements of the non-linear response history procedure would remove any conservatism inherent in all other analysis methods.

REFERENCES

AIJ. (1995). Reconnaissance report on damage to steel building structures observed from the 1995 Hyogoken-Nanbu (Hanshin/Awaji) earthquake, Architectural Institute of Japan, Steel Committee of Kinki Branch, Tokyo, Japan.

AISC. (2005a). Steel Construction Manual, 13th ed., American Institute of Steel Construction AISC, Chicago, Illinois.

AISC. (2005b). ANSI/AISC 360-05. Specification for structural steel buildings, American Institute of Steel Construction AISC, Chicago, Illinois.

AISC. (2005c). ANSI/AISC 341-05. Seismic provisions for structural steel buildings, American Institute of Steel Construction AISC, Chicago, Illinois.

ASCE/SEI. (2006). "Minimum Design Loads for Buildings and Other Structures - including Supplement No. 2." ASCE Standard Number ASCE/SEI 7-05, American Society of Civil Engineers, Reston, VA.

ASCE/SEI. (2007). "Seismic Rehabilitation of Existing Buildings." ASCE Standard Number ASCE/SEI 41-06, American Society of Civil Engineers, Reston, VA.

Astaneh-Asl, A. (1998). "Seismic Design And Behavior of Gusset Plates." Structural Steel And Education Council {Steel Tips}, 209 Vernal Drive, Alamo, California 94507.

Astaneh-Asl, A. (2005). "Design of Shear Tab Connections for Gravity and Seismic Loads." Structural Steel And Education Council {Steel Tips}, 209 Vernal Drive, Alamo, California 94507.

International Code Council (ICC). (2006). International Building Code, Washington, DC.

International Conference of Building Officials (ICBO). (1976). Uniform building code, Whittier, Calif.

Kato, B., Tanaka, A., and Yamanouchi, H. (1980). "A Field Work Investigation of Steel Building Damage Due to the 1978 Miyagiken-oki Earthquake." Proceedings of the Seventh World Conference on Earthquake Engineering, Istanbul, Turkey, 479-486.

Kelly, D. J., Bonneville, D. R., and Bartoletti, S. J. (2000). "1994 Northridge earthquake: damage to a four-story steel braced frame building and its subsequent upgrade." 12th World Conference on Earthquake Engineering, New Zealand Society for Earthquake Engineering, Upper Hutt, New Zealand.

Krawinkler, H., and Martinez-Romero, E. (1989). "Performance Evaluation of Steel Structures in Mexico City." Lessons Learned from the 1985 Mexico City Earthquake, Earthquake Engineering Research Institute, 89-02,113-119.

Liu, J., and Astaneh-Asl, A. (2000a). "Seismic Behavior and Design of Steel Shear Connections with Floor Slab." Proceedings, 12th World Conference on Earthquake Engineering, Auckland, New Zealand, January, 1829.

Liu, J., and Astaneh-Asl, A. (2000b). "Cyclic Behavior of Steel Shear Connections with Floor Slab." Proceedings, 6th ASCCS International Conference on Steel-Concrete Composite Structures. Los Angeles, CA, 745-752.

Liu, J., and Astaneh-Asl, A. (2000c). "Cyclic Behavior and Seismic Design of Steel Shear Connections." Proceedings, International Workshop on Connections in Steel Structures IV, Roanoke, VA, October.

Liu, J., and Astaneh-Asl, A. (2000d). "Cyclic Testing of Simple Connections Including Effects of Slab". Journal of Structural Engineering, January, 32-39.

Liu, J., and Astaneh-Asl, A. (2004). "Investigation of the Cyclic Behavior of Steel Simple Connections". Journal of Structural Engineering, September.

Martinez-Romero, E. (1986). "Damage Assessment and Seismic Behavior of Steel Buildings in Mexico City." Proceedings of the International Conference on The Mexico Earthquakes-1985, Mexico City, Mexico, 409-425.

PEER 2008/08 (2008). Toward Earthquake-Resistant Design of Concentrically Braced Steel-Frame Structures. Patxi Uriz and Stephen A. Mahin. November 2008.

SAC Joint Venture. (1997). "Protocol for Fabrication, Inspection, Testing and Documentation of Beam-Column Connection Tests and Other Experimental Specimens." SAC/BD-97-02, SAC Joint Venture, Sacramento.

Tremblay, R. et al. (1996). "Seismic design of steel buildings: Lessons from the 1995 Hyogo-ken Nanbu earthquake." Canadian Journal of Civil Engineering, 23, 727-756.

Tremblay, R., Timier, P., Bruneau, M., and Filiatrault, A. (1995). "Performance of steel structures during the 1994 Northridge earthquake." Canadian Journal of Civil Engineering, 22, 338-360.

Seismic Damage Analysis Model for RC Structures Based on Concrete Plastic Damage Model

Z.H. Li[1], J. Teng[2] and X.F. He[3]

[1]School of Civil Engineering, Dalian University of Technology, Dalian 116024, P.R. China; PH (86) 411-84706493, FAX (86) 411-84706409; email: lizuohua@dlut.edu.cn
[2]Shenzhen Graduate School, Harbin Institute of Technology, Shenzhen 518055, P.R. China; PH (86) 755-26033806, FAX (86) 755-26033509; email: tengj@hit.edu.cn
3Shenzhen Graduate School, Harbin Institute of Technology, Shenzhen 518055, P.R. China; PH (86) 755-26033506, FAX (86) 755-26033509; email: he_xuefeng@126.com

ABSTRACT

Firstly, a plastic-damage constitutive model for concrete complying with the laws of thermodynamics is proposed based on continuum damage mechanics theory. The damage constitutive equations, damage evolution equations and plastic deformation of concrete are derived. Secondly, Fiber damage analysis model(FDAM) for RC beam-column member is established by analyzing section of fiber beam column element, which was developed with VUEL subroutine based on ABAQUS/Explicit platform, with the uniaxial damage constitutive relations of concrete proposed in present paper being used. The member damage index is defined, which can describe the nonlinear damage behavior of RC members under any loadings. Accuracy of the model is identified preliminarily by comparing with the analysis results of solid element. Finally, a numerical analysis model based on finite element program ABAQUS combined with the proposed damage model is built to analyze the seismic damage of a high-rise structure, and the structure analysis results are compared to the data from shaking table test.

INTRODUCTION

In recent years, the seismic damage model that based on the plasticity and damage mechanics theories has attracted many attentions(e.g. Lee and Fenves, 1998; Wang and Liu, 2001; Li and Wu,2005; Teng and Li, 2006; Wu and Li, 2006). Theoretically, this approach could provide a more robust and broad basis for the research and application of structure seismic analysis. The reinforced concrete members are the

most widely used in structural engineering, so it is more crucial to develop corresponding damage model based on material damage mechanics to understand its mechanical behavior and damage evolution under monotonic/cyclic loadings.

On the other hand, at the aspect of finite element model, the so-called 'fiber method' is currently believed as a promising 'finer' strategy for inelastic structure analysis. The key points of fiber method are, firstly, subdivide member element into longitudinal fibers, and then determine the strains of section points with plan section assumption. After introducing corresponding uniaxial damage constitutive relation for each concrete and rebar fiber (i.e. each section point), the inelastic relation between section resultant forces and section deformations can be derived by integration of the response of the fibers. An especial advantage of the fiber method is that, the inelastic behavior of member section will be simulated at strain-stress level, which provides a practicable way for seismic damage analysis that based on material damage model.

From above considerations, a new energy release rate-based plastic-damage model for concrete, which accounts for the interaction of the damage and plastic deformation, can predict the concrete primary behavior in tension and compression is formulated comply with the basic principles of thermodynamics, and the fiber damage analysis model(FDAM) using fiber method for reinforced concrete members is developed, with uniaxial damage consitutive model for concrete fibers. The task is accomplished by the way of secondary development on ABAQUS/Explicit, which is a famous powerful explicit solver. The member damage index is defined, which can describe the nonlinear damage behavior of RC members under any loadings, and a numerical example of fiber damage analysis model for RC member is given in this paper, with their results compared with results from solid model. Finally, The present model is adopted to analyze seismic damage of a real structure, with their results compared with data from shake table test and which proved the effectiveness of the proposed model and strategy.

DAMAGE ANALYSIS MODEL

Plastic-damage constitutive model for concrete material. A plastic-damage constitutive model for concrete complying with the laws of thermodynamics is proposed based on continuum damage mechanics theory(e.g. Yu and Qian,1993). In order to describe the deformation process resulted from internal energy dissipation and micro change of the structure, the independent internal state variables related with irreversible thermodynamic processes are introduced. The Helmholtz free energy takes the form(Coleman and Gurtin,1967):

$$\psi\left(\boldsymbol{\varepsilon}^e, \boldsymbol{\varepsilon}^p, \boldsymbol{D}\right) = \psi^e\left(\boldsymbol{\varepsilon}^e, \boldsymbol{D}\right) + \psi^p\left(\boldsymbol{\varepsilon}^p, \boldsymbol{D}\right) \tag{1}$$

where $\boldsymbol{D}$ is damage tensor, $\psi^e\left(\boldsymbol{\varepsilon}^e, \boldsymbol{D}\right)$ is elastic Helmholtz free energy, $\psi^p\left(\boldsymbol{\varepsilon}^p, \boldsymbol{D}\right)$

and is plastic Helmholtz free energy.
In the present model, the damage tensor in (1) is substituted by scalar damage variable , which can consider the stiffness degradation of the material, one obtains the following expression for $\psi^e\left(\boldsymbol{\varepsilon}^e, \boldsymbol{D}\right)$:

$$\psi^e\left(\boldsymbol{\varepsilon}^e, D\right) = \frac{1}{2\rho}\boldsymbol{\varepsilon}^e : (1-D)\,\boldsymbol{E}_0 : \boldsymbol{\varepsilon}^e \tag{2}$$

where $\boldsymbol{E}$ is the stiffness tensor, $\boldsymbol{E}_0$ is the initial stiffness tensor, and ρ is the material density.

Based on the Clausius–Duhem inequality (Coleman et al., 1967) for the isothermal case, the damage constitutive equation is given as follows:

$$\boldsymbol{\sigma} = \rho\,\partial\psi^e\left(\boldsymbol{\varepsilon}^e, D\right)\big/\partial\boldsymbol{\varepsilon}^e \tag{3}$$

Generally for the state without damage, there is no plastic deformation occur in the concrete material. In other words, the damage and the plastic deformation will always coexist. The plastic Helmholtz free energy will not be zero when damage appears. But, even up to date, it is difficult to define the expression of plastic Helmholtz free energy directly. In this paper the expression of plastic Helmholtz free energy is given indirectly through a function that is defined using internal variables and elastic Helmholtz free energy, and its expression assumed taking the form as:

$$\psi^p\left(\boldsymbol{\varepsilon}^p, D\right) = F\left(\boldsymbol{\varepsilon}^e, \boldsymbol{\varepsilon}^p\right)\psi^e\left(\boldsymbol{\varepsilon}^e, D\right) \tag{4}$$

where $F\left(\boldsymbol{\varepsilon}^e, \boldsymbol{\varepsilon}^p\right)$ is a function of internal variables.

The damage energy release rate Y may be written in the form:

$$Y = -\rho\frac{\partial\psi}{\partial D} = -\rho\left[\frac{\partial\psi^e\left(\boldsymbol{\varepsilon}^e, D\right)}{\partial D} + \frac{\partial\psi^p\left(\boldsymbol{\varepsilon}^p, D\right)}{\partial D}\right] \tag{5}$$

By substituting (4) into (5), one gets Y expressed by $\psi^e\left(\boldsymbol{\varepsilon}^e, D\right)$ as follows:

$$Y = -\rho\left[1 + F\left(\boldsymbol{\varepsilon}^e, \boldsymbol{\varepsilon}^p\right)\right]\frac{\partial\psi^e\left(\boldsymbol{\varepsilon}^e, D\right)}{\partial D} \tag{6}$$

Thus, Eq. (6) is the control equation of material damage evolution. In this paper $F\left(\varepsilon^e, \varepsilon^p\right) = k\,\varepsilon^p/\varepsilon^e + l$, where k and l are constants.

On the other hand, for the material damage, the Weibull distribution is widely used to describe the distributing rule of the damage and fracture in the rock and the concrete material (e.g. Gao, 1993). In this paper the Weibull distribution hypothesis is also adopted in the determination of the damage variable and damage energy release rate. Therefore, one obtains expressions of D and Y as follows:

$$D = 1 - \exp\left(-\frac{\left(Y - Y_0\right)^a}{b} \right) \tag{7}$$

where Y_0 is initial damage energy release rate, a and b are constants. By substituting (6) into (7), one gets the evolution equation of damage.

The experimental tests show that there a surface (yield surface) in the stress space, where a failure or damage state can be determined. The yield function of Lubliner et al. (1989), with the modifications proposed by Lee and Fenves (1998) that accounts for both tension and compression plasticity is adopted in this work. In terms of effective stresses, the yield function takes the form

$$F = \frac{1}{1-\alpha}\left[\alpha \bar{I}_1 + \sqrt{3\bar{J}_2} + \beta(\tilde{\varepsilon}^p)\left\langle \hat{\bar{\sigma}}_{\max} \right\rangle \right] - c(\tilde{\varepsilon}_c^{\,p}) \tag{8}$$

where $\bar{I}_1 = \mathrm{tr}\,(\bar{\boldsymbol{\sigma}})$ is the first-invariant of the effective stress, $\bar{J}_2 = 1/2\,\bar{\mathbf{s}}:\bar{\mathbf{s}}$ is the second-invariant of the effective deviatoric stress, $\hat{\bar{\sigma}}_{\max}$ is the maximum principal effective stress, $\tilde{\varepsilon}_c^{\,p}$ is the equivalent plastic strain in compression.

The parameters α and β are dimensionless constants which are defined by Lubliner et al. (1989) as follows:

$$\alpha = \frac{\left(f_{b0}/f_0^-\right) - 1}{2\left(f_{b0}/f_0^-\right) - 1} \tag{9}$$

$$\beta(\tilde{\varepsilon}^p) = \left(1-\alpha\right)\frac{c(\tilde{\varepsilon}_c^{\,p})}{c(\tilde{\varepsilon}_t^{\,p})} - \left(1+\alpha\right) \tag{10}$$

where f_{b0} is the biaxial initial yield stress, f_0^- is uniaxial initial compressive yield stress, $\tilde{\varepsilon}_t^{\,p}$ is the equivalent plastic strain in tension.

The shape of the concrete loading surface will be obtained by using a non-associative plasticity flow rule. When the current yield surface F is reached, the material is considered to be in plastic flow state upon increase of the loading. In this work, the flow rule is given as a function of the effective stress $\bar{\boldsymbol{\sigma}}$ by

$$\dot{\boldsymbol{\varepsilon}}^p = \dot{\lambda}^p \frac{\partial F^p}{\partial \bar{\boldsymbol{\sigma}}} \tag{11}$$

where $\dot{\lambda}^p$ is the plastic loading factor, which can be obtained using the plasticity consistency condition, such that

$$F \le 0, \quad \dot{\lambda}^p \ge 0, \quad \dot{\lambda}^p F = 0, \quad \dot{\lambda}^p \dot{F} = 0 \tag{12}$$

Plastic potential F^p adopted in the present model is the Drucker-Prager function expressed as:

$$F^p = \sqrt{2\bar{J}_2} + \alpha^p \bar{I}_1 \tag{13}$$

where is α^p the dilation constant.
By substituting (13) into (11), the evolution law for the plastic strains is obtained

$$\dot{\boldsymbol{\varepsilon}}^p = \dot{\lambda}^p \left(\frac{\bar{\mathbf{s}}}{\|\bar{\mathbf{s}}\|} + \alpha^p \mathbf{I} \right) \tag{14}$$

where $\|\bar{\mathbf{s}}\| = \sqrt{\bar{\mathbf{s}} : \bar{\mathbf{s}}} = \sqrt{2J_2}$, $\mathbf{I}$ is the identity tensor.

Fiber Dmamge Analysis Model(FDAM). The general system equation of structure dynamics can be written in the form

$$\mathbf{M}\ddot{\mathbf{u}} = \mathbf{F} - \mathbf{F}^{\text{int}} \tag{15}$$

where $\mathbf{M}$ is mass matrix, $\mathbf{F}$ is external load vector, and $\mathbf{F}^{\text{int}}$ is defined as internal force at time t. Thus the acceleration, $\ddot{\mathbf{u}}$ can simply obtained by

$$\ddot{\mathbf{u}} = \mathbf{M}^{-1}(\mathbf{F} - \mathbf{F}^{\text{int}}) \tag{16}$$

In practice, the above equation does not usually require solving of the matrix equation, if lumped masses were used, which will derive a diagonal or nearly diagonal mass matrix. Moreover, $\ddot{\mathbf{u}}$ is usually discretized by explicit second order central difference scheme. Therefore, the most important tasks of secondary development in ABAQUS/Explicit are to define the element mass $\mathbf{M}_e$ and element internal force $\mathbf{F}_e^{\text{int}}$, and the global solution is left to the solver itself.

Consider the three dimensional beam-column model in local coordinate system $\bar{x}$-$\bar{y}$-$\bar{z}$, show as in Figure 1, where longitudinal axis $\bar{x}$ is the union of geometric centroids of each section, and $\bar{y}$, $\bar{z}$ are two directions of the section. There are six displacement components and six resultant force components at arbitrary section

$$\bar{\mathbf{u}} = [\bar{u} \quad \bar{w} \quad \bar{v} \quad \bar{\varphi}_x \quad \bar{\varphi}_y \quad \bar{\varphi}_z]^{\mathrm{T}} \tag{17}$$

$$\bar{\mathbf{F}}_s = [\bar{N} \quad \bar{Q}_y \quad \bar{Q}_z \quad \bar{M}_x \quad \bar{M}_y \quad \bar{M}_z]^{\mathrm{T}} \tag{18}$$

where, $\bar{u}$ is axial displacement, $\bar{w}$, $\bar{v}$ are transverse deflections, $\bar{\varphi}_x$ is torsional rotation, and $\bar{\varphi}_y$, $\bar{\varphi}_z$ are bending rotations. Correspondingly, $\bar{N}$ is axial force, $\bar{Q}_y$, $\bar{Q}_z$ are transverse shearing forces, $\bar{M}_x$ is torsional moment, and $\bar{M}_y$, $\bar{M}_z$ are bending moments.

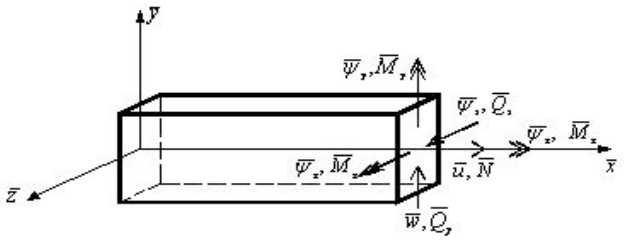


Figure 1. 3D Beam-column model.

Based on Timoshenko Beam Theory and small deformation assumption, we introduce the generalized geometrical relation of the section formulated in vector form

$$\boldsymbol{\varepsilon} = [\,\varepsilon \quad \gamma_y \quad \gamma_z \quad \chi_x \quad \chi_y \quad \chi_z\,]^{\mathrm{T}} = \mathbf{L}\bar{\mathbf{u}} \tag{19}$$

In the section deformation vector $\boldsymbol{\varepsilon}$, the component ε is axial extension, γ_y , γ_z are transverse shearing deformations, χ_x is torsion deformation, χ_y , χ_z are bending curvature. $\mathbf{L}$ denotes the geometrical differential operator matrix. Thus, the generalized section constitutive relation could be formally written as

$$\bar{\mathbf{F}}_s = \bar{\mathbf{K}}_s \boldsymbol{\varepsilon} \tag{20}$$

where $\bar{\mathbf{K}}_s$ is the section stiffness matrix.

For the above model of beam-column, we establish a finite element model that contains two nodes with their local axial coordinates denoted by $\bar{x}_1$ and $\bar{x}_2$, show as Figure 2.

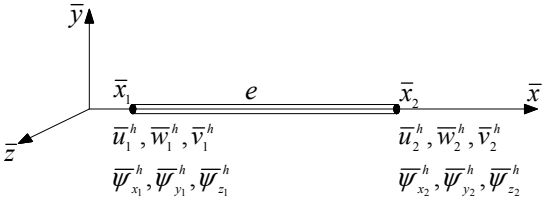


Figure 2. Finite element model.

Therefore, the nodal displacement vector of each element could be written as

$$\bar{\mathbf{u}}_e^h = [\bar{u}_1^h \quad \bar{w}_1^h \quad \bar{v}_1^h \quad \bar{\psi}_{\bar{x}_1}^h \quad \bar{\psi}_{\bar{y}_1}^h \quad \bar{\psi}_{\bar{z}_1}^h \quad \bar{u}_2^h \quad \bar{w}_2^h \quad \bar{v}_2^h \quad \bar{\psi}_{\bar{x}_2}^h \quad \bar{\psi}_{\bar{y}_2}^h \quad \bar{\psi}_{\bar{z}_2}^h]^{\mathrm{T}} \tag{21}$$

Moreover, finite displacement of arbitrary local section

$$\bar{\mathbf{u}}^h = [\bar{u}^h \quad \bar{w}^h \quad \bar{v}^h \quad \bar{\psi}_{\bar{x}}^h \quad \bar{\psi}_{\bar{y}}^h \quad \bar{\psi}_{\bar{z}}^h]^{\mathrm{T}} \tag{22}$$

Obviously, there will be the following interpolating relation between $\bar{\mathbf{u}}_e^h$ and $\bar{\mathbf{u}}^h$

$$\bar{\mathbf{u}}^h = \mathbf{N}\bar{\mathbf{u}}_e^h \tag{23}$$

where $\mathbf{N}$ is formally the displacement interpolating matrix, respectively, the transverse deflections are cubic, bending rotation are quadratic. All of them contain

condensed internal freedoms, and the so-called 'shearing locking' has been avoided. Moreover, both axial displacement and torsional rotation are linear. From Eq.19~Eq.23, the finite deformation and internal force of sections can be written as

$$\bar{\boldsymbol{\varepsilon}}^h = \mathbf{B}\bar{\mathbf{u}}_e^h \tag{24}$$

$$\bar{\mathbf{F}}_S^h = \bar{\mathbf{K}}_s \mathbf{B}\bar{\mathbf{u}}_e^h \tag{25}$$

where geometric matrix $\mathbf{B} = \mathbf{LN}$, which results from $\mathbf{L}$ acting on $\mathbf{N}$. Then, the element internal force vector $\bar{\mathbf{F}}_e^{\text{int}}$ will be derived by virtual displacement theorem

$$\bar{\mathbf{F}}_e^{\text{int}} = \int_{\bar{x}_1}^{\bar{x}_2} \mathbf{B}^{\mathrm{T}} \bar{\mathbf{F}}_S^h \mathrm{d}\bar{x} \tag{26}$$

Besides, the element lumped mass $\bar{\mathbf{M}}_e$ is easy to be formulated for two nodes element model and its formula abbreviated here. But, it should be noted that, in the whole above process, '$\bar{\ }$' means definition in local coordinates system $\bar{x}$-$\bar{y}$-$\bar{z}$, so coordinates transformation should be implemented before the global integrating phase.

In nonlinear explicit dynamic analysis, the main target of 'fiber method' is to calculate section internal force $\bar{\mathbf{F}}_S^h$, and $\bar{\mathbf{F}}_e^{\text{int}}$ will be calculated by integration show as Eq.26.

Take a reinforced concrete beam-column show in Figure 3 as example, the member is longitudinally discretized into *nfib* fibers. The configuration of fibers on sections is displayed in Figure 4, where $(\bar{y}_{ifib}, \bar{z}_{ifib})$ refers to the fiber position in cross section and A_{ifib} is the section area of fiber. Following the plane section assumption, the strain of each fiber can be derived as

$$\varepsilon_{ifib} = \varepsilon + \bar{z}_{ifib}\chi_y - \bar{y}_{ifib}\chi_z = \mathbf{l}_{ifib}^{\mathrm{T}} \bar{\boldsymbol{\varepsilon}}^h \tag{27}$$

where, $\mathbf{l}_{ifib} = [\mathbf{1} \quad \mathbf{0} \quad \mathbf{0} \quad \mathbf{0} \quad \bar{z}_{ifib} \quad -\bar{y}_{ifib}]^{\mathrm{T}}$ Introducing particular uniaxial constitutive relation $\sigma = f(\varepsilon)$ for each fiber respectively, there derived the axial stress of fibers

$$\sigma_{ifib} = f(\varepsilon_{ifib}) \tag{28}$$

Summing all stresses of fibers together, $\bar{\mathbf{F}}_S^h$ will be deduced by virtual displacement theorem

$$\bar{\mathbf{F}}_S^h = (\sum_{ifib=1}^{nfib} \mathbf{l}_{ifib}\sigma_{ifib}A_{ifib}) + \mathbf{l}_{\bar{M}_x}(GJ\chi_x) + \mathbf{l}_{\bar{Q}_y}(GA\gamma_y) + \mathbf{l}_{\bar{Q}_z}(GA\gamma_z) \tag{29}$$

where A is the section area, G is the section shearing modulus, J is the section torsional moment of inertia.

In Eq.29, the effects of torsion and shearing are macroscopically considered at section level, and they are usually assumed to keep elastic in inelastic analysis.

In order to evaluate the nonlinear behavior of RC beam-column member subjected to

arbitrary loading, extreme section damage index of RC member is defined as

$$D_{MC} = \frac{\sum_{i}^{k} D_{ci} A_{cifib}}{\sum_{i}^{k} A_{cifib}}, \quad D_{MT} = \frac{\sum_{i}^{m} D_{ti} A_{tifib}}{\sum_{i}^{m} A_{tifib}} \tag{30}$$

where A_{cifib} is the section area of compressive fiber, A_{tifib} is the section area of tensive fiber.

The last important aspect of our fiber strategy is, the uniaxial constitutive relation of fibers, i.e. the determination of $\sigma = f(\varepsilon)$. Here we adopted uniaxial damage constitutive relation deduced from Eq.3 and its hysterical rule deduced from Eq.15~Eq.16. For steel material in real structure members, we adopted bilinear kinematic hardening model, which is simple but practically effective. The more numerical details will be abbreviated in present paper.

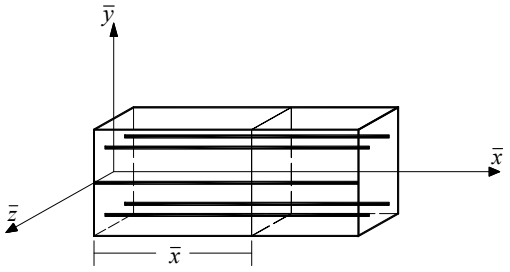


Figure 3. Reinforced concrete beam-column.

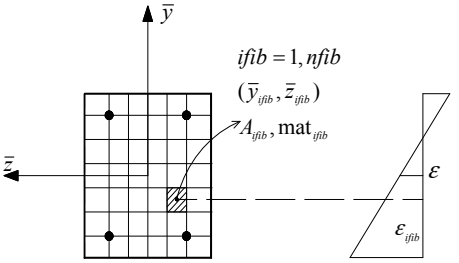
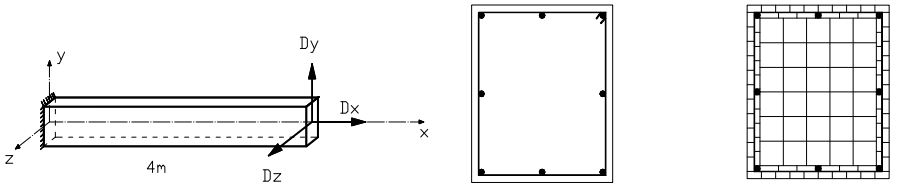


Figure 4. The configuration of fibers on sections.

Numerical Exampel For FDAM. In this section, a numerical example of the present fiber damage analysis model for RC beam-column member is presented, the following properties(see Figure 5) are used: the length is 4m, the cocrete material is C30, the section size is 500mm×600mm. The subdivision of cross section is shown in Figure 9(c). The displacement loading is used: $Dx = -5mm$, $Dy = 20mm$, $Dz = 20mm$.

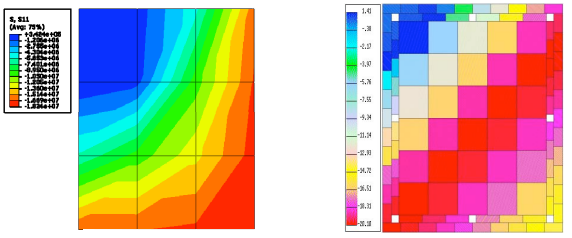


(a) Beam-column member model (b) Rebar of cross section (c) Subdivision of cross section

Figure 5. RC beam-column member.

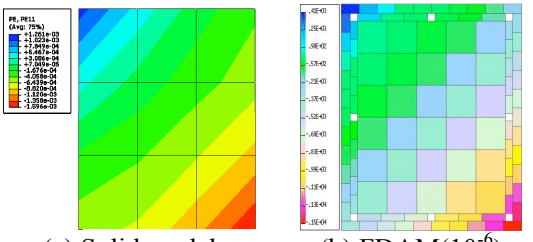
Figure 6~Figure 9 show the stress, the plastic strain and damge distribution of extreme

section for RC member compared with the results of solid model. The results show that the response of fiber damage analysis model for displacement loading is close to the results of solid model. The extreme section damage index of RC member D_{MC}=0.319, D_{MT}=0.0258, the damage evolution of RC member is shown in Figure 10. This example shows that the fiber damage analysis model based on material is reasonable and reliable to evaluate the damage behavior of RC beam-column.



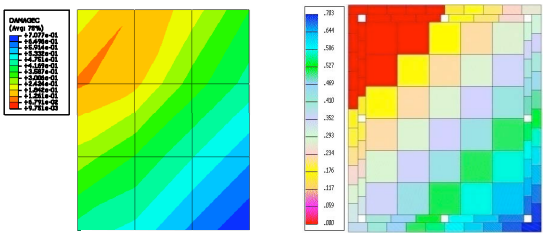
(a) Solid model(Pa) (b) FDAM(MPa)

Figure 6. Stress distribution of section.



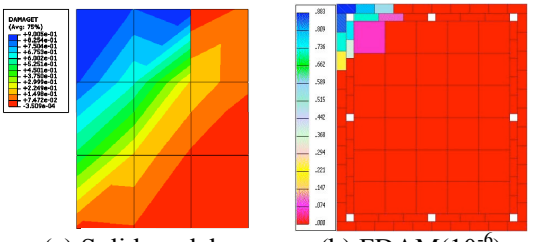
(a) Solid model (b) FDAM(10^{-6})

Figure 7. Plastic strain distribution of section.



(a) Solid model(Pa) (b) FDAM(MPa)

Figure 8. Compression damage distribution of section.



(a) Solid model (b) FDAM(10^{-6})

Figure 9. Tension damage distribution of section.

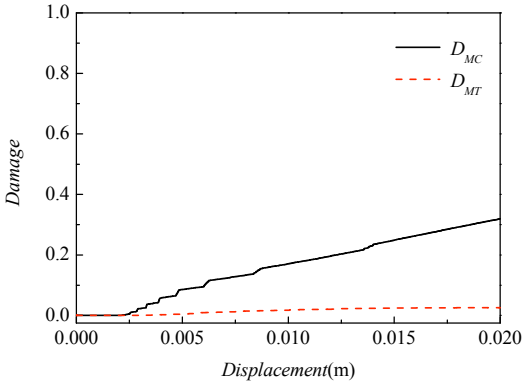


Figure 10. Damage index for RC beam-column member.

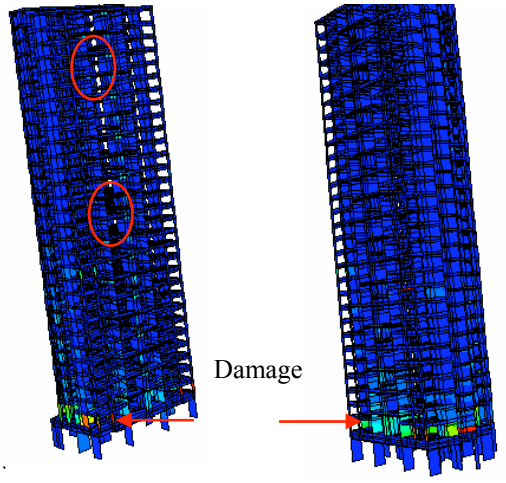
APPLICATION OF STRUCTURAL SEISMIC DAMAGE ASSESSMENT

Based all above proposed models and strategies, the inelastic dynamic analysis

numerical solutions of a high-rise RC structure are given in this section respectively. The structure is the split-level shear wall structure (98.8m), whose girder transfer floor is set on the top of the first floor. The proposed plastic-damage model for concrete is adopted to model the concrete material, and FDAM was adopted to model RC members. Kinematic hardening model is used to model for rebar.

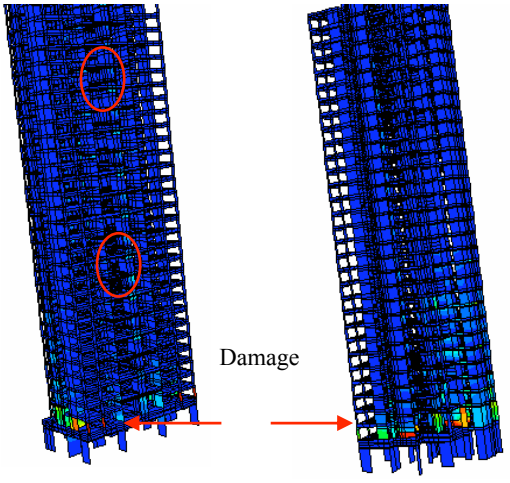
Dynamic elastoplastic analysis and test comparison. Typical earthquake waves including El Centro wave and Taft wave are used as the input data of the earthquake motions, and the excitation in X direction and Y direction is considered respectively. The peak value of acceleration is 220gal.

Theoretically speaking, the dynamic analysis method based on the material damage model can describe the whole damage evolution process and the exact final damage of structure, depending on the degree of finess and exactness of the analysis model. Figure 11 and Figure 12 show the weak portion and the final damage degree of the structure under strong earthquake excitations. The damages are mainly located at the vertical members of upper story of transfer floor, and some coupling beams are also damaged. For many vertical members of the upper story of the transfer floor are destroyed, the structure cannot meet the requirement of No Collapsing Under Strong Earthquake. Figure 13 shows that the seismic damage assessment results closely agree with the shaking table test results. Therefore the seismic damage model based on material damage model can judge the yielding mechanism, weak positions and damaged degree exactly of structures under strong earthquake excitations.



(a) In *X* direction (b) In *Y* direction

Figure 11. Distribution of damage of structure under El Centro wave excitation



(a) In *X* direction (b) In *Y* direction

Figure 11. Distribution of damage of structure under Taft wave excitation



(a) Upper portion of the transfer floor (b) Coupling beam

Figure 13. Damage parts of the structure in shaking table test

CONCLUSION

A plastic-damage constitutive model based on continuum damage mechanics theory is presented in this paper. The formulas of the elastic and plastic Helmholtz free energy are defined to describe the plasticity and damage degradation behavior of concrete. The constitutive relations are validated using the second law of thermodynamics, and the Weibull distribution hypothesis is introduced to simulate the process of damage evolution. The damage constitutive equations, the damage evolution equations and plastic deformation of concrete are presented respectively.

The fiber damage analysis model developed on ABAQUS/Explicit that combined with the proposed uniaxial damage constitutive relations is effective in the damage analysis of RC beam-column. Comparing to the results of solid model, the fiber damage analysis model based on material is reasonable and reliable to evaluate the damage behavior, and can describe the damage evolution process for RC bema-column under loading.

Comparing to the data from shaking table test, the seismic damage assessment of high-rise RC structures based on material damage model is more reasonable and more reliable, to evaluate the seismic performance comprehensively, find out the weak parts effectively and understand the seismic damage evolution process explicitly.

ACKNOWLEDGEMENTS

The authors acknowledge the financial support from the National Natural Science Foundation of China under Grant No. 51008048 and 50938001.

REFERENCES

Bazant Z.P. and Kim S.S. (1979). “Plastic-Fracturing Theory for Concrete”. *J. of the Eng. Mech. Di.*, ASCE, 105(3), 407-428.

Chen A.C.T. and Chen W.F. (1975). "Constitutive Relations for Concrete. *J. of the Eng. Mech. Di.*, ASCE 101(4), 465-481.

Coleman B.D. and Gurtin M.E. (1967). "Thermodynamics with Internal State Variables". *Journal of Chemistry and Physics,* 47, 597-613.

Dragon A. and Mroz Z. (1979). "A Continuum Model for Plastic-brittle Behavior of Rock and Concrete". *International Journal of Engineering Science*, 17(2), 121-137.

Gao F. (1993). "Fractal Property of the Rock Strength and Weibull Modulus". *Chinese Science Bulletin,* 38(15), 1427-1430. (in Chinese)

Grassl P., Lundgren K. and Gylltoft K. (2002), "Concrete in Compression: A Plasticity Theory with A Novel Hardening Law," *International Journal of Solids and Structures,* 39(20), 5205-5223.

Ju J.W. (1989). Energy-based Coupled Elastoplastic Damage Models at Finite Strains. *J. of Eng. Mech.*, ASCE, 115(11), 2507-2525.

Lee J. and Fenves G.L. (1998). "Plastic-Damage Model for Cyclic Loading of Concrete Structures". *J. of Eng. Mech.,* ASCE, 124(8), 892-900.

Li J. and Wu J.Y. (2005). "Elastoplastic Damage Constitutive Model for Concrete Based on Damage Energy Release Rates", Part I: Basic Formulations. *China Civil Engineering Journal*, 38(9), 14-20. (in Chinese)

Lubliner J., Oliver J. and Oller S.(1989). A Plastic-Damage Model for Concrete. *International Journal of Solids and Structures,* 25(3), 299-326.

Onate E., Oller S., Oliver S. and Lubliner, J. (1988). "A Constitutive Model of Concrete Based on the Incremental Theory of Plasticity," *Engineering Computations,* 5(4): 309-319.

Teng J. and Li Z.H. (2006). "Comparison of Different Elastic-Plastic Analysis Method of Complex High-rise Structures under Strong Earthquake Excitations". *4th International Conference on Earthquake Engineering*. Taipei, Taiwan, Paper No. 118.

Wang Z.Y. and Liu J.B. (2001). "The Advances of Studies on Seismic Damage Assessment of Building Structures". *Word Information on Earthquake Engineering*, 17(3), 43-48. (in Chinese)

Wu, J.U., Li, J., Faria, R.(2006). "An energy release rate-based plastic-damage model for concrete". *International Journal of Solids and Structures*. 43, 583–612.

Yu T.Q. and Qian J.C. (1993). Damage Theory and Its Application. *National Defense Industry Press*, Beijing. (in Chinese)

Performance Evaluation of Shear Walls in Existing Wall-type Precast Reinforced Concrete Residential Buildings with New Openings

J. Takagi[1], S. Minami[2], and K. Kitayama[3]

[1] Division of Architecture and Urban Studies, Tokyo Metropolitan University,
1-1 Minami-Osawa Hachioji City Tokyo, Japan;
PH +81-42-677-2798; FAX +81-42-677-2793; email: jtakagi@tmu.ac.jp
[2] Tokyo Metropolitan University (same affiliation and address as above);
PH +81-42-677-1111 (ext.4723); FAX +81-42-677-2793; email: minamis@tmu.ac.jp
[3] Tokyo Metropolitan University (same affiliation and address as above);
PH +81-42-677-2802; FAX +81-42-677-2793; email: kitak@tmu.ac.jp

ABSTRACT

Wall-type precast reinforced concrete (WPC) residential buildings, which are assembled using prefabricated concrete panels for the slabs and walls, were widely constructed during the 1960-70s in Japan. The number of existing WPC residential units constructed before 1980 is approximately 470,000. Although these buildings are of high quality in terms of structural condition, they are not fully utilized due to their small and uniform unit plans that do not suit modern living styles. Creating new openings in the walls could widen the possibility of plan changes during renovation; however, a design methodology for new openings, including the addition of structural reinforcement, has not been developed for this unique structural system. In this research, reinforcement design for new openings was developed and improvement of seismic performance was examined in half-scale cyclic loading tests. Numerical analysis models were also developed and the behavior of the walls was well simulated.

INTRODUCTION

Wall-type precast reinforced concrete (WPC) residential buildings (Figure 1) were widely constructed in Japan from the middle of the 1960s to counter the serious

shortage of housing. Figure 2 shows the annual and accumulative number of WPC units constructed. Approximately 470,000 units were built before 1980. Most of them still exist and maintain good physical condition with precast (PCa) concrete slab and wall panels. Also, their high seismic performance was confirmed from the limited damage observed after the Hanshin-Awaji Earthquake in 1995 (AIJ, 1998). The unit plans for this type of residential building were highly standardized, and each unit area is rather small for modern family use. The buildings typically have five stories without elevators. Stairs were constructed between every two units in the plan and there are no corridors connecting floors, providing both privacy and natural ventilation during summer. With its inconveniences, this housing stock has not been fully utilized despite its good structural condition.



Figure 1. WPC residential buildings

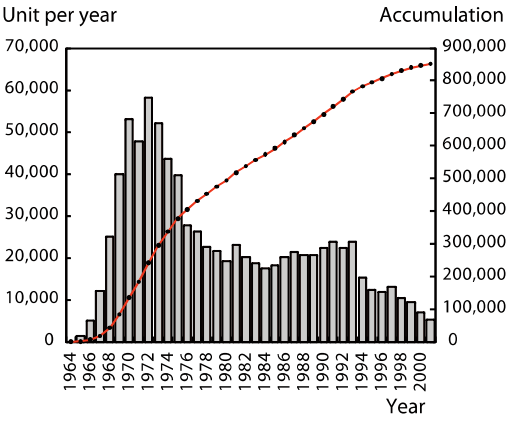


Figure 2. Number of WPC units

In order to activate the housing stock, a renovation design study team in which the authors participated was organized. Barrier-free schemes are proposed considering various aspects including financial feasibility and legal restrictions (Figure 3). In order to provide various unit plans suiting modern life styles, new openings in existing walls are needed in the schemes. However, a methodology for reinforcing the openings in this unique structural system has not yet been developed.

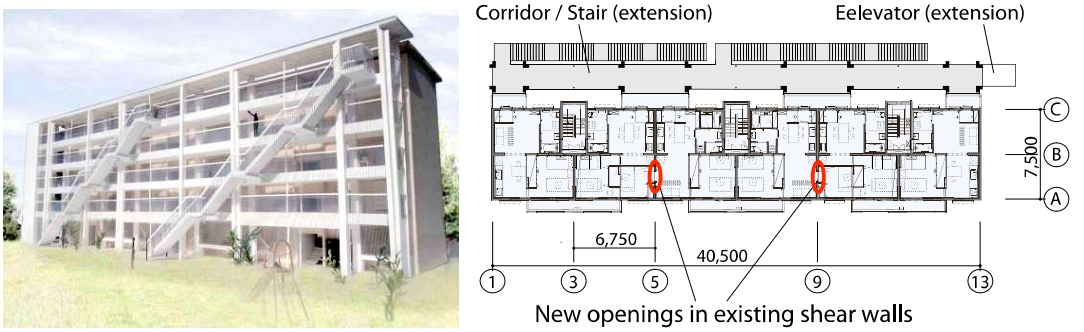


Figure 3. Renovation scheme

In this research, reinforcement design schemes for the new openings in the existing wall panels are developed, and their seismic performance is experimentally evaluated. Also, numerical analysis models for the wall tests are created using inelastic springs for the connections between wall panels.

WPC RESIDENTIAL BUILDINGS

As shown in Figure 4, prefabricated wall and slab panels are assembled for the construction of WPC residential buildings. For the connections between the wall panels, steel plates and welded reinforcements are embedded in the upper and lower sides of the panels (Figure 5). The embedded steel plates are field-welded, and these connections are called "setting bases (SBs)." In addition, there are connections with shear connectors on the vertical sides of the wall panels (vertical connections) as shown in Figure 6. The extended reinforcement is welded to the reinforcement of the horizontally adjacent wall panels, and the gaps between the panels are filled with concrete on site. In the gaps, reinforcement is vertically placed penetrating the slab levels. This reinforcement is called "vertically connecting reinforcement (VCR)," and this works to connect vertically adjacent walls.

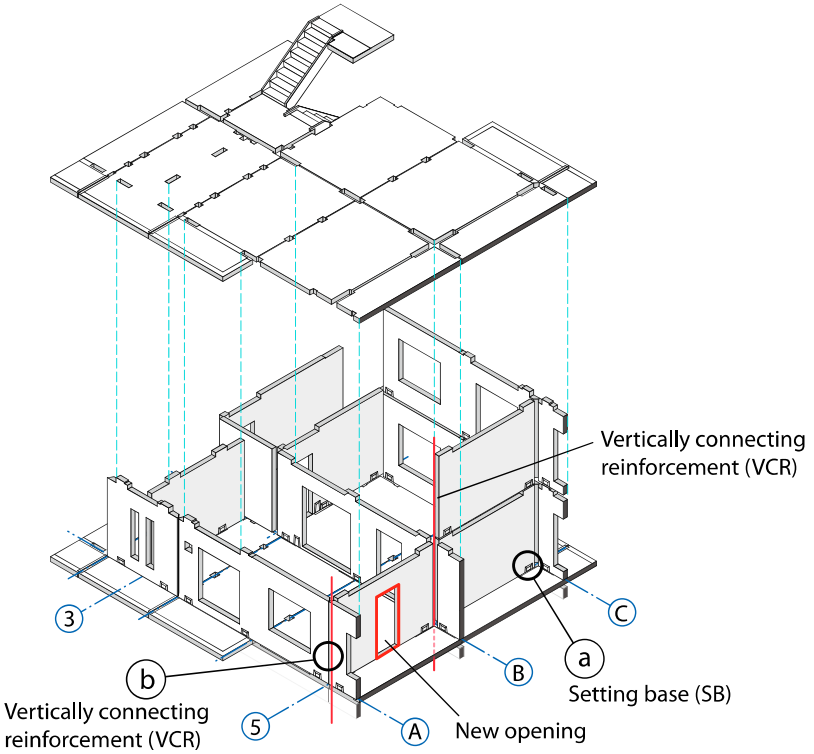


Figure 4. WPC structure

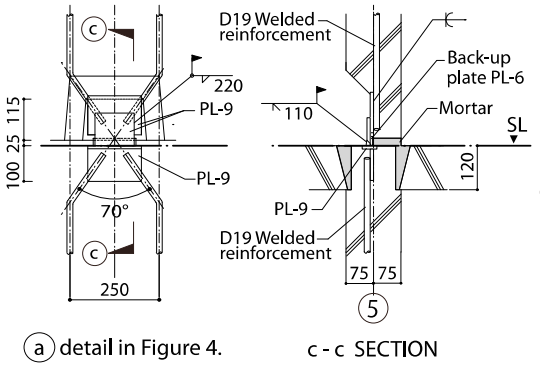


Figure 5. Setting base (SB)

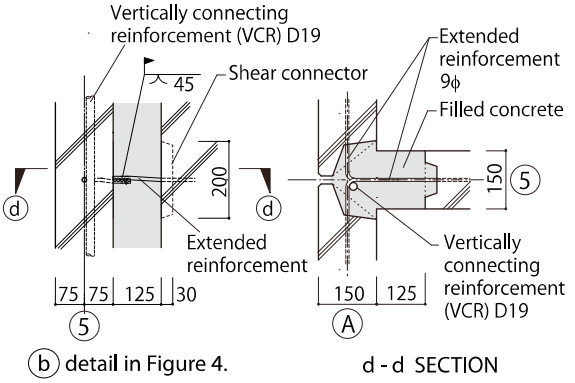


Figure 6. Vertical joint

REINFORCEMENT FOR NEW OPENINGS

Experiencing a significant number of major earthquakes, Japanese seismic design codes have been developed with revisions to design specifications. Consequently, not every existing building necessarily meets all of the current specifications. These existing buildings are not illegal; however, structural reinforcement to meet requirements is needed in the case of major renovation. Generally, this reinforcement is technically difficult and significantly costly. On the other hand, if the renovation is relatively minor, where the number of (partially) structural members demolished is limited, the current design specifications do not apply under the condition that each member (or part of the building) maintains equal or greater structural performance due to the reinforcement involved in the renovation.

Because the seismic performance of the existing WPC residential buildings is generally high, creating new openings in some of the wall panels may not be essential. Depending on the target seismic performance criteria, no reinforcement may be needed. Studying the seismic performance of WPC buildings with new openings is an interesting subject (and this is our future work), and with much consideration given to rapid practical application of the research outcome, our first research objective was to develop reinforcement design schemes for the walls as required by most jurisdictions. (A performance-based design approach, including evaluation of the whole building, takes more time as several issues such as research development, design review, and authorization must be tackled.)

In WPC shear wall panels, there are more than two SBs on the upper and lower sides. The SBs carry pull-up force induced by the overturning moment (OTM) under the seismic lateral load. In the renovation schemes, new openings are placed at

the center of walls, not disturbing the SBs, as shown in Figure 7. The new opening subdivides the wall panel into two. If rocking of these wall panels is the major deformation mode as shown in Figure 7, the resistance capacity of the wall can be significantly reduced. Also, a part of the wall above the new opening is not strong enough to be a coupling beam. Using reinforced concrete (RC) or steel (S) members, reinforcement design schemes are developed by strengthening connections to the walls in the lower story and coupling beams above the new openings.

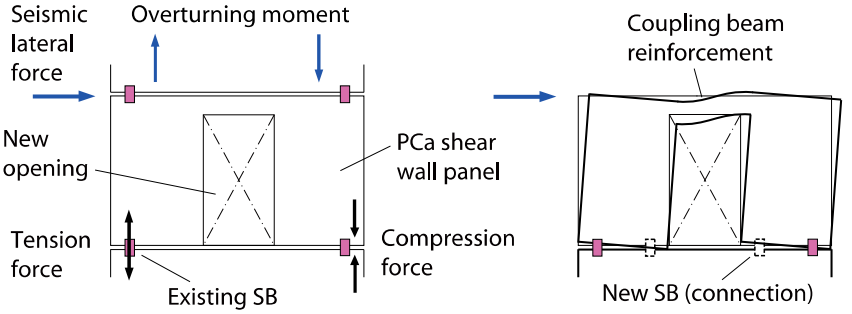


Figure 7. Seismic load resisting system in WPC shear walls

TESTING PROCEDURE

A half-scale experiment was conducted for the shear wall panel on the second floor in the five-story building shown in Figure 3, where there are PCa wall panels on the upper and lower stories and where the seismic lateral load is the greatest. The specimens are composed of a shear wall, part of the walls of the first and third stories, flange walls, and slabs. Stubs are also created at the top and bottom of the specimens for loading. The test parameters are openings in the shear wall, shear-span ratio (H/W), and RC or S reinforcement. Specimens with a small H/W have openings in the first and third stories, while those with a large H/W do not. Eight specimens were created: one with no opening, two with no reinforcement, two with RC reinforcement, and three with S reinforcement. Figure 8 shows the C5S specimen (RC reinforcement with a large H/W) and N5M (no reinforcement with a small H/W). The new RC columns are placed on the side of the new opening in C5S. The columns connect to the new beams under the existing PCa slab panels. A list of specimens with fundamental information is shown in Table 1.

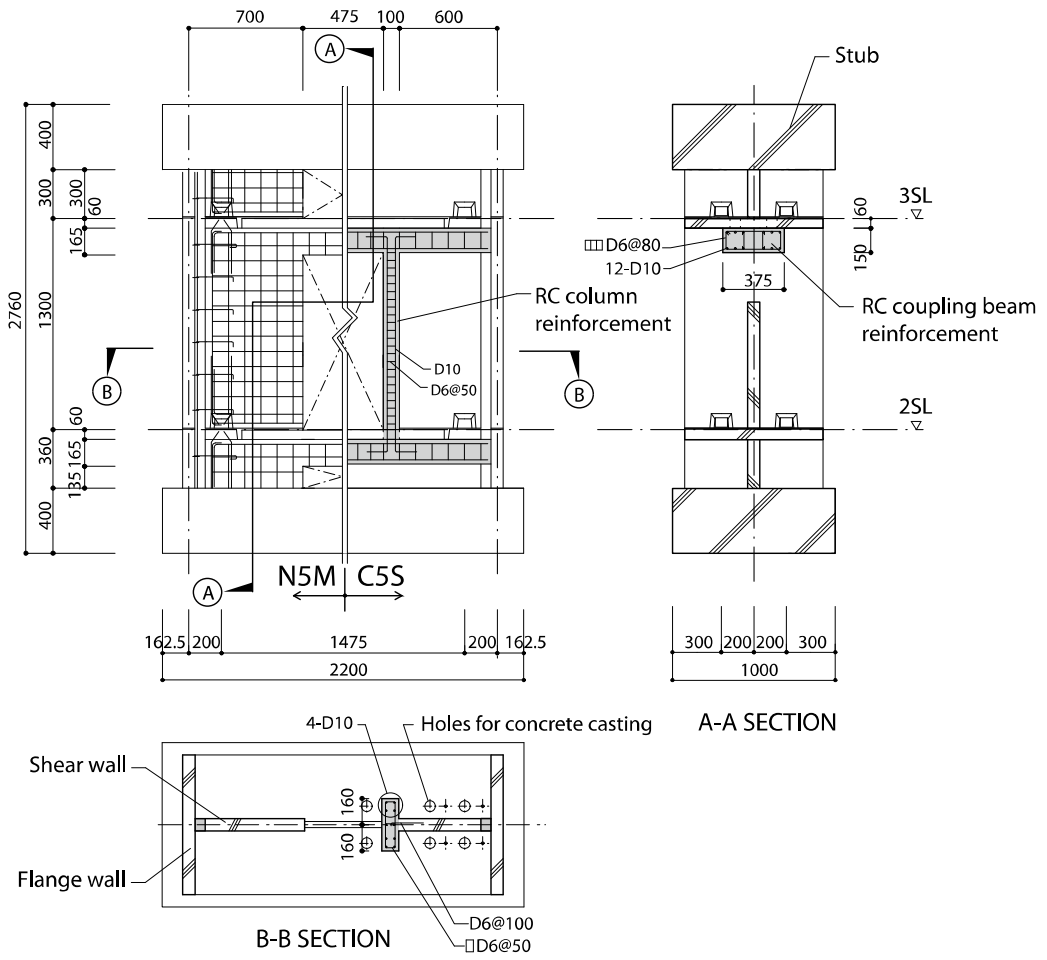


Figure 8. Shear wall test specimens (N5M and C5S)

Table 1. Specimens and fundamental information

Specimen	H/W	Reinforcement	Concrete strength *1) (N/mm^2)			Maximum strength *2) (kN)		Initial stiffness *3) (kN/mm)	Failure mode *4)	Description
			${}_P\sigma_B$	${}_J\sigma_B$	${}_C\sigma_B$	+dir.	-dir.			
W5	1.85 (large)	none	58.6	44.8	-	101	103	166	F	Damage around 2SL SBs
N5S			67.0	48.0	-	105	110	53	F	Failure of 3SL SBs
C5S		RC	58.0	55.2	74.4	154	139	190	F	Damage to first-floor walls under reinforcing columns
S5S		S	66.3	45.7	-	124	117	97	F	
B5S			50.2	59.5	-	113	106	64	F	Damage around 2SL SBs
N5M	1.17 (small)	none	60.8	57.8	-	136	132	40	F	
C5M		RC	52.8	78.8	74.3	289	271	189	F/S	Shear failure (significant damage) of shear walls
S5M		S	51.1	52.4	-	220	235	101	S	

*1) Concrete strength (N/mm^2) on the test day (${}_P\sigma_B$: PCa panels, ${}_J\sigma_B$: joint concrete, and ${}_C\sigma_B$: reinforcing members); *2) Maximum lateral strength (kN) (+dir: positive direction, and -dir: negative direction); *3) Initial stiffness defined as secant stiffness with the origin and strength at R=+0.025%; *4) Failure mode (F: SB failure, and S: shear failure of wall)

Figure 9 shows the loading system of the specimens. Under a constant vertical load, which represents the dead and live load (shown as D in Figure 9), static incremental cyclic load Q (=Q1+Q2) is applied. Coupled vertical force V, which is equivalent to the OTM, is also loaded in proportion to lateral force Q. In order to investigate the influence of the OTM on the behavior of the wall, two shear span ratios (shown as H/W in Figure 9) were prepared: 1.85 (large) and 1.17 (small).

Controlled cyclic lateral displacement is applied to the specimens for rotational deformation, R =0.025%, 0.05%, 0.1%, 0.2%, 0.33%, 0.5%, 0.67%, 1.0%, and 2.0%, with two cycles each except R =0.025% with one cycle, where R is defined as the lateral displacement of the center of the upper stub divided by the height from the top of the bottom stub.

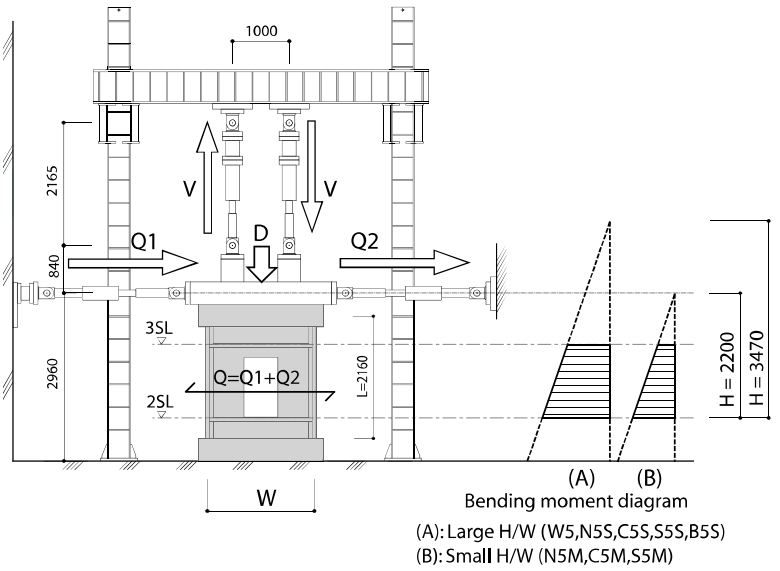


Figure 9. Loading system

TEST RESULTS

Shown in Figure 10 are the crack patterns in the shear walls after loading in W5, N5S, C5S, and C5M, out of the eight specimens. In W5 and N5S, minor cracks were observed in the wall panels and damage is concentrated around the horizontal connections (the SBs and VCRs). Rocking of the wall with failure of the horizontal connections is the overall failure mode in these tests. In N5S, shear cracks were observed; however, they did not directly trigger strength degradation. Regarding behavior of the flange walls, damage was limited to the panels and was observed only at the connections on the upper and lower sides of the panels in all cases.

In C5S, where the new opening is reinforced with RC members and the

H/W is large, several shear cracks were observed in the shear wall panels. Major horizontal cracks were also generated in the wall panel on the first floor. The pull-out force transferred to the wall from the new RC column via the new connected beam was large enough to cause cracks in the wall under the new column. Thus, the connection detail between the wall and the new beam needs to be improved. Although shear cracks were observed in C5S, the primary failure mode is also rocking of the shear wall with failure of the horizontal connections. In C5M, where the new RC columns on the side of the opening penetrate the floor slabs and are embedded in the upper and lower stubs, the walls failed in shear. Because the new columns vertically tighten the wall panels and the H/W is relatively small, failure of the horizontal connections was less significant compared with other tests with a large H/W.

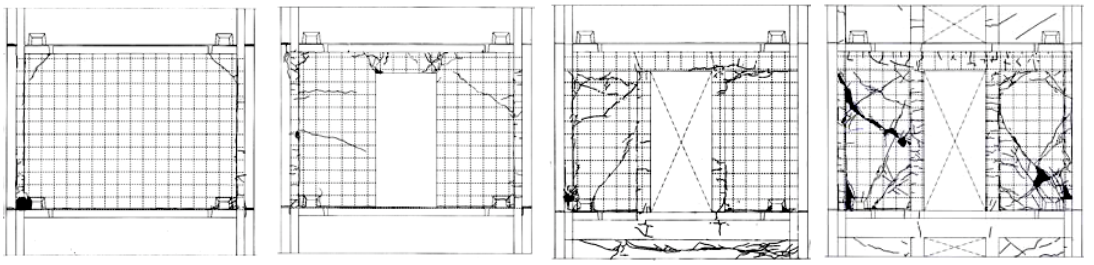


Figure 10. Crack patterns in shear walls

Figure 11 compares the relationships between the lateral force and rotational deformation in the three tests on W5, N5S, and C5S. The difference in the maximum lateral strength of W5 (no opening) and N5S (no reinforcement for the opening) is limited. This is because the failure mode in these tests is rocking with failure of the SBs under a large H/W. Shear failure of the wall was not critical and, consequently, the opening in the wall did not reduce the maximum lateral strength. Contrarily, the initial lateral stiffness and equivalent viscous damping ratio of N5S is approximately 30% and 50% those of W5, respectively; therefore, the difference in their energy dissipation capability is significant.

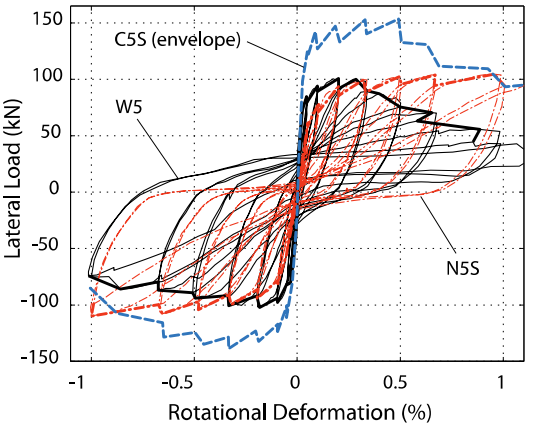


Figure 11. Test results

In C5S, the maximum lateral strength was 140-150% that of W5 and N5S. Similarly, enhancement of seismic lateral strength was observed in other test cases with reinforcement. Although further improvement is needed such as for the connection of the reinforcing and the existing members, the reinforcement design was able to provide equal or greater seismic performance compared to WPC walls without openings.

NUMERICAL SIMULATIONS

In order to simulate the behavior of the WPC wall in the test, numerical analysis models were created. Figure 12 shows two-dimensional models of W5, C5S, and C5M. The models are composed of elastic line elements for the wall panels and inelastic springs for the connections. Shear springs in the shear walls were also included in the models for the small H/W test, where shear failure was observed. The elastic modulus of the concrete was calculated based on the tested concrete strength according to AIJ (2010). In some wall tests, it is observed that rocking of the shear walls is the primary failure mode and behavior of SBs significantly influences the overall behavior of the wall.

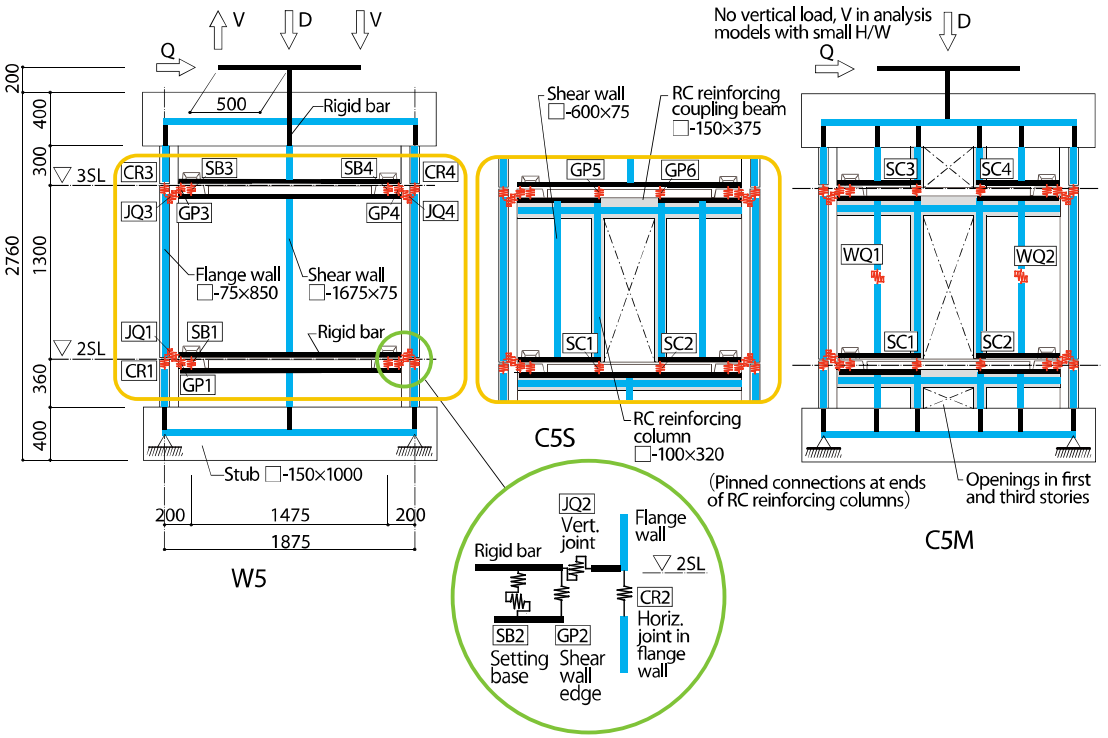


Figure 12. Analysis models

In order to investigate the SB properties, especially pullout tension force and vertical displacement relationships, additional tests were conducted. Shown in Figure 13 is the half-scale specimen of the SB test. Vertical displacement of the specimen composed of an SB and its vicinity in the WPC wall panels on two stories was enforced. The test was performed under two types of loading: one-way tension and cyclic tension-compression. In order to separate the wall panels into two stories, a steel plate was inserted at their boundary. It was expected that the plate would minimize the vertically connecting tensile strength between the concrete panels using a potential manufacturing process.

Shown in figure 14 are the relationships between the controlled vertical displacement and load on the specimens. Peak strength was observed at approximately 8 mm from the vertical displacement with yielding of the reinforcement and fracture of the plate welding. As shown in Figure 14, a tri-linear tensile property of SBs is defined for the analysis models. Calibrating the shear wall simulation with the test, the peak strength is reduced to 75% of the more accurately approximated tri-linear model. A possible physical reason for this reduction is the combination of lateral and vertical force in the wall test.

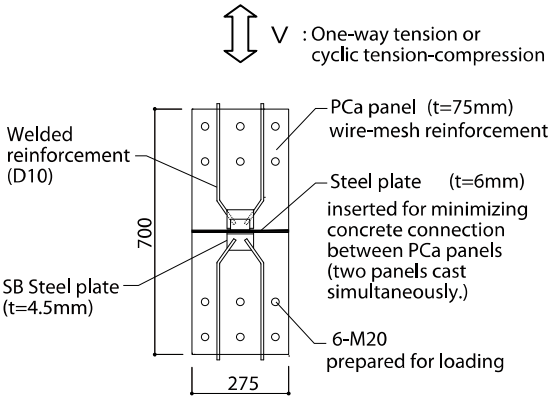


Figure 13. Specimen of SB tests

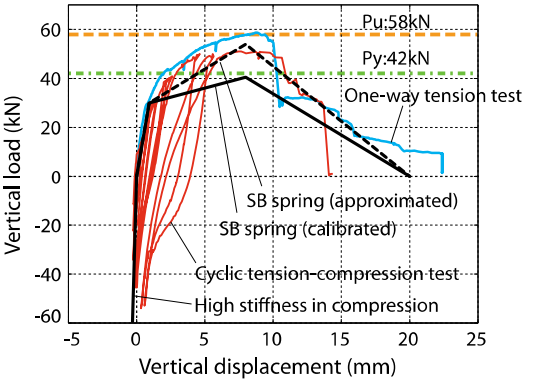


Figure 14. SB test and spring

Other properties of the inelastic springs in the analysis models of the walls are summarized in Table 2. The SB, CR, GP, and JQ spring properties are consistent in the analysis models, while the SC and WQ properties are evaluated for each test with opening reinforcement. Using these simulation models, displacement control static pushover analyses were conducted (MIDAS). Figure 15 shows the analytical results superimposed on the test data. The analyses reasonably simulate the envelope of the cyclic loading test. It is noteworthy that the analyses simulate the failure mode of the WPC walls with reasonable order and accuracy, as well as the strength.

Table 2. Inelastic springs in analysis models

Spring	Direction*	Description
SB	X	Represents sway deformation of shear walls at slab levels Perfect elastic-plastic bi-linear curve with high elastic stiffness and ultimate strength based on Mattock (1972)
	Y+	Represents the tension force and displacement relationships at SBs Tri-linear curve as shown in Figure 14
	Y-	Sufficient strength for compression at SBs Rigid elastic spring
CR	Y+	Represents the tension force and displacement relationships at slab levels at flange walls Tri-linear curve with twice the SB (Y+) curve added to the perfect elastic-plastic curve for VCR
	Y-	Rigid elastic spring
GP	Y-	Rigid elastic spring
JQ	X	Rigid elastic spring, representing condensed horizontal displacement at the shear wall and adjacent flange wall
	Y	Represents shear displacement at vertical connectors between the shear wall and flange wall Perfect elastic-plastic bi-linear curve with rigid elastic stiffness and ultimate strength based on Nakano (2001)
SC	Y+	Represents tension force and displacement relationships at slab levels at new reinforcing columns Perfect elastic-plastic curve with calibrated strength and rigid elastic stiffness
	Y-	Rigid elastic spring
WQ	X	Represents shear deformation of shear walls Quad-linear curve with rigid elastic stiffness (elastic shear deformation simulated by line elements of the walls), shear strength at cracking as 1/3 of the peak strength, which is defined through calibration with the test, R=0.4% for the peak displacement, negative post-peak stiffness (0.5% of the elastic shear stiffness), and 1/2 of the peak strength for the residual strength
	Y	Rigid elastic spring
	R	Rigid elastic spring

* X: horizontal transition, Y: vertical transition (Y+: tension, Y-: compression), and R: rotation
Local coordinate axes of the springs are parallel to the global axes. Freedoms not shown in the table are not constrained.

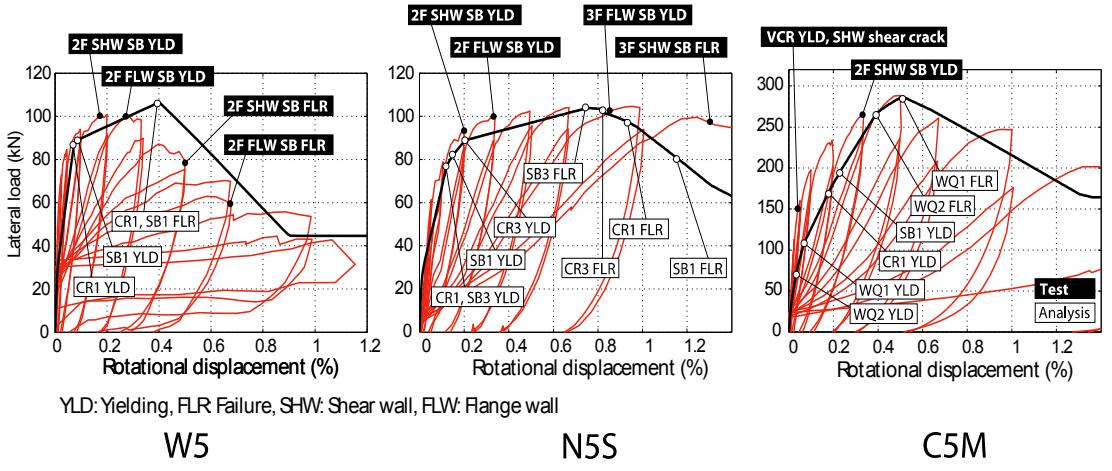


Figure 15. Analysis and test results

CONCLUSIONS AND FUTURE WORK

In this research, reinforcement design for new openings in existing shear walls in wall-type precast reinforced concrete (WPC) residential buildings was developed and improvement of seismic performance was examined through half-scale cyclic loading tests. Furthermore, two-dimensional numerical analysis models, which are composed of line elements for the wall panels and inelastic springs for the connections and shear behavior of the walls, were created. Using the models, the behavior of the tested walls was well simulated. As future work, analysis models are to be further developed for the evaluation of whole building seismic performance.

REFERENCES

Architectural Institute of Japan (AIJ). (1998). *Report on the Hanshin-Awaji Earthquake Disaster Building Series* vol. 2 (in Japanese).

Architectural Institute of Japan (AIJ). (2010). *Standard for Structural Calculation of Reinforced Concrete Structures* (in Japanese).

Mattock, A. H. and N. M. Hawkins. (1972). "Shear Transfer in Reinforced Concrete Recent Research," *PCI Journal*: 3-4

MIDAS Information Technology Co., LTD., Midas GEN ver. 761.

Nakano, K. and Y. Matsuzaki. (2001). "Additional Method of Shear Resistances in Precast Concrete Connections," *J. Struct. Constr. Eng AIJ* no. 550: 151-158 (in Japanese).

ACKNOWLEDGEMENTS

The authors gratefully acknowledge the Ministry of Land, Infrastructure, Transport and Tourism for funding this research. The authors would also like to thank the Housing Research Foundation and the Japan Prefabricated Construction Suppliers and Manufacturers Association for their support.

Structure Failure Mechanism Study Based on Vulnerability Theory

Zhiqiang Zhang[1,2], Guanxing Su[3], Jihong Ye[1,2], Xiaofeng "Bill" Zhang[4]

[1]School of Civil Engineering, Southeast University, 2 Si Pai Lou, Nanjing 210096, China
[2]Southeast University, Key Laboratory of Concrete and Prestressed Concrete Structures of the Ministry of Education, 2 Si Pai Lou, Nanjing 210096, China
[3]Jiangsu Research Institute of Building Science, Nanjing 210008, China
[4]Department of Civil & Environmental Engineering, Temple University, 1947 N. 12th St., Philadelphia, PA 19122; PH (215) 204-3046; FAX (215) 204-4696; email: x.bill.zhang@temple.edu

ABSTRACT

A hexagonal space dome was analyzed to investigate the relationship between structural vulnerability and failure mechanism. The analysis of stress ratios under design loads has shown that the bars that have greater stresses are closely correlated to the deteriorating bars in structural vulnerability. This provides a new approach for structural vulnerability analysis. By calculating the vulnerability parameters of bars of greater stresses, a variety of failure modes can be found and the structural vulnerability can be estimated. Moreover, the relationship between vulnerability characteristic parameters and design ultimate load was discussed by analyzing the structural failure modes under El Centro and artificial earthquake ground motions.

INTRODUCTION

The structural vulnerability theory was introduced by Blockley and others of University of Bristol (Wu, et al, 1993a, 1993b; Blockley 1999; Agarwal, et al, 2001a, 2001b). The structure is vulnerable if the structure fails to a disproportional extent or even collapses under some local destructive effects.

Shen and Zhi (2005) showed that with the increase of load, every latticed shell would collapse finally due to dynamic instability. Some of the latticed shells become instable, while their displacement and internal plastic deformation are very limited, and the collapse due to dynamic instability is abrupt. Other structures undergo large plastic deformations and significant softening before collapsing. They are categorized as strength failure since structures attain large displacements and bars reach their ultimate strengths at failure.

Nodal load-displacement curves can be used to distinguish between structural

dynamic instability and strength failure, as well as other characteristic response indices such as the curve of total load vs. maximum nodal displacement, the proportion of bars entering plasticity, the relative strain of bars, and the total strain energy in the structure.

Under earthquakes, the mechanical behavior of the structure and the damage and collapse modes of the elements are complicated. Strength failure is preferred over dynamic instability to ensure greater structural robustness. For latticed shells, preliminary studies have shown that the differences in height-span ratios, element sections, span lengths, structure forms and connections can lead the structures to different failure mechanisms, namely, strength failure, or dynamic instability. Furthermore, these different parameters can cause the differences in characteristic parameters of structural vulnerability, and subsequently, the results of vulnerability analysis differ. Determining structural failure mechanism involves large amounts of analysis and calculations, resources and time. This paper attempts to find the correlation between the structural vulnerability theory and the structural failure mechanisms by determining structural failure mechanisms from structural vulnerability analysis. The classical 24-bar hexagonal space dome is chosen as the benchmark structure in this preliminary analysis.

VULNERABILITY ANALYSIS OF HEXAGONAL SPACE DOME

The structure of a hexagonal space dome is shown in Figure 1, with geometric and physical parameters as follows: elastic modulus E = 3030 MPa, shear modulus G = 1095 MPa, element cross-section area A = 317 mm^2, R1 = 25 cm, R2 = 43.3 cm, a = 2.0 cm, b = 6.216 cm. The structure is composed of 24 bar elements, and has been used as benchmark structure in many studies. Papadrakakis et al (1986) studied the performance of load-displacement of the structure as a truss system by using two-vector iteration method. Meek and Tan (1984) studied the mechanical behavior of the structure as a frame system by arc-length method. Shen and Chen (1999) analyzed the structure using their nonlinear analysis program SNAP.

Also shown in Figure 1 are the numbering of the nodes and elements of the structure. The structure is clustered in accordance with principles of vulnerability theory, and the results are shown in Figure 2. In the course of clustering, the connection ability of the joints increases until all elements are included. The ultimate value of the connection ability of structural joints is Q = 5.98E18, and the maximum requirement of damage value is 1.65E+008. The results of de-clustering are shown in Table 1. Among all of the failure modes, the resolution is one for the failure mode that is composed of failure event 5, 6, 4 and 3. The index of vulnerability reaches maximum, so this mode is overall collapse.

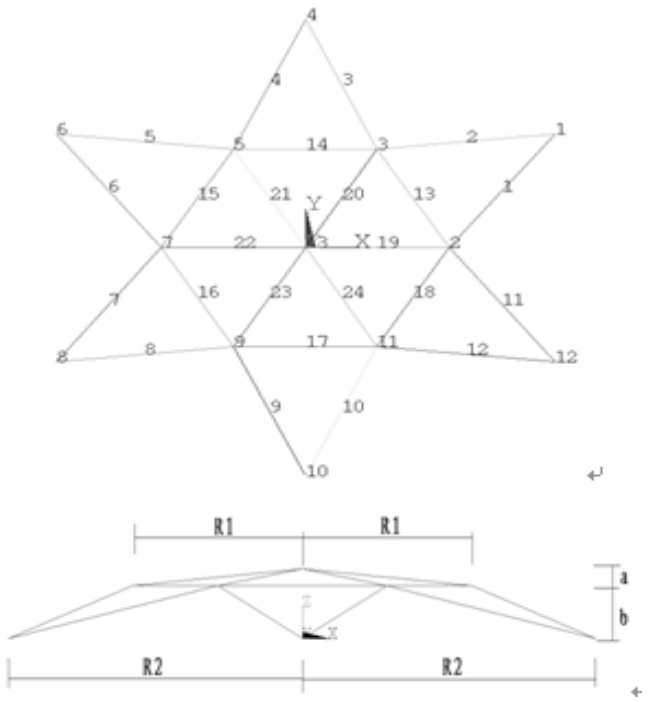


Figure 1. Hexagonal space dome

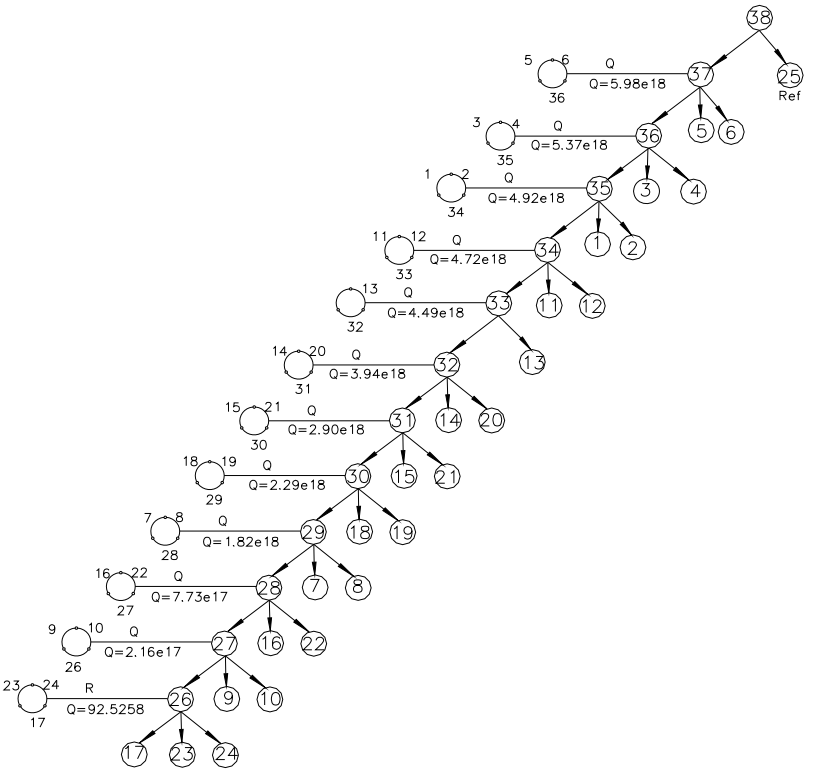


Figure 2. Clustering of hexagonal space dome

Table 1. De-clustering results of hexagonal space dome

Cluster No.	Failure events	Requirement of relative damage	Resolution	Index of vulnerability
37	5，6，4，3	0.065	1	15.358
36	3，4，1，2	0.125	1	7.9987
35	1，2，11，12，13	0.125	1	7.9987
34	8，7，21，15	0.291	1	3.4389
33	20，13，14，21，15，19	0.342	1	2.9204
32	20，14，21，15，19	0.284	1	3.5147
31	21，15，19，18，8，7	0.259	1	3.8530
30	19，18，8，7，16	0.177	1	5.6609
29	8，7，16，22，9	0.177	1	5.6609
28	22，16，9，10	0.177	1	5.6609
27	10，9，24	0.119	0.249	2.0998
26	23	0.056	0.241	4.2951

COMPARISON OF DETERIORATING BARS UNDER STATIC ACTION

In calculating the structural stresses in the bars, two load combinations were considered, one with 1.2 dead load + 1.4 live load, and the other with 1.35 earthquake load by response spectrum analysis + 1.2 gravity load. The results are shown in Table 2. It can be shown that, when the structure is intact, stresses in the deteriorating bars of the overall failure mode are higher than that of other bars. For instance, the bar 6 has the largest stresses in both combinations. In the process of de-clustering, internal forces redistribute with the failure of elements occurs. After bar 5 fails first, deteriorating bars in the structure are bars 6, 4, and 3, and their stresses are relatively high. In the intact structure or the structures with damaged elements, stresses in deteriorating bars from vulnerability analysis are always higher, among the top 50%. Typically, vulnerability analysis does not account for the loading and is only based on the configuration of the structure. The aforementioned observation leads to a new idea in vulnerability analysis – combing the characteristic parameters in vulnerability analysis with the stress determination under actual loading in the structure. Firstly, find elements with high stresses, and then calculate their characteristic parameters and determine the structural vulnerability. Choose the deteriorating bars from the high stressed bars, by trial and error, until the structure becomes mechanism. Based on the characteristic parameters of structural vulnerability, failure modes of overall collapse in different combinations can be determined.

The process of vulnerability analysis of complex structures with a large number of bars is tedious and calculation intensive. This presented method neglects elements of low stresses, therefore reduces the amount of calculation significantly, and in addition, considers the effects of loading.

Table 2. Element stresses in hexagonal space dome

Intact structure					Elem. 5 failed				
Elem. No.	Stress N/mm^2	Elem. No.	Stress N/mm^2	de-clustering	Elem. No.	Stress N/mm^2	Elem. No.	Stress N/mm^2	de-clustering
Combo 1		Combo 2			Combo 1		Combo 2		
6	3.67	6	3.72		4	5.74	4	5.93	
9	3.67	9	3.73		7	5.2	7	5.21	
8	3.36	8	3.42		3	4.83	3	4.97	
7	3.36	7	3.42		15	4.35	15	4.46	
12	3.16	12	3.3		8	3.97	8	4.04	
4	3.16	4	3.3		9	3.49	9	3.59	
2	3.07	2	3.21		10	3.33	10	3.54	
1	3.07	1	3.22		20	3.19	23	3.22	
11	2.96	11	3.12		23	3.17	20	3.2	
3	2.96	3	3.11		1	2.89	1	3.11	
5	2.74	5	2.98	o/a collap. elem. 5,6,4,3	11	2.77	11	2.94	o/a collap. elem. 6,4,3
10	2.74	10	2.99		12	2.5	12	2.73	
16	2.11	16	2.22		18	2.13	18	2.38	
20	2.11	20	2.09		13	2.02	13	2.25	
23	2.11	23	2.13		2	1.63	6	2.2	
19	2.11	19	2.12		24	1.63	2	1.89	
22	2.11	22	2.13		21	1.61	21	1.77	
17	1.82	17	1.98		6	1.47	24	1.73	
15	1.82	15	1.98		17	1.38	17	1.65	
21	1.79	21	1.91		22	1.22	22	1.6	
24	1.79	24	1.91		19	1.2	19	1.34	
14	1.44	14	1.69		16	0.935	16	1.33	
18	1.44	18	1.69		14	0.897	14	1.1	

Table 2. Element stresses in hexagonal space dome (continued)

Elem. 5, 6 failed					Elem. 5, 6, 4 failed				
Elem. No.	Stress N/mm^2	Elem. No.	Stress N/mm^2	De-clustering	Elem. No.	Stress N/mm^2	Elem. No.	Stress N/mm^2	De-clustering
Combo 1		Combo 2			Combo 1		Combo 2		
7	6.96	7	7.1		18	47.4	18	43.7	
8	6.2	8	6.57		1	45.9	1	42.4	
4	5.24	4	5.54		11	42.8	11	39.7	
15	5.07	15	5.02		10	42.2	10	39.1	
1	4.1	1	4.42		12	40.5	12	37.6	
20	3.5	3	4.1		13	33.6	13	31.5	
23	3.5	2	3.74		2	30	2	27.8	
3	3.34	17	3.67		17	28.1	17	26.5	
2	3.25	23	3.56		9	25.3	9	23.8	
17	3.1	20	3.51	o/a collap. elem. 4,3	20	20	20	18.5	o/a collap. elem. 3
12	3.08	12	3.32		23	19.7	23	18.2	
18	2.34	10	2.83		3	16.7	3	16.3	
10	2.24	18	2.68		8	11.2	8	11.3	
22	2.15	22	2.64		21	9.08	21	8.72	
19	2.15	19	2.5		15	9.06	14	8.71	
11	1.95	11	2.33		14	9.06	15	8.7	
9	1.39	9	2.13		24	8.73	24	8.39	
16	1.29	16	1.79		16	5.26	16	5.41	
13	0.372	13	1.3		19	5.12	19	5.34	
21	0.359	21	1.05		22	4.76	22	5.11	
24	0.359	24	0.932		7	4.16	7	5.03	

ANALYSIS UNDER DYNAMIC LOADING

By changing element cross-section area and height-span ratio, seventeen different structures were generated for parametric study. Structural vulnerability analysis was conducted to determine the values of joint connection ability and requirement of damage. Three dimensional earthquake excitations are imposed to the structures with the El Centro record and a response spectrum-compatible artificial wave, as shown in Figure 3. Incremental dynamic analysis was conducted, while the maximum nodal displacements were recorded. From the curve of amplitude of ground motion vs. maximum nodal displacement, the ultimate strengths of structures against instability can be found.

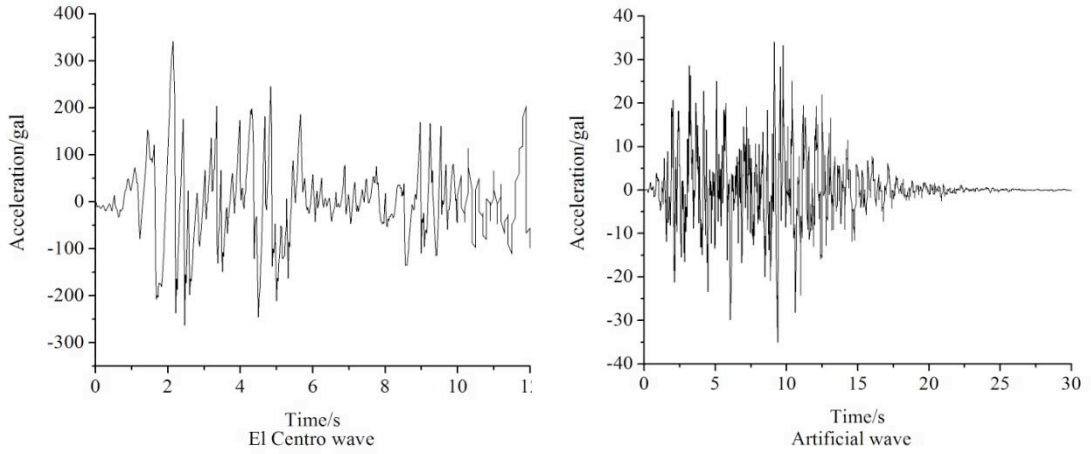


Figure 3. Earthquake ground motions

Joint connection ability vs. ultimate peak acceleration. The values of joint connection ability and requirement of damage were calculated on seven selected models of different element cross-sections, as shown in Table 3. Also shown in Figure 5 are the peak ground acceleration-displacement curves, and in Figure 6 the nodal displacement response-history curves. The peak values for ground acceleration and the ultimate displacements at structural failure can be obtained from figures. For example, in Structure 1, when the peak ground acceleration reaches 1023 gal, some structural elements enter the plastic stage, while the structure retains some bearing capacity at this point. When the amplitude reaches 1074 gal, displacement is much larger. When the amplitude reaches 1091 gal, displacement becomes very large abruptly. The structural stiffness matrix no longer converges. It can be judged that the structure fails completely and no longer has bearing capacity. Therefore, the ultimate strength of the structure in terms of peak ground acceleration is 1074 gal and the corresponding ultimate displacement is 5.68mm. Connection ability values, ground motion peak values and ultimate displacements of different structures are shown in Table 3.

Figure 4 illustrates the relationship between structural joint connection ability and the peak ground acceleration. From Figure 4, it can be observed that the peak ground acceleration increases with the structural joint connection ability, with a nonlinear correlation. As the value of structural joint connection ability increases every 5E18, the peak value of seismic wave increases 3000cm/s^2,1100cm/s^2, 800cm/s^2 and 600cm/s^2, respectively. When joint connection ability value increases to 2E19, the peak value of seismic wave reaches 5500cm/s^2. Therefore, as the same as concentrated load, when the connection ability increases to a certain extent, the peak value of ground motion increases minimally. Connection ability should be chosen rationally to make the structure reach optimal peak value of seismic wave.

Table 3. Parameters of different cross-sections

No.	A cm^2	Con. abil. Q	Req. dam. D_{max}	Vul. ind. φ	El Centro wave			Artificial wave (response spectrum-compatible)		
					a_{peak} cm/s^2	d_{peak} mm	Failure mode	a_{peak} cm/s^2	d_{peak} mm	Failure mode
1	0.8	0.93	4	15.4	1074	5.68	S	1085	3.03	S
2	1.6	7.47	8	15.4	2150	7.90	S	2100	5.03	S
3	2.4	25.2	12	15.4	3096	3.71	D	3185	2.70	D
4	3.2	59.8	16	15.4	4092	3.75	D	4130	2.52	D
5	3.8	103	19	15.4	4774	2.63	D	4924	2.63	D
6	4.1	131	21	15.4	5285	3.36	D	5596	2.75	D
7	4.7	196	24	15.4	6053	2.97	D	6580	2.80	D

NOTE: S - strength failure D - dynamic instability

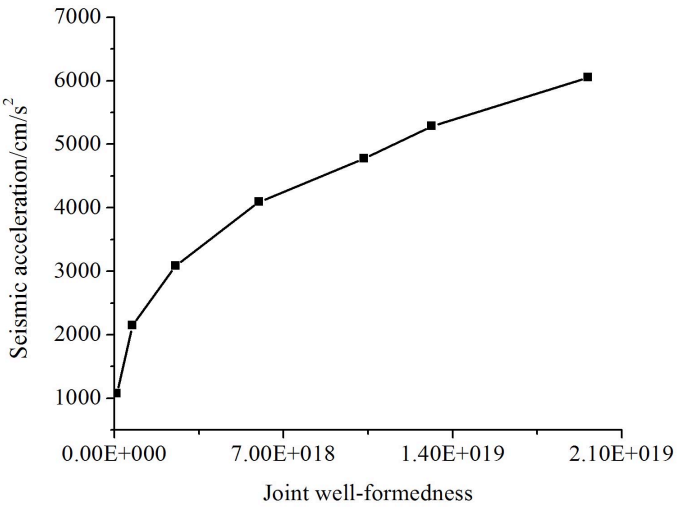
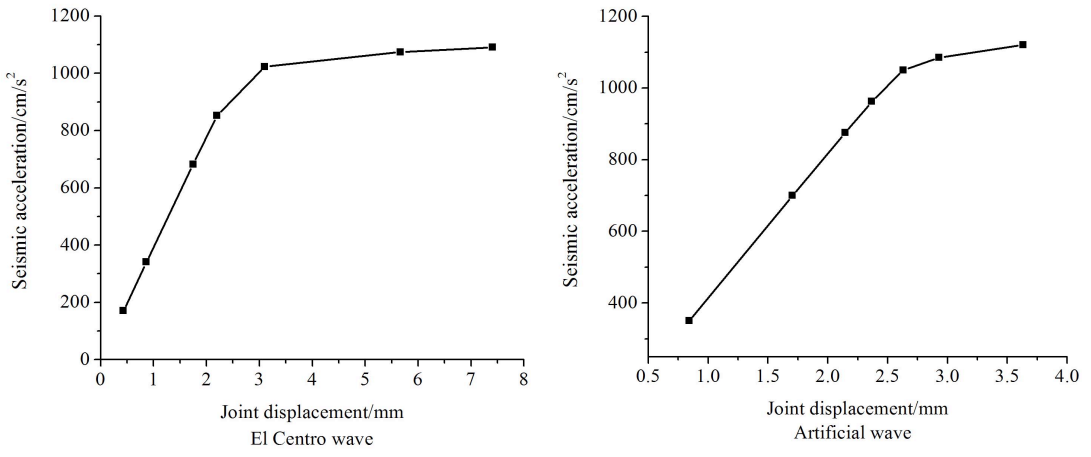
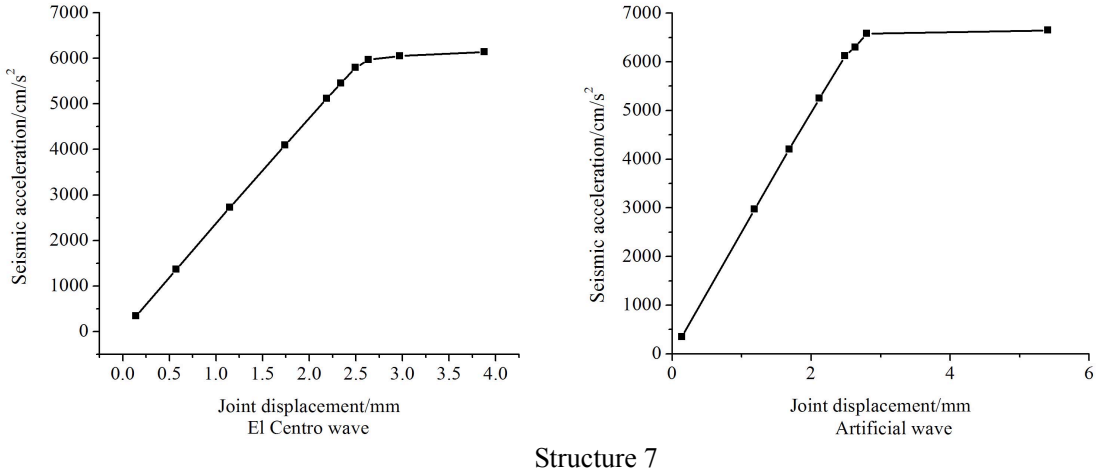


Figure 4. Joint connection ability vs. ultimate peak accel.



Structure 1



Structure 7

Figure 5. Peak ground accel. vs. max. joint displacement

Failure mode and characteristic parameters of structural vulnerability. It can be seen from Table 3, Figures 5 and 6 that the ultimate displacements of Structures 1 and 2 can reach 5.68 mm and 7.90 mm, respectively, under El Centro record, and 3.03 mm and 5.03 mm under the artificial wave. With the increasing amplitude of seismic motion, significant plastic deformations develop in the yielded bars. At the time when the structure collapses, the displacements are comparatively large. So one can judge that Structures 1 and 2 are of strength failure, and corresponding structural connection ability and requirement of damage values are relatively small at this time (see Figures 5 and 6). But the ultimate displacements of Structures 3, 4, 5, 6 and 7 at collapse are comparatively small. It indicates that these structures are of dynamic failure, while corresponding structural connection ability and requirement of damage are relatively large. In case of the same structural configuration, increasing element cross-section is equivalent to increasing grid density. Structural connection ability

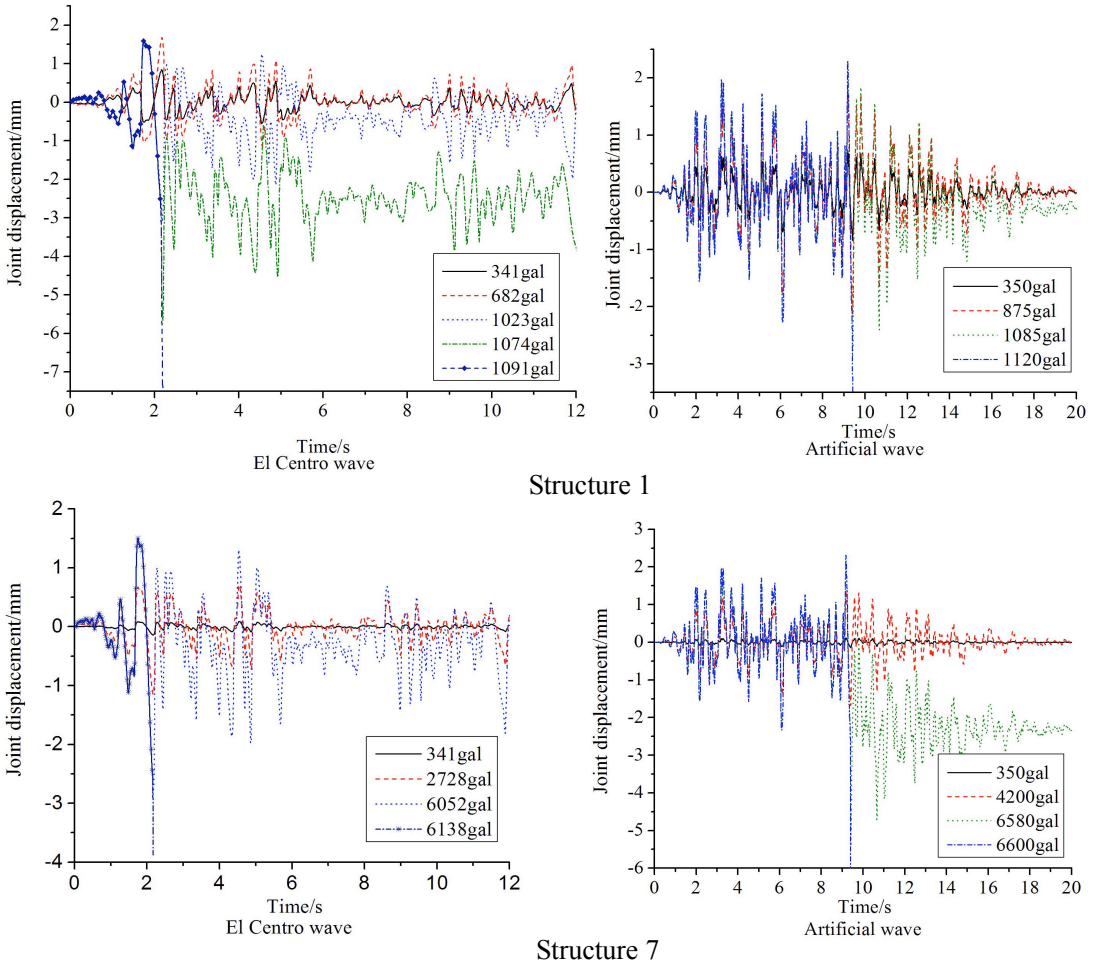


Figure 6. Joint displacement response history

and requirement of damage will change accordingly, and the failure mode changes from strength failure to dynamic instability.

It can be seen that the peak ground acceleration-maximum joint displacement curve has a obvious turning point. This is due to the fact that some of bars in the structure reach inelastic buckling and enter plastic stage under certain peak values of ground motion. Through checking the proportion of the plastic bars, it is found that the hexagonal space dome has a simple form, a small number of elements and most of the bars enter plastic stage simultaneously at a peak ground acceleration, causing an evident turning point in the curve.

Now we change the structural height-span ratio and conduct the structural vulnerability analysis to obtain the joint connection ability and requirement of damage. Similarly the ultimate load and ultimate displacement of the structure can be obtained from the load-displacement curve (see Figures 7 and 8). Failure mode can be determined from the load-displacement curve and response-history curve, as shown in Table 4. Different height-span ratios cause different failure modes. Under El Centro ground motion, structrues with height-span ratios of 1/13, 1/14, and 1/15

are of strength failure mode while ultimate displacements are of large values. Structural failure mode is strength failure under the artificial wave when the span ratio is 1/14 and 1/15.

From analysis above, it can be shown that the structures will fail in strength when values of the connection ability and vulnerability index are small. With the increase of the vulnerability index, the failure mode changes from strength failure to dynamic instability. Structure 15 shows different failure modes under different seismic ground motions.

Table 4. Parameters of different height-span ratio

No.	H/L ratio	Con. abil. Q	Req. dam. D_{max}	Vul. ind. φ	El Centro wave			Artificial wave (resp. spect.-compati.)		
					a_{peak} cm/s^2	d_{peak} mm	Failure mode	a_{peak} cm/s^2	d_{peak} mm	Failure mode
8	1/6	200	1.61	15.8	4160	3.5	D	4505	2.4	D
9	1/7	157	1.62	15.7	4126	2.9	D	4480	2.8	D
10	1/8	126	1.63	15.6	4120	2.6	D	4300	2.0	D
11	1/9	103	1.64	15.5	4116	2.7	D	4200	2.9	D
12	1/10	85.6	1.64	15.4	4110	2.7	D	4165	2.5	D
13	1/11	72	1.65	15.4	4104	3.1	D	4165	2.3	D
14	1/12	59.8	1.65	15.4	4092	3.8	D	4130	2.5	D
15	1/13	52.8	1.65	15.3	4092	4.1	S	4115	2.7	D
16	1/14	45.9	1.65	15.3	4084	6.9	S	4109	4.1	S
17	1/15	40.3	1.66	15.3	4072	7.2	S	4095	5.1	S

NOTE: S - strength failure D - dynamic instability

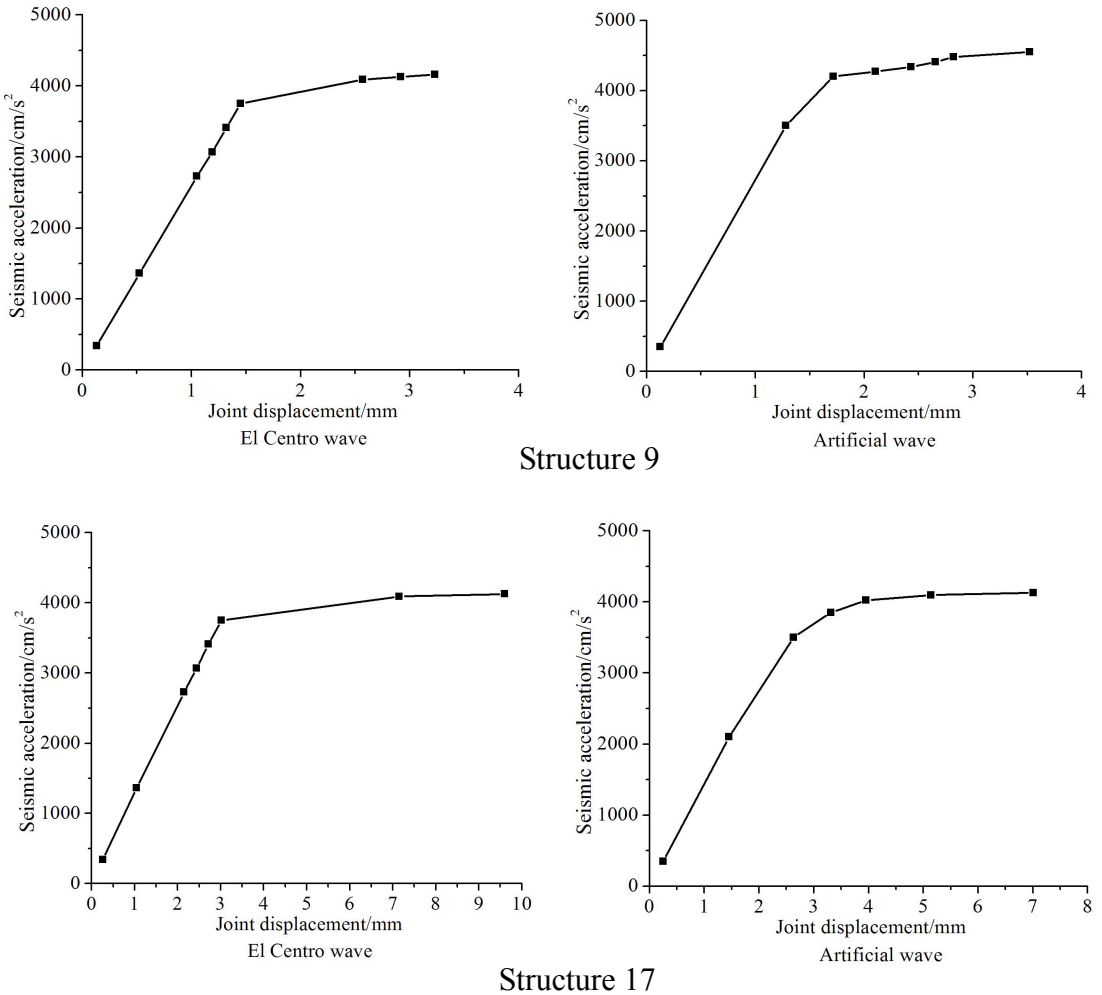


Figure 7. Peak ground accel. vs. max. joint displacement

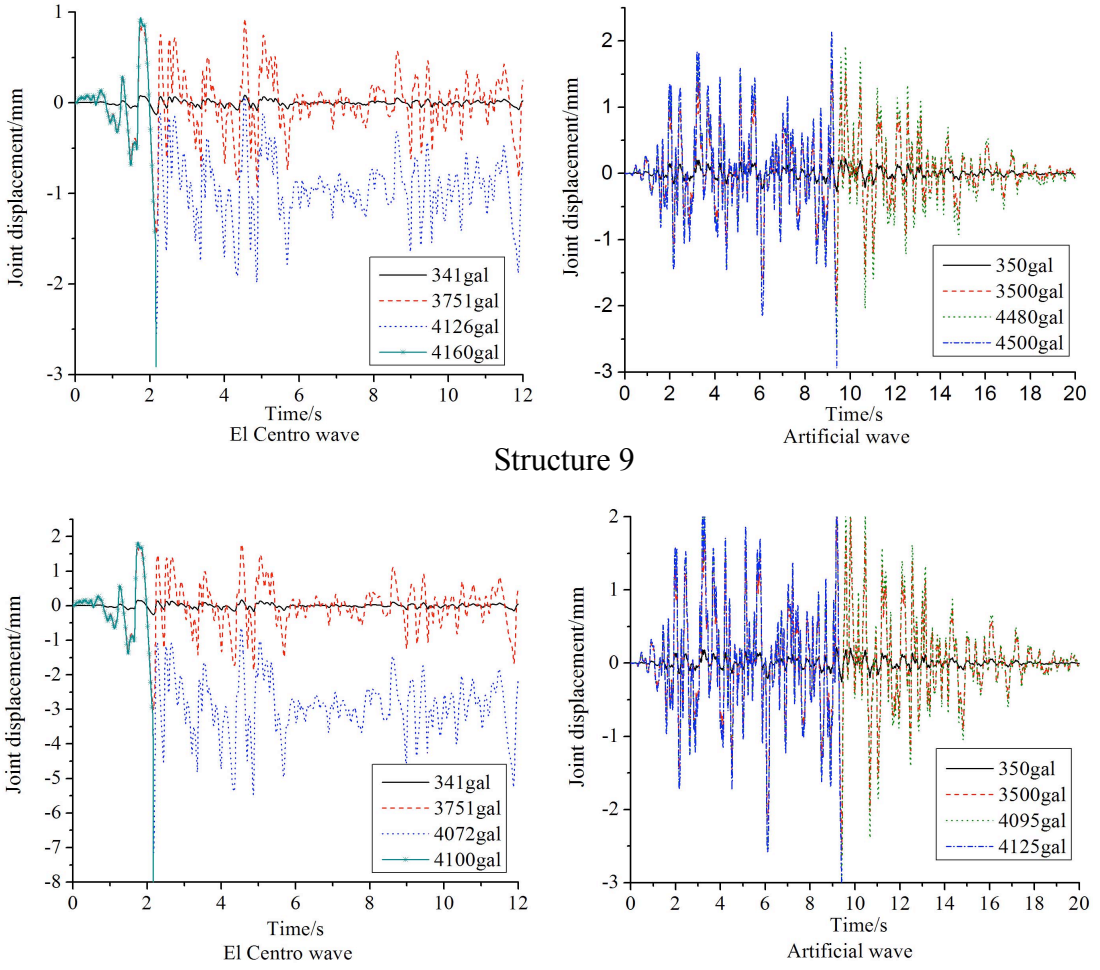


Figure 8. Joint displacement response history

SUMMARY

This paper uses the theory of dynamic instability and failure mechanism to investigate the relationship between failure mechanism and vulnerability theory. A new idea of using vulnerability analysis to determine structural failure mechanism is introduced.

A hexagonal space dome was used as benchmark structure in vulnerability analysis. The relationship between bars of high stresses under load and deteriorating bars with failure mode of overall collapse was studied by calculating stresses in elements under different load combinations. Whether in intact structure or in structure of partial failure, the stresses of deteriorating bars by vulnerability analysis are relatively high. Structural vulnerability analysis provides a new idea of directly

calculating high stress elements' characteristic parameters of vulnerability, finding all failure modes and judging structural vulnerability. The presented method neglects elements with low stresses, which can reduce amount of calculation and account for the effects of loading.

Structural ultimate load and connection ability are nonlinearly correlated. Connection ability should be chosen rationally to ensure the structure reach optimal peak ground acceleration values.

Different member cross-sections and different height-span ratios were studied using incremental dynamic analysis under El Centro record and an artificial ground motion. Different structural failure modes were presented with different element cross-sections and different height-span ratios. Through vulnerability analysis failure mechanisms of different structures are discussed, which reveals strength failure is likely when the connection ability and vulnerability index are small. With the increase of the vulnerability index, the failure mode changes from strength failure to dynamic instability.

REFERENCES:

Agarwal J., Blockley D. I., and Woodman, N. J. (2001a). "Vulnerability of Systems." *Civil Engineering and Environmental System*s, 18(2): 141-165.

Agarwal J., Blockley D. I., and Woodman, N. J. (2001b). "Vulnerability of 3-Dimensional Trusses." *Structura1 Safety*, 23(3): 203-220.

Agarwal, J., Blockley, D. I., and Woodman, N. J. (2003). "Vulnerability of structural systems." *Structural Safety*, 25(3): 263-286.

Blockley, D. I. (1999). "Risk Based Structura1 Safety Methods in Context." *Journal of Structura1 Safety*, 21(4): 335-348.

Blockley, D. I., and Heslop, S. E. (2001). "Managing Vulnerability and Risk for Sustainability." *Civil Engineering and Environmental Systems*, 18(1): 61-86.

Lu, Z., Yu, Y., Woodman, N. J., and Blockley, D. I. (1999). "A Theory of Structura1 Vu1nerability". *The Structural Engineer*, 77(18): 17-24.

Meek, J. L., and Tan, H. S. (1984). "Geometrically Nonlinear Analysis of Space Frames By An Incremental Iterative Technique." *Computer Methods in Applied Mechanics and Engineering*, 47(3): 261-282.

Papadrakakis, M., and Ghionis, P. (1986). "Conjugate gradient algorithm in nonlinear structural analysis problems", *Computer Methods in Applied Mechanics and Engineering*, 59(1), 11–27

Pinto, J. T., Blockley, D. I., and Woodman, N. J. (2002). "The Risk of Vulnerable Failure." *Structural Safety*, 24(2-4): 107-122.

Shen, S., and Chen, X. (1999). *Stability of Latticed Shells*. Science Press, Beijing,

China.

Shen, S., and Zhi, X. (2005). "Failure Mechanism Of Reticular Shells Subjected To Dynamic Actions." China Civil Engineering Journal, 38(1): 11-20.

Su, G. (2010). *Research On Structural Failure Mechanism Based On Vulnerability Theory*, M.S. Thesis, Southeast University, Nanjing, China.

Wu, X., Blockley, D. I., and Woodman, N. J. (1993a). "Vulnerability of Structural Systems Part 1: Rings and Clusters." *Civil Engineering Systems*, 10(4): 301-317.

Wu, X., Blockley, D. I., and Woodman, N. J. (1993b). "Vulnerability of Structural Systems Part 2: Failure Scenarios." *Civil Engineering Systems*, 10(4): 319-333.

Vibration Reduction of a Stadium Corridor Using Tuned Mass Dampers

Zhiqiang Zhang[1,2], Guowei Zhou[3], Aiqun Li[1,2], Xiaofeng "Bill" Zhang[4]

[1]School of Civil Engineering, Southeast University, 2 Si Pai Lou, Nanjing 210096, China
[2]Southeast University, Key Laboratory of Concrete and Prestressed Concrete Structures of the Ministry of Education,2 Si Pai Lou, Nanjing 210096, China
[3]Huasen Architectural & Engineering Designing Consultant Ltd., Nanjing 210096, China
[4]Department of Civil & Environmental Engineering, Temple University, 1947 N. 12th St., Philadelphia, PA 19122; PH (215) 204-3046; FAX (215) 204-4696; email: x.bill.zhang@temple.edu

ABSTRACT

The dynamic characteristics of the long-span corridor in a stadium are usually very complicated. The vibration may be significant when subjected to heavy walking excitations, which requires vibration control systems, such as dampers, to be implemented. In this paper, a stadium corridor using Tuned Mass Dampers (TMDs) for vibration control was studied. The eigenvalue analysis of the corridor showed that a vertical vibration mode is prominent, and the frequency of this mode is close to human fast-walking frequency, which can cause resonance in the corridor. Simulated walking excitation loads were applied to the finite element model. A variety of walking scenarios, and different TMD frequencies and distributions were investigated in order to optimize the frequencies and layout of the TMDs. The analysis results indicated that TMDs can significantly reduce the vibration response of the corridor due to walking, particularly near the resonance frequency. Though the TMDs were tuned to or near the resonance frequency, when subjected to other walking frequencies, the corridor's responses with TMDs also reduced substantially. The sensitivity of TMDs to structural frequency necessitates the field dynamic tests before fine tuning the dampers to optimize the vibration control effects.

INTRODUCTION

Contemporary architectural design evolves with radical changes in functionality, aesthetics, and space arrangement, and brings irregular and unique building configurations. It poses challenges to structural engineers in achieving structural

design to meet the safety and comfort requirements. Shown in Figure 1 is the 3-D model of a stadium, an example of such a challenging structure.

As shown in Figure 1, the bowl is hung at the outer rim by cables to the space trusses at the top. There is no support from the bottom except a few diagonal braces to the giant lattice columns on the left side. The top of the bowl is partially connected to the space trusses. The vertical vibration may be significant because of the low vertical stiffness of the bowl. The ring corridor inside the bowl is supported by vertical posts on the latticed shells of the bowl structure (Figure 2). As a result of the long span, and being supported on the locations where the vertical vibration mode is pronounced, the corridor's vibration may be substantial under human walking excitation, causing discomfort of the occupants and affecting the use of the structure. Therefore, it is necessary to control the vibration of the corridor.

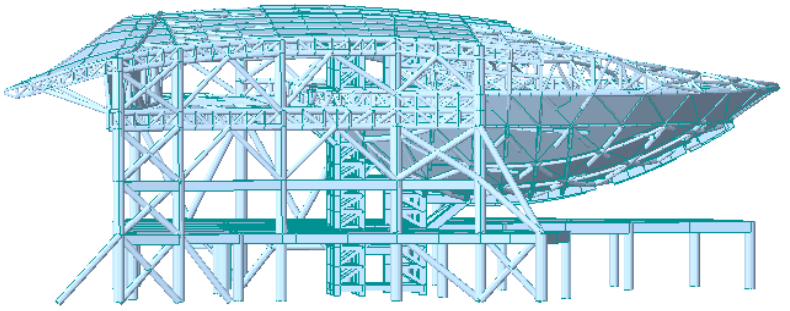


Figure 1. 3-D model of the stadium

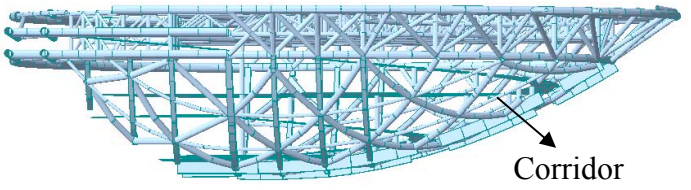


Figure 2. Bowl section and corridor

DYNAMIC ANALYSIS OF THE STRUCTURE

A 3-D finite element model (Figure 1) was developed in MIDAS in order to study the dynamic behavior of the structure, and to provide a basis for the settings of the damper parameters. The space beam element is used to model concrete and steel beams and columns. The shell element is used to model floor slabs, taking account of in-plane and out-of-plane deformations. The cable element is used for the cables

hanging the bowl. Modal analysis is performed using the Ritz vector method by Wilson and others.

The damping ratio varies among different modes for a steel-concrete composite structure like this. To ensure the accuracy of subsequent response history analysis, the method provided by MIDAS is used to calculate the damping ratios of the structure's different modes. The theoretical base is the Stain Energy Weighted Average Method, which averages the strain energy of members of different materials in a mode, weighted by their damping ratios, to obtain the damping ratio of that mode. The damping ratios of the first ten modes are shown in Table 1.

Table 1. Frequencies and damping ratios of the first 10 modes

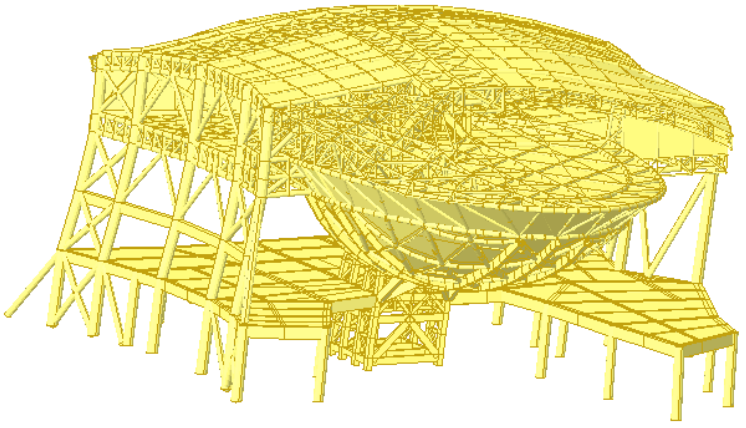
Mode No.	1	2	3	4	5	6	7	8	9	10
Frequency (Hz)	2.34	3.21	3.47	4.53	4.89	6.32	7.20	7.38	7.41	7.48
Damping ratio	0.031	0.027	0.036	0.033	0.044	0.036	0.021	0.025	0.047	0.024

The results of the modal analysis reveal that the vertical vibration mode of the structure is prominent. The second vibration mode turns out to be a vertical mode of the bowl (see Figure 3) and the third mode is a torsion mode. Meanwhile, the corridor shows significant vertical vibration in every mode. Therefore, the vertical vibration is significant for the corridor. The first two modal frequencies of the structure are 2.3Hz and 3.2Hz. Though the first mode is mainly translational, the corridor exhibits certain vertical vibration. The frequencies of 2.3Hz and 3.2Hz are very close to human walking frequencies ranging from 1.8Hz to 2.5Hz, leading to potential resonance in the structure. The structure is adequate in strength. However, the excessive vibration beyond the acceleration tolerance of human comfort may cause psychological panic. Therefore, it is necessary to take measures to damp the vertical vibration of the corridor. The modal periods and vertical participating mass ratios of the top 20 modes are shown in Table 2.

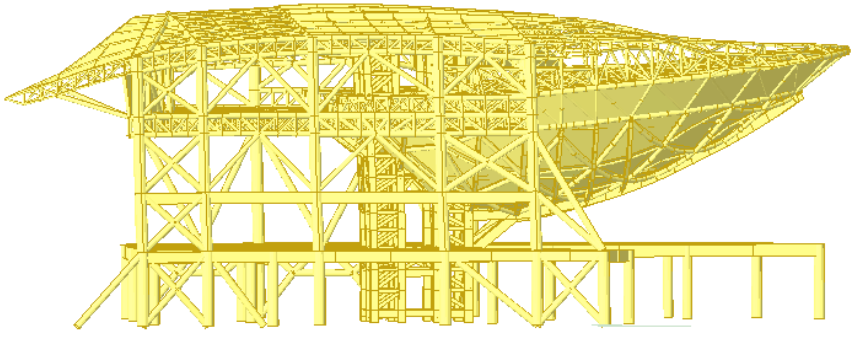
Table 2. Modal properties of first 20 modes

Mode No.	1	2	3	4	5	6	7	8	9	10
Freq. (Hz)	2.34	3.21	3.47	4.53	4.89	6.32	7.20	7.38	7.41	7.48
Vert. parti. mass ratios (%)	0.14	7.90	0.01	2.00	0.51	0.10	1.53	6.62	3.03	3.70
Mode No.	11	12	13	14	15	16	17	18	19	20
Freq. (Hz)	8.07	8.50	8.83	9.56	9.88	10.22	10.39	10.67	10.86	10.95
Vert. parti. mass ratios (%)	3.86	0.01	2.12	4.31	1.26	0.14	1.16	0.14	0	0.42

It can be seen from Table 2 that the 2nd, 8th, 9th and 10th modes are primarily vertical vibration modes, of which the vertical participating mass ratio of the 2nd mode is the largest. The vertical vibration modes are distributed. However, almost every mode has some vertical participating mass. It's observed that significant vertical vibration occurs in every mode in the corridor. With regard to higher order modes, their vibration frequencies are far away from that of the walking excitation, and are less likely to cause resonance. Hence, the vibration control is performed mainly on the first two modal frequencies. Figure 3 shows the first two mode shape.



Mode 1



Mode 2

Figure 3. First two structural vibration modes

During the response history analysis, sixty modes were included for combing. The damping ratios for the first ten modes are shown in Table 1, while the other modes having a uniform damping ratio of 0.035, 0.04, and 0.05, respectively, by input. The analysis demonstrated that the results of using the above three values are almost the same. This indicates that the damping ratios for the upper fifty modes have little

effects on the analysis.

PRINCIPLES AND DESIGN PROCEDURES OF TMD

The main task of controlling the vibration of the corridor under walking excitation is to reduce vertical vibrations. Tuned mass damper (TMD), as a passive control technology, has been successfully used in control of wind-excited vibration in high-rise structures. Numerical studies have shown that TMD can also effectively reduce the vertical vibration of long-span structures.

To maximize the effect of vibration control, the frequency of TMD shall be set near the free vibration frequency of the structure to be controlled. However, the damping effect of TMD is very sensitive to the fluctuations of the free vibration frequency, and there are always discrepancies between the actual free vibration frequencies of the structure and the calculated ones as a result of structural analysis errors and construction variations. Damping effect of TMD will be affected by these factors. More importantly, for the vibration modes lower than the mode being controlled, TMD has a good curbing effect to their response. For the modes higher than the one being controlled, TMD has little damping effect or may even amplify them. Given these characteristics, Clark (1988) proposed the concept of MTMD, which aims at a certain range of frequencies to be controlled, resolving the TMD system of a certain frequency bandwidth into multiple sub-TMD systems to improve the stability of the control system.

With MTMD attached, the dynamic equations of the multi-degree of freedom system under vertical load become:

$$[\mathbf{M}]\{\ddot{\mathbf{x}}\} + [\mathbf{C}]\{\dot{\mathbf{x}}\} + [\mathbf{K}]\{\mathbf{x}\} = \{\mathbf{F}\}$$

Where:

$$[\mathbf{M}] = \begin{bmatrix} \mathbf{M}_S & \mathbf{0} \\ \mathbf{E}^T\mathbf{M}_d & \mathbf{M}_d \end{bmatrix}, \quad [\mathbf{C}] = \begin{bmatrix} \mathbf{C}_S & -\mathbf{E}\mathbf{C}_d \\ \mathbf{0} & \mathbf{C}_d \end{bmatrix}, \quad [\mathbf{K}] = \begin{bmatrix} \mathbf{K}_S & -\mathbf{E}\mathbf{K}_d \\ \mathbf{0} & \mathbf{K}_d \end{bmatrix}$$

$$\{\mathbf{x}\} = \begin{Bmatrix} \mathbf{x}_S \\ \mathbf{x}_d \end{Bmatrix}, \quad \{\mathbf{F}\} = \begin{Bmatrix} f(t) \\ \mathbf{0} \end{Bmatrix}$$

$\mathbf{M_S}$, $\mathbf{C_S}$, and $\mathbf{K_S}$ denote the mass, damping and the stiffness matrices of the main structure, respectively. $\mathbf{M_d}$, $\mathbf{C_d}$, and $\mathbf{K_d}$ denote the mass, damping and the stiffness matrices of the TMD system. $\{\mathbf{x}_d\}$ stands for the displacement vector of each TMD relative to the main structure, only with the vertical component, while horizontal components being zero. $\mathbf{E}$ is the acting position matrix of TMD, where, the j^{th} column vector (with i^{th} element being unity, all others zero) represents that j^{th} TMD is set at the i^{th} node of the structure. *f(t)* is the time history of the walking load, which was obtained by the standard of IABSE.

To reduce the vertical vibration of the corridor, the primary vertical modes must be controlled. In this project, the second mode is the primary vertical mode. Considering the sensitivity of TMD systems to the frequencies, the TMD frequencies need to be fine tuned within the range of frequencies being controlled, to prevent the amplification of other walking frequencies and enhance the stability of the structure. The following are the basic steps of the method.

1. Analyze the structure's dynamic properties. Obtain the vertical vibration mode of the structure and the distribution of the corridor's vertical vibration.
2. Determine the frequency that needs to be controlled according to the results of modal analysis.
3. Locate the TMDs. Generally speaking, installing TMDs targeting a vibration frequency at the peak(s) of the mode shape appears to provide the most damping effect.
4. Add TMDs to the structure, and fine tune the controlling frequency of TMD in a certain spectrum. With the consideration of period change due to the additional masses of TMDs and variations of the walking excitations, determine the most appropriate frequency value(s), to enhance the stability of the system.

COMPARISON OF TMD DESIGNS AND ANALYSIS ON DAMPING

To find out the maximum response locations under the walking load, a group of 30 people were considering walking along the corridor on two floors from Endpoint A to Endpoint B. With two people in a row and the length of the group on the corridor being 14m, that is equivalent to a uniform load of to 0.7kN/m^2, when taking the weight of a person as 70kg, referring to Section 2.2.1 in American Institute of Steel Construction (AISC) Steel Design Guide Series 11 – *Floor Vibrations Due to Human Activity* (Murray et al 1997). The acceleration response was calculated every time the group moving forward by three sections. Then the maximum response was found, which occurred at the exterior on the upper and lower levels, i.e., Node 4999 and Node 5015. Therefore, the locations near these two nodes are the major spots to set TMDs.

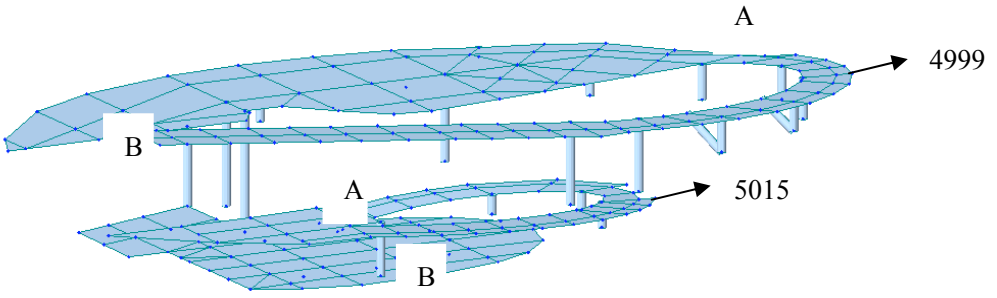


Figure 4. Sketch of the corridor

According to the analysis above, more TMDs are set at the curved segment on the exterior side of the corridor, and fewer near the end points A and B. TMDs are also located on the entrance platforms of the corridor. There are a total of 33 sets of TMD systems over the two corridors. Since the frequencies of walking excitation range from 1.8Hz to 2.5Hz, and the first two natural frequencies of the structure are 2.3Hz and 3.2Hz, the following vibration control schemes are compared: 1) TMDs at 2.5Hz; 2) TMDs at 2.8Hz; 3) TMDs at 3.2Hz. After finding the most effective damping frequency, the TMDs are divided into three groups having different frequencies within the narrow band around that frequency. The damping effects of the above schemes are compared under different loading conditions. The following loading conditions were considered: 1) slow walking, 50 people stretching 20m on the corridor, at the most unfavorable location (i.e., the outermost arc), with a uniform load of 0.7 kN/m^2, and exciting frequency of 1.8Hz, 2.0Hz and 2.2Hz, respectively; 2) fast walking, 30 people stretching 14m on the outermost arc, with a uniform load of 0.7 kN/m^2, and exciting frequency of 2.5Hz and 3.2Hz, respectively. The walking excitation curves are shown in Figure 5.

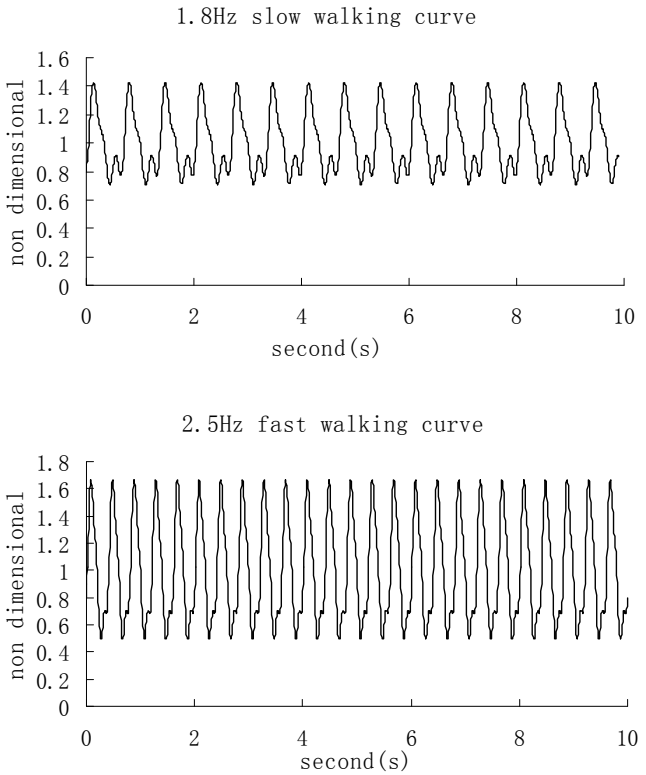


Figure 5. Walking excitations

The comparisons between the acceleration responses of Node 4999 and Node 5015 under each loading condition in three TMD schemes are shown in Table 3.

The following was observed from the analysis, as shown in Table 3. 1) The second vibration mode of the structure plays a decisive role in the response of the corridor, with the frequency of 3.2Hz. 2) The resonance is significant under the walking frequency of 3.2Hz. 3) The responses are much less under the walking frequencies ranging from 1.8Hz to 2.5Hz than that of 3.2Hz, since the resonance frequency is outside this range. 4) As TMDs' tuning frequency increases, the damping effects under different conditions vary. The tuning frequency of 3.2Hz has the best effects on restraining the resonance. But under low excitation frequencies, the damping effects are limited. The tuning frequencies of 2.5Hz and 2.8Hz better restrain vibrations of the lower modes, less effective at 3.2Hz excitation.

Table 3. Acceleration responses of Nodes 4999 and 5015 (mm/s^2)

Tuning frequency		Excitation frequency									
		1.8Hz		2.0Hz		2.2Hz		2.5Hz		3.2Hz	
		Node		Node		Node		Node		Node	
		4999	5015	4999	5015	4999	5015	4999	5015	4999	5015
Before TMD		182	142	207	163	200	160	160	135	665	531
After TMD	2.5Hz	168	128	179	138	176	137	132	101	464	323
	2.8Hz	169	128	179	135	176	133	132	100	353	251
	3.2Hz	175	138	187	145	183	143	143	124	201	183

In order to avoid the resonance, the tuning frequency should be set around 3.2Hz. Table 3 indicates that TMD with one single frequency cannot behave well on both cases of slow and fast walking. Using the concept of MTMD, the whole system of TMDs is divided into three groups. Considering that 3.2Hz is about the upper bound for walking, the groups have the frequencies ranging from 2.8Hz to 3.2Hz. These groups are mostly laid around the peaks of the second mode shape, at the outer side of the arc. TMD with different frequencies are laid in alternative pattern. Doing so reduces TMDs' sensitivity to the excitation frequency, and makes the system to gain damping effects in a wider frequency range. The parameters of the three groups of TMDs are shown in Table 4.

Table 4. TMD system parameters

Number	Mass (kg)	Tuning frequency (Hz)	Period (s)	Stiffness (kN/m)
TMD1	500	3.0	0.333	177.5
TMD2	500	3.1	0.322	189.5
TMD5	500	3.2	0.313	201.9

With the MTMD systems in place, the response accelerations of Nodes 4999 and 5015 under each operating condition are shown in Table 5.

Compared with results in Table 3 and Table 5, it can be seen that after grouping TMDs with separate frequencies within a small range, the responses changed little under the resonance, with significant damping effects. It improved damping effects under slow walking.

Figure 6 shows the comparison of acceleration responses of Nodes 4999 and 5015 before and after TMD installation under the excitation of the frequency of 3.2Hz. It can be seen from Figure 6, before installing TMDs, the structure's acceleration response is of resonance characteristics. After the installation of TMDs, the resonance phenomenon diminishes. At the resonance frequency of 3.2Hz, the damping effect on the acceleration reaches nearly 65%.

Table 5. Max acceleration responses under MTMD (mm/s^2)

Excitation frequency	Node	Before TMD	After TMD	Damping ratios
1.8Hz	4999	182	169	7.14%
	5015	142	129	9.15%
2.0Hz	4999	207	181	12.56%
	5015	163	141	13.50%
2.2Hz	4999	200	175	12.50%
	5015	160	135	15.63%
2.5Hz	4999	160	135	15.63%
	5015	135	110	18.52%
3.2Hz	4999	665	235	64.66%
	5015	531	212	60.08%

CONCLUSIONS

Based on the damping analysis using MTMD on the corridor in a stadium under walking excitations, the following conclusions can be drawn.

1. When the vertical natural frequency of the structure is close to the walking frequency, the resonance response is significant. In order to meet the human comfort requirements, the vibration control should be implemented.
2. TMDs need to be deployed in the vicinity of the peaks of the mode shape corresponding to the frequency to be controlled to achieve the most vibration control effects.
3. TMDs perform the best when tuned to the excitation frequencies. They are less effective to other vibration modes. To control more vibration modes, each group of TMDs should be located at the peaks of the corresponding mode shape.
4. Grouping TMDs into different frequencies within the controlling frequency range

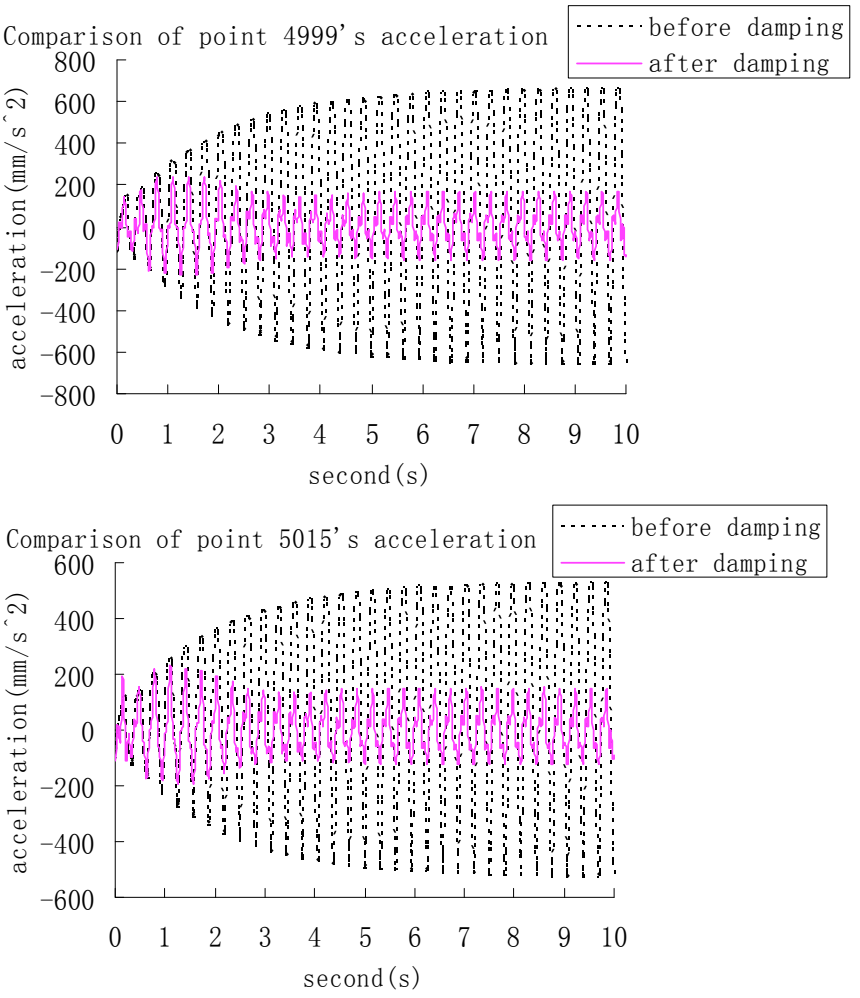


Figure 6. Acceleration responses of Nodes 4999 and 5015 before and after TMD installation

can reduce the amplification of the structure's vibration under other modes.

5. Due to TMDs' sensitivity to the structural free vibration frequencies, it is necessary to conduct field measurements of the dynamic properties of the structures before setting the final damper parameters.

REFERENCES

Clark, A. J. (1988). "Multiple passive tuned mass dampers for reducing earthquake induced building motion." *Proceedings of 9th World Conference on Earthquake Engineering*, Tokyo, Japan, Vol V: 779-784.

Li, A. (2007). *Structural Vibration Control*, China machine press, Beijing, China.

Murray, T. M., Allen, D. E., and Ungar, E. E. (1997). *Floor Vibrations Due to Hunam Activity*, AISC Steel Design Guide Series 11, American Institute of Steel Construction, Chicago.

Wang, Z. (1997). *Vibration Control of Tall Structures*, Tongji University Press, Shanghai, China

Ye, J. (1998). *Theory on Vibration Control of Latticed Shell Structure With TMD,* Post-doctoral research report, Harbin Jianzhu University, Harbin, China.

Ye, Z., Li, A., Ding, Y. (2003). Study on Vibration Energy Dissipation Design of A Pedestrian Bridge, *Special Structures*, 20(1): 68-70.

Zhang, Z., Li, A., and Xu, Y. (2007). "Research on Seismic Vibration Control of Hefei TV Tower with TMD", *Earthquake Resistant Engineering and Retrofitting*, 29(5): 12-16.

The Road Less Traveled – Middlebury, Vermont's Design-Build Cross Street Bridge Project

Gregory S. Goodrich, PE

Vanasse Hangen Brustlin, Inc., 6 Bedford Farms Drive, Suite 607, Bedford, NH 03110; PH (603) 644-0888; FAX (603) 644-2385; email: ggoodrich@vhb.com

Abstract:

From funding to design and construction, the Cross Street Bridge in Middlebury, Vermont is an infrastructure accomplishment that can serve as both inspiration and a blueprint others desiring to integrate infrastructure improvements into the fabric of the community. This paper discusses the development of the bridge —the longest simple span spliced girder known in the US—from conceptual design through final design and construction, providing detail on the team's design-build approach and the challenges faced and overcome.

Background/History:

Middlebury is in the heart of Vermont and home to Middlebury College, one of the country's elite liberal arts schools. The College and the charming New England town both have a rich history but were separated by river with only one narrow crossing. For 60 years the town has wrestled with the issues of funding, location, and consensus about this dilemma while traffic and frustration increased.

The three span Cross Street Bridge is the first major design-build transportation project in the State of Vermont, and with a center span of 240-feet, it boasts the longest simple span precast post-tensioned, spliced concrete girder bridge span known in the United States.

Residents of Middlebury will attest that the idea of a second river crossing was anything but a new initiative. The plan for a new bridge crossing was originally proposed in the 1960's, prompted by the burning of the town's second crossing, the Three Mile Bridge in 1952. Otter Creek bisects the town, separating the downtown shopping district and the college from the emergency services and Route 7, the major north/south highway in the region. The lone crossing for the past 50 years is the Battell Bridge, a narrow stone arch bridge built in the late 1800's. The need for a second bridge to alleviate traffic for residents and visitors and provide additional pedestrian and bicycle facilities was became more urgent as the Battell Bridge aged.

The new bridge, in addition to being the first major transportation design-build project in Vermont required a main span that is now the longest simple span concrete girder in the country, What makes this project even more unique is that the $16 million project received no funding from Federal or State sources; it was funded

entirely by the Town of Middlebury and Middlebury College. Ground breaking was in April 2009 and the bridge opened to the public with great fanfare in October 2010.

Conceptual Design Development:

At the outset of the project, the Town assembled a Bridge Committee comprised of ten local citizens including Town officials, members of the Department of Public Works, , and local volunteers. The committee met regularly with the design-build team to provide feedback on conceptual bridge drawings, graphics, product samples, and other key information pertinent to the development of the project.

Once the project funding was secured by the Town and the VHB/Kubricky Construction design-build team was officially selected and approved, the first challenge was to determine how to deliver a structure with aesthetic significance that would integrate seamlessly into the landscape of this beautiful and historic New England community while also staying within the $16 million project budget. Several goals and considerations were presented by members of the Bridge Committee and the design-build team. Having the Contractor on board from the beginning of design proved to be invaluable to quickly narrow the range of options that would fit within the project budget.

Through engineering studies conducted prior to selection of the design-build team, the location and preliminary layout of the bridge was presented. This layout was expanded upon once the Town determined it would take a design-build approach. The project budget was established first, followed by another important priority for the Town – involving local resources as much as possible. A major regional precast concrete supplier, J.P. Carrara and Sons, based in Middlebury, was brought on board. Carrara specializes in precast, prestressed concrete bridge construction, so the team focused on designing a crossing that would incorporate these materials.

The bridge crossing spans three features: Bakery Lane on the west side, the Otter Creek, and the active Vermont Railway (VTR) on the east side. These features limited the placement of the substructure components. The primary challenge was crossing the Otter Creek at approximately 160-feet between each toe of slope. Crossing Bakery Lane on the west side required 160-feet of superstructure length, as did the railroad crossing on the east side, for a total required superstructure length of 480-feet.

Bridge Concept 1

The first bridge layout proposed two piers placed approximately at the toe of each embankment slope, requiring three span lengths of 160-feet each. This concept utilized 2000 mm tall (6’-6”) 160-foot long precast prestressed New England Bulb Tee (NEBT) girders. At 160- feet long, the NEBT 2000 shape would have maximized J.P. Carrara’s picking weight and transporting length. Another hurdle with this concept was hydraulics. The proposed crossing location for the Cross Street

Bridge is at a bow in the Otter Creek, making it economically impractical to geometrically align each pier with its respective river bank while. This substructure layout proved to be less than ideal from a hydraulic standpoint, and upon further review it was expected that the Vermont Agency of Natural Resources (ANR) would not likely approve of two substructures placed at the toe of each slope in such a configuration.

Bridge Concept 2

The second configuration placed two piers at the top of each river bank, and placed one pier directly in the middle of the channel, creating a bridge crossing with four equal spans of 120-feet long. This configuration incorporated an additional pier and reduced the total number of in-water substructures from two piers to one, requiring fewer cofferdams, reducing the individual precast span lengths from 160-feet to a more reasonable 120-foot span using 42" deep box beams. The design-build team thought that this alternative would be more attractive to the permitting agencies because it only placed one substructure unit in the channel, thereby reducing the overall impacts to the river. Vermont ANR pushed-back challenging the team to find a way to completely span the Otter Creek without permanent channel impact. From this request, the final bridge configuration was born.

Final Bridge Concept: Designing the longest simple span spliced girder known in the US

The third and final bridge configuration presented some significant engineering hurdles. The challenge: span the Otter Creek without permanent channel impacts. The solution: remove the middle support and create a record breaking, 240-foot simply supported center span using precast concrete.

The design team looked at alternatives, one of which was precast, post-tensioned, spliced concrete girder construction. With 120-foot end spans the span ratio of 2:1 would not economically or geometrically accommodate making the bridge continuous for live load, particularly given the close proximity of the railroad on the east side. The vertical clearance required by the railroad, coupled with the profile grade tie-in elevation at the intersection of Pleasant Street at the end of the bridge, made superstructure depths for the east end span relatively shallow, and did not allow for a gradual superstructure depth transition on the east side of the pier in order to effectively establish continuity over the pier. The solution was to create the longest simple span spliced girder known in the US. Through close coordination with Kubricky Construction (the Prime Contractor), and J.P. Carrara, the team began preliminary design on the center span.

Establishing the capabilities of the precast fabricator was critical. J.P. Carrara's maximum crane capacity was 95 tons. Their casting plant configuration could accommodate up to a 10-foot tall girder. J.P. Carrara already owned forms for the NEBT shape; therefore this would be the most economical girder shape for this

application. The team reached out to Corven Engineering, a nationally renowned specialist in post-tensioning construction, for due diligence. Corven conducted a review of the proposed bridge configuration and agreed that it was the most appropriate given the site constraints. They also reviewed the preliminary design and agreed that the proposed girder size and shape was within acceptable design limits. Kubricky and Carrara reviewed the preliminary design and determined that they could build the span within the proposed budget and schedule.

The team scheduled a follow-up meeting with ANR to present the revised bridge layout. The team designed a crossing that would completely span the Otter Creek without permanent channel impacts, however one question remained: would the Agency permit temporary channel impacts in the form of temporary erection towers in order to support the massive girder segments until the post-tensioning could be completed? ANR agreed to permit the temporary channel impacts, and with that, the concept drew one step closer to fruition.

With a viable bridge layout in-hand, the team presented the configuration to the Bridge Committee for approval. From there, the team and the committee presented the layout to the Town Selectboard for final approval, and it passed without exception.

Simultaneously, the team coordinated with the Bridge Committee to develop pier concepts and aesthetic features. Several pier configurations were considered: column bents, wall piers with voided recesses to provide a "window" through the pier, solid wall piers with various arched and vertical recesses, and flared piers. The Town challenged the team to develop a pier that would be unique in its own right and be true to itself– a concrete pier with its own historic significance.

Victor Nuovo, a member of the Bridge Committee and professor emeritus of philosophy at Middlebury College, was a proponent of creating a pier with unique character. He presented photos of a few historic bridges, the Brooklyn Bridge in particular, citing its distinctive visual appeal. These photos provided the initial inspiration for the piers. The team developed a pier concept with telescoping octagonal-shaped end caps, along with two full-height vertical recesses centered on each pier face. The features fit seamlessly with the height-to-width ratio of the piers and visually anchored the massive center span. Extending the ends of the piers beyond the superstructure fascia, and continuing the pier ends above the bridge seats proved to be an effective way of shielding the difference in superstructure depth, which stepped at the pier from a 42-inch deep box beam end span to a 10-foot deep center span NEBT. The pier "end cap" also served to visually break up the sight line along the bridge fascia, thereby providing a graceful and nearly seamless transition from the end span to the center span.

The Town also expressed an interest in visually marking the ends of the channel to motorists on the bridge in an effort to break up the long "viaduct" nature of the bridge and to add aesthetic interest. The Town originally proposed adding "spires" at the pier

locations, which would extend above the roadway to mark the location of the channel. Once the pier shape was developed, the pier end caps were temporarily terminated at the top of sidewalk elevation while alternatives were considered. The design team proposed adding overlooks at the pier location. Since the Cross Street Bridge was intended to serve both motorists and pedestrians, the overlook concept was a natural way to provide pedestrians a place to rest and converse on the bridge while allowing others to pass by. Additionally, the overlooks break up the long superstructure and also serve as a distinguishing feature of the bridge.

Once approved, the final bridge design concept proceeded to the final design phase. The final approved concept was presented to the public at a Town Meeting for direct input prior to beginning final design. There were no bridge design changes or requests from the public meetings as the feedback was overwhelmingly positive. Final bridge design was in full swing by March 2009.

Final Design Development:

The design-build team immediately kicked-off the final design phase of the project, beginning with foundations.

Preliminary bridge borings were taken as part of an engineering feasibility study that had been conducted prior to selection of the design-build team. These select borings were used to develop preliminary foundation concepts in order to project which types of foundations would be suitable at each substructure location. The preliminary geotechnical evaluation suggested that the substructure units on the west side of the Otter Creek would be best supported on piles. The east side required more in-depth discussions due to the presence of a seven to 10 foot deep layer of silt and organic matter on top of very dense and boney glacial till that was thought to be unsuitable for driving piles.

Once the final bridge layout was approved, the team initiated a final subsurface exploration and evaluation program at each proposed substructure location. At the same time, the team began a series of initial coordination meetings between the contractor, geotechnical consultant, and the design engineers to prioritize the design schedule. The team broke-down the bridge components into discrete construction document packages in order to meet the contractor's preferred order of construction sequence.

Expecting that the west abutment and west pier would be founded on piles, the contractor preferred to begin construction there. This decision was aided by the fact that access to the east pier location required a formal Railroad Agreements between the Railroad, the State of Vermont, and the contractor in order to construct the pier on railroad right-of-way, and a superstructure over the railroad corridor. The layout and clearance envelope was subject to Railroad approval prior to the start of construction on the east side.

With the conceptual pier design approved on March 2009 and the ground breaking ceremony scheduled for April 14, 2009, the team worked quickly to produce construction documents for the west pier foundation.

Establishing a Communication Protocol

The team recognized the need for establishing a well-defined "construction communication protocol" for use throughout the project. Given the aggressive schedule and amount of work to be accomplished, the project team defined a process that would guide the project to completion. The project team agreed on a hierarchy of communication that would efficiently channel information between the field and the office while keeping key staff informed without creating unnecessary delays.

To ensure an open flow of communication during the design phase, the team employed weekly scheduled progress conference calls between the contractor, geotechnical consultant, design engineers, and others as needed. This practice proved pivotal in keeping the foundation design and subsurface evaluation on-schedule and in-tune with the contractor's expectations during the early stages of design and construction. The meetings also allowed the design team to explore foundation options on the fly with the contractor available for immediate feedback.

Substructure Construction

As is common for most design-build projects, the substructure is typically designed and constructed prior to final design of the superstructure. The final superstructure configuration had been approved as part of the conceptual design phase, which called for two, 11-foot travel lanes, 4-foot shoulders, 6-foot sidewalks on each side, and three rail anodized aluminum bridge rail with balusters, for a total out-to-out bridge width of 44-feet 8-inches. The spans were set at 120-feet, 240-feet, and 120-feet. These criteria, with the preliminary superstructure design, the preliminary superstructure dead and live loads were calculated and used in the final design of the substructure units, beginning with the west pier.

Due to the advanced construction schedule and the quick turnaround required between approval of the conceptual bridge design and the groundbreaking, the first construction document deliverable was the west pier foundation. This allowed the contractor to order piles and reinforcing steel for the footing prior to releasing construction documents for the intricate pier stem. Since the contractor was to begin pile installation at the west pier, for efficiency he chose to immediately follow with pile installation at the west abutment.

The west pier pile group consists of 30 HP 14x89 piles driven to bedrock, arranged in three rows of 10 vertical piles, each pile approximately 40-feet long. The geotechnical engineer determined that battered piles would not be required given the design loading.

Horizontal loads on the pier were minimized and distributed evenly to each pier by fixing the end spans at the abutments and by releasing both ends of the center span, thereby allowing the longitudinal breaking, thermal, and shrinkage forces to be distributed evenly between both piers ("expansion" style elastomeric bearings were used on each end of the center span, and over the piers on the end spans). Lateral superstructure earthquake loads were transmitted to the piers via cast-in-place "keeper blocks" that were built into each pier bridge seat.

The west abutment pile group consists of a single row of nine vertical HP14x89 piles driven to bedrock, each pile approximately 60-feet long. The pile group was designed to support a continuous stub abutment cap perched atop a wrap-around Mechanically Stabilized Earth (MSE) wall bridge approach. The abutment pile group layout construction documents were broken-out in similar fashion to the west pier foundation in order to allow the contractor to continue pile driving operations prior to the completion of the final abutment cap design. The piles extended through the MSE engineered fill, through a layer of unclassified fill, into glacial till and ultimately set-up on bedrock. The geotechnical engineer was concerned that the unclassified fill would be susceptible to settlement, mostly during construction of the MSE wall, and since the piles had to be driven prior to construction of the MSE wall, the team needed to isolate the piles from potential down-drag induced by the settlement of the MSE wall. This was accomplished by encasing the piles in a 24-inch diameter smooth-wall High Density Polyethylene (HDPE) sleeve that was filled with sand prior to casting the abutment cap.

The abutments were designed to accommodate the longitudinal loads transmitted to them through the fixed bearings. Since the west abutment single row of h-piles were too flexible to resist the longitudinal loads (these loads were not resisted at the piers as the beam ends were placed on expansion bearings over the piers) the loads were resisted via two layers of MSE straps spaced at one foot fastened to the abutment backwall. The straps resist the longitudinal loads traveling away from the abutment (toward the pier). Soil resistance against the cap and backwall was used to resist loads toward the abutment.

The east pier foundation was constructed next. It was initially expected to utilize drilled shafts due to 100+ blow count glacial till under a 10-foot layer of loose silt and alluvial fill material. The contractor preferred to use pile foundations as he could utilize his own labor force instead of hiring a specialty contractor for drilled shaft construction, however, the design team was concerned that the piles would reach refusal without achieving the minimum desired depth of 10-feet. The depth of the loose alluvial fill layer was too deep to consider over-excavating down to the top of the glacial till layer. Over-excavating would require extensive dewatering and cofferdams capable of supporting railroad live load.

The contractor proposed an experimental "test pile" program to evaluate drivability at the east pier. Dynamic pile load tests were completed on each test pile with re-strike in order to confirm proper bearing had been achieved. The test pile program was

successful and h-piles were used at the east pier en lieu of drilled shafts, saving significant project costs.

Upon completion of the east pier stem, the focus turned to the east abutment, which is a traditional spread footing abutment with u-back wingwalls. With firm glacial till only four to seven feet below bottom of footing, and with the water table well below bottom of footing, the contractor elected to simply over excavate the unsuitable material and replace it with a layer of engineered structural backfill.

While the east abutment was being constructed, a second crew began construction on the west abutment MSE wall. The construction of the west abutment MSE wall was relatively routine with the exception of localized over-excavation required to remove pockets of unsuitable organic matter that were found during a series of shallow supplemental field borings taken along the proposed face of MSE wall. The uncontrolled nature of the fill made it imperative that the wall be able to accommodate minor amounts of differential settlement. The approach was isolated from the west abutment by installing 24-inch diameter sleeves over abutment piles to eliminate down drag on the piles in the event that the approach settles. MSE wall construction was ideal for the approach because it can accommodate small amounts of differential settlement since it is relatively flexible in nature.

Final Design Development: (Superstructure)

The keystone of the project was the design and construction of the 240-foot precast, post-tensioned, spliced concrete girder center span. A simple span of this size and type had never been constructed before, and at nearly 10-feet tall, it was also the tallest precast NEBT girder ever constructed in the northeast.

In order to accomplish this engineering feat, VHB teamed with Corven Engineering, post-tensioning design specialists, to perform the final design of the record breaking span. Corven Engineering was initially brought in to provide a peer review of the design concept, and was ultimately engaged to provide final design and construction support during fabrication, erection, and post-tensioning of the span.

Close coordination was required between J.P. Carrara, the precast fabricators, the contractor, and the design team in order to meet the tight schedule and stay on budget for both design and construction.

J.P. Carrara had three initial requirements crucial to the success of fabrication: the girder had to be less than 10-feet tall in order to be able to pick the girder out of the casting bed and load it onto the transport vehicles; the pick weight of each of the girders segments had to be less than 95 tons, the maximum capacity of the cranes in the fabrication plant; and to achieve economical fabrication costs, the design team needed to utilize the NEBT top and bottom flange configuration and configure the girder segment geometry in a way that was compatible with their fabrication beds.

The girder weight and geometry parameters pushed the design capabilities of the girder shape to the absolute maximum of its potential. The girder geometry was tweaked through a series of intermittent reviews by the design team and the fabricator. One of the most significant challenges posed to the design team was the final location of the girder splices. The girders had to be fabricated in three segments. Ideally the splices are located as far from the middle of the span as possible, in order to reduce the applied stress on the splice. The ideal location for the splice was at the quarter-point of the span, or 60-feet from the centerline of bearing. However at 1,700 pounds per linear foot the center segment would weigh over 100 tons. Therefore the final splices were located 65 feet from each pier, making the center segment a total of 108-feet long (accounting for a two-foot splice width), yielding a center segment weight of 92-tons. Each end segment weighed approximately 66-tons, including the massive eight-foot long end blocks.

The girders required five post-tensioning tendons per girder. The top two tendons consist of 19-0.6 inch diameter 270 ksi low-relaxation strands, each requiring approximately 835 kips of jacking force per tendon. The three lower tendons consist of 22-0.6 inch diameter strands, requiring approximately 967 kip of jacking force per tendon. The VSL PT-Plus™ post-tensioning system was selected for use in the girders because it uses corrugated polypropylene plastic ducts, which facilitate tendon installation, increase durability, and enhance corrosion protection of the tendon.

The high post-tensioning anchorage stresses at the end of the girders required heavily reinforced end blocks, the design of which demanded additional coordination between the designers and fabricators. Bar size, spacing, and placement considerations were of critical importance. Through a series of design reviews and interactive comment periods the team swiftly produced a design acceptable to the fabricator.

The balance between fabrication parameters, efficiency, economics, and design performance requirements meant that the design team had to push the envelope by using high performance concrete with a 28-day compressive strength of 10,000 psi. The team was concerned with the ability to place such high-performance concrete in large quantities while achieving proper consolidation in highly congested areas such as the end blocks. The solution was a self-consolidating concrete design mix. The design team requested trial batches to demonstrate the ability to produce a consistent mix with the proper design capabilities. A rigorous quality control program was employed by the fabricator, with independent testing, and additional oversight from the concrete admixture representative throughout the casting process.

The concrete results were incredibly consistent throughout. Proper design strength was achieved in 7-10 days, while the proper release strength was achieved in just less than two days in order to facilitate resetting the casting beds to keep production on-schedule.

The fabricator's casting bed was 270-feet long, which was ideal for casting one entire girder line at a time. Five total casting runs were required (one for each girder line). With a turnover rate of just over a week between castings it took approximately a month and a half to fabricate all five girder lines.

Once on-site, the girder segments were hoisted onto two temporary supports that were erected in the channel. A single 350-ton Manitowoc crane was used to erect the segments, starting with the 64-foot long segments on the east end of the channel, progressing to the 108-foot long center segments, and finishing with the west segments.

Two-foot field closure splices were cast using the same 10,000 psi self-consolidating concrete mix. The close proximity of the concrete plant to the project site made it possible to use such a high-strength mix without compromising the consistency of the mix. One challenge during construction was that the splices had to be cast during the winter, requiring heated curing. The contractor addressed heated curing by threading a two-inch diameter tube with glycol circulating at 180 degrees around each of the splices, covering them with thermal blankets. Continuous recording thermal sensors were strategically placed around each splice to monitor the temperature of the concrete. The sensors were monitored regularly so that adjustments could be made as necessary.

The 240-foot center span was post-tensioned in February 2010. Despite the sub-freezing temperatures of central Vermont, the weather did not significantly slow stressing operations. The crew installed and tensioned nearly 24-miles of post-tensioning strand in approximately three weeks. Upon completion of the stressing operation, the girders lifted off of their temporary supports by approximately 1 inch. The temporary supports were then removed from the channel, and the Otter Creek was finally traversed unobstructed.

The weather did play a role in the progress of the bridge construction, however. Since the tendon stressing operation was completed in mid-winter, it was too cold to initiate grouting of the tendons. The ends of the girders had to be accessible in order to grout, therefore the end spans could not be erected until the grouting was completed. A corrosion inhibitor was installed in the ducts upon completion of stressing operations. The inhibitor was blown out of the ducts in April 2010 in preparation for grouting.

The 120-foot long, 42-inch deep box beams for the end spans were fabricated during the winter months of 2009-2010. Similar to the center span, the box beams also utilized a self-consolidating concrete mix; however, the required design 28-day compressive strength of the box beams was 8,000 psi. Each box beam required 56-0.6 inch diameter 270 ksi low-relaxation prestressing strands, 50 straight strands in the bottom flange, and six straight strands in the top flange. The large number of strands in the box beams created high stress concentrations in the end blocks, and therefore the concrete required release strength of 6,000 psi.

The erection of the box beams on the east side was a carefully coordinated process. The east abutment is perched at the top of a 3:1 spill slope which extends to the railroad at the base of the slope. The location of the railroad and the length of the spill slope limited the contractor's available staging locations for the cranes. Instead of erecting a launching truss to erect the box beams, the contractor elected to utilize a series of three cranes in a choreographed box beam hand-off.

The first crane was placed directly behind the east abutment; the second crane was located at the base of the spill slope, to the east of the railroad, and a third crane adjacent to the pier. The second crane began by picking the west end of the box beam off of the transport dolly by using a sling instead of the lifting loops embedded in the end of the box beam. The transport backed up towards the pier while the crane rotated to the west, walking the end of the beam towards the pier. Once the east end of the box beam was in reach of the crane behind the abutment, the crane finally lifted the east end of the box beam off the transport. At this point, the third crane was in range of the west end of the box beam. This crane engaged lifting loops, which then relieved the middle crane from duty. Finally, the first and the third crane would rotate the box beam over to the abutment and the pier respectively and place the beam on the supports. This process was repeated for each of the 10 box beams on the east end span. The west end span was placed by utilizing two cranes in a conventional manner.

Upon completion of box beam erection, the crew focused on forming and placing the concrete bridge deck. The concrete deck was placed in one continuous operation starting at the west end (the low side) and proceeding to the east. The center span deck slab consists of an eight- inch thick concrete deck with a 28-day compressive strength of 5,000 psi. Each of the two end spans has five- inch minimum thick topping slabs with a required 28-day compressive strength of 4,000 psi. To utilize a single concrete mix design during the continuous deck placement operation, the contractor opted to use the 5,000 psi mix design for each of the three spans. Once cured, the six foot concrete sidewalks and a waterproofing membrane were installed and the deck was paved with three inches of bituminous asphalt.

With the bridge deck complete, one of the more defining features of the bridge was constructed— the overlooks. Four 11-foot wide octagonal shaped overlooks were constructed; one perched on top of each end of each pier, reflecting the shape of the pier ends. With the overlooks complete and the three-rail anodized aluminum bridge rail installed, the bridge was ready for its historic October 30, 2010 ribbon cutting.

Conclusion:

From initial concept through final design, the Cross Street Bridge was a welcomed addition to its unique New England Town. The innovative approach to funding, cutting edge design, and aesthetic detailing, make the Cross Street Bridge truly one of a kind.

Three-Dimensional Effects in Progressive Collapse Modeling

Honghao Li[1] and Sherif El-Tawil[2]

[1]PhD student, Department of Civil and Environmental Engineering, University of Michigan, Ann Arbor, MI 48109; email: honghli@umich.edu
[2]Professor, Department of Civil and Environmental Engineering, University of Michigan, Ann Arbor, MI 48109; email: eltawil@umich.edu

ABSTRACT

This paper highlights the importance of accounting for three dimensional effects when modeling progressive collapse behavior. Two types of nonlinear, inelastic models are first presented: 1) a planar comprised of beam-column elements to represent key structural members, and 2) a 3-D model that accounts for the most important components of the building. After validation, the simulation models are exercised to investigate system robustness when columns are forcibly removed. The importance of 3-D effects is quantitatively investigated through comparisons of system responses captured by the planar and 3-D models. In addition, the effect of modeling the slabs is demonstrated by comparing the responses of a 3-D model without slabs and the same 3-D model, but with slabs. It is shown that the slab plays a crucial role in progressive collapse response.

INTRODUCTION

Planar approximations of system response are made for convenience, because solving such models requires much less computational effort that solving corresponding 3-D models. As such, many of the models in the literature that have been used to study progressive collapse are planar. Planar models typically represent a single frame extracted from a structure, examples of which can be found in Kaewkulchai et al. (2003), Khandelwal and El-Tawil (2007), Khandelwal et al. (2008) Bao et al. (2008), Kim et al. (2009) and Khandelwal et al. (2009). By definition, these models do not explicitly address three dimensional effects, although they could be calibrated to account for some types of 3-D effects in an implicit manner.

It is only recently that 3-D models have come to be used for investigating progressive collapse. One of the earliest examples can be found in Ruth et al (2006), who used 3-D macro-models to show that the dynamic increase factor provided by the then-existing DoD and GSA guidelines is too conservative. However, the Ruth et al. (2006) study did not account for the effect of slabs, which can play a large role in 3-D behavior. Sasani et al. (2008), Szyniszewki (2009) and Mohamed et al. (2009) also used 3-D models to investigate the response of structures under events that could trigger progressive collapse. Other examples can be found in Main (2009), Fu (2009), Fu (2010) and Masoero (2010). Kwasniewski (2009) developed a detailed 3-D model, which was verified and validated by applying a hierarchical approach that included four levels of complexity. Alashker et al (2010) compared the responses of a 3-D

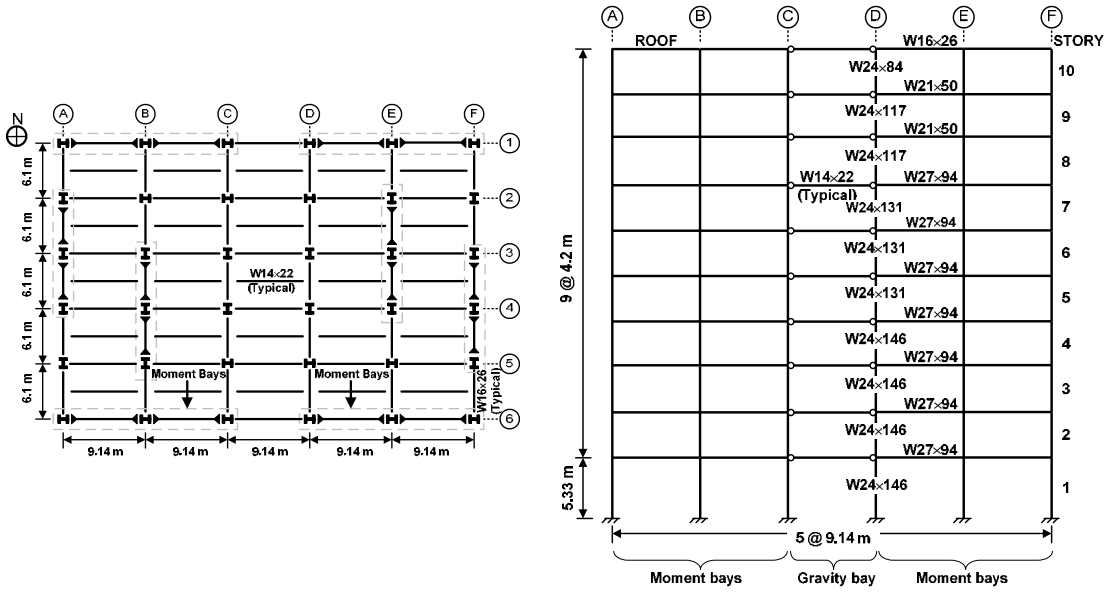
detailed finite element model and a 3-D macro-model subjected to loss of exterior columns. All of the previously discussed efforts to address 3-D behavior were conducted using the finite element method, albeit employing different types of elements. Other approaches for modeling 3-D response can be found in Galal et al (2009), for example, who developed a 3-D model using the Applied Element Method to investigate effect of retrofit strategies on mitigating progressive collapse of steel frame structures.

While it is becoming more clear from accumulating evidence in the literature that accounting for 3-D effects could be significant in progressive collapse modeling, there has not been a systematic study to show how important those effects are. This limitation is addressed herein by comparing between the responses of various types of models. Specifically, the collapse responses of planar and 3-D models of the same system are compared to gain insight into the effects of the various modeling assumptions made and to quantify: 1) the effect of planar versus 3-D models, and 2) the effect of modeling the slab in 3-D systems.

PROTOTYPE STRUCTURE

The National Institute of Standards and Technology (NIST) designed prototype steel framed buildings for the purpose of studying their response to an event which may cause progressive collapse (Liang et al., 2007). The buildings are 10-story office buildings with plan dimensions of 45.7 x 30.5 m and utilize moment-resisting frames as the lateral load resisting system. One of buildings designed by NIST is selected for the study in this paper: namely Building 3, located in Seattle, WA, and categorized as Seismic Design Category D, i.e. SDC-D. The building employs Special Moment Frames (SMF) for lateral force resistance. Design details can be found in Liang et al. (2007) and Khandelwal et al. (2008).

The selected building has a structural system comprised of both moment frames and a gravity system. There are 36 columns, of which 24 belong to moment-resisting bays, while the rest are gravity columns. Beams in the gravity system are connected to columns through shear connections which are comprised of single plate shear tabs that are 9.5 mm thick, made of A36 steel and filet welded to the columns. The beams are bolted to the tabs using 22 mm, A325 high strength bolts. In the moment frames, reduced beam sections (RBS) are used with 50% reduction in RBS flanges. In all moment connections, beams are assumed fully welded to the columns to simplify the modeling process. The structural steel used for all beams and columns is A992 (F_y = 345 Mpa). The plan of Building 3 is shown in Figure 1-a, while the elevation of the E-W frame on axis 6 is shown in Figure 1-b.



(a) Plan view **(b) Elevation**

Figure 1. Prototype building

MODELING APPROACH

The general modeling approach adopted in this study is to model all primary structural elements in the system, within the specific limitations of each model, including all structural members and the connections between them. Since the focus of the study is on nonlinear response, each element's representation permits inelastic response to occur including fracture and separation, where appropriate. To enable realistic simulations of collapse, interpenetration between the various components of each model is prohibited. Therefore, falling components can introduce impact forces on the components with which they come in contact. The simulations are conducted with 5% mass proportional damping and are carried out using the explicit finite element code LS-DYNA (Hallquist 2006).

In both planar and 3-D models, beams and columns are represented using a Hughes-Liu beam-column element formulation, which was shown to be capable of reasonably representing structural response by Khandelwal and El-Tawil (2007). The radius cut reduced beam sections are modeled with a beam element whose cross section is set to the minimum cross section in the reduced section. The failure strain in the macro elements, which triggers deletion of the elements, is based on the work in Khandelwal and El-Tawil (2008).

The composite floor is comprised of a RC slab of thickness 82.5mm sitting on a steel deck with 76 mm depth and connected to the underlying steel beams via shear studs. Steel reinforcement in the RC slab is 0.05927 mm^2/mm in both directions. To avoid the complexity of modeling such a system in detail in the 3-D model, e.g. as in Sadek et al. (2008), a reduced model is employed in this study. The RC floor slab is modeled using fully integrated four-node, isotropic shell elements. A J_2 plasticity

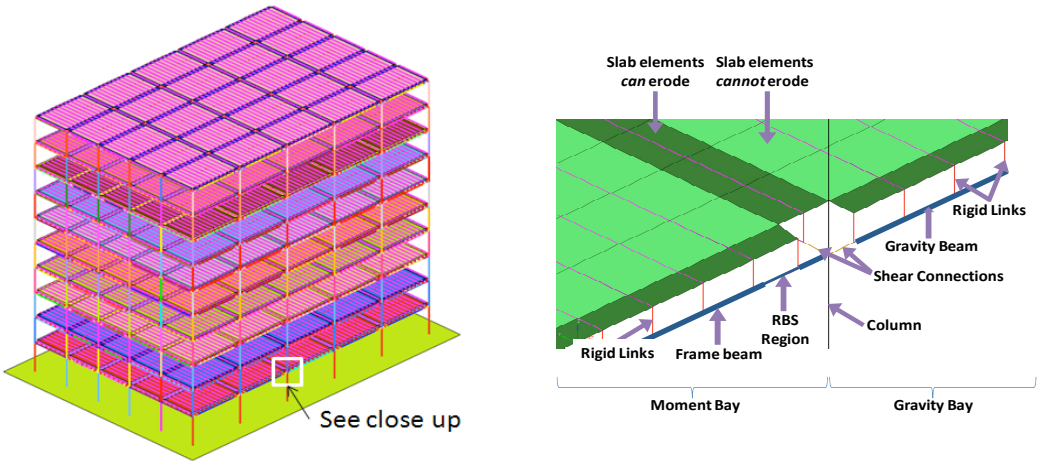
model that can accommodate different tensile and compressive yield responses is used to model the RC slab. Since the steel deck can only develop resistance along the directions of the flutes, its effect is represented using steel bars attached directly to the shell elements. The area of the equivalent steel bars is taken to be 50% of the area of the steel deck based on calibration to Alashker and El-Tawil (2010). To preserve the mass of the slab as it collapses, only peripheral elements are permitted to be deleted while all other slab elements are not allowed to be eliminated. The composite slabs are connected to the steel beams through rigid links to model the composite effect. The model is therefore not purely a macro or micro model, but rather a hybrid, although it is referred to herein as a macro model because of the predominant effect of the macro-elements on collapse response. The total number of the elements used in this model is 63,600. Figure 2-a, shows an overview of the model, while Figure 2-b shows a close up of the shear connections and moment resisting connections. The shear tab is modeled by a single beam element, which has integration points that correspond to the local of individual bolts, as specified in Khandelwal and El-Tawil (2007).

The planar model is essentially a subset of the 3-D model and is a representation of the frame on axis 6 or axis E depending on the column in question. The planar model is extracted from the 3-D model by deleting all but the pertinent elements associated with the pertinent frame. The gravity load from the floor system acting on the frame is computed using the tributary area associated with the frame. To assure that the frame behaves in a reasonable manner, the top flanges of the beams are prevented from moving out of plane to model the stabilizing influence of the slabs.

The 3-D model runs for only 15 minutes to simulate 6-seconds of real time on an AMD Opteron 2435 cluster with 12 CPUs and 24 GB of RAM. The high speed of the model is primarily due to the careful sizing of elements to ensure that they yield as large a time step as possible without compromising accuracy. Since the solution scheme is explicit, the solution time is linked to element characteristics, specifically element size and density.

The proposed models are validated through comparisons to disparate experimental data and the results of more refined models. More details about the material models and validation studies can be found in Alashker et al (2010).

The models employed in this study are designated M2 for the 3-D models and M4 for the planar model. The naming scheme used is selected to match that employed by Alashker et al. (2011). In this paper, simulations were conduct using model M2, but without the slab. The modified M2 model is designated M2-NS (where NS stands for no slab). In M2-NS, it is necessary to keep a small set of peripheral slab elements in each panel in order to maintain the stability of the beams, which tend to undergo lateral torsional buckling when they are left completely unsupported. The slab elements employed in M2-NS are deemed to contribute minimally to the overall structural resistance attributed to the slab system, a fact that was confirmed through sensitivity studies involving subassemblages.



(a) Full 3-D macro-model **(b) Close up of connection region**

Figure 2. Details of the 3-D macro-model (model M2)

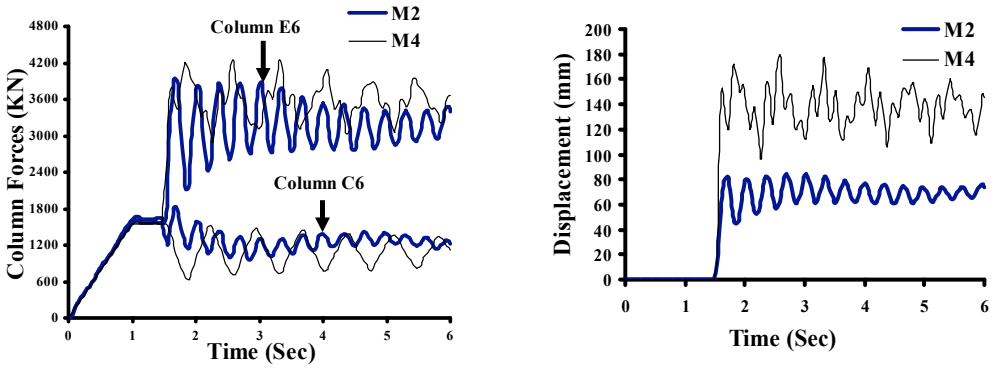
SIMULATION SETUP

The Alternate Path Method (APM) is used to study collapse potential. Gravity loads (i.e. dead load plus 25% of the live loads) are applied gradually within 1 second, followed by a wait period of 0.5 seconds, in order to eliminate dynamic effects. After that, a key element, such as a column is forcibly removed by deleting it instantaneously. It was been shown in Alashker et al (2010) that the proposed loading period is able to yield a reasonable compromise between computational time of the model and prevention of unwanted dynamic effects. The structural system's response to the new boundary conditions is then investigated.

THE COMPARISON BETWEEN RESPONSES OF PLANAR AND 3-D MODELS SUBJECTED TO LOSS OF COLUMNS

A series of nonlinear dynamic analysis are performed with the proposed models. Three first floor column loss cases, which are removal of column at D6, removal of columns D6 and E6 simultaneously and removal of column E5 are carried out and the responses of the planar and 3-D models are compared.

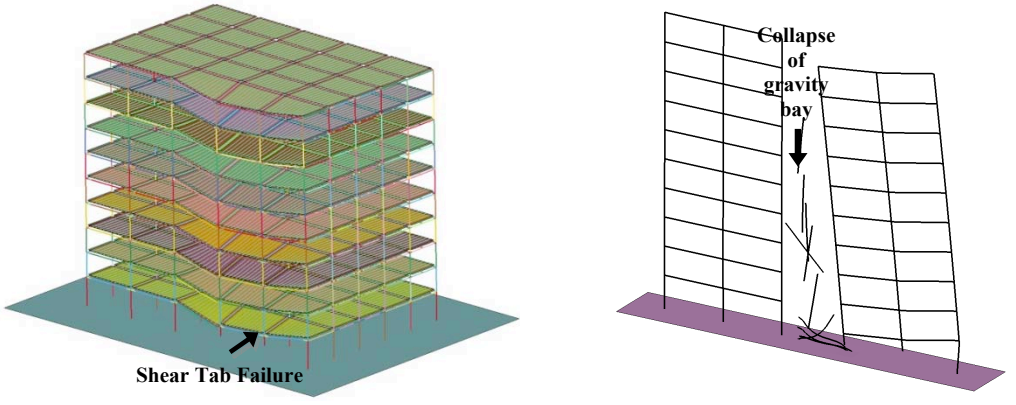
Figure 3 shows a comparison of system responses of M2 and M4 (representing the frame on axis 6) after sudden loss of the exterior column at D6. Cleary, there are substantial differences between the responses of the two models, which are attributed to the slab and other 3-D effects captured by M2 but not M4. These effects appear to play a key role in reducing the overall deflections and promoting load redistribution. For example, the vertical deflection of the node corresponding to the top of the removed column reduces from 128.6 mm in the planar model to 68.3 mm in the 3-D, a 47% reduction. The compressive force in Column C6 is less affected by column removal, losing only 70 kN in M2 versus 479 kN in M4, which highlights again the role of 3-D effects in promoting load redistribution.



(a) Column axial forces **(b) Vertical displacement**

Figure 3. Comparison between the responses of models M2 and M4

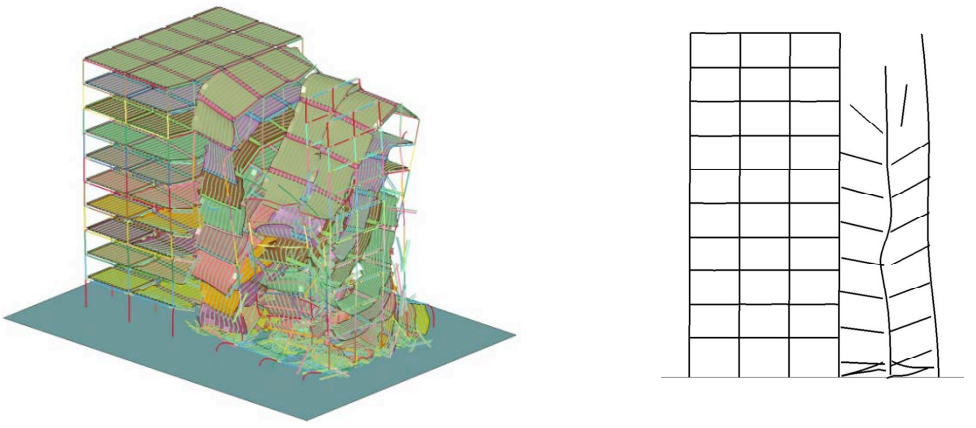
Great differences can be seen between M2 and M4 (representing the frame on axis 6) when exterior columns D6 and E6 are simultaneously removed. As shown in Figure 4, model M4 predicts failure of the system, while M2 shows a controlled response in spite of failure of one of the shear tab connections in bay CD at the first floor. Like the response of M2, failure in M4 initiated at the shear tab connection in bay CD, adjacent to column D6, at the first floor. However, unlike what was captured by M2, shear tab connection failures propagated rapidly upwards all the way to the top floor. At that point, the moment frame spanning columns D6-E6-F6 became unbalanced because it was effectively supported on only one intact column, i.e. F6, and the frame collapsed.



(a) 3-D model response (displacement magnification factor=5) **(b) 2-D model response (displacement magnification factor=1)**

Figure 4. Responses of M2 and M4 subjected to loss of columns D6 and E6 simultaneously

The comparison between the responses captured by M2 and M4 (representing the frame on axis E) after column E5 is removed is shown in Figure 5. It can be seen that system failure occurs in both of the models. In M4, after removal of the column, the shear connections joining the gravity beams to the columns in bays 4-5 and 5-6 failed rapidly and the failures propagated up to the top floor, which induced collapse of these two bays. However, the other three bays remained undamaged. In contrast, widespread collapse occurred in M2. The failures initiates in the slab panels adjacent to the removed column and radiated upwards and outwards to adversely influence the rest of the structure.



(a) 3-D model response **(b) 2-D model response**

Figure 5. Responses of M2 and M4 subjected to loss of columns E5

The 3-D models are considered more realistic than the planar models in that they can capture the effects of the slab and its interaction with the other frame members. The column loss cases discussed above show that there are distinct differences between the results of the planar and 3-D models. When failure is not imminent, e.g. as shown in the case when column D6 is removed, it appears that the slab reduces the deformations that occur and leads to a reduction in the forces that are redistributed to adjacent columns. This can be clearly seen in Figure 3(a), where column E6 in M4 sees a larger increase in load than in M2, whereas Column C6 sees a larger decrease in M4 than in M2. In other words, the slab collaborates with the moment frames to temper the force redistribution that happens when members are removed.

When failure is predicted by model M4, it is not possible to say whether the vulnerability of the structure is overestimated or underestimated. In the studies presented herein, M4 predicted failure when columns D6 and E6 were simultaneously removed, whereas M2 showed that the failure was arrested and did not propagate. On the other hand, when column E5 was removed, M4 predicted failure of the 2 adjacent bays only, whereas M2 showed much more widespread failure. Therefore it is not possible to state with certainty that 2-D models are generally conservative.

EFFECT OF THE SLAB

The previous discussions show that there are substantial differences between the response of planar and 3-D models. It is hypothesized that the slabs are the source of this difference, however that cannot be clearly discerned from the simulations conducted. To clarify the role of the slab in 3-D response, comparisons are made between models M2 and M2-NS. Tables 1 and 2 illustrate these comparisons. Table 1 lists all cases in which collapse is mitigated in the 3-D models. In it, the steady state displacements of the node corresponding to the top of the removed column, computed from both various models, are compared. Table 2 presents cases in which collapse could not be arrested in 3-D models and describes how the models responded during collapse.

An examination of Table 1 shows that the deformations captured by M2-NS are always larger than those captured by M2 and, in fact, are very close to those captured by M4. The only exception is when column E4 is removed, which leads to collapse in M4 (representing the frame on axis E), but not in M2 or M2-NS. However, the displacement in N2-NS reaches 196 mm, which is 3 times the value in M2. Clearly, the slab is exerting much 3-D influence. However, there appear to be other significant sources of 3-D resistance, e.g. coming from out-of-plane structural members, which helped arrest collapse in M2-NS when column E4 was eliminated.

Table 2 reveals that the existence of the slabs is not always beneficial. In cases where D5 or E5 are individually removed, full progressive structural collapse occurs in M2, but not M2-NS, which suffers only partial collapse around the eliminated column. Clearly, the presence of the slab helped promote progressive collapse in these cases. In contrast, when D6/E6 are removed simultaneously, partial collapse also occurs in M2-NS, but collapse is mitigated in M2.

Table 1. Comparison between the responses of the 3D models with and without slabs: progressive collapse is prevented

Column-loss case	Deformation after column loss (steady state)		
	Model M2 (mm)	Model M2-NS (mm)	Model M4 (mm)
D6	69.3	108.1	109.0
E6	26.4	32.1	33.3
F6	45.7	51.8	53.3
E4	65.5	196.1	collapse

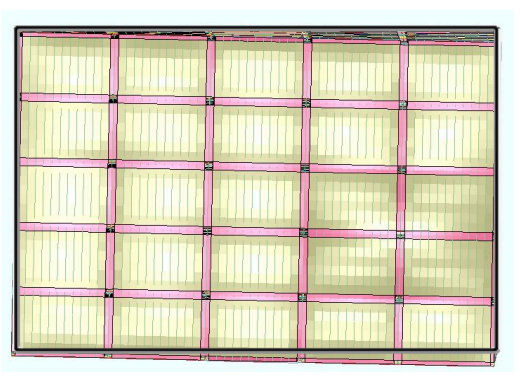
Table 2. Comparison between the responses of the 3D models with and without slabs: progressive collapse occurs

Column-loss case	Response of the model	
	Model M2	Model M2-NS
D5	Full structure collapse	Partial collapse
E5	Full structure collapse	Partial collapse
D6/E6	Collapse mitigated	Partial collapse

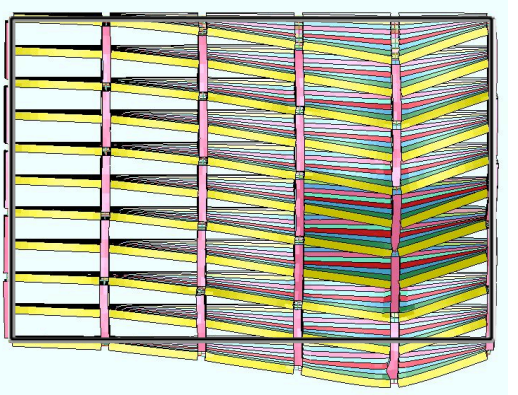
The simulation results shed light on the complex role of the slab in resisting collapse. The results show that when a column in a moment bay is lost and the structure does not collapse, the moment bay containing the removed column will lean towards the location of the removed column. The moment bay will therefore push or pull on adjacent bays in the plane containing the affected moment bay causing the entire frame to also lean in that direction. This effect is equivalent to apply an additional lateral force on to the frame, which results in force redistribution in the columns in the moment. In addition, since the slabs are so stiff in plane, they tend to maintain their rectangular shape, which can lead to global torsional effects.

Figure 6 shows the comparison between the top views of the deformed shape of the models with and without the slabs after loss of E4. The dark lines indicate the outline of the undamaged structure. The global torsional effect is evident in Figure 6(a) and it is clear that the slabs force other moment bays in the system to be mobilized to resist collapse, e.g. the frame on axis F. It can also be seen that the greatest lateral displacement demands may not occur in the frame containing the removed column. In this particular case, the frame on axis F experiences the largest lateral displacement leading to substantial force redistribution in that frame. For example, after loss of E4, the steady state axial force in F5 increases from 1470 kN to 1980 kN, whereas the force in F3 decreases from 1470 kN to 935 kN.

Figure 6(b) shows that for model M2-NS, the frame containing E4 suffers the greatest lateral deformation. Other frames are also being mobilized, but force redistribution in surrounding frames is not as severe as when the slab is present because the other three frames containing moment bays in N-S direction hardly deform laterally. Also evident from a comparison between Figures 6(a) and 6(b) is that a much larger lateral displacement occurs in the frame on axis E in M2 versus M2-NS, which clearly demonstrates the effective role of the slab in this situation.



(a) Deformed shape of M2 (displacement magnification factor=20)



(b) Deformed shape M2-NS (displacement magnification factor=20)

Figure 6. Comparisons of top views of M2 and M2-NS subjected to loss of E4

CONCLUSION

In this paper, planar and 3-D validated models representing the same structure are used to investigate the influence of three dimensional effects on the responses of the structure under column-loss scenarios. Three different models were employed, M2 which is a 3-D model that accounts for the slab, M4, which is derived from M2 but only represent a frame along a single axis, and M2-NS, which is similar to M2, but does not account for the presence of the slab. From the limited simulations presented herein, the following main conclusions can be drawn: (1) 3-D effects are significant and play an important role in determining the response of the structure subjected to sudden column loss; (2) When failure is not imminent, 2-D models can represent the structure reasonably, although they are conservative. However, when failure is predicted, 2-D models may underestimate or overestimate the vulnerability of the structure; and (3) Slabs contributes significantly to reducing the overall deflection of the structure when columns are removed suddenly. The slabs can also help to enhance the integrity of the structure and redistribute the loads when moment columns are removed. However, slabs also lead to more widespread failure if the collapse process is not arrested early on.

REFERENCES

[1] Alashker, Y., Li, H. and El-Tawil, S. (2011), "Approximations in Progressive Collapse Modeling," Submitted to the ASCE Journal of Structural Engineering.

[2] Hallquist, J. (2006), LS-DYNA Keyword User's *Manual, Livermore Software Technology Corporation,* Livermore, CA, Version 971.

[3] Kaewkulchai, G. and Williamson, E. (2003) "Dynamic behavior of planar frames during progressive collapse" *Proceedings of 16th engineering mechanics conference,* 2003.

[4] Khandelwal, K., and El-Tawil, S. (2007) "Collapse behavior of steel special moment resisting frame connections" *Journal of Structural Engineering*, 133(5), 646-655.

[5] Khandelwal, K., El-Tawil, S., Kunnath, S. K., and Lew, H. S. (2008). "Macro-model based simulations of progressive collapse steel frame structures" *Journal of Structural Engineering*, 134(7), 1070-1078.

[6] Bao, Y., Kunnath, S. K., El-Tawil, S., and Lew, H. S. (2008) "Macro-model based simulation of progressive collapse: RC frame structures," *Journal of Structural Engineering*, ASCE, 134(7), 1079-1091.

[7] Kim, J., and Km, T. (2009) "Assessment of progressive collapse-resisting capacity of steel moment frames" *Journal of Constructional Steel Research*, 65(1), 169-179.

[8] Khandelwal, K., El-Tawil, S., and Sadek, F. (2009). "Progressive collapse analysis of seismically designed steel braced frames" *Journal of Constructional Steel Research*, 65(3), 699-708.

[9] Liang, X., Shen, Q., and Ghosh, S. K. (2006) "Assessing ability of seismic structural system to withstand progressive collapse: seismic design and

progressive collapse analysis of steel frame buildings." *Rep. Prepared for SK Ghosh and Associates,* Palatine, Ill.

[10] American Institute of Steel Construction (2005) *Steel Construction Manual*, 13th ed, Chicago.

[11] U.S. General Service Administration (GSA) (2003). *Progressive collapse analysis and design guidelines for new federal office building and major modernization project",* Washington, D.C.

[12] UFC (2009), "*UFC 4-023-03: Design of Buildings to Resist Progressive Collapse*," Department of Defense, Washington, DC

[13] Ruth, P., Marchand, K. A., and Williamson, E. B. (2006) "Static equivalency in progressive collapse alternate path analysis: reducing conservatism while retaining structural integrity," *Journal of Performance of Constructed Facilities*, 20(4), 349-364.

[14] Sasani, M., and Kropelnicki, J. (2008) "Progressive collapse analysis of an RC structure," *Structural Design of Tall and Special Buildings*, 17(4), 757-771.

[15] Szyniszewski, S. (2009) "Probabilistic approach to progressive collapse prevention. Physics based simulations," *The Structures Congress,* 2009.

[16] Mohamed, O. A. (2009) "Assessment of progressive collapse potential in corner floor panels of reinforced concrete buildings," *Engineering Structures*, 31(3), 749-757.

[17] Main, J. A. (2009) " Development of 3D models of steel moment-frame buildings for assessment of robustness and progressive collapse vulnerability," *The Structures Congress,* 2009.

[18] Fu, F. (2009) "Progressive Collapse Analysis of High-rise Building with 3-D Finite Element Modeling Method," *Journal of Constructional Steel Research*, 65(5), 1269-1278.

[19] Fu, F. (2010) "3-D Nonlinear dynamic progressive collapse analysis of multi-storey steel composite frame buildings- parametric study," *Engineering Structures*, 32(12), 3974-3980.

[20] Kwasniewski, L. (2010) "Nonlinear dynamic simulations of progressive collapse for a multistory building," *Engineering Structures*, 32(5), 1223-1235.

[21] Galal, K. and El-Sawy, T. (2010) "Effect of retrofit strategies on mitigating progressive collapse of steel frame structures," *Journal of Constructional Steel Research*, 66(4), 520-531.

[22] Masoero, E., Wittel, F. K., Herrmann, H. J., and Chiaia, B. M. (2010) "Progressive Collapse Mechanisms of Brittle and Ductile Framed Structures," *Journal of Engineering Mechanics*, 136(8), 987-995.

Alternate Path Progressive Collapse Analysis of Steel Stud Bearing Wall Structures

Nabil A. Rahman[1], Ayman Elfouly[2], Michael Booth[3]

[1*] POC. The Steel Network, Inc., Durham, NC 27709; PH (919) 845-1025; FAX (919) 845-1028; email: nabil@steelnetwork.com
[2] Applied Science International, Durham, NC 27709; PH (919) 645-4090; FAX (919) 645-4085; email: elfouly@appliedscienceint.com
[3] The Steel Network, Inc., Durham, NC 27709; PH (919) 845-1025; FAX (919) 845-1028; email: mbooth@steelnetwork.com

ABSTRACT

The Alternate Path Method is used to examine the vulnerability of a 5-story barracks building to progressive collapse based on DoD criteria UFC-4-023-03. The building is composed of composite deck floor system and steel roof trusses, all supported by cold-formed steel stud load bearing walls. Two different wall section removal scenarios at the first story of the building were considered for the analysis. The analysis was performed using the "Extreme Loading® for Structures" software, a 3-dimensional nonlinear dynamic analysis software.

The results show the ability of the composite deck floor slabs to bridge over the removed wall sections. The slabs were able to re-distribute the gravity loads to adjacent wall components, while some of the loads were picked up in tension by the stud walls above the slabs. The study provides a good understanding of the composite deck floor-cold-formed steel stud bearing walls building system in resisting progressive collapse.

INTRODUCTION

In 2001, the Department of Defense (DoD) started to publish design guidelines for structures to resist progressive collapse resulting from an extreme loading event. The design guidelines are given in the Unified Facilities Criteria UFC 4-023-03 "Design of Buildings to Resist Progressive Collapse" (UFC, 2009). This document provides the design requirements necessary to reduce the potential of progressive collapse for new and existing DoD facilities. Since then, engineers are on the lookout for design guides that explain the implementation of DoD guidelines in conventional and new construction systems. This paper provides some guidance for implementing the DoD progressive collapse criteria in buildings constructed with cold-formed steel stud bearing wall systems.

Cold-formed steel load bearing wall systems

The use of cold-formed steel (CFS) load bearing framing in typical mid-rise construction (three to eight stories in height) brings the value of reducing associated construction cost in comparison to other structural framing systems such as reinforced masonry, structural steel and wood. A key component of the cost savings is the lighter mass of the structure, which is the key element to the design of the lateral force resisting system (shear walls) and the foundation. CFS load bearing stud walls must be braced laterally at intermediate points to restrain the studs against lateral and torsional buckling. X-brace flat straps are commonly used in this type of construction to provide the building resistance to lateral wind and seismic forces. The X-brace system provides pre-determined load path for the lateral shear forces, and therefore requires vertical stacking of the shear walls to ensure the load transfer from all floors down to the foundation. The design of cold-formed steel framing in the US is governed by the specification published by the American Iron and Steel Institute (AISI, 2007).

It is important to note that several types of floor systems can be integrated with CFS load bearing walls. Among these types are composite steel deck-concrete slabs (composite deck), CFS joists or open bar joists with a concrete or wood floor diaphragm, and precast hollowcore concrete planks. The composite deck combines the structural advantage of a flat slab with the time saving advantage of a permanent form. The steel deck furnishes the total bottom reinforcement of the composite slab, while additional top reinforcement is required. Due to the composite action between the concrete and the steel deck, the slab can support a greater floor live load compared to a typical reinforced concrete slab of the same depth. More information about CFS load bearing wall systems are given by Rahman (2006, 2007).

DoD progressive collapse design criteria

Unified Facilities Criteria 4-010-01 (UFC, 2007) requires that all new and existing military facilities of three stories or higher be designed to avoid progressive collapse. UFC 4-023-03 (UFC, 2009) offers two general design approaches to reduce the possibility of progressive collapse; Direct Design approach and Indirect Design approach. The Direct Design approach includes the “Alternate Path” method, which is based on flexural performance of the floor system, as the building must bridge across removed vertical supporting elements. The Indirect Design approach includes the “Tie Forces” method, which is based on the catenary (membrane tension) response of the structure, and is used to enhance continuity, ductility and structural redundancy of the building. The level of progressive collapse design and the selection of the design approach and method are based on the Occupancy Category (OC) of the building. This OC is specified in UFC 3-310-01 (UFC, 2005), but also allowed to be specified by the building owner. Engineers dealing with buildings with OC II have the option of using the Alternate Path Method or the Tie Forces Method for the progressive collapse analysis. However, design for buildings with OC III and above must include the Alternate Path Method for the analysis.

The Alternate Path Method follows the LRFD philosophy with load combination for extraordinary events and resistance factors to define design strengths. Three analysis procedures can be used; linear static, nonlinear static and nonlinear dynamic. The estimate of design strength varies depending on the classification of the action; either deformation-controlled or force-controlled action. The nonlinear dynamic analysis selected for this study requires the creation of a three-dimensional model for the primary framing members of the building. Inclusion of secondary framing members in the model is optional, but they must be checked with the results of the analysis if omitted. To perform the analysis, gravity loads and notional lateral loads are to be applied to the model until equilibrium is reached. Then, specified vertical load bearing components (columns or walls) shall be removed from the model and analysis shall continue until maximum displacement of slab is reached, or one cycle of vibration occurs at the location of the removed component. The acceptance criteria are dependent on the structural material. In this study, axial forces are checked as force-controlled action in CFS studs, and displacement is checked as deformation-controlled action in composite deck slab.

Applied Element Method for collapse analysis of structures

The Applied Element Method (AEM) is a nonlinear dynamic analysis method that is capable of predicting, to a high degree of accuracy, the continuum and discrete behavior of structures. The method is proved to track the structural collapse behavior passing through the stages of crack initiation and propagation in tension-weak material, yielding and formation of plastic hinges in ductile material, element separation, element re-contact, and collision with the ground or with adjacent structural components. In the AEM, a structure is modeled as an assembly of small elements. The two elements shown in Figure 1 are assumed to be connected by series of normal and shear springs located at contact points, which are distributed around the element edges. Normal and shear springs totally represent stresses and deformations of the elements. Steel bars in reinforced concrete components are modeled using continuous springs connecting elements together.

Each applied element has six degrees of freedom. These degrees of freedom represent the rigid body motion of the element. Although the element motion is as a rigid body, its internal deformations are represented by its springs' deformation. The global stiffness matrix is determined by summing up the stiffness matrices of springs around each element. Consequently, the developed stiffness matrix has total effects from all of the springs according to the stress status around the element. This technique can be used in both load and displacement control cases, and static and dynamic loads. For more details about the AEM, refer to publications by Meguro and Tagel-Din (2001 and 2002). The AEM is implemented in the Extreme Loading® for Structures (ELS) software (ASI, 2009), which is used to run the analysis in the current study.

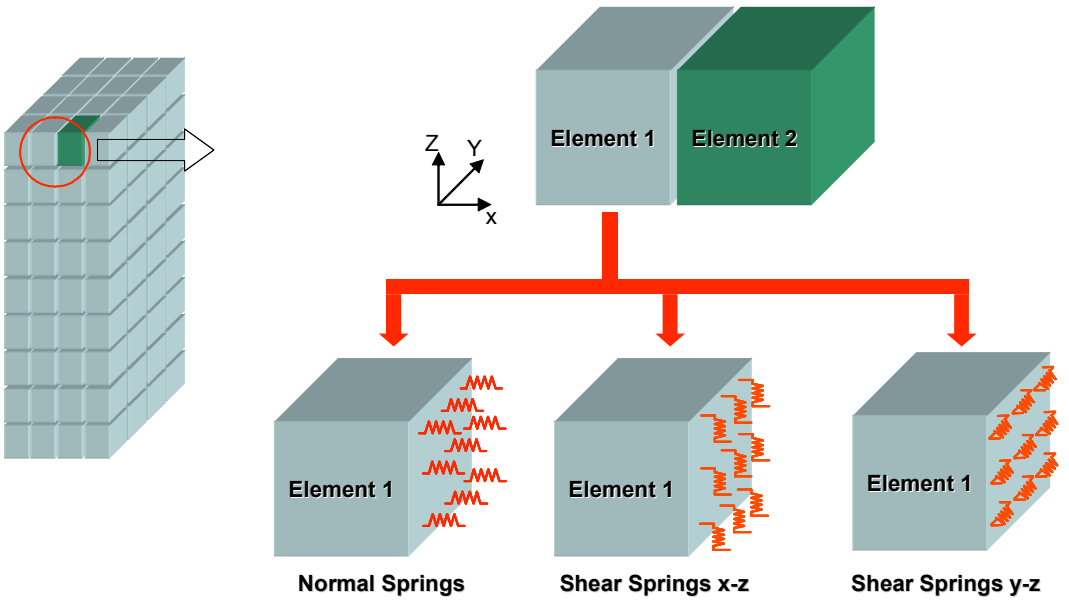


Figure 1. Connectivity springs in the Applied Element Method

BARRACKS BUILDING CASE STUDY

Building Description. Figure 2 shows the elevation, plan view and overall dimensions of the barracks building. The building is a 5-story structure composed of two wing areas and a core area with a typical slab-to-slab height of 3048 mm (120 inch) and first story height of 3200 mm (126 inch). The core area is constructed from structural steel framing, while cold-formed steel stud walls are used in the wing areas as the supporting structure for the gravity loads from the floor slabs and the roof. In the wing areas, the exterior walls on the short side of the building and every separation wall are gravity load bearing walls as shown in Figure 3. The figure also shows the locations of the X-brace strap system, with cold-formed steel stud boundary members, which is used as shear walls to resist lateral loads. The light weight roof trusses are supported on the corridor walls and the exterior walls of the long side of the building. Table 1 shows the schedule of the studs and top and bottom tracks of the main load bearing walls in standard nomenclature. The studs are distributed on typical 406 mm (16 inch) spacing, with weak axis bracing at mid-height. Table 2 shows the schedule of the X-brace shear walls in the longitudinal (east-west) and transverse (north-south) directions. All cold-formed steel (CFS) sections with nomenclature "S" and "T" have 228 MPa (33 ksi) yield strength, and all CFS sections with nomenclature "SG" and "C" have 345 MPa (50 ksi) yield strength. The diagonal straps also have 345 MPa (50 ksi) yield strength.

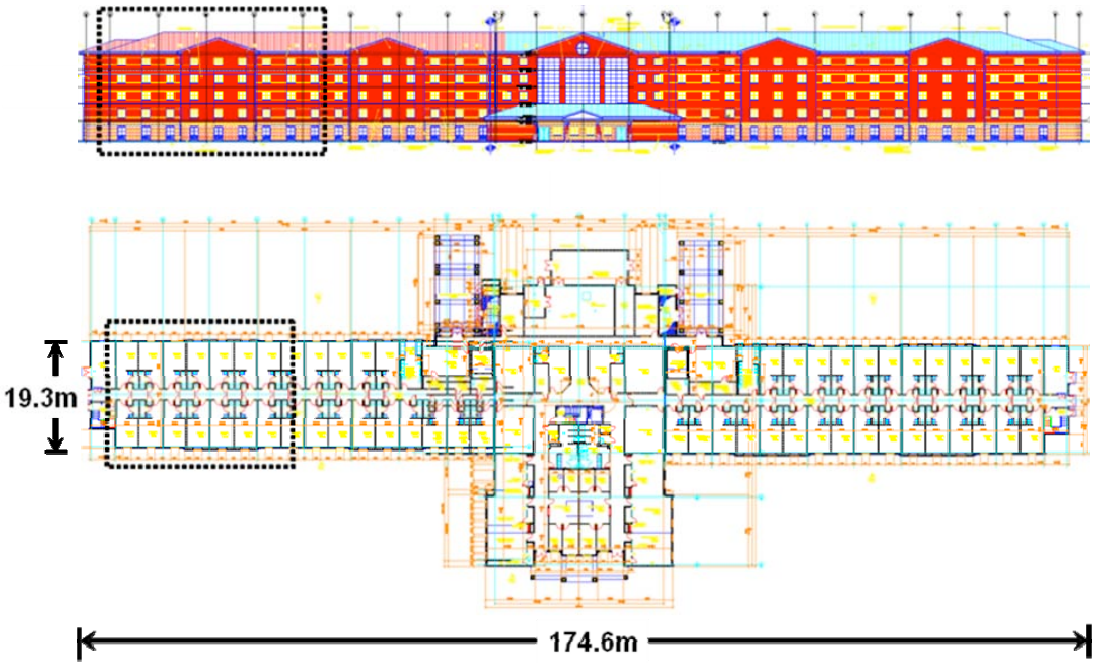


Figure 2. Layout of the barracks building

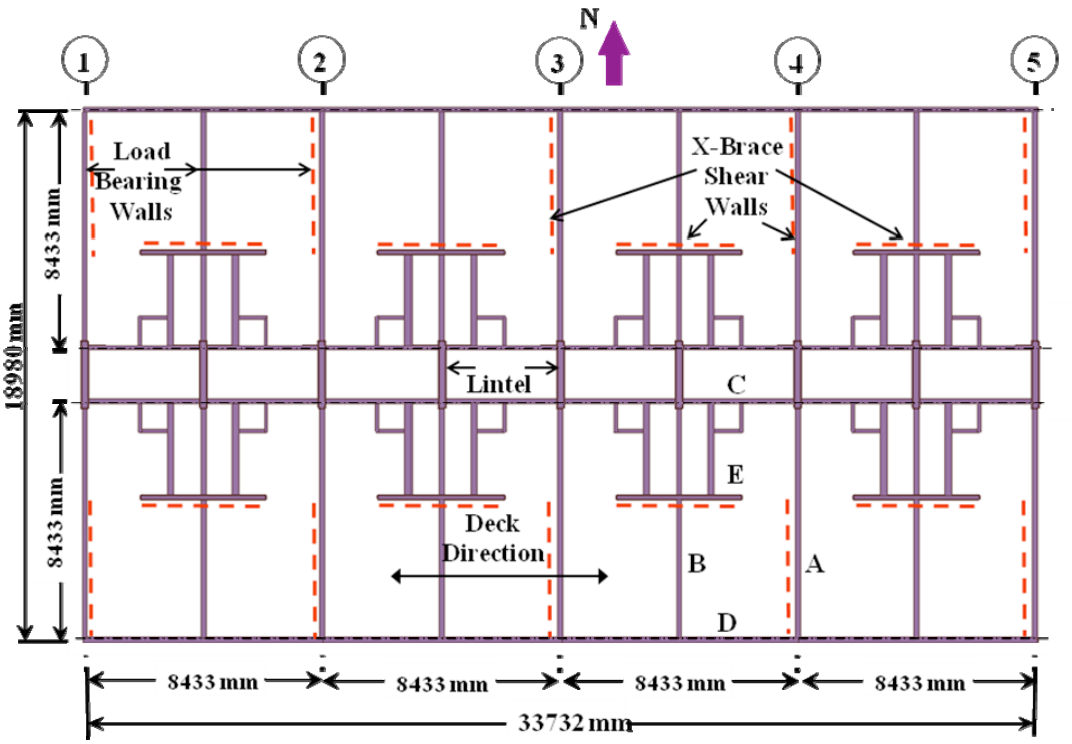


Figure 3. Cold-formed steel framing for wing areas

Table 1. Schedule of load bearing walls (standard nomenclature)

Story	Wall A & B		Wall C	
	Studs	Tracks	Studs	Tracks
5	600S162-43	600T200-43	600S162-43	Built-up section
4	600S162-43	600T200-43	600SG200-43	600T200-43
3	600SG300-43	600T200-43	600SG200-43	600T200-43
2	600SG300-43	600T200-43	600SG200-43	600T200-43
1	600SG300-54	600T200-54	600SG200-43	600T200-54

Story	Wall D		Wall E	
	Studs	Tracks	Studs	Tracks
5	600SG162-43	Built-up section	600S162-33	600T125-43
4	600SG162-43	600T200-43	600S162-33	600T125-43
3	600SG162-43	600T200-43	600S162-33	600T125-43
2	600SG162-43	600T200-43	600S162-33	600T125-43
1	600SG162-43	600T200-43	600S162-33	600T125-43

Table 2. Schedule of X-brace shear walls (standard nomenclature)

Story	Longitudinal Direction (E-W)		Transverse Direction (N-S)	
	Boundary Members	Diagonal Straps	Boundary Members	Diagonal Straps
5	600C250-43	(2) 400-54	600C250-43	(2) 400-54
4	600C250-68	(2) 600-54	600C250-54	(2) 400-54
3	600C250-118	(2) 800-54	600C250-97	(2) 600-54
2	(2)600C250-97	(2) 800-68	(2)600C250-68	(2) 800-54
1	(2)600C250-118	(2) 800-68	(2)600C250-97	(2) 800-54

The floor slab is a composite deck system supported every 4216 mm on separation walls with 50 mm (2 inch) deep, 0.9 mm (30 mil, 20 ga) thick corrugated steel sheet and 100 mm (4 inch) concrete on top of the corrugated sheet. The slab reinforcement includes welded wire mesh 152x152 MW13.3/13.3 (6x6 W2.1/2.1) on top of the deck, and top reinforcement of 16 mm diameter (#5) bars at 150 mm (6 inch) spacing in both directions. The top reinforcement is used as part of a special design requirement for the floor slabs to resist an upward blast pressure specified in a previous version of the UFC 4-023-03. Figure 4 shows the actual cross-section of the composite deck, and the simplified cross-section used in the current numerical analysis model. In the analysis model, the composite deck was simplified into a 150 mm (6 inch) thick concrete slab with a reduced unit weight of the concrete to account for the void space created by the corrugated deck. In addition, the corrugated steel sheet was modeled as an equivalent area of rebar and spacing in the longitudinal direction only, located at the centroid of the deck profile as shown in the figure.

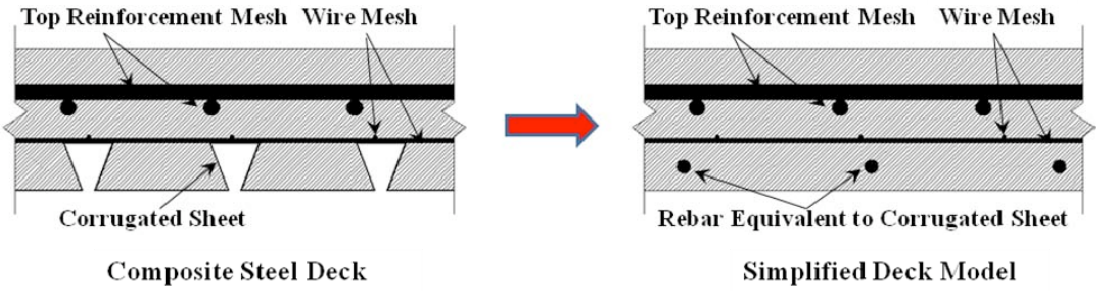


Figure 4. Cross-section of composite steel deck and the simplified model

The connection between the composite deck floor slabs and both the top track of the load bearing walls below and the bottom track of the load bearing walls above uses 4 mm (0.157 inch) diameter powder actuated fasteners. Four fasteners are used at each stud location and one fastener between studs. The steel studs are welded to the top track and the bottom track of the walls at both side of each stud.

Analysis Model. The three-dimensional model of the barracks building was created using the graphical interface and section database of the Extreme Loading® for Structures (ELS) software, Version 3.1. One part of the building, as outlined in Figure 2, and only the first four stories of the building have been considered in the model. This was decided to make the modeling time and analysis time of the building practical. The weight of the fifth story walls was uniformly distributed and added to the weight of the slab below. The weight of the roof trusses was added as line load to the locations of its supporting corridor walls and exterior walls of the long side of the building. Figure 5 shows the three-dimensional model for the part of the building used in the analysis.

All window and door openings on the exterior and the interior of the building were modeled with their appropriate dimensions and framing members. Full connections were used between these framing members attached together, and that between wall studs and their top and bottom tracks. The diagonal straps of the X-brace shear walls were modeled as long tension springs. Powder actuated fasteners for composite deck attachments were modeled as short tension and shear springs. The interface layer between the wall tracks and the composite deck was modeled as material with concrete compressive strength, but with very low shear and tension strengths. Table 3 gives the material properties and strength reduction factors for all components in the numerical model.

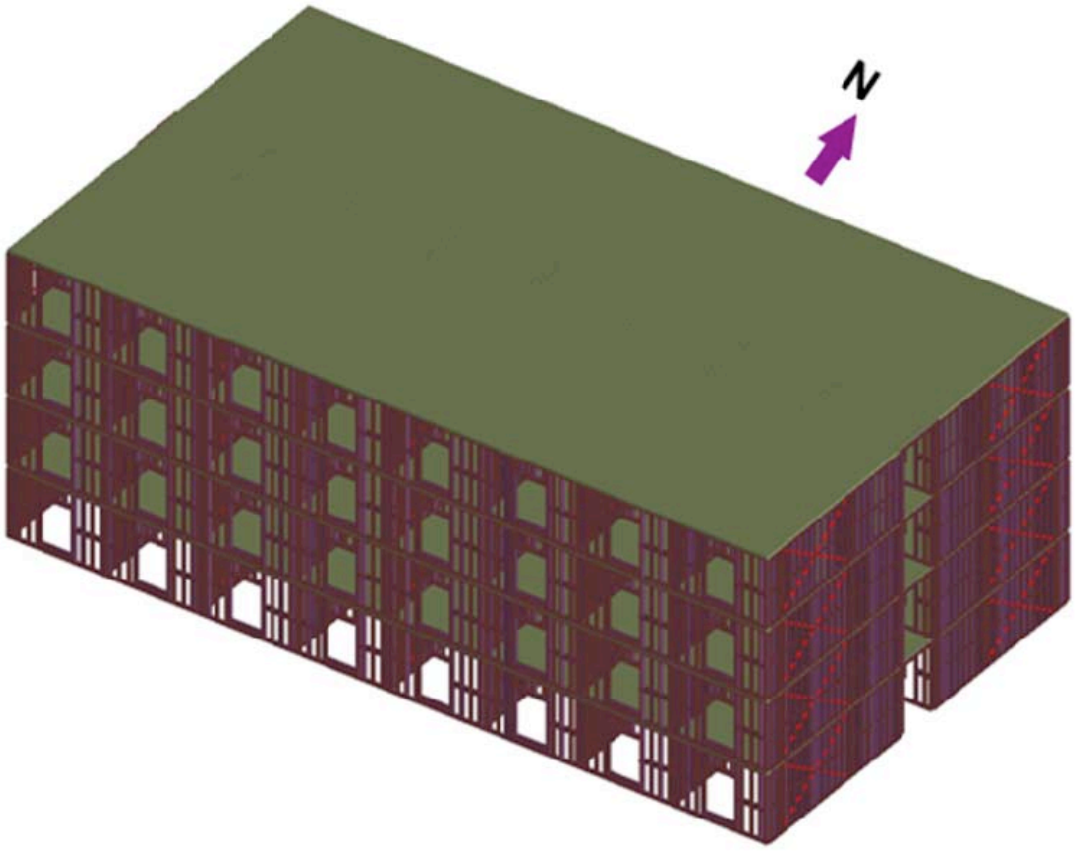


Figure 5. Three-dimensional model of the barracks building

Table 3. Lower bound material properties and strength reduction factors for components

Material	Min. Φ	Type	Young's Modulus (MPa)	Material Strength (MPa) or (kN)
Concrete (ACI 318-08)	0.90	Tension	26,000	$F_c = 27.6$ $F_t = 2.5$
	0.65	Compression and Bearing		
Reinforcement (ACI 318-08)	0.90	Wire mesh and Rebar	200,000	$F_y = 415$ $F_t = 620$
Cold-Formed Steel Framing (AISI S100-07)	0.90	Tension	200,000	$F_y = 228$ or 345 $F_t = 310$ or 450
	0.85	Compression		$F_y = 228$ or 345 $F_t = 310$ or 450
Steel Deck	0.85	Composite Concrete	200,000	$F_y = 275$ $F_t = 415$
Powder Actuated Fasteners	0.5	Deck/Track Connection	200,000	Tension = 4.3 kN Shear = 4.1 kN

Loading and wall removal. The load combination applied for the analysis was "1.2D + 0.5L", as recommend by UFC 4-023-03 for nonlinear dynamic analysis. The total load calculated for floor slabs was 6.3 kN/m^2 (132 psf) and for roof level was 3.7 kN/m^2 (78 psf). Two wall removal scenarios for the Alternate Path Method at the first story of the building were considered in this analysis. Scenario 1 was removal of an exterior wall section at the short side of the building equals to twice the first story height, or 6.4 m. Scenario 2 was removal of a corner wall section of the building equals to the first story height, or 3.2 m, in each direction. The two wall removal scenarios are illustrated in Figures 6 and 7.

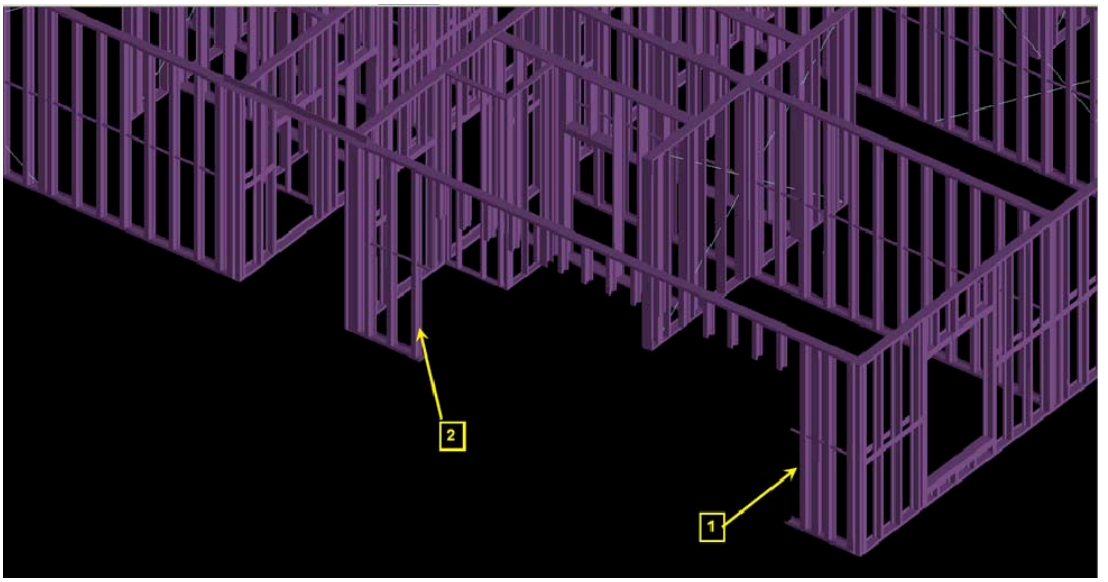


Figure 6. Removal of an exterior wall section of the building

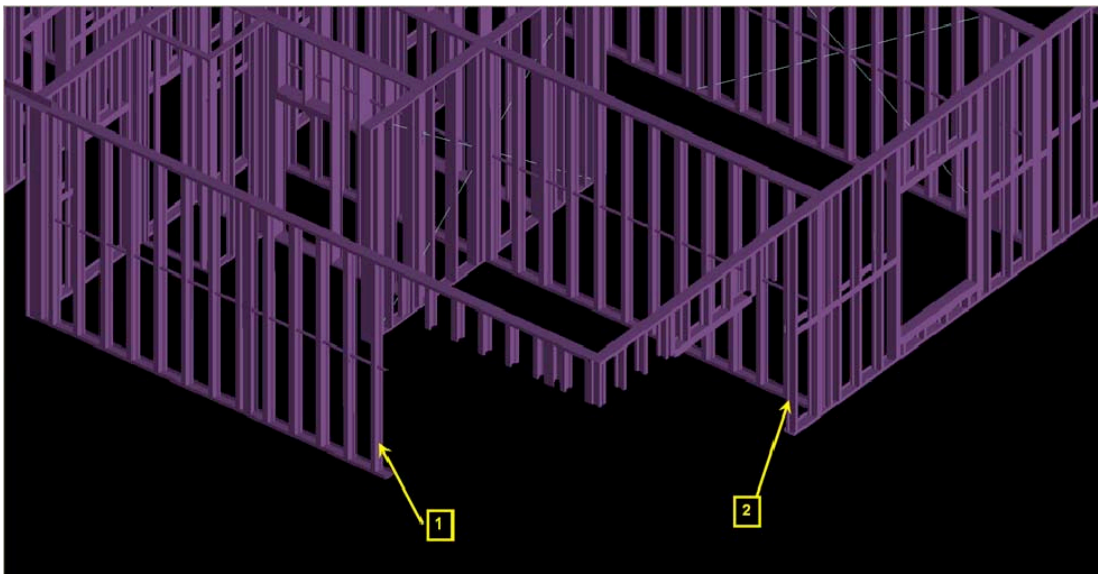


Figure 7. Removal of a corner wall section of the building

RESULTS AND DISCUSSION

There was no progressive collapse or component failure observed in the two wall removal scenarios analyzed in this study. Figure 8 show the deflection history for the floor slabs after wall removal in Scenario 1. Upon removal of the wall section in the model at this location, all the floor slabs started to deflect downward until reaching a maximum deflection of about 3 mm. The deflection stabilized for all floor slabs around an average value of 2.25 mm. Similar deflection behavior was observed for Scenario 2 wall removal with a maximum deflection of 3.5 mm. The limited deflection observed in both scenarios can be attributed to the ability of the composite deck floor slabs to distribute the load in both directions due to the existence of the relatively heavy top reinforcement mesh (16 mm bars every 150 mm). If the special upward blast pressure design requirement did not exist, the top reinforcement could be easily reduced while maintaining the integrity of the floor slabs for the progressive collapse design.

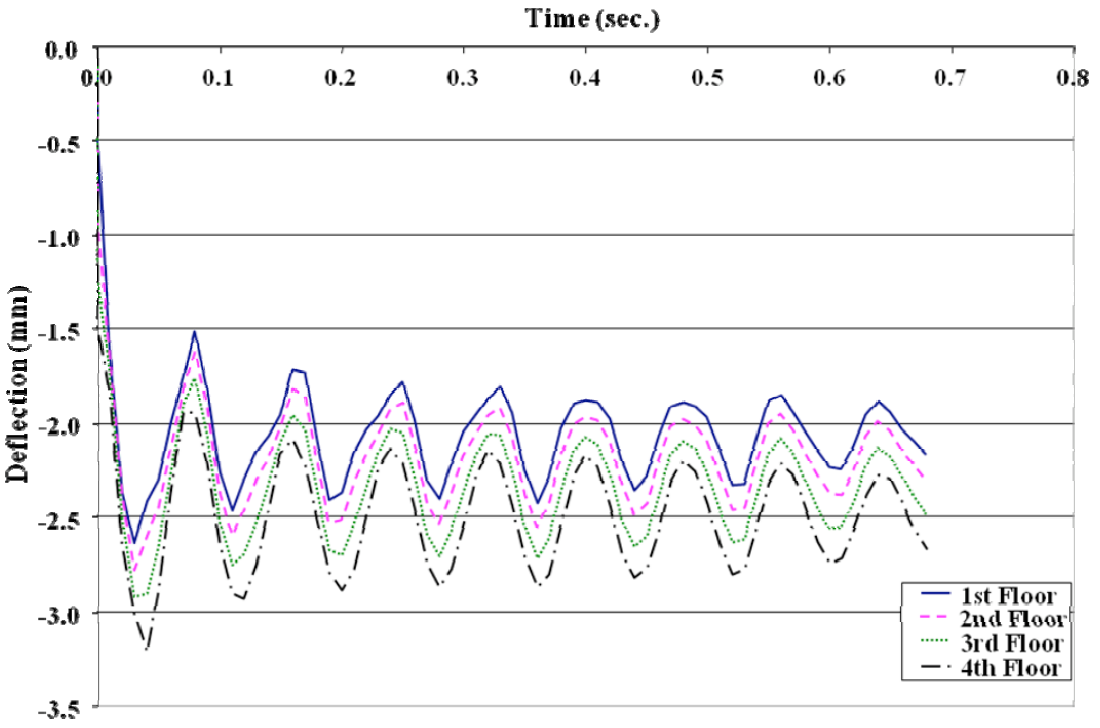


Figure 8. Deflection of floor slabs after wall removal in scenario 1

The axial forces in the adjacent studs to the removed wall sections were monitored before and after wall removal. Table 4 shows the cross sections of the numbered studs, the axial compression forces in the studs prior to wall removal, the sustained axial compression forces in the studs after wall removal, and the LRFD compression strengths of the studs calculated based on the AISI S100-07. It can be noticed that the loss of wall support of the first floor slab of the building caused the load acting on the wall to re-distribute through the slab to the nearest stud support.

The axial forces in the studs increased significantly, but still met the force-controlled acceptance criteria for compression members (ΦP_n) as shown in the table.

Table 4. Axial forces in adjacent studs for wall removals

Scenario and Stud Number	Stud Cross-section	Axial Force Before Wall Removal (kN)	Axial Force After Wall Removal (kN)	LRFD Compression, ΦP_n (kN)
Sc. 1- Stud 1	600SG300-54	8.5	33.7	88.8
Sc. 1- Stud 2	600SG300-54	5.4	24.5	88.8
Sc. 2- Stud 1	600SG300-54	16.5	49.8	88.8
Sc. 2- Stud 2	600SG162-43	5.9	20.2	27.8

The tension forces in the powder actuated fasteners connecting the composite deck floor slabs to the stud walls were also monitored. No failure was observed in these fasteners. The maximum tension force recorded after wall removal was about 0.3 kN, which is less than the acceptance criteria of the fasteners in tension. The tension strength of fasteners is controlled by the pullover strength of the steel sheet around the head of the fastener, ΦPnov, which is calculated as 0.5x4.3 = 2.15 kN.

CONCLUSION

The current study provides a good understanding of the composite deck floor-cold-formed steel stud bearing walls building system in resisting progressive collapse. The results of the study show that the Alternate Path Method coupled with the nonlinear dynamic analysis procedure can be efficiently used to examine the vulnerability of multi-story buildings to progressive collapse based on DoD criteria UFC-4-023-03. The Extreme Loading® for Structures (ELS) software, with its Applied Element Method, assisted in the application of the nonlinear dynamic analysis procedure. The study considered removal of an exterior wall section and a corner wall section at the first story of a 5-story barracks building. The results show the ability of the composite deck floor slabs to bridge over the removed wall sections at the first story of the building. The slabs were able to re-distribute the gravity loads to adjacent wall components, while some of the loads were picked up in tension by the studs above the slabs through the fasteners connecting the slabs to the walls. Although the axial compression forces in the studs adjacent to the removed wall sections increased significantly, the redundancy in the cold-formed steel wall system helped preventing overstressing these studs and exceeding the limit acceptance criteria for compression members.

REFERENCES

American Concrete Institute (ACI). (2008). "Building Code Requirements for Structural Concrete and Commentary." ACI 318-08, Farmington Hills, MI.

American Iron and Steel Institute (AISI). (2007). "North American Specification for the Design of Cold Formed Steel Structural Members." AISI S100-07, Washington, DC.

Applied Science International (ASI). (2009). "Extreme Loading for Structures® Software." Version 3.1, Applied Science International, Durham, NC, USA.

Meguro K. and Tagel-Din H. (2001). "Applied Element Simulation of RC Structures under Cyclic Loading" ASCE, 127(11), 1295-1305.

Meguro K. and Tagel-Din H. (2001). "Applied Element Method for Structural Analysis: Theory and Application for Linear Materials." Structural Eng./Earthquake Eng., International Journal of the Japan Society of Civil Engineers (JSCE), 17(1), 21-35.

Meguro K. and Tagel-Din H. (2002). "AEM Used for Large Displacement Structure Analysis." Journal of Natural Disaster Science, 24(2), 65-82.

Rahman, N., and Booth, M. (2006). "Innovative Mid Rise Construction– Steel Stud Walls with Hollow Core Plank Floor System." STRUCTURE, August 2006, 12-15.

Rahman, N., and Wan, D. (2007). "Innovative Mid Rise Construction– Steel Stud Walls with Hollow Core Plank Floor System- Revisited." STRUCTURE, July 2007, 16-17.

Unified Facilities Criteria (UFC). (2005). "Structural Load Data." UFC 3-310-01, Department of Defense, USA.

Unified Facilities Criteria (UFC). (2007). "DoD Minimum Antiterrorism Standards for Buildings." UFC 4-010-01, Department of Defense, USA.

Unified Facilities Criteria (UFC). (2009). "Design of Buildings to Resist Progressive Collapse." UFC 4-023-03, Department of Defense, USA.

Seismic Behavior of Steel Reinforced Concrete Beam-Columns and Frames

Mark D. Denavit[1], Jerome F. Hajjar[2], and Roberto T. Leon[3]

[1] Graduate Research Assistant, Department of Civil and Environmental Engineering, University of Illinois at Urbana-Champaign, Urbana, IL 61801-2352.
[2] Professor and Chair, Department of Civil and Environmental Engineering, Northeastern University, Boston, MA 02115.
[3] Professor, School of Civil and Environmental Engineering, Georgia Institute of Technology, Atlanta, GA 30332.

ABSTRACT

The ability to perform accurate nonlinear simulations is a key component in the assessment of the behavior of seismic force resisting systems. A three-dimensional distributed plasticity formulation for composite beam-columns suitable for nonlinear static and dynamic analyses of composite seismic force resisting systems has been developed. New uniaxial constitutive relations are developed for the concrete and steel elements to simulate the cyclic response of steel reinforced concrete (SRC) members. The relations account for the salient features of each material, as well as the interaction between the two, including for concrete: varying levels of confinement within a section, cracking, crushing, and spalling, and for steel: cyclic plasticity and residual stresses. The accuracy of the formulation is validated against a comprehensive set of results from monotonically and cyclically loaded beam-column specimens. The formulation is suitable for use in parametric studies to quantify the seismic performance factors of special moment frames using steel reinforced concrete columns and structural steel beams following recommendations of the recently released FEMA P695 report.

INTRODUCTION

Steel-concrete composite columns have been shown to have high strength, stiffness, and ductility. However, there is a lack of quantitatively justified guidance for design of structures with these members. Notably, there is little data is available to justify the structural system response factors (e.g., R, C_d, and Ω_o) given in the specifications. In the current work, we strive to fill these gaps through developing system response factors; assessing beam-column strength; and establishing guidelines for the computation of equivalent composite beam-column rigidity to be used in seismic analysis and design of composite frames. Accurate nonlinear static and dynamic computational formulations are required to achieve these goals. Specifically, for developing rational system response factors, a model should directly simulate all predominate inelastic effects from the onset of yielding through strength and stiffness degradation causing collapse, while being sufficiently robust to track inelastic force redistribution without convergence problems up to the point of collapse (FEMA 2009).

Often, SRC members are modeled with constitutive relations taken directly from structural steel and reinforced concrete theory. This approach neglects the beneficial effects that the composite section provides, namely the added confinement of the concrete by the steel shape and the delay of local buckling in steel shape (although local buckling is often not modeled in structural steel). Several researchers have developed models specifically for use with SRC members (Mirza 1989, Sanz Picon 1992, Elnashai and Elghazouli 1993, El-Tawil and Deierlein 1999, Chen and Lin 2006) that do account for the beneficial effects provided by the composite section. A defining feature among all of these models is the varying levels of concrete confinement assumed throughout the cross-section. The differences between the models arise from the use of different mechanistic assumptions and empirical relations for the various aspects of section behavior (e.g., differences in determination of confining pressure and confinement model). The validity the models and thus their underlying assumptions are shown through comparisons between computation and experimental results. The model presented in this work utilizes a sophisticated finite element as well as comprehensive cyclic constitutive relations. Additionally, extensive validation is performed to ensure accuracy.

THREE-DIMENSIONAL MIXED BEAM FINITE ELEMENT

Frame analyses using distributed-plasticity beam-column elements strike a favorable balance of computational efficiency and accuracy. Additionally, mixed formulations (defined here as treating both element displacements and stress resultants as primary state variables) provide more accurate results with fewer elements as compared to either displacement- or force-based formulations (Alemdar and White 2005). Tort and Hajjar (2010) developed a three-dimensional mixed beam-column element for the analysis of composite frames that include rectangular concrete-filled steel tube members, validating against a large number of experimental tests of composite members and frames. This finite element was adapted and further validated against an additional set of experimental tests on circular concrete-filled steel tube members (Denavit 2009). The element stiffness and internal force are derived in the corotational frame using small strain assumptions. When accompanied with an exact transformation between the corotational and global frame the element is capable of capturing moderate deformation and rotation behavior. The use of independent force interpolation functions provides for a more accurate representation of the nonlinear curvature along the length of a yielded member. Implemented within the OpenSees framework (OpenSees 2011), the element can be used with the wide variety of other elements and solution algorithms available in the framework.

UNIAXIAL CYCLIC CONSTITUTIVE RELATIONS

The formulation relies on accurate constitutive relations to achieve accurate results. The constitutive relations are defined for the finite element at the section level using a fiber model. A fiber model allows the wide variety of behavior exhibited by SRC sections to be described by the integration of uniaxial constitutive relations located throughout the section.

It is desired that the fiber section be defined with minimal input from the analyst. The required input from the analyst includes: basic dimensions (depth of the composite

section, H and width of the composite section, B), dimensions of the steel section (depth, d, flange width, b_f, flange thickness, t_f, and web thickness, t_w), material properties of steel section (yield strength, F_{ys}, ultimate strength, F_{us}, and elastic modulus, E_s), concrete material properties (compressive strength, f'_c), dimensions and material properties of the longitudinal and transverse reinforcement, and fiber density. Using these parameters, the uniaxial constitutive relations and fiber section are defined. Five distinct regions are identified within the section (Figure 1). Separate constitutive relations are defined for each of these regions.

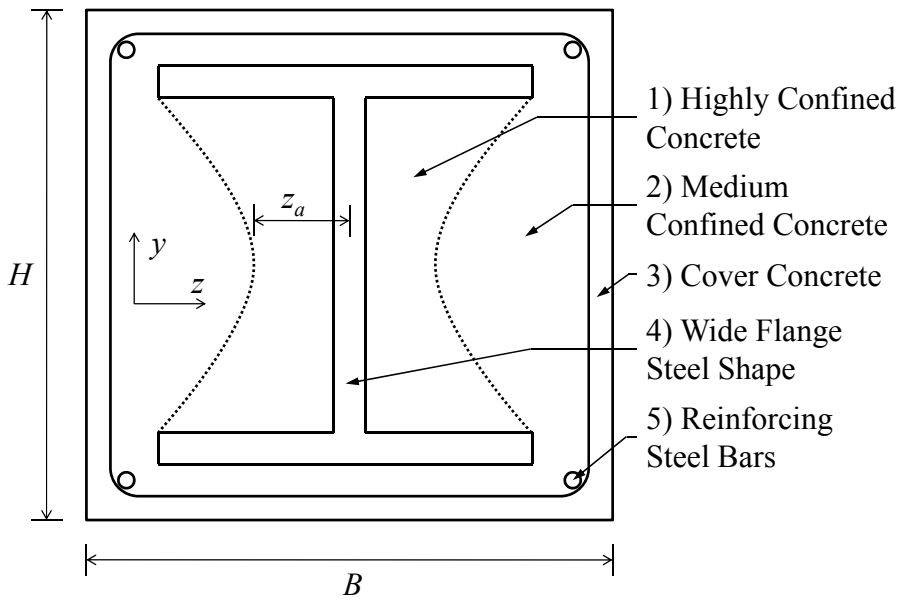


Figure 1. SRC Section

The constitutive relation used for the wide flange steel shape and the reinforcing steel bars is based on the bounding-surface plasticity model of Shen et al. (1995). Modifications were made to model the effects of residual stress within the steel section. The residual stress at a fiber is modeled explicitly as an initial elastic stress in the uniaxial constitutive relation. The Lehigh residual stress pattern (Galambos and Ketter 1958) is used to define the value of residual stress in the steel section with a maximum compressive residual stress of 30% of the yield strength occurring at the flange tips. The confined concrete is assumed to prevent flange and web local buckling and thus, these effects have not been included. In contrast, the model by Elnashai and Elghazouli (1993) is for partially encased composite columns and includes flange local buckling since the concrete only prevents inward buckling of the flange. For simplicity, the wide flange steel section is modeled with sharp corners (i.e., neglecting the fillets).

The constitutive relation for the concrete is based on the rule-based model of Chang and Mander (1994). The backbone stress-strain curve for the concrete is based on the model by Tsai, which is defined by the initial stiffness E_c, peak coordinate ($\varepsilon'_{cc}, f'_{cc}$), and r which acts as a shape factor. The confinement model developed by Mander et al. (1988) for a triaxial state of stress is utilized to determine the peak compressive

strength from the confining pressure in two orthogonal directions (Equations 1 through 5).

$$K = \frac{f'_{cc}}{f'_c} = 1 + A\bar{x}\left(0.1 + \frac{0.9}{1 + B\bar{x}}\right) \tag{1}$$

$$A = 6.8886 - \left(0.6069 + 17.275r\right)e^{-4.989r} \tag{2}$$

$$B = \frac{4.5}{\frac{5}{A}\left(0.9849 - 0.6306e^{-3.8939r}\right) - 0.1} - 5 \tag{3}$$

$$\bar{x} = \frac{f_{l1} + f_{l2}}{2f_c} \quad r = \frac{f_{l1}}{f_{l2}} \quad f_{l1} \le f_{l2} \tag{4}$$

$$\varepsilon'_{cc} = \varepsilon_c\left(1 + 5\left(K - 1\right)\right) \tag{5}$$

where, the strain at peak stress for unconfined concrete, ε_c, is given by Equation 6

$$\varepsilon_c = f_c'^{0.25} \Big/ 1150.0 \tag{6}$$

In order to accommodate low values of r necessary to model high confinement pressures, two values of r are used; one prior to the peak stress reached and one after the peak stress is reached. The value used prior to the peak is based on unconfined concrete, while the one after the peak accounts for the level of confinement and is based on a comparison of the models of Tsai and Popovics (Chang and Mander 1994). These and other parameters for the concrete model are as described in Table 1.

The outermost concrete region of concrete, also termed the cover concrete, is assumed to have zero confining pressure in either direction. Furthermore, it is allowed to spall. Spalling is modeled by modifying the nonlinear compressive backbone curve so that the stress and tangent reduce to and remain at zero after a certain strain. The concrete inside the lateral reinforcing bars is termed the medium confined concrete. In this region, confining pressure is provided by the lateral reinforcing bars. The magnitude of the confining pressure is computed in two orthogonal directions with Equations 7 and 8.

$$f_{ly,medium} = K_e \rho_y F_{yr} \tag{7}$$

$$f_{lz,medium} = K_e \rho_z F_{yr} \tag{8}$$

where, K_e is the ratio of effectively confined cross sectional area to area of the core as defined by Mander et al. (1988), ρ_y, ρ_z are the volumetric ratios of the transverse reinforce steel in either direction as defined by Mander et al. (1988), and F_{yr} is the yield strength of the longitudinal reinforcement.

The concrete between the flanges is termed highly confined concrete. In this region, confining pressure is provided by the lateral reinforcing bars and the steel shape. El-Tawil and Deierlein (1999) developed a mechanism model in which the confining pressure provided by the steel shape acts only in the y direction (Figure 1) and is

computed considering the plastic moment capacity of the flange (Equation 9). The distance between the vertex of the parabola defining the boundary between the highly and medium confined concrete (Figure 1) and the centerline of the steel section is described by Equation 10. This parabolic boundary is modeled explicitly with different constitutive relations on either side. In contrast, the parabolic boundary between the cover and medium confined concrete is implicitly modeled, utilizing the factor K_e to provide average behavior. The difference in handling these two boundaries exists to provide greater accuracy in modeling the boundary between the flanges while retaining the flexibility of different possible configurations of reinforcing steel. A comparison of the monotonic compressive response of the concrete in each of the three regions is shown in Figure 2.

$$f_{ly,high} = f_{ly,medium} + \frac{t_f^2 F_{ys}}{0.75\left(b_f - t_w\right)^2} \tag{9}$$

$$z_a = 0.50 b_f - 0.25\left(d - 2t_f\right) \geq 0.50 t_w \tag{10}$$

The discretization of the fiber section (i.e., computation of location and area of the fibers) is consistent with the geometric description of the cross section presented here. The sum of the area of the fibers for each material type and the total for the section are exact for the selected geometry and do not change with the fiber density. The moment of inertia of the section as computed from the fibers approaches the exact value with increasing fiber density. The discretization is implemented for general three-dimensional analyses as well as for two-dimensional analyses where bending is along either the strong or weak axis. The fiber discretization for two-dimensional analyses takes the form of strips allowing a significant savings in the number of fibers used. The fiber density is defined as the nominal number of fibers along the strong and weak axis with the number of fibers for individual section components (e.g., steel flanges or concrete cover) determined in proportion to their size relative to the entire section. A discretization of 20×20 (or simply 20 for two dimensional analyses) is found to be both accurate and efficient and is used for the analyses presented in this paper.

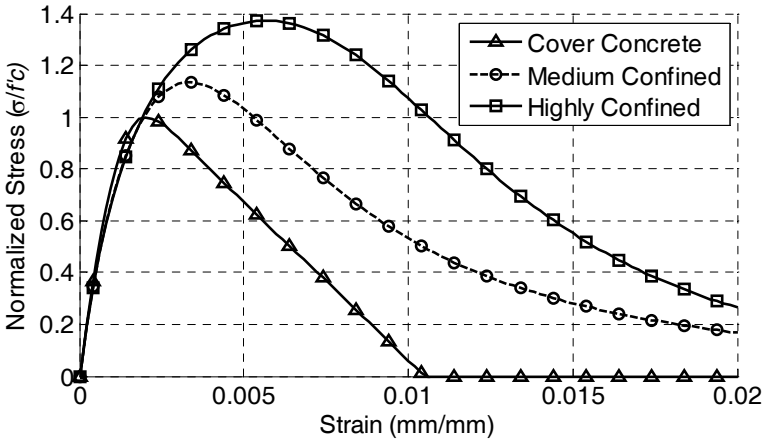


Figure 2. Concrete Constitutive Relations

Table 1. Concrete Material Properties

			Highly Confined	Medium Confined	Cover
	Initial Stiffness	E_c	$E_c[\text{MPa}] = 12,400 + 500 f_c'[\text{MPa}]$		
Compression	Confinement Pressure	f_{ly}	(Equation 7)	(Equation 9)	0
		f_{lz}	(Equation 8)		0
	Peak Stress	f'_{cc}	(Equation 1)		f'_c
	Strain at Peak Stress	ε'_{cc}	(Equation 5)		(Equation 6)
	Shape Factor	r_{pre}	$r_{pre} = f_c'[\text{MPa}]/5.2 - 1.9$		
		r_{post}	$r_{post} = E_c \varepsilon_{cc} / f'_{cc}$		
Tension	Peak Stress	f'_t	$f_t[\text{MPa}] = 0.5\sqrt{f_c'[\text{MPa}]}$		
	Strain at Peak Stress	ε'_t	$\varepsilon_t = 1.23 f_t / E_c$		
	Shape Factor	r	4.0		

VALIDATION OF THE FINITE ELEMENT METHOD

To validate the accuracy the model, a large number of comparative analyses were performed against experimental results. A selection of the validation results for monotonic proportionally loaded beam-columns and cyclic non-proportionally loaded beam-columns is presented here.

Proportionally Loaded Beam-Columns

The most common experimental configuration for testing SRC beam-columns is monotonic proportional loading (Figure 3). Tests of this type have been performed by Virdi and Dowling (1973), Roderick and Loke (1975), Morino et al. (1984) and Wang (1999), and others. Details of four specimens from these experimental studies are presented in Table 2. The results of these experiments are compared to results from analyses conducted using the model presented in this work (Figure 4). When the eccentric of the applied load coincided with one of the principal axes of the column (i.e., strong or weak axis bending), one mid-height lateral deflection is reported. When the applied load induces biaxial bending, two mid-height lateral deflections are reported, one for each of the columns principal axes.

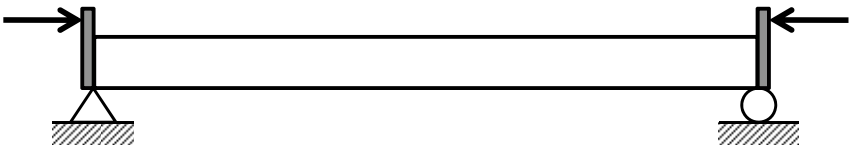


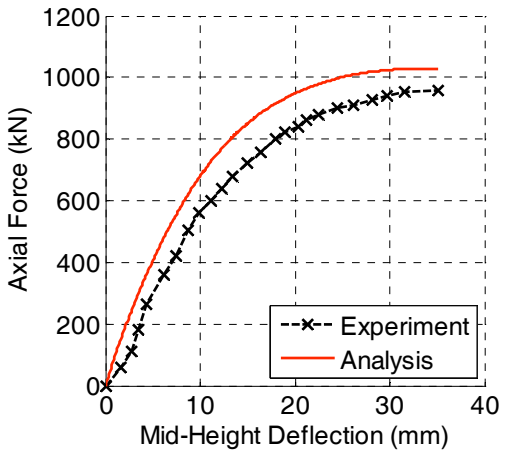
Figure 3. Proportionally Loaded Beam-Column Test Schematic

The results (Figure 4) show a good correlation between experimental and computational results. This is seen in the initial stiffness, peak load, deflection at peak

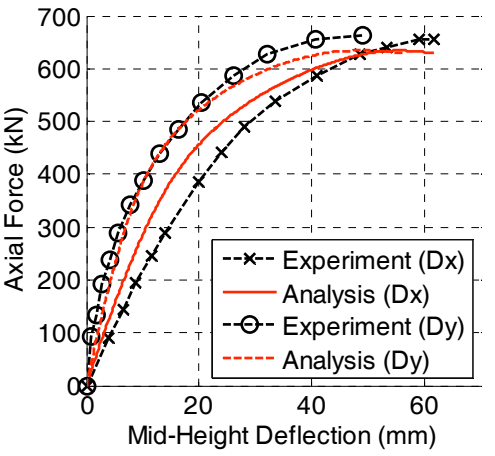
load, post-peak degradation, and ratio of strong and weak axis deflections. The two specimens by Morino et al. (1984) (Figure 4c,d) have a similar cross section and loading angle, but specimen D8-45 has approximately twice the length and eccentricity of B4-45. The higher first- and second-order moments resulted in a significantly lower peak axial load for D8-45. The model predicted the peak axial load accurately for both specimens indicating that model captures well both material and geometric nonlinearity.

Table 2. Proportionally Loaded Beam-Column Specimen Data

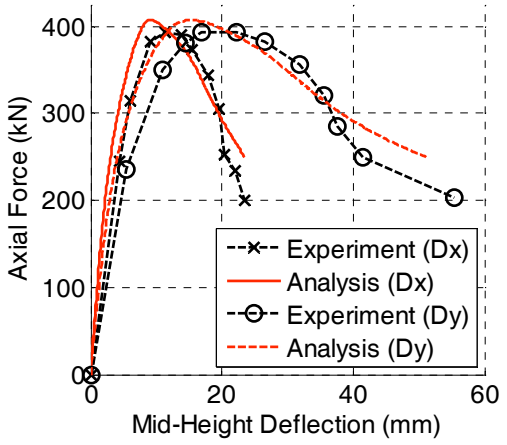
Author	Year	Specimen	H (mm)	B (mm)	f'_c (MPa)	Steel Section	F_y (MPa)	d_b (mm)	F_{yr} (MPa)	L (mm)	Axis	e (mm)
Wang	1999	RSJ1	200	200	55.0	RSJ 102x102	310.0	n/a	n/a	4,000	Strong	55.0
Virdi and Dowling	1973	G	254	254	44.8	UC 6x6@15.7	314.7	12.7	309	7,315	Biaxial	73.4
Morino et al.	1984	B4-45	160	160	23.4	H-100x100x6x8	287.0	4.0	387	2,309	Biaxial	40.0
Morino et al.	1984	D8-45	160	160	22.9	H-100x100x6x8	302.0	4.0	387	4,619	Biaxial	75.0



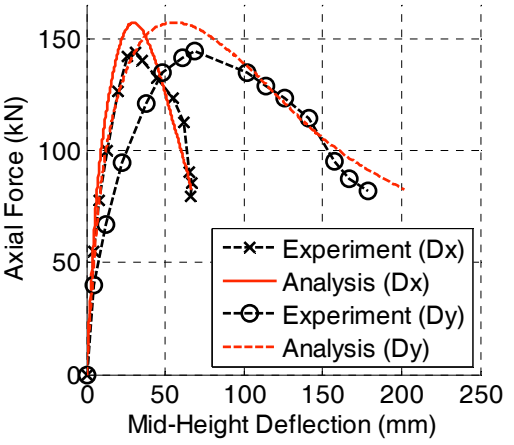
(a) Wang 1999; Specimen: RSJ1



(b) Virdi and Dowling 1973; Specimen G



(c) Morino et al. 1984; Specimen B4-45



(d) Morino et al. 1984; Specimen D8-45

Figure 4. Proportionally Loaded Beam-Column Validation Results.

Cyclically Loaded Beam-Columns

A set of carefully controlled and well documented non-proportionally loaded cyclic SRC beam-columns tests was performed by Ricles and Paboojian (1993, 1994). The specimens were subjected to a constant axial load and cyclically increasing horizontal displacements (Figure 5) which induced strong axis bending in the column.

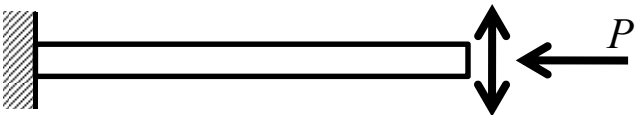
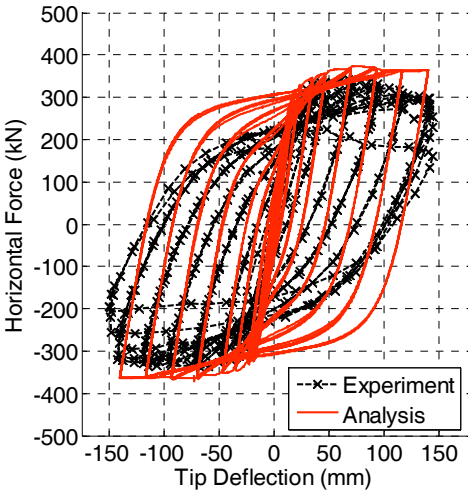
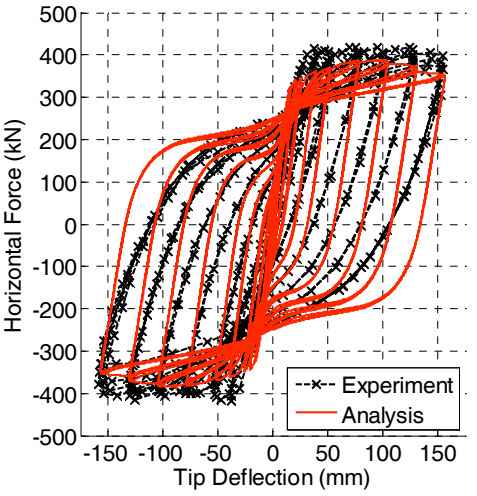


Figure 5. Cyclically Loaded Beam-Column Test Schematic

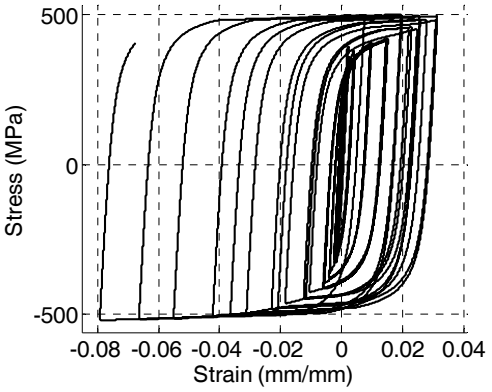
Details of two of specimens from this experimental study are presented in Table 3. The load-deformation results of these experiments are compared to those from analyses conducted using the model presented in this work (Figure 6a,b). Additionally, the stress-strain response from the extreme fiber of the steel section (Figure 6c) and the extreme fiber of the highly confined concrete (Figure 6d) as predicted from the analysis are shown.



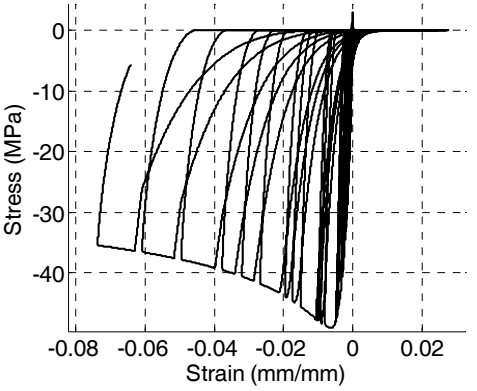
(a) Specimen 6



(b) Specimen 8



(c) Specimen 6, Steel Section Fiber Stress-Strain Relationship



(d) Specimen 6, Highly Confined Concrete Fiber Stress-Strain Relationship

Figure 6. Cyclically Loaded Beam-Column Validation Results.

Table 3. Cyclically Loaded Beam-Column Specimen Data

Specimen	H (mm)	B (mm)	f'_c (MPa)	Steel Section	F_y (MPa)	d_b (mm)	F_{yr} (MPa)	L (mm)	P (kN)
6	406	406	35.8	W8x40	372	28.6	448	1,930	1,490
8	406	406	62.9	W8x40	372	22.2	434	1,930	1,490

The results (Figure 6) show a good correlation between experimental and computational results. The initial stiffness and peak strength are predicted well by the model. The unloading stiffness and yield upon unloading are less accurate, leading to the model predicting fuller hysteresis loops than observed in the experiments. Similar discrepancies between experimental and computational results have been noted in other SRC models (e.g., Elnashai and Elghazouli 1993).

CONCLUSION

A finite element formulation for analysis of SRC members and frames has been presented. The formulation included a mixed based distributed-plasticity beam element and uniaxial constitutive relations. The cyclic uniaxial constitutive relations account for the salient features of SRC behavior. The concrete constitutive relation was based on a rule based model from the literature. Three regions of concrete were defined with separate material properties based on computed levels of confinement pressure. The steel constitutive relation was based on a bounding surface plasticity model from the literature with modifications so that residual stresses could be modeled explicitly within the steel section. A validation was performed showing good correspondence between experimental and computational results for a selection of both monotonic and cyclic tests. The finite element formulation provides an accurate analysis tool for use with composite frames and is suitable for use in parametric studies such as those necessary to develop system behavior factors.

ACKNOWLEDGMENTS

The authors thank Tiziano Perea for his advice in the completion of this work. The work described here is part of a NEESR project supported by the National Science Foundation under Grant No. CMMI-0619047, the American Institute of Steel Construction, the Georgia Institute of Technology, and the University of Illinois at Urbana-Champaign. Any opinions, findings, and conclusions expressed in this material are those of the authors and do not necessarily reflect the views of the National Science Foundation or other sponsors.

REFERENCES

Alemdar, B. N. and White, D. W. (2005). "Displacement, Flexibility, and Mixed Beam-Column Finite Element Formulations for Distributed Plasticity Analysis," *Journal of Structural Engineering*, ASCE, 131(12), 1811-1819.

Chang, G. A. and Mander, J. B, (1994). "Seismic Energy Based Fatigue Damage Analysis of Bridge Columns: Part I - Evaluation of Seismic Capacity," National Center for Earthquake Engineering Research, State University of New York at Buffalo. Department of Civil Engineering, Buffalo, New York.

Chen, C.-C. and Lin, N.-J. (2006). "Analytical Model for Predicting Axial Capacity and Behavior of Concrete Encased Steel Composite Stub Columns," *Journal of Constructional Steel Research*, 62(5), 424-433.

Denavit, M. (2009). "Nonlinear Seismic Analysis of Circular Concrete-Filled Steel Tube Members and Frames," *M.S. Thesis*, University of Illinois at Urbana-Champaign, Urbana, Illinois.

Elnashai, A. S. and Elghazouli, A. Y. (1993). "Performance of Composite Steel/Concrete Members under Earthquake Loading. Part I: Analytical model," *Earthquake Engineering & Structural Dynamics*, 22(4), 315-345.

El-Tawil, S. and Deierlein, G. G. (2001). "Nonlinear Analysis of Mixed Steel-Concrete Frames. II: Implementation and Verification," *Journal of Structural Engineering*, ASCE, 127(6), 656-665.

Federal Emergency Management Agency (FEMA). (2009). Quantification of Building Seismic Performance Factors, FEMA P695, Washington, D.C.

Galambos, T. V., and Ketter, R. L. (1958). "Columns under Combined Bending and Thrust." *Journal of the Engineering Mechanics Division*, ASCE, 85(2), 135-152.

Mander, J. B., Priestley, M. J. N., and Park, R. (1988). "Theoretical Stress-Strain Model for Confined Concrete," *Journal of Structural Engineering*, ASCE, 114(8), 1804-1826.

Mirza, S.A. (1989). "Parametric Study of Composite Column Strength Variability," *Journal of Constructional Steel Research*, 14(2), 121-137.

Morino, S., Matsui, C., and Watanabe, H. (1984). "Strength of Biaxially Loaded SRC Columns," *Composite and Mixed Construction*, ASCE, New York, 185-194.

OpenSees (2011). "Open System for Earthquake Engineering Simulation," Open source software, http://opensees.berkeley.edu.

Ricles, R. and Paboojian S. D. (1993). "Seismic Performance of Composite Beam-Columns," Report No. 93-01, ATLSS Engineering Research Center, Lehigh University, Bethlehem, Pennsylvania.

Ricles, R. and Paboojian S. D. (1994). "Seismic Performance of Steel-Encased Composite Columns," *Journal of Structural Engineering*, ASCE, 120(8), 2474-2494.

Roderick, J. W. and Loke, Y. O. (1975). "Pin-Ended Composite Columns Bent About the Minor Axis," *Civil Engineering Transactions*, 17(2), 51-58.

Sanz Picon, C. F. (1992). "Behavior of Composite Column Cross Sections under Biaxial Bending" *M.S. Thesis*, Cornell University, Ithaca, New York.

Shen, C., Mamaghani, I. H. P., Mizuno, E., and Usami, T. (1995). "Cyclic Behavior of Structural Steels. II: Theory," *Journal of Engineering Mechanics*, ASCE 121(11), 1165-1172.

Tort, C. and Hajjar, J. F. (2010). "Mixed Finite-Element Modeling of Rectangular Concrete-Filled Steel Tube Members and Frames under Static and Dynamic Loads," *Journal of Structural Engineering*, ASCE, 136(6), 654-664.

Virdi, K. S. and Dowling, P. J. (1973). "The Ultimate Strength of Composite Columns in Biaxial Bending," *Proceedings of the Institute of Civil Engineering (London)* 55(2), 251–72.

Wang, Y. C. (1999). "Tests on Slender Composite Columns," *Journal of Constructional Steel Research*, 49(1), 25-41.

Effect of Structure, Soil, and Ground Motion Parameters on Structure-Soil-Structure Interaction of Large Scale Nuclear Structures

L. M. Anderson[1], S. Carey PhD[2], and J. Amin[3]

[1]Bechtel National, Inc., 5275 Westview Drive, Frederick, MD 21703; PH (240) 379-6166; FAX (240) 379-6195; email: lmanders@bechtel.com
[2]Savannah River Nuclear Solutions, LLC., 245-9F Savannah River Site, Aiken, SC 29808; PH (803) 952-3620; email: shawn.carey@srs.gov
[3]Savannah River Nuclear Solutions, LLC., 730-1B Savannah River Site, Aiken, SC 29808; PH (803) 952-8970; email: jayprakash.amin@srs.gov

ABSTRACT

Structure-Soil-Structure Interaction (SSSI) is defined as the effect that a neighboring structure has on the dynamic response of a given structure on a common soil site. The significance of SSSI is sensitive to the characteristics of the soil, structures, and ground motion, as well as the spatial distance between structures.

The Hanford Site, a Department of Energy Facility, contains a complex of structures that exhibit significant SSSI behavior. The SSSI effect is measured in this paper by considering two models, one including the entire complex of structures and one including only the structure that exhibits the most critical SSSI response. The amplification is quanitifed through a comparison of transfer functions and seismic member demand accelerations.

A realistic study of the sensitivity of soil parameters is accomplished by replacing the Hanford Site soil parameters with those of the Savannah River Site (SRS). SRS is also a Department of Energy Facility. As this Site is located in the state of South Carolina, the soil stiffness is less rigid and provides for a practical comparison. The sensitivity of the soil stiffness is quantified by taking a ratio of the response of the combined model to the response of the individual model for both soil types.

INTRODUCTION

The Hanford Waste Treatment Plant (WTP) is a Department of Energy Facility that will vitrify radioactive and chemical tank waste stored at the Hanford Site. The Pretreatment Facility Complex (PTC) houses the first step in the vitrification process. The structures within the PTC are classified as Seismic Category I and must meet the criteria of U.S. Department of Energy Standard 1020 (U.S. Department of Energy, 2002).

The PTC (see Figure 1) is comprised of two small surface-founded structures, the Pretreatment Facility Annex (PTFA) and the Pretreatment Facility Control Building (PTCB), adjacent to one large partially embedded structure, the Pretreatment Facility (PTF). The PTFA and PTCB are separated from the PTF with a seismic gap of less than one foot.

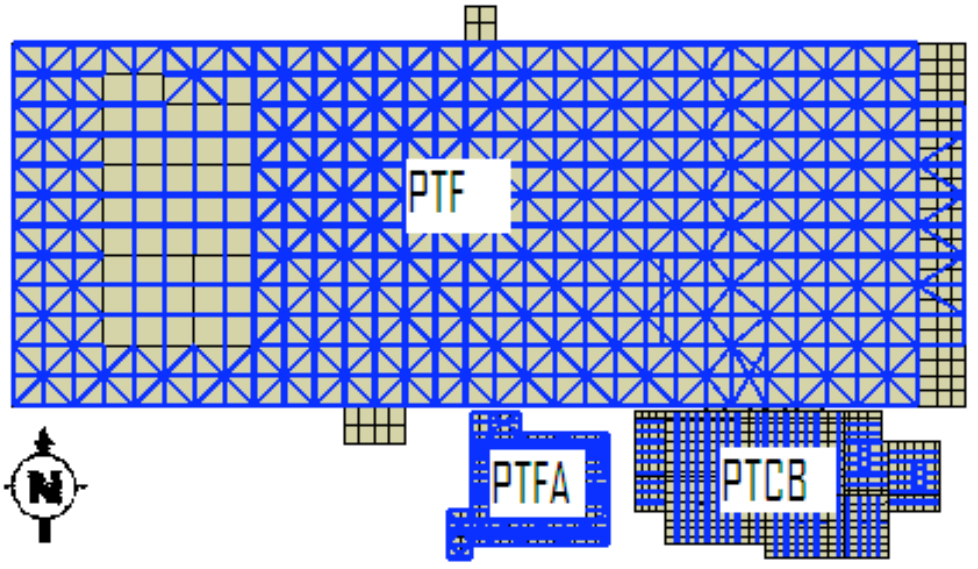


Figure 1. Pretreatment Facility Complex.

The PTF lateral load resisting system consists of concrete shear walls that extend to Elevation (EL) 98'-0" and relatively rigid concrete slab diaphragms. Above EL 98'-0", the roof is designed as a steel framing system that is supported by the concrete shear walls below EL 98'-0" and a steel framing system that surrounds the perimeter of the structure. The PTF exhibits a complex response particularly due to the interaction between the steel and concrete lateral resisting systems.

Lateral loads applied to the PTFA are resisted by a steel framing system, distributed by composite slab diaphragms and a flexible roof diaphragm.

Lateral loads applied to the PTCB are resisted by a concrete shear wall system as distributed by composite floor slab and composite roof slab diaphragms.

The PTCB exhibits a more rigid response than that of the PTFA. The Soil-Structure Interaction (SSI) and Structure-to-Soil-Structure Interaction (SSSI) response of the PTCB is shifted to a more flexible frequency range, which corresponds to a more critical portion of the input response spectra. The PTFA response is more flexible, so the frequency shift when SSI and SSSI are considered is less significant. Therefore, since the PTCB exhibits the most significant SSSI effect, this structure is the focus of the sensitivity studies discussed herein.

SSI RESPONSE OF THE PTCB

Structural Characteristics

The PTCB is a concrete shear wall structure with 1'-6" thick shear walls extending floor to roof and a 4'-0" thick mat. Contributing shear walls are shown highlighted in Figure 2.

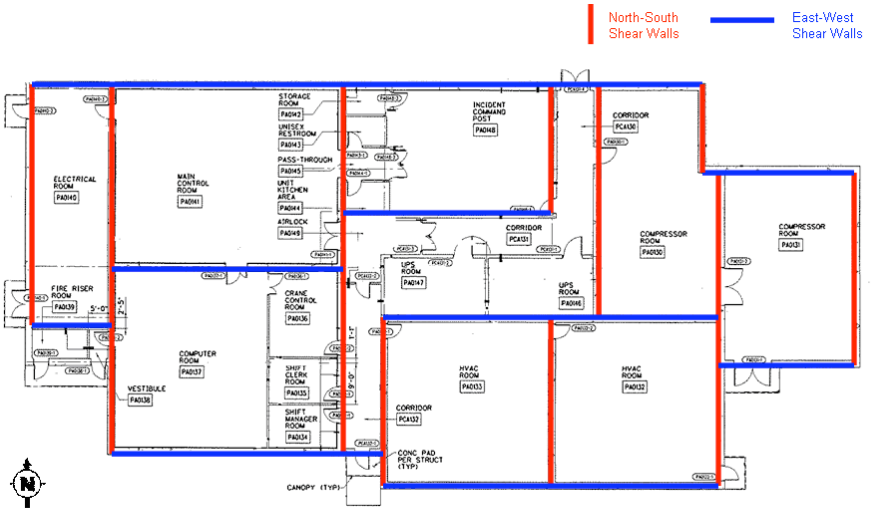


Figure 2. PTCB Shear Walls.

The roof and floors are designed as composite slabs. There are two mezzanine slabs, at EL 15'-0" that cover a small portion of the building footprint. The roof slab elevations range from EL 22'-6" to EL 37'-6".

Hard Rock Analysis

The Hard Rock (HR) analyses and subsequent SSI and SSSI analyses are completed using SASSI2000 (Lysmer et al. 1972, and Lysmer et al. 1999) which provides a linear solution to the SSI problem in the frequency domain.

First, the HR soil case is created with a shear wave velocity of 14,000 fps, to emulate the fixed base condition. Transfer functions are computed at a node on each floor elevation at the same horizontal coordinates. Transfer functions are defined as the ratio of the Fourier amplitude of the frequency dependent seismic response of a given node to that of a control node at the free field where the input seismic motion is applied. For the HR analysis case, the transfer functions provide a visual representation of the structural response.

The HR transfer functions for the EW (x) direction and the NS (y) direction are shown in Figure 3 and Figure 4, respectively.

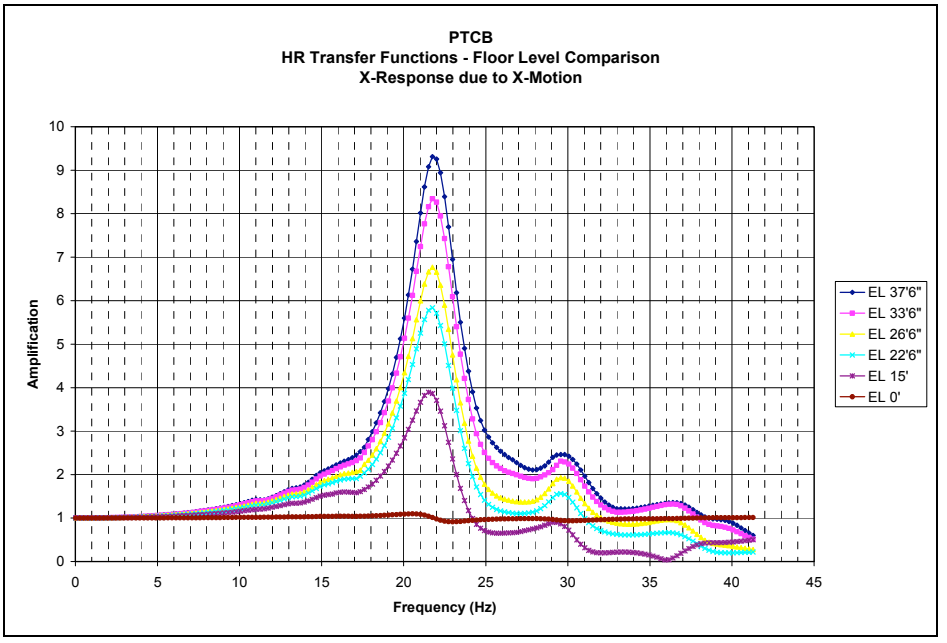


Figure 3. PTCB HR EW Transfer Functions.

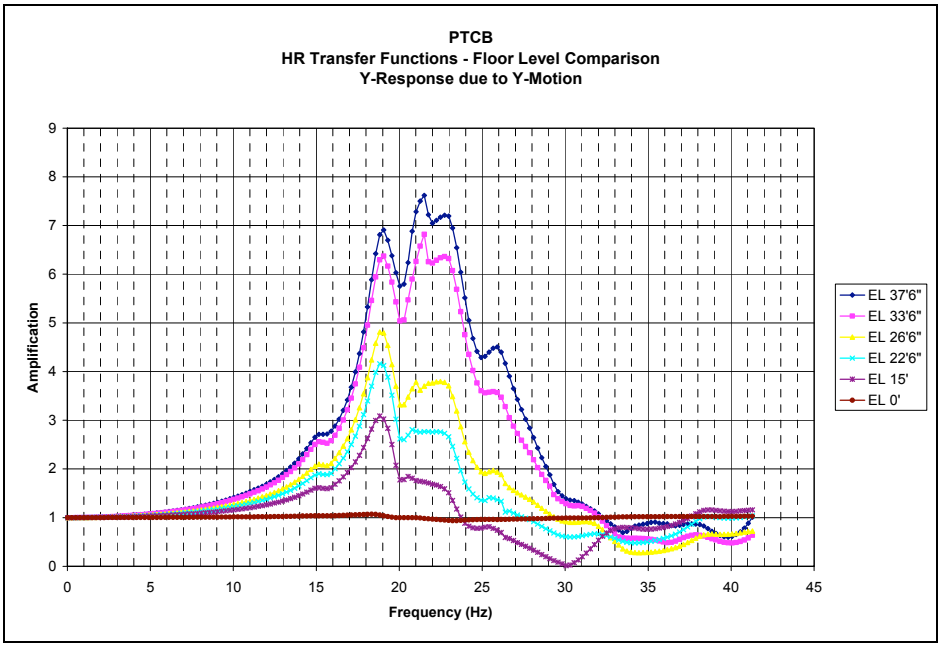


Figure 4. PTCB HR NS Transfer Functions.

The HR analyses indicate that the EW dominant structural mode occurs at approximately 22 Hz and the NS dominant structural modes occur at 19 Hz and 22 Hz. There are more than one dominant modes for the NS direction due to the layout of the NS running shear walls. As shown in Figure 2, the NS shear walls are less regular in placement and length than the EW shear walls.

SSI Analysis

SSI analysis is completed for three strain compatible soil profiles, Upper Bound (UB), Mean (M), and Lower Bound (LB) that are generated through free-field deconvolution analysis. Transfer functions are computed for each soil case and compared for a node at the highest roof elevation due to excitation in the EW and NS directions (see Figure 5 and Figure 6, respectively).

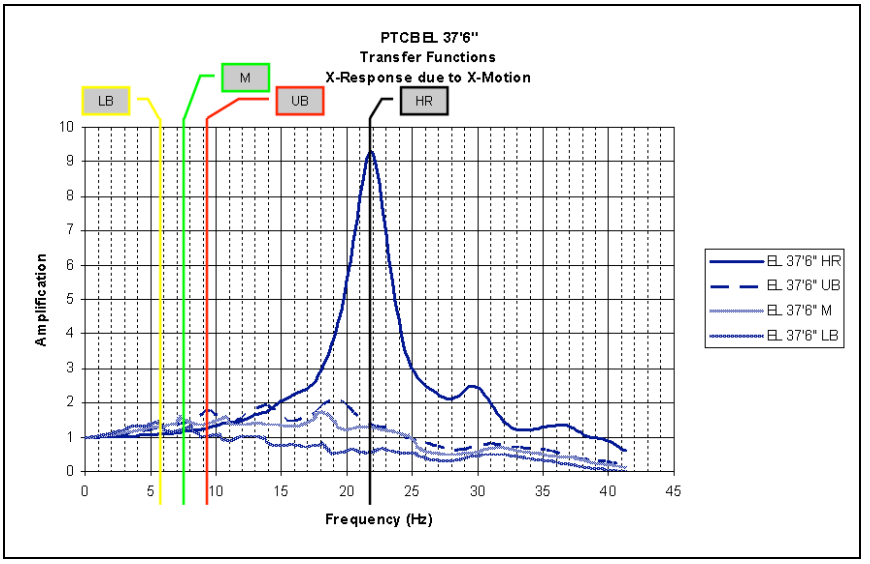


Figure 5. PTCB SSI EW Transfer Functions.

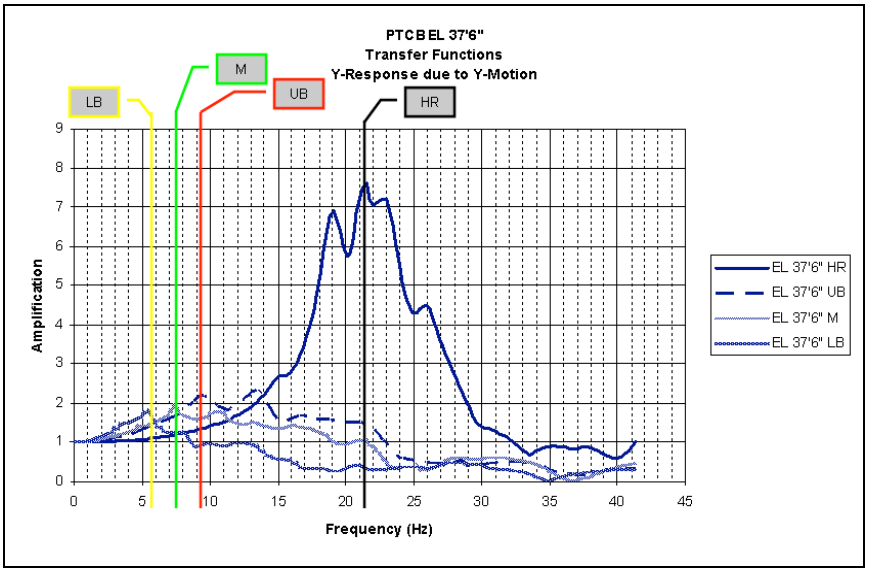


Figure 6. PTCB SSI NS Transfer Functions.

Incorporation of SSI shifts the response of the PTCB into a lower frequency range. For clarity, only the M soil case is shown in the subsequent comparisons.

SSSI RESPONSE OF THE PTCB

Two SSI models are considered for the SSSI analysis. The "combined model" contains the three structures that make up the PTC, with the separation distance of 3'-0" considered. The "individual model" contains only the PTCB without consideration of the adjacent structures in the PTC. Transfer functions are shown for a common node at the center of the PTCB mat in both the individual and combined models (see Figures 7, 8, and 9).

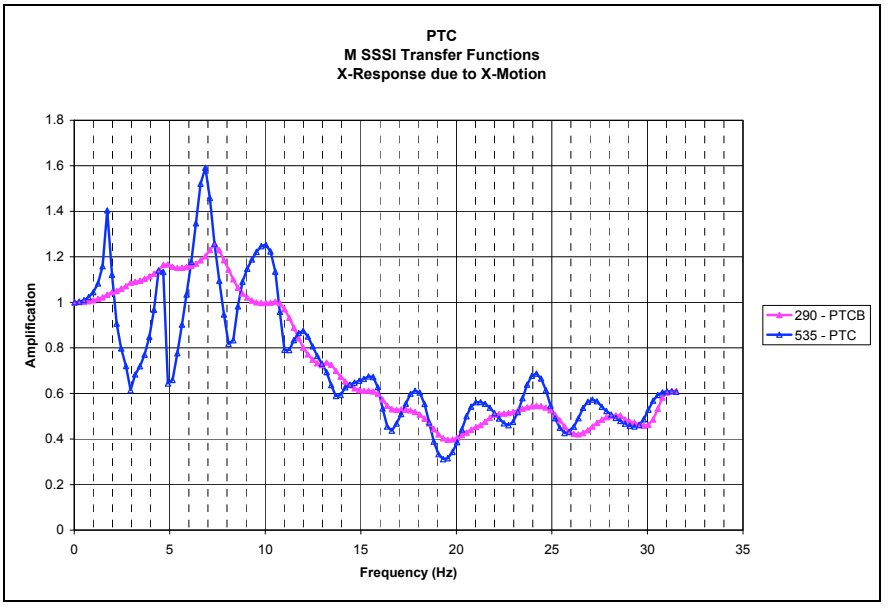


Figure 7. PTCB SSSI EW Transfer Functions.

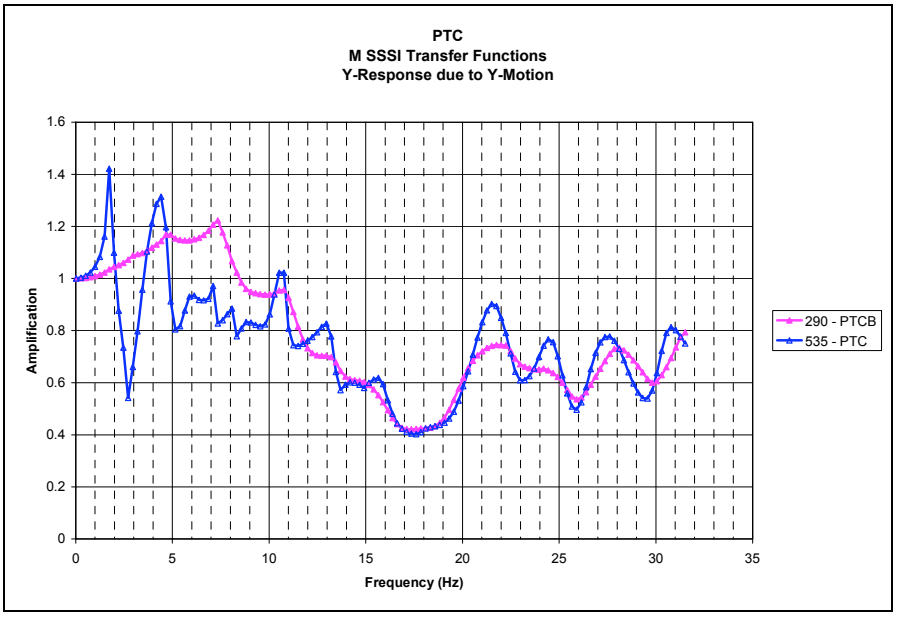


Figure 8. PTCB SSSI NS Transfer Functions.

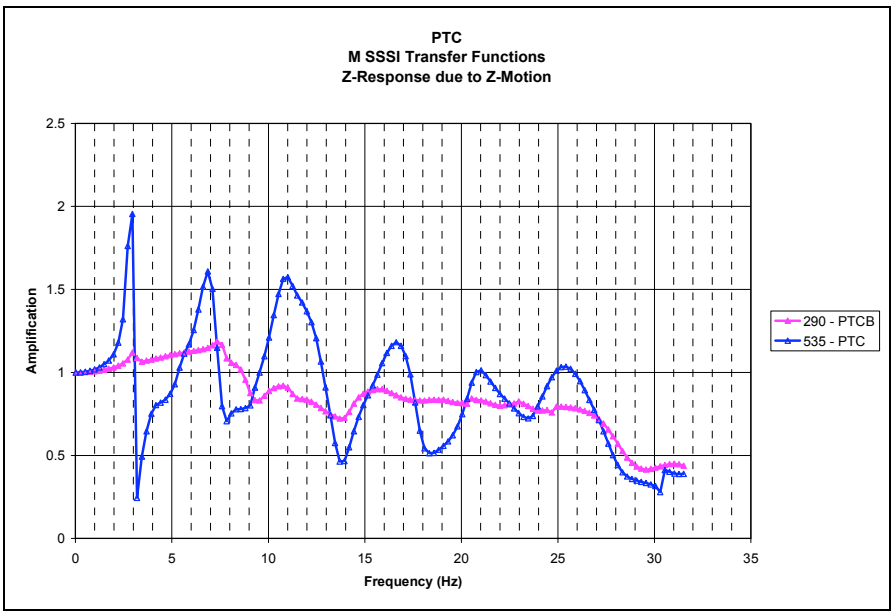


Figure 9. PTCB SSSI Vertical Transfer Functions.

The response of the PTCB in the combined model appears to oscillate about the response of the PTCB in the individual model.

Transfer functions are printed from the combined model for a node at the center of the PTCB mat (Node 535) and a node at the center of the PTF mat (Node 4547) (see Figures 10, 11, and 12).

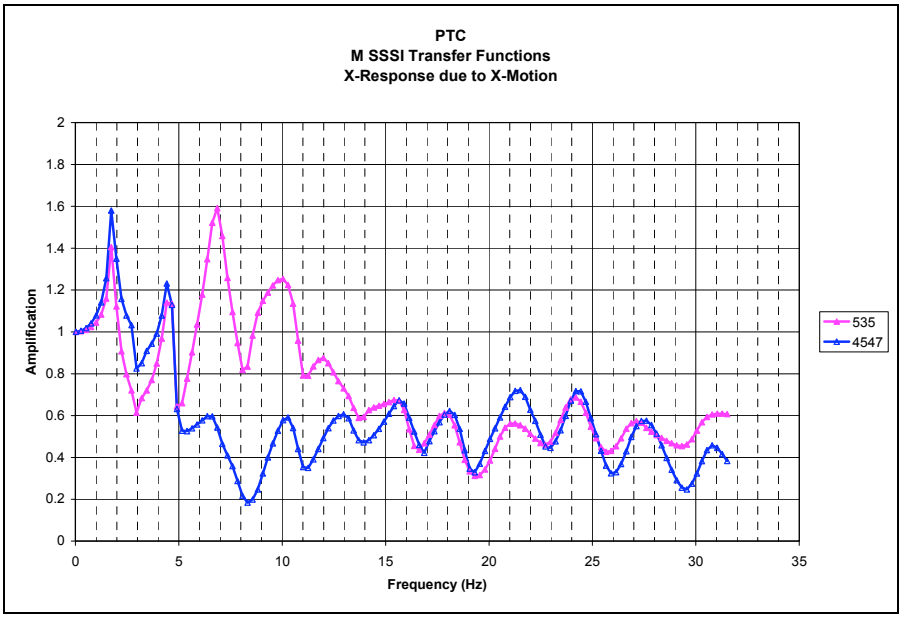


Figure 10. PTC SSSI EW Transfer Functions.

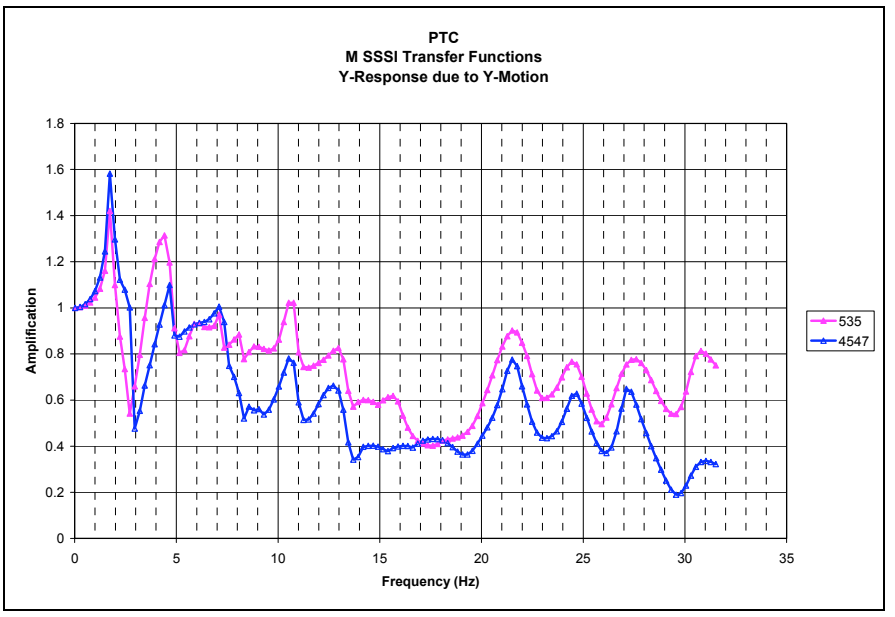


Figure 11. PTC SSSI NS Transfer Functions.

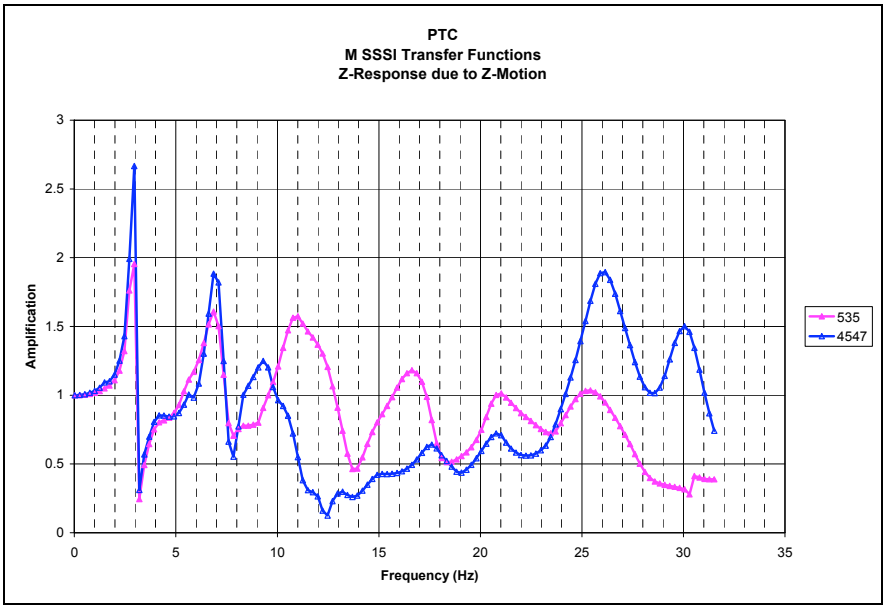


Figure 12. PTC SSSI Vertical Transfer Functions.

The response of the PTCB in the combined model follows the pattern of the PTF response while oscillating about the individual PTCB response. The PTF response exhibits higher energy than that of the PTCB.

Maximum Nodal Accelerations

The site specific input spectra at the free field for the PTC are shown in Figure 13. H1, H2, and VT, correspond to the X, Y, and Z directions, respectively. The input motion is applied to the SSI models.

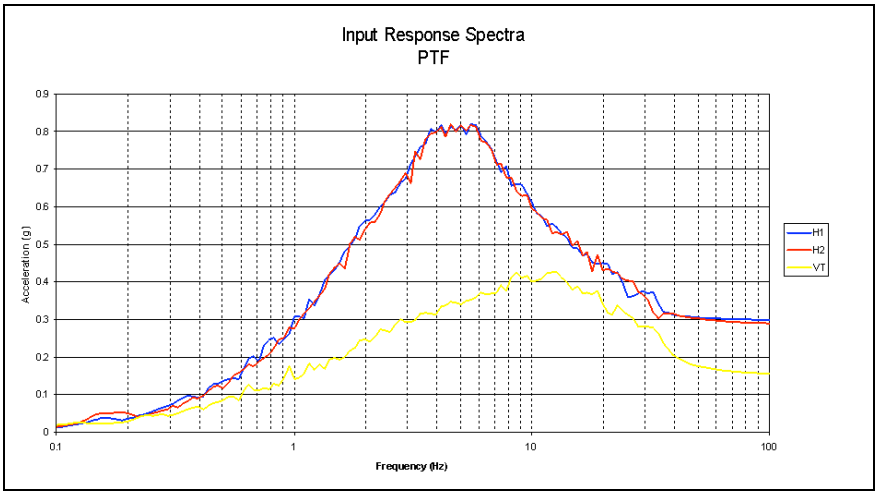


Figure 13. PTC Site Specific Free Field Input Spectra

Maximum accelerations at each node are extracted, in each response direction, due to seismic input in each of the three directions, for each of the three soil cases and then combined for each response direction and enveloped for each soil case. The result is one maximum acceleration, at each node of each model, for each direction.

The SSSI effect with consideration of seismic motion is quantified by computing a weighted average ratio. First, the ratios of the maximum nodal accelerations from the combined model to the individual model are computed for each node. Second, the ratios are weighted by the characteristic nodal mass. Then, the weighted ratios are summed and divided by the total nodal mass of the PTCB.

The weighted average ratios for each direction are shown in Table 1.

Table 1. SSSI Ratios.

X	Y	Z
1.02	1.15	1.33

On average, the incorporation of SSSI effects amplifies the maximum nodal accelerations of the PTCB. When motion is in-plane with the interface, the SSSI amplification is 2%. When motion is out-of-plane with the interface, the SSSI amplification is 15%. When motion is vertical, the SSSI amplification is 33%.

SENSITIVITY OF SOIL PARAMETERS ON SSSI RESPONSE

The sensitivity of soil parameters is studied by replacing the Hanford Site soil parameters (referred to as WTP) with those of Savannah River Site (SRS). The soil stiffness of SRS is less rigid. The Mean shear wave velocities are compared in Figure 14.

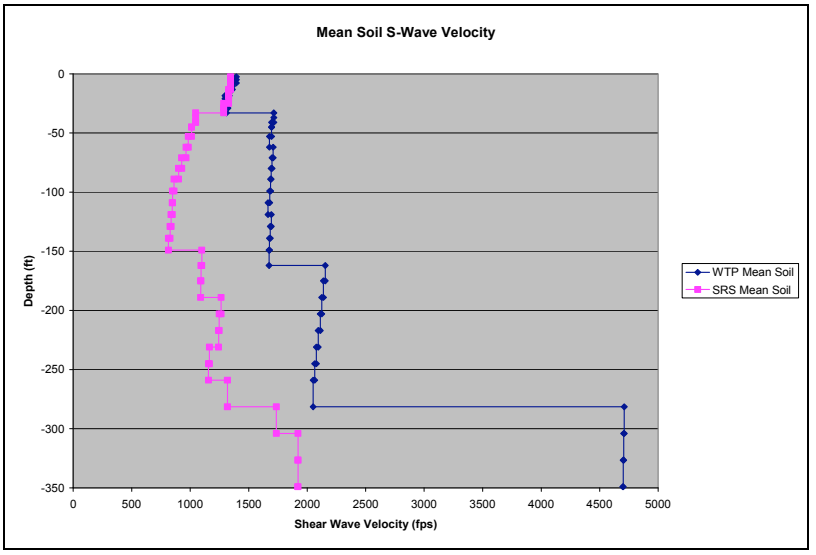


Figure 14. Comparison of Shear Wave Velocities.

Transfer functions are computed for the center node of the PTCB mat in both the combined and individual models. The results are compared for the WTP and SRS soil profiles (see Figures 15, 16, and 17).

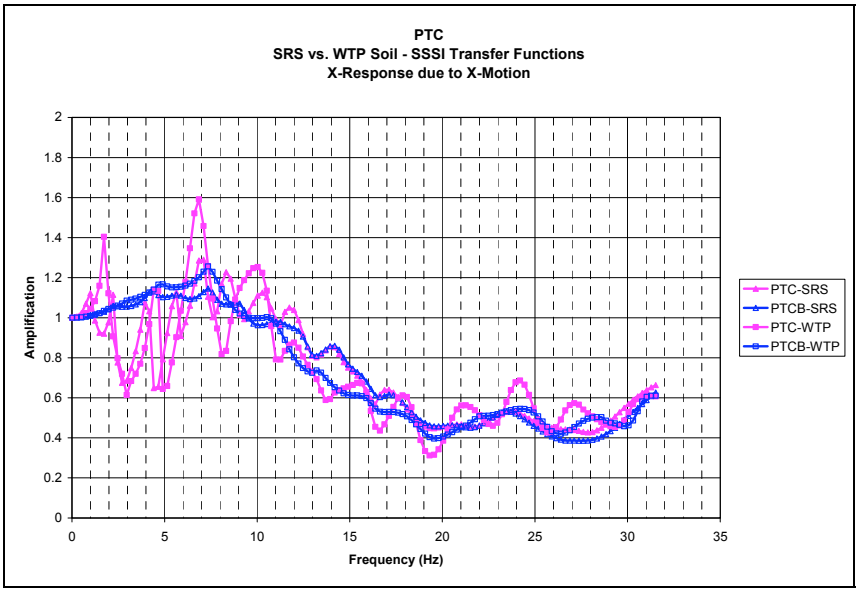


Figure 15. EW Comparison of SSSI Effect WTP vs. SRS Soil.

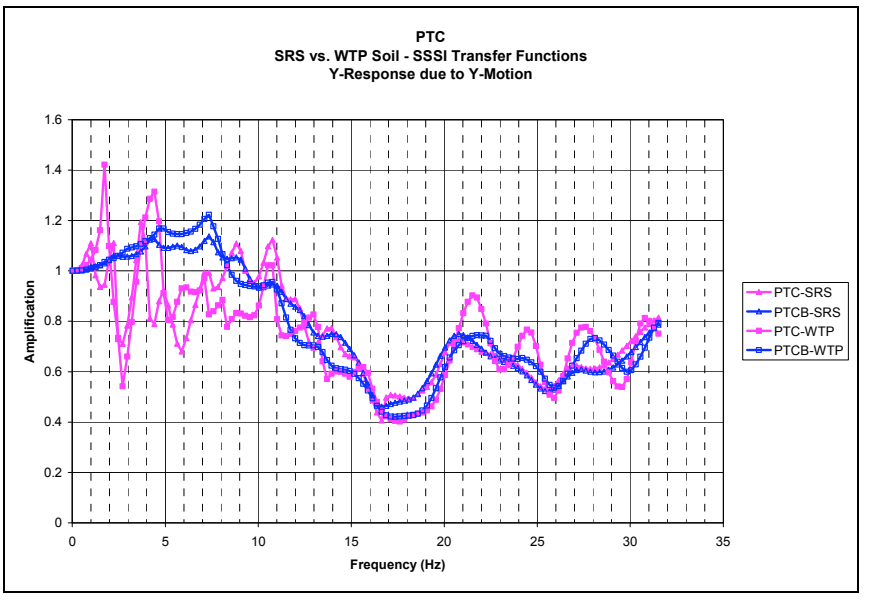


Figure 16. NS Comparison of SSSI Effect WTP vs. SRS Soil.

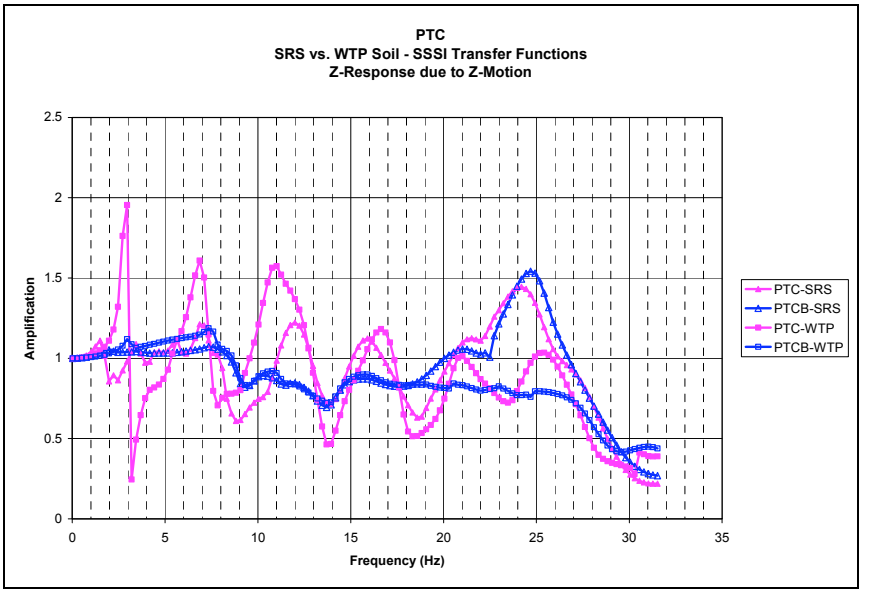


Figure 17. Vertical Comparison of SSSI Effect WTP vs. SRS Soil.

The low frequency energy that is apparent in the response of the model on Hanford Site soil is not evident in the response of the model on Savannah River Site soil. The overall pattern of the transfer functions for the WTP and SRS soil profiles are similar; however, the SRS soil profile provides less SSSI amplification.

The ratio of the combined model response to the individual model response is computed for each frequency and then averaged. The resulting ratios are shown in Table 2.

Table 2. SSSI Ratios by Soil Type.

	SRS Soil	WTP Soil
EW	1.01	1.03
NS	0.97	1.05
Vertical	0.99	1.07

The ratios show that SSSI amplifications are of lesser magnitude when considering a softer soil profile.

CONCLUSION

The Pretreatment Facility Control Building exhibits a significant amplification of seismic demand loads due to the SSSI effect of a larger adjacent structure. Weighted average ratios of maximum nodal accelerations indicate that the SSSI amplifications are most significant in the vertical direction which results in a 33% increase in seismic demand. The amplification in the response perpendicular to the building interface is also significant, resulting in a 15% increase in seismic demand. The amplification of the response parallel to the building interface is less significant, representing only a 2% increase in demand loads.

The Savannah River Site soil profile applied to the Pretreatment Facility Complex structure lowered the SSSI amplification that was apparent with the Hanford Site soil profile. The softer soil generates a smaller SSSI effect than that of the stiffer soil.

REFERENCES

Computers & Structures, Inc. [2000]. "SAP2000, Integrated Software for Structural Analysis & Design", Version 10.0.1, CSI, Berkeley, CA.

Lysmer, J. Tabatabaie-Raissi, M. Tajirian, F. Vahdani, S. and Ostadan, F. [1972], "*SASSI - A System for Analysis of Soil-Structure Interaction*," Report No. UCB/GT/81-02, Geo-technical Engineering, Civil engineering Department, University of California, Berkeley, CA, April.

Lysmer, J. Ostadan, F. and Chin, C.C. [1999], "*SASSI2000 – A System for Analysis of Soil-Structure Interaction*", Revision 1. Geotechnical Engineering Division, Civil Engineering Department, University of California, Berkeley, CA.

U.S. Department of Energy [2002]. "DOE Standard - Natural Phenomena Hazards Design and Evaluation Criteria for Department of Energy Facilities", DOE-STD-1020-2002, U.S. Department of Energy, Washington D.C.

Performance test of secondary mass dampers for vibration control of tall buildings

H. Kim[1], J.-W. Park[2], D.-K. Kim[3], S. Hwang[4]

[1]Assistant Professor, School of Architecture & Civil Engineering, Kyungpook National Univ., Korea, e-mail:hjk@knu.ac.kr
[2]Graduate student, School of Architecture & Civil Engineering, Kyungpook National Univ., Korea, e-mail:unmetoo@knu.ac.kr
[3]Graduate student, School of Architecture & Civil Engineering, Kyungpook National Univ., Korea, e-mail: kdksay0704@knu.ac.kr
[4]Graduate student, School of Architecture & Civil Engineering, Kyungpook National Univ., Korea, e-mail: hsk4298@gmail.com

ABSTRACT

For a secondary mass damper such as tuned liquid damper (TLD) or tuned liquid column damper (TLCD), whose moving mass is liquid, it is impossible to pre-fabricate the damper in a factory for the identification of dynamic properties. Also, it is not easy to pre-fabricate a concrete tuned mass damper (TMD) in a factory whose moving mass is made of concrete. In this paper, an identification method of dynamic properties of secondary mass dampers based on the forced vibration test is presented. Decoupled equations of motion are derived from a coupled equation of motion of building and damper. The decoupled equations of motion are then applied to the system identification using the response of the damper as an input and the response of the building as an output. The proposed method is applied to numerical examples and an actual TMD and TLCD installed in buildings.

INTRODUCTION

As the design and construction of skyscrapers has increased growing in recent years, the interest in the countermeasures to reduce wind-induced motion has gradually increased. In particular, most tall buildings in construction recently have been residential buildings, and thereby the issue of residents' serviceability against wind-induced vibration has received more attention. To solve this matter, it has become a more common practice to install supplementary damping devices for dissipating the energy caused by the external load rather than to increase the lateral stiffness (Soong and Dargush, 1997).

The most typical supplementary damping devices are inter-story installation type dampers and secondary mass dampers (Kim and Adeli, 2005a, Irwin, 2009). The inter-story installation type dampers provide energy dissipation utilizing hysteretic force-displacement behavior induced by inter-story drift. The secondary mass dampers such as a tuned mass damper (TMD), a tuned liquid damper (TLD), and a

tuned liquid column damper (TLCD) are devices relying on the motion of a secondary mass, which is about 0.3 to 1.0% of the entire mass of the building, to counteract the forces acting on a building. Because the secondary mass dampers are often installed on the top floor, they provide fewer architectural constraints than inter-story installation type dampers.

When designing a secondary mass damper, the ratio of moving mass to the first modal mass, or called generalized mass, of a building is determined depending on the required reduction ratio of wind induced vibration. Then, the optimal tuning frequency and damping ratio of the secondary mass damper are calculated based on the determined mass ratio. In the case of a TMD design, the stiffness and number of springs are decided from the optimal frequency ratio, and the damping coefficient and number of oil dampers are decided from the optimal damping ratio (Rana and Soong, 1998, Ghorbani-Tanha et al., 2008).

Before installing a TMD at a site, it requires a free vibration test or human-powered vibration test to be conducted in the factory using a pre-assembled TMD in order to obtain TMD's natural frequency, damping ratio, friction coefficient, restoration force, and other dynamic properties for comparison with designed values. This is to consider discrepancy and tolerance during the fabrication and installation. Especially, the accurate identification of the natural frequency is very important because the control performance of the secondary mass dampers depends significantly on how dampers are properly tuned to the natural frequency of a building. In general, the natural frequency of the pre-assembled TMD is calculated from a spectrum analysis of the response obtained from the free vibration test or human-powered vibration test in the factory, and the damping ratio is calculated using a logarithmic decrement method or half-power method.

In the case of TLD or TLCD, however, it is impossible to perform a factory test using an actual size damper. In addition, in the case of a concrete TMD whose moving mass is composed of concrete rather than steel, the accurate identification of the dynamic properties of the pre-assembled TMD is very difficult because concrete casting at the factory is not feasible.

When the factory test is not viable, the only way to identify the natural frequency and damping ratio of a secondary mass damper is through a force vibration test after installing the damper at the site. In the case of the field test, however, it is very difficult to estimate the dynamic properties accurately using a simple spectrum analysis method and logarithmic decrement method because the responses of a building and a secondary mass damper are coupled in connection to each other. This is because the peak of each response spectrum of damper and building are split into two peaks. That is, the interaction of the building and damper causes the building mode to split into two modes and vice versa.

In this paper, an identification method of the dynamic properties of secondary mass dampers based on the force vibration test is presented. Decoupled equations of motion are derived from a coupled equation of motion of building and damper. The decoupled equations of motion are then applied to the system identification of secondary mass dampers using the response of dampers as an input and the response of the building as an output. For the verification of the proposed method, the dynamic properties of a TMD and a TLCD installed on a single-degree-of-freedom

(SDOF) system are identified through numerical examples. Further, the method is applied to the identification of an actual TMD and TLCD installed in buildings using free vibration responses.

EQUATIONS OF MOTION

TMD. A TMD is a device that increases the damping capacity of a building by installing a secondary mass body with springs and dashpots attached to the building (Figure 1). Since the TMD is installed so that the frequency of this secondary mass body is tuned or close to the natural frequency of the building, the behavior of TMD becomes out of phase to the behavior of the building when the excitation frequency matches the natural frequency of the building resulting in the energy dissipation by the inertial force of the TMD.

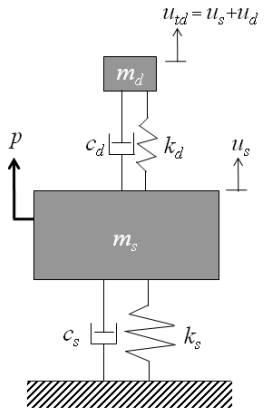


Figure 1. An SOF system with a TMD

The equation of motion of an SDOF system with a TMD can be easily constructed treating the TMD as an additional DOF added to the SODF system. Then, the consequent coupled equation of motion is given as (Den Hartog, 1956, Chopra, 1995)

$$\begin{bmatrix} m_s & 0 \\ 0 & m_d \end{bmatrix}\begin{bmatrix} \ddot{u}_d \\ \ddot{u}_{td} \end{bmatrix}+\begin{bmatrix} c_s+c_d & -c_d \\ -c_d & c_d \end{bmatrix}\begin{bmatrix} \dot{u}_d \\ \dot{u}_{td} \end{bmatrix}+\begin{bmatrix} k_s+k_d & -k_d \\ -k_d & k_d \end{bmatrix}\begin{bmatrix} u_d \\ u_{td} \end{bmatrix}=\begin{bmatrix} p \\ 0 \end{bmatrix} \quad (1)$$

where m_s, c_s, and k_s are mass, damping coefficient, and stiffness of the SODF system, respectively, and m_d, c_d, and k_d are mass, damping coefficient, and stiffness of the TMD respectively, and u_s is the displacement of the SDOF system, and u_{td} is the absolute displacement of the TMD, and p is an external load applied to the SDOF system. It can be seen from Eq. (1) that the response of SDOF system is coupled with that of TMD because there exist non-zero off-diagonal terms.

The natural frequency and damping ratio of TMD can be obtained from Eq. (1) as

$$\omega_d = \sqrt{\frac{k_d}{m_d}} \tag{2.a}$$

$$\xi_d = \frac{c_d}{2m_d\omega_d} \tag{2.b}$$

where ω_d and ξ_d are the natural frequency and damping ratio of TMD, respectively. The ratio of natural frequencies of TMD to that of SDOF system is called frequency ratio, γ, and the ratio of TMD mass to that of SDOF system is called mass ratio, μ, where

$$\gamma = \frac{\omega_d}{\omega_s} \tag{3.a}$$

$$\mu = \frac{m_d}{m_s} \tag{3.b}$$

The optimal frequency and damping ratio of TMD are functions of the mass ratio given in Eq. (3.b) as follows.

$$\gamma_{opt} = \frac{1}{1+\mu} \tag{4.a}$$

$$\xi_{opt} = \frac{1}{2}\sqrt{\frac{3\mu/2}{1+3\mu}} \tag{4.b}$$

The expressions in Eq. (4) are derived assuming free vibration or sinusoidal external loading and zero structural damping ratio. Therefore, the optimal values vary if the external loading is different or there is intrinsic non-zero structural damping ratio. For tall buildings subjected to wind load, however, it is common in practice to design a TMD using optimal parameters by Eq. (4) because the first mode governs the behavior of the tall building and the damping ratio of the building is very small.

In Figure 1, the absolute displacement of TMD is the sum of the displacement of the SDOF system, us, and the relative displacement of TMD to the SDOF system, ud, and it can be expressed as follows.

$$u_{td} = u_s + u_d \tag{5}$$

Using the relative displacement of TMD, Eq. (1) can be re-written as

$$\begin{bmatrix} m_s & 0 \\ m_d & m_d \end{bmatrix}\begin{bmatrix} \ddot{u}_d \\ \ddot{u}_d \end{bmatrix} + \begin{bmatrix} c_s & -c_d \\ 0 & c_d \end{bmatrix}\begin{bmatrix} \dot{u}_d \\ \dot{u}_d \end{bmatrix} + \begin{bmatrix} k_s & -k_d \\ 0 & k_d \end{bmatrix}\begin{bmatrix} u_d \\ u_d \end{bmatrix} = \begin{bmatrix} p \\ 0 \end{bmatrix} \tag{6}$$

The first row of Eq. (6) is

$$m_s\ddot{u}_s + c_s u_s + k_s u_s = p + k_d u_d + c_d \dot{u}_d \tag{7}$$

and the second row of Eq. (6) is

$$m_d\ddot{u}_d + m_d\ddot{u}_s = -k_d u_d - c_d \dot{u}_d \tag{8}$$

Substituting Eq. (8) into Eq. (7) yields

$$m_s\ddot{u}_s + c_s u_s + k_s u_s = p - m_d(\ddot{u}_s + \ddot{u}_d) \tag{9}$$

From Eq. (5), the sum of the absolute acceleration of the SDOF system and the relative acceleration of the TMD in Eq. (9) equals the absolute acceleration of the TMD. Consequently, the equation of motion of SDOF system and TMD can be expressed as follows.

$$m_s\ddot{u}_s + c_s u_s + k_s u_s = p - m_d\ddot{u}_{td} \tag{10.a}$$
$$m_d\ddot{u}_d + c_d \dot{u}_d + k_d u_d = -m_d\ddot{u}_s \tag{10.b}$$

Eq. (10.b) can be further simplified as

$$\ddot{u}_d + 2\xi_d\omega_d\dot{u}_d + \omega_d^2 u_d = -\ddot{u}_s \tag{11}$$

From Eqs. (10.b) and (11), it can be seen that the equation of motion for a TMD subjected to the motion of the SDOF system is identical to that of an SDOF system subjected to an earthquake load. Moreover, it can be recognized that the external force applied to the SDOF system is not included in the equation. Therefore, it can be concluded that the natural frequency and damping ratio of TMD can be identified easily if the acceleration of SDOF system and one of the responses among relative acceleration, relative velocity, and relative displacement of the TMD are known. This can be done by applying any system identification technique using the acceleration of SDOF system as an input and the response of TMD as an output.

Meanwhile, the dynamic properties of the building can be easily obtained from a transient vibration test applying any typical system identification techniques (Ljung, 2007). In the transient vibration test, the movement of TMD should be restrained in order not to provoke any interaction with the building. This condition, however, is often difficult to satisfy in practice. Accordingly, it would be useful if the approximate dynamic properties of the building could be directly identified from an in-situ experiment.

In the in-situ TMD experiment, a free vibration test is often used. The TMD is forced by a hydraulic pump to have an initial displacement and released to move freely, which in turn causes the building to vibrate. In this case, the external force, p, in Eq. (10.a) can be ignored if the magnitude of building vibration is large enough

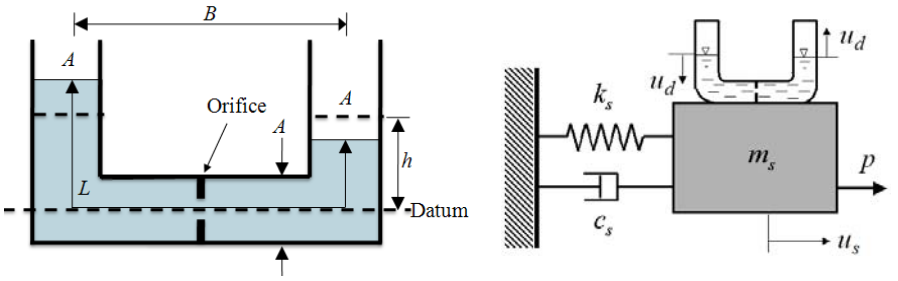
and the applied wind load is negligible. Then, Eq. (10.a) can be simplified as

$$\ddot{u}_s + 2\xi_s\omega_s\dot{u}_s + \omega_s^2 u_s = -\mu\ddot{u}_{td} \tag{12}$$

Similar to the identification of TMD, it can be seen from Eq. (12) that the natural frequency and damping ratio of the building can be obtained by applying any typical system identification technique using a response of TMD as an input and a response of the building as an output.

TLCD. A TLD is similar to a TMD in principle except that a TLD uses liquid (usually water) as a secondary mass body. That is, liquid acts as a moving mass and the liquid sloshing movement absorbs the building's energy if the sloshing frequency is tuned to the natural frequency of the building. In addition to this similarity, a TLD has the advantages of cheap installation cost and ease of maintenance compared to a TMD. Because the control performance of a TLD is close to that of a TMD, it has been increasingly used in practice (Kim and Adeli, 2005b, Kim et al., 2008, Shum et al, 2008).

A TLCD proposed by Sakai et al. (1989) is as one of the TLD variations and particularly designed to maximize the liquid motion energy in the TLD. It is made of a U-shaped tube and dissipates the energy acting on the building by the passage of the liquid through an orifice (Figure 2).



(a) Section of TLCD **(b) An SDOF system with a TLCD**

Figure 2. TLCD system

Unlike a TMD, there is no spring and dashpot between the U-shaped tube of a TLCD and main structure. Therefore, the liquid in the vertical tube is moving together with structure while the external force causes an additional movement of the liquid in the horizontal tube resulting in the following dynamic equilibrium (Chang and Qu, 1998).

$$m_{dh}(\ddot{u}_s + \ddot{u}_d) + m_{dv}\ddot{u}_s + m_s\ddot{u}_s + c_s\dot{u}_s + k_s u_s = p \tag{13}$$

where m_{dh} and m_{dv} are the mass of liquid in the horizontal and vertical tubes, respectively. Eq. (13) can be re-written as

$$(m_s + m_d)\ddot{u}_s + m_{dh}\ddot{u}_d + c_s\dot{u}_s + k_s u_s = p \tag{14}$$

where m_d (= m_{dh} + m_{dv}) is the total liquid mass. From Figure 2, the total liquid mass and mass of liquid in the horizontal tube are calculated as follows.

$$m_d = \rho AL \tag{15.a}$$

$$m_{dh} = m_d \frac{B}{L} \tag{15.b}$$

where ρ is the density of liquid, A is the cross-sectional area of tube, B is the center to center distance between vertical tubes, and L is the total liquid length. The total liquid length, L, is calculated as

$$L = B + 2h \tag{16}$$

where h is the height of water column from the center of the horizontal tube when the liquid is in a state of equilibrium.

When the liquid in a U-shaped tube is moved by the movement of structure, the equilibrium inside the tube is as follows.

$$m_{dh}\ddot{u}_s + m_d\ddot{u}_d + \frac{\rho A\zeta}{2}|\dot{u}_d|\dot{u}_d + 2\rho A g u_d = 0 \tag{17}$$

where g is the gravitational acceleration and ζ is the head-loss coefficient that varies depending on the orifice opening ratio. The natural frequency and damping coefficient of TLCD can be calculated from Eqs. (15) and (17) as follows.

$$\omega_d = \sqrt{\frac{2\rho Ag}{m_d}} = \sqrt{\frac{2g}{L}} \tag{18.a}$$

$$c_d = \frac{\rho A\zeta}{2}|\dot{u}_d| \tag{18.b}$$

It can be seen from Eq. (18.b) that the damping force of a TLCD is not linear unlike a TMD since the absolute value of velocity is included in the damping coefficient.

Using Eqs. (14) and (17), the equation of motion of a SDOF system with a TLCD can be constructed similar to Eq. (1) as follows.

$$\begin{bmatrix} m_s + m_d & m_{dh} \\ m_{dh} & m_d \end{bmatrix}\begin{bmatrix} \ddot{u}_s \\ \ddot{u}_d \end{bmatrix} + \begin{bmatrix} c_s & 0 \\ 0 & c_d \end{bmatrix}\begin{bmatrix} \dot{u}_s \\ \dot{u}_d \end{bmatrix} + \begin{bmatrix} k_s & 0 \\ 0 & k_d \end{bmatrix}\begin{bmatrix} u_s \\ u_d \end{bmatrix} = \begin{bmatrix} p \\ 0 \end{bmatrix} \tag{19}$$

It can be seen from Eq. (19) that the response of the SDOF system is coupled with that of the TLCD because there are non-zero off-diagonal terms in the mass matrix similar to Eq. (1) of the TMD where there are non-zero off-diagonal terms in the damping and stiffness matrix.

In order to identify the dynamic characteristics of a TLCD using the responses of structure and TLCD, the coupled equation of Eq. (17) needs to be derived into the form of Eq. (11). Eq. (17) can be simplified using Eqs. (2.b) and (18) as

$$\ddot{u}_d + 2\xi_d \omega_d \dot{u}_d + \omega_d^2 u_d = -\frac{m_{dh}}{m_d}\ddot{u}_s = -\frac{B}{L}\ddot{u}_s \tag{20}$$

where

$$\xi_d = \frac{c_d}{2m_d\omega_d} \tag{21}$$

Accordingly, if the accelerations of structure and response of a TCLD are available, the natural frequency and damping ratio of a TLCD can be identified using the structural acceleration as an input and the response of a TLCD as an output from Eq. (20) similarly to a TMD. It is important to note that the identified damping ratio of a TLCD is only an equivalent damping ratio unlike a TMD because the damping ratio in Eqs. (20) and (21) includes a nonlinear term. The equivalent damping ratio has been studied by several researchers, and the optimal equivalent damping ratio for the case of sinusoidal load is given by

$$\xi_{opt} = \frac{1}{2}\sqrt{\frac{\gamma(1+\mu-\gamma/4)}{(1+\mu)(1+\mu-\gamma/4)}} \tag{22}$$

Through field experiments on a TLCD, the dynamic properties of a structure can also be approximately calculated from the responses of structure and a TLCD similar to the case of a TMD. First, Eq. (14) can be re-written as

$$(m_s + m_d)\ddot{u}_s + c_s\dot{u}_s + k_s u_s = p - m_{dh}\ddot{u}_d \tag{23}$$

Similar to the free vibration test of a TMD, if the displacement caused by a TLCD is large enough compared to the displacement caused by external forces during the field test of a TLCD, it is possible to ignore the external force term. Then Eq. (23) can be simplified as follows taking into consideration that the mass of TLCD is generally less than 1% of the mass of the structure.

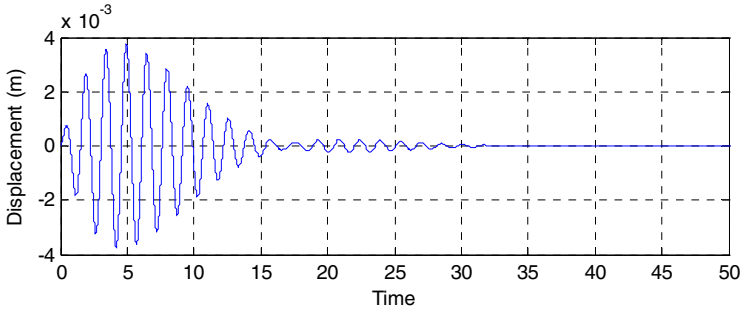
$$\ddot{u}_s + 2\zeta_s \omega_s \dot{u}_s + \omega_s^2 u_s = -\frac{m_{dh}}{m_s}\ddot{u}_d \tag{24}$$

It can be seen from Eq. (24) that the natural frequency and damping ratio of the building can approximately calculated by applying any typical system identification technique using the response of a TLCD as an input and the response of the building as an output in a way similar to the case of a TMD.

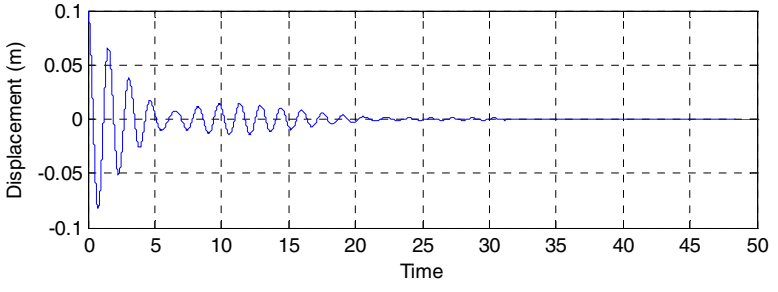
NUMERICAL EXAMPLES

TMD example. A numerical study of an SDOF system with a TMD is performed to investigate the validity of the proposed method for the identification of dynamic properties of TMD and structure. It is assumed that the mass, natural frequency, and damping ration of the SDOF system are 10,449 ton, 0.660 Hz, and 2%, respectively, and the mass of TMD is 100 ton. The corresponding mass ratio of TMD to SDOF system is 0.96 %. From Eq. (4), the optimal natural frequency and damping ratio of TMD are obtained as 0.6537 Hz and 5.91%, respectively.

The free vibration response of the SDOF system is calculated numerically enforcing the initial displacement on the TMD. Figures 3 and 4 present the displacement and acceleration time histories of the SDOF system and TMD, respectively, when the initial displacement of the TMD is 0.09 m. The corresponding power spectral densities (PSD) of the SDOF system and TMD accelerations are shown in Figure 5. From Figure 5, it can be seen that the peak of each PSD of the SDOF system and TMD are split into two peaks near 0.660 Hz, which is the natural frequency of the SDOF system. Consequently, it can be concluded that it is not possible to obtain the natural frequency and damping ratio from PSD using the spectrum analysis method and half-power method due to the interaction of the building and damper.

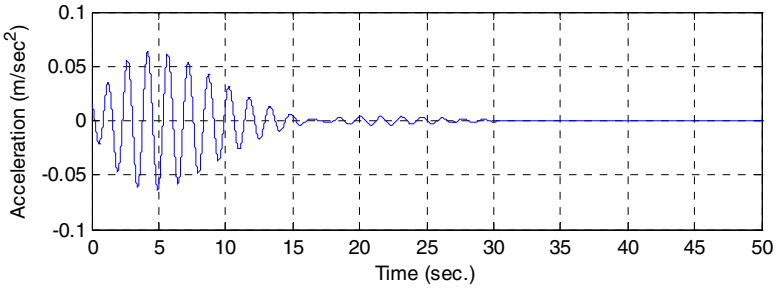


(a) Displacement time history of the SDOF system

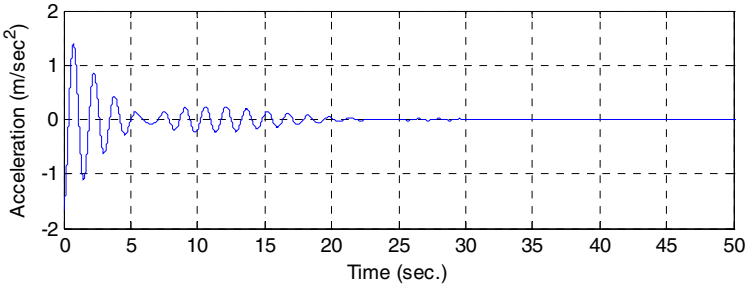


(b) Displacement time history of the TMD

Figure 3. Displacement time histories of the SDOF system and the TMD subjected to the initial TMD displacement of 0.09 m

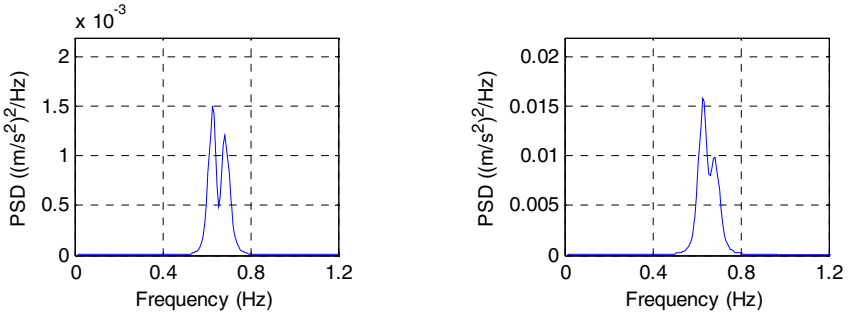


(a) Acceleration time history of the SDOF system



(b) Acceleration time history of the TMD

Figure 4. Acceleration time histories of the SDOF system and the TMD subjected to the initial TMD displacement of 0.09 m



(a) SDOF system **(b) TMD**

Figure 5. PSDs of the SDOF system and TMD accelerations

Using the proposed method, the natural frequency and damping ratio of the TMD can be identified directly from the responses of the SDOF system and TMD. The identified natural frequencies and damping ratios of the TMD found using Eq. (11) are summarized and compared in Table 1. The input for the system identification is the acceleration of the SDOF system while the outputs are the relative displacement and relative acceleration of the TMD. This is to evaluate the identified results depending on the output responses because both the relative displacement and relative acceleration of the TMD can be measured during the free vibration test of the TMD.

Table 1.Identified natural frequency and damping ratio of TMD

Output response	Identified system matrix	Natural frequency (error)	Damping ratio (error)
TMD relative displacement	$\mathbf{A}=\begin{bmatrix} 999.752 & 1000.246 \\ -999.760 & -1000.237 \end{bmatrix}$	0.6538 Hz (0.02 %)	5.91 % (0.00 %)
TMD relative acceleration	$\mathbf{A}=\begin{bmatrix} 999.749 & 1000.248 \\ -999.757 & -1000.240 \end{bmatrix}$	0.6565 Hz (0.43 %)	5.95 % (0.68 %)

The system identification in this study is performed using a Matlab Box-Jenkins model and the state space equation with an order of 2 is used. The system matrix A in Table 1 represents the identified system matrix of the Box-Jenkins model, and the natural frequency and damping ratio are obtained from the eigenvalue analysis using the system matrix A. It can be seen from Table 1 that the identification using both the TMD relative displacement and the relative acceleration yields accurate results with errors of less than 1.0 %.

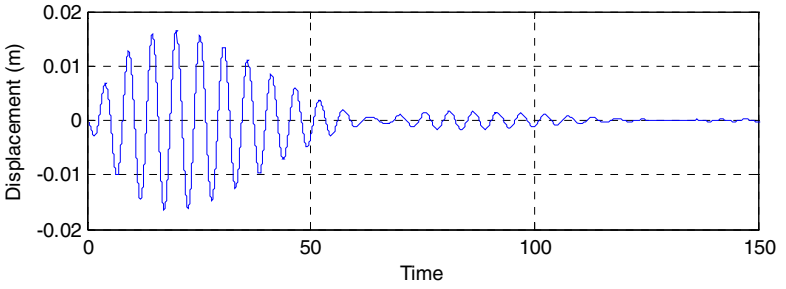
Table 2.Identified natural frequency and damping ratio of SDOF system

Input response	Identified system matrix	Natural frequency (error)	Damping ratio (error)
TMD relative displacement	$\mathbf{A}=\begin{bmatrix} 99.858 & 100.113 \\ -99.945 & -100.027 \end{bmatrix}$	0.6619 Hz (0.29 %)	2.02 % (1.0 %)
TMD relative acceleration	$\mathbf{A}=\begin{bmatrix} 99.861 & 100.111 \\ -99.947 & -100.025 \end{bmatrix}$	0.6604 Hz (0.06 %)	1.98 % (1.0 %)

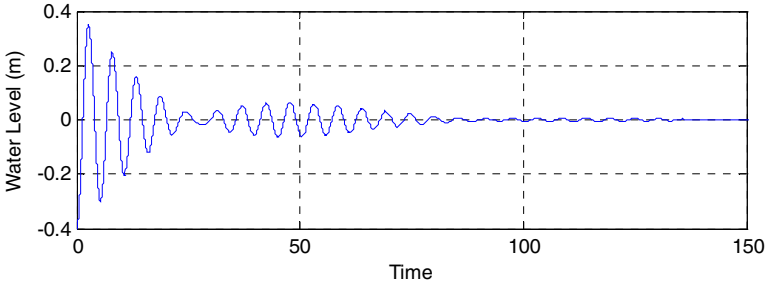
The system identification of the SDOF system is also performed using Eq. (12) and the results are summarized in Table 2. The output for the system identification is the acceleration of the SDOF system while the inputs are the relative displacement and relative acceleration of the TMD. It can be seen from Table 2 that the results using both the TMD relative displacement and the relative acceleration are close to the assumed value. This is because the external force is not considered in the numerical analysis. In contrast, the identified results for the actual building may contain errors to some extent due to external wind load applied to the building during the field test.

TLCD example. The identification of dynamic characteristics of a TLCD and building is performed numerically using a SDOF system. For the numerical simulation, the mass, natural frequency, and damping ratio of the SDOF system are assumed to be 34,153 ton, 0.189 Hz, and 2%, respectively. Further, it is assumed that the mass ratio is 1 % and the ratio the center to center distance between vertical tubes to the total liquid length (B/L) is 0.9. The corresponding optimal natural frequency of

TLCD is 0.187 Hz and the optimal equivalent damping ratio from Eq. (22) is 4.23 %.

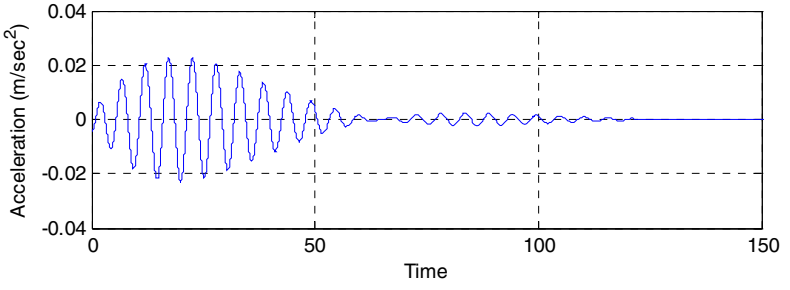


(a) Displacement time history of the SDOF system

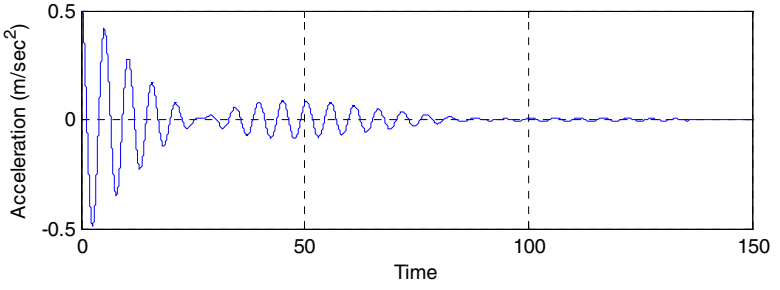


(b) Water level time history of the TLCD

Figure 6. Displacement time histories of the SDOF system and TLCD subjected to the initial TLCD water level of 0.4 m

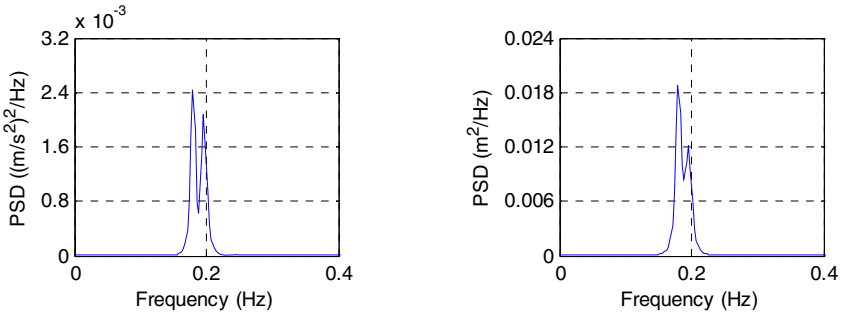


(a) Acceleration time history of the SDOF system



(b) Acceleration time history of the TLCD

Figure 7. Acceleration time histories of the SDOF system and the TLCD subjected to the initial TLCD water level of 0.4 m



(a) SDOF system **(b) TLCD**

Figure 8. PSDs of the SDOF system and TLCD accelerations

The free vibration response of the SDOF system is calculated numerically enforcing the initial water level on the TMD. Figs. 6 and 7 present the displacement and acceleration time histories of the SDOF system and TLCD, respectively, when the initial water level of TLCD is 0.4 m. The corresponding PSDs of the SDOF system and TLCD accelerations are shown in Figure 8. From Figure 8, it can be seen that the peak of each PSD of the SDOF system and TMD are split into two peaks near 0.189 Hz, which is the natural frequency of the SDOF system. Consequently, it can be concluded that it is not possible to obtain the natural frequency and damping ratio from a PSD similar to how it was obtained in a TMD.

In the field test of TLCD, it is impractical to measure the acceleration of water in the TLCD, and only the water level is generally measured using an ultrasonic level probe. Accordingly, the water level in the TLCD and the acceleration of the SDOF system are only used for the system identification in this numerical example. The identified dynamic parameters of the SDOF system and TLCD using Eqs. (20) and (24) are summarized in Table 3. The input and output for the identification of the TLCD are the acceleration of the SDOF system and the TLCD water level, respectively, and the input and output for the identification of the SDOF system are the TLCD water level and acceleration of the SDOF system, respectively.

Table 3.Identified natural frequency and damping ratio of the SDOF system and TLCD

	Identified system matrix	Natural frequency (error)	Damping ratio (error)
TLCD	$\mathbf{A} = \begin{bmatrix} 199.950 & 200.049 \\ -199.954 & -200.045 \end{bmatrix}$	0.1871 Hz (0.01 %)	4.04 % (1.5 %)
SDOF system	$\mathbf{A} = \begin{bmatrix} 19.955 & 20.034 \\ -19.990 & -19.998 \end{bmatrix}$	0.1888 Hz (0.11 %)	1.84 % (8.0 %)

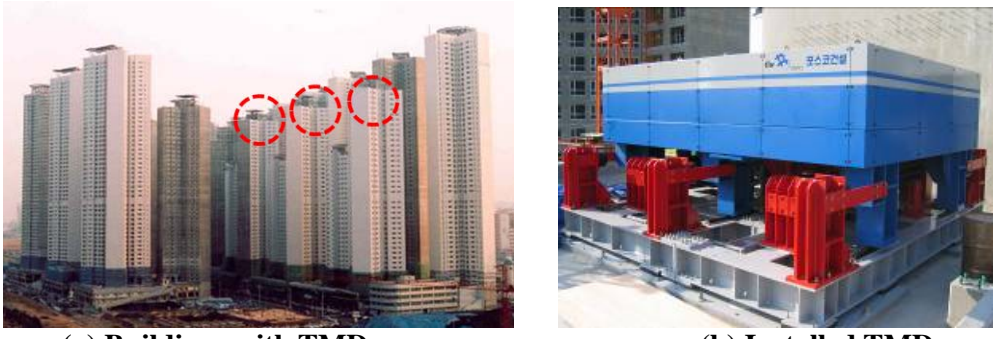
It can be seen from Table 3 that the natural frequencies are quite closely estimated while the damping ratios are identified with relatively large errors. This is

because the damping ratio of a TLCD is a nonlinear value having an absolute value of TLCD water velocity as seen in Eq. (18). Considering that the error is 1.5 % compared to the linearlized optimal equivalent damping ratio of Eq. (21) and the factory pre-assembling test is impossible for a TLCD, however, it can be concluded that the proposed method in this study is effective enough for the identification of a TLCD based on in-situ experiment.

IN-SITU FORCED VIBRATION TEST

TMD test. For the system identification of a TMD through a forced vibration test, the free vibration test was performed in a 50-story building where a TMD is installed. Figure 9(a) depicts the buildings where TMDs are installed and Figure 9(b) shows an installed TMD. The buildings are residential buildings and TMDs are installed in the three buildings marked with dotted circles in Figure 9(a).

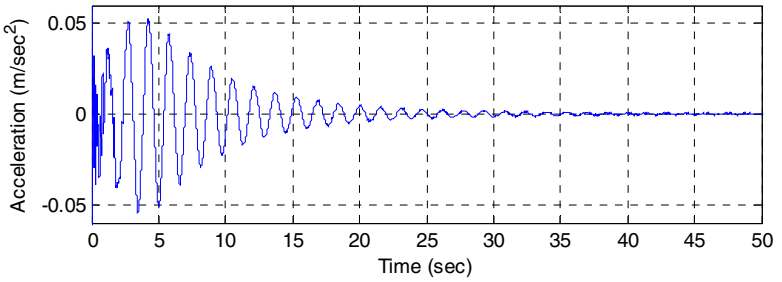
The generalized mass and frequency of the fundamental mode of the building are 10,449 ton and 0.660 Hz, respectively, and the assumed damping ratio for wind design is 2.0 %. The mass of the TMD was designed to be 100 ton, and the natural frequency of TMD was set at 99% of that of the building. The optimal damping ratio of the TMD is 6.0%. Because the moving mass of the TMD installed in the Centum Park project is steel, a pre-assembled test was performed in the factory. The errors of the natural frequency and damping ratio obtained from the factory test were 2.5% and 3.3% respectively.



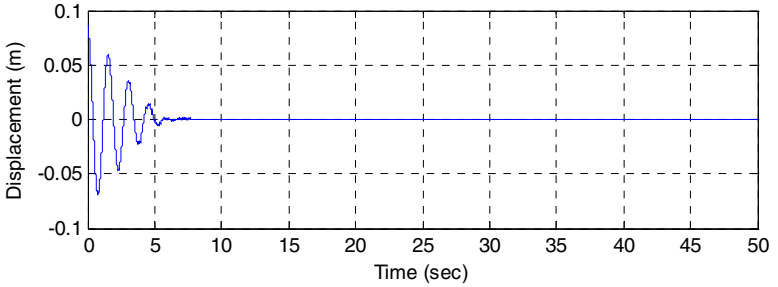
(a) Buildings with TMD **(b) Installed TMD**

Figure 9. Centum Park project, Busan, Korea

A TMD was installed on the roof floor when the concrete work of the structural frame was completed and the forced vibration test was performed at the time of completion of construction including cladding. Figure 10 shows the measured acceleration time histories of the building and the free vibration displacement of the TMD obtained from the forced vibration test on site. The forced vibration test was performed by enforcing an initial displacement of 0.09 m on TMD. It can be seen from Figure 10 that the peak acceleration of the building is about 0.05 m/sec2, which corresponds to the H-90 level according to AIJ2004. This indicates that the acceleration due to the external wind load during the field test was negligible compared to that due to TMD initial displacement.



(a) Accelearation time history of the building



(b) Displacement time history of the TMD

Figure 10. Time histories of the building and TMD obtained from the forced vibration test

The results of system identification using the TMD displacement and building acceleration presented in Figure 10 are shown in Table 4. It can be noted from Table 4 that the identified dynamic parameters of the TMD and building are close to the designed values and the results of the factory test while the natural frequency of the TMD was found to be little greater than the designed value. This is because the TMD is originally tuned to the expected natural frequency based on the testing of a partially completed building.

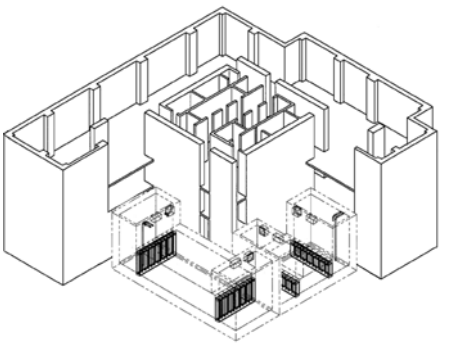
Table 4.Identified natural frequency and damping ratio of the building and TMD

	Natural frequency	Damping ratio
TMD	0.6668 Hz	8.37 %
Building	0.6623 Hz	2.60 %

TLCD test. The forced vibration test was performed for the system identification of the TLCD on a 64-story building where two TLCDs are installed. Figure 11(a) depicts the buildings where TLCDs are installed and Figure 11(b) shows an isometric view of the TLCD floor. The buildings are residential buildings and TLCDs are installed in the all four buildings.



(a) Buildings with TLCD



(b) Isometric view of TLCD floor

Figure 11. The First World project, Incheon, Korea

The generalized mass and frequency of the fundamental mode of the building are 31,145 ton and 0.189 Hz, respectively, and the assumed damping ratio for wind design is 2.0 %. Two perpendicular TLCDs are installed in each building, and the water mass of the larger TLCD is 450 ton. The natural frequency of TLCD is set at 97 % of that of the building. Table 5 shows the results of the building system identification based on the ambient vibration test. It can be noted from Table 5 that the natural frequency shows almost no change but the damping ratio increases significantly by adding water to the TLCD.

Table 5. Identified natural frequency and damping ratio of building based on the ambient vibration test

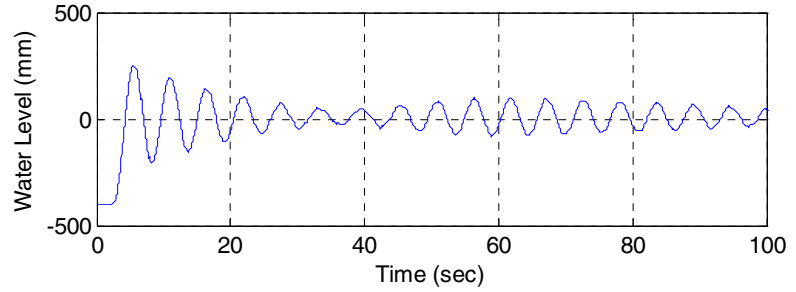
	Natural frequency	Damping ratio
Without TLCD water	0.188Hz	0.47%
With TLCD water	0.189Hz	1.47%

TLCDs were installed on the 66th floor when the concrete work of the structural frame was completed and the forced vibration test was performed at the time of completion of construction. The forced vibration test was performed enforcing an initial water level of 0.4 m on a TLCD. Figure 12 presents the measured TLCD water level and building acceleration obtained from the forced vibration test.

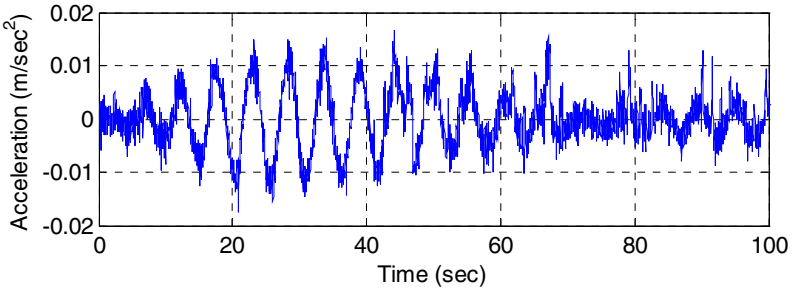
The results of system identification using the TLCD water level and building acceleration presented in Figure 12 are shown in Table 6. For the system identification, a low-pass filter of 1 Hz was used in order to minimize the effect of higher modes and noise. It can be seen from Table 4 that the identified dynamic parameters of the TMD and building are close to the designed values and the results of an ambient vibration test.

Table 6. Identified natural frequency and damping ratio of the building and TLCD

	Natural frequency	Damping ratio
TLCD	0.1788 Hz	3.65 %
Building	0.1854 Hz	1.50 %



(a) Time history of water level in a TLCD



(b) Time history of the building acceleration

Figure 12. Time histories of forced vibration of the building caused by the water oscillation

CONCLUSIONS

In this paper, an identification method for the dynamic properties of secondary mass dampers based on the forced vibration test is presented for the case that the pre-assembled test in a factory is impractical. Decoupled equations of motion are derived from a coupled equation of motion of building and damper. These decoupled equations of motion can be applied to general system identification methods using the responses of the building and damper.

For the verification of the proposed method, the dynamic properties of a TMD and a TLCD install12345ed on a SDOF system were identified through numerical examples, and the method was applied to the identification of an actual TMD and TLCD installed in buildings using free vibration responses. The results of the numerical study and the forced vibration test show that the proposed method is effective in the identification of TMD and TLCD based on the forced vibration test.

REFERENCES

Chang, C.C. and Qu, W.L. (1998), "Unified dynamic absorber design formulas for wind-induced vibration control of tall buildings", The structural design of tall buildings, Vol. 7, No. 2, pp. 147-166.

Chopra, A.K. (1995), Dynamics of structures: theory and applications to earthquake engineering, Prentice, NJ.

Den Hartog, J. P. (1956), Mechanical Vibrations, McGraw-Hill, New York.

Ghorbani-Tanha, A. K., Noorzad, A., and Rahimian, M. (2008), "Mitigation of wind-induced motion of Milad Tower by tuned mass damper", The Structural Design of Tall and Special Buildings, Vol. 18, No. 4, pp. 371–385.

Irwin, P. A. (2009), "Wind engineering challenges of the new generation of super-tall buildings", Journal of Wind Engineering and Industrial Aerodynamics, Vol. 97, No. 7-8, pp. 328-334.

Kim, H. and Adeli, H. (2005a), "Hybrid control of irregular steel highrise building structures under seismic excitations", International Journal for Numerical Methods in Engineering, Vol. 63, No. 12, pp. 1757-1774

Kim, H. and Adeli, H. (2005b), "Wind-induced motion control of 76-story benchmark building using the hybrid damper-TLCD system", ASCE Journal of Structural Engineering, Vol. 131, No. 12, pp. 1794-1802.

Kim, H., Kim, W.-J., Lee, S.-G., Jo, J.-S., Kim, D.-K., and Lee, K.-J. (2008), "Mitigation of Wind-Induced Vibration with Liquid Column Vibration Absorber", Journal Advances in Science and Technology, Vo. 56, pp. 259-264.

Ljung, L. (2007), System Identification Toolbox User's Guide, Mathworks, Natick, MA

Rana, R. and Soong, T.T. (1998), "Parametric study and simplified design of tuned mass dampers", Engineering Structures, Vol. 30, No. 3, pp. 193-204.

Sakai, F., Takaeda, S., and Tamaki, T. (1989), "Tuned Liquid Column Damper – New Type Device for Suppression of Building Vibrations", Proceedings of International Conference on Highrise Buildings, Nanjing, China, pp. 926-931.

Shum, K.M., Xu, Y.L., and Guo, W.H. (2008), "Wind-induced vibration control of long span cable-stayed bridges using multiple pressurized tuned liquid column dampers", Journal of Wind Engineering and Industrial Aerodynamics, Vol. 96, No. 2, pp. 166-192.

Soong, T. T. and Dargush, G. F. (1997), Passive energy dissipation systems in structural engineering , Wiley, New York.

Wu, J.-C., Chang, C.-H., and Lin, Y.-Y. (2009), "Optimal designs for non-uniform tuned liquid column dampers in horizontal motion", Journal of Sound and Vibration, Vol. 326, No. 1-2, pp. 104-122.

A New Structural Modification Approach for Seismic Protection Based on Adaptive Negative Stiffness Device: Conceptual Analysis

D. T. R. Pasala[1], A. A. S. Sarlis[2], Satish Nagarajaiah[1], A. M. Reinhorn[2], M. C. Constantinou[2] and D. Taylor[3]

[1]Rice University, Houston, TX-77005, U.S.A.
[2]University at Buffalo, the State University of New York, Buffalo, NY-14260, U.S.A.
[3]Taylor Devices Inc., North Tonawanda, NY-14120 U.S.A.

ABSTRACT

Column forces, displacements and accelerations experienced by the structure during strong ground motions can be reduced by weakening and (or) softening the structure and adding a supplemental damper. Although this approach proved to be promising analytically, the concept of "structural strength reduction" leads to inelastic behavior and large permanent deformations in the main structural system. In this paper a new concept is developed to emulate weakening in a structural system by adding an "adaptive negative stiffness device" (NSD) and shifting the "yielding" away from the main structural system; leading, to the new idea of "apparent weakening" with reduced inelastic excursions in the main structural system. This is achieved through an adaptive negative stiffness system (ANSS), which is a combination of NSD and a damper. Engaging the NSD at an appropriate displacement (simulated yield displacement), that is well below the actual yield displacement of the structural system, will result in a composite structure-device assembly that behaves like a yielding structure. The NSD has a re-centering mechanism thereby avoiding permanent deformation in the composite structure-device assembly unless, the main structure itself yields. Essentially, a yielding-structure is "mimicked" without any, or with minimum yielding and permanent deformation in the main structure. In summary, the main structural system undergoes less acceleration, less displacements and less base shear, while the ANSS "absorbs" them. This paper presents the working principle and details on development and study of the ANSS/NSD. Through numerical simulations, the effectiveness and the superior performance of the ANSS/NSD as compared to a structural system with supplemental passive dampers is presented.

INTRODUCTION

Conventional structures designed for loads specified by codes undergo significant inelastic deformations during severe earthquakes, leading to stiffness and strength degradation, increased inter-storey drifts, and damage with residual drift. These yielding structures however keep the global forces within limited bounds dictated by the yielding levels. The inelastic effects can be reduced to some extent using passive seismic protection systems in the form of supplemental damping

devices. This approach has emerged as an efficient way to reduce response and limit damage by shifting the inelastic energy dissipation from the framing system to the dampers (Lobo *et al.*, 1993, Constantinou and Symans, 1993, Spencer and Nagarajaiah, 2003). Examples of few such passive systems are base isolation systems (Nagarajaiah et al. 1991, Nagarajaiah *et al.* 2005, 2006; Narasimhan *et al.*, 2006), fluid dampers (Constantinou and Symans, 1993,1997), adaptive tuned mass dampers (Nagarajaiah 2009), adaptive friction dampers (Fenz and Constantinou, 2008), active and semiactive control (Spencer and Nagarajaiah 2003).

Adaptive systems belong to the category of passive seismic protection systems but they are more sophisticated than the regular passive systems. An adaptive system consists of adaptive stiffness and/or damping devices which are capable of changing the stiffness and/or damping of the device depending on the displacement amplitude (Nagarajaiah 2009, Fenz and Constantinou, 2008). These devices are designed to exhibit a force-displacement behavior which upon the addition of structural properties will result in an adaptive system having superior characteristics compared to the original structure. Adaptive systems can also be classified into variable stiffness devices and variable damping devices (Nagarajaiah 2009, Spencer and Nagarajaiah, 2003).

Recently, Iemura and Pradono (2009) proposed pseudo-negative-stiffness dampers (PNSD) that are hydraulic or semiactive or active devices capable of producing negative-stiffness hysteretic loops. It has been shown in their investigations that by adding negative-stiffness hysteretic loops the total force would be lowered significantly. Common passive dampers that act in parallel with the stiffness of structure add to the total force rendering the shear force larger than that due to stiffness of the base-structure alone. Iemura and Pradono (2009) have also reported the applications of PNSD to the benchmark control problems for seismic response reduction. Effectiveness of the proposed method has been validated on three benchmark structures, cable-stayed bridges, buildings, and highway bridges, subjected to various types of recorded ground motions (Iemura and Pradono, 2009). It must be noted that the passive hydraulic dampers cannot "push" the structure is the same direction as the structural displacement; the adaptive NSD proposed in this paper can. Since the NSD has a precompressed spring, it has the ability to push the structure in the same direction as the structural displacement generating the true negative stiffness, instead of pseudo negative stiffness. A hydraulic device that is fully active or semiactive as in the case of PNSD can generate a pseudo-negative stiffness in which case feedback control would be needed to generate the negative stiffness.

All the methods described in this section thus far suffer from one or other limitation: 1) active control devices require feedback and substantial power; 2) semi-active controllers require feedback but nominal power 3) passive control devices may reduce displacement but lead to larger base shear. Combination of adaptive negative stiffness and damping device can result in reduction in base shear and displacement response of the structure. However, to date truly negative stiffness systems have received relatively little attention as compared to aforementioned semiactive or pseudo negative stiffness systems and thus represent a significant gap. Hence, development of new true negative stiffness devices is necessary to reduce the inelastic

behavior excursions in the main structural system. ANSS/NSD can reduce damage in frames by reducing the base shears and deformations and they can also eliminate residual inter-storey drifts.

Reinhorn *et al.* (2005) and Viti *et al.* (2006) introduced the concept of weakening structures (reducing strength and stiffness), while introducing added viscous damping to reduce simultaneously total accelerations and inter-story drifts. Design methodologies for softening the structure (reducing stiffness) and adding damping devices using control theory have been proposed by Cimellaro *et al.* (2009) to determine the locations and the magnitude of weakening and/or softening of structural elements and the added damping while insuring structural stability. A two-stage design procedure was suggested: (i) first using a nonlinear active control algorithm, to determine the new structural parameters while insuring stability, then (ii) determine the properties of equivalent structural parameters of passive system, which can be implemented by removing or weakening some structural elements, or connections, or reduction of stiffness of the main structural elements and by addition of energy dissipation systems. Passive dampers and weakened elements were designed using an optimization algorithm to obtain a response as close as possible to an actively controlled system.

In this study a new concept of ANSS is proposed and the idea of "adaptive weakening." The original stiffness of the main structural system is left unchanged in the proposed ANSS and the "adaptive weakening" occurs due to NSD that mimics the "yielding" thus attracting it away from the main structural system—unlike the weakening concept proposed earlier, wherein the main structural system stiffness itself is reduced.

This paper presents comprehensive details of development and study of the behavior of the ANSS/NSD. The NSD is described in detail and its force-displacement loop is presented. Through numerical simulations it is shown that the concept of ANSS/NSD is very effective in elastic and inelastic structural systems. The effectiveness and the superior performance of the ANSS/NSD as compared to a structural system with supplemental passive dampers when subjected periodic and random input ground motions is demonstrated by numerical results.

PRINCIPLE OF ADAPTIVE NEGATIVE STIFFNESS SYSTEM (ANSS)

From here on adaptive negative stiffness system (ANSS) refers to the assembly of NSD and NPD—damper, unless described otherwise. It can also be simply referred as adaptive system or adaptive stiffness system. The main objective of the adaptive system is to reduce the inelastic excursions of the main structure and reduce the base shear of the structure and at the same time limit the maximum displacement of structure. Adaptive systems belong to the category of passive seismic protection systems but they are more sophisticated than the regular passive systems. The adaptive system that is developed in this work consists of two components that are designed in a two step sequence. First a truly adaptive negative stiffness device, which is capable of changing the stiffness of the device during lateral displacement, is developed based on the properties of the structure. This NSD is designed to exhibit true negative stiffness behavior which upon the addition of structure properties will

result in reduction of the stiffness of the structure and NSD assembly or "adaptive weakening" there by resulting in the reduction of the base shear of the assembly. Then a passive damper is added to reduce the displacements that are caused due to the reduction in stiffness. It has been found through simulation studies that the deformations of the structure and NSD assembly can be reduced using a passive damper--there by reducing the base shear and displacement in a two step process. An alternate explanation to justify the need for a NSD is explained in the next part of this section.

NEGATIVE STIFFNESS DEVICE (NSD)

True negative stiffness means that the force must assist motion, not oppose it as it is in the case of a positive stiffness spring. Psuedo negative stiffness can be accomplished using active or semiactive hydraulic device. In this paper the authors develop a new device that is passive, as it does not need any feedback signal or external power supply to generate the desired force. NSD has a precompressed bar, nonlinear springs and nonlinear damper (Nagarajaiah and Reinhorn, 1994). Schematic diagram showing the configuration of ANSS is shown in Figure 1(a) and the actual NSD placed in a base isolated system is shown in Figure 1(b). The properties of precompressed vertical spring and nonlinear horizontal springs are chosen in such a way that the desired force displacement is achieved. Precompressed bar is placed vertically between the beam and the top of the chevron brace. Since this is an unstable equilibrium for the spring, any inter-storey drift will result in a lateral force that assists the motion. For complete details of the device and its experimental validation the reader is referred to Sarlis *et al*. (2011).

Working principle: Assume a perfectly-linear single degree of freedom structure with stiffness, K_e, and no damping, an NSD with stiffness K_n and a passive damper with damping coefficient C. The force displacement plots are shown in Figure 2(a) (green line is structure, magenta is viscous damper and red is negative stiffness device). By adding NSD to the structure, schematically shown in Figure 2(b), the assembly stiffness reduces to $K_a=K_e–K_n$ beyond the displacement x_1 (shown as blue line in Figure 2(b)). If, F_2 and x_2 are the maximum restoring force and maximum displacement of a perfectly-linear system (green line in Figure 2(b)) then for the same load the maximum restoring force and maximum displacement of the assembly are F_3 and x_3 (blue line in Figure 2(b)), respectively. K_n is designed to achieve the desired reduction in base shear. Force exerted by the NSD is shown as red line in Figure 2(b). Although the reduction in base shear is achieved the maximum deformation of adaptive system is increased in the process when compared with an elastic system.
Deformation of this assembly can be reduced by adding a passing damping device in parallel to the NSD. To demonstrate the concept, a linear viscous damper is used for illustration but a nonlinear damper is a more optimal choice. An optimization needs to be performed to find the best suited nonlinear passive damper (NPD). By adding the viscous damper to the structure along with NSD maximum displacement is reduced resulting in $x_3 < x_2$. Since the assembly of structure and NSD acts like a nonlinear elastic system, viscous damper even with a very small damping coefficient can be

effective. It should be noted that by adding a damper to structure and NSD assembly, base shear of the assembly is not significantly increased.

From Figure 2(a,b,c) it can be seen that there is an offset displacement, x_1, called as "simulate yield-displacement", before the negative stiffness device is engaged. This is to avoid excessive response for relatively small external excitations. For displacements x such that $|x| < |x_1|$ the NSD assembly provides zero force and the structure behaves like the original linear structure. A provision to create this initial gap can be provided in the actual device using a pair of mechanical springs.

Analytical Model: The force in the NSD is given in Eq. (1) (Nagarajaiah and Reinhorn, 1994; Sarlis *et al.*, 2011):

$$F_{NSD} = 2K_h(x)x + K_v\left[\frac{\left(\sqrt{1+\left(\frac{x}{l}\right)^2}-\left(\frac{\Delta}{l}\right)\right)}{\sqrt{1+\left(\frac{x}{l}\right)^2}}\right]x \tag{1}$$

F_{NSD} is the force exerted by the NSD device. x is the horizontal displacement of the structure. K_h and K_v are the stiffness of the nonlinear horizontal spring and linear vertical springs, respectively as shown in Figure 1(a). l is the length of the precompressed spring in the initial position and Δ is the precompression in the vertical spring. By changing the parameters $K_h(x)$, K_v, l and Δ any desired force-displacement curve can be obtained. Initial gap in the NSD can be generated by choosing an appropriate nonlinear elastic spring, $K_h(x)$. A force-displacement loop of NSD—for a particular set of parameters—is shown in Figure 3 (red line), in comparison with the elasto-plastic base-structure (green line) and the structure + NSD (blue line).

PASSIVE DAMPING DEVICE

In the previous section a detailed study on the desired characteristics of NSD was described. Since the NSD reduces the effective stiffness of the structure+NSD assembly increased deformations will result. To limit these deformations a nonlinear passive damper has to be used. Assuming that we have the design ground motion for which the adaptive system has to be designed, the first step is to find the active control force exerted by the output feedback controller to satisfy desired performance specifications. Using optimization method proposed by Cimellaro *et al.* (2009), wherein the optimal properties of the damper, that minimizes the error between the active control force and force exerted by the passive devices, can be found. In this study, with the assumed NSD properties, a linear viscous damper with 20% damping ratio is found to be very effective. Force exerted by the passive damper is given by the following equation

$$F_{NPD} = 2\xi\sqrt{K_e m}\,\dot{x} \tag{2}$$

where, F_{NPD} is the force exerted by the damper, is the damping ratio, K_e is the elastic stiffness of structure and m is the mass of the structure. As mentioned in previous section the main objective of the adaptive system is to reduce the base shear of the structure and at the same time limit the maximum displacement of structure. It will be uneconomical and unrealistic to design devices that will retain the structure in elastic state, without any yielding, after a major earthquake. So, all the studies in this paper involves structure whose properties are representative of a real building and the loading cases for which there is yielding in the structure are also considered.

Ultimate goal of this study is to prove the concept and the effectiveness of the proposed ANSS/NSD analytically and experimentally. All the simulation studies presented in this paper are for a 1:3 scale three storey frame structure developed at University at Buffalo for a study of zipper frames. In the initial phase 2^{nd} and 3rd floors of the frame are braced rendering it essentially as a single degree of freedom system, which is considered in this study. Push-over curve for the zipper frame is obtained using the commercial software with the exact detail. Sivaselvan-Reinhorn model (Sivaselvan and Reinhorn, 2001) is used to capture the bi-linear hysteresis characteristics observed in the three-storey frame. Strength degradation and pinching are ignored. Governing equation of motion for the structure is shown in Eq. 3,4. Simple parameters like K_e and ε are obtained from the push-over curve. Mass of the structure, m, is measured and the values for remaining parameters are obtained using an optimization algorithm. Description of the variables is given in Table-1.

$$m\ddot{x} + \left(2\xi\omega_n m\right)\dot{x} + \alpha\left(1-\varepsilon\right)z + \varepsilon K_e x = -m\ddot{x}_g \tag{3}$$

$$dz/dx = K_e\left(1-\left|z/K_e Y\right|^{\eta}\left(\gamma\,\mathrm{sgn}\left(z\dot{x}\right)+\beta\right)\right) \tag{4}$$

SIMULATION RESULTS

Periodic Ground Motion: For all the results, for periodic input, presented in this work, 10 cycles of sinusoidal input are considered. Excitation frequency is same as the natural frequency of the base structure, $\omega_n = \sqrt{K_e/m}$.

***Elastic Systems*:** For those systems that will remain in elastic region for the design ground motion, NSD is found to be very effective. NSD will reduce the base shear of the structure substantially. To demonstrate this fact, a periodic ground motion is applied to the zipper frame. Amplitude of the ground motion is chosen such that the structure and NSD assembly will remain in elastic region. Adaptive system here refers to the structure and NSD assembly; damper is not used. Response time histories comparing the actual structure and adaptive system (structure + NSD) are shown in Figure 4. It can be seen from results in Figure 4 that all the response characteristics i.e., displacement, velocity and acceleration of the base structure (red curve) are higher that the adaptive system (green curve). Force-displacement behavior of the actual structure and the adaptive system are shown in Figure 5; it is evident from these results that the adaptive system remains in the elastic region whereas the base structure yields. The component forces acting in the adaptive system are shown in Figure 6. "Simulated yield displacement" for the NSD is assumed at a normalized

displacement of 0.25. It should be noted that passive damper is not yet included for the results shown in Figures 4, 5 and 6. For the systems that remain in elastic region, NSD alone is effective for reducing base shear without any increased deformations. A passive damper can be added to reduce the deformation of structure along with the base shear.

Inelastic Systems: The performance of the NSD is further verified for higher input amplitudes. Amplitude of input ground motion is increased so that the adaptive system starts yielding. For yielding structures NSD alone will not improve the performance of the adaptive system. Passive damper has to be added to limit the excessive displacements caused due to reduction in the overall stiffness of the structure.

Passive viscous damper with 20% damping ratio is used in the simulations studies presented in the paper. Three systems are compared after the addition of passive viscous damper (1) Bilinear system (referred to as BS), (2) Bilinear system + passive damper (referred to as PS), and (3) Bilinear system + passive damper + NSD (referred to as ANSS).

For the same input amplitude and 10 input cycles it was found that, by adding the passive damper the deformation of the structure is reduced substantially with a slightly higher base shear (Nagarajaiah *et al.*, 2010). In addition, the acceleration of adaptive system is 40 % less--compared to passive system and base structure system. Due to the presence of NSD in adaptive system the base shear is reduced substantially, whereas in the case of passive system base shear is larger than the case with base structure alone.

To study the efficiency of the ANSS/NSD, performance of the aforementioned systems is verified for Kobe ground motion. The response histories and the force-displacement loops for Kobe earthquake excitation are shown in Figures 7 and 8 respectively. The system with NSD and damper reduces both the displacement and base shear significantly, as evident in Figures 7 and 8.

CONCLUSIONS

A novel and new adaptive negative stiffness system (ANSS) and negative stiffness device (NSD) is proposed and developed in detail in this paper along with a new concept of "adaptive weakening". The proposed NSD does not rely on structural-response feedback and external power supply—unlike previously reported pseudo-negative stiffness devices that do depend on active control—hence, is passive, and exhibits true adaptive negative stiffness behavior by possessing predesigned variations of stiffness as a function of structural displacement amplitude. Addition of NSD to the structural system will result in the reduction of stiffness in the combined system or "adaptive weakening" occurs; however, it is important to note that the stiffness of the base-structure remains unchanged in this study—unlike the concept of weakening proposed earlier wherein the stiffness of the base-structure itself is reduced. Addition of the passive damper reduces the displacements that are caused due to the reduction in effective stiffness.

Effectiveness of the proposed ANSS/NSD in elastic and inelastic structural systems has been demonstrated through the simulation studies for periodic and random input ground motions. It has been shown that the main structural system suffers less force, less displacements and less damage, while the ANSS "absorbs" them.

ACKNOWLEDGEMENTS

Funding by National Science Foundation, grant NSF—CMMI--NEESR-0830391 for this project is gratefully acknowledged.

REFERENCES

Cimellaro, G. P., Lavan, O., and Reinhorn, A. M. (2009). "Design of passive systems for control of inelastic structures." *Earthquake Engineering & Structural Dynamics*, 38(6), 783–804.

Constantinou, M. C., and Symans, M. D. (1993). "Experimental study of seismic response of buildings with supplemental fluid dampers." *The Structural Design of Tall Buildings*, 2(2), 93–132.

Dyck, J., Nagarajaiah, S., and Taylor D. (2006) "Variation of supplemental stiffness and damping using adjustable fluid spring and damper," *Proc. Eighth U. S. National Conf. on Earthquake Eng.*, EERI, CD-ROM.

Fenz, D. M., and Constantinou, M. C. (2008). "Spherical sliding isolation bearings with adaptive behavior: Theory." *Earthquake engineering & structural dynamics*, 37(2), 163–183.

Gluck, N., Reinhorn, A. M., Gluck, J., and Levy, R. (1999). "Design of supplemental dampers for control of structures." *Journal of structural Engineering*, 122(12), 1394.

Iemura, H., and Pradono, M. H. (2009). "Advances in the development of pseudo-negative-stiffness dampers for seismic response control." *Structural Control and Health Monitoring*, 16(7-8), 784–799.

Lobo, R. F., Bracci, J. M., and Shen, K. L. (1993). "Inelastic response of R/C structures with viscoelastic braces." *Earthquake Spectra*, 9, 419.

Nagarajaiah, S., Reinhorn, A. M., and Constantinou, M. C. (1991). "Nonlinear Dynamic Analysis of 3D Base-Isolated Structures." *Journal of Structural Engineering, ASCE*, 117(7), 2035–2054.

Nagarajaiah, S., and Reinhorn, A. (1994). "Applicability of Pseudo-force method to Highly Nonlinear Dynamic Problems." *ASCE: Proceedings of structures congress*, 165–172.

Nagarajaiah, S., and Sahasrabudhe, S. (2006). "Seismic response control of smart sliding isolated buildings using variable stiffness systems: an experimental and numerical study." *Earthquake Engineering & Structural Dynamics*, 35(2), 177–197.

Nagarajaiah, S. (2009). "Adaptive passive, semiactive, smart tuned mass dampers: identification and control using empirical mode decomposition, hilbert

transform, and short-term fourier transform." *Structural Control and Health Monitoring*, 16(7-8), 800–841.

Nagarajaiah, S., Reinhorn, A. M., Constantinou, M. C., Taylor, D., Pasala, D.T.R., and Sarlis, A.A.S. (2010). "Adaptive Negative Stiffness: A New Structural Modification Approach for Seismic Protection." *Proceedings of 5th World Conference on Structural Control and Monitoring*, Tokyo, Japan.

Narasimhan, S., Nagarajaiah, S., Johnson, E. A., and Gavin, H. P. (2006). "Smart base-isolated benchmark building. Part I: problem definition." *Structural Control and Health Monitoring*, 13(2-3), 573–588.

Reinhorn, A. M., Viti, S., and Cimellaro, G. P. (2005). "Retrofit of structures: strength reduction with damping enhancement." *Proceedings of the 37th UJNR panel meeting on wind and seismic effects*, 16–21.

Reinhorn, A. M., Lavan, O., and Cimellaro, G. P. (2009). "Design of controlled elastic and inelastic structures." *Earthquake Engineering and Engineering Vibration*, 8(4), 469–479.

Sahasrabudhe, S., and Nagarajaiah, S. (2005). "Experimental study of sliding base-isolated buildings with magnetorheological dampers in near-fault earthquakes." *Journal of structural engineering*, 131, 1025.

Sarlis, A.A.S., Pasala, D.T.R., Constantinou, M. C., Reinhorn, A. M., Nagarajaiah, S., Taylor, D., and (2010). "Negative Stiffness Device for Seismic Protection of Structures – An Analytical and Experimental Study." *3rd International conference on computational methods in structural dynamics and earthquake engineering*, May 2011.

Sivaselvan, M. V., and Reinhorn, A. M. (2000). "Hysteretic models for deteriorating inelastic structures." *Journal of Engineering Mechanics*, 126(6), 633–640.

Spencer Jr, B. F., and Nagarajaiah, S. (2003). "State of the art of structural control." *Journal of Structural Engineering*, 129, 845.

Symans, M. D., and Constantinou, M. C. (1997). "Seismic testing of a building structure with a semi-active fluid damper control system." *Earthquake Engineering & Structural Dynamics*, 26(7), 759–777.

Viti, S., Cimellaro, G. P., and Reinhorn, A. M. (2006). "Retrofit of a hospital through strength reduction and enhanced damping." *Smart Structures and Systems*, 2(4), 339–355.

Table 1: Description of variables

Description	Variable	Variable	Description
Yield displacement	Y	$\ddot{x}_g$	Ground displacement
Mass	m	ξ	Damping ratio
Pre-yielding stiffness	K_e	ω_n	Natural frequency
Yield strength	K_eY	ε	Post yield stiffness ratio
S-R Model parameter-2	γ		S-R Model parameter-3
S-R Model exponent	η		

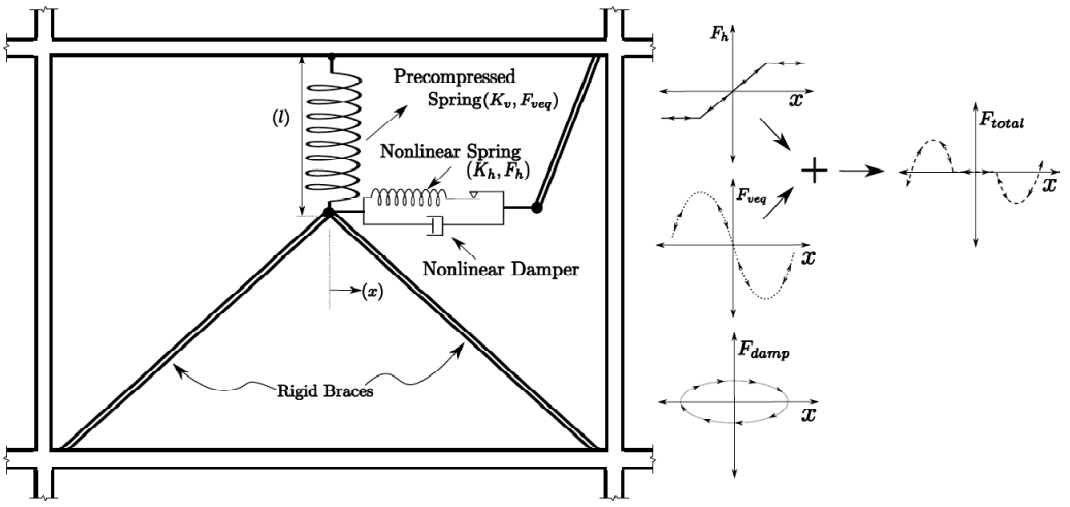


Figure 1(a): The New Concept of ANSS/Negative Stiffness Device—NSD.

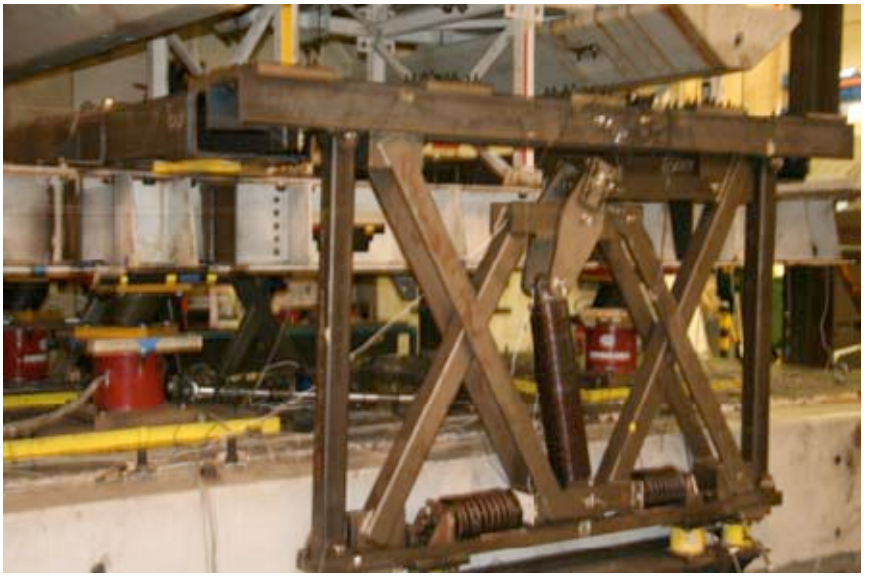


Figure 1(b): NSD placed in a base isolated building tested at SUNY-Buffalo

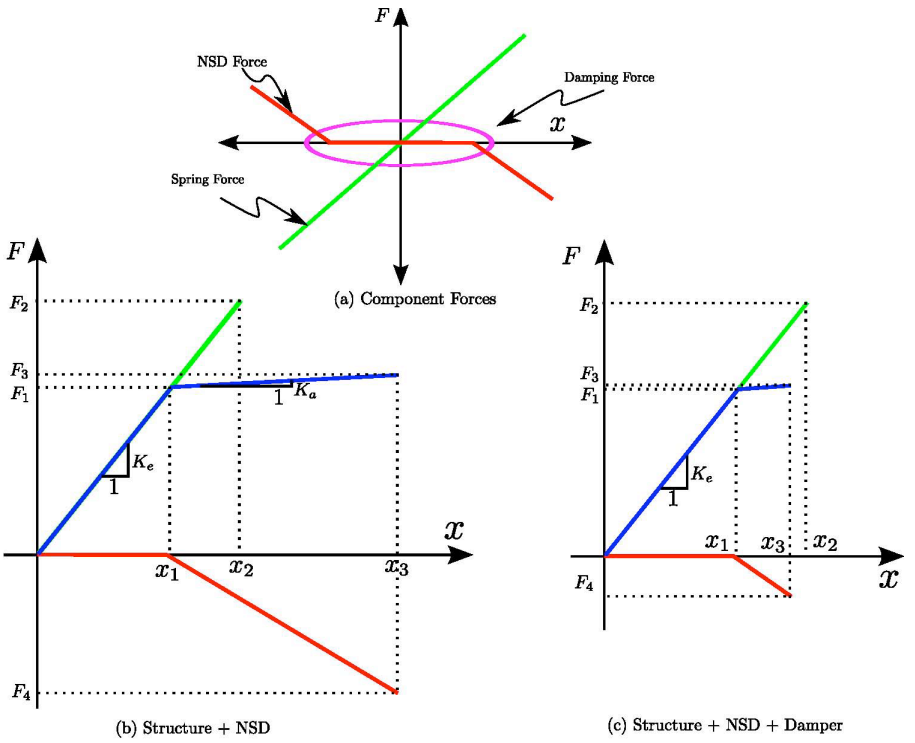


Figure 2: Working principle of ANSS (a) Component F-D plots (b) Linear system with Negative stiffness Device (c) Linear system with Negative stiffness device and Damper [Green- Base-structure, Red- NSD, Blue- Assembly]

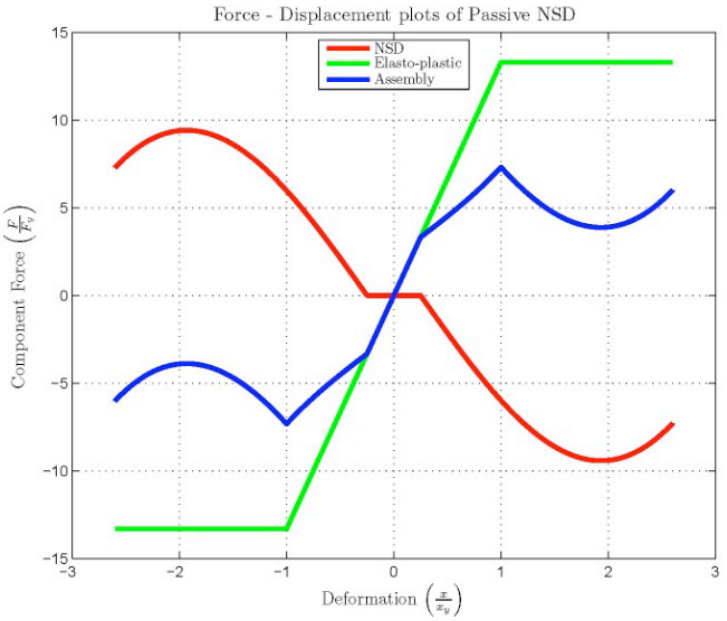


Figure 3: Force-displacement loops of NSD [Green- Base-structure, Red- NSD, Blue- Assembly]

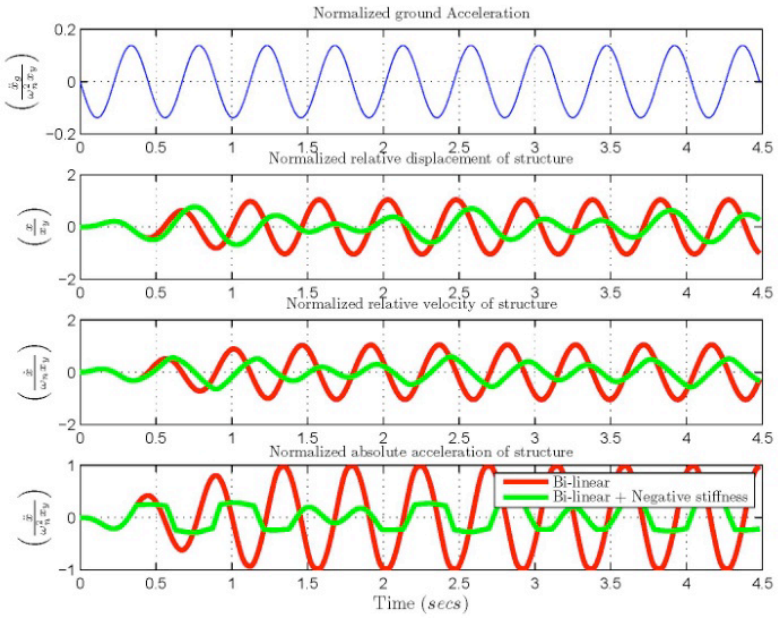


Figure 4: Comparison of responses of system with and without NSD (with the main structure being essentially elastic)

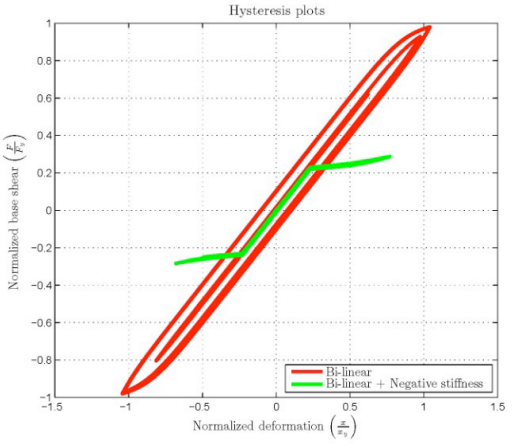


Figure 5: Comparison of hysteresis loops of system with and without NSD (with the main structure being essentially elastic)

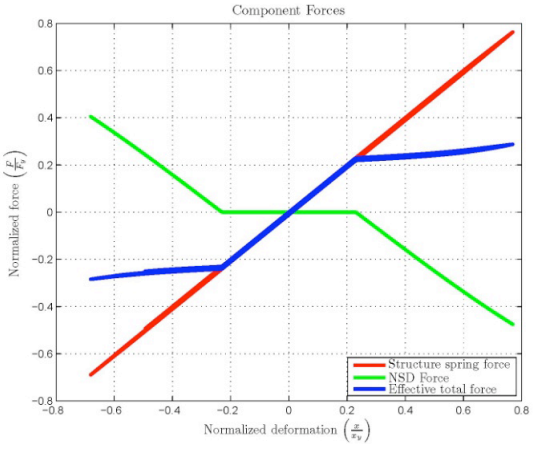


Figure 6: Comparison of component spring forces of the adaptive system (with the main structure being essentially elastic)

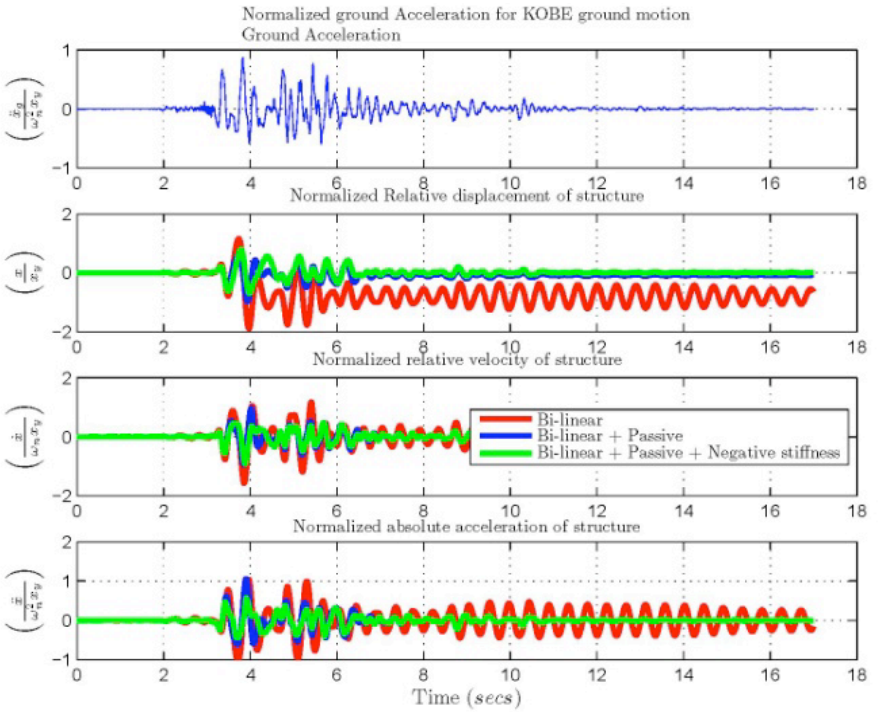


Figure 7: Comparison of responses with and without passive damper/NSD (with structure yielding) under Kobe earthquake excitation.

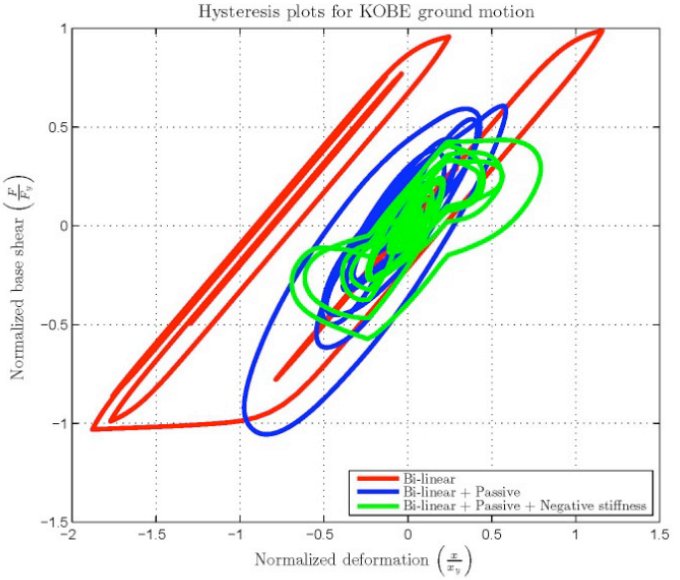


Figure 8: Comparison of hysteresis loops of system with passive damper/NSD (with structure yielding) under Kobe earthquake excitation.

Behavior of Shear Tab Connections under Column Removal Scenario

H. Daneshvar[1] and R. G. Driver[2]

[1] PhD Candidate, Department of Civil and Environmental Engineering, University of Alberta; email: hossein.daneshvar@ualberta.ca

[2] Professor, Department of Civil and Environmental Engineering, University of Alberta; email: rdriver@ualberta.ca

ABSTRACT

Shear connections in beams are conventionally designed to transfer shear forces only. It is assumed that there is no substantial moment transfer due to the fact that beam end rotation is allowable. The shear tab, or fin plate, connection is one of the simplest and most cost-effective shear connection types and, although its behavior under gravity and cyclic loading has been established, its response to the column removal scenario that is commonly considered for progressive collapse analysis is still relatively unknown. In this paper, challenges involved in numerical studies for simulating the performance of shear tab connections when a column has been compromised are discussed. Modeling definitions for performing highly nonlinear analysis are discussed and recommendations are made regarding obtaining verification by available experimental data. Shear, axial force, and moment versus chord rotation diagrams are presented for both numerical and experimental results and conclusion are made.

Introduction

Based on a definition accepted in the literature, connections with moment capacities less than 20 % of the plastic moment capacity of the connected beams are called shear connections (Astaneh-Asl 2005). Shear connections are used conventionally to transfer shear forces exclusively. It is assumed that no moment transfer occurs at simple connections since beam end rotation is permitted. There are several forms of simple connection used in steel structures. The shear tab, or fin plate, connection consists of a plate welded to the supporting column and typically bolted to the supported beam. It is easy to fabricate and is cost-efficient in terms of construction and material. A typical double-sided joint with shear tab connections is depicted in Figure 1.

Table 1 summarizes the types of material usually used in this type of connection in conventional construction.

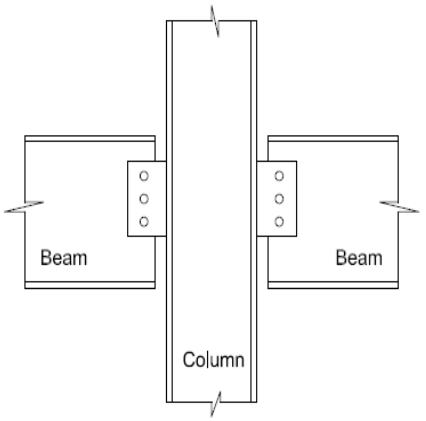


Figure 1. Typical beam-to-column shear tab connection

Table 1. Typical material used for shear tab connections

Component	Material	Description
Plate	A36	-
Bolts	ASTM A325, A490	standard/slotted hole
Welds	E70XX electrode	fillet welds

The behavior of this type of connection under gravity and cyclic load has been established over the past decades (Astaneh-Asl et al. 2002). However, its performance for the progressive collapse scenario has not been established and documented thoroughly. Differences between the behavior of steel connections based on conventional design versus progressive collapse type of design have been described in a paper by the authors (Daneshvar and Driver 2010). Since available progressive collapse guidelines ask designers for robust connections that can resist a "double span" scenario, there is a necessity to investigate this issue. In this paper, challenges involved in numerical studies for simulating the performance of shear tab connections when a column has been compromised are discussed. Various factors involved in modeling for performing highly nonlinear finite element analysis are discussed and results are verified by available appropriately-selected experimental data for the column removal scenario.

Selected Experimental Study

Unfortunately, there are few experimental studies on connection behavior for progressive collapse analysis (Daneshvar and Driver 2010). Experiments conducted by Thompson (2009) have been used to verify the numerical study. A total of nine full-scale tests were carried out at the Milwaukee School of Engineering, keeping the connection depth as the sole varying factor based on AISC's conventional configuration (AISC. 2005). In Figure 2, the test setup and specimen assembly are shown.

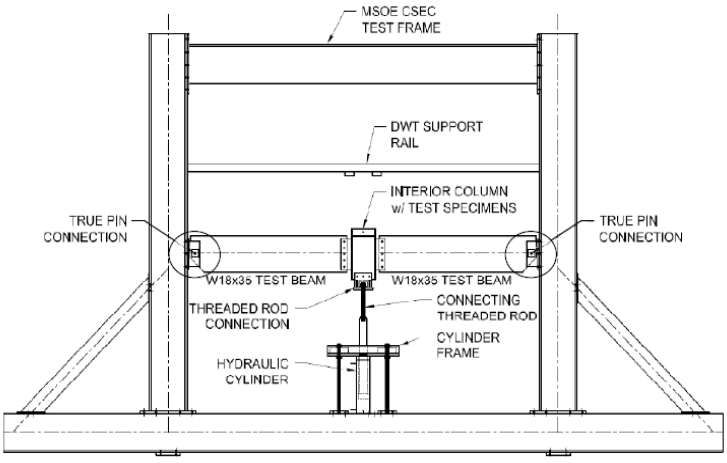


Figure 2. Test setup assembly (Thompson 2009)

The test specimen consisted of a planar two-span beam, with the beams attached to a central column stub by shear tab connections and to "true pin" connections at the far ends of the beams. A vertical displacement was applied to the central stub column in order to simulate a controlled collapse of an interior column (Thompson 2009). The main reasons that this experiment has been selected for the current research are:

- Test configuration: As shown in Figure 2, the test setup simulates a double-span scenario, as described in available progressive collapse design guidelines (e.g., DoD (2009) and GSA (2003));
- Destructive nature of the test: the assembly is pushed down to its ultimate capacity. The connection goes through large rotations, in contrast to many previous tests on the shear tab connections;
- Report of catenary force (axial force): catenary resistance is recognized as one of the main distinguishing factors in the characterization of a connection's robustness for progressive collapse prevention. It is also an alternative path for transferring loads for resisting against collapse after a column has been compromised. Catenary action is explicitly reported in the test report, which is contrary to previous tests on shear tab connections.

Modeling of Steel Connections

Abaqus/CAE (Dassault Systèmes 2009) is used for all stages in the simulation. Finite element models consist of the central column and adjacent beams, as well as the connections with complete detailing, as shown in Figure 3. Shear tabs are welded to the column flange and bolted to beam's web. Since the connection is the point of interest, all characteristic features of the connections are included in the model. The central column is pushed down, while the connection performance is monitored. Model information is summarized in Table 2.

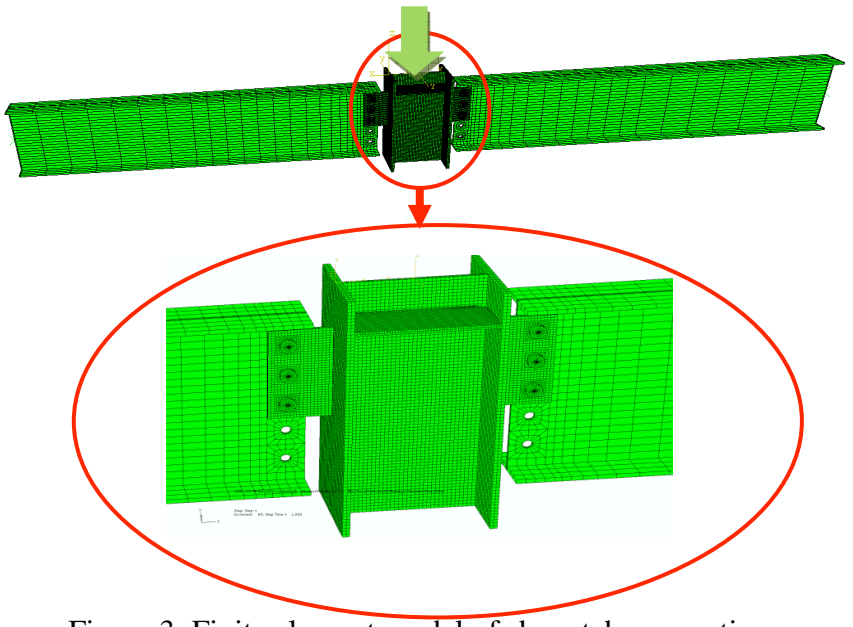


Figure 3. Finite element model of shear tab connection

Table 2. Finite element model summary

Model Summary	No.	Description
Parts	6	beam; stub column; shear tab; bolt; stiffener; rigid plane
Materials	3	A36 (shear tab); A325 (bolts); A992 (others)
Analysis Steps	2	apply pretension; apply vertical displacement
Interactions	13	refer to "boundary nonlinearity" section
Interaction Properties	1	both tangential and normal behavior included
Constraints	6	tying shear tab and stiffeners to stub column
Boundary Conditions	3	avoid out-of-plane displacement; true pin at far ends; two axial springs at far ends of the beams to simulate flexibility of the test setup

In general, the finer the mesh density, the more accurate the result. By increasing the number of elements, convergence to a unique solution can be achieved. This solution is an approximation of the physical model's response. Potential sources of error include the model's geometry, material model, boundary conditions, and loads (Dassault Systèmes 2009). In order to approach the real behavior of the physical model, performing a nonlinear simulation is necessary. Sources of nonlinearity are discussed after the sections on element selection and the mesh refinement analysis.

Element selection

The most comprehensive element family in finite element software is the continuum (solid) element. In this study, three-dimensional (3D) elements are adopted since the problem is 3D in nature. Some studies have established the correlation between two-dimensional and 3D modeling of steel connections (Jaspart 1997). The

incompressibility of plastic deformation in metals imposes some limitations on the types of element suitable for elastic–plastic analysis. This phenomenon may make some elements over-constrained and cause volumetric locking (Epstein and Barrett 2006). Table 3 summarises the properties of different types of continuum elements available in Abaqus.

Table 3. Element types available in Abaqus (Dassault Systèmes 2009)

Element Type	Description
First Order Elements	constant strain throughout the element that prevents mesh locking when the material is approximately incompressible
	accuracy achieved with full integration versus reduced integration depends on the nature of the problem
	recommended in cases of large strains or high strain gradients
Second Order Elements	provide higher accuracy for problems not containing contact simulations or element distortion
	better modeling geometric features, e.g., modeling a curved surface with fewer elements
	very effective in bending-dominated analysis
Reduced-integration Elements	use lower-order integration just for the element matrix, not mass and loading – No locking concern
	reduces the time of analysis, especially in 3D analysis
Full-integration Elements	may suffer from locking behavior, including both shear and volumetric locking
	volumetric locking happens when the material behavior is almost incompressible

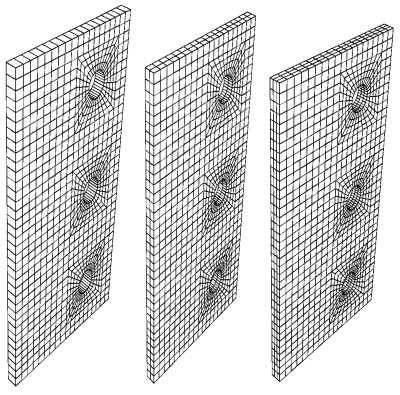
Considering the issues mentioned in Table 2, and taking into account different factors available in the connection assembly model (e.g., presence of large strain and complex contact definition), led to the adoption of a first-order reduced-integration type of element for whole model.

Mesh convergence analysis

In order to make sure that the result of finite element simulation is adequately precise, a mesh refinement study is necessary. Increasing the mesh density leads to a unique value that represents the response of the model. Convergence is obtained when further mesh refinement causes negligible changes in the response. Basically, if the same results are produced with different meshes, it is confirmed that the solution is mathematically accurate (Dassault Systèmes 2009). For the purpose of mesh refinement analysis, the shear tab plate with three holes is isolated from the assembly,

since the main goal of the research is to determine the behavior of the shear tab. Besides, preliminary analyses and experimental evidence show that most of the nonlinear behavior is accumulated in the shear tab region. Instead of including complex bolt–plate interactions, distributed pressure over the bottom half of the holes is considered in order to load the model. In reality, the pressure magnitude varies around the hole circumference, but it is assumed to be uniform. In this study, the influences of mesh density across the thickness of the plate (Figure 4) and mesh density around the holes (Figure 5) are investigated for three particular results: maximum von Mises stress where the shear tab is attached to the stub column (assumed to be fixed), maximum von Mises stress on the bottom surface of the top hole, and vertical displacement of the bottom of the top hole. The results for these two mesh refinement studies are summarized in Tables 4 and 5, respectively.

It is observed that the "normal" mesh density is adequate for both cases, either refining through the thickness or around the hole. There is no considerable advantage in terms of more accurate results that can be obtained using the fine mesh. Besides, the time of analysis would nearly double without getting significant improvements in the results. Although the normal mesh is deemed to be sufficient, appropriate relative mesh density of different parts in the assembly is a big challenge when contact exists. Master and slave surfaces should be defined with respect to associated mesh density.

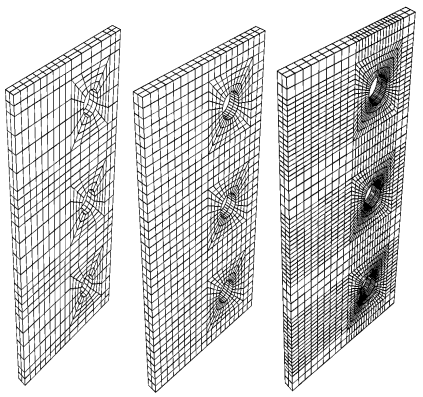


(a) (b) (c)

Figure 4. Mesh refinement across the thickness: (a) Coarse - 1 element in thickness; (b) Normal - two element in thickness; (c) Fine - three elements in thickness

Table 4. Mesh refinement analysis results; refinement across the thickness

Mesh Density (No. of elements in thickness)	Displacement at the bottom of the top hole (mm)	Stress at the bottom of the top hole (MPa)	Stress at the top corner of Shear Tab (MPa)	Relative CPU time
1 (Course)	0.37	279.47	250.31	4.30
2 (Normal)	0.56	276.66	252.97	8.50
3 (Fine)	0.58	277.00	253.27	12.90



(a) (b) (c)

Figure 5. Mesh refinement around the holes: (a) Coarse (b) Normal (c) Fine

Table 5. Mesh refinement analysis results; refinement around the holes

Mesh Density	Displacement at the bottom of the top hole (mm)	Stress at the bottom of the top hole (MPa)	Stress at the top corner of Shear Tab (MPa)	Relative CPU time
Coarse	0.57	273.21	253.43	5.10
Normal	0.56	276.66	252.97	8.50
Fine	0.54	276.63	252.70	16.30

Sources of Nonlinearity

It is necessary to perform nonlinear analysis since the behavior of each component of the connection individually is highly nonlinear, as is the behavior of the whole assembly as a system. All three sources of nonlinearity that are common in structural simulations exist in connection modeling for progressive collapse, including material nonlinearity, geometric nonlinearity, and boundary nonlinearity.

Material nonlinearity

True strain and true stress must be used when plasticity data are being defined in Abaqus. However, most available generic material behavior is in the form of nominal, or engineering, stress versus strain. In order to convert nominal values to true ones, the incompressibility of plastic deformations are taken into account. The conversions are as follows:

$$\sigma_{true} = \sigma_{nom}\,(1 + \varepsilon_{nom})$$

$$\varepsilon_{true} = \ln(1 + \varepsilon_{nom})$$

These equations are valid prior to necking. The strains provided in material test data are the total strains. In order to define the plastic strains, it is necessary to decompose these values into elastic and plastic strain components. Linear interpolation is used

between the data points provided in order to obtain the overall material response. Abaqus assumes a constant stress response outside the range of data provided (Dassault Systèmes 2009).

Geometric nonlinearity

For many structural applications, it is necessary to write the equilibrium equations based on the deformed structure. If loading on the structure causes large deformations, nonlinearity in geometry is involved and superposition cannot be applied. Due to the presence of large deformation in the model under investigation, geometric nonlinearity must be included.

Boundary nonlinearity (contact)

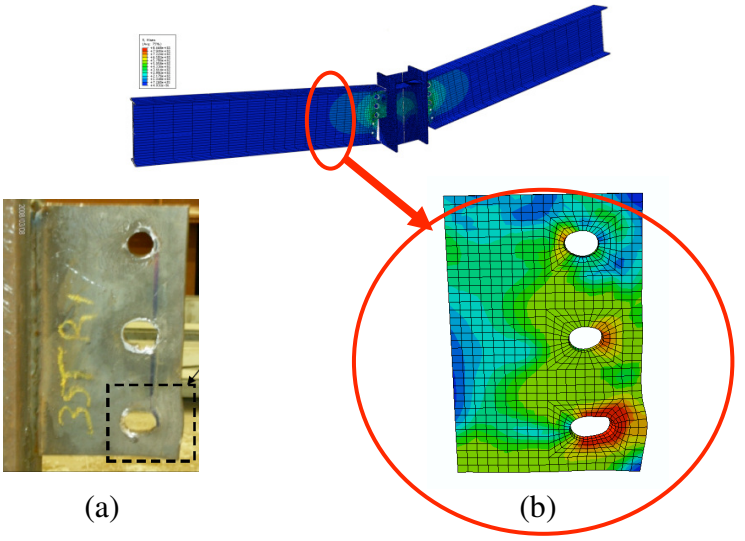
Connection modeling involves contact simulations of different components, allowing transmission of force from one part to another. The mere physical proximity of two surfaces in the connection assembly is not enough for contact definition. Contact behavior is highly nonlinear and causes large and instantaneous changes in the behavior of the assembly. The analysis should detect when the surfaces are separated or in contact in order to apply contact constraint correctly. Contact simulations in Abaqus can be surface-based or element-based. Surface-based contact can be general (automatic) or a contact-pair algorithm (Dassault Systèmes 2009). General contact definitions are highly automated; hence, in models like connections that are complex in terms of the number of interactions, they do not usually lead to a converged solution. Contact-pair algorithms are recommended, although they require more effort in terms of pre-processing. There are a total of six contact pairs in the shear tab connection model: bolt head and shear tab, bolt shank and shear tab, bolt shank and beam web, bolt's nut and beam web, shear tab and beam web, and shear tab and column flange. The "tie constraint" is used to model the last aforementioned contact assuming the welding is flawless.

Relative sliding of the connection's components interacting with each other is another important phenomenon that needs to be included in the model. Abaqus uses two different analysis methods to deal with this phenomenon: small sliding and finite sliding. "Small sliding" is less computationally expensive, but sliding must not exceed a fraction of a typical element dimension (Dassault Systèmes 2009). In the column-removal connection modeling scenario, sliding can be much more than what is assumed to be acceptable in for "small sliding", so the "finite sliding" method must be applied. For tangential behavior, a penalty formulation with a friction coefficient of 0.3 has been used. For normal behavior, a hard-contact formulation with a penalty constraint enforcement method is applied. Nonlinear stiffness behavior has been incorporated and all related parameters are calibrated with experimental data.

Analysis Results

Three tests were carried out on three-bolt shear tab connections (Thompson 2009). Each test produced results for two identical shear tab connections, although their responses might be different. Therefore, six different responses from experiments are available for comparison. The deformed shape of the overall test assembly and a direct comparison of the shear tab deformations observed in the model and the

experiment are shown in Figure 6. It can be seen that there is close similarity between the experiment and the numerical simulation results. Plastic deformation is mostly accumulated around the bottom hole where the failure begins. Besides, the ductility of the system is mostly provided by bearing deformation developed around the holes.



(a) (b)

Figure 6. Deformed shapes of assembly: (a) Shear tab from experiment (Thompson 2009); (b) Shear tab from finite element simulation.

The internal forces—including shear, axial force, and moment—at the bolt line location versus chord rotation of the connection assembly are shown in Figures 7 to 9. The dashed lines and solid lines represent the results of the experiments and simulations, respectively. Figures 7 and 9 verify the simulated model based on acceptable coincidence with the associated experimental results. Based on previous research, the maximum value of rotational demand on a shear connection under gravity load is about 0.03 radians. The maximum rotational demand due to seismic loading is approximately 0.05 radians (Astaneh-Asl 2005). Even the accumulative effect of both gravity and seismic forces is approximately 0.08 radians, which is much smaller than the rotational demand in the column removal scenario.

Figure 8 shows a discrepancy between the experimental and numerical results due to the presence of compression in the finite element curve. Formation of catenary action in the connection assembly is highly dependent on the boundary condition of the test assembly. In other words, the external axial restraint provided by the test setup is very influential on the axial response of the connection as the system goes through large displacements. The precise amount of this external restraint is unknown.

The external restraint provided to the beam and column-stub assembly by the surrounding frame is simulated by axial springs at the far ends of the beams, as mentioned in Table 2. Figure 10 shows the axial response of the connection with different spring stiffnesses. As the stiffness reduces, the compressive force decreases as well. Further study is needed to characterise the influence of support flexibility on the catenary behaviour of shear tab connections under the column removal scenario. Moreover, non-linear springs may be required to achieve an accurate axial response.

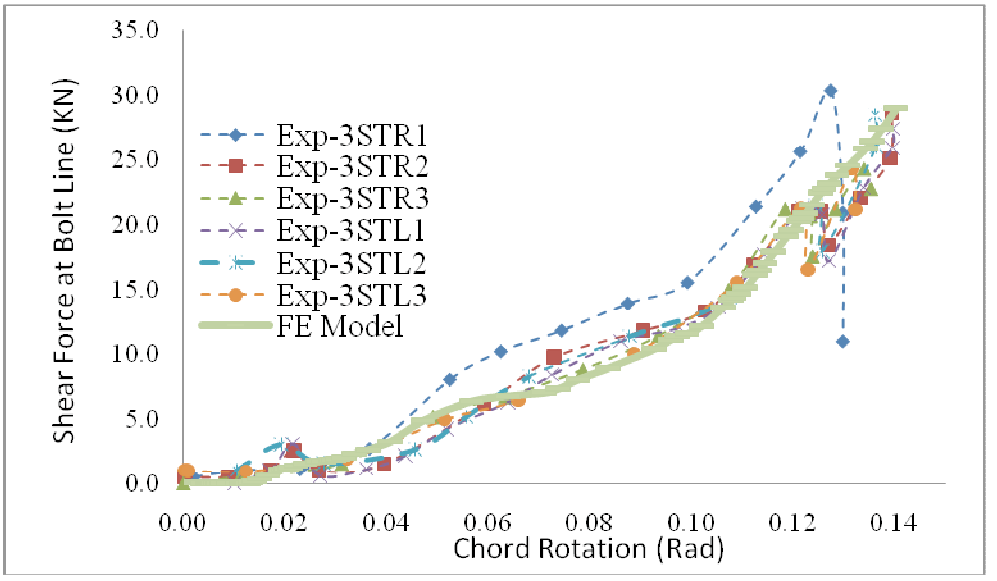


Figure 7. Shear force versus chord rotation curves at the bolt line; Experimental (Thompson 2009) and finite element results.

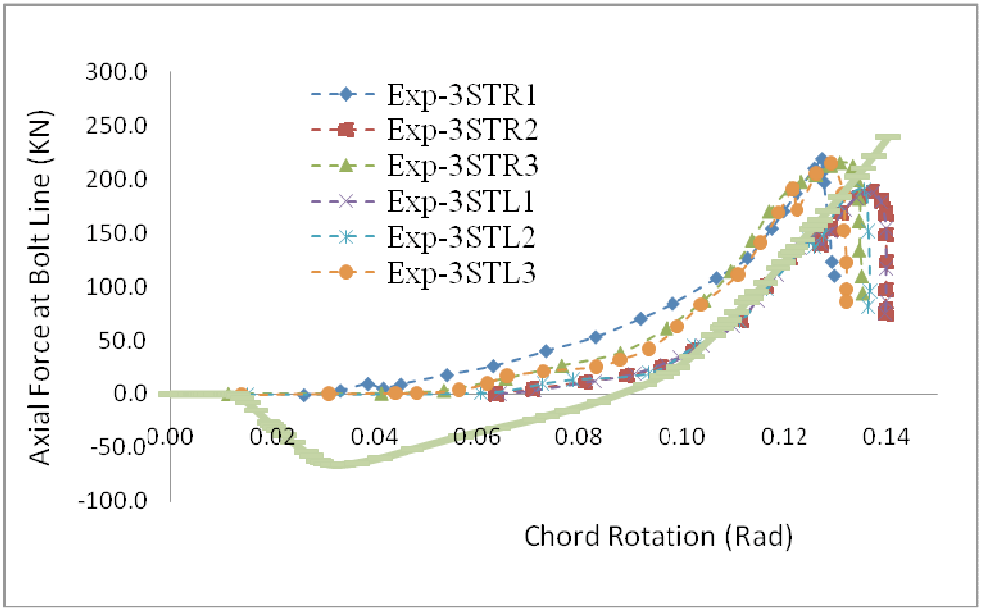


Figure 8. Axial force versus chord rotation curves at the bolt line; Experimental (Thompson 2009) and finite element results.

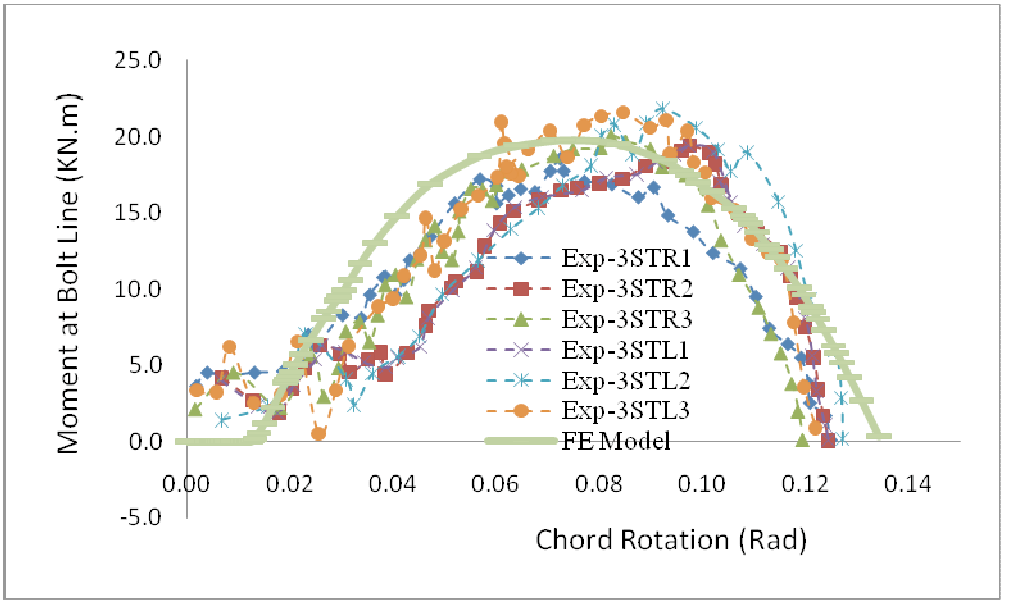


Figure 9. Moment versus chord rotation curves at the bolt line; Experimental (Thompson 2009) and finite element results.

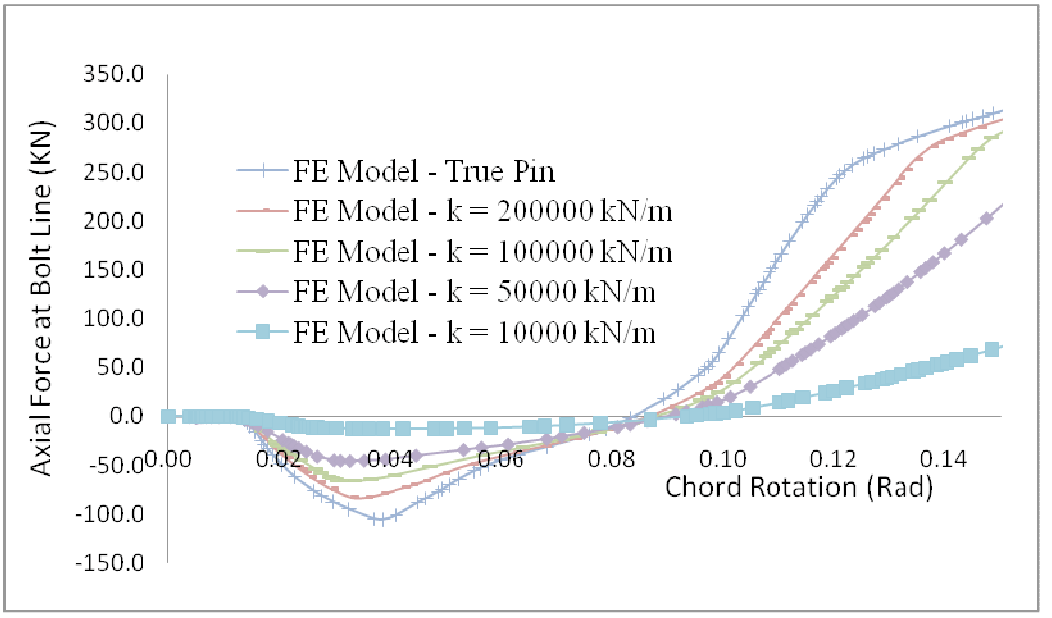


Figure 10. Axial force versus chord rotation curves at the bolt line; Finite element results for different end spring stiffnesses.

Conclusion

The following conclusions can be drawn from the finite element study presented:

- Finite element modeling can be used as an accurate tool to mimic the response of steel connections such as shear tabs in the column removal scenario.

- Nonlinearity definitions, including material, geometric, and boundary (contact) nonlinearities, are the most challenging part of finite element modeling of connections.

- External restraint can influence the catenary behavior of shear tab connections considerably. Axially rigid restraint of the system leads to the development of significant compressive forces before the formation of tensile action. Tensile catenary forces can be counted as an alternative path load when moment resistance has vanished.

- The resulting response curves can be used as input for shear tab connection models in full-building progressive collapse analyses.

REFERENCES

AISC (2005). *Manual of steel construction*, 13th Edition, American Institute of Steel Construction, Chicago, IL.

Astaneh-Asl, A. (2005). "Design of shear tab connections for gravity and seismic loads." *Steel Technical Information and Product Services Report (Steel TIPS).* Structural Steel Educational Council, Moraga, CA.

Astaneh-Asl, A., Liu, J., and McMullin, K.M. (2002). "Behavior and design of single plate shear connections." *Journal of Constructional Steel Research* , 58, 1121-1141.

Daneshvar, H. and Driver, R. (2010). "Application of seismic steel connection experiments to column removal scenario." *2nd Specialty Conference on Disaster Mitigation*. Canadian Society for Civil Engineering Annual Conference, Winnipeg, MB.

Dassault Systèmes, D. (2009). *Abaqus analysis user's manual.* Dassault Systèmes Simulia Corp., Providence, RI.

DoD (2009). *Design of buildings to resist progressive collapse*. Department of Defence, U.S.

Epstein, H.I. and Barrett, C.S. (2006). "Virtual Experiments for Welded Structural Steel Connections." *Practice periodical on structural design and construction*. American Society of Civil Engineers, 11(3), 128-133.

GSA (2003). *Progressive collapse analysis and design guidelines for new federal office buildings and major modernization projects.* General Services Administration, U.S.

Jaspart, O.S. (1997). "Benchmarks for Finite Element Modelling of Bolted Steel Connections". *Journal of Constructional Steel Research* , 43, 17-42.

Thompson, S. L. (2009). "Axial, shear and moment interaction of single plate shear tab connections" *M.S. thesis, Milwaukee School of Engineering.* Milwaukee, WI.

Effect of Regular Perforation Patterns on Steel Plate Shear Wall Column Demands

Hassan Moghimi[1] and Robert G. Driver[2]

[1]PhD Candidate, Department of Civil and Environmental Engineering, University of Alberta, Edmonton, AB, Canada, T6G 2W2; email: moghimi@ualberta.ca
[2]Professor, Department of Civil and Environmental Engineering, University of Alberta, Edmonton, AB, Canada, T6G 2W2; email: rdriver@ualberta.ca

Abstract

Several methods have been proposed to reduce the moment and axial force demands on the columns of steel plate shear walls. One such method is to reduce the strength of the infill plate by introducing a regular pattern of perforations in the form of circular holes. The decrease in shear strength of the system depends on the diameter of the holes and their centre-to-centre distance. It was found using a variety of finite element models that although introducing the perforations may reduce the lateral strength of the system, the total demand on the columns can in some cases actually increase. Also, the perforated system is sensitive to the pattern of holes selected in that a small change in the arrangement of the holes can have a significant effect on the moment demand on the columns. Moreover, the flexibility of the beam-to-column connections affects the column demands considerably and also influences the sensitivity of the column design forces to the pattern of holes selected. An appropriate design method is proposed and the suitability of this system is summarized.

Introduction

Experimental and numerical studies on steel plate shear walls (SPSWs) have shown that they constitute an excellent lateral force resisting system that is characterized by high shear strength and outstanding ductility and redundancy. The high inherent shear strength of the system often results in very thin infill plates being required when using steel grades commonly available in North America. In this common case, handling and welding considerations tend to govern the selection of the infill plate thickness, potentially resulting in a large panel over-strength that leads to excessive demands on the columns under capacity design. This increased demand can have a severe negative impact on the economic competitiveness of the system.

Several methods have been proposed to reduce the moment and axial force demands on the columns of SPSWs arising from the selection of infill plates that are thicker than required to resist the design story shear. These methods can be classified into

two groups. In the first group, the share of the column demands arising from the effect of frame action is reduced by using semi-rigid beam-to-column connections, using reduced beam sections at rigid beam-to-column connections, and/or using a horizontal strut at the mid-height of each story. In the second group, the share of the column demands arising from the effect of tension field action in the infill plates is reduced by decreasing the strength of the infill plates. The use of light-gauge cold-rolled or low yield point steel for the infill plates is one method. The other method is to reduce the strength of the infill plate by introducing a regular pattern of perforations in the form of circular holes. In the latter method, the decrease in shear strength of the system depends on the diameter of the holes and their centre-to-centre distance. It has been intuitively assumed that there is a direct correlation between the reduction of lateral strength of the wall associated with the perforations and the reduction in column demand. In this study, the focus is on the demands on the columns of SPSWs with regular perforation patterns in their infill plates.

Target displacement evaluation

This paper aims to investigate the lateral performance of SPSWs with perforations by comparing them with similar SPSW systems with no perforations in their infill plates. In order to compare the two systems, criteria are needed to make this comparison possible. Most recent studies on SPSW systems have used the capacity design approach as the design method and possibly also for performance checks. However, this method has some shortcomings for seismic design in low and moderate seismic regions, since it can result in very high level design forces that may not occur in the systems in these regions. The capacity design approach is a strength-based method and does not provide any information regarding the lateral deformation of the system when it is under the effect of the design earthquake. Moreover, it cannot be used when different performance objectives are to be satisfied for different seismic hazard levels.

On the other hand, the performance-based design method eliminates the shortcomings mentioned above. In this method, the performance objectives define the status of the building following a design earthquake that represents a desired seismic hazard level. Hence, this method provides a design procedure that allows for the design of lateral force resisting systems for different performance objectives under different seismic hazard levels.

In performance-based design, the target displacement, which is the maximum roof displacement under the design earthquake, δ_r, must be evaluated. Based on the Coefficient Method, the target displacement, δ_t, can be approximated as follows, in terms of the fundamental natural mode of vibration in the direction under consideration:

$$\delta_t = \delta_r = \Phi_{1,r}\, \Gamma_1\, S_d(T_{1e}, \xi_1)\, \psi \qquad (1)$$

where $\varphi_{1,r}$ is the deflection value at the roof level for the fundamental mode shape (which is equal to unity for a normalized mode shape), Γ_1 is the modal mass participation factor for the fundamental mode, $S_d(T_{1e},\xi_1)$ is the spectral displacement at the effective fundamental period (T_{1e}) and its corresponding critical damping ratio (ξ_1) in the direction under consideration, and ψ is a correction factor that takes into account the effects of nonlinear response on the maximum lateral deformation of the system.

The effective fundamental period is the fundamental period of the system, modified to account for yielding in the system (based on the idealized pushover curve) and can be evaluated from $T_{1e} = T_1\sqrt{K_i/K_e}$, where T_1 is the fundamental period, K_i is the elastic lateral stiffness and K_e is the effective lateral stiffness, which is a secant stiffness calculated at a base shear force of 60% of the effective yield strength of the system.

The correction factor ψ takes into account the effects of yielding (coefficient C_1) and pinched hysteresis cycles and cyclic strength and stiffness degradation (coefficient C_2) of the system on the maximum lateral displacement of the system. ASCE 41-06 (2007) defines this correction factor as the product of two factors as follows:

$$\psi = C_1 * C_2 = \left[1 + \frac{R_d - 1}{aT_{1e}^2}\right] * \left[1 + \frac{1}{800}\left(\frac{R_d - 1}{T_{1e}}\right)^2\right] \qquad (2)$$

where a is a site class factor, which is 60 for Site Class D. The correction factors C_1 and C_2 may be selected as unity for periods greater than 1.0 s and 0.7 s, respectively. Also, for systems with no degradation of stiffness and strength, the C_2 coefficient can be selected as 1.0. R_d is the ductility-related force modification factor, as defined in the National Building Code of Canada (NBCC 2005) and FEMA 450 (NEHRP 2004), and is a measure of the extent of nonlinearity in the system. This factor represents the capability of the system to dissipate energy through nonlinear behaviour, and can be defined as the ratio of elastic base shear demand to yield strength of the system.

Normally, for a given design case, the spectral displacement, S_d, for the effective fundamental mode of vibration is evaluated based on following equation:

$$S_d(T_{1e},\xi_1) = S_a(T_{1e},\xi_1)\, g \left(\frac{T_{1e}}{2\pi}\right)^2$$

where S_a is the design spectral acceleration for the effective fundamental period and critical damping ratio of the structure in the direction considered. However, this method is site dependant (depends on seismic hazard and site class at each location) and is not appropriate for general comparisons of different systems. In this study, a standardized seismic hazard independent target displacement has been proposed as a method of comparing different systems. Considering a multi-degree of freedom system designed for a base shear level V_D under monotonically increasing lateral loading, the pushover curve (roof displacement vs. base shear) is similar to Figure 1.

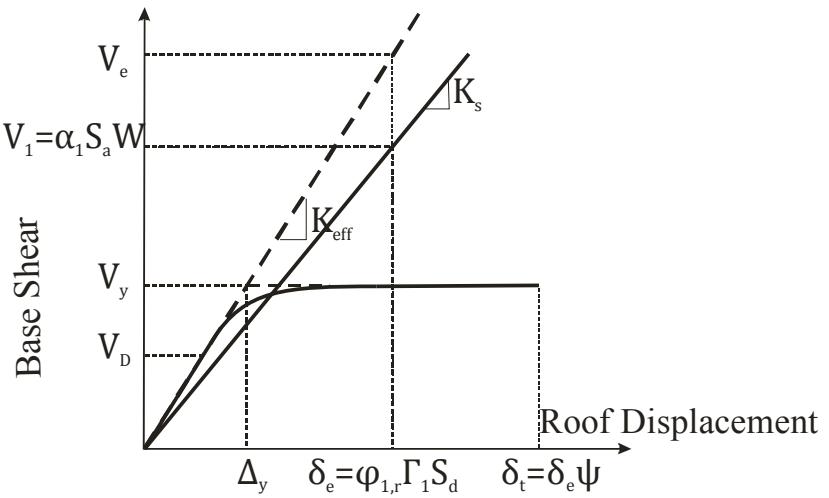


Figure 1. Pushover curve of a general MDOF system.

ASCE 41-06 (2007) defines R_d as the strength ratio of V_1 to V_y, where V_y is the effective yield strength of the system, $\alpha_1 = M_{e1}/M$ is effective mass ratio of the fundamental mode, and M_{e1} and M are the modal effective mass and total seismic mass of the system, respectively. However, defining R_d as this strength ratio does not guarantee that the displacement ratio will be proportional to the stiffness K_{eff} (Figure 1). In this study, R_d is defined as the strength ratio so that the effective stiffness of the system is maintained:

$$R_d = \frac{V_e}{V_y} = \frac{\Phi_{1,r}\Gamma_1 S_d}{\Delta_y} \quad (3)$$

Substituting Equations (2) and (3) into (1), the following equations for target displacement and ductility ratio at the target displacement are obtained:

$$\delta_t = R_d \Delta_y [C_1 C_2] \quad (4)$$

$$\mu_t = \frac{\delta_t}{\Delta_y} = R_d [C_1 C_2] \quad (5)$$

where C_1 and C_2 are defined in Equation (2). Defining R_d based on ASCE 41-06 leads to the following equation for the ductility ratio $\mu_t = [R_d \Gamma_1/\alpha_1][C_1 C_2]$, which yields about 80% larger values for the target displacement. (For a typical SPSW system, the values of Γ_1 and α_1 are fairly constant and can be selected as 1.32 and 0.72, respectively, which makes the coefficient Γ_1/α_1 equal to $1.83 \approx 1.80$).

Equation (5) defines the ductility ratio mainly as a function of R_d. In this study, for any desired level of ductility-related force modification factor, the target displacement is evaluated from Equation (4) and then the performance of the wall has been studied for the ductility ratio obtained from Equation (5).

Numerical Model of Steel Plate Shear Wall System

In order to study the performance of different SPSW systems under pushover analyses and seismic records, a system that was tested previously and proved to have very good response under cyclic loading has been selected and studied. The system is a four-story SPSW (Driver et al. 1997) that was tested under vertical load concurrent with increasing cyclic lateral displacement. The columns were spaced at 3.05 m centre-to-centre and the story height was 1.83 m for the top three story and 1.93 m for the first story. The columns were W310×118 sections, the intermediate beams were W310×60 sections, and the top beam was a W530×82 section. All cross-sections are Class 1 based on S16 (CSA 2009) (or compact based on AISC 360 (AISC 2005)), and they satisfy the stiffness requirements for boundary members of SPSWs (ω_h and ω_L requirements (CSA 2009)). The mean measured infill plate thicknesses were 4.54 mm, 4.65 mm, 3.35 mm, and 3.40 mm, respectively, for stories 1 (base) to 4 (top). Moment connections were used at the beam-to-column joints and all the materials were hot-rolled steel. In the early stages of the experiment, force control was used to control the test, and after achieving the yield lateral displacement for the first story, δ_y, the experiment switched to the displacement control method. Three full cycles were conducted at each deformation stage up to a deformation of $3\delta_y$, and two cycles were used at each deformation step afterward. The system achieved its maximum lateral strength at $5\delta_y$ and its lateral resistance then declined gradually to about 85% of the maximum value at $9\delta_y$. The roof lateral displacement at yield, maximum base shear, and maximum lateral deformation occurred at 32.0 mm, 92.5 mm, and 158 mm, respectively.

The commercial general-purpose finite element code ABAQUS is selected to model this wall. In order to verify the model, first the wall is analysed under the same loading conditions as those used in the experiment. As-built dimensions are used; however, the fish plates are not modelled and the infill plates are connected to the surrounding boundary elements. All infill plates of the wall are modelled using four-node shell elements with reduced integration (S4R element), and frame elements (beams and columns) are modelled using two-node linear beam elements (B31). Material and geometric nonlinearities are both considered. The measured material properties for the beams, columns, and infill plates are used. The von Mises yield criterion, along with the isotropic hardening rule for monotonic loading and kinematic hardening rule for dynamic loading, is used. The effect of residual stresses in the frame members is not considered in the analyses.

The story shear versus story deflection relationships of panel 1 (base) from the analyses are compared with the experimental results in Figure 2. Figure 2(a) shows the response under monotonic loading, where it can be seen that the model provides acceptable results up to the ultimate strength. However, it over-predicts the strength slightly at the early stage of yielding, which is mainly because the monotonic analysis disregards the effect of softening of material due to the cyclic nature of the loading applied to the test specimen. Also, the model does not account for the gradual

degradation of strength exhibited by the test specimen after a story drift of 5δy (lateral displacement 42.5 mm) because the local buckling of the column section and material failure due to tearing of the infill plate are not included in the model.

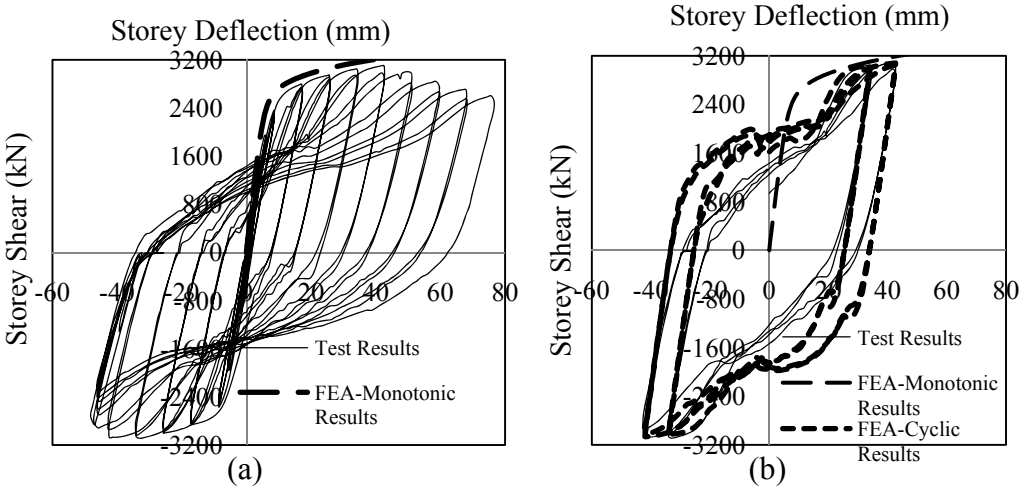


Figure 2. Comparison of test results for panel 1 with FEA results:
(a) Monotonic loading; (b) Cyclic loading.

Figure 2(b) compares experimental results with the cyclic loading analysis results for two excursions at 4δy and two excursions at 5δy. The ultimate load is accurately predicted by the model at each displacement level and even at each excursion. Also, the model predicts the loading and unloading stiffnesses and the deflection at which the tension field in the panel becomes effective well. However, it over-predicts the shear strength of the panel slightly around the zero-displacement regions. In general, the model predicts the monotonic and cyclic responses of the system up to ultimate strength very well and a similar model is used for the pushover analysis discussed in the next section.

Steel plate shear wall systems investigated

In this study, three different steel plate shear wall systems have been considered. Wall A1, shown in Figure 3(a), is the SPSW tested by Driver at al. (1997) and studied in the previous section numerically. Wall A2 is similar to Wall A1, but with simple shear beam-to column connections.

Figure 3(b) shows Wall B1, for which all the properties are similar to Wall A1 except that it contains a regular perforation pattern in all four panels, as permitted by CSA standard S16 (CSA 2009). There are 23 holes in panels 1, 2 and 3, and 18 holes in panel 4. Wall C1, shown in Figure 3(c), is the same as Wall B1, but with a different arrangement of holes; there are 22 holes in panels 1, 2 and 3, and 18 holes in panel 4. Walls B2 and C2 are the same as Walls B1 and C1, respectively, but with simple shear beam-to-column connections.

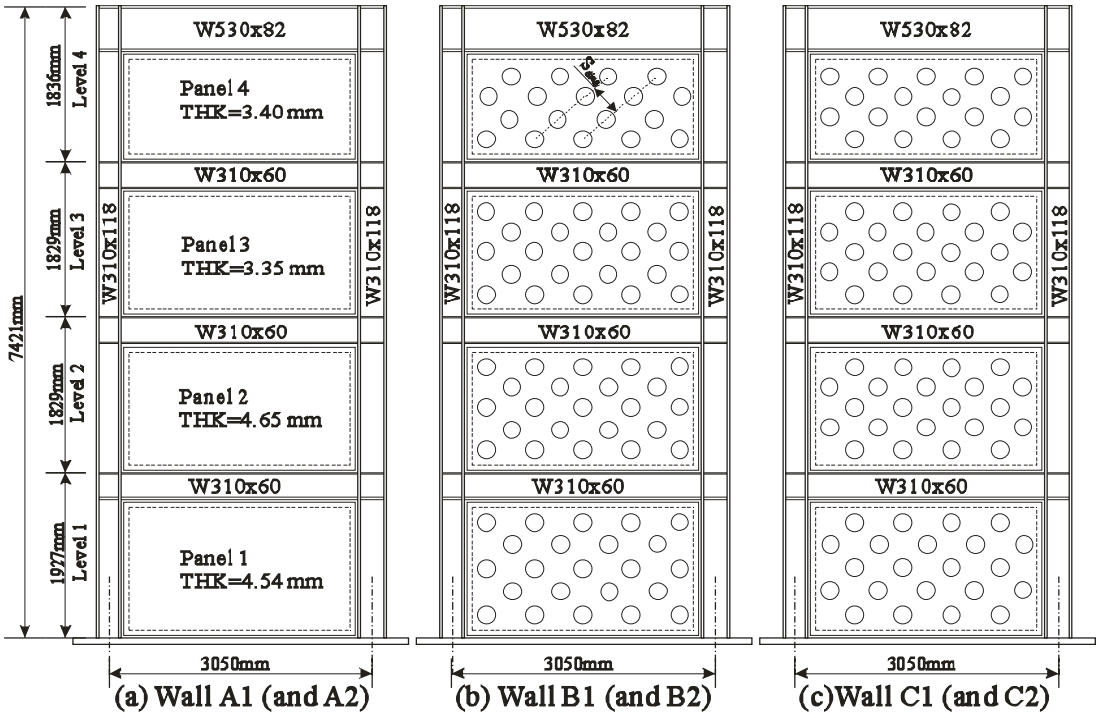


Figure 3. Different systems of SPSWs.

In all perforated walls, the holes are of equal diameter (D = 230 mm) and regularly spaced vertically and horizontally (at a distance of 280 mm) over the entire area of the infill plates. The regular grid of staggered holes allows the development of a diagonal tension field at 45°. The shortest centre-to-center distance between perforations is S_{diag} = 396 mm, which makes the ratio of $D/S_{diag} = 0.58 < 0.6$. The distance between the first hole and surrounding frame members is between D = 230 mm and D+0.7 S_{diag} = 507 mm. Hence, the two perforation patterns satisfy all the requirements of clause 27.9.2.3 of CSA S16-09 for perforated infill plates. Thus, based on this clause, the factored shear resistance of the perforated wall is equal to that of a conventional SPSW times the reduction factor $1-0.7D/S_{diag}$, which for the patterns selected is equal to 0.6.

Performance criteria

Each action is classified as deformation-controlled (ductile) or force-controlled (non-ductile), and all components of each SPSW are primary components (ASCE 2007). When a nonlinear procedure is used, the component capacity for deformation-controlled actions is taken as the permissible inelastic deformation limit considering all coexisting forces and deformations (defined in chapter 5 of the standard, and usually expressed in term of the yield displacement). Conversely, the component capacity for force-controlled actions is taken as the lower-bound strength, evaluated by code design equations and using lower-bound material properties and a strength reduction factor equal to unity.

Flexure of beams is considered to be a deformation-controlled action. Axial compression of columns is considered a force-controlled action, with the lower-bound axial compression capacity P_{CL}. Flexural loading of columns with an axial load at the target displacement less than $0.5P_{CL}$ is considered deformation-controlled. For greater axial loads, it is considered force-controlled. Steel columns subjected to axial tension or combined axial tension and bending moment are considered deformation-controlled. Walls A1, B1, and C1 all use fully restrained moment connections, while Walls A2, B2, and C2 use partially restrained moment connections.

When the criteria of ASCE 41-06 (2007) are used for new buildings, slightly higher than life safety performance levels for a BSE-1 hazard level are needed in order to achieve a system comparable with a similar system designed based on design codes.

Pushover analysis results

In the pushover analyses, a uniform lateral load distribution pattern is used and the effects of gravity loads are considered on the columns of each wall. The pushover curves for all SPSWs investigated are shown in Figure 4. The difference in the curves of Wall A1 and Wall B1 or C1 indicates that the proposed reduction factor based on S16-09 (2009), $1\text{-}0.7*D/S_{diag} \approx 0.6$, provides a conservative evaluation for shear resistance of the perforated walls.

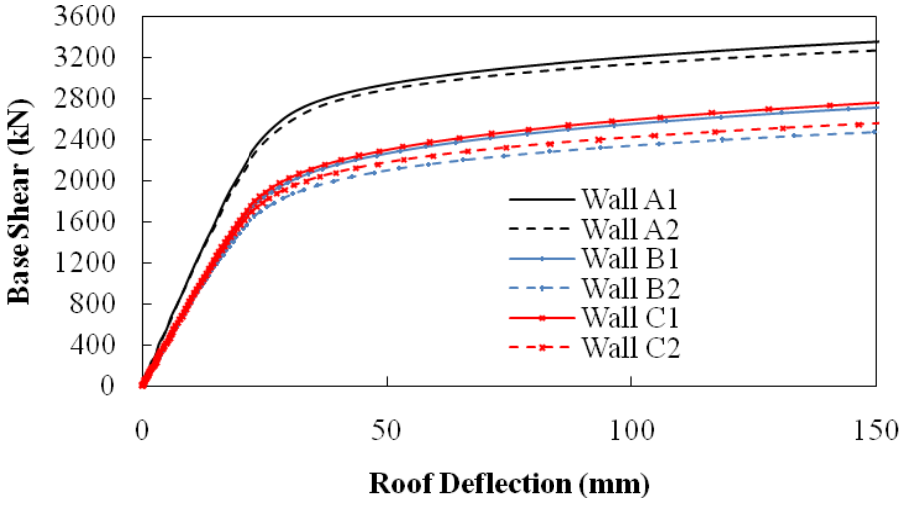


Figure 4. Pushover curves of the SPSW systems.

Previous research has shown that the demand on columns of SPSWs is complex and notably large. Column shear, moment, and axial force demands result from the frame action of the boundary frame and tension field action in the infill plates. The level of the demand depends on the geometry of the system (such as bay width and story height, number of stories, thickness of the infill plate), type of beam-to-column connection (rigid, semi-rigid, and simple), and mechanical properties of the material (especially the infill plate), and can be extremely high in the capacity design method.

In order to design robust and reliable SPSW systems, they should be studied in the context of performance-based design rather than capacity design. In this way, by assuming a desired level of R_d, the target displacement is evaluated from Equation (4). The appropriate values for R_d could be 2, 3.5, and 5, which correspond to limited-ductility (or ordinary), moderate-ductility (or intermediate), and ductile (or special) SPSWs, respectively. At the target displacement, members under deformation-controlled actions must have an expected deformation capacity not less than the maximum deformation demand, and members under force-controlled actions must have a lower-bound strength not less than the maximum force demand.

The axial load and moment internal force demands of both columns of the different walls for $R_d = 2$ and 5, are shown in Figures 5 and 6, respectively. For each level of strength ductility factor, (while the base shear is different) the target displacement for each wall is essentially the same and is equal to 54 mm and 140 mm, for R_d equal to 2 and 5, respectively. Based on the test results (Driver et al. 1997) the 54 mm roof displacement is between the Immediate Occupancy and Life Safety performance levels, and the roof displacement of 140 mm is larger than the Collapse Prevention performance level. As can be seen from Figures 5(a), 5(c), 6(a), and 6(c), the axial force demands for the perforated walls are less than for the solid walls. However, Figures 5(b), 5(d), 6(b), and 6(d) show that the column moment demands for the perforated walls for all connection types tend to be larger than for the solid walls. Also, these figures show that although the difference between Walls B and C are apparently minor, the difference in moment demand is considerable in some regions, suggesting an inherent uncertainty in the response of the perforated SPSWs.

The reason for the higher moment demand is attributed to the fact that the perforated infill plate causes the frame action in the SPSW to increase, since much of the increased demand is located in the connection regions. All in all, the column design demands for perforated walls may be increased in some cases, which is in contrast with the main idea behind the development of the system.

In order to study the actual change in the column demands, design equations are used that take into account the interaction of axial compression and moment. Table 1 shows the compression force–moment interaction results for $R_d = 2$ based on both S16-09 (2009) and AISC 360-05 (2005). The strength ratios presented are the maximum of cross-sectional strength, overall in-plane member strength, and lateral-torsional buckling strength, which in almost all cases is that of the cross-sectional strength. The first two stories of the left columns are subjected to tension loads and they are considered as fully deformation-controlled elements. Also, for the first two stories of the right columns, some of the beam-column strength ratios are greater than 1.0. The reason is attributed to the fact that the design equations are a conservative approximation of true capacities, and also the material models consider strain hardening, while all the interaction equations are checked using yield values. The results show that the perforations increase the interaction values in the upper stories and in the lower stories the improvement is mostly negligible.

Table 2 shows the deformation ductility ratios for $R_d = 2$. For the first two stories of the left columns, which are subjected to tension, the axial ductility ratios are shown. Also, all columns with an axial compressive force at the target displacement that exceeds 50 % of the lower-bound axial compressive strength are considered force-controlled for both axial load and flexure, and are identified in the table by the symbol FC. The results show that the perforations provide limited improvements to the performance of deformation-controlled elements.

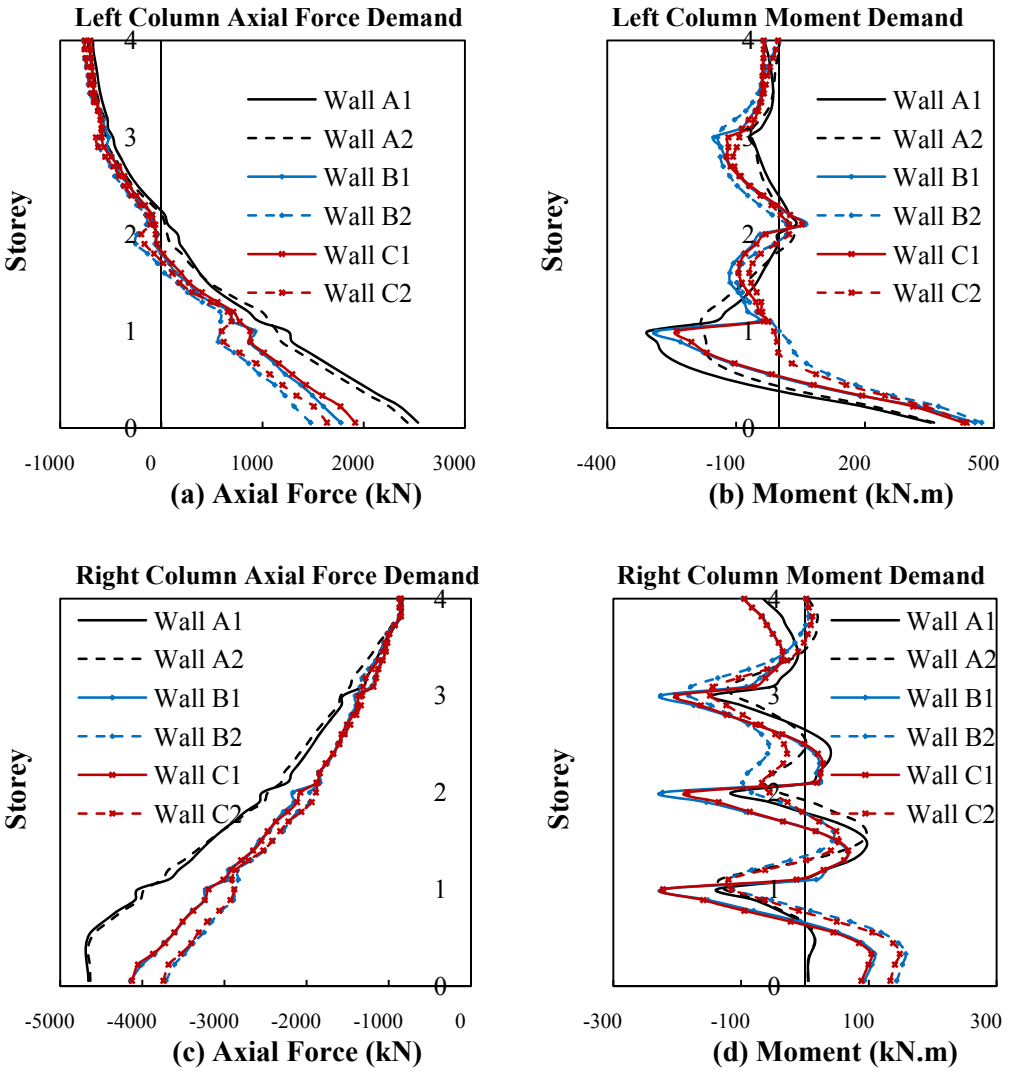


Figure 5. Column internal force demands for $R_d = 2$.

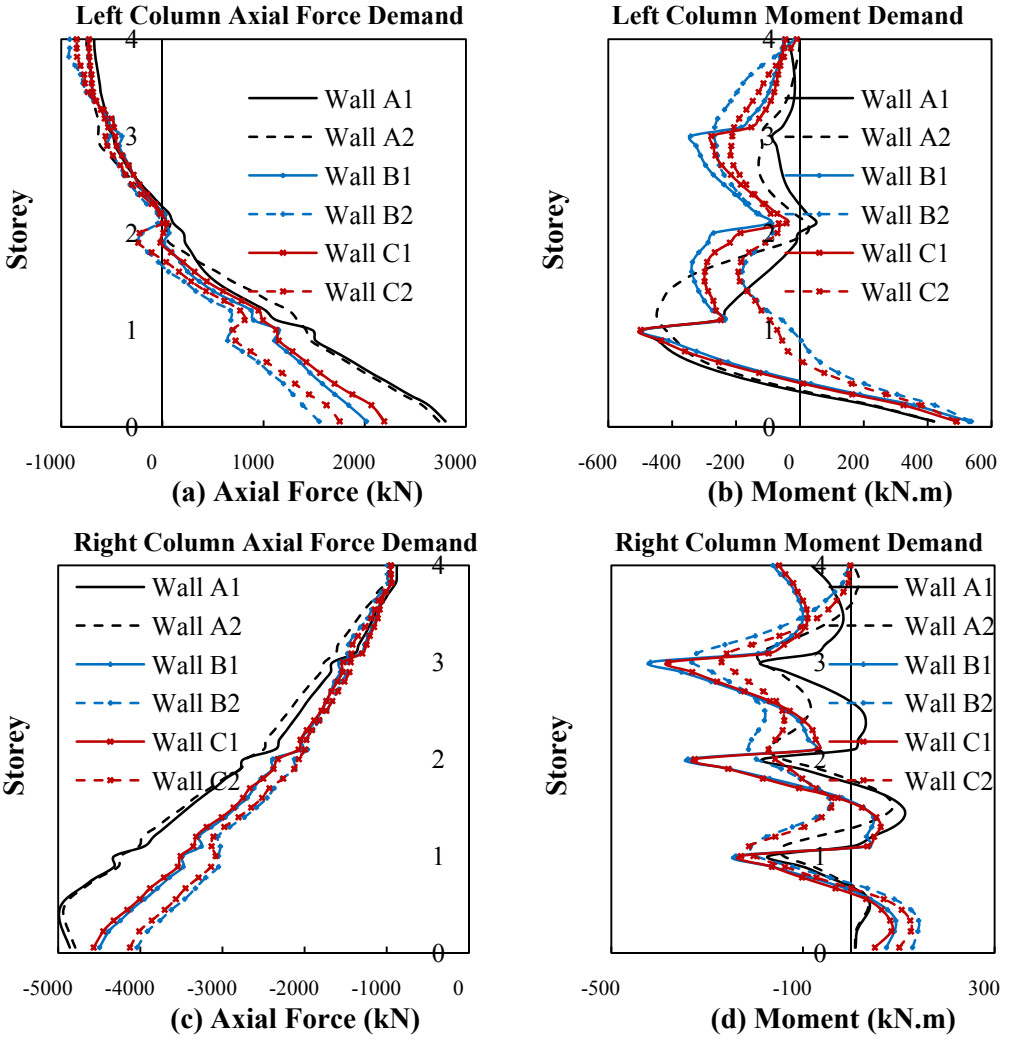


Figure 6. Column internal force demands for $R_d = 5$.

Table 1. Strength ratios for $R_d = 2.0$.

		Wall A1		Wall A2		Wall B1		Wall B2		Wall C1		Wall C2	
	Story	S16	AISC	S16	AISC	S16	AISC	S16	AISC	S16	AISC	S16	AISC
Left Column	1	-	-	-	-	-	-	-	-	-	-	-	-
	2	-	-	-	-	-	-	-	-	-	-	-	-
	3	0.20	0.17	0.21	0.17	0.33	0.31	0.34	0.31	0.29	0.26	0.27	0.24
	4	0.20	0.13	0.21	0.16	0.25	0.21	0.31	0.28	0.23	0.18	0.25	0.21
Right Column	1	1.08	1.11	1.05	1.08	1.03	1.05	1.01	1.01	1.02	1.04	1.00	1.01
	2	0.84	0.74	1.01	1.04	0.79	0.81	0.79	0.81	0.71	0.74	0.80	0.83
	3	0.55	0.56	0.59	0.52	0.62	0.65	0.56	0.57	0.58	0.60	0.50	0.52
	4	0.36	0.20	0.49	0.51	0.39	0.26	0.55	0.57	0.37	0.25	0.49	0.51

Table 2. Deformation (ductility) ratios for $R_d = 2.0$.

		Wall A1		Wall A2		Wall B1		Wall B2		Wall C1		Wall C2	
	Story	θ/θ_y	Δ_{ax}/Δ_{yd}	θ/θ_y	Δ_{ax}/Δ_{yd}	θ/θ_y	Δ_{ax}/Δ_{yd}	θ/θ_y	Δ_{ax}/Δ_{yd}	θ/θ_y	Δ_{ax}/Δ_{yd}	θ/θ_y	Δ_{ax}/Δ_{yd}
Left Column	1	-	0.92	-	0.82	-	0.69	-	0.40	-	0.65	-	0.37
	2	-	0.11	-	0.11	-	0.05	-	0.02	-	0.06	-	0.04
	3	2.45	-	2.44	-	2.54	-	2.67	-	2.38	-	2.22	-
	4	2.05	-	1.93	-	1.55	-	1.44	-	1.49	-	1.33	-
Right Column	1	FC†	-	FC†	-	FC†	-	FC†	-	FC†	-	FC†	-
	2	FC†	-	FC†	-	5.16	-	FC†	-	4.59	-	FC†	-
	3	3.44	-	3.43	-	3.34	-	3.39	-	3.12	-	2.84	-
	4	2.26	-	2.53	-	1.72	-	1.83	-	1.64	-	1.67	-

† FC: Force-controlled element

Conclusion

In this paper, a standardized method has been presented to evaluate the target displacement of any lateral force resisting system in terms of the yield displacement of the system and the ductility-related force modification factor, R_d. Also, it provides a suitable method for comparing different systems with the same value of R_d.

Perforated SPSWs were introduced to alleviate the severe force demands on the columns of SPSWs by degrading the lateral shear resistance of the system. This study has shown that although the perforations reduce the shear capacity of the infill plate considerably, they may not reduce the force demands on the columns, especially at the upper stories where the perforations makes the design strength ratios worse.

Acknowledgements
Funding for this research was provided by the Steel Structures Education Foundation, the Alberta Heritage Foundation, and the University of Alberta.

References

AISC. (2005). *Specification for structural steel buildings. ANSI/AISC 360-05*, American Institute of Steel Construction, Inc., Chicago, IL, United States.

ASCE. (2007). *Seismic Rehabilitation of Existing Buildings. ASCE/SEI 41-06*, American Society of Civil Engineers New York, NY.

CSA. (2009). *CAN/CSA S16-09, Design of Steel Structures*, Canadian Standards Association, Mississauga, ON.

Driver, R.G., Kulak, G.L., Kennedy, D.J.L., and Elwi, A.E. (1997). "Seismic behaviour of steel plate shear walls." Structural Engineering Report 215, Dept. of Civil and Environmental Engineering, University of Alberta, Edmonton, AB.

NBCC. (2005). *National Building Code of Canada*, National Research Council of Canada, Ottawa, ON.

NEHRP. (2004). *Recommended Provisions for Seismic Regulations for New Buildings and Other Structures (FEMA 450). Part 2. Commentary.* 2003 Edition, National Earthquake Hazards Reduction Program, USA

Analysis of Creep Buckling of Steel Columns Subjected to Fire

M. A. Morovat[1], J. Lee[1], M. D. Engelhardt[1], T. A. Helwig[1] and E. M. Taleff[2]

[1]Ferguson Structural Engineering Laboratory, Dept. of Civil, Architectural and Environmental Eng., Univ. of Texas at Austin, 10100 Burnet Road, Building 177, Austin, Texas 78758 USA; PH (512) 471-4476; email: morovatma@mail.utexas.edu, jinwoo@mail.utexas.edu, mde@mail.utexas.edu, thelwig@mail.utexas.edu
[2]Dept. of Mechanical Eng., Univ. of Texas at Austin, Austin, TX 78712 USA; email: taleff@mail.utexas.edu

ABSTRACT

One of the critical factors affecting the strength of steel columns at elevated temperatures is the influence of material creep. Under fire conditions, steel columns can exhibit creep buckling, a phenomenon in which the critical buckling load for a column depends not only on slenderness and temperature, but also on the duration of applied load. Although material creep and consequently the phenomenon of creep buckling can significantly impact the safety of steel columns subjected to fire, they have received relatively little research attention, and are not currently explicitly considered in code-based design formula for columns at elevated temperatures, such as those in the Eurocode 3 or in the AISC Specification.

This paper will propose a preliminary methodology to study the phenomenon of creep buckling in steel columns subjected to fire. Preliminary analytical solutions are presented, and compared with computational predictions for creep buckling. The analytical and computational results clearly indicate that accurate knowledge of material creep is essential in studying creep buckling phenomenon at elevated temperatures. In addition, the results show that neglecting creep effects can lead to erroneous and potentially unsafe predictions of the strength of steel columns subjected to fire.

INTRODUCTION

The essence of performance-based structural fire safety design of steel building structures is the ability to predict thermal and structural response to fire. An important aspect of such predictions is the ability to evaluate strength of columns at elevated temperatures. Columns are critical structural elements, and failure of columns can lead to collapse of a structure. One of the critical factors affecting the strength of steel columns at elevated temperatures is the influence of material creep. Under fire conditions, steel columns can exhibit creep buckling, a phenomenon in which the critical buckling load for a column depends not only on slenderness and temperature,

but also on duration of applied load. This paper presents some results of an on-going research on the phenomenon of high-temperature creep buckling of steel columns.

Creep of Steel at Elevated Temperatures

The term creep refers to time-dependent strain response of materials, or more generally to time- and rate-dependent stress-strain response. At normal temperatures, the stress-strain response of steel shows only a very mild dependence on loading rate, for typical loading rates seen in buildings. Yield stress variations on the order of 10-percent are possible as loading rates are varied (Galambos 1998). Although showing mild rate dependence, steel shows virtually no time-dependent strain (i.e., creep strain) at normal temperatures, and creep effects are normally neglected in the analysis and design of steel structures at normal temperatures. However, as temperature increases, steel exhibits increasingly significant creep effects. The temperature of structural steel members in a building fire can vary widely. However, as a point of reference, unprotected steel in building fires can reach temperatures on the order of 1000 °C (Buchanan 2002). Steel protected with insulation ("fireproofing") can reach temperatures of 550 °C (Buchanan 2002). At these temperatures, the effects of creep on the response of structural steel can be very significant. Creep tests on materials are commonly conducted by subjecting the material to constant stress and temperature, and then measuring strain (creep strain) as a function of time. A typical creep strain versus time curve is shown in Figure 1. This curve is often divided into the three phases of primary, secondary and tertiary creep. In the primary stage, the curve is nonlinear and typically exhibits a decreasing creep strain rate with increase in time. In the secondary stage, the creep strain rate is almost constant, and this stage is often referred to as steady-state creep. In the tertiary stage, the creep strain rate increases with time. For steel, the shape of the curve, the magnitude of the creep strain, and the time scale are highly dependent on temperature and stress levels.

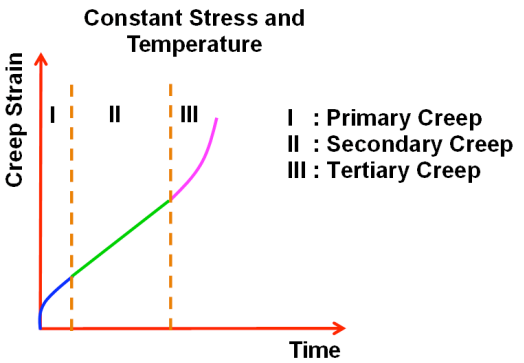


Figure 1. Typical creep strain versus time response under constant stress and temperature.

The creep behavior of steel at elevated temperatures has been studied and reported by several researchers (Norton 1929, Bailey 1930, Dorn 1954, Harmathy 1967, Knight, Skinner and Lay 1971, Williams-Leir 1983, Fields and Fields 1989, and

Luecke et al 2005). One of the simplest and most widely used creep models is the Norton-Bailey model, also known as creep power law (Norton 1929, and Bailey 1930). It should be noted that although the Norton-Bailey law is capable of modeling primary creep, it can define the steady-state or secondary stage of creep more accurately. One of the widely used creep models in structural-fire applications proposed by Fields and Fields (1989) incorporates a power law and represents creep strain, ε_c, in the form of a Norton-Bailey equation as follows:

$$\varepsilon_c = a\, t^b\, \sigma^c \tag{1}$$

In this equation, t is time and σ is stress. The parameters A, B and C are temperature-dependent material properties. Fields and Fields (1989) derived equations for these temperature-dependent material properties for ASTM A36 steel. As a result, the creep model developed by Fields and Fields (1989) were used by NIST in their analysis of the WTC 1 and 2 collapses (NIST 2005). The model developed by Fields and Fields (1989) is capable of predicting creep in the temperature range of 350 °C to 600 °C and for creep strains up to 6-percent. For initial studies of creep buckling of steel columns at elevated temperature, one of the creep models used by the authors was the Fields and Fields (1989) model. The application of this creep model together with observations will be discussed in more detail in the following sections of this paper.

Another creep model used by the authors in their study of creep buckling phenomenon at high temperatures is the one developed by Harmathy (1967). Harmathy (1967) appears to be one of the first investigators who attempted at developing creep formula for structural steels subjected to fire exposure. Harmathy proposed a creep model based on experiments on several structural and prestressing steels including ASTM A36. His model attempts to predict creep strains in both the primary and secondary stages of creep. The model proposed by Harmathy represents creep strain, ε_c, for steel as follows:

$$\varepsilon_c \approx \left(3Z\varepsilon_{c_0}{}^2\right)^{\frac{1}{3}}\theta^{\frac{1}{3}} + Z\theta \quad \text{when} \quad \frac{d\sigma}{dt} = 0 \tag{2}$$

In this equation, θ is the temperature-compensated time in Dorn's creep theory, Z is the slope of the secondary part of the creep curve, also known as the Zener-Hollomon parameter (Zener and Hollomon 1967), and ε_{c0} is the intercept obtained by extending the straight-line section (secondary part) of the $\varepsilon_c(\theta)$ curve to the ε_c axis. The parameters ε_{c_0}, and Z are stress-dependent material parameters.

Although models developed by Fields and Fields (1989) and Harmathy (1967) are referenced by many investigators in the field of structural-fire engineering, their predictions of creep strain for some applied stress levels and temperatures are quite different. As an example, predictions from these two models for ASTM A36 steel are compared and plotted in Figure 2 for an applied stress of 23 ksi at 500 °C. As can be observed from this plot, the differences in the two models are significant. This difference in creep predictions and its impact on creep buckling behavior will be discussed in the following sections and emphasized throughout this paper.

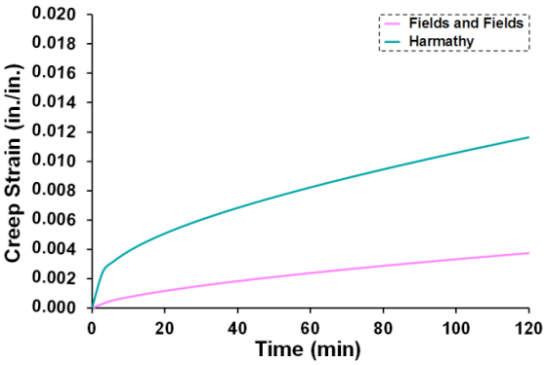


Figure 2. Comparison between Fields and Fields (1989) and Harmathy (1967) models at 23 ksi and 500 °C.

Creep Buckling of Steel Columns at Elevated Temperatures

The term *creep buckling*, as used herein, refers to the phenomenon in which the critical buckling stress for a column depends not only on slenderness and temperature of the column, but also on the duration of the applied load. The concept of creep buckling is illustrated qualitatively in Figure 3. This figure plots buckling stress for a steel column of given effective slenderness KL/r, for different temperatures. Temperature T_1 represents room temperature, for which creep effects are not significant. In this case, the buckling stress is independent of the duration of applied load.

As temperature increases, the initial buckling load (at time zero) decreases, due to the decrease in material strength, modulus and proportional limit. Consequently, the buckling capacity at initial application of load depends only on temperature. This phenomenon has been studied by a number of past investigators. But, as temperature increases and material creep becomes significant, the buckling stress depends not only on temperature, but also on the duration of load application. Thus, in a fire scenario, initially a column at elevated temperature may be safely carrying its load. However, after a period of time, even though the load and temperature have not changed, the column may buckle. This time-dependent creep buckling phenomenon has seen only very limited study in structural-fire engineering research, but is potentially of great importance.

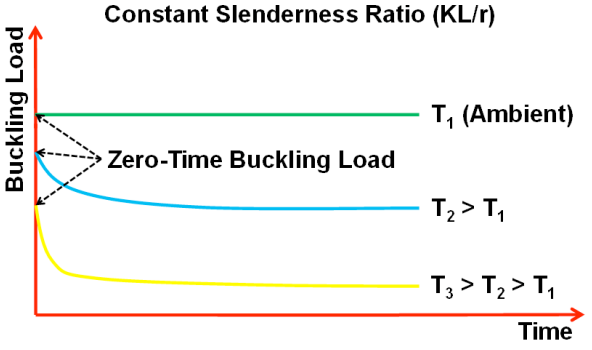


Figure 3. Qualitative representation of creep buckling.

Freudenthal (1946) was one of the first researchers who attempted to solve creep buckling analytically. One year later, Marin (1947) suggested an analytical model to predict creep deflections in columns. Shanley (1952) studied creep buckling behavior of columns for aircraft applications and came up with a model based on the concept of *time-dependent tangent modulus*. A complete account of creep buckling testing programs in the fifties and sixties is provided by Singer, Arbocz, and Weller (2002). Hoff (1957), and Eggwertez (1976) did early work on the effect of creep on high-temperature behavior of steel columns. More recently, Tan et al. (2002) incorporating Harmathy's creep model, developed a finite element program to study the buckling of steel columns at elevated temperatures.

To better evaluate the potential importance of creep buckling in structural-fire engineering applications, preliminary creep buckling analyses have been conducted by the authors. These analyses, analytical and computational, attempt to predict the elevated-temperature creep buckling strength of simply supported steel columns. For these analyses, a W12×120 section made of A36 steel is considered for both the analytical and numerical studies. Moreover, the effective slenderness ratio is kept constant by considering only one single column length of 240 inches.

For the analytical creep buckling studies, the creep buckling model proposed by Rabotnov and Shesterikov (1957) is utilized, along with the creep material models developed by Harmathy (1967) and by Fields and Fields (1989), both for ASTM A36 steel. It should be noted that the model by Rabotnov and Shesterikov (1957) has been adopted, after a fairly comprehensive review of the literature on creep buckling, due to its simple form. In developing their creep buckling model, Rabotnov and Shesterikov (1957) make the fundamental assumption that creep strain rate depends only on the stress and creep strain and not on the history of loading. In other words,

$$f(\sigma, \varepsilon_c, \dot{\varepsilon_c}) = 0 \qquad \text{or} \qquad \dot{\varepsilon}_c = F(\sigma, \varepsilon_c) \tag{3}$$

In which both f and F are functions expressing material creep, ε_c is the creep strain, and $\dot{\varepsilon_c}$ is the creep strain rate. With this assumption, the creep buckling equation can be shown to have the following form,

$$\frac{P_{cr}}{P_E} = \frac{1}{1-[E\lambda/\mu]} \tag{4}$$

in which, E is the temperature-dependent Young's modulus, P_E is the Euler buckling load at elevated temperatures, and λ and μ are material parameters defined as follows,

$$\lambda = \frac{\partial f}{\partial \sigma} \qquad \mu = \frac{\partial f}{\partial \varepsilon_c} \tag{5}$$

Using the material creep models by Harmathy (1967) and Fields and Fields (1989), equations for material parameters μ and λ can be derived according to Equation (5).

Equation (4), which again represents creep buckling capacity, has a simpler form when the material creep model by Fields and Fields (1989) is used to get parameters μ and λ. Equation (4) together with the Fields and Fields (1989) creep material model has the following form,

$$\frac{P_{cr}}{P_E} = \frac{1}{1+[a c\, t^b \sigma^{c-1}]E} \quad \text{or} \quad \frac{P_{cr}}{P_E} = \frac{1}{1+[c\, \varepsilon_c/\sigma]E} \tag{6}$$

Equation (6) clearly shows that at constant stress and temperature, creep buckling capacity is inversely proportional to creep strain. This fact is also represented graphically in Figure 4, in which equivalent creep and creep buckling capacity curves are plotted together at 400 °C. Therefore, like the creep curve at constant stress and temperature, the buckling capacity curve changes with time and ends at a failure point at which the buckling capacity is equal to the applied load. Another useful observation is that there is a specific creep strain corresponding to the buckling failure. The time to reach this specific creep strain and consequently the creep buckling load is considered to be the failure time or time-to-buckle. By considering other constant load levels, one can generate more buckling capacity curves at the same temperature. Figure 5(a) plots these curves, which will be referred to as *iso-load creep buckling capacity curves* at a constant temperature of 400 °C. Again, these curves end at creep buckling loads which are the same as the corresponding applied loads. The envelope to these curves at the buckling failure points is what we refer to as the *creep buckling curve* or the *time-dependent buckling curve* throughout this paper and is shown in Figure 5(b). It is also possible to use Equation (6) directly to solve for creep buckling load. Since at buckling $\sigma = \sigma_{cr} = P_{cr}/A$, Equation (6) can be rewritten as follows,

$$P_{cr} + \left[\frac{acE}{A^{(c-1)}}\right] t^b P_{cr}^c = P_E \tag{7}$$

in which A is the cross sectional area of the column. Equation (7) can be solved iteratively to get the P_{cr} as a function of time at constant temperature. In other words, Equation (7) can be used directly to construct the creep buckling curve at a specific temperature.

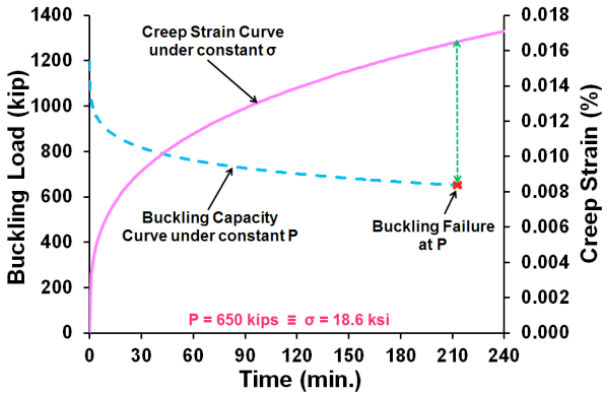


Figure 4. Graphical representation of the concept of creep buckling at 400 °C.

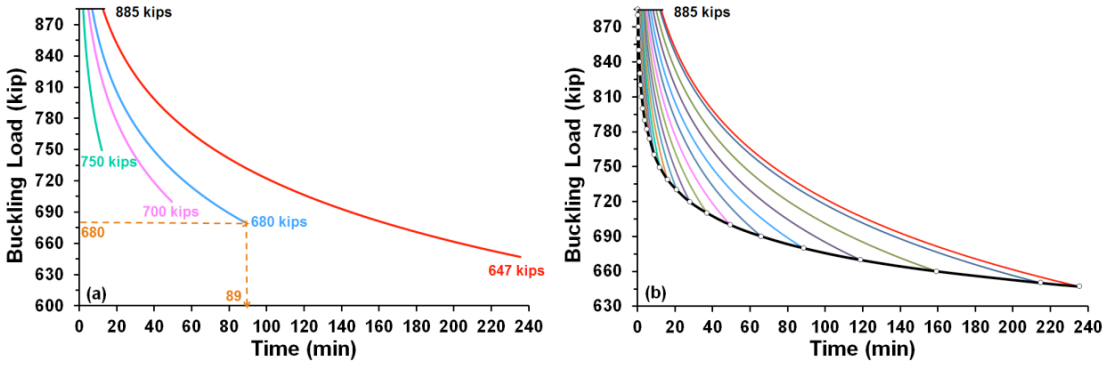
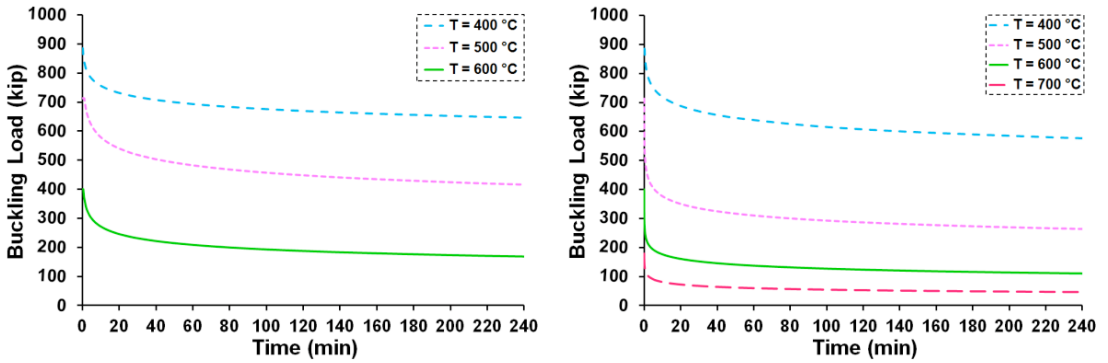


Figure 5. Iso-load buckling capacity curves and the creep buckling envelope at 400 °C.

As a final note on the analytical formulation, it should be added that this method disregards any initial imperfections and assumes a perfectly straight column. Moreover, this method predicts the Euler buckling load as the zero-time buckling load at any given temperature. To be more specific, this method only considers time-dependent inelasticity and ignores time-independent inelasticity due to the applied load at time zero. To have a more sensible model, a cap was placed on the maximum predicted buckling strength to reflect the effects of inelasticity and initial crookedness at time zero. For instance, the Euler buckling load for the column in consideration is 1198 kips at 400 °C. The results of load-deflection analysis on ABAQUS® assuming an initial imperfection of L/1000 and including material inelasticity showed a buckling load of 885 kips, which is shown in Figure 5.

Figures 6(a) and 6(b) show representative results of the analysis considering both material creep models. In these figures, plots of buckling load as a function of time are presented. Results are shown for temperatures of 400 °C to 700 °C. Although this is just a rudimentary study, these results show the potentially enormous impact of creep on buckling. At 500 °C and higher temperatures, the buckling strength of the column after just 20-minutes is reduced to about one-half of its value at initial application of load.



(a) Fields' and Fields' material model **(b) Harmathy's material model**

Figure 6. Analytical predictions of creep buckling using Rabotnov–Shesterikov method.

As a next step, computational predictions of creep buckling were developed using ABAQUS®. In order to simulate creep buckling on ABAQUS®, first, temperature is increased to the desired level, and then a fraction of the zero-time buckling load is applied to the column. No material creep is considered in these two steps. Next, the column is allowed to creep over the time period of 50 hours under the sustained load. Finally, the time-to-buckle due to creep is estimated. It should be pointed out here that to get the zero-time buckling load, an inelastic load-deflection analysis has to be performed. This has been done in ABAQUS® by using a nonlinear analysis scheme called a Riks Analysis. Moreover, to model initial geometric imperfections, an Eigen-value buckling analysis was performed. The initial shape of the column was taken as the shape of the first buckling mode, and the magnitude of the imperfection was chosen as a fraction of the column length. As far as material modeling is concerned, the inelastic material model at elevated temperatures was defined according to Eurocode 3 (2003), and the creep material model is the one proposed by Fields and Fields (1989), explained in the previous section. 3D hexahedral eight-node linear brick elements, C3D8R, have been utilized to model the columns on ABAQUS®.

As an example, the results of creep buckling simulations for the temperature of 500 °C and an initial out-of-straightness of L/1000 are presented in Figure 7 as plots of creep deflection versus time at different load levels. Figure 7 clearly shows that the rate of change of deflection with time increases very slowly up to an inflection point and then increases more rapidly until the column no longer can support its load. The time at which column becomes instable is considered as the failure time or time-to-buckle in this study.

Curves like the one presented in Figure 7 can be used to construct time-dependent column buckling curves, a sample of which is shown in Figure 8. Figure 8 simply presents buckling load as a function of time for different initial imperfections at 500 °C. To better gage the effect of temperature on time-dependent column buckling, Figure 9 compares buckling curves at three different temperatures. As can be expected, the higher the temperature, the more significant are the creep effects on column buckling behavior. It should be emphasized here that creep buckling curves like the ones shown in Figures 8 and 9, clearly show the possible danger of high-temperature design of steel columns just based on the zero-time buckling loads thereby ignoring the effect of duration of the applied load.

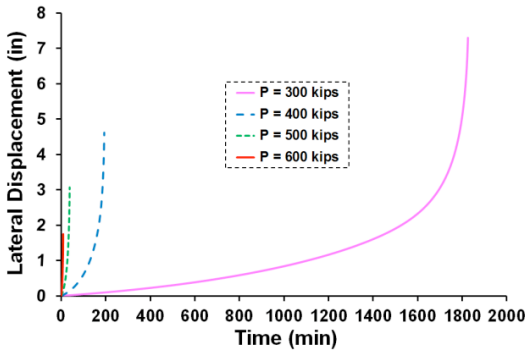


Figure 7. Lateral deflections due to creep at 500 °C and Δ_o = L/1000.

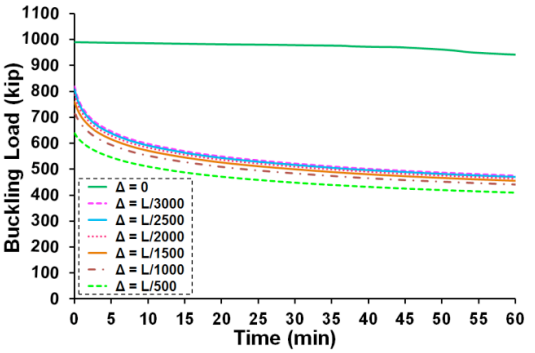


Figure 8. Creep buckling curves at 500 °C considering different initial imperfections.

Creep buckling predictions from analytical and computational methods are compared at 500 °C and presented in Figure 10. The analytical predictions are for a perfect column, while the computational one is for a column with L/1000 initial crookedness. As can be seen in Figure 10, these three curves follow the same trend after about 10 minutes. The difference between these predictions after 10 minutes is related to the difference in predictions of the material models and inclusion of time-independent inelasticity in the computational method. The interesting part though is at times of less than 10 minutes. This initial difference may be related to the effect of initial imperfection on the zero-time buckling load. On the other hand, it can probably also be related to the fact that Harmathy's and Fields' and Fields' models consider primary creep quite differently, especially at high level of stresses as shown in Figure 2. In any event, this seems to be an interesting observation and any solid conclusion requires more accurate experimental information regarding material creep behavior at elevated temperatures.

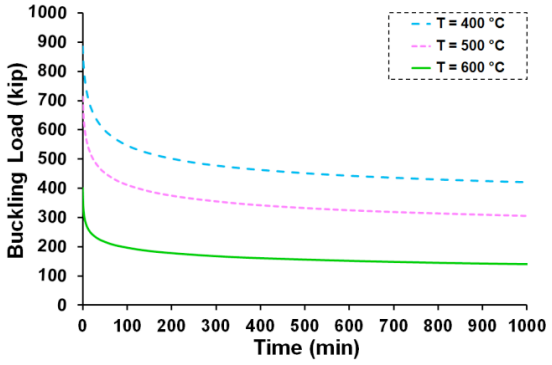


Figure 9. Computational creep buckling curves at Δ_o = L/1000.

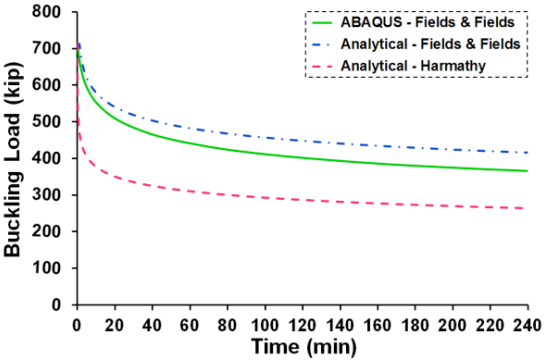


Figure 10. Comparison between analytical and computational creep buckling predictions at 500 °C.

Comparison with AISC and EC3 Predictions

In this section results obtained from analytical and computational creep buckling analyses presented in the previous sections will be compared with the corresponding elevated temperature column strength predictions of AISC (2011) and Eurocode 3 (2003).

It should be pointed out here that formula to predict column strength at high temperatures in Appendix 4 of the 2011 edition of the *AISC Specification for Structural Steel Buildings* are based on work by Takagi and Deierlein (2007). Both the Eurocode 3 column strength formula and that proposed by Takagi and Deierlein predict column strength as a function of temperature, but do not consider duration of load and temperature exposure; i.e., they do not consider creep buckling effects. These formulas are based on computational studies using elevated-temperature stress-strain curves for steel that do not explicitly include creep effects, and are verified against high-temperature column buckling experiments that also did not explicitly consider time dependent effects on buckling.

Figure 11 depicts the comparison of creep buckling predictions from ABAQUS® and Rabotnov-Shesterikov with the ones from Eurocode 3 (2006) and AISC (2011). Generally speaking, it can be observed that code-based predictions underestimate creep buckling time, especially at higher temperatures like at 600 °C as shown in Figure 11(c). The problem with code-based predictions of creep buckling becomes more evident when analytical creep buckling predictions using Harmathy's material creep model are compared against code-based ones, as shown in Figures 11(b), 11(c) and 11(d). It is also interesting to note that as temperatures get higher, analytical and computational buckling predictions using the Fields and Fields material creep model get closer, suggesting that the effect of creep is perhaps more important in overall inelastic buckling behavior at higher temperatures. Observations like these clearly show the significance of the need for more reliable creep data for structural steel.

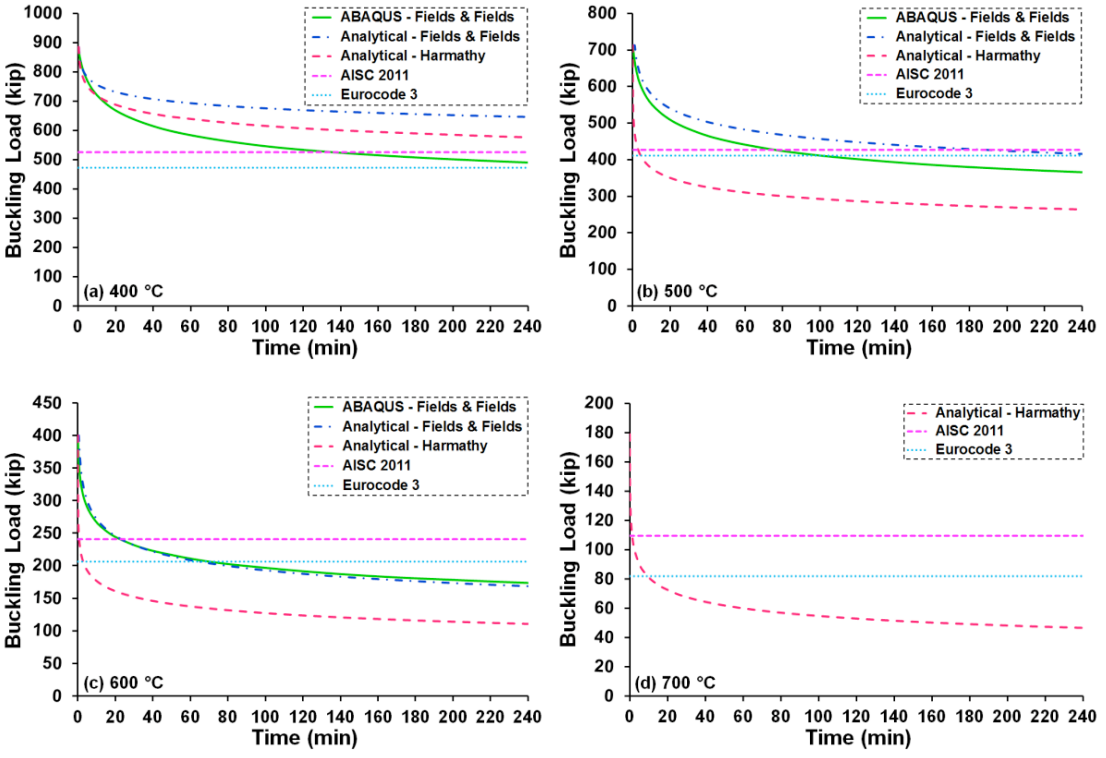


Figure 11. Comparison between computational, analytical, using both Fields and Fields and Harmathy creep models, and code-based creep buckling predictions.

CONCLUSIONS

This paper has presented some results of on-going research on the time-dependent buckling behavior of steel columns subjected to fire. Studies were conducted using a 3D finite element model incorporating both geometric and material nonlinearities. Analytical solutions were also developed to consider material creep effects on the overall time-dependent buckling. A number of factors that influence the time-dependent buckling behavior of steel columns in fire have been investigated, including the initial imperfection of columns.

It is clear from results obtained during this research that having an accurate knowledge of material creep is essential in predicting column buckling behavior at elevated temperatures. In addition, results show that neglecting creep effects can lead to erroneous and potentially unsafe predictions of the strength of steel columns subjected to fire. Columns are critical elements that affect the safety of structures during a fire. Consequently, a thorough understanding of column behavior during fire events is essential for developing appropriate analysis and design approaches. The research presented in this paper is on-going. The next stages of this research will involve a series of elevated temperature experiments on column specimens to provide further understanding of the time-dependent behavior and controlling failure modes of the column as far as creep is concerned. It will also provide further data for validation of modeling techniques.

ACKNOWLEDGMENT

The research reported herein was conducted as part of a research project on *Creep Buckling of Steel Columns Subjected to Fire* supported by the National Science Foundation (NSF Award 0927819). The support of the National Science Foundation and of NSF Program Director M.P. Singh is gratefully acknowledged.

REFERENCES

American Institute of Steel Construction (AISC). (2011). *Specification for Structural Steel Buildings*. Standard ANSI/AISC 360-11, Chicago, IL.

ABAQUS (2007). ABAQUS Version 6.7 User's Manual. Hibbitt, Karlsson, & Sorensen, Inc., Pawtucket, RI.

Bailey, R.W. (1930). "Creep of Steel under Simple and Compound Stress." *Engineering*, 121, 265.

Buchanan, A.H. (2002). *Structural Design for Fire Safety*, John Wiley & Sons Inc., New York.

Dorn, J.E. (1954). "Some Fundamental Experiments on High Temperature Creep." *Journal of the Mechanics and Physics of Solids*, 3, 85.

Eggwertez, S. (1976). "Creep Buckling of Steel Columns at Elevated Temperatures." *10th Congress on Behavior of Building Structures under Fire Effects*, IABSE, 235-240.

Eurocode 3. (2006). "Design of steel structures. Part 1-2: General rules. Structural fire design." EN 1993-1-2 European Committee for Standardization. CEN.

Fields, B.A., and Fields, R.J. (1989). "Elevated Temperature Deformation of Structural Steel." *Report NISTIR 88-3899*, National Institute of Standards and Technology, Gaithersburg, MD.

Freudenthal, A.M. (1950). *The Inelastic Behavior of Engineering Materials and Structures*, John Wiley & Sons Inc., New York.

Galambos, T.V., Editor. (1998). *Guide to Stability Design Criteria for Metal Structures*, 5th Edition, John Wiley & Sons Inc., New York.

Harmathy, T.Z. (1967). "A Comprehensive Creep Model." *Journal of Basis Engineering Transactions*, ASME, 396-502.

Hoff, N.J. (1957). "Buckling at High Temperatures." *Journal of the Royal Aeronautical Society*, 61, 756-774.

Hu, G., Morovat, M.A., Lee, J., Schell E., and Engelhardt, M.D. (2009). "Elevated Temperature Properties of ASTM A992 Steel." *Proceedings*, ASCE Structure Congress 09*,* April 30-May 2, Austin, TX.

Knight, D., Skinner D.H., and Lay, M.G. (1971). *Prediction of isothermal creep*, BHP Melbourne Research Laboratories, Report MRL 18/2, The Broken Hill Proprietary Company Limited Australia, 1-14.

Luecke, W.E., McColskey, J.D., McCowan, C. N., Banovic, S.W., Fields, R. J., Foecke, T., Siewert, T.A., and Gayle, F.W. (2005). *Federal Building and Fire Safety Investigation of the World Trade Center Disaster – Mechanical Properties of Structural Steels (Draft)*, Report NIST NCSTAR 1-3D, National Institute of Standards and Technology, Gaithersburg, MD.

Marin, J. (1947). "Creep Deflections in Columns." *Journal of the Applied Physics***,** 18, 103-109.

Morovat, M.A., Lee, J., Hu, G., and Engelhardt, M.D. (2010). "Tangent Modulus of ASTM A992 Steel at Elevated Temperatures." *Proceedings*, Sixth International Conference on Structures in Fire (SiF' 10), Michigan State University, East Lansing, Michigan, June 2-4, 2010.

NIST (2005) "Component, Connection, and Subsystem Structural Analysis." *Report NIST NCSTAR 1-6c*, National Institute of Standards and Technology, Gaithersburg, MD, September 2005.

Norton, F.H. (1929). *The Creep of Steel at High Temperatures*, McGraw-Hill Book Company Inc., New York.

Rabotnov, G.N., and Shesterikov, S.A. (1957). "Creep Stability of Columns and Plates." *Journal of the Mechanics and Physics of Solids*, 6(27), 27-34.

Shanley, F.R. (1952). *Weight-Strength Analysis of Aircraft Structures*, 1st Edition, McGraw-Hill Book Company Inc., New York.

Singer, J., Arbocz, J., and Weller, T. (2002). *Buckling Experiments: Experimental Methods in Buckling of Thin-Walled Structures*, Volume 2, John Wiley & Sons Inc., New York.

Takagi, J. and Deierlein, G.G. (2007). "Strength Design Criteria for Steel Members at Elevated Temperatures." *Journal of Constructional Steel Research*, 63, 1036-1050.

Tan, K.H., Ting, S.K., and Huang, Z.F. (2002) "Visco-Elasto-Plastic Analysis of Steel Frames in Fire." *Journal of Structural Engineering*, ASCE, 128 (1), 105-114.

Williams-Leir, G. (1983). "Creep of Structural Steel in Fire: Analytical Expressions." *Fire and Materials*, 7(2), 73-78.

Zener, C., and Hollomon, J.H. (1944). "Effect of Strain Rate on the Plastic Flow of Steel." *Journal of Applied Physics*, 15, 22-32.

Punching Shear Failure in Progressive Collapse Analysis

Y. Mirzaei[1] and M. Sasani[2]

[1,2]400 Snell Engineering Center, Department of Civil and Environmental Engineering, Northeastern University, Boston, MA 02115
[1] y.mirzaei@neu.edu and [2] sasani@neu.edu

ABSTRACT

A column failure caused by an explosion, impact, or other accidental events can propagate in a flat plate/slab structure through punching shear and lead to progressive collapse. The local post-punching behavior of flat slabs has been investigated experimentally and theoretically at the EPFL, Switzerland, and a mechanical model capable of predicting this behavior was developed. Using the mechanical model, an analytical model is developed here to estimate the initiation of punching shear failure as well as post-punching shear response of flat plates/slabs. The analytical model is used to study the system level post-punching response of structures and nonlinear dynamic finite element analyses are performed using a general purpose finite element software ABAQUS. The analytical model and the results of system level study can be of interest in assessing progressive collapse resistance of existing structures and in design of new structures.

INTRODUCTION

The term progressive collapse refers to the spreading of an initial local failure triggered by the loss of one or more load carrying members and leading to partial or total collapse of the structure in a manner analogous to the chain reaction. (ASCE/SEI 7, 2010). Following the attacks on the Murrah Federal building in 1995 and on the World Trade Center towers and the Pentagon on September 11, 2001 researchers evaluated progressive collapse resistance of structures (Sozen *et al.,* 1998, Corley *et al.,* 2004, Sasani *et al.*, 2007, Bao *et al.*, 2008) which covers both experimental and analytical studies. One approach based on direct design methods to evaluate progressive collapse of structures is to study the effects of instantaneous removal of load-bearing elements, such as columns. GSA (2003) and DOD (2010) regulations provide threat independent methods and use different scenarios for initiation of local failure to examine potential progressive collapse of structures. These regulations are meant to evaluate general integrity of structures and their capacity to redistribute the loads following removal of only one column. After column removal, the loads previously carried by the column will be dynamically redistributed to the neighboring columns, which could lead to collapse of partially or entire structure. One potential source of progressive collapse in such columns is punching shear caused by the transfer of additional loads from the removed columns. Over the past decades, several collapses due to punching shear failure occurred that resulted in human casualties and large damages. As a local punching failure can trigger progressive collapse, the study

of the post-punching behavior can help adopting constructive solutions to enhance the post-punching behavior of flat slabs and to mitigate the likelihood of the progressive collapse. In this paper, first an analytical model is developed to evaluate punching and post-punching response at a local level, i.e. slab on a single column. In developing this analytical model, experimental studies as well as a mechanical model developed in (Mirzaei Y., 2010) are used. Then to evaluate the effects of punching shear in progressive collapse analysis of structural systems, the response of a flat slab structure following loss of a column is studied leading to punching shear failure in a neighboring column.

POST-PUNCHING TESTS

The post-punching behavior a total of 24 slab specimens with various reinforcement layouts were experimentally evaluated at the EPFL, Switzerland. The effects of tensile reinforcement, integrity reinforcement passing through the column, bent-up-bars, and anchorage details were investigated. All the specimens were identical in geometry but different in reinforcement layout. Slab specimen PM-11 was a square plate with 125 mm thickness and 1500 mm width. The reinforcement ratio was 0.0082 and the concrete compressive strength was 32 MPa. Four integrity reinforcing bars with diameter 12 mm (2×2Ø12) pass through the column with the yield stress of 548 MPa and tensile strength of 625 MPa. A mechanical model was proposed, whose estimation for the PM-11 slab is compared with experimental data later in this paper. Figure 1 shows the test setup as well as the slab geometry (Mirzaei Y. and Muttoni A., 2008). Test results showed that the load-carrying mechanisms that take place after punching failure were related to the well-anchored tensile reinforcement and to the integrity reinforcement passing through the column. The post-punching strength provided by the tensile reinforcement was small because the concrete cover was thin and susceptible to spalling.

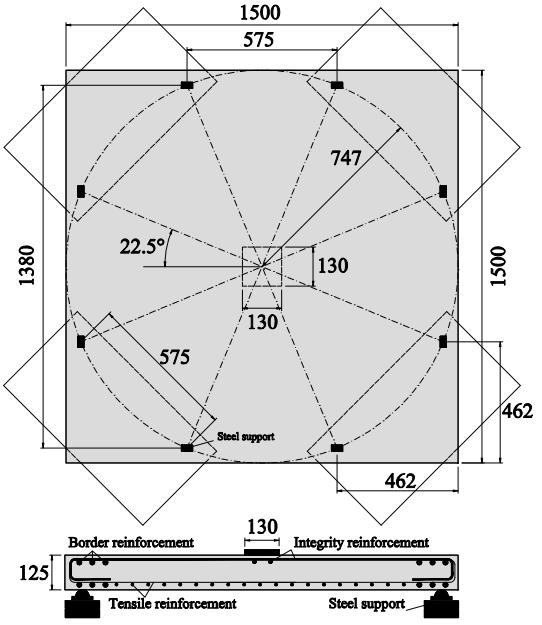


Figure 1. Typical slab plan section [mm].

POST-PUNCHING MECHANISM

Several structural collapses occurred over the past decades due to punching shear failure resulting in human casualties and large damages. These collapses revealed some shortcomings in codes of practice and the necessity of reconsidering punching provisions. The investigations of these collapses showed that the collapse initiated from a local punching failure and propagated throughout the structure likewise a chain reaction or progressive collapse (King *et al.*, 2004). The design of

reinforced concrete flat slabs is governed by deflection at the serviceability limit state and punching shear at the ultimate limit state. When no punching shear reinforcement is provided, failure develops in a brittle manner. Punching shear failure occurs with almost no warning signs, because deflections are small and cracks at the top side of the slab are usually not visible. A large amount of scientific effort has been devoted to the punching shear research and various theories and formulations have been developed. Recently, Muttoni suggested a failure criterion for slabs with and without shear reinforcement which can determine the punching strength mainly as a function of the radial rotation of the slab in the vicinity of the slab-column connection (Muttoni A., 2008). To compute the maximum punching strength, the load-rotation relationship of the slab is also needed for which a mechanical model was proposed based on a quadrilinear moment-curvature relationship for the reinforced concrete section. As a local punching failure can trigger progressive collapse, the study of the post-punching behavior can help adopting constructive solutions to avoid progressive collapse. The post-punching resistance is provided by reinforcing bars passing through the punching cone as they are the only link between the damaged area and the rest of the slab. These reinforcing bars can carry load by developing high tensile stresses accompanied by a significant inclination (Mirzaei Y., 2010).

Mirzaei (2010) developed a mechanical model which is capable of predicting the post-punching behavior of slab column connections as well as the contribution of top and bottom reinforcement to the post failure shear transfer. The model accounts for possible failure modes including the fracture of the bars and the destruction of the concrete over the integrity bars. The destruction of the concrete within and outside the punching cone is treated by considering the pullout behavior of reinforcement embedded in the concrete. The mechanical model calculates the mean axial strain and the rotation of the reinforcing bar for any given deflection. The maximum strain in the reinforcing bar developed in the curvature-influenced zone and then the maximum strain is compared to the ultimate tensile strain. This failure criterion will determine the rupture of the reinforcement.

ANALYTICAL MODEL

Figure 2 shows the geometry as well as a Finite Element Model (FEM) of the PM-11 simply supported reinforced concrete slab tested by (Mirzaei Y. and Muttoni A., 2008). Due to the symmetry and to simplify the analysis only one quarter of the slab is modeled. Because the punching shear is associated with local failure and deformation and the slab deformation away from the failure zone is negligible compared to that at this zone, the concrete is assumed to remain elastic during the analysis. The concrete modulus of elasticity is 33 GPa and its Poisson's ratio is 0.15. The reinforcing steel is modeled as a quadrilinear elastic-plastic material including strain hardening. The elasticity modulus of steel reinforcement is 201 GPa, the yield strength is 548 MPa, and the tensile strength is 625 MPa (Mirzaei Y. and Muttoni A., 2008). The slab thickness is 125 mm and can be modeled as a thin plate. Therefore, the four-node first-order quadrilateral in-plane shell S4R with reduced integration points and finite strains from the ABAQUS element library is used in the model (ABAQUS 2010).

In the load-deflection response of a slab in punching tests two different phases can be distinguished, which are pre-punching and post-punching phases. The finite element modeling of the punching phenomenon is feasible but rather complicated and time consuming. Therefore, to exclude the complexity of the punching calculation, the pre-punching load-deflection response of the slab is analytically calculated by the Critical Shear Crack Theory (Muttoni A., 2008). Then, the result is implemented into the finite element model by using nonlinear connectors. From the basic category of the connections, a Cartesian + Cardan connector has been selected. All the six components of relative motions are available for this connection. The results of the mechanical model are used as the constitutive model for these connectors. Note that the failure zone undergoes large deformations after a column failure, and thus nonlinear constitutive material laws modeling this zone should be applied to simulate the structural behavior realistically.

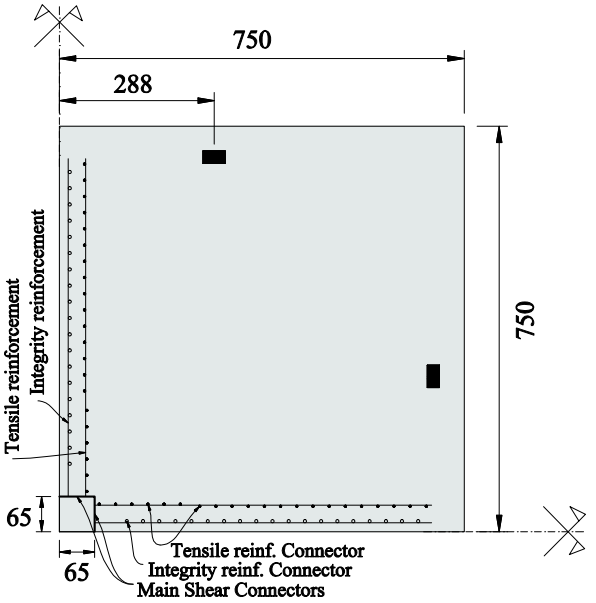


Figure 2. Geometry of the finite element model.

The post-punching strength is mainly provided by the integrity reinforcement passing through the column in the connection zone (Mirzaei Y., 2010). The connection zone shown in Figure 2 connects a rigid zone right above the column to the rest of the slab. In other words, this connection zone simulates the contribution of the reinforcing bars to the shear transfer after a punching shear failure has occurred. The two-node first-order Bernoulli beam element B33 has been chosen in order to simulate the

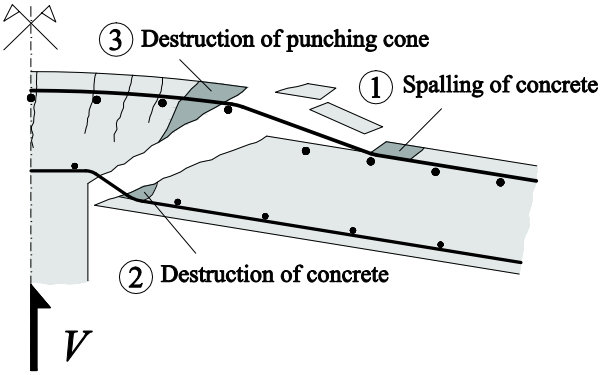


Figure 3. Various critical zones due to interaction between concrete and steel bars

integrity reinforcement passing through the column. This reinforcement will be practically activated as the column punches through the slab. The vertical component of the force developed in the reinforcing bars is the contribution of the integrity reinforcement to the post-punching shear transfer.

In order to better understand the failure process and simulate the failure zone various failure zones are illustrated in Figure 3. Depending on the direction of loading and the thickness of the concrete, three primary failure zones can be characterized in post punching shear, as shown in Figure 3. In zones 2 and 3, the reinforcing bars break the concrete because of the small concrete thickness in these zones. In other words, the thickness of the concrete over the integrity bars at the beginning of the post-punching phase is small. Therefore, reinforcing bars act against concrete with a small thickness and consequently concrete breakout occurs. The progressive destruction of concrete continues up to a certain point at which the thickness of concrete is sufficient to prevent further concrete breakout. Beyond this point, yielding of the bar and crushing of the concrete supporting the bar control the failure process. It has been reported that if the concrete thickness is larger than six to seven times the bar diameter, yielding of the bar and crushing of concrete govern the failure process.

In general, the contribution of the integrity reinforcement to the post-punching strength is governed either by the maximum breakout strength of the concrete above the bar or by the fracture of the integrity bars. For further deflections, the concrete breakout strength remains constant as the thickness of the concrete above the integrity reinforcement is constant. Thus, no further increase in the length of the exposed integrity reinforcement will occur.

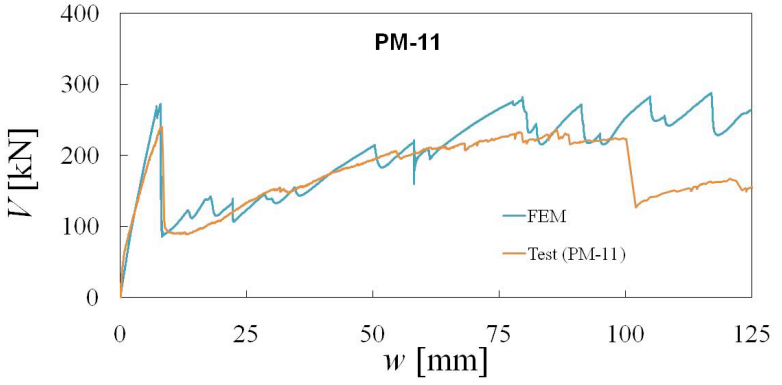


Figure 4. Comparison of analytical and experimental results.

A comparison between the results obtained by the nonlinear FEM and the experimental data is shown in Figure 4. A good agreement can be found between the measured post-punching strength and the one calculated by the nonlinear FEM. The model accounts for the contribution of both well-anchored tensile reinforcement and integrity reinforcement. In this experiment, the tensile reinforcement was well-anchored in the slab which is unlikely in practical projects because of the cut-off points around the zero bending moment areas. The contribution of the well-anchored tensile reinforcement to the post-punching strength could reach 33% of the punching strength and the contribution of the integrity reinforcement reached 65% of the punching strength (Mirzaei Y., 2010).

POST-PUNCHING SHEAR AND PROGRESSIVE COLLAPSE

The implementation of the prescribed post-punching mechanical model in an analytical model in ABAQUS is presented to illustrate the possibility of progressive collapse due to punching failure after a column explosion/removal. To investigate the effects of the post-punching resistance in a concrete slab after a column removal, a sixteen column slab model is considered. Figure 5 shows the geometry of the slab, which is 250 mm thick and has 6m × 6m panels. The column cross sections are 300 × 300 mm. The applied uniformly distributed loads are a total dead load of 8.1 kN/m^2 and a live load of 4 kN/m^2.

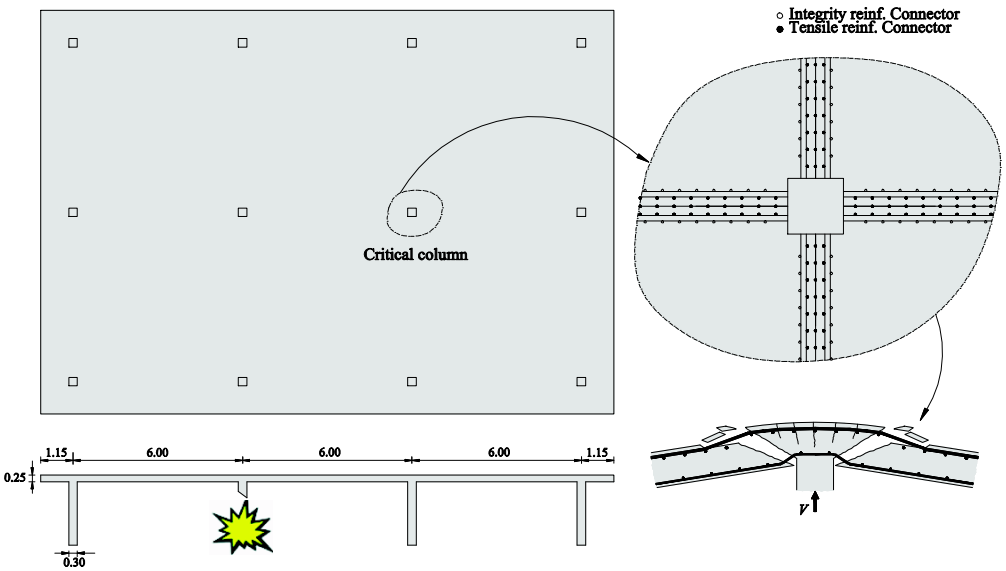


Figure 5. Analytical model of the system level study of progressive collapse due to punching shear failure.

To design the integrity reinforcement, the design load is calculated using load factors of the accidental situation according to ACI 352.1R (2002). The integrity reinforcement is designed by the following equation:

$$A_{si} = \frac{0.5 q_d \ell_1 \ell_2}{\Phi f_y} \tag{1}$$

where A_{si} is the minimum area of the integrity reinforcement in each principal direction placed over the column, q_d is the factored uniformly distributed load but not less than twice the slab service dead load, f_y is the yielding strength of steel, $\Phi = 0.9$ is a shear reduction factor, and ℓ_1 and ℓ_2 are center-to-center span in each principal direction. The quantity of reinforcement A_{si} may be reduced to two thirds of that given quantity for edge connections, and to one-half of that for corner connections.

The Critical Shear Crack Theory proposed by Muttoni (2008) has been used to calculate the up to punching response of the slab-column connection. The post-punching behavior of the slab has been calculated by the mechanical model (Mirzaei Y., 2010). The tensile reinforcement and integrity reinforcement are assumed

to be well-anchored in the slab. The punching strength and post-punching strength are 1067 kN and 899 kN for the interior columns, respectively.

The elements used in the FEM are the same as those described in the previous section for the single column model. This model aims to demonstrate the vulnerability of flat slabs against punching shear failure after a column removal. The load-deflection response of column B is obtained after the removal of column A. The removal of a column influences dynamically the rest of the slab and therefore the structure should be analyzed dynamically. The procedure is described below. The gravity load is applied and the column A top forces and moments are found. Then, the column is removed and its internal forces are applied to the column head. And finally, forces and moments in opposite directions are dynamically applied to the column head and the response of the other columns is studied.

ANALYTICAL RESULTS

The load-deflection response of column B as a result of column A removal is shown in Figure 6.a. It can be seen that the transferred load exceeds the punching strength and therefore the column punches through the slab. One important question is how much post-punching strength and in its turn integrity reinforcement is needed to provide structural safety against progressive collapse in a structure. The punching shear failure occurs at a very small deflection and activates the integrity reinforcement passing through the column. The force developed in the reinforcement increases for further defection. The vertical component of this force is the main contribution to the post-punching strength.

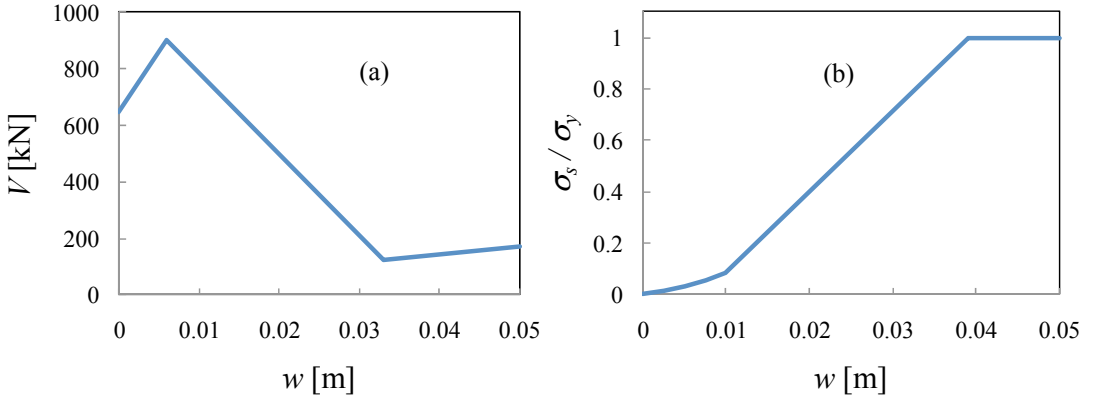


Figure 6 . a) Load-deflection response of column B after the removal of column A and b) evolution of stress in integrity reinforcing bars.

In this analysis, the structure arrived at an equilibrium position soon after the punching shear occurred. However, if the structure required deflecting more to redistribute the loads, the contribution of the integrity reinforcement in transferring load to the column could increase. This increase in the post-punching strength can be helpful in preventing the failure from propagating throughout the structure. The way that a punching shear failure of a slab-column connection can lead to progressive collapse depends not only on the post-punching behavior of the connection but also on

the overall behavior and structural characteristics of the region of the slab surrounding the damaged area and the punching strength of adjacent slab-column connections. Figures 6.b shows the evolution of the stress in reinforcing bars as a function of the vertical displacement. It clearly shows that steel reinforcement exceeds the elastic limit and enters in the plastic region for such small deflection. It has been shown that the integrity reinforcing bars could carry load by developing high tensile stresses accompanied by a significant inclination.

Figure 7 displays the slab deflection contour before and after the punching shear failure of column B. They clearly show that the maximum vertical displacement of the slab occurs at the location of punching shear. It can be seen that the column removal in flat slab structures triggers the failure to the adjacent column. The failure could propagate throughout the structure in the same way leading to the progressive collapse of a large part of the structure. It is shown that the presence of the integrity reinforcement can provide an alternative load path for the load redistribution and prevent the structure from totally collapsing.

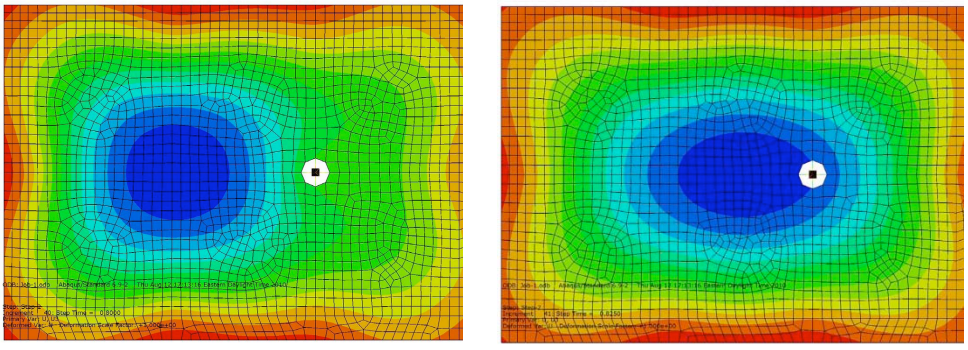


Figure 7. Slab deflection right before (w_{max}=-.00228 m) and right after the punching shear failure of column B (w_{max}=-.00408 m).

CONCLUSIONS

It has been shown experimentally that reinforcing bars play an important role in post-punching behavior as they are the only remaining link between the punching cone and the rest of the slab. Therefore, the load-carrying mechanisms that take place after punching failure are related to well-anchored tensile reinforcement and to integrity reinforcement passing through the column.

A nonlinear finite element model has been developed to simulate the post-punching behavior of flat slabs after a column removal. The performance of reinforcing bars acting against the concrete cover and against the punching cone is fundamentally different. However, a generic procedure was developed capable of predicting the behavior of all possible mechanisms. Within this scope, a series of connector elements has been used and their nonlinear constitutive laws were introduced according to a previously developed mechanical model. The mechanical model is used to determine the mechanical properties of the analytical model of the connection zone, which is between a rigid zone of slab directly above the column and the rest of the slab. The model of the connection zone simulates the contribution of the reinforcing bars to the shear transfer after a punching shear failure. The contribution of

the reinforcing bars to the post-failure shear transfer is simulated using beam element. These elements are practically activated after punching shear failure has occurred. The vertical component of the force developed in these reinforcing bars is the main contribution to the post-punching strength.

The analysis shows that a column removal in a flat slab structure can trigger a punching shear failure at the location of an adjacent column. Such failure potentially can propagate throughout the structure and a series of punching shear failure can occur leading to the progressive collapse of a large part of the structure. The presence of an adequate amount of the integrity reinforcement can provide an alternative load path for the load redistribution and help resist progressive collapse.

ACKNOWLEDGEMENTS

This material is based upon work supported by the U.S. Department of Homeland Security under Award Number 2008-ST-061-ED0001. The views and conclusions contained in this document are those of the authors and should not be interpreted as necessarily representing the official policies, either expressed or implied, of the U.S. Department of Homeland Security.

REFERENCES

ABAQUS (2010). ABAQUS Inc., ABAQUS Standard User's Manual, 6.9 Edition.

ACI 352R (2002). "Recommendations for Design of Beam-Column Connections in Monolithic Reinforced Concrete Structures", ACI-ASCE Committee 352, American Concrete Institute, 37 p., MI.

ASCE/SEI 7 (2010). "Minimum Design Loads for Buildings and Other Structures," Structural Engineering Institute-American Society of Civil Engineers, VA.

Bao, Y., Kunnath, S. K., El-Tawil, S., and Lew, H. S. (2008). "Macromodel-Based Simulation of Progressive Collapse: RC Frame Structures," *Journal of Structural Engineering*, ASCE, Vol. 134, No. 7, pp. 1079–1091.

Corley, W. G. (2004). "Lesson Learned on Improving Resistance of Buildings to Terrorist Attacks," *Journal of Performance of Constructed Facilities*, ASCE, V. 18, No. 2, pp. 68-78.

DOD (2010). "Design of Building to Resist Progressive Collapse," Unified Facility Criteria, UFC 4-023-03, U.S. Department of Defense, Washington, DC.

GSA (2003). "Progressive Collapse Analysis and Design Guidelines for New Federal Office Buildings and Major Modernization Projects," U.S. General Service Administration, Washington, DC.

King S., Delatte N. J.(2004). "Collapse of 2000 Commonwealth Avenue: Punching Shear Case Study", *ASCE Journal of Performance of Constructed Facilities*, Vol. 18 No 1, pp. 54-61, Reston, USA

Mirzaei Y., Muttoni A. (2008). "Tests of the post-punching behavior of the reinforced

concrete flat slabs", IBETON, Switzerland.

Muttoni A. (2008). "Punching shear strength of reinforced concrete slabs without transverse reinforcement", *ACI Structural Journal*, V. 105, N° 4, pp. 440-450.

Mirzaei Y. (2010). "Post-punching behavior of reinforced concrete slabs", EPFL Thesis No. 4613, pp. 230, Lausanne, Switzerland.

Sasani, M., Bazan, M., and Sagirogu, S. (2007). "Experimental and Analytical Progressive Collapse Evaluation of an Actual Reinforced Concrete Structure," *ACI Structural Journal*, V. 104, No. 6, pp. 731-739.

Sozen, M. A.; Thornton, C. H.; Corley, W. G.; and Mlakar, P. F. (1998). "The Oklahoma City Bombing: Structure and Mechanisms of the Murrah Building," Journal *of Performance of Constructed Facilities,* ASCE, V. 12, No. 3, pp. 120-136.

Experimental Evaluation of an Innovative Isolation System for a Lightweight Steel Moment Frame Building at E-Defense

Nhan D. Dao[1], Keri L. Ryan[1], Eiji Sato[2], Taichiro Okazaki[3], Stephen A. Mahin[4], Arash E. Zahgi[1], Kouichi Kajiwara[2], Taizo Matsumori[2]

[1] Civil and Environmental Engineering, University of Nevada, Reno/MS 0258, Reno, NV 89519; email: nhan.unr@gmail.com; keri.ryan@unr.edu; esmailiz@unr.edu
[2]National Research Institute for Earth Science and Disaster Prevention, 1501-21 Nishikameya, Mitsuta, Shijimi-cho Miki, Hyogo, Japan 673-0515; email: eiji@bosai.go.jp; kaji@bosai.go.jp; taizo@bosai.go.jp
[3]Faculty and Graduate School of Engineering, Hokkaido University, Kita 13, Nishi 8, Kita-ku, Sapporo, Hokkaido 060-8628, Japan; formerly NIED; email: tokazaki@eng.hokudai.ac.jp
[4]Civil and Environmental Engineering, 777 Davis Hall, University of California, Berkeley, California, 94720-1710; email: mahin@berkeley.edu

ABSTRACT

In a collaborative effort between NEES TIPS, NIED in Japan, and the NEES Nonstructural Grand Challenge project, a 5-story steel moment frame building will be shaken at the E-Defense facility in Japan. The specimen will be shaken both with and without triple friction pendulum isolators. Nonstructural components including interior walls, ceilings, piping, and concrete cladding panels will be constructed and in the specimen. The isolated specimen will be shaken to a suite of motions representing frequent, design/L2, and MCE/L3 level motions. The tests represent the grandest showcase of the benefit of seismic isolation technology to date, and the primary objective of the tests is to demonstrate that damage free performance can be targeted and achieved against an MCE/L3 earthquake. Limit state tests will illustrate the performance when the demands exceed the displacement capacity of the bearings. The tests will take place over a 3-week time frame in August 2011, with 4 days of shaking anticipated.

INTRODUCTION

Seismic base isolation is recognized as one of the most effective methods to protect both the structure and its contents from large earthquakes. The fundamental horizontal period of the structure is lengthened by installing flexible devices beneath the structure and the base. Lengthening the fundamental period reduces the base shear demand, and increased displacements are accommodated by the isolation system. The hysteretic force-deformation of an isolation system also contributes considerable damping to the dominant response mode so that the input energy to the structure is further reduced.

Analytical and experimental studies on base isolation systems have been carried out during the last four decades. Most research has shown that isolated structures have very good performance (Erduran et. al. 2010, Fan and Ahmadi 1992,

Kelly and Aiken 1991, Samali and Wu 2003). Some studies are concerned about the safety and performance of the isolation system or the isolated building when subjected to extreme ground motions that exceed the design ground motion. Extreme displacement demands of an isolation system subjected to very rare earthquakes may causes these problems: 1) shear failure or buckling of an elastomeric bearing, 2) exhausting the displacement capacity (hitting the rim) of a friction pendulum bearing, 3) pounding against an outer moat retaining wall, or 4) transfer of the force demand accompanied by yielding in the superstructure. Furthermore, some stakeholders (such as the nuclear industry) have become increasingly concerned about the influence of vertical ground acceleration in an isolated structure, since isolation does not specifically protect against vertical motion, and vertical accelerations exceeding 1g have been recorded in recent earthquakes (Clark et. al. 1996, Malushte and Whittaker 2003, Su and Ahmadi 1988).

Most shaking table tests on isolation systems have been conducted on reduced scale models, and lack of full scale testing to demonstrate the reliability of analytical modeling techniques for extreme motions is considered a knowledge gap. The influence of isolation on content response should also be examined, as the overall movement of the building can be considerable. In 2010, E-Defense studied the response of an R/C building isolated with different elastomeric isolator such as high damping rubber and natural rubber with steel dampers, and also with the base of the building fixed. The tests investigated the performance of hospital equipment and several different types of hospital rooms were furnished (Sato et. al. 2010).

The proposed test program will provide additional complimentary data on the response of full-scale isolated buildings. In this testing program, shake table tests of a full scale 5-story steel moment frame building will be conducted. The specimen will be examined both with and without triple friction pendulum isolators, and subjected to several ground motions of varied characteristics and intensity. U.S. style partition walls, ceiling systems, piping components, and exterior cladding panels will be built over portions of the building, and enclosed rooms will house furnishings and other contents. The isolation tests will provide realistic data for examining the response of an isolated structure and contents to extreme earthquakes and evaluating current design and modeling techniques. The response of the fixed base specimen to the same ground motions will provide data for comparing the two configurations.

The test will be performed at Hyogo Earthquake Engineering Research Center, also known as E-Defense, which is accessible to U.S researchers through the NEES/E-Defense collaborative program. This research center hosts the world's largest three dimensional shaking table. The E-Defense shaking table can reproduce the largest three-dimensional ground motions recorded in the 1995 Kobe Earthquake while supporting a test model of 1200 metric tons. At the maximum payload, the E-Defense shake table can produce motions with horizontal acceleration exceeding 0.9g and vertical acceleration exceeding 1.5g. At lower payloads, larger accelerations can be reproduced. The shake table is also capable of producing large motions with low frequency content, as exhibited by the large stroke and velocity capacity (maximum stroke is ±100 cm, maximum velocity is 200 cm/s). The 15 × 20 meter platform is sufficiently large to support a small full scale building.

TEST OBJECTIVES

This research program aims to provide a grand demonstration of effectiveness of seismic isolation for very large ground motions. An international collaboration has been developed that addresses the research concerns for both U.S. and Japan participants. The test objectives are described as follows:

1. Accelerate adoption of protective systems through a full scale, proof-of-concept test. Component tests of isolation devices suggest that scaling effects significantly alter their response trends, while most system level tests have been conducted on reduced-scale specimens. The proposed tests will fill a gap in the existing data while allowing real-life visualization of the behavior of a real building under earthquakes. In this test program, the performance of not only the structure but also nonstructural components and contents will be confirmed. To ensure the educational impact of the tests, we will publicize these tests widely to the U.S. through invited observation, workshops, and media targeted to different audiences. A blind prediction contest is planned; details will be released through NEESComm and at the Structures Congress meeting in 2011.

2. Validate new seismic isolation solutions and design/analysis methods. The proposed tests will examine the new triple friction pendulum isolator that has a limited history of commercial use. The triple pendulum isolator is conducive to a performance-based design approach, wherein the parameters of the isolation system are optimized relative to specific multi-hazard performance criteria. The overriding performance objective is to provide damage-free response against a maximum credible (MCE) or Japan L3 level earthquake. The tests will validate the ability to achieve the performance objective that is targeted in the design process.

3. Extend resiliency to challenging range of critical applications. The test program considers some additional challenges with regard to system configuration and loading conditions. The building structure is lightweight for a traditional elastomeric isolation system. With regarding to load conditions, extreme earthquakes will be applied to the system, including those with large vertical acceleration components or long period, long duration subduction motions.

4. Identify performance limits of the isolation system for extreme motions. The tests will examine the endurance of the devices under long duration motions, and the re-centering capabilities as well as the implications of not re-centering. The specimen is predicted to undergo uplift in some of the simulations. For the motions that produce the largest displacement demands that exceed the isolator capacity, the sliders are predicted to pound against the rim of the bearing, causing a large acceleration wave to propagate through the structure. The influence of this pounding on the performance and safety of the structure will be determined.

SPECIMEN

The specimen to be tested is a 5-story steel moment frame building that has already been constructed (Figure 1). The specimen is approximately 16 meters tall, and asymmetric in plan with dimension of 10 meters by 12 meters (2 bays by 2 bays). The total weight of the building is about 5000 kN, which is well below the maximum capacity of the shaking table so that extreme earthquake ground motions can be

reproduced accurately. The specimen was constructed in September 2008 and used in a test in March 2009 with several different types of inter-story dampers to provide enhanced performance (Kasai et. al. 2010).

The specimen was designed and detailed according to Japanese code and style. The beams and girders are either built-up or rolled wide flange sections, and the columns are cold-formed HSS sections. All girder-to-column and column base connections are fully restrained moment connections. Each girder was constructed in 3 pieces, and bolted together at the approximate inflection points determined by gravity loading. The flanges of the girders are widened near the connections to the column to increase the moment capacity. Floor slabs are composite slabs formed from 75 mm height corrugated steel decks covered by 80 mm normal concrete. The roof slab is a 150 mm normal concrete slab with a flat steel deck; the roof was designed to carry additional loading representative of equipment.

For preliminary analysis, finite element models of the specimen were developed both in SAP2000 and OpenSees. The modeling and analysis is not discussed in detail to preserve the integrity of a planned blind prediction contest.



Figure 1. 5-story steel moment frame specimen.

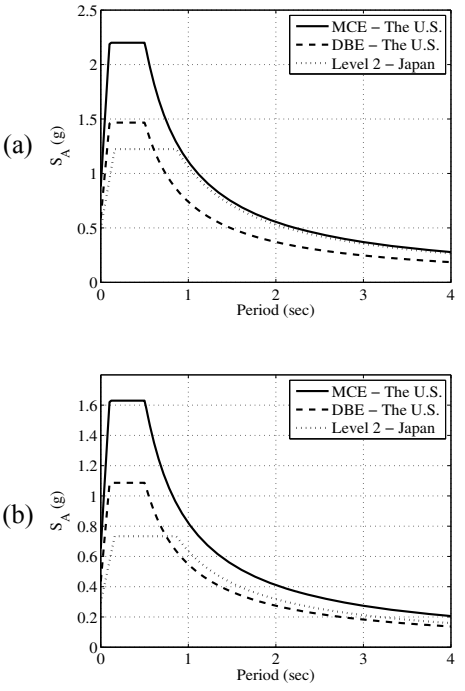


Figure 2. Design spectra for (a) 5% damping and (b) 15% damping.

INPUT GROUND MOTIONS

Design spectra. Design spectra were developed that represent both U.S. and Japan design practice. The design ground motion (DBE) in the U.S. varies as a function of regional seismicity and site conditions. To represent high seismicity, a Los Angeles (CA) location with site class D soil conditions ($V_{s30} = 180$ m/s to 360 m/s) was

selected. These assumptions are consistent with the case study buildings examined in the NEES-TIPS project (Erduran et. al. 2010). Using standard procedures, DBE and MCE design spectra were developed.

The design ground motion for Japan is based on a single "level 2" (L2) design event, where the spectrum is determined as

$$S_A(T) = Z \times G_s(T) \times S_0(T)$$

In this equation, Z is zone factor taken to be 1.0 for most area of the country, $S_0(T)$ defines the default spectrum for engineering bedrock, and $G_s(T)$ is a soil amplification factor that varies with period (Pan et. al. 2005). Soil type II was assumed to be equivalent to U.S. site class D. The U.S. and Japanese design spectra are shown in Figure 2 for damping ratios of both 5% and 15%, the latter which represents the damping in the isolation system.

Selecting ground motions. A number of ground motions have been selected to represent each of the above design spectra and evaluate potential design solutions to satisfy the performance objectives. A subset of these motions will be selected for inclusion in the final test program.

Seven ground motions were selected to represent U.S. spectra; three for the DBE and four for the MCE. The U.S. code requires that appropriate ground motions shall be selected from events having parameters consistent with those that control the MCE, and the motions are scaled to at least 1.3 times the design spectrum over a set period range. However, for the experimental program, records were selected that are rich in long period content and recorded in large earthquakes; the majority of these records are from California earthquakes; both lateral components and the vertical component have been considered. Table 1 indicates the list of records and the characteristics (peak ground acceleration, velocity and displacement of any component) for each record. The scale factor represents the factor by which the record was scaled to match the DBE or MCE spectrum using a similar scaling procedure to the U.S. code. All selected ground motions for the U.S. MCE were scaled down to match the code spectrum, which means that the unscaled motions exceed the MCE level defined by the code. Some of the unscaled records will be included in the test program to represent "beyond MCE" level motions. Figure 3(a) and 3(b) show the response spectra of the records against the 1.3 times DBE and MCE design spectra, as appropriate.

The Japanese code requires all isolated structures to be checked for three standard ground motions: El Centro NS 1940, Taft EW 1952 and Hachinohe EW 1968, scaled to the peak ground velocity of 0.5 m/s; and three additional ground motions that account for the local site effects (Becker et. al. 2010). The subset considered for the experimental program includes El Centro, JMA Kobe (commonly included in the design set for Japan), and Takatori (a strong near fault record). The synthesized Sannomaru record is a long period and long duration record, representative of the motion that would be generated by a deep subduction fault. The Sannomaru record, which has a spectral acceleration that nearly peaks at a period of 3 seconds, is of particular concern due to the large demands and potential resonance effect on long period structures. Table 1 and Figure 3(c) include the statistical information and response spectra for the selected Japanese motions.

Table 1. Parameters of Selected Ground Motions.

Ground motion	Code	Peak A (cm/s^2)	Peak V (cm/s)	Peak D (cm)	Scale Factor
Northridge – Rinaldi	U.S. DBE	809.5	160.3	29.7	0.88
Northridge – Newhall	U.S. DBE	578.6	97.8	38.2	1.32
Turkey – Erzican	U.S. DBE	505.5	84.0	27.6	0.89
Chi Chi TCU 065	U.S. MCE	798.4	126.2	92.6	0.93
Northridge - Sylmar	U.S. MCE	880.2	117.5	54.3	0.85
Loma Prieta - Los	U.S. MCE	947.9	108.7	65.8	0.99
Tabas -Tabas	U.S. MCE	835.6	121.4	95.2	1.11
El Centro N-S	Japan L2	312.8	36.3	21.1	1.38
Kobe - JMA Kobe	Japan L2	805.7	81.6	20.0	1.66
Kobe - Takatori	Japan L2	599.8	127.2	35.8	0.78
Sannomaru	subduction	185.9	51.6	21.7	0.66

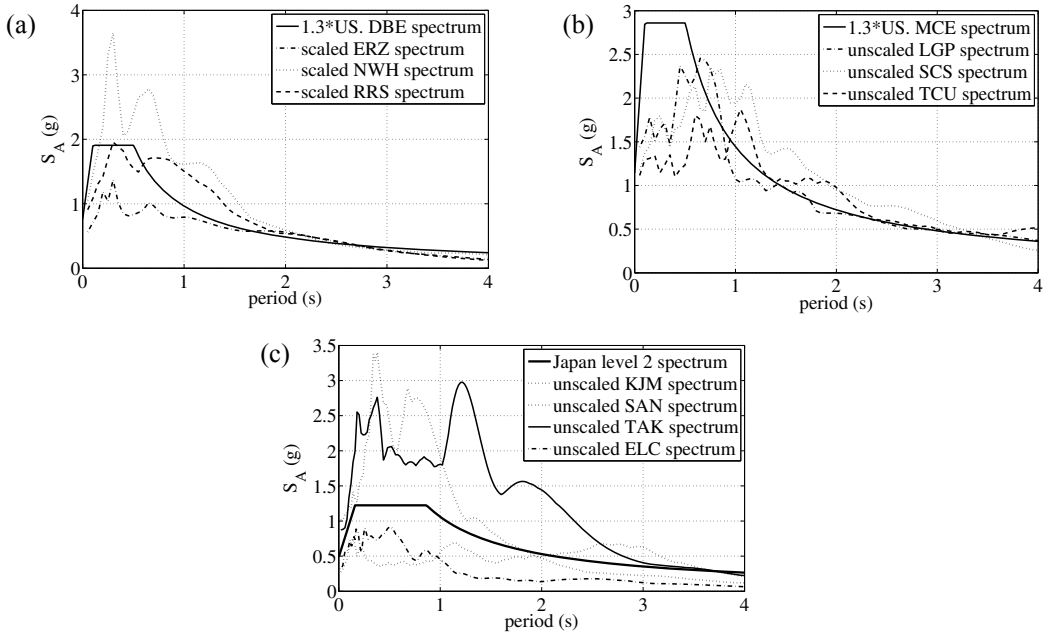


Figure 3. Response spectra of selected records: (a) SRSS spectra for the U.S. DBE, (b) SRSS spectra for the U.S. MCE, and (c) SRSS spectra for Japan L2.

DESIGN OF ISOLATION SYSTEM

Design Strategies. The U.S. code requires that an isolated structure be designed for a force reduction factor $R \leq 2$ in the DBE event, wherein $R = 2$ is permitted for a ductile lateral system while $R = 1$ is required for some types of nonductile systems such as ordinary braced frames. However, because of the inherent overstrength, yielding typically would not be expected in the design event. The U.S. code also requires that interstory drift of the superstructure not exceed 1.5%. For a moment

frame, the drift requirement typically controls the design. The U.S. code does not limit the floor acceleration. The Japanese code permits a small level of yielding in the superstructure for an L2 earthquake event (full plastic hinge formation should be avoided). According to Pan et. al. (2005), while not specifically specified by the code, interstory drift ratio of 1% and the peak floor acceleration of $3\ \mathrm{m/s^2}$ are commonly targeted for isolated buildings in Japan.

However, the above code criteria does not directly consider nonstructural component and content response in the U.S. DBE or Japan L2, and does not consider structural response in the U.S. MCE or Japan L3. In this program, to protect the structure against damage, the isolation system will be designed such that the maximum interstory drift does not exceed 0.5% in MCE/L3. Comparable target drift for the DBE/L2 earthquake is 0.33%. An appropriate performance objective for acceleration sensitive components and contents is being sought, which could be based on floor accelerations, velocity, or floor spectra.

Behavior of Isolators. Nine identical triple friction pendulum isolators provided by EPS Inc. will be used in the test, one beneath each column. Triple friction pendulum bearings consist of two layers of sliders sandwiched between concave sliding surfaces. Static friction between the surfaces resists small lateral loads without deformation, but when the applied lateral force is large enough, the system slides. The combination of vertical force and the curvature of the concave plates provide restoring force while the friction between bearing plates and sliders dissipates the input energy. The general loading behavior of a triple pendulum bearing, which consists of several sliding stages, is described in Fenz and Constantinou (2008).

The bearings selected for the test program have relatively low friction coefficients combined with large lateral displacement capacity designed to provide optimal protection for nonstructural components and contents. The selection of identical pendulum curvature and friction coefficients for the outer sliding surfaces simplifies the force-displacement to a two stage system. The isolator dimensions are shown in Figure 4 and the backbone curve of the isolator is shown in Figure 5. The period of the isolation system depends only on the pendulum lengths and not on supported mass; thus, for each bearing the tangent period at large displacements is 5.6 sec, and the secant period is 4.6 sec at the peak displacement of 112 cm (Fig. 5).

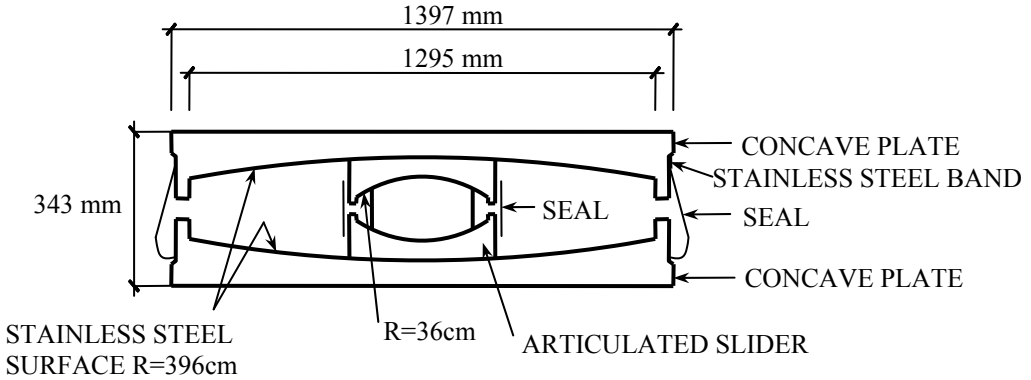


Figure 4. Section view indicating dimensions of isolation bearings

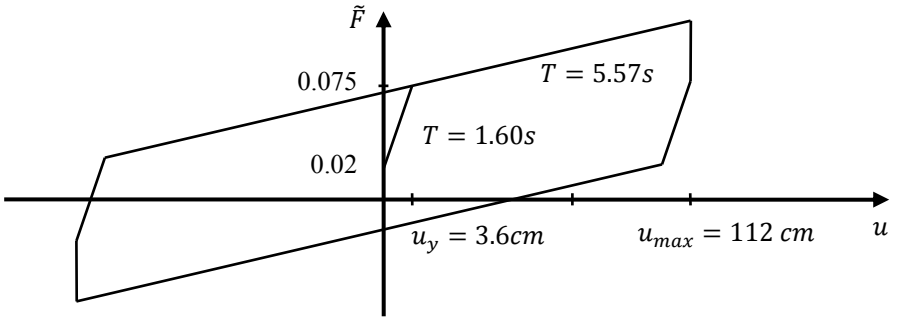


Figure 5. Backbone force displacement of selected triple pendulum isolators

CONNECTION DESIGN

To check performance objective and design the connection, peak responses of isolated structure to the selected ground motions were analyzed. The absolute peak response observed over all of the ground motions in Table 1 are shown in Table 2. The structure easily meets story drift criterion, which is 0.5% for MCE scenario. However, the peak displacement demand observed in the analysis exceeds the capacity, and the effect of sliders pounding against the bearing rims has not yet been considered. Detailed results are not presented to preserve the integrity of the planned blind prediction contest, as mentioned earlier.

For examining behavior of isolators during earthquakes, load cells will be installed beneath each isolator to measure reaction components, as schematically illustrated in Figure 6(a). Two types of load cells are available for use at E-defense. Their properties are shown in Table 3.

Table 2. Peak Responses of Isolated Structure Model to Large Ground Motions.

Peak Isolator Displ. (cm)	Peak Isolator shear (kN)	Peak isolator's vertical reaction (kN)			Peak story drift (%)	Peak floor acc. (g)
		Center isolator	Edge isolator	Corner isolator		
135.4	286.0	1742.4	1382.6	931.5	0.327	0.504

Table 3. Properties of Load Cells.

Type	Number (units)	Height (mm)	Vertical capacity (kN)	Horizontal capacity (kN)
A	44	180	400	250
B	32	195	700	400

Measuring the large forces (Table 2) with available load cells (Table 3) is challenging due to the large overturning effects distributing high axial forces to load cells in the direction of isolator displacements. Previous tests of the isolated hospital at E-Defense did not measure the isolator forces. Optimal arrangements of the load cells have been devised for center, edge, and corner isolators based on the tributary

weight carried by each (Figure 6). The hexagonal configuration distributes the forces and reduces the deformation of connecting plates while minimizing the number of load cells. This configuration possesses identical stiffness in any horizontal direction.

Finite element models were developed in SAP2000 to investigate stress and deformation of connecting plates. The connecting plates were modeled using 8-node solid elements (Figure 7). Forces distributed to load cells were computed by assuming that the connecting plates are plane and stiffness of all load cells are the same. The expected forces in the load cells were applied to the model, and top and bottom plates of load cells were modeled by 4-node shell elements to evenly distribute the forces from the load cells to connecting plates. Table 4 presents the maximum tension and compression forces induced in load cells.

Von Mises stress in the connecting plates is well below the yield stress of the steel, which is 24.82 kN/cm^2. The safety factor is greater than 1.5. The maximum deflection of the plate is 0.784 mm, which is equivalent to a relative deflection $0.96/1000$. This order of flatness is acceptable for friction pendulum bearings.

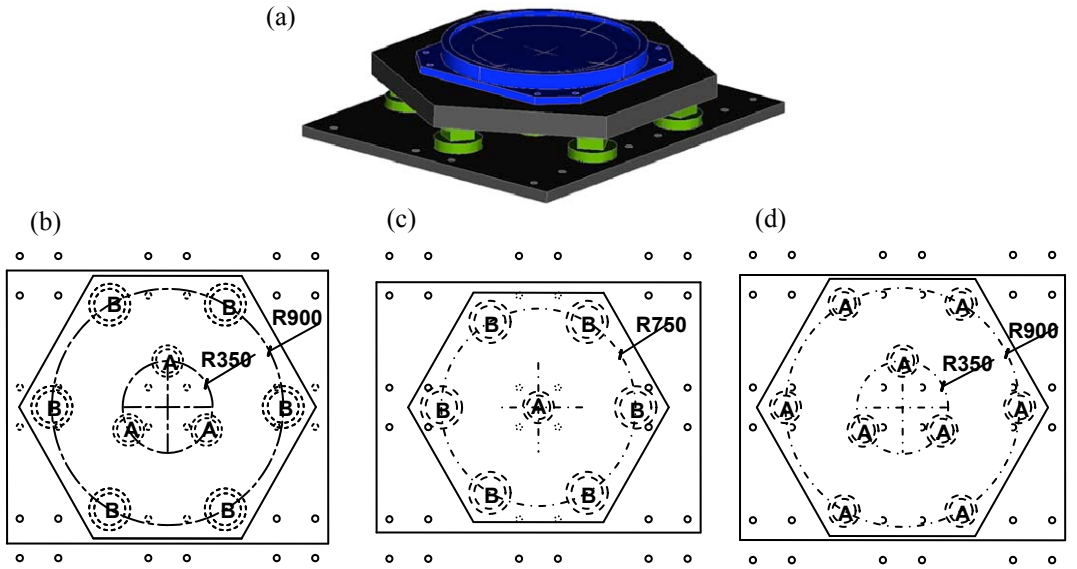


Figure 6. Connection between isolator and shaking table (a) 3-D view; (b)-(d) load cell configuration at center isolator, edge isolators, and corner isolators

Table 4. Peak Forces Induced in Load Cells

Load cell	Max. compression (kN)	Max. tension (kN)	Max. shear (kN)	Status
Type A	388	112	41	OK
Type B	582	192	41	OK

NONSTRUCTURAL COMPONENTS

In recent earthquakes, damage to nonstructural systems resulted in loss of functionality of buildings, including critical facilities, and contributed to major economic losses. Significantly limited data is currently available that address damage

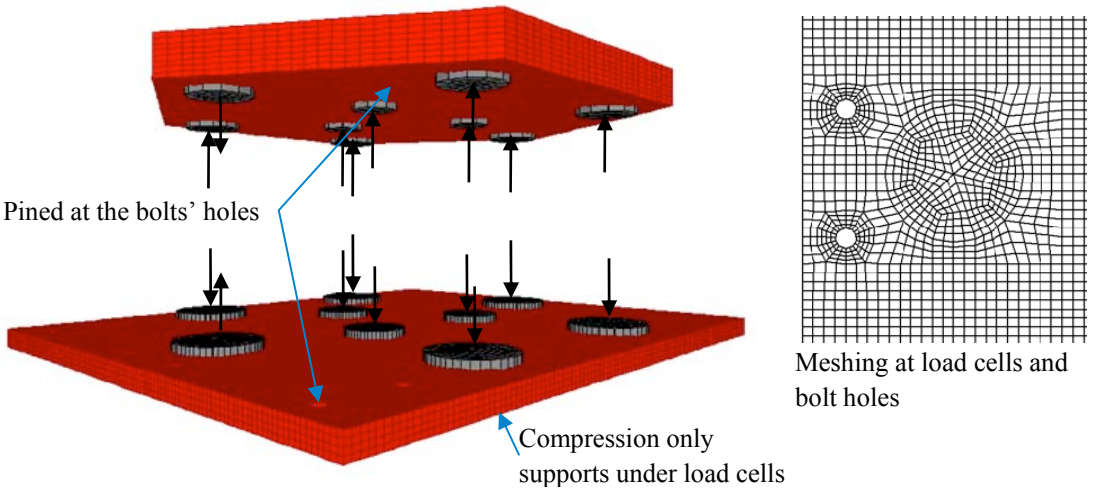


Figure 7. Finite element modeling and analysis of connecting plates.

measures of nonstructural systems that can be used to estimate downtime, repair cost, and life safety threats. In addition to the previously stated objective to demonstrate damage free performance of the building specimen, the experiment presents an excellent opportunity to investigate the seismic response of the full scale nonstructural assemblies in a realistic dynamic environment with interacting together and with the structure.

The NEESR Grand Challenge project "*Simulation of the Seismic Performance of Nonstructural Systems"*, led by PI Emmanuel Maragakis, integrates multidisciplinary system-level studies that develop, for the first time, the simulation capabilities and implementation process for enhancing the seismic performance of ceiling-piping-partition (CPP) nonstructural systems (Maragakis 2011). The Grand Challenge project has formed a collaboration with NEES TIPS and E-Defense to use the experimental setup in Japan as a testbed for installing CPP systems and enhancing the data that will contribute to the project goals.

Ceiling, piping, and partition systems were selected for inclusion in the large scale structure specimen as they account for almost 75% of the total value of critical facilities such as hospitals, schools and offices. The fourth and fifth floors of the test structure were selected to install the CPP systems. A realistic partition layout was designed that offers approximately 1000 sf of enclosed ceiling area. Figure 8 shows the plan layout of these systems. The partitions have been designed with conventional details that are currently in use in residential and commercial buildings, respectively. The ceiling in the fourth floor will be installed without a bracing system, while in the fifth floor the bracing will be included according to the seismic code requirement. Fire suppression sprinkler systems are included to capture dynamic interactions between the ceiling and sprinkler heads. The designed configurations for these systems allows for evaluation of the following effects:

- Comparative performance of CCP systems for isolated and fixed-base structural configurations.
- Interaction of the nonstructural assemblies and structural elements.
- Influence of openings (doors and windows) on response of partitions.
- Influence of corner and T-configuration partition layouts.

- Relative length of partition walls.
- Institutional versus residential partition wall detailing
- Partitions with slip tracks versus fixed tracks.
- Behavior of self-standing partial height partitions (shown as dotted line in Figure 8), which provide an enclosed room for testing furniture and other contents.
- Interaction between partition-ceiling and ceiling–sprinkler piping.
- Dynamic amplification of ceiling relative to structural accelerations.
- Effect of bracing on large areas of ceilings.
- Effect of additional masses such as lighting systems.
- Dynamic response of sprinkler piping system.

Additional plans include the construction and testing of a small section of concrete cladding panels on the building exterior. Details are omitted due to space limitations.

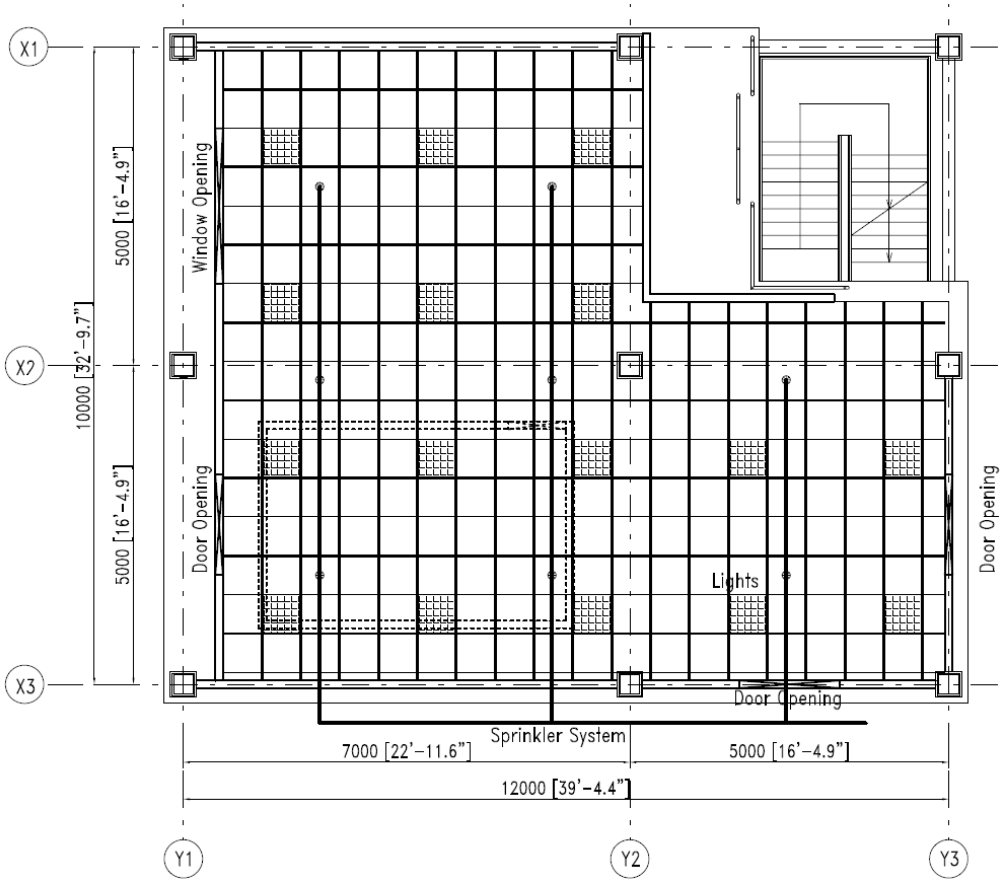


Figure 8. Plan view of interacting ceiling system, exterior wall, and piping planned for 4th and 5th floors of specimen.

CONCLUDING REMARKS

These landmark tests will take place in August/Sept. 2011, where the specimen will occupy the table for a 3 week time frame. Four days of shaking are allocated, with 3 for the isolated specimen (Day 1 = frequent and DBE/L2, Day 2 = MCE/L3, Day 3 = displacement limit tests) and one for the specimen in the fixed-base configuration.

Acknowledgment: This material is based upon work supported by the National Science Foundation under Grants No. CMMI-0724208 and CMMI-0721399. Any opinions, findings, and conclusions or recommendations expressed in this material are those of the author(s) and do not necessarily reflect the views of the NSF.

REFERENCES

Becker, T. C., S. Furukawa, Mahin, S. A., Nakashima, M. (2010). "Comparison of US and Japanese codes and practices for seismically isolated buildings," *Proc., ASCE Structures Congress*, pp. 2330-2338.

Clark, P. W., Higashino, M., Kelly, J. M. (1996). "Performance of seismically isolated structures in the January 17, 1994 Northridge Earthquake," *Proc., Sixth U.S.-Japan Workshop on the Improvement of Building Structural Design and Construction Practices in the United States and Japan*, Victoria, Canada.

Erduran, E., Dao, N. D., Ryan, K. L. (2010). "Comparative response assessment of minimally compliant low-rise conventional and base-isolated steel braced frames," *Accepted to Earthquake Engrg. & Struct. Dyn*.

Fan, F. G., Ahmadi, G. (1992). "Seismic Response of Secondary Systems in Base-isolated Structures," *Engineering Struct*, 14(1):35-48.

Fenz, D. M. and Constantinou, M. C. (2008). "Spherical sliding bearings with adaptive behavior: theory", *Earthquake Engrg. & Struct. Dyn.*, 37(2):163-183.

Kasai, K., et. al. (2010). "Full scale shake table tests of 5-story steel building with various dampers," *Proc., 7th Intern. Conf. on Urban Earthquake Engin. & 5th Intern. Conf. on Earthquake Engin.* Tokyo Inst. Tech., Tokyo, Japan.

Kelly, J. M., Aiken, I. D. (1991). "Experimental studies of the seismic response of structures incorporating base-isolation systems," *Nuclear Engrg. & Des.*, 127(3):329-338.

Maragakis, E. (2011). Simulation of the Seismic Performance of Nonstructural Systems, http://www.nees-nonstructural.org [Jan. 8, 2011].

Malushte, S. R., Whittaker, A. S. (2005). "Survey of past base isolation applications in nuclear power plants and challenges to industry/regulatory acceptance," *18th International Conference on Structural Mechanics in Reactor Technology (SMiRT 18)*, Paper No K10-7. Beijing, China.

Pan, P., Zamfirescu, D., Nakashima, M., Nakayasu, N., Kashiwa, H. (2005). "Base-isolation design practice in Japan: Introduction to the post-Kobe approach," *J. Earthquake Engrg.*, 9(1):147-171.

Samali, B., Wu, Y. M., Li, J. (2003). "Shake table test on a mass eccentric model with base isolation," *Earthquake Engrg. & Struct. Dyn.*, 32(9): 1353-1372.

Sato, E., Kajiwara, K., Furukawa, S., Ji, X., and Nakashima, M. (2010). "Full-scaled shaking table test of a hospital made of a base-isolated four-story concrete structure", *Proc., 9th U.S. National and 10th Canadian Conf. on Earthquake Engrg.*, July 25-29, Toronto, Canada.

Su, L., Ahmadi, G. (1988). "Response of frictional base isolation systems to horizontal-vertical random earthquake excitations," *Prob. Engrg. Mech.*, 3(1):12-21.

UPV Method for Detecting Properties of Carbon-Nanofiber Concrete

T Ravi S Mullapudi[1] and Ashraf Ayoub[2]

[1]PhD Candidate, University of Houston, Department of Civil and Environmental Engineering, W103 Engineering Building 2, Houston, TX 77204, Tel: (281) 217-3936 Fax: 713-743-4260, tsmullapudi@uh.edu
[2]Associate Professor, University of Houston, Department of Civil and Environmental Engineering, N107 Engineering Building 1, Houston, TX 77204-4003, Tel: 713-743-4285, Fax: 713-743-4260, asayoub@uh.edu

ABSTRACT

Concrete is the most widely used construction material, and the addition of carbon-nanofibers (CNF) to concrete has many advantages in both mechanical and electrical properties such as higher strength, a higher Young's modulus, improved fatigue resistance in addition to self-monitoring behavior due to the high tensile strength and high conductivity. In this study, the Ultrasonic Pulse Velocity (UPV) method was used to characterize properties of concrete containing carbon-nanofibers. Concrete strength correlations between pulse velocity, electrical resistance variation and destructive tests were analyzed. The experimental results indicate that the compressive strength, pulse velocity and percent reduction in electrical resistance while loading concrete containing CNF are much greater than those of plain concrete.

INTRODUCTION

Concrete has been used as the major construction material for many years in the field of civil engineering because of its high compressive strength and constructability. Cement, the binding component of concrete, develops micro cracks during casting and loading which weaken the final concrete structure. Micro cracks range in size from picometers to micrometers and eventually lead to abrupt failure if not detected and repaired. In order to restrict the growth of micro cracks, carbon-nanofibers (CNFs) were added to the concrete mix. CNFs have tensile strengths over 7.0 GPa (1015 ksi) and an average length of 20 μm. These characteristics enable the nanofibers to bridge micro cracks and absorb the energy normally released during crack propagation. Addition of the carbon-nanofiber into the concrete increases the strength, ductility and transforms this material into a more robust material. Carbon-fiber concrete is gaining its acceptability during recent years due to the decrease in carbon-fiber cost and increasing demand of superior structural and fundamental properties such as strength, ductility, creep, shrinkage and ductility. Strength of the cement concrete increased with the development of the nanoscale bonding between the CSH and nanofiber which has the ability to hold the cement matrix more strongly than the CSH itself [1].

In recent years, more and more researchers are prone to use the ultrasonic pulse velocity nondestructive technique to test the materials because this technique is easier and more economical than traditional tests. Current research utilized the pulse velocity method to evaluate the properties of the carbon-nanofiber concrete. Lamb [2] analyzed the surface wave propagation for the case of impulse vertical point load with a solution valid for a point far from the source. Lamb's solution was later extended by Nakano [3] for the cases close to the source. Pulse velocity changes with many variables in concrete, including water content, mixing proportions, aggregate type and size, and age of concrete (Tanigawa et al., [4]). Okamoto and Whiting [5] studied the maturity and the pulse velocity to predict the strength of the concrete. Mantrala and Vipulanandan [6] used the pulse velocity method for the evaluation of the differences between polyesterpolymer and polymer. Frearson [7] conducted nondestructive testing and discussed the problems with concrete tests and test results in adverse weather conditions. Gao *et al* [8] indicated that some mechanical and electrical properties of CNFSCC were improved under compression stress, which is the most basic force acting on concrete in reinforced concrete structures. Especially in the aspect of electrical properties, the relationships between electrical resistance variation (ERV) and strain as well as ERV and stress can be established. Therefore, the damage evaluation and self-health monitoring of concrete structures might be easier to carry out since the concrete itself acts as a sensor, resulting in much lower cost of the infrastructure's maintenance and repair. Based on the reasons mentioned above it is feasible and attractive to develop smart high performance carbon-nanofiber concrete by adding CNF to concrete.

EXPERIMENTAL PROCEDURE

MATERIAL PROPERTIES

CNF from Pyrograf Products, Inc. [9] were used in this study. PR-19-XT-LHT-OX is the oxidized product produced by heat-treating the fiber at 1500° C. Heat treatment converts any chemically vapor deposited carbon present on the surface of the fiber to a short-range ordered structure. The inherent conductivity of the fiber is increased following heat treatment. High-range water reducer Glenium 3200 HES, a polycarboxylate admixture from BASF Chemical Co., was used to decrease the viscosity of the concrete [10]. Antifoam agent Antifoam 2210, a silicone–glycol emulsion (polypropylene glycol and polydimethylsiloxane) from Dow Corning, was used for all three kinds of CNFs to reduce the amount of foam produced during mixing and after detergent addition [11]. Low-alkali, type I/II cement was used in all specimens. Crushed limestone with a maximum size of 19 mm was used as coarse aggregate in all specimens. Natural river sand with a fineness modulus of 2.71 was used as fine aggregate in all specimens.

MIXTURE PROPORTIONS

As shown in Table 1, six mixtures were studied. The binder weight is the total weight of cement and CNF. CNFSCC07-LO, CNFSCC10- LO, CNFSCC15-LO,

CNFSCC20-LO and CNFSCC25-LO denote self-consolidating concrete containing the CNF PR-19- XT-LHT-OX in amounts of 0.7%, 1.0%, 1.5%, 2.0% and 2.5% by volume of binder, respectively.

Table 1 Mixing proportions

Mix	Carbon nanofiber (vol% binder)	Water (kg m^{-3} concrete)	Cement (kg m^{-3} concrete)	Coarse aggregate (kg m^{-3} concrete)	Fine aggregate (kg m^{-3} concrete)	High-range water reducer (fl.oz./cw)	Antifoam (fl.oz./cw)
SCC	0	191	480	901	1005	11	0
CNFSCC07-LO	0.7	191	478	902	1008	7	11
CNFSCC10-LO	1	191	478	902	1008	11	11
CNFSCC15-LO	1.5	191	478	902	1008	19	11
CNFSCC20-LO	2	191	478	902	1008	23	11
CNFSCC25-LO	2.5	191	478	902	1008	35	11

TESTING METHODS

DESTRUCTIVE TESTING

Compression tests were conducted using a Tinius Olsen Universal Material Tester with a maximum load capacity of 600 kips according to ASTM rates of 300 lbs s^{-1} in load-control mode and 0.00005" s^{-1} in strain-control mode. The specimens used were 4" by 8" cylinders. A compressometer Standard C 39M-05 load with a digital strain gauge was used to detect strain.

ULTRASONIC PULSE VELOCITY (UPV) TESTING

The device used to measure velocity is ultrasonic pulse velocity meter [12] (V-meter). The V-meter can generate compressive waves traveling along the materials and record the shortest travel time. The wave travel depends upon the amount and dispersion of the carbon-nanofibers. The transit time can be measured with three methods, which are direct, semi direct and indirect method. Direct transmission method is used in this current research because it is more reliable than the other two methods.

The pulse velocity [12] is calculated with the known distance and time as

$$V = D / T \tag{1}$$

whereas V is the pulse velocity, D is the distance between transducers across the diameter, and T is the transit time.

The pulse velocity is measured continuously along the transverse direction of the cylinder throughout the destructive testing. It eases the correlation between pulse velocity, strain and stress at different stages of loading of the cylinder.

ELECTRICAL RESISTANCE VARIATION (ERV) TESTING

The four-probe method was used to determine the volume electrical resistance of the specimens (Fig. 1). The surface of each specimen was ground in order to expose higher densities of CNFs and remove dust from the surface where the wires contact the specimen. Conductive silver epoxy was spread along the wires to hold them in place and ensure continuous contact with the concrete surface. Current was measured across the top and bottom wires using an ammeter with ±0.01 μA accuracy and voltage was measured across the two middle wires using a voltmeter with ±1.0 μV accuracy so that the electrical resistance between the two central wires could be calculated using Ohm's law. A 1.5 V AA battery was used as the voltage source. The original voltage and current readings were recorded as V_0 and A_0, and the original electrical resistance R_0 was calculated. Subsequent voltage and current values were recorded each time the load and strain were recorded during the compressive test. Each strain value, Δ_i, at every time point, i, had corresponding values of voltage and current recorded as V_i and A_i . The electrical resistance R_i and electrical resistance variation Δ_{Ri} were calculated using Eqs. (2) and (3):

$$R_i = V_i / A_i \tag{2}$$

$$\Delta_{Ri} = (R_i - R_0)/R_0 \tag{3}$$

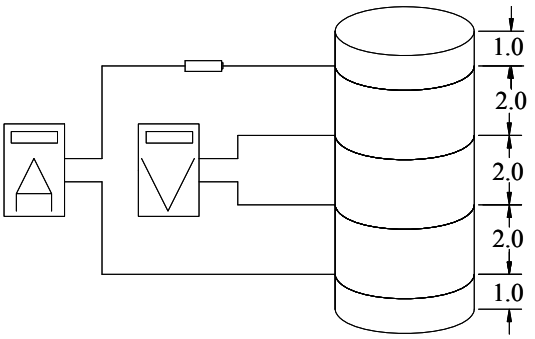


Fig. 1. Cylinder with wires and multimeters attached to measure electric resistance with four probe method.

STRENGTH AND PULSE VELOCITY (V_{PD}) VARIATIONS DURING LOADING

Pulse velocity (V_{PD}) is measured at the middle of the cylinder along the transverse direction throughout the loading and the variation of the pulse velocity (V_{PD}) was compared with stress and strain containing plain Self Consolidated Concrete (SCC) and SCC containing the PR-19-XT-PS-LHT-OX. As the loading increases, compressive strain along the longitudinal direction increases along with the increase of the compressive strength of the concrete. After reaching the peak strength of the concrete, compressive strength reduces with the increase of the compressive strain (Figs. 2 - 3). With the increase of the compressive strain of the concrete along

the longitudinal axis of the cylinder, tensile strain along the transverse direction increases because of the Poisson's effect and that causes damage of the cylinder. Pulse velocity (V_{PD}) is reduced steadily until reaching a strain of about 0.001, and, after that, it is reduced rapidly because of the increase of the damage of the specimen.

For CNFSCC containing PR-19-XT-PS-LHT-OX, the peak compressive strength and pulse velocity (V_{PD}) varies as follows (Figs. 2): CNFSCC10-LO > CNFSCC15-LO > SCC > CNFSCC07-LO > CNFSCC25-LO > CNFSCC20 -LO and is increased 21.4% compared to plain SCC when the CNF concentration is 1.0%. This indicates the threshold of the concentration is around 1.0% and gives higher energy dissipation. From Fig. 2 it is clear that the pulse velocity (V_{PD}) and ductility of CNFSCC10-LO is 20% and 45% higher than the SCC, respectively. Figure 3 shows that the ductility of SCC containing PR-19-XT-LHT-OX is greater than that of plain SCC.

From the above discussion, it is evident that the pulse velocity has a direct correlation between the strength and energy dissipation of the CNF concrete. In next section, the pulse velocity is correlated with the electrical resistance variation.

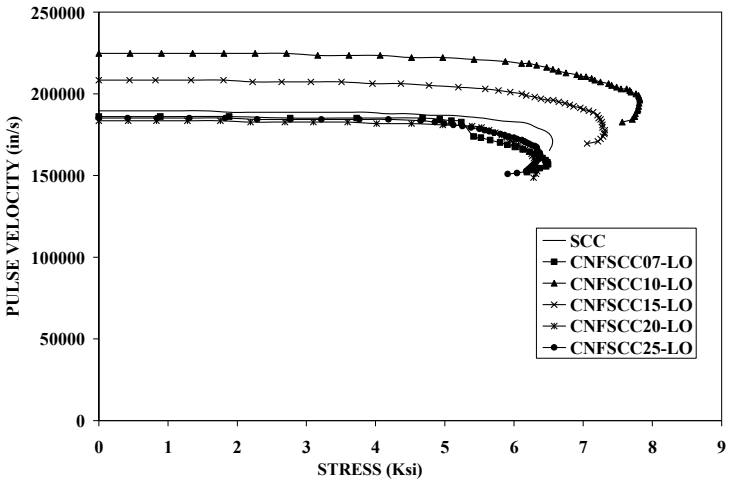


Fig. 2. CNFSCC-LO pulse velocity-stress relation

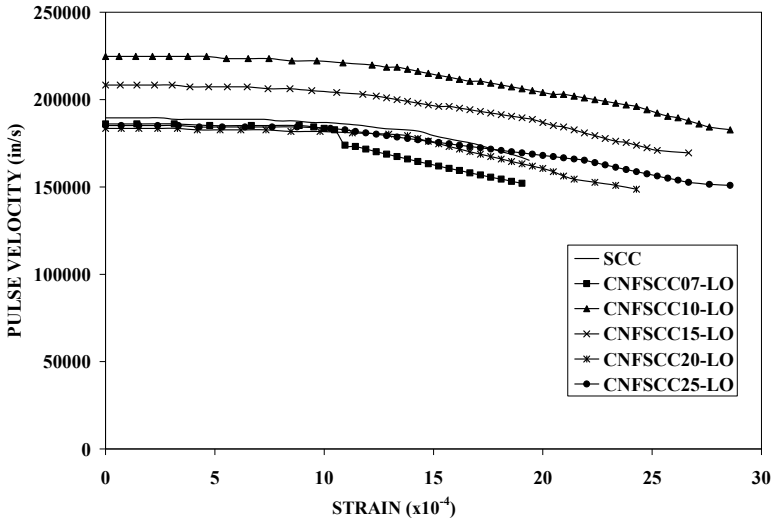


Fig. 3. CNFSCC-LO pulse velocity-strain relation.

PULSE VELOCITY (V_{PD}) *AND ELECTRICAL RESISTANCE (R) VARIATIONS DURING LOADING*

Figures 4– 5 show the relationship between electrical resistance variation Δ_{Ri}, pulse velocity (V_{PD}), stress and strain of each plain SCC and SCC containing the PR-19-XT-PS-LHT-OX. Resistance decreases for all concentrations of fiber. At 1.0% CNF concentration, CNFSCC10-LO exhibits the highest electrical sensitivity with an 80% reduction in electrical resistance. Electrical resistance variation decreases rapidly when the concentration of CNFs is increased from 1.0% to 1.5%. This trend continues at a slower rate for CNF concentrations greater than 1.5%. When the concentration of PR-19-XT-LHT-OX fibers exceeds 2.0%, the percent reduction in electrical resistance is less than 10%. From Figs. 4 and 5 it is evident that the increase of strain and stress reduces the pulse velocity (V_{PD}) and electrical resistance variation. Compared to other mixes CNFSCC10-LO exhibits the higher pulse velocity (V_{PD}) and lower electrical resistance variation.

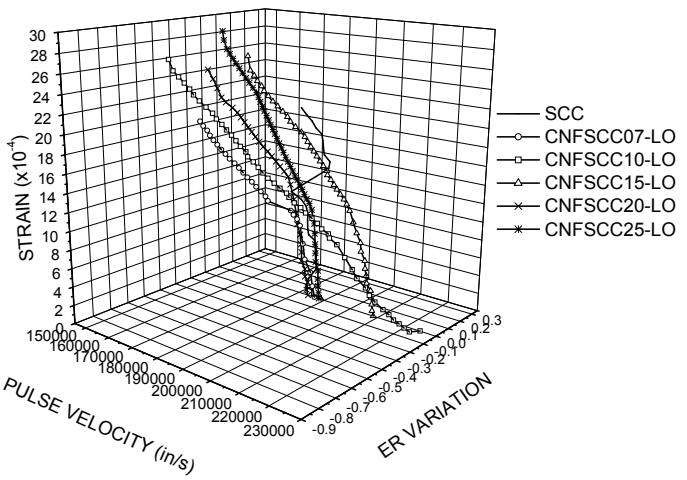


Fig. 4. CNFSCC-LO variation of electrical resistance - pulse velocity - strain

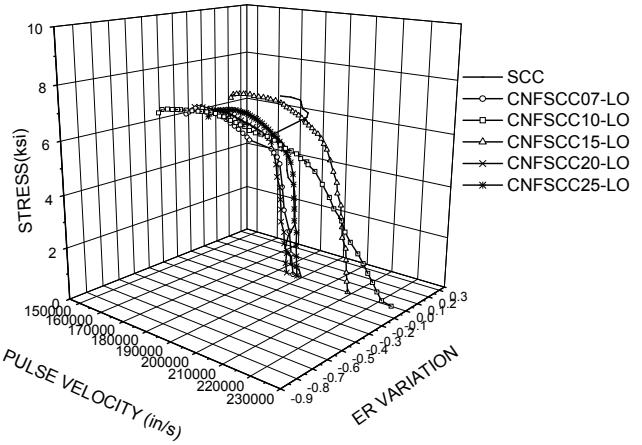


Fig. 5. CNFSCC-LO variation electrical resistance - pulse velocity – stress.

CONCLUSIONS

The results presented in this paper have articulated that the strength and ductility of carbon-nanofiber concrete can be estimated by the pulse velocity method. The ERV of plain SCC is random, so it is impossible to establish the relationship between ERV and strain/stress. Adding CNF decreases the electrical resistance of SCC because it is a semiconductor, but there is a threshold for fiber concentration. If the actual concentration is higher than the threshold, the tunnel conductivity effect of CNF will decrease and the electrical resistance does not change with increasing strain. Well-dispersed CNF in the appropriate concentration allows for the greatest pulse velocity and electrical resistance variation of concrete with increasing strain and, consequently, may be used in applications that require strain monitoring and make concrete itself a sensor. Well-dispersed CNF improves the pulse velocity and strength of concrete. Excess concentration leads to poorly dispersed CNF clumps inside the concrete and has a negative effect on pulse velocity and strength. PR-19-TLHT-OX performs best at concentrations around 1.0%.

REFERENCES

1. Newman J W *Int. SAMPLE Symp. Exhib.* Vol 32 (Covina, CA: SAMPLE) PP 938-44. (1987)
2. Lamb, H. *Royal Society of London Philosophical Transactions Series A*. **203**: 1–42. (1904).
3. Nakano, H. *Japanese Journal of Astrophysics and Geophysics*. 2: **233**–326. (1925).
4. Tanigawa, Y., Baba, K. and Mori, H. American Concrete Institute, Farmington Hills, MI, SP-82, 57-76. (1984).
5. Okamoto, P.A. and Whiting, D. Transportation Research Record. 1458: 85-90 (1994).
6. Mantrala S., Vipulanandan, C. ACI Materials Journal. 92: 660-665 (1995).
7. Frearson, J. Concrete World. 29: 23-24 (1995).
8. Gao, D., Sturm, M., and Mo. Y.L. Electrical resistance of carbon-nanofiber concrete. Smart Mater. Struct. 18, 1–7 (2009).
9. Pyrograf Products, Inc. www.pyrografproducts.com
10. BASF Admixture Systems www.masterbuilders.com 2009.
11. Dow Corning Corporation www.dowcorning.com 2009.
12. ASTM C 597-02. Standard Test Method for Pulse Velocity through Concrete. Annual Book of ASTM Standards. 04.02: 310-313. (2003).

Award Winning Bridges in California Owned and Designed by Caltrans

Authors:

Carl Huang, PE, Professional Engineers in California Government PECG
455 Capitol Mall , Suite 501, Sacramento, CA 98514 PECG@PECG.ORG
Craig Copelan, PE , PECG, ccopelan95694@gmail.com
Ric Maggenti, PE , PECG, PECG@PECG.ORG
Alfred R Mangus PE, MangusAlf@yahoo.com

INTRODUCTION

The California legislature originally authorized state engineering staff to design their own highways and bridges in 1923 [Caltrans 1999] (Figure 1). For approximately eighty-seven years state employees have designed bridges for the state highway and interstate system in California. There are approximately 300 award winning bridges that have been cost effectively designed by state employees and are maintained and operated by Caltrans (www.dot.ca.gov) for the taxpayers of the state of California. The Professional Engineers in California Government (PECG) (www.pecg.org) was created in 1963 as an organization to represent the interests of public employees. PECG's function was primarily to highlight the technical achievements and viewpoints of state employees. In the 1970's with the passage of the Ralph C Dills Act, PECG took over the additional role of representing engineering and related classes in bargaining with their California government employer. Thus the authors as engineers employed by the state of California Department of Transportation belong to both PECG and ASCE. Featured bridges in this short paper and poster are mainly the best known structures recognized by the bridge industry and others as state of the art in bridge engineering. Leading educators such as Professor David Billington believe that structural engineering is an art form with creative individuals due recognition by society, such as award programs (Figure 1). A Bridge Architecture Aesthetics unit has been part of Caltrans structures design since the 1930's. A licensed Architect has managed the unit of technicians, renderers and scale model makers since the 1960's. Caltrans engineers have also designed several notable tunnels and the Webster Precast Concrete Tube, which opened in 1963 (Figure 2).

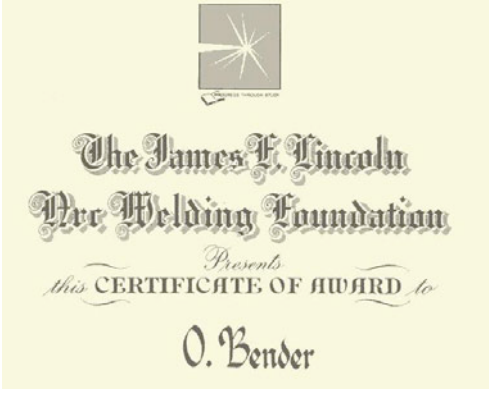


FIGURE.1 NATIONAL CONTEST WINNER [1967]
PHOTO BY OSTAP "JOE" BENDER



FIGURE 2 BUS INSIDE WEBSTER TUBE [1963]
PHOTO BY ALFRED R. MANGUS

ORTHOTROPIC BRIDGES DESIGNED BY CALTRANS

The origin and development of orthotropic steel deck bridges occurred over many years and has many sources [Mangus 1999 & 2005]. In the 1920's steel plates were riveted to steel girders on long span movable bridges to achieve a durable, strong and lightweight superstructure. In 1938 the AISC American Institute of Steel Construction promoted the "Battledeck Bridge System" because the superstructure was made of 100% of welded steel and built tough as a battleship. The German steel industry produced the first orthotropic bridge design manual in 1957 and patented the orthotropic system. In 1963, the American Institute of Steel Construction (AISC) funded and published the "Design Manual for Orthotropic Steel Plate Deck Bridges," authored by Roman Wolchuk [Wolchuk 1963]. Caltrans Engineers researched this technology to bring state of the art seismic resistant design solutions from Europe to California. The authors were instrumental in creating www.orthotropic-bridge.org in 2004 and 2008 for ASCE, which attracted an attendance of about 200 from eleven countries. The FHWA –Federal Highway Administration has a new Orthotropic Bridge Manual in progress which was conceived at the first international orthotropic bridge conference. Active California bridges with orthotropic or 100% steel superstructures designed by Caltrans bridge engineers are summarized in table 1 vs. well known foreign bridges [Huang 2006].

Text In Section	Bridge in Service Name [year open to traffic]	Rib Type	Deck Area (Sq. feet)	Bridge Number (by owner)
1.	Dublin 580/680 Test [1965]	closed	10,880	33-0371G
2.	Ulatis Creek Test [1966]	open	4,420	23-0052R
3.	San Mateo – Hayward [1967]	open	468,875	35-0054
4.	San Diego – Coronado [1969]	closed	122,220	57-0857
TOTAL	**Deck area of CA Orthotropic Bridges**	**both**	**606,395**	
	Akashi-Kaiyo, Japan [1998]	closed	905,093 sq. ft. = 84,086 sq. m.	
	Millau Viaduct, France [2005]	closed	1,989,168 sq. ft. = 184,800 sq.m.	

TABLE 1 CALTRANS DESIGNED ORTHOTROPIC BRIDGES COMPARED TO FOREIGN BRIDGES

WEARING SURFACE TEST BRIDGE AT DUBLIN [1965]

The North 680 to West 580 connector bridge at Dublin, CA [Br. No. 33-371G] [Dec 1965] was built as an experimental bridge to check the accuracy of Caltrans' design software **"*Orthotropic Plate Design*".** This software uses the actual capacities, various trapezoidal ribs, and deck plate thicknesses. The California Department of Transportation (Caltrans) built the I-680 over I-580 Bridge as their test structure. The four span [75-ft + 85-ft + 85-ft + 75-ft] bridge is still in use after 30 years of service, but the wearing surface has been replaced on the thin section. The bridge is 34-ft wide x 320-ft long = 10,880 sq. ft. of deck area [Davis 1964 & 1968].

WEARING SURFACE TEST BRIDGE AT ULATIS CREEK [1966]

The State of California Division of Highways (Caltrans) designed the Ulatis Creek experimental orthotropic bridge lane in 1965. Construction of Caltrans Bridge Number [Br. No. 23-0052R] was completed in 1966. It consists of the two outside lanes of a 5-span bridge for eastbound Interstate I-80. All spans are 26-ft [8-M] long and the orthotropic deck has a "Split-T" superstructure (Figure 3). The bridge design engineers

wanted to test the durability of five types of wearing surfaces. Caltrans San Francisco Bay Toll Crossing engineers supervised this testing, with the most practicable material selected for use as the wearing surface of the San Mateo- Hayward Orthotropic Bridge (Figure 4).



FIGURE. 3 TEST BRIDGE AT ULATIS CREEK [1966]
PHOTO BY ALFRED R. MANGUS

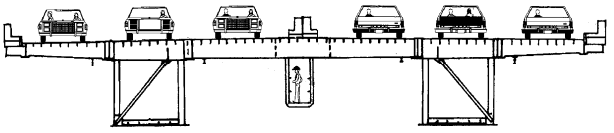


FIGURE 4 CROSS-SECTION SAN MATEO HAYWARD [1967]
DRAWING BY ALFRED R. MANGUS

The Ulatis Creek bridge is 34-ft wide x 130-ft long = 4,420 sq. ft. of Orthotropic steel deck area. The original wearing surface which was selected based upon in service performance at this location for the San Mateo Hayward Bridge is still in place after 43-years, so this bridge has been successful in several ways.

SAN MATEO HAYWARD BRIDGE ACROSS SAN FRANCISCO BAY [1967]

The San Francisco Bay Toll Crossings office (now part of Caltrans) was the designer and owner of the San Mateo – Hayward Bridge. It opened on Oct 31, 1967 and received the ASCE OCEA= Outstanding Civil Engineering Achievement Award of 1968. It received AISC and other awards. This Orthotropic Bridge has two side spans of 375-ft each counterbalancing the main 750-ft span. There are 14 approach spans of 292-ft or 7 on each side of the main span. Thus this bridge has the largest total Orthotropic deck area of all California bridges. The bridge has a width of 85.25 feet, and length of 5,500 feet = 468,875 square feet. It carries six lanes of Route 92 traffic across the San Francisco Bay between the communities of San Mateo and Hayward[Foley 1968][Huang 2005] (Figure 4).

18 TH STREET POC PEDESTRIAN OVERCROSSING [1968]

This orthotropic structure was designed and built as one piece in a fabrication shop. The previous welded steel deck bridge across the freeway used a plate girder as the superstructure. The new steel deck Veerendiel truss superstructure was completely shop prefabricated (Figure 5). It received a James F. Lincoln Arc Welding Award.

SAN DIEGO – CORONADO BRIDGE SAN DIEGO BAY [1969]

The San Diego-Coronado Bridge was completed in June 1969 [BR. NO. 57-0857]. This California toll bridge sweeps across the harbor area of San Diego (Figure 6). The Caltrans bridge design engineers selected a single cell box girder Orthotropic steel deck (continuous length of Orthotropic portion = 573-m). A constant depth box was used for

the 182.88-m + 182.88-m + 152.40-m main spans over the shipping channel. Steel plate girders with concrete deck were used on the remaining length of 1690 m. The area is 19.182-M wide x 518.16-M long = 10,266 sq. meters of steel deck. The bridge was erected in large pieces with the "Marine Boss" barge crane. The sections were field bolted together. The bridge is painted on the inside and outside to resist corrosion and carries six lanes of traffic. It received James F. Lincoln Welding Award and other awards. (Figure 6)



FIGURE 5 18TH STREET PEDESTRIAN OC BY ALFRED R. MANGUS



FIGURE 6 SAN DIEGO CORONADO BRIDGE SUNSET PHOTO PHOTO BY ALFRED R. MANGUS

MOVABLE BRIDGES

The Meridian Cable–Stayed Swing Bridge was completed in June 1977 [Hurdle 1968]. This structure received a lot of publicity because of increasing interest at the time in the development of cable stayed bridge technology. It received a James F Lincoln Arc Welding Award and received considerable attention from the bridge industry after opening to traffic. It is a single swing symmetrical span bridge using steel plate girders and a reinforced concrete deck. The A- frame shaped tower was fabricated from welded steel members.

The Potato Slough moveable bridge across the Sacramento River was completed in 1991(Table 2). It is a single symmetrical swing span bridge using tapered steel plate girders and a reinforced concrete deck. A design model was built and the cast-in-place reinforced concrete sculpture control tower was designed and built. Key dimensions are: Length of largest span: 160.1 ft with a total length: 2,980.1 ft. Deck width: 42.7 ft.

RECOGNITION TO INDIVIDUAL BRIDGE ENGINEERS

The California legislature can rename bridges after Caltrans employees or others. Organizations such as the Western Engineers Society of Pennsylvania' IBC = International Bridge Conference have bestowed recognition upon three bridge engineers who were with the state of California for decades. Art Elliot, James E Roberts and Charles "Chuck" Seim are IBC Roebling Award Winners for a lifetime of achievement in bridge engineering [Wilson 2001]. Other engineers at Caltrans have been bridge design contest winners by various organizations. The late Ostap "Joe" Bender started his career with The California Department of Highways and was a very talented bridge design engineer [Figure 13]. Joe Bender worked on a complete range of interesting bridges

during his career as a public servant and later in private industry. Bender designed steel plate girder structures for highways and railroads, steel box girders, two orthotropic steel deck bridges and an innovative suspension bridge. His concrete bridges include concrete box girders, cast in place concrete boxes and the cast-in-place concrete Pine Valley Bridge. Bridges that he felt that were important for his oral history are: 1957- 5th Street Southbound On-Ramp Overcrossing On Rte 165 In LA County; 1958- Lacy Street Underpass BR#53-1405; 1959- Eagle Point Viaduct BR#4-72 on US 101; 1963- Banner Ridge Overcrossing BR#17-77 On Rte 49 in Nevada County; 1964- Rte 580/680 Separation BR #33-371R/L; 680 / 580 Orthotropic Test Bridge; 1965-Santa Margarita River Bridge, BR#57-07L; 1965- Willow Creek Bridge BR #4-135; 1965 - Cocklebur Overcrossing BR#57-584 on RTE 5; 1965- Klamath River Suspension Bridge At Orleans on Rte 96 BR # 4-69; 1966 - Sacramento River Bridge and Overhead at Brytes Bend BR# 22-26R/L aka Caltrans Worker Memorial Bridge (Figure 12).; 1971-Pine Valley Creek Bridge BR#57-692R/L on Rte 8 (Figure 9).

Bender wrote in a letter in 2001. *"My approach to bridge design is based on several ideas that I have tried to incorporate in my bridges. The selected structure type should first of all:*

1. *Fit the constrains of the site*
2. *Be reasonably economical from the available choices*

Of Secondary concern are (although they may govern the selection):

1. *Appearance*
2. *Local preference*
3. *Research needs*
4. *Advancement of the art of bridge building"*

CONCRETE BRIDGES

Caltrans engineers have designed a wide range of concrete bridges. The award winning lightweight concrete bridge at Napa River has been durable [PCA 1977]. The column heights vary and are flared (Figure 7). The superstructure is variable in depth (Figure 8).

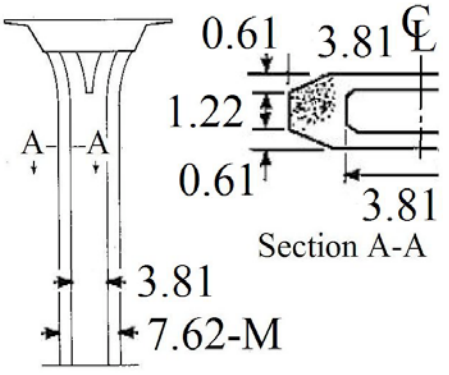


FIGURE 7 NAPA RIVER BRIDGE COLUMN
DRAWING BY ALFRED R. MANGUS

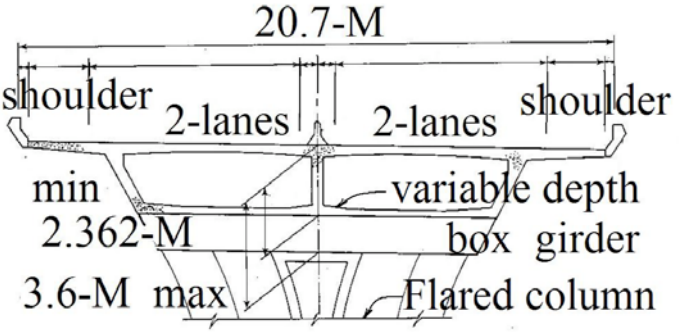


FIGURE 8 NAPA RIVER BRIDGE
DRAWING BY ALFRED R. MANGUS

The Pine Valley Bridge renamed the Nello Greer Memorial Bridge was the first Segmental concrete bridge of either precast or cast-in-place concrete designed and constructed in the USA. Documentaries produced by Caltrans to memorialize the construction of this innovative structure include the "*The Bridge*" which follows the phases of construction of the first segmental concrete bridge in the USA. The 16 minutes of civil engineering content was created by Caltrans Graphic Services with time lapse construction sequences developed by Caltrans Photo Lab.



FIGURE. 9 PINE VALLEY SEGMENTAL PHOTO BY OSTAP "JOE" BENDER



FIGURE 10 DEVILS SLIDE UNOPENED TO TRAFFIC [2011] PHOTO BY KEVIN HARPER

The Director was Richard Jones, cinematographer was John McCue, Audio was by Robert Souza, Art Direction was by David Douglas and Phil Walusek of the Portland Cement Association and "*The Bridge*" features interviews or narration by Caltrans Division of Structures staff, with short discussions on the topic of bridge design by Bert Bezzonne and Ostap "Joe" Bender. Bridge architecture is discussed by Bill Wells and bridge construction by Caltrans Resident Engineer Ralph Sommariva. Film credits recognize Lead Highway Designers Norm Larsen, Nello Greer and Highway Resident Engineer Tom Drake of Caltrans. The General Contractor was SJ Groves of New York City. The prestressing contractor was Dyckerhof and Widmann, Inc., Munich, Germany [ENR 1971].



FIGURE. 11 COCKLEBUR BRIDGE[FOR TANKS] OVER I-5 PHOTO BY OSTAP "JOE" BENDER



FIGURE 12 BRYTES BEND – STEEL TUB PHOTO BY OSTAP "JOE" BENDER

Caltrans bridge design engineers with assistance from the Office of Bridge Architect and Aesthetics staff continue to create beautiful bridges a great recent example is the Devils Slide Bridge on Rte 1 in San Mateo county which will open to traffic in 2011. (Figure 10)

The Cocklebur overcrossing over Interstate 5 is a reinforced concrete box girder with spans of 114`-128`-112` and depth of 10-feet, designed by Ostap Bender. Its unusual depth and non-standard typical section are due to the unusual live loads to support military armored vehicles or the M48A3 Patton Tank. Interstate 5 divides Camp Pendleton Marine Base. This grade separation bridge allows the marines to cross back and forth as needed to complete military exercises. The concrete bridge rails for this structure were unique as they were designed to prevent tanks from accidentally falling onto I-5 traffic (Figure 11).

STEEL BRIDGES

Caltrans engineers have designed a wide range of steel bridges. This includes many normal strength steel plate girder bridges. Caltrans engineers have also designed more complex steel bridges such as curved plate girders, steel arch bridges, steel truss bridges, tub girder bridges, suspension bridges and orthotropic bridges. Brytes Bend Bridge is a steel tub girder twin box superstructure which was fabricated from high strength steel. The steel failed during erection. The general contractor and Caltrans successfully sued the plate steel manufacturer for damages. Although heavily cracked the bridge has been retrofitted and remains in service. In spite of material setbacks the bridge as retrofit to accommodate traffic received AISC and James F. Lincoln Arc Welding Awards. Ostap Joe Bender was lead designer (Figure 12). Caltrans renamed the bridge to honor its maintenance workers. This structure which was renamed the Caltrans Maintenance workers memorial bridge in 2003 honors the 174 Caltrans workers who have been killed in the line of duty since 1923 and the creation of the original highway department.

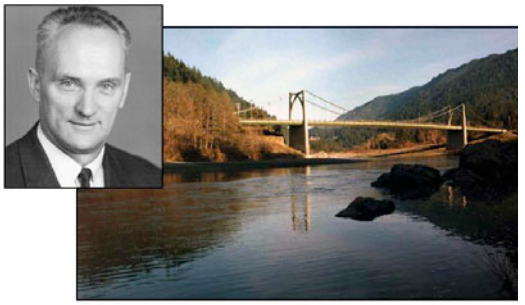


FIGURE 13 BENDER & KLAMATH RIVER SUSPENSION PHOTO BY OSTAP "JOE" BENDER



FIGURE 14 JAMES E. ROBERTS' BRIDGE PHOTO BY JOHN ADAM

SUSPENSION BRIDGES

The Klamath River Bridge at Orleans on Route 96 BR# 4-69 was designed using an aerodynamic wing cross-section shape. The superstructure configuration was influenced

by the world famous British Severn Orthotropic Box girder design (Figure 13). The previous two bridges at this site were suspension bridges built around [1915 timber] and [1940 steel] were carried away by high flood waters. The 1940 AISC Prize winning structure using the traditional stiffening truss of I-Girders, might have survived (Table 2). However large trees floating on top of the flood crest became entangled in the superstructure and facilitated the destruction of the 1940 bridge. The new bridge was completed in 1965 with a Cost: $1,420,000. Spans are 170`-430`-170` width 34-ft depth of only 5`-9". A suspension bridge is usually not the most economical type for a main span length of 430-ft. However the district highway engineers and local area residents favored replacing the 1940's bridge with another suspension span. It still may be the only multi-cell welded steel tub girder with a reinforced concrete deck. The bottom sides are sloped to have an aerodynamic wing shape. The smooth steel soffit will not catch any floating debris and the use of materials creates a very efficient stiffening system. Prefabricated cables were used rather than air spinning. Cast-in place concrete towers were used to eliminate painting. The shape of the towers was selected to match appearance of the 1940's bridge. The bridge received AISC and James F. Lincoln Awards and is featured in two books (Table 2). Designers were Ostap Joe Bender and Bert Bezzonne. PECG members' most recent award from NSBA / AISC was a merit award for the rebuilding of the Fire Damaged MacArthur Maze. Arnold Schwarzenegger's State of the State Address Tuesday, January 8, 2008. **"***In April, a fiery truck crash melted the Bay Area's 580 freeway exchange. Hundreds of thousands of Californians who depended on that interchange foresaw months of delays and stress. Yet it didn't take the expected 150 days to repair. Caltrans, working with contractors, cleared the span in 10 days and then built a new bridge and opened it up in a record 16 days later. Government can work. It can be efficient. It can lead."* – Governor Arnold Schwarzenegger. Film clips of this accelerated bridge repair may be viewed at http://www.amazingmaze.org/ .

THE TUOLUMNE BRIDGE NOW THE JAMES E. ROBERTS MEMORIAL

The Tuolumne River Bridge was selected to be named in honor of Mr. Roberts, because it was one of the first bridges that he was assigned responsibility for as a senior bridge engineer in 1968 with the California Department of Highways [Kempton 11]. Mr. Roberts laid out this Tuolumne River Bridge on a 1200-ft radius horizontal curve to meet the site requirements in December 1967(Figure 14). Computer analysis was required by the designer Mr. Dokken and the design squad because of the bridge's long spans and curved alignment [Dokken 2009]. The Bridge aesthetic unit of the California Department of Highways was called upon to provide architectural enhancements for the structures tall slender columns and sweeping curved spans. The columns were designed with triangular caps to accommodate the superstructure with insets featuring concrete dyed to match the golden California hillsides surrounding the site. Conventional concrete was used for construction of the foundations and the hexagonal columns and lightweight concrete was used for the bridge deck. The superstructure chosen was steel curved girders which were trucked into the site. The location over a future reservoir required that the superstructure be completed quickly and because of the heights above the ground the construction of a concrete superstructure would not have been practical. To accommodate future capacity in this challenging location the structure was designed

Year	Name	Type/class
1935	Sagamore Bridge, Town of Bourne, MA	Honorable Mention
1940	Klamath River Bridge, Humboldt County, CA	First Place
1950	Bridge Over Kern River, Kern County, CA	Honorable Mention
1953	Ninth and Tenth Street Connections, San Francisco, CA	N/A
1954	Indian Creek Bridge, Plumas County, CA	Honorable Mention
1955	Archibald Avenue Bridge, San Bernardino County, CA	Honorable Mention
1955	Distribution Structure Overhead Addition, Oakland, CA	Honorable Mention
1957	Trinity River Bridge, Hoopa, CA	First Honorable Mention
1958	Marsh Rd. Overcrossing, Redwood City Limits, CA	Honorable Mention
1959	Huasna River Bridge, Santa Maria, CA	II-fixed spans under 400 ft
1959	Truckee River Bridge, Truckee, CA	Honorable Mention
1959	Kern Ave. Pedestrian Overcrossing, Mac Farland, CA	Honorable Mention
1959	Grant Line Canal Bridge, Stockton and Tracy, CA	Honorable Mention
1961	Pecwan River Bridge, Weitchpec, CA	Short Span, Merit Award
1962	Elysian Viaduct Bridge, L.A., CA	Medium Span w/fixed span under 400 Ft., Merit Award
1962	Middle Fork Smith River Bridge, Crescent City, CA	Short Span w/fixed spans , Merit Award
1962	South Fork Eel River Bridge of Meyers Flat, Humbolt County, CA	Medium Span w/fixed span under 400 Ft.
1963-64	Webber Creek Bridge, 16 mil. E of Sacramento County Line, CA	Medium Span
1963-64	Vincent Thomas Bridge, San Pedro, CA	Long Span
1963-64	Devil's Canyon Bridge No. 2, 5 mil. E of San Diego County, CA	Short Span
1963-64	Cold Spring Canyon Bridge, Santa Barbara, CA	Long Span
1965	Northbound Route 280/17 Separation, San Jose, CA	Highway Grade Seperation
1965	South Fork Eel Bridge & Separation, Sylvandale, CA	Medium Span High Clearance
1965	Lebec Road Overcrossing, Bakersfield, CA	Highway Grade Separation
1966	Willow Creek Bridge, Willow Creek, CA	Short Span
1966	Route 680/580 Separation, West of San Joaquin County Line, CA	Highway Grade Separation
1967	Dry Creek Bridge, Ione, CA	Short Span
1967	Klamath River Bridge, Orleans, CA	Long Span
1967	Oak Hill Road Overcrossing, South of Victorville, CA	Highway Grade Separation
1967	Merced River Bridge, Bagby, CA	Medium Span Low Clearance
1967	Pioneer Memorial Bridge, Sacramento , CA	Medium span high Clearance
1968	San Mateo-Hayward Bridge, San Mateo and Hayward, CA	Long Span
1968	Eel River bridge and Overhead, Scotia, CA	Med. Span - Low Clearance
1968	South Fork Feather River Bridge, near Feather Falls Butte County, CA	Long Span. Merit
1968	Route 5/99 Separation, Kern county, CA	Hwy Grade Separation
1968	Valencia Blvd. Overcrossing, Valencia, CA	Hwy Grade Separation
1969	Kern River Bridge, Isabella, CA	Medium Span High Clearance
1969	McBean Parkway Overcrossing, Newhall, CA	Hwy Grade Separation
1969	Kern River Bridge, Isabella, CA	Medium Span High Clearance
1970	Sacramento River Bridge at Elkhorn, Sacramento, CA	Medium Span High Clearance, merit
1970	Eugene A. Doran Memorial Bridge (San Mateo Creek Bridge), San Mateo, CA	Medium Span High Clearance
1971	Klamath River (South Rogers Creek) Bridge, Siskiyou County, CA	Medium Span High Clearance
1972	Sacramento River Bridge at Bryte Bend, Sacramento, CA	Medium Span High Clearance
1972	Tuolumne River Bridge, near Sonora, CA	Medium Span Low Clearance
1973	West Connector Viaduct, San Jose, Ca	Elevated Hwys or Viaducts
1975	Kern River Bridge, Kern County, CA	Medium Span Low Clearance

TABLE 2 AISC / NSBA AWARD WINNING STEEL BRIDGES DESIGNED BY PECG MEMBERS

to be widened from 2-lanes of traffic to 4-lanes of traffic. The Roberts Bridge designers received awards from the steel industry an AISC Medium Span Steel Bridge award in 1972 and a James F. Lincoln Arc Welding Award. The AISC Jurors wrote "This ***gracefully sweeping bridge fits beautifully into its setting. The clean curving***

superstructure and the sculptured piers are very pleasing". Mr. Dokken, a former PECG member describes the steel design details [Dokken 2009]. Mr. Roberts was a former PECG State President and a union member for 50-years [Alden 1999] [Roberts 2001].

SEISMIC RETROFIT OF BRIDGES

A major seismic retrofit effort was lead by Mr. Roberts after the Loma Prieta and North Ridge Earthquakes. Standard solutions were developed for standard bridges [Roberts 1999]. Very unique and large bridges required a team of engineers to develop solutions or to evaluate the choices "retrofit or replace" [Roberts & Maroney 1990]. A documentary developed by PECG, The Bridge So Far: A Suspense Story" discusses issues for the replacement bridge systems selected for the East spans of the SFOBB [Copelan 2011]. The west spans of SFOBB are the 2nd most photographed bridge in California. Suspension bridges are more forgiving under seismic loadings, thus a retrofit of extra steel components and other modifications were made for it, as a cost effective solution. The new steel components were made of steel manufactured and fabricated in Brazil. SFOBB West Spans team was awarded ATC-ASCE Seismic Retrofit Project of the Decade in December 2009 at the ATC-SEI-ASCE conference. ATC-SEI- ASCE awards chair Dr Jeremy Isenberg presents five PECG members Dr Lian Duan, Dr Brian Maroney, Rodney "Rod" Simmons, John Fujimoto and Ofelia Alcantara, the lead bridge design engineers. Awards Ceremony. (Figure 15). The West Suspension Spans of the SFOBB Bridge connection San Francisco to Yerba Buena Island is the 2nd most photographed bridge in California. A large team of PECG Engineers contributed to a bridge engineering handbook which has become an industry best seller. Two of the contributing authors Alfred Mangus and Dr. Lian Duan Co-Editor on this bridge engineering handbook are very active in ASCE [Mangus 1999] (Figure 16).



FIGURE 15 PECG ENGINEERS RECEIVE AWARD [2009] COPYRIGHT PHOTO BY ATC-ASCE

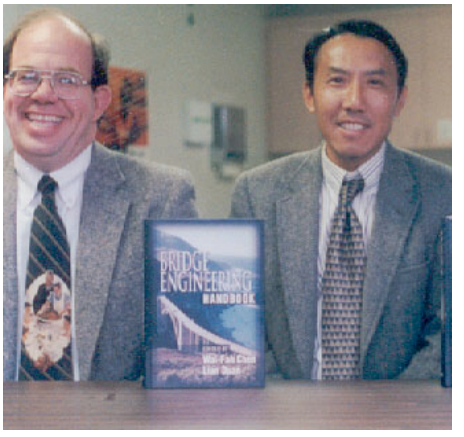


FIGURE 16 PECG ENGINEERS & HANDBOOK COPYRIGHT PHOTO BY A. MANGUS [1999]

A Caltrans Video "No was not an Answer" discusses the reconfiguration of the concrete approach spans in San Francisco for the San Francisco Oakland Bay Bridge. Interviews by District 4 [San Francisco Bay Area and District 59 [Engineering Services – Bridge Structures] Caltrans employees were filmed as a 59-minute documentary by District 4 employees of Caltrans [Copelan 2011].

ACKNOWLEDGEMENT

The authors wanted to thank all of the PECG History Committee Members and other PECG Members and leaders for their review of this paper. A second thank you to PECG for sponsoring the 2004 and 2008 ASCE www.orthotropic-bridge.org and other ASCE venues with the goal of sharing a great deal of very useful information. We also want to thank Mrs. Rita Bender permission to use photo of her late husband, Ostap Joe Bender. We also thank her of copyright release of his bridge photos to ASCE. For more info on Mr. Bender and images please contact her rifibend@comcast.net Mr. John Adam is a licensed Land Surveyor in California and active PECG Member. John's photos have appeared in engineering publications. Alfred R. Mangus was trained as a feature photographer at the Penn State Daily Collegian Newspaper and he has won a national honorable mention in student photo contest by Nikon Corporation with Nutshell Magazine. In closing the authors would like to thank the members of PECG who through their valuable public service provide safe and cost effective transportation on bridges, roads and related infrastructure across the state of California.

REFERENCES

[1] AISC, AISC Prize Bridges -1972, American Institute of Steel Construction pages 8 & 9, 1972 pp 33 [Toulumne River Bridge]
[2] Alden, Don, W., with Oram, Nancy, Eagan, Pat, Starkey, Helen, Rowe, Shirley, "Highway Recollections of James E Roberts", California Department of Transportation [Caltrans], April 26, 1999, pp 83
[3] Caltrans, Historic Bridges of California 1990 -189pages
[4] Copelan, C. Huang, C., Maggenti R. and Mangus, A., Documentaries As A Tool to Inform the Public About Major Infrastructure Projects in California, ASCE Structures Congress SEI , Las Vegas , Nevada 2011
[5] Davis, R. E., "Field Testing Of An Orthotropic Steel Deck Bridge, Vol., 1 and 2", *California Department of Public Works, Division of Highway, Bridge Department*, Sacramento, CA, 1968, 278 pp.
[6] Davis, R. E., Bender, O., "California Builds Experimental Orthotropic Plate Bridge", *Civil Engineering*, ASCE, Vol 34, No. 11, November 1964, pp 62-63.
[7] Dokken, Richard A., Salveson Matthew, "James E. Roberts – More than an Engineer's Engineer". ASCE Structure Magazine, Feb 2009, pp 48-49
[8] ENR "Cantilever Method to debut in US on box girder" Engineering News Record Magazine July 1, 1971 page 13
[9] Foley, E. R. and Murphy J. P., "World's Longest Orthotropic Section Feature of San Mateo-Hayward Bridge", *Civil Engineering*, ASCE, Vol 38, No 4, April 1968, pp. 54-58.
[10] Huang, C., Mangus, A., and Murphy J, (2005) Accelerated Bridge Construction Techniques for Large Steel Orthotropic Deck Bridges" FHWA ABC Symposium Dec. 15-16, at the Sheraton Hotel and Marina in San Diego
[11] Huang, C., Mangus, A., and Murphy J, (2006) "Easy As "ABC" ", *Structure Magazine, A joint Publication of NCSEA – CASE-SEI* October, pp 11 – 15
[12] Hurdle, W. C., "Meridian Bridge" Caltrans Office Of Structure Structures *Bridge Notes Vol. 21 –No. 1 1980 pages 1 to 6*
[13] Kempton, Will, Land, Richard, et al "James E. Roberts Memorial", California Department of Transportation, [Caltrans], DVD, July 14,2006, 59 minutes
[14] Mangus, A, (2005) "Fresh Look at Orthotropic Technology "Public *Roads*, United States Department of Transportation March / Washington D. C. · Vol. 70 · No. 3
[15] Mangus, A, and Shawn, S., (1999) "Chapter 14 Orthotropic Deck Bridges," *Bridge Engineering Handbook*, Chen, W.F., and Duan, L. Editors, CRC Press, Boca Raton Florida
[16] PCA , "Napa River Bridge, Napa California", Bridge Report, Portland Cement Association, 5420 Old Orchard Road Skokie Illinois [SR194.01E], 1977
[17] Pollard, B. , Benoit, J. M., and Pajouhesh D., "Safeguarding Bixby Bridge", *Civil Engineering*, ASCE, Vol. 70, No 1, January 2000, pp. 50-53.
[18] Roberts, James E., Dokken Richard A., *Golden Gate of the Motherload,* Modern Welded Structures, Volume VI, James F. Lincoln Arc Welding, Cleveland, OH, (1st Edition, Nov 1980) pp A-67 to A-70.
[19] Roberts, James E., "Effects of curing and falsework support periods on dead load deflections of reinforced concrete slab bridges: final report / prepared in cooperation with the U.S. Dept. of transportation, Federal Highway Administration" California Department of Highways [Caltrans], 1972,
[20] Roberts, James E.,, *Esthetics in concrete bridge design* / editors, Watson, Stewart C., Hurd, M. K., American Concrete Institute, 1990, 334 pp
[21] Roberts, James E., Maroney Brian "Chapter 40 Seismic Retrofit Practice", *Bridge Engineering Handbook*, 1St ed., Chen, Wai-Fah, Duan Lian Ed., CRC Press, Boca Raton Florida, 1999, pp 43.
[22] Roberts, James E., Maroney Brian, "Theory of California seismic bridge design and analysis for the beginner" (Division of Structures, California Dept. of Transportation, 1990, pp 33.
[23]Roberts, James E., "50-Years – Reflections of a Bridge Engineer, James E Roberts, Technical Advisor to the Director", The ESC = Engineering Service Center Education Committee, California Department of Transportation [Caltrans], DVD, QuickTime, March 14,2001, 58 minutes

[24] Wilson, Bill, "Nothing Earth-Shattering –Roebling Medal ", Roads & Bridges Magazine, August 2001, www.ROADSBRIDGES.com pp 24-25

[25]Wolchuk, R., (1963.)*Design Manual for Orthotropic Steel Plate Deck Bridges*, American Institute of Steel Construction, Chicago, IL.,

Documentaries as a Tool to Inform the Public about Major Infrastructure Projects in California

Authors:

Craig Copelan, PE , PECG, ccopelan95694@gmail.com
Alfred R Mangus, PE, PECG (916)-446-0400 Fax cell (916)-205-1962
MangusAlf@yahoo.com
Ric Maggenti, PE , PECG, PECG@PECG.ORG
Professional Engineers in California Government
455 Capitol Mall, Suite 501, Sacramento, CA 98514

INTRODUCTION

This paper will discuss four award-winning documentaries developed by Professional Engineers in California Government (PECG). These films are entertaining case histories of four major Caltrans construction projects that featured ABC = Accelerated Bridge Construction elements and show how entertaining and informative communication can inform the general public about major construction projects in their community and win the communities support. The organization PECG = Professional Engineers in California Government is union which represents 13, 000 + engineers and related classes of workers employed by the State of California, for more information see the orgainizations web site at www.PECG.org. The organization was formed in 1962 as a professional association in response to member's wishes to promote a positive image for public employees engaged in transportation engineering. The organization produced or provided technical support for each of the documentaries discussed in this paper as a part of that same mission.

THE BRIDGE SO FAR - A SUSPENSE STORY

—The Bridge So Far – A Suspense Story ‖ was the first of a series of documentaries developed by the union, Professional Engineers in California Government. The documentary in addition to discussing the technical issues that surround a major bridge project examines the interplay involved in the development of a transportation mega project within the heart of the busy metropolitan San Francisco Bay area. With a historical perspective that sweeps from the inception of the San Francisco Oakland Bay Bridge in the 1930's to the Loma Prieta earthquake in 1989 when a portion of the bridge collapsed, up to early 2006 and the beginning of bridge construction the documentary provides a rare insight into the workings behind the scenes of a major transportation structural engineering project. The documentary through the use of a humorous and interesting story line provides a

powerful and compelling look at how major engineering projects not only change the places we live but change the way we think about where we live and ourselves. With a scope that includes the collision of politics, community activism, and conflicts between local, state and the Federal governments the film provides entertainment value and a thought provoking message about the staccato steps in the journey a community follows in the development of a new, safe bridge that provides greater mobility for all modes of travel across the Bay between the cities of San Francisco and Oakland. Award winning filmmaker David Brown filmed and produced the entertaining story with all the drama, comedy, optimism, dashed hopes, and plot reversals that can only happen in real life. The 3-D animation was by Rick Pepper and cartoon animation by Charlie Canfield. Movie stills can be viewed at www.thebridgesofar.com/

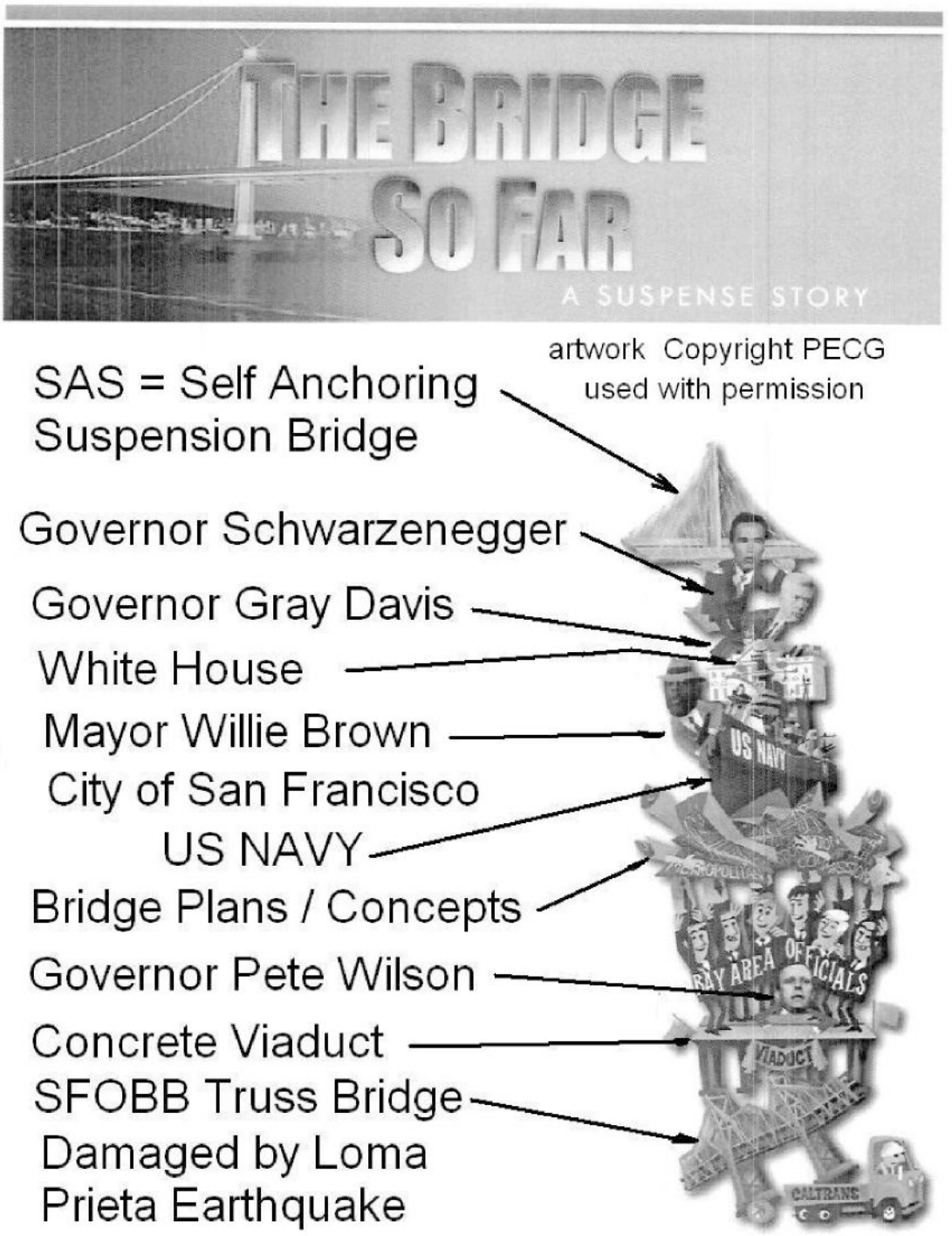


FIGURE 1 CALTRANS IS —CARRYING THE LOAD; MOVIE POSTER ART COPYRIGHT PECG = PROFESSIONAL ENGINEERS IN CALIFORNIA GOVERNMENT

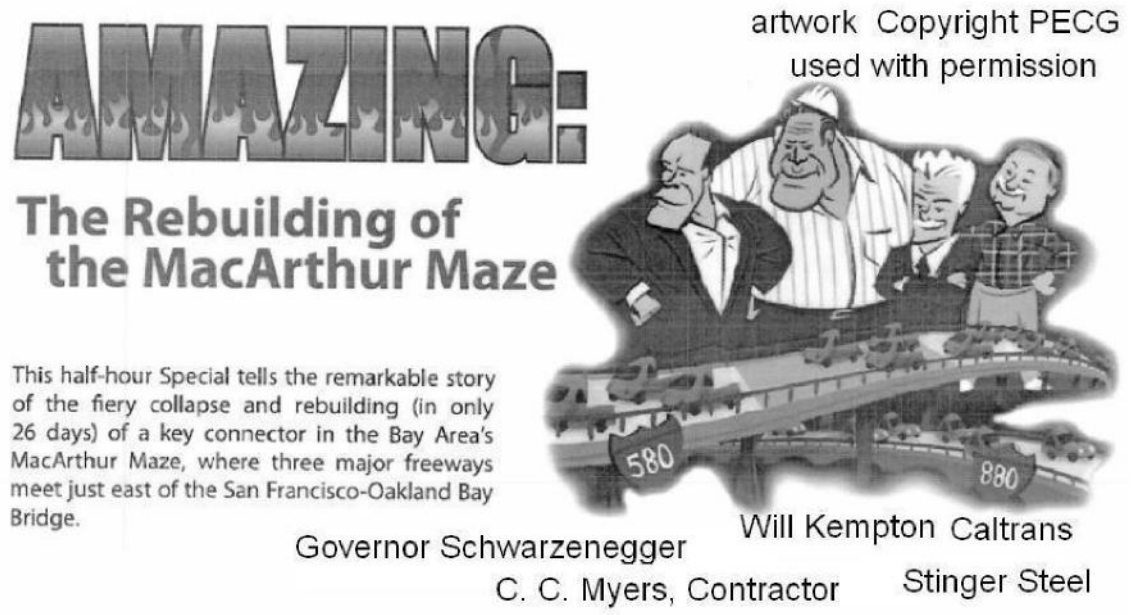
AMAZING: THE REBUILDING OF THE MACARTHUR MAZE

This documentary is destined to be a classic example of ABC Accelerated Bridge Construction. A success story if only for it's for its opening sequence which features the fiery collapse of a major freeway connector in downtown Oakland and then recreates the moments that led up to this conflagration with gripping animated sequences. The Interstate 80/580 connector at the MacArthur Maze links Oakland and San Francisco, on April 29, 2007, a tanker truck carrying fuel overturned, causing a fire to erupt. The heat from the flames caused a 160-foot-long, 45- feet-wide span of the ramp to collapse. With the sudden loss of a structure that serves as a key component in the regional transportation network the documentary begins to tally up the impacts that the loss of a busy thoroughfare which serves in excess of 100,000 vehicles per day and is a primary access point to the San Francisco Oakland Bay Bridge can have upon a city or a region. The cumulative costs in loss of mobility alone can be enormous and in turn justify the use of accelerated construction and emergency contracts with hefty contractor incentives for early completion of a state designed replacement structure to restore what is in essence a lifeline for the movement of goods, services and commute traffic across the San Francisco Bay. Within hours of the conflagration and bridge collapse, state staff met to set priorities, and within nine days of the incident, Caltrans opened the project for bids advertising the project with a $200,000 incentive for each day of completion ahead of schedule. The project had another clause stating that the contractor would be fined $200,000 a day for every 10-minute delay in opening each lane closure. These clauses had a cap of $5 million. The contractor, C.C. Myers, completed the project on May 24, 2009—within an amazing 25 days, earning Myers the full $5 million incentive. The film references previous successful accelerated construction efforts orchestrated by Caltrans after the Northridge earthquake in Los Angeles to quickly replace a major collapsed freeway connector where due to a state of emergency environmental requirements were temporarily put on hold and a contractor was provided with incentives to build a replacement structure designed by the state as quickly as possible with strict oversight provided by state engineering staff to ensure that the final product was built as designed, and would provide the taxpayers with a serviceable and safe replacement structure. This film communicates well the sense of urgency felt by all involved to restore this damaged link in the transportation network quickly and details how incentives are used to provide a contractor with encouragement to complete the job of bridge repair and replacement on an expedited schedule. The contractor Mr. C. C. Myers is featured to good effect throughout the video as he takes an active role in procuring materials, arranging for shipment from locations across the US and works with Caltrans to overcome barriers encountered. The film also does a good job of relaying the sincerity and dedication of the public servants at work in a tense situation.

An enduring testimonial to the value of accelerated construction which features incentives for contractors speeds the contracting process and provides strong engineering oversight by capable state engineering staff was provided in Governor Arnold Schwarzenegger's State of the State Address Tuesday, January 8, 2008.

In April, a fiery truck crash melted the Bay Area's 580 freeway exchange. Hundreds of thousands of Californians who depended on that interchange foresaw months of delays and stress. Yet it didn't take the normal 150 days to repair. Caltrans, working with contractors, cleared the span in 10 days and then built a new bridge and opened it up in a record 16 days later. Government can work. It can be efficient. It can lead."

Movie clips may be viewed at http://www.amazingmaze.org/



prefabricated replacement span. The planning and timing of this work was critical with all construction scheduled to start and complete within Labor Day weekend 2007 with the structure scheduled to reopen for morning commute traffic. The story is told from the perspectives of the contractor the legendary Bay Area figure C. C. Myers, dedicated Caltrans engineers and designers, as well as by reporters who covered the story. The technical details are instructive in this documentary and there is a time lapse sequence that should be a part of any college course that discusses the use of accelerated construction. The project moves smoothly and completes 11 hours ahead of schedule, the documentary makes this a captivating experience that illustrates how all involved must work together to make ABC = Accelerated Bridge Construction work. Award winning filmmaker Movie clips may be viewed at http://www.aspanintime.com/



FIGURE 3. MOVIE POSTER ART COPYRIGHT PECG = PROFESSIONAL ENGINEERS IN CALIFORNIA GOVERNMENT

REBUILDING THE BOAT: FIXING I-5 IN SACRAMENTO REBUILDING THE BOAT: FIXING I-5 IN SACRAMENTO

This documentary follows a construction rehabilitation project located on a busy urban section of I-5 Freeway which follows a depressed alignment through downtown Sacramento California blocks from the State Capitol. Originally conceived as a conventional construction project with lane closures planned for

extended periods, accelerated construction is considered and utilized to reduce construction times and delays for traffic on this key arterial which carries 190,000 vehicles per day. Repair plans were placed out to competitive bidding. General Contractor C. C. Myers was the low bidder and proposed an AC = Accelerated Construction solution as a cost savings under the contract provisions. Myers' revised ABC plan was to reduce construction time from the maximum allowed of 305 days to 34 days total. Caltrans agreed to Myer's ABC Plan and put in place efforts to alert the public about freeway closures and the rerouting of traffic necessary to successfully complete the project. Movie clips may be viewed at http://www.kvie.org/programs/kvie/viewfinder/rebuildingtheboat/

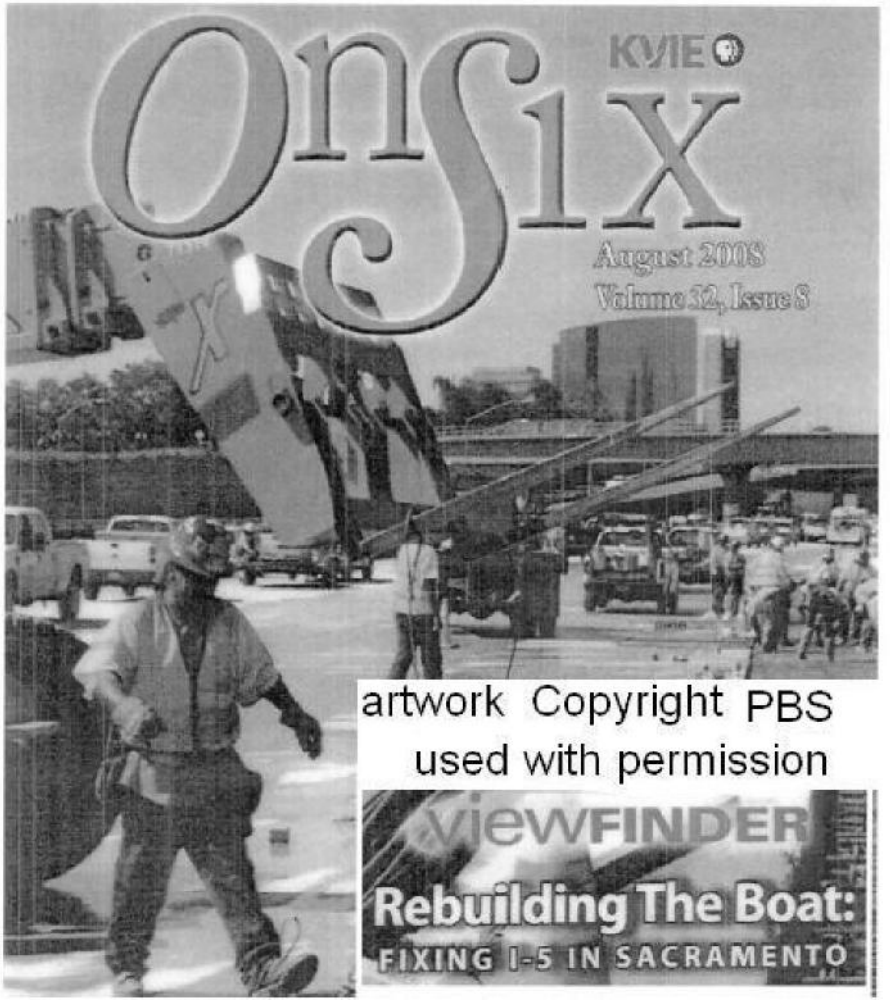


Figure 4. Movie Poster Art copyright PBS = Public Broadcasting System Channel 6 KVIE

THE NEXT FRONTIER: ENGINEERING THE GOLDEN AGE OF GREEN

The Next Frontier: *Engineering the Golden Age of Green* a documentary that focuses on proven renewable, clean civil engineering energy technologies that can improve our future and create a healthier place to life. This film, 56:46 long, is an

entertaining documentary which takes the viewer around the world in search of technologies and policies that will address the serious problem of excessive carbon dioxide emissions and our dangerous dependence on fossil fuels. Successful solutions for Geothermal, Solar, Tidal, and Wind were featured with operators/ users of the technology interviewed by ABC's Good Morning America's Becky Worley. Without the general public's support these technologies will not continue to be expanded, design and built. The documentary informs and simultaneously entertains with film of construction, interviews of key individuals, satirical cartoons and animated graphic of principals and techniques. A successful Tidal power generation in Ireland is featured is movie. The owners' representative and fisherman are interviewed and are pleased with this green coastal energy solution. Wind and solar examples shown are applicable to coastal sites and communities in California or elsewhere. These buildings and alternative energy support facilities require structural engineering design, plus other civil engineering professionals. Movie clips may be viewed at www.thenextfrontiermovie.com/

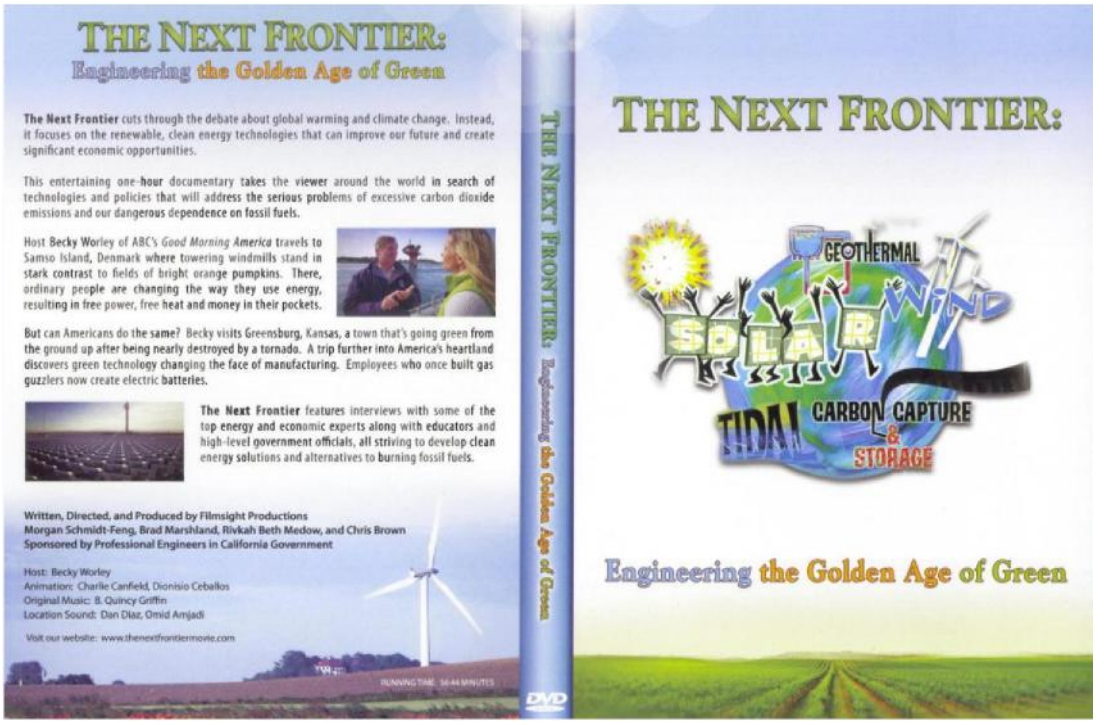


FIGURE 5. THE FIFTH MOVIE OR DVD JACKET'S BACK AND FRONT COVERS. ARTWORK COPYRIGHT AND COURTESY OF PECG

CALTRANS PRODUCED VIDEOS

Caltrans produced documentaries include the —*The Bridge* a construction account of the award winning Pine Valley Bridge. Another Caltrans produced Documentary with companion book Caltrans (2004), —Spanning the Carquinez Strait - The Alfred Zampa Memorial Bridge ‖ , California Department of Transportation Sacramento, CA, 2003 [35 minutes] documents the Alfred Zampa Memorial Orthotropic Suspension Bridge in Crockett-Vallejo California on west bound interstate I-80 [Figure 6]. This was the first aerodynamic orthotropic wing shaped suspension bridge completed in 2003. Contact www.dot.ca.gov/hq/esc/CHPC/historylinks.html the CHPC Caltrans History and Preservation Committee for copies of the booklet and CD-ROM.

A third Caltrans Video —No was not an Answer ‖ discusses the reconfiguration of the approach spans in San Francisco for the San Francisco Oakland Bay Bridge. Interviews by District 4 [San Francisco Bay Area and District 59 [Engineering Services – Bridge Structures] Caltrans employees were filmed as a 59-minute documentary by District 4 employees of Caltrans. A world class bridge crossing in San Francisco Bay for the new East Span portion. Streaming video clips narrated by Caltrans spokesman Bart Ney are available at www.baybridgeinfo.org/ A unique SAS = Self Anchoring Suspension Bridge with an orthotropic superstructure is featured.

CONCLUSIONS

The use of documentaries developed by the Union or Bargaining Unit # 9 Professional Engineers in California Government to highlight the excellent and cost effective Civil Engineering Design and oversight provided by public servants working in the taxpayers interest has been very effective. A successful public education effort by any measure with each of the documentaries receiving broad critical acclaim and distribution through the Public Broadcasting System, of particular note is the documentary ***A Span in Time*** which was recognized with two Emmy Awards.

ACKNOWLEDGEMENT

The authors wanted to thank the leadership of PECG, PBS Channel KVIE of Sacramento and the participants of these projects who shared a great deal of very useful information in and about the documentaries described in this paper. We also want to thank PECG for being a sponsor and the ASCE Structural Engineering Institute of the 2004 and 2008 conferences www.orthotropic-bridge.org/ We would also want like to thank Caltrans for granting reasonable access of Caltrans Copyrighted documents to PECG.

References

BROWN, DAVID, DIRECTOR, DVD, 59 MINUTES, "THE BRIDGE SO FAR, A SUSPENSE STORY ‖ HTTP://WWW.THEBRIDGESOFAR.COM PROFESSIONAL ENGINEERS IN CALIFORNIA GOVERNMENT MEDIA, 455 CAPITOL MALL, SUITE 501 SACRAMENTO, CA 95814 www.thebridgesofar.com/

Brown, David, Director, DVD, 29 MINUTES, "Amazing: the Rebuilding of the MacArthur Maze http://www.amazingmaze.org PROFESSIONAL ENGINEERS IN CALIFORNIA GOVERNMENT MEDIA, 455 CAPITOL MALL, SUITE 501 SACRAMENTO, CA 95814

Brown, David, Director, DVD, 29 MINUTES, "A Span in Time" http://www.aspanintime.com/ PROFESSIONAL ENGINEERS IN CALIFORNIA GOVERNMENT MEDIA, 455 CAPITOL MALL, SUITE 501 SACRAMENTO, CA 95814DVD, 29 MINUTES"

The Effects of Deteriorating Bridges on Bridges on the Bridge Network Connectivity

Keivan Rokneddin[1], Jayadipta Ghosh[1], Jamie E. Padgett[2], Leonardo Duenas Osorio[2]

[1]Graduate Research Assistant, Department of Civil and Environmental Engineering, Rice University, 6100 Main Street, MS-318, Houston, TX 77005; E-mail: keivan@rice.edu

[2]Assistant Professor, Department of Civil and Environmental Engineering, Rice University, 6100 Main Street, MS-318, Houston, TX 77005; PH: 713-348-2325; E-mail: jamie.padgett@rice.edu

The Effects of Deteriorating Bridges on Bridges on the Bridge Network Connectivity

Evaluation of the seismic reliability of aging transportation networks traditionally ignores the deteriorating state of highway bridges. In this study, the present day seismic reliability of bridges in an existing highway network has been evaluated through a time-dependent seismic fragility analysis. An efficient Monte Carlo based algorithm is used to evaluate the network-level reliability of the aging highway bridges without the need to simplify the network layout or change its topology. The criticality of aging bridges is then assessed through different ranking strategies proposed in this study to arrive at an optimized seismic retrofit schedule. The methodology is implemented in a case in the state of South Carolina under a seismic scenario and the proposed ranking strategies are compared to the state of practice methods.

INTRODUCTION

At present more than 26% of highway bridges in the US are either labelled as structurally deficient or functionally obsolete (ASCE 2009) and also a significant percentage of highway bridges are located in regions of moderate to high seismicity (FHWA 2009). Such deteriorating and seismically vulnerable bridges are also a threat to the performance of the transportation network and hence there is an increasing need to quantify such risks to assess network level performance. However, latest studies for aging bridge reliability estimates only considers seismic threats to individual structures without any proper means to integrate into a network level reliability framework to assess the vulnerability of aging transportation networks. Few methodologies exist in literature for reliability assessment of complex transportation networks although they do not take into consideration the effects of aging and deterioration of highway bridges (Liu & Frangopol 2006; Kiremidjian et al. 2007; Ching & Hsu 2007; Fan et al. 2010; Todinov 2007). More recently, (Lee et al. 2010) estimated bridge network reliability by accounting for deteriorated bridge performances of a few structurally similar bridges with corroding bridge columns. In reality, however, transportation networks consist of large number of structurally and geometrically dissimilar aging

bridges with multiple aging components under different exposure conditions (Silano & Brinckerhoff 1993; Hoeke et al. 2009).

The primary objective of network level reliability assessment of transportation systems is to evaluate the probability that the system maintains its functionality over a certain time span. The adapted criterion to assess the functionality in this paper is reachability; i.e. the ability to reach a set of destination nodes in the network starting from the set of origin nodes. There are a few methodologies in the literature to approach such O-D connectivity reliability problem (e.g. [1](; Ching & Hsu 2007; Todinov 2007). A methodology based on crude Monte Carlo simulations (Todinov 2007) has been adapted in this research for network reliability framework for its simplicity and efficiency in applying to large transportation networks. The multiple component deterioration of different bridge categories in a transportation network may readily be integrated into this network reliability approach to evaluate the network level reliability of the transportation system. The fragility of non-bridge segments of a transportation system (highways) may also be considered in the presented network reliability framework; however, such fragilities are negligible compared to the bridge fragilities under seismic events and are therefore not evaluated in this research. The reliability assessment of aging transportation networks is aimed at identifying the most critical bridges in the network and proposing an optimized seismic retrofit schedule. State of the practice to rank bridges following the Seismic Retrofit Manual (Buckle et al. 2006) falls short of taking the topology and system-level reliability of the network into consideration. To address those shortcomings, four other bridge ranking strategies are introduced in this research. The network reliability framework is illustrated in a case study on the bridge network of Charleston, South Carolina, and the performance of the proposed bridge ranking strategies are compared to the current state of the practice.

BRIDGE DETERIORATION MECHANISMS

Aging mechanisms of bridges are highly dependent on the bridge type and proximity and severity to the source of deterioration. Based on proximity to the sea coast, two distinct cases of marine corrosion exposure are considered in the case study: atmospheric and splash. Additionally, the aging mechanisms considered in this study include deteriorations of critical bridge components such as reinforced concrete (RC) columns and bridge bearings. A primary form of deterioration to steel components exposed to the atmosphere is sectional area loss due to corrosion and is found to affect the reinforcing steel in RC columns and anchor bolts and dowel bars in bridge bearings. A vast amount of literature exists on the corrosion deterioration of steel embedded in concrete and regarded as a typical diffusion problem in which the time to initiate corrosion under marine chloride exposure can be expressed as (Bertolini et al. 2004):

$$T_i = \left[\frac{x^{d^2}.R_{cl,0}}{4.k_c k_e.(t_0)^{cl}} \left\{ \text{erf}^{-1}\left(1 - \frac{c_{cr}^d}{c_{s,cl}^d}\right) \right\}^{-2} \right]^{\frac{1}{(1-n_{cl})}} \quad (1)$$

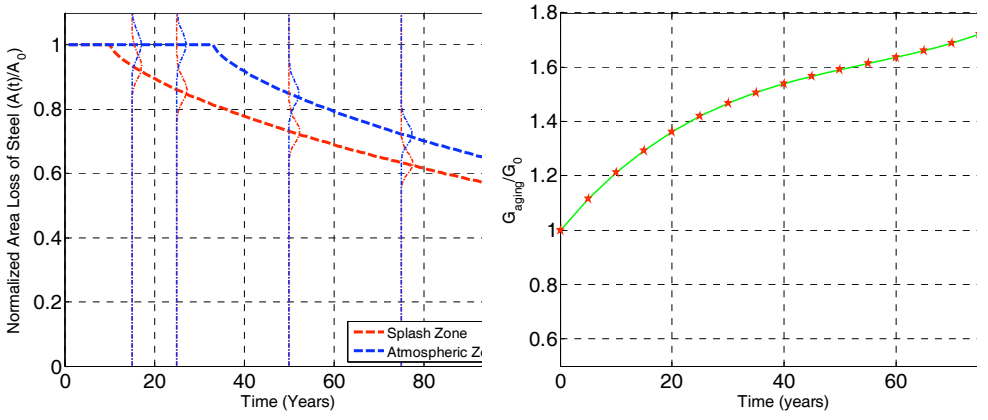
where, x^{d^2} is the design value of cover thickness, $R_{cl,0}$ is the chloride penetration resistance (inverse of diffusion coefficient) determined from compliance tests, k_c is the curing factor, k_e is the environmental factor, t_0 is the

age of concrete when the compliance test is performed, n_{cl} is the age exponent that incorporates the densification of cement paste due to further hydration, c_{cr}^{d} is the design value of surface chloride content, $c_{s,cr}^{d}$ is the critical chloride content beyond which corrosion initiates and erf is the Gaussian error function. Following the corrosion initiation, a time dependent corrosion rate can be assumed following the suggestions by Vu and Stewart (2000) as:

$$i_{corr}(t) = 0.85 i_{corr,0}(t - T_i)^{-0.29} \quad (2)$$

where $i_{corr,0}$ is the corrosion rate at time $t = 0$ years that can be calculated from the water cement ratio in concrete and the reinforcement cover depth (Bertolini et al. 2004; Vu et al. 2005). The impact of severity of exposure condition as mentioned earlier on the deterioration process is shown in figure 1a which depicts the normalized area loss of steel along the service life of the bridge.

While equations 1 and 2 as given above helps to predict the area loss of steel in steel members, often the build up of corrosion debris hinders the free movement of steel bearings leading to potentially 'frozen' bearings with a reduced performance to resist lateral loads during earthquakes. This increase in friction due debris accumulation is assumed to increase from 0.04 to 0.12 at the end of the 75 year bridge service life based on the suggestions of Mander et al. (1996). Additional deterioration mechanisms considered include the increase in shear modulus of elastomeric bearing pads following the model proposed by Itoh and Gu (2009) as shown in figure 1b.



(a) (b)

Figure 1: a) Normalized mean and variance of area reduction of steel reinforcement under different marine exposure conditions and b) Increase in shear modulus of elastomeric bearing pads with aging sue to thermal oxidation.

RELIABILITY ASSESSMENT OF BRIDGE NETWORK

The network level reliability of a transportation system is the probability that the system maintains its functionality under a given seismic event. The functionality in the context of this research is defined as the ability to reach a set of destinations from a set of origins in the network. The connectivity between origin and destination nodes may be lost if enough bridges reach a damage state that involves structural failure or requires temporary closure for inspection/repair to lose all the existing routes from origin to destination nodes.

Some studies have used conventional reliability methods that applicable to sets of parallel and series sub-systems to investigate the reliability problem in transportation systems. Although those methods provide a quick estimate of the network reliability, they may not be realistic enough in large complex networks in which their application requires a lot of simplifications to the topology of the network. A number of Naive Monte Carlo simulation (MC) methods are applicable to solve the described connectivity reliability problem in complex networks without the need for any simplification in the network topology. Another advantage of MC based methods is their capability in considering multiple (O, D) pairs (Ching & Hsu 2007). Since there is often more than one (O, D) pair in real transportation networks, having this capacity is of paramount importance in the network reliability assessment.

The probability of failure of network components is provided as input in any network reliability analysis. MC based methods may incorporate both node (bridge) and link (non-bridge segment of highways) failures in network reliability assessment. In this research, however, the probability of failure of non-bridge components are considered negligible compared to that of the bridges in a seismic event. Therefore, only bridges are assigned a probability of failure in the network. Moreover, only the probability of reaching a certain structural damage state is considered as a failure criterion in bridges. Failure of the network components due to traffic overflow may also be integrated in the model, but such integration involves solving a dynamic traffic assignment problem at each Monte Carlo simulation step which adds significant computational complexity to the network reliability problem. Considering failure due to traffic congestion is on the agenda for future development of this research.

Figure 2 depicts a portion of the bridge network in the county of Berkeley, SC with the identified bridges in the network shown on the map. In network theory, the order of the network is defined as the number of the nodes in the network and is often denoted by n; while the number of the links among the nodes is referred to as the order of the network (m). The depicted bridge network is comprised of 18 bridges with nodes 8 and 6 serving as Origin and Destination nodes, respectively. There are more links connecting the bridges in the network than the minimum number required to maintain the (O, D) connectivity. The existing redundancy in the network provides higher level of reliability since the network may sustain its connectivity in case some of its components lose functionality.

Since the topology of the network cannot be reduced into series and parallel subsets, the conventional network reliability methods for series-parallel systems are not applicable. Nevertheless, combining the components in series or parallel subsets helps to reduce the ultimate computational demand in solving the network reliability problem using Monte Carlo simulations based methods. The naïve Monte Carlo simulation method, referred to as MC hereafter, is illustrated in this section. This approach requires finding the shortest path between Origin and Destination nodes at each round of Monte Carlo simulation based on algorithms such as Dijkstra (Dijkstra 1959). For a single (O, D) pair, each round of Monte Carlo simulation involves a computational complexity of $O(m2.n2.\log(n))$ in this method.

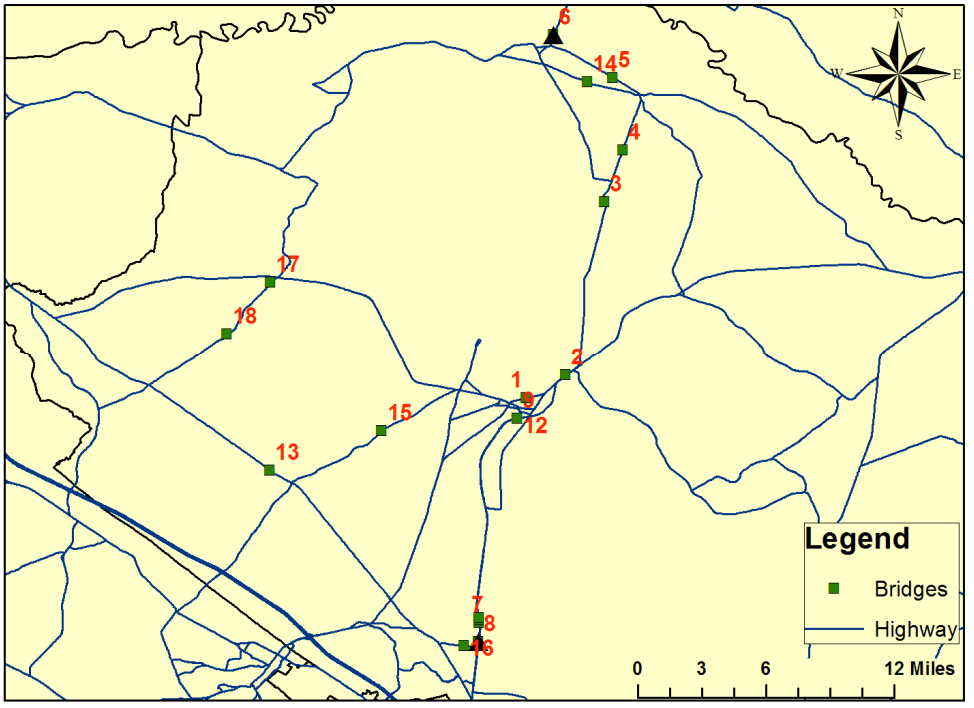


Figure 2: Portion of the bridge network in Berkeley county, SC. The nodes define the location of the identified bridges in the network. Nodes 32 and 27 denote the Origin and Destination nodes, respectively and are shown by dark triangle marks in the figure.

The pseudo-algorithm for MC is brought in Table 2. The bridge reliabilities (one minus probability of reaching the moderate damage state) are stored in a vector (b). At each round of Monte Carlo simulation, a vector of the same size as b (named z) is generated comprising uniformly distributed random numbers in [0, 1]. The values in vectors b and z are compared for each node, and the bridge is assumed to fail in case zi > bi, i being the bridge index. A search for shortest path between Origin and Destination nodes is then performed based on Dijkstra algorithm. An indicator function I[·] stores the cases in which the connectivity is lost in the network. Averaging the indicator function over the number of Monte Carlo simulations (NMC) results in the reliability of the network for the specified (O, D) pair (Todinov 2007).

Table 1: Pseudo-Algorithm for MC reliability method

Procedure MC

Store bridge reliabilities in $\boldsymbol{b}_{n\times 1}$

for $i = 1: N_{MC}$

Generate $\boldsymbol{z}_{n\times 1}$ such that $z_i \in [0\ ,1]$ (Uniformly distributed random number)

Bridge Index(i) = max{0, 1-$\boldsymbol{z}_i/\boldsymbol{b}_i$}

Mark Bridge *i* as failed if *Bridge Index(i) = 0*

Run *Dijkstra (O, D)* to find the shortest path between Origin and Destination nodes

I[·] = 1 if the shortest path is infinite; 0 otherwise

end

$$P_{OD} = \frac{1}{N_{MC}} \sum_{i=1}^{N_{MC}} \mathrm{I}[\cdot]$$

BRIDGE RETROFIT SCHEDULE AND RANKING STRATEGIES

Bridge ranking strategies help to identify the most critical bridges in the chosen network. Traditionally, ranking strategies of bridges are based on the state-of-the-practice methodologies, such as the strategies outlined in the Seismic Retrofitting Manual for Highway Structures (Buckle et al. 2006). In this study, in contrast to state-of-the-practice methodologies, new ranking strategies are proposed that account for topological aspects of the network. These are elaborated in the following sections.

State of the practice methods based on the Seismic Retrofitting Manual for Highway Structures (Buckle et al. 2006)

The state-of-the-practise methodologies can be categorized into two different methods in the increasing order of complexity: Indices Method and the Expected Damage Method. The Indices Method assigns a rank between 0 to 100 to each bridge following an assessment of structural properties of the bridge, seismicity of the region and other socio-economic factors. The Expected Damage Method is mostly based on the cost of repairing the bridge following seismic damage and incorporates the concepts of fragility curves. These reliability curves were however developed for general bridge classes using nonlinear static analysis and without considering the effects of deterioration.

Rankings Based on Network Topology

The seismic retrofit manual emphasizes the significance of network topology in ranking bridges in transportation systems. However, it falls short of providing an explicit approach to account for the topology of network. Two topological metrics are used in this study to incorporate the topology to rank the bridges in a network. *Betweenness Centrality* (*BC*) has been extensively used in the literature since it is considered as a proxy to simulate flow (traffic in case of transportation systems) in complex networks. The *BC* of a given node in the network is defined as the number of geodesic paths passing through that node:

$$BC(i) = \sum_{s,t} n_{st}^{i} \quad (9),$$

where *s* and *t* are pairs of origins and destinations in the network and n_{st}^{i} is an indicator function assuming the value of 1 if node *i* is on the geodesic path from *s* to *t* and zero otherwise. Geodesic path is defined as the shortest path between two nodes in terms of the number of links. Calculating *BC* in a network involves identifying the geodesic paths between all *(O, D)* pairs.

Eigenvalue Centrality (EC) is giving importance to nodes in a network based on the number of their connections and their neighboring nodes. Therefore, nodes directly connected to important nodes are considered more important in this method. The EC vector (X) which includes the value for all the nodes in a network is derived from Equation 10:

$$X = \lambda^{-1} \cdot A \cdot X \quad (10),$$

Where *A* denotes the Adjacency Matrix representing the topology of the network and λ represents the largest eigenvalue of the Adjacency Matrix. Vector *X* from Equation 10 can be computed recursively.

Betweenness Centrality and Eigenvalue Centrality are purely defined based on the network topology and do not take the vulnerability of bridges into account. Therefore, they are not as comprehensive as ranking based on the network reliability method which incorporates both aspects.

Ranking Based on Network Reliability

The MC approach for network reliability evaluation leads to a ranking based on the correlation of failure of individual bridges in the network with the failure in network connectivity. A bridge is deemed more important if its failure is more likely to result in the network connectivity failure. The importance index r, therefore, is defined to account for this conditional probability:

$$r = P(F_{OD}|f_i) \quad (11)$$

where F_{OD} is the event that the connectivity between the *(O, D)* pairs is lost, and f_i is the event that bridge *i* fails (reaches moderate damage state). Obviously, *r* is a probability and therefore varies in *[0, 1]*. Larger *r* values denote more critical nodes.

Ranking based on network reliability takes both network topology and bridge vulnerabilities into account which makes it computationally more expensive. However, its computational complexity is still polynomial in the form of $O(N_{MC}.m^2.n^2.log(n))$.

The described ranking strategies are applied to the bridge network of South Carolina and the rankings are compared next.

Application to the Case Study Network

The proposed time-dependent fragility analysis of aging bridge classes and the network reliability method are applied to the case study network in Figure 2. The described ranking strategies are then applied to identify the location of most critical bridges in the network.

The development of the time-dependent fragility curves and subsequent network reliability analysis requires defining a seismic scenario for the study. The historical seismic events in the region show a pattern of large far in between earthquakes (Padgett et al. 2010). The seismic event with 10% probability of occurrence in 50 years has been adapted for this study based on the seismic deaggregation map of the region, which refers to a magnitude $M_w = 7.3$ event. The historical seismology of the region also suggests a depth of 18 km for the identified seismic event (USGS 2010). Figure 3 shows the PGA contours for the defined scenario event obtained from HAZUZ-MH using western US shallow crustal event for attenuation model. The mean value within each contour is used as the base PGA level to develop the non-linear bridge fragility curves. The bridges in the network are classified by material and construction type using the described strategy. Data from National Bridge Inventory (NBI) has been used to identify bridge characteristics such as the year of construction (to aid in determining the deteriorated present day fragility curves), skew angle, and number of spans for each bridge in the network. The fragility curves

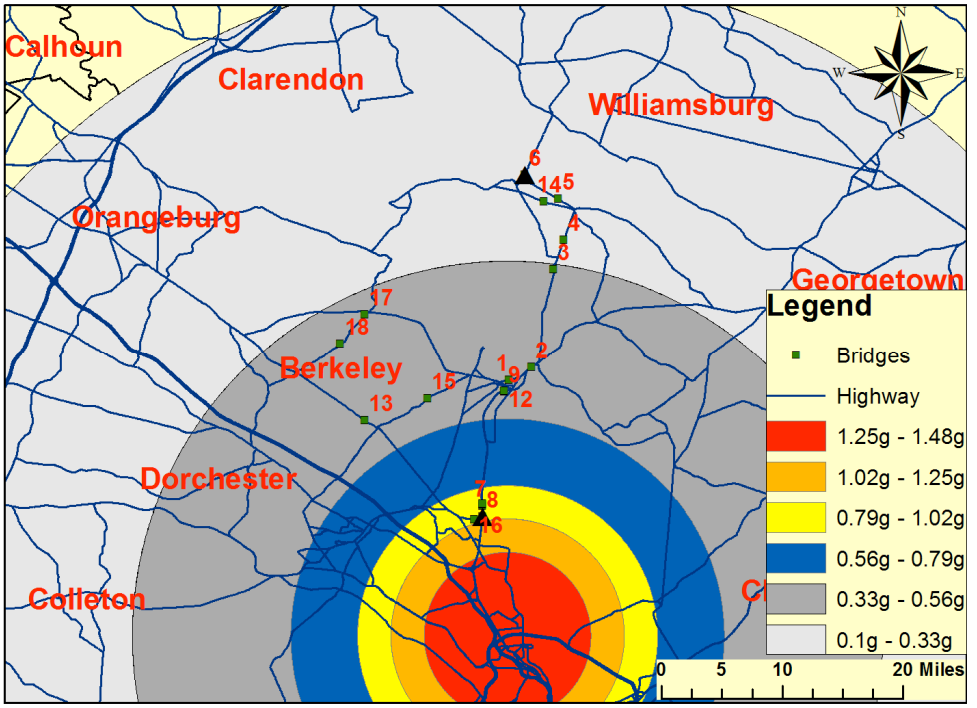


Figure 3: The PGA level contours for the defined seismic scenario

Time dependent fragility curves for aging bridges

An efficient way to quantify the effects of deterioration on the seismic vulnerability of an aging bridge is to evaluate the time dependent vulnerability following the methodology outlined in (Ghosh and Padgett 2010). The general expression representing the time dependent fragility of bridges can be represented as:

$$P[LS(t)|IM] = \Phi\left[\frac{\ln(IM) - \ln\left(med\,(t)\right)}{disp(t)}\right] \quad (3)$$

where, P[LS(t)|IM], is the probability of exceeding limit state LS, conditioned upon a given intensity of ground motion (IM), $\Phi(\cdot)$ is the standard normal cumulative distribution function, and med(t) and disp(t) are the median value and logarithmic standard deviation of the fragility function at time t in the service life of the bridge system. The time dependent fragility parameters, $med(t)$ and $disp(t)$, can be obtained following nonlinear dynamic analysis of the finite element model of the bridge at different times in the service life of the bridge.

For the network under consideration, Table XX shows the type of each bridge, their respective years of construction and the comparison of bridge fragility parameters of the present day bridge to its initial pristine state.

Bridge No.	Bridge Type	Year of Construction	Fragility Parameters (Pristine Bridge)		Fragility Parameter (Present Day Bridge)	
			$med(t)$	$disp(t)$	$med(t)$	$disp(t)$
1	MSSS Concrete Girder	1936	0.42	0.63	0.34	0.56
2	MSC Steel Girder	1944	0.26	0.62	0.25	0.55
3	MSSS Steel Girder	1996	0.30	0.49	0.29	0.48
4	MSC Slab	1997	0.73	0.86	0.73	0.86
5	MSSS Concrete Girder	1983	0.37	0.62	0.36	0.62
6	MSSS Slab	1999	0.56	0.71	0.57	0.71
7	MSSS Concrete Girder	1922	0.63	0.62	0.57	0.62
8	MSSS Concrete Girder	1922	0.63	0.62	0.57	0.62
9	MSSS Concrete Girder	1971	0.51	0.63	0.49	0.58
10	MSSS Slab	1971	0.60	0.71	0.62	0.70
11	MSSS Slab	1971	0.60	0.71	0.62	0.70
12	MSSS Concrete Girder	1971	0.51	0.63	0.49	0.58
13	MSSS Concrete Girder	1938	0.53	0.62	0.48	0.62
14	MSSS Concrete Girder	1983	0.37	0.64	0.36	0.62
15	SS Concrete	2001	2.41	1.00	3.07	1.04
16	MSSS Slab	1966	2.04	0.98	2.05	0.97
17	SS Concrete	1999	2.41	1.00	3.17	1.05
18	SS Concrete	1999	2.41	1.00	3.17	1.05

MSC = Multi-span continuous, MSSS = Multi-span simply supported, SS = Simply Supported

A close observation shows that the most fragile bridges whether in the pristine or aging condition of the network are the MSC Steel and MSSS Steel bridge with the two lowest median value as compared to all bridges in the network. From the

change in their median values however, it can be seen that these two bridges are however not the ones most affected by the effects of deterioration. Aging effects are found to be most predominant for the MSSS Concrete bridges which show the highest percentage changes in median values and hence an increase in the bridge probabilities of failure. For instance bridge numbers 1, 7, 8 and 13 shows a 19%, 11%, 11% and 9% change in bridge failures. A comparison of the time dependent fragility curves for the MSSS Concrete bridge number 1 is shown in figure XX for the pristine bridge at year 1936 and the present day bridge. The multi-span bridges that are least vulnerable to seismic events are the MSSS Slab bridges. It is also seen that the median value of this bridge type (bridge number 16) also increases with age. The same is observed in case of the simply supported bridges. The reason behind this phenomenon is that for certain type of concrete bridges, thermal oxidation of the elastomeric bearing pad increases the lateral stiffness of the bearing and consequently reduces the seismic vulnerability of the bridge. However the increase in median value for the multispan slab bridge is not as dramatic as the single span bridges because of the influence of degrading bridge columns.

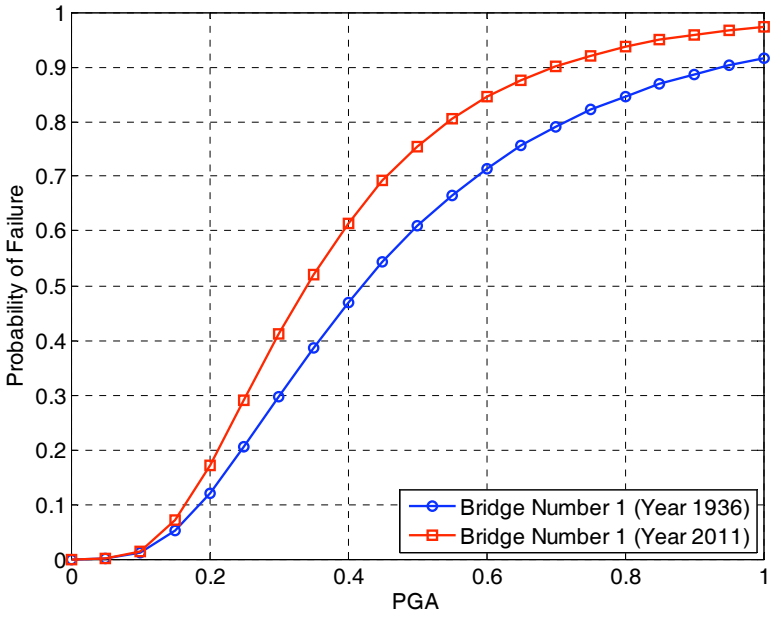


Figure XX: Pristine and deteriorated fragility curves for aging MSSS Concrete girder bridge number 1.

Bridge Network Reliability

The defined seismic scenario and the developed time-dependent fragility curves are employed to evaluate the connectivity reliability of the network depicted in Figure 2. The probabilities of reaching the moderate damage state is used as the failure criteria for the bridges in the network and serve as input to MC reliability method (Table 4).

Table 4: Probabilities of Failure for the Bridges in Figure 2

Bridge ID	Probability of Failure
1	0.679

2	0.859
3	0.802
4	0.077
5	0.207
6	0.086
7	0.777
8	0.777
9	0.440
10	0.705
11	0.705
12	0.440
13	0.450
14	0.209
15	0.032
16	0.201
17	0.030
18	0.030

Following the MC procedure results in a probability of failure of 0.909 (N_{MC} = 1,000,000) for the specified Origin and Destination nodes in Figure 2. The high probability of network failure is associated with the high number of bridges that lie in between nodes 8 and 6. The calculated high probability of network failure is consistent with the fact that most bridges in the network have a relatively high probability of failure and taking into account the number of bridges that lie in between nodes 8 and 6.

Bridge Ranking Strategies

The described different ranking strategies have been employed to identify the critical bridges in the understudy network. Table 5 compares the top five ranked bridges from different strategies. It is clear that while the two state of the practice methodologies result in generally consistent rankings, their results differ from the developed ranking methodologies. The location of critical bridges are also identified on the map of region in Figure 7.

Table 5: Top five ranked bridges in the case study network. Numbers indicate the Bridge ID within the network.

Rank	State of the practice methodologies		Developed Methodologies		
	Indices Method	*Expected Damage Method*	*Eigenvalue Centrality*	*Betweenness Centrality*	*Network Reliability Method*
1	5	5	2	2	6
2	2	14	14	1	8
3	1	2	5	16	16
4	9	1	4	17	17
5	12	9	12	12	13

Both the indices method and the expected damage method adopted from the state of the practice are highly qualitative methods. Based on discrete values of vulnerability ratings for the different bridge components, the top five bridges tied at maximum R = 48.7. The expected damage method depends on the replacement cost of the bridge and hence the number of units in the main span of the bridge. Accordingly, the top bridges as per this strategy are characterized by large number of spans (for example, bridges 5 and 14 have 10 and 11 spans, respectively).

The two topological ranking strategies share two bridges in the top five ranking despite using different concepts. The location of those two nodes, therefore, is critical in the network topology.

The network reliability method is the most comprehensive of the three developed ranking strategies since it takes into account the topological formation of the network as well as individual bridge vulnerabilities. Bridges 6 and 8 are the most critical nodes in network reliability method since survival of Origin and Destination nodes are essential for maintaining connectivity in the network. The other critical bridges are located on the perimeter of the network since the path directly connecting Origin and Destination nodes requires passing through more bridges that are also exposed to higher PGA levels. Therefore, it is likely over each step of Monte Carlo simulations that the connectivity on the direct path is lost while the indirect path maintains connectivity. As the result, the importance index *r* (Equation 10) tends to give higher values to the bridges on the indirect path.

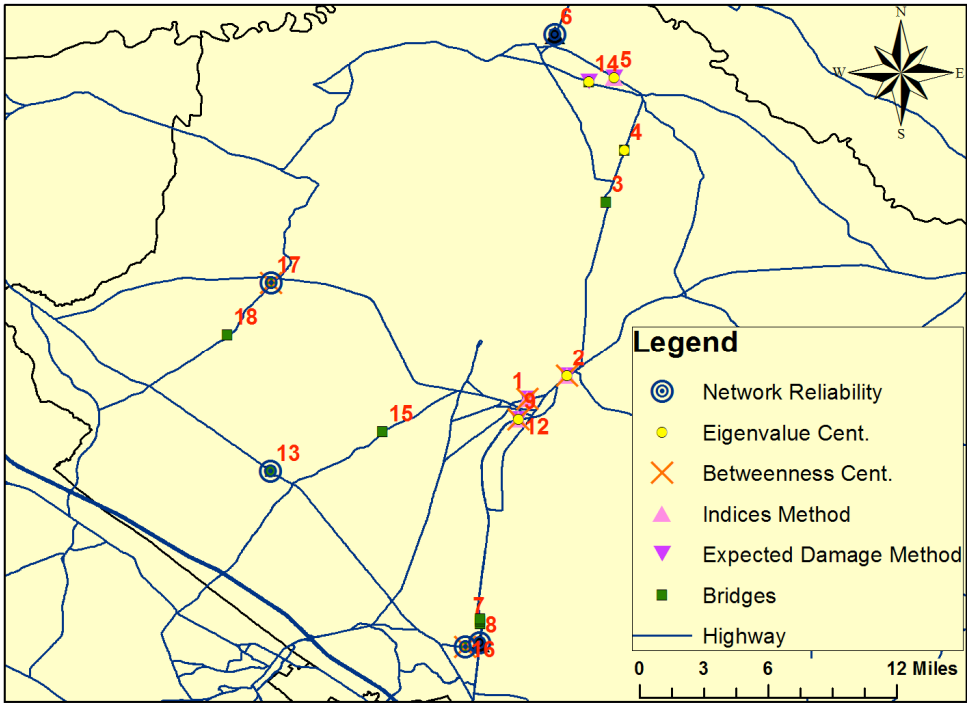


Figure 7: Top five ranked bridges in the network as per the different ranking strategies

Conclusions

Development of time-dependent fragility curves for the bridges in the network enables determining the present day probabilities of failure of deteriorating bridges

in a bridge network. The individual bridge vulnerabilities acquired this way are used to evaluate the network level reliability between a defined set of Origin and Destination pairs. The bridge ranking obtained from the presented MC network reliability approach using time-dependent fragility curves are found to be strikingly different from the qualitative rankings based on the state of the practice methodologies in the seismic retrofit manual.

References

References

ASCE, 2009. ASCE: Infrastructure Fact Sheet. Available at: http://www.infrastructurereportcard.org/sites/default/files/RC2009_bridges.pdf.

Bertolini, L. et al., 2004. *Corrosion of steel in concrete: prevention, diagnosis, repair*, Wiley-VCH.

Broomfield, J.P., 1997. *Corrosion of steel in concrete*, Taylor & Francis.

Buckle, I.G. et al., 2006. *Seismic retrofitting manual for highway structures*, Federal Highway Administration, Office of Research, Development and Technology, Turner-Fairbank Highway Research Center.

Ching, J. & Hsu, W.C., 2007. An Efficient Method for Evaluating Origin-Destination Connectivity Reliability of Real-World Lifeline Networks. *Computer-Aided Civil and Infrastructure Engineering*, 22(8), pp.584–596.

Choe, D. et al., 2008. Probabilistic capacity models and seismic fragility estimates for RC columns subject to corrosion. *Reliability Engineering & System Safety*, 93(3), pp.383-393.

Choe, D. et al., 2009. Seismic fragility estimates for reinforced concrete bridges subject to corrosion. *Structural Safety*, 31(4), pp.275-283.

Dijkstra, E.W., 1959. A note on two problems in connexion with graphs. *Numerische mathematik*, 1(1), pp.269–271.

Fan, Y. et al., 2010. Highway Network Retrofit under Seismic Hazard. *Journal of Infrastructure Systems*, 16(3), pp.181–187.

FEMA, 2003. *HAZUS*, Washington DC: Federal Emergency Management Agency.

FHWA, 1995. *Recording and Coding Guide for the Structure Inventory and Appraisal of Nation's Bridges*, Washington D.C.: U.S. Department of Transportation.

Ghosh, J. & Padgett, J.E., 2010. Aging Considerations in the Development of Time-Dependent Seismic Fragility Curves. *Journal of Structural Engineering*, 136(12), pp.1497-1511.

Hoeke, L.J.L. et al., 2009. Degradation of steel girder bridge bearing systems by corrosion. In *Corrosion 2009, March 22, 2009 - March 26, 2009*. NACE - International Corrosion Conference Series. Atlanta, GA, United states: National Assoc. of Corrosion Engineers International, pp. Carboline; Multi-chem; Corrpo; Champion Technologies; Loresco.

Itoh, Y. & Gu, H.S., 2009. Prediction of Aging Characteristics in Natural Rubber Bearings Used in Bridges. *Journal of Bridge Engineering*, 14, p.122.

Kiremidjian, A., Stergiou, E. & Lee, R., 2007. Issues in seismic risk assessment of transportation networks. *Earthquake Geotechnical Engineering*, pp.461–480.

Le Huy, M. & Evrard, G., 1998. Methodologies for lifetime predictions of rubber using Arrhenius and WLF models. *Die Angewandte Makromolekulare Chemie*, 261-262(1), pp.135-142.

Lee, Y.J. et al., 2010. Post-hazard flow capacity of bridge transportation network considering structural deterioration of bridges. *Structure and Infrastructure Engineering*, 99999(1), pp.1–13.

Liu, M. & Frangopol, D.M., 2006. Probability-based bridge network performance evaluation. *Journal of Bridge Engineering*, 11(5), pp.633–641.

Mander, J.B. et al., 1996. *Response of steel bridge bearings to reversed cyclic loading*, NCEER. Available at: http://bases.bireme.br/cgi-bin/wxislind.exe/iah/online/?IsisScript=iah/iah.xis&src=google&base=DESASTRES&lang=p&nextAction=lnk&exprSearch=8911&indexSearch=ID [Accessed October 19, 2009].

Melchers, R.E. & Frangopol, D.M., 2008. Probabilistic modelling of structural degradation. *Reliability Engineering & System Safety*, 93(3), p.363.

Moore, J. & Fan, Y., 2001. Book review: New Analytical Advances in Transportation and Spatial Dynamics. *Ashgate Publishing Company*.

Nielson, B., 2005. *Analytical fragility curves for highway bridges in moderate seismic zones*. PhD Thesis. Atlanta, Georgia: Georgia Institute of Technology.

Padgett, J.E., DesRoches, R. & Nilsson, E., 2010. Regional Seismic Risk Assessment of Bridge Network in Charleston, South Carolina. *Journal of Earthquake Engineering*, 14(6), pp.918–933.

Padgett, J.E. & DesRoches, R., 2007. Bridge Functionality Relationships for Improved Seismic Risk Assessment of Transportation Networks. *Earthquake Spectra*, 23(1), pp.115-130.

Page, L. et al., 1998. The pagerank citation ranking: Bringing order to the web.

Rix, G. & Fernandez, J., 2004. Earthquake Ground Motion Simulation. Available at: www.ce.gatech.edu/research/mae_ground_motion/ [Accessed October 19, 2009].

Ross, S.M., 2007. *Introduction to probability models*, Academic Press.

Shinozuka, M. et al., 2000. Statistical analysis of fragility curves. *Journal of Engineering Mechanics*, 126(12), pp.1224–1231.

Silano, L.G. & Brinckerhoff, P., 1993. *Bridge inspection and rehabilitation*, Wiley-IEEE.

Sullivan, I. & Nielson, B.G., 2010. Sensitivity Analysis of Seismic Fragility Curves for Skewed Multi-Span Simply Supported Steel Girder Bridges.

TELEATLAS, 2010. Digital Mapping and Navigation Soultions. Available at: http://www.teleatlas.com/index.htm.

Thoft-Christensen, P. et al., 1996. Assessment of the reliability of concrete slab bridges. Available at: http://publications.eng.cam.ac.uk/6361/ [Accessed March 5, 2010].

Todinov, M.T., 2007. *Risk-based reliability analysis and generic principles for risk reduction*, Elsevier.

USGS, 2010. An Updated earthquake Catalog for Stable Continental Regions. Available at: http://earthquake.usgs.gov/research/data/scr_catalog.php [Accessed December 31, 2010].

Vu, K., Stewart, M.G. & Mullard, J., 2005. Corrosion-induced cracking: experimental data and predictive models. *ACI structural journal*, 102(5).

Vu, K.A.T. & Stewart, M.G., 2000. Structural reliability of concrete bridges including improved chloride-induced corrosion models. *Structural Safety*, 22(4), pp.313-333.

Wen, Y.K. & Wu, C.L., 2001. Uniform Hazard Ground Motions for Mid-America Cities. *Earthquake Spectra*, 17(2), pp.359-384.

A study on the minimum column-to-beam moment ratio of steel moment resisting frame with various connection models

Se Woon Choi[1] and Hyo Seon Park[2]

[1]Graduate Student, Department of Architectural Engineering, Yonsei University, Seoul, South Korea; Tel +82-2-2123-2794; FAX +82-2-365-4668; email: watercloud@yonsei.ac.kr
[2]Professor, Department of Architectural Engineering, Yonsei University, Seoul, South Korea; Tel +82-2-2123-2794; FAX +82-2-365-4668; email: hspark@yonsei.ac.kr

Abstract

This paper presents the minimum column-to-beam moment ratio of steel moment resisting frame (SMRF) with various connection models using the non-dominated sorting genetic algorithm-II (NSGA-II). We evaluate the minimum column-to-beam moment ratio of SMRF required to ensure the beam-sway mechanism by the pushover analysis. We investigate the influence of the connections on the minimum column-to-beam moment ratio. We consider WUF-W and RBS as the connection models. The optimal algorithm used in this paper is to minimize the structural weight and the column-to-beam moment ratios through the objective functions and to induce the beam-hinge mechanism through the constraint which is to prevent the formation of plastic hinge at the column part consisting of joints. Using the 3-story example, we compare the minimum column-to-beam moment ratio of SMRF required to ensure the beam-sway mechanism according to the connection models.

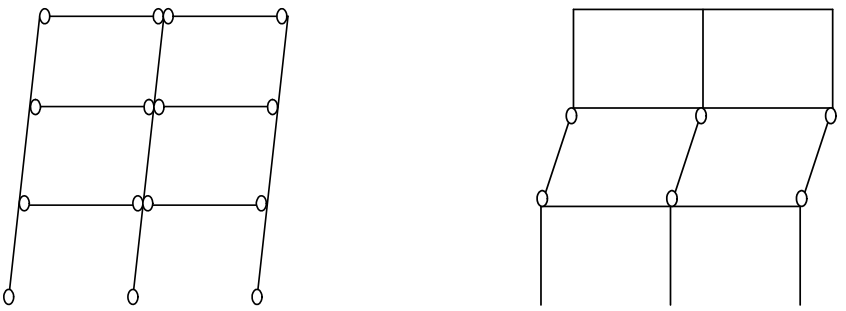
INTRODUCTION

ANSI/AISC 341-05 represents the strong column-weak beam concept to induce the collapse mechanism such as Figure 1(a). The purpose of that is to form plastic hinge at the beam earlier by designing the column moment ratio larger than beam moment ratio like Eq. (1). If the plastic hinge occurs at the column earlier, the plastic deformation concentrates at the certain story owing to the formation of the weak story. The possibility of abrupt collapse of the whole structure also increases by the collapse of column.

$$\sum \frac{M_{pc}^{*}}{M_{pb}^{*}} > 1.0 \tag{1}$$

where,
M_{pc}^{*} is the plastic column moment ratio consists of the relevant connection

M_{pb}^{*} is the plastic beam moment ratio consists of the relevant connection



(a) beam-hinge collapse mechanism (b) column-hinge collapse mechanism

Figure 1. Collapse mechanism types by plastic hinge of moment frame

When performing the dynamic analysis and inelastic analysis, it is known that the brittle fracture can be induced by forming the plastic hinge at column earlier even if satisfying the strong column-weak beam condition because that condition represented by the seismic criteria was set based on the static elastic analysis (Park and Paulay, 1975; Kuntz and Brouning, 2003).

Many research have been studied to solve the strong column-weak beam condition problems (Lee, 1996; Nakashima and Sawaizumi, 2000; Dooley and Bracci, 2001; Kuntz and Brouning, 2003; Medina and Krawinkler, 2005). However, the proposed methods have been induced based on the examples designed by the engineer's experiences, the required minimum moment ratio for inducing the beam-hinge collapse mode has not been defined yet. All the existing researches which were based on linear center-line mode have not considered the effect of the connection which has a major influence on the behavior of moment frame.

Therefore, by using the optimization method, this paper evaluates the required minimum moment ratio inducing the beam-hinge collapse mode of the steel moment frame considering connection. The effects of the minimum moment ratio with different connections are compared through each difference connection modeling. In this paper, WUF-W and RBS are considered as target connection types. The objective functions are defined as the minimization of the structural weights and the minimization of the moment ratio. This paper do not consider the strength condition but the inter-story drift condition because the seismic design for moment frame is determined by inter-story drift condition (Foutch and Yun, 2002; Liu et al., 2005). The constraint condition for the plastic hinge formation of the column is also used to induce the beam-hinge collapse mode of the structure. Finally, the cross-sectional areas of continuous columns are used for the constraint condition to consider the construction of the structures. It is applied to the example of three story steel moment frames with WUF-W and RBS connection respectively, the minimum moment ratio by connections is evaluated.

SEISMIC CONNECTION

The cause of damage by the Northridge earthquake for the steel moment frame was

mainly the brittle fracture of connection such as Figure 2. It was caused by the connection details used in the field.

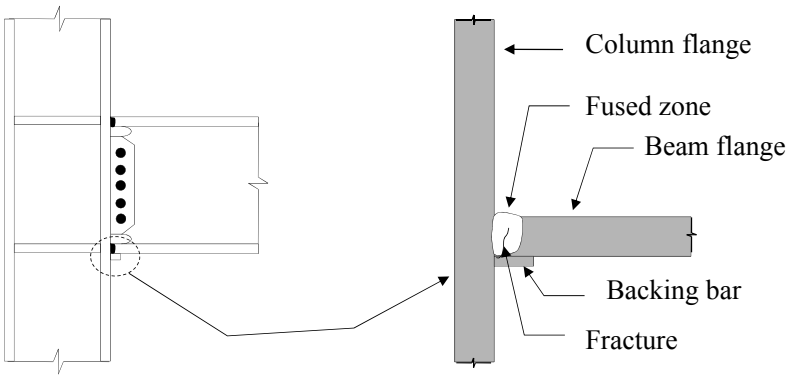
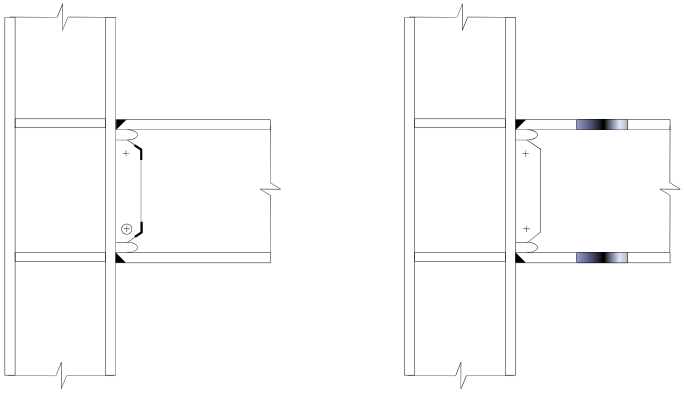


Figure 2. Connection fracture discovered in the Northridge earthquake (FEMA 355d)

Through the SAC project, the solutions for this problem have been researched, as a result, a variety of connection details were represented. According to FEMA 350, WUF-W, RBS, and WFP are suggested as certification connections which can be applied SMF. In this paper, WUF-W and RBS were studied such as Figure 3.



(a) WUF-W (b) RBS

Figure 3. Connection details suggested in FEMA 350

The WUF-W is similar to the existing connection type, but the use of weld metal which has large toughness and the removal of back up bar apply to the WUF-W, so the considerable plastic deformation can be expected at the beam ends. The structural design is performed with the assumption that plastic hinge occurs at the inside of beam near the connection due to the characteristic of good plastic behavior of WUF-W (Kim and Kim, 2009).

The RBS cuts the part of beam flange near the column flange and properly weakens the beam, thereby the RBS induces the location of plastic hinge formation to the inside of beam. The purpose of this is to prevent the brittle fracture of the columns. In the RBS, the type of cutting shape of beam flange is the taper-cut or constant-cut RBS. However, that type has the stress concentration problem, so the radius-cut RBS is the most widely used. The radius-cut RBS is so difficult to express

in the procedure of the structural analysis due to the characteristic of the shape. For this reason, Lee and Chung (2006) proposed the RBS analysis method using the RBS that has the same performance and uniform effective width of the radius-cut RBS, as in Figure 4. The equivalent effective width can be calculated through the Eq. (2)-(4). Please refer to Lee and Chung (2006) for more detail matter.

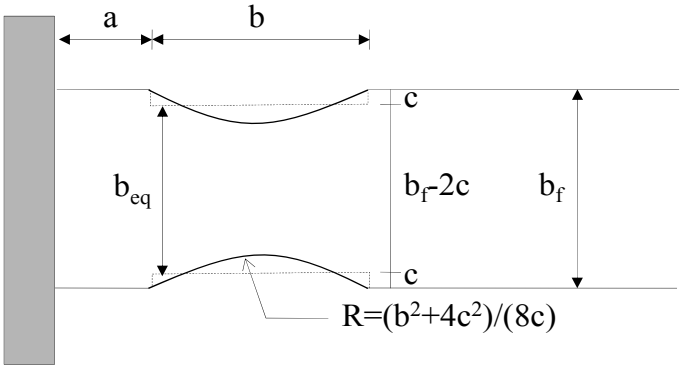


Figure 4. Equivalent effective width of radius-cut RBS proposed by Lee and Chung (2006)

$$X1 = b(\frac{L_b}{2} - (a + /2)) \tag{2}$$

$$X2 = \frac{(L_b - 2a - b)}{\sqrt{\frac{b_f - 2c}{R}}} \tan^{-1}(\frac{b}{2R\sqrt{\frac{b_f - 2c}{R}}}) \tag{3}$$

$$b_{eq} = \frac{X1}{X2} \tag{4}$$

where,
L_b is the effective length of a beam

FEMA 350 represents parameter a, b, and c for determining the shape of RBS such as Eq. (5)-(7).

$$a \cong (0.5 \; to \; 0.75)b_f \tag{5}$$

$$b \cong (0.65 \; to \; 0.85)d_b \tag{6}$$

$$assume \; c = 0.20b_f \tag{7}$$

where,
b_f and d_b are the beam flange width and depth respectively

FORMULATION

Objective functions

This paper uses two objective functions. Because the moment ratio with respect to realistic design must be evaluate to obtain rational conclusion, the first objective function is to minimize the weight of structure as in Eq. (8). By the way, because the purpose of this paper is to evaluate the required minimum column-beam moment ratio inducing beam-hinge collapse mode with difference types of connection, the second objective function is defined as the minimization of the maximum moment ratio among column-beam moment ratio for the design as in Eq. (9). It is used NSGA-II (Deb et al., 2002) which is able to perform multi-objective optimization in order to evaluate two objective functions simultaneously.

$$\min \sum_{i=1}^{m} \rho_i A_i l_i \tag{8}$$

$$\min \alpha_{\max} \tag{9}$$

where,

ρ_i is the density of the i-th element

A_i is the cross-sectional area of the i-th element

l_i is the length of the i-th element

m is the number of elements consisting of the structure

$\alpha_{\max}$ is the maximum plastic moment strength ratio among joints of the structure

ANSI/AISC 341-05 excludes roof joint when examining the moment ratio. This paper also exclude roof joint in the evaluation of moment ratio. To evaluate moment ratio of joint, Eq. (10) is used.

$$\alpha = \sum \frac{(F_y Z)_{column}}{(F_y Z)_{beam}} \tag{10}$$

where,

F_y and Z are the yield stress and plastic section modulus

Constraints

This paper uses three constraints. The first condition constraints on inter-story drift as in Eq. (11). The second condition prevents the plastic hinge from forming at the column ends consist of all joints except the roof joint as in Eq. (12). To consider construction, the third condition is that the cross-sectional areas of lower columns must be greater than or equal to that of upper columns in continuous columns as in Eq. (13).

$$\frac{\Delta}{\Delta_a} \leq 1.0 \tag{11}$$

$$N_{pc} = 0 \tag{12}$$

$$\frac{A^c_{i+1,j}}{A^c_{i,j}} \le 1.0 \tag{13}$$

where,

Δ and Δ_a are the maximum and allowable inter-story drift respectively

N_{pc} is the number of plastic hinges developed on the column part of joints

$A^c_{i,j}$ is the cross-sectional area of the ith floor and jth column

EXAMPLE

This paper uses three story four bay steel moment frame example and evaluates the required minimum moment ratio inducing beam-hinge collapse mode. Please refer to Hasan et al. (2002), Xu et al. (2006) and Gupta and Krawinkler (1999) for details with regard to the condition of the structural design of this example.

The nine design variables(six for columns and three for beams) for the structural optimization are used as in Figure 5. The number of cross-sectional data base whom the design variables of the columns and the beams can randomly select is 16 for the columns and beams respectively. By using ASCE 7-05, the inter-story drift constraint is evaluated.

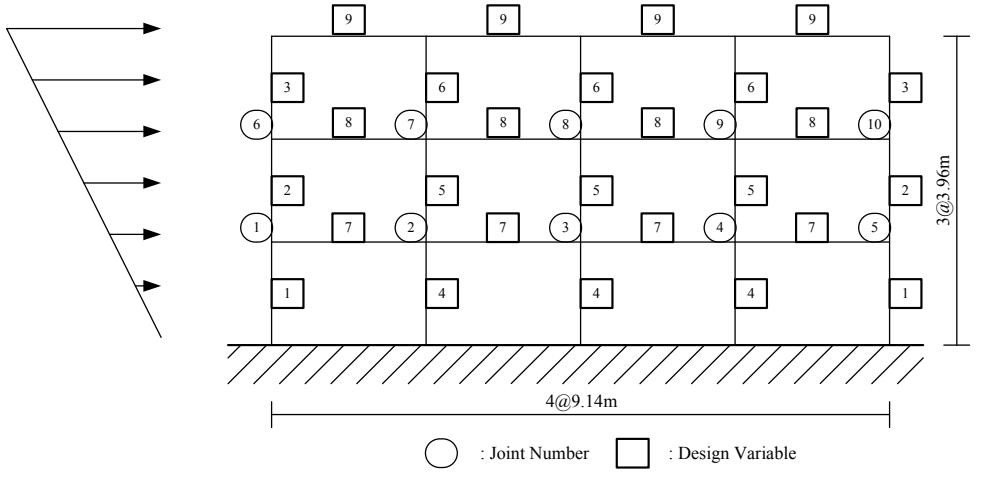
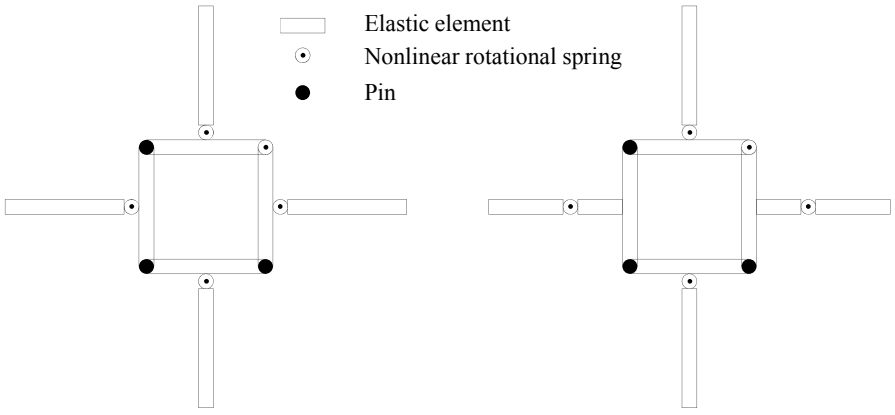


Figure 5. The elevation diagram of the example

The purpose of this paper is to evaluate the required minimum moment ratio inducing beam-hinge collapse mode of the steel moment frame with different types of connection. For this, the connection types for this paper are limited to WUF-W and RBS. By referring FEMA 355f, the analysis modeling for those connections is presented in Figure 6. The parameter a, b, and c determining the shape of RBS as in Eq. (5)-(7) are set to 0.5, 0.85, and 0.2 respectively.

To identify inter-story drift and whether the plastic hinge at the column form or not, linear static analysis and non-linear static analysis are performed respectively, by using OpenSees (2006). For the lateral loads used in non-linear static analysis, the

inverted triangle pattern is used. The target drift is set to be 5% of overall structural height, referring to the maximum inter-story drift ratio, the collapse prevention level, as suggested in FEMA 356.



(a) WUF-W (b) RBS

Figure 6. Analytic modeling of WUF-W and RBS including the panel zone

Through the structural optimization algorithm performance, total 17 feasible solutions(6 solutions for WUF-W and 11 solutions for RBS) are obtained as in Figure 7. As represented in the Table 1., as a result of conforming the constraint ratio of the feasible solution, the constraint ratio of 90% can be verified except each case 1. Each case 1 presents the constraint ratio of 80% levels in the construction constraint condition. This proves the relevance of the constraint conditions.

Both cases represent that the required minimum moment ratio inducing beam-hinge collapse mode decreases as the structural weight increases. However, it is represented that the steel moment frame with RBS requires less moment ratio than the steel moment frame with WUF-W.

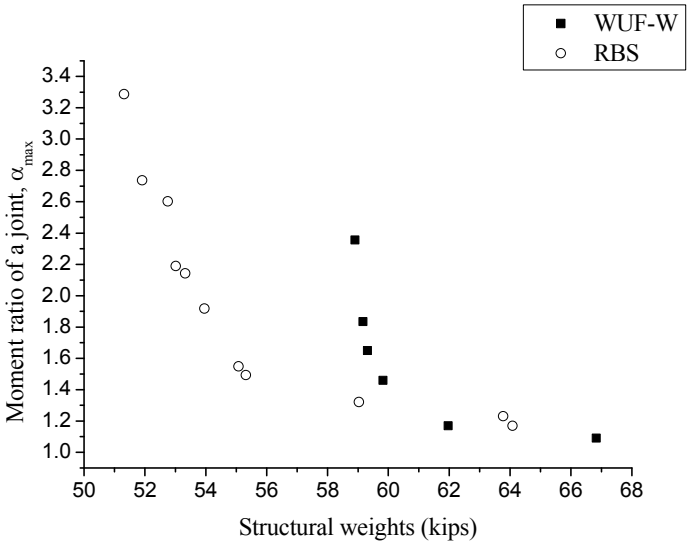


Figure 7. Comparison of the feasible solutions of WUF-W and RBS

Table 1. The values of objective functions and constraints of WUF-W and RBS feasible solutions

Connetion type	Objective functions		Constraints		
	Eq. (8)	Eq. (9)	Eq. (11)	Eq. (12)	Eq. (13)
WUF-W	58.90	2.36	1.00	0.00	0.83
	59.17	1.83	0.99	0.00	1.00
	59.31	1.65	0.99	0.00	1.00
	59.83	1.46	0.98	0.00	1.00
	61.97	1.17	0.98	0.00	1.00
	66.83	1.09	0.96	0.00	1.00
RBS	51.32	3.29	0.97	0.00	0.84
	51.91	2.74	0.97	0.00	1.00
	52.75	2.60	0.96	0.00	1.00
	53.01	2.19	0.97	0.00	1.00
	53.33	2.14	0.95	0.00	1.00
	53.96	1.92	0.94	0.00	1.00
	55.08	1.55	0.99	0.00	1.00
	55.32	1.49	0.97	0.00	1.00
	59.04	1.32	0.99	0.00	1.00
	63.77	1.23	0.95	0.00	1.00
	64.08	1.17	0.98	0.00	1.00

CONCLUSION

According to existing researches, it is known that the ductile behavior of structure can be weakened when the plastic hinge forms in the columns earlier although the strong column-weak beam condition proposed in the criteria is satisfied. A variety of associated researches have limitation that linear center-line model ignoring the effects with respect to panel zone and connection is used. Therefore, this paper evaluates the required minimum moment ratio inducing beam-hinge collapse mode of the steel moment frame by using the optimization algorithm. The analysis modeling of the steel moment frame considers the WFF-W and RBS connections modeling including panel zone.

The proposed method was applied to three story four bay example for verification. Consequently, as the structural weight increases, the required moment ratio deceases. It is also represented that the design with RBS connection has less moment ratio than the design with WUF-W connection under similar structural weight. So, it is judged that the strong column-weak beam condition must be changed according to the connection type.

This research is limited to three story example, and doesn't consider non-linear dynamic behavior. Because it has limitation that doesn't include the analysis of the effects for parameter determining the shape of RBS, it is necessary to conduct the additional study of this.

ACKNOWLEDGEMENTS

This work was supported by the National Research Foundation of Korea(NRF) grant funded by the Korea government(MEST)(No. 2010-0027246).

REFERENCES

American Institute of Steel Construction (AISC). (2005). "ANSI/AISC 341-05 Seismic provisions for structural steel buildings" In: Chicago, I.L.

American Society of Civil Engineers. (2005). *Minimum Design Loads for Buildings and Other Structures (ASCE 7-05)*. American Society of Civil Engineers: New York.

Deb, K., Pratap, A., Agarwal, S., Meyarivan, T. (2002). "A fast and elitist multiobjective genetic algorithm: NSGA-II" IEEE Transactions on Evolutionary Computation, 6(2), pp. 182-197.

Dooley, L. and Bracci, J. M. (2001). "Seismic evaluation of column-to-beam strength ratios in reinforced concrete frames" ACI Structural Journal, ACI, 98(6), pp. 834-851.

Federal Emergency Management Agency (FEMA). 2000. "Recommended seismic design criteria for new steel moment-frame buildings." FEMA 350.

Federal Emergency Management Agency (FEMA). 2000. "State of the art report on connection performance." FEMA 355D.

Federal Emergency Management Agency (FEMA). 2000. "State of the art report on performance prediction and evaluation of steel moment-frame buildings." FEMA 355F.

Federal Emergency Management Agency (FEMA). 2000. "Prestandard and commentary for the seismic rehabilitation of buildings." FEMA 356.

Foutch, D. A., and Yun, S. (2002). "Modeling of steel moment frames for seismic loads" Journal of Construction Steel Research, 58, pp. 529-564.

Gupta A., and Krawinkler H. (1999). "Seismic demands for performance evaluation of steel moment resisting frame structures" The John A. Blume Earthquake Engineering Center, Report No. 132, Dept. of Civil Engineering , Stanford University, Stanford, California.

Hasan, R., Xu, L., Grierson, D. E. (2002). "Push-over analysis for performance-based seismic design" Computers and Structures, pp. 2483-2493.

Kim, T., and Kim, J. (2009). "Collapse analysis of steel moment frames with various seismic connections" Journal of Constructional Steel Research, 65, pp.1316-1322.

Kuntz G. L. and Brouning, J. (2003). "Reduction of column yielding during earthquakes for reinforced concrete frames" ACI Structural Journal, 100(5), pp. 573-580.

Lee, Ch. H., and Chung, S. W. (2007). "A simplified analytical story drift evaluation of steel moment frames with radius-cut reduced beam section" Journal of Constructional Steel Research, 63, pp.564-570.

Lee, H. (1996). "Revised rule for concepts of strong-column weak-girder design" Journal of Structural Engineering, 122(4), pp. 359-364.

Liu, M., Burns, S. A., Wen, Y. K. (2005). "Multiobjective optimization for

performance-based seismic design of steel moment frame structures" Earthquake Engineering and Structural Dynmics, (34), pp. 289-306.

Medina, R. A., and Krawinkler, H. (2005). "Strength demand issues relevant for the seismic design of moment-resisting frames" Earthquake Spectra, 21(2), pp. 415-439.

Nakashima M. and Sawaizumi S. (2000). "Column-to-beam strength ratio required for ensuring beam-collapse mechanisms in earthquake responses of steel moment frames" Proceedings of the 12th World Conference on Earthquake Engineering, New Zealand Society for Earthquake Engineering, paper No. 1109, Auckland, New Zealand.

OpenSees (2006). http://opensees.berkeley.edu/index.php

Park, R., and Paulay, T. (1975). "Reinforced concrete structure" John Wiley and Sons, New York.

Xu, Lei., Gong, Y., Grierson, D. E. (2006). "Seismic design optimization of steel building frameworks" Journal of Structural Engineering, ASCE, 132(2), pp. 277-286.

Steel Plate Shear Walls with Controlled Infill Tension Fields

J. Neal, S.M. ASCE[1], B. Qu, M .ASCE.[2]

[1]Master's Candidate, Department of Civil and Environmental Engineering, California Polytechnic State University, San Luis Obispo, CA 93407; PH (805) 547-2000 FAX (805) 547-2001; Email: joelneal@gmail.com
[2]Assistant Professor, Department of Civil and Environmental Engineering, California Polytechnic State University, San Luis Obispo, CA 93407; PH (805) 756-5645; FAX (805) 756-6330; Email: bqu@calpoly.edu

ABSTRACT

Steel plate shear walls (SPSWs) consist of thin infill steel plates attached to beams, called horizontal boundary elements (HBEs), and columns called vertical boundary elements (VBEs) in building structural frames. Overall capacity of this system is provided primarily by the diagonal tension fields distributed along the entire length of the boundary frame elements due to the yielding of infill steel plates. Capacity design of the boundary frame, as currently designed, may result in very large demand on boundary frame members in some cases. In this investigation, tension field formation was controlled by discontinuous infill-to-boundary frame connections in order to reduce the demand on boundary elements. Finite element (FE) models of this system were developed and analyzed in ABAQUS. Behaviors of such a system (including overall capacity, initial stiffness and demand on boundary frames) were compared with those of the conventional SPSWs. Moreover, analytical models for estimating the plastic strength of SPSWs with discontinuous infill-to-boundary frame connections were presented.

INTRODUCTION

Steel plate shear walls (SPSWs) consist of thin infill steel plates attached to beams, called horizontal boundary elements (HBEs), and columns called vertical boundary elements (VBEs) in building structural frames. As SPSWs deflect horizontally due to the lateral loads, the infill panels buckle followed by the development of plate diagonal tension field actions in the structural frame which provide the lateral resistance to horizontal shear (Thornburn, et al. 1983). SPSWs have been recently used as primary lateral force resisting systems in new and existing building construction (Sabelli and Bruneau 2006). Multiple studies have been performed validating the use of finite element analysis (FEA) as a reasonable tool in determining the overall capacity, stiffness, hysteric behavior, and failure mode of SPSWs.

Design procedures for new SPSWs are now available in the AISC Seismic Provision for Structural Steel Buildings (AISC 2005). This standard, as well as the Canadian code (CSA 2009), indicate that capacity design of the VBEs and HBEs be

used to ensure formation of the infill plate tension field actions and desirable seismic behavior of boundary frames (Elgaaly and Liu 1997; Berman and Bruneau 2008; Qu and Bruneau 2008; Qu and Bruneau 2010a; Qu and Bruneau 2010b).

Moreover, studies on seismic retrofit applications of SPSWs have been performed (Bruneau and Bhagwager 2002; Qu and Bruneau 2008). One important issue recognized from these investigations is that the demand on existing frames, due to the installed infill plates, may exceed their available strength, incurring additional costs for the strengthening work to avoid the premature failure of boundary frame. Also, in some new construction when plate thicknesses greater than required have to be used, due to the unavailability of construction materials, the demand on boundary elements can be of significant magnitude. This is especially problematic in multi-story applications where the bottom-story VBEs accumulate the tension field forces from the upper stories.

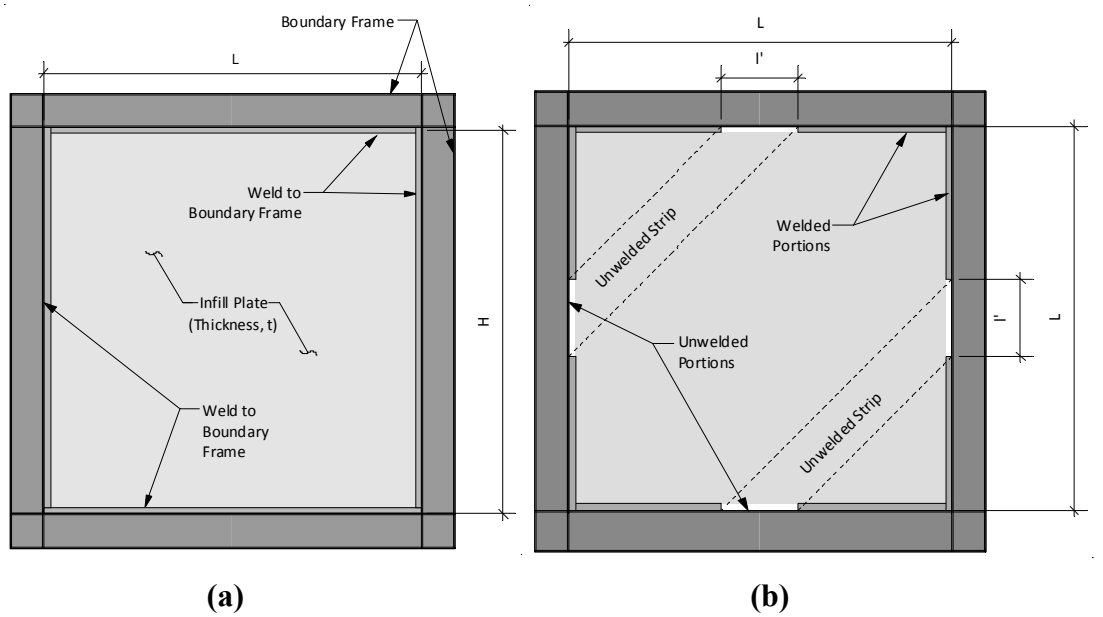
This paper attempts to address these difficulties by limiting the formation of tension fields within the plate by using discontinuous welds to connect the infill plate to the boundary elements. This paper discusses the development of an analytical model to estimate the overall strength and the validation of this model through finite element (FE) models. The overall strength, initial stiffness, and demand on boundary elements are compared between the new SPSWs and traditionally designed SPSWs. The results are used to make recommendations regarding the feasibility of implementing this method of design in common practice.

PROPOSED SYSTEM AND CONVENTIONAL SPSWS

Traditional SPSWs and SPSWs with controlled tension fields are illustrated in Figure 1. As shown, the SPSW with controlled tension fields has discontinuous plate-to-boundary frame connections. Both of these types of SPSWs were studied in this paper. For analysis purposes, the example SPSWs are identical except different plate thickness and plate-to-boundary frame connections. All example walls were modeled and analyzed in Abaqus CAE. Detailed information about the development of these models is presented in the next section.

Initial models consisted of a 3048 mm long, 2.54 mm plate bounded by four pin-ended boundary frame members of equal dimensions. The boundary frame members were specified as W48x355 A572 Grade 50, and the infill plate was ASTM A36 steel. The beams were modeled as 2 discrete beam elements 3048 mm each and the columns as 2 beam elements 3073 mm each. The extra length allowed the columns to be pinned at the base while allowing the bottom beam to freely deflect. The columns, as noted, were pinned at the base to minimize any contribution of the frame to the base shear. The plate was attached to the center-line of the beam elements, and the out-of-plane rotational degree of freedom was fixed at the connection. Since this study focused on the behavior of the plate alone, the boundary

frame members were sized to remain elastic and beam-to-column connections were assumed to be pinned. In addition, strain hardening was not considered. A view of the FEM model is shown in Figure 2.



(a) **(b)**

Figure 1. Conventional SPSWs vs. SPSWs with controlled tension fields

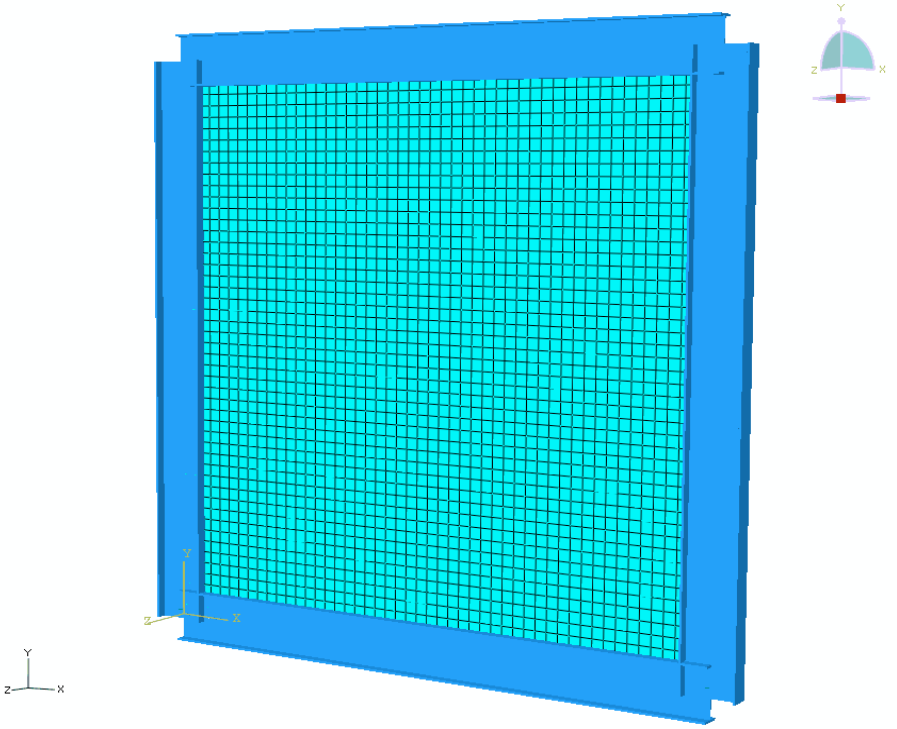


Figure 2. Schematic Abaqus model (Beam elements rendered at 25% scale)

DEVELOPMENT OF FE MODELS

Before the pushover analysis, we performed an initial eigenvalue analysis with a single lateral load applied in-plane at the top of the wall to the boundary frame. The lowest 15 eigenvalues and their graphical representation were recorded, and the coordinates of the lowest 6 eigenvalues that contributed to the known failure state of the model were superimposed onto a new, identical model. The out-of-plane coordinate was slightly displaced according to the eigenvalue shape with a greater emphasis on the lower values. This initial seeding was loaded as an initial condition onto the new model. This was intended to ensure that during pushover the plate failed at it's lowest natural frequencies.

We performed pushover analysis on traditional (fully welded) models by applying a monotonically increasing drift along the top boundary frame beam to a target level at which the wall was fully yielded. The overall base shear was recorded along with the lateral displacement at the upper left corner. The overall base shear was compared to the expected maximum capacity calculated according to Eq. 1. This was intended to calibrate the model and ensure that the control model was producing results in accordance with those predicted by accepted analytical models and previous research (Berman and Bruneau 2003). During analysis, the system reached the yield stress in the plate and remained below the yield stress in the frame. The plate buckled and deformed according to the lower eigenvalues, and all the plate reached the elastic capacity of 36 ksi (248 MPa). The pushover below shows the traditional test model with the maximum calculated shear.

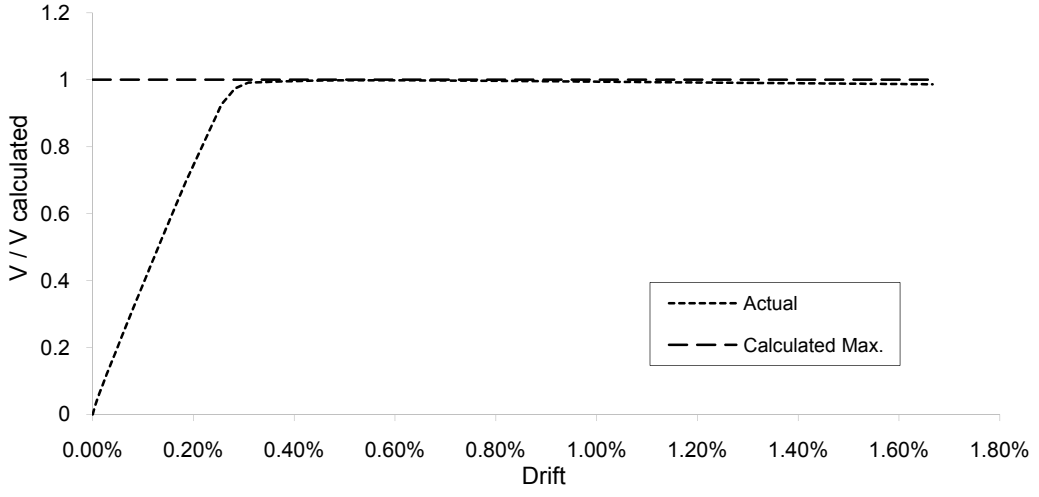


Figure 3. Traditional (fully welded) SPSW pushover curve

This process of modeling the traditional shear walls was performed for various aspect ratios between 0.8 and 2.5 as well as for different plate thicknesses between 3.18 mm and 12.70 mm. Once the models were shown to accurately predict

expected behavior, they were modified to reflect the controlled infill tension assembly.

The controlled infill tension models were formed in the same manner as the traditional walls; however, the constraint connecting the infill plate to the boundary frame was modeled as discontinuous at a ratio equal to the selected weld ratio. The model evaluated here was a 3048 mm x 3048 mm x 2.54 mm infill plate. It was bounded by W48x355 beams and columns as boundary frames, exactly as in the traditional shear wall. A weld ratio of 0.8 was evaluated, so 610 mm at the center of each edge was left unwelded. This configuration also allows the unwelded portions to the beam and column to occur 45 degrees apart corresponding to the tension field angles in typical SPSWs.

SEISMIC PERFORMANCE COMPARISIONS

During the pushover analysis of the tension-controlled system, the frame remained entirely elastic. The plate outside the area bounded by the unwelded portions reached the elastic capacity of 36 ksi (248 MPa), while the areas bounded by unwelded portions reached approximately 50% of elastic capacity, 18 ksi (124 MPa). The edges of those areas reached a higher stress than the center. The model below shows the stress distribution at the final point of the pushover, when maximum capacity has been reached.

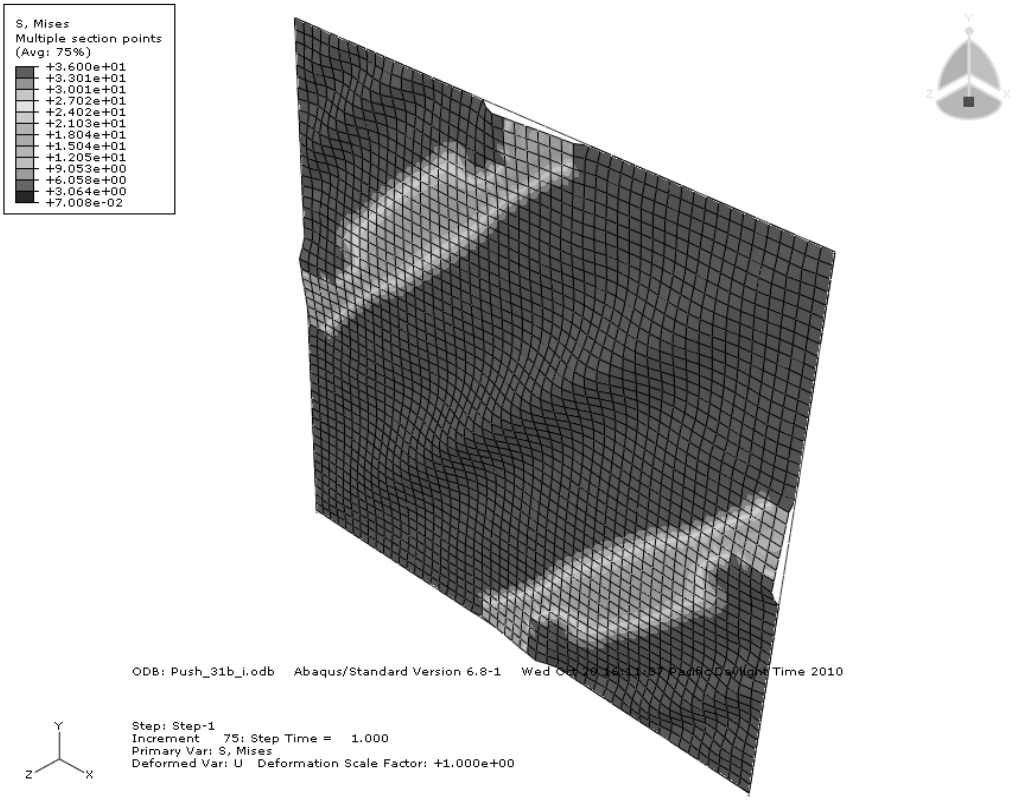


Figure 4. Stress distribution of the SPSWs with controlled tension field actions

The pushover results showed the areas of partial stress add an amount of resistance to the overall base shear, although there is no tension field formed in this area. The contribution of this area is attributed to compressional effects that develop in the plate and vary with plate thickness, length of the diagonal strip of area, and the length of the unwelded portion. These effects are accounted for in the compression effects factor shown in Eq. 4. Multiple plate thicknesses, aspect ratios, and weld configurations were modeled; however, the results here are limited to the test case described above. The traditional shear walls were compared to the plastic capacity model in Eq. 1 while the tension-controlled shear walls were compared to the tension controlled plastic capacity model in Eq. 3.

For the test case presented, the analytical model was found to closely predict the total overall base shear resisted in the FE model (see Figure 5). The first part of the analytical equation, shown in Eq. 2, accurately modeled the tension field contribution of the infill plate by accounting only for tension field formation in the welded areas. The second part of the equation, the compression effect factor, closely modeled the compressive resistance provided by the plate, perpendicular to the direction of tension field formation, by modeling that area as a wide, thin column.

For the model of a 3048 mm x 2.54 mm, 36 ksi (248 MPa) plate with a weld ratio of 0.8, the analytical model predicted the total base shear within 0.10% of the FE results. The analytical equation calculated a shear value of 826.26 kN while the FEM produced a base shear of 827.10 kN. The error increased modestly with thicker plates up to 3.25% for the plates considered in this study. This increase in error with the thicker plate is likely due to the compression effects that occur in the plate in the welded areas that act in addition to the tension fields, as noted by other researchers. (Shishkin et al. 2009). This error value remained small and consistent with error values found in how the fully welded (traditional) SPSWs compare with the plastic capacity model.

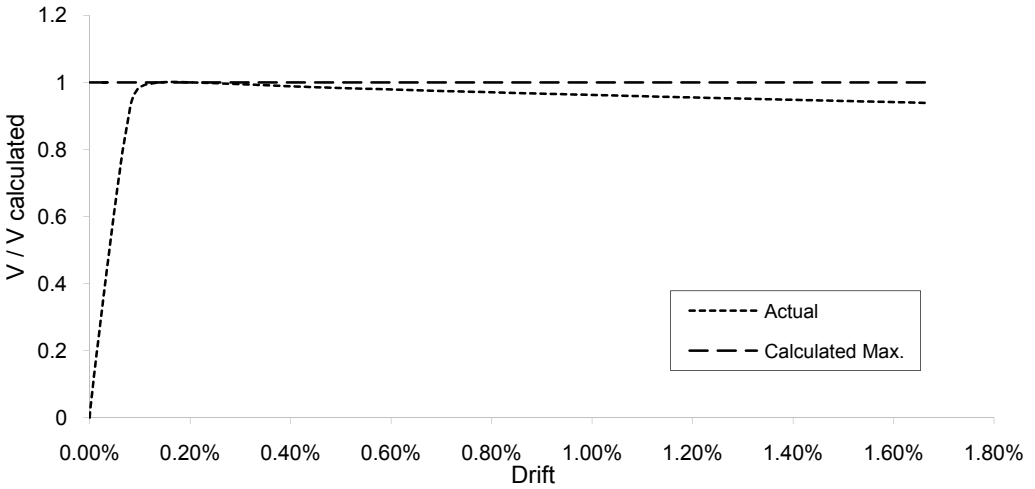


Figure 5. Pushover curve of SPSWs with controlled tension field action

Along with the overall capacity being reduced, the demand on the boundary elements was also reduced. Considering the top beam, since shear demand on the beam is generated by the tension field action, the demand is reduced proportional to how much weld area is reduced, the weld ratio. The moment demand is more dependent on the weld orientation. If load is reduced on the center of the beam, more moment reduction is observed than if the load was reduced on the edges. For the considered SPSW, where the 20% reduction in weld area was at the center of the beam, the moment demand was reduced approximately 25%.

When the tension-controlled system is considered as a method to reduce demand on boundary frames due to oversized infill plates, the overall design characteristics were found to be similar to those of the thinner infill plate. The following figure shows the moment diagram for the top beam in a SPSW where a 6.35 mm plate with a weld ratio of 0.8 was used in lieu of a 5.08 mm plate with a weld ratio of 1.0. For comparison purposes, the full demand of the 6.35 mm plate with a weld ratio of 1.0 is included to show the overall reduction experienced.

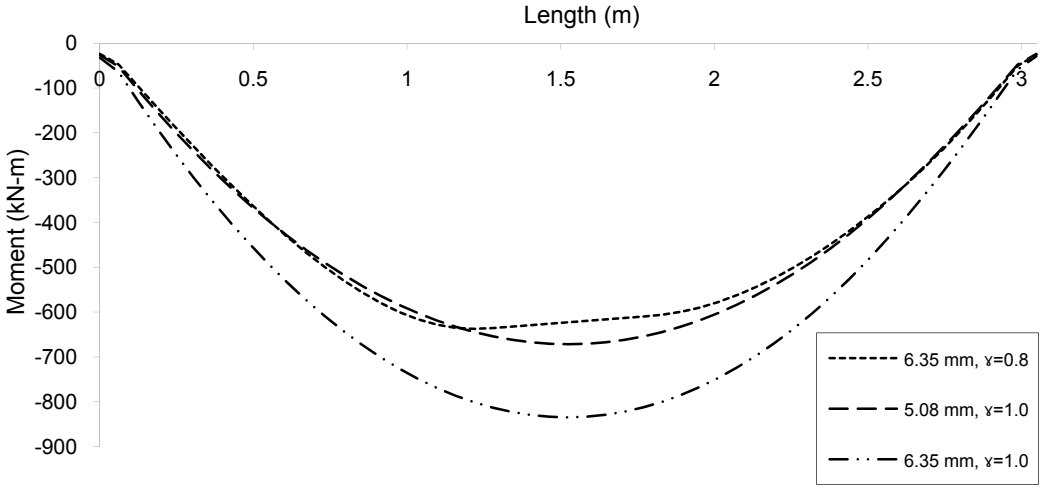


Figure 6. Moment diagrams for top beam

A similar observation was obtained from the demand on VBEs. As shown in Figure 7, bending moment and axial load in the VBEs of the SPSWs with controlled tension field actions closely resembled those of the conventional SPSWs with thinner plate, fully welded. The moment diagram and axial load diagram for the VBEs are shown in Figure 7.

When compared to the traditional SPSWs with both the oversize and normal sized plate, the stiffness of the SPSWs with controlled tension field actions is noticeably less as shown in Figure 8. This difference in stiffness would require the designers to recalculate lateral loads on SPSWs, and such difference would be reduced when the frame moment resisting action provides some stiffness to the overall system.

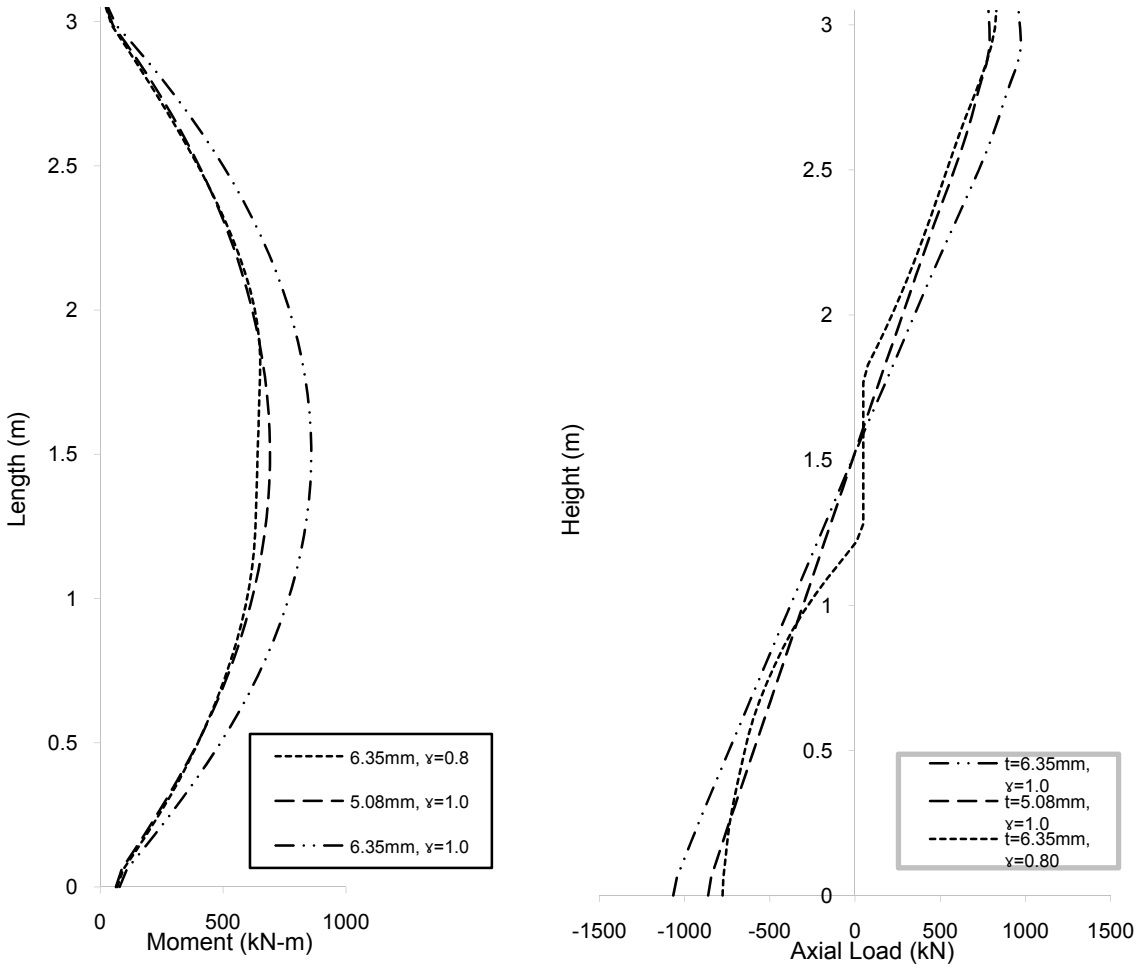


Figure 7. Column demand

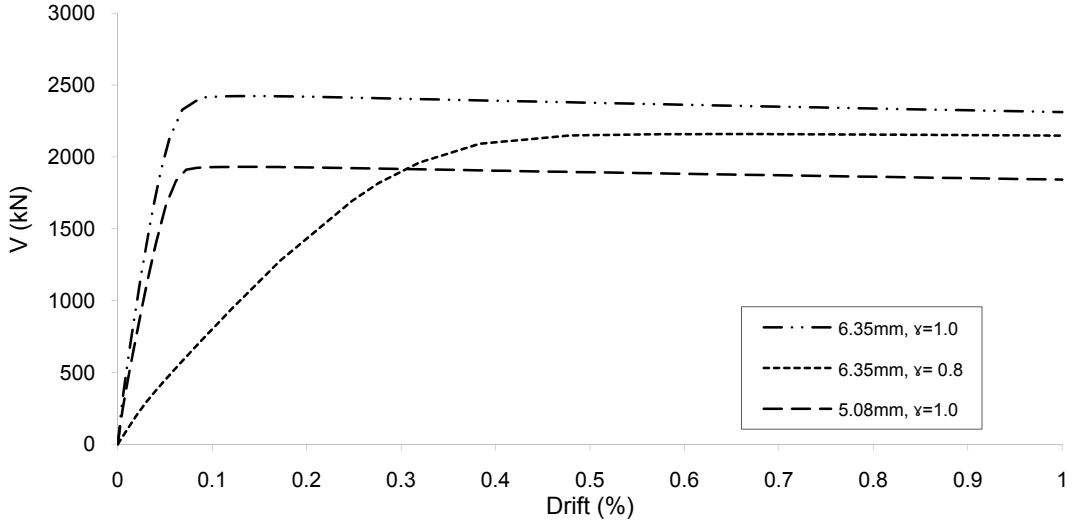


Figure 8. Pushover curves

ANALYTICAL MODELS FOR SHEAR STRENGTH ESTIMATE

Analytical models for calculating plastic strength of conventional SPSWs have been derived and validated by Berman and Bruneau (2003). According to their model, plastic strength of a single story conventional SPSW with pinned beam-to-column and column-to-base connections can be calculated by the following equation.

$$V = \frac{1}{2} F_y t L sin2\alpha \tag{1}$$

where:

V = plastic shear strength
F_y = plate yield strength
t = plate thickness
L = width of the wall
α = tension field angle

Here, the analytical plastic analysis procedure proposed by Berman and Bruneau. (2003) are repeated for the SPSWs with a non-continuous weld, or stitch-weld, connecting the infill plate to the fish-plate and the steel boundary elements. As a result, the ultimate plastic strength of the system, due to tension field action alone, is directly proportional to the weld ratio of the system.

$$V = \frac{\gamma}{2} F_y t L \sin 2\alpha \tag{2}$$

where γ = weld ratio along boundary elements (welded length / total length).

Since the weld ratio is always less than 1.0, the resistance of the wall with discontinuous plate-to-boundary frame connections is lower than that of the same wall with continuous plate-to-boundary frame connections. In addition, it is recognized that Eq. 2 only takes into account the lateral force resistance due to the tension field action. The compressional effects in the infill plate as shown in Figure 4 were not considered. The behavior of the compressional plate zone is similar to a column (i.e. buckle under an increased axial compression). As such, their strength may be considered by the AISC column design equation. As a result, equation for the plastic strength was modified as below

$$V = \frac{\gamma}{2} F_y t L \sin 2a + \Psi \tag{3}$$

where: ψ = compression effect factor,

$$\Psi = F_{CR}\ l'\ t \cos(\alpha) \tag{4}$$

Where: F_{CR} = Compressive stress in the unwelded strip

$$\text{For, } \frac{kL}{r} \le 4.71\sqrt{\frac{E}{F_y}},\ F_{CR} = \left[0.658^{\frac{F_y}{F_e}}\right] F_y \tag{5}$$

$$\text{For, } \frac{kL}{r} > 4.71\sqrt{\frac{E}{F_y}},\ F_{CR} = 0.877 F_e \tag{6}$$

$$\text{Where: } F_e = \frac{\pi^2 E}{\left(\frac{kL}{r}\right)^2} \tag{7}$$

E = elastic modulus of the plate
l' = unwelded length in the top beam
k = slenderness factor = 0.55-0.60
r = radius of gyration

Moreover, the contribution due to the compressional zone should not exceed that of the corresponding tension field action, which means the following equation should be checked.

$$\Psi \le \frac{1}{2} F_y t L (1-\gamma)\cos(\alpha)\sin(2\alpha) \tag{8}$$

The analytical model presented above has been validated by FE results. An example result comparison is given in Figure 5. As shown, reasonable agreements were observed.

CONCLUSION

Behavior of the SPSWs with discontinuous plate-to-boundary frame connections was investigated. Compared with conventional SPSWs, this system exhibits reduced stiffness and reduced demands on boundary frame members. Analytical models developed for calculating the plastic strength of such systems agree reasonable well with the results from FE models.

REFERENCES

American Institute of Steel Construction (AISC). (2005). *Seismic Provisions for Structural Steel Buildings*. American Institute of Steel Construction, Chicago, Illinois.

Berman, J., and Bruneau, M. (2003) "Plastic Analysis and Design of Steel Plate Shear Walls," Journal of Structural Engineering, ASCE, Vol. 129, No. 11, pp. 1148-1156.

Berman, J. W., and Bruneau, M. (2005) "Experimental Investigation of Light-Gauge Steel Plate Shear Walls," Journal of Structural Engineering, ASCE, Vol. 131, No. 2, pp. 259-267.

Berman, J.W. and Bruneau, M. (2008). "Capacity Design of Vertical Boundary Elements in Steel Plate Shear Walls. " AISC Engineering Journal Vol.45, No.1.

Bruneau, M., Bhagwagar, T. (2002). "Seismic Retrofit of Flexible Steel Frames using Thin Infill Panels", Engineering Structures Journal', Vol.24, No.4, pp. 443-453.

Canadian Standards Association (CSA). (2009): *Limit States Design of Steel Structures*. CAN/CSA S16-01. Willowdale, Ontario, Canada.

Sabelli, R., and Bruneau, M. (2006). *Steel Plate Shear Walls* (AISC Design Guide), American Institute of Steel Construction, Chicago, Illinois.

Shishkin, J.J., Driver, R.G., Grondin, G.Y., (2009) "Analysis of Steel Plate Shear Walls Using the Modified Strip Model", ASCE Journal of Structural Engineering, Vol.135, No.11, pp. 1357-1366.

Thorburn LJ, Kulak GL, Montgomery CJ (1983): Analysis of steel plate shear walls. *Structural Engineering Report No. 107*, Department of Civil Engineering, Universtiy of Alberta, Edmonton, Alberta, Canada.

Qu, B., and Bruneau, M. (2008). "Seismic Design of Boundary Frame Members of Steel Plate Shear Walls" Technical Report MCEER-08-0012, Multidisciplinary Center for Earthquake Engineering Research, Buffalo, N.Y.

Qu, B., Bruneau, M.,(2010a). "Behavior of Vertical Boundary Elements in Steel Plate Shear Walls", AISC Engineering Journal, Vol.47, No.2, pp.109-122

Qu, B., Bruneau, M., (2010b). "Capacity Design of Intermediate Horizontal Boundary Elements of Steel Plate Shear Walls", ASCE Journal of Structural Engineering, Vol.136, No.6, pp.665-675.

THE RENOVATION OF FRANKLIN FIELD/ THE CREATION OF THE GEORGE A. WEISS PAVILION

Paul A. Gossen P.E. F.ASCE [1]; Steven P. Emery P.E.[2]

[1] Principal of Geiger Gossen Hamilton Campbell Engineers P.C. , 2 Executive Blvd, Suite 410, Suffern, NY 10901; PH (845) 368-3330; FAX (845) 368-3366; email: pag@geigerengineers.com

[2] Principal of Geiger Gossen Hamilton Campbell Engineers P.C., 2 Executive Blvd, Suite 410, Suffern, NY 10901; PH (845) 368-3330; FAX (845) 368-3366; email: spe@geigerengineers.com

ABSTRACT

As part of the expansion of the athletic program at the University of Pennsylvania in Philadelphia, the space underneath the bleacher area of Franklin Field was recaptured by excavating and then converting the area under the concourse slabs and ramps to a weight training facility. The augmentation has earned the project a LEED Silver Certification.

THE HISTORY OF FRANKLIN FIELD

Franklin Field is the oldest open stadium in the United States. It originally opened in 1903 with wooden bleachers seating 30,000 spectators. In 1922 the stadium was replaced with a concrete structure with a capacity of 50,000 seats. Only 3 years after the rebuilding of the stadium, it was expanded by adding an upper tier with 25,000 more seats. This addition is a independent steel structure, laterally braced by the original concrete frame. In 1983 expansion joints were introduced into the structure.

The stadium is an open-air horseshoe shaped structure and was built on a defunct industrial landfill. The entire stadium, including the "slab on grade", are supported by concrete piles to mitigate possible settlements due to the poor soil condition. Piles are friction piles that penetrate the fill and bear in the underlying glacial till.

The façade of the stadium consists of brick clad columns forming an arcade and supporting the upper concrete rakers. The brick enclosure for these columns terminate in brick arches under the raker beams

THE PROGRAM

In 2007 the Physical Education Department at the University of Pennsylvania in Philadelphia contemplated the expansion of their training facility. One of the possible sites for this expansion was a space under the Franklin Field Football Stadium that had been filled with cinders and debris. The new excavation and enclosing of this area would yield 30,000 sf of usable space. In addition, the expansion of the concourse and upper concourse would be extended from the interior columns to the exterior "arch columns", filling in two floors in the arcade space and adding an additional 20,000 sf of usable space. This scheme enabled a significant increase of usable space while maintaining the historic appearance of the façade.

THE CHALLANGE

The Franklin Field renovation posed several challenges in that new floors were added, column bracing was removed, and the existing façade was uncovered after seven decades. To utilize the new space after excavation, existing piles and pile caps needed to be lowered and existing concrete columns extended. An innovative approach involving a temporary prestressed transfer steel frame was used to support the concrete columns during this phase of work. This approach assured minimum disturbance to and elimination of cracking of the existing concrete structure. No temporary foundation system was required for the temporary support. The frames were designed to be reused for multiple alterations. A soil anchor pinning system was installed to form the new interior retaining wall with no temporary bracing.

DESIGN APPROACH

The University archives contained copies of drawings dating back to the 1923 renovation and subsequent alterations and additions. Unfortunately, some of these drawings were in very poor condition and illegible. The majority of the drawings were architectural details with the most complete and structurally informative documents being the construction drawings of 1983 for the addition of the expansion joints. However, these were only partially accurate because they had been based on assumptions of structural configurations that did not directly affect the construction of the expansion joints. The elevations of the pile caps for the interior columns, for example, varied significantly from the 1983 or original architectural drawings.

The Implementation

The renovation program consisted of several tasks, outlined below.

1. Addition of a new foundation retaining wall ioutside of the exterior brick colonnade to form the exterior wall for the newly excavated area.
To gain as much space as possible for the lower level, the new retaining wall was placed 2 feet in front of the existing masonry arcade columns. The foundation wall is 16 feet high and 16 inch thick. It is laterally braced by the new slab on grade as well as the new concourse framing. The wall is supported by 8"ø steel cased mini piles with a 40 ton capacity.

2. Excavation of the infilled area and placement of a new floor slab; installation of a new retaining wall on the interior side of the new space.
The excavation of the fill underneath the old concourse ramps presented several challenges. The soil in itself was not stable enough for the required vertical cut. Soil nails were installed as the excavation progressed. The cut was periodically sprayed with water to maintain the soil cohesion. After the excavation reached the final vertical elevation, a gunite wall was installed in front of the cut. The wall was cocealed with a CMU wall in front of the gunite wall. A drain gutter was provided between the two walls at the ground floor level to collect any water that might penetrate through the stadia into the soil behind the new gunite wall.

3. Lowering several pile caps and consequently extending their supported columns in the new space.

Four of the existing pile caps extended up to seven feet above the desired elevation for the new lower level floor. They thus interfered with the space to be used for exercise equipment. These pile caps support the concrete columns of the original concrete frame. In order to lower a pile cap, the column above carrying a load of 36 tons, the deal load of the structure, needed to be temporarily supported by other means. Driving new piles next to the existing ones was not feasible due to the site restraints.

A frame was devised that transferred the column load to the pile caps of adjacent columns which were 19'-2 ½" away. The frame was shaped like an "A" and consisted of two HSS 8x8 tubes that formed the A's legs. The top of the "A" lined up with the 16" square column that needed to be suspended and was connected to it through a hanger arrangement. Initially the connection to the concrete column was envisioned to be through a plate welded to the column reinforcement. Tests of sample welds to the reinforcement showed, however, that the welds were too brittle due to the reinforcement's high carbon content. The connection of the hanger to the concrete column was then designed with the use of 16- 1"ø x 8" adhesive fasteners. The base of each HSS 8x8 leg rested next to the adjacent column.

The transfer frame was installed at the concourse level, one story above the pile cap, so that there would be enough room for the demolition of the pile cap and shortening of the piles. The bases of the "A" frame legs were connected to each other by a C10x15.5 tie to resist the spreading force. The center of the tie was spliced by threaded rods tensioned to match the force that would arise when the frame carried the concrete column's calculated dead load. Teflon sheets underneath the bases of the "A" frame legs meant that only small friction forces would resist the prestressing of the tie. The pre-stress forces were monitored by strain gages. The pre-stress in the "A" frame assured that there would be no movement once the column was cut loose from the pile.

The concourse level concrete beams framing into the columns that would support the loaded "A" frame did not have sufficient shear capacity to transfer the load. Shoring underneath the concourse transferred the load directly to the pile caps of these columns. The "A" frame extended from the concourse level to the underside of the concrete raker beam 20 feet above, where it was fastened to provide lateral stability.

4. Removal of the ramp connecting the concourse to the lower level (field level) and replacement of it with a framed floor.
Some of the concrete columns were braced by the ramp and required another means of lateral support for this work phase. Temporary bracing was installed during removal of the ramp and remained until after placement of the new concourse floor.

5. Addition of a new floor to the upper tier between the exterior columns and the extension to upper concourse.
The exterior free standing colonnade consists of masonry encased concrete columns that extend from the foundation to the underside of the raker beams. The masonry encasement at the upper portion forms arches that give the building appearance its special his.toric look Transverse arches connect these columns to the ones that are incorporated into the wall and that support the concourse and upper concourse. new floors were built between these

columns extending the concourse and upper concourse floors into the colonade space. The framing for these floors is steel beams and metal deck with concrete fill. The clearance of the bracing arches and the new upper concourse floor was only three feet. Thus they were removed after the floor framing was installed. This sequence of construction assured continuous bracing of the colonnade columns.

6. Repair of corroded reinforcing and structural steel.
As part of the renovation, the existing structure was evaluated. Parts of the new framed slabs were to be supported from the existing concrete beams. It was observed that many beams had spalled concrete due to reinforcing corrosion. Even some of the steel columns that had been added to support the upper tier showed significant spalling of their concrete enclosures. This was surprising since the beams and columns were previously fitted with a cathodic protection. Once an evaluation of the steel showed that it was sound enough for its structural purpose, the concrete surfaces of the damaged beams and columns were treated with a corrosion inhibiting penetration liquid to slow if not halt further deterioration.

CONCLUSION

The renovation and expansion of the Franklin field to create the George A. Weiss Pavillion presented several design and construction challenges. The successful completion of the work gave the university community a significant and unique usable space for their athletic program without compromising the appearance of one of their historic structures.

Comparison of Hybrid and Emulative Precast Concrete Shear Walls for Seismic Regions

B. J. Smith[1], Y. C. Kurama[2] and M. J. McGinnis[3]

[1]Civil Engineering and Geological Sciences, Univ. of Notre Dame, 156 Fitzpatrick Hall, Notre Dame, IN 46556; PH: (574) 631-5380; email: bsmith24@nd.edu
[2]Civil Engineering and Geological Sciences, Univ. of Notre Dame, 156 Fitzpatrick Hall, Notre Dame, IN 46556; PH: (574) 631-8377; email: ykurama@nd.edu
[3]Civil Engineering, University of Texas at Tyler, 3900 University Blvd, Tyler, TX 75799; PH: (903) 565-5870; email: mmcginnis@uttyler.edu

ABSTRACT

This paper compares the measured lateral load behavior of a 0.4-scale "hybrid" precast concrete wall test specimen with the behavior of a second precast specimen designed to emulate monolithic cast-in-place reinforced concrete shear walls. Both walls have the same overall geometry and are constructed by placing rectangular wall panels across horizontal joints. The lateral resistance at the joints of the "emulative" system is provided by mild [i.e., Grade 400 (U.S. Grade 60)] steel bars, whereas the hybrid wall features a combination of mild steel bars and high-strength unbonded post-tensioning (PT) strands. The mild steel reinforcement at the base of both systems is designed to yield and provide energy dissipation, while the unbonded PT steel in the hybrid system also provides self-centering capability to reduce the residual lateral displacements of the structure after a large earthquake. The comparisons between the two walls focus on the applied lateral load versus displacement behavior, energy dissipation, behavior of the steel reinforcement, and behavior along the critical horizontal base-panel-to-foundation joint. Due to the lack of PT steel, the emulative specimen developed a residual uplift along the entire base-panel-to-foundation joint, resulting in excessive horizontal slip, large strength and stiffness degradation, and significant residual lateral displacements. In contrast, the hybrid specimen showed significantly smaller residual uplift, horizontal slip, and strength and stiffness degradation, resulting in excellent re-centering and energy dissipation with ductile behavior over much larger lateral deformations.

INTRODUCTION AND BACKGROUND

As described in detail in Smith et al. (2011), the hybrid precast wall system investigated in this research utilizes a combination of mild [i.e., Grade 400 (U.S. Grade 60)] steel bars and high-strength unbonded post-tensioning (PT) strands for lateral resistance across horizontal joints. The general test configuration for the hybrid specimen is shown in Figure 1a. Under the application of lateral loads into the nonlinear range, the primary mode of displacement in these walls occurs through gap opening at the base joint. The PT steel is provided by multi-strand tendons placed

inside un-grouted ducts to prevent bond between the steel and concrete. Thus, the tendons are connected to the structure only at end anchorages. The emulative wall configuration (Figure 1b) uses only mild steel reinforcement with no PT steel.

In both systems, the mild steel bars crossing the horizontal joint at the base are designed to yield and provide energy dissipation through the nonlinear lateral displacements of the structure. A pre-determined length of these bars is unbonded at the bottom of the base panel (by wrapping the bars with plastic sleeves) to prevent low-cycle fatigue fracture. In the case of the hybrid wall, both the PT steel and mild steel contribute to the lateral strength of the structure. Upon unloading, the PT steel provides a restoring force to close the gaps and reduce the residual (i.e., permanent) lateral displacements of the wall after a large earthquake. The use of unbonded PT tendons (as compared to bonded tendons) delays the yielding of the strands and reduces the tensile stresses transferred to the concrete (i.e., reduced cracking) as the tendons elongate under lateral loading.

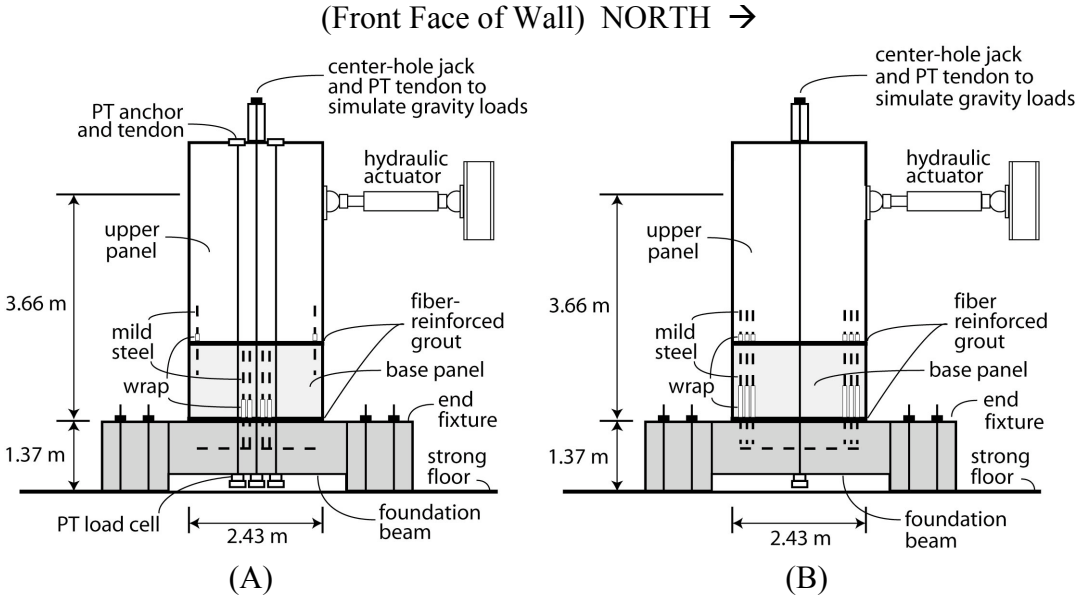


Figure 1. Test configuration: (a) hybrid wall; (b) emulative wall.

According to Chapter 21 of ACI 318 (2008), "a reinforced concrete structural system not satisfying the requirements of this chapter shall be permitted if it is demonstrated by experimental evidence and analysis that the proposed system will have strength and toughness equal to or exceeding those provided by a comparable monolithic reinforced concrete structure satisfying this chapter." The hybrid precast wall system investigated in this research falls within this category of structures that require experimental validation and analysis prior to their use in practice as a primary lateral load resisting system. The roadmap for the seismic performance assessment of hybrid walls is provided by ACI ITG-5.1 (2007), which lays out the minimum experimental evidence needed for the classification of these walls as special reinforced concrete shear walls based on ACI 318. The emulative system in Figure 1b is also not directly permitted by ACI 318, since unlike the requirements for a monolithic cast-in-place reinforced concrete structure, the longitudinal mild steel reinforcement is lumped near the ends of the wall (i.e., there is no distributed steel crossing the horizontal

joints). As compared with a distributed bar arrangement, the lumped reinforcement detail in Figure 1b provides ease of placement during the field erection process.

This paper provides a comparative experimental evaluation of these two precast concrete wall systems under reversed-cyclic lateral loading. Ultimately, the goal of this comparison is to investigate the code approval and validation of the walls according to the guidelines, prerequisites, and requirements in ACI ITG-5.1 and ACI 318.

TEST SET-UP AND SPECIMEN PROPERTIES

The tests conformed to the requirements of ACI ITG-5.1. Schematic drawings of the test setup and specimen details are shown in Figures 1 and 2, respectively. The hybrid specimen was designed as a special reinforced concrete shear wall [within an ASCE 7 (2005) "building frame system"] for a 4-story prototype parking garage with an approximate footprint of 3,770 m^2 (40,600 ft^2) in Los Angeles, CA. Both the hybrid wall and emulative wall tests were conducted at 0.40-scale, which satisfies the minimum scaling limit of ACI ITG-5.1. The specimens featured two panels: the base panel representing the 1st story of the structure and the upper panel representing the 2nd through 4th stories, thereby satisfying the ACI ITG-5.1 requirement for testing multi-panel walls (such that an upper panel-to-panel joint as well as the base-panel-to-foundation joint are evaluated). The 0.40-scale wall length, l_w, was 243 cm (96 in.), base panel height, h_{pb}, was 145 cm (57.5 in.), and wall thickness, t_w, was 15.9 cm (6.25 in.). It was possible to test the upper story panels of the 4-story prototype wall as a single panel since the joints between these upper panels were designed to have no nonlinear behavior and no gap opening. The lateral load was applied 3.66 m (12

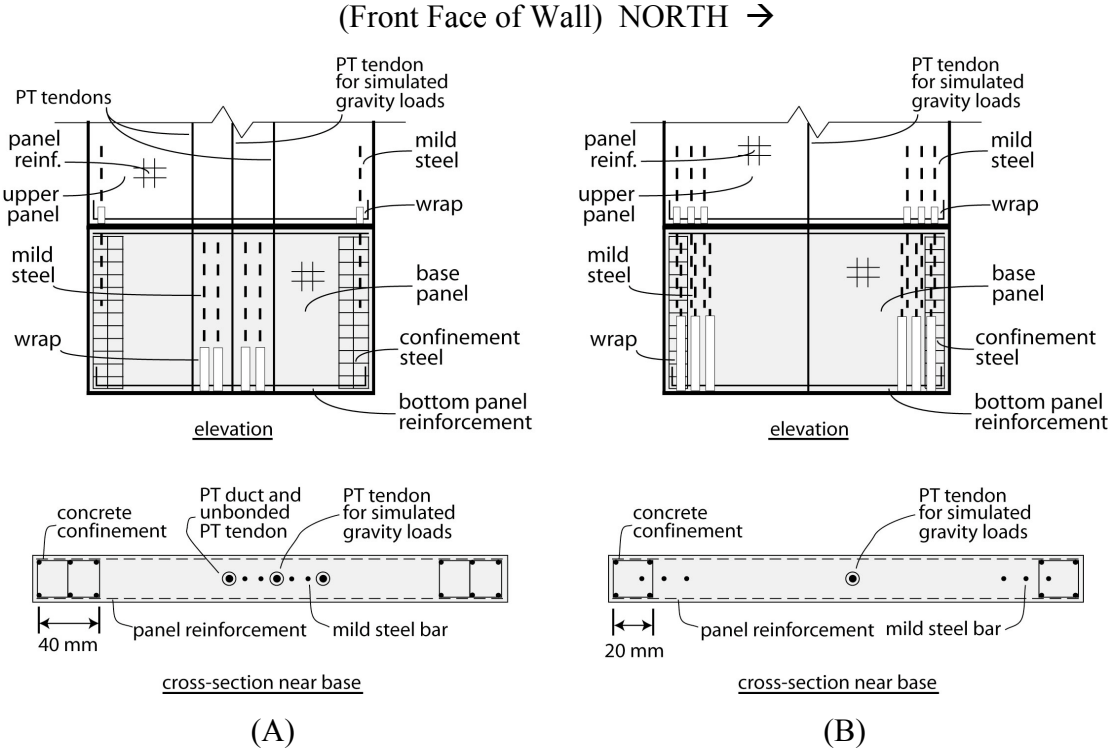


Figure 2. Test specimen details: (a) hybrid wall; (b) emulative wall.

ft) from the wall base (near the resultant location of the 1st mode inertial forces), resulting in a wall base moment to shear ratio of M_b/V_b=1.5l_w. An external downward axial load of about 325 kN (73 kips) was applied at the center of the top of each specimen to simulate the service-level tributary gravity loads acting on the prototype structure.

The hybrid wall specimen was designed using the requirements and guidelines of ACI ITG-5.2 (2009), ACI-318, and ASCE 7 (2005). More information on the design of this wall as well as the results from a pre-test analytical study can be found in Smith and Kurama (2009) and Smith et al. (2011). The structure was designed for a full-scale base moment strength of 24,400 kN-m (18,000 kip-ft) and a "validation-level" wall drift prescribed by ACI ITG-5.1 (2007) as:

$$\Delta_{wm} = 0.9\% \le \left(h_w/l_w\right)0.8\% + 0.5\% \le 3.0\% \quad (1)$$

where, h_w=height to the top of the wall; and l_w=length of the wall. The wall drift, Δ_w is defined as the lateral displacement at the top of the wall divided by the wall height. For the given wall dimensions, the resulting validation-level drift is Δ_{wm}=2.30%.

The design of the emulative wall was conducted for the same lateral force and displacement requirements as the hybrid wall according to ACI 318. Both specimens were designed with minimal overstrength in order to test the limits of the design requirements and procedures. Most of the design parameters remained consistent between the two specimens, with the primary exception of the reinforcement details.

In the hybrid system (Figure 2a), the PT steel consisted of two tendons located 27.9 cm (11 in.) north and south from the wall centerline. The tendons were placed near the wall centerline to reduce the strand strains and also keep the PT ducts away from the critical confined toe regions of the wall. Each tendon contained three 1.3-cm diameter (0.5-in.) strands [design ultimate strength, f_{pu}=1862 MPa (270 ksi)] with an unbonded length from the top of the wall to the bottom of the foundation beam of about 5.48 m (18 ft). The average initial tendon stress, calculated from the measured individual strand forces prior to the application of the lateral load, was f_{pi}=0.54f_{pu}. The mild steel crossing the base joint in the hybrid specimen (i.e., energy dissipating steel) consisted of four 19-mm diameter (U.S. No. 6) bars [measured yield strength, f_{sy}=448 MPa (65 ksi), and yield strain, ε_{sy}=0.0023 cm/cm], with one pair of bars placed 19.0 cm (7.5 in.) north and south from the wall centerline and the other pair 8.9 cm (3.5 in.) north and south from the centerline. The energy dissipating bars were unbonded over a length of 38.1 cm (15 in.) at the bottom of the base panel. Across the upper panel-to-panel joint, only two 19-mm diameter bars were used, with one bar 10.2 cm (4 in.) from each end of the wall. This reinforcement was designed not to yield so as to limit any gap opening along the panel-to-panel joint. To prevent strain concentrations in the panel-to-panel joint reinforcement, a short 7.6-cm length (3-in.) of the bars was unbonded at the bottom of the upper panel. The design unconfined concrete strength for the wall was 41 MPa (6.0 ksi) and the design confined concrete strength (at the toes of the base panel) was 62 MPa (9.0 ksi). The measured unconfined concrete strength for the base panel was 55 MPa (8.0 ksi) on the day that the wall was tested. At the base and panel-to-panel joints, fiber-reinforced grout (with polypropylene microfilament fibers at 0.065% by volume) was used. The test-day strength of the grout at the base joint was 58 MPa (8.4 ksi).

The steel reinforcement crossing the base joint in the emulative specimen (Figure 2b) consisted of six 22-mm diameter (U.S. No. 7) bars [measured yield strength, f_{sy}=427 MPa (62 ksi), and yield strain, ε_{sy}=0.0035 cm/cm], with three bars placed at each end of the wall [located 17.8 cm (7 in.), 30.5 cm (12 in.), and 43.2 cm (17 in.), respectively, from the wall end]. The bars were unbonded over a length of 55.9 cm (22 in.) at the bottom of the base panel. Across the upper panel-to-panel joint, six 22-mm diameter bars were used, with three bars at each end of the wall [located 12.7 cm (5 in.), 25.4 cm (10 in.), and 38.1 cm (15 in.) from the ends of the wall]. As in the case of the hybrid specimen, this reinforcement was designed not to yield so as to limit any gap opening or slip along the panel-to-panel joint. A 7.6-cm length (3-in.) of the bars was unbonded at the bottom of the upper panel to prevent strain concentrations in the joint reinforcement. Similar to the hybrid wall, the design unconfined concrete strength for the emulative wall was 41 MPa (6.0 ksi) and the design confined concrete strength (at the toes of the base panel) was 63 MPa (9.1 ksi). The measured unconfined concrete strength for the base panel of the emulative wall was 45 MPa (6.6 ksi) on the day that the wall was tested, which is smaller than the measured concrete strength for the hybrid wall. The test-day strength of the fiber-reinforced grout at the base joint of the emulative wall was 39 MPa (5.6 ksi).

MEASURED BEHAVIOR OF SPECIMENS

Figure 3 shows the reversed-cyclic lateral displacement history used in the testing of each specimen. The wall drift, Δ_w (positive with the wall displaced southward), was measured as the relative lateral displacement of the wall between the lateral load location and the foundation divided by the height to the lateral load. The hybrid specimen was able to sustain two fully-reversed drift cycles at Δ_w=±2.30% (i.e., the validation-level drift) followed by a greater drift cycle of =±2.95%. In comparison, the emulative wall failed after three fully-reversed drift cycles to Δ_w=±1.15%.

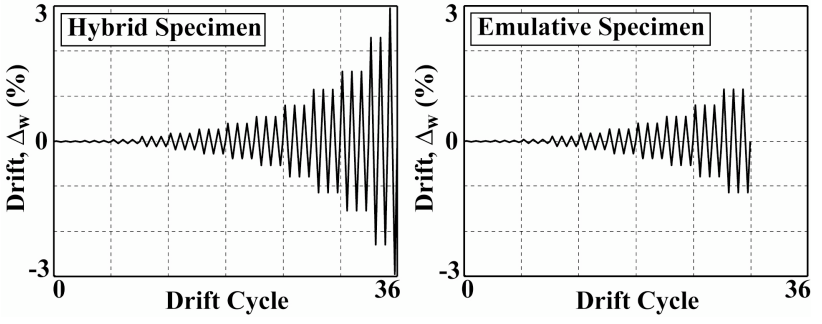
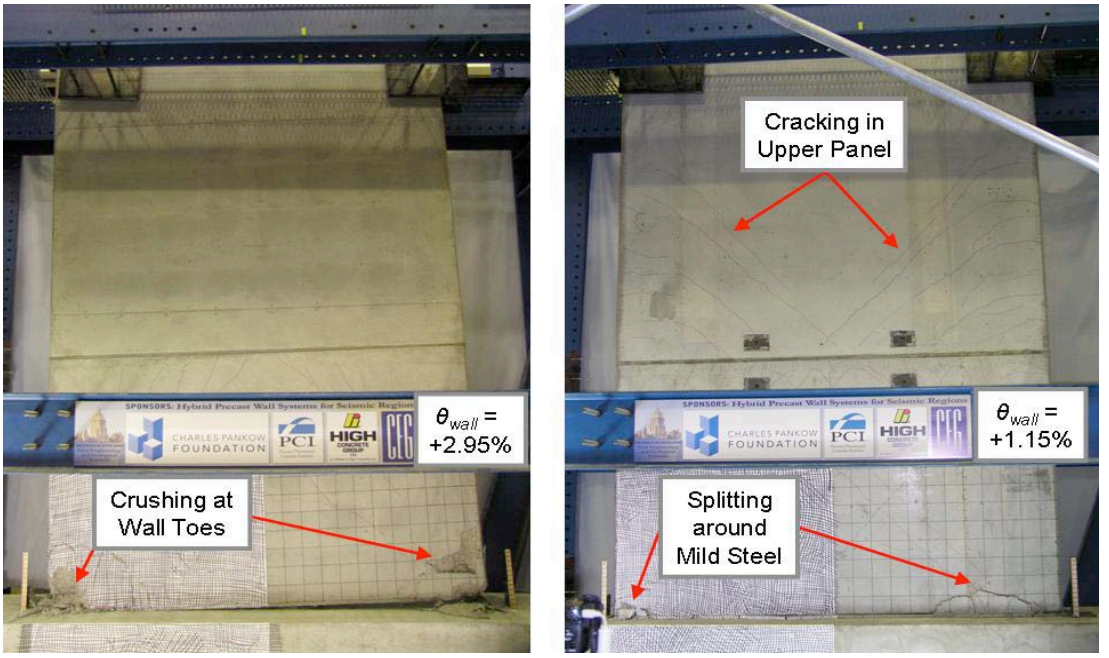


Figure 3. Drift history: (a) hybrid wall; (b) emulative wall.

Figure 4a shows the hybrid specimen at Δ_w=+2.95% (note the gap opening along the base joint at the north end). While crushing of the confined concrete was observed at the wall toes, the total strength loss at the completion of the drift history in Figure 3a was less than 20%, thus satisfying the ACI ITG-5.1 requirement for validation. Additional loading of the wall beyond the required displacement history resulted in further strength loss and subsequent failure of the specimen (defined by ACI ITG-5.1 as the drift at which the total strength loss exceeds 20%). The damage to the wall was limited to the base panel, with no concrete cracking or crushing in the upper panel and no significant gap opening or slip in the upper panel-to-panel joint.

Similarly, Figure 4b shows the emulative wall at the third cycle to Δ_w=+1.15%. While the crack widths generally remained small, the cracking was considerably more extensive than in the hybrid wall and extended high into the upper panel. Failure of the emulative specimen occurred relatively early due to the uplift of the wall from the foundation (i.e., a gap formed along the entire base joint when the wall was returned to Δ_w=0%), which resulted in excessive horizontal slip at the base together with large strength and stiffness degradation. Under load reversal with increasing slip, the concrete around the mild steel bars crossing the base joint began to deteriorate due to the shear force transfer from the bars to the surrounding concrete, eventually resulting in localized splitting of the wall panel around the bars. No significant slip or gap opening was observed in the upper panel-to-panel joint.

(Front Face of Wall) NORTH →

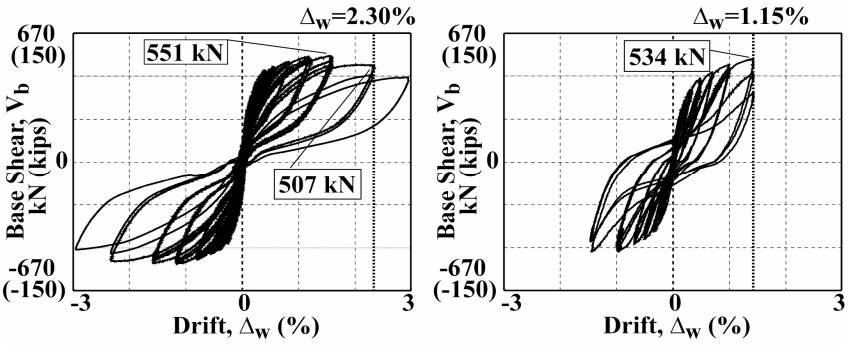


(A) (B)

Figure 4. Observed damage: (a) hybrid wall at Δ_w=+2.95%; (b) emulative wall at Δ_w=+1.15%.

Lateral Load Versus Displacement Behavior. Figure 5 compares the measured base shear force, V_b versus wall drift, Δ_w behaviors for the hybrid and emulative walls. The maximum base shear resistance of the hybrid wall was 551 kN (124 kips) reached at Δ_w=+1.55%, the resistance at the validation drift (Δ_{wm} = +2.30%) was 507 kN (114 kips), and the resistance at Δ_w=+2.95% was 443 kN (99.5 kips). The specimen behaved in a reasonably symmetrical manner in the positive and negative directions, while also exhibiting excellent re-centering capability and energy dissipation. The total strength loss from the maximum base shear resistance to the peak resistance during the final drift cycle to ±2.95% was approximately 19.9% and 13.8% in the positive and negative directions, respectively, which are both within the 20% strength loss limit prescribed by ACI ITG-5.1.

The maximum base shear resistance of the emulative wall was 534 kN (120 kips) reached at Δ_w=+1.15%. Until the yielding of the mild steel bars crossing the base joint, the emulative and hybrid wall behaviors were similar (with the exception of more widespread hairline cracking in the emulative system). However, upon unloading from significant tensile yielding of the mild steel bars, the re-centering capability of the emulative wall was limited. Without the PT force, the restoring effect of the 325-kN (73-kip) tributary gravity load applied at the top of the wall and the 40-kN (9-kip) self-weight of the specimen [total 365-kN (82-kip) gravity load] was not sufficient to fully yield the bars back in compression (i.e. return to essentially zero elongation of the bars) and close the gap at the base joint. Upon reloading, the nonlinear behavior and failure of the wall was dominated by excessive horizontal slip at the base joint, with relatively small gap opening as compared to the hybrid specimen. The behavior of the emulative wall in the positive and negative directions was somewhat unsymmetrical (e.g., the maximum base shear resistance in the negative direction was only 467 kN (105 kips)], which occurred due to different amounts of slip in the two directions. The specimen failed during the third cycle to Δ_w=+1.15%, as the total strength loss from the maximum base shear resistance to the peak resistance was 32.5% in the positive direction (a smaller 11.1% total strength loss occurred in the negative direction).



(A) (B)

Figure 5. Base shear force versus wall drift history: (a) hybrid wall; (b) emulative wall.

Energy Dissipation. The primary source of energy dissipation in both wall systems is the yielding of the mild steel reinforcement over the unbonded length of the bars at the bottom joint. To quantify the energy dissipation of the structure, ACI ITG-5.1 uses the energy dissipation ratio, β, which is defined as "the ratio of the measured energy dissipated by the test module during reversing cyclic displacements between given measured drift angles to the maximum theoretical energy that can be dissipated for the same drift angles." ACI ITG-5.1 requires that β be not less than 0.125 at the validation-level drift.

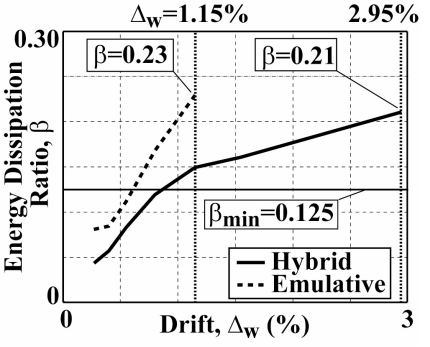


Figure 6. Energy dissipation ratio.

The solid and dashed lines in Figure 6 show the measured energy dissipation ratio, β of the hybrid and emulative walls, respectively, plotted against the wall drift. The last cycle for each drift level was used to calculate β. It can be seen that both

specimens satisfied the ACI ITG-5.1 minimum β requirement at moderate drift levels and continued to exceed the minimum requirement until the end of the test. As expected, the emulative wall demonstrated larger energy dissipation than the hybrid wall since about 41% of the base moment strength of the hybrid wall was provided by unbonded PT steel, which remained linear-elastic during most of the test.

Energy Dissipating Mild Steel Strains. Since the mild steel bars crossing the base-panel-to-foundation joint serve as the main energy dissipater for the wall system, it is essential for these bars to yield significantly but not fracture during the loading history up through the validation drift. Figure 7a shows the four mild steel bars at the base of the hybrid specimen prior to the placement of the concrete. The 38.1-cm (15-in.) long plastic-wrapped unbonded length of the bars can be seen in the photograph. The wrapping was done to reduce the steel strains and thus, prevent low-cycle fatigue fracture as the wall was displaced. Similarly, Figure 7b shows the mild steel bars at the south end of the emulative base panel. Since the reinforcement in the emulative wall was placed at the ends of the panel rather than near the centerline, larger bar elongations were expected. Therefore, a longer 55.9-cm (22-in.) unbonded length was used in the emulative wall.

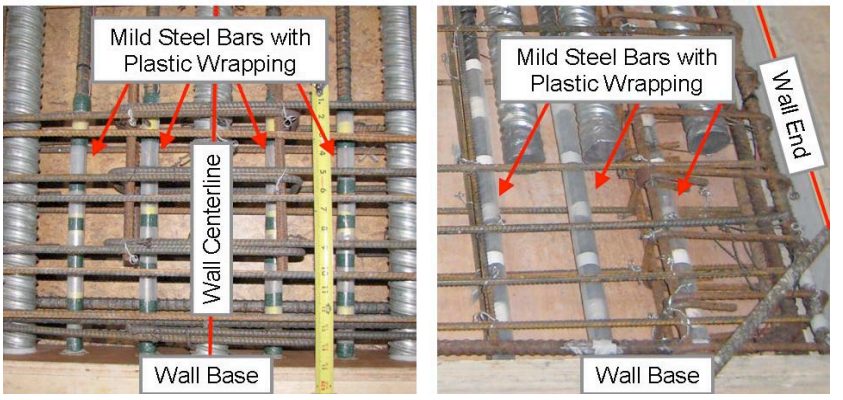


Figure 7. Mild steel bars crossing base joint: (a) hybrid wall; (b) south end of emulative wall.

Figure 8a shows the measured (using strain gauges placed within the unbonded length) and predicted [using the pre-test design procedure described in Smith et al. (2011)] strains for the south intermediate energy dissipating bar in the hybrid specimen [located 8.9 cm (3.5 in.) from the wall centerline]. For clarity, the measured bar strains are shown at the third cycle of each wall drift increment instead of the full cyclic strain history. In general, the measured and predicted strains compare favorably. Note that due to gauge failure,

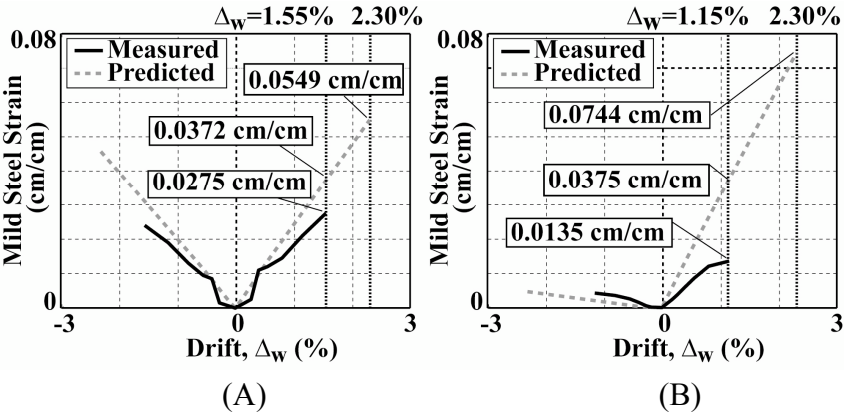


Figure 8. Mild steel strains: (a) hybrid; (b) emulative wall.

measurements could only be taken up to a maximum strain of 0.0275 cm/cm at Δ_w=+1.55%. As designed, the bars yielded (measured yield strain, ε_{sy}=0.0023 cm/cm) relatively early in the loading history and the test was completed with no undesirable behavior of the steel (i.e., no bar fracture, observable slip, or buckling).

Similarly, Figure 8b shows the mild steel strains for the south intermediate bar in the emulative wall [located 30.5 cm (12 in.) from the wall end]. Again, the bars were designed to yield relatively early in the test; however, due to the small gap opening displacements at the base of the wall, the actual axial bar strains remained relatively small. The pre-test design calculations were also based on the axial strains of the bars due to gap opening; and thus, the predictions significantly overestimated the measured strains (e.g., at the maximum drift of Δ_w=+1.15%, the measured and predicted steel strains were 0.0135 cm/cm and 0.0375 cm/cm, respectively).

PT Steel Behavior. The PT steel provides the main restoring force for the hybrid system, ensuring that the gap at the wall base is fully closed upon unloading (which requires that the mild steel bars yield back in compression) and allowing the structure to return to its initial undisplaced position after being subjected to significant lateral loading. Figure 9 depicts this restoring force by plotting the normalized average stress in each of the north and south tendons [calculated as the sum of the measured strand forces divided by $A_p f_{pu}$, where A_p is the total area of the three 1.3-cm diameter (0.5-in.) strands in each tendon and f_{pu}=1862 MPa (270 ksi) is the design strength of the strands]. The differences in the north and south tendon stresses are due to the different elongations of the two tendons as the wall was displaced laterally. Consistent with the design expectations, the PT tendons remained essentially linear-elastic until Δ_w=1.55%, which was possible since the strands were unbonded over their length. The average stresses for the north and south tendons were 0.85 and 0.65f_{pu}, respectively, at the validation-level drift of Δ_{wm}=+2.30%. Considerable stress losses can be seen in the tendons upon unloading from the Δ_w=±2.95% cycle; however, despite this loss, the residual drift of the wall at the end of the test was negligible (see Figure 5a).

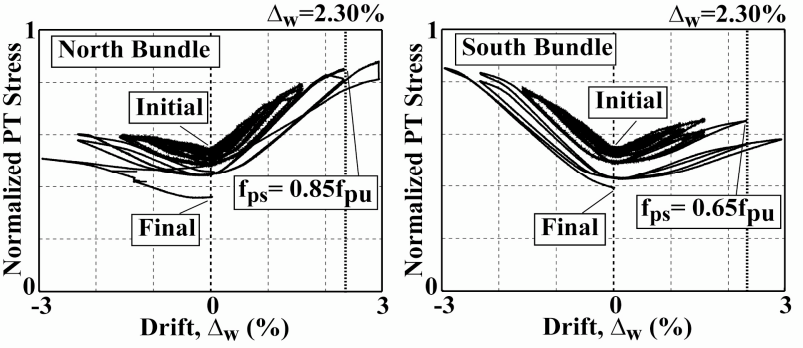


Figure 9. Average PT strand stresses: (a) north tendons; (b) south tendons.

Wall Uplift. The vertical displacement at the top of the wall, which is related to the gap opening along the horizontal joints, can be used to estimate the uplift (or axial elongation) of the test specimens. For this purpose, Figure 10 shows the residual axial elongation measured at the centerline of each wall at the location of the applied lateral load after the completion of each drift series (i.e., after unloading from the last cycle in each drift increment). The accumulation of this residual elongation (upwards

positive) represents a reduction or loss of self-centering. In the hybrid specimen, the axial elongation did not start to accumulate until the Δ_w=±1.55% drift cycles, with a maximum residual elongation of 0.25 cm (0.10 in.) upon unloading from Δ_w=±2.95%. This small amount of uplift did not affect the performance of the wall in any undesirable way. In contrast, the emulative wall accumulated significantly greater axial elongations beginning from the Δ_w=±0.27% cycles, with a maximum uplift of 0.61 cm (0.24 in.) after the last cycle to Δ_w=±1.15%.

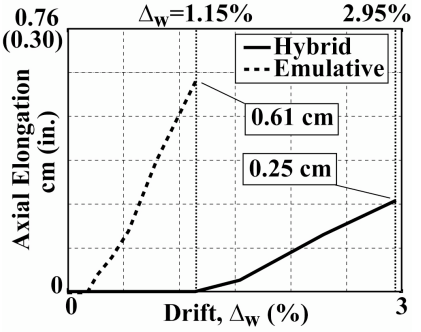


Figure 10. Wall uplift.

The large differences between the axial elongations of the two walls are related to the PT steel. In both specimens, the tensile yielding of the energy dissipating mild steel reinforcement across the base joint resulted in the plastic elongation of the bars during the loading of the wall. Upon unloading of the hybrid specimen, the restoring force provided by the PT steel and the total gravity load [365 kN (82 kips)] caused the mild steel to yield in compression and return to essentially zero elongation, thus fully closing the gap at the base joint. The accumulation of residual axial elongations, which did not start until the Δ_w=±1.55% cycles, coincided with the accumulation of PT stress losses (see Figure 9). In the case of the emulative specimen, once the mild steel bars yielded in tension, the gravity load alone was not large enough to return the bars to the zero elongation state. Over successive loading/unloading cycles with increasing wall drift, the residual tensile deformations in the bars resulted in the complete uplift of the wall (i.e., gap over the entire length of the base joint), overcoming the downward force from the gravity load. As shown in Figure 10, the axial elongation of the emulative specimen accumulated rapidly, ultimately leading to the failure of the structure due to excessive horizontal slip with large strength and stiffness degradation.

Horizontal Slip at Wall Base. By measuring the relative horizontal displacements between adjacent points on either side of the base-panel-to-foundation joint, the horizontal slip at the wall base was determined. The solid lines in Figure 11 show the measured horizontal slip at the centerline of the hybrid wall for loading in the positive and negative directions during the third cycle in each drift series [except for the final drift series where the first cycle (Δ_w=±2.30%) and the third cycle (Δ_w=±2.95%) slips are plotted]. The slip at the base was small [with a maximum slip of about 0.31 cm (0.12 in.) at Δ_w=–2.95%] and did not negatively affect the performance of the wall. Moreover, the crushing of the concrete at the wall toes did not result in a disproportionate accumulation of slip. No slip was observed at the upper panel-to-panel joint of the wall.

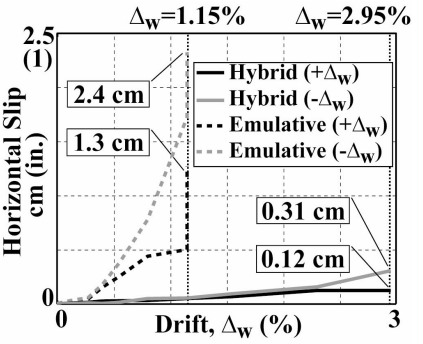


Figure 11. Shear slip at base.

For the emulative specimen (dashed lines in Figure 11), the measured slip at the base joint was much larger, with a maximum value of 2.4 cm (0.93 in.) at the

third cycle of Δ_w=–1.15% [again, the plot shows slip measurements for the third cycle in each drift series, except for the last drift series (Δ_w=±1.15%) where the first and third cycle slips are plotted]. The amount of slip was considerably greater in the negative loading direction. The slip displacements accumulated rapidly beginning from the Δ_w=±0.27% cycles when, as shown in Figure 10, the accumulation of wall uplift also initiated. Upon reloading from a configuration with complete uplift at the base, the mild steel bars were the only components transferring shear forces from the wall into the foundation until the lateral displacement was large enough to close the gap at the compression toe of the wall. The concrete around the mild steel bars began to deteriorate due to this shear force transfer, eventually resulting in the localized splitting of the base panel around the bars (see Figure 4).

At the point when slip at the base joint started to rapidly accumulate in the emulative specimen (i.e., at the first loading of the wall to Δ_w=+0.27%), an estimate of the coefficient of shear friction can be made by dividing the measured base shear force [374 kN (84 kips)] with the compression force transferred through the contact region [comprised of the measured total gravity load, 365 kN (82 kips) and the total force in the tensile mild steel bars, 552 kN (124 kips), where the mild steel stresses were determined using the measured strains and the measured monotonic stress-strain relationship for the bars]. The resulting coefficient of shear friction is equal to 0.41, which is considerably smaller than the value of 0.50 recommended by ACI ITG-5.2 for the base-panel-to-foundation joint. Note that ACI ITG-5.2 also recommends a friction coefficient of 0.60 for the upper panel-to-panel joint; however, an estimate for this coefficient could not be made from the tests since no significant slip was observed at the upper joint of the walls.

SUMMARY AND CONCLUSIONS

This paper compares the measured lateral load behavior of a 0.4-scale hybrid precast concrete shear wall specimen with the behavior of an emulative precast wall. The results demonstrate the tremendous potential for the use of the hybrid wall system as special reinforced concrete shear walls in high seismic regions, while also revealing the potential limitations of the emulative system tested in this research. Based on the measured and observed results, the following conclusions were made:

- The hybrid wall specimen demonstrated full re-centering capability while also providing large energy dissipation due to the combination of unbonded post-tensioning steel with yielding mild steel reinforcement across the base-panel-to-foundation joint.
- The behavior of the hybrid wall was consistent with the design predictions.
- The damage in the hybrid specimen was limited to the base panel.
- The hybrid specimen sustained three fully-reversed drift cycles of magnitude equal to or greater than the validation-level drift prescribed by ACI ITG-5.1.
- While the emulative wall specimen demonstrated excellent energy dissipation from the yielding of the mild steel reinforcement across the base joint, the lack of post-tensioning steel resulted in unsatisfactory re-centering capability.

- Insufficient restoring force allowed the emulative specimen to develop a residual gap along the entire length of the base joint, causing excessive horizontal slip at the base.
- The excessive horizontal slip caused large strength and stiffness degradation of the emulative wall, and ultimately led to the failure of the specimen at a relatively small drift.

ACKNOWLEDGMENTS

This research is funded by the Charles Pankow Foundation and the Precast/Prestressed Concrete Institute (PCI). Additional technical and financial support is provided by the High Concrete Group, LLC, the Consulting Engineers Group, Inc, and the University of Notre Dame. The authors would like to acknowledge the support of the PCI Research and Development Committee as well as the members of the Project Advisory Panel, who include Walt Korkosz (chair) of the Consulting Engineers Group, Inc., Ken Baur of the High Concrete Group, LLC, Neil Hawkins of the University of Illinois at Urbana-Champaign, S.K. Ghosh of S.K. Ghosh Associates, Inc., and Dave Dieter of Mid-State Precast, LP. Additional assistance and material donations have been provided by Jenny Bass of Essve Tech Inc., Randy Ernest of Prestress Supply Inc., Eric Fries of Contractors Materials Company, Chris Lagaden of Ecco Manufacturing, Stan Landry of Enerpac Precision SURE-LOCK, Richard Lutz of Summit Engineered Products, Shane Whitacre of Dayton Superior Corporation, and Steve Yoshida of Sumiden Wire Products Corporation. Any opinions, findings, conclusions, and/or recommendations expressed in this paper are those of the authors and do not necessarily represent the views of the individuals or organizations acknowledged above.

REFERENCES

ACI. (2007). "ACI ITG-5.1-07 Acceptance Criteria for Special Unbonded Post-Tensioned Precast Structural Walls Based on Validation Testing and Commentary." ACI Innovation Task Group 5.

ACI. (2009). "ACI ITG-5.2-09 Design of a Special Unbonded Post-Tensioned Precast Shear Wall Satisfying ACI ITG-5.1 Requirements." ACI Innovation Task Group 5.

ACI. (2008). "ACI 318-08 Building Code Requirements for Structural Concrete (ACI 318-08) and Commentary." ACI Committee 318.

ASCE. (2005). "Minimum Design Loads for Buildings and Other Structures." ASCE/SEI 7-05.

Smith, B. and Kurama, Y. (2009). "Design of Hybrid Precast Concrete Walls for Seismic Regions." *ASCE 2009 Structures Congress*, Austin, TX.

Smith, B., Kurama, Y., and McGinnis, M. (2011). "Design and Measured Behavior of a Hybrid Precast Concrete Wall Specimen for Seismic Regions." *J. of Structural Engineering*. In-print. (preprint article may be accessed from http://ascelibrary.aip.org/).

Evaluation of Ground Motion Scaling Methods for Analysis of Structural Systems

A.P. O'Donnell,[1] O.A. Beltsar,[2] Y.C. Kurama,[3] E. Kalkan,[4] A.A. Taflanidis[5]

[1]Civil Engineering and Geological Sciences, Univ. of Notre Dame, 156 Fitzpatrick Hall, Notre Dame, IN 46556; PH: (617) 797-2311; email: aodonne1@nd.edu
[2]Civil Engineering and Geological Sciences, Univ. of Notre Dame, 156 Fitzpatrick Hall, Notre Dame, IN 46556; PH: (925) 353-0355; email: obeltsar@nd.edu
[3]Civil Engineering and Geological Sciences, Univ. of Notre Dame, 156 Fitzpatrick Hall, Notre Dame, IN 46556; PH: (574) 631-8377; email: ykurama@nd.edu
[4]Earthquake Science Center, United States Geological Survey, 345 Middlefield Rd., Menlo Park, CA 94025; PH: (650) 329-5146; email: ekalkan@usgs.gov
[5]Civil Engineering and Geological Sciences, Univ. of Notre Dame, 156 Fitzpatrick Hall, Notre Dame, IN 46556; PH: (574) 631-5696; email: a.taflanidis@nd.edu

ABSTRACT

Ground motion selection and scaling comprises undoubtedly the most important component of any seismic risk assessment study that involves time-history analysis. Ironically, this is also the single parameter with the least guidance provided in current building codes, resulting in the use of mostly subjective choices in design. The relevant research to date has been primarily on single-degree-of-freedom systems, with only a few studies using multi-degree-of-freedom systems. Furthermore, the previous research is based solely on numerical simulations with no experimental data available for the validation of the results. By contrast, the research effort described in this paper focuses on an experimental evaluation of selected ground motion scaling methods based on small-scale shake-table experiments of re-configurable linear-elastic and nonlinear multi-story building frame structure models. Ultimately, the experimental results will lead to the development of guidelines and procedures to achieve reliable demand estimates from nonlinear response history analysis in seismic design. In this paper, an overview of this research effort is discussed and preliminary results based on linear-elastic dynamic response are presented.

INTRODUCTION

As performance-based considerations become pre-requisite in the seismic design and evaluation of building structures, the use of nonlinear response history analysis (RHA) has gained utmost importance (e.g., for tall or irregular structures, structures with innovative structural systems and materials, and/or structures on soft soil). This rigorous analysis method requires, as input, a suite of ground motion records that have been selected and modified (i.e., scaled) appropriately to make them compatible with the site-specific hazard level(s) considered [e.g., Maximum Considered Earthquake (MCE) level, Design Basis Earthquake (DBE) level]. Ground motion selection and scaling has a large impact on the nonlinear RHA results. In fact, the ground motion record itself is undeniably the most important variable for nonlinear RHA (more than the analytical model parameters) governing the outcome and amount of uncertainty from seismic design.

Ironically, this is also the single parameter with the least guidance provided in current building codes and provisions, resulting in the use of mostly subjective choices in the selection of ground motions for nonlinear RHA.

Most of the research to date on ground motion scaling has been on single-degree-of-freedom systems (Chopra and Chinatanapakdee 2004; Martinez-Rueda 1998) with only a few studies on multi-degree-of-freedom systems (Kalkan and Chopra 2010, 2011; Kalkan and Kwong 2011; Alavi and Krawinkler 2000; Kurama and Farrow 2003; Shome and Cornell 1998). Furthermore, the previous research is based solely on numerical simulations, with no experimental data available for the validation of the results. Consequently, there is currently no consensus on which scaling methods would be best suited to achieve reliable median demand estimates over a wide range of structural properties, seismic hazard conditions, and hazard levels. Considering these issues, the research effort described in this paper is conducting a large number of small-scale shake-table experiments of re-configurable linear-elastic and nonlinear multi-story building frame structures using an exhaustive set of ground motion records. These shake-table tests will form the first experimental study on dynamic response considering a wide range of building properties, lateral strengths, and ground motion records. Ultimately, the results will not only provide the experimental evidence needed to evaluate different ground motion scaling methods, but will also investigate how different site parameters and structure characteristics affect the accuracy and efficiency of the scaling methods. After briefly discussing the current practices and challenges related to ground motion scaling, this paper summarizes the ongoing experimental research effort. Preliminary evaluation results for ground motion scaling are presented based on a linear-elastic test structure.

CURRENT PRACTICE AND CHALLENGES

Procedures for selecting and scaling ground motion records for a site-specific seismic hazard are broadly described in building codes and have been the subject of considerable research in recent years. The ground motion selection and scaling procedures in IBC (ICBO 2006) and CBC (ICBO 2007) are based on ASCE 7-05 (ASCE 2006). According to ASCE 7-05, the average 5%-damped linear-elastic acceleration response spectrum for a set of scaled records should not be less than the design spectrum over the period range from $0.2T_1$ to $1.5T_1$, where T_1 is the fundamental vibration period of the structure being designed. The design value of an engineering demand parameter (EDP) — member deformations, lateral drifts, floor accelerations, etc. — is taken as the average value of the EDP if seven or more records are used in the analysis, or its maximum value over all ground motions if the structure is analyzed for less than seven records (ASCE 7-05 requires a minimum of 3 records). These requirements for ground motion scaling are the same as those in the recently released ASCE 7-10 (ASCE 2010).

To demonstrate the challenges for the reliable use of nonlinear RHA in current practice, Figure 1 shows the estimated peak inter-story drift demands (Morgen and Kurama 2008) for a six-story reinforced concrete frame structure subjected to 10 pairs of "far-fault" MCE ground motion records satisfying the ASCE 7-05 scaling requirement. The drift demands from the 10 pairs of records range from a minimum of slightly less than 1% to a maximum of almost 5%. It is clear that if

only the peak demand from 3 records were used in design, as allowed by ASCE 7-05, then the design outcome (i.e., over-design, under-design, satisfactory) can be drastically altered depending on the records selected. Note that the demands in Figure 1 seem to be highly correlated with the ground motion maximum incremental velocity, MIV (Kurama and Farrow 2003), plotted on the x-axis.

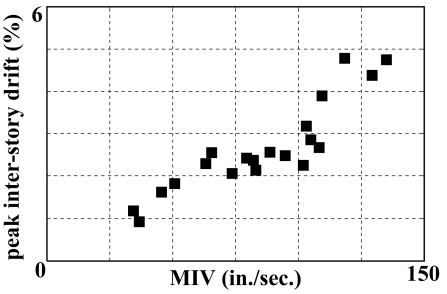


Figure 1. Peak drift demands.

GROUND MOTION SELECTION

Due to lack of specific guidelines, practitioners often select ground motion records based solely on distance, site conditions, and magnitude of the characteristic event expected to dominate the seismic hazard. However, many other factors, such as directivity of the rupture and/or basin effects contribute to the intensity and frequency content of a ground motion at a site. For example, as described in Kalkan and Kunnath (2006, 2008), "forward directivity" (with double-sided pulse) and "fling-step" (with single-sided pulse) motions with long-period, large-amplitude pulses may impose large displacement demands that require the structure to dissipate considerable energy in a single or relatively few cycles.

For the selection of the ground motions in this study, a set of criteria and identification algorithms were set to distinguish earthquake records based on their characteristic attributes associated with source, directivity, site, and/or basin effects (e.g., cyclic versus impulsive records; records with high, mid, or low frequency content; short or long duration records). Basin, duration, and pulse attributes of the records were investigated by frequency domain analyses; whereas, directivity and fling attributes were identified from the orientation of accelerometers relative to the rupture propagation plane. These attributes were then used to categorize a large library of records (PEER Next Generation Attenuation Project Ground Motions database) to facilitate the selection of the most suitable ground motions for different site-specific hazard conditions. Based on this refinement and pre-selection process, a suite of 38 representative near-fault motions (recorded within 20 km of the fault rupture) from a variety of tectonic environments were compiled for the purposes of this research as shown in Table 1.

EXPERIMENTAL STRUCTURE CONFIGURATION

The frame structure selected for the experimental investigation corresponds to a six-story building. As shown in Figure 2(a), the test frame consists of a single bay with center-to-center span length of 30 in. and story height of 17 in. These dimensions, determined based on the size limitations of the shake table, correspond to a building length-scale of, approximately, S_L=1/10. The chosen time scale is S_T=1/3. Two steel plates with total weight of 92.6 lb were securely attached to the midspan of each floor beam, and one plate with weight of 46.3 lb was attached to the midspan of the roof beam.

Table 1. Ground motion records.

EQ File ID	Earthquake Name	Station Name	Year	Magnitude
1058-E	Duzce, Turkey	Lamont 1058	1999	7.14
1059-N	Duzce, Turkey	Lamont 1059	1999	7.14
1061-E	Duzce, Turkey	Lamont 1061	1999	7.14
1062-E	Duzce, Turkey	Lamont 1062	1999	7.14
375-N	Duzce, Turkey	Lamont 375	1999	7.14
531-N	Duzce, Turkey	Lamont 531	1999	7.14
AMA090	Kobe, Japan	Amagasaki	1995	6.90
BOL090	Duzce, Turkey	Bolu	1999	7.14
BRN090	Loma Prieta	BRAN	1989	6.93
CAP000	Loma Prieta	Capitola	1989	6.93
CLS000	Loma Prieta	Corralitos	1989	6.93
CPM000	Cape Mendocino	Cape Mendocino	1992	7.01
DZC270	Duzce, Turkey	Duzce	1999	7.14
FKS090	Kobe, Japan	Fukushima	1995	6.90
FOR000	Cape Mendocino	Fortuna - Fortuna Blvd	1992	7.01
G02000	Loma Prieta	Gilroy Array #2	1989	6.93
G03000	Loma Prieta	Gilroy Array #3	1989	6.93
G04000	Loma Prieta	Gilroy Array #4	1989	6.93
G06090	Loma Prieta	Gilroy Array #6	1989	6.93
GIL067	Loma Prieta	Gilroy - Gavilan Coll.	1989	6.93
GOF160	Loma Prieta	Gilroy - Historic Bldg.	1989	6.93
HEC090	Hector Mine	Hector	1999	7.13
I-ELC180	Imperial Valley-02	El Centro Array #9	1940	6.95
KJM000	Kobe, Japan	KJMA	1995	6.9
LGP090	Loma Prieta	LGPC	1989	6.93
LOB000	Loma Prieta	UCSC Lick Observatory	1989	6.93
NIS090	Kobe, Japan	Nishi-Akashi	1995	6.90
PET090	Cape Mendocino	Petrolia	1992	7.01
PRI000	Kobe, Japan	Port Island (0 m)	1995	6.90
RIO360	Cape Mendocino	Rio Dell Overpass – FF	1992	7.01
SHI000	Kobe, Japan	Shin-Osaka	1995	6.90
SJTE225	Loma Prieta	San Jose - Santa Teresa Hills	1989	6.93
STG000	Loma Prieta	Saratoga - Aloha Ave	1989	6.93
TAK090	Kobe, Japan	Takatori	1995	6.90
TAZ090	Kobe, Japan	Takarazuka	1995	6.90
UC2090	Loma Prieta	UCSC	1989	6.93
WAH090	Loma Prieta	WAHO	1989	6.93
WVC270	Loma Prieta	Saratoga - W Valley Coll.	1989	6.93

The tests were conducted on a medium-size uniaxial earthquake simulator at the University of Notre Dame that consists of a hydraulic actuator/servo-valve assembly and a hydraulic power supply that drive a 4 ft by 4 ft slip table. Figure 2(b) depicts the test frame placed on the shake table, together with the measurement and out-of-plane bracing frames mounted onto the laboratory floor. The test frame was fabricated from extruded aluminum 6105-T5 alloy with a yield strength of 35 ksi. The beam and column member cross-sections were determined to result in strength and

stiffness appropriate with the scale model. The extruded aluminum cross-section in Figure 3(a), oriented in the weak direction (with moment of inertia, I=0.7097 in.^{4} and area, A=3.00 in^2) was used for all beam and column members.

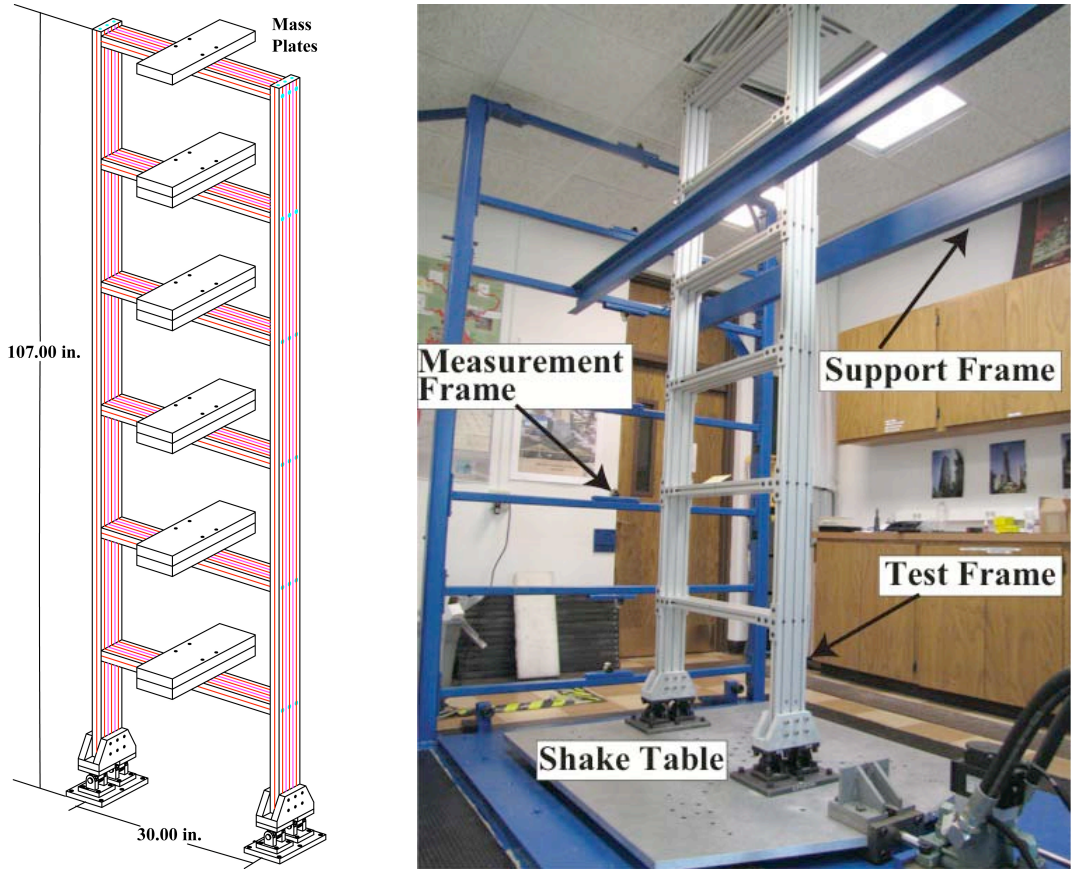
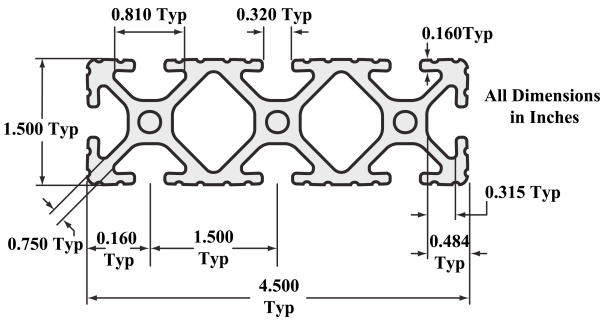


Figure 2. Six-story test frame: (a) schematic; (b) test setup.

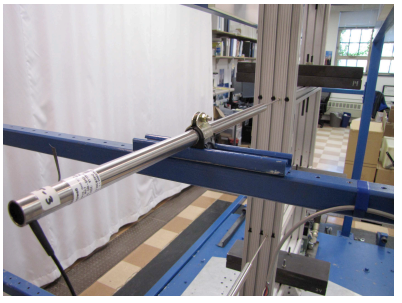
The shake table used in the experimental program can achieve a maximum acceleration of ±4 g with a 1000 lb test load at a nominal operational frequency range of 0-50 Hz. The data acquisition system is capable of recording the table displacements as well as the displacements and accelerations at each floor and roof level of the specimen. The data was collected at a high sampling rate, resulting in close-to-simultaneous excitation and response measurements. The displacements of the structure were measured using seven free unguided LVDTs (six at the floor and roof levels and one at the base) anchored between the test frame and an isolated measurement frame. An example of a mounted LVDT can be seen in Figure 3(b). The clamps used to attach the LVDTs to the measurement frame were engineered to mitigate vibrations.

The column bases were designed and constructed with pinned connections to increase the flexibility of the structure. Figure 3(c) depicts a close-up view of the pinned base connection. Each connection consists of a steel plate bolted to the shake table top, two steel clevises bolted to the plate, and two steel eye brackets inserted into the clevises and bolted to an aluminum fixture at the column base. A tight

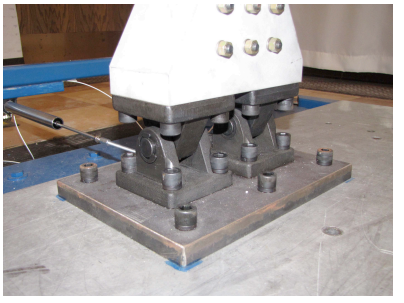
tolerance greased steel pin was used through the eye bracket-to-clevis connection to reduce friction while eliminating backlash effects. To achieve a modular structure, each beam-column connection was constructed using three high-strength bolts passing through the column and screwing into holes tapped into the beam cross section at each end.



(a)



(b)



(c)

Figure 3. Test details: (a) extrusion profile for beam and column members (courtesy 80/20® Inc.); (b) LVDT mounted to frame; (c) pinned connection at column base.

A nonlinear beam-to-column connection is also being constructed as part of this project to allow for the future testing of nonlinear structures with different levels of lateral strength (corresponding to different response modification factors, *R*). As an important feature, the nonlinear connection will also be reconfigurable and reusable, so as to allow for the repeated testing of structures with different lateral strengths under a series of ground motion records. The design of the connection incorporates a friction-fuse concept previously investigated at the University of Notre Dame (Morgen and Kurama 2004). As shown in Figure 4, each beam-to-column connection consists of two components creating 10 rotational friction interfaces in between.

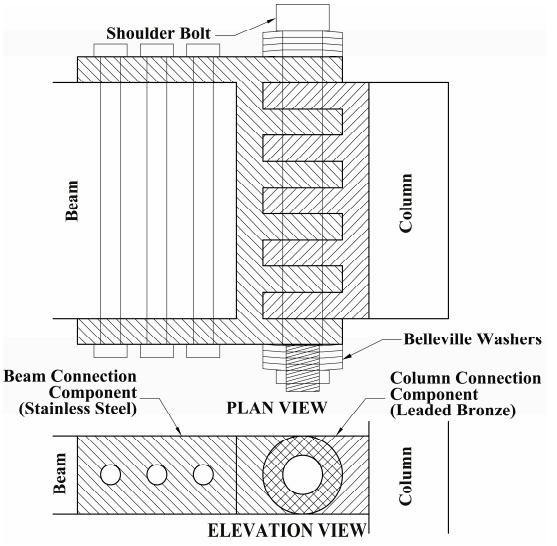


Figure 4. Nonlinear connection.

The nonlinear beam-to-column connection component bolted to the beam end will be fabricated out of stainless steel and the component bolted to the column will be lead-bronze (brass). The use of this alloy at the friction interfaces is desirable because the material continually "self-lubricates" when rubbing against an adjacent metal surface, which helps to reduce the phenomenon of stick-slip and results in a consistent value for the coefficient of friction that is relatively independent of velocity (a desirable characteristic for design and performance). The

friction force can be controlled by the normal force, F_n applied on the interfaces. In the nonlinear beam-to-column connection, this will be achieved using a single high-strength shoulder bolt (see Figure 4) running through the 10 friction interfaces. The prototype connection was designed to produce a total maximum slip moment of about 35 kip-in. at the maximum normal force level. This slip moment was designed to be greater than the yield moment of the aluminum beam cross-section, and thus, it will be used to simulate a linear-elastic structure (R=1). As the normal force is decreased, the connection is allowed to slip at a smaller moment, simulating structures with lower lateral strengths (i.e., R>1) and nonlinear hysteretic response. Belleville washers will be used to maintain a consistent level of normal force across the friction interfaces during each test. After each test, the bolt through each connection will be loosened, the structure will be brought back to plumb, and the connection bolts will be re-tightened to the desired level. A combination of steel shims and Belleville washers will be used to consistently achieve the desired bolt force in each test. Prior to the use of the connections in multi-story frame testing, isolated beam-column subassemblies will be subjected to static and dynamic loads to characterize the nonlinear connection and calibrate the bolt tightening operation as well as the number/arrangement of the shims and Belleville washers to result in the target slip moment levels. This will ensure that the desired connection performance can be achieved with relative certainty and repeatability during the multi-story frame tests.

STATIC BEHAVIOR OF LINEAR-ELASTIC STRUCTURE

To investigate the stiffness characteristics of the linear test structure, monotonic and cyclic pushover experiments were conducted by holding the 4th floor of the frame stationary while displacing the base laterally using the shake table. At the 4th floor level, a steel rod with pin-ended connections (Figure 5) was placed between the test frame and a relatively stiff steel loading frame. As the base of the structure was displaced, the resulting 4th floor force in the pin-ended rod was measured using an intermediary load cell. Two string pot transducers were used to measure the absolute lateral displacements at the base and 4th floor level of the structure (note that the 4th floor displacements were very small but not zero due to the deformations of the loading frame).



Figure 5. Pin-ended rod and load cell assembly.

The 4th floor lateral force versus relative (with respect to base) 4th floor displacement results for the frame during two cycles of loading are shown using the thin black lines in Figure 6. The structure exhibited consistent and repeatable behavior in both the positive and negative loading directions; however, the onset of nonlinear behavior was observed at a relatively small load (about 500 lbs). It was found that the nonlinear behavior occurred as the beam ends lost full contact with the columns due to the stretching of the beam-column connection bolts. The flexibility of the connection bolts also reduced the initial lateral stiffness of the frame (i.e., the beam-to-column connections were not rigid as originally assumed).

Analytical models of the linear-elastic test structure were developed using the OpenSees and DRAIN-2DX programs. The flexibility of the beam-column connections (due to the flexibility of the connection bolts) was modeled by placing linear-elastic zero-length rotational springs at the beam ends. The stiffness of the rotational springs was determined by calibrating the model results (thick gray line) with the linear-elastic range of the measured behavior as shown in Figure 6.

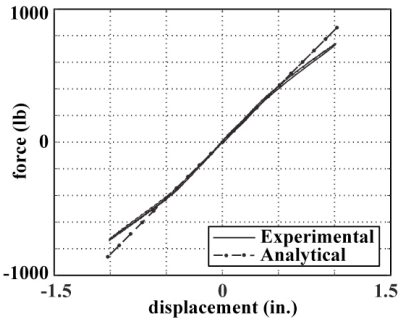
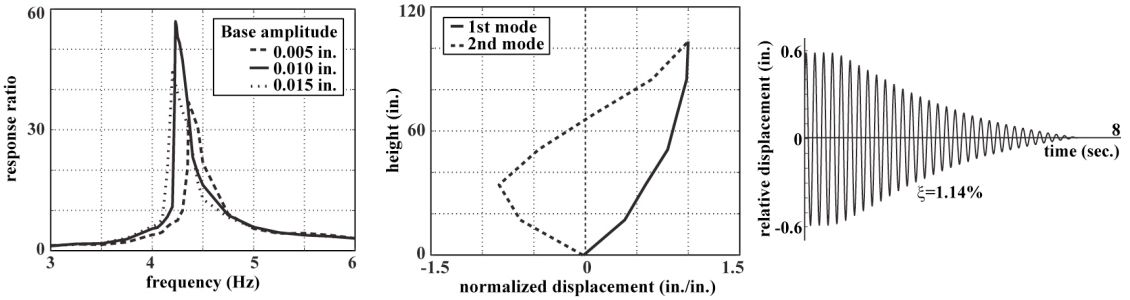


Figure 6. Measured and analytical static behaviors.

Once the nonlinear connection in Figure 4 is constructed and characterized, the hysteretic behavior of frames utilizing these connections will be determined. The analytical modeling of these frames will also utilize zero-length spring elements at the beam ends, but, unlike the linear-elastic frame, these spring elements will have nonlinear hysteretic behavior. The properties of the springs will be determined by calibrating the analytical results with the measured cyclic behavior of the frame, thus providing a full range of prediction tools.

DYNAMIC BEHAVIOR AND IDENTIFICATION

The dynamic characteristics of the linear-elastic structure were investigated by subjecting the frame to a series of sine sweep experiments. The results from three series of sine sweep tests with base excitation amplitudes ranging from 0.005 in. to 0.015 in. can be seen in Figure 7(a), where the y-axis shows the ratio of the relative roof displacement amplitude to the base excitation amplitude and the x-axis shows the frequency of the sine wave exciting the structure. While there is some amplitude dependency, it can be seen that the fundamental frequency of the structure is around f_1=4.35 Hz, (corresponding to a period of T_1=0.23 s), which was found to match very well with the analytical prediction. With the selected time scale of S_T=1/3, the test specimen corresponds to a full-scale structure with a fundamental period of about T_1=0.69 s. The second mode of vibration of the structure was measured to occur at around f_2=16.1 Hz, also with an excellent match with the analytical prediction. The measured mode shapes for the first two modes of vibration can be seen in Figure 7(b). Using the log decrement method on the decay of the measured displacement response at the roof, the damping ratio of the frame was determined as ξ=1.14%. The time-history of the roof displacement used in this calculation can be seen in Figure 7(c).



(a) **(b)** **(c)**

Figure 7. Dynamic behavior: (a) resonance peaks; (b) first and second mode shapes; (c) decay of roof displacement response.

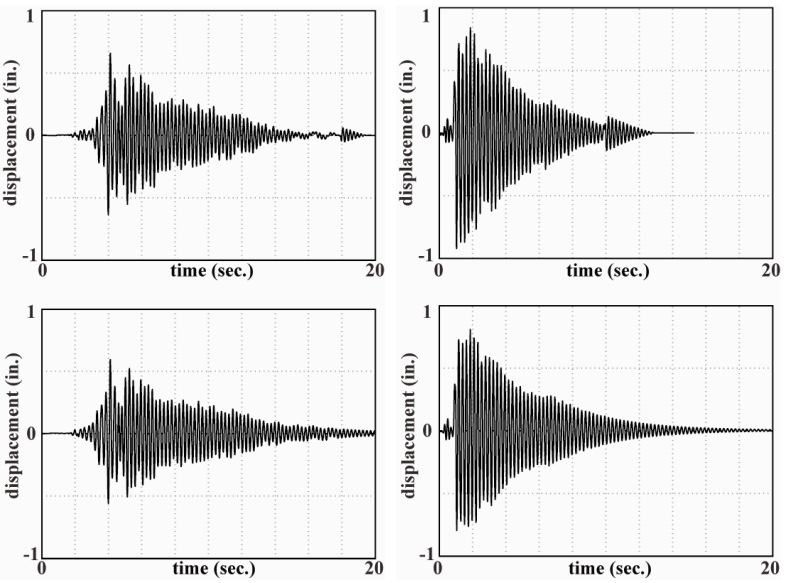


Figure 8. Measured (top) and estimated (bottom) roof displacement responses: (a) AMA090; (b) CPM000.

A subset of earthquake ground motion records was selected and the measured dynamic response of the structure was compared with the estimated response from the OpenSees analytical model as another method of model calibration. Estimated versus measured roof displacement response comparisons from the AMA090 and CPM000 ground motion records can be seen in Figures 8(a) and Figure 8(b), respectively. Once the accuracy of the model was improved and deemed sufficient, the analytical model was subjected to the full suite of 38 ground motion records from Table 1 to guide the shake table tests described in the next section.

GROUND MOTION SCALING FOR LINEAR-ELASTIC RESPONSE

With the characteristics of the linear-elastic structure fully understood and the expected displacement demands from each ground motion estimated by the calibrated analytical model, the test specimen was subjected to five series of shake table tests using 37 ground motions from Table 1 (KJM000 was not used in the experiments due to excessive displacement demands indicated from the pre-test analysis of the structure under this record). The first series of tests subjected the specimen to the unscaled ground motions at full intensity. The second series was conducted with the ground motions scaled to the median linear-elastic single-degree-of-freedom spectral acceleration at the fundamental period of the structure [$\widehat{S_a}(T_1)$]. The effects of uncertainties in structural period estimation (i.e., inaccuracies in period estimation that could be expected in typical design practice) were investigated in the third and fourth test series. For this collection of tests, the ground motion suites were scaled to the median spectral acceleration at $1.3T_1$ and $0.7T_1$ [i.e., $\widehat{S_a}(1.3T_1)$] and $\widehat{S_a}(0.7T_1)$, respectively], representing a 30% error in period estimation. Finally, the fifth series of tests subjected the structure to ground motions scaled to the median maximum incremental velocity ($\widehat{MIV}$) of the suite.

The peak roof displacement demands from the five series of experiments are plotted in Figure 9 and listed in Table 2. It can be seen that the unscaled peak displacement demands are not as strongly correlated to MIV as compared to the correlation with $S_a(T_1)$. As can be expected for a linear-elastic structure, the $\widehat{S_a}(T_1)$

scaling method produced the smallest dispersion in the peak roof displacements. However, the dispersion more than doubled with a 30% error in period estimation, with values similar to the dispersion from the MIV-scaled suite. These results are important in showing that inaccuracies in the estimation of a structure's anticipated period can lead to a much larger dispersion in the seismic demand estimates when compared with the dispersion achieved with the records scaled based on the "exact" period. The remainder of this project will investigate the effects of nonlinear structural response on these findings, including additional scaling methods in the investigation as well.

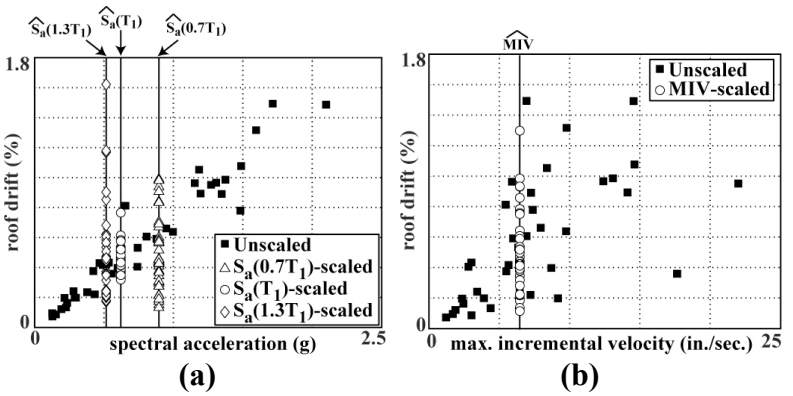


Figure 9. Peak roof displacement demands: (a) plotted against $S_a(T_1)$; (b) plotted against MIV.

SUMMARY AND CONCLUSIONS

This paper describes an ongoing research effort for a novel experimental evaluation of ground motion scaling methodologies for use in nonlinear response history analysis of building structures. The general experimental setup and the features of a 1/10-scale six-storey linear-elastic test frame structure are presented, along with identification results for the static and dynamic properties of the structure. Current efforts for extending the test structure to simulate nonlinear response, reconfigurable to different response modification factors, are also discussed. The test results from the linear-elastic structure stress the potential vulnerabilities of scaling methods that are based on knowledge of the exact properties of the structure. The future extension of this investigation to nonlinear dynamic response, considering a wide range of building properties, lateral strengths, and ground motion records, will ultimately provide guidelines and procedures for appropriate selection and scaling of ground motions for structural engineering practice.

ACKNOWLEDGEMENTS

This research is funded by the National Science Foundation (NSF) under Grant No. CMMI 0928662. The support of Dr. M.P Singh, NSF Program Director, is gratefully acknowledged. The authors would like to acknowledge the project advisory panel, which includes Paulo Bazzurro, AIR Worldwide Corporation, Sigmund Freeman, Wiss, Janney, Elstner Associates, Inc., Vladimir Graizer, U.S. Nuclear Regulatory Commission, Farzad Naeim, John A. Martin and Associates, Inc., and Thomas Sabol, Englekirk & Sabol Consulting Structural Engineers, Inc. The authors also thank Bob St. Henry of NEFF Engineering for his help in the design of the test

frame. The opinions, findings, and conclusions in the paper are those of the authors and do not necessarily reflect the views of the organizations or individuals above.

Table 2. Peak roof displacement responses for five series of linear-elastic tests.

GM Identifier	Unscaled	$\widehat{S_a}(T_1)$	$\widehat{S_a}(0.7T_1)$	$\widehat{S_a}(1.3T_1)$	$\widehat{MIV}$
	in.	in.	in.	in.	in.
1058-E	0.09	0.40	0.43	0.44	0.19
1059-N	0.08	0.35	0.31	0.43	0.36
1061-E	0.10	0.55	0.44	0.39	0.42
1062-E	0.45	0.54	1.03	1.21	0.89
375-N	0.23	0.34	0.16	0.64	0.20
531-N	0.13	0.48	0.32	0.37	0.49
AMA090	0.66	0.38	0.36	0.18	0.39
BOL090	1.11	0.40	0.63	0.32	0.41
BRN090	1.09	0.64	0.46	0.88	0.81
CAP000	0.81	0.33	0.72	0.64	0.66
CLS000	1.36	0.39	0.61	1.22	0.78
CPM000	0.92	0.46	0.48	0.49	0.39
DZC270	1.02	0.43	0.98	0.36	0.45
FKS090	0.44	0.60	0.54	0.19	0.44
FOR000	0.14	0.48	0.45	0.21	0.19
G02000	0.61	0.41	0.59	0.93	0.63
G03000	0.55	0.46	0.32	0.60	0.54
G04000	0.24	0.39	0.19	0.24	0.22
G06090	0.17	0.43	0.40	0.45	0.41
GIL067	0.21	0.45	0.23	0.45	0.33
GOF160	0.21	0.39	0.23	0.26	0.14
HEC090	0.43	0.53	0.14	0.55	0.46
I-ELC180	0.84	0.79	0.87	0.48	0.96
LGP090	0.92	0.41	0.46	0.45	0.78
LOB000	0.25	0.53	0.29	0.42	0.44
NIS090	1.54	0.40	0.73	1.68	1.34
PET090	1.54	0.42	0.87	0.46	0.61
PRI000	0.37	0.40	0.39	0.23	0.12
RIO360	0.41	0.43	0.20	0.58	0.29
SHI000	1.00	0.53	1.02	0.70	1.02
SJTE225	0.42	0.36	0.70	0.63	0.96
STG000	0.63	0.48	0.72	0.58	0.55
TAK090	0.98	0.43	0.60	0.22	0.23
TAZ090	1.00	0.50	0.29	0.52	0.51
UC2090	0.20	0.60	0.47	0.46	0.54
WAH090	0.39	0.54	0.45	0.25	0.43
WVC270	0.68	0.45	0.94	0.48	0.53
MEDIAN	**0.45**	**0.43**	**0.46**	**0.46**	**0.45**
ST. DEV.	**0.42**	**0.09**	**0.25**	**0.31**	**0.27**

REFERENCES

Alavi, B. and Krawinkler, H. "Consideration of near-fault ground motion effects in seismic design," *12th World Conference on Earthquake Engin.*, Paper No. 2665, Auckland, New Zealand, 2000.

ASCE, "Minimum design loads for buildings and other structures," American Society of Civil Engineers, ASCE Standard No. ASCE/SEI 7-05, Reston, VA, 2006.

ASCE, "Minimum design loads for buildings and other structures," American Society of Civil Engineers, ASCE Standard No. ASCE/SEI 7-10, Reston, VA, 2010.

Chopra, A.K., and Chinatanapakdee, C., "Inelastic deformation ratios for design and evaluation of structures: single-degree-of-freedom bilinear systems," *J. of Structural Engineering*, 130(9), 2004, 1304-1319.

International Conference of Building Officials (ICBO), International Building Code, Whittier, CA, 2006.

International Conference of Building Officials (ICBO), California Building Code, Whittier, CA, 2007.

Kalkan E. and Chopra A.K., "Practical guidelines to select and scale earthquake records for nonlinear response history analysis of structures," U.S. Geological Survey Open-File Report 2010-1068, 2010, 126 pp. (available online at http://nsmp.wr.usgs.gov/ekalkan/MPS/index.html)

Kalkan E. Chopra A.K., "Modal-pushover-based ground motion scaling procedure," *J. of Structural Engineering*, 137(3), 2011, (available online at http://nsmp.wr.usgs.gov/ekalkan/MPS/index.html)

Kalkan E. and Kunnath S.K., "Relevance of absolute and relative energy content in seismic evaluation of structures," *Advances in Struc. Eng.*, 11(1), 2008, 17-34.

Kalkan E. and Kunnath S.K., "Effects of fling-step and forward directivity on the seismic response of buildings," *Earthquake Spectra*, 22(2), 2006, 367-390.

Kalkan E. and Kwong N.S., "Documentation for assessment of modal pushover-based scaling procedure for nonlinear response history analysis of "ordinary standard" bridges," U.S. Geological Survey Open-File Report 2010-1328, 58 p. 2011, (available online at http://pubs.usgs.gov/of/2010/1328/).

Kurama, Y. and Farrow, K., "Ground motion scaling methods for different site conditions and structure characteristics," *Earthquake Engineering & Structural Dynamics*, 32(15), 2003, 2425-2450.

Martinez-Rueda, J., "Scaling procedure for natural accelerograms based on a system of spectrum intensity scales," *Earthquake Spectra*, 14, 1998, 135-152.

Morgen, B. and Kurama, Y., "Seismic response evaluation of post-tensioned precast concrete frames with friction dampers," *J. of Str. Eng.*, 134(1), 2008, 132-145.

Morgen, B. and Kurama, Y., "A friction damper for post-tensioned precast concrete beam-to-column joints," *PCI J.*, 49(4), 2004, 112-133.

Shome, N. and Cornell, C., "Normalization and scaling accelerograms for nonlinear structural analysis," *6th U.S. National Conf. on Earthquake Engin.*, Seattle, WA, 1998 (CD-ROM).

Three-Dimensional Tests of Two-Story, One-bay by One-bay, Steel Concentric Braced Frames

Keith Palmer[1], Charles Roeder[2], Taichiro Okazaki[3], Carol Shield[4], Dawn Lehman[2]

[1]Graduate Research Assistant, Dept. of Civil Engineering, University of Washington, Seattle, WA 98195
[2]Professor, Dept. of Civil Engineering, University of Washington, Seattle, WA 98195
[3]Research Fellow, Hyogo Earthquake Engineering Research Center (E-Defense), Miki, Hyogo, 673-0515 Japan
[4]Professor, Dept. of Civil Engineering, University of Minnesota, Minneapolis, MN 55455

Abstract

Steel concentric braced frames (CBFs) are widely used as systems to resist lateral loads induced from wind and seismic loading. Recent research on full-scale CBF subassemblages has shown that current design provisions fall short of the design intent. Additionally, the effect of imposed out-of-plane deformation on the system has never been evaluated experimentally in this manner. This paper describes the design, test setup and experimental results of two tests performed on a two-story, one-bay by one-bay CBFs, an HSS buckling-brace system in a single-story X-configuration, and a buckling-restrained braced frame (BRBF) in a single-diagonal configuration. The design of the gusset plates for the HSS braces followed a balanced design procedure with an elliptical clearance to permit out-of-plane rotation due to brace buckling. The HSS braces fractured at 2% story drift. The BRBF gusset plate design followed current design standards with the BRB cores fracturing at 3.5% story drift prior to any instabilities.

Introduction

Concentric braced frames (CBFs) are widely used as systems to resist lateral loads induced from seismic loading. In high seismic regions, special concentric braced frames (SCBFs) are used. Recent research on full-scale CBF subassemblages has shown that current design provisions fall short of the design intent (Chen et al. 2004, Mahin et al. 2004). Subsequent research has evaluated improvements to the connection design (Yoo et al. 2008). The results have been used to develop a design methodology to balance the multiple yield mechanisms of the frame, most importantly the brace and the gusset plate, to maximize the drift capacity. The process further evaluates all potential failure modes to ensure the desired mechanism occurs and all others are suppressed. This research has resulted in more rational design and detailing rules for SCBFs.

Prior tests performed on braced frames were planar, single and multi-story specimens. The current paper focuses on the full, three-dimensional response of a two-story, one-

bay by one-bay large-scale CBF structure that was tested using the MAST laboratory at the University of Minnesota as part of the NSF-funded project entitled "International Hybrid Simulation of Tomorrow's Braced Frame Systems" through the NEES research program. The test specimen simulated the corner bay of a two-story building system braced in two orthogonal directions. The first test used conventional HSS diagonal braces in a single-story X-configuration in each story. The second test used buckling restrained braces (BRBs) in a single diagonal configuration.

The objectives of the test were: (1) to examine the large-displacement, bi-directional behavior of CBFs and BRBFs, (2) to examine the applicability of the latest design and detailing rules for these systems, (3) to examine the behavior of columns shared by two orthogonal braces, (4) to examine the effect of gusset plates framing into the column web, and (5) to examine the effect of composite concrete slabs on the behavior of CBFs and BRBFs.

Experimental Program

Specimen Description

Two specimens were tested in this research program. Both were nearly full-scale, one-bay by one-bay, two-story frames with braces in two orthogonal bays and framing into a "shared" column. Buckling HSS braces were used in the first test while the second test used BRBs. Fig. 1(a) and 1(b) show the second and third floor plan, respectively, of both test specimens. The braced frames occur along grid lines A and 1 as indicated by the dashed lines near the girders. Note that column A-1 is the "shared" column as the two orthogonal braced bents frame into this column. The second floor deck consists of 2 in. ribbed metal deck topped by 3.25 in. of normal weight concrete for a total depth of 5.25 inches as in typical steel buildings. The third floor slab will be used to transfer the load from the loading beam into the test specimen and as such, required a 10 in. concrete slab.

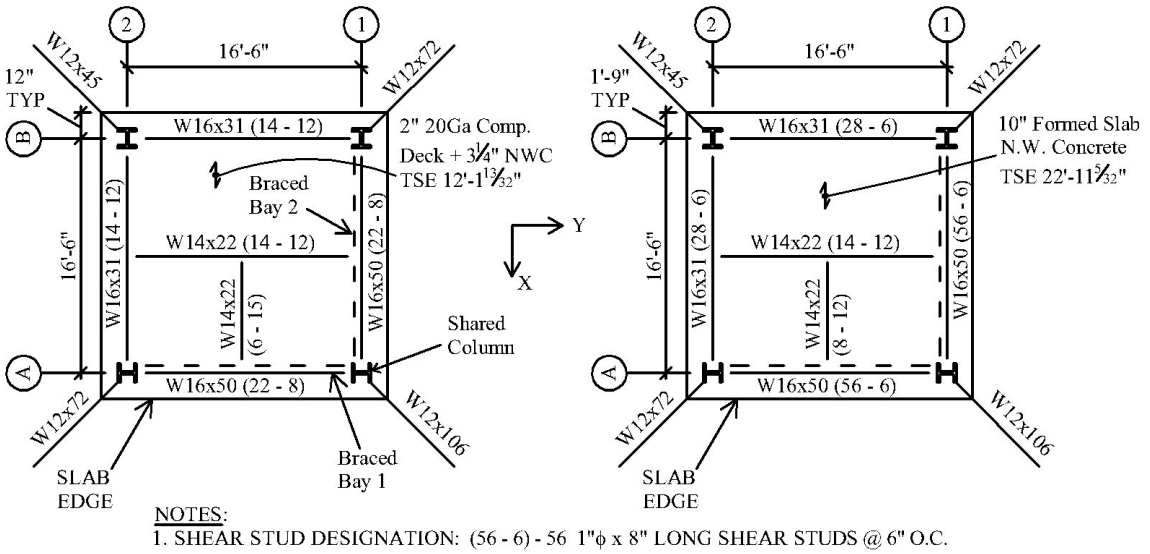


Figure 1. Test specimen floor plans: (a) second floor; (b) third floor plan

The braced frame elevations for the buckling brace frame and the BRBF are shown in Fig. 2(a) and 2(b), respectively. The beam connections in each braced bay are welded flange – welded web (WFWW) connections with demand-critical welds, while those in the other two bays are simple shear connections. The buckling braces were A500B HSS3x3x1/4 while the BRB cores were 46 ksi steel with a design maximum adjusted brace force of 220 kips at 3% story drift. A photo of the test setup showing the strongwalls, crosshead and the first specimen is shown in Fig. 3.

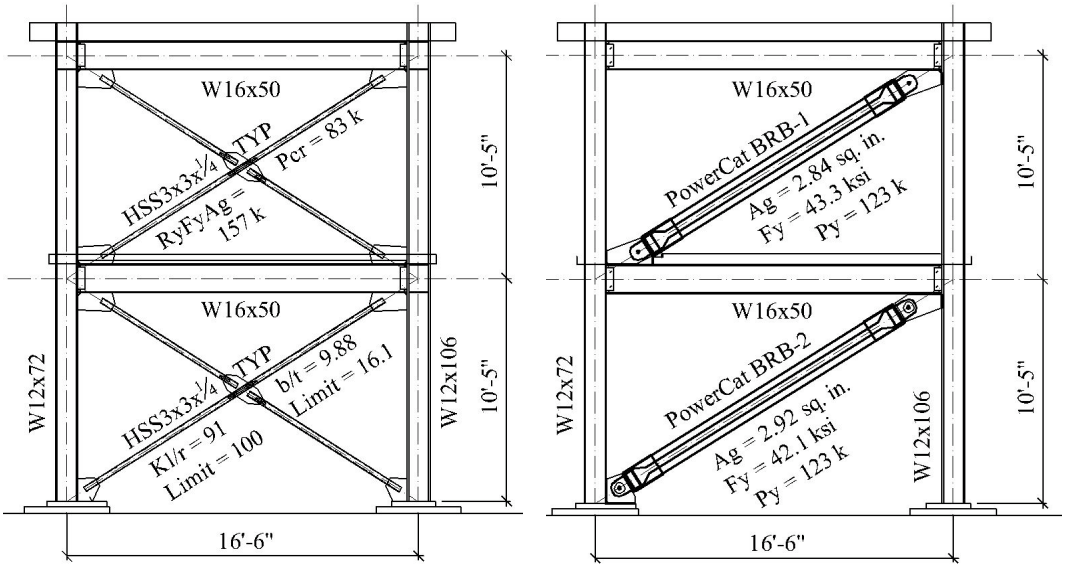


Figure 2. Braced Frame Elevations (a) HSS buckling brace frame; (b) BRBF

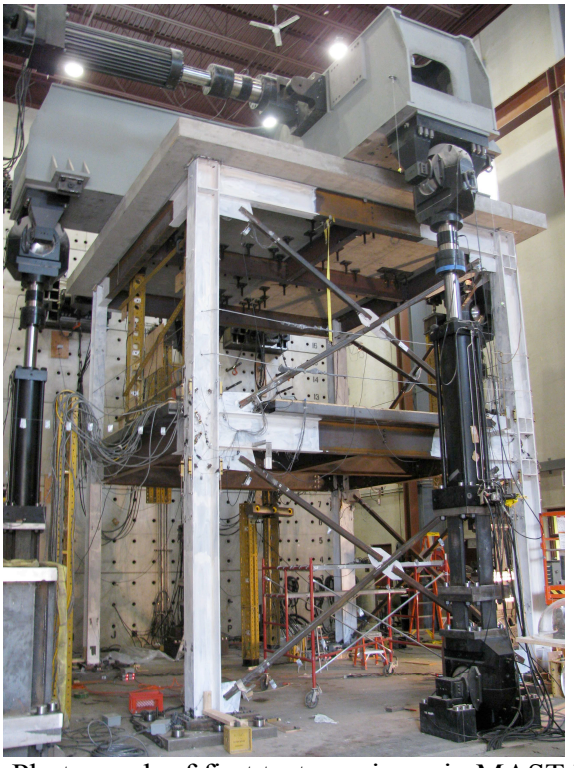


Figure 3. Photograph of first test specimen in MAST lab setup

Specimen Design

The sizes of the HSS buckling braces and BRBs in the test specimen were determined based on the capacity of the MAST lab strongfloor and force actuator system while ensuring that sizes which are typical of current construction could be used. The size of the braces chosen is typical of the upper stories in a mid to high-rise building or the lower stories of a low-rise building. The design of the test frame members followed current design practice based on the AISC Seismic Provisions (AISC 2005b), ASCE 7 (ASCE 2005), and a procedure shown by Lopez and Sabelli (2004). The beams and columns were designed to resist the maximum expected BRB force at $2.0\Delta_{bm}$, where Δ_{bm} is the brace axial deformation corresponding to the design story drift, in combination with the gravity load using the applicable load combinations. The frame beams and columns conform to the strong-column weak-beam philosophy. The demand on the shared column was found assuming 100% of the brace and beam capacities were realized in one direction while 30% of the capacities of these elements were realized in the orthogonal direction.

Gusset Plate Design

HSS Buckling Brace Test Specimen

Current seismic design rules (AISC 2005) require the bracing connection to develop the strength of the brace while accommodating the rotation associated with out-of-plane brace buckling. As shown in Fig. 4(a), accommodation of the rotational capacity is generally accomplished through a linear clearance model, whereby the brace is terminated a distance $2t_p$ before the line of restraint, where t_p is the thickness of the gusset plate. This requirement can result in large buckling lengths of the gusset plate, and consequently, lead to heavy and overly stiff connections that have a detrimental effect on the behavior of the system (Roeder and Lehman 2009).

Based on tests at the University of Washington (UW) of over 30 one-bay, one-story planar CBFs, a new clearance model has been developed that when combined with the proposed balanced design procedure (Roeder et. al. 2005), results in thinner and smaller gusset plates. These thinner gusset plates have been shown to reliably accommodate large out-of-plane gusset rotations at the brace ends and sustain the tensile strength of the brace. This clearance model, called the elliptical clearance model, is shown in Fig. 4(b). A clearance of $8t_p$ has been shown to be the most efficient.

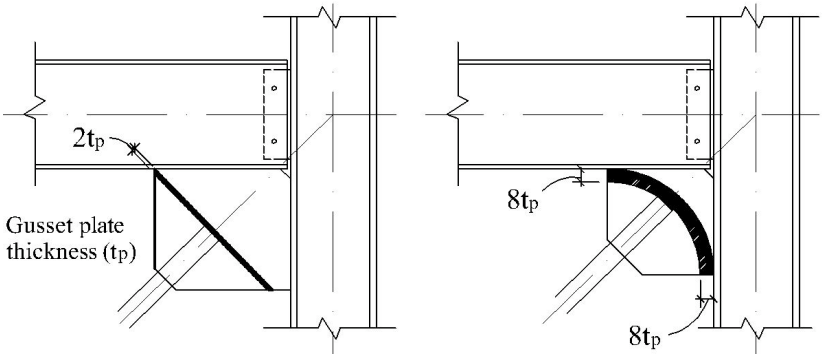


Figure 4. Current and proposed clearance models: (a) AISC $2t_p$ clearance and (b) $8t_p$ elliptical clearance model

The balance factors in the balanced design method are used in a similar manner to the AISC resistance factors except that they are used to achieve ductility and inelastic deformation capacity rather than strength. Smaller balance factors indicate that the exceedance of the considered limit state would cause significant deterioration of strength, stiffness and ductility, and/or that the capacity prediction is less reliable.

Note that the welds connecting the gusset plate to the beams and columns are sized to resist the strength of the gusset plate and not the forces that result from application of the Uniform Force Method (UFM). The buckling lengths of the gusset plates were computed as the average centroidal length and the two lengths at the extreme points of the Whitmore width. An effective length factor, *K*, of 0.65 was used.

Buckling-Restrained Braced Frame

Because BRBs are generally not expected to deform out-of-plane, the clearance model for CBFs does not apply to BRBFs. Given that much less research has been performed on gusset plates for this system, it was decided that the gusset plates in the BRBF specimen would be designed according to the current standards using the uniform force method and the limit states outlined in AISC (2005a) instead of the balanced design approach.

Loading Protocol

Cyclic displacements were applied in each horizontal direction at the top floor while rotation of the crosshead about the vertical axis was maintained at zero to prevent torsional deformation from occurring. Free rotation about both horizontal axes was permitted. To limit the differences between the uni-directional tests performed at UW and those performed here, the same uni-directional displacement histories was used in the current tests that were used in the tests at UW.

The determination of the bi-directional qualities of the bi-directional loading protocol was facilitated by nonlinear time-history analyses of prototype braced frame buildings. Three and 6-story single diagonal BRBF buildings were designed and simultaneously subjected to the X and Y-component of 10 ground motions from the SAC program.

Using rainflow cycle counting, the ratio of the frame damage (cumulative plastic deformation) in X and Y was found for each case and a ratio of 1.5 was chosen. The final displacement-controlled protocol is shown in Figure 5.

Experimental Results

Buckling Brace Test

As discussed earlier, the test specimen was loaded according to Figure 5, where the Y-direction corresponds to that shown in the floor plans in Figure 1. Figure 6 shows the story shear – story drift ratio response for the second floor of each orthogonal braced bent. The top discontinuous brace at the 2nd story fractured during the first negative drift excursion at approximately 2% story drift following the first positive excursion. This drift ratio at fracture is consistent with that observed in two previous tests of a similar single-story X-configuration at UW and those tested by Tremblay et

al (2003). After fracture, the test specimen was unloaded in this frame's direction and uni-directional loading was applied to the specimen in the other direction continuing from the drift at which fracture occurred. The test proceeded until the top discontinuous brace in Braced Bay 2 was deemed close to fracture at approximately 1.7% story drift. The test was stopped prior to brace fracture in this bent to prevent damage to the frame as this frame was to be used again for the BRBF test.

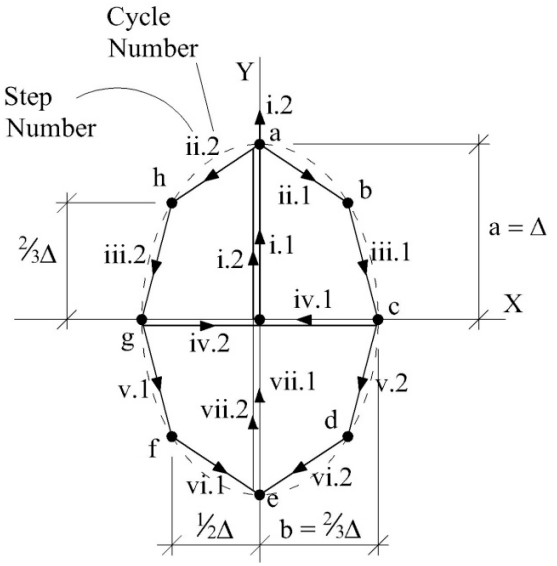


Figure 5. Bi-directional loading protocol "cloverleaf"

Based on brace strain gauge data, and global and local force-deformation curves, brace buckling occurred simultaneously in the discontinuous braces in the 1st and 2nd story of Braced Bay 1 at 0.25% story drift. Yielding of the braces occurred at 0.37% story drift. In the orthogonal direction, brace buckling occurred at 0.22% story drift and yielding at 0.36% story drift. Due to a number of factors including brace end connection stiffness and initial imperfections, brace buckling and subsequent brace damage occurred in only one half of the discontinuous brace while the continuous brace buckled in reverse curvature with the tension brace acting as a lateral support.

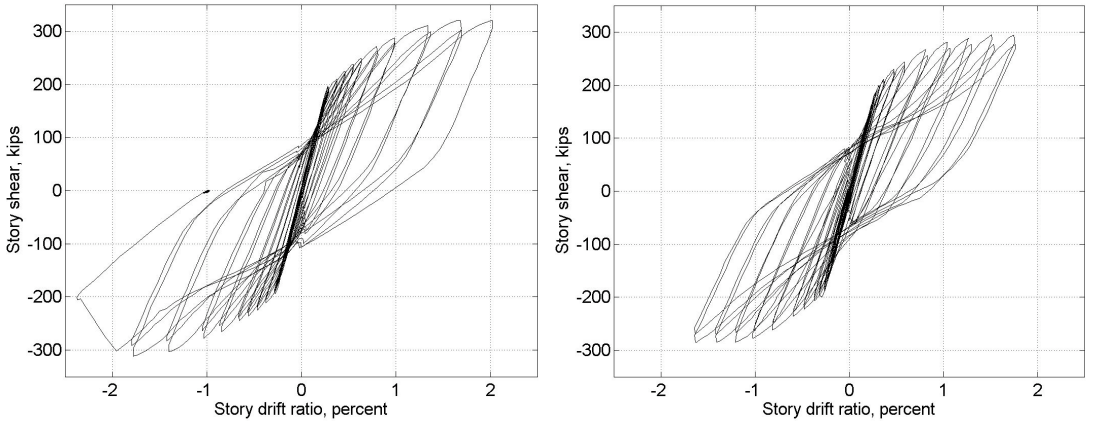


Figure 6. HSS Buckling-brace test 2nd story hysteretic curves: (a) Braced Bay 1 (Y-Direction), (b) Braced Bay 2 (X-Direction)

Prior to brace fracture there was extensive yielding in the gusset plates due to brace axial force and gusset plate bending due to brace buckling. This type of behavior was intended as part of the balanced design philosophy of maximizing energy dissipation and encouraging other yielding mechanisms beyond brace yielding. Slight gusset plate yielding was visually observed (flaking of whitewash) at approximately 0.23% story drift in the corner gussets just prior to brace buckling. Figure 7(a) shows a typical gusset yielding pattern in the corner gusset plates at 2% story drift. This pattern was typical of these joints. Additionally, frame action (opening and closing of the joint) cause additional yielding and deformation in the gusset as seen in the diagonal yield pattern originating at the intersection of the bottom beam flange and column flange shown in Figure 7(a).



Figure 7. HSS buckling-brace test, 2% story drift: (a) Gusset plate yielding, 2nd story corner gusset; (b) Column and gusset plate yielding, base

Column yielding initiated at the base of the three braced frame columns at approximately 0.46% story drift and continued to spread at the bases as the story drift increased. Figure 7(b) shows the yielding at the base of the column in Braced Bay 1 at 2% story drift. Additionally, the web of the beam on the second floor of Braced Bay 1 at the shared column side yielded and deformed at the instant of brace fracture. Up to that point, only limited yielding was observed at this location.

Buckling-Restrained Braced Frame

The BRBF followed the same loading protocol as the first test with the exception of the principal loading direction. Based on the beam web damage described previously, it was decided to make Braced Bay 2 the principal loading direction. Additionally, a web doubler plate with the same thickness as the beam web was attached to the damaged beam web to ensure that would not be the weak link in the BRBF test. It should also be noted that there were initial lateral frame deformations of XX in the Y direction and XX inches in the X direction due to the permanent frame deformation from the first test.

Figure 8 shows the story shear – story drift ratio response for the second floor of each orthogonal braced bent. Yielding of the BRB cores occurred at approximately 0.33% story drift ration in each direction. In the Y-direction, the BRB core fractured at approximately 3.5% average roof drift ratio (RDR) while in the X-direction, the BRB

core fractured at 4.1% RDR. The BRBs in the first story did not fracture as the first story columns resisted a larger amount of the story shear than the second story columns due to the base fixity. After core fracture, the load resisted by each frame was reduced by approximately 40%. The test was continued after core fracture and the frame stiffness remained the same due to the stiffness of the moment frame and the fact that the stiffness of the BRBs at this point was practically zero due to yielding of the BRB core.

At -3.2% RDR, the bottom flange in the second floor beam attached to the shared column in Braced Bay 2 (X-direction) fractured suddenly just outside of the CJP. This occurred after the web at this location exhibited ductile tearing that extended through more than half of the beam web. This tearing was initiated at the erection bolt holes at the beam splice three feet away from the centerline of the column.

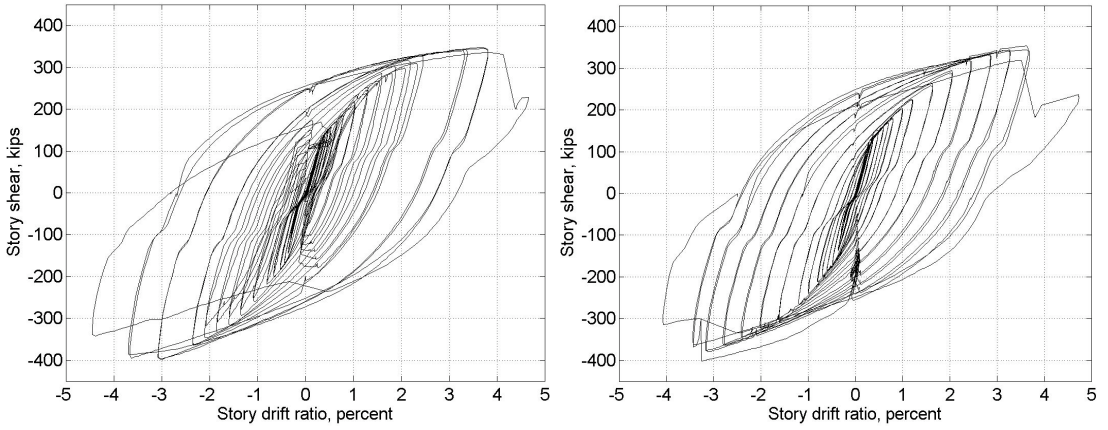


Figure 8. BRBF test 2nd story hysteretic curves: (a) Braced Bay 1, (b) Braced Bay 2

The web and bottom flange of the third floor beam at the shared column side in Braced Bay 1 also exhibited considerable yielding, local buckling and ductile tearing. The tear occurred at the edge of the gusset plate and extended completely through the bottom flange up to approximately ¾ of the beam depth. The braced frame columns yielded considerably at the base and above and below the second and third floor joints. Additionally, local buckling occurred at the base of the two frame columns that the BRBs framed into. This occurred on the side opposite of the gusset plates as shown in Figure 9(b). Column flange and web yielding can also be seen in this photo.

Limited gusset plate yielding was observed and was confined to a localized area approximately one inch square near the gusset-column reentrant corner. Weld tearing occurred in the second and third floor gusset plates at the gusset-column weld. These tears propagated through the total length of the weld and were due to frame action as they initiated when the brace was in compression and the joint was opening. Preliminary analysis indicates that this tearing had limited effect on the overall frame behavior but further analysis is required to fully quantify this.

The BRBs were connected to the gusset plates with pins which limited the amount of moment transferred between these two elements. As a result of fabrication and fit-up

tolerances, which require the hole to be slightly larger than the pin, and yielding of the pin and steel in the vicinity of the pinhole, there was a reduction in frame stiffness as the BRBs underwent a change in the sign of the axial force. This can be seen clearly in the hysteretic curves shown in Figure 8. Additional damage occurring in the frame included panel zone yielding in the columns, tearing at the bolt holes that connected the gravity beams to the braced frame columns, and beam web yielding near the end of the gusset plates. Second floor composite slab damage was limited to hairline cracks around the braced frame columns but were more indicative of shrinkage cracks than flexural cracks.



Figure 9. BRBF test photos: (a) Gusset weld tear, 3.2% story drift; (b) Column local buckling and yielding, 3.2% story drift

Conclusions and Future Work

The out-of-plane loading appeared to have negligible effect on the frame behavior. The HSS braces fractured at 2% story drift which is consistent with previous tests performed on a similar frame loaded uni-directionally at UW. There was considerable gusset plate yielding in the first test which was expected as gusset plate yielding was specifically designed for and deemed a desirable secondary yielding mechanism. Additionally, the elliptical clearance method provided adequate rotation capability of the gusset plates while providing a much more compact design than the $2t_g$ linear offset method most commonly used in practice today.

Similar to the first test, the out-of-plane deformation appeared to have minimal effect on the BRBF behavior. The BRB cores fractured at 3.5 and 4% story drift and no instabilities occurred in the BRB prior to fracture. As BRBs are proprietary and are detailed differently, especially at the ends, this type of behavior may not be typical of all BRBs. Indeed, instabilities have been shown to occur at the end of the BRBs in previous tests that have not been subjected to out-of-plane deformation (Mahin et al. 2004). Frame action, as opposed to brace action, had a dominating effect on the

demands on the gusset-frame welds. The majority of the gusset to column welds tore completely through along their lengths as a result of the joint opening.

Work is ongoing to further analyze the test results with the goals of better quantification of the effect of out-of-plane deformation on the system, the effect of the concrete floor slab, and the demands on the shared column due to bi-directional effects. To aid in this work, 3D finite element models will be developed and calibrated to the test results and parametric studies shall be performed.

Acknowledgements

This is a continuing research project funded by the National Science Foundation through Grant CMS-619161, "NEESR-SG: International Hybrid Simulation of Tomorrow's Braced Frame Systems." Structural steel has been provided by the American Institute of Steel Construction. The authors would like to thank the MAST lab staff for their expertise and hard work.

References

AISC, 2005a, *Steel Construction Manual, 13th Edition*, American Institute of Steel Construction, Chicago, IL. USA.

AISC, 2005b, *Seismic Provisions for Structural Steel Buildings*, American Institute of Steel Construction, Chicago, IL, USA.

ASCE, 2005, *ASCE 7-05 – Minimum Design Loads for Buildings and Other Structures*, American Society of Civil Engineers

Chen, C.H., Hsiao, P.C., Lai, J.W., Lin, M.L., Weng, Y.T. and Tsai, K.C., 2004. "Pseudo-Dynamic Test of a Full-Scale CFT/BRB Frame: Part 2 – Construction and Testing," *13th World Conference on Earthquake Engineering*, Vancouver, B.C., Canada, Paper No. 2175.

Lopez, W. A., Sabelli, R., 2004. "Seismic Design of Buckling-Restrained Braced Frames", *SteelTips*, Structural Steel Educational Council.

Mahin, S., Uriz, P., Aiken, I., Field, C., Ko, E., 2004. "Seismic Performance of Buckling Restrained Braced Frame Systems", *13th World Conference on Earthquake Engineering*, Vancouver, B.C, Canada, Paper No. 1681.

Roeder, C.W., Lehman, D.E., You, J.H., 2005. "Improved Seismic Design of Steel Frame Connections", *International Journal of Steel Structures*, Korean Society of Steel Construction, Seoul, Korea, 5 (2), 141-153.

Roeder, C.W, Lehman, D.E., 2009. "Performance and Behavior of Gusset Plate Connections", *2009 NASCC Conference Proceedings*, Phoenix, AZ, USA.

Trembaly, R., Archambault, M.-H., Filiatrault, A. 2003. "Seismic response of Concentrically Braced Steel Frames Made with Rectangular Hollow Bracing Members", *Journal of Structural Engineering*, 129 (12), 1626-1636.

Yoo, J., Lehman, D.E., Roeder, C.W., 2008. "Influence of connection design parameters on the seismic performance of braced frames", *Journal of Constructional Steel Research*, 64, 607-623.

Design of Normal Strength Concrete Mixtures with Recycled Concrete Aggregates

A.M. Knaack[1] and Y.C. Kurama[2]

[1]Univ. of Notre Dame, Department of Civil Engineering and Geological Sciences, 156 Fitzpatrick Hall of Engineering, Notre Dame, IN, 46556; email: aknaack@nd.edu
[2]Univ. of Notre Dame, Department of Civil Engineering and Geological Sciences, 156 Fitzpatrick Hall of Engineering, Notre Dame, IN 46556; email: ykurama@nd.edu

ABSTRACT

This paper investigates the design of normal strength concrete mixtures that use recycled concrete aggregates as replacement for virgin natural aggregates. Three mix design methods utilizing direct weight replacement, equivalent mortar replacement, and direct volume replacement are compared based on concrete workability, compressive strength, and elastic modulus. A total of 42 mixes were made with different aggregate replacement amounts. It was determined that the concrete workability changes significantly depending on the replacement method used, with the direct volume and equivalent mortar methods resulting in the best and worst workability, respectively. The compressive strength and elastic modulus of the mixes with recycled concrete aggregates showed little variation from concrete with natural aggregates.

INTRODUCTION

Vast amounts of natural aggregates (e.g., crushed stone, gravel) are used for the construction and maintenance of our civil infrastructure. The mining, processing and transportation of these materials consume large amounts of energy and adversely affect the ecology of forested areas and riverbeds. At the same time, about half of the construction and demolition waste in the U.S. consists of old concrete rubble. By recycling the concrete from our existing infrastructure as replacement for virgin coarse aggregates in new construction, it would be possible to substantially reduce the demand for new aggregates.

Recycled concrete aggregates (RCA) can readily pass the prescriptive requirements for coarse aggregates in structural concrete (ASTM 2009); however, the use of recycled concrete as aggregate has been mostly limited to non-structural applications such as sidewalks and sub-base for roadways (FHWA 2008). In particular, almost all of the existing research on RCA concrete (e.g., Buck 1977; Corinaldesi 2010; Dhir et al. 1999; Domingo-Cabo et al. 2009; Etxeberria et al. 2007; Frondistou-Yannas 1977; Hansen 1986; Nishibayashi et al. 1984; Limbachiya et al. 2000; Olorunsogo et al. 2002; Poon et al. 2004; Rahal 2007; Ryu 2002; Sanchez de Juan et al. 2009; Tam et al. 2005; Tavakoli et al. 1996; Topcu and Sengel 2004; Uche 2008; Xiao et al. 2005, 2006) was conducted outside the U.S., limiting the application

of the findings domestically because of variations in materials and quality control. Most of this previous research used simple weight replacement of virgin natural aggregate (NA) with coarse RCA. More recently, a new method dubbed the "equivalent mortar replacement method" was proposed to result in concrete mixes with comparable fresh and hardened properties as concrete made using natural aggregates (Fathifazl et al. 2009). This method accounts for the volume of residual mortar (i.e., mortar left attached to the original aggregate in RCA) so that the resulting concrete mix has the same volume of total mortar (i.e., residual mortar plus fresh mortar) as concrete made with natural aggregates.

Currently, no accepted engineering standard exists for the design of reinforced concrete mixes with significant levels of RCA to result in comparable properties as concrete made using virgin natural aggregates. In the years to come, the renovation of our nation's aging infrastructure will result in both an increase in the supply of recycled concrete and the demand for new concrete. In many cases, the demolished structure may be near the new construction, thus allowing better quality control and reducing transportation costs. To advance the use of RCA in structural concrete, it is essential to develop a mix design methodology that consistently provides desirable fresh and hardened concrete properties using a straightforward proportioning approach. With this objective in mind, this paper provides an experimental evaluation of three aggregate replacement methods: (1) direct weight replacement; (2) equivalent mortar replacement; and (3) direct volume replacement.

AGGREGATE REPLACEMENT METHODS

The three aggregate replacement methods evaluated in this paper are described below.

Direct Weight Replacement (DWR) Method. The direct weight replacement (DWR) method, or some minor variation, has been used almost exclusively throughout the literature, most likely due to its simplicity. In this method, the weight of the total coarse material (i.e., virgin natural aggregate plus RCA) is kept constant for any percentage of aggregate replacement. The corresponding cement content and water content are also kept constant; however, to produce the same volumetric yield, the amount of fine aggregate may be decreased since similar weights of natural aggregate (NA) and RCA may occupy different volumes (depending on the specific gravity). In some variations of the DWR method, the amounts of the both the total coarse aggregate and fine aggregate are adjusted to maintain similar volumetric yields.

Equivalent Mortar Replacement (EMR) Method. The equivalent mortar replacement (EMR) method proposed by Fathifazl et al. (2009) treats RCA as a two-phase material made of residual mortar (RM) and recycled natural aggregate (RNA) rather than as a singular coarse material. The volume of the residual mortar is accounted for so that the resulting concrete mix has the same total mortar volume (i.e., residual mortar plus fresh mortar) as concrete made with virgin natural aggregates. The resulting design relationships between a target natural aggregate concrete (NAC) mix and an EMR mix are given as:

$$V_{RM}^{EMR} + V_{FM}^{EMR} = V_{FM}^{NAC} \quad (1)$$

$$V_{RNA}^{EMR} + V_{NA}^{EMR} = V_{NA}^{NAC} \quad (2)$$

where, V_{RM}^{EMR} = volume of residual mortar (RM) in EMR mix; V_{FM}^{EMR} = volume of fresh mortar (FM) in EMR mix; V_{FM}^{NAC} = volume of FM in NAC mix; V_{RNA}^{EMR} = volume of recycled natural aggregate (RNA) in EMR mix; V_{NA}^{EMR} = volume of virgin natural aggregate (NA) in EMR mix; and V_{NA}^{NAC} = volume of NA in NAC mix.

Equations 1 and 2 dictate that as the volume of RCA is increased in a given volume of concrete, the amount of fresh mortar is decreased while keeping the relative proportions of cement, water, and fine aggregate constant. Because a reduction in fresh mortar causes a reduction in the workability and place-ability of concrete, there is a limit to the maximum amount of aggregate replacement that can be utilized in EMR mixes. As a result, the EMR mixes tested by Fathifazl et al. (2009) used significant amounts of water-reducing admixtures. It was concluded that at similar water and cement contents, EMR mixes had better workability than their NAC counterparts; however, the NAC mixes used in these comparisons did not have any water reducer. Furthermore, while both EMR and DWR methods were evaluated by Fathifazl et al. (2009), the mixes used did not have similar aggregate replacement percentages, thus making direct comparisons very difficult.

Direct Volume Replacement (DVR) Method. The ACI 211 (1991) *Standard Practice for Selecting Proportions for Normal, Heavyweight and Mass Concrete* provides a common method for the proportioning of virgin natural aggregate concrete mixtures based on the absolute volume of each constituent. However, direct volume replacement has not been used in the literature as a method for the design of RCA mixes, and is proposed here as a simple method consistent with standard practice for natural aggregate mix designs. The direct volume replacement (DVR) method treats RCA as a single-phase coarse aggregate where a given volume of NA is replaced by an equal volume of RCA. Since, the resulting volumetric proportions of total coarse aggregate (RCA plus NA), fine aggregate, cement, and water remain constant, there should not be a loss in workability with an increase in the proportion of RCA as long as the inherently greater absorption of RCA (as compared with the absorption of NA) is incorporated into the design.

EXPERIMENTAL PROGRAM

An experimental program was conducted to evaluate the DWR, EMR, and DVR mix design methods on the fresh and hardened properties of concrete with varying amounts of aggregate replacement. The three properties examined are: (1) concrete slump; (2) compressive strength; and (3) modulus of elasticity. A total of 42 mixtures were designed and tested utilizing normal strength concrete.

Aggregates. One type of fine natural aggregate (FA), one type of coarse natural aggregate (NA), and two types of recycled concrete aggregates (RCA) were used in the experimental program. INDOT No. 23 concrete sand was used as the fine aggregate. For coarse natural aggregate, moraine pea gravel (NA-PG) from a local

ready-mix concrete plant was used. These fine and coarse natural aggregates are typical in ready-mix concrete construction.

The first source for recycled concrete aggregate (RCA-ND) was a precast concrete shear wall laboratory specimen previously tested to failure under reversed-cyclic lateral loading at the University of Notre Dame (Smith et al. 2010). The reason for using this test specimen as an RCA source was the availability of detailed information on the mix design as well as the fresh and hardened properties of the source concrete. After the testing of the wall, the precast panels were taken to a recycling facility, where they were crushed to a nominal maximum size of about 5-6 in. The larger pieces were removed by hand and the smaller size fractions were sieved and then combined to produce the desired RCA grading.

The second source for recycled concrete aggregate (RCA-SB) came from a construction recycling yard in South Bend, Indiana. Since this facility takes debris from many sources (e.g., sidewalks, buildings, bridges), the properties of the source concrete are not known. Furthermore, RCA-SB contained approximately 4.0% (by weight) deleterious substances (e.g., brick, asphalt, wood), some of which was manually removed during the sieving, washing, and drying process. It is likely that not all of this material was removed or taken into account when determining the percentage of deleterious material in the RCA.

Table 1 shows the specific gravity [bulk dry, saturated surface dry (SSD), and apparent], absorption, residual mortar content (RMC), and fineness modulus for the aggregates used. The specific gravity and absorption were determined using ASTM C 127 (ASTM 2009b) and ASTM C 128 (ASTM 2009b) for coarse and fine aggregates, respectively, and the fineness modulus of the fine aggregate was determined according to ASTM C 136 (ASTM 2009b). The residual mortar content, which is a measure of the percent (by weight) of residual mortar in the RCA, was determined as described in Abbas et al. (2008). Due to the residual mortar, the specific gravity for RCA is lower than that for NA while the absorption of RCA is greater than that of NA.

Table 1. Natural coarse, recycled, and fine aggregates.

Aggregate	Specific gravity			Absorption (%)	RMC (%)	Fineness Modulus
	Bulk dry	SSD	Apparent			
NA-PG	2.47	2.55	2.70	3.48	-	-
RCA-ND	2.28	2.41	2.63	5.69	60.5	-
RCA-SB	2.13	2.28	2.49	6.73	51.5	-
Sand	2.59	2.63	2.69	1.39	-	2.54

The coarse aggregate gradations used in the research are shown in Figure 1. Since significant variations in aggregate size can produce different fresh and hardened concrete properties (e.g., workability, strength) (Kosmatka et al. 2002), it was necessary to use aggregates with consistent gradation. The source concrete mix design for RCA-ND (Smith et al. 2010), which used ASTM C 33 (ASTM 2009b) No. 8 coarse aggregate [3/8-in. (9.5 mm) nominal maximum aggregate size], was selected as the basis for the aggregate gradation. NA-PG

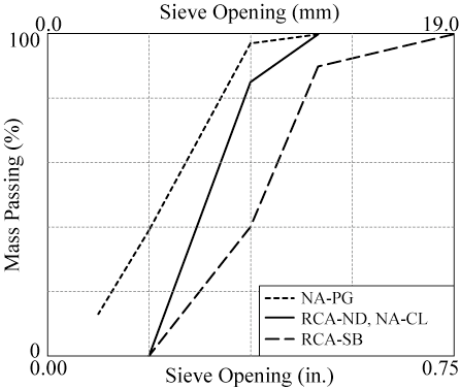


Figure 1. Aggregate gradations.

as acquired from the ready-mix concrete plant followed ASTM No. 8 requirements with no additional gradation necessary; however, RCA-ND was sieved into individual size fractions and recombined to produce gradations similar to ASTM No. 8. RCA-SB was deficient in the No. 4 aggregate size; and thus, a slightly larger gradation following ASTM C 33 No. 7 aggregate was used.

NA Concrete Mix Design. Table 2 lists the dry weight proportions for the target natural aggregate concrete (NAC) mix design that formed the basis for the RCA mixes in this research. The source concrete design for RCA-ND was used as the target NAC mix with NA-PG as the coarse natural aggregate. This mix was originally designed with a water-to-cement (*w/c*) ratio of 0.44 for a target 28-day strength of 6.0 ksi (41.4 MPa), slump of 5±1 in. (127±25 mm), and air content of 5±1.5%. From previous data (Smith et al. 2010), the average measured 28-day strength of the concrete was 6.4 ksi (44.1 MPa). Because the original mix was designed for precast concrete construction, which requires high early concrete strength for removal of formwork, ASTM C 150 Type III (ASTM 2009a) portland cement was used. The concrete also contained Sika® AEA-14 and Sikament® 686 as air-entraining agent (AEA) and high range water reducer (HRWR), respectively.

RCA Concrete Mix Designs. Table 2 also lists the RCA concrete mix designs used in this research by replacing the NA in the target mix design above. The aggregate replacement ratio, R refers to the amount of NA replaced by RCA as given by Equations 3, 4 and 5 for the DWR, EMR, and DVR methods, respectively.

$$R = 1 - W_{NA}^{DWR}/W_{NA}^{NAC} \quad (3)$$

$$R = 1 - V_{NA}^{EMR}/V_{NA}^{NAC} \quad (4)$$

$$R = 1 - V_{NA}^{DVR}/V_{NA}^{NAC} \quad (5)$$

where, W_{NA}^{DWR} = weight of NA in DWR mix; W_{NA}^{NAC} = weight of NA in NAC mix; V_{NA}^{EMR} = volume of NA in EMR mix; V_{NA}^{DVR} = volume of NA in DVR mix; and V_{NA}^{NAC} = volume of NA in NAC mix. Note that the water reducer in each mix was batched proportionally to the amount of cement (per manufacturer's specifications) so as to maintain a consistent composition for the fresh mortar. For the EMR mixes, this resulted in a decrease in the amount of water reducer as R increased (since an increase in R resulted in a decrease in the amount of cement).

Aggregate Preparation. Following dry sieving, the recycled and natural coarse aggregates were washed with water over a No. 8 (2.36 mm) sieve to further remove excess fines. All coarse and fine aggregates were then dried in an oven at 230 °F (110 °C) for at least 24 hours. To ensure that the aggregates did not absorb mix water (in turn pulling water from the cement paste and leading to decreased workability and cement hydration), the aggregates were removed from the oven, batched according to the dry weights in Table 2, blended (if necessary) according to the gradations in Figure 1, and then soaked in water for a period of 18 to 24 hours. After soaking, the excess water was decanted from the aggregates, which were then weighed to determine the amounts of absorbed and residual water on the aggregates. Using the

absorption values from Table 1, the amount of residual water on the aggregates beyond the saturated surface dry (SSD) condition was determined and subtracted from the required mix water for each concrete batch.

Table 2. NA and RCA Normal Strength Concrete Mix Designs

Name	*R*	Water	Cement	NA	RCA	FA	HRWR	AEA
	%	*lb/yd³*	*lb/yd³*	*lb/yd³*	*lb/yd³*	*lb/yd³*	*fl oz/yd³*	*fl oz/yd³*
NA-PG Target	0	253	574	1733	-	1140	60.0	10.0
RCA-ND DWR Method	10	253	574	1560	173	1124	60.0	10.0
	21	253	574	1369	364	1108	60.0	10.0
	31	253	574	1196	537	1093	60.0	10.0
	41	253	574	1023	710	1079	60.0	10.0
	51	253	574	849	884	1064	60.0	10.0
	61	253	574	676	1057	1050	60.0	10.0
	71	253	574	503	1230	1036	60.0	10.0
	81	253	574	329	1404	1021	60.0	10.0
	90	253	574	173	1560	1008	60.0	10.0
	100	253	574	-	1733	994	60.0	10.0
RCA-ND EMR Method	4	239	543	1664	185	1078	56.8	9.5
	9	223	508	1585	396	1007	53.0	8.9
	14	205	466	1495	641	926	49.0	8.1
	20	184	418	1389	926	830	44.0	7.3
RCA-ND DVR Method	10	253	574	1552	173	1140	60.0	10.0
	21	253	574	1374	343	1140	60.0	10.0
	31	253	574	1196	513	1140	60.0	10.0
	41	253	574	1021	681	1140	60.0	10.0
	51	253	574	847	847	1140	60.0	10.0
	61	253	574	674	1012	1140	60.0	10.0
	71	253	574	504	1169	1140	60.0	10.0
	81	253	574	334	1326	1140	60.0	10.0
	90	253	574	166	1482	1140	60.0	10.0
	100	253	574	-	1636	1140	60.0	10.0
RCA-SB DWR Method	10	253	574	1560	173	1114	60.0	10.0
	21	253	574	1369	364	1087	60.0	10.0
	31	253	574	1196	537	1063	60.0	10.0
	41	253	574	1023	710	1039	60.0	10.0
	51	253	574	849	884	1015	60.0	10.0
	61	253	574	676	1057	991	60.0	10.0
	81	253	574	329	1404	942	60.0	10.0
	100	253	574	-	1733	896	60.0	10.0
RCA-SB EMR Method	5	241	548	1646	176	1087	57.3	9.5
	10	229	521	1560	352	1034	54.5	9.1
	15	218	495	1473	528	982	51.7	8.6
	20	206	468	1386	704	929	48.9	8.2
RCA-SB DVR Method	21	253	574	1380	323	1140	60.0	10.0
	41	253	574	1031	631	1140	60.0	10.0
	61	253	574	682	939	1140	60.0	10.0
	81	253	574	333	1248	1140	60.0	10.0
	100	253	574	-	1541	1140	60.0	10.0

Note: 1 lb/yd³ = 0.593 kg/m³; 1 fl oz/yd³ = 38.7 mL/m³

Concrete Slump. Each concrete batch was mixed in a rotating drum mixer according to ASTM C 192 (ASTM 2009b). To determine the workability of each mix, a variation of the ASTM C 143 (ASTM 2009b) slump test was conducted. The ASTM test requires a slump cone with a concrete volume of 0.20 ft^3 (5663 cm^3). However, because of the relatively small amount of RCA available for this project, the batch volume for each mix was limited to 0.12 ft^3 (3398 cm^3) to make four 3 x 6 in. (7.6 x 15.2 cm) cylinders. To allow for the slump measurement of these batches, the dimensions of the ASTM slump cone were scaled by half, thus reducing the required concrete volume to 0.03 ft^3 (721 cm^3). The correlation between the full slump cone and the scaled "mini slump" cone was determined based on two trial batches, one using pea gravel (NA-PG) and the other using crushed limestone (referred to as NA-CL) from a local ready-mix concrete plant. The gradation of NA-CL (Figure 1) was similar to the ASTM No. 8 gradation of NA-PG. The use of these two materials provided slump measurements of concrete with rounded aggregates (pea gravel) as well as angular aggregates (crushed limestone). The concrete batches were based on the target NAC mix design in Table 2 but the amount of water was varied so as to result in varying *w/c* ratios ranging from 0.3 to 0.5. Three mini slump measurements and three standard slump measurements were taken for each mix. The results from the standard and mini slump tests (Figure 2) were compared and linear regression analysis showed that the mini slump test could be used to predict the standard slump test according to Equation 6, with a coefficient of determination of 0.93.

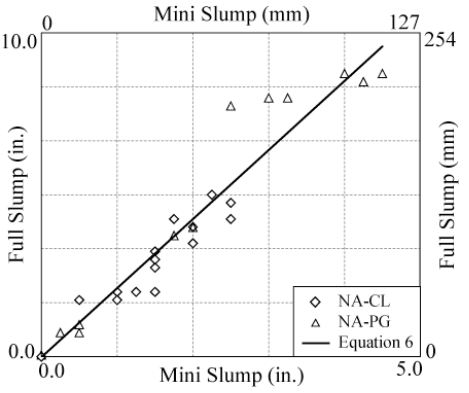


Figure 2. Standard full slump versus mini slump.

$$Full\ Slump = 2.13 * (Mini\ Slump) \quad (6)$$

Note that this regression equation is constrained so that the y-intercept is zero, which does not give the best possible fit but is done to provide a practical relationship without significantly affecting the coefficient of determination.

Curing. Following slump testing, four 3 x 6 in. (7.6 x 15.2 cm) concrete cylinders were made from each batch. Three cylinders were used to determine the compressive strength and stiffness of the concrete, while the fourth cylinder was left unbroken for future reference and microscopic structural analysis and petrography. The cylinders were made using plastic disposable molds, which were capped and stored at room temperature and humidity for approximately one day. The day after casting, the cylinders were removed from the molds and were cured for 27 days in water at room temperature, bringing the total curing duration to 28 days. In accordance with ASTM C 511 (ASTM 2009b), high-calcium hydrated lime (calcium hydroxide) was added to the curing water to prevent the leaching of lime from the concrete cylinders.

Testing. Following the 28-day curing period, the specimens were removed from the curing tank, hand dried using paper towels, and tested in a moist state according to ASTM C 39 (ASTM 2009b). Each cylinder was capped using unbonded steel caps and rubber bearing pads to help maintain an even load distribution during testing. The

testing machine was a Satec© 5590-HVL Universal Testing Machine with a 67 kip (300 kN) axial load capacity. The loading stress rate was held constant at 35 psi/s (241 kPa/s). An Epsilon© 3542RA rock averaging extensometer with 2 in. (5.1 cm) gauge length was used to measure the concrete axial strain. The concrete compressive strength was determined from the peak stress, f_{cm} reached in each test and the secant modulus, E_{sec} was determined as:

$$E_{\text{sec}} = (f_{c2} - f_{c1})/(\epsilon_{c2} - \epsilon_{c1}) \quad (7)$$

where, $f_{c2} = 0.40 f_{cm}$; f_{c1} = stress at ϵ_{c1}; ϵ_{c2} = strain at f_{c2}; and $\epsilon_{c1} = 0.00005$.

RESULTS

The slump, compressive strength, and secant modulus results for the 42 concrete mixes in Table 2 are discussed below. The results are presented as individual data (i.e., not averages) from all of the tests conducted.

Slump. Due to variations in mixture proportions for a given aggregate replacement ratio, *R*, each replacement method may be expected to provide different results for concrete workability. It can be argued that as the ratio of fresh mortar to total coarse material decreases, so too does the concrete workability. As such, the DVR method should not result in a significant decrease in workability provided that similar aggregate gradations are used in the recycled and natural aggregate mix designs and the absorption of the aggregates is accounted for. Conversely, since the DWR and EMR methods decrease the fresh mortar to coarse material ratio, the workability of these mixes is expected to decrease proportionally.

Figure 3 shows the mini slump test results for each of the mix designs. The results show that at the maximum possible replacement ratio of *R*=100%, the DVR method provided similar workability to the target mix design (cases with *R*=0%). The mixes with RCA-SB had slightly smaller slump than the mixes with RCA-ND. This may be attributed to the difference in aggregate gradation (Figure 1), with the nominal maximum aggregate sizes being 1/2 in. (12.5 mm) for RCA-SB and 3/8 in. (9.5 mm) for RCA-ND. In comparison with the DVR method, the DWR method resulted in mini slump values about 0.75 in. (19 mm) less than the target mix design at *R*=100%. The EMR mixes performed the worst and became unworkable at small amounts of replacement, with the mini slump reaching 0 by *R*=20%. Note that as investigated by Fathifazl et al. (2009), it may be possible to reach larger *R* values in EMR mixes by using large amounts of water reducer; however, this was not done in the current research.

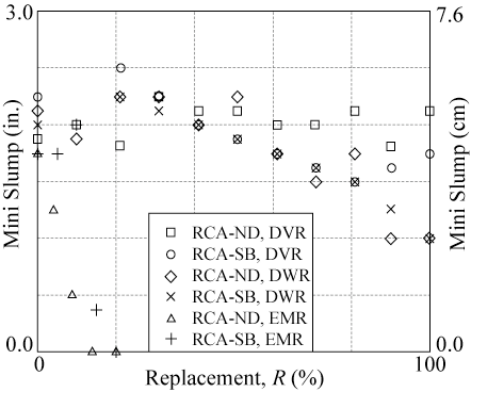


Figure 3. Mini slump.

Compressive Strength. Figures 4a and 4b show the 28-day compressive strength, f_{cm}, results for the mixes with RCA-ND and RCA-SB, respectively. At each replacement ratio, *R*, a minimum of three cylinders were tested for each RCA type and design

method. To ensure repeatability, additional batches of some of the DVR mixes with RCA-ND were made several months after the first batches. Little difference was found in the results from the original and repeated mixes.

From Figure 4, a distinction cannot be made between the compressive strengths of the RCA mixes designed using the DWR, DVR, and EMR methods. In general, each of these design methods was capable of producing RCA concrete (cases with R>0%) with comparable strength as NA concrete (cases with R=0%). No significant trend can be seen as R is increased; however, it is interesting to note that at R=100%, both RCA-ND and RCA-SB concrete were stronger than NA concrete. Furthermore, RCA-SB concrete was only slightly weaker than RCA-ND concrete despite the questionable quality of RCA-SB.

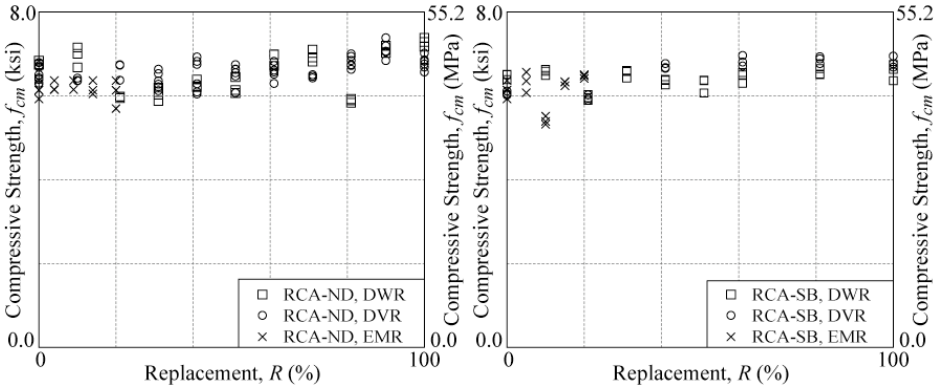


Figure 4. Compressive strength of concrete using: (a) RCA-ND; and (b) RCA-SB.

The slightly higher strengths of RCA concrete as compared with NA concrete could be because of the use of pea gravel (NA-PG) as the coarse natural aggregate in the target mix design. It is also possible that the differences between the aggregate types become more significant for higher concrete strengths. While further research should certainly be conducted on the variability of these results with additional sources of RCA and NA as well as for high strength concrete mixes, it is concluded that compressive strength may not be a limiting factor on the use of RCA in structural normal strength concrete applications.

Modulus of Elasticity. Figure 5 shows the secant modulus, E_{sec} results corresponding to the compressive strength data in Figure 4 (with the exception of the EMR mixes, for which the elastic modulus was not measured). In general, the elastic modulus findings were consistent with those for compressive strength that the replacement ratio and design method did not have a significant effect on the results. Further research is needed on the variability of these results with additional sources of RCA and NA.

For natural aggregate concrete, the elastic modulus is typically considered to vary with compressive strength. Figure 6 shows the variation of elastic modulus with respect to the square root of the compressive strength data from Figures 4 and 5. It can be seen that while the RCA mixes had consistent trends in elastic modulus as the NA concrete and no distinction could be made with respect to the aggregate used, all

of the RCA and NA mixes had elastic modulus values lower than the ACI 318 (2008) modulus (solid line).

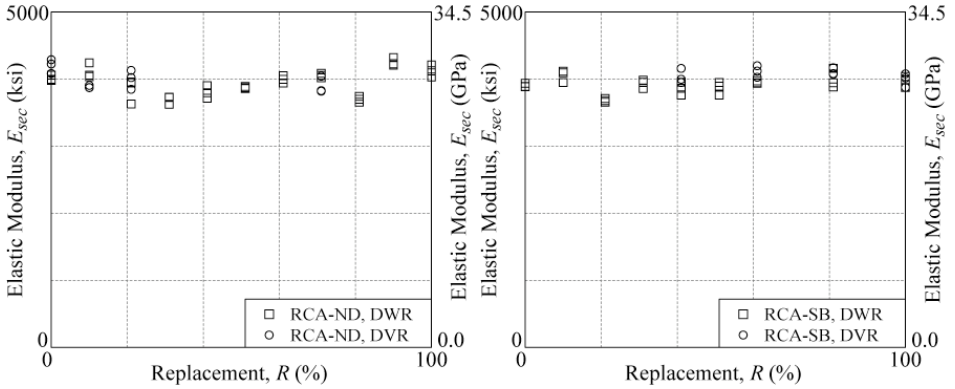


Figure 5. Elastic modulus of concrete using: (a) RCA-ND; and (b) RCA-SB.

SUMMARY AND CONCLUSIONS

This paper investigates the design of normal strength concrete mixtures that use recycled concrete aggregates as replacement for coarse virgin natural aggregates. Three mix design methods utilizing direct weight replacement (DWR), equivalent mortar replacement (EMR), and direct volume replacement (DVR) are compared based on concrete workability, compressive strength, and elastic modulus. The important conclusions from the study are given below. In interpreting these conclusions, it should be emphasized that the results are limited to the materials and mix proportions tested. Ultimately, further research should be conducted on the variability of the results with additional sources of recycled concrete and natural aggregates, as well as for high strength concrete mixes.

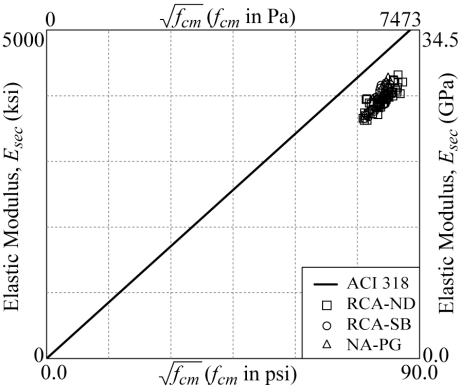


Figure 6. Elastic modulus and compressive strength.

1. The workability of fresh concrete is affected by the aggregate replacement method. The DVR method produced concrete with equivalent workability to the target natural aggregate concrete. While the DWR mixes had somewhat decreased workability than the DVR mixes, the concrete was still easily placed and finished in the cylinder molds. In comparison, the decreased amount of fresh mortar in the EMR method resulted in significantly reduced workability such that aggregate replacement ratios greater than R=20% were not possible without changing the mix proportions or increasing the amount of water reducer.
2. The different natural and recycled concrete aggregates used in this research had a relatively small effect on the compressive strength of the concrete mixes

tested, even at a 100% aggregate replacement ratio. It is concluded that compressive strength may not be a limiting factor on the use of recycled concrete aggregate in structural normal strength concrete applications.

3. For the materials tested, the aggregate replacement mix design method had no distinguishable effect on the compressive strength of concrete.
4. Similar to the compressive strength results, the aggregate type, replacement design method, or replacement amount did not have a significant effect on the elastic modulus of the concrete mixes tested.
5. While the recycled concrete aggregate mixes had consistent trends in elastic modulus as the natural aggregate concrete mixes, all of the specimens tested had elastic modulus values lower than that given by ACI 318 (2008).

REFERENCES

Abbas, A., Fathifazl, G., Isgor, O.B., Razaqpur, A.G., Rournier, B., and Foo, S. (2008). "Proposed Method for Determining the Residual Mortar Content of Recycled Concrete Aggregates." *J. of ASTM International*, 5(1), 1-12.

ACI 318. (2008). *Building Code Requirements for Structural Concrete and Commentary*. American Concrete Institute, Farmington Hills, MI.

ACI Committee 211. (1991). *Standard Practice for Selecting Proportions for Normal, Heavyweight and Mass Concrete*. ACI 211.1-91, American Concrete Institute, Farmington Hills, MI.

ASTM International. (2009a). *Annual Book of ASTM Standards.* 4.01, Philadelphia, PA.

ASTM International. (2009b). *Annual Book of ASTM Standards*. 4.02, Philadelphia, PA.

Buck, A.D. (1977). "Recycled Concrete as a Source of Aggregate." *ACI J.*, 74(6), 212-219.

Corinaldesi, V. (2010). "Mechanical and Elastic Behaviour, of Concrete Made of Recycled-Concrete Coarse Aggregates." *Construction and Building Materials*, 24(9), 1616-1620.

Dhir, R.K., Limbachiya, M.C., and Leelawat, T. (1999). "Suitability of Recycled Concrete Aggregate for Use in BS 5328 Designated Mixes." *Proceedings of ICE: Structures & Buildings*, 134(3), 257-274.

Domingo-Cabo, A., Lazaro, C., Lopez-Gayarre, F., Serrano-Lopez, M.A., Serna, P., and Castano-Tabares, J.O. (2009). "Creep and Shrinkage of Recycled Aggregate Concrete." *Construction and Building Materials,* 23(7), 2545-2553.

Etxeberria, M., Mari, A.R., and Vazquez, E. (2007). "Recycled Aggregate Concrete as Structural Material." *Mat. and Structures*, 40(5), 529-541.

Fathifazl, G., Abbas, A., Razaqpur, A.G., Isgor, O.B., and Foo, S. (2009). "New Mixture Proportioning Method for Concrete Made with Coarse Recycled Concrete Aggregate." *J. of Mat. in Civil Eng.*, 21(10), 601-611.

FHWA. (2008). "Recycled Concrete Aggregate." *Pavements*. Federal Highway Administration, http://www.fhwa.dot.gov/pavement/recycling/rca.cfm.

Frondistou-Yannas, S. (1977). "Waste Concrete as Aggregate for New Concrete." *ACI J.*, 74(8), 373-376.

Hansen, T.C. (1986). "Recycled Aggregates and Recycled Aggregate Concrete Second State-of-the-Art Report Developments 1945-1985." *Materials and Structures*, 19(3), 201-246.

Kosmatka, S.H., Kerkhoff, B., and Panarese, W.C. (2002). *Design and Control of Concrete Mixtures*. 14th Edition. Portland Cement Association, Skokie, IL, 358 pp.

Nishibayashi, S., Yamura, K., and Hayashi, A. (1984). "Elastic-Plastic Properties and Durability of Concrete Made from Recycled Concrete Aggregate Prepared by Crushing Concrete," *Transactions of the Japan Concrete Inst.*, 6, 127-132.

Limbachiya, M.C., Leelawat, T., and Dhir, R.K. (2000). "Use of Recycled Concrete Aggregate in High-Strength Concrete." *Materials and Struct.*, 33(9), 574-580.

Olorunsogo, F. and Padayachee, N. (2002). "Performance of Recycled Aggregate Concrete Monitored by Durability Indexes." *Cement and Concrete Research*, 32, 179-185.

Poon, C.S., Shui, Z.H., Lam, L., Fok, H., and Kou, S.C. (2004). "Influence of Moisture States of Natural and Recycled Aggregates on the Slump and Compressive Strength of Concrete." *Cement and Concrete Res.*, 34(1), 31-36.

Rahal, K. (2007) "Mechanical Properties of Concrete with Recycled Coarse Aggregate." *Building and Environment*, 42, 407-415.

Ryu, J.S. (2002). "An Experimental Study on the Effect of Recycled Aggregate on Concrete Properties." *Magazine of Concrete Research*, 54(1), 7-12.

Sanchez de Juan, M. and Alaejos Gutierrez, P. (2009) "Study on the Influence of Attached Mortar Content on the Properties of Recycled Concrete Aggregate." *Construction and Building Materials*, 23(2), 872-877.

Smith, B., Kurama, Y., and McGinnis, M. (2010). "Design and Measured Behavior of a Hybrid Precast Concrete Wall Specimen for Seismic Regions." *J. of Structural Engineering*, (preprint article may be accessed from http://ascelibrary.aip.org/)

Tam, V.W.Y., Gao, X.F., and Tam, C.M. (2005). "Microstructural Analysis of Recycled Aggregate Concrete Produced from Two-Stage Mixing Approach." *Cement and Concrete Research*, 35(6), 1195-1203.

Tavakoli, M. and Soroushian, P. (1996). "Strengths of Recycled Aggregate Concrete Made Using Field-Demolished Concrete as Aggregate." *ACI Materials J.*, 93(2), 182-190.

Topcu, I.B. and Sengel, S. (2004). "Properties of Concretes Produced with Waste Concrete Aggregate." *Cement and Concrete Research*, 34(8), 1307-1312.

Uche, O.A.U. (2008). "Influence of Recycled Concrete Aggregate (RCA) on Compressive Strength of Plain Concrete." *Continental J. Engin. Sci.*, 3, 30-36.

Xiao, J., Li, J., and Zhang, C. (2006). "On Relationships Between the Mechanical Properties of Recycled Aggregate Concrete: An Overview." *Materials and Structures*, 39(6), 655-664.

Xiao, J., Li, J., and Zhang, C. (2005). "Mechanical Properties of Recycled Aggregate Concrete Under Uniaxial Loading." *Cement and Conc. Res.*, 35(6), 1187-1194.

Buckling Behavior of Shell Elements Subjected to Inelastic Reversed Cyclic Loading

Max Stephens[1], Peter Dusicka[2], Gregory Lewis[1]

[1]Graduate Research Assistant, [2]Associate Professor, Dept. of Civil and Environmental, Portland State University, PO Box 751 CEE, Portland, OR 97207-0751; email: mts@pdx.edu, dusicka@pdx.edu, and gregorylewis3200@gmail.com

ABSTRACT

Shell elements are commonly used over continuum 3D elements to model structural components for computational efficiency when information regarding behavior across the material thickness is not needed. Shell elements are widely believed to effectively capture the global hysteretic behavior of thin walled structural components. The objective of this research was to compare the hysteretic behavior of numerical models of links, such as those used in eccentrically braced frames that consisted entirely of shell and of continuum elements. The geometry, material properties, and loading protocol were consistent in the shell and 3D continuum analyses.

The results captured by the shell-based models exhibited significantly more severe global degradation of the force deformation hysteresis at large inelastic deformations then the 3D continuum elements. This discrepancy was recorded for models of entire links as well as more simplified models. The results of this investigation have brought into question the reliability of shell elements in accurately capturing the buckling behavior of thin walled structural components subjected to extreme cyclic loading.

INTRODUCTION

Shell elements are commonly used in finite element analysis (FEA) to model structures in which the dimension across the thickness is much less than other dimensions in the structure (Simulia, 2010). These elements are formed by combining plate bending and plane stress element formulations to create an element with bending and plane stress degrees of freedom. Shell elements typically used in finite element analysis include 6 degrees of freedom; 3 plate bending, 2 plane stress, and 1 allowing for rotation about the z-axis (Cook, 2002). Shell elements are used in place of full three dimensional elements to increase computational efficiency by decreasing the number of nodes within a model. Thick and thin shell element formulations are available which respectively take into account and ignore transverse shear deformation.

Shell elements are widely believed to effectively capture the global hysteretic behavior of thin walled structural components made from metals. The dimensions across the thicknesses of the plates which make up these components are generally very small relative to the global dimensions of the component. This paper focuses on the uses of this modeling technique for short beam links, such as those used in eccentrically braced frames. Additionally, the performance of such links is generally

assessed based on global hysteretic behavior as opposed to local material behavior and such the performance can be assessed without gathering material information across plate thicknesses. Numerous numerical studies have utilized shell elements to assess the performance of links and stiffened shear panels subjected to cyclic loading including; Berman et al. (2009), Dusicka and Lewis (2007), Alinia and Dastfan (2006), Richards and Uang (2005), Itani et al. (2003), Lee and Yoo (1998).

Due to the widespread use of shell elements to assess the performance of shear links and shear panels, the objective of this study was to assess the cyclic buckling behaviors of structural components modeled using these elements. In this study, the hysteretic responses of a shear link modeled using shell elements and 3D continuum elements were compared. The numerical hysteretic responses were additionally compared to experimental results to assess the validity of modeling shear links using shell and 3D element formulations.

NUMERICAL MODEL

A W12x22 link designed in accordance with the specifications provided in the Seismic Provisions (AISC, 2005) for links in eccentrically braced frames was used for the purpose of this analysis. This link was chosen due to the availability of experimental data while satisfying the compactness requirements in both the flange and the web. The link was classified as long, or flexure dominated, as defined by the requirements specified in the seismic provisions. Specifically, the link length, $e > 2.6M_p/V_p$ where M_p is the plastic moment strength and V_p is the plastic shear strength. The sectional properties of the link were consistent with the dimensions provided for a W12x22 rolled section in the AISC Steel Construction Manual. These properties were used to calculate the plastic shear and moment strengths of the link assuming a nominal yield strength f_y = 50ksi and link length e = 53in. The section properties and calculated nominal strength values are summarized in Table 1. Intermediate stiffeners spaced at 5.9 in were included on one side of the link to provide web stability. End stiffeners were additionally included to shift plastic strain away from the connection zone of the link (Dusicka, 2009). The geometric properties of the stiffeners are summarized in Table 2.

Table 1: Nominal Link Properties.

Beam	Length	Web		Flanges		Nominal Strengths		
	e (in)	h_w (in)	t_w (in)	b (in)	t_f (in)	V_p (kip)	M_p (kip in)	$\frac{2.6M_p}{V_p}$
W12X22	53	11.45	0.26	4.03	0.425	89	1458	42.6

Table 2: Nominal Stiffener Properties.

Stiffener Type	b_s (in)	h_s (in)	t_s (in)	Spacing (in)
Intermediate	1.5	11.45	0.375	5.89
End	5	11.45	0.375	NA

The commercially available FEA program ABAQUS v6.9 (Simulia, 2010) was used to numerically investigate the cyclic behavior of a the link using shell and 3D continuum elements. Three dimensional models were developed, and material as well as geometric non-linearities were incorporated. Model geometry included transverse stiffeners along the effective length of the link, the end stiffeners, and the end plate connection. A model overview for the shell and 3D continuum models is illustrated in Figure 1.

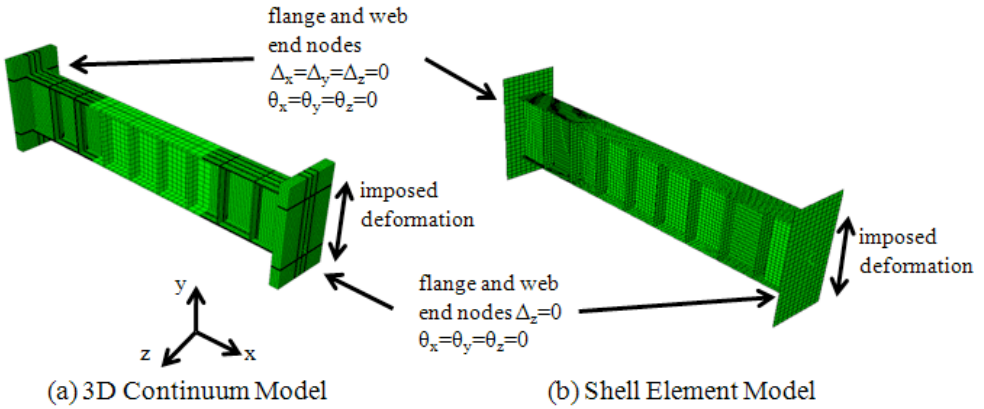


Figure 1: Link Model Overview

To model the cyclic non-linear behavior of steel material in the link, the combined Isotropic/Kinematic hardening formulation was used. The hardening parameters were calibrated using monotonic stress strain data obtained from ASTM tests on the web and flanges of available beam section. As the combined hardening formulation in ABAQUS requires cyclic stress strain data, the cyclic behavior of the steel was approximated by developing a relationship between the monotonic and cyclic behavior of A572 steel using the experimental results from Kaufmann et al. (2001). Modeling material failure was outside the scope of this study, and thereby the material failure characteristics related to fatigue and ductility limits were not included.

The boundary conditions in the models consisted of a fixed-roller system as shown in Figure 1. The nodes at one end of the link were restrained in all degrees of freedom. All rotation and transverse displacement was restrained at the other end of the link, allowing for longitudinal displacement. This ensured that artificially induced internal axial forces were not introduced to the link during loading. Shear was applied by assigning end displacements Δ_y along the y-axis as shown in Figure 1.

To overcome the geometric perfection inherent in numeric modeling, buckling mode shapes were superimposed to introduce imperfections to the model geometry. Elastic Eigen value analyses were conducted to develop the mode shapes of the link. A fraction of the displacements from the first two mode shapes were applied to the link geometry prior to running the non-linear analyses.

Different geometric assumptions and element formulations were used in the shell and 3D continuum models. The shell model was assembled using shell elements located at the center of the plate thickness. Thus in building the model, the effective height of the web, $h_{weff,}$ and stiffeners h_{seff} became $h_{weff} = h_w + t_f$ and $h_{seff} = h_s + t_f$

respectively to maintain the correct web height to thickness aspect ratios; resulting in a 4% height increase in the web and stiffeners. ABAQUS shell element formulations S4, S4R, and S8R were used in the shell model. These elements respectively utilize a linear element formulation with 4-nodes, a linear element formulation with 4-nodes, reduced integration, and hourglass control, and a quadratic element formulation with 8-nodes, reduced integration, and hourglass control. All element formulations included 6 degrees of freedom per node resulting in shell elements with bending, plane strain, and z-axis rotation degrees of freedom (Simulia, 2010). Both Simpson and Gauss integration were used in the shell analysis with 3, 7, and 9 integration points across the shell thicknesses. The continuum model conversely was assembled using ABAQUS 3D continuum elements C3D8. In building the model, the components of the shear link were defined to the geometry provided for a W12X22. C3D8 elements utilize a linear element formulation with 8-nodes and allow for 6 degrees of freedom per node. The components of the W12X22 shear link including the web, flanges, and stiffeners were assembled using ABAQUS tie constraints in both the shell and 3D continuum models (Simulia, 2010).

Global mesh convergence was conducted by analyzing strain values along the flange of the link for both the shell and 3D continuum models. In the shell model, the mesh was refined across the entire length of the link, while in the continuum model the mesh was refined only near the ends of the link where flange buckling was expected to occur. Selective convergence was used in the 3D continuum model for computational efficiency. Final mesh convergence in the 3D continuum model yielded three elements across the web and transverse stiffeners, and four elements across the thickness of the flange.

MONOTONIC BEHAVIOR

Monotonic analyses were conducted on the shell and 3D continuum models to a maximum elastic rotation angle $\gamma = 0.055$rad. The deformation was imposed at one end of the link, and the linear y-axis deformations were translated to elastic rotation angles γ. The monotonic force deformation behaviors observed in the shell and 3D continuum models can be seen in Figure 2, and the yield and ultimate strengths are displayed in Table 3. Changing the integration parameters did not have a noticeable effect on the monotonic behavior of the shell models, and thus only results obtained using Simpson integration with 3 integration points across the shell thickness are shown. Additionally, the monotonic results obtained using the ABAQUS shell elements S4 and S4R were identical, so results obtained using the S4R element have been excluded.

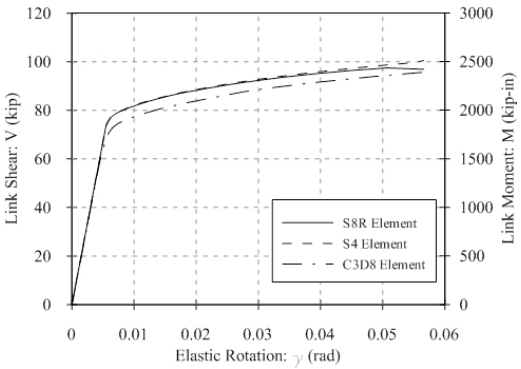


Figure 2: Monotonic Force Deformation Behavior W12x22 Model

The shell and 3D continuum models showed similar monotonic force deformation responses, however minor discrepancies existed in the results. An elastic link stiffness of 13397kip/rad was predicted by all models. The yield strength predicted in both shell models was 11% higher than the yield strength predicted in the 3D continuum model. The discrepancy in yield strength is most likely due to the 4% web height increase in the shell models. Additionally, the model which utilized S8R exhibited signs of strength degradation starting at an elastic deformation angle γ = 0.05rad. While there is no visual indication as to the cause of the strength degradation, it is possibly a result of the fact the quadratic element formulation reduces spurious shear effects by introducing additional nodes to the element. Despite these minor discrepancies, the shell and 3D continuum models predicted similar monotonic global force deformation behaviors for the link.

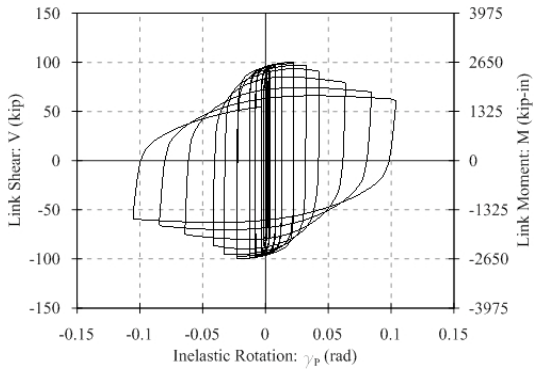
Table 3: Monotonic Yield and Ultimate Strengths W12x22 Model.

	S4 Elements	S8R Elements	C3D8 Elements	% Difference S4/S8R
f_y (kips)	75	75	73	3/3
f_u (kips)	100	97	96	4/1

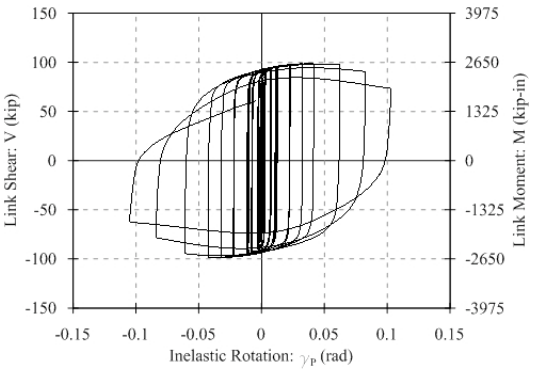
CYCLIC BEHAVIOR

Cyclic analyses were conducted on the shell and 3D continuum models up to a total rotation angle of γ = 0.11rad. Similar to the monotonic analyses, deformations were imposed on one end of the link, and the linear y-axis deformations were translated to elastic rotation angles γ. The imposed displacement history was reversed cyclic in accordance with the specifications provided in the Seismic Provisions (AISC, 2005) for links in eccentrically braced frames. The cyclic force deformation behaviors and back bone curves for the shell and 3D continuum models are shown in Figure 3, and the maximum loads achieved at target deformations are compared in Table 4. In these plots, the elastic deformation contribution has been post-processed, resulting in only the inelastic rotation being shown. Figure 4 shows deformed link shapes at pre and post flange buckling deformation angles for the shell and 3D continuum models. Consistent with the monotonic analysis, all shell models utilized Simpson integration with 3 integration points across the shell thickness, and the results obtained using the

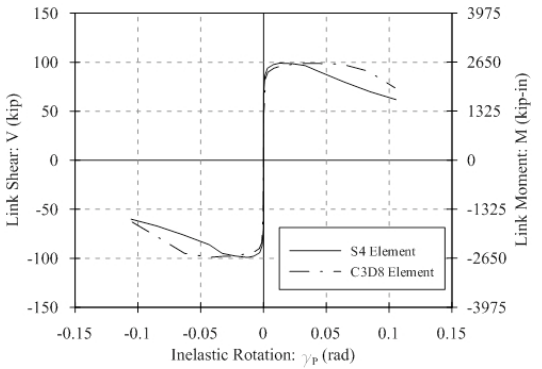
S4R element have been excluded. The cyclic behaviors of the S4 and S8R elements were nearly identical, so results obtained using S8R elements have subsequently been excluded for clarity.



(a) Shell Model



(b) 3D Continuum Model



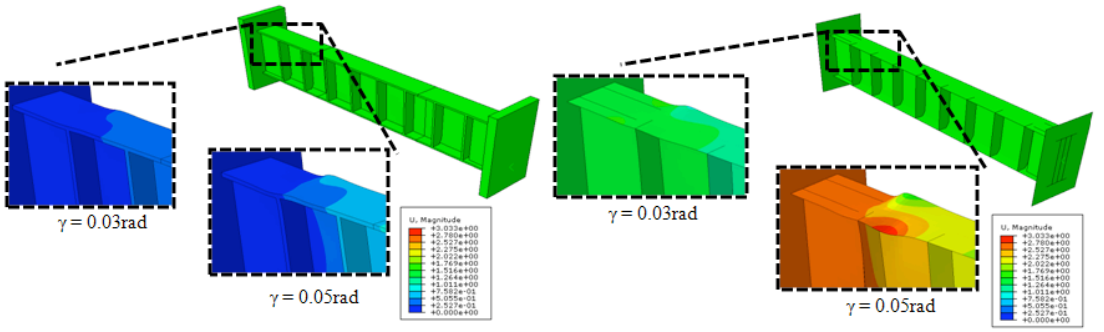
(c) Back Bone Curves

Figure 3: Hysteretic Behaviors and Back Bone Curve Comparison W12x22 Model

Significant differences were observed in the hysteretic behaviors of the shell and 3D continuum models when subjected to cyclic deformations. Similar behaviors were seen at inelastic deformations lower then $\gamma_p = 0.025$rad, however the shell model exhibited large strength degradation at higher rotation angles due to the onset of flange buckling. A stable hysteretic behavior was observed in the shell model through an inelastic rotation $\gamma_p = 0.025$rad before experiencing strength degradation due to flange buckling. The shear capacity continued to decrease through $\gamma_p = 0.105$rad, at which point an overall strength degradation of 38% was observed. The continuum model, on the other hand, exhibited a more stable hysteretic behavior through an inelastic rotation $\gamma_p = 0.065$rad before strength degradation occurred due to the onset of flange buckling. An overall strength degradation of 38% was observed at an inelastic rotation angle $\gamma_p = 0.105$rad, however a majority of this degradation occurred on the last half cycle at $\gamma_p = 0.085$rad. The flange deformations shown in Figure 4 additionally showed discrepancies between the models at common rotation angles. The severity of out of plane flange deformations observed in the shell model were higher than those in the 3D continuum model.

Table 4: Post Buckle Load Difference at Selected Reversals W12x22 Model

γ_p (rad)	S4 Shear (kips)	C3D8 Shear (kips)	% Difference
0.025	100	97	3
0.047	91	99	9
0.075	70	91	23
0.10	63	74	16



(a) 3D Continuum Model (b) Shell Element Model

Figure 4: Deformed Flange Shape Comparison

STRAIN COMPARISON

Although the global behavior was of main interest, the strains in the flanges of the shell and 3D continuum models were also assessed at pre and post buckling rotation angles γ to further quantify differences in post buckling behavior. The ABAQUS cumulative plastic strain variable PEEQ was used for this comparison (Simulia, 2010). Strains were recorded in the top flange half way between the flange edge and web at the termination of the end stiffeners at cyclic reversal points. At this point, out of plane flange deformations were observed. The PEEQ strain in the shell and 3D continuum models is compared in Figure 5.

Flange strains in the shell model were higher than those in the 3D continuum model. The rate of flange strain growth in the shell model increased at a larger rate than the 3D continuum model due to the early onset and severity of flange buckling. The largest strain growth rate difference between the two models was observed after the initiation of flange buckling in the shell model for rotation angles $\gamma > 0.04$rad.

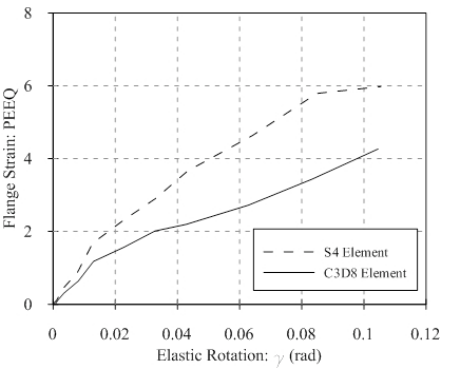


Figure 5: Flange Strain at Reversal Points

SIMPLIFIED MODEL

In an attempt to isolate the causes of the strength degradation observed in the W12x22 link model, simplified shell and 3D continuum models were created. The models consisted of a 10x5x0.5in cantilever plate subjected to displacement controlled cyclic loading. Three dimensional modeling and material and geometric non-linear behaviors were incorporated. The nodes at one end of the beam were restrained in all directions, while all rotation and transverse displacement was restrained at the other end of the link allowing for longitudinal displacement. Material properties for 316 steel provided in ABAQUS example problem 1.1.8 were used in both models. These properties accounted for both the kinematic and isotropic hardening behaviors of steel (Simulia, 2010). S4 elements were used in the shell model, while C3D8 elements were used in the 3D continuum model. The model overview is illustrated in Figure 6.

Global mesh convergence was conducted by analyzing strain values at selected locations on the beam for both the shell and 3D continuum models. Final mesh convergence in the 3D continuum model yielded three elements across the thickness of the beam. Based on the relative simplicity of the models, the mesh distributions used were much finer than the distributions required by the convergence to ensure accurate results were obtained.

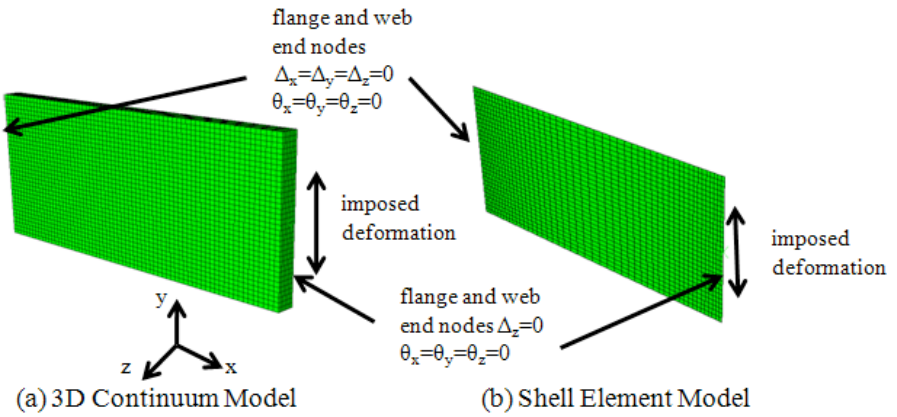
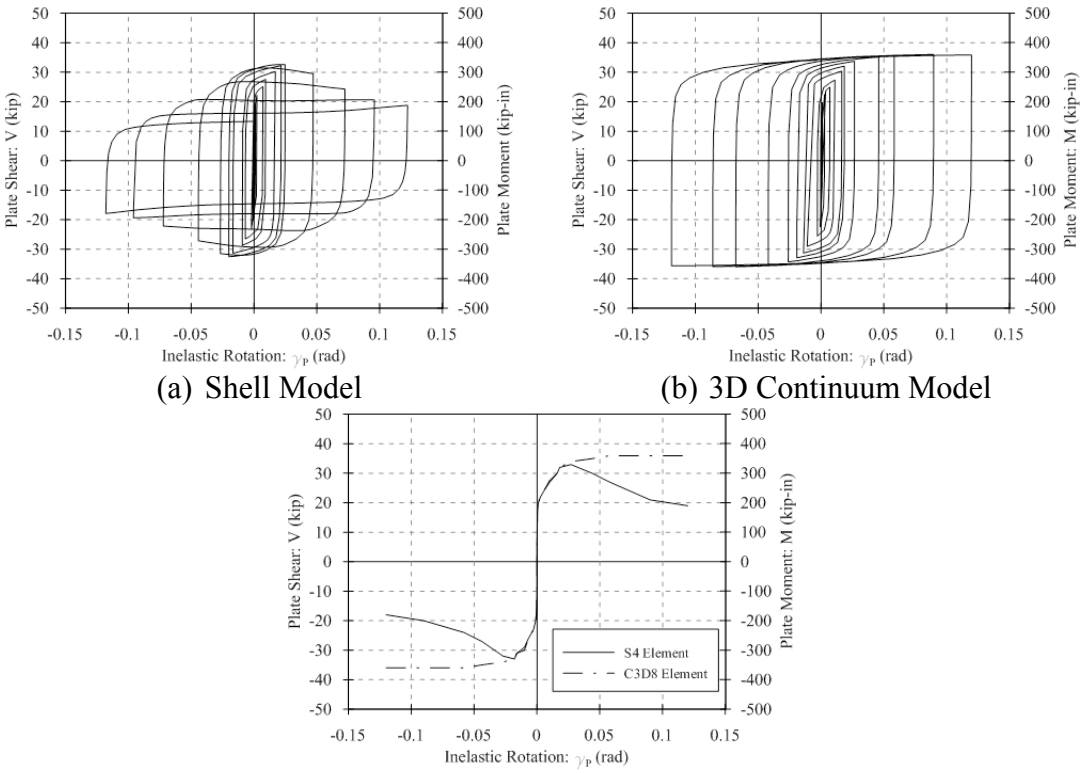


Figure 6: Simplified Model Overview

Cyclic analyses were conducted on the shell and 3D continuum models up to an elastic rotation angle of $\gamma = 0.11$rad. Deformations were imposed on one end of the link, and the linear y-axis deformations were translated to elastic rotation angles γ. The imposed displacement history was reversed cyclic in accordance with the specifications provided in the seismic provisions (AISC, 2005) for links in eccentrically braced frames similar to link models. The cyclic force deformation behaviors and back bone curves for the shell and 3D continuum models are shown in Figure 7, and the maximum loads achieved at target deformations are compared in Table 5.



(a) Shell Model (b) 3D Continuum Model

(c) Back Bone Curves

Figure 7: Hysteretic Behaviors and Back Bone Curve Comparison Simplified Model

Consistent with the results obtained in the full link models, large differences were observed in the hysteretic behaviors of the shell and 3D continuum models. Similar behaviors were recorded for inelastic deformations lower then $\gamma_p = 0.020$rad; however the shell model exhibited large strength degradation and element distortion at higher rotation angles. A stable hysteresis was observed in the shell model through an inelastic rotation angle $\gamma_p = 0.025$rad before strength degradation occurred. An overall strength degradation of 45% was observed at an inelastic rotation $\gamma_p = 0.125$rad. Strength degradation did not occur in the 3D continuum model. The recorded shear capacity of the link continued to increase through an inelastic rotation $\gamma_p = 0.125$rad due to Kinematic and Isotropic hardening effects.

Table 5: Post Buckle Load Difference at Selected Reversals Simplified Model.

γ_p (rad)	S4 Shear (kips)	C3D8 Shear (kips)	Percent Difference
0.025	32	34	5
0.047	30	35	16
0.075	24	36	31
0.098	21	36	43
0.13	19	36	48

EXPERIMENTAL COMPARISON

Experimental data was used to assess the validity of the hysteretic behaviors predicted by the shell and 3D continuum models. An experimental study was conducted by Lewis (2010) to investigate the cyclic performance of W12x22 flexure dominated shear links with intermediate and end stiffeners. The geometry and material properties of the experimental specimen were consistent with the properties used in the shell and 3D continuum models. The link was loaded to failure according the specifications provided in the seismic provisions (AISC, 2005) for links in eccentrically braced frames.

The experimental hysteretic performance of the link was under predicted by the shell model and slightly over predicted by the 3D continuum model. The experimental hysteretic behavior of the link can be seen in Figure 8, and the maximum loads achieved at target deformations are compared in Table 6. Both models accurately predicted the behavior of the shear link in pre buckling deformations through an inelastic rotation angle $\gamma_p = 0.04$rad. The experimental specimen experienced strength degradation for inelastic rotations $\gamma_p > 0.04$rad due to out of plane flange deformation, and an overall strength degradation of 18% was observed before fracture occurred at $\gamma_p = 0.055$rad. For each post flange buckling cycle, the shell and 3D continuum models respectively showed lower and higher shear capacities than were observed in the experimental data. The 3D continuum model, however, more closely predicted the post buckling shear behavior of the link, as the percent difference between the maximum predicted and experimental shear capacities at an inelastic rotation angle $\gamma_p = 0.070$rad were 22% and 2% for the shell and 3D continuum models respectively.

Table 6: Experimental Post Buckling Load Difference at Selected Reversals.

γ_p (rad)	Experimental Shear (kips)	% Difference Shell	% Difference 3D Continuum
0.025	96	5	2
0.047	93	3	6
0.070	89	22	2

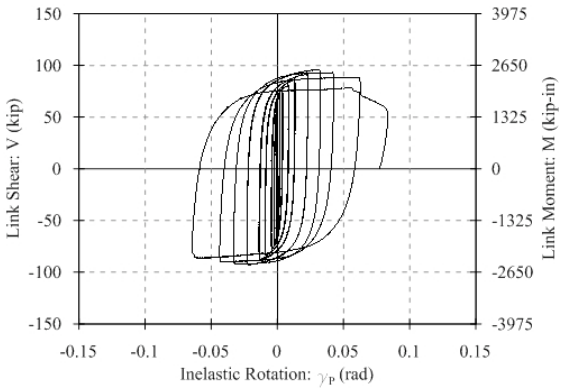


Figure 8: Experimental Hysteretic Behavior of W12x22

CONCLUSIONS

This study presented a comparison between the behavior of a link modeled using shell and 3D continuum elements. The FEA program ABAQUS was used to create shell and 3D continuum models of a W12x22 flexure dominated link with intermediate and end stiffeners. The models were subjected to monotonic and reversed cyclic loading protocols, and the force deformation behaviors were compared. Simplified cantilever beam models were additionally created in an attempt to isolate differences in hysteretic behavior between the shell and 3D continuum models.

The shell and 3D continuum models predicted the same initial link stiffness, but exhibited 11% difference in yield strength when subjected to monotonic and cyclic loading. Similar behaviors were observed between the two models at inelastic deformation angles lower then $\gamma_p = 0.025$rad, however flange buckling developed at lower link deformations in the shell model, and out of plane flange deformations were more severe throughout the cyclic loading protocol. Larger flange strains and strain growth rates were recorded in the shell model due to the relative severity of the flange buckling. Strength degradations were also observed in the simplified shell models. Both the 3D continuum and shell models accurately predicted the experimental hysteretic behavior of the link at low link deformations; however the 3D continuum model more accurately captured the post buckling behavior at large inelastic deformations.

ACKNOLEDGEMENTS

The authors gratefully acknowledge the funding support provided for this research by the National Science Foundation under Grant Award 0830414. However, any opinions, findings, conclusions, and recommendations presented in this paper are those of the writers and do not necessarily reflect the views of any of the sponsors.

REFERENCES

Alinia, M., & Dastfan, M. (2007). Cyclic Behaviour, Deformability and Rigidity of Stiffened Steel Shear Panels. *Journal of Construcional Research* , 554-563.

American Institute of Steel Construction, Inc. (AISC). (2005). *Seismic Provisions for Structural Steel Buildings. Standard ANSI/AISC 341-05.* Chicago, Illinois: American Institute of Steel Construction, Inc.

American Institute of Steel Construction, Inc. (AISC). (2005). *Steel Construction Manual Thirteenth Edition.* Chicago, Illinois: American Institute of Steel Construction, Inc.

Berman, J. W., Okazaki, T., & Hauksdottir, H. O. (2009). Reduced Link Sections for Improving the Ductility of Eccentrically Barced Frame Link-to-Column Connections. *Journal of Structural Engineering* .

Cook, R. D., Malkus, D. S., Plesha, M. E., & Witt, R. J. (2002). *Concepts and Applications of Finite Element Analysis.* New York: John Wiley & Sons. Inc.

Dusicka, P., & Lewis, G. (2007). Numerical Analyes of Cyclic Shear Deformation REsponse of Short Beams with Sandiwch Webs. *Structural Stability Research Council Annual Stability Conference Proceedings* (pp. 585-598). New Orleans: Structural Stability Research Council University of Missouri-Rolla.

Dusicka, P., Berman, J. W., & Purasinghe, R. (2009). Steel Frame Lateral System Concept Utilizing Replaceable Links. *NZSEE Conference.*

Itani, A. M., Lanaud, C., & Dusicka, P. (2003). Analytical Evaluation of Built-Up Shear Links Under Large Deformations. *Computers and Structures* , 681-696.

Lee, S. C., & Yoo, C. H. (1998). Strength of Plate Girder Web Panels Under Pure Shear. *Journal of Structural Engineering* , 184-194.

Lewis, G. R. (2010). Replaceable Shear and Flexure Links for the Linked Column Frame System. *Masters Thesis* . Portland State University.

Richards, P. W.-M. (2005). Effect of Flange Width-Thickness Ratio on Eccentrically Braced Frames Link Cyclic Rotation Capacity. *Journal of Structural Engineering* , 1546-1552.

Simulia. (2010). *Abaqus Users Manual V. 6.9.* Providence, RI: Dassault Systems Simulia.

Seismic Evaluation of Bridge G-947 in Clark County, Nevada Using Nonlinear Static Procedures

Ahmad Saad[1], Aly Said[2], Barbara Luke[3]

[1] Civil and Environmental Engineering Department, University of Nevada, Reno, 1664 N. Virginia Street, Reno, NV, 89557-0258; email: ahmadsaid_eg@hotmail.com
[2] Civil and Environmental Engineering Department, University of Nevada, Las Vegas, 4505 S. Maryland Parkway, Las Vegas, NV 89154-4015; PH (702) 895-2722; FAX (702) 895-3936;email: aly.said@unlv.edu.
[3] Civil and Environmental Engineering Department, University of Nevada, Las Vegas, 4505 S. Maryland Parkway, Las Vegas, NV 89154-4015; PH (702) 895-1568; FAX (702) 895-3936;email: barbara.luke@unlv.edu.

ABSTRACT

Seismic evaluation of one of the most critical bridges in Clark County was performed in this study. The evaluation focused on the performance of the bridge columns under seismic loads in both the transverse and longitudinal directions. The method used for the bridge analysis in this study was the nonlinear static procedure (NSP) introduced by FEMA-356 for the evaluation of buildings. This method was modified to apply on bridges. The acceptance criteria set for the evaluation was the Immediate Occupancy (IO) performance level. Using such performance level was due to the high importance of the bridge and accordingly it is expected to be fully operational after major earthquake events. It was found that deficiencies in bridge performance are attributed to the fact that it was designed and detailed according to older code provisions.

INTRODUCTION

In transportation systems, bridges are vital connective elements. Compared to other highway components, bridges are the most critical components that can be affected by earthquake events. Their damage can severely disrupt the traffic. The resultant disruption from bridge damage by earthquake loads may have a great impact on the economy of the region as well as the post-earthquake emergency response, repair, and reconstruction operations. A large number of bridges were designed and constructed in accordance to older codes. These codes had either no or insufficient seismic design and detailing provisions. In recent earthquakes, a number of bridges did not perform adequately under seismic loads. Despite the fact that they were designed for earthquake resistance, some of them suffered severe damage due to lack of ductility or poor detailing (Priestly *et al.*, 1996).

ANALYSIS PROCEDURES

A pushover analysis is used in this study, the bridge is pushed, using a specific

load pattern, in the direction under consideration until the control node reaches the target displacement. The control node is defined as the node in which its displacement vs. the total base shear creates the pushover curve. The target displacement represents the maximum displacement likely to be experienced by the bridge under the considered earthquake intensity. FEMA-356 (2000) introduced the following equation to calculate the target displacement (δ_t)

$$\delta_t = C_0 C_1 C_2 C_3 S_a \frac{T_e^2}{4\pi^2} g$$

where C_0, C_1, C_2, and C_3 are modification factors to account for different parameters that affect the control node. S_a is the spectral acceleration in (g) corresponding to the effective time period of the bridge (T_e) from the spectral curve.

BRIDGE DESCRIPTION

Bridge G-947 is located at the intersection of the U.S. 95/93 highway (overpass) and both North Main St. and North Casino Center Blvd (underpass). In this study, a segment of the bridge is evaluated. The total length of the studied segment is 255.906 ft, divided into three spans of 79.953 ft, 95.953 ft, and 80 ft long. Figure 1 shows the layout of the whole bridge and the location of the studied part.

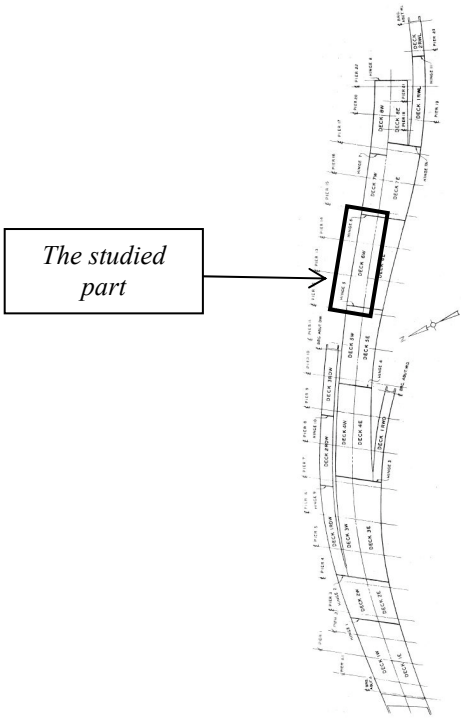


Figure 1 Bridge layout and the location of the studied part

The superstructure of the bridge is a cast-in-place box girder concrete deck that contains five intermediate webs, with a total depth of 5 ft. Each of the bridge

bents in this part of the bridge consists of two columns with integral cap beam in the bridge deck. The cap beam widths are 4.25 ft for pier-13 and 4.50 ft for pier-14.

BRIDGE MODEL

Figure 2 shows the structural model used in the evaluation. A spine model, using frame elements, was developed using SAP2000 with the bridge module. The superstructure was modeled as one element located at the centroid of the deck. Its sectional area is 66.73 ft^2 and the moment of inertias about the Y and Z axes are 259.77 and 11489.19 ft^4, respectively. Where the Y-axis is along the transverse direction and the Z- axis is the vertical axis.

An additional load of 2.067 kip/ft was added to account for the dead load from concrete barriers, pedestrian rails and wearing surfaces overlay. In addition to that, a load of 2.56 kip/ft was added to represent a portion of the live load over the four lanes of the bridge. This portion was chosen to be 25% of the design lane load in the AASHTO (2007) specifications, which is equal to 0.64 kip/ft/lane. All masses were lumped to the nodes. These masses represent the structural components in addition to the aforementioned added loads.

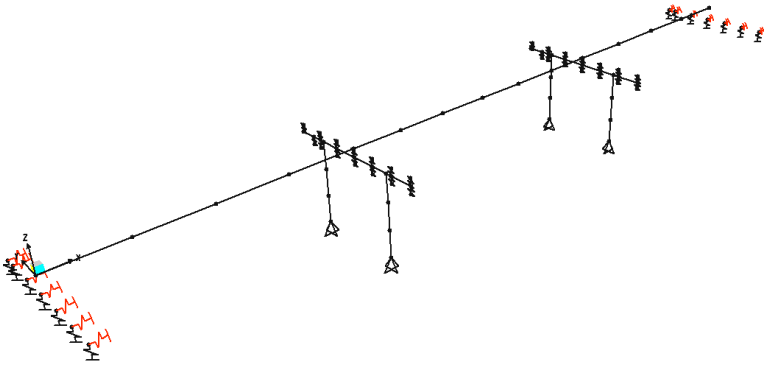


Figure 2 Structural Model using SAP2000

The nonlinearity is represented by the definition of the plastic hinges at the top part of the columns. According to Figure 3, FEMA-356 (2000) specifies the definition of the plastic hinges and the acceptance criteria in different structural members using a generalized load-deformation relationship. This relationship describes the general sequence of stiffness loss of an element. A linear response from "A" to an effective yield at "B" is followed by a linear response at reduced stiffness from "B" to "C", then a sudden reduction in the lateral load resistance to point "D", then response at reduced resistance to "E", and final loss of resistance thereafter (FEMA-356, 2000).

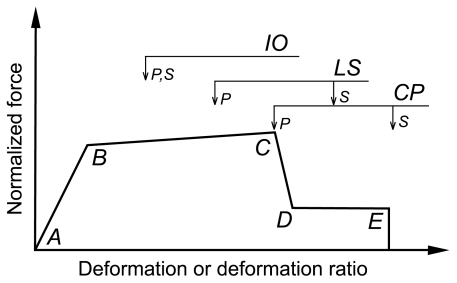
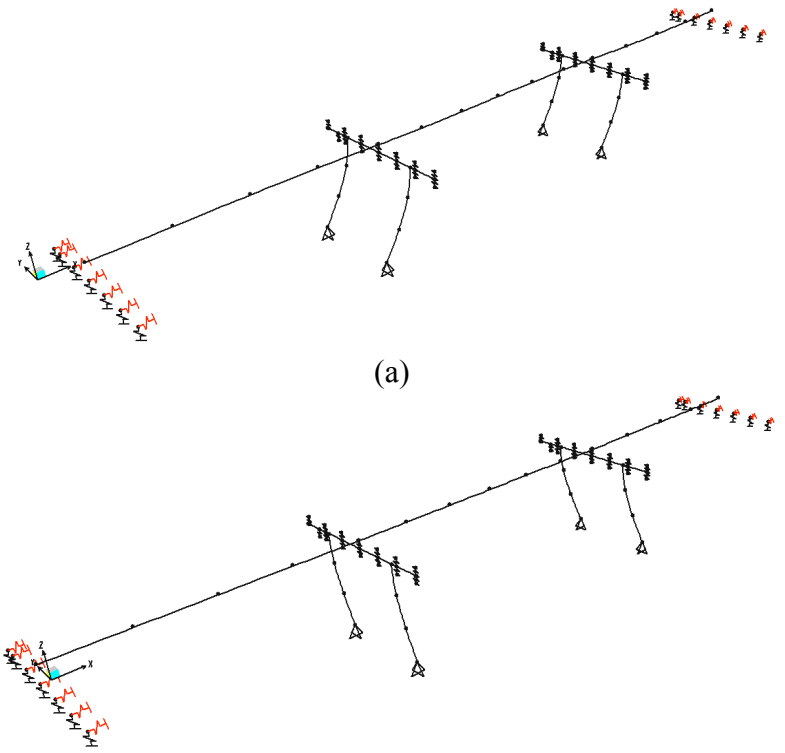


Figure 3. Generalized force-deformation relationship for plastic hinges as defined in FEMA-356 (2000).

MODAL ANALYSIS

Table 1 presents the modal participating mass ratios resulting from the modal analysis of the bridge. It shows that the fundamental modes in the longitudinal and transverse directions are mode-1 and mode-3, respectively. The two mode shapes are illustrated in Figure 4 (a) and (b). The modal participation factors along with the displacements of the control node are used in the calculation of the modification factor "C_0", using the following equation:

$$C_0 = PF \times \phi_{CN}$$



(a)

(b)

Figure 4 The fundamental mode shapes in (a) the longitudinal direction, and (b) the transverse direction of the bridge

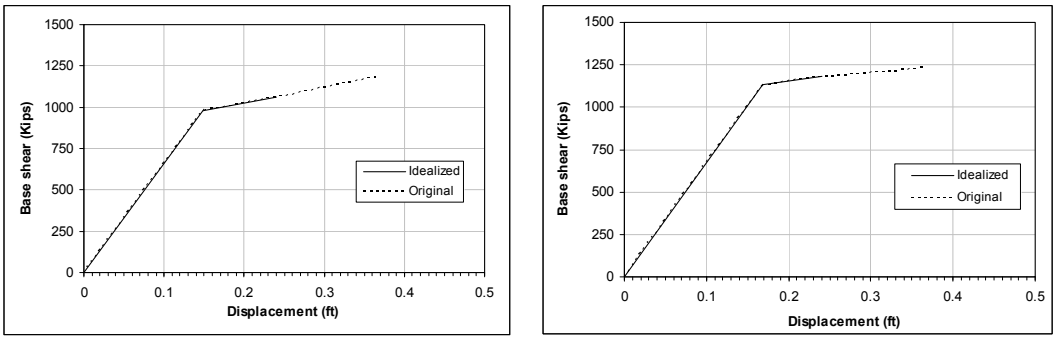
Table 1. Modal participating mass ratios for different modes

Mode	Period (sec)	UX (%)	UY (%)	UZ (%)	Sum UX (%)	Sum UY (%)	Sum UZ (%)
1	1.319	**99.88**	0.00	0.00	99.88	0.00	0.00
2	1.237	0.05	1.43	0.00	99.93	1.43	0.00
3	0.831	0.00	**98.43**	0.00	99.93	99.86	0.00
4	0.276	0.00	0.00	0.00	99.93	99.86	0.00
5	0.203	0.00	0.12	0.00	99.94	99.98	0.00
6	0.203	0.06	0.01	0.00	99.99	99.99	0.00

PUSHOVER ANALYSIS

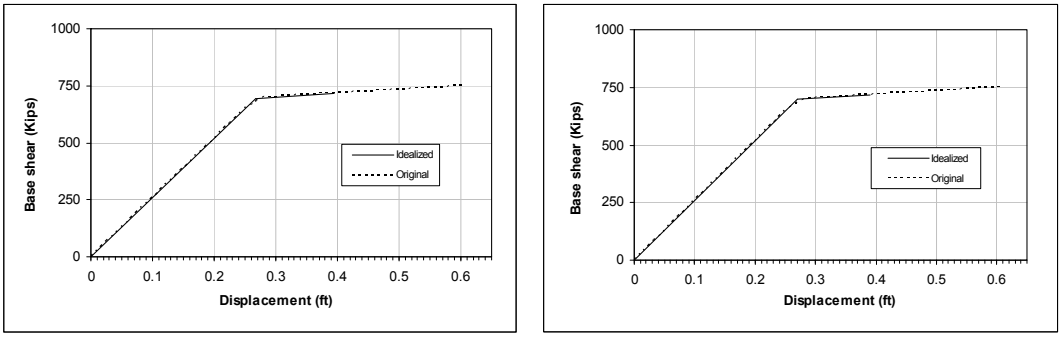
Two load patterns were used in the analysis of the bridge in each of the two principle directions. These load patterns are the "uniform load pattern" and the "modal pattern". The uniform load pattern can be described as a uniform distribution of lateral forces proportional to the distribution of the bridge masses. The modal pattern is a distribution proportional to the deflected shape of the fundamental mode in the direction under consideration. In this case, mode-1 and mode-3 (resulting from the modal analysis) will be used in defining the modal pattern for the longitudinal and the transverse directions, respectively.

Pushover curves were developed based on the four analysis cases and are presented in Figures 5 and 6. The presented pushover curves show that, in all cases, the bridge exceeded the elastic range and plastic hinges were formed.



(a) Uniform load pattern (b) Modal pattern

Figure 5 Pushover curves in the transverse direction using the two load patterns



(a) Uniform load pattern (b) Modal pattern

Figure 6 Pushover curves in the longitudinal direction using the two load patterns

ACCEPTANCE CRITERIA

The acceptance criteria for the plastic hinge rotation values were used. Their values as presented in Table 2. Due to the high importance of the bridge, the acceptance criteria set for the bridge in this study was the immediate occupancy (IO) level. This performance level requires full access to normal traffic immediately following earthquake events.

Table 2 Acceptance criteria for plastic hinge rotations FEMA-356 (2000)

Acceptance Criteria (Performance levels)	Plastic Rotation (radians)
Immediate Occupancy (IO)	0.005
Life Safety (LS)	0.005
Collapse Prevention (CP)	0.01

RESULTS

Plastic hinge rotation values at the target displacements due to different load patterns in the two principle directions were extracted from the analysis results file. When these values are compared with the acceptance criteria for evaluation, about 75% of the plastic hinges violated the acceptance criteria. In the transverse direction, two plastic hinges violated the acceptance criteria in each one of the load patterns. While in the longitudinal direction, all of the plastic hinge rotations in the two load patterns violated the acceptance criteria.

On the other hand, shear force values (demand) on the columns at the target displacements (in all analysis cases) were within the shear capacities of the columns. Accordingly, the design of this bridge is governed by the inadequate development lengths of columns longitudinal reinforcement into the cap beams, and the bridge is at risk of bond slippage at this location under that level of earthquake.

CONCLUSIONS

Evaluation of Bridge G-947 in Clark County, Nevada estimates that the bridge detailing is insufficient to keep it fully operational after a major earthquake event. Using different load patterns in the evaluation process resulted in different values of plastic hinge rotations. Accordingly, it was important to use different load patterns to account for such uncertainty in the behavior of the bridge under lateral loads.

REFERENCES

AASHTO (2007). "*LRDF bridge design specifications*" American Association of State Highway and Transportation Officials Inc., Washington, DC.

AlAyed, H., (2002). "*Seismic analysis of bridges using nonlinear static procedure*". PhD dissertation, Department of Civil and Environmental Engineering, University of Maryland, College Park, Maryland.

CSI (2000). SAP2000 Nonlinear Version 11.0.2 with bridge module, Computers and Structures, Inc., Berkelely, CA.

Federal Emergency Management Agency (FEMA) (1997). "*NEHRP Guidelines for the Seismic Rehabilitation of Buildings*". FEMA-273, Washington, D.C.

Federal Emergency Management Agency (FEMA) (2000). "*Prestandard and Commentary for the Seismic Rehabilitation of Buildings*". FEMA-356, Washington, D.C.

Priestly, M. J. N., Seible, F., and Calvi, G. M., (1996). *Seismic design and retrofit of bridges.* New York: John Wiley & Sons.

Development of Concrete/Cold Formed Steel Composite Flexural Members

N. Wehbe[1] M.ASCE, A. Wehbe[2], L. Dayton[3] M.ASCE and A. Sigl[4] M.ASCE

[1]Civil and Environmental Engineering, South Dakota State University, Box 2219, Brookings, SD 57007; PH (605) 688-4291; FAX (605) 688-6476; email: nadim.wehbe@sdstate.edu
[2]Kiewit Engineering Co., 3555 Farnam St., Omaha, NE 681317; PH (402) 342-2052; FAX (402) 271-2829; email: Alex.Wehbe@kiewit.com
[3]Nucor R&D, 1601 West Omaha Avenue, Norfolk, Nebraska 68701; PH (402) 644-8546; FAX (402-644-8551); email: LDayton@nucor-rd.com
[4]Civil and Environmental Engineering, South Dakota State University, Box 2219, Brookings, SD 57007; PH (605) 688-5427; FAX (605) 688-6476; email: arden.sigl@sdstate.edu

ABSTRACT

Light-gauge steel (LGS) construction is widely used for commercial and industrial buildings. In such construction the wall framing is usually an assembly of cold-formed steel (CFS) studs held between CFS tracks while the floors are normally composite concrete/LGS decks on steel bar joists spanning between load-bearing CFS walls. Heavy hot rolled steel angles or HSS tubes are welded to the top of the CFS load-bearing walls to function as load distribution members (LDM) over the wall studs and as headers over wall openings. The use of hot rolled steel elements results in significant increase in construction cost and time. Such heavy steel elements would be unnecessary if the concrete thickening on top of the CFS wall can be made to act compositely with the CFS track. The resulting concrete/CFS composite beam would be a reinforced concrete beam where the CFS track serves as the tension reinforcement. The continuity at the interface would be provided by stand-off screws that are normally used in the construction of the composite deck.

This research involved experimental and analytical studies to assess the structural performance and failure modes of concrete/CFS track composite beams and to develop optimum beam configurations for use in LGS construction. The parameters included the CFS track thickness, stand-off screw spacing, and stand-off screw configuration. Twenty-seven full-scale specimens were constructed, instrumented, and tested to failure. The flexural and shear strengths, flexural stiffness, and interface shear transfer were investigated. However, only the flexural strength and stiffness are reported in this paper. The results show that concrete/CFS track composite beams can be designed for ductile flexural failure and that the degree of composite action is dependent upon the stand-off screws intensity rather than configuration. Equations for the effective moment of inertia at service loads were derived.

BACKGROUND

Light-gauge steel (LGS) construction is widely used for commercial and industrial buildings. In such construction the wall framing is usually an assembly of cold-formed steel (CFS) studs held between CFS tracks while the floors are normally composite concrete/LGS decks on steel bar joists spanning between load-bearing CFS walls. Heavy hot rolled steel angles or HSS tubes are welded to the top of the CFS load-bearing walls to function as load distribution members (LDM) over the wall studs and as headers over wall openings. Figure 1 shows LGS framing with an HSS tube LDM and header at the top of the CFS wall.



Figure 1. Light-gauge steel framing

The use of hot rolled steel elements results in significant increase in construction cost and time. Such heavy steel elements would be unnecessary if the concrete thickening on top of the CFS wall can be made to act compositely with the CFS track. The resulting concrete/CFS composite beam would be a reinforced concrete beam where the CFS track serves as the tension reinforcement and the track flanges provide resistance to shear. Figure 2 shows the proposed composite beam. The continuity at the interface would be provided by stand-off screws that are normally used in the construction of the composite deck. Figure 3 shows a 2½" long stand-off screw. To the best knowledge of the authors, concrete/CFS composite beams have not been investigated prior to this study.

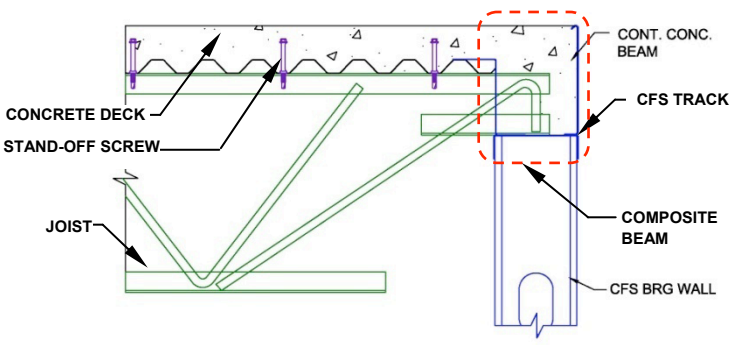


Figure 2. Proposed composite beam



Figure 3. Stand-off Screw

OBJECTIVES AND SCOPE

The main objectives of this study were to assess strength and serviceability of concrete/CFS track composite beams and to develop optimum composite beam configurations for use in LGS construction.

The study comprised both experimental and analytical investigations. Twenty-seven full-scale beam specimens were constructed, instrumented, and tested to failure. The parameters included the CFS track thickness, stand-off screw spacing, stand-off screw configuration, and pour stop engagement. The flexural and shear strengths, flexural stiffness, and interface shear transfer were investigated. However, only the flexural strength and stiffness are reported in this paper.

EXPERIMENTAL WORK

Test Specimens

Five groups of test specimens representing nine different parametric combinations of CFS track thickness, stand-off screw configuration, and engagement of one CFS pour stop were tested. Three identical specimens of each combination were constructed for a total of 27 specimens. The different cross sectional details of the test specimens are shown in Figure 4.

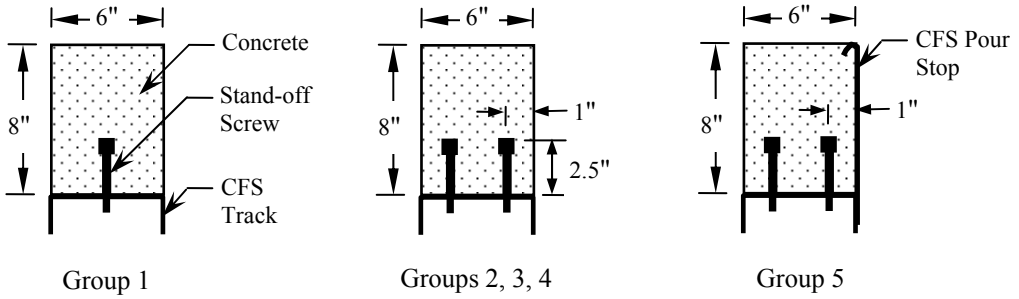


Figure 4. Cross sectional details of the test specimens

Each specimen was 9.75' long and consisted of a 6" wide by 8" deep concrete beam on top of a CFS track. The track web was 6" deep and the track flanges were 2" wide. The concrete section represented the slab thickening on top of a CFS track of a stud wall. Composite action between the CFS track and the concrete was achieved through the use of 2 ½" long by $^{5}/_{16}$" diameter stand-off screw connectors.

Three track thicknesses, 16-gauge, 14 gauge, and 12-gauge, were selected for this study. According to the Steel Stud Manufacturers Association section designation (SSMA, 2010), the track thicknesses used in this study corresponded to CFS sections 600T200-54, 600T200-68, and 600T200-97, respectively. Specimens in Groups 1 and 2 incorporated all three track sections, while specimens in Groups 3, 4, and 5 incorporated only the 600T200-97 track. The track represented the tension reinforcement in the composite beam section. Considering the given track cross sectional areas and an effective tension reinforcement depth, d, measured to the centroid of the track (d = 8.43"), the tension steel ratio was 0.0112, 0.0141, and 0.0201 for specimens with 16-gauge, 14-gauge, and 12-gauge tracks, respectively. For a concrete strength of 3000 psi and steel yield stress of 50 ksi, the maximum and

minimum steel ratios allowed by the ACI code (ACI, 2008) would be 0.0220 and 0.004, respectively.

The stand-off screws were placed in one row for the specimens in Group 1 and in two rows for the specimens in the other groups. The center-to-center screw spacing along the beam's longitudinal axis was 6" for the specimens in Group 1 and Group 2, 4" for the specimens in Group 3, and 12" for the specimens in Group 4 and Group 5. The CFS pour stops were 14-gauge and were used for specimens of Group 5 only. Table 1 shows a matrix of the test specimens. The specimen identification reflects the group number, track thickness, and specimen number within a parametric combination.

Table 1. Matrix of test specimens

Group	Specimens ID	Track Gauge	Track Thickness (1/1000")	Tension Steel Ratio	Screw Placement	Screw Spacing	Pour Stop
1	1-16GA-1, 2, or 3	16	54	0.0112	1 row	6"	No
	1-14GA-1, 2, or 3	14	68	0.0141			
	1-12GA-1, 2, or 3	12	97	0.0201			
2	2-16GA-1, 2, or 3	16	54	0.0112	2 rows	6"	No
	2-14GA-1, 2, or 3	14	68	0.0141			
	2-12GA-1, 2, or 3	12	97	0.0201			
3	3-12GA-1, 2, or 3	12	97	0.0201	2 rows	4"	No
4	4-12GA-1, 2, or 3	12	97	0.0201	2 rows	12"	No
5	5-12GA-1, 2, or 3	12	97	0.0201	2 rows	12"	Yes

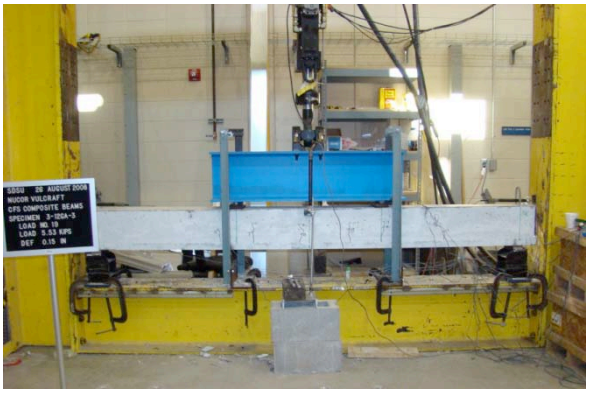
Material Properties

The specified concrete compressive strength was 3000 psi. On the day of testing, the measured compressive strength values varied between 3210 psi and 5100 psi. The measured results are reported in Table 2. The specified yield stresses for the CFS tracks were 42.7 ksi, 47.9 ksi, and 52 ksi for the 12-gauge, 14-gauge, and 16-gauge tracks, respectively. However, coupon testing that was conducted following the completion of the beam specimen testing revealed that the yield stresses of the 12-gauge and the 14-gauge tracks were only 19 ksi and 45 ksi, respectively. The 16-gauge track yield stress was not measured due to lack of coupons from the same heat used to fabricate the tracks. The stand-off screws specified yield stress was 150 ksi.

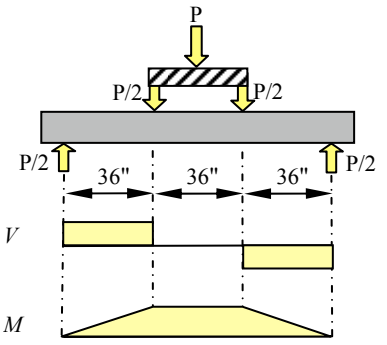
Instrumentation and Test Setup

Strain in the track was measured using surface mounted strain gauges. The gauges were attached to the track at several locations along all three spans. Strain in the concrete was measured using embedded strain gages placed at 1.5" from the top of the section. The mid-span deflection under the applied load was measured by means of a pair of linear variable differential transducers (LVDT). The slip of the concrete relative to the track was measured at both ends of the specimen by means of LVDTs. More details on the instrumentation are provided by Wehbe (2008).

The beam specimen was simply supported at a span of 9.0'. Two equal point loads were applied at the one-third points by means of a 22-Kip hydraulic actuator and a steel spreader beam. The loading was applied in a displacement-controlled mode until failure. Figure 5 shows the test setup.



(a) Specimen Setup



(b) Schematic of the Test Setup

Figure 5. Test Setup

Experimental Results

Overall, the specimens exhibited the same general cracking patterns beginning with initial cracking in the form of pure flexural cracks in the middle span followed by flexural-shear cracks just outside of the middle span. In general, the cracks initiated at locations of stand-off screws. Due to operator error, the loading of Specimen 3-12GA-1 was applied at a high loading rate and the specimen failed immediately after the loading was initiated. Therefore, no data was captured for Specimen 3-12GA-1, but the failure mode was noted. The measured load-deflection relationships are shown in Figure 6.

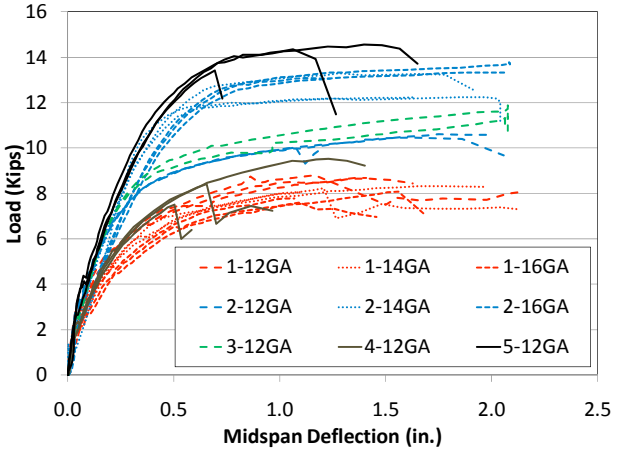
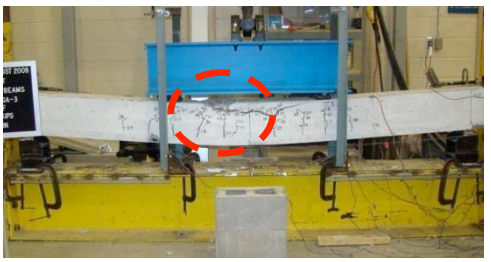
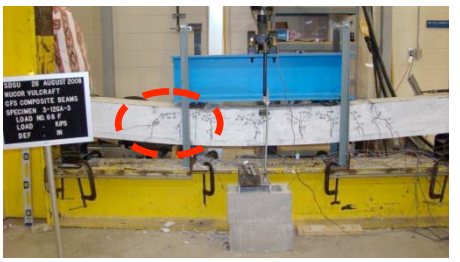


Figure 6. Measured Load-Deflection relationships

The observed failure modes included flexural, shear, and flexural-shear in the concrete section. Specimen 5-12GA-3 failed in a brittle torsional-shear mode as a consequence of the non-symmetric cross sectional stiffness and uneven seating. The observed failure modes are shown in Figure 7. All specimens experienced yielding in the flanges of the track. The yielding extended to the web except in five specimens. In general, the specimens exhibited ductile behavior except for specimens 4-12GA-2, 4-12GA-3, and 5-12GA-3, which failed in shear or torsion. Table 2 shows selected measured results for the tested specimens.



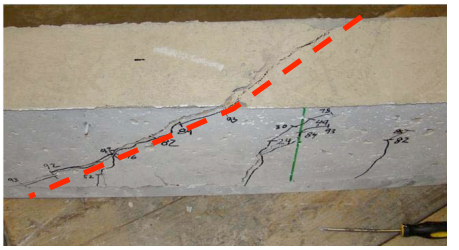
(a) Flexural Failure



(b) Flexural-Shear Failure



(c) Shear Failure



(d) Torsional Failure

Figure 7. Observed failure modes

Table 2. Summary of experimental results

Specimen ID	Concrete Strength (ksi)	1st Crack Type	Load @ 1st Crack (Kips)	Load @ 1st Yield in Track Web (Kips)	Maximum Load (Kips)	Failure Type
1-16GA-1	3.21	Flexural	2.19	-	7.61	Flexural-Shear
1-16GA-2	3.43	Flexural	1.99	7.33	7.79	Flexural-Shear
1-16GA-3	3.43	Flexural	2.10	7.18	8.08	Flexural-Shear
1-14GA-1	3.52	Flexural	1.96	-	8.33	Flexural-Shear
1-14GA-2	3.52	Flexural	2.04	7.27	8.33	Flexural-Shear
1-14GA-3	4.26	Flexural-Shear	2.04	7.26	8.05	Flexural-Shear
1-12GA-1	4.26	Flexural	3.36	6.92	8.69	Flexural-Shear
1-12GA-2	4.26	Flexural	2.42	7.49	8.07	Flexural-Shear
1-12GA-3	4.18	Flexural-Shear	2.47	6.67	8.67	Flexural-Shear
2-16GA-1	4.73	Flexural	1.08	9.62	13.77	Flexural-Shear
2-16GA-2	4.73	Flexural	1.61	9.65	13.33	Flexural
2-16GA-3	4.73	Flexural	1.84	11.24	13.09	Flexural-Shear
2-14GA-1	4.15	Flexural	2.60	13.08	13.29	Flexural
2-14GA-2	4.15	Flexural	1.40	11.02	12.25	Flexural-Shear
2-14GA-3	4.22	Flexural	1.10	9.98	12.25	Flexural
2-12GA-1	4.18	Flexural	3.34	8.36	10.63	Flexural-Shear
2-12GA-2	4.27	Flexural	2.62	8.17	10.05	Flexural-Shear
2-12GA-3	4.27	Flexural	2.87	8.27	10.47	Flexural
3-12GA-1	-	-	-	-	-	Flexural-Shear
3-12GA-2	4.73	Flexural	2.01	8.76	11.87	Flexural-Shear
3-12GA-3	4.59	Flexural	2.11	8.15	11.32	Flexural-Shear
4-12GA-1	4.59	Flexural	1.75	8.47	9.53	Flexural-Shear
4-12GA-2	4.59	Flexural	1.45	-	7.51	Shear
4-12GA-3	4.89	Flexural	1.98	7.13	8.40	Shear
5-12GA-1	4.59	Flexural	2.64	14.10	14.34	Flexural
5-12GA-2	5.10	Flexural	3.55	14.18	14.57	Flexural
5-12GA-3	4.89	Flexural	3.80	-	13.41	Torsional-Shear

ANALYSIS OF RESULTS

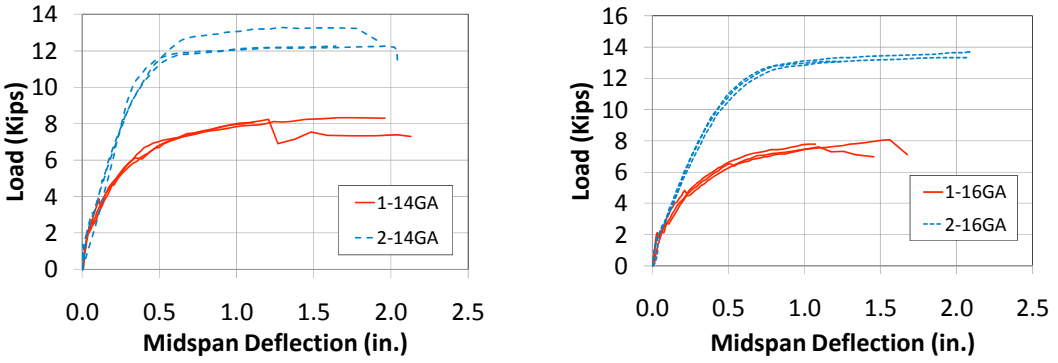
Effect of Stand-Off Screw Density

Relative slip between the concrete and the CFS track was monitored during the test. Table 3 presents the average loads at which the first slip was detected in the specimens of Groups 1 and 2. The results show substantial improvement in composite action when the stand-off screw quantity is increased from 1 screw at 6" to 2 screws at 6".

Table 3. Average load at first relative slip

Track Gauge	Average Load @ 1st Slip (Kips)		Slip Load Ratio (Group 2/Group 1)
	Group 1 (1 screw @ 6")	Group 2 (2 screws @ 6")	
12-Gauge	3.77	5.71	1.37
14-Gauge	3.80	9.50	2.50
16-Gauge	3.33	5.50	1.65

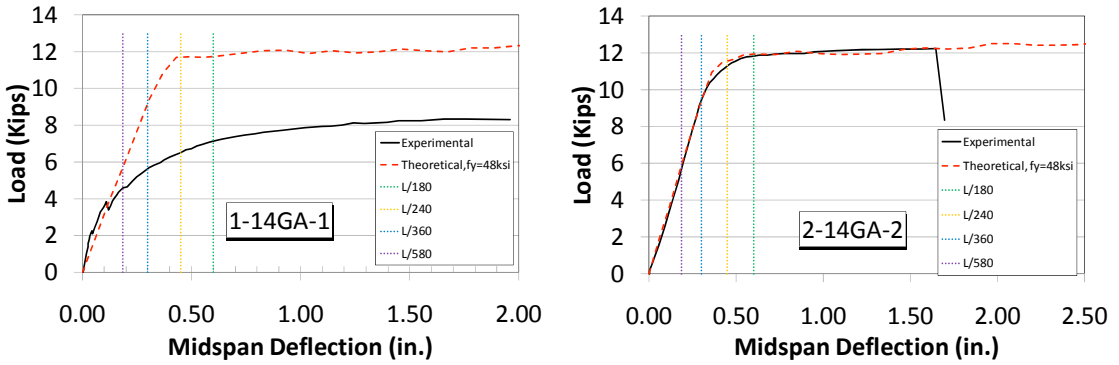
Increasing the stand-off screw density from 1 screw at 6" to 2 screws at 6" also resulted in significant improvement in strength and post-initial cracking stiffness. Figures 7 (a) and 7(b) show measured load-deflection relationships for the 14-gauge and the 16-gauge specimens, respectively. The average strength increased by 53.8% and 72.4% for the 14-gauge and 16-gauge specimens, respectively, and the average effective stiffness, taken at an applied load of 6 Kips, increased by 81.8% and 92.3% for the 14-gauge and 16-gauge specimens, respectively.



(a) 14-gauge, Groups 1 & 2 specimens (b) 16-gauge, Groups 1 & 2 specimens

Figure 7. Comparison of experimental Load-Deflection relationships

Theoretical moment-curvature relationships were used to derive theoretical load-deflection curves. The theoretical moment-curvature relationships were developed using the computer software XTRACT (Imbsen, 2002) and assuming fully composite action. Figure 8 shows theoretical and measured load-deflection relationships for 14-gauge specimens in Groups 1 and 2. Also shown are deflection limits in terms of the span length, L. The results indicate that when the stand-off screw density was 2 screws at 6" (Group 2) or better, slippage was insignificant, the flexural strength was attained, and the theoretical and measured load-deflection relationships were in excellent agreement (Figure 8-b). However, for a stand-off screw density of 1 screw at 6" (Figure 8-a), significant slippage took place and the specimen failed at approximately 33% lower than its theoretical flexural strength.



(a) 14-gauge, Group 1 specimen (b) 14-gauge, Group 2 specimen

Figure 8. Theoretical and experimental load-deflection relationships

Increasing the stand-off screw density from 2 screws at 6" to 2 screws at 4" resulted in nominal increase in strength and stiffness. The average measured strength of Group 3 specimens (2 screws at 4") was approximately 11.7% higher than that of Group 2 specimens (2 screws at 6"). The average effective stiffness, at a load of 6 Kips, of Group 3 specimens was only 3.1% higher than that of Group 2 specimens.

Effect of Stand-Off Screw Configuration

The effect of the stand-off screw configuration was determined by comparing the results of the 12-gauge specimens in Groups 1 and 4. It was found that changing the configuration from one to two rows of screws while maintaining the screw density at 1 screw per foot length had no significant effect on the stiffness of the specimens. The average measured effective stiffness at an applied load of 6 Kips was 21.7 Kip/in and 22.0 Kip/in for the specimens in Groups 1 and 4, respectively.

When 12" screw spacing was used, however, brittle shear failure was observed in two of the three specimens. The shear failure crack in each of the two specimens initiated as a flexure-shear crack that started in an exterior span at the first stand-off screw from the point load. The crack extended vertically along the screw shank, then propagated upward at an inclination towards the point load. Shear failure occurred when the flexural shear crack at the top of the screw suddenly extended in the other direction towards the bottom of concrete as shown in Figure 7(c).

Effect of Track Thickness

Contrary to what was expected, specimens with 12-gauge tracks exhibited lower strength than similar specimens but with 14-gauge and 16-gauge tracks. This was due to the unexpected low yield strength of the 12-gauge tracks. Therefore, no conclusions were made regarding the effect of the track thickness on strength. However, prior to initiation of relative slip, the specimen stiffness would be dependent on the elastic modulus and the cross sectional area of the track. For the same elastic modulus, increasing the track area would cause an increase in stiffness. A comparison among the effective stiffness values at an applied load of 6 Kips is presented in Table 4. The comparison is limited to specimens in Group 2 since the relative slip for that group was negligible at a load of 6 Kips. The results show that

the effective stiffness of the 14-gauge and 16-gauge specimens was 18.8% and 21.5%, respectively, higher than that of the 16-gauge specimens.

Table 4. Average effective stiffness of specimens in Group 2

Track Thickness	Avg. Eff. Stiffness @ Applied Load = 6 Kips (Kip/in)	Stiffness Increase (%)
16-Gauge	27.7	-
14-Gauge	32.9	18.8
12-Gauge	35.3	21.5

Effect of Pour Stop Engagement

The effect of engaging the pour stop was determined by comparing the results of the 12-gauge specimens in Groups 4 and 5. It was found that by engaging the pour stop, the average strength of the test specimens increased by 22.5% while the average effective stiffness at an applied load of 6 Kips increased by 78.9%.

Development of Expressions for the Effective Moment of Inertia

The American Concrete Institute's building code (ACI, 2008) provides an expression (ACI equation 9-8) for determining the effective moment of inertia, I_e, of reinforced concrete members with embedded reinforcement as a function of the applied service load moment. In this study, expressions similar to that of ACI were derived for the composite beams.

The experimental load-deflection results were used to back calculate values for I_e at different applied loads. The elastic modulus of the composite section was assumed to be equal to that of the concrete, E_c, as given by the following ACI expression (ACI, 2008):

$$E_c = 33 w^{1.5} \sqrt{f'_c}$$

where E_c is in psi units, w is the unit weight of concrete in lb/ft^3, and f'_c is the concrete strength in psi. The unit weight of concrete was taken as 145 lb/ft^3.

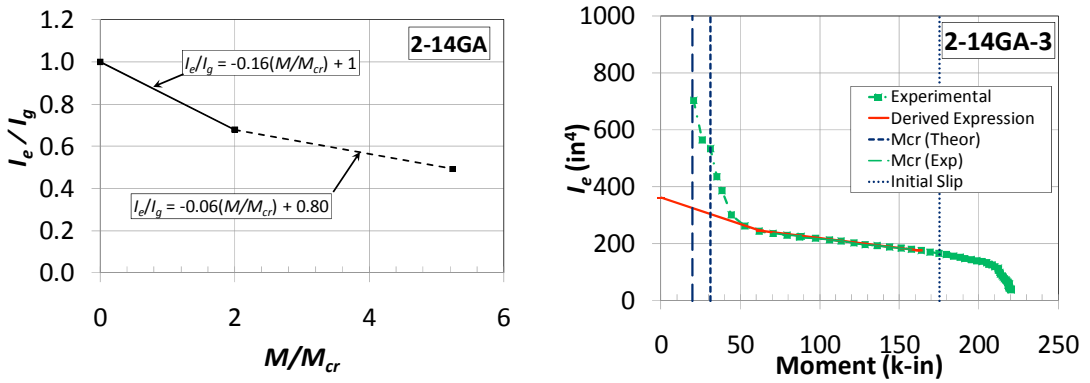
The data set included in the analysis was limited to the range of data points that were deemed to represent service load levels. The upper limit for the service load was considered to correspond to the measured flexural strength divided by a factor of 1.4. The lower limit for the data set was considered to correspond to twice the theoretical cracking moment, M_{cr}, of the composite section. Cracking of concrete in tension was assumed to correspond to a tensile stress equal to the modulus of rupture, f_r, as given by (ACI, 2008):

$$f_r = 7.5 \sqrt{f'_c}$$

where f_r and f'_c are in psi units.

For applied moments less than $2M_{cr}$, the effective moment of inertia was assumed to vary linearly between an upper value equal to the gross moment of inertia, I_g of the composite section at zero moment and a lower value equal to I_e at $2M_{cr}$. For deflection calculations, the effective moment of inertia at mid-span was adopted for the entire beam length as is permitted by ACI (2008). An averaged best-fit line was derived for the calculated I_e for each group of specimens of identical parameters. Figure 9(a) shows the derived expressions for I_e plotted against the

applied moment, M, for the 14-gauge track specimens in Group 2. In the derived expression, I_e is normalized with respect to I_g, and M is normalized with respect to M_{cr}. The derived expressions for I_e for specimen 2-14GA-3 are compared to the experimental data in Figure 9(b).



(a) Derived expressions for I_e (b) Derived and experimental I_e

Figure 9. Derived expression for I_e for specimens 2-14GA

The derived expressions for I_e for specimens with identical parameters are presented in Table 5. Since the expressions were derived for specific specimen configuration, the applicability of each expression is limited. Therefore, additional analytical work is needed to derive a comprehensive and universal expression to replace all the case-specific expressions shown in Table 5.

Table 5. Derived expressions for I_e

Specimen Configuration	Derived Expressions	
	For $0 \le M \le 2M_{cr}$	For $M > 2M_{cr}$
1-16GA	$\left[-0.24\left(M/M_{cr}\right)+1\right] I_g$	$\left[-0.10\left(M/M_{cr}\right)+0.72\right] I_g$
1-14GA	$\left[-0.25\left(M/M_{cr}\right)+1\right] I_g$	$\left[-0.11\left(M/M_{cr}\right)+0.72\right] I_g$
1-12GA	$\left[-0.20\left(M/M_{cr}\right)+1\right] I_g$	$\left[-0.17\left(M/M_{cr}\right)+0.94\right] I_g$
2-16GA	$\left[-0.24\left(M/M_{cr}\right)+1\right] I_g$	$\left[-0.03\left(M/M_{cr}\right)+0.58\right] I_g$
2-14GA	$\left[-0.16\left(M/M_{cr}\right)+1\right] I_g$	$\left[-0.06\left(M/M_{cr}\right)+0.80\right] I_g$
2-12GA	$\left[-0.12\left(M/M_{cr}\right)+1\right] I_g$	$\left[-0.15\left(M/M_{cr}\right)+1.06\right] I_g$
3-12GA	$\left[-0.25\left(M/M_{cr}\right)+1\right] I_g$	$\left[-0.11\left(M/M_{cr}\right)+0.72\right] I_g$
4-12GA	$\left[-0.27\left(M/M_{cr}\right)+1\right] I_g$	$\left[-0.09\left(M/M_{cr}\right)+0.64\right] I_g$
5-12GA	$\left[-0.09\left(M/M_{cr}\right)+1\right] I_g$	$\left[-0.10\left(M/M_{cr}\right)+1.02\right] I_g$

CONCLUSIONS

Based on the results obtained from this study, the following conclusions are made.

1. Concrete/CFS composite beams can be designed for ductile flexural failure.
2. A stand-off screw density of 1 screw at 6" is not adequate for providing full composite action. Early slip was observed in specimens having 1 screw at 6".
3. An increase in the stand-off screw density from 1 screw at 6" to 2 screws at 6" resulted in significant increase in strength and post-initial cracking stiffness. Good composite action was attained when a density of 2 screws at 6" was used.
4. An increase in the stand-off screw density from 2 screws at 6" to 2 screws at 4" resulted in marginal increase in strength and post-initial cracking stiffness.
5. When premature relative slip is prevented, the flexural response of concrete/CFS composite beams can be predicted with good accuracy.
6. For the same stand-off screw density of 2 screws/foot, the flexural stiffness was practically unchanged when the stand-off screw arrangement was changed from 1 screw at 6" to 2 screws at 12". However, using a stand-off screw spacing of 12" may result in brittle shear failure in the concrete.
7. An increase in the track thickness resulted in an increase in stiffness.
8. Engaging the pour stop in the concrete resulted in significant increase in stiffness and strength.
9. Expressions for the effective moment of inertia of the composite beams at service loads were derived. Additional analytical work is needed to derive a universal expression to replace the case-specific expressions.

ACKNOWLEDGEMENT

Funding for this study was provided by NUCOR Corporation in Norfolk, Nebraska. The findings and conclusions of this study are those of the authors and do not necessarily represent the opinion of NUCOR Corporation.

REFERENCES

American Concrete Institute (2008). *"Building Code Requirements for Structural Concrete (ACI 318-08) and Commentary."* Farmington Hills, MI.

Imbsen Software Systems (2000). *"XTRACT Version 2.6.2."* Sacramento, CA.

Steel Stud Manufactures Association (2010). *"Product Technical Information."* www.SSMA.com.

Wehbe, A. P. (2009). *"Experimental Evaluation of Simple Span Cold-Formed Steel and Concrete Composite Beams Utilizing Shearflex® Connectors."* M.S. Thesis. South Dakota State University, Brookings, SD.

An experimental study on the mechanical properties of pultruded CFRP plates at elevated temperatures

Ke Wang, Ben Young, and Scott T. Smith

Department of Civil Engineering, The University of Hong Kong, Pokfulam Road, Hong Kong
Tel (852) 2859-2674; FAX (852) 2559-5337; email: young@hku.hk

ABSTRACT

The use of fibre-reinforced polymer (FRP) composites in civil infrastructure for strengthening and repair applications is becoming more and more widespread. The use of FRP composites for structural members is also gaining popularity. The performance of FRP materials under elevated temperatures is, however, a very real design issue. An accurate understanding of the material properties and behaviour of FRP at such high temperatures are crucial and necessary pieces of information that are surprisingly scarce in the literature. This paper therefore presents the mechanical properties of pultruded carbon fibre-reinforced polymer (CFRP) plates at elevated temperatures. More specifically, CFRP pultruded plate coupons were tested at steady state for temperatures ranging from approximately 20 to 700℃. The tests showed the tensile strength of pultruded CFRP plate to decrease for temperature ranges of 20 to 150℃ and 450 to 706℃. Between these temperature ranges, the tensile strength decreased by a small amount while at 300℃ the ultimate strength was approximately 50 % of the room temperature strength. At the peak temperature of about 700℃, the tensile strength of the FRP plate was as low as 7 % of the room temperature tensile strength.

NOMENCLATURE

E_{normal}= elastic modulus at normal room temperature
T = the temperature of surface of specimen
T_g = the glass transition temperature
$f_{u,T}$=ultimate stress at temperature T℃
$f_{u,normal}$=ultimate stress at normal room temperature (i.e. 22℃)
$\varepsilon_{u,normal}$=strain corresponding to ultimate strength at normal room temperature

INTRODUCTION

Reinforced concrete (RC) infrastructure can be effectively strengthened and repaired with externally bonded fibre-reinforced polymer (FRP) composites or externally mounted post-tensioned FRP tendons and plates. There is an abundance of research related to the experimental validation of these strengthening technologies to RC structural members at room temperature or common operating conditions (e.g. Bank 2006; Hollaway and Teng 2008). There is, however, a distinct lack of research

on the characterisation of FRP construction materials as well as the strengthening of RC structures strengthened with FRP composites at elevated temperatures and fire conditions.

FRP composites consist of fibres embedded in a resin matrix (Hollaway and Teng 2008) and the commonly used carbon and glass fibres can withstand very high temperatures. In the case of carbon fibres this temperature can exceed 2000℃ (Hollaway and Teng 2008). The epoxy used in the resin matrix and also the epoxy used to bond the FRP composite to concrete surfaces can mechanically degrade with increased temperature. Such degradation commences before the glass transition temperature, T_g, is reached and can compromise the ability of the resin matrix to transfer forces amongst the fibres. Another consequence of loss of epoxy integrity is the ability to transfer forces between externally bonded FRP strengthening to the adjacent concrete substrate (Leone et al. 2008). Typically, the T_g can lie in the range of 50 to 90℃ for commercially available products used in civil infrastructure applications (Foster and Bisby 2008). Research on the ability of insulation systems to keep the temperature in the epoxy below critical temperatures for a certain period of time is becoming an active research field (e.g. Kodur et al. 2005; Stratford 2009; Bisby 2003; Hawileh et al. 2009), however, such research is outside the scope of this paper.

Of the limited testing conducted to date on FRP-strengthened RC structural elements such as beams, slabs and columns conducted under elevated temperatures, design guidance has been formulated (Kodur et al. 2007). Such testing (Stratford et al. 2009; Bisby et al. 2005; Gao and Hu 2008; Williams et al. 2008) has considered the behaviour of the entire strengthened member and not the individual materials and components. In addition, such tests were conducted in a transient state manner in which the member was initially loaded and then a fire curve (e.g. Eurocode Part1.2 2002) applied. More recent research (Foster and Bisby 2008) have identified a lack of research and understanding of the mechanical properties of FRP strengthening systems in isolation that are available to the construction industry. This research has also identified a lack of research on the bond between the FRP and the concrete substrate. The work presented in Foster and Bisby (2008) therefore was directed towards enhancing the limited research on the mechanical properties of commercially available FRP materials under elevated temperatures. In their experimental study, they investigated the mechanical properties of FRP bar and plate products under elevated temperatures. To be more precise, Foster and Bisby (2008) conducted tensile coupon tests, single-lap FRP-to-FRP bond tests, direct tension (pull-off) FRP-to-concrete bond tests, and FRP-to-concrete double-lap shear bond tests after exposure to temperatures of up to 400℃. In all tests, the strengths were found to decrease at various rates as the temperatures were increased. While the tests conducted by Foster and Bisby (2008) were focused on post fire behaviour, other researchers such as Eedson et al. (2009) and Chowdhury et al. (2009) have also investigated the behaviour of FRP composite materials for temperatures up to 200℃. Furthermore, Cao et al. (2009) investigated experimentally the tensile properties of CFRP and hybrid FRP sheets at elevated temperatures ranging from 16 to 200℃. They found the strength at elevated temperature to reduce by up to 40 % compared to ambient temperatures. In conclusion, information on the high temperature properties of FRP composites used in civil applications is still quite scarce, especially for the pultruded FRP products which are widely used in civil infrastructure applications.

This paper reports a study on the measurement of the mechanical properties of

CFRP (herein FRP) pultruded plates at temperatures ranging from room temperature (approximately 22℃) up to high temperatures which may be expected in a fire (i.e. 700℃). Flat coupon specimens were prepared from commercially available pultruded FRP plate and then tested to failure in tension in a universal testing machine. The tests were undertaken in a steady state test mode in which the test specimens were heated to a specified temperature and then tested to failure in tension.

EXPERIMENTAL INVESTIGATION

The tensile tests were conducted in a an MTS 810 universal testing machine of 250 kN capacity and the temperature was applied by a high temperature MTS 653 furnace which was controlled by an MTS 409.83 temperature controller. Figure 1 shows the mounted furnace and furnace controller, as well as the grips of the universal testing machine and an FRP test specimen are shown in Figure 1. The furnace, which was capable of reaching a maximum temperature of 1400℃, gained its heat from six pairs of silicon carbide heating elements arranged in three zones. Three external thermocouples were used to measure the surface temperature of the specimens. In addition, the temperature measured from these thermocouples was considered as the real temperature of the specimens in this paper.



Figure 1. Test setup

In all elevated temperature tests, the specimens were heated to a specified temperature then loaded until failure while the target temperature was maintained. After reaching the desired temperature, times of either 5 or 30 minutes were maintained before loading which allowed the epoxy to undergo physical and chemical changes. After such time, tensile load was then applied to the specimens until failure. During the heating up and holding stages the test specimens were unrestrained (i.e. gripped at one end only) in order to enable thermal expansion. After the holding time had been reached, the grips at the originally ungripped end of the specimen were closed and then the specimens tested (while still under the influence of temperature) to failure. The heating rate of the furnace was 50℃ /min. In addition, the tests were undertaken in a ram displacement control mode at a constant rate of 2 mm/min.

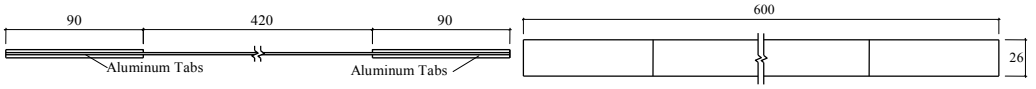
The details of the Sika CarboDur 1214 Pultruded plates used in this study (Sika 2004) are included in Table 1. Tensile coupons were cut to size in the laboratory in accordance with ACI 440.3R-04 (2004) of which the dimensions are shown in Figure 2. An important consideration when testing pultruded FRP plates was to ensure

that rupture failure occurred in the body of the test specimen and away from the grips. For this reason, special attention was given to the design of the grips. Surface roughened aluminium tabs, which provided high contact friction, proved to offer the best gripping due to the ability to prevent crushing of the FRP in the grip region as well as the ability to prevent slippage. The actual cross-sectional dimensions of the test specimens within the centre gauge length region were measured using a micrometer. The measured dimensions were then used to determine the cross sectional-area of each coupon for eventual use in calculating the stress levels.

A total of 31 test coupon specimens were prepared and tested to failure as reported in this paper. The specimens were divided into 2 groups (G1 and G2) as shown in Tables 2 and 3. Group G2 was identical to G1, except for a longer holding time of 30 minutes as compared to 5 minutes for the former.

Table 1. Properties of Sika® CarboDur® Plates 1214 at room temperature (Sika 2004)

Property	Thickness	Fiber content	Tensile strength		Tensile modulus		Strain at rupture
		by volume	Mean value	Min value	Mean value	Min value	
	(mm)	%	(MPa)	(MPa)	(GPa)	(GPa)	%
Sika 1214	1.4	68	3100	>2800	165	160	1.7



(a) Side (b) Front

Figure 2. Schematic of coupon specimen geometry (units: mm)

TEST RESULTS

Table 2. Ultimate stress, failure mode, elastic modulus and strain at break of specimens at room temperature

Group	Specimen Identification[1]	Temperature T (℃)	Ultimate Stress $f_{u,normal}$ (MPa)	Failure Mode[2]	Elastic Modulus[3] E_{normal} (GPa)	Strain at break $\varepsilon_{u,normal}$ (%)
G1 (Room temperature)	SS-22-0-1	22	3239.3	I	188.0	1.70
	SS-22-0-2	22	3169.8	I	193.4	1.65
	SS-22-0-3	22	3052.1	I	193.7	1.61
	SS-22-0-4	22	3072.5	I	191.4	1.57

[1] SS-50-5-1: SS = Steady State, 50 = target temperature of specimen at failure, 5 = holding time at target temperature, 1 = first specimen in sub-series.

[2] Failure modes described in text

[3] For calculation of the ultimate stress and elastic modulus, the composite area and the measured width and thickness of the specimen were used to determine the cross-sectional area of the specimen. The range of strain for calculating elastic modulus is 1000 to 3000 microstrain (ACI440.3R-04 2004).

Table 3. Temperature, ultimate stress and failure mode of tests at elevated temperatures

Group	Specimen Identification[1]	Temperature T (℃)	Holding Time (min□	Ultimate Stress $f_{u,T}$ (MPa)	$\frac{f_{u,T}}{f_{u,normal}}$	Failure Mode[2]
G1 (Temperature Series)	SS-50-5-1	50	5	2889.6	0.922	I
	SS-50-5-2	50	5	3110.7	0.993	I
	SS-100-5-1	98	5	2197.6	0.701	II
	SS-100-5-2	103	5	2137.0	0.682	II
	SS-100-5-3	97	5	2118.1	0.676	II
	SS-150-5-1	146	5	1916.8	0.612	II
	SS-150-5-1	155	5	1792.8	0.572	II
	SS-150-5-1	150	5	1944.0	0.620	II
	SS-200-5-1	211	5	1690.3	0.539	II
	SS-200-5-2	203	5	1720.7	0.549	II
	SS-200-5-3	181	5	1728.9	0.552	II
	SS-200-5-4	198	5	1731.1	0.552	II
	SS-300-5-1	308	5	1664.2	0.531	II
	SS-300-5-2	279	5	1704.4	0.544	II
	SS-300-5-3	300	5	1693.8	0.541	II
	SS-400-5-1	395	5	1501.9	0.479	III
	SS-400-5-2	398	5	1504.2	0.480	III
	SS-400-5-3	420	5	1489.4	0.475	III
	SS-500-5-1	520	5	1354.5	0.432	III
	SS-500-5-2	500	5	1340.8	0.428	III
	SS-600-5-1	623	5	689.5	0.220	III
	SS-600-5-2	625	5	609.1	0.194	III
	SS-700-5-1	706	5	143.5	0.046	IV
	SS-700-5-2	698	5	223.2	0.071	IV
G2 (Time Series)	SS-150-30-1	152	30	1858.0	0.593	II
	SS-150-30-2	180	30	1776.4	0.567	II
	SS-150-30-3	163	30	2002.6	0.639	II

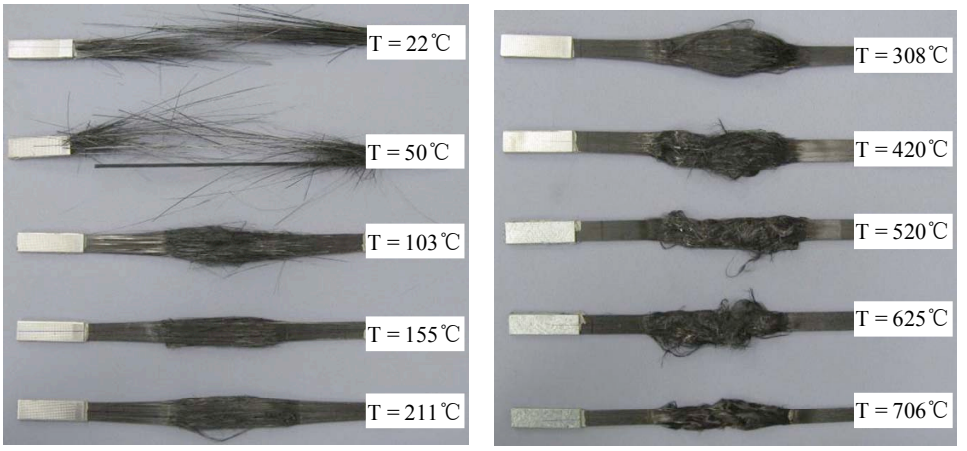
[1] SS-50-5-1: SS = Steady State, 50 = target temperature of specimen at failure, 5 = holding time at target tepperature,1 = first specimen in sub-series.

[2] Failure modes described in text

Time effect. The results of Group G2 tests show that the ultimate strength and failure modes for the specimens were almost the same as compared to the corresponding specimens in Group G1. Such results are shown in Figure 3, as well as Tables 2 and 3. The reason for this behaviour was because there was only a small amount of the

epoxy resin matrix in the specimen. It can therefore be concluded that the holding time of 5 minutes was sufficient, and that the prolonged holding time did not affect the tensile strength of the FRP coupons.

Stress-displacement relationships and failure modes. The tensile stress-displacement curves of G1 exhibit temperature dependent features as observed in Figure 4. It is evident that the ultimate strength deteriorated when exposed to elevated temperature. The stress-displacement relationship is essentially linear from room temperature to temperatures as high as 520℃ right up to rupture failure. In addition, for temperatures ranging from 625℃ to the maximum temperature of 706℃, the stress-displacement relationships become non-linear at high stress levels due to loss of fibres from oxidation.



(a) G1-Temperature series, holding time=5 minutes



(b) G2- Time series, holding time=30 min minutes

Figure 3. Typical failure modes of FRP plates

A brief description of all failure modes encountered in all tests is provided in this section. For Groups G1 and G2, the failure photographs are shown in Figures. 3(a) and (b), respectively, while the types of failure modes are listed Tables 2 and 3. Based on the group G1 test specimens shown in Figure 3(a) for increasing temperature, four different failure modes can be defined which are herein referred to as Modes I, II, III and IV. Each of the failure modes are defined in terms of the temperature ranges extracted directly from the test data provided in Tables 2 and 3.

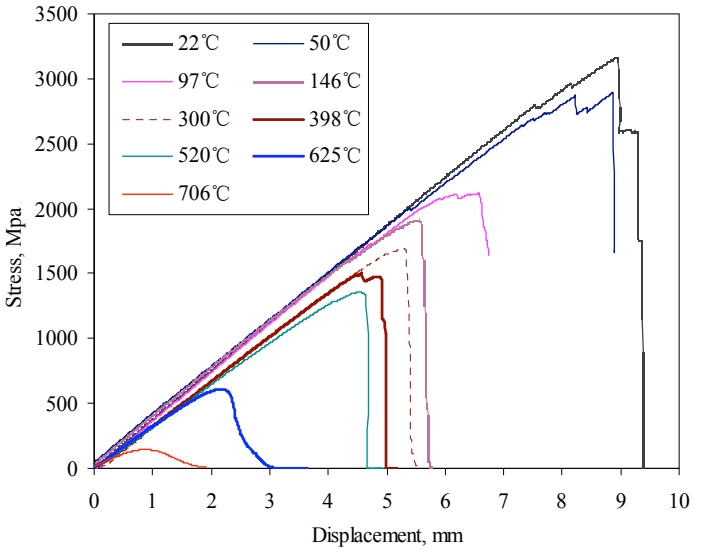


Figure 4. Stress-displacement relationship of G1

Mode I. The temperature of Mode I was relatively low and within the range of 22℃ to 50℃. The specimens failed essentially in a brittle fibre rupture fashion and also simultaneously at different positions along the length of the specimens. The temperature appears to have had little to no effect on the failure mode of these test specimens.

Mode II. For Mode II failing specimens, the rupture position was always within the furnace region. This failure mode occurred between the tested temperature ranges of 97℃ to 308℃. The primary phenomenon for Mode II was softening and gasification of the epoxy resin matrix followed by fibre rupture. Figure 5(a) shows a typical specimen which has failed in a Mode II manner. In this case, part of the epoxy has been lost.

Mode III. From 395℃ to 625℃, the specimens failed in a Mode III manner. In this case, there was no epoxy left on the pultruded FRP plate inside the furnace since the epoxy had self-ignited at about 350℃. Figure 5(b) shows a typical Mode III failed specimen. In this case, the specimen bent freely after the test as all the epoxy had been lost.



(a) Mode II (97℃ to 308℃) (b) Mode III (395℃ to 625℃)

Figure 5. Physical characteristics of the failure mode of types II and III

Mode IV. Mode IV failing specimens endured temperatures from 698 up to 706℃. For such specimens, the epoxy was completely burned and about half of the carbon fibres had oxidised.

Ultimate strength. The reduction factor of the ultimate strength at temperature T to the ultimate strength at room temperature ($f_{u,T}/f_{u,normal}$) at different temperatures is listed in Table 3, and plotted in Figure 6. The vertical axis of Figure 6 represents the strength reduction ratio $f_{u,T}/f_{u,normal}$ and the horizontal axis represents the temperature in degrees Celsius. This figure shows that two large reductions of the failure strength of the test specimens occurred at temperature ranges of 22℃ to 150℃ and 450℃ to 706℃. In addition, there was a gradual reduction in strength and at 300℃ and the ultimate strength of the test specimens reduced to approximately 50% to that of the room temperature strengths. When the temperature rose to around 706℃, the test specimens experienced a significant drop in strength compared with the room temperature strength.

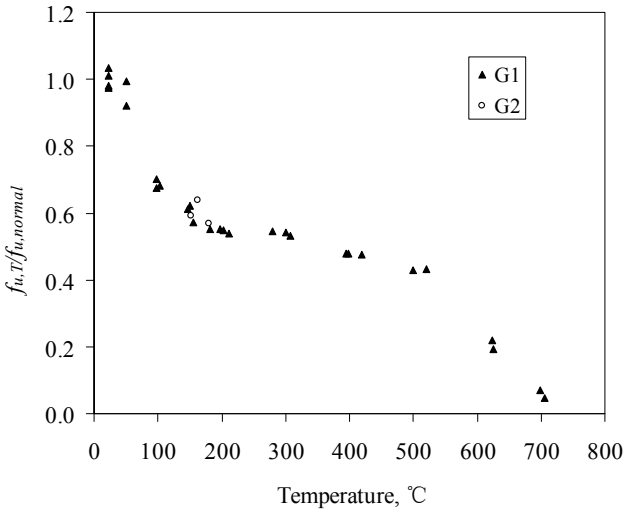


Figure 6. Ultimate plate strength

CONCLUSIONS

This paper has presented the details and results of an experimental investigation on the mechanical properties of pultruded CFRP plates at elevated temperatures ranging from 20 to 700℃ under steady state test conditions. It is important to note here that the results are specific to the type of resin and fibre as well as the fibre volume fraction of the plate tested. The failure modes and ultimate strengths have been discussed in the paper while the stress-displacement relationships have been plotted. The FRP plate was found to ignite when the temperature reached around 350℃ and 600℃. These two self-ignitions were caused by the epoxy matrix transforming into a gaseous state and then by oxidization of the carbon fibres, respectively. Generally, the stress-displacement relation was essentially linear from room temperature to temperatures as high as 520℃. Four different failure modes were

then identified and described, namely (i) rupture of the FRP plate (Mode I), (ii) partial loss of epoxy matrix followed by plate rupture (Mode II), (iii) complete loss of epoxy matrix (Mode III), and (iv) complete loss of epoxy matrix as well as considerable oxidation of the carbon fibres (Mode IV). At a temperature of 300℃, the ultimate strength of the plates reduced to approximately 50% to that of room temperature. In addition, when the temperature rose to around 700℃, the test specimens experienced a significant drop in strength compared to the room temperature strengths.

REFERENCES

Bank, L.C. (2006) *Composites for Construction. Structural Design with FRP Materials*, John Wiley & Sons, USA.

Hollaway, L.C. and Teng, J.G. (2008) *Strengthening and Rehabilitation of Civil Infrastructures Using Fibre-Reinforced Polymer (FRP) Composites*, Woodhead Publishing Limited, Cambridge, UK.

Leone, M., Matthys, S. and Aiello, M.A. (2009) "Effect of elevated service temperature on bond between FRP EBR systems and concrete", *Composites: Part B*, Vol. 40, pp. 85-93.

Foster, S.K. and Bisby, L.A. (2008) "Fire survivability of externally bonded FRP strengthening systems*", Journal of Composites for Construction*, ASCE, Vol. 12, No. 5, pp. 553-561.

Kodur, V.K.R., Bisby, L.A. and Foo, S.H.C. (2005) "Thermal behavior of fire-exposed concrete slabs reinforced with fiber-reinforced polymer bars", *ACI Structural Journal*, Vol. 102, No. 6, pp. 799-808.

Stratford, T.J., Gillie, M., Chen, J.F. and Usmani, A.S. (2009) "Bonded fibre reinforced polymer strengthening in a real fire", *Advances in Structural Engineering*, Vol. 12, No. 6, pp. 867-878.

Bisby, L.A. (2003) *Fire Behavior of Fiber-Reinforced Polymer (FRP) Reinforced or Confined Concrete*, Doctor of Philosophy Dissertation, Department of Civil Engineering, Queen's University, Kingston, Canada.

Hawileh RA, Naser M, Zaidan W, et al. (2009) "Modeling of insulated CFRP-strengthened reinforced concrete T-beam exposed to fire", *Engineering Structures,* Vol. 31, No. 12, pp. 3072-3079.

Kodur, V.K.R., Bisby, L.A. and Green, M.F. (2007) "Preliminary Guidance for the design of FRP-strengthened concrete members exposed to fire", *Journal of Fire Protection Engineering*, Vol. 17, No. 1, pp. 5-26.

Bisby, L.A., Green, M.F. and Kodur, V.K.R. (2005) "Fire endurance of FRP-confined concrete columns", *ACI Structural Journal*, Vol. 10, No. 6, pp. 883-891.

Gao, W.Y. and Hu, K.X. (2008) "Fire resistance research of CFRP-strengthened concrete structures and prospect", *Fiber Reinforced Plastics/Composites*, Vol. 2, pp. 47-52. (in Chinese)

Williams B., Kodur V.K.R., Green M.F., Bisby L. (2008) "Fire endurance of fiber-reinforced polymer strengthened concrete T-beams", *ACI Structural Journal*, Vol. 105, No. 1, pp. 60-67.

BS EN 1991-1-1-2:2002, Eurocode 1: Actions on structures --- Part 1-2: General actions – action on structures exposed to fire, British Standards Institute (BSI), UK.

Eedson, R.T., Bisby, L.A. and Green, M.F. (2009). "Performance of FRP strengthening systems for concrete during exposure to elevated temperatures." Proceedings (CD-Rom), *9th International Symposium on Fiber Reinforced Polymer*

Reinforcement for Concrete Structures (FRPRCS-9), July 13-15, 2009, Sydney, Australia.

Chowdhury, E.U., Eedson, R., Green, M.F., Bisby, L.A. and Benichou, N. (2009) "Mechanical characterization of fibre reinforced polymers materials at high temperature", *Fire Technology*, 45, no. 4, pp. 1-18.

Cao S., Wu, Z. and Wang, X. (2009) "Tensile properties of CFRP and hybrid FRP composites at elevated temperatures", *Journal of Composite Materials*, Vol. 43, No. 4, pp. 315-330.

Sika (2004) *Technical Data Sheet for Sika® CarboDur® Plates*, Sika Hong Kong Pty Ltd.

ACI440.3R-04 (2004) *Guide Test Methods for Fiber-Reinforced Polymers (FRPs) for Reinforcing or Strengthening Concrete Structures*, American Concrete Institute, Farmington Hills, USA.

Inverse Identification of Micromechanics and Fracture Mechanics-Based Damage Evolution Law of Brittle Composites

Shen Shang[1] and Gun Jin Yun[1]

[1]Department of Civil Engineering, The University of Akron, Akron, OH, 44325, USA; ss164@uakron.edu ; gy3@uakron.edu

ABSTRACT

This paper demonstrates identification of parameters associated with damage evolution laws defined in a micromechanics and fracture mechanics-based constitutive model for damage-tolerant brittle composites. A recently developed inverse analysis methodology, called Self-Optimizing Inverse Method (Self-OPTIM), has been extended to the identification of the physics-based damage evolution laws, which has not been achievable. The Self-OPTIM can automatically self-correct the Damage Parameter Set (DPS) based on global in-situ measurements. The material response is obtained from force-driven and displacement-driven nonlinear finite element (FE) simulations. The adopted micromechanics and fracture mechanics-based damage constitutive model can reasonably simulate nucleation and subsequent growth of microcracks within brittle composite materials. It has been implemented within the Self-OPTIM software framework. Numerically simulated synthetic data from an impact tension test are utilized to show successful performance of the proposed damage identification method.

INTRODUCTION

Damage parameter identification techniques and methodologies have received significant attentions in the field of computational damage modeling (Bahloul, 2010; Broggiato and Campana *et al.*, 2007; Celentano and Chaboche, 2007; Cuesta and Alegre *et al.*, 2010; Franulovic and Basan *et al.*, 2010; Hambli, 2002; Munoz-Rojas and Cardoso *et al.*, 2010; Perie and Leclerc *et al.*, 2009). Objectives of the identification of physical damage parameters of materials are two-fold: 1) accessing current damage state of the material to determine the damage initiation; 2) predicting evolutionary behavior of the damage to provide critical information for design of materials.

A strain-rate dependent, micromechanics and fracture mechanics based damage model for brittle materials is adopted in this paper; the model is originated from a micromechanical material model called Statistical CRAck Mechanics (SCRAM) which accounts for opening, shear, growth, and coalescence of an ensemble of cracks (Dienes, 1983). Addessio and Johnson proposed an isotropic constitutive model (ISO-SCRAM) for the inelastic behavior of brittle materials based on the SCRAM (Addessio and Johnson, 1990). Their model is a simplification of SCRAM suitable for predicting the dynamic response of brittle materials under nearly isotropic microcrack distribution. Two different isotropic damage surfaces were used to determine the critical mean crack size for tension and compression cases. In their modeling, the microcrack nucleation rate was expressed as an exponential function of the mean stress as in Reference (Seaman and Curran *et al.*, 1976). Later, a two-step sequential damage model including crack nucleation and crack growth is developed to simulate the crushing behavior of damage-tolerant brittle composite (Lee and Shin, 2003). The constitutive relation and damage evolution law introduced in Reference (Lee and Shin, 2003) is adopted in this paper.

As the damage model is derived in the microscale, identifications of the damage parameters by direct observations need expensive measuring apparatus and complex measurement techniques which challenge the role of numerical simulation (Lauro and Bennani *et al.*, 2001). Most of existing inverse parameter estimation methods has applied optimization techniques which minimize objective functions expressed as differences between the responses from finite element (FE) simulations and measured experimental test data. The objective functions are expressed in terms of the local stress and strain information which only represents the material characteristic on a certain small region of the specimen due to the experiment technique (Celentano and Chaboche, 2007; Franulovic and Basan *et al.*, 2010; Hambli, 2002). Later, the

difference of global displacements (Lauro and Bennani *et al.*, 2001; Xiang and Swoboda *et al.*, 2002), both global displacement and force (Abendroth and Kuna, 2006), and modal characteristics i.e. natural frequencies and/or mode shapes (Friswell, 2007; Singh, 2009) were also implemented into the objective function. In order to improve the performance of the inverse identification technique, micro-scale experimental data (local crack behavior) was applied (Corigliano and Mariani, 2001; Iacono and Sluys *et al.*, 2006). Recently emerging techniques using optical full-field displacement measurements have greatly enhanced performance of the inverse parameters identifications by providing enriched information on deformational characteristics (Grediac and Pierron, 2006; Latourte and Chrysochoos *et al.*, 2008). Furthermore, the displacement fields extracted from the 2D planar based on Digital Image Correlation (DIC) technique were used to the identification of the damage law (Perie and Leclerc *et al.*, 2009). For facilitating use of artificial neural network (ANN)-based material constitutive models, an innovative on-line training methodology, called autoprogressive training, was developed by Ghaboussi, et al. (Ghaboussi and Pecknold *et al.*, 1998). Using their method, ANN material models could be trained by applying only in-site measured global forces and displacements.

In this paper, significant technology advancement in the field of inverse nonlinear constitutive and damage parameter identification has been made by applying the newly developed Self-Optimizing Inverse Method (Self-OPTIM). Unlike other existing inverse parameter identification methods, Self-OPTIM does not need premeasured local reference (i.e. true) stresses and strains in the objective function. Instead, only global boundary force and displacement responses that can readily be measured using conventional sensing techniques are required. It was successfully applied to estimate the cyclic elasto-plastic constitutive model parameters (Yun and Shang, 2010). In the following sections, brief descriptions about the theoretical formulation of the damage model for brittle composite and Self-OPTIM will be recapitulated. In addition, the verification with synthetic data will be carried out to investigate the capacity of the Self-OPTIM method for inverse identification of damage evolution laws of damage-tolerant brittle materials.

RECAPITULATION OF A DAMAGE MODEL FOR BRITTLE COMPOSITE

The composite material used in this paper is assumed to be brittle with isotropic distribution of microcracks. The micromechanics and fracture mechanics-based damage model considers two sequential damage processes: 1) the nucleation of microcracks and 2) the crack growth. The damaged state ω is described as a function

of the physical parameters, that is, the number of microcracks per unit volume (N) and the average size of microcracks $\bar{c}$ as follows (Krajcinovic, 1996)

$$\omega = N\bar{c}^3 \tag{1}$$

Nucleation of Microcracks. When the material reaches an initial damage stage, the crack nucleation will happen. The microcrack nucleation model following the exponential rate equation is presented as (Seaman and Curran et al., 1976)

$$\dot{N} = \begin{cases} \dot{N}_0 \exp\left[\dfrac{(P_s - P_{n0})}{P_1}\right], & P_s > P_{n0} \\ 0, & P_s \le P_{n0} \end{cases} \tag{2}$$

where $\dot{N}_0$ and P_1 are experimentally determined material parameters; P_{n0} designates a threshold stress for the nucleation of microcracks; and P_s is the hydrostatic pressure in the solid material and can be calculated as $P_s = \sigma_{kk}/3$ (Seaman and Curran *et al.*, 1976). An incremental form for a numerical approximation of Eq. (2) by the backward Euler integration scheme can be written as (Lee and Shin, 2003)

$$N_{n+1} = N_n + \Delta t_{n+1}\dot{N}_0 \cdot \exp\left[\frac{(P_s)_{n+1} - P_{n0}}{P_1}\right] \tag{3}$$

Crack Growth Criteria. After further nucleation of microcracks stops, microcracks start to grow. The rate of crack growth is assumed to be a function of overstress, i.e., the distance in the stress space between the current stress and the damage surface. For a stress state that exceeds the current damage threshold, microcracks grow. Two different damage surfaces based on the energy balance of isolated cracks are defined for tension and compression (Addessio and Johnson, 1990). The damage surface for tension case (p~~p~~<0) is expressed as (Addessio and Johnson, 1990)

$$F^n(S_{ij}, p, \bar{c}) = \frac{3}{2}S_{ij}S_{ij} + \frac{45}{4(5-\nu_0)}\left[(2-\nu_0)p^2 - \frac{2K}{\bar{c}}\right] = 0 \tag{4}$$

The damage surface for compression case (p>0) is expressed as (Addessio and Johnson, 1990)

$$F^n(S_{ij}, p, \bar{c}) = \frac{3}{2}S_{ij}S_{ij} - \frac{45}{2(3-2\nu_0^2)}\left[\left(\mu_{fr}p + \sigma_0\right)\left(\mu_{fr}p + \sigma_0 + \sqrt{\frac{\pi K}{\bar{c}}}\right) + \frac{K}{\bar{c}}\right] = 0 \tag{5}$$

where p=-σ_{kk} /3, S_{ij} is the deviatoric stress, σ_0 is the cohesive stress, $_{rf}$ is the coefficient of friction, and K is defined as (Addessio and Johnson, 1990)

$$K = \frac{\pi}{2}\left(\frac{2-\nu_0}{1-\nu_0}\right)K_{IC}G_0 \tag{6}$$

where ν_0 and G_0 are the Possion's ratio and shear modulus of the brittle solids. In addition, K_{IC} is the plane strain fracture toughness.

Rate of Crack Growth. If the state of stress is within the damage surface, the deformation is elastic and no change is made in the mean crack size. If, however, the state of stress is outside the damage surface, then the mean crack size will increase and be determined by integration of the rate of crack growth (Addessio and Johnson, 1990)

$$\dot{\bar{c}} = \beta \dot{c}_{\max} \tanh(d_s) \tag{7}$$

where $\dot{c}_{\max}$ is the shear wave speed ($\dot{c}_{\max} = \sqrt{E^*/\rho^*}$), E* and ρ* are the overall Young's modulus and the density, respectively. β is the scaling factor for crack speed and assumed to be an independent constant, d_s is the measure of the distance the amount by which the state of stress exceeds the damage surface (Addessio and Johnson, 1990)

$$d_s = \frac{3}{2}S_{ij}S_{ij} - F_d \tag{8}$$

in which

$$F_d = \begin{cases} -\dfrac{45}{4(5-\nu_0)}\left[(2-\nu_0)p^2 - \dfrac{2K}{\bar{c}}\right], & p < 0 \\ \dfrac{45}{2(3-2\nu_0^2)}\left[\left(\mu_{fr}p + \sigma_0\right)\left(\mu_{fr}p + \sigma_0 + \sqrt{\dfrac{\pi K}{\bar{c}}}\right) + \dfrac{K}{\bar{c}}\right], & p > 0 \end{cases} \tag{9}$$

The rate equation can be expressed in an incremental form as (Lee and Shin, 2003)

$$\bar{c}_{n+1} = \bar{c}_n + \beta \Delta t_{n+1}\sqrt{\frac{(E^*)_{n+1}}{(\rho^*)_{n+1}}}\tanh(d_s) \tag{10}$$

The effective modulus which is a function of the damage state ω is formulated by using the self-consistent method and differential scheme (Lee and Simunovic, 2006). This micromechanics and fracture mechanics-based damage model was implemented

into the ABAQUS user defined material (UMAT) which accounts for the two-dimensional plane-stress state. The detail formulation can be found in the series research work (Lee and Shin, 2004; Lee and Simunovic, 2006; Lee and Simunovic *et al.*, 2004).

SELF-OPTIMIZING INVERSE METHOD (Self-OPTIM)

A unique capability of the proposed Self-OPTIM method is that it can identify damage related parameters only from global forces and displacements on a partial boundary of tested specimens measured during experimental testing. Details on theoretical fundamentals of the Self-OPTIM methodology can be referred to Reference (Yun and Shang, 2010).

Figure 1 shows a schematic diagram of computational procedures of the proposed Self-OPTIM method.

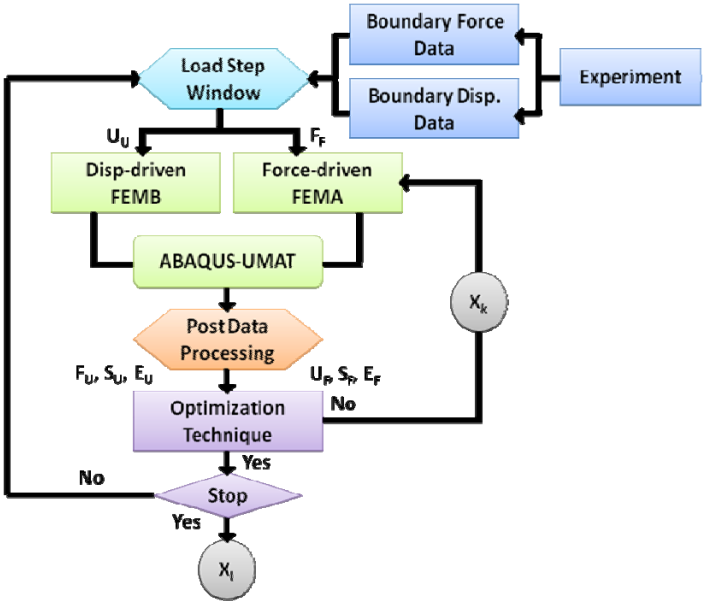


Figure 1 Flowchart of Self-OPTIM Inverse Analysis Method

At the first step, global force and displacement data on the partial boundary are measured from experimental testing. At the second step, an equilibrium path is selected in order to determine the number of load steps and boundary control data used in the identification algorithm. As the third step, these boundary force and displacement data are imposed to the force-controlled nonlinear finite element analysis (FEMA) and the displacement-controlled nonlinear finite element analysis (FEMB), respectively. The two different nonlinear FE simulations are conducted using the UMAT with the updated parameter set under the boundary control data

generated at the second step. At the fourth step, a post processing of FE analyses results automatically extracts two sets of stress and strain data ($\boldsymbol{S}_U$, $\boldsymbol{E}_U$, $\boldsymbol{S}_F$, $\boldsymbol{E}_F$,) at Gauss integration points within the specified elements and two sets of displacement and force data ($\boldsymbol{U}_U$, $\boldsymbol{F}_U$, $\boldsymbol{U}_F$, $\boldsymbol{F}_F$,) of the boundary nodal points from the *.fil* file by using the ABAQUS utility routine *posfil.for*. These steps ranging from Step 1 to Step 4 are repeated under the steady-state genetic algorithm (SSGA). At each generation, the better Damage Parameter Set (DPS) are sought following the SSGA global searching algorithm.

The proposed Self-OPTIM method uses an implicit-explicit objective function defined as a function of the two sets of stresses ($\boldsymbol{S}_{\mathrm{U}}$ and $\boldsymbol{S}_{\mathrm{F}}$), strains ($\boldsymbol{E}_{\mathrm{U}}$ and $\boldsymbol{E}_{\mathrm{F}}$), displacements($\boldsymbol{U}_{\mathrm{U}}$ and $\boldsymbol{U}_{\mathrm{F}}$), and forces ($\boldsymbol{F}_{\mathrm{U}}$ and $\boldsymbol{F}_{\mathrm{F}}$).

$$
\begin{aligned}
OF_{implicit-\exp licit} = {} & W_1 \cdot \sum_{k=1}^{LS}\left[1-\frac{\left\|\sum_{i=1}^{GP}\mathbf{S}_{iU}^{k}\right\|}{\left\|\sum_{i=1}^{GP}\mathbf{S}_{iF}^{k}\right\|}\right]^2 + W_2 \cdot \sum_{k=1}^{LS}\left[1-\frac{\left\|\sum_{i=1}^{GP}\mathbf{E}_{iF}^{k}\right\|}{\left\|\sum_{i=1}^{GP}\mathbf{E}_{iU}^{k}\right\|}\right]^2 \\
& + W_3 \cdot \sum_{k=1}^{LS}\left[1-\frac{\left\|\sum_{i=1}^{NP}\mathbf{U}_{iF}^{k}\right\|}{\left\|\sum_{i=1}^{NP}\mathbf{U}_{iU}^{k}\right\|}\right]^2 + W_4 \cdot \sum_{k=1}^{LS}\left[1-\frac{\left\|\sum_{i=1}^{NP}\mathbf{F}_{iU}^{k}\right\|}{\left\|\sum_{i=1}^{NP}\mathbf{F}_{iF}^{k}\right\|}\right]^2
\end{aligned}
\tag{11}
$$

where W_1, W_2, W_3, and W_4 are weight factors whose values indicate the relative importance of one term compared to the others (Rao, 2009); $\|\cdot\|$ indicates the Euclidean norm; *LS* indicates the number of load steps in current load step window; *GP* indicates the total number of Gauss points in current finite element mesh; *NP* indicates the total number of boundary nodal points. The objective function in Eq. (11) contains implicit full-field stress/strain data and explicit force/displacement data. Fundamentally, the proposed implicit-explicit objective function and updating approach is different from existing model updating techniques which mostly employ explicit data from in-situ measurements or laboratory testing observations. The capacity of the Self-OPTIM method will be verified numerically in the following section.

VERIFICATION WITH SYNTHETIC DATA

A finite element model for a specimen from an impact tension test (Xia and Wang, 1996) is used in this verification test. Using symmetry boundary conditions, only

quarter part of the specimen (6 mm × 4 mm) was modeled by 3mm × 2mm coupon. Both the left and the bottom boundary are constrained on their normal direction. The density, bulk, and shear moduli of the material are used to be known, that is, density ρ=1403 kg/m^3, bulk modulus K=14.02 GPa, and shear modulus =6.28 GPa. The boundary displacement and force data are generated from a displacement-driven simulation with the reference DPS $\boldsymbol{x}_T$=[$\bar{c}_0$ =0.014cm, N_0=1x10^5/cm^3, γ=10 Pa·m, β=1.0x10^{-5}, $\dot{N}_0$ =1x10^5/s/cm^3, P_{n0}=5 MPa, P_1=10 MPa]. Although static analysis is conducted, the rate effect is considered within UMAT by setting the constant time increment Δt in each load step. Thus, the strain rate can be calculated as $\dot{\varepsilon} = \Delta\varepsilon / \Delta t$. The total strain, 0.1, is caused by 200 load steps deformation with the time increment Δt=0.005 s. Therefore, $\dot{\varepsilon}$ =$\Delta\varepsilon/\Delta t$=($\varepsilon^{tol}$/n)/$\Delta t$ =10 s^{-1}. This numerical example is utilized as a reference simulation in the following subsection.

Damage Identification by Self-OPTIM. The steady state genetic algorithm (SSGA) is employed in the Self-OPTIM inverse identification. The preset upper and lower bounds of the DPS are selected ensuring that the randomly selected DPS is permissible for the problem. Even if the SSGA evaluates the objective function only for the two best DPSs in each generation, it is known to converge substantially faster than traditional GA algorithms with comparable searching performance (Yun and Caicedo, 2010).

Table 1 Identification Results by Self-OPTIM

	$\bar{C}_0$ (cm)	N_0 (/cm^3)	γ (Pa m)	β	$\dot{N}_0$ (/s/cm^3)	P_{n0} (MPa)	P_1 (MPa)
$\boldsymbol{x}_T$	0.014	1.00x10^5	10.00	1.00x10^{-5}	1.00x10^5	5.00	10.00
$\boldsymbol{x}_U$	0.018	1.30x10^5	12.00	1.40x10^{-5}	1.30x10^5	7.00	13.00
$\boldsymbol{x}_L$	0.010	0.60x10^5	8.00	0.60x10^{-5}	0.7x10^5	4.00	8.00
$\boldsymbol{x}_I$	0.0143	1.04x10^5	9.50	0.97x10^{-5}	0.85x10^5	4.57	9.71
Initial Error	28.57	30.00	20.00	40.00	30.00	40.00	30.00
	-28.57	-40.00	-20.00	-40.00	-30.00	-20.00	-20.00
Final Error	2.14	4.00	5.32	3.00	15.00	8.60	2.90

In this example, the preset upper and lower bounds of the damage model parameters are assumed have a large initial difference from the true DPS. The algorithm is terminated at 6000th generation. In each generation of the SSGA, a 90% crossover rate and a 30% mutation rate were used. The identification results are summarized in Table 1. All damage evolution related parameters are calibrated accurately except the nucleation rate $\dot{N}_0$. The reason is for a minor role of the nucleation rate in the damage evolution. The number of the microcracks increased only in a small region at the early deformation stage and kept the same state until the end of load steps. Successful identification of the initial mean radius ($\bar{c}_0$) and initial density (N_0) of microcracks implies potential capabilities of the proposed Self-OPTIM method for initial statistical damage assessment, that is, material quality assurance.

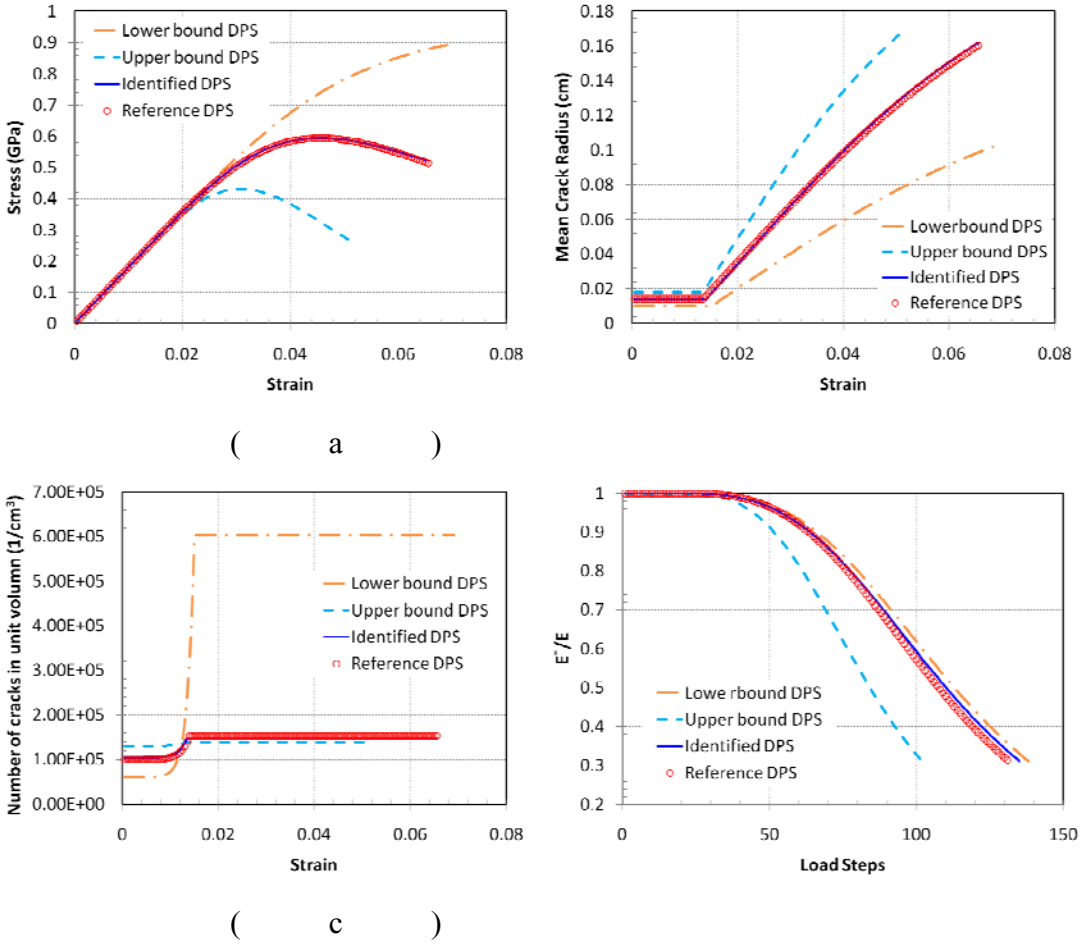


Figure 2 Comparisons of (a) the stress-strain response, (b) the mean crack radius growth and (c) the microcrack nucleation and (d) the degradation of the normalized overall Young's modulus between simulations using the upper bound DPS, lower bound DPS, identified DPS and reference DPS.

The identified response and damage behavior are compared with the result from simulations using the upper and lower bounds DPS, that is, $\boldsymbol{x}_U$, and $\boldsymbol{x}_L$. They are shown in Figure 2. Obviously, the stress-strain response is consistent with the reference. Damage evolution laws could be successfully identified by estimating its associated damage parameters.

CONCLUSIONS

In this paper, a novel method for inverse identification of damage evolution laws of damage-tolerant brittle materials has been proposed. A newly developed model-independent optimization framework, called Self-OPTIM, is combined with a damage model. In the damage model, two independent nonlinear damage modes: 1) nucleation and 2) growth of microcracks, contribute to the degradation of the stiffness. The damage model has limitations in parameter estimations due to its large number of parameters and difficulties in experimental observations. Nevertheless, the Self-OPTIM framework is still capable of finishing the inverse identification problem successfully with an acceptable DPS which reconstructs the global damage behavior consistently as the reference. The progressive damage characteristics in micro-scale are obtained even though Self-OPTIM just used the global boundary displacement and force data which can be easily acquired from the conventional material test.

REFERENCES

Abendroth, M., Kuna, M., (2006). "Identification of ductile damage and fracture parameters from the small punch test using neural networks." *Engineering Fracture Mechanics* 73(6), 710-725.

Addessio, F.L., Johnson, J.N., (1990). "A constitutive model for the dynamic response of brittle materials." *Journal of Applied Physics* 67(7), 3275-3286.

Bahloul, R., (2010). "Optimisation of process parameters in flanging operation in order to minimise stresses and lemaitre's damage." *Materials & Design* 32(1), 108-120.

Broggiato, G.B., Campana, F., Cortese, L., (2007). "Identification of material damage model parameters: An inverse approach using digital image processing." *Meccanica* 42(1), 9-17.

Celentano, D.J., Chaboche, J.L., (2007). "Experimental and numerical characterization of damage evolution in steels." *International Journal of Plasticity* 23(10-11), 1739-1762.

Corigliano, A., Mariani, S., (2001). "Simulation of damage in composites by means of interface models: Parameter identification." *Composites Science and Technology* 61(15), 2299-2315.

Cuesta, I., Alegre, J.M., Lacalle, R., (2010). "Determination of the gurson-tvergaard damage model parameters for simulating small punch tests." *Fatigue & Fracture of Engineering Materials & Structures* 33(11), 703-713.

Dienes, J.K., (1983). "On the stability of shear cracks and the calculation of compressive strength." *Journal of Geophysical Research* 88(Nb2), 1173-1179.

Franulovic, M., Basan, R., Kunc, R., Prebil, I., (2010). "Automation of lcf material model parameters' identification." *Computational Materials Science* 48(3), 529-536.

Friswell, M.I., (2007). "Damage identification using inverse methods." *Philosophical Transactions of the Royal Society a-Mathematical Physical and Engineering Sciences* 365(1851), 393-410.

Ghaboussi, J., Pecknold, D.A., Zhang, M.F., Haj-Ali, R.M., (1998). "Autoprogressive training of neural network constitutive models." *International Journal for Numerical Methods in Engineering* 42(1), 105-126.

Grediac, M., Pierron, F., (2006). "Applying the virtual fields method to the identification of elasto-plastic constitutive parameters." *International Journal of Plasticity* 22(4), 602-627.

Hambli, R., (2002). "Inverse technique identification of material damage law with experimental validation." *International Journal of Manufacturing Technology* 20(3), 223-229.

Iacono, C., Sluys, L.J., van Mier, J.G.M., (2006). "Estimation of model parameters in nonlocal damage theories by inverse analysis techniques." *Computer Methods in Applied Mechanics and Engineering* 195(52), 7211-7222.

Krajcinovic, D., (1996). *Damage Mechanics*, Elsevier, Amsterdam, Netherlands.

Latourte, F., Chrysochoos, A., Pagano, S., Wattrisse, B., (2008). "Elastoplastic behavior identification for heterogeneous loadings and materials." *Experimental Mechanics* 48(4), 435-449.

Lauro, F., Bennani, B., Croix, P., Oudin, J., (2001). "Identification of the damage parameters for anisotropic materials by inverse technique: Application to an aluminium." *Journal of Materials Processing Technology* 118(1-3), 472-477.

Lee, H.K., Shin, D.K., (2003). "Computational approach for modeling of crack nucleation and growth in damage-tolerant brittle materials." *KSCE Journal of Civil Engineering* 7(5), 537-546.

Lee, H.K., Shin, D.K., (2004). "A computational investigation of crack evolution and interactions of microcracks and particles in particle-reinforced brittle composites." *Composite Structures* 64(3-4), 419-431.

Lee, H.K., Simunovic, S., (2006). "Prediction of crack evolution and effective elastic behavior of damage-tolerant brittle composites." *Computer Methods in Applied Mechanics and Engineering* 196(1-3), 118-133.

Lee, H.K., Simunovic, S., Shin, D.K., (2004). "A computational approach for prediction of the damage evolution and crushing behavior of chopped random fiber composites." *Computational Materials Science* 29(4), 459-474.

Munoz-Rojas, P.A., Cardoso, E.L., Vaz, M., (2010). "Parameter identification of damage models using genetic algorithms." *Experimental Mechanics* 50(5), 627-634.

Perie, J.N., Leclerc, H., Roux, S., Hild, F., (2009). "Digital image correlation and biaxial test on composite material for anisotropic damage law identification." *International Journal of Solids and Structures* 46(11-12), 2388-2396.

Rao, S.S., (2009). *Engineering optimization: Theory and practice*. 4th ed. JOHN WILEY & SONS, INC. Hoboken, New Jersey.

Seaman, L., Curran, D.R., Shockey, D.A., (1976). "Computational models for ductile and brittle-fracture." *Journal of Applied Physics* 47(11), 4814-4826.

Singh, K.V., (2009). "Transcendental inverse eigenvalue problems in damage parameter estimation." *Mechanical Systems and Signal Processing* 23(6), 1870-1883.

Xia, Y.M., Wang, X., (1996). "Constitutive equation for unidirectional composites under tensile impact." *Composites Science and Technology* 56(2), 155-160.

Xiang, Z.H., Swoboda, G., Cen, Z.Z., (2002). "Identification of damage parameters for jointed rock." *Computers & Structures* 80(16-17), 1429-1440.

Yun, G.J., Caicedo, J.M., (2010). "A novel evolutionary algorithm for identifying multiple alternative solutions in model updating." *Structural Health Monitoring-An International Journal* Published on-line, doi: 10.1177/1475921710381775

Yun, G.J., Shang, S., (2010). "A self-optimizing inverse analysis method for estimation of cyclic elasto-plasticity model parameters." *International Journal of Plasticity* On-line published, doi:10.1016/j.ijplas.2010.08.003.

Progressive Collapse Analysis of RC Structures Including Beam Axial Deformation

Ali Kazemi[1] and Mehrdad Sasani[2]

[1]400 Snell Engineering Center, Department of Civil and Environmental Engineering Northeastern University, Boston, MA 02115; PH (617) 373-3991; FAX (617) 373-2440; email: a.kazemi@neu.edu
[2]400 Snell Engineering Center, Department of Civil and Environmental Engineering Northeastern University, Boston, MA 02115; PH (617) 373-3991; FAX (617) 373-2440; email: m.sasani@neu.edu

ABSTRACT

Effects of beam growth in progressive collapse resistance of an actual eleven-story reinforced concrete structure are evaluated following predefined initial damage. The initial damage was caused in part by simultaneous explosion (removal) of four adjacent columns, two of which were exterior columns. In addition to the removal of these columns, two beam sections were also exploded. The structure resisted progressive collapse following such severe initial damage. An analytical model of the structure accounting for the interaction between the axial and flexural deformations is developed to study progressive collapse resisting mechanisms. The analytical results show good agreement with experimental data. The main progressive collapse resisting mechanism was the flexural-axial interaction of the second floor deep beams. The Vierendeel frame action of the floors above also contributed to collapse resistance.

INTRODUCTION

Through manmade hazards (accident or act of terrorism), or natural hazards, structures may be subject to conditions that lead to progressive collapse. Progressive collapse is defined as the spread of an initial local failure from element to element, eventually resulting in the collapse of an entire structure or a disproportionately large part of it (ASCE/SEI 7, 2010). Redistribution of loads following an imposed local damage to a structure depends on strength, continuity, redundancy, and deformation and energy dissipation capacities of the structure. From an analytical point of view, progressive collapse occurs when following loss of some structural elements, the structure has its load pattern or boundary conditions changed such that other structural elements are loaded beyond their capacity and fail (Krauthammer et al., 2003).

The Ronan Point apartment building collapse in England, 1968 generated substantial interest in general structural integrity for buildings and the prevention of progressive collapse. A second wave of interest followed the attack on the Murrah Federal building in 1995 and the terrorist attacks on the World Trade Center Towers

and the Pentagon on September 11, 2001. Progressive collapse is by nature a system-level problem where the spread of an initial local failure from element to element eventually results in the collapse of an entire structure or a disproportionately large part of it (ASCE/SEI 7, 2010).

One approach to evaluate progressive collapse of structures is to study the effects of instantaneous removal of a load-bearing element such as a column (GSA, 2003 and DOD 2010). GSA (2003) provides guidelines for progressive collapse analysis of structures based on the alternative path method and mandates instantaneous removal of one load-bearing element with different scenarios as the initiation of damage. DOD (2010) also provides two design methods: one employs the tie force method (indirect design) and the other employs the alternative path method (direct design) under initial damage scenarios in general similar to those of the GSA (2003), that is removal of one load bearing element and evaluating potential progressive collapse of the structure. The level of initial damage in many recent cases of terrorist attacks, however, was by far more significant than removal of one load bearing element. In this study, the progressive collapse resistance of a reinforced concrete structure with discontinuous columns on the floors above, subjected to a severe initial damage is studied experimentally and analytically. The initial damage was set to represent the effects of a severe explosion causing simultaneous loss of four adjacent columns and two beam segments.

BUILDING CHARACTERISTICS

This paper evaluates the progressive collapse resistance of the Crowne Plaza hotel, which was an 11-story structure above the ground located in Houston, TX. The hotel was demolished by implosion after the experiment was concluded. Figure 1 shows a view of the hotel, which had an ordinary reinforced concrete structure. The height of the first story was about 9.14 m. The height of the stories above was 3.05 m. Figure 2 shows the plan of the second floor of the structure. Crosses in the figure show the location of the exploded columns and beam segments. The second floor was a 0.15 m thick two-way slab system supported by 2.057 m deep beams running in both longitudinal and transverse directions. The width of all the longitudinal beams was 0.914 m. The width of transverse beams between axes 3 to 8 was 1.372 m. The cross section of the columns in the first floor between axes 4 to 7 was 0.914 m x 0.914 m. All the columns of floors above were sitting on the longitudinal beams in second floor. The stories above were made of 0.15 m thick two way flat slabs supported by columns. Column dimensions were 0.279 m in the longitudinal and 0.330 m to 0.406 m in the

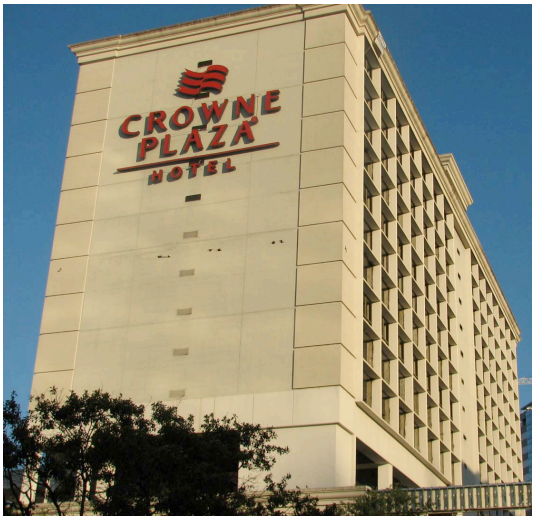


Fig. 1 - View of Crown Plaza Hotel

transverse direction of the structure. The columns on the first floor were spaced at about 9.576 m, while the columns on the floors above were spaced 3.988 m longitudinal direction. This means the columns on the floors above were not continuous to the ground and were supported by the longitudinal beams of the second floor. The structure had an elevator case at the central part of the building and two stair cases at two corners.

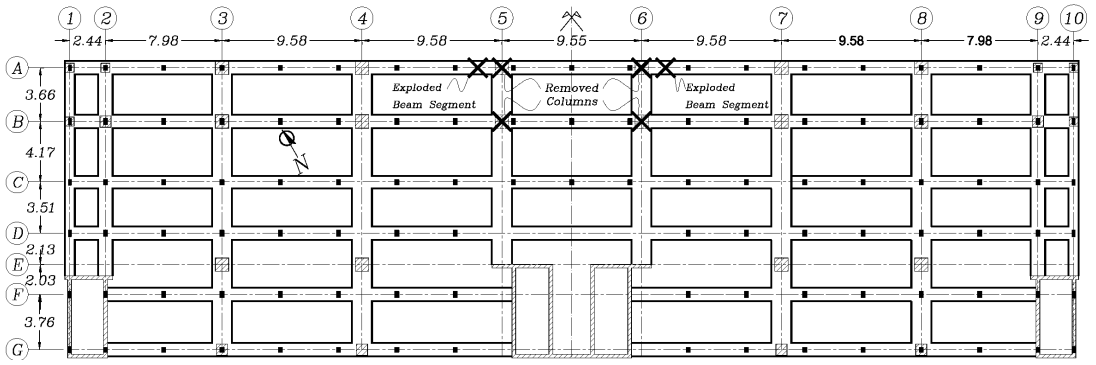


Fig. 2 - Plan of second floor

Compression and tension tests on concrete samples and tension tests on steel samples from the building were conducted. the concrete compressive strength was measured at f'_c= 26.9 MPa for a standard concrete cylinder. The modulus of rupture was determined to be about f_r= 3.4 MPa. The modulus of elasticity of concrete was estimated at 24800 MPa. The yield and ultimate stresses for beam and slab flexural reinforcement were found to be f_y= 517 MPa and f_u= 758 MPa, respectively. The modulus of elasticity of steel was set equal to 200 GPa. The steel ultimate tensile strain was measured at 0.1.

STRUCTURAL MODEL

A three-dimensional finite element model of the structure is developed, using the computer program SAP2000 version 14.1 (2009). Figure 3 shows a three-dimensional view of the second floor of the building and the location of the imposed initial damage. Bernoulli beam elements with localized plastic hinges are used to model material nonlinearity in beams, columns and slab elements. The slab elements in the vicinity of the imposed initial damage (between axes 4 and 7 and between axes A and D) undergo significant structural demand behaving nonlinearly. The slab in this region is modeled by a two-directional grid of beam elements and the slabs away from this area are modeled using elastic four-node shell elements. For the rectangular beams modeling the slabs, due to the fact that the shear flows in a continuum slab and in a two-directional grid of beams are different (MacLeod, 1990) the torsional stiffness of the cross sections were divided by two.

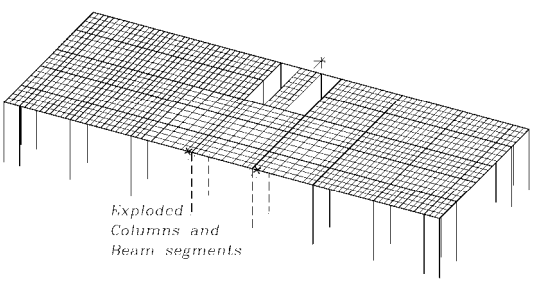


Fig. 3 - Three dimensional view of model

The beams in the second floor are modeled with T- and L-sections. The effective flange width on each side of beams is set equal to four times the slab thickness, 0.61 m (ACI 318, 2008). Geometric nonlinearity is accounted for and the equilibrium equations are written in the deformed configuration of the structure.

To account for torsional cracking an iterative procedure is used in this study. The procedure involves carrying out an analysis with an uncracked section torsional stiffness. Then, wherever the torsional moment exceeds the cracking torsional strength (ACI 318, 2008), the torsional stiffness of the section is reduced to cracked torsional stiffness (Collins and Lampert, 1973). This procedure is repeated until all cracked regions are accounted for. A mass proportional damping ratio of ξ=0.05 in the first vertical vibration mode is used.

The frame elements in the SAP2000 computer program are elastic and linear. One approach to account for plastic behavior in the program is using a localized Moment plastic hinge, which accounts only for flexural plastic deformation. The behavior of a Moment plastic hinge up to the yield point is rigid, which means the hinge has no effect on the response of the element up to the yield point. After the yield point however, the hinge provides plastic deformation to the element (in the vicinity of the hinge). So, the behavior of moment plastic hinges is called rigid-plastic.

The moment-rotation relationship for a moment plastic hinge is obtained under a constant axial force (usually zero) and the interaction of the axial force and the moment (P-M interaction) is not considered. To account for the effect of the axial force and moment interaction, the PMM (the axial force and the bending moment in two directions) plastic hinges are also available in SAP2000. In this type of plastic hinges, the P-M interaction is partially considered at the force level. Therefore, PMM plastic hinges do not include the effect of the interaction between flexural and axial deformations.

Another type of plastic hinge available in SAP2000 is a fiber plastic hinge. In fiber plastic hinges the geometry of the section and the material properties (constitutive laws) are directly used in each time step to obtain the force and deformation response of the sections, and in turn, the elements. That is, in a Fiber Plastic Hinge in addition to flexural, the axial deformation (elastic and plastic) is accounted for. Both moment and fiber plastic hinges are localized plastic hinges represent the behavior of the associated plastic hinge length.

In a localized Fiber Plastic Hinge, in addition to the plastic deformation over the assumed length of the plastic hinge, the so called “elastic” response is also included in the hinge deformation, that is, a fiber plastic hinge is not rigid-plastic. The structural model uses the elastic flexibility of the structural element. Therefore, the elastic flexibility of the region represented by the hinge is double counted. In order to resolve this issue, the solution used in this study is to change the portion of the element represented by a fiber plastic hinge (plastic hinge length) to be axially and flexurally rigid (or have relatively large stiffness to be practically rigid) which in effect diminishes the effect of the elastic flexibility of the structural element. Plastic hinges are used in the elements wherever necessary such as element ends and

longitudinal steel bar cut-off locations. Multiple plastic hinges are used over the length of an element in longitudinal beams in the second floor. In order to avoid plastic hinges with overlapping represented lengths, the lengths of the hinges in second floor beams are set equal to the distance between the hinges (less than half of the beam depth). For the slab elements, the length of all hinges is set equal to one half of the slab thickness or 0.076 m

VERTICAL DISPLACEMENT AND BENDING MOMENTS

Figure 4 shows the vertical displacements at the top of the first floor removed columns A-6 and B-6 obtained from the structural model. The permanent vertical displacements (at the end of vibration) in the second floor at the locations of removed columns A-6 and B-6 are about 66 mm and 46 mm, respectively. The vertical displacements at the top of the removed columns were measured at the site using several displacement sensors. The measured permanent vertical displacements in the second floor at the locations of removed columns A-6 and B-6 were about 56 mm and 43 mm, which are in a reasonable agreement with the analytically obtained displacements.

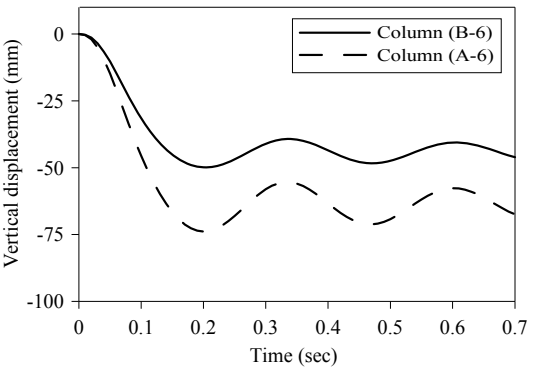


Fig. 4 - Vertical displacement versus time joints A-6 and B-6 on second floor.

Figure 5 shows the bending moment diagram of the beam in the axis B before column removal (under gravity loads) and after column removal (at the peak vertical displacement). After column removal, the central three span beams in the axis B (between axes 4 and 7) bridges over two exploded columns. The maximum negative moment at the face of the beam in axis 7 increases from 1100 kN-m before column removal to 14300 kN-m after column removal, and the maximum positive moment at the mid-span changes from 600 kN-m to 12000 kN-m. Figure 5 shows an about 13 and 20 times increase in the negative (face of the axis 7 transverse beam) and positive (mid-point of the beam) moments of the beam, respectively. The moment-curvature of the section under negative moment and subjected to zero axial load shows all the tensile rebars of the beam section yield under the action of 10700 kN-m. However, the analysis results show that the tensile rebar yielding occurs under a moment of about 13500 kN-m, which is 26% more. This large increase in the yielding moment of the section is due to the effect of an axial compressive force equal to 5100 KN on the section.

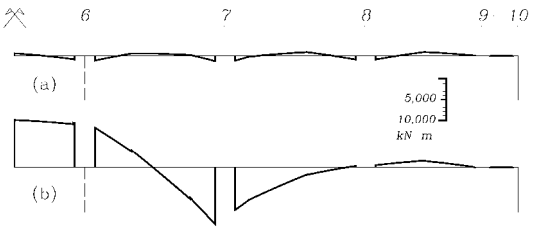


Fig. 5 - Bending moment diagram in axis B (a) before column removal; (b) after column removal at peak vertical displacement

Figures 6 and 7 show the bending moment diagrams of the beams in the axes A and C, respectively. Both figures show the bending moment diagram before column removal (under gravity loads) and after column removal (at the peak displacement of the midpoint of the beam in the axis B). After the removal of the columns and beam segments in the axis A, the left span (between axes 4 and 5) and the right span (between axes 6 and 7) of the beam, lost their connection and behave like cantilevers. The maximum negative moment of the cantilever beam at the face of the transverse beam in axis 7 is 6800 kN-m.

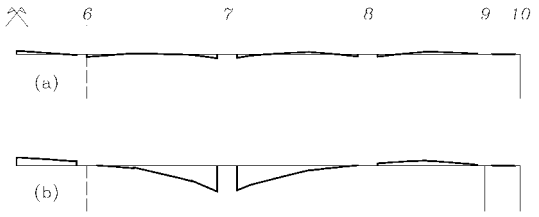


Fig. 6 - Bending moment diagram in axis A (a) before column removal; (b) after column removal at peak vertical displacement

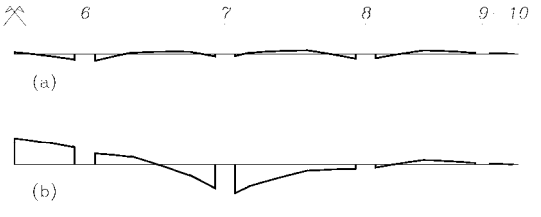


Fig. 7 - Bending moment diagram in axis C (a) before column removal; (b) after column removal at peak vertical displacement

BEAM AXIAL DEFORMATION

Figure 8 shows the axial elongation of the beam centerline of axis B (between axes 4 and 7) versus time. The longitudinal deformation (elongation) of the beam is determined as the relative horizontal displacement between the two end nodes at the intersections of the axis B with axes 4 and 7. Following the formation of cracks the mid-height of the beam section is under tensile strain. As a result, the length of the beam at its centerline increases by the sum of crack widths at the mid-height of the beam section. This phenomenon is known as beam growth (Fenwick and Megget, 1993, and Kim et al., 2004). Yielding of the rebar will influence the tensile strain of the beam centerline and increases the beam growth. In a structure however, because of the beam boundary conditions, such a growth tendency is constrained, which leads to development of compressive axial force to satisfy geometric compatibility. Such a constraint in the structure is provided primarily by the in plane action of the floor system. Analytical results show approximately two thirds of the beam axial compressive force is resisted by the in plane action of the floor system and the remaining one third by the shear forces in columns. The beam compressive force considerably increases the moment capacity of the beam through moment axial force interaction and limits the length of the cracked regions of the beam, both resulting in smaller vertical displacements. As can be seen the maximum elongation of the centerline of the beam is about 4.6 mm.

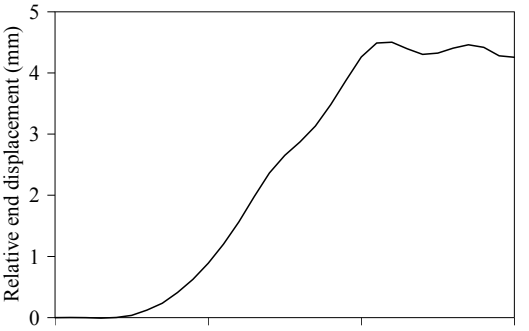


Fig. 8 - Relative horizontal displacement of line B beam between columns B-4 and B-7

Figure 9 shows the axial force of the beam in the axis B at the peak vertical displacement of the midpoint of the beam which is primarily in compression.

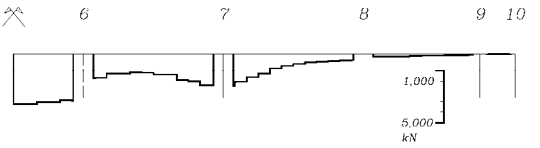


Fig. 9 – Axial compressive force in axis B beam at peak vertical displacement

AXIAL FORCE IN BEAMS

In order to investigate the development of the axial force in the beam and its effect on the system response, let us look at the central part of the structural system in the second floor as shown in Fig.10. Considering section 1-1 in the figure, the relative tendency of the beams to grow and the equilibrium of the longitudinal forces determine if a beam undergoes a tensile or compressive force. The axial tensile forces of the beam elements in axes C and D, and in the longitudinal slab elements, and the horizontal shear forces of the transverse beam and slab elements as well as the column shear forces in the second floor are in equilibrium with the sum of the axial compressive forces developed in the beams of axes A and B.

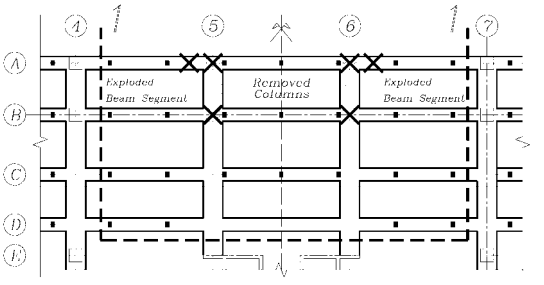


Fig. 10 – Plan of second floor in vicinity of removed columns

All the longitudinal slab elements are subjected to the axial tensile forces. Because the concrete cannot withstand the axial tensile force, it cracks and the slab rebars carry the axial tensile force. As the compressive axial force of the beam in the axes A and B increase, the axial tensile force of the slab elements closer to the axes A and B increase and the slab rebars yield, thus the axial force in the farther elements start to increase rapidly.

The columns of the second floor and the slab elements contribute taking the longitudinal forces by providing shear forces. The results of the analysis show at the peak displacement of the midpoint of the beam in the axis B, the beams in the axes C and D can take about one third of the generated axial compressive force in axes A and B, the slab elements take also about one third by providing tensile axial force. The last one third is provided by the second floor column shear forces and the slab elements satisfying longitudinal force equilibrium.

Figures 11 and 12 show the axial forces in axes A and C, respectively, at the peak vertical displacement in the mid-span of axis B beam. As can be seen, the axial force of the cantilever beam (after beam explosion) in axis A is also compressive, while the axial force in axis C is tensile (positive). The cantilever beam in the axis A, at the 2 m distance from the face of the axis 7 beam has no top rebars except the slab reinforcement. This part of the beam is subjected to a negative moment and cracks under tensile strain at the top of the section. Following the opening of these cracks, the mid height of the section elongates. But the beam is not free to expand, because it is constrained by the floor system. As discussed earlier, because of the beam boundary conditions, compressive axial force will be developed to satisfy

compatibility. The maximum axial compressive force in the cantilever part of the beam in the axis A is 2100 kN. The middle part of the beam in the axis A (between the axes 5 and 6) is subjected to tensile force with the maximum value of 300 kN.

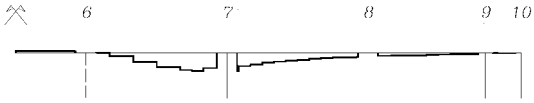


Fig. 11 - Axial force in axis A beam at peak vertical displacement

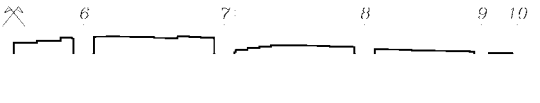


Fig. 12 - Axial force in axis C beam at peak vertical displacement

CONCLUSIONS

Experimental data and analytical results are used to evaluate progressive collapse resistance of an actual eleven-story reinforced concrete structure following severe initial damage. The initial damage imposed on the structure was set to represent the effects of a severe explosion causing the loss of four adjacent columns and two beam segments. The analytical results show that following the imposed initial damage, the bending moments in beams increase by up to about 20 times. Such a significant increase in bending moments, results in considerable cracking of concrete and yielding of reinforcing bars in tension, which in turn leads to beam growth. That is, the tendency in a beam centerline to elongate. This growth tendency in the beams subjected to highest flexural demand, however, is constrained by the floor system, including the other floor beams as well as the slab. The frames of the structure also contribute to constraining beam growth. As a result, significant axial compression can develop in beams subjected to largest force and deformation demands. It is shown in this study that the axial force in critical beams increased the beam yield moment by about 38%. Considering the axial force developed in the critical beams and in turn the increased bending moment capacity significantly improves progressive collapse resistance of the structure.

Two primary gravity load redistribution paths are identified in this structure. One is the flexural-axial response of the second floor deep beams. The other is Vierendeel action of the flat plate structural system in floors above, which reduces the axial compressive force of the columns. The global vertical displacement of the structural model and its local deformation are in good agreement with those of the experimental data.

ACKNOWLEDGEMENTS

This paper is based upon research supported primarily by the NSF Award No. CMMI-0547503. Partial support is provided by the U.S. Department of Homeland Security under Award Number 2008-ST-061-ED0001. The views and conclusions contained in this document are those of the authors and should not be interpreted as necessarily representing the official policies, either expressed or implied, of the National Science Foundation or the U.S. Department of Homeland Security.

REFERENCES

ACI Committee 318 (2008). "Building Code Requirement for Structural Concrete (ACI 318-08) and Commentary (318R-08)," American Concrete Institute, Farmington Hills, MI.

ASCE/SEI 7 (2010). "Minimum Design Loads for Buildings and Other Structures," Structural Engineering Institute-American Society of Civil Engineers, Reston, VA.

Collins, M. P., and Lampert, P. (1973). "Redistribution of Moments at Cracking-The Key to Simpler Torsion Design," *Analysis of Structural Systems for Torsion, SP-35*, American Concrete Institute, Farmington Hills, MI, pp. 343-383.

DOD (2010). "Design of Building to Resist Progressive Collapse," Unified Facility Criteria, UFC 4-023-03, U.S. Department of Defense, Washington, DC.

Fenwick, R. C. and Megget, L. M. (1993). "Elongation and load deflection characteristics of reinforced concrete members containing plastic hinges," Bulletin of NZNSEE, Vol. 26, No. 1, pp. 28-41.

GSA (2003). "Progressive Collapse Analysis and Design Guidelines for New Federal Office Buildings and Major Modernization Projects," U.S. General Service Administration, Washington, DC.

Kim, J., Stanton, J. F. and MacRae, G. A. (2004). "Effect of Beam Growth on Reinforced Concrete Frames." Journal of Structural Engineering, ASCE, Vol. 130, No. 9, pp.1333-1342.

Krauthammer, T., Hall, R. L., Woodson, S. C., Baylot, J. T., Hayes, J. R. and Sohn, Y. (2003). "Development of Progressive Collapse Analysis Procedure and Condition Assessment for Structures," National Workshop on Prevention of Progressive Collapse in Rosemont, IL, Multihazard Mitigation Council of the National Institute of Building Sciences, Washington, DC.

MacLeod, I. A. (1990). "Analytical Modeling of Structural Systems-An Entirely New Approach with Emphasis on Behavior of Building Structures," Ellis Horwood Series in Civil Engineering, UK.

SAP2000 (2009). "SAP2000 Three Dimensional Static and Dynamic Finite Element Analysis and Design of Structures," Analysis Reference, Version 14.1, Computer and Structures, Inc., Berkeley, CA.

Effects of Troweling on Shrinkage of Concrete Treated with an Evaporation Reducer

Vikram C. S. Majeti[1], Christian Dominguez[2], and Craig M. Newtson[2]

[1]Graduate Research Assistant, Department of Civil Engineering, PO Box 30001 MSC-3CE, New Mexico State University, Las Cruces, NM 88003, Ph. 575-646-3801, e-mail: majeti@nmsu.edu
[2] Nuclear/Structural Engineer, PSNS & IMF, Bremerton, WA 98314.
[3]Associate Professor, Department of Civil Engineering, PO Box 30001 MSC-3CE, New Mexico State University, Las Cruces, NM 88003, Ph. 575-646-3801; e-mail: newtson@nmsu.edu

ABSTRACT

This paper presents an investigation into the shrinkage of concrete treated with an evaporation reducer, Confilm®, after placement. Shrinkage tests were conducted on specimens treated with the evaporation reducer both properly and improperly. In the experimental program, concrete was cured under five curing regimens: 1) concrete was dry cured to serve as a basis for comparison, 2) concrete was cured with wet towels to simulate field curing with wet burlap, 3) the evaporation reducer was used as a curing aid to reduce early-age shrinkage in concrete by applying it to the surface before the start of the test and leaving it undisturbed throughout the test, 4) the evaporation reducer was used as a finishing aid during initial finishing (troweling), and 5) the evaporation reducer was again applied just after the concrete surface was floated, but was used as a finishing aid during final finishing (three and a half hours after water was added to the concrete).

Dry curing produced the greatest early-age shrinkage. The reductions in shrinkage observed for wet curing and for the proper use of the evaporation reducer were similar. The effects of troweling the evaporation reducer produced early-age shrinkage that was approximately 75% greater than the shrinkage experienced by concrete properly treated with the evaporation reducer. However, the shrinkage of the concrete treated with Confilm® was still less than the shrinkage observed for concrete cured under wet towels. Consequently, it appears that there is little negative consequence to using Confilm® as a finishing aid. Initial finishing of the concrete treated with the evaporation reducer produced approximately 20% more early-age shrinkage than final finishing. To study the effects of the various curing regimens on tensile strength, four prism specimens were cast and cured along the sides of each shrinkage specimen. From modulus of rupture testing, no statistically significant differences were observed between the curing regimens.

INTRODUCTION AND BACKGROUND

Cracking of concrete due to shrinkage is a primary concern within the concrete industry because such cracks jeopardize the integrity of the structure (Ong and Myint-Lay 2006). The main cause for shrinkage in concrete is moisture loss. The concrete surface shrinks when water evaporates or is used by hydration at a greater rate than the rate at which moisture is replaced by external water (Kwak and Ha 2006). If external water is not available, menisci will be formed in the capillary pores of the hardened cement paste as capillary water is used for hydration or evaporates from the concrete. The surface tension forces cause tensile stress in the concrete. Shrinkage cracks occur when the tensile stresses caused by drying shrinkage are greater than the tensile strength of the young concrete. Repairing bridges that have experienced shrinkage cracking incurs substantial maintenance costs.

The current study deals with the effects of shrinkage in concrete after treating the concrete surface with an evaporation reducer and subjecting the concrete surface to initial and final finishing (troweling) because many concrete finishers like to use certain evaporation reducers as finishing aids. These results are compared with the cases of dry curing, wet curing, and concrete treated with an evaporation reducer used as a curing agent.

The objective of this research was to analyze the effectiveness of an evaporation reducer to control shrinkage on a concrete surface that was troweled (initial and final finishing) after the evaporation reducer was applied. Confilm®, an evaporation reducer produced by BASF Construction Chemicals, LLC-Building Systems was the evaporation reducer used in this work. Confilm® is often used as a finishing aid by concrete finishers. This work focused on evaluating whether or not this practice would be detrimental to concrete quality.

EXPERIMENTAL METHODS

Experiments were conducted to measure shrinkage of concrete treated with an evaporation reducer (Confilm®) over a period of seven days. This section describes the raw materials, the testing apparatus, the preparation of the shrinkage test specimens, and the sequence of operations for conducting the tests used in this research.

Raw materials. Concrete produced for this research was batched in the laboratory. The materials used for preparing concrete were procured locally in Las Cruces, New Mexico. Type I-II Featherlite brand portland cement with a specific gravity of 3.15 was used. Aggregates were obtained from CEMEX, Las Cruces. Fine aggregates were oven dried for at least 24 hours at 110 ± 5 ºC (230 ± 41 ºF) to achieve zero percent moisture. Physical properties for the coarse and fine aggregates are provided in Table 1. After oven drying, the sand was stored in plastic buckets that were tightly covered with plastic to avoid ingress of moisture.

Confilm®, an evaporation reducer, was used in this research. Confilm® is manufactured by BASF Construction Chemicals, LLC. Use of Confilm® is intended to reduce the evaporation of moisture from the surface of concrete and improve the

Table 1. Aggregate properties.

Property	Coarse Aggregate	Fine Aggregate
Bulk Specific Gravity	2.534	2.59
Absorption (%)	1.36	1.23
Fineness Modulus	-	2.48
Dry Rodded Unit Weight	1500 kg/m³ (93.8 lb/ft³)	-

quality of the concrete. In accordance with manufacturer recommendations, one part Confilm® was diluted with nine parts water.

Mixture proportions. Raw materials were proportioned volumetrically, following procedures described by the Portland Cement Association, to produce concrete with a water-cement ratio of 0.5 and a slump of 76.2 to 101.6 mm (3 to 4 inches) (Kosmatka et al. 2002). Because the fine aggregate was sub-angular, the water content of the mixture was reduced by 11.86 kg/m³ (20 lb/yd³). The mixture proportions used in this study are presented in Table 2.

Mixing procedure. The volume of concrete required for each test was greater than the mixing capacity of any individual mixer available. Therefore, the required 0.099 cubic meters (3.5 cubic feet) of concrete was batched in two mixers with 53 percent of the total volume batched in the larger mixer and the remaining 47 percent mixed in the smaller one. Mixing of raw materials was conducted in accordance with ASTM C 192. As soon as the water was added to the concrete mixture, the time was noted as a reference point for all other activities. After mixing, the mixer was emptied into a wheelbarrow and slump of the concrete was measured in accordance with ASTM C 143. If the workability of the concrete was not in the acceptable range of 76 mm to 102 mm (3 to 4 inches), the concrete was discarded. Table 3 presents the measured slump values. After measuring slump, the temperature of the concrete was recorded.

Mold preparation. Molds for the experimental specimens were prepared prior to production of concrete. A 914x457x152 mm (36x18x6 inches) wooden mold was prepared for the shrinkage specimen. The mold was lined with 4 mil thick plastic sheets in two layers. Talcum powder was applied in between the plastic sheet layers to reduce friction and allow free movement of fresh and hardened concrete during shrinkage.

Table 2. Mixture proportions.

Ingredient	kg/m^3	lb/yd^3
Cement	403	680
Coarse Aggregate	909	1533
Fine Aggregate	725	1222
Water	222	374

Table 3. Measured slump for different curing conditions.

Case	Curing Conditions	Slump mm (in)
1	Dry	85 (3.50)
2	Wet towels	80 (3.25)
3	Confilm®	100 (4.00)
4	Confilm® (Initial finishing)	90 (3.75)
5	Confilm® (Final finishing)	85 (3.50)

Four steel prism molds measuring 76.2x102x406 mm (3x4x16 inches) and three steel cylinder molds measuring 102 by 203 mm (4 by 8 inches) were assembled and oil was applied to the inside surface of the molds. The prism molds were placed along the four sides of the wooden mold for the shrinkage specimen so that the prism specimens would be cured in the same environment as the shrinkage specimen.

Specimen preparation. The wooden shrinkage specimen mold was filled with concrete and vibrated using a needle vibrator to achieve uniform consolidation. The concrete was uniformly vibrated for a period of 10 seconds. The companion specimens, 102 by 203 mm (4 by 8 inches) cylinders for testing compressive strength and 76 x 102 x 406 mm (3 x 4 x 16 inches) prisms for testing flexural strength were prepared in accordance with ASTM C 192. The prism specimens were treated with evaporation reducer in the same manner as the shrinkage specimen.

Data acquisition. The system used to measure early-age shrinkage is shown schematically in Figure 1. This system was developed by Lozoya and Newtson (2004). The steel frame supporting the shrinkage measurement system was positioned over the shrinkage specimen in the longitudinal direction as shown in Figure 2. Two steel hangers that were 177.8 x 25.4 x 5mm (7 x 1 x 0.2 inches) were

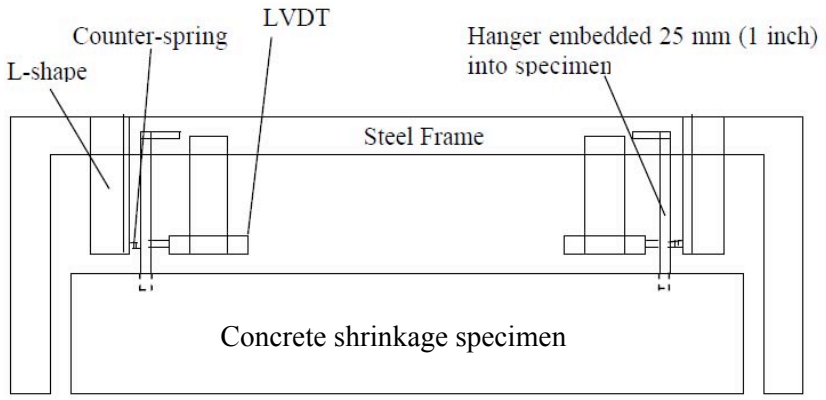


Figure 1. Experimental setup of Lozoya and Newtson (2004).

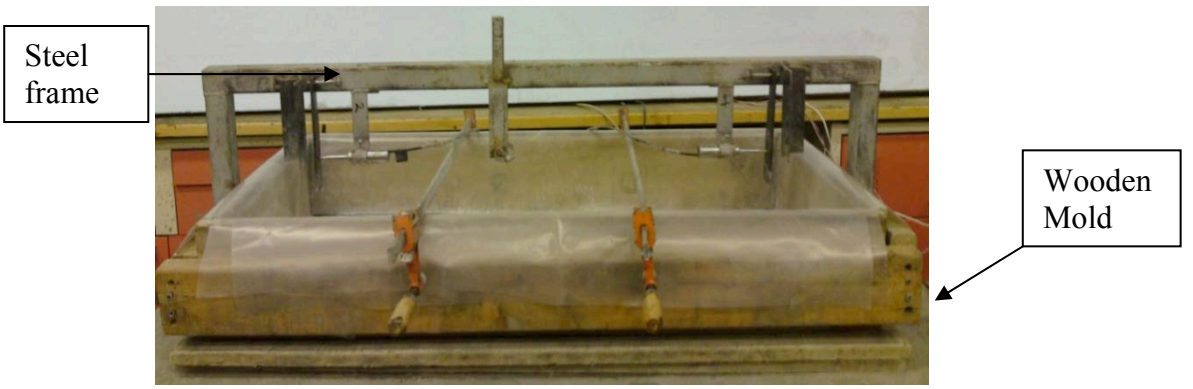


Figure 2. Shrinkage test experimental setup.

hung from metal pins attached to the steel frame and embedded 25mm (1 inch) into the freshly placed concrete. The hangers have a hole through one end that allows them to be hung from the metal pins attached to the frame. The smooth surface of the pin allows the hanger to slide freely. Near the other end, divots were made on both sides of the hangers. One divot served as a resting seat for the head of a LVDT and the divot on the opposite side of the hanger served as a seat for a counter spring. The counter spring is shown in a photograph in Figure 3. The counter springs were attached to the frame at their other ends and had a spring constant equal to that of the springs in the LVDT's. LVDT's (Sensotec model S3C) were inserted through a supporting fixture on the steel frame. The LVDT's were connected to a Superlogics 8017 electronic data acquisition module, which in turn was connected to a computer.

Temperature and relative humidity observations were performed at 15 minute intervals during the initial four hours of the test and then every day at 8:00 am and 10:00 pm local time.

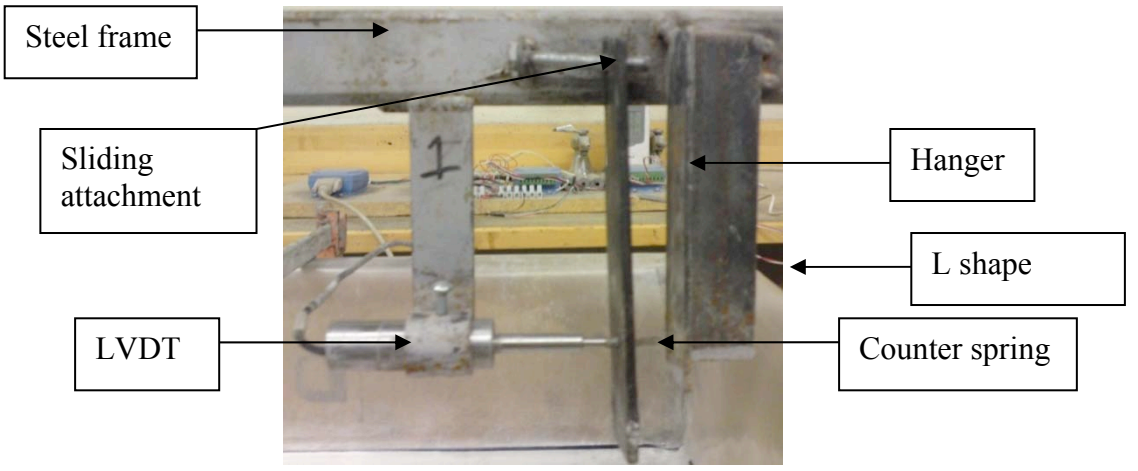


Figure 3. Close up view of hanger and LVDT.

Curing conditions. Experiments were conducted for five curing conditions intended to study the effects of the evaporation reducer (Confilm®). Three experiments were conducted for each case. The five curing conditions investigated were:

1. Concrete was dry cured to serve as a basis for comparison.
2. Concrete was cured with wet towels to simulate field curing with wet burlap.
3. The evaporation reducer was used as a curing aid to reduce early-age shrinkage in concrete. The evaporation reducer was applied to the surface before the start of the test and left undisturbed throughout the test.
4. The evaporation reducer was used as a finishing aid during initial finishing (troweling). The evaporation reducer was applied immediately after the surface was floated, and then the surface was immediately steel troweled.
5. The evaporation reducer was again used as a finishing aid and was applied just after the concrete surface was floated. In this case, the concrete was troweled during final finishing, three and a half hours after water was added to the concrete.

Strength testing. Three cylindrical specimens from each batch were moist cured and four prism specimens were cured alongside each of the shrinkage specimens. All strength specimens were tested at an age of seven days. ASTM C 39 was followed for testing the compressive strength of the cylindrical specimens. Flexural strengths for prism specimens were determined according to ASTM C 78.

RESULTS AND DISCUSSION

Concrete shrinkage was measured for a period of seven days under five different curing conditions. Three tests were performed for each curing condition. This section presents an analysis of the test results and an evaluation of the effectiveness of Confilm® as a curing agent.

Dry Curing. The first curing condition, dry curing, is used as a basis of comparison in evaluating the other test cases. In the dry curing condition, the concrete was air cured without any addition of water or external curing aid. Maximum shrinkage strains observed during the initial 24 hour period and over the seven day period were 258μ and 1208μ, respectively.

Wet towels curing. In the second curing condition, wet towels were placed on the surface of the concrete four hours after water was added to the concrete. The wet towels were rewetted every eight hours. This simulates the use of wet burlap in field curing. A peak shrinkage strain of 212μ was recorded over the seven day period and 78μ was observed during the first 24 hours. Minor expansion was observed during the first few hours of these tests. This is a reduction of 70% and 82% from the shrinkage observed for dry cured concrete at 24 hours and seven days, respectively.

Confilm® curing. The third curing condition studied the effect of Confilm® used as a curing agent on concrete shrinkage. In this case, concrete was treated with Confilm®,

an evaporation reducer, just before the start of the shrinkage tests. The concrete surface was screeded and floated. Then, the evaporation reducer was applied as a thin layer on the concrete surface. In accordance with the recommendations of the manufacturer, Confilm® was applied at a rate of 52.81 ml/m^2 (1.296 x 10^{-3} gal./ft^2). Maximum strains of 48μ and 152μ were observed for 24 hours and seven days, respectively. These shrinkage values are approximately 40% less than the values obtained by wet curing with towels.

Confilm® curing with initial finishing. In the fourth curing condition, the concrete surface was floated immediately after placement and compaction. After floating, Confilm® was applied on the concrete surface at a rate of 52.81 ml/m^2 (1.296 x 10^{-3} gal./ft^2). Then, surface finishing was performed before the start of the test. Use of Confilm® aided in easy and smooth finishing. A maximum 24 hour horizontal shrinkage strain of 93μ was observed by averaging the values from three tests. After seven days, an average horizontal shrinkage strain of 169μ was observed. These shrinkage values are 94% and 11% greater than the shrinkage observed when the Confilm® was used properly.

Confilm® curing with final finishing. In the fifth curing condition, Confilm® was applied to the floated concrete surface at a rate of 52.81 ml/m^2 (1.296 x 10^{-3} gal./ft^2). The concrete surface was finished only after the concrete was initially set. Three and a half hours after adding water to the mixture was considered as the standard time for final finishing. Use of Confilm® again aided in easy and smooth finishing. However, finishing was less smooth than in the initial finishing case since the Confilm® dried somewhat between the time when it was applied and final finishing. The average horizontal shrinkage strains observed for this case during the early-age and long term were 75μ and 167μ, respectively. Figure 10 presents the shrinkage strains versus time. These shrinkage strains are approximately 20% less than the shrinkage observed when the Confilm® was disturbed by initial finishing, and about 60% greater than the shrinkage observed when the Confilm® was used properly.

Comparison of 24 hour shrinkage. Dry curing was considered to be a basis for comparison for the other curing conditions. The maximum average values of 24 hour shrinkage strains obtained for the different tests cases are provided in Table 4. The shrinkage strain of 78μ observed for wet towel curing was 70% less than that from

Table 4. Average shrinkage strains for all curing conditions.

Case	Curing Condition	24-Hour Shrinkage Strain (με)	7-Day Shrinkage Strain (με)
1	Dry	258	1208
2	Wet towels	78	212
3	Confilm®	48	152
4	Confilm® (Initial finishing)	93	169
5	Confilm® (Final finishing)	75	167

dry curing. In the third case, concrete treated with Confilm®, the shrinkage was 82% less than the shrinkage from dry curing. A shrinkage strain reduction of 39% was observed for the Confilm® curing case when compared with wet curing.

In the fourth case, even though lower shrinkage strains were observed by 64% when compared to dry case, the shrinkage strain was greater by 18% and 94% than the shrinkage strains for Cases 2 and 3, respectively. It appears that initial finishing disrupted the evaporation barrier provided by Confilm® which allowed a moderate increase in shrinkage, lowering the evaporation. For the final case, Confilm® with final finishing, the shrinkage strain was less than the shrinkage from Cases 1, 2, and 4 by 71%, 4%, and 23%, respectively. However, it was greater than Case 3 by 58%. Noticeable differences in shrinkage strain were observed between Cases 4 and 5 (initial and final finishing respectively) only when compared with Case 2. When compared with concrete shrinkage strain from Case 2 (78μ), there was an increase in Case 4 by 18% and a decrease by 4% in Case 5. Since the shrinkage from Case 5 was comparable to the shrinkage from Case 2, it appears that using Confilm® as an aid for final finishing is a reasonable practice. The 24 hour shrinkage strains for the different cases are plotted in Figure 4.

Comparison of seven day shrinkage. The horizontal shrinkage strains observed over a period of seven days are compared in Figure 5. Figure 6 illustrates the same shrinkage strains for the different curing conditions, but excludes the dry curing condition. The maximum shrinkage strains recorded at the end of seven days are tabulated in Table 4. The shrinkage from dry curing was much greater than the other values since no curing aid was provided. In the second case, where wet towels were placed on the surface of concrete, the shrinkage strain decreased by 82% when compared to dry curing. This observation is consistent with results from Lozoya and Newtson (2004). In the third case, treatment of the concrete with Confilm® reduced

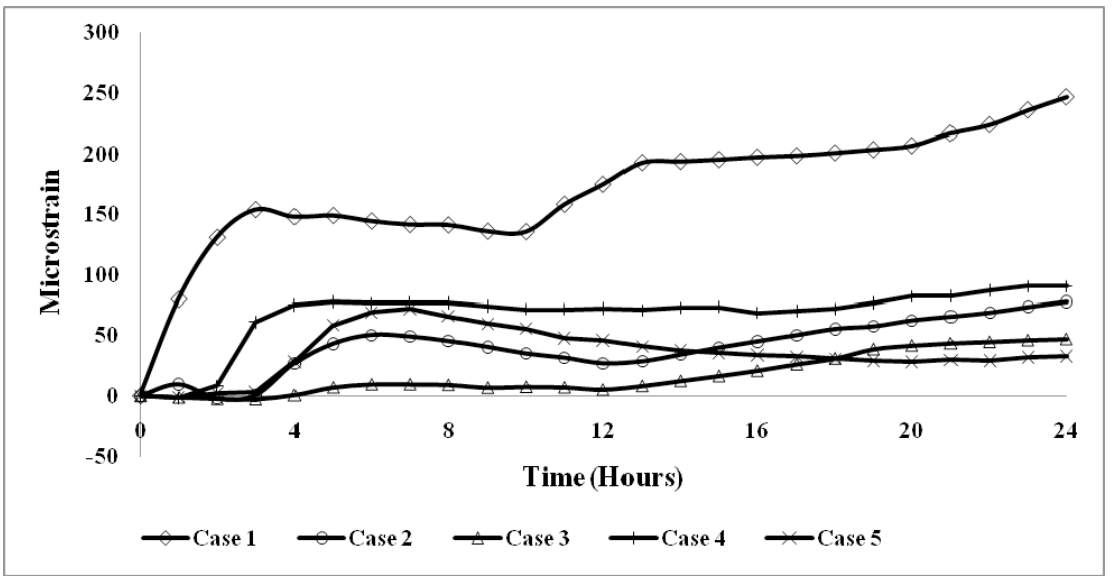


Figure 4. Average 24 hour shrinkage strains.

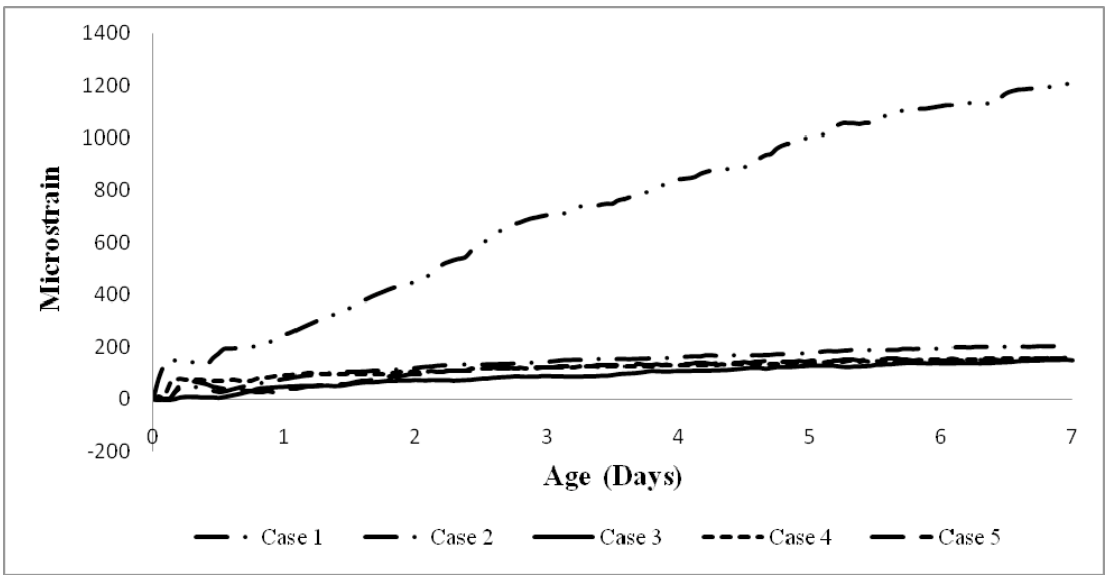


Figure 5. Average seven day shrinkage strains.

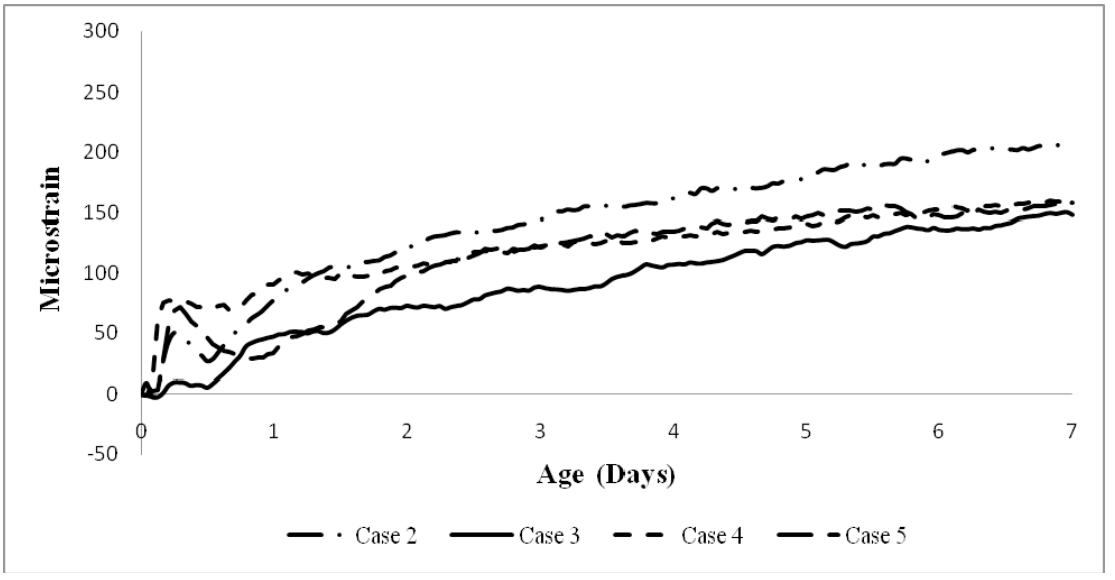


Figure 6. Average seven day shrinkage strains for Cases 2-5.

the shrinkage strain by 87% and 28% when compared with dry cured concrete and concrete cured using wet towels, respectively. The increased shrinkage observed when using wet towels may indicate that when the towels dry, water is wicked from the concrete. Alternatively, the addition of water may lower the temperature of the concrete and cause greater thermal shrinkage.

The shrinkage strain observed for Case 4 is greater than the shrinkage from Case 3, by 10%. This increase is likely due to the finishing after application of

Confilm®. This finishing might have slightly disturbed the Confilm® barrier over the concrete surface that prevents loss of moisture from the concrete.

Lower shrinkage strains were observed for Confilm® curing with initial finishing when compared to the dry curing and wet curing conditions by 86% and 20%, respectively. This reduction indicates that Confilm®, even when misused, generates a barrier over the concrete surface that prevents loss of moisture from concrete and reduces shrinkage.

The shrinkage strain experienced by concrete treated with Confilm® that was disturbed by final finishing (167μ) was similar to the shrinkage of concrete treated with Confilm® disturbed by initial finishing (169μ). Since both finishing operations on Confilm® treated surfaces resulted in less shrinkage than wet curing with towels, it appears that using Confilm® as a finishing aid has little negative consequence.

Tensile strength results. Prism specimens were placed and cured along each side of the shrinkage specimens to monitor the effect of curing in each test case except for the dry test case. They were treated in the same manner as the shrinkage specimen. At an age of seven days, these prism specimens were tested for flexural strength according to ASTM C 78. The average flexural strength values are tabulated in Table 5. These values ranged from 3.74 MPa to 4.55 MPa (542 psi to 660 psi).

The greatest flexural strength was observed for the prisms produced for the dry curing case. However, this set of prisms was moist cured (not cured beside the shrinkage specimens). Consequently, the high strength is not a reflection of the curing method for the shrinkage tests. From Table 5, the specimens treated properly with Confilm® had slightly greater flexural strength than the concrete cured with wet towels. It was also observed that finishing after treating with the evaporation reducer slightly decreased the flexural strength of concrete. However, neither of these observations appear to be statistically significant.

Compressive strength results. The same mixture proportions were used for all of the concrete produced for this research. Quality of the concrete was monitored by testing companion specimens for compressive strength. Cylindrical specimens of size 102 by 203 mm (4 by 8 inch) were used as companion specimens. After demolding, the cylindrical specimens were moist cured for seven days. Then, the specimens were tested for compressive strength according to ASTM C 39. The average compressive strength values are provided in Table 5. These values ranged from 28.6 MPa to 38.0 MPa (4150 psi to 5520 psi). The cylinders produced for the dry cured case had the

Table 5. Average strength results.

Case	Curing Condition	Modulus of Rupture MPa (psi)	Compressive Strength MPa (psi)
1	Dry	4.48 (650)	38.0 (5520)
2	Wet towels	3.93 (570)	32.9 (4780)
3	Confilm®	4.14 (600)	30.7 (4450)
4	Confilm® (Initial finishing)	3.85 (559)	32.9 (4770)
5	Confilm® (Final finishing)	3.74 (542)	28.6 (4150)

greatest strength which indicates that this mixture is a little different from the other mixtures. If this is the case, the shrinkage for the dry curing case may also be erroneously high. However, the magnitude of the expected increase would not be expected to change the conclusions drawn from the shrinkage results. If the dry case were omitted from analysis, there would be no changes to the conclusions drawn about the effectiveness of Confilm®.

CONCLUSIONS

Shrinkage cracking is a serious problem affecting the durability, serviceability and maintenance costs for concrete structures. Shrinkage cracks occur on a concrete surface when loss of moisture causes tensile stresses that exceed the tensile strength of concrete. Moisture loss is caused by environmental factors like high wind velocity, low relative humidity, and extreme differences between air and concrete temperatures. Water-to-cement ratio, cement type, cement content, aggregate properties, and degree of hydration of the cement also affect the development of shrinkage. Shrinkage in concrete can be controlled to a certain degree by wet curing the concrete and allowing uninterrupted hydration of the cement. Other methods of limiting moisture loss include the use of evaporation reducers such as Confilm®. However, concrete finishers often like to use Confilm® as a finishing aid. Disturbing the evaporation barrier with finishing operations is widely thought to harm the concrete. Consequently, this practice is generally considered to be unacceptable.

To study the effects of misusing the evaporation reducer (Confilm®) as a finishing aid on concrete shrinkage, five sets of shrinkage tests were performed by varying the curing conditions. The following conclusions were drawn from the results of the testing:

1. Wet curing with towels reduced shrinkage by 80% compared to dry curing. This observation was consistent with results from Lozoya and Newtson (2004).
2. Using Confilm® as a curing aid (no troweling) resulted in 30% less shrinkage than wet curing with towels. The difference in shrinkage between these two cases may have been partly due to external water decreasing the temperature of the wet cured concrete which would increase shrinkage.
3. Disturbing the Confilm® barrier by finishing, increased the early-age shrinkage strains by 94% compared to concrete treated with Confilm® properly.
4. Even though the shrinkage strains measured at the end of seven days were similar for both initial and final finished concrete treated with Confilm®, these values are greater than the concrete treated with Confilm® alone. This indicates that disrupting the evaporation barrier increases shrinkage. However, the shrinkage strains for the troweled Confilm® cases were less than the shrinkage from wet curing with towels. Therefore, it appears that using Confilm® as finishing aid has little negative consequence.

5. Troweling a concrete surface treated with Confilm® in a final finishing operation resulted in shrinkage that was only slightly less than the shrinkage observed for initial finishing.
6. No significant difference in flexural strength values were observed between the curing methods used in this research.

REFERENCES

Kosmatka, S. H., Kerkhoff, B., and Panarese, W. C., (2002). "Design and Control of Concrete Mixtures," 14th Edition, Portland Cement Association, Skokie, Illinois, USA.

Kwak, H. G., and Ha, S. J., (2006). "Plastic Shrinkage Cracking in Concrete Slabs. Part I: A Numerical Model," *Magazine of Concrete Research,* 58(8), 505-516.

Lozoya, J., and Newtson, C. M.,(2004). "Effects of Early Misting on Concrete Shrinkage," Proceedings, Advancing Concrete Through Science and Engineering, RILEM, March 2004, Evanston.

Ong G. K. C., and Myint-Lay, K., (2006). "Applications of Image Analysis to Monitor Very Early Age Shrinkage," *ACI Materials Journal,* 103(3), 169-176.

I35w Bridge Collapse: Lessons Learned and Challenges Revealed

S. Hao
ACII, INC. P.O. Box 8090, Wilmette, IL 60091-8090
Tel: (847) 920-9475; FAX (847) 256-3014; Email: hao0@suhao-acii.com

ABSTRACT

This article discusses the issues in structural design revealed by the highway I35W Bridge's collapse that occurred at August 1st, 2007, based on an analysis of the bridge's original design drawings, a series of detailed finite elements computations, and the material evidences disclosed by National Safety Transportation Safety Board (NTSB) official investigation. These issues include (i) the redundancy consideration for multi-span bridge; (ii) the reason for those undersized designs in that bridge; (iii) the effects of lateral force on gusset plates' load capacity in steel-truss structure; (iv) the criterion of gusset plate's stability and a thin-plate theory-based model for load-rating. This analysis concludes that the lessons learned from the I35W Bridge may have certain significance for the safety assessments of those similarly-structured steel bridges. A bridge's service life is 75 years or longer. According to a NTSB's document [37], there are more than hundreds this kind of aged bridges still in service [4].

1.INTRODUCTION

The past century can be remembered as the most successful period for bridge engineering, which has also brought up great challenges to bridge engineers to digest rapidly-developed ideas, new tools, and novel methodologies in related engineering sciences while to assure new designs and existing bridges' operation being safe, economic, and technologically advancing. While enjoying great success for decades, we did have suffered several significant setbacks. One example is the collapse of the Minneapolis I35W highway bridge.

August 1st of 2007, 6:05PM, the interstate I35W Bridge in the City Minneapolis, Minnesota, collapsed suddenly. The 8 traffic-lane, 1000-foot-long deck of the 1907-foot-long bridge fell into Mississippi River within seconds, resulted in 13 fatalities and 145 injuries, see Figs. 1, 2.

Designed in 1964 and opened to traffic at 1967, the I35W Bridge stretches from north to south over the Mississippi River in the City Minneapolis in Hennepin County, Minnesota. The major part of the bridge is a 1000 foot (304.8 meters) long, 108 foot (32.92 meters) wide, three-span steel deck-truss superstructure, which collapsed completely. The bridge originally had six traffic lanes. After two major rehabs in last century, it has been widened into eight lanes with two auxiliary lanes and its concrete deck has been reinforced from 6.5 inches to 8.5 inches thick. NTSB's official investigation [1,2] indicates that, at the moment of the collapse, two lanes of the bridge were occupied by piled construction materials and heavy trucks; four lanes were opened to traffic; and the other two lanes were empty.

This article summarizes an independent investigation of this disaster based on material evidences and advanced computations. The theoretical background and the analytical methodologies applied can be found, for examples, those in the references list [5-26, 30-33,43-

46,50-51]. A part of preliminary results of this analysis have been submitted to the related investigation and administrative agencies since the second week after the bridge's collapse [27,28].

This article is organized as follows: the next section introduces the structural and material's models applied in the analysis. The third section analyzes the results obtained and compares the data with materials' evidences. The following section discusses the reasons that had caused this bridge's undersized design. The fifth section explores further the underlying structural issues that triggered the collapse, from which the lessons learned do have certain significance for the procedure of gusset plates' assessment currently applied. A model based on two-dimensional plate buckling theory has been introduced. The last section summarizes the conclusions.



(a) The I35W Bridge (right) at 1970. (b) August 2nd, 2007

Fig. 1 Minneapolis I35W Bridge: Before and after the collapse

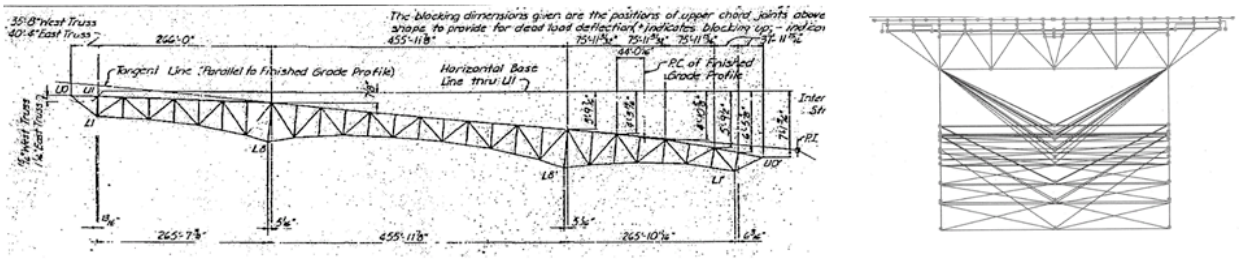


Fig. 2. layout of the superstructure: (a) main frame; (b) lateral bracings and floor trusses

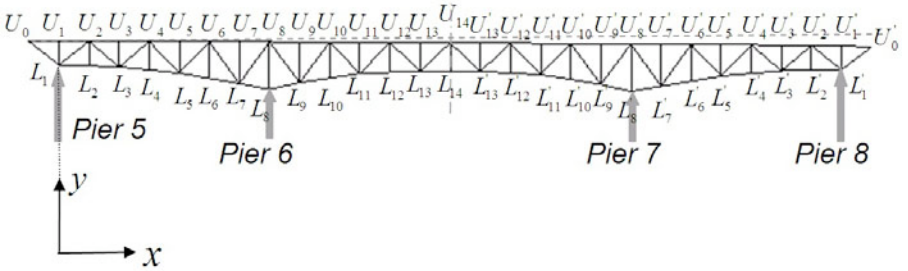
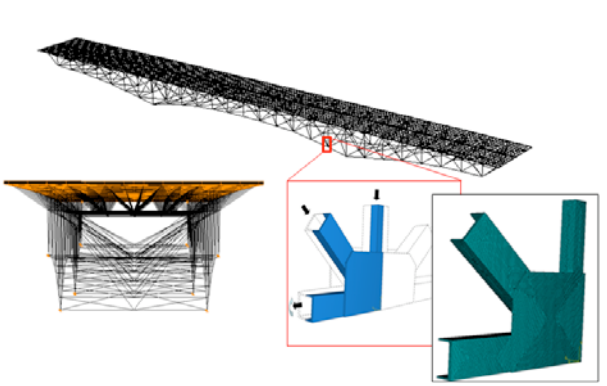


Fig. 3 Nodes and support piers of the main truss frame, where *U* and *L* stand for the nodes on upper and lower chords, respectively; a prime is attached to denote the nodes in south half span (right).

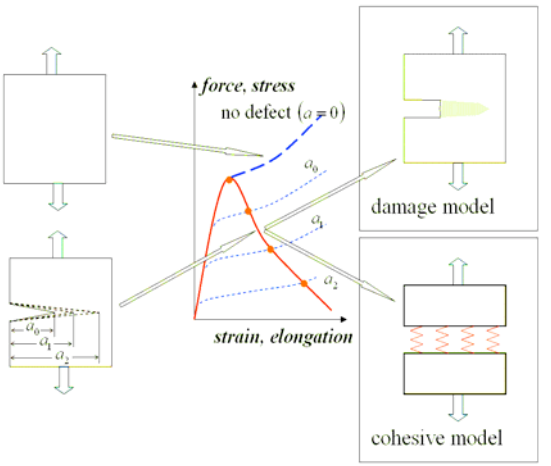
2. METHODOLOGY AND MODEL APPLIED

2.1 Structural Model: As depicted in Fig. 2, the steel superstructure of I35W Bridge contains three parts: (i) two main truss-frames, west and east; (ii) lateral bracings and 27 floor trusses, (iii) reinforced concrete-slab deck. Fig. 3 is a two-dimensional model of the bridge's main frame and the locations of major gusset plates, i.e. the nodes in the truss-network. Additional subscript "*E*" or "*W*" may be used in the following text to denote a node at eastern or western main frame. As illustrated in Fig. 4a, a two-level computational model has been developed, i.e. using 3D finite element to obtain force-deflection behavior of gusset plate, which is implemented into truss network of the bridge superstructure.

2.2 Materials Model: A structural failure is often started by material's failure in one or several key-structural components, which introduces extra complexities to an analysis of a structural collapse like I35W Bridge. In a new sustainable structure's design, it is generally required to keep the stress level in all components within material's yield limit. By contrast, a failure means applied stress reaches a material's strength limit while the material's strain surpasses yield strain. As explained by the example in Fig. 4b, for the defect-free plate under uniaxial tension on left-upper corner, the corresponding average stress-strain curve is the solid line that linearly increases from the origin and connects the thick dash line that ascends nonlinearly, plotted in middle. A material's failure is the result of evolution of one or many defects. When a defect in the form of crack exists in the plate, as plotted in the lower-left, the average stress-strain relations can be represented by the linearly solid line connected with these thin short-dashed lines corresponding for different crack lengths. When the material elements at crack tip fails, the crack grows, for example, from a_0 to a_2, the plate's elongation will increase continuously while applied stress decreases, as illustrated by the solid line connected through the dots. For common 30-50 grade mild structural steels at room temperature, such a crack growth is an accumulation of micro-scaled damages in the form of voids nucleation, growth and coalescence [9-13,30-33]. The "spring model" or "cohesive model", developed in [12,13], have been implemented into finite element analysis to count such a damage-induced material's failure.



(a)



(b)

Fig. 4: (a) A two-level 3D FE Models of the bridge; (b) Model to represent a material failure, e.g. damage-induced-crack, resulted structural failure.

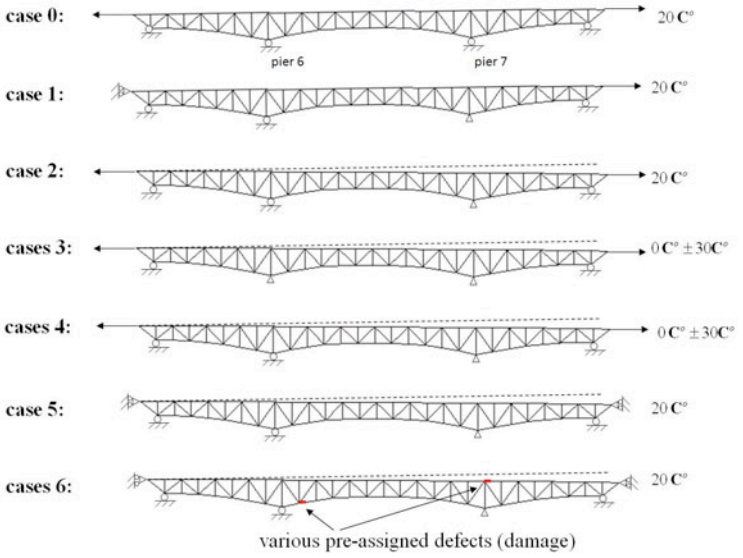
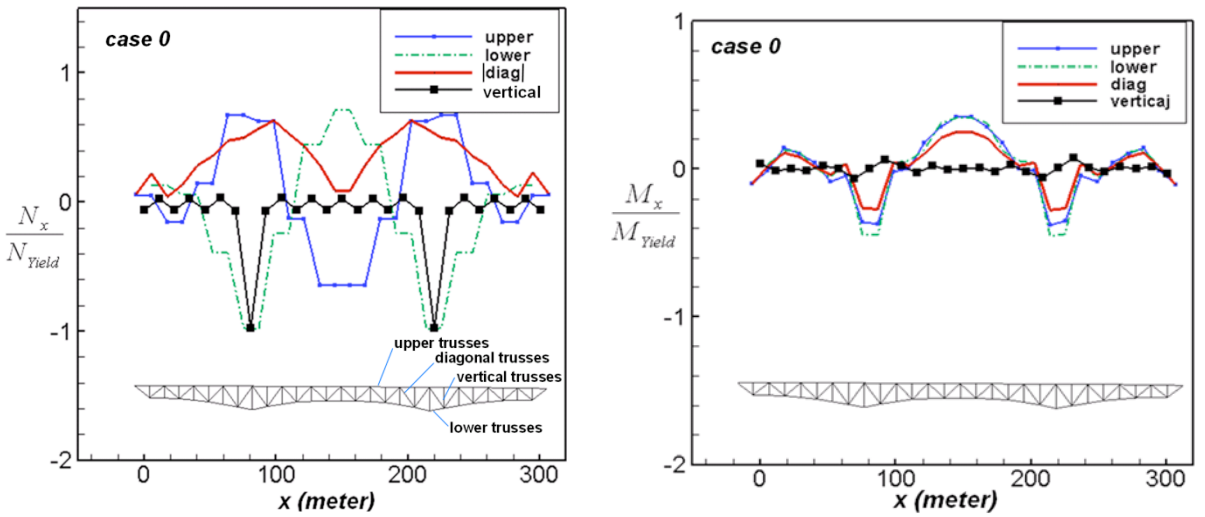


Fig. 5: Cases analyzed: Case 0: flat deck; all support bearing are rollers; **case 1**: the same as 0 but the pier 7 bearing was locked; **case 2**: design condition - the same as 1 but with deck slope; **case 3**: design condition but with locked pier 6 bearing, temperature varies; **case 4**: design condition, temperature varies; **case 5**: design condition, horizontally confined; **case 6**: design condition but with pre-existing defects at various gusset plates; see [27a]. Each case contains several respective sub-cases with different parameters.

2.3 Cases Analyzed: in the first report that was finished seven weeks after the disaster [27a], a primary object was to identify the locations that might initiate the failure through computer simulations of various possible failure processes, so as to assist official investigation to identify the actual location and causes. Due to limited data and information at the time, 2D and 3D computer simulations for about 20 cases (Fig. 5) of the bridge's superstructure's failure have been performed to consider various circumstances which include (a) the effects of supporting bearing conditions to superstructure's load path and stress amplitude; (b) whether the bridge-deck's slop (about 1 degree, see Fig. 2) caused extra horizontal forces; (c) temperature's change-induced thermal stresses, which include two cases: day-night and seasonal shifts caused uniform changes and the case with non-uniform temperature distribution, for example, the upper chords (the trusses near deck) are warmer than other parts; (d) pre-existing defects at various locations.

3. RESULTS AND DISCUSSION

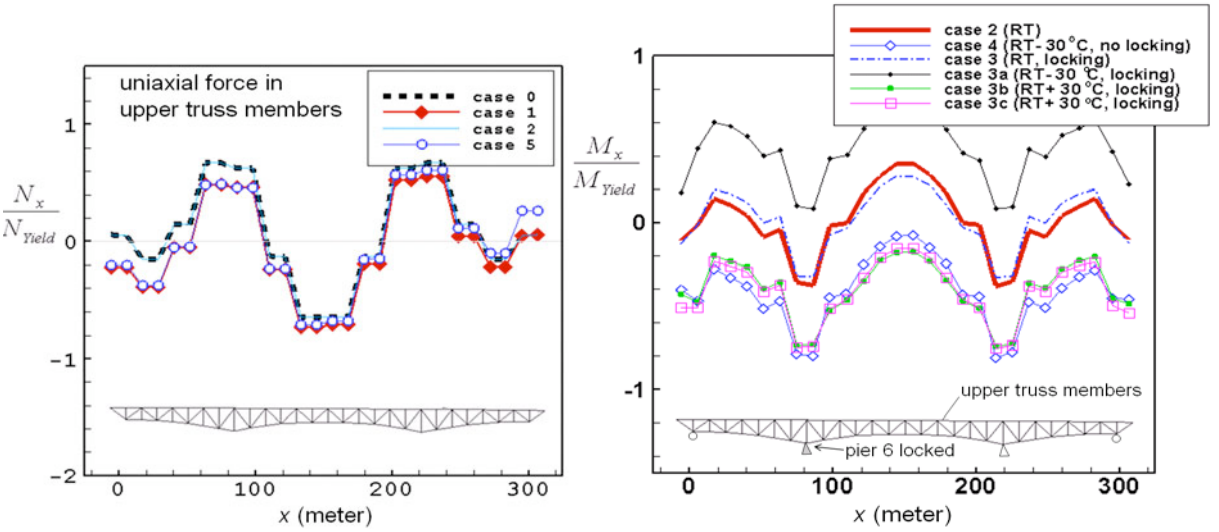
3.1 Forces and Bending Moments Distributions: Plotted in Fig. 6(a) are the uniaxial forces in the four groups of truss members in main frame, which are upper chords, lower chords, truss diagonals, and truss verticals. The force in upper chords, the solid line connecting small solid dots, reaches its positive maximum above the piers of center span while the negative maximum at the center. By contrast, the force in lower chords, the light dash-dot line, has a positive peak at the center and two negative maximums above the piers. The distribution of the force in truss diagonals (solid line) is characterized by the peaks around the spots where the upper chord's force decreases from positive to negative while the lower chord's force inversely uprises. As plotted in Fig. 6(b), the bending moment in truss-verticals is ignorable whereas that in other reaches positive maximum in the centre of middle span and negative maximum just above two piers. In this case the bending moment in the diagonal members is generally lower than that in upper and lower chords.



(a) (b)

Fig. 6 (a) Uniaxial force in the four groups of major truss members in main frame, where N_x is the uniaxial force and N_{Yield} is that when material yields; (b) the bending moment distributions, where M_x is in-plane moment and M_{Yield} is the moment at yield. No bearing-lock or temperature change (case 0).

Fig.7(a) shows a comparison of the upper chords' uniaxial forces for the cases 0,1,2, and 5, which indicates that the deck's slope and the horizontal constraint/forces from approaching spans do not have remarkable effects on this force's distribution. By contrast, Fig.7(b) are the bending moments in upper chords when temperature changes while supporting bearings are locked, i.e. the cases 3 and case 4 in Fig. 5, respectively; compared with the case 2 that is the normal design condition. It demonstrates a significant combined effect of temperature change and locked bearing. In practice, severe corrosion may drastically increase the friction resistance of a bridge's roller bearing; an extreme case is that a roller bearing eventually is fully locked so it becomes a pin point that does not allow horizontal movement. This induces considerable high thermal stress when temperature changes, as demonstrated by this plot.



(b)

Fig. 7: The same plots as that in Fig. 6 but considering temperature change and locked bearings, where RT refers to room temperature; (a) Uniaxial forces in upper chords and (b) the corresponding bending moment.

3.2 Scenario of the Collapse: Now we discuss the following two issues: the sequence of the bridge's superstructure's collapse and what we can learn from it. One may notice that the force and bending moment distributions in Figs.6 and 7 are nearly symmetric to the central span of the bridge. Just after the disaster, there was an argument regarding the sequence of the failure, i.e., which approach of the bridge failed first. An opinion gained many echoes was that all structural components between the two piers over the river failed almost simultaneously, i.e. a horizontal fall of the central span. To clarify this issue, Fig.8 are the photographic pictures recorded by Army Engr. Corp. from south side of the bridge, which was reported by medium (CNN). The water splashes at the moment that middle span was fallen, i.e. Fig. 8(d), reveals the collapse initiated from south side [27a]. The north approach span failed subsequently without showing any capacity to resist the collapse.

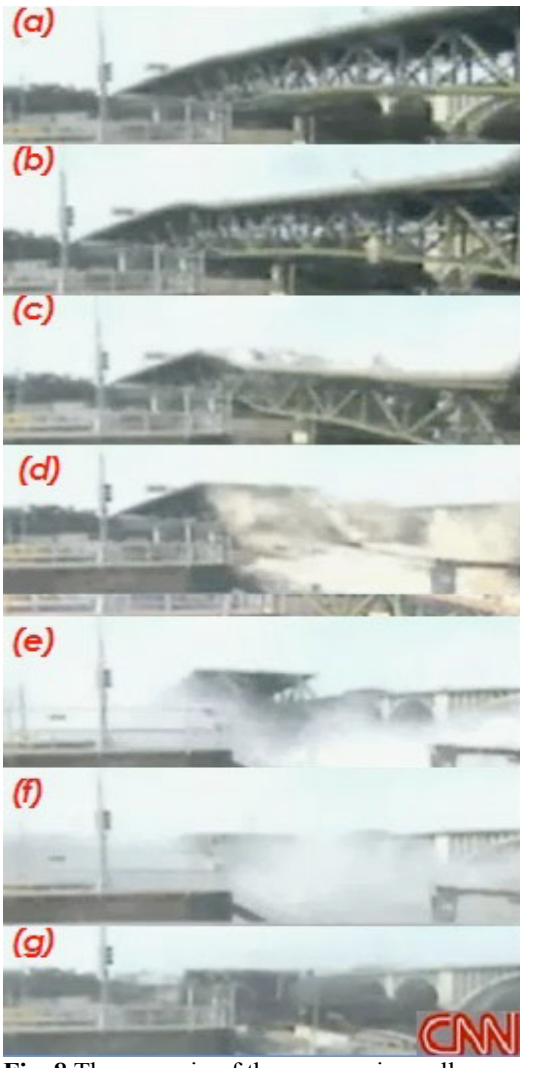


Fig. 8 The scenario of the progressive collapse presented by I35W (Army Corps' Video)

In bridges' design, the three-span like I35W is a common structure; the underlying idea is to gain long central span with minimized cost. This can be explained by the influence-line solutions in Fig. 9. By comparing the bending moments in the three cases with the same middle span length "b" and under the same distributed load "q", one can find that the maximum bending moment of the case (a) is about 80% higher than that in case (c); similarly, the moment of case (b) is about 20% higher than case (c).

However, from the viewpoint of structural integrity, the advantage of the three-span design (c) is traded-off by lower redundancy. This is because, when one of three spans is severely damaged or fails, the force distributions in other two shift back to the situation similar to the case (a). Such a scenario is illustrated in Fig. 10. This, the author believes, was a reason that caused the progressive collapse of I35W Bridge. This leads to a conclusion that states as following: to avoid a similar progressive collapse that occurred in I35W Bridge, an additional safety factor may be necessary for those key single-load path structural components in a multi-span bridge if its design of load capacity is merely based on the influence-line analysis described in Fig. 9(c).

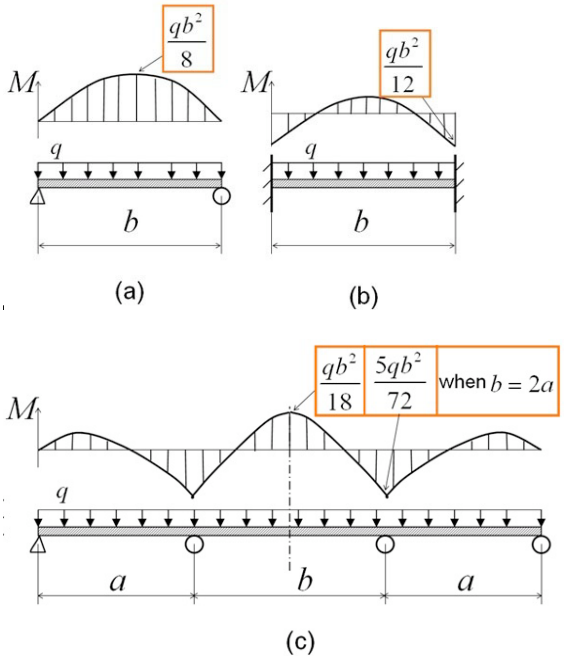


Fig. 9 The influence-line solutions explain the benefit of a three-span bridge's design like that in I35W because the peak bending moment in case (c) is much lower than that in case (a) and case (b) for the same span length "*b*" and uniformly distributed load density "*q*".

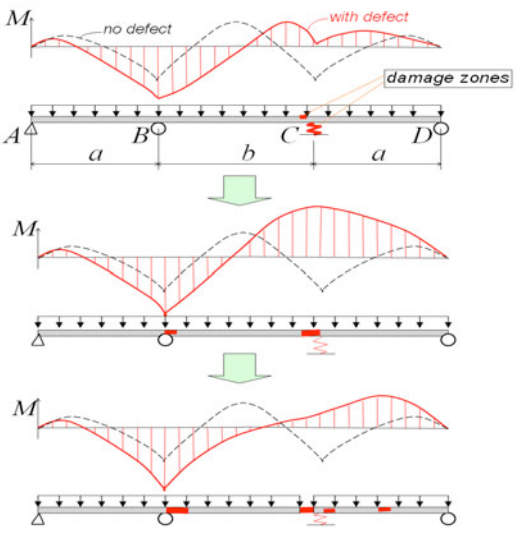


Fig. 10 A scenario that a material's failure induces a progressive structural failure in a three-span bridge, where the material's failure occurs first at the location just above the bearing support C, which results in the material's failure around the bearing support B; subsequently the beam AB becomes a simple span that is the same as the case (a) in Fig. 9.

3.3 Where the Collapse Started: The early study [27a] suggested that damage-induced material's failure caused the structural failure. Such a material's damage can be, for example, fatigue-induced cracks or significant corrosion-resulted section loss. Obviously, an undersized design has the same effect as such a damge. Three possible failure patterns were focused, see Fig. 11, and the case (c) was considered as mostly close to reality [27a]. Although this simulation was done just a couple of weeks after the collapse (submitted to NTSB at August 17th, 2007), it does demonstrate significant deflection around the node U'9 and U'10. The "undersized" gusset plate U'10 actually initiated the bridge's failure[1,2,41].

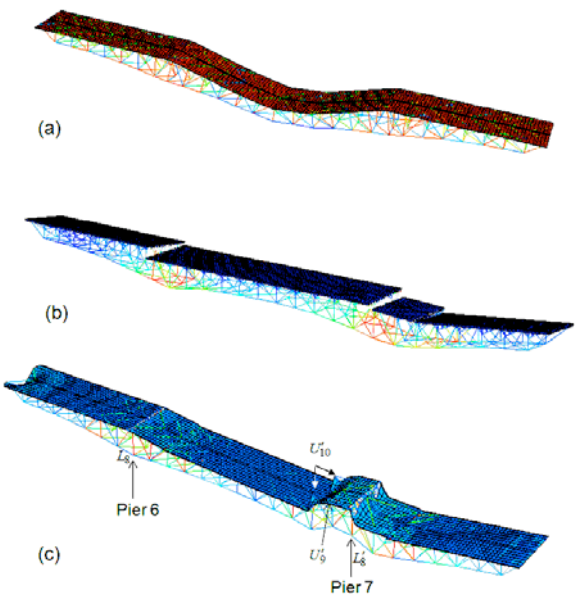


Fig. 11. Three failure patterns of the bridge

3.4 NTSB's Findings and Conclusions: after thorough examination of the wrecked pieces of the bridge, at January 15, 2008 and November of 2008, respectively, NTSB has released the results of the official investigation [1,41], which disclosed that the gusset plates at the nodes U10,U'10,L11,L'11 in main frames of central span and U4, L3,U'4,L'3 of the approach-spans are undersized, which are half inch thick.

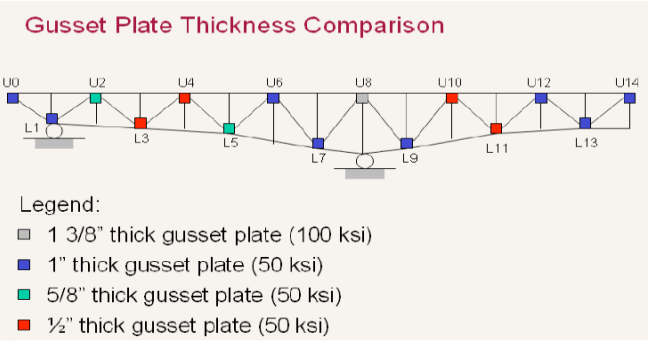
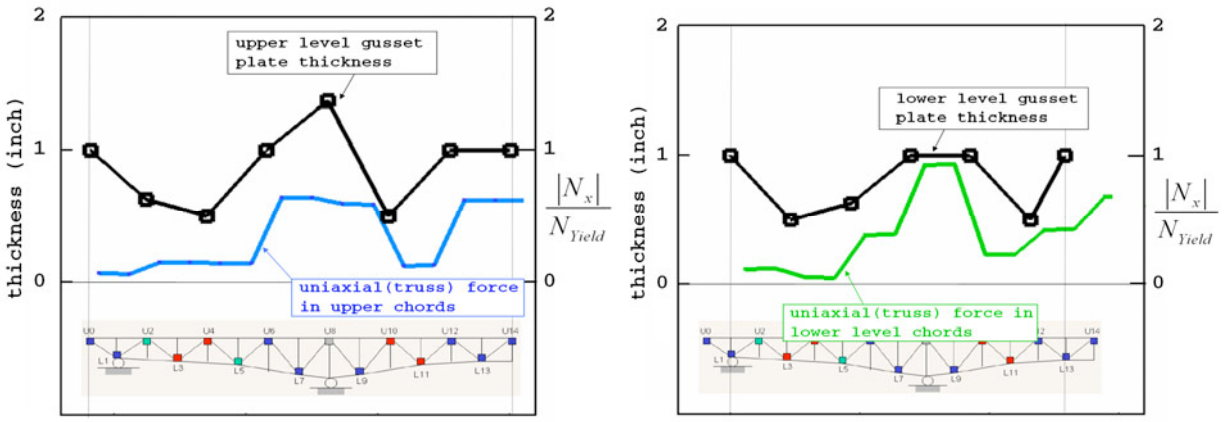


Fig. 12 Gusset Plates Thickness in I35W Bridge[1,41]

By contract, all other gusset plates in the nodes that connect four or five truss members were one inch in thickness or more, see Fig. 12. Also, the NTSB's analyses of the video recorded at the instance of the collapse indicates that the half-inched gusset plate at node U'10 failed first, which triggered the subsequent collapse of the bridge. The record of the design firm of the I35W bridge reveals the bridge designed without appropriated calculation, which resulted in the undersized gusset plates.



(a) (b)

Fig. 13 Comparisons between the gusset plate thickness and the uniaxial forces in horizontal truss members plotted in Fig. 7a: (a) upper chords; (b) lower level chords.

4. WHY THE GUSSET PLATES UNDERSIZED

Plotted in Fig.13 are the comparisons between the actual gusset thicknesses from Fig. 12 and the uniaxial forces of upper and lower-chards that were given in Fig. 6(a). An obvious coincidences between the force distributions and gusset thicknesses can be seen except near the end nodes (U_0, L_1). All half-inch gusset plates (U_4, U_{10}, L_3, L_{11}) are at or close to the locations with the lowest truss force. This fact seems implying that the plates' thicknesses were designed based on the forces in horizontal trusses.

However, by checking the results plotted in Fig. 6(a) carefully, one can find another fact: the force in diagonal member almost reaches its peak value at the location, for example, between

$U_{10}L_9$ and $U_{10}L_{11}$, where the upper and lower chords forces change signs. The reason is obvious: at this location the diagonal truss $U_{10}L_9$ transfers the deck load-induced compression force flow in middle upper chords of central span into lower chords and supporting bearings; whereas $U_{10}L_{11}$ transfers the tension force flow in middle lower chords into upper chords above the piers; whereby the gusset plates like L_9, U_{10} and L_{11} are the "pivots" for these load paths of force flows, as explained in Fig. 14.

Therefore, a statement has been given in the third paragraph, section 5 of the report [27a]: "Due to the limited computation capability in past, it seems that the original design and subsequent early investigations could only treat the 9340 bridge* as a truss-assembled structure, which led to the focus onto the forces and damage conditions in truss members….". Obviously, the truss force in upper and lower level chords had been used as the governing parameters for the gusset plate design, whereas the corresponding stress concentration in the gusset plates did not obtain sufficient consideration at the time.

Based on an examination of all original design drawings and the material evidences disclosed by NTSB's investigation, several other "undersized" structural components have also been identified in the analysis [29]. These components are the upper and lower chords attached to those undersized gusset plates in Fig. 12. It has been found that the thicknesses of upper chords' wall and gusset plates are actually proportional to the bending moment solution of the one-dimensional influence line analysis illustrated in Fig. 10c. This fact reveals that the NTSB-disclosed undersized gusset plates are the consequence of a bias toward a "one-dimensional model" in the original design, which did not give sufficient consideration to the effects of the forces from diagonal truss members input into gusset plates [29].

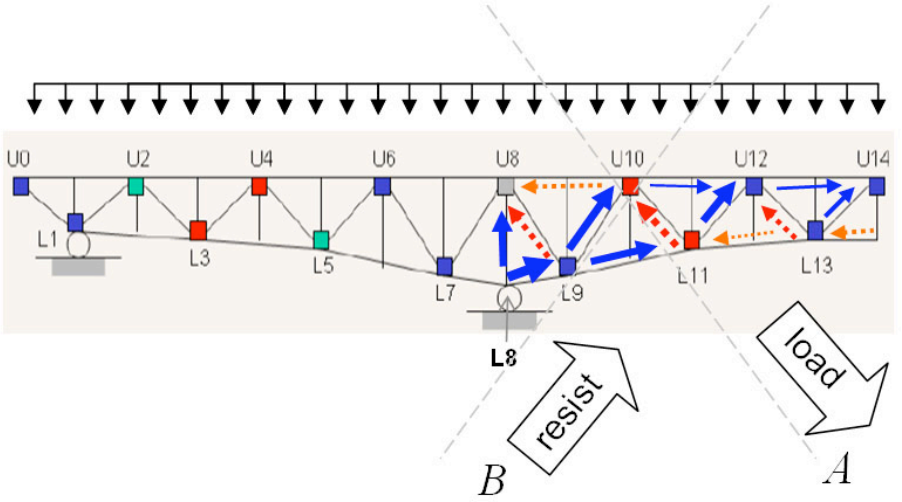


Figure 14 An illustration of the main "load path" in central span of I35W, where the blue solid-line arrows represent compression and the red dotted line arrows represent tension. The compression is mainly corresponding to the resistance from the pier and the global bending moment; whereas the tension is mainly corresponding to span's weight and deck load. The gusset plates U10, L11, U12 are the pivots to balance load and resistance forces transferred by diagonal members. The major function of vertical trusses is to provide redundancy to the truss cells except the member L8-U8.

* The I35W Bridge is numbered as 9340 in national bridge inventory.

5.“TRUSS APPROXIMATION” AND GUSSET PLATE

A practical question is: how to determine a gusset plate’s capacity in practical applications? Conventional consideration treats gusset plates as additional stiffeners that do not have significant effect to a truss network load capacity. The author of this paper had also been convinced for while that “truss-approximation”, i.e. omitting bending moment and shear in slender structural members of a truss network, was good enough for applications. Under this approximation, a gusset, which fastens connected truss-members, becomes a “hinge” that allows free rotation between adjacent members because of no bending moment exists. This approximation generally provides acceptable accuracy for long beams/trusses while significantly simplifies analysis, which has been successfully applied over centuries. However, it should be noticed that the resulted “hinge approximation” implies the ignorance of the secondary stress caused by bending moment at a gusset plate and the corresponding stress concentration. These stresses may not have significant effect to truss members but can be crucial for a gusset plate. To demonstrate this point, two simple examples are given in Fig. 15 to explain the differences.

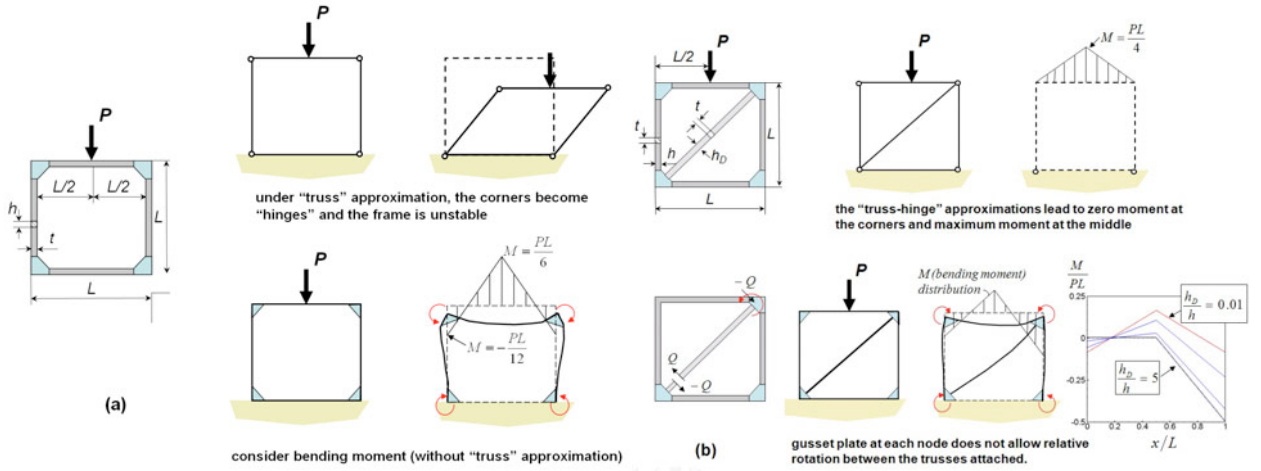


Fig. 15 (a) The truss-cell is an unstable structure when hinges are at the corner. By contrast, gusset plates keep the adjacent trusses perpendicular to each other, resulted in the bending moments at the corners; (b) An additional diagonal bracing stabilizes the frame; the bending moments become more remarkable at the upper-right node gusset and its amplitude increases when the ratio of the widths of diagonal bracing (h_D) and vertical trusses (h) increases; when this ratio is large, the upper horizontal truss is like a cantilever fixed at right end by the gusset plate.

Fig. 15(a) shows a square truss-cell that is unstable when the nodes at the corners are hinges. Adding gusset plates to keep the adjacent trusses perpendicular to each other, which makes the cell becomes a stable frame but results in bending moment at the gusset. When an additional diagonal truss is added to the cell in (a), as illustrated in Fig. 15(b), the cell becomes a stable structure despite hinges at the nodes. The corresponding bending moment in upper chord is plotted when a concentrated force is imposed. As a comparison, the lower part of this figure is an analytical solution when the nodes are stiffened by gusset plates; stronger diagonal member results in higher bending moment at the node, hence, the gusset plate.

It is no doubt that “truss approximation” can provide satisfied solution for the uniaxial forces of slender members in many cases. However, when force flows in a truss-network are not uniform, instead, varying drastically, the corresponding bending moments, particularly, at gusset

plates, can be remarkable. This may occur at least under the following three conditions: (i)concentrated load presents; (ii) inhomogeneous internal stress, for example, thermal stress; (iii) residual stresses caused by, for example, in-appropriated welding or cambering. For a structural member like a gusset plate with complicated geometry, a bending moment-induced stresses and corresponding stress concentration may have substantial effects on its load capacity and fatigue life. The effect of bending moment can be viewed directly by the numerical analysis presented in Fig.9(c), which shows significant relative rotation between adjacent trusses around those pivotal nodes such as U10, L11 when the superstructure starts to fail. This result can be verified by the bowing of the actual U'10 gusset plate observed four years before the bridge's collapse, see Fig. 16(a), which could be caused by a past deck's overload or the result of cambering during erection. In either case, such a bowing implies reduction of the gusset's load capacity and, thus, its vulnerability to this kind of loads applied later.

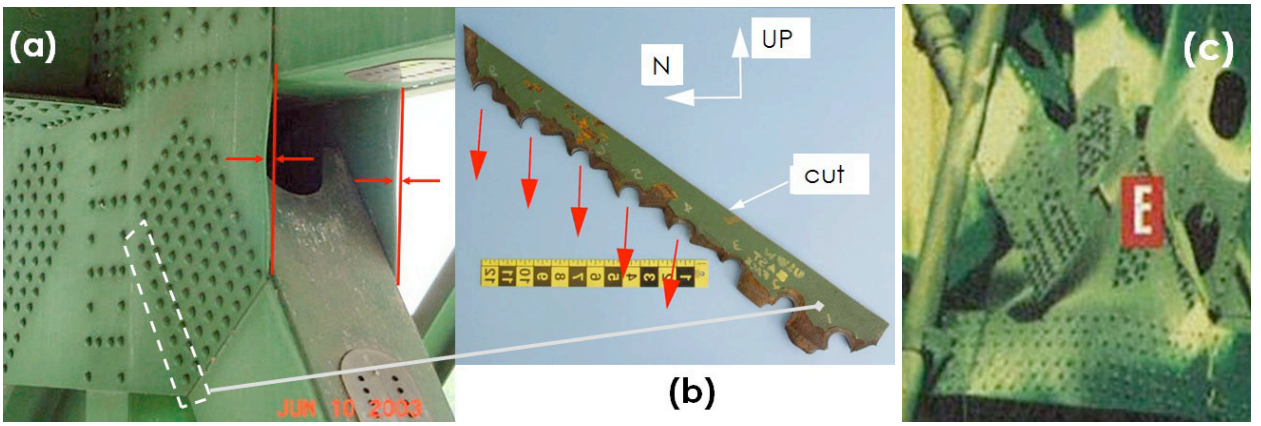


Fig. 16 Three patterns of gussets' failures:(a) bowing, I35W Bridge's gusset plate U10' [2]; (b) a cut of the U10' plate's lower part; (c) buckling due to the large ratio of unbraced length /gusset thickness, which occurred in the highway I90 Grand River Bridge, Ohio, 1997 [47];

6. GUSSET PLATES' LOAD RATING

6.1 Failure patterns of gusset plates: The gusset plates' failure in I35W Bridge is not a unique case. Fig. 16(c) shows a gusset's buckling that occurred 1997 at the Grand River Bridge that carried highway I90 of Ohio [47,48]. Therefore, it can be assure that gusset plate may fail at least by three different patterns: (i) bending and associated rotation-induced bowing, on the part of a gusset plate with free-edge between two adjacent trusses, see Fig. 16(a); (ii) tension-dominated ductile failure between the edges of two adjacent trusses, which can be a cause or the result of a bowing presented at another edge of one truss, or occurs independently; (iii) buckling in the unbraced area in the front of an attached truss, which may be accompanied by bowing nearby, as demonstrated in Fig. 16(c).

Most gusset plates in steel bridges are made of 30-70 grade mild steels. This class of steels often fails in the form of ductile fracture except under some particular circumstances such as temperature below ductile-brittle transition point or within the area near or at a welded joint. For a thin gusset plate, buckling or bowing is when compression force reaches instability limit when applied stress may be much lower than yield strength. By contrast, a tension-dominated failure is an accumulation of shear deformation along slip-planes of polycrystalline matrix at yield limit, which may present in two modes: the out-plane shear that induces necking; and the

in-plane shear that often starts at a free edge with stress concentration, for example, a rivet's hole or a crack, and then leads to a Lude's band. Both modes present in Fig. 16(b) but within different areas.

6.2 Load-rating gusset plates: The "bowing" of the U'10 gusset plate of I35W in Fig. 16a is considered as an early warning sign. That tragedy proofs a failure of such a gusset can lead to entire bridge's fall. Therefore, in a new truss-bridge's design or an aged bridge's load-rating, a practical issue is to identify its load capacity based on each structural components' capacities including all gusset plates, whereby the following two steps are essential:

1) Compute the forces and bending moments input into a gusset plate in a truss bridge, if the "truss approximation" applies, it should be aware of the corresponding deviation in result.
2) Determine the limit state for each gusset plate within engineering acceptable accuracy.

To this end, a procedure and associated computer programs have developed to investigate the failure process of I35W Bridge based on the theories and methodologies introduced in [5-26, 30-33,43-46,50-51]. A series of in-depth three-dimensional computations of I35W Bridge under the actual live loads at the instance of collapse, see Fig. 17, as well as the bridge under various design conditions, have been performed [28,29] according to original design drawings and in the light of the material evidences of NTSB's investigation[1,2] and FHWA's technical advisory [3].

In addition to the discussions of more undersized-components disclosed from original design drawings and the evidence of the one-dimensional influence line solution-biased original design, another conclusion obtained in [29] is that the nodes connecting floor trusses and main truss-frame, see Fig. 17b, was inappropriately designed. This is because it actually divides deck load to two high-amplitude force flows input into a weak gusset plate, i.e. compression on the plate's top and downward tension on its bottom edge. The particular structural features presented in this part and the implications to load capacity are to be discussed in follows because they can be useful for other gusset plates' load rating in general.

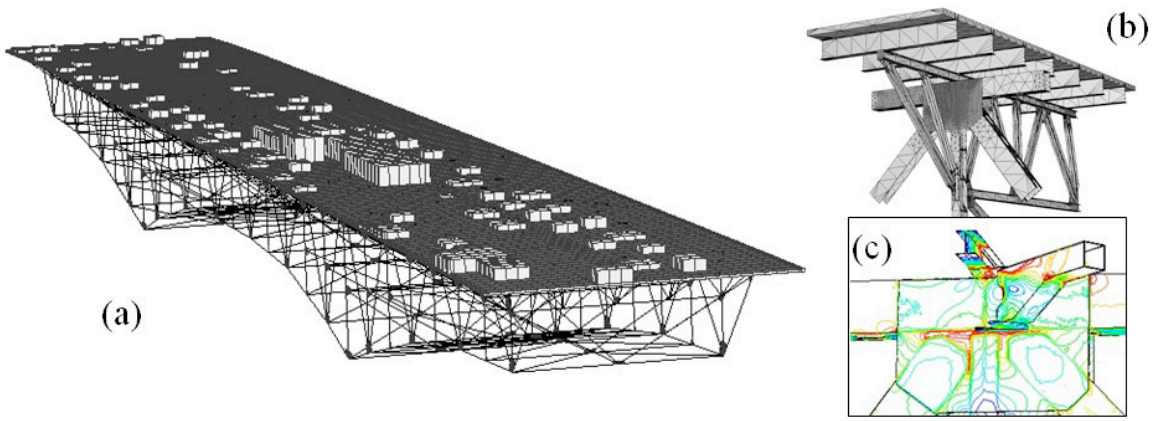


Figure 17. (a) A fully-scaled computation of I35W Bridge [29] based on design drawings and live load at the time of collapse, where the trucks, cars, and construction materials are represented by the brick elements with the densities corresponding to their weights; (b) a finite element model for the connection between floor truss and main flame at the node U10; (c) computed stress contour on an inside gusset plate[27b], which indicates the stress on the inside horizontal lateral bracing introduces lateral force that affects the deformation of the gusset plate.

Plotted in Fig. 18 are the computed uniaxial stress in the floor trusses that connect the south U10' and U11' gusset plates of I35W. Here we focus on the stress distribution in the diagonal

members of the floor truss attached to U10', which is plotted as the empty diamonds linked by dash lines. One may notice that the two highest stress peaks occur in the diagonal members just inside the gusset plate on each side, by which the amplitude of the peak near western U10' is about 13% higher than that near the eastern U10'. This difference is denoted as *Qp* in the figure, which, obviously, is caused by the eccentric deck live load at the moment of the collapse, see Fig. 19a. Another notable phenomenon in Fig. 18 is the difference in stress level between the diagonal floor trusses member inside and outside a gusset, denoted as Q_D (on left).

In original design drawings the inside floor truss-diagonal near the gusset was made of W12x92 H-beam; the insider floor truss bottom chord was W12x85 H-beam; and the two outside floor truss-diagonals were W8x35 and W10x54, respectively. Therefore, the magnitude of Q_D implies that, at the node below the gusset plate, the outwards lateral force from the inside truss-diagonal was about 2.6 time higher than the sum of the inwards lateral forces input from the two outside diagonal members. Their resultant must be balanced by the tensions in the floor truss bottom chord, the horizontal force component in the diagonal lateral bracing, and the lateral shear in the main flame vertical truss. According to Fig. 18 there is no significant stress in the bottom chord; whereas the inside diagonal lateral bracing is a very slender beam that has very limited capacity to carry horizontal force. Therefore, the majority of the horizontal resultant is balanced by the lateral shear of the main flame's truss vertical, which is denoted as Q_M in the figure. Q_M produces a bending moment to the attached gusset plate, denoted as *M*.

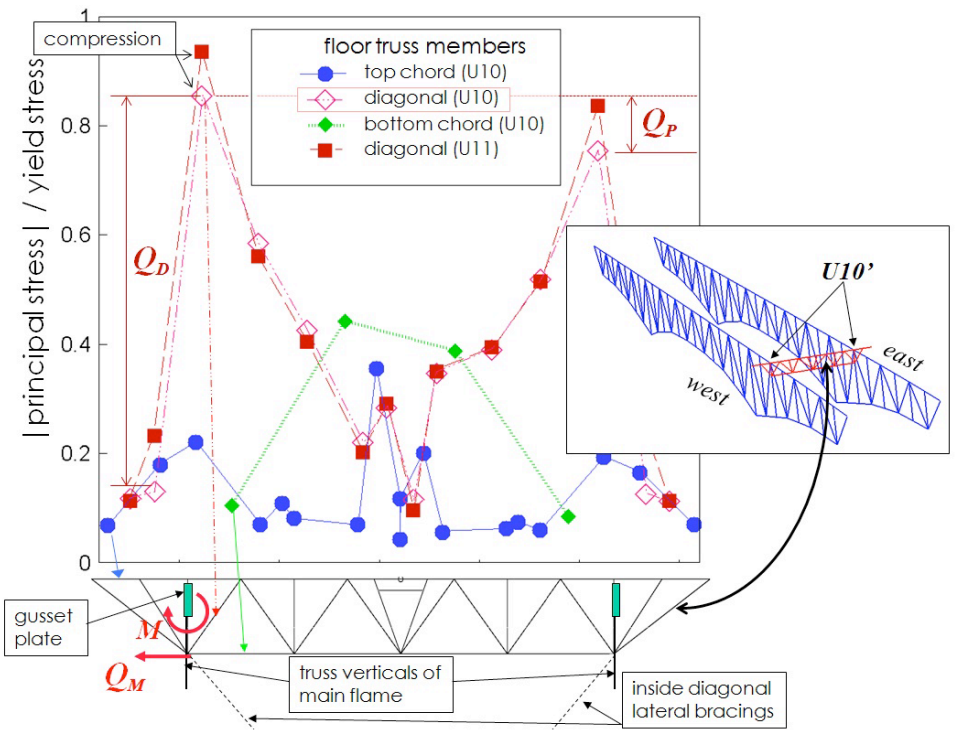
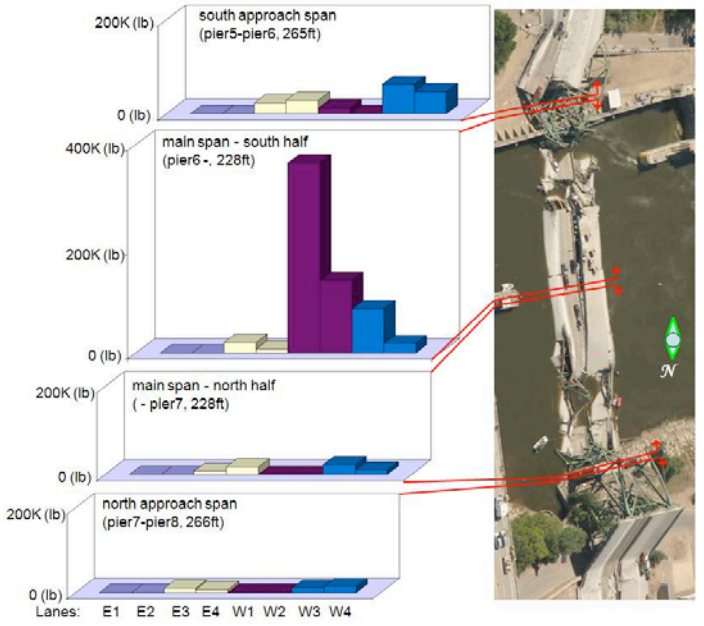


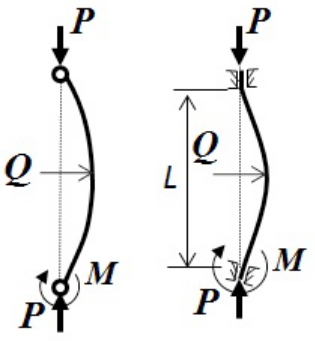
Fig. 18 Stress distribution in floor trusses connect to U10' and U11', which result in the out-of-plane force Q_M and bending moment *M* onto the gusset plate; see the discussion in the text.

On the other hand, the Q_P in Fig. 18 represents the difference of the forces that the floor truss input to eastern and western main flames, respectively. Again, because the stresses on the two

ends of the floor truss' horizontal members attached to the two main flames are almost equal, Q_P should be balanced by the lateral shear on main truss vertical and the horizontal lateral bracings between the two main flames, i.e. the one horizontally attached to the gusset plate in the computation of Fig. 17(c). Fig. 19(a) gives the deck load's distribution of the I35W Bridge when it collapsed; although the majority of the live loads was on the western side, it should be noticed that the stock-piled construction materials, which is the heaviest part of entire live-load, were on the lane W1 that is just beside the central line. This can be a reason that the difference Q_P is less than 15% of the total force in the floor truss diagonal. Obviously, there is no need to address the fact that the deck load-induced vertical force on the western gusset plate is much higher than that on the eastern side. In Fig. 19(a) the live-load on the lane W1 equals the weight of several design trucks (80 kips each). In practical application, a worst scenario could be the case that multiple presence of heavy trucks line on one side of a bridge's deck, for example, the lane W4 in Fig. 19(a). Under this situation, Q_P can be significantly higher.



(a)



(b)

Fig. 19 (a) I35W Bridge's deck live load distribution at the moment of collapse, which causes the difference Q_P in Fig. 18; (b) Eular's instability models with lateral force and bending moment under two boundary conditions; for gusset plate, the lateral force and bending moment are out-of-plan force and moment.

The forces Q_P and Q_D in Fig. 18 introduce extra out-of-plane force Q_M and bending moment M to the gusset plate, as illustrated at the left-low corner of Fig. 18. These kinds of lateral forces and moments generally may have significant impact to the gusset and the attached truss-verticals' stabilities. For an engineering evaluation, conventional procedure often simplifies a structure into a one-dimensional model, then applying Eular's instability criterion, as illustrated in Fig. 19b. This criterion is exact for long slender structures such as bars and columns. For a two-dimensional structure like a gusset plate, Eular's criterion is generally over-conservative when all external forces lie in the same plane as the plate does. However, for either a one-dimensional bar or a two-dimensional plate, when lateral force or out-of-plane bending presents, see Fig. 19b, corresponding modifications are necessary. Theoretical solutions of lateral forces have already been obtained for one-dimensional bar, for examples, see [5,6]. Theoretical

analyses in these literatures indicate that, when an out-of-plane force Q or bending moment M is proportional to in-plane compression force P, for an elastic slender structure component the following relationship holds:

$$M_{\max} \propto \frac{P^2}{1-(P/P_E)} \tag{1}$$

where $M_{\max}$ is the maximum bending moment in the component; P_E is the Eular's prediction of the load at onset of instability. This relationship implies that a lateral load does not have strong effect on the instability load. However, the maximum bending moment may increase drastically because it is proportional to the square of in-plane load. This may cause material's yielding earlier than the case without out-of-plane forces, resulted in reduction of system stiffness and subsequent loss of stability even when applied load is still lower than Eular's prediction [50, 51].

A thin-plate theory [5,6] based model has been developed, see Fig. 20, which partitions a gusset plate into several zones characterized by different failure modes and the model enables to obtain analytical or semi-analytical solution for each mode. This is because a gusset plate's un-braced area is generally one order greater than its thickness. Such a thin plate may fail through two mechanisms: tension-induced material failure or buckling under compression, as discussed early in this paper. Accordingly, the two cases in Fig. 16 demonstrate the three corresponding patterns: (i) buckling at unbraced area due to compression, Fig. 16c; (ii) compression-induced bowing of the triangle area of a gusset, Fig. 16a; (iii) tension induced necking in another triangle area of the gusset, together with shear failure around rivets, Fig. 16b. These patterns may occur concurrently or a dominant one triggers another. The challenges for design and load-rating a gusset plate are to identify the key parameters that are able to characterize geometric complexities and to compute the limit load at critical conditions considering lateral perturbation.

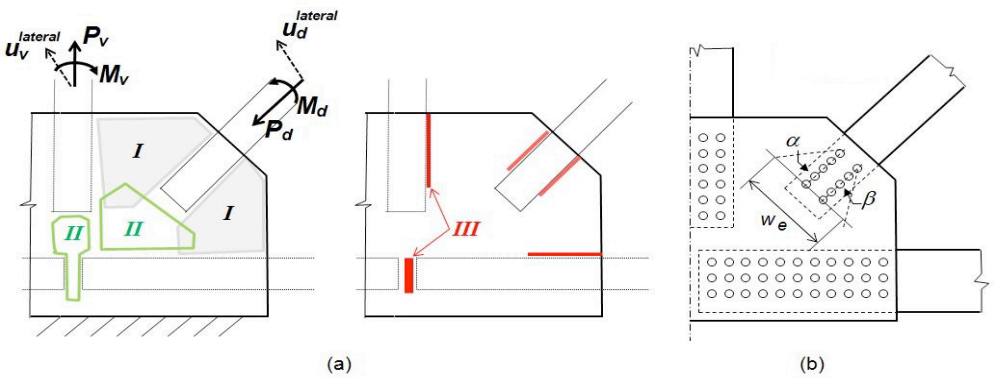


Fig. 20 A thin-plate theory based model[49a] to analyze gusset plate: (a) the gusset plate is parttioned into three characteristic zones that may be governed by different failure modes: I. bowing/necking, II. buckling, III. shear failure dominates; (b) a proposed "Modified Whitmore Model (WWH) where the angles α and β are determined by local geometries.

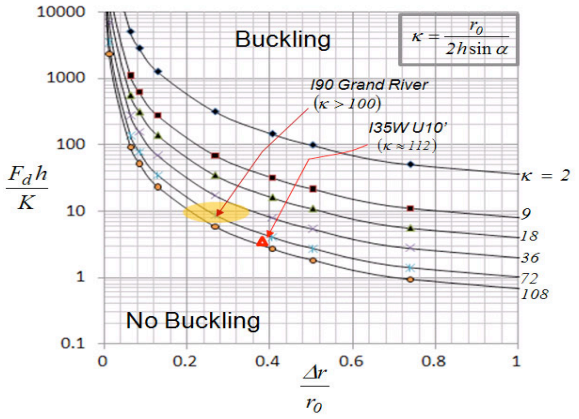


Fig. 21 A semi-analytic solution of gusset buckling based on Von Karman's thin plate instability theory[38]. For a given geometric parameter κ, each curve in this chart defines the corresponding critical load at buckling for a modified Whitmore mode [49a,b]; F_d: the critical load at buckling

For buckling, a group of semi-analytical solutions has been obtained based on Von Karman's thin plate stability theory [38] after some additional geometric modifications to the Whitemore model. Introductions of this theory and related applications can be found, for examples, in [5,6,40]. Further theoretical developments of structural stability can be found, for examples, in [43,44,50-51]. According to this theory, the stability of this fan-shaped is governed by the stationary solution of the following equilibrium condition (in polar coordinate system):

$$K\Delta\Delta w = N_{rr}\frac{\partial^2 w}{\partial r^2} + N_{\theta\theta}\left(\frac{\partial w}{r\partial r} + \frac{\partial^2 w}{r^2\partial\theta^2}\right) - 2N_{r\theta}\left(\frac{\partial w}{r^2\partial\theta} - \frac{\partial^2 w}{r\partial\theta\,\partial r}\right) \quad \text{where} \quad K = \frac{Eh^3}{12(1-v^2)} \tag{2}$$

where $N_{rr}, N_{\theta\theta}, N_{r\theta}$ denote the in-plane radial, hoop, and shear force densities, respectively; w is out-of-plane displacemen. The solved force is plotted in Fig. 21 after normalization.

Conclusions

To avoid a progressive collapse that occurred in I35W Bridge, additional safety margin, i.e., an enlarged safety factor for ASD-Allowable Stress Design (or η_R in LRFD), is necessary for all key single load-path structural members in a multi-span bridge if this bridge's design is merely based on the one-dimensional influence-line analysis explained in Fig. 9(c).

Roller bearing condition is crucial for maintaining an aged bridge's safety operation. Corrosion or other deterioration induced roller bearing lock may result in significant thermal stresses in a bridge.

Stress concentration and bending moment: bending moment and induced-stress concentration around truss-joints may have remarkable effect on bridge's load capacity and fatigue life. Due to the limited computational means in past, these effects might be treated in an *ah hoc* way, for example, large safety factor. In order to avoid over-conservative or risky designs, relatively accurate computation is necessary.

Effects of lateral forces: based on NTSB's material evidences, the results of this analysis suggest three failure modes of gusset plates, i.e. buckling, bowing, and tension-induced necking; the necking is an out-of-plane shear failure, which is essentially the same as an in-plane shear failure in ductile steels. The three failure modes may occur at different areas in a gusset, depending upon the forces and bending moments input from attached trusses. Obviously, the amplitudes of these forces are strongly depending upon deck's live load distribution, bearings' condition, and the details of superstructure's design. Both the eccentric

deck's live load and the inappropriated design of the joint between floor truss and main trusses frames in I35W caused remarkable out-of-plane (lateral) force and bending moment.

Load-rating gusset: this analysis concludes that the lateral forces involved in I35W Bridge's failure may present in other similarly-structured truss bridges, which may significantly reduce a gusset plate's capacity, especially, against buckling, because of localized nonlinear effects. To accurately capture these kinds of load paths, three-dimensional consideration and detailed computation are necessary.

Based on the theories introduced in [5,6] and Von Karman's thin plate stability formulation[38], a semi-analytical solution for a modified Whitmore model of gusset plate's stability has been developed.

ACKNOWLEDGMENTS

The author would like to express his appreciations to Mr. Foster, Mr. Bagnard, Mr. Wildey, Mr. Collions (NTSB), Mr. M. Lwin, Mr. M. Kerley, E. Wasserman, Dr. Ian Friedland, Dr. B. V. Johnson, Mr. C. Puzey, Mr. R. Pratt,, Mr. H. Capper, Mr. N. McDonald, Mr. A. P. Yannotti, Mr. K. Thompson(AASHTO), Prof. T. Galambos(UM), Prof. Z. Bazant and Prof. J. Shofer(NWU), Prof. T. Oden(UTX) for the discussions in past two years. The author thanks Northwestern University Library for the convenience provided during this research.

REFERENCES

[1] National Transportation Safety Board (NTSB), "Safety Recommendation (H08-1)", Jan., 2008, Washington, D. C.

[2] National Transportation Safety Board (NTSB), "Highway Accident Report Interstate 35W Collapse Over the Mississippi River Minneapolis, Minnesota, August 1, 2007", *NTSB/HAR-08/03, Nov. 14, 2008*, NTSB, Washington, D. C.

[3] Gee, King W. (2008), "Load-carrying Capacity Consideration of Gusset Plates in Non-load-path-redundant Steel Truss Bridges", *FHWA Technical Advisory T 5140.29*., Jan. 15, 2008. FHWA, Washington, D. C.

[4] Reid, R. L. (2008), "The Infrastructure Crisis", *Civil Engineering Magazine*, January, 2008.

[5] Bazant, B. "Stability of Structures: Elastic, Inelastic, Fracture, and Damage Theories", Mineola, Dover Pub. 2001

[6] Galambos V. Theodore, "Structural Stability of Steel Concepts and Applications for Structural Engineers", John, Willies & Son, 2008

[7] Hill R., 1951, "Mathematic Theory of Plasticity", *Oxford University Express*.

[8] Timoshenko, S. P. and Goodier, J. N., 1970, "Theory of Elasticity", *McGraw-Hill*.

[9] Hutchinson, J. W., *Singular Behavior at the End of a Tensile Crack in a Hardening Material*, J. Mech. Phys. Solids, 1968,. **16(1)**, p. 13-31.

[10] Rice, J. E., Rosengren, G. F., Plan Strain Deformation near a Crack Tip in a Power-Law Hardening Material, J. Mech. Phys. Solids, 1968,. **16(1)**, p. 1-12.

[11] Liebowitz, H., *Fracture, An Advanced Treatise. Edited by H. Liebowitz*. 1968, New York: Academic Press.

[12] Rice J.R., and Levy N., *A Line-Spring Model for Surface Crack.* J. Appl. Mech., 1972. 39(1), pp. 185-191.

[13] Needleman, A., *A continuum model for void nucleation by inclusion debonding*. J. Appl. Mech., 1987. 54(3): p. 525-531.

[14] Zienkiewicz, O.C., Taylor, R. L., *The Finite Element in Engineering Science,*. 1972: McGraw Hill.

[15] Oden, J.T., *Finite Elements of Nonlinear Continua*. 1972, New York: McGraw-Hill Book Company.

[16] Hughes, T.J.R., *The Finite Element Method*. 1987, New Jersey: Prentice-Hall.

[17] Belytschko, T., Liu, W.K., and Moran, B., *Nonlinear Finite Elements for Continua and Structures*. 2000, New York: John Wiley & Sons.

[18] Reddy, J. N., *Mechanics of Laminated Composite Plates and Shells. Theory and Analysis*, 2nd ed., CRC Press, Boca Raton, FL, 2004.

[19] Bathe K-J., Finite Element Procedure, Prentice-Hall Inc., 1996.

[20] Fisher, J. W., 1984, Fatigue and Fracture of Steel Bridges, Wiley Interscience pub..

[21] Sureash, S., 1998, Fatigue of Materials, 2nd Ed., Cambridge Univ. Press.

[22] McDowell, D.L., Gall, K.A. Horstemeyer, M.F. and Fan, J., Eng. Frac. Mech., 70 (2003) 49–80.
[23] Frangopol, D. et al.(2009)"Multi-criteria Optimization of Life-Cycle Maintenance Programs using Advanced Modeling and Computational Tools", in "Trends in Civil and Structural Computing", Saxe-Coburg Publications.
[24] Maragakis, E., B. M. Douglas, and C. Qingbin, "Full-Scale Field Capacity Tests of a Railway Bridge."
[25] Sternberg, E. and Lee, G. C. , 2006,. Meeting the challenge of facility protection for homeland security. J. Homeland Security and Emergency Management, February 2006
[26] Mertz D. R., Load and Load Combination, in: STEEL BRIDGE DESIGN HANDBOOK, National Steel Bridge Alliance (NSBA), Chicago, Illinois, 2006.
[27a] Hao, S., "I-35W Report I", submitted to NTSB http://www.suhao-acii.com/files/Report_SuHao_Sep22_2007
[27b] Hao, S., "Why the Gusset Plates of I-35W Bridge Are "Undersized?", submitted to NTSB at 3/6/2008. http://www.suhao-acii.com/files/Report2_March2008.pdf
[28] Hao, S., "I-35W Reprot IV: A Complete Load Rating of I35W Bridge", (Submitted to NTSB at May, 2009).
[29] Hao, S. (2008), "A Note of I35W Bridge Collapse", ASCE, J. Bridge Engineering, Sept/Oct, 2010, pp.608-618.
[30] K. Ravi-Chandar and W.G. Knauss (1984) "An Experimental Investigation Into Dynamic Fracture – IV", On the Interaction of Stress Waves with Propagating Cracks," International Journal of Fracture 26 189-200.
[31] Rice, J.R., and Tracey, D.M., *On the ductile enlargement of voids in triaxial stress field.* Journal of the Mechanics and Physics of Solids, 1969. **17**: p. 2-15.
[32] Gurson, A. L. (1977) "*Continuum Theory of Ductile Rupture by Void Nucleation and Growth: Path I-Yield Function and Flow Rules for Porous Ductile Media*". J. Eng. Mat. Tech. 99, p. 2-17
[33] Tvergaard, V. (1982): *On Localization in Ductile Materials Containing Spherical Voids*. Int. J. Fract. 18, p. 237.
[34] Hao, S. and W. Brocks, "*The Gurson-Tvergaard-Needleman-Model for Rate and Temperature-Dependent Materials*", Computational Mechanics, Volume 20, Page 34, 1997.
[35] Hao, S. W.K. Liu, G.B. Olson, and B. Moran, "*Multi-Scale Constitutive Model and Computational Framework for the Design of Ultra-High Strength, High Toughness Steels*", Computer Method in Applied Mechanics and Engineering, Volume 193/17-20, Pages 1865-1908, 2004.
[36] Hao, S., W. K. Liu, *Moving particle finite element method with superconvergence: Nodal integration formulation and applications*, Computer Method in Applied Mech. and Eng., 196, pp 6059-6072, 2006.
[37] NTSB: "*Data Report: State-by-State Bridge Counts*", by Price, J. M., March. 12, 2008.
[38] Von Karman, T., "*Festigkeitsprobleme im Maschinenbau*," in *Encylop¨adie der Mathematischen Wissenschaften*, IV/4C, 1910, 311-385.
[39] Whitmore, R.E., "*Experimental investigation of stresses in gusset plates*", Bulletin No. 16, Engineering Experiment Station, University of Tennessee, 1952.
[40] Bloom, F. and Coffin D, Handbook of Thin Plate Buckling and Postbuckling, Chapman and Hall/CRC, 2000.
[41] Holt R. and Hartmann J., FHWA, Turner-Fairbank Research Center Report, Jan. 12, 2008.
[42] Ibrahim, F., "*Load Rating Evaluation of Gusset Plates in Truss Bridges*" , FHWA, Feb. 2008
[43] Hutchinson, J.W., He, M.Y., Evans, A. G., "*The Influence of Imperfections on the Nucleation and Propagation of Buckling Driving Delaminations"*, J. Mech. Phys. Solids, 48, (2000), pp.709-734.
[44] Hill, R., Hutchinson, J. W., *"Bifurcation Phenomena in the Plate Tension Test"*, J. Mech. Phys. Solids, 25, (1875), pp.239-264
[45] Schwalbe, K.-H. and Cornec, A. "*The engineering treatment model (ETM) and its practical application*", Fatigue Fract. Enyn 9 Mat, Struct, V.14, 405-412, 1991
[46] Hao, S., A. Cornec, Schwalbe, K.-H., "*Engineering Treatment Model(ETM) for Crack Driving Force Estimation of Structures With Stress Concentration*", ASME, Trans., J. Pressure Vessels Tech., V.115, pp.164-170, 1993.
[47] Huckelbridge, A., Palmer, D., Snyder R., "*Grand Gusset Failure*", Civil Engineering Magazine, Sept. 1997
[48] Bagnard, M., "*Gusset Plate Inspection Issues*", Presentation, Nov. 2008.
[49a] Hao, S., "Rating Gusset", a proposal submitted to AASHTO-T14, July, 2009.
[49b] Hao, S., Proceedings of the ASME (American Society of Mechanical Engineers) Annual Congress 2010, November 12-18, 2010, Vancouver, paper number IMECE2010-38312
[50] Hutchinson, J.W. and Koiter, W.T., "Postbuckling Theory," *Appl. Mech. Rev.*, 23, 1970, 1353-1366.
[51] Needleman, A., "Post-bifurcation Behavior and Imperfection Sensitivity of Elastic-Plastic Circular Plates," *Int. J. Mech. Sci.*, 17, 1975, 1-13.

Characterization of Mortar Using Calcified Cell-$CaCO_3$ by Microbial Biomineralization

Wha-Jung Kim[1], Woo-Young Chun[1], Jun-Seok Park[1], Chang-Joon Lee[1]

[1]School of Architecture and Civil Engineering, Kyungpook National University, Daegu 702-701, Korea; TEL +82-53-950-5596; FAX +82-53-950-6590; E-mail: kimwj@knu.ac.kr, cwy@knu.ac.kr, junseok@knu.ac.kr, cjlee4@knu.ac.kr

ABSTRACT

The limestone composed of calcium carbonate is an important resource as the main material for the cement, which is the basis of all construction materials, and most calcium in natural environment takes the morphology of calcium carbonate. This paper presents a basic study on the development of construction materials in an eco-friendly manner by using biomineralization of effective microorganisms.

Micro-biologically induced calcite precipitation (MICP) was achieved using the effective microorganism, *Sporosarcina pasteurii* ATCC11859, an aerobic bacterium pervasive in natural soil deposits. This study searched beneficial microorganisms inhabiting on the based experimental method (16S rDNA base sequence analysis, the EDTA titration method, and X-ray diffraction analysis) of using standard cultured microorganism, *Sporosarcina pasteurii* ATCC11859, to separate and identify eight new beneficial microorganisms, *Sporosarcina soli* KNUC401, *Bacillus massiliensis* KNUC402, *Arthrobacter crystallopoietes* KNUC403, *Lysinibacillus fusiformis* KNUC404, *Halomonas aquamarina* WC-1, *Halomonas hydrothermalis* WC-2, *Bharhavaea cecembensis* JC-1, *Microoccus yunnanensis* JC-2, producing calcite (a mineral morphology of calcium carbonate), for basic research. The result of this study, bio-mineral characteristics of these microorganisms, has been researched. This research, which used eight newly identified effective microorganisms, may be premature for its application to actual situation and thus needs further consideration for advanced research in the future. The effect of the application of calcified Cell-$CaCO_3$ to mortar performance can lead to the development of a new material that will contribute to alleviation of environmental problems as well as facilitation of concrete remediation and repair work.

The results of this experiment showed formation of calcite and hardening of mortar surface. Scanning electron micrographs (SEM) verified formation with precipitated calcite forming bonds at particle-particle contacts. X-ray diffraction (XRD) analysis confirmed that the observed calcite was comprised of calcium carbonate. Additionally, the basic experiment indicated that mortar pores could be filled by calcified Cell-$CaCO_3$ with microorganisms and calcite complex structure.

INTRODUCTION

The ancient earth crust was covered with volcanic rock and meteorite materials, and microorganisms have taken an important role of various chemical process of the earth such as bioleaching of a variety of metals including steel and circulation of organic materials. The microorganisms have been involved in the interaction with control factors of the earth chemical through these bio-chemical processes [11]. Development and synthesis of nano materials by microbial biomineralization are currently in early investigation stage, and the possibility of using particles of uniform size and regularity, which are produced by microorganisms in the process of adaptation to environment and preservation of species, as functional nano materials has been examined [10]. Limestone among these rocks formed by microorganisms has built vast sedimentary basin from continental shelf to ocean floor, and a huge amount of carbon dioxide in the earth crust has been contained in the limestone through

this sedimentation of the earth chemical process. Limestone is a sedimentary rock composed of calcium carbonate, and its component, calcium, is the most abundant element after carbon and silicon [1]. The limestone composed of calcium carbonate is an important resource as the main material for the cement, which is the basis of all construction materials, and most calcium in natural environment takes the morphology of calcium carbonate. Calcium carbonate is largely classified into three types of crystallization-calcite, aragonite, and vaterite, and it is used mainly as a filler material. There chemical and organic processes of calcium carbonate production in natural environment. When these processes occur continuously and simultaneously, bio-chemical reaction accompanied by micro-chemical process takes place. This reaction is called biomineralization by microorganisms [2].

Additionally, the technique to use microbial biomineralization for the improvement of surface quality and functionality of concrete has been proven to be possible by earlier research finding of such a microbe, i.e. *Sporosarcina pasteurii* ATCC1189, which inhabits the soil to form calcite as a mineral morphology (crystallization) of calcium carbonate [3,4,5,9]. Although a lot of researches in construction material field have been conducted to eradicate harmful contagious germs and fungi, there are a few researches on the improvement of quality and functionality of concrete by using microorganisms. Previous research trend to apply these microorganisms to concrete has been carried out preliminarily with their application to mortar. Since the best pH environment for *Sporosarcina pasteurii* inhabiting the soil is around 9 but the pH of cement environment is strong alkaline with pH of 12, its long-term survival has been the research issue for many studies [6,7,8,12]. Accordingly, if microorganisms with similar characteristics of producing calcite, a mineral morphology of calcium carbonate, like *Sporosarcina pasteurii*, but having a longer life in concrete can be identified for its use in concrete, it should be very advantageous and thus a merit for this research. This study searched beneficial microorganisms inhabiting concrete structure based on the experimental method of using standard cultured microorganisms, *Sporosarcina pasteurii* (ATCC1189), to separate and identify eight new beneficial microorganisms, *Sporosarcina soli* KNUC401, *Bacillus massiliensis* KNUC402, *Arthrobacter crystallopoietes* KNUC403, *Lysinibacillus fusiformis* KNUC404, *Halomonas aquamarina* WC-1, *Halomonas hydrothermalis* WC-2, *Bharhavaea cecembensis* JC-1, *Microoccus yunnanensis* JC-2, producing calcite (a mineral morphology of calcium carbonate), for basic research. The result of this research, bio-mineral characteristics of these microorganisms, has been reported [14].

This study presents in-depth characterization of these eight newly identified microorganisms, producing calcite, in terms of their contribution to improvement of construction structure as well as the evaluation of Cell-$CaCO_3$ preparation in accordance with the calcite production performance of these microorganisms. This useful Cell-$CaCO_3$ was applied to mortar for the purpose of the improvement in the quality and performance of concrete in this study to evaluate the compressive strength property in relation to various curing conditions. Then, the mortar was forced to crack for the investigation of the crack filling ability of these microorganisms by calcite production. Finally, the direction for future research and the possibility for future development are discussed.

NEWLY IDENTIFIED CALCITE-FORMING EFFECTIVE MICROORANISMS

This study uses MICP (micro-biologically induced calcite precipitation) by eight newly identified microorganisms by 16S rDNA sequence analysis as shown in table 1 in addition to the typical microorganisms, *Sporosarcina pasteurii* ATCC11859, which inhabits the soil and produces calcite as previously discussed. The 16S rDNA sequence analysis among the methods for identification of microorganisms computes the similarity and evolutionary distance between cultured microorganisms based on the previously analyzed data of the microorganisms.

Table 1. List of newly identified calcite-forming effective microorganisms

No	Job Type	Isolate No.	Nearest neighbor based on 16S rRNA sequence (Accession No.)	Similarity (%)
1	**Identify**	KNUC401	*Sporosarcina soli* (GQ214000)	**98.83**
2		KNUC402	*Bacillus massiliensis* (GQ213997)	**96.60**
3		KNUC403	*Arthrobacter crystallopoietes* (GQ213998)	**99.85**
4		KNUC404	*Lysinibacillus fusiformis* (GQ213999)	**100.00**
5		WC-1	*Halomonas aquamarina* (AJ306888)	**99.56**
6		WC-2	*Halomonas hydrothermalis* (AF212218)	**98.21**
7		JC-1	*Bharhavaea cecembensis* (AM286423)	**99.58**
8		JC-2	*Microoccus yunnanensis* (FJ214355)	**99.29**

[Computational method of micro-biological evolutionary distance]

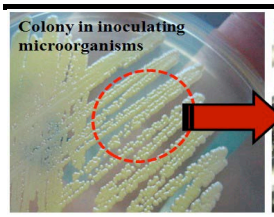
K = -(1/2)In{(1-2P-Q)(1-2Q)1/2} *K : Micro-biological evolutionary distance

*P,Q denotes the replacement ratio for each metastasis type and changeover type among rDNA replacement ratios

It analyzes rDNA sequence of 1,300～1,400bp for the identification of microorganisms. Similarity between cultured microorganisms was determined by the computational method of micro-biological evolutionary distance, and the evolutionary distance between organisms is proportional to the number of transition of DNA elements during the evolution process. There are various types of DNA element transition. Sometimes, several transitions take place in the same place of DNA sequence, and other types of transition occur. Changeover-type transition (pyrimidine from purine or the reverse transition) is known to occur easily by metastatic transition (the distance between purine and pyrimidine or the distance between pyrimidine) [13]. The equation for similarity analysis is based on this property of DNA element transition, and there are only about 4,000 species that have been identified so far according to microbiology reports. If the similarity between cultured microorganisms is below 98.5%, it is regarded as a new species. It is current situation that this type of research dealing with the use of microorganisms in construction material field does not exist, and these eight newly identified effective microorganisms resources not only suggest a basic direction for future research but also are expected to have an academic merit in consideration of their environmental benefit.

The mechanism of micro-biologically induced calcite precipitation (MICP) is very complex. As it was discussed in our previous research [15], the bio-chemical precipitation of $CaCO_3$ in natural environment is generally accompanied with biomineralization of microorganisms. These microorganisms produce $CaCO_3$ on their surface to protect themselves from outside environment. This biomineralization attracts various cations (elements like magnesium, sodium, potassium, calcium, etc.) including Ca^{2+} from the surrounding environment and combines the cations to the cell membrane of these microorganisms to contribute to the precipitation of $CaCO_3$. The precipitated $CaCO_3$ takes the form of a composite Cell・$CaCO_3$ produced by the combination of a cell and inorganic molecule ($CaCO_3$), and is crystallized with continuous activity of the microorganisms. The precipitated $CaCO_3$ is produced not by pure chemical reaction but by bio-chemical reaction. The cell membrane of calcite-forming effective microorganisms as shown in table 2 takes negative electric charge and attracts various cations including Ca^{2+} from the surrounding environment to precipitate $CaCO_3$ on its cell membrane. Our previous research found based on previous research trend that *Sporosarcina pasteurii* ATCC11859, which inhabits the frequently studied soil for the purpose of the improvement in the quality and performance of concrete and forms endospore at extremely hostile environment, produced urease by its metabolism in the urea environment and contributed to the precipitation of $CaCO_3$ on its cell membrane as grown in the Urea-$CaCl_2$ culture medium.

Table 2. Mechanism of $CaCO_3$ precipitation by calcite-forming effective microorganisms





$Ca^{2+} + Cell \rightarrow Cell \cdot Ca^{2+}$

$Cl^- + HCO_3^- + NH_3 \Leftrightarrow NH_4Cl + CO_3^{2-}$

$Cell \cdot Ca^{2+} + CO_3^{2-} \rightarrow Cell \cdot CaCO_3\downarrow$

[Composition of Urea-$CaCl_2$ culture medium]

Make up to 1L of distilled water

1) Nutrient Broth [NB] : 3g (0.3%)

2) Ammonium chloride [NH_4Cl] : 10g (1%)

3) Sodium bicarbonate [$NaHCO_3$] : 2.12g (CO_3^{2-} 25.2mM)

- Adjusting pH concentration to 6.0 with shaking
- Autoclave for 15min. at 121℃

4) Urea [$CO(NH_2)_2$] : 20g (2%)

5) Calcium chloride [$CaCl_2$] : 3.70g (Ca^{2+} 25.2mM)

The bio-chemical mechanism of $CaCO_3$ production on the surface of microorganisms grown in the Urea-$CaCl_2$ culture medium discussed in this section is an important factor of influence of urease to the $CaCO_3$ precipitation. This study prepared culture medium for continuous research and considered the interaction with microorganisms. Since the mechanism of $CaCO_3$ precipitation is very complex, it can be subjected to the influence of the concentration of microorganisms, ion strength (the total of all ions in the solution), pH of the solution, etc. before the contribution of $CaCO_3$ to the improvement in the dynamic performance of concrete. Urease is an enzyme for the hydrolysis of urea to form ammonia and carbon dioxide. This urease action increases the surrounding pH due to the ammonia generated from the hydrolysis of urea and produces carbon dioxide to create an environment conductive to the precipitation of $CaCO_3$.

EVALUATION OF CALCIUM CARBONATE CRYSTALLINITY BY CALCITE-FORMING EFFECTIVE MICROORANISMS

Cell-$CaCO_3$ precipitation reactivity. Previous research found that *Sporosarcina pasteurii* ATCC11859, which likes alkaline environment around pH 9 and forms endospore in harsh environment, produced urease from urea by its metabolism, and contributed to the production of calcite. This experiment used Urea-$CaCl_2$ culture medium to investigate the calcite production of the eight newly identified effective microorganisms in the same urea environment. The Urea-$CaCl_2$ culture medium is chemically composed of 1) 3g (0.3%) of NB (Nutrient Broth) in powder state for the growth of the microorganisms, 2) 10g (1%) of water-soluble Ammonium chloride for the reaction during Calcium carbonate precipitation, 3) 2.12g of Sodium bicarbonate (CO_3^{2-} 25.2mM), 4) 20g (2%) of urea, and 5) 3.70g of Calcium chloride (Ca^{2+} 25.2mM) in 1L distilled water. These eight newly identified useful microorganisms for this experiment were visually verified through a microscope to produce mineral crystal of $CaCO_3$ in the same environment used for the previous experiment with *Sporosarcina pasteurii* ATCC11859, i.e. solid Urea-$CaCl_2$ agar culture medium as shown in figure 1. The biomineralization of calcium carbonate in the Urea-$CaCl_2$ culture medium is initiated by chemical reaction of Ca^{2+}, ionized form of calcium chloride in aqueous solution, and bicarbonate (HCO_3^-) from sodium bicarbonate to produce calcium carbonate ($CaCO_3$) and hydrogen ion (H^+) in the solution [$Ca^{2+} + HCO_3^- \rightarrow CaCO_3 + H^+$]. Here, calcium carbonate ($CaCO_3$) and hydrogen ion (H^+) is the product of a pure chemical reaction, and carbonate ion (CO_3^{2-}) mainly remains in the form of bicarbonate (HCO_3^-) ion in the solution before the production of calcite ($CaCO_3$). The second process of making urease by microorganisms involves raising pH around the microorganisms by ammonia (NH_3) generated from hydrolysis of urea and promotes production of calcite ($CaCO_3$) by emitting carbon dioxide (CO_2). Ammonium chloride (NH_4Cl) in the Urea-$CaCl_2$ culture medium is used in the production of calcite by microorganisms by reacting with carbonate (CO_3^{2-}). The

chemical reaction leaves chloride ion (Cl^-), bicarbonate (HCO_3^-), and ammonia (NH_3) in the aqueous solution, and this reaction can be reversed so that a balanced state is reached depending on the pH of the solution [$Cl^- + HCO_3^- + NH_3 \Leftrightarrow NH_4Cl + CO_3^{2-}$]. Here, MICP, the production of calcite by microorganisms, is subjected to metabolism of the microorganisms, and it is a much more complicated process than regular chemical method.

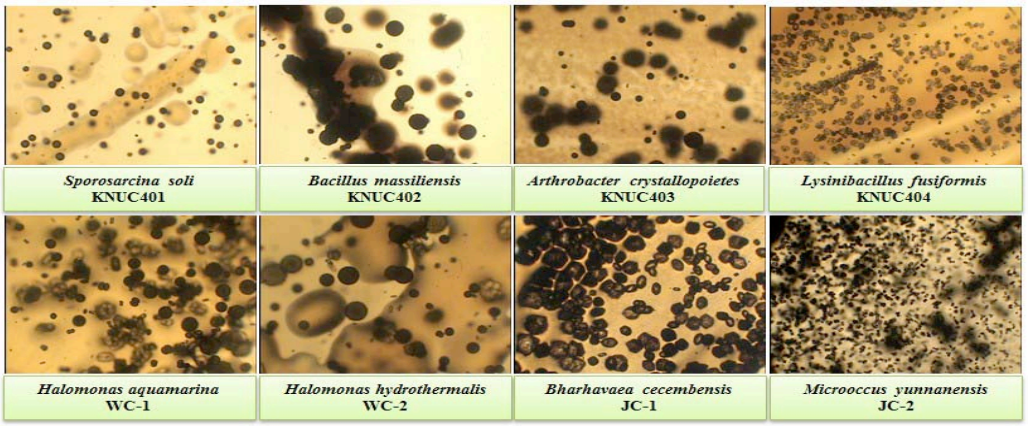


Figure 1. Micro-biologically induced calcite precipitation by effective microorganisms in the Urea-$CaCl_2$ culture medium

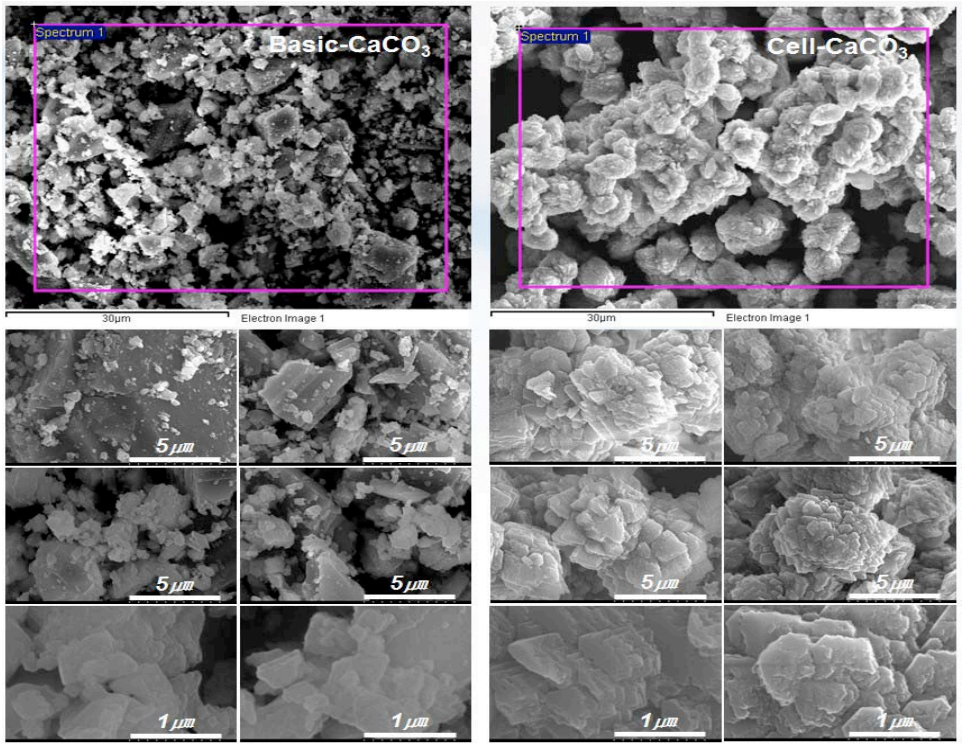


Figure 2. Comparison of scanning electron micrographs of micro-biologically induced calcite precipitation by effective microorganisms

Calcite-forming effective microorganisms in the Urea-$CaCl_2$ culture medium generate ammonia through hydrolysis of urea during the process of making urease to change the surrounding pH to alkaline of pH 9 and emit carbon dioxide to protect themselves from harsh

surrounding environment to form a crystallization of calcium carbonate (Cell-$CaCO_3$), i.e. calcite, on their cell membranes. The crystallized morphology of Cell-$CaCO_3$ formed in solid Urea-$CaCl_2$ liquid culture medium was identified as a particle, of which substituent molecules was combined by metabolism of the microorganisms, in the figure 2. Its magnified image in 1㎛ caliber shows a structure of very minute crystals formed by the microorganisms and combined with themselves.

Calcite crystallinity by effective microorganisms. This experiment is a preliminary investigation of bio-mineral production of calcite by microorganisms and evaluates the calcite crystallinity by metabolism of the microorganisms. The test method involves preparation by 500㎖ of Urea-$CaCl_2$ liquid culture medium for separate inoculation was applied in previous research, and eight newly identified effective microorganisms inhabiting and separated from natural environment, in order to determine the crystallinity of the mineral produced by microorganisms. They were cultured for 7 days in a 180rpm shaking incubator at 30℃. The culture was filtered through 0.45㎛ membrane filter, and the crystal structure of the mineral produced by the microorganisms was analyzed by X-ray diffraction (XRD) as shown in figure 3. All of the mineral crystals precipitated by eight calcite-forming effective microorganisms separated from natural environment were determined to be a mineral morphology of calcium carbonate (calcite) by XRD analysis.

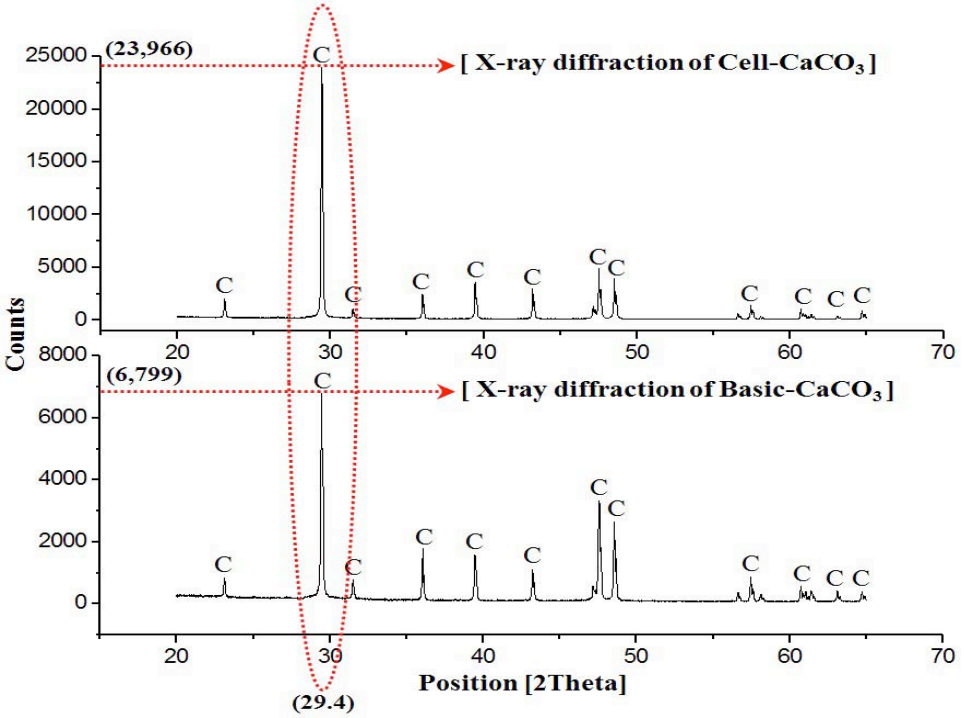


Figure 3. Comparison of X-ray diffraction analysis of micro-biologically induced calcite precipitation by effective microorganisms

The test for the evaluation of calcite crystallinity produced by microbial metabolism in the Urea-$CaCl_2$ liquid culture medium found that urease was produced from urea, and all of the previously discussed *Sporosarcina pasteurii* ATCC11859 and newly identified eight calcite-forming effective microorganisms resources, which produce a mineral morphology of calcite, exhibited the characteristics of forming calcite for the calcium carbonate crystallinity in the Urea-$CaCl_2$ liquid culture medium. Moreover, the crystal structure of the calcite with and without microorganisms differed greatly as shown in figure 3 of XRD analysis.

Thus, all of the eight calcite-forming effective microorganisms separated from natural environment, which produce urease in the Urea-$CaCl_2$ liquid culture medium and contribute to the precipitation of calcite, exhibited the characteristics of making the crystal structure of the calcite crystal structure by their metabolism. The crystal phase, morphology, and particle size of the calcite precipitated by microorganisms in the Urea-$CaCl_2$ liquid culture medium vary by the composition of the culture solution, pH, temperature, supersaturating, agitating speed, added ions, etc. The calcite synthesized in the culture solution mainly exhibited three types of crystal shape (spindle-regular quadrangular pyramid, chain, and rhombohedron). Each oxygen element of carbonate, CO_3, generally combines with two Ca elements of cation layer close to one carbon element.

However, all of the calcium carbonate and the crystal structure of mineral in the Urea-$CaCl_2$ liquid culture medium by eight calcite-forming effective microorganisms exhibited rhombohedral structure with lattice constants of a=4.99Å, c=17.06Å, and Ca and CO_3 ions alternate each other to form a layer of a little distorted shape with CO_3 in one layer combined to six oxygen elements.

EFFECT ON THE COMPRESSIVE STRENGTH OF MORTAR MIXED WITH MICROBIAL BIOCHEMICAL CALCIUM CARBONATE

Experimental methods. This experiment evaluates compressive strength of mortar to apply bio-mineral production of calcite to improvement of mortar performance. The size of the mortar specimen was 50.8×50.8×50.8mm, and the materials used for the preparation of 1 set (18 specimens each) were 1,308g of ordinary Portland cement, 3,924g of river sand passing through 1.2mm sieve, and 720㎖ of mixing solution. Distilled water only and included Basic-$CaCO_3$ and Cell-$CaCO_3$ in the Urea-$CaCl_2$ liquid culture medium were used as mixing solution depending on the experimental setting as shown in table 3. For the application of biomineralization to improvement of mortar performance, $CaCO_3$ solution in the Urea-$CaCl_2$ liquid culture medium of pH 7 was prepared of distilled water. $CaCO_3$ solution in the Urea-$CaCl_2$ liquid culture medium is used in microbial experiment. The biggest reason for using $CaCO_3$ solution in the Urea-$CaCl_2$ liquid culture medium instead of water in the application of microorganisms to mortar mix is because it can restrain or buffer the change of the environment around the microorganisms.

Table 3. Experimental composition of mortar mix

Group	Name	Mixing materials	Mortar mixing water	Specimens total
Control group	**W**	- Cement 1,308g - Sand 3,924g, - Mixing water 720 ㎖ to 18EA(1SET) of mortar specimens	Distilled Water only	**18EA (6SET)**
Experimental group	**BC**		Included Basic-$CaCO_3$ solution in the Urea-$CaCl_2$ liquid culture medium	**18EA (6SET)**
	MC		Included Cell-$CaCO_3$ solution in the Urea-$CaCl_2$ liquid culture medium	**18EA (6SET)**
Total				**54EA (18SET)**

[$CaCO_3$ solution in the Urea-$CaCl_2$ liquid culture medium]

1) 720 ㎖ of distilled water containing NB(nutrient broth) 2.16g and NH_4Cl 7.2g, $NaHCO_3$ 7.2g, $CaCl_2$ 12.6g, Urea($CO(NH_2)_2$) 14.4g
2) Make the calcite-forming microorganisms of step 1 up to 10 ㎖ with distilled water
3) Shaking incubation to adjusting pH concentration to 7.0 with calcite-forming microorganisms

This method is used to obtain the best realistic experimental result for the evaluation of compressive strength of mortar mixed with $CaCO_3$ solution in the Urea-$CaCl_2$ liquid culture medium. The mortar specimens not mixed with $CaCO_3$ were set as control group of pure distilled water and Included $CaCO_3$ solution in the Urea-$CaCl_2$ liquid culture medium. All specimens were prepared in the set of six each (for a total of 18 specimens each) to make it one group. A total of three groups were fabricated to make a total of eighteen each (for a total of 54 specimens each). All mortar specimens mixed with and without microorganisms were demolded after 24 hours and cured at constant temperature of 25℃ and humidity of 50% by a thermo-hydrostat for 28 days. They were divided into groups of two depending on the curing condition (air and water). Compressive strength of the mortar specimens was measured at 3 days, 7 days and 28 days, and the surface of the mortar specimen was kept completely dry for the compressive strength measurement

Experimental results. The mortar specimen mixed with Cell-$CaCO_3$ manifested 23.96% and 18.26% and 9.67% increase in compressive strength at 3 days and 7 days and 28 days, respectively, of air curing.

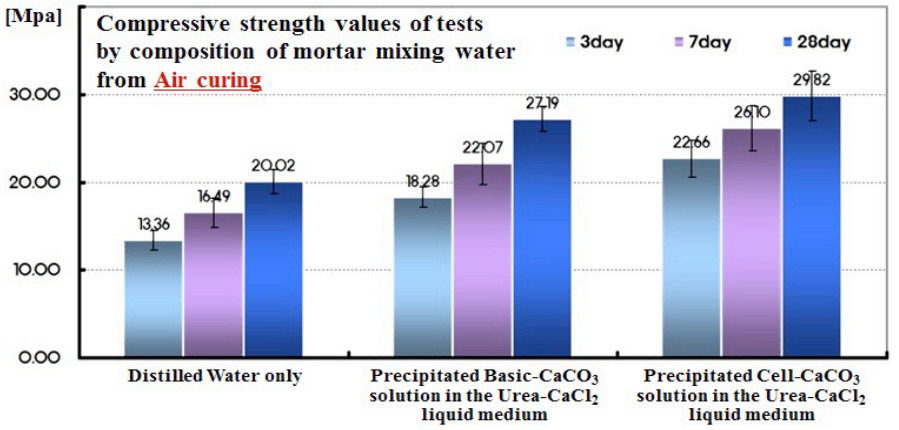


Figure 4. Compressive strength values of tests from air curing by different types of mortar mixing water

Additionally, the mortar specimen mixed with Cell-$CaCO_3$ manifested 43.48% and 13.80% and 8.05% increase in compressive strength at 3 days and 7 days and 28 days, respectively, of water curing.

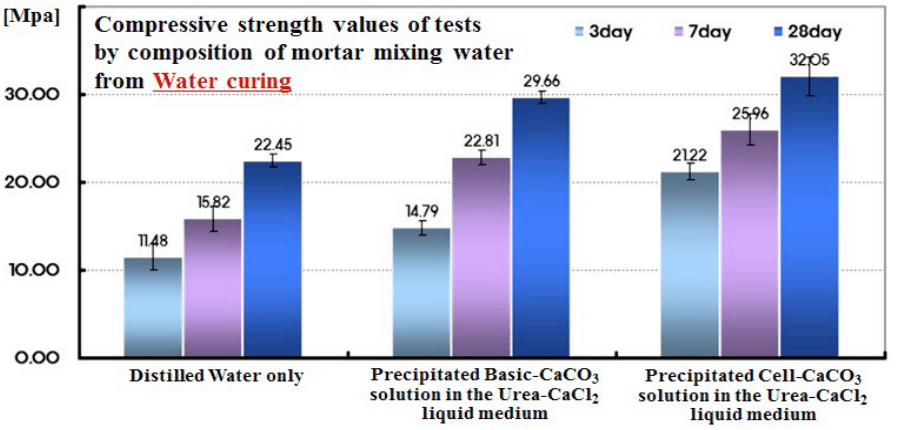


Figure 5. Compressive strength values of tests from water curing by different types of mortar mixing water

Among these specimens, the compressive strength of mortar specimens mixed with Cell-$CaCO_3$ increased by 69.61% and 58.28% and 48.95% at 3days and 7 days and 28 days, respectively, of air curing in comparison to the compressive strength of ordinary mortar specimens. Moreover, the compressive strength of mortar specimens mixed with Cell-$CaCO_3$ increased by 84.84% and 64.10% and 42.76% at 3day and 7 days and 28 days, respectively, of water curing as shown in figure 4 and 5. Of particular notice here is that the compressive strength of mortar specimens increased significantly in comparison to control group specimens not subjected to $CaCO_3$ treatment. This means that the $CaCO_3$ affects the mortar strength to a certain degree and that the overall increase in the compressive strength of mortar is caused by the presence of certain quantity of bio-organic materials.

Additionally, the use of Cell-$CaCO_3$ in the application of microorganisms to mortar in high pH environment showed more effectiveness in the growth of microorganisms in strong alkaline cement environment. Thus, it is deemed that more investigative studies are needed to understand accurately the role of interaction between microorganisms applied to mortar for the improvement of mortar compressive strength after micro-biologically induced calcite precipitation.

MORTAR CRACK REPAIRING BY MICROBIAL BIOCHEMICAL CALCIUM CARBONATE PRECIPITATION

Experimental methods. This experiment examines filling of crack artificially induced in mortar by using micro-biologically induced calcite precipitation (MICP). The specimen was prepared by mixing 30g of cement, 10g of sand, and 15g of distilled water in Petri dish of 5cm to the thickness of 0.5cm. The artificial crack was induced by drying the specimen at 60℃ right after mixing.

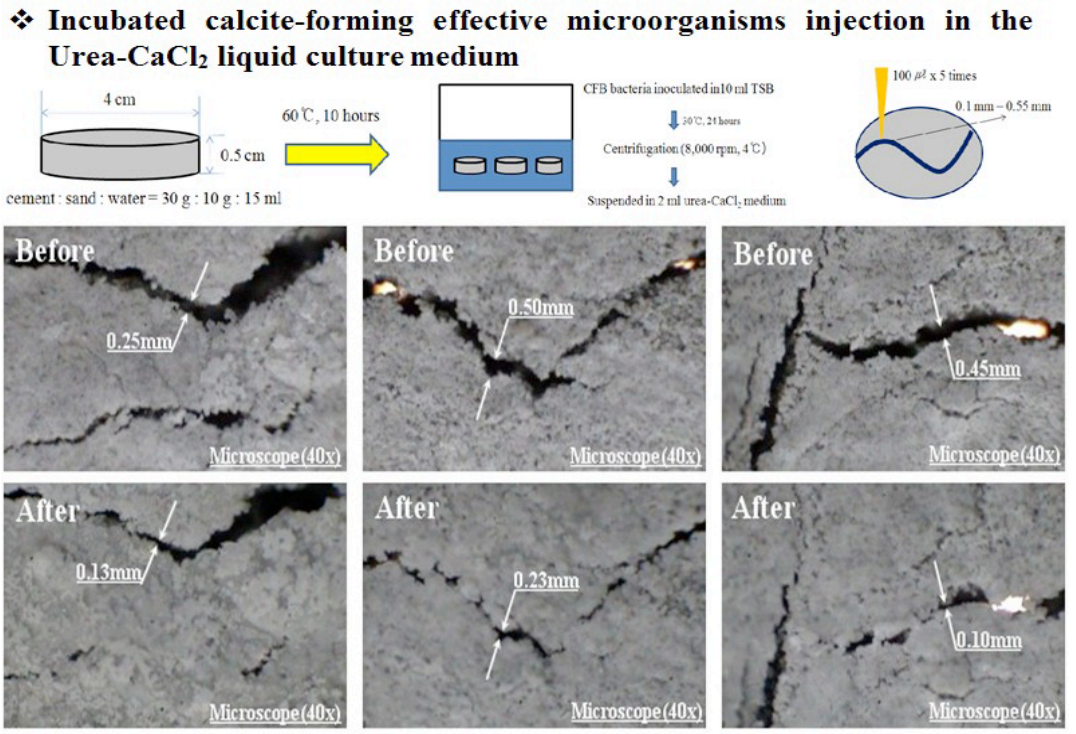


Figure 6. Repairing of crack in mortar from injection of calcite-forming effective microorganisms by micro-biologically induced calcite precipitation

This prepared specimen was cured in water for 7 days to remove unhydrated cement slurry remaining on the surface and in crack of the mortar, and the specimens to be used for the examination of crack filling capability was selected arbitrarily for the crack width between minimum hair thickness of 0.1mm and maximum thickness of 0.7mm. The selected Microorganisms inoculated and cultured in 30㎖ Urea-$CaCl_2$ liquid culture medium of pH 6.0 for calcite precipitation was injected into the crack in mortar. The injection method involved using pipet of 100㎕ capacity to dispense 100㎕ culture solution containing the selected microorganisms to the crack center five times a day for 3 days. This experimental setup was kept at constant temperature of 30℃ and humidity of 60% to examine the crack-filling capacity of the microorganisms by MICP. The evaluation was conducted by inspection with microscope of 40x magnifying power at the same place for 20 days.

Experimental results. The experimental result showed that the filling capacity of microorganisms in the Urea-$CaCl_2$ liquid culture medium and dispensed into artificially induced crack in mortar was somewhat effective in filling the mortar crack by MICP as shown in figure 6. Since crack filling capacity of microorganisms depends on the growth of the microorganisms at right humidity and oxygen supply, it was more effective in smaller and shallower crack site than in wider and deeper crack site. It was also found that the calcite precipitated in mortar crack during the growth of the microorganisms was the major material for the increase in compressive strength of mortar.

CONCLUDING REMARKS

This study investigated the application of Micro-biologically Induced Calcite Precipitation (MICP) to the development of next-generation smart concrete in consideration environmental issues. Calcite is formed by biomineralization of microorganisms in this study. The possibility of using calcite-forming microorganism, *Sporosarcina soli* KNUC401, *Bacillus massiliensis* KNUC402, *Arthrobacter crystallopoietes* KNUC403, *Lysinibacillus fusiformis* KNUC404, *Halomonas aquamarina* WC-1, *Halomonas hydrothermalis* WC-2, *Bharhavaea cecembensis* JC-1, *Micrococcus yunnanensis* JC-2, for the production and precipitation of calcite has been proposed in various studies to improve the quality and performance of concrete. This study applied this property of microorganisms to produce and precipitate calcite for the purpose of improving concrete performance and quality. In addition to previously reported *Sporosarcina pasteurii* ATCC11859, eight additional microorganisms inhabiting natural environment were identified by 16S rDNA sequence analysis. These newly identified microorganisms were found to be effective in production of calcite, and the calcium carbonate crystallinity by MICP was evaluated.

These effective microbial resources were first applied to mortar environment for the aforementioned purpose of improving the performance and quality of concrete. The compressive strength of the mortar specimens was evaluated by curing conditions, and artificial crack was induced in the mortar to examine the filling capacity of the microorganisms by MICP. The effects of the application of these useful microorganisms include not only concrete repairing function but also the development of new environment-friendly materials for improved concrete performance. This research theme will continue to be one of the most important research subjects in the future. Additional merit of this study is the use of microorganisms actually inhabiting in concrete structure and producing calcite in natural environment.

These microorganisms surviving in the natural environment for long times are not only safe environmentally but also effective as a new material of low-loading to environment. This research development of using effective microorganisms is not in the state of practical implementation, and more thorough investigations are needed in the future in order to secure

definite foundation for its use in terms of improving the quality and performance of concrete. Nonetheless, the changeover to new paradigm or idea based on such existing concepts as the theme of this study will certainly prepare the foundation for more advanced research in the future as shown in figure 7.

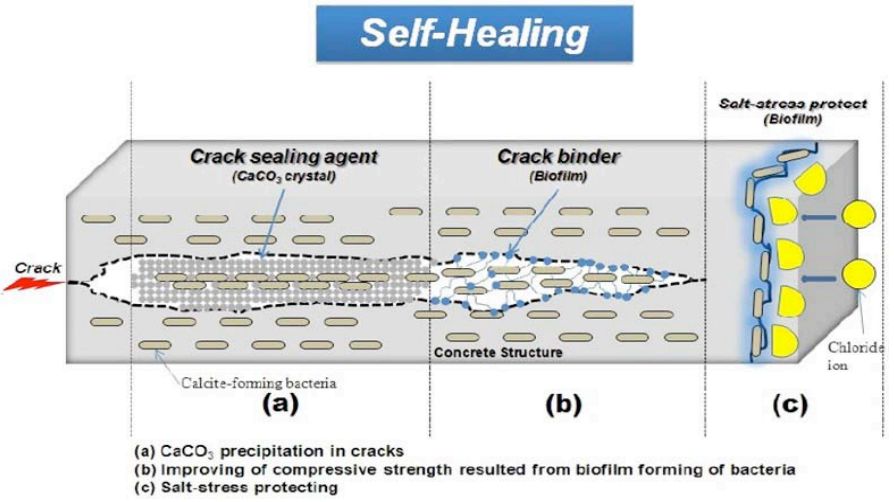


Figure 7. Repair mechanism of self-healing of crack in the concrete sections by calcite-forming effective microorganisms

ACKNOWLEDGMENT

This work was supported by the National Research Foundation of Korea (NRF) Korea grant funded by the Korea government (MEST) [Project No: NRF-2008-314-D00463, NRF-2010-0015142].

REFERENCES

1. ETHEL V. LYON, (1968), "The Literature of Cement, Lime, Plaster, and Gypsum," *Jamerican Chemical Society*, Vol. 78, pp. 122–141.
2. Stocks-Fischer, S., Galinat, J.K., and Bang, S.S., (1999), "Microbiological Precipitation of $CaCO_3$", *Soil Biology and Biochemistry*, Vol. 31, pp. 1563-1571.
3. Ramakrishnan, V., Ramesh, K.P., and Bang, S.S. (2000), "Bacterial Concrete", *Proceedings of SPIE's 2000 Symposium on Smart Materials*, Vol. 4234, Melbourne, Australia, pp. 168-176.
4. Bang, S.S., Galinat, J.K., and Ramakrishnan, V. (2001), "Calcite Precipitation Induced by Polyurethane-Immobilized *Bacillus pasteurii*", *Enzyme and Microbial Technology*, Vol. 28, pp. 404-409.
5. Bachmeier, K., Williams, A.E., Warmington, J., and Bang, S.S. (2002), "Urease Activity in Microbiologically-Induced Calcite Precipitation", *Journal of Biotechnology*, Vol. 93, pp. 171-181.
6. Rapolu, R., Panchalan, R.K., Ramakrishnam, V., and Bang, S.S. (2004), "Durability Characterization of Bacterial Concrete - A Smart Biomaterial", *Proceedings of the ICFRC International Conference on Fibre Composites, High Performance Concretes and Smart Materials*, Chennai, India, pp. 1047-1056.
7. Vemuri, S.L., Panchalan, R.K., Rapolu, R., Ramakrishnan, V., and Bang, S.S. (2004), "Experimental Investigation of the Plastic Shrinkage Crack Reduction Potential of Bacteria

in Concrete", *Proceedings of the International Conference on Advances in Concrete and Construction (ICACC)*, Hyderabad, India, pp. 125-139.
8. Bang, S.S. (2004), "The present and future of biosealant in crack remediation", *Proceedings of the ICFRC International Conference on Fibre Composites, High Performance Concretes and Smart Materials*, Chennai, India, pp. 991-1001.
9. Ramakrishnan, V., Panchalan, R.K., and Bang, S.S. (2005), "Bacterial Concrete - A Concrete for the Future in Serviceability of Concrete", *American Concrete Institute*, SP-225, pp. 37-54.
10. Han, C. S., Lee, H. Y., and Roh. Y. (2006), "On Biologically Produced Nanomaterials", *Int. J. Nanotechnol.*, Vol. 3, No. 2-3, pp. 236-252.
11. Roh, Y., Gao, H., Vali, H., Gao, W., Kennedy, D. W., Yang, Z., Gao, W., Dohnalkova, A. C., Stapleton, R. D., Moon, J. W., Phelps, T. J., Fredrickson, J. K., and Zhoe, J., (2006), "Metal Reduction and Iron Biomineralization by a Psychrotolerant Fe(III)-Reducing Bacterium, Shewanella sp. Strain PV-4." *Applied and Environmental Microbiology*, Vol. 72, No. 5, pp. 3236-3244.
12. Achal V., Mukherjee A., Basu P.C. and Reddy M.S. (2009), "Lactose Mother Liquor as an Alternative Nutrient Source for Microbial Concrete Production by *Sporosarcina Pasteurii*", *Journal of Industrial Microbiology and Biotechnology*, Vol. 36, pp. 433-438.
13. Benjamin S. W. (2009), *Microbes and Society*, World Science Publishing, pp. 120-128.
14. Sung-Jin Park, Yu-Mi Park, Woo-Young Chun, Wha-Jung Kim and Sa-Youl Ghim., (2010), "Calcite-Forming Bacteria for Compressive Strength Improvement in Mortar", *Journal of Microbiology and Biotechnology*, Vol. 20, No. 4, pp. 782-788.
15. Wha-Jung Kim, Sung-Tae Kim, Sung-Jin Park., Sa-Youl Ghim, and Woo-Young Chun, (2009), "A Study on the Development of Self-Healing Smart Concrete Using Microbial Biomineralization", *Journal of the Korea Concrete lnstitute*, Vol. 21, No. 4, pp. 501-511.